



Mathematical Model for Design of Battery Electrodes

II. Current Density Distribution

W. G. Sunu* and B. W. Burrows*

Gould Research Center, Rolling Meadows, Illinois 60008

ABSTRACT

A model that predicts the current density and potential distributions as a function of depth of discharge, discharge rate, and grid design has been developed for application to lead-acid batteries. The calculated potential distributions are in excellent agreement with the observations reported in a companion paper. The effects of the ohmic resistance of electrodes on capacity and distributions of potential, current density, and local active material utilization are discussed. It is demonstrated that the model can be used to optimize the design of grids or current collectors commonly used in lead-acid batteries.

In a prior paper (1), a mathematical model was described for predicting the potential distribution over the surface of electrodes. This model was an extension of that introduced by Tiedemann *et al.* (2). In this model, the current density was assumed to be uniform over the electrode surface. Excellent agreement was found between the potential distribution predicted by the model and that measured experimentally in lead-acid cells immediately after the start of discharge, *i.e.*, for plates in the fully charged state. While extremely valuable in evaluating various grid designs, one would also like to know the current density distribution and hence the distribution of active material utilization during discharge. To obtain this information the assumption of uniform current density distribution must be removed.

Previously (3), we reported potential distributions measured on lead-acid electrodes of the motive power type and calculated the corresponding current density distribution based on the model of Tobias and Wijsman (4). This approach is limited, however, to simple current collector geometries and to steady-state conditions.

In this paper, we extend the model described in a companion paper (1) to handle a nonuniform distribution of current density. Our approach is similar to those reported by Vaaler and Brooman (5) and by Tiedemann and Newman (6). Vaaler and Brooman presented a model without the restriction of uniform current density distribution by treating the negative electrode as an equipotential surface. Later, Tiedemann and Newman reported a more comprehensive model which included the effect of cell polarization derived from a porous electrode model. Their mathematical descriptions were derived for symmetrical electrodes. Applications of these models have also been reported (7, 8).

The model presented here describes the details of grid design variations in asymmetrical electrodes (both electrically and geometrically). Cell polarization correlation was taken from experimental data. The model includes the effects of active material conductivity, electrode polarization, nonuniform current density distribution, and grid design variations (number of hori-

zontal and vertical members, plate dimensions, single or multiple tabs and their locations, taper members, and diagonals of varying length, size, and their locations). It predicts (i) cell voltage, (ii) potential distributions on both positive and negative electrodes, (iii) current density distributions, and (iv) distribution of local active material utilization over the electrode surface all as a function of the discharge time, discharge rate, and grid design.

Experimental

A 12V automotive battery was assembled in the laboratory using factory-pasted plates. The battery contained six cells connected electrically in series in which each cell had five positive and six negative plates. The positive grid was 1.6 mm thick and weighed 58.9g. The negative grid was 1.2 mm thick and weighed 45g. Both grids were 120 mm high and 142 mm wide. The weight of the pasted positive electrode was 156g and the pasted negative weighed 119g.

To allow measurement of resistances of terminals, intercell connectors, and tabs, Teflon coated gold wires were attached to both ends of each component. The specific gravity of the electrolyte solution was adjusted to 1.265 g/cm³ after formation. The terminal voltages and potential losses across the terminals, tabs, and intercell connectors were measured during discharge at different rates (25-500A) and temperatures (22°, 50°, and -18°C). The terminal battery voltages obtained at room temperature were used for comparison with model predictions. The potentials measured at various locations on positive and negative electrodes were reported previously (1).

To solve the grid model, it is necessary to measure the resistance of each grid segment between two adjacent nodes. The positive grid consists of 27 horizontal members and 10 vertical members, resulting in a total of 243 (27 × 9) horizontal segments and 260 (26 × 10) vertical segments. Likewise, the negative grid contains 220 (20 × 11) horizontal segments and 228 (19 × 12) vertical segments. The resistance of each of these grid segments was measured from horizontal and vertical bars cut from standard grids.

Mathematical Model

The overall mathematical framework used in this study is summarized in the flow diagram in Fig. 1.

* Electrochemical Society Active Member.

Key words: lead-acid battery, grid, current collector, modeling, optimization.

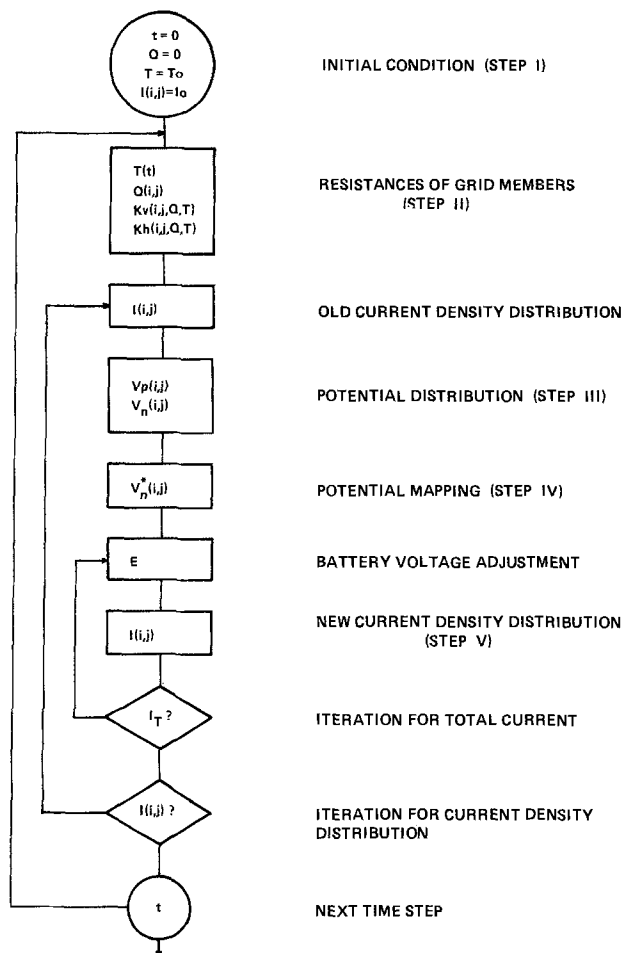


Fig. 1. Flow diagram showing the calculation steps used in this model.

The indices i and j represent i th horizontal and j th vertical members, respectively, counted from a corner closest to the tab location. The model is described by several calculation steps. As an initial condition, a uniform current density distribution was assumed (Step I). The resistance of each grid segment at (i, j) and contributions of the active material conductivity were determined for a given temperature T , and the state of discharge, Q (Step II). Using the current density distribution calculated in the previous iteration step, the potential distribution on the positive plate, $V_p(i, j)$, and that on the negative plate, $V_n(i, j)$, were calculated (Step III). In Step IV the potential distributions on the negative plate were superimposed over each location of the positive node to get $V_n^*(i, j)$. In Step V, the current density distribution $I(i, j)$ was determined at each positive node using an empirical voltage-current-time relationship. The battery voltage E was adjusted until the integral of the current density distribution, I_T , equaled the applied current density. Steps III-V were repeated with respect to current density distribution.

The convergence criterion was 10^{-5} , which is defined by the ratio of the difference between two successive current densities at each node to the present value. If this condition is satisfied at all nodes, the computation continues to the next time step of discharge, namely, Step II. Usually, iteration steps of less than four were needed for a converged solution at each time step. Detailed descriptions of each step are given below.

Grid member resistances.—Step II.—The cell temperature and the amount of active material (PbO_2 in the positive and Pb in the negative electrode) vary with time during discharge. Thus, the resistance of

each grid segment has to be corrected for the cell temperature change and for the active mass contribution. The grid member conductance, the reciprocal of the resistance, at a given temperature can be estimated by

$$K_h(i, j) = \frac{K_{hg}(i, j) + K_{ha}(i, j, Q)}{1 + B_t(T - 298)} \quad [1]$$

$$K_v(i, j) = \frac{K_{vg}(i, j) + K_{va}(i, j, Q)}{1 + B_t(T - 298)} \quad [2]$$

where T is the cell temperature in K; $K_{hg}(i, j)$ is the conductance of the horizontal grid segment between nodes (i, j) and $(i, j + 1)$; $K_{vg}(i, j)$ is the conductance of the vertical grid segment between nodes (i, j) and $(i + 1, j)$; $K_{ha}(i, j, Q)$ and $K_{va}(i, j, Q)$ are horizontal and vertical components of the active material conductance of a pellet, respectively; B_t is the temperature coefficient of resistance.

The temperature of the lead-acid cell was estimated by a simple heat balance equation of

$$\frac{dT}{dt} = \frac{hA}{mC}(T - T_a) + \frac{3600}{4.184} \frac{Q}{mC} \quad [3]$$

where

$$Q = I_c \left[E_o - \frac{T}{nF} \left(\frac{\partial S}{\partial w} \right)_{P,T} - E \right]$$

where T is the average cell temperature (K); T_a is the ambient temperature; t is the discharge time in hours; m is the weight of the cell (3548g); C is the heat capacity per unit weight of the cell (cal/g/K); Q is the heat generation rate (J/sec); hA is the overall heat transfer coefficient, h , multiplied by the surface area of the cell, A ; I_c is the current per cell (A); n is the number of electrons in the cell reaction; F is the Faraday constant; E_o is the reversible cell potential; E is the terminal voltage of a cell; S is the entropy; w is the reaction progress variable. The heat capacity of the present test cell in the fully charged state was estimated as 0.222 cal/g/K and the hA as 394 cal/K/hr.

The effect of the active material conductivity on the plate resistance was included using the method discussed in the previous paper (1). The active material conductivity, K_a ($\Omega^{-1} \text{cm}^{-1}$), is defined by the conductivity of a porous active mass element of a unit volume. With this definition of K_a , the vertical (K_{va}) and horizontal (K_{ha}) components of the active material conductance of a pellet can be determined from

$$K_{va}(i, j, Q) = K_a(Q) \frac{d_t a}{b} \quad [4]$$

$$K_{ha}(i, j, Q) = K_a(Q) \frac{d_t b}{a} \quad [5]$$

$$K_a(Q) = K_o \left[1 - \frac{Q(i, j)}{Q_o} \right] \quad [6]$$

where d_t is the plate thickness and a and b are lengths of the vertical and horizontal grid segments, respectively; K_o is the conductivity of a porous active material at the fully charged state and 25°C ; Q_o is the theoretical ampere-hours of active material at the fully charged state; Q is the ampere-hours removed from the active material at (i, j) . The conductivity of the porous active material, K_a , was approximated by a linear function with the depth of discharge at each node, $Q(i, j)$. The active mass conductivity at the fully charged state, K_o , was reported as $1969 \Omega^{-1} \text{cm}^{-1}$ for the negative and $32 \Omega^{-1} \text{cm}^{-1}$ for the positive electrode (1).

Potential distribution of grids.—Step III.—A mathematical model for predicting the potential distribution of a plate was reported in our previous paper (1),

assuming that the current density is uniform over the plate. The grid was treated as a resistance network of connecting nodes where the grid members intersect and Kirchoff's law was applied to each node. Four equations were used to describe four different situations shown in Fig. 2, which could arise with the presence of diagonal members. The same equations were used in this paper except for the term "apparent current density." The apparent current density used in paper I was the constant value, I , but this was replaced with $I(i, j)$ to describe the apparent current density as a function of the location of each node. The equations corresponding to Eq. [1]-[4] of paper I are rewritten as

$$[V(i, j) - V(i-1, j)] K_v(i-1, j) + [V(i, j) - V(i, j-1)] K_h(i, j-1) + [V(i, j) - V(i, j+1)] K_h(i, j) + [V(i, j) - V(i+1, j)] K_v(i, j) + 2I(i, j) A(i, j) = 0 \quad [7]$$

$$[V(i, j) - V(i, j-1)] K_h(i, j-1) + [V(i, j) - V(i-1, j)] K_v(i-1, j) + [V(i, j) - V(i, j+1)] K_h(i, j) + [V(i, j) - V(i+1, j)] K_v(i, j) + [V(i, j) - V_d(i-1, j-1)] K_d(i-1) + [V(i, j) - V_d(i+1, j)] K_d(i) + 2I(i, j) A(i, j) = 0 \quad [8]$$

$$[V(i, j) - V(i, j-1)] K_h(i, j-1) + [V(i, j) - V(i-1, j)] K_v(i-1, j) + [V(i, j) - V_d(i, j)] K_h(i, j) (b/c) + [V(i, j) - V(i+1, j)] K_v(i, j) + 2I(i, j) A(i, j) = 0 \quad [9]$$

$$[V_d(i, j) - V(i, j)] K_h(i, j) (b/d) + [V_d(i, j) - V(i-1, j)] K_d(i-1) + [V_d(i, j) - V(i, j+1)] K_h(i, j) (b/e) + [V_d(i, j) - V(i+1, j+1)] K_d(i) = 0 \quad [10]$$

where $V(i, j)$ is the potential at the node (i, j) ; $V_d(i, j)$ is the node potential of a diagonal member at an intersection between (i, j) and $(i, j+1)$; $K_h(i, j)$ is the conductance of the horizontal grid segment between nodes (i, j) and $(i, j+1)$; $K_v(i, j)$ is the conductance of the vertical grid segment between nodes (i, j) and $(i+1, j)$; $K_d(i)$ is the conductance of a diagonal member segment between the i th row and the $(i+1)$ th row; $I(i, j)$ is the apparent current density at node (i, j) ; $A(i, j)$ is the area bounded by dotted lines (see Fig. 2) from which the node (i, j) collects current from the active material; $a, b, c, d,$ and e are the distances of segments as shown in Fig. 2.

Thus, a grid which has M horizontal members, N vertical members, and N_d additional nodes created by diagonal members can be described by $MN + N_d$ equations and by an $[MN + N_d, 2(N + d) + 1]$ matrix where d is the number of diagonal members. Refer to paper I for a detailed explanation.

The resultant matrix was solved with an HP9835 minicomputer using the technique described by Prokopius (9). At a specified discharge time and temperature and with the given resistances of grid members and the given current density distribution, the potentials in each electrode can be determined independently at all nodes. As the nodes in the negative electrode are not aligned with those in the positive electrode, the calculated grid potentials in the negative electrode were superimposed, with a linear approximation, over the location of the positive nodes. In this way, potential losses in both electrodes were determined at each location of positive nodes.

Voltage-current-time-relationship.—From the potential losses in both electrodes, the current density

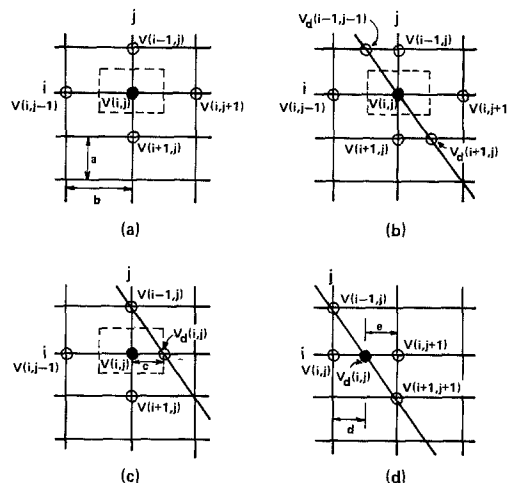


Fig. 2. Notation for indexing of nodes: (a) orthogonal intersections; (b), (c), and (d) represent three situations for diagonal members intersecting horizontal segments.

can be calculated at each positive node if a well-defined voltage-current-time relationship is given. The relationship used in this study was the four parameter analytical expression reported by Shepherd (10)

$$E = E_s - N_s I_c - \frac{R I_c}{1 - \frac{(I_c t)}{Q}} \quad [11]$$

where $E_s, N_s, R,$ and Q are fitting parameters; I_c is the current per cell in amperes; t is the time of discharge in hours; and E is the terminal voltage of the cell. This equation was derived such that the parameters $E_s, N_s I_c, R I_c,$ and Q represent equilibrium cell potentials, resistive potential losses in the cell, activation overpotentials at the fully charged state, and the cell capacity in Ah, respectively (10).

Equation [11], however, is inadequate to determine the effect of grid potential losses on the current density distribution along the electrode surface, as it is described by an overall terminal voltage E and a total current applied to the cell, I_c . In order to describe the local current density distribution, Eq. [11] was rewritten as

$$E = E_s - V_p(i, j) - V_n^*(i, j) - N I(i, j) A_s - \frac{R I(i, j) A_s}{1 - \frac{t I(i, j) A_s}{Q}} \quad [12]$$

where A_s is the total apparent surface area of positive electrodes in a cell, $I(i, j)$ is the apparent current density at node (i, j) , E is the terminal voltage of a cell, $N I(i, j) A_s$ is the resistive loss in the cell other than from the grid resistance, $V_p(i, j)$ is the potential loss in the positive grid between a tab and a node (i, j) , and $V_n^*(i, j)$ is the potential loss in the negative grid between a tab and a hypothetical node at the same location as the positive node (i, j) .

The overall applied current per cell, I_c , used in Eq. [11] is replaced with the local current density, $I(i, j)$, multiplied by the total apparent surface area of positive electrodes per cell, A_s . The grid resistance is excluded from N_s of Eq. [11] and represented with $V_p(i, j)$ and $V_n^*(i, j)$. The parameter N in Eq. [12] is then regarded as the resistive component in the cell other than grids.

Equation [12] becomes identical to Eq. [11] for an ideal cell of zero grid resistance, where the potential losses in the grids are absent and the current density is uniform over the plate. Under this conditions, the

term, $I(i, j)A_s$, equals I_c with the term $V_p(i, j) + V_n^*(i, j)$ being zero.

The fitting parameters (E_s , N , R , and Q) can be determined in two ways. Experimentally, they can be determined from polarization curves of an ideal cell of zero grid resistance using small cells (e.g., with an apparent surface area of 1 cm^2) or cells having highly conductive plates (e.g., lead-coated copper grids). Alternatively, they can be determined from a best fit between model predictions and polarization curves of cells of finite grid resistance. The latter approach was used here.

Current density distribution.—Step V.—The local current density at node (i, j) can be calculated from Eq. [12] for a given cell voltage E . The total current per plate, I_T , then can be determined from the integral of the current density over the electrode surface

$$I_T = \sum_{i=1}^M \sum_{j=1}^N A(i, j) I(i, j) \quad [13]$$

where $A(i, j)$ is the area from which a node (i, j) collects current from active materials. The $A(i, j)$ is $\frac{1}{4}$ ab at the corner of the plate, $\frac{1}{2}$ ab at the node on the frame, and ab at the node other than on the frame members. If the calculated total current, I_T , is different from the applied current, I_c/N_p , where N_p is the number of positive plates per cell, then the cell voltage E was adjusted to calculate a new set of current density distributions. This calculation was repeated until the calculated total current, I_T , agreed with the applied current (I_c/N_p) within $10^{-3}\%$ deviation.

Results

Fitting parameters (E_s , N , R , and Q) in Eq. [12] were determined from a best fit between model predictions and discharge curves of a standard 12V battery measured at different rates (25-500A). They were $E_s = 2.0468$, $N = -0.00153$, $R = 0.09167$, and $Q = 48.0794$. The voltage of a 12V battery was evaluated from

$$E_b = 6E + R_b I_c$$

where E_b is the terminal voltage of a 12V battery, E is the voltage of a cell, I_c is the current per cell, and R_b is the sum of resistances of two terminals, five intercell connectors, and tabs used in battery assembly. The R_b was measured as $1.865 \text{ m}\Omega$.

The calculated and measured polarization curves are compared in Fig. 3. The dashed lines represent predicted polarization curves of a battery containing ideal

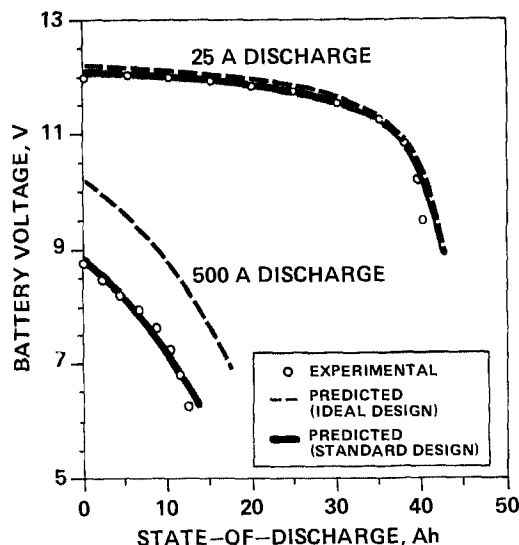


Fig. 3. Comparison between observed and predicted polarization curves for a 12V automotive battery containing 11 plates per cell.

plates of zero grid resistance and thus correspond to Eq. [11]. Solid lines represent the polarization curves predicted for a battery consisting of standard plates. A good agreement was found between data and predictions except for near the end of discharge where polarization increases rapidly.

Figure 3 shows that the ideal zero resistance grid has a negligible effect on the low rate capacity at 25A (or 14.7 mA/cm^2) but results in a significant capacity improvement at 500A (or 293 mA/cm^2). At a cut-off voltage of 7.2V, the predicted cranking capacity of the standard battery is 10 Ah and that of a battery employing the ideal grid design is 16.4 Ah, leading to a possible 64% improvement. This is an upper limit which may be obtained by grid design modifications with no changes in the plate thickness and apparent current density.

In Fig. 4, the potential distributions predicted at the fully charged state are compared with data (dashed curves) reported in our previous paper (1). The model predictions were obtained using resistances measured from each grid member segment and without the assumption of uniform current density distribution over the plate surface. It is shown that the agreement is excellent with an average deviation being less than 5%.

Normalized current density distributions predicted for different states of discharge are shown in Fig. 5 and 6. At 500A, the initial current density distribution is extremely nonuniform, being 51-73% higher near the

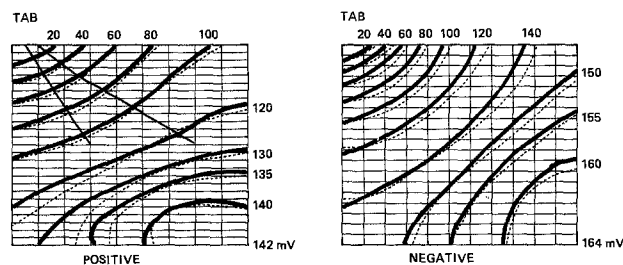


Fig. 4. Comparison of initial grid potential distribution (in mV) between prediction (solid line) and data (dashed line) for discharge at 500A per battery or 100A per plate at 22°C .

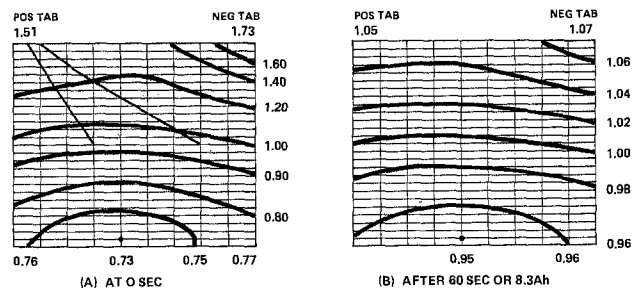


Fig. 5. Normalized current density distribution plotted at different states of discharge at 500 A/battery or 100 A/plate. Average current density is 293 mA/cm^2 .

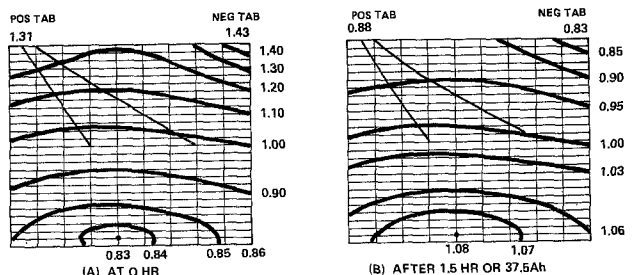


Fig. 6. Normalized current density distribution plotted at different states of discharge at 25 A/battery or 5 A/plate. Average current density is 14.67 mA/cm^2 .

tab compared to the average current density and 27% lower near the bottom. As discharge continues, the current density distribution becomes more uniform because the upper part of the plate, which has been deeply utilized, polarizes more than the bottom. After a 60 sec discharge or 8.33 Ah, the cell voltage drops to 7.5V with the current density distribution being nearly uniform.

During constant current discharge at 25A, the current density distribution at the fully charged state is less pronounced than the case of 500A discharge but still is substantial, being 31-43% higher near the tab than the average and 17% lower near the bottom (see Fig. 6A). The current density distribution becomes essentially uniform after 0.5 hr of discharge or 12.5 Ah. After 1.5 hr of discharge (or 37.5 Ah), the current density near the bottom is significantly higher than that near the tab. Clearly, electrode polarization, which depends on the local active material utilization, is the major controlling factor compared to grid resistive losses in determining the current density distribution near the end of 25A discharge.

The local active material utilization at a node can be calculated by integrating the current density of the same node with respect to time. The results are shown in Fig. 7 and 8. The local active material utilization (Ah/cm²) was multiplied by the total surface area of positive plates in the 11-plate cell (i.e., 1700 cm²) for the purpose of comparing directly with the overall ampere-hours discharged. With a discharge rate of 500A, the distribution of the active material utilization was highly nonuniform throughout the discharge even after 60 sec. The active material near the bottom of the plate is utilized much less compared to that near the top (see Fig. 7B). Discharge could continue further to more fully utilize the active material in the lower portion of the electrode but the battery voltage would be less than 7.2V, a voltage considered as a lower limit for engine starting.

During discharge at 25A, the distribution of active material utilization is more uniform compared to that of 500A discharge but still is significantly nonuniform as shown in Fig. 8A. However, near the end of discharge, the active material is more evenly utilized over the plate surface (see Fig. 8B). As most of the

active material has been deeply utilized, further discharge would lead to a rapid voltage drop caused by the depletion of electrolyte in the pores of the electrode.

Discussion

In optimizing the design of batteries for high specific power applications, the aim is to maximize the high rate performance while minimizing the weight of grids. The high rate performance of a plate of a given electrode thickness can be improved by reducing the plate resistance. Reducing the weight of grids is desirable as it makes it possible to provide more active material in a given electrode volume, thus increasing the overall electrode capacity. Therefore, it is important to quantify the relationships between resistive losses in the grid, grid weight, grid design variations, and the high rate performance.

Experimental quantification of the effect of grid design variations requires a large number of tests and in practice is impractical in view of time and effort involved in preparing grids of various designs. These effects were illustrated here using the model predictions. The eight different grid configurations studied in our previous paper (1) were used for purposes of comparing the effects of different grid designs. These were selected to illustrate the effects on the cell performance of varying (i) number, length, and location of diagonal members; (ii) number and location of tabs; and (iii) number and size of internal grid members.

In our earlier work (1), we used the tab-to-corner potential difference as a measure for the cell performance. In the present work, the calculated cell capacity to a 7.2V cutoff is used. The detailed grid configurations of interest were shown in Fig. 1A of our companion paper (1). The grid weight of each configuration was calculated based on the data in Table III of the same paper (1). The model was applied to eight different 11-plate batteries containing negative and positive plates of the same kind, namely; E-B, F-A, G-D, O-L, P-M, Q-N, U-R, and V-S (see Fig. 1A of paper I). Also included was the combination E-A, a configuration presently being used in automotive batteries and used as an experimental reference in this work.

The predicted cranking capacities (at 500A per battery with a 7.2V cut-off voltage at 22°C) for these eight different grid configurations are plotted in Fig. 9 against the total weight of grids in the batteries. The ideal case is that of grid with zero resistance. The capacity for such a hypothetical situation is 16.4 Ah and is shown as the dashed line in Fig. 9. The capacity of the battery using production grids (combination E-A) was 10 Ah both as measured and as predicted from the model. For a double tab design (combination Q-N) the cranking capacity is predicted to be 14.2 Ah but with an increase of 7% in total grid weight. This improvement in capacity is due to the reduction in grid potential losses to 160 mV per cell from 305 mV per cell in the standard design. The light weight grid configuration (V-S combination) has a tab at the 1/4W position from the corner, two diagonals, and more than half of the internal horizontal members removed. A battery design of this configuration results in the reduction of the grid weight by 35% or 1.2 kg/battery with the cranking capacity no less than obtained with the standard battery.

The accuracy of the model was verified by the good agreement between measured and predicted potential distributions. To use the model as a means of predicting the cell capacity, Shepherd's voltage-current-time relationship was used with fitting parameters evaluated near the range of the current of interest. Generally, this equation was quite satisfactory. But near the end of discharge or during high rate discharge where the cell voltage drops rapidly, a greater de-

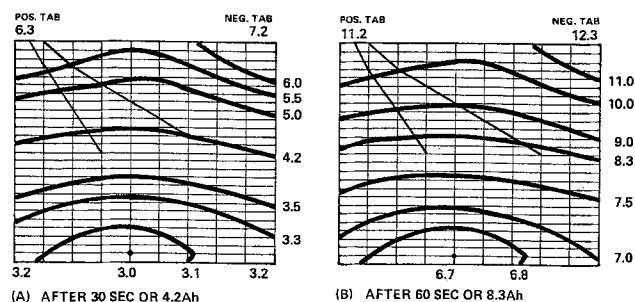


Fig. 7. Distribution of local state-of-discharge expressed as Ah/battery for a current of 500 A/battery or 100 A/plate at 22°C.

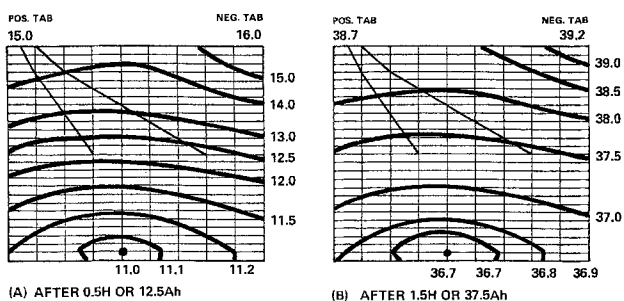


Fig. 8. Distribution of local state-of-discharge expressed as Ah/battery for a current of 25 A/battery or 5 A/plate at 22°C.

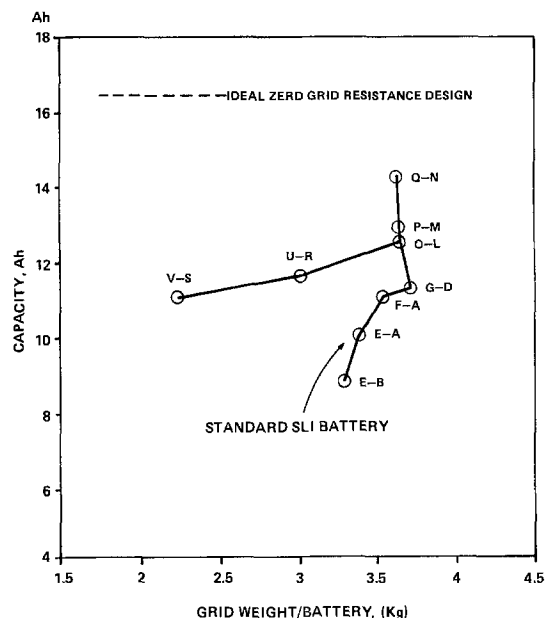


Fig. 9. SLI battery capacities (at 500A and 22°C) predicted for nine different grid combinations are plotted as a function of the total grid weight. Detailed grid configurations were shown in the Appendix of the companion paper (1).

viation occurred which reduces the accuracy of the capacity predictions in Fig. 9.

The present model can be used to predict the effects on the cell performance of a variety of grid design variations such as tab location, number and location of diagonal members, number and size of grid members, tapered configuration of frame and internal grid members, and the size of each pellet. However, the present model does not predict the effects on the cell voltages of electrode design or operation variables such as plate thickness, porosity, paste density, active surface area, thickness of the separator, and initial electrolyte concentration. A model for describing these electrode effects is being developed and will be reported in the future.

Conclusion

A mathematical model was developed that predicts the transient, two-dimensional (along the width and

the height of the electrode) behaviors of lead-acid cells (i.e., cell voltage, current density distribution, grid potential losses, the distribution of local active material utilization, and cell capacity) as a function of the depth of discharge, discharge rate, and grid design variations. An excellent agreement was found between data and predicted potential distributions. It was demonstrated that the model can be used (i) to describe detailed physical changes occurring in the electrode during discharge, (ii) to quantify the interactions between grid design, grid weight, and the cell performance, and (iii) to optimize the design of grids or current collectors for a variety of applications through a computer-aided design approach.

Acknowledgment

The authors wish to thank Mrs. J. Rudolph for her assistance.

Manuscript submitted Jan. 8, 1983; revised manuscript received Aug. 1, 1983. This was Paper 281 presented at the Detroit, Michigan, Meeting of the Society, Oct. 10-15, 1982.

REFERENCES

1. W. G. Sunu and B. W. Burrows, *This Journal*, **129**, 688 (1982).
2. W. H. Tiedemann, J. Newman, and F. Desua, *Power Sources*, 6, D. H. Collins, Editor, p. 15 (1977).
3. W. G. Sunu and B. W. Burrows, *This Journal*, **128**, 1405 (1981).
4. C. W. Tobias and R. Wijsman, *ibid.*, **100**, 459 (1953).
5. L. E. Vaaler and E. W. Brooman, Paper 780221, SAE Congress and Exposition, Detroit, MI (1978).
6. W. H. Tiedemann and J. Newman, in "Battery Design and Optimization," S. Gross, Editor, pp. 23, 39, The Electrochemical Society Softbound Proceedings Series, Princeton, NJ (1979).
7. L. E. Vaaler, E. W. Brooman, and H. A. Fuggiti, *J. Appl. Electrochem.*, **12**, 721 (1982).
8. W. H. Tiedemann and J. Newman, Paper 5378, 1981 Summer National Meeting of the American Institute of Chemical Engineers (1981).
9. P. R. Prokopius, NASA Technical Memorandum, NASA TM X-3359 (1976).
10. C. M. Shepherd, *This Journal*, **112**, 252, 657 (1965).

The Electrochemical Oxidation of Polyacetylene and Its Battery Applications

G. C. Farrington¹ and B. Scrosati

Instituto di Chimica Fisica, Universita di Roma, Pzlle. Aldo Moro, Rome, Italy

D. Frydrych and J. DeNuzzio

Department of Materials Science, University of Pennsylvania, Philadelphia, Pennsylvania 19104

ABSTRACT

When oxidized in a nonaqueous cell containing 1.0M LiClO₄ in propylene carbonate, polyacetylene develops a voltage of 3.4-4.0V vs. Li/Li⁺ ClO₄⁻. Oxidation levels at least as high as [CH(ClO₄)_{0.10}]_x can be produced electrochemically and then reduced to the undoped state with nearly 100% coulombic efficiency. The electrochemical doping (oxidation) process is only efficient when carried out with a minimum of liquid electrolyte under ultraclean conditions. Similar results are observed with a LiAsF₆ electrolyte. Polyacetylene is an extraordinary material of great importance for electrochemistry. However, on the basis of this and other published research, it is not yet clear that it offers major advantages over current electrodes for high energy density nonaqueous batteries.

Polyacetylene is a fascinating new material with extraordinary electrochemical properties. It is a simple conjugated organic polymer which can easily be synthesized by the catalytic polymerization of acetylene. Polyacetylene films can be chemically oxidized and reduced by a variety of species, such as halogens (I and Br) and various organo-alkali metal reagents, such as n-butyl lithium and sodium naphthalide. These reactions are generally referred to as p-doping (oxidation) or n-doping (reduction). They produce compounds of the type (CHX_y)_x and (M_yCH)_x, in which y is typically in the range of 0-0.1. What is most unusual about polyacetylene is that p- or n-doping transforms it from a virtual electronic insulator into a lustrous polymer with an electronic conductivity typical of metals (1).

The reversible oxidation and reduction of polyacetylene can also be carried out electrochemically in nonaqueous electrolytes containing appropriate dissolved anions or cations. These reactions were first described by Nigrey *et al.* (2). The electrochemical potentials of oxidized polyacetylene films (X = I, AsF₆, Br, ClO₄) are typically 3-4V vs. the Li/Li⁺ electrode. The potentials of the reduced films (M = Li, Na) are about 0.5-1.5V vs. that of Li/Li⁺. Nigrey *et al.* (2) and MacInnes *et al.* (3) first suggested that the oxidized and reduced polyacetylenes might be used as high voltage anode/cathode couples in nonaqueous electrochemical cells.

The general goals of our research have been to examine those aspects of the chemistry and electrochemistry of polyacetylene which influence its potential application in batteries. This paper summarizes our investigations of the stability and electrochemical oxidation of polyacetylene in propylene carbonate containing LiClO₄ or LiAsF₆.

Stability

Polyacetylene exists in *cis* and *trans* isomers (Fig. 1). *Trans* polyacetylene is the thermodynamically stable form. The *cis* isomer can be produced by polymerization at low (-78°C) temperatures, but it is unstable toward isomerization, which can be induced by heating or by doping with various chemical species (5, 6, 7). Polyacetylene also self-reacts, forming cross-links and defects. These reactions occur rapidly at elevated temperatures (150°-260°C) (5).

The stability of polyacetylene has been studied by various authors (8, 9, 10, 11). In the absence of a

¹Permanent address: Department of Materials Science, University of Pennsylvania, Philadelphia, Pennsylvania 19104.

Key words: cathode, current efficiency, discharge, polymers.

supply of counterions, virgin and doped polyacetylene are extremely reactive with oxygen. When films are exposed to small concentrations of oxygen for short times, the reaction appears to be reversible. However, during longer exposure, oxygen irreversibly attacks the polymer chain and degrades the conjugated bond network. Oxidation also embrittles the material. Similar reversible and irreversible reactions are observed with other oxidants. We have observed that iodine-doped polyacetylene irreversibly degrades above 60°C, and films doped with bromine irreversibly degrade above about 40°C (11). There are initial indications (11, 12) that films doped with AsF₆⁻ and ClO₄⁻ are somewhat more stable.

Electrochemical Experiments

MacDiarmid *et al.* first demonstrated that films of polyacetylene prepared by the Shirakawa technique can be readily doped to semiconducting and metallic states with a wide variety of chemical species (13, 14, 15). Interest in the electrochemistry of polyacetylene began with the demonstration by Nigrey *et al.* (2) that polyacetylene can be electrochemically oxidized to

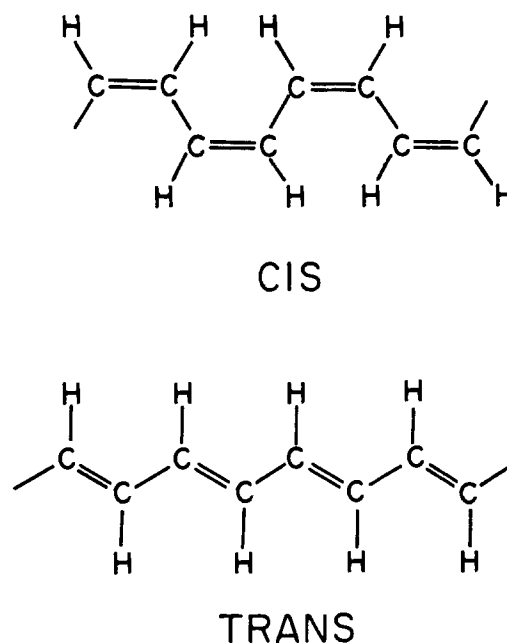


Fig. 1. Polyacetylene isomers

the metallic state in reactions that are the electrochemical equivalents of the chemical doping reactions. Many additional investigations of the electrochemical reactions of polyacetylene have been reported (16-21).

Our research has examined the oxidative (p-doped) electrochemical reactions of polyacetylene in propylene carbonate containing LiClO_4 or LiAsF_6 . Its principal goals have been to explore the reversibility, coulombic efficiency, and electrochemical potentials associated with the reactions at various levels of doping (values of y in $[\text{CHX}_y]_x$).

The polyacetylene films used in these experiments were prepared by the technique first described by Shirakawa (4). Polyacetylene was transferred and stored under vacuum, and manipulated and studied in an inert atmosphere dry box.

Experiments were carried out with electrochemical

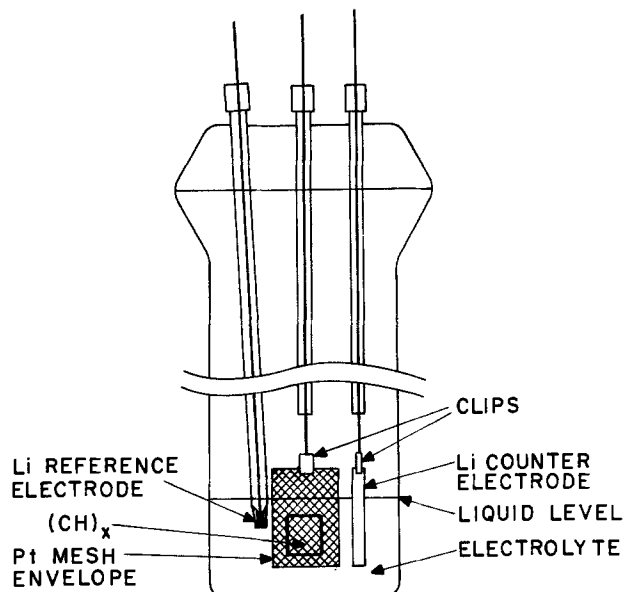


Fig. 2. Larger volume electrochemical cell

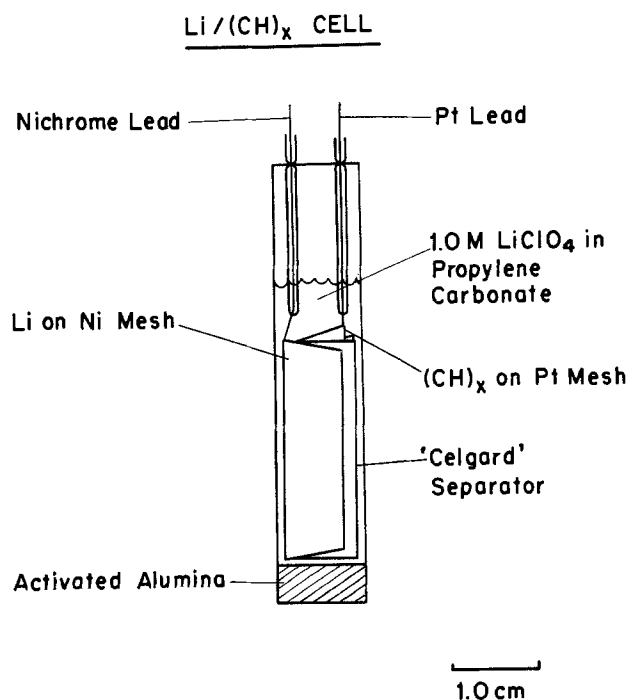


Fig. 3. Sealed electrochemical cell of small electrolyte volume

cells of the types shown in Fig. 2 and Fig. 3. Electrolytes were prepared from Burdick and Jackson propylene carbonate which was distilled and then percolated through neutral activated alumina (Fisher or Woelm). The electrolyte salts were LiAsF_6 (U.S. Steel, Electrochemical Grade), LiClO_4 (Alfa-Ventron), and LiClO_4 (Anderson Physics). The salts were dried at 180°C before use. After the salts were dissolved, the electrolyte solutions were purified by a second percolation through activated alumina.

Results

Series A.—The first series of experiments was carried out using the electrochemical cell shown in Fig. 2 and electrolytes prepared from LiAsF_6 and from LiClO_4 obtained from Alfa-Ventron. Data from one set of experiments using LiAsF_6 are described first. These experiments used a sample of polyacetylene of about 0.7 cm^2 in area (2.8 mg), held in Pt mesh, along with approximately 10 cm^3 of 0.95M LiAsF_6 in propylene carbonate.

The cell was first studied without any polyacetylene in order to determine the electrochemical stability of the electrolyte. The working electrode was a large piece of Pt mesh, about 2 cm^2 in area, normally used to hold the sample of polyacetylene. While the potential was slowly swept from 2.7 to 4.0V vs. Li/Li^+ at 2 mV/sec, background currents of less than $3\text{ }\mu\text{A}/\text{cm}^2$ were observed between 3.2 and 3.75V. Around 3.8V, the current began to rise and reached a value of about $20\text{ }\mu\text{A}/\text{cm}^2$ at 4.0V. The solvent had a good window of stability in the potential range of 3.2 to 3.75V vs. Li/Li^+ , but decomposed at an increasing rate at higher potentials.

With the polyacetylene sample in place, appreciable oxidation began at around 3.4V and the current rose to just over $3\text{ mA}/\text{cm}^2$ at 4.0V. Reduction was observed when the sweep was reversed.

The polyacetylene sample was then repeatedly oxidized and reduced to determine the maximum oxidation level which could be achieved and the reversibility of the reaction. To oxidize the film, the potential was increased in 100 mV steps from 3.5 to 3.9V. The experiment was first carried out without a sample of polyacetylene. The control experiment demonstrated that negligible background current passed up to potentials of 3.9V. With a sample in place, currents upon initial polarization were much larger, typically $0.5\text{--}1\text{ mA}/\text{cm}^2$, on the basis of the geometric area of one side of the polyacetylene. At each potential, the current decayed rapidly to a value that remained approximately constant. The magnitude of the limiting current increased with increased polarization voltage (see Table I).

A separate experiment under essentially identical conditions was designed to determine the coulombic efficiency of the oxidation/reduction process. This experiment started with a fresh sample of polyacetylene, which attained an open-circuit voltage of 2.49V vs. Li/Li^+ . The film was oxidized (charged) by increasing its potential from 2.6 to 3.7V in 100 mV steps. At any given potential, the potential was increased when the current had decayed to approximately 10% of its peak value. To reduce the film (discharge), the po-

Table I.

Potential (V) (Charge)	I Limiting ($\mu\text{A}/\text{cm}^2$)
3.5	20
3.6	24
3.7	57
3.8	157
3.9	571
Total	

tential was stepped immediately to 3.6V and then to 3.0V in 100 mV steps. Again, the potential was decreased whenever the current decreased to 10% of its initial value at any potential. A final discharge step at 2.5V was carried out for 24 hr. Table II summarizes the results. The maximum oxidation level attained (y in $[\text{CHX}_y]_x$) was 0.11, based on the total charge passed. However, the total charge recovered during discharge indicated a real y value of only 0.023. This yielded an apparent efficiency of charge storage and recovery only about 22%.

We observed similar results in other experiments of this type. Because this behavior might have been the result of some curious chemistry of the AsF_6^- ion, the experiments were repeated with an electrolyte of 1.0M LiClO_4 in propylene carbonate. However, all of the results were consistent, regardless of the electrolyte salt. In all cases, the coulombic efficiency of the polyacetylene electrode was very low. The charge recovered upon reduction indicated that a maximum oxidation level of no greater than 0.02-0.03 could be achieved before the oxidation process became very inefficient.

Series B.—The results of Series A are inconsistent with previous reports by MacDiarmid and co-workers (see, for example, 2, 16-21) which have indicated that polyacetylene can be oxidized to y values of 0.07 with coulombic efficiencies of over 90%. They obtained these results with electrochemical cells containing very small amounts of electrolyte.

We evaluated one cell of this type, which was prepared by members of Professor MacDiarmid's research group. It contained a polyacetylene electrode about 1.12 cm^2 in area (2.7 mg). The polyacetylene was separated from a lithium electrode with Celgard™, a porous polymeric separator. The electrode package was packed into the upper part of a small glass cell (see Fig. 3). The lower part was filled with activated alumina.

The cell had undergone five charge-discharge cycles before it was given to us under the conditions of 0.050 mA/cm^2 charge followed by discharge at 0.500 mA/cm^2 and an additional exhaustive controlled potential discharge at 2.5V vs. Li/Li^+ . We then carried out seven additional cycles. Table III summarizes the results.

In each cycle, the polyacetylene electrode film was oxidized at a constant current of 50 $\mu\text{A}/\text{cm}^2$. During

Table II.

Potential (V) (Charge)	*Q (C)	% Cumulative oxidation or reduction
2.6	0.0002	
2.7	0.0004	
2.8	0.0005	
2.9	0.0005	0.01
3.0	0.0010	0.02
3.1	0.0020	0.03
3.2	0.0045	0.07
3.3	0.0095	0.14
3.4	0.0190	0.28
3.5	0.1017	1.10
3.6	0.1070	1.90
3.7	1.1740	11.00
Total charge:	1.4203	
(Discharge)		
3.6	0.0001	
3.5	0.0124	0.09
3.4	0.0211	0.25
3.3	0.0211	0.41
3.2	0.0117	0.50
3.1	0.0046	0.53
3.0	0.0033	0.56
2.5	0.2425	2.30
Total charge:	0.3168	
Efficiency:	22%	

* Not cumulative.

Table III.

% Oxidation*	Reduction current (mA/cm^2)	Q_0/Q_1 (%)**	Q_0/Q_1 Total %†
6.96	0.56	48.7	92.1
6.96	0.56	48.6	92.2
7.00	0.56	52.7	92.1
6.00	0.56	45.3	94.3
3.00	0.28	50.0	90.0
6.00	0.28	66.5	90.7
6.00	0.14	60.5	84.8

* 100y in $(\text{CHX}_y)_x$, oxidized at 0.050 mA/cm^2 ; ** at constant current; † constant current plus additional controlled-potential discharge at 2.5V.

oxidation, the potential of the cell slowly rose from about 3.79V at $y = 0.03$ to 3.9V at $y = 0.07$. The cell was then discharged at three different currents: 500 $\mu\text{A}/\text{cm}^2$, 250 $\mu\text{A}/\text{cm}^2$, and 120 $\mu\text{A}/\text{cm}^2$, in separate experiments. At all three discharge currents, the cell potential immediately fell to about 3.4V. It then continued to decrease until it reached 2.5V. The constant-current discharge was changed to an extended controlled-potential discharge at that potential.

About 50% of the charge could be removed during the constant current discharge at 500 $\mu\text{A}/\text{cm}^2$ before the cell potential reached 2.5V. At the lower discharge currents, 60-65% of the charge was removed before the potential reached 2.5V. The initial peak currents during controlled potential discharge were 500-800 $\mu\text{A}/\text{cm}^2$. After about 1 hr, the current decayed to less than 50 $\mu\text{A}/\text{cm}^2$. After 15 hr at 2.5V, the current was less than 1 $\mu\text{A}/\text{cm}^2$. The controlled potential discharges extracted an additional 30-40% of the initial oxidation charge, which yielded overall coulombic efficiencies of 85-95%.

Series C.—Another cell of this design (Fig. 3) was prepared. It used a polyacetylene sample of 1.3 cm^2 (2.86 mg) supported on Pt mesh of about 2 cm^2 . The lithium counterelectrode was formed by pressing lithium ribbon into a nickel support mesh, and was about 3 cm^2 in area. The electrodes were separated by a Celgard K-442 polypropylene sheet. The cell contained about 1g of activated alumina (Woelm) as a continuous getter for impurities and about 1 cm^3 of electrolyte prepared from Burdick and Jackson UV-grade propylene carbonate which had been vacuum distilled and contained 1.0M LiClO_4 . After one freeze-pump-thaw cycle, the cell was sealed under vacuum.

The cell was charged at a constant current density of 50 $\mu\text{A}/\text{cm}^2$ (based on the area of one side of the polyacetylene) and later discharged in two steps, first at 500 $\mu\text{A}/\text{cm}^2$ until the potential reached 2.5V, and then in an extended controlled-potential discharge at 2.5V. The controlled-potential discharge was generally carried out for about 16 hr, during which the cell current decayed to less than 1 $\mu\text{A}/\text{cm}^2$. A typical plot of current vs. time during controlled-potential discharge is shown in Fig. 4.

The results of this experiment are summarized in Table IV, which presents the final open-circuit voltage attained after charging as a function of oxidation level. It also indicates the fraction of charge recovered during constant-current discharge and the total charge recovered at constant current and controlled potential. The data are listed in the order of increasing oxidation level. The real order in which the experiments were carried out is indicated by the numbers in brackets after each value of y . Figure 5 plots the open-circuit voltage after charging as a function of oxidation level.

The results on coulombic efficiency clearly demonstrate that nearly all of the charge injected during oxidation can be recovered if the reduction begins immediately. However, regardless of the oxidation level, only about half of the charge can be recovered under the constant-current conditions used (500 $\mu\text{A}/$

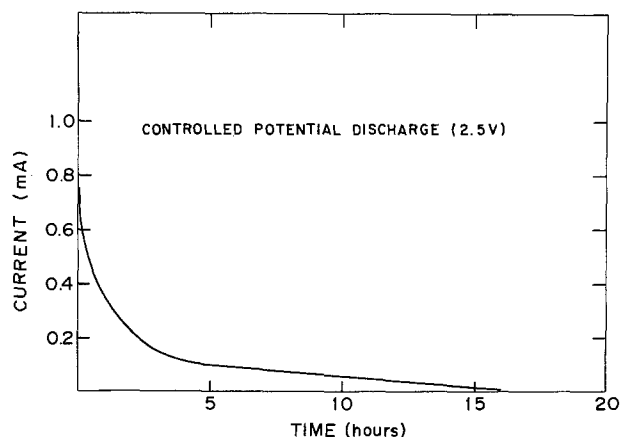


Fig. 4. Discharge of polyacetylene cathode at controlled potential of 25V vs. Li/Li⁺.

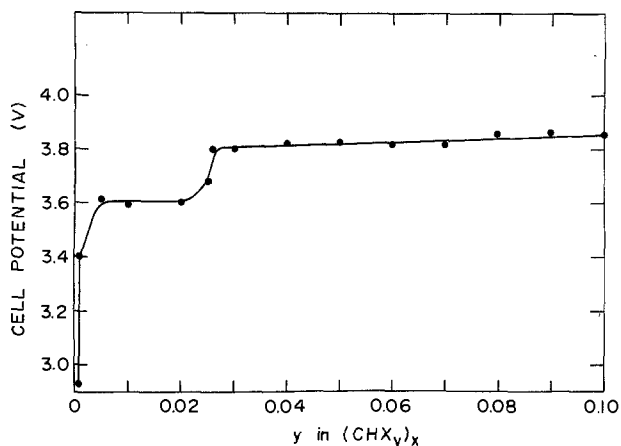


Fig. 5. Open-circuit potential of Li/[CH(ClO₄)_y]_x as function of y. Cell oxidized at 50 μA/cm² constant current.

cm²). The remainder can only be extracted at lower rates.

To measure the rate of self-discharge of the cell, the polyacetylene was first charged to a y level of 0.03 and then discharged using the usual constant-current/controlled-potential sequence. In one experiment the discharge began immediately, in the other it was delayed while the cell stood on open circuit for 40 hr. The results are summarized in Fig. 6. Immediate constant current discharge recovered 41% of the

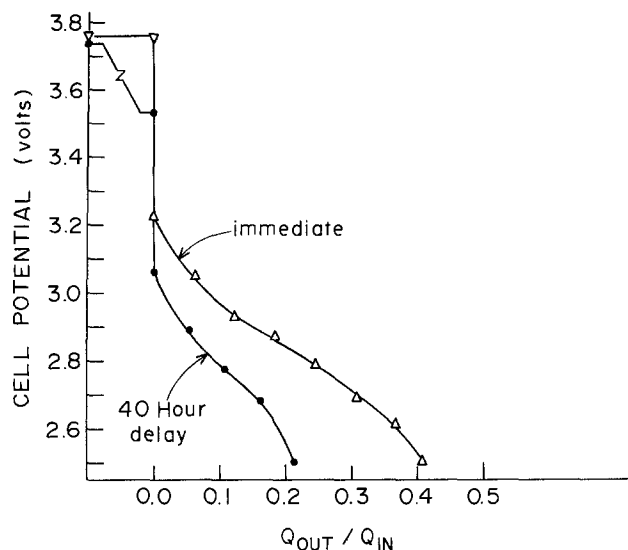


Fig. 6. Immediate and delayed constant current (500 μA/cm²) reduction of polyacetylene originally oxidized to a level of $y = 0.03$ at 50 μA/cm² in an LiClO₄-PC electrolyte. Charge fraction refers to fraction of the original doping level recovered upon reduction.

charge; an additional 56% was recovered during the subsequent controlled-potential discharge for a total coulombic efficiency of 97%. The initial open-circuit potential was high, but dropped sharply as the result of cell resistance when the discharge current was applied. In the other experiment, the 40 hr delay resulted in a decrease in the open-circuit potential of the cell. No change in the cell IR drop was observed. But, constant current discharge recovered only 21% of the initial charge. A total of 61% was recovered after the controlled-potential step.

Discussion

Our experiments confirm previous reports of MacDiarmid *et al.* (16-19) that polyacetylene can be reversibly oxidized (p-doped) to compositions of (CH[ClO₄]_{0.10})_x and then reduced with nearly 100% coulombic efficiency. The results also illustrate several aspects of the stability, variation in electrochemical potential, and electrochemical reversibility of polyacetylene. These are discussed in this section, which also reviews the prospects for polyacetylene as a cathode material in nonaqueous batteries.

Our results confirm that the oxidation of polyacetylene is highly efficient if carried out with a minimum of electrolyte under ultraclean conditions (for example, 2-3 mg of polyacetylene with about 1 cm³ of electrolyte sealed under vacuum with Al₂O₃—experimental Series B and C). However, poor coulombic efficiencies were observed when the same amount of film was in contact with about 10 cm³ of electrolyte in a cell which was not sealed under vacuum, but merely operated in a dry box. We assume that the inefficiency observed with the latter cell was the result of impurities in the electrolyte, although no thorough study of the impurity content of the various electrolytes used in this investigation has been carried out.

The observation that even cells which use a minimum of electrolyte can yield poor coulombic efficiencies during initial oxidation/reduction cycles (see, for example, Table IV, cycle 1) suggests that polyacetylene is extremely sensitive to the presence of traces of impurities in the electrolyte. The first oxidation/reduction cycles with a polyacetylene electrode may actually help purify the electrolyte. Whether impurities are in fact the major cause of poor efficiency, however, cannot be confirmed without a more detailed study of electrolyte/polyacetylene interactions.

Table IV.

% Oxidation*	Final potential (V)	Q _o /Q _i (%)**	Q _o /Q _i Total %†	Cycle
0.50	3.61	19.7	100.0	18
1.00	3.59	2.1	100.0	12
2.00	3.60	2.4	100.0	16
2.50	3.68	3.5	93.2	20
2.69	3.80	46.3	96.9	3
3.00	3.80	39.2	73.1	1
3.00	3.80	21.3	62.0	2
3.00	3.80	41.6	96.8	8
4.00	3.81	43.3	89.0	4
4.00	3.83	45.5	92.5	5
4.00	3.84	45.5	94.4	6
5.00	3.84	46.6	89.7	7
5.00	3.84	46.9	92.5	9
5.00	3.82	46.1	93.0	10
6.00	3.82	44.2	95.4	14
7.00	3.82	41.6	95.6	19
8.00	3.86	50.9	88.9	11
8.00	3.86	46.9	94.1	15
9.00	3.86	44.6	91.2	17
10.00	3.85	48.7	87.6	13

* 100y in (CHX_y)_x; ** at constant current of 500 μA/cm²; † constant current plus additional controlled potential discharge at 2.5V.

We have also observed that only about 50% of the charge stored in oxidized polyacetylene ($x = \text{ClO}_4$) at a current density of $50 \mu\text{A}/\text{cm}^2$ can be recovered at a constant-current discharge of about $500 \mu\text{A}/\text{cm}^2$ before the potential of the electrode drifts sharply toward negative values. The remainder of the stored charge appears to be accessible, but only upon extended controlled-potential discharge at 2.5V vs. Li/Li^+ . These results imply that slow diffusion of ClO_4^- in polyacetylene may hinder the recovery of a large fraction of the stored charge. Results which also imply that the slow diffusion of anions in polyacetylene may limit the rate of its electrochemical reactions have been presented by Will (23).

The results shown in Fig. 6 also suggest that even under carefully controlled conditions, oxidized polyacetylene ($x = \text{ClO}_4$) undergoes considerable loss of charge upon standing on open circuit for 40 hr. This might be the result of the diffusion of ClO_4^- species deep into the polyacetylene fibrils or of slow self-discharge with the nonaqueous electrolyte. It might also be caused by the irreversible chlorination of polyacetylene by ClO_4^- .

There is no doubt that many of the oxidized polyacetylene compositions are thermodynamically unstable toward irreversible oxidation of the conjugated-polymer backbone. As mentioned earlier in this paper, irreversible halogenation begins at $40^\circ\text{--}60^\circ\text{C}$ with Br^- or I^- as the doping ion. The stability of ClO_4^- -doped compositions appears to be considerably greater, although recent reports of Abe *et al.* (24) and Winkle *et al.* (25) indicate that extended electrochemical cycling of polyacetylene with ClO_4^- may slowly result in its irreversible chlorination. It may be that the degree of irreversible oxidation of polyacetylene is negligible if it is cycled within a carefully defined potential range. Further investigations of its long-term cycle life as a function of doping level are needed to resolve this point.

In measuring the open-circuit potential of ClO_4^- -doped polyacetylene as a function of ClO_4^- content (see Fig. 5), we observed two potential plateaus. This behavior contrasts with the smooth increase in open-circuit potential with doping level reported by Kaneto *et al.* (16). Our data were obtained at somewhat lower currents than those used by Kaneto *et al.* ($20 \mu\text{A}/\text{mg}$ film [$50 \mu\text{A}/\text{cm}^2$] vs. up to $100 \mu\text{A}/\text{mg}$ film) and are also based on complete oxidation/reduction cycles to oxidation levels chosen in a semi-random order. The data are quite consistent. They were not obtained at inappropriately high current densities or electrode potentials. Why two plateaus are observed is not clear. However, Abe *et al.* (24) have recently reported similar results. Perhaps two plateaus are an artifact, perhaps not. Nevertheless, these results underscore the need for a careful study of the interrelationship of the preparation conditions, structure, and morphology of polyacetylene and its electrochemical characteristics.

All of these results underscore the fact that the most desirable properties of polyacetylene—high electronic conductivity, oxidizing and reducing power, and utility as an electrochemical electrode—are observed with compositions that often are highly reactive or unstable. Polyacetylene is an extremely sensitive electrode material which must be handled carefully during cell assembly, used only with highly pure electrolytes, and cycled within strict potential limits.

Possible battery applications of polyacetylene have been widely discussed. Three types of batteries using polyacetylene as an electrode material have been suggested (3). The first uses p-doped polyacetylene as a cathode material, most likely with a lithium or similarly high energy-density anode; the second uses n-doped polyacetylene as an anode in combination with a cathode such as TiS_2 ; and the third is an all-poly-

acetylene battery in which the n-doped material is the anode and the p-doped form is the cathode.

On the basis of the information which has been published so far, two major factors appear to impede the application of polyacetylene in high energy-density rechargeable batteries. The first is the instability of both virgin and doped polyacetylene, which has already been discussed in this paper. The other is its apparently low gravimetric- and volumetric-energy-densities, in either the p-doped (cathode) or n-doped (anode) form.

To put polyacetylene in perspective, Table V compares the characteristics of a typical oxidized polyacetylene cathode composition, $[\text{CH}(\text{ClO}_4)_{0.10}]_x$ with TiS_2 , and a polyacetylene anode composition, $[\text{Li}_{0.10}\text{CH}]_x$ with pure Li. Note that it takes about twice the weight and nearly ten times the volume of the oxidized polyacetylene to store the same charge as TiS_2 . The characteristics of n-doped polyacetylene are similar.

These calculations consider only charge and not cell voltage. To include voltage, Table VI summarizes four possible battery couples involving the anodes and cathodes drawn from Table V. The characteristics presented for polyacetylene n-doped with Li are based on currently available experimental results. Kaner *et al.* (26) and Huq *et al.* (27) have indicated that n-doping of polyacetylene occurs readily in a highly pure electrolyte of 1.0M LiClO_4 in tetrahydrofuran (THF). Coulombic efficiencies for charge and immediate discharge are nearly 100% for doping levels up to 0.08. Above $y = 0.08$, the efficiency decreases in this particular electrolyte. The potential of the $(\text{Li}_y\text{CH})_x$ electrode varies from about 1.5V at $y = 0.01$ to 0.5V for $y = 0.08$.

As Table VI shows, the voltage of a $\text{Li}/[\text{CH}(\text{ClO}_4)_{0.10}]_x$ cell is about 50% higher than a comparable Li/TiS_2 cell. Its price is increased weight and volume. Similarly, cells involving $(\text{Li}_y\text{CH})_x$ anodes sacrifice considerable potential, weight, and volume compared to their Li counterparts. One additional difference between the cathode materials is worth noting. Cells using TiS_2 have an invariant salt concentration in the electrolyte, whereas cells using polyacetylene cathodes inject additional electrolyte salt (here LiClO_4) into the electrolyte during the discharge process. Sufficient solvent must be present to accommodate the additional salt.

We have not attempted to estimate energy densities for complete cells. In such estimates, much depends on the specifics of design. It is especially difficult to extrapolate the characteristics of active materials to the performance of a finished system when a radically different electrode material is being considered. Never-

Table V. Theoretical gravimetric and volumetric energy densities of selected electrodes

Electrode	Gravimetric g/eq	Volumetric cm^3/eq
TiS_2	111.0	34.2
$[\text{CH}(\text{ClO}_4)_{0.10}]_x$	229.0	327.0
Li	6.9	12.9
$[\text{Li}_{0.10}\text{CH}]_x$	137.0	195.0

Table VI. Theoretical energy densities of selected couples

Couple	Voltage (V)	Energy density (W-hr/kg)
Li/TiS_2	2.0	454
$\text{Li}/[\text{CH}(\text{ClO}_4)_{0.10}]_x$	3.0	341
$(\text{Li}_{0.10}\text{CH})_x/\text{TiS}_2$	1.0	108
$(\text{Li}_{0.10}\text{CH})_x/[\text{CH}(\text{ClO}_4)_{0.10}]_x$	2.0	146

Voltages are estimated operating voltages.

theless, the results currently available for the electrochemical performance of polyacetylene cathodes and anodes suggest that they are considerably less interesting as high energy density cathode and anode materials than materials such as TiS_2 (28) and Li.

We have also made no attempt to estimate the potential power densities that might be achieved with polyacetylene electrodes. If energy densities are difficult to estimate, power densities are more so, since power density is largely an engineering parameter. However, current data do not indicate that polyacetylene is a major breakthrough in achieving high power densities.

All of these estimates would be changed if the maximum oxidative doping level of polyacetylene could be increased to 0.20 or 0.30 with high coulombic efficiency. On the basis of what we currently know, increasing the doping level would require either decreasing the voltage of the polyacetylene cathode or identifying a non-aqueous electrolyte that is stable at potentials above 3.9-4.0V vs. Li/Li^+ . Currently, the charging process in propylene carbonate containing LiClO_4 becomes inefficient above $y = 0.10$. In this range, the electrode potential is greater than 3.9V vs. Li/Li^+ , and the non-aqueous electrolyte begins to decompose. Similarly, n-doped polyacetylene would be a more attractive anode if it could store more charge at potentials closer to that of pure lithium.

Unfortunately, too little is understood about the electrochemical reactions of polyacetylene to know whether, for example, the present doping levels are limited by an intrinsic characteristic of the doped state or by an extrinsic factor such as the morphology of the polymer. Logical directions for polyacetylene research include a search for new dopants and electrolytes which will permit the material to be cycled efficiently to higher doping levels. In addition, the relationship between the structure of doped polyacetylenes and their electrochemical behavior must be understood to determine whether the currently achieved capacities might be increased by changing the physical characteristics of the material.

To understand the structural/compositional/property relationship in polyacetylene is an exciting challenge for electrochemical research. Perhaps polyacetylene or some other polymer yet to be discovered will revolutionize batteries; perhaps not. Regardless, polyacetylene is a remarkable material which opens up new areas of electrochemistry and deserves continued research.

Acknowledgment

The authors thank Professor A. MacDiarmid and co-workers of the University of Pennsylvania for providing the polyacetylene films used in these experiments.

Manuscript submitted April 13, 1983; revised manuscript received July 5, 1983.

The University of Pennsylvania assisted in meeting the publication costs of this article.

REFERENCES

- A. G. MacDiarmid and A. J. Heeger, *Syn. Met.*, **1**, 101 (1979-1980).
- P. J. Nigrey, A. G. MacDiarmid, and A. J. Heeger, *J. Chem. Soc., Chem. Commun.*, 594 (1979).
- D. MacInnes, Jr., M. A. Drury, P. J. Nigrey, D. P. Nairns, A. G. MacDiarmid, and A. J. Heeger, *ibid.*, 317 (1981).
- T. Ito, H. Shirakawa, and S. Ikeda, *J. Polymer Sci., Polym. Chem. Ed.*, **12**, 11 (1974).
- M. Rolland, P. Bernier, S. Lefrant, and M. Aldissi, *Polymer*, **21**, 1111 (1980).
- J. M. Pochan, D. F. Pochan, H. Rommelmann, and H. W. Gibson, *Macromol. Chem.*, **14**, 110 (1981).
- T. Ito, H. Shirakawa, and S. Ikeda, *J. Polym. Sci., Polym. Chem. Ed.*, **13**, 1943 (1975).
- M. Aldissi, M. Rolland, and F. Schue, *Phys. Status Solidi B*, **68**, 733 (1982).
- J. M. Pochan, H. W. Gibson, F. C. Bailey, and D. F. Pochan, *Polym. Commun.*, **21**, 250 (1980).
- D. J. Berets and D. S. Smith, *Trans. Faraday Soc.*, **64**, 823 (1968).
- R. Huq and G. C. Farrington, Submitted to *This Journal*.
- M. Rolland, S. Lefrant, M. Aldissi, P. Bernier, E. Rzepka, and F. Schue, *J. Electron. Mater.*, **10**, 619 (1981).
- H. Shirakawa, E. J. Louis, A. G. MacDiarmid, C. K. Chiang, and A. J. Heeger, *J. Chem. Soc., Chem. Commun.*, 578 (1977).
- C. K. Chiang, M. A. Drury, S. C. Gau, A. J. Heeger, E. J. Louis, A. G. MacDiarmid, Y. W. Park, and H. Shirakawa, *J. Am. Chem. Soc.*, **100**, 1013 (1978).
- S. C. Gau, J. Milliken, A. Pron, A. G. MacDiarmid, and A. J. Heeger, *J. Chem. Soc., Chem. Commun.*, 662 (1979).
- K. Kaneto, M. Maxfield, D. P. Nairns, A. G. MacDiarmid, and A. J. Heeger, *J. Chem. Soc., Faraday Trans.*, **78**, 3417 (1982).
- J. H. Kaufman, J. W. Kaufer, A. J. Heeger, R. Kaner, and A. G. MacDiarmid, *Phys. Rev. B*, **26**, 2327 (1982).
- J. H. Kaufman, E. J. Mele, A. J. Heeger, R. Kaner, and A. G. MacDiarmid, *This Journal*, **130**, 571 (1983).
- A. Feldblum, J. H. Kaufman, S. Etemad, A. J. Heeger, T.-C. Chung, and A. G. MacDiarmid, *Phys. Rev. B*, **26**, 815 (1982).
- P. Nigrey, D. MacInnes, Jr., D. P. Nairns, A. G. MacDiarmid, and A. J. Heeger, *This Journal*, **128**, 1651 (1981).
- A. F. Diaz and T. C. Clarke, *J. Electroanal. Chem.*, **111**, 115 (1980).
- M. Maxfield, Personal communication.
- F. G. Will, Abstract 554, p. 838, The Electrochemical Society Extended Abstracts, Vol. 1983-1, San Francisco, May 8-13, 1983.
- K. Abe, F. Goto, T. Yoshida, and H. Morimoto, Abstract 553, p. 836, The Electrochemical Society Extended Abstracts, Vol. 1983-1, San Francisco, May 8-13, 1983.
- M. R. Winkle, R. T. Gray, and M. J. Hurwitz, *This Journal*, **130**, 242C (1983).
- M. R. Winkle, R. T. Gray, and M. J. Hurwitz, Abstract 27, p. 45, The Electrochemical Society Extended Abstracts, Vol. 1982-2, Detroit, Oct. 17-21, 1982.
- R. Huq and G. C. Farrington, Unpublished results.
- M. S. Whittingham, *Science*, **192**, 1126 (1976).

Electrochemical Tunnel Etching of Aluminum

R. S. Alwitt* and H. Uchi¹

United Chemi-Con, Incorporated, Northbrook, Illinois 60062

T. R. Beck*

Electrochemical Technology Corporation, Seattle, Washington 98107

R. C. Alkire*

Department of Chemical Engineering, University of Illinois, Urbana, Illinois 61801

ABSTRACT

Anodic dissolution of aluminum in hot chloride solutions produces a high density of fine etch tunnels that extend along [100] directions. Tunnels evolve from cubic etch pits when all but one of the pit wall surfaces become passivated; dissolution then occurs at the one active face at a rate that may initially be as high as 20 A/cm². Tunnels have square cross sections with sides ~1 μm and aspect ratios as high as 100:1. Tunnel growth may be considered a unique form of pitting corrosion in which dissolution and passivation occur simultaneously with a sustained balance between the two processes.

Anodic dissolution of aluminum in hot chloride solutions produces a high density of fine tunnels that extend along [100] directions. Tunnel etching is used commercially to process tonnage quantities of foil for use as electrodes in aluminum electrolytic capacitors. The tunnels in these foils are typically 1-2 μm wide, 40-50 μm long, and present at a density of the order 10⁷ cm⁻² (1, 2).

Tunnel attack of aluminum was first reported in a study of tap water corrosion of 2S alloy (3). Edeleanu studied these structures in some detail, as part of a larger study on the propagation of corrosion pits (4). Corrosion scientists have generally not paid much attention to tunnel attack, perhaps because it appears to be a secondary feature of pitting attack at room temperature.

Tunnel growth is difficult to study because it is accompanied by general crystallographic attack that masks tunnel initiation and confounds measurements of tunnel length. We were fortunate to find a combination of pretreatment/etch/metal that produces a uniform dispersion of nucleation sites with a high probability that each site develops into a tunnel. This made possible a detailed and quantitative study of tunnel growth and morphology without interference from general crystallographic attack. We present here the results of that study and we discuss the phenomenon as it may relate to pitting corrosion. A model describing electrochemical events in the tunnels is under development by the authors.

Experimental

Specimens were 100 μm-thick, 0-temper, 99.99% Al capacitor-grade foil from Toyo Aluminum Company.² This foil is fabricated to have a high cubicity texture, so the surface is composed mostly of (100) planes and tunnels grow normal to the surface. Similar foil is available from other major aluminum suppliers, but each may require a different pretreatment to get a uniform dispersion of tunnels.

Specimens were cleaned by immersion for 10 min at room temperature in either 1N NaOH or 1N HCl, rinsed, and then immediately transferred to the electrochemical cell. Anodic dissolution was in 1N HCl at a constant nominal cd of 50 or 200 mA/cm² for times between 0.1 and 100 sec, and at temperatures 40°-97°C. The potential was measured vs. a saturated calomel

electrode at room temperature, using a Luggin probe with tip placed 1-2 mm from the Al surface.

This high-purity metal did not undergo general corrosion in the HCl etchant, even at elevated temperatures, during the time required for these experiments. The distribution of initial etch pit sites is more uniform in HCl than in NaCl solutions, and no solid oxidation product is formed in bulk solution in HCl. The appearance of the tunnels produced in acid and neutral chloride solutions is identical.

Tunnel features were studied by examination of oxide replicas in the scanning electron microscope (SEM). Barrier oxide films 75 nm thick were deposited on the specimen surface and then the metal was dissolved in warm Br₂-methanol solution. The outside film surface was mounted on the specimen stub so that the tunnels extended toward the viewing direction. These films are self-supporting and consume only 25 nm of Al metal, so no significant smoothing effects are introduced at the magnifications used in this study.

Results

Qualitative aspects of tunnel growth.—The sequence of tunnel growth is illustrated in Fig. 1 for specimens that had been cleaned in NaOH and then etched at 90°C, 200 mA/cm². At 0.2 sec, only a dispersion of small cubic pits is present; the shallow scallops covering the surface are from the NaOH pretreatment. At 1.0 sec, the pit depth is significantly greater than width, i.e., the tunnel structure has started. At 90°C, and also at lower temperatures, initially only cubic pits are present and tunnels become evident between 0.5 ~ 1.0 sec.

At 5.0 sec, tunnels are well-developed along the three (100) directions. The tunnels extending parallel to the original surface lie just under the surface and originate from a side wall of a cubic pit. Small etch pits are seen that started some time after the first pits and will develop into later generations of tunnels. No general surface attack is evident.

At 10 sec, the tunnel array has a density of vertical tunnels on the order 10⁶ cm⁻² and exhibits a range of lengths and widths. Tunnels are straight, symmetrical, and usually tapered, although parallel-sided tunnels are frequently seen. At 90°C, the tunnel width at the base is generally 1.0 ~ 2.5 μm on a side, but occasionally some wider tunnels are seen. If etching at 90°C is continued, say, for 30 sec, tunnels will be 70-80 μm long and will have tapered to a width of ~0.25 μm.

Width measurements at specified tunnel heights for short tunnels superpose similar data for long tunnels.

* Electrochemical Society Active Member.

¹ Present address: KDK, 363, Arakawa, Takahagi-shi, Ibaraki-ken, 318, Japan.

² 3-1 Marunouchi, Chiyoda-ku, Tokyo 100, Japan.

Key words: metals, SEM, corrosion, dissolution.

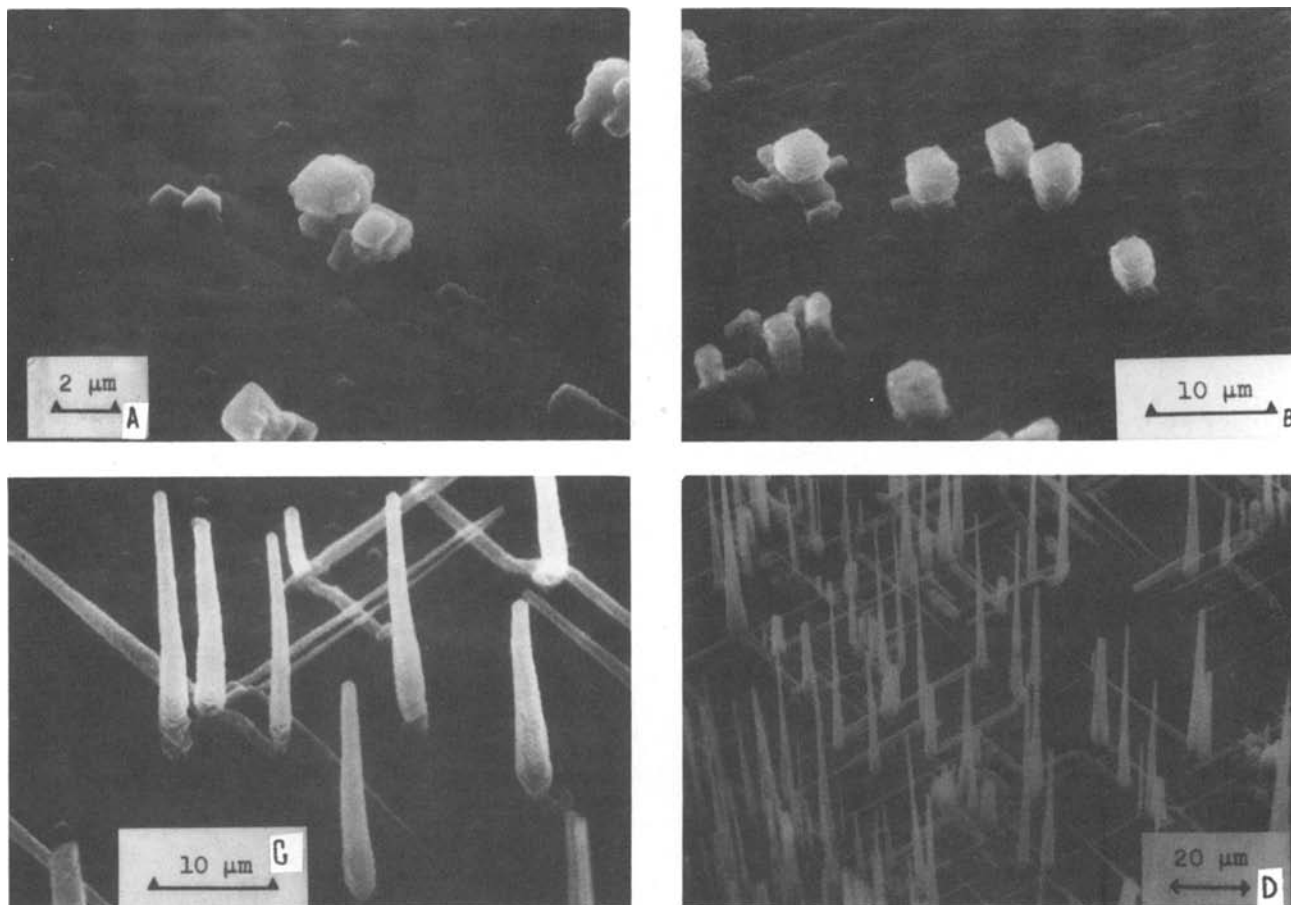


Fig. 1. Tunnel growth sequence at 200 mA/cm², 90°C. A: 0.2 sec; B: 1.0 sec; C: 5.0 sec; D: 10.0 sec. NaOH pretreatment

That lateral dimensions do not change with time means that all dissolution takes place at the tunnel tip. This is a critical feature of tunnel growth. Dissolution occurs in one direction and wall surfaces are passive.

Figure 2 shows some structural details of tunnels grown at 70°C, 200 mA/cm² for 5 sec. The tunnels have square cross section and the tip surface is smooth, although sometimes what appears to be growth facets are present, as on the right. There is a well-defined right angle edge between tip face and wall; no rounded contours are evident. Crystal structure not only determines the direction of tunnel growth, but the tunnels grow by crystallographic dissolution. In contrast to the flat, generally featureless tip surface, the walls are highly rippled with matching contours on adjacent walls. The wall-ripple density is the same at 90° and 70°C, $\sim 10^5$ cm⁻¹.

It was thought that because of the active nature of

the tunnel tip dissolution might occur for some interval that would alter the tip appearance after the external current was shut off. To prevent any open-circuit attack, an etch was performed at 90°C in which the current was stepped to a cathodic pulse of 50 mA/cm² for 20 msec prior to open circuit. The appearance was unchanged by this procedure, suggesting no significant open-circuit attack. A more thorough evaluation of the potential distribution following current reversal is needed to determine how much dissolution may occur during the reversal transient.

The structural details of tunnels from an etch in 1N NaCl (5) were found to be identical to those of the tunnels from an HCl etch. The electrolyte composition in the restricted geometry of the tunnels is determined mostly by the dissolution rate of aluminum and will be a concentrated AlCl₃ solution, independent of the nature of the cation in the bulk solution.

Lower temperatures tend to produce wider tunnels. The widest tunnels observed in this study were about 7 μm, in samples etched at 60° and 65°C. No tunnels initiated if the temperature were below 60°C, confirming an observation made by Jackson (2). However, tunnels would continue to grow at lower temperature after tunnels had started at a higher temperature. For example, after 5 sec at 90°C, the temperature was lowered to 40°C by rapid addition of cold etchant, and the etch was continued for 20 sec. A tunnel that propagated during this period is shown in Fig. 3. The wider end section of the tunnel developed during the 40°C etch.

Quantitative aspects of tunnel growth.—Tunnel lengths were measured from micrographs like those in Fig. 1. Using the convention that the longest tunnels had initiated when the current was switched on, length vs. time was determined for these first generation tunnels. Different etch conditions were used and

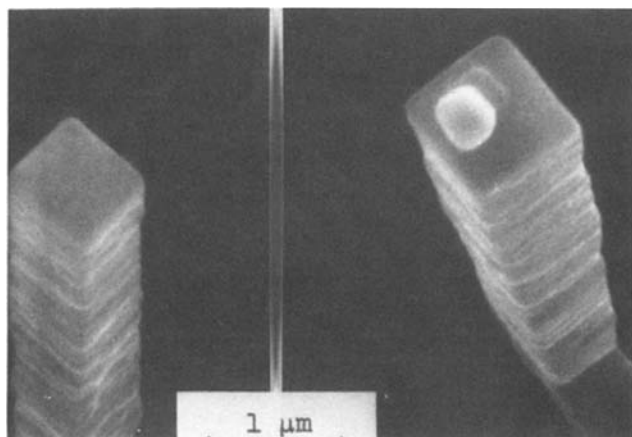


Fig. 2. Tunnel tips at 70°C, 200 mA/cm², 5 sec

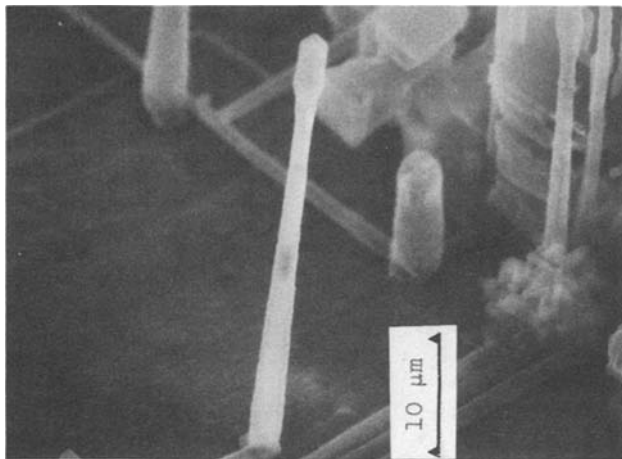


Fig. 3. Effect of temperature decrease from 90°C to 40°C during etch at 200 mA/cm². NaOH pretreatment.

the several sets of data are plotted in Fig. 4. At longer times, the tunnel density is so high that the location of a tunnel base is obscured in 45° views. In those cases, the specimens were examined in cross sections prepared with conventional metallographic techniques.

From Fig. 4, it is seen that neither pretreatment nor nominal cd had an effect on individual tunnel growth rate, although tunnel density and tunnel width depended on these particular conditions. Conditions that affect tunnel initiation do not necessarily have any effect on subsequent tunnel growth.

The initial tunnel growth rate increased with increasing temperature. At 70° and 80°C, the growth rate was constant up to ~55 μm length and decreased slightly at longer lengths. The dashed portion of the 70° curve indicates that tunnels perforated the specimen at 80 sec. Therefore, a longer tunnel length would have been recorded if a thicker foil had been used.

Tunnel growth at 90° and 97°C was quite different than at the lower temperatures. Up to 65-70 μm, the length increased as $t^{0.7}$, and the growth stopped when tunnels reached a length of 70-90 μm.

Initial growth rate vs. $1/T$ is shown in Fig. 5. An additional data point at 60°C (not shown in Fig. 4) is also included. An apparent activation energy of 15 kcal/mol describes the process over the whole temperature range.

The relationship between growth rate and cd at the tunnel tip is given by the relation

$$i = \left(\frac{zF\rho}{M} \right) \frac{dl}{dt} \quad [1]$$

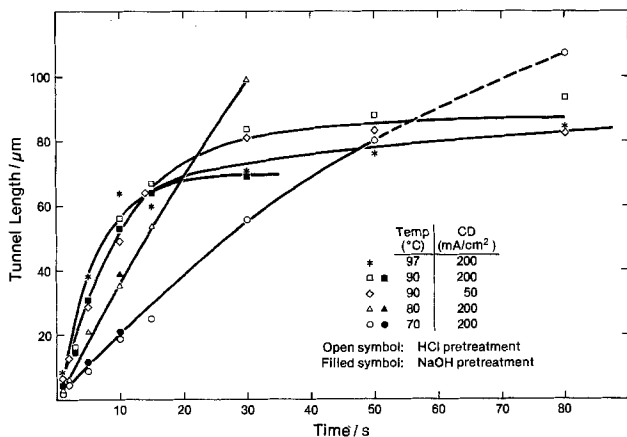


Fig. 4. First generation tunnel lengths. Open symbols for HCl pretreatment and filled symbols for NaOH pretreatment. ○: 70°C, 200 mA/cm²; △: 80°C, 200 mA/cm²; ◇: 90°C, 50 mA/cm²; □: 90°C, 200 mA/cm²; *: 97°C, 200 mA/cm².

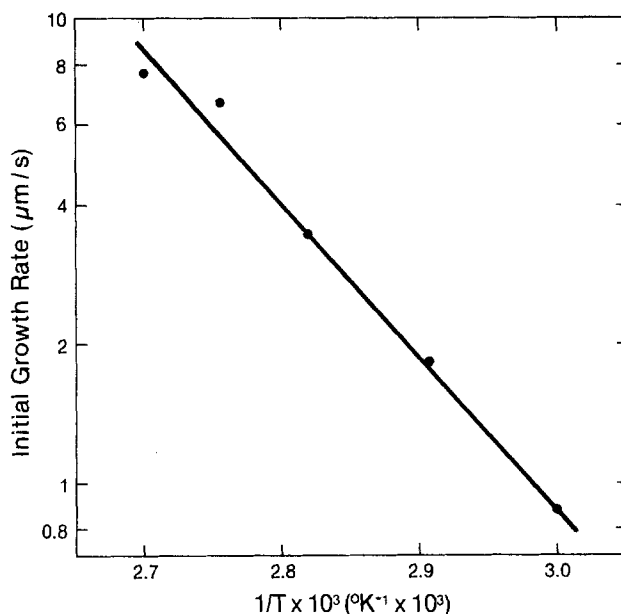


Fig. 5. Initial growth rate vs. reciprocal absolute temperature

For Al, $z = +3$, $\rho = 2.7$ g/cm³, and $M = 27$, so i (A/cm²) = $2.9 dl/dt$ (μm/sec). At 97°C, the initial cd was more than 20 A/cm², and at 60°C the initial cd was more than 2 A/cm². The latter is still quite high.

The metal weight loss during etching is 10-15% greater than calculated for the Faradaic charge. There is also a quantity of H₂ evolved from the surface that is equivalent to the excess weight loss. The gas may be evolved from the tunnels, but this has not been directly observed. This occurs to the same extent in neutral NaCl solutions as in the acid solutions used here.

The open-circuit potential was in the range -1.03 to -1.08V (SCE). Upon application of the current, the potential increased to ca. -0.8V SCE and then remained constant (± 5 mV). The voltage rise at 50 mA/cm² is shown in Fig. 6. The potentials include 10 ~ 20 mV IR drop between foil and Luggin probe, depending on the probe location with each specimen. A plateau during the first second is prominent at 70°C but gets smaller as temperature increases. This could be associated with either pit nucleation or tunnel initiation. Steady-state tunnel growth occurs at constant electrode potential.

When the cd was increased to 200 mA/cm² in 50 mA/cm² steps, the potential increased in equal increments, and the slope of the polarization line was close to the value estimated for the ohmic drop between Luggin probe and working electrode. Thus, ohmic polarization controls the i - V curve. This is in agreement with the observation that tunnel growth rate did not vary with nominal cd (Fig. 4). Extrapolation of such

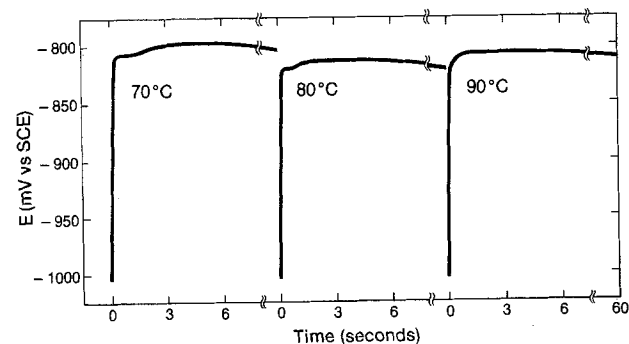


Fig. 6. Electrode potential (SCE) vs. time at 50 mA/cm² and several temperatures.

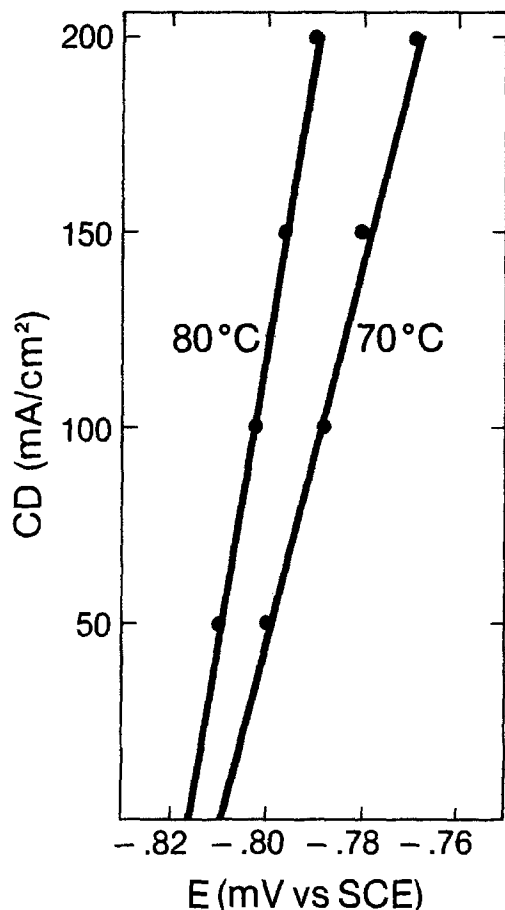


Fig. 7. Dependence of electrode potential on cd at 70°C and 80°C.

data to zero cd, as in Fig. 7, gives an estimate of E_{A1} free of external IR, but includes the IR drop within the tunnels. Measurements at temperatures from 60° to 90°C gave a temperature dependence of E_{A1} of about -1 mV/degree.

Effect of open-circuit and step changes.—To get an idea of how rapidly tunnel growth can be quenched, the galvanostatic etch was interrupted for brief open-circuit intervals. For example, at 90°C and 200 mA/cm², the etch was interrupted at 5 sec for an interval of 43 msec and then continued for a total etch time of 10 sec. The longest tunnel length seen in this specimen was 30 μ m, which is typical of a 5 sec etch period (see Fig. 4). This experiment was repeated at 70°C and 200 mA/cm², applying a 43 msec interrupt at 15 sec with a total etch time of 30 sec. The tunnel lengths were characteristic of a 15 sec etch period.

Thus, 43 msec on open circuit is sufficient to quench tip dissolution. This was the shortest interval used in these experiments and may be longer than the minimum time needed for tip passivation.³ At the time the open-circuit interval was applied, the tip cd was 15 and 5.5 A/cm² at 90° and 70°C, respectively.

Instead of an open-circuit interval, the nominal cd was reduced from 200 to 50 mA/cm² over the 43 msec span. An etch for 5 sec at each cd (10 sec total) produced tunnels 50 μ m long. This is the same as for a steady cd, indicating that the step had no effect on tip cd. The reduction in nominal cd was accommodated by an instantaneous reduction in active area, as shown in Fig. 8. The nonactive tip area was repassivated at the same potential that supported active dissolution on the rest of the tip face.

³ Conditions recently described for a commercial etch process using pulsed d.c. indicate that an open-circuit interval of about 1 msec may cause tip passivation (13).

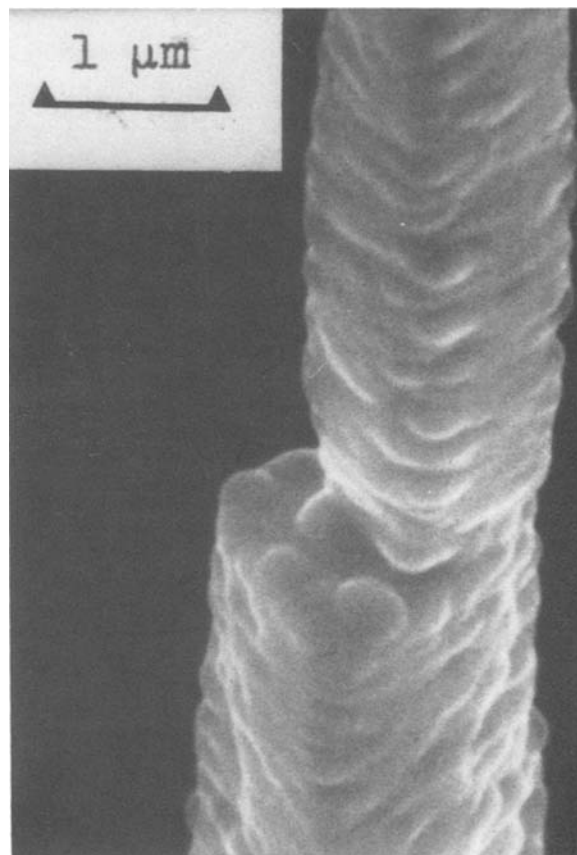


Fig. 8. Step change in cd from 200 mA/cm² (5 sec) to 50 mA/cm² (5 sec) at 90°C.

An increase in temperature causes a wide tunnel to break up into smaller tunnels. Figure 9 shows tunnels that were grown first at 65°C and then had hot etchant rapidly added to raise the temperature to 90°C. For smaller tunnels to form it is necessary for passive zones to develop on the wide tunnel tip. From this, we infer that the passivation process occurs more readily at higher temperature. The limiting tunnel length at 90° and 97°C (Fig. 4) must be owing to passivation of the tip occurring more easily at these temperatures than at lower temperatures.

Discussion

There are many common features of tunnel dissolution and pitting corrosion. Tunnel growth occurs in the neighborhood of the pitting potential (2, 6), and in this potential region the aluminum undergoes crystallographic attack (7). Dissolution at a high cd in restricted geometry creates a local electrolyte composition substantially different from the bulk. In this environment hydrogen evolution accompanies metal dissolution. Repassivation is a rapid process and occurs at the dissolution potential under some conditions (8).

Tunnel growth may be considered a special form of pitting corrosion. Its unique features are simultaneous dissolution and passivation on adjacent surfaces, and sustained balance between these two processes.

In our experiments, pit nucleation and growth during the first tenths of a second are similar to the events reported for initial pitting of iron and nickel (9) in that crystallographic pits with characteristic dimensions of a few microns are produced. The tunnel structure starts when dissolution becomes limited to one pit face due to passivation of the other faces. An elevated temperature seems necessary for this passive film to nucleate.

The reactions taking place at the tunnel tip are most likely the same as occur during conventional

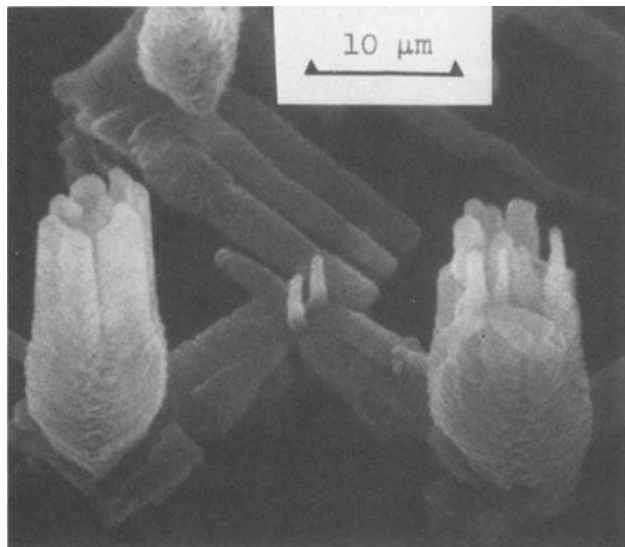


Fig. 9. Effect of temperature increase from 65°C to 90°C at 200 mA/cm².

pitting at this potential. This would be dissolution across an adsorbed chloride layer or perhaps a thin barrier salt layer (9, 10); any thicker layer is precluded by the crystallographic nature of the attack. Tip passivation may result from transport of water across this film to the metal surface to form an oxide monolayer that blocks metal ion transport.

It is difficult to determine whether the etch tunneling process proceeds under transport or under activation control. Seeming to point to activation control are data at and below 80°C for which the tunnels grow at a constant rate as etching proceeds. However, since there is a significant *IR* drop along a tunnel, the potential at the tunnel tip must decrease during etching but still have no effect on dissolution rate. For example, at 80°C the growth rate is constant at 10 A/cm²; if the solution resistivity is 1 Ω-cm, then the *IR* drop increases 1 mV per μm of tunnel length.

At 90°C, the tunnels grow at a decreasing rate, at constant potential, as etching proceeds. One might, therefore, expect the growth rate to decline as $t^{1/2}$ under diffusion control, or as t^1 under ohmic control. The observed dependence of $t^{0.7}$ is intermediate between these and suggests mixed control.

The activation energy over the temperature range under study was found to be 15 kcal/mol. This is in the lower range of values associated with chemical reactions, and is higher by severalfold than values associated with diffusion or conduction through liquids. However, because an activation energy of 15 kcal/mol is in the range observed for diffusion in solids, one could not rule out diffusion control in a salt film formed at the tunnel tip.

There are two ways to sustain tunnel growth. The first is to have parallel reactions of tip dissolution and wall passivation. The rate at which a unit step is dissolved must equal the rate at which a unit length is passivated. There appears to be no inherent limitations in fitting any of the experimental observations to such a model. The presence of a passivating wall film that can spread relatively easily may be the necessary qualitative difference between wall and tip that sustains tunnel growth. Any model based on this idea

must provide a means for limiting one reaction to the wall and another to the tip.

The second way to make a tunnel is by sequential dissolution and passivation. A sequence consists of initiation of a pit at the tunnel tip, pit growth to fill the tunnel cross section, and passivation of this new surface. A new breakdown event on the tip face then starts the next cycle. Within the context of this model, the wall ripples may be the height of each sequence step and the tip facets are stages in pit growth. A serious shortcoming of this hypothesis is that since each sequence step requires initiation of wall passivation, it cannot easily account for continued tunnel growth after a step change to low temperature. Also, it is not clear why the center line of the tunnel remains fixed during growth. Dissolution on the tip face is expected to spread symmetrically from the breakdown point. This does not happen. Instead, dissolution stops near the previous wall boundary, independent of the point of initiation.

Tunnel growth during anodic dissolution is not unique to aluminum. A high density of microscopic tunnels propagating along crystallographic directions has been observed in stainless steel during stress-corrosion cracking (11), and in GaP and n-type GaAs during dissolution in methanolic Cl solution (12). These are not cubic systems, as is aluminum. It is not known if these all form by a similar mechanism.

Acknowledgment

We appreciate the assistance of Mr. A. Ohtake with some of the experimental measurements. The work of one of the authors (T. R. B.) was supported by the Office of Naval Research (N00014-76-C-0495 and N00014-82-C-0052). The work of another (R. C. A.) was supported by the National Science Foundation (NSF-DMR 82-00781) at the University of Illinois at Urbana-Champaign.

Manuscript submitted March 4, 1983; revised manuscript received Aug. 1, 1983. This was Paper 66 presented at the Detroit Meeting of the Society, Oct. 17-21, 1982.

United Chemi-Con, Incorporated assisted in meeting the publication costs of this article.

REFERENCES

1. C. G. Dunn, R. B. Bolon, A. S. Alwan, and A. W. Stirling, *This Journal*, **118**, 381 (1971).
2. N. F. Jackson, *Electrocomponent Sci. and Tech.*, **2**, 33 (1975).
3. E. C. Pearson, H. J. Huff, and R. H. Hay, *Can. J. Tech.*, **30**, 311 (1952).
4. C. Edeleanu, *J. Inst. Metals*, **89**, 90 (1960-1961).
5. C. K. Dyer, Unpublished results.
6. H. Fickelscher, *Werkst. Korros.*, **33**, 146 (1982).
7. J. A. Richardson and G. C. Wood, *Corros. Sci.*, **10**, 313 (1970).
8. A. Broli and H. Holtan, *ibid.*, **13**, 237 (1973).
9. H.-H. Strehblow and J. Weners, *Z. Phys. Chem.*, **98**, 198 (1975); H.-H. Strehblow and M. B. Ives, *Corros. Sci.*, **16**, 317 (1976).
10. T. R. Beck and R. C. Alkire, *This Journal*, **126**, 1662 (1979).
11. N. A. Nielsen, *Corrosion*, **27**, 173 (1971); M. F. Dean, F. H. Beck, and R. W. Staehle, *ibid.*, **23** (1967).
12. B. D. Chase and D. B. Holt, *This Journal*, **119**, 314 (1972); M. M. Faktor, D. G. Fiddymont, and M. R. Taylor, *ibid.*, **122**, 1566 (1975).
13. European Patent Appl. 81201307.6, Int. Cl. H01G9/04, publ. No. 0054990 (A1) (1982).

A Simple Phase Transition Model for Metal Passivation Kinetics

G. L. Griffin

Department of Chemical Engineering and Materials Science, University of Minnesota, Minneapolis, Minnesota 55455

ABSTRACT

We present a minimal parameter kinetic model which describes the corrosion and passivation of metal surfaces. Two elementary steps are included, namely, the oxidation of surface metal atoms to produce adsorbed cations, and the subsequent dissolution of these cations into the electrolyte. Oxide layer formation is represented by two-dimensional condensation of adsorbed cations to produce a continuous phase; statistics of the condensation process are treated at the mean field level. The structure and magnitude of the i - V curve in the active-passive transition region is calculated for two cases: the limit of maximum passivation hysteresis (spinodal decomposition of the oxide phase), and the limit of zero hysteresis (equilibrated phase transition). Methods for analyzing experimental i - V curves to yield the rate constants associated with the model are presented.

Passivation plays a crucial role in the corrosion resistance and electrochemical behavior of many metals. The remarkable nature of the passivation effect is shown most clearly by polarization curves (i - V plots) of the active-passive transition region, which reveal that the oxidation current passes through a maximum and then actually decreases with increasing anodic polarization.

Detailed measurements of the passivation process have been performed for metals covering much of the periodic table (1, 2), using a variety of experimental techniques, many of which are considerably more sophisticated than simple i - V curve measurements (3). These results have provided both qualitative and quantitative evidence for a wide range of microscopic reactions, reflecting the fact that the formation of passive layers in real systems involves a complex and inter-related set of processes.

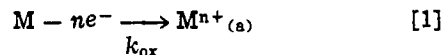
As a result of this complexity, there appears to be a shortage of experimentally useful kinetic models that are simple enough to provide an overall description of the active-passive transition region with a minimal number of kinetic parameters, but which contain parameters that have an interpretable physical significance (4-9). Such models, provided that their limitations and assumptions are clearly understood, can be a valuable aid to the experimenter.

In this paper, we describe a simple kinetic model for the passivation process which nevertheless can account for all of the characteristic features of the classical i - V curve for the active-passive transition. The model contains only two elementary rate processes, namely, the oxidative hydrolysis of surface metal atoms to produce adsorbed cations, and the dissolution of these cations away from the electrode surface. Passivation is effected by assuming that the rate of cation dissolution decreases as the cation coverage increases, due to the stabilizing influence of oxide lattice bond formation. After developing the model, we next examine the predicted i - V curves for two extremes of passivation behavior: the limit of maximum hysteresis, where the phase transition between isolated cations and a condensed oxide layer occurs via spinodal decomposition; and the limit of a fully equilibrated phase transition, where the i - V curve will track the "tie line" describing a first-order phase transition between dilute and condensed cation layers. For each limit, equations are developed which permit the kinetic parameters of the model to be determined directly from experimentally measured i - V curves.

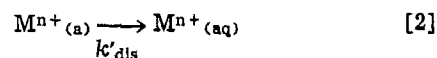
Development of the Model

We begin by assuming that there are two elementary steps which determine the overall mechanism of corrosion and passivation: oxidative hydrolysis of surface metal atoms to form adsorbed cations

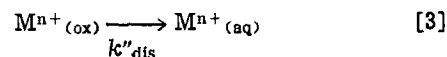
Key words: metals, electrode, corrosion, passivity.



followed by dissolution of cations into the electrolyte phase. The latter process may involve cations that are isolated on the electrode surface



as well as cations incorporated into the oxide layer



In particular, we do not explicitly consider the elementary steps by which isolated cations are incorporated into the oxide layer.

Instead, we further assume that the only feature which distinguishes an isolated adsorbed cation from a cation in the oxide layer is the presence of a full complement of nearest neighbor cations. This permits us to treat the surface adsorbate layer as a lattice gas of interacting cations, for which isolated cation behavior is obtained in the limit as $\theta \rightarrow 0$ and oxide-like behavior is obtained as $\theta \rightarrow 1$.

Finally, we assume that the dissolution rate constants defined in reactions [2] and [3] can actually be thought of as the two limiting extremes of a single, coverage dependent dissolution rate constant, $k_{dis}(\theta)$

$$k'_{dis} = k_{dis}(\theta = 0) \text{ and } k''_{dis} = k_{dis}(\theta = 1) \quad [4]$$

The coverage dependence of $k_{dis}(\theta)$ is assumed to arise from the fact that the difficulty of dissolving a cation will increase with the number of nearest neighbor cations, due to the formation of lattice oxide bonds. With this assumption, it becomes possible to describe cation dissolution using a single rate constant, which does, however, depend strongly on the average cation coordination number at each value of θ .

The exact form of an analytic expression used for $k_{dis}(\theta)$ will depend on the nature of the microscopic interactions and on the level of approximation used to solve the population statistics of the cation layer lattice. For our present purposes, the assumption of pairwise additive interactions in the mean field approximation provides a suitable illustration of the effects we wish to describe. At this level of approximation, the average desorption energy associated with cation dissolution, E_d , will be linearly proportional to cation coverage

$$E_d = E_d^0 + n_s \omega \theta \quad [5]$$

where n_s is the saturation number of nearest cation neighbors surrounding a surface cation in the oxide lattice, and ω is the effective interaction energy between neighboring cations. The latter will include the decrease in solvation energy produced by exclusion of water ligands from a cation when a new oxide

bond is formed, as well as the metal-oxygen bond energy. Other factors which influence passive layer stability (e.g., anion concentration, pH, etc.) will also be included in the effective value of ω .

If Eq. [5] is assumed to describe the average cation dissolution energy, then the rate constant for cation dissolution becomes

$$k_{\text{dis}} = k^{\circ}_{\text{dis}} \exp(-\beta\theta) \quad [6]$$

where $\beta = n_s\omega/RT$ and k°_{dis} represents the dissolution rate constant for an isolated adsorbed cation. Since this average rate constant describes the dissolution of all cations (isolated and oxide-incorporated), the rate expression for the dissolution current, i , becomes

$$i = k^{\circ}_{\text{dis}}\theta \exp(-\beta\theta) \quad [7]$$

At steady state, of course, this will equal the rate of cation formation by reaction [1]. We expect that reaction [1] will only occur on that fraction of the metal surface which is not covered by adsorbed cations. Further, we expect that the rate constant for the oxidative hydrolysis process will have the Tafel-like behavior typically associated with charge transfer processes. Thus we assume a rate expression for cation formation of the form

$$i = k^{\circ}_{\text{ox}}(1 - \theta) \exp(BV) \quad [8]$$

where $B = \alpha F/RT$ is the Tafel coefficient.

To obtain an analytical expression for the corrosion current using either Eq. [7] or [8], we must first find an expression relating θ and V . Eliminating i from Eq. [7] and [8] and rearranging, we can write

$$V = \frac{1}{B} [-\beta\theta + \ln(k^{\circ}_{\text{dis}}/k^{\circ}_{\text{ox}}) + \ln(\theta/1 - \theta)] \quad [9]$$

The key feature of Eq. [9] is that for $\beta > 4$, there will be potentials at which more than one value of θ satisfies the equation. In other words, multiple steady-state solutions for $\theta(V)$ exist. This can be shown by examining the sign of the first derivative of Eq. [9] with respect to θ .

This is illustrated in Fig. 1, where we show $\theta(V)$ based on Eq. [9] for the case of $\beta = 6$. The sigmoidal behavior produces a potential region where three distinct values of θ satisfy Eq. [9]. This behavior is en-

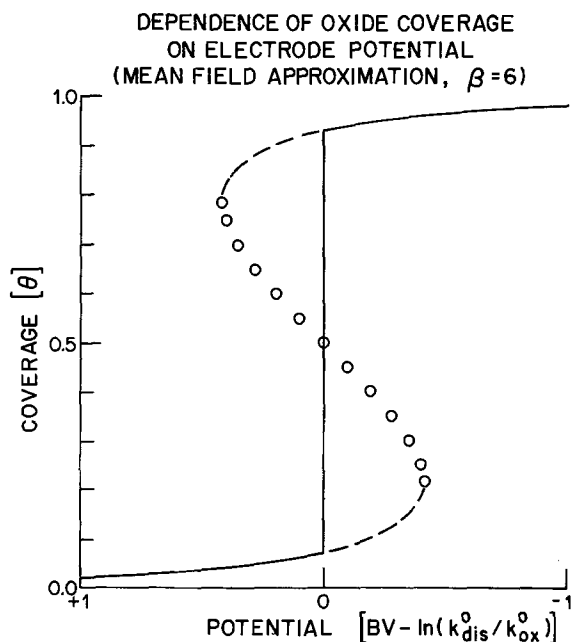


Fig. 1. Adsorbed cation coverage as a function of electrode potential, assuming a cation interaction parameter $\beta = 6$. (cf. Eq. [9]).

tirely analogous to a van der Waals loop (10), and represents the mean field approximation to a phase transition between isolated cations (dilute phase) and a continuous oxide layer (condensed phase). The vertical tie line passing through $\theta = 1/2$ represents the first order phase transition predicted by more exact statistical mechanical treatments. The dashed portions of the upper and lower branches that extend beyond the phase transition tie line represent excursions into the metastable regions of the condensed and dilute phase θ - V curves, respectively. Physically, these regions are accessible if a nucleation barrier for phase transformation is present, which prevents the condition of the cation layer from reversibly evolving along the phase transition tie line. The open circles represent the unstable region of the solution.

For larger values of β , the potential range of the multiple solution region increases. For smaller values of β , the range decreases, until multiplicity vanishes at $\beta = 4$. For $\beta < 4$, only a single-valued, nonsingular solution for $\theta(V)$ exists.

Examples of i - V curves calculated using these results for $\theta(V)$ are shown in Fig. 2. The parameters used in Eq. [7] and [8] are: $k^{\circ}_{\text{ox}} = 8 \times 10^{32}$ mA/cm²; $B = 57.6$ V⁻¹; and $k^{\circ}_{\text{dis}} = 1300$ mA/cm² (11). The interaction parameter, β , is varied between 0 and 6, in order to show the influence of attractive interactions (i.e., oxide formation) on the shape of the i - V curves. For reference, the asymptotic behavior limits (Tafel-like metal dissolution and constant rate oxide dissolution) are also shown.

For the extreme case of $\beta = 0$, no current maximum is observed. This illustrates that a simple two-step

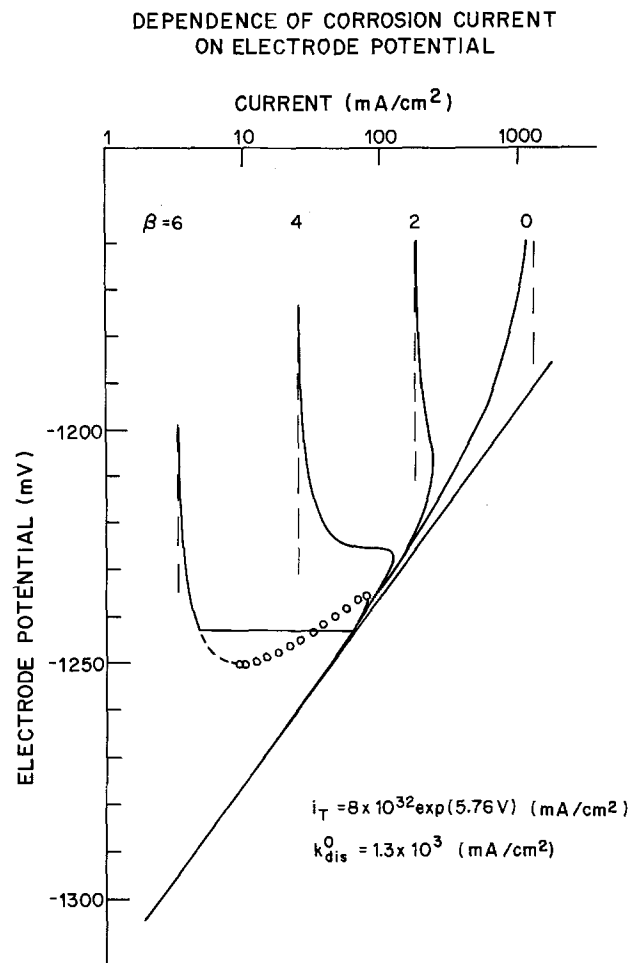


Fig. 2. Current density-potential curves calculated for different values of the cation interaction parameter, $0 \leq \beta \leq 6$. Other rate parameters fixed: $k^{\circ}_{\text{ox}} = 8 \times 10^{32}$ mA/cm²; $B = 57.6$ V⁻¹; $k^{\circ}_{\text{dis}} = 1300$ mA/cm².

model based only on cation formation and uniform oxide dissolution (cf. Eq. [1] and [3] alone) cannot account for classic passivation behavior.

For $\beta = 2$, a current maximum is observed. For $\beta = 4$, which represents the critical value of the interaction constant in the mean field theory, the maximum value of the derivative of the current with respect to potential in the passivating region reaches infinity (at $\theta = \frac{1}{2}$).

For $\beta = 6$, the sigmoidal shape of the $\theta = V$ curve shown in Fig. 1 results in a multivalued analytic form for the i - V curve in the active-passive transition region. If the cation layer is fully equilibrated when the potential passes through this region, we would expect the i - V curve to follow the discontinuity represented by the horizontal tie line. If a nucleation process is required to convert between isolated cations and an oxide layer, then the i - V curve will follow the metastable branch dictated by the direction of the potential sweep. In the latter case, hysteresis would be expected around the active-passive transition.

Discussion

Clearly, the use of a two-step, variable rate constant model based on a mean field treatment is a gross approximation to the complex molecular behavior associated with the formation and destruction of the passive layer at a real metal surface. In particular, the assumption that the passive oxide layer can be modeled as a saturated monolayer of cations represents a serious restriction. Of equal concern is the use of a linear coverage dependence for the effective dissolution energy (cf. Eq. [5]), when in reality the value of E_d represents an average over a complicated distribution of step, ledge, and kink cation sites in the passive film. However, the most important feature of passive layer behavior is contained in the model, namely, the fact that the rate of cation dissolution must be treated as a function of cation (oxide) coverage.

With these cautions in mind, we proceed to examine the limiting behavior and major structural features of the i - V curves predicted using this model. Our goal is to relate these experimentally measurable features to the microscopic rate parameters for a given system.

Asymptomatic behavior.—Cathodic potentials.—At sufficiently negative values of the potential, θ will approach zero (cf. Fig. 1). As seen from Eq. [8], the observed current will approach the Tafel-like limit assumed for metal dissolution from an oxide-free surface

$$i_T = k_{ox} \exp(BV) \quad [10]$$

Anodic potentials.—At sufficiently positive potentials, θ will approach unity. As seen from Eq. [7], the observed current will approach the constant value characteristic of oxide dissolution in the passive region

$$i_p = k_{dis} \exp(-\beta) \quad [11]$$

We note that if i_p is known experimentally, then k_{dis} can be determined using this equation, provided that the value of β can be found independently (see below).

Structural features.—Maximum hysteresis.—The distinguishing feature of i - V curves in the active-passive transition region is the magnitude and shape of the current maximum. As noted in the description of Fig. 1 and 2, the branch of the analytic θ - V curve which the actual i - V curve will track is determined by the size of the nucleation barrier associated with the cation layer phase transition. We will first consider the situation resulting for the maximum barrier, in which case the i - V curves will extend into the metastable region all the way to the spinodal decomposition points.

Differential of Eq. [7] shows that the maximum current in this case occurs at $\theta_m = 1/\beta$. We can also see that within the context of the present model, a metal

surface will not show a maximum in its i - V curve unless $\beta > 1$. In other words, the latter condition represents the minimum necessary cation interaction energy to produce a passivating oxide layer.

We can find the relative amplitude of the current maximum by substituting θ_m back into Eq. [7]. The ratio of the maximum current, i_m , to the limiting current at potentials well into the passive region, i_p , is then

$$i_m/i_p = [\exp(\beta - 1)]/\beta \quad [12]$$

Thus a comparison of experimentally determined values of i_m and i_p will provide an estimate of β .

The potential at which the maximum current occurs, V_m , is found by substituting θ_m into Eq. [9]

$$V_m = \frac{1}{B} [\ln(k_{dis}^0/k_{ox}^0) - \ln(\beta - 1) - 1] \quad [13]$$

Thus k_{dis}^0 and β can be determined by solving any two of the Eq. [11]-[13] simultaneously. Comparison of the values obtained using alternative methods will provide a consistency check for the apparent accuracy of the model, since the experimental quantities i_p , i_m , and V_m are all independently determined.

The spinodal decomposition points of the metastable branches of the θ - V curve (Fig. 1) are located where the derivative of Eq. [9] with respect to θ vanishes. The coverages at these two points, θ^\pm , are given by

$$\theta^\pm = \frac{1}{2} \pm \sqrt{\frac{1}{4} - \frac{1}{\beta}} = \frac{1}{2} \pm \gamma \quad [14]$$

provided that $\beta \geq 4$.

The potential at each end point is found by substituting Eq. [14] into Eq. [9]. The potential range between the two points, ΔV , which corresponds to the maximum range that can be expected for a hysteresis loop, is then

$$\Delta V = \frac{1}{B} \left[2\beta\gamma - 2 \ln \left(\frac{\frac{1}{2} + \gamma}{\frac{1}{2} - \gamma} \right) \right] \quad [15]$$

Equilibrated phase transition.—For systems where there is no nucleation barrier for conversion between the dilute and condensed phases of the cation layer, there will be no hysteresis loop during a cyclic potential sweep. Instead, the i - V curve will track the phase transition tie line when passing through the active-passive transition region. The potential of this tie line, $V_{1/2}$, is given by

$$V_{1/2} = \frac{1}{\beta} \left[\ln(k_{dis}^0/k_{ox}^0) - \frac{\beta}{2} \right] \quad [16]$$

(cf. Eq. [9], with $\theta = \frac{1}{2}$). Thus, for materials which do not show hysteresis, Eq. [16] should be used instead of Eq. [13] for determining k_{dis}^0 and β from experimental results.

If the i - V curve tracks the equilibrium tie line, then we also note that the maximum current will not reach the value predicted by Eq. [12]. Instead, the maximum will occur at the intersection of the phase transition tie line and the high current low coverage branch of the i - V curve.

In this case, an exact analytic expression cannot be written for the maximum current in the absence of hysteresis, i_m^* . However, a reasonable approximation can be obtained by substituting $V_{1/2}$ from Eq. [16] into Eq. [8], and setting $\theta = 0$. This procedure will overestimate i_m^* by at most a factor of two, in the limiting case of $\beta = 4$. For values of $\beta > 4$, the approximation rapidly approaches the correct value, as seen either from Fig. 2 or Eq. [14] (note that $0 < \theta_m^* < \theta^-$). The equation relating i_m^* to i_p becomes

$$i_m^*/i_p = \exp(\beta/2) \quad [17]$$

Equation [17] should be used instead of Eq. [12] to estimate β for systems which do not show hysteresis.

Finally, we note that many real systems would be expected to show hysteresis behavior somewhere between the extremes of spinodal decomposition and equilibrated phase transition. Solution in this case will require knowledge of the nucleation barriers for the oxide layer phase transition, which generally is not available. However, one simplified case can be considered. If we assume that the coverage supersaturation at the nucleation threshold is the same for phase transitions in either direction, then comparison of Eq. [9] and [16] shows that $V_{1/2}$ is equal to the arithmetic average of the observed potential limits of the hysteresis loop, V_+ and V_-

$$V_{1/2} = (V_+ + V_-)/2 \quad [18]$$

Equation [18] provides a method to evaluate $V_{1/2}$ for systems which exhibit limited hysteresis. (Equation [18] is accurate in fact even for the limit of spinodal decomposition). Values of β and k_{dis}^0 can then be determined as above.

Summary

We have described a minimal parameter model which can reproduce the important features of the i - V curve in the active-passive transition region. The physical significance of each parameter in the model has been discussed, along with methods for determining the values of the parameters using experimental measurements. While the model is only an approximation to most real systems, we believe that it does provide a basis for proposing and evaluating more complicated passivation mechanisms. To this end, future work should be done both to assess the utility of the model for correlating experimental data and to theoretically examine approaches to loosening the restrictions imposed by the assumptions of the model.

Acknowledgment

This work was supported by the Corrosion Research Center at the University of Minnesota, through Department of Energy Grant No. DE-AC02-79ER10450.

Manuscript submitted March 16, 1983; revised manuscript received Aug. 3, 1983.

REFERENCES

1. N. D. Tomashov and G. P. Chernova, "Passivity and Protection of Metals Against Corrosion," Plenum Press, New York (1967).
2. "Passivity of Metals," R. P. Frankenthal and J. Kruger, Editors, The Electrochemical Society, Princeton, NJ (1978).
3. I. Epelboin and M. Keddam, in "Passivity of Metals," R. P. Frankenthal and J. Kruger, Editors, p. 184, The Electrochemical Society, Princeton, NJ (1978).
4. N. Sato, in "Comprehensive Treatise of Electrochemistry," Vol. 4, J. O'M. Bockris, B. E. Conway, E. Yeager, and R. E. White, Editors, p. 193, Plenum Press, New York (1981).
5. N. Sato, in "Passivity of Metals," R. P. Frankenthal and J. Kruger, Editors, p. 29, The Electrochemical Society, Princeton, NJ (1978).
6. V. Brusic, in "Oxides and Oxide Films," Vol. 1, J. W. Diggle, Editor, p. 1, Marcel Dekker, New York (1972).
7. K. J. Vetter, *Electrochim. Acta*, **16**, 1923 (1971).
8. U. Ebersbach, K. Schwabe, and K. Ritter, *ibid.*, **12**, 927 (1967).
9. A. A. Elmiligy, D. Geona, and W. J. Lorenz, *ibid.*, **20**, 273 (1975).
10. J. E. Mayer and M. G. Mayer, "Statistical Mechanics," p. 273, Wiley, New York (1940).
11. I. Sanghi and M. Fleischman, *Electrochim. Acta*, **1**, 161 (1959).

Diffusion Controlled and Transient Photocurrents of Photo-Oxidation Reactions at Polycrystalline α - Fe_2O_3

M. Anderman* and John H. Kennedy*

Department of Chemistry, University of California, Santa Barbara, California 93106

ABSTRACT

Steady-state photooxidation currents at polycrystalline α - Fe_2O_3 electrodes with low band bending were found to depend significantly on the reducing agents present in the electrolyte. Photooxidation of water at low band bending exhibited only transient character. Diffusion-controlled photocurrents for the photooxidation of I^- and $\text{Fe}(\text{CN})_6^{4-}$ in acidic solutions, and OH^- in unbuffered neutral solution were observed at an α - Fe_2O_3 RDE and could be fitted to the Levich equation. The steady-state and the transient photocurrents are analyzed and discussed in terms of cathodic back-reaction of intermediate products with conduction band surface forbidden electrons.

The semiconductor/electrolyte interface has been extensively studied in the last decade or so primarily because of its possible use for solar energy conversion. When an ideal semiconductor is brought into contact with a redox couple in solution, equilibration of the electrochemical potentials of the semiconductor and the redox couple will occur. If the electrochemical potential of the solution was initially more positive than that of an n-type semiconductor (the important case for solar energy conversion at n-type semiconductors), equilibration will result in the formation of a depletion layer inside the semiconductor with upward bending bands (1). This electric field will drive electron holes that may be generated by $>$ bandgap illumination toward the surface, and will drive photogenerated electrons toward the semiconductor bulk. Thus, one

can obtain a photopotential and a photocurrent between the illuminated semiconductor anode and a dark metallic cathode that is immersed in the same solution (1).

Under potentiostatic conditions and a reversible electrolyte couple the ideal model predicts: (i) onset of photocurrent will occur promptly following the onset of depletion layer formation, i.e., just anodic to the so-called flatband potential (V_{FB}); (ii) when a specific adsorption of the redox couple does not occur, the photocurrent should depend on the light intensity and on the semiconductor properties but should be independent of the redox couple; and (iii) no dark current is expected for a stable ideal semiconductor when the electrode potential is within the gap of the semiconductor.

The behavior of practical semiconductor anodes is usually less than ideal. Thus, (i) the onset of steady-

* Electrochemical Society Active Member.
Key words: α - Fe_2O_3 photoanode, diffusion-controlled photocurrent, RDE photoanode, transient photocurrent.

state photocurrent often occurs a few hundred millivolts anodic to the observed V_{FB} ; (ii) in a few cases (2-4) it has been found that the photocurrent does depend upon the reduced species even when no shift of V_{FB} by specific adsorption could be detected; and (iii) dark current of various magnitude has frequently been observed in the forbidden potential zone.

Since these three deviations from ideality will usually result in a decrease of the optimal photoconversion efficiency, it is important to investigate them. We have extended our studies on polycrystalline α - Fe_2O_3 anodes in aqueous solution to the use of the rotating ring-disk electrode (RRDE). With it, the diffusion dependence of the photocurrent was studied and the oxidation products were analyzed. A light shutter to investigate transient currents has also been employed. It was found that not only may the redox species influence the photocurrent but that there exists a potential range in which water oxidation is completely deactivated by a coupled cathodic reaction, while the photooxidation of some reducing agents occurs under quantitative diffusion-limited conditions. The results are discussed in terms of a back-reaction of the water oxidation products with surface forbidden electrons.

Experimental

Polycrystalline α - Fe_2O_3 electrodes doped with 1 atom percent (a/o) SiC were prepared by sintering the appropriate pressed powder mixture at 1360°C for 14-20 hr as described earlier (5). Gold was sputtered on the back surface to form ohmic contact. To assemble the α - Fe_2O_3 electrode as a disk onto the Pine Instrument AFDTI36 Ring (demountable)-Disk Electrode Assembly, the following procedure was used. The electrode was contacted to a stainless steel pin with silver epoxy. The back surface was then insulated with black wax and a suitable Teflon cup was glued to the back surface using 5 min epoxy resin and Loctite 404 industrial adhesive. While it is generally desirable to polish a disk electrode for RRDE experiments, we found that polishing decreased the photoactivity of the surface probably by introducing surface defects. Thus, the flatness of the pellet surface was simply measured with a micrometer and only those electrodes that were perfectly perpendicular to the pin holder with deviations from flatness smaller than 50 μ m were used. After this check, the electrode and the Teflon back support were gently machined on the edge to the exact diameter of the RRDE disk (0.625 cm diam, 0.307 cm² area), leaving the Teflon cup a few micrometers oversize for a press fit. A small amount of Halocarbon 25-5S grease was applied around the electrode sides to ensure a good seal. The electrode was then pressed into the ring disk assembly, washed with acetone and deionized water, and was then ready for use. The ring electrode was platinum. The only problem encountered with this procedure was that sometimes the halocarbon grease seal had to be renewed after a few days of operation.

The electrochemical cell was a 200 ml all quartz cylinder covered with a Teflon lid. The cell included a SCE reference, Pt wire counterelectrode separated from the main compartment by fritted glass, and gas entry tubes. The light source was a 150W xenon lamp that delivered a light intensity of \sim 500 mW/cm² at the electrode surface. The light path included a shutter (1 in.), IR filter, reflecting mirror, and a 10 cm quartz lens. The light beam reached the electrode through the bottom of the cell, and hence, passed through \sim 8 cm of electrolyte solution.

The electrochemical instrumentation consisted of a Pine Instrument RDE-3 dual potentiostat in conjunction with X-Y recorder and a Tektronix 564B storage oscilloscope. A Pine Instrument ASR motor with rotation speeds of 0-3820 rpm (0-400 sec⁻¹) was used. The light shutter was Uniblitz 225L driven by a Uni-

blitz SD 122 electronic shutter drive unit that was pulsed by a Hewlett-Packard 3311A function generator. Opening time of the shutter was 2.0-2.5 msec.

The experiments in neutral solutions were carried out with a CO₂-free electrolyte. Cell resistance was \sim 100 Ω arising predominantly from the bulk resistance of the α - Fe_2O_3 electrode.

Results

Photocurrent-potential curves for a polycrystalline α - Fe_2O_3 electrode in 1M NaOH is given in Fig. 1. Curve 2 is the steady-state photocurrent as recorded at a scan rate of 10 mV/sec. Curve 1 shows the transient peak values that were taken pointwise with the oscilloscope at 50 mV intervals. The transient peak exhibited a first-order decay into the steady-state value with a lifetime of $<$ 2 msec. When the shutter was turned off, a cathodic transient peak of slightly lower magnitude and similar lifetime was observed, in agreement with earlier reports (6-8). The transient and the steady-state photocurrent converged into one curve about 800 mV past the onset of the transient photocurrent.

The V_{FB} of similar α - Fe_2O_3 electrodes, determined by Kennedy and Frese (9) from extrapolation of Mott-Schottky plots, was $-0.73V$ vs. SCE in 2M NaOH. However, in this work we have used a much simpler and satisfactory method to measure V_{FB} . The electrode potential was stepped from the onset of the steady-state photocurrent in the cathodic direction in intervals of 25-50 mV. At some point the anodic transient peak disappeared, and the electrode showed no photoeffect. If the electrode was stepped further in the cathodic direction, a small cathodic transient photoeffect was evident. The potential at which no photoeffect was observed is taken to be V_{FB} . Surprisingly, this simple method gave highly reproducible results. The experimental uncertainty for a specific electrode was $<$ 50 mV, and the variation among different samples was $<$ 100 mV. From this method, V_{FB} in 1M NaOH was $-0.8 \pm 0.1V$ vs. SCE, in good agreement with previous data (9-11).

In 1M HClO₄ with no added redox couple, the general picture was similar (curves 1 and 3 of Fig. 2). Anodic transient photoeffects started \sim 0.1V vs. SCE while steady-state photocurrent began only at \sim 0.5V vs. SCE. The two curves converged \sim 1V anodic to the onset of the transient photocurrent.

Addition of 0.1M NaCl to the 1M HClO₄ solution had no effect on the transient photocurrent. However, the steady-state photocurrent moved cathodically (curve 2 of Fig. 2) so that it was between the transient and the steady-state photocurrents of the chloride-

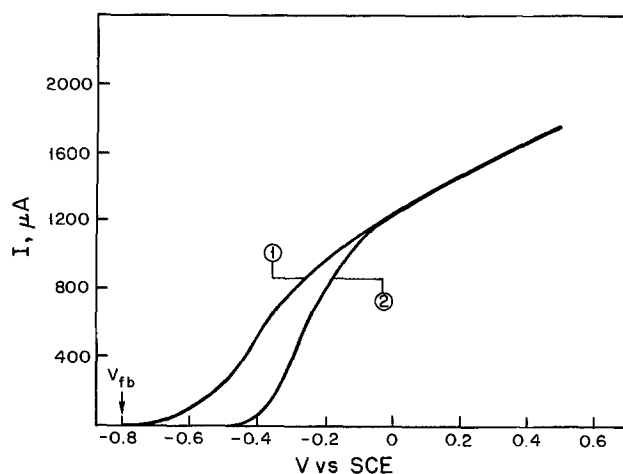


Fig. 1. Photocurrent-potential curves for a polycrystalline α - Fe_2O_3 electrode in 1M NaOH. 1, Transient photocurrent taken pointwise with an oscilloscope, and 2, steady-state photocurrent taken with a scan rate of 10 mV/sec. Electrode area = 0.307 cm².

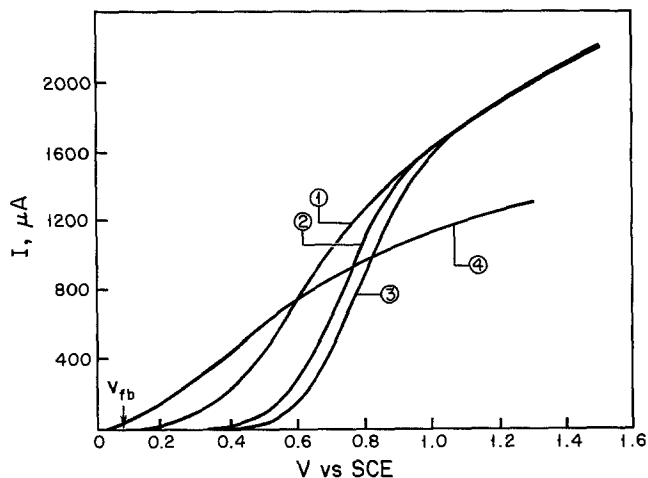


Fig. 2. Photocurrent-potential curves for $\alpha\text{-Fe}_2\text{O}_3$ in 1M HClO_4 . 1, Transient photocurrent with no added redox species or in 0.1M NaCl or in 0.1M KBr. It is also the steady-state photocurrent-potential curve for 0.1M KBr/1M HClO_4 . 2, Steady-state curve for 0.1M NaCl/1M HClO_4 . 3, Steady-state curve for 1M HClO_4 (H_2O oxidation). 4, Steady-state and transient curve for 0.01M KI/1M HClO_4 uncorrected for light absorption by the colored solution.

free solution. The convergence of the transient and the steady-state photocurrents now occurred at a less anodic potential. The effect of bromide was even more pronounced. In fact, the transient and the steady-state photocurrents were essentially identical, except for a small difference near the onset potential, and they were also identical to the transient values for 0.1M NaCl and halide-free solutions. V_{FB} for all solutions as determined by the procedure described above was $0.1 \pm 0.1\text{V vs. SCE}$.

Curve 4 in Fig. 2 is the corresponding curve for a 0.01M KI/1M HClO_4 solution. It must be noted that the measured photocurrent was reduced due to absorption of light by the colored solution. In this case, no transient effect was seen. The onset of the photocurrent was around 0.05V vs. SCE , and the V_{FB} measurement gave $0.0 \pm 0.1\text{V vs. SCE}$. It appears from these results that I^- was the only species that affected V_{FB} by specific adsorption on the electrode surface.

Even here, the effect was rather small, only 50-100 mV. It is important to note that only transient effects that have a lifetime $\cong 2$ msec (the opening time of the shutter) could be detected. Dark current, observed $\sim 1.5\text{V vs. SCE}$, was only slightly affected by the addition of halide ions to the solution. Dark current was more dependent upon the specific electrode used.

Next, the dependence of the photocurrent on the rotation rate of the disk electrode for halide-containing solutions was measured. Figure 3 shows a photocurrent-potential curve at a rotation frequency of 196 sec^{-1} for $2.88 \times 10^{-4}\text{M KI/1M HClO}_4$ solution. It can be seen that the photocurrent was composed on two separate oxidation waves. The first one almost reached a plateau value that was dependent upon rotation speed (Fig. 3 inset) but was practically unchanged when the light intensity was reduced by a factor of two. The second oxidation wave started at the same potential at which the steady-state photooxidation of water was observed in the halide-free solution and exhibited the same general shape. Also, the dependence of the photocurrent on the rotation speed diminished as the electrode potential was scanned anodically from the plateau region. On the other hand, the dependence of the photocurrent upon the light intensity grew, reaching a linear dependence at 1.5V vs. SCE .

For a diffusion-limited current (I_{dl} , mA) at an RDE, Levich gives (12)

$$I_{dl} = 0.62nFAD^{2/3}\nu^{-1/6}\omega^{1/2}C_b \quad [1]$$

where n is the number of electrons transferred in the reaction, F is the Faraday constant, A is the electrode area (cm^2), D is the diffusion coefficient (cm^2/sec), ν is the kinematic viscosity (cm^2/sec), ω is the angular velocity (rad/sec), and C_b is the concentration of the diffusing species (M) in the bulk solution.

Thus for diffusion-limited current at an RDE, the current should depend on the square root of the rotation speed. Figure 4 is I_{dl} vs. $\omega^{1/2}$ for the photocurrent values at 0.45V vs. SCE taken from the curves shown in Fig. 3 (inset). An excellent straight line was obtained clearly indicating that the photocurrent was diffusion limited at that potential. The theoretical slope of the line in Fig. 4 can be calculated from Eq. [1] if the various factors are known. A value for D of $1.72 \times 10^{-5}\text{ cm}^2/\text{sec}$ for I^- (13), and $\nu = 10^{-2}\text{ cm}^2/\text{sec}$ were used. However, the value of n depends on the

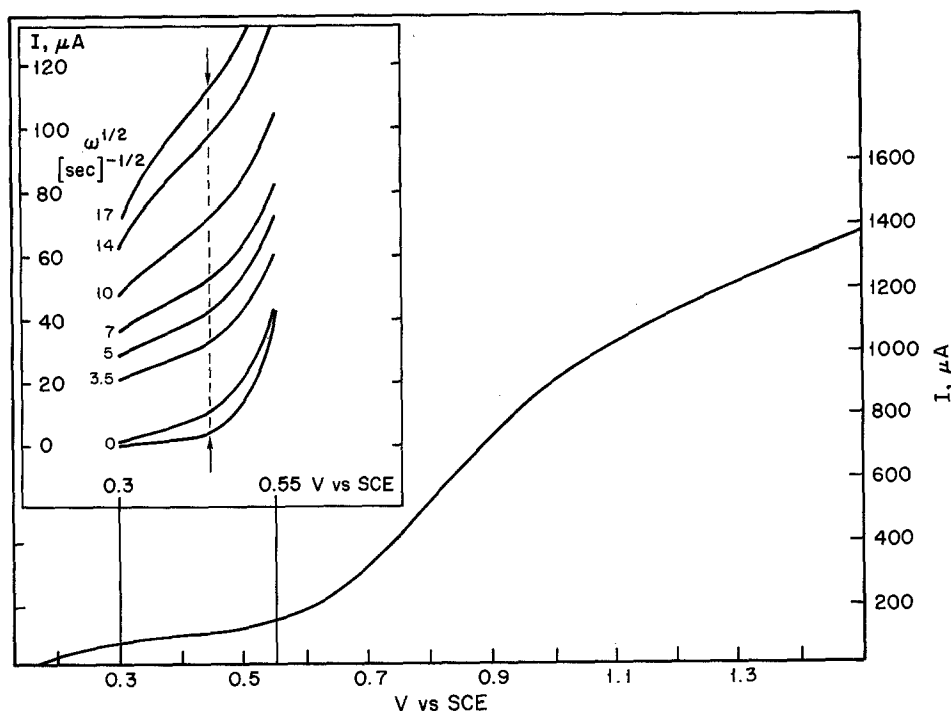


Fig. 3. Photocurrent-potential curve for an $\alpha\text{-Fe}_2\text{O}_3$ electrode in $2.88 \times 10^{-4}\text{M KI/1M HClO}_4$. Rotation frequency: 196 sec^{-1} ; scan rate: $10\text{ mV}/\text{sec}$. Inset: Photocurrent-potential curves in the plateau region of Fig. 3 as a function of the rotation frequency.

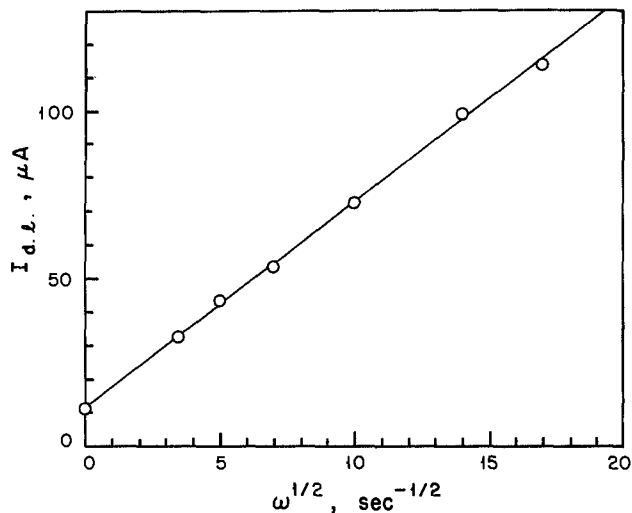
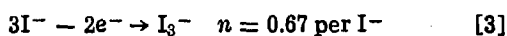
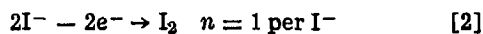


Fig. 4. Levich plot (I_{d1} vs. $\omega^{1/2}$) for the photocurrent values at 0.45V vs. SCE from the data shown in Fig. 3 (inset, broken line).

relative amounts of I_3^- and I_2 at the surface (14)



By using $K = 710 \text{ M}^{-1}$ (15) as the formation constant of I_3^- and taking into account the difference between the diffusion coefficient of I^- and I_2 (14), a value of $n = 0.87$ was calculated for these conditions. With these values inserted into Eq. [1]

$$\frac{dI_{d1}}{d\omega^{1/2}} = 6.7 \mu\text{A}\cdot\text{sec}^{1/2} \quad [4]$$

in reasonable agreement with the experimental slope of $6.1 \mu\text{A}\cdot\text{sec}^{1/2}$. The small difference may be attributed to adsorption of I_2 on the surface (16), which will change the average value of n . Adsorption of I^- is also the most likely explanation for the nonzero intercept seen in Fig. 4.

A detailed study of photooxidation competition at an $\alpha\text{-Fe}_2\text{O}_3$ photoanode using the ring electrode will be given in a separate publication (17). However, it can be noted here that the collection efficiency for I_2 at the ring approached 100% (of the theoretically expected value) up to 0.5V vs. SCE and declined sharply at higher potentials.

In a similar way, Br^- and Cl^- in acidic solution and all halides in neutral or moderately basic solution ($\text{pH} < 12.4$) exhibited photocurrents dependent upon the rotation speed in the potential region cathodic to the onset of steady-state photocurrent for the oxidation of water (OH^-). However, for these solutions, the photooxidation of water began before a diffusion-limited plateau current for X^- was achieved and no calculations as above could be made.

Figure 5 shows I-V curves for a $6 \times 10^{-4}\text{M}$ $\text{Fe}(\text{CN})_6^{4-}/1\text{M}$ HClO_4 solution at various rotation speeds. Figure 6 is a Levich plot for these data. As in the case of I^- , the photocurrent showed a diffusion-limited plateau current with an excellent fit to the Levich Eq. [1]. In this case, the photocurrent values were almost identical to the dark current values that were obtained at a Pt disk electrode of the same size in the same solution (curve 1 in Fig. 6). The diffusion coefficient for $\text{Fe}(\text{CN})_6^{4-}$ calculated from Eq. [1] using the slope of the line in Fig. 6 was $0.52 \times 10^{-5} \text{ cm}^2/\text{sec}$ and compared very well with the value of $0.50 \times 10^{-5} \text{ cm}^2/\text{sec}$ in 1M KCl reported by Jahn and Vielstich (18).

Figure 7 shows I-V curves for an $\alpha\text{-Fe}_2\text{O}_3$ electrode in an unbuffered $2 \times 10^{-4}\text{M}$ $\text{OH}^-/1\text{M}$ NaClO_4 solution at various rotation speeds. This measurement was

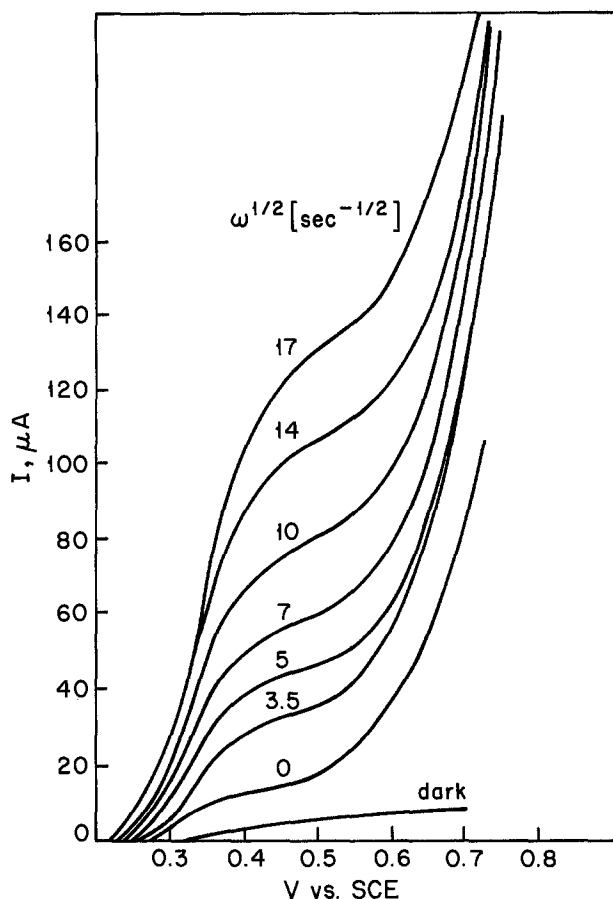


Fig. 5. Photocurrent-potential curves for an $\alpha\text{-Fe}_2\text{O}_3$ electrode in $6 \times 10^{-4}\text{M}$ $\text{Fe}(\text{CN})_6^{4-}/1\text{M}$ HClO_4 for the first oxidation wave at various rotation frequencies.

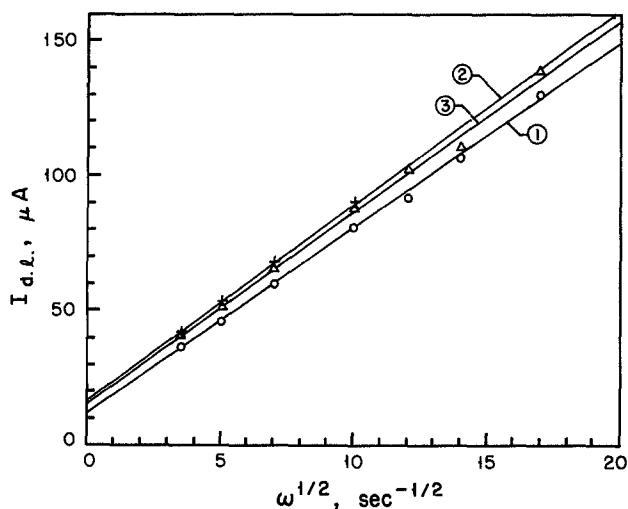


Fig. 6. I_{d1} vs. $\omega^{1/2}$ plots for $6 \times 10^{-4}\text{M}$ $\text{Fe}(\text{CN})_6^{4-}/1\text{M}$ HClO_4 . 1, Pt disk in the dark, 0.7V vs. SCE. 2 and 3, Two samples of $\alpha\text{-Fe}_2\text{O}_3$ disk electrodes with data taken at 0.5V vs. SCE.

carried out under N_2 or N_2/O_2 atmosphere to eliminate the influence of dissolved CO_2 on the pH. Also, a single compartment cell was used for these studies to maintain constant pH and this was verified experimentally.

As with I^- and $\text{Fe}(\text{CN})_6^{4-}$, the photocurrent in dilute base exhibited a diffusion-limited plateau region before it rose to what is apparently a second oxidation wave. A plot of Eq. [1] for photocurrent at 0.25V vs. SCE is given in Fig. 8. If the diffusing species is assumed to be OH^- and its concentration is used in Eq. [1], the calculated diffusion coefficient is 2×10^{-5}

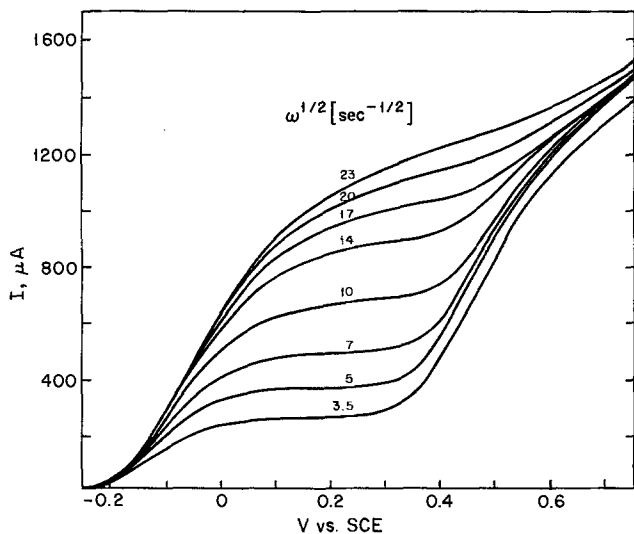


Fig. 7. Photocurrent-potential curves for an $\alpha\text{-Fe}_2\text{O}_3$ electrode in an unbuffered $2 \times 10^{-4}\text{M OH}^-/\text{NaClO}_4$ solution at various rotation frequencies.

cm^2/sec . This value is significantly smaller than the typical reported values of $4.5\text{--}5.0 \times 10^{-5} \text{ cm}^2/\text{sec}$ (19). This experiment was repeated several times with varying OH^- concentration, supporting electrolyte, and electrode. In all cases, Levich plots were quite linear and I_{dl} depended linearly with $[\text{OH}^-]$ as predicted. At the same time, the slope was always about one-third of the calculated one.

Discussion

The results as shown in Fig. 1-8 and the additional data described above have shed some new light on the behavior of semiconductor photoanodes. It is the transient photocurrent at these electrodes that behaves as expected at an ideal semiconductor. The transient photocurrent turns on right at V_{FB} and it is independent of the redox couple in solution for a given V_{FB} . It depends linearly on the light intensity and is independent of the rotation speed. The transient photocurrent shifts 59 mV/pH (9) as does V_{FB} (1), while the shift of the steady-state photocurrent may be somewhat different (5). Thus, the transient photocurrent is controlled solely by solid-state processes.

The degree to which this is also true for the steady-state photocurrent depends on the nature of the charge transfer at the electrode surface.

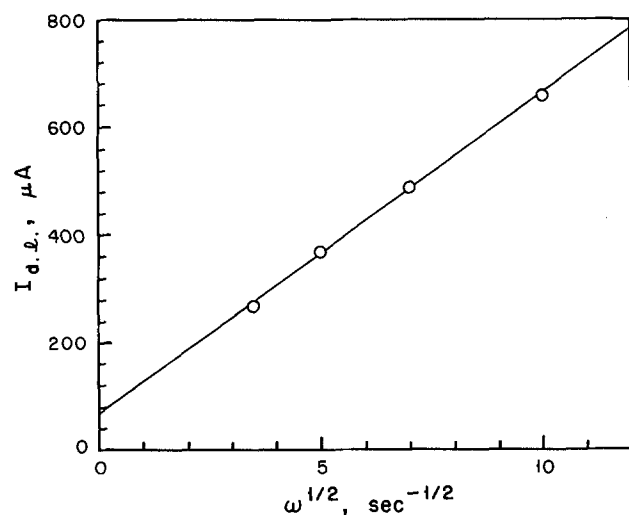


Fig. 8. I' vs. $\omega^{1/2}$ plot for the data in Fig. 7 taken at 0.25V vs. SCE . Rotation frequencies: $12.25\text{--}100 \text{ sec}^{-1}$.

Thus, redox species with fast charge-transfer kinetics exhibit almost ideal behavior even for the steady-state photocurrent. This is the case for I^- and $\text{Fe}(\text{CN})_6^{4-}$. As the charge-transfer kinetics become less rapid, as for Cl^- and H_2O , the photocurrent no longer behaves ideally. Hardee and Bard (6) proposed cathodic dark current coupled to the anodic photocurrent as responsible for the transient effects they observed. Curran and Gissler (7) and, more recently, Iwanski *et al.* (8) have also studied these effects. Back-reaction of photooxidation products (or more likely, intermediates) with conduction band electrons via surface states is the probable cause of the several observations reported here. At very small band bending, just anodic to V_{FB} , electrons may still be accessible at the surface. Highly reactive photooxidized species, such as H_2O^+ , $\cdot\text{OH}$, $\text{Cl}\cdot$, *etc.*, are capable of capturing these electrons causing a cathodic current component equivalent to the anodic photocurrent component. This results in no net steady-state photocurrent. As the band bending increases, the availability of electrons at the surface decreases so that the cathodic current component also decreases. Therefore, the anodic steady-state photocurrent increases. Finally, at sufficiently large band bending no electrons are available to react at the surface and the cathodic current component disappears. At this potential, the steady-state photocurrent will converge with the transient photocurrent and will also be independent of the redox species present. The amount of band bending required to overcome the cathodic current component clearly depends on the affinity of the photooxidized species for electrons, and the observed order: H_2O^+ , $\cdot\text{OH}$, Cl^- , Br^- , I^- , $\text{Fe}(\text{CN})_6^{3-}$ is expected from electronegativity considerations.

A rather exceptional result that emphasizes the importance of the process described above is displayed in Fig. 3 and 5. Under conditions at which water is thermodynamically oxidizable by the photogenerated hole and is present in large excess at the surface, diffusion-controlled oxidation of I^- or $\text{Fe}(\text{CN})_6^{4-}$ with no oxidation of water was observed. Theoretical analysis of the influence of mass transfer and light flux on the photocurrent at photoelectrodes has recently been published by Bruckenstein and Miller (20).

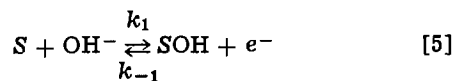
We now turn to the results of Fig. 7 and 8. First it should be noted that the consumption of OH^- at the surface will cause the surface pH to drop. This, in turn, will change the adsorption equilibrium at the surface involving $\text{OH}^-/\text{H}_2\text{O}$ and will change V_{FB} (1). A less anodic V_{FB} means smaller band bending and a correspondingly smaller photocurrent. Thus, scanning of the potential in the plateau region ($0.1\text{--}0.3\text{V vs. SCE}$ in Fig. 7) hardly changes the band bending but mainly affects the $\text{OH}^-/\text{H}_2\text{O}$ adsorption equilibrium. When the surface pH drops to ~ 3.5 , the flux of H^+ (H_3O^+) away from the electrode surface becomes large enough to maintain a steady-state pH value at the surface. From that point, scanning the potential will increase the band bending and also the photocurrent. According to this model, the second oxidation wave corresponds to photocurrent at a surface pH of ~ 3.5 . The amount of OH^- depletion at the surface will depend on the normal diffusion-convection parameters, and hence, Levich behavior is expected.

An additional factor is that H_2O , which is a weaker nucleophile than OH^- , requires larger band bending to overcome back-reaction of intermediates. Thus, the first wave could be due to OH^- oxidation while the second wave is due to direct H_2O oxidation. From these experiments, there is no unambiguous way to distinguish between these two models.

Another observation needing discussion is the slope in Fig. 8. The good slopes observed for I^- and $\text{Fe}(\text{CN})_6^{4-}$ exclude the possibility of experimental error. However, the OH^- oxidation reaction is not a

one-step electron-transfer reaction, and the smaller slope is likely to be caused by the more complex kinetics.

Damjanovic (21) has summarized many of the possible paths for electrochemical O₂ evolution. Many of these paths can be generalized under the following reaction scheme (22)



where *S* stands for surface active site and *k* is the rate constant for the particular step. If reaction [5] occurs under diffusion-controlled conditions, its rate, *v*, will be

$$v_1 = K_D[\text{OH}^-] \quad [7]$$

where *K_D* is the appropriate diffusion factor which, in the case of an RDE, is

$$K_D = 0.62 AD^{2/3} \nu^{-1/6} \omega^{1/2} \quad [8]$$

The rate of the back-reaction, *v*₋₁, is

$$v_{-1} = k_{-1}[\text{SOH}] \quad [9]$$

where *k*₋₁ is a potential (band bending) dependent rate constant. The rate of reaction [6] will be

$$v_2 = k_2[\text{SOH}] \quad [10]$$

At a steady state, as is assumed for the case of an RDE

$$v_1 = v_{-1} + v_2 \quad [11]$$

Solving for the steady-state concentration of SOH one obtains

$$[\text{SOH}] = \frac{K_D[\text{OH}^-]}{k_2 + k_{-1}} \quad [12]$$

If reaction [6] includes the slow step, the current will be

$$\begin{aligned} I' &= nFv_2 = \frac{k_2}{k_2 + k_{-1}} FK_D[\text{OH}^-] \\ &= \frac{k_2}{k_2 + k_{-1}} 0.62 AFD^{2/3} \nu^{-1/6} \omega^{1/2} [\text{OH}^-] \quad [13] \end{aligned}$$

While the linear dependence upon [OH⁻] and ω^{1/2} is retained, the values of the pseudo diffusion-limited current, *I*'_{dl}, are reduced by a factor, *k*₂/(*k*₂ + *k*₋₁), due to the back-reaction of equation [5], i.e.

$$I'_{dl} = \frac{k_2}{k_2 + k_{-1}} I_{dl} \quad [14]$$

The fit between the derivation above and the previous results is straightforward. Reaction [5] in the forward direction is responsible for the transient photocurrent while in the backward direction is responsible for the cathodic transient. Reaction [6] is a measure of the steady-state photocurrent. Experimentally it was found that *k*₂/(*k*₂ + *k*₋₁) ≈ 0.3 so that the steady-state photocurrent occurs at a rate that is only one-third of the rate of the forward reaction [5], at that particular band bending.

While it is not possible to be more specific about the nature of the adsorbed intermediates, which in fact are not yet known even for metal electrodes, the gen-

eral scheme presented above fits all the experimental results reported in this work quite nicely.

Conclusions

The following have been observed and discussed for polycrystalline α-Fe₂O₃ photoanodes.

1. The transient photocurrent fits the ideal semiconductor/electrolyte interface model.

2. The availability of surface-forbidden electrons at the surface to react with highly active intermediates causes a decrease in the steady-state photocurrent at low band bending in the presence of redox species exhibiting slow charge-transfer kinetics.

3. Photoelectrochemical reactions that occur under diffusion control in aqueous solution have been established.

The extension of these observations to other non-ideal semiconductors is possible and should be investigated. TiO₂ and WO₃ have shown dependence of the photocurrent on redox species (2-4) and are likely candidates to exhibit similar behavior to that reported here for polycrystalline α-Fe₂O₃.

Acknowledgments

This work is supported by the Division of Chemical Sciences, Office of Basic Energy Science, U.S. Department of Energy. The authors also thank Mr. Vince Lamarca for generous technical assistance with the RRDE assembly. Support from University Energy Research Group is acknowledged.

Manuscript submitted April 30, 1983; revised manuscript received July 29, 1983.

REFERENCES

- H. Gerischer, *Top. Appl. Phys.*, **31**, 115 (1979).
- T. Kobayashi, H. Yoneyama, and H. Tamura, *J. Electroanal. Chem.*, **124**, 179 (1981).
- K. Hirano and A. J. Bard, *This Journal*, **127**, 1056 (1980).
- W. A. Gerrard, *J. Electroanal. Chem.*, **86**, 421 (1978).
- J. H. Kennedy and M. Anderman, *This Journal*, **130**, 848 (1983).
- K. L. Hardee and A. J. Bard, *ibid.*, **124**, 215 (1977).
- J. S. Curran and W. Gissler, *ibid.*, **126**, 56 (1979).
- P. Iwanski, J. S. Curran, W. Gissler, and R. Memming, *ibid.*, **128**, 2128 (1981).
- J. H. Kennedy and K. W. Frese, Jr., *ibid.*, **125**, 723 (1978).
- R. K. Quinn, R. D. Nasby, and R. J. Baughman, *Mater. Res. Bull.*, **11**, 1011 (1976).
- K. G. McGregor, M. Calvin, and J. W. Otvos, *J. Appl. Phys.*, **50**, 369 (1979).
- V. G. Levich, "Physicochemical Hydrodynamics," Prentice-Hall, Englewood Cliffs, NJ (1962).
- P. Beran and S. Bruckenstein, *Anal. Chem.*, **40**, 1044 (1968).
- J. D. Newson and A. C. Riddiford, *This Journal*, **108**, 699 (1961).
- R. A. Skoog and D. M. West, "Analytical Chemistry," 2nd Ed., Holt, Rinehart and Winston, Inc., New York (1974).
- J. H. Kennedy, R. Shinar, and J. P. Ziegler, *This Journal*, **127**, 2307 (1980).
- J. H. Kennedy and M. Anderman, *ibid.*, Submitted.
- D. Jahn and W. Vielstich, *ibid.*, **109**, 849 (1962).
- A. C. Riddiford, *Adv. Electrochem. Electrochem. Eng.*, **4**, 47 (1966).
- S. Bruckenstein and B. Miller, *This Journal*, **129**, 2029 (1982).
- A. Damjanovic, in "Modern Aspects of Electrochemistry," J. O'M. Bockris and B. E. Conway, Editors, No. 5, p. 369, Plenum Press, New York (1969).
- C. Iwakura, K. Fukuda, and H. Tamura, *Electrochim. Acta*, **21**, 501 (1976).

Electrochemical and Photoelectrochemical Behavior and Selective Etching of III-V Semiconductors in H_2O_2 as Redox System

Eduard Haroutiounian and Jean-Paul Sandino

R.T.C. La Radiotechnique-Compelec, Laboratoire de Chimie, 92156 Suresnes, Cedex, France

Paul Cléchet,* Didier Lamouche, and Jean-René Martin

Laboratoire de Physicochimie des Interfaces, Ecole Centrale de Lyon, B.P. 163, 69130 Ecully, France

ABSTRACT

Basic electrochemical processes at GaAs, GaAsP, and GaAlAs electrodes were studied in H_2O_2 aqueous solutions at several pH values. An analytical automatic system, which directly plots gallium concentration vs. potential, allows the collection of information on corrosion processes. The approach of making continuous analysis of gallium ions, while dissolving the semiconductor at a preselected potential, was used in conjunction with impedance and ellipsometric measurements in order to study interfacial phenomena. On the basis of these results, a mechanism for chemical corrosion (etching) which involves electrons captured from semiconductor surface states by H_2O_2 was proposed. Anodic polarization can also induce corrosion by hole generation in the valence band or by avalanche breakdown. As expected, pH plays a fundamental role in the corrosion process through the solubility shift of the oxide layer. Further consideration is given to the effect of illumination, with special emphasis on p-type semiconductors, for which it can lead to an inhibition effect on corrosion via a current doubling mechanism. Finally, application of selective etching is described for GaAs, GaAlAs, and GaAsP hetero structures.

Selective etching has been the subject of a number of investigations of interest in connection with III-V semiconductor devices, heterojunction laser technology, and more general multilayer device technology (1, 2). For practical purposes, the dissolution is generally carried out by using redox etchants, without a thorough knowledge of the mechanisms leading to the selective corrosion phenomenon (3-6). The result is a semiempirical approach which is time consuming when a new specific problem is encountered.

Solar energy conversion has stimulated fundamental research in the field of semiconductor electrochemistry (7-9), and processes associated with semiconductor interfaces are now better understood. However, this knowledge is still very difficult to exploit directly for the investigation of redox systems that might be suitable for selective etching. From a practical point of view, it means that the corrosion behavior of a particular semiconductor has still to be explored in detail experimentally. To solve such problems, the choice of the perfect tool is not obvious. Since corrosion involves electron exchange through a solid-liquid interface, it follows that electrochemical tools seem to be the most appropriate. In the first instance, current-voltage curves are generally obtained. However, it has been observed in oxidizing media, and this point will be discussed at length later in this paper, that the anodic corrosion current of a n-type semiconductor in the dark is sometimes exactly compensated for by electrons captured by the etchant over a large potential range (2, 10-13). No information can be obtained about the corrosion rate for such situation from classical voltamperometry. This necessitates an alternative way of gaining further insight into the electrochemical behavior of semiconductors.

The rotating ring-disk electrode (RRDE), which has been largely used for semiconductor corrosion studies (see, for example, Ref. 14-17), does not perfectly suit our gas evolving etchant (H_2O_2). Direct sequential chemical analysis of corrosion products may give valuable information, especially since the gallium ion concentration vs. time can be converted into current voltage curves. Such a method would be tedious and time consuming unless a fast automatic system for

Ga analysis were available. Consequently, we have developed a method of investigation based on the use of an automatic colorimetric system. Gallium analysis is performed at the outlet of a three-electrode micro-electrochemical cell.

As shown later, this method, which can be adapted to redox couples other than the H_2O_2 used here, can lead to better knowledge of the dissolution process and thus can make the choice of selective etching criteria easier. In the future, this technique might be considered as a complementary tool for electrochemical studies involving, i.e., RRDE. In this study, impedance-electrode measurements and ellipsometry were also used in order to complete the information gained from the gallium concentration curves.

Experimental

Materials.—Unless otherwise specified, the III-V samples used in this study were (100) single crystals. n-Type gallium arsenide was Si-doped bulk material with donor density $N_D \sim 10^{18} \text{ cm}^{-3}$, n-type $\text{Ga}_{0.7}\text{Al}_{0.3}\text{As}$ (Si doped, $N_D \sim 2 \cdot 10^{17} \text{ cm}^{-3}$), and $\text{GaAs}_{0.6}\text{P}_{0.4}$ (Te doped, $N_D \sim 4 \cdot 10^{16} \text{ cm}^{-3}$) were vapor phase epitaxial layers grown on (100) GaAs substrate, with a typical thickness of 20 μm . Experiments on GaAs were performed after etching in $\text{H}_2\text{SO}_4/\text{H}_2\text{O}/\text{H}_2\text{O}_2$ (3:1:1) in order to remove the superficial damaged layer. The ohmic contacts were made using alloyed tin on the back of the GaAs substrate under N_2 or H_2/N_2 controlled atmosphere.

Apparatus.—The microelectrochemical cell with continuous electrolyte flow (4 ml min^{-1}) is shown Fig. 1. Its general design was drawn from Ref. (18) with some modifications. The electrode (0.2 cm^2) can be illuminated, via an optical fiber, with a 100W halogen lamp. In order to prevent thermal effects due to IR radiation, a filter (wavelength bandpass: 400-650 nm) and an absorption cell filled with water (2 cm thickness) were used.

Experiments were performed using a conventional potentiostatic system (Tacussel Solea S.A.). Successive preselected potentials were applied to the semiconductor electrode for 10 min while the electrolyte flow leaving the cell was analyzed. For each voltage, the static current was measured in order to get the corresponding current-voltage curves which, for simplicity, have been drawn as continuous lines in

* Electrochemical Society Active Member.

Key words: etching, semiconductor, H_2O_2 , photoelectrochemistry, corrosion mechanism, passivation, semiconductor technology, GaAs/GaAsP/GaAlAs.

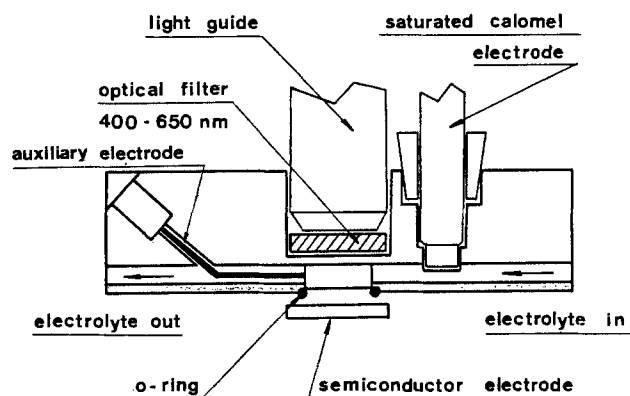


Fig. 1. Plan of the microelectrochemical cell

the various figures. Between two consecutive steps, etching of the semiconductor surface was carried out with the help of the etchant solution described in the previous section and a bypass system. All potentials are expressed with respect to the saturated calomel electrode (SCE).

Electrolyte.—The choice of the electrolytes and redox system was dictated by experience, since citric acid and H_2O_2 are frequently used for GaAs etching as complexing electrolyte and oxidizing agent, respectively. Moreover, this mixed solution has good selectivity properties for GaAsP/GaAs heterostructures, since only the latter product dissolves. Given the poor buffer capability of citric acid, we also used a phosphate buffer in medium pH range. Experiments in highly acidic and alkaline media were also carried out by adding H_3PO_4 or NaOH to the solutions. In every case, and unless otherwise specified, a 0.1M concentration for electrolyte and 1% (33.3 ml of 30% H_2O_2 per liter) for H_2O_2 was chosen for experimental convenience. Sodium hydroxide was used for pH adjustments.

Gallium analysis.—At the outlet of the microelectrochemical cell, Ga was analyzed through a colorimetric automatic system (Auto Analyser II, Technicon). The measurement involved the following stages: (i) decomposition of excess H_2O_2 by hydroxylamine treatment; (ii) formation of a colored Ga-rhodamine complex; (iii) extraction of this complex by CCl_4 ; (iv) optical absorption measurements of the organic phase with a spectrophotometer (working wavelength 550 nm).

A calibration curve was drawn with standard solutions of gallium (the stock solution was prepared from high purity Ga metal dissolved in HCl) in the concentration range of interest ($0-50 \mu g ml^{-1}$). Under our experimental conditions, As and Al ions do not interfere in the Ga determination. Relative standard deviation of the calibration curve was 2%. For experiments involving GaAlAs material, a correction factor was used in order to take into account the presence of 30% of aluminum. Conversion of gallium concentrations into current was made by assuming a six-hole corrosion process (19). In order to distinguish clearly the current-voltage curves and the gallium concentration-voltage curves in the text and figure captions, we use $I = f(V)$ for the former and $I_{Ga} = f(V)$ for the latter.

Impedance and ellipsometric measurements.—Ellipsometric measurements were carried out with an automatic spectroellipsometer (20). In addition, capacitance measurements were performed with a potentiostatic system, using an ATNE lock-in amplifier and a Hewlett-Packard Model 3325-A function generator, which were controlled by an Apple II microcomputer. The GaAs electrode's area was $0.71 cm^2$. Unless otherwise specified measurements were made

Table I. Flatband potentials of n-type GaAs, $GaAs_{0.6}P_{0.4}$, and $Ga_{0.7}Al_{0.3}As$

pH	n-GaAs	n-GaAs _{0.6} P _{0.4}	n-Ga _{0.7} Al _{0.3} As
0 (H_2SO_4 , 0.5M)	-1.02 ^a -1.08 ^b	-1.28 ^a -1.42 ^c	-1.12 ^a -1.70 ^d
14 (NaOH, 1M)	-1.86 ^a -1.88 ^b	-2.0 ^a -2.20 ^c	-2.0 ^a -2.4 ^d

^a Our results.

^b Extrapolated values from (21).

^c GaAs_xP_{1-x}: $x = 0.39$, extrapolated values from (22).

^d Ga_{1-x}Al_xAs: $x = 0.27$, extrapolated values from (22).

at a frequency of 1 kHz. Flatband potentials of the freshly etched (called "clean" surface in the text, this term being further justified at the end of the next section) n-type semiconductors, obtained by extrapolation of Mott-Schottky plots calculated from a series equivalent circuit, at two pH's, are shown in Table I. The measured capacitances showed only a weak frequency dependence. The results were perfectly reproducible even after numerous voltage scans. These results are in good agreement with those of other authors (21, 22), except for those of GaAlAs (22). The reason for this discrepancy is not known. The pH dependence of the flatband is about 60 mV per pH unit, except for GaAsP (51 mV per pH unit).

Results and Discussion

n- and p-Type GaAs.—In order to have a better understanding of the mechanism by which a semiconductor like GaAs corrodes in H_2O_2 aqueous solution, bearing in mind that such corrosion might be used for selective etching of heterostructures, it is interesting to compare Fig. 2 and 3, which show the results obtained on n- and p-type GaAs in an acidic 1% H_2O_2 medium, at room temperature.

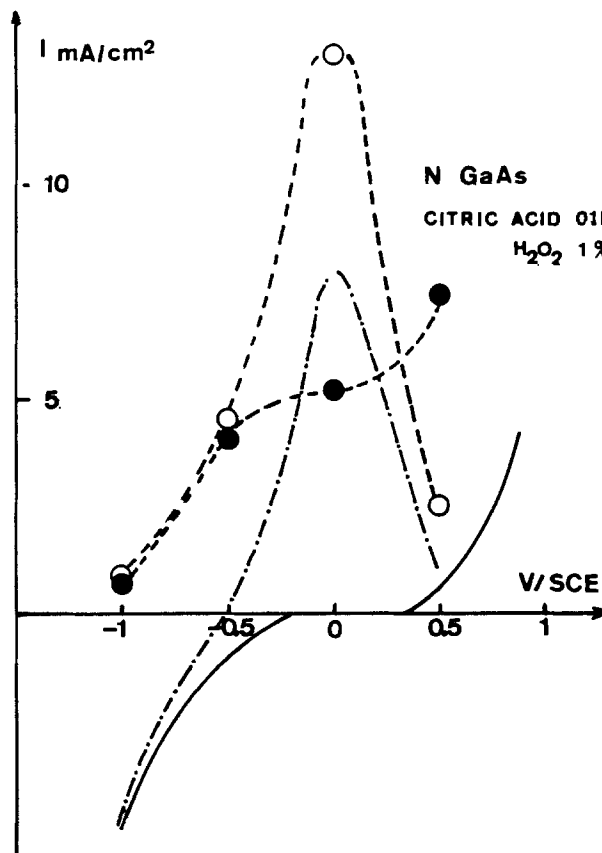


Fig. 2. $I = f(V)$ and $I_{Ga} = f(V)$ curves (see text) for n-type GaAs in 0.1M citric acid and 1% H_2O_2 . ---●--- I_{Ga} in the dark. ---○--- I_{Ga} under illumination. ——— $I = f(V)$ in the dark. ——— $I = f(V)$ under illumination.

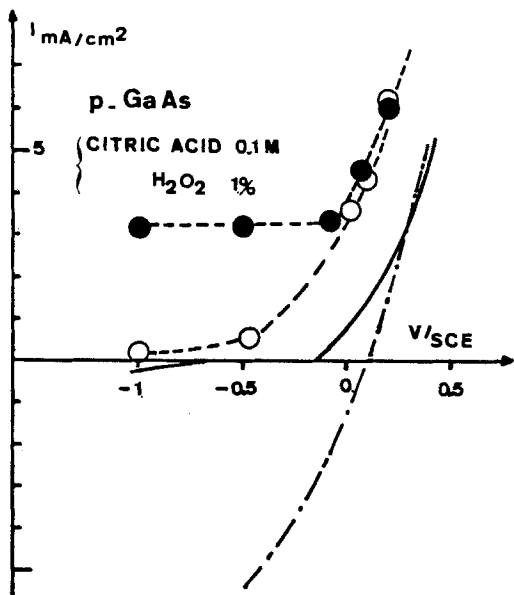


Fig. 3. $I = f(V)$ and $I_{Ga} = f(V)$ curves for p-type GaAs in 0.1M citric acid and 1% H_2O_2 . Symbols are the same as used in Fig. 2.

With n-type GaAs, in the dark, on anodic scanning, we observe that corrosion begins at about $-1.0V$. The $I_{Ga} = f(V)$ curve thus exhibits a characteristic plateau before a sharp increase when the potential reaches $+0.5V$. As previously stated, the lack of faradaic current in a large range of potential where corrosion occurs (approximately -0.2 to $+0.4V$) should be noted. Under illumination, the corrosion is accelerated and a maximum appears in the $I_{Ga} = f(V)$ curve at about the same voltage as the photocurrent peak (see below). This corresponds to a passivation of the semiconductor.

With p-type GaAs in the dark, the results are comparable. Over a large range of potential (between -1.0 and $0.0V$), the corrosion rate remains constant and, as observed with n-type GaAs, this corrosion is not accompanied by a faradaic current.

The behaviors of these two kinds of materials differ strongly under illumination. With p-type, we observe that the corrosion does not increase with illumination, as it does for n-type GaAs; rather it vanishes when a cathodic photocurrent arises.

In order to explain this difference, we must consider the flatband values of these materials at this low pH ($-1.15V$ for n-type and $+0.15V$ for p-type, respectively) and the peculiar redox properties of H_2O_2 (23, 24). It is well known that H_2O_2 is a strong bifunctional oxidant whose two-step reduction involves an OH^\cdot radical intermediate. Two "microscopic" standard redox potentials correspond to these two successive steps, the values of which have been estimated by Memming to be widely separated from that of the global H_2O_2/OH^- system ($+1.54V$). According to Fig. 4, with p-type GaAs, hydrogen peroxide is capable of giving rise to a current doubling process (23, 24) where each photon induces a two-electron transfer across the interface. The capture of a photoexcited electron from the conduction band creates an OH^\cdot radical (which has empty levels of low energy) which is then able to inject a hole into the valence band of GaAs. The electric field within the depleted layer being directed towards the bulk semiconductor, the injected holes are driven in this direction. This prevents surface corrosion. This is the reason why no corrosion is observed under illumination with p-type GaAs. This current doubling on p-type GaAs has very recently been observed by Gerischer *et al.* (25). With n-type GaAs, current doubling is no longer possible, according to the direction of the electric field, which is now

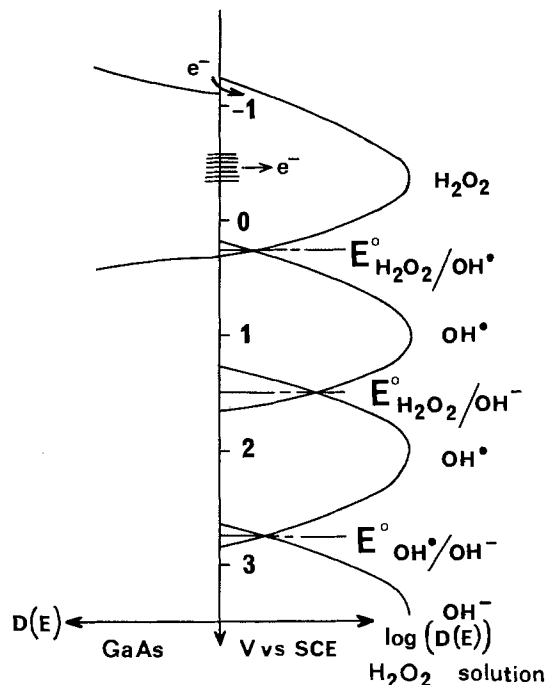


Fig. 4. Energy diagram at pH 2 of the GaAs- H_2O_2 interface (24). This diagram supposes an equal concentration of all the redox species. The stationary concentration of OH^\cdot being small (24), the overlap of the conduction band and of H_2O_2 is probably much better than represented here.

directed towards the surface for this range of potential. Electrons are driven to the bulk, and holes to the surface, where they contribute to semiconductor dissolution while an anodic photocurrent appears (Fig. 2). This situation (increase of I_{Ga}) appears as soon as the electrode potential becomes positive of the flatband potential of the material.

The shapes of the curves of Fig. 2 and 3 are easy to interpret at high anodic and cathodic polarization.

With n-type GaAs in the dark (Fig. 2), the sharp increase of the corrosion at strong anodic polarization follows exactly the increase of the anodic current. It has been shown that this wave is an avalanche breakdown wave which depends on doping level and crystallographic defects of GaAs (26). The discrepancy observed between the breakdown voltage shown in Fig. 2 and 5, at the same pH, probably results from the

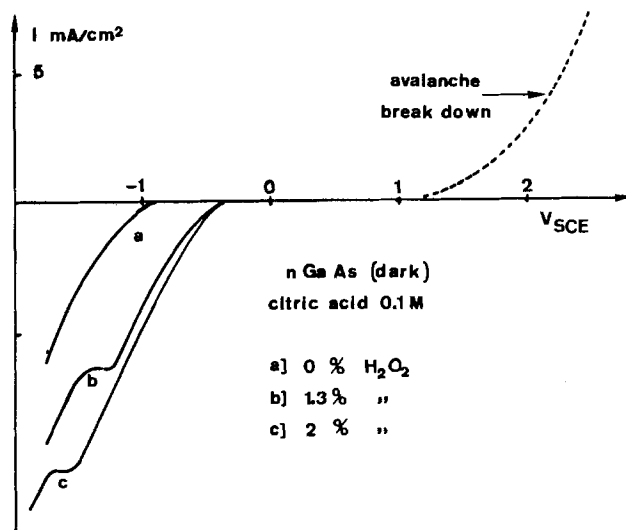


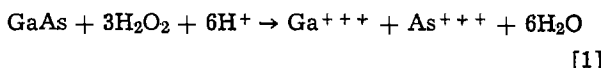
Fig. 5. Voltamperometric curves for n-type GaAs in the dark in 0.1M citric acid and several H_2O_2 concentrations. Voltage scanning rate: 100 mV min^{-1} .

batch origin of the GaAs substrate. For lower potentials, in the dark, the anodic breakdown current disappears while corrosion, as for p-type samples, decreases. The difference lies in the fact that for more negative potentials (less than $-0.3V$), a large cathodic wave arises and at the same time corrosion stops. It is logical to postulate that this corrosion suppression at low potential is a consequence of the electrolytic reduction of H_2O_2 at the interface by electrons from the conduction band, which accumulate when the electrode potential approaches its flatband value. This reduction of H_2O_2 at n-type GaAs electrode under cathodic polarization is indicated by the mass-diffusion limited waves of Fig. 5. The same explanation is given by Gerischer *et al.* for the observed chemical stability of n-type GaAs in Br_2 solution under cathodic polarization (12).

With p-type GaAs in the dark (Fig. 3), such a rapid reduction of H_2O_2 does not occur at the surface under cathodic bias, so the corrosion plateau remains flat even at $-1.0V$. For potentials more positive than $-0.2V$, the large anodic wave, which is accompanied by a strong corrosion, probably results from the hole accumulation in the valence band and from the resulting breaking of the chemical bonds of the semiconductor. Illumination has no influence here, because of the migration of the holes towards the bulk semiconductor.

The final point concerns how corrosion can occur in the dark, without electron transfer, in the intermediate range of potentials ($-0.5 < V < +0.5$ for n-type and $V < 0V$ for p-type).

Such corrosion can only be explained by a purely chemical process, *i.e.*, by an exactly compensated exchange of electric charges between the semiconductor, which is oxidized, and the oxidant, which is reduced. This process can be represented by the following schematic reaction



The nature of the resulting species depends on the pH and complexing power of the electrolyte. This is evidently the process by which chemical etching of the semiconductor proceeds at the rest potential.

The problem is thus to explain how such a reduction of H_2O_2 , at intermediate potential, can be initiated by high energy electrons (Fig. 4), since from the classical theory of electron transfer (7, 9, 10), these electrons can only be captured from the conduction band, whose electron concentration, for these two materials in the dark, is poor. In the absence of pinning of the Fermi level, the electron concentration increases as the potential of the semiconductor becomes more cathodic, but this increase is therefore not consistent with the observed voltage independence of chemical corrosion (see Fig. 3). Another explanation must be found.

It is well known that a high concentration of surface and interface states is always present at the surface of GaAs, especially near the middle of the bandgap (27, 28) and if the surface is oxygen covered (29, 30) as after etching by acidic H_2O_2 mixture (31). According to experiments conducted *in vacuo*, these electronic states often result from dangling bonds or a different band structure of surface atoms which have a high reactivity for the solvent (32). This is certainly the case for our highly reactive acid etched surfaces. If an electron from such a surface state (examples of which are drawn Fig. 4) is transferred to an adsorbed H_2O_2 molecule, it will lead to a short lived $OH\cdot$ radical, which is consequently attached to a surface atom with a weakened bond to the surface. This $OH\cdot$ radical is thus in a favorable situation to capture, directly, a second electron from the same atom, without the constraint of equality between donor and acceptor electronic states levels required by the faradaic transfer

through the Helmholtz layer. This leads to a still less strongly attached atom and to the progressive corrosion of the electrode.

This mechanism may explain why the chemical corrosion is potential independent and why it occurs in particular at the rest potential, *i.e.*, under the etching conditions, ($-0.075V$ for p-type and $-0.245V$ for n-type in our case).

Under illumination, for p-type material, electrons are available in the conduction band, which, by means of a current doubling mechanism, prevent the corrosion from continuing (Fig. 3). The current doubling phenomenon is thus more rapid than the chemical corrosion process. This is in agreement with the large photocathodic wave seen in Fig. 3. On the contrary, as previously stated, with n-type semiconductors, photoholes which appear in the valence-band contribute to corrosion by chemical bond breaking (Fig. 2).

This analysis shows that, in addition to anodic electrochemical corrosion resulting from hole accumulation in the valence band (p-type) or breakdown (n-type) and the photoelectrochemical corrosion by photoholes (n-type), simple chemical corrosion is another very important means of corrosion which probably does not only occur by hole injection into the valence band. Without any doubt, surface states play a very important role in the etching mechanism, and this fact is emphasized by the polishing or defect-revealing ability of this kind of etch.

Other semiconductors and pH effect.—Figures 6 and 7 show that in the same acidic corrosive medium, the behavior of GaAsP and GaAlAs can be explained using similar arguments. The values of the flatband potentials of these materials, which are slightly more negative than GaAs (Table I), support this argument. We observe that GaAsP (Fig. 6) exhibits a much lower chemical corrosion rate than the two other n-type materials (compare Fig. 2, 6, and 7).

An etchant is generally composed of an oxidant (here H_2O_2) and an acidic or basic solubilizing agent of the amphoteric oxide which grows at the surface of the semiconductor (33). Figure 8 shows that the etching rate (*i.e.*, the chemical corrosion at the rest potential) of GaAs in H_2O_2/H_3PO_4 mixtures at various pH's in the dark support this definition. The solubility of GaAs increases strongly in the regions of low and

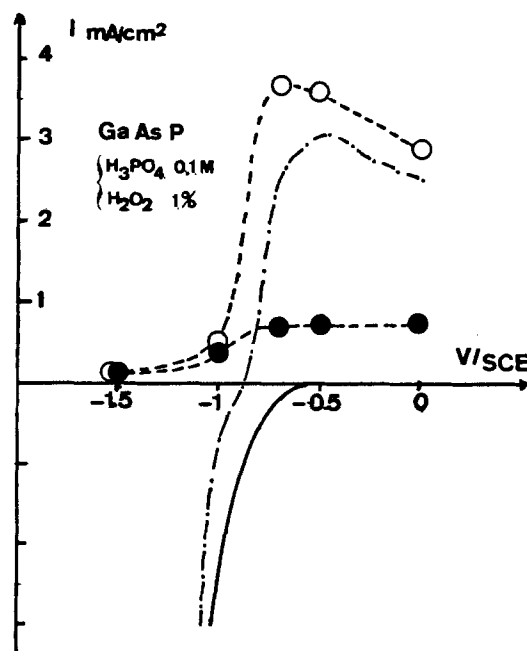


Fig. 6. $I = f(V)$ and $I_{GaAsP} = f(V)$ curves for n-type GaAsP in H_3PO_4 0.1M and 1% H_2O_2 . Symbols are the same as used in Fig. 2.

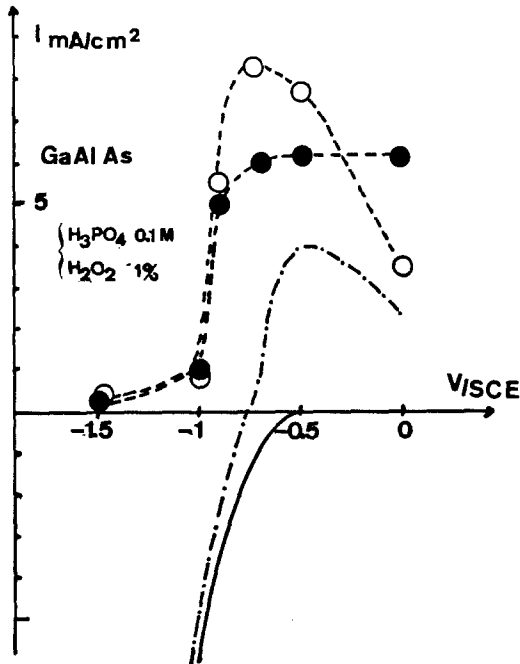


Fig. 7. $i = f(V)$ and $i_{Ga} = f(V)$ curves for n-type GaAlAs in H_3PO_4 0.1M and 1% H_2O_2 . Symbols are the same as used in Fig. 2.

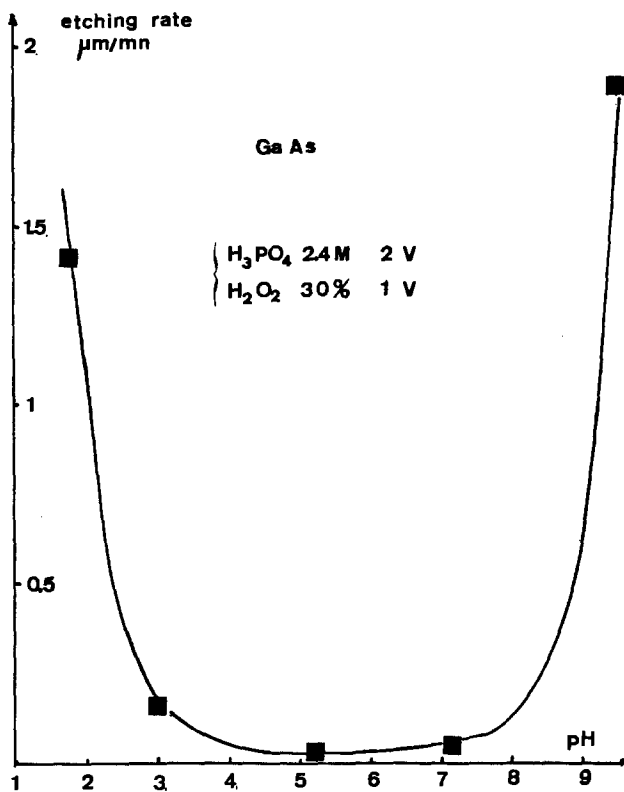


Fig. 8. Etching rate vs. pH curves in the dark of n-type GaAs in 1:2 H_2O_2 30% and H_3PO_4 2.4M mixture.

high pH when the solubility of the oxides of the different elements of which the semiconductor is composed are known to be large (34). Thus, etching of III-V semiconductors is only efficient at low and high pH and is slow at intermediate values when the low solubility of the oxide protects the material. The two other materials show curves similar to the curve of Fig. 8, except for the lower solubility of GaAsP, which has been already noted. In acidic or alkaline media, this poor etching rate of GaAsP offers selective properties for the removal of GaAs with respect to GaAsP layers in the GaAs/GaAsP heterostructure.

The effect of pH on the etching rate is clearly illustrated by the form of the curves of Fig. 9 obtained at pH 7. The chemical corrosion plateaus practically disappear, while the passivation peaks become very pronounced. Passivation, for these three materials, is very effective for voltages exceeding somewhat the passivation peaks.

On the other hand, at pH 13, Fig. 10-12 show that chemical dissolution is effective again and that the passivation becomes less pronounced.

In the absence of passivation, the corrosion rate is practically proportional to H_2O_2 concentration, as shown Fig. 10 and 12, in the cathodic range of potential (compare the values for i_{Ga} respectively with 1 and 0.5% of H_2O_2). When passivation occurs (as, for example, for GaAlAs and GaAs under illumination at 0.0V), oxide layer formation governs the dissolution process and proportionality with H_2O_2 concentration no longer holds.

All these observations are consistent with a corrosion mechanism which involves competition between the rates of oxide formation and dissolution. The second phenomenon prevails at low and high pH. However, it can also be noted that illumination sometimes reinforces passivation (see Fig. 2, 7, 10, and 12, for instance).

Passivation and oxide layer growth.—Spectroellipsometric and impedance measurements were carried out in order to reveal the effect of oxide growths on the dissolution phenomenon in H_2O_2 . n-Type GaAs was used exclusively for this study.

First, capacitance measurements and Mott-Schottky plots were obtained in citric and phosphoric 0.1M media at pH 2 and 7 without H_2O_2 and for "clean" surface n-GaAs. The data were taken at 1 and 10 kHz. From the Mott-Schottky plots of Fig. 13 we obtained donors densities (N_D) of about 7.1×10^{17} for 10 kHz and 1 kHz, which shows, as previously stated, a very

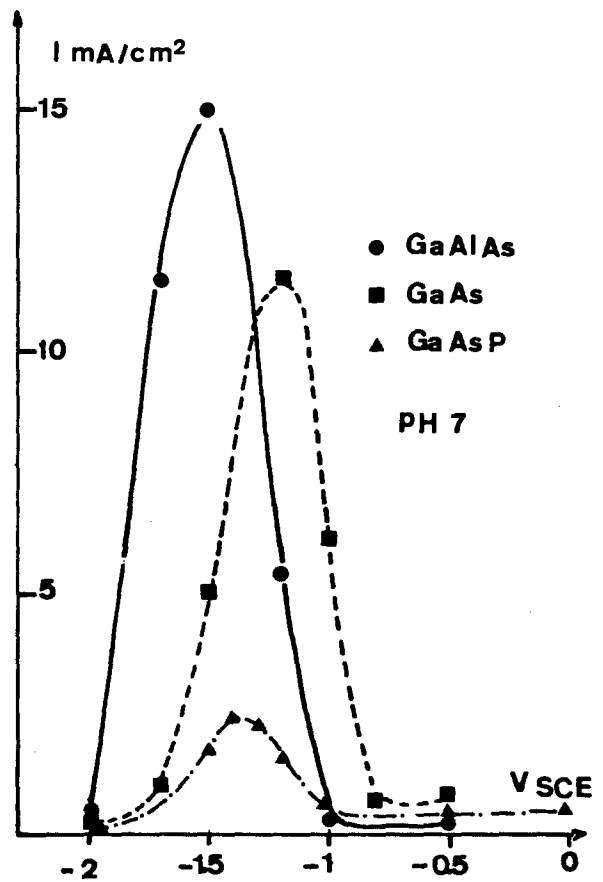


Fig. 9. $i_{Ga} = f(V)$ for n-type GaAs, GaAlAs, and GaAsP in H_3PO_4 0.1M and H_2O_2 1% at pH 7.

weak frequency dependence and a good agreement with the predicted values. No account was taken of

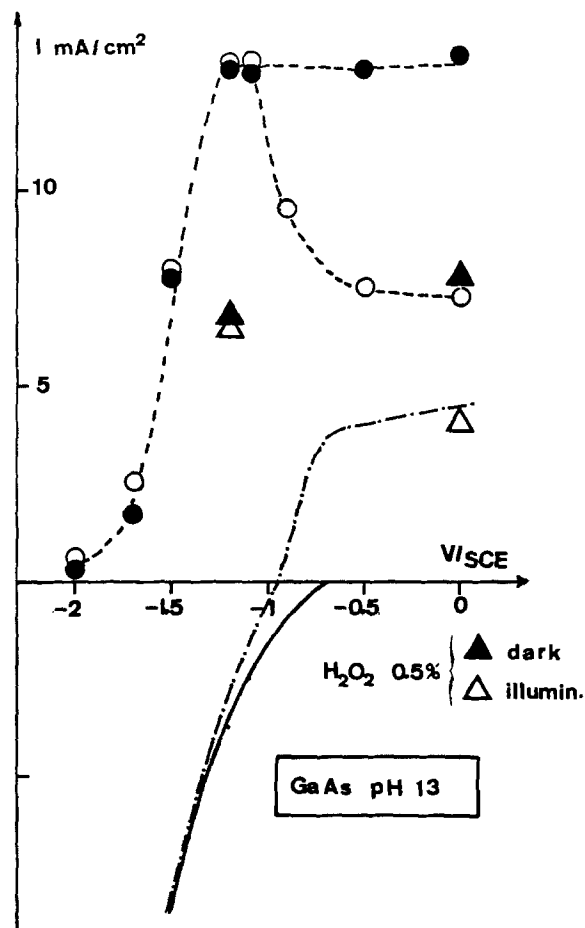


Fig. 10. $I = f(V)$ and $I_{Ga} = f(V)$ for n-type GaAs in H_3PO_4 0.1M and 1% H_2O_2 at pH 13. Symbols are the same as used in Fig. 2 except for 0.5% H_2O_2 solution.

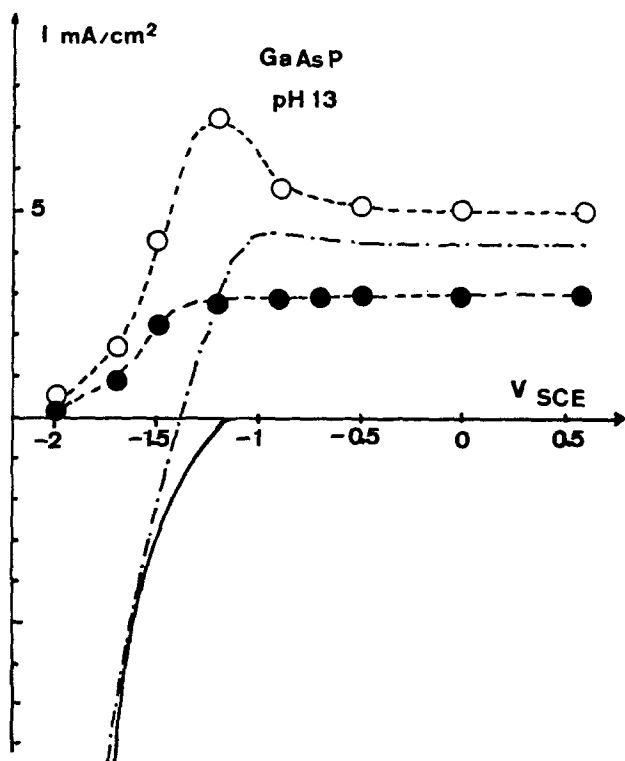


Fig. 11. $I = f(V)$ and $I_{Ga} = f(V)$ for n-type GaAsP under the same conditions as Fig. 10.

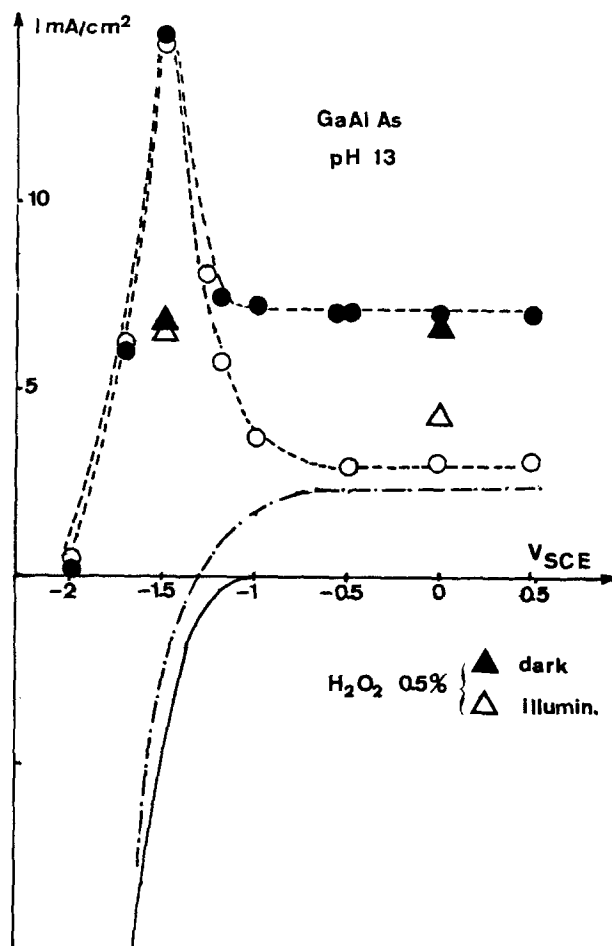


Fig. 12. $I = f(V)$ and $I_{Ga} = f(V)$ for n-type GaAlAs, in the same conditions as Fig. 10.

surface roughness for the calculation of the doping level. The corresponding flatband potentials were frequency independent and compared favorably, allowing for the observed pH dependence with the values of Table I. Experimental values of these flatband potentials are identical for both solutions (citric and phosphoric), indicating that for a given sample in indifferent electrolyte this quantity is determined by the pH solely. Hence for practical convenience, further experiments were made in a phosphoric medium. The linearities over a large range of potentials of the Mott-Schottky plots (about 1.5V), as well as the perfect reproducibility of these plots even after numerous scans up to the highest voltage attained in capacitance measurements (deep depletion situation), show that the GaAs surface can be considered, from a practical point of view to be oxide free, even if such freshly etched surfaces cannot be considered as completely exempt of oxygen (31). It was impossible to detect the presence of oxide by ellipsometry on surfaces so prepared. This justifies our term "clean."

A second series of capacitance measurements were performed in a H_3PO_4 0.1M + H_2O_2 1% pH 7 medium. These results, which are not shown here, should be discussed in conjunction with the $I_{Ga} = f(V)$ curve for the n-GaAs of Fig. 9. Several points should be emphasized: (i) the range of potential where Mott-Schottky behavior was observed was very reduced compared to that in the previous media. (ii) The shape of the Mott-Schottky plots seemed to be very time dependent.

These two points clearly support the assumption that in such a medium and for the considered range of potential, changes in the GaAs surface occur in agreement with the observed corrosion and passivation of this material under these conditions.

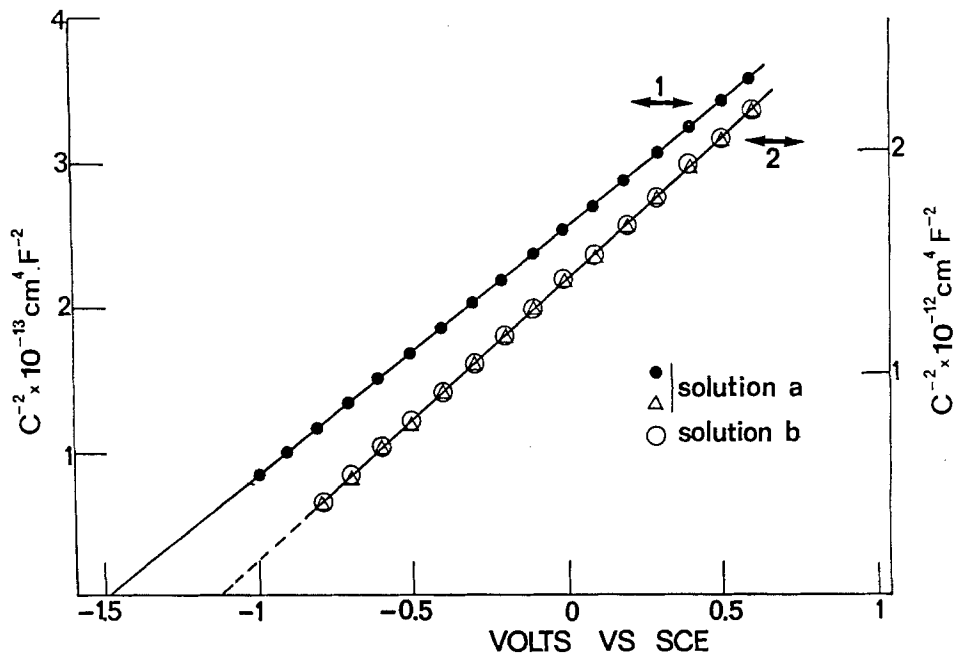


Fig. 13. Mott-Schottky plots for "clean" (1) and oxidized (2) n-type GaAs in: a. H_3PO_4 0.1M at pH 7. b. H_3PO_4 0.1M + 1% H_2O_2 at pH 7. Frequency: 1 kHz.

In an attempt to explain such an evolution, further experiments were made on the basis of the $I_{\text{Ga}} = f(V)$ curve of Fig. 9.

First, a "clean" n-type GaAs electrode was held at -1.4V , i.e., on the cathodic side of the passivation peak, for more than 2h, the differential capacitance being periodically and automatically measured after a fast microcomputer monitored shift of the potential (less than 1s) to 0.0V. The measured capacitance at 0.0V remained perfectly constant and equal to that of the "clean" surface at the same voltage ($2 \cdot 10^{-7} \text{ F} \cdot \text{cm}^{-2}$ [see Fig. 13]) in all cases. The "new" smooth and polished surface appeared to be oxide free by ellipsometric measurements, as the "clean" surfaces were.

Second, a "clean" electrode was held at -0.75V , i.e., on the other side of the passivation peak. Capacitance measurements were performed for more than 10h in the same way as before. A fast increase followed by a slow continuous decrease of the capacitance was observed. Ellipsometric measurements proved the growth of an oxide layer which appeared to be linked with the change of the electrode capacitance.

Third, Mott-Schottky plots were obtained for such a deliberately oxidized sample in the different media: H_3PO_4 0.1M, pH 7 and H_3PO_4 0.1M + 1% H_2O_2 , pH 7. The results showed a good linearity for both solutions over a large range of potentials. This shows that the oxide evolution rate could be neglected during these experiments. Figure 13 shows that plots obtained in both media were identical, but were shifted towards positive potentials compared with the plots obtained for the "clean" sample in the first solution. It is worth noticing that such a phenomenon in a nonaqueous medium, probably due to a large potential drop across the oxide layer, has already been reported by Morisson *et al.* (27), as has been the lower slope for the oxidized sample compared with the "clean" one. We have no explanation for this phenomenon (note the two scales used in Fig. 13).

All these experiments clearly confirm that in H_2O_2 medium: (i) the decrease of the n-GaAs dissolution rate, above -1.1V (Fig. 9) is due to a passivation of the semiconductor caused by the growth of an oxide layer. (ii) the GaAs surface on the cathodic side of these passivation peaks can be considered oxide free.

Application: selective etching.—From a knowledge of the $I_{\text{Ga}} = f(V)$ curves it is possible to explore a new way of selective etching of the three III-V semiconductors considered here. Referring to the previous

sections concerning the behavior of these materials at pH 7 (when the passivation is very efficient) between -1.5 and -1.1V , GaAlAs is protected against corrosion by passivation, while GaAs dissolves. The same is observed for GaAsP between -1.3 and -1.1V . If the voltage of a heterostructure involving GaAs and GaAlAs, or GaAsP, is fixed within these ranges, dissolution of GaAs alone will occur. This selective process of dissolution involves both the choice of an applied voltage and the passivation phenomenon in oxidizing media. Usually these methods are used independently of each other, the latter being carried out at rest potential etching.

Preliminary experiments have been performed on a GaAs/GaAlAs heterostructure at -1.2V in a H_3PO_4 0.1M + 1% H_2O_2 aqueous solution at pH 7. Dissolution began from the GaAs surface. The approximate observed selectivity ratio (etching rate of GaAs upon etching rate of GaAlAs) was about 10, further experiments are needed for a better determination of this ratio.

It is worth noting that afterwards GaAlAs interface exhibits a smooth, mirrorlike surface. This is probably due to the fact that at this potential (-1.2V) the remaining oxide layer is thin and helps the polishing process by a diffusion mechanism. The quality of the surface after such selective attack appears to be one of the most important advantages of the method.

The same technique was applied to GaAs/GaAsP heterostructure. In this case, the nature of the surface is satisfactory enough for practical applications but the smoothness is not as marked as for GaAlAs. Therefore, for this last type of heterostructure there is no great advantage in using the technique with applied voltage, since, as already stated, selectivity is obtained directly in acid or alkaline media at the rest potential.

The experiments described above show that a precise knowledge of electrochemical behavior permits a rapid determination of possible selective etching procedures.

Conclusions

Using impedance and ellipsometric measurements, we have shown that a method based on direct analysis of corrosion products of the semiconductor under corrosion conditions leads to a better understanding of the corrosion mechanisms involved for the III-V compounds concerned in this study. The etching behavior of H_2O_2 appears to be controlled by an oxide

layer formation which depends to a great extent on the pH. From this result new experimental conditions may be established in order to solve practical problems concerning selective etching.

Acknowledgments

We are pleased to acknowledge that this work was supported by the French Direction des Recherches et Etudes Militaires (DRET) under contract no. 80-34-169-00-470-75-01. We would like to thank Dr. J. Joseph and Dr. A. Gagnaire for their useful contribution (ellipsometric measurements) and D. Richartz (RTC) for his technical assistance.

Manuscript submitted June 2, 1982; revised manuscript received ca. Nov. 1, 1982.

Ecole Centrale de Lyon assisted in meeting the publication costs of this article.

REFERENCES

- R. P. Tijburg and T. Van Dongen, *This Journal*, **123**, 687 (1976).
- L. Hollan, J. C. Tranchant, and R. Memming, *ibid.*, **126**, 855 (1979).
- R. A. Logan and F. K. Reinhart, *J. Appl. Phys.*, **44**, 4172 (1973).
- C. E. Hurwitz, J. A. Rossi, J. J. Hsien, and C. M. Wolfe, *Appl. Phys. Lett.*, **27**, 241 (1975).
- J. L. Merz and R. A. Logan, *J. Appl. Phys.*, **47**, 3503 (1976).
- J. L. Merz, R. A. Logan, and A. M. Sergent, *IEEE J. Quantum Electron.*, **qe-15**, 72 (1979).
- R. Memming, *Philips Tech. Rev.*, **38**, 160 (1978/1979).
- "Photoeffects at Semiconductor-Electrolyte Interfaces," A. J. Nozik, Editor, A.C.S. Symp. Series No. 146, American Chemical Society, Washington, DC (1981).
- S. R. Morrison, "Electrochemistry at Semiconductor and Oxidized Metals Electrodes," Plenum Press, New York (1980).
- H. Gerischer, in "Physical Chemistry, an Advanced Treatise," Vol. IX-A, p. 483, H. Eyring, Editor, Academic Press (1970).
- R. Memming and G. Schwandt, *Electrochim. Acta*, **13**, 1299 (1968).
- H. Gerischer and W. Mindt, *ibid.*, **13**, 1329 (1968).
- H. Gerischer and W. Mindt, *Surf. Sci.*, **4**, 440 (1966).
- R. Memming, *Ber. Bunsenges. Phys. Chem.*, **81**, 732 (1977).
- T. Inoue, T. Watanabe, A. Fujishima, and K. Honda, *This Journal*, **127**, 719 (1977).
- K. W. Frese, Jr., M. J. Madou, and S. R. Morrison, *J. Phys. Chem.*, **84**, 3172 (1980).
- B. Miller, S. Menezes, and A. Heller, *J. Electroanal. Chem.*, **94**, 85 (1978).
- T. Ambridge and M. M. Faktor, *J. Appl. Electrochem.*, **5**, 319 (1975).
- W. W. Harvey, *This Journal*, **114**, 473 (1967).
- A. Gagnaire and J. Joseph, *C.R. Acad. Sci., Ser. B*, **293**, 357 (1981).
- F. Cardon and W. P. Gomes, *J. Phys. D.*, **11**, L63 (1978).
- F. El Halouani, H. Traore, G. Allais, and A. Deschanvres, *Surf. Sci.*, **79**, 498 (1979).
- R. Memming, *This Journal*, **116**, 785 (1969).
- R. Memming, in "Electroanalytical Chemistry," A. J. Bard, Editor, Vol. 11, p. 1, M. Dekker, Inc., (1979).
- H. Gerischer, N. Müller, and O. Haas, *J. Electroanal. Chem.*, **119**, 41 (1981).
- J. C. Tranchant, L. Hollan, and R. Memming, *This Journal*, **125**, 1185 (1978).
- K. W. Frese and S. R. Morrison, *ibid.*, **126**, 1235 (1979).
- J. M. Palau, E. Testemale, and L. Lassabatere, *J. Vac. Sci. Technol.*, **19**, 192 (1981).
- W. E. Spicer, I. Lindau, P. Skeath, and C. Y. Lu, *ibid.*, **17**, 1019 (1980).
- E. Kamieniecki and G. Cooperman, *ibid.*, **19**, 453 (1981).
- A. Munoz-Yague, J. Piqueras, and N. Fabre, *This Journal*, **128**, 149 (1981).
- H. Gerischer, D. M. Kolb, and J. K. Sass, *Adv. Phys.*, **27**, 437 (1978).
- D. W. Shaw, *This Journal*, **127**, 874 (1981).
- M. Pourbaix, "Atlas d'Equilibres Electrochimiques," Gauthier-Villars et Cie, Editor, Paris (1963).

Catalytic Activity of Iron, Nickel, and Nickel-Phosphorus in Electroless Nickel Plating

J. Flis¹ and D. J. Duquette

Department of Materials Engineering, Rensselaer Polytechnic Institute, Troy, New York 12181

ABSTRACT

The catalytic activity for electrooxidation of hypophosphite and electroless nickel plating on iron, nickel, and electrolessly plated nickel (with 2.2-2.9 weight percent (w/o) P) was investigated in an ammoniacal solution of pH 8.8 at 50°C by potential measurements and linear sweep voltammetry from -0.3V to 0.92V vs. SCE. Cathodic polarization of any of the substrates (in 0.1M H₂SO₄) before testing or permeation of hydrogen through iron foils during testing reduced the incubation time for electroless plating, increased anodic dissolution of the substrates in the passive region, and increased the hypophosphite electrooxidation on nickel and nickel-phosphorus at potentials of thermodynamic stability for nickel oxides or hydroxides. The nickel-phosphorus substrate exhibited significantly higher activity than pure nickel, in a similar manner to the effect of cathodic polarization. The effect of cathodic polarization and hydrogen is associated with the electrochemical reduction of surface oxides, whereas the higher activity of nickel-phosphorus deposits (as compared to that of pure nickel) is explained by the lower protectivity of surface oxides on these deposits.

Electroless nickel plating from hypophosphite solutions proceeds spontaneously on many metal surfaces (1-5), although the specifics of this process may be of a different nature. Some noble metals (palladium,

rhodium, nickel, cobalt, gold) possess an intrinsic catalytic ability to induce electrooxidation of hypophosphite, and electroless nickel plating; whereas some active metals become catalytic due to the deposition of nickel from a solution by a displacement reaction. The latter phenomenon has been shown for iron, aluminum, and beryllium (2), gallium and thallium (6), magnesium, zinc, and manganese. The

¹On leave from Institute of Physical Chemistry, 01-224 Warszawa, Poland.

Key words: electroless, nickel plating, iron, nickel, nickel-phosphorus.

catalytic activity of copper has been shown to be strongly affected by surface oxides (7). The activation of copper or its alloys by anodic treatment (4) or by the addition of chloride ions to a given plating solution (8) is evidently associated with the removal of these surface oxides.

Nickel and iron induce spontaneous electroless plating of nickel, but the presence of surface oxides may considerably prolong incubation times and decrease the adhesion of the deposits to the substrates. Investigations by Gaigher and van Wyke (9) showed that contamination of a nickel substrate due to exposure to laboratory air resulted in a blocky discontinuous growth of nickel electrodeposits, in contrast to smooth monolayer-type growth for uncontaminated surfaces.

The catalytic activity of a nickel surface for dehydrogenation of hypophosphite diminishes with time (2, 3) in the absence of Ni^{2+} ions. However, it is sustained in the presence of these ions, even at concentrations as low as $2 \times 10^{-3}\text{M}$ (2). Gutzeit (2) indicated that the concentration of Ni^{2+} ions in the solution remains constant during a given experiment. Nevertheless, it seems that a small amount of deposition of electroless nickel is also possible, giving rise to the continuation of the catalytic activity.

Epifanova *et al.* (10) showed that the catalytic activity of electroless nickel for oxidation of hypophosphite was distinctly higher than that of pure nickel. This was explained in terms of the catalytic action of phosphorus. It is possible that the higher catalytic activity of nickel-phosphorus deposits when compared to that of nickel may also be due to other reasons, such as less vulnerability to oxide formation or other surface contamination, or to hydrogen absorbed by the deposits during plating. The effect of surface conditions on growth of the deposits was stressed by Cavallotti and Salvago (6). Inhibition of electroless plating and of hypophosphite electrooxidation by oxy-anions, oxides, or dissolved oxygen has been reported by several authors (7, 11-13).

Hydrogen has been shown to accelerate electroless plating, both by participation in the reduction of Ni^{2+} ions (1-3, 14), and also by reduction of surface oxides (13). On the other hand, hydrogen may diminish the catalytic activity of substrates, as it was observed for palladium (13).

The present work was undertaken in order to determine the effect of surface oxides and of hydrogen on the incubation time for electroless plating and on the catalytic activity for electrooxidation of hypophosphite on substrates of iron, nickel, and nickel-phosphorus.

Investigations were carried out in an ammoniacal hypophosphite solution, in which electroless plating produced nickel-phosphorus deposits with 2.2-2.9 w/o P (13). The catalytic activity and electrochemical behavior of the substrates were examined by potential measurements and linear sweep voltammetry.

Experimental

Tests were carried out on annealed Armco iron, 99.9% pure nickel, and preformed electroless nickel-phosphorus deposits containing 2.2-2.9 w/o P.

Specimens of Armco iron were electropolished in a solution of 940 ml acetic acid (glacial) + 60 ml perchloric acid, at 40-60V, while specimens of nickel were electropolished in a solution of 100 ml H_2SO_4 + 75 ml H_2O , at 5-6V; both at room temperature. Specimens were subsequently washed in distilled water, dried in air, and then masked with (MicroshieldTM) lacquer to obtain an uninsulated surface area of 1 cm^2 . The lacquer remained adherent and stable for periods of approximately 2 hr. Nickel-phosphorus deposits of $\sim 3 \mu\text{m}$ thickness were grown on electro-

Table I. Composition of electrolytes

Solution designation	$\text{NaH}_2\text{PO}_2 \cdot \text{H}_2\text{O}$ (g/liter)	$\text{NiSO}_4 \cdot 6\text{H}_2\text{O}$ (g/liter)	KNa tartrate $\text{KNaC}_4\text{H}_4\text{O}_6 \cdot 4\text{H}_2\text{O}$ (g/liter)	28% NH_4OH (ml/liter)	Conc H_2SO_4 (ml/liter)
Plating solution	13.25 (0.125 mol/liter)	13.1 (0.05 mol/liter)	28.1	70	ca. 15
Supporting solution	—	—	28.2	70	ca. 15
Supporting solution with Ni^{2+} ions	—	13.1	28.2	70	ca. 15
Supporting solution with sodium hypophosphite	13.25	—	28.2	70	ca. 15

polished nickel by immersion into a plating solution (cf. Table I) at 50°C for 30 min.

Specimens were examined under the following conditions: (i) electropolished (iron or nickel) or freshly deposited (nickel-phosphorus), tested within 1 hr after preparation. (ii) As (i), followed by cathodic polarization in 0.1M H_2SO_4 at a current density of $100 \text{ A} \cdot \text{m}^{-2}$ for 10 min and tested immediately after polarization and rinsing with distilled water. (iii) As (i), aged in air at 50°C for 28 hr. (iv) As (i), immersed into 0.1M NaOH at 25°C, for 30 min. (v) Electropolished iron with continuous permeation of hydrogen.

A schematic drawing of a specimen instrumented for hydrogen permeation is shown in Fig. 1. A 0.10 mm thick membrane of annealed Armco iron was glued to a glass tube which then was filled with 0.1M H_2SO_4 . The outer portion of the membrane served as the specimen's reaction surface. Permeation of hydrogen through this surface was achieved by cathodic polarization of the inner surface at a current density of $100 \text{ A} \cdot \text{m}^{-2}$. The rate of hydrogen permeation through Armco iron membranes was determined electrochemically (15) in separate experiments. In these experiments, the diffusion sides of the membranes were electroplated with palladium and the membranes were clamped between the two compartments of the electrolytic permeability cell. The diffusion compartment contained 0.02M NaOH with a reference electrode of $\text{Hg}/\text{HgO}/0.02\text{M NaOH}$. A typical current transient for hydrogen permeation during cathodic polarization of a membrane is shown in Fig. 2. No hydrogen gas bubbles were observed during the permeation experiments.

Specimens were examined in the solutions listed in Table I, prepared from reagent grade chemicals and distilled water. Sulfuric acid or, if necessary, NH_4OH , was added in amounts appropriate to adjust the pH of the solutions to 8.8. Measurements were carried out on stationary specimens at $50.0 \pm 0.5^\circ\text{C}$ in solutions deaerated by purging with pure nitrogen.

Measurements involved monitoring of open-circuit electrode potentials, and of linear sweep voltammograms. Potentials were measured against saturated calomel electrode (SCE) at 25°C via a Luggin capillary. Voltammetric measurements were performed using single cathodic sweeps at a rate of 1 mV/sec, beginning at -0.3V vs. SCE .

Results

Open-circuit potentials.—Changes of electrode potential for the substrates after immersion into electroless plating solutions are shown in Fig. 3 and 4. The rest potential of the electroless plating was approximately -0.87V (7, 13). The time required to reach this potential is defined as the incubation time and characterizes the ability of the substrates to become active for electroless plating.

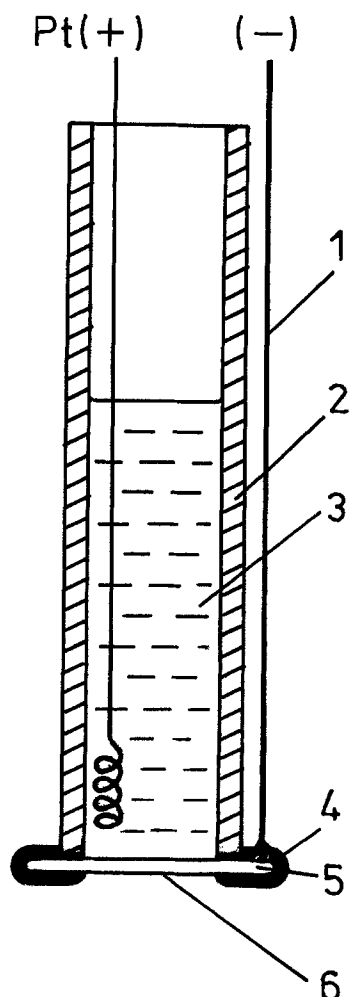


Fig. 1. Schematic drawing of a specimen unit for continuous permeation of hydrogen. (1) insulated wire, (2) glass tube, (3) 0.1M H_2SO_4 , (4) epoxy resin, (5) 0.10 mm thick iron membrane, (6) specimen surface.

Figure 3 shows that electropolished iron becomes active after achieving a potential arrest at approximately $-0.5V$. These potential arrests virtually dis-

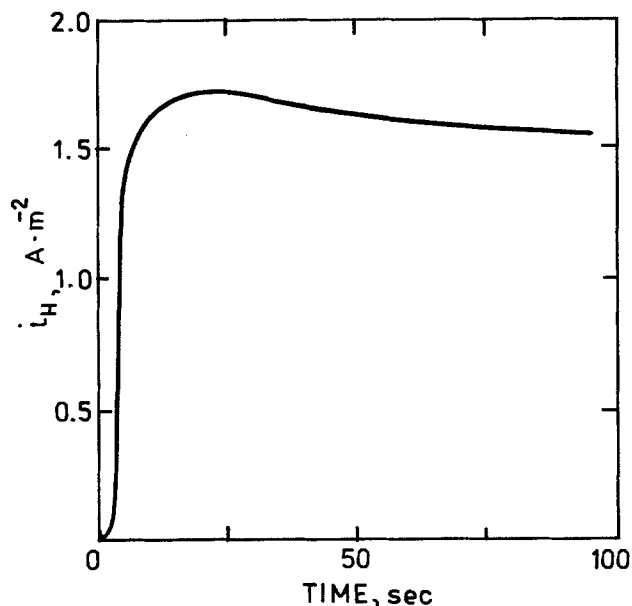


Fig. 2. Permeation of hydrogen (i_H) through a 0.10 mm thick iron membrane during cathodic polarization at $100 A \cdot m^{-2}$ in 0.1M H_2SO_4 , $50^\circ C$.

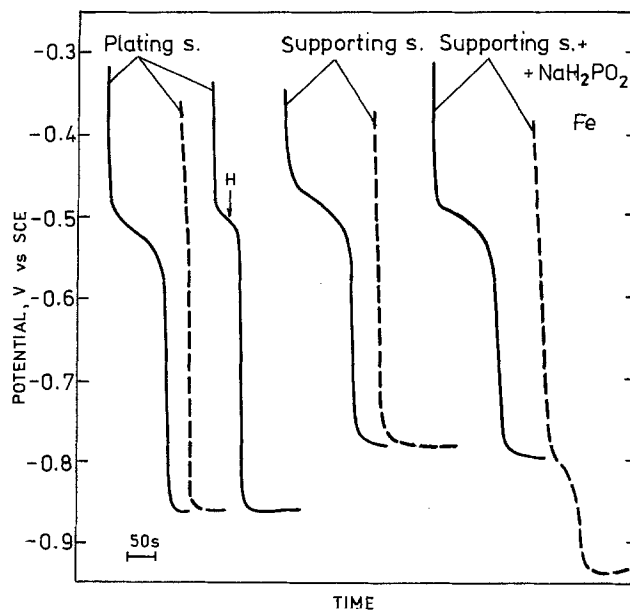


Fig. 3. Open-circuit potential of electropolished iron (full lines) and of iron after cathodic polarization in 0.1M H_2SO_4 (dashed lines) upon immersion into the plating, supporting, and supporting + NaH_2PO_2 solutions. An arrow with "H" indicates the start of hydrogen permeation through an iron membrane.

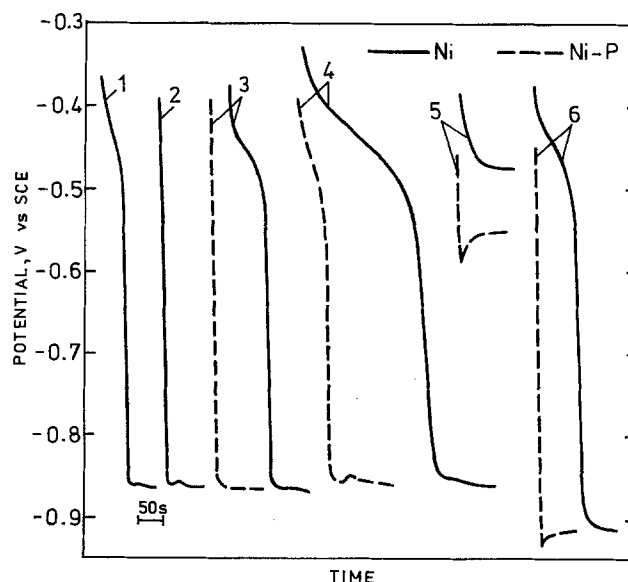


Fig. 4. Open-circuit potential of nickel and nickel-phosphorus deposits after immersion into the plating solution (curves 1-4), supporting solution (5) and supporting with NaH_2PO_2 (6): (1) electropolished nickel, (2) nickel after cathodic polarization, (3) after exposure to air at $50^\circ C$ for 28 hr, (4) after exposure to 0.1M $NaOH$ for 0.5 hr.

appeared when specimens were cathodically polarized in 0.1M H_2SO_4 before testing. Permeation of hydrogen through iron membranes also diminished the extent of the potential arrest.

In the supporting solution (Table I), the rest potential of iron was approximately $-0.78V$. With a hypophosphite addition, the potential was nearly the same on an electropolished surface, but on cathodically polarized surfaces it shifted to approximately $-0.92V$, after a brief arrest at $-0.78V$.

The incubation time for plating on electropolished nickel (Fig. 4) was shorter than that for iron, and was also substantially diminished by cathodic prepolarization. Potential arrests were observed at approximately $-0.45V$.

On nickel-phosphorus deposits, the potential arrests observed at -0.45V were significantly shorter than those observed on nickel, indicating higher activity of these deposits for the initiation of electroless plating. In solutions without Ni^{2+} ions, potentials on nickel-phosphorus dropped to lower values than on nickel.

Voltammetric measurements.—Measurements were made in the supporting solution with and without the additives essential for plating (cf. Table I), by scanning the potential in the cathodic direction from -0.3 to -0.92V or lower. Potential scanning was initiated immediately upon immersion.

Voltammograms on electropolished and cathodically polarized iron are shown in Fig. 5 and 6. Electrooxidation of hypophosphite in the solution without Ni^{2+}

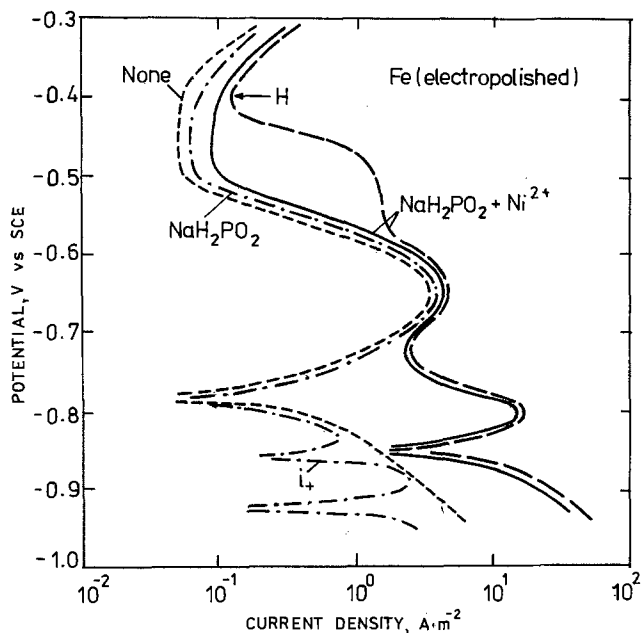


Fig. 5. Voltammograms for electropolished iron in the supporting solution with and without other components (cf. Table I), beginning at -0.30V . An arrow with "H" indicates the start of hydrogen permeation through an iron membrane. Below the discontinuities the current is cathodic, except where anodic current is denoted by $i+$.

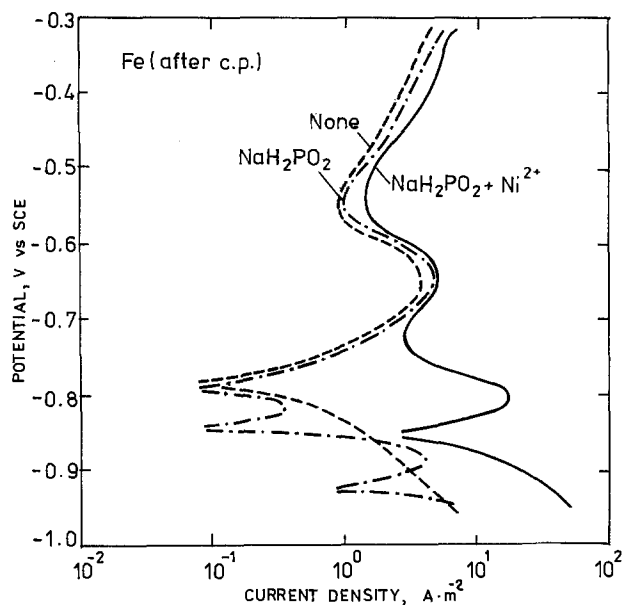


Fig. 6. Voltammograms for iron after cathodic polarization in $0.1\text{M H}_2\text{SO}_4$, measured in the supporting solution with and without other components, beginning at -0.3V .

ions began at approximately -0.83 and -0.81V on electropolished and cathodically polarized iron, respectively. This was indicated by a deflection of the cathodic curves at these potentials, followed by the appearance of anodic current loops. In the solution containing Ni^{2+} ions, the electrooxidation of hypophosphite began at approximately -0.70V .

Permeation of hydrogen through the specimen's surface caused an increase in anodic current in the passive region, but did not affect the electrooxidation of hypophosphite. Cathodic polarization of specimens prior to testing also increased the anodic current in the passive region, without affecting the electrooxidation of hypophosphite (Fig. 6).

Voltammograms on nickel and nickel-phosphorus in various solutions are shown in Fig. 7-10. The curves were measured after cathodic polarization labeled "c.p." of specimens in $0.1\text{M H}_2\text{SO}_4$. These voltammograms show that the nickel-phosphorus deposits were significantly more active than pure nickel. The higher activity of the deposits was indicated by higher anodic currents at noble potentials in all solutions, by the occurrence of a peak at around -0.78V in the plating solution, and by a steeper rise in cathodic currents at approximately -0.75V in the supporting solution with Ni^{2+} ions.

As in the case for iron, cathodic polarization of nickel and nickel-phosphorus in $0.1\text{M H}_2\text{SO}_4$ before testing considerably increased anodic currents at noble potentials. At more active potentials, current increases were not significant. The effect of cathodic polarization was evident in essentially the same potential range for both materials.

Discontinuities in the voltammograms measured in the solutions without NaH_2PO_2 (Fig. 8 and 9) indicate mixed rest potentials. Currents measured noble to these potentials represent anodic dissolution of the substrates. The voltammograms show that the anodic dissolution rate of nickel-phosphorus was higher than that of nickel and that cathodic prepolarization increased the rate of dissolution of both substrates.

At potentials noble to -0.5V , anodic currents measured in the hypophosphite containing solutions (Fig. 7 and 10) were virtually identical to those measured in the hypophosphite-free solutions (Fig. 8 and 9)

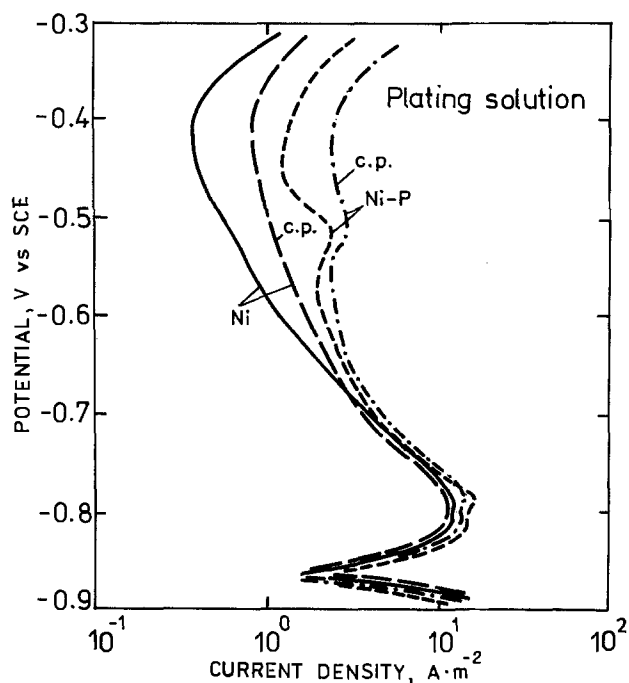


Fig. 7. Voltammograms for nickel and nickel-phosphorus deposits in the plating solution, beginning at -0.3V . Curves denoted by "c.p." were measured after cathodic polarization in $0.1\text{M H}_2\text{SO}_4$.

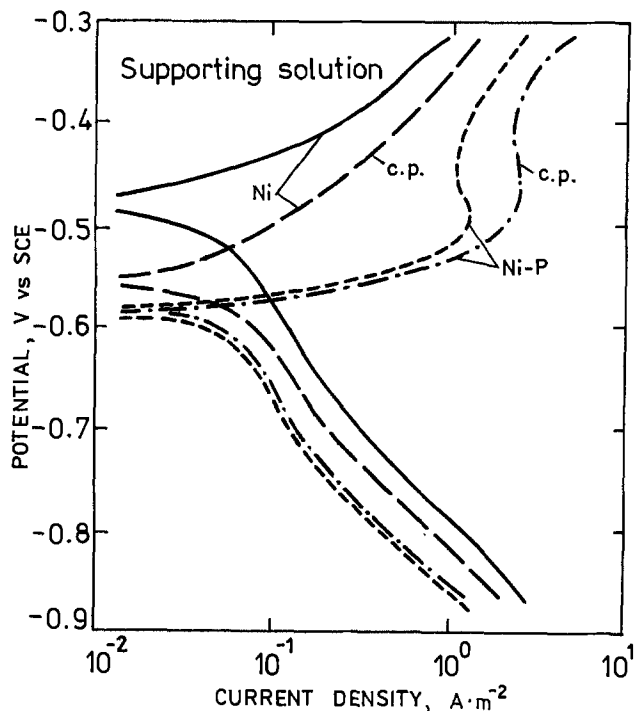


Fig. 8. Voltammograms for nickel and nickel-phosphorus deposits in the supporting solution.

on each substrate. This suggests that at these potentials the measured current was associated primarily with anodic dissolution of the substrates, and that the electrooxidation of hypophosphite either did not take place or was negligible. An anodic current measured at more active potentials was evidently associated with electrooxidation of hypophosphite. This shows that the hypophosphite electrooxidation became significant at the potentials corresponding to rest potentials in the hypophosphite-free solutions. The higher anodic dissolution current corresponds to higher electrooxidation current near the corrosion potentials.

In the plating solution (Fig. 7) the electrooxidation current of hypophosphite, active to -0.75V , reached

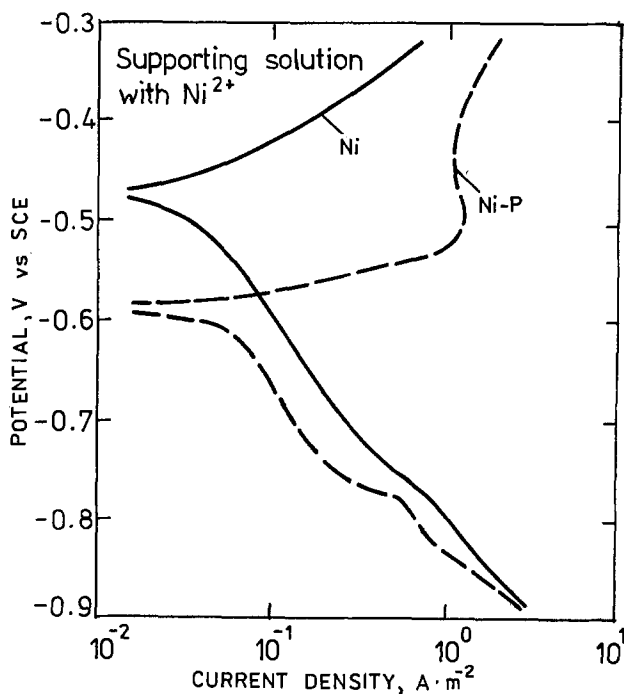


Fig. 9. Voltammograms for nickel and nickel-phosphorus deposits in the supporting solution with added Ni^{2+} ions.

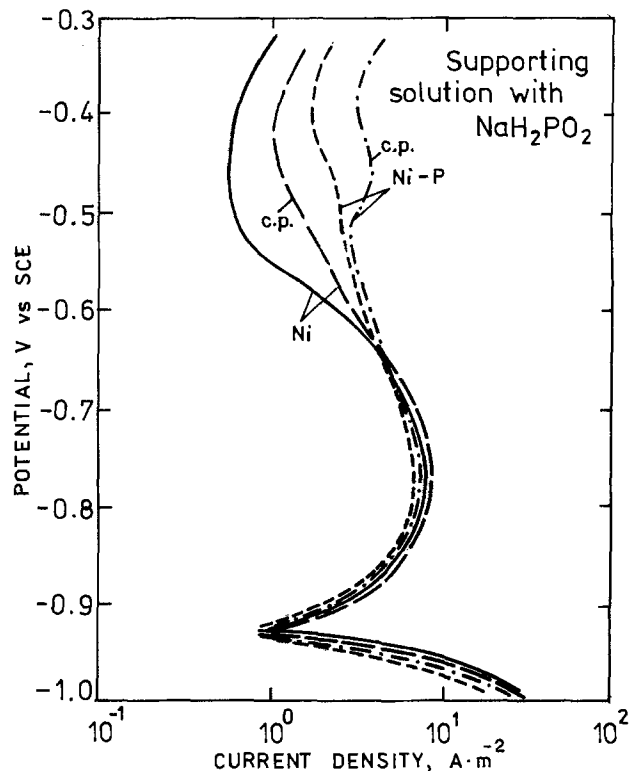


Fig. 10. Voltammograms for nickel and nickel-phosphorus deposits in the supporting solution with added NaH_2PO_2 .

higher values than in the solution without Ni^{2+} ions (Fig. 10). On nickel-phosphorus deposits, in the plating solution, the increase in the current active to -0.75V was greater than on pure nickel and showed a distinct peak at -0.78V . Nickel showed only a slight tendency to form a peak at this potential.

The increase in the electrooxidation current in the plating solution active to -0.75V coincided with the start of electrolytic deposition of nickel on the substrates. The latter can be seen from cathodic curves in the supporting solution with added Ni^{2+} ions (Fig. 9). The increased electrooxidation current in the plating solution thus results from electrolytic deposition of nickel on the substrates.

Discussion

Measurements of open-circuit potentials show that the incubation time for electroless nickel plating on the respective substrates decreased in the sequence: iron > nickel > nickel-phosphorus. Oxidation of specimens prior to immersion increased the incubation time, while cathodic polarization decreased it. On iron, the incubation time was also lowered by saturation of the surface with hydrogen as indicated by permeation plateaus.

The major part of the incubation times was associated with potential arrests in the range of -0.45V for nickel and of -0.5V for iron. Voltammograms in the supporting electrolyte showed that the potential arrest for iron was in the passive-active region, while that for nickel was approximately at the corrosion potential (Fig. 8). This suggests that these potential arrests are associated with oxide dissolution.

The decrease in incubation time resulting from cathodic prepolarization or by permeation of hydrogen can also be attributed mainly to the reduction of surface oxides. This is evidenced by higher anodic currents in the passive region on iron (Fig. 5 and 6), and also on nickel and nickel-phosphorus above their corrosion potentials (Fig. 8).

Cathodic polarization leads to the reduction of surface oxides and presumably saturates the specimen surfaces with hydrogen. This absorbed hydrogen may

contribute to reduction of oxides or hydroxides which form thereafter, especially upon immersion into the plating solution. Formation of oxides or hydroxides on the substrates in the plating solution can be surmised from the values of pH and of initial potentials, which indicate thermodynamic stability for oxides or hydroxides (16).

The voltammograms show that electrooxidation of hypophosphite started at potentials at which oxides should be reduced. On iron, this occurred at ca. -0.82V , which is approximately the equilibrium potential of the $\text{Fe}(\text{OH})_2/\text{Fe}$ reaction (16); while on nickel and nickel-phosphorus this occurred at approximately the corrosion potentials. At this potential, surface oxides should be reduced to a great extent, though not completely (17-19). The effects of hydrogen and of cathodic prepolarization on the initiation of plating and on the hypophosphite electrooxidation are associated with the reduction of surface oxides. The hypophosphite electrooxidation was not affected at more active potentials. Nor was the hypophosphite electrooxidation affected by evolution of hydrogen at ca. -0.7V , as has been reported for palladium (13).

The greater efficiency of the nickel-phosphorus substrate (compared to that of nickel) can also be explained in terms of surface oxides. Larger anodic dissolution currents on nickel-phosphorus than those on nickel indicate that the oxide layers on nickel-phosphorus were less protective, which may result from thinner, less stable, or discontinuous oxides. Thus, the incubation time for nickel-phosphorus was shorter and hypophosphite electrooxidation in the noble potential region was greater than are observed for nickel. At potentials active to -0.65V in the solution without Ni^{2+} ions, hypophosphite electrooxidation was essentially identical for nickel and for nickel-phosphorus. This indicates that the intrinsic catalytic activity of the two substrates is nearly the same. The difference in the activity occurs essentially because of the presence of surface oxides and can be attributed to the difference in the protective properties of the oxide layers on these substrates. The explanation of Epifanova *et al.* (10), which invokes a catalytic action of phosphorus in electroless deposits, does not seem to be appropriate for the present case. The surface of nickel-phosphorus deposits is probably less contaminated with residual oxides or other species at more negative potentials. This explains the steeper rise in the electrodeposition current of nickel at -0.75V on these deposits than on nickel (Fig. 9). It is suggested that faster electrodeposition of fresh nickel on nickel-phosphorus deposits from the plating solution is responsible for the higher electrooxidation current on these deposits below -0.75V (Fig. 7). The freshly electrodeposited nickel should possess high catalytic activity owing to low contamination of its surface.

Electrolytic deposition of nickel from a plating solution (active to -0.75V) enhanced the hypophosphite electrooxidation on nickel and nickel-phosphorus, whereas on iron it initiated the hypophosphite electrooxidation at approximately this potential (Fig. 5 and 6). In the solution without Ni^{2+} ions, the hypophosphite electrooxidation on iron began at -0.81V or below. This shows that for iron in the plating solution, electrolytic deposition of nickel occurs during the spontaneous potential shift, followed by electrooxidation of hypophosphite. This is in accord with the conclusion of Gutzeit (2).

Conclusions

Cathodic polarization of iron, nickel, and nickel-phosphorus in $0.1\text{M H}_2\text{SO}_4$ before testing considerably diminished incubation times for electroless nickel plating on these substrates. A similar effect was caused by permeation of hydrogen through the iron surface.

Potential scans from -0.3 to -0.92V vs. SCE showed that cathodic polarization and/or the presence of hydrogen in the substrates increased anodic dissolution of the substrates in the passive region, and increased the hypophosphite electrooxidation on nickel and nickel-phosphorus in the potential range of thermodynamic stability of nickel oxides or hydroxides.

The activating effect of cathodic polarization and hydrogen can be entirely ascribed to the reduction of surface oxides.

Nickel-phosphorus deposits showed lower incubation times for electroless plating of nickel, greater anodic dissolution in the passive region, and greater hypophosphite electrooxidation in the presence of oxides than those observed for nickel. This is attributed to lower protectiveness of surface oxides on these deposits.

Acknowledgment

This work was supported by International Business Machines Corporation.

Manuscript submitted March 7, 1983; revised manuscript received July 29, 1983.

REFERENCES

1. A. Brener and G. E. Riddell, *J. Research Natl. Bur. Standards*, **37**, 31 (1946); *ibid.*, **39**, 385 (1947).
2. G. Gutzeit, *Plating*, **1158**, 1275, 1377 (1959); *ibid.*, **63** (1960).
3. K. M. Gorbunova and A. A. Nikiforova, "Physico-Chemical Principles of Nickel Plating," *Izd. Akad. Nauk SSSR, Moscow* (1960); *Eng. Trans.* **63-11003**, U.S. Dept. of Commerce (1963).
4. G. G. Gavrillov, "Chemical (Electroless) Nickel Plating," Portcullis Press, Redhill (1979).
5. G. Salvago and P. L. Cavallotti, *Plating*, **665** (1972).
6. P. L. Cavallotti and G. Salvago, *Electrochim. Metall.*, **3**, 23 (1968).
7. J. Flis and D. J. Duquette, Submitted to *This Journal*.
8. V. S. Epifanova, Yu. V. Prusov, and V. N. Flerov, *Zashch. Met.*, **14**, 226 (1978).
9. H. L. Gaigher and G. N. van Wyke, *Electrochim. Acta*, **18**, 849 (1973).
10. V. S. Epifanova, Yu. V. Prusov, and V. N. Flerov, *Elektrokhimiya*, **13**, 1611 (1977).
11. N. Feldstein and P. R. Amodio, *This Journal*, **117**, 1110 (1970).
12. C. Gabrielli and F. Raulin, *J. Appl. Electrochem.*, **1**, 167 (1971).
13. J. Flis and D. J. Duquette, *This Journal*, **131**, 51 (1984).
14. K. N. Gorbunova and A. A. Nikiforova, *Zh. Fiz. Khim.*, **28**, 883 (1954).
15. M. A. V. Davanathan and Z. Stachurski, *Proc. R. Soc. London, Ser. A*, **270**, 91 (1962).
16. M. Pourbaix, "Atlas of Electrochemical Equilibria," Pergamon Press, London (1964).
17. N. Sato and K. Kudo, *Electrochim. Acta*, **19**, 461 (1974).
18. B. MacDougall and M. Cohen, *This Journal*, **121**, 1152 (1974).
19. Woon-kie Paik and Z. Szklarska-Smialowska, *Surf. Sci.*, **96**, 401 (1980).

Morphological Instability in Nonsteady Galvanostatic Electrodeposition

I. Effect of Surface Diffusion of Adatoms

Ryoichi Aogaki and Tohru Makino¹

Department of Chemistry, The Institute of Vocational Training, 1960, Aihara, Sagamihara, 229, Japan

ABSTRACT

In non-steady galvanostatic deposition without any surface diffusion, it has already been reported that the average size of crystals formed on an electrode surface decreases with deposition time since large number of crystal nuclei are successively generated due to high supersaturation of adatoms. However, when the crystal sizes become extremely small, it is necessary to consider the effect of the surface diffusion on crystal morphology. Therefore, we attempted to derive a degree of surface irregularity (dsi) equation including the surface diffusion to examine the time dependence of the maximum dis (dsi_{max}). It was found that the dsi_{max} value obtained here becomes smaller with time than that neglecting surface diffusion. The relation between the spatial wavelength (λ_{max}) corresponding to dsi_{max} and deposition time was obtained for the case where the surface diffusion cannot be disregarded, i.e., λ_{max} initially decreases, but approaches a certain constant value with time. Regarding λ_{max} as a measure of crystal size, it was obviously concluded that since the surface diffusion hinders the growth of crystal particles which develop from nuclei, the sizes do not decrease even after a long time passes. Moreover, as dsi_{max} is taken as a measure of increasing height of surface irregularity, it became clear that the surface diffusion also suppresses the growth rates of crystal peaks.

In galvanostatic deposition under diffusion control, owing to high supersaturation, a large number of crystal nuclei grow to form minute roundish particles without particular crystal faces. It has been pointed out that such growth is attributed to instability accompanied with the diffusion of depositing ions (1, 2, 9). Furthermore, a general expression for the variation of the surface morphology with increasing deposition time was derived for when the transition from thermodynamic equilibrium to nonequilibrium takes place (3). After drawing three-dimensional contour plotting obtained from the theory, the average particle size and standard deviation were calculated. The results were compared with statistical data obtained from SEM photographs by means of image analysis; both results were in good agreement (4).

According to this theory, as the bulk concentration decreases and the current density increases, the particle size decreases with time, and finally converges into zero (2). This is an extreme case, but to some extent such a prediction may be possible in a case of low concentration and high current density.

We attempted to improve the theory by introducing the effect of surface diffusion of adatoms. In order to make clear the mechanism of unstable growth, a thermodynamic condition was considered.

Theoretical

Diffusion of active ions in the electrolytic solution.—Following the concentration change of depositing ions near the electrode surface, which arises from sudden deposition, a nonsteady mass transfer occurs near the electrode. We assume that the solution is in a stationary state and contains a lot of supporting electrolyte so that the migration of the ions due to the presence of electric field can be neglected and there is no mass flow caused by fluid motion.

First, we consider a case where any fluctuations do not exist. Taking the electrode surface equal to the x-y plane, the concentration distribution in the present case has only one component in the z-direction perpendicular to the surface; i.e., the diffusion equation neglecting the terms of migration and mass flow (5)

$$\frac{\partial C^*(z, t)}{\partial t} = D \frac{\partial^2 C^*(z, t)}{\partial z^2} \quad [1]$$

¹ Present address: AHS Japan Company, 2-10-12, Akasaka, Minato-ku, 107, Japan.

Key words: unstable crystal growth, galvanostatic deposition, morphology.

is obtained, where $C^*(z, t)$ is the depositing ion concentration in nonfluctuated state, D is the diffusion coefficient, and t is deposition time. On the other hand, the fluctuation of the concentration, $c(x, y, z, t)$, imposed on this system can be written as follows (2)

$$\frac{\partial c(x, y, z, t)}{\partial t} = D \nabla^2 c(x, y, z, t) \quad [2]$$

where the migration and mass flow effects are also disregarded. Such fluctuation component is generally expressed by the superimposition of Fourier components, as long as they are sufficiently small compared with the nondisturbed component. Thus, a single component corresponding to a set of wave number, (k_x, k_y) as was shown in the preceding paper (2), is represented as follows

$$c_k(x, y, z, t) = c^0(z, t) \exp [i(k_x x + k_y y)] \quad [3]$$

where the subscript k means that the component corresponds to a single wave number, $k \equiv \sqrt{k_x^2 + k_y^2}$. Then substituting Eq. [3] into Eq. [2] under a quasi-steady condition

$$\left| \frac{\partial c^0(z, t)}{\partial t} \right| \ll |Dk^2 c^0(z, t)|$$

using the variable separation method, the general solution for $c^0(z, t)$ is obtained. It is

$$c^0(z, t) = (A_1 e^{-kz} + A_2 e^{kz}) \beta(t) \quad [4]$$

Here, A_1 and A_2 are arbitrary constants, and $\beta(t)$ is a function of the time. Because we should abandon a solution diverging in the bulk solution ($z \rightarrow \infty$), $A_2 = 0$ must be held. The following equation is derived

$$c^0(z, t) = A_1 e^{-kz} \beta(t) \quad [5]$$

[3] can be written as

$$c_k(x, y, z, t) = A_1 e^{-kz} \beta(t) e^{i(k_x x + k_y y)} \quad [3.1]$$

Thermodynamic condition accompanied with mass transfer.—In the electrolyte solution, the electrochemical potential of solute species, because of the electrode reaction, varies with location; consequently, the species transfer according to the inequalities of the potentials. This is a thermodynamical dissipative process. It is assumed that the species transfer in keeping local equilibrium (10). From this assumption, it can be

derived that the variation of the potential, Ψ , is equal to zero at all places of the electrolyte solution, and

$$\delta\Psi(x, y, z, t) = 0 \quad [6]$$

This relation is the necessary condition for $\Psi(x, y, z, t)$ to be minimum. If the temperature and pressure can be regarded as locally homogeneous, we can take $\Psi(x, y, z, t)$ as the electrochemical potential of active ionic species in the presence of a large amount of supporting electrolyte. Measuring the electrode potential, $V(x, y, z, t)$, at an arbitrary point of the solution with an electrode reversible to the active ions, if the potential in the bulk solution is taken as the standard, a relation is given in the form

$$\Psi(x, y, z, t) = n\mathbf{F}V(x, y, z, t) \quad [7]$$

Substituting [7] into [6], it follows that

$$\delta V(x, y, z, t) = 0 \quad [8]$$

However, the mass transport of the active ionic species induces the flow of electrolytic current in the solution. In the presence of a large amount of supporting electrolyte, the electrolytic current density is approximated (2) by

$$\vec{J}(x, y, z, t) = -\sigma \left[\nabla V(x, y, z, t) - \nabla H(x, y, z, t) - \frac{\Phi(x, y, t)}{n\mathbf{F}} \delta(z - Z) \right] \quad [9]$$

where σ is the electric conductivity of the bulk solution, $H(x, y, z, t)$ is the overpotential of the depositing ion, and $\Phi(x, y, t)$ is the surface potential arising from surface deformation. And $\delta(z - Z)$ is $\{0, 0, \delta(z - Z)\}$ where $\delta(z - Z)$ is the δ -function, and $z = Z$ is the equation of the electrode surface. Integrating Eq. [9] from a point (x, y, ∞) , of the bulk solution to a point, $(x, y, Z - 0)$, nearly inside the electrode, the equation

$$V(x, y, Z - 0, t) - V(z = \infty) = \frac{1}{\sigma} \int_{z=0}^{\infty} J_z(x, y, z, t) dz + H(x, y, Z, t) - H(z = \infty) - \frac{\Phi(x, y, t)}{n\mathbf{F}} \quad [10]$$

is obtained. Here, $V(z = \infty)$ and $H(z = \infty)$ are the electrode potential and concentration overpotential of the bulk solution, respectively, which take constant values. And $J_z(x, y, z, t) < 0$ is defined for cathodic deposition. Taking the variation of both sides of [10], the equation

$$\delta V(x, y, Z - 0, t) = \frac{1}{\sigma} \int_z^{\infty} j_z(x, y, z, t) dz + \eta(x, y, Z, t) - \frac{\phi(x, y, t)}{n\mathbf{F}} \quad [11]$$

is derived. Here, $j_z(x, y, z, t)$, $\eta(x, y, Z, t)$, and $\phi(x, y, t)$ are the fluctuation components of the electrolytic current in the z -direction, the concentration overpotential, and the surface potential, respectively. In terms of Eq. [8], Eq. [11] yields the following equation

$$\frac{1}{\sigma} \int_z^{\infty} j_z(x, y, z, t) dz + \eta(x, y, Z, t) - \frac{\phi(x, y, t)}{n\mathbf{F}} = 0 \quad [12]$$

Mass balance of adatoms at the electrode surface.—Active ionic species diffusing through the solution receive electrons to deposit as adatoms on the electrode surface. Then they move according to the difference of the chemical potential which changes with location, and is finally incorporated into the crystal lattice. The process mentioned above is schematically shown in Fig. 1. Conventionally, the interface between the double layer and the solution is denoted as $z =$

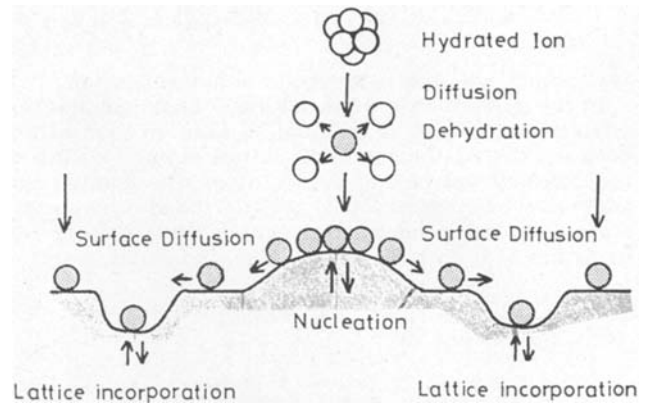


Fig. 1. Schematic diagram for the mass balance near the electrode. At the electrode surface, both the surface diffusion and nucleation simultaneously occur. Since the electron exchanging process is not rate determining, it is assumed that the adatoms are kept in equilibrium with the lattice atoms.

$Z + 0$ while the one between the double layer and the crystal lattice is as $z = Z - 0$. As shown in Fig. 1, the mass balance in the double layer is clearly written as follows

$$\frac{\partial C_{ad}(x, y, t)}{\partial t} + \nabla_{\perp} \cdot \vec{J}_{surf} = J_{flux}(z = Z + 0) - J_{flux}(z = Z - 0) \quad [13]$$

where C_{ad} is the surface concentration of the adatoms and $\nabla_{\perp} = (\partial/\partial x, \partial/\partial y)$. J_{surf} is the mass flux of the adatoms on the surface, namely

$$\vec{J}_{surf} = -D_{ad} \nabla_{\perp} C_{ad}(x, y, t) + b C_{ad}(x, y, t) \vec{f} \quad [14]$$

Here, D_{ad} is the diffusion coefficient of the adatom, and b is its mobility, which should satisfy the Einstein relation

$$b = \frac{D_{ad}}{RT} \quad [15]$$

\vec{f} is a motive force originated from the potential difference caused by surface deformation. Thus in the present case, the equation

$$\vec{f} = -\nabla_{\perp} \phi(x, y, t) \quad [16]$$

is derived (1). $J_{flux}(z = Z + 0)$ denotes the mass flux of the active ions going vertically into the double layer through the solution. The explicit form is represented by

$$J_{flux}(z = Z + 0) = D \{ \vec{n} \cdot \nabla C(x, y, z, t) \}_{z=Z+0} \quad [17]$$

where \vec{n} is a unit vector normal to the double layer surface. $J_{flux}(z = Z - 0)$ is the mass flux of the adatoms coming in and out of the interface between the double layer and the metal lattice. This process properly takes place at the active sites, such as kinks and steps.

As a result, the deposition continuously proceeds and the surface morphology changes with time. The variation can be described by

$$\frac{\partial Z(x, y, t)}{\partial t} = \Omega \left\{ \frac{\partial C_{ad}(x, y, t)}{\partial t} + J_{flux}(z = Z - 0) \right\} \quad [18]$$

Moreover, substituting Eq. [18] into Eq. [13], the rate equation of the surface height

$$\frac{1}{\Omega} \frac{\partial Z(x, y, t)}{\partial t} + \nabla_{\perp} \cdot \vec{J}_{\text{surf}} = J_{\text{flux}}(z = Z + 0) \quad [19]$$

is obtained, where Ω is the molar volume of metal.

In the present case, it is naturally assumed that the adatom concentration is equal to that in equilibrium between the adatoms and the lattice atoms.² Owing to the constant activity of lattice atom, the equilibrium adatom concentration, C_{ad}^* is concluded to be constant; i.e., independent of location. Thus, taking the variation of both sides of Eq. [19], it follows that

$$\frac{1}{\Omega} \frac{\partial \zeta(x, y, t)}{\partial t} = \frac{D_{\text{ad}}}{RT} C_{\text{ad}}^* \nabla_{\perp}^2 \phi(x, y, t) + D \left\{ \frac{\partial c(x, y, z, t)}{\partial z} \right\}_{z=Z} \quad [20]$$

where $\zeta(x, y, t)$ is the fluctuation component of the surface height.

Other relations.—The nondisturbed concentration of the active ionic species in the solution connected with an electrode has the relation

$$C^*(Z, t) = C^*(Z^*, t) \quad [21]$$

and the fluctuation component is expressed as

$$c(x, y, Z, t) = c(x, y, Z^*, t) + L(t)\zeta(x, y, t) \quad [22]$$

where Z^* is the average, nondisturbed height of the electrode surface, and $L(t)$ is the nondisturbed concentration gradient of the depositing ion, or

$$L(t) = \left\{ \frac{\partial C^*(z, t)}{\partial t} \right\}_{z=Z^*} \quad [23]$$

The concentration overpotential in the presence of a lot of supporting electrolyte is given in the form

$$H(x, y, z, t) = \frac{RT}{nF} \ln \left\{ \frac{C(x, y, z, t)}{C^*(z = \infty)} \right\} \quad [24]$$

where $C^*(z = \infty)$ is the constant concentration of active ions in the bulk of the solution. Taking the variation on both sides of [24], the equation

$$\eta(x, y, z, t) = \frac{RT}{nF} \frac{c(x, y, z, t)}{C^*(z, t)} \quad [25]$$

is obtained.

The fluctuation component of the electrolytic current has a well-known relation for the mass flux of depositing ion at an electrode surface, i.e.

$$\vec{n} \cdot \vec{j}(x, y, z, t) = -nFD\{\vec{n} \cdot \nabla c(x, y, z, t)\}_{z=Z} \quad [26]$$

Since the current density is conserved in the solution, the following conservative equation for current fluctuation is derived

$$\nabla \cdot \vec{j} = 0 \quad [27]$$

The increment of the surface potential due to surface deformation (11) is given as

$$\phi(x, y, t) = -\Omega\gamma \nabla_{\perp}^2 \zeta(x, y, t) \quad [28]$$

where γ is the surface energy of the electrode.

Derivation of dsi equation.—Before treating all the equations with regard to various fluctuations, we have to solve Eq. [1] for the case of galvanostatic dif-

fusion. Fortunately, this solution for surface concentration is the well-known Sand's equation (8)

$$C^*(z = Z^*) = C^*(z = \infty) + \frac{2J_z^*}{nF} \sqrt{\frac{t}{\pi D}} \quad [29]$$

As shown in the previous paper (2), as long as the fluctuation is small compared with the nondisturbed component, an arbitrary fluctuation can be decomposed into numerous Fourier components as well as the concentration fluctuation in Eq. [3]. The fluctuation of the surface irregularity is

$$\zeta_k(x, y, t) = \zeta^{\circ}(t) \exp[i(k_x x + k_y y)] \quad [30]$$

The current density fluctuation in the z-direction is

$$j_{zk}(x, y, z, t) = j_z^{\circ}(z, t) \exp[i(k_x x + k_y y)] \quad [31]$$

The fluctuation of the concentration overpotentials is

$$\eta_k(x, y, z, t) = \eta^{\circ}(z, t) \exp[i(k_x x + k_y y)] \quad [32]$$

whether or not this system is stable can be completely determined by examining the above components with a single set of wave numbers, (k_x, k_y) .

Substituting Eq. [3], [5], [29], [30], [31], and [32] into Eq. [12], [20], [22], [25], [26], and [28], respectively, and making the procedure similar to that in the preceding paper (2), the dsi equation is obtained as follows (see Appendix)

Step 1: $0 \leq t \leq t^*$

$$\begin{aligned} & \ln\{\zeta_k(x, y, t)/\zeta_k(x, y, 0)\} \\ &= -\frac{\sigma\Omega^2\gamma k^3 t}{(nF)^2} + \frac{\pi\sigma\Omega RTk}{2D(nF)^4 J_z^{*2}} (-nFJ_z^* + \Omega\gamma\sigma k^2) \\ & \cdot \left\{ \alpha \ln \left(\frac{\alpha}{\alpha + 2nFJ_z^* \sqrt{Dt/\pi}} \right) + 2nFJ_z^* \sqrt{Dt/\pi} \right\} \\ & \quad - \frac{D_{\text{ad}}C_{\text{ad}}^* \Omega^2 \gamma t}{RT} k^4 \quad [33] \end{aligned}$$

where $\alpha = D(nF)^2 C^*(z = \infty) + \sigma RT$, and t^* denotes the transition time when the surface concentration of the depositing ion falls to zero, or

$$t^* = \frac{\pi D(nF)^2 C^*(z = \infty)^2}{4J_z^{*2}} \quad [34]$$

Step 2: $t > t^*$

$$\begin{aligned} & \ln\{\zeta_k(x, y, t)/\zeta_k(x, y, 0)\} \\ &= -\frac{\pi\sigma\Omega^2 D\gamma C^*(z = \infty) k^3}{4J_z^{*2}} \\ & + \frac{\pi\sigma\Omega RTk}{2D(nF)^4 J_z^{*2}} (-nFJ_z^* + \Omega\gamma\sigma k^2) \\ & \cdot \left\{ \alpha \ln \left(\frac{\alpha}{\sigma RT} \right) - D(nF)^2 C^*(z = \infty) \right\} \\ & \quad - \frac{\Omega J_z^* k}{nF} (t - t^*) - \frac{D_{\text{ad}}C_{\text{ad}}^* \Omega^2 \gamma t}{RT} k^4 \quad [35] \end{aligned}$$

These results indicate that the surface diffusion term, $D_{\text{ad}}C_{\text{ad}}^* \Omega^2 \gamma k^4 t / RT$, simply adds to the dsi equations which were previously derived. Thus, the following approximated equations are obtained

$0 \leq t \leq t^*$

$$\begin{aligned} & \ln\{\zeta_k(x, y, t)/\zeta_k(x, y, 0)\}_{\text{app}} \\ &= \frac{\Omega t k}{nFRT} \left[-RTJ_z^* - \Omega\gamma k^2 \left\{ nFDC^*(z = \infty) \right. \right. \\ & \quad \left. \left. + \frac{4}{3} J_z^* \sqrt{\frac{Dt}{\pi}} \right\} \right] - \frac{D_{\text{ad}}C_{\text{ad}}^* \Omega^2 \gamma t}{RT} k^4 \quad [36] \end{aligned}$$

² According to the measurements by Bockris *et al.* (6, 7), the equilibrium concentration of adatoms at Ag electrode does not depend upon the bulk concentration of Ag ions and is likely to keep constant.

and

$t > t^*$

$\ln\{\xi_k(x, y, t)/\xi_k(x, y, 0)\}_{\text{app}}$

$$= \frac{\Omega k}{3nFRT} \left\{ -3RTJ_z^* t - nFD\Omega\gamma C^*(z = \infty)t^*k^2 \right\} - \frac{D_{\text{ad}}C_{\text{ad}}^*\Omega^2\gamma t}{RT} k^4 \quad [37]$$

Because the surface diffusion term always takes negative value and has the 4th power of wave number, it is concluded that the surface diffusion suppresses the unstable growth. Considering the relationship between the wave number and the wavelength ($\lambda = 2\pi/k$) it is predicted that the effect of the surface diffusion becomes significant with the decreasing crystal size.

Discussion

Occurrence of unstable growth.—From the dsi equations obtained, it is concluded that the dsi becomes positive for certain wave numbers only when the current density is negative, and that the dsi is negative for all wave numbers when the current density is positive. This means that the crystal growth becomes unstable only in cathodic deposition; i.e., the initial surface fluctuations in thermodynamic equilibrium develop with increasing time until the surface irregularities macroscopically emerge.

The process of the unstable growth is schematically explained in Fig. 2. In cathodic deposition, the concentration of the depositing ion increases with increasing distance from the electrode surface, so that the top parts of the surface fluctuation tend to protrude into higher concentration regions of the solution than the bottoms. Thus, the mass flux at the top becomes larger than the bottom. Moreover, the concentration in the neighborhood of the top parts is prevented from reducing by the following manner. The surface potential ($\phi[x, y, t]$) is positive at a convex part, where the fluctuation of the cathodic current density ($j_z[x, y, z, t]$) in the z -direction takes a negative value because the nonfluctuated cathodic current is defined negative and the mass transfer of ionic species is greater than that of concave parts. So, $\int_z^\infty j_z(x, y, z, t) dz < 0$ is obtained. From Eq. [12], at a convex portion

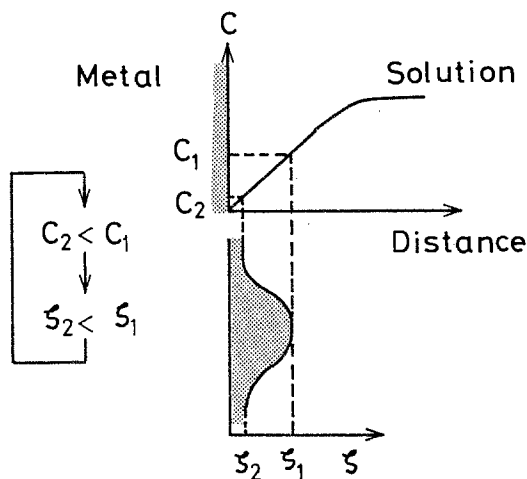


Fig. 2. Process of the occurrence of instability. In cathodic deposition, the concentration distribution of metal ions has a positive slope, so that the higher part (ξ_1) of the surface irregularity tends to protrude into higher concentration region than the lower part (ξ_2). The surface concentration of metal ion C_1 at ξ_1 becomes higher than C_2 at ξ_2 . The mass flux at ξ_1 increases more rapidly than at ξ_2 ; the higher the part, the more projects.

$$\eta(x, y, Z, t) = -\frac{1}{\sigma} \int_z^\infty j_z(x, y, z, t) dz + \frac{\phi(x, y, t)}{nF} > 0 \quad [38]$$

is derived. In other words, the concentration overpotential fluctuation, $\eta(x, y, Z, t)$ at a convex portion is positive. Therefore, using Eq. [25], the surface concentration fluctuation, $c(x, y, Z, t)$, at a top part is found to be positive, while $c(x, y, Z, t)$ at the bottom is negative. As a result, a convex part is always surrounded by higher concentration of the depositing ion than is a concave part. This effect is thought to support the unstable process mentioned above, so that the unstable growth proceeds.

Effect of the surface diffusion of adatoms.—Using the relationship obtained, dsi- λ curves were tentatively drawn (Fig. 3). The value of concentration C_{ad}^* , 8.0×10^{-6} mol/m², was obtained by averaging the experimental data of Bockris *et al.* (6, 7). It was found that every dsi- λ curve has a maximum value, dsi_{max}. It and the corresponding wavelength, λ_{max} , were plotted against the deposition time, as shown in Fig. 4 and 5.

In Fig. 4, it can be seen that as the deposition time elapses, due to the effect of the surface diffusion, the increasing rate of the dsi_{max} becomes slower than that in the case disregarding such effect. On the other hand, the surface diffusion affects the value of λ_{max} more drastically than that of dsi_{max}. Figure 5 indicates the result of a comparison of λ_{max} considering the effect of the surface diffusion with λ_{max} neglecting it. In the case where the surface diffusion is hindered, λ_{max} rapidly decreases with the deposition time. In such case, it can be expected that as time elapses, much more pronounced nucleation growth successively takes place, so that the average crystal dimension de-

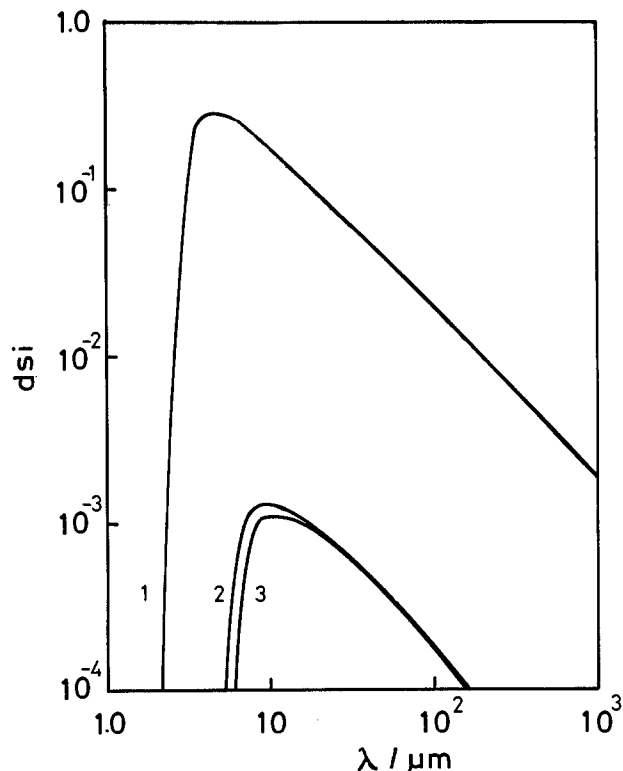


Fig. 3. Variation in the degree of surface irregularity (dsi) with wavelength (λ) in Ag deposition after a constant current step is applied: $J_z^* = -100$ Am⁻²; $C^*(z = \infty) = 56.8$ mol m⁻³; $\sigma = 1.7 \times 10^2$ Ω⁻¹m⁻¹; $\gamma = 1.1$ Jm⁻²; $D_{\text{ad}} = 2.2 \times 10^{-10}$ m²s⁻¹; $C_{\text{ad}}^* = 8.0 \times 10^{-6}$ mol m⁻²; $D = 1.55 \times 10^{-9}$ m²s⁻¹; $n = 1$; $F = 9.65 \times 10^4$ C eq⁻¹; $R = 8.31$ J deg⁻¹ mol⁻¹; $T = 300$ K; $\Omega = 1.05 \times 10^{-5}$ m³mol⁻¹. 1: $t = 10$ s; 2: $t = 1.0$ s; 3: $t = 0.1$ s.

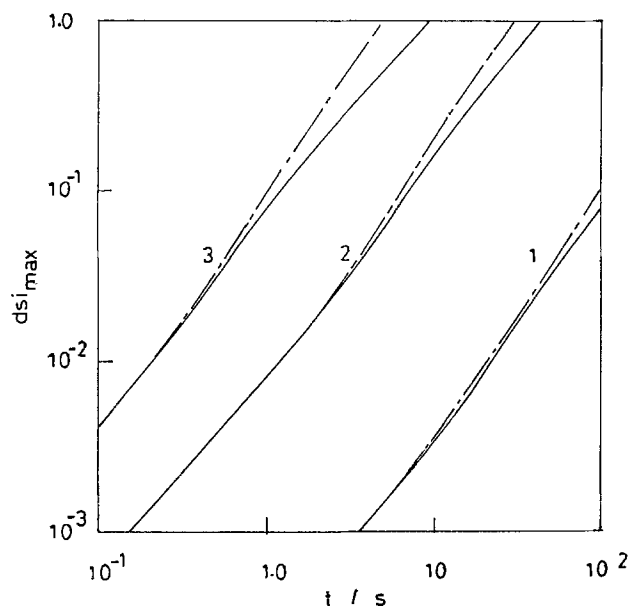


Fig. 4. Dependence of the maximum degree of surface irregularity (dsi_{max}) on the deposition time for various current densities at the bulk concentration of Ag ion. $C^*(z = \infty) = 56.8 \text{ mol m}^{-3}$; $\gamma = 1.0 \text{ Jm}^{-2}$. —: $D_{ad} = 2.2 \times 10^{-10} \text{ m}^2\text{s}^{-1}$; - - - -: $D_{ad} = 0.0 \text{ m}^2\text{s}^{-1}$. 1: $J_z^* = -50 \text{ Am}^{-2}$; 2: $J_z^* = -100 \text{ Am}^{-2}$; 3: $J_z^* = -300 \text{ Am}^{-2}$. Other data are the same as in Fig. 3.

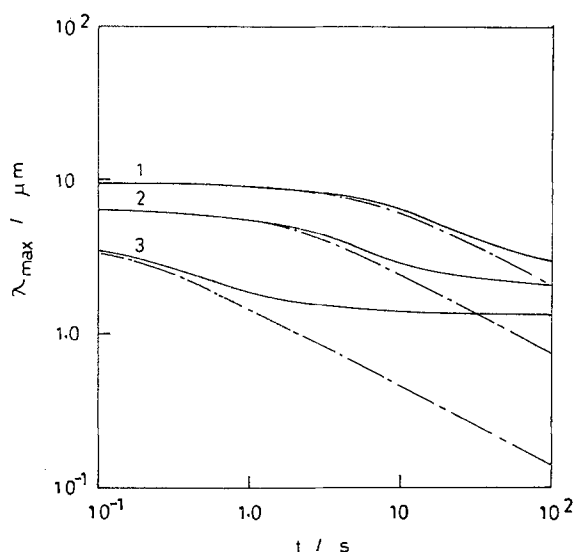


Fig. 5. Dependence of the wavelength (λ_{max}) corresponding to dsi_{max} on the deposition time for various current densities at the bulk concentration of Ag ion. $C^*(z = \infty) = 56.8 \text{ mol m}^{-3}$; $\gamma = 1.0 \text{ Jm}^{-2}$. —: $D_{ad} = 2.2 \times 10^{-10} \text{ m}^2\text{s}^{-1}$; - - - -: $D_{ad} = 0.0 \text{ m}^2\text{s}^{-1}$. 1: $J_z^* = -50 \text{ Am}^{-2}$; 2: $J_z^* = -100 \text{ Am}^{-2}$; 3: $J_z^* = -300 \text{ Am}^{-2}$. Other data are the same as in Fig. 3.

creases without limit with time. The growth rates of the crystals increase violently with the increasing time.

This prediction seems insufficient, particularly for the case where λ_{max} starts to decrease to an infinitesimal value at a relatively early stage of the deposition; we have not observed such extremely small particles as were predicted. If we introduce the effect of the surface diffusion, λ_{max} indeed decreases at an early stage, but finally converges a certain finite value; obviously, such insufficiency as was mentioned above is improved.

This tendency becomes much clearer for the case of low bulk concentration and high current density. Figure 6 shows the time dependence of dsi_{max} in the case of flow concentration, and Fig. 7 represents the relationship between the deposition time and λ_{max} in the same case. As shown in Fig. 6, the surface diffusion

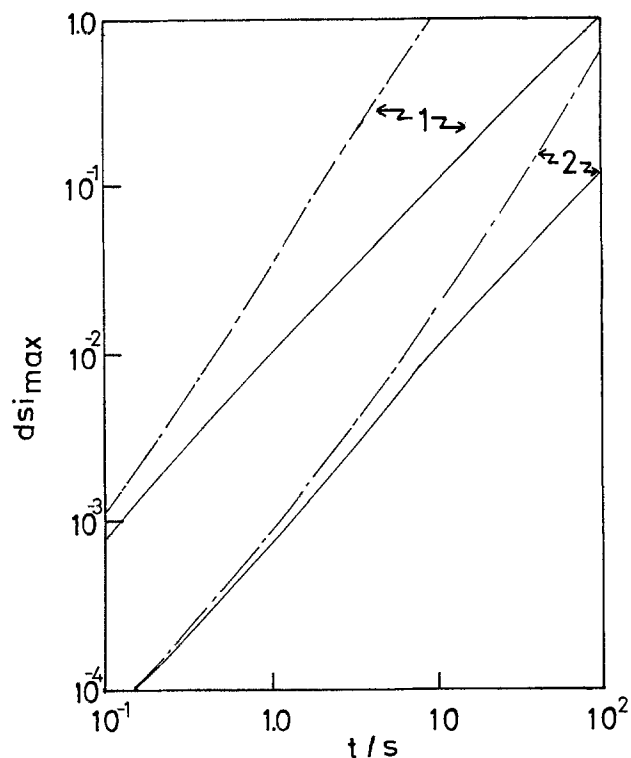


Fig. 6. Plots of the dsi_{max} vs. the deposition time for the galvanostatic Ag deposition on an Ag electrode at the bulk concentration of 5.68 mol m^{-3} . $\gamma = 1.0 \text{ Jm}^{-2}$. —: $D_{ad} = 2.2 \times 10^{-10} \text{ m}^2\text{s}^{-1}$; - - - -: $D_{ad} = 0.0 \text{ m}^2\text{s}^{-1}$. 1: $J_z^* = -50 \text{ Am}^{-2}$; 2: $J_z^* = -10 \text{ Am}^{-2}$. Other data are the same as in Fig. 3.

drastically hinders the increase of the dsi_{max} value. In Fig. 7, it is shown that λ_{max} vs. deposition time behaves much differently from that displayed in Fig. 5; from the early stage, it takes a constant value and decreases no more with time.

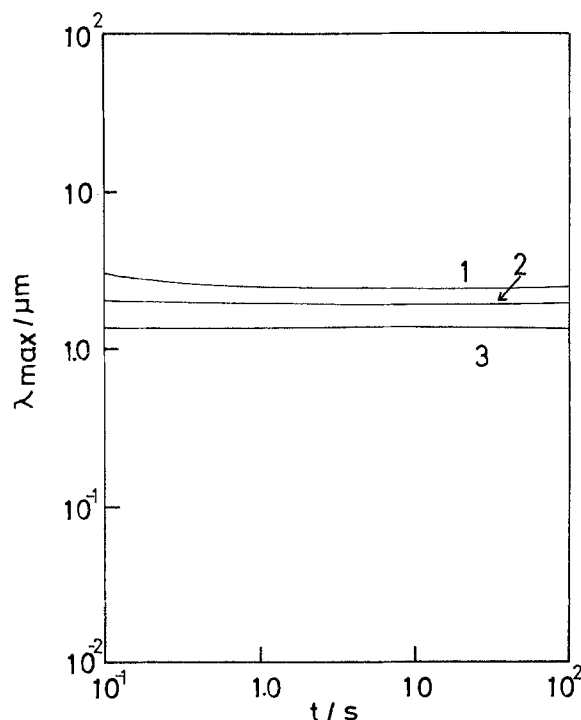


Fig. 7. Plots of λ_{max} vs. the deposition time for the galvanostatic Ag deposition on an Ag electrode at the bulk concentration of 5.68 mol m^{-3} . $\gamma = 1.0 \text{ Jm}^{-2}$. 1: $J_z^* = -50 \text{ Am}^{-2}$; 2: $J_z^* = -100 \text{ Am}^{-2}$; 3: $J_z^* = -300 \text{ Am}^{-2}$. Other data are the same as in Fig. 3.

Applying the conclusion obtained above to the actual system, it can be said that the particle sizes do not change after a long time passes. However, if the surface diffusion of adatoms is suppressed by some reasons, for example, the competitive adsorption of other species (which has an inhibiting effect for the metal adatoms), the theory disregarding the surface diffusion may still be important. In that case, nucleation growth may occur vigorously everywhere on the electrode surface.

Conclusion

Because of the large contribution of the surface diffusion of adatoms during galvanostatic deposition it can be proved that particle size decreases with deposition time into the infinitesimal dimension. After a certain period of time, the crystals formed on the electrode tend to keep their sizes constant. At the same time, the growth rate of the crystal is somewhat suppressed. However, when the surface diffusion of adatoms is blocked by the intense adsorption of other chemical species, the equations neglecting the surface diffusion are, as before, important to explain the rapid growth of minute crystal particles.

Manuscript submitted Nov. 29, 1982; revised manuscript received ca. July 26, 1983.

The Institute of Vocational Training assisted in meeting the publication costs of this article.

APPENDIX

On taking each variation of $\vec{J}(x, y, z, t)$, $V(x, y, z, t)$, $H(x, y, z, t)$, and $\Phi(x, y, t)$ in Eq. [9] and using Eq. [8], the following equation is obtained

$$\vec{j} = \nabla\eta(x, y, z, t) - \frac{\phi(x, y, t)}{nF} \delta(z - Z) \quad [\text{A-1}]$$

Substituting Eq. [A-1] into Eq. [27] in the solution, it follows that

$$\nabla^2\eta(x, y, z, t) = 0 \quad [\text{A-2}]$$

The fluctuations can be expressed in terms of their numberless Fourier components, so that Eq. [A-2] must also hold for $\eta_k(x, y, z, t)$ with a single set of wave numbers, k_x and k_y . Substituting Eq. [32] into Eq. [A-2], and adopting a boundary condition ($\eta_k[x, y, z, t] \rightarrow 0$ at $z \rightarrow \infty$), the solution of $\eta_k(x, y, z, t)$ is derived as

$$\eta_k(x, y, z, t) = B_1 e^{-kz} \xi(t) \exp[i(k_x x + k_y y)] \quad [\text{A-3}]$$

where $\xi(t)$ is an arbitrary function of t , and B_1 is an arbitrary constant. From Eq. [A-3], it is obvious that the z -component, $j_{zk}(x, y, z, t)$, has the following relationship with $\eta_k(x, y, z, t)$ in an electrolyte solution

$$j_{zk}(x, y, z, t) = \sigma \frac{\partial}{\partial z} \eta_k(x, y, z, t) \quad [\text{A-4}]$$

By means of Eq. [31], [A-3] and [A-4], $j_{zk}(x, y, z, t)$ is explicitly expressed as

$$j_{zk}(x, y, z, t) = -\sigma B_1 k e^{-kz} \xi(t) \exp[i(k_x x + k_y y)] \quad [\text{A-5}]$$

On the other hand, as far as the surface irregularity is small, normal unit vector (\vec{n}) of the surface can be approximated parallel to the z -axis, so that Eq. [26] can be rewritten as

$$j_{zk}(x, y, z, t) = -nFD \left\{ \frac{\partial c_k(x, y, z, t)}{\partial z} \right\} \text{ for } z = Z \quad [\text{A-6}]$$

Using Eq. [3], [A-3], and [A-6], current density fluctuation ($j_{zk}[x, y, z, t]$) has a relation with concentration fluctuation, ($c_k[x, y, z, t]$) at the electrode surface

$$j_{zk}(x, y, Z, t) = -nFDkc_k(x, y, Z, t) \quad [\text{A-7}]$$

A substitution of Eq. [22] into Eq. [25] yields the following equation

$$\eta_k(x, y, Z, t) = \frac{RT}{nF} \frac{c_k(x, y, Z^*, t) + L(t) \zeta_k(x, y, t)}{C^*(Z, t)} \quad [\text{A-8}]$$

From Eq. [28] and [32], the relation between ϕ_k and ζ_k is obtained

$$\zeta_k(x, y, t) = \Omega\gamma k^2 \phi_k(x, y, t) \quad [\text{A-9}]$$

where $\zeta_k(x, y, t)$ is surface potential with a single set of wave number. By means of Eq. [A-5] and [A-7], the equation

$$\int_Z^\infty j_{zk}(x, y, z, t) dz = nFDc_k(x, y, Z^*, t) \quad [\text{A-10}]$$

is derived. Substitution of Eq. [A-8], [A-9], and [A-10] into Eq. [12] yields the following equation

$$c_k(x, y, Z, t) = \frac{\sigma\{\Omega\gamma C^*(z = Z^*)k^2 - RTL(t)\}}{(nF)^2 DC^*(z = Z^*) + \sigma RT} \zeta_k(x, y, t) \quad [\text{A-11}]$$

Using Eq. [A-6] and [A-7], it follows that

$$\left\{ \frac{\partial c_k(x, y, z, t)}{\partial z} \right\}_{z=Z^*} = -kc_k(x, y, Z^*, t) \quad [\text{A-12}]$$

From Eq. [20], the following equation concerning the fluctuation components having a single set of wave number is obtained

$$\frac{1}{\Omega} \frac{\partial \zeta_k(x, y, t)}{\partial t} = \frac{D_{ad}}{RT} C_{ad}^* \nabla^2 \zeta_k(x, y, t) + D \left\{ \frac{\partial c_k(x, y, z, t)}{\partial z} \right\}_{z=Z^*} \quad [\text{A-13}]$$

Substituting Eq. [A-9], [A-11], and [A-12] into Eq. [A-13], one finally derives the dsi equation

$$\ln \{\zeta_k(x, y, t)/\zeta_k(x, y, 0)\} = \int_0^t f(k, t) dt \quad [\text{A-14}]$$

where

$$f(k, t) = \frac{\sigma\Omega Dk\{RTL(t) - \Omega\gamma C^*(z = Z^*)k^2\}}{(nF)^2 DC^*(z = Z^*) + \sigma RT} - \frac{D_{ad}C_{ad}^*\Omega^2\gamma}{RT} k^4 \quad [\text{A-15}]$$

LIST OF SYMBOLS

t	deposition time, s
t^*	transition time when surface concentration falls to zero, s
x, y, z	variables in Cartesian-coordinate system, m
Z	electrode surface height, m
Z^*	nonperturbed component of Z , m
$Z + 0$	the interface between the double layer and the solution, m
$Z - 0$	the interface between the double layer and the crystal lattice, m
$\zeta(x, y, t)$	fluctuation component of the surface height, m
$\zeta_k(x, y, t)$	equation of $\zeta(x, y, t)$ with a single set of wave numbers (k_x, k_y), m
$\zeta^0(t)$	amplitude of $\zeta_k(x, y, t)$, m
$C(x, y, z, t)$	concentration of depositing ion, mol m^{-3}
$C^*(z, t)$	nonperturbed component of $C(x, y, z, t)$, mol m^{-3}
$C^*(z = \infty)$	bulk concentration of depositing ion, mol m^{-3}
$C^*(z = Z)$	nonperturbed component of $C(x, y, z, t)$ at $z = Z$, mol m^{-3}
$C^*(z = Z^*)$	nonperturbed component of $C(x, y, z, t)$ at $z = Z^*$, mol m^{-3}
$c(x, y, z, t)$	fluctuation component of $C(x, y, z, t)$, mol m^{-3}
$c_k(x, y, z, t)$	equation of $c(x, y, z, t)$ with a single set of wave numbers [k_x, k_y], mol m^{-3}
$c^0(z, t)$	amplitude of $c_k(x, y, z, t)$, mol m^{-3}
$C_{ad}(x, y, t)$	adatom concentration, mol m^{-2}
C_{ad}^*	equilibrium adatom concentration, mol m^{-2}
$J(x, y, z, t)$	current density, $A m^{-2}$
$J_z^*(t)$	nonperturbed z -component of $\vec{J}(x, y, z, t)$, $A m^{-2}$

$\vec{j}(x, y, z, t)$	fluctuation component of $\vec{J}(x, y, z, t)$, $A\ m^{-2}$	k_x, k_y	x - and y -components of wave number, m^{-1}
$j_z(x, y, z, t)$	z -component of $j(x, y, z, t)$, $A\ m^{-2}$	n	electron number exchanging at the electrode per one species
$j_{zk}(x, y, z, t)$	equation of $j_z(x, y, z, t)$ with a single set of wave numbers ($[k_x, k_y]$), $A\ m^{-2}$	\vec{n}	unit vector normal to the electrode surface
$j_z^\circ(z, t)$	amplitude of $j_{zk}(x, y, z, t)$, $A\ m^{-2}$	Φ	surface potential arising from surface deformation, $J\ mol^{-1}$
\vec{J}_{surf}	mass flux of adatom, $mol^{-1}m^{-1}$	ϕ	perturbed component of Φ , $J\ mol^{-1}$
$J_{flux}(z = Z + 0)$	mass flux of depositing ions entering vertically to the double layer, $mol^{-1}m^{-2}$	$\Psi(x, y, z, t)$	electrochemical potential of depositing ions, V
$J_{flux}(z = Z - 0)$	mass flux of adatoms coming in and out of the interface between the double layer and the metal lattice, $mol^{-1}m^{-2}$	$\delta\Psi(x, y, z, t)$	variation of $\Psi(x, y, z, t)$, V
$V(x, y, z, t)$	electrode potential, V	α	$= D(nF)^2 C^*(z = \infty) + \sigma RT$
$V(z = \infty)$	$V(x, y, z, t)$ at the bulk solution, V	$\beta(t)$	arbitrary function of deposition time
$\delta V(x, y, z, t)$	variation of $V(x, y, z, t)$, V	$\xi(t)$	arbitrary function of deposition time
$H(x, y, z, t)$	concentration overpotential of depositing ion, V	λ	wave length, m
$H(z = \infty)$	$H(x, y, z, t)$ at the bulk solution, V	λ_{max}	wave length corresponding to dsi_{max} , m
$H^*(z = Z^*)$	nonperturbed component of $H(x, y, z, t)$ at $z = Z^*$, V	$\delta(z - Z)$	$\delta = \{0, 0, \delta(z - Z)\}$
$\eta(x, y, z, t)$	fluctuation component of $H(x, y, z, t)$, V	$\delta(z - Z)$	δ -function
$\eta_k(x, y, z, t)$	equation of $\eta(x, y, z, t)$ with a single set of wave numbers (k_x, k_y), V	γ	surface energy, Jm^{-2}
$\eta^\circ(z, t)$	amplitude of $\eta_k(x, y, z, t)$, V	Ω	molar volume of crystal, m^3mol^{-1}
D	diffusion coefficient of depositing ions, m^2s^{-1}	σ	electric conductivity, $\Omega^{-1}m^{-1}$
D_{ad}	surface diffusion coefficient of adatoms, m^2s^{-1}	∇	$= (\partial/\partial x, \partial/\partial y, \partial/\partial z)$
F	Faraday constant, $96,500\ C\ eq^{-1}$	∇_{\perp}	$= (\partial/\partial x, \partial/\partial y)$
R	gas constant, $8.31\ Jdeg^{-1}mol^{-1}$		
T	absolute temperature, K		
$L(t)$	concentration gradient of depositing ion at the electrode surface, $mol\ m^{-4}$		
A_1	arbitrary constant, $mol\ m^{-3}$		
A_2	arbitrary constant, $mol\ m^{-3}$		
B_1	arbitrary constant, $mol\ m^{-3}$		
b	mobility of adatom, $mol\ m^{-2}J^{-1}s^{-1}$		
dsi	degree of surface irregularity		
dsi_{max}	maximum value of dsi		
\vec{f}	motive force on the electrode surface, Nm^{-1}		
i	$\equiv \sqrt{-1}$		
k	wave number, m^{-1}		

REFERENCES

1. R. Aogaki, K. Kitazawa, Y. Kose, and K. Fueki, *Electrochim. Acta*, **25**, 965 (1980).
2. R. Aogaki and T. Makino, *ibid.*, **26**, 1509 (1981).
3. R. Aogaki, *This Journal*, **129**, 2442 (1982).
4. R. Aogaki, *ibid.*, **129**, 2447 (1982).
5. J. Newman, "Electrochemical System," Chap. 11, Sec. 73, Prentice-Hall, Inc., Englewood Cliffs, NJ (1973).
6. W. Mehl and J. O' Bockris, *Can. J. Chem.*, **37**, 190 (1959).
7. W. Mehl and J. O. Bockris, *J. Chem. Phys.*, **27**, 817 (1957).
8. K. J. Vetter, "Electrochemical Kinetics," p. 207, Academic Press, New York (1967).
9. T. Makino and R. Aogaki, *Denki Kagaku*, **51**, 287 (1983).
10. P. Glansdorff and I. Prigogine, "Thermodynamic Theory of Structure, Stability and Fluctuations," Chap. 2, Wiley-Interscience, London (1971).

Morphological Instability in Nonsteady Galvanostatic Electrodeposition

II. Experimental Demonstration of the Surface Diffusion Effect of Adatoms by Means of Image Analysis

Ryoichi Aogaki and Tohru Makino¹

Department of Chemistry, The Institute of Vocational Training, 1960, Aihara, Sagamihara, 229, Japan

ABSTRACT

In nonsteady galvanostatic deposition, where the surface diffusion of adatoms often plays an important role, the variations in surface morphology of electrodes during deposition was examined experimentally. When the surface diffusion can be ignored, as has been reported, nucleation growth caused by high supersaturation of adatoms at an electrode surface is so violent that the average crystal size becomes smaller with increasing deposition time. In extreme cases particle dimensions diverge into zero after long periods. A large discrepancy exists between the actual deposition and theoretical prediction. To deal with this difficulty, the introduction of surface diffusion is sufficient. Surface diffusion tends to suppress the development of the surface irregularities arising from nucleation growth, and consequently the average size of the crystals formed on the electrode increases somewhat with increasing deposition time. This was ascertained by several experiments concerning Ag deposition on Ag electrodes.

As shown in the previous paper (1), the surface diffusion of adatoms in galvanostatic deposition becomes

very important when the deposition occurs at low concentration and high current density. Under such conditions, electrodeposition theoretically allows the crystal sizes formed on electrode surface to decrease infinitely, since many crystal peaks continuously emerge through the nucleation because of the high

¹ Present address: AHS Japan Company, 2-10-12, Akasaka, Minato-ku, 107, Japan.

Key words: galvanostatic deposition, unstable crystal growth, morphology, image analysis.

supersaturation of adatoms. The surface diffusion seems to relieve such difficulty. In Ref. (1), it is predicted that the crystal size reaches a constant value after a certain deposition time elapses.

However, that prediction concerning the surface diffusion effect was derived from the behavior of $dsi-\lambda$ curves, not from the actually calculated crystal sizes, which are obtained only from three-dimensional contour plotting by means of computer graphics.

In the present paper, using the procedures of calculation obtained from another previous paper (2), we simulated the surface morphology in view of the surface-diffusion effect to obtain the crystal-size distribution. After a comparison of the results with experimental data given by image analysis of SEM photographs of electrodeposited surface, the effect of surface diffusion on crystal particle size was examined.

Experimental

Experiments were carried out for Ag deposition on Ag electrodes in a solution of $AgClO_4$ with a supporting electrolyte of $1M HClO_4$. The Ag electrodes were polycrystallines with $0.5 cm^2$ area, and they were 99.99% pure. They were chemically polished in a chromic acid/hydrochloric acid/nitric acid mixture, according to the Levinstein and Robinson method (9). Immediately after washing them several times in twice-distilled water with a supersonic washer, the polished planar electrode was set on an electrode cell and soaked in the electrolytic solution. The electrode cell was mainly composed of Teflon plates (see Fig. 1). So electrodes could be easily attached to the cell, they were inserted from the back of the cell using a screwed Teflon rod connected with a Pt wire. All the experiments were carried out in the stationary solution. Thus, the solution near the electrode surface was protected from any movement of the solution by the cylindrical wall part of a Teflon plate in front of the electrode. The Teflon plate and electrode were made to come closely into contact to inhibit the disturbance caused by the leakage of the solution through the gap between them. Then, the cell was immersed in the solution for the polished surface to face downward. This prevented the agitation of the solution from natural convection because the liquid containing a large amount of depositing ions was heavier than the dilute one. Consequently, potential-time curves under galvanostatic conditions were in good agreement with those predicted by the usual nonsteady diffusion equation (3).

The electrolytes used were $AgClO_4$ and $HClO_4$, both of reagent grade and made by Wako Pure Chemical Industries. The solutions were prepared with twice-

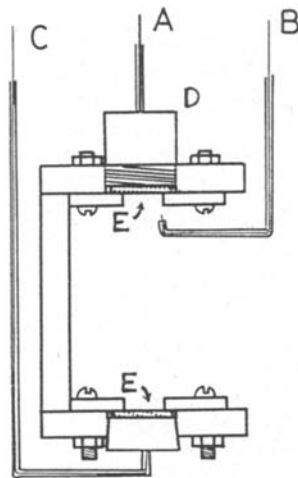


Fig. 1. Schematic representation of the electrolytic cell. A: working electrode; B: reference electrode; C: counterelectrode; E: Ag plate.

distilled water and they were deaerated before and after each experiment with bubbling nitrogen. Immediately after being deposited galvanostatically for a given period of time, the samples were again rinsed to be dried by N_2 gas. SEM photographs of the samples were then taken. From the photographs, the statistical properties of the crystal size, including the average diameter and standard deviation, were computed by means of a Toyo Ink Company, Luzex 500 Image Analyzer. The diameter of a crystal was defined as that of a circle equivalent to the area.

Calculations

The surface morphology was drawn in three-dimensional contour plotting, which was calculated in accordance with the procedures mentioned previously (2). Assuming a rectangular electrode surface divided into a mesh of 128×128 points, random numbers generated by computer were assigned to each point. Interpolation between neighboring mesh-point data yielded a matrix with 256×256 data points, which corresponded to the initial fluctuation ($\zeta[x, y, 0]$) of surface height arising from microscopic deposition and dissolution of metal.

The initial fluctuation ($\zeta[x, y, 0]$) exists in thermodynamic equilibrium between metal adatoms and ions near the electrode. When the ions are deposited on the surface by the application of a current galvanostatically, the electrode system transfers to a nonequilibrium state. Subsequently, the metal ions successively diffuse according to the electrode reaction. Initial microscopic surface fluctuations simultaneously develop to yield many macroscopic crystal peaks. This process can be expressed in the following equation of Fourier image functions

$$Z(k_x, k_y, t) = F(k_x, k_y, t) Z(k_x, k_y, 0) \quad [1]$$

where $Z(k_x, k_y, 0)$ and $Z(k_x, k_y, t)$ are the image functions of the initial surface fluctuation and the fluctuation at $t = t$, respectively. $F(k_x, k_y, t)$ is the transfer function concerning galvanostatic deposition. This is described by two different expressions of dsi which are given in Ref. (1).

$$t \leq t^*$$

$$F(k_x, k_y, t) = \exp \left[\frac{\Omega t k}{nFRT} \left\{ -RTJ_z^* - \Omega \gamma k^2 \left(nFDC^*(z = \infty) + \frac{4}{3} J_z^* \sqrt{\frac{Dt}{\pi}} \right) - \frac{D_{ad} C_{ad}^* \Omega^2 \gamma t}{RT} k^4 \right\} \right] \quad [2]$$

$$t^* < t$$

$$F(k_x, k_y, t) = \exp \left[\frac{\Omega k}{3nFRT} \left\{ -3RTJ_z^* t - nFD\Omega \gamma C^*(z = \infty) t^* k^2 \right\} - \frac{D_{ad} C_{ad}^* \Omega^2 \gamma t}{RT} k^4 \right] \quad [3]$$

where t^* denotes the transition time when the surface concentration of depositing ions falls to zero, or

$$t^* = \frac{\pi D (nF)^2 C^*(z = \infty)^2}{4J_z^{*2}} \quad [4]$$

All the notations of parameters in these equations are the same as in Ref. (1).

The initial surface fluctuation ($\zeta[x, y, 0]$) determined at the 256×256 data points was converted to its Fourier image function ($Z[k_x, k_y, 0]$) using two-dimensional Fourier transform for x - and y -coordinates. Describing the procedure mathematically

$$Z(k_x, k_y, 0) = \frac{1}{2\pi} \int_{-\infty}^{\infty} \int_{-\infty}^{\infty} \zeta(x, y, 0) \exp[-i(k_x x + k_y y)] dx dy \quad [5]$$

is obtained. Then, the image function ($Z[k_x, k_y, t]$) at $t = t$ is computed by means of Eq. [1]. Finally, surface morphology at $t = t$ is given by the following Fourier inversion

$$\zeta(x, y, t) = \frac{1}{2\pi} \int_{-\infty}^{\infty} \int_{-\infty}^{\infty} Z(k_x, k_y, t) \exp[i(k_x x + k_y y)] dk_x dk_y \quad [6]$$

From $\zeta(x, y, t)$, we know how the crystal peaks are distributed over the surface, which are defined as the parts above the root-mean-square height of $\zeta(x, y, t)$. Their average size and standard deviation can then be calculated. In these calculations, the surface diffusion coefficient and surface energy, which are unknown parameters, can be determined by curve fitting of the results to the experimental data.

Results and Discussion

Figure 2 is an SEM photograph of the minute crystal particles generated during galvanostatic deposition. Figure 3 represents the three-dimensional contour plotting of the surface morphology under the same conditions as in Fig. 2. Both figures have similar morphological features. Using the image analyzer, the crystal particles in Fig. 2 and 3 were converted into circles having areas equivalent to the particles. The diameters were defined as the crystal sizes. Figure 4 is a histogram of the crystal size distribution. It was obtained from the SEM photographs. From the surface morphology obtained theoretically, another histogram of crystal size distribution is given in Fig. 5. After confirming that the histograms had Gaussian distributions, the mean crystal sizes and standard deviations were obtained from both experiments and calculations.

At first, crystal size-time curves were experimentally obtained. Then, utilizing the surface diffusion coefficient and surface energy, which had already been determined by fitting the calculated data to observed ones, theoretical crystal size-time curves were calculated, where the average value of the data measured by Bockris *et al.* (4, 5) was used as the adatom concentration, *i.e.*, $C_{ad}^* = 8.0 \times 10^{-6} \text{ mol/m}^{-2}$. Figure 6 shows the results of the computation, where the diffusion coefficient determined is $D_{ad} = 1.6 \times 10^{-10} \text{ m}^2\text{s}^{-1}$, which is in good agreement with the value of $5.0 \times 10^{-10} \text{ m}^2\text{s}^{-1}$ predicted by Bockris *et al.* (8). In the figure, it is obvious that there is a large difference of the time dependence of crystal size as expected for the two cases, regardless of whether the surface diffusion is disregarded or not.

In the present case, the average size which is different from that in Ref. (7) increases to some extent

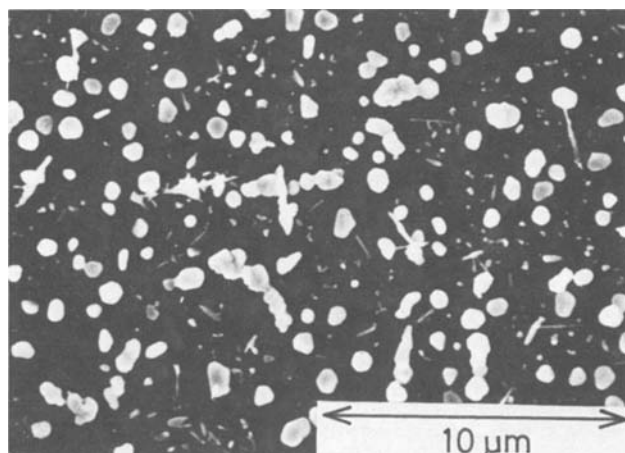


Fig. 2. SEM photograph of the crystal peaks formed on an Ag electrode in galvanostatic diffusion-controlled deposition in a solution of $56.8 \text{ mol/m}^{-3} \text{ AgClO}_4 + 10^3 \text{ mol/m}^{-3} \text{ HClO}_4$. Deposition time is 10s, and current density is -100 Am^{-2} .

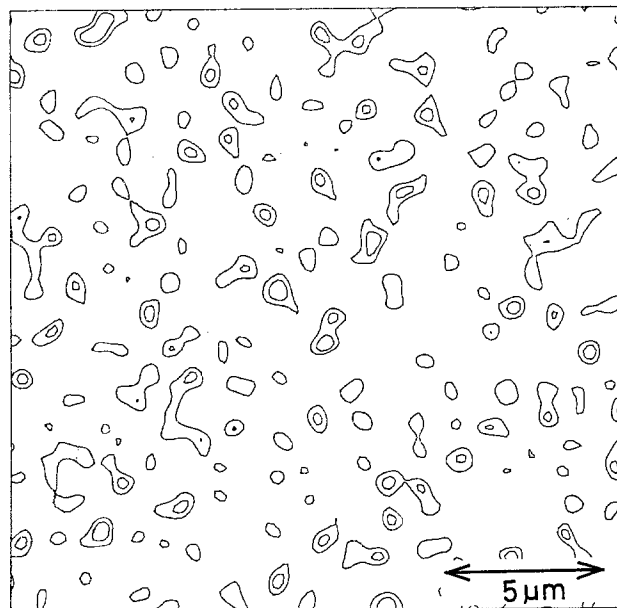


Fig. 3. Theoretical three-dimensional contour line plotting of an Ag surface deposited from a 56.8 mol m^{-3} Ag ionic solution with a large amount of supporting electrolyte at a time of 10s after a constant current step with a density of -100 Am^{-2} applied. Every contour line is plotted at intervals of the standard deviation of surface height. $D: 1.55 \times 10^{-9} \text{ m}^2\text{s}^{-1}$; $\gamma: 0.55 \text{ Jm}^{-2}$; $\Omega: 1.03 \times 10^{-5} \text{ m}^3\text{mol}^{-1}$; $\sigma: 1.7 \times 10^2 \text{ } \Omega^{-1}\text{m}^{-1}$; $D_{ad}: 1.6 \times 10^{-10} \text{ m}^2\text{s}^{-1}$; $C_{ad}^*: 8.0 \times 10^{-6} \text{ mol/m}^{-2}$; $T: 300\text{K}$.

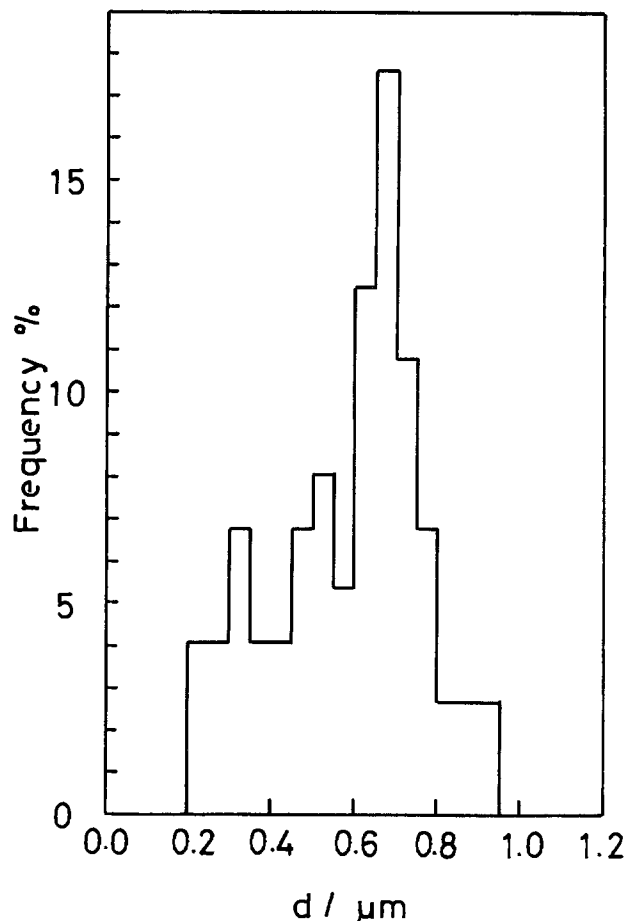


Fig. 4. Crystal size distribution formed on an Ag electrode in galvanostatic diffusion-controlled deposition in a solution of $56.8 \text{ mol m}^{-3} \text{ AgClO}_4 + 10^3 \text{ mol m}^{-3} \text{ HClO}_4$. Deposition time is 3.0s, and current density is -100 Am^{-2} . The size of a crystal is defined as the diameter of a circle equivalent to its area.

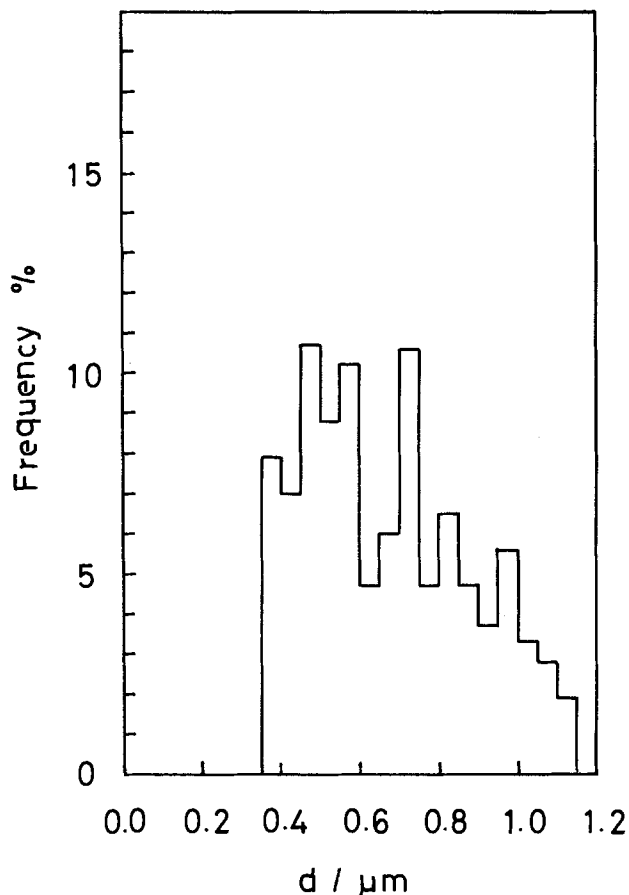


Fig. 5. Theoretical crystal size distribution formed on an Ag electrode in galvanostatic diffusion-controlled deposition in a 56.8 mol m^{-3} Ag ionic solution. Deposition time is 5.0s, and current density is -100 Am^{-2} . Crystal size is defined as the diameter of a circle equivalent to a peak area in a three-dimensional contour line plotting. Other parameters used for calculation are the same as in Fig. 3.

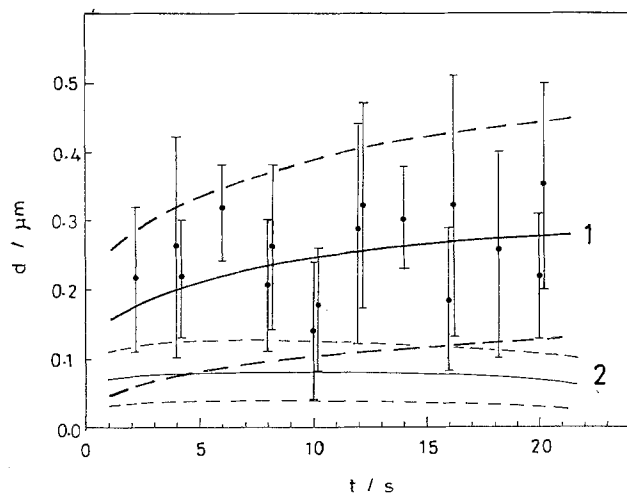


Fig. 6. Crystal size distribution developed on an Ag electrode as a function of deposition time. Bulk concentration is 5.68 mol m^{-3} , and current density is -10 Am^{-2} . Solid dots represent the average values of crystal sizes, and the bars above and below the dots are upper and lower error limits. The numbered curves correspond to the two cases. Curve 1; $D_{ad}: 1.6 \times 10^{-10} \text{ m}^2 \text{ s}^{-1}$. Curve 2; $D_{ad}: 0.0 \text{ m}^2 \text{ s}^{-1}$. Other parameters used for calculation are; $D: 1.55 \times 10^{-9} \text{ m}^2 \text{ s}^{-1}$; $\gamma: 1.9 \times 10^{-2} \text{ J m}^{-2}$; $\Omega: 1.03 \times 10^{-5} \text{ m}^3 \text{ mol}^{-1}$; $\sigma: 1.7 \times 10^2 \text{ J m}^{-2}$; $C_{ad}^*: 8.0 \times 10^{-6} \text{ mol m}^{-2}$; $T: 300\text{K}$.

with increasing time. In Ref. (7) it was shown that the average size decreases with deposition time. This

was attributed to the high supersaturation of adatoms, which promotes the successive formation of a number of new crystal nuclei. In order to better examine the surface diffusion effect, another experiment and calculation were carried out (see Fig. 7). Ignoring the surface diffusion, we see that at the beginning, the average crystal size increases with increasing time, and after reaching a maximum value at a certain deposition time, it begins to decrease with time. This means that the crystal growth originated by nucleation has a certain induction time, which was predicted in Ref. (6). The presence of the induction time may be because the supersaturation of adatoms drastically increases after surface concentration falls to zero.

However, the surface diffusion of adatoms mitigates the nucleation growth because deposited adatoms rapidly move to other active sites, such as kinks and steps.

The effect of current density on crystal growth was examined. Figure 8 shows the results at a current density higher than in Fig. 6. The bulk concentration was the same as in Fig. 6, and the values of the surface diffusion coefficient (D_{ad}) and the surface energy

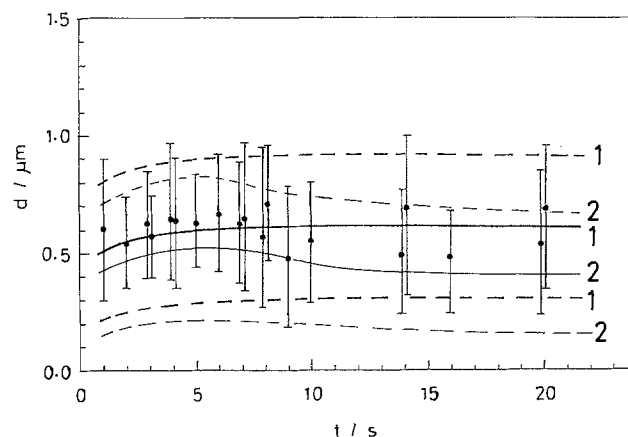


Fig. 7. Crystal size distribution developed on an Ag electrode as a function of deposition time. Bulk concentration is 56.8 mol m^{-3} , and current density is -100 Am^{-2} . Curve 1; $D_{ad}: 1.6 \times 10^{-10} \text{ m}^2 \text{ s}^{-1}$. Curve 2; $D_{ad}: 0.0 \text{ m}^2 \text{ s}^{-1}$. Other parameters used for calculation are the same as in Fig. 3.

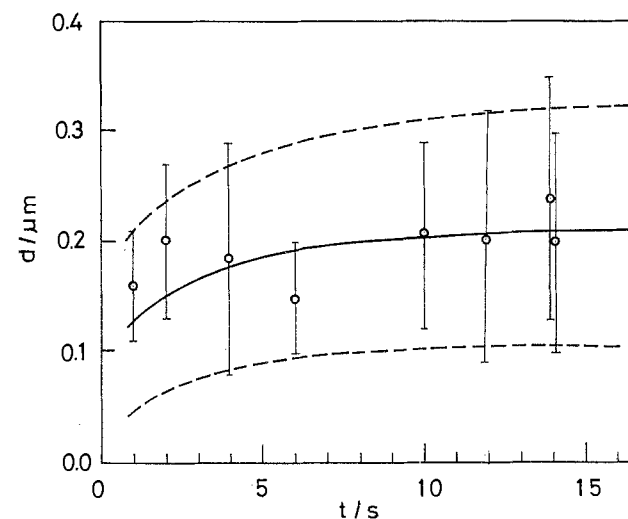


Fig. 8. Crystal size distribution developed on an Ag electrode as a function of deposition time. Bulk concentration is 5.68 mol m^{-3} , and current density is -50 Am^{-2} . Curve 1; $D_{ad}: 1.6 \times 10^{-10} \text{ m}^2 \text{ s}^{-1}$. Curve 2; $D_{ad}: 0.0 \text{ m}^2 \text{ s}^{-1}$. Other parameters used for calculation are the same as in Fig. 6.

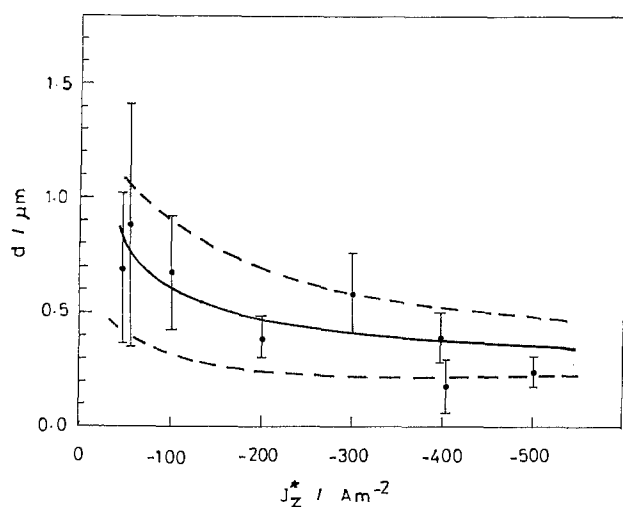


Fig. 9. Dependence of Ag crystal size distribution on the current density. Deposition time is 6.0s, and the bulk concentration of AgClO_4 in a 10^3 mol m^{-3} HClO_4 solution is 56.8 mol m^{-3} . Solid dots represent the average values of crystal sizes and, the bars above and below the dots are upper and lower error limits. The solid line is the theoretical average value and the dotted lines depict the theoretical upper and lower error limits. D : $1.55 \times 10^{-9} \text{ m}^2 \text{ s}^{-1}$; γ : 0.55 J m^{-2} ; Ω : $1.03 \times 10^{-5} \text{ m}^3 \text{ mol}^{-1}$; σ : $1.7 \times 10^2 \text{ } \Omega^{-1} \text{ m}^{-1}$; D_{ad} : $1.6 \times 10^{-10} \text{ m}^2 \text{ s}^{-1}$; C_{ad}^* : $8.0 \times 10^{-6} \text{ mol m}^{-2}$; T : 300K.

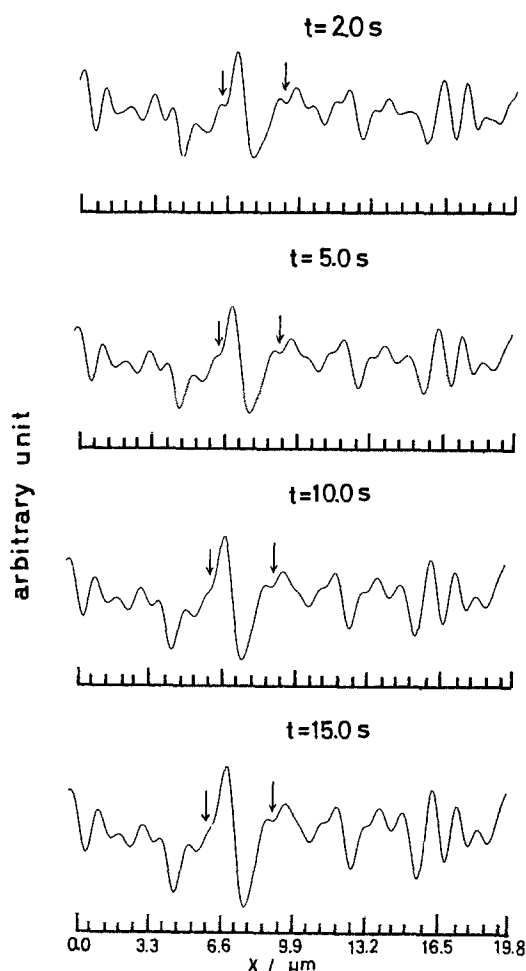


Fig. 10. Time variation in the height of the cross-sectional profile for the silver electrode surface at a given point ($y = 5.0 \text{ } \mu\text{m}$). Current density is -100 A m^{-2} , and bulk concentration is 56.8 mol m^{-3} . Other parameters are the same as in Fig. 9.

(γ) used for the calculations were also the same as in Fig. 6. The experimental values seem to agree well with the theoretical curves. This suggests that the electrode surface has values of D_{ad} and γ independent of the current density as long as the bulk concentration remains constant. In order to make sure of this fact, galvanostatic deposition with a constant bulk concentration was performed at various current densities. At the same time, the average size and its standard deviation of the crystals were calculated with the constant D_{ad} and γ which had already been obtained. As shown in Fig. 9, the experimental results are in good agreement with the theoretical computations. It can be concluded that in galvanostatic deposition, D_{ad} and γ depend only on the bulk concentration and not on the current density, and that the average size decreases with decreasing bulk concentration.

When surface diffusion does not contribute as much to crystal growth, many new crystal peaks emerge (7). This phenomenon was detected in profiles drawn by computer, such as appears in Fig. 10. It can be seen in Fig. 10 that the peaks do not develop vertically and that no new peaks protrude into the solution. This confirms that surface diffusion suppresses the development of the new crystals.

Conclusion

In galvanostatic deposition, the surface diffusion of adatoms becomes important at low bulk concentration and high current density, where the electrode surface has a tendency to form new crystal peaks with increasing time because of the high supersaturation of adatoms. If in this case the surface diffusion of the adatoms is hindered for some reason, the nucleation is likely to yield a number of small crystal peaks. Consequently, the average size of the crystal peaks decreases with increasing time. Also, it can be concluded that an induction period is needed for crystal formation arising from nucleation. At the beginning of deposition, supersaturation is not enough to generate new peaks due to nucleation, and so the peaks which have already existed grow to rather larger sizes. Minute new crystals start to grow when supersaturation reaches a sufficiently high value. The average particle size-deposition time curve, therefore, depicts one maximum value which seems to correspond to the induction time of nucleation. Surface diffusion suppresses such decreasing of the average size since it obstructs new nucleation growth.

In cases where surface diffusion is more active, new crystal growth caused by nucleation cannot be found in galvanostatic deposition. Both the calculation and experiment supported this prediction.

Acknowledgment

The authors wish to thank Professor S. Yamauchi of the University of Tokyo for displaying the results of our calculation by computer graphics. The discussion with Professor Yamauchi was quite helpful in establishing some of the results presented herein.

Manuscript submitted Nov. 29, 1982; revised manuscript received ca. July 26, 1983.

The Institute of Vocational Training assisted in meeting the publication costs of this article.

REFERENCES

1. R. Aogaki and T. Makino, *This Journal*, **131**, 40 (1984).
2. R. Aogaki, *ibid.*, **129**, 2442 (1982).
3. K. J. Vetter, "Electrochemical Kinetics," p. 207, Academic Press, New York (1967).
4. W. Mehl and J. O'M. Bockris, *Can. J. Chem.*, **37**, 190 (1959).
5. W. Mehl and J. O'M. Bockris, *J. Chem. Phys.*, **27**, 817 (1957).

6. R. Aogaki and T. Makino, *Electrochim. Acta*, **26**, 1509 (1981).
7. R. Aogaki, *This Journal*, **129**, 2447 (1982).
8. J. O'M. Bockris and G. A. Razumney, "Fundamental Aspects of Electrocrystallization," p. 64, Plenum Press, New York (1967).
9. H. J. Levinstein and W. H. Robinson, *J. Appl. Phys.*, **33**, 3149 (1962).

Nucleation and Growth of Electroless Nickel Deposits on Molybdenum Activated with Palladium

J. Flis¹ and D. J. Duquette

Rensselaer Polytechnic Institute, Materials Engineering Department, Troy, New York 12181

ABSTRACT

Early stages of electroless nickel plating from an ammoniacal hypophosphite solution of pH 8.8 at 50°C with palladium-activated Mo were investigated using TEM and SEM, potential measurements, and LSV. It was shown that activation of molybdenum in a PdCl₂/HCl solution resulted in the formation of palladium islands on the substrate. In the plating solution, the nickel deposition took place simultaneously, but it took place independently on the palladium islands and on the molybdenum substrate. It was concluded that the nickel deposition on the molybdenum substrate occurred upon a thin layer of nickel, electrolytically deposited during a spontaneous potential shift. The role of the palladium islands was to catalyze electrooxidation of hypophosphite and induce the potential shift. A potential arrest at -0.7V vs. SCE was observed on the palladium with a concomitant decrease in the oxidation rate of hypophosphite. This phenomenon was ascribed to competitive adsorption of hydrogen and possibly to poisoning of the palladium by a hydride (β -PdH). In systems of palladium with molybdenum and palladium with nickel, a synergistic effect of small amounts of one metal on the catalytic activity of the other was observed.

Electroless chemical deposition of nickel from aqueous solutions, described first by Brenner and Riddell in 1946-1947 (1), proceeds spontaneously only on some metals, such as nickel, cobalt, palladium, iron, aluminum, gold, and zinc. A few of these possess intrinsic catalytic activity, while others (*e.g.*, iron and aluminum) are believed to acquire catalytic activity after initial deposition of nickel. Nickel deposition can take place due to a displacement reaction in a plating bath (2) or by an electroplated nickel "strike."

A common method for activation of noncatalytic substrates involves immersion into HCl solutions of PdCl₂, RhCl₂, or SnCl₂. Marton and Schlesinger (3) used the SnCl₂-PdCl₂ treatment for obtaining small catalytic sites on dielectric substrates. They found that on the activated dielectric substrates the deposition of nickel starts only at certain specific sites and leads to the formation of islands. On nickel and palladium, nickel deposition is homogeneous and shows no island structure. The substrates investigated differed in their electron conductivity as well as in catalytic activity; dielectric substrates are nonconducting and nonactive; whereas nickel and palladium are conducting and highly active.

The objective of this work is to examine the nucleation and growth of nickel deposits on a nonactive metallic substrate of molybdenum after activation in a PdCl₂/HCl solution. Electroless nickel plating on molybdenum is described elsewhere (4-6). These investigations were carried out in order to determine the distribution of palladium on activated molybdenum substrates, and to examine the growth of nickel deposits on a heterogeneous surface of molybdenum and palladium.

The plating was carried out in an ammoniacal hypophosphite solution. Deposits were examined using transmission electron microscopy (TEM), scanning electron microscopy (SEM) and energy dispersive spectroscopy (EDS). The catalytic activity and electrochemical behavior of molybdenum with palladium

were evaluated on the basis of potential measurements and linear sweep voltammetry (LSV). These types of measurements are justified in view of the widely accepted opinion that electroless deposition involves a charge-transfer mechanism. Electrochemical measurements in studies of electroless deposition have been described by other investigators (7-14).

Experimental

The substrates examined were 99.7% molybdenum rolled sheet containing ~0.3% metallic impurities, and electrodeposited palladium.

The molybdenum was electropolished in a solution of 12.5% H₂SO₄ (by volume) in ethanol, rinsed with distilled water and methanol, and then masked with lacquer to obtain an uninsulated surface area of 1 cm². Thin foils for TEM were prepared by the double-jet electropolishing technique in a solution of 12.5% H₂SO₄ in methanol at -50°C. Activation was achieved by immersion into solutions of 1 g/l PdCl₂ = 1 ml/l concentrated HCl for chemical and structural analyses, or 0.2 g/l PdCl₂ + 0.2 ml/l HCl for electrochemical studies, for periods of 5-300s. This was followed by washing in distilled water and methanol. Molybdenum specimens for SEM and EDS examinations were activated by placing droplets of a PdCl₂/HCl solution on the surface.

Palladium substrates were obtained by Pd electrodeposition on pure copper from a solution of 0.8 g/l PdCl₂ · 2H₂O + 60 g/l NaOH. The electrodeposition was carried out at room temperature at a current density of 100 A/m² for 200s, producing palladium layers of approximately 1 μ m in thickness.

In some experiments, specimens were cathodically polarized in 0.1M H₂SO₄ at a current density of 100 A/m² for 600 sec prior to testing. Specimens were examined in the solutions listed in Table I. Sulfuric acid (98%) was added in amounts appropriate for adjusting the pH of the solutions to 8.8 (at 25°C). All measurements were carried out on stationary specimens at 50.0° ± 0.5°C (pH at 50°C was 8.3) in a 250 ml

¹On leave from Institute of Physical Chemistry, 01-224 Warszawa, Poland.

Key words: electroless, nickel plating, molybdenum, palladium.

round-bottom flask provided with a reflux condenser, Luggin capillary, and a platinum wire as an auxiliary electrode. The solutions were deaerated by purging with pure nitrogen.

Electrochemical examinations involved (a) monitoring of open-circuit electrode potentials upon immersion of specimens into solutions, and (b) LSV measurements. Potentials were measured against saturated calomel electrode (SCE) at 25°C via a Luggin capillary. Voltammetric measurements were performed using single cathodic sweeps at a rate of 1 mV/s, beginning at -0.3V vs. SCE.

Uptake of hydrogen into the palladium substrates in the plating solution was determined by an electrochemical permeation method (15). Palladium was electrodeposited on a $50\ \mu\text{m}$ -thick membrane of Armco iron. The reverse (diffusive) side was electroplated with nickel from a Watt's solution at $100\ \text{A}/\text{m}^2$ for 100s. The diffusion compartment in the electrolytic permeability cell contained 0.02M NaOH, with a reference electrode of Hg/HgO/ 0.02M NaOH.

The growth rate of electroless deposits was determined gravimetrically on the platinum wire, which was electroplated with a nickel layer $\sim 0.2\ \mu\text{m}$ thick. (Deposited for 30 min after reaching a mixed potential of -0.87V .) The deposits were dissolved in concentrated HNO_3 and analyzed for phosphorus content by the molybdophosphoric acid method (16) with absorbance measurements being made at 380 nm.

Results

Open-circuit potential of molybdenum and palladium-activated molybdenum.—Changes of electrode potential of the substrates upon immersion into the plating solution are shown in Fig. 1. The rest potential was about -0.4V . Molybdenum alone did not fall below -0.5V , and no plating occurred on this substrate. Activation of molybdenum with palladium resulted in a potential shift to $\sim -0.87\text{V}$, (characteristic for the electroless plating in the solution examined). Two potential arrests tended to appear on the potential/time curves: the first at about -0.5V , and the second at about -0.7V . The former arrest decreased with increasing activation time (i.e., increasing amount of palladium deposited on the surface), whereas the latter increased with the activation time. Cathodic polarization of specimens prior to testing virtually eliminated both potential arrests.

Open-circuit potential of palladium.—Changes of the potential on palladium subjected to various surface treatments in different solutions are shown in Fig. 2. As in the case of palladium-activated molybdenum, the mixed potential of electroless deposition was about

Table I. Composition of solutions

Solution designation	$\text{NaH}_2\text{PO}_3 \cdot \text{H}_2\text{O}$ g/l	$\text{NiSO}_4 \cdot 6\text{H}_2\text{O}$ g/l	KNa tartrate $\text{KNaC}_4\text{H}_4\text{O}_6 \cdot 4\text{H}_2\text{O}$ g/l	28% NH_4OH ml/l	98% H_2SO_4 ml/l
Plating solution	13.25 (0.125 mol/l)	13.1 (0.05 mol/l)	28.2	70	ca. 15
Supporting solution	—	—	28.2	70	ca. 15
Supporting solution with Ni^{2+} ions	—	13.1	28.2	70	ca. 15
Supporting solution with sodium hypophosphite	13.25	—	28.2	70	ca. 15

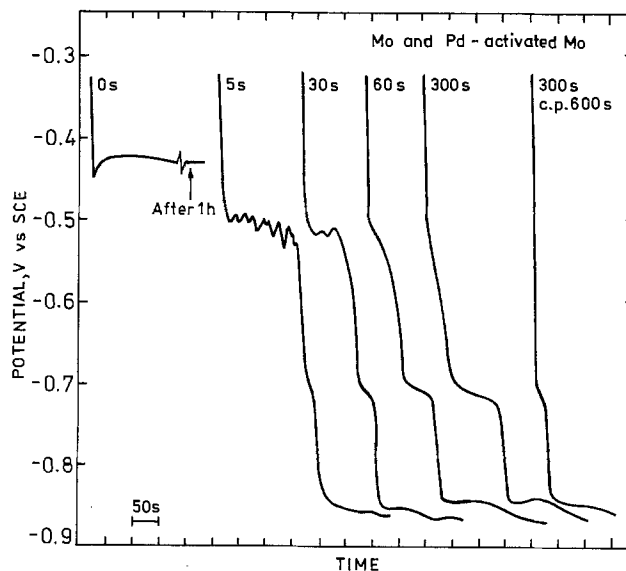


Fig. 1. Open-circuit potential of molybdenum after immersion into the plating solution. Parameter is the time in seconds of palladium activation in the solution of $1\ \text{g}/\text{l}$ $\text{PdCl}_2 + 1\ \text{ml}/\text{l}$ HCl . Cathodic polarization prior to testing (cp) was carried out in 0.1M H_2SO_4 at $100\ \text{A}/\text{m}^2$ for 600s.

-0.87V . In the supporting solution with hypophosphite (no Ni^{2+} ions), the potential dropped to values of about -0.92V . A potential arrest at -0.7V was observed in both solutions. After the oxidizing surface treatments (aging in air or immersion into 0.1M NaOH), substrates showed an additional potential arrest at about -0.5V . Cathodic polarization prior to testing eliminated the arrest at -0.5V and substantially reduced the time of arrest at -0.7V . In the supporting solution (no hypophosphite or Ni^{2+} ions), the stationary potential was about -0.4V .

Growth rate and phosphorus content in the deposits.—At the mixed potential of -0.87V , the average growth rate of the deposits on nickel-covered platinum was $14 \pm 3\ \text{mg} \cdot \text{m}^{-2} \cdot \text{s}^{-1}$. Assuming a density of the deposits of $7.85\ \text{kg}/\text{l}$ (17), this would correspond to an increase in thickness at a rate of $(1.8 \pm 0.4) \times 10^{-3}$

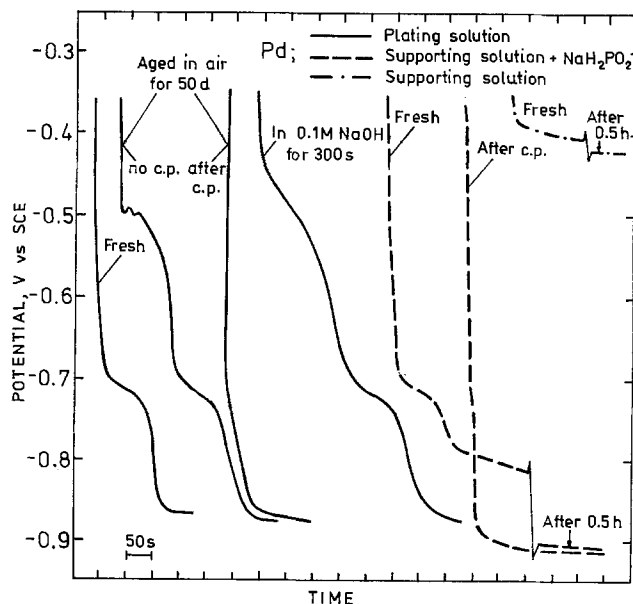


Fig. 2. Open-circuit potential of palladium upon immersion into various solutions after surface treatments as indicated at the curves.

$\mu\text{m} \cdot \text{s}^{-1}$. The deposits contained from 2.2 to 2.9 weight percent (w/o).

Voltammetric measurements.—To comply with the extent and direction of the open-circuit potential shifts (Fig. 1 and Fig. 2), the potential was scanned from -0.3V to -0.92V or below. Voltammograms for molybdenum, palladium-activated molybdenum, and palladium in the supporting solution with and without other components essential for plating (cf. Table I) are shown in Fig. 3, 4, and 5, respectively.

The polarization curves of molybdenum (Fig. 3) in the supporting solution and in the solution with sodium hypophosphite (NaH_2PO_2) were similar, indicating that hypophosphite did not undergo electro-oxidation on this substrate. However, the anodic current of elec-

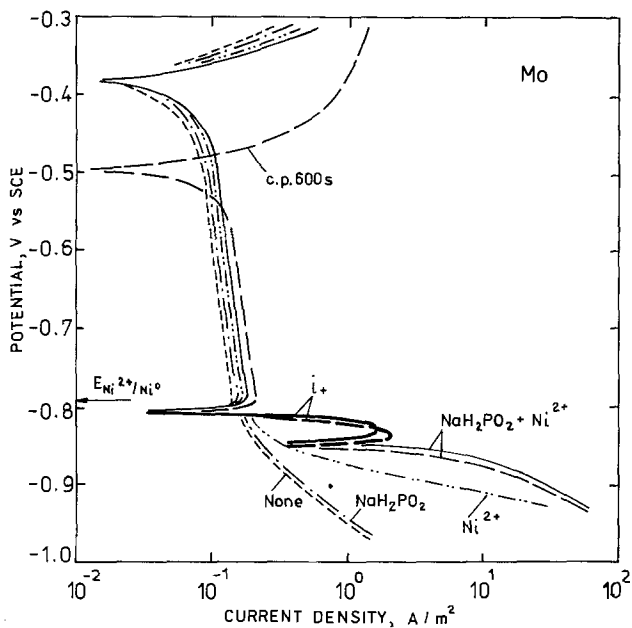


Fig. 3. Voltammograms on molybdenum in the supporting solution without and with other components (see Table I), starting at -0.3V .

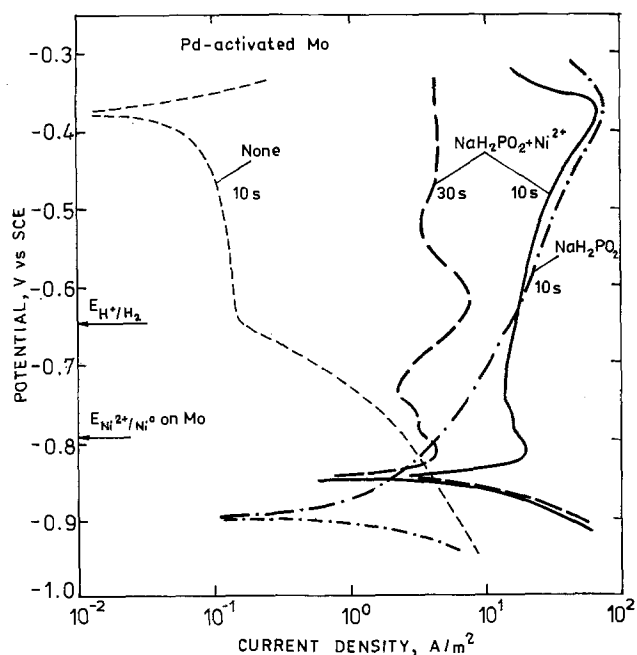


Fig. 4. Voltammograms on molybdenum and palladium-activated molybdenum in the supporting solution without and with other components, starting at 0.3V . Parameter is the time of activation in solution of $0.2\text{ g/l PdCl}_2 + 0.2\text{ ml/l HCl}$.

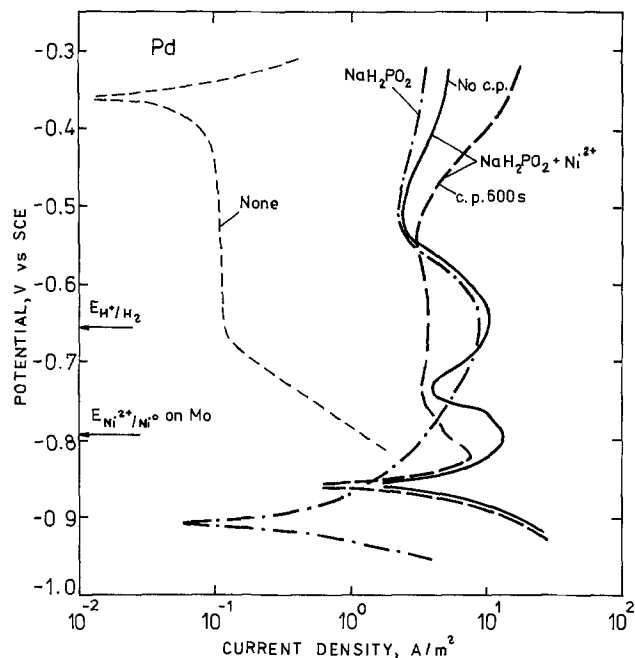


Fig. 5. Voltammograms on palladium in the supporting solution without and with other components.

tro-oxidation of hypophosphite appeared in the solution with NaH_2PO_2 and Ni^{2+} ions (plating solution). It started at the potential of nickel deposition, as seen from the curve for the solution with Ni^{2+} ions. Electro-oxidation of hypophosphite took place on a layer of nickel, electrolytically deposited on molybdenum during the potential scan (in Fig. 3 the potential of nickel deposition is shown as $E_{\text{Ni}^{2+}/\text{Ni}^0}$).

Cathodic polarization of specimens in $0.1\text{M H}_2\text{SO}_4$ prior to testing shifted the corrosion potential of molybdenum towards negative values, but did not affect electro-oxidation of hypophosphite.

Deposition of palladium significantly activated the molybdenum substrate both with respect to electro-oxidation of hypophosphite and its evolution of hydrogen (Fig. 4). Hydrogen evolution started at a potential of -0.65V , whereas electro-oxidation of hypophosphite took place over the entire potential range. Activation with palladium for a longer immersion time (30s) resulted in a decrease of anodic current and in the appearance of a distinct maximum in current at a potential of about -0.65V , as compared to the shorter immersion time (10s). Common for the immersion times of 10 and 30s was a maximum at about -0.82V . In the solution with NaH_2PO_2 (without Ni^{2+} ions), the anodic current decreased steadily with decreasing potential.

Voltammograms for palladium (Fig. 5) resembled those for the palladium-activated molybdenum. Cathodic polarization of palladium prior to testing increased the anodic current at the start of the potential scan and smoothed the curves, eliminating the maximum observed at -0.65V .

The voltammograms allow an interpretation of some of the features of the potential/time curves (Fig. 1, 2). The potential arrests at about -0.5V were associated with the corrosion potentials of the substrates (as indicated by discontinuities on the voltammograms), while the rest potential of -0.87V in the plating solution was the mixed potential of electrochemical processes involving oxidation and reduction of hypophosphite, evolution of hydrogen, and reduction of Ni^{2+} ions. In the absence of Ni^{2+} ions, the mixed potential was -0.92V .

The potential arrests on the palladium containing substrates at -0.7V may be associated with the decreasing anodic current for electro-oxidation of hypophosphite in this potential region (Fig. 4, 5). A rela-

relationship between the potential arrests and the decreasing current is also apparent from the effects of cathodic polarization, which reduces the potential arrests and also smoothes the voltammetric curves, eliminating the decrease in anodic current (Fig. 5).

The decrease in anodic current on palladium below about -0.65V appears to be associated with hydrogen, which begins to evolve at about this potential. This can be deduced from the voltammograms in the supporting solution, which show an increase of the cathodic current above -0.65V (Fig. 4, 5). There is also a relationship between the potential arrests at -0.7V and hydrogen evolution which can be deduced from a simultaneous measurement of the open-circuit potential and of hydrogen permeation (Fig. 6). Figure 6 shows that the potential arrest on palladium electrodeposited on an iron membrane began simultaneously with the permeation of hydrogen through the membrane. A rapid potential drop below about -0.78V was accompanied by a marked increase in the hydrogen permeation rate.

TEM examinations.—An electron micrograph of a molybdenum foil after activation in a PdCl_2/HCl solution is shown in Fig. 7. Palladium was deposited in small islands (black spots in the micrograph) between 0.01 and $0.1\ \mu\text{m}$ in diameter. The distribution of the palladium islands was random, and no correlation with dislocations or grain boundaries in the foil was observed. Large portions of the molybdenum surface remained free of palladium deposits.

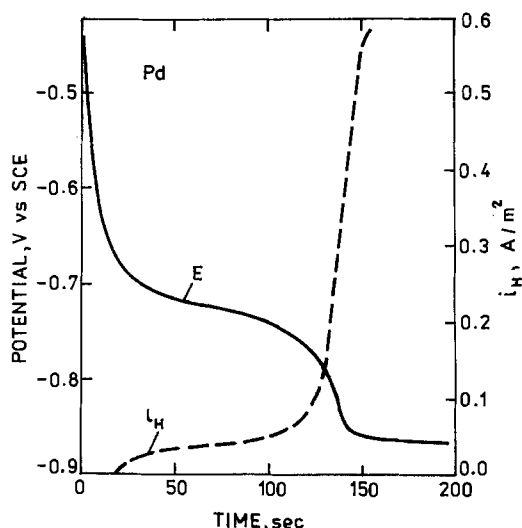


Fig. 6. Open-circuit potential (E) of palladium electrodeposited on iron membrane and permeation (i_H) of hydrogen through the membrane upon exposure to the plating solution.

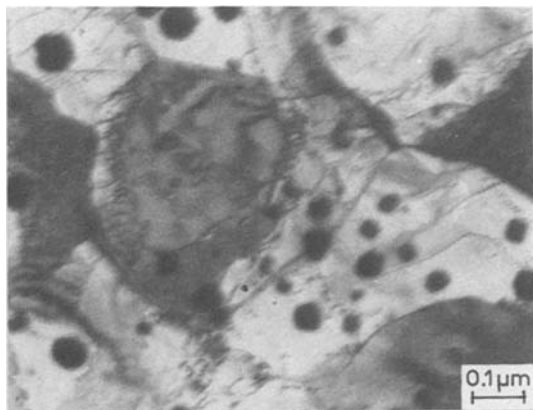


Fig. 7. Electron micrograph of a molybdenum foil after immersion into solution of $0.2\ \text{g/l PdCl}_2 + 0.2\ \text{ml/l HCl}$ for 10s. Black spots are deposits of palladium.

Figure 8 shows a palladium-activated foil of molybdenum after immersion in the plating solution until the open-circuit potential dropped to -0.80V . Upon attaining this potential, the foil was quickly withdrawn from the solution and rinsed with distilled water and methanol. The black spots shown in Fig. 8 are islands of palladium-nickel deposits as identified by electron diffraction. The micrograph shows that at the early stages of electroless nickel plating, the deposition of nickel is not confined to the palladium islands, but proceeds simultaneously on the entire molybdenum surface, without connection with the islands. Radial spreading of nickel deposits grown on the palladium islands was not observed.

SEM and EDS examinations.—SEM and EDS were used to examine more advanced stages of electroless nickel plating. In order to simulate the palladium islands, isolated droplets of the activating solution of $1.0\ \text{g/l PdCl}_2 + 1.0\ \text{ml/l HCl}$ were placed on molybdenum surface. Figure 9 shows an SEM micrograph of the molybdenum surface with a circular spot formed by a droplet of the activating solution. As determined by EDS, the white area in the center of the spot was a deposit of palladium, whereas the white flowerlike features were corrosion products containing oxygen and chlorides. The dark patches in the central area as well as the isolated white dots indicate that the palladium deposit on the molybdenum substrate was not uniform.

Specimens with the spots of palladium were in part masked with a lacquer and exposed to the plating solu-

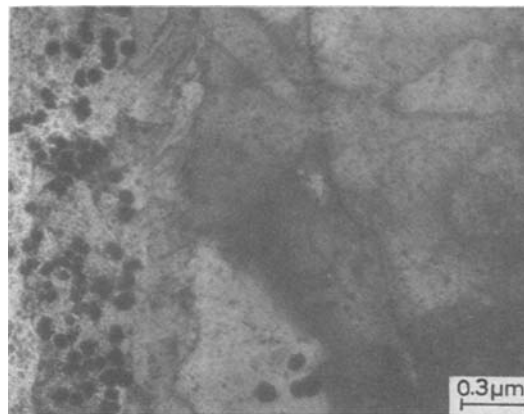


Fig. 8. Electron micrograph of a palladium-activated molybdenum foil after immersion into the plating solution until open-circuit potential reached -0.80V . Black spots are deposits of palladium. Small gray circular patches are presumably deposits of nickel.

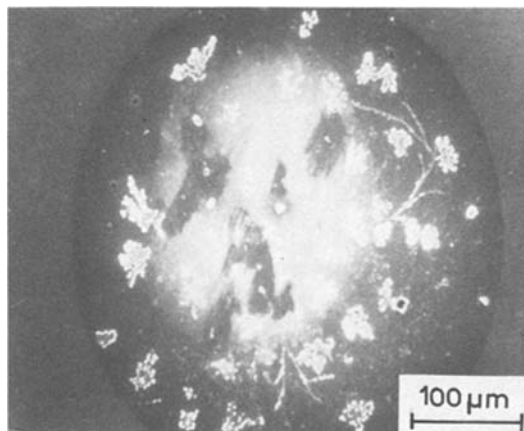


Fig. 9. SEM micrograph of a circular spot on molybdenum, formed by a droplet of activating solution of $1\ \text{g/l PdCl}_2 + 1\ \text{ml/l HCl}$. White diffused area in the center is deposited palladium. White flower-like features are corrosion products.

tion. The time of the plating was measured from the moment of attainment of an open-circuit potential of -0.80V and was varied from 8 to 40s.

An SEM micrograph of a partially masked specimen plated for 10s is shown in Fig. 10. A comparison of the masked and exposed areas indicates that deposition of nickel occurred both on the palladium-containing spots and on the surrounding molybdenum surface. The nickel deposit on the molybdenum surface was thinner than that on the palladium surface, and it differed in appearance.

This growth pattern continued for all of the times used. The nickel deposit on the molybdenum and palladium substrates after plating for 40s is shown in Fig. 11. The deposit on the molybdenum surface still remained thinner than that on the palladium surface. No indication of enlargement and coalescence of the nickel deposits growing on the palladium spots was ever observed.

As shown in Fig. 11, nickel deposition on the molybdenum surface after 40s was highly nonuniform. According to analysis by EDS, the dark stripes and patches indicated bare surface of molybdenum, with only a small amount of nickel.

Elemental analysis of the deposits grown on the molybdenum and palladium substrates also was performed by EDS. EDS spectra from molybdenum substrates (with and without palladium activation) after plating for various times are shown in Fig. 12. It can be seen that the energy peak of nickel in the region with palladium appeared sooner and was markedly higher than that of the molybdenum region without

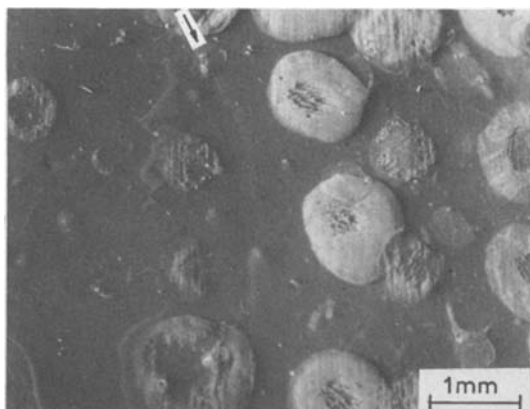


Fig. 10. SEM micrograph of molybdenum substrate with circular spots formed by droplets of the activating solution, after plating of an unmasked area for 10s. Nickel plated areas are brighter than unplated ones. Arrow indicates a border between a masked area (to the left) and plated area (to the right).

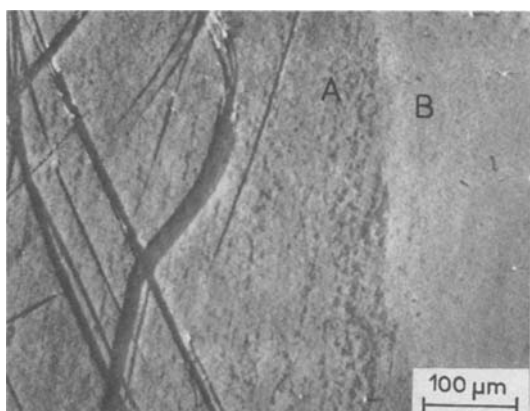


Fig. 11. SEM micrograph of nickel deposit on (A) molybdenum region and (B) palladium-containing region after plating for 40s.

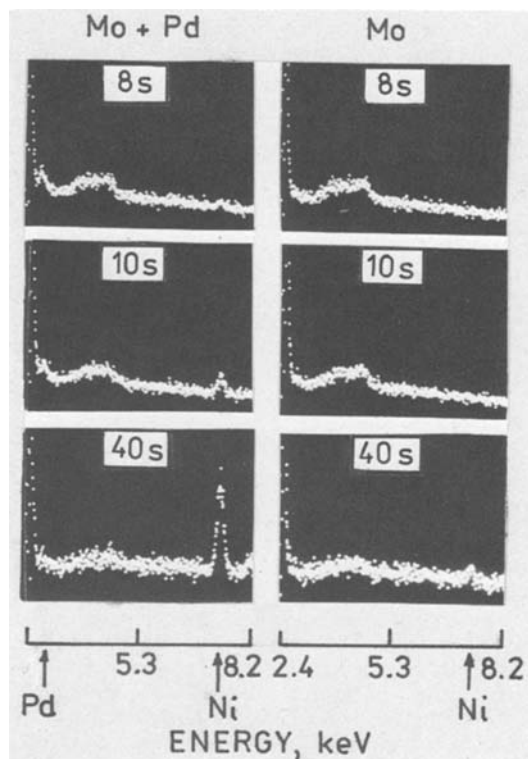


Fig. 12. EDS spectra from the molybdenum substrates with and without palladium after plating for 8, 10, and 40s. Arrows indicate peaks of palladium ($\text{Pd}_{L\alpha 1} = 2.838\text{ keV}$) and of nickel ($\text{Ni}_{K\alpha 1} = 7.477\text{ keV}$).

palladium. After plating for 40s, the nickel peak on molybdenum with palladium was about six times higher than the nickel peak on molybdenum itself.

The SEM and EDS examinations suggest that the rate of nickel deposition on palladium is considerably higher than that on molybdenum, both for the initial stage of a plating time of 8 or 10s (Fig. 10, 12) and also for its more advanced stage of 40s (Fig. 11, 12). Alternatively, there may be a delay in the initiation of plating. On the basis of the determined average rate of the nickel deposition ($1.8 \times 10^{-3} \mu\text{m} \cdot \text{s}^{-1}$), it can be estimated that after 10s of plating, the average thickness of the deposit was about 50 lattice parameters of nickel. This might lead to supposition that the effect of a substrate should disappear at about this thickness of nickel deposits. However, the deposits obviously were not continuous (note stripes in Fig. 11).

Discussion

These microscopic investigations have shown that electroless deposition of nickel on molybdenum around palladium spots proceeds simultaneously with and independently of the deposition on the palladium spots. Growth by coalescence of the deposits on palladium spots was not observed. The growth of nickel deposits on the molybdenum surface indicates that the catalytic activity of palladium spots is not restricted only to the spots themselves, but it is also transmitted to other noncatalytic areas of a metal substrate. It is suggested that this transmission occurs by an electrochemical effect of palladium, involving catalytic electro-oxidation of H_2PO_2^- with a resultant potential shift to negative direction and an accompanying electrolytic deposition of nickel.

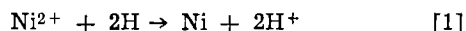
As shown in the voltammetric curves (Fig. 3-5), hypophosphite undergoes electro-oxidation on palladium in the entire range of open-circuit potentials on the substrates examined. In the plating solution, this leads to a potential shift to -0.87V (Fig. 1, 2). If this potential shift occurs on molybdenum, then at about -0.78V nickel will start to deposit electrolytically and electro-oxidation of hypophosphite will follow on the deposited

nickel. This is apparent from Fig. 3, which shows a positive current of electro-oxidation of hypophosphite in the plating solution. Evidently, this is a consequence of the preceding nickel deposition on molybdenum. Growth of electroless nickel deposits on molybdenum around palladium islands can be regarded as a result of electrolytic deposition of nickel, which is a good catalyst for electroless plating. The electrolytic deposition of nickel under open-circuit conditions occurs during the spontaneous potential shift, when the potential falls below about -0.78V . This potential shift results from electro-oxidation of hypophosphite, which in turn is initiated by palladium areas. Electroless nickel deposition on molybdenum surfaces thus are a result of a secondary electrochemical effect of palladium, which provides nonactive molybdenum with a thin layer of active nickel.

Similarly, a preliminary deposition of nickel during the spontaneous potential shift also occurs on palladium. This suggestion is supported by the voltammograms in Fig. 4 and Fig. 5, which show that the anodic current of electro-oxidation of hypophosphite in the solution with Ni^{2+} ions increases with the decreasing potential (below about -0.75V) and reaches a maximum; whereas in the absence of Ni^{2+} ions, the current steadily decreases. The increase of the current in the solution with Ni^{2+} ions can be explained by electrolytic deposition of some amounts of nickel, which causes an enhancement of the catalytic activity of the palladium substrate.

Preliminary deposition of small amounts of nickel results in a discontinuous and porous layer constituting a heterogeneous surface of nickel and palladium. Thus, the enhancement of the catalytic activity of palladium occurred when both metals, palladium and nickel, were simultaneously present on the surface. This suggests a synergistic relationship between these two metals. This synergistic effect can also be observed for palladium with molybdenum. The voltammograms in Fig. 4 show that the anodic current of electro-oxidation of hypophosphite on palladium-activated molybdenum was higher after a short activation time (10s) than after a longer activation time (30s).

The synergistic effect of palladium and nickel in the electro-oxidation of hypophosphite may be responsible for the observation that the growth of electroless nickel deposits on palladium spots is faster than on the molybdenum surface (Fig. 10-12). If the electroless deposits were continuous and free of pores, the growth should be controlled by the catalytic activity of the deposits only and be the same on the palladium and molybdenum substrates. However, the growth rate does depend on the type of substrate. This can be ascribed to porosity of the deposits and to the effect of the substrate exposed through the pores. Alternatively, the faster growth of the electroless deposits on the palladium spots may be explained in terms of the mechanism proposed originally by Gorbunova and Nikofova (18) involving reduction of Ni^{2+} ions by hydrogen atoms



It is possible that the initiation of nickel deposition on the palladium spots is accelerated through the above reaction, for which an additional source of hydrogen can be hydrogen absorbed in the palladium. Subsequent growth would thus be supported by the co-deposition of both H and Ni. This effect of absorbed hydrogen on the rate of the electroless plating is not straightforward. Cathodic polarization considerably activates the substrates, diminishing the potential arrests at -0.5 and -0.7V (Fig. 1, 2). This could be due in part to absorbed hydrogen and also to the reduction of surface oxides.

On the other hand, there is an indication that hydrogen inhibited electro-oxidation of hypophosphite. This is indicated by the potential arrest on palladium at

about -0.7V (Fig. 1, 2) and the decreasing current of anodic oxidation of hypophosphite (Fig. 4, 5), which coincided with the start of hydrogen evolution at -0.65V (Fig. 4, 5) and its permeation through the metal (Fig. 6). The inhibiting effect of hydrogen may be due to its adsorption on the surface and possibly to the formation of palladium hydride $\beta\text{-PdH}$. Adsorption of hydrogen will be competitive to the adsorption of hypophosphite, and thus will decrease the adsorption and the oxidation rate of the latter. Competitive adsorption of hydrogen was suggested by Sazonova *et al.* (14) as being responsible for a decrease in adsorption of dimethylamine borane on platinum. Hydrogen may also form the hydride $\beta\text{-PdH}$ that can markedly diminish the catalytic activity of palladium (20, 21). It is noteworthy that the anodic current from the oxidation of hypophosphite in the absence of Ni^{2+} ions steadily decreased with potential (Fig. 4, 5), which may be attributed to the increasing amount of hydrogen adsorbed on and by palladium.

The geometrical pattern of discontinuities in the electroless nickel deposits on the palladium surface (Fig. 11) may have many explanations. Generally, it may be associated with high internal stresses and with poor adhesion of the deposits to the substrate. Adhesion of deposits is normally related to the binding and interfacial energies and also to the lattice parameter mismatch between deposit and substrate (22). In considering these factors, it is important to note that the molybdenum substrate is not really a bare metal, but is largely covered with oxides. According to potential-pH diagrams (23), under conditions of electroless nickel plating in the solution examined, an oxide of the MoO_2 type is possible and must be taken into account when adhesion of the electroless nickel deposits to molybdenum is being considered.

Conclusions

Electroless nickel deposition was examined on molybdenum which was activated with palladium by immersion into a PdCl_2/HCl solution. This procedure results in the formation of palladium islands on the molybdenum substrate. In the hypophosphite plating solution, the nickel deposition takes place on the palladium islands and on the molybdenum substrate simultaneously and independently. The deposition on the palladium islands appears to be considerably faster than that on the molybdenum substrate. On the basis of voltammetric measurements it is concluded that the electroless nickel deposition on the molybdenum substrate actually occurs upon a thin layer of nickel, which is electrolytically deposited during a spontaneous potential shift in the cathodic direction. The palladium islands act as catalysts for electro-oxidation of hypophosphite, which in turn causes the potential shift.

Voltammograms indicate that the anodic current associated with oxidation of hypophosphite on palladium is increased when small amounts of molybdenum or nickel are also present on the surface. This suggests that small amounts of one metal can exert a synergistic effect on the catalytic properties of another. This effect explains the observation that the growth of nickel deposits on molybdenum with palladium is more rapid than that on molybdenum alone under the same electrochemical conditions.

Cathodic polarization prior to plating results in substantial activation of the substrates. This activation can be attributed to removal of oxide layers rather than to an effect of absorbed hydrogen on the plating process.

Upon immersion of palladium into the plating solution a potential arrest is observed at about -0.7V . This potential arrest coincides with a decreasing electro-oxidation rate of hypophosphite and with the evolution of hydrogen. This phenomenon may be ascribed both to the competitive adsorption of hydrogen on the palladium surface, which may decrease the adsorption and the oxidation rates of hypophosphite, and to a decrease

in the catalytic activity of palladium, which may be due to the formation of β -PdH.

Acknowledgments

The authors would like to express thanks to M. Lambert for helpful consulting on the TEM, SEM, and EDS investigations. This work was supported by International Business Machines Corporation.

Manuscript submitted Jan. 27, 1983; revised manuscript received Aug. 2, 1983.

Rensselaer Polytechnic Institute assisted in meeting the publication costs of this article.

REFERENCES

1. A. Brenner and G. E. Riddel, *J. Res. Natl. Bur. Stand.*, **37**, 31 (1946); **39**, 385 (1947).
2. G. Gutzeit, *Plating*, **46**, 1158, 1275, 1377 (1959); **47**, 63 (1960).
3. J. P. Marton and M. Schlesinger, *This Journal*, **115**, 16 (1968).
4. G. A. Walker and C. C. Goldsmith, *Thin Solid Films*, **53**, 217 (1978).
5. I. M. Kvokova and L. E. Chalykh, *Zashch. Met.*, **6**, 240 (1970).
6. G. G. Gavrillov, "Chemical Electroless Nickel Plating," Portcullis Press, Redhill (1979).
7. R. M. Lukes, *Plating*, **51**, 1066 (1964).
8. M. Paunovic, *ibid.*, **55**, 1161 (1963).
9. F. M. Donahue and C. U. Uy, *Electrochem. Acta*, **15**, 237 (1970).
10. N. Feldstein and T. S. Lancsek, *This Journal*, **118**, 869 (1971).
11. G. A. Sadakov and Z. K. Slepenskova, *Sov. Electrochem.*, **12**, 14 (1976).
12. S. M. El-Raghy and A. A. Abo-Salama, *This Journal*, **126**, 171 (1979).
13. T. Osaka, H. Takematsu, and K. Nihei, *ibid.*, **127**, 1021 (1980).
14. D. Aikens and F. Pushpanaden, Private communication.
15. M. A. V. Devanathan and Z. Stachurski, *Proc. Roy. Soc.*, **270A**, 91 (1962).
16. "Colorimetric Determination of Nonmetals," D. F. Boltzand and J. A. Howell, Editors, J. Wiley and Sons, New York (1977).
17. "Symposium on Electroless Nickel Plating," ASTM Special Tech. Publ., No. 265, p. 29 (1959).
18. Gabrielli and Raulin, *J. Appl. Electrochem.*, **1**, 167 (1971).
19. K. M. Gorbunova and A. A. Nikofofova, *J. Phys. Khim.*, **28**, 3, 883, 897 (1954).
20. S. V. Sazonova, K. M. Gorbunova, and M. V. Ivanov, p. 736, Extended Abstracts of the 32nd ISE Meeting, Dubrovnik, 1981.
21. A. Couper and D. D. Eley, *Discuss. Faraday Soc.*, **8**, 172 (1950).
22. J. J. S. Scholten and J. A. Konvalinka, *J. Catal.*, **5**, 1 (1966).
23. B. Lewis and J. C. Anderson, "Nucleation and Growth of Thin Films," Academic Press, New York (1977).
24. M. Pourbaix, "Atlas of Electrochemical Equilibria," Pergamon Press, London (1964).

Cathode Characteristics of Organic Electron Acceptors for Lithium Batteries

Shin-ichi Tobishima, Jun-ichi Yamaki, and Akihiko Yamaji

Nippon Telegraph and Telephone Public Corporation, Ibaraki Electrical Communication Laboratory, Tokai, Ibaraki-ken, 319-11, Japan

ABSTRACT

Discharge and charge characteristics of cathode-active materials for lithium batteries were studied. Electron acceptors of charge transfer complex with high electron affinity were examined as cathode-active materials because they were expected to have high cell voltage. These electron acceptors are 2,4,7-trinitro-9-fluorenone (TNF), 2,4,5,7-tetranitro-9-fluorenone, 7,7,8,8-tetracyanoquinodimethane, 9,10-phenanthrenequinone, and 13 other compounds. Among these compounds, TNF showed the highest discharge capacity (1050 A-hr/kg) and the highest energy density (2030 W-hr/kg). Cycle lives of TNF were 400 and 54 times at charge-discharge capacity of 100 of A-hr/kg (1.2 electron transfer per 1 mol TNF) and 200 A-hr/kg (2.4 electron transfer per 1 mol TNF), respectively. The cycle tests indicate reversibility of TNF up to two-electron transfer.

Lithium organic-electrolyte batteries are of great interest as power sources for electronic devices because of their high energy density. Characteristics of lithium batteries, such as discharge capacity, cell voltage, energy density, and rechargeability, are affected by the selection of cathode-active materials. In order to discover the best cathode-active materials, many materials have been examined over the last several years (1-3). Most of those compounds are inorganic compounds. However, N-halogen compounds (4) and pyromellitic dianhydride (5) are organic cathode-active materials. It was reported (6) that, theoretically, organic compounds had much higher electrochemical capacities than inorganic compounds. Furthermore, organic compounds, having high electron affinity, are expected to have high cell voltage.

In this work, 17 organic compounds, which are known as electron acceptors of charge transfer complex, are tested as cathode-active materials for lithium batteries. These electron acceptors were chosen for two reasons. First, many of these compounds have high

electron affinity. Second, there is a possibility that these compounds will react with lithium reversibly, at least for one electron transfer process (7). This could mean that these organic compounds can be used as rechargeable cathode-active materials.

Experimental

2,4,5,7-tetranitro-9-fluorenone and 7,7,8,8-tetracyanoquinodimethane were obtained from Aldrich Chemical Company. Other cathode-active materials were obtained from Tokyo Kasei Company.

A test cell was used to evaluate cathode-active material properties. It had a flat configuration, as shown in Fig. 1. The lithium electrode area was 3.14 cm². The cathode electrode area was 4.91 cm². Current density was calculated using the lithium electrode area. Cathode mixtures were prepared by mixing appropriate amounts of the active materials and acetylene black, obtained from Denkikagaku Kogyo Company. A carbon felt sheet (Nippon Carbon Company) was used to prevent direct reaction between the cathode-active

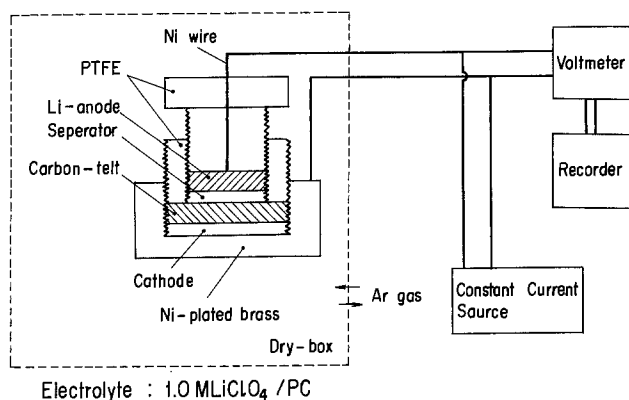


Fig. 1. Test cell configuration and measuring system

material and lithium metal. The electrolyte used was 1 or 1.25M LiClO_4 (Kanto Chemicals Company) solution in propylene carbonate (Tokyo Kasei Company). Water content was less than 200 ppm (Karl Fischer method). Porous polypropylene sheet (Polyplastic Company) was used as the separator. Lithium disk anodes were prepared by pressing in lithium wires (Merck Company). All cells were constructed and tested in a dry box filled with argon gas.

Results and Discussion

Discharge characteristics of organic electron acceptors coupled with lithium.—Organic electron acceptors used in this work are 2,4,7-trinitro-9-fluorenone (TNF), 7,7,8,8-tetracyanoquinodimethane (TCNQ), 9,10-phenanthrenequinone (PQ), 2,3-dichloro-5,6-dicyanobenzoquinone (DDQ), and 13 other compounds, many of which are aromatic compounds. Figure 2 shows the chemical structure of TNF, PQ, TCNQ, and DDQ.

Lithium cells were discharged at a constant current of 1 mA (0.32 mA/cm^2). Figure 3 shows the relation between electron affinity (8) of organic electron acceptors used and the corresponding cell voltage measured at the initial flat part of discharge curves. Cell voltage was found to have the tendency to increase with increases in electron affinity.

Figure 4 shows discharge curves of TNF and 2,4,5,7-tetranitro-9-fluorenone (TENF). Figure 5 shows discharge curves of TCNQ, PQ, fluorenone, and fluorene. Most of the discharge curves showed two flat parts,

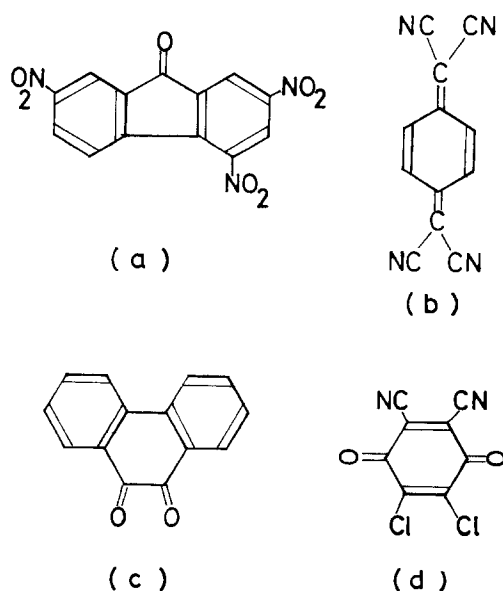


Fig. 2. Chemical structure of a: TNF; b: TCNQ; c: PQ; and d: DDQ.

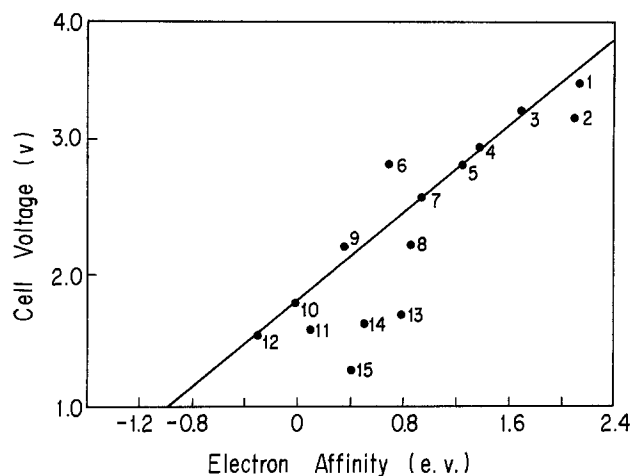


Fig. 3. Relation between initial cell voltage and electron affinity of organic electron acceptors. 1: 2,3-dichloro-5,6-dicyanobenzoquinone ($\text{C}_6\text{Cl}_2\text{O}_2[\text{CN}]_2$); 2: tetracyanoethylene ($\text{C}_2[\text{CN}]_4$); 3: 7,7,8,8-tetracyanoquinodimethane ($\text{C}_6\text{H}_4\text{C}_2[\text{CN}]_4$); 4: bromanil ($\text{C}_6\text{Br}_4\text{O}_2$); 5: chloranil ($\text{C}_6\text{Cl}_4\text{O}_2$); 6: p-benzoquinone ($\text{C}_6\text{H}_4\text{O}_2$); 7: 2,4,7-trinitro-9-fluorenone ($\text{C}_{13}\text{H}_5\text{N}_3\text{O}_7$); 8: pyromellitic dianhydride ($\text{C}_6\text{H}_2[\text{CO}]_4\text{O}_2$); 9: m-dinitrobenzene ($\text{C}_6\text{H}_4[\text{NO}_2]_2$); 10: phthalonitrile ($\text{C}_6\text{H}_4[\text{CN}]_2$); 11: phenanthrene ($\text{C}_{14}\text{H}_{10}$); 12: naphthalene (C_{10}H_8); 13: perylene ($\text{C}_{20}\text{H}_{12}$); 14: anthracene ($\text{C}_{14}\text{H}_{10}$); 15: pyrene ($\text{C}_{16}\text{H}_{10}$).

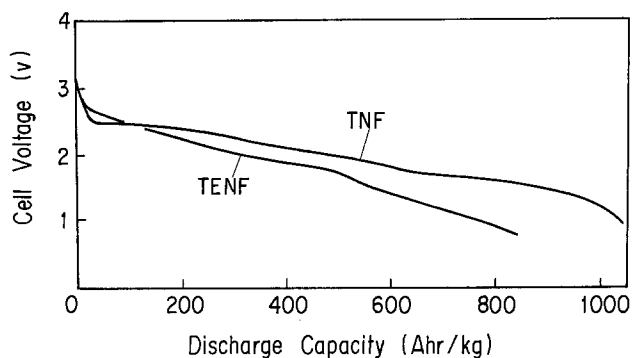


Fig. 4. Discharge curves of TNF and TENF at 1 mA

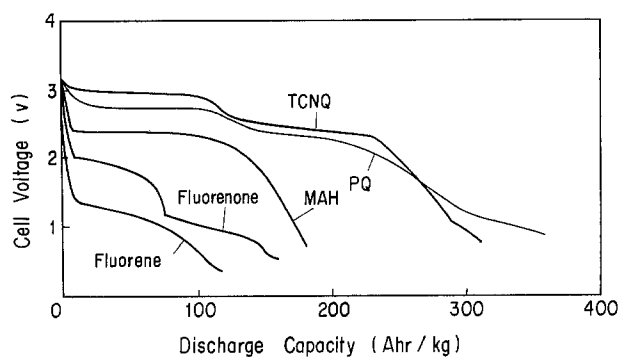


Fig. 5. Discharge curves of TCNQ, PQ, MAH, fluorenone, and fluorene at 1 mA.

which were followed by a gradually decreasing part. In cases of TNF and TENF, two flat parts were not clearly observed because the difference between voltages in the first part and in the second part was small (about 0.24V). The discharge capacity of the first part was a little higher than that of the second part. The discharge capacity of each part was nearly equal to that calculated on the basis of one electron transfer. It has been reported (9, 10, 11) that π -conjugated organic compounds are generally reduced through stepwise two-electron transfer in nonaqueous media.

Table I. Discharge characteristics of organic electron acceptors

Cathode-active material	Molecular weight	Energy ^a density (W-hr/kg)	Discharge ^a capacity (A-hr/kg)	Average voltage (V)	Utilization (%) ^b		Electron transfer number	Discharge current density (mA/cm ²)
					1st step	2nd step		
TNF	315.21	2030	1050	1.92	96	82	11.9	0.32
TENF	360.19	1590	810	1.96	86	85	10.5	0.32
TENF ^d		1910	960	2.00			12.7	0.32
PQ	208.22	710	320	2.20	88	84	2.56	0.32
TCNQ	204.19	370	300	1.58	89	79	2.30	0.32
9-fluorenone	180.21	270	170	1.62	53	50	1.10	0.32
MAH	98.06	250	180	2.18	51		0.54	0.32
anthracene	178.23	195	160	1.22	72	37	1.06	0.32
pyrene	202.26	180	125	1.20	61	52	1.12	0.32
phenanthrene	178.23	140	120	1.17	36	28	0.80	0.32
perylene	252.32	116	70	1.65	65 ^c		1.30	0.32
fluorene	166.22	112	108	1.04	39	28	0.68	0.32
naphthalene	128.17	101	65	1.55	41		0.40	0.32
PDA	218.12	279	135	2.07	55 ^c		1.10	1.00
o-chloranil	245.88	250	106	2.30	18		0.48	1.00
m-DNB	168.11	225	110	2.05	31	37	0.68	1.00
o-bromanil	423.70	210	85	2.50	67		1.34	1.00
p-benzoquinone	108.10	71	71	2.53	11		1.12	1.00
phthalonitrile	128.30	39	38	1.02	18		0.18	1.00
TCNE	128.09	25	13	1.92	6		0.06	1.00
DDQ	227.01	19	16	1.19	16		0.16	1.00

Cathode mixture: active material 0.05g; AB 0.05g.

^a Values were based only on the cathode-active material weight and up to 1V.

^b Values were based on one-electron transfer per cathode 1 mol.

^c Values were based on two-electron transfer per cathode 1 mol.

^d Cathode mixture: TENF 0.03g; AB 0.1 g.

TNF: 2,4,7-trinitro-9-fluorenone; TENF: 2,4,5,7-tetranitro-9-fluorenone;

PQ: 9,10-phenanthrenequinone; TCNQ: 7,7,8,8-tetracyanoquinodimethane; MAH: maleic anhydride;

PDA: pyromellitic dianhydride; m-DNB: m-dinitrobenzene; TCNE: tetracyanoethylene;

DDQ: 2,3-dichloro-5,6-dicyanobenzoquinone.

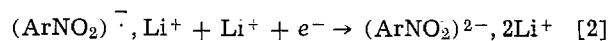
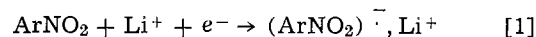
These facts indicate that the cathode reactions, corresponding to the first and second plateau, are the production of radical anion and dianion, respectively. Details of the third reaction mechanism are not clear, but the reaction may be the opening of benzene rings and/or reaction of various functional groups, such as —CN, —NO₂, —Cl, and —Br, with lithium.

Table I summarizes the discharge characteristics of various organic electron acceptors used in these cells. Discharge capacity and energy density were calculated only on the basis of cathode materials. TNF showed the highest discharge capacity (1050 A-hr/kg) and the highest energy density (2030 W-hr/kg). TENF showed a 810 A-hr/kg discharge capacity and a 1590 W-hr/kg energy density.

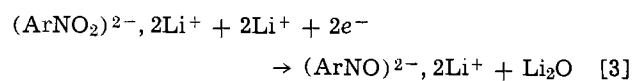
From the discharge test results, it was found that TNF, TCNQ, and PQ showed high cell voltage, as well as high energy density. Other compounds, such as DDQ, bromanil, and chloranil, showed rather low energy density (see Table I). In the next section, more detailed cathode characteristics of TNF, TCNQ, and PQ are discussed.

2,4,7-trinitro-9-fluorenone (TNF; *m/o* 315.21; C₁₃H₅N₃O₇).—As mentioned earlier, TNF showed the highest discharge capacity (1050 A-hr/kg up to 1V at constant current of 1 mA). This value corresponded to about 12 Li mols per 1 mol TNF. The reason for this reaction mechanism is not perfectly clear, but one possible explanation is mentioned below. The initial TNF reaction seems to be the stepwise formation of radical anion and dianion, according to Eq. [1] and

[2]. This explanation is supported by the literature on cyclic voltammetry of TNF (11) and the reduction of aromatic nitro compounds (ArNO₂) in nonaqueous media (9, 12).



Although what further reduction mechanisms there might be is not clear, nitro function in the dianion seems to react electrochemically with lithium. The reduction of the dianion is supposed to occur, according to Eq. [3], as is the formation of nitroso function. This reaction is analogous to the reaction between aromatic nitro compounds and C₆H₅Li (12).



Assuming Eq. [1], [2], and [3], eight-electron transfer per mol TNF is possible. As a further reduced prod-

uct, $\text{Ar} >\text{NLi}$ and/or $\text{Ar} >\text{NOLi}$ is possible (12).

Discharge-capacity dependence on the acetylene black (AB) contents in cathode mixtures was measured galvanostatically at 1 mA for each cell, where AB contents varied from 0% to 91%. AB compositions and their effect on the discharge characteristics of TNF are summarized in Table II. Capacity and energy density increased with increasing AB contents and

Table II. Cathode composition and discharge characteristics

Cathode composition			Capacity based on only TNF weight (A-hr/kg)	Energy density on only TNF weight (W-hr/kg)	Cell capacity (mhr)
TNF (g)	AB (g)	AB content (%)			
0.05	0.000	0.00	295	603	14.8
0.05	0.025	33.3	425	821	21.3
0.05	0.050	50.0	1050	2030	52.5
0.01	0.100	90.9	1150	2040	11.5
0.00	0.100	100.0	(29*)		2.9

* Based on AB weight.

1.0V cut-off, 1 mA.

TNF: 2,4,7-trinitro-9-fluorenone; AB: acetylene black.

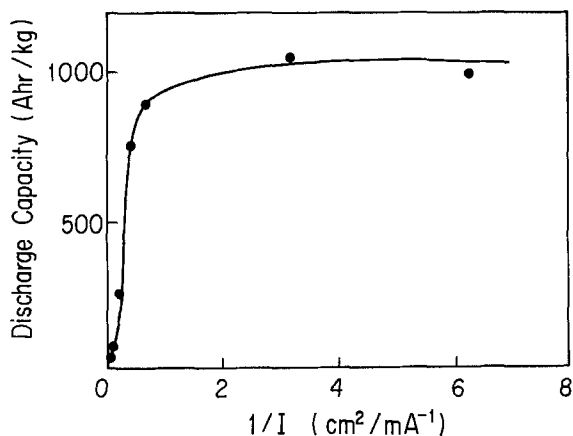


Fig. 6. Discharge capacity dependence on current density, 1V cutoff, TNF/Li cell.

saturated at a maximum value near 1000 A-hr/kg and 200 W-hr/kg.

Since discharge capacity also depends on discharge-current density, the effect of current density on the discharge capacity of TNF was studied. A cathode mixture was made of 0.05g TNF and 0.05g AB. Results are shown in Fig. 6. Discharge capacity increased with decreasing discharge current and it attained a maximum value of about 1000 A-hr/kg at a current density of 1 mA/cm². These two experiments suggest that 100% discharge capacity for the TNF cathode is about 1000 A-hr/kg.

To examine the possibility of cycling TNF cathode material, a cycling test of TNF coupled with lithium was carried out at various charge-discharge capacities (from 50 A-hr/kg to 550 A-hr/kg). The results for charge-discharge capacity of 50 A-hr/kg are shown in Fig. 7. This value corresponded to 0.59 Li mols per 1 mol TNF. The numbers shown in Fig. 7 are cycle number. Cells were tested up to 700 times.

The charge-discharge test of the blank test cell, with a cathode containing only AB, was performed under the same conditions as in the TNF cell test. The charge-discharge capacity was 100 A-hr/kg and the current density was 0.32 mA/cm². The relationship between the minimum or maximum charge voltage and cycle number, together with the blank results, are summarized, in Fig. 8 and Fig. 9. Curves "a" and "b" in Fig. 8 show minimum discharge voltages of the TNF cell and the blank cell, respectively. Curves "a" and "b" in Fig. 9 show maximum TNF cell voltages and the blank cell, respectively. Minimum TNF cell voltage was 2.5V at the first cycle and becomes lower with increasing of cycle numbers. However, its value was 1.8V even at the 100th cycle. In cases of the blank test (curve "b" in Fig. 8), minimum voltage is about 1.2V from the first to the 35th cycle. Maximum charge voltage of the TNF cell (curve "a" in Fig. 9) shows a relatively constant value of 3.7V from the first to the 100th cycle. However, in the blank cell (curve "b" in Fig. 9), its value is more than 10V at the 45th cycle. From these results, it can be concluded that the TNF cathode reacts with lithium reversibly.

Table III summarizes the cycling test condition and the TNF cathode cycle life. Cycle life was expressed as a cycle number where discharge voltage was higher than 1V. Cycle numbers for 50 A-hr/kg and 100 A-hr/kg discharge capacities were 691 times and 400 times, respectively. However, in the case of 200 A-hr/kg, cycle number was 54 times. In case of more than 200 A-hr/kg, cycle life was rather low. Table III also indicates that TNF rechargeability becomes poor by reacting with three mols of lithium per one mol TNF.

The rechargeability of TNF coupled with lithium was observed for up to two lithium reactions for 1 mol TNF. This fact agrees with the results of cyclic voltammetry of TNF in nonaqueous solutions (11), which show the formation of reversible TNF dianion.

7,7,8,8-tetracyanoquinodimethane (TCNQ; *m/o* 204.19; C₁₂H₄N₄).—As mentioned earlier, the TCNQ cell

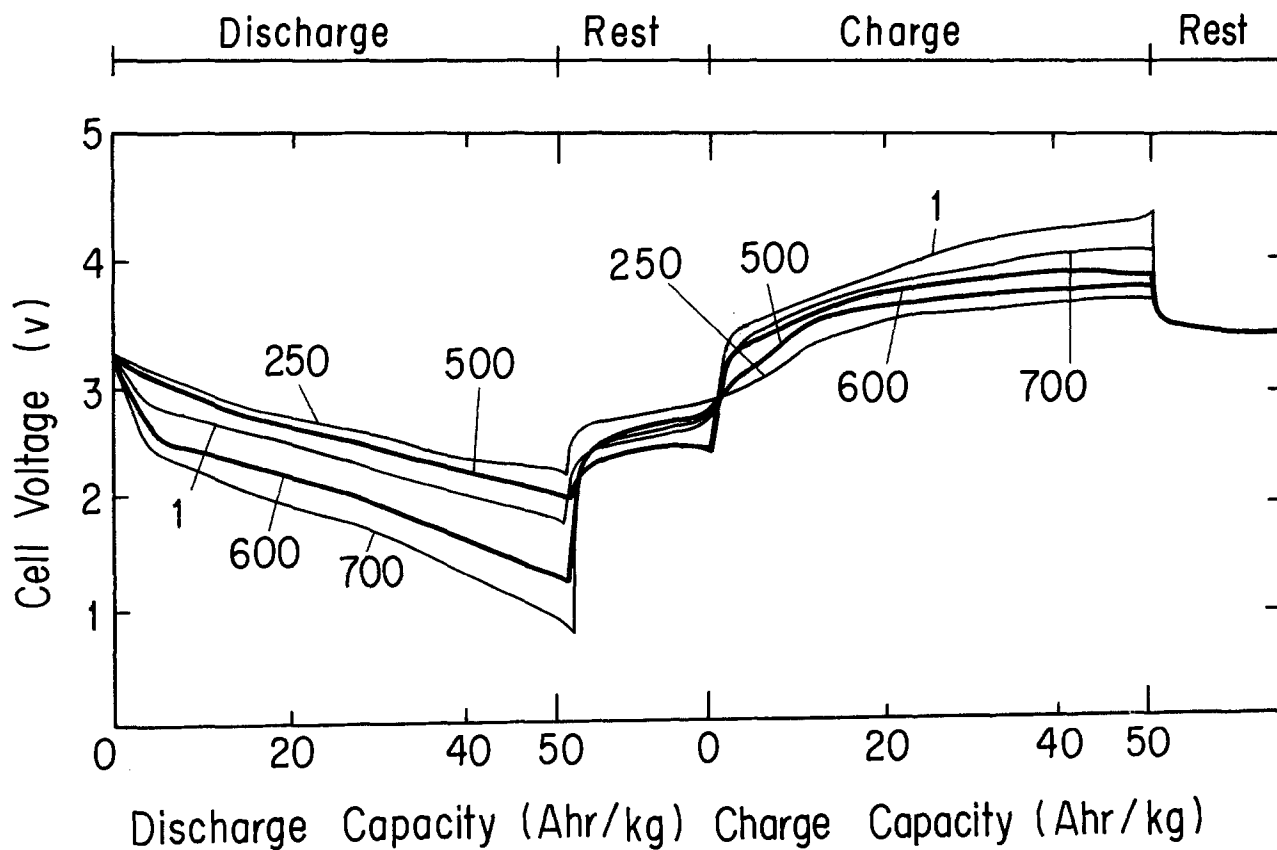


Fig. 7. Charge-discharge curves of Li/TNF cell at 50 A-hr/kg depth

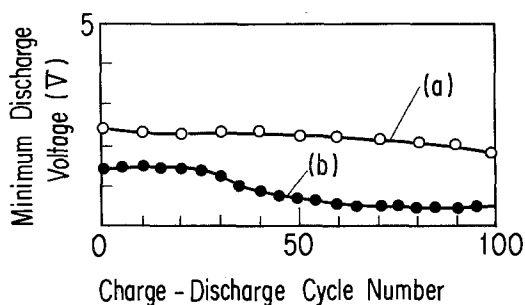


Fig. 8. Relation between minimum discharge voltage and charge-discharge cycle numbers of (a) TNF/Li cell and (b) blank cell.

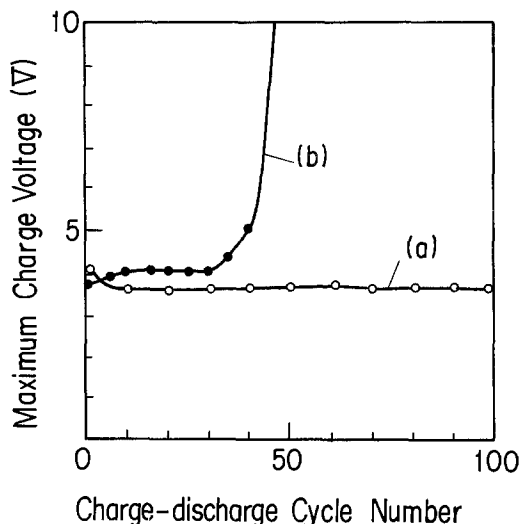


Fig. 9. Relation between maximum charge voltage and charge-discharge cycle numbers of (a) TNF/Li cell and (b) blank cell.

Table III. Charge-discharge characteristics of TNF coupled with lithium

Charge-discharge capacity (A-hr/kg)	Electron transfer number ^a	Cycle number ^b
50	0.59	691
100	1.2	400
200	2.4	54
300	3.5	15
400	4.7	7
550	6.4	2

Electrolyte: 1.25N LiClO₄-propylene carbonate; charge-discharge current density: 0.32 mA/cm²; cathode mixture: TNF 0.01g, AB 0.01g.

^a Calculated value corresponding to charge-discharge capacity.

^b Cycle number, where discharge voltage is higher than 1V.

showed a discharge capacity of 300 A-hr/kg up to 1V. This value corresponds to 2.3 mol of Li per 1 mol TCNQ. The suspicion that there is a cathode reaction is supported by stepwise formation of the radical anion

(TCNQ⁻) and dianion (TCNQ²⁻), for the reasons mentioned below. TCNQ is known to react with at least 1 mol of Li per 1 mol TCNQ by the reaction involving n-C₄H₉Li (13). TCNQ⁻ (14) and TCNQ²⁻ (15) are reported as the reduction products of TCNQ. Polarographic results of TCNQ in nonaqueous solution (15), show two-step reduction mechanism. Cell voltages calculated from half-wave potential are about 3.2 and 2.7V, respectively. This fact agrees with the TCNQ discharge test result; i.e., the discharge curve showed two flat parts and decreasing third part, and cell voltage was 3.1V at the first flat part and 2.6V at the second flat part. Discharge capacity at the first flat part and the second flat part is near that calculated based on one-electron transfer at each flat part of discharge (0.89 e⁻ at the first and 0.79 e⁻ at the second).

In sum, the initial reaction seems to be the formation TCNQ⁻ and TCNQ²⁻. The third reaction mecha-

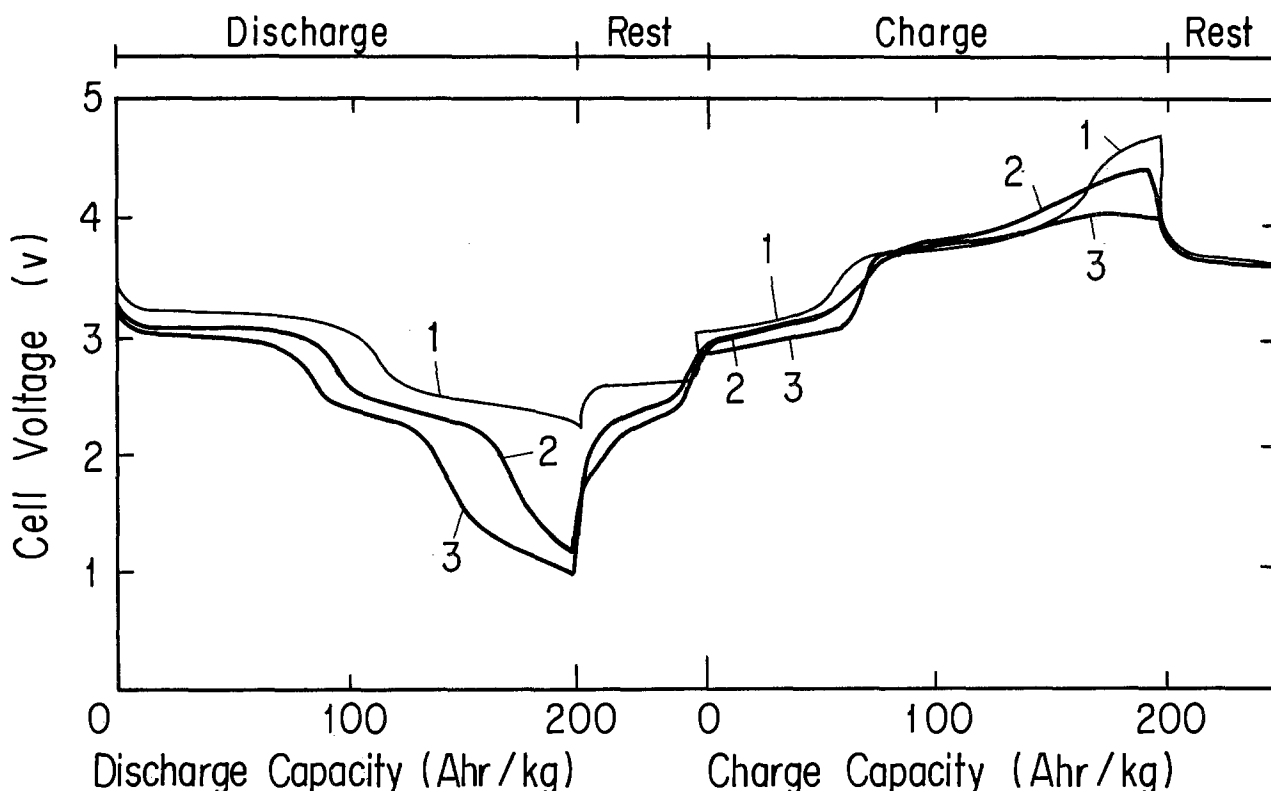


Fig. 10. Charge-discharge curves of TCNQ/Li cell at 200 A-hr/kg depth

nism is not clear, but the formation of LiCN may occur, because cell voltage at the third part of discharge is higher than that of the cathodic reaction of propylene carbonate with lithium (this value is reported as about 0.6V vs. Li (16)) or that of AB. Therefore, it was expected that TCNQ could be cycled up to two-electron transfer. A cycle test on TCNQ was carried out at 200 A-hr/kg charge-discharge capacity, which corresponds to 1.8 mols Li per 1 mol TCNQ.

Figure 10 shows the TCNQ cell charge-discharge curves. At the first cycle, both discharge and charge curves showed only two flat parts. With increasing cycle numbers, the discharge curve showed two flat parts and a third part, but the charge curve did not show a distinct third part. With increasing cycle numbers, utilization decreased at the first and the second flat parts, based on two-electron transfer. Utilizations of the first cycle, second cycle, third cycle, and fourth cycle were 1.58, 1.35, 1.16, and 1.02 e^- , respectively. The cycle number was 4, where discharge voltage was higher than 1V. So, the cathode reaction at the third part of the discharge is probably irreversible. One possible explanation for this fact is that third electrochemical reaction included the formation of insoluble and irreversible LiCN.

9,10-phenanthrenequinone (PQ; m/o 208.22; C₁₄H₈O₂).—As mentioned earlier, the PQ cell showed 310 A-hr/kg discharge capacity up to 1V. This value corresponded to 2.4 mol Li per 1 mol PQ, when the AB/PQ weight ratio was 1. We feel the cathode reaction is a

stepwise formation of $PQ^{\cdot-}$ and PQ^{2-} for the reasons mentioned below. Quinones are known to be reduced stepwisely by a two-electron transfer process (17). Radical anion and dianion are reported to be reduction products (17, 18). Polarographic results of PQ in nonaqueous solution (19) show a two-step reduction mechanism. Cell voltages, calculated from half-wave potential, are about 2.8 and 2.3V, respectively. This agrees with the discharge test results; i.e., the discharge curve showed two flat parts and a decreasing third part. Cell voltage is 2.7V at the first flat part and 2.2V at the second flat part of the discharge. The discharge capacity at the first and the second flat parts of discharge is near that calculated from one-electron transfer at each part (0.88 e^- at the first and 0.84 e^- at the second).

The initial PQ cathode reaction seems to be the formation of $PQ^{\cdot-}$ and PQ^{2-} . The third reaction mechanism is not clear, but the Li₂O formation may occur for the reasons mentioned in the TCNQ section.

The discharge capacity dependence on AB contents was measured galvanostatically at 1 mA. Results are shown in Fig. 11. Discharge capacity and energy density, based on PQ weight, increased with increasing AB contents and saturated to maximum values near 350 A-hr/kg and 750 W-hr/kg, respectively. From the results, it is found that the addition of 50 w/o or more than AB to PQ is necessary to achieve a good cathode efficiency.

Cycle tests of PQ were carried out at 200 A-hr/kg, which corresponded to 1.6 mols Li per 1 mol PQ. Figure 12 shows the result. The cycle number, where discharge voltage was higher than 1V, was only 2. The discharge voltage at the 5th cycle was 0.8V. The discharge curves showed two flat parts and a third part with increasing cycle numbers, but the charge curves did not show a distinct third part. This fact may be attributed to the formation of irreversible and insoluble Li₂O, as mentioned previously.

Conclusion

Cathode characteristics of organic electron acceptors for lithium batteries were examined. Based on the results, the following conclusions were reached.

1. Cell voltage is proportionally increased with increasing electron affinity of organic electron acceptors.

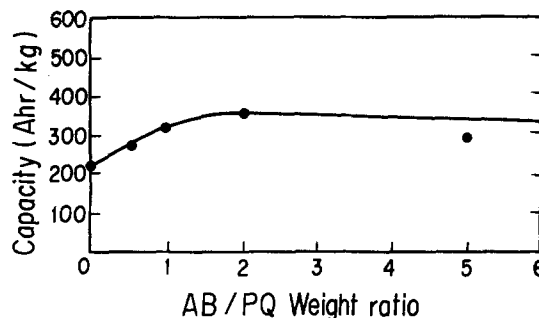


Fig. 11. Discharge capacity dependence of Li/PQ cell on AB contents, 1V cutoff.

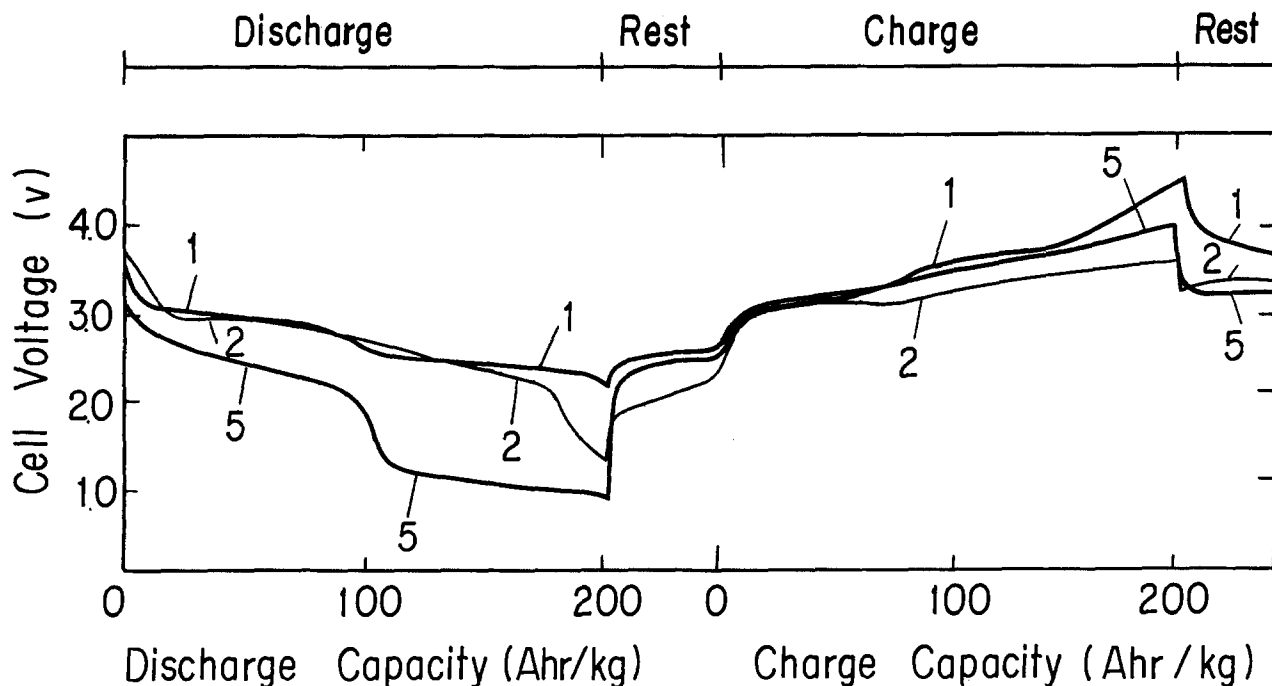


Fig. 12. Charge-discharge curves of PQ/Li cell at 200 A-hr/kg depth

DDQ, TCNQ, bromanil, chloranil, and TNF show high cell voltage values of 3.4, 3.1, 3.0, 2.9, and 2.6V, respectively.

2. TNF shows the highest discharge capacity (1050 A-hr/kg) and the highest energy density (2030 W-hr/kg) of the materials examined for this work. TENF and PQ show energy density values of 1580 W-hr/kg and 710 W-hr/kg, respectively. However, the discharge capacities of DDQ, bromanil, and chloranil are rather low.

3. TNF rechargeability is good up to a capacity of two-electron transfer per 1 mol TNF. The cycle life of TNF at 100 A-hr/kg is 400 times and that at 50 A-hr/kg is about 700 times.

For lithium secondary batteries, TNF is a promising cathode-active material.

Acknowledgment

The authors would like to express their gratitude to Mr. T. Inamura for his helpful guidance and discussion during the course of this research.

Manuscript submitted Dec. 14, 1981; revised manuscript received ca. May 15, 1983.

The Nippon Telegraph and Telephone Public Corporation assisted in meeting the publication costs of this article.

REFERENCES

1. M. S. Whittingham, *Prog. Solid Chem.*, **12**, 41 (1978).
2. D. W. Murphy and F. A. Trumbore, *J. Crystal*

Growth, **39**, 185 (1977).

3. J. N. Carides and D. W. Murphy, *This Journal*, **124**, 1309 (1977).
4. D. L. Williams, J. J. Byrne, and J. S. Driscoll, *ibid.*, **116**, 2 (1969).
5. T. Ohzuku, H. Wakamatsu, Z. Takehara, and S. Yoshizawa, *Electrochim. Acta*, **24**, 723 (1977).
6. H. Alt, H. Binder, A. Kohling, and G. Sundstede, *ibid.*, **17**, 873 (1972).
7. M. E. Peover, "Electroanalytical Chemistry," Vol. 3, p. 1, Marcel Dekker, New York (1967).
8. M. Ichikawa, M. Soma, T. Onishi, and K. Tamura, *Bull. Chem. Soc. Jpn.*, **40**, 1294 (1967).
9. J. S. Dunning and D. N. Bennion, *This Journal*, **117**, 485 (1970).
10. P. H. Given and M. E. Peover, "Advances in Polarography," Vol. 3, p. 948, Pergamon, Oxford (1959).
11. J. E. Kuder, J. M. Pochan, S. R. Turner, and D. F. Hinman, *This Journal*, **125**, 1750 (1978).
12. P. Buck, *Tetrahedron Lett.*, 1563 (1967).
13. M. S. Whittingham and M. B. Dines, *This Journal*, **124**, 1387 (1977).
14. Z. G. Soos and D. J. Klein, *J. Chem. Phys.*, **55**, 3284 (1971).
15. S. G. Clarkson, B. C. Lane, and F. Basolo, *Inorg. Chem.*, **11**, 662 (1972).
16. A. N. Dey, *Thin Solid Films*, **43**, 131 (1977).
17. C. K. Man and K. K. Barnes, "Electrochemical Reactions in Nonaqueous Systems," p. 190, Marcel Dekker, New York (1970).
18. J. N. Butler, *J. Electroanal. Chem.*, **14**, 89 (1967).
19. T. G. Edwards and R. Grinter, *Trans. Faraday Soc.*, **69**, 1070 (1968).

K₂CO₃ Solid Electrolyte as a CO₂ Probe: Decomposition Measurements of CaCO₃

Richard Côté, and Christopher W. Bale*

Département de Génie Métallurgique, Ecole Polytechnique, Station A, Montréal, Québec, H3C 3A7 Canada

Michel Gauthier*

Institute de Recherche d'Hydro-Québec, Varennes, Québec, J0L 2P0 Canada

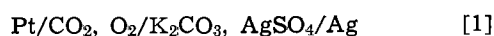
ABSTRACT

An electrochemical cell using a K₂CO₃ solid electrolyte has been employed as a gas probe to measure the equilibrium partial pressure of carbon dioxide in CO₂/synthetic air mixtures at 1 atm total pressure in the temperature range of 575-1025 K. Stable reversible emf's have been obtained in gas mixtures containing as little as 9 ppm CO₂ in air. The carbonate cell has also been used to measure the standard Gibbs energy change associated with the dissociation of calcium carbonate into calcium oxide and carbon dioxide in the temperature range of 725-975 K. The thermodynamic results are in good agreement with the published data from the literature, thus validating the use of K₂CO₃ as a CO₂ probe.

The use of solid-state galvanic cells as experimental tools for measuring thermodynamic properties of materials and gases is well established. One general category of solid electrolytes that has recently received attention in our laboratories is represented by the chemical formula A_nBX_m. Our efforts have been mainly devoted to the behavior of alkali sulfates in sulfur/oxygen atmospheres (1-3). For example, K₂SO₄, though entirely cation conducting, has been successfully employed as a solid electrolyte in measurements of the equilibrium partial pressures of SO₂ (and SO₃) in SO₂/O₂ gas mixtures in the temperature range of 873-1173 K. Stable reversible emf's have been obtained in SO₂/air gas mixtures containing as little as 0.1 ppm SO₂. K₂SO₄ has also been used to measure metal oxide-

sulfate thermodynamic equilibria in the Ni-NiSO₄, MgO-MgSO₄, and Mn₂O₃-MnSO₄ systems (4).

By comparison, the use of K₂CO₃ as a solid electrolyte for measuring the equilibrium partial pressure of CO₂ in gases has received little attention. Except for preliminary measurements obtained at 1000 K that have been included in a former publication (1) and in an internal report at IREQ (5), no systematic work has been published on the K₂CO₃(s)/CO₂(g), O₂(g), Pt electrode. The previously published results have shown that the following cell could be used at 1000 K to measure the equilibrium partial pressure of CO₂ in air



(working) (reference)

In the present investigation, this design was modified and the following cell used

* Electrochemical Society Active Member.

Key words: electrochemical cell, potassium carbonate, calcium carbonate, decomposition, carbon dioxide, probe, thermodynamics.

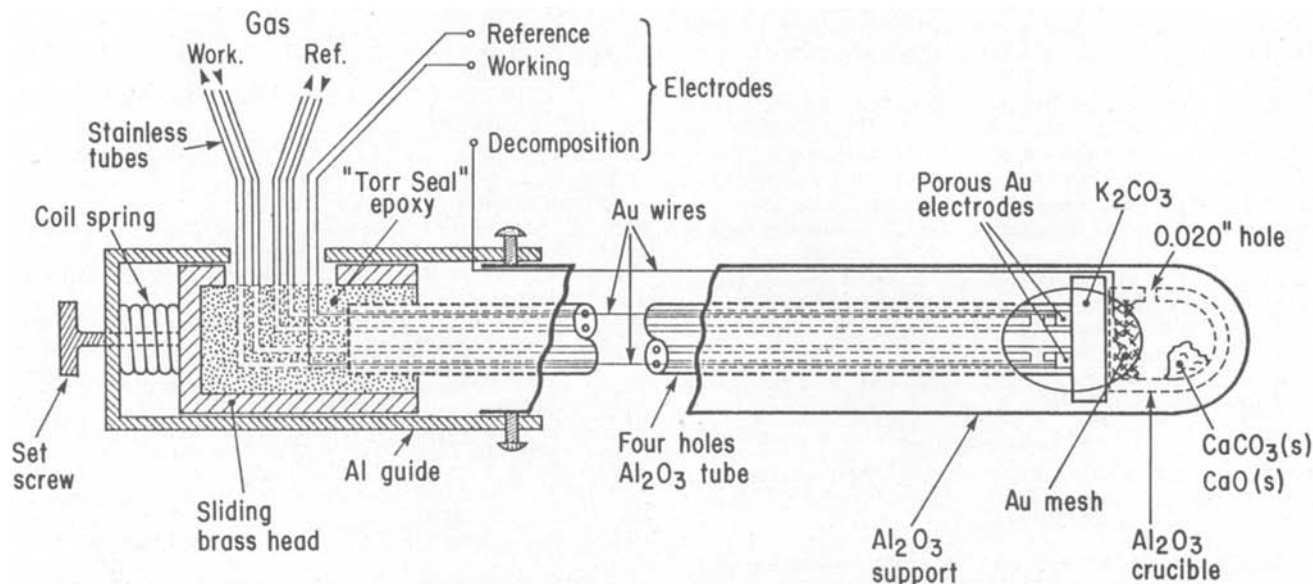
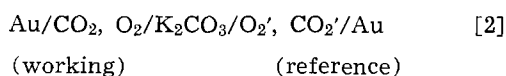
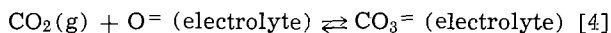
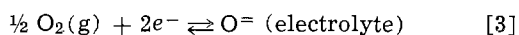


Fig. 1. Schematic representation of the K_2CO_3 concentration cell used in the present investigation

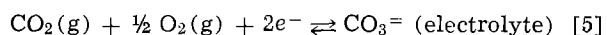


The Ag^+/Ag reference was replaced by a controlled CO_2/O_2 gas mixture, since the latter enables the partial pressure of CO_2 to be defined at different values. Also, Au electrodes were used, since it was observed that Pt tends to react with the K_2CO_3 solid electrolyte at high temperatures.

By analogy with the mechanism proposed by Salzano and Newman (6) for half-cells of the type Pt, SO_2 , O_2/SO_4^{2-} , it is assumed that the following reactions take place at each electrode



which lead to the overall electrode reaction



Therefore, the Nernst equation for the electromotive force of the carbonate cell is

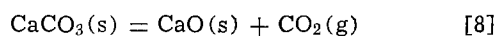
$$E = \frac{RT}{2F} \ln \frac{P_{CO_2} P_{O_2}^{1/2}}{P'_{CO_2} P'_{O_2}^{1/2}} \quad [6]$$

By defining P'_{O_2} and P'_{CO_2} at the reference electrode, it is possible to deduce the value of P_{CO_2} at the working electrode from measurements of the cell emf if P_{O_2} is also known.

If the oxygen potential at both electrodes is that of air, i.e., $P_{O_2} = P'_{O_2} = 0.21$ atm, then Eq. [6] simplifies to

$$E = \frac{RT}{2F} \ln \frac{P_{CO_2}}{P'_{CO_2}} \quad [7]$$

For the case where P_{CO_2} at the working electrode is the product of dissociation of calcium carbonate, the following chemical reaction takes place in this electrode compartment



If the activities of CaO and $CaCO_3$ are unity, the standard Gibbs energy change of Eq. [8] is given by

$$\Delta G^\circ = -RT \ln P_{CO_2} \quad [9]$$

Hence, the emf measurements can be used to deduce the standard Gibbs energy change of $CaCO_3$ decomposition if the value of P_{O_2} at the working electrode is also known.

Experimental

The carbonate electrochemical cell used in the present investigation is schematically illustrated in Fig. 1. The cell design is similar to that described in an earlier publication on sulfate concentration cells (4). The cell contained two gas circulating electrodes and one metal oxide-carbonate-gas electrode. The emf given by Eq. [7] was measured between any two of the electrodes.

The 99.96% purity K_2CO_3 (see Table I) solid electrolyte pellet (1 cm diam \times 0.5 cm thick) was prepared by pressing K_2CO_3 powder at 4000 kg/cm² and then sintering at 1025 K for a period of 48 hr. Since K_2CO_3 is hygroscopic, precautions were taken to ensure that the humidity levels were kept at a minimum.

The gas circulating electrodes were CO_2 /air mixtures (9–12,000 ppm CO_2) flowing at controlled rates (40–500 ml/min measured at 298 K) over Au gauzes in contact with the electrolyte surface. The large gold-electrolyte contact surface promoted the electrode equilibria. In the case of CO_2 /air mixtures greater than 1000 ppm CO_2 , the mixtures were prepared by injecting an appropriate quantity of pure CO_2 measured with a gas syringe into plastic 10 liter Mylar bags already filled with synthetic air. The precision of the value of P_{CO_2} in the preparation of these mixtures was about 3%. Commercially analyzed gas mixtures stored in cylinders were used for CO_2 levels of less than 1000 ppm. For these cases the precision of the values of P_{CO_2} was of the order of 1%.

The calcium carbonate-oxide-gas electrode consisted of a 1 ml alumina crucible initially containing pure calcium carbonate (calcite) powder (see Table I). In order to prevent any reaction between the calcium and potassium carbonates, it was important to avoid physical contact between the powder and the electrolyte. An Au gauze connected to an Au wire was used as the electrode. The gold served to separate the

Table I. Principal impurities in K_2CO_3 and $CaCO_3$

Impurities in $CaCO_3$		Impurities in K_2CO_3	
SO ₄	0.003%	SO ₄	0.004%
Ba	0.005%	N	0.001%
Cl	0.0003%	Cl	0.003%
Fe	0.0005%	Fe	0.0005%
Pb	0.0003%	Pb	0.0005%
Sr	0.05%	PO ₄	0.001%
Mg	0.0005%	Mg	0.01%
Na	0.002%	Na	0.02%
K	0.003%		

powder mixture from the electrolyte as well as promote the electrode equilibria. The alumina crucible had a small hole (1 mm diam) in its wall and was exposed to air on the outside of the crucible. The hole was small enough so that only small amounts of CO₂ diffused out of the crucible, and the partial pressure of CO₂ inside was fixed by the calcium carbonate dissociation given by Eq. [9]. The hole was large enough to enable the air to slowly diffuse into the chamber so that when P_{CO₂} was small, the equilibrium partial pressure of O₂ was effectively 0.21 atm. A similar design has been successfully employed in the study of metal sulfate/oxide equilibria (4).

At high temperatures K₂CO₃ becomes ductile. A slight pressure applied to the housing (Fig. 1) caused a slight deformation of the pellet which resulted in gastight electrode compartments. In the case of the gas circulating electrodes, the seals were tested by connecting each compartment to a mercury manometer and changing the total pressure by 10 cm of mercury. The compartment was considered gastight if the meniscus in the manometer remained stable for at least 30 min.

The cell temperature was maintained at ± 1 K by use of a 45 cm horizontal Lindberg 940W furnace. The temperature was measured by two previously calibrated Chromel-Alumel-type K thermocouples placed on both sides of the electrolyte pellet, as shown in Fig. 1. The thermocouple emf signals were measured by a Keithley Model 191 multivoltmeter and showed the cell to be isothermal. The precision of the temperature measurements was estimated to be 1 K. All cell emf signals between the two circulating gas electrodes or between the circulating gas reference electrode and the carbonate-oxide-gas electrode were measured by a Tacussel Aries 20,000 high impedance (10¹⁴Ω) multivoltmeter. The thermocouple and cell emf's were also recorded on a two-pen SEFRAM chart recorder.

Results and Discussion

At the reference electrode, the equilibrium partial pressures of oxygen, carbon dioxide, and the other gaseous species at 1 atm total pressure and a fixed temperature can be calculated from the initial composition of the gas mixture prepared at 298 K. The results of the free energy minimization calculation performed at the F*A*C*T thermodynamic data treatment center (7) are shown in Table II, where the equilibrium partial pressures of the principal species have been calculated at 1025 K from an initial gas mixture of P_{CO₂} = 12,000 ppm in air. It is clear from Table II that CO₂, O₂, and N₂ are the prominent stable gaseous species, and that P'_{O₂} effectively remains at 0.21 atm, since the initial concentration of CO₂ is dilute. However, at much higher concentrations of CO₂ and for higher temperatures it is evident that P'_{O₂} would no longer be 0.21 atm. In such cases, the simplified Nernst relation given by Eq. [7] would no longer be valid. Instead, it would then be necessary to measure P'_{O₂} and use this equilibrium value in the expanded Nernst Eq. [6]. This, however, was not necessary in the present study, since P_{CO₂} = 12,000

Table II. Computed equilibrium partial pressures of gas species at 1025 K and 1 atm from an initial gas mixture of 12,000 ppm CO₂ in air

Species	Pressure (atm)	Species	Pressure (atm)
N ₂	0.781	NO ₃	0.274 (10 ⁻¹³)
O ₂	0.208	N ₂ O ₃	0.688 (10 ⁻¹⁷)
CO ₂	0.119 (10 ⁻¹)	N ₂ O ₄	0.507 (10 ⁻¹⁹)
NO	0.505 (10 ⁻⁶)	N	0.115 (10 ⁻²¹)
NO ₂	0.222 (10 ⁻⁶)	N ₂ O ₅	0.192 (10 ⁻²²)
O	0.149 (10 ⁻⁸)	CNO	0.425 (10 ⁻²⁴)
N ₂ O	0.373 (10 ⁻¹⁰)	CN	0.166 (10 ⁻⁴⁰)
CO	0.361 (10 ⁻¹¹)	C	0.159 (10 ⁻⁴⁴)
O ₃	0.126 (10 ⁻¹¹)		

ppm and T = 1025 K were the maximum concentration and temperature employed.

Circulating gas electrode emf's.—In Fig. 2 are plotted the experimental emf results in the temperature range 525–1025 K for measurements made between the circulating gas electrodes for two series of experiments corresponding to two concentrations of CO₂ in synthetic air at the reference electrode. In the first series, measurements were made with the reference electrode fixed at 1,099 ppm CO₂, and the working electrode varied from 90.9 to 12,000 ppm CO₂. In the second series, the reference electrode was 948 ppm CO₂, and the working electrode 9.1 ppm CO₂. Measurements were made after increasing or decreasing temperatures as shown, and in all cases the flow rate of the gas in each electrode was 200 ml/min (measured at 298 K) at a total pressure of 1.0 atm. During the course of the experiments the solid electrolyte pellet was often examined and replaced. No discoloration or contamination of the pellet was ever detected.

The solid lines in Fig. 2 correspond to the theoretical values obtained from the simplified Nernst relationship of Eq. [7]. The agreement between the theoretical and measured values is good, except for the case where the concentration of CO₂ is 9.1 ppm. The theoretical values are also compared in Table III with the linear expression of emf as a function of T obtained from a least square regression analysis of the results. EMF data are often extrapolated down to 0 K in order to determine enthalpy values. The nonzero values of "a" in Table III calculated from the experimental data illustrate the weakness of such extrapolations.

In Fig. 3 are plotted, at selected temperatures, the measured emf (obtained from the regression analysis of Table III) as a function of P_{CO₂} for the case of 1099 ppm CO₂ at the reference electrode. The solid lines in this figure correspond to the theoretical values of Eq. [7].

From Fig. 2-3 and Table III it can be seen that in most cases there is good agreement between the measured and theoretical values, particularly when the concentrations of CO₂ at the two electrodes are similar. During the course of the experiments the electrodes were often short-circuited for several seconds, and the time required to return to a stable emf was recorded. It was noted that the response time for stable emf's varied from less than 1 sec to several minutes, depending upon the cell temperature and

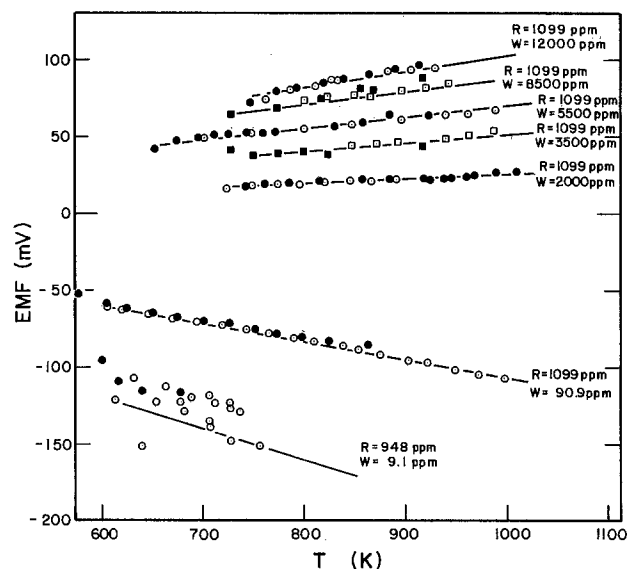


Fig. 2. EMF results for the circulating gas electrode. ● ■: After temperature increase; ○ □: after temperature decrease; —: calculated from Eq. [7]. R: reference electrode; W: working (measuring) electrode.

Table III. Comparison of measured and theoretical electromotive force using circulating gas electrodes

CO ₂ concentration (ppm)		Electromotive force (mV) $E = a + bT$				
Working electrode	Reference electrode	Measured (regression)		Standard deviation	Theoretical (Eq. [7])	
		a	b		a	b
9.1	984	33.04	-0.224	4.33	0	-0.200
90.9	1099	12.73	-0.119	1.15	0	-0.107
2,000	1099	-3.23	0.029	0.64	0	0.026
3,500	1099	-4.54	0.057	0.47	0	0.050
5,500	1099	7.21	0.060	0.55	0	0.069
8,500	1099	14.87	0.071	0.50	0	0.088
12,000	1099	7.39	0.095	1.06	0	0.103

concentration of CO₂ at the working electrode. The response time was longest at low temperatures and/or low concentrations of CO₂. The results were rejected in those cases where the emf did not return to its previous value or when stable values were difficult to obtain. For the case where the concentration of CO₂ at the working electrode was 9.1 ppm, it became increasingly difficult to obtain stable values at the lower temperatures. It was impossible to obtain a stable emf below 575 K even after 1 hr regardless of the concentration of CO₂.

Although the upper temperature limit was set at 1025 K, there appears to be no reason why reversible emf's could not be obtained up to the melting point of K₂CO₃ (1174 K). However, the electrolyte pellet may become too soft to support the cell housing (Fig. 1) at such temperatures.

In Fig. 4 are plotted the measurements of the emf at 923 K as a function of flow rate of gas (measured at 298 K) in the working electrode. The concentrations of CO₂ were fixed at 2000 and 1099 ppm in the working and reference electrodes, respectively. The flow rate in the reference electrode was maintained at 200 ml/min. It was found that the measured emf was independent of flow rate in the range 100-400 ml/min. Using the same temperature and gas mixtures, and a flow rate of 200 ml/min in both circulating electrodes, an experimental run which lasted 40 days was carried out. At all times the difference between the measured and the theoretical emf (23.80 mV) was never greater than 1.5 mV. This confirmed the stability of the Au supporting electrodes.

Decomposition of CaCO₃.—In Fig. 5 are plotted 31 emf measurements made between the calcium carbonate-oxide-gas electrode and the circulating gas reference electrode containing a concentration of 1050 ppm CO₂ in air flowing at 200 ml/min through the gas compartment. Measurements were made after both

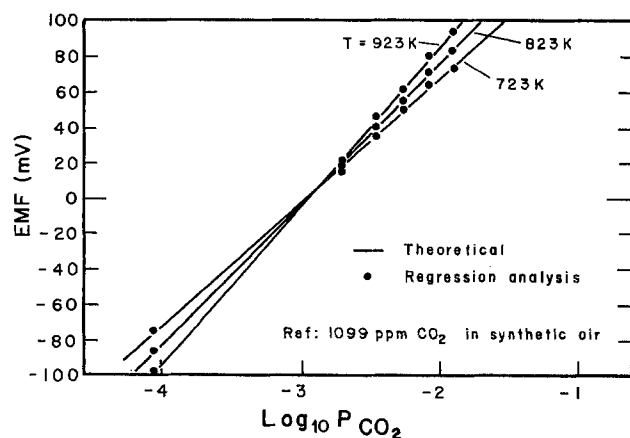


Fig. 3. EMF at selected temperatures as a function of P_{CO_2} . ●: Present investigation (regression analysis); —: calculated from Eq. [7].

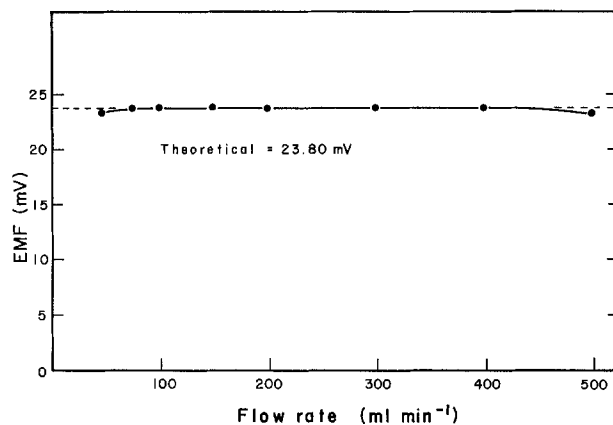


Fig. 4. EMF results at 923K as a function of flow rate with 2000 and 1099 ppm CO₂ in air in the working and reference electrodes, respectively.

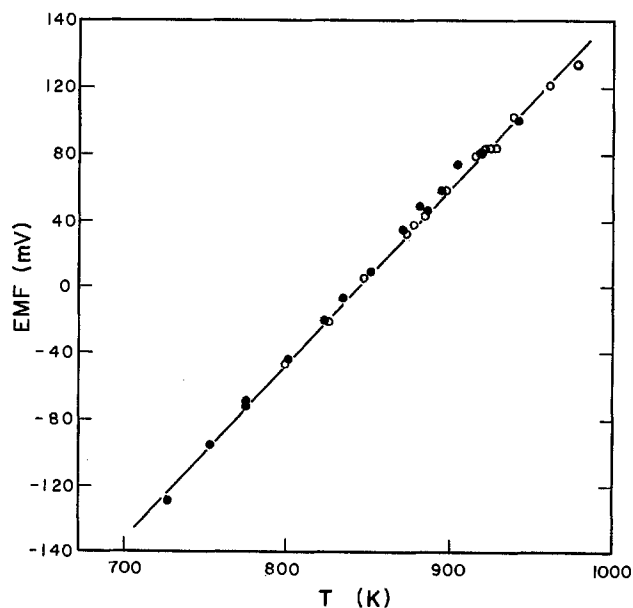


Fig. 5. EMF results for CaCO₃ dissociation with 1050 ppm CO₂ in air at the reference electrode. ●: Temperature increase; ○: temperature decrease; —: regression analysis of the results.

increasing and decreasing temperatures. Figure 5 summarizes the results of four different experimental runs using different samples of K₂CO₃ electrolyte and CaCO₃ powder. Examination of the cell at the end of each run showed that the electrolyte remained uncontaminated and that the calcium carbonate had not completely dissociated.

Stable emf's were obtained in the temperature range 725-975 K. Measurements made outside this range were rejected. At temperatures much higher than 975 K, the dissociation partial pressure of CO₂ becomes so large that the partial pressure of O₂ defined by air diffusing into the crucible can no longer be approximated at 0.21 atm, and so Eq. [7] is no longer valid. At 725 K, the dissociation partial pressure of CO₂ is approximately 10⁻⁵ atm; below this temperature it becomes too small to be measured. This is the same limit of CO₂ detection that was observed using the synthetic CO₂/air mixtures described previously.

Assuming a temperature independent enthalpy and entropy of dissociation of calcium carbonate, a linear least squares regression analysis of the measurements leads to the following expression for the temperature dependence of the standard Gibbs energy change of Eq. [9]

$$\Delta G^\circ = 169.55 - 0.1443 T \text{ kJ } (T = 725-975 \text{ K}) \quad [10]$$

(standard deviation = 0.41 kJ)

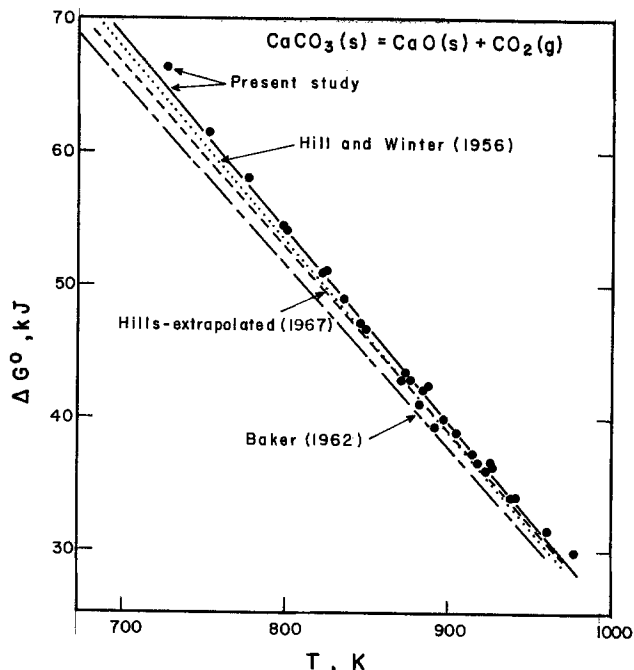


Fig. 6. Comparison of the data for the standard Gibbs energy change of the reaction; $\text{CaCO}_3(\text{s}) = \text{CaO}(\text{s}) + \text{CO}_2(\text{g})$.

This computed free-energy expression is compared with the data published in the literature in Fig. 6 and in Table IV. The results are in very good agreement with the data of Hill and Winter (8), who measured the total pressure of dissociation in the same temperature range as the present study. The difference between the results of the present study and the data of Hills (9) and Baker (10), which were obtained at higher temperatures, can be attributed to the effect of the small temperature dependence of the enthalpy and entropy of the reaction.

Error analysis.—There are several factors which can cause errors in the measured P_{CO_2} . As well as errors in preparing the reference gas mixture and measuring the cell temperature and emf, errors can be created by impurities in the gas mixtures.

Theoretical calculations using the F*A*C*T thermodynamic data treatment center (7), show that trace impurities of SO₂ and Cl₂ and even H₂O can have catastrophic effects upon the K₂CO₃ electrolyte due to the formation of K₂SO₄, KCl, and KOH.

Stable emf's are most difficult to obtain at low concentrations of CO₂ and low temperatures, particularly when there is a large difference in CO₂ concentration (and hence large emf) between the two electrode compartments.

The error in the measured concentration of CO₂ with respect to the error in the measured emf (ΔE), at a given temperature can be derived from Eq. [7] and is given by

$$\% \text{ error} = \left(1 - \exp \left[\frac{2F\Delta E}{RT} \right] \right) \times 100 \quad [11]$$

Table IV. Comparison of thermodynamic data for the reaction*

Source	ΔH° (kJ)	ΔS° (J/K)	Temp (K)
Hill and Winter (8)	168.41	143.9	722-1177
Baker (10)	161.34	137.2	1175-1483
Hills (9)	163.64	138.5	973-1173
Present study	169.55	144.3	725-975

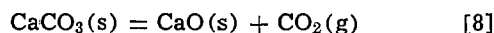
* Reaction: $\text{CaCO}_3(\text{s}) = \text{CaO}(\text{s}) + \text{CO}_2(\text{g})$.

In the case of the results of the circulating gas electrode, assuming a precision of 1.5 mV in the measured emf's for concentrations of CO₂ > 100 ppm, it follows from Eq. [11] that at 873 K there will be a maximum error of 3.9% in the measured P_{CO_2} at these concentrations. This error decreases with increasing temperature.

With respect to the measurements of the CaCO₃ decomposition, if we assume an error of ± 1 K in the value of the temperature, and an improbable error of 2 mV in the measured emf, it follows from Eq. [7] that overall precision in the measured Gibbs energy will be in the order of 500J. This value compares favorably with the experimental standard deviation of 0.41 kJ.

Summary

The equilibrium partial pressure of carbon dioxide in CO₂/synthetic air mixtures has been successfully measured by an electrochemical concentration cell using K₂CO₃ as a solid electrolyte in the temperature range 575-1025 K. Reversible emf's were obtained for mixtures containing as little as 9 ppm CO₂ in air. The cell response was less than 1 sec at high concentrations of CO₂ at high temperatures. An error analysis indicated a precision of 3-4% of the value of CO₂ for concentrations above approximately 100 ppm CO₂. The cell was used to measure the thermodynamic properties of calcium carbonate dissociation in the temperature range 725-975 K. By a least squares analysis applied to the results, the following free energy expression was calculated



$$\Delta G^\circ = 169.55 - 0.1443T \text{ kJ} \quad (T = 725-975 \text{ K}) \quad [10]$$

with a standard deviation = 0.41 kJ. An error analysis indicated a precision of 500J. The measured change in Gibbs energy is in good agreement with the published data from the literature, thus validating the use of K₂CO₃ as a CO₂ probe.

Manuscript submitted Dec. 4, 1982; revised manuscript received Sept. 7, 1983.

The Institute de Recherche d'Hydro-Québec assisted in meeting the publication costs of this article.

REFERENCES

- M. Gauthier and A. Chamberland, *This Journal*, **124**, 1579 (1977).
- M. Gauthier, A. Chamberland, A. Bélanger, and M. Poirier, *ibid.*, **124**, 1584 (1977).
- M. Gauthier, A. Bélanger, Y. Meas, and M. Kleitz, in "Solid Electrolytes," P. Hagenmuller and W. Van Gool, Editors, Chap. 12, Academic Press, New York (1978); M. Gauthier, R. Bellemare, and A. Bélanger, *This Journal*, **123**, 371 (1981).
- M. Gauthier and C. W. Bale, *Metall. Trans.*, **14B**, 117 (1983).
- P. Gervais, A. Chamberland, and M. Gauthier, IREQ Internal Report No. 1475.
- F. J. Salzano and L. Newman, *This Journal*, **119**, 1273 (1972).
- C. W. Bale, A. D. Pelton, and W. T. Thompson, "F*A*C*T — Facility for the Analysis of Chemical Thermodynamics," User's Manual Edition 1, McGill University/Ecole Polytechnique, Quebec (1979); supplement "Equilib" (1981).
- K. J. G. Hill and E. R. S. Winter, *J. Phys. Chem.*, **60**, 1361 (1956).
- A. W. D. Hills, *Inst. Min. Met. Trans., Sec. C*, **76**, 241 (1967).
- E. H. Baker, *J. Chem. Soc.*, **122**, 464 (1962).

Determination of Activity Coefficients for KCl at Elevated Temperatures

W. F. Bogaerts* and A. A. Van Haute

Leuven University (K. U. Leuven), Institute for Industrial Chemistry de Croylaan 2, B-3030 Leuven (Heverlee), Belgium

ABSTRACT

A real breakthrough in high temperature-high pressure electrochemical measurements will depend on the availability of precision reference electrode systems, which in turn require an accurate knowledge of activity coefficients of the reference electrolyte solution. The paper summarizes available literature and evaluates different approximating equations. It also derives a new calculation method, which is applied on KCl electrolytes and which seems to provide very accurate results for activity coefficients at temperatures up to 300°C. Reliable data have been derived for KCl concentrations up to about 4 molal.

The Ag/AgCl/KCl reference electrode system is frequently used in high temperature-high pressure electrochemical measurements. In order to calculate the Nernstian response of the system as a function of temperature, activity coefficients at each temperature must be known. Unfortunately, literature data on high temperature activity coefficients are rather scarce, particularly on KCl electrolytes.

An array of useful experimental results for simple aqueous solutions at elevated temperatures is listed in Table I (γ_{\pm} : mean molal ionic activity coefficient; ϕ : molal osmotic coefficient).

As can be seen in Table I, a complete set of activity data for NaCl is readily available for temperatures up to 300°C (8, 9, 11-13). Data for the KCl-H₂O system, however, are not, except for some recently published, isolated data in the 200°-250°C range (40). In spite of the general observation that the individual ionic character of the different alkali metal halides (and probably most 1:1 electrolytes) is much less pronounced at high temperatures (14, 15), there is a considerable difference between the activity coefficients for NaCl and KCl at room temperature (e.g., for 1m NaCl and KCl at 25°C, $\gamma_{\pm} = 0.657$ and 0.604, respectively). This indicates that the NaCl data cannot be directly applied to the KCl system over the whole temperature range, as has been done in some earlier electrochemical investigations at moderately high temperatures.

Existing Equations

Different ways have been suggested in the literature to derive approximate KCl activity coefficients from available data on other systems or from values at lower temperatures.

Based on lower temperature observations, Danielson (23) and Seys (24, 25) assumed that $(\partial \ln \gamma_{\pm} / \partial T)_m$ is the same for NaCl and KCl solutions. By combining this expression with the least squares fit cubic function of $\ln \gamma_{\pm}$ vs. T given by Gardner (8) for NaCl solutions, and fitting the equation to the activity coefficient value of 1m KCl at 25°C, Danielson obtained for 1 molal KCl solution

$$\ln \gamma_{\pm}(T) = 2.113 - 0.0213T + [0.5897 \times 10^{-4}]T^2 - [0.568 \times 10^{-7}]T^3 \quad [1]$$

where T is in degrees Kelvin.

Following the same procedure, similar expressions may be derived for other concentrations

$$\begin{aligned} 0.5\text{m KCl: } \ln \gamma_{\pm}(T) &= 2.005 - 0.0196T \\ &+ [0.5325 \times 10^{-4}]T^2 - [0.501 \times 10^{-7}]T^3 \quad [2] \end{aligned}$$

* Electrochemical Society Active Member.
Key words: electrolyte, electrode, emf.

$$\begin{aligned} 2.0\text{ m KCl: } \ln \gamma_{\pm}(T) &= 1.597 - 0.0181T \\ &+ [0.5266 \times 10^{-4}]T^2 - [0.543 \times 10^{-7}]T^3 \quad [3] \end{aligned}$$

$$\begin{aligned} 3.0\text{m KCl: } \ln \gamma_{\pm}(T) &= 0.884 - 0.0127T \\ &+ [0.3999 \times 10^{-4}]T^2 - [0.459 \times 10^{-7}]T^3 \quad [4] \end{aligned}$$

Seys (24, 25) has used a graphic extrapolation method, based on the same principle, for estimating mean ionic activity coefficients of 0.01N-0.1N KCl solutions at elevated temperatures. Although the basic equation of these methods can hardly be assumed to be exact at each temperature, fairly good approximations may be expected at elevated temperatures and rather low concentrations.

Another approximate calculation technique has been derived by Cobble (26)

$$\log \gamma_{\pm}(T) = \log \gamma_{\pm}(25^{\circ}\text{C}) - [I^{1/2}/(1 + I^{1/2})] \cdot [A\gamma^T - A\gamma^{25^{\circ}\text{C}}] \quad [5]$$

which may be obtained by using an extended form of the Debye-Hückel equation (Guggenheim equation)

Table I. Activity-related data on high temperature aqueous solutions

Ref.	Reported data type	Experimental method*	Solute	Temp (°C)	Molality
(1)	γ_{\pm}, ϕ	emf	NaCl	15-45	0.002-0.1
(2)	γ_{\pm}	emf	NaCl	15-50	0.01-1.0
(3)	γ_{\pm}, ϕ	emf	KCl	15-45	0.002-0.1
(4)	γ_{\pm}, ϕ	bp	NaCl	60-100	0.05-4.0
(5)	γ_{\pm}, ϕ	bp	KBr	60-100	0.1-4.0
(6)	ϕ	vp	NaCl	25-100	1.0-6.1
(7)	ϕ	vp	NaCl	125-270	1.0-3.0
(8)	ϕ, γ_{\pm}	vp	NaCl	125-270	0.5-3.0
(9)	γ_{\pm}	comp	NaCl	25-300	1.0-3.0
(10)	ϕ	vp	NaCl	125-300	0.1-1
(11, 12)	ϕ, γ_{\pm}	vp	NaCl	75-300	(0)-sat
(13)	γ_{\pm}	vp	NaCl	130-350	0.5-5.0
(11)	ϕ	vp	MgSO ₄	75-200	0.4-1.5 (4)
(11)	ϕ	vp	MgCl ₂	75-300	0.4-5
(14)	ϕ, γ_{\pm}	vp	MgCl ₂	25-300	(0)-sat
(15)	ϕ	vp	Li-, Na-, CsCl	0-300	1
(16)	ϕ	isop	a.o.KCl†	99.6	(0.8-5)
(17)	ϕ	isop	a.o.KCl†	121.1	(0.5-6.5)
(18)	ϕ	isop	a.o.KCl†	140.3	(0.25-10)
(38, 39)	ϕ	isop	Li-, K-, CsCl	110-200	(1)-(3)-7)
(40)	ϕ, γ_{\pm}	isop	Li-, K-, CsCl	225, 250, 0-90	(0.7-8), (1.46-8)
(19)	γ_{\pm}	emf	HCl	0-90	0.001-0.1
(20)	γ_{\pm}, ϕ	emf	HCl	25-275	0.001-1.0
(21)	γ_{\pm}	emf	HCl	25-200	0.01-0.1
(22)	γ_{\pm}	emf	HBr	25-200	0.001-1.0

* emf: electrochemical cell; bp: boiling point elevation; vp: vapor pressure lowering; comp: γ_{\pm} values computed from osmotic coefficients given in Ref. (4, 7); isop: isopiestic comparison (vs. NaCl).

† Data reported on (NaCl), KCl, LiCl, CsCl, Na₂SO₄, BaCl₂, MgSO₄, and UO₂SO₄.

$$\log \gamma^{\pm} = -A\gamma^T \cdot |z_+ \cdot z_-| \cdot [I^{1/2}/(1 + I^{1/2})] \\ + 2[\nu_+ \cdot \nu_-/\nu] \cdot B_{(m)} \cdot m \quad [6]$$

and assuming that the concentration dependent parameter $B_{(m)}$, which varies from solute to solute, is independent of the temperature. $A\gamma^T$ is given as

$$A\gamma^T = [2\pi N_{APW}/2.303]^{1/2} \cdot [e^2/\epsilon kT]^{3/2} \quad [7]$$

Values of $A\gamma^T$ taken from Cobble (26) and Silvester and Pitzer (36), are given for different temperatures in Table II. These data are preferred over those of Cohen (37) or Dobson (27), since the former are based on a fitting of more literature data.

The assumption that $B_{(m)}$ is independent of temperature has been proven to be incorrect (9, 12, 27), and deviations from the predicted behavior (Eq. [5]) may be expected. The usefulness of the method has been tested by Macdonald (28) for low concentrations of HCl and HBr (0.001, 0.01, and 0.1m). Additional tests for higher concentrations and for NaCl solutions are shown in Fig. 1 and 2.

The differences between calculated and measured activity coefficients are rather small at lower temperatures and/or low concentrations. For the NaCl-H₂O system, Eq. [5] gives values which are too low in the lower temperature range and too high at the higher temperatures (> approximately 250°C). Deviations increase with increasing concentration.

Dobson (27), using a Guggenheim-type expression for $\log \gamma^{\pm}$ with two terms

$$\log \gamma^{\pm} = [-z^2 \cdot A\gamma^T \cdot I^{1/2}/(1 + I^{1/2})] \\ + B \cdot I + C \cdot I^{3/2} \quad [8]$$

and trying to take into account the temperature dependence of these correction terms (cf. B of Eq. [6]), gives the following equation for the mean ionic activity coefficient of KCl

$$\log \gamma^{\pm}(T) = -[A\gamma^T \cdot I^{1/2}/(1 + I^{1/2})] \\ + [-0.134964 + 0.599323 \times 10^{-3} \times T] \cdot I \\ + [0.052002 - 0.20659 \times 10^{-3} \times T] \cdot I^{3/2} \quad [9]$$

An analogous expression is given for HCl

$$\log \gamma^{\pm}(T) = -[A\gamma^T \cdot I^{1/2}/(1 + I^{1/2})] \\ + [0.232448 - 0.2172 \times 10^{-3} \times T] \cdot I \\ + [0.40129 - 0.16861 \times 10^{-3} \times T] \cdot I^{3/2} \quad [10]$$

Equation [9] and [10] were said to represent activity coefficients up to at least 5m and 150°C.

The validity of these equations for estimating activity coefficients at elevated temperatures has been tested in Fig. 1 and Tables III and IV. Up to about 0.1m, Eq. [10]

Table II. Debye-Hückel parameter $A\gamma^T$ at different temperatures

T (°C)	$A\gamma^T$	T (°C)	$A\gamma^T$
10	0.4977	140	0.6693
20	0.5053	150	0.6894 (0.6899)*
25	0.5094	160	0.7106
30	0.5139	170	0.7331
40	0.5234	175	0.7451
50	0.5339	180	0.7570
60	0.5453	190	0.7824
70	0.5575	200	0.8094 (0.8097)*
75	0.5641	220	0.8690
80	0.5707	225	0.8863
90	0.5847	240	0.9381
100	0.5997	250	0.983 (1.012)*
110	0.6156	260	1.020
120	0.6325	275	1.095 (1.198)*
125	0.6415	280	1.120
130	0.6504	300	1.248 (1.294)*
		325	1.475
		350	1.881 (2.026)*

* Ref. (37).

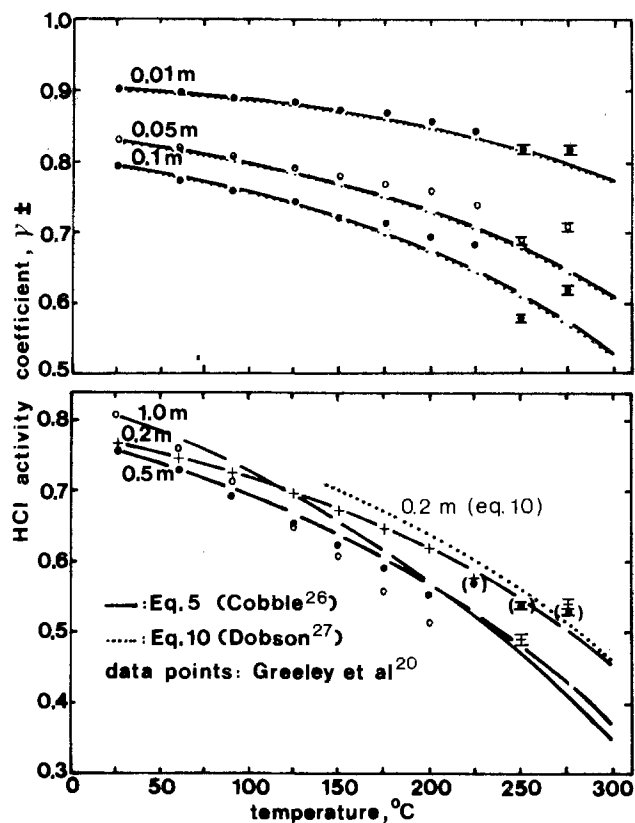


Fig. 1. Mean ionic activity coefficients for HCl solutions as a function of temperature (full lines: calculated using Eq. [5] (26); dotted lines: Eq. [10] (27); experimental data points are taken from (20).

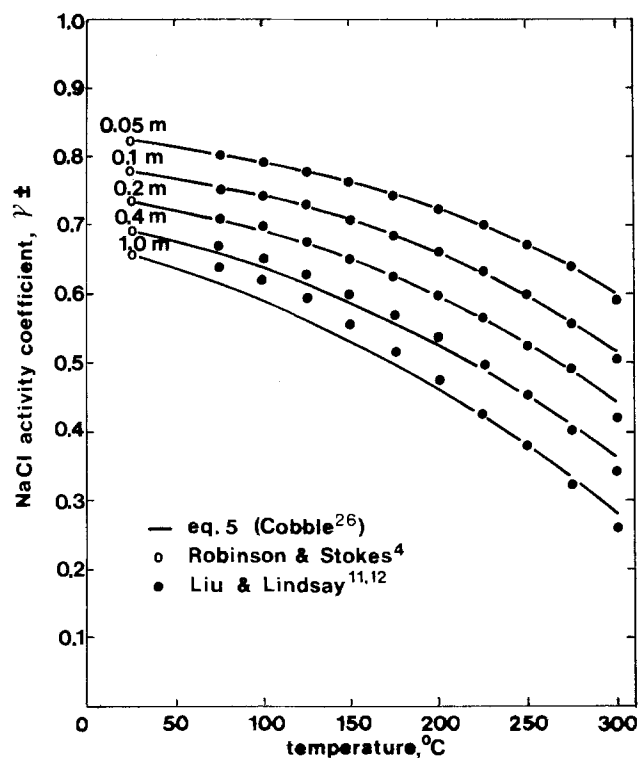


Fig. 2. Mean ionic activity coefficients for NaCl in aqueous solutions as a function of temperature (full lines: calculated using Eq. [5] (26); data points are taken from (4, 11, 12).

for HCl gives practically the same values as Eq. [5]. From 0.2m on, however, very large errors are found, even at low temperatures. Therefore, the equation for HCl activity coefficients as presented by Dobson in Ref. (27) is considered to be in error. There may also

Table III. Estimation of mean ionic activity coefficients for a 1m KCl solution at elevated temperatures by means of different equations

T (°C)	$(\phi_{\text{NaCl}} - \phi_{\text{KCl}})_{\text{est}}$	$\gamma_{\pm\text{NaCl}}/\gamma_{\pm\text{KCl}}$ Eq. [17]	$\gamma_{\pm\text{NaCl}}$ Ref. (11, 12)	$(\gamma_{\pm\text{KCl}})_{\text{est}}^a$ cf. Eq. [17]	$\gamma_{\pm\text{KCl}}^b$ Eq. [11]	$\gamma_{\pm\text{KCl}}^c$ Eq. [5]	$\gamma_{\pm\text{KCl}}^d$ Eq. [9]
75	0.036	1.075	0.640	0.596	0.576	0.568	0.591
100	0.035	1.073	0.624	0.582	0.563	0.545	0.580
125	0.033	1.068	0.594	0.556	0.547	0.519	0.568
150	0.029	1.060	0.557	0.526	0.525	0.491	0.548
175	0.025	1.051	0.517	0.492	0.496	0.460	(0.526)
200	0.020	1.041	0.474	0.455	0.459	0.428	(0.499)
225	0.019	1.039	0.428	0.412	0.413	0.392	(0.467)
250	0.018	1.037	0.378	0.365	0.360	0.350	(0.410)
275	0.013	1.026	0.323	0.315	0.302	0.308	(0.384)
300	0.008	1.016	0.261	0.257	0.243	0.258	(0.330)

* Data given by Holmes and Mesmer are 0.412 at 225°C and 0.368 at 250°C (40), respectively.

^a Own derivation; ^b Danielson equation; ^c Cobble equation; ^d Dobson equation.

Table IV. Comparison of calculated and observed mean ionic activity coefficients of a 0.1m KCl solution at different temperatures

T (°C)	$\phi_{\text{NaCl}} - \phi_{\text{KCl}}$ Ref. (1, 3)	$\gamma_{\pm\text{NaCl}}/\gamma_{\pm\text{KCl}}$ Eq. [17]	$\gamma_{\pm\text{KCl}}$ cf. Eq. [17]	$\gamma_{\pm\text{KCl}}$ observed; Ref. (3)	$\gamma_{\pm\text{KCl}}$ Eq. [9]
15	0.0053	1.0107	0.7700	0.7697	—
25	0.0056	1.0113	0.7681	0.7679	0.7610
30	—	—	—	—	0.7598
35	0.0057	1.0115	0.7653	0.7649	—
40	—	—	—	—	0.7568
45	0.0055	1.0111	0.7618	0.7617	—

be some doubt about the usefulness of Eq. [9], especially for temperatures higher than 150°C. This is indicated in Table III and IV. KCl activity coefficients larger than the ones which have been estimated for NaCl are calculated by means of Eq. [9] at the elevated temperatures.

Development of More Reliable Data

Another method, which might provide more reliable results in our case (but which implies the availability of some osmotic data) is similar to the idea suggested by Lindsay *et al.* (14).

Experimental osmotic coefficient data are correlated by a general equation of the form

$$\phi = 1 - DH(\beta, m) + Bm + Cm^2 + \dots \quad [11]$$

which is related through the Gibbs-Duhem relation

$$\phi(T, m) = 1 + \frac{1}{m} \int_0^m m \cdot d \cdot \ln \gamma_{\pm}(T, m) \quad [12a]$$

or

$$\phi(T, m) = 1 + \ln \gamma_{\pm}(T, m) - \frac{1}{m} \int_0^m \ln \gamma_{\pm}(T, m) \cdot dm \quad [12b]$$

to an extended form of Debye-Hückel equation with both a linear and a quadratic correction term

$$\ln \gamma_{\pm} = -[\alpha m^{1/2}/(1 + \beta m^{1/2})] + 2Bm + 1.5Cm^2 \quad [13]$$

The coefficients β (which contains the ion-size parameter), B , and C are adjustable temperature dependent parameters. $DH(\beta, m)$ is the Debye-Hückel term, given by

$$DH(\beta, m) = [\alpha/\beta^3 \cdot m] ([1 + \beta m^{1/2}] - 2 \ln [1 + \beta m^{1/2}] - [1 + \beta m^{1/2}]^{-1}) \quad [14]$$

where α is the Debye-Hückel limiting slope ($\alpha = A\gamma^T \cdot \ln 10$).

Up to 1m, the experimental NaCl osmotic coefficients could best be represented by putting $C = 0$ in Eq. [11] (14)

$$\phi = 1 - DH(\beta, m) + Bm \quad [15]$$

According to Fig. 3, it seems reasonable that the KCl osmotic coefficients can also be described by a similar equation.

Additionally, if the β parameters can be assumed to be equal for NaCl and KCl,¹ then

$$\phi_{\text{NaCl}} - \phi_{\text{KCl}} = [B_{\text{NaCl}} - B_{\text{KCl}}] \cdot m \quad [16]$$

It follows that

¹ This is not unreasonable, since ion size parameters for NaCl and KCl may be expected to be nearly equal (35). A value of $\beta = 1.5$ is typical. Even if the best fitting β_{KCl} is slightly different from β_{NaCl} , we can assume a coefficient β'_{KCl} which is equal to β_{NaCl} . Differences, introduced by using this new β'_{KCl} value, may be cancelled by a modified value for B_{KCl} .

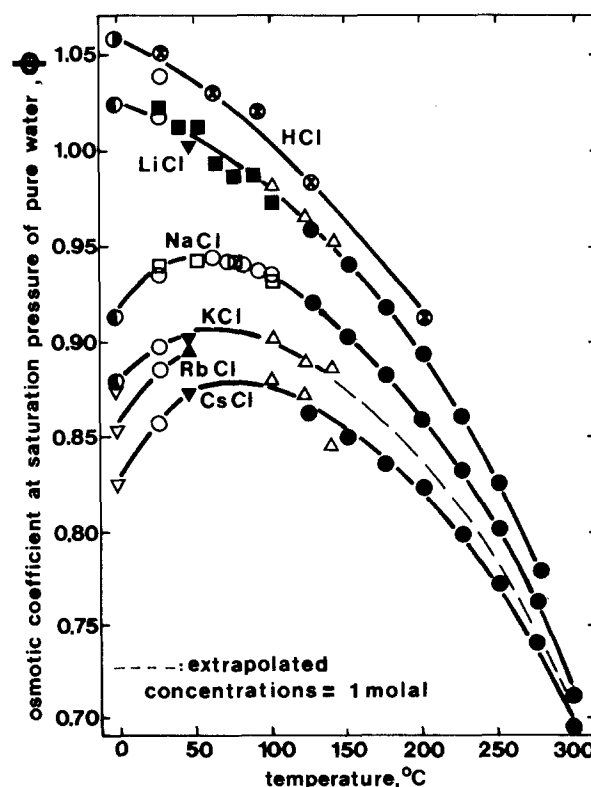


Fig. 3. Temperature dependence of osmotic coefficients of 1m alkali metal chlorides and HCl. Compilation of data from different sources: ● Ref. (15); ○ Ref. (4); ⊙ Ref. (29); ⊚ Ref. (30); ⊠ Ref. (20); ▲ Ref. (31); △ Ref. (16-18); ▼ Ref. (32); ▽ Ref. (33); ■ Ref. (41); □ Ref. (34).

$$\ln [\gamma_{\pm \text{NaCl}} / \gamma_{\pm \text{KCl}}] = 2[B_{\text{NaCl}} - B_{\text{KCl}}] \cdot m \quad [17]$$

Values of ΔB ($\equiv B_{\text{NaCl}} - B_{\text{KCl}}$) may be directly estimated from the plots of ϕ vs. temperature for the 1 molal solutions (Fig. 3). The corresponding values of $(\phi_{\text{NaCl}} - \phi_{\text{KCl}})$, $\gamma_{\pm \text{NaCl}} / \gamma_{\pm \text{KCl}}$, and $\gamma_{\pm \text{KCl}}$ are shown in Table III. Extrapolation errors may be expected to be lower than ca. 1%.

The same procedure can be followed at other concentrations. However, since less osmotic coefficient data are available at these concentrations (Table I), many data must be extrapolated, and the expected accuracy will be smaller.

A test for the accuracy of the method is shown in Table IV. Remarkably good agreement is obtained between the activity coefficients calculated by means of the present method and values and tabulated in standard texts. Extremely close agreement is also obtained with the experimental data of Holmes and Mesmer at 225° and 250°C (40).

It may be concluded that the above method seems to provide very reliable results for calculating high temperature activity data. However, sufficient osmotic data must be available. Up to about 150°C, these may be provided by results of Soldano *et al.* (16-18). At more elevated temperatures, only sporadic results are available (14, 38, 40), and extrapolations and interpolations are necessary. Data obtained from the other equations might provide additional results (cf. Table III).

The final results of the calculations based on Eq. [17] are presented in Fig. 4. Some experimental data points and results obtained by other equations are also shown.

Conclusions

Available activity coefficients for different solutions at elevated temperatures have been summarized in Table I. Sufficient data for KCl solutions, which are of particular interest for high temperature electrochemical measurements, are not present; at least not up to temperatures of about 300°C, which are especially impor-

tant for a number of power generating or cooling systems.

Different ways suggested in the literature for deriving approximate KCl activity coefficients from available data on other electrolytes or from values at lower temperatures have been evaluated. None seems to be completely satisfying, and a new calculation method has been derived. The latter is based on the knowledge of activity data for NaCl and a limited number of osmotic coefficients or KCl solutions at elevated temperatures. Reliable data for KCl activity coefficients have been calculated in this way for temperatures up to 300°C and concentrations up to about 4 molal (Fig. 4). If additional osmotic data for KCl at higher concentrations become available—such as those of Holmes and Mesmer at 225° and 250°C—extensions are easily possible and more precise activity coefficients can be obtained at higher concentrations.

Comparison of data for NaCl and KCl clearly shows that a substitution of KCl activity coefficients by NaCl values, as has been done in most of the earlier electrochemical corrosion studies at elevated temperatures, can lead to imprecise or erroneous conclusions, especially at lower or intermediate temperatures and at moderate or higher solute concentrations.

Manuscript submitted April 7, 1983; revised manuscript received July 26, 1983.

Leuven University assisted in meeting the publication costs of this article.

LIST OF SYMBOLS

I	ionic strength ($= 0.5 \sum_i m_i z_i^2$)
z_+, z_-	electronic charges of the positive and negative ions
ν_+, ν_-	stoichiometric coefficients ($\nu = \nu_+ + \nu_-$)
N_A	Avogadro's number
ρ_w	density of water
T	absolute temperature (degrees Kelvin)
ϵ	dielectric constant of pure water
k	Boltzmann's constant
e	absolute electronic charge

REFERENCES

- G. J. Janz and A. R. Gordon, *J. Am. Chem. Soc.*, **65**, 218 (1943).
- A. H. Truesdell, *Science*, **161**, 884 (1968).
- W. J. Hornibrook, G. J. Janz, and A. R. Gordon, *J. Am. Chem. Soc.*, **64**, 513 (1942).
- R. A. Robinson and R. H. Stokes, "Electrolyte Solutions," 2nd rev. ed., p. 480, Butterworths, London (1959); compilation of data from R. P. Smith and D. S. Hirtle, *J. Am. Chem. Soc.*, **61**, 1123 (1939).
- R. A. Robinson and R. H. Stokes, "Electrolyte Solutions," 2nd rev. ed., p. 480, Butterworths, London (1968); compilation of data from G. C. Johnson and R. P. Smith, *J. Am. Chem. Soc.*, **63**, 1351 (1941).
- H. F. Gibbard, G. Scatchard, R. A. Rocesseau, and J. L. Creek, *J. Chem. Eng. Data*, **19**, 281 (1974).
- E. R. Gardner, P. J. Jones, and H. J. de Nordwall, *Trans. Faraday Soc.*, **59**, 1994 (1963).
- E. R. Gardner, *ibid.*, **65**, 91 (1969).
- H. C. Helgeson, *Am. J. Sci.*, **267**, 729 (1969).
- C. Liu and W. T. Lindsay, *J. Phys. Chem.*, **74**, 341 (1970).
- C. Liu and W. T. Lindsay, "Thermodynamic Properties of Aqueous Solutions at High Temperatures," Final report to Office for Saline Water under Contract No. 14-01-0001-2126, U.S. Government Printing Office, Washington, D.C. (1971).
- C. Liu and W. T. Lindsay, *J. Solution Chem.*, **1**, 45 (1972).
- N. A. Atonov, V. N. Gilyarnov, V. I. Zarembo, and M. K. Federov, *Zh. Prikl. Khim.*, **49**, 120 (1976).
- W. T. Lindsay and C. Liu, *NACE*, **4**, 139 (1976).
- W. T. Lindsay and C. Liu, *J. Phys. Chem.*, **75**, 3723 (1971).
- C. S. Patterson, L. O. Gilpatrick, and B. A. Soldano, *J. Chem. Soc.*, **120**, 2730 (1960).
- B. A. Soldano and C. S. Patterson, *ibid.*, **122**, 937 (1962).

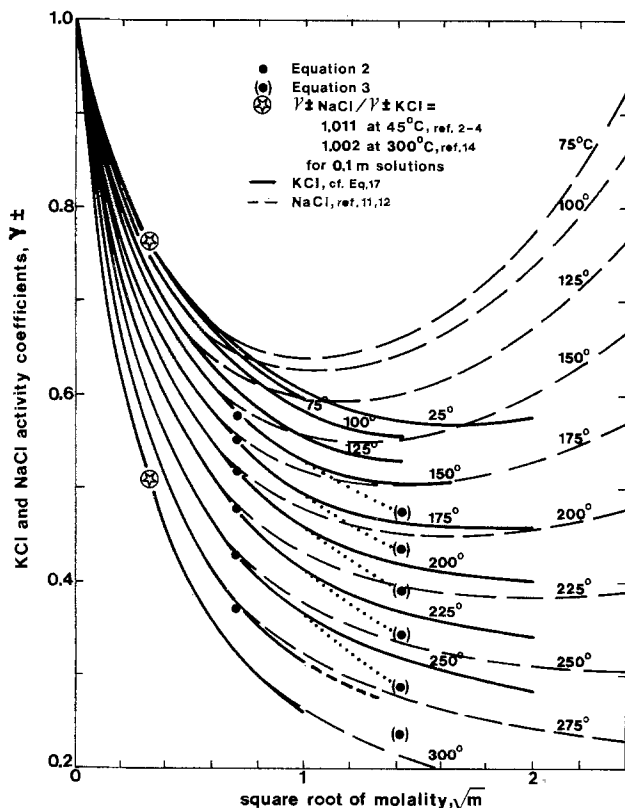


Fig. 4. Estimated mean ionic activity coefficients for KCl solutions at elevated temperatures. Broken lines indicate NaCl activity coefficients for comparison.

18. B. A. Soldano and M. Meek, *ibid.*, **123**, 4424 (1963).
19. R. G. Bates and V. E. Bower, *J. Res. Nat. Bur. Stand.*, **53**, 283 (1954).
20. R. S. Greeley, W. T. Smith, M. H. Lietzke, and R. W. Stoughton, *J. Phys. Chem.*, **64**, 1445 (1960).
21. T. Izaki and K. Arai, *Suiyokai-Shi*, **16**, 367 (1968).
22. M. B. Towns, R. S. Greeley, M. H. Lietzke, and R. W. Stoughton, *J. Phys. Chem.*, **64**, 1861 (1960).
23. M. J. Danielson, *Corrosion*, **35**, 200 (1979).
24. A. A. Seys, A. A. Van Haute, and T. Fujii, *NACE*, **4**, 467 (1976).
25. A. A. Seys, Ph.D. Thesis, University of Leuven, Belgium (1972).
26. J. W. Cobble, *J. Am. Chem. Soc.*, **86**, 5394 (1964).
27. J. V. Dobson, "Advances in Corrosion Science and Technology," Vol. 7, p. 224 (1980).
28. D. D. Macdonald, "Modern Aspects of Electrochemistry," Vol. 11, p. 141 (1975).
29. G. Scatchard and S. S. Prentiss, *J. Am. Chem. Soc.*, **55**, 4355 (1933).
30. H. M. Chadwell, *J. Am. Chem. Soc.*, **49**, 2795 (1927).
31. L. L. Makarov, Y. G. Vlasov, and V. I. Isotov, *Russ. J. Phys. Chem.*, **38**, 1297 (1964).
32. K. L. Hellams, C. S. Patterson, B. H. Prentice, and N. J. Taylor, *J. Chem. Eng. Data*, **10**, 323 (1965).
33. G. Karagunis, A. Hawkinson, and G. Damköhler, *Z. Phys. Chem. (Leipzig)*, **151**, 433 (1930).
34. H. F. Gibbard, Ph.D. Thesis, M.I.T., Cambridge, MA (1966).
35. J. O'M. Bockris and A. K. Reddy, "Modern Electrochemistry 1," 3rd ed., p. 244, Plenum, New York (1977).
36. L. F. Silvester and K. S. Pitzer, *J. Phys. Chem.*, **81**, 1822 (1977).
37. P. Cohen, "The Chemistry of Water and Solutions at High Temperatures for Application to Corrosion in Power Systems," Report to the US Atomic Energy Commission (1972).
38. H. F. Holmes, C. F. Baes, and R. E. Mesmer, *J. Chem. Thermodyn.*, **10**, 983 (1978).
39. H. F. Holmes and R. E. Mesmer, *ibid.*, **13**, 1035 (1981).
40. H. F. Holmes and R. E. Mesmer, *J. Phys. Chem.*, **87**, 1242 (1983).
41. H. F. Gibbard and G. Scatchard, *J. Chem. Eng. Data*, **18**, 293 (1973).

Anodic Iridium Oxide Films

XPS-Studies of Oxidation State Changes and O₂-Evolution

R. Kötz, H. Neff, and S. Stucki

Brown Boveri Research Center, 5405 Baden, Switzerland

ABSTRACT

The anodic oxidation of iridium and O₂ evolution on iridium oxide films in 1N H₂SO₄ has been investigated using x-ray photoelectron spectroscopy. The binding energy of the O 1s level decreases with anodic polarization of the electrode while the relative amount of oxygen compared to iridium remains constant. The XPS results are consistent with a model of subsequent deprotonation of the anodic iridium oxide upon anodic polarization. A reaction path for O₂ evolution and corrosion on iridium oxide is proposed. Valence band spectra of the oxide surfaces confirm the proposed model.

Iridium oxide films have attracted much attention recently for two reasons. First, these films exhibit high electrocatalytic activity for the anodic oxygen evolution (1, 2). Second, the anodic iridium oxide films show a pronounced electrochromic effect (3).

The electrocatalytic properties of iridium oxide films for the O₂ evolution reaction in acid electrolytes are excellent. They are only exceeded by those of the ruthenium oxide. Both materials, however, suffer from substantial corrosion during O₂ evolution at high current densities. The favored anode catalyst for water electrolysis in acid electrolytes turns out to be a mixed oxide of ruthenium and iridium (4).

In order to gain a further understanding of the O₂ evolution mechanism on the mixed oxides, we have investigated the anodic behavior of the single components. Recently, we proposed a model for the O₂ evolution reaction and corrosion on ruthenium oxides, based mainly on XPS results (5). O₂ evolution and corrosion on ruthenium starts from a surface site with Ru in the hexavalent state. After two consecutive deprotonation steps, oxygen is released from RuO₄.

In the present study, we have applied x-ray photoelectron spectroscopy (XPS) in order to determine changes in the composition of the iridium oxide electrode surface leading to the O₂ evolution reaction. On a metallic iridium electrode, oxygen evolution is preceded by the formation of a thin oxide layer. This was demonstrated by Mozota and Conway using voltammetry (6) and recently in our laboratory with the aid of XPS (7). The thickness of this oxide layer can be increased substantially by periodic potential cycling. Oxide layers grown by potential cycling exhibit an

electrochromic effect, which results from a reversible redox reaction of the iridium in the bulk of the film. Because of the electrochromic effect, which might be useful for display applications, the charge storage mechanism in iridium oxides has been investigated extensively (3, 8-11). McIntyre *et al.* (8) have demonstrated that the electrochromism is due to a cation-insertion mechanism. In an aqueous electrolyte, the charge arising from the oxidation or reduction of the film is compensated by a transfer of protons between the bulk of the film and the electrolyte. The stoichiometry of the transferred proton is either H⁺ or H₃O⁺. It is, however, not clear whether the above mechanism, which has been proved with a mildly surface-insensitive technique (Rutherford backscattering spectroscopy), holds also for the surface of the oxide where O₂ evolution should take place. In addition, it has to be examined whether an analogous mechanism with proton transfer can be formulated for the oxygen evolution reaction.

XPS has been used effectively as a surface-sensitive technique in several studies of electrochemically modified electrode surfaces (12). Although there are still some questions as to what extent the electrochemical interface is preserved upon emersion and transfer to the vacuum chamber, the successful correlation of XPS results and electrochemical parameters demonstrates the usefulness of this *ex situ* method for electrode surface analysis (13).

Experimental

The XPS measurements were performed in a Kratos ES 300 electron spectrometer using non-monochromatized AlK_α radiation. The overall spectral resolution was 1.2 eV, and the measured binding energies were

calibrated against the Au $4f_{7/2}$ line at 84.0 eV. The photoelectrons were detected at normal emission.

The electrochemical experiments were performed in 1N H_2SO_4 using the standard three-electrode potentiostatic arrangement. All potentials are quoted with respect to the saturated calomel electrode (SCE). The anodic iridium oxide films were grown by periodically stepping the potential of a metallic iridium working electrode between $-0.25 V_{SCE}$ and $+1.30 V_{SCE}$ with a step frequency of 1 Hz.

The iridium electrodes were prepared as thin films by rf sputtering from an iridium target (4N) onto glass substrates. Iridium oxide films were also prepared by reactive sputtering of iridium in an Ar atmosphere with an O_2 partial pressure of 10^{-3} Torr (2).

Before any sequence of electrochemical measurements, the iridium samples were Ar ion sputtered until no oxygen or carbon was detectable by XPS. The electrodes were removed from the electrolyte under potential control and immediately transferred to the electron spectrometer using a fast insertion lock.

Results

In Fig. 1, voltammograms are shown for a metallic iridium electrode and an anodic iridium-oxide film obtained by potential cycling. The charge storage capacity of the oxide is clearly reflected by the considerable broadening of the voltammogram above $0.5 V_{SCE}$. At more cathodic potentials, the measured current is comparable to that of the clean metal surface. The wave at $0.7 V_{SCE}$ for the iridium oxide is accompanied by a coloration of the film from clear to dark blue in an anodic potential scan. Similar curves have been measured and discussed before by several authors (8-11).

The oxide formed on an iridium metal electrode due to one anodic scan up to $1.3 V_{SCE}$ appears to have properties comparable to those of the thick anodic oxide. The pronounced waves in the voltammogram of the oxide at $0.7 V_{SCE}$ and at $1.15 V_{SCE}$ are also indicated in the cathodic potential scan of the iridium metal electrode at $0.75 V_{SCE}$ and $1.1 V_{SCE}$, respectively.

XPS results of anodic iridium oxide films are displayed in Fig. 2. The anodic films were grown to a moderate thickness by potential cycling and removed

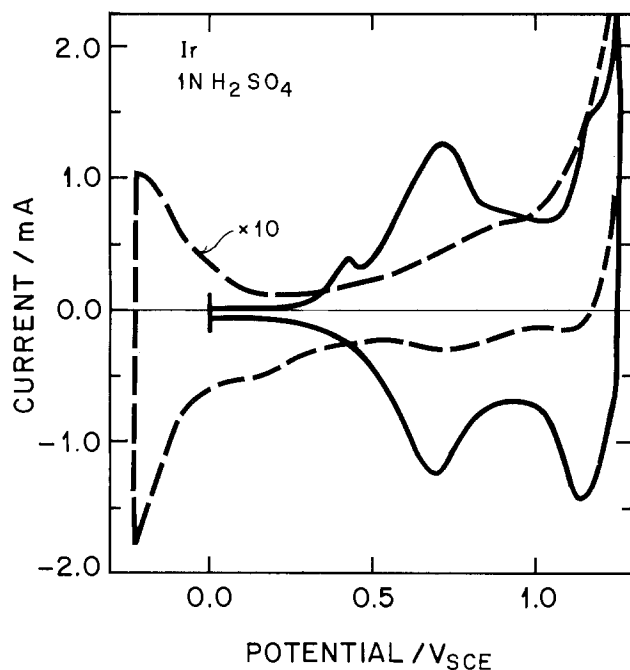


Fig. 1. Voltammogram of iridium (---) and an anodic iridium oxide film (—) in 1N H_2SO_4 . Scan rate: 100 mV/s; temperature: $25^\circ C$; area = $1 cm^2$.

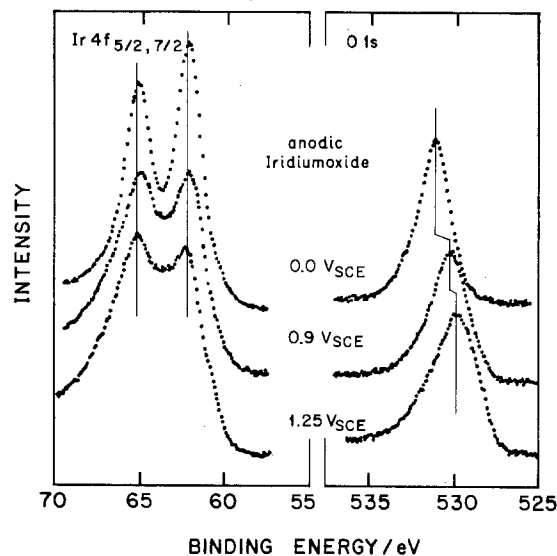


Fig. 2. X-ray photoelectron spectra of Ir $4f_{5/2,7/2}$ and O $1s$ levels of an anodic iridium oxide film exposed to 1N H_2SO_4 at different potentials (15 min).

from the electrochemical cell at the respective potentials. The position of the Ir $4f$ bands is found to be independent of the electrode potential. Compared to the Ir $4f_{7/2}$ binding energy of 60.9 eV for the metal (14), the Ir $4f$ levels of the anodic oxide shift to a higher binding energy by 1.5 eV, indicating a surface layer with Ir in a higher oxidation state.

A more pronounced dependence on the electrode potential was observed for the O $1s$ level (Fig. 2). At 0.0V, where the oxide is bleached, the O $1s$ binding energy is 531.2 eV. Upon anodic polarization, the O $1s$ level shifts to lower binding energies of 530.5 eV and 529.8 eV, at $0.9 V_{SCE}$ and $1.25 V_{SCE}$, respectively. If the potential is kept at $1.5 V_{SCE}$, where O_2 evolution occurs and the anodic oxide starts to corrode, the O $1s$ level shifts back to 530.4 eV (not shown in Fig. 2, but see Table I). In addition to the shift in binding energy, a significant broadening of the O $1s$ structure is noticed. The FWHM value increases from 2.1 eV at $0.0 V_{SCE}$ to 2.9 eV and 3.2 eV at $0.9 V_{SCE}$ and $1.25 V_{SCE}$, respectively.

The thermal stability of the surface species formed at different electrode potentials was tested by varying the temperature of the substrate in the vacuum chamber. Figure 3 shows the O $1s$ - and Ir $4f_{7/2}$ -level positions as a function of temperature. While the O $1s$ binding energies differ significantly at room temperature for the various electrode potentials, a common binding energy is reached at $230^\circ C$ ($E_B = 530.5 \pm 0.2$ eV). The oxide species formed at $0.9 V_{SCE}$ appears to be the most stable configuration. In contrast to the O $1s$ levels, the Ir $4f_{7/2}$ levels shift to lower binding energies independent of the electrode potentials. The decrease in Ir $4f_{7/2}$ binding energy is probably due to dehydration or decomposition of the anodic oxide.

In order to provide complementary information about the electronic properties of the oxide surfaces,

Table I. XPS-binding energies (± 0.1 eV) and intensity ratios for anodic iridium oxide at different potentials (V_{SCE}) and temperatures ($^\circ C$). For the O $1s$ level FWHM-values are given in brackets. Electrolyte: 1 N H_2SO_4 .

Temperature	Potential	Ir $4f_{7/2}$	O $1s$ (ΔE_B)	O $2s$	I_{O1s}/I_{Ir}
RT	0.0	62.4	531.2(2.1)	24.3	2.9
	0.9	62.3	530.5(2.9)	23.1	2.9
	1.25	62.4	529.8(3.2)	22.5	3.1
320°	1.5	62.5	530.4(3.1)	—	—
	0.0	61.1	530.6(2.6)	—	1.2
	0.9	61.3	530.5(2.9)	—	1.6
	1.25	61.9	530.3(3.1)	—	2.3

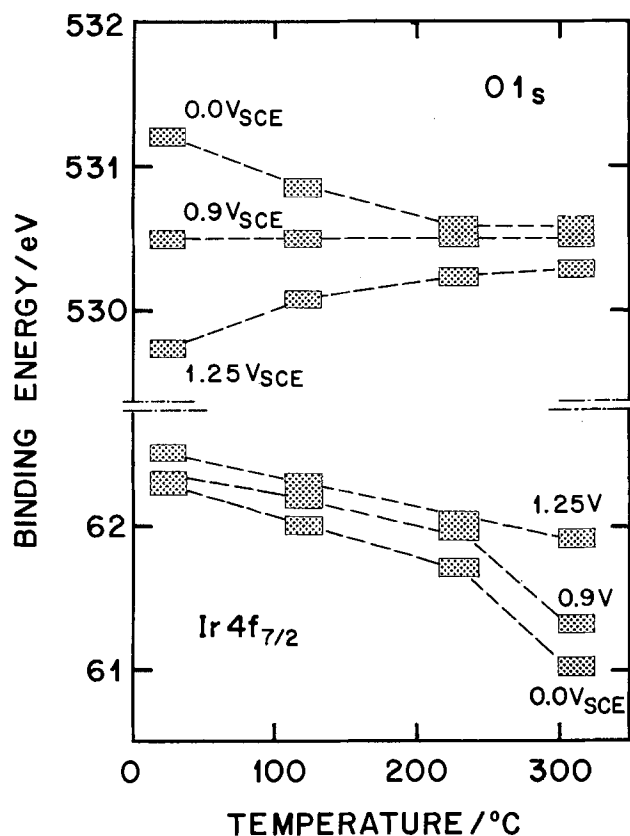


Fig. 3. Binding energies of the O 1s and Ir 4f_{7/2} levels as a function of substrate temperature.

XP spectra were recorded of the valence band region. In Fig. 4, the spectra of the clean polycrystalline iridium surface and of the oxides after polarization at 0.0V and 1.25V are plotted. The spectrum of the clean surface exhibits the broad, rather structureless 5d-

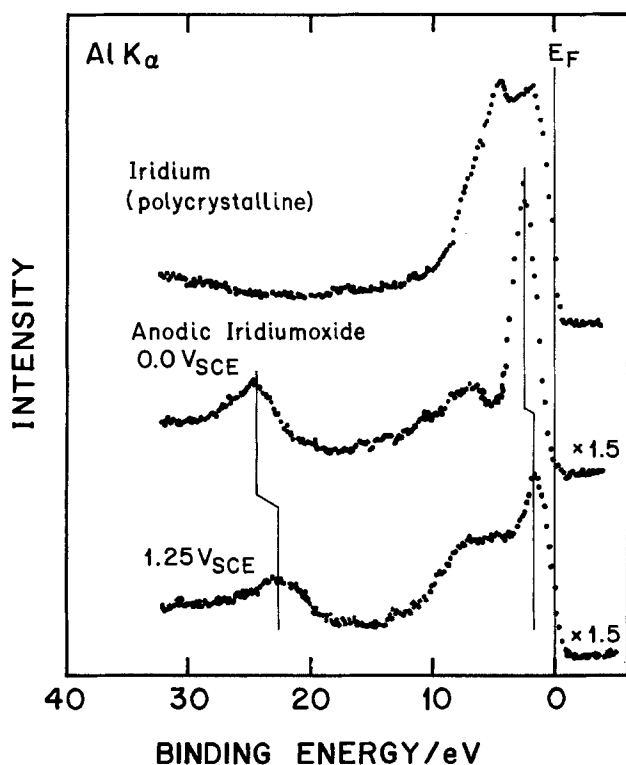


Fig. 4. X-ray photoelectron spectra of the valence band region of clean iridium and anodic iridium oxide films polarized at 0.0 V_{SCE} and 1.25 V_{SCE}. AlK_α excitation, normal emission.

band of Ir, extending to about 8 eV below the Fermi level (15). After electrochemical oxide formation, O 2s emission is evidenced at 24.3 eV and 22.5 eV. The strong maximum right below the Fermi level for both polarizations can be attributed to the *t*_{2g} band of the respective compound, assuming octahedrally coordinated iridium (16). At 0.0V, this band is located at 2.5 eV with virtually zero electron density at the Fermi level, while at 1.25V, the center of the *t*_{2g} emission shifts to 1.8 eV, giving rise to a nonzero electron density at *E*_F. In addition, a pronounced drop in emission intensity from the *t*_{2g} band is noticeable upon anodic polarization.

The emission characteristics in the O 2p energy region are also dependent on the electrode potential. The maximum at 7.0 eV in the spectrum for the electrode polarized at 0.0V changes to a broad plateau between 4.0 eV and 8.0 eV.

Discussion and Conclusions

Several mechanisms have been suggested for the charge storage process in iridium oxide films (8 and references therein), the majority of which assume a change in the Ir valence state from III to IV across the wave at 0.7 V_{SCE} of the voltammogram. Our XPS results for the Ir 4f binding energy, which was found to be potential independent (Fig. 2), do not contradict this assumption. However, a definite correlation of the experimental binding energy of the Ir 4f level with an oxidation state of III or IV cannot be made from available data. A binding energy of 62.4 eV might be interpreted as iridium being in a trivalent state or as a hydrated iridium dioxide with iridium in the tetravalent state. For IrCl₃, a Ir 4f binding energy of 62.6 eV has been found by Folkesson (17). On the other hand, the Ir 4f level at 61.9 eV (16) for the iridium dioxide might be shifted to higher binding energies as a consequence of hydration. This has been observed before for ruthenium oxide films (5, 18). The relatively shallow minimum between the two spin-split Ir 4f levels for the electrodes polarized at 0.9V and 1.25V (Fig. 2) may indicate the presence of higher oxides. A similarly unsatisfactory situation with respect to the interpretation of Ir 4f binding energies of iridium oxide films was encountered by Kim *et al.* (14). Therefore, the following discussion of the XPS data will be restricted to the O 1s level.

According to the oxide path (19) for the oxygen evolution reaction and to the models which have been suggested for the charge storage mechanism, there are three oxygen species, which may contribute to the intensity of the O 1s core level: (i) oxide, (ii) hydroxide, and (iii) water. The binding energies of these species on Ir were established from the following data (see Table II). For single-crystalline IrO₂, the O 1s binding energy was determined to be 529.8 eV (16). In our laboratory, we found a binding energy of 529.6 eV for polycrystalline IrO₂. Chemisorbed oxygen on Ir exhibits a binding energy of 529.8 (20). For hydroxides

Table II. XPS-binding energies (± 0.1 eV) of some relevant samples

Sample	Ir 4f _{7/2}	O 1s	References
Anodic iridium oxide	62.4	531.2	This work
		530.5	
		529.8	
IrO ₂	61.8	529.8	(16)
	61.8	529.6	This work
IrCl ₃	62.6		(17)
H ₂ O on Ir	—	533.1	This work
	—	532.1	(26)
	—	533.4	(23)
	—	533.2	(25)
	—	532.4	(24)
OH on Ir	—	530.5	(26)
	—	531.0	(24)
	—	531.5	(23)
	—	530.8	(25)
FeOOH	—	530.3/531.5	(22)
Ni(OH) ₂	—	531.4	(21)

of nickel (21) and iron (22, 23), a somewhat higher binding energy of 531.5 eV has been reported. A binding energy around 531 eV has been measured for hydroxyl species adsorbed on metals (24-26). We have found a binding energy of 533.1 eV for water adsorbed on Ir. This is in agreement with several other investigations of different metals (24-26).

Assuming that only these three species, with approximate binding energies of 529.6 eV (oxide), 531.0 eV (hydroxide), and 533.1 eV (water), contribute to the XPS spectra, we have deconvoluted the measured O 1s bands. It is evident in Fig. 5 that the contribution of hydroxide species to the overall O 1s signal decreases with anodic polarization. Simultaneously, the photoemission intensity originating from O 1s levels of oxide species increases. The shift of the O 1s level to lower binding energies at anodic potentials can thus be understood as a consequence of decreased OH contribution and increased oxide intensity. At a potential of 0.0V, only hydroxide is found on the surface of the anodic oxide layer. Further information about the chemical composition of the electrode surface can be gained from an analysis of the relative intensity of the O 1s and Ir 4f_{7/2} levels. Taking into account a relative scattering cross section of 0.86 for Ir 4f and 0.338 for O 1s (27), and an analyzer sensitivity proportional to the kinetic energies (FRR mode), we find a constant oxygen/iridium ratio of 3.0 ± 0.2 for all three polarizations. These results demonstrate that upon anodic polarization the total amount of oxygen species stays constant, while the contribution of oxide species grows at the expense of hydroxide species.

Based on the above findings, we propose a mechanism for anodic processes on iridium which is sketched in Fig. 6. Starting from Ir(OH)₃, a deprotonation step leads to the formation of IrO(OH)₂ with Ir in the tetravalent state. As indicated in Fig. 6, this first deprotonation step is connected with the coloration of the oxide film. After two additional deprotonation steps, IrO₃ is formed, with Ir in the hexavalent state, where oxy-

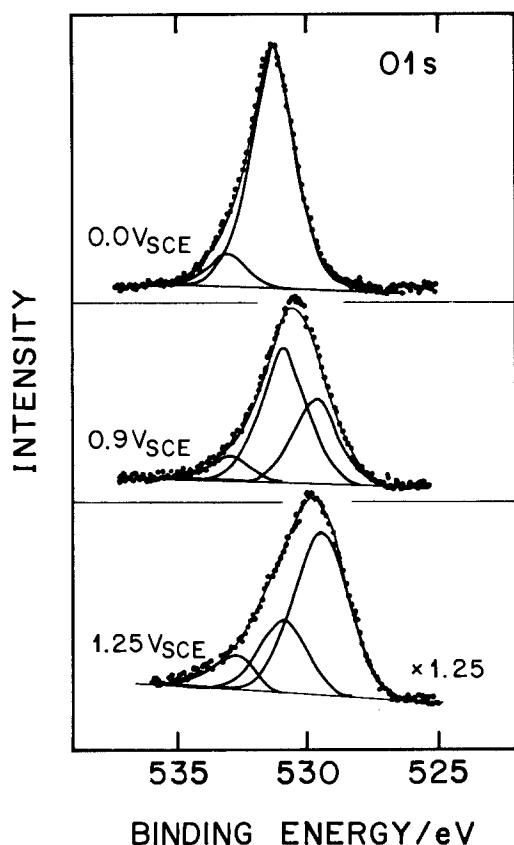


Fig. 5. Deconvoluted O 1s levels of anodic iridium oxide films at different potentials.

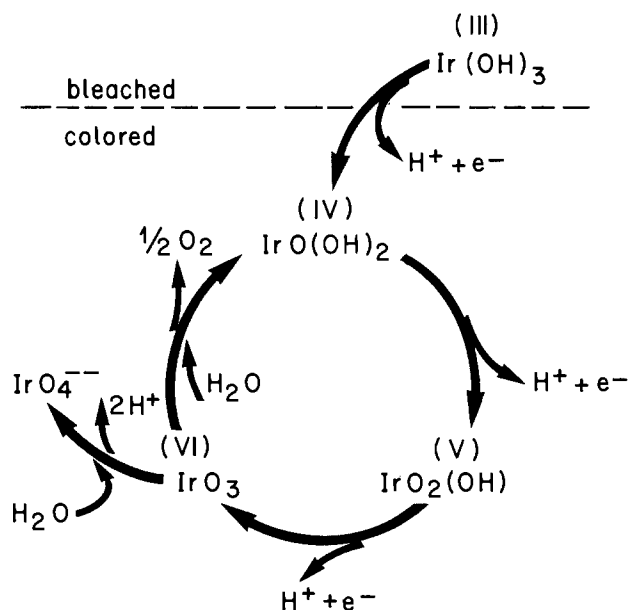
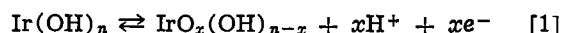


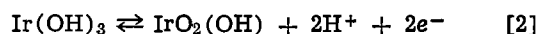
Fig. 6. Model for charge storage and oxygen evolution on iridium electrodes.

gen is split off. Simultaneous uptake of one water molecule leads back to tetravalent iridium as the starting position for the cycle. Alternatively, IrO₃ may corrode into the electrolyte as IrO₄²⁻ ion (28). A similar mechanism has been suggested recently for O₂ evolution on Ru (5).

In order to decide whether the anodic charge storage process occurring in the bulk of the oxide holds also for the oxide surface, the first step of our proposed mechanism in Fig. 6 (Ir(OH)₃ → IrO(OH)₂) should be compared with known models describing the bulk reaction. Gottesfeld and Srinivasan suggested a model based on ellipsometry results which is in complete agreement with our findings (9). According to the redox reaction



with $n = 3$ and $x = 1$, a proton is ejected from the oxide film upon coloration. A similar model was proposed by Michell *et al.* (10). These authors, however, found a transfer of two electrons for the bleaching mechanism ($n = 2$, $x = 2$ in Eq. [1]), which might be due to the wide potential step ($-0.2 \text{ V}_{\text{SCE}}$ to $1.25 \text{ V}_{\text{SCE}}$). For a potential step this wide, our model also suggests the transfer of two electrons according to $n = 3$ and $x = 2$



The second step (see Fig. 6), however, does not change the color of the oxide layer and is connected with the wave at $1.15 \text{ V}_{\text{SCE}}$ of the voltammetry curve.

The absence of significant amounts of H₂O in the spectra of the O 1s level and the potential-independent O/Ir ratios indicate that free H₃O⁺ ions, liberating one H⁺, are the external proton source or sink during the redox reactions. Water, bound to the solid and serving as "vehicle" for the proton, would give rise to an increase in O/Ir ratio upon bleaching. This has been suggested by McIntyre (8) and Burke and Whelan (11). If only free protons are considered, the mechanism based on RBS measurements suggested by McIntyre (8) predicts also a constant O/Ir ratio. The constant O/Ir ratio at the oxide surface is in discord with the OH⁻ insertion mechanism proposed by Beni *et al.* (29) for the bulk of the oxide. Obviously, at the immediate surface of the oxide, protons are readily available from the bulk electrolyte, according to the Grothuss mechanism, without strong interaction of

H₂O with the surface. It is, however, possible that water bound to the surface evaporates or dissociates after emersion under UHV conditions.

With respect to O₂ evolution, it is obvious that the proton ejection step can be applied consecutively in order to provide the amount of electrons required to liberate oxygen from IrO₃. Although relatively stable in alkaline electrolytes, IrO₃ decomposes readily in dilute sulfuric acid with simultaneous O₂ evolution (30). Further oxidation of iridium to an oxidation state higher than the hexavalent state is very unlikely, because the existence of such a species has not been established. Therefore, our model is consistent with the known electrochemical oxide path (19), if Ir in the tetravalent state is assumed to be the surface site. As has been discussed before for ruthenium (5), the species representing the starting position of the O₂ evolution cycle has to have a relative stability on the respective substrate in order to prevent heavy corrosion. The thermodynamic stability of iridium compounds with Ir in the tetravalent state is well known and was confirmed by our results (Fig. 3) for the species involved in anodic oxidation. It can be shown by voltammetry that on Ir, as well as on polycrystalline or amorphous IrO₂, a film is generated during O₂ evolution with properties similar to those of anodic iridium oxide. We assume, therefore, that our model for O₂ evolution and corrosion holds not only for thick anodic iridium oxide films, but also for IrO₂ and Ir anodes.

The valence band spectra (Fig. 4) corroborate our interpretation of the core-level data. The change in valence state from Ir(III) to Ir(V), which did not show up as a chemical shift in the core level spectra, gives rise to the reduction of emission intensity of the t_{2g} band. Upon anodic polarization, more electrons per iridium atom are needed to fill the O 2p shell. Despite its higher total population of electrons in the iridium d-band (t_{2g}), the hydroxide at 0.0 V_{SCE} has a much lower density of occupied states near the Fermi level. This result is consistent with the rather low electronic conductivity found for bleached anodic iridium oxide film in electrochemical experiments. At potentials cathodic of 0.25 V_{SCE}, electrode reactions like H adsorption or underpotential deposition of Cu or Ag (31) take place only at the metal/oxide interface.

At a potential of 1.25V, the valence band spectrum is in good agreement with published data for IrO₂, with emission from M-O σ and M-O π orbitals at 7.9 eV and 5.7 eV (16, 32). In addition, the position of the t_{2g} band at 1.8 eV indicates that oxide species dominate at 1.25 V_{SCE}. At 0.0 V_{SCE}, the O 2p region is characterized by a strong band at 7.0 eV with a weak shoulder at 10 eV. We attribute the band at 7.0 eV to the M-O π band, while that at 10 eV is likely to have OH σ-bonding character (22, 33, 34). Thus, the spectrum at 0.0 V_{SCE} is dominated by hydroxyl species. The above assignment, which appears to be rather ambitious in view of the low resolution of our XPS valence-band data, was confirmed by UPS measurements on the same samples using He II excitation with a much better resolution and signal-to-noise ratio. The UP spectra revealed bands at 2.5 eV (t_{2g}), 6.5 eV (M-O π) and 10.3 eV (O-H σ) for the sample polarized at 0.0V and 1.8 eV (t_{2g}) and 5.3 eV (M-O π) and 8.0 eV (M-O σ) for 1.25 V_{SCE} polarization (35).

In conclusion, we have demonstrated with the aid of XPS that oxygen evolution on anodic iridium oxide is preceded by consecutive deprotonation steps during the anodic potential scan. Upon deprotonation, the relative amount of oxygen is constant while the O 1s binding energy decreases. The shift in O 1s binding energy is due to a transition from oxygen bound as hydroxide to oxygen bound as oxide.

The first of these deprotonation steps goes together with the known electrochromic effect in anodic iridium oxides. Upon coloration, the stoichiometry at the immediate oxide surface changes from Ir(OH)₃ to

IrO(OH)₂. Oxygen evolution starts from the latter species along the known electrochemical oxide path.

Acknowledgments

The excellent technical assistance of W. Foditsch is gratefully acknowledged. This work was supported by the Nationaler Energie Forschungs Fond.

Manuscript submitted Feb. 18, 1983; revised manuscript received ca. July 21, 1983.

Brown Boveri Research Center assisted in meeting the publication costs of this article.

REFERENCES

1. S. Trasatti and G. Lodi, in "Electrodes of Conductive Metallic Oxides," S. Trasatti, Editor, p. 521, Elsevier, Amsterdam (1980).
2. S. Hackwood, L. M. Schiavone, W. C. Dautremont-Smith, and G. Beni, *This Journal*, **128**, 2569 (1981).
3. S. Gottesfeld, J. D. E. McIntyre, G. Beni, and J. L. Shay, *Appl. Phys. Lett.*, **33**, 208 (1978).
4. K. Müller, G. Scherer, and S. Stucki, in "Extended Abstracts of 32 I.S.E. Meeting," Vol. I, p. 28 (1981).
5. R. Kötz, H. J. Lewerenz, and S. Stucki, *This Journal*, **130**, 825 (1983).
6. J. Mozota and B. E. Conway, *This Journal*, **128**, 2142 (1981).
7. R. Kötz, H. J. Lewerenz, P. Brüesch, and S. Stucki, *J. Electroanal. Chem.*, **150**, 209 (1983).
8. J. D. E. McIntyre, S. Basu, W. F. Peck, Jr., W. L. Brown, and W. M. Augustyniak, *Phys. Rev. B*, **25**, 7242 (1982).
9. S. Gottesfeld and S. Srinivasan, *J. Electroanal. Chem.*, **86**, 89 (1978).
10. D. Mitchell, D. A. J. Rand, and R. Woods, *ibid.*, **84**, 117 (1977).
11. L. D. Burke and D. P. Whelan, *ibid.*, **124**, 333 (1981).
12. P. M. A. Sherwood, *Surf. Sci.*, **101**, 619 (1980) and references therein.
13. W. N. Hansen, D. M. Kolb, D. L. Rath, and R. Wille, *J. Electroanal. Chem.*, **110**, 369 (1980).
14. K. S. Kim, C. S. Sell, and N. Winograd, in "Proceedings of the Symposium on Electrocatalysis," W. M. Breiter, Editor, p. 242, The Electrochemical Society Softbound Proceedings Series, Princeton, NJ (1974).
15. N. V. Smith, G. K. Wertheim, S. Hüfner, and M. M. Traum, *Phys. Rev. B*, **10**, 3197 (1974).
16. G. K. Wertheim and H. J. Guggenheim, *ibid.*, **22**, 4680 (1980).
17. B. Folkesson, *Acta. Chem. Scand.*, **27**, 287 (1973).
18. K. S. Kim and N. Winograd, *J. Catalysis*, **35**, 66 (1974).
19. J. O'M. Bockris, *J. Chem. Phys.*, **24**, 817 (1956).
20. P. A. Zhdan, G. K. Boreskov, A. I. Boronin, W. F. Egelhoff, Jr., and W. H. Weinberg, *Surf. Sci.*, **61**, 25 (1976).
21. K. S. Kim, W. E. Baitinger, J. W. Amy, and N. Winograd, *J. Electr. Spectros.*, **5**, 351 (1974).
22. K. Wandelt, *Surface Science Reports* **2**, 1-121 (1982).
23. A. G. Akimov, *Elektrokhimiya*, **15**, 1510 (1979).
24. G. B. Fisher and J. L. Gland, *Surf. Sci.*, **94**, 446 (1980).
25. C. Benndorf, C. Nöbl, and F. Thieme, *ibid.*, **121**, 249 (1982).
26. T. S. Wittrig, D. E. Ibbotson, and W. H. Weinberg, *ibid.*, **102**, 506 (1981).
27. M. Cardona and L. Ley, in "Photoemission in Solids I," Vol. 26 of Topics in Applied Physics, M. Cardona and L. Ley, Editors, p. 82, Springer, New York (1978).
28. L. D. Burke, in "Electrodes of Conductive Metallic Oxides," S. Trasatti, Editor, p. 141, Elsevier, Amsterdam (1980).
29. G. Beni, C. E. Rice, and J. L. Shay, *This Journal*,

- 127, 1342 (1980).
 30. L. Wöhler and W. Witzmann, *Z. Anorg. Chem.*, **57**, 323 (1908).
 31. R. Kötz and S. Stucki, Unpublished results.
 32. J. Riga, C. Tenret-Noel, J. J. Pireaux, R. Caudano, and J. J. Verbist, *Physica Scripta*, **16**, 351 (1977).
 33. G. B. Fisher and B. A. Sexton, *Phys. Rev. Lett.*, **44**, 683 (1980).
 34. A. Spitzer and H. Lüth, *Surf. Sci.*, **120**, 376 (1982).
 35. H. Neff and R. Kötz, To be published.

The Insulator-Electrolyte Interface: Photoelectrochemistry of Red HgI_2

H. von Känel, E. Kaldis, and P. Wachter

Laboratorium für Festkörperphysik ETH, 8093 Zürich, Switzerland

H. Gerischer*

Fritz-Haber-Institut der Max-Planck-Gesellschaft, Faradayweg 4-6, D-1000 Berlin 33, Germany

ABSTRACT

Highly insulating red HgI_2 shows a very small quantum yield for both anodic and cathodic polarization. This is due to the poor charge separation made by an insufficient electric field strength in the wide space-charge layer characteristic of lightly doped materials. Quantum efficiencies exceeding 50% can be obtained for anodic polarization, however, through the artificial generation of a space-charge layer. In this approach, use is being made of the photoconductivity of HgI_2 . Illuminating the sample with light of wavelengths close to the bandgap of 2.1 eV at 300 K, leads—in conjunction with the trapping processes occurring in HgI_2 —to a potential distribution similar to an n-doped semiconductor. We discuss the dependence of the spacial and temporal buildup of this potential distribution on the external parameters such as the illumination intensities, wavelengths, and bias. Included is a discussion of the corrosion mechanisms of HgI_2 .

Red (tetragonal) mercuric iodide has been experiencing continued interest throughout this century. Beginning with investigations of its photoconductivity (1) and its exciton structure (2), emphasis has shifted toward the application of HgI_2 as a nuclear detector and spectrometer (3).

Tetragonal HgI_2 has a bandgap of 2.1 eV at room temperature and exhibits a very high resistivity (1)—typically $10^{13} \Omega\text{cm}$ —despite a remarkable amount of elemental impurities (4, 5). Insulating materials have not been commonly used for photoelectrochemical studies so far because of the lack of efficient separation of the electron-hole pairs created within the penetration depth of suprabandgap light. The separation of charge carriers usually (except in extremely thin crystals) requires a strong electric field such as is present in the depletion region at the interface between an electrolyte and a suitably doped and biased semiconductor. Recently, however, it has been shown that a potential distribution reminiscent of that of a doped semiconductor can be obtained by illuminating the investigated insulator with two light sources simultaneously (6). In this new approach, the appropriate doping for the formation of a depletion layer at the interface is achieved by making use of the photoconductivity of the crystal; i.e., one of the two light sources provides radiation which is only weakly absorbed and hence produces (mobile and fixed) charge carriers throughout the bulk of the sample. Under suitable conditions the quantum yield for nonpenetrating (suprabandgap) radiation of the second light source is thus increased dramatically.

Double-beam experiments have been reported in a number of previous publications (7). They usually deal with relatively highly doped semiconductors, however, and the change of the potential distribution in them is of a different nature than that reported here. One exception is an article on the surface-photovoltage diffusion-length measurement in amorphous silicon (8).

* Electrochemical Society Active Member.

Key words: photoconductivity, photodoping, potential distribution.

In this paper we present a study of the photoelectrochemical properties of red HgI_2 , as well as its corrosion behavior. We use the techniques mentioned above.

Experimental Procedures

Crystal growth and characterization.—The single crystals used in this work were grown by static sublimation from prepurified material. A detailed discussion of the growth and characterization processes has already been published (4). Here we want to stress the relatively high degree of perfection and conventional purity of these crystals. We are supported by the following: (i) low etch-pit concentration ($<10^3/\text{cm}^2$) of the as-grown crystal faces; (ii) lack of striations common to the usually applied temperature oscillation growth methods (9); (iii) annealing at 75° in iodine atmosphere of the single-crystal plates ($\approx 5 \times 5 \text{ mm}$, 2 mm thick) used in this investigation. These plates were cleaved from the as-grown crystals and etched in an alcoholic solution of KI before annealing.

Compared with HgI_2 from other laboratories, the purity of our crystals is high (5). However, spark-source mass spectrographic analysis revealed that our crystals contained several thousand ppm of hydrocarbon impurities. This led to the suggestion that our HgI_2 -crystals were actually clathrates or intercalates of the layer structure (4). The influence of this effect on the measured physical properties is presently not known.

Electrode preparation.—Like many workers before, we used carbon contacts in order to avoid a chemical reaction with the HgI_2 . The crystals were mounted on a brass rod surrounded by a piece of Teflon tubing. Before embedding the electrode in silicone rubber, the crystals were usually thinned down to an appropriate thickness of $\approx 0.1\text{--}0.2 \text{ mm}$ by peeling off successive layers with a self-adhesive tape. In order to remove any surface damage, the electrodes were etched in 1M KI for up to 1 min. By this method a perfectly smooth and shiny surface was obtained.

Electrolyte.—The support electrolyte used in all the experiments was 0.5M K_2SO_4 in triple-distilled water,

in which HgI_2 is stable in the dark. $\text{Fe}^{2+}/\text{Fe}^{3+}$ did not affect the stability in the dark, nor did it suppress photocorrosion at all. The only way to substantially reduce the degradation of the electrode surface by the anodic photocorrosion (described in more detail below) was found to be the use of a solution containing the complex HgI_4^{2-} ($2 \times 10^{-2} - 0.1\text{M}$). The solution was prepared by adding one mol fraction of HgCl_2 to the support electrolyte in addition to about four mol fractions of KI, the exact amount being chosen in a way that led to a small amount of precipitated red HgI_2 ; the solution was saturated with HgI_2 .

Experimental setup.—In the electrochemical cell, a platinum wire served as the counterelectrode, and a saturated calomel electrode served as the reference. Instead of a potentiostat, an ordinary power supply was used which allowed the application of voltages up to 70V between the counterelectrode and the working electrode. The working electrode was grounded via the measuring resistor (100Ω – $1\text{M}\Omega$, depending on the current to be measured).

Steady-state measurements.—The photocurrent spectra and the current-potential curves were obtained by chopping the monochromatized beam of a high pressure xenon lamp at $\approx 15\text{ Hz}$, and recording the corresponding voltages across the measuring resistor with a PAR lock-in amplifier. As will be described below, the quantum efficiency for monochromatic light was very low unless the electrode was illuminated in addition with a long-wavelength light source. This was achieved by filtering the light from a tungsten-filament lamp through 8 cm of triple-distilled water and a Schott filter with an absorption edge just below that of HgI_2 (OG 590 or RG 610). The intensity of this broad-band light was varied either by operating the lamp at 12V or 6V or by inserting a neutral-density filter into the beam. We did not measure the absolute intensity of this light source. The room temperature optical properties (reflection and absorption) were measured by standard techniques.

Time-dependent properties.—These were obtained with essentially the same setup except that both light sources could be chopped either simultaneously or interchangeably and at different frequencies. The signals were recorded by means of a signal averager.

Results

Steady-State Photocurrent Measurements

We observed a pronounced asymmetry between anodic and cathodic polarization of the electrode. Numerous other workers have reported analogous observations in photoconductivity measurements. The photoresponse was restricted to a small region at or near the negative electrode (1). This corresponds to the anodic polarization in our photoelectrochemical experiments, since in them the crystal-front surfaces were at the lower potential. In Fig. 1 the photocurrent-potential curves for an anodically polarized electrode in $0.5\text{M K}_2\text{SO}_4 + 0.1\text{M HgI}_4^{2-}$ illuminated with strongly absorbed light of $\lambda = 550\text{ nm}$ and with sub-bandgap radiation of different intensities (given in arbitrary units) are shown. The filter used for the sub-bandgap illumination was OG 590. If the additional broad band light source is operated at high enough intensity (i.e., at 12V, with no neutral-density filters introduced into the beam), then the current-potential curves and the associated quantum efficiency are the same for Schott filters RG 610 and OG 590. Using filters with a higher or lower lying cutoff leads to lower quantum efficiencies.

The intensity of the monochromatic light beam was $\approx 180\ \mu\text{W}/\text{cm}^2$. The most pronounced feature of Fig. 1 is the steep rise of the photocurrent at small potentials for high-intensity sub-bandgap radiation (top curve). This indicates the formation of a barrier region

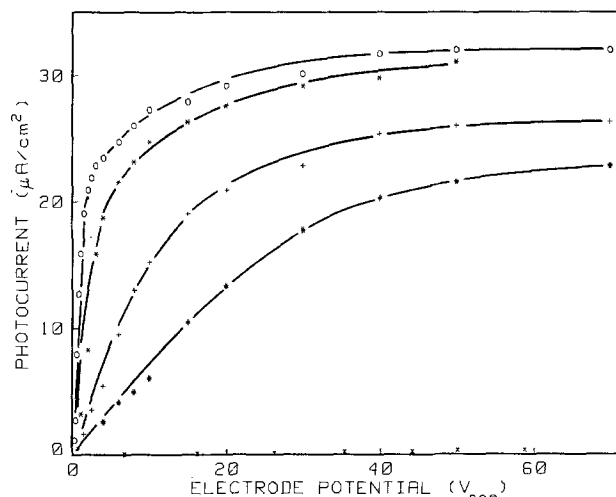


Fig. 1. Photocurrent-potential curves at an HgI_2 electrode in $0.5\text{M K}_2\text{SO}_4 + 0.1\text{M HgI}_4^{2-}$. The electrode is illuminated by a chopped monochromatic light source ($\lambda = 550\text{ nm}$, intensity $\approx 180\ \mu\text{W}/\text{cm}^2$) and by steady-state sub-bandgap light (tungsten lamp, filtered through H_2O and Schott glass OG 590). The intensity of the latter is highest for the top curve O (100% in relative units), and decreases steadily for the other curves (curve \star : 14%; $+$: 2.3%; $\#$: 0.65%; \times : monochromatic illumination only).

at the electrode surface. For monochromatic illumination alone ($\lambda = 550\text{ nm}$), the photocurrent-potential curve nearly coincides with the potential axis (bottom curve in Fig. 1). The photocurrent is smaller by about two orders of magnitude ($\approx 0.3\ \mu\text{A}/\text{cm}^2$ at 50 V_{SCE}).

All measurements in Fig. 1 were performed by applying a voltage of 70V first and then recording the photocurrent as a function of decreasing cell voltage. Before any change of the intensity of the sub-bandgap radiation, the initial voltage of 70V was reapplied. After a waiting period, the associated value for the photocurrent was found to be equal to the original one (hence ruling out a serious degradation of the surface). The waiting period became longer the smaller the intensity of the sub-bandgap light.

Other time-dependent effects were observed at low voltages. After any change of voltage, the photocurrent slowly decreased for several minutes. This transient effect became more pronounced at lower sub-bandgap intensities. For the top curve in Fig. 1, the effect was observed below $\approx 0.5\text{ V}_{\text{SCE}}$ only, for the bottom curve below 10 V_{SCE} .

The linearity of the photocurrent with the monochromatic light intensity depends strongly on the intensity of the additional sub-bandgap light source (Fig. 2). In Fig. 2, curves a, b, and c represent the photocurrent (electrode potential 60 V_{SCE}) as a function of intensity. The full curves in this double log-plot correspond to a linear relationship (slope = 1). The additional light source was operated at 12V with OG 590 (curve a), at 12V with RG 610 (curve b), and at 6V with RG 610 and an additional neutral density filter of 0.1% transmittance (curve c).

For the sake of clarity, only the curves showing the most pronounced behavior have been displayed in Fig. 2. At $\lambda = 600\text{ nm}$ (curve b) the linearity is not influenced at all by changes of the intensity of the second light source. The opposite is true at 550 nm: for high intensity sub-bandgap illumination (curve a), deviations from the linear relationship occur around $1\text{ mW}/\text{cm}^2$. On decreasing the intensity of the long wavelength light source, these deviations occur at lower and lower intensities until for curve c there is no linear relationship in the entire investigated range. In fact, the photocurrent is even partly quenched in this case, as can be seen by reducing the intensity of the monochromatic beam to the lowest value of 180

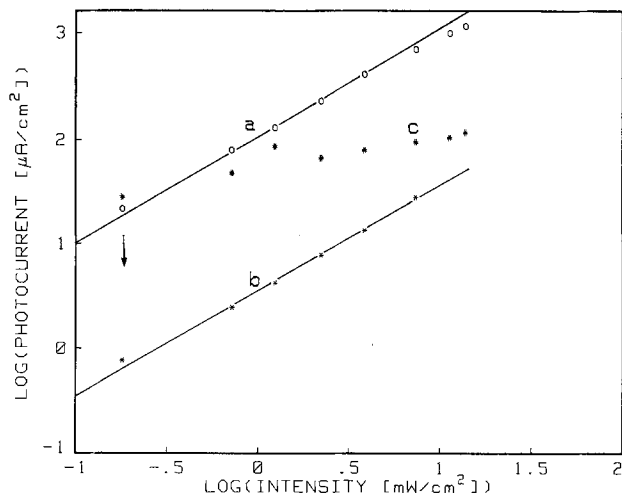


Fig. 2. Dependence of the photocurrent on the intensity of the monochromatic illumination. Electrode potential 60 V_{SCE}, electrolyte 0.5M K₂SO₄ + 2 × 10⁻²M HgI₄²⁻. Curves a (λ = 550 nm) and b (λ = 600 nm) correspond to intense illumination with sub-bandgap light (curve a: tungsten lamp 12V, filter OG 590; curve b: 12V, RG 610). For curve c (λ = 550 nm) the intensity of the long-wavelength radiation was much smaller (tungsten lamp 6V, filtered with RG 610 and 0.1% neutral-density filter). The full curves have a slope of 1; they correspond to a linear relationship.

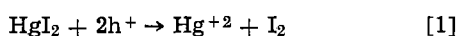
μW/cm² (see tip of the arrow in Fig. 2). The original value of the photocurrent at this intensity can be restored by illuminating the sample with long wavelength light of higher intensity (e.g., as in curve a) for several minutes.

Figure 3 shows the quantum efficiencies (uncorrected for reflection losses) of an HgI₂ electrode in 0.5M K₂SO₄ + 0.1M HgI₄²⁻ for anodic (curves a and c) and cathodic (curve b) polarization.

For curves a and b, the electrode was illuminated by monochromatic light only. In both cases the response was limited to a narrow spectral region around the onset of the interband absorption (insert Fig. 3). The anodic photocurrent changed drastically upon illumination of the electrode with a second lamp (curve c) providing sub-bandgap radiation (Schott filter RG 610). For the low monochromatic light intensity used in this measurement (approximately 50 μW/cm² on average), the apparent quantum efficiency remained at around 50% in the spectral range between 450 nm and 570 nm. Taking into account the reflection losses at the surface (R ≈ 20% at 550 nm) leads to a corrected quantum efficiency larger than 60%. For cathodic polarization, however, the quantum efficiency was not altered by the additional illumination of the electrode. Hence, the mentioned asymmetry between anodic and cathodic polarization became even much more pronounced when the electrode was illuminated with the second light source. An additional, even more dramatic manifestation of this asymmetry was found in the frequent breakdowns encountered in the cathodic case (under illumination), sometimes at voltages as low as 1V. No breakdowns happened for the anodic polarization up to the highest applied voltage (70V).

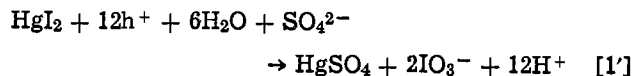
Photocorrosion

Anodic photocorrosion.—Mercury is already in its highest oxidation state (2+) in HgI₂. It is clearly the iodide which is oxidized in an anodic reaction. The electrode was photocorroded in 0.5M K₂SO₄ for a time sufficient to yield 10⁻⁴M I₂ if iodide were oxidized to I₂ according to



No elemental iodine could be detected, however, by the very sensitive iodo-starch reaction. We have to con-

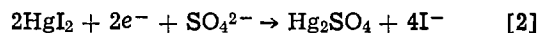
clude that iodide is oxidized to a higher oxidation state. The reaction can be tentatively formulated as



Since IO₃⁻ is a strong oxidizing agent, it should be able to oxidize I⁻ to I₂ in an acidic solution. After adding a few drops of HCl and KI solution to the electrolyte, the iodo-starch reaction indeed indicated the presence of I₂.

Optical examination of the electrode surface revealed clear signs of photocorrosion even for intensities as low as 50 μW/cm² and after a few minutes of exposure. This was accompanied by a marked decrease of the photocurrent at wavelengths below 560 nm. Addition of Fe²⁺ (up to 0.1M) did not result in any visible reduction of the photocorrosion. The introduction of the solution containing the HgI₄²⁻ complex (see preparation of the electrolyte) did, however, result in a visibly slower rate of deterioration of the surface, at least at low intensities. The oxidation of adsorbed HgI₄²⁻ to iodate represents a competing reaction that could lead to slower photocorrosion. The photocurrent was indeed stable for a much longer time (several hours at low intensities) with this electrolyte.

Cathodic polarization.—Cathodic photodecomposition of HgI₂ might in principle lead to the reduction of Hg²⁺ to either Hg⁺ or Hg⁰. After illumination of the electrode with filtered white light (OG 590, for which the photocurrent at -0.7 V_{SCE} was 0.3 μA) for 2h, a yellow layer was observed on top of the electrode. This reaction product was light sensitive and assumed a grayish coloration upon illumination with white light. Since it does not seem to be soluble in KI (which Hg₂I₂ would be) the reaction product probably consists of Hg₂SO₄. The most likely reaction mechanism is thus



Transient Effects

In order to shed some light on the role played by the additional long-wavelength light source, particularly with regard to the time-dependent effects already mentioned above, we decided to look at the time dependence of the photocurrent signal itself. In the first experiment the sample was illuminated with monochromatic light (λ = 550 nm) only. The long-wavelength illumination was then switched on. In order to be able to distinguish between the two contributions to the photocurrent, the monochromatic beam was chopped with 1.5 Hz. In Fig. 4 two such sets of measurements are displayed (upper curves: total photocurrent; lower curves: photocurrent due to the sub-bandgap illumination alone). Both were taken on the same electrode. The middle curves (#) show the behavior of the virgin electrode (never before illuminated), while the others (*) were taken after the electrode had been illuminated several times. The most striking feature of all these curves is the extremely slow rise of the photocurrent associated with the monochromatic radiation (given by the difference of the total photocurrent and the sub-bandgap contribution in Fig. 4). Moreover, this risetime diminishes when the electrode has been illuminated for some time before the experiment (top curve in Fig. 4). By contrast, the initial risetime of the photocurrent due to the sub-bandgap illumination is always fast (we have no explanation for the hump seen in the lower of the [#] curves in Fig. 4). The decay time after switching off the sub-bandgap radiation is nothing on the scale of Fig. 4 both for the total and for the photocurrent due to the penetrating radiation alone (examine also Fig. 5 for this point).

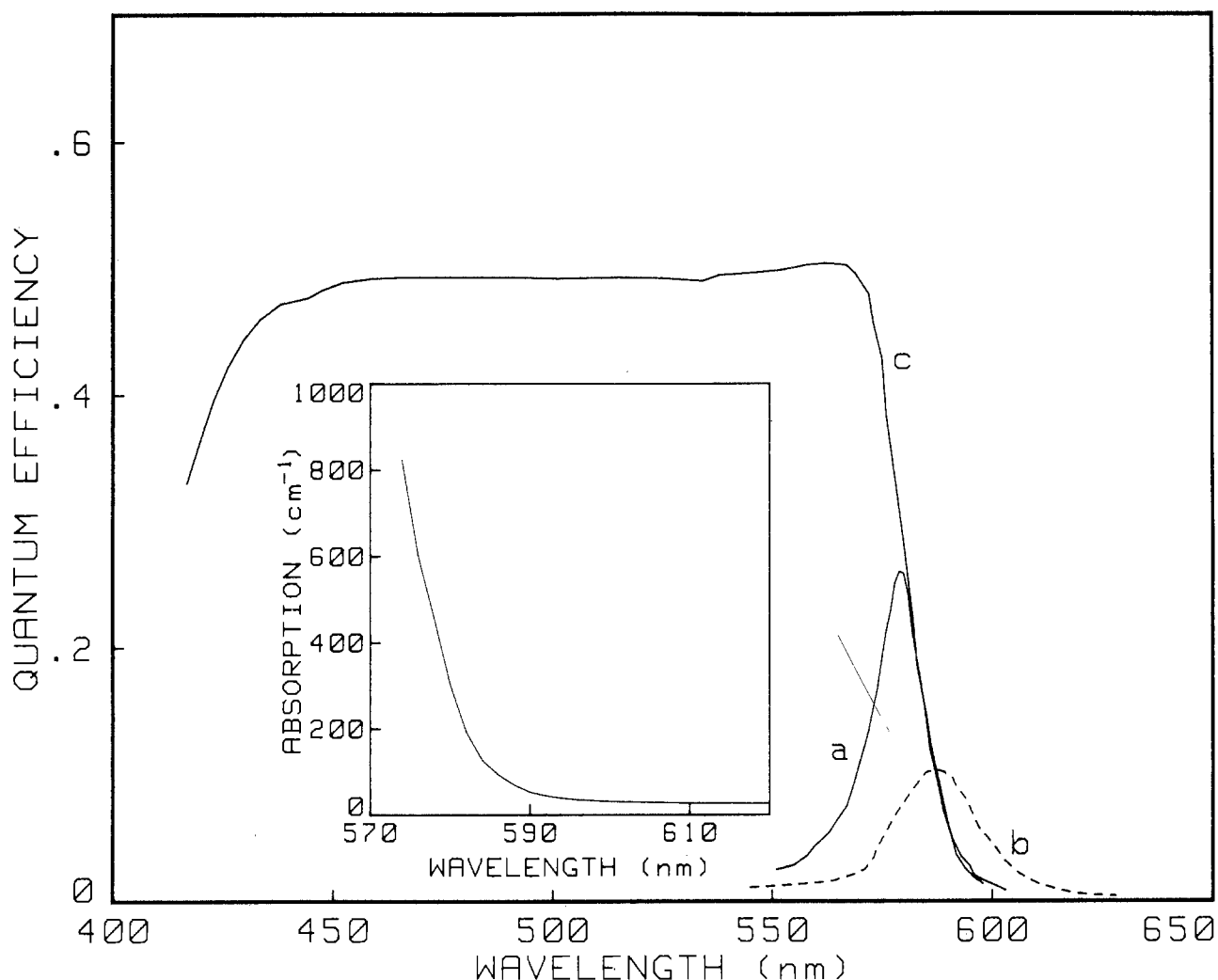


Fig. 3. Quantum efficiency with monochromatic illumination alone ($50 \mu\text{W}/\text{cm}^2$) for anodic (a) and cathodic (b) polarization and with additional long-wavelength illumination (c, anodic polarization). The insert shows the absorption coefficient around the onset of the inter-band transition. The electrolyte was $0.5\text{M K}_2\text{SO}_4 + 2 \times 10^{-2}\text{M Hgl}_4^{2-}$, electrode potential 20V_{SCE} .

Since the risetime observed in Fig. 4 depend so strongly on the history of a sample and because of the considerable variation from sample to sample, our dis-

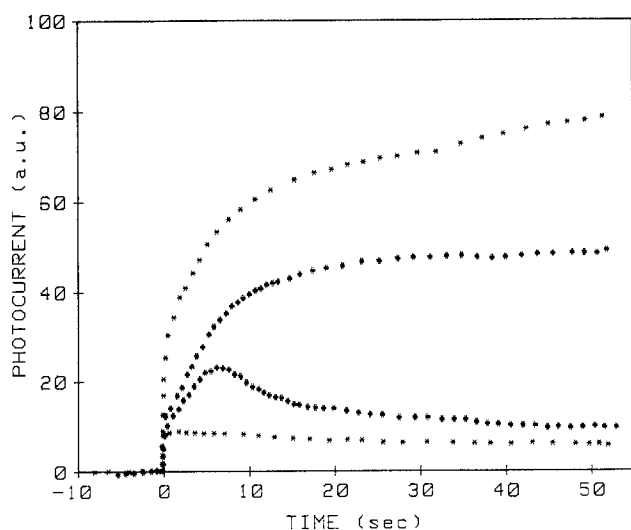


Fig. 4. Time dependence of the photocurrent signal ($\lambda = 550 \text{nm}$) after switching on the sub-bandgap radiation (at $t = 0\text{s}$). Electrode potential 20V_{SCE} ; electrolyte $0.5\text{M K}_2\text{SO}_4 + 2 \times 10^{-2}\text{M Hgl}_4^{2-}$. The lower curves show the photocurrent due to the sub-bandgap radiation alone, the upper ones the total photocurrent. #: virgin electrode which was never illuminated before; *: same electrode after having been illuminated for several minutes.

cussion will be limited to the qualitative features of these experiments. The important result pertaining to Fig. 4 is that the risetime of the photocurrent after the initial application of the long-wavelength radiation is much longer than the decay time after shutting it off. Those two times may be expected to be of a different physical origin.

The situation is quite different once the sample has been irradiated for some time with sub-bandgap light

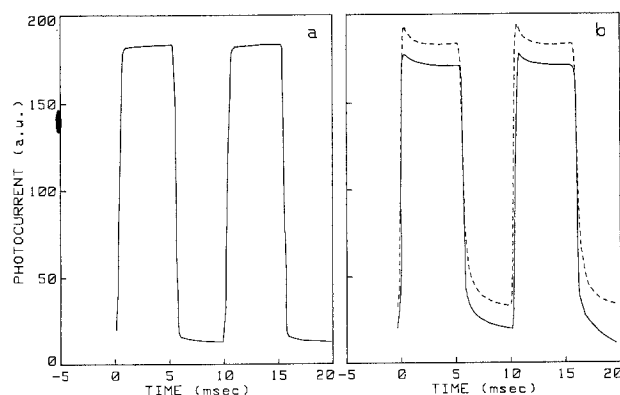


Fig. 5. a: Photocurrent signal for chopped monochromatic illumination ($\lambda = 550 \text{nm}$, $\nu = 100 \text{Hz}$) and continuous sub-bandgap radiation with electrode potential 10V_{SCE} ; b: photocurrent signal for continuous monochromatic ($\lambda = 550 \text{nm}$) and chopped (100Hz) sub-bandgap illumination with electrode potential 10V_{SCE} (full curve) and 20V_{SCE} (dashed curve). Same electrolyte as in Fig. 4.

(i.e., after reaching the saturation region in Fig. 4). The risetime then decreases dramatically. This is shown in Fig. 5 where the monochromatic light beam has been chopped at 100 Hz for continuous illumination by the sub-bandgap source (Fig. 5a) and vice versa (Fig. 5b). A comparison of Fig. 5a and Fig. 5b shows that the amplitude of the modulation of the photocurrent is practically the same in both cases. Hence, the risetime of the photocurrent associated with the onset of the sub-bandgap illumination is now of the same order of magnitude as the decay time after entering the dark phase (Fig. 5b). The risetime observed here must thus be due to a different mechanism than that one seen in Fig. 4.

Figure 5b also shows that in the dark phase of the sub-bandgap radiation (with monochromatic illumination), the photocurrent does not decay to zero (the photocurrent for monochromatic radiation alone, i.e., with no second lamp present at all, would be much smaller on this scale. See also Fig. 1). This becomes more pronounced the higher the electrode potential, as can be seen in Fig. 5b. Here the full curve is for a potential of 10 V_{SCE} and the dashed one for 20 V_{SCE}.

Discussion

Before we enter the discussion of the experimental results presented above, we should like to summarize the main points again:

1. The photocurrent response of HgI₂ to monochromatic light alone is limited to a narrow spectral region near the absorption edge.

2. For anodic polarization, the quantum efficiency is increased drastically for wavelengths below 570 nm when the electrode is illuminated in addition to sub-bandgap light of high enough intensity. The cathodic photocurrent, however, is little affected.

3. For a high enough intensity of the sub-bandgap illumination, the photocurrent due to the monochromatic light saturates at relatively low voltages, indicating the formation of a depletion region near the electrode surface.

4. The photocurrent varies linearly with the intensity of short-wave ($\lambda \leq 560$ nm) monochromatic radiation only for as long as the intensity of the additional light is high enough. If it is not, the response to the short-wavelength radiation may be quenched.

5. The improvement of quantum efficiency after switching on the sub-bandgap light source is a very slow process. It takes up to tens of minutes for low intensities of the sub-bandgap illumination. This risetime is fastest for high sub-bandgap intensities and high voltages.

6. Once the space-charge configuration leading to high quantum efficiency has been established by prolonged illumination with sub-bandgap light, and after a (short) dark phase of the latter (in which the current decays almost to zero), the rise of the photocurrent is faster by several orders of magnitude upon renewed illumination of the electrode (the monochromatic source being on continuously).

Most of the phenomena described above have been observed at relatively high electrode potentials (≥ 3 V_{SCE}, with the exception of the current-potential curves). Thus, the kinetics of the charge transfer at the HgI₂/electrolyte interface may be expected to be of minor importance for our discussion. We have to deal with the solid-state properties of HgI₂ exclusively. Our main task is of course to explain the mechanism for the drastic increase of the quantum efficiency brought about by the illumination of an anodically polarized electrode with a second light source providing broad-band long-wavelength radiation with a cutoff close to the absorption edge of HgI₂ (in the following, this is called penetrating radiation). The high absorption coefficient ($K \approx 10^4$ cm⁻¹ at $\lambda = 550$ nm (10)) leads to a very short penetration depth

for wavelengths beyond the absorption edge. In case of a linear potential distribution within the sample, the electric field strength would be below 10⁴ V/cm even for the highest applied voltage of 70V and the thinnest crystals (≈ 0.1 mm). This would clearly be insufficient for efficient carrier separation, especially in view of the rather small hole mobility encountered in these compounds (3, 11). In fact, if we assume such a linear potential distribution in the dark, it is easy to see that illuminating the electrode with light of a short penetration depth could influence this potential distribution in a way detrimental to carrier separation. Due to their higher mobility, the electrons diffuse faster toward the back contact than toward the holes. The electric field generated by the resulting charge distribution is thus opposed to the external field (the electrode being polarized anodically). The total electric field in the generation region is therefore definitely too weak. This situation is pictured in Fig. 6a; which shows the electric potential for anodic polarization in the dark (curve 1) and under illumination by monochromatic light only ($\lambda < 570$ nm, curve 2). The corresponding band diagram is shown in Fig. 6b. The experimental results provide compelling evidence for a profound change of the potential distribution upon the simultaneous illumination of the electrode by penetrating radiation. The effective range of wavelengths of this additional light is confined to a rather narrow spectral region near the onset of the absorption in HgI₂. In other words, in order to be efficacious, the long wavelength photons must be able to cause inter-band transitions and hence produce additional mobile carriers of both signs in the bulk of the electrode. Sub-

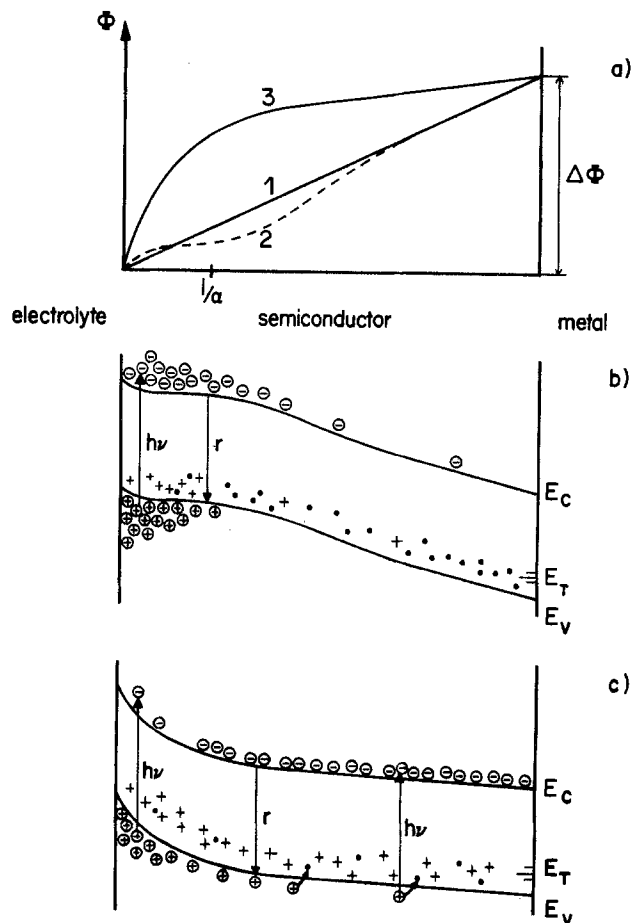


Fig. 6. a: Approximate potential distribution in an anodically biased ($\Delta\Phi$) HgI₂ electrode in the dark (1), for monochromatic (suprabandgap) illumination alone (2), and for additional continuous illumination with sub-bandgap photons (3). b: Band diagram corresponding to illumination mode 2. The dots in the figure represent empty hole traps. c: Band diagram for illumination mode 3.

sequently, the holes become trapped in the bulk, so that the steady-state photocurrent is mainly carried by electrons. (There is a marked difference in mobilities for electrons [$\approx 100 \text{ cm}^2/\text{Vs}$] and holes ($\approx 4 \text{ cm}^2/\text{Vs}$), as has been shown by many authors (3, 11).

Hence the irradiation of the sample with penetrating radiation leads to a shift of the electron Fermi level from a value near the middle of the bandgap towards the conduction band. The insulator is thus transformed into an effective n-type semiconductor with a carrier concentration depending on the intensity of the penetrating radiation. The trapped holes play the role of the positively charged donors in an ordinary semiconductor. (Curve 3 of Fig. 6a shows qualitatively the potential distribution for this situation, and Fig. 6c shows the corresponding band diagram [both again for anodic polarization].)

With this picture in mind, we see that the asymmetry between cathodic and anodic polarization immediately becomes apparent. In the cathodic case, both the increased recombination rate due to the accumulation of electrons at the surface and the poor mobility of the holes lead to a negligible photocurrent for nonpenetrating (i.e., short wavelength) radiation. In the anodic case, however, the electric field in the depletion region (Fig. 6c) will be able to separate the charge carriers produced by the nonpenetrating radiation. This will happen only if the ratio between the barrier's height and width is high enough. The barrier height and width are controlled not only by the applied voltage, but also by the intensity of the long-wavelength radiation, since the latter controls the doping level. In the depletion approximation, the barrier width depends on the inverse square root of the doping concentration. We are now able to explain the nonlinear intensity dependence of the photocurrent for nonpenetrating radiation (Fig. 2), and for low-level penetrating radiation. Only if the intensity of the latter is made high enough, so a depletion region forms, does one get a linear relationship over an appreciable range of intensities. Under the same conditions, the saturation at low potentials (Fig. 1) and the high quantum efficiency follow suit.

Without a more detailed investigation (by other means) of the trapping processes occurring in our HgI_2 crystals, it does not seem appropriate to construct an artificial trapping model which might explain the time dependence of the photocurrent shown in Fig. 4 and 5.

It is, however, possible to give some qualitative arguments on the basis of the available experimental evidence. Figure 4 suggests a very slow buildup of the space-charge layer under sub-bandgap illumination which could result from the slow filling of deep hole traps. The latter might then be expected to be sufficiently long lived so that once they have been gen-

erated, the response is governed by other processes which may very well be much faster (Fig. 5b). For a detailed discussion of these phenomena, the recombination mechanisms and eventual electron trapping will have to be taken into account.

Conclusions

We have shown that red HgI_2 , which is a material with an extremely high resistivity, can be optically doped so that photoelectrochemical investigations become feasible. A model has been proposed in which holes generated throughout the bulk by weakly absorbed long-wavelength light are trapped and so act as ionized donors and convert the insulator into an effective n-type semiconductor. This greatly affects the potential distribution near the electrolyte interface. The much-improved carrier separation leads to a pronounced enhancement of the otherwise poor quantum yield up to values above 50% over a wide spectral range.

The dependence of the steady-state photocurrent on applied potential and light intensity and the observed transient effects are in agreement with the model mentioned above.

Acknowledgments

Many valuable discussions with Dr. B. Bressel and Dr. M. Piechotka are gratefully acknowledged. We thank Ms. M. Lübke and Mr. J. Müller for their technical help in some of the experiments and the NEFF for financial support.

Manuscript submitted April 19, 1983; revised manuscript received Aug. 7, 1983.

REFERENCES

1. R. H. Bube, *Phys. Rev.*, **106**, 703 (1957).
2. E. F. Gross, *Sov. Physics Uspekhi*, **5**, 195 (1962).
3. R. C. Whited and M. M. Schieber, *Nucl. Instr. Meth.*, **162**, 113 (1979).
4. T. Kobayashi, J. T. Muheim, P. Waegli, and E. Kaldis, Submitted to *This Journal*.
5. J. T. Muheim, T. Kobayashi, and E. Kaldis, Submitted to *Nucl. Instr. Meth.*
6. H. Gerischer, M. Lübke, and B. Bressel, Submitted to *This Journal*.
7. W. Siripala and M. Tomkiewicz, *This Journal*, **130**, 1062 (1983), and references therein.
8. A. R. Moore, *J. Appl. Phys.*, **54**, 222 (1983).
9. M. M. Schieber, I. Beinglass, G. Dishon, and A. Holzer, in "Current Topics in Nuclear Science," Vol. 2, E. Kaldis and A. J. Scheel, Editors, p. 279, North Holland, Amsterdam (1977).
10. T. M. Brahim, Report CEA-R-5169 of the Commissariat à l'Énergie Atomique, CEN-Saclay, 91191 Gif-sur-Yvette Cédex France (1982).
11. R. Minder, G. Majni, C. Canali, G. Ottaviani, R. Stuck, J. P. Ponpon, C. Schwab, and P. Siffert, *J. Appl. Phys.*, **45**, 5074 (1974).

Hydrodynamic Studies on a Vertical Electrolyzer with Gas Evolution under Forced Circulation

F. Hine,* M. Yasuda,* Y. Ogata, and K. Hara
Nagoya Institute of Technology, Nagoya 466, Japan

ABSTRACT

The electrical resistance of the gas-solution mixture and the hydrodynamic pressure drop in a vertical cell operated under forced circulation of the electrolytic solution were measured. They strongly depended on the electrode configuration and the cell geometry, especially in narrow channels. One must be careful designing electrolyzers with gas evolution, otherwise the cell voltage increases extensively. Relationships among the electrical resistivity, the gas void fraction, the flow rate or the Reynolds number, the friction factor, and others are obtained.

The electrolyte conductivity in electrolyzers decreases when the solution contains gas bubbles, resulting in high cell voltage. The flow of the gas-solution mixture in a vertical cell depends on the configuration of the electrolyzer and is classified into three types: blocked convection, natural circulation, and forced circulation (1). Of these, blocked convection is undesirable, especially in narrow channels since separation of gas bubbles from the two-phase mixture is difficult. Electrolyte circulates by gas lift when a downcomer is provided, which is a common feature of water electrolyzers and chlor-alkali cells. The gas voidage in the electrolysis zone, and hence the ohmic voltage drop, are decreased by natural circulation in this case. The gas voidage can be further reduced by forced circulation, however, it is rarely used because a circulation pump is required. Most experiments described here were conducted under forced circulation to clarify the hydrodynamic behavior of the vertical cell with gas evolution since the analysis of natural circulation of electrolyte was somewhat complicated. The results obtained are, of course, applicable to cells under natural circulation when appropriate assumptions and/or modifications are used.

The anolyte and/or catholyte of the membrane-type chlorine cell are circulated between their compartments and respective reservoirs to maintain the solution composition and temperature. Also, the current efficiency is improved somewhat by solution circulation, probably due to reduced concentrations of NaCl and NaOH near the membrane in both sides.

Generally speaking, the interelectrode gap or the distance between the electrode and the separator must be small for reducing the IR drop and cell voltage. But good design is important otherwise the gas voidage in the narrow channel increases, resulting in large IR drop.

Nonflat plate electrodes such as perforated plate, mesh, and expanded metal can release electrolytic gas bubbles in the space in the rear of the electrode (2, 3), but these electrodes result in friction loss of solution flow.

This work deals with the hydrodynamic behavior of a vertical cell equipped with gas evolving electrodes of various kinds and the voltage characteristics of these systems.

Experimental Procedure

The flow sheet is illustrated in Fig. 1. The electrolyte 0.2N NaOH, was pumped into the bottom part of cell through the flowmeter, and was sent back to a 30 liter reservoir where the solution temperature was controlled by both an electric heater (1 kW) and a cooling water coil.

* Electrochemical Society Active Member.

Key words: bubble effects, electrolyte conductivity, flat plate electrode, forced circulation, friction factor, gas void fraction, mesh electrode, pressure drop, vertical cell.

A vertical PVC pipe (19 mm inner diam and 64 cm long), equipped with two platinized Pt foil electrodes of 23 mm length and 3 mm width, was located above the test cell to determine the conductance of the two-phase mixture and hence, the gas void fraction at the cell top (ϵ_T). The relationship between the gas voidage and the conductance was calibrated prior to the measurement.

The returned solution was reserved in the cushion tank during the conductivity measurement to avoid any disturbance of the leakage current from the electrolyzer. Gas was purged out from the cushion tank and the reservoir.

Two Luggin-Haber probes were positioned at the center of the electrolyzer to evaluate the gas voidage (ϵ_C) at the point from the solution IR drop perpendicular to the electrodes. One probe protruded 1-5 mm, depending on the electrode spacing, from the flat plate counterelectrode, and another Luggin was located just at the electrode surface.

The pressure drop between the top and the bottom of the electrolyzer was measured by a manometer connected with the pressure taps located at the respective points. The distance between two taps was 90 cm, but the pressure drop presented in the text was on the basis of 1m in distance.

The electrolyzer, made of Lucite resin, is shown in Fig. 2. The flat plate counterelectrode and the flat plate test electrode were made of a Type 304 stainless

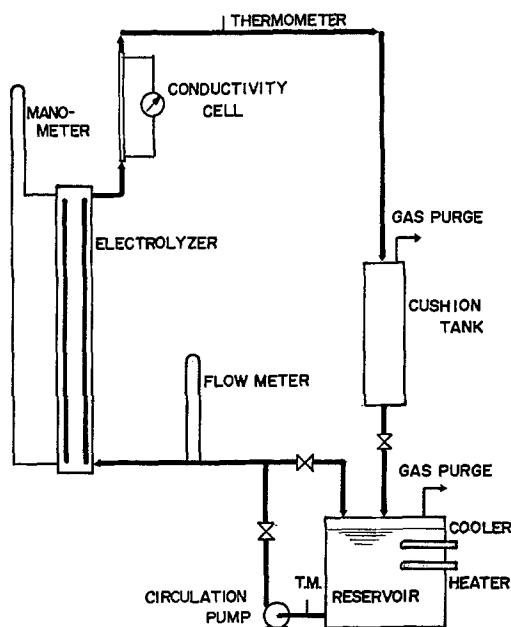


Fig. 1. Flow sheet

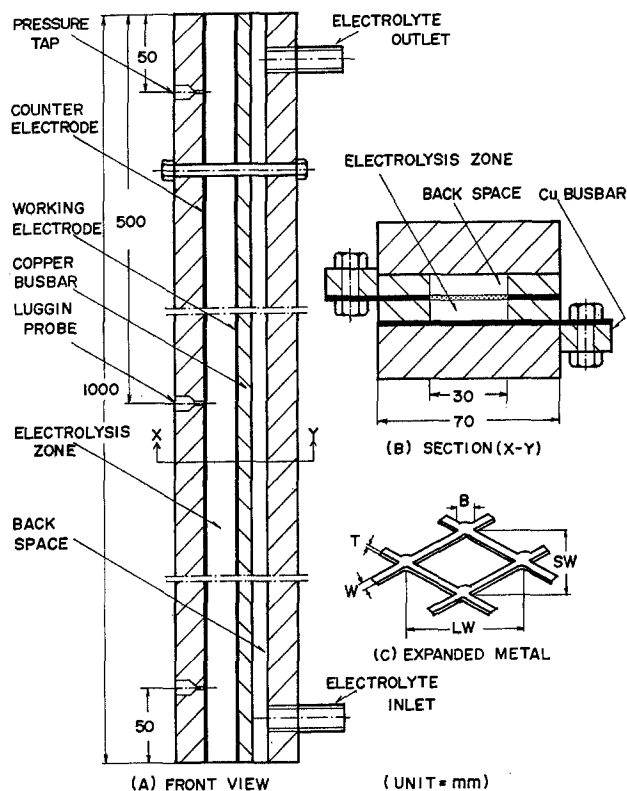


Fig. 2. Electrolytic cell (A and B) and expanded metal (C)

steel sheet (100 cm long, 9 cm wide, and 2 mm thick). A heavy copper bus bar was bonded at the end of the steel plate longitudinally to avoid voltage drop in the electrode hardware. These electrodes were clamped together with a plastic spacer, and hence, the working area was 96 cm long and 3 cm wide.

The electrode gap was varied in the range 1-20 mm with various spacers. The width of the space in the back of the nonflat plate electrode was also varied with the spacers in the range 2.5-7.0 mm (see Fig. 2B).

The nonflat plate electrodes include the mesh electrodes (ME) and the expanded metal electrodes (EX). The perforated plate electrode was also employed as reference. A mesh, 96 cm long and 3 cm wide, was soldered to the window frame (100 cm long and 9 cm wide) to fabricate the mesh electrode. Some examples of the meshes and expanded metals tested are listed in Table I. These materials were made of Type 304 stainless steel with some exceptions, due to availability in the market. Generally, the test electrode was used as cathode, and the counterelectrode as anode.

Table I. Geometry of nonflat plate electrodes

Mesh				
No.	Wire diam (mm)	Open size (mm)	Percent open	Resistance ^a (mΩ)
ME-2	0.67	2.49	62.1	7.20
4	0.60	1.36	48.1	4.67
5	1.20	1.30	27.0	2.17
12	0.254	0.592	49.0	18.50
14	0.254	0.381	36.0	10.55
L ¹	2.0 (2.4) [*]	2.2	22.7	0.50

^{*} transverse

Expanded metal								
No.	Dimensions (mm) ^a					Resistance (mΩ) ^a		
	T	W	B	LW	SW	Percent open	Longitudinal	Transverse
EX-1	0.4	0.6	1.8	6.2	3.2	41	1.86	0.90
2	0.5	0.7	2.4	8.2	3.6	36	2.30	1.07

¹ Cold rolled ² For 1 cm × 1 cm ³ See Fig. 1C

Caustic soda solution (0.2N NaOH) was electrolyzed. The operating temperature was 50°C. The physico-chemical properties of the electrolytic solution at 50°C are as follows

$$\text{Specific resistance} = 16.4 \Omega \text{ cm}$$

$$\text{Viscosity} = 0.006101 \text{ g/cm sec}$$

$$\text{Density} = 1.0215 \text{ g/cm}^3$$

During electrolysis, hydrogen and oxygen evolved at the cathode and the anode, respectively, and mixed together because there was no separator between two electrodes. Thus, $\frac{1}{2}$ mol H₂ and $\frac{1}{4}$ mol O₂ were evolved for 1F. These gas bubbles cover the electrode surface and the overvoltage increases. On the other hand, the electrolyte resistance is increased by dispersion of bubbles. However, the surface coverage is small since the solution flow diverts gas bubbles from the electrode in a vertical cell.

The electrolytic current was varied in the range 0-100A. The average current density was 34.7 A/dm² at 100A of total current for a flat plate electrode.

The flow rate of solution was varied from 30 to 300 cm³/sec. The interelectrode gap was a simple flow channel when a flat plate was used as the test electrode. On the other hand, the electrolytic solution could pass through the nonflat plate electrode to the back space, and hence, the actual flow rate in the electrolysis zone decreased.

Results and Discussion

Flat plate electrode.—The terminal voltage of the cell equipped with the flat plate electrode decreased with increase in the flow rate, especially at high currents, and approached asymptotes as illustrated in Fig. 3A. At high flow rates, the terminal voltage was almost linear with electrolytic current since the gas voidage was small even at large currents (Fig. 3B). The cell voltage increased rapidly with an increase in

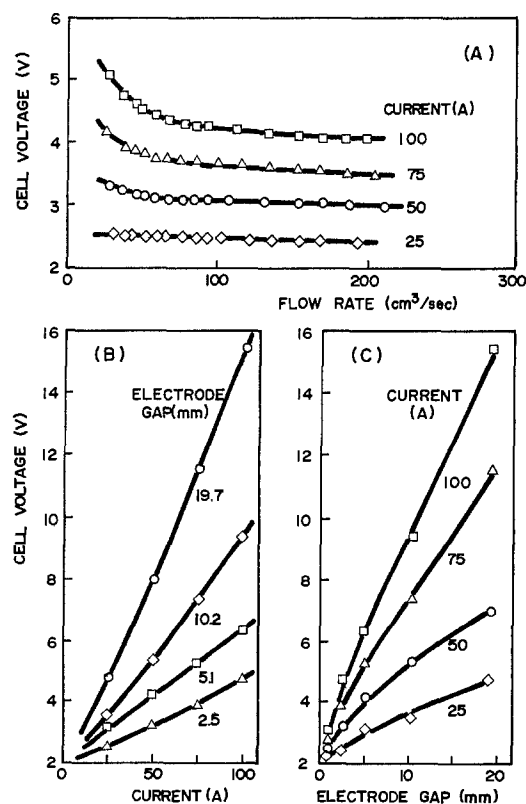


Fig. 3. Cell voltage as a function of the solution flow rate (A), the electrolytic current (B), and the electrode gap (C). Electrode = flat plate. (A) Electrode gap = 2.5 mm. (B and C) Solution flow rate = 40 cm³/sec.

the electrode gap, especially for a small gap (Fig. 3C) because of the distribution of bubbles across the electrode gap in a wide channel; that is, most of the bubbles are crowded next to the electrode, and only solution flows in the center of the channel, while bubbles are uniformly distributed in a narrow channel. It differs from the results obtained under natural circulation and blocked convection (1, 2), where the cell voltage rises greatly when the electrode spacing becomes small because of large gas voidage.

Figure 4A shows examples of the solution resistivity and the gas voidage as functions of the flow rate. The gas void fraction (ϵ) is represented by Eq. [1]

$$\epsilon = \frac{Q_G}{Q_G + sQ_S} \quad [1]$$

Generally, the slip ratio (s) for the gas-solution mixture in electrolytic cells is considered to be unity (4, 5). Also, the electrical resistivity of the two-phase mixture (ρ) is a function of ϵ such as

$$\frac{\rho}{\rho_0} = \frac{1 + 0.5\epsilon}{1 - \epsilon} \quad \text{Maxwell} \quad [2]$$

and

$$\frac{\rho}{\rho_0} = (1 - \epsilon)^{-1.5} \quad \text{Bruggeman} \quad [3]$$

Although many have discussed the accuracy of these equations (6), no significant difference is found in the range $\epsilon < 0.3$ (7-10). The gas void fraction on the right side in Fig. 4A was calculated from Eq. [2].

Table II shows the voltage balance of the cell with a flat plate electrode. At low currents, the solution IR drop was only one tenth of the cell voltage when the solution flow rate was large. On the other hand, it becomes the largest component of the terminal voltage at large amperages and small flow rates because the reduced resistivity (ρ/ρ_0) increases with an increase in the amperage and a decrease in the flow rate. The resistivity ρ is almost independent of the interelectrode gap since the gas voidage is a function of the amperage or the gas evolution rate and the solution flow rate (see Eq. [1]).

The potential drop, $E_d + \Sigma\eta$, in Table IIB is 0.15V larger than that of Table IIA, probably due to a small deviation of the position of the Luggin probe and the electrode gap during fabrication of the cell. Deviation of the distance by 0.1 mm causes a voltage drop of 60 mV at 35 A/dm², for example.

The pressure drop vs. flow rate curve is almost independent of the electrolytic current at flow rates more than 100 cm³/sec as shown in Fig. 5 because the gas void fraction is almost negligible even at large

Table II. Voltage balance with a flat plate electrode (Interelectrode gap = 2.5 mm)

(A) At flow rate = 150 cm ³ /sec				
	Current, A			
	25	50	75	100
Anode potential, E_A^*	0.76	0.78	0.79	0.80
Cathode potential, E_C^*	-1.47	-1.51	-1.53	-1.55
Decomposition voltage, E_d				
+ overvoltages, $\Sigma\eta$	2.23	2.29	2.32	2.35
Solution IR drop, IR_{s01}	0.21	0.71	1.12	1.71
Terminal voltage, V_T^{**}	2.44	3.00	2.44	4.06
(B) At 100A (= 34.7 A/dm ²)				
	Flow rate, cm ³ /sec			
	30	50	100	150
Reduced resistivity, ρ/ρ_0	1.75	1.40	1.23	1.17
Solution voltage drop, IR_{s01}^{***}	2.49	1.99	1.75	1.66
Terminal voltage, V_T	5.00	4.55	4.25	4.15
$V_T - IR_{s01} = E_d + \Sigma\eta$	2.51	2.56	2.50	2.49

* V vs. Hg/HgO

** $V_T = E_d + \Sigma\eta + IR_{s01}$

*** Estimated IR drop free of bubble = 1.42V.

amperages. At low flow rates, the pressure drop became negative, depending on the amperage, due to gas lift. It suggests circulation of the two-phase flow in a closed loop in the cell. The flow pattern in a cell with a perforated electrode is illustrated in Fig. 1 in the previous paper (2). Contribution of such complicated flow to the reduction of the gas void fraction in the interelectrode gap was small. Therefore, an appropriate design of the cell, especially the down-comer or the back space, is important if one seeks to decrease the gas voidage by means of natural circulation.

The pressure drop in the cell equipped with an expanded metal electrode is significantly large compared to the flat plate electrode, due to turbulence of the solution flow, as illustrated by the dotted line in Fig. 5.

Thorpe *et al.* proposed the frictional pressure drop multiplier (Ψ) as follows (5)

$$\Psi = \frac{\Delta P_T}{\Delta P_S} \quad [4]$$

Vogt introduced a coefficient K , which is a function of ϵ (10)

$$\frac{dP_T}{dx} = K \frac{dP_S}{dx} \quad [5]$$

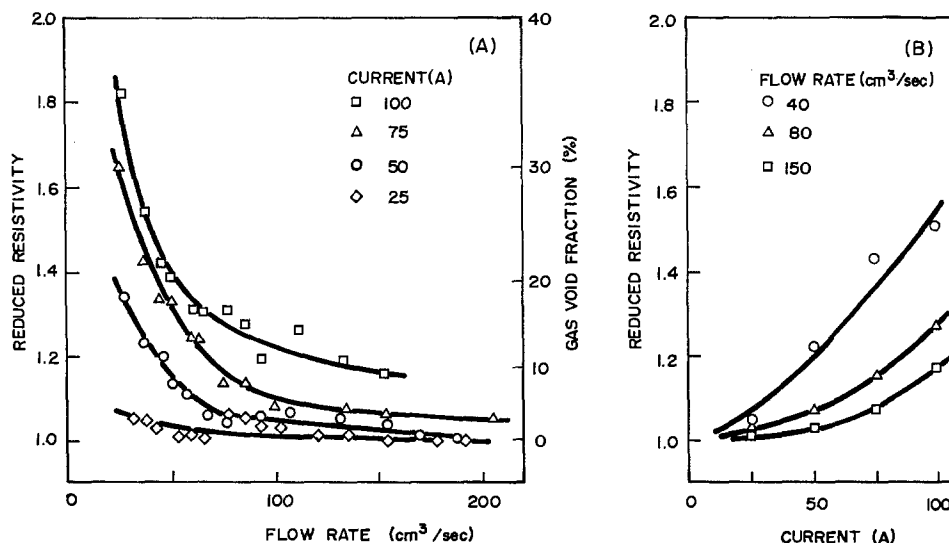


Fig. 4. Reduced resistivity (ρ/ρ_0) as a function of the solution flow rate (A) and the electrolytic current (B). Electrode = flat plate; electrode gap = 2.5 mm.

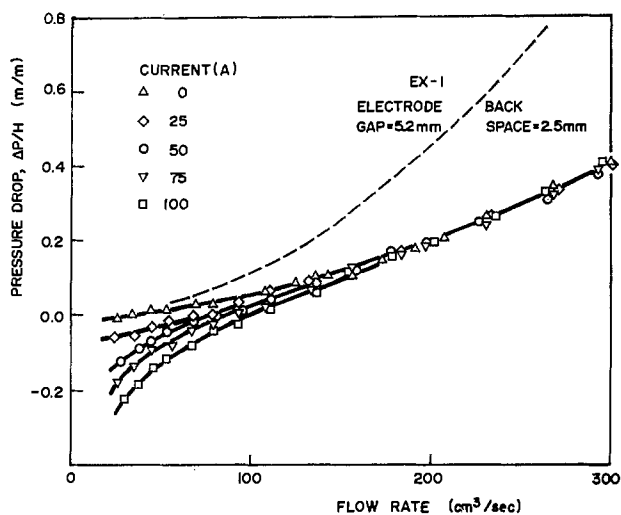


Fig. 5. Pressure drop vs. solution flow rate curves. Electrode = flat plate; electrode gap = 5.1 mm.

$$K = \frac{1}{1 - \epsilon} \frac{f_T}{f_S} = \frac{(1 + \epsilon)^n}{1 - \epsilon} \quad [6]$$

where n is an exponent depending on the flow velocity, e.g., $n = 1$ for laminar flow and $n = 0$ for fully developed turbulent flow. Correlation between Ψ and K is as follows

$$\Psi = \int_0^H K \frac{dx}{H} \quad [7]$$

For fully developed turbulent flow, Vogt obtained Eq. [8]

$$\Psi = \frac{1 - 0.5\epsilon_T}{1 - \epsilon_T} \quad [8]$$

The multiplier Ψ evaluated with the experimental results was a function of the gas void fraction and the electrode gap, as shown in Fig. 6, a power law, Eq. [9], fit the data better than Eq. [8]

$$\Psi = \left(\frac{1 - 0.5\epsilon_T}{1 - \epsilon_T} \right)^m \quad [9]$$

$$m = 840d + 0.5 \quad [10]$$

If $n = 0.25$, we obtain

$$\Psi = \left(\int_0^H \frac{[1 + \epsilon_T(x/H)]^{0.25} dH}{1 - \epsilon_T(x/H)} \right)^m \quad [11]$$

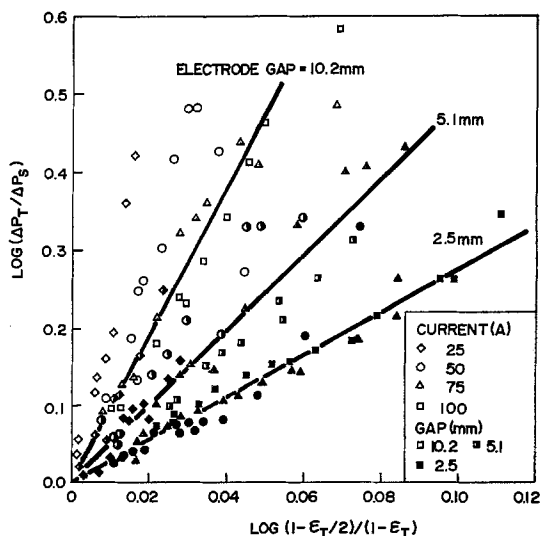


Fig. 6. Frictional pressure drop multiplier (Ψ) vs. gas void fraction at the cell top. Electrode = flat plate.

$$m' = 750d + 0.8$$

[12]

This equation is too complicated for practical use, and it gives almost the same results as Eq. [9]. Although a simple form of Ψ can be found (11), it deviates significantly from experiments.

Because the frictional pressure drop multiplier depends on the geometry of the flow channel, as shown by Eq. [9] and [11], further work is required.

Nonflat plate electrodes.—Most of the mesh electrodes tested showed high voltages compared to the flat plate electrode as shown in Fig. 7. The voltage with the expanded metal electrode was almost the same as with the flat plate electrode, and a few materials such as ME-4 were preferable.

The cell voltage was almost independent of the mesh size when the back space was small, but the voltage of the cell having a large back space increased as the mesh became lighter because the two-phase mixture could not escape from the electrolysis zone to the back space. That is, the actual flow rate in the electrolysis zone becomes small at a given flow rate when the back space is large, resulting in large gas voidage.

If the back space was too large and the mesh was so tight the two-phase mixtures could not penetrate it, the cell voltage rose greatly as the interelectrode gap decreased, just as the voltage of narrow cells having a pair of the flat plate electrodes was high (1). The current distribution near the nonflat plate electrode causes a large solution IR drop, especially in the narrow channel. Both oxygen and hydrogen overvoltages on the nonflat plate electrode are high because of reduction of the electrode area, which also causes high cell voltage.

The reduced resistivity at the cell top and at the center of the cell are shown in Fig. 8. The resistivity of the two-phase flow at the cell top is of course independent of the electrode configuration, but is only a function of the gas void fraction (Fig. 8A).

On the other hand, the resistivity of the two-phase system in the electrolysis zone depends greatly on the electrode configuration, as shown in Fig. 8B. Note that the resistivity in the electrolysis zone is significantly larger than at the cell top when a badly designed electrode is employed, suggesting very large gas voidage in the electrolysis zone in comparison with that in the back space. The expanded metal electrodes, both EX-1 and EX-2 in this figure, can release electrolytic gases to the back side, resulting in low gas voidage and cell voltage.

In the previous paper (9), assumptions of a linear distribution of a population of gas bubbles along the vertical flat plate electrode and also uniform distribution perpendicular to the electrode, agreed with the

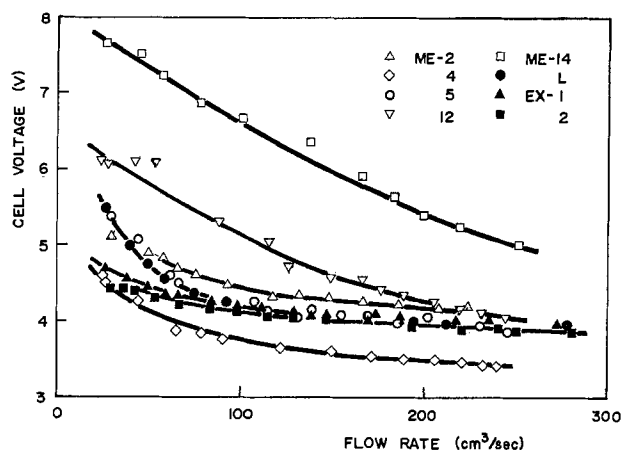


Fig. 7. Cell voltage vs. solution flow rate curves. Electrode = nonflat plate; electrode gap = 1.1 mm; back space = 7.0 mm; electrolytic current = 100A.

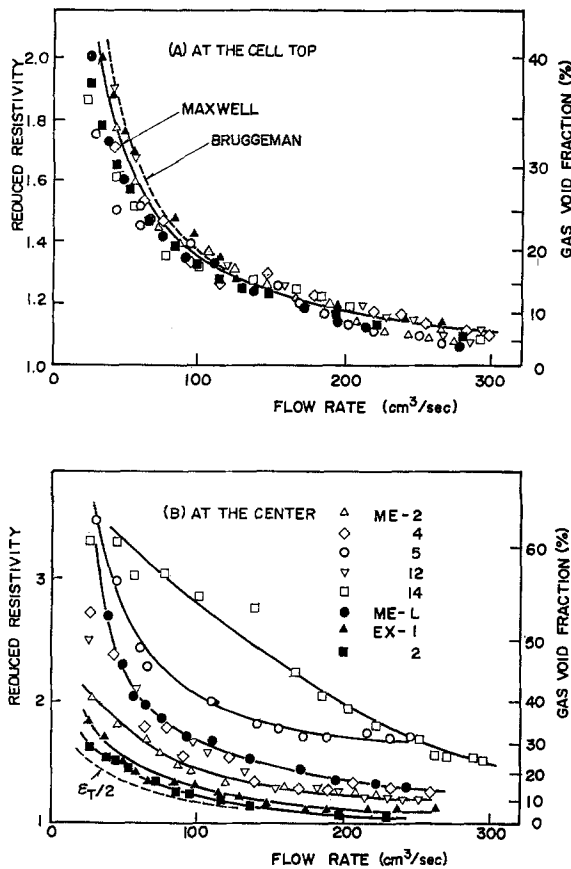


Fig. 8. Reduced resistivity (ρ/ρ_0) vs. solution flow rate curves at the cell top (A) and at the center (B). Electrode = nonflat plate; electrode gap = 1.1 mm; back space = 7.0 mm; electrolytic current = 100A.

experiment. An estimated gas void fraction with an assumption of $\epsilon_c = \epsilon_T/2$ is illustrated by the dotted line in Fig. 8B. All of the experimental data with the mesh electrodes are significantly larger than the dotted line.

Although a large portion of electrolytic gas bubbles can escape from the electrolysis zone to the back side through the mesh, the interelectrode space is still crowded with a swarm of gas bubbles, and its gas voidage is greater than that in the back space and also that with a simple assumption: $\epsilon_c = \epsilon_T/2$.

The cell geometry such as the ratio of the electrode spacing (d) to the depth of the back space (d_B) is also an important factor of ρ/ρ_0 and ϵ , as shown in Fig. 9, for example. A straight line in the figure shows $\epsilon_c = \epsilon_T/2$. The gas voidage in the electrolysis zone is almost equal to that in the back space if the ratio d/d_B is large. On the other hand, a narrow space between two electrodes was crowded with a swarm of gas bubbles and the gas void fraction increased greatly because most of the solution passed through the back space (Fig. 9A). The gas voidage in the cell equipped with EX-1, for example, was almost uniformly perpendicular to the electrode since the electrode permitted the gas bubbles to escape (Fig. 9B).

Since a mesh in the flow behaves as a turbulent promoter, the pressure drop of the channel is increased by its insertion, as shown in Fig. 10 (also see Fig. 6). The pressure drop in the channel with ME-5 was very large since this mesh was composed of thick wires. The expanded metal showed a large pressure drop due to its configuration. Two meshes, ME-12 and ME-14, showed a relatively small resistance to the two-phase flow since these meshes were fabricated with thin wires and tight. The pressure drop is, of course, a function of the cell geometry as well.

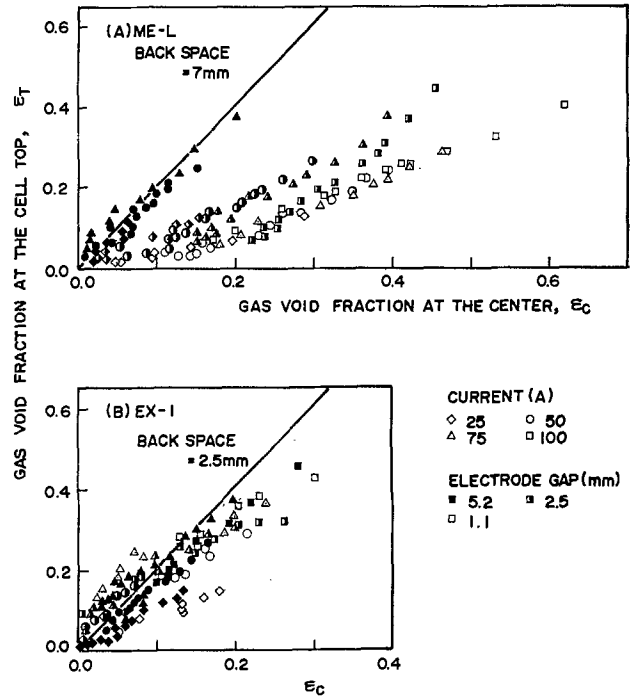


Fig. 9. Gas void fraction at the cell top and at the center.

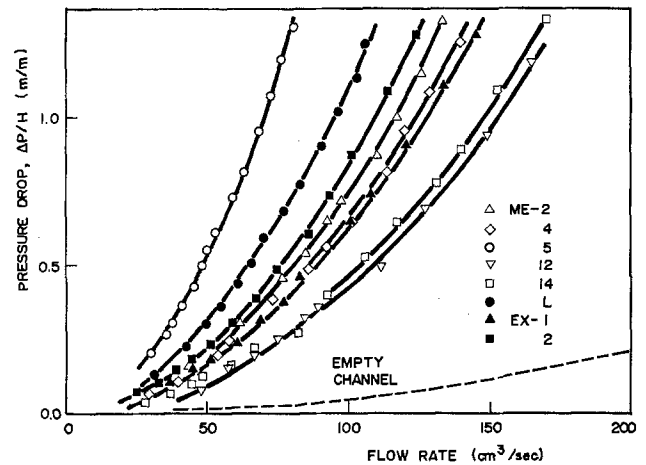


Fig. 10. Pressure drop vs. flow rate curves in the single-phase flow (zero current). Electrode = nonflat plate; electrode gap = 1.1 mm; back space = 2.5 mm.

The pressure drop (ΔP_S) is represented as follows

$$\Delta P_S = 4f \frac{u_s^2}{2g_c} \frac{H}{D_e} \quad [13]$$

where the equivalent diameter of the flow channel is roughly shown by Eq. [14]

$$D_e = \frac{2w(d + d_B + t)}{w + d + d_B + t} \quad [14]$$

The friction factor is a function of the Reynolds number Re and the slope of the logarithmic plots of f vs. Re are almost independent of the inserts, as shown in Fig. 11. Consequently, we have an equation

$$f = f_1 Re^{-0.126} \quad (400 < Re < 2000) \quad [15]$$

where f_1 is the standard friction factor at $Re = 1$, and is a function of the insert.

The pressure drop vs. flow rate curves were almost independent of the rate of gas evolution even at large currents, except at low flow rates, smaller than 50 cm³/sec, where the pressure drop became negative due to the gas lift.

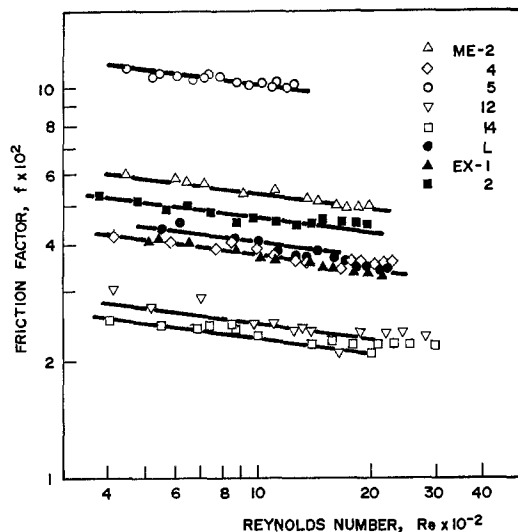


Fig. 11. Friction factor vs. Reynolds number in the single-phase flow. Electrode = nonflat plate; electrode gap = 1.1 mm; back space = 2.5 mm.

The frictional pressure drop multiplier in the channel equipped with a mesh electrode agrees well with Eq. [9], as shown in Fig. 12, and the exponent m varies linearly with the cell geometry ($d + d_B$), as shown in Fig. 13.

Conclusion

The cell voltage decreased with increasing flow rate since the gas void fraction decreased. The voltage of the narrow channel equipped with a pair of the flat plate electrodes was low when the flow rate of electrolyte was large enough.

The terminal voltage of the cell equipped with the nonflat plate electrode was rather high compared to that with the flat plate electrode. Therefore, careful selection of the electrode material and appropriate design of the cell equipped with the nonflat plate electrode are of great importance since the cell voltage is sensitive to the bubble effects.

The mesh electrodes of ca. 50% open yielded the lowest cell voltage. Tight meshes woven with heavy wire retard gas bubbles passing through. However, the overvoltage and the electric resistance of these electrodes, and hence the cell voltage, are relatively low.

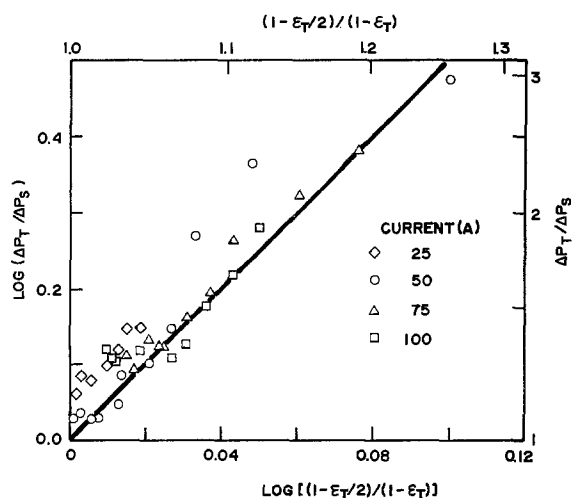


Fig. 12. Frictional pressure drop multiplier (Ψ) vs. gas void fraction at the cell top. Electrode = ME-2; electrode gap = 1.1 mm; back space = 7.0 mm.

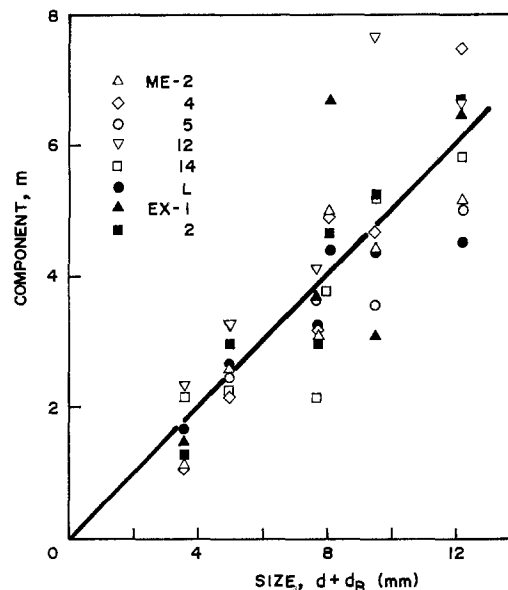


Fig. 13. Component m vs. cell size ($d + d_B$)

The expanded metal electrode permits gas bubbles to escape and contributes to the reduction of the cell voltage even at low flow rates.

The logarithmic plots of the friction factor vs. the Reynolds number was linear, and the slope was independent of the electrode configuration. The standard friction factor f_1 depends on the type of electrode.

The friction loss with the mesh electrode woven with thin wires less than 0.6 mm in diam was small. The friction loss with heavy wire mesh was large. Cold rolling enabled the reduction of the hydraulic resistance of mesh, whereas the open area was decreased.

The frictional pressure drop multiplier Ψ was related to the gas void fraction with a simple equation. Consequently, these factors are useful for designing a vertical cell equipped with either a flat plate electrode or a nonflat plate electrode operated under forced circulation of electrolytic solution. The experimental results are also applicable for a cell operated under natural circulation.

Manuscript submitted Jan. 19, 1983; revised manuscript received Aug. 1, 1983.

LIST OF SYMBOLS

d	density of bubble-free solution, kg/m ³
d	electrode spacing, m
d_B	depth of back space, m
D_e	equivalent diameter of channel, m
E_d	decomposition voltage, V
f	friction factor
f_1	standard friction factor
f_s	friction factor for single-phase flow
f_T	friction factor for two-phase flow
g_c	conversion factor for gravity acceleration, kg m/sec ² kg
H	electrode height, m
K	coefficient
m, m'	components
n	component
$\Delta P_S, dP_S$	pressure drop of single-phase flow, kg/m ²
$\Delta P_T, dP_T$	pressure drop of two-phase flow, kg/m ²
Q_S	solution flow rate, m ³ /sec
Q_G	gas evolution rate, m ³ /sec
s	slip ratio
t	electrode thickness, m
u_S	flow velocity of solution, m/sec
w	electrode width, m
x	distance, m
e	gas void fraction
e_C	gas void fraction at the center of cell
e_T	gas void fraction at the cell top
ρ	electrical resistivity of gas-solution mixture, Ω m

ρ_0	electrical resistivity of bubble-free electrolyte, $\Omega \text{ m}$
Ψ	frictional pressure drop multiplier
η	overvoltage, V

REFERENCES

1. F. Hine and K. Murakami, *This Journal*, **127**, 292 (1980).
2. F. Hine and K. Murakami, *ibid.*, **128**, 64 (1981).
3. J. Jorne and J. F. Louvar, *ibid.*, **127**, 298 (1980).
4. J. E. Funk and J. F. Thorpe, *ibid.*, **116**, 48 (1969).
5. J. F. Thorpe, J. E. Funk, and T. Y. Bong, *J. Basic Eng.*, **173**, March (1970).
6. R. E. Meredith and C. W. Tobias, in "Advances in Electrochemistry and Electrochemical Engineering," Vol. II, C. W. Tobias, Editor, p. 15, Interscience Publ., New York (1962).
7. R. E. Meredith and C. W. Tobias, *This Journal*, **108**, 286 (1961).
8. L. L. L. Sigrist, O. Dossenbach, and N. Ibl, *J. Appl. Electrochem.*, **10**, 223 (1980).
9. F. Hine, M. Watanabe, M. Yasuda, and M. Kutata, Paper 412 presented at The Electrochemical Society Meeting, Montreal, Que., Canada, May 9-14, 1982.
10. H. Vogt, *J. Appl. Electrochem.*, **12**, 26 (1982).
11. H. Akagawa, *Nippon Kikai Gakkai Ronbunshu*, **23**, 292 (1957).

Conductivity of Anodic Silver Chloride during Formation

Theodore R. Beck* and David E. Rice

Electrochemical Technology Corporation, Seattle, Washington 98107

ABSTRACT

Silver electrodes were anodized in KCl, NaCl, LiCl, and HCl solutions of concentration greater than 4N. High field conduction was exhibited by the growing AgCl film during the anodizing process at current densities greater than 1 mA/cm². The high field barrier film reverts to a porous high conductivity film at applied potentials greater than 20V or when the anodizing current is interrupted or briefly reversed.

Anodic silver chloride films for Ag/AgCl reference electrodes are commonly formed in 0.05N KCl or 0.1-1N HCl at current densities of 0.4-10 mA/cm² (1). Under these conditions, porous anodic films form with specific conductivities that are 10-100 times (1-4) that of bulk AgCl. The conductivities of these films increase with the concentration and conductivity of the electrolyte in which they are measured, indicating a predominance of pore conduction.

The present work deals with formation of anodic AgCl films in concentrated (4-15N) solutions of KCl, NaCl, LiCl, and HCl. For these electrolytes, there is a region of current densities in which AgCl films exhibit high field conduction, *i.e.*, exponential relation of current density to potential, during the anodizing process. There is no systematic relation of the film conductivity to solution conductivity for the high field films, indicating a bulk film effect. This region is illustrated in Fig. 1. The high field conduction region occurs at concentrations well above common usage for anodizing silver for reference electrodes, which may account for it not being previously observed and studied.

Experimental

Anodizing experiments were conducted with silver disk or rectangular electrodes imbedded flush in epoxy resin insulation. Silver from three sources was used: 99.999% pure bead (Cominco), an unknown but high purity rod, and 99.9% pure wire. The respective dimensions of the silver electrodes were: $d = 1.8 \text{ mm}$, $A = 2.5 \text{ mm}^2$, length = 2 mm; $1.6 \times 3.2 \text{ mm}$ rectangle, $A = 5.0 \text{ mm}^2$, length = 25 mm; $d = 0.75 \text{ mm}$, $A = 0.44 \text{ mm}^2$, length = 25 mm. Pretreatment was sanding with no. 600 silicon carbide paper and rubbing with a cotton swab under the electrolyte solutions. Solutions were made from ACS specification chemicals and distilled water.

A Princeton Applied Research 173 potentiostat was used for the constant current experiments with a platinum counterelectrode. The silver electrodes were mounted in the anode facing up position so that events could be observed under a 60 \times binocular microscope.

* Electrochemical Society Active Member.

Key words: films, electrode, current density, transients.

Potential transients of the silver electrodes were measured in respect to a saturated calomel electrode. Slow low current density transients were recorded on a strip chart recorder, and fast high-current density transients were recorded on a storage oscilloscope. All experiments were carried out at room temperature, $21^\circ \pm 2^\circ\text{C}$.

Results and Discussion

Constant current experiments.—A typical potential transient at constant current is shown in Fig. 2. Five distinct regions of potential were observed over most of the range of current densities for high field conduction shown in Fig. 1, although at the higher current densities the regions A and B were indistinct. In region A, the potential at low current densities was close to that of the reversible Ag/AgCl couple. The silver surface color gradually turns brown during the period of region A, and at the end of region A, a wave of different texture is seen moving from the edges to the center of the electrode. No visible change is seen in region B. At the beginning of region C, small gas

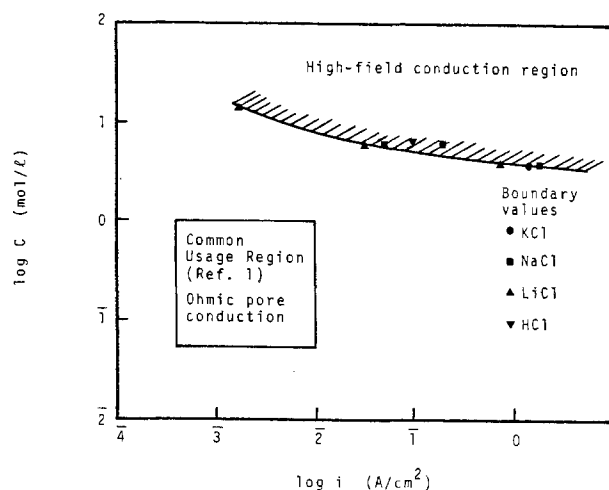


Fig. 1. Current density-concentration region for high field conduction compared to region of common usage.

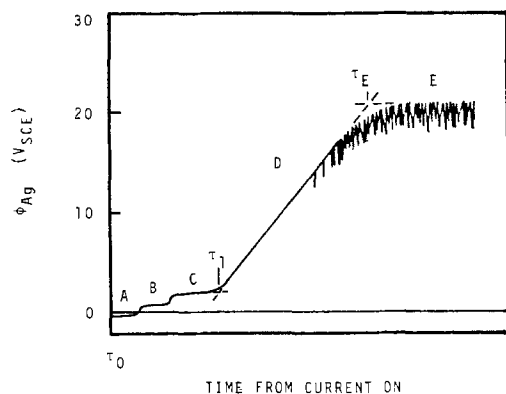


Fig. 2. Typical potential transient at constant current. Time scale is approximately 100s down to 0.1s depending on current density from 10^{-3} to 10 A/cm 2 .

bubbles sprout from the surface. Starch-iodide paper touched to the removed electrode turned blue, indicating that the bubbles were chlorine. During region C, a whitish haze appears over the surface and increases with time of anodizing.

Region D is a nearly linear rise in potential with time. No visible change occurs on the surface other than a decrease in the gas evolution rate. The slope of the region D curve increases with current density. As region E is approached, occasional spikes of decreasing potential occur. The frequency increases with time and in region E the spikes become a continuous band. Zones of intense agitation and evolution of microbubbles are seen to move around the electrode surface during region E. The potential of region E is nearly independent of current density.

The only reasonable phenomenon that could cause such a large increase in potential in region D is increase in AgCl film resistance due to thickening with time. The AgCl thickness for a dense film would vary with time as

$$l = \frac{iM}{zF\rho} (\tau - \tau_1) \quad [1]$$

and the conductivity is defined by

$$\kappa = \frac{il}{\Delta\phi} \quad [2]$$

A constant slope in region D shows that AgCl conductivity is constant at constant current density, and it can be readily shown that

$$\kappa = \frac{Mi^2}{zF\rho(d\phi/d\tau)} \quad [3]$$

The value of $M/zF\rho$ is 2.67×10^{-4} cm 3 /C for AgCl.

Values of κ calculated from Eq. [3] and experimental data for three concentrations of chloride solutions are given in Fig. 3. Because of the high solubility of LiCl, a wide range of concentrations was possible with LiCl. Current density was based on geometric area; no correction was made for surface roughness. Within experimental error, no difference was observed in conductivities for the three electrodes with purities from 3-9 to 5-9.

Conductivity is seen to vary as the first power of current density in Fig. 3. A linear relationship of conductivity to current density in Fig. 3 is consistent with high field conduction

$$i = i_0 \exp\left(\frac{\beta\Delta\phi}{l}\right) \quad [4]$$

for which the integral conductivity, Eq. [2], is

$$\kappa = \beta i / \ln(i/i_0) \quad [5]$$

The term $\ln(i/i_0)$ varies slowly with current density as discussed further on. The higher measured conduc-

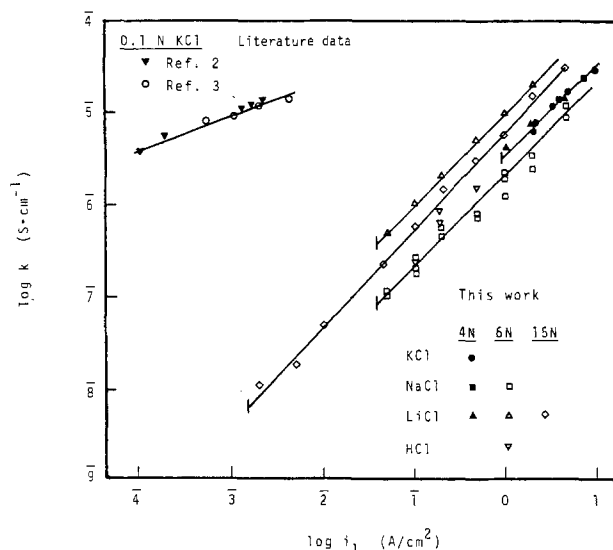


Fig. 3. Calculated conductivities of AgCl during anodizing in chloride solutions at constant current (region D, Fig. 2) compared to literature data for conductivity of AgCl after formation in lower concentration chloride.

tivities in the 6N and 15N LiCl solutions are not explained at this time.

The vertical bar at the lower end of the line for each concentration in Fig. 3 indicates the current density below which region D of Fig. 2 is not observed. These are the values plotted in Fig. 1. At lower current densities the region C is extended and becomes noisy or the potential goes into violent fluctuations. Some published conductivities for preformed AgCl from the common usage region of Fig. 1 are given in Fig. 3 for comparison.

The theoretical value of β based on an ion hopping model (5) is

$$\beta_{\text{Theor}} = \frac{\alpha z F a}{RT} \quad [6]$$

For $\alpha = 0.5$ and the hop distance, a , equal to the sum of ionic diameters of Ag $^+$ and Cl $^-$, $2(1.26 + 1.81) = 6.14$ Å (6), the value of β_{Theor} at 294 K is 1.2×10^{-6} cm/V. The experimental values in Fig. 3 ($\beta = \kappa \ln(i/i_0)$ at $i = 1$ A/cm 2) are 2-4 times this value, which may be attributed in part to the term $\ln(i/i_0)$ and in part to surface roughness.

The true current density should be smaller by the roughness factor, γ , and the true conductivity calculated by means of Eq. [3] should be smaller by a factor of γ^2 . The result in Fig. 3 is that the plotted experimental conductivity is high by a factor of γ . Birss and Wright (7) observed a roughness factor of 2-4 by EDL capacitance measurements for silver surfaces polished with up to 1200 grade emery paper. In our experiments, some electropolishing is to be expected under the growing AgCl films.

Superimposed triangular wave.—To confirm that the growing AgCl films conduct by the high field mechanism, fast transient experiments were conducted during film growth in region D. A 10 Hz triangular current wave of amplitude $\pm 1.1 i_1$ was superimposed for a second or less on the steady anodizing current i_1 at certain potentials, ϕ_1 . Current-voltage curves were displayed on the storage oscilloscope. Results of a set of experiments in saturated LiCl are shown in Fig. 4. The curves are clean and reproducible at a frequency around 10 Hz, whereas lower frequencies disturbed the anodizing current for too long a time and high frequencies gave hysteresis loops. The curves go smoothly through the origin and give negative potentials at negative current densities; the Ag/AgCl reversible potential is essentially equal to the SCE

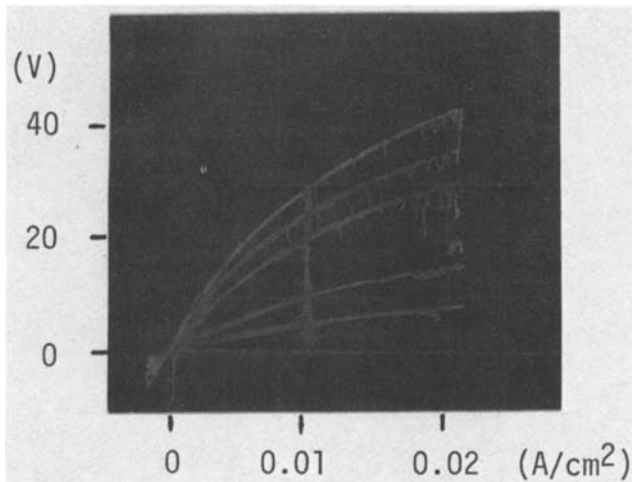


Fig. 4. Potential-current density transients for 10 Hz triangular current density wave superimposed on the steady $i_1 = 0.01 \text{ A/cm}^2$ at various potentials. ϕ_1 , in region D (Fig. 2), saturated LiCl, 5 mm^2 electrode.

potential within the accuracy of the scale of Fig. 4. Increase in the amplitude of the triangular current density wave in the negative direction gave a sharp decrease in magnitude of the potential (higher conductivity), which, however, recovered to the Fig. 4 displayed potentials on the positive sweep. This sharp decrease in potential (increase in conductivity) for a large negative current density sweep and recovery of potential suggests incipient pore or crack formation and healing.

Data from Fig. 4 are plotted semilogarithmically in Fig. 5 in accordance with the high field equation. The curves become linear at the high current density ends but deviate at the low current density ends. Extrapolation of the linear region to zero potential in Fig. 5 gives $i_0 = 0.0022 \pm 0.0005 \text{ A/cm}^2$ in the high field equation. Since the curves in Fig. 4 go linearly through the origin and are logarithmic in Fig. 5 at higher current densities, the hyperbolic sine function was fit to the data.

$$i = 2i_0 \sinh\left(\frac{\beta \Delta \phi}{l}\right) \quad [7]$$

The inverse function

$$\sinh^{-1}\left(\frac{i}{2i_0}\right) = \frac{\beta}{l} \Delta \phi \quad [8]$$

was used to replot data from Fig. 4 with $i_0 = 0.0022$

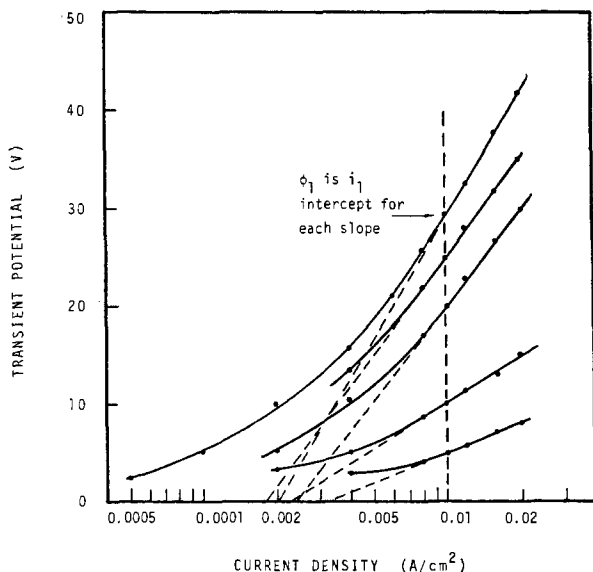


Fig. 5. Replot of Fig. 4 curves on semilogarithmic coordinates

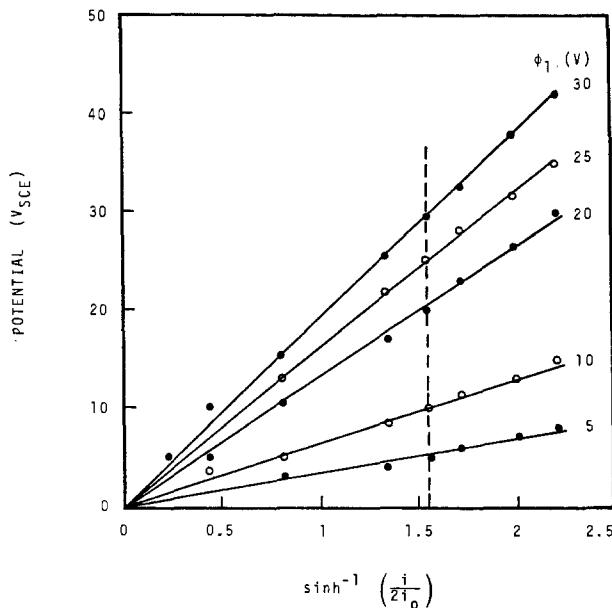


Fig. 6. Replot of Fig. 4 curves in accordance with hyperbolic sine function. ϕ_1 is the quasi steady-state potential at which the triangular wave is superimposed. $i_0 = 0.0022 \text{ A/cm}^2$, $i_1 = 0.01 \text{ A/cm}^2$.

A/cm^2 . As shown in Fig. 6, the data plot as straight lines using Eq. [8]. Conductivity of anodically forming silver chloride appears to follow a function analogous to the Butler-Volmer equation of electrochemical kinetics.

Discussion.—The slopes of the lines in Fig. 6 can be used to calculate the parameter, l/β

$$\frac{l}{\beta} = \frac{d\phi}{d \sinh^{-1}\left(\frac{i}{2i_0}\right)} \quad [9]$$

The value of l at each potential, ϕ_1 , can be determined from Eq. [1] if τ_1 is defined. The value of τ_1 was determined from the zero potential intercept of the plot of the slopes of the curves in Fig. 6 vs. time from τ_0 (Fig. 2). The value of $\tau_1 = 53 \text{ sec}$ found corresponds approximately to τ_1 shown in Fig. 2. In other words, it appears that most of the current density in regions A, B, and C builds porous AgCl and generates chlorine, rather than contributing to the barrier layer.

Values of i_0 for experiments over a range of anodizing current densities, i_1 , for which measurements were feasible are plotted in Fig. 7. The linear least squares fit to these data in logarithmic coordinates gives

$$i_0 = 0.089 i_1^{0.81} \quad [10]$$

for $0.003 < i_1 < 0.06 \text{ A/cm}^2$.

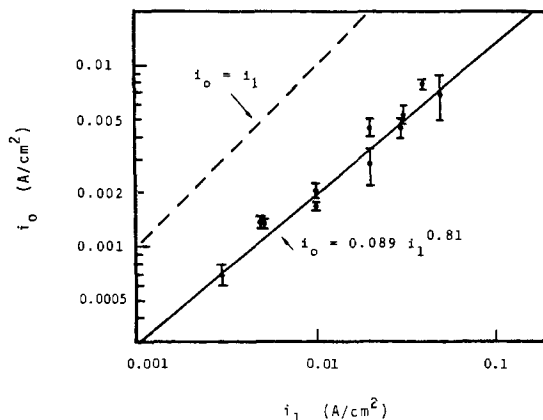


Fig. 7. Relation of i_0 to i_1

The value of i_0 is not constant, but varies as the 0.81 power of the base applied current density, i_1 . Assuming Eq. [10] to apply over the whole range of the experiments, $0.001 < i_1 < 10$ A/cm², the value of $\ln(i_1/i_0)$ in Eq. [5] for steady-state anodizations varies from 1.11 to 2.86.

The extrapolated current density at which $i_1 = i_0$, and below which low field or ohmic conduction would always be expected, is $i_1 = i_0 = 3.0 \times 10^{-6}$ A/cm², a value outside of the possible range of the present experiments. The low field conductivity from Eq. [7] would be

$$\kappa_\Omega = 2i_0\beta \quad [11]$$

The extrapolated lower limit i_0 and $\beta = 5 \times 10^{-6}$ cm/V from Fig. 3 in Eq. [11] give $\kappa_\Omega = (2)(3 \times 10^{-6})(5 \times 10^{-6}) = 3.0 \times 10^{-11}$ S · cm⁻¹. This value is in approximate agreement with the intrinsic conductivity from the paper by Corish and Jacobs (8), extrapolated to a temperature of 298 K. These results indicate that the conductivity of silver chloride at the high current densities ($>10^{-3}$ A/cm²) reported herein are due to the intrinsic conductivity of AgCl rather than extrinsic conductivity from impurities which give a value of about 10^{-7} S · cm⁻¹ (8, 9) for 5-9 purity silver chloride and 3×10^{-6} S · cm⁻¹ (8) for 3-9 AgCl. These literature conductivities were measured at small current densities with impedance bridges. Impurities in the silver electrodes would be expected to be divalent and less noble than silver and be oxidized into the silver chloride as ionic impurities.

Interruption of the current during the anodizing process in region D of Fig. 2 for periods of seconds or more followed by reapplying the current results in a restart through regions A to D. The periods of regions A, B, and C are shorter and the initial slope in region D steeper to the potential at which the current was interrupted compared to the first curve. The slope then becomes the same as the first curve. These data suggest that pores or cracks form in the barrier film when the current is interrupted and heal when the current is turned on again.

The noise and erratic potentials in region C at low current densities also indicate an instability and opening of pores or cracks. The rapid decrease in the absolute value of the negative potential (increased conductivity) at negative current densities in the superimposed triangular current density wave (Fig. 4 type experiment) also indicates opening of pores. The time for the conductivity to increase at negative current density in the negative sweep was observed to be about 20 msec. Even more rapid cracking and healing is noted in Fig. 4 for the thicker films. The time for the shortest excursions in potential (conductivity increase) is less than a line width in Fig. 4, ~ 0.2 msec.

The noise and the potential plateau in region E, Fig. 2, also suggest a continuous widespread fracture and healing process in the AgCl film. The accompanying intense agitation by microbubbles of chlorine is also consistent with Cl⁻ discharge at high overpotential at the base of cracks in the AgCl layer. The existence of region E suggests that the thicker AgCl layer is under considerable mechanical strain. Since the potential of region E is nearly independent of current density in the region $10^{-3} < i < 10$ A/cm² for a given electrolyte, the AgCl film thickness in region E is nearly independent of current density. The thickness is

$$l_E = \beta \Delta \phi_E / \ln(i/i_0) \quad [12]$$

from Eq. [5] and [2]. The barrier AgCl film thickness in region E is therefore about $l_E = (5 \times 10^{-6} \text{ cm/V})(20\text{V}) = 1 \times 10^{-4}$ cm or on the order of one micrometer, neglecting $\ln(i/i_0)$.

Bro and Marincic (10) observed a potential-time dependence like that in Fig. 2 on galvanostatic charging of silver in 2M ZnCl₂, 0.5M NaClO₄ solution at

0.15 A/cm² but did not try to explain it. They attributed their plateau at 30V to Joule heating of their thin electrodes and onset of boiling. A much smaller temperature rise is expected for the relatively more massive silver electrode used in the majority of the present experiments in which the 5 mm² rod was 25 mm long. The heat generated in the growing AgCl film from τ_1 to τ_E in Fig. 2 is

$$Q_g = \int_{\tau_1}^{\tau_E} i \phi d\tau \quad [13]$$

Substitution of $i d\tau$ from Eq. [3] and [5] into Eq. [13], assuming $\phi = 0$ at $\tau = \tau_1$ and neglecting $\ln(i/i_0)$ gives

$$Q_g = \frac{\beta z F \rho}{M} \int_0^{\phi_E} \phi d\phi = \frac{\beta z F \rho \phi_E^2}{2M} \quad [14]$$

The heat generated in an AgCl film in region D, irrespective of current density, is approximately

$$Q_g = \frac{(5 \times 10^{-6})(20^2)}{(2)(2.67 \times 10^{-4})} = 3.75 \text{ J/cm}^2 \quad [15]$$

The sensible heat that can be absorbed by the silver rod is

$$Q_s = \rho_s l_s C_p \Delta T \quad \text{J/cm}^2 \quad [16]$$

If all of the heat generated is absorbed by the silver rod, the temperature rise is

$$\Delta T = \frac{3.75}{\rho_s l_s C_p} \quad [17]$$

Handbook values of silver density and specific heat (10) and $l = 2.5$ cm give

$$\Delta T = (3.75)/(10.5)(2.5)(0.234) = 0.61^\circ\text{C} \quad [18]$$

The time constant for heat flow into the silver rod is

$$\tau = \frac{l^2}{(k_s/\rho_s C_p)} \quad [19]$$

which for handbook data (10) for silver gives

$$\tau = (2.5)^2(10.5)(0.234)/4.19 = 3.7 \text{ sec} \quad [20]$$

All experiments at current densities < 0.1 A/cm² had $(\tau_E - \tau_1) > 3.7$ sec so that temperature rise would have been of no consequence. At 10 A/cm², the value of $(\tau_E - \tau_0)$ (Fig. 2) is about 0.03 sec and $(\tau_1 - \tau_0)$ is small at this current density. This value gives a heat conduction length of 0.2 cm from Eq. [19]. The temperature rise of this length in Eq. [17] gives $\Delta T = 7.6^\circ\text{C}$ so that temperature rise should not have caused a significant error in any of the experiments with the silver rod or for the 5-9 Ag electrode which had about 0.2 cm length in the epoxy resin. The temperature rise should actually be smaller than these calculated values due to conduction of heat to the epoxy resin surrounding the silver anodes and to transport of heat to the electrolyte solution. The temperature rise at the worst case by conduction within the AgCl barrier layer at 20V is calculated to be less than 0.5°C at 10 A/cm² using a typical handbook value of conductivity for alkali halide salts of ~ 50 mW · cm⁻¹ · K⁻¹ (6).

A question is whether chloride ion can be transported from solution to the silver chloride surface fast enough during the anodizing process. This question can be answered by comparing the time $(\tau_E - \tau_0)$ in Fig. 2 to the time to deplete Cl⁻ at the surface according to Sand's equation

$$i_- = \frac{\frac{1}{2}z_-FC_- \sqrt{\frac{\pi D_-}{\tau}}}{(1 - t_-)} \quad [21]$$

Experimental values of τ_E vs. i in Fig. 8 are compared to Eq. [21] for $C_- = 6 \times 10^{-3}$ mol/cm³, $D_- = 1 \times 10^{-5}$ cm²/sec, and $t_- = 0.6$. Results in Fig. 8 show that chloride ion depletion is not a limiting factor in reaching region E in 6N Cl⁻ solutions.

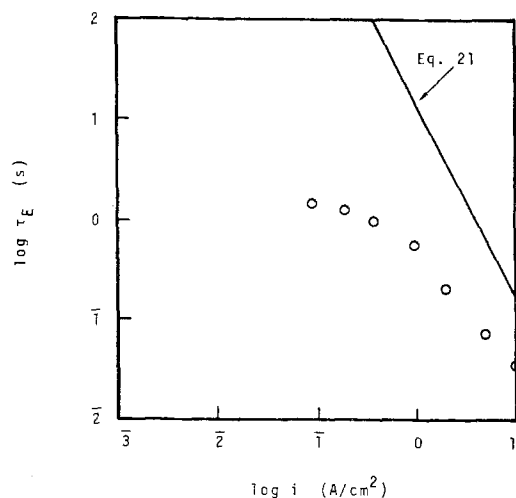


Fig. 8. Comparison of time to reach region E to time for Cl^- ion depletion (Eq. [21]) as a function of current density in $6N \text{ Cl}^-$.

Events in regions A, B, and C of Fig. 2 may now be speculated upon. Region A is probably dissolution of silver ion to form a supersaturated solution of AgCl which precipitates AgCl particles at the end of region A as observed for other metals and their salts (12, 13). Region B may be the filling in of further AgCl between the first particles by the mechanism of AgCl^{n-n+1} complex formation and transport described by Katan, Szpak, and Bennion (14). As the voids between particles fill in, the actual current density and overpotential rise at the end of region B until chloride ion discharges at the silver surface to form Cl_2 . The voids continue to fill during region C until virtually complete coverage by AgCl at the metal surface, and then the high field conduction process can start. There is apparently a competition between filling the voids and cracking of the existing AgCl layer. High chloride ion concentration which promotes AgCl^{n-n+1} formation, and high current densities, favor the void filling process over the cracking process and thus, the formation of the barrier AgCl film.

Formation of a barrier layer film has been reported by Birss and Wright (15) for silver in $1N \text{ NaI}$ solution at a current density of about 0.2 A/cm^2 . They did not observe the barrier type AgI effect in $0.1N \text{ NaI}$. These observations are in accord with the relative solubilities of the silver halide complexes in chloride and iodide solution. Figure 1 shows that the boundary chloride concentration at a current density of 0.2 A/cm^2 is about $5N$. The solubility of AgCl in $5N$ chloride is about $10^{-2}N$ (15). Silver iodide has this solubility in $0.9N$ iodide (16), which is between the concentrations forming and not forming barrier-type AgI of Birss and Wright (15). Their conductivity of AgI at 0.2 A/cm^2 of 8.7×10^{-5} is about two orders of magnitude larger than the corresponding value for AgCl in Fig. 3.

Conclusions

The following conclusions are made concerning anodic formation of silver chloride in concentrated chloride solutions.

1. A barrier layer film of AgCl exhibiting high field conduction forms at high current densities in KCl, NaCl, LiCl, and HCl solutions at concentrations greater than $4N$.

2. A superimposed triangular current density on the anodizing current density, i_1 , gives a response that can be fit by the expression

$$i = 2i_0 \sinh \left(\frac{\beta \Delta \phi}{l} \right)$$

in which $\beta \cong 5 \times 10^{-6} \text{ cm/V}$ and i_0 is a function of the base current density, i_1 .

3. The barrier film reverts to a porous condition at $\Delta \phi > 20V$ or when the anodizing current is interrupted or briefly reversed.

Acknowledgment

This work was supported by the National Institute of Neurological and Communicative Disorders and Stroke, National Institutes of Health, Bethesda, MD, under Contract No. NIH-N01-NS-0-2316.

Manuscript submitted April 18, 1983; revised manuscript received July 18, 1983. This was Paper 485 presented at the Washington, DC, Meeting of the Society, Oct. 9-14, 1983.

Electrochemical Technology Corporation assisted in meeting the publication costs of this article.

LIST OF SYMBOLS

a	ionic hop distance, cm
A	area, cm^2
C	concentration, $\text{mol} \cdot \text{cm}^{-3}$
C_p	specific heat, $\text{J} \cdot \text{g}^{-1} \cdot \text{K}^{-1}$
d	diameter, cm
D	diffusivity, $\text{cm}^2 \cdot \text{sec}^{-1}$
F	the Faraday, $96,500 \text{ C} \cdot \text{equiv.}^{-1}$
i	current density, $\text{A} \cdot \text{cm}^{-2}$
i_0	exchange current density, $\text{A} \cdot \text{cm}^{-2}$
k	thermal conductivity, $\text{W} \cdot \text{cm}^{-1} \cdot \text{K}^{-1}$
l	length or thickness, cm
M	molecular weight, $\text{g} \cdot \text{mol}^{-1}$
Q	heat flux, $\text{J} \cdot \text{cm}^{-2}$
R	gas constant, $8.314 \text{ J} \cdot \text{mol}^{-1} \cdot \text{K}^{-1}$
t	transference number, dimensionless
T	temperature, K
z	valence, $\text{equiv.} \cdot \text{mol}^{-1}$
α	fraction of ionic hop distance to top of energy barrier
β	high field exponential constant, $\text{cm} \cdot \text{V}^{-1}$
κ	electrical conductivity, $\text{S} \cdot \text{cm}^{-1}$
κ_0	low field conductivity, $\text{S} \cdot \text{cm}^{-1}$
ρ	density, $\text{g} \cdot \text{cm}^{-3}$
τ	time, sec
ϕ	potential, V

REFERENCES

- G. J. Janz and D. J. G. Ives, *Ann. N.Y. Acad. Sci.*, **148**, 210 (1968).
- L. J. Kurtz, *Compt. Rend. U.R.S.S.*, **11**, 283 (1935).
- H. Lal, H. R. Thirsk, and W. F. K. Wynne-Jones, *Trans. Faraday Soc.*, **47**, 70 (1951).
- W. Jaenicke, R. P. Tischer, and H. Gerischer, *Z. Electrochem.*, **59**, 448 (1955).
- L. Young, "Anodic Oxide Films," Academic Press, New York (1961).
- "CRC Handbook of Chemistry and Physics," 58th Ed., CRC Press, Cleveland OH (1978).
- V. I. Birss and G. A. Wright, *Electrochim. Acta*, **27**, 1429 (1982).
- J. Corish and P. W. M. Jacobs, *J. Phys. Chem. Solids*, **33**, 1799 (1972).
- C. Wagner, *Trans. Faraday Soc.*, **34**, 851 (1938).
- P. Bro and N. Marincic, *This Journal*, **116**, 1338 (1969).
- E. R. G. Eckert and R. M. Drake, Jr., "Heat and Mass Transfer," 2nd Ed., p. 498, McGraw Hill, New York (1959).
- H. C. Kuo and D. Landolt, *Corros. Sci.*, **16**, 915 (1976).
- T. R. Beck, *This Journal*, **129**, 2412 (1982).
- T. Katan, S. Szpak, and D. N. Bennion, *ibid.*, **121**, 757 (1974).
- V. I. Birss and G. A. Wright, *Electrochim. Acta*, **27**, 1439 (1982).
- W. F. Linke, in "Solubilities," 4th Ed., Vol. 1, p. 67, D. Van Nostrand Co. Inc., New York (1958).

Defect Structure and Electrical Properties of Undoped and Cr-Doped CoO

Janusz Nowotny and Irene Sikora

Institute of Catalysis and Surface Chemistry, Polish Academy of Sciences, 30-239 Kraków, Poland

Mieczyslaw Rekas

Institute of Materials Science, Academy of Mining and Metallurgy, 30-059 Kraków, Poland

ABSTRACT

Seebeck coefficient and electrical conductivity are measured at 1300 K vs. oxygen partial pressure in the p_{O_2} range between $2.12 \cdot 10^4$ -23 Pa. Comparative analysis of both parameters indicates that the mobility term for electron holes in undoped CoO is changing vs. oxide composition. Its average value is: $\mu_h = 0.33 \pm 0.03 \text{ cm}^2 \text{ V}^{-1} \text{ sec}^{-1}$. Singly ionized cation vacancies were established as predominant defects for undoped CoO and doubly ionized cation vacancies for CoO-Cr₂O₃ solid solutions. No simple relationship is observed between the concentration of Cr incorporated into CoO and the generated hole concentration as predicted by the controlled valency theory. In contrast to this theory, the experimental data indicate a strong decrease of the Fermi energy E_F vs. Cr concentration for CoO-Cr₂O₃ solid solutions. Accordingly, significant interaction between point defects in Cr-doped CoO crystal is postulated. The application of the Debye-Huckel theory for strong electrolytes allows for the calculation of E_F which is in an agreement with experimental results. The defect equilibrium constants are calculated for formation of singly and doubly ionized cation vacancies in CoO at 1300 K

$$K_v' = [V_{Co}'] [h'] f_h' f_v' p_{O_2}^{-1/2} = 6.3 \pm 2.0 \cdot 10^{-8} [\text{Pa}^{-1/2}]$$

and

$$K_v'' = [V_{Co}''] [h']^2 f_v'' f_h^2 p_{O_2}^{-1/2} = 1.2 \pm 0.5 \cdot 10^{-11} [\text{Pa}^{-1/2}]$$

The electrical conductivity method is frequently used in studies of structural properties of ionic crystals (1-3). The interest in this method is generated because of its high sensitivity to defect structure. In these studies, it is generally considered that electrical conductivity is proportional to concentration of electronic carriers generated during ionization of crystal point defects. This requires an assumption that the mobilities of electronic carriers are independent of their concentration and thus, of crystal composition. This is usually accepted for oxides exhibiting lower concentration of defects. However, if an increasing concentration of defects leads to their mutual interactions, the mobility term is changing. Then the correct interpretation of electrical conductivity data should involve independent discussion of both concentration and mobility.

The effect of changing mobility of electronic carriers vs. crystal composition is not significant in the interpretation of thermoelectric power data which enables one to directly calculate the concentration of electronic carriers in the crystal. Furthermore, comparative studies of both electrical conductivity and thermoelectric power enable determination of the mobility term.

The purpose of the present work is to perform comparative studies of both electrical conductivity and Seebeck effect for an oxide crystal as a function of its composition. Both undoped CoO and CoO-Cr₂O₃ solid solutions were chosen as model systems.

Properties of undoped CoO were the subject of numerous studies (4-9). Recent works strongly indicate that electrostatic interactions between point defects are rather important. The interactions producing a marked deviation from the ideal point defect theory were observed by Chen, and Mason (10) who studied Seebeck effect vs. p_{O_2} . Morin and Dieckmann (11) have also found variations of chemical diffusion coefficient vs. crystal composition that is considered in terms of defect interactions. Although different observations were reported elsewhere (9), there has been a gradual

Key words: Seebeck effect, electrical conductivity, nonstoichiometry, Fermi energy, thermopower, cobaltous oxide, point defect interactions.

accumulation of data indicating that the deviation from ideality must be taken into account for undoped CoO, especially at higher activity close to CoO-Co₃O₄ phase boundary and at lower temperatures (10). One may expect that these interactions should have an effect on the mobility of electronic carriers as well. Comparative study of both electrical conductivity and Seebeck effect is a possible quantitative approach of solving this question.

Cr-doped CoO is even a better object for studies of defect interactions since in this case, the concentration of defects may be easily controlled within the solubility region of the CoO-Cr₂O₃ system, which amounts to 1 atomic percent (a/o) at 1000°C (12).

Definition of Terms

The electrical conductivity of a predominantly p-type semiconductor may be expressed as

$$\sigma = B \mu_h [h'] e \quad [1]$$

where: B is the constant value involving sample geometry in cm^{-1} , μ_h is the mobility of electron holes in $\text{cm}^2 \cdot \text{V}^{-1} \cdot \text{sec}^{-1}$, $[h']$ is the concentration of electron holes in cm^{-3} , and e is the elementary charge in C. For a metal deficient oxide Me_{1-y}O , lattice electroneutrality requires the correlation between the concentrations of quasifree holes and cation vacancies as predominant lattice defects

$$[h'] = 2[V''_{Me}] + [V'_{Me}] \quad [2]$$

where V'_{Me} and V''_{Me} are singly and doubly ionized cation vacancies, respectively.

At lower temperatures, formation of neutral vacancies V^x_{Me} should also be taken into account.

Depending on temperature and crystal composition, the following three limiting cases may be considered

$$[V^x_{Me}] \gg [V'_{Me}] + [V''_{Me}] \quad [3]$$

$$[V'_{Me}] \gg [V^x_{Me}] + [V''_{Me}] \quad [4]$$

$$[V''_{Me}] \gg [V^x_{Me}] + [V'_{Me}] \quad [5]$$

where

$$[V^x_{Me}] + [V'_{Me}] + [V''_{Me}] = y$$

Accordingly, assuming application of the mass action law to defects in crystal, the following relationships may be written for the concentration of predominant defects as a function of T and p_{O_2} when the crystal is in equilibrium with p_{O_2} in the gas phase

$$[V_{Me}^x] = \text{const. } p_{O_2}^{1/2} \exp\left(-\frac{\Delta H_f}{RT}\right) \quad [3a]$$

$$[V_{Me}'] = [h\cdot] = \text{const. } p_{O_2}^{1/4} \exp\left[-\frac{\frac{1}{2}\Delta H_f}{RT}\right] \quad [4a]$$

$$[V_{Me}''] = \frac{1}{2} [h\cdot] = \text{const. } p_{O_2}^{1/6} \exp\left[-\frac{\frac{1}{3}\Delta H_f}{RT}\right] \quad [5a]$$

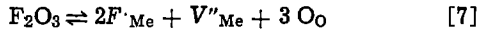
Generally for ionized defects we may write

$$[V_{Me}^{z\cdot}] = \frac{1}{z} [h\cdot] = \text{const. } p_{O_2}^{1/n} \exp\left[-\frac{\frac{2}{n}\Delta H_f}{RT}\right] \quad [6]$$

where constant involves the entropy term, ΔH_f is formation enthalpy of defects in crystal, and z is ionization degree of cation vacancies which may be related to n

$$n = 2(z + 1) \quad [6a]$$

When trivalent cations F^{3+} are substituted into the lattice exhibiting a deficit of metal $Me_{1-y}O$



and assuming that $[h\cdot] \ll [V_{Me}'']$, the lattice electro-neutrality condition acquires the simple form

$$[V_{Me}'] = \frac{1}{2} [F_{Me}'] \quad [8]$$

Then application of the mass action law leads to the relation

$$[V_{Me}''] = \text{const. } p_{O_2}^{1/4} \exp\left[-\frac{\frac{1}{2}\Delta H_f}{RT}\right] \quad [9]$$

In both thermal and chemical equilibrium $1/n$ in Eq. [6] may be expressed as

$$\left\{ \frac{1}{n} = \frac{\partial \ln [h\cdot]}{\partial \ln p_{O_2}} \right\}_{T=\text{const.}} \quad [10]$$

Assuming that $\mu_{h\cdot}$ is independent of crystal composition, we obtain by combination of Eq. [1] and [10]

$$\left\{ \frac{1}{n} = \frac{\partial \ln \sigma}{\partial \ln p_{O_2}} \right\}_{T=\text{const.}} \quad [11]$$

Determination of thermoelectric power α enables one to calculate the Fermi energy of crystal E_F and, therefore, the concentration of electronic carriers, independently of a knowledge of the mobility term $\mu_{h\cdot}$, which is rather difficult to determine. For p-type semiconductors, α is intercorrelated with E_F and thus with $[h\cdot]$ according to the relation

$$\alpha = \frac{k}{e} \left(\frac{E_F}{kT} + \frac{S_V}{k} \right) \quad [12]$$

where: E_F is the Fermi energy, S_V is the parameter referring to vibrational entropy associated with the polaron environment, and k is the Boltzmann constant ($8.6173 \cdot 10^{-5} \text{ eV} \cdot \text{K}^{-1}$). Taking into account the Fermi-Dirac statistics

$$\left\{ \frac{[h\cdot]}{N_{h\cdot}} = \{1 + \exp(E_F/kT)\}^{-1} \right\} \quad [13]$$

where $N_{h\cdot}$ is density of states, Eq. [12] assumes the form

$$\alpha = \frac{k}{e} \ln \frac{N_{h\cdot} - [h\cdot]}{[h\cdot]} + \frac{S_V}{k} \quad [14]$$

Assuming $N_{h\cdot} \gg [h\cdot]$, the simple Maxwell-Boltzmann statistics may be applied. Consequently

$$\alpha = \frac{k}{e} \ln \frac{N_{h\cdot}}{[h\cdot]} + \frac{S_V}{k} \quad [15]$$

Assuming $E_F \gg kT$, Eq. [13] assumes the form

$$E_F = kT \ln \frac{N_{h\cdot}}{[h\cdot]} \quad [16]$$

Assuming S_V is independent of crystal composition, the combination of Eq. [11] and [15] leads to the expression

$$\left\{ \frac{1}{n} = -\frac{\partial \alpha}{\ln p_{O_2}} \cdot \frac{k}{e} \right\}_{T=\text{const.}} \quad [17]$$

A difference in the value of $1/n$ calculated according to Eq. [11] on one hand, and [17] on the other, results in the mobility term $\mu_{h\cdot}$, which may vary with composition. Combining Eq. [1] and [15], we obtain the expression which enables one to calculate the mobility term

$$\ln \mu_{h\cdot} = \ln \sigma + \frac{e\alpha}{k} - \frac{S_V}{k} - \ln B - \ln N_{h\cdot} - \ln e \quad [18]$$

Experimental

The preparations were obtained by annealing of co-precipitated mixtures of both cobalt and chromium hydroxides at 1270 K for 5 hr. The preparation procedure, determination of Cr concentration, and spectral analysis of impurities are described elsewhere (12). The measuring setup for Seebeck effect and electrical conductivity is shown in Fig. 1. The CoO sample in the form of a pellet was placed between the two Pt measuring electrodes [Fig. 1 (3)]. The temperature gradient across the pellet was achieved by two heating elements [Fig. 1 (10)] located on both sides of the pellet. The measuring setup was placed inside the aluminum tube [Fig. 1 (6)]. The required oxygen activity in the chamber was achieved by Ar-O₂ mixture flowing through the measuring tube. Before taking the measurements, the sample was standardized by heating at 1300 K in air and in argon until a constant value of electrical conductivity in the two consecutive runs was reached.

The Seebeck voltage ΔV was measured for six to eight different temperature gradients. The Seebeck coefficient α was calculated from slopes of ΔV vs. ΔT dependences

$$\alpha = \frac{\partial V}{\partial T} \cong \frac{\Delta V}{\Delta T} \quad [19]$$

The electrical conductivity was measured by the classical four-probe method for five different voltages ranging between 0.5-5V (3).

Results and Discussion

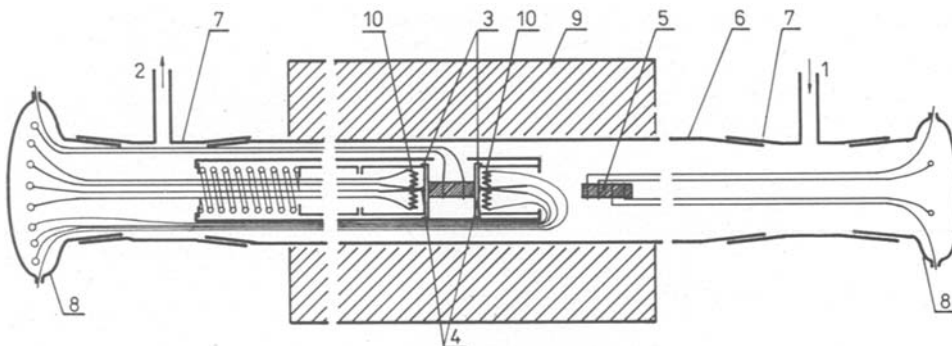
Undoped CoO.—The obtained experimental data as well as the calculated values of α at p_{O_2} ranging from $2.12 \cdot 10^4$ to 23 Pa and $T = 1300$ K are listed in Table I and illustrated in Fig. 2. The following relationships may be written for σ and α vs. p_{O_2} , respectively

$$\ln \sigma = 1.74 + 0.258 \ln p_{O_2} \quad [20]$$

$$\alpha_{\text{exp}} = 0.352 - 0.0205 \ln p_{O_2} \quad [20a]$$

Therefore, we obtain for n , respectively

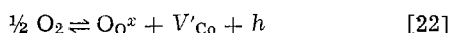
Fig. 1. Measuring setup for Seebeck effect and electrical conductivity. (1) Gas inlet, (2) gas outlet, (3) measuring Pt electrodes, (4) thermocouples PtRh10-Pt, (5) oxygen gauge CoO, (6) aludum tube, (7) Pyrex joints, (8) Pt wires sealed through Pyrex glass, (9) furnace, (10) microheaters.



$$n = 3.88 \pm 0.12 \quad [21]$$

$$n = 4.20 \pm 0.24 \quad [21a]$$

Both Eq. [20] and [21] indicate that singly ionized cation vacancies predominate in CoO for the conditions under study. Therefore, the following equilibrium should be considered



for which the equilibrium constant is

$$K_{V'} = [V'_{\text{Co}}][h]p_{\text{O}_2}^{-1/2} \quad [23]$$

Therefore, we assume the condition [4] and Eq. [4a] for calculation of $[V'_{\text{Co}}]$ in undoped CoO. Appropriately, the electroneutrality condition of the lattice Eq. [2] may be reduced to the form

$$[V'_{\text{Co}}] = [h] \quad [24]$$

Combining Eq. [15] and [23], we may calculate the entropy term

$$\frac{S_V}{k} = \frac{1}{2} \left\{ \ln K_{V'} + \frac{1}{2} \ln p_{\text{O}_2} \right\} + \frac{e\alpha}{k} - \ln N_{h'} \quad [25]$$

Assuming full ionization of cation vacancies in CoO, ($N_{h'} = 1$) and also taking $K_{V'}$ after Kofstad (1)

$$K_{V'} = 10^{-2} \exp(-13,000/RT)$$

Equation [25] leads to

$$\frac{S_V}{k} = -0.868 \pm 0.080$$

This value is close to that determined for the wustite phase by Seltzer and Hed (2) ($S_V/k = -0.89$).

According to the theory of small polarons, S_V may be evaluated as (13)

$$\frac{S_V}{k} = \beta E_m/kT \quad [26]$$

where E_m = activation energy of mobility, and

$$\beta \leq 1$$

According to Fisher and Tannhauser (4), S_V for CoO is close to zero around $p_{\text{O}_2} = 1$ Pa and increases at very low p_{O_2} values. Generally, the component of α resulting from S_V in Eq. [15] remains within $10 \mu\text{V K}^{-1}$ (14).

Table I. Determined values of α_{exp} and $\ln \sigma$ as well as calculated α_{calc} for undoped CoO

$\ln p_{\text{O}_2}$ [p_{O_2} in Pa]	α_{exp} [$\text{mV} \cdot \text{K}^{-1}$]	α_{calc} [$\text{mV} \cdot \text{K}^{-1}$]	$\ln \sigma$ [σ in Ω^{-1}]
9.97	0.391	0.374	1.294
8.67	0.412	0.402	0.983
8.12	0.415	0.414	0.889
7.26	0.434	0.432	0.710
7.19	0.425	0.434	0.685
3.16	0.527	0.521	-0.452

Thus, for CoO it is negligible. Generally, it seems that for semiconductors for which conduction occurs according to a "hopping mechanism" and also for smaller deviations from stoichiometry, this assumption seems to be valid. If this is assumed, Eq. [25] leads to

$$N_{h'} = 0.43 \pm 0.03$$

This value seems reasonable if a significant concentration of defects is taken into account, as is the case for CoO where the defects in crystal cannot be considered as an ideal solution (10, 11).

Accordingly, assuming $S_V = 0$ and $N_{h'} = 0.43$, we may calculate α from Eq. [15] (see Table I). As it results from the above consideration, both presented assumptions (*i.e.*, $N_{h'} = 1$, $S_V/k = 0.868$ or $N_{h'} = 0.43$, $S_V = 0$) provide a satisfactory agreement with the experiment. However, the second possibility is more consistent with the theory of thermoelectric phenomena in crystals. Therefore, in the considerations below we assume that $S_V = 0$ and $N_{h'} = 0.43$. A good agreement between experimental α_{exp} and calculated α_{calc} values is observed. The inverse of oxygen exponent n (Eq. [6]), computed from both σ and α , is close to 4,

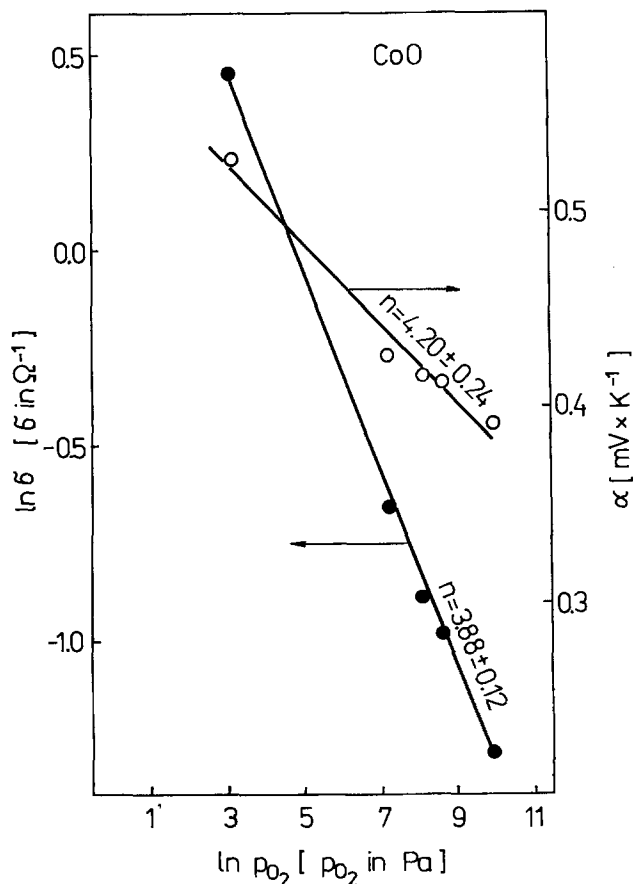


Fig. 2. $\ln \sigma$ and α vs. $\ln p_{\text{O}_2}$ for undoped CoO at 1300 K ($B = 3.7 \text{ cm}^{-1}$).

Table II. Parameter n in Eq. [8] reported in literature

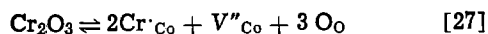
No.	Authors	n	p_{O_2} range (Pa)	T (K)	Experimental method
1.	Fisher and Tannhauser (4)	1/3.8-1/4.3 1/5.7-1/6.1	10^5 – 10^{-1} 10^{-1} – 10^{-7}	1190-1620	electrical conductivity
2.	Morin (6, 7)	1/4	10^5 – 10^2	1270	electrotransport
3.	Mrowec and Przybylski (15)	1/4.0-1/3.4	$6.7 \cdot 10^4$ – 66.7	1570	volumetry
4.	Carter and Richardson (11)	1/3.4	$5.6 \cdot 10^2$ – 10^5	1420	gravimetry
5.	Chowdhry and Coble (9)	1/3.8-1/4.2	10^4 – 10^5	1170-1310	electrical conductivity

which is in agreement with singly ionized cation vacancies as major type of defects as postulated in the literature at higher p_{O_2} (4, 5). Table II summarizes some data of n for CoO (4, 6, 7, 15, 16).

The observed difference in n determined in the present work from σ on one side (3.88) and from α on the other (4.20) is beyond experimental error. In determination of n , we usually assume that $\mu_{h^{\cdot}}$ is constant vs. oxide composition (1, 3). However, this assumption is not obvious for CoO. Therefore, assuming that $n = 4.20$, determined from α , is correct, Eq. [18] was applied to calculate the mobility term $\mu_{h^{\cdot}}$ which is listed in Table III. Its average value in the p_{O_2} range under study yields $\mu_{h^{\cdot}} = 0.329 \text{ cm}^2 \text{ V}^{-1} \text{ sec}^{-1}$. This value is in good agreement with that given by Fisher and Tannhauser (4) ($\mu_{h^{\cdot}} = 0.4 \text{ cm}^2 \text{ V}^{-1} \text{ sec}^{-1}$). However, in contrast to literature reports (8, 17), the present work indicates that $\mu_{h^{\cdot}}$ for CoO varies with p_{O_2} vs. crystal composition.

CoO-Cr₂O₃ solid solutions.—Crystals of three different concentrations of chromium were prepared containing 0.048, 0.49, and 0.90 a/o Cr. These concentrations are well below the solubility limit of Cr in CoO which amounts 1 a/o (12).

Figure 3 illustrates, as example, the dependence of both $\ln \sigma$ and α vs. $\ln p_{O_2}$ at 1300 K for $[\text{Cr}] = 0.048$ a/o. The parameters n determined from both σ (n_{σ}) and α (n_{α}) are shown in Table IV. As can be seen, both sets of data are close to four, which is in agreement with the substitutional mechanism of Cr incorporation into CoO



where the electroneutrality condition requires

$$[\text{Cr}'_{\text{Co}}] = 2[V''_{\text{Co}}] \quad [28]$$

The experimental values of Fermi energy (E_F)_{exp} were determined from Eq. [12]. Curve 1 in Fig. 4 illustrates (E_F)_{exp} vs. $[\text{Cr}'_{\text{Co}}]$ at $p_{O_2} = 2.12 \cdot 10^4$ Pa. As seen, (E_F)_{exp} initially slightly increases by 0.03 eV and then sharply

Table III. Mobility of electron holes $\mu_{h^{\cdot}}$ calculated from Eq. [1] and [18] ($B = 3.75 \text{ cm}^{-1}$)

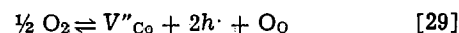
$\ln p_{O_2}$ (p_{O_2} in Pa)	$\mu_{h^{\cdot}}$ ($\text{cm}^2 \text{ V}^{-1} \text{ sec}^{-1}$)
9.97	0.367
8.67	0.343
8.12	0.323
7.26	0.337
7.19	0.296
3.16	0.310
Avg. 0.329 ± 0.025	

Table IV. Parameter n determined from σ (n_{σ}) and α (n_{α}) for CoO-Cr₂O₃ solid solutions at $T = 1300$ K

No.	Cr concentration (a/o)	n_{σ}	n_{α}
1.	—	3.88 ± 0.12	4.20 ± 0.24
2.	0.048	4.14 ± 0.07	4.25 ± 0.36
3.	0.49	4.60 ± 0.20	4.52 ± 0.21
4.	0.90	3.83 ± 0.12	4.37 ± 0.38

decreases by 0.11 eV, relative to the value for undoped CoO. This final decrease of (E_F)_{exp} is in apparent contradiction with the controlled valency theory. According to this theory, the formation of donor centers causes an increase in E_F .

Assuming doubly ionized cation vacancies V''_{Co} as predominant defects in CoO-Cr₂O₃ solid solutions, the following equilibrium should also be taken into account.



for which the equilibrium constant is

$$K_{V''} = [V''_{\text{Co}}][h^{\cdot}]^2 p_{O_2}^{-1/2} \quad [30]$$

Considering the condition Eq. [28], we obtain for $[h^{\cdot}]$

$$[h^{\cdot}] = p_{O_2}^{1/4} (2K_{V''})^{1/2} [\text{Cr}'_{\text{Co}}]^{-1/2} \quad [31]$$

Assuming that for CoO $S_V = 0$, and considering Eq. [16] and [31] we may express E_F vs. $[\text{Cr}'_{\text{Co}}]$

$$E_F = \frac{kT}{2} \ln [\text{Cr}'_{\text{Co}}] - \frac{kT}{2} \left\{ \ln 2K_{V''} + \frac{1}{2} \ln p_{O_2} \right\} + kT \ln N_{h^{\cdot}} \quad [32]$$

Equation [32] enables one to calculate theoretical changes of E_F vs. $[\text{Cr}'_{\text{Co}}]$. For calculations, we assume that for undoped CoO the concentration of impurities

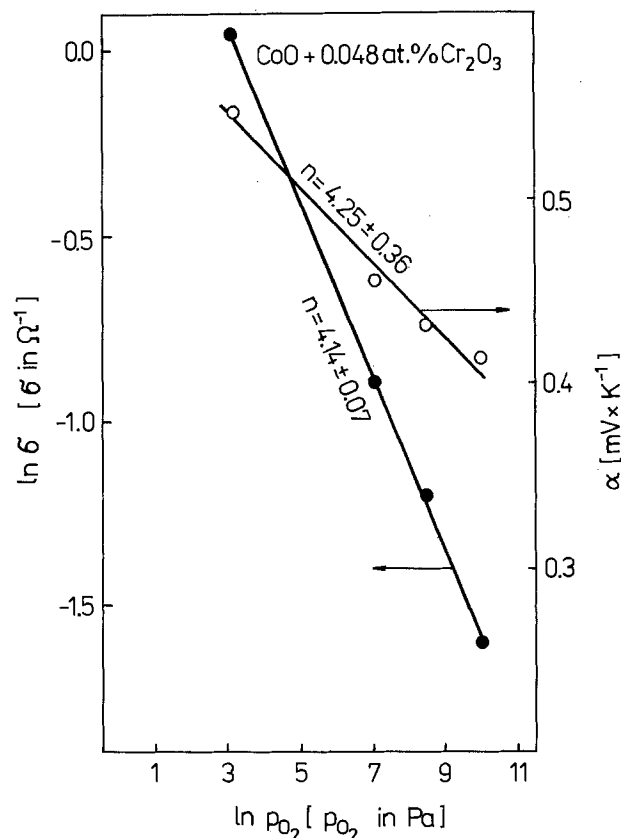


Fig. 3. $\ln \sigma$ and α vs. $\ln p_{O_2}$ for CoO + 0.048 a/o Cr at 1300 K

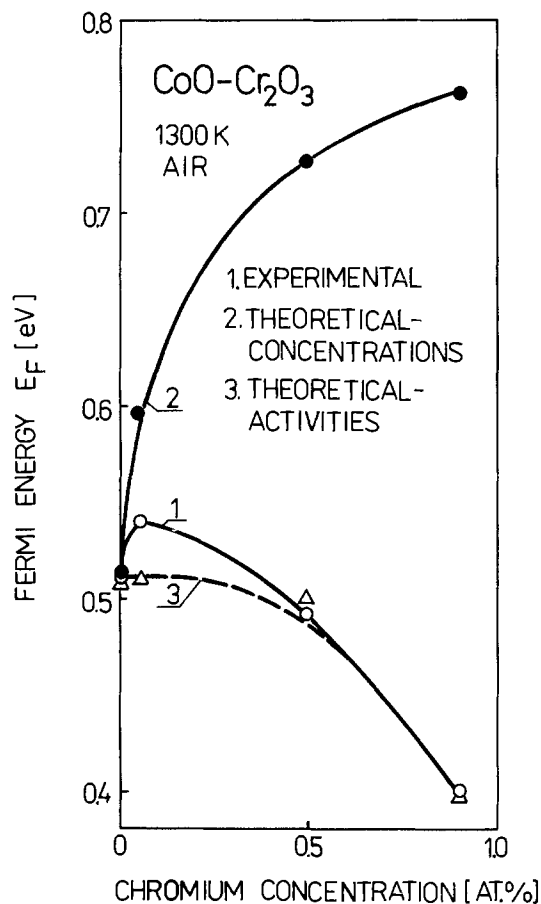


Fig. 4. Fermi energy E_F plotted vs. $[CrCo]$. (1) Experimental data, (2) calculated relative changes of E_F using concentrations of defects, (3) theoretical dependence E_F vs. $CrCo$ calculated using defect activities.

forming donor centers equals 0.01 a/o (12). This value was substituted in Eq. [32] instead of $[CrCo]$ for the undoped sample of CoO. The calculations lead to relative changes of E_F vs. $[CrCo]$ which is illustrated by curve 2 in Fig. 4. The observed increase of ΔE_F is consistent with the generally acknowledged classical considerations resulting from the ideal point defect theory. As seen, however, there is a considerable discrepancy between the theoretical dependence and experimental results. The discrepancy indicates that the generally assumed defect structure model of CoO considering isolated point defects is not satisfactory. The model should involve interactions between defects as has been already considered (10, 11). These interactions are not negligible for undoped CoO and become considerable for Cr-doped CoO.

Equation [23] and [30] as well as corresponding electroneutrality conditions Eq [24] and [28], involving isolated point defects, enable one to calculate defect concentrations for undoped CoO (Fig. 5) and Cr-doped CoO (Fig. 6, 7). Formation of aggregates of four vacancies was postulated by Catlow and Stoneham (18) for CoO as well as for NiO and MnO. Formation of defect complexes was also considered by Perkins and Rapp (19) for NiO-Cr₂O₃ solid solutions. The picture is even more complicated if cation interstitials are involved, as it has been postulated by Stiglich *et al.* (20) and by Mrowec *et al.* (15). Although the discussion on the defect structure model for CoO is still open, the results presented in this work indicate that the simple classical model involving unassociated point defects is not satisfactory. Therefore, in the considerations presented below, activities of defects are used instead of concentrations and the Debye-Hückel theory is applied to calculate appropriate equilibrium constants and resulting Fermi energy changes.

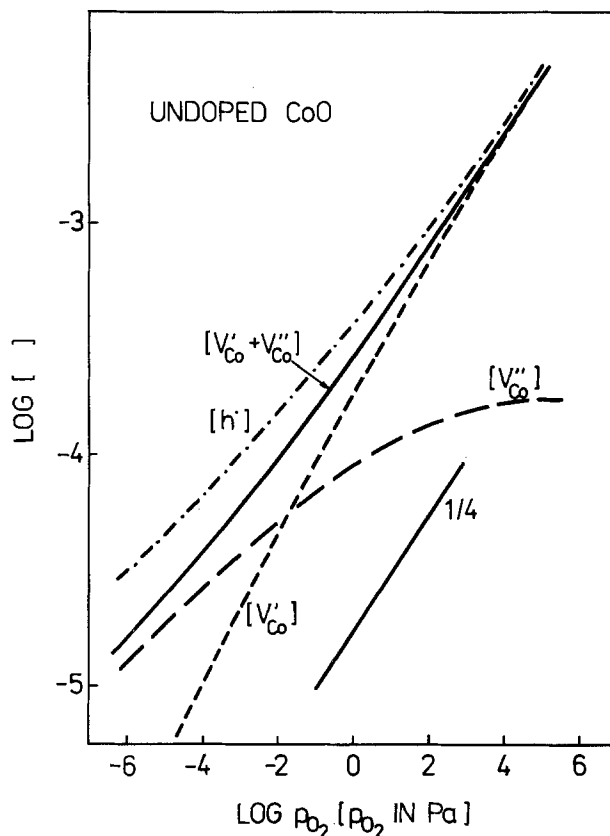


Fig. 5. Concentration of defects in undoped CoO at 1300 K

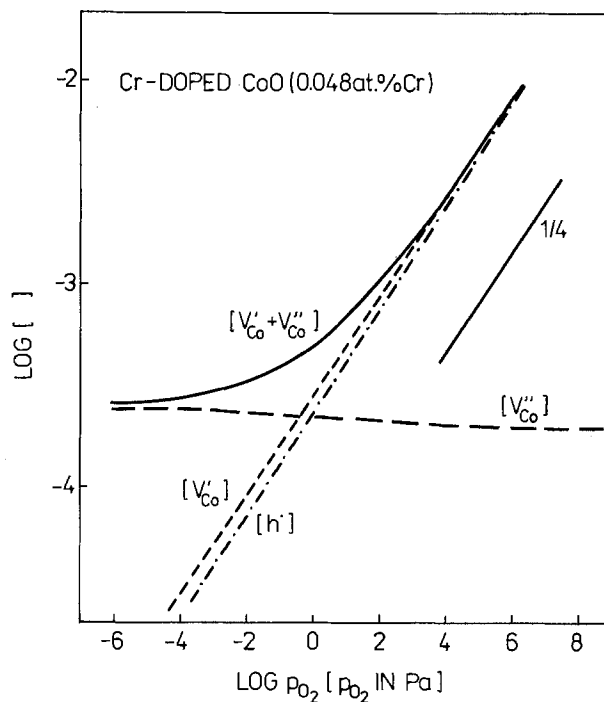


Fig. 6. Concentration of defects in Cr-doped CoO (0.048 at.% Cr) at 1300 K.

Considering activities, Eq. [23] and [30] assume the following forms

$$K^*_{v'} = \frac{[V'Co][h] \cdot f_h \cdot f_{v'}}{p_{O_2}^{1/2}} \quad [33]$$

$$K^*_{v''} = \frac{[V''Co][h]^2 \cdot f_h^2 \cdot f_{v''}}{p_{O_2}^{1/2}} \quad [34]$$

The Debye-Hückel theory for strong electrolytes was applied to calculate the activity coefficients

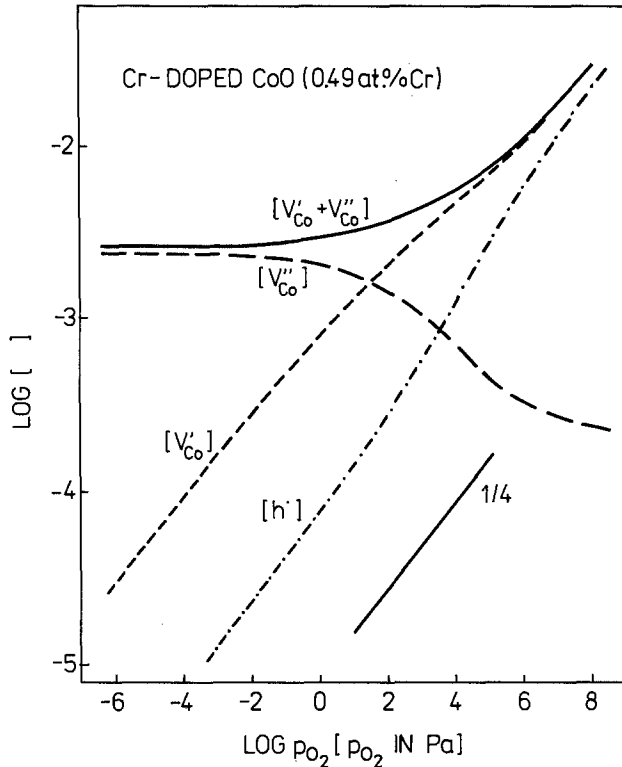


Fig. 7. Concentration of defects in Cr-doped CoO (0.49 a/o Cr) at 1300 K.

$$\ln f_i = -\frac{1}{2\epsilon} \cdot \frac{z_i^2 e^2 N_A}{RT} \cdot \frac{H}{1+a} \quad [35]$$

where ϵ is the dielectric constant of the solvent, z_i is the charge of the ion, N_A is Avogadro's number, a is the distance between ions, and

$$H = \sqrt{\frac{4\pi e^2}{kT} \sum_{i=1}^n N_i z_i^2} \quad [36]$$

where N_i is the number of ions in cm^3 and the other parameters have their traditional meaning. For calculations, it has been assumed that $\epsilon = 12.9$ (21) and

$$a = \frac{a_0}{\sqrt{2}} = 3.01 \cdot 10^{-8} \text{ cm}$$

where a_0 is the lattice parameter equal to 0.426 nm (4.26Å) (4). In calculations of ionic force

$$I = \frac{1}{2} \sum_{i=1}^n N_i z_i^2 \quad [37]$$

the following defects were considered: $h\cdot$, V'_{Co} , V''_{Co} , and $\text{Cr}\cdot_{\text{Co}}$. Therefore, considering appropriate simple electroneutrality conditions [24] and [28], we obtain

$$I = [h\cdot] \quad [38]$$

for undoped CoO and

$$I = \frac{1}{2} \{2[h\cdot] + 3[\text{Cr}\cdot_{\text{Co}}]\} \quad [39]$$

for CoO-Cr₂O₃ solid solutions.

As results from Eq. [35]

$$f_{h\cdot} = f_{V'} = f_{\text{Cr}\cdot} = f \quad [40]$$

and

$$f_{V''} = f^4 \quad [41]$$

The calculated values of activity coefficients as well as equilibrium constants are listed in Table V and VI for

Table V. Equilibrium constant $K_{V'}$ for undoped CoO at 1300 K

No.	$\ln p_{\text{O}_2}$ (p_{O_2} in Pa)	f	$K_{V'}$ ($\text{Pa}^{-1/2}$)	$K^{*V'}$ ($\text{Pa}^{-1/2}$)
1.	9.97	0.491	$1.56 \cdot 10^{-7}$	$3.75 \cdot 10^{-8}$
2.	8.67	0.516	$1.83 \cdot 10^{-7}$	$4.88 \cdot 10^{-8}$
3.	3.12	0.520	$2.25 \cdot 10^{-7}$	$6.08 \cdot 10^{-8}$
4.	7.19	0.532	$2.84 \cdot 10^{-7}$	$8.03 \cdot 10^{-8}$
5.	3.16	0.656	$1.99 \cdot 10^{-7}$	$8.58 \cdot 10^{-8}$

* Average value 1-5 $6.3 \pm 2.0 \cdot 10^{-8}$

Table VI. Equilibrium constant $K_{V''}$ for CoO-Cr₂O₃ solid solutions at 1300 K

No.	$\ln p_{\text{O}_2}$ (p_{O_2} in Pa)	f	$f_{V''}$	$K_{V''}$ ($\text{Pa}^{-1/2}$)	$K^{*V''}$ ($\text{Pa}^{-1/2}$)
0.048 a/o Cr					
1.	-9.97	0.499	0.062	$4.46 \cdot 10^{-8}$	$6.91 \cdot 10^{-10}$
2.	-8.29	0.517	0.071	$2.48 \cdot 10^{-12}$	$4.71 \cdot 10^{-11}$
3.	-7.11	0.540	0.085	$6.91 \cdot 10^{-11}$	$1.73 \cdot 10^{-12}$
4.	-3.16	0.436	0.036	$5.84 \cdot 10^{-9}$	$4.08 \cdot 10^{-11}$
0.49 a/o Cr					
5.	-9.97	0.399	0.025	$1.08 \cdot 10^{-9}$	$4.37 \cdot 10^{-12}$
6.	-8.29	0.469	0.028	$1.37 \cdot 10^{-9}$	$6.41 \cdot 10^{-12}$
7.	-3.16	0.434	0.035	$1.75 \cdot 10^{-9}$	$1.17 \cdot 10^{-11}$
0.90 a/o Cr					
8.	-9.97	0.347	0.014	$5.47 \cdot 10^{-9}$	$9.55 \cdot 10^{-12}$
9.	-8.14	0.363	0.017	$5.49 \cdot 10^{-9}$	$1.03 \cdot 10^{-11}$
10.	-6.88	0.366	0.018	$7.01 \cdot 10^{-9}$	$1.68 \cdot 10^{-11}$
11.	-3.16	0.383	0.021	$6.82 \cdot 10^{-9}$	$2.12 \cdot 10^{-11}$

* Average value 5-11 $1.2 \pm 5 \cdot 10^{-11}$

undoped CoO and Cr-doped CoO samples. As can be seen, the equilibrium constants, $K^{*V'}$ and $K^{*V''}$ calculated from activities, show significantly smaller changes compared to those calculated from concentrations, except in the case of $K_{V''}$ data for the CoO sample containing the smallest concentration of Cr (0.048 a/o). As one can expect in this case, the simple electroneutrality condition [28] is not valid. Therefore, the average values of the equilibrium constants were calculated for positions 5-11 (Table VI). Accordingly, the general electroneutrality condition involving both singly and doubly ionized cation vacancies should be applied

$$[V'_{\text{Co}}] + 2[V''_{\text{Co}}] = [h\cdot] + [\text{Cr}\cdot_{\text{Co}}] \quad [42]$$

Taking into account Eq. [33], [34], [40], and [41], we obtain

$$f^6 [h\cdot]^2 [h\cdot] + [\text{Cr}\cdot_{\text{Co}}] - K^{*V'} p_{\text{O}_2}^{1/2} [h\cdot] f^4 - 2K^{*V''} p_{\text{O}_2}^{1/2} = 0 \quad [43]$$

Values of $[h\cdot]$ were calculated from Eq. [43] for a given $K_{V'}$ and $K_{V''}$. The successive approximations method was applied for calculations of consistent values $[h\cdot]$ and f . Thus, determined values of $[h\cdot]$ served to calculate E_F vs. $[\text{Cr}\cdot_{\text{Co}}]$ from Eq. [16]. This dependence, which is illustrated by curve 3 in Fig. 4, shows a satisfactory agreement with experimental data, again with the exception of the case where the concentration of chromium is the smallest.

Conclusions

Comparative studies of electrical conductivity and of Seebeck effect enables one to determine the mobility of electron holes. The mobility term is changing vs. oxide composition which is an indication of defect interactions in undoped CoO.

The results presented here indicate that the simple defect model involving unassociated point defects is not adequate to describe defect structure of Cr-doped CoO.

Manuscript submitted June 30, 1982; revised manuscript received ca. Jan. 31, 1983.

REFERENCES

1. P. Kofstad, "Nonstoichiometry, Diffusion and Electrical Conductivity in Binary Metal Oxides," John Wiley and Sons, Inc., New York (1972).
2. M. S. Seltzer and A. Z. Hed, *This Journal*, **117**, 815 (1970).
3. J. Nowotny and A. Sadowski, *J. Am. Ceram. Soc.*, **62**, 24 (1979).
4. B. Fisher and D. S. Tannhauser, *J. Chem. Phys.*, **44**, 1663 (1966).
5. A. Dugnesnoy, F. Marion, and C. R. Hend, *C.R. Acad. Sci.*, **256**, 2862 (1963).
6. F. Morin, *Can. Metall. Q.*, **14**, 105 (1975).
7. F. Morin, *This Journal*, **126**, 760 (1979).
8. R. Dieckmann, *Z. Phys. Chem., N.F.*, **107**, 189 (1977).
9. U. Chowdhry and R. L. Coble, *J. Am. Ceram. Soc.*, **65**, 336 (1982).
10. H. C. Chen and T. O. Mason, *ibid.*, **64**, C-130 (1981).
11. F. Morin and R. Dieckmann, *Z. Phys. Chem., N.F.*, **129**, 219 (1982).
12. J. Nowotny, I. Sikora, and J. B. Wagner, Jr., *J. Am. Ceram. Soc.*, **65**, 192 (1982).
13. R. R. Heikes and R. W. Ure, "Thermoelectricity," Interscience Publishers, Inc., New York (1961).
14. I. G. Ostin and N. F. Mott, *Adv. Phys.*, **18**, 41 (1969).
15. S. Mrowec and K. Przybylski, *Rev. Int. Hautes Temp. et Refract.*, **14**, 285 (1977).
16. R. E. Carter and F. D. Richardson, *J. Metals*, **6**, 1244 (1954).
17. J. E. Stroud, I. Bransky, and N. M. Tallan, *J. Chem. Phys.*, **58**, 1263 (1971).
18. C. R. A. Catlow and A. M. Stoneham, *J. Am. Ceram. Soc.*, **64**, 234 (1981).
19. R. A. Perkins and R. A. Rapp, *Metall. Trans.*, **4**, 193 (1973).
20. J. J. Stiglich, D. H. Whitmore, and J. B. Cohen, *J. Am. Ceram. Soc.*, **56**, 211 (1973).
21. J. P. Cyr, These d'Etat No AO 12542, l'Institut National Polytechnique de Lorraine, 1976.

Photoelectrochemistry of WSe₂ Electrodes

Comparison of Stepped and Smooth Surfaces

H. J. Lewerenz,^{*1} H. Gerischer,^{*} and M. Lübke

Fritz-Haber-Institut der Max-Planck-Gesellschaft, Faradayweg 4-6, D-1000 Berlin 33, Germany

ABSTRACT

Smooth and stepped surfaces of n-WSe₂ have very different properties for adsorption and charge transfer. Adsorption of OH⁻ and I⁻ is strong at stepped surfaces, but not observable at smooth surfaces. This is apparent in flatband potential measurements. Photocurrent voltage curves indicate in the steady state slow charge transfer rates with all redox couples. This leads to an inversion at smooth parts of the surface, while the high recombination rate at steps prevents accumulation and makes them a sink for holes. I⁻ reacts faster than other redox couples with holes, and catalyzes further hole transfer. The presence of I₂ in the solution modifies the surface chemically, and the blocking character of the contact is lost.

Low susceptibility to photocorrosion has advanced the use of layered compound transition metal dichalcogenides in liquid-junction solar cells. Considerable stability and solar conversion efficiencies have been reported (1-5). This stability against photocorrosion, particularly for photoanodes, has been attributed to phototransitions involving quasi-intrametallic d-bands. These leave M-X bonds largely unaffected (1, 2). This, however, can only be expected for perfect Van der Waals planes. From growth process, the materials are known to exhibit a varying number of steps, which have been discovered to act as recombination centers and to limit conversion efficiencies. They also enhance photocorrosion (6-7).

For fundamental investigations, the morphological surface anisotropy of MX₂ (M = W, Mo; X = S, Se) electrodes provides the opportunity to study two distinctly different types of surfaces *in situ*. At steps, strong covalent bonds can be formed with components of the ambient, but the smooth surfaces are mainly interacting via weak Van der Waals bonding with the environment.

At steps, the chemical interaction with electrolyte species is considerably stronger and introduces a variety of reaction possibilities. Adsorption (or chemisorption) can occur. This affects the surface-state energy and density distribution. Examples of this will be given in this paper.

The general coexistence of smooth and stepped regions, whose relative areas vary for each crystal and depend on the surface preparation, makes it impossible to prepare reproducible electrode surfaces. One can only demonstrate the general trend by comparing samples with large differences in surface perfection with respect to their electrochemical behavior. We report here such results obtained with WSe₂ crystals. The well-known effectiveness of the I₃⁻/I⁻ redox couple for high charge transfer rates and reduction of corrosion (8, 9) deserves investigation, particularly of its microscopic interaction with stepped and smooth surfaces. An understanding of the role of steps and other surface imperfections on the photoredox reactions and photocorrosion is important for an understanding of limits and possible improvements of liquid-junction solar cells made with these materials.

Experimental

The n-WSe₂ crystals used were grown by standard chemical transport reaction (10). Smooth and structured crystals were selected from the same batch upon visual inspection with a light microscope. Ohmic contacts were made with Hg-In amalgam, followed by Ag-epoxy (Epoxy Prod. 40773) making contact to a copper rod, which was then encapsulated with insulating epoxy (Scotchcast 3M No. 4). Experiments were performed with a standard three-electrode potentiostatic arrangement using a Pt counterelectrode and a saturated calomel electrode (SCE) as reference electrode. All potentials are referred to SCE. All current potential curves were measured with rotating electrodes. Solutions were made from triple-distilled water

^{*} Electrochemical Society Active Member.

¹ Present address: Hahn-Meitner-Institut für Kernforschung Berlin GmbH, Bereich Strahlchemie, Glienicke Str. 100, D-1000 Berlin 39, Germany.

Key words: semiconductor, chemisorption, overvoltage, surfaces.

and analytical-grade chemicals. The differential capacitance has been measured by standard techniques at 800 Hz. Illumination was provided by a 100W tungsten-iodine lamp with 5 mW/cm².

Results

The opportunity to monitor the interaction of electrolyte species with a semiconductor surface is provided by capacitance measurements. Corresponding flatband potentials (U_{FB}), extrapolated from Mott-Schottky plots, allow the determination of the semiconductor band-edge positions.

Figure 1 shows the influence of I^- concentration on the flatband potential of a smooth and two stepped WSe₂ electrodes. For the smooth sample, very little dependence is noted, but the stepped samples have a much more negative U_{FB} and show a further cathodic shift when the I^- concentration is changed from $10^{-4}M$ to $10^{-1}M$. Because of high Faradaic currents, U_{FB} could not be determined for I^- concentration higher than $10^{-2}M$ at the stepped-III anode with the highest surface imperfection. Figure 2 shows the influence of pH on the flatband potential of smooth and two highly structured WSe₂ electrodes (stepped I and stepped II) in three supporting electrolytes. For the smooth sample, no measurable dependence of flatband potential on OH^- concentration is found. The stepped samples show pronounced changes with pH in K_2SO_4 and KCl but not in KI . Changes are largest in K_2SO_4 . For $pH < 1$, the value of U_{FB} of a stepped sample is almost identical to that of a smooth electrode. The overall change in flatband potential between pH 1 and 11 is $\Delta U_{FB} = -0.25V$. At the steepest part of the curve around $pH = 5$, the slope dU_{FB}/dpH reaches 46 mV/pH. For a solution with 1M Cl^- , U_{FB} at this particular stepped electrode is shifted at pH 1 towards more negative values than the smooth sample, but approaches the values in K_2SO_4 for $pH > 7$. In 1M KBr , U_{FB} is shifted somewhat more cathodically at pH 1, and in 1M KI the shift of U_{FB} reaches 200 mV. The influence of pH was no longer detectable in 1M KI solution within the error limits of our measurements.

The influence of the surface structure of WSe₂ on photocurrent voltage curves for two different redox

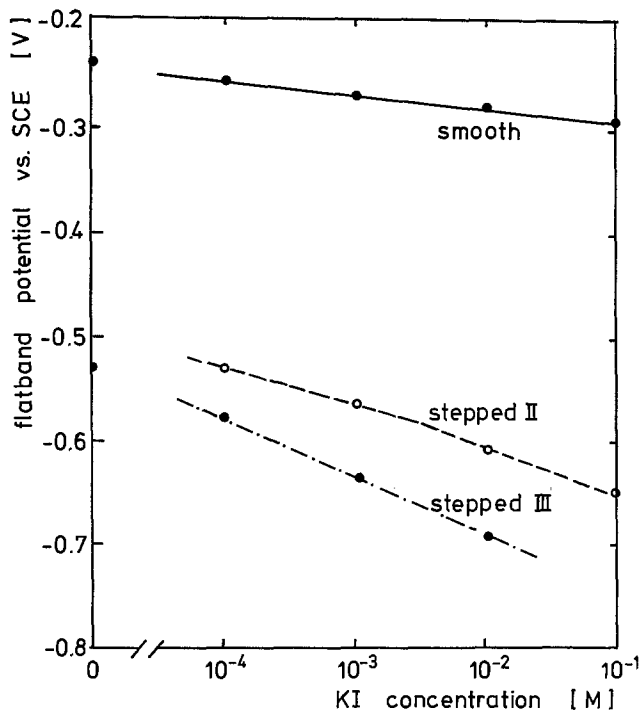


Fig. 1. Flatband potentials of smooth and stepped WSe₂ electrodes in dependence on the KI -concentration. Electrolytes: 1M KCl , pH 6. Flatband from Mott-Schottky plots at 800 Hz.

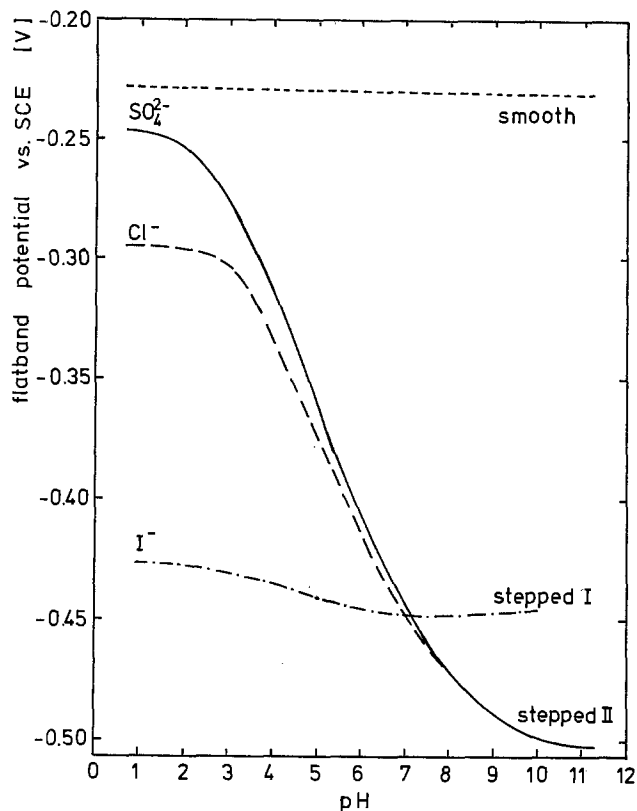


Fig. 2. pH dependence of the flatband potentials of smooth and stepped WSe₂ electrodes with different anions: 0.5M K_2SO_4 , 1M KCl , 1M KI .

electrolytes is displayed in Fig. 3. In I^- , the smooth surface shows a photocurrent onset at $-0.2V$, and a relatively steep increase and saturation at $+0.8V$. The stepped sample shows a delayed onset in photocurrent and a considerably smaller slope of the $I-V$ curve. It does not reach saturation upon polarizing to $+1.1V$. The behavior of these electrodes in $Fe(CN)_6^{4-}$ is considerably worse with respect to the photocurrent voltage characteristics. Although the onset of the photocurrent coincides for the smooth electrode for both electrolytes, the raise with potential is much lower for $Fe(CN)_6^{4-}$ than for I^- . The photocurrent of the stepped electrode in $K_4Fe(CN)_6$ is further reduced, and is approximately 1/6 of the current of the smooth electrode in KI at 1.0V. Also indicated in Fig. 13 are the respective dark currents for the smooth and the

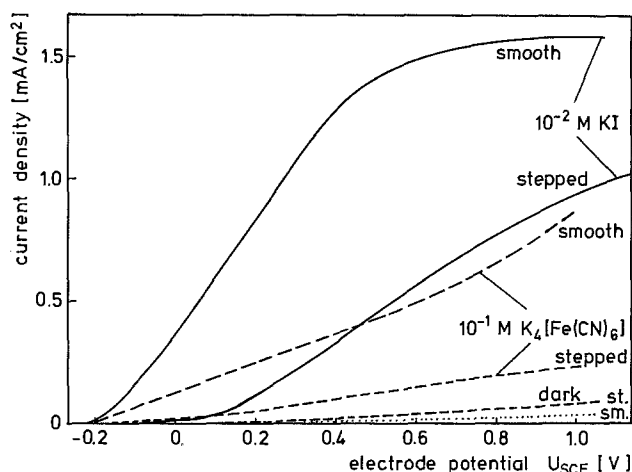


Fig. 3. Photocurrent voltage curves at smooth and stepped WSe₂ electrodes with different concentrations of $K_4Fe(CN)_6$ or KI in 1M KCl , pH 6.

stepped sample. It is shown that the anodic dark currents increase with surface imperfection.

The influence of I^- on the photocurrents was further examined by changing the I^- concentration and monitoring the I-V curves on stepped and smooth samples (Fig. 4). It is noted that upon increasing the I^- concentration on a stepped sample up to $10^{-3}M$ KI, no distinct difference in photoresponse compared to the base line in KCl is found. A substantial increase in current and shift to more negative bias, however, is observed for $10^{-1}M$ KI and much more so if the concentration is increased to $5.5M$. On the smooth electrode, a deviation from the curve recorded in KCl is already found for $10^{-3}M$ KI. This improves further upon increased I^- concentration. The steepness of the photocurrent voltage curve on the smooth electrode is considerably higher, and the photocurrent reaches the saturation region at much less positive bias.

A very drastic change of the surface chemistry occurs if I_3^- is present in the electrolyte. Electrodes with a large number of steps lose their blocking character in the potential range above 0V (SCE) in the dark, and their current voltage curves pass the open-circuit potential linearly. This potential approaches the redox potential of the electrolyte.

Figure 5 shows the potential dependence of the currents passing in the dark the contact between an iodine and iodide containing electrolyte and n-WSe₂ samples with four different surface morphologies. The currents increase with surface distortion. They are very small for the smoothest electrode and largest for the edge of a crystal exposed to solution.

Discussion

Influence of surface morphology.—The results are evidence of the influence of surface structure on the photoelectrochemical behavior of layered semiconductors, and the exceptional role of the I^-/I_3^- redox couple in the charge transfer reactions at the WSe₂ electrolyte interface. This is similar to experience with

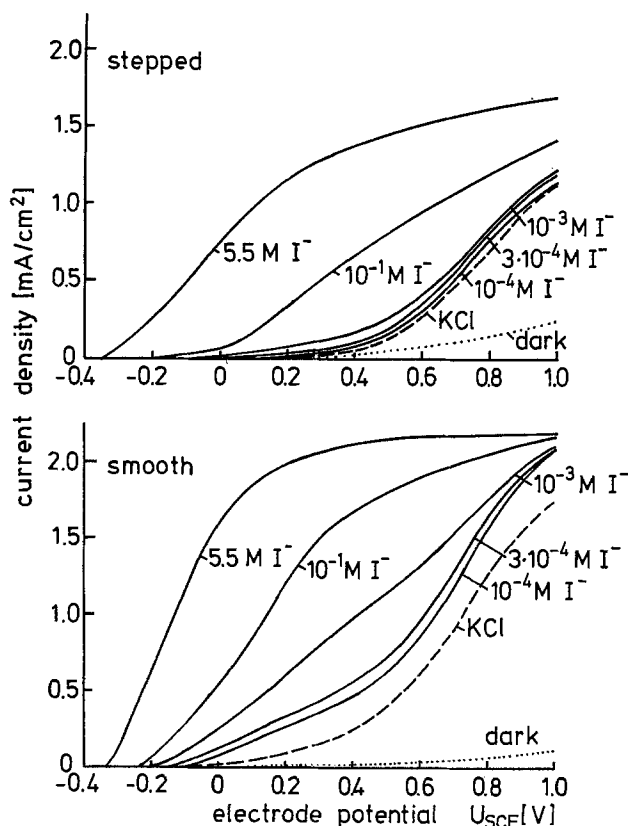


Fig. 4. Photocurrent voltage curves for stepped WSe₂ and smooth WSe₂ electrode with different KI-concentrations in 1M KCl. Both crystals are from the same growth batch.

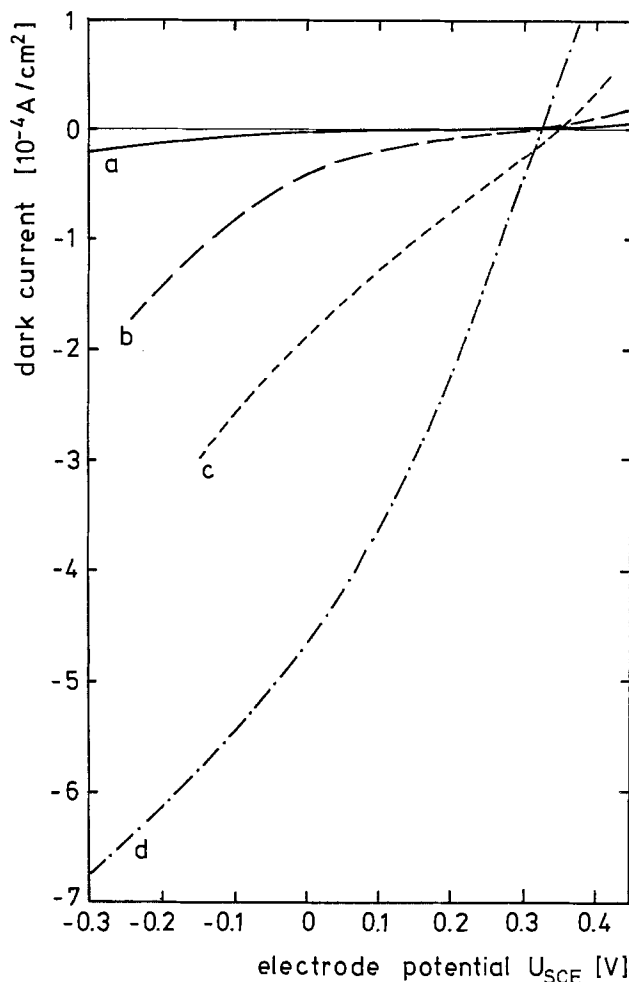


Fig. 5. Current-potential curves for 4 WSe₂ samples with different surface structures in solution of 1M KCl + $10^{-2}M$ KI + $1.5 \times 10^{-3}M$ KI₃. a = very smooth (as grown), b = relatively smooth, c = stepped, d = edge of a crystal (surface || \vec{c}).

MoSe₂ electrodes (11). The s-p bonding orbitals between metal and chalcogene atoms are located below the d_{z²} orbitals, which form the uppermost valence band (12). The d_{z²} orbitals are shielded by the Se layers from interaction with the ambient. W atoms at steps and other surface defects can interact strongly with components of the electrolyte because the d orbitals of the W atom there are not shielded against external reactants. These unsaturated bonds of the W atoms can overlap with electronic orbitals of components of the electrolyte and form new chemical bonds, particularly those with nucleophilic reactants, like OH⁻ and the halide ions. Chemical modification of such surface sites will introduce surface or interface states in the semiconductor-energy gap which act as recombination centers. The poor solar-cell performance of stepped WSe₂ electrodes has mainly been attributed to this effect (13, 14).

Our experiments show that this interaction occurs already in the dark and leads to the negative shift of the flatband potential for electrodes with stepped surfaces, since the adsorption of negative charge on the surface leaves behind a positive counter charge in the solution at a distance of the Helmholtz double-layer dimension (Fig. 1, 2). The size of this shift depends necessarily on the number of surface sites where such an interaction is possible. Saturation of the reactive sites is approached at high concentrations of the interacting species in the electrolyte. On the most stepped surface with a large excess of such sites in Fig. 1, a flatband-potential shift of 59 mV per concentration decade is approached. Figure 2 displays the relative

binding of SO_4^{2-} , Cl^- and I^- with respect to OH^- at steps. SO_4^{2-} appears to have negligible interaction, but I^- is much more strongly bound than OH^- and occupies all the accessible chemisorption sites. Therefore, the pH has little effect on U_{FB} in the presence of a high concentration of KI. Cl^- and Br^- do not interact as well as OH^- . Quantitative relations are difficult to obtain because of the limited control and reproducibility of surface preparation.

Smooth surfaces.—Photocurrents in the presence of redox systems increase only very slowly with positive bias. The reason for the delayed onset of the photocurrents relative to the position of the flatband potentials and the sluggish increase with bias could be a shift of the band-edge position. This comes about because of the charging of surface states, which can capture holes and accumulate positive charge to a sufficiently large amount. Since the missing voltage drop of the space charge layer would in this case appear in the Helmholtz double layer, a high number of surface states would be needed. The inertness to adsorption of these planes makes it difficult to assume this for a smooth Van der Waals plane. Fermi-level pinning appears, therefore, insufficient as an explanation for the photocurrent-voltage characteristics of the smooth electrodes.

A more plausible explanation is the assumption that the electron transfer rate is slow, and leads to an accumulation of holes underneath the interface. This explanation has been discussed by Reichmann (15), and Albery *et al.* (16). In this case, an inversion layer is formed as was indicated already for MoSe₂ electrodes by capacity- and surface-conductivity measurements under illumination (17).

The formation of an inversion layer will also affect the position of the bandedges to some extent. The additional electric charge in an inversion layer can create a considerably increased field strength at the surface, which extends through the Helmholtz double layer.

The additional voltage drop in the Helmholtz double layer due to this effect cannot, however, be as large as that generated by a high concentration of charged surface states, but this effect will nonetheless contribute to the slow increase of the photocurrents with bias.

Stepped surfaces.—At the surfaces with a large number of steps, surface recombination is enhanced considerably. There is also some evidence that dislocations or other structural defects are concentrated in the bulk near steps and increase the rate of recombination in this region of the bulk (14). This leads to a very inhomogeneous concentration distribution of holes in the space charge layer. We can assume that holes are consumed much faster by recombination at steps and in the surrounding bulk than at smooth parts of the surface. The result is that the concentration of holes around steps is much lower than at the smooth parts, and a large concentration gradient between smooth-surface areas and steps will exist. This causes a preferential transport of holes to the steps, as displayed in Fig. 6. The higher hole mobility parallel to the layers will further contribute to the increased drift of holes to steps on the surface.

If the flatband potential is shifted at the stepped electrodes to more negative values by the adsorption of anions which can be oxidized by holes, such as I^- ions, the consumption of this negative surface charge can reverse the shift of U_{FB} , as was observed for adsorbed S^{2-} on CdS (18). This is, however, unlikely for solutions with very high I^- concentration, because the adsorption of I^- is a fast reaction, and with a large excess of iodide the generated iodine will quickly be desorbed by complexation with I^- ions. It must be mentioned that accumulation of positive charge in surface states at steps also contributes to the slow increase of the photocurrent with applied voltage. This comes about by an increase of the voltage drop in the Helmholtz double layer and a corresponding shift of the bandedges to more positive potentials. The predom-

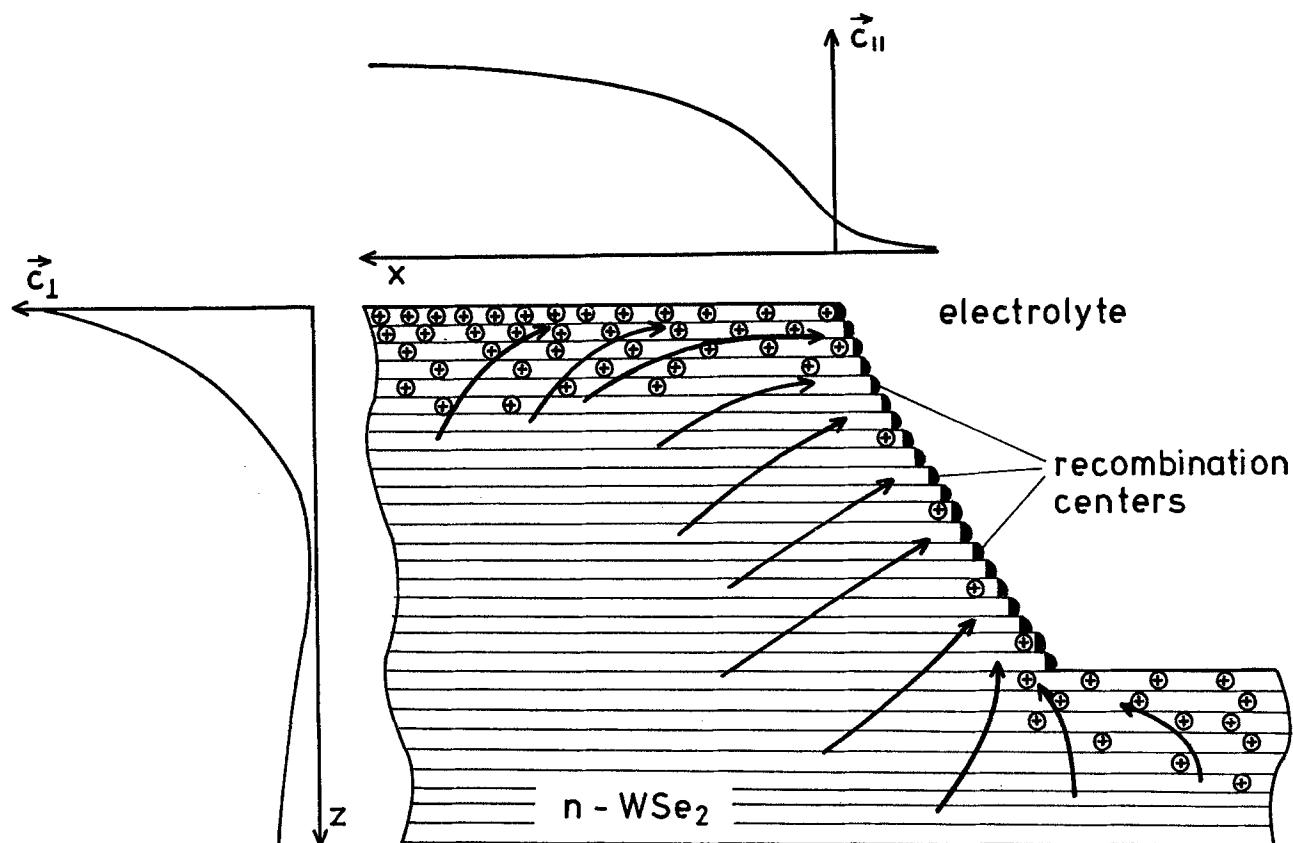


Fig. 6. Schematic representation of the motion of photogenerated minority carriers near the edge of a step. Hole-concentration profiles parallel and perpendicular to the \vec{z} -axis are also indicated.

inant effect of the steps, however, seems to be the increase of the recombination rate.

The specificity of the iodide redox reaction.—In the absence of specific adsorption, the interaction between the holes and the ions in solution will be very weak due to the small overlap between the d_{z^2} orbitals and the highest occupied orbital of the redox species. Consequently, the charge transfer rate is low. These unfavorable conditions are less important for iodide for two reasons. First, its solvation shell is more weakly bound, and the ion itself may be able to approach the surface closer than other redox ions. Second, the iodine atom as the reaction product appears to interact more vigorously even with the smooth surface. This will affect the transition state in which electron transfer occurs and reduce the activation barrier for hole transfer. The adsorbed I atoms will further catalyze the electron transfer from I^- ions to holes and enhance the formation of the I_2 molecule in the second step of this redox reaction. However, one still needs a very high concentration of I^- to make the electron transfer reaction at the WSe_2 surface so fast that the surface concentration of holes is drastically reduced at the smooth electrodes and the flux of minority carriers to the surface can approach its limiting value (cf. Fig. 4).

At the stepped electrodes, the I^- ions are adsorbed and can react with holes easily. However, this enhanced charge transfer rate has to compete with the increased rate of recombination. The catalytic effect of adsorbed I atoms on the rate of hole transfer to other I^- ions can obviously not fully compensate for the increased losses by recombination. The overall result is still a slower increase of the photocurrent with the bias applied than at the smooth surfaces.

If iodine is present in the electrolyte, the surface seems to change completely in chemical character, at least around steps and other defects. A layer with a high concentration of surface states is formed. The layer catalyzes electron transfer to and from the conduction band to an extent that dark currents passing continuously the abscissa close to the equilibrium po-

tential of the redox system become possible (cf. Fig. 5). The chemical nature of this surface modification remains to be determined.

Manuscript submitted April 4, 1983; revised manuscript received July 27, 1983.

REFERENCES

1. H. Tributsch, *Ber. Bunsenges. Phys. Chem.*, **81**, 361 (1977).
2. H. Tributsch, *This Journal*, **125**, 1086 (1978).
3. J. Gobrecht, H. Gerischer, and H. Tributsch, *Ber. Bunsenges. Phys. Chem.*, **82**, 1331 (1978).
4. H. J. Lewerenz, A. Heller, and F. J. DiSalvo, *J. Am. Chem. Soc.*, **102**, 1877 (1980).
5. B. A. Parkinson, T. E. Furtak, D. Canfield, K. Kain, and G. Kline, *Faraday Discuss. Chem. Soc.*, **70**, 233 (1980).
6. W. Kautek, H. Gerischer, and H. Tributsch, *Ber. Bunsenges. Phys. Chem.*, **83**, 1000 (1979).
7. W. Kautek and H. Gerischer, *Surf. Sci.*, **119**, 46 (1982).
8. H. Tributsch, *Solar Energy Mater.*, **1**, 257 (1979).
9. H. Gerischer and M. Lübke, *Ber. Bunsenges. Phys. Chem.*, **87**, 123 (1983).
10. H. Schäfer, in "Chemical Transport Reactions," Academic Press, New York (1964).
11. W. Kautek and H. Gerischer, *Electrochim. Acta*, **26**, 1771 (1981).
12. B. L. Evans, in "Physics and Chemistry of Materials with Layer Structures," Vol. 4, P. A. Lee, Editor, p. 1, D. Reidel Publishing Co., Dordrecht-Holland (1976).
13. H. J. Lewerenz, A. Heller, H. J. Leamy, and S. D. Ferris, in "Photoeffects at Semiconductor-Electrolyte Interfaces," A. J. Nozik, Editor, p. 17, ACS Symp. Ser. 146, Washington (1981).
14. H. J. Lewerenz, S. D. Ferris, C. J. Doherty, and H. J. Leamy, *This Journal*, **129**, 418 (1982).
15. J. Reichmann, *Appl. Phys. Lett.*, **36**, 574 (1980).
16. W. J. Albery, P. N. Bartlett, A. Hammett, and M. P. Dare-Edwards, *This Journal*, **128**, 1492 (1981).
17. C. D. Jaeger, H. Gerischer, and W. Kautek, *Ber. Bunsenges. Phys. Chem.*, **86**, 20 (1982).
18. R. H. Wilson, *This Journal*, **126**, 1187 (1979).

Technical Notes

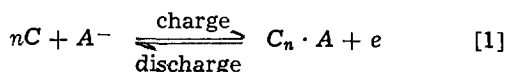


Graphite Fiber as a Positive Electrode of Rechargeable Lithium Cells

Yoshiharu Matsuda,* Masayuki Morita, and Hidenori Katsuma

Department of Industrial Chemistry, Faculty of Engineering, Yamaguchi University, Tokiwa-dai, Ube, Yamaguchi, Japan

Graphite compounds have gained interest as possible positive electrodes for rechargeable lithium cells. Their charge-discharge characteristics have been studied in organic electrolytic solutions such as sulfolane (1), dimethylsulfoxide (2, 3), and propylene carbonate (4, 5). The charge-discharge reactions of graphite positives are believed to involve the intercalation-deintercalation process shown in Eq. [1]



* Electrochemical Society Active Member.

Key words: lithium cell, graphite fiber, rechargeability, anion intercalation.

where n is an integer and A^- denotes an anion (2-5). Cell performance is dependent on the variety of the graphite. Bennion *et al.* (2) and Ohzuku *et al.* (5) presented some high-efficiency charge-discharge cycles using pyrolytic graphite positives. It is held that the edge face (parallel plane to the c -axis of the crystal) of the graphite structure is effective for the intercalation reaction (4). This note presents the use of carbon (graphite) fibers with surfaces consisting mainly of the edge face of the graphite. The charge-discharge behavior of the graphite fiber electrode was studied in propylene carbonate (PC) solutions of $LiClO_4$, $LiBF_4$, and $LiPF_6$. The results are discussed from the standpoint of the structure change.

Experimental

A felt of graphite fiber (Nihon Carbon Company, Limited, GF-25A) was used as the test electrode. It was characterized by x-ray diffraction analysis and scanning electron microscopy (SEM). The felt was cut into disks of 12.5 mm diameter (average weight; 0.038g), and then mounted on a Teflon holder with a Pt current-collector. The apparent surface area exposed to the solution was 0.5 cm².

The solvent PC was purified and dehydrated by the usual methods, as described elsewhere (6, 7). The electrolytic salts (LiClO₄, LiBF₄, and LiPF₆) were extra-pure grade. They were used after drying under reduced pressure for 24 hr or more (7). The concentration of the electrolyte was 1.0 mol dm⁻³. The water contents of the solution were less than 80 mg dm⁻³.

The charge-discharge characteristics were investigated using a half-cell test with an excess of the electrolytic solution (about 100 cm³). A beaker-type cell with a Pt counterelectrode (16 mm × 28 mm) was used. A SCE was used as the reference electrode. The electrode potential is reported against the Li/Li⁺ couple. The potential of the Li/Li⁺ vs. SCE was directly determined by separate experiments. It was -3.0V. The felt electrode was charged at a constant current of 0.1 mA (0.02 A dm⁻²) for 60 min. Discharging was done without a break at the same current density until the electrode potential was 3.0V (vs. Li/Li⁺). The charge-discharge cycle was repeated at least six times. These electrochemical measurements were carried out under a dry N₂ atmosphere at 298 K.

Results and Discussion

Figure 1 shows SEM photographs of the graphite fiber before its electrochemical use. The maximum length of the fiber was about 3 mm, and the average diameter was 10-15 μm. The x-ray diffraction pattern of the graphite fiber is shown in Fig. 2. This indicates that the (100) plane of the graphite structure, as well as the (002) or (004) plane, is highly developed

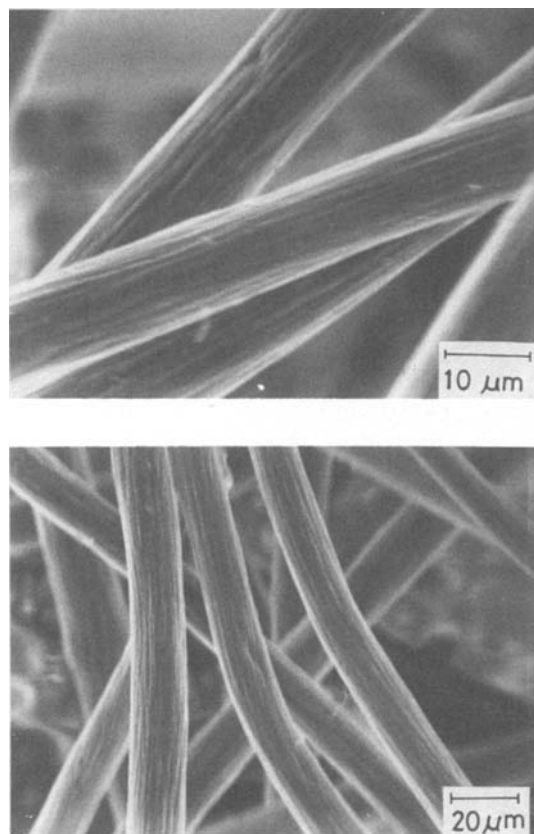


Fig. 1. SEM photographs of the graphite fiber

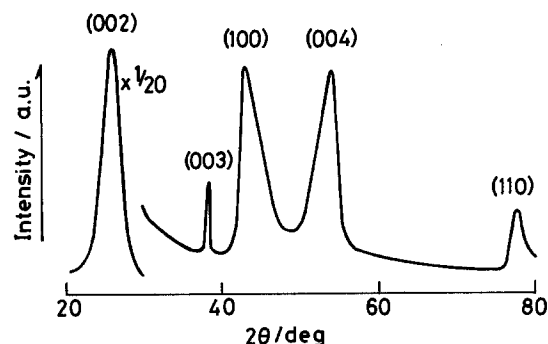


Fig. 2. X-ray diffraction pattern of the graphite fiber electrode

in the fiber. Thus the plane parallel to the c-axis (so-called edge face) of the graphite crystal is preferentially exposed at the surface of the fiber.

The charge-discharge curves of a graphite fiber electrode are shown in Fig. 3, where the charge (or discharge) time of 60 min corresponds to a capacity of 24 C g⁻¹. The charging potentials remained almost constant after the first 30 min, and the curves scarcely varied with increasing cycle numbers. During discharge, potential plateaus, which might be attributable to the deintercalation of the anion, were observed. These results are similar to those in dimethylsulfite solution, as reported by Deshpande and Bennion (3). There is no evidence for intercalation *per se*, but the data would be consistent with the formation of a graphitic acid salt as reported in works on aqueous solutions (8, 9). The coulombic capacities (A-hr discharged) tended to increase with continued cycling. The variation in the x-ray diffraction pattern of the fiber was investigated during the charge-discharge process. The intensity of each diffraction peak fell off with repeated cycling; though shifts in the diffraction angles were not observed. This indicates a decreasing crystallinity of the graphite with cycling. The increase in the coulombic capacity with repeated cycling is probably related to the lowered degree of crystallinity. On the other hand, the coulombic effi-

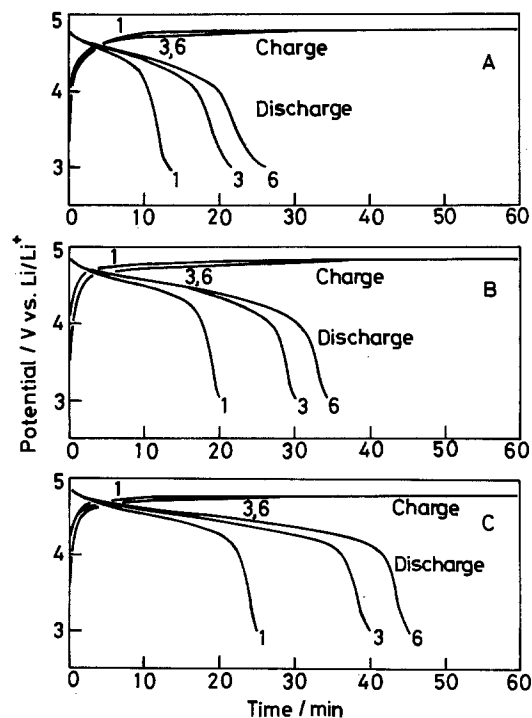


Fig. 3. Charge-discharge curves of the graphite fiber electrode. A: in 1.0 mol dm⁻³ LiClO₄; B: in 1.0 mol dm⁻³ LiBF₄; C: in 1.0 mol dm⁻³ LiPF₆.

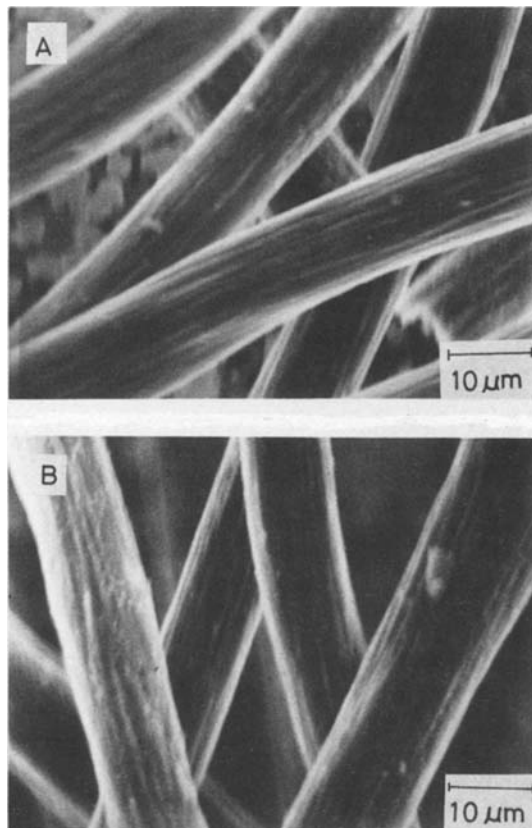


Fig. 4. SEM photographs of the graphite fiber after 6 charge-discharge cycles. A: in $1.0 \text{ mol dm}^{-3} \text{ LiClO}_4$; B: in $1.0 \text{ mol dm}^{-3} \text{ LiPF}_6$.

ciency of the charge-discharge cycle (A-hr discharged/A-hr charged) increased in the order of $\text{ClO}_4^- < \text{BF}_4^- < \text{PF}_6^-$. Such differences in the efficiency could result from the difference in the extent of intercalation during the charge. Purity of the salt is probably not a main factor in the cycle efficiency because the impurity contents were low (e.g., $< 1\%$ in LiPF_6 and $< 0.1\%$ in LiBF_4) even in the solution

prepared. The cycle efficiency would depend on the kind of anion to be intercalated, though the reason for the difference in the reactivity was not clarified in the present work.

There was little change in the appearance of the fiber electrode after the charge-discharge cycles, although the results of x-ray diffraction analysis showed a decrease of graphite structure in the fiber. Figure 4 shows SEM photographs of the graphite fiber after the sixth discharge in the LiClO_4 and LiPF_6 solutions. There was little change in shape of the fiber except for some roughness of the surface. This should be an important feature for the electrode of secondary cells, and it suggests that such fiber electrodes abounding with the edge face of the crystal are favorable for practical use. However, further attempts should be made to improve charge-discharge efficiency, and the long-term characteristics of the cycling should also be investigated for realizing a practical rechargeable cell.

Acknowledgment

The authors would like to acknowledge that this work was supported by the Grants in Aid for Scientific Research (No. 00555313 and 56850187) from Japan Ministry of Education and that some reagents were presented by Morita Chemical Industries, Ltd.

Manuscript submitted April 15, 1983; revised manuscript received July 25, 1983.

Yamaguchi University assisted in meeting the publication costs of this article.

REFERENCES

1. A. Brenner, *This Journal*, **118**, 461 (1971).
2. J. S. Dunning, W. H. Tiedemann, L. Hsueh, and D. N. Bennion, *ibid.*, **118**, 1886 (1971).
3. S. L. Deshpande and D. N. Bennion, *ibid.*, **125**, 687 (1978).
4. Y. Takada and Y. Miyake, *Denki Kagaku*, **43**, 329 (1975).
5. T. Ohzuku, Z. Takehara, and S. Yoshizawa, *ibid.*, **46**, 438 (1978).
6. Y. Matsuda, Y. Ōuchi, and H. Tamura, *J. Appl. Electrochem.*, **4**, 53 (1974).
7. Y. Matsuda, *Denki Kagaku*, **48**, 665 (1980).
8. J. O. Besenhard and H. P. Fritz, *Z. Anorg. Allg. Chem.*, **416**, 106 (1975).
9. F. Beck, H. Junge, and H. Krohn, *Electrochim. Acta*, **26**, 799 (1981).

Repassivation Behavior of Two Glassy Alloys in Sulfuric Acid with and without Chloride Ions

Ronald B. Diegle,^{*,1} and David M. Lineman²

Battelle Columbus Laboratories, Columbus, Ohio 43201

The excellent corrosion resistance of certain Cr-containing glassy alloys has been attributed to the presence of very protective passive films, particularly hydrated chromium oxyhydroxide (1, 2). The degree of enrichment of Cr^{3+} in such films can be greater than that in films formed on crystalline stainless steels containing comparable levels of alloyed Cr. P in the glassy structure greatly facilitates enrichment of Cr^{3+} into the passive film (1, 3, 4); analysis of repassivation transients (2, 5, 6) has suggested that P accelerates dissolution of the unfiled alloys, and that this intensified dissolution promotes the formation of passive films

that are highly enriched in Cr^{3+} . The work reported here was undertaken to analyze the repassivation behavior of certain glassy alloys as influenced by the metalloids P, B, and Si, and by chloride ion in solution.

Experimental

Compositions of the alloys that were used are given in Table I. The alloys designated 2826A and Si/B were glassy, and they were procured from Allied Chemical Corporation and prepared at Battelle, respectively; both were made by the melt spinning process. The T316 stainless steel was procured from a commercial vendor and it was included so that repassivation behavior of the glassy alloys could be compared with that of a crystalline Cr-containing stainless steel. Current transients were generated by scratching specimens that were potentiostated relative to a satu-

* Electrochemical Society Active Member.

¹ Present address: Sandia National Laboratories, Albuquerque, New Mexico 87185.

² Present address: Corning Glass Works, Corning, New York 14870.

Key words: amorphous, corrosion, passivity, transients.

Table I. Compositions of alloys

Alloy	Composition, atomic percent ^a							
	Fe	Ni	Cr	Mn	Mo	P	B	Si
2826A	32	36	14	—	—	12	6	—
Si/B	32	36	14	—	—	—	12	6
T316	65	11	18	2.0	1.4	0.0	—	2.0

^a Compositions of 2826A and T316 were quoted by suppliers and Si/B was analyzed at Battelle.

rated calomel electrode (SCE) in 1N H₂SO₄, with or without addition of 1N NaCl. Scratching was performed with a spring driven sapphire stylus (7), and the transients were recorded on a waveform recorder (Physical Data Model 514A). This recorder could sample the signal at intervals as short as 0.5 μsec, and thus it was more than adequate for resolving current-time behavior in the 10⁻³-1 sec range. The alloy electrodes were first abraded with 600 grit SiC paper to create a standard surface finish, then rinsed with acetone, air dried, and mounted to a Teflon holder prior to scratching. The average scratch area for each type of alloy was determined after several scratch events by means of a high power optical microscope equipped with a filar eyepiece. The scratches were approximated as being rectangular in cross section and sufficiently shallow that the area of the inside walls of the scratch could be ignored. Several areas were measured and then averaged for use in calculating current densities. (Only the scratch area, not the total exposed electrode area, was used to calculate current density.)

Results

Potentials in the passive range of polarization behavior were selected for the scratching experiments so that well-developed passive films would form on the scratched areas. Anodic polarization curves for the three alloys are shown in Fig. 1 for 1N H₂SO₄. T316 steel was polarized to 0.20V (SCE), which was in the passive potential region in both 1N H₂SO₄ and 1N H₂SO₄ + 1N NaCl. A potential further into the passive region was selected for the two glassy alloys, namely, 0.60V (SCE); however, because this value exceeded the critical pitting potential of the Si/B alloy in 1N H₂SO₄ + 1N NaCl, a potential of 0.20V (SCE) was used for the Si/B alloy in Cl-containing 1N H₂SO₄. It was not considered critical to use the same potential for all three alloys because neither the passive film compositions nor the current passed should depend strongly on the applied potential over this potential range.

Shown in Fig. 2 are typical current density-time plots measured at passive potentials. Two distinct regions are evident. In region 1, the current density decreased linearly with a slope of about -1 sec⁻¹. After about

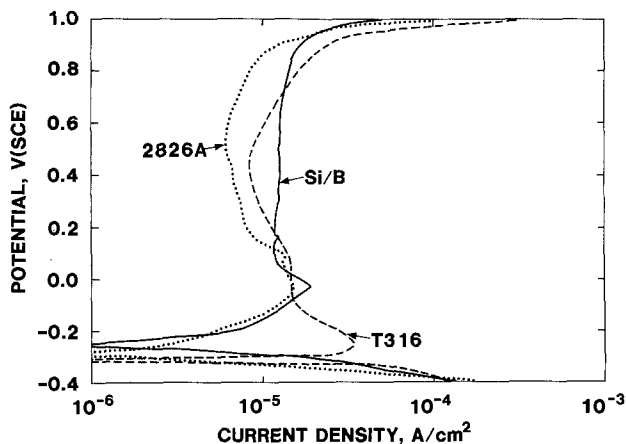


Fig. 1. Polarization curves obtained in deaerated 1N H₂SO₄ at room temperature. Scan rate = 1 mV/sec.

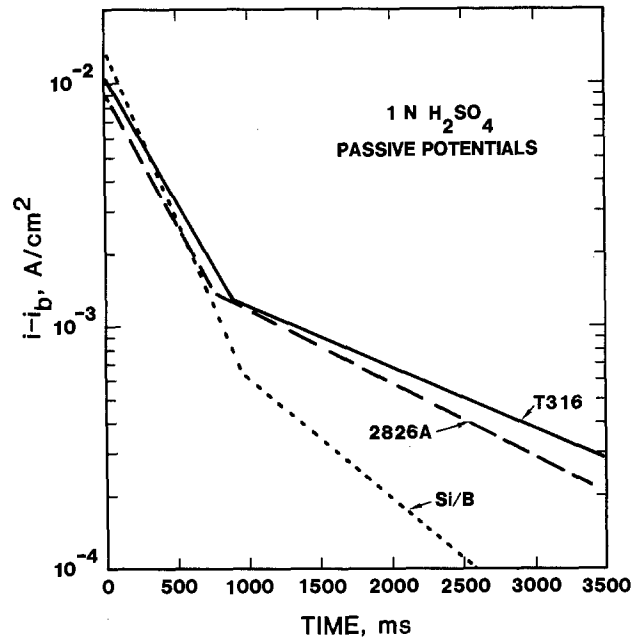


Fig. 2. Typical anodic current transients obtained in 1N H₂SO₄. $i_b \approx 4 \cdot 10^{-5}$, $4 \cdot 10^{-5}$, and $2 \cdot 10^{-4}$ A/cm² for 2826A, Si/B, and T316, respectively.

700-1000 msec had elapsed, the current density decreased at a slower rate, denoting region 2 behavior. The current density-time relationship was of the form

$$(i - i_b) = (i_p - i_b) 10^{st} \quad [1]$$

in which i is current density, i_p is the peak current density measured, i_b is the background or steady-state current density, s is the slope of the data in either region 1 or 2, and t is the time after i_p occurred. This equation was integrated between appropriate limits to calculate the charge density passed in region 1, Q_1 , and in region 2, Q_2 . Repassivation parameters are presented in Table II, and they are the mean values from, typically, three replicate experiments for each alloy. The effect on repassivation of adding 1N NaCl to the electrolyte is shown in Fig. 3. The two stage semilogarithmic current decay still occurred, but the dissolution current was substantially increased for the Si/B alloy. Repassivation parameters measured in the presence of NaCl are presented in Table III.

Discussion

Hashimoto *et al.* (6) measured repassivation transients on glassy Fe-10Cr-13B-7X alloys in 0.1N H₂SO₄, where X = Si, B, or P. They showed that P caused the most rapid current decay after abrasion, and Si the least rapid, although they did not analyze quantita-

Table II. Repassivation parameters measured in deaerated 1N H₂SO₄ at passive potentials^a

Alloy	Potential [V(SCE)]	$i_p - i_b$ (mA/cm ²)	Q_1 (mC/cm ²)	Q_2 (mC/cm ²)	s_1 (sec ⁻¹)	s_2 (sec ⁻¹)
T316	0.20	11.0	4.1	1.7	-1.09	-0.25
2826A	0.60	11.9	3.6	1.8	-1.05	-0.38
Si/B	0.60	9.5	2.8	0.4	-1.37	-0.53

^a Results quoted are averages of, typically, three measurements.

Table III. Repassivation parameters measured in deaerated 1N H₂SO₄ + 1N NaCl at passive potentials^a

Alloy	Potential [V(SCE)]	$i_p - i_b$ (mA/cm ²)	Q_1 (mC/cm ²)	Q_2 (mC/cm ²)	s_1 (sec ⁻¹)	s_2 (sec ⁻¹)
T316	0.20	3.3	10.2	5.1	-1.23	-0.26
2826A	0.60	1.5	5.8	2.4	-0.99	-0.40
Si/B	0.20	530.0	200.0	107.0	-1.06	-0.47

^a Results quoted are averages of, typically, three measurements.

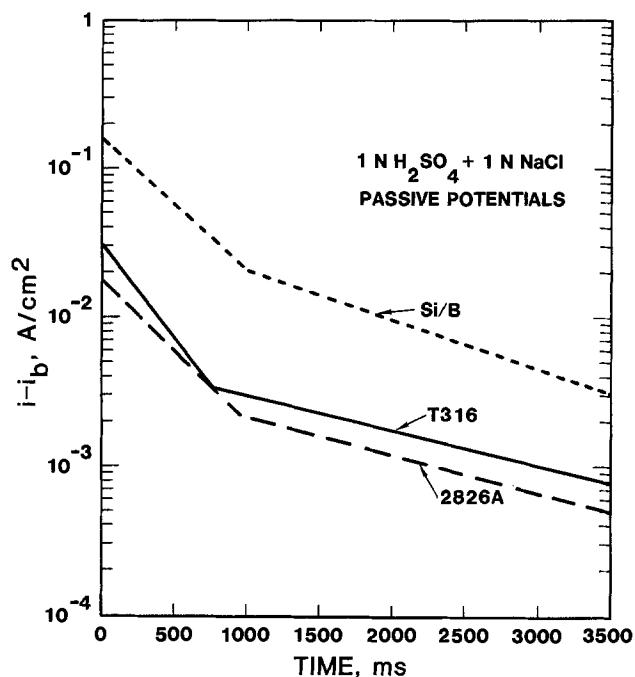


Fig. 3. Typical anodic current transients obtained in 1N H_2SO_4 + 1N NaCl. $i_b \approx 3 \cdot 10^{-5}$, $7 \cdot 10^{-4}$, and $1 \cdot 10^{-3}$ A/cm 2 for 2826A, Si/B, and T316, respectively.

tively the kinetics of current decay. Reference to Fig. 2 shows that the repassivation rate for the Si/B alloy was somewhat faster than that of 2826A, and thus our results regarding the influence of metalloids are somewhat at variance with these workers. However, the presence of chloride ion markedly differentiated the effects of P from Si in promoting rapid repassivation, as evident in Fig. 3 and Table III.

It is interesting to compare the Q_1 values to the charge required to form one monolayer of passive film. As a first approximation and to simplify the calculation, it was assumed that the only cation present in the film was Cr^{3+} . This was not strictly true, yet under some conditions the cationic fraction of Cr, relative to Fe, Ni, and other cations, can indeed be large, especially at potentials well cathodic to transpassive behavior (2, 4). Second, the film composition was taken to be $CrO(OH) \cdot H_2O$ because $CrO_x(OH)_{3-2x} \cdot nH_2O$ has been postulated, based on extensive XPS analysis, to comprise a substantial proportion of the passive film on glassy Cr-containing alloys exhibiting high corrosion resistance (1, 2); for this calculation x was taken to be 1. An estimate of the monolayer equivalent charge density (MEQ) was made for a film of the above composition with a density of 3 g/cm 3 and thickness of 0.3 nm.

The calculated charge density is 0.34 mC/cm 2 , in agreement with the lower range of 0.4-0.7 mC/cm 2 calculated by Frankenthal for Fe-24Cr (8). However, if the film is pure $CrO(OH) \cdot H_2O$ and selective dissolution of Cr from the alloy does not occur, then Fe and Ni must be dissolved into solution; this dissolution would increase the total measured charge to 1.4 mC/cm 2 , provided that P and B (in 2826A, e.g.) are not oxidized. [Both elemental and oxidized P have been found in the passive film on a glassy alloy (9).] If all of the P and B are oxidized to P^{5+} and B^{3+} , then the MEQ is increased further to 2.0 mC/cm 2 . These calculated values of 1.4-2.0 mC/cm 2 are less than the experimental values of 2.8-4.1 mC/cm 2 in Table II. Although the agreement is reasonable given the uncertainties in scratch area and film composition, the larger experimental values suggest that a portion of the measured Q_1 charge represents alloy dissolution in addition to repassivation. [Growth to more than one monolayer is ruled out because region 1 obeys semilogarithmic

growth kinetics, which is expected for monolayer film formation when metal dissolution is rate controlling (10).] The MEQ's for T316 and Si/B alloys are, respectively, 1.3 and 1.5 mC/cm 2 . They are also less than the Q_1 values in Table II, again suggesting that some alloy dissolution accompanied repassivation.

The effect of chloride addition to the electrolyte was to intensify dissolution during repassivation of T316 and especially Si/B, as reflected by increases in $i_p - i_b$ and Q_1 . The effect was very pronounced for Si/B, as shown in Table III. Addition of chloride did not, however, greatly alter the rate of repassivation, s_1 .

Concerning region 2, it was observed that if current density were plotted vs. time on log-log coordinates (not shown), the curves became linear at the time in which region 2 behavior was established in semi-log plots, i.e., about 700-1000 msec. The linearity is suggestive of a high field oxide growth mechanism, although the variable slopes in this work precluded unequivocal identification of a recognized growth rate law. Note that the Q_2 values in Table III are equivalent to about one additional monolayer of $CrO(OH) \cdot H_2O$ except for the Si/B alloy; it is not known why this value is so small. The addition of 1N NaCl to the H_2SO_4 moderately increased Q_2 for T316 steel and profoundly increased Q_2 for the Si/B alloy.

The repassivation behavior of the two glassy alloys and T316 steel is similar in form, as evident by the two stage semilogarithmic current decay in Fig. 2 and 3. The inclusion of T316 steel in this study was not intended to imply that it is a compositional analog to the glassy alloys; rather, it was included as being representative of Cr-containing crystalline stainless steels; and therefore, this similarity in current decay was unexpected. The presence of chloride ion had little effect on repassivation of 2826A, whereas it increased the region 1 dissolution, Q_1 , of T316. This difference in Q_1 presumably resulted from the ability of 2826A to incorporate Cr^{3+} at relatively high cationic concentrations into the passive film, as demonstrated by the XPS work of Hashimoto and co-workers (11). However, Cr in the glassy alloy structure is not a sufficient condition for excellent passivity, as evident from the large amount of dissolution accompanying repassivation of the Si/B alloy in chloride-containing H_2SO_4 . The combination of 14% Cr, 12% P, and 6% B showed a considerably faster repassivation rate than 14% Cr, 12% B, 6% Si in chloride-containing 1N H_2SO_4 , but unexpectedly and for yet unknown reasons the reverse is true in 1N H_2SO_4 without chloride ions. In both of these environments, the behavior of 2826A was only slightly faster than T316 steel. As expected, the repassivation rates were slower and required more dissolution to accomplish repassivation in the chloride-containing environment than in the environment without chlorides. The excellent chemical stability of 2826A supports the contention (3) that a synergism exists between Cr and P in glassy alloys, and that P can greatly increase the ability of Cr to confer passivity in very corrosive electrolytes.

Acknowledgments

This research was supported by Battelle's Corporate Technical Development Center. The authors are pleased to acknowledge helpful comments on the manuscript by R. P. Frankenthal of Bell Laboratories and K. Hashimoto of The Research Institute for Iron, Steel, and Other Metals.

Manuscript submitted Feb. 22, 1983; revised manuscript received Aug. 12, 1983.

Sandia National Laboratories assisted in meeting the publication costs of this article.

REFERENCES

1. K. Asami, K. Hashimoto, T. Masumoto, and S. Shimodaira, *Corros. Sci.*, **16**, 909 (1976).
2. K. Hashimoto, M. Naka, J. Noguchi, K. Asami, and

- T. Masumoto, in "Passivity of Metals," R. P. Frankenthal and J. Kruger, Editors, pp. 161-167, The Electrochemical Society, Princeton, NJ (1978).
3. K. Hashimoto, M. Naka, J. Noguchi, K. Asami, and T. Masumoto, in "Passivity of Metals," R. P. Frankenthal and J. Kruger, Editors, pp. 162, 168, 169, The Electrochemical Society, Princeton, NJ (1978).
 4. T. Masumoto and K. Hashimoto, *Ann. Rev. Mater. Sci.*, **8**, 215 (1978).
 5. K. Hashimoto, K. Osada, T. Masumoto, and S. Shimodaira, *Corros. Sci.*, **16**, 71 (1976).
 6. K. Hashimoto, M. Naka, K. Asami, and T. Masumoto, *Boshoku Gijutsu*, **27**, 279 (1978).
 7. A. K. Agrawal and R. B. Diegle, Paper 21 presented at The Electrochemical Society Meeting, Minneapolis, MN May 10-15, 1981.
 8. R. P. Frankenthal, *This Journal*, **116**, 580 (1969).
 9. T. Thomas, Private communication.
 10. D. A. Vermilyea, in "Advances in Electrochemistry and Electrochemical Engineering," P. Delahay and C. W. Tobias, Editors, pp. 241-242, Interscience, New York (1963).
 11. K. Hashimoto, *Suppl. Sci. Rep. RITU*, **A**, 203 (1980).

The Determination of Ammonia in Copper Pyrophosphate Plating Solution

Thomas M. Tam* and John S. Zevely

Lockheed Missiles and Space Company, Process Control Engineering, Sunnyvale, California 94086

Copper pyrophosphate solutions are commonly used for plating through-holes in printed circuit boards. Precise monitoring and control of several of the solution constituents is essential for achieving a good quality copper deposit. Recently, a cyclic voltammetric (CV) stripping technique has been shown to provide a measure for the concentration of effective brightener (1) and nitrite, NO_2^- (2), in this solution. We have found that the CV technique can also be used to monitor the concentration of ammonia, NH_3 , in the solution.

Ammonium hydroxide or ammonia gas is added to the solution to produce a more uniform and lustrous deposit and to improve anode corrosion during electroplating. Excess ammonia can cause the formation of cuprous oxide which can hinder the adhesion of the copper deposit to the circuit board (3). For this reason, ammonia in the solution needs to be controlled. The desired range of total ammonia in the solution is 0.06-0.18M.

Experimental

Equipment.—The CV experiments described herein were performed using a platinum working electrode, platinum auxiliary, and Ag/AgCl reference electrodes. The apparatus has been described elsewhere (2). No routine maintenance of the electrodes was required after initial setup.

The pH of the solutions was measured using an Altex (gel-filled) combination pH electrode. The electrode was calibrated against pH 10 and 7 buffer solutions. An Orion Ammonia electrode was used to measure ammonia in the solutions. The electrode was prepared according to the manufacturer's procedure for measuring the ammonia content of solutions with salt content above 1M, and was calibrated using 1M potassium pyrophosphate solutions which contained known amounts of NH_4NO_3 . These pyrophosphate solutions had ionic strengths ($\mu = 10$) similar to those of the copper pyrophosphate solutions used in this study. The pH of the pyrophosphate solutions was adjusted to 12 to ensure that NH_3 was the major species in solution. The membrane of the electrode was replaced when it became discolored or when stable readings could not be achieved. This occurred after 1-2 days of extensive use. It was necessary to recalibrate the electrode after about 2 hr of use. The concentrations of NH_3 in the test solutions were determined by using the calibration curve.

* Electrochemical Society Active Member.

Key words: analysis, electrode, voltammetry.

The pH and ammonia electrodes were connected to an Orion Model 901 Ionalyzer, which gives a digital read out.

Solution.—The copper pyrophosphate solutions used were prepared by dissolving copper pyrophosphate ($\text{Cu}_2\text{P}_2\text{O}_7 \cdot 3\text{H}_2\text{O}$) and potassium pyrophosphate ($\text{K}_4\text{P}_2\text{O}_7$) in deionized water. Pure pyrophosphate solutions were prepared with $\text{K}_4\text{P}_2\text{O}_7$ only. The pH of the solutions was adjusted with concentrated potassium hydroxide or nitric acid.

Ammonium nitrate (NH_4NO_3) was added to copper pyrophosphate solutions to vary the amount of NH_3 in the solutions. The loss of NH_3 was kept to a minimum by making the measurements within 15 min after the solutions were prepared.

Current determinations at -0.26V (Fig. 1).—The current at -0.26V is due to ammonia (see Results and Discussion) and significant background current (i_b). This i_b is difficult to reproduce. To correct for it, the following procedure was used: A straight line was drawn from -0.125 to -0.425V assuming that the i_b increases linearly in this region. The difference in cur-

¹ All voltages reported herein are with respect to the Ag/AgCl electrode.

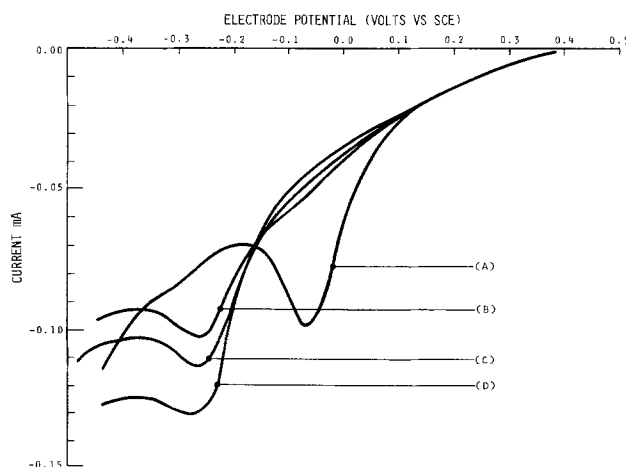


Fig. 1. Variation of cathodic peaks of copper pyrophosphate solutions with respect to NH_4NO_3 . Experimental conditions, see Fig. 2, pH = 8.80. $[\text{NH}_4\text{NO}_3] = 0.0\text{M}$ (A); 0.056M (B); 0.088M (C); 0.153M (D).

rent between the total current and i_b at $-0.26V$ is due to ammonia.

Results and Discussion

Ogden and Tench have reported the stripping cyclic voltammogram of copper pyrophosphate solutions (1). They observed a small oxidation peak at $0.2V$ and the corresponding reduction peak at $-0.3V$. We have found that when NH_3 is not present in the copper solution, a similar cathodic peak is observed between -0.15 and $0.0V$ (Fig. 2). This peak is due to reduction of platinum oxide (4).

When ammonia is added to the solution, a peak at $-0.26V$ is observed (Fig. 1). As the pH of the solution is adjusted above 8.8, an additional peak at $-0.38V$ is observed.

The characteristics of these peaks are as follows:

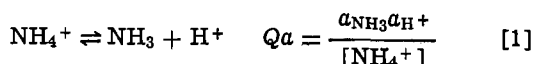
1. $-0.15-0.0V$ peak: this peak exists both in pyrophosphate and copper pyrophosphate solutions. The position of the peak is pH dependent (Fig. 2), and the intensity of the peak is inversely proportional to the amount of NH_4NO_3 added.

2. $-0.26V$ peak: this peak exists only when NH_4NO_3 is added to copper pyrophosphate solutions. Its intensity is directly proportional to the amount of NH_4NO_3 added. Also, as the NH_4NO_3 concentration is maintained constant, and the pH is changed from 8.0 to 9.0, the intensity of the peak increases.

3. $-0.38V$ peak: this peak shows up only in copper pyrophosphate solution when the pH is adjusted above 8.8 (Fig. 2).

These results are consistent with the interpretation that NH_3 , OH^- , and copper pyrophosphate ions are the active species that cause the changes of these peaks. The main concern of this study is the characterization of the peak at $-0.26V$. To accomplish this, the relation between NH_3 and copper pyrophosphate complexes was first investigated.

An Orion Ammonia electrode was used to measure the activity of NH_3 in two sets of solutions. The solutions in Set A are copper pyrophosphate solutions, and those in Set B are pyrophosphate solutions. Both solutions contained various amounts of NH_4NO_3 . The data shown in Table I are explained in terms of the dissociation of NH_4^+



where a_{NH_3} and a_{H^+} are the activities of NH_3 and H^+ measured by the ammonia and pH electrodes, respectively. The Qa term is the equilibrium quotient as defined. Notice the a_{NH_3} values in both sets with a comparable amount of NH_4NO_3 added to them, are quite similar. In addition, Qa in both cases is not significantly different and is constant.

The major chemical species in the copper solutions are: $[Cu(P_2O_7)_2^{6-}] = 0.35M$ and $[P_2O_7^{4-}] = 0.27M$. The equilibrium between copper (II) mono- and di-

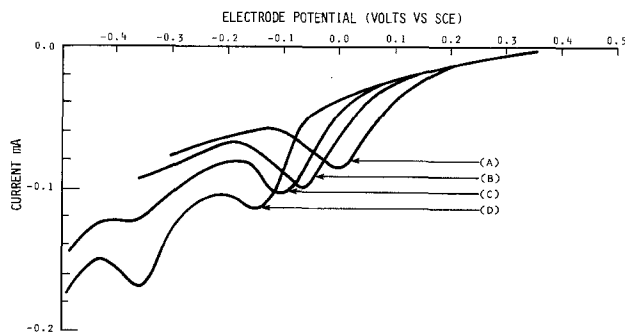
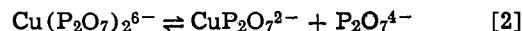


Fig. 2. Variation of cathodic peaks of copper pyrophosphate solutions with respect to pH. $[Cu(P_2O_7)_2^{6-}] = 0.35M$. pH = 8.00 (A); 8.82 (B); 9.14 (C); 9.50 (D). Sweep rate = 40 mV/sec; rotation speed = 3000 rpm; temperature = $25^\circ \pm 1^\circ C$.

pyrophosphate complexes in the pH range of about 8-9 is shown in Eq. [2]



A treatment of this equilibrium (5) permits the evaluation of the concentration of $CuP_2O_7^{2-}$ ions. Its concentration is calculated to be approximately $10^{-4}M$. If either copper species will complex with NH_3 , their concentration in solution should be enough to affect the a_{NH_3} measured (Table I). The dissociation quotient Qa , also would not be a constant value as reported. If therefore can be concluded that the $Cu(P_2O_7)_2^{6-}$ and $CuP_2O_7^{2-}$ do not form significant amounts of copper ammonia complexes. The changes in current density of the peak at $-0.26V$ measured from the cyclic voltammograms correlate with changes in the a_{NH_3} . This relationship is shown in Fig. 3. When the $Cu(P_2O_7)_2^{6-}$ concentration is varied between 0.31-0.41M the intensity of the peak remains constant. (These are the control limits for our production baths.) We have stated that the $-0.26V$ peak exists only when both copper and NH_3 are present in solution. However, the copper species do not complex with ammonia. We therefore assign this peak to the reduction of copper on a platinum surface with NH_3 adsorbed on it



The peak at $-0.38V$ can be assigned to the reduction of Cu^{2+} on a platinum surface with OH^- adsorbed on it. No quantitative data however has been obtained regarding this peak.

Peak assignment.—The overall assignments of the anodic and cathodic peaks on the cyclic voltammogram of the copper pyrophosphate solution are as follows (Fig. 4): (A) oxidation of NO_2^- and organic impurities (7); (B) reduction of platinum, (C) reduction of $Cu(P_2O_7)_2^{6-}$ on Pt- NH_3 surface; (D) reduction of $Cu(P_2O_7)_2^{6-}$ on Pt- OH^- surface; (E) reduction of $Cu(P_2O_7)_2^{6-}$ on Pt-Cu surface; (F) oxidation of Cu^0 .

Table I. Activity of ammonia in $Cu(P_2O_7)_2^{6-}$ and $P_2O_7^{4-}$ solutions

	Solution (A) ^a			Solution (B) ^b		
	$[NH_4^+] \times 10^{-2}M$	$a_{NH_3} \times 10^{-4}M$	$Qa \times 10^{-13}M$	$[NH_4^+] \times 10^{-2}M$	$a_{NH_3} \times 10^{-4}M$	$Qa \times 10^{-13}M$
pH = 8.80 ± 0.01	2.2	4.0	3.0	2.1	4.0	3.0
	3.2	6.3	3.1	3.3	4.7	2.3
	5.3	9.2	2.8	5.5	8.0	2.3
	9.2	17.0	3.0	8.9	12.0	2.2
	15.3	30.0	3.0	15.7	21.0	2.1
pH = 8.31 ± 0.01	1.7	1.0	2.9	1.7	0.6	1.7
	3.3	2.0	2.9	3.4	1.4	2.1
	5.0	2.9	2.9	5.4	2.8	2.6
	9.1	6.2	3.5	9.3	4.7	2.5
	15.2	22.0	3.5	15.1	5.6	1.8
			Average: 3.1 ± 0.3			2.2 ± 0.4

^a $[Cu(P_2O_7)_2^{6-}] = 0.35M$; $[P_2O_7^{4-}] = 0.30M$; $\mu = 10$.

^b $[P_2O_7^{4-}] = 1.0M$; $\mu = 10$.

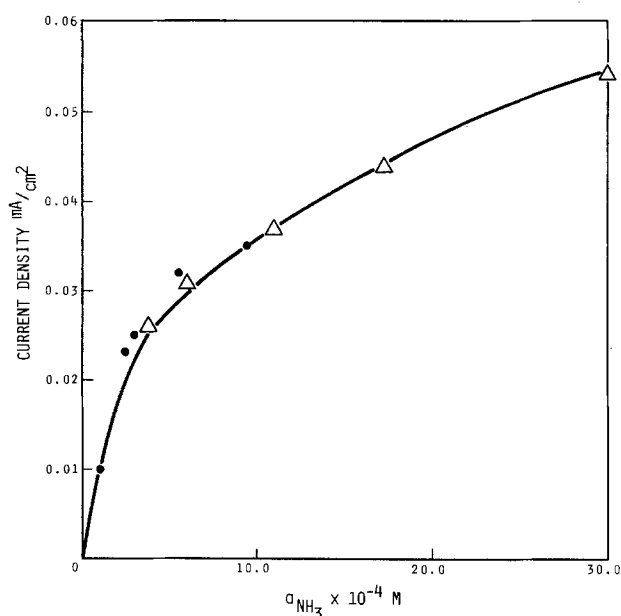


Fig. 3. Dependence of current density (-0.26V) vs. α_{NH_3} . Experimental conditions, see Fig. 2. pH = 8.80 (Δ); 8.30 (\bullet).

Conclusions

It has been shown that the CV technique can be used to monitor the concentration of effective brightener (1), the buildup of nitrite (2), and organic impurities (7) in copper pyrophosphate plating solutions. In this study, we have identified a cathodic peak at -0.26V due to the presence of NH_3 . The current of the peak is proportional to the α_{NH_3} in the solution. The CV unit is not as sensitive (minimum limit $\sim 1 \times 10^{-4}\text{M}$, NH_3) as the Orion Ammonia electrode (minimum detection limit $\sim 10^{-6}\text{M}$, NH_3). It is, however, a much more durable system. The concentration range of the ammonia in the copper pyrophosphate bath is well above the limit of the unit.

From the equilibrium study, we found that under these experimental conditions, less than 2% of the

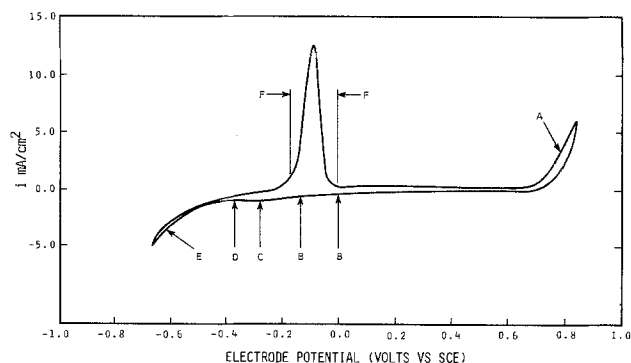


Fig. 4. Peak assignments on the cyclic voltammogram of $\text{Cu}(\text{P}_2\text{O}_7)_2^{8-}$. Experimental conditions, see Fig. 2; pH = 8.65. Peak assignment, see text.

NH_4^+ dissociates to give NH_3 . There is no evidence to show that NH_3 forms complexes with the copper species present. This result was somewhat surprising. The most likely function of ammonia is to modify the surface that copper is plated on (6).

Manuscript submitted July 11, 1983; revised manuscript received Sept. 6, 1983.

Lockheed Missiles and Space Company assisted in meeting the publication costs of this article.

REFERENCES

1. D. Tench and C. Ogden, *This Journal*, **125**, 194 (1978).
2. T. M. Tam and G. A. Fung, *ibid.*, **130**, 874 (1982).
3. T. W. Dini, "Modern Electroplating," 3rd ed., F. A. Lowenheim, Editor, p. 205, Wiley Interscience, New York (1974).
4. A. Damjanovic, L. S. R. Yeh, and J. F. Wolf, *This Journal*, **127**, 1945 (1980).
5. J. I. Watters and A. Aaron, *J. Am. Chem. Soc.*, **75**, 611 (1953).
6. C. Ogden and D. Tench, *This Journal*, **128**, 539 (1981).
7. C. Ogden and D. Tench, *Plating Surf. Fin.*, **66**, 45 (1979).

Composition and Crystallinity of Electroless Nickel

Kazuyuki Sugita and Nobuo Ueno

Department of Image Science and Technology, Faculty of Engineering, Chiba University, Chiba, Japan 260

In the literature dealing with the deposition product of electroless nickel, several studies have been focused on the evaluation of properties, such as coercivity (1, 2), electrical resistivity (3, 4), and mechanical strength (5), and their correlation to phosphorus or boron content in the deposit, degree of crystallinity, and size or orientation of grains. It is known that the composition and structure of the deposit, in turn, depend on the substrate for deposition (1, 2), method of activation or acceleration (3, 6), type of plating bath (ligand or buffer system and reducing agent) (1-3), and plating conditions including concentration of each component, pH of plating bath, bath temperature, and plating duration (1, 5, 7, 8).

For the nickel deposited from the plating solutions, in which NaH_2PO_2 is employed as the reducing agent, it was reported that the deposit was a Ni-P binary alloy (2, 5, 7). As-plated nickel deposited from acidic solution had a higher phosphorus content and was

Key words: alloy, analysis, deposition, ESCA.

amorphous, while the nickel from alkaline solution had a lower phosphorus content and was crystalline (5, 7). On the other hand, Schwartz and Mallory have found that two Ni-P alloys containing approximately the same amount of phosphorus exhibited different magnetic behavior even after heat-treatment, if they were prepared from different solutions (2). The initial structure of nickel film as-plated from electroless solution is generally considered to be metastable, but it is transformed to a more stable state by aging or heat-treatment. The structure and property of aged deposits should have the correlation with the composition, if they are thoroughly heat-treated to attain to the most stable state which is determined by the phosphorus content. The result suggests that the structure of electroless nickel may not be determined only by the phosphorus content.

The purpose of this study is to analyze composition and crystallinity of the nickel deposits simultaneously and to find out what factors other than phosphorus

content govern the structure and property of the Ni-P alloy.

Experimental

Specimen preparation.—The substrate was the poly-(4,4'-bisphenylene ether pyromellitimido) film Torey 25KA, which was preliminarily activated with palladium for electroless plating. Other chemicals used in this study were of extra pure grade. The substrates were immersed in the electroless solution for nickel deposition. The formulation of electroless solutions and plating conditions are listed in Table I.

The nickel deposited above pH 10.7 at 60°C was metallic film tinged with black, while the deposits below pH 10.2 at 60°C and those below pH 10.4 at 52°C were lustrous silver. The rate of deposition showed a maximum at pH 10.2-10.5 when the bath temperature was kept constant, and pH was changed as a parameter in the range from 8.5 to 10.7. The maximum rate of deposition at 60°C was calculated to be 0.34 μ /min at pH 10.2, assuming that the density of the deposit equals that of pure nickel. The rate is very close to the value at 70°-75°C reported in the literature (2).

The nickel deposited on the polyimido film was scraped off and used as the sample for x-ray diffraction measurement and elemental analysis.

Composition of electroless deposits.—Nickel and phosphorus contents were measured first by chemical analysis: the nickel was determined by the dimethylglyoxime method (9), and the phosphorus was by the ammonium molybdophosphate method (10). The detailed procedure in the literature was modified until reproducible values were obtained: when nickel metal and phosphorus pentaoxide of extra pure grade chemicals were employed as the standard, the observed values coincided to the theoretical within relative errors of ± 4 and $\pm 2\%$, respectively.

Then, some of the nickel deposits on the polyimido film were analyzed with a VG Scientific ESCA Lab-5 Spectrometer which uses $AlK\alpha$ line as the x-ray source before and after argon ion etching.

X-ray diffraction.—X-ray reflection from the nickel deposits was measured with a Rigakudenki Diffractometer using $FeK\alpha$ or $CuK\alpha$ line.

Electron transmission microscopy and diffraction.—Clean substrates of glass, on which copper film was preliminarily vacuum-evaporated, were immersed in the electroless nickel solution and the plating was initiated by contacting with an aluminum wire for an instant (7). At the completion of a plating run, the copper substrate was stripped from the deposits in an aqueous solution of chromic acid (500 g/liter) and sulfuric acid (50 g/liter) (8). A Japan Electron Optics JEM-T6S and a Hitachi HU-11D electron microscopes were used for the measurements. The former was operated at 60 kV and the latter at 75 kV.

Results and Discussion

Composition of nickel deposits.—Nickel and phosphorus contents in the nickel, which was deposited from the plating solutions of various pH are illustrated in Fig. 1. It was found that the deposits contained a few weight percent of phosphorus and, besides nickel and phosphorus, a few weight percent of other compo-

Table I. Electroless solution and plating conditions

Constituents, g/liter	Literature (2)	This study
Nickel sulfate $NiSO_4 \cdot 6H_2O$	25	25
Sodium hypophosphite $NaH_2PO_2 \cdot H_2O$	25	15-50
Sodium pyrophosphate $Na_2P_2O_7$	50	50
pH	10.0-10.5	8.5-10.7
Bath temperature	70°-75°C	50°-60°C
Plating duration	5 min	1-4 min

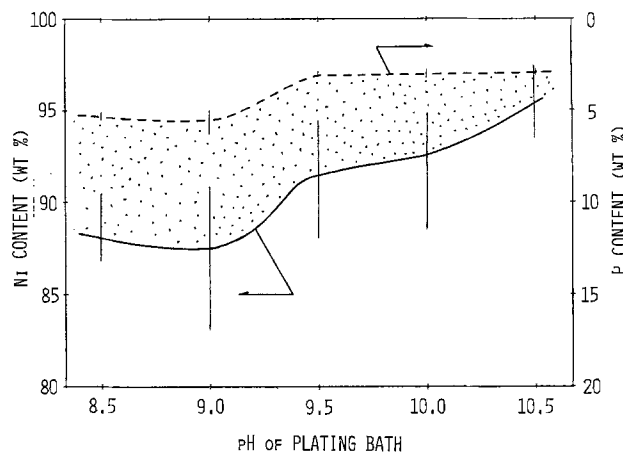


Fig. 1. Nickel and phosphorus contents in deposits from plating bath of various pH [NaH_2PO_2 conc: 25 g/liter, 55°C]; dotted area: other component(s) than Ni and P.

nent(s). The amount of impurities, phosphorus and other component(s), was smaller in the range of pH 9.5-10.5 than in the range of pH 8.5-9.0. Correlation between composition of the deposits and concentration of the reducing agent, NaH_2PO_2 , was studied and is shown in Fig. 2. The amount of impurities was depressed by lowering concentration of NaH_2PO_2 . It is found that the phosphorus and other component(s) incorporated in the nickel deposit can be controlled by concentration of NaH_2PO_2 as well as pH of the plating solution.

The deposits from plating solutions of pH 9.0 and 10.0 were taken as an example with higher content of impurities (designated as Deposit-9, hereafter) and another with lower content of impurities (designated as Deposit-10, hereafter), respectively. They were studied by ESCA. The normalized spectra are shown in Fig. 3 and the peak intensities are in Table II. The first spectrum was run on the surface of the nickel deposit film without argon ion etching, and the second and the third ones were after argon ion etching down to depths of 5 and 20Å, respectively. The etched depth was estimated by the sputter yield of the iron film. The N_{1s} peak due to the substrate of polyimido was not detected, until the nickel film was etched about 100Å deep.

At the surface of the nickel films, P_{2p} and O_{1s} peaks, as well as Ni_{2p} peak due to nonmetallic nickel, were observed for both Deposit-9 and Deposit-10. By the way, the peaks around 860 eV of binding energy are the satellite ones. At a depth of 5 or 20Å, Ni_{2p} peak due to nonmetallic nickel was still intense for Deposit-

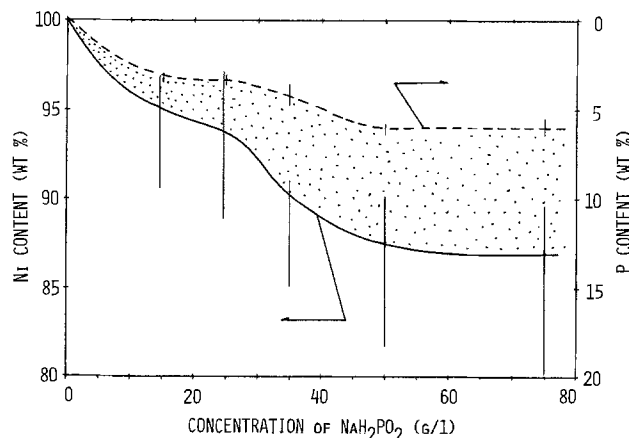


Fig. 2. Nickel and phosphorus contents in deposits from plating bath of various NaH_2PO_2 conc [pH 10.0, 55°C]; dotted area: other component(s) than Ni and P.

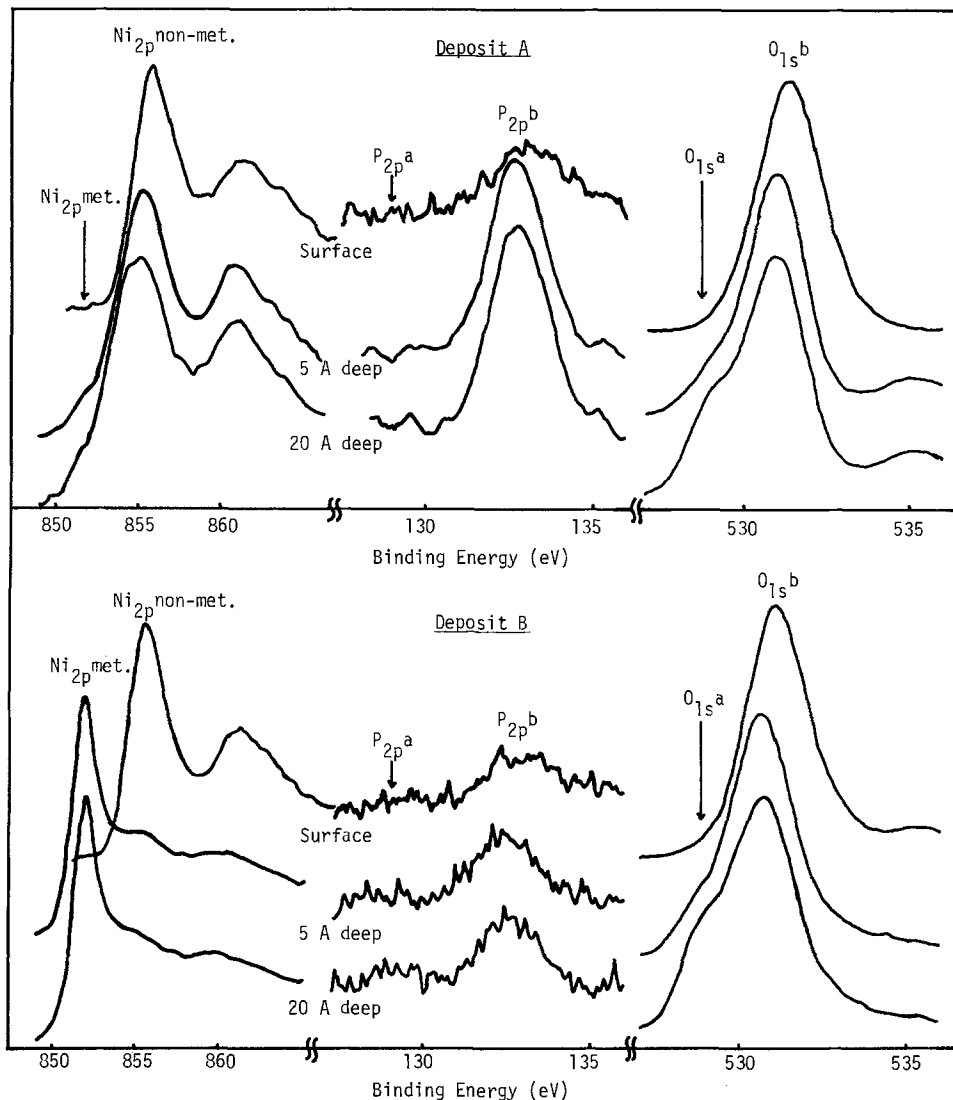


Fig. 3. Normalized ESCA spectra of nickel deposit film [NaH_2PO_2 conc: 25 g/liter, 55°C]; upper: Deposit-9 from plating bath of pH 9.0, lower: Deposit-10 from plating bath of pH 10.0.

9, while Ni_{2p} peak due to metallic nickel became dominant for Deposit-10. P_{2p} and O_{1s} peaks at a depth of 5 or 20 Å were as intense as those at the surface in the case of Deposit-9. The intensity of P_{2p} and O_{1s} peaks at a depth of 5 or 20 Å was much smaller than that at the surface in the case of Deposit-10. The peak intensities were consistent with the results of chemical analysis: intense for Deposit-9 (P; 6.3%, others; 7.2%), but weak for Deposit-10 (P; 3.2%, others; 2.0%).

The results indicate that metallic nickel is contained in Deposit-10, while most of Deposit-9 is composed of nonmetallic nickel. Shift of binding energy of 3-4.5 eV cannot be ascribed to the difference between crystalline and amorphous states, but indicates different valence states of nickel, metallic and nonmetallic. Then, it is considered that Deposit-9 with higher impurity content is nonmetallic or intermetallic compound. Moreover, it is confirmed that oxygen is contained, more or less, in the nickel deposit, and that the deposit is not a Ni-P binary alloy but ternary or quaternary, since hydrogen is difficult to be detected by this method.

Crystallinity of nickel deposits.—The crystallinity was investigated both by x-ray diffraction and by electron transmission diffraction. The former reveals the value averaged over many nickel grains, while the latter examines the value of a comparatively narrow area.

An influence of the substrate on the crystallinity of the deposits was suggested (2). In our study, x-ray diffraction was observed on the nickel deposit on the

polyimido film, and electron diffraction was on the deposit on the copper. The coincidence of the results by x-ray diffraction with those by electron diffraction indicates that the crystallinity of the deposit did not depend on the substrate in this system.

Graham *et al.* studied effects of variation in phosphorus content of electroless nickel deposited from alkaline-chloride-citrate and acid-sulfate baths, and established that increase of phosphorus content brings about decrease of crystallinity and that an abrupt change in the structure occurs at phosphorus content of about 7% (5). Chow *et al.* demonstrated that nickel film deposited from an alkaline-citrate bath assumes a crystalline structure when the solution is strongly alkaline (pH 10 or above) (7).

In this study, it was found that the nickel deposits from the pyrophosphate bath were crystalline above pH 9.4 when the concentration of NaH_2PO_2 was kept constant at 25 g/liter, or below 35 g/liter of NaH_2PO_2 concentration when pH was kept constant at 10.0. The deposit from the plating solution containing 15 g/liter of NaH_2PO_2 at pH 10.0 was as highly crystalline as the nickel which was vacuum-evaporated. When these results of crystallinity are considered together with those of composition mentioned above, it is concluded that decrease of crystallinity is caused by increase of oxygen (or oxygen and hydrogen) content(s) as well as increase of phosphorus content, and that amorphous nickel is composed of nonmetallic compound. The nickel deposits, which contained less than 4 weight percent (w/o) of phosphorus and more than 92 w/o of nickel, were crystalline and metallic.

Table II. Peak intensity of ESCA spectrum

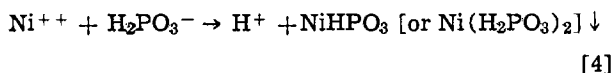
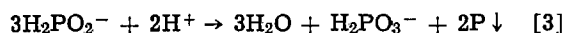
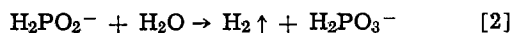
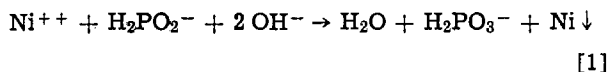
Sample	Peak B.E. (eV) Depth	Ni _{2p}		P _{2p}		O _{1s}	
		metallic 851.80-851.95	nonmet. 854.95-856.35	a 128.70-129.55	b 132.40-133.10	a 528.60-528.95	b 530.55-531.25
Deposit-9	0 ^A	0	1794 (100)	0	61 (3.4)	0	3185 (178)
	5	291 (10)	2887 (100)	0	124 (4.3)	304	4563 (158)
	20	166 (15)	1101 (100)	0	132 (12.0)	1142	4594 (417)
Deposit-10	0	0	1554 (100)	7	41 (2.6)	0	3253 (209)
	5	4707 (89)	5304 (100)	14	76 (1.4)	173	1767 (33)
	20	6448 (86)	7539 (100)	18	85 (1.1)	503	1853 (25)

* The number in parentheses indicates intensity relative to Ni_{2p} peak.

** Deposit-9 and Deposit-10 are those from plating bath of pH 9.0 and pH 10, respectively.

Impurity in nickel deposits.—Considerable amount of oxygen was directly detected by ESCA with Deposit-9 even after the surface layer of nickel oxide was etched away by argon ion bombardment. The oxygen incorporated in Deposit-10 was not negligible, either. Then, the impurity was found to be composed of phosphorus and oxygen (or phosphorus, oxygen, and hydrogen).

Since both the phosphorus component and the other components(s) increased as the concentration of NaH₂PO₂ increased, it should be reasonable to consider that they came from the hypophosphite ion. Therefore, the results suggest the possibility that the nickel deposit may contain, besides nickel phosphide, nickel phosphite as an impurity which was formed by oxidation of hypophosphite. The reactions which take place in the plating bath, including the side reactions, can be expressed by the following equations



where, Eq. [1] is the main reaction of the electroless deposition which gives metallic nickel (4).

In conclusion, the nickel film deposited from the ammoniacal pyrophosphate bath is not merely a Ni-P binary alloy, but contains oxygen (or oxygen and hydrogen). The crystallinity has a close relation to the amount of the impurities. The as-plated nickel can be

kept as metallic and highly crystalline as the vacuum-evaporated one by controlling pH and concentration of the reducing agent. On the contrary, electroless deposition of amorphous nickel, which is composed of non-metallic compound, is also possible.

Acknowledgment

The authors wish to thank Dr. Kozo Tsunoyama and Miss Takako Hane of Research Laboratories, Kawasaki Steel Corporation for their valuable assistance in the ESCA experiments. Thanks are also to Mrs. Kieko Harada for her helpful suggestions, and to Messrs. Yoshitomo Nabeoka, Shinya Maruyama, Masato Nagasawa, Hiroshi Ito, Masahiro Onuma, and Yasunori Doi for their contribution to this research.

Manuscript submitted April 19, 1983; revised manuscript received Aug. 9, 1983.

REFERENCES

1. G. S. Albert, R. H. Wright, and C. C. Parker, *This Journal*, **113**, 687 (1966).
2. M. Schwartz and G. O. Mallory, *ibid.*, **123**, 606 (1976).
3. N. Hedgecock, P. Tung, and M. Schlesinger, *ibid.*, **122**, 866 (1975).
4. B. K. Singh and R. N. Mitra, *ibid.*, **127**, 2578 (1980).
5. A. H. Graham, R. W. Lindsay, and H. J. Read, *ibid.*, **112**, 401 (1965).
6. J. P. Marton and M. Schlesinger, *ibid.*, **115**, 16 (1968).
7. S. L. Chow, N. E. Hedgecock, M. Schlesinger, and J. Rezek, *ibid.*, **119**, 1614 (1972).
8. T. Watanabe and Y. Tanabe, *Mater. Sci. Eng.*, **23**, 97 (1976).
9. "Bunseki-kagaku Binran," pp. 108, 109, Society of Analytical Chemistry of Japan, Maruzen (1971).
10. "Bunseki-kagaku Binran," p. 204, Society of Analytical Chemistry of Japan, Maruzen (1971).



Tungsten Etching in CF_4 and SF_6 Discharges

C. C. Tang* and D. W. Hess*

Department of Chemical Engineering, University of California, Berkeley, California 94720

ABSTRACT

Plasma etching characteristics of tungsten films are studied in CF_4 and in SF_6 discharges. The etch rates are investigated as a function of electrode temperature, oxygen and hydrogen additions, system pressure, and RF power. Relative fluorine atom concentrations are determined by optical emission spectroscopy. Results indicate that tungsten etching is primarily controlled by fluorine atoms generated in the discharge in CF_4 plasmas or when oxygen is added to the etch gases. In pure SF_6 , SF_x species may play an important role in the etch process. Hydrogen additions scavenge fluorine atoms and generate residues which inhibit etching.

Due to the fine line geometries required for very large scale integration (VLSI), intense interest has developed in RF glow discharge etching of metal films. Since aluminum and its alloys are widely used for interconnections in integrated circuits, much of the work in plasma etching of metals has centered around these materials. However, as the need for lower resistivity and improved contact barriers arises, refractory metals such as tungsten receive increasing attention. Thus, an understanding of the chemistry of plasma-enhanced etching of these materials is necessary.

Tungsten plasma etching has been performed both in barrel and in parallel plate reactors. The primary gases used have been CF_4 and CF_4/O_2 mixtures (1, 2) although reactive ion etching (RIE) of tungsten in SF_6 has also been reported (3). It is believed that fluorine atoms formed by electron impact dissociation of fluorine containing molecules react with the tungsten surface to form tungsten hexafluoride as the final etch product. There are no reports concerning the use of chlorinated gases to etch tungsten. Most likely this is due to the lower volatility of tungsten chlorides (WCl_5 , bp 275.6°C; WCl_6 , bp 346.7°C) compared to tungsten hexafluoride (WF_6 , bp 17.5°C).

Maeda *et al.* (1) etched tungsten with pure CF_4 in a barrel reactor at 13.56 MHz. They reported that there was no etch rate dependence on temperature or on etch time. In addition, it was found that the etch rate and the fluorine atom emission intensities both decreased with increasing pressure. They conclude that the etching of tungsten was limited by the supply of active species. Kumar *et al.* (2) reported the etching of tungsten using 4% O_2 in CF_4 in an electrodeless chamber. The etch rate increased with RF power sub-linearly.

Wolfe *et al.* (3) reported the reactive ion etching of tungsten using SF_6/O_2 mixtures at a pressure of 10 mtorr. The etch rate of tungsten decreased monotonically with the addition of oxygen. At an SF_6/O_2 flow ratio of 5.7, the etch rate of tungsten increased with pressure from 80 nm/min at 5 mtorr to 200 nm/min at 30 mtorr.

This paper presents the results of a study initiated to investigate the plasma-enhanced etching of tungsten films. The effect of substrate temperature, RF

power, gas pressure, and oxygen and hydrogen additions to CF_4 and SF_6 etch gases are studied in a parallel plate plasma etching system. Optical emission spectroscopy is used as a diagnostic tool to determine relative fluorine atom concentrations in the etching atmospheres.

Experimental Procedures

Unless otherwise noted, the tungsten films were obtained via plasma-enhanced deposition from WF_6 and H_2 (4). The depositions were carried out at an electrode temperature of 350°C, and RF frequency of 4.5 MHz, an H_2/WF_6 ratio of 3, a pressure of 200 mtorr, and a power density of 0.12 W/cm². Sputtered films were deposited in a Perkin Elmer Randex sputtering system at 20 mtorr and 0.55 W/cm². The tungsten films used for etching studies were typically 0.4 μm thick, deposited onto borosilicate glass substrates. In all cases, the surface area of tungsten etched was 6.5 cm².

Plasma etching was performed in a 14 in diam stainless steel radial flow reactor with 7 in diam stainless steel electrodes. The samples were positioned on the lower grounded electrode, which was separated from the upper powered electrode by a distance of 2 in. The lower electrode was heated resistively by a ring heater affixed to the underside of the electrode. Since no cooling capabilities were available in this particular reactor, the minimum electrode temperature utilized for the present study was 60°C. This temperature allowed etch times greater than 15 min to be used without any detectable increase in electrode temperature as measured by a shielded chromel-constantan thermocouple.

The pumping system consisted of a 50 cfm corrosion resistant mechanical vacuum pump with a liquid nitrogen cold trap positioned between the pump and the etch chamber. The pressure was altered by throttling the pump at a fixed flow rate. A capacitance manometer was used to determine chamber pressure.

The etch gases used in this study were CF_4 (99.7%) and SF_6 (99.99%) obtained from Matheson Gas Products. No further purification was attempted. Oxygen (99.99%) was obtained from a liquid source, and was passed through a Matheson no. 451 purifier before being mixed with CF_4 or SF_6 . The flow rates of individual gases were controlled by Tylan mass flow controllers, and the gases were mixed prior to entering the etch chamber. Etch rates were determined gravimetrically

* Electrochemical Society Active Member.

by weighing samples before and after specific etch times.

In order to separately evaluate the effect of various plasma parameters on tungsten etch rates and fluorine atom densities, a set of standard etch conditions was established. The conditions used were; 50W (0.2 W/cm²), at 4.5 MHz, 200 mtorr pressure, 60°C electrode temperature, total flow rate of 75 sccm, 60°C electrode temperature, total flow rate of 75 sccm, and gas mixtures of 10% O₂ in either CF₄ or SF₆.

Optical emission studies were performed using a Plasmatherm (Model PSS-2) Plasma Scan Emission Monitoring System. The monochromator was positioned at a 4 in diam quartz window to monitor emission intensities. Relative fluorine atom densities were determined by using argon (2% of the feed gas) as a tracer or "actinometer," and recording emission intensities of Ar (750.4 nm) and F (703.7 nm) as a function of plasma parameters (5). No change in F atom emission intensity was observed for Ar additions up to 4%.

Results and Discussion

The etch depth of tungsten films in SF₆/O₂ or in CF₄/O₂ plasmas increases linearly with etch time. Further, when this linear relationship is extrapolated, the line passes through the origin, indicating that no lag time or initiation period exists at the start of tungsten etching. Such results are in sharp contrast to those observed during aluminum etching, wherein an induction period is typically observed (6). The cause of this difference in etch behavior is due to the fact that the native tungsten oxide does not present a barrier to plasma etching, whereas native aluminum oxide does. Aluminum forms strong bonds with oxygen. However, tungsten forms an unstable oxide (volatile above 800°C). A second consideration with regard to the observed etch differences between tungsten and aluminum relates to the heats of formation of the compounds involved in the two chemical systems. The heat of formation of the etch product WF₆ (-421 kcal/mol) is much higher than those of the oxides (WO₂, -136 kcal/mol; W₂O₅, -169 kcal/mol; WO₃, -201 kcal/mol), whereas the heat of formation of AlCl₃ (-140 kcal/mol) is considerably lower than aluminum oxide (-398 kcal/mol). These thermodynamic data are consistent with the observations that ion bombardment is needed to assist native aluminum oxide removal, while ion bombardment is not necessary for tungsten oxide etching. Indeed, tungsten can be etched in a barrel reactor with an etch tunnel that isolates the wafers from energetic ion bombardment (1).

Temperature dependence of etch rates.—Arrhenius plots of the etch rate of tungsten in 90% SF₆/10% O₂ and in 90% CF₄/10% O₂ plasmas are shown in Fig. 1. The apparent activation energy for both etching reactions is 0.2 eV/mol. The agreement of activation energies for tungsten etching in CF₄ and in SF₆ plasmas suggests that the active etchant species and the reaction mechanism may be the same for both etch gases. The higher etch rates observed with SF₆ over CF₄ plasmas are apparently due to the higher fluorine atom concentrations in SF₆ plasmas (see optical emission studies described below).

The temperature dependence of tungsten etching observed in the present study disagrees with the results of Maeda *et al.* (1). Maeda used pure CF₄ to etch tungsten in a barrel reactor. They reported that the etch rate did not depend upon substrate temperature between 25° and 320°C. Differences in these two studies are probably due to the variation in fluorine atom concentration between CF₄ and CF₄/O₂ plasmas. Clearly, a much lower concentration of fluorine atoms is present in CF₄ relative to CF₄/O₂ plasmas (see below). Since fluorine atoms appear to be the primary etchant for tungsten in these discharges, the discrepancies between this study and that of Maeda suggest

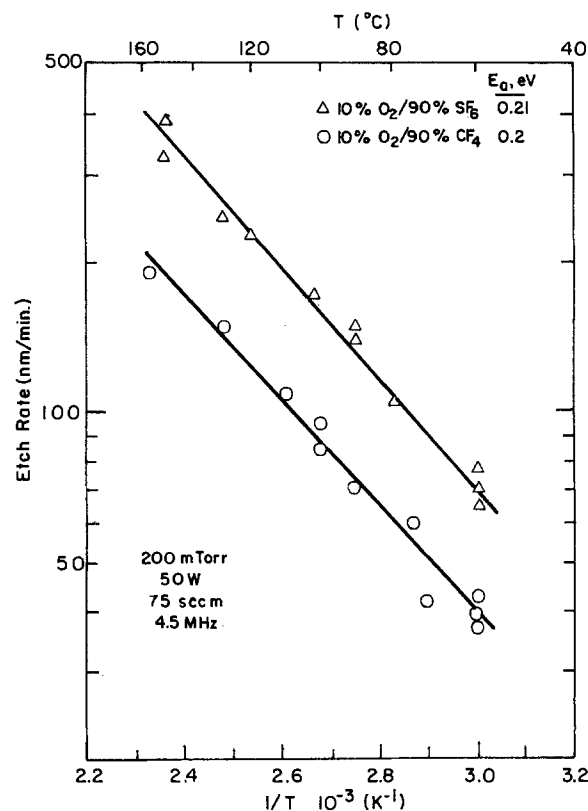


Fig. 1. Arrhenius plots of tungsten etch rate in CF₄/O₂ and SF₆/O₂ discharges.

basic differences in the rate-controlling steps for CF₄ vs. CF₄/O₂ plasmas.

In pure CF₄ discharges, the etch rate is most likely limited by reactant supply. That is, the generation of active species in the plasma, which is independent of temperature, is rate limiting. Further, fluorocarbon radicals generated in pure CF₄ plasmas may polymerize and deposit on tungsten surfaces. The removal of these polymers or residues on tungsten surfaces must be considered in the etching mechanism. However, the addition of oxygen greatly increases the supply of fluorine atoms. Consequently, the reactant supply is no longer rate limiting; instead, a surface reaction step becomes rate limiting in CF₄/O₂ plasma etching of tungsten. In addition, oxidation of fluorocarbon radicals precludes the deposition of fluorocarbon polymers.

Oxygen additions.—The effect of oxygen additions to CF₄ on the relative fluorine atom density and on the tungsten etch rate is shown in Fig. 2. Although both fluorine atom density and etch rate go through a maximum, the peak etch rate does not coincide with the maximum fluorine atom density. Such trends are identical to those observed in the CF₄/O₂ plasma etching of silicon (7, 8). These results also substantiate the claim that fluorine atoms are the primary etchant for tungsten in CF₄/O₂ discharges. As in the case of silicon etching (7), oxygen additions to CF₄ enhance the production of fluorine atoms and reduce carbon containing residues, thereby increasing the tungsten etch rate. Further, since fluorine and oxygen atoms compete for surface adsorption sites, a non-coincidence of the tungsten etch rate and the maximum fluorine atom concentration results, exactly analogous to that observed in silicon etching (7).

If direct electron impact excitation from the ground state to the emitting state is the dominant excitation process, then (5) the optical emission intensity, I_x , is given by $I_x = CN_x[X]$, where C is a constant, $[X]$ is the ground state concentration of species, X , and $N_x = k_x n_e$ is the excitation efficiency, a product of the rate

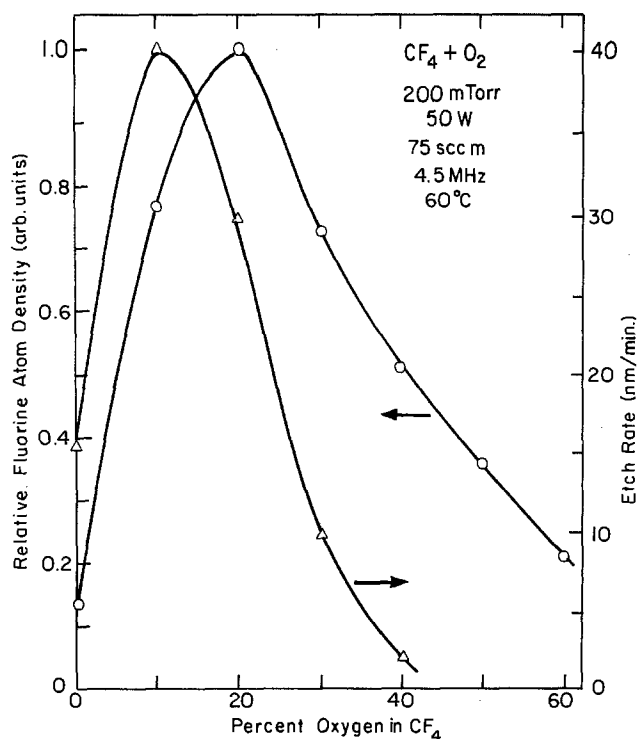


Fig. 2. Etch rate of tungsten and relative fluorine atom density as a function of oxygen concentration in CF_4 plasmas.

constant for direct excitation (k_x) and the electron density (n_e). The normalized excitation efficiency observed for argon atoms in this study is shown as a function of oxygen addition in Fig. 3. For comparison, these efficiencies are also given for results reported in Ref. (5) and (8). In all cases, the excitation efficiency decreases as the oxygen concentration increases. However, results reported in this study and in Ref. (8) are essentially the same, while the data from Ref. (5)

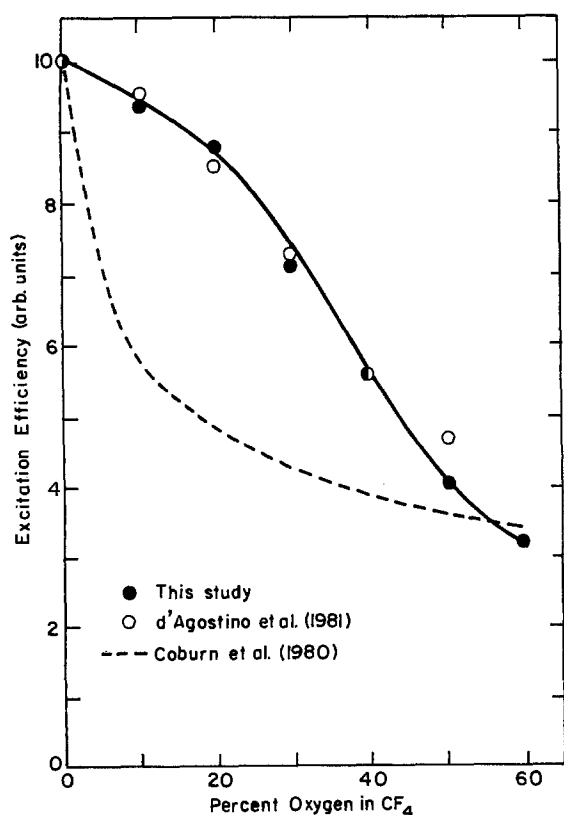


Fig. 3. Comparison of excitation efficiency as a function of oxygen concentration in CF_4 .

shows a more rapid initial drop in excitation efficiency with oxygen content. In large part, the nonconstant pressure conditions in the study of Ref. (5) (36 mtorr at 0% O_2 , 44 mtorr at 20%, 37 mtorr at 66% O_2) may be the cause of this difference.

The observed decrease in the excitation efficiency of Ar and F atoms suggests that the enhanced fluorine atom concentration caused by oxygen addition cannot be due to an increase in the dissociation rate of CF_4 [threshold energy for CF_4 dissociation and argon excitation energy are quite similar, 12 and 13.5 eV (3), respectively]. Thus, the enhanced fluorine atom density due to oxygen additions must be a result of reactions between oxygen atoms and radicals formed by the dissociation of CF_4 . Oxygen reacts with CF_x radicals to liberate fluorine atoms, thus minimizing CF_x and F recombination. Indeed, many reaction schemes are possible and these have been discussed previously (7).

Tungsten etch rates and relative fluorine atom concentrations in SF_6 plasmas are shown as a function of oxygen content in Fig. 4. Again, the maximum observed in the fluorine atom density is consistent with that displayed by CF_4/O_2 plasmas and is in agreement with results reported for silicon etching in SF_6/O_2 plasmas (9, 10). In a manner identical to CF_4/O_2 mixtures, enhanced fluorine atom production via oxygen additions to SF_6 can be explained by reaction of oxygen with SF_x radicals. Possible reaction schemes for SF_6/O_2 plasmas are discussed in Ref. (9).

The maximum etch rate shown in Fig. 4 occurs with a pure SF_6 discharge, which is in agreement with results reported on reactive ion etching of tungsten in SF_6/O_2 discharges as a function of oxygen addition (3). However, the maximum fluorine atom density which is four times higher than in a pure SF_6 discharge, occurs at 30% oxygen. Clearly, competitive adsorption between oxygen and fluorine atoms on a tungsten surface cannot explain the maximum etch rate at such low fluorine atom concentrations.

It is expected that the primary free radicals generated in SF_6 plasmas are SF_5 and SF_3 (11). When SF_5 and SF_3 migrate to the tungsten surface, they can undergo dissociative chemisorption to form F, SF_4 , and SF_2 . Thus, in addition to electron impact dissociation of SF_6 , another source of fluorine atoms is available. Therefore, if such dissociative chemisorption occurs, SF_x radicals may play an important role in

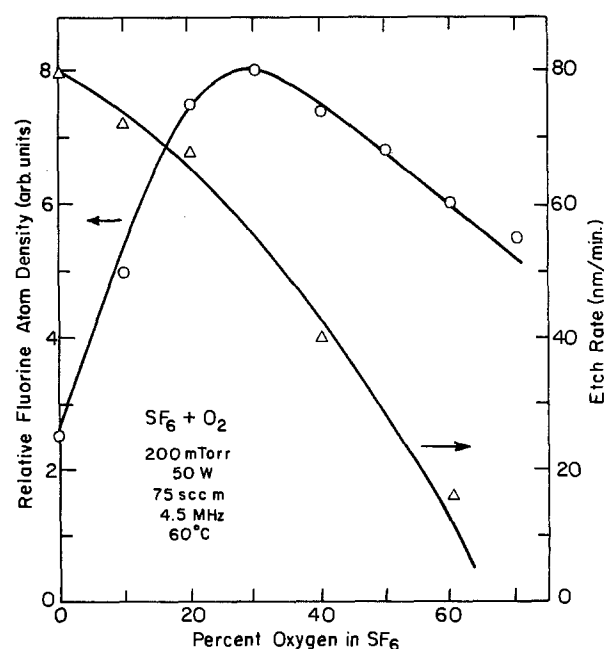


Fig. 4. Etch rate and relative fluorine atom density as a function of oxygen concentration in SF_6 plasmas.

tungsten etching in pure SF_6 discharges. Further support for these conclusions arises from the observation that the apparent activation energy for tungsten etching in a pure SF_6 discharge is 0.07 eV/mol. However, stable oxyfluorides form in SF_6/O_2 plasmas (9), so that fluorine atoms may be the important etchant species in the presence of even small concentrations of oxygen. Currently, the reasons for the striking differences between the etch behavior of silicon and tungsten in pure SF_6 vs. SF_6/O_2 plasmas are unclear; nevertheless, in light of the above results, the differences are probably related to variations in surface chemistry between these two film materials.

Sulfur hexafluoride has a higher F/S ratio and weaker sulfur-fluorine bonds than the corresponding F/C ratio and carbon-fluorine bonds in CF_4 . As a result, a higher fluorine concentration exists in SF_6/O_2 discharges. This explains the higher tungsten etch rate in SF_6/O_2 than in CF_4/O_2 discharges. In addition, sulfur forms compounds that are more volatile than similar carbon compounds. This is consistent with the fact that no sulfur or sulfur compounds are detected by Auger analyses after tungsten etching in pure SF_6 discharges. Therefore, residues may not be a great concern in these plasmas.

Hydrogen additions.—Hydrogen additions to CF_4 decrease the fluorine atom concentration dramatically due to the formation of relatively stable HF. Indeed, the emission intensity of fluorine (703.7 nm) quenches to zero after 10% hydrogen is added to CF_4 . No etching is observed and the weight of the sample increases as a result of a film being deposited on the tungsten surface. A postetch Auger spectrum of the tungsten surface shows W, C, O, and F. Apparently, a fluorocarbon film with tungsten incorporation forms from simultaneous tungsten etching and plasma polymerization. These results are similar to previous reports of simultaneous aluminum etching and chlorocarbon film formation (12). In the present study, hydrogen atoms are efficient scavengers of fluorine atoms causing an increase in the concentration of gas phase fluorocarbon unsaturates which are precursors to polymer formation. When the polymer film completely covers the tungsten surface, the film inhibits the etching of tungsten. Such observations are in agreement with silicon etching studies using CF_4/H_2 mixtures (13).

The addition of hydrogen to SF_6 discharges significantly decreases the tungsten etch rate. The rate falls from 80 to 25 nm/min with 10% H_2 added to SF_6 . However, the relative fluorine atom density is higher with 10% hydrogen addition than with pure SF_6 discharges. The reasons for such observations are unknown, but the results again suggest that SF_x radicals may be important in the etching of tungsten. Of course, the decreased etch rate due to hydrogen additions also results from competitive chemisorption on the tungsten surface between hydrogen and fluorine atoms or SF_x radicals.

Although Auger analysis did not detect sulfur on the tungsten surface during etching in SF_6/O_2 plasmas, a yellow deposit was observed on the base plate of the reactor. Auger confirmed that this deposit was sulfur. Apparently ion bombardment of the wafer combined with the slightly elevated electrode temperatures in this study, assist sulfur removal from the tungsten surface, thereby precluding deposition on the film.

Pressure dependence.—The dependence of the etch rate of tungsten and of the relative fluorine atom density on the reactor pressure are illustrated in Fig. 5 and 6 for CF_4/O_2 and SF_6/O_2 , respectively. Clearly, the etch rate and the relative fluorine atom density vary greatly with pressure in CF_4/O_2 and SF_6/O_2 plasmas; however, the functional relationship of etch rate with pressure in CF_4/O_2 and SF_6/O_2 is quite dif-

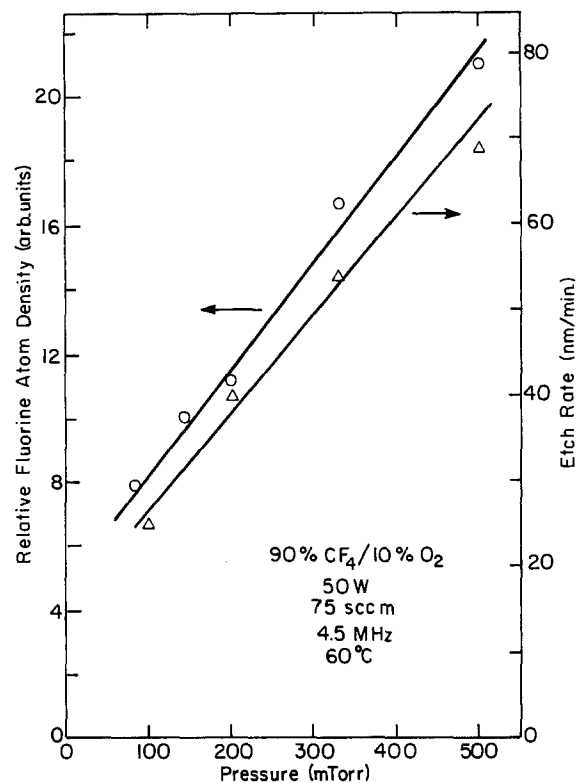


Fig. 5. Etch rate and relative fluorine atom density as a function of pressure in a 90% $\text{CF}_4/10\% \text{O}_2$ discharge.

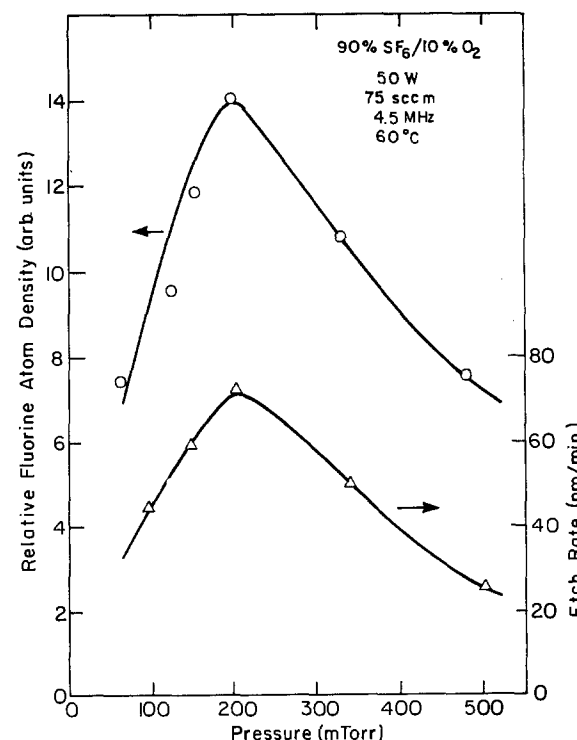


Fig. 6. Etch rate and relative fluorine atom density as a function of pressure in a 90% $\text{SF}_6/10\% \text{O}_2$ discharge.

ferent. As shown in Fig. 5, the etch rate and the relative fluorine atom density in CF_4/O_2 both increase linearly with pressure in the range of 100–500 mtorr. Unlike CF_4/O_2 , the etch rate and the relative fluorine atom density in SF_6/O_2 plasmas increase with pressure and exhibit a maximum at 200 mtorr as indicated in Fig. 6. Above 200 mtorr, the etch rate and the relative fluorine density both decrease as the pressure increases.

The results of Fig. 5 and 6 can be explained by considering plasma energetics. As the total pressure increases, the ion energy drops; thus, the etch process will become more dependent upon a mechanism involving neutral reactive species. Therefore, the pressure dependence of the etch rate should be dominated by the relative abundance of neutral etchant species. As shown in Fig. 5 and 6, the functional relationship between the etch rate and the relative fluorine density and the pressure dependence in their respective plasmas are quite similar. Again, this indicates that the active etchant for tungsten is fluorine atoms.

An investigation of the excitation efficiencies of argon in both CF_4/O_2 and in SF_6/O_2 plasmas, indicate that the efficiencies decrease monotonically with increasing pressure. Although the electron density increases with pressure, the average electron energy, which is principally a function of the ratio of the electric field to the pressure (E/P), decreases with increasing pressure (14). The formation of excited argon species generally involves electrons with energies > 13.5 eV. This corresponds to electrons in the high energy tail of the electron energy distribution function. Naturally, the energies of these electrons are extremely sensitive to pressure variation.

Several factors are involved in the effect of pressure on fluorine atom density. (i) The collision rate of gas molecules with electrons will increase as pressure increases, thereby altering the generation rate of fluorine atoms; (ii) the electron energy decreases with a pressure increase which decreases the generation rate of fluorine atoms; and (iii) the fluorine atom residence time will increase with pressure, thereby increasing the fluorine atom density. These phenomena have opposing effects on fluorine atom density. As a result, the fluorine atom density reaches a maximum at a certain pressure which depends on the chemical system.

Comparison of the dependence of the fluorine atom density on pressure in CF_4 and in SF_6 discharges (Fig. 5 and 6) suggests that the electron energy in SF_6 plasmas is more sensitive to pressure variation than in CF_4 plasmas. Such conclusions are confirmed by measurement of the excitation efficiency of argon in these two plasma atmospheres. The normalized excitation efficiency in SF_6 discharges decreases much faster with pressure increases than in CF_4 discharges.

For comparison to the PECVD results, the etch rate of sputtered tungsten films was determined as a function of pressure. The dependence of etch rate on CF_4/O_2 pressure was identical to that shown in Fig. 5. However, the sputtered films etched at a rate 15% lower than the PECVD films. This result is probably due to the higher density of sputtered (19 g/cm^2) vs. PECVD (16.8 g/cm^3) films.

RF power.—Both the electron density and the average electron energy increase with RF power; thus, the rate of ionization, excitation, and dissociation of gas phase molecules increases. As a result, both the excitation efficiency and the relative fluorine atom density should increase with RF power in CF_4/O_2 and in SF_6/O_2 discharges. As shown in Fig. 7, this is the trend observed for SF_6/O_2 discharges. The identical situation is noted for CF_4/O_2 plasmas, except that the etch rates are lower than those observed for SF_6/O_2 by approximately a factor of 2.5. Clearly, this result is due to the lowered fluorine atom density in CF_4/O_2 compared to SF_6/O_2 plasmas.

Summary

Tungsten films can be etched in CF_4 and in SF_6 discharges. Unlike certain other metal films, the native oxide on tungsten does not inhibit etching. Therefore, reproducible and controllable etch rates can be routinely achieved in CF_4/O_2 and in SF_6/O_2 plasmas.

The etch rate of tungsten is strongly dependent upon oxygen additions. A maximum etch rate is observed

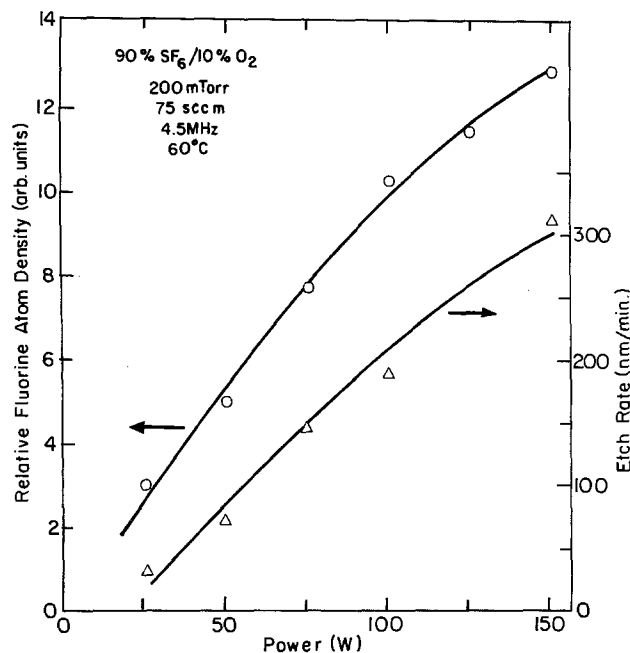


Fig. 7. Etch rate and relative fluorine atom density as a function of RF power in a 90% $\text{SF}_6/10\%$ O_2 discharge.

in 90% $\text{CF}_4/10\%$ O_2 plasmas, which is analogous to the trend observed in silicon etching in CF_4/O_2 discharges. With SF_6 , oxygen additions decrease the etch rate even though the fluorine atom density reaches a maximum at 30% O_2 . Such results suggest that SF_x radicals may play an important role in pure SF_6 plasma etching of tungsten. The increased etch rate observed in SF_6/O_2 compared to CF_4/O_2 discharges is due to the higher fluorine atom density in SF_6 plasmas. This fact, coupled with the observation that the apparent activation energy is identical for tungsten etching (between 60° and 160°C) in CF_4/O_2 and in SF_6/O_2 plasmas, indicates that fluorine atoms are the primary etchant in these atmospheres, and that the same reaction mechanism is probably operative in both discharges. With 90% $\text{CF}_4/10\%$ O_2 or 90% $\text{SF}_6/10\%$ O_2 plasmas, increases in RF power increase tungsten etch rates.

Hydrogen additions to CF_4 and to SF_6 result in a scavenging of fluorine atoms, thereby decreasing the overall etch rate, and generating residues of carbon or sulfur. However, Auger results suggest that sulfur is easily sputtered from the wafer during etching in SF_6 plasmas.

Acknowledgments

The authors would like to thank Plasma Therm Incorporated for donation of the Plasmascan Emission Monitoring system used in this study. This investigation was supported by the Army Research Office under Contract No. DAAG29-83-K-0039.

Manuscript submitted April 14, 1983; revised manuscript received Aug. 1, 1983.

REFERENCES

1. K. Maeda and K. Fujino, *Denki Kagaku*, **43**, 22 (1975).
2. R. Kumar, C. Ladas, and G. Hudson, *Solid State Technol.*, **19**, (10), 54 (1976).
3. J. W. Randall and J. C. Wolfe, *Appl. Phys. Lett.*, **39**, 742 (1981).
4. J. K. Chu, C. C. Tang, and D. W. Hess, *ibid.*, **41**, 75 (1982).
5. J. W. Coburn and M. Chen, *J. Appl. Phys.*, **51**, 3134 (1980).
6. D. W. Hess, *Plasma Chem. Plasma Proc.*, **2**, 141 (1982).
7. C. J. Mogab, A. C. Adams, and D. L. Flamm, *J. Appl. Phys.*, **49**, 3796 (1978).
8. R. d'Agostino, F. Cramarossa, S. DeBenedicts, and

- G. Ferraro, *ibid.*, **52**, 1259 (1981).
 9. R. d'Agostino and D. L. Flamm, *ibid.*, **52**, 162 (1981).
 10. R. d'Agostino, V. Colaprico, and F. Cramarossa, *Plasma Chem. Plasma Proc.*, **1**, 365 (1981).

11. J. J. Wagner and W. Brandt, *ibid.*, **1**, 201 (1981).
 12. A. G. Nagy and D. W. Hess, *This Journal*, **129**, 2530 (1982).
 13. L. M. Ephrath, *ibid.*, **126**, 1419 (1979).
 14. A. T. Bell, *Solid State Technol.*, **21**, (4), 89 (1978).

Deviation from Stoichiometry of Boron Monophosphide

C. J. Kim* and K. Shono**

Sophia University, Faculty of Science and Technology, Kioicho-7, Chiyoda-ku, Tokyo 102, Japan

ABSTRACT

The deviation from stoichiometry of boron monophosphide (BP) was controlled by heat-treatment. The BP of n-type conductivity was caused by anti-site phosphorus or by phosphorus vacancy. The BP of p-type conductivity was caused by anti-site boron or by boron vacancy.

Boron monophosphide (BP) is one of the III-V compound semiconductors. It is well known that BP grows on Si substrate by the thermal reaction of B_2H_6 and PH_3 in H_2 (1). Two possible causes of the donor or the acceptor in the BP have been reported (2). This work shows that the excess or lack of boron or phosphorus determines the conduction type and resistivity of the BP.

Experimental Procedure

The experimental apparatus for the growth of BP on Si substrate has already been reported (3). n-Type BP (100) was grown at $950^\circ C$, and p-type BP (100) at $1080^\circ C$ on the Si (100) substrate. Characteristic crystalline imperfections such as {111} twins, {211} twins, and {111} planar defects, exist at early growth of BP less than 300\AA thick (4). However, the half-order streak pattern observed by reflection electron diffraction (RED) from the surface of the 500\AA -thick BP shows a BP (100)-c (2×2) surface structure (5).

The BP compound decomposes easily when exposed in hydrogen at temperatures greater than $900^\circ C$. After the epitaxial growth of the BP, the BP surface was covered to 500\AA with Si_3N_4 deposited at $680^\circ C$ by the thermal reaction of SiH_4 and NH_3 in N_2 . Then, the sample was heated in N_2 . After the heat-treatment, the Si_3N_4 was removed by etching in hydrofluoric acid. The BP is chemically stable and cannot be attacked. The conduction type of the BP was determined by measuring thermoelectric power. The resistivity of the BP was measured with the four-point probe method or by measuring the ohmic current through the BP. The BP was removed by plasma etching in a mixture of CF_4 (98%) and O_2 (2%) or by a selective removing method (6). By measuring the sheet resistance and junction depth of the diffusion layer formed in the Si substrate during the heat-treatment, the amount of boron or phosphorus diffused from the as-grown BP was determined. The complementary error function profile was assumed.

Experimental Results

Resistivity of as-grown BP.—n-BP (100) can be grown on Si (100) at $950^\circ C$, and p-BP (100) at $1080^\circ C$. The flow rate of PH_3 and B_2H_6 has to be varied according to the growth temperature. The resistivity can be measured by the four-point probe method for n-BP grown on a highly doped p-Si substrate and for p-BP grown on a highly doped n-Si substrate by assuming p-n junction isolation. The resistivity obtained is

10^{-2} - 10^{-3} Ω -cm for both as-grown n- and as-grown p-BP.

Conduction type and resistivity of BP after heat-treatment.—After as-grown n- or p-BP covered with Si_3N_4 is heated in N_2 , a resistor with two Al electrodes, as shown in the inset of Fig. 1, is made to measure the resistivity of the BP. A diffusion layer is formed in the Si substrate having the same type of conductivity as the BP. The results are summarized in Fig. 1 for as-grown n-BP, and in Fig. 2 for as-grown p-BP.

The as-grown n-BP shows a high resistivity for 8 min of heat-treatment at $1200^\circ C$ and for 30 min at $1100^\circ C$. For longer heat-treatment times, it changes to p-BP. The resistivity of the p-BP decreases to as low as 10^{-2} Ω -cm as the heat-treatment time increases. The treatment temperature of $1050^\circ C$ is a characteristic one, where the resistivity is over 10^{10} Ω -cm for the heat-treatment time of more than 2 h. The conduction type cannot be determined by the

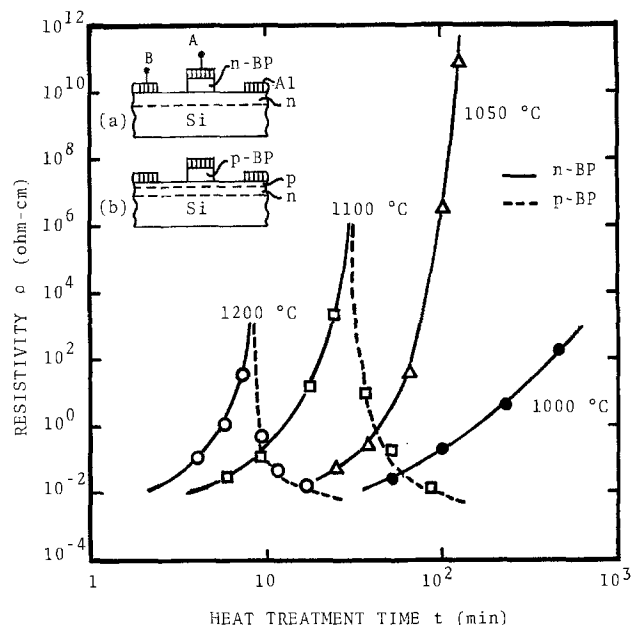


Fig. 1. Resistivity and conduction type of BP as a function of heat-treatment time. Starting n-BP was grown at $950^\circ C$. Inserts (a) and (b) are cross-sectional views of samples for the measurement of current-voltage characteristics through BP, after (a) the phosphorus diffusion layer is formed from n-BP in the Si substrate and (b) the boron diffusion layer is formed from p-BP over the phosphorus diffusion layer.

* Electrochemical Society Student Member.

** Electrochemical Society Active Member.

Key words: stoichiometry, BP, heat-treatment.

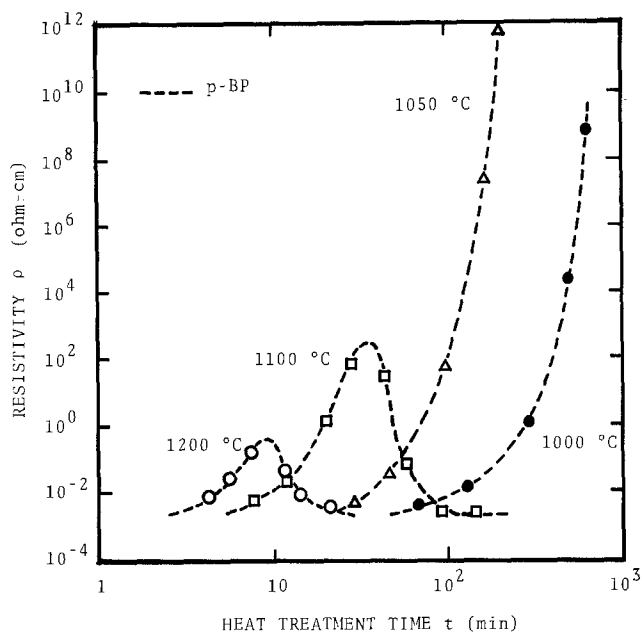


Fig. 2. Resistivity and conduction type of BP as a function of heat-treatment time. Starting p-BP was grown at 1080°C.

conventional thermoelectric power method. At 1000°C, the n-BP does not change its conduction type, and its resistivity increases gradually as the heat-treatment time is increased.

For the as-grown p-BP of Fig. 2, no change of the conduction type can be observed. However, for 1200° and 1100°C, a peak was observed in the resistivity. For treatment time greater than 8 min at 1200°C and for 30 min at 1100°C, the resistivity decreased as the heat-treatment time increased. The final value of the resistivity is less than 10^{-2} Ω -cm. At 1050°C, a resistivity of more than 10^{10} Ω -cm was obtained for the heat-treatment time of more than 3 h, and the conduction type could not be measured by the conventional thermoelectric power method. At 1000°C, the type of conductivity did not change from p-type for heat-treatment time of more than 10 h.

By the heat-treatment at 1100°C for 30 min on the as-grown p-BP, p-BP acquires a resistivity of 150 Ω -cm. When given subsequent heat-treatment at 1000°C for several hours, a conversion of the conduction type from p-BP to n-BP was observed.

Diffusion layer formed in Si substrate.—It was found that n-BP acts as a source diffusing phosphorus into the Si substrate and that p-BP diffuses boron into the Si substrate. If a p-Si substrate is employed for the growth of n-BP, and an n-Si substrate is employed for the growth of p-BP, diffusion layers are found in the Si substrate.

Representative results for as-grown n-BP for heat-treatment at 1100°C are shown in Fig. 3. For a heat-treatment time of less than 30 min, an n-type diffusion layer was formed in the Si substrate. The junction depth (x_j) increases in proportion to the square root of the heat-treatment time (t), and the sheet resistance (R_s) decreases in proportion to the square root of t . After 30 min, a p-type diffusion layer appeared on the n-type diffusion layer. Its junction depth (x_{jB}) seems to increase linearly with the increase of the heat-treatment time. The sheet resistance R_{sB} decreases steeply in comparison with that of R_s .

Discussion

Total amount of phosphorus or boron in as-grown BP.—The resistivity of as-grown n- or p-BP in the range from 10^{-2} to 10^{-3} Ω -cm gives a carrier concentration of 10^{20} – 10^{21} cm^{-3} when assuming an electron or hole mobility of about $15 \text{ cm}^2/\text{V} \cdot \text{s}$ (7). As-grown

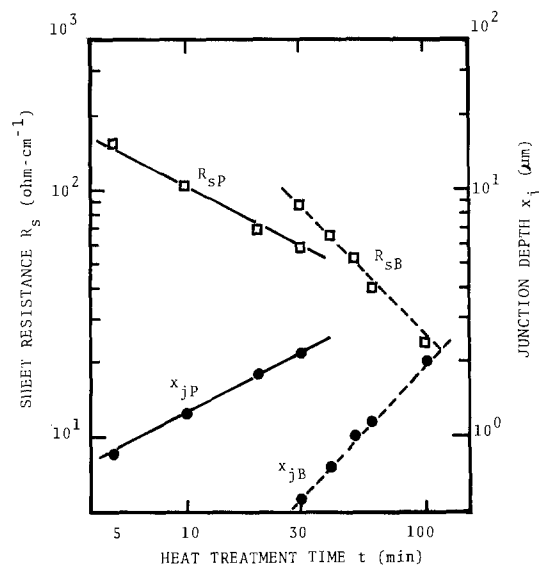


Fig. 3. Junction depth (x_j) and sheet resistance (R_s) of phosphorus or boron-diffusion layer formed in Si substrate. The heat-treatment temperature was 1100°C.

n-BP acts as a diffusion source of phosphorus, which forms an n-type diffusion layer in the Si substrate. A double donor of anti-site phosphorus is a cause of as-grown n-BP (2). As-grown p-BP acts as a diffusion source of boron, which forms a p-type diffusion layer in Si substrate. A double acceptor of anti-site boron is a cause of as-grown p-BP. The excess amount of phosphorus or boron contained in the as-grown BP is estimated to be in the range of 10^{15} to 10^{16} cm^{-2} for the BP thickness of 500Å employed in the experiment.

Total amount of phosphorus or boron diffused into the Si substrate.—From the sheet resistance (R_{sP}) and the junction depth (x_{jP}) given in Fig. 3, the phosphorus surface concentration (C_{SP}) can be obtained by applying Irvin's curve (8). As shown in Fig. 4, C_{SP} is constant at about 5.0×10^{19} cm^{-3} . The total amount of phosphorus (Q_P) diffused into the Si substrate, which is almost in proportion to the square root of t , reaches about 2×10^{15} cm^{-2} . After 25 min of heat-treatment, Q_P reaches a saturation point. The diffusion coefficient of phosphorus (D_P) can be estimated to be: $D_P = 5.5 \times 10^{-13}$ cm^2/s . This value is almost the same

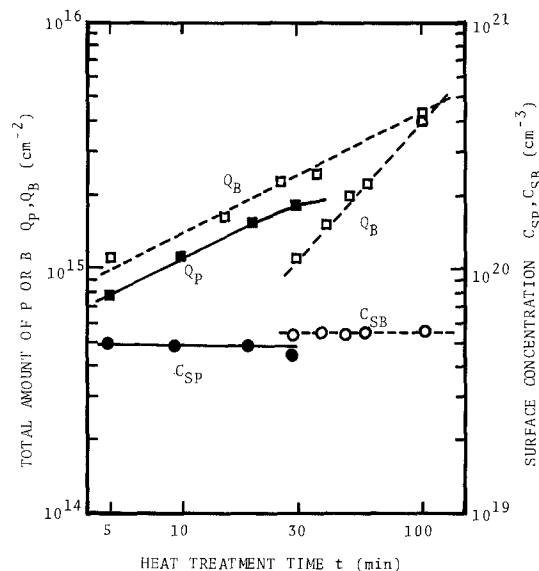


Fig. 4. Surface concentration and total amount of phosphorus and boron diffused into Si substrate from the BP. The heat-treatment temperature was 1100°C.

as the well-known phosphorus diffusion coefficient at 1100°C (9).

The boron surface concentration (C_{SB}) and the total amount of boron (Q_B) diffused over the phosphorus diffusion layer are also obtained. A simple calculation employing t gives the result of Fig. 4. C_{SB} is a constant of about $5.3 \times 10^{19} \text{ cm}^{-3}$, a value larger than that for phosphorus. Q_B seems to increase linearly with t . However, by employing the actual time of boron diffusion, which is given as $(t - 25)$ min for 1100°C, the total amount of boron (Q_B') shown in Fig. 4 becomes in proportion to the square root of t .

Qualitative characteristics of BP according to the heat-treatment are summarized in Fig. 5. At heat-treatment temperatures greater than 1050°C, the as-grown n-BP finally changes to p-BP. By observing the diffusion layer formed in the Si substrate, it was confirmed that the n-BP acted as a phosphorus diffusion source ("1" in Fig. 5) and that the p-BP as a boron diffusion source ("3" in Fig. 5). The total amount of phosphorus for 8 min at 1200°C, for 25 min at 1100°C, and for 120 min at 1050°C is almost the same as the same level as the excess amount of phosphorus contained in the as-grown n-BP (i.e., about $2.5 \times 10^{15} \text{ cm}^{-2}$). Boron diffusion can be explained as due to a boron vacancy formation after stoichiometric composition. The amount of boron vacancy in p-BP was ascertained to be almost equal to the total amount of boron diffused into the Si substrate over the n-type diffusion layer.

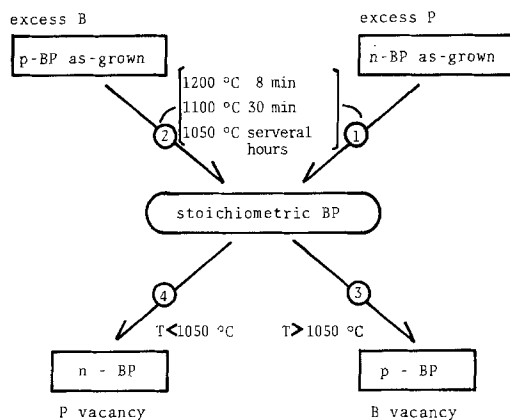


Fig. 5. Qualitative characteristics of BP due to the heat-treatment.

For as-grown p-BP, with the heat-treatment greater than 1050°C, as-grown p-BP keeps the p-type conductivity. The first boron diffusion into the Si substrate from p-BP ("2" in Fig. 5) comes from the excess boron on regular phosphorus sites, and the second one ("3" in Fig. 5) comes from a boron on the regular lattice sites, resulting in a boron-vacancy formation.

A phosphorus-vacancy formation ("4" in Fig. 5) can also be expected. It was confirmed that the stoichiometric BP after a preliminary heat-treatment for 30 min at 1100°C of as-grown n- or p-BP finally changed to n-BP after several hours of heat-treatment at 1000°C. In this case, the analysis of the phosphorus diffusion layer was difficult, because C_{SP} is lower than C_{SB} , and the total amount of phosphorus is too small for diffusion temperatures less than 1050°C.

Conclusion

The deviation of BP from stoichiometry determines its conduction type. The type obtained is determined by heat-treatment after the BP surface was covered with Si_3N_4 . n-BP is given by anti-site phosphorus or phosphorus vacancy, and p-BP is given by anti-site boron or boron vacancy.

Manuscript submitted May 4, 1983; revised manuscript received Aug. 4, 1983. This was Paper 205 presented at the Montreal, Que., Canada, Meeting of the Society, May 9-14, 1982.

Sophia University assisted in meeting the publication costs of this article.

REFERENCES

1. M. Takigawa, M. Hirayama, and K. Shono, *Jpn. J. Appl. Phys.*, **13**, 411 (1974).
2. K. Shono, H. Otake, and J. Bloem, *J. Cryst. Growth*, **45**, 187 (1978).
3. K. Shono and C. J. Kim, *ibid.*, **56**, 511 (1982).
4. Y. Hirai and K. Shono, *ibid.*, **41**, 124 (1977).
5. C. J. Kim, M. Iida, and K. Shono, *Proc. Fac. Eng. Tokai Univ.*, **8**, 31 (1982).
6. M. Takigawa, T. Sato, and K. Shono, *This Journal*, **122**, 824 (1975).
7. K. Shono, T. Takenaka, and M. Takigawa, "Proc. 12th Intern. Conf. on the Physics of Semiconductors," 286 (1974).
8. J. C. Irvin, *Bell Syst. Tech. J.*, **41**, 387 (1962).
9. R. B. Fair and J. C. C. Tsai, *This Journal*, **124**, 1107 (1977).

A Method of Forming Contacts Between Two Conducting Layers Separated by a Dielectric

E. R. Sirkin* and I. A. Blech**

Xerox Corporation Palo Alto Research Center, Palo Alto, California 94304

ABSTRACT

A technique for vertically interconnecting two conducting layers separated by an insulator is described. The technique offers advantages over present methods, including complete step coverage over vertical via walls and a planarized surface. In addition, this technique can be extended easily to form multiconductor-insulator interconnects. Moreover, as device dimensions are reduced to the micron and submicron level, the planarization and therefore the interconnection will improve. The method will have applications in integrated electronics and perhaps integrated optics and other semiconductor devices.

Integrated circuits contain several electrically conducting layers such as the silicon itself, polycrystalline silicon, and one or more layers of metallization. The conductors are separated by dielectric layers which are preferentially etched to make interlayer contacts. The interlayer contacts are traditionally made by etching holes (vias) in the dielectric prior to the deposition of the top conductor. The disadvantages of this method are: (i) incomplete metal coverage over the via sidewall, and (ii) creation of a nonplanar structure.

The present paper describes a procedure which overcomes both disadvantages using a planarization technique. A similar technique has been suggested previously (1).

Interconnect Technique

The planarization consists of six basic steps.

First, deposition of a thick conductor layer having a thickness at least equal to the sum of the standard first-level conductor and the insulator thicknesses.

Second, formation of pillars on the first conductor (rather than vias) by etching part of the thick conductor (Fig. 1a).

Third, definition of the first-level conductor (Fig. 1b).

Fourth, deposition of a thick insulator layer.

Fifth, application of a viscous thick layer (e.g., photoresist) to a thickness greater than the pillar height in a manner which results in a planar surface (Fig. 1c).

Sixth, etchback of the thick viscous and insulator layers at similar rates (thereby exposing the top of the conducting pillars [Fig. 1d]).

Seventh, formation of the top conductor (Fig. 1e).

Experimental

Starting materials consisted of polished 3 in 20-50 Ω -cm $\langle 100 \rangle$ p-type Si wafers with 75 nm of thermally grown SiO_2 . Deposition of the first conductor, 1300 nm Al, was accomplished in a Balzers Model 450 PM Magnetron Sputterer. Shipley Microposit 1400-26 positive photoresist was spun over the metal surface and exposed using a reticle opposite in polarity to that of a standard via pattern. The photoresist was developed and the aluminum wet etched to form pillars 750 nm high (Fig. 1a). Next, the first-level metal mask was defined, and the metal etched (Fig. 1b). The resulting structure, as seen in Fig. 2, a scanning electron micrograph (SEM micrograph), shows 750 nm-high pillars extending from the remaining aluminum film, which is 550 nm thick.

The insulating layer, a 4% by weight phosphorous-doped SiO_2 film, was deposited at 400°C to a thickness of 850 nm in a low temperature chemical vapor depo-

sition (CVD) system. This thickness is somewhat less than that prescribed according to Fig. 1c. As a consequence, after planarization the metal pillars were coplanar with the SiO_2 surface over the bottom metal film, but not with the SiO_2 surface over the field regions of the wafer. This technique, however, can be easily extended so as to produce truly planar surfaces by depositing a thicker dielectric (as illustrated in Fig. 1). Measurements made using a Tencor Alphastep profilometer showed that the metal step heights were reproduced after SiO_2 deposition, thereby indicating good conformal coverage. Shipley 1400-33 Microposit photoresist was spun over the insulating SiO_2 layer using a Machine Technology, Incorporated Omnichuck at a spin speed of 2840 rpm. To ensure good uniformity, the resist was dispensed while the wafer spun at ~ 90 rpm. Hexamethyldisilazane was also applied prior to the resist to ensure good adhesion. The wafer was then baked at 180°C for 30 min. Duplication of this procedure on a test wafer without the SiO_2 and metal layers indicated a photoresist index of refraction of 1.65 and a thickness of 2240 nm. A photoresist thickness

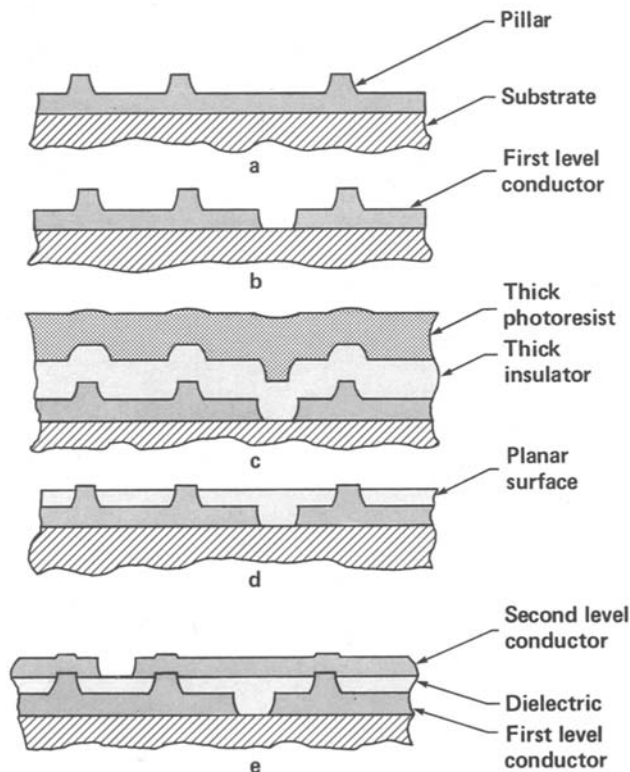


Fig. 1. Schematic drawings showing the proposed method of vertically connecting two conductors.

* Present address: Zoran Corporation, Sunnyvale, California 94086.

** Present address: Department of Materials Engineering, Technion, Haifa 32000, Israel.

Key words: etching, contacts, integrated circuits.

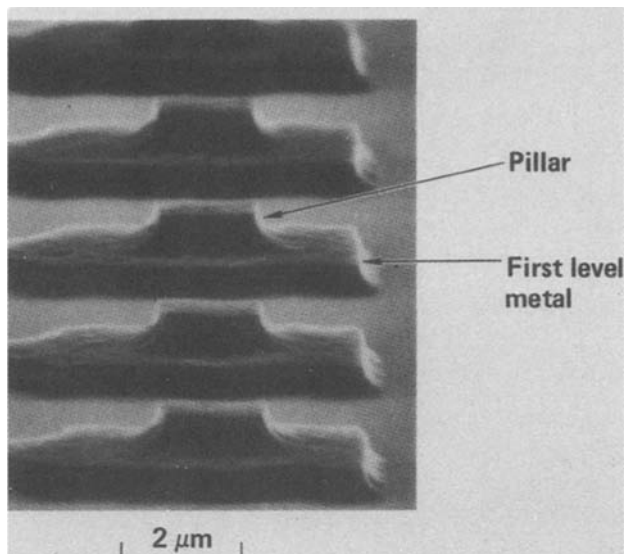


Fig. 2. SEM micrograph of the etched first conductor showing the pillar interconnects.

of 2240 nm, as measured in the field, on wafers with etched-metal structures was verified with a Nanometrics Nanospec. Measurements on the Tencor Profilometer indicated that the step height of 750 nm resulting from the metal pillars was reduced to 50 nm. Thus, the metal steps were planarized.

The metal pillars were exposed by etching back the resist and SiO_2 layers above the pillars. This was accomplished in an Applied Materials AME 8110 Reactive Ion Etcher. By varying the $\text{CHF}_3:\text{O}_2$ gas ratio while maintaining all other etch parameters, constant etch-rate curves were generated for the SiO_2 and the planarizing photoresist (Fig. 3). Etch conditions were chosen so that the oxide and photoresist etched at the same rate. As a consequence, the planar resist surface profile is transferred into the oxide surface. A similar planarization approach was previously described by Adams and Capio (2). Figure 4, an SEM micrograph, shows the etched back structure with the pillar-top surface exposed. Calculations indicated that for the etch cycle used, the final photoresist thickness over the SiO_2 layer in the field should be 530 nm. The measured thickness was 512 nm, verifying that the etch performance was consistent with predictions. This resist layer was next stripped in an asher.

Prior to depositing the second conducting layer, the surface of the wafer was exposed to an RF backscatterer in the magnetron sputterer in order to remove the native oxide on top of the conducting pillars. Without breaking vacuum, a thin layer 100 nm of Ti-10%W alloy followed by 1000 nm of Al-2%Cu were sputtered on the wafer. The only purpose for depositing the TiW was to provide an etch stop in case the wafer had to be stripped and etched further in the Reactive Ion Etcher.

The top metal layer was defined by wet etching both the Al-2%Cu and TiW layers. The completed structure, consisting of interconnected first- to second-level metal stitchthroughs, is shown in Fig. 5. A cross section of the interconnecting structure showing the bottom-level metal, the interconnecting pillar, the insulating oxide film, and the top-level metal is shown in Fig. 6. The first-level metal and field regions are uniformly covered by the deposited oxide ensuring electrical insulation between the two conducting layers. The utility of the planarization technique is demonstrated by the pillar structure, which does not suffer from step coverage problems normally encountered in via etching followed by metal deposition. Moreover, the plasma-etched insulating oxide surface, over the first-level metal, is coplanar with the top surface of the pillar.

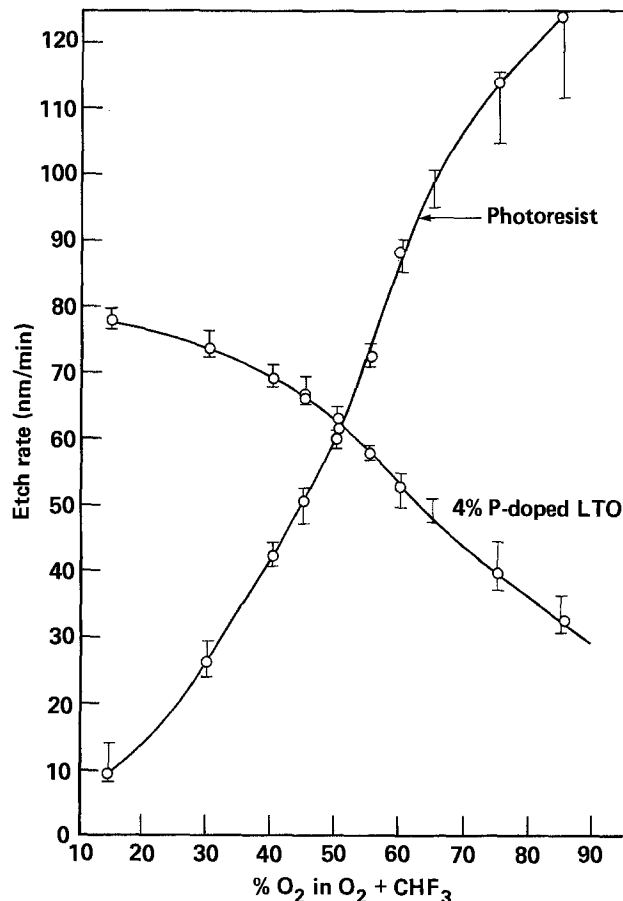


Fig. 3. Etch rates of 4% p-doped SiO_2 and planarizing photoresist as a function of O_2 gas concentration.

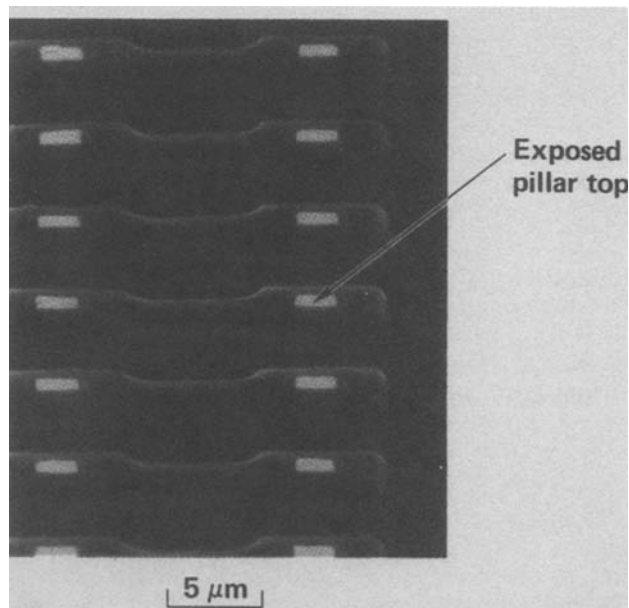


Fig. 4. SEM micrograph of planarized SiO_2 surface with pillar interconnect exposed.

This enhances step coverage and photolithographic definition in subsequent processing steps. The top-pillar surface is clearly in direct physical contact with the top-level metal.

Results

Electrical probe measurements were taken in order to ensure that contacts were made between the first and second conducting layers by the interconnecting pillars and wherever there were no pillars that the two conducting films were electrically isolated. The

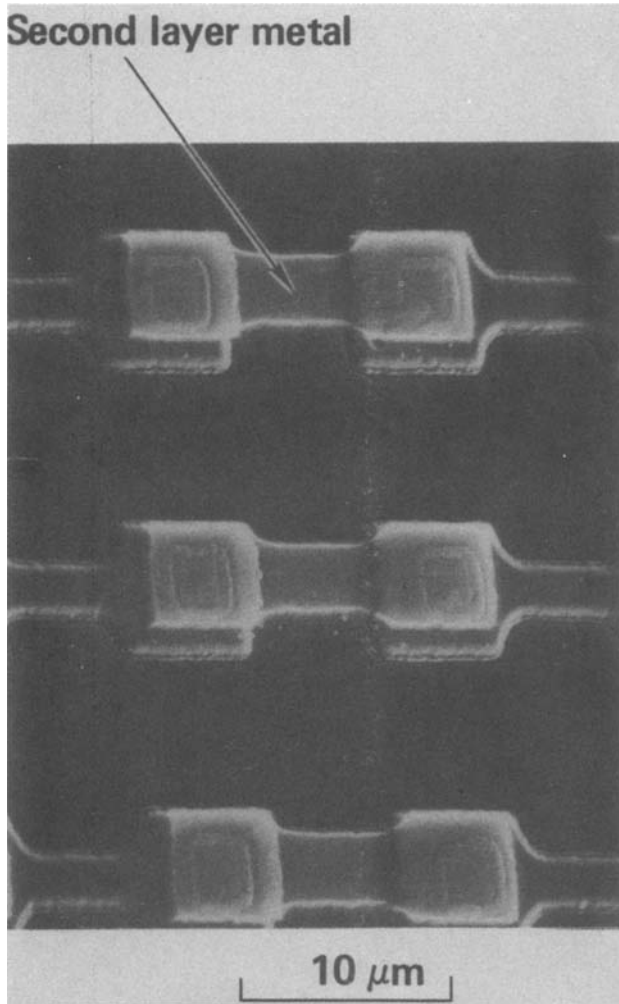


Fig. 5. SEM micrograph of the completed interconnect structure on a stitchthrough test pattern.

pattern used to test electrical continuity between the two metal layers was a standard stitchthrough pattern consisting of 108 rows of 20 contacts per row. Each contact size was $2 \times 2 \mu\text{m}$ (area = $4 \mu\text{m}^2$). A standard overlapping meander structure with 3600 crossovers was used to test electrical isolation.

The first- and second-level metal widths were $4 \mu\text{m}$. Testing of these structures on a wafer processed according to the procedure given in the previous section did not result in a positive continuity test. However,

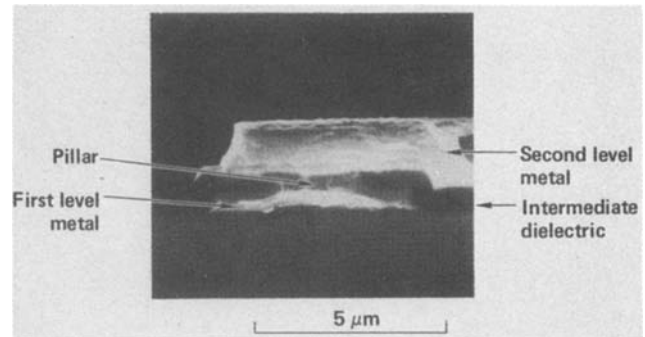


Fig. 6. SEM micrograph of a cross section through a pillar interconnect.

after the wafer was given a standard sintering treatment (450°C for 30 min in a reducing atmosphere of 15% N_2 and 85% H_2) contact was made and showed that all of the 2160 contacts in the stitchthrough were electrically conducting. The measured resistance was 500Ω , indicating a resistance of 0.25Ω per contact. Allowing 0.18Ω for the metallization, the net contact resistance is 0.07Ω per contact (or $\sim 3 \times 10^{-9} \Omega\text{-cm}^2$ specific contact resistivity). On the same die, the meander structures showed electrical isolation up to 15V dc.

Conclusions

A technique for interconnecting two conducting layers separated by an insulating film has been demonstrated. The technique does not suffer from step coverage problems encountered in standard via-interconnect fabrication. The surface of the intermediate insulating film is coplanar with top of the interconnecting metal (pillars), and provides a smooth surface for the second-level metallization. This technology can be readily extended to multilevel (>2) interconnects.

Acknowledgments

We appreciate the assistance of Dr. H. Van der Plas for depositing the Al films, and Mr. R. Allen for exposing the wafers.

Manuscript submitted July 8, 1983; revised manuscript received Sept. 1, 1983.

Xerox Corporation assisted in meeting the publication costs of this article.

REFERENCES

1. J. R. Kitcher, *IBM Tech. Disc. Bull.*, **23**, 1395 (1980).
2. A. C. Adams and C. D. Capio, *This Journal*, **126**, 1042 (1979).

Chemical Etching of GaAs

Sadao Adachi and Kunishige Oe

Nippon Telegraph and Telephone Public Corporation, Musashino Electrical Communication Laboratory, Musashino-shi, Tokyo 180, Japan

ABSTRACT

A new HCl:CH₃COOH:K₂Cr₂O₇ system which is particularly suitable for use in etching solutions of GaAs crystals has been developed. This system can be classified into two individual regions, A and B, according to etching characteristics. The solutions in region A are light orange in color, while those in region B are dark brown. The rate-limiting process is the reaction rate limited in region A, and the diffusion limited in region B. This system, especially in Region A, provides high-quality etched surfaces without any undesirable roughness or etch pits. Etching rates for (001) GaAs vary from 0.01 to 1 μm/min, depending on the component proportion of the solutions and/or on the normal K₂Cr₂O₇ aqueous solution. Ordinary mesa-shaped structures have been formed on etching stripes in (001) GaAs parallel to the [110] and $\bar{1}\bar{1}0$ directions. The system does not erode photoresists, and so is attractive for a variety of GaAs device applications.

Chemical etching is one of the most commonly employed techniques in the semiconductor device and materials science fields. A number of investigators have reported on the etching characteristics of GaAs crystals (1). Recently, we have studied the preferential etching characteristics of GaAs in solutions of various etchant systems (HCl, HNO₃, HBr, etc.) and have demonstrated geometrically etched profiles produced in the (001) planes of GaAs by employing these etchant systems (2). Important factors determining the choice of an etchant are, generally, the etching rates for the materials in question, the degree of surface quality, the solution chemical aggressiveness toward photoresist masks, and the desired etching profile for the relevant purpose.

The most commonly used etchants for GaAs are various compositions of Br₂-CH₃OH, H₂SO₄-H₂O₂-H₂O, and NH₄OH(NaOH)-H₂O₂-H₂O (1). These solutions, however, tend to erode photoresist masks such as AZ-1350J, and often provide little degree of reproducibility of etched-depth control. In the fabrication of GaAs electron devices, e.g., field effect transistors (FET's), the thickness of the active layer must be controlled with sufficient accuracy. Various depth profiles (impurity concentration, mobility, etc.) must be exactly measured by using etch removing techniques to characterize various kinds of devices based on such material properties.

In this paper, a new etching solution composed of HCl, CH₃COOH, and K₂Cr₂O₇ aqueous solution is developed for the etching of GaAs. This system can be classified into two regions (A and B), according to the etching characteristics. Region A is the chemical-reaction rate-limited process, while region B is the diffusion-limited one. This solution does not erode photoresists such as AZ-1350J, and gives high-quality etched surfaces. Etching rates for (001) GaAs vary from 0.01 to 1 μm/min, depending on the component proportion of the solutions and/or on the normal K₂Cr₂O₇ aqueous solution. Such features are attractive for a variety of GaAs device applications.

Experimental

The GaAs single crystals employed were Si-doped, n-type with carrier densities in the region of 10¹⁸ cm⁻³. Studies were also performed on Cr-doped, semi insulating GaAs crystals, and it was found that the etching rates were not affected by conductivities of the wafers. All the wafers used were of (001) surface orientation with an uncertainty of one degree or less. After being mirror-like finished, degreased, and rinsed in deionized water, they were chemically etched in an H₂SO₄:H₂O₂:H₂O = 3:1:1 solution for 1 min at 80°C.

Key words: GaAs, chemical etching, etching rate, etching profile.

The etching solution was prepared by mixing HCl, CH₃COOH, and K₂Cr₂O₇ aqueous solution. The chemicals used were all of reagent grade. They were as follows: HCl (12N), CH₃COOH (17N), K₂Cr₂O₇ (purity ≅ 99.8%), and H₂O (deionized water). The composition dependence of the etching rate was measured by changing the proportions of these etching solutions. A large quantity of solution was prepared to prevent the etching temperature from rising and the etching solution composition from varying during the experiments. Etching was carried out in a temperature-regulated water vessel without illumination and stirring. The etching solution temperature was varied between 5° and 60° ± 0.5°C. The etchant was freshly mixed prior to each experiment.

Etching studies were performed for the etching selected regions of (001) surface GaAs through windows in AZ-1350J photoresist mask. The desired geometries, in this case the window width of 30 μm, were defined by standard photolithography techniques (3). After etching, removing the AZ-1350J mask, and rinsing in deionized water, the etched depths were measured from a step height between the etched and unetched surfaces using an interference microscope. Etching profiles were also observed on the (110) and $\bar{1}\bar{1}0$ planes perpendicular to the wafer surface under an optical microscope.

Etching Rate

The purpose of this section is to present accurate data of the etching rate as a function of composition proportion in the HCl:CH₃COOH:(1N-K₂Cr₂O₇) system. The etching kinetics will be mentioned in detail in the next section. The dependence of the etching rate on composition *m* of the etchant HCl:CH₃COOH:(1N-K₂Cr₂O₇) = *m*:1:1 by volume ratio (hereafter referred to as HCl-*m*11) for (001) GaAs at 20°C is shown in Fig. 1. The K₂Cr₂O₇ solution was prepared by dissolving 14.7g K₂Cr₂O₇ in deionized water (100 cm⁻³). The data show that the etching rate increases with increasing *m* in the lower *m*-value region and is nearly constant in the higher *m*-value region (*m* ≅ 2.0). For *m*-values lower than 1.5, the etchants are transparent and light orange in color. The etchants with *m* ≅ 1.5, on the other hand, are dark brown in color. The etchants, especially in the region of *m* < 1.5, provide high quality etch-pit free GaAs surfaces.

Figure 2 shows the dependence of the etching rate on composition *n* of the etchant HCl:CH₃COOH:(1N-K₂Cr₂O₇) = 1:*n*:1 by volume ratio (HCK-1*n*1) for (001) GaAs at 20°C. As clearly seen in the figure, the etching rates decrease gradually with increasing *n*. In this case, the etchants are transparent and light orange in color within our experimental range. An etched-surface quality is also very good within our measured *n*-value range.

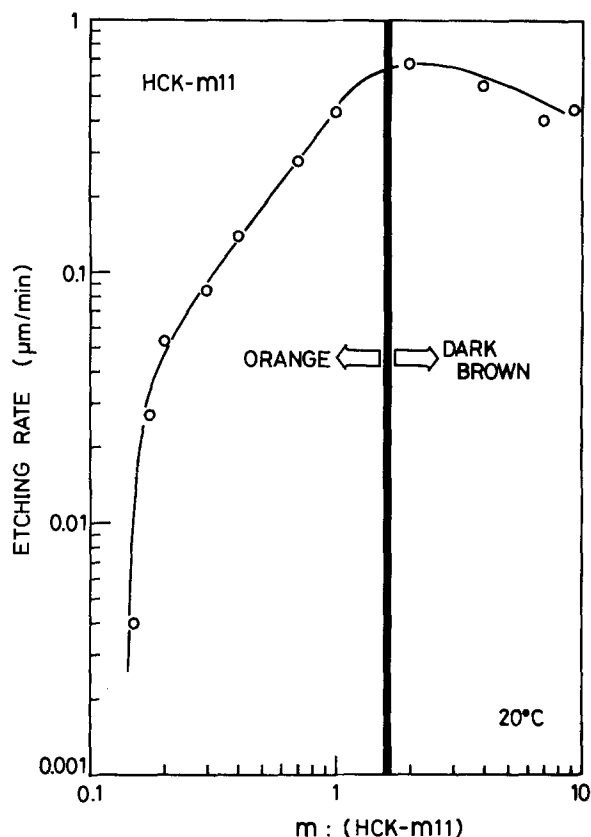


Fig. 1. The dependence of the etching rate on composition m of the etchant $\text{HCl}:\text{CH}_3\text{COOH}:(1\text{N}-\text{K}_2\text{Cr}_2\text{O}_7) = m:1:1$ (HCK-m11) for (001) GaAs at 20°C .

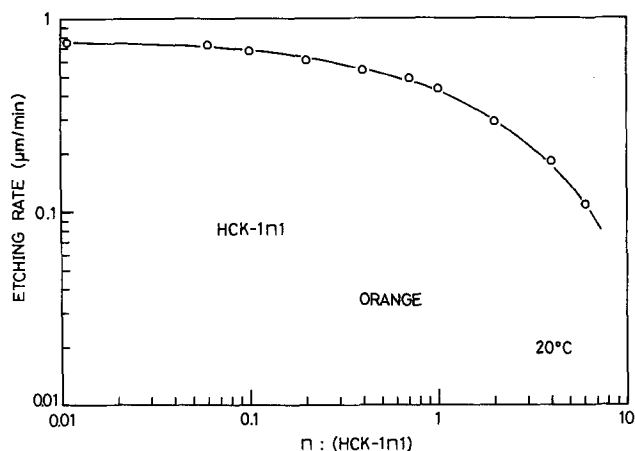


Fig. 2. The dependence of the etching rate on composition n of the etchant $\text{HCl}:\text{CH}_3\text{COOH}:(1\text{N}-\text{K}_2\text{Cr}_2\text{O}_7) = 1:n:1$ (HCK-1n1) for (001) GaAs at 20°C .

The dependence of the etching rate on composition l of the etchant $\text{HCl}:\text{CH}_3\text{COOH}:(1\text{N}-\text{K}_2\text{Cr}_2\text{O}_7) = 1:1:l$ by volume ratio (HCK-11l) for (001) GaAs at 20°C is shown in Fig. 3. The etching rate increases with increasing l , peaking at $l \approx 0.7$ ($\approx 0.49 \mu\text{m}/\text{min}$), and then decreases with increasing l . The etchants are dark brown in color for the l -values lower than 0.55, and light orange in the region of $l \approx 0.55$. The etchants also provide high-quality etch-pit free GaAs surfaces within our experimental range.

The etchants, such as $\text{HCl}:\text{CH}_3\text{COOH}$ and $\text{CH}_3\text{COOH}:(1\text{N}-\text{K}_2\text{Cr}_2\text{O}_7)$ mixtures do not etch GaAs, but the $\text{HCl}:(1\text{N}-\text{K}_2\text{Cr}_2\text{O}_7)$ mixture etches GaAs sufficiently. Figure 4 shows the etching rate as a function of the solution of $(1\text{N}-\text{K}_2\text{Cr}_2\text{O}_7)/\text{HCl}$ by volume ratio for (001) GaAs at 20°C . It can be seen that the etching rate is proportional to this ratio in the lower ratio

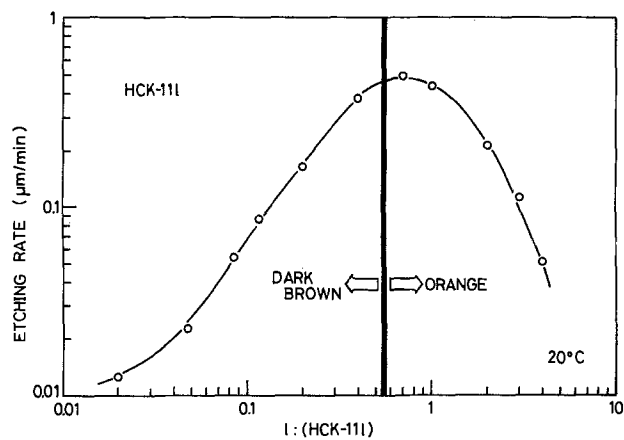


Fig. 3. The dependence of the etching rate on composition l of the etchant $\text{HCl}:\text{CH}_3\text{COOH}:(1\text{N}-\text{K}_2\text{Cr}_2\text{O}_7) = 1:1:l$ (HCK-11l) for (001) GaAs at 20°C .

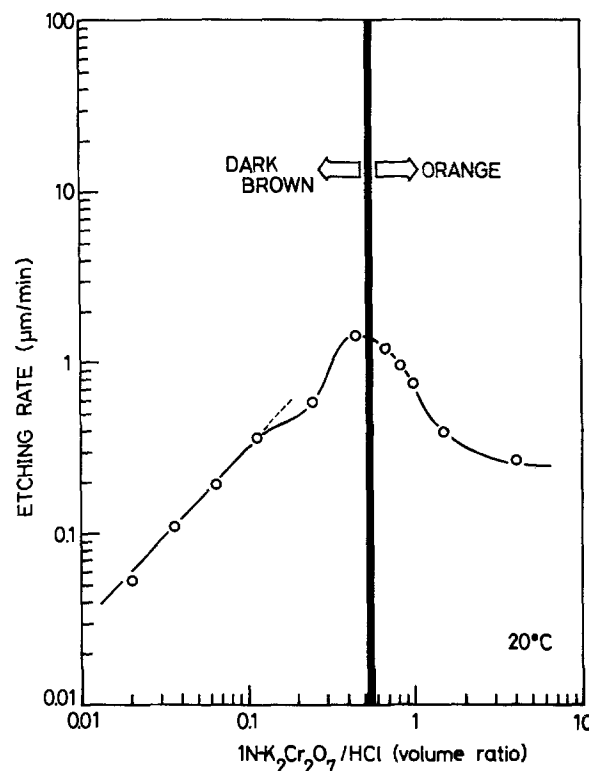


Fig. 4. The dependence of the etching rate on volume ratio of the $(1\text{N}-\text{K}_2\text{Cr}_2\text{O}_7)/\text{HCl}$ etchant for (001) GaAs at 20°C .

region, showing a maximum at $(1\text{N}-\text{K}_2\text{Cr}_2\text{O}_7)/\text{HCl} \approx 0.7$, and then decreases gradually with increasing ratio. The etched-surface quality is good within our experimental range.

Dissolution Process

We showed in Fig. 1-4 accurate experimental data of the etching rate as a function of composition proportion in the $\text{HCl}:\text{CH}_3\text{COOH}:(1\text{N}-\text{K}_2\text{Cr}_2\text{O}_7)$ system. It was found that the etchants' being light orange in color provide good reproducible etching rates and high-quality etched surfaces, their being dark brown does not. In this section, we shall investigate in detail the dissolution mechanism of this system on GaAs of (001) surface orientation.

Figure 5 shows the triangular coordinate system that was used to represent the composition of the $\text{HCl}:\text{CH}_3\text{COOH}:(1\text{N}-\text{K}_2\text{Cr}_2\text{O}_7)$ system. Each vertex corresponds to 100% of one of the constituents. This figure presents the composition of the etchant by volume of the constituents. Shown in the figure are lines

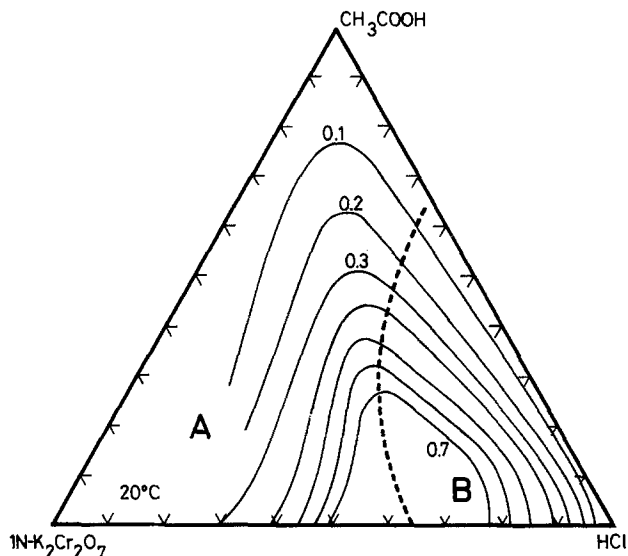


Fig. 5. Constant etching rate curves for (001) GaAs in the system $\text{HCl}:\text{CH}_3\text{COOH}:(1\text{N}-\text{K}_2\text{Cr}_2\text{O}_7)$, at 20°C . The numbers represent etching rates in $\mu\text{m}/\text{min}$.

of constant etching rate with its increment of $0.1 \mu\text{m}/\text{min}$, plotted as a result of a large number of individual determinations. The triangular diagram can be divided into two individual regions, A and B. A corresponds to the light orange solution and B to the dark brown solution. The boundary between the regions A and B is given by the dashed line. As shall be shown, these regions exhibit different etching characteristics.

The etched depth as a function of time for (001) GaAs in the light orange (HCK-111) and dark brown solution (HCK-511) is shown in Fig. 6. The data were taken at 20°C . The stirring effect was examined for

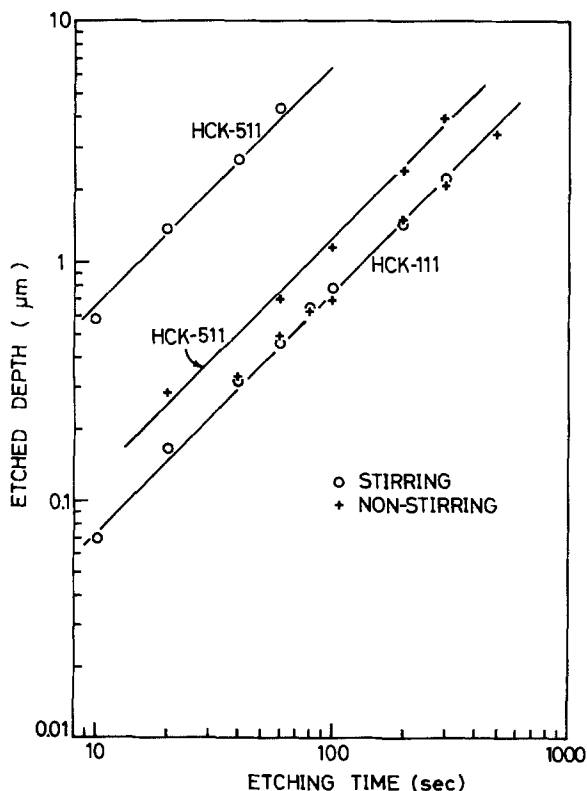


Fig. 6. Relation between etched depth and etching time for (001) GaAs in the solutions of $\text{HCl}:\text{CH}_3\text{COOH}:(1\text{N}-\text{K}_2\text{Cr}_2\text{O}_7) = 1:1:1$ (HCK-111) and $\text{HCl}:\text{CH}_3\text{COOH}:(1\text{N}-\text{K}_2\text{Cr}_2\text{O}_7) = 5:1:1$ (HCK-511) at 20°C .

these solutions by stirring the samples by hand. As clearly seen in the figure, the etched depths were found to have a nearly linear dependence on etching time for both the solutions with and without stirring. It is noted that the light orange solution did not show a clear stirring effect, as the dark brown solution did.

Figure 7 shows the temperature dependence of the etching rate in the light orange (HCK-111) and dark brown (HCK-511) solutions. The etching rates were found to increase exponentially with increasing etchant temperature in each etchant. The activation energies were determined to be 11.6 kcal/mol for the HCK-111 and 4.6 kcal/mol for the HCK-511 etchant.

It is well known that the dissolution process is either reaction-rate limited or diffusion limited (4-6). The reaction-rate limited process is a function of the chemical reaction rate, while the diffusion-limited process depends on the transport of etchant molecules by diffusion. The former process has a linear dependence of the etched depth d on etching time t , i.e., $d \propto t^{1.0}$, while the latter process has in general a relation of $d \propto t^{0.5}$. The diffusion-limited process usually has lower activation energy than the reaction-rate limited process, and is therefore relatively insensitive to temperature variations. In fact, Iida and Ito (7) have studied the etching characteristics of (001) GaAs in the $\text{H}_2\text{SO}_4:\text{H}_2\text{O}_2:\text{H}_2\text{O}$ system and obtained activation energies of $6-8 \text{ kcal/mol}$ in high H_2SO_4 solutions (diffusion limited) and $8-11 \text{ kcal/mol}$ in low H_2SO_4 solutions (reaction-rate limited). Moreover, the diffusion-limited process shows notable stirring effect on the etching rate; the reaction-rate limited process does not. From these considerations, one can conclude that the light orange and dark brown solutions are due to the chemical-reaction rate-limited and diffusion-limited etching processes, respectively.

Figure 8 shows the etching rate as a function of normal k ($k\text{N}-\text{K}_2\text{Cr}_2\text{O}_7$) in the $\text{HCl}:\text{CH}_3\text{COOH}:(k\text{N}-\text{K}_2\text{Cr}_2\text{O}_7) = 1:1:1$ solution taken at 20°C . The etching rate increases with increasing normal k in the region up to $k \approx 0.2$, and then saturates with k in the region higher than 0.2 . In the low- k region ($k \leq 0.2$), the dependence of the etching rate R on k can be expressed exactly by $R \propto k^{1.0}$. For the k -value lower than 0.2 , the etchants are dark brown in color (diffusion-limited process). The etchants with $k > 0.2$, on the other hand, are light orange (reaction-rate limited process).

The microscopic etching mechanisms under consideration are thought to be very complex, since the dependence of the etching rates for (001) GaAs on the etchant-component proportions does not have simple linear relations; it indicates complicated behavior (see Fig. 1-4). Thus, at present, we cannot formulate

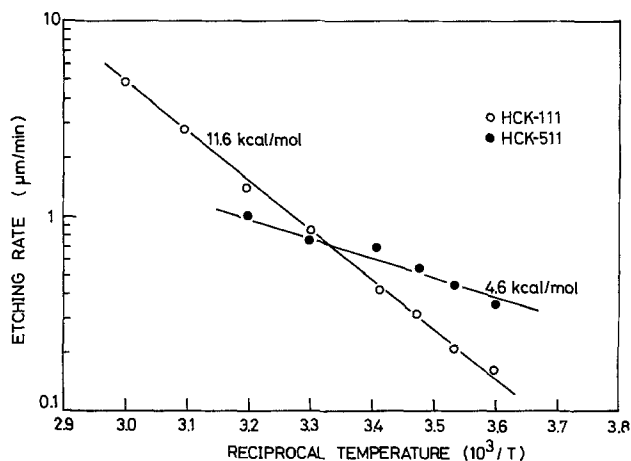


Fig. 7. Temperature dependence of the etching rate in the solutions of $\text{HCl}:\text{CH}_3\text{COOH}:(1\text{N}-\text{K}_2\text{Cr}_2\text{O}_7) = 1:1:1$ (open circles) and $\text{HCl}:\text{CH}_3\text{COOH}:(1\text{N}-\text{K}_2\text{Cr}_2\text{O}_7) = 5:1:1$ (filled circles).

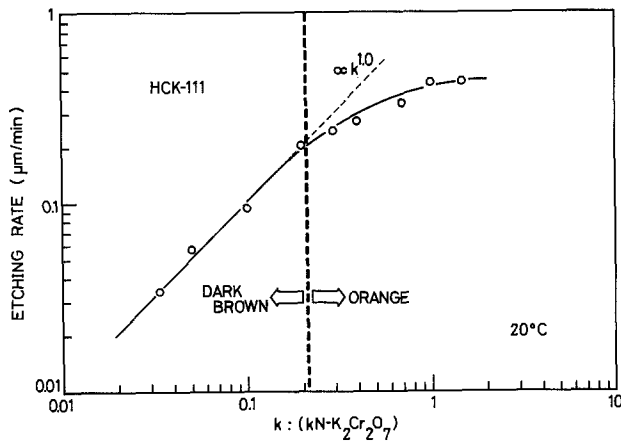
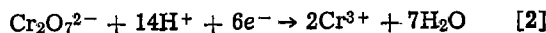
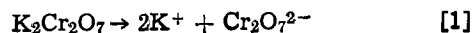


Fig. 8. Etching rates as a function of normal k ($kN\text{-}K_2Cr_2O_7$) in the solution of $HCl:CH_3COOH:(kN\text{-}K_2Cr_2O_7) = 1:1:1$ for (001) GaAs at $20^\circ C$.

rate equations of dissolution processes for GaAs by taking into account the etchant-component proportions. However, one can expect from a phenomenological aspect the following etching kinetics. The chemical reaction in the light orange solutions may be formally represented by the equations



The $Cr_2O_7^{2-}$ ion provides the light orange color, and its oxidation action would oxidize GaAs. The oxidized products can, then, be easily dissolved by HCl. As can be seen in Fig. 5, CH_3COOH acts only as a diluent for these kinetics. The rate-limiting process is thought to be the surface reaction, such as oxidation of GaAs and dissolution of oxidized products. The case for the dark brown solutions should essentially be the same as for the light orange. The dark brown color would arise from various kinds of chromates. The rate-limiting process, however, is the diffusion of oxidizing agents. One can also point out that the $K_2Cr_2O_7$ aqueous solution in this system contributes to produce etch-pit free, high-quality surfaces and, moreover, to increase the etching rates of (001) GaAs with increasing its normal, k (see Fig. 8).

Etching Profile

Etching profiles are examined by cleaving the (001) GaAs wafer in orthogonal directions along the (110) and $(\bar{1}10)$ planes. The profiles of (001) GaAs etched through AZ-1350J mask in the HCK-111 (light orange) solution are shown in Fig. 9a. It is clear from the figure that the profiles change in shape with a crystallographic rotation of 90° about the [001] axis and that they exhibit clear crystal habits. The etching profile of the (110) cleavage plane exhibits the ordinary mesa-shaped plane forming an angle of about 70° with respect to the (001) surface plane. The profile of the $(\bar{1}10)$ cleavage plane also indicates the inclined plane whose side forms an angle of about 35° with respect to the (001) surface plane. The etch-revealed plane forming an angle of about 70° with respect to the (001) surface plane, observed on the (110) cleavage plane, corresponds to the $\{2\bar{2}1\}$ crystallographic plane. The $\{2\bar{2}1\}$ plane, in principle, forms an angle of 70.5° with respect to the (001) surface plane. The inclined plane forming an angle of about 35° with respect to the (001) surface plane, observed on the $(\bar{1}10)$ cleavage plane, corresponds to the $\{112\}$ crystallographic plane. This plane, in principle, forms an angle of 35.3° with respect to the (001) surface plane.

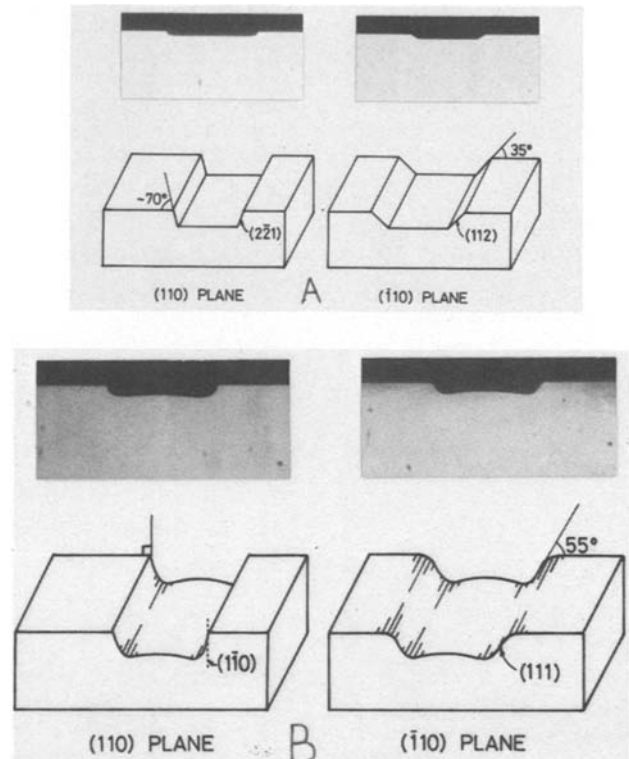


Fig. 9. A: etching profiles of (001) GaAs etched in the solution of $HCl:CH_3COOH:(1N\text{-}K_2Cr_2O_7) = 1:1:1$ at $20^\circ C$. B: etching profiles of (001) GaAs etched in the solution of $HCl:CH_3COOH:(1N\text{-}K_2Cr_2O_7) = 5:1:1$ at $20^\circ C$.

The etching profiles of (001) GaAs etched through AZ-1350J mask in the HCK-511 (dark brown) solution are shown in Fig. 9b. This solution provides the ordinary mesa-shaped structures with roundish tails at the etched bottoms for both the (110) and $(\bar{1}10)$ cleavage planes. The profiles, however, do not exhibit clear crystal habit. The tangents of the etch-revealed walls form angles of 90° and 55° with respect to the (001) surface planes for the (110) and $(\bar{1}10)$ cleavage planes, respectively.

It is known (7) that the reaction-rate limited etchant usually produces a flat-etched bottom, but the diffusion-limited one provides a roundish tail near the frame of the window, similar to the present results (see Fig. 9a and b). We have found that all the light orange solutions studied produce the flat-etched bottoms and that all the dark brown solutions provide the roundish tails at the etched bottoms.

Conclusion

A new etching solution composed of HCl, CH_3COOH , and $K_2Cr_2O_7$ aqueous solution has been developed for the etching of GaAs. This system can be classified into two individual regions, A and B, according to the etching characteristics. The solutions in Region A are light orange in color, while those in Region B are dark brown in color. The rate-limiting process is determined to be the reaction-rate limited in Region A and the diffusion-limited in Region B. This system does not erode photoresists such as AZ-1350J, and provides high-quality etched surfaces without any undesirable roughness or etch pits. Etching rates for (001) GaAs vary from 0.01 to $1 \mu m/min$, depending on the component proportion of the solutions. The rates increase linearly with increasing the normal $K_2Cr_2O_7$ aqueous solution in the low normal region ($\leq 0.2N$) and then saturate in the higher normal region. This system, especially in Region A, has reproducible etching rates and is thereby useful for GaAs device processing. The etching profiles are also

examined by cleaving the wafer in orthogonal directions along the (110) and ($\bar{1}\bar{1}0$) planes. Ordinary mesa-shaped structures have been formed on etching stripes in (001) GaAs with shiny flat-etched bottoms in the solutions of Region A, and with roundish tails at the etched bottoms in the solutions of Region B.

Acknowledgments

The authors wish to thank K. Kumabe, S. Shimada, and N. Kuroyanagi for their continual encouragement.

Manuscript submitted March 25, 1983; revised manuscript received July 11, 1983.

Nippon Telegraph and Telephone Public Corporation assisted in meeting the publication costs of this article.

REFERENCES

1. See, for example, W. Kern, *RCA Rev.*, **39**, 227 (1978).
2. S. Adachi and K. Oe, *This Journal*, **130**, 2427 (1983).
3. S. Adachi and H. Kawaguchi, *ibid.*, **128**, 1342 (1981).
4. H. C. Gatos and M. C. Lavin, *J. Phys. Chem. Solids*, **14**, 169 (1960).
5. M. Otsubo, T. Oda, H. Kumabe, and H. Miki, *This Journal*, **123**, 676 (1976).
6. Y. Mori and N. Watanabe, *ibid.*, **125**, 1510 (1978).
7. S. Iida and K. Ito, *ibid.*, **118**, 768 (1971).

Chromium and Manganese Redistribution in Semi-insulating GaAs

M. Oshima, K. Watanabe, and S. Miyazawa

Nippon Telegraph and Telephone Public Corporation, Musashino Electrical Communication Laboratory, Musashino, Tokyo 180, Japan

ABSTRACT

Cr and Mn redistribution in various semi-insulating GaAs substrates annealed with or without encapsulation have been investigated quantitatively using secondary ion mass spectrometry (SIMS) and photoluminescence (PL). Mn was incorporated into Cr-depleted sites (Ga vacancies). Cr out-diffusion can be explained by simple diffusion theory having critical Cr depletion concentration under which no Cr depletion and Mn accumulation occur. While stress-enhanced diffusion takes place without Mn incorporation in capped annealing, a large Cr out-diffused area appears in the case of capless (face-to-face) annealing of high-dose implanted GaAs. This may be attributed to defects and surface dissociation.

Semi-insulating GaAs substrates provide active layers for high-speed GaAs IC devices after ion implantation and annealing processes. However, it has been reported that these substrates, usually doped with Cr, are thermally unstable, and show type conversion during heat-treatment. These phenomena (1-3) are reportedly due to Cr out-diffusion and Mn accumulation at the surface, where Mn serves as shallow acceptors. However, the relationship between Cr depletion and Mn accumulation has not been quantitatively discussed yet.

This paper aims at a better understanding of this relationship during various kinds of heat-treatment. Cr and Mn redistribution are discussed in terms of SIMS depth profiles from their dependence on annealing time, ambient gases, annealing temperature, Cr concentration in substrates, capping films, and ion implantation. Redistribution mechanisms are also discussed.

Experimental

Semi-insulating, Cr-doped wafers used in this study were of (100) orientation and grown by the horizontal Bridgeman technique (HB) and the liquid encapsulation Czochralski (LEC) method. Their initial preparation was the same as that reported by Watanabe *et al.* (4). Annealing was performed at 700°-900°C. The ambient gas was H₂ purified by a Pd diffuser. In the case of As₄/H₂, the mixture gas was supplied by H₂ passing through a GaAs chunk strainer held at the annealing temperature. Therefore, the As₄ atmosphere was not the same as controlled atmosphere technique (CAT). The estimated arsenic partial pressure is lower than 5×10^{-4} torr at 800°C (5). Ion implantation of Cr was done at room temperature at 300 keV with a dose of 10^{13} - 10^{15} cm⁻². Sputtered SiO₂ and plasma CVD Si₃N₄ films were used as capping layers.

An ion microanalyzer with O₂ primary ion bombardment was used to obtain the Cr, Mn, and other impurity depth profiles. Calibration of atomic concentration was established using standards prepared by ion

implantation. The Cr detection limit was examined using an epitaxially grown undoped GaAs film grown on GaAs substrate. The minimum detectable concentration of Cr was 5×10^{14} cm⁻³. Talystep was employed to measure the resultant crater depth. While an area of 250 μm square was sputtered, secondary ions were collected from the 60 μm-diam central area. The depth resolution was checked using a 8600Å Mo film on a Si substrate. From the width of the interface $\Delta d/d$ (the depth resolution) was found to be 8.7%, mainly due to knock-on effects and sputter redeposition.

Photoluminescence measurements were carried out at 4.2 K with the sample immersed in liquid He, using an Ar laser as the excitation source.

Redistribution Resulting from Capless Annealing

Figure 1a and 1b show Cr and Mn depth profiles for samples annealed in two different furnaces at 800°C for 1h in H₂ flow without capping layers. Both samples were from the same wafer. There is a remarkable difference in the amount of accumulated Mn, while the Cr profiles look alike. This is one of the reasons why we believe the Mn mainly originates from the ambient gas, presumably from heaters through the quartz tube.

A second reason is the large amount of accumulated Mn in the depleted region. If all the Mn concentrated at the surface is to have come from the bulk material, then it must have diffused distances of up to 100 times the thickness of this surface region. In order to estimate the diffusion length of Mn in GaAs at 800°C for 1h, we employed the diffusion coefficient with As reported by Sze (6). It comes to only about 2 μm at most, which is too small to account for the Mn accumulation.

A third reason is that when the sample was annealed again after polishing off about 10 μm from the surface, similar depth profiles of Cr and Mn were obtained. While Klein *et al.* (2) reported that Mn began to be depleted by the sequential heating and removal of Mn which diffused to the surface, we observed almost the same Mn accumulation after the heat/polish cycle.

Key words: SIMS, GaAs depth analysis, annealing redistribution.

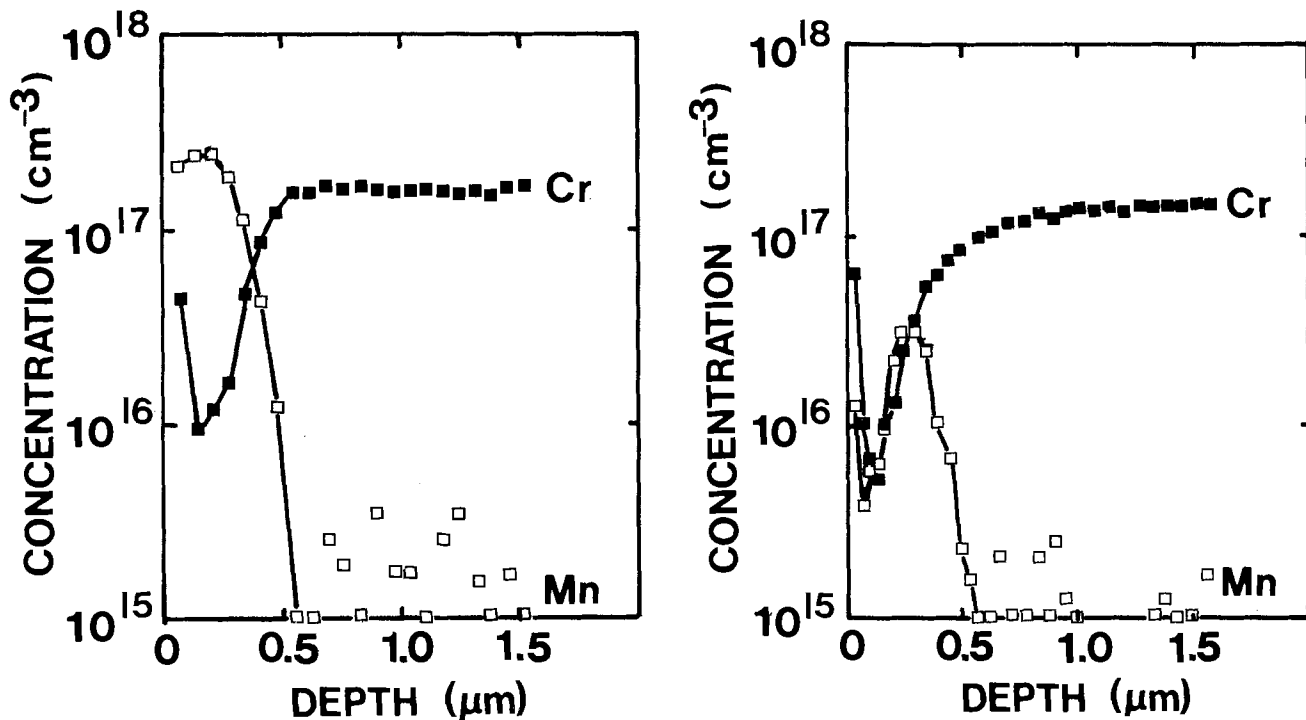


Fig. 1. Cr and Mn redistribution of GaAs substrates annealed in two different furnaces at 800°C for 1h in H₂ without encapsulation

Figure 2 shows PL spectra of the sample used in Fig. 1a. Peak A is reportedly carbon-related (carbon shallow acceptors), and peak B is due to Mn occupying Ga vacancies (7). Peaks at 1.375 and 1.34 eV are attributable to peak B's LO phonon replica and its 2 LO phonon replica, respectively. Interestingly, after being incorporated into the GaAs, Mn diffuses into the Cr-depleted region and occupies Ga vacancies dur-

ing H₂ annealing, although the diffusion coefficient of Mn is reportedly larger than that of Cr.

In order to understand the redistribution mechanism, the dependence of the Cr-depletion depth on annealing time was investigated. Figure 3 shows the depth of the Cr out-diffused region, which is defined as the depth where the Cr concentration becomes 84% of the original value, as a function of annealing time. Here, 84% is the value of $\text{erf}(x/2\sqrt{Dt})$, when the x is equal to $2\sqrt{Dt}$. Open circles indicate H₂ ambient gas, and open squares (8) As₄/H₂ (H₂ flow with a GaAs strainer). Estimated values were calculated using the reported Cr diffusion coefficient (9) and the first term ($\text{erf}[x/2\sqrt{Dt}]$) of the equation reported by Smith *et al.* (10). Although the rough estimation (solid line) shows slightly higher values than experimental results, it is evident that the diffusion process is dominant in Cr redistribution, judging from the proportionality of

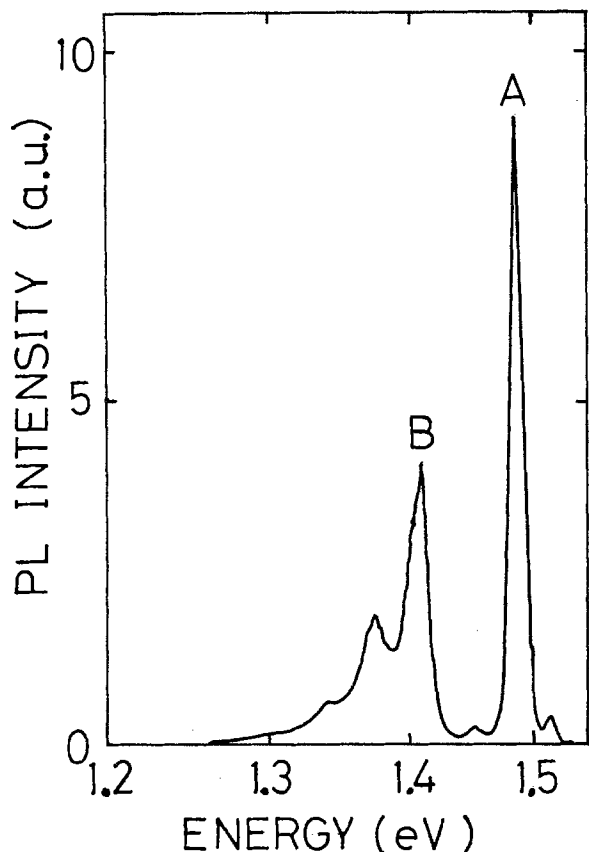


Fig. 2. GaAs photoluminescence spectra at 4.2 K. Sample is the same as Fig. 1a.

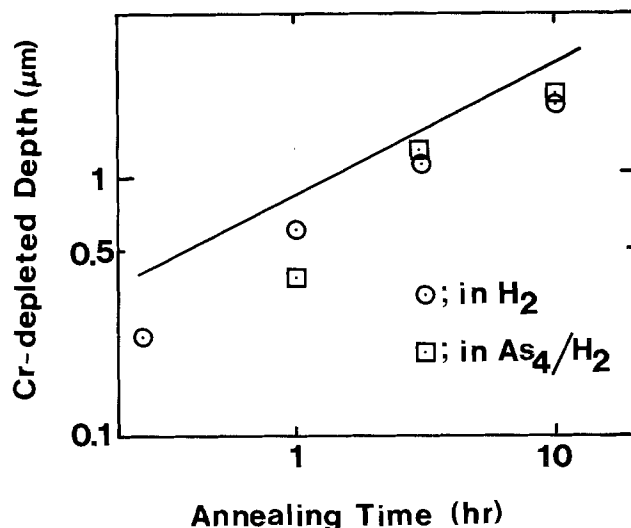


Fig. 3. Cr depleted depth as a function of annealing time. Samples are annealed at 800°C in H₂ (circles) and in As₄/H₂ (squares) without encapsulation. Solid line indicates the estimated value from the reported Cr diffusion coefficient in GaAs.

the depletion depth to \sqrt{t} . The discrepancy between estimation and experiment might be attributed to surface reactions forming volatile Cr compounds.

Kasahara *et al.* (11) reported that Cr redistribution is controlled by the partial pressure of arsenic during annealing, since the interfacial conductance decreases with high arsenic partial pressure. However, our results show no significant difference in Cr out-diffusion under various ambient gases up to annealing time of 1h. This is probably because our atmosphere of As_4/H_2 did not reach the sufficient arsenic pressure to prevent the loss of As and dissociation of GaAs.

Next, we investigated the dependence of Cr and Mn redistribution on the original substrate Cr concentration. Figure 4 shows Cr depth profiles in GaAs substrates with three different Cr concentrations. Curves (a) and (b) are for Cr-doped HB crystals, and curve (c) is for undoped LEC. Annealing was performed at 800°C for 1h in H_2 . While (a) and (b) show Cr depletion, (c) shows no change in the Cr profile. Mn accumulated in Cr-depleted regions. As a result, there was almost no Mn accumulation in the case of (c).

These results suggest two important points. First, there might be a minimum or critical Cr concentration for Cr depletion. The level is about $5 \times 10^{15} \text{ cm}^{-3}$, which is in good agreement with other authors' results (12, 13). Therefore, no Cr depletion takes place for Cr content substrates lower than that critical level. This critical concentration shows no dependence on annealing temperature. This suggests that it might not be due to thermal equilibrium considerations. More detailed work should be done.

Second, Mn was incorporated mainly into Cr-depleted sites. Zucca (14) reported that Mn diffusivity is large under a condition of V_{Ga} population excess. Sze (6) reported a dependence of the Mn diffusion coefficient on the presence or absence of As in the ambient gas, which in turn would strongly effect the number of As vacancies in the lattice. The precise role of Ga and As vacancies in the redistribution of Cr and Mn is still the subject of active discussion.

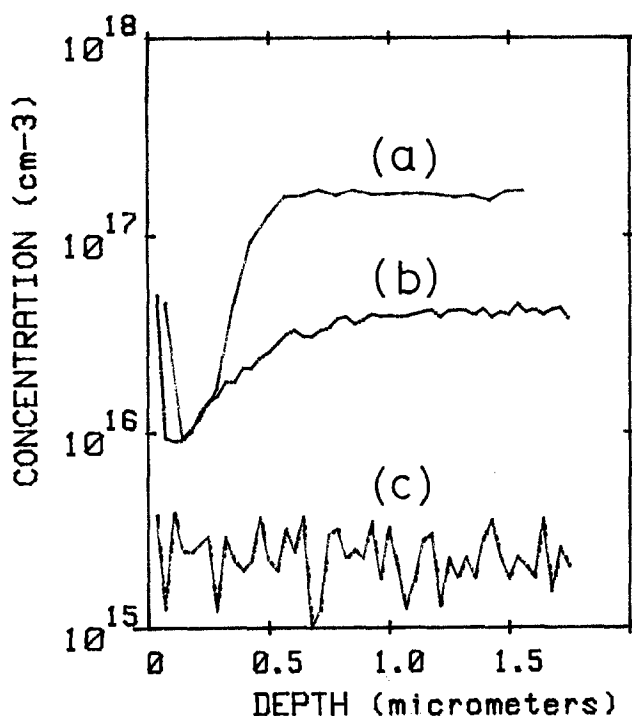


Fig. 4. Cr depth profiles as a function of Cr concentration in GaAs. (a) and (b) indicate HB Cr-doped substrates, and (c) LEC. Annealing was performed at 800°C for 1h without encapsulation. Mn profiles, which are not shown here, are located only in the Cr-depleted region.

Redistribution Resulting from Cr Ion Implantation

Cr ion-implanted samples were annealed to investigate their Cr-depletion behavior. Figure 5a, 5b, and 5c show Cr-implanted GaAs substrates with 10^{13} , 10^{14} , and 10^{15} cm^{-2} doses at 300 keV, respectively. In Fig. 5a, most of the implanted Cr on interstitial sites out-diffused, and Mn accumulation took place to the same degree as in the unimplanted samples, indicating that the Cr on Ga site was also depleted. In this case, the accumulation of Cr at the surface and the bump located around $R_p + \Delta R_p$ reported by Simondet *et al.* (15) were not observed. In Fig. 5b, Cr also out-diffused toward the surface and piled up with the surface concentration exceeding the solid solubility limit in GaAs ($2-3 \times 10^{17} \text{ cm}^{-3}$).

When the dose exceeded the amorphous limit, a large area of Cr depletion appeared, extending to the same depth as the region of Mn accumulation, as shown in Fig. 5c. The Cr depth profile does not look like the error function as predicted by simple diffusion theory. This may be due to the existence of a critical Cr concentration which limits the minimum Cr level. Even taking into account the amorphous area that would be caused by the dosage and the energy used, this region of enhanced Cr out-diffusion seems to be too deep. In the sample annealed at 850°C, Cr depletion extended to a depth of 9 μm . This result is quite different from that (see Fig. 5) reported by Simondet *et al.* (15). Their sample was annealed at 772°C for 15 min, after an implantation of $3 \times 10^{14} \text{ Cr cm}^{-2}$ at 190 keV.

We consider this enhancement of Cr out-diffusion to be mainly due to surface dissociation, while Magee *et al.* (16) reported that out-diffusion was enhanced by defects created by implantation. The sample in Fig. 5c showed considerable surface roughness compared to lower dosed samples, which may have been caused by surface thermal dissociation. Figure 6a shows an SIMS secondary ion image of $^{69}\text{Ga}^+$, and Fig. 6b an image taken by a Nomarski interference microscope. Although an $^{75}\text{As}^+$ ion image could not be obtained because of the low ionization yield of As (about 3 orders of magnitude lower than Ga), As^+ depth profiles show that the surface region of this highly dosed sample was more As deficient than the other samples. We consider this surface roughness to be due to Ga droplets (several microns diameter) resulting from in-stensate surface dissociation, which might be enhanced by the recrystallization of the amorphized region.

The difference between our results and those reported by Simondet *et al.* can be attributed to this surface morphological change. Udagawa *et al.* (17) reported that the agreement between calculations of Cr depletion profiles and experimental results were poor when samples were annealed for long times. This discrepancy was reportedly caused by the slightly matte surface, indicating the initiation of thermal dissociation. Further investigation will be needed to discover the cause of this surface morphological change.

Redistribution Resulting from Capped Annealing

Finally, in order to compare these results with capped annealing, SIMS analysis was performed on GaAs substrates capped with 3000Å SiO_2 or 1600Å Si_3N_4 films. Here, appropriate electron bombardment during depth profiling was employed to prevent charging up.

Figure 7a and 7b show As, Cr, and Mn depth profiles of GaAs. These samples were annealed in H_2 for 1h at 800°C. The As^+ pile up at the interface might be attributed to the well-known SIMS interface effect. When these samples were analyzed after removal of these films using $HF + H_2O$ solution, Cr showed the same profiles as before with a completely flat As^+ profile, and no Mn was detected in either case. The amount of Cr piled up at the surface proved to be equal

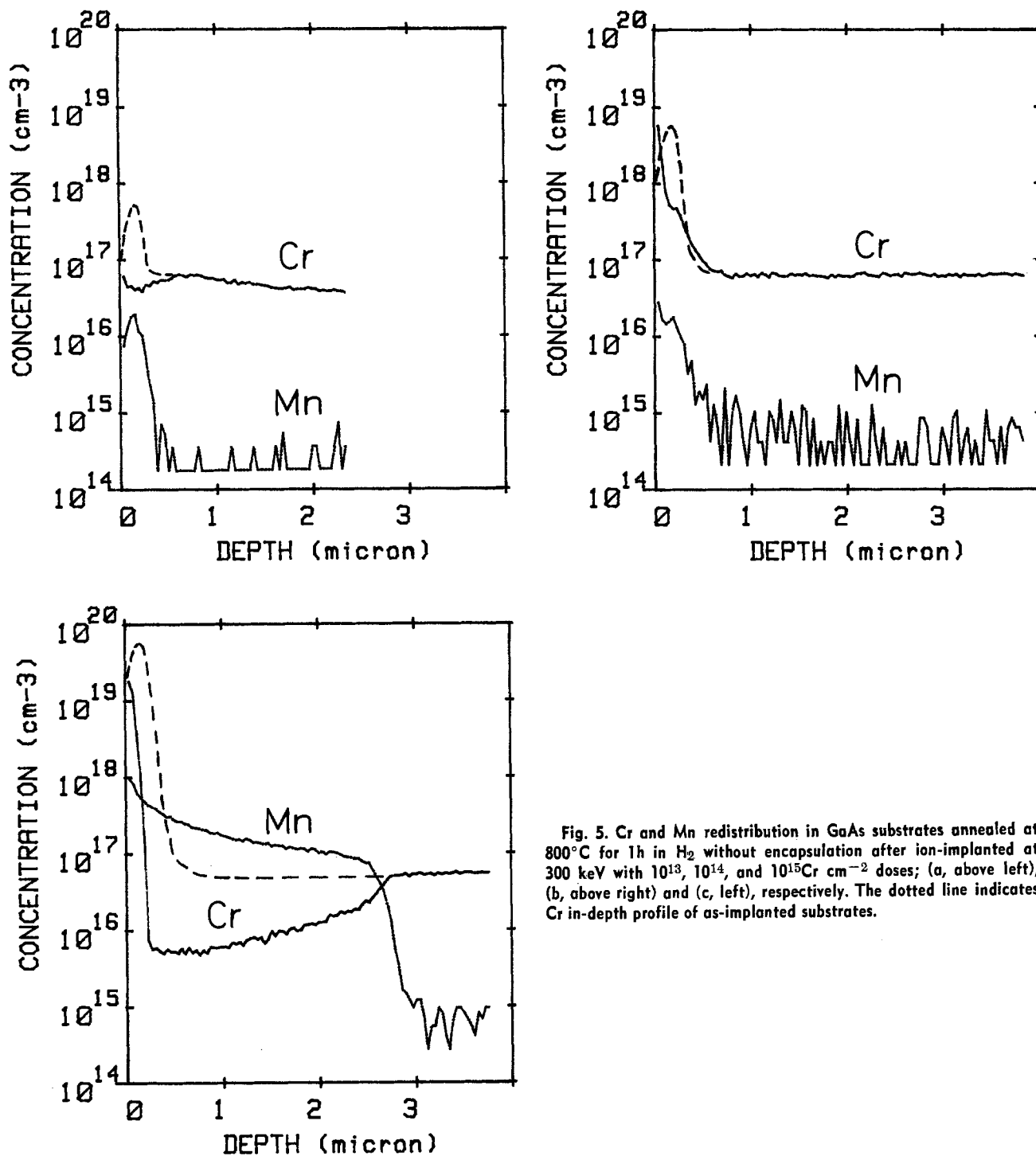


Fig. 5. Cr and Mn redistribution in GaAs substrates annealed at 800°C for 1h in H₂ without encapsulation after ion-implanted at 300 keV with 10^{13} , 10^{14} , and 10^{15} Cr cm⁻² doses; (a, above left), (b, above right) and (c, left), respectively. The dotted line indicates Cr in-depth profile of as-implanted substrates.

to that depleted from the bulk, within an uncertainty of 20%, indicating that Cr does not out-diffuse into capping films even when annealed at 800°C. In addition, these films were found to prevent Mn invasion from the ambient gas into the GaAs.

Note that the Cr and Mn ion intensity observed in the capping layers is anomalously high. Actually, the Cr and Mn concentrations are very low, but the ion intensities are greatly enhanced in the capping layers by SIMS matrix element effects. This was experimentally verified by SIMS on Si₃N₄ films which had undergone the same Cr implantation.

Since the Cr-depleted regions were about 4 times as deep as those observed in capless annealing, the stress field caused by capping layers is thought to enhance Cr out-diffusion. This strain field could arise from thermal mismatch between the capping film and the GaAs.

As was the case for capless annealing, a critical Cr concentration for Cr depletion was observed. (In both

cases, the substrate Cr concentration was well below the solid solubility limit.) Figure 8 shows the Cr depth profiles of GaAs subjected to capped annealing at 800°C in H₂. While curve A shows Cr depletion, the Cr profile (B) (18) is not changed by annealing. Therefore, it can be said that substrates with a Cr concentration lower than the critical level (about 5×10^{15} cm⁻³) do not suffer Cr depletion in capped annealing. Although the mechanism by which this critical Cr concentration for depletion occurs is not clear at present, it is probably not due to thermal equilibrium considerations, since the critical Cr concentration does not depend on annealing temperature.

The Cr depletion depth is plotted in Fig. 9 as a function of $1/T$ (annealing temperature). The solid line indicates the estimated value from simple diffusion theory. Here we used $D = 4.3 \times 10^3 \exp(-3.4/kT)$ (7). The circles indicate capless annealing, the triangles ion-implantation (with a 10^{15} cm⁻² dose), and the squares capped annealing. There have been many

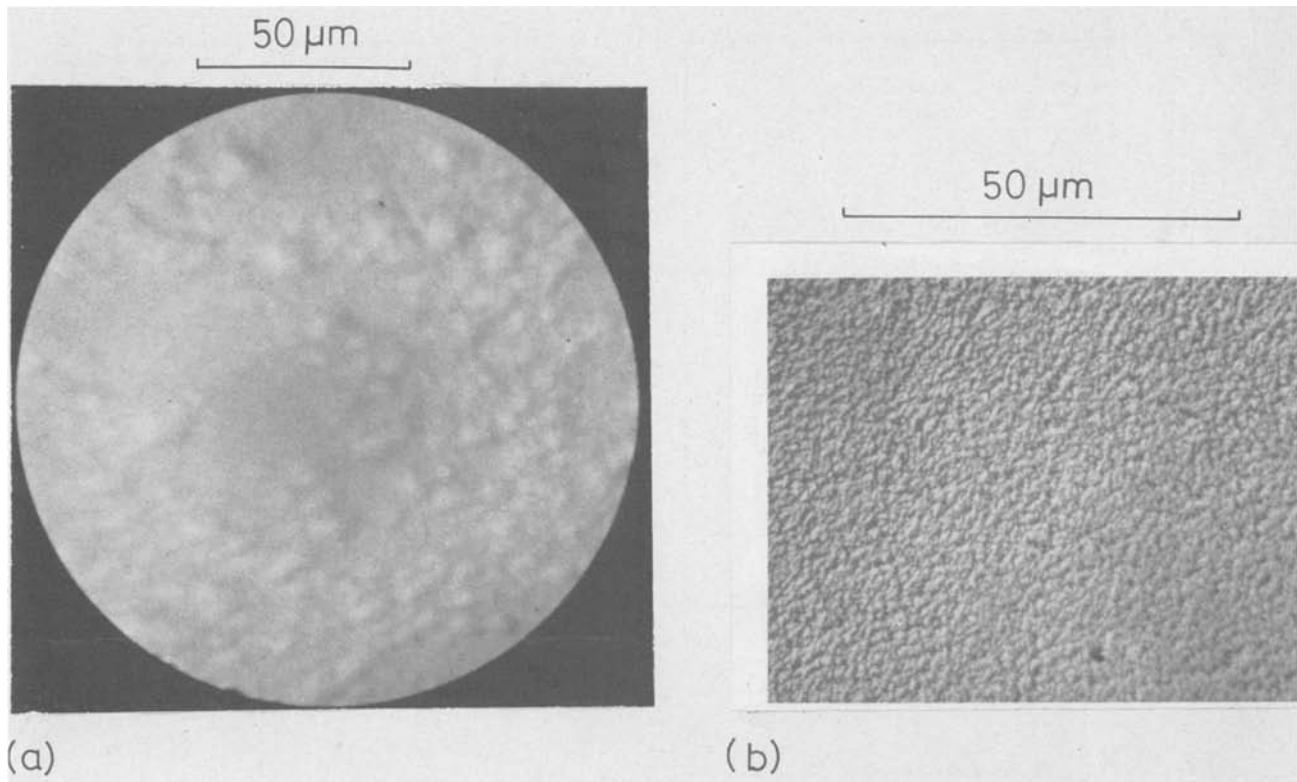


Fig. 6. $^{69}\text{Ga}^+$ secondary ion image by SIMS (a), and photograph by Nomarski differential interference microscope (b). Sample is the same as Fig. 5c. In this case, SIMS spatial resolution was about $1\ \mu\text{m}$, which was verified using $1\ \mu\text{m}$ line and space patterns fabricated by electron beam exposure system and reactive sputter etching. $^{75}\text{As}^+$ ion image could not be observed because of its weak ionization yield.

different diffusion coefficients for Cr in GaAs values reported. Sato (21) reported $1.6 \times 10^{-12}\ \text{cm}^2/\text{s}$ at 800°C , determined by an analysis of the conductive layer thickness resulting from capped annealing of Cr-doped GaAs. Wilson *et al.* (22) reported $D_{800^\circ\text{C}}$ to be $6.7 \times 10^{-12}\ \text{cm}^2/\text{s}$ from a depth analysis of Cr in Cr-doped GaAs with an epitaxially grown GaAs layer. This is large compared to other values. Kasahara *et al.* (11)

reported $D = 6.3 \times 10^5 \exp(-3.4/kT)$ using the diffusion equation with the interfacial conductance (23). Judging from Fig. 4 by Kasahara, the pre-exponential term might be 6.3×10^3 , which fixes $D_{800^\circ\text{C}}$ at $6 \times 10^{-13}\ \text{cm}^2/\text{s}$. Simondet *et al.* reported $D = 2 \times 10^{-14}\ \text{cm}^2/\text{s}$ at 772°C from a "crude calculation" using SIMS depth profiles of Cr in-diffusion in implanted and annealed GaAs. This seems too small, if defect-enhanced diffu-

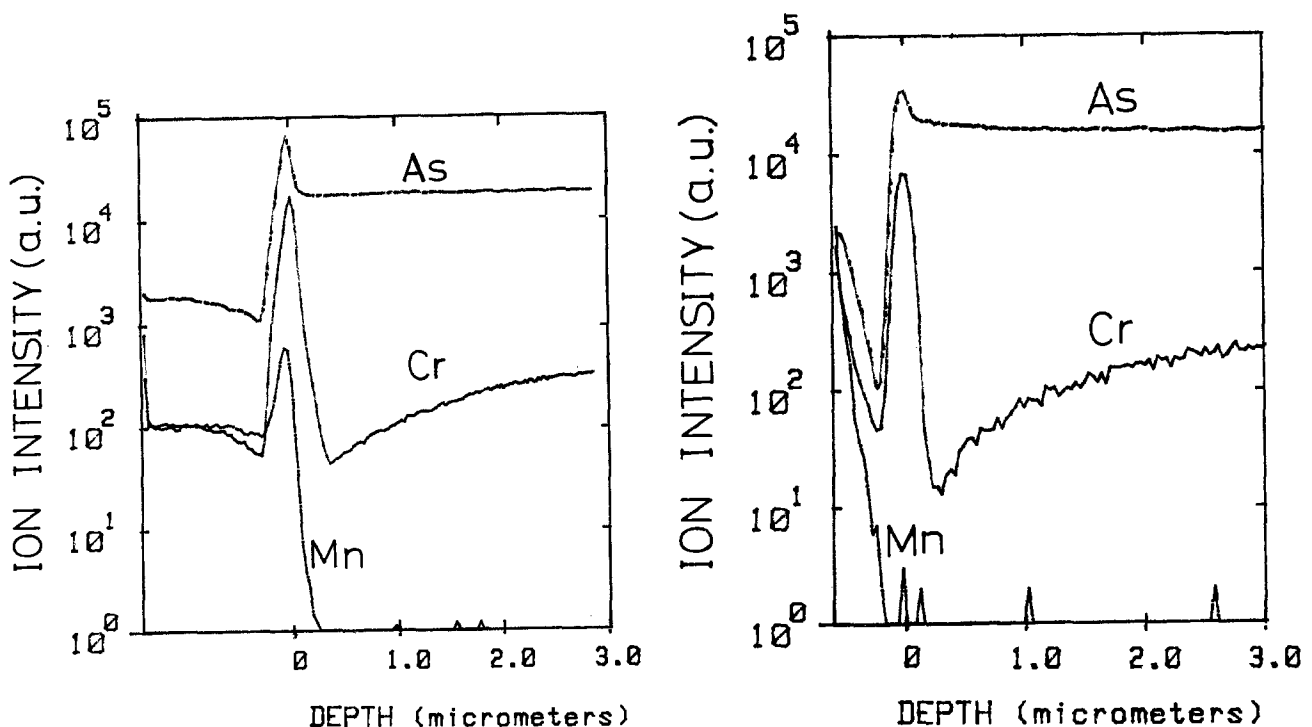


Fig. 7. As, Cr, and Mn depth profiles of GaAs substrates capped with 3000\AA SiO_2 (a, left) and 1600\AA Si_3N_4 (b, right) films. Annealing was performed at 800°C for 1h in H_2 . Electron bombardment was employed during analysis for preventing charging-up.

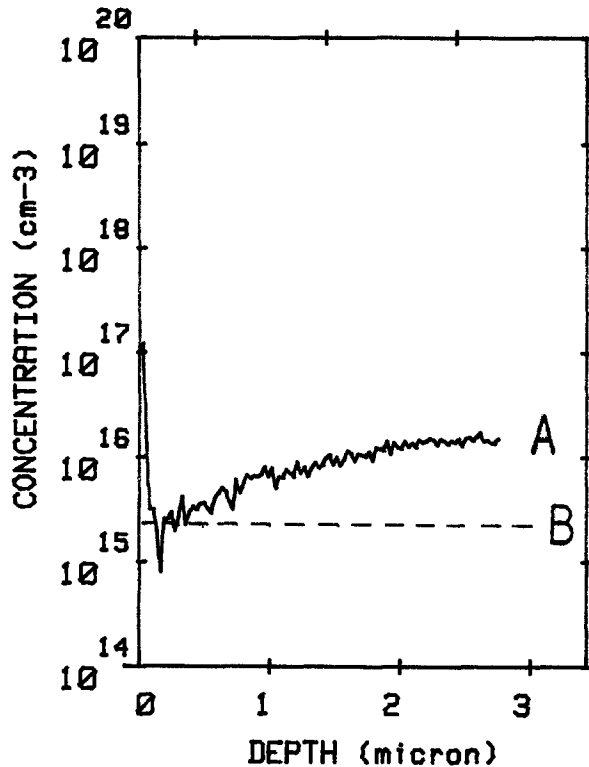


Fig. 8. Cr depth profiles of GaAs substrates with different Cr concentration. Samples (A,B) were annealed at 800°C for 1h in H₂ with 3000Å SiO₂ films for encapsulation. SIMS analysis was performed after removal of capping films. In the case of B, no Cr depletion was observed.

sion caused by ion implantation is taken into account. Therefore, the value given in Ref. 7 is adopted in this work.

From this graph (Fig. 9), three important results can be pointed out. First, capless annealing causes Cr depletion, which can be explained by simple diffusion theory in both HB and LEC crystals. However, in annealing at 750°C, Cr depletion and Mn accumulation are limited only to a shallow region. Kasahara *et al.* (11) reported that almost no Cr out-diffusion was observed after annealing at 700°C. At these low temperatures, the surface reaction necessary to allow Cr to evaporate might be the rate-determining process for Cr depletion. In the case of capped annealing a deep depleted region was observed even for 700°C annealing. This may be because no surface reaction is necessary.

The second point to note is the enhancement of Cr out-diffusion by ion implantation-induced defects. Deveaud *et al.* (24) reported that implanted (600 keV) Cr diffuses rapidly when annealed at 800°C ($D_{800-C} > 10^{-12}$ cm²/s). Since our result at 800°C roughly corresponds to $D = 5 \times 10^{-12}$ cm²/s, it is clear that defects by ion implantation definitely act to enhance Cr out-diffusion. Perhaps the large activation energy (about 5 eV) is due to surface dissociation reactions in addition to defect-enhanced diffusion.

Finally, in capless annealing, Cr depletion is enhanced with an activation energy similar to that observed after capless annealing.

Conclusions

Cr and Mn redistribution during heat-treatment has been investigated using SIMS and PL. Mn was found to be incorporated mainly from the ambient gas into Cr-depleted sites. Cr out-diffusion can be explained by simple diffusion theory, except for low-temperature annealing, where surface reaction effects might dominate behavior. Cr out-diffusion is strongly enhanced in samples undergoing capped annealing or high-dose

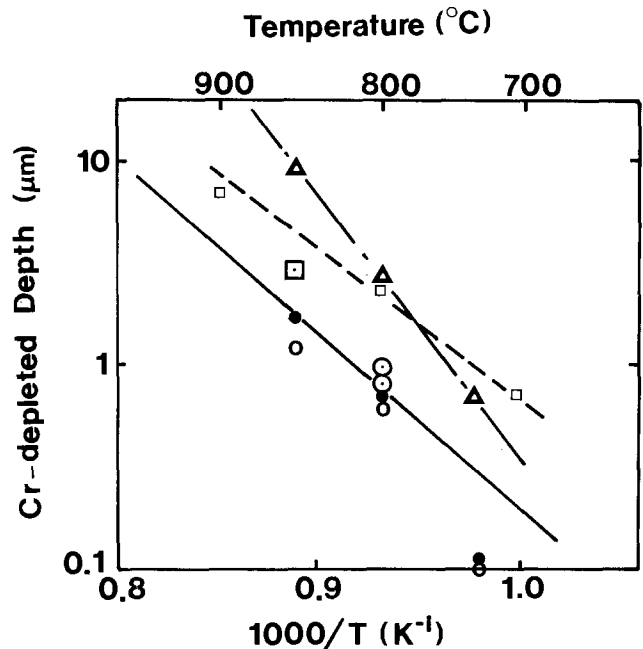


Fig. 9. Cr-depleted depth as a function of $1/T$. T stands for annealing temperature. Solid line indicates the estimated value from Cr diffusion coefficient in GaAs. 1. Capless annealing: Open circles: HB crystal ($\text{Cr}:1.4 \times 10^{17}$ cm⁻³). Solid circles: LEC crystal ($\text{Cr}:4 \times 10^{16}$ cm⁻³). Circles with dot: after Vasudue *et al.* (19). Triangles: ion implanted with 10^{15} cm⁻² dose. 2. Capped annealing. Squares: HB crystal. Squares with dot: after Hopkins (20).

ion implantation. This enhancement is attributed to stress fields in the former case, and defects and surface dissociation in the latter. There exists a critical Cr concentration for Cr depletion. GaAs substrates with lower Cr content than this do not exhibit Cr depletion regardless of whether they have undergone capless or capped annealing.

Acknowledgments

The authors wish to express their sincere thanks to M. Yamaguchi, S. Hattori, M. Ohmori, and Y. Imamura for their discussion and support during the course of this work. One of the authors (K. W.) thanks Y. Matsuoka for his discussion. Thanks are also due to S. Nojima for providing us with the GaAs substrates.

Manuscript submitted Nov. 9, 1982; revised manuscript received Sept. 9, 1983. This was Paper 243 presented at the Montreal, Que., Canada, Meeting of the Society, May 9-14, 1982.

Nippon Telegraph and Telephone Public Corporation assisted in meeting the publication costs of this article.

REFERENCES

- J. B. Clegg, G. B. Scott, J. Hallais, and A. Mircea-Roussel, *J. Appl. Phys.*, **52**, 1110 (1981).
- P. B. Klein, P. E. R. Nordquist, and P. G. Siebenmann, *ibid.*, **51**, 4861 (1980).
- H. Kanber, M. Feng, and J. M. Whelan, *Appl. Phys. Lett.*, **40**, 960 (1982).
- K. Watanabe, Y. Matsuoka, Y. Imamura, and T. Ito, in "1981 Gallium Arsenide and Related Compounds," T. Sugano, Editor, p. 383, The Institute of Physics (1981).
- J. R. Arthur, *J. Phys. Chem. Solids*, **28**, 2257 (1967).
- S. M. Sze, "Physics of Semiconductor Devices," p. 31, Wiley Interscience, New York (1969).
- W. E. Lum and H. H. Wieder, *Appl. Phys. Lett.*, **31**, 213 (1977).
- K. Watanabe, Personal communication.
- J. H. Crawford and L. M. Slifkin, "Point Defects in Solids 2," p. 224, Plenum Press, New York (1975).
- F. M. Smith and R. C. Miller, *Phys. Rev.*, **104**, 1242 (1956).
- J. Kasahara and N. Watanabe, *Jpn. J. Appl. Phys.*,

- 19, L151 (1980).
12. A. M. Huber, G. Morillot, N. T. Linh, P. N. Favennec, B. Deveaud, and B. Toulouse, *Appl. Phys. Lett.*, **34**, 858 (1979).
 13. T. J. Magee, R. D. Ormond, C. A. Evans, Jr., R. J. Blattner, R. M. Malbon, D. S. Day, and R. Sankaran, *ibid.*, **38**, 559 (1981).
 14. R. Zucca, *Inst. Phys. Conf. Ser.* no. 33b, 228 (1977).
 15. F. Simondet, C. Venger, G. M. Martin, and J. Chaudmont, *ibid.*, no. 45, 100 (1980).
 16. T. J. Magee, H. Kawayoshi, R. D. Ormond, L. A. Christel, J. F. Gibbons, C. G. Hopkins, C. A. Evans, Jr., and D. S. Day, *Appl. Phys. Lett.*, **39**, 906 (1981).
 17. T. Udagawa, M. Higashiura, and T. Nakanishi, in "Semi-insulating III-IV Materials," G. J. Rees, Editor, p. 108, Shiva, Nottingham, England (1980).
 18. S. Nojima, Personal communication.
 19. P. K. Vasudev, R. G. Wilson, and C. A. Evans, Jr., *Appl. Phys. Lett.*, **36**, 837 (1980).
 20. G. G. Hopkins, *et al.*, *ibid.*, **36**, 989 (1980).
 21. Y. Sato, *Jpn. J. Appl. Phys.*, **12**, 242 (1973).
 22. R. G. Wilson, P. K. Vasudev, D. M. Jamba, C. A. Evans, Jr., and V. R. Deline, *Appl. Phys. Lett.*, **36**, 215 (1980).
 23. R. C. Miller and F. M. Smith, *Phys. Rev.*, **107**, 65 (1957).
 24. B. Deveaud and P. N. Favennec, *Solid State Commun.*, **24**, 473 (1977).

Electrochemical Deposition of Photosensitive CdTe and ZnTe on Tellurium

Hendrik J. Gerritsen¹

Institut für Angewandte Physik der Universität Karlsruhe, Karlsruhe, Germany

ABSTRACT

Two methods to prepare Cd and Zn telluride layers electrochemically on a Te electrode situated in 0.1M CdSO₄ electrolyte are described. Crystalline, photoelectrochemical, and spectral sensitivity properties of the layers are described. The simplicity of the preparational methods and the various interesting semiconductor and photochemical properties of the resulting telluride layers lend themselves well to instructional purposes.

A great many electrochemical deposition methods for cadmium and bismuth chalcogenides have been reported in the literature. CdS and Bi₂S₃ have been formed by anodic deposition on Cd and Bi, respectively, in S²⁻ containing aqueous electrolyte (1, 2, 3). While large photo quantum efficiency was reported for Bi₂S₃ (4), layers of CdSe similarly prepared were less satisfactory because of their thinness (5).

Cathodic coprecipitation of photosensitive cadmium selenide and telluride layers on a variety of substrates from aqueous solution containing CdSO₄ and SeO₂ or TeO₂ has been reported (6, 7, 8). This method has more recently been extended to nonaqueous electrolytes as well (9, 10).

What will be described in this paper is the electrochemical deposition of cadmium and zinc telluride on a tellurium electrode as substrate in 0.1M CdSO₄ electrolyte. Two different modes of operation were studied. In one, called Method I, no bias was applied between the electrodes, in the other, Method II, the tellurium electrode was biased strongly positively. The crystalline and photoelectrical properties of layers prepared by these two methods are described and compared with each other. Causes for the differences are discussed.

Experimental

A tellurium rod and a cadmium strip were hung in a 0.1M solution of cadmium sulfate in water and connected with each other via a 20 kΩ variable resistor and a microamp meter (see Fig. 1). A high impedance voltmeter was connected across the two electrodes, and N₂ could be bubbled through the electrolyte. A variable external potential (V) was applied in some of the experiments.

To prepare ZnTe, a metal zinc strip and a 0.1M ZnSO₄ solution were used instead. Contact to the cadmium or zinc metal was made by spotwelding a Pt wire to one side of the 0.5 × 5 cm metal foil 0.05 cm thick.

Te was also contacted with Pt wire, usually by sending an electrical current through the wire and pressing the red glowing platinum wire into the Te rod. Some experiments were performed starting from small chunks of Te, which were melted under a slow stream of dry nitrogen in a Pyrex mold. In that case, the contacting wire (platinum or standard tinned copper wire) was placed with the Te in the mold and became embedded into the molten Te. The heat of a Bunsen burner (450°C) sufficed to melt the tellurium. The mold was covered with a lid to minimize contact with the air and because Te tends to sublime and its

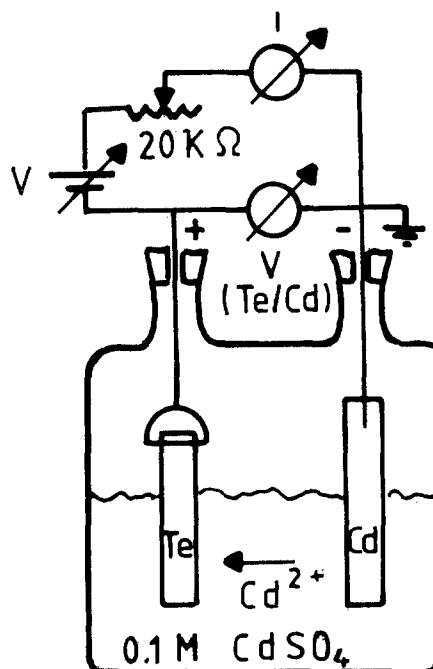


Fig. 1. Basic setup to grow and measure CdTe and ZnTe layers

¹Permanent address: Department of Physics, Brown University, Providence, Rhode Island 02912.

Key words: cadmium, photocurrent, polycrystalline deposit, preparation, telluride, zinc.

vapors are poisonous. The tellurium rod could be lifted easily out of the mold since Te shrinks upon cooling.

The Cd and Zn used were 99.97% pure; the Te was 99.99% pure. The electrodes were degreased with acetone, and the metals further cleaned by immersion in diluted HCl and rinsing in distilled water. The tellurium was cleaned by immersion and stirring in 5% (by volume) Br₂ in methanol for 10 min, followed by more stirring in the solution which was gradually diluted with methanol, ending up with pure methanol. After this treatment the polycrystallinity of the Te surface was clearly visible to the eye.

Method I

Cadmium.—In this very simple method, the cadmium and tellurium in the 0.1M CdSO₄ solution form a battery. The open voltage of this battery is about 0.63V, although one Te electrode that had been freshly etched for a long time (1h in 5% bromo methanol) gave 0.85V. Measurements of the potential of the Cd and Te vs. a saturated calomel reference electrode in the 0.1M solution gave -0.69V for the Cd. This was in fair agreement with the calculated value of -0.66V. For the Te, it varied from -0.06V to +0.16V depending on the degree of etching previously given.

The current that flows when one connects the Cd and Te via a 20 kΩ resistor corresponds to a flow of Cd²⁺ onto the Te followed by formation of CdTe. In minutes, the initially large current decays to a fraction of a milliamp, and the variable resistor is reduced to zero. In most of the experiments N₂ was bubbled through the electrolyte at a slow rate, but in the few experiments where this was omitted and the electrolyte exposed to the open ambient air, the resultant films were not noticeably different. Almost all the experiments on film growth were performed in the dark for reasons that will soon become apparent.

The progress of film formation was followed by visual observation, by measurement of the short-circuit photocurrent of the layer upon brief illumination, and by measurement of the open-circuit photovoltage. A 6 mW HeNe laser with wavelength of emission at 633 nm was the illumination; it illuminated the telluride layer in the cadmium sulfate solution.

Initially the color of the CdTe layer forming on the silvery Te substrate was golden, and the short-circuit current, observed on the μA meter, did not change much upon illumination. After 4h of growth the short-circuited dark current of +4 μA (flowing externally from the Te to the Cd) increased to +5 μA upon laser illumination. As a function of time of film growth, a color mosaic develops of gold, red, blue, and purple areas, the dark current decreases steadily, and the photocurrent increases. The size of the color domains appears to be similar to that of the polycrystalline areas previously observed on the Te substrate, that is, from 1 to 10 mm². After 70h of growth, the photocurrent of the purple areas is typically +180 μA, and that of the golden-bronze areas is only +50 μA, while the open-circuit voltage was 290 mV. The time of appearance of the color mosaic did depend on the previous etch given to the Te; a Te electrode that had been given a long etch developed the colors after only 24h. Film growth after one week was very slow, but a small current kept flowing, the color mosaic assumes deeper colors, and the photosensitivity increases still slowly in time. A tellurium electrode made by melting Te chunks in a Pyrex form and placing them in the electrolyte in air (no N₂ used) and short-circuited with the Cd electrode behaved in a manner similar to that of the polycrystalline Te rod; it was very sensitive to daylight.

It should be mentioned that no growth occurred on a piece of tellurium which was left for two weeks in the solution and was not externally connected with the cadmium electrode.

Zinc.—Less effort was expended to grow ZnTe by this method than was spent on CdTe. It appeared that

Method II worked better for zinc telluride than Method I. The battery Zn/0.1M ZnSO₄/Te has an initial voltage of 1.2V. After shortening via a 20 kΩ resistor for two days in open air, the dark current was still rather large, +20 μA. With laser light this current increased to +23 μA. The layer had a gold/bronze color with indication of a mosaic structure in the shades of gold, similar to, but much less colorful, than that observed in the CdTe layer.

Method II

This method was discovered accidentally when an attempt was made to reverse the flow of positive metal ions by biasing the Te electrode positively with respect to the metal electrode. While a fair degree of electrocleaning was obtained by applying a bias of about +0.9V (Te w.r.t. Cd) and drawing a small reversed current for typically one day, a very different behavior was observed when a large reverse current was maintained.

Layers with optimal photosensitivity were obtained by maintaining a current flow of -5 mA going from Te to the metal in the liquid for about 10 min. This requires a bias increased gradually from +1.3 to 4.5V. The resultant layers were shiny black, with some indication of colors in the CdTe layer. Exclusion of air by bubbling through of N₂ appears not to make much difference.

Results and Discussion

Current-voltage measurements.—The measurement setup was identical to that used to grow the layers, as in Fig. 1. Keithley Instruments Electrometers 610C or 602 (battery operated) were used for the electrical measurements, while the light intensity of the HeNe laser was measured with a photometer/radiometer system, EG&G Model 450.

Figure 2 shows the results of a CdTe and a ZnTe layer. The CdTe was grown with Method I (though CdTe layers grown with Method II have a similar i-V characteristic); the ZnTe was grown with Method II. A rectifying barrier between 0 and +0.5V is evident in both. A positive current is defined as a current that flows in the same direction as the current in the short-circuited, unbiased battery that is in the liquid from the metal towards the tellurium. In the metal-tellurium battery, the Te has the positive potential w.r.t. the metal. Therefore, the potential will be chosen as that of the Te w.r.t. the metal. When the Te, covered with the telluride layer, is biased negatively, the photo-effects are at their largest, but also a very large dark current begins to flow. This was identified in the Cd system as the reduction of Cd²⁺ at the CdTe layer, forming Cd dendrites along crystallite boundaries and along edges. The right side of the i-V characteristic shows blocking, but above +0.5V, current begins to flow, again leading to formation of the telluride by Method II.

An explanation of the general features of these curves must include the semiconductor properties of the telluride layer and the nature of the electrolyte, in which the positive metal ions play a special role. If one assumes that p-type metal tellurides are formed, which cover themselves with an n-type inversion layer at the electrolyte interface, one has an explanation for the direction of the short-circuited photocurrent, which is carried in the liquid by Cd²⁺ and is discharged at the CdTe layer by the photoelectrons present at the interface. Application of a positive bias blocks that photocurrent. However, one has a problem understanding the dark current behavior. If the p-n junction is as postulated, then forward current should flow when the CdTe (and thus the Te) is given a positive bias, while blocking is expected for Te at negative potential. A possible explanation for the phenomenon shown in Fig. 2 is that for negative bias, the metal ions discharge on the telluride, and the charge transfer takes place by tunneling through the very thin n-layer. In the positive bias direction, electrolysis of the electrolyte would

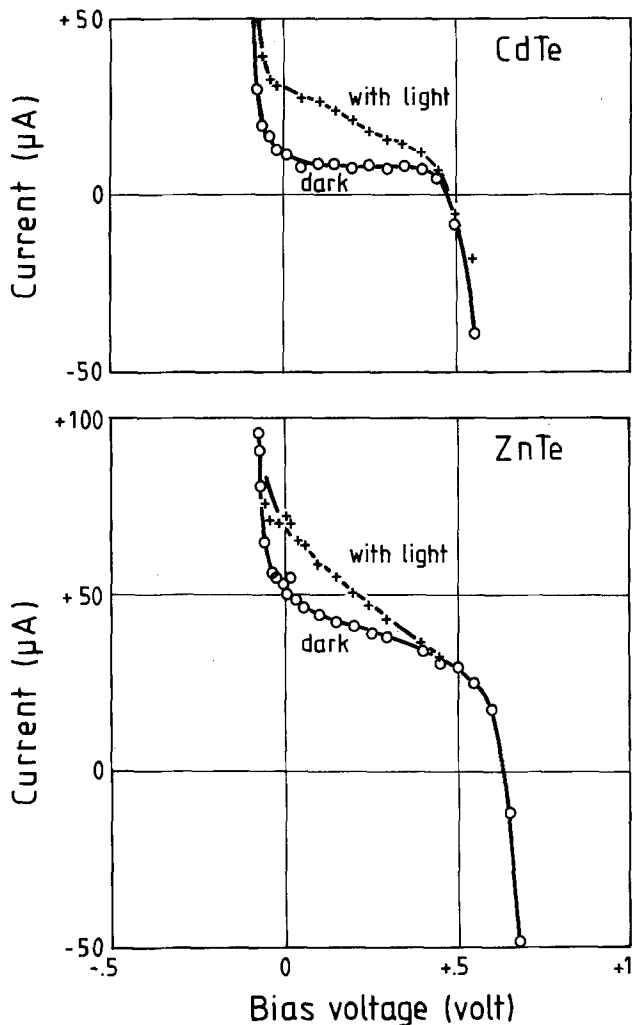


Fig. 2. C-V characteristics of CdTe and ZnTe layers

have to take place to provide the necessary carriers and charge transfer. It seems plausible that this requires voltages above +0.5V.

In order to obtain additional confirmation regarding this explanation, experiments were done with 2 mm-thick melt-grown polycrystalline crystals of p-CdTe and of n-CdSe, grown by a modified Bridgman technique, as shown in Fig. 3 and 4. Except for the difference in slope, caused by the rather large (15 kΩ) resistance of the melt-grown CdTe, Fig. 3 is in all essential points identical with Fig. 2. In contrast, in the low resistivity in n-CdSe one sees the reversal of the direction of photocurrent, as expected, and also the extreme blocking (both semiconductor and electrolyte are blocking) and large forward current. A similar characteristic was observed when the same n-CdSe disk was placed in a 1M polysulfide solution, a common electrolyte for this material (Fig. 5). Since there was now a photocurrent at zero bias, this electrolyte could be used as a photovoltaic cell, while it could not be so used in the CdSO₄ solution.

Two attempts were made to grow n-type CdTe on Te. These attempts were inspired by the results obtained in the cathodic codeposition method (8), in which additions of small quantities of In₂(SO₄)₃ changed the p-type into n-type material. Layers grown from 0.1M CdSO₄, to which in one experiment was added 0.001M In₂(SO₄)₃, and in a second experiment 0.01M InCl₃, by both Methods I and II, came out as p-type with characteristics not much different from undoped layers. Perhaps the fact that the layers are grown on Te, which is a p-dopant for CdTe, explains this negative result.

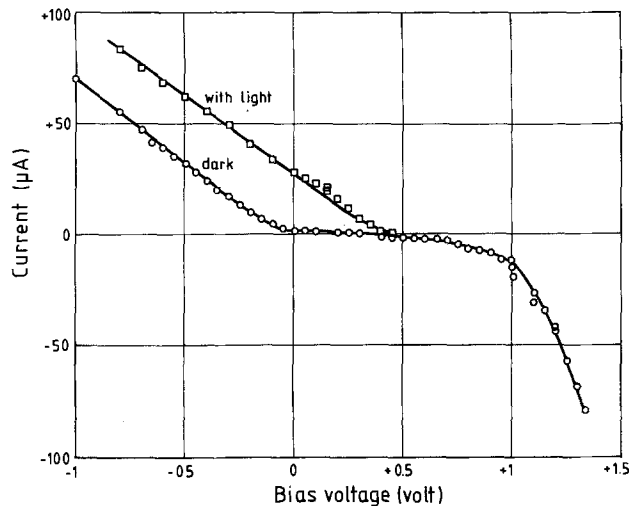


Fig. 3. C-V characteristics of polycrystalline p-CdTe

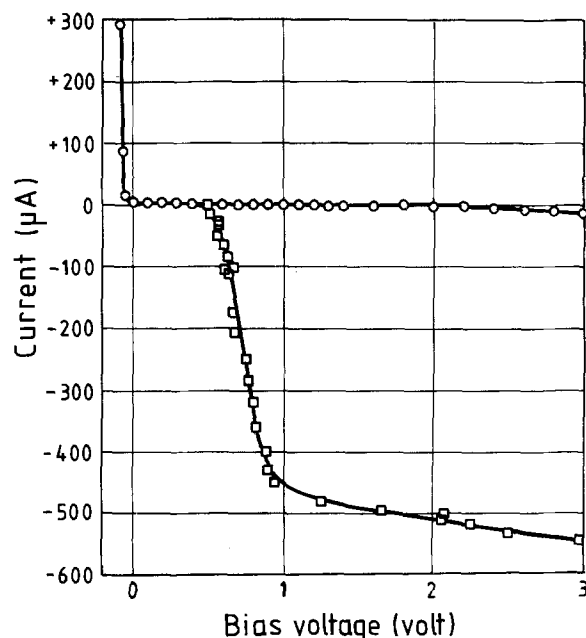


Fig. 4. C-V characteristics of polycrystalline n-CdSe in 0.1M CdSO₄

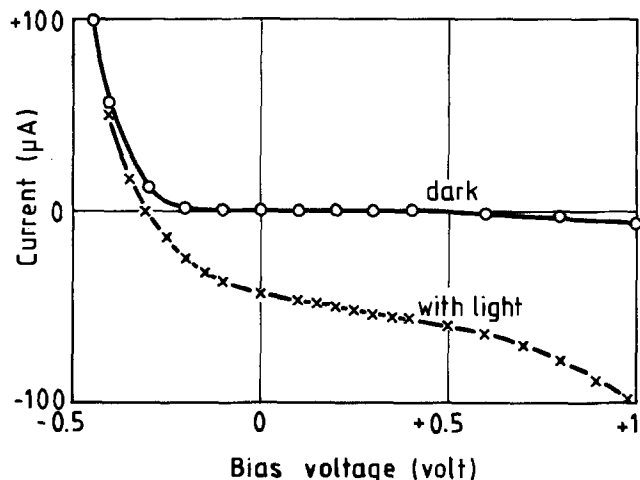


Fig. 5. C-V characteristics of polycrystalline n-CdSe in polysulfide solution.

Light damage and recovery.—This effect was studied in CdTe layers and consists of the following observation: when the layer is illuminated by a light beam, the

closed-circuit photocurrent rises rapidly, comes to a standstill and then decreases. The speed of decrease depends on the intensity. At the same time, one observes a whitish-gray spot on the layer. After several hours in the dark, the spot disappears, and the layer recovers. The study of this effect was important for two reasons: first, to assure that the photomeasurements done on the layers could be performed under conditions (short pulses of low intensity light) where the effect was absent; second, the curious dark recovery held out some possible hope for semiconductor systems in which light damage occurs.

Quantitatively, the 6 mW laser beam illuminating one of the sensitive, purple areas on a CdTe film grown for one week by Method I gave a 200 μA short-circuit photocurrent, which decayed to 100 μA in 45s, leaving a gray white spot of 3 mm diam. Leaving the cell short-circuited in the dark results in the shrinking and final disappearing of the spot after about 8h while the photocurrent is back at 200 μA . If one disconnects the short between the Cd and Te, recovery occurs after about 2½h. Chemical analysis determines that the spot consists of Cd metal, as is to be expected. As soon as photocurrent flows in this system, cadmium plates out on the CdTe. However, the recovery occurs because the cadmium spot acts as the electrode of a Cd/Te battery which forms CdTe probably by Cd movement along the layer and inward. If one keeps the Te and Cd electrodes connected, the spot experiences competition from the Cd^{2+} flow of the latter and is expected to disappear slower than when the Te and Cd electrodes are disconnected. This form of recovery will of course proceed slower and slower the thicker and longer the telluride layer has grown. It would be interesting to see if a slightly negative bias of the CdTe w.r.t. the Cd electrode might make the spot grow by selective Cd plating. Such an effect would be similar to chemical development in photography and might improve the sensitivity of this layer, which is presently about 500 mJ/cm^2 for clearly visible spots. The spectral range and reversibility makes this simple system of some potential interest as photographic material for study of near IR lasers.

For comparison, light damage experiments were performed on the 2 mm-thick melt-grown polycrystalline p-CdTe sample in the same setup. There too, the light created cadmium at the surface, but recovery did not occur. A clean Te rod was placed in the solution and externally connected to the CdTe sample which had the Cd spot. In the course of several minutes most of the Cd had migrated off from the CdTe sample and onto the Te rod.

Photovoltaic characteristics.—A CdTe layer grown for 1 week by Method I was used in the configuration of Fig. 1. It was illuminated by a spread-out 5 mW laser beam, and the i/V plot was obtained by varying the load resistance from 0 to 20 k Ω . The experiment was done in a time short compared to the time it takes the Cd layer formed to reduce the photocurrent. The result is shown in Fig. 6a and compared with the characteristics of the 2 mm-thick, low-ohmic, polycrystalline n-CdSe in a solution of polysulfide consisting of 1M each of NaOH, Na_2S , and S with Pt as counter-electrode. The p-CdTe layer had an efficiency of 0.2%; the best efficiency measured for a similar layer has been 0.4%. In comparison, the p-CdTe polycrystalline crystal of 2 mm thickness showed a 0.55V open-circuit voltage and a photovoltaic efficiency of 16% at low light levels where the resistive voltage drop across the crystal does not limit the current or the measured efficiency appreciably.

Spectroscopic characteristic.—Figure 7 shows the spectral characteristics measured for the two type CdTe layers discussed in the text and a polycrystalline CdTe disk. The values on the ordinate represent the short-circuit photocurrent in a cell consisting of the CdTe

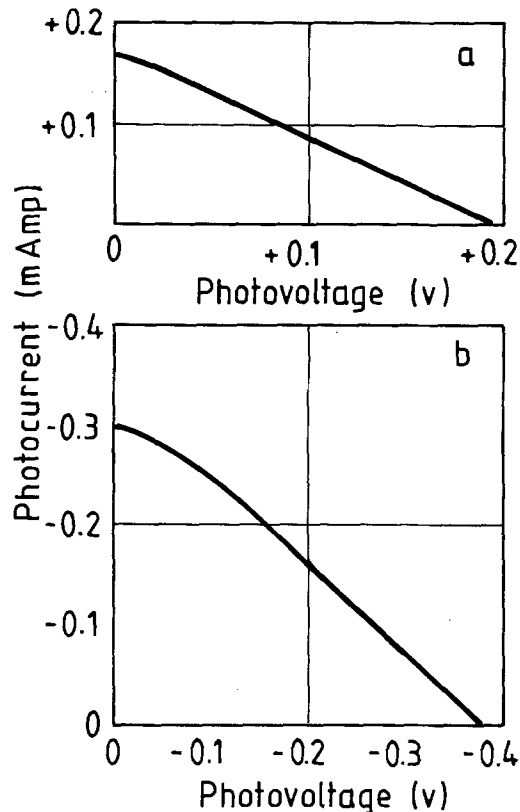


Fig. 6. Photovoltaic characteristics: (a) electrodeposited CdTe on Te, (b) polycrystalline n-CdSe in polysulfide solution.

layer on Te (or the CdTe disk), a Cd electrode, and 0.1M CdSO_4 electrolyte. The monochromator used was a prism-type Zeiss M4G11 which was illuminated with a 50W tungsten/halogen lamp and calibrated with a photometer/radiometer system EG&G Model 450. The room temperature bandgap of single-crystal CdTe is about 1.5 eV, corresponding to 826 nm. Of interest is the rather steep rise in photocurrent with decreasing wavelength for both the melt-grown CdTe and the layer grown by Method I, while the photocurrent in the layer grown by Method II rises slowly and does not seem to reach its plateau at 500 nm.

A similar difference between single crystals (steep rise) and electrodeposited layers (gradual) has also been reported for CdSe (11), and for CdS (12). The explanation for the observations in Fig. 7 would then be that the electrodeposited p-CdTe layer grown

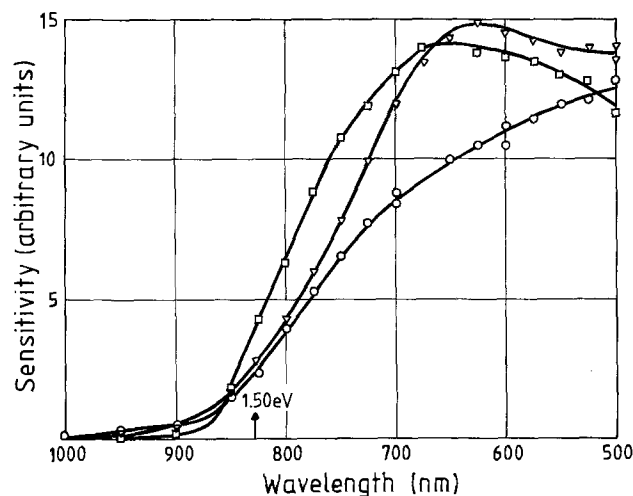


Fig. 7. Spectral sensitivity of polycrystalline CdTe (\square); CdTe layer grown on Te without bias (Method I) (∇); CdTe layer grown with positive bias on Te (Method II) (\circ).

by Method II contains such a high density of acceptors ($>10^{18} \text{ cm}^{-3}$) that the space charge region is thin compared to the penetration depth of the light. Going towards shorter wavelengths decreases this penetration depth and produces more photocurrent in the space-charge region. It is significant that the CdTe layers prepared by Method I behave like melt-grown polycrystalline CdTe. ZnTe prepared by Method II was also measured (Fig. 8) and behaved similarly to the CdTe grown by Method II, with the exception that its bandgap is wider. That layer too seems to contain a high density of acceptors.

Mechanism of layer formation.—Method I is straightforward; the Cd/CdSO₄/Te battery operates by migration of Cd²⁺ from the Cd to the Te electrode, discharge of the Cd²⁺ to Cd, and subsequent formation of CdTe. Cd requires some time to diffuse through this layer to recombine with Te, as demonstrated by the gradual disappearance of a light-damage Cd spot at the surface of the layer. The growth speed of a single-crystal CdTe domain seems dependent upon the crystal domain orientation of the Te substrate, as evidenced by the difference of interference colors in the color mosaic.

Method II involves most likely a positive tellurate ion, perhaps injected into the solution as HTeO₂⁺ (13 and 8) that combines with Cd²⁺ from the solution and settles down on the Te electrode as CdTe. The resultant free positive charge presumably oxidizes water to O₂, though the exact mechanism has not been studied.

Crystalline and mechanical properties of the layers.—The layers of CdTe grown by Method I attach themselves very strongly to the Te substrate. Their lively colors are due to a combination of interference and absorption effects and indicate: (i) their thickness is of the order of 0.1 to 0.2 μm; (ii) the domains of area 1-10 mm² are single crystals. Well-defined Laue back-

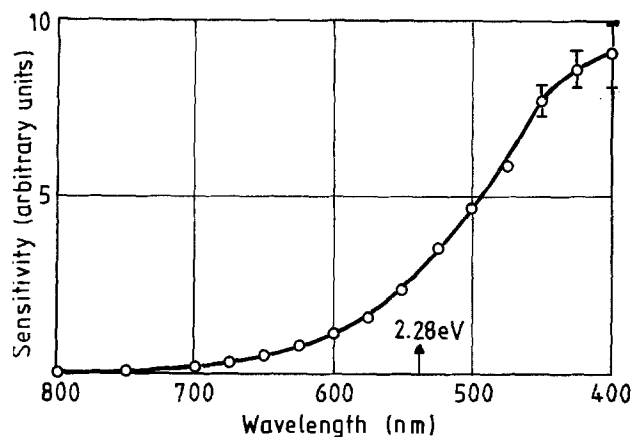


Fig. 8. Spectral sensitivity of electrodeposited ZnTe on Te

scattering spots of the CdTe layers showed that the various differently colored areas correspond to various single- or twin-crystal orientations.

The layers grown by Method II are black in appearance and attach well, but not as strongly to the tellurium as the layers grown slowly by Method I. There were no single-crystal lines observable in the Laue pattern of these layers. Chemical analysis and photo response indicate that both layers are metal telluride, but the stoichiometry has not been determined.

Conclusions

Two electrochemical deposition methods for the preparation of CdTe and ZnTe have been described. The layers have interesting properties in particular that single-crystal domain telluride layers can be prepared electrochemically. The many photoelectrochemical effects observable in this simple system make it attractive for educational purposes as well, particularly since the toxicity aspects (cadmium sulfate solution) are not especially hard to control.

Acknowledgments

I want to thank the Deutsche Forschungsgemeinschaft for financial support, the Department of Physics at the University of Karlsruhe for their great hospitality and, in particular, Dr. W. Ruppel and Dr. P. Würfel for several helpful discussions, and Mr Schiefferdecker for some help with the experiments.

Manuscript submitted Nov. 29, 1982; revised manuscript received July 21, 1983.

The Universität Karlsruhe assisted in meeting the publication costs of this article.

REFERENCES

1. B. Miller and A. Heller, *Nature*, **262**, 680 (1976).
2. L. M. Peter, *Electrochim. Acta*, **23**, 165 (1978).
3. J. Vedel, M. Soubeyrand, and E. Castel, *This Journal*, **124**, 177 (1977).
4. L. M. Peter, *J. Electroanal. Chem.*, **98**, 49 (1979).
5. W. A. Gerrard and J. R. Owen, *Mater. Res. Bull.*, **12**, 677 (1977).
6. G. Hodes, J. Manassen, and D. Cahan, *Nature*, **261**, 403 (1976).
7. S. Chandra and R. K. Pandey, *Phys. Status Solidi A*, **59**, 787 (1980).
8. M. P. R. Panicker, M. Knaster, and F. A. Kröger, *This Journal*, **125**, 567 (1978).
9. A. S. Baranski and W. R. Fawcett, *ibid.*, **127**, 766 (1980).
10. A. S. Baranski, W. R. Fawcett, A. C. McDonald, R. M. de Nobriga, and J. R. MacDonald, *ibid.*, **128**, 963 (1981).
11. K. Colbow, D. J. Harrison, and B. L. Funt, *ibid.*, **128**, 547 (1981).
12. L. M. Peter, in "Semiconductor Liquid-Junction Solar Cells," Adam Heller, Editor, p. 236, The Electrochemical Society Softbound Proceedings Series, Princeton, NJ (1977).
13. M. Pourbaix, "Atlas d'Equilibres Electrochimiques," Gauthier-Villars et Cie, Paris (1963).

Pairing Effects in the Luminescence Spectrum of $\text{Zn}_2\text{SiO}_4\text{:Mn}$

D. J. Robbins,^{*,1} E. E. Mendez, E. A. Giess, and I. F. Chang*

IBM T. J. Watson Research Center, Yorktown Heights, New York 10598

ABSTRACT

High resolution, low temperature photoluminescence spectra of manganese-doped willemite ($\text{Zn}_2\text{SiO}_4\text{:Mn}$) single crystals have been measured. "Hot" bands on the zero-phonon lines of the ${}^4\text{T}_1$ excited state of $\text{Mn}_{\text{Zn}}^{2+}$ on inequivalent sites are observed at low Mn concentration between 4 K and 29 K. Their appearance is attributed to vibronic (Ham) quenching of the first-order spin-orbit interaction in the ${}^4\text{T}_1$ excited state, by analogy with known properties of $\text{Mn}_{\text{Zn}}^{2+}$ in ZnS and ZnSe. At higher Mn concentration, additional lines appear which are assigned to Mn pair centers involving substitution on nearest neighbor Zn sites. Electron microprobe analysis shows that the segregation coefficient of Mn incorporation in the crystal increases as the Mn concentration in the melt increases. This is indicative of pairwise incorporation during growth, and consistent with the optical detection of Mn pairs in the crystals at higher Mn concentrations. The measured luminescence decay times depend on both Mn concentration and temperature of the crystals, due to thermally activated energy transfer between Mn centers.

Manganese-doped willemite finds practical application as a green-emitting phosphor in both fluorescent lamp and display devices (1). In the particular case of cathode ray tube devices, the basic $\text{Zn}_2\text{SiO}_4\text{:Mn}$ system (designated P1) (2) is typically employed in high luminance applications, and when co-doped with arsenic (designated P39) (2) it is used as an anti-flicker phosphor for information display. The luminescence in all these phosphor applications is that of the divalent Mn^{2+} ion substituted on Zn sites (3). Optimization of phosphor efficiency and lifetime, two important practical quantities, depends critically on the details of impurity incorporation in the willemite lattice (4). In this paper, we report a high resolution spectroscopic study of Mn incorporation in willemite, together with measurements of luminescence lifetime as a function of both Mn concentration and temperature.

The willemite lattice has two inequivalent Zn sites, both having four nearest neighbor oxygen ions in a slightly distorted tetrahedral (T_d) configuration (5, 6). Two inequivalent Zn tetrahedra and one Si tetrahedron alternate in chains parallel to the c-axis; these chains are linked on a threefold screw axis in such a way that neighboring inequivalent Zn tetrahedra form pairs by sharing corners, the pair axes lying approximately parallel or perpendicular to the crystal c-axis. Nearest neighbor cation interactions between ions on Zn sites therefore occur between the inequivalent Zn sites. Luminescence is assigned to transitions between the spin-orbit components of the ${}^4\text{T}_1$ excited state and the ${}^6\text{A}_1$ ground state of Mn^{2+} in T_d coordination (7). EPR studies (8) originally showed that Mn could be incorporated on both Zn sites. Low temperature photoluminescence spectra (9-12) excited by broad band, high-energy radiation revealed two zero phonon lines (ZPL's) which were attributed (12) to $\text{Mn}_{\text{Zn}}^{2+}$ ions on the two inequivalent Zn sites, designated A and B sites. The sharp ZPL's were reported (12) at 2.455 eV (504.6 nm) for the Mn_A centers and 2.404 eV (515.3 nm) for the Mn_B centers, and confirmed by Fern and Chang (13). The energy difference was suggested to be consistent with the difference in crystal field strength estimated from differences in Zn—O bond lengths at the two sites. However, the spectral resolution achievable in these earlier studies was limited by the use of polycrystalline material. In particular, the line broadening observed at high Mn concentrations (12) precluded the observation of impurity interaction effects at higher doping levels.

For the present study, single crystals of Zn_2SiO_4 including both Mn and As impurities have been used

(14). Preparation of the material in single crystal form allows better control of impurity incorporation and offers the possibility of improved spectral resolution through reduction of inhomogeneous line broadening. Selective excitation of the Mn_A and Mn_B centers has been achieved using various lines from an Ar^+ laser, allowing spectral isolation of luminescence from the lower energy Mn_B centers for the first time. The Ar^+ laser lines at 501.7 and 514.4 nm provide near-resonant excitation of the Mn_A and Mn_B centers, respectively, and under this condition of near-resonance additional fine structure has been observed at low temperature in the region of the ZPL's. The experimental procedures employed in this study are outlined in the section on experimental techniques, and the results reported in the results section. The significance of these results is discussed more fully later, and comparisons are made with the properties of $\text{Mn}_{\text{Zn}}^{2+}$ in ZnS and ZnSe, where analogous effects of Mn impurity concentration and temperature on the optical spectra have been reported.

Experimental Techniques

Single crystals of Zn_2SiO_4 in the form of hexagonal prisms several millimeters in size were grown between 1300° and 960°C by the slow cooling (1°C/hr) of molten solutions of composition $5\text{Zn}_2\text{SiO}_4 + 3\text{Pb}_2\text{ZnSi}_2\text{O}_7$. Mn and As impurities were introduced as MnF_2 and As_2O_5 , respectively. Crystal compositions were determined with an Applied Research Laboratory's Scanning Electron Microprobe Quantometer, using the characteristic MnK_α , AsL_α , and PbM_α lines for low level impurities and Mn° , GaAs , and Pb° as reference materials. Arsenic is incorporated into the willemite crystals to a lesser degree than Mn, the segregation coefficient for As being more than an order of magnitude lower than that for Mn. Little, if any, Pb is soluble in willemite grown in this way. Further discussion of the crystal growth and analysis procedures is given in Ref. (14).

High resolution, low temperature PL spectra were measured using a Spex 1402 0.75m double monochromator and cooled RCA C31034A (GaAs) phototube, with excitation by selected lines from the Ar^+ laser. The samples were mounted in a variable-temperature cryostat. Luminescence decay times were measured between 5-300 K using a mechanical shutter in the laser beam. In order to improve signal/noise ratio in the decay curves when a narrow bandpass in the detection monochromator was used, signals from repeated pulses were added using a Nicolet 1174 signal averager.

Results

Chemical analysis and buoyancy density measurements have indicated a nonstoichiometric crystal for-

* Electrochemical Society Active Member.

¹ On leave from: Royal Signals and Radar Establishment, Malvern, England.

mula $Zn_{1.96}Si_{1.04}O_{4.04}$ for the willemite lattice (14). The results of 14 separate microprobe analyses on Mn-doped crystals show that the number of Mn atoms per formula unit incorporated in the willemite crystal (denoted $[Mn]_x$) is not a simple linear function of the mol fraction of MnF_2 in the growth melt (denoted $[Mn]_m$). The data points are plotted in Fig. 1, and the line represents a least squares fit giving the relationship

$$[Mn]_x \cong 75[Mn]_m^2 + 0.6[Mn]_m + 0.0007 \quad [1]$$

This equation has been used to estimate the Mn concentration in crystals used in the spectroscopic measurements for which no microprobe analyses were available. The results are shown in Table I. The fractional substitution of Mn for Zn in the willemite lattice is then approximately equal to $[Mn]_x/1.96$, allowing for the nonstoichiometry of the crystal formula.

Figure 2 shows the low temperature Mn^{2+} luminescence spectra excited by different lines of the Ar^+ laser. The two ZPL's, attributed to the high energy (Mn_A) and low energy (Mn_B) sites, are clearly seen. The relative intensities of these two ZPL's vary with excitation energy, even for relatively high-energy and nonresonant excitation using laser lines at 473 and 458 nm. This variation presumably reflects differences in the absorption spectra of Mn^{2+} ions on the inequivalent Zn sites. The laser line at 514.5 nm (2.41 eV) is at too low an energy to excite luminescence from the Mn_A centers, and the lowest curve in Fig. 2 therefore represents the emission spectra from Mn_B centers alone. This is the first time that luminescence from the two inequivalent Mn centers in willemite has been clearly separated, and the technique reveals the vibronic sideband associated with the Mn_B site without interference from sidebands of the higher energy Mn_A site which are otherwise present.

Figure 3 shows the luminescence spectrum excited at 458 nm at a series of temperatures between 4.2 and 29 K. These spectra were measured with a lower resolution detection monochromator, but the resolution is adequate to show that the ZPL's for both Mn_A and Mn_B sites have the "hot" components which appear as shoulders ~ 1 meV to high energy of the main lines as the temperature is increased. The effect is illustrated with better resolution for the Mn_B center in Fig. 4; the upper figure shows the temperature dependence for a crystal of low Mn concentration ($\sim 0.3\%$ Mn substituted for Zn), and the lower figure for a high Mn concentration ($\sim 3\%$ Mn). The dependence of lineshape on temperature and the appearance of the hot band 1.2 meV above the main line are most marked for the sample with lower Mn concentration.

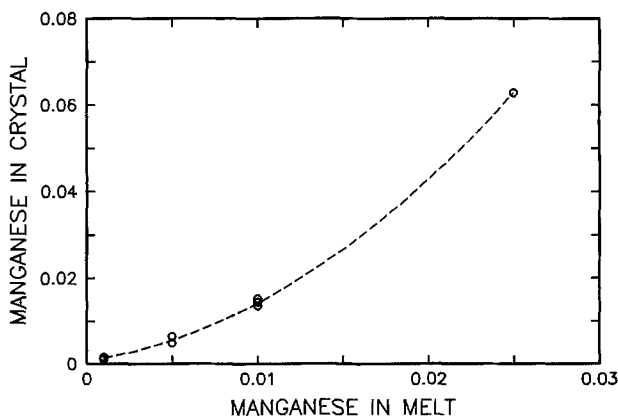


Fig. 1. A plot of the number of Mn atoms per formula unit of willemite vs. the number of mols of MnF_2 in the growth melt. Each melt contained 0.433 mols Zn. The data points represent 14 independent microprobe analyses. The fitted line is described by Eq. [1].

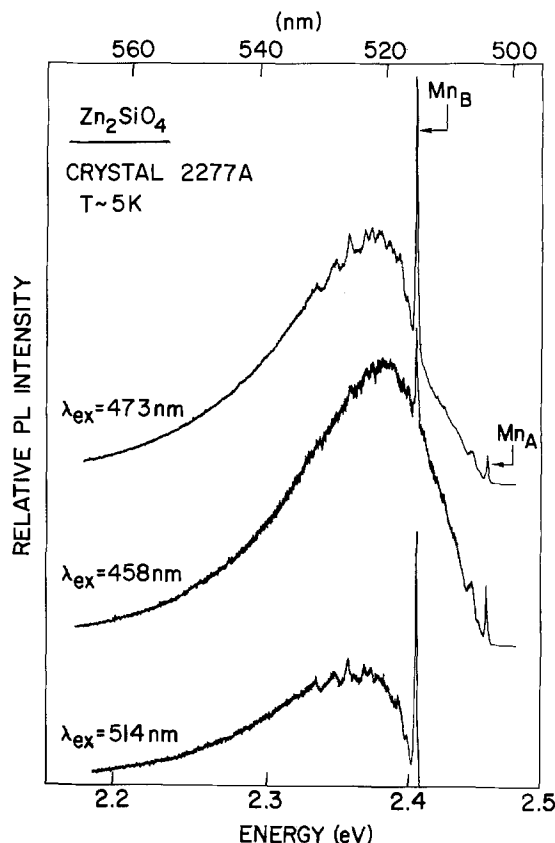


Fig. 2. Low temperature photoluminescence spectra of a Zn_2SiO_4 :Mn crystal excited by different lines of an Ar^+ laser. The laser line at 514 nm falls between the ZPL's for Mn_A and Mn_B centers, allowing isolation of luminescence from Mn_B centers.

Stevens and Vink (12) noted that higher concentrations of Mn impurity ($> 1\%$) produced spectra in which the ZPL's for both Mn_A and Mn_B centers were less well resolved. However, this broadening is not simply the result of decreasing crystal perfection, and near-resonant excitation of the two centers reveals additional fine structure in the region of the ZPL's. Near-resonant excitation of the Mn_A centers is achieved with the 501.7 nm (2.47 eV) Ar^+ line, the 5 K ZPL luminescence for a series of crystals with increasing Mn concentration being shown in Fig. 5. The

Table I. Estimated Mn concentration in willemite crystals (Eq. [1])

Crystal	$[Mn]_m^*$	$[Mn]_x$
2277A	0.005	0.006
2298A	0.005	0.006
2279A	0.010	0.014
2159B	0.020	0.043
2299A	0.020	0.043
2228A	0.025	0.063

* Growth melt contains 0.433 mol Zn.

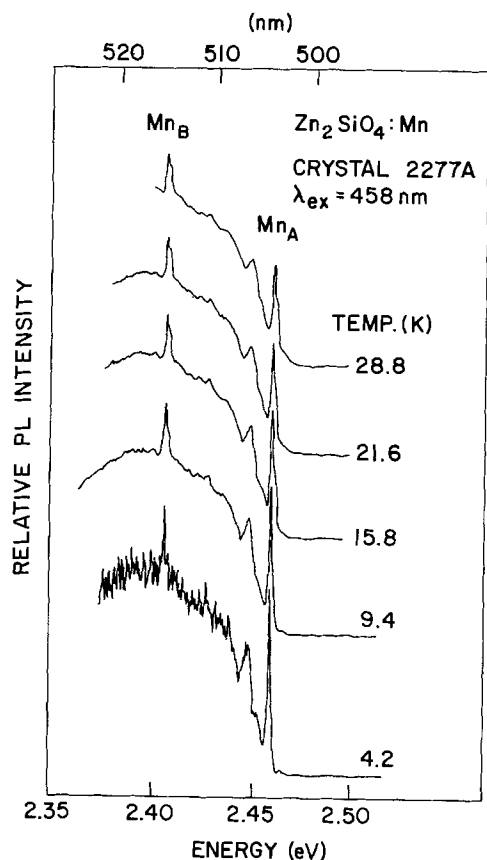


Fig. 3. Low resolution photoluminescence spectra of a $Zn_2SiO_4:Mn$ crystal at different temperatures. As temperature increases, "hot" bands appear as shoulders on the high-energy side of the ZPL's for both Mn_A and Mn_B centers.

solid arrows indicate the peak energy of the single ZPL observed at low temperature for crystals with low Mn concentration. As the Mn doping level increases additional lines appear, mainly to higher energy (indicated by broken arrows), and steadily increase in intensity until they constitute the major features for crystal 2228A. Similar near-resonant excitation of the Mn_B centers is achieved with the 514.5 nm (2.41 eV) Ar^+ line, the corresponding ZPL luminescence being illustrated in Fig. 6. Again the low Mn concentration crystals show a single ZPL at low temperature with additional lines increasing in intensity as the Mn doping level increases. However, for these Mn_B centers the major new lines appear at lower energy than the ZPL observed at low Mn concentration. The observation of single ZPL's for Mn_A and Mn_B centers at low concentration can be attributed to the dominance of isolated Mn_{Zn}^{2+} impurities at low doping levels. The appearance of additional ZPL's which increase in intensity with increasing Mn concentration is characteristic of Mn-Mn pair interactions. As discussed in the following section, the fact that the barycenter of the Mn_A luminescence shifts to higher energy, while that of the Mn_B luminescence shifts to lower energy, with increasing Mn concentration suggests that the dominant interaction involves nearest neighbor Mn_A - Mn_B pairs in the willemite lattice. It can also be seen from Fig. 5 and 6 that whereas the changes in lineshape correlate strongly with changes in Mn doping level, there is no evidence for spectral features correlating with the As concentration which could be attributed to interaction between Mn_{Zn}^{2+} and the As impurity.

The decay curves for the Mn_A and Mn_B centers at various temperatures were separately measured using near-resonant excitation, with the detection monochromator tuned at the appropriate ZPL energy. The

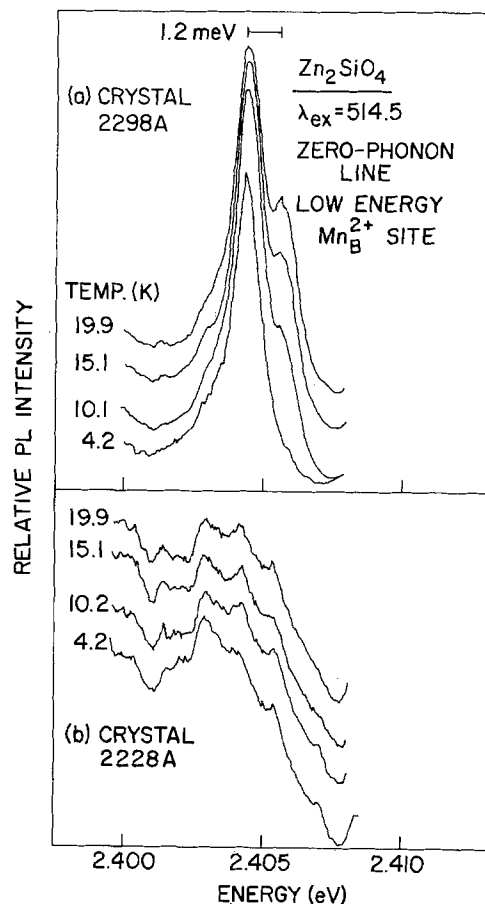
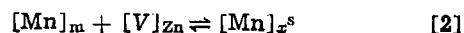


Fig. 4. High resolution photoluminescence spectra of the ZPL region for Mn_A centers at different temperatures: (a) low Mn concentration and (b) high Mn concentration. The "hot" band in (a) is ~ 1.2 meV above the ZPL (cf. Fig. 3).

decays were in general not simple exponentials; the time to decay to $1/e$ of the initial intensity ($t_{1/e}$) for a series of crystals is given in Table II for the Mn_A centers and in Table III for the Mn_B centers. At low temperature the Mn_B decay is independent of Mn concentration. However, the decay time decreases as the temperature increases, the effect being more significant at high doping levels. Only small differences in decay time were observed at low temperature for crystal 2228A when the detection monochromator was set on the peak of ZPL's attributed to single Mn_B centers and to Mn_A - Mn_B pairs. The decay of the Mn_A centers, on the other hand, is measurably different for high and low Mn concentrations, but the change with temperature is smaller than for the Mn_B luminescence. The decay times observed at ~ 5 K for low Mn concentrations are in good agreement with values reported by Stevels and Vink (12), viz., 12 ms and 15 ms for Mn_A and Mn_B sites, respectively, at 1.6 K.

Discussion

Figure 1 demonstrates that the relationship between Mn incorporation in a crystal and the melt concentration includes both linear and quadratic terms. A quadratic dependence is indicative of Mn pairing during growth, as shown by the following argument. Since the substitution of Mn^{2+} for Zn^{2+} in the lattice maintains charge neutrality, and assuming that activities are proportional to concentration in the melt and crystal (i.e., approximately ideal behavior), the thermodynamics of Mn incorporation can be described by the law of mass action as follows. If $[V_{Zn}]$ and $[MnMn]_x$ are the zinc vacancy and Mn-pair concentrations in the growing crystal, then the incorporation of Mn as single ions is given by



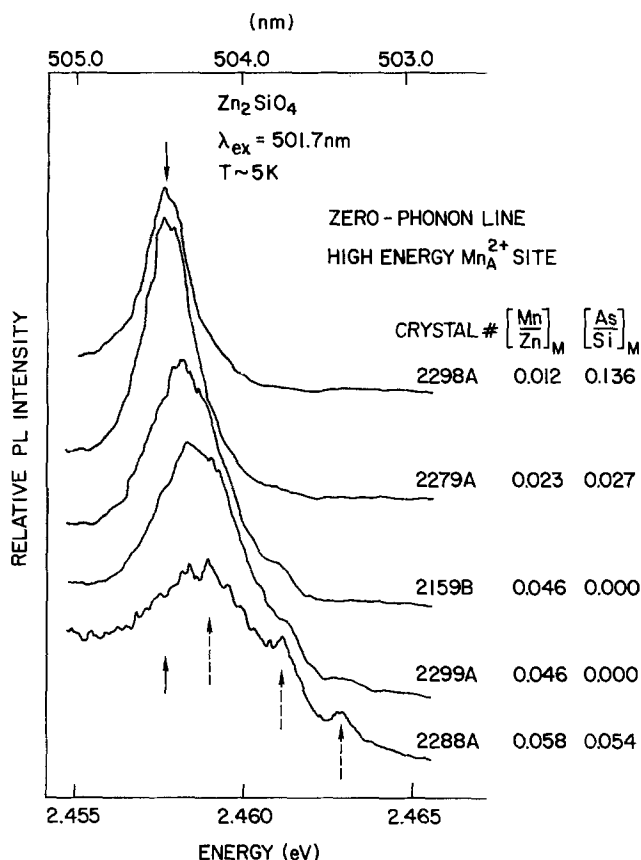


Fig. 5. High resolution photoluminescence spectra of the ZPL region for Mn_A centers for crystals with varying Mn concentration. The solid arrows indicate the ZPL energy at low Mn concentration, due to single ions. The broken arrows indicate lines appearing at high Mn concentration and attributed to pairs. $[Mn/Zn]_m$ and $[As/Si]_m$ indicate the molar ratios of Mn/Zn and As/Si in the growth melt, respectively. The estimated Mn concentration in each crystal is given in Table I.

$$\frac{[Mn]_x^s}{[Mn]_m[V_{Zn}]} = K_s(T) \quad [3]$$

and as Mn-Mn pairs by

$$2[Mn]_m + 2[V_{Zn}] \rightleftharpoons [MnMn]_x \quad [4]$$

$$\frac{[MnMn]_x}{[Mn]_m^2[V_{Zn}]^2} = K_p(T) \quad [5]$$

The concentration of Mn incorporated in the crystals in the form of pairs is

$$[Mn]_x^p = 2[MnMn]_x \quad [6]$$

The total Mn concentration in the crystal is then given by

$$[Mn]_x = [Mn]_x^p + [Mn]_x^s = \{2K_p(T)[V_{Zn}]^2 + K_s(T)[V_{Zn}]\} [Mn]_m \quad [7]$$

Table II. $t_{1/e}$ for Mn_A^{2+} site (excitation 501.7 nm) (ms)

Sample	$\left[\frac{Mn}{Zn}\right]_m$	$T(^{\circ}K)$					
		5°	68°	98°	138°	198°	266°
2298A	0.011	10.7	10.7	12.8	9.9	9.1	8.3
2228A	0.057	8.8	8.0	8.8	6.1	5.2	5.3

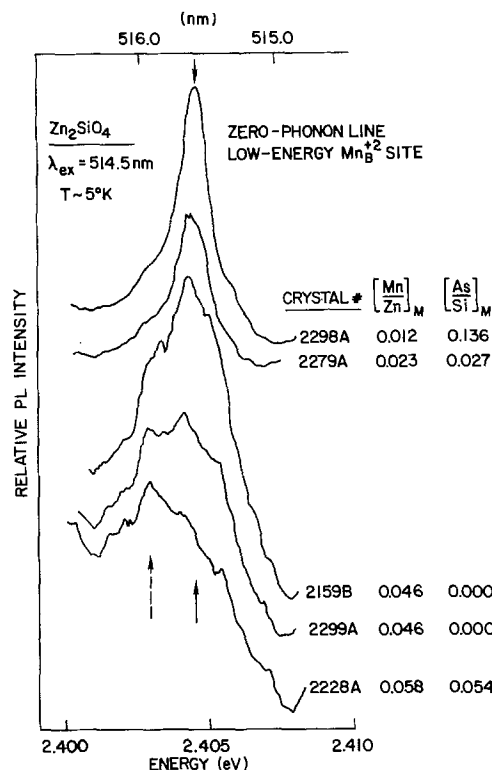


Fig. 6. High resolution photoluminescence spectra of the ZPL region for Mn_B centers for crystals with varying Mn concentration. See caption to Fig. 5 for details.

The quadratic term only appears for pairing during the growth process, which must be energetically favored in order to be significant. The high resolution optical spectra provide evidence for dominant nearest neighbor Mn_A - Mn_B pair formation in the crystals at higher Mn concentrations. It may therefore be the case that strain energy associated with incorporation of Mn in willemite is minimized if two Mn ions substitute simultaneously in neighboring inequivalent zinc sites rather than as separated, isolated ions. Further work to establish the dependence of pairing on growth temperature and on zinc vacancy concentration is required to provide more insight into the mechanism of Mn incorporation.

The observation of "hot" bands in luminescence 1.2 meV ($\sim 10 \text{ cm}^{-1}$) to high energy of the ZPL's for both Mn_A and Mn_B single-ion centers in willemite is entirely analogous to the luminescence of Mn_{Zn}^{2+} in ZnS and ZnSe (15, 16). There, "hot" bands are found $\sim 10 \text{ cm}^{-1}$ and $\sim 11.5 \text{ cm}^{-1}$, respectively, above the lowest ZPL for the Mn ions in T_d symmetry, i.e., substitutional on cubic zinc sites. In addition, luminescence excitation spectra (15, 17) for ZnS:Mn and ZnSe:Mn reveal that the "hot" band arises from a second ZPL lying above the lowest energy line. Con-

Table III. $t_{1/e}$ for Mn_B^{2+} site (excitation 514.4 nm) (ms)

Sample	$\left[\frac{Mn}{Zn}\right]_m$	$T(^{\circ}K)$						
		5°	20°	34°	59°	88°	127°	297°
2277A	0.011	15.6	15.1	14.5	15.1	-	11.8	8.3
2159B	0.045	15.6	15.1	14.5	13.4	-	-	5.6
2228A	0.057	15.6	15.1	13.4	10.5	7.5	5.1	2.7

sideration of first-order spin-orbit coupling in the 4T_1 excited state of Mn^{2+} in T_d symmetry predicts the following order of components (7): $\Gamma_6 < \Gamma_8(3/2) < \Gamma_7, \Gamma_8(5/2)$, using standard notation (18). The observation of only two ZPL's has been attributed to a complete vibronic quenching of the first-order spin-orbit coupling by strong coupling to a phonon mode of e-symmetry (the Ham effect) (15, 17). The second-order spin-orbit coupling is not quenched by the vibronic coupling, resulting in assignment of the two lines as transitions to the doubly degenerate levels represented as (15)

$$(i) \quad |\Gamma_7\rangle \text{ and } (3/\sqrt{10})|\Gamma_8(3/2)\rangle \\ - 1/\sqrt{10}|\Gamma_8(5/2)\rangle \quad (\text{lower energy})$$

$$(ii) \quad |\Gamma_6\rangle \text{ and } (1/\sqrt{10})|\Gamma_8(3/2)\rangle \\ + 3/\sqrt{10}|\Gamma_8(5/2)\rangle \quad (\text{higher energy})$$

This assignment is supported in the case of ZnS:Mn and ZnSe:Mn by analysis of Zeeman and uniaxial stress data (15, 17). The separation of the two components depends on second-order spin-orbit interactions summed over all multiplets of the d^5 configuration which differ by not more than one electron from the configuration of the 4T_1 state. A similar assignment must be supposed for the two lines in Fig. 4(a), although it is remarkable that almost identical behavior should be observed for Mn^{2+} in Zn_2SiO_4 when the crystal field parameters and the phonon spectrum are very different from the zincblende semiconductors ZnS (16, 18).

Mn pairs have also been observed in ZnS (16, 19), with antiferromagnetic spin coupling producing additional luminescence lines to low energy of the ZPL for isolated Mn_{Zn}^{2+} centers. In the case of ZnS, pairing occurs between Mn ions on equivalent sites. However, for willemite the nearest neighbor interactions involve the inequivalent Zn sites, with the possibility of Zn_A - Zn_B pairs having axes approximately parallel or perpendicular to the crystal c-axis. The most appropriate model for the Mn-Mn interaction in an ionic compound like willemite is likely to be multipolar (20), the leading term being the dipole-dipole coupling in the T_d symmetry field, with electron exchange small. The interaction between nearest neighbor inequivalent Mn_A - Mn_B centers is then best described as a second-order Davydov interaction between non-degenerate transition dipoles on the two centers, which are mixed via the crystal potential. The effect can be illustrated schematically by a simple perturbation argument. Denoting the ground state wavefunctions of isolated Mn_A and Mn_B centers as $|\phi_A\rangle$, $|\phi_B\rangle$, and using primes for the excited states (taken to be nondegenerate for simplicity), the zero-order wavefunctions for the ground and lower excited states of a nearest neighbor pair are given by the products

$$\psi_g = |\phi_A\rangle |\phi_B\rangle \quad [8]$$

$$\psi_{e^A} = |\phi_A'\rangle |\phi_B\rangle \quad [9]$$

$$\psi_{e^B} = |\phi_A\rangle |\phi_B'\rangle \quad [10]$$

The Hamiltonian for the pair is of the form

$$\mathcal{H} = \mathcal{H}_A + \mathcal{H}_B + \mathcal{H}_{AB} \quad [11]$$

where \mathcal{H}_A , \mathcal{H}_B are the Hamiltonians for the isolated Mn centers, and \mathcal{H}_{AB} represents the pair interaction, which is assumed small. Using perturbation theory, and retaining only the second-order terms involving the excited states, the energies of the pair states are

$$E_g = E_A^0 + E_B^0 + \langle \phi_A \phi_B | \mathcal{H}_{AB} | \phi_A \phi_B \rangle \quad [12]$$

$$E_{e^A} = E_A' + E_B^0 + \langle \phi_A' \phi_B | \mathcal{H}_{AB} | \phi_A' \phi_B \rangle + \frac{E_{AB}^2}{\Delta} \quad [13]$$

$$E_{e^B} = E_A^0 + E_B' + \langle \phi_A \phi_B' | \mathcal{H}_{AB} | \phi_A \phi_B' \rangle - \frac{E_{AB}^2}{\Delta} \quad [14]$$

where E_A^0 , E_B^0 and E_A' , E_B' are the energies of ground and excited states for isolated Mn_A and Mn_B centers, and

$$E_{AB}^2 = |\langle \phi_A' \phi_B | \mathcal{H}_{AB} | \phi_A \phi_B' \rangle|^2 \quad [15]$$

$$\Delta = (E_A' - E_A^0) - (E_B' - E_B^0) \quad [16]$$

The transition to the higher excited pair state therefore occurs at an energy

$$(E_{e^A} - E_g) = (E_A' - E_A^0) + D_A + \frac{E_{AB}^2}{\Delta} \quad [17]$$

where

$$D_A = \langle \phi_A' \phi_B | \mathcal{H}_{AB} | \phi_A' \phi_B \rangle \\ - \langle \phi_A \phi_B | \mathcal{H}_{AB} | \phi_A \phi_B \rangle \quad [18]$$

and $(E_A' - E_A^0)$ is the transition energy at an isolated Mn_A center. The transition to the lower pair state occurs at an energy

$$(E_{e^B} - E_g) = (E_B' - E_B^0) + D_B - \frac{E_{AB}^2}{\Delta} \quad [19]$$

where

$$D_B = \langle \phi_A \phi_B' | \mathcal{H}_{AB} | \phi_A \phi_B' \rangle \\ - \langle \phi_A \phi_B | \mathcal{H}_{AB} | \phi_A \phi_B \rangle \quad [20]$$

and $(E_B' - E_B^0)$ is the transition energy at an isolated Mn_B center. The net effect of the Mn_A - Mn_B pairwise interaction is, therefore, to produce shifts (δE^A , δE^B) in the transition energies compared with the isolated centers, where

$$\delta E^A = D_A + \frac{E_{AB}^2}{\Delta} \quad [21]$$

$$\delta E^B = D_B - \frac{E_{AB}^2}{\Delta} \quad [22]$$

If the differential first-order terms D_A , D_B are small, the second-order interaction predicts an upward shift in energy for transitions at the Mn_A center in the pair, and a downward shift for transitions at the Mn_B center. This is the sense of the barycenter shifts illustrated in Fig. 5 and 6, and it is for this reason that we propose a dominant nearest neighbor Mn_A - Mn_B pairing to explain the changes in lineshape observed at higher Mn doping levels. The appearance of extra lines in addition to the barycenter shifts for the pairs can be accounted for in terms of the known degeneracy of the Mn_A and Mn_B excited states (discussed in the previous paragraph), and the possibility of forming inequivalent pairs of different symmetry. However, no detailed treatment of the pair fine structure will be attempted here.

The antiferromagnetic spin coupling between nearest neighbor Mn_{Zn}^{2+} ions on equivalent sites in ZnS produces a low temperature, pair luminescence decay time approximately an order of magnitude faster than that for single ions (19). The corresponding ZPL for the spin-coupled pair is shifted ~ 15 meV to low energy (19). However, the predominantly second-order interaction between inequivalent nearest neighbor sites in willemite gives pair line shifts which are much smaller, ~ 1 meV. This weakening of the pair interaction, combined with spectral overlap resulting from larger linewidths, may explain why no significant difference in decay time at low temperature was observed in willemite when the detection monochromator was tuned to lines attributed to pairs and to single ions. Nevertheless, the luminescence decay for both Mn_A and Mn_B sites becomes faster as tempera-

ture increases. Tables II and III show that the effect is greater as the Mn concentration increases, i.e., as the Mn inter-center energy transfer becomes more facile, indicating a thermally activated energy transfer to centers with larger recombination rates. Preliminary measurements (21) on a number of crystals suggest that the luminescence efficiency at room temperature does not decrease markedly at higher Mn doping levels. The decrease in decay time at higher Mn concentrations therefore probably does not reflect a "concentration-quenching" (20) at nonradiative centers in the crystals, but rather an energy transfer to complex centers involving Mn^{2+} ions with faster radiative rates. The probability of exciting such centers is presumed larger at higher temperatures and higher Mn concentration due to the increased rate of inter-center energy transfer in the crystal. The sensitivity of the Mn_A decay rate to the Mn concentration even at low temperature (Table II) may indicate a significant nonthermal component in energy transfer from the higher energy Mn_A centers to Mn_B centers. Further efficiency measurements are required to confirm the possible usefulness of variations in Mn concentration for control of decay time in phosphors based on the $Zn_2SiO_4:Mn$ system.

Acknowledgments

The authors wish to thank F. Cardone, J. Kuptsis, and R. Savoy for carrying out the microprobe analyses, and C. F. Guerci for assistance in sample preparation. They are also grateful to P. Avouris for loan of equipment, and to D. B. Dove, N. Caswell, and D. T. J. Hurle for their useful comments.

Manuscript submitted Feb. 11, 1983; revised manuscript received July 18, 1983. This was Paper 513 presented at the Montreal, Quebec, Canada, Meeting of the Society, May 9-14, 1982.

IBM T. J. Watson Research Center assisted in meeting the publication costs of this article.

REFERENCES

- H. W. Leverenz, "Luminescence of Solids," John Wiley and Sons, New York (1950).
- "Optical Characteristics of CRT Screens," JEDEC Publication 16-C, Nov. 1975, Electronic Industries Association, Washington DC.
- I. F. Chang and G. A. Sai-Halasz, *This Journal*, **127**, 2458 (1980).
- J. M. Brownlow and I. F. Chang, *SID/IEEE Display Research Conference Proceedings*, 66-71, 1982.
- M. A. Simonov, P. A. Sandomirskii, Yu. K. Egorov-Tismenko, and N. V. Belov, *Sov. Phys. Dokl.*, **22**, 622 (1977).
- K-H. Klaska, J. C. Eck, and D. Pohl, *Acta Crystallogr.*, **B34**, 3324 (1978).
- A. M. Clogston, *J. Phys. Chem. Solids*, **7**, 201 (1958).
- H. K. Perkins and M. J. Sienko, *J. Chem. Phys.*, **46**, 2398 (1967).
- C. C. Vlam, *J. Opt. Soc. Am.*, **41**, 558 (1951).
- D. T. Palumbo and J. J. Brown, *This Journal*, **117**, 1184 (1970).
- G. A. Sai-Halasz, Unpublished work.
- A. L. N. Stevels and A. T. Vink, *J. Lumin.*, **8**, 443 (1974).
- R. Fern and I. F. Chang, Unpublished work.
- E. A. Giess, C. F. Guerci, J. D. Kuptsis, I. F. Chang, and D. J. Robbins, *J. Crystal Growth*, **60**, (1982).
- R. Parrot, C. Naud, C. Porte, D. Fournier, A. C. Boccara, and J. C. Rivoal, *Phys. Rev. B*, **17**, 1057 (1978).
- W. Busse, H-E. Gumlich, A. Geoffroy, and R. Parrot, *Phys. Status Solidi B*, **93**, 591 (1979).
- D. Fournier, A. C. Boccara, and J. C. Rivoal, *J. Phys. C.*, **10**, 113 (1977).
- G. K. Koster, J. O. Dimmock, R. G. Wheeler, and H. Statz, "Properties of the Thirty-Two Point Groups," MIT Press, Cambridge, Mass.
- W. Busse, H-E. Gumlich, B. Meissner, and D. Theis, *J. Lumin.*, **12/13**, 693 (1976).
- R. K. Watts in "Optical Properties of Ions in Solids," B. di Bartolo, Editor, Plenum Press, New York (1975).
- N. S. Caswell, Private communication.

Archival Life of Tellurium-Based Materials for Optical Recording

G. M. Blom* and D. Y. Lou

Philips Laboratories, Briarcliff Manor, New York 10510

ABSTRACT

The archival life of digital optical recording air-sandwich disks is described in this paper. The optically sensitive materials are tellurium-based alloys, and the substrates are polymethylmethacrylate. Various techniques such as reflection, transmission, signal-to-noise ratio, and bit-error rate measurements are used to characterize degradation. It is demonstrated that bit-error rate measurements are by far the most sensitive. It is shown that elemental tellurium, when stored under normal office conditions, has an archival life of at least several years when the optical disk is in the form of an air-sandwich disk. Tellurium alloys fabricated into an air-sandwich disk have a projected archival life of at least ten years. The projections are based on bit-error rate measurements on air-sandwich disks stored under accelerated degradation conditions for periods of several years. Storage conditions which allow condensation of water vapor must be avoided. Experiments with disks having trilayers and containing the normally excellent tellurium alloys show rapid degradation. Such degradation is believed to result from electrochemical corrosion.

Digital optical recording (DOR) is a new technology which has been proven on a pilot production scale to be capable of storing large amounts of data (1-9). Large area and volumetric densities have been achieved. Densities as high as 10^{11} bits per 12 in diam disk and up to 5×10^{11} bits per surface of a 16 in diam disk have been demonstrated. The thickness of a two-sided air-sandwich disk and its protective cartridge is about 1 cm. Hence, densities per area and volume are significantly enhanced compared to current

magnetic recording technology. It seems likely that commercial products will be introduced in the near future in an office environment and as data processing peripherals. In either case, media are required on which the information is stored.

The three parameters most important for a successful optical recording media are archival life, resolution, and sensitivity (10). Several materials such as organic dyes (4), tellurium and other metal trilayers (11-12), amorphous materials (13), magneto-optical materials (6), textured surfaces (14), silicides (15), and, of course, tellurium-based alloys (9) have been investi-

* Electrochemical Society Active Member.
Key words: films, optics, corrosion, failure.

gated by many researchers. Most of these materials have shown to have adequate performance characteristics as far as resolution and sensitivity are concerned. This is especially true as long as the highest storage densities are not required. Currently, tellurium alloys are the only group of materials on which sufficient data have been collected concerning archival life. It will be shown that archival life with these alloys is excellent. It was shown previously (16) that the archival life of air-sandwich disks with elemental tellurium was several weeks when stored under accelerating conditions. The magnitude of the acceleration factor was unknown at that time.

In this paper, we will discuss the various criteria which are commonly used for measuring archival lives of optical recording media. It will be demonstrated that the bit-error rate (BER) is a much more sensitive parameter than other commonly measured parameters, such as reflectivity, transmission, and signal-to-noise ratio (SNR). Nevertheless, the other parameters are useful for initial screening new materials for their archival quality in optical recording technology. Subsequently, various storage conditions and their possible influence on the archival life of the optical disk will be discussed. This will also uncover information regarding conditions and precautions which must be adhered to and taken for storage of these disks under normal operating conditions. The storage conditions are not arbitrarily selected: they take into consideration that the DOR disk is packaged in the well-known air-sandwich disk. We will describe the air-sandwich disk that uses polymethylmethacrylate (PMMA) substrates in some detail and elaborate on its features.

Air-Sandwich Disk

The air-sandwich disk, shown schematically in Fig. 1, consists of two PMMA substrates each coated with a 30 nm layer of elemental tellurium or a tellurium alloy. Sometimes a polymer or acrylic subbing layer is applied on the substrates prior to metal deposition. Many subbing layers have a detrimental effect on disk archival life. The data reported here refer to disks without subbing layers. The two individual disks are separated by spacers at the inner and outer radii of the information band. Typically, the information band is between 70 and 145 mm radius for a 300 mm diam disk. The inner spacer is usually PMMA, which is bonded with transfer adhesive to the two individual disks. An alternative method uses a hot-melt adhesive that also serves as a spacer. The width of this spacer extends from the inner radius of the disk, i.e., 35-55 mm. The outer spacer of the air-sandwich disk is either an adhesive open-cell foam strip, 5 mm wide, or 3 mm of hot melt followed by a 2 mm acrylic adhesive for added strength. All spacers are 1 mm thick. Of course, metal film is deposited on the inside surfaces of the air-sandwich disk.

The advantages of the air-sandwich structure are that the sensitive material is protected from environmental effects such as dust and operator handling, as well as

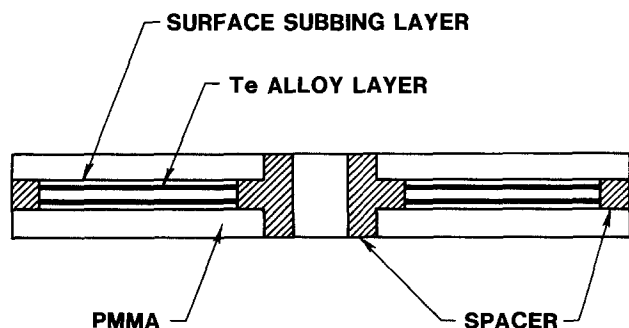


Fig. 1. Schematic diagram of air-sandwich disk

that any particles and smudges, such as fingerprints, are out of focus as a result of the substrate thickness being 1-1.2 mm. Because the tellurium is inside the structure, the operators are protected from the possible harmful effects of tellurium. Also, one has a two-sided disk.

The tellurium alloys are made by mixing the appropriate elements, sealing them in a quartz ampul, and heating the ampul at a temperature of about 600°C. The alloy is vacuum deposited by flash evaporation on the PMMA substrate, which is maintained at room temperature. The average evaporation rate is 0.1 nm/s.

We find it essential to use air-sandwich disks for archival testing, because testing of single disks is complicated by the lack of protection of the metal film from the environment. The air-sandwich structure was found to be necessary for continuous optimum performance. Alternative protective structures for the sensitive media can be devised, however, we find the air-sandwich disk structure simple to fabricate as well as easy to operate, and it attains excellent archival life properties.

Measured Parameters

To obtain information concerning the archival properties of an optical recording medium, possible changes of optical parameters as a function of time must be measured. Optical reflection and transmission are often chosen for measurement. They are useful for initial screening, since they help ascertain if a new material has any potential as an optical recording medium. These two parameters can be measured without performing optical recording. We found, as is shown in Fig. 2, that consistent optical transmission is a prerequisite for good archival life, but by no means is it sufficient. The optical reflection, measured at 488 nm, of our tellurium alloy is typically 44%, while the transmission is typically 7%. The uniformity of these parameters within the disk and between disks is $\pm 10\%$ relative, corresponding to a thickness variation of ± 2 nm.

Another parameter for determining archival life of DOR disks is the signal-to-noise ratio (SNR). Of course, this requires that actual recording must be

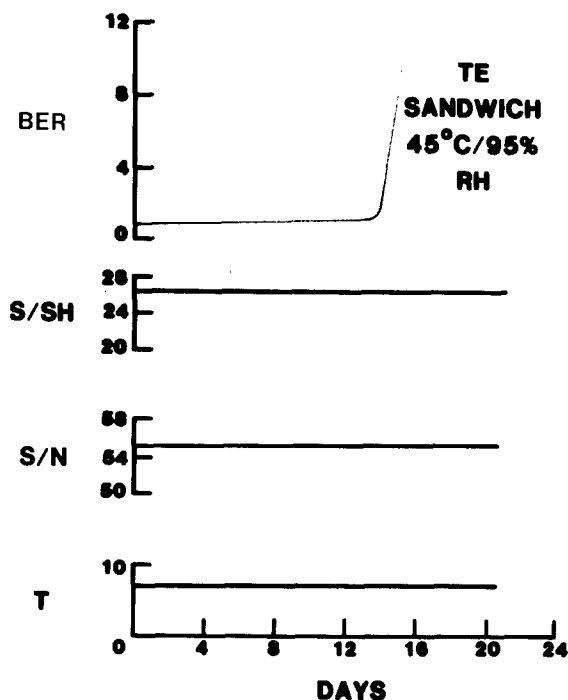


Fig. 2. Comparison of various media parameters, such as BER, signal-to-second harmonic (S/SH), signal-to-noise ratio (S/N), and optical transmission (T) as a function of storage time, indicating that BER is the most sensitive parameter.

performed. Sometimes video information is recorded off the air, and the SNR is measured over a 4.2 MHz bandwidth. However, for digital optical recording, one must recognize that translation from SNR to bit-error rates is not necessarily straightforward. We have measured the SNR of digital information (at 4.2 MHz bandwidth) and, as shown in Fig. 2, it was found to be a prerequisite for good archival life. However, the fact that SNR remains unchanged does not necessarily imply that the digital recording medium is stable. Similarly, we have measured the signal-to-second harmonic ratio and found a comparable behavior as for the SNR.

The parameter which we find must be measured for determining archival life properties of optical recording media is the bit-error rate. In all cases the presented data apply to the uncorrected or raw BER. The uncorrected BER provides true disk characterization. Upon applying error correction codes, the combination of the disk BER and the correcting electronics results in a corrected BER. It will be shown later that with uncorrected BER's of 10^{-4} corrected BER's of better than 10^{-9} can be obtained.

In Fig. 2 we have plotted the BER as a function of time for an air-sandwich disk coated with 30 nm of elemental tellurium. Also plotted are SNR, optical transmission, and signal-to-second harmonic ratio (S/SH) for this same disk. It can be seen that the BER catastrophically increased after about 2 weeks storage at a temperature of 45°C and a relative humidity of 95%, while the other three parameters shown in Fig. 2 were still unchanged even after 3 weeks. This demonstrates that the BER must be directly measured in determining the archival life of DOR media.

The reason for the above-mentioned observation is that transmission and reflection measurements are macroscopic parameters. The areas involved in these measurements are typically large compared to the spot size used for actual recording. While the SNR and S/SH ratios require actual recording, the measured values represent an average of a microscopic parameter over a large area. Hence, changes in the 10^{-4} range cannot be measured. The BER, however, is a bit-by-bit comparison of the recorded information, and it simply counts the number of times that a bit does not correspond to what was recorded. BER is a microscopic measurement. Therefore, it is sensitive to levels much lower than 10^{-4} , as when we observed BER's of 10^{-7} . Consequently, we will use BER to determine archival life of our media.

Storage Conditions

In order to generate meaningful archival data, one must specify the storage conditions for the DOR air-sandwich disks. One expects to specify test conditions which accelerate the degradation phenomena in a specific, well-known way. This assumes that one knows the temperature dependence of the chemical reactions responsible for degradation, e.g., an exponential relation with temperature. In the case of semiconductors this is generally a safe assumption. For DOR air-sandwich disks with tellurium alloys as the sensitive media this is not necessarily the case. It is expected that elevated temperatures and elevated relative humidities accelerate the degradation reactions. Since we are operating with PMMA substrates, a practical upper temperature for these tests is approximately 45°C. At higher temperatures, the PMMA deforms irreversibly. Consequently, one of the storage conditions which was selected is 45°C and 95% relative humidity (RH). Another storage condition is room ambient, which is an average temperature of 22°C and an average RH of 50%. In order to differentiate between the influence of elevated temperature and increased RH, another storage condition is 45°C and 50% RH. A cyclic storage condition where the temperature was changed between

25° and 45°C with 8h cycles, ramps of 2h, and a constant RH between 90 and 95% was also used. As expected, no degradation of the recording media was observed when stored at 0°C. Hence, as far as media testing is concerned, we have four different storage conditions: (i) 45°C and 95% RH, (ii) room ambient, (iii) 45°C and 50% RH, and (iv) cyclic. Temperatures around 0°C were used to test the strength of the seal. Many adhesives work well at room temperature and higher, but becomes brittle at freezing temperatures. Thus, low temperature tests were performed on blank disks to select the proper sealing technology.

Archival Life

Miller modulated pseudorandom bit patterns were recorded on air-sandwich disks and in some cases on single, open disks. The recorder had a He-Ne laser, a data rate of 2 Mbit/sec, and a spot size of 0.8 μm FWHM. The spot was focused through the PMMA substrate onto the elemental tellurium or the tellurium alloy. When measuring the average BER, a band of about 1 cm wide was recorded with the bit pattern generated and compared by an HP 8088A. In other measurements, the recording consisted of a single track of data divided into 32 sectors, each with protection bits, clock-synchronization bits, etc. Bit by bit comparisons were made. BER values, as well as various statistical information about the error distributions, could be obtained.

Typical BER results for medium-quality single open disks coated with 30 nm of elemental tellurium are shown in Fig. 3. Clean room (class 100) ambient storage conditions are designated by the open circles, and the 45°C/95% RH storage conditions are depicted by the triangles. For single open disks stored at 45°C/95% RH, catastrophic degradation occurs after 2 days. However, storing such disks under clean room ambient conditions, we observed that even after 2 yr they still had an unchanged BER. While we do not suggest using such open single disks these results show that elemental tellurium, when properly stored, is a good DOR medium.

BER data on air-sandwich disks coated with 30 nm of elemental tellurium are shown in Fig. 4. Room

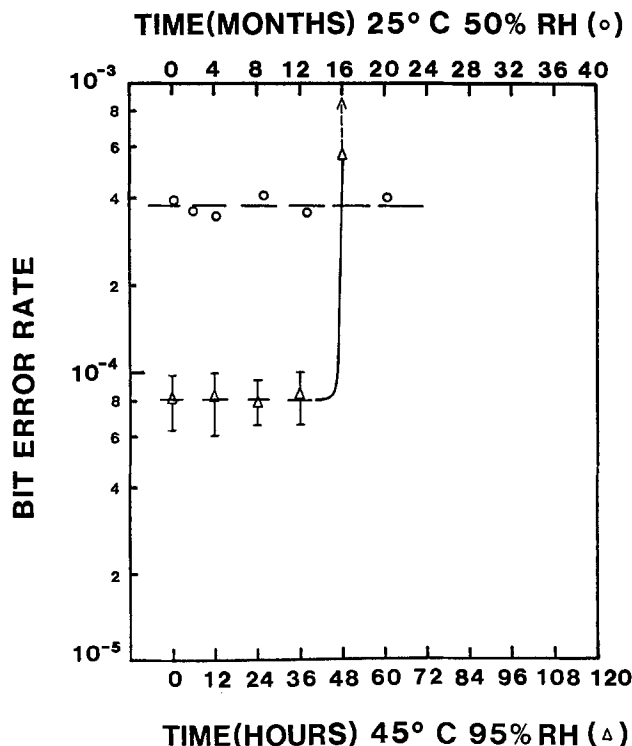


Fig. 3. Degradation characteristics of a single open disk coated with 30 nm elemental tellurium.

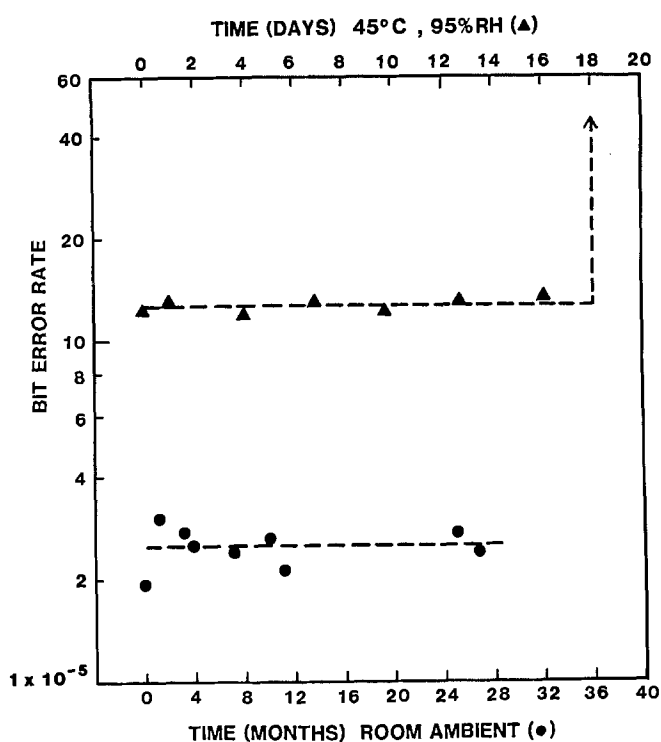


Fig. 4. Degradation characteristics of an air-sandwich disk coated with 30 nm elemental tellurium.

ambient and 45°C/95% RH are the storage conditions. Again these are typical results. Storing at the accelerated conditions shows that catastrophic degradation occurs after about 2.5 weeks. Comparing the 45°C/95% RH data in Fig. 3 and 4 indicates that nearly an order of magnitude is gained in storage time for an air-sandwich configuration compared with a single open disk. As would be expected from the data shown in Fig. 3, it is seen in Fig. 4 that room ambient storage shows no change in BER data after 2 yr. Dividing the storage times to catastrophic degradation obtained from Fig. 4 results in an acceleration factor greater than 45. Again we confirm here that elemental tellurium as a medium is far better, as we have often claimed, especially if used in combination with the air-sandwich disk configuration.

Alloying of selenium in the tellurium results in a significant improvement for the archival life of DOR disks. The data shown in Fig. 5 and 6 are BER data as a function of storage time for single open disks and air-sandwich disks containing 30 nm of the tellurium-selenium alloy. For single open disks stored at 45°C/95% RH and recorded with pseudorandom data, catastrophic degradation occurs after 3 weeks. This is approximately one order of magnitude longer than with elemental tellurium; significant improvement is obtained. Storing an air-sandwich disk at the accelerated conditions of 45°C/95% RH shows that even after nearly 2 yr no change has occurred in the BER; and an improvement of at least 30 is obtained. Figure 6 also shows the data for room ambient storage and the single open disk for comparison.

While the average BER is a simple and useful description of disk performance, the possibility of applying error correcting codes to the recovered data means that we also need information about the statistical distribution of the errors. Figure 7 shows such a distribution. It was measured over about 10^9 bits, and is the distribution of the lengths of burst errors detected on a typical medium-quality disk. Most of the errors are randomly occurring single-bit errors. Relatively simple error correcting algorithms are readily available, and have been used in recordings with BER's of better than 10^{-9} .

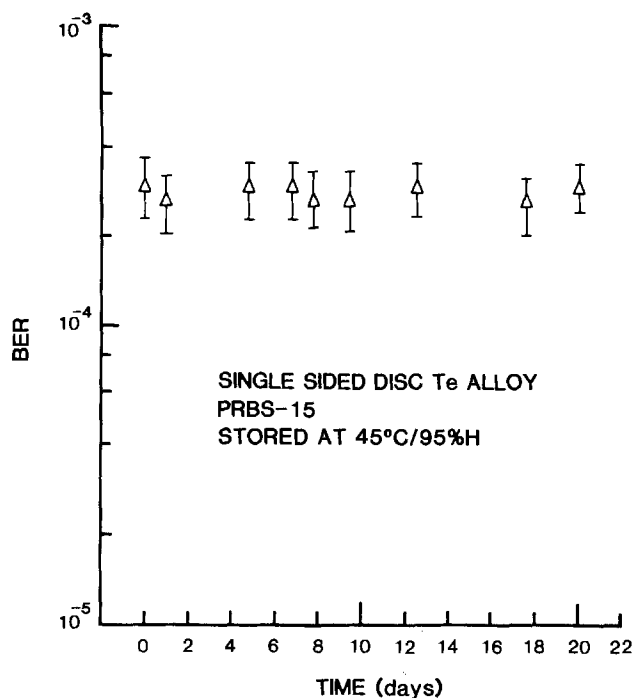


Fig. 5. BER as a function of storage time for a single open disk stored at 45°C and 95% RH, coated with 30 nm tellurium alloy and recorded with a pseudorandom bit sequence.

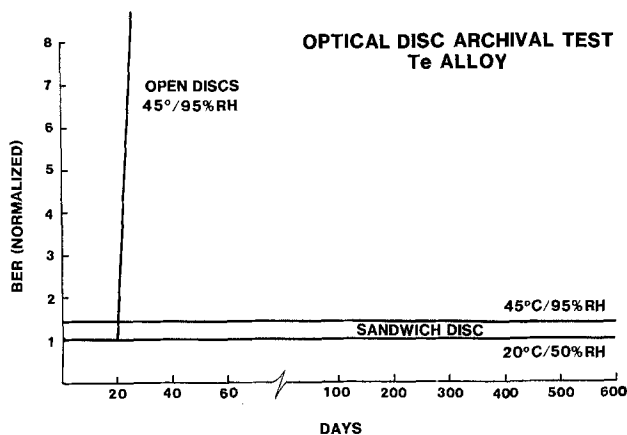


Fig. 6. Normalized BER as a function of storage time for tellurium alloy coated disks stored under various conditions.

Discussion

Improvements in storage times between air-sandwich disks and single open disks of 10 and 30 were established for disks containing elemental tellurium and Te-Se alloys, respectively. These improvements are attributed to two possible factors. One is that the air-sandwich structure protects the metal film from immediate exposure to water vapor and chemical pollutants in the air. The other is that the air-sandwich protects the metal film from dust. Dust probably contains metal particles, for which it has been established that corrosion is enhanced significantly when contacted by the Te or Te-Se film in the presence of water vapor. The electrochemical potential difference between a metal particle and the sensitive film is believed to be a major factor for this rapid degradation. Since the air-sandwich disks are fabricated in a class 100 clean room, the air-sandwich disks are like miniature clean rooms themselves. Single open disks stored in a dust-free (class 100 clean room) condition show an archival life of at least 20 months.

From the acceleration factors stated earlier, up to at least 45, one can conclude that the air-sandwich disks

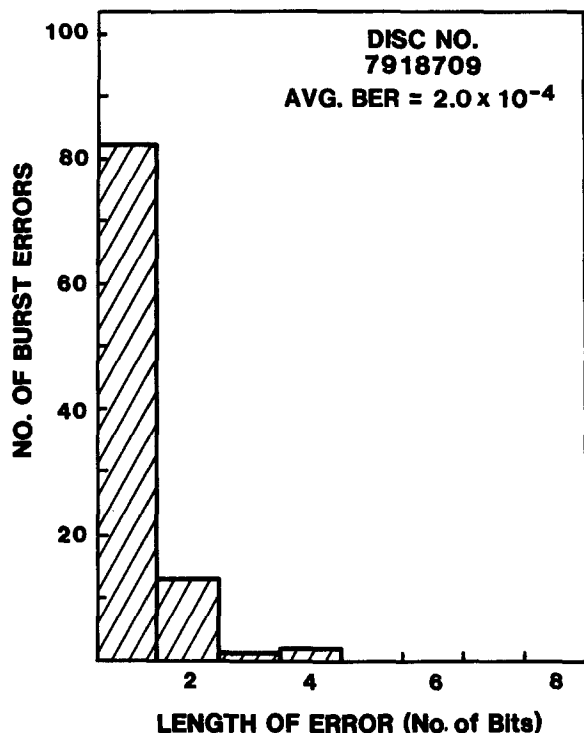


Fig. 7. Bit error distribution of a typical disk

containing the Te-Se alloy have an archival life of at least 20 yr and possibly as high as 75 yr under normal ambient conditions. The uncorrected or raw BER data, being in the 10^{-5} to 10^{-4} range, together with the BER distribution data (Fig. 7) and the application of error correcting codes, show that our data demonstrate that sufficient archival life exists for our DOR medium. In magnetic recording, BER's of at least 10^{-8} are required for sufficient archival life; however, this pertains to measurements after at least sector rewrites and is therefore not equivalent to our uncorrected BER. As stated earlier, correcting algorithms have been used to obtain BER's of better than 10^{-9} . Sufficient archival life is often specified as 10 yr under normal storage and operating conditions as are currently used in data storage operations. Thus, we conclude that our DOR medium is superior to the current archival medium, *i.e.*, magnetic tape. For comparison,

we tested a magnetic tape at the $45^{\circ}\text{C}/95\%$ RH conditions. It was observed that the data was unretrievable after a few days of storage.

From our measurements, we can conclude that the storage conditions of $45^{\circ}\text{C}/95\%$ RH indeed accelerate the degradation for elemental tellurium and for tellurium alloys on single open disks and most likely also for air-sandwich disks with the alloy. However, from the limited data at $45^{\circ}\text{C}/50\%$ RH, where no degradation was observed after more than a year of storage, and from the earlier shown data, we cannot draw conclusions concerning the degradation mechanism itself. Also, the cyclic storage conditions for which we have not shown data because of redundancy indicate that this environment gives the same BER data as a function of time as the $45^{\circ}\text{C}/95\%$ RH conditions. Possibly, longer storage times would allow such differentiation. Our main objective is to demonstrate that a tellurium alloy is an excellent DOR medium for storage times of up to 10 yr.

Measurements of shelf-life of optical recording disks coated with elemental tellurium have been reported earlier (17). In these measurements, the recording sensitivity was measured as a function of storage time. It was shown that high-humidity storage conditions degrade the films rapidly; this agrees with our archival data.

In addition to the single-layer films deposited on the PMMA substrates, we have also looked at the application of this alloy in a trilayer or bilayer configuration. Figure 8 is an optical micrograph of what happens to a bilayer consisting of 100 nm of aluminum covered with about 20 nm of our tellurium alloy upon storage for a few days at $45^{\circ}\text{C}/95\%$ RH. Large corroded areas are observed. While the original BER was about 10^{-4} , the data could not be retrieved after this storage time. We believe that such degradation results when two different metals are in contact with each other, or, in the case of the trilayer, separated by a dielectric several tens of nm thick. As is well known in metallurgy, an electrochemical potential difference is set up in such a structure. In the presence of any water vapor, a corrosion process can be activated. This can either oxidize the mirror, *i.e.*, the aluminum, or the sensitive medium, *i.e.*, the tellurium alloy. This corrosion process proceeds much faster than the simple oxidation degradation occurring with single tellurium alloy films in air-sandwich disks. It is likely to be a mechanism similar to the corrosion/degradation process observed in single open disks when stored at $45^{\circ}\text{C}/95\%$ RH.

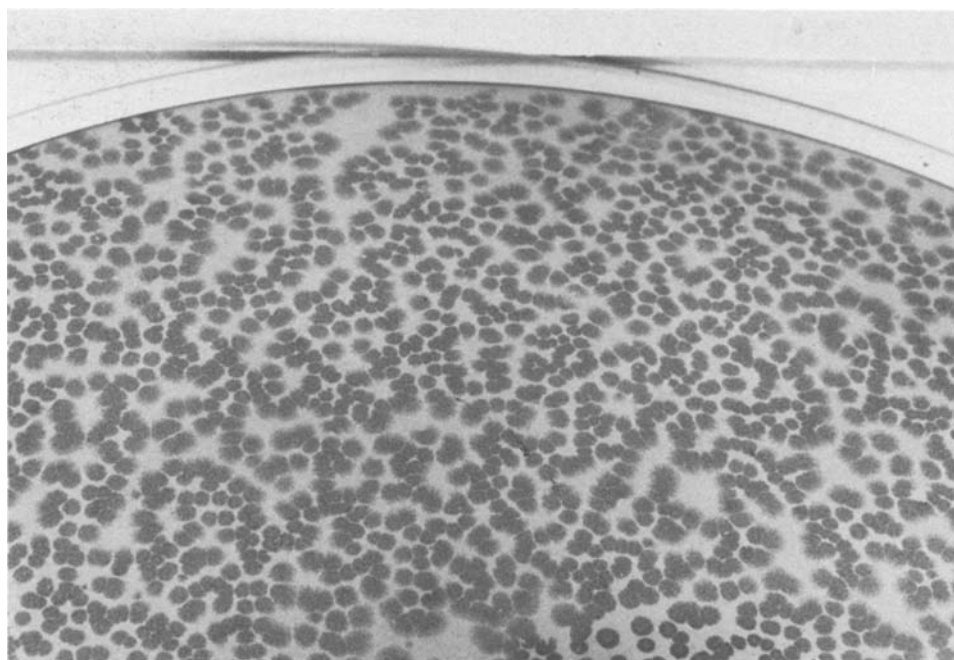


Fig. 8. Photograph of a bilayer disk containing the tellurium alloy showing severe degradation. Degradation is believed to result from electrochemical corrosion.

The fact that the PMMA substrates which we have used in this study are very permeable to water vapor, and to a lesser degree to other possible pollutants, apparently plays no major role. Degradation is no problem. The only condition which we found must be adhered to is that condensation of water vapor must be prevented. This is easy to accomplish even for storage at 45°C/95% RH. One simply must not put the disk after removal from the environmental chamber directly onto a cold table. No condensation was observed when the disks were left in ambient conditions after removal from the environmental chambers. In fact, the permeability of PMMA to water vapor is an advantage. From separate experiments we concluded that the equilibrium water vapor pressure inside the air-sandwich disk is established in approximately 10 min. This certainly helps to prevent condensation of water vapor, since the equilibrium water vapor pressure is obtained very rapidly.

Conclusion

Tellurium alloys deposited on PMMA substrates and fabricated into air-sandwich disks have proven to have an archival life, when stored at 45°C and 95% relative humidity, of at least 2 yr. From our data on elemental tellurium we conclude that the acceleration factor is at least 10, and possibly as much as 45. Hence, an archival life for the air-sandwich disk with the alloy can safely be extrapolated to an archival life of at least 10 yr when the disks are stored and used in normal computer room environments. This shows a significant improvement over magnetic tape, the current medium for long-term storage.

Acknowledgments

The authors like to thank S. Spedaro and M. Jaso for the disk fabrication, J. Nadan and J. Deasis for the bit by bit disk testing, and G. Kenney for his constant encouragement in this work.

Manuscript submitted June 6, 1983; revised manuscript received Aug. 26, 1983.

Philips Laboratories assisted in meeting the publication costs of this article.

REFERENCES

1. A. E. Bell, R. A. Bartolini, and F. W. Spong, *RCA Rev.*, **40**, 345 (1979).
2. G. Kenney, D. Lou, R. McFarlane, A. Chan, J. Nadan, T. Kohler, J. Wagner, and F. Zernike, *IEEE Spectrum*, **16**, no. 2, 33 (1979).
3. K. Bulthuis, M. G. Carasso, J. P. Heemskerck, P. J. Kivits, W. J. Kleuters, and P. Zalm, *ibid.*, **16**, no. 8, 26 (1979).
4. D. Howe, J. Wrobel, J. Bodenheimer, H. Thomas, and D. Lind, Conference on Lasers and Electro-Optical Systems, San Diego, August, 1980.
5. S. Yonezawa, T. Maede, T. Sudujama, and H. Takahashi, Conference on Lasers and Electro-Optical Systems, San Diego, August, 1980.
6. H. Heitmann, L. Sander, M. Urner-Wille, and K. Witter, *J. Mag. Mater.*, **21**, 233 (1980).
7. M. de Haan, Conference on Lasers and Electro-Optical Systems, San Diego, August, 1980.
8. R. McFarlane, G. Blom, A. Chan, S. Chandra, E. Frankfort, G. Kenney, D. Lou, J. Nadan, and J. Hafner, *Opt. Eng.*, **21**, 913 (1982).
9. D. Y. Lou, G. M. Blom, and G. C. Kenney, *J. Vac. Sci. Technol.*, **18**, 78 (1981).
10. G. M. Blom and D. Y. Lou, Society of Photographic Scientists and Engineers, Las Vegas, March 15-19, 1981.
11. A. E. Bell and F. W. Spong, *IEEE J. Quantum Electron.*, **qe-14**, 487 (1978).
12. G. M. Blom, *Appl. Phys. Lett.*, **35**, 81 (1979).
13. A. E. Bell and F. W. Spong, *ibid.*, **38**, 920 (1981).
14. H. G. Craighead, R. E. Howard, P. F. Liao, D. M. Tennant, and J. E. Sweeney, *ibid.*, **40**, 662 (1982).
15. K. Y. Ahn, T. H. DiStefano, S. R. Herd, N. J. Mazzeo, and K. N. Tu, *J. Appl. Phys.*, **53**, 6360 (1982).
16. D. Y. Lou, *This Journal*, **128**, 699 (1981).
17. A. Milch and P. Tasaico, *ibid.*, **127**, 884 (1980).

Protection of n-GaAs Photoanodes by Photoelectrochemical Grafting of Poly (3-Methyl-thiophene) and Poly (3,4-Dimethyl-thiophene) Films

G. Horowitz, G. Tourillon,* and F. Garnier

Laboratoire de Photochimie Solaire, C.N.R.S., 94320 Thiais, France

ABSTRACT

Very adhesive poly (3-methyl-thiophene) and poly (3,4-dimethyl-thiophene) films were photoelectrochemically grown on platinum-plated n-GaAs electrodes. The stability of poly (3-methyl-thiophene)-coated photoanodes is dependent on the nature of the counterion used during the synthesis of the polymer. Best results were obtained with SO_3CF_3^- . No film peeling was observed after a 17 h run in a $\text{Fe}(\text{CN})_6^{4-/3-}$ aqueous solution under 30 mW/cm² tungsten lamp illumination. This is attributed to the greater density and smaller porosity of the polymer grown with this counterion. However, corrosion of the photoanode occurred, because of the reduction of the polymer to its neutral form where its conductivity is drastically lowered. Reduction of the polymer film was also observed with poly(3,4-dimethyl-thiophene), but a comparison between the absorption spectra of electrochemically and chemically reduced polymers suggests that the electrochemical reduction is not complete. This can account for the lack of photocorrosion of GaAs after a 4 h run in a $\text{Fe}(\text{CN})_6^{4-/3-}$ electrolyte. The use of more oxidizing redox couples prevented the reduction of the polymer film, but led to a rapid photodissolution of the electrode.

The development of semiconductor-based photoelectrochemical (PEC) solar cells is mainly limited by the problem of photodegradation of small bandgap electrodes. A good stabilization of GaAs has been obtained by adding selenide to the electrolyte (1-3). More recently, polymer coatings have been employed to protect semiconductor photoelectrodes. One of the most reported polymers is polypyrrole, which has been

shown to be a good conducting electrochemically synthesized organic polymer on Au or Pt electrodes (4). Long term stabilization (up to 450h) has been reported on polypyrrole-protected n-Si in various aqueous solutions (5-7). Protection of n-GaAs by polymer coating seems to be a more difficult task. The reported stabilities in aqueous solution are 10-20 min with polypyrrole (8) and 2h with polystyrene pendant $\text{Ru}(\text{bpy})_3^{2+}$ complex (9). It has been shown recently that other conducting organic polymers of the same group as polypyrrole can be electrochemically gener-

* Electrochemical Society Active Member.

Key words: photoelectrode stabilization, conducting polymer, gallium arsenide.

ated, e.g., polythiophene and polyfuran (10). In this paper, we show that very adhesive films of poly(3-methyl-thiophene) and poly(3,4-dimethyl-thiophene), hereafter called PMeT and PMe₂T, can be photoelectrochemically grafted on platinum-plated n-GaAs. The protection of the electrodes is shown to be dependent on the nature of the counterion. Corrosion or passivation of the GaAs surface may occur, depending on the counterion and the monomer. An attempt is made to explain the lack of long-term stabilization of n-GaAs by means of conducting organic polymers.

Experimental

Electrodes were prepared from (100) and (111) n-GaAs wafers purchased from RTC-Caen (France). The doping level ranged from 1.5 to 2.5 × 10¹⁶ cm⁻³. Ohmic contacts were made by evaporating Au-Ge alloy and annealing at 400°C under N₂ atmosphere. A copper wire was attached to the back contact with silver epoxy cement. The wafers were then mounted on glass tubes with Torr Seal (Varian) resin. The active surface was polished with 1 μm diamond paste and etched in 5% bromine-methanol for 5-10s. It was then rinsed thoroughly with ethanol.

The platinum electroplating was carried out in the dark under -0.6 to -0.7 V/SCE cathodic polarization in an aqueous solution of (NH₄)₂PtCl₆ and LiClO₄. Electrodeposition of polymers was performed under tungsten illumination (ca. 30 mW/cm²) in acetonitrile solutions containing 0.1M supporting salt and 1M distilled 3-methyl or 3,4 dimethyl-thiophene. The supporting electrolyte was LiClO₄, Bu₄NBF₄, or Bu₄NSO₃CF₃. The quantity of deposited Pt, as well as the polymer film thickness, were followed by using a digital coulometer. Interferometric measurements that were carried out on platinum electrodes showed a linear variation of the thickness of electrodeposited PMeT films as a function of the charge, with a slope of 10 Å/mC × cm⁻². This value was used for determining the film thickness on platinized GaAs. The stability of protected n-GaAs photoanodes was tested by measuring the short-circuit current vs. time of an illuminated cell with a load resistance of 1Ω. Electrolytes were prepared with reagent-grade chemicals and distilled water. Stability tests were performed in two different redox solutions: (i) 0.1M K₃Fe(CN)₆ and 0.1M K₄Fe(CN)₆ in 0.1M KCl (pH = 7.3), and (ii) 0.1M FeCl₂ and 0.1M FeCl₃ in 0.1M HCl (pH = 1.0). I⁻/I₃⁻ and Br⁻/Br₂ aqueous solutions were prepared as follows: 1M KI, 0.1M I₂, 0.2M KCl and 0.2M KBr, 0.02M Br₂, 0.1M KCl. Illumination was obtained with a tungsten lamp and was roughly estimated as 30 mW/cm² with no correction for absorption by the solution and polymer film.

Results

Table I gives the polymerization-onset potentials of pyrrole and thiophene derivatives on Pt and illuminated platinum-plated n-GaAs electrodes. Attempts to grow polythiophene derivative films on naked GaAs led to very inhomogeneous films, probably because corrosion competes with polymerization at the potentials used. No improvement was obtained by etching the electrode in 1:1 H₂SO₄/H₂O₂ solution, or by ruthenium pretreatment (1). Very adhesive films could be grown on platinum-plated GaAs electrodes. The best results were obtained with a charge of 10 mC/cm², corresponding to a thickness of about 20Å of platinum. Scanning electron micrographs of a platinized electrode showed that Pt films are not continuous and tend to leave uncovered islands. However, continuous polymer films could be grown on such pretreated electrodes.

Linear sweep cyclic voltammograms of PMeT-covered Pt and illuminated platinized-GaAs electrodes are shown in Fig. 1. It must be pointed out that the oxidation peak is observed on GaAs only under illumination, whereas the reduction peak can also be obtained in dark. The 0.6V cathodic shift of the peaks is similar to the one observed on the polymerization onset potentials.

The adhesion of polymer films was checked by applying a piece of adhesive tape on the electrode and peeling it off. No removal of the polymer film was obtained for both PMeT and PMe₂T.

The corrosion behavior of a naked GaAs electrode in an aqueous solution depends on the pH of the electrolyte (11, 12). At neutral pH (electrolyte i), both As₂O₃ and Ga₂O₃ are stable, and GaAs is rapidly covered with an oxide layer, leading to a sharp decrease of the photocurrent, as shown by the dashed curve in Fig. 2. In acidic electrolyte (ii), Ga₂O₃ is completely soluble, and a continuous dissolution of the electrode is observed, without any decrease of the photocurrent. Platinization did not change the corrosion behavior of GaAs, probably because of the discontinuous character of the electrodeposited Pt films.

The evolution of the photocurrent with time in electrolyte i is shown in Fig. 2, 3, and 4 for different polymer films. The rapid decrease occurring within the first minute is associated with an electrochemical reduction of the film to its neutral form. This reduction is evidenced by the change of color from dark blue to red for PMeT, and from dark blue to pale blue for PMe₂T films. It has also been verified by measuring the rest potential of the electrode in an acetonitrile solution of the supporting salt. The film could then be reoxidized to its conducting form. The rapid decrease of the photocurrent can then be attributed to the increase of the ohmic resistance of the polymer film, as will be discussed in the following section.

Figure 2 corresponds to a PMeT-BF₄⁻ film. It is worth noting the increase of the photocurrent during the first hour. During the course of the experiment, a white insoluble deposit appeared on the surface, which gradually covered the electrode, leading to a decrease of the photocurrent. The experiment was interrupted after 3h and the electrode was rinsed in distilled water and blown dry. The deposit appeared as little pellets of oxide that have grown over the polymer film. This latter was still covering the whole electrode surface. After removing the oxide pellets, polymer film corrosion pits could be seen on the electrode. The j-v characteristic measured before the stability test is shown in the inset of Fig. 2. The values for the parameters of the corresponding power curve are the following. Short-circuit current density: 5.7 mA/cm². Open-circuit voltage: 0.54V. Fill factor: 0.50. The power efficiency at 30 mW/cm² is thus 5%. An efficiency of 10.5% has been reported for polypyrrole-coated n-GaAs in methanol (8). Attempts to obtain power curves for uncoated GaAs failed because of the rapid passivation of the electrode.

Similar behavior was observed with PMeT-ClO₄⁻ films, with a photocurrent maximum occurring after only 15 min.

The photocurrent vs. time behavior of a PMeT-SO₃CF₃⁻ film covered electrode is shown in Fig. 3. No deposit appeared over the film after 17h. We observed a slow decay of the photocurrent, which can

Table I. Polymerization onset potential on platinum and illuminated platinized n-GaAs electrodes. Electrolytic solution: CH₃CN-0.1M, supporting salt-1M monomer. The onset potentials do not depend on the nature of the supporting salt.

Monomer	Polymerization onset potential (V vs. SCE)	
	Pt	Illuminated n-GaAs/Pt
Pyrrole	0.8	0.2
3-Me Thiophene	1.4	0.8
3,4-Me ₂ Thiophene	1.3	0.7

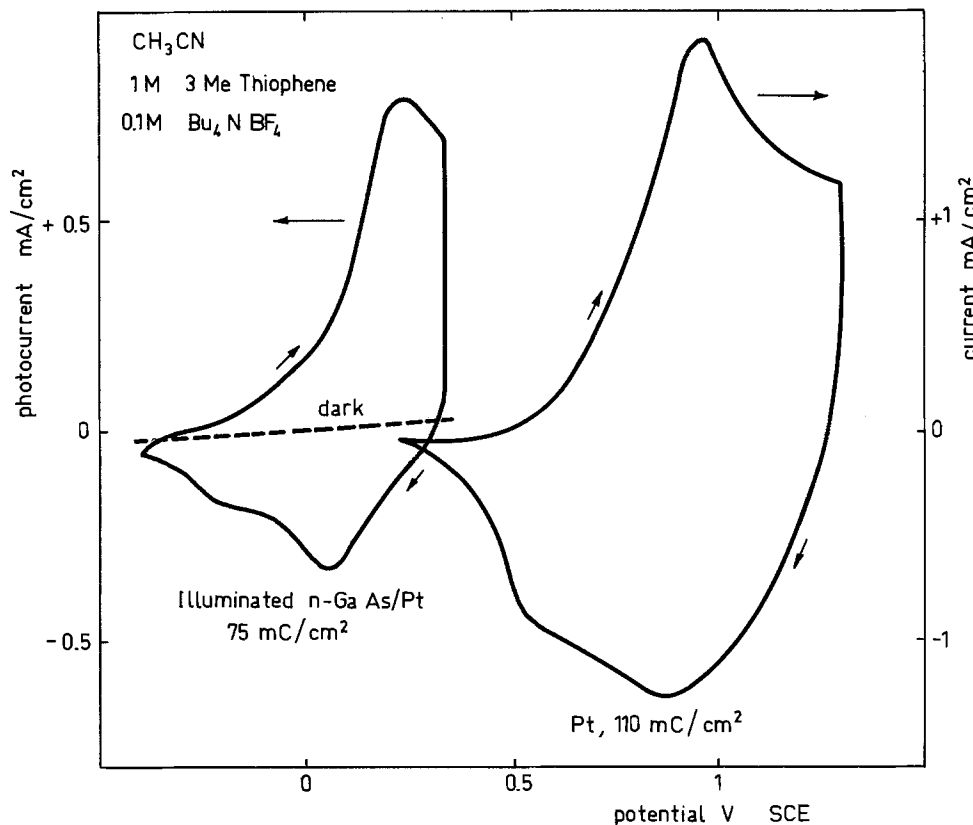


Fig. 1. Cyclic voltammogram of PMeT-BF_4^- on platinum and illuminated platinized-n-GaAs electrodes. Illumination by a tungsten lamp at 30 mW/cm^2 . Scan rate: 50 mV/s .

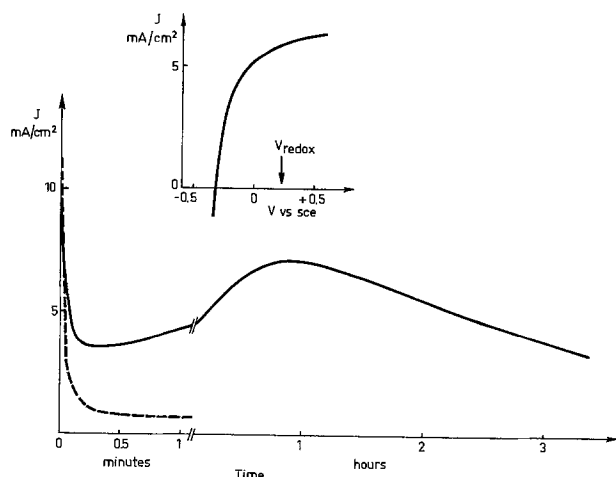


Fig. 2. Short-circuit current vs. time for a bare (---) and PMeT-BF_4^- -coated platinized (—) n-GaAs photoanode, in aqueous $0.1 \text{ M K}_3\text{Fe(CN)}_6$, $\text{K}_4\text{Fe(CN)}_6$, KCl solution. The polymer layer is 1000 \AA thick. Illumination by a tungsten lamp at about 30 mW/cm^2 . A voltammetric curve for the protected electrode is shown in the inset (scan rate: 200 mV/s).

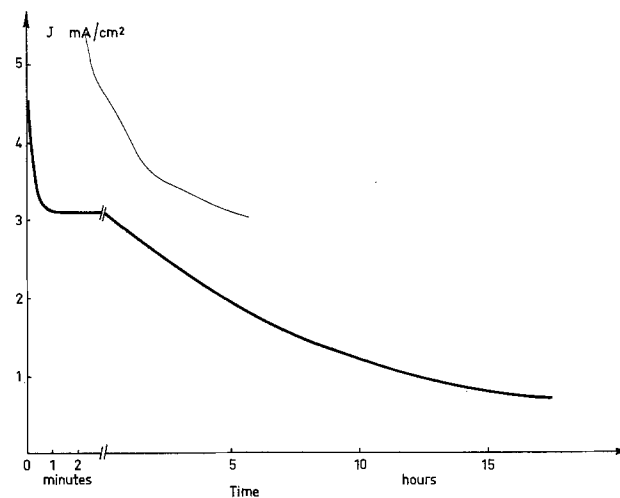


Fig. 3. Same as Fig. 2 for a $\text{GaAs/Pt/PMeT-SO}_3\text{CF}_3^-$ electrode. Film thickness: 1000 \AA .

be attributed to the passivation of the semiconductor. Some corrosion pits were visible at the electrode surface after removing the polymer film.

The best protection was obtained with $\text{PMe}_2\text{T-SO}_3\text{CF}_3^-$ films, as shown in Fig. 4. No deposits on the film or corrosion pits on the electrode were observed after a 4h run under tungsten lamp illumination.

Experiments in solution *ii* led to similar results with all the polymer films. After about 1h under illumination, the film cracked and peeled off the electrode. Dissolution of GaAs occurred during the course of the experiment.

Finally, Fig. 5 shows the correlation between the equilibrium redox potential and the open-circuit voltage (V_{oc}) for a GaAs/Pt/PMeT photoanode. V_{oc} was taken as the difference between the onset of the photocurrent and the redox potential. The linear variation

observed has also been reported for other GaAs/polymer PEC cells (8, 9), and suggests the absence of Fermi level pinning, at least within the voltage range $0.2\text{--}0.8 \text{ V/SCE}$.

Discussion

The lack of long-term stabilization of polymer-coated n-GaAs in aqueous solutions originates from film peeling that occurs after 10–20 min with polypyrrole (8), and 2h for polystyrene $\text{Ru}(\text{bpy})_3^{2+}$ complex (9). With PMeT and PMe_2T , one of the most remarkable features is that film peeling only occurs after a significant corrosion of the photoanode. This is particularly evident in solution *ii*, where the GaAs dissolution is not prevented by the polymer, and where the film peels off the electrode only after a substantial corrosion of the electrode. Moreover, a $\text{PMeT-SO}_3\text{CF}_3^-$ -coated electrode could be run for 17h in solution *i* without any film peeling.

The explanations can be given for the corrosion of polythiophene protected electrodes; first, the reduc-

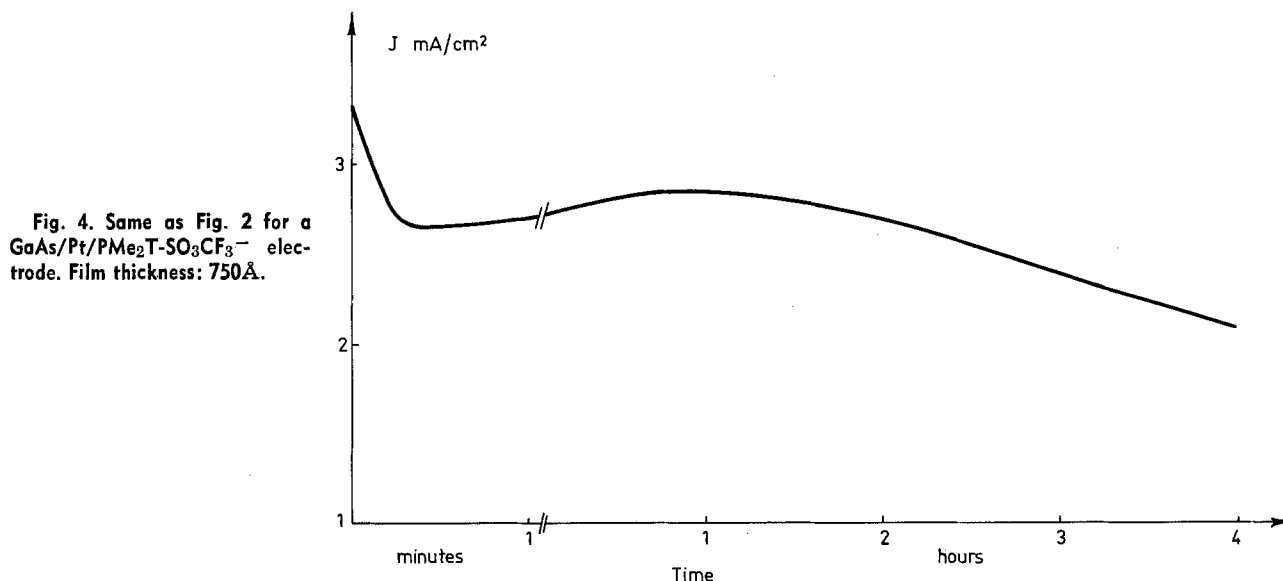


Fig. 4. Same as Fig. 2 for a GaAs/Pt/PMe₂T-SO₃CF₃⁻ electrode. Film thickness: 750Å.

tion of the film to its neutral (semiconducting) form, and second, the porosity of the film.¹

The porosity of the polymer is clearly shown by the growth of oxide pellets over the film with PMeT-BF₄⁻ and PMeT-ClO₄⁻ in electrolyte *i*. This feature cannot be explained without assuming that Ga or As ions are able to get through the polymer to the electrolyte. The porosity of PMeT films seems to be dependent on the nature of the counterion used for the electrochemical synthesis, since no oxide growth was observed with SO₃CF₃⁻. This is clearly shown by the scanning electron micrographs of reduced PMeT films, grown on platinum electrodes shown in Fig. 6, which reveal

¹One of the referees suggested that the photocurrent bump in Fig. 2 and 4 could be due to a light filtering effect originating from a decrease of the polymer absorption (see Fig. 7) as it is reduced. This can be discarded, since the reduction occurs within the first minute of the stability test, whereas the photocurrent increase is a much longer process.

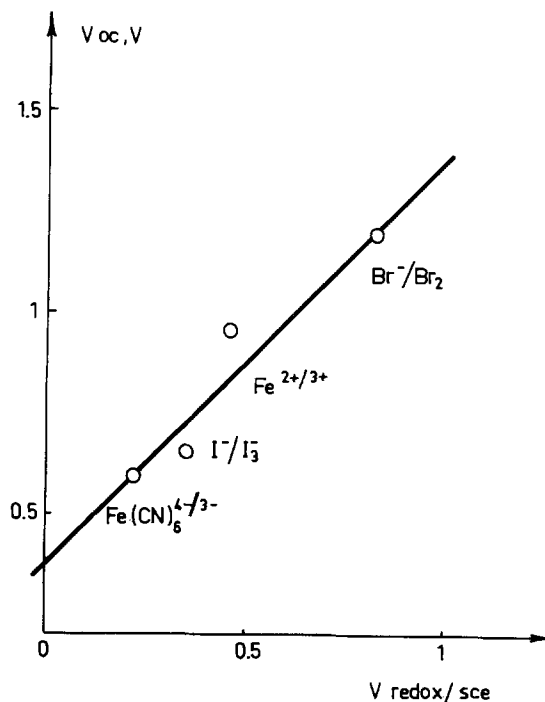


Fig. 5. Open-circuit voltage of a GaAs/Pt/PMeT-BF₄⁻ photoanode-Pt counterelectrode PEC cell as a function of the redox potential of the electrolyte. The illumination is a 30 mW/cm² tungsten light. Polymer film thickness: 1000Å.

a much higher degree of porosity of films originally grown with ClO₄⁻ counterion. The more space filling character of SO₃CF₃⁻ films could be attributed to a better match between the sizes of the thiophene mole-

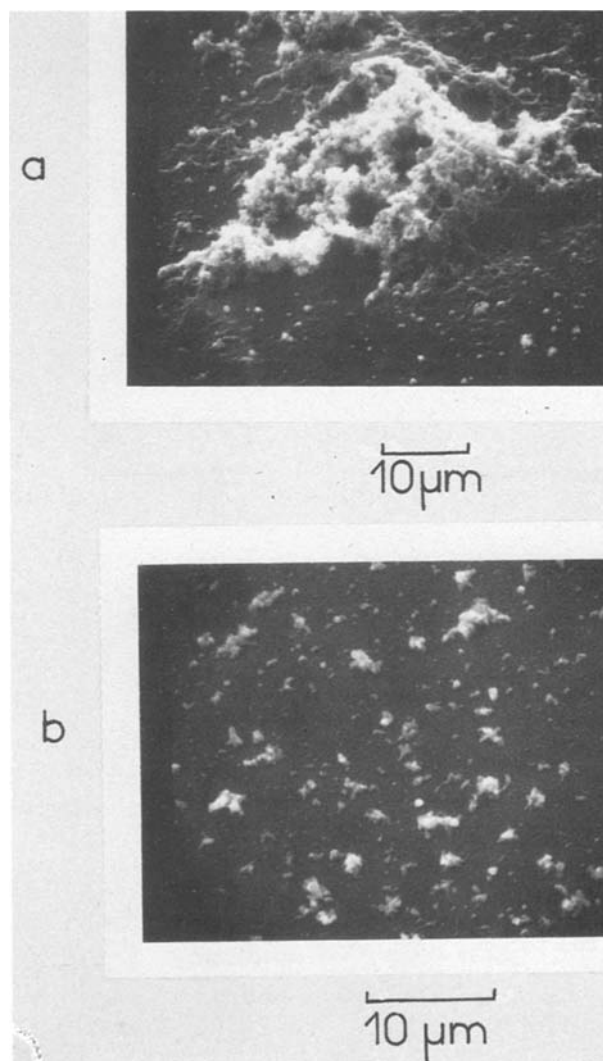


Fig. 6. Scanning electron micrograph of 3000Å-thick reduced PMeT films on platinum. (a) Film grown with ClO₄⁻ counterion. (b) Film grown with SO₃CF₃⁻ counterion.

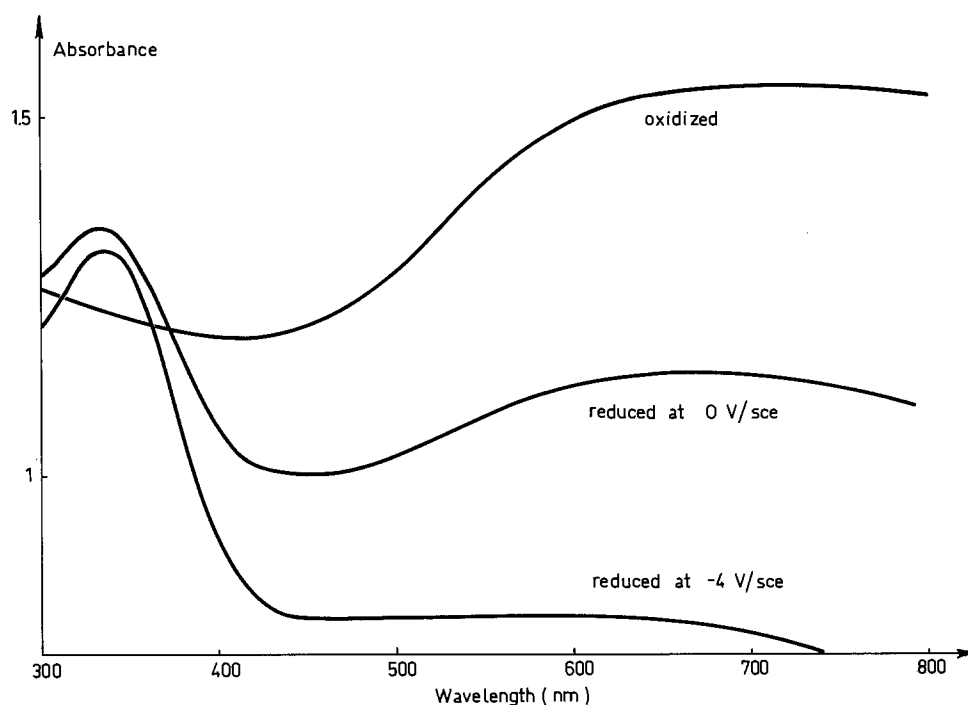


Fig. 7. Absorption spectra of oxidized and electrochemically reduced $\text{PMe}_2\text{T-C1O}_4^-$ films. The spectrum of the film reduced at -4V/SCE is equivalent to the one obtained for chemically reduced polymer. Polymer film thickness: 1000\AA . PMe_2T films grafted on semi-transparent Pt electrodes.

cule and the counterion. Studies of PMeT grown on Pt substrates have shown a higher density of the polymer with SO_3CF_3^- counterion, which could be explained by a smaller distance between the polymer chains (13).

Reduction of the polymer film occurred in both electrolytes *i* and *ii*. It is shown by the rapid photocurrent drop that takes place within the first minute of the experiment. The reduction was clearly evidenced by putting back the electrode in an acetonitrile solution where the PMeT film could be reoxidized as described in the previous section. A probable explanation of the polymer reduction is a positive shift of the redox peaks of PMeT from their position in acetonitrile; a shift of ca. 0.35V has been observed on Pt/ PMeT electrodes (14). Corrosion of the photoanode could then occur, because the photocarriers are not drained rapidly enough towards the electrolyte through the polymer film. The polymer reduction can also account for the low power efficiency (5%) observed on PMeT -coated GaAs photoanodes.

The reduction of the polymer induces a change of its color and absorption spectrum. A complete dedoping can be obtained chemically in ammonia. This gives red PMeT and yellow PMe_2T . The red color is also obtained on electrochemically reduced PMeT . Furthermore, elemental microanalysis showed a doping level of 0.005% for chemically reduced and 0.010% for electrochemically reduced (at -0.2V/SCE) poly-3-methylthiophene. For comparison, the doping level of the conducting form is about 30%. The corresponding conductivities are $30 (\Omega \times \text{cm})^{-1}$ for the oxidized form and $10^{-7} (\Omega \times \text{cm})^{-1}$ for the reduced form (these values were measured on pressed pellets). Then, the PMeT -coated electrodes are worked with a neutral (quasi-insulating) protective film; this explains the corrosion observed in electrolyte *i*.

The pale blue color of reduced- PMe_2T films indicates that the reduction of this film is only partial. Absorption spectra of oxidized and reduced- PMe_2T films are shown in Fig. 7. These spectra were measured on PMe_2T films grafted on semitransparent Pt electrodes. A complete electrochemical reduction of the film, leading to an absorption spectrum similar to the one measured on chemically reduced PMe_2T , is only obtained at a highly reducing potential (-4V/SCE). The polymer film reported in Fig. 4 is then only partly dedoped. This explains the smaller value of the initial

photocurrent drop, and can account for the better stability of a PMe_2T -coated GaAs photoanode.

The reduction of the polymer film could be prevented by using a more oxidizing redox couple. A trial has then been performed with a Br^-/Br_2 aqueous solution. The experiment led to a rapid corrosion of the photoanode with the formation of white insoluble Ga and As bromide. However, the blue color of the PMeT film proves that it has stayed in its conducting form. The open-circuit voltage measured in this redox couple is surprisingly high: 1.20V , approaching the bandgap of GaAs (1.42eV). It can be compared to the value reported by Noufi *et al.* on polypyrrole-coated GaAs (8): 1.37V in $\text{Fe}(\text{CN})_6^{4-/\text{Fe}(\text{CN})_6^{3-}}$, NaOH aqueous solution. It must be noted that the values reported in Fig. 5 cannot be related to corrosion, since they have been measured at open circuit, with no net current flowing through the electrode.

Conclusion

Electrodeposition of PMeT and PMe_2T films on GaAs seems to be more difficult than on polypyrrole. Pre-deposition of platinum was necessary in order to obtain homogeneous films. However, very adhesive films were grown. They resist to the adhesive-tape peel test, and still adhered to the electrode even when corrosion evolved. The protection against photocorrosion is only partial, because of the porosity of the film and its reduction to its neutral form. Long-term stabilization could be reached if a compromise is found between the nonreduction of the polymer film, which requires a higher oxidizing redox couple, and the enhanced corrosion of GaAs with such a couple.

Manuscript submitted June 1, 1983; revised manuscript received Sept. 7, 1983.

REFERENCES

1. B. A. Parkinson, A. Heller, and B. Miller, *Appl. Phys. Lett.*, **33**, 521 (1978); *This Journal*, **126**, 954 (1979).
2. R. Noufi and D. Tench, *This Journal*, **127**, 188 (1980).
3. A. Bourrasse, H. Cachet, G. Horowitz, and S. Le Crom, *Rev. Phys. Appl.*, **17**, 801 (1982).
4. A. F. Diaz, K. K. Kanazawa, and G. P. Gardini, *J. Chem. Soc., Chem. Commun.*, 635 (1979); K. K. Kanazawa, A. F. Diaz, W. D. Gill, P. M. Grant, G. B. Street, G. P. Gardini, and J. F. Kwak *Synth. Met.*, **2**, 329 (1979/1980); A. F.

- Diaz, J. M. Vasquez-Vallejo, and A. Martinez-Duran, *IBM J. Res. Develop.*, **25**, 42 (1981).
5. R. Noufi, A. J. Frank, and A. J. Nozik, *J. Am. Chem. Soc.*, **103**, 1849 (1981).
 6. F. R. F. Fan, B. L. Wheeler, and A. J. Bard, *This Journal*, **128**, 2042 (1981).
 7. T. Skotheim, I. Lundström, and J. Prejza, *ibid.*, **128**, 1625 (1981); T. Skotheim, L. G. Petersson, O. Inganas, and I. Lundström, *ibid.*, **129**, 1737 (1982).
 8. R. Noufi, D. Tench, and L. F. Warren, *ibid.*, **127**, 2310 (1980).
 9. K. Rajeshwar, M. Kaneki, and A. Yamada, *ibid.*, **130**, 38 (1983).
 10. G. Tourillon and F. Garnier, *J. Electroanal. Chem.*, **135**, 173 (1982).
 11. S. M. Park and M. Barber, *ibid.*, **99**, 67 (1979).
 12. H. Cachet, R. Calsou, M. Froment, and H. Mathlouthi, *J. Molec. Spectrosc. Electron.*, **7**, 9 (1982).
 13. G. Tourillon and F. Garnier, *J. Polymer Sci.*, To be published.
 14. G. Tourillon and F. Garnier, *J. Electroanal. Chem.*, To be published.

Modification of Schottky Barriers in Silicon by Reactive Ion Etching in NF_3 Gas Mixtures

T. P. Chow

General Electric Corporate Research and Development, Schenectady, New York 12345

S. Ashok

Engineering Science Program, The Pennsylvania State University, University Park, Pennsylvania 16802

B. J. Baliga and W. Katz

General Electric Corporate Research and Development, Schenectady, New York 12345

ABSTRACT

The effect of reactive ion etching on silicon surfaces with NF_3 diluted with argon and nitrogen was studied. Similar to the pure NF_3 case, the Schottky barrier height was increased for p-Si and decreased for n-Si. This barrier modification was most effective at ~10% NF_3 , while the silicon-etch rate was reduced by an order of magnitude, as compared to pure NF_3 . The degree of ion bombardment, as inferred from substrate dc bias, reached a maximum at ~20% NF_3 for argon-diluted cases, but increased monotonically from pure NF_3 to pure N_2 for nitrogen-diluted cases. Optical emission spectra indicated that atomic fluorine concentration decreases with increasing diluent content for both plasmas, with molecular nitrogen being the major product detected.

Reactive ion etching (RIE) is becoming a commonly used processing technique in patterning high-resolution structures in integrated circuits, because it combines the high selectivity of plasma etching with the anisotropy of sputter etching. Various thin film materials have been etched under a wide range of conditions (1). However, the surface properties of silicon after RIE have not been investigated in detail. In prior works, fluorocarbons were usually used, and several structural (TEM and RHEED) and electrical measurements (MOS retention time, DLTS) were performed on the etched surfaces (2-5). Also of relevance are two previous studies using low-energy ion beams to simulate the damages created during plasma etching, one using argon (6), and another using chlorine and fluorine as well as argon (7). All these studies indicated that plasma-induced damages result in changes in Schottky barriers and carrier lifetime, but high-temperature annealing can at least partially eliminate these changes. Our interests in studying the phenomenon of RIE-related damages are in its applications for controllably modifying Schottky barrier heights. An alternative technique towards this end is low-energy implantation of dopant atoms (8, 9).

In this paper, an examination of silicon surfaces after RIE with NF_3 -based plasmas by Schottky-diode characteristics and secondary ion mass spectrometry (SIMS) is reported. The discharge characteristics were monitored *in situ* with optical emission spectroscopy and substrate dc voltage measurements; they too are reported herein.

Experimental Procedure

The RIE was performed in a commercial, parallel-plate-type reactor (Plasmatherm PK 1241). p-Type, (111)-oriented and n-type, (100)-oriented, silicon

Key words: discharge, diodes, surfaces, spectra.

wafers with a resistivity of 1-4 Ω -cm were cleaned in the usual manner prior to loading into the reactor. They were then etched with 50-200W of RF power. The dc bias developed on the RF electrode was monitored, but the plasma potential was not directly measured. The conditions used for the RIE were: gas flow rate of 5-10 sccm, pressure of 60-90 mtorr, substrate temperature of 40°C, etching time of 10 min, and electrode spacing of ~5 cm. An automated optical spectrometer scanning between 200 and 800 nm was used to analyze the plasma emission spectrum. After RIE and a standard cleaning cycle with $\text{H}_2\text{O}_2/\text{H}_2\text{SO}_4$, hot nitric acid, and HF dip, gold dots (1 mm diam and 2000Å thick) were e-beam evaporated using shadow masks. Back ohmic contacts were formed by evaporating ~1 μm of Al. (The back side of the n-type wafers were implanted with phosphorus at $1 \times 10^{15}/\text{cm}^2$ and then activated before RIE and Al deposition.) On some samples, Al was used to check the effect of the Schottky metal. SIMS was performed with a Cameca IMS 3-f ion microscope with a cesium primary beam of impact energy of 17 keV and negative ion sampling.

Results

Previously, we have reported that RIE with pure NF_3 leads to a gradual increase in Schottky barrier in p-Si and a decrease in n-Si with increasing applied RF power up to 200W (10). After RIE, the silicon surface was examined with SIMS to determine the composition of the surface layers. A marked increase in fluorine (M/e of 19) was found; its integrated intensity is shown in Fig. 1 as a function of applied RF power. It was also determined that fluorine was present only up to ~500Å. Other species, such as SiN^- and AlO^- , were also found to be significantly higher on the etched surfaces, but no systematic dependences on RF power were seen. The origins of the nitrogen and aluminum species are attributed to NF_3 , and reactor electrodes

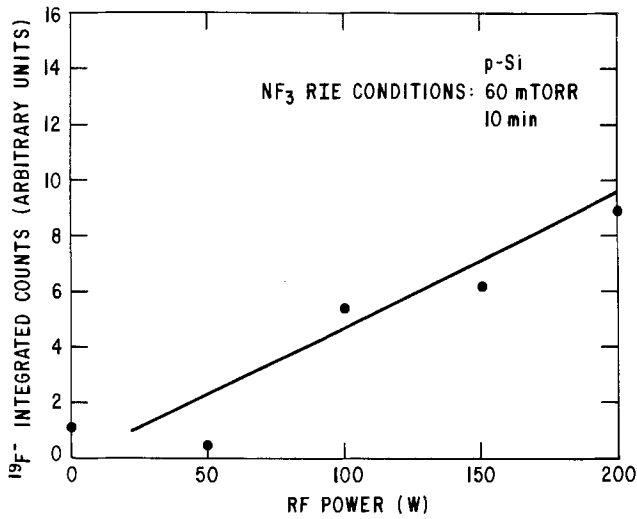


Fig. 1. Integrated intensity of fluorine ions ($M/e = 19$) on NF_3 -etched silicon surface, as detected by SIMS, as a function of the applied RF power.

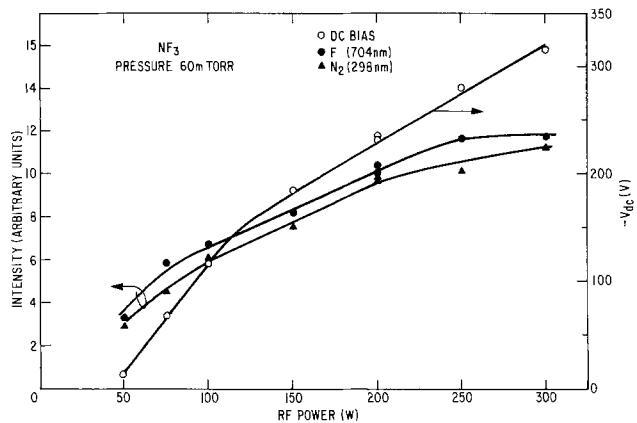


Fig. 2. Optical emission intensity of atomic fluorine (703.7 nm) and molecular nitrogen (297.7 nm) and substrate dc bias vs. applied RF power in 100% NF_3 plasmas at 60 mTorr for an unloaded reactor.

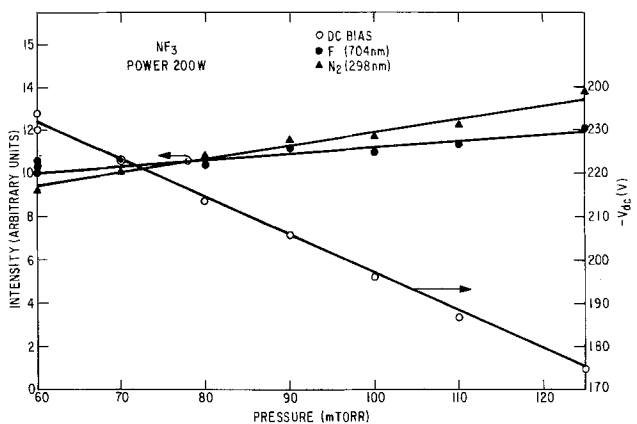


Fig. 3. Optical emission intensity of atomic fluorine (703.7 nm) and molecular nitrogen (297.7 nm) and substrate dc bias vs. pressure in 100% NF_3 plasmas at 200W for an unloaded reactor.

and chamber walls, respectively.

For 100% NF_3 plasmas, the optical emission intensities of atomic fluorine and molecular nitrogen, as well as the substrate dc bias, increases with increasing RF power (Fig. 2). This increase is due to the enhanced dissociation of the NF_3 molecules. However, the substrate bias decreases rapidly at higher pressures, while the optical emission intensities of both

F and N_2 increase slightly, as shown in Fig. 3.

One of the major limitations of using pure NF_3 plasma for Schottky barrier tailoring is its extremely fast silicon etch rate (11, 12). It has been previously demonstrated that inert gases can be used as diluents in reducing poly-Si and $MoSi_2$ etch rates (12). Under the present conditions used for RIE, pure NF_3 plasmas etched crystalline silicon quickly (~ 5000 Å/min), but diluting to only 10-20% with argon or nitrogen reduced the etch rate by about an order of magnitude. Figure 4 illustrates this trend for the case of 200W and 60 mtorr at 40°C. Also shown is the etch rate of a positive photoresist (AZ1470) which hardly changes with dilution.

In general, the Schottky barriers were modified in these diluted plasmas in a way similar to those obtained with NF_3 alone. The I-V characteristic of an unetched Au/n-Si device is shown in Fig. 5, together

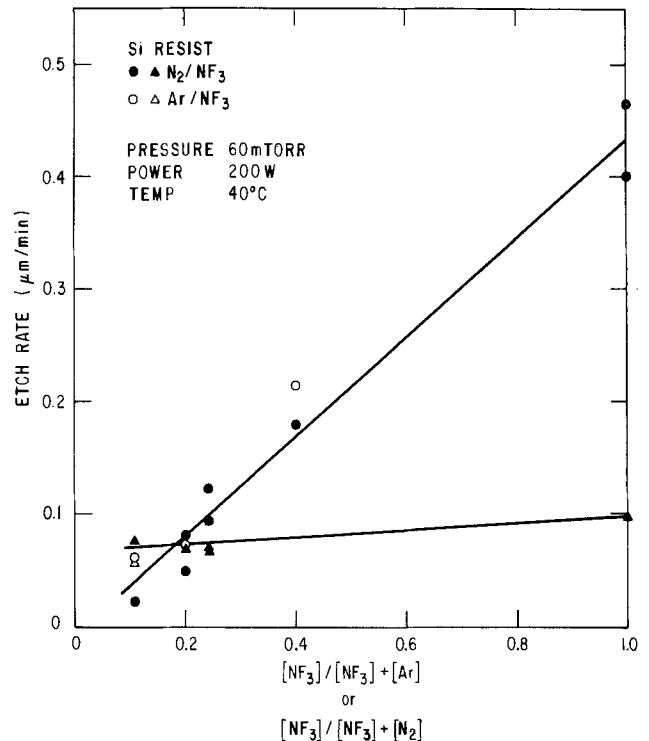


Fig. 4. The silicon and positive photoresist (AZ1470) etch rates as a function of concentration of NF_3 diluted with argon and nitrogen. An RF power of 200W, a pressure of 60 mTorr, and a substrate temperature of 40°C were used.

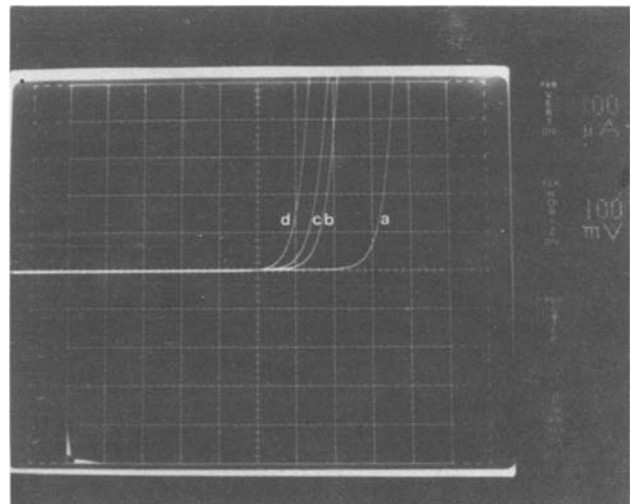


Fig. 5. I-V characteristics of Au/n-Si diodes after RIE (200W and 60 mTorr) in various NF_3/Ar gas mixtures. a: unetched (control). b: 42. c: 24. d: 11% NF_3 in argon.

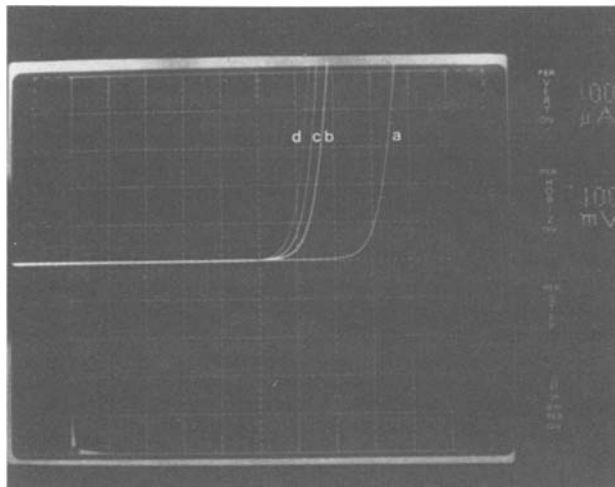


Fig. 6. I-V characteristics of Au/n-Si diodes after RIE in various NF_3/N_2 gas mixtures. a: unetched (control). b: 32. c: 24. d: 11% NF_3 in nitrogen.

with those of samples etched in 11, 24 and 42% NF_3 in NF_3 /argon. A decreasing barrier is seen with decreasing NF_3 content. Figure 6 shows the I-V characteris-

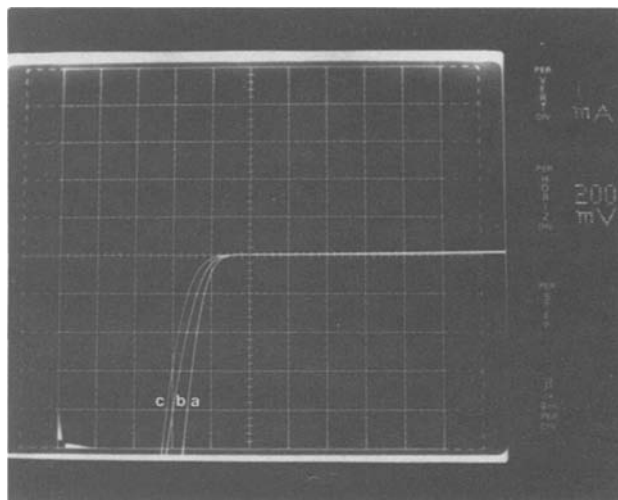


Fig. 8. I-V characteristics of Au/p-Si diodes after RIE in various NF_3/N_2 gas mixtures. a: 32. b: 24. c: 11% NF_3 in nitrogen.

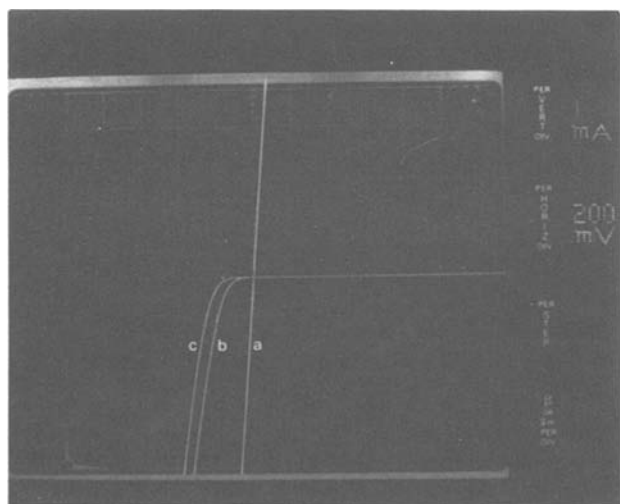


Fig. 7. I-V characteristics of Au/p-Si diodes after RIE in various NF_3/Ar gas mixtures. a: unetched (control). b: 24. c: 11% NF_3 in argon.

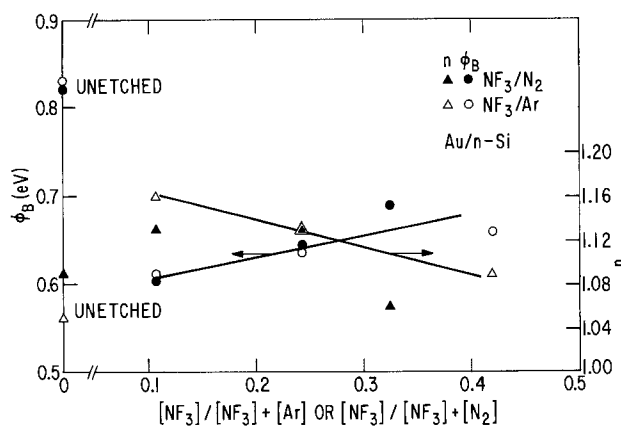


Fig. 9. Schottky barrier height (ϕ_B) and ideality factor (n) of Au/n-Si diodes as a function of gas composition of NF_3/Ar and NF_3/N_2 plasmas.

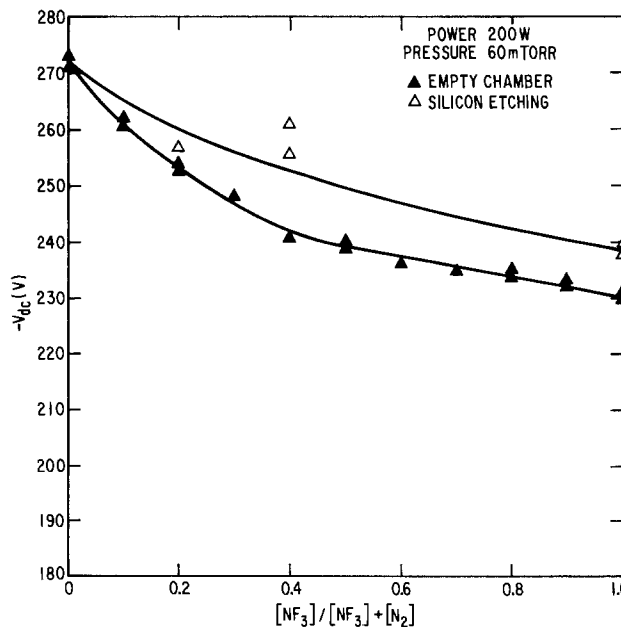
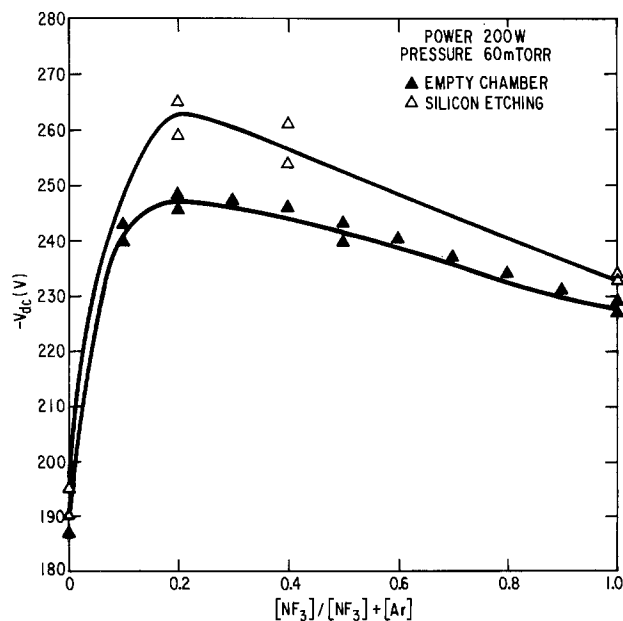


Fig. 10. Substrate dc bias vs. gas composition of (a, left) NF_3/Ar and (b, right) NF_3/N_2 plasmas at 200W and 60 mTorr

tics of Au/n-Si samples etched in nitrogen-diluted NF_3 plasmas. A similar decreasing trend in barrier height can also be observed. Figure 7 and 8 show the I-V behavior of gold/p-silicon diodes exposed to NF_3/Ar and NF_3/N_2 plasmas, respectively. An increase in barrier height was seen with decreasing NF_3 percentage when compared to the unetched sample.

By measuring log current *vs.* voltage under forward and reverse biasing conditions, the Schottky barrier height and ideality factor can also be deduced. These two parameters are shown in Fig. 9 as a function of gas composition of both Ar- and N_2 -diluted plasmas for the Au/n-Si devices. A larger barrier-height change is accompanied by a greater deviation from unity of the ideality factor. For the p-Si devices, large values of n (1.3-1.5) were obtained. Similar characteristics were observed for devices with aluminum for the Schottky metal.

Substrate dc bias can be used to infer the degree of ion bombardment during RIE. Generally, it is higher during silicon etching than in an unloaded chamber. Also, different variations in this voltage were observed, dependent on whether argon or nitrogen was used for dilution. When the plasma becomes less NF_3 rich with argon addition, the voltage increases up to $\sim 20\%$ of NF_3 . Further dilution leads to a gradual drop until pure argon is reached (Fig. 10a). A monotonic increase has been observed with increasing nitrogen content, and the maximum occurs at pure N_2 (Fig. 10b). Despite the different trends described, the dc biases for these two types of plasmas at the composition of most interests (10-20% NF_3) only differs slightly.

When the gas composition varies, there are substantial changes in concentrations of constituent atoms and molecules. These changes were monitored with optical emission spectroscopy for reactor under empty and silicon-loaded conditions. In these plasmas, the major spectral lines have been attributed to atomic fluorine (703.7 nm), argon (706.7 nm), and molecular nitrogen (297.7 nm). While the most intense N_2 line is at 337.1 nm, we have chosen to monitor the 297.7-nm line because its intensity range is closer to those of argon and fluorine. Spectral lines that may be traceable to atomic nitrogen, F_2 or NF_x ($x = 1, 2, 3$) were not identified.

In general, atomic fluorine concentration (as inferred from line intensity) decreases with increasing

dilution. Since atomic fluorine is believed to be the species responsible for silicon etching in fluorine-based plasmas (13), the decrease in silicon with decreasing NF_3 percentage can be explained by the decrease in reactant concentration. The presence of a silicon wafer on the cathode ($\sim 10\%$ area coverage) drastically reduces the 703.7-nm line intensity (by $\sim 70\%$). As shown in Fig. 11, for either an empty or silicon-loaded reactor, the decrease in fluorine emission varies linearly with decreasing NF_3 percentage, except at the extremes of the composition range. Furthermore, there is little difference between the Ar- and N_2 -diluted cases (Fig. 11a *vs.* b), indicating that nitrogen does not significantly suppress fluorine generation. However, such a correlation was not observed for NF_3 diluted with He in a dc hollow-cathode reactor (14). The reason is probably because of the difference in diluent nature (helium *vs.* argon and nitrogen) and in reactor configuration. While the variation of the other constituents (mostly argon and/or nitrogen) is monotonic for argon-diluted NF_3 , it is not for the N_2 -diluted ones (Fig. 12 and 13). As expected, the molecular nitrogen intensity increases with increasing nitrogen content, but at $\sim 10\%$ NF_3 it reaches a local minimum, probably due to other competing reactions involving fluorine and nitrogen atoms. Furthermore, it can be noted that in the NF_3/Ar case, the steep decrease in argon line intensity also occurs at low NF_3 percentage. In contrast to fluorine, loading the reactor with silicon only changes the levels of argon and nitrogen slightly, confirming their inert chemical nature in the etching reactions.

When only inert gases (argon and nitrogen) were used for RIE, the Schottky barrier change is very much dependent on reactor background-gas levels and chamber conditioning. Hence, they cannot be used reliably for the Schottky barrier modification. The exact nature of the damage has not been studied here, but it has been proposed (7) that it is a complex formed by a defect with a halogen atom.

Summary

Reactive ion etching of silicon surfaces with NF_3 diluted with nitrogen and argon have been shown to result in Schottky barrier shifts similar to those obtained with pure NF_3 . However, while NF_3 plasma

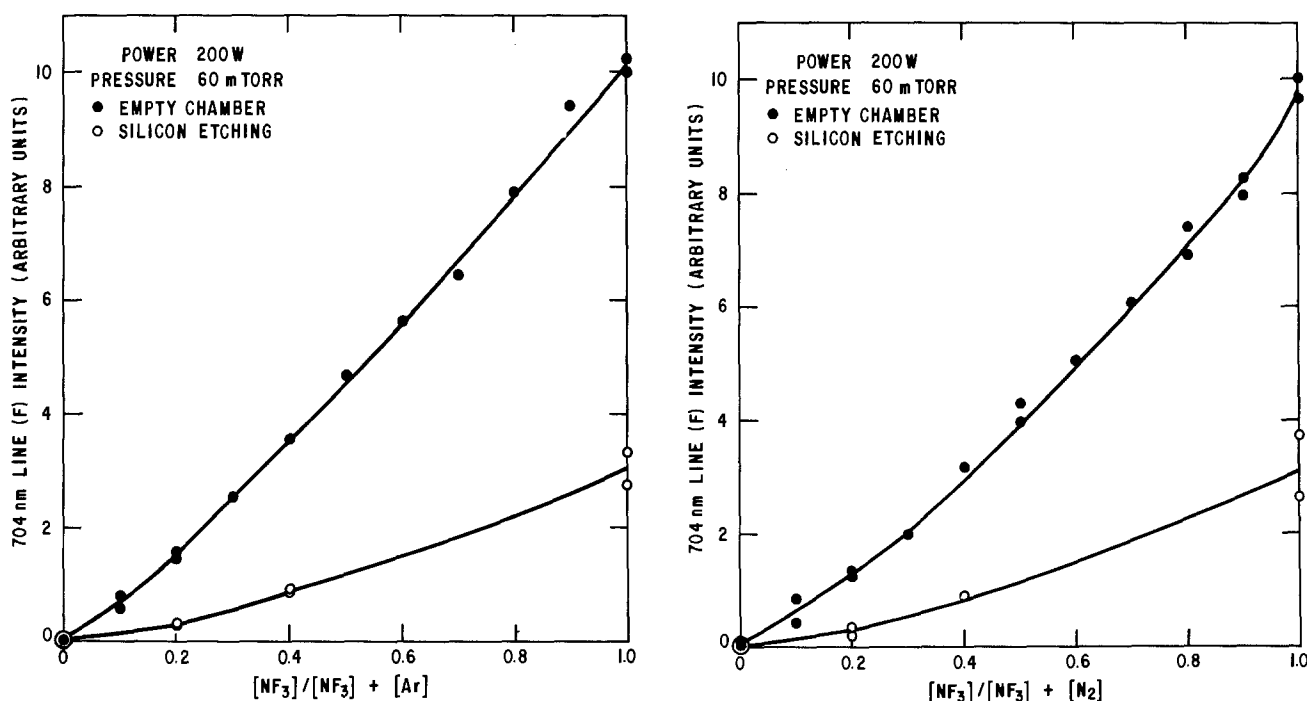


Fig. 11. Optical emission intensity of atomic fluorine (703.7 nm) as a function of gas composition of (a, left) NF_3/Ar and (b, right) NF_3/N_2 plasmas.

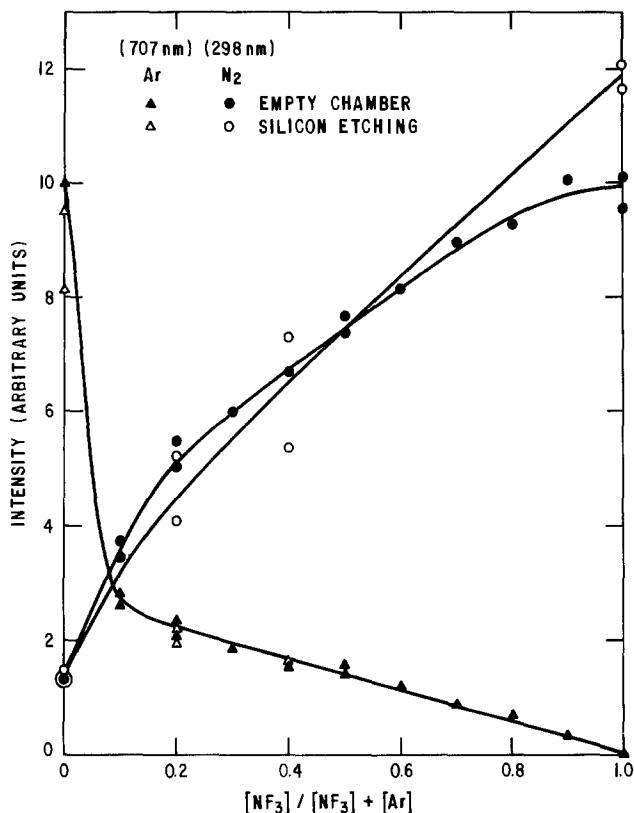


Fig. 12. Optical emission intensity of atomic argon (706.7 nm) and molecular nitrogen (297.7 nm) as a function of gas composition of NF_3/Ar mixtures.

etched silicon at a relatively high rate, the diluted plasmas only etched silicon at much reduced rates (about 10% of that in NF_3). The degree of ion bombardment upon argon and nitrogen addition follows different trends, reaching a maximum at 80% Ar dilution. Optical emission spectra showed that fluorine concentration increases with increasing NF_3 percentage. Molecular nitrogen is the major reaction product detected.

Acknowledgment

We would like to thank P. A. Maciel and G. Smith for technical assistance.

Manuscript submitted July 5, 1983; revised manuscript received July 18, 1983. This was Paper 175 presented at the San Francisco, California, Meeting of the Society, May 8-13, 1983.

General Electric Company assisted in meeting the publication costs of this article.

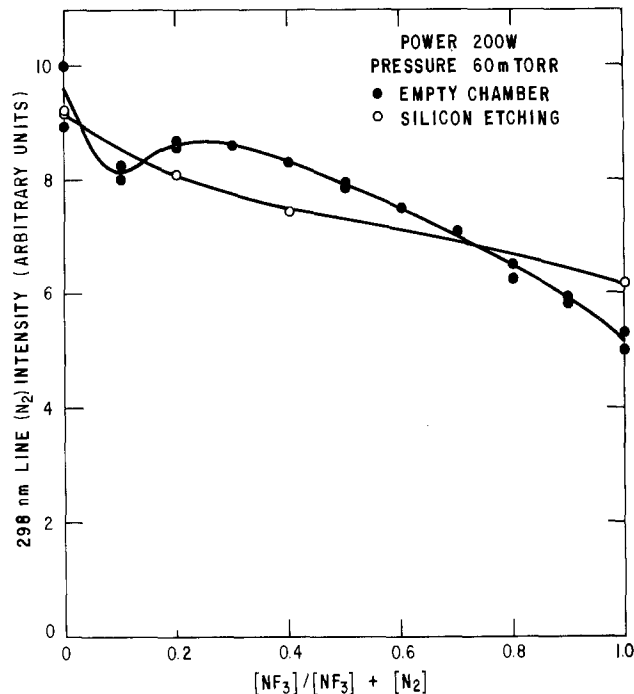


Fig. 13. Optical emission intensity of molecular nitrogen (297.7 nm) as a function of gas composition of NF_3/N_2 mixtures.

REFERENCES

1. L. M. Ephrath, *IEEE Trans. Electron Devices*, ed-28, 1315 (1981).
2. L. M. Ephrath and R. S. Bennett, *This Journal*, 129, 1822 (1982).
3. C. Ransom, T. I. Chappell, L. M. Ephrath, and R. S. Bennett, Abstract 215, p. 346, The Electrochemical Society Extended Abstracts, Vol. 82-1, Montreal, Que., Canada, May 9-14, 1982.
4. S. Pang, D. D. Rathman, D. J. Silversmith, R. W. Mountain, and D. D. DeGraff, Abstract 185, p. 289, The Electrochemical Society Extended Abstracts, Vol. 82-2, Detroit, Michigan, October 17-21, 1982.
5. M. O. Watanabe, M. Taguchi, K. Kanzaki, and Y. Zohta, *Jpn. J. Appl. Phys.*, 22, 281 (1983).
6. S. Ashok, S. J. Fonash, and R. Singh, *Appl. Phys. Lett.*, 39, 423 (1981).
7. G. Greeuw and J. F. Verwey, *Solid-State Electron.*, 26, 241 (1983).
8. J. M. Shannon, *ibid.*, 19, 537 (1976).
9. R. L. Thornton, *Electron Lett.*, 17, 485 (1981).
10. S. Ashok, T. P. Chow, and B. J. Baliga, *Appl. Phys. Lett.*, 43, 687 (1983).
11. D. H. Bower, *This Journal*, 129, 795 (1982).
12. T. P. Chow and A. J. Steckl, *J. Appl. Phys.*, 53, 5531 (1982).
13. D. L. Flamm, V. M. Donnelly, and J. A. Mucha, *ibid.*, 52, 3633 (1981).
14. N. J. Ianno, K. E. Greenberg, and J. R. Verdeyen, *This Journal*, 128, 2174 (1980).

(100) Silicon Etch-Rate Dependence on Boron Concentration in Ethylenediamine-Pyrocatechol-Water Solutions

N. F. Raley,* Y. Sugiyama,¹ and T. Van Duzer

Department of Electrical Engineering and Computer Sciences and the Electronics Research Laboratory, University of California, Berkeley, California 94720

ABSTRACT

The (100) silicon etch-rate dependence on boron concentration in ethylenediamine-pyrocatechol-water (EPW) solutions at 110°C has been measured by successive etching of boron-diffused silicon. The etch rate begins to decrease near 10^{19}cm^{-3} and decreases approximately as the fourth power of doping over three orders of magnitude in etch rate. The etch-rate ratio between heavily and lightly doped silicon appears insensitive to pyrazine concentration from 0.01 to 6.0g/liter E, oxygen exposure of the etch solution, and light. The etch-rate decrease is sensitive to hole concentration and not to atomic concentration of boron or stress. The etch-rate dependence may be explained by assuming that the hydrogen-evolution cathodic half-reaction of the oxidation-reduction reaction is the rate-determining step. The reason for the etch-rate decrease as the hole concentration increases is given in terms of increased Auger recombination of large numbers of electrons chemically produced at the silicon surface during etching. Excellent agreement with experiment is obtained. Similarities of this etch system and the phenomenon of silicon staining are discussed in terms of oxidation-reduction reactions. Application to control of thickness and uniformity of boron-doped silicon membranes is discussed.

Boron-doped silicon membranes have been fabricated using ethylenediamine-pyrocatechol-water (EPW) etching solutions for a variety of purposes: as thin substrates to reduce backscattering in electron (1) or ion beam lithography (2), to reduce scattering of transmitted radiation in x-ray lithography (3), as thin highly doped barriers for Josephson junctions or super-Schottky diodes (4), as ink-jet nozzles (5), and for the fabrication of micromechanical beams used in accelerometers (6, 7). In almost all cases, boron diffusions are used to stop the EPW-etchant attack on silicon. Thus far, there has been very little work reported on the etch-rate dependence on boron or on the basic etchant system itself. Finne and Klein (8) first reported the etchant but did not find any etch-rate dependence up to $8 \times 10^{17}\text{cm}^{-3}$ boron. It was reported later that the etchant stopped at $7 \times 10^{19}\text{cm}^{-3}$ (9), but there was no detailed measurement of the transition region. Reisman *et al.* (10) discovered the effect of pyrazine and oxygen-induced benzoquinone catalysts on the etch rate for lightly doped silicon in EPW solutions. This is important, since the pyrazine and quinone concentration in commercially available ethylenediamine and pyrocatechol, respectively, varies from lot to lot. They briefly report the etch-rate dependence on boron in bulk silicon wafers at two levels of heavy doping for high pyrazine/low benzoquinone etch solutions and find the etch rate to be small but finite in the 10^{20}cm^{-3} range. Seidel and Csepregi (11) reported a stronger etch-rate dependence on doping in epitaxial layers than that reported by Reisman *et al.* They used a similar etch solution, except with somewhat lower pyrazine concentration and unknown benzoquinone content. Initial experiments in our laboratory had indicated an etch rate approximately an order of magnitude smaller than that obtained by Reisman *et al.*, although still non-zero. There has been no indication in the literature of the effect of pyrazine or benzoquinone on the heavy doping etch rate or etch-rate measurements on diffused layers. Also, there has been no report on the mechanism of the decrease of etch rate for EPW solutions. As a consequence of the scarcity of data, membrane formation has been a trial and error process.

The purpose of the present investigation is to study the etch-rate dependence on boron concentration in

diffused layers, as this is the most common method of dopant introduction in the fabrication of silicon membranes. The effect of catalyst concentration and the dependence of the etch rate on light are also analyzed. Possible mechanisms for the etch-rate decrease with doping are considered, and oxidation-reduction reactions are proposed to explain the observations. Design curves are calculated using the etch-rate dependence and the diffusion profile employed in this study as an aid in the determination of etching time needed in order to obtain desired membrane thickness and/or uniformity. The principles used here can be applied to any known concentration profile.

Experimental

The starting wafers used in this study were 51-76 mm diam, nominal (100) orientation ($\sim \pm 1^\circ$), 1-10 $\Omega\text{-cm}$, 300 μm thick, and polished on one side. The wafers were of p-type conductivity in most cases. However, no difference was observed in etching with n-type wafers.

Sample preparation.—Two different methods of etch-rate measurement were used, as shown in Fig. 1. In the method shown in Fig. 1a, etching was done from the most heavily doped side of the wafer in such a way as to make a measurable step. In the method shown in Fig. 1b, etching was done from the more lightly doped side of a thick membrane (4), and the remaining membrane thickness was measured by observing the minimum energy for transmission of an electron beam.

We will describe first the fabrication procedure for the etch-step method shown in Fig. 1a. The wafers were first degreased in trichloroethylene, acetone, and methyl alcohol and then rinsed in deionized water and dried in nitrogen gas. Following a 5s dip in buffered HF ($\text{NH}_4\text{F}:\text{HF} = 5:1$), the wafers were cleaned for 10 min in $\text{H}_2\text{SO}_4:\text{H}_2\text{O}_2 = 4:1$ solution. Final cleaning was done in RCA-1 solution ($\text{NH}_4\text{OH}:\text{H}_2\text{O}_2:\text{H}_2\text{O} = 1:1:5$) for 15 min at 75°C. Oxide on the wafers was then removed in buffered HF. The wafer was rinsed, dried, and immediately loaded lying horizontally on a quartz boat in the boron predeposition furnace. The gas flows were 210 cm^3/min of 1000 ppm $\text{B}_2\text{H}_6/\text{Ar}$, 13 cm^3/min O_2 , in a carrier gas of 1.3 liter/min N_2 and were set 30 min prior to wafer loading. The temperature was measured using a Chromel-Alumel thermocouple connected to an Omega 199 thermocouple meter with an accuracy of $\pm 2^\circ\text{C}$. The diffusion was performed at 950°C for 45 min.

* Electrochemical Society Student Member.

¹ On leave from the Electrotechnical Laboratory, Ibaraki, Japan.

Key words: anisotropic silicon etching, silicon membranes, boron concentration profiles.

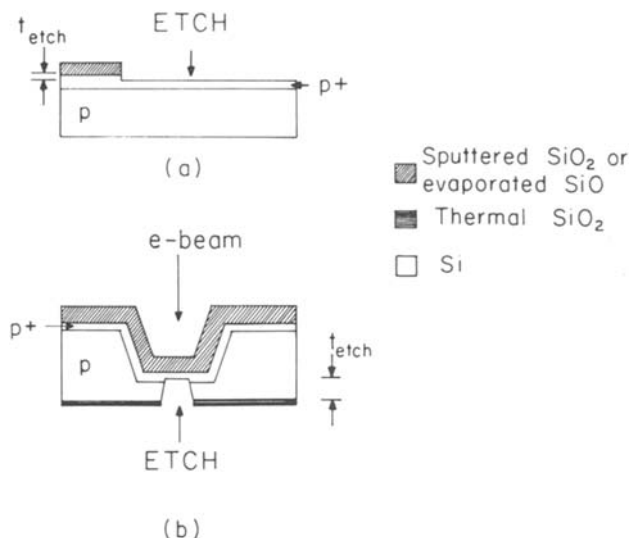


Fig. 1. Sample geometries used to study successively etched silicon: (a) direct etch-step method; (b) electron-transmission method. The thickness of the oxide layers is in the range 2000-5000Å in both cases. In method (b), the thickness and area of the thick membrane are 1.5 μm and 100 μm × 100 μm; the thickness and area of the thin membrane are ~0.3 μm and 10 μm × 10 μm.

The ~1000Å thick boron glass formed on the wafer was removed by dilute HF (HF:H₂O = 1:20) for 1 min in the dark. The etching was done in the dark to prevent stain formation on the heavily doped p-type silicon surface, which occurs especially in dilute HF solutions in bright light (12). No stains were observed, especially after a subsequent RCA-1 clean designed to remove them. In order to remove the SiB phase layer (~50Å) under the glass, a wet oxidation at 800°C for 15 min was performed, which grew ~200Å oxide. The phase layer was removed because it has properties different from boron-doped silicon and knowledge of its etching properties were not desired in this study.

After BHF etching of the phase layer oxide, sputtered SiO₂ or evaporated SiO was deposited as an etchant mask. In the first experiments, SiO₂ sputtering was performed at a base pressure of ~10⁻⁶ torr in 8 mtorr Ar:O₂ = 4:1 gas at ~1.4 W/cm² power density for 3h, giving about 6000Å. However, this process was found to cause sputter damage, as evidenced by sheet resistance increases of 10-20% after sputtering, indicating that the electrically active concentration profile had been altered (refer to Results section). In order to avoid damage, 1500Å SiO layers deposited at 15Å/s in 10⁻⁶ torr vacuum were used instead, with no measurable sheet-resistance change. The wafers were then scribed into 5/8 in. × 1/2 in. rectangles. Wax was applied along one edge (~1/8 in. wide) and baked until hard; the mask layer was subsequently etched in BHF in the dark. After wax removal and cleaning, the wafers were ready for silicon etching.

The fabrication scheme for the electron-beam-transmission method shown in Fig. 1b was somewhat more involved (4). First, a silicon wafer was anisotropically etched to about 1-5 μm thickness over ~100 × 100 μm area. Thermal oxide (~2000Å) was grown on both sides of the wafer and stripped off the etched side. The p⁺ diffusion/wet oxidation as described above was performed. The bottom window (~10 × 10 μm) in thermal oxide was opened using conventional electron-beam lithography techniques. Then, SiO₂ or SiO was deposited as before on top as an etchant mask but was not patterned. This scheme allowed etch rate measurement of the diffusion profile at lower concentration (~5 × 10¹⁹ cm⁻³) without the need for prolonged etching of the highly doped (~1.5 × 10²⁰ cm⁻³) surface region.

Silicon etching.—The silicon etching apparatus is shown in Fig. 2. Nitrogen is bubbled into the solution through a quartz diffuser at 160 cm³/min in order to minimize the oxidation of the solution and to provide stirring. Cool water is circulated in the upper jacket in order to condense evaporated solution vapor onto the walls. It is then fed back into the solution through a teflon valve. The solution level does not change over many hours of etching. The temperature is monitored by a thermometer placed in the etch bath and is maintained at 110° ± 1°C. The wafers are held in place by the removable quartz holder.

The chemical proportions of the etchant used were 17 ml E: 3g P: 8 ml W. The ethylenediamine was made by J. T. Baker and the pyrocatechol was made by MCB Company. The pyrazine concentration in a particular batch of ethylenediamine was measured by ultraviolet absorption at 3150Å wavelength with a Carey 219 spectrophotometer using a volumetric technique. It was initially desired to keep the pyrazine concentration low in the etch rate experiments in order to minimize its effect. It was discovered later, however, that high pyrazine levels did not seem to significantly effect the etch-rate ratio between heavy and light doping.

The silicon etchings were performed about 1h after the solution was mixed in order to allow stabilization of the solution temperature and gas-flow rate. The color of the etch solution at this time was pale amber; the color darkened slightly after many hours of etching but never assumed the deep-red coloration which is characteristic of EPW-etch solutions substantially exposed to air. Both heavily and lightly doped wafers were etched at the same time in order to best characterize the etch-rate ratio. After loading of the wafers in the quartz holder, a 5s BHF dip followed by 30s running DI rinse was done to remove the native oxide and rinse off HF. The wafers were immediately inserted into the silicon etch without drying in order to prevent reformation of the native oxide. At this point, the silicon surface was always hydrophobic. After silicon etching, the wafers were first rinsed in running DI water for 15s to remove most of the silicon etchant. This was followed by a 5s BHF and a 30s final DI water rinse. The silicon surface was again hydrophobic. After residual organic removal steps and a subsequent BHF dip, the silicon steps were measured and the etch process repeated. All etchings were performed under yellow lighting except where otherwise noted.

Measurement accuracies.—The etch-step method shown in Fig. 1a was used for most of the measurements of heavy doping etch rate. The etched-silicon step was measured indirectly as the difference of the total step (oxide and silicon) and the oxide thickness.

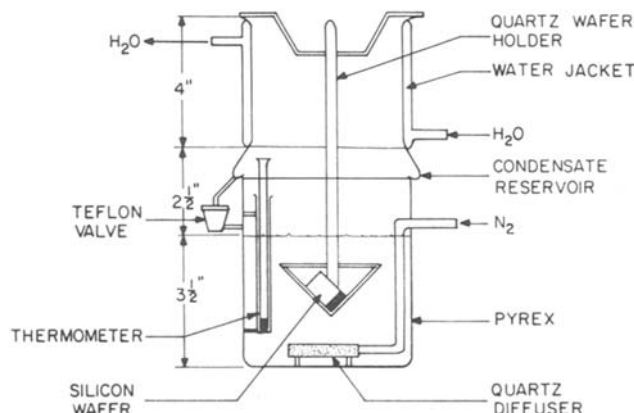


Fig. 2. Schematic diagram of the silicon etching apparatus with reflux column. The wafers are loaded through the top of the beaker. The condensate is fed back into the etch solution.

The total step was measured using a Tencor α -step depth profiler. Oxide thickness was measured using a Gaertner L119 ellipsometer. The total step and oxide thickness were in the 2000-5000Å range. The difference between the measurements of the depth profiler and the ellipsometer on a 4700Å thermal-oxide calibration standard was $\sim 100\text{Å}$; the measurement uncertainties were ± 50 and $\pm 5\text{Å}$, respectively. We estimate a worst case error in etch depth of $\sim 150\text{Å}$. However, the oxide mask was removed from time to time on some samples and the silicon steps (about 400-1000Å) were measured directly, using only the depth profiler, as a check against the indirect method. In most cases, the indirect steps measured were in agreement with the more accurate direct measurements. For the direct method, the difference between the α -step and ellipsometer on a 770Å oxide standard was very small (30Å); the depth profiler measurement uncertainty was also reduced to $\pm 20\text{Å}$. Thus, the worst case accuracy in etch steps in these experiments is 50Å out of 400Å minimum etch steps (less than 15%).

In the second method, the silicon thickness after etching was determined by finding the maximum electron-beam voltage at which the transmitted beam current was zero. Thickness was then calculated using appropriate electron-range formulas, taking into account the thickness of the oxide mask (13). The details of this thickness-measurement technique will be published elsewhere. It is sufficient to say that the uncertainty using this technique is, at worst, $\pm 100\text{Å}$ out of typical 1000Å silicon thickness etched (about $\pm 10\%$).

The light-doping etch rate was measured using the first method on bulk silicon, without the diffused layer, with 5000Å thermal or sputtered SiO_2 as the mask. Typical etch steps measured were 3-30 μm with about $\pm 10\%$ error. Approximately $\pm 5\%$ of this error is attributable to variation of the etch rate over the etching time due to solution oxygenation (refer to Results section).

Concentration profile.—The atomic concentration of boron in both damage-free and sputter-damaged profiles was determined by secondary ion mass spectrometry (SIMS) using a CAMECA Model IMS-3f with a negative oxygen ion as the sputtering ion to enhance yield. The ion beam was scanned over a 400 μm area on a control chip from the same diffused wafer used in the silicon etching experiments at a beam energy of ~ 5 kV, ~ 1 μA current at $\sim 10^{-8}$ torr chamber pressure. The sputter etch rate was ~ 500 Å/min. As boron naturally occurs as B10 and B11 isotopes, both singly charged B10 and B11 ions were monitored, and their contributions added to obtain the total boron concentration. The accuracy in boron concentration is generally quoted as being in the ± 10 -20% range or less, depending on the accuracy of the measurement of a B11 ion implanted calibration standard and the physical and chemical similarity between sample and standard. As discussed in the Results section, the accuracy for our profiles is $\sim \pm 5\%$, which is probably due to our relatively simple analytical situation. The depth scale accuracy is determined by the accuracy in measurement of the final sputtered crater depth ($\sim \pm 5\%$) and the linearity of etch depth with time ($\sim \pm 5\%$). The total depth scale error, then, is $\sim \pm 10\%$.

Spreading resistance measurements were also performed using Solid State Measurements Model ASR-100 as a check of the electrical profile. The bevel angle used was $\sim 0.25^\circ$ and the probe step increment ~ 3.0 μm , giving a profile depth increment of 150Å. The probe spacing used was 20 μm with a probe weight of 5.0g.

Profile sheet resistance measurements were made using a standard four-point probe technique with 0.67 mm probe spacing in order to compare to calculated sheet resistance. A Keithley Model 225 current source

provided 1 mA current and separate Keithley Model 169 multimeters monitored the probe current and voltage. The worst case accuracy in measured sheet resistance was $\sim \pm 5\%$. The measured sheet resistance variation over a 25×25 mm area for a given diffusion run was $\pm 0.5\%$. It was $\pm 4.0\%$ from run to run.

The profile in the surface region of sputter-damaged samples was investigated using the incremental sheet resistance (ISR) technique (14) using the method illustrated in Fig. 1a to successively etch silicon. Even though finiteness of the sample size ($\frac{1}{2}$ in. \times $\frac{1}{2}$ in.) was taken into account, it was relatively unimportant as the sample-size correction factor was approximately 0.96. As a direct consequence, the electrical shunting effect of the nearby unetched heavily doped region under the oxide mask was unmeasurable for the maximum etched depth encountered in these experiments ($\sim 1000\text{Å}$), as was confirmed by measured values of sheet resistance for samples with and without this region present.

Oxygen, pyrazine, and light effects.—The surface of a boron-diffused wafer ($\sim 1.2 \times 10^{20}$ cm^{-3}) and a bulk wafer ($\sim 1.6 \times 10^{19}$ cm^{-3}) were etched at various levels of solution oxygenation using the method shown in Fig. 1a with an SiO_2 mask. Some etching experiments were performed in an open beaker in order to further expose the etch solution to oxygen. These experiments were done at low pyrazine concentration (~ 0.01 g/liter E) in order to isolate the effect of oxygen. The etch rate at the surface of the boron-diffused wafer was also measured at high pyrazine levels (~ 6 g/liter E) and in various light intensities ranging from etching in the dark to etching under illumination of a 650W lamp held 6 in. from the etch solution.

Results

Etch solution characterization.—The absorbance at 3150Å wavelength of typical ethylenediamine used to determine the etch-rate dependence on boron concentration is plotted in Fig. 3 as a function of pyrazine concentration added. The absorbance is given by

$$\text{abs} = \log_{10} (I_i/I_t) \quad [1]$$

where I_i is the transmitted intensity through an empty reference quartz cell and I_t is the transmitted intensity through an identical quartz cell filled with ethylenediamine. According to Beer's law (15), $I_i/I_t = 10^{\alpha c l}$ where α is the absorption coefficient per unit concen-

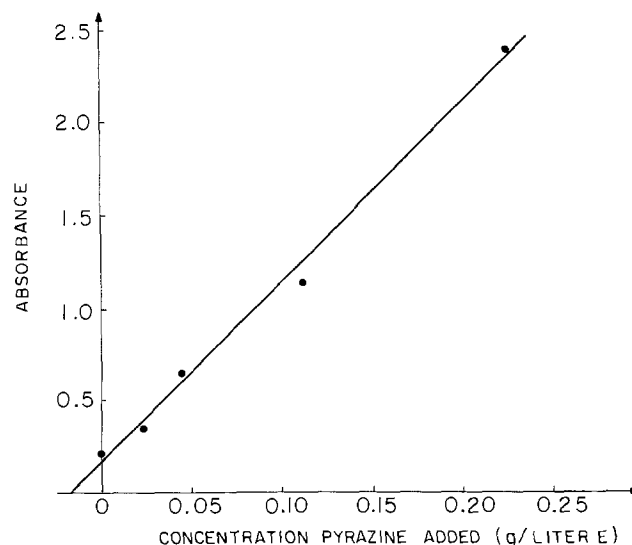


Fig. 3. Absorbance of typical ethylenediamine as a function of added pyrazine at 3150Å wavelength. Cell path length is 1 cm. The data are described by this equation: absorbance = 9.79 (pyrazine added) + 0.16. Original pyrazine concentration determined here is 0.016 g/liter E.

tration of absorbent in a nonabsorbing medium, c is the concentration of absorbent, and l is the cell path length. In this case

$$\text{abs} = alc \quad [2]$$

and

$$d(\text{abs})/dc = al \quad [3]$$

assuming that the absorption coefficient α is a constant and independent of concentration c . In our case, pyrazine is the absorbent and ethylenediamine is the non-absorbing medium. Referring to Fig. 3, if we assume that the absorbance is zero for pyrazine-free ethylenediamine, then the original pyrazine concentration is approximately 0.016 g/liter E. The slope $d(\text{abs})/dc$ for our 1 cm cell was determined to be $9.79 \text{ (g/liter)}^{-1}$. The slope obtained by Reisman *et al.* (10) for a 0.1 mm path length, when corrected to 1 cm path length using Eq. [3], gives $10.3 \text{ (g/liter)}^{-1}$, in good agreement with our result.

The typical etch rate for lightly doped silicon as a function of time after solution mixing is shown in Fig. 4. Note that the initial etch rate is $27.5 \mu\text{m/h}$. Assuming that the activation energy of 8.4 kcal/mol (10) is independent of pyrazine concentration c_p to values as low as 0.01 g/liter E, then

$$\log ER_{110\text{-C}} = 1.694 + 0.134 \log c_p \quad [4]$$

which gives $c_p = 0.013 \text{ g/liter E}$, in good agreement with the measured result of 0.016 g/liter E, using ultraviolet absorption. Note that the etch rate in Fig. 4 increases gradually as a function of time. An "oxygen-enhancement factor" F_{O_2} is defined as

$$F_{O_2} = ER_0(t)/ER_0(0) \quad [5]$$

for low pyrazine solutions used here. It is a measure of solution oxygenation. The enhancement factor ranged from 1.07 to 1.72. In other experiments performed in open beakers, values as large as 2.92 were obtained. We believe this is because of exposure of the solution to oxygen due to backstreaming from the etch beaker top or to oxygen impurity in the nitrogen bubbling gas. We also believe this exposure is responsible for the slight change in etch-solution coloration after many hours of etching. Reisman *et al.* (10) have seen a similar effect when oxygen is bubbled into an etch solution initially free of oxygen. However, they observed more drastic change in solution color from pale amber to deep red. As mentioned before, the color change in our samples was not drastic. This is most likely due to the difference in levels of oxygen exposure.

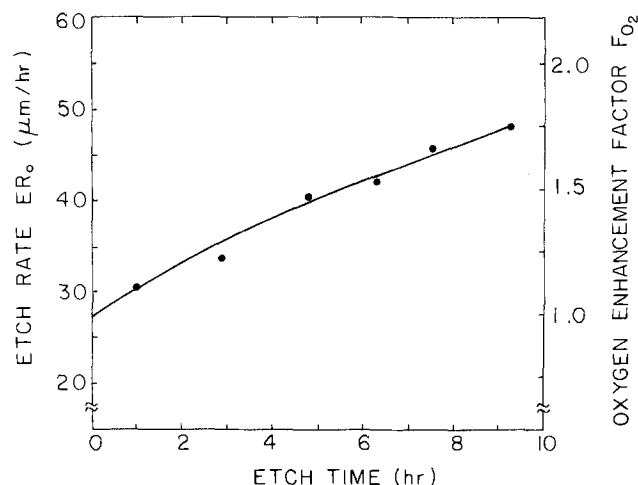


Fig. 4. Typical light doping (1-10 $\Omega\text{-cm}$) etch rate (ER_0) as a function of time after mixing. The solution proportions are 17 ml E: 3g P: 8 ml W and 0.016 g/liter E pyrazine. The etch temperature is 110°C . The oxygen enhancement factor F_{O_2} is the ratio of etch rate at time (t) to initial etch rate.

In general, we have not observed haze due to low pyrazine concentration on the lightly doped or heavily doped silicon surfaces, as was seen by Reisman *et al.* Haze was observed on only one occasion with a 10^{19} cm^{-3} doped wafer.

Concentration profiles.—The SIMS and spreading resistance results for the profile used for the etch-rate dependence are shown in Fig. 5a. The SIMS profile is only accurate past the first 150Å; the corresponding time is required for the sputter-etch rate to stabilize because of the layer of native oxide (16). The depth at which the etch rate became stable was verified to be $\sim 150\text{Å}$ by observing the point at which the B⁺10 and B⁺11 ion current ratios with respect to total ion current were within a few percent of their steady-state values. The fact that the proportions of B10 and B11 were 23% and 77%, respectively, which is close to the proportions in naturally occurring boron (20% and 80%) (17), is a good indication that the calibration factors for B10 and B11 ions are the same and that there is negligible interference from Si^{2+} 30 ion in the B10 signal.

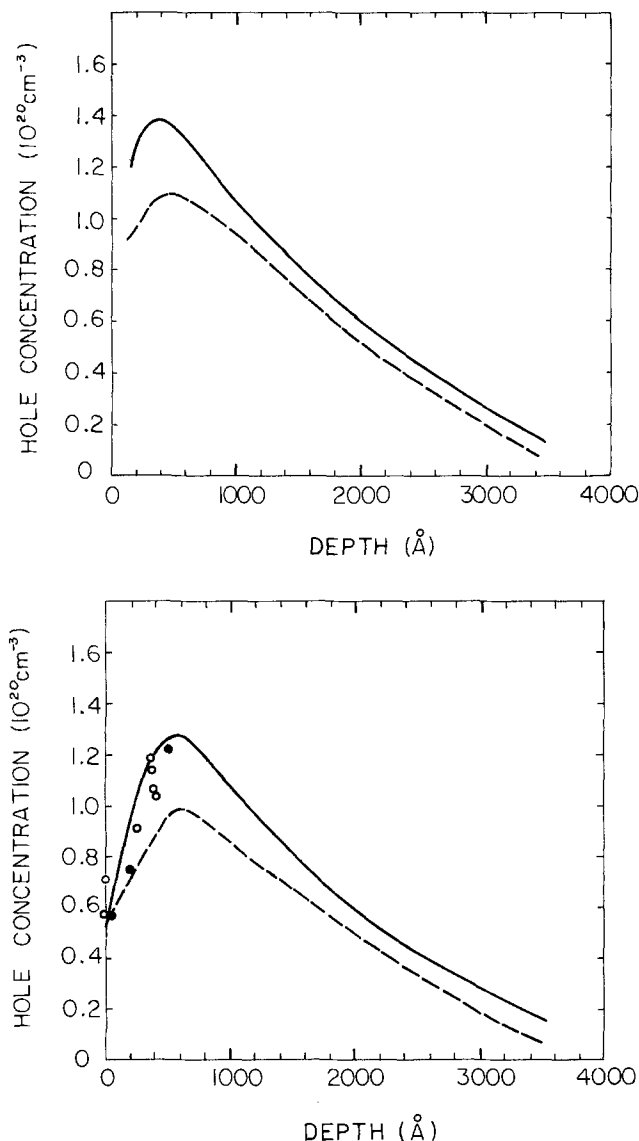


Fig. 5. Hole concentration as a function of depth. (a, top) un-damaged samples. — SIMS. --- spreading resistance. The concentration reduction from the surface to $\sim 350\text{Å}$ is due to the boron segregation effect. (b, bottom) sputter-damaged samples: ● incremental sheet resistance. --- spreading resistance. — resultant profile. Concentrations (○) derived from etch-rate data in the damaged region using Eq. [10] show good agreement with profile.

There is a concentration reduction from the surface to approximately 350Å depth due to segregation of boron into the oxide during the 800°C wet oxidation step. The extrapolated concentration value at the surface, neglecting the segregation effect, is $\sim 1.5 \times 10^{20} \text{ cm}^{-3}$, which is very close to the expected solid solubility of boron in silicon at the diffusion temperature (18). Furthermore, since the boron concentration in our profile is always less than the expected solid solubility, the existence of electrically inactive boron caused by boron precipitation is unlikely.

The sheet resistance ρ_s of an arbitrary doping profile $N_B(x)$ is

$$\rho_s = \frac{1}{\int_0^\infty [1/\rho(x)] dx} \quad [6]$$

where the resistivity $\rho(x) = 1/qp(x)\mu(x)$, q is the electronic charge, and the hole concentration $p(x)$ and mobility $\mu(x)$ are some functions of $N_B(x)$. The sheet resistance calculated for the SIMS profile using precise values for resistivity as a function of unprecipitated boron concentration (19) is very close to the measured value, as seen in Table I. This value is not very sensitive to the first 150Å, assuming that the concentration is $\sim 10^{20} \text{ cm}^{-3}$, so the fact that the profile is not well known there does not appreciably affect the result. Note also that since the measurement uncertainty in sheet resistance is $\pm 5\%$ and that the integrated doping profile gives the measured sheet resistance result, the doping uncertainty in this case is closer to $\pm 5\%$ than $\pm 10\text{-}20\%$.

The solid-solubility concentration and integrated-sheet resistance results allow us to conclude that the doping profile is correct and boron precipitation unlikely. In addition, since differences between boron concentration and hole concentration due to deionization effects are not observed at high concentrations (19), we have plotted the SIMS result as hole concentration in Fig. 5a.

Comparison of the spreading resistance profile to the SIMS profile indicates that the profile shapes are in qualitative agreement. However, the calculated sheet resistance for the spreading resistance profile does not give quantitative agreement with the measured sheet resistance value, as seen in Table I. For this reason and the fact that the interpretation of raw data is more straightforward in SIMS analysis, the concentration values used here are those determined from the SIMS profile.

The profiles for those samples that were sputter damaged are shown in Fig. 5b. The SIMS profile was the same as that for undamaged samples, indicating that boron was not displaced and that the SIMS sputter etch rate was unaffected by the damage. The electrically active concentration for depths less than 625Å was determined by the incremental sheet resistance technique assuming a bulk mobility value of 53 cm^2/sec (19). The concentration in this depth range is less than the boron concentration determined by SIMS. This is consistent with the idea that the sputter damage creates donor traps at energy levels within the silicon-forbidden gap, which compensate the boron

acceptors (20, 21). We believe that there is no damage past 625Å, however, so that the profile there is identical to the SIMS profile. This supposition is supported by the fact that a maximum in electrical concentration as obtained from spreading resistance data and a minimum in silicon etch rate were found to occur at approximately 600Å depth. The calculated sheet resistance for the resultant profile is very close to the measured value, as seen in Table I. It should be noted that the donor traps cause $\sim 50\%$ max increase in ionized scattering centers relative to the ionized boron impurity; however, this increase should have negligible effect on the hole mobility used to determine the hole concentration in the damaged region, since the hole mobility is relatively independent of the scattering center concentration for concentrations in the $\sim 10^{20} \text{ cm}^{-3}$ range (19). The interest in the damaged samples derives from the fact that the effects of boron and hole concentration on the etch rate can thereby be isolated, as we see below.

Etch-rate dependence on hole concentration.—The successive etching aspect of the experiment made it possible to express the etch-rate data as etch-time integrals between position x and a common fixed reference point $x_r > x$ in the concentration profile as

$$t_{\text{etch}} = \int_x^{x_r} dx/ER_p(x) \quad [7]$$

where $ER_p(x)$ is the concentration-dependent etch rate, and t_{etch} is the time required to etch from x to x_r . If we multiply Eq. [7] by the light-doping etch rate ER_0 and define the etch-rate ratio $ERR(x) = ER_p(x)/ER_0$, then

$$G(x) = ER_0 t_{\text{etch}} = \int_x^{x_r} dx/ERR(x) \quad [8]$$

or

$$ERR(x) = -\frac{1}{dG(x)/dx} \quad [9]$$

We use the etch-rate ratio so as to be able to compare etch-rate results obtained under different levels of etch solution oxygenation with different light doping etch rates.

A good fit to the data is $\ln G(x) = -ax + b$, where $a = 26.01$ and $b = 5.365$ with $G(x)$ in microns, and x is the distance from the surface in microns. In this case, $ERR(x) = 1/aG(x)$. The etch-rate ratio so determined as a function of position was then transformed to a function of hole concentration using the SIMS profile in Fig. 5a. The data were then fit to a straight line on a log-log scale using the least squares method as

$$ERR(p) = 2.8 \times 10^{-3} p^{-4.3} \quad [10]$$

which is valid for concentrations in the range from $\sim 3.0 \times 10^{19} \text{ cm}^{-3}$ to $1.28 \times 10^{20} \text{ cm}^{-3}$.

This result is plotted in Fig. 6 along with assorted etch-rate ratios measured on bulk wafers. Note that the etch-rate ratio begins to decrease at approximately 10^{19} cm^{-3} . The etch-rate ratio found by Reisman *et al.* (10) for bulk wafers using 6 g/liter E pyrazine-etch solutions is shown in Fig. 6 for comparison. Approximately $\pm 10\%$ etch-rate variation for concentrations less than 10^{19} cm^{-3} is observed and is most likely due to differences in misorientation of the different wafers from true (100) orientation, as observed by Finne and Klein for wafers of nominal (111) orientation (8). Finally, one can see using Eq. [10] that the etch-rate ratio for the practical maximum boron concentration in silicon is $\sim 1.4 \times 10^{-4}$ for $2.0 \times 10^{20} \text{ cm}^{-3}$ boron doping. This corresponds to less than 1 Å/min for a typical light doping etch rate of 25 $\mu\text{m}/\text{h}$.

Important secondary results can be derived from consideration of the etch-rate data obtained for sputter-damaged samples. In the damaged region, the etch-

Table I. Comparison of measured sheet-resistance values to calculated sheet-resistance values based on profiles obtained using various methods (SIMS, ISR, spreading resistance). Results for undamaged and sputter-damaged samples are shown.

Sample	Profile sheet resistance ρ_s (Ω/\square)		
	Measured	Calculated	
		SIMS/ISR	Spreading resistance
Undamaged	41.5	41.6	54.0
Sputter-damaged	45.3	45.2	61.0

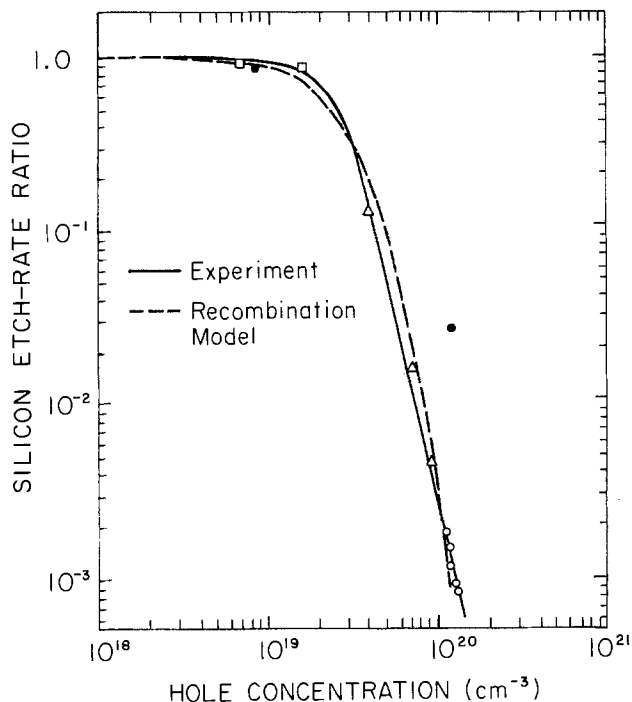


Fig. 6. Etch-rate ratio as a function of hole concentration. \circ etch step. Δ electron-beam transmission. \square bulk wafers. The solution proportions are 17 ml E:3g P:8 ml W and 0.016g pyrazine/liter E. The etch temperature is 110°C. \bullet indicate data of Reisman *et al.* for 6g pyrazine/liter E "B" etch (10).

rate ratio was significantly larger and hole concentration smaller than the ratio and concentration observed before damage, respectively; however, the boron concentration remained unchanged. This result indicates that the etch-rate ratio depends directly on the concentration of holes and not on the concentration of boron. Furthermore, for a given etch-rate ratio at a given depth, the effective hole concentration was calculated using Eq. [10] and plotted in Fig. 5b in the damaged region from the surface to 600Å depth. There is good agreement between the calculated points and the hole concentration profile obtained using the incremental sheet resistance method. This result indicates that the only effect of the sputter damage on the etch-rate ratio is to reduce the hole concentration through boron compensation so that Eq. [10] is still valid. This conclusion is in agreement with the observation that the heavy doping etch rate increases significantly as a result of sputter damage, whereas the light doping etch rate does not change appreciably compared to etch rates of undamaged samples.

Oxygen enhancement effects.—The effect of the oxygen enhancement factor (F_{O_2}) on the etch-rate ratio is shown in Fig. 7. We will consider data at a negligibly low (~ 0.01 g/liter E) level of pyrazine, so that the effects of pyrazine as an additional variable are eliminated. For high boron concentrations ($\sim 1.2 \times 10^{20}$ cm $^{-3}$), it appears that the etch-rate ratio is nearly independent of F_{O_2} for values of 1.20-2.32. This covers most of the range of factors (1.07-1.74) encountered in the experiments used to determine the etch-ratio dependence on hole concentration. Similarly, for lower boron concentrations ($\sim 1.6 \times 10^{19}$ cm $^{-3}$), the etch-rate ratio is seen to be independent over the 1.10-2.77 measured range. Due to the small oxygenation effect ($\sim 20\%$) on the etch-rate ratio compared to the doping effect, correction of the data presented in Fig. 6 to the oxygen-free condition was deemed unnecessary.

Pyrazine effects.—The effect of high pyrazine level on the etch-rate ratio is shown in Fig. 7, at high boron

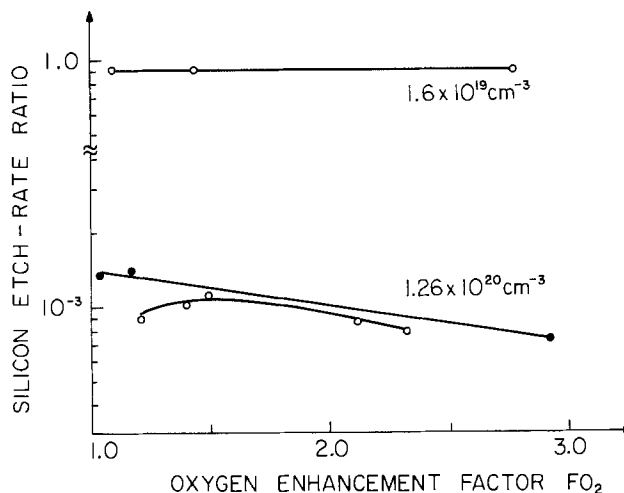


Fig. 7. Etch-rate ratio as a function of oxygen enhancement factor for various hole and pyrazine concentrations. \circ ~ 0.01 g/liter E. \bullet 6 g/liter E.

concentrations only. First, note that the etch-rate ratio is relatively independent of F_{O_2} from 1.04 to 2.92 at 6 g/liter E pyrazine concentration. The etch-rate ratio of 10^{-3} ($\pm 25\%$) is very close to that for ~ 0.01 g/liter E pyrazine. Consequently, at any value of F_{O_2} , the etch-rate ratio is relatively independent of pyrazine level.

One must be aware that when a fresh etch solution of large pyrazine content (~ 6 g/liter E) is oxygenated, the light doping etch rate actually decreases with increasing oxygen until a minimum is reached, and then increases monotonically. Therefore, for initial oxygenation times, $F_{O_2} < 1.0$, this makes it difficult to compare high pyrazine-etch rate results to etch-rate results obtained with low pyrazine-etch solutions at the same oxygen level where $F_{O_2} > 1.0$. Furthermore, it is possible to infer two different oxygen levels from the same F_{O_2} factor due to the nonmonotonic dependence of etch rate on oxygen level. To avoid these difficulties, we define the oxygen factor for high pyrazine-etch solutions to be the value that would have been obtained at the oxygenation time of interest if the pyrazine concentration were approximately zero (in our case, ~ 0.01 g/liter E). This assumes identical oxygenation conditions and that the presence of pyrazine does not affect the oxygenation of the solution (production of benzoquinone). In this way, over a wide range of pyrazine concentration, comparison of etch-rate results is facilitated and the oxygen factor truly reflects the extent of solution oxygenation.

Light effects.—The etch-rate ratio for the diffused surface was independent of incident light in the range studied for low pyrazine levels and $F_{O_2} > 1.4$. The value of light doping etch rate was also independent of light, as has been observed by Reisman *et al.* (10), since the etch rate followed a continuous oxygen-enhancement curve independent of light conditions. No difference was observed between white and yellow light. The approximate light intensity incident on the etching apparatus ranged from 0 to 0.44 W/cm 2 (650W Sunn gun with 3400 K filament temperature). No measurements of etch solution absorption were made in the visible region (4000-7000Å). However, we believe that not more than $\sim 50\%$ of the light incident on our etch apparatus is absorbed by the solution before reaching the wafers. Otherwise, one would not be able to see the wafers in the etch bath as easily as is now possible. This conclusion agrees with the absorption measurements made by Reisman *et al.* (10) where little absorption was found in the visible region. Therefore, the maximum light intensity incident on the wafers was ~ 0.22 W/cm 2 .

Discussion

Any proposed etch mechanism must explain the critical concentration at which the etch-rate ratio decreases, the -4.3 power-law dependence on hole concentration, and the insensitivity of the etch-rate ratio to oxygen, pyrazine, and light. One mechanism could be the formation, at high boron concentrations, of slowly etched SiB_4 precipitates, whose rate of formation is proportional to the fourth power of boron doping. However, as the boron doping in the experiments conducted here is less than the solid-solubility concentration, boron should not precipitate. In addition, we have shown that the boron doping is completely electrically active; that would not be the case for higher resistivity precipitates (22).

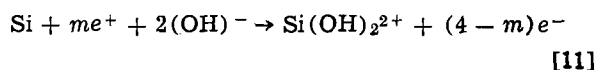
A second mechanism could be that the decrease in etch rate is caused by an increase in boron-induced stress. The etch-ratio dependence on hole concentration would be replaced by a similar dependence on tensile stress, since tensile stress is directly proportional to boron doping in the heavily doped region (23), and the boron is assumed to be electrically active. This mechanism would explain the critical concentration level, since the concentration at which measurable tensile stress is developed for boron in silicon ($\sim 10^{19} \text{ cm}^{-3}$) (23) is close to the concentration at which the etch-rate ratio decreases. However, the reason for the fourth power dependence is not obvious. To explain the etch-rate increase in damaged samples, it might be supposed that the argon-sputter damage relieves tensile stress in the damaged region. This is conceivable, since any implanted argon atoms would tend to expand the silicon lattice due to their larger atomic diameter and offset the contraction caused by the smaller diameter boron atoms. However, it is necessary to explain the fact that the etch-rate ratio in the damaged region also depends on hole concentration in the same way as in undamaged regions. This requires that the net tensile stress in the damaged region has the same dependence on net hole concentration as boron-induced stress on boron doping (the net hole concentration is given by the difference between the boron concentration and compensating donor-trap concentration). This situation seems unlikely, as the process of stress creation in the damaged and undamaged cases is quite different. In the undamaged case, the tensile stress simply increases in direct proportion to the hole concentration, which depends on the number of boron atoms on substitutional lattice sites. In the sputter-damaged case, it is supposed that dechanneled argon atoms displace silicon atoms to interstitial sites to create divancies (21) which act as the donor traps previously mentioned. The stress in this situation, however, depends on the relative position of the displaced silicon atoms, the implanted argon atoms, the original boron atoms (all of which can be on substitutional or interstitial sites), and the divancies. The situation is further complicated by argon damage and atom depth distributions, which are not necessarily the same. This makes it possible that trap concentration has little causal relation to the argon concentration at a given depth. Since the embedded argon atoms would be a main source of stress relief, the relation between net hole concentration and net tensile stress at a given depth is indirect, unlike the direct dependence in the undamaged case.

To test the stress hypothesis further, lightly doped p-type wafers were stressed in a cantilever-beam fashion with one end fixed and the other end deflected to provide the desired stress. The maximum stress level at the fixed end was calculated from elementary beam mechanics (24) to be $9.8 \times 10^8 \text{ dynes/cm}^2$ for a strain of 7.5×10^{-4} , which corresponds to $\sim 1.4 \times 10^{20} \text{ cm}^{-3}$ boron-doped silicon with no applied stress (23). The etch rate was measured using the etch-step method in Fig. 1a with thermal SiO_2 masks and with

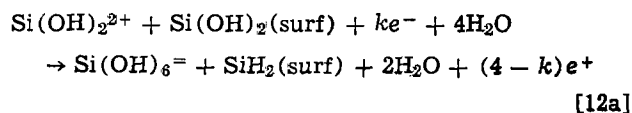
the silicon beam in tension and compression. No etch-rate decrease was observed at various positions along the beam compared to the unstressed condition. Even though the stress levels required to simulate BO_3 molecules (25) formed in the silicon lattice may be somewhat larger than those used here for boron, it seems reasonable to conclude that stress is not a factor.

Nevertheless, a variation of the stress mechanism has been proposed by Palik *et al.* to account for the etch-rate decrease in KOH-etch solutions (25). They propose that the boron-induced strain in the silicon lattice at high doping levels promotes the formation of a slowly etched surface layer. However, one must exercise caution in applying their results to our experiments. Their investigation utilizes a different etch solution (KOH and water) at a lower etch temperature (25°C) with no complexing agent. Even for KOH solutions at a higher etch temperature (60°C), the etch-rate dependence on boron concentration is different from that obtained for EPW solutions (11). It is also well known that the magnitude and orientation dependence of etch rate of lightly doped silicon in KOH solutions (26) is different from that in EPW solutions (8). Consequently, the rate-determining reaction may be different for the two solutions, even though the main solution constituents believed to be responsible for etching (OH^- and H_2O) are the same. Furthermore, one would expect that, as a result of sputter damage and the consequent increase in defect concentration, the surface layer proposed by Palik *et al.* (25) would be more likely to form and decrease the etch rate. This is contrary to our observations. Finally, we obtain excellent agreement between experiment and the theory based on a mechanism different from strain-induced formation of surface layers which we now develop.

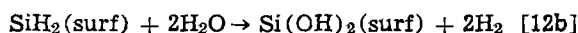
It is now clear that any proposed mechanism for the etch-rate decrease must incorporate the fact that the etch-rate ratio depends on the hole concentration. It is well known that free electrons and/or holes are often involved in the chemical reactions that take place in the etching of semiconductors (27, 28). Finne and Klein (8) proposed that the reactions involved in EPW etching of silicon were ionization of the ethylenediamine base in solution, oxidation-reduction of the silicon surface forming hydrous silica and hydrogen, and complexing of the hydrous silica to a complex pyrocatecholate. Since the ionization step occurs very rapidly and the complexing step does not normally limit the etch rate (8), the rate-determining step for the total reaction must be either the oxidation or reduction reaction. We propose that the rate-determining step for the etching of both heavily and lightly doped silicon is the reduction reaction. The proposed oxidation-reduction reactions are: for oxidation



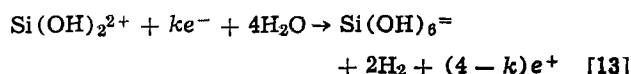
and for reduction



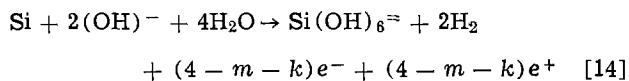
which is followed by



where e^+ signifies a hole, e^- an electron, and (surf) indicates that the corresponding chemical reactant is attached to the silicon surface. The values of the coefficients m and k are such that $0 < m < 4$ and $0 < k < 4$, since the oxidation state of silicon is four. The overall reduction reaction is then



Combining Eq. [11] and [13], the net oxidation-reduction reaction is



which is the same as that proposed by Finne and Klein except for the addition of free carriers. Note that the net numbers of electrons and holes in Eq. [14] are equal in order to maintain charge neutrality. The reactions in Eq. [11] and [12] are similar to those proposed by Turner (29) for germanium. Here, the monolayer of hydroxide maintained at the silicon surface is indicated by $\text{Si}(\text{OH})_2(\text{surf})$. The reactions are different from those of Turner in three ways: (i) the $\text{Si}(\text{OH})_2^{2+}$ at the surface is converted into $\text{Si}(\text{OH})_6^-$, which dissolves in solution; (ii) the silicon hydride decomposes in the presence of water to evolve two mols of hydrogen gas (30) and to regenerate the hydroxide monolayer; and (iii) the number of holes and electrons involved are generalized. The first two differences are necessary in order for the reactions to agree with the observations of Finne and Klein; the third difference is to facilitate comparisons. In anode/cathode experiments on germanium, Turner (29) found $m \sim 2$ and $k \sim 4$; we also believe that $k \sim 4$, which fits our etch-rate dependence results (Fig. 6), but that $m \sim 0$. This is explained in the recombination model section.

It is important to note that if Eq. [13] is the etch-rate determining step and the reverse reaction is negligible, then the total etch rate is proportional to the production rate of hydrous silica and hydrogen. This production rate is, in turn, proportional to the product of the deficient reactant concentrations. Assuming in Eq. [13] that the electrons needed are deficient for heavily doped boron surfaces, then the etch rate is

$$ER(p) \propto n^k = n^4 \quad [15]$$

where n is the free-electron concentration at the silicon surface being etched. For lightly doped surfaces, the electron concentration is not deficient. This fixes the etch rate at a value corresponding to some electron concentration n_0 , where n_0 is the electron concentration below which the etch-rate ratio is 1.0. Therefore, the etch-rate ratio is

$$ERR(p) = (n/n_0)^4 \quad [16]$$

valid for p such that $ERR(p) \leq 1.0$. Note that even though a fourth power dependence of reaction rate on concentration is uncommon, it has also been observed in the formation of donor states in heat-treated silicon (31). Finally, even though the oxidation-reduction reaction product $\text{Si}(\text{OH})_6^-$ proposed by Finne and Klein appears in Eq. [14], it has not been experimentally verified in EPW solution to our knowledge. This may be because $\text{Si}(\text{OH})_6^-$ is very quickly converted into a complex pyrocatecholate (8) and therefore not easily observable. An alternative choice of reaction product is $\text{SiO}_2(\text{OH})_2^-$ as determined by Palik *et al.* for silicon etching in KOH solution (32) (Eq. [13] would then require two mols of water instead of four in order to remain balanced). However, the important point here is that the fourth power dependence is still valid as it derives from the fact that four electrons are needed to reduce hydrogen to form the silicon hydride surface layer and is independent of the particular silicon-etch product which goes into solution.

Recombination model.—The source of the electron concentration n and its dependence on the boron doping must now be determined. It is unlikely that the source of electrons is the semiconductor near the surface, as the electron concentration at the point of

etch-rate decrease ($\sim 10^5 \text{ cm}^{-3}$) is too low to explain the fact that the etch rate is independent of light. The approximate electron concentration induced by light of the intensity used is $\sim 10^{15} \text{ cm}^{-3}$, and it seems improbable that diffusion away from the surface or recombination would prevent greater than 10^5 cm^{-3} effective concentration due to light from reaching the surface. Electron supply from the semiconductor bulk is not important, since there appears to be no etch-rate difference for diffusions into p or n substrates.

We propose, then, that the supply of electrons is generated by the chemical reaction at the semiconductor surface and not provided by the semiconductor near the surface or in the bulk. Specifically, the oxidation reaction in Eq. [11] generates electrons which can be used in the reduction reaction in Eq. [13]. This explains our choice for $m \sim 0$ in Eq. [11] with $k \sim 4$; four electrons must be chemically generated in Eq. [11] to satisfy the four electrons needed in Eq. [13]. Otherwise, electron sources other than chemical generation would be required in order for the net oxidation-reduction reaction in Eq. [14] to proceed, which we have shown to be unlikely. The idea that free carriers are generated at silicon surfaces during chemical etching is not a new one; it was proposed by Turner (28) to explain results obtained using the HF-HNO_3 system to etch silicon. For example, if the chemical generation rate of electrons is greater than the generation rate due to light, the mechanism of electron supply through chemical generation would explain the fact that light has no noticeable effect on the etch rate in the range studied.

One can calculate the relative magnitudes of the chemical and light generation rates. From the known etch rate of (100) silicon in EPW solution and knowledge of silicon bond density and lattice constant, it is found that $\sim 10^{17} \text{ e/cm}^2 \text{ s}$ are needed to etch silicon at its maximum rate; these are presumably supplied chemically. In order to calculate the electron generation rate due to light, we assume that only those electrons generated within a specific distance from the surface can participate in the etch reaction. It will be shown later that this distance is $\sim 100 \text{ \AA}$. Assuming a light intensity of 0.22 W/cm^2 corresponding to the maximum intensity used in these experiments, the useful electron generation rate due to light is then $\sim 8 \times 10^{15} \text{ e/cm}^2 \text{ s}$, more than an order of magnitude smaller than the chemical generation rate.

Assuming that the electron supply is predominantly generated chemically with negligible contribution from the semiconductor, we propose that the etch-rate decrease is due to fewer electrons recombining at the surface, since the enhanced recombination of electrons near the surface increases with boron doping. In this model, the electron concentration generated by the oxidation reaction in Eq. [11] is independent of surface hole concentration, and the electrons are injected into the semiconductor to a distance L_{eff} from the surface, which is probably about 100 \AA . The tendency for these injected electrons to recombine at the surface and participate in the reduction reaction in Eq. [13] increases as the time taken to reach the surface from the injection distance L_{eff} decreases. The time taken to reach the surface is L_{eff}/s_0 where s_0 is the surface recombination velocity. Similarly, the tendency for these electrons to recombine in the semiconductor en route to the surface is proportional to the inverse of the electron lifetime τ_n . Therefore, the concentration of electrons n recombining at the surface is

$$n = \left[\frac{s_0/L_{\text{eff}}}{s_0/L_{\text{eff}} + 1/\tau_n} \right] n_0 \quad [17]$$

where n_0 is the maximum concentration of electrons recombining at the surface. It has been reasonably assumed that since the injection distance L_{eff} is suffi-

ciently close to the surface, the electron velocity at any depth from the surface to L_{eff} is well approximated by the surface velocity s_0 . When the electron lifetime is large compared to the transit time, $n = n_0$ and the etch rate is the light doping etch rate. Substituting Eq. [17] into Eq. [16] and rearranging, the etch-rate ratio is

$$ERR = \left[\frac{1}{1 + L_{\text{eff}}/s_0\tau_n} \right]^4 \quad [18]$$

In layers heavily doped with boron in approximately $10 \mu\text{s}$ lifetime intrinsic silicon material and free of diffusion-induced defects, the lifetime τ_n is dominated by Auger recombination and given by K/p^2 , where p is the hole concentration and $K = 8.33 \times 10^{30} \text{ cm}^{-6} \cdot \text{s}$ (33, 34). Inserting this expression into Eq. [18], we obtain

$$ERR(p) = \left[\frac{1}{1 + (p/p_c)^2} \right]^4 \quad [19]$$

where

$$p_c = (s_0K/L_{\text{eff}})^{1/2} \quad [20]$$

If we fit Eq. [19] at $p = 10^{20} \text{ cm}^{-3}$ where $ERR = 2.8 \times 10^{-3}$, then $p_c = 5.5 \times 10^{19} \text{ cm}^{-3}$. Equation [19] is plotted for this value of p_c in Fig. 6; the agreement with experiment is very good. Using Eq. [20], $s_0/L_{\text{eff}} = 3.63 \times 10^8 \text{ s}^{-1}$. We assume that the surface recombination velocity s_0 is determined by the monolayer of hydroxide maintained at the silicon surface during etching. For reasonable values of capture cross section $\sigma \sim 10^{-15} \text{ cm}^2$, thermal velocity $v_{\text{th}} \sim (3kT/m)^{1/2} \sim 1.32 \times 10^7 \text{ cm/s}$, and trap density $N_t \sim 10^{10} \text{ cm}^{-2}$ representative of thin oxide layers on silicon (35), $s_0 \sim 1.32 \times 10^2 \text{ cm/s}$ and $L_{\text{eff}} \sim 36\text{\AA}$. This indicates that the doping profile is sampled over a very small depth and that the concentration being etched can be considered constant and equal to the surface concentration, as has been tacitly assumed in all the etching experiments. Note that we have assumed a one-dimensional path for the injected electrons. In reality, the silicon surface is composed of local, adjacent oxidation and reduction sites, and the injected electrons travel a curved two-dimensional path from an oxidation site surface through the semiconductor to an adjacent reduction site surface. The distance L_{eff} can then be seen to be somewhat larger than the average oxidation-reduction site separation.

Pyrazine and oxygen effects.—The independence of etch-rate ratio from pyrazine and oxygen content seen in our experiments can be explained by considering their effect on the etch-rate determining step. It has been shown in the model presented here that the reduction half-reaction in Eq. [13] is the etch-rate determining step over the range of contaminant levels studied. We propose that the effect of pyrazine and oxygen is to increase the rate of the oxidation-reduction reaction in Eq. [14] without affecting the complexing step; this, in turn, means that these contaminants increase the rate of the reduction half-reaction. This can be seen from the following argument. Reisman *et al.* (10) reported that in the case of pyrazine additions to the etch bath there was a tendency for residues to form on the silicon surfaces unless additional pyrocatechol was added. They concluded that pyrazine increases the rate of the oxidation-reduction reaction, and residues form if the complexing step becomes the rate-determining step because of a lack of pyrocatechol. Reisman *et al.* also reported that "B" etch (18.8 ml E: 3g P: 6 ml W, presumably with no pyrazine) that has been oxygenated increases the overall etch rate, but no residues are formed. The "B" etch has nearly the same composition as that used by Finne and Klein, in which the complexing step is saturated for the amount of pyrocatechol used. The pyrazine content in the latter was $\sim 1.1 \text{ g/liter E}$;

therefore, the complexing step was surely saturated for $\sim 0 \text{ g/liter E}$ in "B" etch, and the only way oxygen could increase the etch rate would be to increase the oxidation-reduction reaction.

Therefore, as pyrazine and/or oxygen levels increase, it may be possible to increase the rate of the reduction reaction so that it is larger than the complexing step. In this case, the reduction reaction will no longer be the rate-determining step, and Eq. [15] will be invalid. In addition, residues will appear if the complexing step becomes the rate-determining step. However, Eq. [15] has been found to be in good agreement with our experiments, and residues were not observed. Therefore, we believe that the light and heavy doping etch-rate determining step remained the reduction reaction over the range of pyrazine and oxygen levels considered here so that the etch-rate ratio was independent of these contaminants.

Different rate-determining steps for light and heavy doping etching may explain the fact that Reisman *et al.* observed an etch-rate ratio at a hole concentration of $1.2 \times 10^{20} \text{ cm}^{-3}$ more than an order of magnitude higher than observed here, using high pyrazine "B" etch (refer to Fig. 6). A possible scenario of etch-rate increase due to pyrazine would be as follows. Suppose the high pyrazine level increased the rate of the reduction reaction by a factor of ten with respect to the rate with low pyrazine level. For initial etch-rate ratios less than 0.1, the reduction reaction would still be the rate-determining step for the heavy doping etch rate since the dopant limiting effect is dominant. However, the rate-determining step of the light doping etch rate may be changed to the complexing step. This is plausible, since Reisman *et al.* did observe residue formation. The rate of the complexing step would be less than that of the reduction reaction; suppose that the effective light doping etch rate increases by a factor of two. In this case, the etch ratio would increase by a factor of five due to pyrazine. If this analysis is valid, then the etch ratio may not be independent of pyrazine for levels above 6 g/liter E . The fact that their experiments were conducted on bulk wafers should not be an important difference according to the model presented here. However, if the resistivity of their wafers was $0.002 \Omega\text{-cm}$ instead of $0.001 \Omega\text{-cm}$, there would be good agreement with our results.

Silicon staining correlation.—Finally, the correlation between the etch-ratio decrease and the silicon staining phenomenon (12, 36, 37) is further evidence for the proposed oxidation-reduction reactions. Both effects are predominant for heavily boron-doped (100) silicon for concentrations greater than $\sim 10^{19} \text{ cm}^{-3}$. For high boron concentration, the common silicon stain compounds SiH_x , SiO_y , or SiH_xO_y , where $1.0 < x < 2.0$ and $1.0 < y < 2.0$, can be formed if any of the reactants in the stain reaction are of insufficient concentration to allow the reaction to go to completion. This is correlated to the observed decrease in etch rate because of insufficient electron concentration. The reduction reaction in Eq. [12a] could be the stain reaction since the possibility of the formation of silicon hydride exists. Furthermore, in a way analogous to that by which insufficient oxidizing agent can cause staining (12), it is possible that it is also caused by electron concentration deficiency.

For heavy n-type doping less than $8 \times 10^{19} \text{ cm}^{-3}$, the etch rate is found to decrease only slightly (10), which correlates with the fact that the stain phenomenon occurs to a lesser extent than with heavy boron doping. In the heavy n-type doping case, the rate-determining step may be the oxidation reaction Eq. [11]. From arguments similar to those used in the case of heavy p-type doping, any holes needed in the oxidation reaction are assumed to be chemically generated. However, the onset of near-surface recombina-

tion of these holes should occur at considerably higher n-type doping (as opposed to p-type doping) because the surface recombination velocity s_0 for holes is larger than that for electrons. This is because the hole traps are likely to be associated with surface $(OH)^-$ ions whereas the electron traps are associated with surface H^+ ions (38); since there are more larger $(OH)^-$ ions near the surface in basic solution than smaller H^+ ions, the trap density and capture cross section are correspondingly larger for holes than for electrons. In addition, the dependence of etch rate on n-type doping should be slight, since $m \sim 0$ in Eq. [11]. These may be the reasons that the etch rate is only slightly dependent on heavy n-type doping in the range studied. Similarly, little or no silicon hydride stain would be formed, since the reduction reaction (Eq. [12a]) would go further to completion than with p-type material due to the large electron concentration with n-type doping; also, little or no silicon hydroxide stain would be formed in the oxidation reaction (Eq. [11]) because the hole-reactant concentration should be only slightly deficient based on the slight decrease in etch rate.

The previous discussion might seem to indicate that the stain would always form at high boron dopings in the etch-ratio experiments. However, the silicon hydride stain is removed easily in alkaline solutions with $pH > 9$ (36). As the pH of the EPW solution was measured to be about 10 and may actually be as high as 11, one can be sure that silicon etching was not impeded by a surface layer of stain residue.

Applications

For applications, it is useful to be able to calculate the resultant membrane thickness for a given concentration profile and etch conditions; this can be done using Eq. [8] and Eq. [10] and numerical integration. For an initial silicon thickness x_i , the final membrane thickness x_f can be plotted as a function of the product of light doping (1-10 Ω -cm) etch rate and etch time. This calculation was done for $x_i = 1 \mu m$ and $5 \mu m$ for the SIMS profile in Fig. 5a and is shown in Fig. 8. For known $x_i = 1 \mu m$ and light doping etch rate $ER_0 \sim 60 \mu m/h$ (measured prior to membrane etching), the etch time is determined to be approximately 20 min to obtain a 1000 \AA -thick membrane. These curves can be easily extended to larger initial thicknesses by calculating the additional light doping etch time needed to etch to the thicknesses that appear in Fig. 8. Note that the membrane can be etched away entirely in about 2h for $ER_0 \sim 60 \mu m/h$ due to the finite etch rate even at high doping. Note

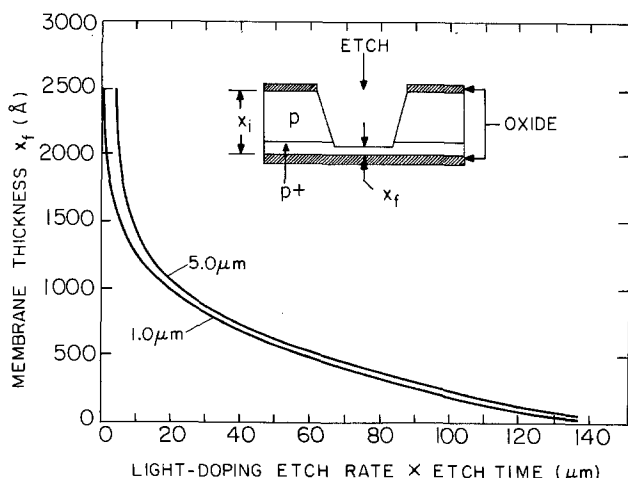


Fig. 8. Final membrane thickness x_f as a function of product of light doping etch rate and etch time with initial silicon thickness x_i as parameter. The SIMS concentration profile used is shown in Fig. 5a.

also for a variation in x_i of 1-5 μm , the uniformity in final thickness is $\sim 50\text{\AA}$ out of 500 \AA or $\pm 5\%$.

This point is elaborated in Fig. 9. The variable t_{crit} is the time needed to etch from the thinnest region of the sample to the position x_{crit} at which the boron concentration equals p_{crit} . The quantity p_{crit} is the hole concentration at which the etch rate has reduced to 90% of its maximum value; referring to Fig. 5a and Fig. 6, $p_{crit} \sim 1.3 \times 10^{19} \text{ cm}^{-3}$ at $x_{crit} \sim 3500\text{\AA}$. The variable Δx is the initial thickness variation of the sample and is set for purposes here from 0.1 to 10 μm in Fig. 9. Note that $\Delta x = 4 \mu m$ represents the thickness variation shown in Fig. 8. Final membrane thickness variation is the ratio of maximum thickness difference over the sample to the thickness at the thinnest region, which gives worst case results. The results differ by only a few percent if normalized to the average membrane thickness.

Note that the uniformity for our particular profile is best near 50 μm on the abscissa. Note also that $\Delta x = 10 \mu m$ corresponds to etching thick bulk wafers with typical $\pm 5 \mu m$ thickness variation over the wafer diameter, giving $\sim 16\%$ min. final membrane variation. On the other hand, $\Delta x = 0.1 \mu m$ can correspond to the double-etch scheme as described by Huang and Van Duzer (4), where less than 0.2% variation over the wafer can be expected. In addition, the thickness variation over individual membranes in these two cases can be considerably less than the variations stated over the whole wafer because of the smaller etching area and corresponding smaller value of Δx . Finally, large-area membranes ($\sim 0.9 \text{ cm} \times 0.9 \text{ cm}$) were found by Rutherford backscattering to have approximately 7% thickness variation (39). Assuming 10 μm initial thickness variation over a 51 mm diam wafer, then $\Delta x \sim 2 \mu m$ over each of these large-area membranes. Using the stated etch conditions (39) of 50 $\mu m/h$ light doping etch rate and assuming a minimum etch time of 1h with 25 μm initial silicon thickness, $ER_0 \times (\text{etch time} - t_{crit}) \sim 50(1-25/50) \mu m \sim 25 \mu m$. The thickness variation calculated in Fig. 9 is $\sim 4\%$, in reasonable agreement with the observed result. An exact comparison is not possible, since these diffusions were performed at 1050°C for 15 min and the calculation applies for a 950°C, 45 min diffusion.

A secondary application of the etch-rate dependence is to the measurement of electrically active surface concentration in heavily doped boron layers for concentrations in the range $\sim 0.5-1.5 \times 10^{20} \text{ cm}^{-3}$, pro-

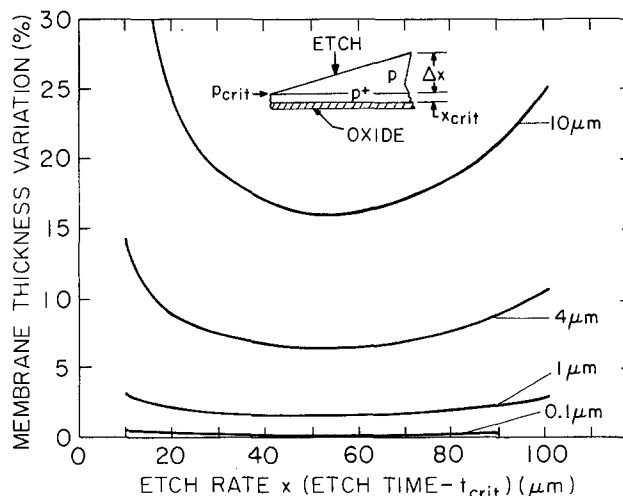


Fig. 9. Membrane thickness variation as a function of product of light doping etch rate and etch time after the critical concentration p_{crit} is reached where $p_{crit} = 1.3 \times 10^{19} \text{ cm}^{-3}$. The parameter is the initial thickness variation Δx . The etched sample (insert) is shown at a total etch time equal to t_{crit} . The SIMS concentration profile used is shown in Fig. 5a so that $x_{crit} \sim 3500\text{\AA}$.

vided that the profile variation at the surface is not too large. Analytical techniques such as SIMS and spreading resistance profiling often give questionable results at the surface ($\sim 100\text{\AA}$) because of physical limitations. This was the case for the profile in Fig. 5a, where the surface concentration was determined instead by etch rate to be $\sim 1.1 \times 10^{20} \text{ cm}^{-3}$.

Conclusions

The etch-ratio dependence of (100) silicon in EPW solutions for high boron doping has been found to decrease at $\sim 10^{19} \text{ cm}^{-3}$ and follows a -4.3 power law dependence on doping over three orders of magnitude of etch-rate ratio. The etch rate is determined by the hole concentration and not by stress due to substitutional boron.

The etch-rate ratio appears independent of solution oxygenation and pyrazine content in the ranges studied, since the reduction reaction rate-determining step is unchanged as a function of these contaminants. The etch-rate ratio is independent of light intensity in the range studied, since the number of electrons generated by light that participate in the etch reaction is far smaller than the number of electrons generated by the chemical etching reaction at the silicon surface. Furthermore, the independence of etch-rate ratio from light intensity has been shown to indicate that the number of electrons generated chemically is large compared to the equilibrium electron concentration.

An etching model has been proposed in which the electrons injected into the semiconductor by the oxidation reaction return to and recombine at the surface and thereby participate in the reduction reaction. It is proposed that the etch-rate decrease with increased hole concentration is due to insufficient electrons recombining at the surface because of enhanced Auger recombination in the semiconductor. An equation for the etch-rate ratio which assumes that the reduction reaction is the rate-determining step is derived and gives excellent agreement with experiment. The oxidation-reduction reactions proposed can also explain the correlations between the dependence of the etch-rate ratio on heavy boron doping and the silicon staining phenomenon.

Design curves for membrane fabrication are presented as a guide in the calculation of etch time needed to obtain desired membrane thickness. It is shown that the final membrane thickness variation over a wafer can be as small as 0.2%, depending on the etch conditions, the initial thickness difference over the sample, and the doping profile. The etch-rate ratio can also be used to determine the hole concentration at heavily boron-doped silicon surfaces.

Acknowledgments

This work was supported in part by AFOSR (JSEP) F49620-79-C-0178. The authors would like to acknowledge the help of C. Evans for the SIMS measurement, D. Dickey for the spreading resistance profiles, J. Kiely and A. Waterhouse for the ultraviolet absorption measurements, and D. McDaniel, D. Rogers, and R. Hamilton for their technical assistance. One of us (N. Raley) appreciates the stimulating discussions with R. Ruby and C. Drowley and the encouragement and support provided by R. Frustino throughout the course of this work.

Manuscript submitted Jan. 5, 1983; revised manuscript received July 29, 1983.

The University of California assisted in meeting the publication costs of this article.

REFERENCES

1. I. Adesida, R. Shimizu, and T. E. Everhart, *J. Appl. Phys.*, **51**, 5962 (1980).
2. J. L. Bartelt, C. M. McKenna, and C. W. Slayman, Abstract 277, p. 454, The Electrochemical Society Extended Abstracts, Montreal, Que., Canada, May 9-14, 1982.
3. C. J. Schmidt, P. V. Lenzo, and E. G. Spencer, *J. Appl. Phys.*, **46**, 4080 (1975).
4. C. L. Huang and T. Van Duzer, *IEEE Trans. Electron Devices*, **ed-23**, 579 (1976).
5. E. Bassous, *ibid.*, **ed-25**, 1178 (1978).
6. K. E. Petersen, A. Shartel, and N. F. Raley, *ibid.*, **ed-29**, 23 (1982).
7. R. D. Jolly and R. S. Muller, *This Journal*, **127**, 2750 (1980).
8. R. M. Finne and D. L. Klein, *ibid.*, **114**, 965 (1967).
9. A. Bohg, *ibid.*, **118**, 401 (1971).
10. A. Reisman, M. Berkenblit, S. A. Chan, F. B. Kaufman, and D. C. Green, *ibid.*, **126**, 1406 (1979).
11. H. Siedel and L. Csepregi, Abstract 123, p. 194, The Electrochemical Society Extended Abstracts, Montreal, Que., Canada, May 9-14, 1982.
12. D. G. Schimmel and M. J. Elkind, *This Journal*, **125**, 152 (1978).
13. H. J. Fitting, *Phys. Status Solidi A*, **26**, 525 (1974).
14. R. P. Donovan and R. A. Evans, NBS Special Publication no. 337, p. 123 (1970).
15. R. P. Bauman, "Absorption Spectroscopy," pp. 14-15, John Wiley & Sons, New York (1962).
16. W. K. Hofker, "Implantation of Boron in Silicon," Philips Research Reports Supplement no. 8, p. 38 (1975).
17. "Handbook of Chemistry and Physics," 54th edition," R. C. Weast, Editor, p. B-8, CRC Press (1973-1974).
18. G. L. Vick and K. M. Whittle, *This Journal*, **116**, 1142 (1969).
19. W. R. Thurber, R. L. Mattis, Y. M. Liu, and J. J. Filliben, *ibid.*, **127**, 2291 (1980).
20. E. Grusell, S. Berg, and L. P. Andersson, *ibid.*, **127**, 1573 (1980).
21. L. P. Andersson and A. O. Ewvaraye, *Vacuum*, **28**, 5 (1978).
22. E. Arai, H. Nakamura, and Y. Terunuma, *This Journal*, **120**, 980 (1973).
23. F. H. Horn, *Phys. Rev.*, **97**, 1521 (1955).
24. R. J. Roark and W. C. Young, "Formulas for Stress and Strain," pp. 89-96, McGraw-Hill, New York (1975).
25. E. D. Palik, J. W. Faust, Jr., H. F. Gray, and R. F. Greene, *This Journal*, **129**, 2051 (1982).
26. D. F. Weirauch, *J. Appl. Phys.*, **46**, 1478 (1975).
27. W. H. Brattain and C. G. B. Garrett, *Bell Syst. Tech. J.*, **34**, 129 (1955).
28. D. R. Turner, *This Journal*, **107**, 810 (1960).
29. D. R. Turner, *ibid.*, **103**, 252 (1956).
30. E. G. Rochow, "Chemistry of the Silicones," p. 6, John Wiley & Sons, New York (1946).
31. W. Kaiser, H. L. Frisch, and H. Reiss, *Phys. Rev.*, **112**, 1546 (1958).
32. E. D. Palik, H. F. Gray, and P. B. Klein, *This Journal*, **130**, 956 (1983).
33. J. D. Beck and R. Conradt, *Solid State Commun.*, **13**, 93 (1973).
34. J. Dziewior and W. Schmid, *Appl. Phys. Lett.*, **31**, 346 (1977).
35. A. S. Grove, "Physics and Technology of Semiconductor Devices," pp. 130-145, John Wiley & Sons, New York (1967).
36. R. J. Archer, *J. Phys. Chem. Solids*, **14**, 104 (1960).
37. K. H. Beckmann, *Surf. Sci.*, **3**, 314 (1965).
38. S. G. Ellis, *J. Appl. Phys.*, **28**, 1262 (1957).
39. N. W. Cheung, *Rev. Sci. Instrum.*, **51**, 1212 (1980).

Low Resistance Contacts for Lead-Sulfide-Selenide Diode Lasers

D. E. Swets and C. R. Harrington

General Motors Research Laboratories, Physics Department, Warren, Michigan 48090-9055

ABSTRACT

Cryogenically cooled lead-sulfide-selenide ($\text{PbS}_{1-x}\text{Se}_x$) diode lasers have been used in vehicle exhaust gas measurements. Diodes with a continuous wave (cw) operating temperature above 95 K would permit cooling with a small microminiature refrigerator. This would greatly enhance the possibility of practical applications. One important factor that prevents higher operating temperatures is the heat generated at the electrical connections to the diode (produced at the contact resistance, R_c). Reproducible low R_c was not obtained for PbS and $\text{PbS}_{1-x}\text{Se}_x$ of low x compositions by the contact formation technology developed for PbSnTe and $\text{PbS}_{1-x}\text{Se}_x$ of high x . A new method, in which the crystal surfaces are electrolytically etched (in HBr) followed by a nitric acid rinse, has resulted in a low R_c for all $\text{PbS}_{1-x}\text{Se}_x$ compositions.

Operation of $\text{PbS}_{1-x}\text{Se}_x$ diode lasers at temperatures above 95 K is desirable for various practical applications. One factor that limits the operating temperature is the ohmic heat (I^2R_c) generated at the metal-semiconductor interface when a current (I) is passed through a contact resistance (R_c). For higher temperature of operation, R_c should be as low as possible.

The contact formation procedure developed for $\text{Pb}_{1-x}\text{Sn}_x\text{Te}$ crystals resulted in low R_c routinely (1). When that fabrication procedure was applied to $\text{PbS}_{1-x}\text{Se}_x$ crystals, R_c was low for PbSe, but very high for PbS. A high p-type carrier concentration is necessary for a low R_c . This is more difficult to achieve and maintain in PbS than in PbSe, due to the nature of their respective pressure-temperature-composition phase diagrams. Results on mixed composition crystals with $x = 0.18, 0.38,$ and 0.60 were inconsistent.

An attempt was made to determine which processing step, or steps, were responsible for the high R_c . Careful examination of the various steps suggested the following. (i) The most likely cause of the large differences in R_c is the etching step. (ii) Improper crystal handling (lapping, polishing, etc.), plating, and mounting can cause poor R_c . This, however, is true for all crystal compositions and was not the cause of the difference in R_c results between PbS and PbSe. (iii) It was also determined by tests with n-type and p-type samples (rather than p-n junction diodes) that low R_c was easily achieved on clean untreated n-type PbS (i.e., facets or cleaved surfaces). Low R_c was not achieved on similar p-type surfaces without etching.

Experimental

Low resistance contacts to PbSnTe and PbSe crystals can be formed by squirting a stream of concentrated HBr over lapped p-type surfaces and then rinsing in a stream of deionized water. Concentrated HBr was also used on PbS by Ralston *et al.* (2), who reported low R_c (10 m Ω at 15 K) for their diodes. We were unable to reproduce their results. Tests were devised to determine any differences between HBr etching of PbSe and PbS. One such test was made to verify a suspected difference in etch rate.

Similar sized crystals of PbTe, PbSe, and PbS were weighed and then immersed in HBr for 3 min and rinsed. The etch rate was determined by the loss of weight during the etch. Table I shows the etch rate for PbS to be much greater than for PbSe or PbTe. The high etch rate was related to the R_c for PbS, but the mechanism was not known. (See Discussion.)

Electrolytic etching of $\text{PbS}_{1-x}\text{Se}_x$, with HBr as the electrolyte, was studied as an alternative to mechanical lapping and polishing, and also for stripe geometry applications. Etching with the sample as the anode and a platinum cathode produces a red or yellow "film"

on the sample (depending on composition). This film can be removed by a reverse polarity etch or by a nitric acid rinse. This procedure resulted not only in good material removal, but also in low R_c . The electrolytic etch-nitric acid rinse (E-N) method was optimized and found to give consistently low R_c on both PbS and PbSe. The best results were obtained when the electrolyte was one part HBr, one part H_2O for PbSe (1:1) and 1:3 for PbS.

The current density was held at 20 mA/cm². The voltage was typically between 50 and 100 mV depending on electrolyte concentration, crystal size, and crystal composition. Sample area was $\sim 7 \times 10^{-4}$ cm². Under these conditions the etch rate was ~ 2 $\mu\text{m}/\text{min}$. Both the electrolyte and the HNO_3 rinse were at room temperature.

The following comparison was made between the HBr squirt etch method and the E-N method: several as-cleaved n-type PbS and PbSe crystals were converted to p-type by annealing at 700°C with a p-type source. The crystals were then etched by one of three methods: HBr-squirt, HNO_3 alone (dipped in a beaker), or the E-N method. In all cases, the samples were rinsed in deionized H_2O after etching. All other processing steps were similar for all samples. Electroplated layers of gold, palladium, gold, and indium (in that order) formed the contacts (3). The samples were tested for R_c at 77 K. The results (shown in Fig. 1) illustrate the lower R_c (17 m Ω) obtained on PbS with the E-N method compared to the HBr squirt method (3 Ω). Also, the E-N method is superior to the HNO_3 alone, i.e., the electrolysis improves the R_c .

The results of a similar test on PbSe are given in Fig. 2. The E-N method was superior in this case also. A third study of R_c on PbS as a function of hole concentration is shown in Fig. 3. In this test, all the crystals were etched using the E-N method, but had different hole concentrations due to annealing at temperatures of 900°, 700°, and 400°C. The results illustrate that even with electrolytic etching, R_c will be high when the hole concentration is too low. (The 400°C anneal resulted in a carrier concentration of $\sim 10^{18}/\text{cm}^3$.) This result was expected, but is included to illustrate the importance of achieving as high of a hole concentration as possible on the PbS crystal surface.

Discussion

Auger surface analysis showed that both PbSe and PbS have similar trace amounts of Br and O, regardless of how they were etched (each etched by the squirt or E-N methods). It is evident that the residue cannot

Table I. Etch rate comparison

Material	HBr etch rate (mg/min)
PbS	23.0
PbSe	0.37
PbTe	0.10

¹ Auger analysis of the film on PbSe showed it to be $\sim 100\text{\AA}$ thick and contain excess bromine and oxygen. The chemical and physical properties of the film suggest the compound SeOBr_2 or $\text{PbOSe}_2\text{Br}_2$.

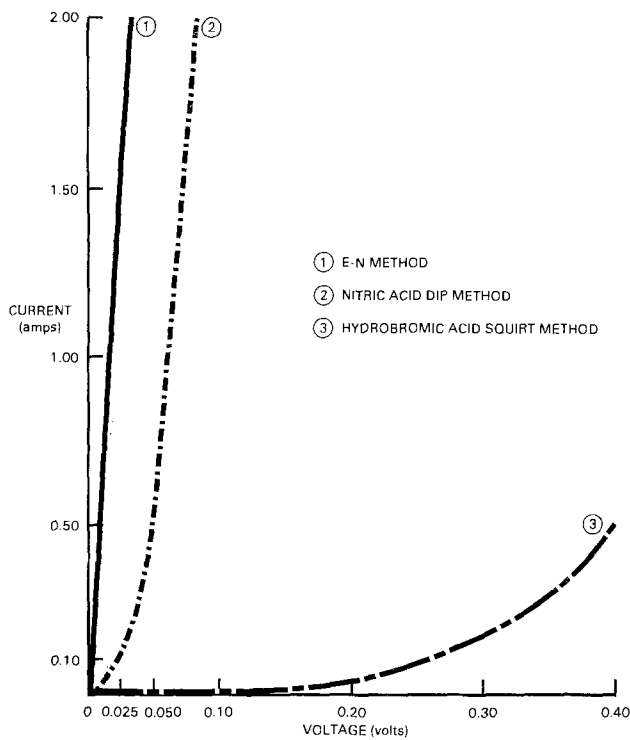


Fig. 1. *i*-*V* curves of p-type PbS etched by three methods

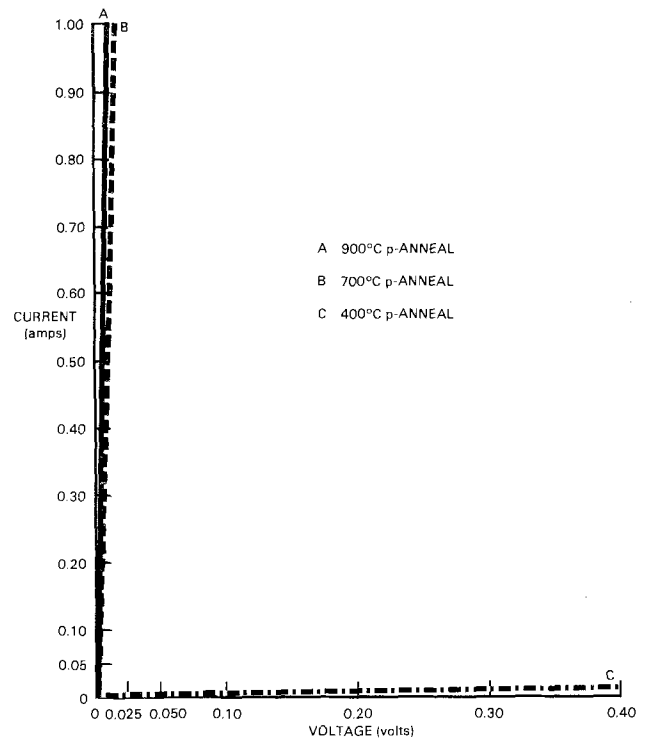


Fig. 3. *i*-*V* curves of E-N etched PbS annealed at various temperatures to show effect of hole concentration.

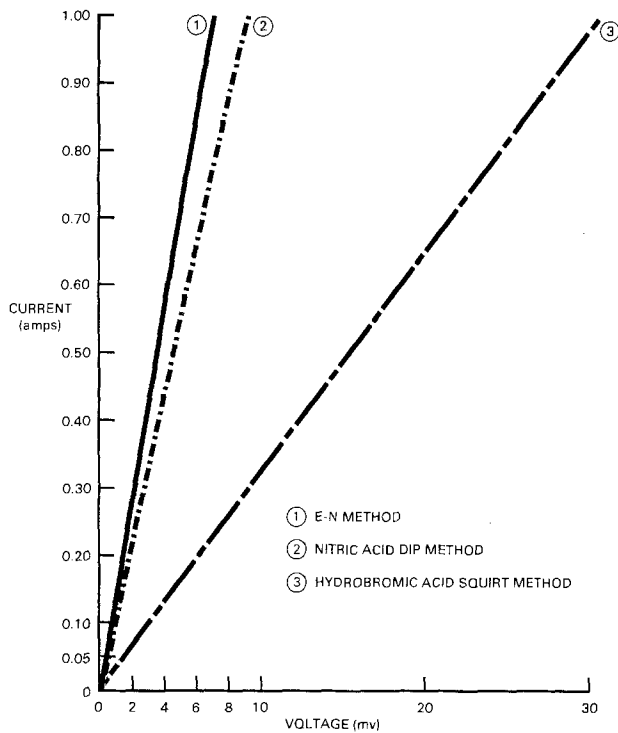


Fig. 2. *i*-*V* curves of p-type PbSe etched by three methods

account for the difference in R_c by different etching methods. SEM studies showed a considerable surface texture difference between squirt and E-N etched samples, especially on PbS (see Fig. 4). The E-N method produces a coarse textured high surface area on PbS, whereas the squirt method polishes PbS and leaves the surface relatively smooth. In Fig. 4a, the original surface had been lapped, yet squirt etching made it smoother.

In the case of PbSe, the slower etch rate of the squirt method preserves the coarse texture produced by prior lapping, i.e., there is no polishing effect. The E-N method also produces a coarse texture, but the difference between squirt and E-N etching is not as pro-

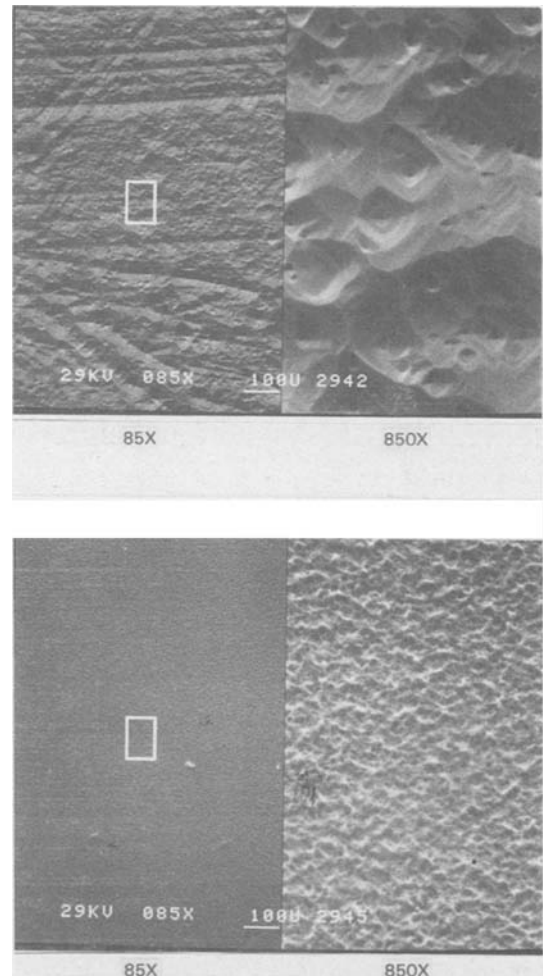


Fig. 4. (a, top) PbS surface after HBr squirt etch. SEM photos at 85 and 850 \times . (b, bottom) PbS surface after E-N etch. SEM photos at 85 and 850 \times .

nounced. It is then hypothesized that the key to achieving low R_c is the ability to achieve and maintain a coarse surface texture and that in the case of PbS, such a surface can be formed during electrolyte etching in HBr. Furthermore, this texture is maintained during subsequent etching in HNO_3 . Simply dipping a PbS crystal in HNO_3 also produces a rough texture but results in a somewhat higher and less ohmic R_c . We were not able to show by Auger analysis any evidence of selective etching which might make the surface metal rich and improve bonding to the metal layers.

The present result is consistent with an earlier finding that coarse surface texture is required for making stable low resistance contacts to $\text{Pb}_{1-x}\text{Sn}_x\text{Te}$ (4). The E-N method developed in this study has enabled us to produce coarse textured surfaces on crystals (such as PbS) that have a high etch rate in HBr solutions.

Summary

The following statements summarize our findings:

1. The hydrobromic acid squirt etching method developed for making low resistance contacts to PbSnTe and high x $\text{PbS}_{1-x}\text{Se}_x$ does not work reproducibly for $\text{PbS}_{1-x}\text{Se}_x$ of low x .

2. Electrolytic hydrobromic acid etching, followed by a nitric acid rinse, gives low R_c for $\text{PbS}_{1-x}\text{Se}_x$ of all compositions.

3. High R_c was related to a low carrier concentration in some PbS crystals.

4. Studies with Auger spectroscopy showed that poor R_c was probably not due to an insulating film or residue from the etching.

5. Scanning electron microscope studies showed that HBr squirt etching polishes PbS and results in a low surface area texture. The electrolytic etch results in a high surface area texture. This difference in texture may explain the differences in ohmic contact resistance observed, but more study is needed to determine the nature of the surfaces after etching and their reactions with the contact material.

Acknowledgments

The authors wish to thank W. Lo for helpful suggestions, S. Gaarenstroom and R. Waldo for Auger analyses and W. Lange for SEM studies.

Manuscript submitted Feb. 14, 1983; revised manuscript received June 13, 1983.

General Motors Research Laboratories assisted in meeting the publication costs of this article.

REFERENCES

1. W. Lo, D. E. Swets, and G. P. Montgomery, Jr., "New $\text{Pb}_{1-x}\text{Sn}_x\text{Te}$ Crystal Growth Method and Sb-Diffused Diode Laser Performance," General Motors Research Memorandum 32-1862, April 30 (1975).
2. R. W. Ralston, *et al.*, *J. Appl. Phys.*, **45**, 1323 (1974).
3. W. Lo, *ibid.*, **52**, 900 (1981).
4. W. Lo, *Appl. Phys. Lett.*, **28**, 154 (1976).

Optical Measurement of Carrier Profiles in Silicon

T. Motooka, T. Warabisako, and T. Tokuyama

Hitachi Limited, Central Research Laboratory, Kokubunji, Tokyo 185, Japan

T. Watanabe

Hitachi Limited, System Development Laboratory, Tama, Kawasaki 244, Japan

ABSTRACT

A new method to determine depth profiles for carrier concentration in semiconductor has been developed using infrared ellipsometry. The method is based on theoretical calculations which have shown that a carrier profile can be sensitively described by its infrared ellipsometric parameters as function of the incident angle. Through measuring ellipsometric parameters and performing computer analysis, carrier profiles for shallow-doped samples made by arsenic ion implantation were nondestructively determined. The results are in good agreement with those from the conventional anodization stripping method.

The depth profile of the carrier concentration in silicon is a fundamental parameter for determining device characteristics. Thus, measurement of carrier concentration profiles is inevitable for semiconductor process technologies. However, conventional measuring methods, *e.g.*, the anodization stripping (1) or capacitance methods (2), are destructive, and are so laborious that they have been obstacles to the development of LSI technologies.

Several workers have performed optical measurements of carrier concentrations in silicon. Rawlins (3) measured the resistivity of epitaxial layer by the infrared attenuated reflection method. Jastrzebski *et al.* (4) determined the lateral changes of carrier concentrations in silicon wafers by measuring CO_2 laser transmittance. In their papers, the depth profiles were assumed to be homogeneous. Abe and Kato (5) and Wagner and Schafer (6) tried to measure carrier concentration depth profiles by infrared reflectance and transmittance spectroscopy (2.5–20 μm). Since reflectance or transmittance measurements are not so accurate, it has proven difficult to accurately determine the depth profiles with these methods.

In the present paper, we show a new measuring method which makes it possible to nondestructively determine depth profiles in less than 15 min using infrared ellipsometry.

In the present paper, we show a new measuring method which makes it possible to nondestructively determine depth profiles in less than 15 min using infrared ellipsometry.

Principle

Our new method is based on ellipsometry. When linearly polarized light is incident to a sample surface with incident angle θ , reflected light is generally elliptically polarized, as shown in Fig. 1. Mathematically, this transformation can be described as follows. If electric vectors of the incident (reflected) light are decomposed into the *s*- and *p*-polarized waves (E_s and E_p [E'_s and E'_p]) then they are connected in the manner

$$\begin{pmatrix} E'_s \\ E'_p \end{pmatrix} = \begin{pmatrix} R_s \exp(i\phi_s) & 0 \\ 0 & R_p \exp(i\phi_p) \end{pmatrix} \begin{pmatrix} E_s \\ E_p \end{pmatrix} \quad [1]$$

Key words: semiconductor, infrared, ellipsometry.

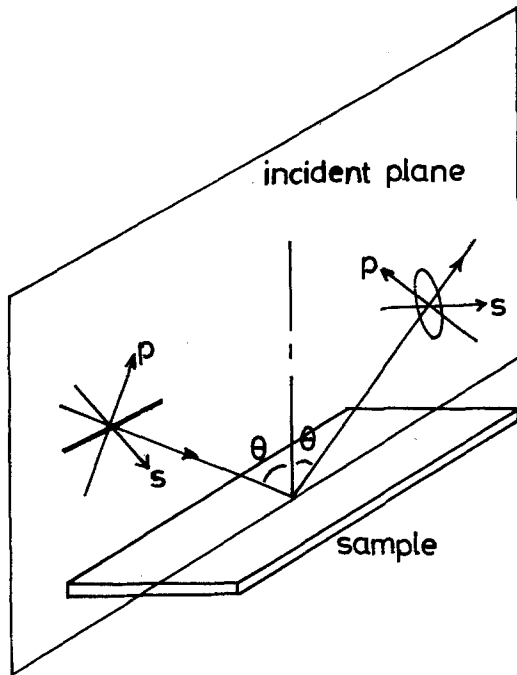


Fig. 1. Reflection ellipsometry. Incident linearly polarized light, with incident angle θ , is generally transformed into elliptically polarized light after reflection from the sample surface. Electric fields associated with incident and reflected light are decomposed into s- and p-axes, which are defined as those perpendicular and parallel to the incident plane, respectively.

where $R_s(R_p)$ and $\phi_s(\phi_p)$ are changes in the amplitude and phase for the s- or p-polarized wave after reflection. Ellipsometry determines the Δ and ψ , which are defined as

$$\Delta = \phi_p - \phi_s \text{ and } \tan \psi = R_p/R_s \quad [2]$$

These ellipsometric parameters are determined through the Maxwell equations (7)

$$\text{rot}\mathbf{E} = i(\omega/c)\mathbf{H} \text{ and } \text{rot}\mathbf{H} = -i(\omega/c)\epsilon(\omega)\mathbf{E} \quad [3]$$

Here, ω is the angular frequency of the incident light, and $\epsilon(\omega)$ is the dielectric function of the sample and is used to describe the electrical or optical properties of the sample. In this way, we can investigate the sample properties by ellipsometry.

The dielectric function for a doped semiconductor (8) is

$$\epsilon(\omega) = \epsilon_\infty - \frac{4\pi N e^2}{m^* \omega^2} \frac{1}{1 + i/\omega\tau} + \epsilon_b(\omega) \quad [4]$$

where ϵ_∞ is the dielectric constant of a nondoped sample. The second term is due to intraband transitions and is directly proportional to free electron or hole concentration, i.e., carrier concentration, N . Here m^* is the carrier effective mass, e is the electron charge, and τ is the carrier relaxation time. The third term concerns real interband transitions and can be neglected if we use infrared light.

In the case of silicon, $\epsilon_b(\omega)$ can be neglected if we use an infrared light with wavelength longer than 1.09 μm , and m^* is 0.27 m_0 (m_0 : electron rest mass) for n-type doping (9). The used τ value is 1×10^{-14} sec, which approximately corresponds to the value at the electron concentration of $5 \times 10^{19} \text{ cm}^{-3}$.

From now on, we will fix ω at the value corresponding to a CO_2 laser with 10.6 μm wavelength, and instead of a dielectric function we will use the optical constants defined by

$$\sqrt{\epsilon} = n + ik \quad [5]$$

Here, n is the refractive index, and k is the extinction coefficient.

Figure 2 shows the infrared optical structure of the sample. The first layer is impurity doped, and in this

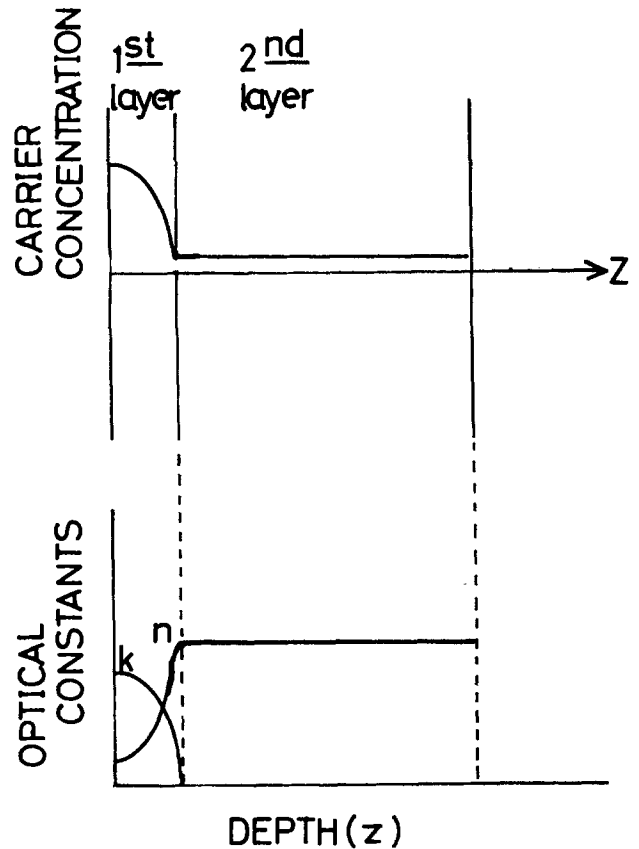


Fig. 2. The optical model of impurity doped semiconductor wafer. The first layer is inhomogeneous with the optical constant distributions $n(z)$ and $k(z)$. The second layer is a homogeneous thick substrate with homogeneous optical constants.

layer carriers are usually distributed as shown. The second layer is the substrate, and in this layer carrier concentration is homogeneous. The corresponding optical constants are calculated by Eq. [4] and Eq. [5]. Once these optical constants are determined, the ellipsometric parameters Δ and ψ can be calculated by solving the Maxwell equations. In this calculation, it was necessary to get rid of the interference effect in the thick transparent substrate (10).

Figure 3 shows an example of calculated Δ and ψ values. In this example, carrier profiles are assumed to be Gaussian distributions with three widths (W) and incident angles are changed from 0 to 85 degrees. This calculation indicates that each carrier distribution corresponds to each (Δ, ψ) locus when the incident angle changes continuously. In fact, the one-to-one correspondence can be proven for the box-type profiles. The proof is shown in the Appendix.

Generally, for each carrier profile $[N(z)]$ the optical constant distribution is uniquely determined by the equation

$$n(z) + ik(z) = \left[\epsilon_\infty - \frac{4\pi N(z) e^2}{m^* \omega^2} \frac{1}{1 + i/\omega\tau} \right]^{1/2} \quad [6]$$

If we consider the n - k plane and the third axis z (depth), each carrier profile is uniquely transformed into the spatial curve shown in Fig. 4a. Considering the Δ - ψ plane and the third axis θ (incident angle), spatial curve a corresponds to spatial curve b . Although an exact mathematical proof of the one-to-one correspondence between these two spatial curves has not been arrived at, we have concluded that this correspondence is correct from computer experiments.

This one-to-one correspondence means that it is possible to construct the carrier profile from the experimental (Δ, ψ) values for various incident angles.

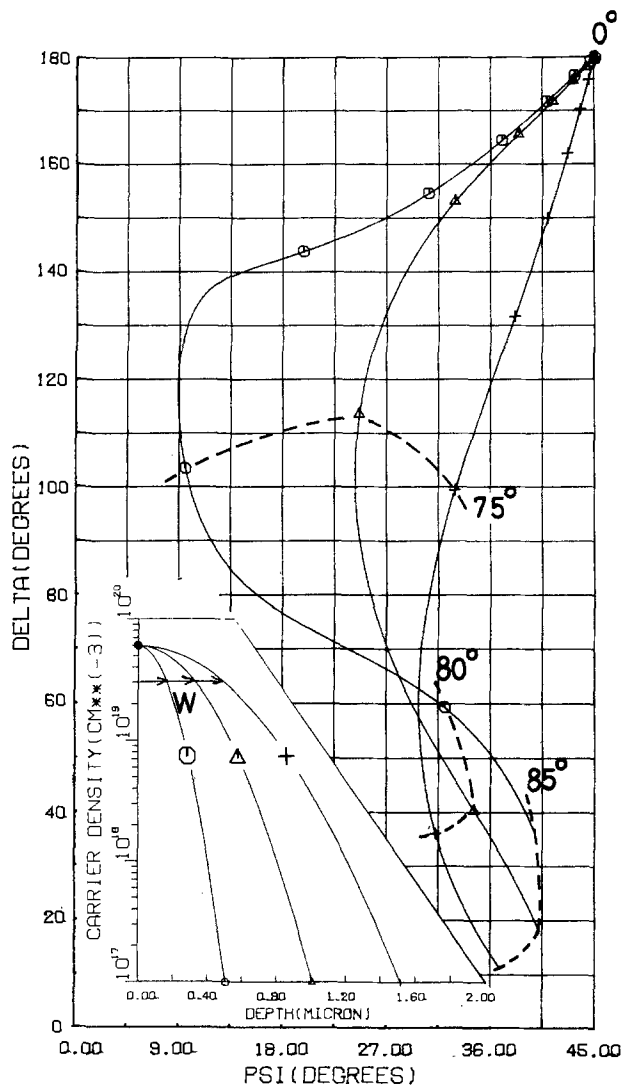


Fig. 3. Calculated Δ - ψ curves. Carrier profiles are assumed to be Gaussian distributions, $N(Z) = N_0 \exp(-Z^2/W^2)$, where $N_0 = 6 \times 10^{19} \text{ cm}^{-3}$ and $W = 0.18, 0.36, \text{ and } 0.54 \text{ }\mu\text{m}$. The substrate is a non-doped silicon wafer with a $100 \text{ }\mu\text{m}$ thickness. Incident angles are changed from 0 to 85 degrees and the symbols are marked every five degrees for each line.

Experiments and Analysis

Figure 5 shows a schematic diagram of our carrier profiler. The light source is a CO₂ laser. The CO₂ laser beam is linearly polarized by the metal grid polarizer and impinges upon the silicon wafer with incident angle θ . The reflected light becomes elliptically polarized, and Δ and ψ for this ellipse are determined by the rotating analyzer method (11). The apparatus are all controlled by a minicomputer, and the ellipsometric parameters Δ and ψ for each incident angle θ are obtained automatically. The obtained (Δ, ψ) values are input to a large computer to determine the carrier profile, as will be shown later.

An example of some experimental results is shown in Fig. 6. The sample for this experiment was made by arsenic ion implantation at an energy of 40 keV and a dose of $5 \times 10^{15} \text{ cm}^{-2}$, followed by isothermal annealing at 1000°C for 40 min. We chose four incident angles (65°, 69°, 73°, and 77°) near the Brewster angle, because Δ is usually very sensitive to the sample properties near this angle.

In order to determine the carrier profile from these data we introduced an appropriate carrier profile model for ion implanted samples as shown in Fig. 7. This profile model has four adjustable parameters: N_0 , P , W_1 , and W_2 . By adjusting these parameters, a wide

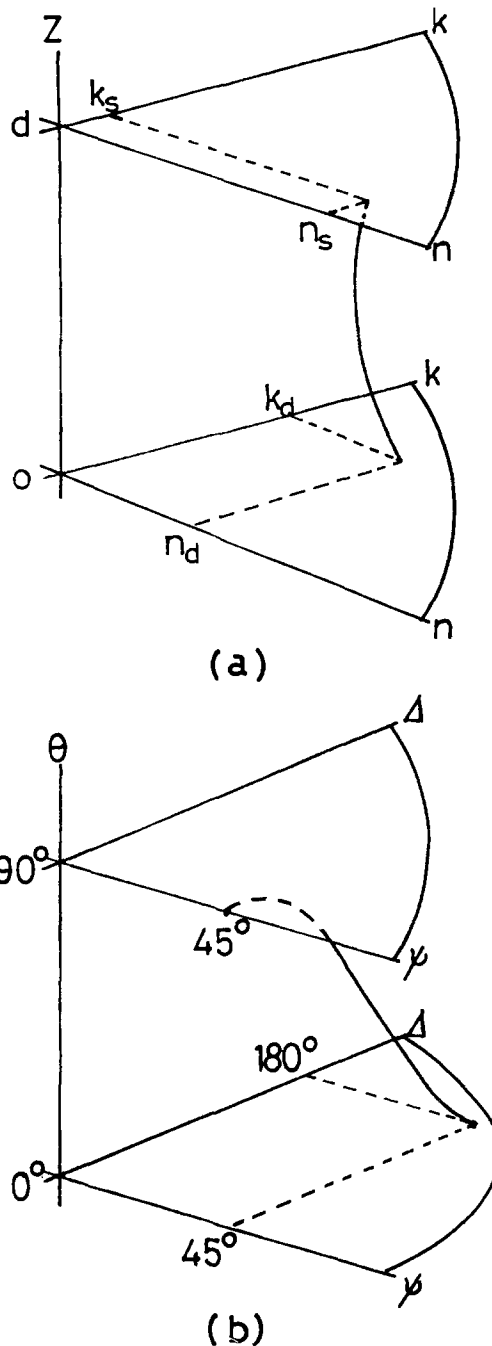


Fig. 4. General relation between carrier profile and Δ - ψ curve. a: Each carrier profile uniquely corresponds to the spatial curve in n - k - z space. b: The spatial curve in (a) corresponds to the spatial curve in Δ - ψ - θ space.

range of carrier profiles can be included in this model. Using a large computer, these four parameters were optimized for the calculated (Δ, ψ) values to fit the experimental ones. The moving range of the four parameters were $10^{17} \leq N_0 \leq 5 \times 10^{20} \text{ cm}^{-3}$, $0 \leq P \leq 3 \text{ }\mu\text{m}$, $0 \leq W_1 \leq 10 \text{ }\mu\text{m}$, and $0 \leq W_2 \leq 3 \text{ }\mu\text{m}$. The optimized values were $N_0 = 1.3 \times 10^{20} \text{ cm}^{-3}$, $P = 0.23 \text{ }\mu\text{m}$, $W_1 = 5.0 \text{ }\mu\text{m}$, and $W_2 = 0.098 \text{ }\mu\text{m}$. Results are shown in Fig. 6. The theoretical Δ - ψ curve is shown as a solid line.

The discrepancy between the theoretical and experimental values in Fig. 6 is attributed to the following reasons. (i) There exists some experimental errors in the ellipsometric measurements. In our experimental apparatus, we estimate these errors at about three degrees for both Δ and ψ . (ii) The true carrier profile may not be exactly described by the profile model shown in Fig. 7.

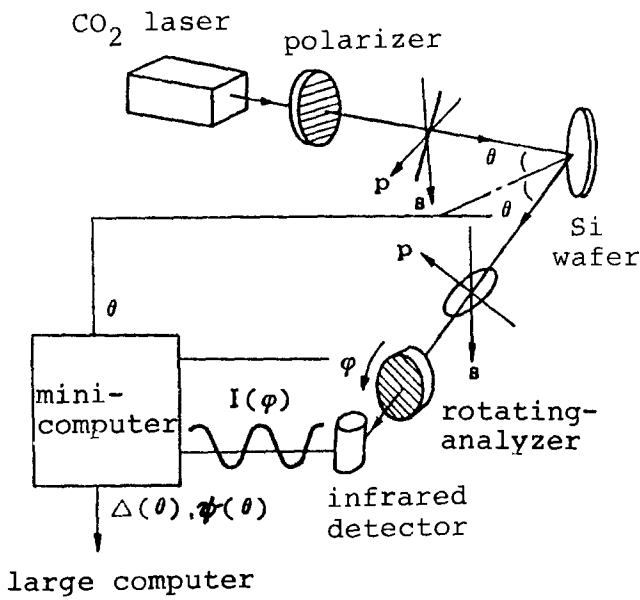


Fig. 5. Schematic diagram of the carrier profiler

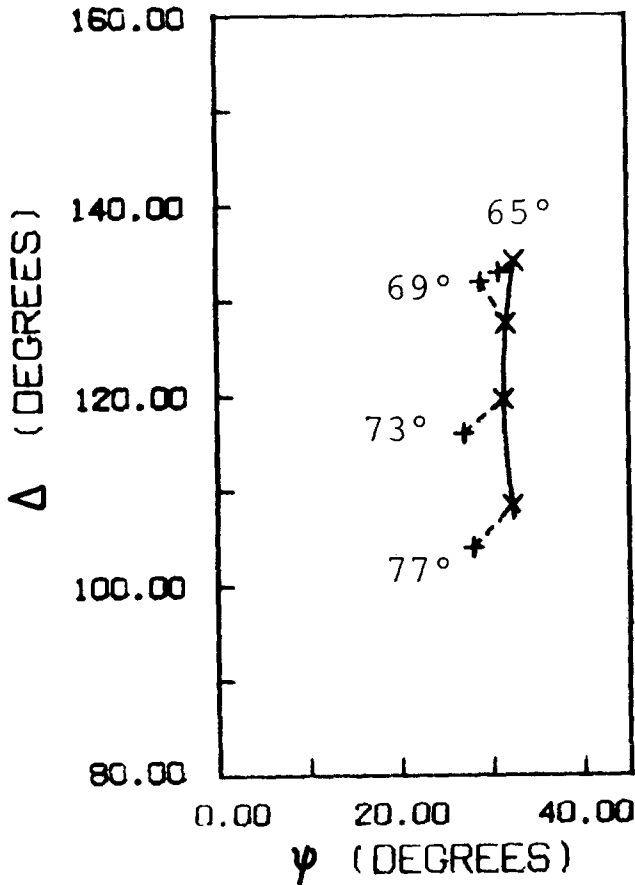


Fig. 6. Experimental results and how they fit the theoretical values. The (+) symbols represent the experimental (Δ, ψ) points for the selected incident angles. The (x) symbols represent the theoretical (Δ, ψ) points. Each is connected with its corresponding experimental points by a broken line. The solid line shows the (Δ, ψ) locus when θ continuously changes from 65 to 77 degrees.

Figure 8 shows the carrier profile of the sample. The solid line represents the carrier corresponding to the theoretical Δ - ψ curve. The (+) symbols represent the carrier profile determined by the conventional anodization stripping method. Both are in good agreement.

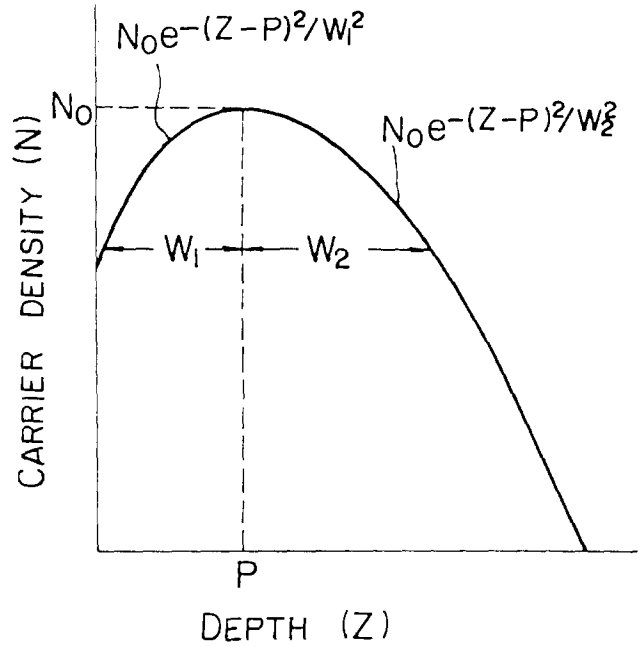


Fig. 7. Carrier profile model. The profile is assumed to be Gaussian: $N(Z) = N_0 \exp[-(Z - P)^2/W_1^2]$ for $Z \leq P$ and $N_0 \exp[-(Z - P)^2/W_2^2]$ for $Z > P$. Here, N_0 is the peak carrier concentration, P is the peak depth, W_1 and W_2 are the two widths of the Gaussian distributions.

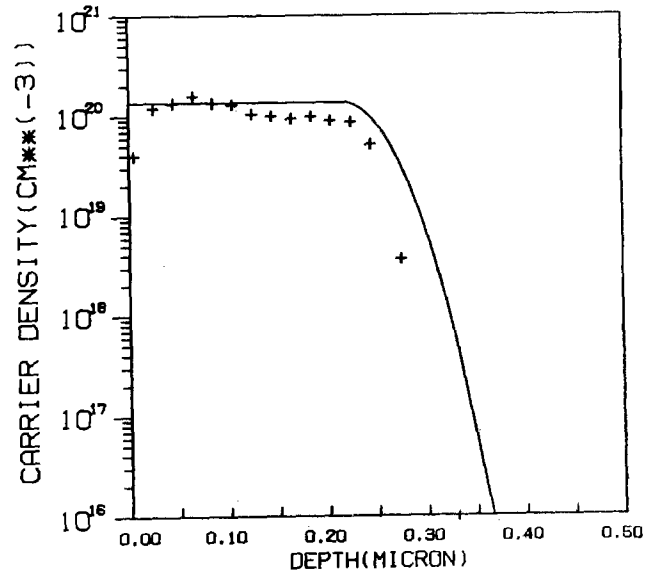


Fig. 8. Carrier profile. The solid line shows the carrier profile determined by our method, and the (+) symbols show the profile determined by the conventional destructive method.

Conclusions

The features of our method are outlined in Table I and compared with those for conventional methods. Comparison is made with respect to measurable range, resolution, and turnaround time. The measurable range and the resolution of our method were estimated by assuming the experimental errors to be one degree for both Δ and ψ .

The weak point in our method is the minimum detectable density, i.e., 10^{17} cm^{-3} . This limit is deduced from Eq. [4]; the dielectric function becomes insensitive to the carrier density when the ratio of the plasma frequency to the incident light frequency ($[4\pi N e^2 / \epsilon_0 m^*]^{1/2}$) becomes small. This ratio is ~ 0.01 for CO_2 laser wavelength and the carrier density of 10^{17} cm^{-3} . However, the difficulty can be avoided if

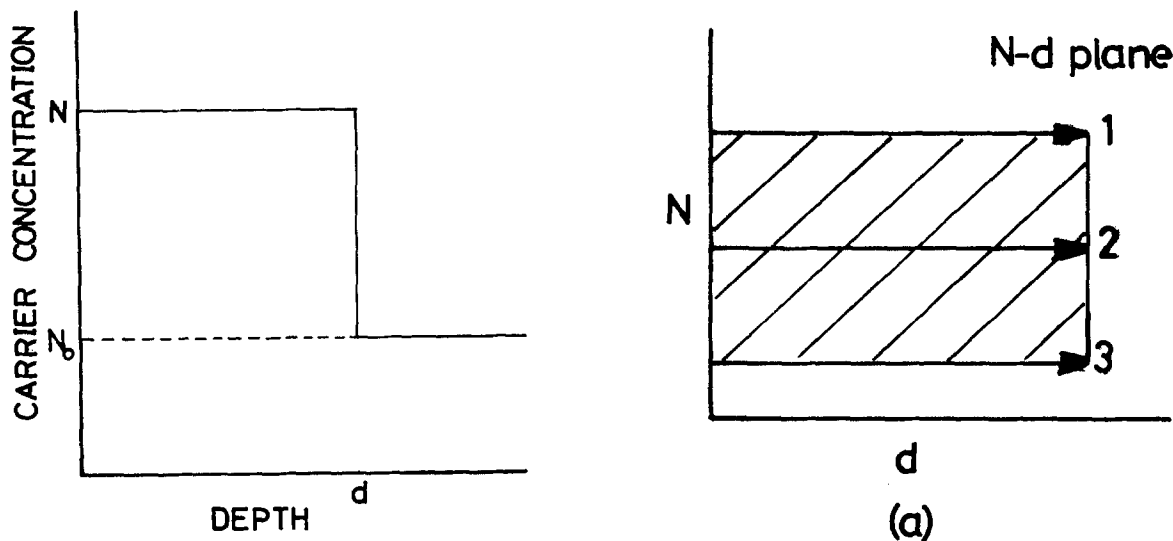


Fig. 9. A box-type profile. The first layer is a homogeneously doped layer with carrier concentration N and thickness d . The second layer is substrate with carrier concentration N_0 .

we use a longer wavelength. For example, if we use a light source with a wavelength of $30 \mu\text{m}$, then the minimum detectable density goes down to 10^{16} cm^{-3} .

In summary, our method is superior to conventional methods, and will become an efficient tool for developing LSI technologies.

APPENDIX

Let us show the one-to-one correspondence between the Δ - ψ curve and the carrier profile in the case of the box-type profile as shown in Fig. A-1. For a proof, we introduce complex variable $\rho = \tan\psi \exp(i\Delta)$ instead of Δ and ψ . For the box profiles, ρ can be described (12) as

$$\rho = \frac{D + Ex + Fx^2}{A + Bx + Cx^3} \quad \text{[A-1]}$$

where

$$x = \exp \left[i \frac{4\pi d}{\lambda} (\epsilon - \sin^2\theta)^{1/2} \right] \quad \text{[A-2]}$$

λ is the incident light wavelength, θ is the incident angle, and d and ϵ are, respectively, the depth and the dielectric constant of the first layer with carrier concentration N . In Eq. [A-1], $A, B, C, D, E,$ and F are the functions of $\lambda, \theta, N,$ and N_0 (carrier concentration of the substrate).

Each box profile is represented by one point in the N - d plane. This point is transformed into the point in the complex ρ -plane through Eq. [A-1] and [A-2]. Mathematically, ellipsometry defines a mapping from the N - d plane to the ρ -plane.

Let us consider the properties of this mapping. Any region of the N - d plane can be covered by the lines parallel to the d -axis as shown in Fig. A-2a. These lines are transformed into the x -plane through Eq. [A-2]. Figure A-2b shows three examples of this mapping. General properties are as follows: all $d = 0$ points in the N - d plane correspond to the $(1, 0)$ point in the x -plane, and as d increases along with the line, the x -locus makes a spiral curve converging on the $(0, 0)$ point in the limit $d \rightarrow \infty$. For small N , the x -locus is like a circle, and as N becomes larger, the x -locus spirals inward.

Since N is constant on each line, $A, B, C, D, E,$ and F in Eq. [A-1] are constants on each line. Thus, ρ is a rational function of x ; that is, Eq. [A-1] represents a conformal mapping from the x -plane to the ρ -plane, as illustrated in Fig. A-2c. This means that the one-to-one correspondence between the x - and ρ -loci is fulfilled unless $\rho'(x) = 0$ ($'$ means the derivative about

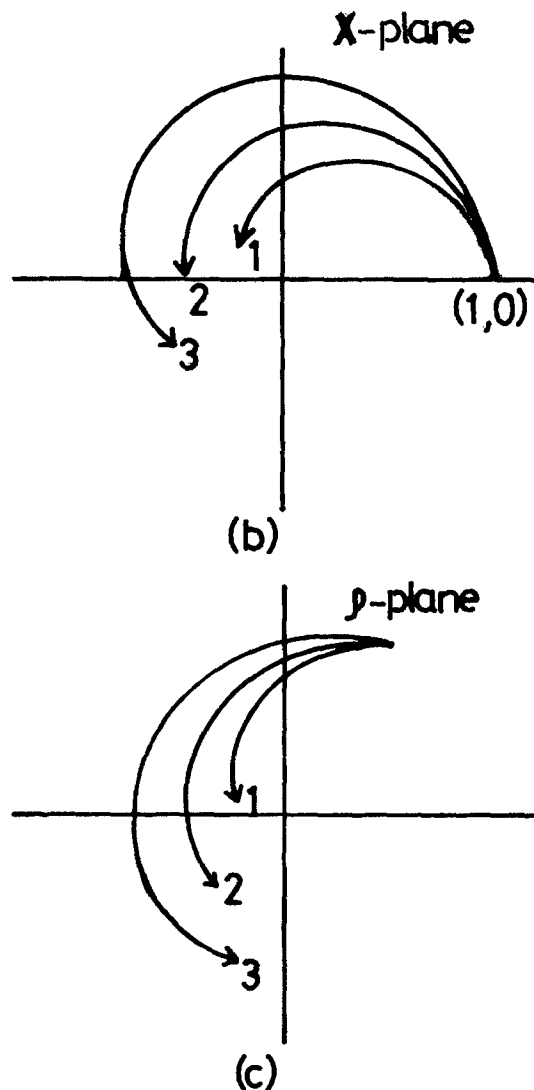


Fig. 10. Mapping by ellipsometry. a: any region of the N - d plane is covered by the lines like 1, 2, and 3. b: schematic diagram of x -loci corresponding to the lines 1, 2, and 3. c: conformal mapping from x -plane to ρ -plane.

x). Generally, there exist three x -points that satisfy $\rho'(x) = 0$. However, we can always select an incident angle to avoid $\rho'(x) = 0$. Thus, one-to-one correspond-

Table I. Features of respective carrier profile measurement methods

		Measurable range		Resolution		Turnaround time	Remarks
		Density (cm^{-3})	Depth (μm)	Depth (μm)	Area (mm^2)		
Conventional method	Anodization stripping method	$10^{19.5} \times 10^{20}$	0-10	~ 0.05	~ 10	4-5 hr	Destructive
	Capacitance method	$10^{15}-10^{18}$	0.2-10	~ 0.01	~ 1	4-5 hr	Destructive
Our method	Polarization of reflected light	$10^{17.5} \times 10^{20}$	0-10	≤ 0.01	≤ 1	≤ 15 min	Noncontact and nondestructive

ence between x - and ρ -points can be concluded. Moreover, if there is no crossing between the x -loci, the

one-to-one correspondence between N - d and ρ -points is fulfilled.

If the range of the N - d plane becomes larger, the crossing between two x -loci occurs as shown in Fig. A-3. In this example, two points, (N_1, d_1) and (N_2, d_2) are transformed into the same point in the x -plane. However, even in this case, it is possible to discriminate between (N_1, d_1) and (N_2, d_2) by measuring the ellipsometric parameters at the two incident angles.

Let us introduce z (depth) and θ (incident angle) as the third axes in the N - d and ρ -planes, respectively. All the box-type carrier profiles are represented by the straight lines in the N - d - z space, and these lines have the one-to-one correspondence to the curves in the ρ - θ space.

Acknowledgments

The authors would like to thank N. Natsuaki and K. Ohyu for their helpful discussions and sample preparations. The kind encouragement of M. Tamura is also gratefully acknowledged.

Manuscript submitted Dec. 3, 1982; revised manuscript received July 27, 1983. This was Paper 188 presented at the Montreal, Que., Canada, Meeting of the Society, May 9-14, 1982.

Hitachi, Limited assisted in meeting the publication costs of this article.

REFERENCES

1. R. Baron, G. A. Shifrin, and O. J. Marsh, *J. Appl. Phys.*, **40**, 3702 (1969).
2. J. A. Copeland, *IEEE Trans. Electron Devices*, **ed-16**, 445 (1969).
3. T. G. R. Rawlins, *This Journal*, **111**, 810 (1964).
4. L. Jastrzebski, J. Lagowski, and H. C. Gatos, *ibid.*, **126**, 260 (1979).
5. T. Abe and T. Kato, *Jpn. J. Appl. Phys.*, **4**, 742 (1965).
6. H. H. Wagner and R. R. Schafer, *J. Appl. Phys.*, **50**, 2697 (1979).
7. R. M. A. Azzam and N. M. Bashara, "Ellipsometry and Polarized Light," North-Holland, Amsterdam (1977).
8. H. Ehrenreich and M. H. Cohen, *Phys. Rev.*, **115**, 786 (1959).
9. W. G. Spitzer and H. Y. Fan, *Phys. Rev.*, **106**, 882 (1957).
10. T. Motooka, *J. Opt. Soc. Am.*, **71**, 884 (1981).
11. P. S. Hauge and F. H. Dill, *IBM J. Res. Develop.*, **472** (1973).
12. R. M. A. Azzam and N. M. Bashara, "Ellipsometry and Polarized Light," p. 289, North-Holland, Amsterdam (1977).

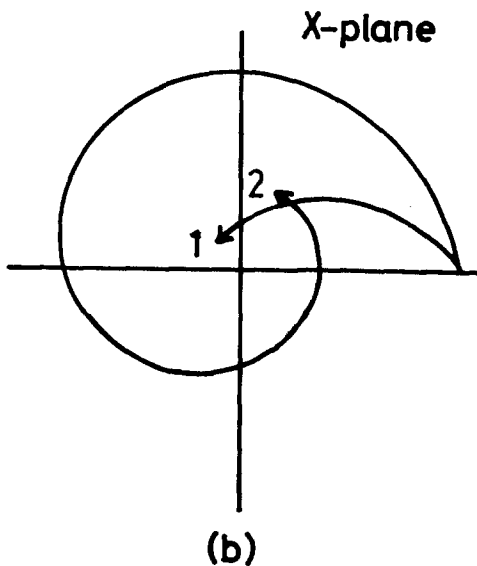
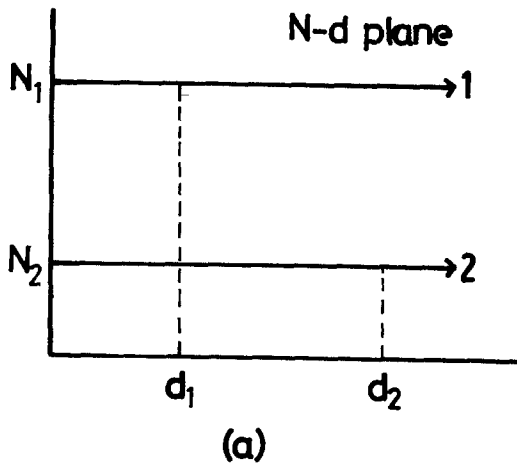


Fig. 11. Crossing between the two x -loci. Two points in the N - d plane, (N_1, d_1) and (N_2, d_2) , are transformed into the same point in the x -plane.

The Effects of Substrate Oxygen Content and Preannealing on the Properties of Silicon Epitaxial Layers

R. K. Tsui,* J. A. Curless, F. Secco d'Aragona,* and P. L. Fejes

Motorola, Incorporated, Semiconductor Research and Development Laboratories, Phoenix, Arizona 85008

ABSTRACT

A study was carried out to evaluate whether the quality of Si epitaxial layers could improve if they were deposited on substrates intrinsically gettered through thermal annealing. Three different two-step procedures were used to preanneal the substrates prior to deposition. Optical microscopy revealed the presence of defect-free (denuded) zones at the surfaces of preannealed substrates only when the initial concentrations of interstitial oxygen in the substrates were $>1.5 \times 10^{18}$ atoms cm^{-3} , and if the high temperature step of the preannealing was carried out in a nonoxygen ambient. While the density of oxidation-induced stacking faults in the epitaxial layers showed no such dependence, the minority carrier generation lifetimes in the layers were strongly dependent on the oxygen content and thermal history of the substrates. Layers deposited on preannealed substrates of high initial oxygen content exhibited the greatest lifetimes. It is believed that oxygen precipitates and related defects, when present in a substrate, getter metallic impurities introduced during processing away from the epitaxial layer and thus improve lifetimes. Such gettering appeared to be most effective when the substrates had both surface denuded zones and high densities of bulk defects.

During the past several years, there has been an extensive amount of research in the area of intrinsic gettering in Si (1). Currently, the majority of the Si material used for electronic device fabrication is grown by the Czochralski (Cz) technique, and the incorporation of oxygen in the Si during Cz growth is well known. The general idea behind intrinsic gettering is to make use of selective thermal annealing to cause the grown-in oxygen to precipitate in the bulk region of a wafer and to out-diffuse from the surface regions, resulting in the formation of defect-free surface regions. Devices subsequently fabricated in such defect-free regions have been reported to exhibit better yield and/or performance (2, 3). This is because of the higher degree of crystallographic perfection of the surface region, and the gettering ability of the precipitates and related defects in the bulk to suppress structural defect formation and reduce contamination by impurities in the surface region of the wafer (4, 5).

The majority of studies on intrinsic gettering to date, however, has been focused on bulk wafers. Relatively little work has been published about the effects of intrinsic gettering on the quality of epitaxial layers. There have been reports on the suppression of epitaxial stacking fault formation by reducing the nucleation sites for these stacking faults through the gettering action of SiO_2 precipitates formed in the substrates (6, 7). It has also been reported that minority carrier generation lifetimes in epitaxial layers can be improved by using as substrates high oxygen content wafers that have been intrinsically gettered prior to deposition (8). Thus it appears that epitaxial layer quality can be improved if through successful intrinsic gettering the substrate provides a defect-free surface region (the so-called denuded zone) to form a good epi/substrate interface, and bulk defects to act as sinks for contaminating impurities.

Recently, however, it has been reported (9) that a high temperature anneal as used in the earlier studies (2, 4, 8) can no longer consistently induce the intrinsic gettering effect in the higher quality Si wafers currently available. The reason suggested is that as crystal growth techniques improved, wafers nowadays contain smaller and fewer grown-in nuclei for the formation of oxygen precipitates and related defects (9, 10). Consequently, a single high temperature anneal may not always induce the higher density of bulk defects necessary for effective intrinsic gettering. Instead, two-step

annealing procedures must be used (9-11). Here the low temperature annealing step creates nuclei and causes grown-in nuclei to grow in size. On the other hand, the high temperature step causes dissolution of nuclei and out-diffusion near the wafer surfaces as well as the growth of oxygen precipitates and related defects in the bulk. Two-step annealing procedures can much more consistently result in the formation of surface denuded zones and a high density of bulk defects. So far, there apparently has been only one published report on the deposition of epitaxial Si on substrates in which denuded zones have been formed and the reduction of epitaxial microdefects achieved by two-step annealing (12). In this paper, we report our findings on the effects of various two-step substrate preannealing procedures on the structural and electrical properties of epitaxial layers subsequently deposited on those substrates.

Experimental Procedures

The substrates used in the present study were dislocation-free, p-type (B-doped, ~ 60 - $110 \Omega\text{-cm}$), 76 mm diam Cz wafers of (100) orientation. All the wafers were from the same ingot, which was treated, in accordance with common manufacturing practices, with a donor thermal anneal at 650°C for 1.5h prior to processing. The interstitial oxygen and substitutional carbon concentrations in these wafers were determined by measuring the room temperature infrared (IR) absorption at wavelengths around $9 \mu\text{m}$ (13) and $16 \mu\text{m}$ (14), respectively, and using the appropriate scaling factor to multiply the absorption coefficient, α . In the case of substitutional carbon, its concentration (C_{sub}) is given by the relation (C_{sub}) = $1.1 \times 10^{17} \alpha$ atoms cm^{-3} (ASTM F123-74). The concentration of interstitial oxygen (O_{int}) is given by the relation (O_{int}) = $4.81 \times 10^{17} \alpha$ atoms cm^{-3} (ASTM F121-79). The initial (i.e., prior to any two-step annealing) concentration of interstitial oxygen, (O_{int})_i, in each wafer was determined, and the range was from 8.48×10^{17} to 2.03×10^{18} atoms cm^{-3} . The initial values of (C_{sub}) in these wafers were low, ranging from 4×10^{16} atoms cm^{-3} in those from the tang end of the ingot to not detectable ($<1 \times 10^{16}$ atoms cm^{-3}) in those from the seed end. All the concentration data described in this paper were obtained from IR absorption measurements made using a Perkin-Elmer 180 double-beam spectrophotometer. During the course of the study, IR absorption in some wafers was also measured using a Nicolet 170 SX Fourier Transform IR spectrophotometer. The two different techniques gave values of (O_{int}) with ex-

* Electrochemical Society Active Member.

Key words: epitaxial silicon, intrinsic gettering, minority carrier generation lifetime.

cellent agreement. All wafers were scribe marked for identification.

The wafers were then divided into four groups. After being cleaned, each of the first three groups was heat-treated using a different two-step preannealing procedure. The wafers in the fourth group were set aside as controls and were not annealed. The three different preannealing procedures used were: (i) a low/high anneal consisting of 16h at 800°C in N₂ followed by 18h at 1050°C in O₂ (Procedure 1), (ii) a low/high anneal consisting of 16h at 650°C in N₂ followed by 4h at 1050°C, all in N₂ (Procedure 2), and (iii) a high/low anneal consisting of 4h at 1050°C in N₂ followed by 64h at 650°C in O₂ (Procedure 3). According to published results and studies in our laboratory (10, 15, 16), these procedures have been found to cause the formation of bulk precipitates and denuded zones in wafers with high (O_{int})_i. On completion of the anneals, surface oxides were stripped off using HF and the final concentration of interstitial oxygen, (O_{int})_f, in each wafer was determined from IR absorption measurements as described above.

Next, epitaxial deposition was made on all four groups of wafers. After being cleaned, the wafers were loaded onto an Applied Materials AMC 7600 reactor. Then approximately 0.1-2.0 μm of Si was removed from the surface of each substrate by *in situ* HCl etching at approximately 1160°-1200°C. Finally, approximately 10-15 μm of p-type (B-doped, ~1 Ω-cm) epitaxial layers were deposited at 1150°-1160°C, using SiCl₄ as the Si source, and at a rate of approximately 0.65-1.0 μm min⁻¹.

After deposition of the epitaxial layers, each of the four groups of wafers was divided into two lots. One lot was wet oxidized for the evaluation of oxidation-induced stacking faults (OISF), and the other lot set aside for electrical characterization. The wafers were thus divided into a total of eight different lots. The wet oxidation procedure consisted of: (i) ramp up from 650° to 1050°C in N₂ + 1% O₂, (ii) 2h at 1050°C in H₂ + O₂ (torch used, plus 2% HCl added for the last 45 min), and (iii) ramp down from 1050° to 650°C in N₂. The surface oxide layers (~7000Å) formed on each of the wafer so oxidized were then stripped off with HF, and the wafer was cleaved into two halves such that the cleavage plane was (110) oriented. Cleaved halves were then immersed for 1 min in a Secco etch (17) which has an etch rate of ~1.5 μm min⁻¹. Structural defects thus delineated were observed using optical microscopy. The OISF density in the epitaxial layer was measured at four points that lay in a straight line parallel and close to the cleaved edge. Two of the points were 38 mm apart and equidistant from the center of the cleaved edge. The other two were 56 mm apart and also equidistant from the center of the cleaved edge. The cleavage plane was examined to determine if a denuded zone was present in the substrate. Wafers from four of the eight lots were so studied.

MOS capacitors were fabricated onto the surfaces of the epitaxial layers of the other four lots of wafers set aside for electrical characterization. The fabrication procedure basically consisted of: (i) growing ~1000Å of gate oxide at 1050°C on the epitaxial layer surface, (ii) an ion implantation of B (using an energy of 50 keV and a dosage of 10¹⁵ ions cm⁻²) into the back side of the substrate to facilitate the making of ohmic contacts, (iii) a postimplantation anneal at 900°C in N₂ for 0.5h, (iv) a front-side deposition of ~10,000Å of Al, (v) photolithographic patterning and etching to form capacitors (26 mils diam) and guard rings (separated from the capacitor by a 0.2 mil gap), and (vi) an anneal at 465°C in forming gas for 0.5h. Using these capacitors, measurements of capacitance and current transients were made after the capacitors were pulsed into deep depletion. The epitaxial minority carrier generation lifetime (τ) was deduced from these measurements

using calculations based on the Zerbst method (18, 19) with τ being determined from the slope of a curve which is a plot of the measured generation current *vs.* the normalized depletion depth. The measurement system consisted of a Princeton Applied Research 410 C-V plotter and a Keithley 619 electrometer/multimeter, controlled by a Hewlett Packard 85 desktop computer system, and a probe station. Measurements were made inside a dark enclosure at either room temperature or 40°C. Due to the time consuming nature of each measurement, only four or five capacitors per wafer were sampled. These capacitors were located typically at four points lying on the two orthogonal diameters of the wafer with each point approximately 20 mm from the wafer center. In some cases the capacitor at the wafer center was also used for the measurement.

Results and Discussion

Oxygen precipitation and denuded zone formation.—The reduction of (O_{int}), defined as $\Delta(O_{int}) = (O_{int})_i - (O_{int})_f$, that had occurred in the substrate wafers due to preannealing Procedures 1-3 are shown in Fig. 1, as a function of (O_{int})_i. The data indicated that the magnitude of $\Delta(O_{int})$ depended strongly on (O_{int})_i. In the cases where Procedures 2 and 3 were used (see Fig. 1b and 1c, respectively), $\Delta(O_{int})$ became significant (>1 × 10¹⁷ atoms cm⁻³) once (O_{int})_i exceeded approximately 1.4-1.5 × 10¹⁸ atoms cm⁻³. Furthermore, for substrates with (O_{int})_i > 1.9 × 10¹⁸ atoms cm⁻³, preannealing with Procedure 2 clearly resulted in higher values of $\Delta(O_{int})$ than those obtained using Procedure 3. However, as shown by Fig. 1a, preannealing with

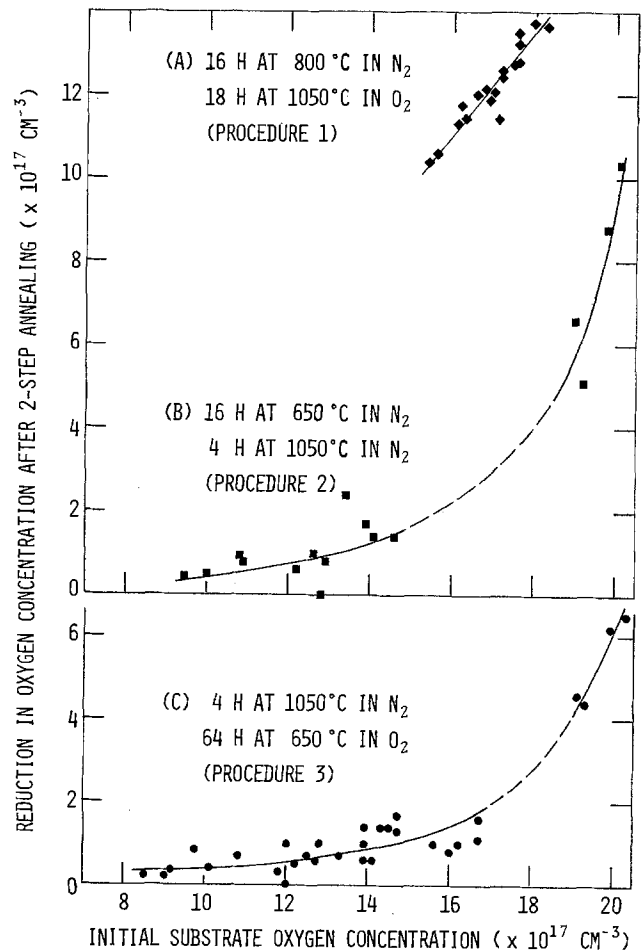


Fig. 1. Reduction in the interstitial oxygen concentration [$\Delta(O_{int})$] as a function of the initial concentration of interstitial oxygen [(O_{int})_i] in substrates: (A) preannealed using Procedure 1 (◆), (B): preannealed using Procedure 2 (■), (C): preannealed using Procedure 3 (●).

Procedure 1 resulted in even higher $\Delta(O_{\text{int}})$, at least when $(O_{\text{int}})_i > 1.5 \times 10^{18}$ atoms cm^{-3} . It is generally agreed that some outdiffusion of oxygen from the surface regions of a wafer occurs during the high temperature annealing. If the amount of interstitial oxygen so lost from a substrate during two-step annealing is neglected, $\Delta(O_{\text{int}})$ is then indicative of the amount of interstitial oxygen that has precipitated due to the pre-annealing procedure.

Data gathered by observing the Secco-etched (110) cleavage planes of the wet-oxidized wafers tend to support this (see Table I). Substrates that had $(O_{\text{int}})_i > 1.5 \times 10^{18}$ atoms cm^{-3} and were preannealed using Procedures 1-3 exhibited a high density of defects. On the other hand, substrates with $(O_{\text{int}})_i < 1.5 \times 10^{18}$ atoms cm^{-3} had been preannealed using Procedures 2 and 3, but these substrates showed very little, if any, defects. When present, the density of these defects increased with increasing $\Delta(O_{\text{int}})$, as can be seen in Fig. 2. While it is apparent that Procedures 1-3 all caused the formation of oxygen precipitates and related defects in the substrates, no denuded zones were observed in those substrates preannealed using Procedure 1 (see Fig. 2d). Conversely, denuded zones with thicknesses of 20-40 μm were found in all the substrates with $(O_{\text{int}})_i > 1.5 \times 10^{18}$ atoms cm^{-3} and preannealing using Procedure 2 (see Fig. 2c) or Procedure 3 (see Fig. 2a and 2b). In the substrates that were not preannealed (controls), no defects could be seen when their cleavage planes were observed under the optical microscope, irrespective of $(O_{\text{int}})_i$.

The absence of denuded zones in substrates preannealed using Procedure 1 led to the speculation that because the high temperature (1050°C) step was carried out in an O_2 ambient the out-diffusion of dissolved oxygen from the surface regions of the substrates was retarded. Subsequent split-lot experiments in which wafers were annealed using Procedure 1 with the 1050°C step being carried out in either a N_2 or O_2 ambient were performed. Denuded zones were observed in wafers annealed with the 1050°C step carried out in a N_2 ambient. However, the thicknesses of these denuded zones were much thinner ($< 10 \mu\text{m}$) than those obtained using Procedures 2 and 3. Again, no denuded zones were found in wafers annealed with the 1050°C step carried out in an O_2 ambient. These evaluations were carried out immediately after the two-step annealing and not after epitaxial deposition as in the original experiments. Thus the possibility that the *in situ* epi etch-back (of $\sim 2 \mu\text{m}$) removed a very thin denuded zone can be ruled out. Furthermore, a dry oxidation of 18h at 1050°C will only consume about 3500Å of Si, an amount that is insignificant in the consideration for denuded zone formation.

It is possible that after 16h at 800°C, relatively large-sized precipitates and/or nuclei form near wafer surfaces, and the subsequent step at 1050°C becomes less effective in causing their dissolution and out-diffusion in order to form denuded zones. Carrying out the 1050°C step in O_2 makes this even less effective. The experimental results discussed so far do indicate that $(O_{\text{int}})_i$, the annealing sequence (high/low vs. low/

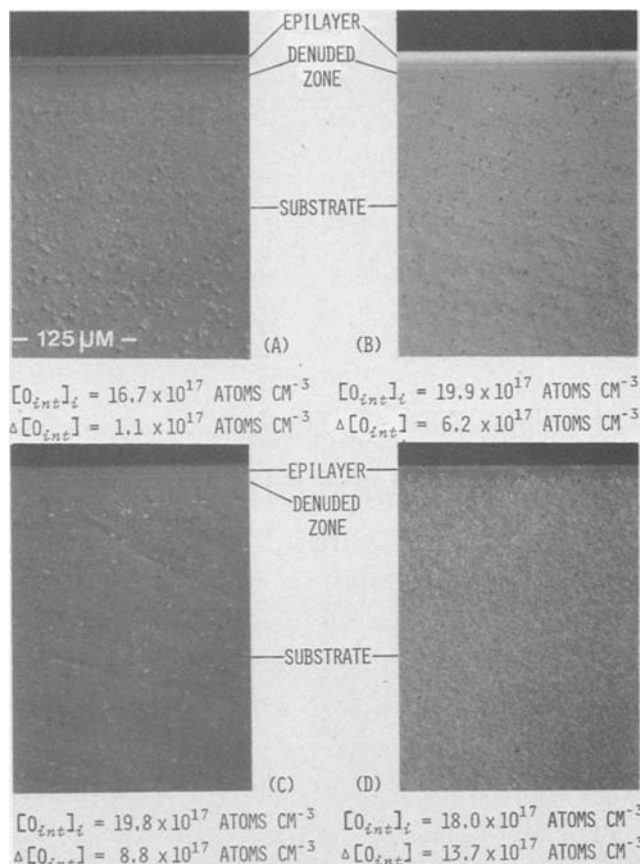


Fig. 2. Optical micrographs of Secco-etched (110) cleavage planes of wafers with substrates. (A) and (B): preannealed using Procedure 3. (C): preannealed using Procedure 2. (D): preannealed using Procedure 1. $(O_{\text{int}})_i$ and $\Delta(O_{\text{int}})$ for each substrate are given beneath the corresponding micrograph.

high), and the annealing ambient are among the factors that influence the way in which oxygen precipitation occurs.

Oxidation induced stacking faults in the epitaxial layers.—The structural characteristics of the epitaxial layers were examined after wet oxidation and Secco etching. The OISF density in the layers deposited on substrates that were preannealed using Procedures 2 and 3 as well as on substrates that were not preannealed (controls) are shown in Fig. 3, as a function of $(O_{\text{int}})_i$ in the substrates. Each data point represents the averaged density, and the spread between the maximum and minimum densities observed is also indicated.

The data do not indicate a strong correlation between OISF density and $(O_{\text{int}})_i$. Densities in general were lowest in epitaxial layers deposited on substrates preannealed using Procedure 2 (see Fig. 3b) and highest in layers deposited on control substrates, especially for those with high values of $(O_{\text{int}})_i$ (see Fig. 3a). It appears that while successful intrinsic gettering through the use of two-step annealing greatly reduces the OISF density on the surfaces of wafers (10, 16), the effect is less pronounced in epitaxial layers deposited on such two-step annealed substrates.

Finally, while the highest OISF densities shown in Fig. 3 were $< 800 \text{ cm}^{-2}$, densities in layers deposited on substrates preannealed using Procedure 1 were $> 10^4 \text{ cm}^{-2}$. It is known that dislocation loops are generated at oxygen precipitates (5). The heavy precipitation that had occurred throughout these substrates after preannealing with Procedure 1 (with no denuded zones formed) most likely resulted in a high density of dislocations at the substrate surfaces. These dislocations in turn gave rise to defective epi/substrate

Table I. Oxygen precipitation in the substrates as observed on Secco-etched (110) cleavage planes

Substrate preanneal procedure	Initial substrate oxygen concentration (cm^{-3})	
	$< 1.5 \times 10^{18}$	$> 1.5 \times 10^{18}$
800°/1050°C (Procedure 1)	No precipitation	Precipitation
650°/1050°C (Procedure 2)		No denuded zone
1050°/650°C (Procedure 3)	No precipitation	Precipitation with denuded zone
None (Control)		No precipitation

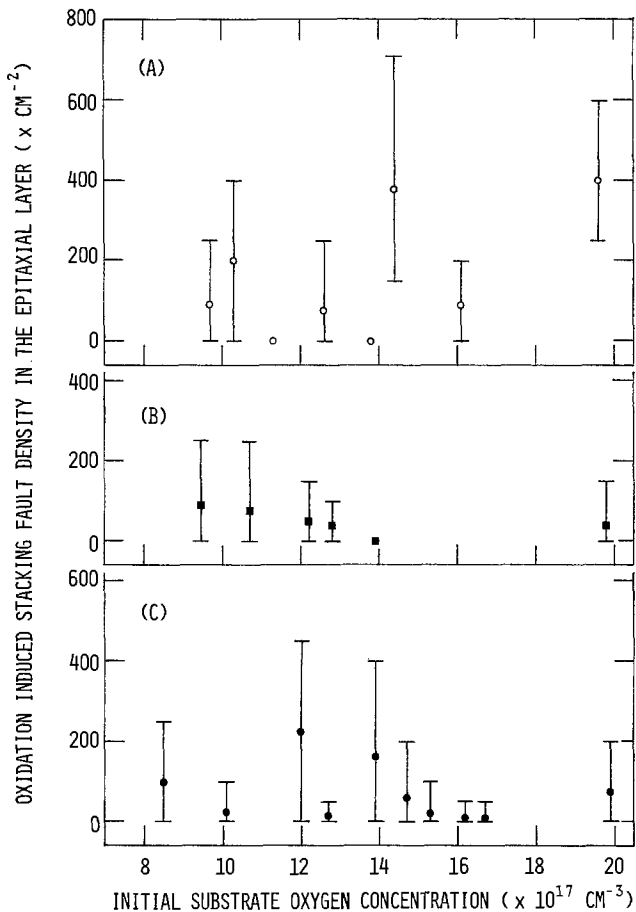


Fig. 3. Oxidation induced stacking fault (OISF) density in epitaxial layers as a function of $(O_{\text{int}})_i$ in substrates. (A): not preannealed (\circ). (B): preannealed using Procedure 2 (\blacksquare). (C): preannealed using Procedure 3 (\bullet).

interfaces on the subsequent deposition of the epitaxial layers, and allowed dislocations to propagate through the growing layers. The presence of these dislocations in the epitaxial layers created a large number of centers to nucleate OISF on the subsequent oxidation of Fig. 2d. The significantly higher OISF density in these layers compared to those observed in the other three lots of wafers (*i.e.*, $>10^4$ vs. $<800 \text{ cm}^{-2}$) is indicative of poorer structural quality. This is reflected in the electrical properties of these layers, as will be described below.

Minority carrier generation lifetime in the epitaxial layers.—Figure 4 shows τ in the epitaxial layers as a function of $(O_{\text{int}})_i$ in the substrates. Each data point corresponds to the averaged lifetime, and the spread between the maximum and minimum values of τ determined is also shown. The response time of the experimental setup limited the lowest measurable value of τ to $0.1 \mu\text{s}$. Epitaxial layers with $\tau < 0.1 \mu\text{s}$ are indicated by arrows (see lower left portion of Fig. 4); solid arrowheads indicate that the substrates had been preannealed using Procedures 2 or 3, and open arrowheads indicate control substrates.

First we will discuss the values of τ in layers deposited on substrates preannealed using Procedure 1 (as indicated by the symbol \blacklozenge and all located in the lower right portion of Fig. 4). In this group, the values of τ were low (typically $< 1 \mu\text{s}$), a fact that is not unexpected in view of the poor structural quality of these epitaxial layers (OISF density $> 10^4 \text{ cm}^{-2}$). The rest of the data in Fig. 4 show the following trends (see Table II for a summary). (i) For the epitaxial layers deposited on substrates with $(O_{\text{int}})_i < 1.2 \times 10^{18}$ atoms cm^{-3} , the values of τ were below the measure-

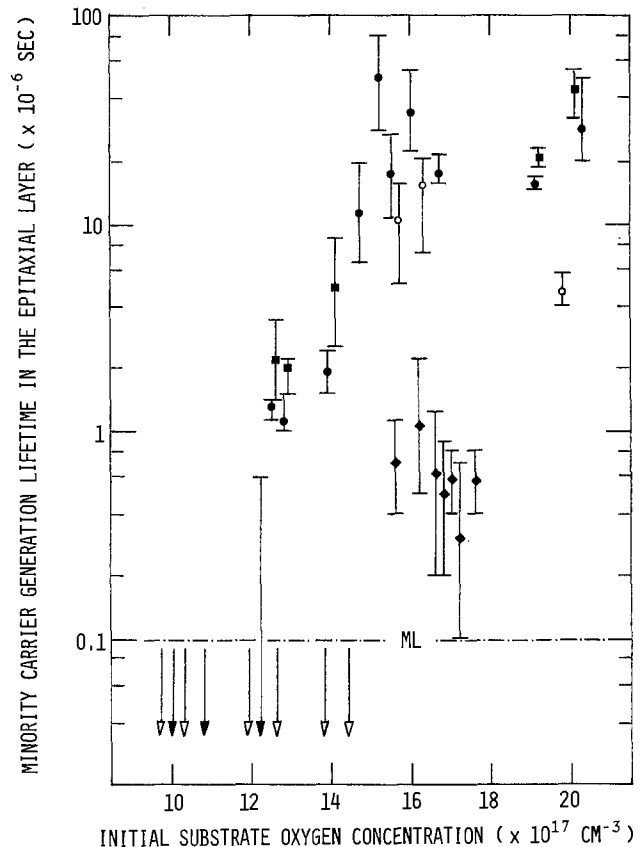


Fig. 4. Minority carrier generation lifetime (τ) in epitaxial layers as a function of $(O_{\text{int}})_i$ in substrates. Layers with $\tau < 0.1 \mu\text{s}$ are indicated by arrows, with solid arrowheads for substrates preannealed using Procedure 2 or 3 and open arrowheads for control substrates. All other symbol designations are the same as in Fig. 1 and Fig. 3.

ment limit of $0.1 \mu\text{s}$, irrespective of whether the substrate had been annealed. (ii) In cases where the substrates had $(O_{\text{int}})_i$ in the range of ~ 1.2 - 1.5×10^{18} atoms cm^{-3} , the values of τ in layers deposited on substrates preannealed using Procedures 2 and 3 (indicated by the symbols \blacksquare and \bullet , respectively, in Fig. 4) increased from ~ 1 to $\sim 10 \mu\text{s}$ as $(O_{\text{int}})_i$ increased. τ in layers deposited on control substrates remained $< 0.1 \mu\text{s}$. (iii) When the substrates had $(O_{\text{int}})_i > 1.5 \times 10^{18}$ atoms cm^{-3} , the values of τ in layers deposited on substrates preannealed using Procedures 2 and 3 increased to as high as $80 \mu\text{s}$ and averaged around 20 - $40 \mu\text{s}$, with no strong dependence on $(O_{\text{int}})_i$. The lifetimes in layers deposited on control substrates were now measurable, but their values were typically a factor of 2-3 lower than those in layers deposited on preannealed substrates with comparable $(O_{\text{int}})_i$. (iv) For substrates with $(O_{\text{int}})_i$ in the range of $\sim 1.2 \times 10^{18}$ to 2.0×10^{18} atoms cm^{-3} , τ in a layer deposited on a substrate preannealed using Procedure 2 was always slightly higher than that in a layer deposited on a substrate with comparable $(O_{\text{int}})_i$ but preannealed using Procedure 3.

Table II. Minority carrier generation lifetimes in epitaxial layers deposited on preannealed (using Procedures 2 and 3) and control (not preannealed) substrates

Initial substrate oxygen concentration (cm^{-3})	Epitaxial minority carrier generation lifetime (μs)	
	Preannealed substrate	Control substrate
$< 1.2 \times 10^{18}$	< 0.1	< 0.1
1.2 - 1.5×10^{18}	~ 1 - 10	< 0.1
$> 1.5 \times 10^{18}$	~ 20 - 40	~ 5 - 15

The lifetime data for epitaxial layers deposited on substrates preannealed using either Procedure 2 or 3 can be explained if defects in the bulk regions of these substrates had given rise to gettering effects in the cases where $(O_{\text{int}})_i$ was high. As mentioned earlier, it had already been determined that either Procedure 2 or 3 could create denuded zones and bulk defects in substrates with $(O_{\text{int}})_i > 1.5 \times 10^{18}$ atoms cm^{-3} . Intrinsic gettering effects would thus be expected to be highest in such substrates; values of τ in the layers deposited on such substrates indeed were consistently the highest. As $(O_{\text{int}})_i$ in the substrates gradually decreased below $\sim 1.5 \times 10^{18}$ atoms cm^{-3} , corresponding decreases in $\Delta(O_{\text{int}})$, together with the absence of bulk defects and denuded zones, had been observed. Gettering effects would be expected to diminish as well, and values of τ did drop from ~ 10 to ~ 1 μs as $(O_{\text{int}})_i$ in the substrates decreased from ~ 1.5 to $\sim 1.2 \times 10^{18}$ atoms cm^{-3} . It was not possible to determine if this trend continued when $(O_{\text{int}})_i$ in the substrates was $< 1.2 \times 10^{18}$ atoms cm^{-3} , since values of τ in layers deposited on such substrates were below 0.1 μs . It is not unreasonable to expect τ to eventually level off at a lower limit of < 0.1 μs when $(O_{\text{int}})_i$ in the substrates were so low that no gettering effect whatsoever was induced through preannealing.

As for the cause of the degradation in τ and the nature of the gettering mechanism, there does not appear to be a direct correlation to OISF densities in the epitaxial layers. Whereas the difference in values of τ were large (< 0.1 μs vs. > 10 μs), there were no significant differences in OISF densities between the layers deposited on substrates of varying $(O_{\text{int}})_i$ values and preannealed using Procedures 2 and 3 (see Fig. 3b and 3c). Furthermore, even the highest densities in these cases (which tended to be found in layers deposited on preannealed substrates with low $(O_{\text{int}})_i$; this class of layers had $\tau < 0.1$ μs) were much lower than the OISF densities in layers deposited on substrates preannealed using Procedure 1 (< 500 vs. $> 10^4$ cm^{-2}). Nevertheless, this latter class of layers still had $\tau > 0.1$ μs consistently.

However, it has been reported that OISF-related degradation in electrical properties was observed only when the stacking faults were decorated with impurities (20, 21). It has also been reported that metallic impurities such as Fe, Cr, Ni, Cu, and Au could often be introduced as contaminants during epitaxial processing (22, 23). It has been shown that intrinsic gettering as induced by two-step annealing has the ability to make use of bulk defects to getter heavy metals such as Cu away from the surface denuded zone (24). It is possible that in the present study impurities and/or impurity-decorated stacking faults in the epitaxial layer had a strong influence on τ . Preannealing of substrates with low $(O_{\text{int}})_i$ did not result in the formation of bulk precipitates and related defects, and thus no sinks were provided to getter metallic impurities out of the epitaxial layers. As $(O_{\text{int}})_i$ in the preannealed substrates increased, the gettering effect began to come into play, with maximum effectiveness being achieved in substrates with high $(O_{\text{int}})_i$ where both denuded zones and bulk defects were formed. In the substrates preannealed using Procedure 1, bulk defects were present, but the gettering effectiveness was probably reduced because of the absence of denuded zones.

In fact, the proposed model could explain all the τ data except for those in layers deposited on control substrates with high $(O_{\text{int}})_i$. Even though no bulk defects were observed in these substrates under the optical microscope (and none were expected since these substrates were not preannealed), the values of τ in the layers deposited on these substrates were substantially higher than those in layers deposited on control substrates with low $(O_{\text{int}})_i$. This phenomenon has been

observed previously (8). It is possible that in control substrates microprecipitates of oxygen too small in size to be detected using optical microscopy, but still possessing a certain degree of gettering ability, exist. These microprecipitates are believed to be present in the as-grown Si crystal and can act as nuclei for further precipitation on receiving subsequent thermal annealing. The growth or dissolution of these microprecipitates is dependent on $(O_{\text{int}})_i$ and the temperature of the subsequent anneal (25). For a given value of $(O_{\text{int}})_i$, there is at each temperature a critical size above which a microprecipitate will grow and below which it will shrink or dissolve. In the control substrates with low $(O_{\text{int}})_i$, it is possible that these microprecipitates were smaller than the critical size at the high temperature experienced during epitaxial processing, and the microprecipitates would dissolve. The critical size is smaller, though, for the same temperature in the control substrates with high $(O_{\text{int}})_i$. Thus the microprecipitates in these substrates would not shrink or dissolve and might possibly provide some ability to getter metallic impurities, though not as effectively as high $(O_{\text{int}})_i$ substrates preannealed using Procedure 2 or 3. Further work is necessary to get a better understanding of the mechanisms involved in control substrates with high $(O_{\text{int}})_i$.

Finally, it should be mentioned that while lifetime is strongly dependent on measurement technique and resistivity of the material (26), as well as on the thermal processing the material has received (23), it is not directly related to the oxygen content of the material. The lifetimes of material grown by the float-zone technique can be very high, even though such material contains much less oxygen than Cz material. However, the results of the present study do indicate that oxygen precipitates and related defects, when present in the bulk region of a wafer, getter impurities away from the wafer surfaces and so remove the lifetime degrading effects of the impurities. Since oxygen precipitation depends on the oxygen concentration of the material, lifetime is thus indirectly related to oxygen content.

Summary

Silicon epitaxial layers have been deposited on preannealed (prior to deposition) and control (not preannealed) substrates with initial concentrations of interstitial oxygen ranging from $8\text{--}20 \times 10^{17}$ atoms cm^{-3} . All the substrates were wafers taken from the same ingot of Si to eliminate variations that could possibly arise due to different thermal histories during crystal growth. Three different two-step preannealing procedures were used, including high/low and low/high temperature anneals in different ambients. The degrees of oxygen precipitation due to the preannealing were monitored. Surface denuded zones free of precipitates and related defects, as observed using optical microscopy, were found in preannealed substrates only when their initial concentrations of interstitial oxygen were $> 1.5 \times 10^{18}$ atoms cm^{-3} and when the high temperature step of the preannealing was carried out in a nonoxygen ambient.

Minority carrier generation lifetimes (determined using measurements of capacitance relaxation time) in the epitaxial layers deposited on substrates with low initial oxygen concentrations ($\lesssim 1.2 \times 10^{18}$ atoms cm^{-3}) were below the measurement limit of 0.1 μs , irrespective of whether the substrates had been preannealed or not. The lifetimes of layers deposited on control substrates with high initial oxygen concentrations averaged ~ 10 μs . Lifetimes in layers deposited on preannealed substrates with high initial oxygen concentrations averaged another factor of 2-3 higher (and reached as high as 80 μs) if the substrates had surface denuded zones. In both cases, high initial oxygen concentration meant $> 1.5 \times 10^{18}$ atoms cm^{-3} .

It is believed that oxygen precipitates and related defects, when present in the substrate, getter metallic impurities introduced during processing away from the epitaxial layer and thus improve lifetimes. Such gettering appeared to be most effective when the substrates had both surface denuded zones and high densities of bulk defects. Of the three different two-step substrate preannealing procedures used, the low/high procedure of 16h at 650°C/4h at 1050°C (all in N₂) appeared to provide somewhat better gettering (in terms of generally lower densities of oxidation induced stacking faults and higher lifetimes in the epitaxial layers) than the high/low procedure of 4h at 1050°C in N₂/64h at 650°C in O₂.

Acknowledgments

Thanks are due to R. M. Boyle for carbon and oxygen concentration measurements, J. W. Rose and P. J. Tobin for the epitaxial depositions, A. L. Turley for technical assistance, H. M. Liaw and C. J. Varker for helpful discussions, and S. Hill and S. Trower for manuscript preparation.

Manuscript submitted March 3, 1983; revised manuscript received July 30, 1983.

Motorola, Incorporated assisted in meeting the publication costs of this article.

REFERENCES

1. For example, see in "Semiconductor Silicon 1981," H. R. Huff, R. J. Kriegler, and Y. Takeishi, Editors, The Electrochemical Society Softbound Proceedings Series, Pennington, NJ (1981).
2. T. Y. Tan, E. E. Gardner, and W. K. Tice, *Appl. Phys. Lett.*, **30**, 175 (1977).
3. G. A. Rozgonyi and C. W. Pearce, *ibid.*, **32**, 747 (1978).
4. S. Kishino, S. Isomae, M. Tamura, and M. Maki, *ibid.*, **32**, 1 (1978).
5. W. K. Tice and T. Y. Tan, *ibid.*, **28**, 564 (1976).
6. G. A. Rozgonyi, R. P. Deysher, and C. W. Pearce,

- This Journal*, **123**, 1910 (1976).
7. L. E. Katz and D. W. Hill, *ibid.*, **125**, 1151 (1978).
 8. K. H. Yang, H. F. Kappert, and G. H. Schwuttke, *Phys. Status Solidi A*, **50**, 221 (1978).
 9. S. Kishino, M. Kanamori, N. Yoshihiro, M. Tajima, and T. Iisuka, *J. Appl. Phys.*, **50**, 8240 (1979).
 10. K. Nagasawa, Y. Matsushita, and S. Kishino, *Appl. Phys. Lett.*, **37**, 622 (1980).
 11. K. Yamamoto, S. Kishino, Y. Matsushita, and T. Iizuka, *ibid.*, **36**, 195 (1980).
 12. H. Tsuya, K. Tanno, and F. Shimura, *ibid.*, **36**, 658 (1980).
 13. W. Kaiser and P. H. Keck, *J. Appl. Phys.*, **28**, 882 (1957).
 14. R. C. Newman and J. B. Willis, *J. Phys. Chem. Solids*, **26**, 373 (1965).
 15. M. Ogino, T. Usami, M. Watanabe, H. Sekine, and T. Kawaguchi, Paper 435 presented at The Electrochemical Society Meeting, Hollywood, FL, Oct. 5-10, 1980.
 16. F. Secco d'Aragona, R. K. Tsui, H. M. Liaw, and P. L. Fejes, To be published.
 17. F. Secco d'Aragona, *This Journal*, **119**, 948 (1972).
 18. M. Zerbst, *Z. Agnew. Phys.*, **22**, 30 (1966).
 19. F. P. Heiman, *IEEE Trans. Electron Devices*, **ed-14**, 781 (1967).
 20. K. V. Ravi, C. J. Varker, and C. E. Volk, *This Journal*, **120**, 533 (1973).
 21. Y. Ichida, T. Yanada, and S. Kawado, in "Lifetime Factors in Silicon, ASTM STP 721," p. 107, American Society for Testing and Materials, Philadelphia (1980).
 22. C. W. Pearce and R. G. McMahon, *J. Vac. Sci. Technol.*, **14**, 40 (1977).
 23. K. Graff and H. Pieper, in "Lifetime Factors in Silicon, ASTM STP 721," p. 136, American Society for Testing and Materials, Philadelphia (1980).
 24. S. Kishino, K. Nagasawa, and T. Iisuka, *Jpn. J. Appl. Phys.*, **19**, L466 (1980).
 25. Y. Matsushita, *J. Cryst. Growth*, **56**, 516 (1982).
 26. B. Ross, in "Lifetime Factors in Silicon, ASTM STP 721," p. 14, American Society for Testing and Materials, Philadelphia (1980).

Characteristics of Sputter-Deposited Mo Films

Masamitsu Suzuki and Kazuyoshi Asai

Nippon Telegraph and Telephone Public Corporation, Atsugi Electrical Communication Laboratory, Tokyo, Japan

ABSTRACT

Plasma etching characteristics and electrical resistivities for sputtered Mo films on GaAs substrates were studied. The plasma etching rate of the films depends largely on deposition rate. High etching rates and electrical resistivities are obtained by lowering deposition rates. Anisotropies both in the side etching rates and electrical resistivities are found in intermittently deposited Mo films resulted from rotating the substrate holding table. It is concluded from SEM, x-ray, and Auger analyses that the principal factors dominating these film characteristics are the anisotropically grown grains caused by oblique incident-angle deposition and oxygen adsorption in grain boundaries of the Mo films.

Molybdenum films have been used in Si MOS LSI's as gates and interconnections (1, 2, 3) because of their thermal stability (4), low resistivity (5), and plasma etching availability (6). The authors have proposed using Mo films as the self-aligned submicron Schottky gates for GaAs IC's (7).

In this paper, detailed studies on the plasma etching characteristics and the electrical resistivities of sputtered Mo film deposited on GaAs substrates are described. Mo films were prepared by sputter deposition for good adhesion on GaAs substrates. As for Mo film patterning, a CF₄ + 5% O₂ plasma etching technique was adopted because of its superior etching controllability over wet etching.

It was found that the resistivity and etching rate of Mo film largely decrease with an increasing sputter

deposition rate. Lateral anisotropic characteristics were also found in the films deposited by intermittent deposition (ID). These resulted from rotating the substrate holding table in our film deposition setup, shown in Fig. 1.

To explain these facts, the structure of the sputtered Mo films and the effect of O₂ absorption were studied.

Experimental

Molybdenum films were deposited on semi-insulating (100) GaAs wafers with planar magnetron sputtering equipment. A diagram showing the substrate holding table and the sputter target is presented in Fig. 1. The Mo target was located off the rotating axis of the substrate holding table, and was 65 mm above the sample zone. The table rotated at speeds between 0 and 6 rpm. Target and table diameters were 10 cm

Key words: films, metals, integrated circuits, etching.

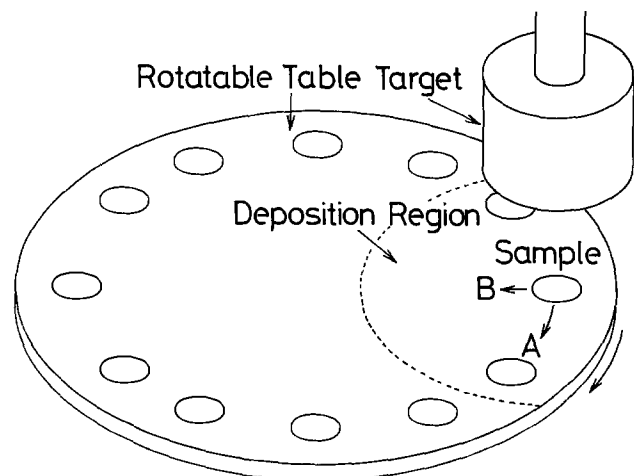


Fig. 1. A bird's eye view of planar magnetron sputter deposition equipment.

and 35 cm, respectively. The depositing area was 3 times larger than the Mo target, that is, about 30 cm diam. Argon pressure during film deposition was set at 4×10^{-3} torr. RF or dc power was applied to the target. The thickness of the Mo films prepared was about $0.3 \mu\text{m}$.

When the table was rotated during deposition, Mo film was deposited intermittently on the substrate, because the substrate repeatedly passes the deposition region (ID Mo). When the table was stationary and the substrate was fixed under the target, Mo was deposited on the substrate surface continuously (CD Mo). To clarify further explanations, axes A and B are defined with respect to the table rotating and radial directions, respectively, as shown in Fig. 1.

The Mo films were etched by $\text{CF}_4 + 5\% \text{O}_2$ plasma in a barrel-type etcher with an Al etch tunnel. Etching pressure and power were 0.3 torr and 50W, respectively. Under these conditions, GaAs substrates were not etched. The amounts of the Mo etched in both depth and side directions were measured by Talystep and SEM, respectively. Using Mo stripes $3 \mu\text{m}$ wide and $832 \mu\text{m}$ long, which were delineated by ion milling, Mo film resistivities were measured in the A and B directions. Molybdenum film structures were examined by SEM and x-ray diffraction. Oxygen absorption was measured by Auger electron spectroscopy.

Results

Plasma etching characteristics.—Molybdenum film etching rates vs. sputter deposition rates are shown in Fig. 2. Table I lists the sample preparation conditions used throughout this study. In the case of ID films, deposition rates indicate average deposition rates defined by a ratio of the film thickness to the total deposition time including nondepositing intervals. The ID cases are shown on the left of the dashed division line in Fig. 2; the CD cases are shown on the right. From these results, the following characteristics can be stated: (i) vertical depth etching is faster than side etching in all cases; (ii) in the case of ID Mo films, side etching in direction B is faster than in direction A;

Table I. Sample preparation conditions

No.	Sputter power	Deposition mode	Table rotation speed	Deposition rate
1	dc 150W	Intermittent deposition (ID)	6 rpm	123 A/min
2	RF 500W			145 A/min
3	dc 335W			245 A/min
4	dc 720W			442 A/min
5	dc 150W	Continuous deposition (CD)	0 rpm	700 A/min
6	RF 500W			870 A/min
7	dc 335W			1400 A/min

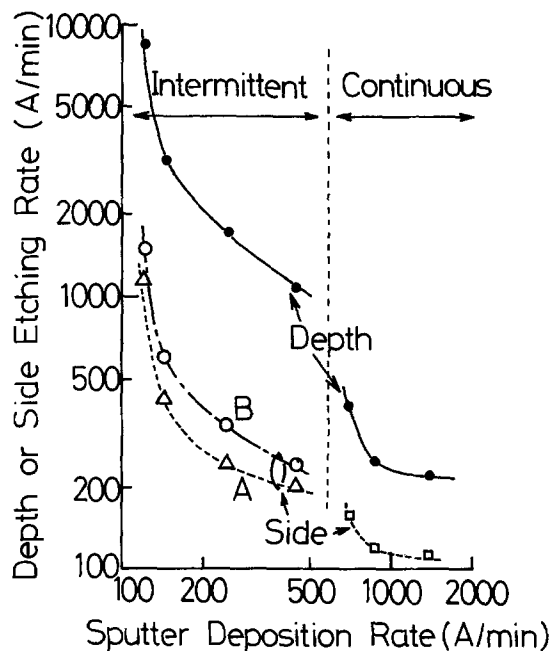


Fig. 2. Relation between etching rates and sputter deposition rates for sputtered Mo films. The deposition rate for the ID Mo films indicates the average deposition rate defined by the ratio of film thickness to total deposition time. Etching rates for CD Mo films are on the right of the dashed division line; etching rates for ID Mo films are on the left. A and B indicate side etching rates in the directions A and B, respectively. For sample preparation conditions, see Table I.

(iii) both vertical and side etching rates decrease rapidly with increasing sputter-deposition rates and are independent of RF and dc power sources.

It may be noted that the etching characteristics are discontinuous between the ID and the CD cases. When parameters a , b , and c are defined as: $a = (\text{vertical etching rate})/(\text{side etching rate along A direction})$; $b = (\text{vertical etching rate})/(\text{side etching rate along B direction})$; $c = a/b$, the differences on the etching properties are represented by these parameters. Here, $a = 6.9$, $b = 5.2$, $c = 1.3$ for the ID cases, and $a = b = 2.2$, $c = 1$ for the CD cases. This suggests an abrupt change in Mo film structure between the ID and CD Mo films.

Different edge shapes between ID and CD line patterns delineated by plasma etching also were observed by SEM, as shown in Fig. 3. In the ID Mo films, edge shape is anisotropic. That is, the line edge parallel to direction A shows many deep notches (Fig. 3a), and the line edge parallel to B is smoother (Fig. 3b). In the CD Mo films, the line edge has neither anisotropic shapes nor notches (Fig. 3c).

Another difference between etching characteristics for these two mode films was observed in SEM photographs shown in Fig. 4. In the case of ID Mo films, isolated columnar crystal grains were observed in a slightly etched film (Fig. 4a). In the case of CD Mo film, such columnar grains are not seen in a slightly etched film; the film seems to be uniformly etched (Fig. 4b).

These observations about the pattern edge shapes and the slightly etched surfaces suggest that ID Mo films have some irregular grain structure while CD Mo films have uniform grain structure.

Electrical resistivity.—Figure 5 shows resistivities for both ID and CD Mo films as a function of the sputter deposition rates. The resistivities for the ID Mo films show anisotropies similar to the side etching rates as presented with two separate curves on the left of the dashed division line in the figure. The resistivities for the CD Mo films are shown on the right of the dashed division line. From Fig. 5, it is also clear

that for both CD and ID cases film resistivity decreases with increasing film deposition rate.

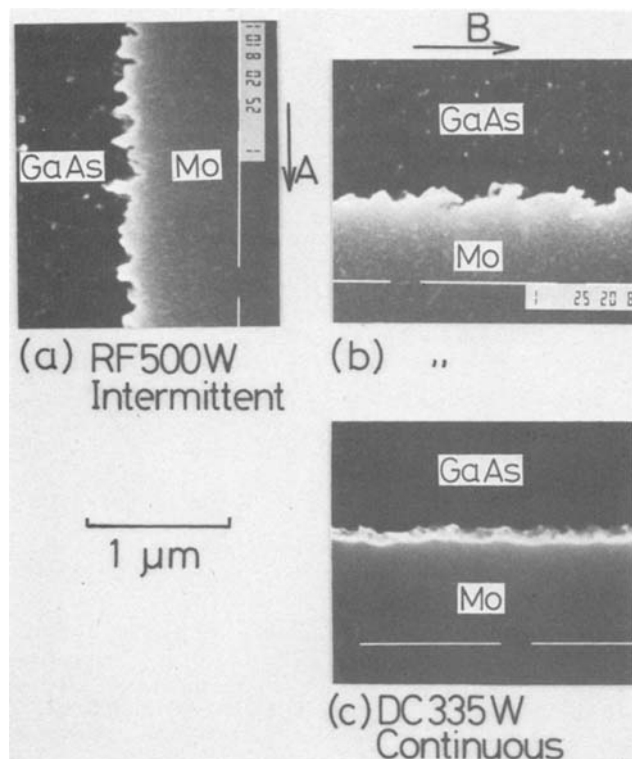


Fig. 3. SEM photographs of pattern edge shapes for Mo films etched with a photoresist masking. The photoresist has been removed. (a) and (b) are pattern edges parallel to directions A and B for the same intermittently deposited Mo film, respectively; (c) is the pattern edge of the continuously deposited Mo film. Sample preparation conditions: (a) and (b) ID, RF 500W, 6 rpm, 145 Å/min; (c) CD, dc 335W, 1400 Å/min.

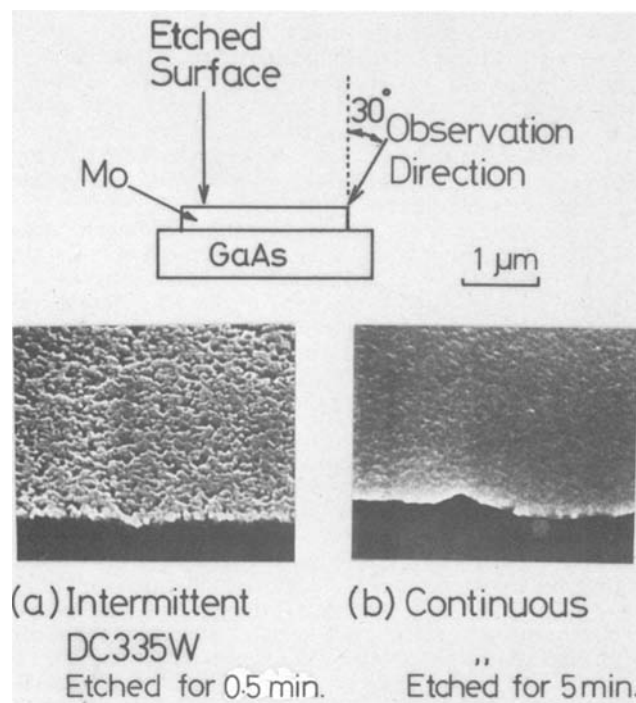


Fig. 4. SEM photographs of Mo films' slightly etched surfaces. (a) Intermittently deposited Mo film, (b) continuously deposited Mo film. Sample preparation conditions: (a) ID, dc 335W, 6 rpm, 245 Å/min; (b) CD, dc 335W, 1400 Å/min.

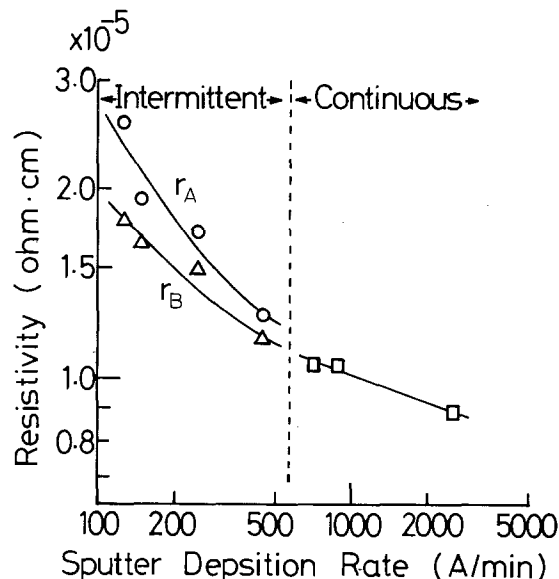


Fig. 5. Electrical resistivities vs. sputter deposition rates. r_A and r_B are resistivity values in directions A and B, respectively. Resistivities of the continuously deposited Mo films are isotropic. For sample preparation conditions, see Table I.

Discussion

Structural anisotropy of Mo films.—To investigate the cause of the anisotropies observed in side etching rates and electrical resistivities of the ID Mo films, more precise analyses were performed. First, x-ray diffraction was measured. A clear and large intensity peak of x-ray diffracted by (110) crystal planes of Mo and small peaks diffracted by other crystal planes such as (211) were observed for all Mo films studied. Figure 6 shows intensity ratios $I_{(211)}/I_{(110)}$ vs. sputter deposition rate. The CD Mo films are better ordered in the (110) direction, while the ID Mo films include many (211) directed grains (the fully disordered value of $I_{(211)}/I_{(110)}$ is 0.39 from ASTM).

The table rotation was first suspected to cause these anisotropies. Figure 7 shows plots of resistivities r_A , r_B and the ratio of r_A/r_B vs. rotation speed. The results show that the table rotation speed does not affect the anisotropies. Consequently, another possible cause of the anisotropy, the oblique angle between the incident Mo particles and the substrate surface, was investigated.

Experiments to investigate the oblique angle deposition effect were set up, as shown in the inset in Fig. 8. In the experiment, the substrates were tilted from

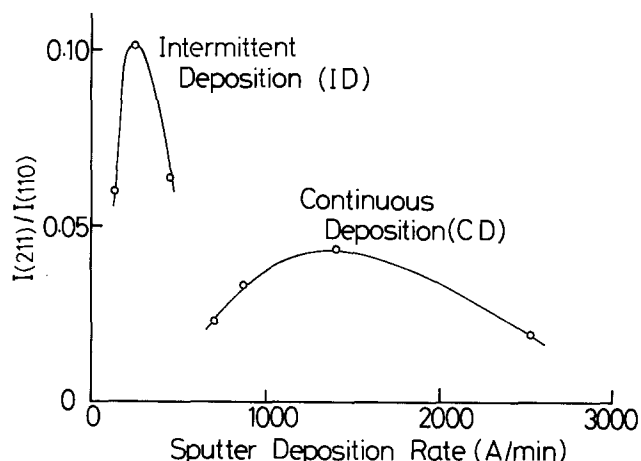


Fig. 6. Ratios of $I_{(211)}$ to $I_{(110)}$ vs. sputter deposition rates, where $I_{(211)}$ and $I_{(110)}$ are diffracted x-ray intensities from (211) and (110) crystal plane of molybdenum, respectively. For sample preparation conditions, see Table I.

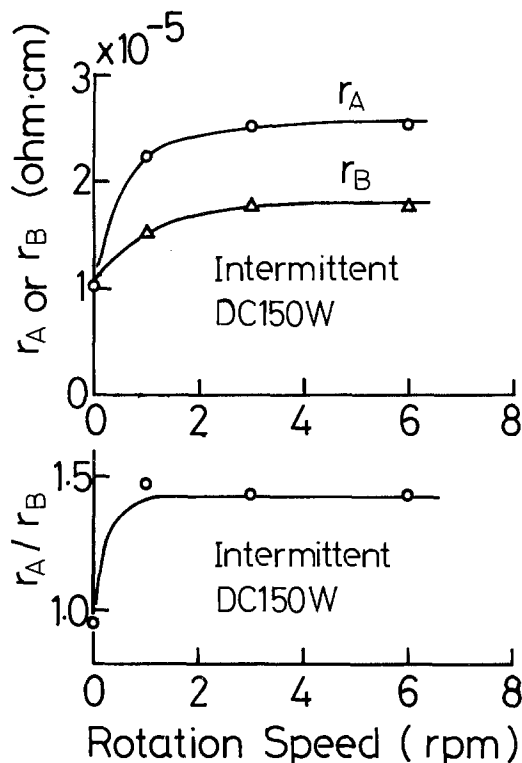


Fig. 7. Dependences of intermittently deposited Mo film resistivities r_A and r_B and ratio r_A/r_B on table rotation speed. Sample preparation condition: ID, dc 150W, 123 Å/min.

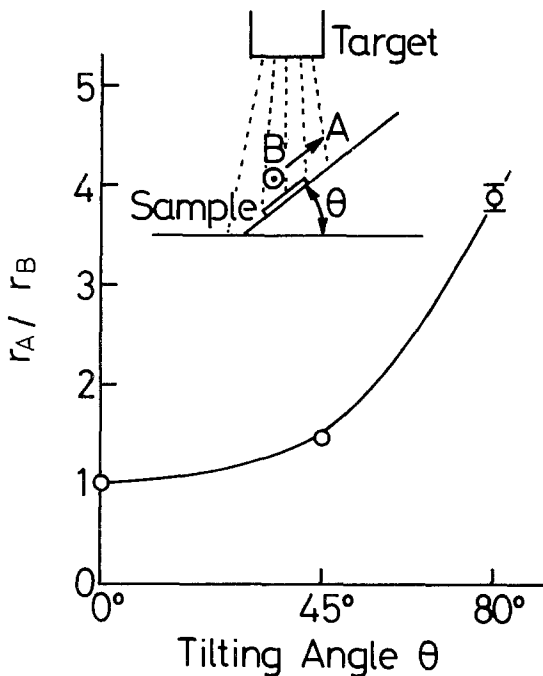


Fig. 8. Anisotropic resistivities of Mo films continuously deposited on a tilted GaAs substrate. Plot shows r_A/r_B vs. tilting angle θ . The directions A and B are the same as in Fig. 1, at 0 degrees. Sample preparation condition: CD, dc 335W.

0 to 80 degrees, and Mo was deposited with CD mode. The resistivities r_A and r_B of the Mo films were measured along the slope direction A and the direction B perpendicular to the direction A, respectively. They are plotted vs. tilting angle in Fig. 8. The marked anisotropy can be seen. The ratio r_A/r_B increases prominently with the tilt angle increase.

This anisotropy was found to be induced by structural anisotropy of the film. Figure 9 shows SEM photographs of the 70° tilt-angle deposited Mo film.

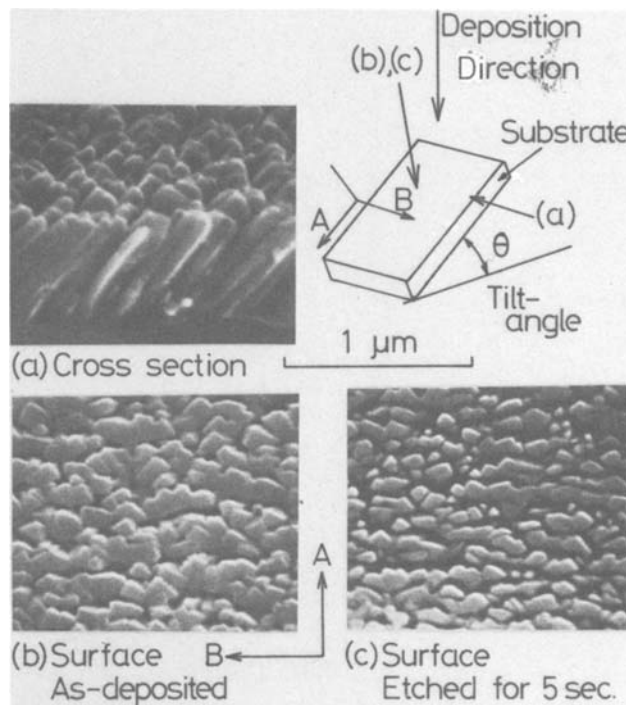


Fig. 9. SEM observations for anisotropic film structure of a tilt-angle deposited Mo film. Tilt angle is 70° . (a) Cross section parallel to direction A, (b) surface of the as-deposited film observed from deposition direction, (c) the Mo film surface etched for 5s, observed from the deposition direction. Sample preparation condition: same as in Fig. 8.

Columnar crystal grains growing toward the depositing direction are seen in Fig. 9a, which shows a cross section along the A direction. The photographs in Fig. 9b and 9c are viewed from the vertical direction of the film surface. Figure 9b shows an as-deposited surface and Fig. 9c shows a surface etched by plasma for 5s. The anisotropic grain structure is clearly observed. The grains have a tendency to grow faster in the B direction and slower in the A direction, resulting in a platelet-like grain. This platelet-like grain shape causes anisotropy in resistivity of the tilt-angle deposited Mo film. Furthermore, fast grain boundary etching is evident in Fig. 9c, which shows a deep grain boundary, which resulted after only 5s of plasma etching, and grains isolated from each other. The notched edges shown in Fig. 3 also related well with these anisotropic grain shapes.

In the real film deposition, when the divergent projection of the sputtered Mo particles is taken into account, as illustrated in Fig. 10, the substrates on the rotating table were subjected to the tilted state repeatedly. Consequently, oblique deposition can be reasonably viewed as the cause of the anisotropy of the intermittently deposited films.

Oxygen enhanced etching at Mo grain boundaries.— It has been reported (5) that EB-evaporated Mo film consists of columnar crystal grains, and that its electrical resistivity is affected strongly by oxygen content in grain boundaries. It is felt that sputtered Mo films also include oxygen in grain boundaries, and that the percentage of oxygen affects their resistivities. ID Mo films are expected to contain more oxygen than CD Mo films because of oxygen absorption during nondeposition intervals. This speculation is consistent with larger resistivities for ID Mo films as shown in Fig. 5. Furthermore, the additional oxygen absorption in ID cases is confirmed by AES analysis. Figure 11 shows Auger profile data on O_2 contents for an ID Mo film. The depth profile of O_2 is wavelike. The wavelength for the O_2 signal just coincides with sputter deposited film thickness/rotation. The peaks of the profile indi-

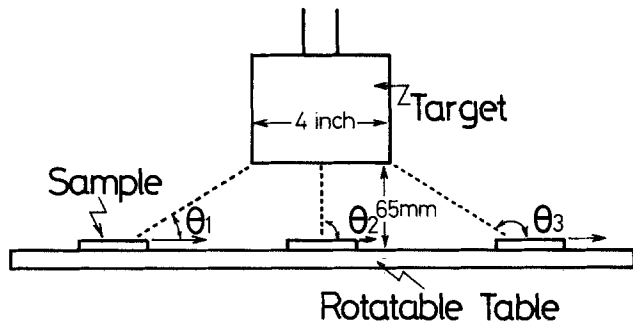


Fig. 10. Tilt angle deposition in the intermittent deposition. Tilt angle changes with the table rotation.

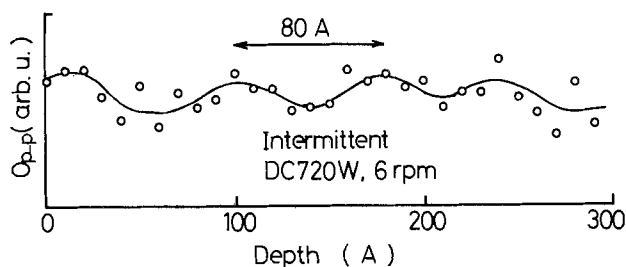


Fig. 11. Auger profile data on O_2 contents of the intermittently deposited Mo film. Sample preparation condition: ID, dc 720W, 6 rpm, 442 Å/min.

cate the presence of the additionally absorbed oxygen in the ID Mo film.

In order to verify the oxygen-enhanced etching phenomenon, oxygen annealed Mo films were prepared and etched. Figure 12 shows etching amounts vs. etching time for the CD Mo films, in their as-deposited state, annealed at 460°C for 3 min each in N_2 or H_2 atmosphere (line 1), and annealed in O_2 atmosphere (line 2). The CD Mo films annealed in N_2 or H_2 atmosphere exhibit the same etching rate as that of the as-deposited sample. However, for the CD Mo films annealed in O_2 atmosphere, a surface layer $\cong 1000\text{Å}$ thick was etched with the same rate (5200 Å/min) as that of the ID films. These results seem to support the possibility that oxygen absorbed in the grain boundaries of Mo film during the deposition periods accelerates the CF_4 plasma etching rate, especially in the ID Mo films.

Conclusions

Plasma etching and electrical resistivity characteristics for sputtered Mo films were studied. Both etching rate and resistivity depend largely on deposition rate. Anisotropies in both characteristics, which were

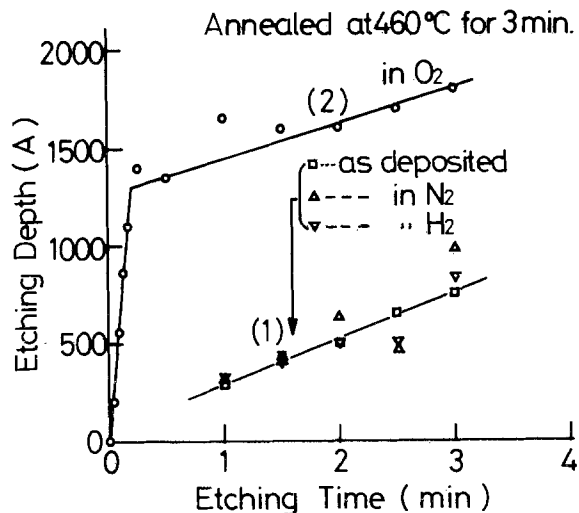


Fig. 12. Etching characteristics of continuously deposited Mo films annealed in various atmospheres. (1): as-deposited and annealed in N_2 or H_2 flow. (2): annealed in O_2 . Sample preparation condition: CD, dc 335W, 1400 Å/min.

observed in the intermittently deposited Mo films, are the results of the oblique incident-angle deposition and the oxygen absorption at grain boundaries.

Acknowledgment

The authors wish to express their gratitude for the useful discussions with Mr. K. Kurumada and Dr. M. Ohmori and encouragement from Drs. Y. Kato and Y. Suemune.

Manuscript received Feb. 14, 1983; revised manuscript received June 13, 1983.

The Nippon Telegraph and Telephone Public Corporation assisted in meeting the publication costs of this article.

REFERENCES

1. D. M. Brown, W. E. Engeler, M. Garfinkel, and P. V. Gray, *This Journal*, **115**, 874 (1968).
2. H. Oikawa, T. Wada, and T. Amazawa, *Rev. Electr. Commun. Lab.*, **24**, 407 (1976).
3. T. Mano, K. Takeya, K. Kiuchi, T. Ogawa, and K. Hirata, ISSCC Dig. Tech. Paper, 234 (1980).
4. S. D. Mukherjee, D. V. Morgan, and M. J. Howes, *J. Vac. Sci. Technol.*, **16**, 138 (1979).
5. H. Oikawa, *ibid.*, **15**, 1117 (1978).
6. M. Oda and K. Hirata, Proceedings of The Second Symposium on Dry Processes, 87, Oct. (1980).
7. M. Suzuki, K. Asai, and K. Kurumada, IECCE Japan, ED82-46, 77 (1982).

High Concentration Sb Diffusion into Silicon Using Auxiliary Wafers and Optimum Conditions

Mitsuo Nanba and Hirotsugu Kozuka

Hitachi Limited, Central Research Laboratory, Kokubunji, Tokyo 185, Japan

Shuichi Nakamura

Hitachi Limited, Device Development Center, Kodaira, Tokyo 187, Japan

ABSTRACT

The optimum condition for Sb diffusion into silicon using a silicon wafer lapped with Al_2O_3 powder and a sapphire wafer as an auxiliary wafer has been determined. To obtain higher Sb concentrations—as high as the solid solubility of Sb into silicon—the Sb_2O_3 vaporized source concentration has to be kept over 0.4 mol percent (m/o) during diffusion. A nonoxidizing atmosphere and a small distance between the diffusion and auxiliary wafers are desirable. Although sheet conductance obtained by utilizing a lapped silicon wafer depends on the number of uses it has, that obtained by the sapphire wafer is independent of use number. When Al_2O_3 is present on the diffusion wafer beforehand, the diffusion concentration increase is similar to that with the auxiliary wafers with Al_2O_3 on their surface. The process presented here has no effect on phosphorus impurity diffusion. The solubility change of elemental Sb in the multicomponent glass film grown on the diffusion wafer is presented to explain the higher Sb concentration when Al_2O_3 is present.

In bipolar IC fabrication, Sb-buried layers are more effective than As-buried layers for lowering auto-doping from the buried layer during epitaxial growth (1). However, two problems remain in conventional Sb-diffusion processes. One is diffusion-induced defects such as erosions (2, 3), which hinder normal epitaxial growth and decrease device yield. The other is difficulty in obtaining high carrier concentrations at the surface of the diffused layer (4). Although SbCl_3 and $\text{Sb}(\text{C}_2\text{H}_5\text{O})_3$ have been proposed as dopant sources to avoid the former problem, the latter problem has yet to be resolved (5).

Recently, a new Sb-diffusion technique that avoids both these problems has been presented (6-8). This new technique uses auxiliary silicon wafers lapped with Al_2O_3 powder. Diffusion wafers in this method are set face to face with auxiliary wafers in an open-tube system using Sb_2O_3 . The behavior of the new diffusion process has already been investigated, and it has been confirmed that the effect of the auxiliary wafer on Sb diffusion was due to the presence of the Al_2O_3 on its wafer surface (9).

However, the effects of the auxiliary wafer and diffusion conditions have not yet been explained. These conditions include dopant-source concentration, diffusion atmosphere, diffusion temperature, and so on. This work describes optimum conditions and the diffusion mechanism for this new diffusion technique.

Experimental Procedures

Sample preparation.—Diffusion silicon wafers employed in this study were Czochralski-grown (CZ) (100) oriented, p-type with a resistivity of 10-30 Ω -cm. Four different types of auxiliary wafers were prepared. Auxiliary wafers in the first group were silicon wafers polished with no. 1200-1500 Al_2O_3 . Those in the second, third, and fourth groups were wafers deposited with chemical vapor deposition (CVD) Al_2O_3 film (about 50-100 nm thick), wafers implanted with a dose of 1×10^{15} Al^+ ions/ cm^2 at 47 keV, and sapphire single-crystal wafers.

When auxiliary wafers of the first group were utilized, the sheet conductance (σ_s) of the diffusion wafer depended on the number of uses of the auxiliary wafers. Therefore, the wafers of these groups were changed every experiment unless specifically designated.

Key words: glass, solubility, mass spectroscopy.

Diffusion was performed through a two-zone furnace system, as shown in Fig. 1. Dry nitrogen was used as a carrier gas. To investigate σ_s dependence on an oxidizing atmosphere, a little dry oxygen gas was mixed into the nitrogen gas. In the first furnace zone, Sb_2O_3 powder was charged in a Pt boat and heated to either 750° or 800°C. In the second, diffusion and auxiliary wafers were set on a fused-silica holder at 1025°-1200°C. The distance d between the diffusion and auxiliary wafers was varied from 2 to 32 mm to determine the influence of d on σ_s .

To evaluate the applicability of our process to impurities other than Sb, phosphorus diffusion was carried out with liquid-source POCl_3 . The source liquid was maintained at 20°C. A large flow (3000 cm^3/min) of nitrogen was sent through the diffusion tube. During impurity deposition, a low flow (150 cm^3/min) of nitrogen was bubbled through the POCl_3 . A low flow of oxygen (50 cm^3/min) was mixed in to facilitate POCl_3 decomposition into P_2O_5 .

Sample analysis.—Concentration profiles of Sb in the diffusion wafers were obtained by a differential conductivity method (10). Sheet resistance (ρ_s) of the diffusion layer was measured with a four-point probe after the glass was etched away. The σ_s is obtained from the reciprocal of this ρ_s measurement. The concentration of Sb in the glass layer grown on the diffusion wafer was measured by ion microanalyzer (IMA). These

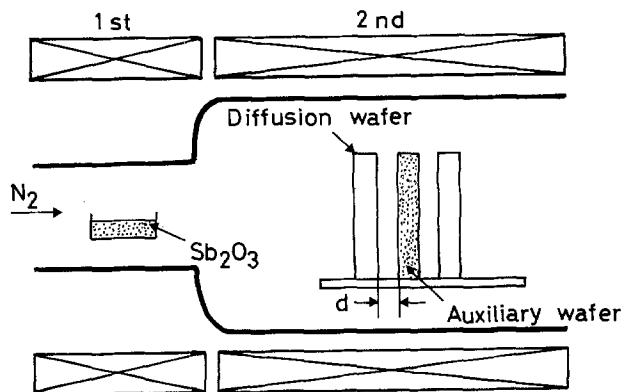


Fig. 1. Experimental apparatus. Diffusion was mainly executed at the condition of 2 mm for distance (d) between the diffusion and auxiliary wafers.

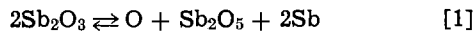
samples for IMA were sputter etched using 13 keV O^+ ions at a rate of about 6 nm/min. The glass thickness grown on the samples was measured by ellipsometry.

Results

Influence of dopant-source concentration.—The diffusion of Sb was carried out using both the new and conventional processes at Sb_2O_3 dopant-source concentrations in the carrier gas in the range of 0.1–1.0 m/o. In this new process, the silicon wafers polished with No. 1200–1500 Al_2O_3 were used for the auxiliary wafers. The glass layer grown on the diffusion wafers was measured by IMA. The relative intensity of ^{122}Sb in the layer is shown in Fig. 2. This intensity directly corresponds to its concentration. Accordingly, it becomes evident that glass concentration using conventional technique is proportionate to dopant-source concentration. However, the glass concentration in the new process varies at approximately the square of the dopant-source concentration. This suggests that the Sb glass-formation mechanism obtained by the new process differs entirely from that obtained by conventional processes.

The Rutherford backscattering (RBS) spectra for the diffusion wafer at 0.65 m/o of source concentration has already been reported (6). Sb yield in a glass layer obtained by this technique was about 10% of that obtained by conventional techniques. At the same source concentration in Fig. 2, it could be confirmed that the Sb concentration in a glass layer using the new technique is also about 10% of that obtained by the conventional one.

The thickness of the glass layer observed under dopant conditions similar to Fig. 2 is given in Fig. 3. In the glass layer, oxygen is formed by the reaction



Generally, the glass thickness is proportionate to the oxygen concentration. Therefore, if the chemical equilibrium Eq. [2] is formed

$$\frac{(O)(Sb_2O_5)(Sb)^2}{(Sb_2O_3)^2} = K \quad [2]$$

where K is equilibrium constant, the thickness is proportionate to the square root of Sb_2O_3 source concentration. This agrees with the experimental data of conventional method. However, although the thickness

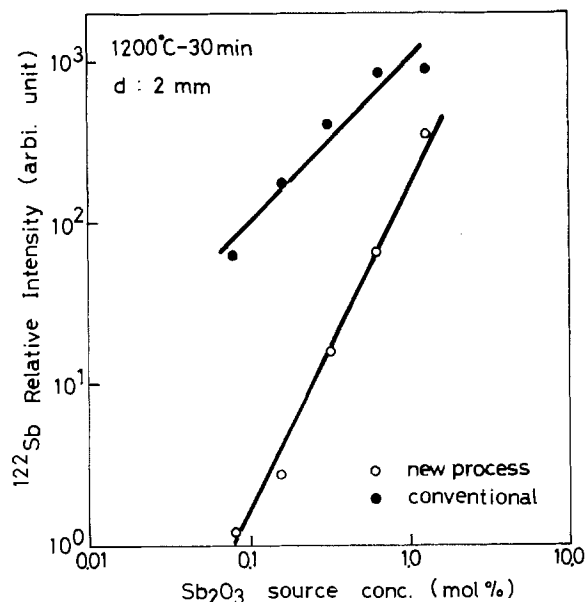


Fig. 2. Normalized ^{122}Sb intensity in the glass layer grown on the diffusion wafer vs. Sb_2O_3 source concentration. \circ and \bullet indicate the intensity obtained by the new and conventional processes, respectively.

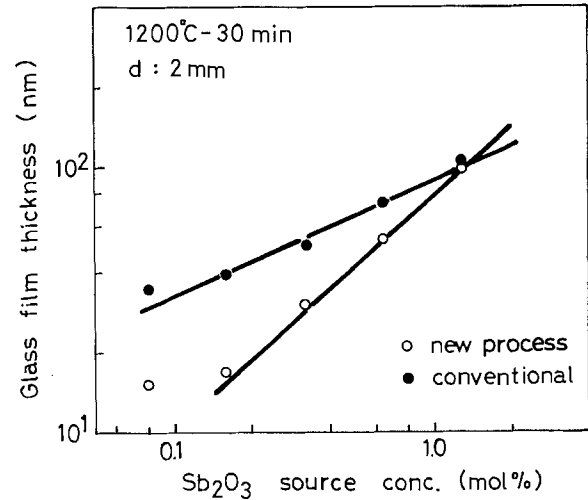


Fig. 3. Glass film thickness dependence on Sb_2O_3 source concentration.

obtained by the new process is proportionate to source concentration, this may be because the $(Sb)^2$ term of Eq. [2] is close to constant in the presence of Al_2O_3 in the glass layer on the diffusion wafer (9).

The relation of diffusion wafer σ_s and Sb_2O_3 source concentration are shown in Fig. 4. The σ_s using the new process strongly depends on source concentration. At a source concentration of less than 0.2 m/o, the technique has a negative effect on high concentration Sb diffusion. This is because σ_s 's obtained by the new process are lower than those obtained by a conventional one.

σ_s 's obtained by conventional processes are independent of those in the range 0.1–0.4 m/o, and slightly increase in the region over 0.4 m/o.

The reason σ_s in the new process rapidly decreased at source concentrations below 0.2 m/o is important in understanding the diffusion mechanism obtained from the new technique.

Diffusion under variant source concentrations.—The diffusion process described above was carried out at a constant-source concentration for the entire diffusion time. Here, to determine the dependence of diffusion behavior on time, this source concentration was controlled as shown in Fig. 5a.

The resultant surface concentration C_0 and carrier concentration profiles of the Sb diffusion layer are shown in Fig. 5b and Fig. 6. Distribution results labeled 15 min, 30 min, and 60 min in Fig. 6 correspond to diffusion time. The C_0 obtained by conventional processes is nearly constant during diffusion time. How-

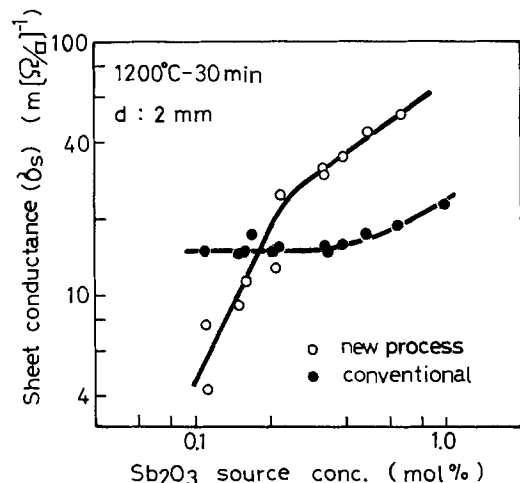


Fig. 4. Relation between σ_s and Sb_2O_3 source concentration

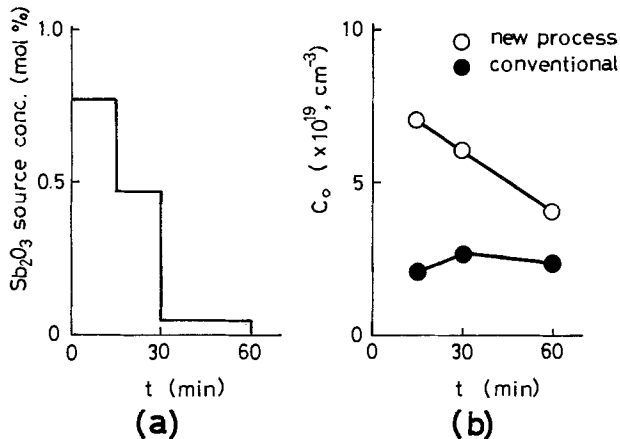


Fig. 5. Sb_2O_3 source concentration vs. diffusion time (a), and surface concentration C_o obtained by these source conditions (b).

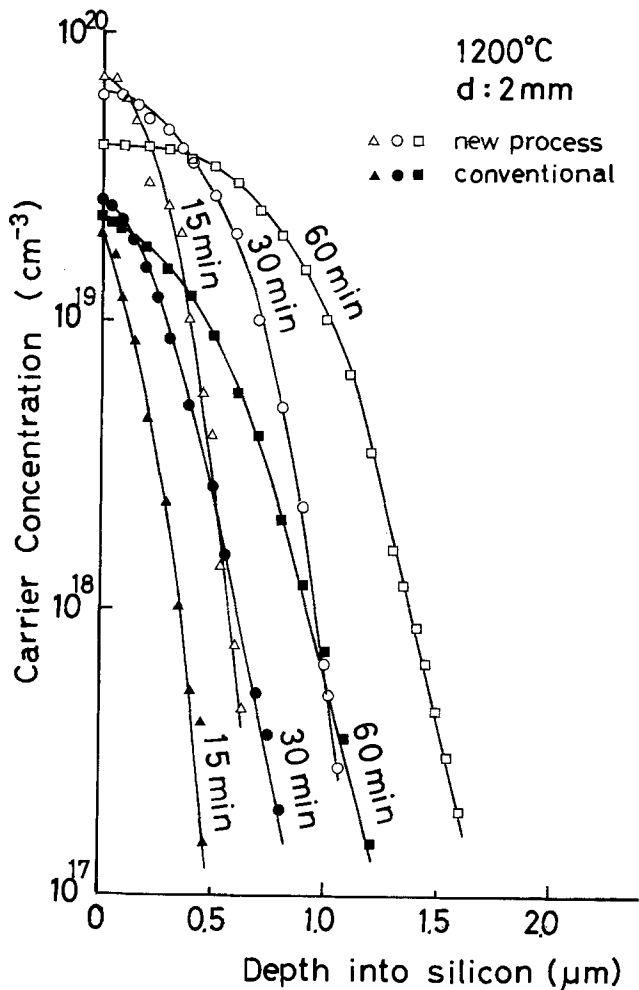


Fig. 6. Carrier concentration profiles obtained by the new (Δ , \circ , \square) and conventional (\blacktriangle , \bullet , \blacksquare) processes.

ever, the C_o in our process at 15, 30, and 60 min of diffusion time was 7.0×10^{19} , 6.0×10^{19} , and 4.0×10^{19} cm $^{-3}$, respectively. Large decreases in C_o occurred between 30 and 60 min. These correspond to the decrease of Sb_2O_3 source concentration from 0.47 to 0.05 m/o. Thus, it provides that diffusion in the new process is very sensitive to dopant-source concentration. Both constant-source concentration through the diffusion time and its being above 0.4 m/o are necessary for our process.

This may mean that the interface condition between the glass layer and silicon substrate with the new technique is affected by Sb_2O_3 concentration in the

gas phase. However, that obtained by conventional methods is stable and similar to the results shown in Fig. 4.

Effect of oxygen in the carrier gas.—An effect of oxidizing atmosphere is shown in Fig. 7. Even when the $O_2/(N_2 + O_2)$ ratio is changed to 0, 1, 2, and 4%, results obtained by conventional processes are approximately 14.9 m(Ω/\square) $^{-1}$ in all cases and hardly change. In contrast, σ_s obtained by the new process become 40.0, 31.3, 26.3, and 16.7 m(Ω/\square) $^{-1}$ at the respective ratios, and gradually decrease as the O_2 content increases.

A previous paper (9) reported that comparison of the Sb concentration at the silicon surface C_o with the Sb concentration at glass-silicon interface C_r for elemental Sb produced good results. Therefore, it was concluded that carrier concentration in silicon depended on the concentration of elemental Sb at the glass-silicon interface. From this point of view, it can be assumed that the C_r levels obtained by the new process decrease as oxygen increases. The reason for the C_r decrease is not clear. However, in our process there is no doubt that something effective for high-concentration Sb diffusion onto the diffusion wafer depends on several diffusion conditions.

Here the C_r of the conventional process cannot be high in comparison with that obtained by the new process, because the C_o obtained by the former process is lower than that obtained by the latter process, as shown in Fig. 6. On the contrary, the Sb concentration in the glass layer on the diffusion wafer in the conventional process is higher than that in the new process, as shown in Fig. 2. Thus, it should be considered that the Sb concentrations in glass layer are no relation to the C_r . The factors which determine the C_r will be described in another section.

Dependence on the diffusion temperature.—Let σ_s^p and σ_s^c be defined as the sheet conductance obtained by the new process and by conventional processes, respectively (6). The value $\sigma_s^p - \sigma_s^c$ should reveal the effect on Sb diffusion obtained by the new technique.

The relationship between vicinity distance d and the $\sigma_s^p - \sigma_s^c$ with diffusion temperature as a parameter is given in Fig. 8. Here, σ_s^c are 23, 3.1, 0.78, and 0.25 m(Ω/\square) $^{-1}$ at diffusion temperatures of 1200°, 1100°, 1050°, and 1025°C, respectively.

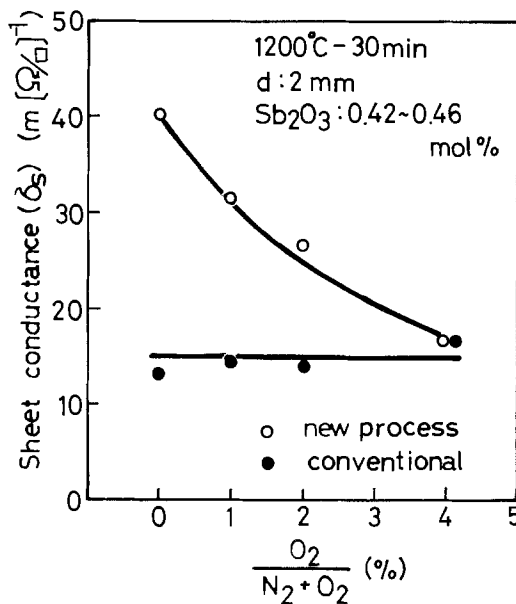


Fig. 7. Effect of oxygen content in nitrogen carrier gas on diffusion.

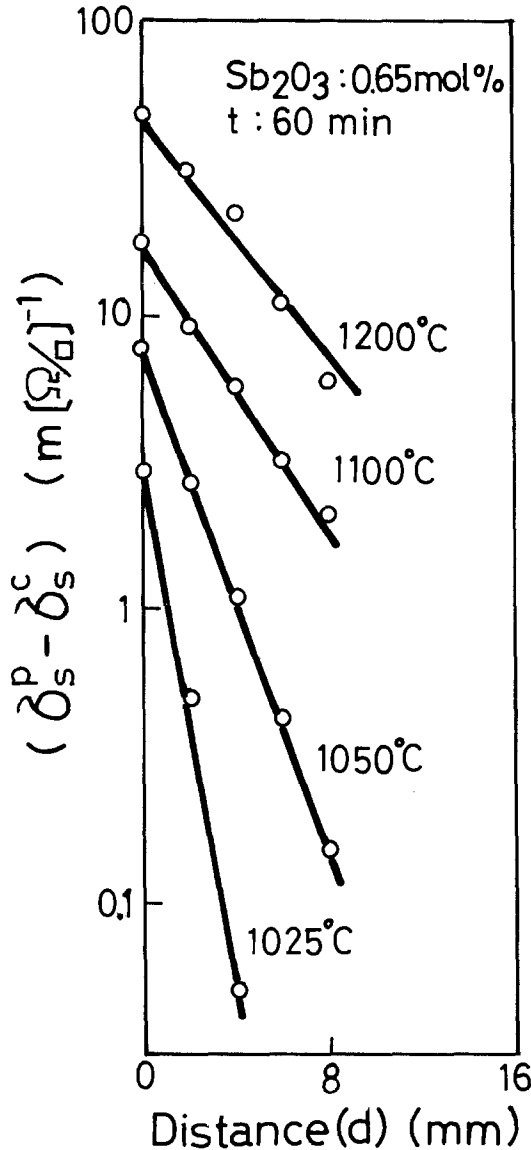


Fig. 8. The $(\sigma_s^p - \sigma_s^c)$ vs. d with diffusion temperature (1025°-1200°C) as a parameter. The σ_s^p and σ_s^c show σ_s obtained by the new and conventional techniques.

As distance d between the diffusion and auxiliary wafers becomes smaller, $\sigma_s^p - \sigma_s^c$ of the wafer increases remarkably. When distance d is about 6-8 mm or greater, the effect of the auxiliary wafer decreases drastically, and σ_s^p attained becomes identical to σ_s^c realized by conventional methods.

From the dependence of $\sigma_s^p - \sigma_s^c$ on diffusion temperature, it is known that distance d which is effective in our process decreases with diffusion temperature. The relation between $\sigma_s^p - \sigma_s^c$ and d in Fig. 8 is represented by

$$(\sigma_s^p - \sigma_s^c) = \sigma_{s0} \exp(-d/\lambda') \quad [3]$$

where σ_{s0} and λ' are functions of diffusion temperature and source concentration. σ_{s0} and λ' correspond to the increase in Sb amount created by the effect of the auxiliary wafer and mean free distance of the material diffused from the auxiliary wafer surface to the diffusion one.

The λ' values obtained from Fig. 8 are 4.3, 3.6, 1.9, and 1.05 mm for diffusion temperatures 1200°, 1100°, 1050°, and 1025°C, respectively. λ' should correspond to the diffusion length of activated species emitted from the surface of auxiliary wafer. The species are perhaps Al-Sb complex oxide.

Dependence upon distance d at various source concentrations.—At a source concentration under 0.2 m/o,

diffusion using the new technique has a negative effect on high-concentration Sb diffusion, as seen in Fig. 4. The d in that diffusion was 2 mm and smaller than λ' at 1200°C, as shown in Fig. 9. If d is larger than λ' , it is expected that σ_s attained with this new condition will differ from those attained with the former one. Therefore, the relationship between σ_s and d with source concentration as parameters were examined. The result is shown in Fig. 10. At a 0.17 m/o source concentration, σ_s obtained by the new process is also lower than that obtained by conventional processes. However, σ_s increases with d , and σ_s with a d of 32 mm is nearly equal to that obtained for the conventional processes.

In high and low source concentrations, the effects of the new process vary drastically as d decreases.

Comparison between Al_2O_3 -lapped wafer and sapphire.—When silicon wafers are lapped with no. 1200-1500 Al_2O_3 as the auxiliary wafer, σ_s of the diffusion wafer depends on the number of uses of the auxiliary wafer. Therefore, these wafers were changed every experiment. To clarify the role of the auxiliary wafer in the diffusion runs, these wafers were not changed; they were used sequentially.

Variation of σ_s obtained with these polished silicon wafers is shown in Fig. 11 by \circ . In this figure, the σ_s variation obtained with the sapphire single-crystal wafers as an auxiliary wafer is denoted by Δ . Compared with σ_s obtained by Si and sapphire wafers, it becomes clear that in practical use the latter auxiliary wafer is more useful than the former. Therefore, the result shows that Al_2O_3 is effective for Sb diffusion.

With the decrease of σ_s obtained by sequential use of the Al_2O_3 lapped wafer, it is assumed that the Al_2O_3 on the surface of the auxiliary wafer is diffused out during the diffusion procedure (9). Hence, the Al_2O_3 concentration reached on the diffusion wafer is lower than that which could contribute to higher concentra-

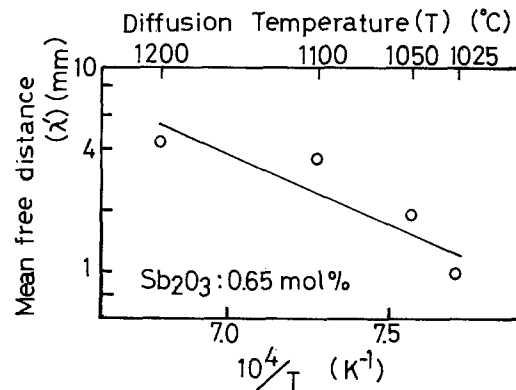


Fig. 9. Dependence of mean free distance λ' of the material out-diffused from the surface of the auxiliary wafer on diffusion temperature T .

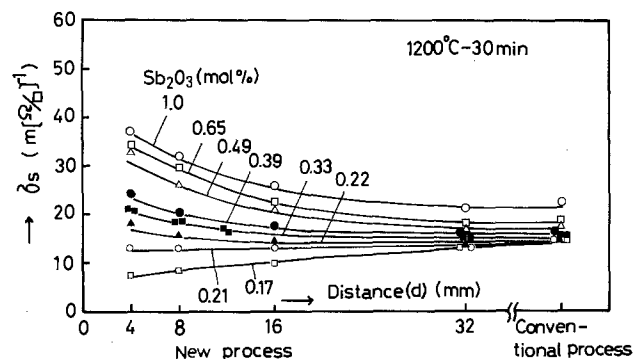


Fig. 10. σ_s dependence on d for the new process

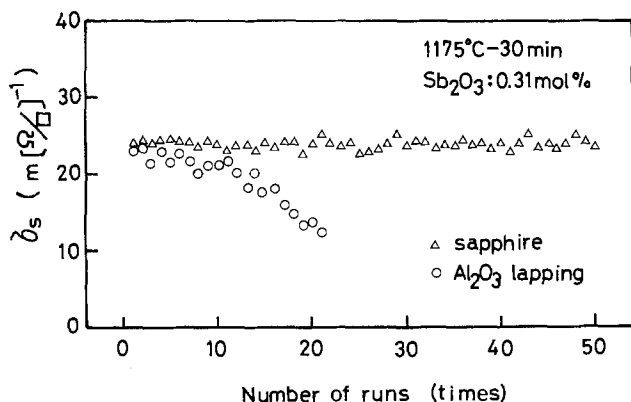


Fig. 11. Comparison of diffusion using Al_2O_3 -lapped wafer (\circ) and sapphire (\triangle) as auxiliary wafers.

tion Sb diffusion in the diffusion wafer, as shown in Fig. 11.

Diffusion in the auxiliary wafer itself.—The dependence of σ_s on the four different types of auxiliary wafers is shown in Table I. In this table, "Diffusion wafers" indicates that σ_s was measured for diffusion wafers utilizing four different types of auxiliary wafers, and "Auxiliary wafers themselves" shows that the σ_s was measured for the auxiliary wafer (CVD- Al_2O_3 , Al^+ implantation).

Since σ_s of "Diffusion wafers" are higher (46.08 – $54.95 \text{ m}[\Omega/\square]^{-1}$) than those obtained by conventional method ($16.64 \text{ m}[\Omega/\square]^{-1}$), it becomes apparent that all these auxiliary wafers bring desirable results. Such results confirm that the effect of the auxiliary wafer on Sb diffusion is due to Al_2O_3 presence on its surface (9), as seen in Fig. 11.

However, the σ_s of "Auxiliary wafers themselves" should be noted. The σ_s for " Al^+ implantation" is $40.82 \text{ m}(\Omega/\square)^{-1}$, and suitably high as compared with that obtained by conventional methods. Therefore, it is shown that the effect of Al (probably from the Al_2O_3 because of changes occurring during prethermal treatment for diffusion) presented on the diffusion wafer itself beforehand is similar to that of auxiliary wafers, which have Al_2O_3 on their surfaces. The σ_s for "CVD- Al_2O_3 " ($29.85 \text{ m}(\Omega/\square)^{-1}$) is not so large as those obtained by conventional methods. This takes in consideration the fact that CVD- Al_2O_3 film (about 50–100 nm thick) on the wafer acts as a diffusion mask during the initial period of diffusion.

Phosphorus diffusion using auxiliary wafers.—It is expected that the new process using auxiliary wafers may be useful in impurity diffusions other than Sb. However, the new process has no appreciable effect on diffusion with a phosphorus oxychloride (POCl_3) source, as is shown in Table II. This shows that the new process is useful for limited impurities. These are difficult to diffuse in a surface concentration as high as the

Table I. Sheet conductance (σ_s) obtained by the new and conventional techniques. In the new technique four different types of auxiliary wafers were used. Diffusion temperature, diffusion time, and distance (d) were 1200°C , 45 min, and 4 mm, respectively

Techniques		Sheet conductance σ_s ($\text{m}(\Omega/\square)^{-1}$)
Conventional		16.64
Diffusion wafers	New process (Used auxiliary wafers)	
	sapphire	54.35
	CVD- Al_2O_3	54.95
	Al_2O_3 lapping	52.36
	Al^+ implantation	46.08
Auxiliary wafers themselves	CVD- Al_2O_3	29.85
	Al^+ implantation	40.82

Table II. Sheet conductance of phosphorus-diffused layer using and without auxiliary wafer lapped with Al_2O_3 powder

Impurity	Conditions	Sheet conductance σ_s ($\text{m}(\Omega/\square)^{-1}$)	
		New process	Conventional
Phosphorus	900°C 30 min	44.3–48.1	47.6–50.3
	990°C 30 min	155.0–168.1	163.9–172.4
	1100°C 30 min	498.2–434.8	434.8–469.5

solid solubility (12). Our phosphorus diffusions were executed at high concentration conditions as described, in the section on experimental procedure. Further investigation will be necessary at the lower flow ($<150 \text{ cm}^3/\text{min}$) condition of nitrogen bubbled through the POCl_3 .

Discussion

It was confirmed that σ_s obtained by the new technique rapidly decreased at dopant-source concentrations below 0.2 m/o, and became lower as compared with that obtained by the conventional technique (Fig. 4). However, in such low dopant-source concentrations, if d between the diffusion and auxiliary wafers was increased, σ_s obtained by our technique was increased to as much as that by the conventional technique, as seen in Fig. 10. Furthermore, the diffusion of the new process was dependent upon several diffusion conditions.

To obtain high concentrations of Sb diffusion with our process, source concentrations have to be kept as high as 0.4 m/o throughout the diffusion procedure. The σ_s obtained by the new process gradually decreased as O_2 content increased. However, continuous presence of Al_2O_3 on the auxiliary wafer was necessary for higher concentration diffusion. Results described above are too complex to discuss briefly. A similar phenomenon is not seen anywhere but in our reports (6, 9).

Here, the effects of elemental Sb can be assumed. Elemental Sb is created on the auxiliary wafer using Al_2O_3 and is emitted toward the diffusion wafer. When Sb diffusion is carried out at 1200°C for 30 min in a 0.65 m/o source concentration, the thickness of the glass layer obtained by conventional techniques ($\sim 71 \text{ nm}$) is roughly similar to that obtained by the new technique ($\sim 56 \text{ nm}$).

This glass should be produced according to a chemical reaction such as



If the glass layer is assumed to be twice that of the Sb atomic radii (1.45\AA), the layer obtained by our technique is 193 layers. Because the Sb atom concentration is $3.3 \times 10^{22} \text{ atoms/cm}^3$, the amount of elemental Sb per layer is about $1.0 \times 10^{15} \text{ atoms/cm}^2$. Therefore, the total formation amount of elemental Sb in the glass layer is high ($\sim 10^{17} \text{ cm}^{-2}$) and similar to that obtained by the conventional method. Consequently, it is difficult to justify that such high concentrations of elemental Sb at the interface are affected by the amounts of elemental Sb emitted from the auxiliary wafer. Another model is necessary.

For the above reasons, it is important for understanding our diffusion mechanism to know why surface concentrations obtained by conventional techniques are lower than those obtained by the new technique.

A large quantity of Al, probably Al_2O_3 , was detected in the glass layer grown in the diffusion utilizing an auxiliary wafer (9). The Al_2O_3 is transferred from the auxiliary wafer. This Al_2O_3 transfer is supported by the described results (Fig. 11).

At present, considerations, such as that the solid solubility of elemental Sb in the glass layer depends on the amount of Al_2O_3 present in the layer, most

naturally explain the diffusion mechanism obtained by the new process.

Here, the chemical reaction and transfer path of elemental Sb are as shown in Fig. 12.

When a Sb_2O_3 source is supplied, Sb_2O_3 reacts with the Al_2O_3 on the surface of the auxiliary wafer and produces $(\text{Al-Sb})\text{O}_x$.

The $(\text{Al-Sb})\text{O}_x$ is diffused toward the diffusion wafer by gas phase diffusion.

However, Sb_2O_3 reacts with Si (diffusion wafer) and produces SiO_2 and elemental Sb, as is seen in Eq. [4]. The SiO_2 forms a glass layer.

Elemental Sb is divided into four components. First is the component diffused into Si (Sb_A in Fig. 12). The second is that in glass (Sb_B). The third and fourth are those that diffused out into the gas phase (Sb_C), and that diffused into auxiliary wafers (Sb_D), respectively.

Thus, either by decreasing distance d (Fig. 8) or by increasing Sb_2O_3 source concentration (Fig. 4), the $(\text{Al-Sb})\text{O}_x$ amounts reached on the glass layer increase. Therefore, the elemental Sb concentration at the glass-silicon interface grows as the effect of the new process reveals.

At a low Sb_2O_3 source concentration, the Sb_2O_3 concentration in the glass layer becomes smaller. Therefore, elemental Sb concentration drops drastically (Fig. 4).

At a low Sb_2O_3 source concentration and at a small distance between the diffusion and auxiliary wafers, σ decreases more as compared to the conventional process, because Sb_2O_3 source is consumed by the auxiliary wafer (Fig. 10).

According to these considerations, the key in interpreting the diffusion mechanism may be the solubility change of elemental Sb in the multicomponent glass (SiO_2 , Al_2O_3 , Sb_2O_3 , and elemental Sb). However, to support this diffusion model, the effective concentrations of Sb_2O_3 and Al_2O_3 in the glass layer on the surface of the diffusion wafer will have to be revealed.

The optimum diffusion conditions for higher Sb concentration using the new process are shown in Fig. 13. The optimum conditions are the region divided by the definite concentration of the host (Sb_2O_3) and the assisting impurity concentration (Al_2O_3). At lower concentrations of both Sb_2O_3 and Al_2O_3 , the surface concentration of Sb diffusion obtained by the new process is lower than that obtained by the conventional one (Fig. 4, 10). When the host source and the assisting concentration increase, the surface concentration of the diffusion wafer increases to as high as the solid solubility of Sb in silicon. However, when these concentrations increase more, two problems result. One is

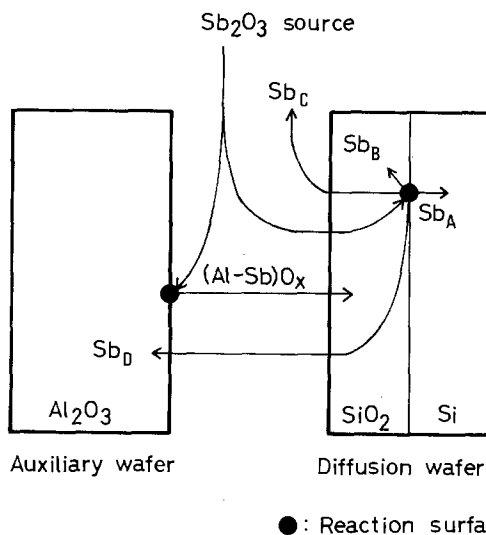


Fig. 12. Assumption of chemical reaction and transfer path of elemental Sb in the new diffusion process.

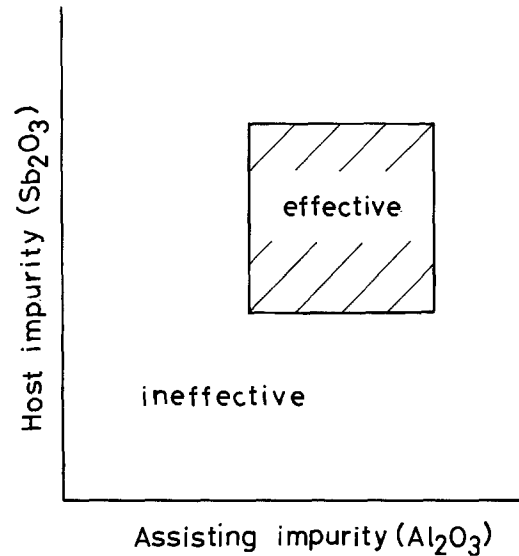


Fig. 13. Conception of optimum diffusion conditions for higher Sb concentration.

surface defects, such as surface erosion (2). The other is contamination by the assisting Al_2O_3 impurity.

Furthermore, in the diffusion described (6, 9), the only usable material is Al_2O_3 . However, it is expected that some other material might also prove usable, as shown in Fig. 13. Such details can be clarified in further investigations.

Conclusion

The optimum conditions for higher Sb diffusion into silicon with auxiliary wafers were clarified. The following results were obtained from the new diffusion process: 1. To obtain higher Sb concentration diffusion using an auxiliary wafer, Sb_2O_3 source concentration in a nitrogen carrier gas has to be kept as high as 0.4 m/o during the entire diffusion process.

2. When a very small amount of oxygen is mixed into the nitrogen carrier gas, the sheet conductance obtained by the new process decreased.

3. Both high Sb_2O_3 source concentration and a small distance between the diffusion and auxiliary wafers are effective in the new process.

4. Although the sheet conductance obtained by utilizing an Al_2O_3 -lapped wafer depends on the number of uses, that obtained by a sapphire wafer is independent of the number of uses.

5. When Al_2O_3 is present on the diffusion wafer beforehand, the effect of Al_2O_3 on Sb diffusion is almost the same as that of auxiliary wafers having Al_2O_3 on their surface.

6. The new process has no effect on phosphorus diffusion.

7. To explain diffusion behavior, solubility change of elemental Sb in the multicomponent glass is discussed.

Acknowledgment

We are indebted to Minoru Wada and Hitoshi Tsuyama for the concentration profile measurement and IMA analysis, respectively. We are also indebted to Dr. Kunihiro Yagi and Akira Shintani for their support in sample preparation and useful discussions.

Manuscript submitted May 16, 1983; revised manuscript received Aug. 2, 1983.

Hitachi Limited assisted in meeting the publication costs of this article.

REFERENCES

1. G. Mitsunashi, *NEC Res. Dev.*, **36**, 68 (1975).
2. A. LaRocque, R. Yatsko, and A. Quade, *This Journal*, **105**, 254C (1958).

3. A. Goetzberger, *Solid-State Electron.*, **5**, 61 (1962).
4. F. L. Gittler and R. A. Porter, *This Journal*, **117**, 1551 (1970).
5. W. R. Runyan, "Silicon Semiconductor Technology," p. 146, McGraw-Hill Co., New York (1965).
6. M. Nanba, *This Journal*, **128**, 420 (1981).
7. C. Munakata, M. Nanba, and S. Matsubara, *Jpn. J. Appl. Phys.*, **20**, L137 (1981).
8. C. Munakata, K. Yagi, T. Warabisako, M. Nanba, and S. Matsubara, *ibid.*, **21**, 624 (1982).
9. M. Nanba, H. Kozuka, and K. Usami, *Appl. Phys. Lett.*, **39**, 235 (1981).
10. E. Tannenbaum, *Solid-State Electron.*, **2**, 123 (1961).
11. C. S. Fuller and J. A. Ditzenberger, *J. Appl. Phys.*, **27**, 544 (1956).
12. F. A. Trumbore, *Bell System Tech. J.*, **39**, 205 (1960).

A Scanning Auger Electron Spectroscopic Study of Particulate Defects in Metallurgical-Grade Silicon

J. H. Thomas III,* R. V. D'Aiello, and P. H. Robinson*

RCA Laboratories, Princeton, New Jersey 08540

ABSTRACT

Metallurgical-grade silicon, used as a substrate material for low-cost epitaxial solar cells, purified by the heat-exchange method leaves some metallic particulate residue in the purified ingots. Scanning Auger electron spectroscopy has been used to elementally identify the particulate residue exposed in sections from purified ingots. Particle composition (V, Ti, Ni, Fe, Al, and C rich silicon) was found to be position sensitive within an ingot and to depend on the source of MG feedstock.

An alternate low-cost method of producing silicon solar cells uses commercial metallurgical-grade silicon as a substrate material (1). Various methods have been described to improve the quality of this silicon

such as the heat-exchange method (HEM) (1). In these studies (1), it was shown that residue contamination in the substrate produces defects in the epitaxial silicon layer and results in a lower cell yield. The composition, nature, and distribution of defects or impurities within a refined ingot is important to the characterization of the refining process as well as

* Electrochemical Society Active Member.
Key words: heat-exchange method, solar cells, metallic impurities.

INGOT 015 TE 9 DEFECT
SEM (60x)

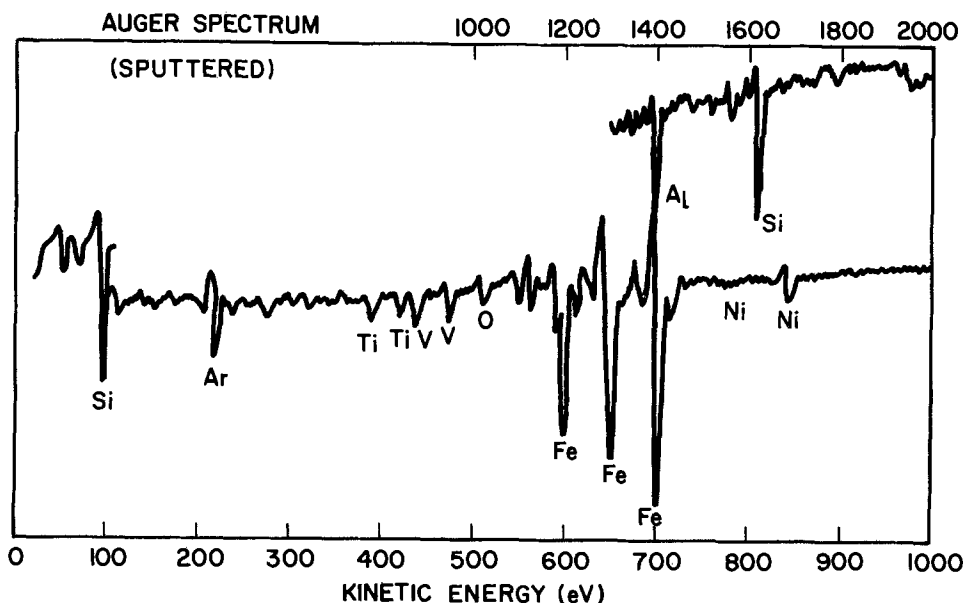


Fig. 1. Ingot 015. (Top) Micrograph of a typical defect (60 \times). (Bottom) Auger spectrum of this defect after sputtering 10 min.

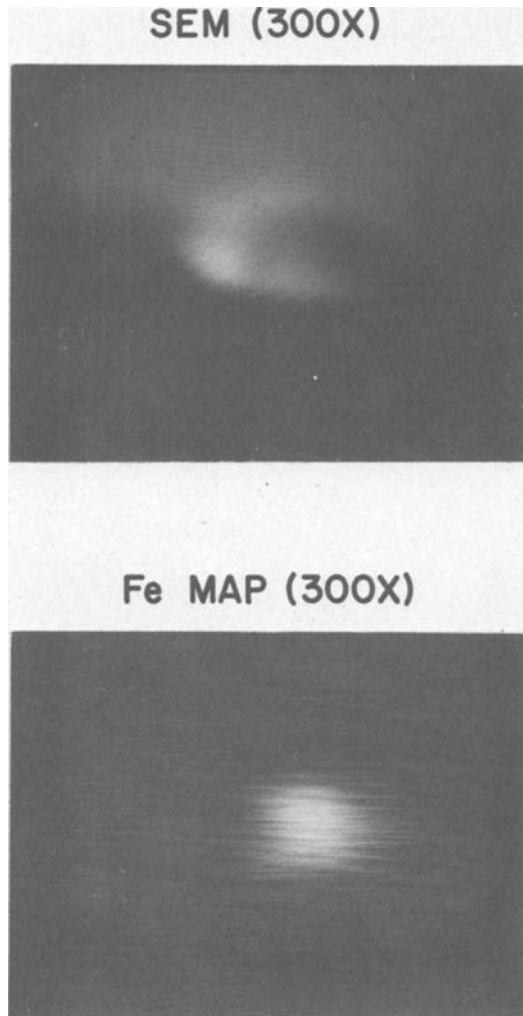


Fig. 2. Ingot 015. (Top) Micrograph of the defect in Fig. 1 at 300 \times . (Bottom) Fe Auger elemental map (300 \times) showing Fe distribution (after sputtering).

understanding the contamination of the epitaxial silicon layer.

Small beam Auger electron spectroscopy has been applied with considerable success to the characterization of solar cell materials (2-7). The general methodology of application is well established. However, surface studies using this technique must be viewed with caution, especially on topographically rough surfaces such as those encountered in this work (7). In this paper, results of an Auger electron spectroscopic study of defects in HEM refined metallurgical-grade silicon are presented. The elemental composition and compositional variations of particulate defects were studied with respect to their position in the ingot.

Sample Preparation

The details of silicon refinement using HEM are described elsewhere (1, 8). Ingots of Hanna Mining Company feedstock (8) (Ingot 015) and Silicon Smelters, Limited, South Africa feedstock (8) (Ingot 020) silicon were refined by double solidification using the heat-exchange method. Slabs were sliced from the top, middle, and bottom of the ingots to study the distribution of particles in the resolidified material.

The slabs of silicon were polish-etched in an HF:HNO₃(1:6) etchant (8). The silicon immediately surrounding defects near the surface of a slab etched faster than the "bulk" silicon, leaving a pit and exposing the surface of the defect at the bottom of the pit. Pits and defects vary from ~10 to 500 μm in diameter. Some defects are larger since they occur along

extensive grain boundaries. A total of six samples (top, middle, and bottom of Ingot 015 and Ingot 020) were studied by Auger electron spectroscopy.

Instrumental Approach

Scanning Auger microprobe (SAM) studies were performed using a Physical Electronics Industries Model 545 system equipped with a Physical Electronics Industries Model 20-015 rastered ion gun for sputter microsectioning samples in depth. This system maintains a base pressure of less than 3×10^{-10} torr. Sputtering was performed by backfilling the vacuum system to a static pressure of 5×10^{-5} torr argon. Argon sputter rates were about 50 $\text{\AA}/\text{min}$ (relative to Ta₂O₅) at 2 keV ion energy. Auger measurements and video display were performed at an electron beam potential of 3 keV using an electron beam current to give a beam size of about 10 μm FWHM. Spectra were obtained using processed modulation to the CMA in the derivative mode. Micrographs were obtained by measuring the sample absorbed current. Auger elemental maps were made by adjusting the spectrometer to a given elemental peak and using this analog signal to Z-modulate the monitor oscilloscope with raster position. Most mappings were obtained at a lock-in time constant with 20 ms and required 1 min per frame. Elemental line scans were obtained by scanning the electron beam in the X direction with Y = 0 (midpoint of the micrograph) and displaying the Auger intensity as Y modulation on the oscilloscope.

Metallic Defects

Figure 1 shows a typical defect from Ingot 015 (top) taken in the absorbed current mode at 60 \times ($E_e = 3$ keV). At this magnification, not much detail is observed. The defect appears as a mound (~100 μm diam) at the bottom of a shallow etch pit. Because of the intrinsic 5-10 μm resolution of this instrument, higher magnification does not yield any further detail. The majority of the defects studied were similar in appearance at this resolution. The electron beam size was sufficiently small so that the beam could be centered on the defect and Auger analysis performed at this point.

The crater region was sputter cleaned for 10 min removing about 500 \AA of material (relative to the sputter rate of Ta₂O₅) and an Auger spectrum of the defect was obtained. This spectrum is shown in Fig. 1 below the micrograph of the defect. The spectrum is displayed from 0 to 1000 eV for the lower trace and from 1000 to 2000 eV for the upper trace. The lower trace shows the elements Si, Fe, Ni, Ti, V, O, and Ar, and the upper trace shows Si and Al. This spectrum is qualitatively representative of most of the Auger spectra taken in this study. Two points must be made: (i) all the defects studied contain silicon as a major constituent and (ii) argon is observed as a result of implantation due to sputtering at 2 keV and will henceforth be ignored. Sputtering sequentially removes carbon contamination revealing an oxygen-rich surface. The most significant peaks aside from Si were Fe and Ni. Al, Ti, and V are observed under the oxide layer that measures perhaps 100 \AA thick. Further sputtering does not significantly change the spectrum as shown.

Semiquantitative analysis was performed by measuring the peak-to-peak signal intensities and applying tabulated elemental sensitivity factors as described in Ref. (9). This procedure yields a normalized surface composition of Si (50%), Al (16%), Fe (29%), Ni (2.5%), V (1.5%), Ti (1%), and O (1%) at a depth of 500 \AA . Data are accurate to within a factor of $\pm 30\%$. Therefore, the major constituents of this typical defect are Fe and Al in addition to Si. It is possible that conditions are favorable for silicide formation and the defect represents a combination of Fe_xSi compounds. This procedure is useful to determine qualitatively an ordering of elemental composition for a given signal strength. Unfortunately, true quantitative analysis is not possi-

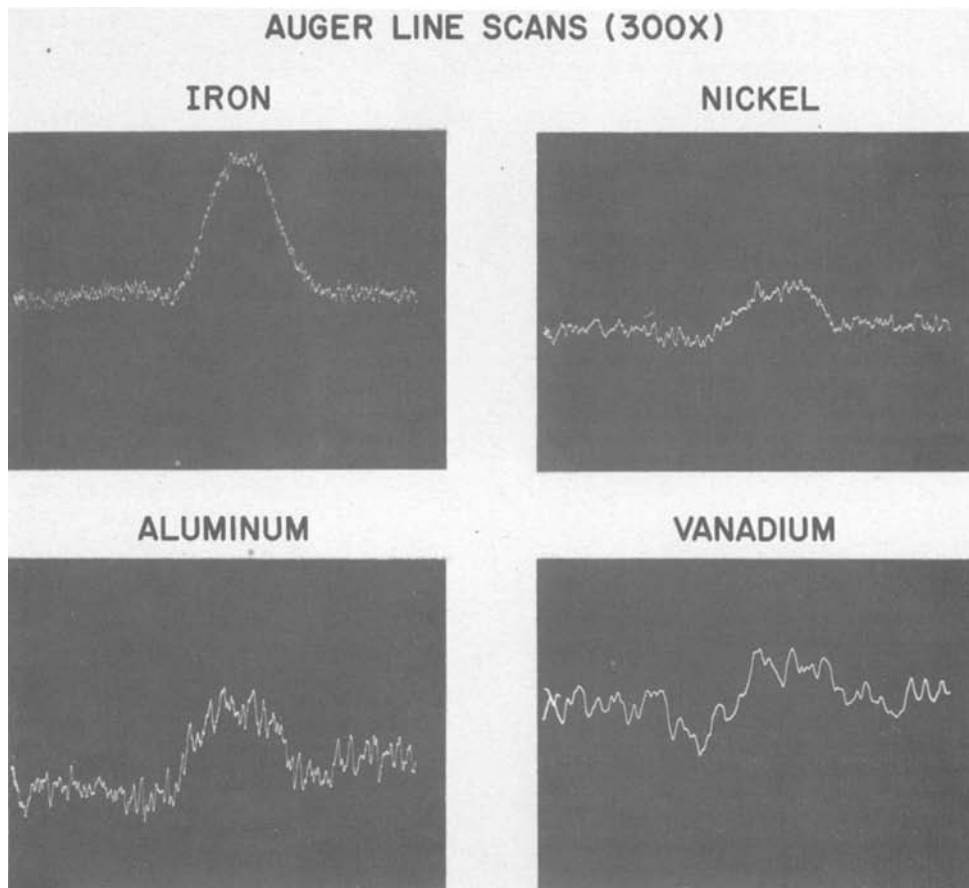


Fig. 3. Ingot 015. Auger elemental line scans are shown for Fe, Ni, Al, and V at 300X. Lines are taken at the midpoint of the 300X micrograph (Fig. 2).

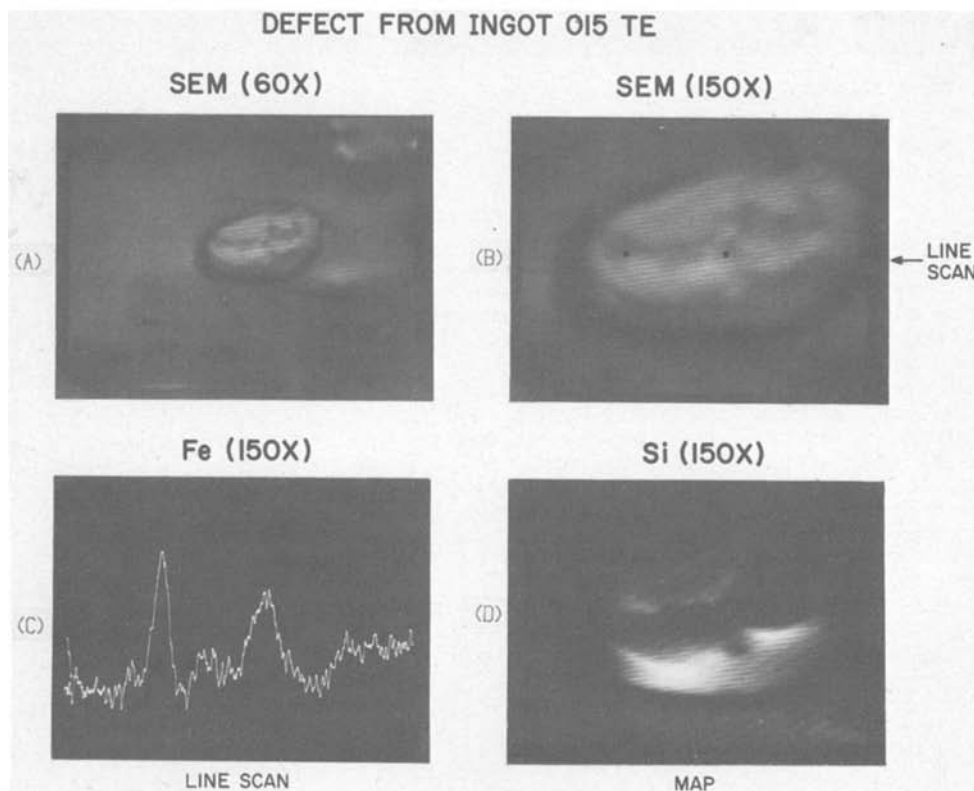


Fig. 4. Ingot 015 (top). (A) Micrograph of another defect (60X). (B) Same defect at (150X). (C) Fe line scan showing two prominent peaks [dots on micrograph (B)] due to topography. (D) Silicon Auger elemental map showing topographically enhanced features. Note the substrate is silicon.

ble due to surface topography effects that dominate the Auger signal intensity (10), in this case, of extremely rough defects at the bottom of etch pits. In addition, quantitative analysis requires a detailed knowledge of many other factors, e.g., preferential sputtering. This is beyond the scope of this study.

Figure 2 shows an absorbed current micrograph of the same defect at 300X. Immediately below the micrograph is shown the corresponding Fe Auger map. The Fe map was obtained by using the 702 eV LMM Fe transition (the most intense peak in the derivative spectrum). The most intense portion of the Fe map

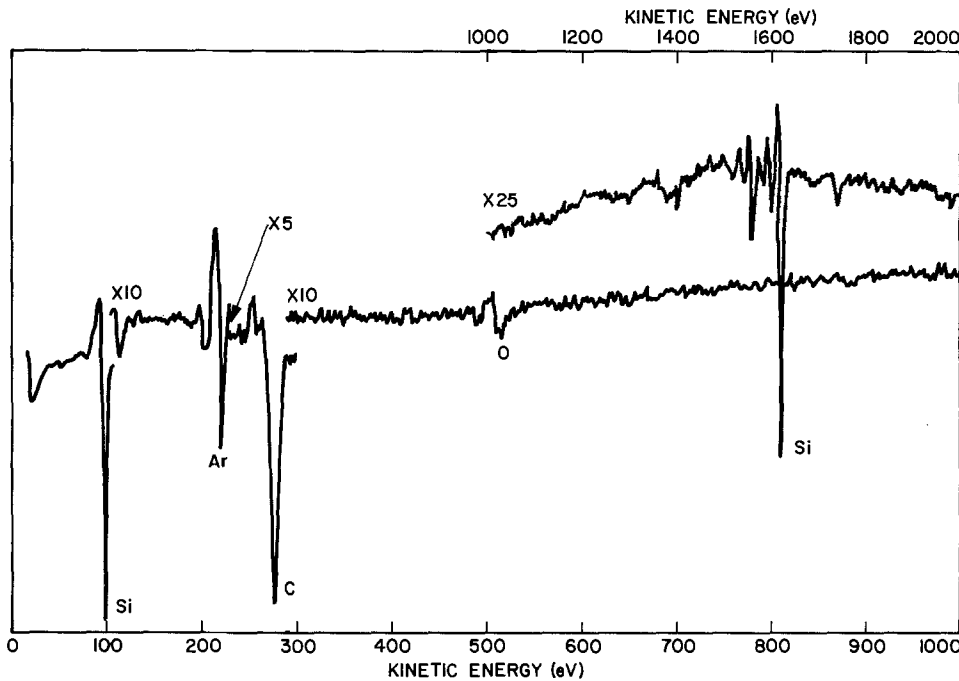


Fig. 5. Ingot 020. Auger spectrum of a carbide-like defect after sputtering 20 min.

may correspond to a peak in Fe concentration. The Fe peak does not correspond exactly to the "geometric" center, but lies slightly to the right-hand side of the observed defect. The dark regions in the map may correspond to lower Fe but not necessarily zero Fe due to the reduction in sensitivity at the small time constants required to perform an analog map.

By plotting the Auger peak amplitude as a function of X position (Y is centered on the micrograph), a more quantitative evaluation of the elemental concentration gradient can be obtained. Figure 3 summarizes line scans for Fe (702 eV), Ni (856 eV), Al (1389 eV), and V (470 eV) for this defect. All the elements shown have similar distributions across the defect and reach a maximum concentration near the center of the defect region. This distribution is representative of many of the defects studied. In performing Auger analysis of defects, it is therefore necessary to characterize the position (X, Y) where the electron beam is placed.

Topographic Effects

Some defects show considerable concentration variation across the sputtered cross section. An example of this behavior is shown in Fig. 4. Two absorbed-current micrographs are shown at 60 and 150 \times . Even with the poor resolution of the electron beam, surface details are readily observed. To demonstrate the effects of topography on the apparent elemental composition of the defect, a Si (91 eV) elemental map and an Fe (702 eV) elemental line scan at 150 \times are included. The Si map shows features similar to the micrograph. Since the substrate is Si, the bright regions of the map are due to topographically enhanced Si detection or electron emission and probably represent an overall change in the electron yield in this region. Auger spectra show that Si is actually less concentrated in this defect region. The Fe line scan is equally dramatic, showing two peaks in Fe concentration. The Fe concentration peaks occur at the black dots on the 150 \times micrograph. Again, Auger spectra show that in fact the low Fe concentration region between the peaks correlates with an overall reduction in detected current (electron yield). Although topography tends to reduce the apparent usefulness of the mapping technique, elemental intensity correlations with micrograph features aid in the understanding of the chemical composition of the defects.

Carbide/Oxide Defects

Most of the defects studied contain heavy elements: Fe, Ni, V, Ti, etc. There are a few defects that appear

similar in physical structure ($\sim 100 \mu\text{m}$ diam at the bottom of an etch pit) but contain no detectable heavy elements. A sample Auger spectrum from a defect in Ingot 020 (bottom) is shown in Fig. 5. Auger peaks are observed for Si, C, O, and Ar after sputtering the surface for ~ 10 min. Using the peak-to-peak amplitudes with appropriate elemental sensitivity factors (9), the Si to C ratio is found to be 2. This indicates that Si is in the form of a carbide, Si_2C . Figure 6 shows a 300 \times

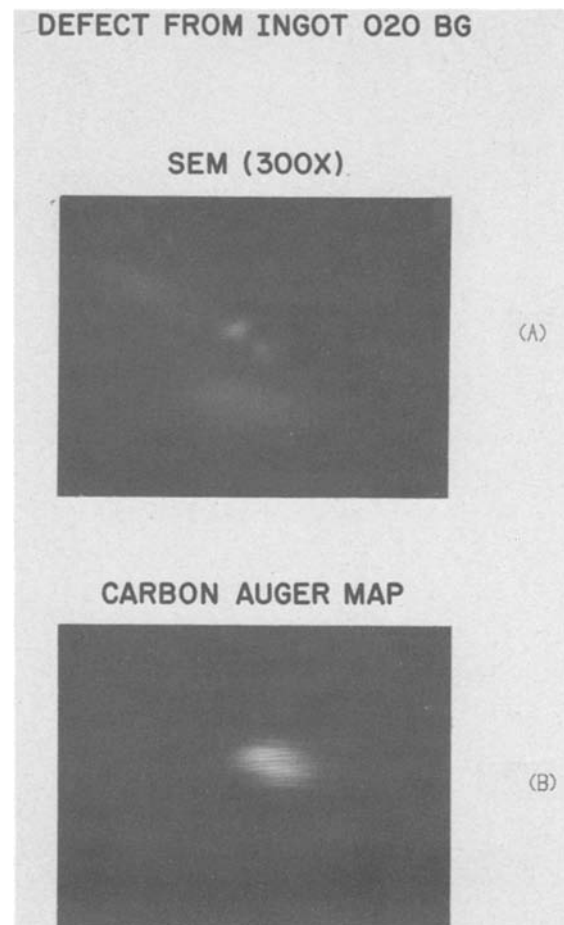


Fig. 6. Ingot 020 (bottom). (A) Micrograph of the defect of Fig. 5 (300 \times). (B) Carbon Auger elemental map (300 \times).

micrograph and a corresponding carbon elemental map. Carbon is peaked in the center of the defect region.

Defect Compositional Gradients

To characterize and summarize defect compositional variations from Ingots 015 and 020, Auger spectra were obtained after sputtering each defect ~10 min. Peaks were observed for Si and Al, Fe, Ni, V, Ti, O, C, and S and varied with ingot and position within the ingot. Amplitudes varied with the type of defect, heavy metal, or carbide. The electron beam was positioned with the aid of the micrographs and subsequent elemental mapping information. An assessment of the amplitudes of the observed Auger peaks was used to qualitatively rank the ingots corresponding elemental concentration as large, medium, or small. These data were used to generate Fig. 7 and 8 which summarize the elemental composition of 20 defects studied from the two ingots. Detected elements are listed in the left column. The position of the sample in the ingot and the defect number are listed horizontally; each column represents the qualitative magnitude of the elemental concentration; the largest circle corresponds to the largest in rank and the smallest to the smallest in rank. In this way, the defect elemental composition can be viewed as a function of position in the ingot.

Although only four defects at most were studied at each ingot position, trends are readily observed from Fig. 7 and 8. In Ingot 015, most of the defects studied contain heavy elements (Fe, etc.). No carbide-type defects were observed within the sample of nine defects studied. Heavy element concentration, that is, the number of heavy elements incorporated in the defects, appears to be more concentrated at the ingot top. Fe-rich defects or Al-rich defects occur at the bottom. Also, O and S are more prevalent at the bottom of this ingot. V was not detected at the bottom. In comparison,

defects in Ingot 020 are Fe-rich throughout but a significant number of carbide-rich defects are also observed in the middle and bottom. In general, Ingot 020 contains fewer metallic elements, excluding Fe, than does Ingot 015. The gradient in the ingot is for heavy metal containing defects or particles to be concentrated at the ingot top and the lighter oxide/carbide type defects to be concentrated toward the bottom of the ingot.

Conclusions

Particulate defects in metallurgical-grade silicon are easily observed by Auger electron spectroscopy using a modest spatial resolution. Ion microsectioning by sputter profiling shows that the defects are composed of silicon alloyed or compounded with metals (Fe, Ni, Ti, V, and Al), as observed in some earlier studies of similar material (11), and carbon or oxygen to form carbides or oxides (12). Depth profiling the particles shows that the surface is oxide-rich and the bulk (>500Å) is relatively uniform in composition. Defect composition is position-dependent within a given ingot with light element-rich defects concentrated at the bottom and heavier element-rich defects concentrated at the top. This distribution is not consistent with what is expected or observed in studies (11) by other methods. Considerable differences in composition were noted for defects from Ingot 015 as compared with Ingot 020. This is due to the differences in impurities found in the raw feedstock materials used in forming the silicon ingots. In general, this study has demonstrated the utility of scanning Auger electron spectroscopy as applied to defect characterization in metallurgical grade silicon. It is also shown that impurities detected by bulk analysis methods (8) segregate as silicide-like particles during solidification.

Acknowledgments

The author wishes to thank G. O. Fowler and E. M. Botnick for obtaining the Auger data.

This work was partially supported by SERI/DOE under subcontract number XS-0-9100-3.

Manuscript submitted June 21, 1983; revised manuscript received Sept. 6, 1983.

RCA, David Sarnoff Research Center assisted in meeting the publication costs of this article.

REFERENCES

- C. P. Khattak, M. Basaran, F. Schmid, P. H. Robinson, R. V. D'Aiello, and A. H. Firester, in "Proceedings of the 15th IEEE Photovoltaic Specialists Conference," IEEE, Orlando, FL (1981).
- L. L. Kazmerski, in "Applied ESCA," F. Ho and H. Windawi, Editors, Wiley-Interscience, New York (1982).
- L. L. Kazmerski, P. J. Ireland, and T. F. Cizek, *J. Vac. Sci. Technol.*, **17**, 23 (1980).
- L. L. Kazmerski and P. J. Ireland, *ibid.*, **17**, 528 (1980).
- B. W. Lee, J. M. Kuo, B. LaLevic, and W. A. Anderson, *ibid.*, **19**, 696 (1981).
- P. H. Holloway, *Adv. Electron. Electron Phys.*, **54**, 241 (1980).
- R. J. Blattner, *Microstruct. Sci.*, **8**, 63 (1980).
- R. V. D'Aiello, *et al.*, SERI Final Report SERI/TR-0-9100-2, January (1982).
- L. E. Davis, N. C. MacDonald, P. W. Palmberg, G. E. Rich, and R. E. Weber, "Handbook of Auger Electron Spectroscopy," Physical Electronics Ind., Eden Prairie, MN (1976).
- C. S. Fadley, *Prog. Solid State Chem.*, **11**, 265 (1976).
- L. P. Hunt, V. D. Dosaj, J. R. McCormick, and L. D. Crossman, in "Proceedings of the 12th IEEE Photovoltaic Specialists Conference," pp. 125-129, IEEE, Baton Rouge, LA (1976).
- T. G. Digges, M. H. Le'pold, K. M. Koliwad, G. Turner, and G. D. Cumming, in "Proceedings of the 12th IEEE Photovoltaic Specialists Conference," pp. 120-124, IEEE, Baton Rouge, LA (1976).

Defect Characterization

Ingot - 015

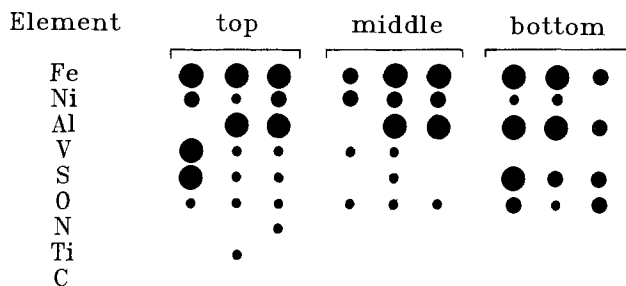


Fig. 7. Ingot 015. Defect characterization and distribution in the ingot.

Defect Characterization

Ingot - 020

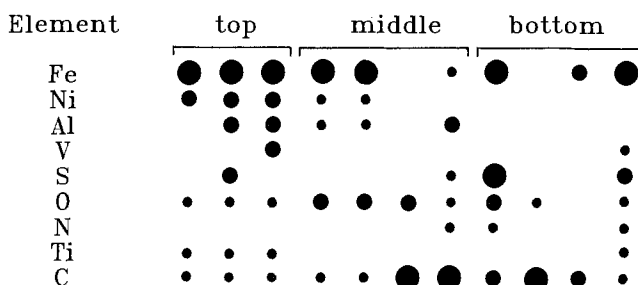


Fig. 8. Ingot 020. Defect characterization and distribution in the ingot.

Oxidation Phenomena of Polysilicon/Tungsten Silicide Structures

N. Hsieh

Fairchild Camera and Instrument Corporation, Advanced Research and Development Division, Palo Alto, California 94304

L. Nesbit

IBM General Technology Division, Essex Junction, Vermont 05452

ABSTRACT

In order to increase the conductivity of polysilicon lines used in polysilicon VLSI technology, silicides (e.g., WSi_2 , MoSi_2 , and TaSi_2) are presently being considered as overlays on the polysilicon lines. One advantage of a polysilicon/silicide structure is that, presumably, it is an oxidizable, self-passivating structure. Under certain oxidation conditions similar to those employed in polysilicon FET processing, voids may develop in the polysilicon layer and/or undesirable oxides lacking structural integrity may develop on the silicide surface. The oxidation mechanisms governing these phenomena are herein discussed.

As semiconductor device dimensions continue to decrease, the need to enhance the conductivity of doped polysilicon interconnections and gate electrodes in VLSI circuits becomes increasingly acute. Refractory metal silicides (e.g., TiSi_2 , WSi_2 , MoSi_2 , and TaSi_3) are presently being considered as overlays to, or replacement for, polysilicon lines as a means of increasing the conductivity of these lines while still retaining an oxidizable structure for self-passivation (1). This structure, consisting of a metal silicide layer directly on top of a polysilicon film, is referred to as the "polycide" structure while the word "silicide" refers only to the metal silicide layer on top of the polysilicon film.

The kinetics of the oxidation of the polysilicon/silicide (polycide) structure have been previously reported (2, 3). It has been found that atoms from the underlying polysilicon layer diffuse through the silicide film to the top silicide surface, where the silicon is oxidized, while the silicide layer itself is not oxidized. We have found (4) that, under certain oxidizing conditions, voids may form in the polysilicon layer and/or undesirable oxides which lack structural integrity may grow on the top surface of the silicide layer.

Geipel, *et al.* (5) have reported extensively on the microstructural, processing, and MOS characteristics of the polycide films. The purpose of this present article is to elaborate on the oxidation characteristics of the polycide structure and, in particular, to specify the conditions under which the aforementioned oxidation phenomena take place.

Experimental Procedure

In order to fully investigate the oxidation characteristics of the polycide structure, various silicon/silicide structures were formed. The standard procedure for forming the polycide structure consists of first depositing 400 nm of *in situ* phosphorus-doped polysilicon on 45 nm of thermal oxide grown on a $\langle 100 \rangle$ p-type silicon substrate. A 350 nm layer of WSi_2 is then coevaporated on top of the polysilicon layer in a dual *e*-beam evaporator. The entire structure is then annealed at 1000°C (1273 K) for 30 min in an inert ambient in order to homogenize and to lower the resistivity of the WSi_2 layer. The blanket polycide structure is then patterned by CF_4/O_2 plasma etching, using photoresist as an etch mask. The patterned polycide film is subsequently subjected to a dry-wet-dry oxidation process at 1000°C (1273 K) so as to form about 240 nm of oxide on top of the WSi_2 layer and a substantial oxide

layer along the edges of the patterned polycide structure.

In order to elucidate the polycide oxidation characteristics and the ensuing results, two slightly different structures were also formed and investigated. In one case, the polysilicon layer was deposited by *e*-beam evaporation of intrinsic silicon onto the thermal oxide which was immediately followed by the coevaporation of the WSi_2 layer. Thus, the intrinsic polysilicon and the WSi_2 layers were deposited sequentially in the same *e*-beam evaporator without breaking the evaporator vacuum between the deposition of the two layers. The resulting structure is similar to that of the usual polycide structure except that the polysilicon layer is intrinsic (undoped) instead of being doped with phosphorus. Some of the resulting blanket films were subsequently annealed and oxidized, while other films were annealed, patterned, and then oxidized.

A second structure was also formed which started with 45 nm of thermal oxide grown on a $\langle 100 \rangle$ p-type silicon wafer. The oxide was patterned to form 2 μm wide openings down to the substrate. A layer of WSi_2 was then coevaporated onto the oxide pattern and annealed at 1000°C (1273 K) in an inert atmosphere. This procedure resulted in regions of WSi_2 on top of 45 nm of oxide (regions A) and regions of WSi_2 on top of bare silicon (regions B), as illustrated in Fig. 1. This structure was then subjected to a dry-wet-dry oxidation cycle which resulted in the growth of 500 nm of oxide over both regions A and B.

Results and Discussion

Voids.—We have observed that the oxidation of the polysilicon/ WSi_2 structure under the aforementioned conditions results in the formation of voids in the polysilicon layer, as indicated in Fig. 2. In the patterned polycide structure, the voids form first and are largest near the edges of the patterned polycide structure. Smaller voids are generally observed away from the patterned edges. The voids range in size from a few tens of nanometers to over a micron in diame-

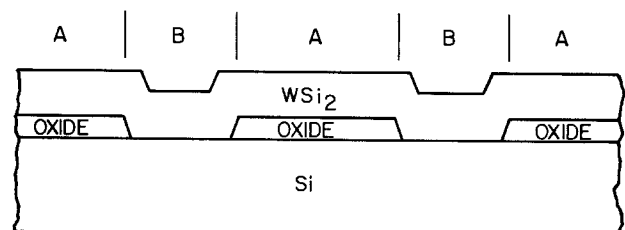


Fig. 1. Patterned oxide structure with WSi_2 coevaporated over the entire structure.

Key words: tungsten, tungsten silicide, silicide, polycide, refractory materials.

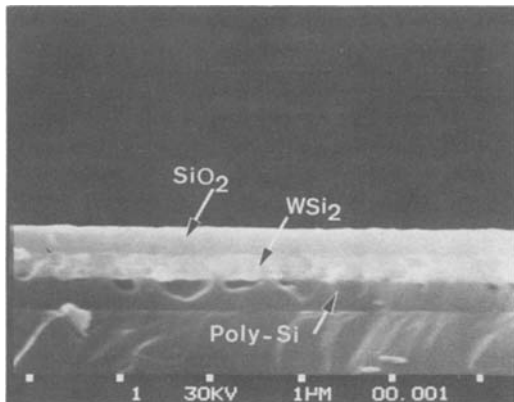


Fig. 2. Large voids are observed in the polysilicon layer of an oxidized polysilicon/ WSi_2 blanket structure.

ter. The smaller voids are bounded by the polysilicon/ WSi_2 interface whereas the larger voids span the entire thickness of the polysilicon film.

Crowder and Zirinsky (3) have shown that the oxidation mechanism of a polysilicon/ WSi_2 structure involves the diffusion of silicon atoms from the polysilicon layer to the top surface of the silicide film where the silicon is oxidized. Throughout the oxidation process, the silicide film remains relatively inert. The presence of voids in the polysilicon layer in the present experiments apparently results from a net flux of silicon atoms from this layer with an insufficient counterflux of other atoms.

The nonuniform distribution of the voids in the polysilicon layer and their variation in size indicates that vacancy supersaturation and nucleation occur at preferred sites. One possible cause of this effect is the presence of a silicon diffusion barrier, such as a polysilicon native oxide, at the polysilicon/silicide interface. This diffusion barrier would inherently have attendant weak points or pinholes through which the silicon could easily diffuse. Hence, these points would become sites for void nucleation and growth.

In order to ascertain if a polysilicon native oxide was present, and acting as at least a partial diffusion barrier, a layer of intrinsic silicon and a film of WSi_2 were sequentially deposited in an *e*-beam evaporator without breaking the evaporator vacuum of 5×10^{-6} torr between depositions. In this manner, the presence of a polysilicon native oxide was minimized, if not totally eliminated. Oxidation of blanket films produced in this manner resulted in no voids in the polysilicon layer. Thus, pinholes in the polysilicon native oxide contribute to the formation of large discrete voids in the polysilicon layer. (Although the *e*-beam evaporated polysilicon also differs from the conventional doped CVD polysilicon in that the latter has a high concentration of phosphorus, later experiments show that phosphorus is unrelated to void formation.)

In order to gain a more quantitative understanding of the factors contributing to the void formation, the pinholes in the polysilicon native oxide were simulated by $2 \mu\text{m}$ wide strips deliberately etched into a thermally grown oxide on a silicon wafer. (See Fig. 1.) Since the native oxide thickness on a bare, lightly doped single-crystal silicon wafer is believed to be thinner than that on heavily doped polysilicon, the presence of any native oxide on the silicon wafer in the etched spaces may be assumed not to inhibit the diffusion of silicon from the substrate. (Indeed, the experimental results support this assumption.) After deposition and annealing of the WSi_2 film on the patterned oxide, the wafer was oxidized and a uniformly thick 500 nm oxide was grown over both regions A (WSi_2 on oxide) and B (WSi_2 on the silicon substrate). Where a $2 \mu\text{m}$ wide B region lies between two $2 \mu\text{m}$

wide A regions or between a $2 \mu\text{m}$ and a $30 \mu\text{m}$ wide A region, voids do not form in the silicon substrate in the B regions (see Fig. 3). However, voids are observed exclusively in the silicon substrate in those B regions which separate two $30 \mu\text{m}$ wide A regions, as shown in Fig. 4.

Two things are immediately evident from Fig. 3 and 4. First, the role of phosphorus in void formation is excluded since the voids also form in the lightly boron-doped substrate, in a similar fashion to the voids which form in the phosphorus-doped polysilicon layer. Second, the micrographs clearly show the consumption of silicon atoms from the wafer, where the silicon diffusion is uninhibited. The consumption of silicon atoms either results in the movement of the WSi_2/Si interface (Fig. 3) or in the formation of voids (Fig. 4).

The relative area ratios of the silicon source (B regions) to the silicon drain (A regions) contributes to the formation of voids in the silicon substrate during oxidation. If A_A and A_B are the respective areas of regions A and B, and if $A_A/A_B = 15/2 = 7.5$, as in the case of Fig. 3, then voids do not form in the underlying silicon. Rather, the WSi_2 layer moves towards the silicon substrate in the opposite direction of the silicon flux. If $A_A/A_B = 30/2 = 15$, then voids will form in the silicon substrate, as observed in Fig. 4. These results indicate that the formation of voids in the polycide structure is dependent upon the local area fraction of the pinholes in the polysilicon native oxide. If the ratio of the oxidized area to the (polysilicon native oxide) pinhole area is large, then there is a high flux of silicon atoms through the pinhole. This results

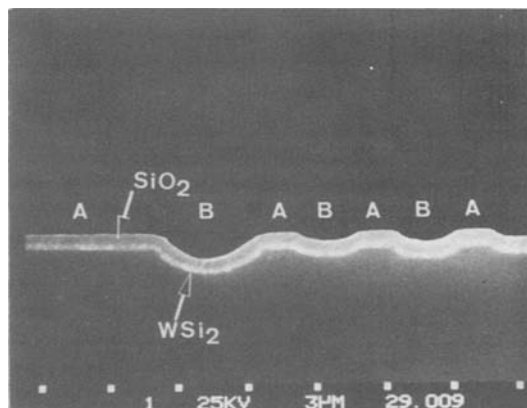


Fig. 3. A cross-sectional view of alternating regions A ($\text{WSi}_2/\text{SiO}_2/\text{Si}$ substrate) and B (WSi_2/Si substrate). A uniformly thick oxide layer has grown over both structures. No voids are observed at the WSi_2/Si substrate interface. The A region at the left is $30 \mu\text{m}$ wide.

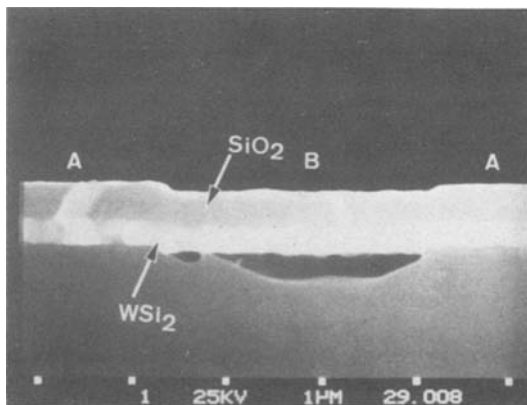


Fig. 4. A similar cross section to that in Fig. 3, except that the area ratio of region A to region B is much greater than 1. Large voids have formed in the silicon substrate in region B which is adjacent to two $30 \mu\text{m}$ wide A regions.

in a supersaturation of vacancies at the pinhole and subsequent void formation.

Based on the findings of Crowder and Zirinsky (3), it had been anticipated that the WSi_2 film would migrate toward the substrate during the oxidation process and thus provide the necessary flux of atoms to counter the flux of silicon atoms supplying the oxidation reaction. This is the case in Fig. 3, where A_A/A_B is small. In the case where voids form, however, the movement of the WSi_2 layer toward the substrate is almost nonexistent, so as not to be sufficient to offset the flux of silicon atoms from the polysilicon layer. Consequently, there is a net flux of vacancies from the free surface to the polysilicon layer.

This phenomenon of vacancy flux to counter an atomic flux is similar to the Kirkendall effect, after the work of Smigelskas and Kirkendall (7). If the excess vacancy concentration or vacancy supersaturation becomes great enough, vacancies will condense to form voids. Based on classical nucleation theory, Seitz (8) and Barnes and Mazey (9) concluded that homogeneous nucleation of voids by the accumulation of individual vacancies is improbable. However, if the vacancies condense on relatively large defects, i.e., by heterogeneous nucleation, the required supersaturation for void nucleation may be considerably less than that for homogeneous nucleation. In particular, Resnick and Seigle (10) and Balluffi (11) have concluded that the vacancy supersaturation need only be on the order of one percent for heterogeneous nucleation of voids. The observation that the smaller voids are bounded by the polysilicon/silicide interface implies that this interface acts as the nucleation site for the voids.

The predominance of voids at the edges of the patterned polycide structures results from the fact that the polysilicon layer in these regions must supply silicon for the oxidation of both the top polycide surface and the side of the patterned structure. Hence, the critical supersaturation for void formation occurs first at the edges of the patterned polycide structure and later within the interior of the pattern.

Once a void nucleates, it continues to grow and to act as a sink for vacancies, and as a source for silicon atoms. This feature of voids results from the void/polysilicon surface acting as a high diffusivity path for the silicon atoms from the interior of the polysilicon layer up to the polysilicon/silicide interface. Vignes and Badia (12) demonstrated in the Fe-Ni system that the presence of voids results in an abnormal increase in the interdiffusion coefficient. Therefore, the presence of voids enhances rather than inhibits the kinetics of the diffusing specie(s).

Once the silicon atoms from the polysilicon layer reach the silicide layer, they are capable of rapid lateral diffusion. Hence, the oxide on the silicide surface is of a uniform thickness despite a nonuniform distribution of voids in the polysilicon layer. From our oxide pattern in Fig. 1, it is apparent that the lateral silicon diffusion in WSi_2 is rapid enough to assure uniform oxide growth to a lateral range of at least 15 μm during oxidation. The high lateral diffusivity is apparently oxidation-induced where a lateral vacancy flux exists.

In order to analyze the factors contributing to the formation of voids, the diagram in Fig. 5 shows the basic structure involved in the potential formation of voids. Area A represents the total oxidized area that is supplied by the diffusion of silicon atoms from the WSi_2/Si interface of area a . A differential volume of $dV = a \cdot d$ is constructed just below this interface in order to monitor the atomic fluxes. The thickness, d , of this differential volume may be chosen to be sufficiently small so that the atomic and vacancy concentrations may be regarded as constant within this volume. Also, the atomic/vacancy diffusion through the

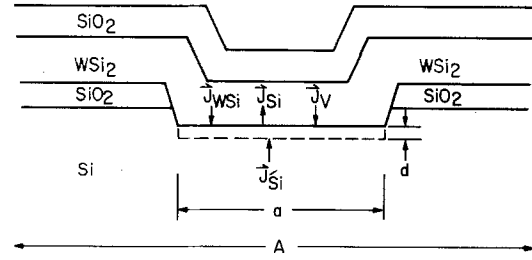


Fig. 5. Schematic of the patterned oxide structure with coevaporated WSi_2 after oxidation. The appropriate diffusive fluxes are also shown.

perimeter of this volume may be assumed to be negligible.

Consider three major atomic fluxes, \vec{J}_{Si} , \vec{J}_{WSi_2} , and \vec{J}'_{Si} , associated with this volume, dV . \vec{J}_{Si} is the flux of silicon atoms from dV to the oxidizing interface, \vec{J}_{WSi_2} is the flux of silicide molecules into dV , and \vec{J}'_{Si} is the flux of silicon atoms from the bulk silicon to dV by self-diffusion from the substrate.

In nonsteady-state conditions, the net atomic flux of atoms or molecules into dV will be negative due to a loss of silicon atoms. In order to conserve space or lattice sites within dV , there must be a counterflux of vacancies, \vec{J}_V , into dV , presumably from the oxidizing free surface. Therefore

$$\vec{J}_V + \vec{J}_{Si} + \vec{J}_{WSi_2} + \vec{J}'_{Si} = 0 \quad [1]$$

From Fick's second law, the relationship between \vec{J}_V and the vacancy concentration is

$$\nabla \cdot \vec{J}_V = - \frac{\partial N_V}{\partial t} \quad [2]$$

By applying Gauss's theorem to dV

$$\vec{J}_{V1} \cdot S_1 - \vec{J}_{V2} \cdot S_2 = - \int \left(\frac{\partial N_V}{\partial t} \right) dV - \frac{\partial}{\partial t} \int N_V dV \quad [3]$$

where \vec{J}_{V1} and \vec{J}_{V2} are the vacancy fluxes at the top and bottom surfaces of dV , respectively. Since areas S_1 and S_2 are both equal to area a , and since N_V is assumed to be constant throughout dV , Eq. [3] becomes

$$(\vec{J}_{V1} - \vec{J}_{V2})a = - \frac{\partial N_V(a \cdot d)}{\partial t} \quad [4a]$$

or

$$\vec{J}_{V1} - \vec{J}_{V2} = - d \frac{\partial N_V}{\partial t} \quad [4b]$$

At the top surface of dV , $\vec{J}'_{Si} = 0$; therefore, from Eq. [1]

$$\vec{J}_{V1} = - (\vec{J}_{Si} - \vec{J}_{WSi_2}) \quad [5]$$

where proper sign considerations have been taken. At the bottom surface of dV , $\vec{J}_{WSi_2} = \vec{J}_{Si} = 0$ or

$$\vec{J}_{V2} = - \vec{J}'_{Si} \quad [6]$$

Substituting Eq. [5] and [6] into Eq. [4], we get

$$\vec{J}_{Si} - \vec{J}_{WSi_2} - \vec{J}'_{Si} = d \left(\frac{\partial N_V}{\partial t} \right) \quad [7]$$

\vec{J}_{Si} is the flux of silicon atoms to be oxidized and it may be expressed as

$$\vec{J}_{\text{Si}} = \frac{\rho}{M} \frac{A}{a} \frac{dl}{dt} \quad [8]$$

where ρ is the density and M is the molecular weight of SiO_2 formed over area A on top of the silicide film. The variable l is the top oxide layer thickness and dl/dt is the oxidation rate.

Although no explicit expressions can be written for \vec{J}_{WSi} and \vec{J}'_{Si} , they are both driven by the vacancy concentration in dV . Therefore, to a first-order approximation

$$\vec{J}_{\text{WSi}} + \vec{J}'_{\text{Si}} = \alpha N_V \quad [9]$$

where α is a proportionality constant, assumed to depend only on temperature. Substituting Eq. [8] and [9] into Eq. [7], we arrive at the expression

$$\frac{\partial N_V}{\partial t} = \frac{\rho}{M} \frac{A}{a} \frac{dl}{dt} - \frac{\alpha N_V}{d} \quad [10]$$

In order to solve Eq. [10], we assume at $t = 0$ that the vacancy concentration is $N_V(0)$ and, afterward, a constant oxidation rate $dl/dt = r$ is maintained. It is easy to show then that

$$N_V(t) = \frac{\rho}{M} \frac{A}{a} \frac{r}{\alpha} \left[1 - \exp\left(-\frac{\alpha}{d} \cdot t\right) \right] + N_V(0) \exp\left(-\frac{\alpha t}{d}\right) \quad [11]$$

Equation [11] describes the change of vacancy concentration at the silicon surface immediately below the WSi_2 layer. For times $t \gg d/\alpha$, the exponential terms become negligible, and a steady-state value of N_V is reached, namely

$$N_V = \frac{\rho}{M} \frac{A}{a} \frac{r}{\alpha} \quad [12]$$

The steady-state value of N_V is proportional to the oxidation rate r and to the area ratio A/a . In practice, the oxidation rate does change with time (e.g., when an oxide layer has grown sufficiently thick that the oxidation rate becomes parabolic). However, the basic conclusion that N_V is proportional to r holds if the oxidation rate does not change appreciably over time on the order of d/α .

For a given oxidation rate or a set of oxidation rates, the area ratio parameter A/a will determine the steady-state vacancy concentration. If N_V is below a critical value N_V^c , no voids will form, but the WSi_2/Si interface will migrate toward the substrate due to the \vec{J}_{WSi} flux. If N_V exceeds N_V^c , vacancies will condense to form voids. The results depicted in Fig. 3 and 4 show the role the area ratio parameter A/a plays in determining whether or not N_V exceeds N_V^c .

In order to confirm the dependency of void formation on the oxidation rate, dl/dt , the structure in Fig. 1 was capped with 50 nm of CVD oxide prior to thermal oxidation. In this manner, the initial oxidation rate was substantially reduced from that of the uncapped structure. Accordingly, no voids formed in the B regions, even when the area ratio was as large as 15.

The vacancy concentration times α is shown in Fig. 6 as a function of oxidation time and area ratio, A/a . The curves are based upon oxidation rate data produced by Roberts (13) and upon Eq. [10]. As can be observed from the graph, the structure with the A/a ratio represented by curve 1 has the highest vacancy concentration at the start of the wet oxidation cycle, and it is this structure that results in voids in the substrate. The oxidation conditions represented by curves 1 and 2 do not result in voids in the substrate. Thus, the critical vacancy concentration to nucleate voids must lie between the peak concentrations of curves 1 and 3 for this structure.

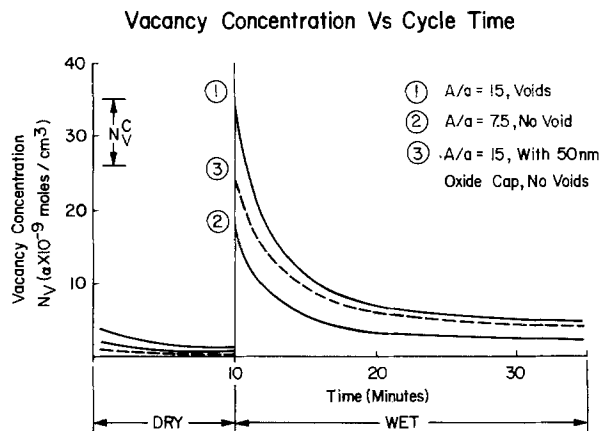


Fig. 6. Vacancy concentration in the substrate as a function of the patterned oxide structure in Fig. 5 and of the oxidation cycle.

Silicide oxidation.—Another phenomenon that may occur upon oxidation of the polycide structure is that the silicide layer itself may be oxidized. Several authors have looked at the oxidation of tungsten silicide films deposited on SiO_2 (2, 14-16), on single-crystal silicon (14), and on polysilicon (2, 16). Mohammadi *et al.* (14) have demonstrated that dry oxidation of WSi_2 films on SiO_2 at 1000°-1200°C results in the formation of SiO_2 and WO_3 , the latter of which is a volatile oxide at these temperatures. Sinha (15) has shown that when WSi or WSi_2 are deposited on SiO_2 and oxidized at temperatures at or above 900°C, the silicon in the silicide film oxidizes first and then the remaining free tungsten oxidizes.

This results in the silicide film breaking up and lifting off the substrate in localized areas, and the oxidation is then regarded as being "destructive." Zirinsky *et al.* (2) have demonstrated that, when deposited on polysilicon, the WSi_2 layer maintains its integrity when subjected to steam oxidation.

In the course of the present experiments, blanket WSi_2 films were deposited on polysilicon films and on oxidized silicon wafers. These films were then oxidized at 1000°C in wet oxygen (steam) for 12 or 22 min; the results are shown in Fig. 7. The lighter regions on the wafers are where the silicide layer has been destructively oxidized. After an oxidation time of 12 min, more than half of the WSi_2 layers on the SiO_2 film has oxidized. After 22 min, nearly all of the silicide layer on the SiO_2 film had oxidized, but only a small portion of the silicide on the polysilicon film had oxidized. The results of this experiment suggest that the presence of an underlying oxide film results in the oxidation of the silicide layer, and the rough oxide region propagates with oxidation time.

An SEM micrograph of a region where the silicide film in the polycide structure had begun to oxidize is

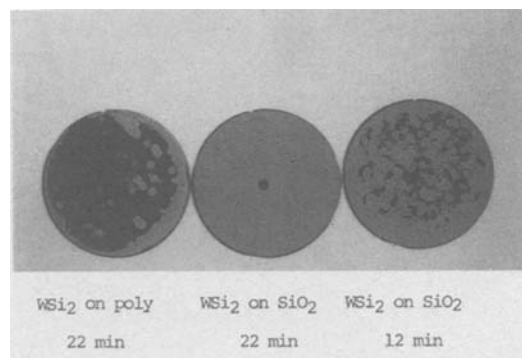


Fig. 7. Blanket WSi_2 films on polysilicon or on SiO_2 . The wafers have been oxidized in wet oxygen at 1000°C for the specified times. The light regions are where the WSi_2 layer has been "destructively" oxidized.

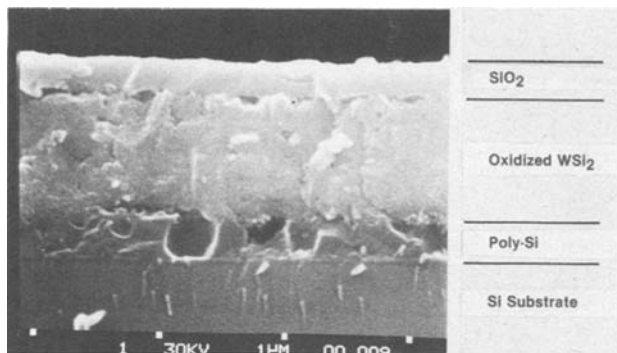


Fig. 8. The polycide structure in which the silicide layer has been oxidized. Voids are observed in the polysilicon layer and at the silicide/oxide interface.

shown in Fig. 8. In the micrograph, voids are present in the polysilicon film, indicative of pinholes in the polysilicon native oxide. The oxidized silicide layer is $0.95 \mu\text{m}$ thick, which is about three times thicker than the as-annealed silicide film. Finally, a layer of presumably SiO_2 is on top of the oxidized silicide layer, and small voids are observed at the SiO_2 /silicide interface. The expansion of the silicide film and the formation of voids at the SiO_2 /silicide interface probably result from the formation of the volatile WO_3 compound within the silicide film.

Although silicon diffuses from the polysilicon layer during the oxidation process, apparently the rate of silicon oxidation is greater than the diffusional supply of silicon from the polysilicon layer. Consequently, the silicide film itself also starts to oxidize. This is believed to occur when there are extended native oxide regions on the polysilicon layer, so that the A/a ratio is very large.

Summary

Several unique features, with regard to the oxidation of the polycide structure, have been discussed in this paper and are summarized as follows:

1. Upon oxidation of the polycide structure, voids may form in the polysilicon layer. These voids nucleate at the polysilicon/silicide interface and grow into the polysilicon film itself.

2. The voids are due in part to a polysilicon native oxide which acts as a barrier to the diffusion of silicon from the polysilicon to the top silicide surface. The diffusion of silicon from the polysilicon films takes place at localized regions at the silicide/polysilicon interface where there are believed to be pinholes in the native oxide.

3. As a result of the localized diffusion of silicon from the polysilicon layer, there is a counterflux of vacancies from the free surface to the polysilicon layer. These vacancies condense to form voids in the polysilicon layer.

4. Two process and/or material parameters influence the formation of voids in the polysilicon layer. The first of these is the relative area of pinholes in

the polysilicon native oxide. If the ratio of the area being oxidized, A , to the area of the pinhole in native oxide, a , is nearly equal to 1, then voids are not likely to form. If, however, $A/a \gg 1$ then voids will tend to form. Consequently, voids are more prevalent near the edges of patterned polycide structures than in the interior of such structures. The second factor which promotes void formation is a high oxidation rate.

5. Despite the formation of voids in the polysilicon layer, the oxide above the silicide film is of uniform thickness and does not reflect the presence or absence of voids in the underlying polysilicon film. This uniform oxide thickness results from the rapid lateral diffusion of silicon in the silicide film relative to the oxidation rate of silicon at the oxide/silicide interface.

6. Under certain oxidation conditions, the silicide layer itself may oxidize, resulting in an expansion or thickening of the silicide layer up to three times its original thickness. The oxidation of the silicide layer is favored by the same oxidation conditions that promote voids in the polysilicon layer, namely, rapid oxidation rates and an oxide layer which inhibits the diffusion of silicon from an underlying silicon source.

Acknowledgments

The authors would like to thank B. L. Crowder for pointing out the role of polysilicon native oxides. We also wish to thank H. J. Geipel, E. E. Gardner, and P. C. Velasquez for many helpful discussions during the course of this work.

Manuscript submitted May 4, 1983; revised manuscript received Sept. 6, 1983.

IBM General Technology Division assisted in meeting the publication costs of this article.

REFERENCES

1. S. P. Murarka, *J. Vac. Sci. Technol.*, **17**, 775 (1980).
2. S. Zirinsky, W. Hammer, F. d'Heurle, and J. Baglin, *Appl. Phys. Lett.*, **33**, 76 (1978).
3. B. L. Crowder and S. Zirinsky, *IEEE J. Solid-State Circuits*, **sc-14**, 291 (1979).
4. N. Hsieh and L. A. Nesbit, Abstract 161, p. 425, The Electrochemical Society Extended Abstracts, Vol. 80-1, St. Louis, MO, May 11-16, 1980.
5. H. J. Geipel, N. Hsieh, M. H. Ishaq, C. W. Koburger, and F. R. White, *IEEE Trans. Electron Devices*, **ed-27**, 1417 (1980).
6. B. L. Crowder, Private communication.
7. A. Smigelskas and E. Kirkendall, *Trans. AIME*, **171**, 130 (1947).
8. F. Seitz, *Acta Metall.*, **1**, 355 (1953).
9. R. S. Barnes and D. J. Mazey, *ibid.*, **6**, 1 (1958).
10. R. Resnick and L. L. Seigle, *Trans. AIME*, **209**, 87 (1957).
11. R. W. Balluffi, *Acta Metall.*, **2**, 194 (1954).
12. A. V. Vignes and D. M. Badia, in "Diffusion Processes," J. N. Sherwood, A. V. Chadwick, W. M. Muir, and F. L. Swinton, Editors, p. 275, Gordon and Breach Science Pub., New York (1971).
13. S. Roberts, Private communication.
14. F. Mohammadi, K. C. Saraswat, and J. D. Meindl, *Appl. Phys. Lett.*, **35**, 529 (1979).
15. A. K. Sinha, *J. Vac. Sci. Technol.*, **19**, 778 (1981).
16. F. Mohammadi and K. C. Saraswat, *This Journal*, **127**, 450 (1980).

Minimum Wafer Thickness by Rotated Ingot ID Wafering

C. P. Chen and M. H. Leipold

Jet Propulsion Laboratory, California Institute of Technology, Pasadena, California 91190

ABSTRACT

The efficient utilization of materials is critical to certain device applications such as silicon for photovoltaics or diodes and gallium-gadolinium-garnet for memories. A variety of slicing techniques has been investigated to minimize wafer thickness and wafer kerf. This paper presents the results of analyses of ID wafering of rotated ingots based on predicted fracture behavior of the wafer as a result of forces during wafering and the properties of the device material. The analytical model indicated that the minimum wafer thickness is controlled by the depth of surface damage and the applied cantilever force. Both of these factors should be minimized. For silicon, a minimum thickness was found to be approximately 200×10^{-6} m for conventional sizes of rotated ingot wafering. Fractures through the thickness of the wafer rather than through the center supporting column were found to limit the minimum wafer thickness. The model suggested that the use of a vacuum chuck on the wafer surface to enhance cleavage fracture of the center supporting core and, with silicon, by using $\langle 111 \rangle$ ingots could have potential for reducing minimum wafer thickness.

Some devices are much more dependent on material cost than others. Such devices include photovoltaics, high power diodes, and magnetic bubble memories. Improved wafering technology to reduce both wafer thickness and kerf loss has been employed in an attempt to increase material utilization. One approach which has been proposed and investigated is to rotate the ingot during ID wafering. This permits the use of thinner blades because of the reduced depth of cut. Additionally, the smaller lever arm of the unsupported wafer should reduce stresses and tendency to fracture. The apparent advantages of this technique have not been realized in practice and this study was made in an attempt to analyze the reasons for the unsatisfactory performance and to determine if fundamental limitations existed or if further modifications to the technique might be useful. Experimental efforts to use rotated ingot ID wafering generally resulted in fracture of the wafers as wafer thickness was reduced. The failure usually took the form of circular cracking often to the point where the entire center of the wafer was broken out. This occurred in spite of efforts to precisely align the axis of the rotated ingot perpendicular to the ID blade.

In a previous paper, Ref. (1), fracture mechanics analysis was utilized to derive an equation describing the stress conditions of a wafer during conventional ID wafering. This equation predicted the minimum wafer thickness as a function of diameter for ID sawing. The required wafer thickness increased with increasing wafer diameter and, for silicon, was appreciably smaller than existing SEMI standard.

In this paper, fracture mechanics concepts were extended to analyze the loading conditions of a wafer during rotation ingot ID wafering. It is anticipated that this analytical model can provide a guideline estimating the allowable wafer thickness *vs.* diameter for rotation ingot ID wafering in terms of fracture mechanics parameters. The analysis was conducted for silicon but would be applicable to other materials using appropriate input data.

Fracture Mechanics Model

A wafer with center support subjected to a cantilever force can be considered to represent the stressed condition of a wafer during rotation ingot ID wafering as shown in Fig. 1. The diameter of the rigid center support, d , can be considered to be the diameter of the center core (uncut area) during rotation ingot wafering. The applied cantilever force, P , on the wafer may be due to saw blade vibration and surface tension; it increases with cutting rate (1). The force on a wafer during slicing could be either a distributed loading or

a concentrated force. In either case, an equivalent concentrated force P (as shown in Fig. 1) could be used to describe the force conditions affecting a wafer during rotation ingot ID slicing.

Fracture of materials is the result of the extension of a pre-existing flaw under stress. Fracture mechanics defines that (for a given stress level) the flaw size required for the onset of rapid propagation and fracture is called the critical crack size (a_c). This critical size in turn depends upon the values of the critical stress intensity factor (K_{IC}) for the material. Therefore, the fracture strength of material is controlled by a_c and K_{IC} of the material. For a small semicircular flaw, the relationship equation of fracture stress (σ) as a function of a_c and K_{IC} was derived (1) and can be approximately expressed as

$$\sigma = \frac{K_{IC}}{\sqrt{\pi a_c}} \quad [1]$$

Thus, to determine the failure in any direction, it is necessary to determine σ from K_{IC} and a_c . K_{IC} is a material constant, although directional, and a_c is a function of wafering technology, related to the surface damage.

Application of a force P at the edge of the wafer results in a stress both in the wafer and in the center support (see Fig. 1). These stresses can result in failure by propagation of microcracks in directions A or B, respectively. The propagation through the wafer thickness (A direction) destroys the wafer; propagation through the central core (B direction) results in a usable wafer with a central nib.

Considering first the stress in the wafer (failure in direction A), the maximum stress in the wafer was

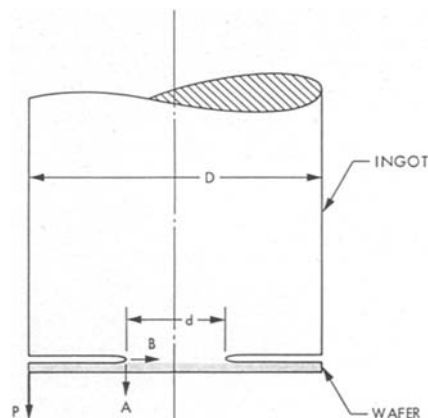


Fig. 1. A circular thin wafer, center supported, is subjected to a cantilever force P .

Key words: silicon, photovoltaic, fracture mechanics analysis.

found to occur at the edge of the center support and can be expressed analytically (2) in an equation

$$\sigma_A = \frac{P}{t^2} \beta \tag{2}$$

where σ_A = stress in the wafer at the edge of the center support, P = applied cantilever force, t = wafer thickness, $\beta = \frac{3}{\pi} \sum_0^\infty e_n$, and $\sum_0^\infty e_n$ is Fourier series in which e_n is a function of ν = Poisson's ratio, d = diameter of center support, D = wafer diameter, $n = 0, 1, 2, \dots \infty$.

Substituting Eq. [1] into Eq. [2], the wafer thickness, t , can be written as

$$t^2 = \frac{\sqrt{\pi a_{cA}}}{K_{IC}} P_A \beta \tag{3}$$

where a_{cA} = critical flaw size for propagation in direction A and P_A = allowable force to cause crack propagation in direction A. A computer calculation of β as a function of d/D for n up to 30 and $\nu = 0.22$ for silicon (3) is shown in Fig. 2. Thus Eq. [3] expresses the relationship between the required wafer thickness and diameter.

Next, considering the tendency of the stress in the center support to cause crack propagation in direction B, the fiber stress, σ_B can be expressed from structure analysis (4) as follows

$$\sigma_B = \frac{16P_B D}{\pi d^3} \tag{4}$$

Substituting Eq. [1] into Eq. [4], the allowable applied force (P_B) of the center core in terms of wafer diameter and fracture mechanics parameters, can be written in the form

$$P_B = \frac{\sqrt{\pi}}{16} \frac{K_{IC} d^3}{\sqrt{a_{cB}} D} \tag{5}$$

In this equation, P_B and a_{cB} are allowable force and critical crack size, respectively, for the center core. However, in this case, the total length of the crack in B direction should be the depth of the cut plus the surface damage flaw in the center core.

Application of Analytical Model to Silicon

Application of the model to ID wafering of rotated ingots is straight-forward. The analysis here will be limited to silicon but can be applied to other materials. The fracture mechanics studies (5) on single crystal silicon found that the critical stress intensity factor K_{IC} in several crystalline planes is as follows

$$\begin{aligned} K_{IC} &= 0.82 \text{ MNm}^{-3/2} \text{ in } \{111\} \\ K_{IC} &= 0.90 \text{ MNm}^{-3/2} \text{ in } \{110\} \\ K_{IC} &= 0.95 \text{ MNm}^{-3/2} \text{ in } \{100\} \end{aligned} \tag{6}$$

Thus the easy fracture direction is {111}. However, because the differences in K_{IC} are small, the difference

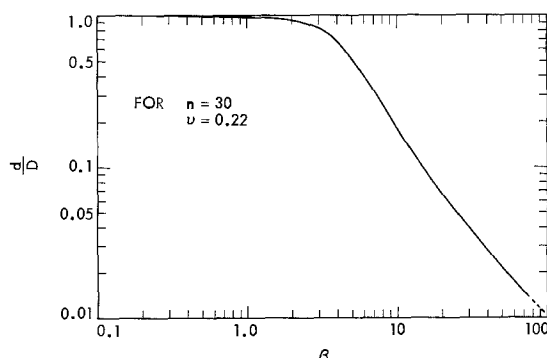


Fig. 2. Factor β as function of d/D for silicon

will be ignored and all calculations will use {111} fracture data. Figure 3 shows the difference between {100} and {111} fracture in the B direction. The typical wafer surface damage from ID sawing was measured (6) and found to be approximately 50 μm or

$$a_c = 50 \times 10^{-6} \text{m} \tag{7}$$

Substituting these values of K_{IC} and a_c into Eq. [3], the allowable applied force, P_A , for wafer failure at several wafer thicknesses for slicing $100 \times 10^{-3} \text{m}$ ingots is shown in Fig. 3. Equation [3] shows that P_A decreases with increasing a_{cA} .

As shown in Fig. 3, the minimum required wafer thickness without cracking at the very small values of d (e.g., $3 \times 10^{-3} \text{m}$) is very sensitive to the force P (in general $P = P_A = P_B$). Therefore, decreasing the cutting rate near the small d region is very important for rotation ingot wafering in order to minimize deflection of the wafer and P .

Predictions for the wafering operation from Fig. 3 can be summarized as follows:

1. At each wafering thickness, the allowable force on the wafer decreases with decreasing center core diameter. In other words, the probability of cracking a wafer during rotation ingot wafering increases with increasing depth of cutting.

2. The allowable applied force P for a wafer decreases very rapidly as the center core diameter is reduced to a very small value (e.g., $3 \times 10^{-3} \text{m}$). Therefore, cracks in the wafer in direction A are usually found near the center of the wafer from rotation ingot wafering.

3. During typical conventional ID slicing at a cutting rate of $51 \times 10^{-3} \text{m/min}$, "P" has been estimated (1) to be 0.5N. Using $P = 0.5 \text{N}$, a $200 \times 10^{-6} \text{m}$ -thick wafer is very likely to crack at $d = 50 \times 10^{-3} \text{m}$, and a $300 \times 10^{-6} \text{m}$ -thick at $d \approx 14 \times 10^{-3} \text{m}$.

A successful rotation ingot wafering occurs when a wafer is broken off from the ingot at the center core without generating cracks in the wafer. According to this model, the force for crack propagation in the "B" direction must be reached before that in the "A" direction. As mentioned before, the total crack size in Eq. [5] is expressed as

$$a_{cB} = \frac{1}{2} (D - d) + a_c \tag{8}$$

Since $a_c \ll \frac{1}{2} (D - d)$, the crack size in B direction can be written as follows

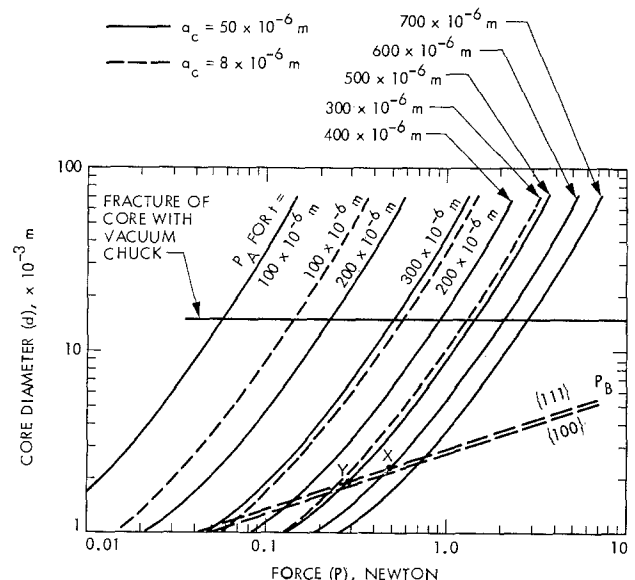


Fig. 3. Fracture force (P) vs. core diameter for rotated ingot wafering of 100 mm wafers.

$$a_{cB} = \frac{1}{2} (D - d) \quad [9]$$

Substitution of Eq. [9] into [5], the allowable fracture force (P_B) of the center core is written in a form

$$P_B = \frac{\sqrt{2\pi}}{16} \frac{d^3}{D\sqrt{D-d}} K_{IC} \quad [10]$$

Using $K_{IC} = 0.82 \text{ MNm}^{-3/2}$, the fracture force P_B in Eq. [10] for the center support core in B direction as a function of core diameter is plotted in Fig. 3. If any applied force P_B is again equivalent to 0.5N, the fracture of the wafer center supporting core for a $100 \times 10^{-3}\text{m}$ diameter wafer can occur. In Fig. 3, at $d = 2.3 \times 10^{-3}\text{m}$, Eq. [5] states that P_B vs. the d is independent of the wafer thickness. Thus $600 \times 10^{-6}\text{m}$ thick wafers can be sliced at regular cutting speed (P equivalent = 0.5N) and the center core will fracture at $2.3 \times 10^{-3}\text{m}$ (see point X on Fig. 3). A $500 \times 10^{-6}\text{m}$ thick wafer can be sliced by reducing cutting force (0.5N) from near $d = 3.5 \times 10^{-3}\text{m}$ at a rate following its P vs. d curve to $d = 1.9 \times 10^{-3}\text{m}$ where fracture of the center core occurs at $P = 0.29\text{N}$ (see point Y on Fig. 3). Wafer thickness smaller than $300 \times 10^{-6}\text{m}$ is possible as the force P be further reduced to smaller than 0.05N. This analytically calculated d value and wafer thickness have the same magnitude as that observed in typical silicon wafers (7).

Special procedures in wafering have demonstrated the ability to reduce surface damage to $8 \times 10^{-6}\text{m}$ (8). Substituting $a_{cA} = 8 \times 10^{-6}\text{m}$ into Eq. [3], the curves of P vs. d for $t = 100 \times 10^{-6}\text{m}$, $200 \times 10^{-6}\text{m}$, and $300 \times 10^{-6}\text{m}$ are plotted in Fig. 3. The intersections of these curves and P_B curves suggest that a minimum wafer thickness can be further reduced to less than $200 \times 10^{-6}\text{m}$. Therefore, this analytical model suggests that it is very important to minimize the wafer surface damage and the applied force, especially at small d region, to achieve the minimum usable wafer thickness.

The present rotation ingot wafering of silicon is mostly carried out with $\langle 100 \rangle$ ingots. Because the fracture strength of the material is directly proportional to K_{IC} , as shown in Eq. [1], the allowable fracture force for the center core in $\langle 100 \rangle$ can be greater than that in $\langle 111 \rangle$ axis, because K_{IC} on $\{100\}$ is greater than K_{IC} on $\{111\}$ as shown in Eq. [6]. Thus, if $\langle 111 \rangle$ ingots were used, easier fracture in the central core would occur. However, the difference is small for silicon, as shown in Fig. 3. A possible useful feature of $\langle 111 \rangle$ silicon ingot is that the fracture surface of silicon in $\{111\}$ was found (5) to be a clean cleaved fracture, while fracture surface in other crystalline planes reveals rough crack branching.

It may also be possible to control fracture by increasing the applied stress in B direction. This might be accomplished by means of a uniform force on the wafer parallel to its axis (e.g., by a vacuum chuck). The application of a vacuum chuck to rotation ingot wafering is shown schematically in Fig. 4. The total vacuum force on a wafer can be calculated by

$$F = q \frac{\pi D^2}{4} \quad [11]$$

where q = vacuum pressure, max q is 1 atm = 0.1 MNm^{-2} .

The relationship of D and d can be expressed in a form

$$\frac{D}{d} = \frac{\sqrt{\sigma_n}}{q} \quad [12]$$

where σ_n = nominal stress in the center core.

Because of the existence of stress concentration in a deep groove, Eq. [12] can be rewritten as

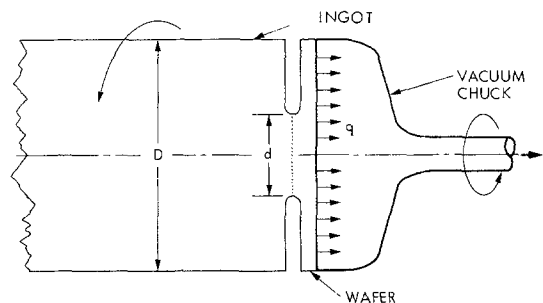


Fig. 4. Schematic showing the application of vacuum chuck to rotation ingot wafering.

$$\frac{D}{d} = \frac{\sqrt{\sigma_c}}{k_t q} \quad [13]$$

where k_t = stress concentration factor in the bottom of the groove and σ_c = stress on the flaw.

The stress concentration factor, k_t , for a grooved bar in tension is normally determined from the ratio of groove root radius (r) and d and D . For rotation ingot ID slicing, the typical value of r/d is very small (e.g., 0.02), and D/d is very large (e.g., 20). Available data (9) do not cover the appropriate range of values for r , d , and D , and thus k_t is imprecise. However, this factor in a machined notch of brittle materials has a very large value because microcracks are usually found in the bottom of the notch. The radius of the microcrack (r) may be on the order of 10^{-9}m and the value of r/d can be an extremely small value. K_t is taken conservatively here as 15, but could easily be as high as several hundred.

Assume that

$$\begin{aligned} D &= 100 \times 10^{-3}\text{m} \\ k_t &= 15 \\ K_{IC} &= 0.82 \text{ MNm}^{-3/2} \\ a_{cB} &= 50 \times 10^{-6}\text{m} \end{aligned}$$

Substituting these values into Eq. [1] and [13], the calculations indicated that the fracture of the center core occurs at $D/d = 6.6$ or $d = 15 \times 10^{-3}\text{m}$, as indicated by the line in Fig. 3. In this case, considerable saving in cutting time and blade wearing can be expected. In addition, this auxiliary force on the wafer can increase the clearance for the blade. It should be noted that it is important to use an ingot in which minimum K_{IC} is aligned parallel to the wafer surface ($\{111\}$ for Si) to maintain clean cleaved fracture in B direction as mentioned previously.

These results suggest that rotational ID wafering does have potential for very thin wafers. The analysis should be interpreted only that such an approach is possible. Technical difficulties, such as proper lubrication, minimization of vibration, and control of blade entry into the ingot, are not minor.

Conclusions

1. An analytical model of a thin circular wafer, supported by a center core and subjected to an equivalent cantilever force at the wafer edge was used to describe the loading condition of a wafer during rotation ingot ID wafering.

2. A fracture mechanics concept was found to be useful to derive the relationship equation for the allowable wafer thickness vs. diameter as

$$t^2 = \frac{\sqrt{\pi a_{cA}}}{K_{IC}} P_A \beta \quad [14]$$

where β is a factor relating to the ratio of D and d and Poisson's ratio ν .

3. It is important to reduce applied force "P" by minimizing saw vibration and cutting rate in order to

maintain minimal wafer thickness, especially at small center core diameter.

4. The allowable thickness is dependent upon the depth of surface damage (flaw size a_c) of the wafer. The minimum wafer thickness can be further reduced to approximately 200×10^{-6} m for the conventional wafer diameters of 100×10^{-3} m when the depth of wafer surface damage can be reduced to less than 8×10^{-6} m.

5. Proper alignment of easy fracture direction ($\{111\}$ for silicon) with the wafer surface and use of a vacuum chuck to assist fracture in the center core direction is shown to have great potential to obtain minimum thickness wafers. Considerable saving in cutting time can be expected.

Acknowledgments

The work described in this paper was performed by the Applied Mechanics and Solar Energy Conversion Systems sections of the Jet Propulsion Laboratory, California Institute of Technology, for the U.S. Department of Energy through an agreement with NASA.

Manuscript submitted Nov. 29, 1982; revised manuscript received Sept. 9, 1983.

The Jet Propulsion Laboratory assisted in meeting the publication costs of this article.

REFERENCES

1. C. P. Chen, *This Journal*, **129**, 2835 (1982).
2. Von H. Reissner, *Ingenieur-Archiv*, **1**, 72 (1929).
3. C. St. John, *Phil. Mag.*, **32**, 1193 (1975).
4. F. R. Shanley, "Strength of Materials," Chap. 15, McGraw-Hill, New York (1957).
5. C. P. Chen and M. H. Leipold, *Am. Ceram. Soc. Bull.*, **59**, 469 (1980).
6. R. L. Meek and M. C. Huffstutler, Jr., *This Journal*, **116**, 893 (1969).
7. G. F. Fiegl, Siltec, Final Report, DOE/JPL-955282-81, December 1981.
8. T. S. Kuan, K. K. Shih, J. A. Van Vechten, T. Baum, and W. A. Westdorp, *Jpn. J. Appl. Phys.*, **21**, L143 (1982).
9. R. E. Peterson, "Stress Concentration Design Factors," p. 33, John Wiley & Sons, New York (1953).

The Semiconductor-Electrolyte Interface

Photocurrent and Related Parameters in Cadmium Telluride

J. L. Sculfort,* R. Triboulet,¹ and P. Lemasson*

Laboratoire d'Electrochimie Interfaciale du CNRS 92195 Meudon Principal Cedex, France

ABSTRACT

The CdTe-aqueous electrolyte interface is studied both in the dark and under illumination for n- and p-type single crystals. From the anodic and cathodic currents are deduced information about the stability of the semiconductor electrode which agrees fairly well with decomposition potentials calculated from thermodynamic data. For n- and p-CdTe, hydrogen evolution prevails to cathodic decomposition. For n-CdTe, linear Schottky plots are obtained only after a photoetching in 1M NaOH solution. The flatband potential then measured is consistent with that obtained for p-CdTe. Both are pH independent. The minority carrier diffusion length and the Urbach's slope are deduced from photoelectrochemical measurements. They change with the dopant and the free carrier concentration and agree with each other. Information is then obtained about the quality of the samples.

The II-IV compound cadmium telluride presents different properties (energy gap ca. 1.5 eV, direct transition, n- or p-type conductivity, large atomic numbers of the components, etc.) which make it attractive for applications as different as gamma and x-ray detectors or photovoltaic devices (1). However, the practical use of this material up to now is limited mainly by the imperfections of the crystalline structure both in the bulk and in surface. For example, the diffusion length of the minority carrier, a parameter which reflects the perfection of the crystal, remains generally small (ca. 1 μ m) thus limiting, e.g., the efficiency of CdTe solar cells.

In electrochemistry, cadmium telluride received attention mainly in view of solar applications. However, n-CdTe presents a poor stability under illumination in aqueous solvents; further, the problems of the electrode surface preparation are numerous and not yet solved (2). The p-type cadmium telluride also received attention, but the flatband potential value severely hinders its use as a photocathode in a liquid photovoltaic cell though the electrochemical behavior appears to be simpler than for n-type (3).

In the present work, we present the electrochemical behavior of n- and p-type CdTe in supporting electrolyte (pH range 0-14) both in the dark and under il-

lumination. Thus an attempt is presented to correlate the nature of the dopant and the free carrier density with two selected physical parameters (minority carrier diffusion length and Urbach's slope of the absorption tail).

Experimental

Single crystal cadmium telluride wafers are cut from ingots grown either by a Bridgman technique (n-type) or the traveling heater method (THM) (p-type). Various doping and free carrier concentrations are used:

n-type: 1.5×10^{15} cm⁻³ not intentionally doped
 8×10^{17} cm⁻³ In doped

p-type: 4×10^{15} cm⁻³ not intentionally doped
 3×10^{16} cm⁻³ and 7×10^{16} cm⁻³ P doped.

The electrode surface in contact with the electrolyte is ca. 10 mm² and the back face is provided with an ohmic contact:

n-type: In-Hg amalgam under H₂ atmosphere for 2 mn at 300°C

p-type: a chemical deposit of gold is diffused by heating to 300°C in H₂ atmosphere for 3 mn

In each case, a gold wire is soldered to the ohmic contact and the electrodes are glued in epoxy resin except the front face which is polished to a mirror finish (dia-

* Electrochemical Society Active Member.

¹ Permanent address: Laboratoire de Physique des Solides, CNRS 92195 Meudon Principal Cedex, France.

Key words: II-VI semiconductor, electrode, optics, doping.

mond paste 0.25 μm). Prior to electrochemical operation, the electrodes are chemically etched: 15s in 1% bromine-methanol solution at ca. 5°C (n-type) and 3 mn in 10M NaOH solution at 40°C (p-type). These etchants preserve the surface stoichiometry of the samples and avoid the growth of oxide layers that are too thick (4).

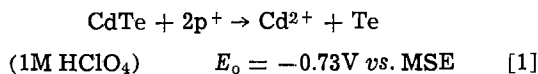
Electrolytes are prepared from Millipore purified water and high purity grade chemicals (Merck suprapur). Stirring of the solution is achieved by gas bubbling (O_2 or Ar) when necessary. The reference electrode is a mercury-mercurous sulfate electrode denoted by MSE (0V vs. MSE = +0.65V vs. NHE). NHE: normal hydrogen electrode.

A 250W tungsten halogen lamp is used as a light source, and light fluxes are measured by means of a silicon photodiode (PIN 10D-SB, UDT). Measurements consist mainly of steady-state current voltage curves in the dark and under illumination and of impedance measurements. Further details about the experimental techniques have already been published (5).

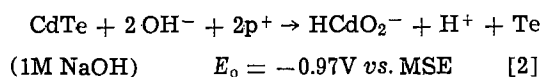
Results and Discussion

Steady-state current-voltage curves for n- and p-type CdTe in the dark and under illumination at pH 0 and 14 are presented in Fig. 1 and 2. The main results coming from these measurements are collected in Table I and II. We notice first that the observed reduction and oxidation currents, correlated to reactions, are in good agreement for n- and p-type electrodes both at pH 0 and 14. Further experiments at intermediate pH values have been achieved whose results match well those reported here; therefore in the following we deal only with pH 0 and 14. Thermodynamic energy values used in the computation of the standard potentials E_0 are taken from the literature (6).

Oxidation reactions.—According to previous work (3a), possible decomposition reactions are



pH = 14



Such reactions are possible with n-type materials in the dark only at large band bendings. They can take place at illuminated n-type electrodes or p-type electrodes in the dark as soon as holes are available in surface.

Experimentally, anodic reactions are observed at potentials E_{ox} such as

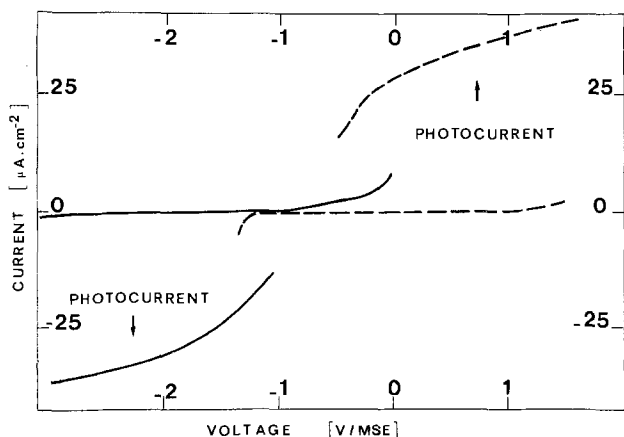


Fig. 1. Typical current and photocurrent (modulated) vs. potential characteristics for CdTe/1M NaOH junctions. The photocurrent is measured at 850 nm. n-CdTe: $1.5 \times 10^{15} \text{ cm}^{-3}$, dashed line; p-CdTe: $3 \times 10^{16} \text{ cm}^{-3}$, full line.

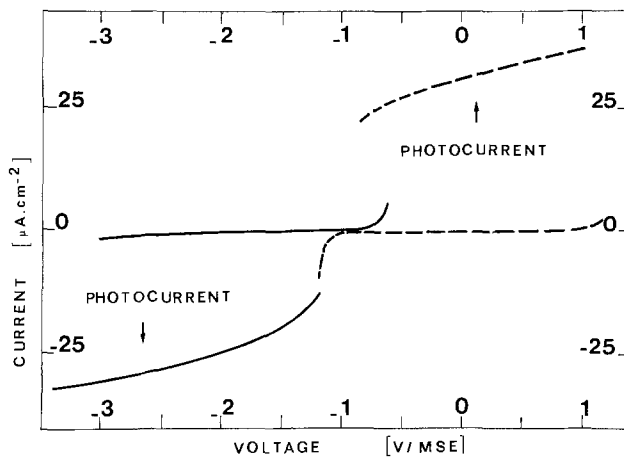


Fig. 2. Typical current and photocurrent (modulated) vs. potential characteristics for CdTe/1M HClO_4 junctions. The photocurrent is measured at 850 nm. n-CdTe: $1.5 \times 10^{15} \text{ cm}^{-3}$, dashed line; p-CdTe: $3 \times 10^{16} \text{ cm}^{-3}$, full line.

$$\text{pH} = 0 \quad \begin{cases} \text{n-type (illuminated)} & E_{\text{ox}} \cong -0.8\text{V vs. MSE} \\ \text{p-type (dark)} & E_{\text{ox}} \cong -0.8, -0.7\text{V vs. MSE} \end{cases}$$

$$\text{pH} = 14 \quad \begin{cases} \text{n-type (illuminated)} & E_{\text{ox}} \cong -0.8\text{V vs. MSE} \\ \text{p-type (dark)} & E_{\text{ox}} \cong -0.95\text{V vs. MSE} \end{cases}$$

At both pH's, the experimental potential values are in good agreement with the thermodynamic reactions reported in Eq. [1]-[2]. From the above considerations, it is possible to deduce that the oxidation process of CdTe takes place without energy barrier as soon as the free carriers involved (holes) are available in sufficient amount close to the semiconductor surface.

In the dark, at n-CdTe electrodes, anodic decomposition takes place at potentials greater than +0.8 to +1.0V and only for free carrier densities sufficiently large ($> 10^{17} \text{ cm}^{-3}$). We deduce then that the associated processes do not involve holes from the valence band but electrons from species in solution which are injected in the conduction band by tunneling. Such processes necessitate large band bendings and have been observed with other n-type semiconductors such as ZnSe (7).

Reduction reactions.—These processes seem more complicated than in the former case due to the possibility of hydrogen evolution.

Experimental evidence of cathodic currents takes place in the following potential ranges (Table II)

$$\text{pH} = 0 \quad \begin{cases} \text{n-type (dark)} & E_{\text{red}} \leq -0.8, -1.0\text{V vs. MSE} \\ \text{p-type (illuminated)} & E_{\text{red}} \leq -0.7\text{V vs. MSE} \end{cases}$$

$$\text{pH} = 14 \quad \begin{cases} \text{n-type (dark)} & E_{\text{red}} \leq -1.0\text{V vs. MSE} \\ \text{p-type (illuminated)} & E_{\text{red}} \leq -1.0\text{V vs. MSE} \end{cases}$$

These experimental values must be correlated with the thermodynamic data (3a)

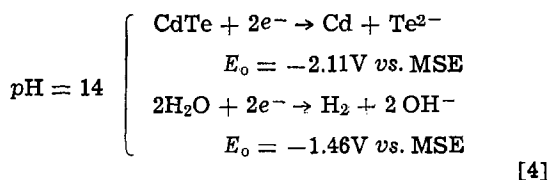
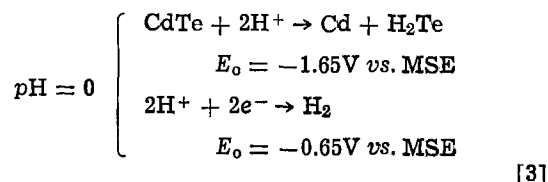


Table I. Anodic and cathodic currents at the CdTe/1M HClO₄ interface

Potential (V)	-3.0	-1.8	-1.65	-1.2	-0.8	-0.73	-0.7	-0.65	-0.3	+1.0
n-CdTe	← reduction					← no current			→ oxidation →	
n-CdTe	← reduction					oxidation			→	
p-CdTe	← reduction	← no current						→ oxidation		
p-CdTe	← reduction						→ oxidation			
particular indications a)		V_{fb}^n	E_d^n			E_d^p		H^+/H_2	V_{fb}^p	

a) V_{fb}^n is the flat band potential for n-CdTe ; V_{fb}^p for p-CdTe

E_d^n : standard potential of the cathodic decomposition $CdTe + 2H^+ + 2e^- \rightarrow Cd + H_2Te$

E_d^p : standard potential of the anodic decomposition $CdTe + 2p^+ \rightarrow Cd^{++} + Te$

Table II. Anodic and cathodic currents at the CdTe/1M NaOH interface

Potential (V)	-3.5	-2.11	-1.8	-1.46	-1.2	-1.0	-0.97	-0.8	-0.3	+0.8
n-CdTe	← reduction					← no current			→ oxidation →	
n-CdTe	← reduction					no current			→ oxidation →	
p-CdTe	← reduction	← no current						→ oxidation		
p-CdTe	← reduction						→ oxidation			
particular indications a)		E_d^n	V_{fb}^n	H_2O/H_2			E_d^p		V_{fb}^p	

a) V_{fb}^n and V_{fb}^p have the same meaning as in table I.

E_d^n : standard potential of the cathodic decomposition $CdTe + 2e^- \rightarrow Cd + Te^{--}$

E_d^p : standard potential of the anodic decomposition $CdTe + 2OH^- + 2p^+ \rightarrow HCdO_2^- + H^+ + Te$

It appears that hydrogen evolution reaction may compete with decomposition. At p-type electrodes and for small photon fluxes ($< 10^{14} \text{ cm}^{-2}$), hydrogen can be experimentally produced without further modification of the electrochemical behavior. At n-type materials, hydrogen evolves in the dark at potential below $-1.0V$ vs. MSE and the electrode remains unperturbed. The latter case will be discussed later together with the determination of the flatband potential value.

However, at p-type electrodes and pH's 0 and 14 a cathodic decomposition of the semiconductor together with hydrogen evolution can be evidenced for large band bendings (potential below $-3V$ vs. MSE) and large photon flux thus suggesting that decomposition is a slow process as compared to hydrogen evolution.

Influence of dissolved oxygen.—This influence is noticeable with p-type materials for which a dark cathodic current exists correlated to the presence of

oxygen in solution. This dark current is diffusion limited thus suggesting that oxygen reduction takes place by hole injection into the semiconductor valence band. Due to the lack of influence of the addition of H_2O_2 in solution, the mechanisms of oxygen reduction are not yet clear.

Flatband potential.—In the previous sections, the slight influence of pH on the experimental potential values must be outlined. Such an observation suggests that the flatband conditions do not depend on the pH. In this direction, determination of the flatband potential V_{FB} has been achieved both by capacitance (C) and modulated photocurrent (i_{ph}) measurements. In the latter case, a linear plot i_{ph}^2 vs. V enables the determination of V_{FB} (8).

N-type.—A good Schottky behavior (linear plot C^{-2} vs. V) is obtained only after a photoetching of the electrode (3 mn at $V = +1.0V$ vs. MSE in 1M NaOH solution). The importance of photoetching for II-VI semiconductor electrodes has recently received particular attention (9). This treatment is necessary to obtain reproducible results in the whole pH range. Results are presented in Fig. 3. We found

$$V_{n_{FB}} \simeq -1.8V \text{ vs. MSE}$$

a result in fair agreement with literature (2). This value is almost pH independent.

P-type.—The Schottky behavior is obtained with only the chemical etching (see above). The result is

$$V_{p_{FB}} \simeq -0.3V \text{ vs. MSE}$$

The plot of i_{ph}^2 vs. V is shown in Fig. 3 and is pH independent.

We observe that

$$|V_{n_{FB}} - V_{p_{FB}}| \sim E_g = 1.5 \text{ eV}$$

The invariance of V_{FB} with pH may probably be accounted for by a specific interaction between the aqueous electrolyte and the telluride anion of CdTe. Such a behavior has already been observed for other II-VI compounds, especially for CdS (10), and explained by a similar argument.

We now compare the potential V_{H_2} at which hydrogen evolution takes place at n-CdTe (see above) and $V_{n_{FB}}$. We have

$$V_{H_2} \simeq -1.0V \text{ vs. MSE}$$

and the difference

$$|V_{H_2} - V_{n_{FB}}| \simeq 0.8V$$

is very large. A similar phenomenon is observed with many other n-type semiconductors and particularly n-GaP for which a specific interaction with H^+ ions has been invoked (11). In view of the results obtained with p-CdTe electrodes, a similar assumption seems possible here.

Material characterization.—The above results suggest that the conditions can be fulfilled in order to achieve a photoelectrochemical determination of a physical parameter such as the minority carrier diffusion length L . These conditions have been detailed elsewhere (12), and we do not emphasize them in this paper. We only mention that the L determination lies on the use of the Gärtner model (13) for the description of the i_{ph} vs. V characteristic.

Fulfillment of conditions

$$\begin{cases} \alpha L \ll 1 & \alpha = \text{optical absorption coefficient} \\ \alpha W \ll 1 & W = \text{space charge region width} \end{cases} \quad [5]$$

enables us to express the photocurrent i_{ph} as

$$i_{ph} = K\alpha(W + L) \quad K = \text{constant} \quad [6]$$

By plotting i_{ph} (in arbitrary units) vs. W (computed by the Schottky relation), the determination of L becomes simple. The L values for CdTe are reported in Table III and can be compared to other results (13). We notice that for similar doping and free carrier densities, our results are in fair agreement with those obtained by other methods. The L values we obtain are rather small ($< 1 \mu m$) and verify a posteriori condition [5] and justify the method. Generally, small L values have been obtained for CdTe which are attributed to defects in the material. Another possibility to correlate the defect density (connected with the dopant) with a physical parameter is given by the Urbach's rule which indicates that the optical absorption tail obeys the analytical equation

$$\alpha = \alpha_0 \exp[S(E_g - E)] \quad [7]$$

where α_0 is a constant, E_g the energy gap, E the photon energy, and $S (= \sigma/kT)$ is Urbach's slope. The complete Urbach's rule which includes the variation with temperature of S has already been extensively studied for CdTe (14). Different interpretations are possible for relation [7] (15), we only keep in mind that

Fig. 3. Reciprocal squared capacitance and squared photocurrent vs. potential plots for CdTe/1M NaOH junctions. ●: n-type; $V_{n_{FB}} = -1.8V$ vs. MSE. Capacitance measured at 100 kHz. ○: p-type; $V_{p_{FB}} = -0.3V$ vs. MSE. Wavelength 850 nm.

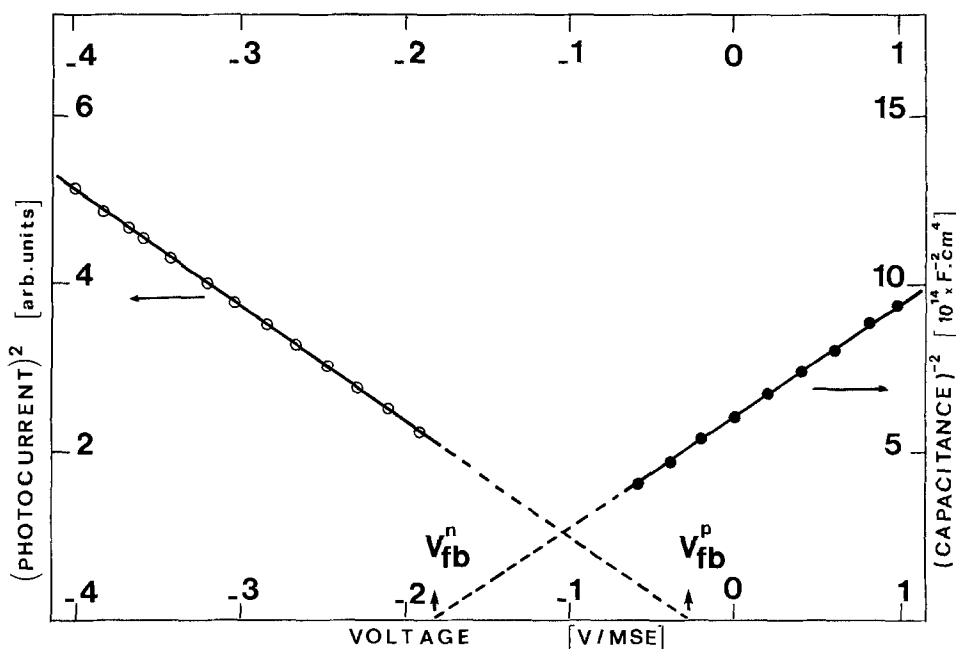


Table III. Minority carrier diffusion length (L) and Urbach's slopes (S) deduced from photoelectrochemical measurements. The free carrier concentration (N) is measured by Hall effect (Van der Paw)

Conduction	p	p	p	n	n
Dopant	Undoped	P	P	Undoped	In
N (cm^{-3})	4×10^{15}	3×10^{16}	7×10^{16}	1.5×10^{15}	8×10^{17}
S (eV^{-1})	93	35	27	94	52
L (μm)	0.85	0.15	0.09	0.25	0.15

Urbach's slope is directly connected with the defects of a semiconductor and their ionization, possibly introduced by a dopant, and that a small value of S corresponds to a large amount of defects (Fig. 4).

In the absorption tail, the α values are low and conditions [5] hold. Thus, the related photocurrent i_{ph} can be expressed by relation [6] which combined with Eq. [7] leads to

$$i_{\text{ph}} = K\alpha_0 (W + L) \exp [S(E_g - E)] \quad [8]$$

This equation indicates that the photocurrent tail and the absorption tail may lead to similar information about the defects in a semiconductor (S value).

Equation [8] is verified with our CdTe samples and the results which are independent of the band bending in the semiconductor are reported in Table III. We notice that a doping with phosphorus leads to S values much smaller than in the other cases. This observation may probably be correlated with the particular property of P to produce defects in CdTe (16).

Summary

The CdTe-aqueous electrolyte interface presents behavior which is analyzed carefully. The information deduced from electrochemical measurements indicates that this interface presents a reproducible Schottky behavior which enables us to determine the minority carrier diffusion length and the Urbach's slope of a set of different CdTe samples. These parameter determinations may be accurately compared to others and enable us to produce information about the defects in the CdTe single crystals.

Manuscript submitted June 12, 1983; revised manuscript received Sept. 20, 1983.

REFERENCES

- For general information, see e.g., Proceedings of the 2nd Symposium on Cadmium Telluride, Strasbourg, 1976, edited in *Revue Phys. Appl.* 12 (1977); K. Zanio, in "Cadmium Telluride—Semiconductors and Semimetals," Vol. 13, R. K. Willardson and A. C. Beer, Editors, Academic Press, New York (1978).
- (a) A. Aruchamy and M. S. Wrighton, *J. Phys. Chem.*, **84**, 2848 (1980); (b) A. Heller, K. C. Chang, and B. Miller, *J. Am. Chem. Soc.*, **100**, 684 (1978); (c) C. Vasquez-Lopez, F. Sanchez-Sinencio, J. S. Helman, J. L. Peña, A. Lastras-Martinez, P. M. Raccach, and R. Triboulet, *J. Appl. Phys.*, **50**, 5391 (1979); (d) S. Tanaka, J. A. Bruce, and M. S. Wrighton, *J. Phys. Chem.*, **85**, 3778 (1981); (e) A. E. Rakhshani and L. E. Lyons, *Aust. J. Chem.*, **35**, 1949 (1982).
- (a) J. O'M. Bockris and K. Uosaki, *This Journal*, **124**, 1348 (1977); (b) J. O'M. Bockris, K. Uosaki, and H. Kita, *J. Appl. Phys.*, **52**, 808 (1981); (c) Y. Nashimoto, S. Fuyuki, T. Akutagawa, and S. Hayakawa, *Jpn. J. Appl. Phys.*, **20**, 565 (1981).
- P. Gaugash and A. G. Milnes, *This Journal*, **128**, 924 (1981).

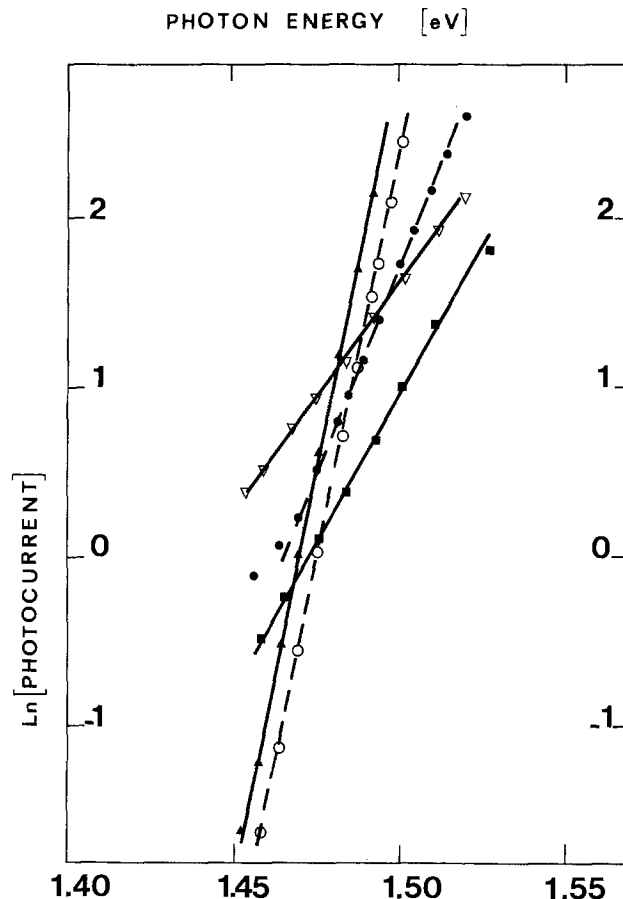


Fig. 4. Urbach's slopes are deduced from Ln (photocurrent) vs. photon energy plots at fixed electrode potential. The slope is independent of the potential. Full line: p-CdTe \blacktriangle undoped, $4 \times 10^{15} \text{ cm}^{-3}$; \blacksquare P-doped $3 \times 10^{16} \text{ cm}^{-3}$; \blacktriangledown P-doped, $7 \times 10^{16} \text{ cm}^{-3}$. Dashed line: n-CdTe \circ undoped, $1.5 \times 10^{15} \text{ cm}^{-3}$; \bullet In-doped, $8 \times 10^{17} \text{ cm}^{-3}$.

- J. Gautron, P. Lemasson, F. Rabago, and R. Triboulet, *ibid.*, **126**, 1868 (1979).
- W. H. Latimer, "Oxidation Potentials," 6th ed., Prentice Hall, New York (1964).
- P. Lemasson and J. Gautron, *J. Electroanal. Chem.*, **119**, 229 (1981).
- P. Lemasson, A. Etcheberry, and J. Gautron, *Electrochim. Acta*, **27**, 607 (1982).
- R. Tenne, N. Müller, Y. Mirovsky, and D. Lando, *This Journal*, **130**, 852 (1983).
- T. Watanabe, A. Fujishima, and K. Honda, *Chem. Lett.*, 897 (1974).
- H. Yoneyama, S. Mayumi, and H. Tamura, *This Journal*, **125**, 68 (1978).
- (a) J. Gautron and P. Lemasson, *J. Cryst. Growth*, **59**, 332 (1982); (b) A. Etcheberry, M. Etman, B. Fotouhi, J. Gautron, J. L. Sculfort, and P. Lemasson, *J. Appl. Phys.*, **53**, 8867 (1982).
- (a) P. Gaugash and A. G. Milnes, *This Journal*, **128**, 921 (1981); (b) L. Tarricone, N. Romeo, G. Sberveglieri, and S. Mora, *Solar Energy Mater.*, **7**, 343 (1982); (c) D. R. Wight, D. Bradley, G. Williams, M. Astles, S. J. C. Irvine, and C. A. Jones, *J. Cryst. Growth*, **59**, 323 (1982).
- C. Konak, J. Dillinger, and V. Prosser, in Proc. Int. Conf. II-VI Compounds, Providence, R.I., 1967, D. G. Thomas, Editor, p. 856, Benjamin, New York (1967).
- (a) D. L. Dexter, *Phys. Rev. Lett.*, **19**, 383 (1967); (b) D. J. Dow and D. Redfield, *Phys. Rev.*, **B5**, 594 (1972).
- F. A. Selim and F. A. Kröger, *This Journal*, **124**, 401 (1977).

End Point Detection for Reactive Ion Etching of Aluminum

Kwang O. Park and Fredrick C. Rock

GTE Laboratories Incorporated, Advanced Components Technology, Waltham, Massachusetts 02254

The fabrication of VLSI circuits requires many steps of delicate dry etching processes to delineate fine-line patterns. In dry etching processes, a viable technique that enables the detection of the completion of an etching process is required to prevent over or under-etching. In a typical end-point detection scheme, a particular chemical species produced during the etching process is observed by monitoring a relevant spectral line as the etching process consumes the substrate material. The time to terminate the process can then be inferred from the changes in chemical composition of the plasma. In the past, when Al was etched especially in the pure CCl_4 , SiCl_4 , or BCl_3 gas, the 261 nm band has been used for end-point detection. This is because it is a major molecular AlCl emission band in the UV range overshadowing the 522-nm emission in the visible range. In this note we report results on the use of the 522 nm band emitted from molecular AlCl for end-point detection of Al etch in the free chlorine containing gas plasma and the relative merits of this procedure.

Etching was performed in a planar-type etcher with parallel-plate electrodes, as shown in Fig. 1. Chamber pressure during etching was maintained at 0.6 torr. A 13.56 MHz RF power supply was employed in this experiment. A monochromator (Instrument SA Model H-2) was used to take emission spectrum. A signal from a band of interest was obtained by tuning the monochromator to the peak of the band, and the intensity *vs.* time profile was recorded on a strip chart recorder. A Hamamatsu Model R928 photomultiplier was used as the detector.

Al and its alloys have been reactively ion etched effectively in plasmas consisting of SiCl_4 , Cl_2 , and BCl_3 gases (1, 2). The transient emission spectrum measured from a plasma consisting of 130 cm^2 SiCl_4 , 100 cm^2 Cl_2 , and 50 cm^2 BCl_3 is shown in Fig. 2. It has been found experimentally that this particular gas composi-

tion results in an excellent etch rate (about 400 nm/min at 0.5W/cm² applied power density) with an anisotropic profile and quickly removes native aluminum oxide. The spectrum shows Cl_2 bands at 257 and 307 nm, SiCl bands at 282 and 287 nm, and BCl bands at 272 and 278 nm. All of these molecules are reactant species in the plasma. The spectrum also shows additional bands at 261 and 522 nm due to molecular AlCl (3), which is the major reaction product of Al etching (2). The 261-nm band is assigned to the transition $\text{A}^1\Pi \rightarrow \text{X}^1\Sigma$ in the singlet state, and the 522-nm band may be attributable to the transition $\text{B}^3\Sigma \rightarrow \text{A}^3\Pi$ in the triplet state (4). Atomic Al(1) lines at 394 and 396 nm are also seen. Several of these bands have been previously used for end-point detection. Specifically, the 261-nm band due to AlCl has been widely used for this purpose because it is well resolved and is of high intensity during Al etch with CCl_4 , SiCl_4 , BCl_3 , etc. (5-7). When Al is etched, especially with mixtures of SiCl_4 , Cl_2 , and BCl_3 , the 261-nm band has a high intensity when there is aluminum remaining. This high intensity starts to fall as the etching is completed. However, there is an overlapping intense and broad Cl_2 band at 257 nm which is reduced during the etching and begins to return as the etching approaches completion (8). The result is that the signal at 261 nm first decreases as the etching is completed and then begins to increase again as the Cl_2 band returns, as shown in Fig. 3. Consequently, end-point detection with this signal can be uncertain, especially when Cl_2 gas is added to the other gases to enhance Al etch rates. The intensity of the 261-nm signal is expected to in-

Key words: end point detection, RIE of Al, optical emission spectroscopy.

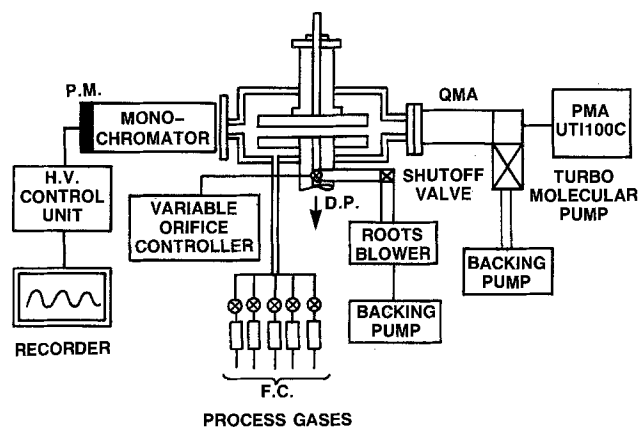


Fig. 1. Schematic of the experimental etcher (PK2440 PE/RIE system) with a monochromator and a QMA.

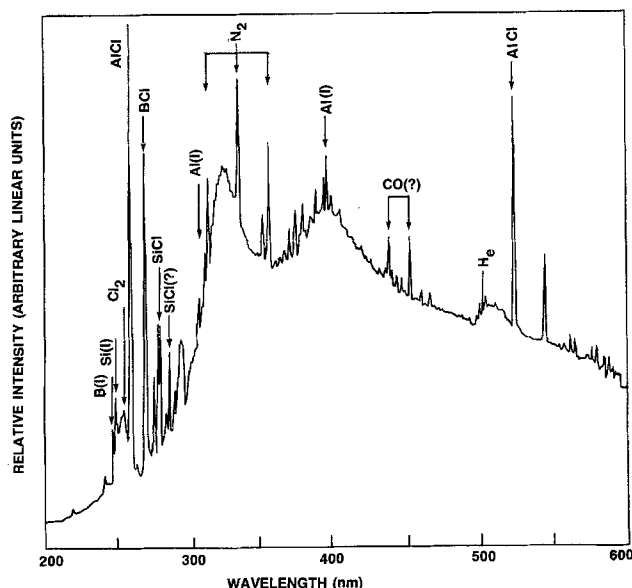


Fig. 2. Transient optical emission spectrum of the $\text{SiCl}_4 + \text{Cl}_2 + \text{BCl}_3$ plasma during Al RIE. This spectrum is uncorrected for system response.

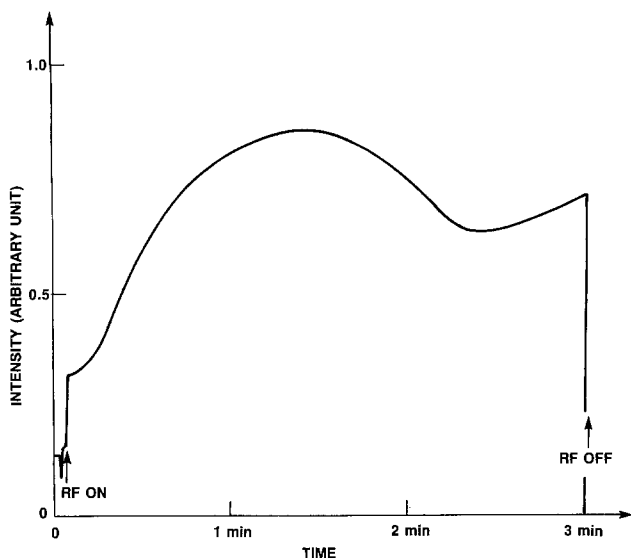


Fig. 3. Intensity vs. time of the 261 nm band during Al + 1%Si etching.

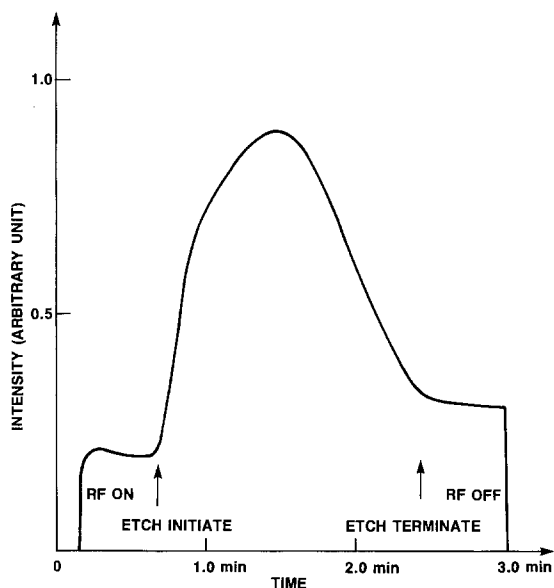


Fig. 4. Intensity vs. time of the 522 nm band during Al + 1%Si etching.

crease sharply once etching is initiated. It then reaches a steady-state maximum. However, it has been observed that in Al etching there is always an induction period of some degree which is associated with the removal of native aluminum oxide (2). The duration of an induction period depends strongly on the quality of Al films, the composition of etchant gases used, and other factors, including the environmental conditions of the etching chamber. The initial gradual increase in the intensity of the 261-nm signal, as shown in Fig. 3, is attributable to the slow etching caused by native aluminum oxide. The extent of the duration of the peak intensity is related to the Al film thickness and

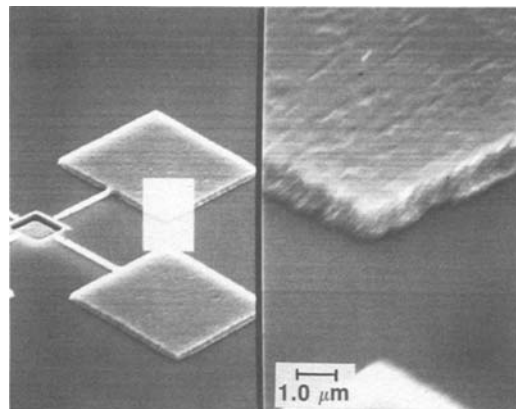


Fig. 5. An SEM picture of 1 μm -thick Al + 1%Si film which was etched using the end-point detection technique shown in Fig. 4.

the etch rate. However, while Al(1) lines at 394 and 396 nm are free from interference, they tend to have low intensities and sometimes are difficult to find. The 522 nm band not only has a high intensity, but also is well isolated and easy to locate because it is free from interference with the neighboring bands.

Figure 4 shows the actual use of the 522-nm signal for end-point detection during reactive ion etching of three sample 3-in wafers 1 μm thick Al + 1%Si films with an above-mentioned gas mixture. Some delay in 522 nm emission after initiation of the RF discharge is apparent in Fig. 4. This is because of the time required for the proper matching of the system impedance. As the etching is completed, the signal intensity starts to fall; it drops eventually to the sustaining level of the discharge. The end point of the etching is clearly evident because there are no conflicting emissions overlapping the 522 nm band signal near the end of the etching process. To clear the residues remaining on the substrate, the substrate was deliberately over-etched by extending the etching period by about 20% past indicated etch completion. Figure 5 shows an SEM picture of 1.0 μm thick Al + 1%Si film, which was etched employing the 522 nm end-point detection technique.

Manuscript submitted March 14, 1983; revised manuscript received July 29, 1983.

GTE Laboratories assisted in meeting the publication costs of this article.

REFERENCES

1. R. F. Reichelderfer, *Solid State Technol.*, **25**, 160 (1982).
2. K. Tokunaga, F. C. Redeker, D. A. Danner, and D. W. Hess, *This Journal*, **128**, 851 (1981).
3. "Tables of Constants and Numerical Data," Simone Bourcier, Editor, Pergamon Press Ltd., Oxford (1970).
4. D. Sharma, *J. Astrophysics*, **113**, 210 (1951).
5. K. O. Park, Abstract 196, p. 318, The Electrochemical Society Extended Abstracts, Vol. 83-1, San Francisco, California, May 8-13, 1983.
6. B. J. Curtis, *Solid State Technol.*, **23**, 129 (1980).
7. C. S. Korman, *ibid.*, **25**, 115 (1982).
8. J. E. Spencer and B. Y. Shu, Abstract 151, p. 239, The Electrochemical Society Extended Abstracts, Vol. 82-2, Detroit, Michigan, October 17-21, 1982.

Improved Conductivity in Polysilicon Films by Pre-annealing

C. P. Wu and G. L. Schnable

RCA Laboratories, Princeton, New Jersey 08540

B. W. Lee¹ and R. Stricker²

RCA Solid State Division, Somerville, New Jersey 08876

Doped polycrystalline silicon is used as MOS transistor gates and interconnects in many kinds of micro-electronic devices and integrated circuits. The polysilicon film is usually deposited by low-pressure chemical vapor deposition (LPCVD) techniques, and subsequently doped by either a POCl_3 diffusion process at approximately 1000°C for 30 min, or by ion implantation followed by annealing at between 850 and 950°C . Doping of polysilicon films by ion implantation is becoming more popular because often it means fewer processing steps and/or lower processing temperatures, which is important for VLSI fabrication.

With ion implantation for doping polysilicon films, it is difficult to obtain sheet resistivities below $40\text{-}50 \Omega/\square$, because a large fraction of the implanted atoms diffuse to the polysilicon grain boundaries upon postimplant annealing, become trapped and, therefore, do not contribute to electrical conductivity (1). The electrical conductivity of doped polysilicon thin films can be influenced by many factors (1-8), including crystallite size and orientation; potential barriers (8), dopant (4, 5) and oxygen segregation (6) at grain boundaries; and stress and other effects. Increased polysilicon conductivity has been achieved by pulsed (9, 10) or cw laser annealing (11-13), which affords a means to increase the active carrier concentrations and to increase the size of the crystallites and so achieve higher conductivity in polysilicon films.

Recently, we have found that significantly lower resistivity of ion-implanted polysilicon films can be obtained by preannealing at a temperature between 1000° and 1200°C for 30 min in an inert ambient prior to doping the polysilicon by ion implantation, or by POCl_3 diffusion (14). The polysilicon film samples were prepared by LPCVD at 620°C . The films were $0.5 \mu\text{m}$ thick, deposited on $0.5 \mu\text{m}$ of SiO_2 thermally grown on (100)-orientation single-crystal silicon wafers. This ensured that there would be no epitaxial regrowth during the preannealing process. It is also the configuration in which doped polysilicon films are most frequently used in integrated circuits.

Except for the controls, the samples were preannealed at temperatures ranging from 1000° to 1200°C for 30 min in dry nitrogen prior to doping by ion implantation. They were then ion-implanted either with $^{31}\text{P}^+$ ion at 50 keV with a fluence of 10^{16}cm^{-2} , or with $^{11}\text{B}^+$ ions at 50 keV with a fluence of $6 \times 10^{15} \text{cm}^{-2}$. All samples were capped with $\sim 0.5 \mu\text{m}$ of SiO_2 by CVD at 450°C to prevent cross contamination before furnace annealing at 950°C for 30 min to activate the implanted atoms. The capping oxides were then stripped and the sheet resistivities were evaluated using four-point probes.

Table I summarizes the results of sheet resistivity measurements by four-point probes on ion-implanted polysilicon films that were preannealed at $1000^\circ\text{-}1200^\circ\text{C}$. The control samples were not preannealed, and their sheet resistivities are in the range usually obtained. Samples preannealed at 1000°C showed a slight improvement in sheet resistivities; this varied from 6% to 9%. Substantial improvements in sheet re-

sistivities were obtained for 1100°C preanneal, 30% for the ^{31}P -implanted polysilicon sample and 48% for the ^{11}B -implanted sample. These improvements increased to well over 50% if higher preanneal temperatures could be tolerated. Obviously, higher preanneal temperatures and/or longer preanneal times resulted in the growth of larger average crystallite size and, therefore, fewer grain boundaries to trap the implanted ions.

The above-described experiments were repeated with LPCVD amorphous silicon deposited at 560°C . Polysilicon formed from amorphous silicon is currently being used instead of LPCVD polysilicon in many device and circuit applications because of its improved surface smoothness (15-19). Table II summarizes the results of preannealing of LPCVD amorphous silicon films prior to doping by POCl_3 diffusion at 950°C for 30 min, or by ion-implantation (and subsequent post-implant anneal at 950°C for 30 min). For samples doped by the POCl_3 diffusion technique, the improvements are 11% for preannealing at 1000°C and 23% at 1100°C . Results for the ion-implanted samples show improvements varying from 4% for samples preannealed at 1000°C to 32% at 1100°C . Thus, preannealing of silicon films deposited in either polycrystalline or amorphous form results in substantial improvement in film resistivity, even for conventional doping with a POCl_3 source, which can be considered to provide an infinite source of dopant impurities. Scanning electron microscopy was used to examine the various samples in the above experiments, and no detectable change in surface roughness could be observed at 20K magnification. Similar results were obtained by Harbeke *et al.* (15).

Table I. Sheet resistivities of polysilicon films deposited in polysilicon form (LPCVD at 620°C), preannealed at different temperatures, followed by doping by ion implantation and subsequent annealing

Preanneal temp. (30 min preanneal)	Sheet resistivity, Ω/\square	
	^{31}P implant, 50 keV, 10^{16}cm^{-2} dose	^{11}B implant, 50 keV, $6 \times 10^{15} \text{cm}^{-2}$ dose
Control (no preanneal)	48.6 ± 2.2	87.5 ± 0.7
1000°C	44.1 ± 0.7	82.5 ± 1.8
1050°C	43.1 ± 0.7	63.1 ± 0.5
1100°C	34.3 ± 0.8	45.1 ± 0.1
1150°C	26.9 ± 1.2	36.8 ± 0.2
1200°C	22.3 ± 0.1	33.5 ± 0.1

Table II. Sheet resistivities of polysilicon films which were deposited in amorphous form (LPCVD at 560°C), preannealed at different temperatures, followed by doping by conventional diffusion (POCl_3) or by ion implantation and subsequent annealing

Preanneal in N_2 (30 min preanneal)	Sheet resistivity, Ω/\square		
	POCl_3 diffusion	^{31}P implant, 50 keV, 10^{16}cm^{-2} dose	^{11}B implant, 50 keV, $6 \times 10^{15} \text{cm}^{-2}$ dose
Control (no preanneal)	15.2 ± 0.5	61.6 ± 0.3	76.0 ± 0.6
1000°C	13.6 ± 0.2	59.2 ± 0.9	72.9 ± 0.4
1100°C	11.7 ± 0.2	42.1 ± 0.4	52.0 ± 0.3

¹Present address: Dept. of Electrical Engineering, Rutgers University, Piscataway, NJ 08854.

²Present address: Western Electric, Allentown, PA 18103.

Key words: ion implantation, diffusion, anneal, CVD.

In conclusion, we have shown that a preannealing step of 1100°C for 30 min in dry nitrogen, applied to either polysilicon films or LPCVD amorphous silicon films, can substantially improve sheet conductivity and be incorporated into many IC processes, in which such preannealing can precede source and drain implants to minimize dopant diffusion.

Manuscript received June 8, 1983.

RCA Laboratories assisted in meeting the publication costs of this article.

REFERENCES

1. L. L. Kazmerski, in "Polycrystalline and Amorphous Thin Films and Devices, L. L. Kazmerski, Editor, pp. 59-128, Academic Press, New York (1980).
2. Y. Wada and S. Nishimatsu, *Denki Kagaku*, **47**, 118 (1979).
3. T. I. Kamins, *J. Appl. Phys.*, **42**, 4357 (1971).
4. B. Swaminathan, E. Demoulin, T. W. Sigmon, R. W. Dutton, and R. Reif, *This Journal*, **127**, 2227 (1980).
5. M. M. Mandurah, K. C. Saraswat, C. R. Helms, and T. I. Kamins, *J. Appl. Phys.*, **51**, 5755 (1980).
6. D. Redfield, *Appl. Phys. Lett.*, **40**, 163 (1982).
7. C. Dianteill and A. Rocher, *J. Phys. Paris*, **43**, C1 (1982).
8. N. C.-C. Lu, L. Gerzberg, C.-Y. Lu, and J. D. Meindl, *IEEE Trans. Electron Devices*, **ed-30**, 137 (1983).
9. C. P. Wu and C. W. Magee, *Appl. Phys. Lett.*, **34**, 737 (1979).
10. S. Onga, S. Kohyama, K. Shibata, Y. Nagakubo, and H. Iizuka, *Jpn. J. Appl. Phys.*, **19**, 133 (1980).
11. A. Gat, L. Gerzberg, J. F. Gibbons, T. J. Magee, J. Peng, and J. D. Hong, *Appl. Phys. Lett.*, **33**, 775 (1978).
12. H.-S. Lee, *ibid.*, **38**, 770 (1981).
13. H.-S. Lee, *Solid-State Electron.*, **24**, 1059 (1981).
14. B. W. Lee, R. E. Stricker, C. P. Wu, and G. L. Schnable, in "Proceedings of the Symposium on VLSI Technology, Systems, and Applications," p. 279, Taipei, China (1983).
15. G. Harbeke, L. Krausbauer, E. F. Steigmeier, A. E. Widmer, H. F. Kappert, and G. Neugebauer, *Appl. Phys. Lett.*, **43**, 249 (1983).
16. L. Faraone, in "INFOS 83 Abstracts," p. 59, International Conference on Insulating Films on Semiconductors, Eindhoven, The Netherlands (April 1983).
17. J. T. McGinn, H. F. Kappert, L. Krausbauer, J. M. Shaw, and A. E. Widmer, Abstract 415, p. 647, The Electrochemical Society Extended Abstracts, Vol. 83-1, San Francisco, California, May 8-13, 1983.
18. G. Harbeke, E. F. Steigmeier, and A. E. Widmer, Abstract 416, p. 649, *ibid.*
19. E. Kinsbron, M. Sternheim, and R. Knoell, *Appl. Phys. Lett.*, **42**, 835 (1983).

Use of a Liquid Electrolyte Junction for the Measurement of Diffusion Length in Silicon Ribbon

Ronald H. Micheels

Mobil Solar Energy Corporation, Waltham, Massachusetts 02254

R. David Rauh*

EIC Laboratories Incorporated, Newton, Massachusetts 02158

In the last 10 years there has been a rapid expansion in the technology of silicon sheet growth (1). A key parameter for the evaluation of this material for photovoltaic applications is the minority carrier diffusion length. For single crystal and epitaxial silicon the surface photovoltage (SPV) technique (2) is a standard ASTM test method for the determination of minority carrier diffusion length (3). However, the conductive oxide glass pressure contact which is used to detect the surface photovoltage in the ASTM method is unsuitable for sheet silicon because of the uneven nature of the surfaces. The liquid-semiconductor junction, which acts very much like a Schottky barrier (4), lends itself very well to the problem of contacting irregular surfaces. The feasibility of using a liquid junction for diffusion length measurement was first demonstrated by Fabre *et al.* (5), who reported spectral response measurements of Si photoelectrodes. More recently Moore (6) has applied the liquid junction to measurement of diffusion lengths in n-type amorphous silicon using the SPV method. We would like to report the successful application of a liquid electrolyte-semiconductor junction to the measurement of SPV diffusion lengths in p-type, polycrystalline silicon ribbon. The use of the liquid junction greatly reduces the time and labor involved in the measurement compared to that required with a more conventional Al-Schottky barrier process which was previously employed in this laboratory (7). By using the liquid junction it has been found possible

to measure samples directly from crystal growth, thus eliminating etching or any other sample processing.

The p-type Si ribbon used in this study was grown by the edge-defined film-fed growth (EFG) technique (8) with a typical resistivity of 3-5 Ω -cm and thickness in the range of 0.25-0.40 mm. A Teflon cell, shown in Fig. 1, was used to hold 1×2 in. ribbon samples. A 0.1M solution of tetrabutylammonium perchlorate ($(C_4H_9)_4NClO_4$) in methanol was used as the electrolyte. Initial measurements were made with 0.002M methylviologen hydrate added to the solution to form a redox couple with a potential near the conduction band. However, it was found that the addition of methylviologen was unnecessary due to the Fermi level pinning effect produced by surface states at the silicon-solution interface (9). A Pt wire was used as a solution reference electrode. A layer of In foil was pressed against the ribbon to make the back contact. Subsequent to this study it was found that a sheet of silver impregnated rubber (Chomerics Materials Incorporated, Woburn, Massachusetts) was a more practical contact material. A 2V reverse bias voltage was applied across the liquid junction to prevent any significant band bending from occurring at the back contact, which is weakly rectifying in nature. The SPV apparatus basically consists of a chopped monochromator light source with a feedback control circuit which adjusts the light intensity to maintain a constant photovoltage at the sample junction. The monochromator wavelength is stepped through 12 points between 870 and 1000 nm. The $1/e$ penetration depth of the light

* Electrochemical Society Active Member.

Key words: semiconductor, cell, photovoltaic.

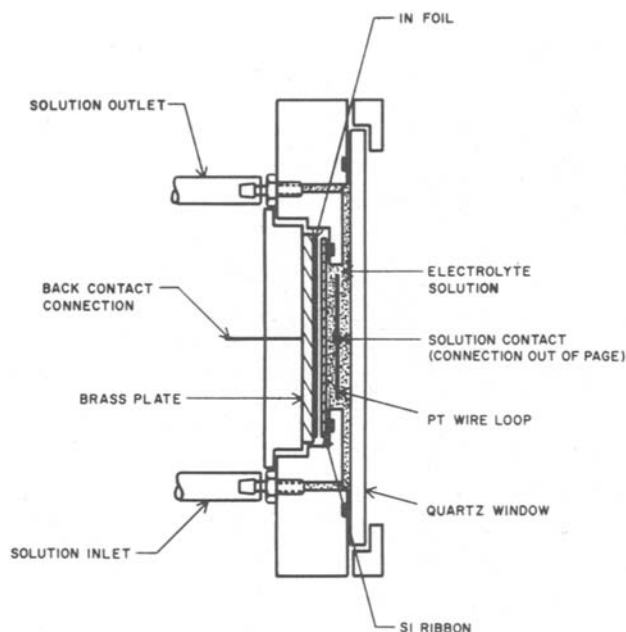


Fig. 1. Cross section of liquid junction cell

$(1/\alpha)$ ranges from 22 to 120 microns between these wavelengths. The data are collected and fitted with a computer. The apparatus and data analysis is described in more detail in Ref. (7). The absorption coefficients used in the analysis were determined from absorption and reflection spectra of polished ribbon samples and are given in Table I.

In order to determine whether the minority carrier diffusion lengths (L_n) measured with the liquid junction cell were correct, two comparison experiments were conducted in which samples were measured both with an aluminum-Schottky barrier and with the liquid junction. In the first experiment a set of 7 Si ribbon and 5 float-zone Si samples were processed into Al-Schottky diodes with sintered Al back contacts, using the procedure given in Ref. (7). The float-zone samples were annealed at 1200°C for various times up to 1h in an Ar/O₂ ambient which degraded the diffusion lengths from 145 down to 14 microns. The L_n values were measured, and the samples were then etched in a 50% solution of HF in H₂O to remove the Al-Schottky barrier from the front surface. The samples were then remeasured with the liquid junction cell. The L_n results which are plotted in Fig. 2a indicate that both junctions yield the same L_n values with experimental error. A least squares fit of the data gives a slope of 1.00 ± 0.05 and an intercept of 2 ± 3 microns, with standard deviations given for the uncertainties. One problem encountered with some of the samples measured with the liquid junction was a slow exponentially decaying component in the photovoltage, having a magnitude of 5-15% of the initial photovoltage. The decay typically had a time constant in the range of 3-5 min and significantly decreased in magnitude after the cell was illuminated with strong white light (50 mW/cm²) for 1 min. This slow decay in the photovoltage was not observed with Al-Schottky junctions, indicating that it is a surface phenomenon occurring in the vicinity of the silicon-electrolyte interface. In the second experiment a set of 33 ribbon samples was measured with the liquid junction cell, unetched, as received from crystal growth. The photovoltages observed in these samples were in general lower by a factor of 3-5 than the etched samples previously mea-

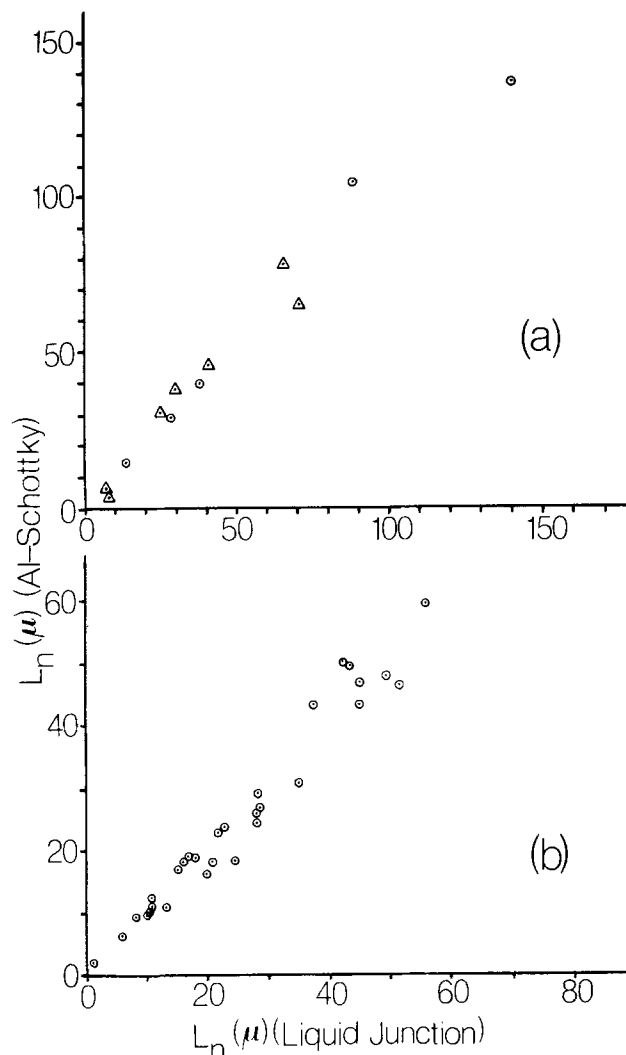


Fig. 2. Comparison of diffusion lengths measured with the liquid junction vs. an Al-Schottky junction. (a) Etched samples with sintered Al back contacts, measured with liquid junction subsequent to measurement with Al-Schottky barrier: Δ ribbon samples, \odot O₂ at annealed float zone Si samples. (b) Ribbon samples measured, unetched, with liquid junction first and then with Al-Schottky barrier after etching.

sured, but the drift problem was no longer present. The samples were subsequently etched for 90s in a standard 4:1 (HNO₃/HF) solution and for 15s in a 9:1 etch, to remove the SiC/SiO₂ surface films formed in crystal growth. Next, the samples were treated with a 3:1 30% H₂O₂/H₂SO₄ solution for 1 min to produce a thin oxide layer on the surface and a 125Å Al film was evaporated on the front surface to form a transparent Schottky barrier. The diffusion lengths were then remeasured and the results for both junctions are plotted against each other in Fig. 2b. The least squares fit of this data gives a slope of 0.998 ± 0.038 and an intercept of 0.2 ± 1.1 microns, confirming that both types of junctions yield the same results. It should be noted that the differences in transmission and reflectance between the Si-Al junction and the liquid junction were found to be insignificant over the wavelength range used.

In order to verify that the nonohmic pressure contact to the back of the samples was not introducing any error into the L_n measurements, a set of 8 unetched ribbon samples was measured with the liquid junction cell and then remeasured after being provided with an

Table I. Absorption coefficients of Si ribbon

λ (nm)	870	900	910	920	930	940	950	960	970	980	990	1000
α (cm ⁻¹)	446	329	293	261	232	206	182	160.3	139.4	119.5	100.6	83.1

ohmic back contact. The ohmic contact was formed by etching the back surface with 4:1 and 9:1 etchants and then rubbing on a layer of GaIn eutectic alloy. The addition of the ohmic back contact did not have any effect on the L_n values measured.

In conclusion, the liquid-electrolyte junction described here provides a practical means of measuring the SPV diffusion length of p-type EFG Si ribbon and should be applicable to other types of sheet grown Si.

Acknowledgments

The authors would like to thank Grant Hayes and Steven Monteiro for their assistance in this work. The work performed at EIC Laboratories was supported by the Office of Naval Research.

Manuscript submitted May 20, 1983; revised manuscript received Aug. 25, 1983. This was Paper 352 presented at the Washington, DC, Meeting of the Society, Oct. 9-14, 1983.

Mobil Solar Energy Corporation assisted in meeting the publication costs of this article.

REFERENCES

1. T. F. Ciszek, in "Materials and New Processing Technologies for Photovoltaics," J. P. Dismukes, E. Sirtl, P. Choudhury, and L. P. Hunt, Editors, p. 70, The Electrochemical Society Softbound Proceedings Series, PV 82-8, Pennington, NJ (1982).
2. A. M. Goodman, *J. Appl. Phys.*, **32**, 2550 (1961).
3. ASTM F 391-78, 1979 Annual Book of ASTM Standards, part 43, p. 770, American Society for Testing and Materials, Philadelphia (1979).
4. A. Nozik, *Ann. Rev. Phys. Chem.*, **29**, 189 (1978); J. Reichman, *Appl. Phys. Lett.*, **36**, 574 (1980).
5. E. Fabre and M. Mautref, *Acta. Electron.*, **18**, 336 (1975).
6. A. R. Moore, *Appl. Phys. Lett.*, **40**, 403 (1982).
7. R. O. Bell and G. M. Freedman, in, 13th IEEE Photovoltaics Specialists Conference, p. 89, IEEE, New York (1978).
8. F. V. Wald, in "Crystals: Growth, Properties and Applications," Vol. 5, J. Grabmaier, Editor, Chap. 5, pp. 147-198, Springer-Verlag, Berlin (1981).
9. A. J. Bard, A. B. Bocarsly, F. R. F. Fan, E. G. Walton, and M. S. Wrighton, *J. Am. Chem. Soc.*, **102**, 3671 (1980).



The Current-Voltage Characteristics of MOS Structures as Measured with Triangular and Sinusoidal Voltage Sweep Methods

K. Nitsch, I. Turlik, and M. Slaby

Institute of Electron Technology, Technical University of Wrocław, Poland

The triangular voltage sweep method has been generally used for evaluating the mobile charge concentration (1,2,3). The fundamental analytical expression and the method for estimating the mobile charges concentration with current-voltage characteristics to the triangular voltage have been presented in papers by Marciniak and Tangena (3,4). It has been shown that the fundamental relations of the TVS method enables one to determine the mobile charge density in MOS structures when a sinusoidal signal of a low frequency is used. It is also possible to use the same measurement system for investigating the dielectric relaxation effects with a small dc signal. This is an additional advantage of the method proposed here (5).

The equivalent conditions of both methods have been defined by the comparison of TVS and SVS characteristics.

THE RESPONSE OF THE MOS STRUCTURE TO SINUSOIDAL AND TRIANGULAR SIGNALS IN A QUASI-EQUILIBRIUM STATE

The essential condition for identification of the mobile charge in dielectric films of the MOS structure is a quasi-equilibrium state during the experiment; that is, under sweep conditions so slow that the ionic charge distribution can equilibrate continuously with the externally applied voltage (1). Usually in the TVS method, this quasi-equilibrium condition can be realized experimentally at the elevated temperatures in the range above 150°C at sweep rates less than 100 mV/s.

Based on the analysis of current-voltage characteristics of MOS structures in a quasi-equilibrium state presented by Kuhn, the current response of the MOS structure to an ac signal may be written as

$$i = - \frac{dQ(V,t)}{dt} = \frac{d}{dt} \int_0^V C(V) dV + \frac{d}{dt} \int_{x_0}^{x_1} \rho(x,t) dx \quad [1]$$

where: $Q(V,t)$ is the total charge induced at the semiconductor electrode; $C(V)$ is the differential MOS capacitance; $\rho(x)$ is the mobile charge concentration in the dielectric layer; and x_0 is the thickness of the dielectric layer (the direction of the x-coordinate is chosen so that $x=0$ for the metal-dielectric surface, and $x=x_0$ for the dielectric-semiconductor surface).

For the triangular signal, $V = \pm \alpha t$, and using $d/dt = \pm \alpha d/dV$ from Eq. [1] we obtain

$$i(V) = \pm \alpha C(V) \pm \alpha \frac{d}{dV} \int_{x_0}^{x_1} \rho(x,V) dx \quad [2]$$

Further, if we choose a sinusoidal signal as the applied voltage, $V = V_m \cdot \sin \omega t$, and using $d/dt = \pm V_m \omega \cos \omega t$, we can get the following form

$$i(V) = \pm V_m \omega \cos \omega t C(V) \pm V_m \omega \cos \omega t \frac{d}{dV} \int_{x_0}^{x_1} \rho(x,V) dx \quad [3]$$

Thus, it is possible to calculate the density of mobile charges in quasi-equilibrium conditions for triangular and sinusoidal signals from Eq. [2] and [3], respectively

$$\rho_0 = \frac{1}{\alpha} \int_{-V_0}^{V_0} [i(V) - \alpha C(V)] dV \quad [4]$$

$$\rho_0 = \frac{1}{V_m \omega \cos \omega t} \int_{-V_0}^{V_0} [i(V) - V_m \omega \cos \omega t C(V)] dV \quad [5]$$

Comparing Eq. [4] and [5], we notice that the density of the mobile ion charge defined by a triangular signal is equivalent to the density determined by a sinusoidal one when

$$\alpha = V_m \omega \cos \omega t \quad [6]$$

For $\omega t=0$ we obtain

$$\omega = \frac{\alpha}{V_m} \quad [7]$$

This allows one to measure the frequency of a sinusoidal signal corresponding to the applied potential sweep rate in the TVS method. For example, using $V_m=5V$ and the typical values of the potential sweep rate ($\alpha=5\div 50$ mV/s) for the quasi-equilibrium state, we obtain the frequency range of a sinusoidal signal

$$\omega = 10^{-3} \div 10^{-2} \text{ Hz} \quad [8]$$

The density of the mobile charge defined by Eq. [4] and [5] is directly proportional to the area between the polarization current curve and the envelope of the rectangle or the ellipse corresponding to the capacitance of the dielectric layer (in practice, at elevated temperature, $C(V) \approx C_{OX}$ in all the range of applied voltages) (Fig. 1).

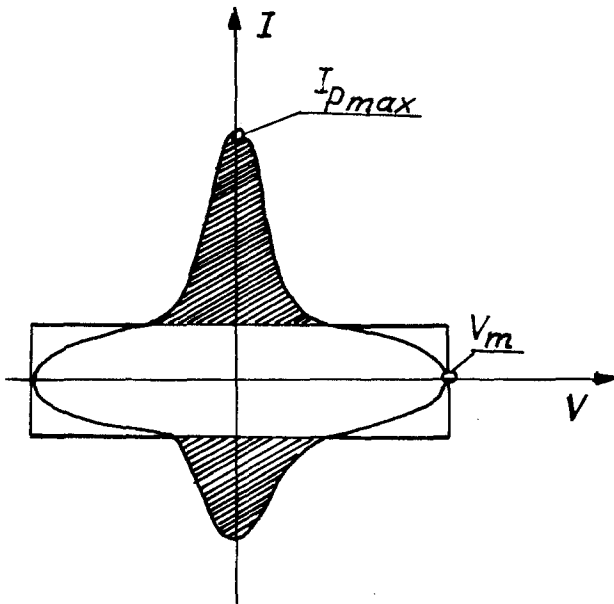


Fig. 1. Illustration for determining the density of the mobile charge by TVS and SVS methods.

The formula for calculating the density of the mobile ion charge using the TVS method has the following form (3)

$$Q = g \frac{kT}{q} \frac{I_p \text{ max}}{\alpha} \quad [9]$$

For a sinusoidal signal, this formula may be written as

$$Q = g \frac{kT}{q} \frac{I_p \text{ max}}{V_m \omega} \quad [10]$$

The quality evaluation of the dielectric layer can also be made by measuring the material parameters by means of a small ac signal of a very low frequency (5) in the same measurement system.

A typical I-V characteristic of an ac small signal is shown in Fig. 2.

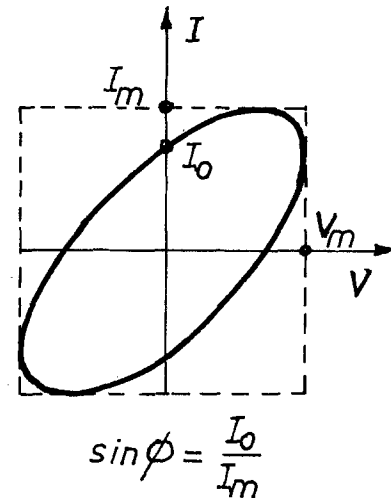


Fig. 2. I-V characteristic of MOS structure for a small ac signal at an elevated temperature.

The material parameters (the components of the complex capacitance $C^*=C' + jC''$ and $\tan \delta$) can be determined from the following relationships

$$C' = \frac{I_0}{V_{\text{max}}} \quad [11]$$

$$C'' = \frac{\sqrt{I_{\text{max}}^2 - I_0^2}}{V_{\text{max}}}$$

$$\tan \delta = \sqrt{\frac{I_{\text{max}}^2}{I_0^2} - 1}$$

Taking into account the geometrical capacitance, we can estimate the components of the complex permittivity.

RESULTS AND DISCUSSION

The I-V characteristics of the MOS structures have been measured for comparison of

the results of TVS and SVS methods. The MOS structures were formed by the thermal oxidation of the n-type silicon wafers of a resistivity $\rho = 3 \div 6 \Omega \text{ cm}$ with the aluminum gate. The thickness of the oxide layer was 100 nm, and the contacts were made by evaporated aluminum dots about 1mm diam and $0.3 \mu\text{m}$ thick. Some measurement results have been shown in Fig. 3 and 4.

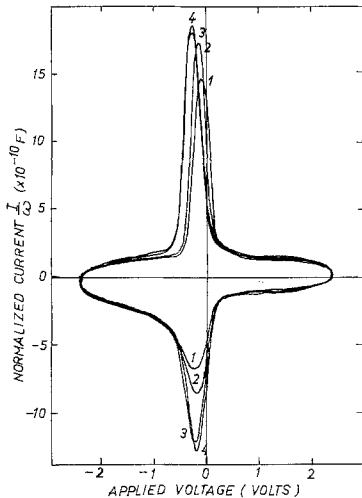


Fig. 3. Experimental SVS characteristics for $T = 480 \text{ K}$. (1) $\omega = 0.4 \text{ Hz}$; (2) $\omega = 0.2 \text{ Hz}$; (3) $\omega = 0.04 \text{ Hz}$; and (4) $\omega = 0.02 \text{ Hz}$.

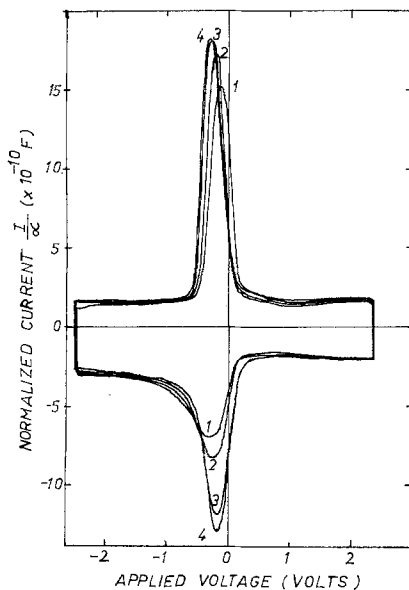


Fig. 4. Experimental TVS characteristics for $T = 480 \text{ K}$. (1) $\alpha = 1 \text{ V/s}$; (2) $\alpha = 0.5 \text{ V/s}$; (3) $\alpha = 0.1 \text{ V/s}$; and (4) $\alpha = 50 \text{ ms/s}$.

The current-voltage characteristic was measured using Keithley 610C electrometer, Hewlett Packards H203A function generator and a slow triangular wave function generator.

The measured frequency was chosen according to Eq. [7]. The concentration of the mobile charge has been evaluated based on the I-V characteristics of the MOS structures for the sinusoidal and triangular voltage sweep methods. The agreement of results for both methods has been obtained, however, the differences in measured values were caused by the integration error of the experimental curve ($\pm 1\%$). Table I shows the typical values of Q measured using TVS methods.

Table I.

TVS		SVS	
$\alpha \left[\frac{\text{mV}}{\text{s}} \right]$	$Q [10^{-10} \text{C}]$	$\omega [\text{Hz}]$	$Q [10^{-10} \text{C}]$
50	8.62	$2 \cdot 10^{-2}$	8.68
100	5.53	$4 \cdot 10^{-2}$	5.53
500	4.94	$2 \cdot 10^{-1}$	4.91

The results obtained using the TVS and SVS methods confirm that these methods are equivalent, because the results are nearly the same. Thus, the TVS and SVS methods can be used interchangeably depending on the measurement setup. The differences in values of the mobile charge concentration for both methods are contained within the range of the method's error. The advantage of applying this method is the possibility of determining the dielectric parameters. These parameters can be obtained in the known way from I-V characteristics during one measurement cycle. Results of the SVS method may be compared in a simple way with results obtained by the TVS method according to the relationship in Eq. [6] given in this paper.

REFERENCES

1. N.J. Chou, *This Journal*, **118**, 601 (1971).
2. M. Kuhn and D.J. Silversmith, *ibid.*, **118**, 966 (1971).
3. H. M. Przewlocki and W. Marciniak, *Phys. Status Solidi A*, **29**, 265 (1975).
4. A.G. Tangena, J. Middelhoek, and N.F. de Rooij, *J. Appl. Phys.*, **49**, 2876 (1978).
5. R.J. Kriegler and R. Bartnikas, *IEEE Trans. Electron Devices*, **20**, 722 (1973).

Manuscript submitted Aug. 12, 1981.

Determination of the Minimum Surface Enrichment of Molybdenum Required to Inhibit Active Dissolution of an Fe-Cr-Ni-Mo Alloy

R. C. Newman* and E. M. Franz

Brookhaven National Laboratory, Materials Technology Division, Upton, New York 11973

It is becoming clear that molybdenum inhibits localized corrosion of stainless steels through its effect on the anodic dissolution kinetics, rather than by any mechanism which could be discovered by analyzing the fully developed passive film. Wanklyn (1) has emphasized the importance of MoO_2 as a compound which is readily formed and is stable at relatively active potentials in mildly acidic solutions. It is also kinetically stable in strongly acidic solutions because of the necessity for reductive dissolution as Mo^{3+} . In the passive state at much higher potentials there is a tendency for depletion of Mo in the passive film. Hashimoto et al (2) and Goetz and Landolt (3) have both detected high concentrations of Mo on surfaces subjected to prolonged active dissolution. The chemical state of Mo in these experiments is controversial - perhaps $\text{Mo(VI)}(2)$. Brox and Olefjord (4), using an Fe-Cr-Mo alloy, showed in addition that elemental Mo was enriched in the surface following active dissolution, and suggested that an "intermetallic surface phase" was present. With respect to localized corrosion, it is likely that Mo is enriched on the surface during the small amount of dissolution which precedes repassivation of an incipient localized corrosion site; the excess Mo may then dissolve during prolonged passivation, or may be present so locally that it cannot be detected by surface analysis. In the present work we have measured the charge density required to deactivate freshly generated surfaces of an Fe-Cr-Ni-Mo alloy in the range of potentials where rapid active dissolution occurs in the absence of Mo. This charge density is used to calculate the maximum possible surface coverage of Mo as a function of exposure time of the new surface.

A novel dual electrode assembly was used to compare the bare surface behavior of Fe-Cr-Ni and Fe-Cr-Ni-Mo alloys (compositions in Table 1). Annealed 1 mm plates of both alloys were mounted on edge in a block of epoxy resin, with a spacing between them of about 1 mm, and ground to a 600 grit finish. A separate electrical connection was made to each specimen (Figure 1). The specimen block was fixed to the

bottom of a plastic cell containing a platinum counter electrode and a saturated calomel reference electrode (SCE). Two Stonehart model BC1200 potentiostats were used in the inverted mode to control the potentials of the two specimens at the same value, with the platinum counter electrode grounded. The two current outputs were fed through 60 Hz filters to two channels of a Nicolet digital oscilloscope (model 2090). A diamond pencil was used to make a single scratch across the width of both electrodes. Although the width and depth of the scratches were only reproducible to within about 25%, they were always constant to within 10% across both electrodes for a given scratch. This gave a high degree of confidence in the comparison of the bare surface behavior of the two alloys. The scratch width was $75 \pm 20 \mu\text{m}$, with a depth of about $20 \mu\text{m}$; the apparent scratch area was therefore taken as $0.1 \pm 0.03 \text{ mm}^2$. The scratch currents were low enough (and the solution conductivities high enough) that no noticeable interactions occurred between the ohmic potential fields of the two electrodes. The maximum IR drop to a scratch was less than 10 mV (5).

Most of the measurements were made using 1.5M H_2SO_4 at 22°C; a few were made with 1M HCl. For the sulfuric acid, both electrodes were passivated at +300 mV (SCE) before pulsing to the potential of interest; reactivation was slow enough to permit scratching in the active range with a low base current. For HCl, where passivation of one alloy was not possible, the electrodes were coated with a thin layer of lacquer and the scratches made through this layer.

Molybdenum sharply reduced the anodic current densities in the active range, as shown for sulfuric acid in Figure 2. The steady-state active to passive transition for alloy A was at $-275 \pm 5 \text{ mV}$ for this solution. When the alloys were scratched in the passive range for 1.5M H_2SO_4 , their current decays were virtually indistinguishable as shown in Figure 3. This is evidence that Mo does not influence the early growth of the passive film, and therefore that its effects should be sought in the active

*Electrochemical Society Active Member

range of potentials. Figure 4 shows the transients obtained at -300 mV, where passivation did not occur; very similar results were obtained in both H₂SO₄ and HCl at -350 mV. Both alloys showed an initial current peak, but within 200 ms the current on the Mo alloy (B) had fallen sharply below its companion. After 2 s the ratio of the currents was about 10, and alloy A had almost reached its steady state. By comparing this steady state with that of the surface as a whole, it was shown that the estimate of the scratch area was accurate and that the roughness of the scratch was comparable with that of a 600 grit finish. Using the apparent scratch area, the charge density passed on alloy B after 2 s was about 3.5 mC/cm². For a mean oxidation number of just over 2 and a roughness factor of about 2 for the scratched surface, this represents at most 5 atom layers of alloy oxidized (the roughness factor is not likely to be less than 2). For a bulk Mo concentration of 2.7 wt.% (1.6 at.%), the maximum possible surface concentration of Mo at this stage is therefore no more than 8 at.%. The initial peak seen for both alloys is probably due to preferential dissolution of iron, leaving a surface enrichment of nickel and chromium - it is notable that the charge density under this peak (~4 atom layers) would leave about one monolayer of (Cr + Ni) if iron was perfectly selectively dissolved.

Mechanism of Molybdenum Effect

The present results could be consistent with several possible effects of molybdenum, of which we will give two examples. First, Mo may be retained in the elemental form during preferential dissolution of iron; 8 at.% is then a reasonable surface concentration at which agglomeration of Mo atoms might begin to occur, for instance at surface steps (the mean Mo-Mo distance being between 3 and 4 substrate lattice spacings). Frankenthal (6) showed that the first stages of passivation of Fe-Cr alloys required charge densities equivalent to less than one monolayer of oxidized metal, and concluded that most of the initial current decrease involved deactivation of heterogeneities; if these were already saturated with elemental Mo, then the active current density could also be dramatically reduced by quite small coverages of Mo. Second, 8 at.% Mo may be sufficient to cover most of the surface if it reacts to form a hydrated oxide monolayer such as MoO₂·2H₂O (7). The main drawback of this mechanism is that bulk MoO₂ is not stable at pH = 0 and E_H ≈ -100 mV; however, thermodynamic data for the "two-dimensional" phase are not available. On balance we favor the accumulation of elemental Mo (to ~8 at.%) as the primary deactivating process; under appropriate conditions, this may be

followed by formation of a 2- or 3-dimensional network containing Mo(IV). Experiments with Fe-Cr-Mo alloys, where active dissolution occurs at lower potentials, are in progress and should resolve the role of MoO₂.

Conclusions

1. 1.6 at.% Mo does not affect the first few seconds of repassivation of an Fe-Cr-Ni alloy in 1.5M sulfuric acid.
2. 1.6 at.% Mo sharply decreases the active current density on a new surface after the passage of a quantity of charge equivalent to about 5 atom layers of alloy.
3. These results show that molybdenum acts at a sub-monolayer level in its primary inhibiting effect on active dissolution of stainless steels in sulfuric or hydrochloric acid, but has no effect on the repassivation rate in sulfuric acid.

Kenneth Sutter assisted with the experimental measurements. This work was sponsored by the US Department of Energy, Division of Basic Energy Sciences (contract DE-AC02-76CH00016).

1. J.N. Wanklyn, *Corros. Sci.* 21, 211 (1981).
2. K. Hashimoto, K. Asami and K. Teramoto, *Corros. Sci.* 19, 3 (1979).
3. R. Goetz and D. Landolt, *Electrochim. Acta* 27, 1061 (1982).
4. B. Brox and I. Olefjord, *Proceedings of 5th International Symposium on Passivity*, Bombannes, France, 1983 (in press).
5. H.J. Pearson, G.T. Burstein and R.C. Newman, *J. Electrochem. Soc.* 128, 2297 (1981).
6. R.P. Frankenthal, *J. Electrochem. Soc.* 116, 580 (1969).
7. M. Pourbaix, "Atlas of Electrochemical Equilibria in Aqueous Solutions", p. 277. Pergamon Press, 1966.

Table 1 Compositions of Alloys

wt.%	Cr	Ni	Mo	Fe
A	18.7	10.3		bal.
B	16.6	11.0	2.7	bal.

Key words : alloy, corrosion, passivity

Manuscript submitted Aug. 9, 1983.

Brookhaven National Laboratory assisted in meeting the publication costs of this article.

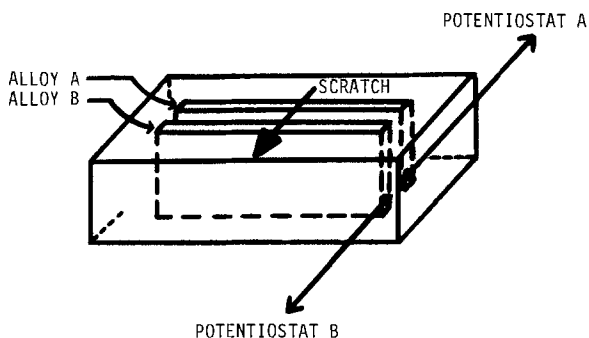


Fig. 1 Specimen assembly for comparative scratching electrode measurements.

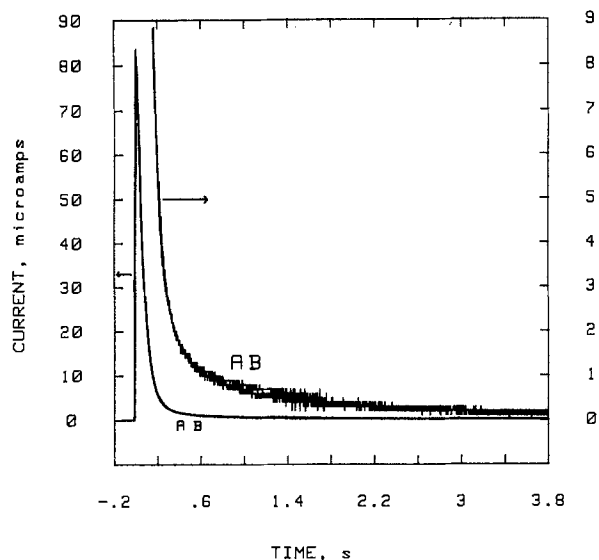


Fig. 3 Repassivation kinetics of alloys A and B in 1.5M H₂SO₄ at +350 mV (SCE). Scratch area was 10⁻³ cm².

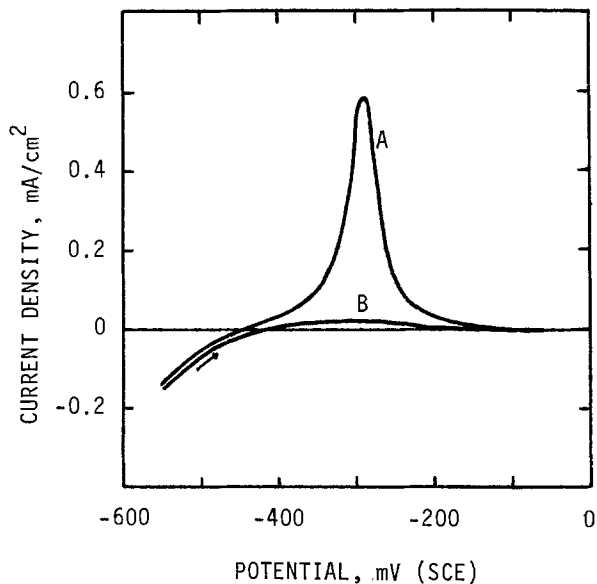


Fig. 2 Anodic polarization behavior of alloys A and B in 1.5M H₂SO₄ at 22°C. Potential sweep rate was 1 mV/s. Pretreatment was 600 grit grinding plus -1.0 V (SCE) for 60 s.

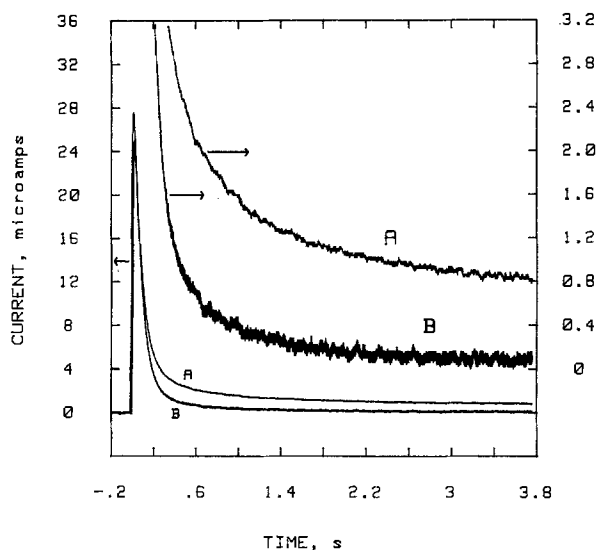


Fig. 4 Decay of active current for alloys A and B scratched in 1.5M H₂SO₄ at -300 mV (SCE). Scratch area was 10⁻³ cm².

Photoelectrochemical Response of GaPc-Cl Thin Film Electrodes Using Two Photon Sources and Two Illumination Directions

W. Buttner, P. Rieke, and N. R. Armstrong*

Department of Chemistry, University of Arizona, Tucson, Arizona 85721

The measurement of photocurrent response as a function of illumination wavelength, photocurrent spectroscopy, has been used in the characterization of many semiconductors and photoconductors (1-6). In our own studies of thin films of tri- and tetravalent metal phthalocyanines (Pc) and silicon phthalocyanines, photocurrent action spectra have been used to verify the identify of the majority photoproduced charge carriers, and estimate their average diffusion length (ℓ) before recombination (5, 6). The photocurrent spectra were found to depend upon the direction of illumination. For frontside illumination, illumination from the electrolyte side, the photocurrent spectra mimicked the absorbance spectra, a broad featureless peak between 550 and 850 nm. With backside illumination (made possible by illumination through the semitransparent conductive substrate) two maxima were observed at 575 and 795 nm with severe attenuation of the photocurrent in the highly absorbing region between these two peaks. This directional effect is explained by considering the relationships between the point of carrier creation, the direction in which it must migrate and the thickness of the GaPc-Cl film. The experimentally determined condition of oxidative current implies that either hole must move towards the dye/electrolyte interface or electrons must move in the opposite direction. Since in frontside illumination the photocurrent response parallels the absorption spectra we must conclude that the photocurrent does not depend on the penetration depth of the light, ($1/\beta$) where β is the absorption coefficient ($10^4 \leq \beta \leq 10^5 \text{ cm}^{-1}$ between 550 and 850 nm). Thus holes must be the mobile, photoproduced charge carrier. With backside illumination highly absorbed photons having a small penetration depth create holes very near the substrate/Pc interface. The photocurrent maxima occur

at the condition where $1/\beta = d - \ell$, where d is the thickness of the Pc film and ℓ is the average diffusion length before recombination (5). Using thin GaPc-Cl films (<200 nm), we estimate that $1/\beta \approx 5 \times 10^{-5} \text{ cm}$ at 575 nm and 795 nm. Estimates of the film thickness, $d \approx 700 \text{ nm}$, ascertained from visible spectra of the dissolved Pc film in pyridine, allows an estimation of $\ell = 200 \text{ nm}$ for Figure 1a.

Previous experiments have shown that polychromatic illumination of the Pc film produces photocurrents that seem to be in excess of those predicted by experiments using monochromatic sources (5-9). Photocurrents observed voltammetrically using polychromatic sources also show little dependence upon illumination direction in contrast to illumination with monochromatic sources. Figures 1, b-d, indicate the reason for these observations. The action spectra shown were all obtained using a monochromatized Xenon arc source, modulated at 100 Hz, and lock-in-amplifier (Ortec-Brookdeal) detection of the photocurrent response from the i/V converter of the potentiostat (ECO 551). Figures 1 b-d represent spectra obtained by backside illumination with that "probe" source and frontside illumination using an unmodulated "pump" laser source. In the case shown, a 632.8 nm He-Ne was used, but qualitatively similar results have been obtained using CW lasers at 514.7 nm, 457.1 nm (Argon ion laser) and 325 nm (He-Cd laser). As the power of the CW source was increased, the modulated photocurrent at each wavelength increased and the photocurrent maxima converged slightly, corresponding to a shift in the wavelength maxima of up to 25 nm. The ratio of β at 600 nm to that at 575 nm is ca. 1.5 to 1, $1/\beta$ decreases by a corresponding amount which indicates that ℓ has increased from 200 nm to ca. 350 nm. Since ℓ is a potential dependent parameter, a similar effect could also be produced by

*Electrochemical Society Active Member.

increasing the applied bias potential to the photoelectrode. If taken to its theoretical limit (which is generally not practical), the backside action spectra should converge on the frontside action spectrum or the absorbance spectrum.

The idea of using one modulated and one unmodulated illumination source has been previously reported for various photocurrent spectroscopies (1, 10). In most cases it was necessary for the modulated probe source and the CW pump source to illuminate the electrode at the electrolyte interface, since the electrodes were not thin films nor were they on optically transparent backings. As shown in Figure 2 for our experiments, the absorption profiles of the opposed pump source and probe source will overlap different regions dependent upon the absorptivity, β , of each. The pump source may produce charge carriers that occupy trap or recombination sites near the front surface -- the greatest distance away from the origin of the photoproduced holes. The presence of high concentrations of unmodulated charge carriers from the pump source increases the overall conductivity of the Pc film, allowing for a more efficient harvesting of the modulated carrier from the Au/Pc interface. The backside-induced photocurrent increases in accordance with the increase in λ to λ' .

The photocurrent enhancement at 632.8 nm using a modulated, low power, He-Ne source and two different pump sources is quantitated in Fig. 3. The maximum photocurrent enhancement obtained is greater than a factor of 2 for the 514.5 nm pump and slightly less than a factor of two for the 457.9 nm pump -- normalization to the absorptivities as these two wavelengths shows these enhancements to be nearly equal. The maximum enhancement is obtained with only small additions of pump power, corresponding to a probe-to-pump flux ratio of up to 300:1. Beyond this point the effect of each pump source decreases and the photocurrent enhancement saturates. In this same region of pump

flux to the frontside of the Pc film, the total photocurrent (a.c. + d.c.) increased non-linearly with increasing light flux ($i \propto I^{0.65}$). Such a non-linear relationship coincides with the expectations of the model of Rose which postulates a distribution of shallow and deep hole traps in the band gap region of the photoconductor (11). Experiments in progress also show that the effect of the pump light source may also be to reduce the barrier height for charge transfer at the Au/Pc interface which should likewise yield a non-linear photocurrent vs. light intensity dependence.

Polychromatic illumination of the Pc film and other photoconductor thin films results in a sizeable fraction of the charge carriers produced being used to create a more conductive channel for a small hole population, which actually produces the photocurrent response. Further optimization of these photoconductive materials requires that the barriers to hole transport be significantly reduced, i.e., that λ be made comparable or larger than the Pc film thickness. Two-photon photocurrent spectroscopies are promising in their ability to quantitate the effect on photoelectrochemical performance of defect states. These experiments also suggest ways by which the photoconductivity of thin films for photoelectrochemical or reprographic applications might be controlled using multiple sources which illuminate the photoconductor from two different directions.

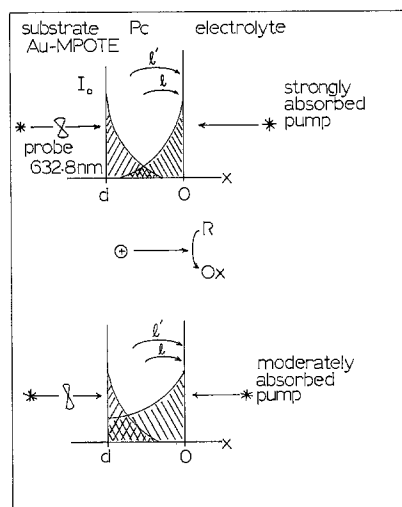
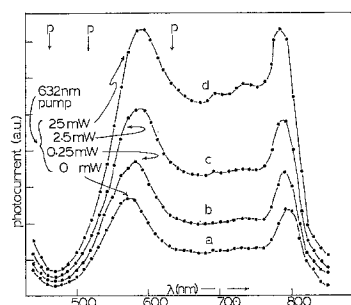
This research was supported by grants from the National Science Foundation, CHE 17571, and from IBM Corporation. We also gratefully acknowledge the use of a He-Cd laser for these and subsequent studies from the San Francisco Laser Center. We also thank Prof. J. E. Pemberton of this Department for the loan of the argon ion laser. P. Rieke acknowledges support in the form of the C. S. Marvel Graduate Fellowship.

References

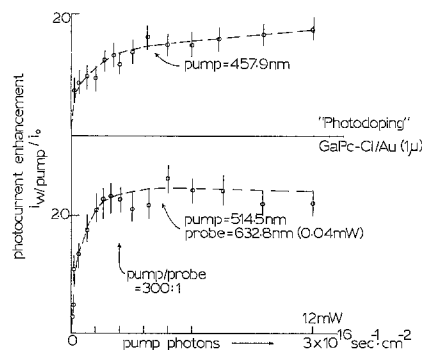
1. A. Heller, K. C. Chang, and B. Miller, *J. Electrochem. Soc.* **124** (1977) 697.
2. G. Kline, K. Kam, D. Canfield and B. A. Parkinson, *Solar Energy Materials*, **4** (1981) 301.
3. L. R. Faulkner, ACS Symp. #184, "Interfacial Photoprocesses: Energy Conversion and Synthesis," M. S. Wrighton, ed., Amer. Chem. Soc., Washington, D. C., 1980, pp. 113-139 and references therein.
4. A. K. Gosh, D. L. Morel, T. Feng, R. F. Shaw and C. A. Rowe, *J. Appl. Phys.* **45** (1974) 230.
5. P. C. Rieke, C. L. Linkous and N. R. Armstrong, *J. Phys. Chem.* (in press).
6. T. Mezza, N. R. Armstrong and M. Kenney, *J. Electroanal. Chem.* (submitted).
7. T. Mezza, C. L. Linkous, V. R. Shepard, N. R. Armstrong, R. Nohr and M. Kenney, *J. Electroanal. Chem.*, **124** (1981) 311.
8. C. Linkous, T. Klofta and N. R. Armstrong, *J. Electrochem. Soc.*, **130** (1983) 1050; and C. Linkous, Ph. D. Dissertation, Michigan State University, 1983.
9. P. Rieke and N. R. Armstrong, *J. Amer. Chem. Soc.* (in press).
10. J. F. McCann and M. Skvillas-Kazacos, *J. Electrochem. Soc.* **130** (1983) 1451.
11. A. Rose, "Concepts in Photoconductivity and Allied Problems," R. E. Krieger Pub. Co., N. Y., 1978, pp. 69-91.

Figure Captions

1. Photocurrent action spectrum (lock-in amplifier output vs. wavelength) for a GaPc-Cl/Au-MPOTE electrode immersed in a pH=4 (0.2 M KHP), 0.05 M hydroquinone solution, held at a bias potential of +0.4 volts vs. Ag/AgCl. a) Backside illumination using a monochromatized (2 nm bandpass) Xenon arc lamp. Spectrum corrected for lamp/monochromator power transmission fluctuations. No added pump. b)-d) As in (a), but with CW, 632.8 nm He-Ne laser, illumination of the front surface of the Pc film at the pump power densities shown (laser diffused to ca. 1 cm²).



Manuscript submitted Aug. 29, 1983;
revised manuscript received Sept. 8, 1983.





REVIEWS AND NEWS

Reports on Electrochemical Society Summer Fellowship Awards

During the summer of 1983, the following graduate students received \$1500, representing the three Summer Fellowship Awards of The Electrochemical Society.

Ms. Rosalie G. Tompson, University of Missouri-Columbia, was designated as the winner of the Edward Weston Fellowship.

Mr. Bob L. Wheeler, The University of Texas at Austin, was awarded the Colin Garfield Fink Fellowship.

Mr. David F. Tessier, University of Ottawa, Canada, was selected as the recipient of the Joseph W. Richards Fellowship.

The Summer Fellowship Awards are made "without regard to sex, citizenship, race, or financial need, to a fellow or teaching assistant pursuing work between the degrees of B.S. and Ph.D. on a subject in a field of interest to The Electrochemical Society." They are intended to cover a period during which the recipient has no financial support for the continuance of his or her work.

The Edward Weston Summer Fellowship Report

Ms. Tompson's report is given below.

The goal of this work was to use inelastic electron tunneling spectroscopy (IETS) to study the reaction of SOCl_2 with aluminum oxide and, in particular, to determine intermediate products in the reaction. IETS (1) is a sensitive technique for detecting monolayer coverages of a molecular species adsorbed on an oxide layer. Tunnel junctions are fabricated as a sandwich of metal (usually Al), metal oxide, dopant (molecule of interest), and metal (usually Pb). To obtain spectra, the junctions are cooled to 4.2 K, and a variable d-c bias voltage and an a-c modulation signal are applied. Peaks in the resulting second harmonic vs. bias voltage correspond to the vibrational frequencies of the dopant molecule and phonons of the sandwiching metal electrodes. The useful range is 30 meV (240 cm^{-1}) to 500 meV (4000 cm^{-1}). Previously, IETS has been successfully used in our laboratory to determine the reaction intermediates of the CCl_2 /aluminum oxide system (2).

This project was based on literature studies of the reactions of SOCl_2 with metals and metal oxides (most notably with Li in a Li/ SOCl_2 battery system). These studies had indicated that metal chlorides, free sulfur, and SO_2 could be expected to result from such a reaction. Other products could include SO_2Cl_2 , S_2Cl_2 , SCl_2 , S_2O , and HCl (from reaction with water on the aluminum oxide surface). Reaction intermediates might also be seen (e.g., various metal chloride and sulfur chloride radicals, SO and SO radicals and SOCl^-). Further, sulfur bonded to bare Al atoms of the oxide surface might possibly be observed although such bonds are often difficult to detect with tunneling. The first step in the process was to fabricate aluminum oxide tunnel junctions doped with SOCl_2 . The usual doping and fabrication procedures, and modifications thereof, did not provide high quality junctions or spectra. Junctions doped with 4-12 μl of pure SOCl_2 were unusable since the SOCl_2 reacted strongly with the thin oxide layer and the underlying Al. Junctions doped with 4-12 μl of SOCl_2 dissolved in benzene at concentrations ranging from 0.1 to 10% SOCl_2 by volume were also of poor quality (low resistance with noisy spectra). The spectra from these junctions, however, did yield surprising results. No metal chloride stretches were seen, nor were there any other stretches observed which involved chlorine. There were indications of Al-S bonds, of SO_2 and other sulfur-oxygen type bonds, and possibly of benzene on the surface. One possible interpretation of these results is that the SOCl_2 chlorinated the benzene before the solution was applied to the metal oxide surface. As a consequence, the complex was adsorbed on the oxide surface. Previously, benzene when used as a solvent has not been seen in tunneling spectra. Since these spectra were noisy, the results obtained are not yet conclusive. Current plans include attempting to fabricate tunnel junctions with very small amounts of pure SOCl_2 .

REFERENCES

1. P. K. Hansma, "Tunneling Spectroscopy Capabilities, Applications, and New Techniques," Plenum Press, New York (1982).
2. R. M. Ellialtioglu, H. W. White, L. M. Godwin, and T. Wolfram, *J. Chem. Phys.* **72**, 5291 (1980).

The Colin Garfield Fink Summer Fellowship Report

Mr. Wheeler's report is given below.

A method for the simultaneous determination of the absorption coefficient, α , and the minority charge carrier diffusion length, L , of semiconductor electrodes was evaluated. The method is based on electronically differentiating the photocurrent as a function of applied potential and, hence, is called the differential photocurrent (DPC). This method, first proposed by Sukegawa *et al.* (1) for solid-state devices, involves the simultaneous modulation of the incident radiation (at f_1) and the applied potential (at f_2) with detection of the intermodulation photocurrent (at $|f_2 - f_1|$). α and L were determined for a p-GaP single-crystal in contact with an aqueous Eu^{3+} solution. The values for α were $400 \text{ nm} - 8.1 \times 10^4 \text{ cm}^{-1}$ and $450 \text{ nm} - 6.9 \times 10^4 \text{ cm}^{-1}$. The value of L determined for the sample was $0.10 \pm 0.01 \mu\text{m}$. The values agree quite well with literature values. The DPC technique has the advantage that the measurements are conducted with the semiconductor in the same configuration normally used in photoelectrochemical cells. One drawback, however, is that any deleterious effects the electrolyte has on the semiconductor, such as surface recombination or the formation of surface states, could affect the measurement. An additional complication is a filter effect caused by the species produced at the photoelectrode. This effect would be absent in solid-state measurements on step junctions and care must be used in matching the wavelengths of interest to regions where the redox couple to be used does not absorb. In addition, the method is very model dependent (*i.e.*, the photocurrent is fit to the Gärtner model, and any inaccuracies in the model will be manifested in the results). Apart from the determination of α and L , this method holds promise as a means for detecting surface states which play a role in the production of the photocurrent. When the photocurrent increases steadily towards saturation as a function of the reverse bias, as predicted by the well known Gärtner model, the differential photocurrent decreases monotonically and reaches zero as the photocurrent reaches saturation. Any inflection in the steady increase in the photocurrent will be magnified in the plot of the differential photocurrent with respect to reverse bias. This inflection in the photocurrent can be attributed to surface states acting as recombination sites. This has been illustrated by a plot of the differential photocurrent vs. voltage for n-MoSe₂, which has been shown by the a-c impedance technique to have surface states. At the same potential at which the states were found by a-c impedance, a large dip occurs in the differential photocurrent. However, except for determining the energy distribution of the surface states with respect to the bandedges, no quantitative information appears readily available.

In addition, polycrystalline films of MoSe₂ were studied. The films were grown by vapor transport from MoSe₂ powder and I₂ as a transport agent. The chemicals were placed in a quartz tube and evacuated at liquid nitrogen temperature and sealed. The tube was then placed in a split tube furnace kept at 900°C for approximately one week. At that time, a suitable portion of the tube was held under running water to condense the I₂ vapor. Polycrystalline films of MoSe₂ had grown above the original charge. The films were quite sturdy and could be removed from

the quartz in most cases. Electrodes were made with both the rough surface, which was towards the charge during growth, and the smooth surface, which was against the quartz tube, exposed to the electrolyte. Preliminary results show that both types of electrodes were able to photo-oxidize bromide.

REFERENCES

1. T. Sukegawa, *et al.*, *IEEE Trans. Electron Devices*, **ed-27**, 1251 (1980).
2. B. L. Wheeler, *This Journal*, Submitted for publication.

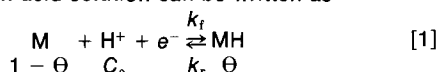
The Joseph W. Richards Summer Fellowship Report

Mr. Tessier's report is given below.

The electrochemical hydrogen evolution reaction (HER) has proved a useful model system in the study and kinetic treatment of simple, as well as of more complex electrode reactions (1,2). Much work has been done on the elucidation of the rate-determining step(s) in the HER at metals of widely differing adsorptive and catalytic properties and from diverse electrolyte solutions (3-5). Of equal interest has been the question of the mechanism and molecular mechanics of the initial step, in acid media, of the discharge of the hydrated proton and the transfer and chemisorption of the resulting H atom on the electrode surface.

Comparative studies at various metal electrodes on the discharge of, and H₂ evolution from the unhydrated H₃O⁺ ion as found in salt-like strong acid "monohydrates" and from H⁺_{aq} in solutions of the same acid in excess water have recently been reported by Conway and Tessier (6). The steady-state polarization behavior at Hg electrodes differed markedly from that at the more catalytic Ni and Pt surfaces. In particular, at Pt and Ni, the observed rates of the HER from 1M CF₃SO₃H are ca. 10-25× greater than from the monohydrate, CF₃SO₃-H₃O⁺; this order was found to be reversed at Hg cathodes. The temperature dependence of the HER was discussed in terms of current ideas about electron and proton transfer in electrochemical reactions, the state of hydration of H⁺, and the role of discharge from paired CF₃SO₃⁻ and H₃O⁺ ions.

Linear potential sweep cyclic voltammetry experiments allow the elementary H-adsorption/desorption step in the HER at Pt to be studied independently from the overall H₂ evolution process. The electrochemical reaction responsible for the formation of adsorbed H at Pt in acid solution can be written as



where Θ is the fractional coverage of the surface by H, k_f and k_r are the indicated rate constants, C_0 is the concentration of H⁺ in the outer Helmholtz plane, and the surface concentration of metal sites is represented by the quantity $(1 - \Theta)$.

In the absence of mass-transport limitations and of diffuse double layer effects, the net current density for reaction [1] at any potential, E , is given by (7)

$$-Qd\theta/dt = i = -Q\{k_f(1 - \Theta)C_0 \exp(-\beta FE/RT) - k_r\Theta \exp[(1 - \beta)FE/RT]\} \quad [2]$$

In a linear potential sweep experiment, $E = E_{in} + St$, and under reversible conditions (low sweep rate, S), the coverage Θ adjusts to an equilibrium value for every value of potential, corresponding to the electrochemical adsorption isotherm for H on M. However, at relatively higher sweep rates, the current is determined increasingly by one or other of the two terms in Eq. [2], and the peak potential $E_{p,irr}$ progressively differs from that obtaining under reversible conditions, $E_{p,rev}$ (7).

Under completely irreversible conditions, at a sufficiently high sweep rate, the quantity $E_p = E_{p,irr} - E_{p,rev}$ is given by (7)

$$E_p = b \log(S_{0,p,c}) = b \log(-S) \quad [3]$$

where $b = RT/\beta F$ and $S_{0,p,c} = (RT/\beta F) k_f^{(1-\beta)} k_r^\beta C_0^{(1-\beta)}$. Thus a Tafel-like extrapolation of E_p vs. $\log(S)$ to $E_p = 0$ yields $\log(S_{0,p})$, the reversibility parameter, which is related to the standard rate constant k_0 by

$$S_{0,p} = (RT/\beta F) k_0 C_0^{(1-\beta)} \quad [4]$$

The characteristic rate parameter, k_0 , derived from the estimated $S_{0,p}$ for the elementary H-adsorption/desorption process

at Pt is then susceptible to a temperature study so that an analysis of the activation parameters analogous to that reported previously for the overall HER from H⁺ in different states of hydration (6), can be made.

This part of the work, concerned with the temperature dependence of the kinetics of the H-adsorption process at Pt, was carried out during the tenure in 1983 of the Joseph W. Richards Summer Fellowship of the Electrochemical Society.

Experimental

The potentiodynamic sweep method was employed as described elsewhere (7). A Nicolet 2090 digital oscilloscope served to record the i - E profiles. An internal reference electrode or a specially-made low-impedance reference electrode compartment was used in the measurements at high sweep rates. Cell design and minimization of the Pt working electrode surface area reduced the magnitude of IR losses which were offset by means of an adjustable positive feedback IR-drop compensator (12). High purity CF₃SO₃H solutions were prepared from the purified monohydrate as described previously (6). The anhydride, (CF₃SO₂)₂O, prepared by the dehydration of the acid over "P₂O₅" (13), was reacted with D₂O to yield CF₃SO₃-D₃O⁺ which was further purified.

The anodic H-desorption process was studied since, at higher S , the conjugate H-adsorption/desorption peaks overlap and are obscured by the onset of H₂ evolution currents. A slow (1 Vs⁻¹) cathodic sweep and a cathodic potential holding period of 0.2s was used in order to achieve surface equilibration prior to the analytical anodic scans.

Results

Typical cyclic voltammograms obtained at Pt electrodes in the "monohydrate" salt CF₃SO₃-H₃O⁺ and 1M aqueous CF₃SO₃H are shown in Fig. 1.

In the 1M solution, the H-adsorption region of the i - E profile is similar to that previously observed in HClO₄ solutions (7), indicating a relatively small degree of specific adsorption of the anion. The competitive adsorption of CF₃SO₃⁻, e.g., with SO₄²⁻, PO₄³⁻, and ClO₄⁻, has been studied previously by cyclic voltammetry in dilute aqueous solution (8), and it was concluded that CF₃SO₃⁻ is adsorbed to approximately the same extent as ClO₄⁻. Electrical double layer capacitance studies at Hg have indicated that the anion is not strongly adsorbed at this metal either (9).

In the acid monohydrate, the H adsorption region is appreciably shifted to less positive potentials as is evident in the cyclic voltammogram (Fig. 1); also the onset of surface oxidation of Pt is shifted to more anodic potentials. Both these observations probably result from greater anion adsorption in the monohydrate "melt". Such effects on the Pt profile are known to occur in the presence of strongly adsorbed anions, e.g., in sulfuric acid solutions containing even trace quantities of halide ions (10, 11).

The characteristic sweep rates, $S_{0,p}$, above which the anodic desorption of H from Pt is kinetically irreversible, is shown in the plot of E_p vs. $\log(S)$ plot in Fig. 2. $S_{0,p}$ for the 1M solution is com-

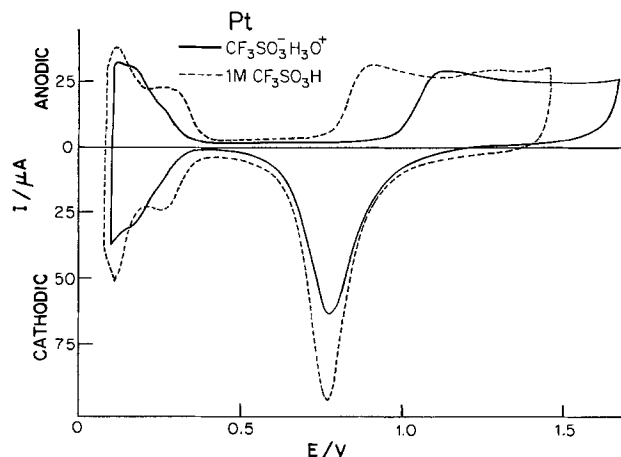


Fig. 1. Cyclic voltammetry i - E profiles for CF₃SO₃-H₃O⁺ and 1M CF₃SO₃H at 313 K at a Pt electrode. Sweep rate 92 mV s⁻¹.

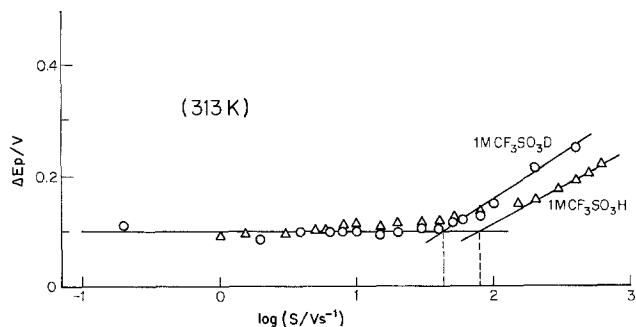


Fig. 2. Tafel-type plots for H-desorption from Pt in $\text{CF}_3\text{SO}_3\text{H}$ solutions at 313 K.

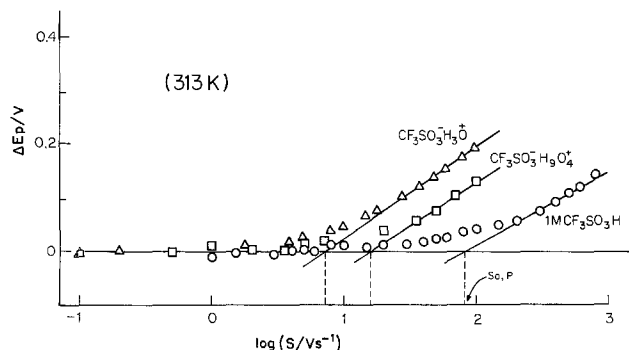


Fig. 3. Tafel-type plots for H- and D-desorption from Pt in 1M $\text{CF}_3\text{SO}_3\text{H(D)}$ at 313 K.

parable to the values reported for HClO_4 solutions (7). In the monohydrate, a smaller value of $S_{o,p}$ is observed; slower kinetics were also observed under steady-state polarization for the HER at Pt from the monohydrate as compared with the 1M acid solution (6), in contrast to the steady-state behavior at Hg. Note that in dilute acid media, the presence of strongly adsorbed anions on the Pt electrode surface has been shown to increase the rate of H-desorption (7).

Apparent activation energies, ΔH_{app}^\ddagger , were determined from plots of $S_{o,p}/T$ ($\propto k_0$) vs. T^{-1} derived from experiments over the temperature ranges 273–333 K (1M aq $\text{CF}_3\text{SO}_3\text{H}$) and 313–345 K ($\text{CF}_3\text{SO}_3^- \text{H}_3\text{O}^+$). The resulting ΔH_{app}^\ddagger values and the derived frequency factor ratio, corrected for double layer effects (6), appear in Table I. The frequency factor ratio, $A(1\text{M})/A(\text{H}_3\text{O}^+) = 73$ is significantly greater than the value of $ca. 10^{-1}$ for the steady-state HER at Pt (6). This difference is primarily due to the comparable ΔH_{app}^\ddagger values for the H-desorption reaction in these two solutions; the changes in the rates themselves between the two solutions are similar for the overall HER, and for the elementary H-desorption process. Based on the observed frequency factor ratios, the conjugate H-adsorption/desorption reactions do not

Table I. ΔH_{app}^\ddagger value and derived frequency factor ratio corrected for double layer effects

Solution	$\Delta H_{app}^\ddagger/\text{kJ mol}^{-1}$	$S_{o,p}/\text{V s}^{-1}$
$\text{CF}_3\text{SO}_3^- \text{H}_3\text{O}^+$	24.4	7.3
1M $\text{CF}_3\text{SO}_3\text{H}$	19.7	82.0

Frequency factor ratio $A(1\text{M})/A(\text{H}_3\text{O}^+) = 73$ at 313 K.

seem to be important in determining the rate of the HER at Pt from these solutions. However, there may be some similarity in behavior of the HER at Hg (where electron transfer is believed to be rate determining), and of the H-desorption reaction at Pt.

The H/D kinetic isotope effect was also investigated for the H-desorption process and the E_p vs. $\log(S)$ plot for the 1M $\text{CF}_3\text{SO}_3\text{H(D)}$ is shown in Fig. 3. A decrease in $S_{o,p}$ of $ca. 2x$ was found on substitution of D for H. Further work is currently in progress on the study of the H/D isotope effect on this reaction at Pt in the 1M aqueous and the monohydrate solutions as a function of temperature.

The results described briefly above, combined with other work related to the HER, will be presented in detail in a forthcoming publication. Additional experimental studies on the growth of surface oxide films at Pt in the novel $\text{CF}_3\text{SO}_3^- \text{H}_3\text{O}^+$ "melt" will also be reported shortly.

Acknowledgment

Support of this work by the Joseph W. Richards Summer Fellowship is gratefully acknowledged. The recipient is grateful for the continuing generous help and guidance of Professor B. E. Conway.

REFERENCES

1. A. N. Frumkin, in "Advances in Electrochemistry and Electrochemical Engineering," Vol. 3, P. Delahay and K. Tobias, Editors, p. 287, Wiley Interscience, New York (1963).
2. J. O'M. Bockris, in "Modern Aspects of Electrochemistry," Vol. 1, J. O'M. Bockris and B. E. Conway, Editors, Butterworths, London (1954).
3. See the bibliographies in Ref. (1) and (2).
4. B. E. Conway and J. O'M. Bockris, *J. Chem. Phys.*, **26**, 532 (1957).
5. R. Parsons, *Trans. Faraday Soc.*, **47**, 1332 (1951).
6. B. E. Conway and D. F. Tessier, *Int. J. Chem. Kinet.*, **13**, 925 (1981).
7. H. Angerstein-Kozłowska and B. E. Conway, *J. Electroanal. Chem.*, **95**, 1 (1979).
8. G. W. Walker, Ph.D. Dissertation, The American University, Washington D.C., (1981); G. W. Walker and R. T. Foley, Paper 491 presented at The Electrochemical Society Meeting, Minneapolis, MN, May 10–15, 1981.
9. E. R. Gonzalez and S. Srinivasan, *Electrochim. Acta*, **27**, 1425 (1982); E. R. Gonzalez, R. Naranjo, K.-L. Hsueh, and S. Srinivasan, *ibid.*, **28**, 165 (1983).
10. D. M. Novak and B. E. Conway, *J. Chem. Soc., Faraday Trans. I*, **77**, 2341 (1981).
11. J. Mozota and B. E. Conway, *ibid.*, **78**, 1717 (1982).
12. J. Mozota and B. E. Conway, *Electrochim. Acta*, **28**, 1 (1983).
13. T. Gramstad and R. N. Hazeldine, *J. Chem. Soc.*, 4069 (1957).



Chemical Reactions in Lithium Sulfur Dioxide Cells Discharged at High Rates and Temperatures

W. L. Bowden, L. Chow, D. L. Demuth, and R. W. Holmes

Duracell Laboratory, Duracell Laboratory for Physical Science, Burlington, Massachusetts 01803

ABSTRACT

The discharge capacity of Li/SO₂ cells was examined at high current and temperatures. D cells rated at 8 Ah delivered over 7 Ah at 5A current and 55°C, while cells discharged at 72°C gave 7 Ah at 3A. The cells were analyzed for residual lithium and sulfur dioxide. Spent cathodes were analyzed by infrared spectroscopy. A parasitic reaction was found in which Li₂S₂O₆ and S were formed, presumably by reaction of Li₂S₂O₄ with SO₂. This reaction became noticeable only under extreme combination of high rate and temperature.

Lithium/SO₂ cells are useful power sources for devices requiring high drain performance at low temperatures. Such cells generally are of a jelly roll design with layers of lithium foil, separator, and porous carbon cathode. The electrodes are surrounded by a highly conductive nonaqueous electrolyte consisting of an organic solvent (usually acetonitrile), a salt (usually lithium bromide), and sulfur dioxide, which serves as a soluble cathode material (1). In the course of cell discharge the lithium anode is oxidized, and the SO₂ soluble cathode is reduced. The discharge product, identified as lithium dithionite (2), precipitates in the porous cathode and eventually may passivate it. Such cells have open-circuit voltages near 3V and discharge at around 2.8V, delivering 140-150 Wh/lb over the cells' life (3, 4). Typical SO₂ D cells have short-circuit currents of over 100A and can deliver 30A pulses at specific powers of over 300 W/lb. In the course of discharging cells at elevated temperatures, it was observed that some cells delivered less than the usual capacity. We discharge a number of LO25SX and LO26SX D-type SO₂ cells at different rates and temperatures to determine the extent and magnitude of this decline in capacity. We used infrared spectroscopy and specific chemical analysis to identify products of the cells. We report the results here.

Experimental

The LO26SX, a hermetically sealed spirally wound D cell, was selected as a test vehicle for this study. The LO26SX is distinguished by its balanced cell chemistry in which the ratio of Li metal and SO₂ soluble cathode is near unity. This particular cell is rated at 8 Ah at 267 mA at 25°C. Capacities were calculated to a 2V cutoff and cells used for chemical analyses were not discharged below 2V. Cells were discharged at 21°, 55°, and 72°C on selected loads, as well as at constant currents, with data collection either by a Linseis LD-12 recorder or an HP 1000 computerized data-acquisition system.

Cells which were used for chemical analysis were placed in a specially made stainless steel bomb and punctured. The volatile acetonitrile and SO₂ were

withdrawn under vacuum and collected by cooling a flask with liquid nitrogen. The sulfur dioxide removed from the cell was then determined iodometrically. The remaining cell with its electrodes was then transferred to an argon-filled glove box and disassembled. Residual lithium was estimated by weighing the remaining anode. The carbon cathode was then analyzed by a variety of methods. Sulfur in the discharged cathode was determined gravimetrically by extracting the cathode with CH₂Cl₂ in a Soxhlet extractor. The CH₂Cl₂ was then removed with a rotary evaporator and the remaining sulfur weighed. Dithionite was determined by leaching the cathode with deaerated pH 10 buffer. The leachate was analyzed for dithionite by adding an aliquot to an excess of the Cu(II) ammine complex and spectrophotometrically measuring the destruction of Cu(II) (5). Dithionate was determined by first oxidizing the leachate with alkaline KMnO₄. The MnO₂ product was removed by filtering. All sulfur oxyanions except dithionate are converted to sulfate in this step. The solution of dithionate was then digested with metavanadate in H₂SO₄. The dithionate was then determined by back titration with KMnO₄ (6).

The extremely interesting compound lithium dithionite (Li₂S₂O₄) was prepared by reduction of sulfur dioxide with the lithium benzophenone ketyl. THF was refluxed with CaH₂ under argon for several days and then distilled into a carefully dried flask. The flask was taken into an argon-filled glove box where a slight excess of vacuum-dried benzophenone was dissolved in the THF. To this solution small pieces of lithium foil were added with stirring. The solution rapidly turned the intense blue of the benzophenone radical ion. Sulfur dioxide was then bubbled into this solution through a fritted-glass tube. The blue color of the solution rapidly disappeared, replaced by a milky white suspension in the THF. The white solid was collected by filtering, washed with CS₂ to remove any sulfur, and washed with CH₃CN to remove residual benzophenone. Purity was determined to be approximately 70% by Rohm's method (5). Lithium dithionate was prepared by oxidation of SO₂ with MnO₂ to form a mixture of manganous dithionate and sulfate. The sulfate and Mn(III) were removed by precipitation with hot saturated Ba(OH)₂. The result-

Key words: lithium, sulfur dioxide, nonaqueous electrolyte, high temperature discharge, capacity loss, decomposition, lithium dithionite, infrared, thermal analysis.

ing barium dithionate hydrate crystallized after water was removed with a rotary evaporator. The BaS_2O_6 was dissolved in water and converted to $Li_2S_2O_6$ by precipitating the Ba^{2+} with Li_2SO_4 solution. The extremely soluble $Li_2S_2O_6$ was isolated as a crystalline hydrate after reducing the solution in volume. Anhydrous material was obtained by vacuum drying at approximately $60^\circ C$. Lithium thiosulfate was prepared by metathesis of potassium thiosulfate with $LiClO_4$ in water. The slightly soluble $KClO_4$ was filtered off and the $Li_2S_2O_6$ crystallized on cooling after the solution was concentrated. The remaining sulfur oxyanions were obtained from Ventron or Pfaltz & Bauer. Infrared spectra were recorded with a Perkin-Elmer Model 683 spectrometer. The solid samples were finely ground with KBr in an agate mortar and pressed into a disk to give consistent samples. Considerable care was required to get a satisfactory spectrum of a discharged cathode because of the carbon present. Best results were obtained by using a very dilute KBr pellet combined with expansion of the transmittance scale.

Results

Cell testing.—Standard LO26SX cells were discharged at 21° , 55° , and $72^\circ C$ on loads varying from 0.4 to 55Ω . Capacities, shown in Tables I-III, were calculated to a 2V cutoff. Cell capacity is shown as a function of load and discharge temperature in Fig. 1. The increased currents drawn from the cells have little effect on capacity at $21^\circ C$, where the LO26SX delivers near its rated 8 Ah at currents of over 6A. As the temperature is increased, cell capacity remains essentially unchanged at lower currents with cells delivering the 8 Ah rated capacity on 5Ω load (approximately 0.55A). The combination of high current and high temperature resulted in a decreased cell capacity. This decrease can amount to 3.5 Ah under the extreme conditions on $72^\circ C$ temperature and 0.4Ω load.

From the plot in Fig. 1, it is clear that the LO26SX drops below the rated 8 Ah capacity only under high current discharge and high temperatures. The results at 21° , 55° , and $72^\circ C$ clearly show that the progressive nature of this phenomenon with temperature. The heat generated by the cell on discharge also plays an important role. The voltage and wall temperature of an LO26SX cell discharged at 2A are shown in Fig. 2. The wall temperature rose to some $89^\circ C$ during the discharge, and it can be safely presumed that more severe temperatures could be measured internally. The decline in capacity only at high currents and high tem-

Table I. Discharge of LO26SX cells at ambient temperature

Cell no.	Load (Ω)	Hr of service	Capacity (Ah)
9A	0.4	1.244	7.949
9B	0.4	1.228	7.890
10A	0.4	1.261	7.997
10B	0.4	1.239	7.862
10C	0.4	1.307	8.368
11H	0.4	1.096	6.944
11K	0.4	1.194	7.572
9H	0.6	1.951	8.537
9I	0.6	1.857	8.089
10H	0.6	1.836	8.030
10I	0.6	1.840	8.020
11A	0.6	1.981	8.637
11B	0.6	1.902	8.357
11C	0.6	1.966	8.590
11I	0.8	2.657	8.908
11J	0.8	2.674	8.946
6G	1.0	3.188	8.619
6I	2.0	6.351	8.817
6H	5.0	15.833	8.931
14D	5.0	14.856	8.378
14E	5.0	14.703	8.286
14F	5.0	14.401	8.115
7G	55.0	167.29	8.761
7H	55.0	172.48	9.041
7I	55.0	169.02	8.851

Table II. Discharge of LO26SX cells at $55^\circ C$

Cell no.	Load (Ω)	Hr of service	Capacity (Ah)
9F	0.4	0.751	4.898
10F	0.4	0.907	5.834
11G	0.6	1.359	5.965
9G	0.8	2.399	8.027
10G	0.8	2.555	8.457
6D	1.0	3.246	8.686
12D		3.266	8.666
12E		3.174	8.465
12F		3.182	8.458
6F	2.0	6.192	8.538
6E	5.0	15.158	8.524
7D	55.0	165.07	8.612
7E	55.0	151.58	7.867
7F	55.0	150.39	7.847

Table III. Discharge of LO26SX cells at $72^\circ C$

Cell no.	Load (Ω)	Hr of service	Capacity (Ah)
9D	0.4	0.694	4.499
10D	0.4	0.666	4.307
11E	0.6	1.077	4.754
9E	0.8	1.863	6.270
10E	0.8	2.067	7.001
6A	1.0	3.204	8.633
12A	1.0	2.535	6.751
12B	1.0	2.491	6.597
12C	1.0	2.454	6.507
14A	1.0	2.539	6.774
14B	1.0	2.561	6.803
14C	1.0	2.451	6.529
6C	2.0	5.779	7.995
6B	5.0	15.410	8.696
7A	55.0	170.87	8.903
7B	55.0	154.43	8.032
7C	55.0	151.95	7.902

peratures is due to an internal temperature well over $72^\circ C$. At these high temperatures, side reactions may occur which are unimportant at lower temperatures.

Analysis of cells.—We evaluated the processes taking place in the cell by infrared spectroscopy and

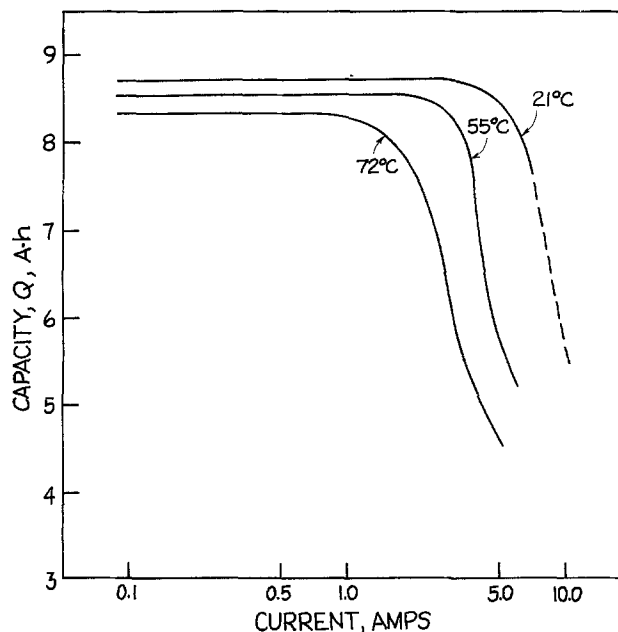


Fig. 1. Capacity to 2V of LO26SX cells as a function of average discharge current.

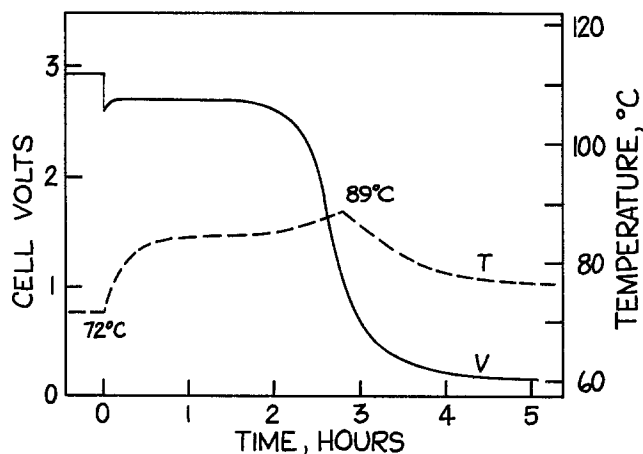


Fig. 2. Cell voltage and wall temperature vs. time for LO26SX cell discharged at 2A at 72°C.

specific chemical analysis. Infrared spectroscopy is a particularly suitable technique for studying the cathode, since it can detect relatively unstable materials *in situ* before possible reaction during extraction or isolation procedures. After some preliminary experiments with mulls, we selected dilute samples of finely ground cathode in KBr as a sampling technique. Infrared spectra of cathode from cells discharged at room temperature and 72°C at 1Ω are shown in Fig. 3 and 4. Both cathode spectra are characterized by absorbances at approximately 1090, 1020, and 905 cm⁻¹, while the cathode discharged at elevated temperature has three additional bands at 1240, 1170, and 970 cm⁻¹. A series of spectra of cathodes from cells discharged under increasingly severe conditions revealed that the bands at 1240, 1170, and 970 become relatively more intense as the severity of temperature and rate increases.

The increase in intensity of the new bands led us to suspect that at high rates and temperatures the expected Li₂S₂O₄ (lithium dithionite) product might either decompose or fail to form. To test this hypothesis we had a number of cells analyzed for sulfur dioxide and lithium dithionite after discharge. Results are shown in Table IV. As shown by the data in Table IV, cells discharged at high rates and currents had substantially less dithionite than calculated from the diminished capacity, and only approximately 50% as much as cells discharged at room temperature. The analyses of discharged cell cathodes clearly showed that new chemistry was appearing under the extremely severe discharge conditions. To see whether this new chemistry was due to dithionite decomposition, we compared the infrared spectra of Na₂S₂O₄ before and after heating at 5°C/min in a sealed Ni-monic crucible in a Mettler TA2000 DTA. The DTA exotherm occurred at 192°C. The only identified decomposition product was Na₂S₂O₃ from its IR. We noted that the IR of Na₂S₂O₄ was not similar to that of a discharged cathode containing Li₂S₂O₄ and specu-

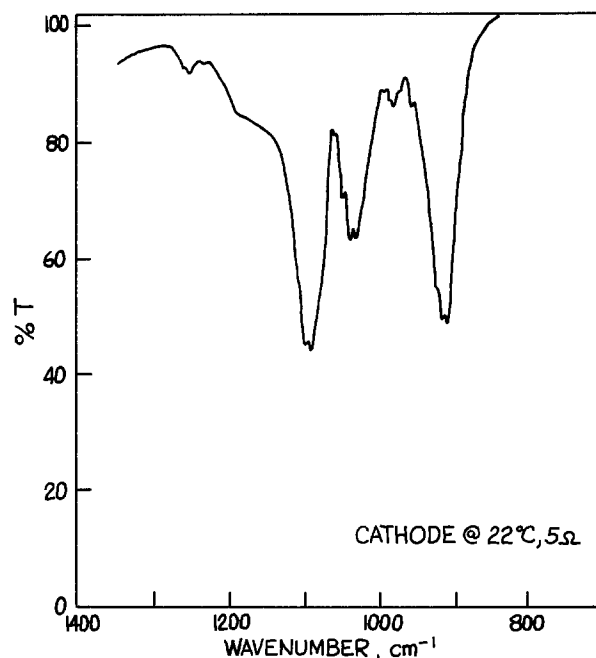


Fig. 3. Infrared spectrum of cathode from an LO26SX cell discharged at 22°C, 5Ω load.

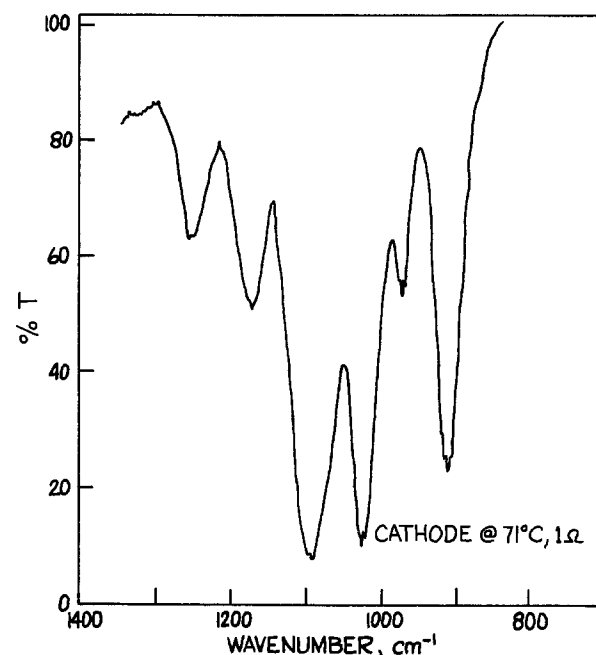


Fig. 4. Infrared spectrum of cathode from an LO26SX cell discharged at 71°C, 1Ω load.

lated that Li₂S₂O₄ might react differently from Na₂S₂O₄. An authentic solid sample of Li₂S₂O₄ was prepared by oxidation of lithium-benzophenone ketyl

Table IV. Analysis of LO25SX and LO26SX cells for Li₂S₂O₄ and SO₂

Cell no.	Temp (°C)	i (A)	Q (Ah)	Grams SO ₂ (found)	Grams S ₂ O ₄ ⁻² (found)	Grams* S ₂ O ₄ ⁻² (calc.)	% S ₂ O ₄ ⁻² yield
LO26SX							
1	72	1Ω (2.5A avg)	5.47	9.45	9.46	13.06	72.4
2	72		5.46	9.90	8.90	13.03	68.3
3	25		6.82	6.41	15.87	16.28	97.5
4	25		7.14	6.09	15.67	17.05	91.9
LO25SX							
D5	71	1Ω (2.5A)	6.22	10.20	11.06	14.86	74.4
C3	71		5.53	11.95	9.87	13.21	74.7
D4	25	22Ω (0.13A)	8.58	5.38	19.17	20.52	93.4
C4	25		8.49	5.10	20.44	20.29	100.7

* The calculated amount of dithionite is based on the assumed cell reaction: 2Li + 2SO₂ → Li₂S₂O₄.

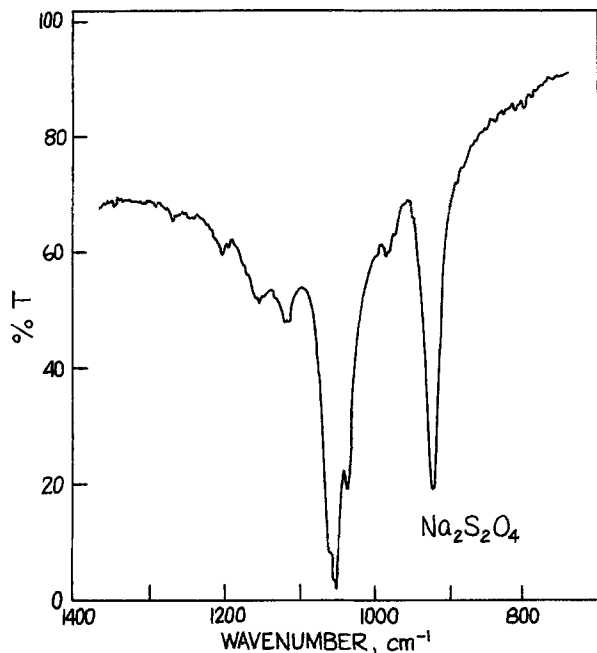


Fig. 5. Infrared spectrum of $\text{Na}_2\text{S}_2\text{O}_4$

by SO_2 in carefully dried THF. Quantitatively our product was only about 70% pure. The infrared spectrum of this material (Fig. 6) was almost identical to that of a discharged cathode. Thermal analysis demonstrated that $\text{Li}_2\text{S}_2\text{O}_4$ showed no reaction below 170°C , only slightly lower than $\text{Na}_2\text{S}_2\text{O}_4$. This was somewhat unexpected given the difficulty of preparing $\text{Li}_2\text{S}_2\text{O}_4$. Figure 7 shows the DSC results for $\text{Li}_2\text{S}_2\text{O}_4$ heated at $40^\circ\text{C}/\text{min}$ in a Perkin-Elmer DSC-4.

Examination of cathode spectra from cells tested at high temperature pointed to the presence of a dithionate in the cathode. A commercial sample of $\text{Na}_2\text{S}_2\text{O}_6$ is shown in Fig. 8. The absorbance at 1240 cm^{-1} is very similar to that in the cathode spectrum, while the band at 1000 cm^{-1} could be masked by the 1020 cm^{-1} dithionite band. A specific analysis for dithionate determined that 0.055 mols of $\text{Li}_2\text{S}_2\text{O}_6$ were present in a cell discharged at 72°C on 1Ω load. We prepared an authentic sample of $\text{Li}_2\text{S}_2\text{O}_6$ and found its IR pattern to be similar to that of $\text{Na}_2\text{S}_2\text{O}_6$. A dis-

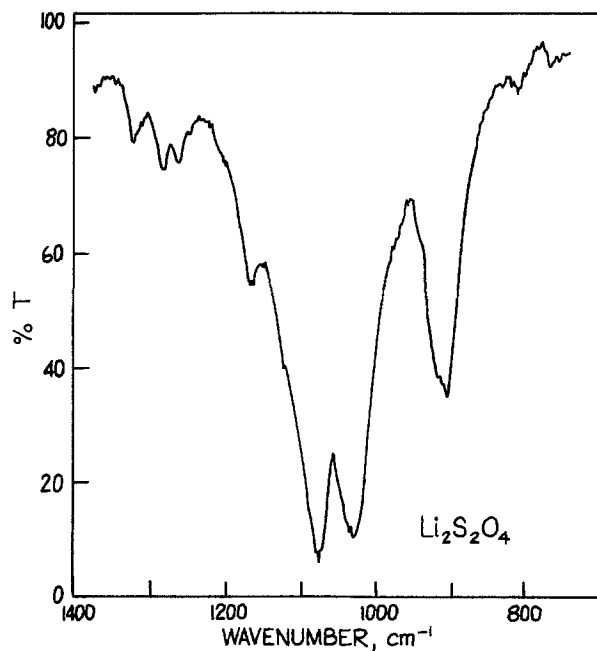


Fig. 6. Infrared spectrum of $\text{Li}_2\text{S}_2\text{O}_4$ prepared by reduction of SO_2 with benzophenone ketyl.

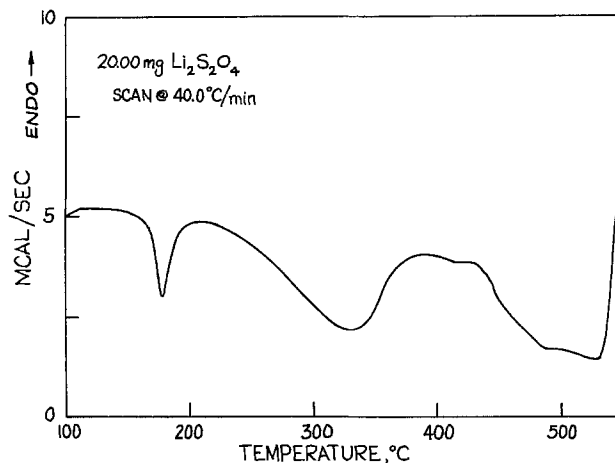


Fig. 7. Differential scanning calorimetry at $40^\circ\text{C}/\text{min}$ of prepared sample of $\text{Li}_2\text{S}_2\text{O}_4$.

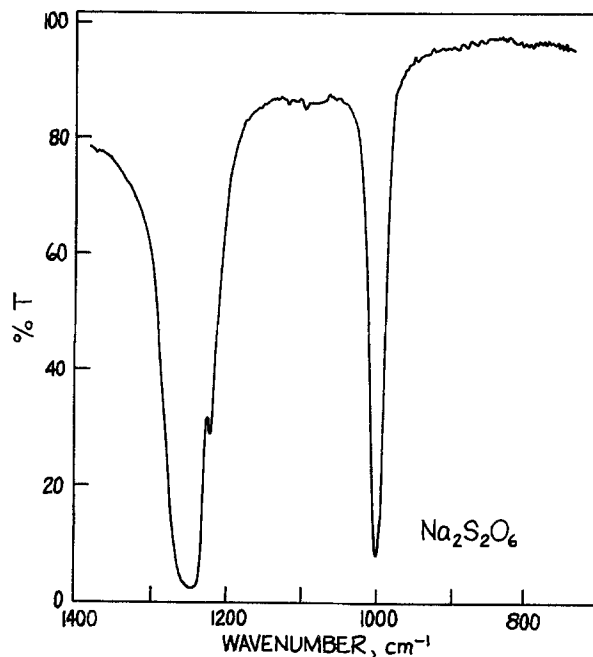


Fig. 8. Infrared spectrum of $\text{Na}_2\text{S}_2\text{O}_6$ showing absorbances at 1240 and 1000 cm^{-1} .

charged cell was analyzed for sulfur by leaching the cathode with methylene chloride. The solid product (0.96g) was identified as elemental sulfur by its characteristic powder diffraction pattern. While this identified two products of the high temperature reaction, namely, S and $\text{Li}_2\text{S}_2\text{O}_6$, there were still two absorbances in the infrared which had not been assigned, 1170 and 970 cm^{-1} . To identify the source of these absorptions a number of salts of sulfur oxyanions were examined by IR. The unassigned absorbances are not due to Li_2SO_4 , Li_2SO_3 , or $\text{Li}_2\text{S}_2\text{O}_3$, as shown by Fig. 9, for example. The anions $\text{S}_2\text{O}_7^{2-}$ and $\text{S}_4\text{O}_6^{2-}$ were also eliminated. The IR spectra of $\text{K}_2\text{S}_2\text{O}_5$ and $\text{Na}_2\text{S}_2\text{O}_5$ were generally similar, and we suggest that $\text{Li}_2\text{S}_2\text{O}_5$ is also present in the cathode, as shown in Fig. 10.

To determine whether this capacity degradation at high current and temperature was related strictly to cell discharge or could be created in storage of partly discharged cells, LO26SX cells were 50% discharged at 25°C and then stored at 72°C for a week. At the end of the week the infrared spectra of the cathodes showed only the three absorbances due to lithium dithionite. This observation suggests that the reactions responsible for the capacity decline occur mainly during the formation of lithium dithionite rather than as a subsequent reaction in the cell.

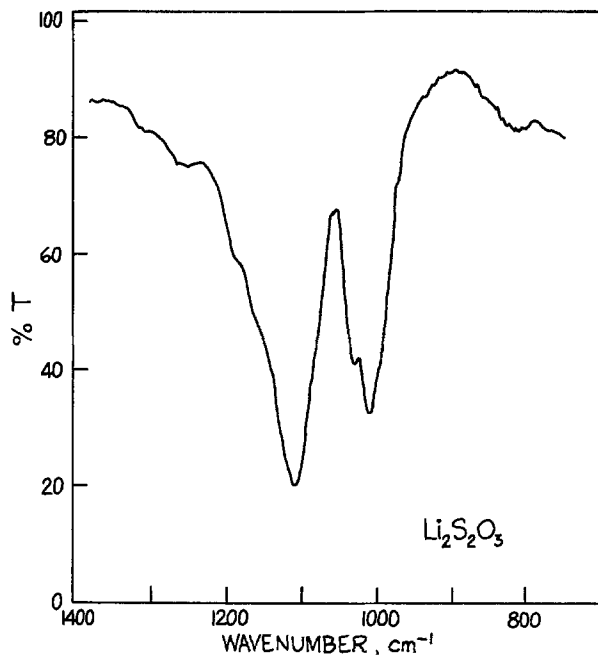


Fig. 9. Infrared spectrum of Li₂S₂O₃, for comparison with spectra of discharge products.

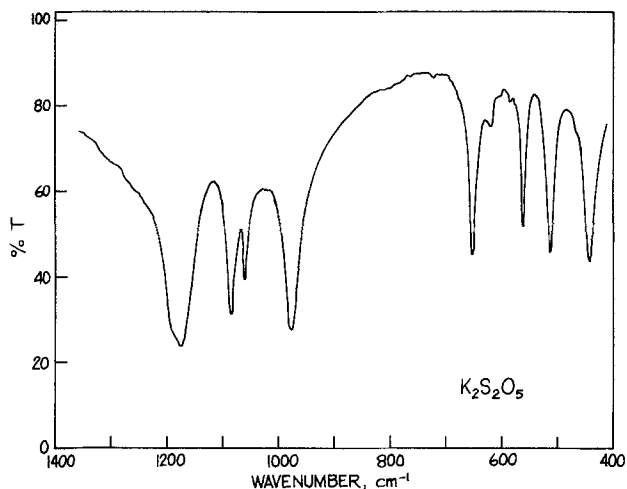
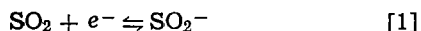


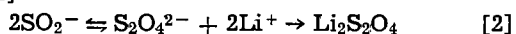
Fig. 10. Infrared spectrum of K₂S₂O₅ showing the absorbances at 1170 and 970 cm⁻¹.

Discussion

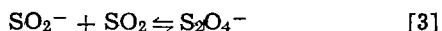
The reduction of SO₂ in aprotic solvents is known to occur via an initial one-electron transfer to form a radical anion, (8, 9). In extremely dilute solutions in a coordinating medium like DMF, the electron transfer process is reversible



The SO₂⁻ radical anion itself is an unstable species and may react by a variety of methods. In acetonitrile solvent with a Li⁺ supporting electrolyte, the most easily available mode of reaction is dimerization to dithionite followed by rapid precipitation of the lithium salt (2, 13). This dithionite formation from the short-lived radical ion occurs almost quantitatively in SO₂ cells discharged at 25°C, as shown by the average dithionite yield of 95.9% based on the stoichiometry in reactions [1] and [2]

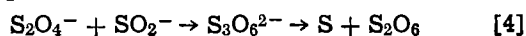


In DMF or under more unusual conditions the SO₂⁻ radical ion may coordinate with SO₂ to form a complex ion (8, 10)



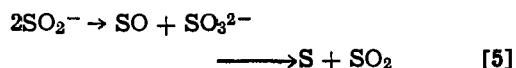
We suggest that this complex ion might react further with the radical ion to form a dianion, apparently similar to trithionate, which would decompose to give the

detected products of lithium dithionate and sulfur

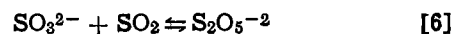


The characteristic 1200 cm⁻¹ band of trithionate was never observed in a cathode IR spectrum, however.

The SO₂⁻ ion has also been found to disproportionate in solution to give sulfite and sulfur monoxide. The sulfur monoxide is extremely unstable and will disproportionate to rapidly form sulfur and SO₂ (11)

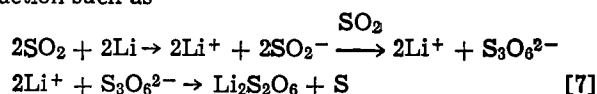


The sulfite ion itself is known to form pyrosulfite in aqueous solutions (12). Thus we have a plausible mechanism for explaining the presence of pyrosulfite as well



It is at least as notable that the infrared spectra gave negative evidence for the presence of two expected byproducts, Li₂SO₄ and Li₂S₂O₃. The lithium sulfate had been found on analysis of cells stored for extremely long times at high temperatures, while thio-sulfate has been proposed as a cell product in certain circumstances. The different pattern of products clearly points to the electron transfer involving SO₂⁻ being involved in these reactions, as opposed to slow side reactions involving the LiBr and SO₂ electrolyte components.

The amount of dithionate found, 0.055 mols, corresponds roughly to the capacity decrease in such a cell. It is quite tempting to ascribe the capacity loss to a reaction such as



In this reaction three equivalents of SO₂ produce two of current with formation of S and Li₂S₂O₆. Coupled with disproportionation of the SO₂ radical ion to eventually form S and Li₂S₂O₅, this offers a facile explanation for the capacity loss phenomenon, although the available data are far from definitive.

Conclusion

Lithium/sulfur dioxide cells discharged under conditions of high current and high temperature deliver less capacity than cells discharged at the same currents at room temperature or at elevated temperature and low rates. Analysis of these cells with diminished capacity revealed substantially less Li₂S₂O₄ discharge product than in normally discharged cells. The quantity of dithionite present was only 75% of that expected from the cell capacities. The loss in capacity is also accompanied by side reactions forming elemental S, Li₂S₂O₅, and Li₂S₂O₆. It is likely that these side reactions occur during discharge, since partly discharged cells stored at 72°C do not show spectroscopic evidence of deterioration. The side reactions appear to lead to premature cathode passivation, since cells had both Li and SO₂ present at the end of discharge. Our results show that the redox chemistry of SO₂ in organic solvents is a complex problem. Cell capacity and cell chemistry are both sensitive to factors which are not yet completely understood.

Manuscript submitted June 23, 1983; revised manuscript received Sept. 19, 1983.

Duracell, Incorporated assisted in meeting the publication costs of this article.

REFERENCES

1. A. N. Dey and R. W. Holmes, *This Journal*, **127**, 1877 (1980).
2. P. Bro, H. Y. Kang, C. R. Schlaikjer, and A. H. Taylor, *IECEC '75 Rec.*, 432 (1975).
3. D. Linden and B. McDonald, *J. Power Sources*, **5**, 35 (1980).
4. P. Bro, R. W. Holmes, N. Marincic, and A. H. Tay-

- lor, in "Proc. Ninth Int. Symp. Power Sources," Joint Services Electrical Power Sources Committee, p. 703, Brighton, England (1974).
5. T. J. Rohm, Paper presented at 10th NERM, American Chemical Society, Boston, MA.
 6. H. Crossland and N. Hofmann-Bang, *Acta Chem. Scand.*, **15**, 1064 (1961).
 7. G. Pass and H. Sutcliffe, "Practical Inorganic Chemistry," p. 24, Chapman and Hall, London (1968).
 8. R. P. Martin and D. T. Sawyer, *Inorg. Chem.*, **11**, 2644 (1972).
 9. R. Bonnetterre and G. Caquis, *J. Electroanal. Chem.*, **32**, 215 (1971).
 10. C. L. Gardner, D. T. Fouchard, and W. R. Fawcett, *This Journal*, **128**, 2337 (1981).
 11. P. Schenck and R. Steudel, in "Inorganic Sulfur Chemistry," H. C. Nickless, Editor, pp. 405-408, Elsevier, New York (1968).
 12. M. Schmidt and W. Siebert, in "Comprehensive Inorganic Chemistry," Vol. II, J. C. Bailor, H. J. Emeléus, R. Nyholm, and A. F. Trotman-Dickenson, Editors, pp. 795-933, Pergamon Press, Oxford, England (1973).
 13. M. W. Rupich, L. Pitts, and K. M. Abraham, *This Journal*, **129**, 1857 (1982).

Electrochemical and Ellipsometric Investigations of Passive Films Formed on Iron in Borate Solutions

I. The Kinetics of Film Growth on Iron at Constant Anodic Potentials

Z. Szklarska-Smialowska¹ and W. Kozlowski

Institute of Physical Chemistry, Polish Academy of Sciences, Warsaw, Poland

ABSTRACT

The kinetics of passive film formation on iron in borate buffer solution has been studied at different anodic potentials. The process of film growth has been found to occur in four distinct stages. About 80-90% of the total film thickness formed in 1h grows during the initial two stages which last for only 1-3s (depending upon potential). The electric field strength across the film is not constant but decreases with progressing film growth. The thickness of the film determined ellipsometrically is less than that calculated from the electric charge consumed. The process of anodic film formation is accompanied by the dissolution of iron which occurs over the whole range of potentials.

The rates at which passive films grow on the surface of iron have been studied either by electrochemical techniques, in which the anodic current density is measured as a function of time (1, 2), or ellipsometrically by measuring the optical parameters for the evolving film (3-6). This latter technique directly yields the film thickness as a function of time which can be used to test various models for the growing anodic film. In the majority of cases, ellipsometric measurements began approximately 1 min after a constant anodic potential was applied, i.e., at a time subsequent to the development of a major part of the film. As far as we are aware, only in two studies (3, 6) have attempts been made to determine the rate of film growth during the initial minute following the application of the potential.

A particularly large body of information on the initial process of film growth on iron has been provided by Kruger and Calvert (3). They found that film growth occurs in three stages. In the first stage, a linear relationship exists between the film thickness and the square root of time. The authors (3) suggest that during this stage the film growth is controlled by the diffusion of OH⁻ ions to the electrode surface. During the second stage, a number of complex processes occur which cannot be characterized by any simple rate law. The third stage, i.e., that of the steady-state growth, can be described equally well by either a logarithmic or inverse logarithmic law. From the inverse logarithmic relationship, the so-called jump distance has been estimated to be 10Å, and the activation energy equal to 1.8 eV. This value of the jump distance is much larger than the value expected for Fe₂O₃, which is about 3Å. It is worth mentioning that other authors (4, 5) have also found jump distances much larger than 3Å.

Many theoretical models have been proposed to explain the kinetics and mechanisms of film growth on metals. The inverse logarithmic model proposed by

Mott and Cabrera (7) assumes field-assisted cation diffusion and uniform field strength across the film. The logarithmic model of Fehlner and Mott (8) proposes that anion diffusion is responsible for film growth and that the field strength in the film is independent of thickness. Another logarithmic model developed by Sato and Cohen (9) postulates that field-assisted place exchange of metal-oxygen pairs is responsible for film thickening. This model is applicable to very thin films only. Chao *et al.* (10) recently proposed a model based on the movement of point defects in a chemical potential and electrostatic field. These authors propose that oxygen anions are responsible for growth of the primary passive film.

Most models presented to date consider passive films to be semiconductors or "incipient" semiconductors by virtue of dielectric breakdown (10). A different approach has been adopted by Cahan and Chen (11). In their "chemiconductor" model, the passive film on iron is pictured as an insulating ferric oxyhydride. Small nonstoichiometry, primarily due to Fe²⁺ near the metal-film interface and to Fe⁴⁺ near the film-solution interface, affect the local conductivity in the film.

The objective of the present work was to use electrochemical and ellipsometric techniques to characterize the kinetics of film growth on iron in borate buffer solution of pH 8.45. Experimental data has been collected from the first few moments (~0.2s) to up to 1h after the application of a constant anodic potential. Particular emphasis has been placed on correlating the results obtained using the electrochemical and ellipsometric techniques, so that a consistent picture can be developed of the evolution of the passive film as a function of time.

Experimental Procedure

An Armco iron specimen with an exposed area of 0.5 cm² was mounted in a Teflon holder. The specimen surface was first mechanically ground with emery papers finishing with 800 grit, then polished with 1

¹ Present address: Department of Metallurgical Engineering, The Ohio State University, Columbus, Ohio 43210.

μm diamond paste, and finally electropolished in a mixture of glacial acetic acid and perchloric acid (20:1) at a current density of $2 \text{ A} \cdot \text{cm}^{-2}$ for 2-5s. This treatment did not cause etching or roughness. Before initiating experimental measurements, the specimen was washed with distilled water and methanol.

Two borate buffer solutions of pH 8.45 were used: $0.02\text{M H}_3\text{BO}_3 + 0.005\text{M Na}_2\text{B}_4\text{O}_7$ (solution 1); and $0.15\text{M H}_3\text{BO}_3 + 0.0357\text{M Na}_2\text{B}_4\text{O}_7$ (solution 2). These solutions were prepared using Analytical Reagent grade chemicals and triple distilled water. The solutions were deaerated by bubbling argon (99.99%) for at least 24h before the experiment. All measurements were made at 22°C .

The ellipsometer used was a Rudolf Research Model 2000 equipped with a revolving analyzer. The light source was a tungsten iodine lamp from which monochromatic light of 546.1 nm wavelength was obtained using an interference filter.

The McCrackin (12) computer program was used to evaluate the optical constants of iron and of the film formed on it. In the case of double layer films, the refractive indexes were calculated on the assumption that these films were composed of two homogeneous layers, one on the top of another, with different optical constants.

Before measurements of the optical constants of iron, the specimens were cathodically reduced with a current density of $0.02 \text{ A} \cdot \text{m}^{-2}$ during 20 min. During the last period of the cathodic reduction, the solution in the electrolytic cell was exchanged.

Optical parameters were measured for films formed at constant potentials at 100 mV intervals over the range of -0.5 to 0.8V .

The Δ and Ψ parameters were measured with an accuracy of $\pm 0.03^\circ$ and $\pm 0.01^\circ$, respectively, which corresponded to an accuracy of film thickness determination of ± 0.01 to $\pm 0.02 \text{ nm}$.

All potentials are referred to the saturated calomel electrode. The kinetics of film growth were studied for periods extending from about 0.2s to 60 min after application of the potential, during which time changes in the optical parameters and current densities were recorded.

Results

In order to characterize electrochemically the studied system, anodic polarization curves were obtained in both solutions at a scan rate of 1V per min (Fig. 1). The maximum current corresponding to the active/passive transition occurred at -0.6V . The passive potential region extended up to 0.85V . The current density in the whole potential region was higher in the more concentrated solution (solution 2).

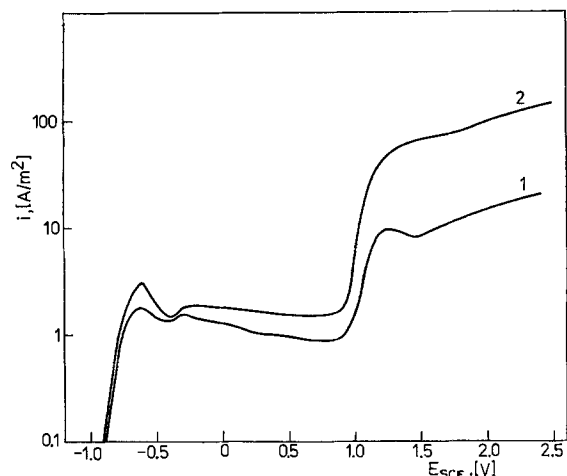


Fig. 1. Anodic polarization curves for Armco iron in: solution 1 $0.02\text{M H}_3\text{BO}_3 + 0.005\text{M Na}_2\text{B}_4\text{O}_7 \cdot 10 \text{ H}_2\text{O}$ pH 8.45; and solution 2 $0.15\text{M H}_3\text{BO}_3 + 0.375\text{M Na}_2\text{B}_4\text{O}_7 \cdot 10 \text{ H}_2\text{O}$ pH 8.45.

The optical parameters of films obtained after passivation of the iron for 60 min in both solutions are shown in Fig. 2. The values of n (refractive index) and k (absorption coefficient) changed significantly in the range of potentials from -0.5 to about -0.1V in solution 1 and from -0.5 to -0.3V in solution 2. Within these potential regions, the values of n and k increased in solution 1 from 2.1 to 2.45 and from 0.09 to 0.22, respectively and in solution 2 from 1.7 to 2.2 and from 0.06 to 0.15, respectively. In stagnant solutions, a second layer developed on those films which exhibited lower optical parameters ($n = 1.6-1.8$ and $k = 0.015-0.05$). In stirred solutions, this second layer was not formed.

In the second potential region, i.e., from -0.1 to 0.8V in solution 1 and from -0.3 to 0.8V in solution 2, the films could be described by only one value of n and k in both stirred and unstirred solutions. As shown in Fig. 2, these values also changed with the passivation potential, but this effect was less pronounced in the second potential region. In solution 1, n increased from 2.45 to 2.6 and k from 0.22 to 0.36, while in solution 2, n increased from 2.2 to 2.5 and k from 0.15 to 0.25.

As is clearly shown in Fig. 3, the changes in optical parameters occurred only during the initial 30s of polarization; after this both n and k reached time independent values in both solutions.

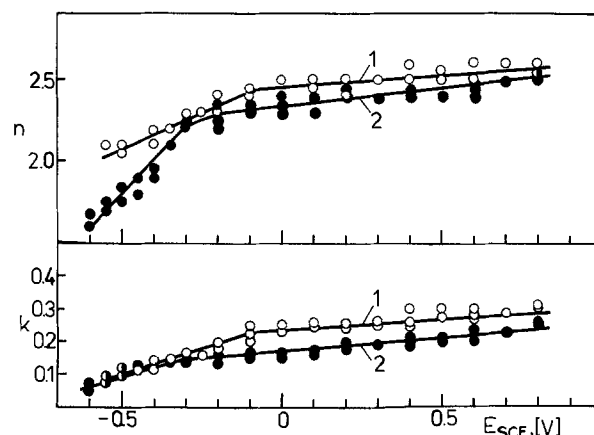


Fig. 2. Dependence between optical parameters n and k and potential measured in solutions 1 and 2.

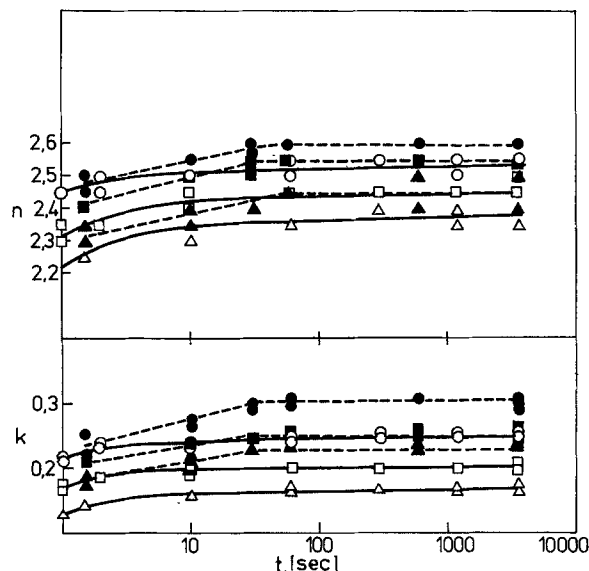


Fig. 3. Optical parameters n and k vs. time measured in solutions 1 (dashed line) and 2 (solid line) at 0.0V (Δ , \triangle), 0.4V (\square , \blacksquare), and 0.8V (\circ , \bullet).

Due to film thickening, the current density decreases with increasing passivation time at constant potential. An example is given in Fig. 4. In solution 1, at potentials ranging from 0 to 0.8V, the dependence of $\log i$ on $\log t$ is nonlinear in the initial period from 0.2 to 1.2s, thereafter, two linear regions can be distinguished: from 1.2 to 5-10s; and from 5-10 to 1200-1800s. After this period, i drops below $0.01 \text{ A} \cdot \text{m}^{-2}$. At the same passivation potentials, the initial current density is higher in the more concentrated solution 2 than in solution 1 and in the initial second, the i vs. t curve is more pronounced in solution 1, and within the third passivation region, the slopes of all i vs. t curves are similar.

An example of the relationship between film thickness (d) as determined ellipsometrically in solution 1 and $\log t$ is plotted for different passivation potentials in Fig. 5. In this figure, I denotes the initial process of oxidation lasting from about 0.2 to 0.5s. It is noted that d is a nonlinear function of $\log t$ and is potential dependent. Within the next region (II), the relationship between d and $\log t$ is linear. Higher rates of film growth and larger film thicknesses are observed with increasing potential. This oxidation stage ends at ~ 2 s at 0.6V and at ~ 6 s at -0.2 V. The third stage (III) of

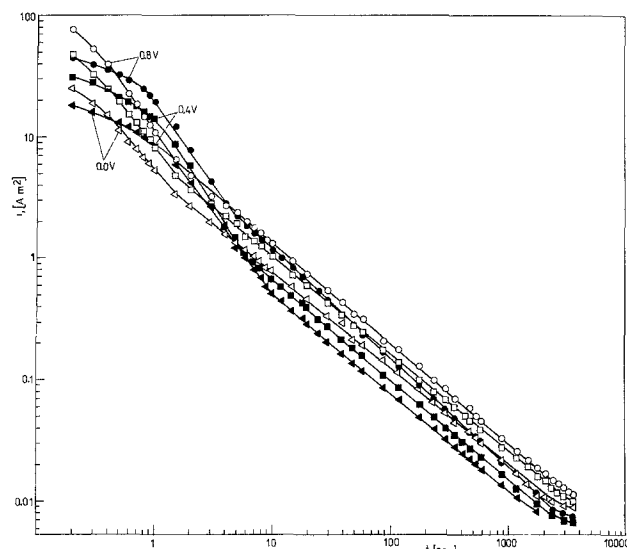


Fig. 4. Changes of current density during passivation of iron in solutions 1 (▲●) and 2 (△□○) at 0.0, 0.4, and 0.8V.

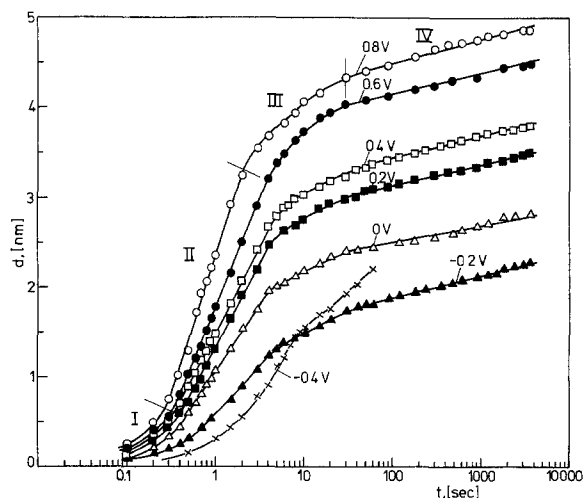


Fig. 5. Dependence between film thickness determined ellipsometrically and passivation time in solution 1 at different potentials. Consecutive steps of film formation at 0.8V are marked in the graph.

approximately 8-30s duration is characterized by intermediate oxidation rates between stages II and IV. This stage can be regarded as transition from stage II to IV. In the fourth stage (IV), the relationship between d and $\log t$ is linear and the oxidation rate is relatively low. Relationships between d and $\log t$ measured in solution 2 do not differ substantially from those obtained in solution 1.

From these data it is apparent that, at a given anodic potential, 80-90% of the film thickness attained in 1h of passivation is formed within the initial 10-30s.

Figures 6 and 7 show the effect of potential on film thickness at the end of each passivation stage in solutions 1 and 2, respectively. In Fig. 8, the film thickness measured in solution 1 is plotted as a function of the charge density (Q) calculated from the $\log i$ vs. $\log t$ curve. It should be noted that in Fig. 8 only the final three stages of film growth can be distinguished, as the initial stage of about 2s duration cannot be calculated by the technique employed. The same types of curves were obtained in solution 2.

Discussion

These ellipsometric measurements indicate that the optical parameters of passive films formed in 1h are potential dependent. Two potential regions can be distinguished. In the first region, which occurs at more negative potentials, the composition and properties of the film, as characterized by its optical parameters,

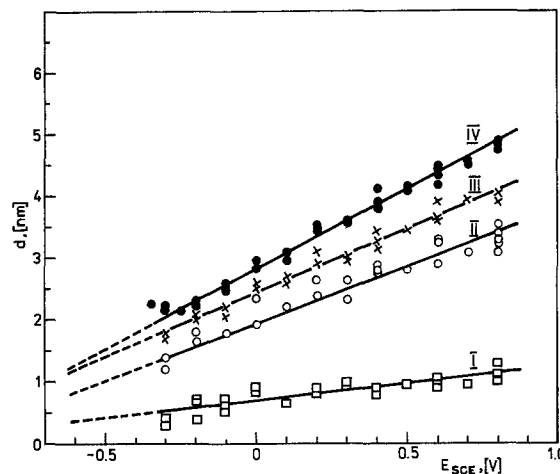


Fig. 6. Thickness of film formed in solution 1 measured at the end of each consecutive step of film growth as a function of potential.

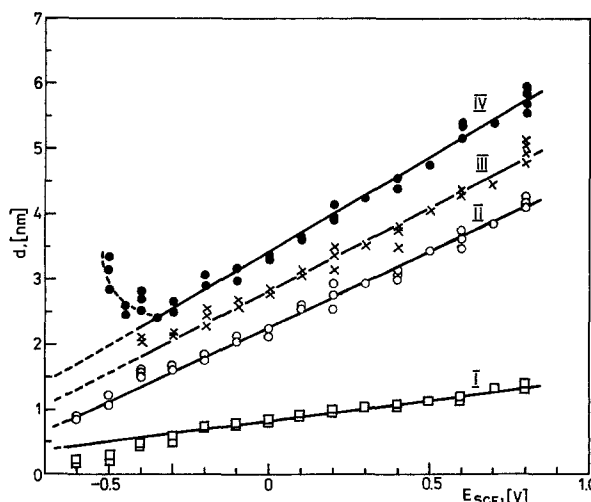


Fig. 7. Thickness of film formed in solution 2 measured at the end of each consecutive step of film formation as a function of potential.

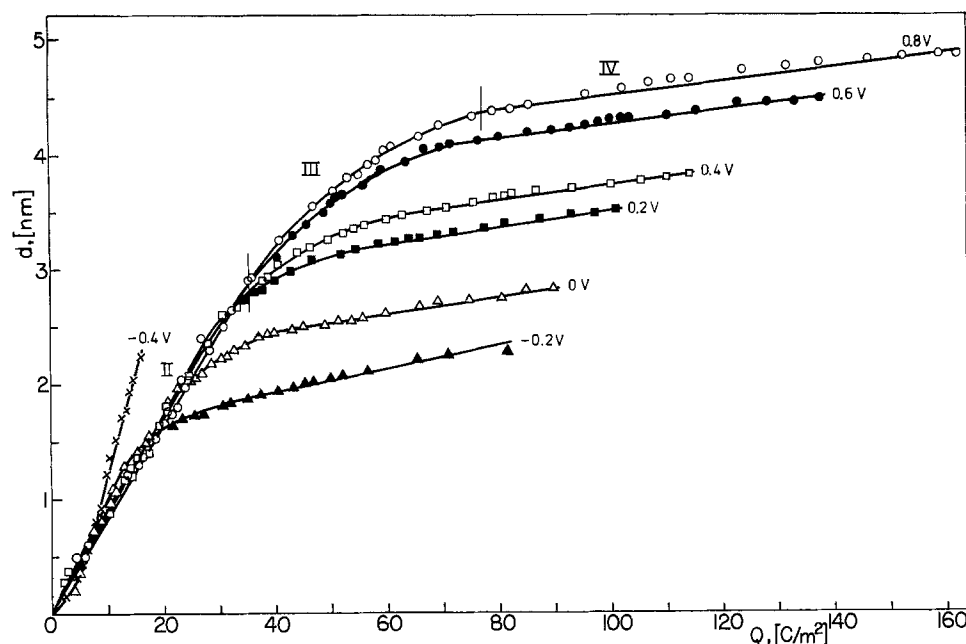


Fig. 8. Dependence between film thickness measured ellipsometrically in solution 1 vs. potential and charge density.

change more significantly with passivation potential. Also, the refractive indexes of the film are relatively low, suggesting the formation of hydroxides or oxyhydroxides. In the second region, at more anodic potentials, the effect of potential is less pronounced, and the optical parameters suggest that the film is composed of oxides and hydroxides. Initially, the values of n and k vary as a function of time, but in about 10-30s they assume constant levels.

Some characteristic differences occur in the optical parameters of films formed in solution 1 as compared with those formed in solution 2. At the same passivation potential, lower n and k values were measured in solution 2. This suggests that films formed in solution 2 are relatively less dense and contain a greater ratio of oxyhydrates to oxides. Furthermore, a greater amount of boron may be occluded from solution 2 as boron is incorporated in films formed in borate solutions (13-15).

Simultaneous ellipsometric and current decay measurements at constant potential show that film growth occurs in several stages. Four stages can be distinguished in plots of film thickness vs. log time, but only three stages appear in plots of d vs. charge density (Q), because the method employed for the determination of Q does not reveal the initial stage I.

Based on the film thickness as a function of potential data shown in Fig. 6 and 7, the field strength values (ϵ) corresponding to different passivation periods have been calculated using the formula

$$\epsilon = \frac{\Delta V}{\Delta d} \quad [1]$$

where V is the applied anodic potential, and d is film thickness. The results given in Table I indicate that the average field strength is the highest in stage I and decreases significantly during the following passivation periods as d and t increase.

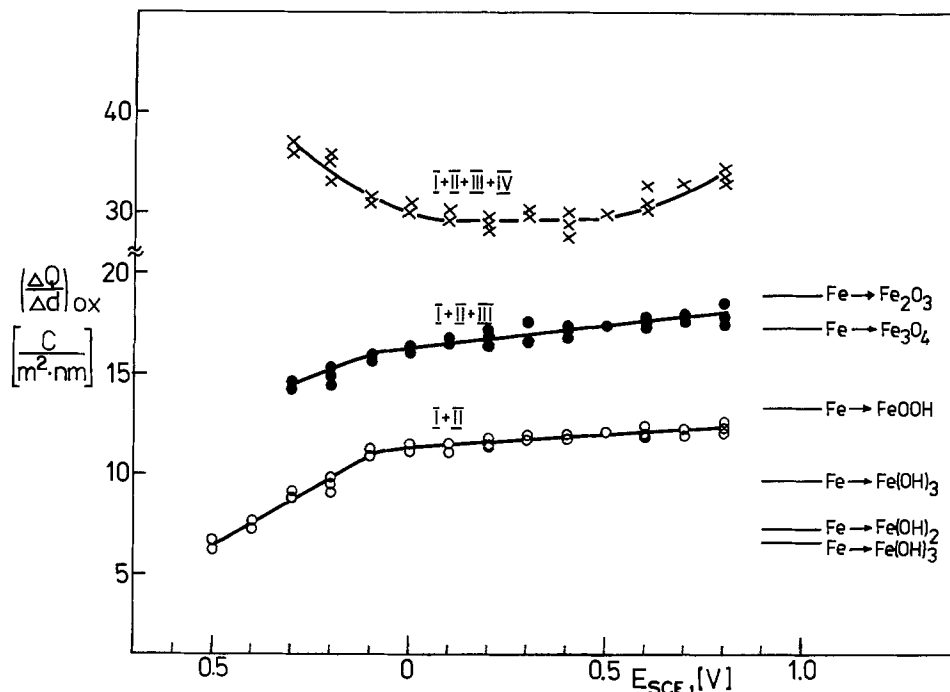
Table I. Mean field strength of passive films, ϵ (in $V \cdot cm^{-1}$)

Passivation period	Solution 1 ϵ	Correlation coefficient	Solution 2 ϵ	Correlation coefficient
Stage I	1.8×10^7	0.74	1.6×10^7	0.96
Stage I + II	5.4×10^6	0.92	4.3×10^6	0.99
Stage I + II + III	4.9×10^6	0.97	4.0×10^6	0.98
Stage I + II + III + IV	3.9×10^6	0.98	3.5×10^6	0.98

Using all of the electrochemical and ellipsometric data, the anodic charge per unit volume of film during each passivation period has been calculated as shown in Fig. 9 for solution 1. The charges consumed in stages I and II and I-III are greater in solution 1 than in solution 2, but the total charge consumed after polarization for 1h is greater in solution 2. In Fig. 9, the ratios of $\Delta Q/\Delta d$ for different oxides, hydroxides, and oxyhydroxides of iron are also included. For these calculations, the following densities (expressed in $g \cdot cm^{-3}$) have been taken into consideration: Fe_2O_3 5.249; Fe_3O_4 5.18; γ - $FeOOH$ 4.09; $Fe(OH)_3$ 3.6 and 2.44; and $Fe(OH)_2$ 3.4. As noted before, two potential regions in the relationship between oxidation potential and n and k are noted in Fig. 9. For states I and II and I-III, the increase in $\Delta Q/\Delta d$ is more pronounced at lower potentials. This is especially true in solution 1. However, for the total I-IV period, increases in $\Delta Q/\Delta d$ are more pronounced at higher potentials. By comparing the theoretical values of $\Delta Q/\Delta d$ with experimental data, it can be assumed that within the first potential region between -0.5 and $0V$ the film being formed contains iron in the oxidation state of $+2$ and $+3$. The charge per unit volume corresponds approximately to that of $Fe(OH)_3$ and $Fe(OH)_2$. The increase in $\Delta Q/\Delta d$ with increasing potential can be attributed to a larger Fe^{3+}/Fe^{2+} ratio and to a reduced content of water in the film. The fact that the charge associated with stages I and II is less than the theoretical value for γ - $FeOOH$ formation seems to suggest that hydroxides are also formed.

The effects of potential on $\Delta Q/\Delta d$ for stages III and IV in solution 1 are shown in Fig. 10. During stage III in both solutions, these ratios increase with increasing potential from about $-0.2V$, but are only slightly affected by changes in E . It is evident that for both stage II and IV, the values of $\Delta Q/\Delta d$ greatly exceed those theoretically predicted for any oxide or hydroxide of iron. The omission of surface roughness coefficient which is estimated at 1.2-1.6 (16-18) cannot be the main reason for this discrepancy, because to match the experimental results with theoretical values one should assume a roughness coefficient for film IV to be 7-8 which would be unrealistic. Another reason may be associated with the occurrence of the iron dissolution in addition to film formation. To determine whether dissolution may occur during the anodic oxidation of iron in borate solution, colorimetric analyses were made on specimens after 45h of anodic polarization at various potentials in solution 1. Unfortunately,

Fig. 9. Effect of potential on Q/d for stages I and II, I-III, and I-IV of passivation in solution 1.



the analytic technique employed was not precise enough to determine the amount of iron dissolved in short time periods. The results plotted in Fig. 11 indicate that in addition to Fe^{3+} , small amounts of Fe^{2+} are also present. In this figure, the calculated amounts of Fe^{3+} which can be dissolved during ellipsometric measurement for 1h are indicated by dashed lines for both solution 1 and 2. Based on the charge density values used in film formation at various potentials and on the calculation of the charge densities required to form films of thicknesses determined ellipsometrically, the excess of the charge was estimated. For this estimate, a roughness coefficient of 1.0 was used. In solution 1, the film was assumed to be Fe_2O_3 having a density of $5.0 \text{ g} \cdot \text{cm}^{-3}$. In solution 2, an average value for the assumed mixture of Fe_2O_3 with FeOOH corresponding to the formula $\text{Fe}_2\text{O}_{2.25}\text{OH}$ provided a density of $4.7 \text{ g} \cdot \text{cm}^{-3}$. The estimated excess charge was used to calculate the amount of Fe^{3+} dissolved. These calculations indicated that larger amounts of iron were dissolved during passivation in solution 2 than in solution 1.

If it is assumed that the dissolution rate does not change with time, the amount of Fe^{3+} determined analytically after 1h of passivation was less than that estimated. This difference could be attributed to a time-dependent dissolution rate where the rate decreases

with increasing passivation time, and/or to the occurrence of iron in the film at a valency higher than 3+.

As stated earlier, the development of passive films at constant anodic potentials has been found to occur in four stages. This agrees in essence with the findings of Kruger and Calvert (3), but we have found an additional stage so that our stages I and II appear as stage I in their study.

Stage I.—It is impossible, in practice, to determine the effect of oxidation time on film thickness in stage I as it lasts for only 0.2s, and a very thin film forms in this stage. Presumably, its thickness does not exceed a unit cell of Fe_2O_3 , i.e., about 0.83 nm. It appears reasonable that initially an adsorption film forms which is then transformed into a tridimensional phase film.

Stage II.—After a critical film thickness is attained at the end of stage I, the growth rate increases and d becomes a linear function of $\log t$. At the beginning of stage II, d is a function of \sqrt{t} , and 70-80% of the film developed in this stage grows at a square root relationship between thickness and time (Fig. 12). It was found that the growth rate was higher in solution 2, but the duration of proportionality between d and \sqrt{t} was shorter in solution 2 than in solution 1.

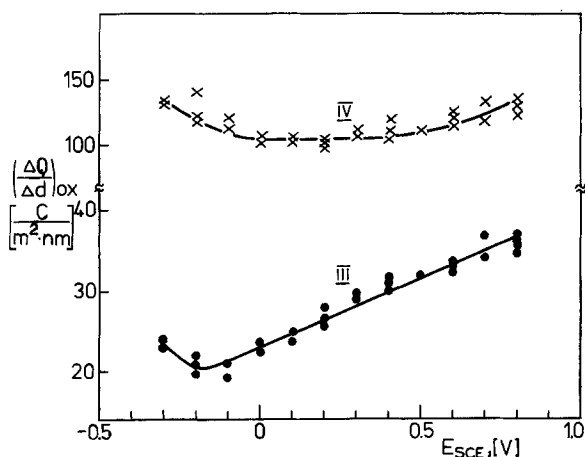


Fig. 10. Q/d as a function of potential for oxidation stages III and IV in solution 1.

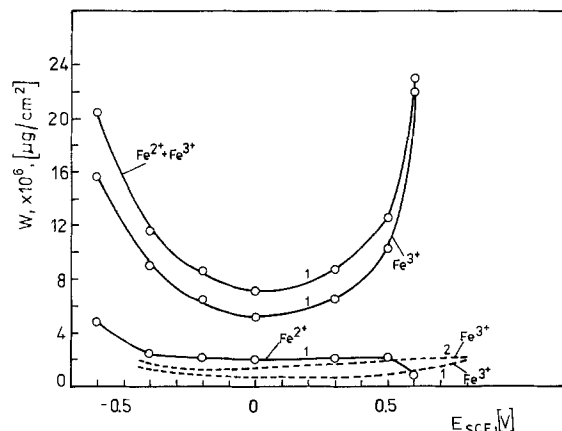


Fig. 11. Concentration of Fe^{3+} and Fe^{2+} determined colorimetrically (solid line) and concentration of Fe^{3+} in solutions 1 and 2 estimated from the surplus of charge (dashed line).

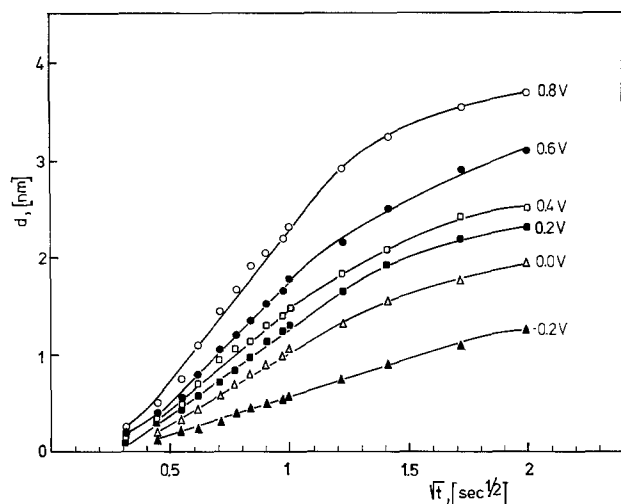


Fig. 12. Dependence of film thickness on time for films grown in solution 1.

A linear relationship occurs between t and the anodic charge density, Q . This appears to indicate that the total charge is used in the formation of only one compound. Calculations have shown that, during film growth in both solutions, the field strength decreases significantly in this stage, from about $10^7 \text{ V} \cdot \text{cm}^{-1}$ to $4\text{--}5 \times 10^6 \cdot \text{cm}^{-1}$.

It should be noted that during the initial period of stage II, two linear relationships are effective as follows

$$1/d = A + B \log t \quad [2]$$

and

$$1/d = A' + B' \ln t/d^2 \quad [3]$$

Constants B and B' are linear functions of the passivation potential, but the "jump distance" calculated on these bases is approximately 10^{-3} nm instead of the predicted value of about 0.3 nm . This suggests that in stage II the inverse logarithmic model of film growth is not valid.

Stage III.—The film growth rate in this stage is intermediate between those in stage II and IV. A slight increase in optical parameters is noted suggesting either (i) changes in the composition of the whole film or (ii) formation of a new layer on top of the previous film. The first assumption should be rejected as it has been shown by cathodic reduction experiments that the film formed in stage II does not change its properties (21).

The relationship between film thickness and charge density is not linear which appears to indicate that complicated processes occur in this stage. During part of this stage, a linear dependence is observed between both d and $1/d$ vs. t . However, calculations based on the inverse logarithmic relationship indicate jump distance values of approximately 0.01 nm instead of the predicted 0.3 nm .

Stage IV.—In agreement with Kruger and Calvert (3) and Lukac *et al.* (5), stage IV is the steady-state growth stage which can be described by either a logarithmic or inverse logarithmic rate law. The use of Eq. [2] for calculation of the jump distance gives values of 0.94 and 0.86 nm for solutions 1 and 2, respectively, while the respective values obtained using Eq. [3] are 0.92 and 0.83 nm .

Assuming that the film growth kinetics are controlled by a diffusion process with no ion migration, the following equation can be used to calculate the apparent diffusion coefficients that are effective during the various oxidation stages observed up to $t = 60 \text{ min}$

$$d = \sqrt{6Dt} \quad [4]$$

where D is the effective (apparent) diffusion coefficient

(diffusivity), and d is the film thickness (diffusion distance) attained in oxidation time t . The data plotted in Fig. 13-15 for films obtained at passivation potentials of $0, 0.2, 0.4,$ and 0.8 V indicate that in the majority of instances D is a linear function of d . Only for the time period covering stages I-III in solution 2 do

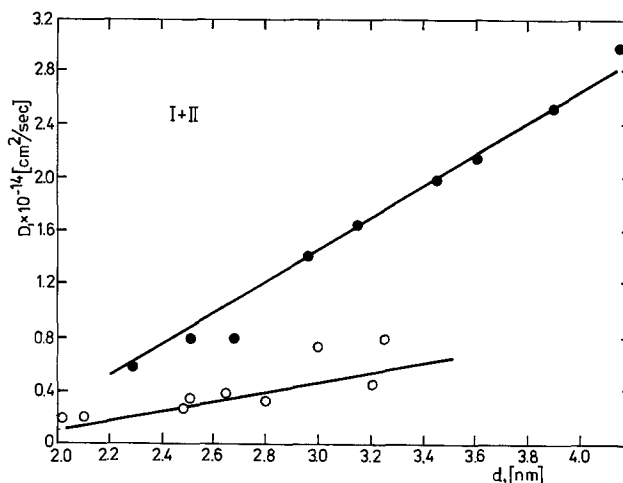


Fig. 13. Apparent diffusion coefficient as a function of film thickness at the end of the period of time covering stages I and II in solutions 1 (\circ) and 2 (\bullet).

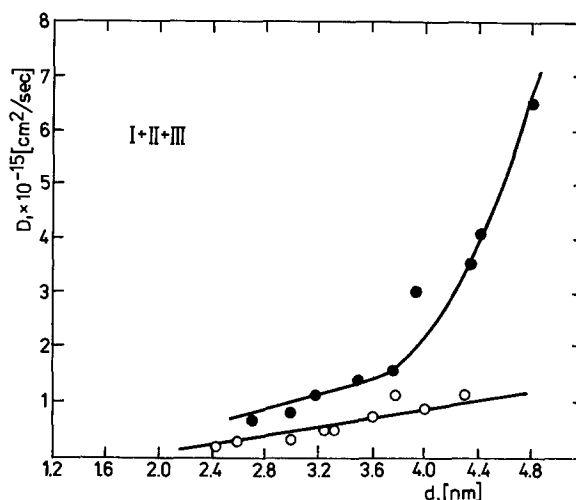


Fig. 14. Apparent diffusion coefficient as a function of film thickness at the end of the period of time covering stages I-III in solutions 1 (\circ) and 2 (\bullet).

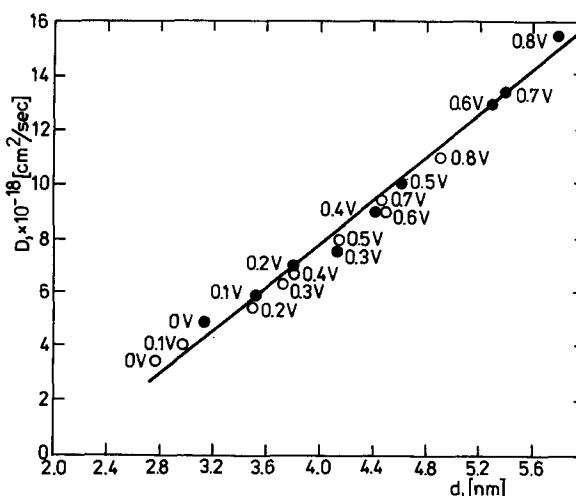


Fig. 15. Apparent diffusion coefficient as a function of film thickness after 60 min of passivation in both solutions 1 and 2.

two experimental points deviate greatly from the linear relationship. For films of the same thickness formed in the time periods covering stages I and II and I-III, calculations lead to much higher D values for films formed in solution 2 as compared with solution 1. Calculations also show that the apparent diffusivities in stages I and II are four orders of magnitude larger, and in stages I-III are three orders of magnitude larger than D values computed for the whole passivation time of 60 min (Fig. 15). The conclusion can be drawn, therefore, that the outermost film layer formed in stage IV is primarily responsible for the sharp decline of the film growth rate and for the increased passivity of iron.

The D values calculated for stages I and II are of the order 10^{-14} $\text{cm}^2 \cdot \text{s}^{-1}$, hence too small to correspond to diffusion processes occurring in an aqueous electrolyte, and they should be attributed to the diffusion of some species in the solid film. Even though the apparent diffusion coefficient was calculated on the basis of a simplified assumption, the results indicate that the properties are not homogeneous to the whole film. It appears reasonable to conclude that either different species control diffusion in stage IV than in preceding stages or significant changes occur in the composition of the outermost film layer during stage IV.

It is generally accepted that passive films on iron contain water. For example, Rahmer (19) found that the amount of water diminishes with passivation time. According to Konno and Nagayama (13), external film layers contain less water than internal ones. Okamoto (20) claims that the concentration of water in the passive film on stainless steels decreases when both the anodic potential and passivation time are increased. Sato (21-23) assumes that the inner part of the film is anhydrous while the outer part is hydrated.

The ellipsometric data indicate that with increasing potential the film increases in density. This effect is more pronounced in stage I than in stage III, and probably is due to increased concentration of iron cations and decreased concentration of water in the latter stage.

No change in the optical parameters between stages I-III and stage IV are revealed ellipsometrically, but this may be due to the relative thinness of the outermost layer, and hence its insignificant contribution to the optical properties of the whole film obtained in 60 min. Distinction between the inner and outer layer would be possible if the optical parameters of both layers were significantly different, which does not seem to occur.

Calculated D values for films obtained in both solutions 1 and 2 during the total passivation period (stages I-IV, $t = 60$ min) are identical and suggest that the external layers in these two solutions are the same.

As is known (24, 25), ions derived from the electrolyte (for example, Cl^-) may be incorporated in the external and, as we believe, most protective film layer; this seems not to occur in the internal layer. It can be assumed, therefore, that the external layer is composed of hydroxides together with anions incorporated from the electrolyte. The presence of water (hydroxyl ions) might be responsible for the more protective properties of the outer film layer. For example, the high resistance of Fe-Cr alloys is attributed to the presence of chromium hydroxide in the passive film (26). However, some more sophisticated experiments should be made to verify the above interpretation.

On the basis of the data obtained, it can be stated that the kinetics of film growth on iron is a very complicated process which cannot be described satisfactorily by any of the existing models as there is insufficient information in the mechanisms of processes occurring in different stages of film growth. For example, little useful basic data exists on: (i) the effect

of pH and electrolyte composition on film growth, especially in the initial stage; (ii) the distribution of Fe^{3+} , Fe^{2+} , H^+ (OH^-), and O^{2-} in the film at different anodic potentials; and (iii) the quantity of iron dissolved during anodic passivation under various experimental conditions.

Conclusions

1. In both solutions examined, the electric charge consumed in film formation in the initial period of anodic oxidation (stages I and II, $t > 1$ s) is less than the theoretical charge calculated for Fe_2O_3 formation, even if the roughness coefficient is not considered. This implies that, during this initial oxidation period, compounds with lower densities form, such as hydroxides or oxyhydroxides.

2. With increasing oxidation time, the charge consumed per unit of film volume increases to values exceeding that required for Fe_2O_3 formation.

3. Oxidation occurs in four distinctive stages characterized by different rates of film growth and different values of the electric field.

4. The electric field strength decreases as oxidation proceeds from stage I to stage IV.

5. The film formed in stage I is very thin, probably monolayer or less.

6. The film formed in stage II is thickest and grows at the highest rate relative to the other oxidation stages.

7. The growth rate in stage II increases with increasing anodic potential, but the effect of potential is insignificant in both stages III and IV.

8. The optical constants of the film change significantly in stage II and slightly in stage III, but remain constant in stage IV.

9. In stage II, the film thickness is a linear function of \sqrt{t} , while films formed in stages III and IV grow according to a logarithmic rate law.

10. None of the existing models can be applied to the experimentally observed kinetics of film growth on iron in borate solutions.

11. Growth of anodic films on iron in borate solutions is accompanied by the transmission of iron ions to the electrolyte.

Manuscript submitted Jan. 11, 1983; revised manuscript received Sept. 23, 1983.

REFERENCES

1. N. Sato and M. Cohen, *This Journal*, **111**, 512 (1964).
2. R. V. Moshtev, *Ber. Bunsenges. Phys. Chem.*, **71**, 1079 (1967).
3. J. Kruger and J. P. Calvert, *This Journal*, **114**, 43 (1967).
4. K. N. Goswami and R. W. Staehle, *Electrochim. Acta*, **16**, 1895 (1971).
5. C. Lukac, J. B. Lumsden, S. Smialowska, and R. W. Staehle, *This Journal*, **122**, 1571 (1975).
6. C. T. Chen, B. D. Cahan, and E. Yeager, *Tech. Rep. 48*, Case Western Reserve University, Cleveland, OH (1979).
7. N. Cabrera and N. F. Mott, *Rep. Prog. Phys.*, **12**, 163 (1948-1949).
8. F. P. Fehlner and N. F. Mott, *Oxid. Met.*, **2**, 59 (1970).
9. N. Sato and M. Cohen, *This Journal*, **111**, 519 (1964).
10. C. Y. Chao, L. F. Lin, and D. D. Macdonald, *ibid.*, **128**, 1187 (1981).
11. B. D. Cahan and C. T. Chen, in "Corrosion and Corrosion Protection," R. P. Frankenthal and F. Mansfeld, Editors, p. 37, The Electrochemical Society Softbound Proceedings Series, Pennington, NJ (1981).
12. L. McCrackin, "A Fortran Program for Analysis of Ellipsometry Measurements," U.S. Govt. Printing Office, Washington, DC (1969).
13. M. Seo, M. Sato, J. B. Lumsden, and R. W. Staehle,

- Corros. Sci.*, **17**, 209 (1977).
14. H. Konno and M. Nagayama, in "Passivity of Metals," R. P. Frankenthal and J. Kruger, Editors, p. 585, The Electrochemical Society Softbound Proceedings Series, Princeton, NJ (1978).
 15. M. Fischer, W. Gruner, and J. Reinhard, *Corros. Sci.*, **15**, 279 (1975).
 16. M. Nagayama and M. Cohen, *This Journal*, **109**, 781 (1962); **110**, 670 (1963).
 17. J. Ord and J. Bartlett, *ibid.*, **112**, 160 (1965).
 18. J. W. Schulze and U. Stimming, *Z. Phys. Chem. N.F.*, **98**, 285 (1975).
 19. D. Rahner, Ch. Dörfel, and W. Forker, in "III Mezhd. Nauchn. Konf. po Probl. Korr. SEV," Vol. 2, p. 185, Warszawa (1980).
 20. G. Okamoto, *Corros. Sci.*, **13**, 471 (1973).
 21. Z. Szklarska-Smialowska and W. Kozłowski, *This Journal*, To be published.
 22. N. Sato, K. Kudo, and T. Noda, *Electrochim. Acta*, **16**, 1909 (1971).
 23. N. Sato, K. Kudo, and T. Noda, *Corros. Sci.*, **10**, 785 (1971).
 24. N. Sato and K. Kudo, *Electrochim. Acta*, **16**, 447 (1971).
 25. Z. Szklarska-Smialowska, H. Viefhaus, and M. Janik-Czachor, *Corros. Sci.*, **16**, 649 (1976).
 26. A. E. Yaniv, J. B. Lumsden, and R. W. Staehle, *This Journal*, **124**, 490 (1977).
 27. K. Asami, K. Hashimoto, and S. Shimodaira, *Corros. Sci.*, **18**, 151 (1978).

Halide Nuclei Theory of Pit Initiation in Passive Metals

T. Okada

Industrial Products Research Institute, Ministry of International Trade and Industry, Yatabe, Tsukuba, Ibaraki 305, Japan

ABSTRACT

A kinetic approach is used to test the theory of pit initiation in passive metals in contact with a solution containing aggressive ions. A new process, hemispherical halide nuclei formation at the surface of the passive film and inward growth under restricted conditions, is introduced. The possibility of nuclei growth is discussed, taking into account the irreversible thermodynamic stability of the system. The direction of the irreversible change of a system consisting of the metal substrate, the passive film, the halide nuclei, and the solution is determined using the general evolution criterion of irreversible thermodynamics proposed by Glansdorff and Prigogine. A critical radius of the halide nucleus r^* is deduced. This radius must be surpassed for growth and pitting to take place. The present theory explains the nature of the pit initiation processes, especially some characteristic values of the pitting phenomenon, such as the critical pitting potential and the induction period of pit nucleation.

Pitting is a specific feature of localized corrosion in which areas of a passive metal surface break down locally as a result of preferential attack by aggressive ions in a corrosive environment. Pitting has attracted much attention recently because of its practical implications. According to the "Alles oder Nichts-gesetz" of passivity (1), active and passive areas should not coexist on a uniform metal surface. However, during the pitting process, the condition of the metal-solution interface at the bottom of the pit becomes different from the rest of the metal surface (2, 3). Once the surface of a passive metal is destroyed locally, this itself brings about a more corrosive environment, due to the local halide ion concentration, a change in the pH of the local solution, and the subsequent local polarization at the pit bottom. Thus, pitting turns out to be a stable condition (4).

Generally, two stages of the pitting process are considered by most authors (3, 5): the stage of pit initiation which terminates with the appearance of the first pit after a certain time of incubation, and the stage of pit propagation and its preservation due to the subsequent local corrosive environment. The former stage is assumed to include the degeneration of the passive film, but this mechanism is not yet clear. The process of pit generation is regarded as a stochastic process (6), which turns to the next stage where local dissolution proceeds at the pits thus formed.

Sometimes shallow hemispherical pits are observed during pitting corrosion of aluminum or stainless steel (3). These cases resemble the situation during electropolishing of the metal. Here the continuation of the dissolution reaction caused by a degeneration of the metal surface is more significant than the change in composition of the solution at the pit bottom (7). It seems plausible that the degeneration of the metal surface occurs prior to the appearance of the pits.

Key words: pitting corrosion, irreversible thermodynamics, halide nucleation, initiation.

Vetter (8) and Vermilyea (9) stressed in their theory of pitting corrosion that when the potential of a passive metal was shifted anodically in halide solutions, the state changed from the passive film being stable to the metal halide being stable thermodynamically. This theory appears to be valid, especially when electropolished-like pitting is considered. However, these authors only examined the interchange between two phases, the metal oxide and the metal halide, from the point of view of thermodynamic stability, and did not microscopically consider how the metal halide was generated on the surface of a passive metal.

On the other hand, according to the "transitional halide complex" theory of pitting corrosion (10), pitting starts at the point where sufficient halide ions jointly adsorb on the passive film so that they form a transitional complex with a lattice cation at the passive film-solution interface. This idea seems attractive, because it deals with the formation of a metal halide from a microscopic point of view.

In this study, an attempt was made to describe the process of pit initiation beginning with the premise that pitting occurs through formation of metal halides on the passive film, thereby taking into account the microscopic stability of the halides. A theoretical basis is presented, with the assumption that the process of pit initiation consists of passive film degeneration by halide nuclei formation on the film and growth inwards.

The model.—Figure 1 illustrates the process of pit formation on a passive metal. Suppose that a halide "nucleus", hemispherical in shape and with a radius r , is formed on the passive film surface of thickness L . If this nucleus is stable and grows continuously, it will penetrate the passive film which protects the metal surface. Then the uncovered metal dissolves rapidly through the nonprotective metal halides, thus forming a pit. But if this nucleus is not stable and does not grow, it disappears and the metal remains in a passive state.

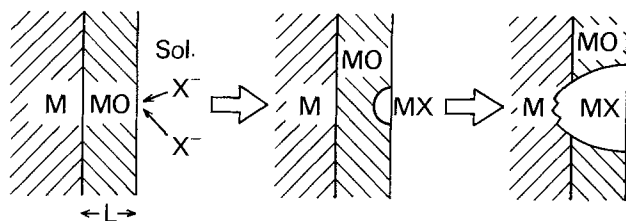


Fig. 1. Illustration of a process leading to pit initiation. M: metal, MO: passive film, MX: metal halide, Sol.: solution.

Whether the nucleus grows or not should be determined referring to the irreversible thermodynamic stability conditions, because the system under consideration is in a nonequilibrium state. As will be shown later, the nucleus starts to grow in a stable manner when its radius passes the critical value r^* , but it eventually disappears when the radius is smaller than r^* . This situation resembles the case of the precipitation of a solute from a saturated solution, in which a critical radius also exists for the formation of a solute nucleus (11).

Theory

The general evolution criterion.—One of the most general relationships so far obtained in irreversible thermodynamics which indicates the direction of the irreversible change of a system is the so-called general evolution criterion proposed by Glansdorff and Prigogine (12)

$$\delta_X P \equiv \int_k \sum J_k d_i X_k dV \leq 0 \quad [1]$$

That is, in a system of time-independent boundary conditions, an irreversible change proceeds so that the time derivative of the forces multiplied by the conjugated fluxes becomes negative until the system reaches a steady state. Suppose that the temperature is kept constant so that the heat flux can be ignored. Then the processes occurring in the system shown in Fig. 1 are: the transport of ion species in the passive film; the interface reaction where the metal oxide changes into the metal halide; and the transport of species through the metal halide and the dissolution reaction at the interface between the passive film or the metal halide and the solution, so that

$$\delta_X P = \delta_X P_{MO} + \delta_X P_{MO/MX} + \delta_X P_{MX} + \delta_X P_{MX/S} + \delta_X P_{MO/S} \quad [2.1]$$

with

$$\delta_X P_{MO} = \int_{MO} \sum_k J_k d_i X_k dV_{MO} \quad [2.2]$$

$$\delta_X P_{MO/MX} = \int_{MO/MX} \sum_k J_k d_i X_k dS_{MO/MX} \quad [2.3]$$

$$\delta_X P_{MX} = \int_{MX} \sum_k J_k d_i X_k dV_{MX} \quad [2.4]$$

$$\delta_X P_{MX/S} = \int_{MX/S} \sum_k J_k d_i X_k dS_{MX/S} \quad [2.5]$$

$$\delta_X P_{MO/S} = \int_{MO/S} \sum_k J_k d_i X_k dS_{MO/S} \quad [2.6]$$

in which V_{MO} is the volume of the passive film, $S_{MO/MX}$ is the interface between the oxide and the halide nuclei, V_{MX} is the volume of the halide nuclei, and $S_{MX/S}$ and $S_{MO/S}$ are the halide nuclei-solution and the oxide-solution interfaces, respectively

Processes occurring within the system are depicted schematically in Fig. 2. The constituent metal and the oxygen ions take part in the transport processes in the passive film. The x-axis is perpendicular to the metal surface and is directed towards the solution. For simplicity, only one-dimensional transport along the x-axis will be taken into account. Designating the metal and the oxygen ions as M and O, respectively, the flux of each species per unit cross section in the oxide film is

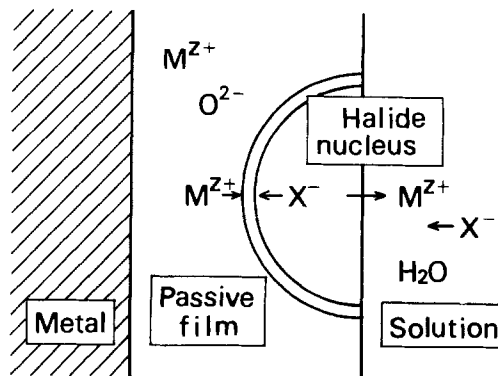


Fig. 2. Schematic representation of processes occurring within the system consisting of the metal, the passive film, the halide nucleus, and the solution.

expressed by the following transport equation (13, 14)

$$J_i = \frac{z_i}{|z_i|} \nu_i n_i a \exp \left(- \frac{U_i - \alpha_i |z_i| F a \Delta \Phi_0 / \delta}{RT} \right), \quad i = M, O \quad [3]$$

where ν_i is vibrational frequency, n_i is concentration of i-species in the oxide layer, a is "jump-distance", α_i is "transfer coefficient", z_i is charge of the ionic species, $\Delta \Phi_0$ is potential difference within the oxide layer, and δ is thickness of the oxide layer.

The force corresponding to each flux is

$$X_i = - \frac{1}{T} \frac{\partial \tilde{\mu}_i}{\partial x}, \quad i = M, O \quad [4]$$

where $\tilde{\mu}_i$ is the electrochemical potential of i-species in the oxide layer. Suppose that a major part of the gradient of electrochemical potential arises from the electric field in the oxide layer, and that the potential changes linearly through the oxide layer, so that

$$X_i = \frac{1}{T} z_i F \frac{\Delta \Phi_0}{L - r'}, \quad i = M, O \quad [5]$$

Here r' is the "thickness" of the metal halide in the simplified model in which hemispherical halide nuclei are scattered over the surface of the passive film surface, and accordingly, would have the order of magnitude

$$r' = \gamma r \quad [6]$$

where the ratio of the area occupied by the halide nuclei on the surface of the passive metal is designated as γ .

Consider now the imaginary time derivative δr of the radius r of the halide nucleus. The resultant change of the force δX_i would be expressed as follows

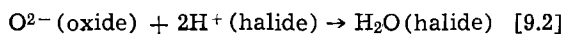
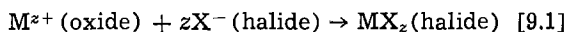
$$\delta X_i = \frac{z_i F}{T} \left\{ \frac{\delta \Delta \Phi_0}{L - r'} + \frac{\gamma \Delta \Phi_0}{(L - r')^2} \delta r \right\}, \quad i = M, O \quad [7]$$

Using the above relationship, Eq. [2.1] can be written as

$$\begin{aligned} \delta_X P_{MO} &= \frac{1}{T} \{ z F J_M - 2 F J_O \} \left\{ \frac{\delta \Delta \Phi_0}{L - r'} \right. \\ &\quad \left. + \frac{\gamma \Delta \Phi_0}{(L - r')^2} \delta r \right\} \left(L - \frac{2}{3} \pi r^3 N \right) S \\ &= \frac{1}{T} I^\circ \left(\delta \Delta \Phi_0 + \frac{\gamma \Delta \Phi_0}{L - r'} \delta r \right) \quad [8] \end{aligned}$$

where I° is the total current passing from the metal to the solution, S is the surface area of the metal in contact with the solution, and N is the number of halide nuclei generated per unit area of the metal surface.

The following reactions are considered to occur at the interface between the halide nuclei and the passive oxide



The partial reaction current density of the respective reactions, i_M and i_O , can be expressed as follows if the backward reaction rate is ignored

$$i_M = k_M \exp \left[\frac{\mu_M(1)}{RT} \right] \exp \left[\frac{z\mu_X(2)}{RT} \right] \exp \left(\frac{\alpha_M z F \Delta \Phi_{MO/MX}}{RT} \right) \quad [10.1]$$

$$i_O = k_O \exp \left[\frac{\mu_O(1)}{RT} \right] \exp \left[\frac{2\mu_H(2)}{RT} \right] \exp \left(\frac{2\alpha_O F \Delta \Phi_{MO/MX}}{RT} \right) \quad [10.2]$$

where k_M , k_O are the rate constants, $\mu_M(1)$, $\mu_O(1)$ are chemical potentials of M^{z+} and O^{2-} , respectively, in the passive film at the interface with the halide nuclei, $\mu_X(2)$, $\mu_H(2)$ are chemical potentials of X^- and H^+ , respectively, in the halide nuclei at the interface with the oxide, α_M , α_O are transfer coefficients, and $\Delta \Phi_{MO/MX}$ is the Galvani potential difference at the interface between the oxide and the halide nuclei. The chemical affinity of each reaction is

$$A_M = \mu_M(1) + z\mu_X(2) + zF\Delta\Phi_{MO/MX} \quad [11.1]$$

$$A_O = \mu_O(1) + 2\mu_H(2) - 2F\Delta\Phi_{MO/MX} \quad [11.2]$$

So that Eq. [2.3] becomes

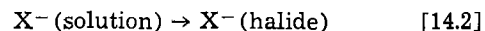
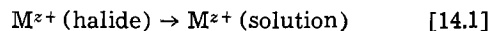
$$\delta_X P_{MO/MX} = \frac{2\pi r^2 NS}{T} \left\{ \frac{i_M}{zF} [\delta\mu_M(1) + z\delta\mu_X(2) + zF\delta\Delta\Phi_{MO/MX}] - \frac{i_O}{2F} [\delta\mu_O(1) + 2\delta\mu_H(2) - 2F\delta\Delta\Phi_{MO/MX}] \right\} \quad [12]$$

Transport of M^{z+} , X^- , H^+ , and H_2O occurs in the halide nuclei. Suppose that the ionic conductance is relatively high in the halide so that a linear relation holds between the fluxes and the forces. In this case, Eq. [2.4] could be written as (Appendix A)

$$\delta_X P_{MX} = \frac{2\pi r^2 NS}{3T} \left\{ J'_M \left[\delta\mu_M(2) - \delta\mu_M(3) + zF\delta\Delta\Phi_X - \frac{J'_M}{\bar{n}'_M v'_M} \delta\tau \right] + J'_X \left[\delta\mu_X(2) - \delta\mu_X(3) - F\delta\Delta\Phi_X - \frac{J'_X}{\bar{n}'_X v'_X} \delta\tau \right] + J'_H \left[\delta\mu_H(2) - \delta\mu_H(3) + F\delta\Delta\Phi_X - \frac{J'_H}{\bar{n}'_H v'_H} \delta\tau \right] + J'_W \left[\delta\mu_W(2) - \delta\mu_W(3) - \frac{J'_W}{\bar{n}'_W v'_W} \delta\tau \right] \right\} \quad [13]$$

where J'_M , J'_X , J'_H , J'_W are fluxes of M^{z+} , X^- , H^+ , and H_2O , respectively, in the halide nuclei; $\mu_i(2)$, $\mu_i(3)$ ($i = M, X, H, W$) are chemical potentials of each species in the halide at the interface with the oxide and with the solution, respectively; \bar{n}'_i ($i = M, X, H, W$) is the average concentration of each species within the halide; and v'_i ($i = M, X, H, W$) is the mobility per unit force of each species within the halide.

The following reactions might proceed at the interface between the halide and the solution



Ignoring the backward rate, the partial reaction current density of each reaction is

$$i'_M = k'_M \exp \left(\frac{\mu_M(3)}{RT} \right) \exp \left(\frac{\alpha'_M z F \Delta \Phi_{MX/S}}{RT} \right) \quad [15.1]$$

$$i'_X = k'_X \exp \left(\frac{\mu_X(4)}{RT} \right) \exp \left(\frac{\alpha'_X F \Delta \Phi_{MX/S}}{RT} \right) \quad [15.2]$$

where k'_M , k'_X are the rate constants, $\mu_X(4)$ is the chemical potential of X^- in the solution, α'_M , α'_X are transfer coefficients, and $\Delta \Phi_{MX/S}$ is the Galvani potential difference at the interface between the halide nuclei and the solution. The chemical affinity of each reaction is

$$A'_M = \mu_M(3) - \mu_M(4) + zF\Delta\Phi_{MX/S} \quad [16.1]$$

$$A'_X = \mu_X(4) - \mu_X(3) + F\Delta\Phi_{MX/S} \quad [16.2]$$

Equation [2.5] becomes

$$\delta_X P_{MX/S} = \frac{\pi r^2 NS}{T} \left\{ \frac{i'_M}{zF} [\delta\mu_M(3) - \delta\mu_M(4) + zF\delta\Delta\Phi_{MX/S}] + \frac{i'_X}{F} [\delta\mu_X(4) - \delta\mu_X(3) + F\delta\Delta\Phi_{MX/S}] \right\} \quad [17]$$

Following the same procedure as stated above for the reactions occurring at the interface between the oxide and the solution where the halide nuclei is not generated, it might be true for Eq. [2.6] that

$$\delta_X P_{MO/S} = \frac{(1-\gamma)S}{T} \frac{i''_M}{zF} [\delta\mu_M(3') - \delta\mu_M(4') + zF\delta\Delta\Phi_{MO/S}] \quad [18]$$

where i''_M is the dissolution current density of M^{z+} through the oxide-solution interface; $\mu_M(3')$, $\mu_M(4')$ are the chemical potentials of M^{z+} within the oxide and the solution, respectively, at the oxide-solution interface; and $\Delta \Phi_{MO/S}$ is the Galvani potential difference at the oxide-solution interface. It is assumed that the passive film does not grow or dissolve at the interface with the solution and, consequently, that the steady dissolution of M^{z+} takes place while the reaction participated in by O^{2-} is nearly in equilibrium.

Equations of continuity.—A relationship should exist between the fluxes for each portion of the system; the metal, the passive oxide, the halide nuclei, and the solution. Here fluxes are described in a steady state and no materials or charges are accumulated or consumed locally because the change of the system proceeds very slowly.

The total current I° from the metal to the solution is written as if there is no electron conduction in the oxide layer

$$I^\circ = (zFJ_M - 2FJ_O)S = I_M + I_O \quad [19]$$

where I_M and I_O are the contributions by M^{z+} and O^{2-} , respectively, to the total current I° . I° can be divided into two parts; I , which flows through the halide nuclei into the solution, and I' , which flows directly through the oxide-solution interface

$$I^\circ = I + I' \quad [20]$$

The change in the current I° resulting from the change in τ is mainly due to I , because the current density of dissolution through the halide nuclei is much larger

than that through the oxide-solution interface, so that

$$\delta I^\circ \stackrel{\circ}{=} \delta I \quad [21]$$

It is obtained from Eq. [3] and [19] that

$$\delta I^\circ = \frac{\alpha_M z F a I_M + 2\alpha_O F a I_O}{RT} \left\{ \frac{\delta \Delta \Phi_O}{L - r'} + \frac{\gamma \Delta \Phi_O}{(L - r')^2} \delta r \right\} \quad [22]$$

it was assumed here that $\delta n_i/n_i \stackrel{\circ}{=} 0$ ($i = M, O$) in the oxide film. Equation [3] then becomes

$$\delta_X P_{MO} = \frac{1}{T} \frac{RT(L - r') I^\circ}{\alpha_M z F a I_M + 2\alpha_O F a I_O} \delta I^\circ \quad [23]$$

It can be written at the oxide-halide nuclei interface that

$$I = 2\pi r^2 NS (i_M + i_O) \quad [24]$$

Taking the derivative of Eq. [24] and using Eq. [10.1] and [10.2]

$$\begin{aligned} i_M [\delta \mu_M(1) + z \delta \mu_X(2)] + i_O [\delta \mu_O(1) + 2 \delta \mu_H(2)] \\ = \frac{RT}{2\pi r^2 NS} \left(\delta I - \frac{2}{r} I \delta r \right) \\ - (i_M \alpha_M z F + 2i_O \alpha_O F) \delta \Delta \Phi_{MO/MX} \quad [25] \end{aligned}$$

Assuming that M^{z+} and O^{2-} are nearly in equilibrium in the oxide film so that

$$2\delta \mu_M(1) + z \delta \mu_O(1) = 0 \quad [26]$$

and further assuming that an approximation of the equilibrium condition holds between the chemical potentials of H^+ and X^- in the halide

$$\delta \mu_H(2) + \delta \mu_X(2) = 0 \quad [27]$$

Substituting Eq. [25]-[27] into Eq. [12], and assuming for simplicity that

$$\alpha_O \stackrel{\circ}{=} -\alpha_M \quad [28]$$

it is shown that

$$\begin{aligned} \delta_X P_{MO/MX} = R \frac{i_M + i_O}{zF i_M - 2Fi_O} \left(\delta I - \frac{2}{r} I \delta r \right) \\ + \frac{2\pi r^2 NS}{T} (1 - \alpha_M) (i_M + i_O) \delta \Delta \Phi_{MO/MX} \quad [29] \end{aligned}$$

It can be written for the transport of species within the halide nuclei that

$$I = \pi r^2 NS (zF J'_M - F J'_X + F J'_H) \quad [30]$$

Taking the derivative of Eq. [30] and rearranging

$$\begin{aligned} zF \bar{n}'_M v'_M [\delta \mu_M(2) - \delta \mu_M(3)] \\ - F \bar{n}'_X v'_X [\delta \mu_X(2) - \delta \mu_X(3)] \\ + F \bar{n}'_H v'_H [\delta \mu_H(2) - \delta \mu_H(3)] = \frac{1}{\pi r NS} \delta I - \frac{I}{\pi r^2 NS} \delta r \\ - (z^2 F^2 \bar{n}'_M v'_M + F^2 \bar{n}'_X v'_X + F^2 \bar{n}'_H v'_H) \delta \Delta \Phi_X \quad [31] \end{aligned}$$

It is assumed that an approximation of equilibrium condition holds between the chemical potentials of M^{z+} and X^- and between the chemical potentials of H^+ and X^- in the halide

$$\delta \mu_M(s) + z \delta \mu_X(s) = 0, \quad s = 2, 3 \quad [32.1]$$

$$\delta \mu_H(3) + \delta \mu_X(3) = 0 \quad [32.2]$$

Substituting Eq. [27], [31], [32.1], and [32.2] into Eq. [13] and ignoring the flux of H_2O , it can be shown that

$$\begin{aligned} \delta_X P_{MX} = \frac{2\pi r^3 NS}{3T} \left\{ \frac{I \delta I}{\Lambda_X (\pi r^2 NS)^2} - \left[\frac{1}{\Lambda_X} \left(\frac{I}{\pi r^2 NS} \right)^2 \right. \right. \\ \left. \left. + \frac{J^2_M}{\bar{n}'_M v'_M} + \frac{J^2_X}{\bar{n}'_X v'_X} + \frac{J^2_H}{\bar{n}'_H v'_H} \right] \frac{\delta r}{r} \right\} \quad [33] \end{aligned}$$

where

$$\begin{aligned} \Lambda_X &\equiv z^2 F^2 \bar{n}'_M v'_M + F^2 \bar{n}'_X v'_X + F^2 \bar{n}'_H v'_H \\ &= \frac{z n'_M \lambda'_M}{T'_M} \quad [34] \end{aligned}$$

and λ'_M and T'_M are the ionic equivalent conductance and the transport number of M^{z+} , respectively, in the halide.

The following equation holds at the interface between the halide nuclei and the solution

$$I = \pi r^2 NS (i'_M + i'_X) \quad [35]$$

Taking the derivative of Eq. [35] and using Eq. [15.1] and [15.2]

$$\begin{aligned} i'_M \delta \mu_M(3) + i'_X \delta \mu_X(4) = \frac{RT}{\pi r^2 NS} \left(\delta I - \frac{2I}{r} \delta r \right) \\ - (\alpha'_M z F i'_M + \alpha'_X F i'_X) \delta \Delta \Phi_{MX/S} \quad [36] \end{aligned}$$

Disregarding the chemical potential change of ions in the solution

$$\delta \mu_i(4) = 0, \quad i = M, X \quad [37]$$

and assuming for simplicity that

$$\alpha'_M = \alpha'_X \quad [38]$$

Eq. [17] can be rearranged as follows

$$\begin{aligned} \delta_X P_{MX/S} = \frac{R}{zF} \left(1 + \frac{i'_X}{i'_M} \right) \left(\delta I - \frac{2I}{r} \delta r \right) \\ - \frac{\pi r^2 NS}{T} \left[\frac{\alpha'_M}{zF} \left(1 + \frac{i'_X}{i'_M} \right) (zF i'_M + F i'_X) \right. \\ \left. - (i'_M + i'_X) \right] \delta \Delta \Phi_{MX/S} \quad [39] \end{aligned}$$

The chemical potential of M^{z+} at the interface between the passive film and the solution does not shift greatly, so that

$$\delta \mu_M(3') = \delta \mu_M(4') = 0 \quad [40]$$

Then Eq. [18] becomes

$$\delta_X P_{MO/S} = \frac{1}{T} I \delta \Delta \Phi_{MO/S} \quad [41]$$

From Eq. [2], [21], [23], [29], [33], and [41] it is shown that

$$\begin{aligned} T \delta_M P = \left\{ \frac{RT(L - r') I^\circ}{\alpha_M z F a I_M + 2\alpha_O F a I_O} + \frac{2}{3\Lambda_X} \frac{I}{\pi r NS} \right. \\ \left. + \left[\frac{i_M + i_O}{zF i_M - 2Fi_O} + \frac{1}{zF} \left(1 + \frac{i'_X}{i'_M} \right) \right] RT \right\} \delta I \\ - \left\{ \frac{2}{3} \pi r^2 NS \left[\frac{1}{\Lambda_X} \left(\frac{I}{\pi r^2 NS} \right)^2 + \frac{J^2_M}{\bar{n}'_M v'_M} \right. \right. \\ \left. \left. + \frac{J^2_X}{\bar{n}'_X v'_X} + \frac{J^2_H}{\bar{n}'_H v'_H} \right] + \left[\frac{i_M + i_O}{zF i_M - 2Fi_O} \right. \right. \\ \left. \left. + \frac{1}{zF} \left(1 + \frac{i'_X}{i'_M} \right) \right] RT \frac{2I}{r} \right\} \delta r + (1 - \alpha_M) I \delta \Delta \Phi_{MO/MX} \\ + \left(1 - \frac{\alpha'_M}{zF} \frac{zF i'_M + F i'_X}{i'_M} \right) I \delta \Delta \Phi_{MX/S} + I \delta \Delta \Phi_{MO/S} \quad [42] \end{aligned}$$

Empirical relations.—The current I passing through the halide nuclei increases with an increase in r , because the current coming out of the metal substrate concentrates mostly on the halide nuclei in spite of the large resistance of the oxide film. The following relationship is now assumed

$$I = A \pi r^2 NS \quad [43]$$

here A and χ are constants. χ takes a value between 1 and 2. A is almost the dissolution current per cross section of the halide nuclei (Appendix B), and can be expressed empirically using the externally applied potential of the metal E and the concentration of X^- in the solution C_X

$$A \stackrel{\circ}{=} i = k_X C_X^n \exp\left(-\frac{\xi FE}{RT}\right) \quad [44]$$

where k_X , n , and ξ are constants.

The current passing through the interface between the oxide and the halide nuclei can be expressed empirically as

$$I = 2\pi r^2 NSK \exp\left(\frac{\beta F \Delta \Phi_{MO/MX}}{RT}\right) \quad [45]$$

where K and β are constants. From Eq. [43] and [45]

$$\delta \Delta \Phi_{MO/MX} = -\frac{2-x}{r} \frac{RT}{\beta F} \delta r \quad [46]$$

Similarly, the current passing through the interface between the halide nuclei and the solution can be expressed empirically as

$$I = \pi r^2 NSK' \exp\left(\frac{\beta' F \Delta \Phi_{MX/S}}{RT}\right) \quad [47]$$

where K' and β' are constants. From Eq. [43] and [47]

$$\delta \Delta \Phi_{MX/S} = -\frac{2-x}{r} \frac{RT}{\beta' F} \delta r \quad [48]$$

The potential difference at the oxide-solution interface is assumed to be nearly constant

$$\delta \Delta \Phi_{MO/S} \stackrel{\circ}{=} 0 \quad [49]$$

Actually, the composition of the solution in contact with the halide nuclei differs from that of the solution in contact with the passive film so that a potential difference should arise within the solution due to the ion transport, but this effect can be disregarded. Equation [42] can be rewritten using Eq. [43], [44], [46], [48], and [49], as

$$\delta_X P = F(L, r, i) \delta r \quad [50.1]$$

with

$$F(L, r, i) \equiv \frac{I}{r} \frac{R}{F} \left[\lambda_L X \left(\frac{L}{a} - \frac{\gamma}{a} r \right) - (2-x) \lambda_I - \frac{\lambda_X}{\Lambda_X} \frac{F}{RT} i r^{\chi-1} \right] \quad [50.2]$$

Here λ_L , λ_I , and λ_X are positive constants defined by

$$\lambda_L \equiv \frac{I_M + I_0}{\alpha_M z I_M + 2\alpha_0 I_0} \quad [50.3]$$

$$\lambda_I \equiv \frac{i_M + i_0}{z i_M - 2i_0} + \frac{1}{z} \left(1 + \frac{i'_X}{i'_M} \right) + (1-\alpha) \frac{1}{\beta} + \left(1 + \frac{\alpha'_M}{z} \frac{z i'_M - i'_X}{i'_M} \right) \frac{1}{\beta'} \quad [50.4]$$

$$\lambda_X \frac{I^2}{\Lambda_X r^2 NS} \equiv \frac{2}{3} \pi r^2 NS \left[-(\chi-1) \frac{1}{\Lambda_X} \left(\frac{I}{\pi r^2 NS} \right)^2 + \frac{J^2_M}{\bar{n}'_M v'_M} + \frac{J^2_X}{\bar{n}'_X v'_X} + \frac{J^2_H}{\bar{n}'_H v'_H} \right] \quad [50.5]$$

and have an order of magnitude of 1 (Appendix C).

Pit initiation.—According to Eq. [1], the whole system changes irreversibly so that the right-hand side of Eq. [50.1] becomes negative. Therefore, if $F(L, r, i)$ is negative, then $\delta r > 0$, and the halide nuclei would start to grow. In Fig. 3, the change of $F(L, r, i)$ with r was illustrated schematically. If there were a halide

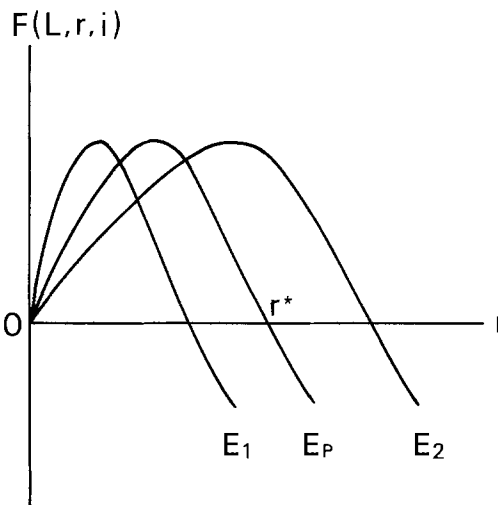


Fig. 3. Variation of $F(L, r, i)$ (case $\chi \stackrel{\circ}{=} 2$ in Eq. [50.2]) as a function of the radius r of the halide nuclei. $E_1 > E_p > E_2$, E_p : pit initiation potential at which $r^* = r_{max}$.

nucleus whose radius were larger than the critical radius r^* , it would grow continuously until it broke through the passive film and caused pitting.

For simplicity let χ be 2, since the current coming out of the metal substrate easily concentrates in the halide nuclei because the passive film is not thick enough. The critical radius r^* in this case is

$$r^* = \frac{2\lambda_L \frac{L}{a}}{2\lambda_L \frac{\gamma}{a} + \pi \frac{\lambda_X}{\Lambda_X} \frac{F}{RT} i} \quad [51]$$

It can be seen from Eq. [44] and [51] that r^* increases proportionally to the passive film thickness L , and decreases with the increase in the potential of the metal E and the X^- concentration C_X in the solution.

In order for pitting to occur, r^* must be smaller than the maximum statistically attainable value r_{max} .¹ Equation [51] gives at $r^* = r_{max}$

$$\pi \frac{\lambda_X}{\Lambda_X} \frac{F}{RT} k_X C_X^n \exp\left(\frac{\xi FE_p}{RT}\right) = 2\lambda_L \frac{1}{a} \left(\frac{L}{r_{max}} - \gamma \right) \quad [52]$$

Consequently, a pit will form when the potential E exceeds E_p , as shown in Eq. [52]. This potential can be referred to as the pit initiation potential, or the potential of pit nucleation.

Discussion

An irregular current oscillation was observed before pit formation when the metal was polarized anodically in solutions containing halide ions (17). This observation agrees qualitatively with the present theory in which it was assumed that the pit is not generated immediately at the flaw of the passive film, but after the "halide nuclei" grow inwards or diminish at the surface of the passive film.

Substituting Eq. [B.1] and [B.5] into Eq. [51] and using the relationship

$$\Lambda_X R_X \stackrel{\circ}{=} 1 \quad [53]$$

the potential difference within the halide nuclei at the pit initiation potential can be estimated

$$\lambda_X \Delta \Phi_X \frac{F}{RT} \stackrel{\circ}{=} 2\lambda_L \frac{1}{a} (L - \gamma r_{max}) \quad [54]$$

¹ r_{max} can be replaced by L when the passive film is not very thick. Usually, r_{max} would have a value in nanometers.

The thickness of the passive film might be measured in nanometers or some tens of nanometers, whereas a would be several tenths of a nanometer so that L/a would have the magnitude of several tens of nanometers. It can be concluded from the above equation that $\Delta\phi_x$ is larger than some tenths of volts at the pit initiation potential. This implies that the pit initiation potential becomes more positive than the thermodynamically estimated potential for the halide formation on the surface of the metal by an order of magnitude of 1V.

If the passive film thickness is not very thick, then $x \approx 2$ in Eq. [43]. Equation [52] holds in this case, which states that pits will appear as the concentration C_x increases and the potential of the metal exceeds E_p . Equation [52] further predicts the relationship

$$E_p = \text{const.} - \frac{nRT}{eF} \ln C_x \quad [55]$$

which agrees with many experimental results (15, 18, 19).

On the other hand, if the passive film is thick, x in Eq. [43] is less than 2, so that there should be cases where pit initiation and passive film breakdown cannot occur when the film thickness increases with the increase in the potential or when it increases at a constant potential with time.

The induction period τ is considered to be one of the most characteristic variables of the pit initiation process. This is the time required for the first appearance of the pit after the establishment of conditions for pitting (19, 20). Suppose that the critical radius r^* , which is the minimum necessary size for growing halide nuclei, is given by Eq. [51]. The volume of the nucleus is $2\pi r^{*3}/3$. A sufficient number of X^- should be supplied by transportation at the passive film-solution interface so that this size of nucleus can appear by fluctuation or by any other process.² The time required to meet this condition can be regarded as τ , then the relationship

$$\sqrt{\tau} \propto r^* \quad [56]$$

should exist between τ and r^* . Equation [56] coupled with Eq. [44] and [51] leads to

$$\ln \tau = \text{const.} - 2n \ln C_x - \frac{2eFE}{RT} \quad [57]$$

Hoar and Jacob (10) experimentally obtained the relationship

$$\ln \tau = \text{const.} - m \ln C_x \quad [58]$$

and Heusler and Fisher (20) stressed the relationship

$$\ln \tau = \text{const.}/(\ln C_x/C_{xc})(\ln C_H/C_{hc})(E - E_p) \quad [59]$$

where C_{xc} and C_{hc} are the critical concentrations of X^- and H^+ , respectively, above which pitting can occur. The above two relationships coincide qualitatively with Eq. [57].

Aggressive ions are known to cause passive film thinning (19), which accelerates the pit formation. It should also be mentioned that once a flaw in the passive metal is attacked by aggressive ions, this creates preferential penetration of these ions at that point. These effects make the pitting phenomenon more complicated and are therefore not considered explicitly in this study.

Manuscript submitted Dec. 7, 1982.

Industrial Products Research Institute assisted in meeting the publication costs of this article.

² It should be noticed that halide formation has become thermodynamically stable under these conditions, and that halide nucleation is possible if one only considers the local situation around a halide nucleus to be generated. However, the irreversible system as a whole does not permit the stable existence of halide nuclei whose radius is less than r^* .

APPENDIX A

Let the x-axis pass through the center of a hemispherical halide nucleus into the solution. The flux of each species within the halide is considered to be so fast because of the high ionic conductance that it can be expressed similarly to the case of the transport of ions in solution, i.e.

$$J'_i = -n'_i v'_i \frac{\partial \tilde{\mu}_i}{\partial x}, \quad i = M, X, H, W \quad [A.1]$$

where n'_i , v'_i , and $\tilde{\mu}_i$ are the concentration, the mobility per unit force, and the chemical potential, respectively, of the i-species in the halide. In general, the flux can be expressed as a function of y' , the radial distance from the x-axis. Assuming that the electrochemical potential changes linearly along with the x-axis

$$J'_i(r') = \bar{n}'_i v'_i \frac{\tilde{\mu}_i(2, y') - \tilde{\mu}_i(3)}{\sqrt{r^2 - y'^2}} \quad [A.2]$$

where \bar{n}'_i is the average concentration of i-species within the halide, $\tilde{\mu}_i(2, y')$ is the chemical potential of i-species upon the interface between the oxide and the halide at the distance y' from the x-axis.

Let the equelectrochemical potential plane be parallel to the interface between the solution, so that

$$\tilde{\mu}_i(2, r') = [\tilde{\mu}_i(2, 0) - \tilde{\mu}_i(3)] \frac{\sqrt{r^2 - y'^2}}{r} + \tilde{\mu}_i(3) \quad [A.3]$$

Equations [A.2] and [A.3] give

$$J'_i(r') = J'_i = \bar{n}'_i v'_i \frac{\tilde{\mu}_i(2, 0) - \tilde{\mu}_i(3)}{r} \quad [A.4]$$

Then Eq. [2.4] leads to

$$\delta_x P_{MX} = \frac{2}{3} \pi r^3 NS \frac{1}{T} \bar{\Sigma} \bar{n}'_i v'_i \frac{\tilde{\mu}_i(2, 0) - \tilde{\mu}_i(3)}{r} \left[\frac{\delta \mu_i(2, 0) - \delta \mu_i(3)}{r} + z_i F \frac{\delta \Delta \phi_x}{r} - \frac{J'_i}{\bar{n}'_i v'_i} \frac{\delta r}{r} \right] \quad [A.5]$$

Designating $\tilde{\mu}_i(2, 0) = \tilde{\mu}_i(2)$, Eq. [A.5] becomes Eq. [13]. It should be noted that the rate and the affinity of the interfacial reactions between the oxide and the halide nuclei could be a function of y' generally, but such effects were disregarded here and they were all represented by those at $y' = 0$, i.e., at the deepest point of the halide nuclei (see Eq. [12]).

APPENDIX B

Suppose that the halide nucleus is an ionic conductor. If the specific resistance of the halide is designated by R_x , then

$$I = \frac{1}{R_x} \frac{\pi r^2 NS}{r} \Delta \phi_x \quad [B.1]$$

and

$$\delta I = \frac{I}{r} \delta r + \frac{\pi r NS}{R_x} \delta \Delta \phi_x \quad [B.2]$$

In the case where the halide nuclei have a very high ionic conductivity, so that the potential difference through the halide nuclei is substantially determined by the potential of the metal and is almost constant through the progress of the irreversible change, i.e.

$$\delta \Delta \phi_x \stackrel{\circ}{=} 0 \quad [B.3]$$

Eq. [B.2] becomes

$$\delta I = \frac{I}{r} \delta r \quad [B.4]$$

This case corresponds to $x = 1$ in Eq. [43].

On the other hand, in the case where the dissolution reaction rate through the halide nuclei can be assumed for hemispherical pitting corrosion (15, 16)

$$I = 2\pi r^2 NSi \quad [\text{B.5}]$$

here i is a dissolution current per unit of interface area of the halide nucleus which contacts with the oxide. In this case, $x = 2$ in Eq. [43]. Comparison of Eq. [B.1] or [B.5] with Eq. [43] would yield

$$A \doteq i \quad [\text{B.6}]$$

APPENDIX C

The case of $x = 2$ would be enough to verify the point. With the use of Eq. [30] and [34]

$$\begin{aligned} & \frac{2}{3} \pi r^2 NS \left[-\frac{1}{\Lambda_X} \left(\frac{I}{\pi r^2 NS} \right)^2 \right. \\ & \quad \left. + \frac{J_M^2}{\bar{n}'_M v'_M} + \frac{J_X^2}{\bar{n}'_X v'_X} + \frac{J_H^2}{\bar{n}'_H v'_H} \right] \\ & = \frac{2}{3} \pi r^2 NS [\bar{n}'_X v'_X (F n'_H v'_H J'_M \\ & - z F n'_M v'_M J'_H)^2 + \bar{n}'_H v'_H (F n'_X v'_X J'_M \\ & + z F \bar{n}'_M v'_M J'_X)^2 + \bar{n}'_M v'_M (F n'_H v'_H J'_X \\ & + F \bar{n}'_X v'_X J'_H)^2] / \bar{n}'_M v'_M \bar{n}'_X v'_X \bar{n}'_H v'_H \\ & \quad (z^2 F^2 \bar{n}'_M v'_M + F^2 \bar{n}'_X v'_X + F^2 \bar{n}'_H v'_H) \\ & = O \left(\frac{I^2}{\Lambda_X r^2 NS} \right) > 0 \quad [\text{C.1}] \end{aligned}$$

The left-hand side of Eq. [C.1] is put to $\lambda_X I^2 / \Lambda_X r^2 NS$.

REFERENCES

- U. F. Frank, *Z. Elektrochem.*, **62**, 649 (1958).
- W. Schwenk, *Corros. Sci.*, **3**, 107 (1963).
- H. Kaesche, "Die Korrosion der Metalle," Chap. 9, Springer-Verlag, Berlin (1966).
- T. Okada and T. Hashino, *Corros. Sci.*, **17**, 671 (1977).
- N. D. Greene and M. G. Fontana, *Corrosion.*, **15**, 25t (1959).
- N. Sato, *This Journal*, **123**, 1197 (1976).
- T. P. Hoar, D. C. Mears, and G. P. Pothwell, *Corros. Sci.*, **5**, 279 (1965).
- K. J. Vetter, *Ber. Bunsenges. Phys. Chem.*, **69**, 683 (1965).
- D. A. Vermilyea, *This Journal*, **118**, 529 (1971).
- T. P. Hoar and W. R. Jacob, *Nature*, **216**, 1299 (1967).
- A. W. Adamson, "Physical Chemistry of Surfaces," Chap. 7, Interscience Publishers, New York (1967).
- P. Glansdorff and I. Prigogine, "Thermodynamic Theory of Structure, Stability and Fluctuations," Chap. 9, Wiley-Interscience, New York (1974).
- W. Jost, "Diffusion in Solids, Liquids, Gases," Chap. 3, Academic Press, New York (1960).
- K. J. Vetter, "Electrochemical Kinetics," Chap. 6, Academic Press, New York (1967).
- H. J. Engell and N. D. Stolica, *Z. Phys. Chem. N.F.*, **20**, 113 (1959).
- E. Brauns and W. Schwenk, *Werkst. Korrosion*, **12**, 73 (1961).
- W. P. Iverson, *This Journal*, **115**, 617 (1968).
- H. P. Leckie and H. H. Uhlig, *ibid.*, **113**, 1262 (1966).
- M. Janik-Czachor, *ibid.*, **128**, 513C (1981).
- K. E. Heusler and L. Fisher, *Werkst. Korrosion*, **27**, 551 (1976).

Polarization Behavior of the Nickel Electrode in Molten Sulfides

C. T. Liu* and O. F. Devereux*

Department of Metallurgy and Institute of Materials Science, University of Connecticut, Storrs, Connecticut 06268

ABSTRACT

Polarization behavior of the Ni-200 electrode in 75% Na₂S-25% FeS at 1000°C under H₂-0.32% H₂S at 1 atm is linear over an overpotential range of $-600 \leq \eta \leq 600$ mV and is consistent with resistance polarization in the electrolyte. Similar polarization behavior of the 304 stainless steel electrode and of the Ni-200 electrode in 85% Na₂S-15% NiS suggests that the charge transfer mechanism is a sulfide/polysulfide exchange reaction. Nonelectrode dissolution of nickel in the 75% Na₂S-25% FeS melt occurs at 1.6×10^{-6} g cm⁻² s⁻¹, apparently due to oxidation by H₂S. Anomalously high dissolution rates are attributed to trace polysulfide.

The virtual omnipresence of sulfur in fossil fuels raises concern regarding sulfur-caused corrosion in high temperature fuel utilization and conversion processes. In particular, coal conversion processes operate under conditions of low oxygen potential (1), in which many metal sulfides are stable (2), and at temperatures sufficient for these sulfides to be molten, rendering reactor structures subject to catastrophic failure by hot corrosion (3). Similar concerns may be voiced concerning the sodium-sulfur battery, which operates at considerably lower temperatures (ca. 400°C) in the presence of sodium polysulfide (3). Considerable insight with regard to reaction rates and mechanisms in such hot corrosion processes may be gained through electrode polarization studies; our recent experience with the nickel electrode in molten sodium carbonate (4) prompted the following study of the polarization behavior of nickel electrodes and of the nonelectrode dissolution of nickel in molten sulfide mixtures.

Experimental System

Our polarization cell has been described previously (5). It is limited to temperatures not greatly in excess of 1000°C, and employs a reference electrode which is, in effect, reversible to sodium ion (6). The latter fact led us to consider sodium sulfide (Na₂S) as the corrosive electrolyte; however, the melting point of this compound has been reported as 1180°C, prohibitively high for our apparatus (7-10). (Other values as low as 950°C have been reported (11-13). These values, however, may be due to partial oxidation of the sulfide samples investigated; Courtois (8) reported a melting point of 1180°C for Na₂S, but a liquidus temperature of 950°C for the 87% Na₂S-13% Na₂SO₄ solution.) Consequently, we selected ferrous sulfide (FeS) as a melting point lowering solute, primarily because of the availability of considerable data on the Na₂S-FeS system (12, 14, 15), although in retrospect another alkali sulfide might have been preferable. We used the eutectic composition of 25 weight percent (w/o) FeS, melting at 650°C, reported

* Electrochemical Society Active Member.

Key words: electrode, nickel, sulfide, dissolution, polarization.

by Kopylov and Novoselov (14) to exist between Na_2S and $5\text{Na}_2\text{S} \cdot 2\text{FeS}$. A crude DTA measurement of this mixture gave a melting point of 686°C in reasonable agreement with the published value. Although FeS nominally displays excellent electronic conduction (it may contain as much as 20% excess sulfur and is, therefore, a p-type semiconductor through formation of Fe^{+3}), Velikanov *et al.* (15) reported that conductivities of molten Na_2S -FeS mixtures vary only slightly with composition up to 45 mol percent (m/o) (48 w/o) FeS, implying that in this range melt conductivity is primarily ionic. The equilibrium between solid iron and the 75% Na_2S -25% FeS melt at 1000°C was estimated (16) to occur at $P_{\text{H}_2\text{S}}/P_{\text{H}_2} = 2.4 \times 10^{-3}$, while the equilibrium between solid nickel and the nickel-saturated sulfide melt at 1000°C was given by Nagamori and Ingraham (17) as $P_{\text{H}_2\text{S}}/P_{\text{H}_2} = 4.0 \times 10^{-3}$, delineating a narrow range of gas compositions in which both the electrolyte and the nickel electrodes are stable. The cell environment was fixed at the midpoint of this range ($P_{\text{H}_2\text{S}}/P_{\text{H}_2} = 3.2 \times 10^{-3}$) using a certified standard mixture from the Matheson Company.

Experimental Procedure

Dissolution and polarization experiments were conducted in a vertical tube furnace with proportioning temperature control. The electrolyte cell was housed in a closed end mullite tube, 3.5 in. od, which terminated in a vacuum-tight water-cooled flange which permitted electrical, mechanical, and gas flow feed-throughs. Nickel specimens were prepared from Ni-200 rod 0.25 in. diam, mechanically polished with 600 grit SiC paper, and washed and dried prior to use. Specimens were approximately 0.4 in. long (ca. 2.3 cm^2 exposed surface) and were cemented to alumina tubes with alumina cement (Ultra-Bond 552, Aremco Products, Incorporated). The alumina tubes in turn passed through the vacuum flange closing the top of the furnace tube and permitted positional control through sliding O-ring seals as well as housing electrode wires during polarization. Approximately 100g of electrolyte was employed in each run. This was contained in a recrystallized alumina crucible for dissolution experiments, or graphite crucible for polarization experiments. The latter also served as counterelectrode. Ferrous sulfide was purchased as 99+ % FeS from Great Western Inorganics Company; Na_2S was prepared by dehydrating reagent-grade $\text{Na}_2\text{S} \cdot 9\text{H}_2\text{O}$ from J. T. Baker Chemical Company in two stages: first, the hydrated sulfide was stored in a desiccator, which was evacuated daily, for several weeks; this removed approximately 70% of the water. Afterward, the desiccated sulfide was slowly heated to 200°C under a 1 torr vacuum and stored in a desiccator for future use. Thermogravimetric analysis demonstrated that this procedure removed 95% of the water, and that heating to higher temperatures was counterproductive in that sulfate was formed.

The components of the electrolyte were thoroughly mixed, then held at 200°C in the cell overnight under the $\text{H}_2\text{S}/\text{H}_2$ mixture. Subsequently the cell was slowly heated to 1000°C and held for a minimum of 1h to complete moisture removal and permit reduction of any sulfate present. The initial flow rate of the cell gas was $25 \text{ cm}^3/\text{min}$; prior to melting of the electrolyte it was set at $100 \text{ cm}^3/\text{min}$ for the remainder of the experiment. Equilibrium calculations indicated that the electrolyte was stable against oxidation at air-leak rates approximating the gas flow rate, while Kopylov's data indicate that Na_2S is stable against hydration at $P_{\text{H}_2\text{O}} = 1 \text{ atm}$ at temperatures above 190°C (18).

Potentiostatic polarization measurements were performed using the nickel specimen as working electrode, the graphite crucible as counterelectrode, and the previously described reference electrode (6). Potential

was fixed by standard instrumentation, employing a fixed step rate of $2 \text{ mV}/20\text{s}$. The potential sweep was from maximum cathodic potential (-800 mV) to maximum anodic potential (400 mV), and then back to maximum cathodic potential. Polarization data were directly recorded as potential *vs.* log current.

Several nonelectrode dissolution experiments were performed simultaneously by the simple expedient of suspending several mounted specimens over the melt at once. At the onset of the test, one specimen would be lowered into the melt, followed by the others at fixed intervals of 10 or 20h. No significant weight change occurred prior to immersion; *i.e.*, the nickel specimens were in theory and in fact inert to the cell atmosphere. Weight change was established by weighing clean specimens before and after immersion.

Results

Polarization was linear over the potential range studied; a typical curve, redrawn from the as-recorded semi-log plot, is shown in Fig. 1. The abscissa is not normalized to unit area because of the obvious change in specimen surface area that occurred during each test. The initial (cathodic-to-anodic) polarization curve has a slope of 0.78Ω ; this value was typical. In some, but not all, runs the anodic curve showed a slight hysteresis; Fig. 1 shows a slope of 1.02Ω for the anodic portion of the anodic-to-cathodic polarization. Using an aqueous electrolyte of known conductance, we estimated the cell constant to be 1.4 cm^{-1} ; with this value and the conductance measured by Velikanov, *et al.* (15) for 62% Na_2S -38% FeS at 1000°C , $1.8 \Omega^{-1} \text{ cm}^{-1}$, the electrolyte resistance was estimated as 0.78Ω . This excellent agreement (again, the data of Velikanov, *et al.* show very little variation with composition in this range) strongly implies that the observed polarization is attributable to ohmic resistance of the electrolyte. In agreement with this a comparable experiment using a different working electrode, 304 stainless steel, gave a cell resistance of 0.80Ω , demonstrating little, if any, effect of electrode material on cell resistance. The cell resistance at 900°C , using the nickel electrode, was found to be 0.75Ω , implying an activation energy for electrolytic charge transport of -1.16 kcal/mol . This may be meaningful; cell resistance was found to be reproducible and small, negative activation energies have been reported for other salts (11).

Nonelectrode weight loss measurements from three runs (thirteen specimens) are plotted in Fig. 2. All measurements save those for the longest immersion

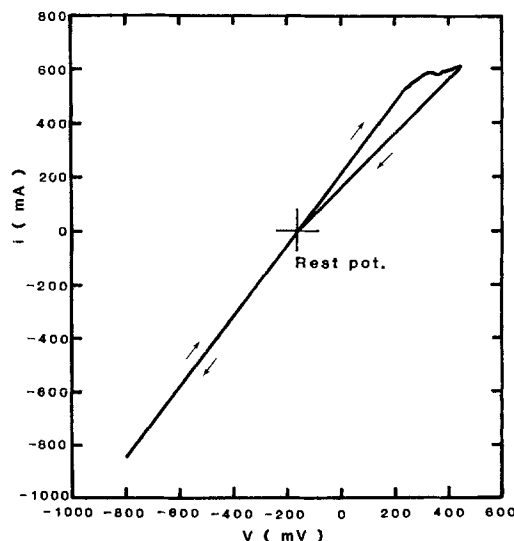


Fig. 1. Linear polarization plot for Ni-200 in 75% Na_2S -25% FeS at 1000°C . Initial specimen area: 2.3 cm^2 . Potential measured vs. $\text{CO}, \text{CO}_2(\text{Pt})|\text{Na}_2\text{CO}_3$ electrode (0.38 atm CO , 0.62 atm CO_2).

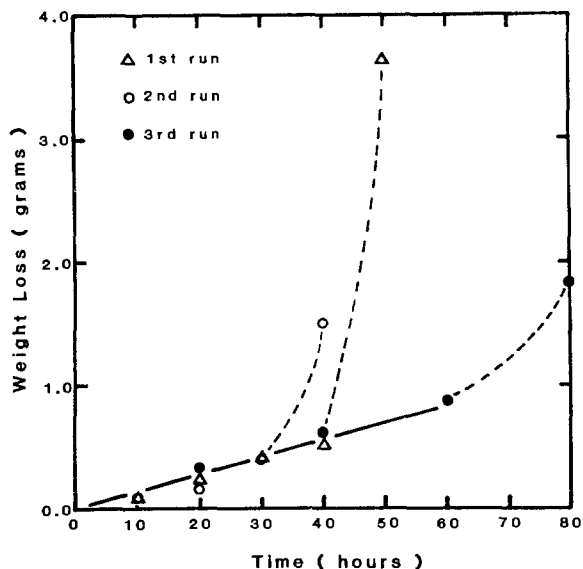
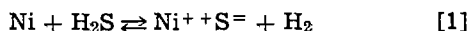


Fig. 2. Nonelectrode weight loss measurements for Ni-200 in 75% Na₂S-25% FeS at 1000°C. Initial specimen area: 2.3 cm².

time in each run fit a linear dissolution rate of 3.7×10^{-6} g s⁻¹, or 1.6×10^{-6} g cm⁻² s⁻¹. This is clearly attributable to oxidation of nickel by H₂S



which must occur until the melt approaches saturation with nickel sulfide; that is, the value for $P_{\text{H}_2\text{S}}/P_{\text{H}_2}$ employed for these experiments is just below the value at which nickel and nickel-saturated nickel sulfide are in equilibrium ($a_{\text{Ni}} \sim a_{\text{NiS}} \sim 1$), while the electrolyte for these studies initially contains no nickel ($a_{\text{NiS}} = 0$) and never attains more than a few percent nickel ($a_{\text{NiS}} \ll 1$). In each run the specimen immersed first (i.e., that with the longest immersion time) shows a disproportionately high dissolution; this is discussed in the next section.

Discussion

The Butler-Volmer equation, which describes the net rate of a single electrode reaction controlled by electron transfer, is written

$$i = i_0 [e^{(1-\beta)\eta_a F/RT} - e^{-\beta\eta_a F/RT}] \quad [2]$$

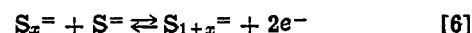
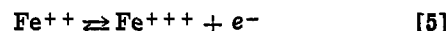
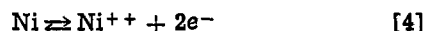
where i is the observed current, i_0 is the exchange current, η_a is the activation overpotential, β is a symmetry factor ($0 < \beta < 1$), and R , T , and F have their usual meanings. The exponential terms may be expanded, and when η_a is sufficiently small, Eq. [2] reduces to

$$i = i_0 \eta_a F/RT \quad [3]$$

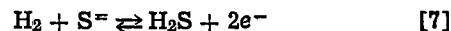
i.e., linear activation polarization. The region of validity of Eq. [3] is greatest when $\beta = 0.5$, in which case it may be shown that the linear relation is about 10% in error when $|\eta_a| = 1.5 RT/F$, or 0.165V at 1000°C. The region of validity is smaller for other values of β , approaching 0.022V as β approaches either 0.0 or 1.0. Linearity of current with potential was observed, however, over a significantly greater overpotential range, from -600 to +600 mV. Invoking a simple model, that the observed overpotential may be regarded as the sum of a charge transfer overpotential and an ohmic potential drop in the electrolyte, it is clear that only a small portion of the observed overpotential is attributable to charge transfer and that the remainder is ohmic. This is, of course, in agreement with the excellent correlation between measured cell resistance and published conductance values (15). As a corollary to this observation, the exchange current density must be relatively large to permit a cell current of 850 mA (current density ~ 370 mA cm⁻²) to be carried within the linear

range of Eq. [2]. That is, the overpotential is clearly the sum of two linear contributions; that due to conduction in the electrolyte is inherently linear, while that due to charge transfer is linear only if i_0 is greater than the ratio of the maximum current at which linearity is observed to the maximum value of $\eta_a F/RT$ at which linearity can be observed. Thus, we may infer that $i_0 \geq 370/1.5 = 250$ mA cm⁻².

We may postulate as likely candidates for the mechanism of charge transfer at the electrode surface the reactions



and



Of these, the similarity of the polarization behavior of Ni-200 and 304 stainless steel electrodes suggests that reaction [4] is not dominant. Similarly, a single polarization experiment performed with a nickel electrode in an electrolyte of 85% Na₂S-15% NiS yielded a curve identical to those obtained with the 75% Na₂S-25% FeS electrolyte, demonstrating that reaction [5] is not dominant.¹ Reaction [7] does not seem the probable charge transfer mechanism because it must necessarily experience concentration polarization; oxidation of CO and of H₂ at the nickel electrode in molten sodium carbonate at substantially higher pressures entails limiting diffusion currents of the order of a few mA/cm² (4, 19), values inconsistent with the high currents passed by this electrode.

Thus, by elimination we infer that the predominant charge transfer mechanism is a sulfide/polysulfide exchange. In this context, the departure from linearity seen during anodic polarization and the increased cell resistance during the anodic portion of the anodic-to-cathodic sweep could be interpreted as a concentration polarization involving sulfide by the following argument: as noted above, the measured overpotential may be regarded as the sum of an activation or charge transfer overpotential and an ohmic potential difference

$$\eta = \eta_a + \eta_r \quad [8]$$

From Eq. [3]

$$\eta_a = \frac{iRT}{i_0 F} \quad [9]$$

and, writing the ohmic resistance of the cell as r and the electrode area as A

$$\eta_r = iA r \quad [10]$$

or

$$\eta = \left(\frac{RT}{i_0 A F} + r \right) iA \equiv iA r_{\text{eff}} \quad [11]$$

where, again, iA is the measured cell current. The effective resistance of the cell (r_{eff}) increased from 0.78 to 1.02Ω as a result of anodic polarization. Inasmuch as the value of r_{eff} during subsequent cathodic polarization is not affected, it is clear that the parameter that controls the change in slope is not electrode area (A), but the exchange current density (i_0) for the anodic reaction. This parameter is proportional to the product of reactant activities (21), e.g., from reaction [6] $i_0 \propto a_{\text{S}_x} a_{\text{S}^{2-}}$, or, if $x = 1$ and transfer of a single electron is rate controlling, $i_0 \propto a_{\text{S}^{2-}}$. From the foregoing estimate that $i_0 \geq 250$ mA cm⁻² and given that $A = 2.3$ cm², it is clear that $RT/i_0 A F \leq 0.2\Omega$, which is close in magnitude to the observed change in r_{eff} . The mecha-

¹ Although in analogy to iron, nickel has higher oxidation states, the large positive free energy change for the reaction $\text{Fe}_2\text{O}_3 + 2\text{NiO} \rightleftharpoons 2\text{FeO} + \text{Ni}_2\text{O}_3$ ($\Delta G^\circ = 75.9$ kcal/mol at 25°C (13, 20)), suggests that these will be formed only at more oxidizing potentials than that required for formation of Fe³⁺.

nism for the change in slope is, thus, as follows: during initial anodic polarization the activity of sulfide, $a_{S^{2-}}$, at the electrode surface is large and the exchange current density is appreciably in excess of its minimum value, 250 mA cm^{-2} . During this portion of the polarization sweep, charge transfer polarization is insignificant in comparison to the ohmic potential difference. However, as a result of anodic polarization, the anolyte is enriched in polysulfide (S_{1+x}^{2-}) and the activity of sulfide is correspondingly decreased. The resulting decrease in the magnitude of the exchange current density causes a significant charge transfer contribution to the total overpotential; the effective increase in the cell resistance due to this effect can be 0.2Ω (approximately equal to the observed change) without entailing a substantive departure from linearity. The customary approach to asymptotic behavior associated with concentration polarization is, in fact, seen at the upper end of the cathodic-to-anodic sweep in Fig. 1; this region of the curve was somewhat smoother and of more traditional appearance in other experiments. This concentration polarization persists, i.e., η_a remains inversely proportional to the reduced value of i_0 , as long as the electrode is anodic. When the electrode becomes cathodic, reaction [6] reverses, S_{1+x}^{2-} is consumed, and the activity of sulfide is restored to its initial value.

Following both polarization and dissolution experiments in the 75% Na_2S -25% FeS melt, substantial quantities of a cubic Ni-Fe precipitate (Ni:Fe \sim 4:1) were recovered. We attribute this to a loss of sulfur from the melt due to reduction by hydrogen, coupled with a narrowing of the stoichiometric range of NiS and FeS as the melt was cooled to room temperature, rather than to cathodic reduction of the metals.

The disproportionately high weight loss of the first specimen immersed in each dissolution experiment is consistent with the existence of a low level of polysulfide ion in the as-melted electrolyte. Thomas and Rule have reported that sodium disulfide is extremely stable (22), and Tegman's postulated distributions of the concentrations of $S^=$, $S_2^=$, . . . $S_8^=$ as functions of equilibrium P_{S_2} (23) suggest at least trace levels of $S_2^=$ in our system, for which $P_{S_2} = 5.3 \times 10^{-8}$ atm. In our preparation of anhydrous Na_2S we observed a faint yellow color, which is associated with the presence of the disulfide Na_2S_2 (10, 24). The disulfide ion would function as an oxidizing agent, and the presence of 1% Na_2S_2 in the 100g melt would account for the dissolution of 0.6g of nickel via the reaction



which is of the order of the anomalous initial weight loss.

Figure 3 shows a polished section through the near-surface region of a specimen subsequent to a dissolution experiment. The high intra- and intergranular void density in this region is quite suggestive of hydrogen injection under the influence of a large fugacity gradient due to reaction [1], although a somewhat comparable structure with evidence of sulfide inclusions has been noted in gas-phase attack of iron by H_2S (25). However, EDX analysis showed no indication of sulfur in the sample shown in Fig. 3.

Conclusions

Polarization of Ni-200 and 304 stainless steel electrodes in 75% Na_2S -25% FeS and 85% Na_2S -15% NiS melts at 1000°C is linear over an overpotential range of -600 (cathodic) to 600 mV (anodic), with a cell resistance consistent with published values for conductivity of the electrolyte. Charge transfer overpotential can account for only a small portion of the measured overpotential and is apparently unrelated to corrosion of the electrode: It is attributed to a sulfide/polysulfide exchange reaction with an exchange current density in

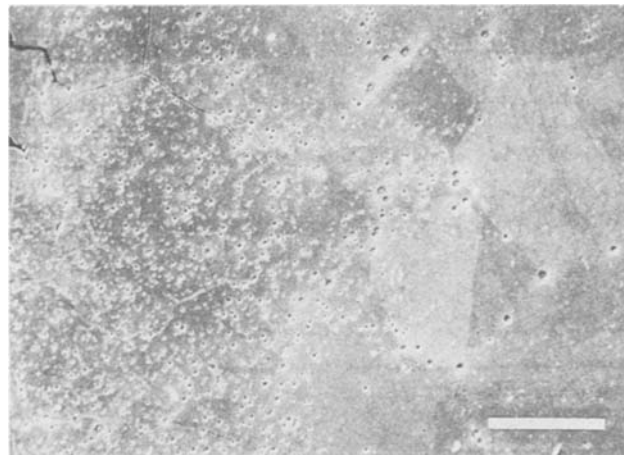


Fig. 3. SEM micrograph of section through a Ni-200 specimen exposed to 75% Na_2S -25% FeS for 10h at 1000°C . The specimen surface is seen at the upper left-hand corner. Marker is $100 \mu\text{m}$.

excess of 250 mA cm^{-2} . Nonelectrode dissolution of nickel in the 75% Na_2S -25% FeS melt at 1000°C occurs at $1.6 \times 10^{-6} \text{ g cm}^{-2} \text{ s}^{-1}$, corresponding to a dissolution current at the rest potential of $5.3 \times 10^{-3} \text{ A cm}^{-2}$. An anomalously high initial dissolution rate is attributed to trace polysulfide in the melt.

Acknowledgment

The authors are pleased to acknowledge the support of the U.S. Department of Energy through contract no. DE-AC02-76ER02960.

Manuscript submitted Jan. 27, 1983; revised manuscript received Sept. 6, 1983.

The University of Connecticut assisted in meeting the publication costs of this article.

REFERENCES

1. K. Natesen and O. K. Chopra, in "High Temperature Alloys," Z. A. Foroulis and F. S. Petit, Editors, p. 493, The Electrochemical Society Softbound Proceedings Series, Princeton, NJ (1977).
2. E. A. Gulbransen and S. A. Jansson, in "High-Temperature Metallic Corrosion of Sulfur and Its Compounds," Z. A. Foroulis, Editor, The Electrochemical Society Softbound Proceedings Series, Princeton, NJ (1970).
3. Panel Report on Corrosion in Energy Systems, Division of Materials Sciences, U.S. Department of Energy, University of Illinois (1979).
4. O. F. Devereux, K. Y. Kim, and K. S. Yeum, *Corros. Sci.*, **23**, 205 (1983).
5. K. Y. Kim and O. F. Devereux, *ibid.*, **22**, 21 (1982).
6. K. Y. Kim and O. F. Devereux, *This Journal*, **125**, 1796 (1978).
7. G. Brauer, "Handbook of Preparative Inorganic Chemistry," 2nd ed., p. 360, Academic Press, New York (1963).
8. M. Gaston Courtois, *C.R. Hebd. Seances Acad. Sci.*, **208**, 200 (1939).
9. N. I. Kopylov and S. S. Novoselov, *Russ. J. Inorg. Chem.*, **9**, 1038 (1964).
10. E. Rosen and R. Tegman, *Chem. Scr.*, **2**, 221 (1972).
11. G. J. Janz, "Molten Salt Handbook," p. 16, 300, Academic Press, New York (1967).
12. L. V. Steck, M. Slavin, and O. C. Ralston, *J. Am. Chem. Soc.*, **51**, 3241 (1929).
13. O. Kubaschewski and C. B. Alcock, "Metallurgical Thermochemistry," 5th ed., p. 380, Pergamon Press, London (1979).
14. N. I. Kopylov and S. S. Novoselov, *Metall. Khim. Prom. Kaz.*, **1**, 53 (1962).
15. A. A. Velikanov et al., *Izv. Vyssh. Uchebn. Zaved. Tsvetn. Metall.*, **4**, 148 (1975).
16. C. T. Liu, M.S. Thesis, University of Connecticut, Storrs, Connecticut (1982).
17. M. Nagamori and T. R. Ingraham, *Metall. Trans.*, **1**, 1821 (1970).
18. N. I. Kopylov, *Russ. J. Inorg. Chem.*, **13**, 276 (1968).

19. K. Y. Kim and O. F. Devereux, in "Proceedings of an International Conference on High Temperature Corrosion," p. 539, San Diego, March 2-6, 1981, NACE, Houston (1983).
20. M. Pourbaix, "Atlas d'Equilibres Electrochimiques," p. 331, Gauthier-Villars & Cie., Paris (1963).
21. K. J. Vetter, "Electrochemical Kinetics," Academic Press, New York (1967).
22. J. S. Thomas and A. Rule, *J. Chem. Soc.*, **111**, 1063 (1917).
23. R. Tegman, *Chem. Scr.*, **9**, 158 (1976).
24. P. J. Walker, *J. Cryst. Growth*, **47**, 598 (1979).
25. R. Boland and O. F. Devereux, *Metall. Trans.*, **10A**, 1959 (1979).

Solution of Some Integral Equations Occurring in the Theory of Electrochemical Nucleation and Growth

S. Fletcher*

CSIRO, Institute of Energy and Earth Resources, Division of Mineral Chemistry, Port Melbourne, Victoria 3207, Australia

ABSTRACT

A formula is derived for the average value of any crystal growth parameter observed during electrochemical nucleation and growth. The formula contains a Volterra integral equation of the first kind and therefore cannot always be solved explicitly. However, it can be solved under certain conditions, and these are discussed. The most important solutions are collected into tables.

A large part of electrochemical nucleation theory deals with the prediction of the time evolution of the mean value properties of ensembles of crystals (1-3). The purpose of the present work is to describe some new solutions to this problem for the special case where all crystals have the same geometry, grow by the same mechanism, and are independent of each other and of electrode boundaries. Solutions are established using integral equation methods. As usual in the theory of integral equations, the Dirichlet notation $y = f(x)$ is used to mean both " y is a function of x " and " $f(x)$ is the value of the function y at a particular x ." Throughout the text, parentheses, (), are reserved for this notation, square brackets, [], for multiplication, and braces, { }, for functionals. The superscript primed, as in the function $f'(x)$, denotes the first derivative of the function with respect to the argument x .

Derivation of Ensemble Average Quantities in Terms of Integral Equations

We begin with an example. Suppose we are interested in the total volume of an ensemble of hemispherical crystals which are nucleating and growing on a battery plate over the interval $(0, t)$. One way to write this is as the sum of the volumes of all of the crystals considered independently (4)

$$V_N(t) = \sum_{j=1}^{N(t)} \frac{2\pi}{3} R_1(\tau_j, t)^3 \quad [1]$$

Where $R_1(\tau, t)$ is the radius of one crystal that appeared at time τ and is observed at time t , and $N(t)$ is the experimentally observed number of crystals at time t . Another way of writing $V_N(t)$, valid for large $N(t)$, is to approximate it by its expectation value $E\{V_N(t)\}$. This latter approach, which is useful when the τ_j are closely spaced, is used in the present work. In particular, $N(\tau)$ is chosen to be so large that it can be described by a continuous real-valued function of τ over at most a finite number of intervals in the range $0 \leq \tau \leq t$. Thus $N(\tau)$ is assumed to be arbitrarily close to its expectation value $E\{N(\tau)\}$, and since the conditional probability density of the times τ at which crystals appear has the form (4)

$$p(\tau|0 \leq \tau \leq t) = \begin{cases} \frac{N'(\tau)}{N(t)}, & 0 \leq \tau \leq t \\ 0, & \text{otherwise} \end{cases} \quad [2]$$

then it follows that the expectation value of the volume of one crystal is

$$E\{V_1(t)\} = \int_0^t \frac{2\pi}{3} R_1(\tau, t)^3 p(\tau|0 \leq \tau \leq t) d\tau \quad [3]$$

given only that all crystals grow via the same mechanism. Hence the expectation value of the total volume $V_N(t)$ of the ensemble of crystals is

$$E\{V_N(t)\} = \int_0^t \frac{2\pi}{3} R_1(\tau, t)^3 N'(\tau) d\tau \quad [4]$$

which is therefore a good approximation to Eq. [1] when $N(\tau)$ is large.

The above approach is easily generalized to the expectation values of other crystal growth parameters. Defining some extensive property $\lambda_N(t)$ of an ensemble of $N(t)$ crystals, then its expectation value is clearly

$$E\{\lambda_N(t)\} = \int_0^t \lambda_1(\tau, t) N'(\tau) d\tau \quad [5]$$

where $\lambda_1(\tau, t)$ is the value of λ for one crystal appearing at time τ and observed at time t , and the whole equation has the form of a Volterra integral equation of the first kind (5, 7).

A specialization of Eq. [5] of some experimental interest occurs when $\lambda_1(\tau, t)$ has a power law dependence on crystal radius, for crystal growth in any number of dimensions. In this case, the expectation value of $\lambda_N(t)$ can be expressed in the form

$$G(t; \kappa) = \int_0^t R_1(\tau, t)^\kappa N'(\tau) d\tau \quad [6]$$

where $G(t; \kappa)$ is some function of time for a specified κ . Experimental parameters that can be represented in this way include crystal volumes, surface areas, peripheral lengths, and electrical charges. The first derivative of Eq. [6] is interesting too. This is because other experimental parameters, such as linear crystal growth rates and electrical currents, have representations in

* Electrochemical Society Active Member.

Key words: electrodeposition, crystallization, kinetics, nucleation.

the form $G'(t; \kappa)$. Such derivatives are obtained by applying the generalized Leibnitz formula (8) to Eq. [6]. Hence, if $R_1(t, t) = 0$ then

$$G'(t; \kappa) = \int_0^t \kappa R_1(\tau, t)^{\kappa-1} \frac{\partial}{\partial t} R_1(\tau, t) N'(\tau) d\tau \quad [7]$$

Explicit Formulas for Ensemble Average Quantities for Cases Where Crystal Radii Have Power-Law Dependences on Elapsed Time

To compare theoretical and experimental values of ensemble average quantities it is desirable to solve Eq. [6] and [7] for specified $N(t)$ and $R(t)$. Of particular interest in electrochemical nucleation theory is the case when the kernel $R_1(\tau, t)^\kappa$ is a function of $[t - \tau]$ only (1, 2), for in that case the radius of a crystal appearing at time τ and observed at time t depends only on the elapsed time $[t - \tau]$, not on some complex parameter connected with time varying growth rates in the interval (τ, t) . Then Eq. [6] takes the form of a convolution integral of the first kind

$$H(t; \kappa) = \int_0^t R_1(t - \tau)^\kappa N'(\tau) d\tau \quad [8]$$

and from this a number of solutions can be obtained by means of Laplace transforms and the convolution theorem. A particularly interesting subset of solutions is that for which $R_1(t - \tau)^\kappa$ has a power-law dependence on elapsed time $[t - \tau]$, as is expected for crystal growth under interfacial control at constant potential (1, 2). Then Eq. [6] can be written in the form

$$M(t; y) = \int_0^t [t - \tau]^y N'(\tau) d\tau \quad [9]$$

which is soluble under a very wide range of conditions (9), being related to the Riemann-Liouville fractional integral of order $(y + 1)$.

Another advantage of seeking conditions for which the kernel $R_1(\tau, t)^\kappa$ has a power-law dependence on elapsed time is that the derivative of Eq. [9] is easily found. Thus

$$M'(t; y) = \int_0^t y [t - \tau]^{y-1} N'(\tau) d\tau \quad [10]$$

which is also related to the Riemann-Liouville fractional integral. In fact, it follows by induction from Eq. [9] and [10] that for a power-law dependence of $R(\tau, t)^\kappa$ on $[t - \tau]$ not only can crystal growth parameters be discussed in terms of Eq. [9] but so can their n -fold derivatives. This useful property means that, on the power-law model, the solutions of both Eq. [6] and [7] can be obtained directly by solution of Eq. [9].

Some explicit solutions of Eq. [9] are collected in Table I for various assumed functional forms of $N'(t)$, and some other forms of Eq. [9] are listed in Table II for certain values of y . Using the results in these tables it is possible to reconstruct all the known formulas for ensemble average quantities arising in nucleation/growth at constant potential (1, 2). Many new results can be derived also. To illustrate this assertion, two new formulas are now derived for electrical currents caused by two-dimensional nucleation and crystal growth.

Two Solutions of the Integral $M(t; y)$ of Experimental Interest

Power-law appearance rate and power-law growth rate of crystals in two-dimensional nucleation and growth.—A "classical" problem in electrocrystallization theory is the derivation of the electrical current caused by the two-dimensional nucleation and growth of independent circular crystals, in response to a potential step (1-3). The general result is found from Eq. [6] and [7]. It is

Table I. Solutions of the integral $M(t; y)$ for various assumed forms of $N'(t)$

$N'(t)$	$M(t; y)$
1	$\frac{t^{y+1}}{y+1}$
t^x	$\frac{\Gamma(y+1)\Gamma(x+1)}{\Gamma(x+y+2)} t^{x+y+1} = B(x+1, y+1) t^{x+y+1}$
$\sum_{x=0}^{\infty} \left(\frac{a_x t^x}{x!}\right)$	$\sum_{x=0}^{\infty} \left(\frac{a_x \Gamma(y+1)}{\Gamma(x+y+2)} t^{x+y+1}\right), \quad x = 0, 1, 2, \dots$
$t^x(t+a)^{x+1}$	$\frac{\Gamma(y+1)\Gamma(x+1)}{\Gamma(x+y+2)} t^{x+y+1} \alpha^{x+1} {}_2F_1\left(x+1, -(x+1); x+y+2; -\frac{t}{\alpha}\right)$
$t^x \exp(-\alpha t)$	$\frac{\Gamma(y+1)\Gamma(x+1)}{\Gamma(x+y+2)} t^{x+y+1} {}_1F_1(x+1; x+y+2; -\alpha t)$
$M(t; x)$	$\frac{\Gamma(y+1)\Gamma(x+1)}{\Gamma(x+y+2)} M(t; x+y+1)$

Table II. Other forms of the integral $M(t; y)$ for various assumed values of y

y	Other form
0	$M(t; 0) = N(t) - N(0)$
1	$M(t; 1) = \int_0^t \int_0^t N'(\tau) d\tau dt$
0, 1, 2, ...	$M(t; y) = y! \int_0^t \int_0^t \dots \int_0^t N'(t) \dots dt dt dt$ ($y+1$)-fold
$y > -1$	$M(t; y) = \Gamma(y+1) \int_0^t \int_0^t \dots \int_0^t N'(t) \dots dt dt dt$ ($y+1$)-fold
$-1 < y < 0$	$N(t) = \frac{1}{\Gamma(y)\Gamma(1-y)} \int_0^t [t-\tau]^{y-1} M(\tau; y) d\tau$ (Abel's inversion formula)

$$I(t) = \frac{Q_{\text{mon}}}{A} \int_0^t 2\pi R_1(\tau, t) R'_1(\tau, t) N'(\tau) d\tau \quad [11]$$

Now let us assume that at constant potential the number of crystals has a power-law dependence on time

$$N(t) = at^x \quad [12]$$

Let us also assume that the radius of a circular crystal has a power-law dependence on elapsed time after nucleation

$$R_1(\tau, t) = b[t - \tau]^y \quad [13]$$

Then from Eq. [9] and Table I, we deduce

$$I(t) = \frac{Q_{\text{mon}}}{A} \pi a b^2 \frac{\Gamma(2y+1)\Gamma(x)}{\Gamma(2y+x+1)} [2y+x] t^{2y+x-1} \quad [14]$$

and if x and y are non-negative integers

$$I(t) = \frac{Q_{\text{mon}}}{A} \pi a b^2 \frac{(2y)! x!}{(2y+x-1)!} t^{2y+x-1} \quad [15]$$

A useful check on this result is that the cases of $(x, y) = (0, 1)$ and $(1, 1)$ are the familiar ones of instantaneous and progressive nucleation, respectively (1-3).

An active site model.—This model is identical to that considered above except that the number of crystals is controlled by the activation rate of special sites at which nucleation is preferred (4). Assuming a first-order depletion rate of sites, $N(t)$ is given by the following Fredholm integral equation of the first kind

$$N(t) = \int_0^{\infty} N_0 \left[1 - \exp\left(-\frac{\alpha t}{N_0}\right) \right] \Phi(\alpha) d\alpha, \quad \alpha > 0 \quad [16]$$

where N_0 is the total number of active sites and $\Phi(\alpha)$ is the probability density of sites having activation rate α . (It is assumed that α is not time varying.) This equation simplifies if all active sites have the same probability of nucleation; in that case

$$N(t) = N_0 \left[1 - \exp\left(-\frac{\alpha t}{N_0}\right) \right] \quad [17]$$

Inserting this equation instead of Eq. [12] into Eq. [11] leads to the analogue of Eq. [15]

$$I(t) = \frac{Q_{\text{mon}}}{A} \pi a b^2 t^{2y} {}_1F_1\left(1; [2y + 1]; -\frac{\alpha t}{N_0}\right) \quad [18]$$

where the function ${}_1F_1(a; c; z)$ is Kummer's confluent hypergeometric series (8), and y is given by Eq. [13]. A check on this result is the substitution $y = 1$, which yields

$$I(t) = \frac{Q_{\text{mon}}^2}{A} \pi a b^2 \left[\frac{N_0}{\alpha} \right]^2 \left[\frac{\alpha t}{N_0} + \exp\left(-\frac{\alpha t}{N_0}\right) - 1 \right] \quad [19]$$

a formula already known in the literature (2).

Conclusions

A general equation has been derived for ensemble average values of crystal growth parameters arising in electrochemical nucleation and growth (Eq. [5]). The equation has the form of a Volterra integral equation of the first kind. For cases of crystal growth in which the Volterra kernels had power-law dependences on elapsed time after nucleation, it was shown that the Volterra integral could be replaced by a simpler integral of the Riemann-Liouville type (Eq. [9]). Solutions of this last integral were tabulated for forms of $N'(t)$, and values of y , of interest to electrochemists (Tables I and II). To illustrate the use of these tables, two new formulas were derived for electrical currents caused by two-dimensional nucleation and growth. The formulas were checked by showing that well-known results were recovered when appropriate assumptions were made.

Acknowledgments

This work was sponsored by the International Lead-Zinc Research Organization, (ILZRO), a project ZE-295, and the Australian National Energy, Research, Development, and Demonstration Council (NERDDC). Their financial support is gratefully acknowledged. I also thank Dr. I. Grey for his comments on the manuscript.

Manuscript received March 8, 1983.

CSIRO assisted in meeting the publication costs of this article.

LIST OF SYMBOLS

V_N	total volume of N crystals considered independently
$R_1(\tau, t)$	radius of one crystal appearing at time τ and observed at time t
$p(\tau)$	probability density of times τ at which crystals appear
$p(\tau 0 \leq \tau \leq t)$	conditional probability density of times τ at which crystals appear, given that they appear only in the range $0 \leq \tau \leq t$
$N(t)$	number of crystals at time t
$N'(t)$	appearance rate of crystals at time t [i.e., the first derivative, with respect to time, of $N(t)$]
$E(x)$	expectation value of x
$I(t)$	electrical current at time t ...
$I_1(\tau, t)$	electrical current at time t due to a single crystal appearing at time τ
Q_{mon}	electrical charge required to form a monolayer
A	electrode area
$\lambda_N(t)$	any time varying property of an ensemble of crystals
$G(t; \kappa)$	a Volterra integral equation of the first kind for specified κ
$H(t; \kappa)$	a convolution integral equation of the first kind for specified κ
$M(t; y)$	an integral equation of importance in nucleation theory, related to the Riemann-Liouville fractional integral of order $(y + 1)$
a, b, x, y	numerical constants
(a, b, c, z)	(in Dirichlet notation). Variables of hypergeometric series
α	constant activation rate of sites
${}_1F_1(a; c; z)$	Kummer's confluent hypergeometric series (8)
${}_2F_1(a, b; c; z)$	Gauss's hypergeometric series (8)
$\Gamma(a)$	gamma function (8)
$\gamma(a, z)$	incomplete gamma function (8)
$B(a, z)$	beta function (8)

REFERENCES

1. J. A. Harrison and H. R. Thirsk, in "Electroanalytical Chemistry," Vol. 5, A. J. Bard, Editor, pp. 67-148, Academic Press, New York (1971).
2. A. Bewick and M. Fleischmann, in "Topics in Surface Chemistry," E. Kay and P. S. Bagus, Editors, pp. 45-74, Plenum Press, New York (1978).
3. S. Fletcher, *J. Electroanal. Chem.*, **118**, 419 (1981).
4. S. Fletcher and T. Lwin, *Electrochimica Acta*, **28**, 237 (1983).
5. W. Pogorzelski, "Integral Equations and their Applications," Vol. 1, Pergamon Press, Oxford (1966).
6. F. Smithies, "Integral Equations," Cambridge University Press, Cambridge, England (1958).
7. F. G. Tricomi, "Integral Equations," Interscience Publishers Inc., New York (1957).
8. M. Abramowitz and I. Stegun, "Handbook of Mathematical Functions," Dover Publications Inc., New York (1965).
9. "Tables of Integral Transforms," Vol. II, A. Erdelyi, Editor, McGraw-Hill Inc., New York (1954).

Initiation of Electroless Nickel Plating on Copper, Palladium-Activated Copper, Gold, and Platinum

J. Flis* and D. J. Duquette

Materials Engineering Department, Rensselaer Polytechnic Institute, Troy, New York 12181

ABSTRACT

The catalytic activity of copper, palladium-activated copper, gold, and platinum for electro-oxidation of hypophosphite and electroless nickel plating was investigated in an ammoniacal solution of pH 8.8 at 50°C by potential measurements and linear sweep voltammetry from -0.3 to -0.92V vs. SCE. Early stages of nickel plating on copper-palladium substrates were studied by scanning electron microscopy in conjunction with EDAX. It was found that palladium-activated copper and gold were catalytically active in the entire range of potentials examined; copper was active below -0.6; platinum was not active at all. Small amounts of electrolytically deposited nickel considerably increased the electro-oxidation rate of hypophosphite on copper, gold, and palladium. TEM examinations showed that activation of copper in a PdCl₂/HCl solution resulted in the deposition of palladium in the form of separate patches. Electroless nickel deposition on copper substrates with separate palladium spots took place on copper and palladium independently of each other. The deposition on palladium was faster than that on copper. It was concluded that the activation of copper substrates around palladium spots occurred solely through a spontaneous potential shift, induced by electro-oxidation of hypophosphite on the palladium spots. It was suggested that small amounts of one metal synergistically enhanced the catalytic activity of the other metals.

Electroless nickel plating (1-3) is an autocatalytic process whose initiation is the result of the catalytic activity of a given substrate. After initiation of the plating, the process proceeds spontaneously on the deposited-nickel layer. It is believed that the rate of film growth is largely determined by the activity of the newly formed nickel layer. This is certainly true for thick layers; however, the growth of thin layers may still be affected by the substrate.

The authors of this work have previously reported (4) that the growth of nickel deposits on palladium occurred more rapidly than the growth on molybdenum, even when the deposits were of the order of 17 nm thick. This enhanced growth may be caused by small amounts of palladium being exposed in the deposit, and it may indicate a synergistic effect of small amounts of palladium on the catalytic activity of subsequent nickel deposits. A synergistic effect of one metal on catalytic activity of another metal seemed to appear in systems of palladium with nickel and palladium with molybdenum (4). This effect may account for the observation by Lelental (5) that electroless deposits of nickel on copper had higher catalytic activity than on nickel alone. It can be expected that small amounts of nickel, deposited at the start of plating, may also alter the catalytic activity of a substrate. This can be important, especially for substrates with generally poor catalytic activity and for substrates whose inherent activity is masked by surface reaction products.

The objective of this work was to investigate the initiation and early growth of electroless nickel plating on copper, palladium-activated copper, gold, and platinum. These metals were chosen because of differences in catalytic activity and in other chemical properties, characteristic of the elements of the VIII and IB groups of the periodic table. Palladium and gold are

* On leave from Institute of Physical Chemistry, 01-224 Warszawa, Poland.

Key words: electroless, nickel plating, copper, palladium, gold.

good catalysts for electroless nickel plating (1); copper can be made active by an anodic treatment (3) or by addition of chloride ions into the bath (6, 7); platinum is not active under open-circuit conditions (1). The inertness of platinum is in contrast to the behavior of other transition metals, which are good catalysts both for electroless nickel plating and for hydrogenation-dehydrogenation reactions (1, 2).

This work examines the effects of early nickel deposits on the catalytic activity of the substrates and the effects of palladium and copper substrates on more advanced stages of electroless nickel plating in an ammoniacal hypophosphite solution.

Experiments

Investigations were performed on 0.1 mm-thick foils of high purity copper, on vacuum deposited gold, and on platinum wire.

The copper foil was electropolished in a solution of 20% HNO₃ in methanol at a voltage of 6V at about 0°C, rinsed with distilled water and methanol, and then masked with lacquer to obtain an uninsulated-surface area of 1 cm². Thin foils for TEM were prepared by double-jet electropolishing in a solution of 33% HNO₃ in methanol at a temperature below -20°C. Activation of copper was achieved by immersion into a solution of 1 g/l PdCl₂ + 1 ml/l concentrated HCl or 0.2 g/l PdCl₂ + 0.2 ml/l HCl for 5s (for electron microscopy). Specimens for SEM and EDAX examinations were activated by placing separate droplets of the solution of 1 g/l PdCl₂ + 1 ml/l HCl on the surface and leaving them until dry.

Gold substrates were obtained by vacuum evaporation of gold on electropolished copper foils.

Platinum wires were cleaned in 35% HNO₃ and then cathodically polarized in 0.1M H₂SO₄ at a current density of 100 A · m⁻² for 600s.

Specimens were examined in the solutions listed in Table I. The solutions were prepared from analytical-grade reagents and distilled water. Sulfuric acid (98%)

Table I. Composition of solutions

Solution designation	NaH ₂ PO ₃ ·H ₂ O, g/l	NiSO ₄ · 6H ₂ O, g/l	KNa tartrate KNaC ₄ H ₄ O ₆ · 4H ₂ O, g/l	28% NH ₄ OH, ml/l	98% H ₂ SO ₄ , g/l
Plating solution	13.25 (0.125 mol/l)	13.1 (0.05 mol/l)	28.2	70	~ 15
Supporting solution	—	—	28.2	70	~ 15
Supporting solution with Ni ²⁺ ions	—	13.1	28.2	70	~ 15
Supporting solution with sodium hypophosphite	13.25	—	28.2	70	~ 15

was added in amounts appropriate for adjusting the pH of the solutions to 8.8 (at 25°C). All measurements were carried out on stationary specimens at $50.0 \pm 0.5^\circ\text{C}$ (pH at 50°C was 8.3) in a 250 ml round-bottom flask provided with a reflux condenser, Luggin capillary, and a platinum wire as an auxiliary electrode. The solutions were deaerated by purging with purified nitrogen gas.

Electrochemical examinations involved (i) monitoring of open-circuit electrode potentials after immersion of the specimens into the solutions, and (ii) linear sweep voltammetric (LSV) measurements. Potentials were measured against saturated calomel electrode (SCE) at 25°C via Luggin capillary, and throughout this paper are referred to as SCE. Voltammetric measurements were performed using a single cathodic sweep at a rate of $1\text{ mV} \cdot \text{s}^{-1}$, beginning at -0.3V .

The growth rate of the deposits at controlled potentials was determined from weight gains.

Results

Open-circuit potential.—Changes of electrode potentials of the substrates after immersion into the plating solution or a similar solution without Ni^{2+} ions are shown in Fig. 1. All potentials shifted in the cathodic direction on immersion, but only in the cases of palladium-activated copper and gold did they reach a potential of about -0.87V (characteristic of electroless plating of nickel). The potentials of copper and of platinum attained stationary values of about -0.45 and -0.65V , respectively, at which no plating took place. In the solution without Ni^{2+} ions, the potential of gold dropped to a value about 0.5V more negative than that in the plating solution.

As determined previously (4), the electroless nickel deposits contained from 2.2 to 2.9 weight percent (w/o) P.

Voltammetric measurements.—The measurements were made in the supporting solution with and without components essential for plating (cf. Table I) by scanning the potential in the cathodic direction from -0.3 to -0.92V or below. This potential range and direction of scanning were chosen in order to model

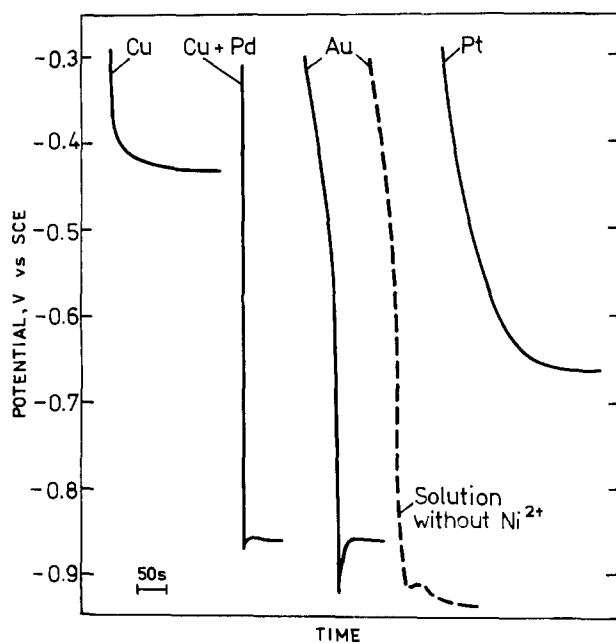


Fig. 1. Open-circuit potential of copper, palladium-activated copper (activation in the solution of $1\text{ g/l PdCl}_2 + 1\text{ ml/l HCl}$ for 5s), gold, and platinum after immersion into a plating solution (solid lines) or into a supporting solution with NaH_2PO_2 but without Ni^{2+} ions (dashed line).

the spontaneous shift of potential under open-circuit conditions (Fig. 1). Voltammograms for the substrates examined are shown in Fig. 2-5.

From Fig. 2 it can be seen that electro-oxidation of hypophosphite on freshly electropolished copper started at potentials slightly below -0.6V . This was manifested by the appearance of anodic current loops in the solutions containing NaH_2PO_2 . In solutions without NaH_2PO_2 , the current was cathodic in this potential region. The electro-oxidation current was diminished when the solution was aerated or when air-formed film was present on the copper surface. In order to grow the oxide film, electropolished specimens were kept in air for two weeks. Figure 3 shows that the anodic current loop on copper with an air-formed oxide appeared at more negative potentials than on freshly electropolished copper. On freshly electroplated copper a significant difference was observed

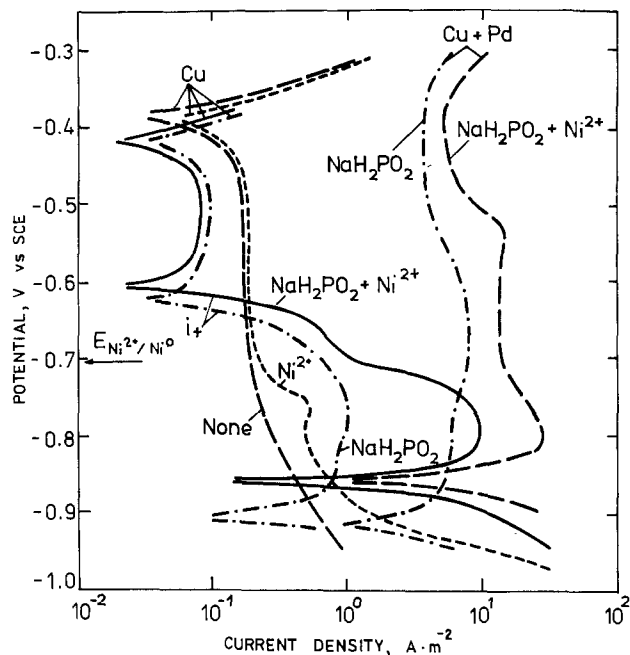


Fig. 2. Voltammograms on freshly electropolished copper and palladium-activated copper (activation in $0.2\text{ g/l PdCl}_2 + 0.2\text{ ml/l HCl}$ for 5s) in the supporting solution with and without other components (cf. Table I), starting at -0.3V . Below the discontinuities in the curves the current is cathodic, except where the anodic current is denoted by i_+ .

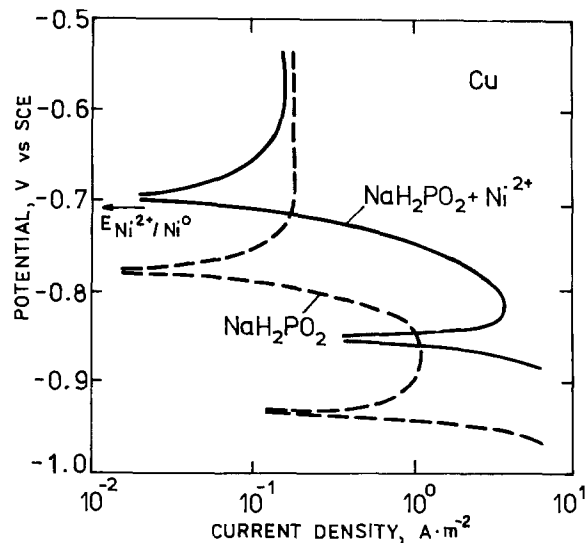


Fig. 3. Voltammograms on electropolished copper, stored in laboratory air for two weeks.

between anodic current loops in the NaH_2PO_2 containing solution with and without Ni^{2+} ions, when potentials were below about -0.7V (Fig. 2). The anodic current in the solution without Ni^{2+} ions decreased, whereas in the solution with Ni^{2+} ions it increased markedly at potentials below -0.7V . From the curve in the solution with added Ni^{2+} ions alone it can be concluded that the reduction of Ni^{2+} ions began at about -0.7V .

The marked increase in the electro-oxidation current in the plating solution below -0.7V can thus be associated with electrolytic deposition of nickel on the copper substrate. It may also be noted that electro-oxidation on copper with an air-formed oxide (Fig. 3) started at approximately the same potential as the deposition of nickel, and may be related to the nickel deposition.

An increase in the electro-oxidation current below the potential of electrolytic deposition of nickel was also apparent for the palladium-activated copper (Fig. 2), and for gold (Fig. 4). Electro-oxidation of hypophosphite on these substrates took place in the entire potential range from -0.3V through the mixed potentials. At potentials below -0.7V , the anodic current decreased in the solution without Ni^{2+} ions, and in the solution with Ni^{2+} ions it increased with a maximum at approximately -0.8V .

Voltammograms on platinum (Fig. 5) in the supporting solution and in the solution with NaH_2PO_2 were similar, indicating that hypophosphite did not undergo electro-oxidation on this substrate in the potential range examined. However, an anodic current was observed as a deflection in the cathodic current curve below -0.8V in the solution with NaH_2PO_2 and Ni^{2+} ions (plating solution). The deflection started at a potential at which there also appeared a deflection of a cathodic curve in the supporting solutions with Ni^{2+} ions. The latter deflection showed a decrease in the hydrogen-evolution current caused by deposition of nickel on platinum. This potential is designated as $E_{\text{Ni}^{2+}/\text{Ni}^0}$. Evidently, electro-oxidation of hypophosphite occurred on a layer of nickel, electrolytically deposited on platinum during the potential scan.

The Tafel slopes for the cathodic curves of hydrogen evolution in the supporting solution were about 250, 120, and 60 mV/decade on copper, gold, and platinum, respectively.

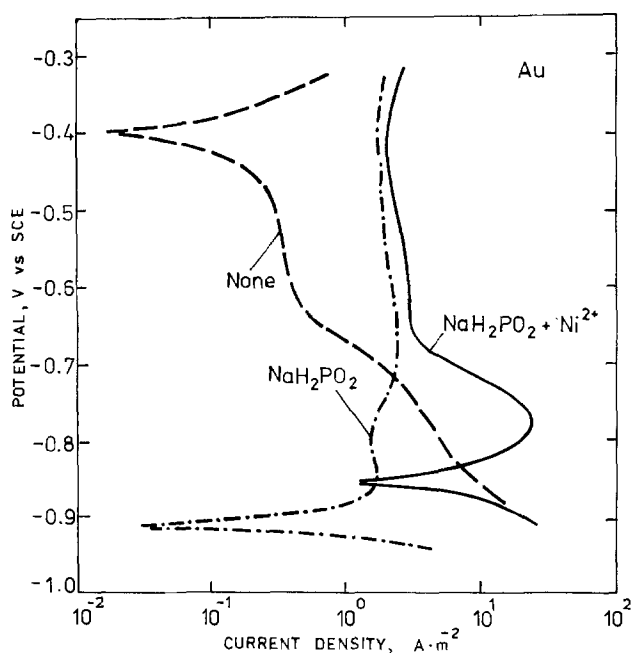


Fig. 4. Voltammograms on gold in the supporting solution as a function of solution additives, starting at -0.3V .

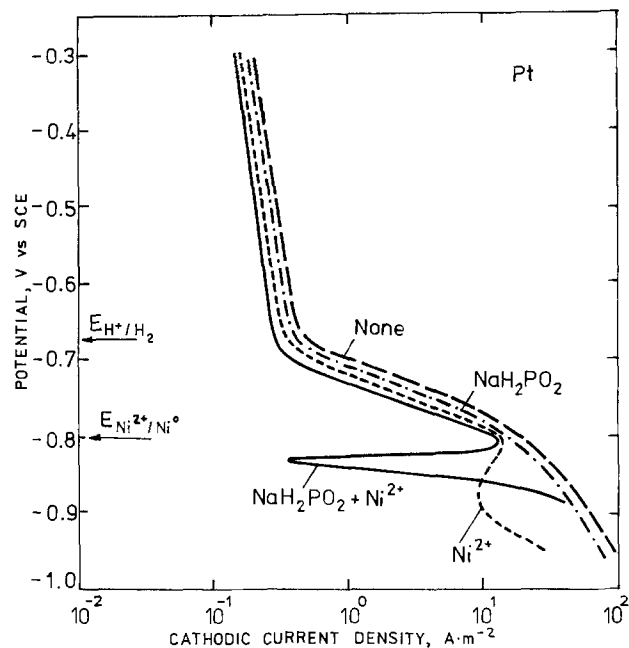


Fig. 5. Voltammograms on platinum in the supporting solution as a function of solution additives, starting at -0.3V .

Discontinuities in the voltammograms correspond to rest potentials. They indicate that in Fig. 1, the rest potential of copper (-0.45V) was at its corrosion potential, and that of platinum (-0.65V) corresponded to the potential of the hydrogen electrode. The plateau potential of -0.87V observed in the plating solution was a mixed potential for electroless nickel plating. In the absence of Ni^{2+} ions, the mixed potential was -0.92V .

The voltammograms shown in Fig. 2 and 4 suggest that electrolytic deposition of nickel on copper and gold started at around -0.7V . In order to determine the deposition of nickel at specific potentials, plating was performed on copper under potentiostatic conditions. Average deposition rates were evaluated from weight gains after potentiostatic polarization in the plating solution for periods ranging from 15 min to 2h. Results are given in Fig. 6. The deposition was already discernible at -0.725V , and increased with decreasing potential, attaining a Tafel-type dependence with a slope of 90 mV/decade below -0.78V . These results provide evidence that deposition of nickel on copper started at least at -0.725V , or about 0.15V more positive than the plateau potential of electroless nickel plating (Fig. 1).

TEM, SEM, and EDAX examination.—An electron micrograph of a copper foil after activation in a PdCl_2/HCl solution is shown in Fig. 7. The elongated black patches and smaller gray dots are deposits of palladium. The micrograph shows that the copper substrate surface contains islands of palladium rather than uniform coverage. Nevertheless, it was highly active for electro-oxidation of hypophosphite and for nickel plating (Fig. 2).

In order to examine the palladium islands in more detail, separate droplets of the activating solution of 1 g/l PdCl_2 + 1 ml/l HCl were placed on a copper surface and allowed to dry. Figure 8 shows an SEM micrograph of the copper surface, with two circular spots formed by droplets of the activating solution. A part of one of the spots is shown at higher magnification in Fig. 9. The irregular black features are sites of localized dissolution of copper (pits), around which enhanced deposition of palladium occurred (light diffuse features). The small white islands ($\sim 0.2\ \mu\text{m}$ diam) are palladium.

These features indicate that there were areas on the activated copper surface, such as the pits or regions

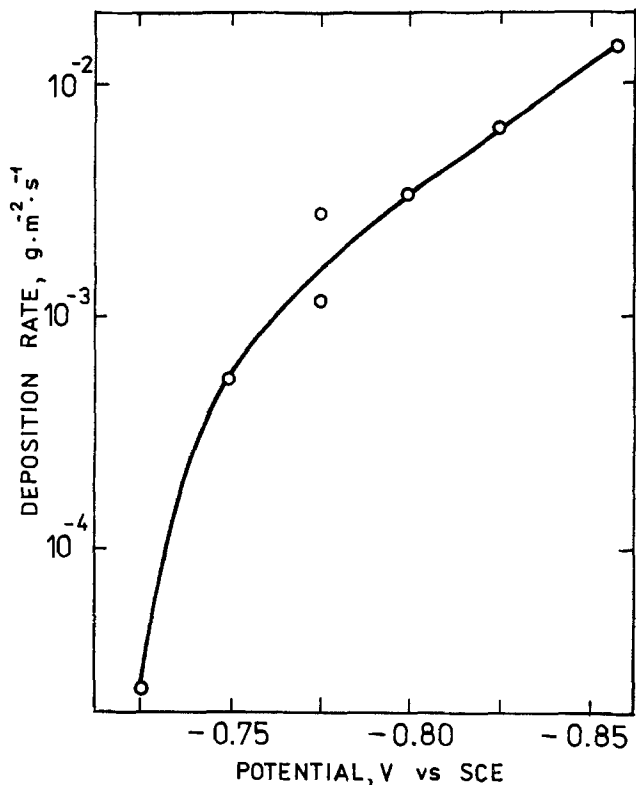


Fig. 6. Potential dependence of the rate of nickel deposition on copper in the plating solution. The slope of the linear portion is 90 mV/decade.

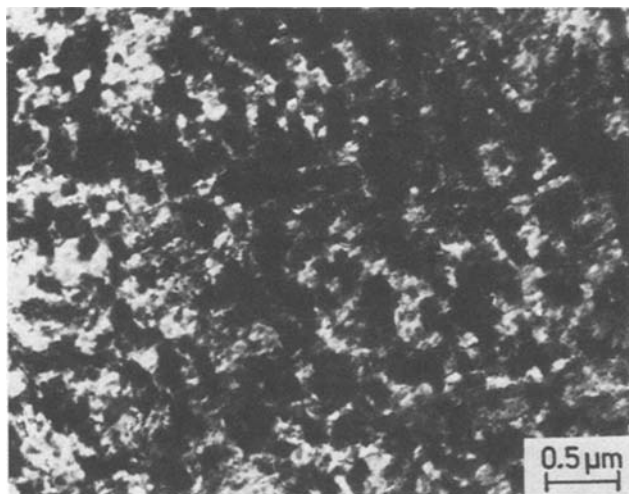


Fig. 7. Electron micrograph of a copper foil after immersion into a solution of 0.2 g/l PdCl₂ + 0.2 ml/l HCl for 5s. The black patches are deposits of palladium.

between the islands, which remained free of palladium. Nickel plating on these areas would be expected to occur differently from plating on the deposited palladium.

Specimens containing palladium deposits were partly masked with lacquer and exposed to the plating solution. The time of plating was measured from the moment when the open-circuit potential attained a value of -0.80V, and varied from 1 to 12s.

Figure 10 shows the interface between palladium containing and palladium-free surfaces, after plating for 3s. The small black dots on the palladium-deposited surface are corrosion pits in copper; and the dark patches on the palladium-free surface are discontinuities in the nickel deposit. The discontinuities are characteristic of early stages of nickel plating. They

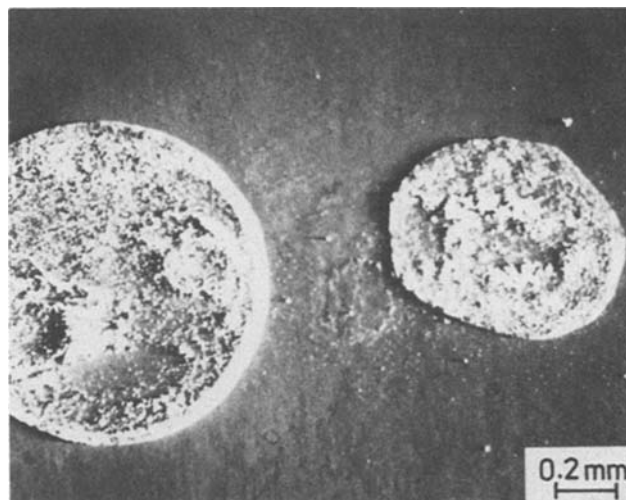


Fig. 8. SEM micrograph of a copper substrate with palladium containing circular spots, formed by droplets of an activating solution of 1g/l PdCl₂ + ml/l HCl.

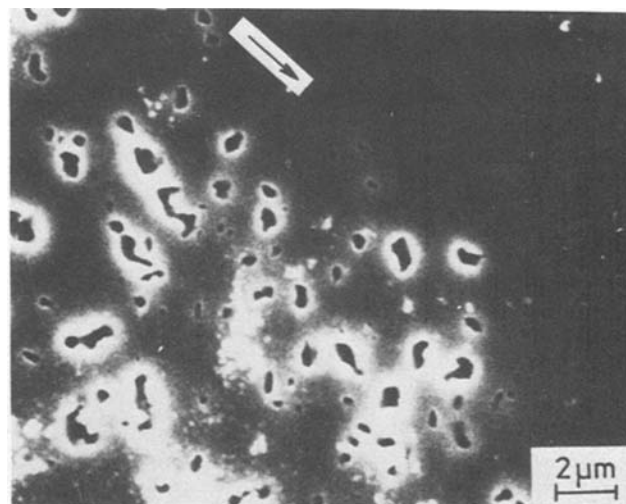


Fig. 9. SEM micrograph of the copper substrate as in Fig. 8, showing the palladium containing spot (below arrow) at higher magnification. The irregular black sites are corrosion pits, while the diffuse lighter regions around them are deposits of palladium.

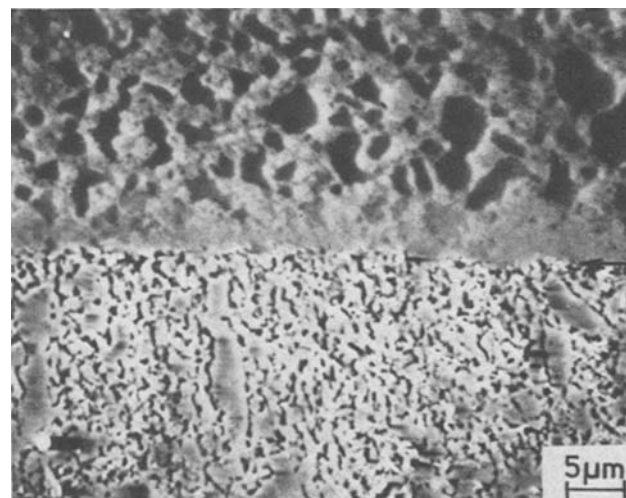


Fig. 10. SEM micrograph of nickel deposits on copper substrate with palladium (below arrow) and without palladium (above arrow), after electroless plating for 3s. Note the nonuniformity of the deposit on the copper substrate without palladium.

also occurred on the palladium-deposited surfaces when the plating time was shorter (1s). As the nickel deposits became thicker, the discontinuities disappeared.

The difference in the appearance of nickel deposits on the areas with and without palladium indicates that the rate of deposit on the copper surface was slower than that on the palladium surface, or, alternatively, that the initiation of nickel deposition is delayed on copper relative to palladium. This implies independent nucleation of the deposits on each of the surfaces. An enhanced deposition of nickel on the copper surface occurred only in the regions adjacent to palladium, suggesting a short-range effect of the palladium.

The independent nucleation on the two substrates was observed to be independent of plating time. SEM micrographs of partially masked specimens plated for 6 and 12s are shown in Fig. 11 and 12, respectively.

The independence of the nickel deposition on copper and palladium was also shown by the EDAX examinations. The EDAX spectra from copper substrates with and without palladium, after plating for various times, are shown in Fig. 13. It can be seen that the nickel peak on the spectrum from copper with palladium appeared earlier and was larger than the nickel peak from copper alone. This indicates that the rate of

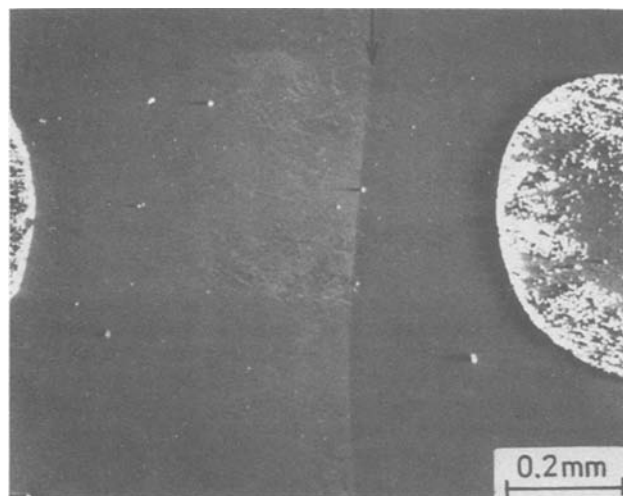


Fig. 11. SEM micrograph of a copper substrate with palladium containing spots, after plating of an unmasked area (left from arrow) for 6s.

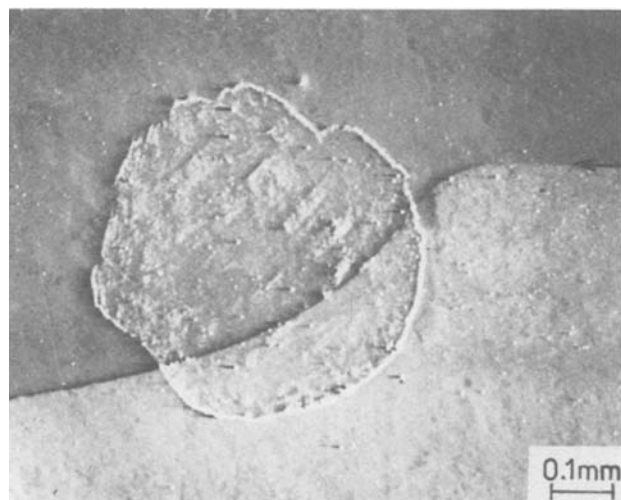


Fig. 12. SEM micrograph of a copper substrate with a palladium containing spot, after plating of an unmasked area (below arrow) for 12s.

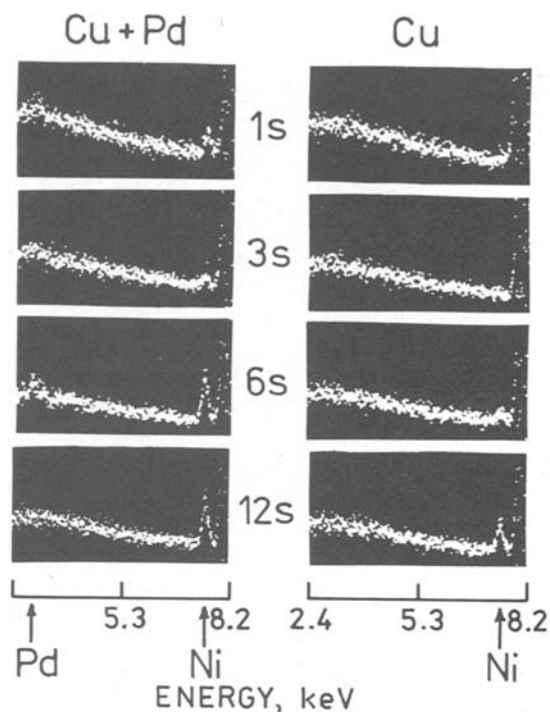


Fig. 13. EDAX spectra from a copper substrate with and without palladium, after electroless plating for 1, 3, 6 and 12s. Arrows indicate x-ray energy peaks of palladium ($\text{Pd } L_{\alpha 1} = 2.383 \text{ keV}$) and nickel ($\text{Ni } K_{\alpha 1} = 7.477 \text{ keV}$).

nickel deposition on palladium was greater than on copper alone. After plating for 12s, the nickel peak on copper with palladium was about 1.6 times higher than the peak on copper alone. From the data shown in Fig. 6, it follows that the deposition rate at an open-circuit potential of -0.86V was about $15 \text{ mg} \cdot \text{m}^{-2} \cdot \text{s}^{-1}$. Assuming the density of deposits to be approximately 7.85 kg/l (8), the deposit on copper after a 12s plating would be expected to be about 23 nm thick (65 lattice parameters of nickel), and the deposit on copper with palladium to be about 37 nm thick (105 lattice parameters). It should be noted that the effect of the palladium on the deposition process was still observed after this thickness of nickel deposit accumulated.

Discussion

This work agrees with earlier results (1-3), which showed that gold and palladium-activated copper exert high catalytic activity for electroless nickel plating, while copper alone and platinum are not active under open-circuit conditions. Voltammetric measurements have shown that electro-oxidation of hypophosphite occurs on gold and palladium-activated copper at their open-circuit potentials, and that on copper it occurs only at more negative potentials. On platinum it does not occur unless nickel is electrolytically deposited on this substrate.

It is apparent that the catalytic activity of the substrates cannot be directly related to their electronic structure, in particular, to the filling of d electron shells. In electrocatalysis, it is essential that reacting species first adsorb on the catalytic surface before any charge transfer takes place. It has been suggested that in the electro-oxidation of hypophosphite the reacting species are hypophosphite anions (1-3). Adsorption of these ions on an electrode surface takes place by displacement of other species such as oxides, adsorbed water molecules, or organic compounds.

Presumably, platinum lacks catalytic activity for electroless plating as a result of chemisorption of non-reacting species, which prevents adsorption of hypophosphite anions. The presence of a strongly adsorbed species on platinum is suggested by the high value of

the Tafel slope in the solutions used (~ 60 mV/decade, see Fig. 5). This value is twice as large as the Tafel slope observed on platinum in acid media [32 mV/decade at 50°C (9)]. A large value of the Tafel slope for hydrogen evolution also was observed on copper electrodes. In the supporting solution the slope was measured as 250 mV/decade (Fig. 2); in acid media it is 128 mV/decade at 50°C (9). Nevertheless, the lack of catalytic activity at noble potentials can be associated with the presence of surface oxides rather than adsorbed organic species. The significance of oxide films in diminishing the catalytic activity of copper is apparent from Fig. 2 and 3.

The catalytic activity of the substrates is effective only during the initiation period. This activity is altered as soon as nickel deposits begin to form. The voltammetric measurements have shown that on copper, palladium-activated copper, and gold, the catalytic activity increased markedly at a potential of approximately -0.7V , when nickel started to deposit. Apparently, at this potential nickel was deposited electrolytically without the participation of hypophosphite and accordingly was free of phosphorus. In practice, the phosphorus-free nickel will be expected to electrolytically deposit during the spontaneous potential shift, before the subsequent electroless deposition of phosphorus containing layers. The nickel thus deposited induces subsequent electro-oxidation of hypophosphite on platinum substrates (Fig. 5), and also considerably increases the electro-oxidation current on all other substrates (Fig. 2 and 4). The increase of the electro-oxidation current on copper and gold results primarily from the higher activity of nickel itself. However, it is also possible that small amounts of nickel act synergistically with the substrates. A synergistic action has been suggested previously in the systems of molybdenum with palladium and of palladium with nickel (4). Synergism seems to be also plausible for substrates of copper or gold with nickel. This suggestion for the copper-nickel system can be supported by the observation of Lelental (5), who showed that the catalytic activity of nickel with copper was higher than that of pure copper.

The occurrence of a synergistic effect appears to be ever more probable for the palladium-nickel system. The high catalytic activity of palladium is further increased at the start of nickel deposition at about -0.7V , as seen for the palladium-activated copper in Fig. 2. Also, electroless nickel deposition on the palladium spots occurred more rapidly than that on the copper substrate (Fig. 10 and 13), and continued to be more rapid for a significant period, even when the palladium could be expected to be almost entirely covered with the nickel deposit.

Under open-circuit conditions copper did not initiate electroless plating, because its corrosion potential ($\sim -0.45\text{V}$) was more noble than the potential region of catalytic activity (below -0.6V). In order to activate copper, the electrode potential must be shifted below at least -0.6V . It is suggested that the activation of copper by isolated patches or spots of palladium is accomplished solely by the potential shift resulting from electro-oxidation of hypophosphite on the palladium patches or spots.

At potentials active to $\sim -0.6\text{V}$, the copper substrate becomes active, and below about -0.7V it is additionally activated by electrolytically deposited nickel. Electro-oxidation of hypophosphite and electroless plating on the copper substrate thus proceed independently of the palladium patches or spots.

The activation of the copper by palladium spots is limited to the initiation period. This is demonstrated by the independent growth of the nickel deposits on copper and the palladium spots (Fig. 10 and 13), and by the lack of any radial spreading of nickel deposits growing on the palladium spots.

Initial deposits of palladium and nickel on copper differed in appearance from those on molybdenum (4). On copper the palladium deposits were irregular and diffuse (Fig. 7), while on molybdenum they were circular and sharply defined. Nickel deposits on molybdenum had elongated discontinuities, while on copper they were free of such discontinuities. It was also observed that adhesion of electroless nickel to copper was stronger than to molybdenum. The difference in the appearance and adhesion of the deposits on copper and molybdenum is largely associated with the absence or presence of surface oxides. The potential-pH diagrams of these metals in water (10) indicate that, at the pH and potentials prevailing during electroless plating, the copper substrates should be free of oxides, but that the molybdenum substrates may be covered with MoO_2 .

Conclusions

Potential scans from -0.3 to -0.92V vs. SCE indicated that electro-oxidation of hypophosphite in an ammoniacal solution occurred on gold and on palladium-activated copper over the entire potential range, while on copper it occurred only below -0.6V . In the presence of air-formed oxides, the electro-oxidation on copper started at more negative potentials. Platinum was not catalytically active in the potential range examined; however, electro-oxidation of hypophosphite on this substrate occurred after nickel had been electrolytically deposited during the potential scan.

Small amounts of electrolytically deposited nickel strongly enhanced the electro-oxidation current of hypophosphite on copper, gold, and palladium. This can be associated with the high catalytic activity of freshly deposited nickel and/or with a synergistic effect of small amounts of nickel on the catalytic properties of the other metals.

Activation of copper by immersion into a PdCl_2/HCl solution resulted in the formation of separate palladium patches on the copper substrate. In the plating solution, the nickel deposition on copper with individual palladium spots took place on the palladium spots and on copper independently of each other, the deposition on the palladium spots being considerably faster than that on copper.

It is concluded that the activation of the copper surface surrounding separate palladium spots occurs solely through a spontaneous potential shift due to the electro-oxidation of hypophosphite on the palladium spots. No radial spreading of nickel deposits growing on the palladium spots was observed.

Acknowledgments

The authors wish to express thanks to Michael R. Lambert for his helpful consultation on the TEM, SEM, and EDAX investigation. The work was supported by IBM Corporation.

Manuscript submitted Feb. 22, 1983; revised manuscript received Aug. 1, 1983.

Rensselaer Polytechnic Institute assisted in meeting the publication costs of this article.

REFERENCES

1. A. Brenner and G. E. Riddel, *J. Res. Nat. Bur. Stand.*, **37**, 31 (1946); *ibid.*, **39**, 385 (1947).
2. G. Gutzeit, *Plating*, **68**, 1158, 1275, 1377 (1959); **69**, 63 (1960).
3. G. G. Gavrilov, "Chemical (Electroless) Nickel Plating," Portcullis Press, Redhill (1979).
4. J. Flis and D. J. Duquette, Submitted to *This Journal*.
5. M. Lelental, *ibid.*, **122**, 486 (1975).
6. D. G. McBride, *Plating*, **9**, 32, 358 (1972).
7. V. S. Epifanova, Yu. V. Prusov, and V. N. Flerov,

- Zashch. Met.*, **14**, 226 (1978).
8. "Symposium on Electroless Nickel Plating," ASTM Special Tech. Publ. no. 265, 29 (1959).
9. J. O'M. Bockris and Srinivasan, "Fuel Cells:

- Their Electrochemistry," p. 130, McGraw-Hill Book Co., New York (1969).
10. M. Pourbaix, "Atlas of Electrochemical Equilibria," Pergamon Press, London (1964).

Electrodeposition of Copper on Platinum (111) Surfaces Pretreated with Iodine.

Studies by LEED, Auger Spectroscopy, and Electrochemistry

John L. Stickney, Stephen D. Rosasco, and Arthur T. Hubbard

Department of Chemistry, University of California, Santa Barbara, California 93106

ABSTRACT

Studies by low energy electron diffraction (LEED) and Auger spectroscopy of copper electrodeposited on well-characterized platinum (111) surfaces from aqueous sodium perchlorate solutions are reported. Prior to electrodeposition, the platinum (111) surface was pretreated with I_2 vapor in ultrahigh vacuum to form a Pt(111) ($\sqrt{7} \times \sqrt{7}$) R19.1°-I superlattice, which protected the platinum surface and the surface of the electrodeposit from attack by the electrolyte and contamination by residual gases. The results were as follows: electrodeposition took place in two narrow, overlapping underpotential deposition linear scan voltammetric peaks followed by one conventional bulk copper deposition peak. Underpotential deposition produced an ordered layer. The first underpotential deposition peak formed a (3×3) superlattice in which the unit cell contained four iodine atoms and a comparable number of Cu atoms per nine surface Pt atoms ($\theta_{Cu} = \theta_I = 4/9$). At completion of the underpotential deposition process a (10×10) coincidence lattice was present in which $\theta_{Cu} = 8/9$ and $\theta_I = 4/9$. The iodine Auger signal was not appreciably affected by Cu deposition, indicating that the iodine atoms were present in the topmost layer of the surface at all Cu coverages.

Electrodeposition and electrocrystallization are the subject of numerous interesting studies (3). Surface structure of an electrodeposit at the atomic level is an aspect about which there is little information, however, since most work has dealt with conventional (i.e., structurally undefined) surfaces. In two previous articles we reported studies of electrodeposited silver on iodine-pretreated Pt(111) by LEED (1, 2) and quantitative Auger spectroscopy (2). Studies by LEED of the structures of a wide variety of surfaces in ultrahigh vacuum have revealed that structures resembling single-crystal planes are formed on the surface of a single crystal only under very special circumstances (4). Chemisorbed layer structure is likewise a sensitive function of many variables (4). Each stage of underpotential deposition is sensitive to surface structural characteristics, as evidenced directly by data in the previous articles (2, 3) and indirectly by results reviewed in (5) and (6). In particular, studies of deposition of copper on conventional Pt surfaces have been reported (6, 7). Vapor deposition of metals on well-characterized surfaces has been the subject of studies (8). Halogen chemisorption on well-defined surfaces is also beginning to receive attention (9-12). In the present article we report an exploration of the structure and composition of copper electrodeposited on well-characterized iodine-pretreated Pt(111) surfaces using LEED, Auger spectroscopy, and cyclic voltammetry. The purpose of pretreating the Pt(111) surface with iodine vapor (9) was to protect the Pt(111) substrate and the electrodeposited copper from side reactions with the electrolyte and residual gases (11).

Experimental

The instruments and procedures employed for these studies were described in previous articles (1, 9, 10, 13-15). The Pt(111) single-crystal electrode was oriented and polished so that all six faces were crystallographically equivalent. Before each use, the crystal was cleaned by Ar^+ ion bombardment and annealed by resistance heating, after which LEED and Auger spectroscopic characterization confirmed that an

ordered, atomically clean Pt(111) surface was present. After treatment with an I_2 vapor beam equivalent to 10^{-6} torr (9) for several minutes, the crystal was again characterized. The resulting Pt(111) ($\sqrt{7} \times \sqrt{7}$) R19.1°-I superlattice (9) was then valved off from the LEED chamber, brought to ambient pressure with argon, and the electrochemical cell was introduced. The cell was then rinsed and filled with electrolyte, the crystal immersed into the solution, and voltammetric current-potential scans run. Electrode potentials were measured with respect to a Cu/Cu^{2+} ($10^{-3}M$ in $1M$ $NaClO_4$) half-cell; however, for the sake of continuity, potentials are reported with respect to the $Ag/AgCl$ ($1M$ $NaCl$) reference, based upon direct comparative measurements involving the two half-cells. All apparatus contacting the solutions were constructed of Pyrex glass and Teflon, and thoroughly cleaned to remove surfactants. Solutions were prepared with water pyrolyzed with oxygen (16), distilled, and then saturated with pure nitrogen. Following completion of the electrolysis, the electrolyte was drained away, the crystal was rinsed with water, and the electrochemical cell was valved off from the crystal. After sorption and cryogenic pumping (5 min), the crystal was characterized once again by LEED and Auger spectroscopy. At the end of the procedure, copper was removed by electrolysis followed by brief ion bombardment. Each result was verified at least five times. These electrodeposition processes proved to be highly reproducible.

Results

Pt (111) and iodine.—The clean Pt (111) surface yielded the ideal (1×1) LEED pattern reported by other workers (17) (Fig. 1a) corresponding to the hexagonal (111) surface structure shown in Fig. 2a. Saturation of the surface produced the LEED pattern shown in Fig. 1b, corresponding to the Pt (111) ($\sqrt{7} \times \sqrt{7}$) R19.1°-I structure shown in Fig. 2b. This " $\sqrt{7}$ " surface, previously shown to be resistant to attack by a variety of solvents, surfactants, and electrolytes (1, 2, 11) was the starting point for the electrodeposition studies described in this article.

Auger spectra of the Pt (111) surface (Fig. 3a) contained only transitions assignable (18) to Pt, in agreement with previous work (19). Auger spectra of the Pt (111) ($\sqrt{7} \times \sqrt{7}$) R19.1°-I surface (Fig. 3b) contains a doublet due to iodine (507 and 518 eV) and Pt intensities decreased to 65% of the levels for clean Pt (111). Previously reported (1, 2, 9, 10) quantitative Auger (14) results were duplicated in this work; at maximum clarity of the $\sqrt{7}$ LEED pattern, the surface unit cell contained three iodine atoms per seven surface Pt atoms ($\theta_1 = 3/7 = 0.43$). Numerous replicate LEED patterns and Auger spectra were obtained for this superlattice. No evidence of beam damage or other artifacts was found. Auger data are summarized in Table I.

Immersion of the surface in aqueous solutions.—

Previous work has shown that the $\sqrt{7}$ superlattice is stable toward the argon atmosphere, aqueous perchlorate electrolytes, and evacuation (1, 2). No changes in Auger spectrum or LEED pattern were found after evacuation of the crystal following exposure to the argon atmosphere, or immersion into 1M aqueous perchlorate containing dilute Cu^{2+} (followed by rinsing with water). That is, aqueous $\text{HClO}_4/\text{NaClO}_4/\text{Cu}(\text{ClO}_4)_2$ mixtures did not react chemically with the $\sqrt{7}$ surface, and were removed by water, which evaporated without detectable residues. These tests illustrate the passivating influence (11) of iodine atoms chemisorbed on Pt (20). Without such pretreatment, platinum reacted with perchloric acid during emersion (removal) or evacuation with partial loss of surface order and formation of a deposit of chlorine and oxygen (13). Pretreatment of the surface with iodine was therefore helpful in maintaining the surface in a well-defined state for the purposes of the present experiments.

Electrodeposition of copper.—When immersed at open circuit into aqueous Cu^{+2} (10^{-3}M) in 1M HClO_4 ($\text{pH} = 3$), the $\sqrt{7}$ surface yielded the current-potential trace (21) shown in Fig. 4; the figure shows the first scan starting from the rest potential. This negative going initial scan consisted of two narrow (10 mV full width at half of maximum) underpotential deposition peaks very close together (0.252 and 0.244V vs. Ag/AgCl), and a wave for deposition of bulk copper with a half-wave potential of about -0.03V . A wave rather than a peak resulted from the use of a very slow scan rate (0.28 mV/s) combined with slight vibration of the crystal. The heights and areas of the first two peaks were independent of Cu^{2+} concentration above about 10^{-4}M and were directly proportional to scan rate, as expected for underpotential deposition (5, 6). The third peak was proportional to Cu^{2+} concentration and displayed the morphology of a process controlled by

the diffusion of Cu^{2+} . When the direction of potential scan was reversed, the corresponding dissolution peaks were observed. Noticeable differences in morphology between negative and positive going scans indicate that these processes involve small but not negligible activation energy. As can be seen from Fig. 4, the deposition trace contains barely perceptible shoulders on the two prominent underpotential peaks. When a second cycle was recorded, minor changes in morphology occurred, particularly the disappearance of the small shoulders. Otherwise the traces were constant. Appearance or disappearance of those small shoulders correlated with the presence or absence of a slight excess of iodine above that required to form the $\sqrt{7}$ superlattice. When Cu^{2+} was omitted from the solution, the voltammetric current was negligible (less than 1% of the corresponding peak height). This lack of background current further illustrates the passivating effect of iodine pretreatment (20, 22), and incidentally testifies to the purity of the reagents and the structural regularity of the substrate.

Electronic integration of the electrolysis current as a function of time yielded the coulometric data in Table I, in which Q represents the charge ($\mu\text{C}/\text{cm}^2$) to deposit copper, starting from the initial potential (typically 0.365V) and scanning to the specified potential at which the electrode was emersed from the solution. The electrolytic charge to return to 0.365V (via the positive going dissolution scan) corresponded very closely to that for the deposition scans in the potential range from 0.365 to -0.10V . Packing density of copper was calculated by means of the Faraday law

$$Q - Q_b = nFA\Gamma_{\text{Cu}} \quad [1]$$

where A is the geometric area of the single-crystal electrode (0.7723 cm^2), Γ_{Cu} is the packing density expressed in mols/ cm^2 , and n is the number of electrons to reduce the Cu^{2+} ion. The magnitude of n was assumed to be two in this system, since Auger spectra did not indicate the presence of counterions (Fig. 3c) necessarily present if the adsorbed copper atoms were partially charged. Also, this n value is consistent with structures indicated by the LEED patterns, as described below. A similar situation was reported in a previous work (2). Dividing Γ_{Cu} by the packing density of Pt atoms in the Pt (111) plane converts the results into more familiar units

$$\theta_{\text{Cu}} = \Gamma_{\text{Cu}} / (2.490 \times 10^{-9}) \quad [2]$$

Based upon coulometric data, the two underpotential deposition peaks taken together (from the starting point of the scan, 0.365V, to completion of the peaks at 0.200) resulted in deposition of $\theta_{\text{Cu}} = 0.84$, which is noticeably less than a full monolayer. It is not possible

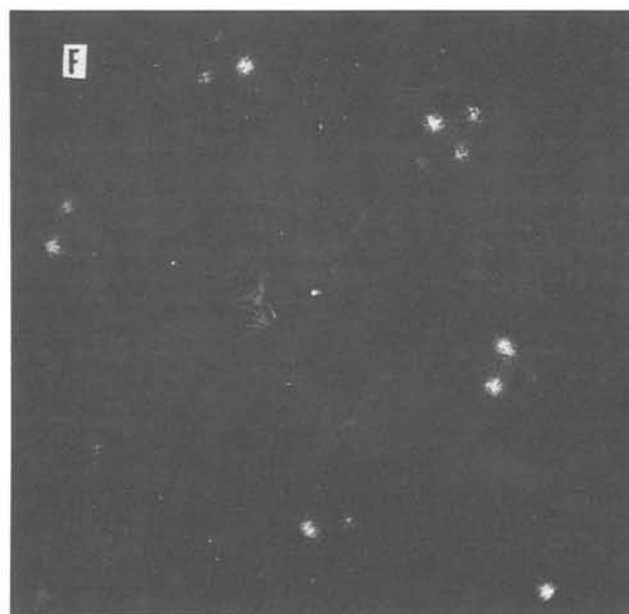
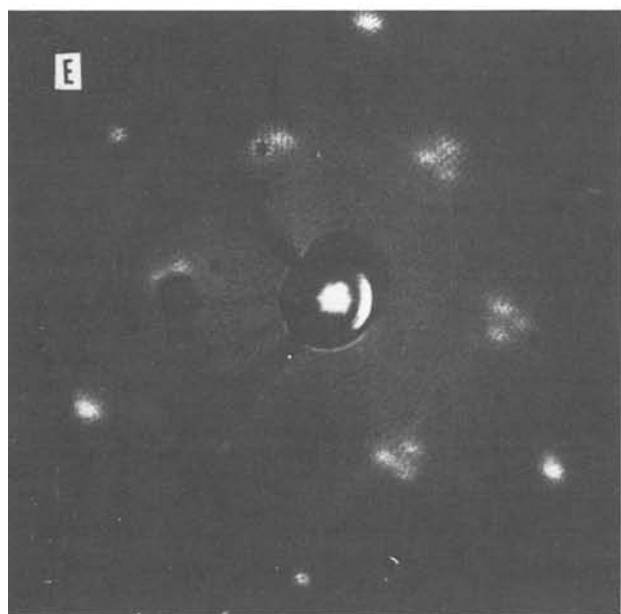
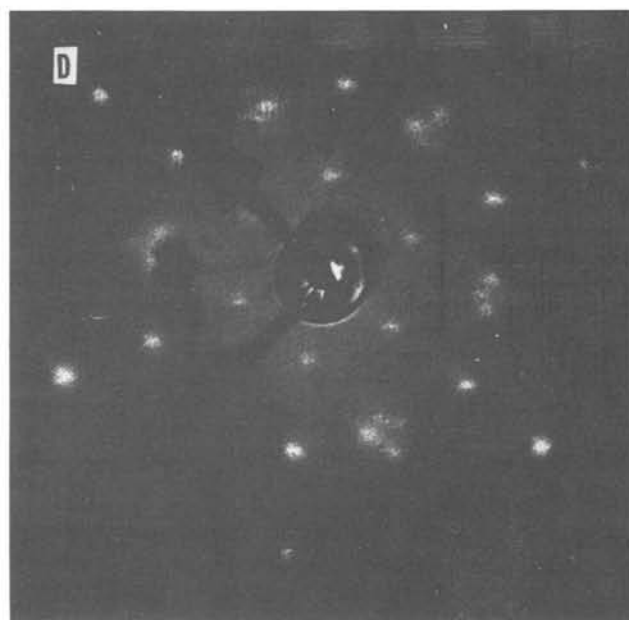
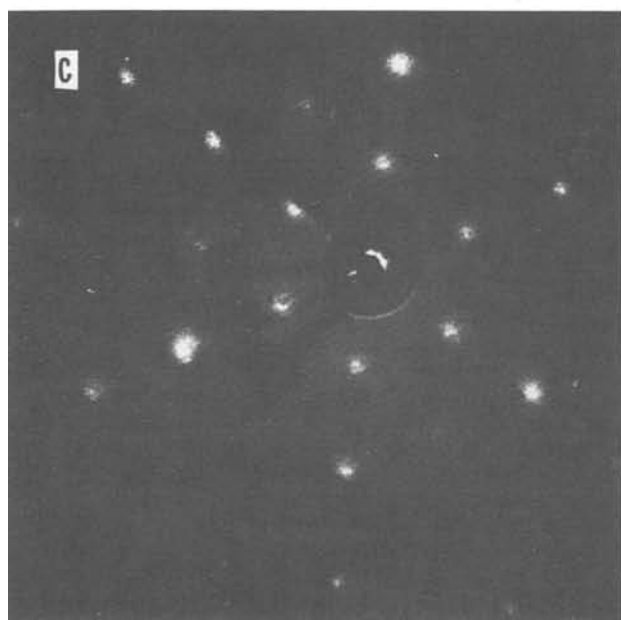
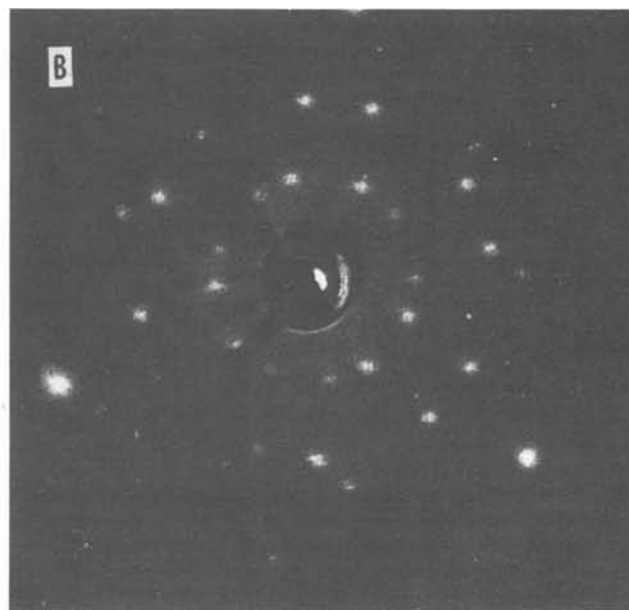
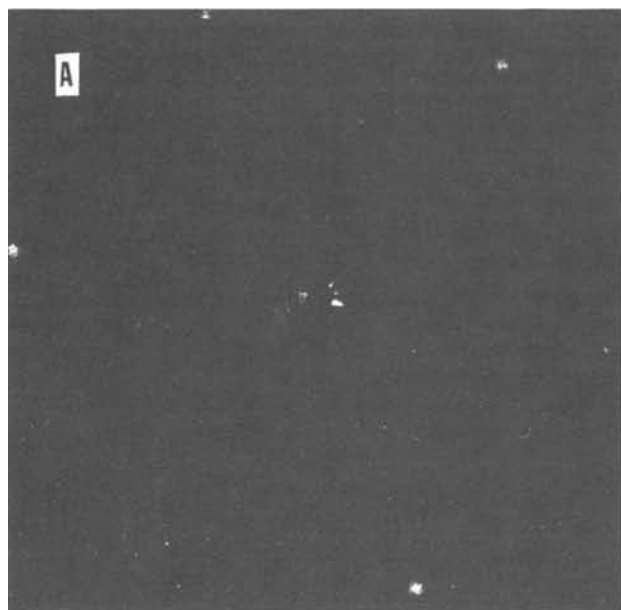
Table I. Electrochemical, Auger and LEED data for electrodeposited copper

Surface treatment	Voltammetry ¹			Auger spectroscopy ¹		LEED pattern
	Emersion potential, V	$(Q - Q_b)/A$, ² $\mu\text{C}/\text{cm}^2$	θ_{Cu} , from Eq. [1], [2]	Relative iodine Auger signal	Relative platinum Auger signal, 160 eV	
I_2 vapor ³	—	—	—	1.00	0.66	$(\sqrt{7} \times \sqrt{7})\text{R19.1}^\circ$
Atop UPD peak 1	0.252	118	0.250	1.00	0.63	(3×3)
Between UPD peaks	0.248	177	0.370	1.00	0.54	$(3 \times 3) +$
Atop UPD peak 2	0.244	253	0.530	0.91	0.47	(10×10)
After UPD peak 2	0.200	403	0.840	0.90	0.31	$(3 \times 3) +$
After UPD on ion-bombarded surface	0.150	425	0.886	—	—	(10×10)
After UPD on pre-electrolyzed surface	0.150	514	1.070	—	—	Diffuse

¹ Experimental conditions for Auger spectroscopy, as in Fig. 3; for voltammetry, as in Fig. 4.

² After pretreatment with I_2 vapor, the iodine Auger current was 1.06 nA, corresponding to an iodine atom packing density (θ_1) of 0.45.

³ Background charge densities, Q_b/A , were as follows: 31 $\mu\text{C}/\text{cm}^2$ at 0.252V; 32 at 0.248; 34 at 0.244; 45 at 0.200; 91 at 0.150 (I.B.), and 91 at 0.150 (pre-electrolyzed).



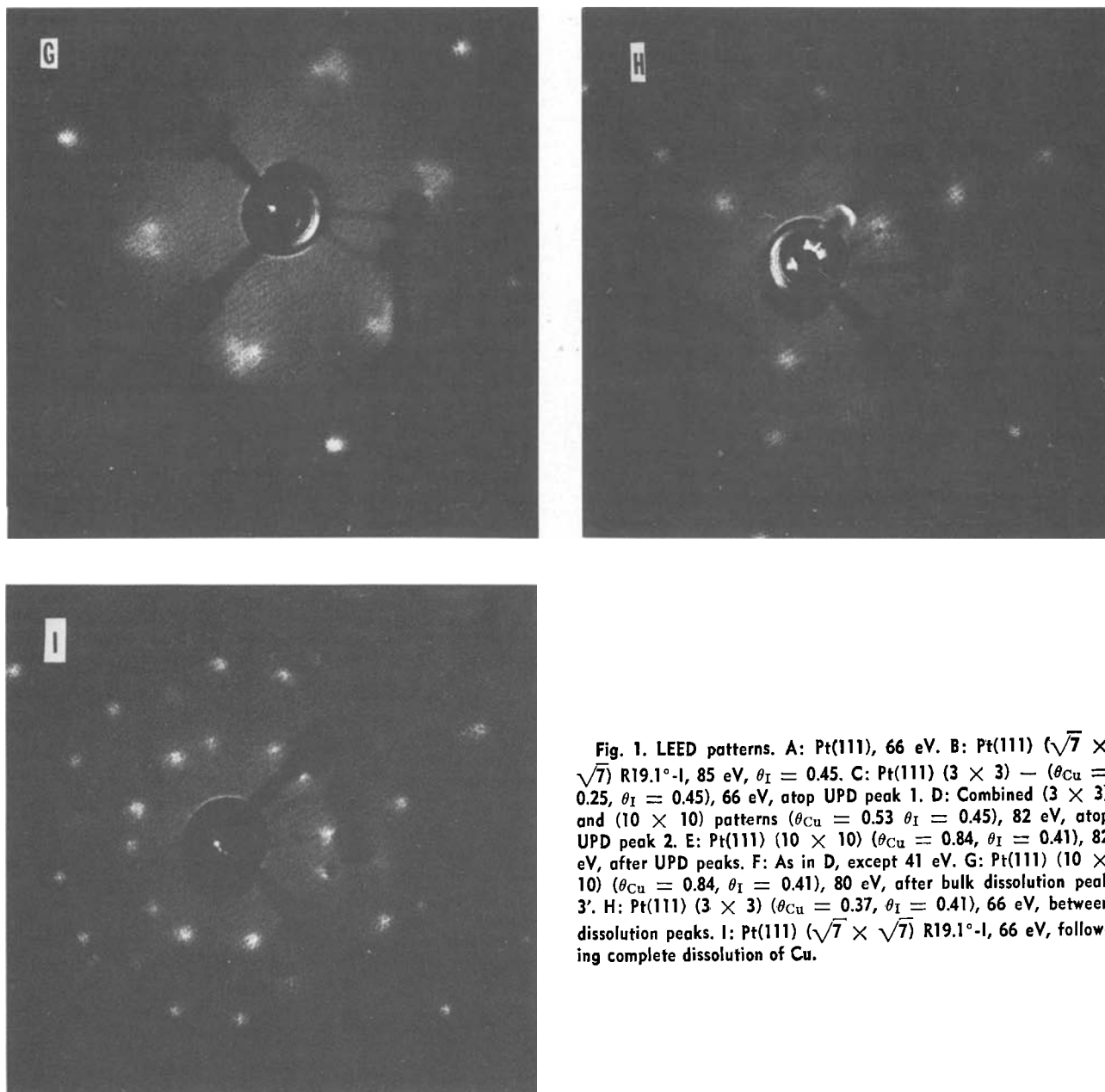


Fig. 1. LEED patterns. A: Pt(111), 66 eV. B: Pt(111) ($\sqrt{7} \times \sqrt{7}$) R19.1°-I, 85 eV, $\theta_I = 0.45$. C: Pt(111) (3×3) — ($\theta_{Cu} = 0.25$, $\theta_I = 0.45$), 66 eV, atop UPD peak 1. D: Combined (3×3) and (10×10) patterns ($\theta_{Cu} = 0.53$, $\theta_I = 0.45$), 82 eV, atop UPD peak 2. E: Pt(111) (10×10) ($\theta_{Cu} = 0.84$, $\theta_I = 0.41$), 82 eV, after UPD peaks. F: As in D, except 41 eV. G: Pt(111) (10×10) ($\theta_{Cu} = 0.84$, $\theta_I = 0.41$), 80 eV, after bulk dissolution peak 3'. H: Pt(111) (3×3) ($\theta_{Cu} = 0.37$, $\theta_I = 0.41$), 66 eV, between dissolution peaks. I: Pt(111) ($\sqrt{7} \times \sqrt{7}$) R19.1°-I, 66 eV, following complete dissolution of Cu.

to separate the areas of the two peaks without making assumptions regarding their morphologies.

Auger spectra of electrodeposited copper.—Auger spectra observed following electrodeposition of Cu onto the $\sqrt{7}$ surface are typified by Fig. 3c, obtained on completion of the first underpotential deposition peak. Only peaks due to I, Pt, and Cu are present in the spectra. A striking feature of the spectra is that the iodine Auger signal, seen as a doublet at 507 and 518 eV, was influenced only slightly by deposition of Cu; while the Pt signals steadily vanished as the Pt was covered over with Cu. Clearly, iodine always constituted the outermost surface layer. Each new Cu layer was apparently located beneath the iodine layer. Multiple cycles of Cu deposition and dissolution spanning periods of 1h or more did not lead to removal of iodine, even though the solution contained no dissolved iodine. Removal of iodine occurred only when the surface was strongly anodized. Potentials greater than 1.0V were required (20). This dissolution process gave rise to a prominent positive peak at 1.0V (2)



Of the Auger signals attributed to Cu (18), only the

peak at 920 eV was resolvable from signals due to Pt (Fig. 3c). The signal-to-noise characteristics of the Cu peaks were judged insufficient for quantitation in the present experiments.

LEED patterns of electrodeposited copper.—LEED patterns, obtained for deposition of amounts of Cu on the $\sqrt{7}$ surface corresponding to emersion at various points along the voltammetric curve, are shown schematically in Fig. 4. Photographs of the LEED patterns appear in Fig. 1. Sharply defined LEED patterns were present at all stages of Cu deposition or dissolution. Accordingly, the structure of the surface was readily monitored. Stability of the electrode potential of the system is illustrated by the observation that for deposition of copper, emersion, rinsing with distilled water at open circuit, examination by LEED and Auger, and immersion back into Cu^{2+} solution at open circuit, the rest potential was found to be close to the initial emersion potential. Subsequent voltammetry showed no changes from the behavior represented by Fig. 4, indicating the absence of any reconstruction during rinsing, LEED examinations, etc.

Simple immersion and emersion at 0.365V without appreciable electrodeposition conserved the $\sqrt{7}$ LEED

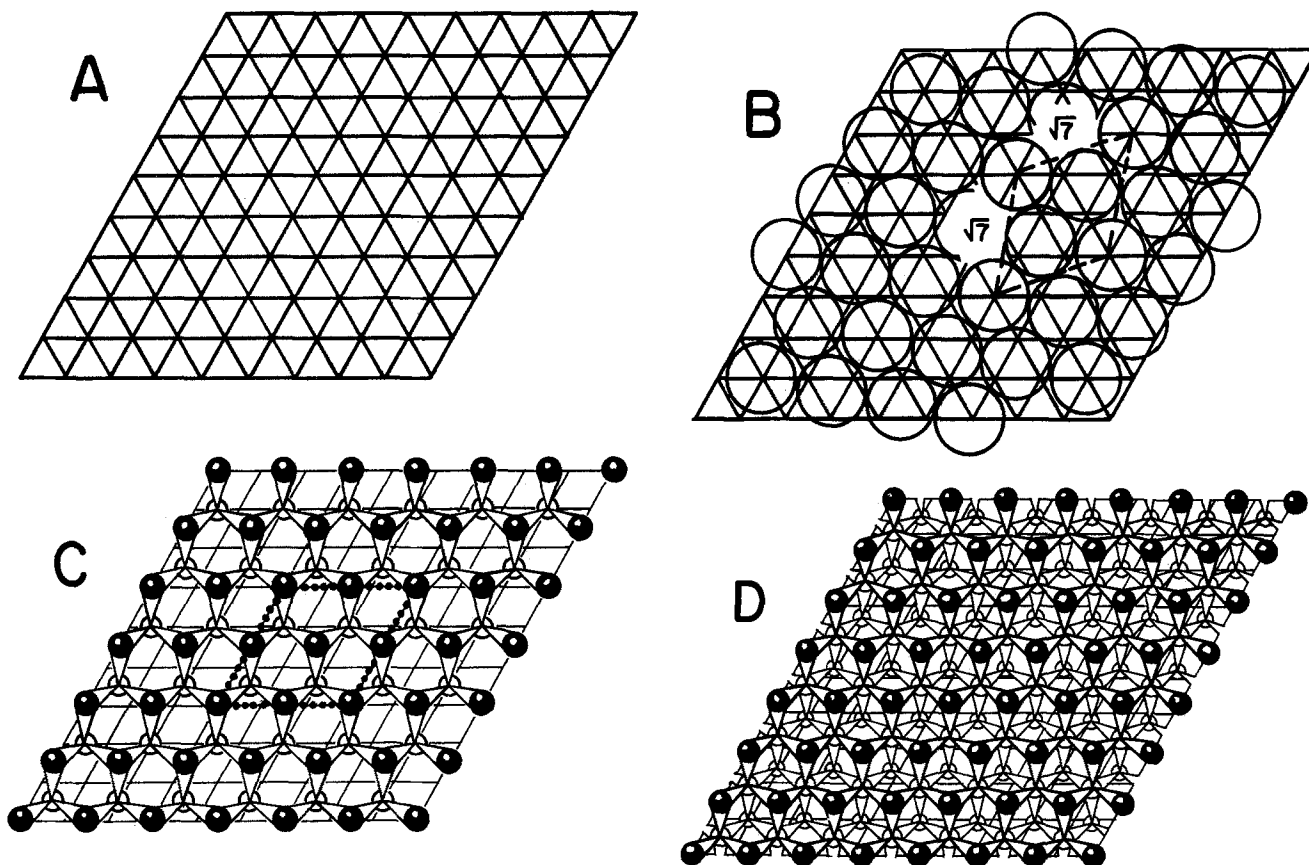


Fig. 2. Surface structures. A: Pt(111) (1×1) clean surface structure; Pt surface atoms are located at points of intersection of the grid. B: Pt(111) ($\sqrt{7} \times \sqrt{7}$) $R19.1^\circ$ -1 superlattice; circles represent van der Waals radii of I atoms. C: Pt(111) (3×3) ($\theta_{Cu} = \theta_I = 4/9$); CuI(111) layer forming a (3×3) coincidence lattice with Pt(111); solid circles represent I atoms; open circles, Cu atoms. D: Pt(111) (10×10) ($\theta_{Cu} = 8/9$, $\theta_I = 4/9$).

pattern unchanged from that prior to immersion. At the top of the first underpotential peak, the LEED pattern was (3×3) (Fig. 1c, 0.252V, $\theta_{Cu} = 0.25$). LEED observations made at several points along the first peak revealed that the $\sqrt{7}$ pattern faded and the (3×3) beams brightened as deposition proceeded. Beginning near the midpoint between the underpotential peaks, the (3×3) pattern began transforming into the (10×10) pattern, as shown at two different beam energies in Fig. 1e and 1f, in which spots forming rhombic groups of four spots located near the integral-index, and ($\pm 1/3$, $\pm 2/3$) and equivalent positions displayed the greatest intensity. Beam intensity varied sharply with energy as usual. As a result not all of the beams were visible at any given energy. At completion of the UPD peaks, the Cu coverage was $\theta_{Cu} = 0.84$.

When the direction of potential scan was reversed, dissolution of the Cu deposits occurred (peaks 1', 2', and 3' of Fig. 4). LEED patterns obtained at various stages during dissolution appear in Fig. 1g through 1i. As can be seen, these patterns were equivalent to those observed at the same Cu coverages during deposition. Complete dissolution of Cu occurred, producing the $\sqrt{7}$ pattern (Fig. 1i) equivalent to that observed prior to deposition (Fig. 1b). Oxidative dissolution of adsorbed iodine atoms and oxidation of the Pt surface commenced at about 0.95V, as usual (20), and produced a disordered oxygenous layer.

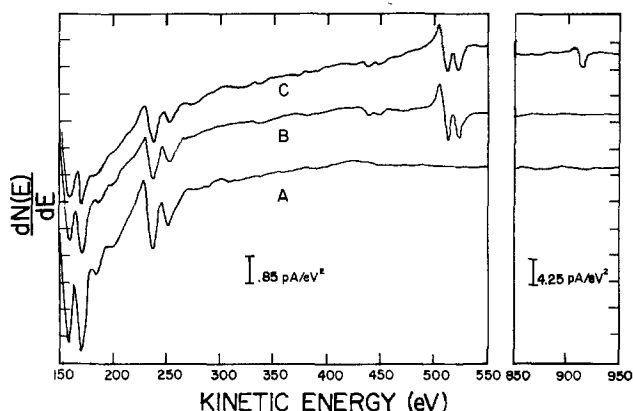


Fig. 3. Auger spectra. A: Clean surface, Pt(111). B: Pt(111) ($\sqrt{7} \times \sqrt{7}$) $R19.1^\circ$ -1 (spectrum was the same after immersion in 1M HClO₄). C: Between UPD peaks 1 and 2.

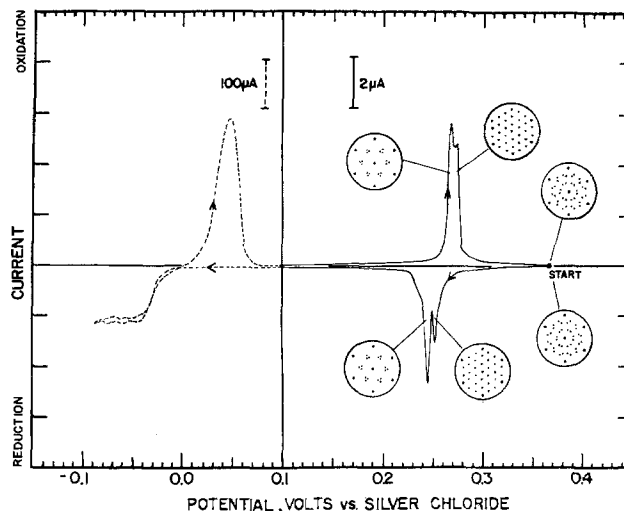


Fig. 4. Cyclic current-potential curve for deposition of Cu at the Pt(111) ($\sqrt{7} \times \sqrt{7}$) $R19.1^\circ$ -1 surface. Experimental conditions: 10^{-3} M Cu²⁺ in 1M NaClO₄. Scan rate, 0.28 mV/s.

Effect of surface disorder on electrodeposition.—Pt (111) surfaces which had been subjected to ion-bombardment or electrochemical oxidation and reduction were subjected to electrodeposition under conditions identical to those described above for the $\sqrt{7}$ superlattice.

Ion-bombardment of the Pt (111) surface for a few minutes (500 eV Ar⁺ ions, 5.6 μ A/cm²) caused the LEED pattern to become diffuse, as usual. Subsequent treatment with I₂ vapor produced a disordered adsorbed layer having an iodine Auger signal about 20% weaker than for the $\sqrt{7}$ superlattice.

One cycle of electrolytic oxidation and reduction of the $\sqrt{7}$ surface (a scan at 10 mV/s from 0.2 to 1.2 to 0.0 and back to 0.2V vs. AgCl, in 1M HClO₄ electrolyte saturated with iodine) produced a diffuse LEED pattern and an iodine Auger signal which was a few percent weaker than for the $\sqrt{7}$ superlattice.

A comparison of the behavior of surfaces thus prepared toward voltammetric electrodeposition of Cu is provided in Fig. 5, where the first sweep is shown in each case. As can be seen, one effect of the disorder introduced either by ion-bombardment or by electrolytic redox was to degrade the sharply defined voltammetric peaks into a broad hump having no distinguishable fine structure. LEED patterns for Cu electrodeposited on the disordered surfaces were diffuse. A 10 mV shift of the underpotential deposition process toward less positive potentials was found for the disordered surfaces. The amount of Cu electrodeposited at underpotential increased somewhat because of the disorder; the increase was most noticeable (27%) for the electrolyzed surface.

Discussion

LEED patterns obtained for amounts of deposited Cu present at numerous points along the cyclic current-potential curves were sharply defined, demonstrating that underpotential deposition of Cu on Pt (111) ($\sqrt{7} \times \sqrt{7}$) R19.1°-I is an ordered process at all stages. This rule is illustrated by the LEED photograph in Fig. 1d, which was obtained midway through

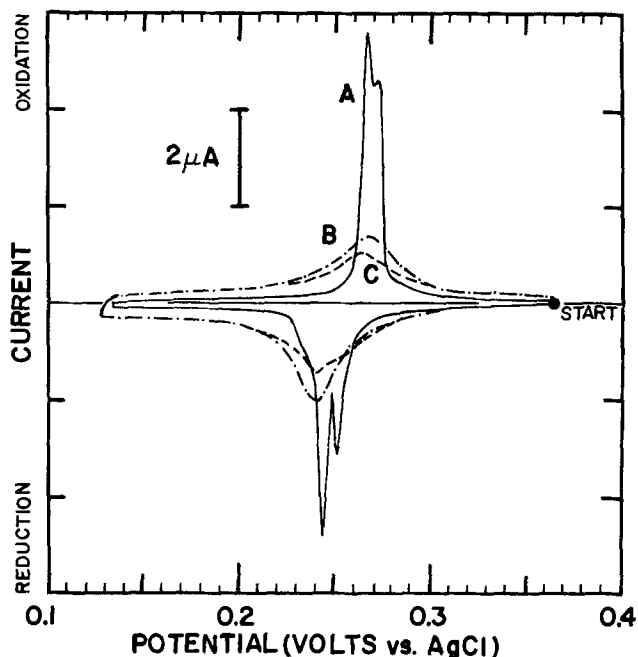


Fig. 5. Electrodeposition of Cu at the $\sqrt{7}$ superlattice and surfaces disordered by ion-bombardment or electrolytic cycling. A: — Pt(111) ($\sqrt{7} \times \sqrt{7}$)R19.1°-I surface. B: - - - ion bombarded, then saturated with I₂ vapor. C: ···· electrolytically cycled, then saturated with aqueous I₂. Experimental conditions as in Fig. 4.

the underpotential deposition process; spots of the (3 × 3) and (10 × 10) patterns are present. That is, each new structure formed on a portion of the surface, leaving the remainder of the surface unchanged until the entire surface was converted to the new structure. Similar results were found for Ag on the $\sqrt{7}$ surface (1, 2).

It can be seen from the data in Table I, that the first stage of Cu underpotential deposition (peak 1 of Fig. 4) forms a surface unit cell having (3 × 3) symmetry and containing four iodine atoms and a comparable number of Cu atoms per nine surface Pt atoms. Qualitative LEED does not define the locations of atoms in the interior of the unit cell, however. A model structure consistent with the results appears in Fig. 2c. In constructing this model, the Cu and I atoms were assigned to their relative positions parallel to the (111) plane in the cubic (zinc blende, also called sphalerite) structure of CuI (23). In the (111) direction of CuI, the Cu and I atoms form a hexagonal network with a Cu-I interatomic distance of 2.63Å. Superimposed on Pt (111), this hexagonal network would form the (3 × 3) lattice illustrated in Fig. 2c. The distance between Cu atoms is somewhat smaller in CuI (3.72Å) than in the (3 × 3) superlattice (4.16Å). A relaxation of that sort is attributable to differences in bonding of the bilayer in CuI relative to adsorption on Pt (111). Iodine was assigned to the upper plane and Cu to the lower plane in agreement with the constancy of Auger intensity for iodine. Placement of the CuI bilayer in relation to the Pt (111) net is arbitrary at this time. The qualitative significance of this model is that the spectacular stability and orderedness of the (3 × 3) structure appears to stem from its close relationship to the (111) plane of crystalline CuI.

Stable (3 × 3) structures have been reported for chemisorption systems involving HBr (24), Cl₂, and Br₂ (12a) on Pt (111), and Br₂ (12d) on Ag (111). A considerably less stable (3 × 3) structure was formed by treatment of the Pt (111) surface with I₂ vapor (12a) or an aqueous solution of I₂ (11). This lesser stability of the (3 × 3) structure in the absence of Cu is attributable to the lack of a simple bilayer structure such as CuI (111).

A related structure was postulated to explain the (3 × 3) LEED pattern for electrodeposited Ag on Pt (111)-I (2), in view of the observation that the Cu coverage ($\theta_{Cu} \leq 4/9$) is less than that for the corresponding Ag structure ($\theta_{Ag} = 5/9$). This surface structural difference finds a parallel in the structural differences which exist between solid AgI and CuI. For instance, AgI adopts hexagonal (wurzite) and cubic (zinc blende) structures, while CuI exhibits only the zinc blende structure (23).

Upon completion of the underpotential peaks ($\theta_{Cu} = 0.84$) and continuing into deposition of bulk Cu, the LEED pattern contained fractional-index beams at some of the positions characteristic of Pt (111) (10 × 10) symmetry (Fig. 1d-g). The brightest of these fractional-index beams were present as rhombic groups located near the ($\pm 1/3$, $\pm 2/3$) and equivalent positions, as well as near the integral-index beams. This same LEED pattern was observed for Cu (111) after saturation with Cl₂ vapor (12d); that is, electrodeposition of Cu on a halogen pretreated Pt (111) surface produced the same LEED pattern as halogen adsorption on a Cu (111) single-crystal surface. The rhombuses of 1/10-index spots are parallel to the larger rhombuses defined by the (1 × 1) unit mesh. Accordingly, the fractional-index mesh is not rotated and therefore the R30° aspect of the ($6\sqrt{3} \times 6\sqrt{3}$) R30° structure proposed in Ref. (12d) cannot be correct, although $6\sqrt{3} = 10.39$ is close to the observed unit mesh size of (10 × 10). Accordingly, this is a (10 × 10) pattern with systematic absences. A model structure consistent with these observations is shown in Fig.

2d. This structure is derived from the previous one (Fig. 2c) by adding one Cu atom at each unoccupied center of the large equilateral triangles formed by the previously deposited Cu atoms, and compressing the resulting superlattice slightly along the furrows of the Pt (111) surface. The resulting structure preserves the original CuI (111) bilayer structure, while forming an octahedral environment around the Cu atoms in the bilayer, adding a second layer of Cu atoms. Pairs of Cu atoms are separated by distances of approximately $\sqrt{3}$ and $\sqrt{3}/2$ in the $R30^\circ$ direction, but achieve exactly (10×10) registry with the Pt (111) substrate. Slight compression of the lattice is understandable in terms of increased rigidity of the superlattice when another layer of Cu atoms is added to the original CuI bilayer. In keeping with the experiment, the structure of this (10×10) superlattice would not permit deposition of further Cu without bond breaking, disruption of the structure, or other difficult steps. Similar LEED patterns have been reported for Kr on the basal plane of graphite by Chinn and Fain (25), and for I on Ag (111) and Au (111) by Farrell *et al.* (12), and for Cl on Ni (111) by Erley and Wagner (26). For each of these latter systems, a $(\sqrt{3} \times \sqrt{3}) R30^\circ$ LEED pattern appeared (12) at a halogen packing density of $\theta = 1/3$, followed by the complete (10×10) or related pattern at higher packing densities. In agreement with these observations, the (10×10) structure in Fig. 2d is closely related to the intermediate (3×3) structure (Fig. 2c) and also to the preceding intermediate state consisting of halogen atoms chemisorbed on the (111) plane (Fig. 2b). Formation of this structure would require only small adjustments in atomic coordinates and does not appear to involve any difficult stages.

Dissolution of Cu preserved the LEED patterns observed with the corresponding coverage along the deposition scans. Removal of Cu was apparently quantitative, since the familiar $(\sqrt{7} \times \sqrt{7}) R19.1^\circ$ LEED pattern (Fig. 1b) reappeared (Fig. 1i) following the final dissolution peak (1' of Fig. 4). Clearly, the deposition and dissolution processes approached structural reversibility under the conditions of these experiments.

Comparison of LEED data for vapor-deposited metals (8) with patterns observed for electrodeposited Ag (1, 2) and Cu reveals some interesting differences. Vapor deposits tend to give complex LEED patterns resembling coincidence lattices, and in many cases are disordered until annealed, whereas the electrodeposits reported here were formed in an ordered state at room temperature. A clear analogy exists between I, which preserves surface order and cleanliness in the deposition of Ag and Cu on Pt, and As which promotes epitaxy in vapor deposition of Ge on GaAs (27). The $(\sqrt{7} \times \sqrt{7}) R19.1^\circ$ LEED pattern observed for I_2 (9, 12a) and HI (10) on Pt (111) has been reported also for Na on Ag (111) and Bi on Cu (111) (8b).

Acknowledgments

Acknowledgment is made to the National Science Foundation, the Air Force Office of Scientific Research, and the Donors of the Petroleum Research Fund administered by the American Chemical Society for support of this research.

Manuscript submitted March 28, 1983; revised manuscript received Sept. 2, 1983.

The University of California assisted in meeting the publication costs of this article.

REFERENCES

1. A. T. Hubbard, J. L. Stickney, S. D. Rosasco, M. P. Soriaga, and D. Song, *J. Electroanal. Chem.*, **150**, 165 (1983).
2. J. L. Stickney, S. D. Rosasco, D. Song, M. P. Soriaga, and A. T. Hubbard, *Surf. Sci.*, **130**, 326 (1983).
3. (a) E. Budevski, *Electrochem. Metallorum*, **1**, 131 (1966); (b) J. H. deBoer, Editor, "Reactivity of Solids," Elsevier, New York (1961); (c) R. H. Doremus, Editor, "Growth and Perfection of Crystals," John Wiley and Sons, New York (1958); (d) M. Fleischmann and H. R. Thirsk, in "Advances in Electrochemistry and Electrochemical Engineering," P. Delahay, Editor, Interscience, New York (1963); (e) A. N. Frumkin, *This Journal*, **107**, 461 (1960); (f) H. C. Gatos, Editor, "Symposium on Surface Chemistry of Metals and Semiconductors," John Wiley and Sons, New York (1960); (g) J. J. Gilman, Editor, "The Art and Science of Growing Crystals," John Wiley and Sons, New York (1963); (h) T. P. Hoar, in "Modern Aspects of Electrochemistry," J. O'M. Bockris, Editor, Vol. 2, p. 262, Butterworths, London (1959); (i) N. Pangarov, *J. Electroanal. Chem.*, **9**, 70 (1965); (j) R. Piontelli, G. Poli, and G. Seravello, in "Transactions of the Symposium on Electrode Processes," E. Yeager, Editor, pp. 67-107, John Wiley and Sons, New York (1961); (k) R. Piontelli, *Electrochem. Metallorum*, **1**, 5 (1966); (l) D. R. Turner, "The Surface Chemistry of Metals and Semiconductors," John Wiley and Sons, New York (1960); (m) G. Wranglen, *Electrochim. Acta*, **2**, 130 (1966).
4. (a) E. Bauer, in "Techniques of Metals Research," R. F. Bunshah, Editor, Vol. 2, p. 559, Wiley-Interscience, New York (1969); (b) C. B. Duke, *Adv. Chem. Phys.*, **27**, 1 (1974); (c) P. J. Estrup, in "Characterization of Metal and Polymer Surfaces," Vol. 1, L. H. Lee, Editor, p. 187, Academic Press, New York (1977); (d) T. W. Haas, G. J. Dooley, III, J. T. Grant, A. G. Jackson, and M. P. Hooker, *Prog. Surf. Sci.*, **1**, 155 (1971); (e) A. Ignatiev, *Am. Lab.*, **5**, 12 (1972); (f) J. J. Lander, *Prog. Solid State Chem.*, **2**, 26 (1965); (g) J. W. May, *Ind. Eng. Chem.*, **57**, 19 (1965); *Adv. Catal.*, **21**, 151 (1970); (h) J. B. Pendry, "Low-Energy Electron Diffraction," Academic Press, London (1974); (i) E. N. Sickafus and H. P. Bonzel, *Prog. Surf. Membr. Sci.*, **4**, 115 (1971); (j) G. A. Somorjai, *Surf. Sci.*, **34**, 156 (1973); (k) G. A. Somorjai and H. H. Farrell, *Adv. Chem. Phys.*, **20**, 215 (1971); (l) G. A. Somorjai and L. L. Kesmodel, *MTP Int. Rev. Sci.*, **7**, 1 (1975); (m) J. A. Strozier, D. W. Jepsen, and F. Jona, in "Surface Physics of Materials," J. M. Blakely, Editor, Chap. 1, Academic Press, New York (1975); (n) M. A. Van Hove, *Surf. Sci.*, **80**, 1 (1979); (o) M. B. Webb and M. C. Legally, *Solid State Phys.*, **28**, 301 (1973).
5. (a) D. M. Kolb, M. Przanyski, and H. Gerischer, *J. Electroanal. Chem.*, **54**, 25 (1974); (b) E. Schmidt and H. R. Gygg, *ibid.*, **12**, 300 (1966); (c) K. Juttner and W. J. Lorenz, *Z. Phys. Chem.*, **122**, 163 (1980); (d) W. J. Lorenz, H. D. Herman, N. Wüthrich, and F. Hilbert, *This Journal*, **121**, 1167 (1974); (e) D. M. Kolb, in "Advances in Electrochemistry and Electrochemical Engineering," Vol. 11, H. Gerischer and C. W. Tobias, Editors, p. 125, John Wiley and Sons, New York (1978).
6. (a) R. Adzic, V. Jovancevic, and M. Podlavicky, *Electrochim. Acta*, **25**, 1143 (1980); (b) R. Adzic, *Inst. J. Chem.*, **18**, 166 (1979); (c) A. Bewick and B. Thomas, *J. Electroanal. Chem.*, **85**, 329 (1977); *ibid.*, **84**, 127 (1977); (d) A. Budnioc, *ibid.*, **123**, 365 (1981); (e) B. F. Conway and H. Angerstein-Kozłowska, *ibid.*, **113**, 63 (1980); in "Electrode Processes 1979," S. Bruckenstein, B. Miller, J. D. E. McIntyre, and E. Yeager, Editors, p. 271, The Electrochemical Society Softbound Proceedings Series, Princeton, NJ (1980); (f) K. Engelsmann, W. J. Lorenz, and E. Schmidt, *J. Electroanal. Chem.*, **114**, 1 (1980); *ibid.*, **114**, 11 (1980); (g) N. Furuya and S. Motoo, *ibid.*, **72**, 165 (1976); (h) W. Gorski and J. Lipkowski, *ibid.*, **133**, 253 (1982); (i) A. Hamelin and A. Katayama, *ibid.*, **117**, 221 (1981); (j) A. Hamelin, A. Katayama, G. Picq, and P. Vennereau, *ibid.*, **113**, 293 (1980); (k) J. A. Harrison and P. J. Stronach, *ibid.*, **72**, 239 (1976); (l) T. Hinoue, S. Okazaki, and T. Fujinaga, *ibid.*, **133**, 195 (1982); (m) R. Lacmann and J. Möller, *Electrochim. Acta*, **20**, 805 (1975); (n) W. Paatsch, *This Journal*, **124**, 1505 (1977);

- (o) R. Piontelli, *J. Chim. Phys.*, **46**, 288 (1949); (p) S. T. Rao and R. Weil, *This Journal*, **127**, 1030 (1980); (q) T. O. Sedgwick and J. E. Smith, Jr., *ibid.*, **123**, 254 (1976); (r) W. G. Sherwood, D. F. Untereker, and S. Bruckenstein, *ibid.*, **125**, 384 (1978); (s) W. G. Sherwood and S. Bruckenstein, *ibid.*, **125**, 1098 (1978); (t) S. Szabo and F. Nagy, *J. Electroanal. Chem.*, **70**, 357 (1976); (u) P. E. Untereker, W. G. Sherwood, and S. Bruckenstein, *This Journal*, **125**, 380 (1978); (v) V. A. Vicente and S. Bruckenstein, *J. Electroanal. Chem.*, **82**, 187 (1977); (w) Z. Yoshida and S. Kihara, *ibid.*, **86**, 167 (1978).
7. (a) B. J. Bowles, *Electrochim. Acta*, **15**, 589 (1970); (b) M. W. Breiter, *This Journal*, **114**, 1125 (1967); *ibid.*, **115**, 2197 (1968); (c) S. Bruckenstein and D. T. Napp, *J. Am. Chem. Soc.*, **90**, 6303 (1968); (d) S. H. Cadle and S. Bruckenstein, *Anal. Chem.*, **43**, 932, 1858 (1971); (e) D. M. Kolb and R. Kötzt, *Surf. Sci.*, **64**, 698 (1977); (f) D. M. Kolb, R. Kötzt, and K. Yamamoto, *ibid.*, **87**, 20 (1979); (g) D. T. Napp, D. C. Johnson, and S. Bruckenstein, *Anal. Chem.*, **39**, 481 (1967); (h) C. L. Scottichini and C. N. Reilley, *J. Electroanal. Chem.*, **139**, 233, 247, 265 (1982); (i) G. W. Tindall and S. Bruckenstein, *Anal. Chem.*, **40**, 1051, 1637 (1968); *ibid.*, **41**, 2119 (1969).
8. (a) J. P. Biberian and G. A. Somorjai, *J. Vac. Sci. Technol.*, **16**, 2073 (1979); (b) G. E. Rhead, *ibid.*, **13**, 603 (1976); F. Delamare and G. E. Rhead, *Surf. Sci.*, **35**, 185 (1973); (c) E. Bauer, *ibid.*, **7**, 351 (1967); E. Bauer and H. Poppa, *Thin Solid Films*, **12**, 167 (1972); E. Bauer, H. Poppa, G. Todd, and P. R. Davis, *J. Appl. Phys.*, **48**, 3773 (1977); *ibid.*, **45**, 5164 (1974); (d) P. J. Goddard, J. West, and R. M. Lambert, *Surf. Sci.*, **71**, 447 (1978); P. J. Goddard and R. M. Lambert, *ibid.*, **107**, 519 (1981); (e) W. Hoesler and W. Moritz, *ibid.*, **117**, 196 (1982); (f) W. Schlenk and E. Bauer, *ibid.*, **93**, 9 (1980); (g) M. Hanbucken and H. Neddermeyer, *ibid.*, **114**, 563 (1982); (h) K. Takayanagi, D. M. Kolb, K. Kambe, and G. Lehmpfuhl, *ibid.*, **100**, 407 (1980); (i) L. G. Feinstein, E. Blanc, and D. Dufayard, *ibid.*, **19**, 269 (1970); (j) C. Argile and G. E. Rhead, *ibid.*, **53**, 659 (1975); (k) R. A. Armstrong, *ibid.*, **50**, 615 (1975); (l) C. Binns and C. Norris, *ibid.*, **116**, 338 (1982); (m) J. M. Charig and D. K. Skinner, *ibid.*, **19**, 283 (1970); (n) E. Gillet and B. Gruzza, *ibid.*, **97**, 553 (1980); (o) D. C. Jackson, T. E. Gallon, and A. Chambers, *ibid.*, **36**, 381 (1973); (p) T. Koshikawa and R. Shimizu, *Jpn. J. Appl. Phys., Suppl. 2, Pt. 2*, 637 (1974); (q) P. W. Palmberg and T. N. Rhodin, *J. Appl. Phys.*, **39**, 2425 (1968); (r) R. K. Quinn, M. L. Knotek, and N. R. Armstrong, *This Journal*, **123**, 1794 (1976); (s) A. Sepulveda and G. E. Rhead, *Surf. Sci.*, **66**, 436 (1977); (t) M. Sunjic, D. Sokcevic, and J. W. Gadzuk, *Jpn. J. Appl. Phys., Suppl. 2, Pt. 2*, 753 (1974); (u) H. Tokutaka, K. Nishmori, and K. Takashima, *Surf. Sci.*, **86**, 54 (1979).
9. T. E. Felter and A. T. Hubbard, *J. Electroanal. Chem.*, **100**, 473 (1979).
10. G. A. Garwood, Jr. and A. T. Hubbard, *Surf. Sci.*, **92**, 617 (1981).
11. J. Y. Katekaru, J. F. Hershberger, G. A. Garwood, Jr., and A. T. Hubbard, *ibid.*, **121**, 396 (1982).
12. (a) H. H. Farrell, *ibid.*, **100**, 613 (1980); H. H. Farrell, M. M. Traum, N. V. Smith, W. A. Royer, D. P. Woodruff, and P. D. Johnson, *ibid.*, **102**, 527 (1981); S. A. Cochran and H. H. Farrell, *ibid.*, **95**, 359 (1980); (b) P. D. Johnson, *ibid.*, **102**, 527 (1981); (c) W. Erley, *ibid.*, **94**, 281 (1980); (d) P. J. Goddard, K. Schwaha, and R. M. Lambert, *ibid.*, **71**, 351 (1978); P. J. Goddard and R. M. Lambert, *ibid.*, **67**, 180 (1970); (e) F. Forstmann, W. Berndt, and P. Büttner, *Phys. Rev. Lett.*, **30**, 17 (1973); (f) W. Berndt, *Jpn. J. Appl. Phys., Suppl. 2, Pt. 2*, 653 (1974); (g) G. Rovida and F. Pratesi, *Surf. Sci.*, **51**, 270 (1975); G. Rovida, F. Pratesi, and E. Ferroni, *J. Catal.*, **41**, 140 (1976); G. Rovida, F. Pratesi, M. Maglietta, and E. Ferroni, *Jpn. J. Appl. Phys., Suppl. 2, Pt. 2*, 117 (1974); (h) E. Zanazzi, F. Jona, D. W. Jepson, and P. M. Marcus, *Phys. Rev. B*, **14**, 432 (1976); (i) N. R. Avery, *Surf. Sci.*, **43**, 101 (1974); (j) D. G. Fedak, J. V. Florio, and W. D. Robertson, in "The Structure and Chemistry of Solid Surfaces," G. A. Somorjai, Editor, John Wiley and Sons, New York (1969); (k) E. Bestel, K. Schwaha, and F. P. Netzer, *Surf. Sci.*, **83**, 439 (1979); (l) G. G. Price, K. J. Rawlings, and B. J. Hopkins, *ibid.*, **95**, 245 (1980); *ibid.*, **85**, 379 (1979); (m) R. G. Jones and D. L. Perry, *ibid.*, **88**, 331 (1979); P. A. Dowben and R. G. Jones, *ibid.*, **84**, 449 (1979); *ibid.*, **88**, 348 (1979); (n) D. L. Fehrs and R. E. Stickney, *ibid.*, **17**, 298 (1969); (o) C. W. Jowett and B. J. Hopkins, *ibid.*, **22**, 392 (1970); (p) K. Faulian and E. Bauer, *ibid.*, **70**, 271 (1978); (q) J. D. McKinley, *J. Chem. Phys.*, **40**, 120 (1964); (r) P. H. Citrin, P. Eisenberger, and R. C. Hewitt, *Phys. Rev. Lett.*, **41**, 309 (1978); P. H. Citrin, P. Eisenberger, and R. C. Hewitt, *J. Vac. Sci. Technol.*, **15**, 449 (1978); (s) J. D. Head, K. A. R. Mitchell, and L. Noodleman, *Surf. Sci.*, **61**, 661 (1976); (t) R. A. Marrow and R. M. Lambert, *ibid.*, **71**, 107 (1978).
13. R. M. Ishikawa and A. T. Hubbard, *J. Electroanal. Chem.*, **69**, 317 (1976); R. M. Ishikawa, J. Y. Katekaru, and A. T. Hubbard, *ibid.*, **86**, 271 (1978).
14. J. A. Schoeffel and A. T. Hubbard, *Anal. Chem.*, **49**, 2330 (1977).
15. A. T. Hubbard, *Acc. Chem. Res.*, **13**, 177 (1980); *J. Vac. Sci. Technol.*, **17**, 49 (1980).
16. B. E. Conway, H. Angerstein-Kozłowska, and W. B. A. Sharp, *Anal. Chem.*, **45**, 1331 (1973).
17. A. E. Morgan and G. A. Somorjai, *J. Chem. Phys.*, **51**, 3309 (1969); C. W. Tucker, Jr., *Surf. Sci.*, **2**, 516 (1964); *Appl. Phys. Lett.*, **3**, 98 (1963); *J. Appl. Phys.*, **35**, 1897 (1964); J. M. Charlot and R. Deleight, *C. R.*, **259**, 2977 (1964); G. A. Somorjai, P. C. Stair, T. J. Kaminska, and L. L. Kesmodel, *Phys. Rev. B*, **11**, 623 (1975).
18. W. A. Coghlan and R. E. Clausing, *At. Data*, **5**, 317 (1973).
19. D. L. Fehrs and R. E. Stickney, *Surf. Sci.*, **17**, 298 (1969); C. W. Jowett and B. J. Hopkins, *ibid.*, **22**, 392 (1970); K. Faulian and E. Bauer, *ibid.*, **70**, 271 (1978); N. J. Taylor, *Rev. Sci. Instrum.*, **40**, 792 (1969).
20. R. F. Lane and A. T. Hubbard, *J. Phys. Chem.*, **79**, 808 (1975).
21. P. Delahay, "New Instrumental Methods in Electrochemistry," p. 115, Interscience, New York (1954).
22. A. T. Hubbard, R. A. Osteryoung, and F. C. Anson, *Anal. Chem.*, **38**, 692 (1966).
23. L. C. Pauling, "The Nature of the Chemical Bond," 3rd ed., p. 244, Cornell University Press, Ithaca, NY (1960).
24. G. A. Garwood, Jr. and A. T. Hubbard, *Surf. Sci.*, **112**, 281 (1981).
25. M. D. Chinn and S. C. Fain, Jr., *Phys. Rev. Lett.*, **39**, 146 (1971).
26. W. Erley and H. Wagner, *Surf. Sci.*, **66**, 371 (1977).
27. (a) R. S. Bauer and J. C. McMenamin, *J. Vac. Sci. Technol.*, **15**, 1444 (1978); (b) W. Mönch and H. Gant, *ibid.*, **17**, 1094 (1980).

Extension of Darby's Model of a Hydrophylic Gas Fed Porous Electrode

R. E. White,* M. A. Nicholson,* L. G. Kleine, J. Van Zee,** and R. Darby

Department of Chemical Engineering, Texas A&M University, College Station, Texas 77843

ABSTRACT

A model presented previously by one of the authors (1,2) is reviewed and extended. Aspects of this model which were not previously available in the open literature are considered, and the model is extended to include previously neglected terms in the governing differential equations, fractional reaction orders in the current density-overpotential expression, and mass-transfer coefficients to account for mass-transfer resistance of the reactants to the faces of the porous electrode. The model is used to predict quantities of interest for oxygen reduction in an acidic aqueous solution in a porous carbon electrode.

Many models of gas fed hydrophylic porous electrodes have been proposed as reviewed recently by Chizmadzhev and Chirkov (3) and by Tilak *et al.* (4). Unfortunately, neither of these reviews mentions Darby's model (1, 2) which is based essentially on measurable quantities of the wettable porous electrode of interest and the transport and kinetic properties of the reactants involved. The purpose of this work is to extend Darby's homogeneous model (1) and to present predictions based on this model which include fractional reaction orders and external mass-transfer coefficients for the reactants.

Homogeneous Model

Darby's (1) homogeneous model is a conceptualization of the chemical, electrochemical, and physical processes that occur within a hydrophylic gas fed porous electrode. Figure 1 schematically presents the representation used here for a region of a gas fed porous electrode which is assumed to be small compared to the dimensions of the electrode. Note that the figure shows the gas pore to be open at both ends, which may be the case in some small volume elements within the electrode; however, the figure does not mean that large gas channels exist from the gas side to the electrolyte side of the electrode. A closer look at Fig. 1 reveals that the gaseous reactant in the pore is assumed to be in local chemical equilibrium with the liquid phase as indicated by $C_{G1}(z)$, which represents the liquid phase composition of the gaseous reactant at the gas-liquid interface (where a liquid pore intersects a gas pore). Further inspection of Fig. 1 indicates that the concentration of the dissolved gaseous reactant varies with depth (y) into the liquid filled pore as indicated by $C_G(y, z)$. Also, note that the coordinate y is normal to the gas-liquid interface and, consequently, is not in the same direction with respect to z for all pores (see Fig. 1 and the List of Symbols).

Once the gaseous reactant has dissolved into the electrolyte at the mouth of a liquid-filled pore, the dissolved gas diffuses into the pore and reacts along the walls of the pore. It is assumed here that no concentration gradient exists across the liquid-filled pore. The flux of the dissolved gaseous reactant (N_G) is given by

$$N_G = -D'_{GJ} \frac{dC_G}{dy} + \frac{C_G}{C} (N_G + N_J) \quad [1]$$

where J represents the liquid phase solvent whose concentration is approximately C and

$$D'_{GJ} = D_{GJ} \frac{\phi_1}{\tau} \quad [2]$$

(ϕ_1 and τ will be discussed later). Since C is typically

* Electrochemical Society Active Member.

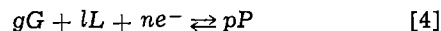
** Electrochemical Society Student Member.

Key words: fuel cell, diffusion, mass transport.

$\gg C_G$, Eq. [1] can be simplified to

$$N_G = -D'_{GJ} \frac{dC_G(y, z)}{dy} \quad [3]$$

The electrochemical reaction that occurs along the pore walls is



and the material balance for the dissolved gaseous reactant is

$$\frac{dN_G}{dy} = -\frac{gi'_{os}}{nF} \left[\left(\frac{C_G(y, z)}{C_{G0}} \right)^{g'} \left(\frac{C_L(z)}{C_{L0}} \right)^{l'} \exp \left(\alpha \frac{nF}{RT} \eta \right) \right] \quad [5]$$

where cathodic current density and overpotential have been chosen to be positive in order to be consistent with Darby (1, 2). The boundary conditions that apply are as follows

$$\text{at } y = 0 \quad C_G = C_{G1}(z) \quad [6]$$

and

$$\text{as } y \rightarrow \infty \quad C_G(y, z) = 0, \text{ and } \frac{dC_G}{dy} = 0 \quad [7]$$

which when applied to Eq. [5] yields

for $g' = 1$

$$C_G = C_{G1} \exp(-K_1^{1/2} y) \quad [8]$$

and

for $g' \neq 1$

$$C_G(y, z) = C_{G1}(z) \left\{ \frac{g' - 1}{2^{1/2} (g' + 1)^{1/2}} \xi_1 + 1 \right\}^{2/(1-g')} \quad [9]$$

where

$$\xi_1 = y K_1^{1/2} [C_{G1}(z)]^{(g'-1)/2} \quad [10]$$

and

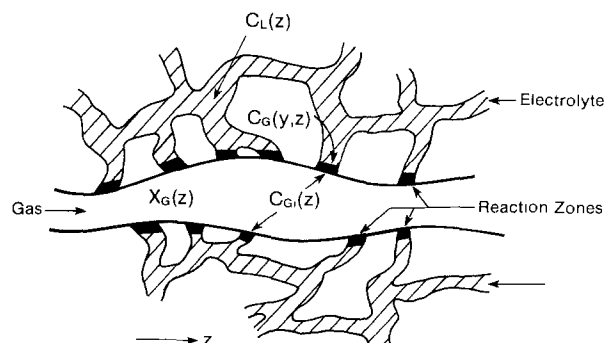


Fig. 1. Schematic of the homogeneous model for a single gas pore (1).

$$K_1 = \frac{i_0 s g}{D'_{GJ} n F C_{G_0} g'} \left[\left\{ \frac{C_L(z)}{C_{L_0}} \right\}^{1'} \exp \left\{ \frac{\alpha n F}{RT} \eta \right\} \right] \quad [11]$$

It is important to note that Eq. [8] and [9] apply only when the dissolved gaseous species is consumed.

Equation [9] can be used to derive an expression for the rate of consumption of the gaseous reactant per unit of electrode volume (R_G)

$$R_G = -a_g D'_{GJ} \frac{dC_G}{dy} \Big|_{y=0} \quad [12]$$

which by using Eq. [9] becomes

$$R_G = a_g D'_{GJ} \left\{ \frac{2K_1}{g' + 1} \right\}^{1/2} [C_{Gi}(z)]^{(g'+1)/2} \quad [13]$$

where a_g is the surface area of the gas-filled pores per unit of electrode volume and will be discussed below.

The dissolved gas that is consumed by the electrochemical reaction must be supplied by diffusion of the gaseous reactant from the electrode/gas interface. This gives rise to the material balance equation for the gaseous reactant within the gas-filled pores

$$\frac{dN_G}{dz} + R_G = 0 \quad [14]$$

The flux of the gaseous reactant (N_G) is

$$N_G = -D'_{GI} \frac{P_0}{RT} \frac{dX_G}{dz} + X_G(N_G + N_I) \quad [15]$$

where

$$X_G = P_G/P_0 \quad [16]$$

and

$$D'_{GI} = D_{GI} \frac{\phi_g}{\tau} \quad [17]$$

(ϕ_g will be discussed presently). Since $N_I = 0$ (I represents N_2 typically), Eq. [15] can be simplified to

$$N_G = -\frac{P_0 D'_{GI}}{RT(1 - X_G)} \frac{dX_G}{dz} \quad [18]$$

Substitution of Eq. [13] and [18] into Eq. [14] and letting

$$\xi = z/d \quad [19]$$

yields

$$\frac{d}{d\xi} \left\{ \frac{D'_{GI} P_0}{(1 - X) RT} \frac{dX_G}{d\xi} \right\} = d^2 a_g D'_{GJ} \left\{ \frac{2K_1}{g' + 1} \right\}^{1/2} [C_{Gi}(z)]^{(g'+1)/2} \quad [20]$$

Equation [20] can be simplified by using Eq. [11] for K_1 , Henry's law for $C_{Gi}(z)$ and C_{G_0}

$$C_{Gi}(z) = X_{Gi}(z) \frac{CP_0}{H} \quad [21]$$

where at $z = 0$ (for no mass-transfer resistance to the electrode from the bulk gas)

$$C_{G_0} = C_{Gi}(z=0) = X_{G_0} \frac{CP_0}{H} \quad [22]$$

and the definition of the mol fraction of the liquid reactant (X_L)

$$X_L = C_L(z)/C \quad [23]$$

and its value at the electrode/electrolyte interface at $z = d$ (for no mass-transfer resistance to the electrode from the bulk electrolyte)

$$X_{L_0} = C_{L_0}/C = C_L(z=d)/C \quad [24]$$

When mass-transfer resistance occurs, \bar{X}_{G_0} still repre-

sents the mol fraction of the gaseous reactant in the bulk gas, but $X_G(\xi = 0)$ is no longer equal to X_{G_0} and similarly for $X_L(\xi = 1.0)$ and X_{L_0} . Since $X_G = X_{G_0}$, substitution of Eq. [21]-[24] into Eq. [20] yields

$$\frac{d}{d\xi} \left\{ \frac{1}{1 - X_G} \frac{dX_G}{d\xi} \right\} = K_G X_G^{(g'+1)/2} X_L^{1/2} \quad [25]$$

where

$$K_G = \frac{a_g d^2 RT}{D'_{GI} (g' + 1)^{1/2}} \left\{ \frac{2i_0 s g D'_{GJ} C}{n F P_0 H X_{G_0} X_{L_0}} \right\}^{1/2} \left\{ \exp \left\{ \alpha \frac{nF}{RT} \eta \right\} \right\}^{1/2} \quad [26]$$

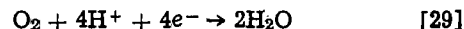
A similar equation can be derived for the mol fraction of the liquid reactant. The starting point is a flux expression for the liquid phase reactant

$$N_L = -CD'_{LJ} \frac{dX_L}{dz} + X_L(N_L + N_J) \quad [27]$$

where

$$D'_{LJ} = D_{LJ} \phi_l / \tau \quad [28]$$

N_J and N_L are often related in a simple manner through the stoichiometry of the electrochemical reaction. For the case considered here, the electrochemical reaction is



in an aqueous solution.¹ Thus, J is H_2O and H^+ is the liquid reactant L . Then, according to Eq. [29], the flux of J is related simply to the flux of L

$$N_J = -\frac{1}{2} N_L \quad [30]$$

which when substituted into Eq. [27] yields

$$N_L = \frac{-CD'_{LJ}}{1 - \frac{X_L}{2}} \frac{dX_L}{dz} \quad [31]$$

Equation [4] (or [29]) shows that the rate of consumption of the liquid reactant is related simply to the rate of consumption of the dissolved gaseous reactant

$$R_L = \frac{l}{g} R_G \quad [32]$$

The liquid phase reactant must be supplied from the bulk electrolyte as described by the material balance equation for L

$$\frac{dN_L}{dz} + R_L = 0 \quad [33]$$

Substitution and simplification as before yields

$$\frac{d}{d\xi} \left(\frac{1}{1 - \frac{X_L}{2}} \frac{dX_L}{d\xi} \right) = K_L X_G^{(g'+1)/2} X_L^{1/2} \quad [34]$$

where

$$K_L = \frac{a_g l d^2}{D'_{LJ} (g' + 1)^{1/2}} \left\{ \frac{2i_0 s D'_{GJ} P_0}{g n F C H X_{G_0} X_{L_0}} \right\}^{1/2} \exp \left\{ \frac{\alpha n F}{2RT} \eta \right\} \quad [35]$$

Equations [25] and [34] are the governing equations for the mol fractions of the gaseous reactant within the gas-filled pores (X_G) and of the liquid reactant within the liquid-filled pores (X_L). The boundary con-

¹ It should be noted that in systems operating above the boiling point of the electrolyte the water produced in Eq. [29] would evaporate and leave the cell via the gas phase.

ditions for these equations are as follows

at $\zeta = 0$

$$\frac{dX_L}{d\zeta} = 0 \tag{36}$$

$$k_{mg} [X_G(\zeta = 0) - X_{G0}] = -\frac{D'_{GI}}{d} \frac{dX_G}{d\zeta} \tag{37}$$

and

at $\zeta = 1$

$$\frac{dX_G}{d\zeta} = 0 \tag{38}$$

$$k_{ml} [X_L(\zeta = 1) - X_{L0}] = \frac{D'_{LJ}}{d} \frac{dX_L}{d\zeta} \tag{39}$$

where k_{mg} and k_{ml} are external mass-transfer coefficients. (Note that when both k_{mg} and k_{ml} become infinitely large, Darby's original boundary conditions are obtained.) Values for k_{mg} and k_{ml} can be predicted for simple systems such as flow between flat plates [see Ref. (5), *e.g.*,] and can be determined experimentally for more complicated systems.

Before proceeding with a solution of the governing equations for $X_G(\zeta)$ and $X_L(\zeta)$, let us consider the distribution of the porosity of the electrode between the gas and liquid pores. The differential pressure ($P = P_0 - 1$ atm) determines the fraction of the porosity (ϕ) filled with gas (ϕ_g) and the fraction filled with liquid (ϕ_l) by assuming that the radius of the largest flooded pore is

$$r_e = \frac{2\gamma \cos \theta}{P} \tag{40}$$

Equation [40] states that the gas pressure in the gas-filled pores is balanced by the surface tension of the liquid in the flooded pores. If we assume that the pores wet easily, all pores larger than r_e will be gas-filled and all pores smaller than r_e will be flooded. A cumulative pore size distribution function [$f(r_e)$] can be defined as the fraction of the total pore volume which has pore radii greater than r_e

$$f(r_e) = \int_{r_e}^{\infty} \alpha(r) dr \tag{41}$$

where $\alpha(r)$ is the pore size distribution function and is assumed here to be normal

$$\alpha(r) = \frac{1}{\sigma\sqrt{\pi}2} \exp \left[-\frac{1}{2} \left(\frac{r - \bar{r}}{\sigma} \right)^2 \right] \tag{42}$$

where \bar{r} and σ represent the mean pore radius and the standard deviation of the distribution, respectively. Substitution of Eq. [42] into Eq. [41] yields

$$f(r_e) = \int_{r_e}^{\infty} \left\{ \frac{1}{\sigma\sqrt{\pi}2} \exp \left[-\frac{1}{2} \left(\frac{r - \bar{r}}{\sigma} \right)^2 \right] \right\} dr \tag{43}$$

which can be rewritten in a more convenient form by first breaking the integral into two parts

$$f(r_e) = \int_0^{\infty} \left\{ \frac{1}{\sigma\sqrt{\pi}2} \exp \left[-\frac{1}{2} \left(\frac{r - \bar{r}}{\sigma} \right)^2 \right] \right\} dr - \int_0^{r_e} \left\{ \frac{1}{\sigma\sqrt{\pi}2} \exp \left[-\frac{1}{2} \left(\frac{r - \bar{r}}{\sigma} \right)^2 \right] \right\} dr \tag{44}$$

and by defining a dimensionless pore radius r'

$$r' = \frac{1}{\sqrt{2}} \frac{r - \bar{r}}{\sigma} \tag{45}$$

Then, in terms of r' Eq. [44] becomes

$$f(r'_e) = \int_0^{\infty} \frac{1}{\sigma\sqrt{\pi}2} \exp(-r'^2) \sigma\sqrt{2} dr' - \frac{1}{\sigma\sqrt{\pi}2} \int_0^{r'_e} \exp(-r'^2) \sigma\sqrt{2} dr' \tag{46}$$

or

$$f(r'_e) = \frac{1}{2} - \frac{1}{\sqrt{\pi}} \int_0^{r'_e} \exp(-r'^2) dr' \tag{47}$$

which simplifies to

$$f(r'_e) = [1 - \text{erf}(r'_e)]/2 \tag{48}$$

Thus, the fraction of the porosity filled with gas (ϕ_g) is simply

$$\phi_g = \phi f(r'_e) \tag{49}$$

and the fraction filled with liquid (ϕ_l) is

$$\phi_l = \phi - \phi_g \tag{50}$$

Both ϕ_g/τ and ϕ_l/τ are used to modify the free stream diffusion coefficients (see Eq. [2] and [17]). The value used here for τ was chosen arbitrarily. (It may be possible to determine a value for τ by measuring both ϕ and D'_{GJ} .)

The porosity (ϕ), gas phase porosity (ϕ_g), and the BET-type specific surface area (a) can be used to determine an expression for the surface area of the gas-filled pores per unit of electrode volume (a_g).

The desired expression for a_g can be obtained by assuming that the pores are tortuous cylinders with a mean pore radius of \bar{r} and by considering the ratio of a to ϕ

$$\frac{a}{\phi} = \frac{\frac{\text{pore wall surface area}}{\text{electrode volume}}}{\frac{\text{pore volume}}{\text{electrode volume}}} = \frac{2\pi\bar{r}\tau d}{\pi\bar{r}^2\tau d} = \frac{2}{\bar{r}} \tag{51}$$

or

$$\frac{a}{\phi} \bar{r} = 2 \tag{52}$$

(or some other constant). If Eq. [52] is true for the electrode as a whole, then it is reasonable to assume that it is also true for the gas-filled pores

$$\frac{a_g}{\phi_g} \bar{r}_g = 2 = \frac{a}{\phi} \bar{r} \tag{53}$$

where \bar{r}_g is the mean pore radius of the gas-filled pores which can be normalized in a manner similar to r_e

$$\bar{r}'_g = \frac{1}{\sqrt{2}} \frac{\bar{r}_g - \bar{r}}{\sigma} \tag{54}$$

Expressions for \bar{r}'_g and then a_g can be obtained in terms of the pore size distribution parameters (\bar{r}, σ) as follows. Since \bar{r}'_g is defined to be the normalized pore radius such that one-half of the gas pore volume is contained in pores with radii larger than \bar{r}'_g , the cumulative pore size distribution function $f(\bar{r}'_g)$ is simply one-half of the cumulative pore size distribution for the gas-filled pores [$f(r'_e)$]

$$f(\bar{r}'_g) = f(r'_e)/2 \tag{55}$$

An expression for \bar{r}'_g can be obtained from Eq. [55] by using an equation for $f(\bar{r}'_g)$ which is analogous to Eq. [48] for $f(r'_e)$

$$[1 - \text{erf}(\bar{r}'_g)]/2 = f(r'_e)/2 \tag{56}$$

which can be rearranged to

$$\text{erf}(\bar{r}'_g) = 1 - f(r'_e) \tag{57}$$

or

$$\bar{r}'_g = \text{erf}^{-1} [1 - f(r'_e)] \tag{58}$$

Then according to Eq. [49] and [50], Eq. [58] can be written as

$$\bar{r}'_g = \text{erf}^{-1}(\phi_1/\phi) \quad [59]$$

which when combined with Eq. [54] yields an expression for \bar{r}'_g

$$\bar{r}'_g = \bar{r} + \sqrt{2} \sigma \text{erf}^{-1}(\phi_1/\phi) \quad [60]$$

Substitution of Eq. [60] into Eq. [53] yields

$$a_g = \frac{a\bar{r}'\phi_g/\phi}{\bar{r} + \sqrt{2} \sigma \text{erf}^{-1}(\phi_1/\phi)} \quad [61]$$

which, by using Eq. [48]-[50], becomes the desired expression for a_g

$$a_g = \frac{a\bar{r}'(1 - \text{erf } r'_e)}{2\{\bar{r}' + \sqrt{2} \sigma \text{erf}^{-1}[(1 + \text{erf } r'_e)/2]\}} \quad [62]$$

Figure 2 shows the dependence of a_g on the difference between the gas pressure and the electrolyte pressure (P). As shown in Fig. 2, a_g is very sensitive to P from about 7 to 12 psi.

Results and Discussion

The apparent current density (total current/projected area of the electrode) of the porous electrode can be determined from the flux of the gaseous reactant into the porous electrode

$$\frac{gi}{nF} = N_G|_{\zeta=0} \quad [63]$$

which by using Eq. [18] becomes

$$i = \frac{K_A}{1 - X_G} \frac{dX_G}{d\zeta} \Big|_{\zeta=0} \quad [64]$$

where

$$K_A = \frac{nFP_0 D'_{GI}}{gdRT} \quad [65]$$

The gradient of the mol fraction of the gaseous species ($dX_G/d\zeta$) needed in Eq. [64] can be determined from $X_G(\zeta)$ which can be obtained by solving Eq. [25] and [34] subject to the boundary conditions given by Eq. [36]-[39]. Darby (1) found $X_G(\zeta)$ [and $X_L(\zeta)$] by assuming that X_G and $X_L \ll 1$ so that the governing equations for X_G and X_L become

$$\frac{d^2 X_G}{d\zeta^2} = K_G X_G^{(g'+1)/2} X_L^{l'/2} \quad [66]$$

$$\frac{d^2 X_L}{d\zeta^2} = K_L X_G^{(g'+1)/2} X_L^{l'/2} \quad [67]$$

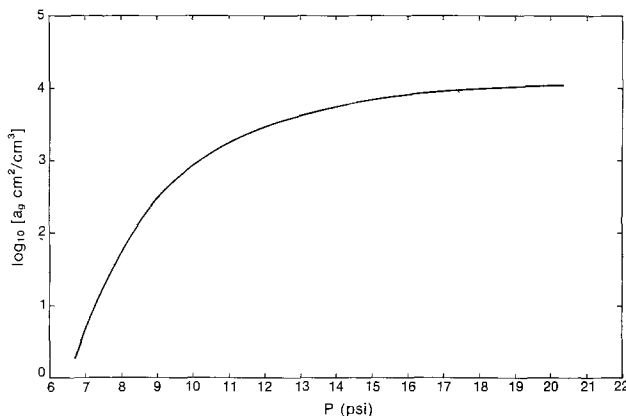


Fig. 2. Dependence of the surface area of the gas pores per unit of electrode volume (a_g) on the differential pressure across the electrode (P).

According to Sepa *et al.* (6), $g' = 1$ and $l' = 1$ or 1.5 for reaction [29] depending on the overpotential. Darby (2) solved approximately Eq. [66] and [67] for $g' = 1$ and $l' = 1$ by assuming that

$$X_G = X_{G0} \left[1 - b \left(\zeta - \frac{\zeta^2}{2} \right) \right] \quad [68]$$

and

$$X_L = X_{L0} [a' + (1 - a') \zeta^2] \quad [69]$$

which satisfy the boundary conditions (Eq. [36]-[39]) for infinitely large external mass-transfer coefficients and by substituting Eq. [68] and [69] into Eq. [66] and [67] and evaluating the result at $\zeta = 0$ to determine a' and b

$$a' = 1 + \frac{K_L^2 X_{G0}^2}{8X_{L0}} - \left[\left(1 + \frac{K_L^2 X_{G0}^2}{8X_{L0}} \right)^2 - 1 \right]^{1/2} \quad [70]$$

$$b = K_G (X_{L0} a')^{1/2} \quad [71]$$

Finally, application of Eq. [64] gives the desired expression for the current density

$$i = X_{G0} K_A b \quad [72]$$

Again, Eq. [72] is based on the assumption that X_G and X_L are both much less than 1 which is not a good assumption if X_{G0} and X_{L0} are on the order of 0.1 as is the case here. To relax this assumption, Eq. [25] and [34] were solved by using Newman's numerical technique (5, 7) for the fixed and variable parameters considered here as shown in Table I (see Table II for a typical set of calculated parameter values).

Figure 3 shows a comparison between the predicted mol fraction distributions for the simplified and complete governing equations cases, and Fig. 4 presents a comparison of the predicted current densities for both cases. Also shown in Fig. 4 is the predicted limiting current density according to Austin (8, Eq. 6.38a)

$$i_L = \left(\frac{nFD'_{GI}}{d} \right) \frac{X_{G0} P_0 f}{RT} \quad [73]$$

where

$$f = \frac{\ln[(1 - X_{G0})^{-1}]}{X_{G0}} \quad [74]$$

Table I. System parameters used for calculations

Fixed Parameters	
Gas phase	$X_{G0} = 0.21$
Electrolyte	$X_{L0} = 0.127$, $C = 0.05$ mol/cm ³ , $\gamma = 75$ dyn/cm, $\theta = 0^\circ$
Henry's law constant	$H = 3.99966 \times 10^{10}$ dyn/cm ²
Porous medium characteristics	$\phi = 0.5$, $\tau = 15$, $d = 0.2$ cm, $\sigma = 5 \times 10^{-5}$ cm, $\bar{r} = 1.5 \times 10^{-4}$ cm, $a = 1.5 \times 10^4$ cm ² /cm ³
Molecular diffusivities	$D_{GI} = 0.2$ cm ² /s $D_{LI} = 2 \times 10^{-5}$ cm ² /s $D_{GI} = 1 \times 10^{-5}$ cm ² /s
Kinetic parameters	$n' = 4$, $\alpha = 1/2$, $i_{0S} = i_0/d$, $g' = 1.0$, $T = 298.15$ K
Stoichiometric coefficients	$g = 1$, $l = 4$, $n = 4$
Variable Parameters (with typical values)	
Gas phase	$P_0 = 1.6212 \times 10^6$ dyn/cm ²
Kinetic parameters	$i_0 = 10^{-5}$ A/cm ² , $l' = 1.0$, $\eta = 0.1V$

Table II. Calculated parameters for $g' = 1.0$, $i_0 = 10^{-5}$ A/cm², $l' = 1.0$, $P_0 = 1.6$ atm, and $\eta = 0.1V$

$$\begin{aligned} \phi_1 &= 0.4867 \\ \phi_g &= 0.0133 \\ a_g &= 2.29 \times 10^2 \text{ cm}^2/\text{cm}^3 \\ K_G &= 2.19 \\ K_L &= 3.12 \\ K_A &= 2.23 \times 10^{-2} \text{ A/cm}^2 \end{aligned}$$

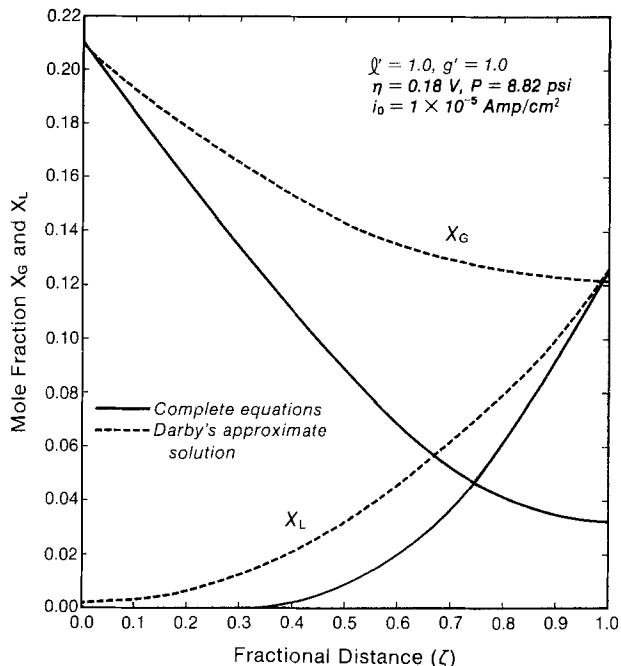


Fig. 3. Mol fraction distributions for the complete governing equations model (Eq. [25] and [34]) with infinitely large k_{mg} and k_{ml} , and Darby's approximate solutions (Eq. [68] and [69]) to the simplified governing equations (Eq. [66] and [67]).

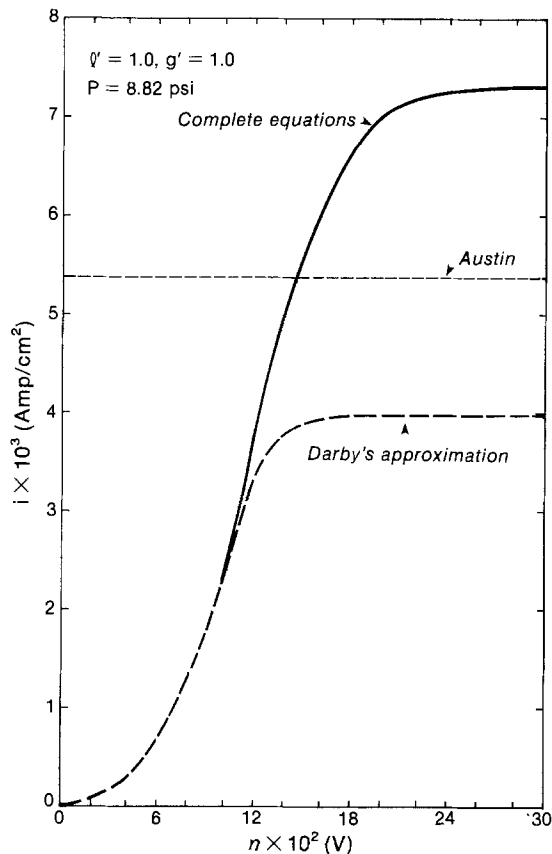


Fig. 4. Comparison of predicted current densities by the complete model with infinitely large k_{mg} and k_{ml} , Darby's approximate solutions, and Eq. [73] for the limiting current density with $i_0 = 10^{-5}$ A/cm².

Substitution of the appropriate values from Tables I and II into Eq. [73] and [74] gives $i_L = 5.27 \times 10^{-3}$ A/cm². Notice in Fig. 4 that for large values of η , the predictions of the complete model are significantly different from those of Darby's approximate solution. This is due to the importance of the neglected terms in the governing differential equations for the two cases (compare Eq. [25] and [66] and Eq. [34] and [67]). It is interesting that the prediction of the limiting cur-

rent density by Austin's equation falls between these two cases. This is due to using an effective diffusion coefficient for oxygen (D'_{GI}) in Austin's equation which is the same as the effective diffusion coefficient (D'_{GI}) used in both of the other cases. If D'_{GI} is determined by multiplying D_{GI} by ϕ/τ , instead of ϕ_g/τ , then the limiting current density predicted by Austin's equation is 37.6 (i.e., ϕ/ϕ_g) times larger than that shown in Fig. 4.

The limiting current density for the complete model (as shown in Fig. 4) is plotted in Fig. 5 together with other limiting current density values at different differential pressures P . Also shown in Fig. 5 are the limiting current density predictions of Darby's approxi-

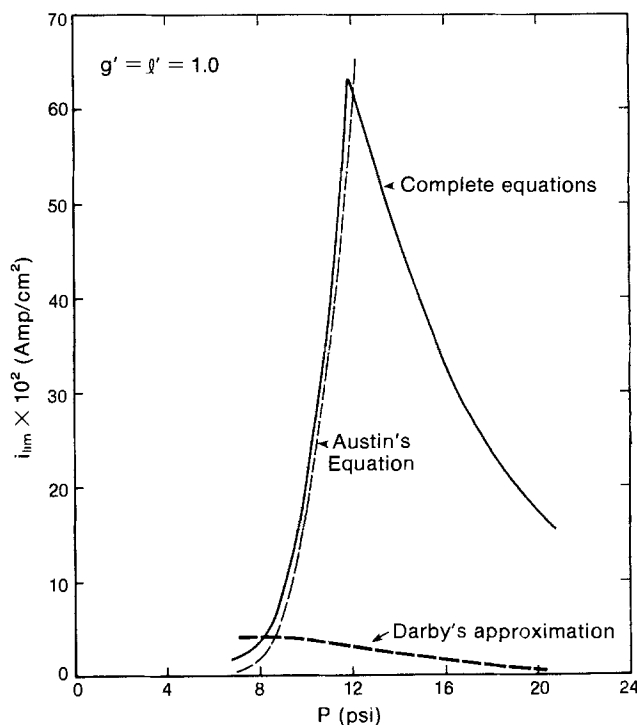


Fig. 5. Limiting current density dependence upon P for the complete model with infinitely large k_{mg} and k_{ml} , Darby's approximate solution, and Eq. [73] with $i_0 = 10^{-5}$ A/cm².

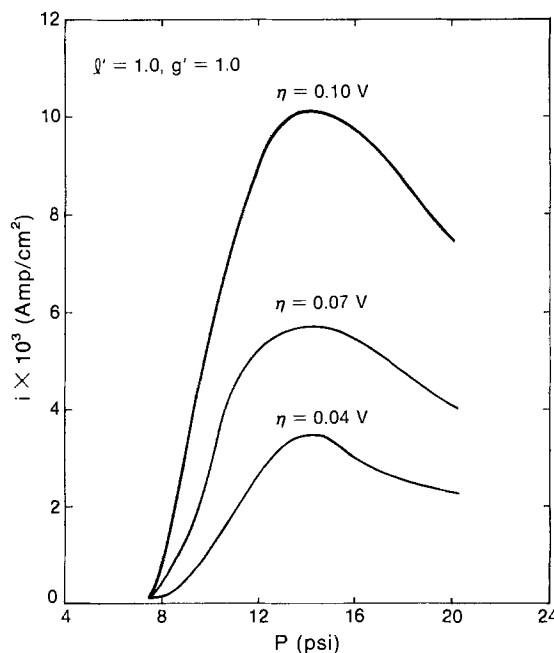


Fig. 6. Predicted current density dependence on η and P for the complete model with infinitely large k_{mg} and k_{ml} where $i_0 = 10^{-5}$ A/cm².

mate solution and Eq. [73] again with D'_{GI} determined with ϕ_g instead of ϕ (note that ϕ_g depends upon P). Figure 5 clearly shows that a maximum limiting current density is predicted at approximately $P = 12$ psi for the system considered here.

Figure 6 shows how the current density below the limiting current density depends on the differential pressure (P) for various values of η . Experimental current density values (3) have a similar dependence on P and η as shown in Fig. 7. Figures 6 and 7 are presented here for qualitative comparison only, since not enough information is available for a quantitative comparison between Darby's model and the experimental data presented in Fig. 7.

Figures 8 and 9 demonstrate how the kinetic parameters l' and i_0 effect the predicted current densities. These figures show that predicted current densities depend upon these parameters to the extent that it should be possible to determine values for l' and i_0 by

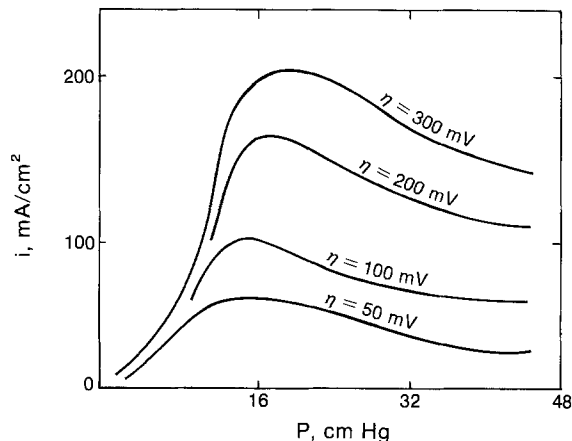


Fig. 7. Experimental current density (3) dependence on η and P .

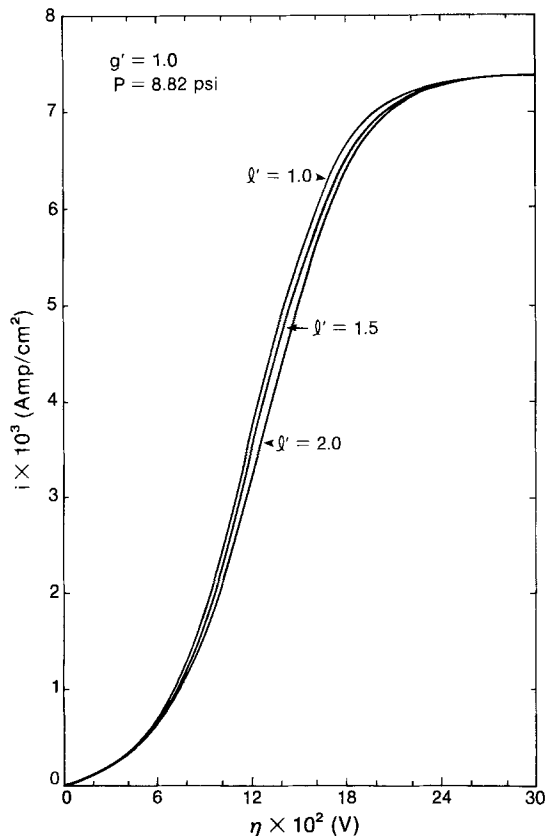


Fig. 8. Comparison of predicted current densities for various liquid reactant reaction orders for the complete model with infinitely large k_{mg} and k_{ml} when $i_0 = 10^{-5}$ A/cm².

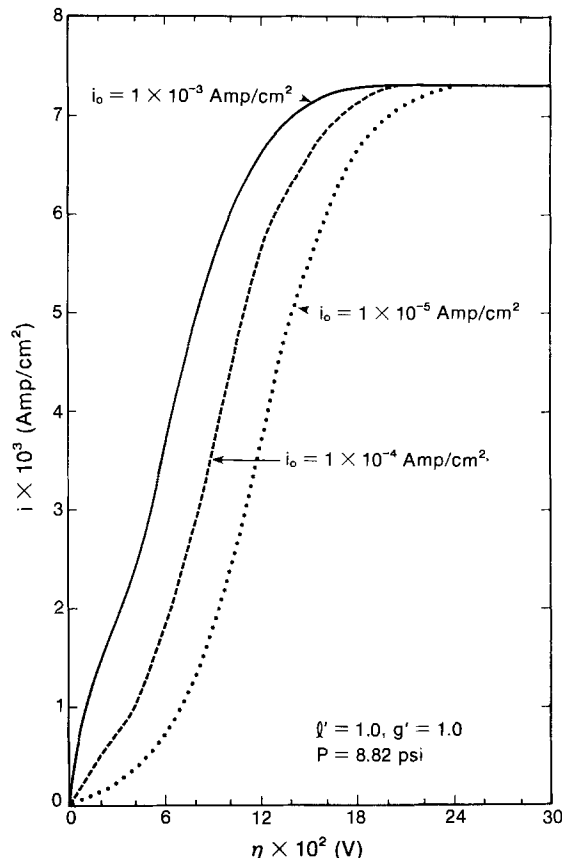


Fig. 9. Effect of the exchange current density on the predicted current densities for the complete model with infinitely large k_{mg} and k_{ml} .

comparison of data to predicted values using least squares, nonlinear fitting, for example.

Finally, the effect of the external mass-transfer coefficients is demonstrated in Fig. 10 and 11. Figure 10 shows how the mass-transfer resistance to the electrode can alter the mol fraction distributions within the electrode, and Fig. 11 presents the effect of finite values of k_{mg} and k_{ml} on the predicted current density. Figure 11 clearly demonstrates that for large values of η the predicted current density can be reduced significantly if external mass-transfer resistance of the reactants to the electrodes is important.

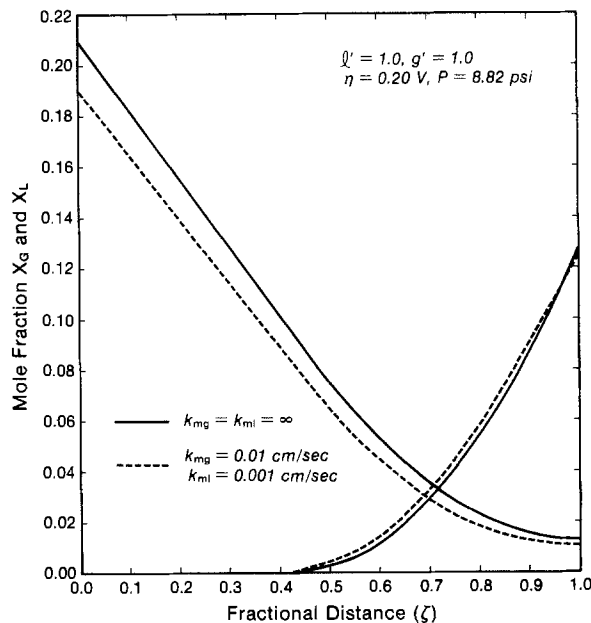


Fig. 10. Effect of external mass-transfer coefficients (k_{ml} and k_{mg}) on the predicted mol fractions for the complete model when $i_0 = 10^{-5}$ A/cm².

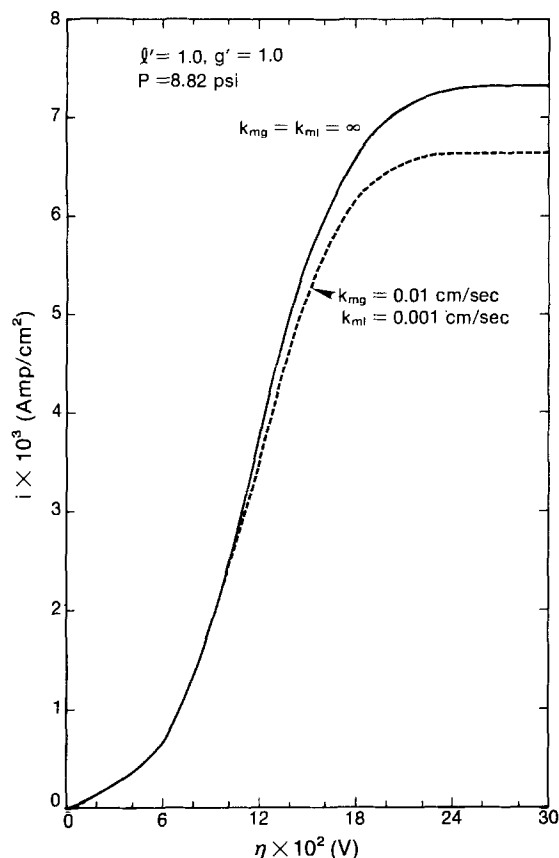


Fig. 11. Effect of external mass-transfer coefficients (k_{m1} and k_{mg}) on the predicted current densities for the complete model when $i_0 = 10^{-5}$ A/cm².

Conclusion

Darby's model of a gas fed hydrophilic porous electrode is useful because it includes important features of hydrophilic porous electrodes which are often neglected. For example, it includes a pore size distribution for a porous electrode which can be determined experimentally and used in the model.

The extensions presented here (considering the complete governing equations, fractional reaction orders, and mass-transfer coefficients) should aid in data analysis and electrode design.

Acknowledgments

The authors acknowledge gratefully the support of this work by the Dow Chemical Company.

Manuscript submitted March 18, 1983; revised manuscript received Sept. 13, 1983.

LIST OF SYMBOLS

a	specific surface area, cm ² /cm ³
a_g	gas pore surface area per unit electrode volume, cm ² /cm ³
C	total liquid phase concentration, mol/cm ³
C_L	concentration of liquid reactant, mol/cm ³
C_{Gi}	concentration of the dissolved gas G at the gas-liquid interface, mol/cm ³
C_{Go}	concentration of gaseous reactant at the gas-electrolyte interface at $z = 0$ (see Eq. [22]), mol/cm ³
d	electrode thickness, cm
D_{GI}	diffusivity of the gas phase reactant in gas phase inert component, cm ² /s
D'_{GI}	effective diffusivity of gas phase reactant in gas phase inert component in a porous medium, cm ² /s
D_{GJ}	diffusivity of the gas phase reactant in liquid phase solvent, cm ² /s
D'_{GJ}	effective diffusivity of the gas phase reactant in liquid phase solvent in a porous medium, cm ² /s
D_{LJ}	diffusivity of liquid phase reactant in liquid solvent, cm ² /s

D'_{LJ}	effective diffusivity of the liquid phase reactant in porous medium, cm ² /s
F	Faraday's constant, 96487C/mol
$f(r'_e)$	fraction of total pore volume in gas-filled pores (i.e., cumulative pore size distribution for r'_e)
g	stoichiometric coefficient for gas phase reactant in overall electrode reaction
g'	reaction order with respect to gas phase reactant
H	Henry's law constant, dyn/cm ²
i	current density, A/cm ²
i_0	exchange current per unit of projected area of the electrode, A/cm ²
i'_0	exchange current per unit of active catalytic surface area, A/cm ²
K_A	parameter used to calculate i , A/cm ²
K_G	dimensionless parameter for gas phase component
K_L	dimensionless parameter for liquid phase component
k_{mg}	gas phase mass-transfer coefficient, cm/s
k_{ml}	liquid phase mass-transfer coefficient, cm/s
l	stoichiometric coefficient for liquid phase reactant
l'	reaction order with respect to liquid phase reactant
N_i	molar flux of species i ($i = G, J, I, L$), mol/cm ² -s
n	number of electrons involved in overall electrode reaction
n'	number of electrons in electrode reaction
P	differential pressure = $P_0 - 1.01325 \times 10^6$ dyn/cm ²
P_G	partial pressure of the gaseous reactant G , dyn/cm ²
P_0	absolute gas pressure, dyn/cm ²
R	gas constant, 8.3143J/mol-K
r_e	radius of a pore in which gas-liquid interface will be located, cm
$\frac{r'_e}{\bar{r}}$	normalized radius of the largest flooded pore
\bar{r}	mean pore radius, cm
\bar{r}_g	mean pore radius of gas-filled pores, cm
\bar{r}'_g	normalized mean pore radius of gas-filled pores
s	specific accessible catalytic surface area, cm ² /cm ³
T	absolute temperature, K
X_G	mol fraction of gas phase reactant
X_{Go}	mol fraction of gaseous reactant at the bulk phase-electrode interface ($\xi = 0$)
X_L	mol fraction of liquid-phase reactant
X_{Lo}	mol fraction of liquid reactant-bulk phase ($\xi = 1$)
y	depth into a liquid filled pore, normal to the gas-liquid interface, not in the same direction with respect to z for all pores, cm
z	distance from the bulk gas-electrode interface into the porous electrode, cm

Greek Symbols

α	transfer coefficient
$\alpha(r)$	pore size distribution, cm ⁻¹
η	polarization (driving force), V
γ	surface tension of electrolyte, dyn/cm
ϕ	porosity
ϕ_g	porosity of gas-filled pores
ϕ_l	porosity of liquid-filled pores
σ	standard deviation of pore size distribution function, cm
τ	tortuosity
θ	contact angle, degrees
ξ	dimensionless coordinate, z/d

REFERENCES

1. R. Darby, *Adv. Energy Convers.*, **5**, 43 (1965).
2. R. Darby, LTV Research Center Report 0-71000/34-26, Dallas, Texas (1963).
3. Yu. A. Chizmadzhev and Yu. G. Chirkov, in "Comprehensive Treatise of Electrochemistry," Vol. 6, E. B. Yeager, J. O'M. Bockris, B. E. Conway, and S. Sarangapani, Editors, p. 317, Plenum Press, New York (1983).
4. B. V. Tilak, R. S. Yeo, and S. Srinivasan, in "Comprehensive Treatise of Electrochemistry," Vol. 3,

- J. O'M. Bockris, B. E. Conway, E. Yeager, and R. E. White, Editors, p. 39, Plenum Press, New York (1981).
5. J. S. Newman, "Electrochemical Systems," Prentice-Hall, Inc., Englewood Cliffs, NJ (1973).
6. D. B. Sepa, M. V. Vojnovic, and A. Damjanovic,

- Electrochim. Acta*, **26**, 781 (1981).
7. R. E. White, *Ind. Eng. Chem. Fundam.*, **17**, 367 (1978).
8. L. G. Austin, in "Handbook of Fuel Cell Technology," C. Berger, Editor, Prentice-Hall, Inc., Englewood Cliffs, NJ (1968).

Electrochemical Photocapacitance Spectroscopy Method for Characterization of Deep Levels and Interface States in Semiconductor Materials

Ron Haak and Dennis Tench

Rockwell International Science Center, Thousand Oaks, California 91360

ABSTRACT

The recently developed electrochemical photocapacitance spectroscopy (EPS) method for characterization of deep levels in semiconductors is described. Topics discussed include the advantages of the method, experimental considerations, and the determination of state densities and kinetic parameters (associated with state population/depopulation). Both steady-state and transient capacitance changes are treated mathematically. Data for n-GaAs, p-GaAs, n-CdSe, a-Si and p-Zn₃P₂ are presented to illustrate the wide applicability of the method and its sensitivity to both bulk and interface states, including those observed by other characterization methods.

Electrochemical photocapacitance spectroscopy (EPS) has recently been shown to be a sensitive means for characterization of deep levels in semiconductor materials (1). In the present paper, the EPS technique is described and illustrative results are presented for a variety of single-crystal and polycrystalline materials. Since the intent of the authors is to encourage and facilitate use of EPS by both physicists and electrochemists, considerable detail is given in areas expected to be unfamiliar to either group of scientists. It should also be emphasized that the focus here is on covering the practical aspects of applying the method rather than on providing a comprehensive quantitative treatment.

EPS Method

In EPS, the capacitance of a reverse-biased semiconductor electrode is measured as a function of the wavelength of incident sub-bandgap light. The electrostatic situation and possible phototransitions for an n-type semiconductor are depicted in Fig. 1. In the dark, all of the negative charge in the electrolyte Helmholtz layer must be compensated by fixed ionized donors so that the space-charge layer extends deep into the semiconductor. At sufficiently anodic bias voltages (except at very high charge-carrier concentrations), the space-charge capacitance is generally small ($<0.1 \mu\text{F}/\text{cm}^2$) compared to the Helmholtz layer capacitance ($\sim 20 \mu\text{F}/\text{cm}^2$). In this case, the impedance of the interfacial region is dominated by the space charge, so that additional charge, introduced by optical population/depopulation of traps or interface states, significantly affects the thickness of the space-charge layer and is readily detected as a change in capacitance. Transitions from bandgap states (electron traps) into the conduction band introduce additional fixed positive charge to the semiconductor space-charge region (or at the interface), reducing the thickness of the space-charge layer and increasing the capacitance. Similarly, transitions from the valence band to bandgap states (hole traps) result in a decrease in capacitance. Charge may also be introduced into the semiconductor space-charge region by localized transitions from the ground state

to an excited state of an impurity (or defect center), followed by thermal injection of charge into one of the semiconductor bands (see Fig. 1). For p-type semiconductors, the capacitance change associated with a given type of transition is opposite in sign to that for an n-type material.

Typical plots of capacitance vs. wavelength (for sweeps from low to high photon energies) yield a series of plateaus and/or peaks, each corresponding to the population/depopulation of a given bandgap state. Plateaus are obtained for transitions that directly involve one of the semiconductor bands and can consequently be effected by light covering a wide range of energies above a certain threshold. Peaks are obtained for localized transitions which are effected only by light of a relatively specific energy. The onset energy of the capacitance change yields the energy of the state, relative to the appropriate bandedge. For localized transitions, the peak energy may be more de-

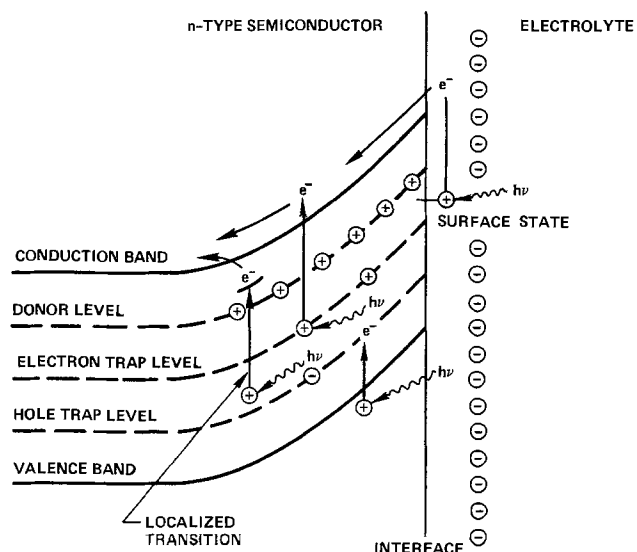


Fig. 1. Schematic representation of a reverse-biased n-type semiconductor, and typical phototransitions involved in electrochemical photocapacitance spectroscopy.

Key words: semiconductor traps, electrochemical detection, gallium arsenide, cadmium selenide, amorphous silicon, zinc phosphide.

scriptive. When trap saturation is attained, *i.e.*, all states of a given energy are populated/depoppedulated by the available light, the magnitude of the capacitance change yields the density of states. Otherwise, the latter can often be determined from the time dependence of the photocapacitance after initiating illumination. In many cases, bulk and interface states can readily be distinguished from the effect of the electrode bias voltage, which determines the thickness of the space-charge layer and thus the number of bulk states responding but has little effect on the potential drop at the interface, *i.e.*, across the Helmholtz region.

The advantages of the EPS method can be summarized as follows. First, charged or discharged states produced by phototransitions generally accumulate in the space-charge layer or at the interface, causing an integral effect on the capacitance so that the sensitivity of EPS is greatly enhanced in comparison to techniques based on simple photocurrent measurements. Also, in contrast to EPS, techniques based on a net flow of current cannot readily distinguish the effects of charge transfer mediators in the solution from those associated with interface states. Compared to the analogous solid-state photocapacitance technique, EPS is also more sensitive, since leakage currents can be considerably reduced in electrochemical systems by adjusting the availability of electronic states in the electrolyte, and the monolayer-sharp junction with transparent electrolytes permits more light to be focused on the area of interest, *i.e.*, the space-charge region. In addition, compared to techniques like deep level transient spectroscopy (DLTS), EPS is relatively straightforward and can be performed rapidly, since the blocking contact is formed simply by immersing the semiconductor in an electrolyte, and measurements are performed at ambient temperature and pressure. Although slower wavelength scans requiring several hours may be required to study slow states or to minimize data scatter, EPS spectra with good resolution can often be obtained over a 2 eV range in 15 min. With the proper choice of electrolyte, EPS is also nondestructive. On the other hand, since EPS is an *in situ* electrochemical technique, the electrolyte can be chosen to permit characterization of electronic states associated with the semiconductor-electrolyte interface or passive films, *e.g.*, oxides. EPS could also be used for electrochemical profiling, in which layers of the semiconductor are electrochemically dissolved between measurements. It should also be mentioned that EPS is sensitive to both donor and acceptor states in the same material, whereas minority carrier traps are extremely difficult to characterize by DLTS. EPS may also be applicable to the characterization of oxide films on metal electrodes.

Density of bulk states.—In calculating densities of states, it is convenient to assume that exhaustive depletion of charge carriers within the semiconductor space-charge region prevails; this is justified for the small photocapacitance changes normally observed. In this case, the contribution of ionized bulk states of density n to the capacitance C is given by the well-known Mott-Schottky (2, 3) expression

$$\frac{1}{C^2} = -\frac{8\pi E}{\epsilon_{sc} e n} \quad [1]$$

for which kT/e and the potential drop in the electrolyte have been neglected (other symbols are defined below). The net number of ionized states, which determines the magnitude of the measured capacitance, is equivalent to the net semiconductor charge resulting from the equilibrium between thermal and optical emission/capture processes for both positively and negatively charged centers. Since we are concerned with the change in capacitance associated with optical population/depopulation of specific deep levels, it is appropriate to write the net density of ionized states (n_t) as

$$n_t = n_i + n_o \quad [2]$$

where n_t is the density of optically populated/depoppedulated traps of a specific energy, and n_o is the net density of ionized states present under illumination with light of energy just below the onset of the transition of interest. Note that the sign of the change in charge produced by the specific phototransition under study must be considered, *i.e.* n_t increases when the existing space charge is enhanced and decreases when it is diminished.

Rewriting Eq. [1] in terms of n_t and n_o and substituting in Eq. [2], we obtain

$$n_t = \pm \frac{8\pi E}{\epsilon_{sc} e} (C_o^2 - C^2) \quad [3]$$

where C is the capacitance measured with light of sufficient energy for population/depopulation of the trap, C_o the capacitance measured with light of energy just below the onset for the trap under study, E the electrode bias potential *vs.* U_{FB} (flatband potential), ϵ_{sc} the semiconductor dielectric constant, and e the electronic charge. Thus, the density of bulk traps (per cm^3) populated/depoppedulated by illumination can be readily calculated from the associated photocapacitance change according to

$$n_t = \pm \frac{1.4 \times 10^{20} E}{\epsilon_{sc}} (C_o^2 - C^2) \quad [4]$$

where capacitance is in $\mu\text{F}/\text{cm}^2$, and E is in volts *vs.* U_{FB} . When the trap is initially populated/depoppedulated totally and is fully depoppedulated/populated (saturated) by the light, $n_t = N_t$ (the total trap density). This is the case for a sufficiently deep trap (for which thermal emission is negligible) when the associated capacitance plateau or peak is insensitive to the light intensity. An implicit assumption, of course, is that the population of only one trap level changes in the spectral region of interest.

Density of interface states.—For the treatment given here, it is assumed that interface states do not themselves respond to the measurement voltage perturbation and, therefore, affect the capacitance (only when charged) via a change in the potential distribution between the semiconductor space charge region and the electrolyte Helmholtz layer.¹ In this case, we rewrite the Mott-Schottky expression still assuming that the semiconductor space-charge capacitance dominates the electrode impedance, but now allowing for the electrode potential being distributed between the semiconductor and the electrolyte, *i.e.*

$$\frac{1}{C^2} = -\frac{8\pi \Delta\phi_{sc}}{\epsilon_{sc} e n_o} \quad [5]$$

and since

$$\Delta\phi_{sc} = E - \Delta\phi_H \quad [6]$$

and

$$\Delta\phi_H = \frac{e n_i}{C_H} \quad [7]$$

where $\Delta\phi_{sc}$ is the potential drop across the semiconductor space-charge region, n_o the bulk charge-carrier concentration, $\Delta\phi_H$ the potential drop across the electrolyte Helmholtz layer, n_i the density of ionized interface states (per cm^2), and C_H the capacitance of Helmholtz layer. Thus we have

$$\frac{1}{C^2} = -\frac{8\pi (E - \Delta\phi_H)}{\epsilon_{sc} e n_o} = -\frac{8\pi E}{\epsilon_{sc} e n_o} + \frac{8\pi e n_i}{\epsilon_{sc} n_o C_H} \quad [8]$$

Since $\Delta\phi_{sc} \cong E$ when $n_i = 0$

$$\frac{1}{C^2} = \frac{1}{C_o^2} - \frac{8\pi n_i}{\epsilon_{sc} n_o C_H} \quad [9]$$

¹Note that in the absence of interface states the potential drop across the Helmholtz layer is practically constant with electrode potential over the range of interest to the present work.

so that

$$n_i = \pm \frac{\epsilon_{sc} n_o C_H}{8\pi} \left(\frac{1}{C_o^2} - \frac{1}{C^2} \right) \quad [10]$$

where C is the capacitance with interface states ionized, and C_o the capacitance in the absence of interface state ionization.

Taking $C_H = 20 \mu\text{F}/\text{cm}^2$, which is its typical value (4), we have

$$n_i = 8.7 \times 10^{-7} \epsilon_{sc} n_o \left(\frac{1}{C_o^2} - \frac{1}{C^2} \right) \quad [11]$$

where capacitance is in $\mu\text{F}/\text{cm}^2$.

Deep level kinetic characteristics.—The kinetics of processes involved in filling and emptying deep trap levels can also be studied by EPS. In this case, the photocapacitance transients are measured after initiation and after interruption of illumination. The general expression² for the change in the concentration of ionized states with time is

$$\frac{dn_s}{dt} = k_i(N_s - n_s) - k_n n_s \quad [12]$$

where n_s is the density of ionized states, N_s the total density of trap states, k_i the ionization constant, k_n the neutralization constant, and t time. Note that k_i and k_n include terms for both thermal and optical processes.

Integration of Eq. [12] yields

$$\ln [(k_i + k_n)n_s - k_i N_s] = - (k_i + k_n)t + K \quad [13]$$

where K is the integration constant.

The components of k_i and k_n depend on the nature of the state. For a state that becomes more positive when ionized

$$k_i = e_n^t + e_n^o + c_p \quad [14]$$

$$k_n = e_p^t + e_p^o + c_n \quad [15]$$

whereas for a state that becomes more negative when ionized

$$k_i = e_p^t + e_p^o + c_n \quad [16]$$

$$k_n = e_n^t + e_n^o + c_p \quad [17]$$

where e_n^t and e_p^t are thermal emission rate constants, e_n^o and e_p^o optical emission rate constants, and c_n and c_p capture rates for electrons and holes, respectively. The various processes involved can be visualized with the aid of Fig. 2. Note that an increase in positive charge produces an increase in C for an n-type semiconductor but a decrease for a p-type material; a decrease in positive charge produces the opposite effects.

The capture rates include a factor for the appropriate minority carrier concentration, *i.e.*

²The treatment given here is similar to that presented by Miller *et al.* (5) except that the equations are derived in terms of ionized states.

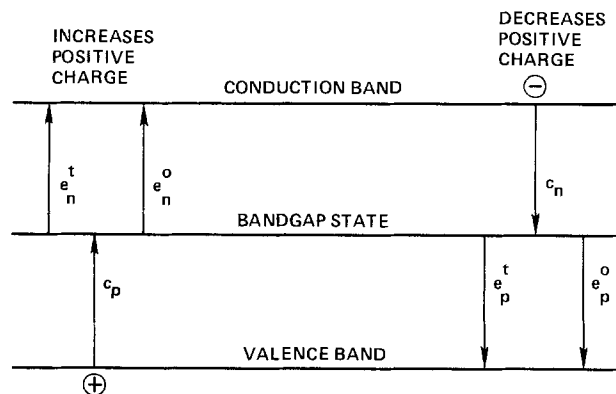


Fig. 2. Schematic diagram depicting the various ionization and neutralization processes for a semiconductor bandgap state.

$$c_n = \sigma_n \nu_n n \quad [18]$$

$$c_p = \sigma_p \nu_p p \quad [19]$$

where σ_n and σ_p are capture cross sections, ν_n and ν_p average thermal velocities, and n and p charge carrier concentrations. Equations [18] and [19] are for electrons and holes respectively.

Deep levels in wide-bandgap materials.—Of special interest from a practical standpoint is the characterization of deep traps in relatively wide-bandgap extrinsic semiconductors, for which thermal emission processes and the concentration of minority carriers can often be ignored. For a specific example, consider an n-type material containing a deep electron trap that is neutral when filled and positively charged when empty. In this case, e_n^t and c_p are taken as zero, *i.e.*

$$k_i = e_n^o \quad [20]$$

and

$$k_n = e_p^t + e_p^o + c_n \quad [21]$$

First consider repopulation of the states in the dark after at least a portion of them have been ionized by illumination. Since e_n^o and e_p^o are also zero in this case, $k_i = 0$ and $k_n = e_p^t + c_n$, so that Eq. [13] reduces to

$$-\ln n_s = (e_p^t + c_n)t + K \quad [22]$$

Substitution of n_t and n_i from Eq. [3] and [10] for n_s yields

$$-\ln \left[\frac{8\pi E}{\epsilon_{sc} e} (C_o^2 - C^2) \right] = (e_p^t + c_n)t + K \quad [23]$$

for bulk states, and

$$-\ln \left[\frac{\epsilon_{sc} n_o C_H}{8\pi} \left(\frac{1}{C_o^2} - \frac{1}{C^2} \right) \right] = (e_p^t + c_n)t + K \quad [24]$$

for interface states. Solving for K at $t = 0$, we have

$$\ln \left(\frac{C_o^2 - C_t^2}{C_o^2 - C_{t=0}^2} \right) = - (e_p^t + c_n)t \quad [25]$$

for bulk states, and

$$\ln \left[\left(\frac{1}{C_o^2} - \frac{1}{C^2} \right) / \left(\frac{1}{C_t^2} - \frac{1}{C_{t=0}^2} \right) \right] = - (e_p^t + c_n)t \quad [26]$$

for interface states (where C_t and $C_{t=0}$ represent C at time t and $t = 0$, respectively).

Thus, plots of $\ln [(C_o^2 - C_t^2)/(C_o^2 - C_{t=0}^2)]$ for bulk states or $\ln [(1/C_o^2 - 1/C_t^2)/(1/C_o^2 - 1/C_{t=0}^2)]$ for interface states *vs.* time should yield a straight line of slope $(e_p^t + c_n)$. For states sufficiently above the valence band in energy, e_p^t can also be taken as zero and c_n is obtained directly. When this is not the case, c_n , which is proportional to n , can be evaluated from the effect of injecting a known concentration of majority carriers (electrons). This can be accomplished by momentarily reducing the bias voltage (6). Alternatively, in electrochemical systems, it is possible to adjust the dark current, which determines the overall value of n through the space charge region by adding appropriate solution redox couples that inject majority carriers into the semiconductor. The more negative the redox potential of the couple, the greater the tendency to inject electrons. It should be mentioned that analogous procedures could be used to evaluate minority carrier capture rates from EPS measurements. In this case, minority carriers would be injected by momentarily forward biasing the semiconductor (6) or employing solution redox couples that are sufficiently positive for n-type semiconductors or sufficiently negative for p-type materials.

Now consider the change in photocapacitance with time after initiating illumination. Since $n_s = 0$ at $t = 0$,

Eq. [13] becomes

$$-\frac{1}{(k_1 - k_n)} \ln \left[1 - \frac{(k_1 + k_n)}{k_1 N_s} n_s \right] = t \quad [27]$$

Having determined k_n from photocapacitance decay studies we can readily calculate k_1 when N_s is known, *i.e.*, when trap saturation can be attained. Otherwise, k_1 and N_s can be determined by iteration to attain the best fit for Eq. [27]. If the photon flux (I) is known, the optical cross section (σ_n°) can be extracted from e_n° (which equals k_1 in this case) since $e_n^\circ = \sigma_n^\circ I$.

Experimental Considerations

Electrolyte selection.—For studies of a specific electrochemical system, EPS measurements are, of course, made *in situ* in the electrolyte of interest. In other cases, however, an electrolyte must be selected.

Interface states associated with oxygen adsorption or surface oxides can readily be studied by EPS in aqueous solutions, in which oxide interfacial structures are apparently stable. Note that for n-CdSe (see Results section), interface states associated with oxygen adsorption are found to be practically unchanged in aqueous systems compared to the vacuum. In EPS, the environment, *i.e.*, electrode potential and solute/solvent, can also be easily varied. Such studies can provide valuable information about oxidation/passivation phenomena.

In cases for which there is flexibility in the choice of electrolyte for EPS measurements, two prime considerations are the electrolyte optical transmission and electrical conductivity. Ideally, the electrolyte should be transparent to light ranging in energy from the bandgap down to midgap, which permits the entire bandgap region to be probed (via transitions involving both bands). Solvents that are sufficiently polar can generally be rendered electrically conductive via dissolution of appropriate salts. Tetraalkylammonium salts are typically used with the nonaqueous solvents.

Optical transmission spectra for some key solvents are shown in Fig. 3 and 4; the cell path length was 1.0

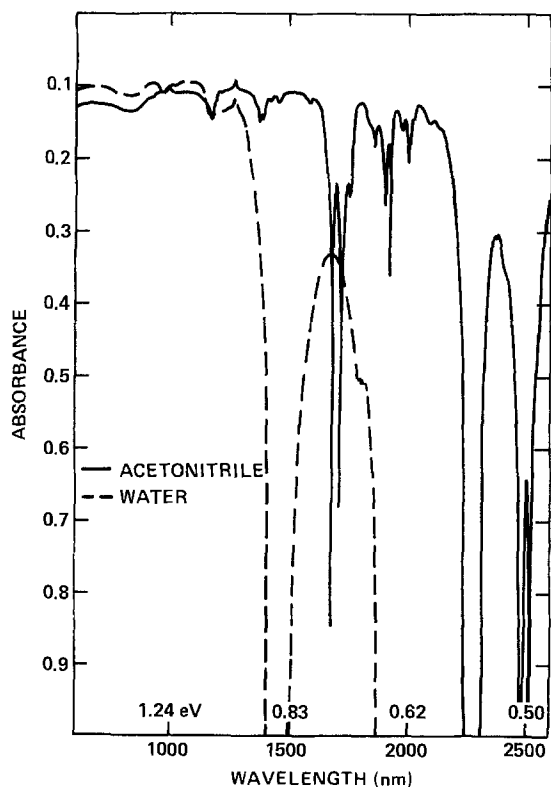


Fig. 3. Optical absorption spectra for water and acetonitrile (1.0 mm path length).

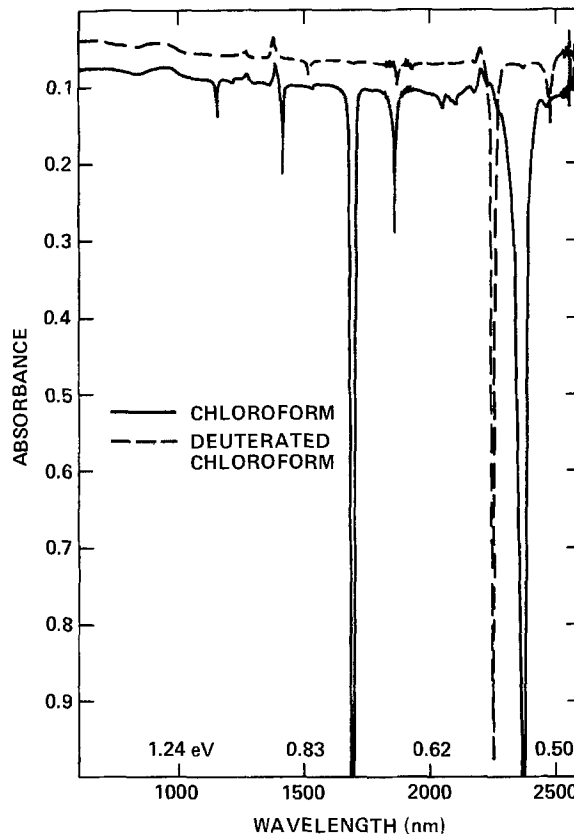


Fig. 4. Optical absorption spectra for chloroform and deuterated chloroform (1.0 mm path length).

mm, which is approximately equivalent to the thickness of electrolyte through which light passes in the EPS cell used in the present work. The useful range for water (Fig. 3), which is limited by the onset of absorption associated with O-H stretching, is seen to extend down to about 0.9 eV (1350 nm). Note that the transmission cutoff for alcohols would be similar to that of water. Acetonitrile (Fig. 3) exhibits no significant absorption features down to about 0.75 eV (1650 nm) where the onset of sharp absorption peaks associated with the C-H bond is observed. At energies between 0.75 and 0.55 eV, several sharp spectral features are evident, but considerable light transmission also occurs. Thus, acetonitrile can be used with little concern down to 0.75 eV, and between 0.75 and 0.55 eV with caution. In all cases, EPS spectra should be closely examined to determine which features might result from solvent absorption. The effects of the latter can be checked by varying the solvent or the thickness of the electrolyte layer in the light path. Chloroform, which contains only one C-H bond, exhibits significantly weaker absorption (the only pronounced spectral features are two sharp peaks at 0.52 and 0.73 eV) so that its useful range extends to at least 0.5 eV (Fig. 4). The effects of solvent absorption features associated with hydrogen can be even further reduced by use of deuterated solvents. Figure 4 also shows the transmission spectrum for deuterated chloroform (a readily available solvent); the good transmission characteristics extend to beyond 0.5 eV (the only pronounced spectral feature is a sharp peak at 0.55 eV), permitting bandgaps in the 1 eV range to be probed.

Another consideration in selecting a solvent is the stability of the semiconductor in the electrolyte. Although chemical instability may be a problem in some cases, the primary concern is the effect of photogenerated minority carriers, which migrate to the interface and can result in dissolution of the semiconductor and/or film formation. It should be emphasized at the outset that, in our experience, such effects are gen-

erally small and do not appreciably affect short-term EPS measurements. In the case of bulk states, even long-term measurements may not be affected by a slow rate of photodissolution, but film formation, when it occurs, is likely to cause the baseline capacitance to drift with time, making quantitative inferences more difficult. For studies of interface states, both photodissolution and film formation are likely to affect the structure of the interfacial region and interfere with EPS measurements. It should be mentioned that although the less polar nonaqueous solvents generally provide greater inherent stability against semiconductor photodissolution, there is also a greater tendency toward film formation in such media.

Photodissolution and film formation processes can generally be greatly suppressed or practically eliminated by incorporation of suitable redox species in the electrolyte. In this case, photogenerated minority carriers are removed as they arrive at the interface (before semiconductor degradation can occur) by reaction with the redox species, which is simultaneously converted to another soluble species. The stabilizing effect of redox species is to some extent reflected in the redox couple potential, but other factors are also important in this respect, and the effect of the couple on the interface characteristics and dark current must be considered. For example, specific adsorption of redox species can affect the interfacial structure and the semiconductor/electrolyte potential distribution, and may result in an increase in dark current. Ideally, both halves of the couple should be transparent to light in the energy range of interest (or be present in small concentration) and should not adsorb strongly on the semiconductor. Fortunately, a large number of redox couples have been studied for use in stabilizing electrochemical solar cells; even the least stabilizing of those reported in the literature would probably be effective for the extremely small currents flowing during EPS measurements.

It should also be mentioned that some electrolyte redox species may exchange electrons with interface states, affecting their population and hence the magnitude of any corresponding EPS spectral feature. Such effects may be undesirable in some cases, but can also be exploited to investigate the extent to which a particular interface state mediates electron transfer between the semiconductor and the electrolyte. Charge transfer mediation undoubtedly plays an important role in the functioning of many electrochemical systems, particularly those involving electrocatalysis, but its fundamental aspects have remained obscure.

Measurement frequency.—The voltage perturbation frequency employed in EPS measurements can to some extent be used as an adjustable parameter to maximize the signal to noise ratio and, in that manner, the sensitivity to capacitance changes. In this case, the frequency is chosen to yield a relatively large value for the capacitive reactance, as indicated by a large phase shift (70° – 90°) between the voltage perturbation and the current response. When there is appreciable frequency dispersion, this procedure will lead to some uncertainty in the calculated densities of states, but the associated error is generally very small for smooth single-crystal electrodes and is typically much less than an order of magnitude even for polycrystalline materials. In any case, measurements made at a given frequency should provide a relative measure of the density of a particular state.

Errors associated with frequency dispersion can be minimized if the source of the dispersion is known. Generally speaking, high frequency measurements, for which the effects of surface inhomogeneities and lattice defects are minimal, are considered more reliable. This is often not the case for polycrystalline films having appreciable porosity, since, because of the tortuous current paths involved, a large portion of the perturba-

tion voltage at high frequencies may fall across the electrolyte rather than the semiconductor. Therefore, for porous films low frequency measurements may be more reliable.

Measurements at various perturbation frequencies can also provide additional information. For example, the exchange of electrons between interface states and electrolyte species in response to the voltage perturbation, which may occur under some bias potential conditions, is likely to be a relatively slow process which contributes to the measured capacitance only at low frequencies. In this case, the associated EPS spectral feature will vanish as the perturbation frequency is increased,

Electrode bias voltage.—The electrode bias potential is typically varied over the range where the semiconductor is reverse biased and the dark current is minimal. As already mentioned, the magnitude of EPS spectral features associated with bulk states generally varies linearly with the space-charge depletion width, whereas those associated with interface states are relatively potential insensitive. Thus, bulk and interface states can typically be distinguished from the effect of the electrode bias potential. Identification made in this way can readily be verified by changing the solvent or adding surfactants to the electrolyte. The surfactants typically have a large effect on the energies/population of interface states but have little effect on the EPS characteristics of bulk states.

Changes in the population of interface states with electrode bias voltage can also be detected by EPS. In this case, the magnitude of the photocapacitance change corresponding to the interface state should vary rather abruptly over a limited potential range as the state population changes; this contrasts with the Mott-Schottky behavior associated with a bulk state. It should also be mentioned that the potential dependence of the population of an interface state is likely to be affected by the presence of redox species in the electrolyte, which can exchange charge with the state.

Experimental Details

Figure 5 shows a block diagram of the apparatus used in the present work. Complete computer control was provided by a Hewlett Packard 9826 desktop computer. The real and imaginary components of the electrode impedance were determined by a Solartron Model 1172 frequency response analyzer which automatically averages over many perturbation cycles. The perturbation voltage was typically 10 mV (rms), although larger voltages are sometimes used for highly resistive materials. The impedance of the counterelectrode (Pt) and lead inductance effects were eliminated from the measurement by use of a Stonehart Model BC 1200 potentiostat (which employs a dual working electrode lead) in the three-electrode mode. A Tektronix Model AM501 differential amplifier was employed between the potentiostat and the frequency response analyzer. Monochromatic illumination (1 – 2 mW/cm²) having a bandwidth of ~ 8 nm (depending on the slit dimensions and diffraction grating) was provided by a 1000W tungsten-halogen lamp³ via an Instruments SA Model HT-20 turret monochromator. Appropriate ordering/neutral density filters were inserted automatically.

With the apparatus described here, capacitance changes of 0.01% can be measured. This corresponds to a detectability limit for both bulk and interface states (the latter expressed per cm²) of 0.02% of the overall charge carrier concentration.

The electrochemical cell was glass with a quartz optical window and a Teflon top through which cell connections were made. The electrolyte volume was ~ 200 ml. An inert atmosphere was maintained via

³ The spectral output for this lamp is relatively monotonic; for most other light sources, particularly Xe lamps, it is important to take into account intensity variations with wavelength.

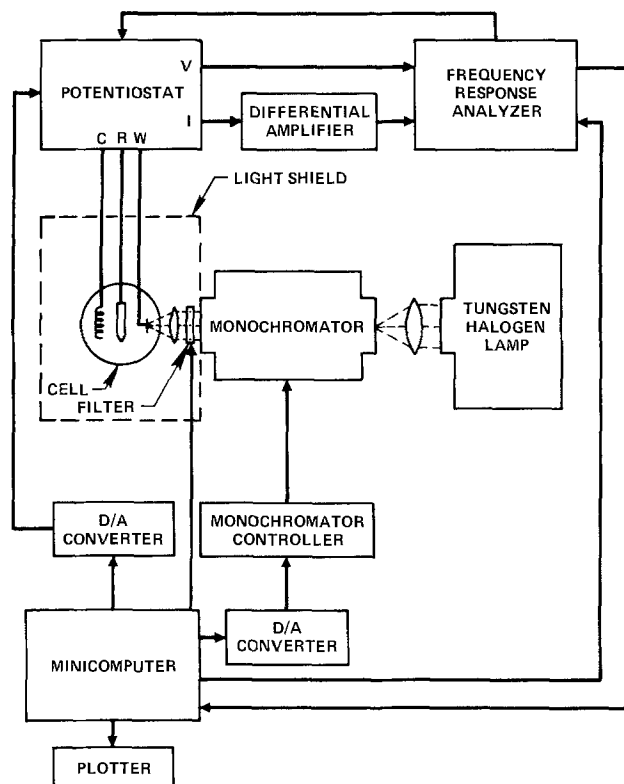


Fig. 5. Block diagram of the EPS apparatus

argon bubbling through the solution. The platinum counterelectrode was isolated from the main cell compartment via a glass frit. The reference electrode was a double junction saturated calomel electrode (SCE) or Ag/AgCl in aqueous solutions, and an Ag/Ag⁺ (acetonitrile/0.1M AgNO₃/0.1M tetraethylammonium perchlorate) in nonaqueous electrolytes. All bias voltages are given relative to the flatband potential (U_{FB}), which was determined by ac impedance measurements as a function of potential (values typically agreed with those observed for photocurrent onset).

Semiconductor electrodes, with appropriate ohmic contacts, were mounted in polyester resin (Torr Seal, Varian, Incorporated) so that only the desired surface was exposed to the electrolyte. The area of the exposed semiconductor surface was usually 0.2 cm², permitting total illumination of the surface. For larger electrodes, the dark capacitance associated with the unilluminated portion of the exposed surface was subtracted from all measured capacitance values. Single crystal electrodes were generally polished using aqueous slurries of successively finer alumina powders to a particle size of 0.3 μ m before etching; thin film materials received no mechanical pretreatment. The following etching procedures were used. GaAs electrodes were immersed in 50/50 volume percent (v/o) H₂SO₄/H₂O₂ (30%) for ~10s. CdSe electrodes were etched in ~50 v/o HNO₃ for ~10s, then dipped in aqueous polysulfide solution (1.0M S + 2.5M Na₂S + 1.0M KOH) to remove excess Se from the surface. Amorphous Si specimens were used as obtained. Zn₃P₂ electrodes were etched in 1 v/o bromine/methanol for 5-10s.

Results and Discussion

Deep traps in n-GaAs.—The sensitivity of EPS to some of the more common deep traps in n-GaAs is illustrated by the spectrum for horizontal Bridgman material (<100>) shown in Fig. 6; corresponding phototransitions are depicted in the insert. The important features apparently correspond to the "B" state (7, 8) (decrease in capacitance at 0.73 eV), the "EL2" level (9, 10) (increase in C at 0.83 eV), chromium (11) (peak at 0.92 eV superimposed on EL2 wave), and an

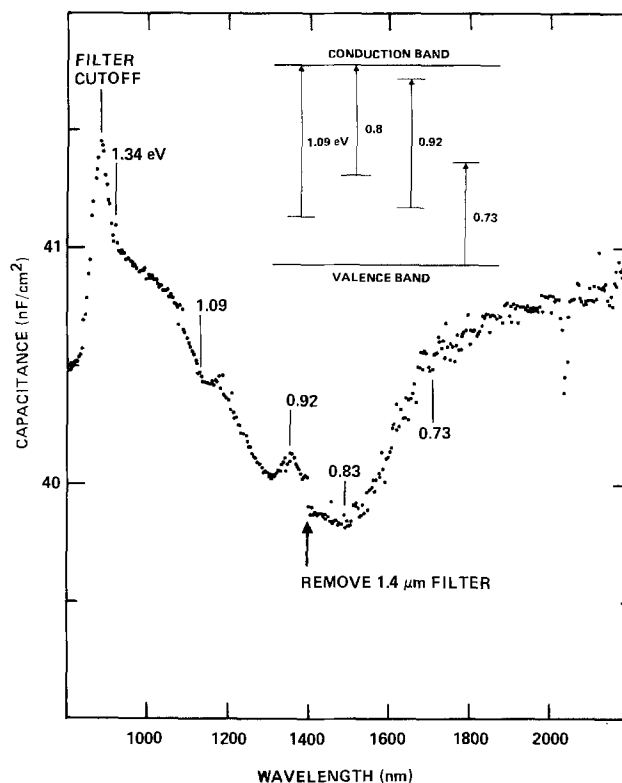


Fig. 6. EPS spectrum (measured at 5 kHz) and associated energy levels/phototransitions for n-GaAs (0.5V vs. U_{FB}) in 0.1M tetraethylammonium perchlorate/acetonitrile solution.

unidentified donor state at 1.09 eV. All of these transitions exhibit the electrode-potential dependence expected for bulk states. Some surface pretreatments introduce an additional donor state at about 0.70 eV which apparently resides at the interface, since the associated capacitance change is potential independent. Based on the capacitance changes, the densities of all bulk states detected are $\sim 10^{14}/\text{cm}^3$, which are reasonable values when compared to literature data for similar material. Also secondary ion mass spectroscopy (SIMS) analysis indicated that the chromium concentration in our material was $2 \times 10^{14}/\text{cm}^3$.

Comparison with DLTS.—A direct comparison between EPS and DLTS was made for a liquid-encapsulated Czochralski (LEC) p-GaAs specimen (<100>); a typical EPS spectrum and the assumed phototransitions are shown in Fig. 7. With DLTS, only the hole trap (acceptor level) corresponding to the sharp capacitance increase at 0.69 eV in the EPS spectrum was detected. Both methods yielded about the same density, for this state, $10^{15}/\text{cm}^3$. Three additional states were detected by EPS, corresponding to a capacitance decrease at ~0.74 eV (electron trap), a peak at 0.9 eV (probably a localized impurity transition), and an increase in capacitance at 1.06 eV (hole trap). Although the sum of the energies of the 0.69 and 0.74 eV levels corresponds closely to the bandgap (1.42 eV), complementary transitions involving the same center are not involved. This was shown clearly from the time dependence of the capacitance upon shifting the wavelength from one value to another or interrupting illumination. For example, if 1500 nm light is blocked, the capacitance rapidly increases to a slowly decaying value because the lifetime of the occupied 0.74 eV level is relatively short (<1s), whereas that of the occupied 0.69 eV hole trap is very long (at least several minutes).

Interface states at n-CdSe.—The sensitivity of EPS to interface states is best illustrated by data obtained for n-CdSe, for which interface states associated with

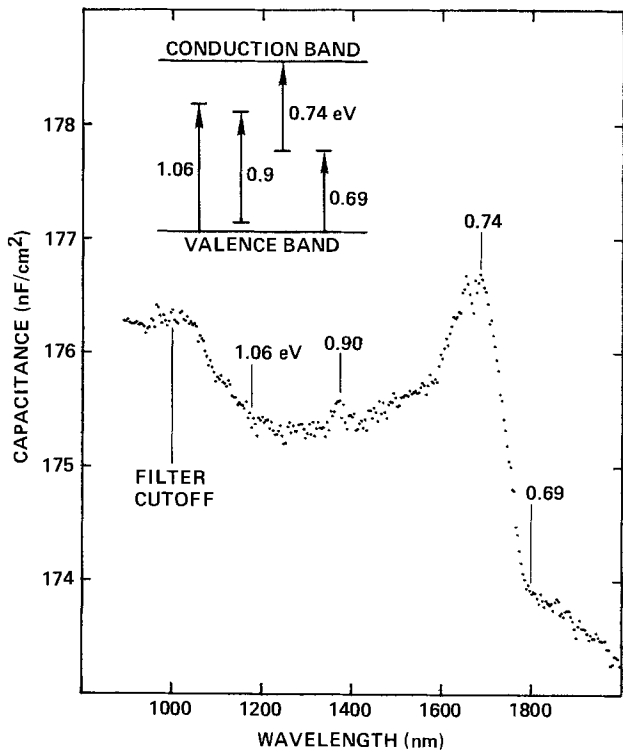


Fig. 7. EPS spectrum (measured at 10 kHz) and associated energy levels phototransitions for LEC p-GaAs (0.4V vs. U_{FB}) in 0.1M tetrabutylammonium perchlorate/0.1M benzoquinone/acetonitrile.

oxygen adsorption play a dominant role (12, 13). Figure 8 shows an EPS spectrum and associated phototransitions for a chemically etched single crystal of

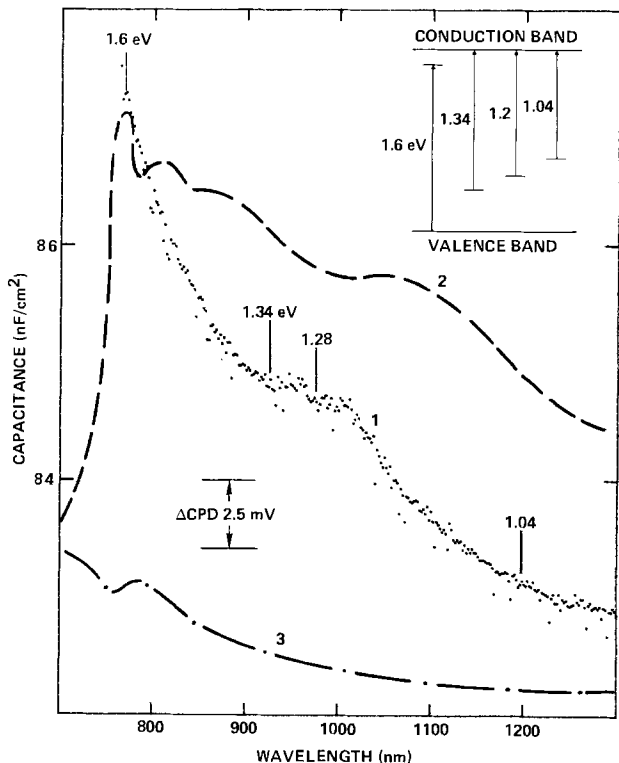


Fig. 8. EPS spectrum (measured at 5 kHz) for chemically etched single-crystal n-CdSe (0.7V vs. U_{FB}) in 0.5M KOH solution (curve 1) and surface photovoltage spectra for oxygen-adsorbed (curve 2) and vacuum-cleaved (curve 3) single-crystal n-CdSe. Surface photovoltage data taken from Ref. (12); Δ CPD = change in contact potential difference. Reproduced with permission of North Holland Publishing Company, Amsterdam, from *Surf. Sci.*, 69, 62 (1977).

n-CdSe (cleaved perpendicular to c-axis) in a basic aqueous electrolyte (curve 1), as well as surface photovoltage spectra (curve 2 and 3) reported by Brillson (12) for oxygen-adsorbed (70% coverage) and vacuum-cleaved (LEED-ordered) single-crystal n-CdSe surfaces. Three capacitance increases/plateaus, associated with transitions from donor states at 1.04, 1.28, and 1.34 eV to the conduction band, are evident. Note that there is also a barely discernible capacitance decrease at \sim 1.6 eV, which corresponds to a transition from the valence band to an ionized donor state located just below the conduction band; this state occurs in much higher concentrations in some polycrystalline materials.

The similarity between the surface photovoltage spectrum for the oxygen-adsorbed surface and the EPS spectrum is striking, indicating that the surface oxide structure is similar in the two environments and that the same bandgap states are involved. The 1.04 eV transition, and possibly the transition at 1.28 eV (not resolved by the vacuum technique), must involve interface states associated with oxygen adsorption, since no change in surface photovoltage was observed for the vacuum-cleaved CdSe (curve 3) in this energy range. The 1.34 eV transition is apparently intrinsic to CdSe, since it is evident in the photovoltage spectra for both vacuum-cleaved and oxygen-adsorbed CdSe crystals. EPS data for n-CdSe single crystals with various surface pretreatments also indicate that both the 1.04 and 1.34 eV transitions are associated with interface states. For example, although the same transitions are observed in all cases, concentrations of the 1.04 and 1.34 eV states are reduced by photoetching and greatly increased by mechanical polishing. EPS data for n-CdSe in aqueous solutions also correlate extremely well with other solid-state literature data for oxygen-adsorbed surfaces [e.g., (13)]. As an indication of the sensitivity of the EPS method, the concentration of the 1.04 eV interface state calculated according to Eq. [2] from the data in Fig. 8 is $3 \times 10^{12}/\text{cm}^2$, and that of the 1.28 eV state is $5 \times 10^{11}/\text{cm}^2$.

Amorphous silicon.—EPS has also been applied successfully to characterization of amorphous silicon. Figure 9 shows an EPS spectrum on three different scales

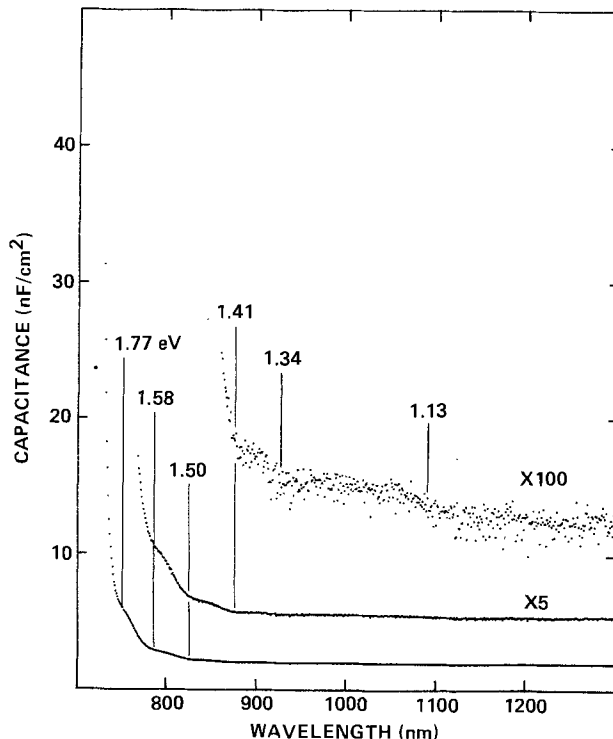


Fig. 9. EPS spectrum for a-Si (measured at 10 kHz) in 0.1M tetrabutylammonium perchlorate/acetonitrile.

(offset) for an a-Si specimen (deposited on stainless steel) in an acetonitrile electrolyte. Two relatively weak transitions (onsets at 1.13 and 1.34 eV) and four stronger transitions (onsets at 1.41, 1.50, 1.58, and 1.77 eV) are resolved as a series of plateaus, all corresponding to excitations from states within the mobility gap to the conduction band. Apparently, both band-tail states and gap states (14) in a-Si can be detected by EPS.

Kinetic studies.—Finally, EPS evaluation of deep-level kinetic parameters will be illustrated for one specific case. Figure 10 shows a typical EPS spectrum obtained for thin film p-Zn₃P₂ (prepared by chemical vapor deposition on tungsten-coated silicon steel). Note that at wavelengths longer than 1100 nm the capacitance scale is 100-fold more sensitive and the EPS curve is offset. There are two well-defined peaks (0.74 and 1.02 eV) presumably corresponding to localized impurity transitions, and two capacitance increases (onsets at 1.08 and 1.27 eV) corresponding to transitions from the valence band to bandgap states. The 1.08 eV level is apparently an interface state since it varies considerably with surface pretreatment, sometimes obscuring the 1.02 eV peak. The other states apparently reside in the bulk.

Consider the 0.74 eV bulk state in p-Zn₃P₂. The time dependence of the photocapacitance after initiation and interruption of 1680 nm illumination is shown in Fig. 11. Figure 12 shows a plot of $\ln [(C_o^2 - C_t^2)/(C_o^2 - C_{t=0}^2)]$ vs. time in the dark, which, according to Eq. [25], should yield a straight line of slope k_n . The good linearity at longer times is evident. Note that the initial rapid decrease in C , which results in a non-zero intercept, is probably caused by edge effects. Figure 13 shows the photocapacitance rise data from Fig. 11 and the theoretical curve (solid line) obtained by computer fitting the data to Eq. [27] using the k_n value from Fig. 12; the good fit is evident. Calculated values for N_s and k_o are also given in Fig. 13. The value for N_s ($1.4 \times 10^{16}/\text{cm}^3$) is slightly higher than that calculated from the overall capacitance change ($8.5 \times 10^{15}/\text{cm}^3$), since trap saturation had not been attained. In cases for which the capacitance change is independent

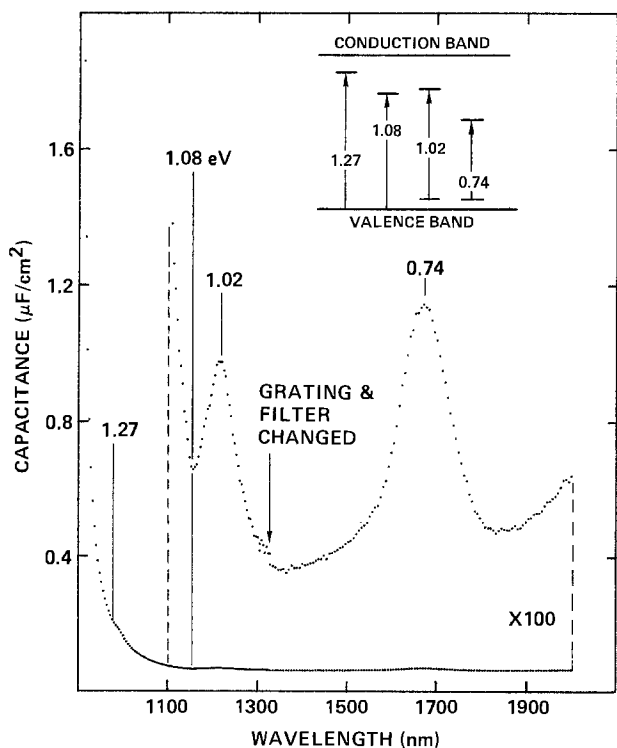


Fig. 10. EPS spectrum (measured at 5 kHz) for thin film p-Zn₃P₂ (0.3V vs. U_{FB}) in 0.1M tetrabutylammonium perchlorate/acetonitrile.

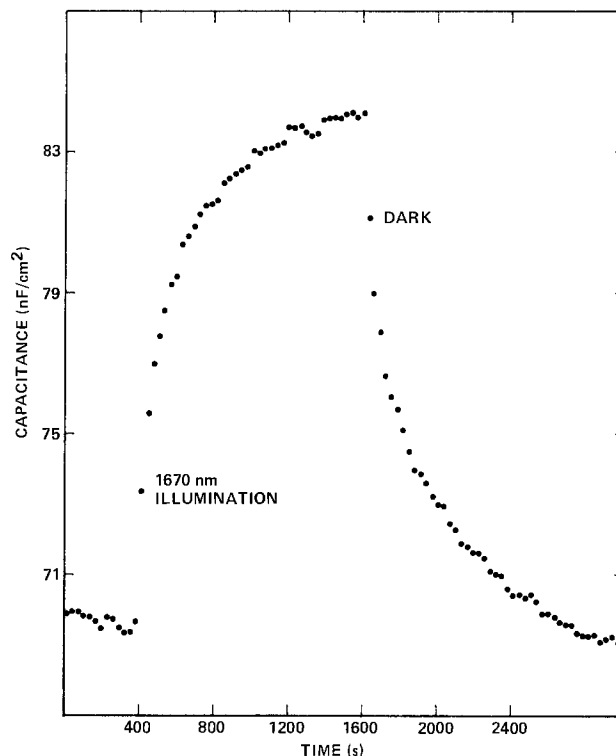


Fig. 11. Photocapacitance time dependence for the 0.74 eV state in thin film p-Zn₃P₂ after initiation and interruption of 1680 nm illumination. Conditions same as in Fig. 10.

of illumination intensity, the two calculated values for N_s are found to be equivalent.

Summary and Conclusions

EPS has been demonstrated to be an extremely sensitive means for characterization of deep electronic levels in a wide variety of semiconductor materials. Application of the method, which is nondestructive and provides *in situ* electrochemical information, is relatively straightforward and rapid; the blocking contact

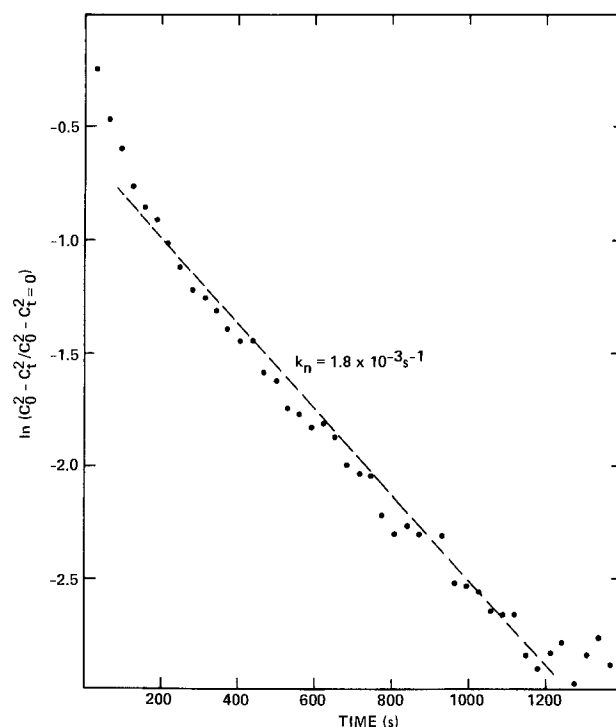


Fig. 12. Decay plot according to Eq. [25] for the data in Fig. 11

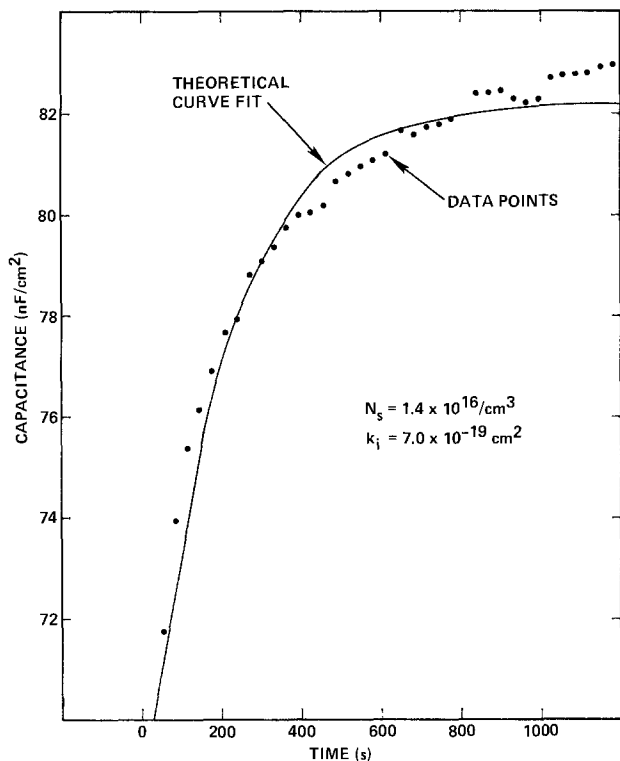


Fig. 13. Computer fit to the photocapacitance-rise data from Fig. 11, and calculated N_s and k_i values according to Eq. [27] for a bulk state.

being formed simply by immersing the semiconductor in a liquid electrolyte and measurements are made at ambient temperature and pressure. Information concerning the energetic location, density, and population/depopulation kinetics for both bulk and interface states is provided.

Acknowledgments

This work was partially supported by the Solar Energy Research Institute under Subcontract no. XG-0-9276. The authors thank Dr. Thomas McMahon of the Solar Energy Research Institute and Dr. Ting Chiu of Southern Methodist University for providing the a-Si and Zn_3P_2 specimens, respectively. The authors are also indebted to Dr. Kenneth Elliott, who provided the GaAs specimens and performed the DLTS measurements, and Dr. William Southwell, who provided the curve-fitting program used in the transient analyses.

Manuscript submitted July 5, 1983; revised manuscript received ca. Aug. 22, 1983.

Rockwell International Science Center assisted in meeting the publication costs of this article.

REFERENCES

1. R. Haak, C. Ogden, and D. Tench, *This Journal*, **129**, 891 (1982).
2. N. F. Mott, *Proc. R. Soc. London, Ser. A*, **171**, 27 (1939).
3. W. Schottky, *Z. Phys.*, **118**, 539 (1942).
4. J. O'M. Bockris and A. K. N. Reddy, in "Modern Electrochemistry," Vol. 2, p. 754, Plenum Press, New York (1970).
5. G. L. Miller, D. V. Lange, and L. C. Kimmerling, *Ann. Rev. Mater. Sci.*, **7**, 377 (1977).
6. C. H. Henry, H. Kukimoto, G. L. Miller, and F. R. Merritt, *Phys. Rev. B*, **7**, 2499 (1973).
7. D. V. Lang and R. A. Logan, *J. Appl. Phys.*, **47**, 1533 (1976).
8. A. Mitonneau, G.M. Martin, and A. Mircea, *Electron. Lett.*, **13**, 666 (1977).
9. A. Ashby, G. G. Roberts, D. J. Ashen, and J. B. Mullin, *Solid-State Commun.*, **20**, 61 (1976).
10. G. M. Martin, A. Mitonneau, and A. Mircea, *Electron. Lett.*, **13**, 191 (1977).
11. D. Bois, *J. Phys. (Paris)*, **35**, C3-241 (1974).
12. L. J. Brillson, *Surf. Sci.*, **69**, 62 (1977).
13. J. E. Ture, G. J. Russell, and J. Woods, *J. Cryst. Growth*, **59**, 223 (1982).
14. R. A. Gibson, P. G. LeComber, and W. E. Spear, *Solid-State Electron. Dev.*, **2**, 53 (1978).

Performance and Discharge Characteristics of Ca/LiCl, LiNO₃/LiNO₃, AgNO₃/Ni Thermal Battery Cells

G. E. McManis,* M. H. Miles,* and A. N. Fletcher*

Chemistry Division, Research Department, Naval Weapons Center, China Lake, California 93555

ABSTRACT

Thermal battery cells utilizing molten LiNO₃ as an oxidizing electrolyte with calcium anodes have been characterized for high rate discharge conditions. The presence of small amounts of AgNO₃ greatly improves the cathode reaction. Half-cell studies of anode characteristics show little variation of anode potential with temperature. Gassing at the anode-electrolyte interface increases with temperature and current density. Overall anode consumption rates increase with increasing temperature, while anode coulombic efficiencies drop at high rates of discharge (300 mA/cm²). Cathode half-cell data reveal that high rate reduction of AgNO₃ dissolved in LiNO₃ yields masses of dendritic growth at low temperatures (260°-275°C) while at higher temperatures (> 400°C) correspondingly fewer dendritic structures are observed. Cell experiments show anticipated current-voltage-temperature relationships, effectively mirroring half-cell experiments. Cell voltages sustain over 2V at 75 mA/cm² for periods which vary according to temperature of discharge.

Extensive research has been directed toward the development of a new generation high power-density thermal battery system for high rate discharge applications to replace the Ca/LiCl-KCl/CaCrO₄ system, which has been in use since World War II. The Ca/CaCrO₄ system exhibits a highly complex cathodic reaction. Furthermore, CaCrO₄ is a known carcinogen, and chromium is a strategic material with minimal

* Electrochemical Society Active Member.

U.S. reserves (1). An ideal thermal battery system would be capable of rapid activation, achieving high energy and power densities over a wide operating range of temperatures, and sustaining high current densities without utilizing strategic or toxic materials.

Much progress has been made in the development of new anode materials (LiAl, LiSi, LiB) and in the development of transition-metal sulfide cathodes (FeS, FeS₂), but the electrolyte most commonly used re-

mains the LiCl-KCl eutectic melting at 352°C (2). A lower electrolyte melting point would minimize both the quantity of pyrotechnic heating material and the quantity of insulation required for cell activation and discharge.

Lithium nitrate is a strong oxidizing agent with the dried reagent grade melting near 255°C. As an oxidizing salt, the need for a separate cathodic layer (such as CaCrO_4) is eliminated (3). The calcium anode in contact with molten LiNO_3 without added halide passivates, and rapidly forms a nonstoichiometric calcium oxide film. This film prevents reaching the true equilibrium potential and the passage of large current densities (4). The addition of halides produces corrosive attack of the film with subsequent pitting and thinning of the film allowing for high rate discharge at useful potentials (4-6). Chloride ion concentrations over 20 mol percent (m/o) have been found optimum for high rate discharges (7).

Although nitrate species are reducible, the electrode product of insoluble Li_2O precipitates on the cathode and prevents high rate discharge due to film resistivity (8, 9). The presence of AgNO_3 in the LiNO_3 electrolyte allows the reduction of silver ions to be utilized as the cathodic reaction, as well as the reduction of nitrate ions (10). The silver-ion reduction in molten LiNO_3 has been shown to sustain 100 mA/cm^{-2} without severe polarization.

A thermal battery system utilizing these concepts has evolved with a cell configuration of Ca/LiCl , $\text{LiNO}_3/\text{LiNO}_3$, AgNO_3/Ni . LiNO_3 is incorporated into a fiberglass binder/separator with LiCl layered near the anode and a layer of AgNO_3 in LiNO_3 with Cab-o-Sil binder near the cathode current collector. Such a design assures Cl^- concentration and isolation at the anode-electrolyte interface and maximizes the AgNO_3 concentration near the nickel current collector. The fiberglass LiNO_3 separator effectively prevents the formation of dense insoluble resistive AgCl layers. The catholyte layer of AgNO_3 in LiNO_3 with Cab-o-Sil binder allows for an optimal concentration of AgNO_3 near the cathode. The Cab-o-Sil serves to improve the low temperature characteristics by controlling catholyte flow and dendritic growth of silver reduced onto the Ni current collector.

Experimental

Nickel current collectors were cut from 0.010 in. thickness of Ni (99.9%, ROC/RIC), leads were 18 gauge Ni wire and spot-weld attached. Anodes were constructed by spot welding disks punched from Ca ribbon of 0.020 in thickness (99%, ROC/RIC) to Ca/Fe bimetal disks. Both the Ca foil and the bimetal disks were degreased in dichloroethane and cleaned in a dilute solution of HNO_3 in dimethylformamide until no dark oxide film was visible prior to spot welding.

LiCl (Mallinkrodt, Analytical Reagent), KCl (Matheson, ACS reagent), LiNO_3 (Baker, "Baker-Analyzed" Reagent), and LiNO_2 (Great Western Inorganics, 99% pure, monohydrate) were dried overnight at 125°C under vacuum prior to use. Some decomposition of the $\text{LiNO}_2 \cdot \text{H}_2\text{O}$ was noted, and weight loss was consistent with the loss of a water of hydration. AgNO_3 (Baker and Adams, ACS Reagent) was ground to a fine powder by mortar and pestle before use.

Anode performance experiments to determine current-voltage-temperature-calcium consumption relationships were conducted in porcelain crucibles (Coors) with 0.25 in diam anodes, Pt foil counterelectrodes, and Ag/Ag^+ reference electrodes. Temperature control was to $\pm 10^\circ\text{C}$ on a thermostated porcelain-surface hot plate.

Cathode performance characteristics for deposition potential and deposit morphology experiments were conducted in similar crucibles with 20 m/o AgNO_3 in

LiNO_3 solutions. Temperature control was $\pm 10^\circ\text{C}$. The solution was quiescent except for convective currents.

Cell testing procedures have been discussed previously (7). Anode vs. reference-electrode potentials were determined with a digital electrometer (Keithley Model 615). Galvanostatic conditions were maintained using a constant current source (Keithley Model 225). Temperature was monitored by a digital thermometer with analog output (Fluke Model 2165A). Cell voltages, applied current, and temperature were monitored by multimeters (Hewlett-Packard Model 3938A) and logged by a thermal printer (Hewlett-Packard Model 5051A). Other data channels were monitored on y vs. t recorders.

Results and Discussions

Anode performance characteristics.—Previous work showed that chloride ion concentration near the anode has a great influence on open-circuit and high current-density anode potentials (4, 7). Beyond 20 m/o, added Cl^- does not influence performance significantly. The thin layer of high Cl^- concentration near the anode allows for optimum discharge characteristics, but gives poor activation times because of the time required for solvation of the LiCl prior to depassivation of the anode. The effect of temperature on anode potential is minimal, as shown in Fig. 1. The duration of discharge for identical anodes, however, is seen to drop significantly at higher temperatures because of the rapid chemical oxidation of Ca by the LiNO_3 electrolyte. The variation in the amount of calcium was held to less than $\pm 0.25 \times 10^{-4}$ mols Ca (less than 10 m/o).

In Fig. 2, similarly treated anodes were discharged to 0.0V (vs. Ag/Ag^+ reference). As is shown, peak anode coulombic efficiency and consumption minimum occur in the region of about 310°C. Comparison to Fig. 1 reveals no significant difference in discharge curves other than time above 2V and a slightly higher anode potential at 310°C. It is thus apparent that anode film thickness, as governed by the corrosive activity of Cl^-

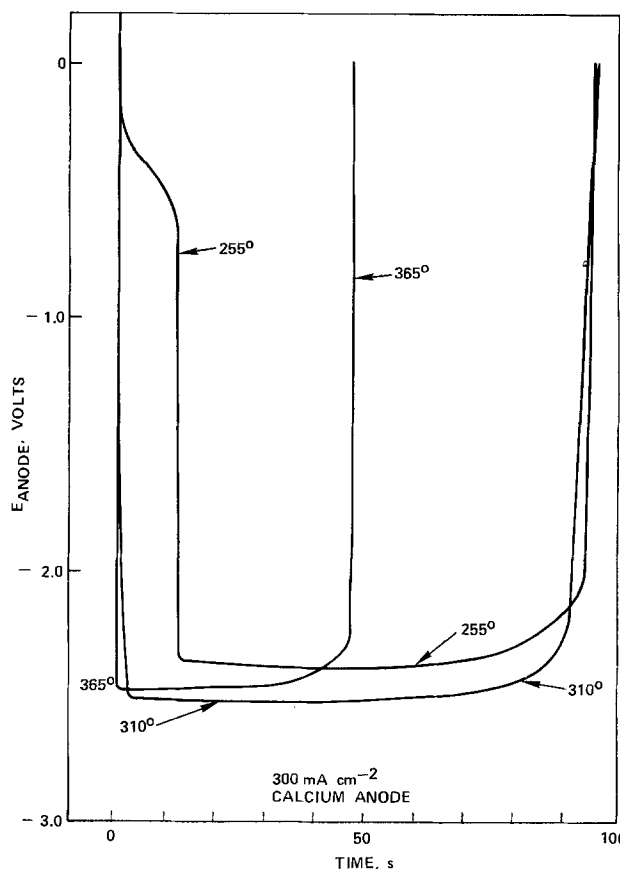


Fig. 1. Effect of temperature on calcium anode discharge curves at $300 \text{ mA}/\text{cm}^{-2}$ in LiNO_3 .

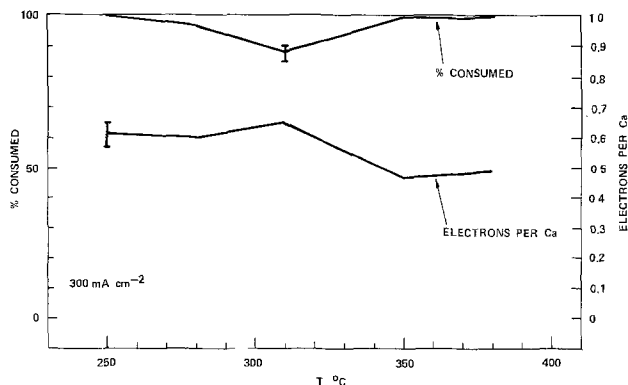


Fig. 2. Effect of temperature on anode consumption and anode efficiency for constant current discharges at 300 mA/cm^2 in LiNO_3 .

anions, limits discharge time and gradual film buildup at intermediate temperatures, allows for polarization, and hence less than 100% utilization of the calcium metal. At temperatures of 365°C and higher, the chemical oxidation rate is extremely rapid. The electrochemical oxidation is thus competing with rapid film formation by the direct reaction of Ca and LiNO_3 , and cell discharge times are shortened and coulombic efficiency is lowered.

Figure 3 shows that the performance of the calcium anode is better at 305°C than at either 275° or 375°C . Anode polarization is significant at current densities above 100 mA/cm^2 at both 275° and 375°C . The 305°C discharges up to 200 mA/cm^2 show a nearly linear anode potential vs. $\log i$ relationship.

Previous studies (7, 11) of large cells containing LiClO_4 have revealed that calcium anode deflagrations occur at high temperatures because of O_2 generation at the anode-electrolyte interface. During the present studies on molten nitrates, it was noted that gas evolution at the anode electrolyte interface was a function both of temperature and of current density. This gassing is due to the chemical reaction of calcium with

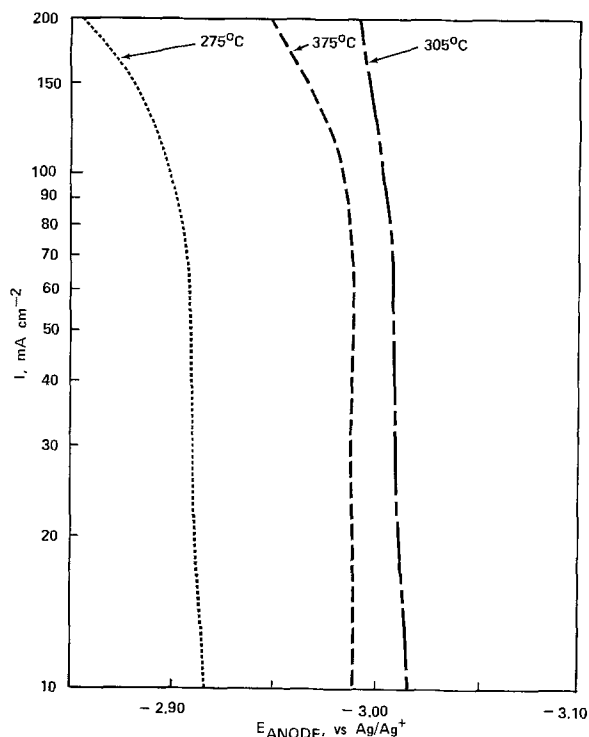
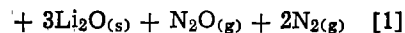
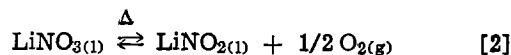


Fig. 3. Effect of temperature on anode potentials at various current densities in LiNO_3 .

molten nitrates to produce N_2O and N_2 but not O_2 (12)



The comparative voltammetric stability of the calcium anode at low temperatures despite vigorous gas evolution suggests that the reaction does not produce oxygen. At higher temperatures (over 425°C) Ca/LiCl, $\text{LiNO}_3/\text{LiNO}_3$, AgNO_3/Ni cells show occasional anode deflagrations, which may be due to O_2 generation by the thermal decomposition of LiNO_3 , as in Eq. [2].



Cyclic voltammetric studies have noted an increase in nitrite oxidation-wave peak currents consistent with LiNO_3 thermal decomposition in the region of 400° - 500°C (9, 13). Other workers have reported that the decomposition becomes appreciable only above 720 K (447°C) (13).

The alternative decomposition reaction (Eq. [3]) has been reported to be negligible up to 600 K (327°C) (13). Thermogravimetric analysis (TGA) of LiNO_3 confirms those reports, but reveals that above 550°C , decomposition to the oxide becomes quantitative



The use of fiberglass binders in molten LiNO_3 appears to be feasible only for short-term (less than 20 min) battery applications. LiNO_3 attacks SiO_2 over a period of time at temperatures up to 350°C with a more rapid attack at higher temperatures. Pure molten LiNO_2 immediately attacks SiO_2 , forming jellylike SiO_3^{2-} compounds. Much of the observed attack of LiNO_3 on SiO_2 may be attributed to the combined aggressive activity of Li^+ and NO_2^- . The NO_2^- species must be characterized as a definite binder aggressor.

Anode efficiency and consumption are complex functions of anode size and available calcium. It should be remembered that CaO is formed both by the chemical and the electrochemical reactions.

Cathode performance characteristics.—Half-cell studies of the silver ion cathode center on the morphologic characteristics of deposited silver metal and the deposition potential as a function of temperature. Galvanostatic depositions on nickel substrates at high rates show large masses of dendritic material when the electrolyte is at 260° - 285°C . Above 400°C , little dendritic growth is seen because of the extreme oxidizing nature of the molten LiNO_3 electrolyte.

Cell performance characteristics.—A total of 48 Ca/LiCl, $\text{LiNO}_3/\text{LiNO}_3$, AgNO_3/Ni thermal battery cells were discharged at constant temperature and constant current. In Table I, data are shown for constant temperature, constant current discharges at 261° , 310° , and 400°C . Data (where relevant) are indicated as mean \pm standard deviation of the individual values. Below 250°C , LiNO_3 is solid, and the cell is not electrochemically active. At temperatures over 425°C , anode deflagrations prompted by O_2 generation from the thermal decomposition of nitrate occur.

Figure 4 represents a typical complete cell discharge for a $1/2$ in diam cell approximately 4 mm thick utiliz-

Table I. Cell discharge characteristics

Parameter	261°C	310°C	400°C
Temperature	261°C	310°C	400°C
Number of tests	4	3	8
Peak cell voltage (75 mA/cm ²)	$2.46 \pm 0.09\text{V}$	$2.57 \pm 0.04\text{V}$	2.42 ± 0.28
Time above 80% peak voltage	$89.7 \pm 7.7\text{s}$	$90 \pm 4\text{s}$	$70 \pm 4\text{s}$
e ⁻ /Ca	0.61 ± 0.04	0.643 ± 0.005	0.53 ± 0.13
Deflagrations	0	0	2

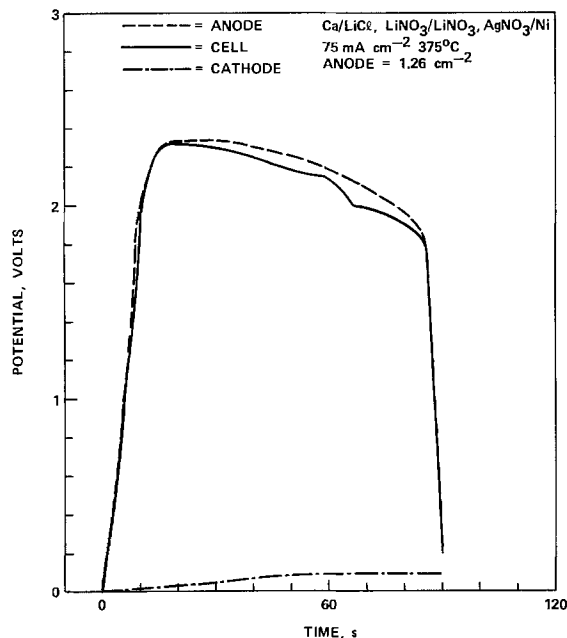


Fig. 4. Single cell discharge at 75 mA/cm^2 using a 1.26 cm^2 cell.

ing the catholyte layer at 12 weight percent (w/o) Cab-o-Sil in (20 m/o AgNO_3 + 80 m/o LiNO_3) with applied facial pressure ($\sim 10^5 \text{ Pa}$). Oxide ions generated at the cathode form both CaO and Li_2O . The resistive effects of oxide precipitation and anode passivation produce lower cell voltages than those seen in half-cell discharges from the outset of discharge. Cell resistance is found to increase to a maximum at the end of discharge. Overall anode potential shows somewhat poorer performance than in half-cell tests. This is probably because of silver ion migration to form resistive AgCl , and blocking of active anode sites by insoluble resistive CaO .

Conclusion

Thermal battery cells based on the system Ca/LiCl , $\text{LiNO}_3/\text{LiNO}_3$, AgNO_3/Ni show promise for thermal

battery high rate discharge applications without utilizing strategic or toxic materials. While cell performance characteristics have yet to be fully optimized, 1.26 cm^2 cells producing over 2V at 75 mA/cm^2 have been demonstrated with 60s discharge times. Anode functional range is between $275^\circ\text{--}425^\circ\text{C}$ with applied facial pressure and a minimal amount of calcium. Anode potential is relatively insensitive to temperature, but discharge capacity is optimized at about 310°C for $75\text{--}100 \text{ mA/cm}^2$ discharge rates.

Manuscript submitted Jan. 9, 1983; revised manuscript received ca. Aug. 1, 1983.

The Naval Weapons Center assisted in meeting the publication costs of this article.

REFERENCES

1. D. G. Altenpohl, in "Materials in World Perspective," pp. 24-25, Springer Verlag, New York (1980).
2. C. W. Jennings, in "The Primary Battery," Vol. II, G. W. Heise and N. C. Cahoon, Editors, pp. 263-293, John Wiley and Sons, Inc., New York (1975).
3. A. N. Fletcher and D. A. Fine, in "Proceedings of the 28th Power Sources Conference," Atlantic City, NJ, June 12-15, 1978, The Electrochemical Society, Inc., pp. 92-94 (1979).
4. M. H. Miles, *J. Appl. Electrochem.*, **11**, 325 (1981).
5. M. H. Miles, D. A. Fine, and A. N. Fletcher, *This Journal*, **125**, 1209 (1978).
6. M. H. Miles and A. N. Fletcher, *J. Appl. Electrochem.*, **10**, 251 (1980).
7. G. E. McManis, M. H. Miles, and A. N. Fletcher, in "Proceedings of the 30th Power Sources Conference," Atlantic City, NJ, June 7-12, 1982, The Electrochemical Society, Inc., In press.
8. A. N. Fletcher, M. H. Miles, and M. L. Chan, *This Journal*, **126**, 1496 (1979).
9. M. H. Miles and A. N. Fletcher, *ibid.*, **127**, 1761 (1980).
10. M. H. Miles, G. E. McManis, and A. N. Fletcher, Paper 586 presented at The Electrochemical Society Meeting, Denver, Colorado, Oct. 11-16, 1981.
11. M. H. Miles and A. N. Fletcher, *This Journal*, **128**, 1489 (1981).
12. B. J. Brough and K. H. Kerridge, *Inorg. Chem.*, **4**, 1353 (1965).
13. K. H. Stern, *J. Phys. Chem. Ref. Data*, **1**, 747 (1972).

The Lithium-Boron Alloy Anode in Molten Nitrate Electrolytes

G. E. McManis,* M. H. Miles,* and A. N. Fletcher*

Chemistry Division, Research Department, Naval Weapons Center, China Lake, California 93555

ABSTRACT

Potentiostatic studies of Li(B) anodes in molten LiNO_3 at 300°C indicate that at 80% peak open-circuit voltage, a broad flat discharge at 780 mA cm^{-2} is obtained. Galvanostatic discharge studies show stable anode potentials more negative than -3V (vs. Ag^+/Ag) in LiNO_3 at 300 mA cm^{-2} over a temperature range of $270^\circ\text{--}350^\circ\text{C}$. At temperatures above 350°C , deflagrations of the anode were often observed, particularly after deep discharge. Electrolyte composition is a key factor in determining the current density-potential and potential-temperature characteristics of the Li(B) anode in molten nitrates. Experiments in equimolar $\text{LiNO}_3\text{--KNO}_3$ exhibit open-circuit anode potentials up to 0.2V less electronegative to that seen in equimolar $\text{LiNO}_3\text{--NaNO}_3$ electrolyte. In a like fashion at 300 mA cm^{-2} and 300°C , the use of $\text{LiNO}_3\text{--KNO}_3$ equimolar electrolyte results in Li(B) anode potentials up to 0.45V more positive than those seen in $\text{LiNO}_3\text{--NaNO}_3$ equimolar electrolyte and up to 0.85V more positive than that seen in LiNO_3 electrolyte. Single cell tests integrating the Li(B) anode with existing silver ion cathode technology exhibit stable cell potentials in excess of 3V at 300 mA cm^{-2} at 300°C . The two phase composition of the Li(B) alloy allows for exceptional anode stability at the high anode potential of elemental lithium.

The lithium-boron alloy has been developed as an alternative anode material for thermal battery applications demanding high cell voltages, high discharge

* Electrochemical Society Active Member.

Key words: cell, current density, fused salts, oxidation.

rates, and good energy and power density characteristics. Previous studies by other workers have been done in LiCl-KCl eutectic electrolyte and have characterized the Li(B) alloy as a two phase composite material having a refractory Li_7B_6 matrix supporting intersti-

tial elemental lithium which acts as the anode material to produce potentials near those of free elemental lithium (1-12).

The Li_7B_6 matrix retains structural integrity up to 600°C or higher (1, 4, 5) in LiCl-KCl electrolyte. The structural integrity of the anode is particularly important above 188°C where interstitial elemental lithium is molten and labile. Elemental lithium within the matrix "wicks" to the anode-electrolyte interface similar to the behavior of nickel-feltmetal-lithium anodes, thus presenting a continually renewed lithium surface for electrochemical reaction (1, 4, 5). This capability allows for extremely high discharge rates with reported discharges to 8000 mA cm^{-2} in LiCl-KCl eutectic electrolyte without severe anode polarization (5).

Molten nitrate electrolytes are attractive media for thermal battery applications because of their oxidizing nature, low toxicity, and low melting points. In electrochemical cells utilizing active metal anodes in molten nitrates, corrosion processes are inhibited through the formation of nonstoichiometric passivating oxide films (13, 14). The thickness, structural integrity, and ionic conductivity regulate cation migration across the film and hence the current density which may be passed without extensive anode polarization due to cation accumulation within the film (13, 14).

The presence of aggressive species at the film-electrolyte interface that compete for adsorption with passivating nitrate anions introduces corrosive attack at the film. Adsorbed nitrate anions tend to "heal" the film while the addition of an aggressive anionic species (e.g., Cl^- , Br^- , or I^-) produces breaks and localized pitting corrosion on the anode (14). Film breakdown allows for free passage and migration of cationic species and thus an unimpeded anode reaction at close to the equilibrium potential (13).

Previous studies in molten nitrate electrolytes have considered primarily the calcium anode in systems with either added halide or oxyhalide anion species (13-17). A relatively tight calcium oxide film is rapidly formed on the calcium anode in molten LiNO_3 . This film acts to polarize the anode by retaining cationic species within the film unless depassivating halide species attack. Potentiostatic experiments reveal a surge of current indicative of film breakdown immediately on addition of Cl^- , Br^- , or I^- species (13). Thermal battery cells based on calcium anodes in molten lithium nitrate electrolytes utilize a thin layer of LiCl near the anode which attacks the passive film on solvation by molten LiNO_3 at activation (15).

The molten nitrate electrolyte thermal battery cells, as previously reported, utilize the reduction of silver ions as the major cathode reaction (15, 17, 18). This is accomplished by utilizing a catholyte layer composed of 20 mol percent (m/o) AgNO_3 in LiNO_3 that is rendered immobile by the addition of 12 weight percent (w/o) Cab-O-Sil as a binder. The electrolyte per se is LiNO_3 with a fiberglass (SiO_2) binder.

The objective of this work was to integrate extant molten nitrate thermal battery cell technology with the Li(B) alloy anode material to achieve a thermal battery cell capable of the high cell voltages and high rate discharges characteristic of lithium anodes while retaining the low melting point and oxidizing advantages of the molten nitrate electrolyte. Li(B) availability and experimental considerations limited work presented here to electrolyte temperatures over 250°C . A future communication will discuss Li(B) anode behavior below 250°C in molten nitrates.

Experimental

All salts were reagent grade and were dried overnight under vacuum at 125°C - 130°C prior to use. The electrolyte wafers were constructed by dipping fiberglass filter paper disks (Gelman Type A, 0.3 mm thickness and 6.35 mm diam) into molten electrolyte. The

electrolyte wafers were immediately assembled into cells to minimize moisture pickup.

Anodes were constructed by punching disks (6.35 mm diam) from 75 atom percent (a/o) (65 w/o Li) Li(B) foil (0.5 mm thickness) in an argon-filled dry box and prompt spotwelding of Li(B) disks to a stainless steel backing followed by spotwelding a nickel lead wire. Completed anodes were used immediately. An L-shaped reference electrode (0.1m Ag^+/Ag) was used to monitor anode potential.

Cyclic voltammetric and potentiostatic experiments were conducted either in platinum crucibles where the crucible acted as counterelectrode or in porcelain crucibles where a platinum screen acted as the counterelectrode. Cyclic voltammetric experiments utilized a Pt working electrode, while a Li(B) working electrode was used in potentiostatic experiments. Cyclic voltammograms were generated using a Princeton Applied Research Model 173 potentiostat with a PAR Model 175 universal programmer.

Galvanostatic experiments utilized a Keithley Model 225 constant current source and a Hewlett-Packard data acquisition system which has been previously described (15). Temperature measurements utilized Chromel-Alumel thermocouples with a digital thermometer (Fluke, Model 2165A). Cell testing technique has been previously described (15, 16).

Results and Discussion

At current densities of 300 mA cm^{-2} , cell voltages of approximately 3V are obtained as shown in Fig. 1. The cell construction featured the lithium (boron) alloy anode in contact with a LiNO_3 binder wafer which, in turn, contacted a layer of $\text{AgNO}_3\text{-LiNO}_3$ in binder with a platinum cathode current collector. During discharge, slight gassing was noted at the anode-electrolyte interface.

Half-cell studies of Li(B) anode discharges revealed an extremely high current density capability when potentiostated at 80% of the peak open-circuit voltage. Figure 2 demonstrates the potentiostatic discharge of a Li(B) anode at -2.56V vs. the Ag^+/Ag reference. The broad flat characteristic curve corresponds to a current density of 780 mA cm^{-2} which represents the maximum sustained current density for the Li(B) anode in molten LiNO_3 assuming an 80% peak voltage cutoff.

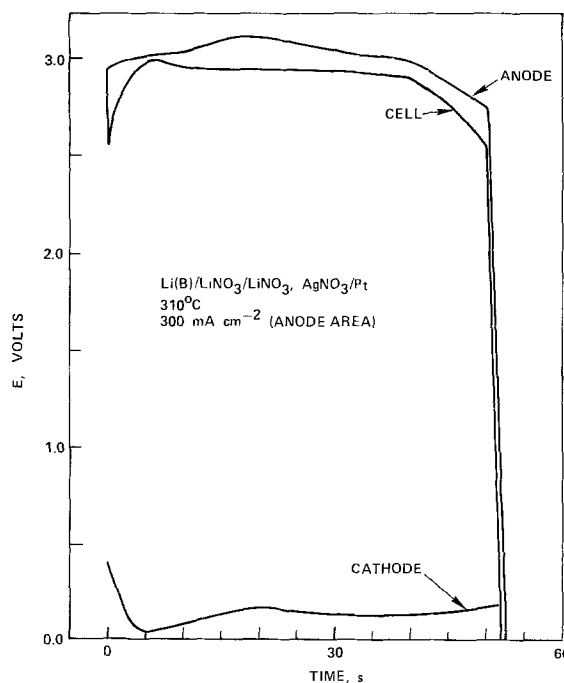


Fig. 1. Cell discharge at a constant current density of 300 mA cm^{-2} (anode area) at 310°C . Peak cell potential = 3.02V .

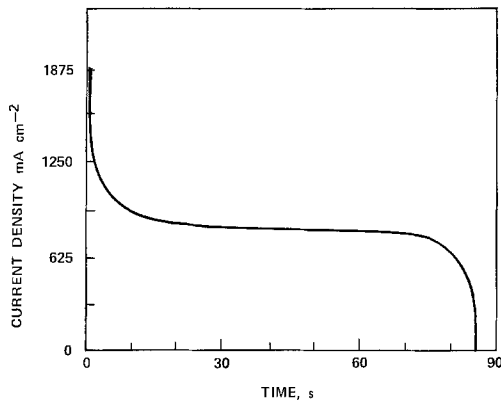


Fig. 2. Potentiostatic discharge of the Li(B) anode at 290°C in LiNO_3 . Open-circuit potential was -3.2V vs. Ag^+/Ag . The anode was potentiostated at 80% peak OCV (-2.56V).

The electrolyte composition is also a major factor in determining anode performance characteristics below 350°C. Figure 3 illustrates the effect of varying electrolyte composition on anode current-potential relationships at 300°C. It is evident that in equimolar $\text{LiNO}_3\text{-KNO}_3$ severe anode passivation occurs at 300 mA cm^{-2} while in LiNO_3 and in equimolar $\text{LiNO}_3\text{-NaNO}_3$ electrolytes much less polarization due to passivation is noted.

The passive film on Li(B) alloy anodes differs qualitatively from that seen on Ca anodes. The addition of LiCl to $\text{LiNO}_3\text{-KNO}_3$ electrolytes with Li(B) anodes at 300 mA cm^{-2} serves only to cause the anode potential to become less electronegative. This is in contrast to Ca anodes that polarize severely in pure molten LiNO_3 at 300 mA cm^{-2} , but show a decrease in passivation as halide concentration increases.

The Li(B) anode may be modeled as a molten lithium liquid phase supported on a rigid matrix of Li_7B_6 . Elemental lithium is held within the matrix by its own surface tension and, as the reaction proceeds, expended lithium at the anode-electrolyte interface is replaced by fresh elemental lithium "wicking" from the depths of the anode. The actual lithium-electrolyte interface is governed by a Li_2O film (19, 20) but, owing to the mechanical instability of a film floating on a molten anode, passivating or blocking effects are minimal (13, 14).

Li(B) anodes often deflagrate in molten nitrate electrolytes at temperatures above 350°C. The prediction to deflagrate at high electrolyte temperatures is accentuated during deep discharge. At 380°C, the tendency for anode deflagration decreases in the order $\text{KNO}_3 \gg \text{NaNO}_3 \gg \text{LiNO}_3$. The probability of anode deflagration drops with temperature. Below 350°C in molten LiNO_3 electrolyte, the Li(B) anode is relatively stable and deflagration-free.

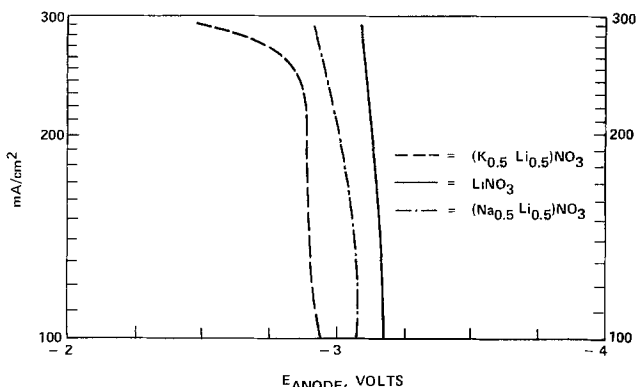


Fig. 3. Effect of current density on anode potential in various molten nitrate electrolytes at 300°C.

During the discharge of Li(B) anodes, significant anode oxidation products precipitated and were identified as elemental boron resulting from oxidation of the supportive Li_7B_6 matrix to lithium ions and elemental boron. The degree of attack in the Li_7B_6 matrix is dependent on temperature, current density, and electrolyte composition with greater amounts of elemental boron precipitate noted in KNO_3 and NaNO_3 containing electrolytes than in LiNO_3 electrolytes.

Addition of KO_2 to a $\text{LiNO}_3 \cdot \text{KNO}_3$ melt with a Li(B) anode was observed to increase the corrosion rate of the Li_7B_6 matrix. In addition, Li(B) anodes immersed in molten NaNO_3 or KNO_3 showed immediate formation of an elemental boron precipitate followed by deflagration of the anode. These results suggest that O_2^{2-} and O_2^- species that exist in NaNO_3 and KNO_3 melts are aggressive agents against the Li_7B_6 matrix. In LiNO_3 containing melts, O_2^{2-} and O_2^- species exist at much lower concentrations than the more stable O^{2-} ion. However, owing to the observed corrosive power of O_2^{2-} and O_2^- , even small amounts in the nitrate melt are sufficient to severely degrade the Li_7B_6 matrix. The presence of O_2^{2-} and O_2^- species has also led to corrosive attack on such inert metals as Pt and Ni in molten nitrates (21).

In high temperature melts (over 350°C), two factors predispose the anode to deflagration. First, electrolyte attack on the supportive matrix increases to form larger and larger surface pools of elemental lithium and, secondly, the surface tension of the lithium within the matrix decreases according to the relation (22-24)

$$\gamma = \gamma_0 (1 - T/T_c)^n \quad [1]$$

where γ is the surface tension and T_c is the critical temperature of the molten metals; n relates a scaling constant which may be assumed to be unity (22-24). As the surface tension of the elemental lithium decreases, the "wicking" rate increases and the net area of exposed lithium increases. The freshly exposed lithium reacts rapidly with the melt but, owing to the mechanical instability of a film on a liquid surface, unpassivated Li is continuously exposed. The reaction of the melt with freshly exposed lithium becomes dominant at higher temperatures and, as its rate increases, so does the likelihood of thermal runaway and anode deflagration. Also, as the anode area increases, so does the quantity of resistive Li_2O precipitate formed and thus, cell potential and anode potentials reflect a growing resistive Li_2O layer.

As would be expected from the above model, a significant temperature-potential relationship is noted at applied current. Anode potentials at open circuit and at 100 mA cm^{-2} as a function of temperature are shown in Fig. 4. Figure 5 illustrates the effect of varying current density on anode potentials at three fixed temperatures.

A thermodynamic examination of Li(B) cells is complicated by the role that the Li_7B_6 matrix and its reaction products may play in the discharge reaction.

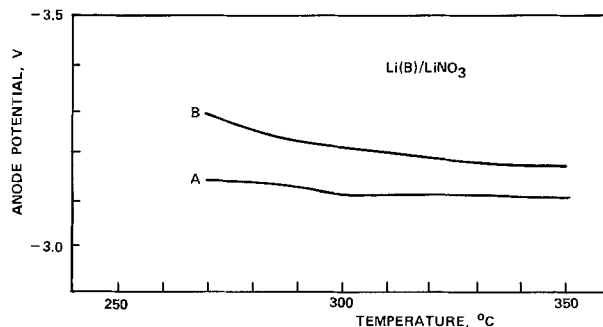


Fig. 4. Effect of temperature on anode potential in molten LiNO_3 electrolyte. B is open-circuit potential, A is potential at 100 mA cm^{-2} .

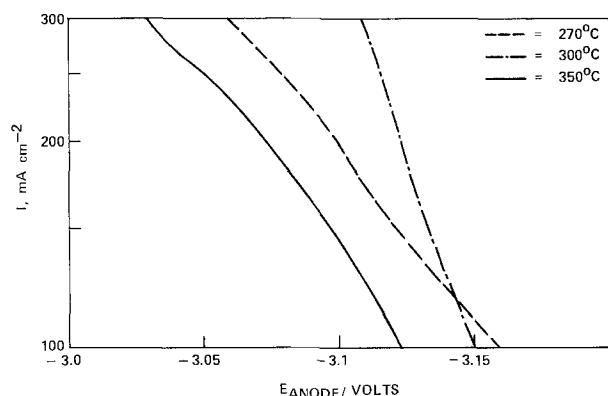
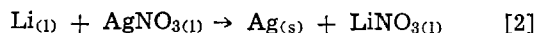


Fig. 5. Effect of current density on anode potential at three temperatures in LiNO_3 electrolyte.

Previous calculations have indicated the high theoretical anode and cell potentials possible with elemental lithium/molten nitrate electrolytes (19, 20).

Cyclic voltammetric studies at 100 mVs^{-1} of the LiNO_3 electrolyte before and after Li(B) anode discharge reveal an extensive nitrite oxidation peak appearing after discharge and no anomalous peaks which might be associated with lithium-boron oxides or electroactive anode reaction products. It should be noted that elemental boron is insoluble and readily precipitates.

Assuming the Li_7B_6 matrix is inert and that the reaction is chiefly lithium oxidation, the thermodynamic calculations for the cell reaction



yields $\Delta G^0 = -79.4 \text{ kcal at } 300^\circ\text{C}$, hence $E^0 = 3.44\text{V}$.

Summary

An examination of the Li(B) alloy anode in molten nitrate electrolytes reveals high rate discharge characteristics in the temperature region $270^\circ\text{--}350^\circ\text{C}$.

Galvanostatic studies show no appreciable anode polarization in molten LiNO_3 at 300 mA cm^{-2} . High current density polarization is more evident in $\text{LiNO}_3\text{--NaNO}_3$ and $\text{LiNO}_3\text{--KNO}_3$ electrolytes.

Above 350°C , anode degradation in molten nitrate electrolytes is severe and deflagration may occur. This is attributed to both an increase in the Li_7B_6 degradation reaction rate and to the increased mobility and fluidity of elemental lithium within the Li_7B_6 matrix.

Potentiostatic studies of the Li(B) alloy anode at 300°C in LiNO_3 at 80% peak open-circuit voltage reveal a flat discharge rate at approximately 780 mA cm^{-2} . This high current density is approximately an order of magnitude above that obtainable in conventional Ca/LiCl , KCl/CaCrO_4 thermal battery cells.

Single cell tests at 300 mA cm^{-2} utilizing a Ag^+ cathode in conjunction with the Li(B) anode in molten LiNO_3 demonstrate concept feasibility at high rate discharges with cell voltages of approximately 3V.

Acknowledgment

The authors wish to thank Dr. S. Dalleck and B. F. Larrick of the Naval Surface Weapons Center, White

Oak, Maryland, for fruitful discussions and for providing Li(B) samples. Financial support for this work was funding from the Navy's Block Program "High Energy Batteries for Weapons" (SF 65-571-692).

Manuscript submitted Dec. 27, 1982; revised manuscript received ca. Aug. 1, 1983.

Naval Weapons Center assisted in meeting the publication costs of this article.

REFERENCES

1. R. Swarc, R. D. Walton, S. Dalleck, and B. Filarick, *This Journal*, **129**, 1168 (1982).
2. S. D. James, *J. Appl. Electrochem.*, **12**, 317 (1982).
3. S. Dalleck, D. W. Ernst, and B. F. Larrick, *This Journal*, **126**, 866 (1979).
4. L. E. DeVries, L. D. Jackson, and S. D. James, *ibid.*, **126**, 993 (1979).
5. S. D. James and L. E. DeVries, *ibid.*, **123**, 321 (1976).
6. S. Dalleck and B. F. Larrick, in "Proceedings of the 30th Power Sources Symposium," Atlantic City, NJ, June 7-10, 1982, The Electrochemical Society, Inc., p. 42 (1983).
7. B. F. Larrick, S. D. James, and R. Swarc, in "Proceedings of the 28th Power Sources Symposium," Atlantic City, NJ, June 12-15, 1978, The Electrochemical Society, Inc., p. 95 (1979).
8. S. Dalleck, D. W. Ernst, and B. F. Larrick, NSWC/WOL TR 77-67, Naval Surface Weapons Center, Silver Spring, MD, January 11, 1978.
9. D. G. Simons, M. D. Brown, D. J. Lano, and J. G. Brennan, NSWC TR 79-95, Naval Surface Weapons Center, Silver Spring, MD, March 1, 1979.
10. W. P. Kilroy and I. Angres, NSWC/WOL TR 77-129, Naval Surface Weapons Center, Silver Spring, MD, November 10, 1977.
11. S. D. James and L. E. DeVries, NSWC/WOL TR 78-22, Naval Surface Weapons Center, Silver Spring, MD, March 1, 1976.
12. D. Ernst, *This Journal*, **129**, 1513 (1982).
13. M. H. Miles, *J. Appl. Electrochem.*, **11**, 325 (1981).
14. M. H. Miles, D. A. Fine, and A. N. Fletcher, *This Journal*, **125**, 1209 (1978).
15. G. E. McManis, M. H. Miles, and A. N. Fletcher, in "Proceedings of the 30th Power Sources Symposium," Atlantic City, NJ, June 7-10, 1982, The Electrochemical Society, Inc., p. 39 (1983).
16. M. H. Miles and A. N. Fletcher, *J. Appl. Electrochem.*, **10**, 251 (1980).
17. M. H. Miles and A. N. Fletcher, *This Journal*, **128**, 1489 (1981).
18. M. H. Miles, G. E. McManis, and A. N. Fletcher, Paper 586 presented at The Electrochemical Society Meeting, Denver, CO, Oct. 11-16, 1981.
19. J. Poris, I. D. Raistrick, and R. A. Huggins, in "Lithium Batteries," H. V. Venkatesetty, Editor, p. 459, The Electrochemical Society Softbound Proceedings Series, Pennington, NJ (1981).
20. I. D. Raistrick, J. Poris, and R. A. Huggins, in "Lithium Batteries," H. V. Venkatesetty, Editor, p. 477, The Electrochemical Society Softbound Proceedings Series, Pennington, NJ (1981).
21. M. H. Miles and A. N. Fletcher, *This Journal*, **127**, 1761 (1980).
22. A. A. Adamson, in "The Physical Chemistry of Surfaces," 2nd ed., pp. 53-58, John Wiley and Sons, New York (1967).
23. E. A. Guggenheim, *J. Chem. Phys.*, **13**, 253 (1945).
24. A. V. Grosse, *J. Inorg. Nucl. Chem.*, **24**, 147 (1962).

The Electrocatalysis of Oxygen Evolution on Perovskites

John O'M. Bockris* and Takaaki Otagawa*†

Department of Chemistry, Texas A&M University, College Station, Texas 77843

ABSTRACT

Measurements of the oxygen evolution reaction have been made on eighteen substituted perovskites containing first-row transition metal ions. Rates are reported at equilibrium and at an overpotential of 0.3V. Electrode kinetic parameters are given, including roughness factors. The rate does not depend on semiconductor-type properties. It increases as the pH of zero charge, at which the occupancy of OH⁻ and H⁺ at the interface becomes equal, moves in an alkaline direction, with decrease of magnetic moment, with decrease of stability of the perovskite lattice, with decrease of the enthalpy of formation of the transition metal hydroxides, and with increase in the number of d-electrons in the transition metal ion. The accuracy of the roughness factor measurements are affected by weakness in knowledge of true double layer capacities. The value assumed here, 60 μF cm⁻², may be accurate to only ±100%. Models are given which suggest that the pores are active throughout. The correlations between the rate and electronic properties are consistent with rate-determining steps which involve desorption of OH radicals, e.g., M^z-OH + OH + ^{z,d,s}M^z . . . H₂O₂ + e⁻. An MO discussion suggests that the electrocatalysis increases with increased occupancy of the antibonding orbitals of M^z-OH. Earlier interpretations include the concept that an increase of the rate occurs because of increasing overlap between the e_g orbitals of the transition metal ion and the sp_σ orbital of O. However, this theory is based on only three different materials, in which rate-determining step changes. An interpretation based upon nonstoichiometry is shown to be consistent with observed trends, but insufficient to explain their magnitude. The electrical and chemical contributions to the rate are analyzed. The value of α is related via bond strength considerations to the M^z-OH bond strengths. The relative electrocatalysis discussed is limited to an overpotential which corresponds to a practical range of rates on the faster catalysts. A volcano relation for oxygen evolution on perovskites seems likely. Future electrocatalysts are predicted.

General concepts of electrocatalysis based on the fundamental aspects of the rate equation for electron transfer, particularly for hydrogen evolution and oxygen reactions on phase oxide-covered (or free) metals, have been thoroughly discussed by Appleby (1).

The first attempt to rationalize the electrocatalysis of oxygen evolution was made by Ruetschi and Delahay (2) in 1955. They plotted the overpotential at constant current density against M-OH bond strength [but cf., Conway and Bockris (3)].

More recently, several theoretical approaches to rationalize the electrocatalysis of oxygen evolution on oxides have been made by Tseung and Jasem (4), Trasatti (5) and Matsumoto *et al.* (6-10).

Tseung and Jasem (4) suggested that there is a correlation between the redox potential of an oxide couple of the electrocatalyst and the reversible potential of the oxygen evolution reaction. No mechanistic rationalization was suggested. Correspondingly, Trasatti (5) found that a somewhat volcano-shaped curve could be obtained by plotting overpotentials as a function of the enthalpy change for the lower-to-higher oxide transition in the catalyst.

Between 1977-1981, Matsumoto *et al.* (6-11), developed the theory of σ* band formation. The essential condition for high catalytic activities of oxygen evolution on perovskites is that a broad σ* band is formed and that the transition metal cation exists in a higher oxidation state. These authors' concepts do not involve chemical bonding.

In this work, a systematic investigation was made to correlate the electrocatalytic properties of perovskites (ABO₃) for oxygen evolution with their electronic structures, with stress upon the characterization of the bonding of surface oxygenated intermediates, as a correlating factor.

Experimental

Preparation of perovskites.—The transition metal oxides with substituted perovskitic structure [(A_{1-x}A_{x'}BO₃), where A is a lanthanide (mainly La), A' is an alkaline earth (mainly Sr), and B is a first-row transition metal] were chosen in order to study the electrocatalytic activities for oxygen evolution systematically.

* Electrochemical Society Active Member.

† Present address: Argonne National Laboratory, EES Division, Argonne, Illinois 60439.

Key words: electrocatalysis, oxygen evolution, perovskite.

The addition of the A' ion was necessary to give sufficient conductivity for most of the compounds.

The perovskites were synthesized by high temperature solid-state reactions (11-20). Binary oxides or carbonates with high purity (~99.999%, Aldrich or Alfa) were used as starting materials. The appropriate amount of each reagent required to give the desired metal ion stoichiometry was weighed and mixed mechanically for 2h. The uniformly mixed powder was then placed in a Pt-covered Alundum combustion boat (Fisher) and fired in an appropriate atmosphere (12-20) at 1100°-1400°C for a total of 30-70h, with frequent regrinding and refring of the products. The pure lanthanum nickelate crystals were synthesized by a coprecipitation technique (21). X-ray diffraction patterns were taken for each powder to confirm the compound concerned. The electrodes (in pellet form) were then made by pressing powders at 300 kg cm⁻² and sintering at 1000°C. No binder was added.

Solid-state surface studies.—The resistivities and Hall effects for the surface of pellets were obtained by the method of van der Pauw (22). Impedance measurements were carried out by a lock-in analyzer approach (23). Measurements of the magnetic susceptibilities were carried out by the Faraday method (24). The physicochemical characterizations of La_{0.9}Sr_{0.1}CoO₃ electrodes by XPS are reported elsewhere (25).

Electrochemical kinetic studies.—Electrode kinetic parameters were determined mainly in 1M NaOH by potentiostatic current/time relations at varying potentials. A PAR Model 173 potentiostat/galvanostat, fitted with a PAR Model 376 current/voltage converter, was used to control the electrode potential. The detailed procedures for the steady-state potentiostatic experiments to obtain various kinetic parameters are described elsewhere (26).

Surface areas.—The surface areas of powders and electrodes were determined by BET and by double layer charging curves, respectively.

Cyclic voltammograms, taken in the flat double layer (dl) charging region and limited to a 50 mV potential range, were used to obtain a dl capacitance (27, 28). This value was then used to determine the roughness factor by assuming a theoretical value of the dl capacitance for a smooth surface. The potential was swept by connecting the output of a PAR Model 175 universal

programmer to the external potential signal input of the potentiostat. An X-Y recorder (Hewlett Packard Model 7010B) was used to plot the current/potential curves. Errors in, and the significance of, these surface area measurements are discussed below.

Measurements of acid-base properties.—The potentiometric acid-base titration method (29-33) was used to investigate the concentration of OH⁻ groups on the surface of perovskites in powdered form in aqueous solution. The experiments were made using a pH meter (Orion Research Model 811) with a combination pH electrode (Silver-Silver Chloride Internals, Miniature, Sargent-Welch, cat. no. S-30078-10). A glass titration cell, containing a water jacket, was used. A powder of ~0.3g was introduced into an aqueous solution¹ (25 ml) of 0.004M KOH and 0.01M KCl (J. T. Baker Chemical Company) and kept suspended overnight. Stirring was accomplished by means of a Teflon-covered magnet and a magnetic stirrer (Thermolyne Corporation Model S-7805). A constant temperature circulator (HAAKE Model FK) was used to keep the solution temperature at 25°C. The titration cell was sealed carefully and was under a CO₂-free N₂ stream, to avoid any CO₂ contamination from air, throughout the experiments. The titrant was 0.1M HCl (J. T. Baker Chemical Company). A microburette with a Teflon plug stopcock (Sargent-Welch, cat. no. S-10945-50C) was used.

Then, the titration was carried out by adding 0.05-0.1 ml quantities of the titrant successively. pH values were continuously recorded on an X-t recorder (Fisher Recordall Series 5000) to ensure the establishment of a steady state.

The titration curve thus obtained was compared with that previously obtained in the blank solution to determine the excess OH⁻ charge on the surface and, thus, to obtain the pH at which the amount of OH⁻ and H⁺ at the surface becomes equal (zero point of charge [zpc]).

Results and Experimental Rate Correlations

Solid-state parameters.—Solid-state parameters are summarized in Table I.

¹ This gives rise to a pH value of ~11.4. It is important to keep the powder in an alkaline solution initially, since perovskite-type oxides tend to dissolve in a strong acid solution.

The electrodes were all p-type semiconductors; the charge carrier densities were 10¹⁷-10¹⁸ cm⁻³, and the resistivities were 10⁻³-10⁻¹ Ω cm. The Hall mobility averaged around 30 cm² V⁻¹ s⁻¹. The Mott-Schottky plots indicated a p-type semiconductor behavior at the surface with a flatband potential of 0.20-0.50 (V vs. NHE).

The magnetic susceptibility (Fig. 1) varies with temperature and also varies greatly among the perovskites examined. LaNiO₃ showed a paramagnetism (even below 100 K), while La_{0.9}Sr_{0.1}CoO₃ showed a ferromagnetism with T_c = 221 K (i.e., La_{0.9}Sr_{0.1}CoO₃ becomes paramagnetic at room temperature). Strong ferromagnetism and antiferromagnetism were observed at room temperature, on La_{1-x}Sr_xMnO₃, and La_{1-x}Sr_xFeO₃, respectively (T_c for LaMnO₃ was 346 K).

Surface areas.—The BET measurements showed surface area values of ~15 m² g⁻¹ for powders and varied little among the compounds (Table I). The values of 15 m² g⁻¹ are in agreement with those obtained in an examination of perovskites by Crespin and Hall (35a). However, they differ from values observed by Matsumoto *et al.* (11), who obtained a value in the region of 2 m² g⁻¹. Doubtless these differences arise from differences in particle size of starting materials.

Typical cyclic voltammograms at various sweep rates for La_{0.9}Sr_{0.1}MnO₃ and La_{0.9}Ce_{0.1}CoO₃ are presented in Fig. 2. The anodic and cathodic currents were equal in magnitude, and the charging current was linear with the sweep rate. The dl capacitance was calculated from the slope of the charging current vs. sweep rate. The roughness factors were then determined by assuming a dl capacitance of 60 μF cm⁻², according to the views of Levine and Smith for oxide surfaces (34).

The dl capacitance values and roughness factors on various perovskite electrodes are summarized in Table I. The electrochemically active surface areas (roughness factors) were 100-1000 in terms of the ratio of the active to the apparent external surface area. The electrode prepared by a coprecipitation technique (LaNiO₃) extended this factor to about 5000.

Surface charges.—Figure 3 shows a typical titration curve on LaCoO₃. The coverage (θ [surface charge density, q_±]) vs. pH relations of cobaltates is shown in Fig. 4. 1.4 × 10¹⁵ sites cm⁻² was assumed to be a full

Table I. Physicochemical and solid-state properties of perovskites

Perovskite	BET area† (m ² g ⁻¹)	zpc† (pH)*	C _{DL} (F cm ⁻²) ^b	Roughness factor ^c	ρ (Ω cm) ^d	μ _H (cm ² V ⁻¹ s ⁻¹) ^e	n (cm ⁻³) ^f	V _{fb} (V vs. NHE) ^g	μ _{eff} [†] (μB) ^h
LaNiO ₃	15.2	8.9	3.4 × 10 ⁻¹	5.6 × 10 ²	1.22 × 10 ⁻³	3.15 × 10 ¹	1.63 × 10 ²⁰	0.30	1.43
LaNiO ₃ *	12.8	9.2	4.5 × 10 ⁻³	7.5 × 10 ²	5.49 × 10 ⁻²	2.68 × 10 ¹	4.25 × 10 ¹⁸	0.25	
LaCoO ₃	12.6	6.7	1.4 × 10 ⁻²	2.4 × 10 ²	4.22	2.65 × 10 ¹	5.39 × 10 ¹⁶	0.65	2.92
La _{0.9} Sr _{0.1} CoO ₃	18.1	7.2	7.2 × 10 ⁻³	1.2 × 10 ²	4.18 × 10 ⁻²	3.55 × 10 ¹	4.21 × 10 ¹⁸	0.39	3.95
La _{0.9} Sr _{0.1} CoO ₃	14.5	8.2	9.0 × 10 ⁻²	1.5 × 10 ³	4.38 × 10 ⁻⁴	2.25 × 10 ²	6.35 × 10 ¹⁹	0.09	
La _{0.9} Ce _{0.1} CoO ₃	9.6	7.3	6.3 × 10 ⁻³	1.0 × 10 ²	7.44	7.05	1.19 × 10 ¹⁷	0.40	
La _{0.9} Th _{0.1} CoO ₃ †	8.4	7.1	1.1 × 10 ⁻²	1.8 × 10 ²	1.54	6.01 × 10 ¹	6.74 × 10 ¹⁶	0.25	
Nd _{0.9} Sr _{0.1} CoO ₃	9.0	7.4	7.0 × 10 ⁻²	1.2 × 10 ³	8.92 × 10 ⁻²	9.99 × 10 ¹	7.02 × 10 ¹⁷	0.28	
Gd _{0.9} Sr _{0.1} CoO ₃ ‡	15.8	6.5	6.0 × 10 ⁻²	1.0 × 10 ³	3.48	1.73 × 10 ²	1.04 × 10 ¹⁶	0.54	
La _{0.9} Sr _{0.1} FeO ₃	8.1	7.6	3.6 × 10 ⁻²	6.0 × 10 ²	1.80	5.82 × 10 ¹	5.97 × 10 ¹⁶	0.50	
La _{0.9} Sr _{0.1} FeO ₃	19.3	8.6	2.0 × 10 ⁻¹	3.3 × 10 ²	1.46 × 10 ⁻¹	9.39 × 10 ¹	4.55 × 10 ¹⁷	0.46	(3.11-4.65) [†]
LaMnO ₃	21.2	7.0	4.0 × 10 ⁻²	6.7 × 10 ²	1.62	2.75 × 10 ¹	1.40 × 10 ¹⁷	0.02	14.95
La _{0.9} Sr _{0.1} MnO ₃	9.8	7.3	8.4 × 10 ⁻³	1.4 × 10 ²	8.20 × 10 ⁻¹	1.73 × 10 ¹	2.96 × 10 ¹⁷	-0.02	
La _{0.9} Sr _{0.1} MnO ₃	14.6	8.2	7.3 × 10 ⁻²	1.2 × 10 ³	2.89 × 10 ⁻¹	1.16 × 10 ¹	1.87 × 10 ¹⁸	0.10	
La _{0.9} K _{0.1} MnO ₃	9.5	7.6	4.4 × 10 ⁻²	7.3 × 10 ²	2.81 × 10 ⁻¹	1.39 × 10 ¹	1.60 × 10 ¹⁸	-0.01	
La _{0.9} Ca _{0.1} MnO ₃	14.9	8.2	4.6 × 10 ⁻³	7.6 × 10 ²	2.01 × 10 ⁻²	1.81 × 10 ²	1.57 × 10 ¹⁹	0.18	
La _{0.9} Sr _{0.1} CrO ₃	25.4	5.7	7.8 × 10 ⁻²	1.3 × 10 ³	6.54 × 10 ⁻¹	2.51 × 10 ¹	3.81 × 10 ¹⁷	0.17	
LaVO ₃	19.4	6.6	4.7 × 10 ⁻²	7.8 × 10 ²	2.60	2.00 × 10 ¹	1.20 × 10 ¹⁷	0.37	(1.16-2.18) [†]

† Values for powders.

* Zero point of charge: the pH at which the amount of OH⁻ and H⁺ at the surface becomes equal

^b Double layer capacitance by the cyclic voltammetric method.

^c Roughness factor, calculated by assuming a dl capacitance of 60 μF cm⁻² for a smooth oxide surface (34).

^{d, e, f} Resistivity, Hall mobility, and carrier density, measured at 50 Hz, respectively (25).

^g Flatband potential in 1M NaOH, measured at 5-100 Hz (25).

^h Effective magnetic moment in Bohr magnetons (25).

[†] Values for LaFeO₃ and SrFeO₃.

[‡] Values for La_{0.9}Sr_{0.1}CrO₃ and LaCrO₃.

* X-ray analysis showed that this substance consisted of LaNiO₃, La₂NiO₅, and NiO, as a mixed multiphase.

† X-ray analysis showed a multiphase (perovskite and ThO₂) and a poor crystallinity for La_{0.9}Th_{0.1}CoO₃ and Gd_{0.9}Sr_{0.1}CoO₃, respectively.

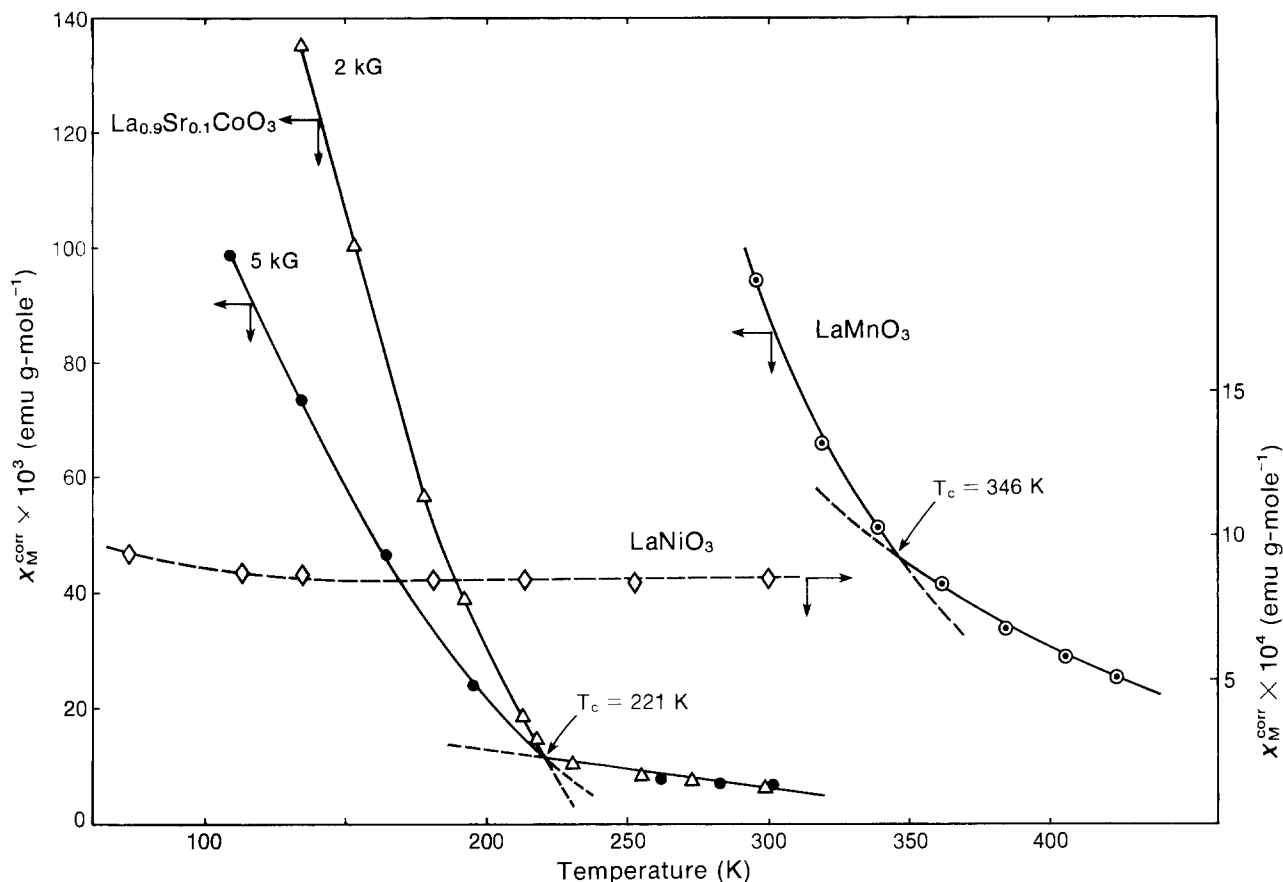


Fig. 1. Temperature dependence of magnetic susceptibility. A magnetic field of 5 kG was used for LaNiO_3 and LaMnO_3 . T_c designates Curie temperature.

coverage (35a). The values of q_{\pm} were estimated from the difference between the titration curves, with and without powders, using the following relation (29, 31)

$$q_{\pm} = \frac{F \cdot \Delta V \cdot C}{S \cdot \omega} \quad [1]$$

where F is the Faraday constant, ΔV the difference in the volume of the titrant (0.1M HCl) in the presence and/or absence of the powder at a given pH, C is the concentration of the titrant (0.1M), and S is the BET surface area and ω is the amount of powder used.

The surface charge depends linearly on pH. The figures reveal several different linear sections of the coverage vs. pH relation for each material. At pH in the alkaline region, the coverage approaches $100 \mu\text{C}$ of OH^- per actual BET-based cm^2 of the electrode material in powdered form. A similar tendency was observed on the other perovskites.

These values may be compared with those in the literature. Thus, Levine and Smith (34) show a theoretical plot for the charge as a function of pH which is similar, though slightly more curved, to that of the experimental values obtained here. Aktinson *et al.* (33a) obtained coverage-pH data for, e.g., FeOOH in KCl, which resemble in shape those obtained in the present work. In particular, the work of Kita *et al.* (29), who worked in the presence of KCl, had straight line sections in charge-pH plots similar to those observed here.

It is possible to derive capacitances from the measurements obtained here (cf. Fig. 4) by assuming that the behavior of the surface is Nernstian (32) whereupon

$$C = \frac{\delta q}{\delta V} = \frac{\delta q}{\delta \text{pH}} \cdot \frac{\delta \text{pH}}{\delta V} \quad [2]$$

with

$$\frac{\delta V}{\delta \text{pH}} = 0.059$$

On the basis of Eq. [2], capacitance values of approximately $200 \mu\text{F cm}^{-2}$ in the vicinity of zpc are obtained for most of the perovskites studied.

In comparison with this are the values quoted by Levine and Smith (34) where the maximum values are said to be $160 \mu\text{F cm}^{-2}$ for SiO_2 and ZnO , and the work of Bowden *et al.* (33b) who give values of about $200 \mu\text{F cm}^{-2}$ for most oxides other than SiO_2 . Thus, our present values are clearly consistent with those in the literature. It could be that they may need, however, correcting downwards because we have used, in the evaluation of the area, the BET values for packed powders, whereas the values in dispersions would be expected to be somewhat higher (35b).

The values of the pH at which the surface-adsorbed OH^- and H^+ are equal (zpc) were 7-9 (pH) (Table I). This value increased with an increase in the degree of Sr substitution.

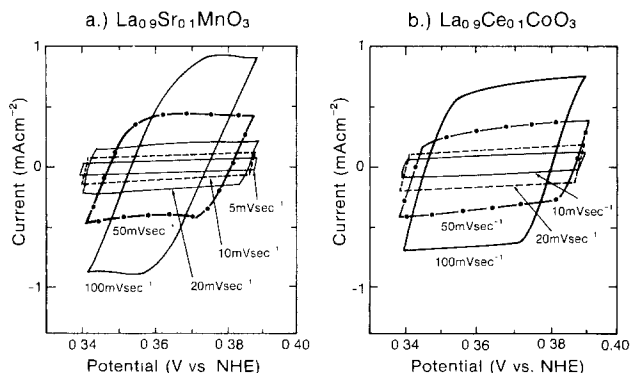


Fig. 2. Cyclic voltammograms, limited to the potential range of 0.34-0.39 (V vs. NHE), in O_2 -saturated 1M NaOH at 25°C , for $\text{La}_{0.9}\text{Sr}_{0.1}\text{MnO}_3$ (a) and $\text{La}_{0.9}\text{Ce}_{0.1}\text{CoO}_3$ (b).

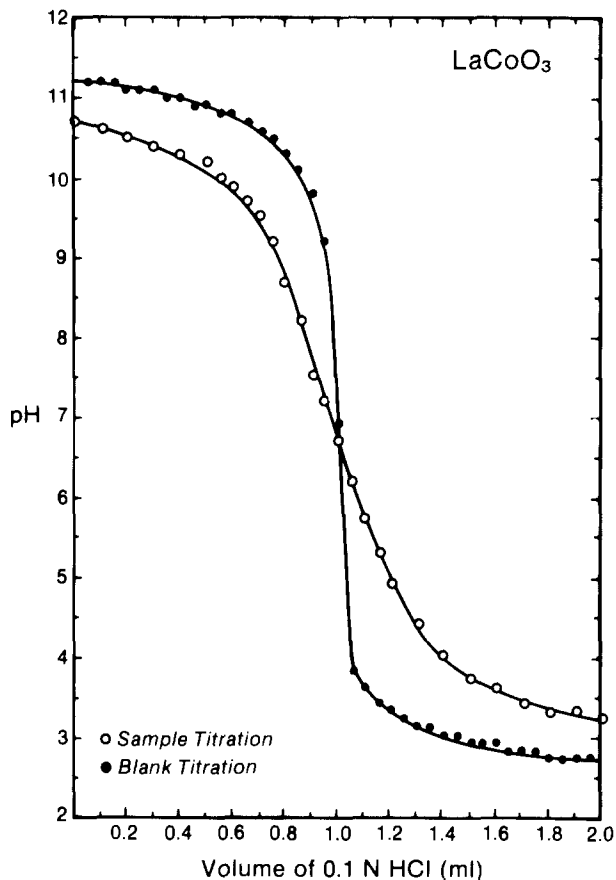


Fig. 3. Typical titration curve of perovskite powder (LaCoO_3). Electrolyte: 0.004M KOH + 0.01M KCl (25 ml). 0.3g of powder was used.

Kinetic parameters for oxygen evolution on perovskites.—The potential vs. $\log i$ plots for $\text{La}_{1-x}\text{Sr}_x\text{CoO}_3$ are presented in Fig. 5. The Tafel slopes for oxygen evolution at lower overpotentials were 43, ~65, ~120,

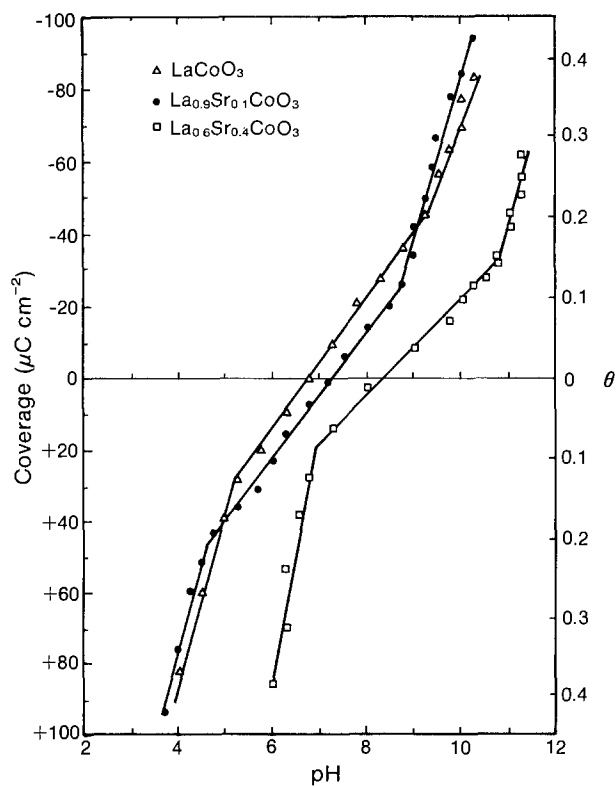


Fig. 4. Coverage (surface charge density) of cobaltates as a function of pH. 1.4×10^{15} sites cm^{-2} was used for full coverage.

~125, 200, and 175-235 mV/decade^{-1} for LaNiO_3 , $\text{A}_{1-x}\text{A}'_x\text{CoO}_3$ ($\text{A} = \text{La, Nd, Gd}$; $\text{A}' = \text{Sr, Ce, Th}$), $\text{La}_{1-x}\text{Sr}_x\text{FeO}_3$, $\text{La}_{1-x}\text{A}'_x\text{MnO}_3$ ($\text{A}' = \text{Sr, K, Ca}$), $\text{La}_{1-x}\text{Sr}_x\text{CrO}_3$, and $\text{La}_{1-x}\text{Sr}_x\text{VO}_3$, respectively. The reaction order, with respect to OH^- , was close to unity.

Table II summarizes the kinetic parameters for oxygen evolution (26). Current densities are expressed in terms of real surface area, taking into account the roughness factors. It is interesting to note that the reaction order in Table II shows a decrease which parallels the decrease of α or the increase of Tafel parameter a . The reaction order may be a sensitive parameter with oxides and may be related to the details of the mechanism. An example of such mechanisms to account for this parallelism is fully discussed elsewhere (26).

Correlations with physicochemical properties.—Flat-band potential (V_{FB}), carrier density (n), and Hall mobility (μ_{H}) are typical bulk properties of semiconducting perovskite-type oxides. However, no obvious correlations between catalytic activities and the parameters were found.

A fair correlation was found between the electrocatalytic activities and the pH at which the surface-adsorbed H^+ and OH^- are equal (zpc). The catalytic activity increases as the zpc becomes more alkaline. However, some scatter was observed in this correlation and it is possible that this arose from the fact that the solutions in which the zero point of charge was measured contained Cl^- , which could have been adsorbed to a different extent upon the various perovskites (although KCl concentration was 10^{-2}M , the adsorption would not be expected to have been great).

The reaction rates for oxygen evolution on perovskites are plotted against magnetic moments (μ_{eff}) in Fig. 6. The values of μ_{eff} for $\text{La}_{1-x}\text{Sr}_x\text{FeO}_3$ were estimated from those for LaFeO_3 and SrFeO_3 . The plot for LaMnO_3 was omitted, since it gave an anomalously

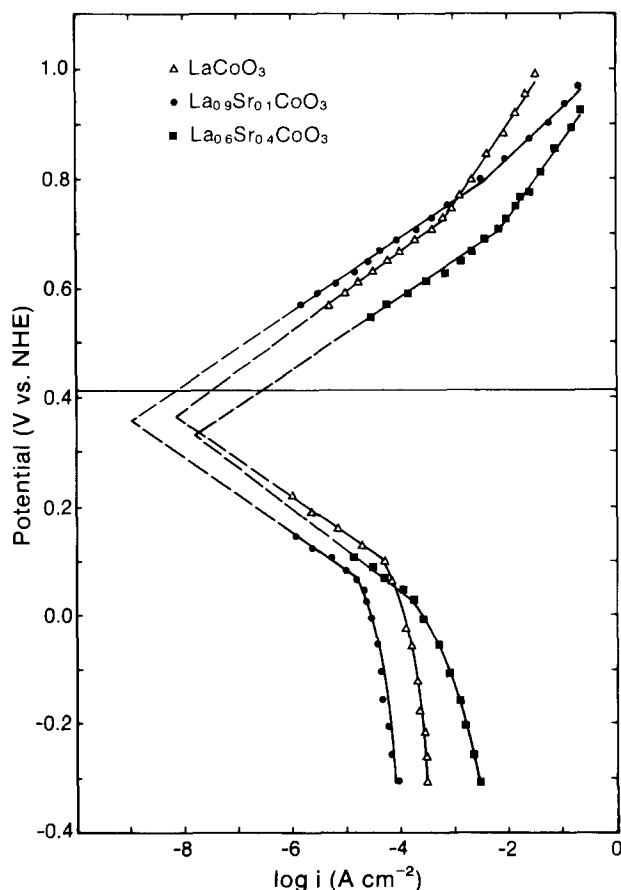


Fig. 5. Potential vs. $\log i$ plots on cobaltates in 1M NaOH at 25°C (iR corrected).

Table II. Kinetic parameters based on real surface areas for oxygen evolution on perovskites

Electrode	Roughness factor ^a	Tafel slope (V decade ⁻¹) ^b	α^c	Reaction order ^d	i_0 (A cm ⁻²) ^e	i (A cm ⁻²) ^f at $\eta = 0.3V$	$a(V)^g$
LaNiO ₃ ^h	5.6×10^3	0.043	1.37	0.95	1.1×10^{-12}	1.3×10^{-5}	0.51
LaNiO ₃ ⁱ	7.5×10^3	0.065	0.91	1.10	7.8×10^{-11}	2.9×10^{-6}	0.66
LaCoO ₃	2.4×10^3	0.070	0.84	0.70	1.5×10^{-10}	1.6×10^{-6}	0.69
La _{0.9} Sr _{0.1} CoO ₃	1.2×10^3	0.066	0.89	0.98	6.6×10^{-11}	2.5×10^{-6}	0.67
La _{0.8} Sr _{0.2} CoO ₃	1.5×10^3	0.064	0.92	0.84	2.1×10^{-10}	1.0×10^{-5}	0.62
La _{0.9} Ce _{0.1} CoO ₃	1.0×10^3	0.062	0.95	0.94	1.1×10^{-10}	6.9×10^{-6}	0.62
La _{0.8} Th _{0.2} CoO ₃ ^j	1.8×10^3	0.065	0.91	0.70	2.5×10^{-11}	1.0×10^{-6}	0.69
Nd _{0.8} Sr _{0.2} CoO ₃	1.2×10^3	0.065	0.91	0.85	3.3×10^{-11}	1.4×10^{-6}	0.68
Gd _{0.8} Sr _{0.2} CoO ₃	1.0×10^3	0.070	0.85	0.68	4.0×10^{-11}	7.2×10^{-7}	0.73
La _{0.7} Sr _{0.3} FeO ₃	6.0×10^2	0.130	0.45	0.82	4.2×10^{-9}	5.0×10^{-7}	1.09
La _{0.5} Sr _{0.5} FeO ₃	3.3×10^3	0.110	0.54	0.75	1.7×10^{-9}	8.1×10^{-7}	0.97
LaMnO ₃	6.7×10^2	0.126	0.47	0.65	2.1×10^{-10}	5.0×10^{-8}	1.22
La _{0.9} Sr _{0.1} MnO ₃	1.4×10^3	0.125	0.47	0.65	5.1×10^{-10}	1.3×10^{-7}	1.16
La _{0.8} Sr _{0.2} MnO ₃	1.2×10^3	0.125	0.47	0.60	5.9×10^{-10}	1.6×10^{-7}	1.15
La _{0.8} K _{0.2} MnO ₃	7.3×10^2	0.125	0.47	0.65	1.9×10^{-10}	5.3×10^{-8}	1.21
La _{0.2} Ca _{0.8} MnO ₃	7.6×10^2	0.130	0.45	0.63	1.7×10^{-9}	3.5×10^{-7}	1.14
La _{0.8} Sr _{0.2} CrO ₃	1.3×10^3	0.200	0.30	0.25	1.4×10^{-9}	3.2×10^{-6}	1.77
LaVO ₃	7.8×10^3	0.175	0.34	~ 0	5.1×10^{-10}	2.7×10^{-6}	1.63

^a Roughness factor, calculated by assuming a dl capacitance of $60 \mu F cm^{-2}$ for a smooth oxide surface (34).

^b Tafel slope in the lower overpotential region.

^c Transfer coefficient: $\alpha = 2.3RT/bF$, where b is a Tafel slope.

^d Reaction order with respect to OH⁻ at constant potentials.

^e Exchange current density in terms of real surface area.

^f Current density in terms of real surface area for oxygen evolution at an overpotential of 0.3V.

^g Tafel line intercept (Tafel parameter a): $a = -b \log i_0$.

^h LaNiO₃ prepared by a coprecipitation technique.

ⁱ Multiphase; LaNiO₃ + La₂NiO₄ + NiO.

^j Multiphase; La_{0.8}Th_{0.2}CoO₃ + ThO₂.

high value of μ_{eff} ($\mu_{eff} = 14.94$). However, this value is indicative of a strong ferromagnetism and was associated with a poor catalytic activity. If one ignores the plot for La_{0.8}Sr_{0.2}CrO₃, which showed little oxygen evolution due to instability under the anodic condition, it may be seen in Fig. 6 that the electrocatalytic activity decreases as the magnetic moment increases. or as the magnetism changes from paramagnetism to ferro/antiferromagnetism.

Correlations with thermodynamic properties.—Nakamura *et al.* (36) studied the chemical stability of perovskites LaBO₃ (B = V, Cr, Mn, Fe, Co, Ni) by thermogravimetry at 1000°C in a controlled P_{O2} atmosphere. The stability limits of the perovskite phases expressed in terms of $-\log P_{O_2}^*$ (P_{O2}^{*} = critical oxygen partial pressure in bar) were greater than 21.1 for LaCrO₃ and LaVO₃, 16.95 for LaFeO₃, 15.05 for LaMnO₃, 7.0 for LaCoO₃, and ~ 0.6 for LaNiO₃; hence, lattice oxygens become easily released in this sequence. The electrocatalytic activities of oxygen evolution are plotted against this critical oxygen partial pressure in Fig. 7.

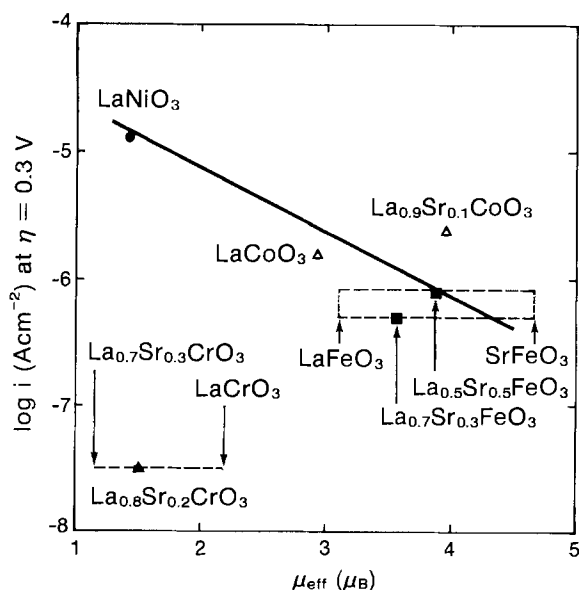


Fig. 6. Current density (based on real surface area) for oxygen evolution on perovskites at an overpotential of 0.3V vs. effective magnetic moment, μ_{eff} .

There is a tendency that the lesser the stability at 1000°C, the better the electrocatalysis.

The reaction rates of oxygen evolution on perovskites are plotted against ΔH_f° of the hydroxides and M-OH bond strength in Fig. 8 and 9, respectively. The M-OH strength was calculated, based on the method of Ruetschi and Delahay (2), with corrections made by including the electronegativity term, as suggested by Conway and Bockris (3). Table III summarizes these thermodynamic properties. A linear correlation, limited to the descending branch of a volcano curve, is seen (Fig. 9); the electrocatalysis decreases as the M-OH bond strength increases.

The thermodynamic data to which reference can be made here are unfortunately not those of the perovskite itself, nor to that of the substituted perovskites containing, *e.g.*, strontium. Appropriate thermodynamic data have not yet been published for these materials. What we have used here, encouraged by the correlations obtained, are data for the corresponding oxides, *e.g.*, Cr(OH)₃, etc. We have limited these oxides to those of the trivalent metal. This arises out of the evidence from the work of Nakamura *et al.* (20), and also some ESCA measurements (25) referred to below, that the surface of La_{0.9}Sr_{0.1}CoO₃ consists of the trivalent cobalt and oxygen vacancies over the range of potentials which we used in the present work.

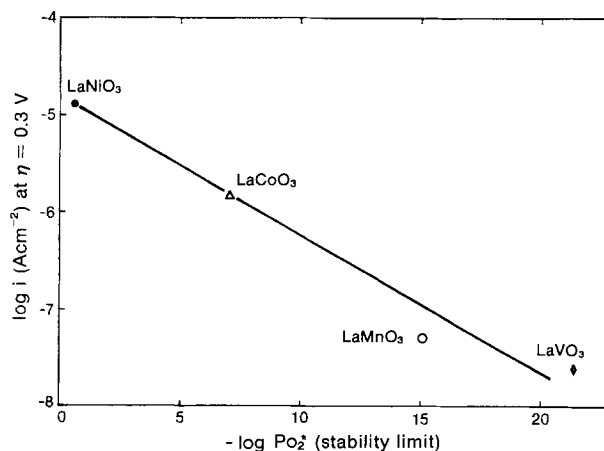


Fig. 7. Current density (based on real surface area) for oxygen evolution on perovskites at an overpotential of 0.3V vs. the stability limits of perovskites in terms of $-\log P_{O_2}^*$ at 1000°C.

Table III. Thermodynamic properties of transition metals and related hydroxides and oxides

Transition metal	ΔH_f° (kcal mol ⁻¹) ^a		ΔH_f° (kcal mol ⁻¹) ^b 2M ^{III} O → M ₂ ^{III} O ₃	χ_M (eV) ^c	M-OH bond strength (kcal mol ⁻¹)		
	M ^{III} (OH) ₃	M ₂ ^{III} O ₃			D _{cov} (M-OH) ^d	D _{ion} (M-OH) ^e	D(M-OH) ^f
Ni	-162.6	-112.0†	-13.0	1.75	64.6	57.5	122.1
Co	-176.6	-115.0†?	-21.5*	1.70	69.2	61.2	130.4
Fe	-197.0	{ -161.9† -196.5	{ -69.2 -57.0*	1.64	76.0	65.8	141.8
Mn	-212.0	{ -191.9† -232.1	-45.1	1.60	81.0	69.0	150.0
Cr	-247.1	-269.7	-102	1.56	92.7	72.2	164.9
V	?	-290.0	-96.0	1.45	107.0*?	81.5	188.5?

^a Standard enthalpy of formation; † Hydrated oxides (37, 38).

^b Enthalpy change for the lower-to-higher oxide transition; * lower oxide is M₂O₃ (5, 38, 39).

^c Electronegativity (Allred-Rochow) values for transition elements in the valence (II) (40).

^d D_{cov}(M-OH) = 10.35 - ΔH_f[°]/3, where 10.35 (kcal mol⁻¹) and ΔH_f[°] are the enthalpies of formation of OH(g) (37) and M^{III}(OH)₃, respectively (2).

^e D_{ion}(M-OH) = 23.06 (χ_M - χ_{OH})², where χ_{OH} was estimated as ~3.3 (40).

^f D(M-OH) = D_{cov}(M-OH) + D_{ion}(M-OH).

^g ΔH_f[°] for V₂O₅ was used.

Correlations with d-electron configuration.—In Fig. 10, the catalytic activities for oxygen evolution on perovskites are plotted against the number of d-electrons of each transition metal ion in perovskites. The number of d-electrons was assigned based on the trivalent transition metal ions in perovskites. The reaction rate increases with an increase of the number of d-electrons.

Discussion

Degree of validity of the roughness factor measurements.—There are two assumptions in the roughness factor measurements: (i) the only reason for the difference of the capacitance observed is due to roughness; double layer capacitance for the perovskite per real unit area is that of a nonpolarizable interface which has a capacitance per real square centimeter of 60 μF cm⁻²,² (ii) The capacitances used in the determinations were those of the solid/solution interface and not, e.g., those of the Schottky barrier within the semiconductor.

² Utilizing a similar method, it would be possible to select 16 μF cm⁻² as the reference value, because this is the capacitance of the Hg/solution interface on the negative branch. However, the present work was carried out (cf. Fig. 11) in a region near or positive to the flatband potential, and, hence, the more appropriate capacitance for reference is that of the Hg/solution interface on the positive branch. This is less constant in numerical value. 60 μF cm⁻² has been taken as a typical value (34).

In respect to the comparison with Hg, the validity is lessened by the discovery of Frumkin *et al.* (41), that the dl region on various metals which do not adsorb H significantly varies from ca. 16 to ca. 25 μF cm⁻² on the negative branch. Indeed, it has been suggested that the Thomas-Fermi screening length in a metal contributes to the net dl capacitance and could make the true values of this quantity a parameter characteristic of the metal (42, 43) [however, the limits of this variation do not seem to exceed the range 16-25 μF cm⁻² (41)].

These contributions lessen the numerical certainty of the method used. Because of these intrinsic difficulties, the roughness factors probably do not have absolute significance better than ±100%.

It is interesting to note that the electrochemical and BET areas are not parallel. A parallelity would be expected if the samples used for both methods had been the same (44). Unfortunately, it was not possible to subject the pellets which were used as the electrodes to a BET examination because the BET apparatus which was available was not sufficiently sensitive to register pressure changes with pellets. Therefore, lightly packed powders were used and this difference in form is probably the origin of the fact that there is no constant ratio between the electrochemical and BET measurements.

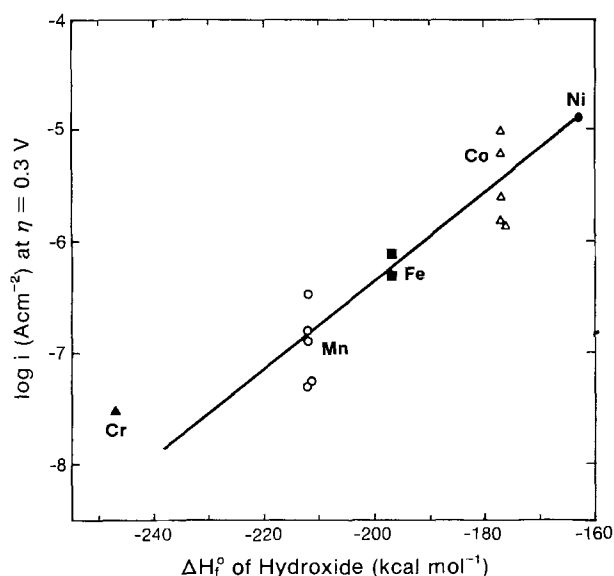


Fig. 8. Current density (based on real surface area) for oxygen evolution on perovskites at an overpotential of 0.3V vs. enthalpy of formation of corresponding hydroxides: M^{III}(OH)₃. The transition metal ions (M) in perovskites are indicated with different symbols.

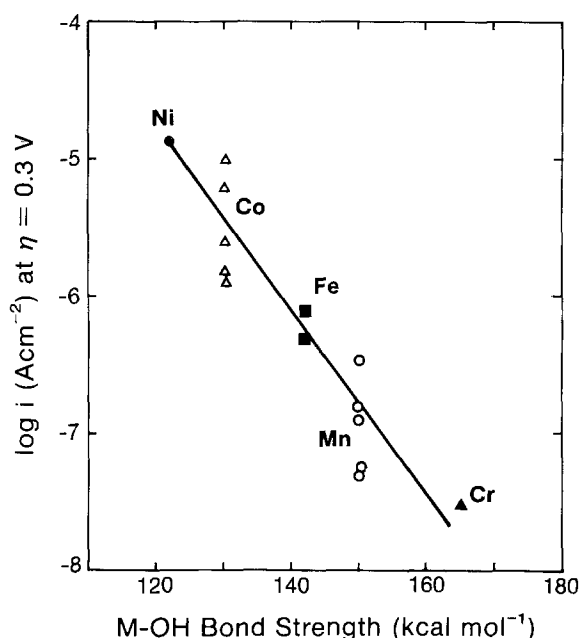


Fig. 9. Current density (based on real surface area) for oxygen evolution on perovskites at an overpotential of 0.3V vs. M-OH bond strength. The transition metal ions (M) in perovskites are indicated with different symbols.

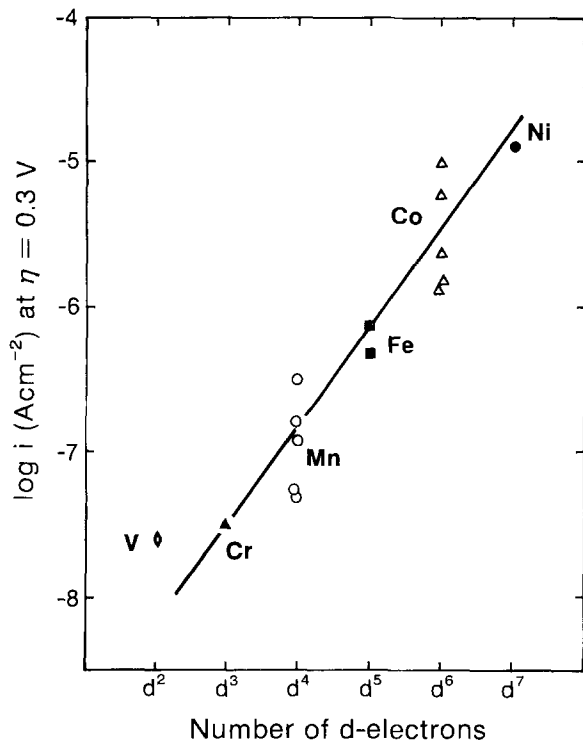


Fig. 10. Current density for oxygen evolution on perovskites at an overpotential of 0.3V vs. number of d-electrons of transition metal ions in perovskites. The transition metal ion in perovskites are indicated with different symbols.

With respect to the dl nature of the capacitance observed, this would depend on the shape of the capacitance/potential curve. An example is shown in Fig. 11. There are clearly three regions. In the cathodic side, a Mott-Schottky plot is visible. In the anodic region positive to ca. 0.8V (NHE), a pseudo-capacitance region is visible and correlates with the region of measurements of O_2 evolution. The values of capacitance in the region near 0.4V and positive to it, including the characteristic hump, seem likely to represent predominantly dl capacitances. The potential range of 0.34-0.39V was used in the determination of the dl capacitance by the cyclic voltammetry technique on the substance shown ($Nd_{0.9}Sr_{0.1}CoO_3$).

Pseudo-capacitance effects which could arise from the oxidation of the B^{III} - B^{IV} certainly should not be expected in the range in which the capacities have been taken because of the evidence from the ESCA data

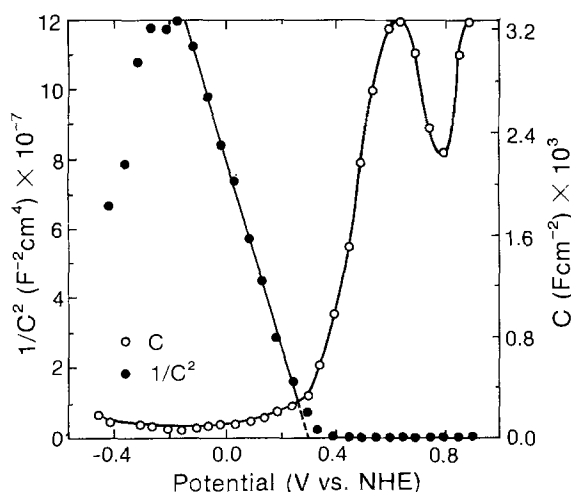


Fig. 11. Capacitance vs. potential plot and Mott-Schottky plot on $Nd_{0.9}Sr_{0.1}CoO_3$ in O_2 -saturated 1M NaOH at 25-100 Hz. Values are expressed in terms of geometric surface area.

that, in the case of the cobalt perovskites, the cobaltic ions remain the dominating occupiers of the surface, together with some oxygen vacancies which would increase with the value of substitution, x (25). It must be recalled that there is only a very small potential range in which the capacitance values were taken. This range was particularly chosen so that it was outside indications of pseudo capacitance or the influence of the possible space charge in the perovskite, as shown in, e.g., Fig. 11.

A rationalization of the change in properties from those characteristic of a semiconductor (see also values of carrier densities in Table I) and those of a metal can be made on the basis of the specific adsorption of OH^- ions. In Fig. 4, it is shown that at $pH \sim 12$ in the region of potential at which the measurements were made (open-circuit potential), OH^- ions are strongly adsorbed.³ It is shown elsewhere (26) that an occupancy of $\sim 10\%$ of the surface states would make changes of potential in the Helmholtz layer ~ 100 times greater than changes within the semiconductor. It is noteworthy that on $Nd_{0.9}Sr_{0.1}CoO_3$, the OH^- adsorption becomes detectable at about 0.2V (NHE), near the region at which the capacitance/potential curve changes its nature (i.e., metallization begins).

Porosity and activity on perovskites.—The large roughness factor raises the question of a model by which so much of the interior surface of these microporous electrodes could be active. One may justify the order of magnitude of the surface area by the following example. Suppose the porous electrode consists of uniform cylindrical pores of 1 μm diam; its porosity is 50%, and the depth of a pore is 0.5 mm. The real area of such a body per apparent square centimeter of surface is 1000 cm^2 . Various assumed shapes and depths of pores gave results in this order (46).

The real exchange current density (i_0) for oxygen evolution on perovskites was typically varied over the range 10^{-12} - 10^{-9} A cm^{-2} (Table I). This observation indicates that the oxygen evolution reaction is highly irreversible; therefore, the diffusion impedance becomes small in influence, and the reactivity would be expected to spread uniformly to a considerable fraction of the interior surface of the microporous electrodes (47). The highest real current density was 10^{-5} A cm^{-2} ; bubbles tended to form at about 10^{-3} A cm^{-2} . Most of the internal area is, therefore, free of bubbles.⁴

One may, therefore, regard the microporous perovskite electrodes as planar electrodes in dealing with their kinetics. This view may be supported by the following observations made on RuO_2 electrodes. In the case of Ti-supported RuO_2 electrodes, in which RuO_2 layers are highly porous with large surface area values, it has been shown that the rate of chlorine evolution was independent of both the roughness factor and the oxide loading of these anodes (48), while the oxygen evolution rates were dependent upon the true (rather than the apparent) area of these electrode surfaces (49). This observation indicates that the chlorine evolution reaction, which is highly reversible, occurs mainly at the external surface of these microporous electrodes, while a much greater degree of the electrode area is active in oxygen evolution.

Interpretation of rate correlations.—The following observations can be made based on the rate correlations given in the Results section.

³ The values of adsorption of OH^- on perovskites (e.g., on manganese) correspond to those near full coverage. But this would not be possible if there were a charge retention of unity [anion repulsion (45)]. Hence, the highly covered surfaces indicate OH^- ions, i.e., partial charge transfer and the consequent formation of quantum states in the surface associated with such bonding.

⁴ The freedom from bubbles and low diffusional impedance leaves only a potential ohmic impedance to reduce the activity of the pores. In an ideal cylindrical pore 0.05 cm deep, and with a maximum real current density of 10^{-5} A cm^{-2} , the ohmic p.d. in the pore is 10⁻⁶V.

First, anodic oxygen evolution on perovskites occurs on metallized structures. Thus, no correlation exists between reaction rates and V_{FB} . Bond, rather than band, concepts should be stressed (50).

Second, the value of the pH at which the concentration of OH^- and H^+ particles is equal (zpc) is a measure of OH^- bond strength of the surface to OH^- . It was found that a weak correlation exists between $(i)_{0.3V}$ and the pH of zero charge. Those perovskites which have a more alkaline pH of zero charge would tend to have a weaker bond strength of OH^- .

Third, ferro-antiferromagnetism in perovskites lies in the superexchange interaction between the transition metal ion and the lattice oxygen (13, 51-53). Hence, a strong interaction would be expected between the transition metal ion and the oxygenated species on the perovskites which exhibit a ferro/antiferromagnetism. This would explain the correlation in Fig. 6, in the sense that electrocatalysis of oxygen evolution decreases as the bond strength of $\text{M}^z\text{-OH}$ increases (cf. Fig. 9).⁵

Fourth, the tendency, shown in Fig. 7, to increase catalysis with decreased stability of the oxide may indicate that a high catalytic activity for oxygen evolution on perovskites is associated with ease of loss of lattice oxygens and/or ease of formation of oxygen vacancies, i.e., weaker bonding of oxygenated species to the lattice.

Fifth, the d-correlation shown in Fig. 10 suggests that the reaction site for oxygen evolution on a perovskite-type oxide is a first-row transition metal ion (B ion).

Sixth, in gas phase catalysis, a double peak pattern predicted by crystal-field effects on bond strength is observed (55, 56). The observed d-correlation in Fig. 10 does not follow a double peak pattern, indicating that the crystal-field effect upon electrocatalysis is not significant in perovskites. This observation may suggest that a rearrangement of d-electron configuration occurs at the surface of a perovskite as a result of more splittings of d-orbitals due to the unsaturated coordination (57). This new d-electron configuration could have a decisive role in electrocatalysis in terms of bond formation between an intermediate and the surface.

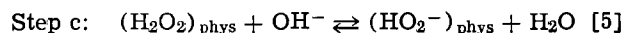
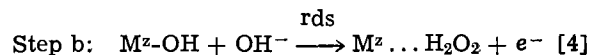
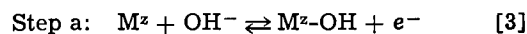
Seventh, it has been shown that electrocatalysis of oxygen evolution on perovskites depends primarily on the local interaction between a reaction site (transition metal B ion) and an intermediate. The observations in Fig. 8 and 9 suggest that the reaction rate of oxygen evolution on perovskites is determined by the difficulty of removal of OH intermediates, rather than adsorption of OH intermediates. Breaking of the $\text{M}^z\text{-OH}$ bond is involved in the rate-determining step.

Therefore, it seems reasonable to assume that a common rate-determining step occurs in a path of oxygen evolution reaction on a series of perovskite-type oxides. The correlation between rate at a constant potential and the calculated value of bond strength (Fig. 9) is an analog of a similar correlation observed for hydrogen evolution (3), in which rate-determining electrochemical desorption occurs on the various transition metals.

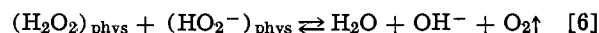
Electrocatalysis in terms of a rate-determining OH desorption mechanism.—The facts adduced above show that the likely mechanism underlying electrocatalysis of oxygen evolution on perovskites involves a rate-determining M-OH desorption (M is B ion in ABO_3). However, it has been found (58, 59) that there are a number of individual kinetic characteristics of the electrolytic oxygen-evolution reaction that demand some variation in the details of the mechanism, and an investigation (26) has shown that consistency can

be brought to these facts by the assumption that differing M-OH bond strengths among the perovskites give rise to different isotherms.

The mechanism⁶ found most consistent with the kinetics data is



Step d:



Two dimensional potential-energy diagrams, based on a Morse function approach (60, 61), for the proposed mechanism for oxygen evolution, are qualitatively shown in Fig. 12.

In Step a, the water molecule, originally adsorbed to a reaction site (M^z) can be replaced by an OH^- ion by means of proton transfers. Hence, a successful electron transfer (transmission coefficient $\kappa \sim 1$) may occur.

In Fig. 12, the dashed curve represents a situation with a lower adsorption energy for OH species as expected in nickelates, i.e., a smaller activation energy for Step b. Ferrites would be expected to have a higher adsorption energy and, hence, a larger activation energy. This view is consistent with the correlations shown in Fig. 6, 7, 8, and 9.

Electrocatalysis in terms of MO theory.—A schematic of a model for the active surface of the perovskite is shown in Fig. 13. The $\{001\}$ plane containing the transition metals is likely to be an active reaction surface. A simple model of such an oxide surface is the MO_5 (M is a transition metal ion; O is an oxygen ion) cluster; 3d (e_g, t_{2g}) levels will split further because of the lower symmetry near the surface.

According to the calculations for SrTiO_3 by Wolfram *et al.* (57, 62, 63), the e_g levels of the MO_6 cluster (bulk) split into the $d_{x^2-y^2}$ and d_{z^2} levels, with the d_{z^2} state lying below the $d_{x^2-y^2}$ state at the surface. The t_{2g} levels split into the double degenerated d_{xz} and d_{yz} states and the singlet d_{xy} state. These energy levels are schematically shown in the upper part of Fig. 14.

Assuming that these d-levels calculated for SrTiO_3 also hold for other perovskites, one may assign the d-electron configuration of the transition metal ion at

⁶ In the case of lanthanum nickelate, the participation of lattice oxygens is considered (26), which gives the reaction order with respect to OH^- as unity.

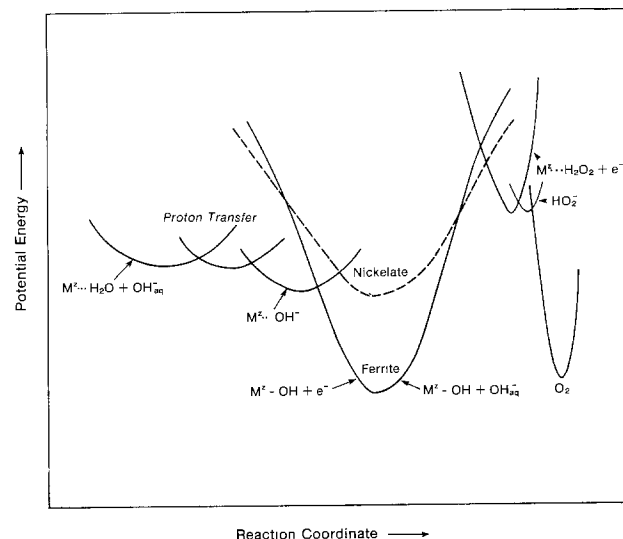


Fig. 12. Potential energy diagrams for a rate-determining OH desorption mechanism.

⁵ Well-known suggestions by Tseung (54), which relate the paramagnetism of O_2 to its positioning on the electrode surface, apply to the O_2 reduction process, but O_2 cannot be involved in the rate determining in the evolution reactions reported here.

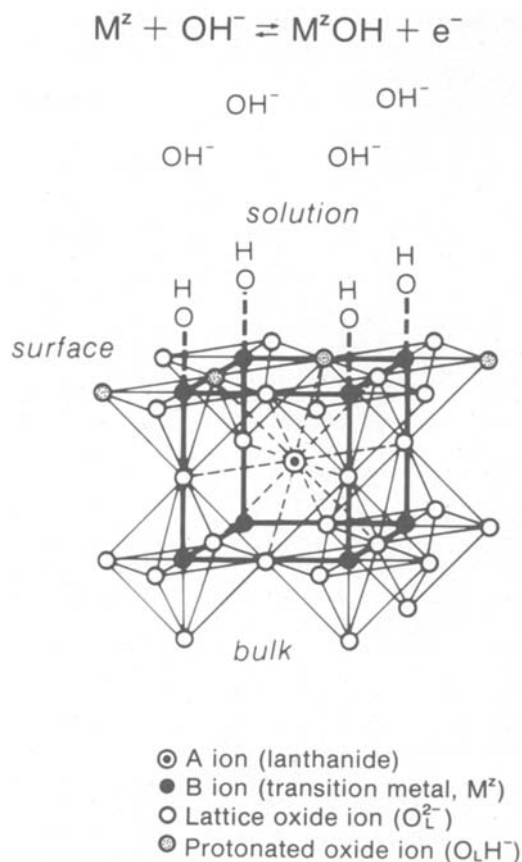


Fig. 13. Schematic model for the active surface of the perovskite, in which transition metal B ion is electrochemically active.

the surface of perovskite-type oxides, as shown in Fig. 14. The energy differences can be seen only qualitatively. In cobaltates, a high spin configuration (64) is shown. A low spin configuration is also possible. It can be seen in Fig. 14 that the d_{z^2} orbital will be occupied by an electron only in cobaltates or nickelates.

A likely electronic structure of OH is: $1s^2 2s^2 (2p_x + 1s)^2 2p_x^2 2p_y^1$ (57). The bonding state is an oxygen $2p_z$ orbital σ -bonded to a hydrogen $1s$ state. The oxygen $2p_x$ and $2p_y$ orbitals remain as nonbonding.

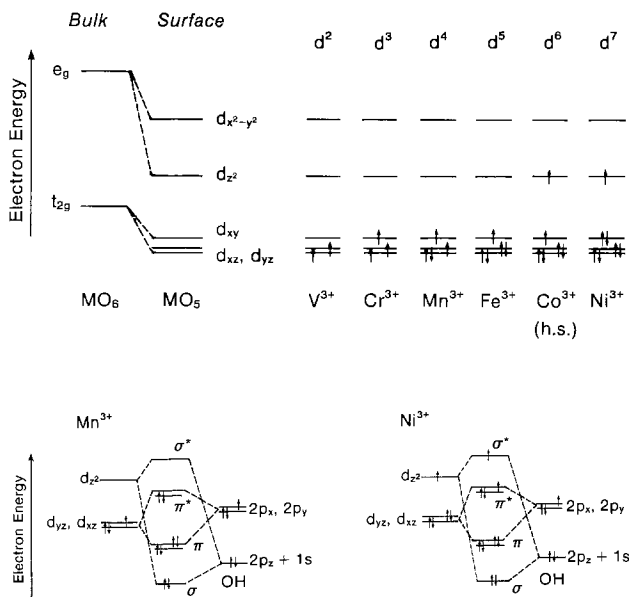


Fig. 14. d -electron configuration of transition metal ions at the surface of perovskites (above); MO diagrams for the M^z -OH bonding at the surface of perovskites; manganites and nickelates (below).

The possible orbital interactions between a transition metal ion at the surface of perovskites and an OH species are as follows. The d_{z^2} of a transition metal ion⁷ will overlap with the $2p_z + 1s$ orbital of an OH, forming σ -type orbitals, while the d_{xz} (d_{yz}) orbital will interact with the $2p_x$ ($2p_y$) of an OH, giving π -type orbitals. Neither the $d_{x^2-y^2}$ nor the d_{xy} orbital will mix with the OH orbitals, because of symmetry conservation.

Based upon the d -electron configuration and the possible orbital overlaps, MO diagrams for the M^z -OH bonding at the surface of perovskites are shown for manganites and nickelates in the lower part of Fig. 14. The following observations can be made from the qualitative MO diagrams.

First, the OH species is a saturated ligand, having almost filled p -orbitals. Therefore, the contribution of π -bondings, i.e., back bonding (65), to the M^z -OH bonding would be negligible, especially in the case of Co^{3+} or Ni^{3+} .

Second, since the bonding orbitals of M^z -OH are readily occupied by electrons from OH species, electrons from the d -orbitals of the surface transition metal in perovskites will occupy the antibonding orbitals of M^z -OH. Thus, it is expected that the bond strength of M^z -OH would decrease as the number of d -electrons increases.

Third, it has been postulated that the bond order is approximately proportional to the bond energy (66). The estimated bond orders for M^z -OH bonding at the surface of perovskites decrease in the following sequence. $V^{3+}:2.5$, $Cr^{3+}:2.5 > Mn^{3+}:2 > Fe^{3+}:1.5 > Co^{3+}:1-1.5^8 > Ni^{3+}:1$. The trend in bond order is in agreement with that bond strength determined thermodynamically (Fig. 9).

Fourth, electrons in the d_{z^2} orbital, e.g., in Ni^{3+} or high spin Co^{3+} , may play an important role in achieving high reaction rates, since these electrons tend to occupy the σ^* antibonding of M^z -OH, resulting in a weaker bond.

Fifth, the observed poor catalytic ability on vanadates and/or chromites may be interpreted by the fact that a higher oxidation state easily forms on these materials (38), forming a too stable surface complex of OH species. Thus, these perovskites cannot serve as electrocatalysts, since further reactions, which lead to the formation of oxygen, have difficulty in proceeding.

Earlier interpretations.—Matsumoto *et al.* have contributed many publications (6-11, 67) in which an interpretation of the relative reaction rates measured according to the geometric surface are given. The essence of their view concerns the overlap integrals between the sp_σ orbital of O (or O containing species) and the e_g orbital of the transition metal ion, which are seen as being related to the σ^* character of the bands in the perovskite.

According to them, the important part of the evolution of oxygen depends upon the discharge of H_2O or OH^- to adsorbed OH through the σ^* band, which is assumed to extend to the surface. The rate-determining steps assumed by Matsumoto *et al.* are based on experiments with only three transition metals, namely, Mn, Fe, and Co. These elements and their perovskites are taken, in their view, to give rise to a rate-determining step of the discharge of OH^- for the Mn containing compounds (6). For the iron and cobalt compounds, they conclude that $MOH + OH^- \rightarrow MO^- + H_2O$ is the rate-determining step (7, 8, 10).

The introduction of band theory by Matsumoto *et al.* is appreciated, although it has some counter difficulties in neglecting bond concepts which seem fruitful in catalytic discussions. The principal difficulty is the

⁷ The x -axis is taken in the direction perpendicular to the reaction surface in Fig. 13.

⁸ B.O. = 1 for low spin. B.O. = 1.5 for high spin.

lack of possibility of making plots with their work that extend over more than three materials. It is easy to change the rate-determining step and obtain agreement with Tafel slopes in ad hoc manner if there is no requirement for consistency within a group of materials. In the present work, (e.g., as shown in Fig. 10) there is a consistent correlation between the current at an overpotential of 0.3V and six different materials. It is difficult to avoid the conclusion that the rate-determining step in this group must be the same and to see this as a more likely model than that of Matsunoto *et al.* with changing rate-determining steps. A more certain judgment with respect to their work, compared with our own, must await a provision of data involving more transition metals.

Trasatti (5) [cf. Tseung and Jasem (4)] considers that a volcano relation should exist for the electrocatalysis of oxides in the sense that the rate should at first increase with the enthalpy change of the lower-to-higher oxide transition and then decrease (after the enthalpy has reached about 80 kJ mol⁻¹). Some degree of structural rationalization can be seen in the sense that adsorption of a component (e.g., OH) on the oxide concerned would be expected to parallel the heat of formation on the compound in the next valency state. Conversely, Trasatti does not relate his observations to any particular mechanism for oxygen evolution and, correspondingly, to any rate-determining step, although the direction of the dependence of the rate upon bonding considerations would vary with this.

Plotting our data as a function of the enthalpy change of the lower to the higher oxide transition (ΔH_t°) gives the correlation shown in Fig. 15, which is consistent with those made in Fig. 7, 8, and 9. There is, thus, consistency between the detailed mechanistic view suggested here and the more general indications of Trasatti (5) [cf. those of Tseung and Jasem (4)]. Thus, the parameter of ΔH_t° would be expected to be parallel to the M-OH bond strength.

Potential of comparison for electrocatalysis.—Normally, the i_0 values are used in electrocatalytic comparisons (1). However, such values may not offer useful data from the viewpoint of a comparison of rates at practical current densities. Table II shows that LaNiO₃ has an i_0 value among the lowest of the materials examined, but, as a consequence of the low Tafel slope, the value of the real current density passed at an overpotential of 0.3V is the highest observed (21).

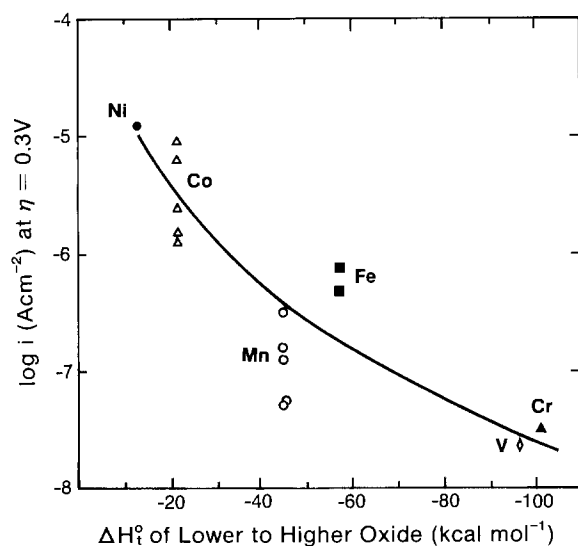


Fig. 15. Current density (based on real surface area) for oxygen evolution on perovskites at an overpotential of 0.3V vs. enthalpy change of lower-to-higher oxide transition. The transition metal ions in perovskites are indicated with different symbols.

It is clear that the practically important region for comparison is that of the low overpotential section of the Tafel region, and here the overpotential of 0.3V has been arbitrarily chosen as the comparison potential.

However, such use of current density at a certain overpotential means that if the Tafel slopes differ, as they do here (see Table II), there will be a different electrical contribution to the rate, i.e., interpretations of electrocatalysis cannot be made on the basis of bonding considerations alone without relating the change of such contributions to other factors (e.g., radical coverage which may alter Tafel slopes and, therefore, the electrical contribution for a given overpotential). Table IV shows the contribution to the rate of the $e^{\alpha n F/RT}$ term in the Tafel equation.

Of relevance here is the plot of the overall transfer coefficient (α) as a function of the number of d-electrons in the transition metal ions of perovskites (Fig. 16). Thus, α increases smoothly with the number of electrons which occupy the d-levels. This can be seen to influence directly the strength of OH bonds to the transition metal ion, when the latter becomes weaker as the d-occupancy increases. In turn, the steady-state OH coverage affects the isotherm effective in the kinetics and changes α , i.e., changes the electrical contribution to the free energy of activation.

Therefore, the general rule found here, that increasing weakening of the M-OH bond for the group of perovskites concerned increases the rate, is unimpaired by considerations which separate chemical and electrical contributions to practical values of the catalysis. But the discussion shows that the relative rate of oxygen evolution on these catalysts is strictly dependent upon a choice of potential range. The present range considered refers to current densities of over 100 mA cm⁻² (based on geometric area) on the better catalysts.

The effect of substitution and nonstoichiometry.—In order to obtain sufficient conductivity in the perovskites (ABO₃), it is necessary to substitute some of the A ions by ions of lower valency, e.g., Sr²⁺. When a certain amount of divalent strontium substitutes for the trivalent lanthanum in a perovskite, there may be two results to compensate for the change of charge. Some of the B³⁺ ions can be changed into B⁴⁺. Alternatively, oxygen vacancies can be introduced.

We choose to accept the latter model because of the work of Nakamura *et al.* (20). These workers examined the perovskite La_{0.9}Sr_{0.1}CoO₃ in respect to the rate of oxygen desorption from the surface. They concluded that the effect of the increase of the Sr²⁺ content x is to introduce oxygen vacancies rather than Co⁴⁺ ions. Additional evidence was obtained in our own work in examining the same substance by ESCA (25). The results show that in the potential range for

Table IV. Overpotential contributions to the rate of the oxygen-evolution reaction at constant overpotential on different groups of perovskites

Transition metal in perovskite	θ^\dagger	Tafel slope	α	$e^{\alpha n F/RT}*$
Ni	$\theta \rightarrow 0$	$\frac{2RT}{3F}$	1.5	4×10^7
Co	$0.2 < \theta < 0.8$	$\frac{F}{2RT}$	1.0	1×10^6
Fe, Mn	$\theta \rightarrow 1$	$\frac{F}{2RT}$	0.5	3×10^3
V, Cr	?	$> \frac{2RT}{F}$	> 0.5	$< 10^2$

[†] Coverage of M²⁺-OH.
* $\eta = 0.3V$.

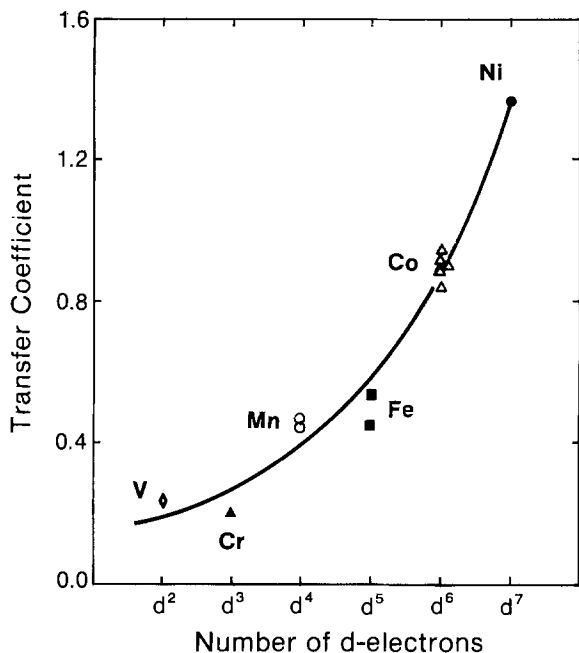


Fig. 16. Transfer coefficient of oxygen evolution at lower overpotentials on perovskites vs. number of d-electrons of transition metal ions in perovskites. The transition metal ions in perovskites are indicated with different symbols.

oxygen evolution reaction there existed in the surface of the perovskite only Co^{III} and oxygen vacancies. On this basis it is assumed that a similar model exists for the rest of the perovskites reported on in this paper.

In Fig. 17 it is shown that some increase in the current at constant overpotential occurs with x . This is indeed consistent with our model, according to which the rate of oxygen evolution would increase with an increasing lessening of the B-OH bond strength, and also with the description of Nakamura *et al.* (20), who found that the desorption of O increases in rate as the Sr²⁺ content increases, i.e., as the number of oxygen vacancies is increased. Thus, the increase of oxygen vacancies can be seen as a decrease in the average bonding energy of O to the lattice.

A contrast in this view can be seen with that which would arise had it been assumed that the effect of increasing the substitution x upon the lattice is to cause a corresponding number of Co⁴⁺ ions to exist in the

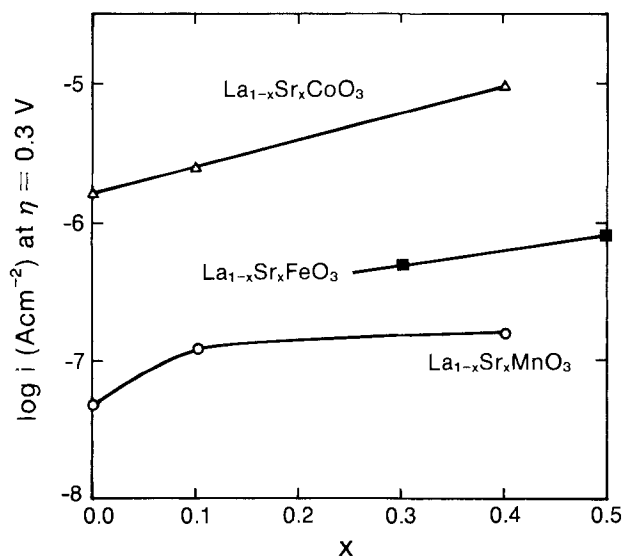
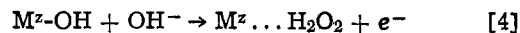


Fig. 17. Current density (based on real surface area) for oxygen evolution on perovskites at an overpotential of 0.3V vs. degree of Sr-substitution, x .

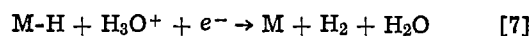
surface. Then, as x increases, the B-OH bond strength would increase and one would expect, on the present model, for the rate to fall. The fact that Fig. 17 shows, however, an increase in the rate is consistent with the weakening of M-O bonding in the lattice, which corresponds to the introduction of oxygen vacancies.

Our view is consistent with the prediction of Trasatti (5) that an important factor in oxide electrocatalytic activity is related to the degree of nonstoichiometry. However, it correspondingly shows that this is not the main factor involved in the variation of the electrocatalytic activity, which changes over three orders of magnitude with alteration of the transition metal ion at constant stoichiometry.

A volcano relationship?—The data in the present paper suggest that rate increases as M^z-OH decreases. A rate-determining step consistent with this is (*inter alia*)



The analogy which this step forms to that in hydrogen evolution on transition metals (1, 3)



suggests that, as the bonding to the oxide surface further weakens, the rate of Eq. [4] increases sufficiently so that another reaction in the same kinetic sequence becomes rate determining. By analogy with the situation in hydrogen evolution, this would be



An elementary consideration of potential energy surfaces shows that the dependence of rate upon M^z-OH would reverse in trend; the rate would decrease with increasing occupancy of the antibonding orbital of M^z-OH. Thus, a plot of rate at a given overpotential against some measure of M^z-OH strength would pass through a maximum. Such a plot is shown in Fig. 18. A similar suggestion, without mechanistic commitment, has been made by Trasatti for oxide catalysts (5).

A low value of ΔH_f^o of Rh₂O₃, -68.3 kcal mol⁻¹ (37) (cf. Table III), suggests that the perovskites with a second-row transition metal ion, e.g., La_{1-x}Sr_xBO₃ (B = Mo, Ru, Rh) (68, 69), may exhibit a very weak bonding of M^z-OH, and, hence, could be members of the left-hand branch of a volcano plot. The molybdenum containing compound may show a faster rate than the other compounds mentioned because of the relatively high ΔH_f^o of MoO₂ [-130 kcal mol⁻¹ (37)].

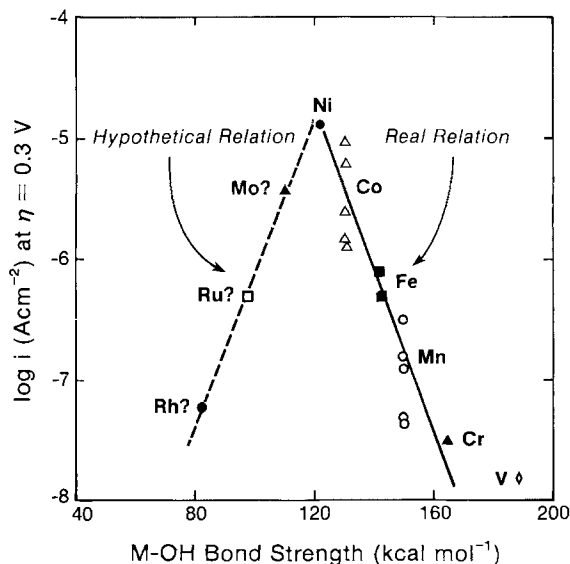


Fig. 18. Hypothetical volcano plot for oxygen evolution on perovskites. Transition metal B ions in perovskites are indicated with different symbols.

It must be stressed that the points shown in Fig. 18 refer to speculative predictions of oxygen evolution on perovskites containing the metals indicated. They have, for example, nothing to do with expectations of the relative oxygen-evolution rate on, e.g., RuO_2 (or NiO) where there is evidence that the rate predicted here for perovskites would be reversed for oxides (59).

Prediction of electrocatalysis.—Figure 19 gives the plots of Tafel line intercepts (Tafel parameter a)⁹ of oxygen evolution vs. the number of d-electrons of transition ions in the various perovskite-type oxides. This correlation in terms of number of d-electrons can be further rationalized by plotting Tafel line intercepts against the number of electrons occupying the antibonding orbitals of $\text{M}^z\text{-OH}$ (cf. Fig. 14), as shown in Fig. 20. In Fig. 20, the electrocatalytic activity based on Tafel line intercepts increases as the number of electrons occupying the antibonding orbitals increases.

Thus, lanthanum nickelate (LaNiO_3) gives the highest electrocatalytic activity among the perovskites studied (21). The high catalytic activity observed on the NiCo_2O_4 spinel (4) is in agreement with this prediction, since it contains catalytically active species, Ni^{II} and Co^{III} .

On the basis of Fig. 20, one might predict that LaCuO_3 (71) would be a better catalyst than LaNiO_3 , since its d^8 electrons would contain a greater number of antibonding positions. However, instability of the Cu^{III} compounds would be expected in aqueous solution (72); it is possible that stabilization could be achieved by replacing some Cu^{3+} by Cu^{2+} in a compound such as $\text{La}_{1-x}\text{Ce}_x\text{CuO}_3$.

Stability of electrocatalysts.—Some of the catalysts examined were polarized for times up to 40h. A typical example obtained on $\text{La}_{0.9}\text{Sr}_{0.1}\text{CoO}_3$ is shown in Fig. 21. Under the anodic polarization at 25 mA cm^{-2} , the electrode potential rose gradually during the first 26h. It became constant after 20h. XPS study showed that the cobalt species present was only Co^{III} at the surface after this anodic polarization (25).

⁹This method of comparing electrocatalysis has been used particularly by Srinivasan *et al.* (70).

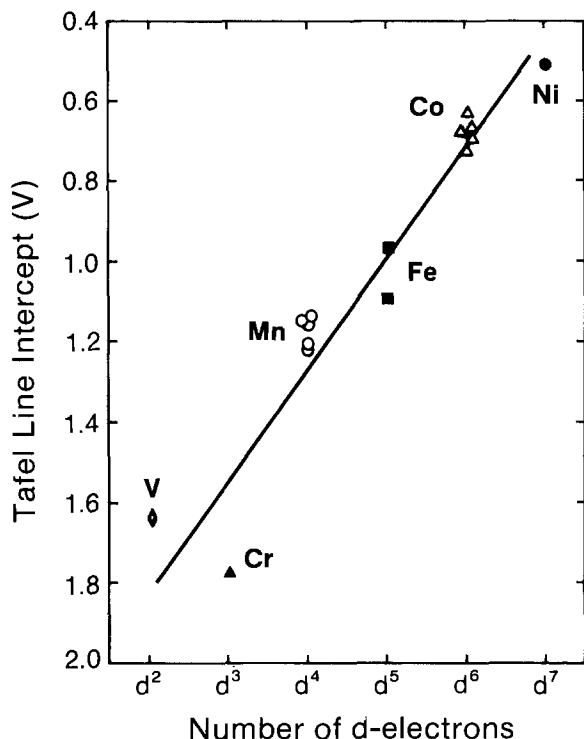


Fig. 19. Tafel line intercept (Tafel parameter a , based on real surface area) of oxygen evolution on perovskites vs. number of d-electrons of transition metal ions in perovskites. The transition metal ions in perovskites are indicated with different symbols.

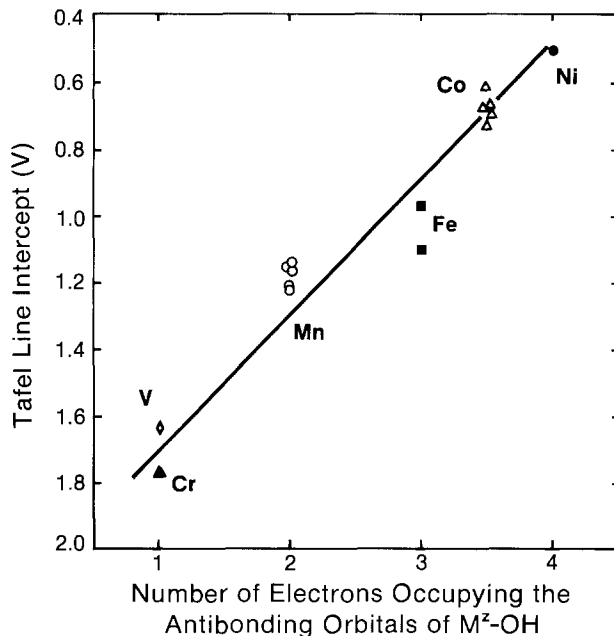


Fig. 20. Tafel line intercept (Tafel parameter a , based on real surface area) of oxygen evolution on perovskites vs. number of electrons occupying the antibonding orbitals of $\text{M}^z\text{-OH}$. The averaged values for high spin and low spin cases were used for cobaltates. The transition metal ions in perovskites are indicated with different symbols.

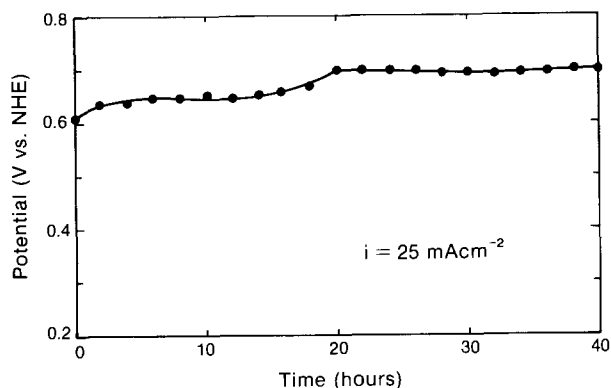


Fig. 21. Time variation of potential on $\text{La}_{0.9}\text{Sr}_{0.1}\text{CoO}_3$ electrodes in O_2 -saturated 1M NaOH at 25°C under a galvanostatic condition.

Also, LaNiO_3 exhibited a stable performance for over 70h at 100 mA cm^{-2} , which corresponds to an overpotential of 300 mV.

Summary

An increase in the catalytic activity for electrolytic evolution of oxygen on perovskites occurs in parallel with a high occupancy of antibonding orbitals of $\text{M}^z\text{-OH}$.

Acknowledgments

The authors are grateful to Professor S. Trasatti, Dr. A. Damjanovic, Dr. A. J. Appleby, and Dr. O. J. Murphy for helpful critical discussion of this work. The support of this work by the Robert A. Welch Foundation (Grant no. A-740) is gratefully acknowledged.

The authors are also grateful to Dr. M. B. Hall for a helpful discussion on MO theory and to Mrs. Lynn McCartney-Murphy for her editing and typing of this manuscript.

Manuscript submitted Dec. 20, 1982; revised manuscript received July 12, 1983.

Texas A&M University assisted in meeting the publication costs of this article.

REFERENCES

1. A. J. Appleby, in "Modern Aspects of Electrochemistry," Vol. 9, J. O'M. Bockris and B. E. Conway, Editors, p. 369, Plenum Press, New York (1973).
2. P. Ruetschi and P. Delahay, *J. Chem. Phys.*, **23**, 556 (1955).
3. B. E. Conway and J. O'M. Bockris, *J. Chem. Phys.*, **26**, 532 (1957).
4. A. C. C. Tseung and S. Jasem, *Electrochim. Acta*, **22**, 31 (1977).
5. S. Trasatti, *J. Electroanal. Chem.*, **111**, 125 (1980).
6. Y. Matsumoto and E. Sato, *Electrochim. Acta*, **24**, 421 (1979).
7. Y. Matsumoto, J. Kurimoto, and E. Sato, *J. Electroanal. Chem.*, **102**, 77 (1979).
8. Y. Matsumoto, H. Manabe, and E. Sato, *This Journal*, **127**, 811 (1980).
9. Y. Matsumoto and E. Sato, *Electrochim. Acta*, **25**, 585 (1980).
10. Y. Matsumoto, S. Yamada, T. Nishida, and E. Sato, *This Journal*, **127**, 2360 (1980).
11. Y. Matsumoto, H. Yoneyama, and H. Tamura, *J. Electroanal. Chem.*, **83**, 167 (1977).
12. G. V. Subba Rao, B. M. Wanklyn, and C. N. R. Rao, *J. Phys. Chem. Solids*, **32**, 345 (1971).
13. C. N. R. Rao, *J. Indian Chem. Soc.*, **51**, 979 (1974).
14. H. Obayashi, T. Kudo, and T. Gejo, *Jpn. J. Appl. Phys.*, **13**, 1 (1974).
15. D. S. Rajoria, V. G. Bhide, G. R. Rao, and C. N. R. Rao, *J. Chem. Soc. Faraday Trans. 2*, **70**, 512 (1974).
16. T. Katsura, K. Kitayama, T. Sugihara, and N. Kimizuka, *Bull. Chem. Soc. Jpn.*, **48**, 1809 (1975).
17. B. C. Tofield, *J. Solid State Chem.*, **12**, 270 (1975).
18. R. J. H. Voorhoeve, J. P. Remeika, and L. E. Trimble, *Ann. N.Y. Acad. Sci.*, **272**, 3 (1976).
19. C. P. Khattak and D. E. Cox, *Mater. Res. Bull.*, **12**, 463 (1977).
20. T. Nakamura, M. Misono, and Y. Yoneda, *Bull. Chem. Soc. Jpn.*, **55**, 394 (1982).
21. T. Otagawa and J. O'M. Bockris, *This Journal*, **129**, 2391 (1982).
22. L. J. van der Pauw, *Philips Res. Rep.*, **13**, 1 (1958).
23. R. A. Fredlein and A. J. Bard, *This Journal*, **126**, 1892 (1979).
24. L. N. Mulay, in "Physical Methods of Chemistry," Part IV, A. Weissberger and B. W. Rossiter, Editors, p. 521, Wiley-Interscience, New York (1972).
25. J. O'M. Bockris, T. Otagawa, and V. Young, *J. Electroanal. Chem.*, In press.
26. J. O'M. Bockris and T. Otagawa, *J. Phys. Chem.*, In press.
27. G. Singh, M. H. Miles, and S. Srinivasan, in "Electrocatalysis on Non-Metallic Surfaces," NBS Special Publ. no. 455, A. D. Franklin, Editor, p. 289, U.S. Government Printing Office, Washington, DC (1976).
28. R. S. Yeo, J. Orehotzky, W. Visscher, and S. Srinivasan, *This Journal*, **128**, 1900 (1981).
29. H. Kita, N. Henmi, K. Shimazu, H. Hattori, and K. Tanabe, *J. Chem. Soc., Faraday Trans. 1*, **77**, 2451 (1981).
30. G. A. Parks, *Chem. Rev.*, **65**, 177 (1965).
31. J. W. Murray, *J. Colloid Interface Sci.*, **46**, 357 (1974).
32. D. N. Furlong, D. E. Yates, and T. W. Healy, in "Electrodes of Conductive Metallic Oxides," S. Trasatti, Editor, p. 367, Elsevier, New York (1981).
33. (a) R. J. Aktinson, A. M. Posner, and J. P. Quirk, *J. Phys. Chem.*, **71**, 550 (1967); (b) J. W. Bowden, M. D. A. Bolland, A. M. Posner, and J. P. Quirk, *Nature*, **245** (1973).
34. S. Levine and A. L. Smith, *Discuss. Faraday Soc.*, **52**, 290 (1971).
35. (a) M. Crespini and W. K. Hall, *J. Catal.*, **69**, 359 (1981); (b) M. A. F. Pyman and A. M. Posner, *J. Colloid Interface Sci.*, **66**, 85 (1978).
36. T. Nakamura, G. Petzow, and L. J. Gauckler, *Mater. Res. Bull.*, **14**, 649 (1979).
37. "Handbook of Chemistry and Physics," 60th Edition, E. O. Smythe, Editor, p. E655, The Chemical Rubber Co., Cleveland (1979).
38. M. Pourbaix, "Atlas of Electrochemical Equilibria in Aqueous Solutions," p. 334, Pergamon Press, New York (1966).
39. K. Klier, *J. Catal.*, **8**, 14 (1967).
40. J. E. Huheey, "Inorganic Chemistry," 2nd Edition, pp. 162-171, Harper and Row, New York (1978).
41. A. Frumkin, B. Damaskin, N. Grigoryev, and I. Bagotskaya, *Electrochim. Acta*, **19**, 69 (1974).
42. O. K. Rice, *Phys. Rev.*, **31**, 1051 (1928).
43. A. A. Kornyshev, W. Schmickler, and M. A. Vorontyev, *Phys. Rev. B*, **25**, 5244 (1982).
44. L. D. Burke and O. J. Murphy, *J. Electroanal. Chem.*, **96**, 19 (1979).
45. J. O'M. Bockris and M. A. Habib, *Z. Phys. Chem.*, **98**, 43 (1975).
46. T. Otagawa, Ph.D. Thesis, Texas A&M University, College Station, TX (1983).
47. S. Srinivasan, H. D. Hurwitz, and J. O'M. Bockris, *J. Chem. Phys.*, **46**, 3108 (1967).
48. L. D. Burke and J. F. O'Neill, *J. Electroanal. Chem.*, **101**, 341 (1979).
49. L. D. Burke, O. J. Murphy, J. F. O'Neill, and S. Venkatesan, *J. Chem. Soc. Faraday 1*, **73**, 1659 (1977).
50. F. S. Stone, *J. Solid State Chem.*, **12**, 271 (1975).
51. G. H. Jonker and J. H. Van Santen, *Physica*, **19**, 120 (1953).
52. J. B. Goodenough, in "Progress in Solid State Chemistry," Vol. 5, H. Reiss, Editor, p. 143, Pergamon Press, Oxford (1971).
53. H. Taguchi, M. Shimada, and M. Koizumi, *Mater. Res. Bull.*, **13**, 1225 (1978).
54. A. C. C. Tseung, *This Journal*, **125**, 1660 (1978).
55. D. A. Dowden, *Catal. Rev.*, **5**, 1 (1971).
56. A. Cimino and S. Carra, in "Electrodes of Conductive Metallic Oxides," S. Trasatti, Editor, p. 97, Elsevier, New York (1980).
57. T. Wolfram, F. J. Morin, and R. Hurst, in "Electrocatalysis on Non-Metallic Surfaces," NBS Special Publ. no. 455, A. D. Franklin, Editor, p. 21, U.S. Government Printing Office, Washington, DC (1976).
58. A. Damjanovic and B. Javanovic, *This Journal*, **123**, 374 (1976); A. Damjanovic, J. F. Wolf, and S. L. Soled, *ibid.*, To be published.
59. S. Trasatti and G. Lodi, in "Electrodes of Conductive Metallic Oxides," S. Trasatti, Editor, p. 521, Elsevier, New York (1981).
60. B. E. Conway and J. O'M. Bockris, *Can. J. Chem.*, **35**, 1124 (1957).
61. B. E. Conway and J. O'M. Bockris, *Electrochim. Acta*, **3**, 340 (1961).
62. T. Wolfram, R. Hurst, and F. J. Morin, *Phys. Rev. B*, **15**, 1151 (1977).
63. T. Wolfram and S. Ellialtioglu, in "Theory of Chemisorption," J. R. Smith, Editor, p. 149, Springer-Verlag, Berlin (1980).
64. G. H. Jonker, *Philips Res. Rep.*, **24**, 1 (1969).
65. J. E. Huheey, "Inorganic Chemistry," 2nd Edition, p. 402, Harper and Row, New York (1978).
66. R. L. Dekock and H. B. Gray, "Chemical Structure and Bonding," p. 199, Benjamin, Menlo Park, CA (1980).
67. H. Tamura, H. Yoneyama, and Y. Matsumoto, in "Electrodes of Conductive Metallic Oxides," S. Trasatti, Editor, p. 261, Elsevier, New York (1980).
68. K. Kamata, T. Nakamura, and T. Sata, *Mater. Res. Bull.*, **10**, 373 (1975).
69. J. R. Bouchard and J. F. Weiher, *J. Solid State Chem.*, **4**, 80 (1972).
70. M. H. Miles, Y. H. Huang, and S. Srinivasan, *This Journal*, **125**, 1931 (1978).
71. J. B. Goodenough, N. F. Mott, N. Pouchard, G. Demazeau, and P. Hagenmuller, *Mater. Res. Bull.*, **8**, 647 (1973).
72. F. A. Cotton and G. Wilkinson, "Advanced Inorganic Chemistry," New York (1972).

Adsorption of 3-phenyl-1-propanol on Gold Electrode from Perchloric Acid Solutions

K. Katoh and M. Koseki

Department of Applied Chemistry, Faculty of Engineering, Niigata University, 2-8050, Ikarashi, Niigata, 950-21, Japan

ABSTRACT

Adsorption parameters of 3-phenyl-1-propanol and some other ω -phenyl alkanols were calculated after the isotherm of $\theta/(1-\theta)^n = K_{\text{ads}} \cdot X_{\text{org}}$. The adsorption peaks appeared at 0.70 and 0.35V (*vs.* SCE) for the adsorbate. The peak near 0.70V seems to be due to π -electron interaction of the benzene ring and another peak at 0.35V to the alcohol group as side chain. The peak height of coverage-potential curve at 0.35V became larger depending upon the number of carbon atoms in the aliphatic alcohol group on the benzene ring. The differential capacity was measured by a rapid rectangular single-pulse technique, and the voltage-time curve was memorized electrically set by a "Wave Memory." Then, the reproducibility of the capacity measurement became approximately within $\pm 6\%$. The values of n and the standard free energy of adsorption (ΔG°) of the adsorbate at 0.70V were calculated as 2.8 and -7.4 kcal/mol, respectively.

In the adsorption of benzene compounds on electrode surface, the π -electron interaction between the adsorbed molecule and the electrode surface plays a dominant role (1). As reported in a previous paper (2), the adsorption peak of benzoic acid appears at 0.60V (*vs.* SCE), and the peak seems to be due to adsorption of benzene ring by its π -electron interaction on the gold electrode. In this report, adsorption of 3-phenyl-1-propanol (PPA) on gold electrode was studied. The adsorption peak was found at 0.70V. However, we found out that the new peak appeared at 0.35V. Peak height of the coverage-potential curve became larger depending upon the number of carbon atoms in the aliphatic alcohol group on the benzene ring from the coverage data of benzyl alcohol, 2-phenyl ethanol, and 3-phenyl-1-propanol. Kinetic parameters were calculated after the concept of competitive adsorption by Bockris and Swinkels (3, 4), Dahms and Green (5), and Conway and Dhar (6). They assumed that one molecule of an organic substance took the place of n molecules of water on the electrode surface. Lawrence and Parsons (7) calculated the n value from the geometrical ratio of the area occupied by the organic molecule to the one by water molecule. Dahms and Green (5) calculated the value for adsorption of aromatic hydrocarbons on gold electrode with radiotracer technique.

Experimental

Gold electrode.—The gold electrode which was used as the working electrode which was made from polycrystalline pure gold (99.99%, Tokuriki Manufacturing Company Limited) and was sheathed in a Teflon rod (2). The electrode surface was polished before each series of electrochemical works with very fine emery papers and then polished with dilute suspension of 600 mesh dichromium trioxide polishing powder. The electrode surface was reduced by setting the potential near -0.20 V for 20 min or more. The surface condition of the reducing process was observed by drawing a cyclic voltammetric curve of the gold electrode. The apparent surface area of the electrode was 0.049 cm², and the roughness factor as calculated with the method of Brummer and Makrides (8) was 1.4.

Counter and polarizing electrodes.—A gold cylindrical mesh and plate were used as counter and polarizing electrodes, respectively. All potentials were measured against SCE. The electrochemical cell contained main and standard cell units of SCE with a Haber-Luggin capillary. The standard cell was separated from the main cell by a glass frit and a closed stopcock.

Key words: adsorption, gold electrode, 3-phenyl-1-propanol, differential capacity.

Measurements.—Perchloric acid solution (0.1M) was prepared as the supporting electrolyte. PPA as the adsorbate was dissolved in the solution. All the experiments were carried out at 30°C in thermostated solutions which were deoxygenated with pure nitrogen gas bubbling. The working gold electrode was polarized by a potentiostat (HA 101, Hokuto Denko Company Limited). The potentials and currents were checked by a digital multimeter (DMM-126A, TOA Electronics, Limited) during the run.

Differential capacity measurement was performed with rapid rectangular single pulse techniques (9). This method consists of measuring the slope of a voltage-time curve of the working electrode at the onset, or at a time close to it, of a rectangular current pulse. The voltage-time curves were memorized by a set of "Wave Memory" (E-5001, NF Circuit Design Block Company, Limited) with 2 ms/word input and displayed them on a X-Y recorder (at 10 ms/word) output or on an oscilloscope. The differential capacities were computed from the curves by our original computer program. This was based on Barradas and Valeriotte's (10). The reproducibility of the capacity data became less than 6% in the range of 0.0-0.9V.

Results and Discussion

Coverage-potential curves.—Differential capacities were measured in the range -0.2 - 0.9 V with 0.05 V step for 1.0×10^{-2} to 1.0×10^{-4} M of PPA aqueous solutions. The capacity-potential curves in 0.1M perchloric acid with different additions of PPA are shown in Fig. 1. Schmid and Hackerman (11) described the magnitude of the capacities. The shapes of the capacity-potential curves were dependent on the exposed face of gold electrode and the concentration of perchloric acid as the supporting electrolyte. In the capacity-potential curve of 0.1M perchloric acid in Fig. 1, the magnitude of the capacities was a little lower than the data of Schmid and Hackerman, and the shape was close to the results of a (110) face single-crystal gold electrode for 0.1M of the acid (11). The differential capacity data of the saturated PPA solution (0.04M) were calculated by the straight line relationship between logarithmic concentration of an adsorbed substance and its capacity (12). The calculated differential capacities were used as the ones of full coverage.

Coverages were calculated with the simplified form (14) from Frumkin's model (13)

$$C = C_0(1 - \theta) + C_1 \cdot \theta \quad [1]$$

where C_0 is the capacity of the supporting electrolyte, C_1 the one of full coverage, and C the capacity for coverage θ .

Coverage-potential curves are shown in Fig. 2 from 1.0×10^{-4} to 0.01M of PPA; the curve of 2-phenyl

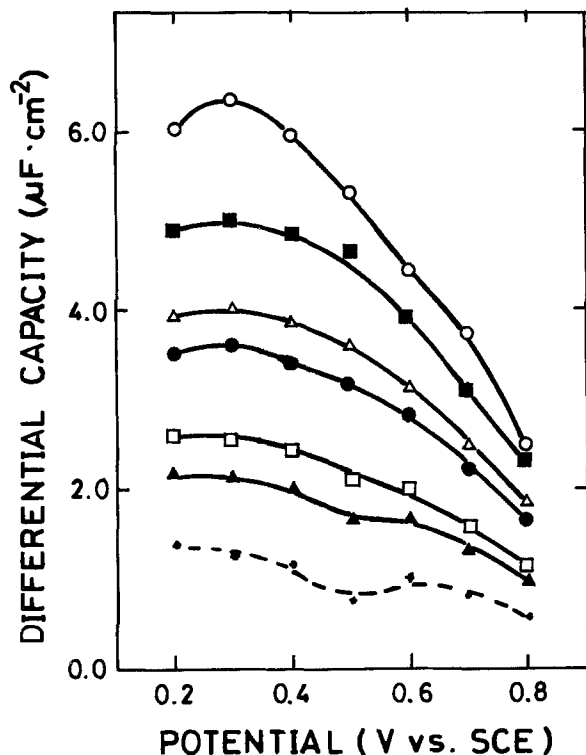


Fig. 1. Differential capacity-potential curves of 3-phenyl-1-propanol in 0.1M perchloric acid solutions. ○: 0.1M perchloric acid. ■: 1.0×10^{-4} M PPA. △: 5.0×10^{-4} M PPA. ●: 1.0×10^{-3} M PPA. □: 5.0×10^{-3} M PPA. ▲: 1.0×10^{-2} M PPA. -●-: 0.04M (sat.) PPA.

ethanol (EPA) of 5.0×10^{-4} M (dotted line) is presented for comparison. The adsorption maximum of their solutions of PPA showed at 0.35 and 0.70V. In the case of EPA solutions, the peak heights at 0.35V were relatively smaller than the ones at 0.70V. In

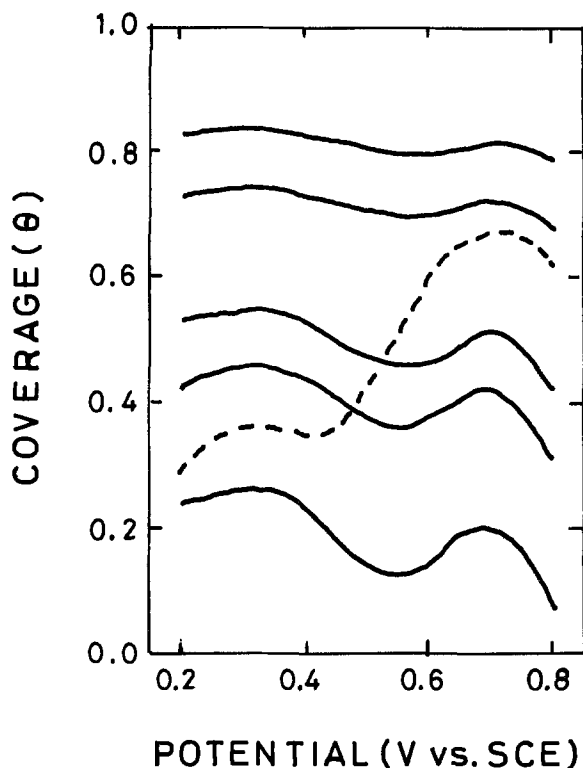
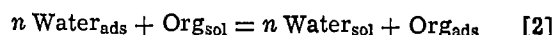


Fig. 2. Coverage-potential curves of 3-phenyl-1-propanol. Solid lines, from bottom to top, 1.0×10^{-4} M, 5.0×10^{-4} M, 1.0×10^{-3} M, 5.0×10^{-3} M, and 1.0×10^{-2} M PPA. Dotted line, 5.0×10^{-4} M PEA.

PPA solutions, the heights at 0.35V became larger than the ones at 0.70V in any concentration.

Calculations of adsorption parameters.—For selection of adsorption isotherm, an excellent review was presented by Conway *et al.* (15). The problems of molecular size factor and evaluation of interaction terms in adsorption isotherms were reported by Conway and Dhar (16). Adsorption of a solute from a solution must be a competitive process between the adsorbate molecule and the solvent one. The competitive adsorption of two species from a liquid phase has been treated by numerous authors by means of Langmuir isotherm (17-19). Temkin's isotherm was applied to the adsorption of neutral molecules by Delahay and Mohilner (20). The competitive adsorption of species with different sizes was discussed by Dahms and Green (5), Bockris and Swinkels (3, 4), and Conway and Dhar (6).

After Dahms and Green (5), an equilibrium is assumed to be established between solvent, adsorbed solvent, organic species in aqueous solution, and adsorbed organic species



where n is the number of adsorbed water molecules which occupy the same surface area as one molecule of the adsorbate.

Under ideal conditions, the electrochemical potential of the adsorbed organic entity in Eq. [2] may be written

$$\bar{\mu}_{\text{org, ads}} = \bar{\mu}_{\text{org, ads}}^{\circ} + RT \ln \theta \quad [3]$$

and the electrochemical potential of the adsorbed water is given by

$$\bar{\mu}_{\text{w, ads}} = \bar{\mu}_{\text{w, ads}}^{\circ} + RT \ln (1 - \theta) \quad [4]$$

The electrochemical potentials of the adsorbate in aqueous solution are written by

$$\bar{\mu}_{\text{org, sol}} = \bar{\mu}_{\text{org, sol}}^{\circ} + RT \ln X_{\text{org, sol}} \quad [5]$$

$$\bar{\mu}_{\text{w, sol}} = \bar{\mu}_{\text{w, sol}}^{\circ} + RT \ln X_{\text{w, sol}} \quad [6]$$

where $X_{\text{org, sol}}$ and $X_{\text{w, sol}}$ are the mol fractions of organic and water, respectively.

The difference in standard free energy is expressed by using the electrochemical potentials

$$\Delta \bar{G}^{\circ} = \bar{\mu}_{\text{org, ads}}^{\circ} - \bar{\mu}_{\text{org, sol}}^{\circ} - n(\bar{\mu}_{\text{w, ads}}^{\circ} - \bar{\mu}_{\text{w, sol}}^{\circ}) \quad [7]$$

Dahms and Green obtained finally the following isotherm from dilute aqueous solutions of the organic adsorbate

$$\frac{\theta}{(1 - \theta)^n} = X_{\text{org, sol}} \cdot \exp\left(-\frac{\Delta \bar{G}^{\circ}}{RT}\right) = K_{\text{ads}} \cdot X_{\text{org, sol}} \quad [8]$$

where $X_{\text{org, sol}}$ represents the mol fraction of the organic species in the solution, and K_{ads} is the adsorption equilibrium constant expressed with mol fraction.

Equation [8] can be expressed by using mol concentration (c)

$$\frac{\theta}{(1 - \theta)^n} = B \cdot c \quad [9]$$

where B is the adsorption equilibrium constant expressed with mol concentration. B is related to K_{ads} as $K_{\text{ads}} = 55.5 \times B$ (6). The relationship between coverage and $\log c$ for PPA is shown in Fig. 3. The observed values (plots) agreed with the solid line which was calculated from Eq. [9] as $n = 2.8$, except at higher coverages. In the case of higher coverages, the interaction parameter (a) should be considered. Various isotherms with the parameter a were proposed by Frumkin (17), Hill (21), and others.

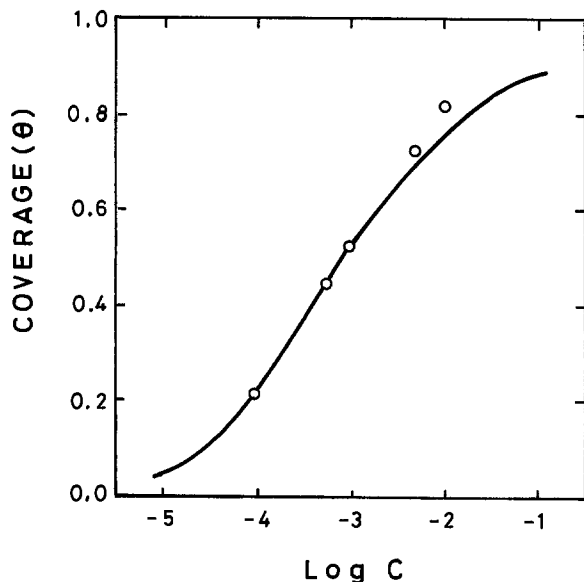


Fig. 3. Coverage-log c curve of 3-phenyl-1-propanol. Open circle: experimental values. Solid line: calculated line with Eq. [9] as $n = 2.8$.

The Eq. [9] can be modified by introducing the a as follows

$$B \cdot c = \frac{\theta}{(1 - \theta)^n} \exp(-2a\theta) \quad [10]$$

This equation was proposed by Parsons (22). From Eq. [10], values of a were calculated as 0.13 and 0.37 for 0.01 and 0.005M of PPA, respectively. The positive value of a means an attractive interaction between the adsorbed molecules. The other parameters are shown in Table I for benzyl alcohol (BZA), EPA, and PPA.

The values of $\Delta\bar{G}^\circ$ (at 30°C) at 0.70V for benzene (23), BZA, and PPA were -4.9 , -7.5 , and -7.4 kcal/mol, respectively. Thus, the two ω -phenyl alcohols seem to adsorb strongly and benzene weakly among these compounds on a gold electrode.

According to the experimental results, the adsorption peaks appeared at 0.65, 0.70, and 0.70V for BZA, EPA, and PPA, respectively. These peaks seem to be due to the interaction between π -electrons of the benzene rings and the electrode surface. A peak at 0.35V seems to be due to the alcoholic groups as side chains. This conclusion was supported by the evidence that the n -propyl alcohol was adsorbed on a gold electrode at 0.35V. Thus, PPA showed a two-position adsorption at 0.35 and 0.70V on a gold electrode. Taking into account the geometric ratios of the ω -phenyl alkanols to water molecules, the values of n in Table I are reasonable.

Conclusion

In the differential capacity measurements by a rapid rectangular single pulse technique, the "Wave

Table I. Adsorption parameters of benzyl alcohol, 2-phenyl ethanol and 3-phenyl-1-propanol

Compd.	BZA*	EPA*	PPA	
Ads. max.	0.65V	0.70V	0.35V	0.70V
n	3.7	2.9	3.2	2.8
$\Delta\bar{G}^\circ$	-7.5 ± 0.5	-8.6 ± 0.5	-7.7 ± 0.5	-7.4 ± 0.4
$K_{\text{ads}} (\times 10^6)$	2.57 ± 0.15	1.55 ± 0.09	3.71 ± 0.22	2.26 ± 0.14

* The data were obtained with Pt (counter, polarizing) and Au (working) electrodes.

Memory" was successfully employed for the voltage-time curve measurements. The calculation process of the capacities became easier and faster then, and the reproducibility of the capacity data was less than 6%.

3-phenyl-1-propanol showed a two-position adsorption at 0.35 and 0.70V vs. SCE on a gold electrode. The adsorption peak at 0.70V seems to arise from the interaction between the π -electron of the benzene ring and the electrode surface. Another peak at 0.35V seems to be due to an adsorption of alcoholic group on the benzene ring.

The peak heights of coverage-potential curves at 0.35V increased with the number of carbon atoms in the alcoholic groups.

The values of n at 0.70V for benzyl alcohol, 2-phenyl ethanol, and 3-phenyl-1-propanol were 3.7, 2.9, and 2.8, respectively. These values were reasonable, taking into account the geometric ratios of the ω -phenyl alkanols to water molecules.

The standard free energy of adsorption $\Delta\bar{G}^\circ$ for benzyl alcohol and 3-phenyl-1-propanol at 0.70V were -7.5 and -7.4 kcal/mol, respectively.

Acknowledgment

The authors are grateful to Dr. Koei Minagawa for his valuable suggestions on this report. The authors also like to express their gratitude to Mr. A. Kimura for his helpful assistance with the experimental work.

Manuscript submitted Nov. 18, 1982; revised manuscript received Sept. 2, 1983.

Niigata University assisted in meeting the publication costs of this article.

REFERENCES

1. A. N. Frumkin and B. B. Damaskin, in "Modern Aspects of Electrochemistry," Vol. 1, J. O'M. Bockris and B. E. Conway, Editors, p. 149, Butterworth, Washington (1964).
2. K. Katoh and G. M. Schmid, *Bull. Chem. Soc. Jpn.*, **44**, 2007 (1971).
3. J. O'M. Bockris and D. A. J. Swinkels, *This Journal*, **111**, 736 (1964).
4. J. O'M. Bockris, M. Green, and D. A. J. Swinkels, *ibid.*, **111**, 743 (1964).
5. H. Dahms and M. Green, *ibid.*, **110**, 1075 (1963).
6. B. E. Conway and H. P. Dhar, *Electrochim. Acta*, **19**, 445 (1974).
7. J. Lawrence and R. Parsons, *J. Phys. Chem.*, **75**, 3577 (1969).
8. S. B. Brummer and A. C. Makrides, *This Journal*, **111**, 1122 (1964).
9. J. S. Riney, G. M. Schmid, and N. Hackerman, *Rev. Sci. Instrum.*, **32**, 588 (1961).
10. R. G. Barradas and E. M. L. Valeriotte, *This Journal*, **117**, 650 (1970).
11. G. M. Schmid and N. Hackerman, *ibid.*, **109**, 243 (1962).
12. B. B. Damaskin, O. A. Petrii, and V. V. Batrakov, "Adsorption of Organic Compounds on Electrodes," p. 85, Plenum Press, New York (1971).
13. A. N. Frumkin, *Z. Physik.*, **35**, 792 (1926).
14. M. W. Breiter, *Electrochim. Acta*, **7**, 533 (1962).
15. B. E. Conway, H. Angerstein-Kozłowska, and H. P. Dhar, *Electrochim. Acta*, **19**, 455 (1974).
16. B. E. Conway and H. P. Dhar, *Surf. Sci.*, **44**, 261 (1974).
17. A. N. Frumkin, *Z. Physik. Chem.*, **116**, 466 (1925).
18. E. Blomgren and J. O'M. Bockris, *J. Phys. Chem.*, **63**, 1425 (1959).
19. R. G. Barradas and B. E. Conway, *Electrochim. Acta*, **5**, 349 (1961).
20. P. Delahay and D. M. Mohilner, *J. Am. Chem. Soc.*, **84**, 4247 (1962).
21. T. L. Hill, *J. Chem. Phys.*, **20**, 141 (1952).
22. R. Parsons, *J. Electroanal. Chem.*, **7**, 136 (1964).
23. T. Takamura, K. Takamura, and F. Watanabe, *Surf. Sci.*, **44**, 93 (1974).

Adatom Coverage Dependences and Specificity Effects on the Rate of Formic Acid Electro-oxidation at Polycrystalline Platinum

Mani Shabrang,* Haruo Mizota, and Stanley Bruckenstein*

Department of Chemistry, State University of New York at Buffalo, Buffalo, New York 14214

ABSTRACT

The catalysis and inhibition of formic acid electro-oxidation that may accompany metal-submonolayer formation on polycrystalline platinum was studied quantitatively using the rotating ring-disk electrode (RRDE) technique. Under controlled flux conditions one can attain limiting current behavior for the oxidation of formic acid and thereby determine the upper limit for the optimum adatom coverage for lead and bismuth. These values are found to be 30-35% of the real area of the platinum electrode. The electro-oxidation experiments in this paper are correlated with the literature dealing with polycrystalline and single-crystal studies of hydrogen adsorption and formic acid oxidation at platinum to explain differences of the behavior of various underpotential deposited (UPD) species. The poisoning of the electro-oxidation process of formic acid requires the presence of adsorbed hydrogen or unhindered access to the first adsorbed intermediate COOH that is produced. During the initial stages of UPD, submonolayers of silver or copper do not deposit significantly on Pt(100), the plane that is responsible for most of the electro-oxidation of formic acid. Therefore, UPD silver or copper cannot inhibit poisoning of the formic acid oxidation process by decreasing hydrogen adsorption, or restricting access to COOH via a third body mechanism. Bismuth, lead, and other UPD species with radii larger than platinum do deposit significantly on Pt(100) at low UPD coverages, and can therefore slow the poisoning of the formic acid process on this plane.

Research on the oxidation of formic acid on noble metals and its electrocatalysis has been going on for more than a century (1-3). Interest in this process has gained considerable momentum in the past two decades due to the process's significance in the fuel cell technology and because of the simplicity of the formic acid molecule provides a model for the electro-oxidation of other organic fuels. A formic acid oxidation mechanism that describes the principal experimental results involves, as the initial stage, an oxidative electroadsorption step (4, 5) resulting in the weakly adsorbed carboxyl adradial, COOH, and H⁺. The carboxyl adradial is bonded to one electrode site and may then either be electro-oxidized directly to CO₂ and H⁺ or react with other adsorbed species on the platinum surface and transform into organic poisons. These poisons inhibit further oxidation of formic acid by blocking those reaction sites required in the initial stage of the oxidation. The similarity between adsorption products produced from formic acid and methanol oxidation under potentiodynamic (4) and potentiostatic (6, 7) control, and that the initial interaction of CH₃OH with an activated electrode results in the loss of the three hydrogens on the carbon atom (8), led Capon and Parsons to deduce that the chemical composition of the major poisoning species in formic acid oxidation is COH, which is strongly adsorbed at three adjacent electrode sites. A minor poisoning species, with the structure C(OH)₂ occupying two adjacent sites, has also been suggested as being involved in the inhibition process (4). A detailed review of the work in acidic media prior to 1973 (9) and the interpretation of the cyclic voltammograms on noble metals (10) are available.

Significant catalysis of the oxidation of formic acid is caused by the presence of submonolayer amounts of some foreign metal atoms, *e.g.*, Hg (11), Tl, Cd, Bi, and Pb (12). These submonolayers form by the underpotential deposition (UPD) on platinum and other noble metals. Also, other strongly adsorbed species, such as SH⁻, CH₃CN, etc., catalyze the electro-oxidation of formic acid (11). UPD of Cu and Ag on platinum inhibit this reaction (12). Two theories are currently used to explain the catalytic effect of UPD monolayers: (i) UPD prevents hydrogen adsorption on platinum and thereby interferes with COH formation (12, 13); and (ii) the UPD species functions as a so-called

"third body" which diminishes the probability of an encounter between two adsorbed species that results in the formation of poisons (11, 14). A similar process is believed to decrease the hydrogen evolution rate along with UPD of copper (15). The poisoning of the hydrogen evolution process by species such as R-CN, S, and SH⁻ is also explained through this effect. Thus, the word "catalysis" is used in the context of formic acid electro-oxidation in the sense of preventing a decrease in the initially rapid rate, rather than increasing the initial rate at an activated electrode.

In this work, the rotating ring-disk electrode (RRDE) technique was applied to study the effect of varying UPD submonolayer coverages of lead and bismuth on the catalysis of formic acid electro-oxidation at platinum electrodes in acidic media. Concentrations of formic acid in the range of 10⁻⁶ to 10⁻²M were used. Under these conditions, mass-transfer limited currents could be achieved that not only allowed the study of the catalytic effects in a simple manner, but also made possible the control of the rate of electrode poisoning during the establishment of the UPD adatom equilibrium-coverage isotherm. The electrocatalysis by UPD lead and bismuth and the inhibition effects of UPD copper and silver are explained in terms of platinum site preference on Pt(100) and Pt(111) of the UPD species and the formic acid oxidation reactions.

Experimental

Chemicals and equipment.—Solutions were prepared with water purified in a Milli-Q™ Reagent-Grade Water System (Millipore Corporation, Bedford, Massachusetts). Reagent grade chemicals were used in the preparation of the supporting electrolyte and stock solutions. Concentrations reported for formic acid assumed 90% purity of the reagent-grade formic acid. Nitrogen was used to remove oxygen from the solutions.

Experiments were performed at 25° ± 0.5°C. Electrode potentials were measured using a saturated calomel electrode (SCE).

All electrode potentials reported in the text are given *vs.* SCE. Note that the term "underpotential" is used in the text, and that it differs from the term "potential." The "underpotential" is the quantity most closely related to the equilibrium isotherm for the adatom being studied. For example, it is advantageous to describe processes involving the UPD of lead in terms of its underpotential, where the "underpotential" is the difference between the potential applied to the

* Electrochemical Society Active Member.

Key words: surface coverage, formic acid oxidation, electrocatalysis, underpotential deposition, platinum active sites, third body effect.

disk electrode and the potential of a bulk lead electrode in that particular solution.

Unless otherwise stated 0.12M HClO₄ solution was used as the supporting electrolyte.

The two platinum-ring, platinum-disk electrodes used in the experiments were constructed in this laboratory. Their dimensions were: (i) disk radius of 0.38 cm; ring-inner radius of 0.40 cm; and ring-outer radius of 0.49 cm. (ii) disk radius of 0.38 cm; ring-inner radius of 0.40 cm; and ring-outer radius of 0.52 cm. Teflon was used as the insulating material. The ring-disk electrode parameters N (16) and $\beta^{2/3}$ (17) were $N = 0.38$ and $\beta^{2/3} = 1.08$ for the first electrode, and $N = 0.42$ and $\beta^{2/3} = 1.4$ for the second electrode. These electrodes were polished before each experiment to a final mirror finish using 0.05 μ β -alumina on Buehler microcloth (Buehler Limited, Evanston, Illinois). The counterelectrode was a platinum wire. The electrode rotator was manufactured by Pine Instruments Company (Grove City, Pennsylvania).

The design of the four-electrode potentiostat has been described elsewhere (18). An Eclipse S/200 mini-computer (Data General Corporation, Southboro, Massachusetts) was the basis of a digital data-acquisition system developed in this laboratory (19, 20). All experimental sequences were computer controlled and the data were stored on magnetic-disk cartridges.

Preparation of lead-ring, platinum-disk electrode.—Hydrogen evolution on platinum strongly interferes with lead deposition from Pb²⁺ solutions in acidic media ($E^\circ = -367$ mV) and a meaningful convective-diffusion controlled current for the reaction $\text{Pb}^{2+} + 2e \rightarrow \text{Pb}$ at the ring electrode cannot be attained under these conditions. A simple pretreatment of the ring electrode (19), which forms a few monolayers of the UPD metal, does not yield reproducible ring responses for collection and shielding experiments. Hence, prior to each UPD experiment between 50 and 100 monolayers of lead were deposited on the ring electrode from a 0.015M Pb(II)/1M NaClO₄ solution (slightly acidified to pH = 5 by HClO₄) at -0.55 V (very low current density) while the disk electrode was potentiostated at $+0.5$ V. The ring currents for the reduction of Pb²⁺ that were then observed in dilute solutions of Pb²⁺ (10^{-6} – 10^{-4} M) were stable to within 5%, provided the ring electrode had been potentiostated at negative potentials (< -0.55 V). Thick lead deposits were avoided in order to minimize variations in the collection efficiency.

The ring pretreatment for the bismuth UPD studies followed the procedure of Reidhammer *et al.* (19).

Calculation of lead and bismuth coverage.—The surface coverage of adatom (θ) is defined in terms of the number of platinum surface sites occupied by the adatom. The number of occupied platinum surface sites is calculated from the charge required to form one monolayer of adsorbed hydrogen, as determined in the manner described below, minus the charge required to oxidize adsorbed hydrogen from an electrode on which adatoms have adsorbed. The determination of the bismuth adatom surface coverage was based on the procedure described by Cadle and Bruckenstein (25), who in turn used the approach originally suggested by Bowles (26). The charge required to form one monolayer of bismuth atoms from Bi³⁺ is, on this basis, 460 $\mu\text{C cm}^{-2}$ for an electrode with a roughness factor of 1.43 (25). For lead (atomic radius = 1.75Å), a close packed layer was assumed. This corresponds to a value of 260 $\mu\text{C cm}^{-2}$ for the charge required to form a monolayer from Pb²⁺ (27, 28). All coverages reported have been corrected for the surface roughness of the platinum disk electrode.

Determination of platinum-disk area by hydrogen adsorption charge measurement.—The surface roughness of the platinum-disk electrode was determined according to the modified procedure suggested by

Biegler *et al.* (21) and adopted by Capon and Parsons (4); the charge in the area bounded by the horizontal portion of the current-potential (i - E) curve after oxide reduction, and the potential at the current minimum just before the rising portion of the hydrogen evolution curve corresponded to a fractional hydrogen coverage of 0.77. In 0.12M HClO₄, the potential range for current integration is between $+0.16$ and -0.23 V. This procedure has also been verified using independent ring-disk electrode techniques (22).

First, the electrode was potential cycled between oxygen and hydrogen evolution for a few minutes in the supporting electrolyte (at 0.2 V s⁻¹) and reproducible i - E curves were obtained. Next, the disk was potentiostated at 0.0V for 15s and then at 1.2V for 60s. The potential of a stationary disk was then scanned cathodically at several scan rates. The charge required for hydrogen adsorption was measured and averaged and the surface roughness calculated using the generally accepted value of 210 $\mu\text{C cm}^{-2}$ for the monolayer charge density of adsorbed hydrogen (23). The precision and reproducibility of this method is the same as other recently proposed methods for platinum surface area measurement that are also based on hydrogen-adsorption charge (24). The platinum electrode surface roughness typically ranged from 1.8 to 2.6.

Determination of the Nernst potential for Pb²⁺ solutions in 0.12M HClO₄.—The equilibrium (Nernst) potential (E_N) was determined by measuring the open-circuit potential of the lead-ring electrode of the RRDE at a rotation speed of 2500 rpm before and after each experiment. The experiments, repeated daily, yielded a value of -0.492 ± 0.003 V for 10^{-4} M Pb solution.

The open-circuit potential of the lead-ring electrode in the pretreatment solutions was -0.418 ± 0.002 V. The Nernst potentials for bismuth were measured according to Ref. (19) and (25).

Disk potential programming for the determination of UPD coverage of lead and bismuth.—The disk-program sequence for lead coverage determination is shown schematically in Fig. 1. The purpose of the steps are as follows: (A) Removes any lead and oxidizable impurities from the electrodes. (B) Reduces the platinum oxide formed in step A. Electrode rotation is stopped during this step in order to minimize mass transfer of Pb²⁺ to the disk. (C) Removes unwanted UPD lead formed during step B by an anodic pulse of short duration. (D) Deposits UPD lead at the disk potential of interest and sets the desired rotation speed simultaneously. (E) Strips lead by potential-scanning in a positive direction (linear scan rate = 200 mV s⁻¹).

The ring-shielding response during step D and the ring-collection response during step E were recorded and processed to determine UPD coverages.

The ring- and disk-potential sequences used by Reidhammer *et al.* (19) were followed (with addition of step C above) for the determination of underpotential bismuth coverage.

Results and Discussion

Irreversible deposition of bismuth on platinum.—Irreversible deposition of UPD bismuth on platinum has already been demonstrated by the RRDE technique (25). During the stripping of UPD bismuth only 90% leaves the platinum surface and the remaining 10% is irreversibly adsorbed. This 10% must be taken into account when calculating the UPD bismuth coverage, for once Bi³⁺ has been introduced into the solution, the platinum surface will never be entirely free of bismuth after the first UPD deposit forms. Only mechanical polishing can remove this irreversibly adsorbed bismuth.

In the case of lead, however, no measurable irreversible UPD occurs on platinum. No significant differences were detected (between 0.0 and 1.2V among the disk current-disk potential (i_D - E_D) curves obtained by

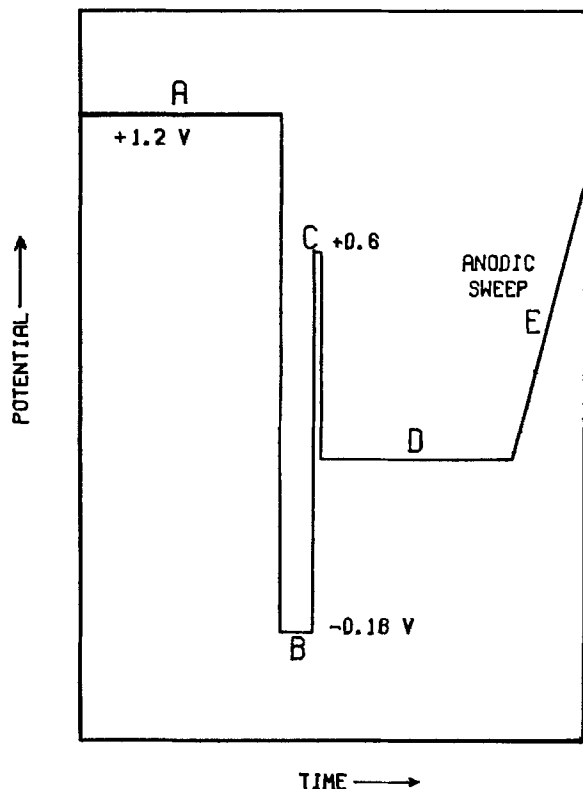


Fig. 1. Potential program sequence for UPD lead on a bare platinum electrode. Details and significance for each step is given in the text.

repetitive scanning (from -0.5 to $1.2V$) a freshly made and polished platinum electrode in $0.12M$ $HClO_4$, and the same thoroughly rinsed electrode that was subjected to any one of the following treatments in which the electrode was: (i) subjected to 30 min of continuous deposition and stripping of lead monolayers, (ii) exposed for 12h to $0.1M$ lead nitrate solution, or (iii) tested for irreversible deposition on an oxidized electrode (25).

After a bulk lead deposit is stripped off the platinum-ringing electrode, it must be potential-cycled a few minutes in $HClO_4$ solution before it recovers the original platinum i - E characteristics in the oxide-formation region.

Behavior of lead in the UPD region.—The difference between the work functions of lead and platinum is about 1.4 eV. This produces a UPD region for lead of $\sim 0.6V$ that begins, in a $10^{-5}M$ solution of Pb^{2+} , just negative of platinum oxide formation and extends well into the hydrogen evolution region. The UPD behavior of lead at platinum in acidic solutions can only be studied practically in the region positive of the hydrogen evolution. This UPD region coincides with the formic acid oxidation region.

A typical platinum disk (i_D - E_D) curve (29), along with the corresponding lead-ring current, disk potential (i_R - E_D) curve at a ring potential of $E_R = -0.6V$ is shown in Fig. 2. Shielding of the ring begins at a disk potential of $+0.05V$.

Unlike the UPD behavior of lead at gold (30), where more than one UPD current peak is observed (31), the ring-collection current accompanied the electro-oxidation (stripping) of the UPD lead from the platinum-disk surface shows only one prominent peak. Hydrogen evolution obscures the stripping process of bulk lead in acidic ($pH < 4$) solutions. The unshielded lead-ring electrode current is slightly higher than the lead convective-diffusion current for a $10^{-5}M$ Pb solution ($11.5 \mu A$) probably because hydrogen evolution occurs at the ring electrode edges, or on bare Pt sites.

An example of the effect of the plating time on disk-stripping and ring-collection currents is shown in Fig.

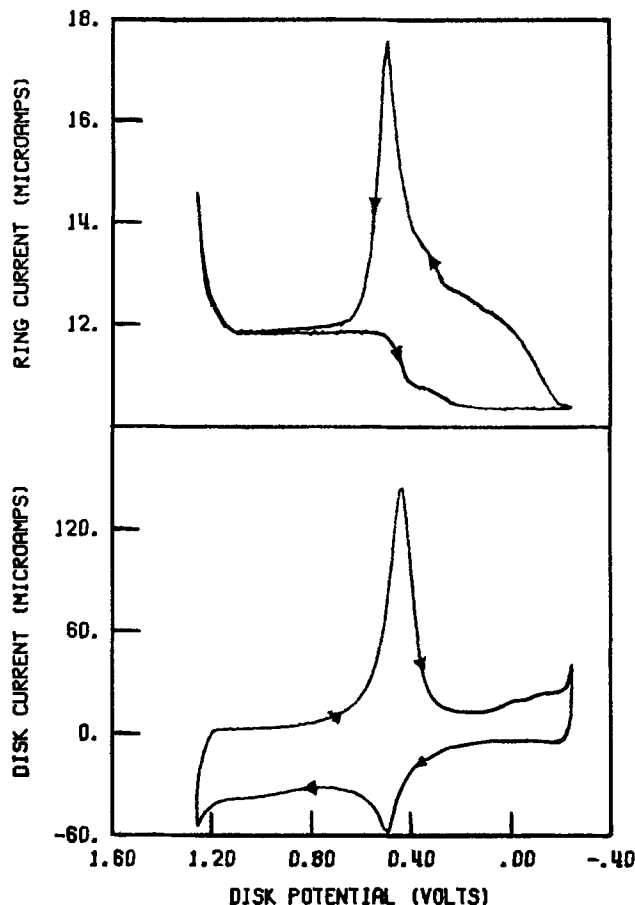


Fig. 2. Disk current-disk potential curve and corresponding ring current-disk potential curve for the second electrode in $1 \times 10^{-5}M$ Pb^{2+} - $0.12M$ $HClO_4$ solution $E_R = -0.6V$ (vs. SCE), $\omega = 2500$ rpm, and scan rate = 50 mV s^{-1} .

3 for $10^{-5}M$ Pb^{2+} in $0.12M$ $HClO_4$ at an underpotential, $E_{UPD} = +0.5V$ (step D in Fig. 1). E_{UPD} is the difference between the potential applied to the disk electrode and the potential of a bulk lead electrode in the solution being studied. The growth of the lead UPD deposit is virtually complete after 20, 45, and 200s in 10^{-4} , 10^{-5} , and $10^{-6}M$ solutions of Pb^{2+} , respectively. The effect of disk plating potential on disk-stripping and ring-collection currents (step E in Fig. 1) is shown in Fig. 4 for $E_{UPD} > +0.5V$. The time response of the disk electrode current and the ring electrode shielding current during the adsorption of lead on the platinum disk are shown in Fig. 5 for different values of E_{UPD} . The ring current becomes unshielded as the disk current drops to zero. The interpretation of the transient behavior for the ideal system of silver UPD on gold was taken from Swathirajan and Bruckenstein (32).

The procedures for the determination of coverage by using the underpotential ring-collection (Fig. 4) and ring-shielding (Fig. 5) responses are described in detail elsewhere (19, 33, 34). The lead UPD coverage values obtained by these two independent methods agree within 5%, while individual experiments are reproducible within 2% from day to day. The total lead coverage as a function of the E_{UPD} is shown in Fig. 6. This isotherm agrees with the isotherm reported by Schmidt and Wuthrich (35), who employed the thin layer-twin electrode technique.

Limiting currents for the formic acid oxidation at an RDE.—According to Capon and Parsons (4), in the region where H_{ad} is thermodynamically unstable, the disproportionation reaction [2], which involves the formic acid molecule ($pK_{diss} = 3.75$), occurs parallel to the main oxidation pathway, reaction [1]

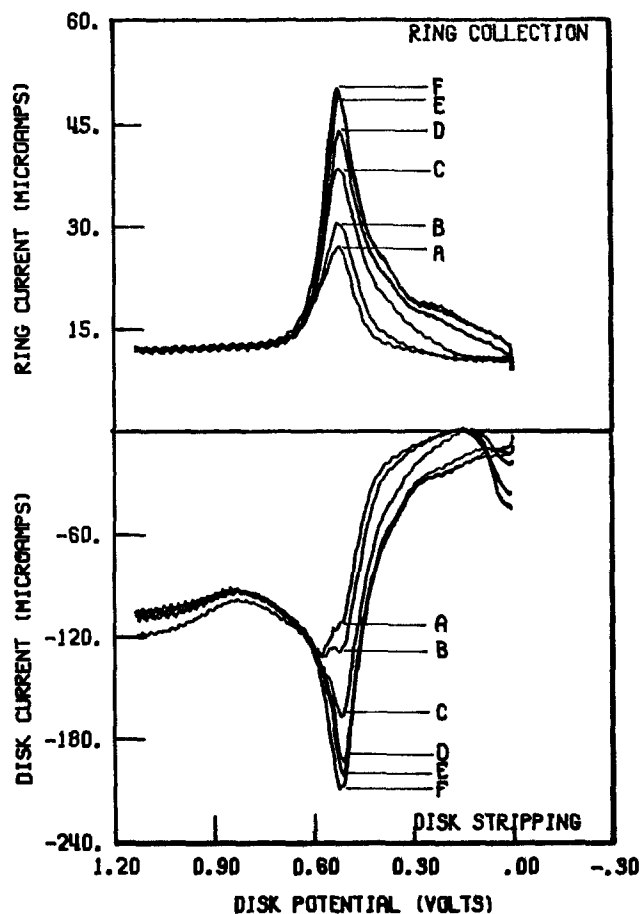


Fig. 3. Effect of plating time on disk-stripping and ring-collection currents for $E_{UPD} = +0.5V$ in $10^{-5}M Pb^{2+}$ - $0.12M HClO_4$ solution. Deposition times are: 5s (A), 7s (B), 10s (C), 15s (D), 30s (E), and 45s (F) $E_R = -0.6V$ (vs. SCE), $\omega = 2500$ rpm, and scan rate = 200 $mV s^{-1}$.

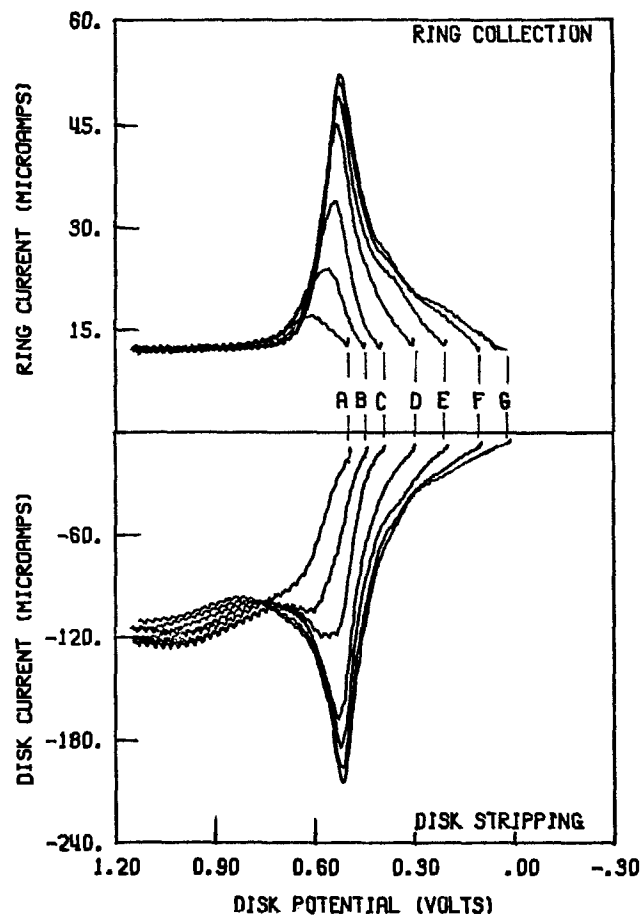
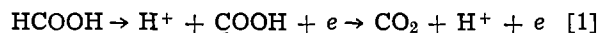
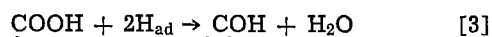


Fig. 4. Effect of plating potential on disk-stripping and ring-collection currents in $10^{-5}M Pb^{2+}$ - $0.12M HClO_4$ solution. E_{UPD} values are $+1.0V$ (A), $+0.95V$ (B), $+0.9V$ (C), $+0.8V$ (D), $+0.7V$ (E), $+0.6V$ (F), and $+0.5V$ (G). $E_R = -0.6V$ (vs. SCE), $\omega = 2500$ rpm, and scan rate = 200 $mV s^{-1}$.



Reaction [2] is the principal poisoning reaction.

Decreasing the supply of dissolved $HCOOH$ should preferentially reduce the rate of poison formation. The latter rate is slow (4) as compared to the rate of the main current producing reaction sequence, Reaction [1], which becomes mass-transport limited. However, in the hydrogen adsorption region, the main poisoning reaction



is very fast (4), and the surface becomes inactivated before mass transport of formic acid becomes rate determining.

As expected, outside the H_{ad} region formic acid oxidation indeed exhibits limiting current behavior at low concentrations (10^{-5} - $10^{-2}M$) in the presence of lead or bismuth at platinum RDE. Figures 7 and 8 show typical i - E curves for the first disk electrode in $2 \times 10^{-3}M$ formic acid solutions. At low rotation speeds a wider limiting current potential range can be achieved under potentiodynamic conditions before the surface is deactivated by the poisoning species or the surface oxides.

The plot of the limiting current (obtained during the positive going potential scan) vs. $\omega^{1/2}$ is linear between 400-3600 rpm for 10^{-3} to 5×10^{-3} concentrations of $HCOOH$ in the presence of $10^{-4}M$ bismuth or lead. The diffusion coefficient for formic acid, calculated from the improved form of the Levich equation, assuming a two-electron overall reaction, is $0.97 \times 10^{-5} cm^2 s^{-1}$ in the presence of lead and $0.98 \times 10^{-5} cm^2 s^{-1}$ in the presence of bismuth. The value obtained from a Kou-

tecky-Levich analysis of the kinetics in $1.52 \times 10^{-3}M$ formic acid in $2 \times 10^{-2}M HCOONa$ and $1M KCl$ is $1.5 \times 10^{-5} cm^2 s^{-1}$ (36).

It is interesting to note that in the presence of bismuth (Fig. 8), a wider limiting current potential range is obtained during the positive going potential scan, since part of the adatom layer always remained on the surface.

The limiting current at the rotating platinum-disk electrode is not maintained, if the potential is held constant in the UPD region. Enough $HCOOH$ eventually diffuses to bare platinum surface sites and then participates in the disproportionation reaction [2]. The disk current decays steadily, and the surface continues to poison until no sites are available for the initial oxidative electroadsorption step (reaction [1]). The decay rates vary with underpotential, a result that demonstrates the effect of the UPD coverage on the rate of the poison formation. During the initial stages of the poisoning process, this variation in poisoning rate can be correlated with the instantaneous adatom coverage determined in the presence of formic acid. In Fig. 9 the time dependence of the limiting current decay is shown as a function of potential in the presence of lead adatoms. Because of the changing adsorption characteristics of electrodes held at constant potential (10, 37), we did not attempt to study the initial poisoning rates quantitatively. However, these rates increase with an increase of the mass-transfer rates to the electrode.

Determination of UPD coverage in the presence of formic acid.—In $0.1M$ unstirred solutions of $HCOOH$ several minutes are required for the platinum surface to become saturated by the organic residues formed at $0.0V$ (4). This saturation time is longer than 20s when

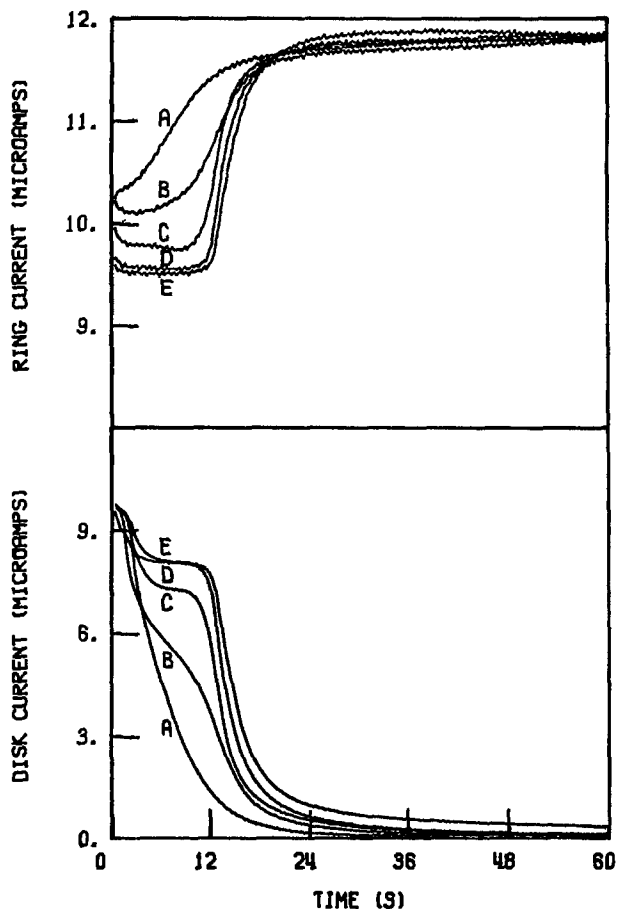


Fig. 5. Time dependence of disk- and ring-electrode currents at various underpotentials in $10^{-5}M Pb^{2+}$ - $0.12M HClO_4$ solution. E_{UPD} values are $+0.9V$ (A), $+0.8V$ (B), $+0.7V$ (C), $+0.6V$ (D), $+0.5V$ (E). $E_R = -0.6V$ (vs. SCE) and $\omega = 2500$ rpm.

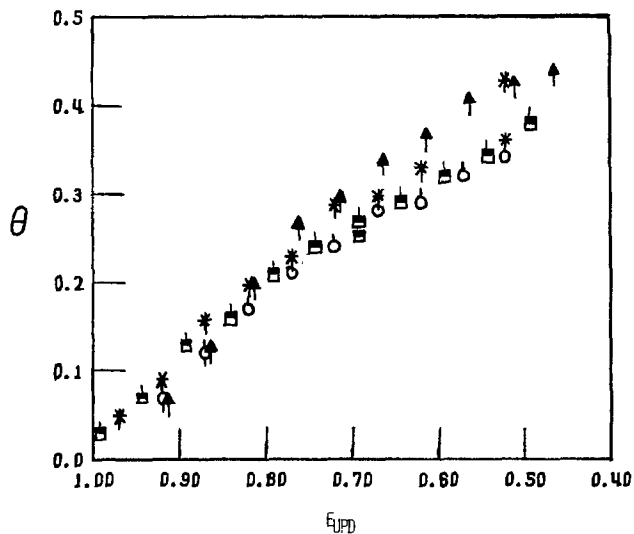


Fig. 6. Lead coverage on platinum (θ) as a function of electrode plating potential (vs. SCE). Concentrations of Pb^{2+} in $0.12M HClO_4$ is $10^{-4}M$ (\uparrow), $10^{-5}M$ ($*$), $2 \times 10^{-6}M$ (\square), $10^{-6}M$ (\circ).

the disk electrode rotates at 600 rpm (38). Therefore, we conclude that at concentrations of formic acid below $10^{-3}M$ and for cation concentrations above $10^{-5}M$, the formation of adsorbed intermediates is slow and that the available platinum surface is not appreciably reduced, while Pb^{2+} and Bi^{3+} ions reach equilibrium coverage. The conditions for this assumption are best at anodic potentials ($>0.0V$) where the organic residues are less stable (4) and equilibrium UPD coverage is reached rapidly because of lower equilibrium coverage values. For example, in $10^{-4}M Pb^{2+}$ solutions,

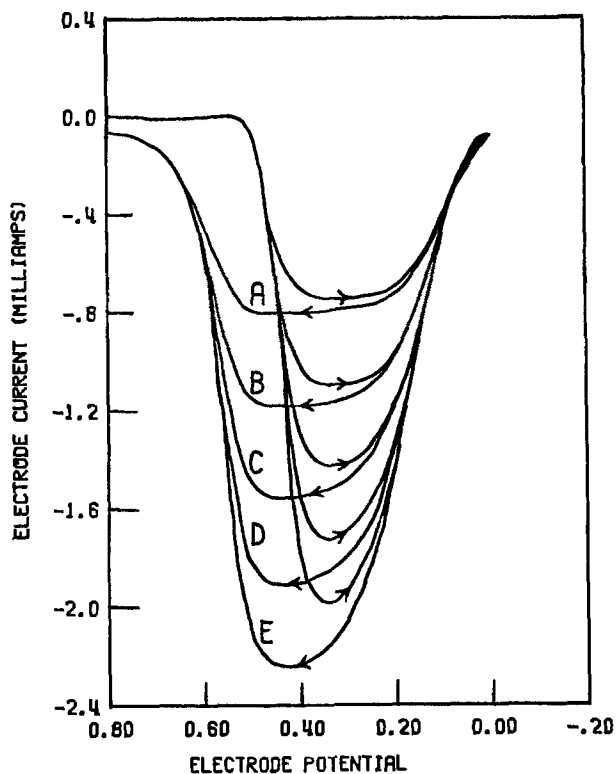


Fig. 7. Disk electrode $i-E$ curves for $2 \times 10^{-3}M$ formic acid in $0.12M HClO_4$ in the presence of $10^{-4}M Pb^{2+}$ showing the dependence of the limiting currents on the rotation speed. $\omega = 400$ rpm (A), 900 rpm (B), 1600 rpm (C), 2500 rpm (D), and 3600 rpm (E). Scan rate = $50 mV s^{-1}$.

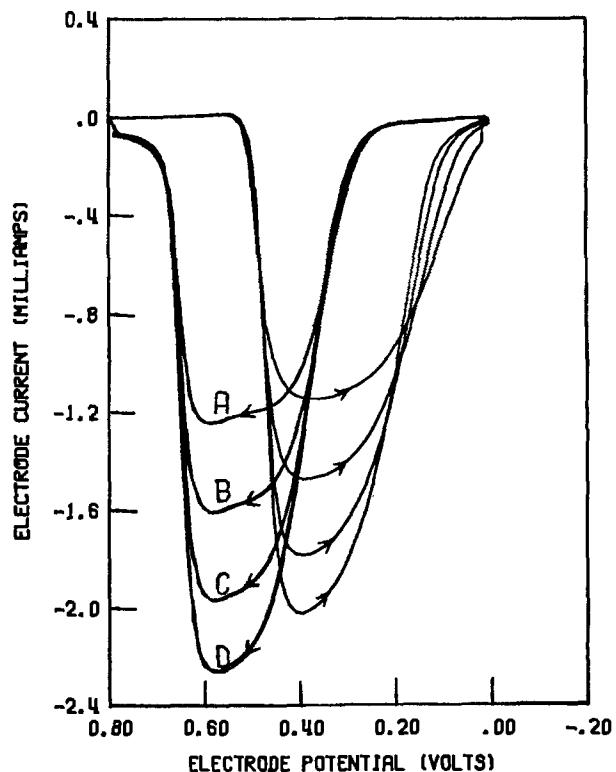


Fig. 8. Disk electrode $i-E$ curves for $2 \times 10^{-3}M$ formic acid in $0.12M HClO_4$ in the presence of $10^{-4}M Bi^{3+}$ showing the dependence of the limiting current on the rotation speed. $\omega = 900$ rpm (A), 1600 rpm (B), 2500 rpm (C), and 3600 rpm (D). Scan rate = $50 mV s^{-1}$. First electrode.

equilibrium surface coverage at $0.3V$ ($\sim 25\%$) is established in less than 5s at 2500 rpm.

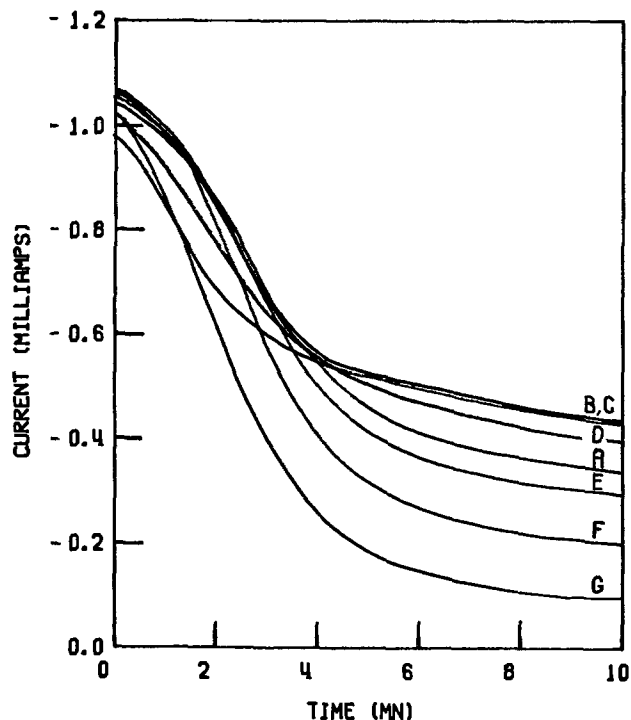


Fig. 9. Decay of the limiting current as a function of potential for second electrode in 2×10^{-3} solution of HCOOH in 0.12M HClO_4 and in the presence of 10^{-4}M Pb^{2+} . $\omega = 900$ rpm. The electrode potential was held at 0.20V (vs. SCE) (A), 0.25V (B), 0.28V (C), 0.32V (D), 0.36V (E), 0.38V (F), and 0.42V (G).

The effect of the formic acid concentration on the ring-collection current peak is shown in Fig. 10 for 10^{-4}M Pb^{2+} . At high concentrations of formic acid, the UPD lead coverage does not have time to reach its equilibrium value before products from the poisoning reaction cover a significant fraction of the electrode surface. This effect is more pronounced at lower concentrations of the cation. We assume that the equilibrium adatom isotherm and the equilibrium isotherm for the organic residues are relatively independent of one another.

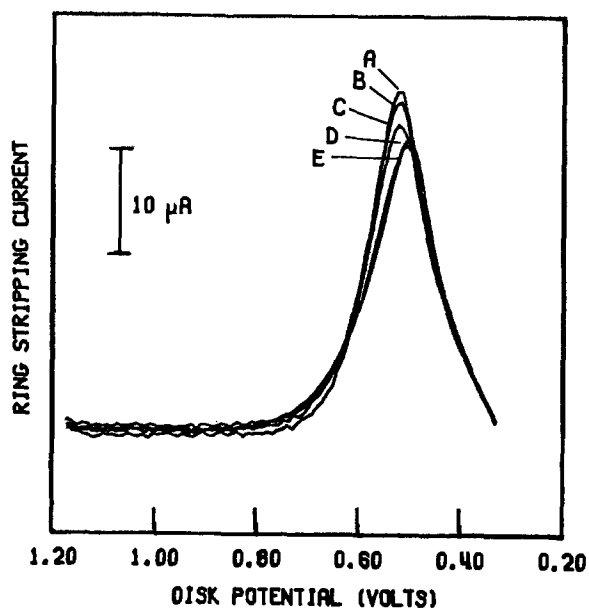


Fig. 10. Effect of the formic acid concentration on the ring electrode collection currents for 10^{-4}M Pb^{2+} in 0.12M HClO_4 . Ring potential = -0.6V (vs. SCE). No HCOOH (A), $5 \times 10^{-5}\text{M}$ (B), 10^{-3}M (C), $2 \times 10^{-3}\text{M}$ (D), and $5 \times 10^{-3}\text{M}$ (E). $\omega = 2500$ rpm. Scan rate = 200 mV s^{-1} . First electrode.

The formic acid oxidation current, 10 min after establishing an equilibrium lead coverage, was obtained at a number of underpotentials at 400 and 900 rpm. These data were used to obtain plots of formic acid oxidation current vs. lead UPD coverage, and are shown in Fig. 11. The slowest rate of poisoning occurs at a lead coverage range of $(30 \pm 3)\%$.

The optimum lead adatom coverage value reported by others (39) was about 50%. We suggest that these higher coverage estimates (39, 40) result from the way in which the microscopic area of the platinum electrode was determined. The potential just before the rise of the current due to a hydrogen evolution on the platinum electrode corresponds to a hydrogen coverage of 0.77 (4, 21), not unity. The unity assumption that was made leads to an underestimate of $\sim 20\%$ of the microscopic platinum surface area, and the reported values of 50% would then become $50 \times 0.77 = 39\%$.

Previous workers have determined adatom coverages by integrating stripping peaks. Since there is a change in point of zero charge with UPD coverage, there could be a systematic error associated with a charging current that accompanies the change in coverage (41, 42). However, under certain conditions the potential scan can lead to a compensating charging current. This entire matter is discussed elsewhere (31).

The optimal bismuth coverage occurs at $(35 \pm 3)\%$ also, as is seen in Fig. 12. In this case again the HCOOH oxidation current becomes insignificant at $\theta = 50\%$.

The optimal adatom coverages for maximum electrocatalysis reported above constitute the upper coverage limit for such measurements. Experiments performed at higher HCOOH concentrations in unstirred solutions (12, 39) must result in a significant partial coverage of the platinum surface by the organic poisons before UPD equilibrium is reached. Therefore, UPD coverages estimated under such conditions will yield coverage values lower than the true ones.

Inhibition effects by UPD.—The underpotential deposition of copper or silver on platinum inhibits the oxidation of formic acid (12). This effect is more pronounced with silver. Both silver and copper are not electrocatalysts for the formic acid oxidation reaction; therefore, it is not surprising that when they cover the

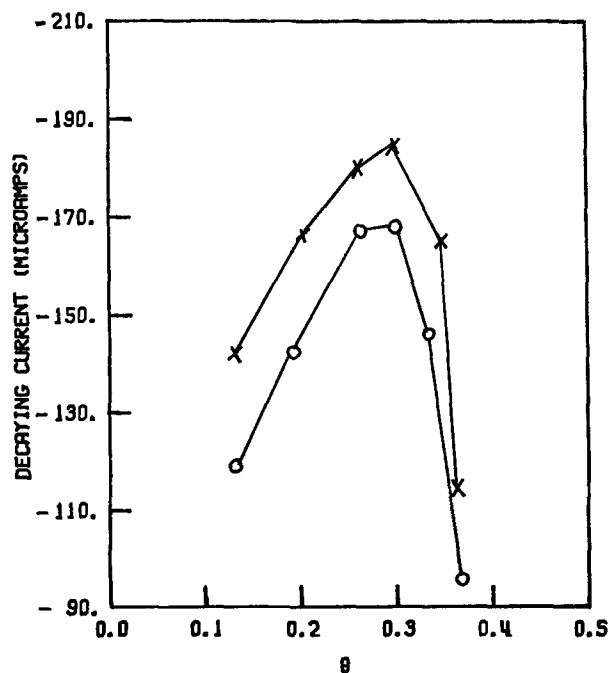


Fig. 11. Formic acid oxidation current as function of lead monolayer coverage on platinum. The points were sampled after a 10-min wait at 400 rpm (O) and 900 rpm (X). Lead concentration: 10^{-4}M . Second electrode.

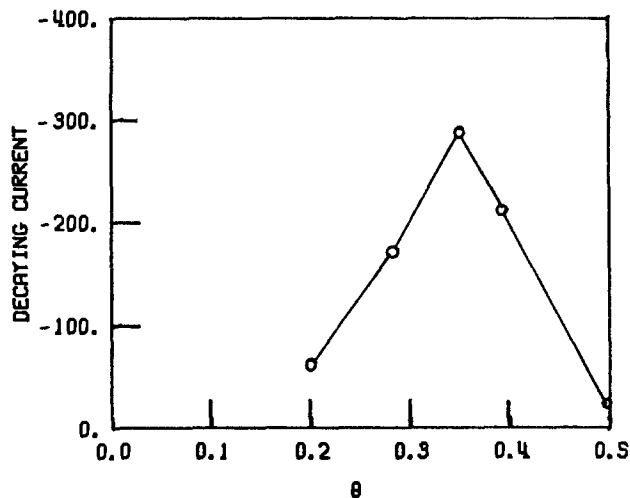


Fig. 12. Formic acid oxidation current as a function of bismuth monolayer coverage on platinum. The points were sampled after a 90s wait at 2500 rpm. Bismuth concentration: $5 \times 10^{-5}M$. First electrode.

platinum surface by more than a monolayer the oxidation process stops. Reaching monolayer coverage is possible, under equilibrium conditions, in the potential region where formic acid oxidation takes place (excluding the formic acid third anodic peak). However, even a very small UPD silver coverage on platinum has an inhibiting effect.

In Fig. 13 the effect of $5 \times 10^{-6}M$ Ag^+ on the $i-t$ curve of $10^{-3}M$ $HCOOH$ in $0.12M$ $HClO_4$ is shown. The potential was jumped to $+0.29V$ after the electrode pretreatment (steps A, B, and C in Fig. 1). More than 20s was required for equilibrium silver coverage to be reached in $2 \times 10^{-5}M$ silver solutions (43). In $5 \times 10^{-6}M$ solutions of Ag^+ , the UPD rate was much slower, $\sim 50s$ (32). If a third-body (11, 14) catalytic mechanism were operative over the entire polycrystalline platinum surface, the Ag adatoms would prevent poison formation (11, 14) during the initial stages of UPD. However, this result was not found.

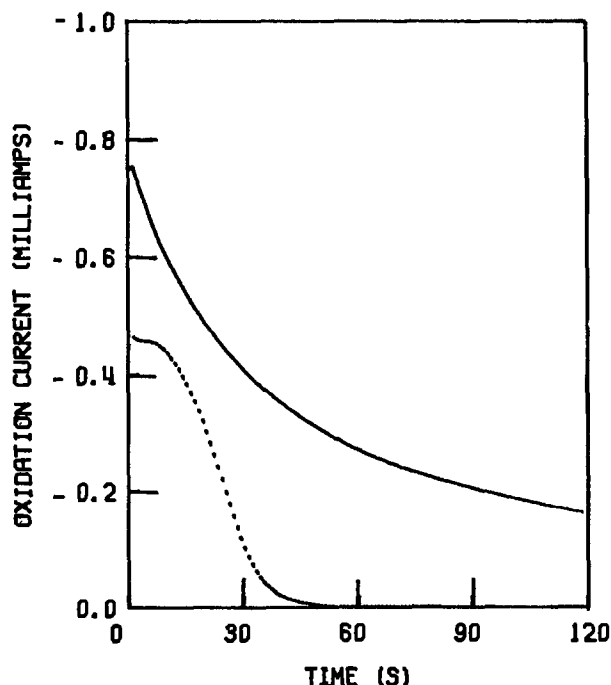


Fig. 13. Effect of silver UPD on the oxidation current of $10^{-3}M$ $HCOOH$ in $0.12M$ $HClO_4$. The potential was jumped to $+0.29V$ (vs. SCE) after the electrode pretreatment. Solid curve: no Ag^+ . Dotted curve: $5 \times 10^{-6}M$ Ag^+ . $\omega = 2500$ rpm. Second electrode.

Potentiodynamic experiments also show this accelerated poisoning effect. Figure 14 shows the $i-E$ curve in the same solution used in Fig. 13. Equilibrium silver coverage is not reached at a high potential scan rate of 200 $mV s^{-1}$ in very dilute solutions; however, the formic acid oxidation current is substantially decreased. Likewise, no catalysis occurs during the initial stages of the copper underpotential deposition.

Clearly, the hydrogen inhibition, or the third-body mechanism, does not apply to formic acid oxidation in the case of submonolayer amounts of silver and copper. However, these kinetic data can be explained using the results of recent studies at single-crystal platinum, as can the electrocatalysis by UPD lead, bismuth, and other UPD species of atomic radii greater than platinum.

The oxidation of formic acid is strongly dependent on the platinum plane at which it occurs (44). In particular, the UPD studies of formic acid oxidation lie in the potential region where the oxidation in the absence of UPD occurs principally at Pt(100), since the rate at Pt(100) is about ten times the rate at Pt(111) (44). The rate on Pt(110) is also significant: about 40% of Pt(100). Thus, if any adatom is preferentially deposited on Pt(111) during its initial stages of UPD, the hydrogen inhibition or third-body effect will operate solely on this plane, which contributes only to a small extent to the total formic acid oxidation current. Simultaneously, the Pt(100) and Pt(110) planes, which have little or no adsorbed adatoms, will poison quickly, and the total external current will drop rapidly. If the adatom deposits to a significant extent on Pt(100) and Pt(110) during its initial stages of UPD, it will inhibit hydrogen adsorption and will also be available as a third body, and thus inhibit the poisoning process on the faces which are most responsible for the oxidation current. As will be shown below, silver and copper initially deposit on Pt(111) at $\theta < 0.5$, while lead, bismuth, and other adatoms with radii larger than that of platinum do not preferentially deposit on Pt(111) at low UPD coverages.

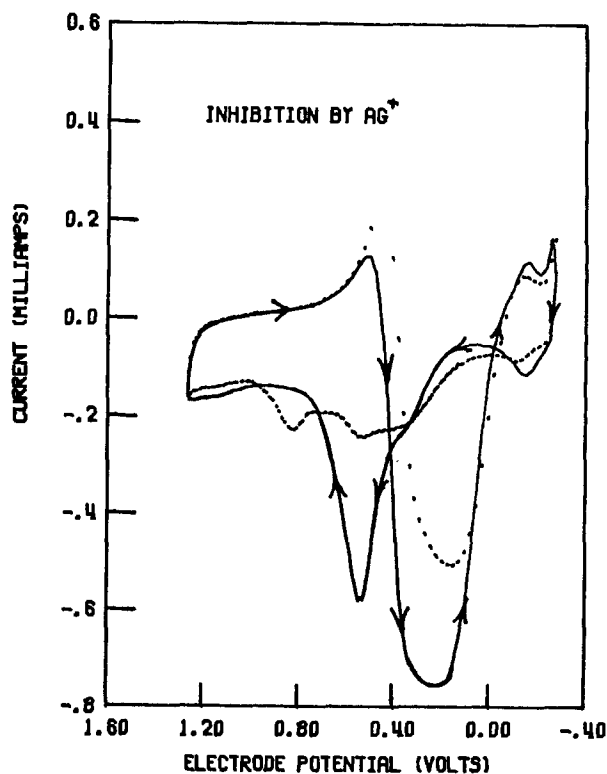


Fig. 14. Effect of silver UPD on the $i-E$ curve of $10^{-3}M$ $HCOOH$ in $0.12M$ $HClO_4$. Solid curve: no Ag . Dotted curve: $5 \times 10^{-6}M$ Ag^+ . $\omega = 2500$ rpm. Scan rate = 200 $mV s^{-1}$. Second electrode.

Low surface coverages (<0.5) of silver, copper, and adatoms preferentially inhibit the adsorption of weakly bound hydrogen sites on polycrystalline platinum (29, 45). These weakly bound hydrogen sites have been associated with Pt(111) (46-48). We conclude that the initial stages of UPD of silver and copper at polycrystalline platinum occur at Pt(111) on sites having similar surface energies. In contradistinction, lead and bismuth show no significant preferential inhibition of the various hydrogen adsorption sites at low UPD coverages (29), and therefore a significant amount of adatom deposition can occur on Pt(100) and Pt(110). Thus, the initial stages of adatom coverages of silver, copper, lead, and bismuth meet the requirements set forth in our hypothesis for explaining the differences in electrocatalytic behavior of different adatoms.

In general, adatoms with radii greater than that of platinum tend to be more randomly distributed on the various platinum faces of polycrystalline substrate, and so should show electrocatalysis of the formic acid oxidation process at polycrystalline platinum. For example, mercury, with a radius greater than platinum, catalyzes formic acid electro-oxidation (11) and shows no preferential inhibition of hydrogen adsorption (29).

Figure 15 illustrates the various points made above. It contains the I_D-E_D curves for the UPD-catalyzed electro-oxidation of $10^{-3}M$ formic acid solution in $0.12M$ $HClO_4$ at different lead ion concentrations. It is clear from the positive-to-negative potential scans that substantial poisoning by reaction [2] to form COH occurs until at least $10^{-5}M$ lead ion is present in solution and that increasing the concentration of lead ion to as high as $10^{-3}M$ improves this particular problem only slightly.

It is also clear that a very low concentration ($10^{-6}M$) of lead ion catalyzes the oxidation of formic acid only modestly compared to a solution without any lead ion during the positive-to-negative potential scan. This is the potential region in which the poisoning process to COH occurs via reaction [2]. During the negative-to-positive potential scan, the extent of poisoning is markedly reduced by the presence of $10^{-6}M$ lead ion. In the potential region more negative than 0 V, the poisoning process to form COH proceeds via electroadsorbed hydrogen according to reaction [3]. This poisoning inhibition indicates that low surface coverages of lead readily block those surface sites upon which hydrogen electroadsorbs. This conclusion is consistent with our previous comments and does not imply that UPD lead is adsorbed on only one kind of surface site. Also, we note that the poisoning path through electroadsorbed hydrogen is significantly suppressed by low coverages of UPD lead, a result consistent with the possibility of

UPD lead to block two adsorbed hydrogen atoms per lead atom.

The UPD catalytic effect during the positive-to-negative potential scan is strongly concentration and potential dependent for potentials in the range $+0.23$ to $-0.10V$. This dependence arises from three sources, one that increases the rate of oxidation and two that decrease it.

Up to the optimum surface coverage at a given scan rate, poisoning is suppressed by higher UPD coverages. This optimum coverage is reached at different potentials for different solution concentrations of lead ion because the nonequilibrium surface coverage is proportional to both solution concentration and time (and hence potential). After the optimum coverage is exceeded, physical blocking of platinum sites interferes with the primary electro-oxidation path of formic acid. Also, the rate of the uncatalyzed electro-oxidation of formic acid decreases for classical electrochemical reasons, i.e., the rate constant of reaction [1] decreases as the potential decreases. The interplay of these three factors will result in an optimum solution concentration of lead ion for the catalytic process at a particular rotation speed for a given rate of potential scan in the positive-to-negative direction.

The negative-to-positive potential scan $I-E$ curves merge, for practical purposes, for lead-ion concentrations above $10^{-5}M$ when the potential is more positive than $0.25V$. This situation arises because the surface coverage of UPD lead approaches equilibrium in these solutions at the experimental scan rate. Coverage is determined by potential. The observed differences between the $I-E$ curves under discussion arise from the slight concentration dependence of isotherm depicted in Fig. 6.

The interpretation of potentiodynamic data is complicated, as was realized by previous workers who used cyclic voltammetry at a stationary electrode to study the oxidation of formic acid (12). The use of the rotating disk and ring-disk electrodes simplifies this interpretation by providing reliable estimates of UPD surface coverage during the potential scan.

Conclusions

The residues formed on the surface of a platinum electrode during the electro-oxidation of formic acid can decrease the amount of the platinum surface area available for the underpotential deposition process of a foreign adatom necessary to catalyze the oxidation reaction. The amount of this decrease will be determined by the concentrations of the dissolved species. The surface of the platinum electrode not covered with organic residues must be determined in order to calculate the actual adatom coverage during the formic

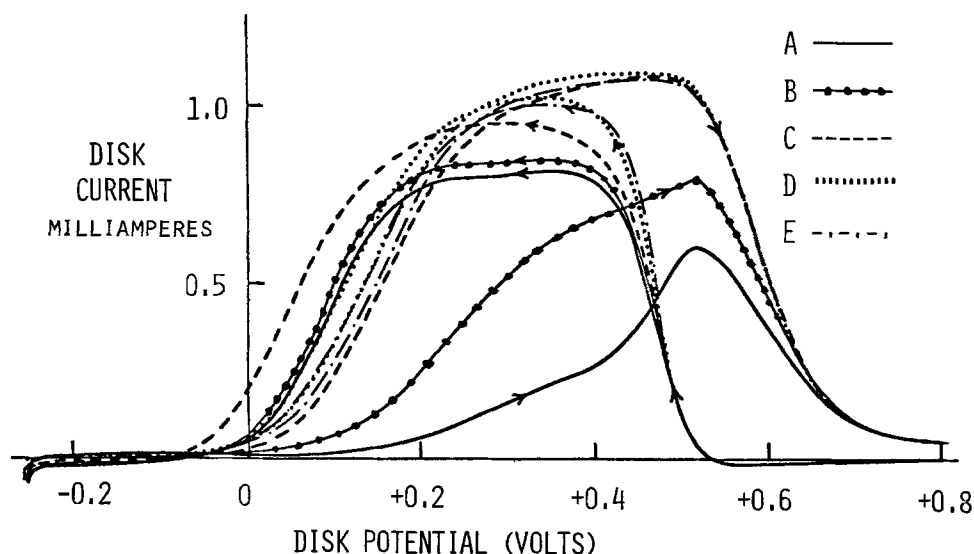


Fig. 15. Effect of lead ion concentration on cyclic voltammograms at a rotating disk electrode. $1 \times 10^{-3}M$ $HCOOH$ in $0.12M$ $HClO_4$. $\omega = 2500$ rpm. Potential scan rate is 50 mV s^{-1} , and scan limits are 1.15 to $-0.25V$ (vs. SCE). $i-E$ curves are these obtained on repetitive scanning. No Pb^{2+} (A), $10^{-6}M$ Pb^{2+} (B), $10^{-5}M$ Pb^{2+} (C), $10^{-4}M$ Pb^{2+} (D), and $10^{-3}M$ Pb^{2+} (E).

acid oxidation process. This problem can be minimized by using low concentrations of formic acid and enhanced mass transfer of the UPD species. Under these conditions, a limiting formic acid oxidation current can be obtained over a wide potential region at the rotating disk electrode. The decay of this limiting disk current can then be monitored as a function of the adatom surface coverage, which is determined by using the ring electrode of the RRDE.

The dependence of the oxidation current of formic acid and the selectivity for adatom UPD on the orientation of the crystal planes of platinum explains why adatoms with radii greater than the platinum atom are capable of catalyzing formic acid oxidation, while very low coverages of atoms with smaller radii appear to have substantial inhibiting effects.

Acknowledgment

This work was supported by the Air Force Office of Scientific Research under AFSOR Grants no. 78-3621 and 83-0004.

Manuscript submitted Jan. 10, 1983; revised manuscript received ca. Aug. 27, 1983.

REFERENCES

- H. S. C. Deville and H. Debray, *Compt. Rend.*, **78**, 1782 (1874).
- E. Muller, *Z. Elektrochem.*, **29**, 264 (1923).
- B. E. Conway and M. Dzieciuch, *Can. J. Chem.*, **41**, 21, 55 (1963).
- A. Capon and R. Parsons, *J. Electroanal. Chem.*, **44**, 205 (1973).
- M. W. Breiter, *Electrochim. Acta*, **10**, 503 (1965).
- M. W. Breiter, *J. Electroanal. Chem.*, **19**, 131 (1968).
- V. N. Kamath and H. Lal, *ibid.*, **19**, 137 (1968).
- B. I. Podlovchenko and E. P. Gorganova, *Dokl. Akad. Nauk SSSR*, **156**, 673 (1964).
- A. Capon and R. Parsons, *J. Electroanal. Chem.*, **44**, 1 (1973).
- A. Capon and R. Parsons, *ibid.*, **44**, 239 (1973).
- H. Angerstein-Kozłowska, B. MacDougall, and B. E. Conway, *This Journal*, **120**, 756 (1973).
- R. R. Adzic, D. N. Simic, D. M. Drazic, and A. R. Despic, *J. Electroanal. Chem.*, **61**, 117 (1975); **65**, 587 (1975); **80**, 81 (1977).
- R. R. Adzic, *Isr. J. Chem.*, **18**, 166 (1979).
- B. E. Conway, H. Angerstein-Kozłowska, and G. Czartoryska, *Z. Phys. Chem.*, **112**, 195 (1978).
- N. Furuya and S. Motoo, *Denki Kagaku*, **41**, 307 (1973).
- W. J. Albery, D. T. Napp, and S. Bruckenstein, *Trans. Faraday Soc.*, **62**, 1932 (1966).
- W. J. Albery and S. Bruckenstein, *ibid.*, **62**, 1920 (1966).
- D. T. Napp, D. C. Johnson, and S. Bruckenstein, *Anal. Chem.*, **39**, 481 (1967).
- T. M. Riedhammer, L. S. Melnicki, and S. Bruckenstein, *Z. Phys. Chem.*, **111**, 177 (1978).
- J. D. Jolson, Ph.D. Thesis, State University of New York at Buffalo (1978).
- T. Biegler, A. J. Rand, and R. Woods, *J. Electroanal. Chem.*, **29**, 269 (1971).
- D. F. Untereker and S. Bruckenstein, Unpublished results.
- S. Gilman, in "Electroanalytical Chemistry," Vol. 2, A. J. Bard, Editor, p. 129, Marcel Dekker, New York (1967).
- G. G. Barna, S. N. Frank, T. H. Teherani, *This Journal*, **129**, 746 (1982).
- S. H. Cadle and S. Bruckenstein, *Anal. Chem.*, **44**, 1993 (1972).
- B. J. Bowles, *Nature (London)*, **212**, 1456 (1966).
- A. R. Nisbit and A. J. Bard, *J. Electroanal. Chem.*, **6**, 332 (1963).
- M. M. Nicholson, *J. Am. Chem. Soc.*, **79**, 7 (1957).
- S. H. Cadle and S. Bruckenstein, *Anal. Chem.*, **43**, 1858 (1971).
- V. A. Vicente and S. Bruckenstein, *ibid.*, **45**, 2036 (1973).
- S. Swathirajan, H. Mizota, and S. Bruckenstein, *J. Phys. Chem.*, **86**, 2480 (1982).
- S. Swathirajan and S. Bruckenstein, *This Journal*, **129**, 1202 (1982).
- G. W. Tindall and S. Bruckenstein, *Electrochim. Acta*, **16**, 245 (1971).
- L. S. Melnicki, Ph.D. Thesis, State University of New York at Buffalo (1984).
- E. Schmidt and N. Wuthrich, *J. Electroanal. Chem.*, **40**, 399 (1972).
- B. Gostisa-Mihelcic and W. Vielstich, *Ber. Bunsenges. Phys. Chem.*, **77**, 476 (1973).
- S. Schuldiner and B. J. Piersma, *J. Phys. Chem.*, **74**, 2823 (1970).
- D. R. Rhodes and E. F. Steigelmann, *This Journal*, **112**, 16 (1965).
- D. Fletcher and V. Solis, *J. Electroanal. Chem.*, **131**, 309 (1982).
- N. Furuya and S. Motoo, *ibid.*, **98**, 189, 195 (1979).
- D. M. Kolb, in "Advances in Electrochemistry and Electrochemical Engineering," Vol. 3, P. Delahay and C. W. Tobias, Editors, p. 211, John Wiley and Sons, Inc., New York (1963).
- S. Swathirajan and S. Bruckenstein, *J. Electroanal. Chem.*, **146**, 137 (1983).
- L. S. Melnicki, T. M. Reidhammer, and S. Bruckenstein, in "Electrode Processes," S. Bruckenstein, J. D. E. McIntyre, B. Miller, and E. Yeager, Editors, p. 305, The Electrochemical Society Soft-bound Proceedings Series, Princeton, NJ (1979).
- J. Clavilier, R. Parsons, R. Durand, C. Lamy, and J. M. Leger, *J. Electroanal. Chem.*, **124**, 321 (1981).
- C. L. Scortichini and C. N. Reilley, *J. Catal.*, **79**, 138 (1983).
- E. Yeager, W. O'Grady, M. Woo, and P. Hagans, *This Journal*, **125**, 348 (1978).
- A. Hubbard, R. Ishikawa, and J. Kutakaru, *J. Electroanal. Chem.*, **86**, 271 (1978).
- P. N. Ross, *Surf. Sci.*, **102**, 463 (1981).

The Transport and Kinetics of Photogenerated Carriers in Colloidal Semiconductor Electrode Particles

W. John Albery* and Philip N. Bartlett*

Department of Chemistry, Imperial College, London SW7 2AY, England

ABSTRACT

The transport and kinetics of photogenerated majority and minority carriers in a spherical semiconductor particle of colloidal size are considered. The Poisson-Boltzmann equation is solved for the sphere, and the potential distribution in the particle is obtained. The recombination of the carriers according to Hall-Shockley-Read kinetics gives rise to a number of different cases, for which equations describing the flux of photogenerated species in the external solution are obtained. Kinetic case diagrams show how the different cases are related to each other and how they depend upon such variables as the irradiance, the Fermi level in the electrolyte, the surface rate constants, and the radius of the particle. Three different strategies which could lead to devices for efficient solar energy conversion are found and discussed.

The use of semiconductor particles as microheterogeneous electrodes for solar energy conversion (1, 2) or photocatalysis (3, 4) has aroused considerable interest. In discussing these systems most authors have assumed that the semiconductor particles behave in a similar fashion to macroscopic electrodes made of the same material. For instance, Grätzel and Frank (5) have published a simple description of the response of a particle to a pulse of light. In this paper we present a more complete theoretical description of the photogeneration of holes and electrons in the particle, their transport and recombination kinetics, and the kinetics of their reactions at the surface of the particle. We give expressions for the efficiency of the particle system and how it depends upon the above-mentioned parameters. We show that the particles behave very differently from their macroscopic analogues. We find a number of different kinetic cases, and from these cases we deduce that there are three different ways of achieving efficient solar energy conversion. The conditions for these three different strategies are derived and discussed. Throughout we present the theory for p-type particles.

Model

We consider a spherical particle of radius r_s doped so that the Debye length of the material is L_D ; the absorption coefficient for the light (α) gives rise to an absorption length, L_e , where $L_e = \alpha^{-1}$. We assume that the particle is so small that $r_s \ll L_e \sim 10^{-4}$ cm, leading to uniform irradiance (I) inside the particle and uniform photogeneration of holes and electrons (g), where

$$g = I/L_e \quad [1]$$

In this paper we consider only the steady state. Under steady-state conditions, the net flux of electrons (j) leaving the conduction band of any particle must balance the net flow of holes from the valence band. The collection efficiency (N) of the particle is then the ratio of photogenerated electrons or holes leaving the particle compared to the number of photons absorbed by the particle. Using Eq. [1]

$$N = \frac{4\pi r_s^2 j}{(4/3)\pi r_s^3 g} = \frac{j}{1/3 r_s g} = \frac{3jL_e}{I r_s} = \frac{j}{J} \quad [2]$$

The parameter J ($= 1/3 I r_s L_e^{-1}$) describes the inward flux of photons that are absorbed by each particle. In writing Eq. [2], we assume that the loss of electrons and holes from the particle takes place in a reasonably uniform fashion all over the surface of the particle. A more complicated situation will be found if, for instance, the particle is coated with Pt in a

single localized patch. Under these conditions the transport and kinetics of the carriers will depend upon the detailed geometry of the coating, and one cannot expect to devise a general theory for such a situation. Providing that the materials like Pt are dispersed over the whole surface, we can describe the kinetics of the removal of electrons or holes by the following equations

$$j = k_n' n_s = k_p' p_s - k_{-p}' \quad [3]$$

where n_s is the surface concentration of electrons in the conduction band, and p_s is the surface concentration of holes in the valence band. In Eq. [3] we assume (for a p-type particle) that there is no thermal injection of electrons from the solution into the conduction band, but with k_{-p}' we allow for the thermal injection of holes (majority carriers) into the valence band. In the dark $j = 0$, and we can define p_s^D , the surface concentration of holes in the dark, as

$$p_s^D = k_{-p}'/k_p' \quad [4]$$

This concentration is fixed by the redox systems in the electrolyte. Using Eq. [4] we can eliminate k_{-p}' from Eq. [3] to obtain

$$j = k_p' (p_s - p_s^D) \quad [5]$$

The rate constants k_n' and k_p' are electrochemical rate constants with units of cm/s^{-1} . If either reaction is confined, say to Pt covering an area A on the surface, then

$$k_n' = k_n'' (A/4\pi r_s^2)$$

where k_n'' is the rate constant for the Pt catalyst.

Distribution of Potential

Since the particle has spherical geometry, we cannot assume, as others have done (5), that the width of the depletion layer is given by the equation for a planar macroscopic electrode; we must solve the Poisson-Boltzmann equation for the sphere. For the depletion layer, the Poisson-Boltzmann equation may be written in dimensionless variables as follows

$$\rho^{-2} \frac{\partial}{\partial \rho} \left(\rho^2 \frac{\partial \theta}{\partial \rho} \right) = 1 \quad [6]$$

where

$$\rho = r/L_D \quad [7]$$

$$\theta = \phi F/RT$$

r is the distance from the center of the particle, and ϕ is potential measured with respect to the center of the particle so that $\phi = 0$ at $r = 0$.

Integration of Eq. [6] yields

$$\theta = \frac{1}{6} (\rho - \rho_w)^2 (1 + 2\rho_w/\rho) \quad [8]$$

* Electrochemical Society Active Member.
Key words: solar energy conversion, photogenerated carriers, colloidal semiconductors.

where we have used the boundary conditions that θ and $(\partial\theta/\partial\rho) = 0$ at $\rho = \rho_W$, the inside edge of the depletion layer. For large particles where the width of the depletion layer is small compared to the radius of the particle, $\rho \approx \rho_W$ throughout the depletion layer, and Eq. [8] simplifies to

$$\theta = \frac{1}{2} (\rho - \rho_W)^2$$

This is the same result as for a planar electrode. For a thin depletion layer close to the surface of the sphere, the spherical geometry does not affect the potential distribution.

For small colloidal particles $r_s \sim 10^{-6}$ cm, the radius of the particle may be smaller than the width of the depletion layer, so that $\rho_W = 0$, with $\theta = 0$ and $(\partial\theta/\partial\rho) = 0$ at $r = 0$. Equation [8] then simplifies to

$$\theta = \rho^2/6 \quad [9]$$

Under these conditions, the whole of the particle is depleted of majority carriers and there is no field-free region.

We now discuss the conditions under which Eq. [9] will hold. In Fig. 1 we compare the potential distribution in a macroscopic planar electrode with that in a small spherical particle. For both cases we assume that the Fermi level is fixed by a redox couple in the electrolyte which has shifted its position by an amount corresponding to θ_F from its position at flatband. In the planar case (assuming no Fermi-level pinning), this means that θ_F describes the potential drop across the depletion layer of width W . For the particle, r_s is too small for this full potential difference to be developed. From Eq. [9] the maximum value of θ is

$$\theta_s = \frac{1}{6} (r_s/L_D)^2 \quad [10]$$

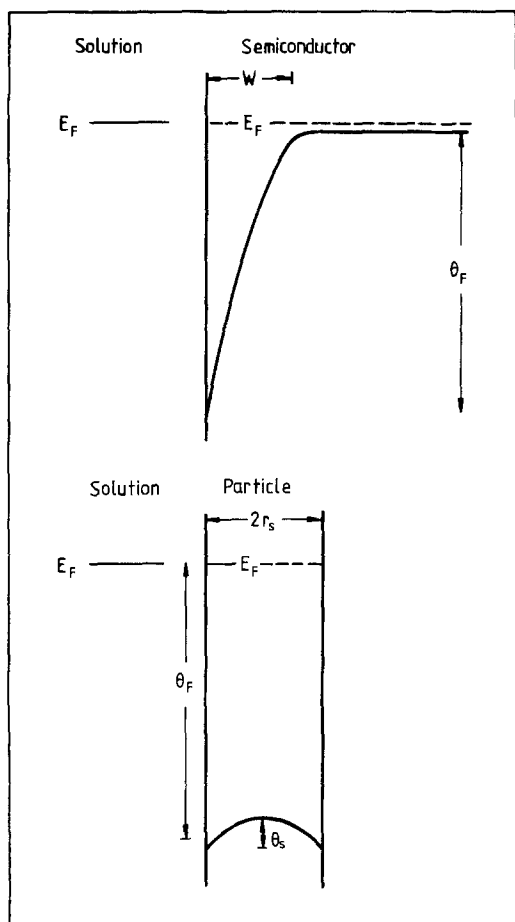


Fig. 1. Comparison of the potential distribution and Fermi levels for a macroscopic planar electrode and for a spherical particle.

Hence the particle will be completely depleted and Eq. [9] will hold when

$$\frac{1}{6} \left(\frac{r_s}{L_D} \right)^2 = \theta_s < \theta_F = \frac{1}{2} \left(\frac{W}{L_D} \right)^2$$

or when

$$r_s < 3^{1/2} W = (6 \theta_F)^{1/2} L_D \quad [11]$$

For colloidal particles where r_s is, for instance, 10^{-6} or smaller, it is likely that the condition in Eq. [11] will be satisfied, that is, that the particle will be completely depleted of its majority carriers and that the potential distribution will be given by Eq. [9]. This is a major difference between the small spherical particle and the macroscopic electrode. Furthermore, since θ_s may be much smaller than θ_F , there may be much less potential difference within the particle than within the macroscopic depletion layer. An even more extreme situation is when $r_s > 6^{1/2} L_D$ giving $\theta_s < 1$. Under those conditions the particle can be treated as being field free. Finally, θ_F may be related to p_{FB}^D

$$\theta_F = \ln p_{FB}^D - \ln p_s^D \quad [12]$$

where p_{FB}^D is the concentration of majority carriers in the dark at flatband and is equal to the charge-carrier density of the macroscopic material. The parameter θ_F plays the same role for semiconductor particles as the electrode potential does for the macroscopic case.

Transport in the Particle

The differential equation describing the photogeneration of the minority carriers, their transport by diffusion and by migration, and their recombination may be written, using Eq. [9], as

$$\frac{D_n}{r^2} \frac{\partial}{\partial r} \left(r^2 \frac{\partial n}{\partial r} - \frac{nr^3}{3L_D^2} \right) + \begin{matrix} \text{Diffusion} & \text{Migration} & \text{Generation} \\ \text{(or drift)} & & \end{matrix} - \begin{matrix} \text{Recombination} \\ v = 0 \end{matrix} = g \quad [13]$$

where n is the concentration of electrons and v is the rate of recombination. Integration of Eq. [13] shows that providing

$$g \ll D n_s / L_D^2 \quad [14]$$

then the distribution of n is given by a Boltzmann distribution in the potential described by Eq. [9].

Substitution from Eq. [1], [2], and [3] allows us to rewrite the condition in Eq. [14] as

$$1 \ll \frac{N}{3} \frac{D_n}{L_D} \frac{r_s}{k_n' L_D} \quad [15]$$

In Eq. [15] it is likely that both D_n/L_D are larger than k_n' and r_s is larger than L_D ($\theta_s > 1$). Hence, unless N is very small, the condition in Eq. [15] is likely to hold, and the electrons will obey a Boltzmann distribution. The low value of N will be obtained when recombination kinetics are very rapid, and under these conditions the last two terms in Eq. [13] could give a uniform distribution in the particle. Such cases are so inefficient as to be uninteresting and will not be further considered. A similar argument can be used for the holes. The conclusion that both electrons and holes obey the Boltzmann distribution agrees with our earlier work (6) on recombination in the depletion layer of macroscopic electrodes. Figure 2 shows the resulting concentration profiles for the electrons and holes.

It should be noted that the characteristic time for the transport of the electrons in the depleted particle is given by L_D^2/D_n and not r_s^2/D_n as stated by Grätzel and Frank (5). Migration is more efficient than diffu-

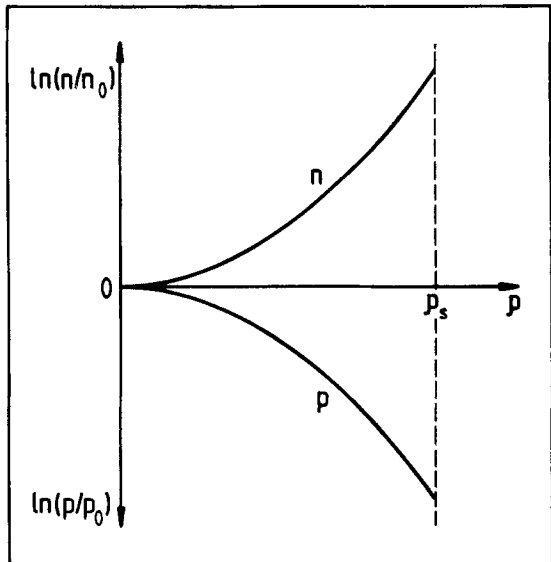


Fig. 2. Typical concentration profiles for electrons and holes inside a p-type spherical particle where $\rho = r/L_D$ and ρ_s is the surface of the particle.

sion, and the field assists the transport. It is, therefore, even more certain that carriers photogenerated in a small particle will reach the surface before being destroyed by recombination. Grätzel and Frank assume that once a carrier has reached the surface it is bound to be lost from the particle. We do not agree with this assumption. Next we explore the fate of the carriers. Will they be lost from the particle through the k_n' and k_p' reactions or will they recombine in the particle?

Recombination Kinetics

In our previous work (6) we expressed the equation for the Hall-Shockley-Read (7, 8) model in kinetic terms

$$\frac{1}{v} = \frac{1}{k_I n} + \frac{1}{k_{II} n p} + \frac{1}{k_{II} p} \quad [16]$$

I II III

In this equation n and p are given by the Boltzmann distributions

$$n = n_s \exp(\theta - \theta_s) \quad [17]$$

and

$$p = p_s \exp(\theta_s - \theta) \quad [18]$$

Because the particle is small, it is unlikely that all three terms in Eq. [16] will be significant. We therefore consider in turn four cases, I, II, III, and I/III. In the last case terms I and III become equal at some value of r inside the particle.

As shown in Fig. 3, the main losses from recombination for case I occur near the surface and for case III at the center. For case II the Boltzmann factors cancel out, and the loss is uniform throughout the particle. For case I/III, case I is found (low value of n) near the center and case III near the surface; the maximum loss is at the boundary between the two cases.

The general expression for N is

$$N = 1 - \frac{\int_0^{r_s} r^2 v dr}{\frac{1}{3} g r_s^3} \quad [19]$$

The problem is to work out the value of the integral and the numerator of Eq. [19] using Eq. [2], [3], [5], [7], [9], [16], [17], and [18]. The detailed working is given in the Appendix, and the results are collected in Table I. We also include expressions for a field-free particle which will arise when $\theta_s < 1$ and the field is negligible.

We now discuss these expressions. The terms in the denominators compare the rate constants for recombination k_I , k_{II} , and k_2 with the rate constants for reaction at the surface k_n' and k_p' . For case I ($\theta_s > 1$), we may write

$$\frac{3k_I L_D^2}{k_n' r_s} = \frac{k_I}{k_n'} \left(\frac{\partial \theta}{\partial r} \right)_s^{-1} \quad [20]$$

This may be compared with the similar expression for the macroscopic case (9) where

$$\frac{k_I}{k_n'} \frac{L_D}{(2\theta_0)^{1/2}} = \frac{k_I}{k_n'} \left(\frac{\partial \theta}{\partial x} \right)_0^{-1} \quad [21]$$

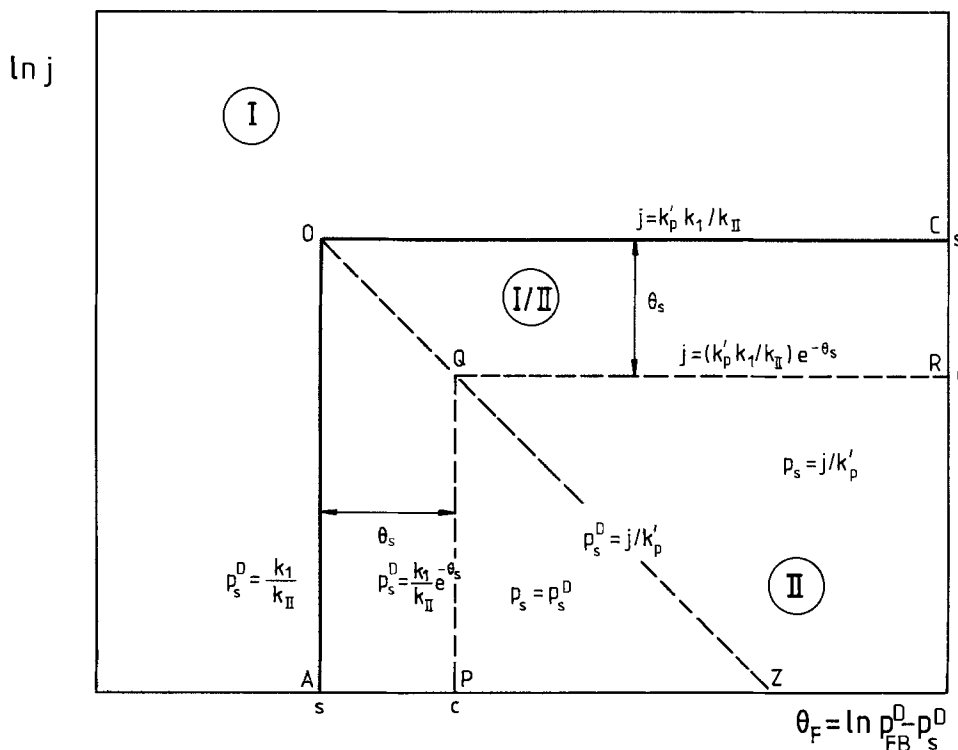


Fig. 3. Kinetic case diagram for case A (see Eq. [27]) and for $\theta_s > 1$. The conditions and the zones of dominance for the different kinetic cases are displayed as a function of the flux j and the position of the Fermi level described by θ_F . For the mixed I/II zone, the boundary is at the surface of the particle on the solid lines passing through O and at the center of the particle on the broken lines passing through Q.

Table I. Results for N

Case ^a	$\theta_s = r_s^2/6L_D^2$ ^b	N
I	$\theta_s > 1$	$\frac{1}{1 + 3 k_1 L_D^2/k_n' r_s}$
	$\theta_s < 1$	$\frac{1}{1 + k_1 r_s/3k_n'}$
II ^c		$\frac{1}{1 + \frac{k_{11} r_s}{3 k_n'} \left[p_s D + \frac{N I r_s}{3 k_p' L_e} \right]}$
III ^d	$\theta_s > 1$	$\frac{1}{1 + \frac{k_2 L_D^3 C \exp(\theta_s)}{r_s^2} \left[\frac{3 p_s D L_e}{N I r_s} + \frac{1}{k_p'} \right]}$
	$\theta_s < 1$	$\frac{1}{1 + \frac{k_2 r_s}{3} \left[\frac{3 p_s D L_e}{N I r_s} + \frac{1}{k_p'} \right]}$
I, III ^{e,f}	$\theta_s > 1$	$\frac{1}{1 + \frac{3\pi}{2} \frac{L_D^2 r_s}{r_s^2} \left[\frac{k_1 k_2}{k_n'} \left\{ \frac{3 p_s D L_e}{N I r_s} + \frac{1}{k_p'} \right\} \right]^{1/2}}$

^a Cases I, II, and III refer to the dominant term in Eq. [16] for Hall-Shockley-Read kinetics.

^b $\theta_s > 1$ corresponds to particles with field. $\theta_s < 1$ means that the particles are field free.

^c The same result is obtained regardless of the size of θ_s .

^d $C = (3/2) (6\pi)^{1/2} = 6.51$.

^e There is no result for $\theta_s < 1$ because under these conditions there can be no shift in mechanism from I to III.

$$r_s^2 = r_s^2 + 3L_D^2 \ln \left[\frac{k_2 k_n'}{k'} \left\{ \frac{3 p_s D L_e}{N I r_s} + \frac{1}{k_p'} \right\} \right]$$

The inverse gradients in Eq. [20] and [21] describe the distances near the surface over which θ decreases by 1 or the concentration of electrons falls to e^{-1} of its value at the surface. The recombination in this distance can compete with the loss through the surface. Further into the particle (or macroscopic electrode), the field keeps the concentration of minority carriers so low that recombination is negligible. This is not true for the field-free case, where recombination takes place throughout the particle. The denominators of the other three cases in Table I contain 3 terms. This is because the concentration of holes may be dominated by either the concentration in the dark (p_s^D), with negligible perturbation by the light or by the photo-generated concentration. Inspection shows that the ratio of the last two terms in each case is the same. From Eq. [2] and [5]

$$p_s^D + \frac{N I r_s}{3 k_p' L_e} = p_s \quad [22]$$

For case II the exponential terms for the loss by recombination cancel out so that there is a uniform velocity of reaction throughout the volume of the particle. Both the recombination and the loss of minority carriers are proportional to n and so

$$\frac{k_{11} r_s p_s}{3 k_n'} = \frac{(4/3) \pi r_s^3 k_{II} p_s n_s}{4\pi r_s^2 k_n' n_s}$$

In this case the result does not depend upon the field. For case III, where the recombination is proportional to the concentration of holes, with the field, the largest concentration (p_0) is at the center and maintains its value for a sphere of radius of about $3L_D$. From Eq. [2] $3L_e/N I r_s = j^{-1}$ and so

$$\frac{k_2 L_D^3 C \exp(\theta_s) p_s}{r_s^2} \cdot \frac{3L_e}{N I r_s} = \frac{k_2 L_D^3 C p_0}{r_s^2 j}$$

This ratio compares the loss of holes by k_2 in the cen-

tral sphere with the loss through the surface. For the field-free case, the ratio is $1/3 k_2 r_s p_s/j$, and recombination takes place throughout the sphere.

Case I/III is more complicated. The parameter r_s describes the radius where term I and term III in Eq. [16] are equal. The rate of recombination is largest at this value, and r_s can vary between r_s , which corresponds to the boundary with case I, and L_D , which corresponds to the boundary with case III. Inspection shows that as a rough approximation the term in the denominator of case I/III is the geometric mean of those in terms I and III. This case does not exist for $\theta_s < 1$, because it is the field which changes the kinetics.

Kinetic Case Diagrams

We now discuss how the different cases in Table I are related to each other as a function of first the flux (j), of carriers leaving a particle, and second, the concentration of majority carriers in the dark, which is related by Eq. [12] to θ_F . The quantities j and θ_F are the analogues of the photocurrent and electrode potential for a macroscopic electrode. For a particle, θ_F will be fixed by the redox couples present in the electrolyte solution. We start by considering the cases where $\theta_s > 1$ and a field is present in the particle.

From Eq. [16] the boundaries between the different cases are as follows

$$I/II \quad p = k_1/k_{II} \quad [23]$$

$$II/III \quad n = k_2/k_{II} \quad [24]$$

The boundary between I and I/III will be when $\theta_s = \theta_s$ or from Eq. [A-16]

$$k_1 n_s = k_2 p_s \quad [25]$$

The boundary between I/III and III will be when $\theta_s = 0$ or from Eq. [A-16]

$$(k_1 p_s/k_2 n_s) = \exp(2\theta_s) \quad [26]$$

We find that depending on the ratio $(k_p' k_1/k_2 k_n')$ three different types of behavior can be found

$$(k_p' k_1/k_n' k_2) < 1 \quad [27]$$

$$1 < (k_p' k_1/k_n' k_2) < \exp(2\theta_s) = \exp \left[\frac{1}{3} (\tau_s/L_D)^2 \right] \quad [28]$$

$$\exp(2\theta_s) < (k_p' k_1/k_n' k_2) \quad [29]$$

We now consider each case in turn. Figure 3 shows the kinetic case diagram for Eq. [27]. The main zones on the diagram are the cases described by Eq. [27] and [28] with a small intermediate zone. The case described by (Eq. [29]) (the $k_2 p$ term) does not appear because the kinetic condition in Eq. [17] for Eq. [27] assumes that inside the particle the product $k_2 p$ will always exceed $k_1 n$. The reason for this is that k_p' is sufficiently small for it to be difficult for the holes to be lost at the surface. The dotted line OQZ divides the Eq. [28] case into a zone where the concentration of holes is determined by the unperturbed dark concentration (p_s^D) and a zone where the photogenerated concentration is significantly larger than p_s^D ; under these conditions the reaction at the interface is irreversible. The boundaries are then determined by Eq. [23]; the solid lines show where the terms are equal at the surface, and the broken lines where they are equal at the center of the particle. It is satisfactory that, apart from numerical terms, the expression for N for case II in Table I agrees with that for case I on the boundaries; the second term in the denominator for case II is dominant on the vertical boundaries, and, using Eq. [2] ($j = 1/3 N I r_s/L_e$), the third term on the horizontal boundaries.

Next we consider the intermediate case described by Eq. [28], where the kinetic ratio is roughly in balance. The kinetic case diagram is shown in Fig. 4. Comparing the horizontal lines, comparison with Fig. 3 shows that the boundaries OA and PQR are the same. The line QZ still separates the zones where the concentration of holes is determined by the thermal concentration or by the photogeneration. The boundaries OD, OB, and XY are given by Eq. [25], [24], and [30], respectively. The parameter θ_*^L is the limiting value of θ_* , and describes the location of the reaction zone for the I/III case inside the particle at the point where on increasing the irradiance the case II region ceases to exist

$$\exp(\theta_*^L - \theta_s) = (k_2 k_n' / k_1 k_p')^{1/2} \quad [30]$$

Above the line XQZ increasing irradiance increases j , n , and p , but does not alter the relative balance of

$k_1 n$ and $k_2 p$. Hence θ_* does not change; it remains equal to θ_*^L . Depending on the kinetics, θ_*^L can vary between 0 and θ_s . When θ_*^L is equal to θ_s nearly all the particle has case I kinetics. Under these conditions, Fig. 4 reduces back to Fig. 3 with the points O and X coincident and the line OB a distance θ_s above QR. Again it is satisfactory that the different expressions for N in Table I are in reasonable agreement on the boundaries.

Finally we turn to case C, expressed by Eq. [29], where the ratio is now large. The kinetic case diagram is shown in Fig. 5. Because of the large kinetic ratio at high irradiance there are not many holes (k_p' is large), and so term III will dominate the whole of the particle. Comparing Fig. 4 and 5 the boundaries OA, OB, OD, and PQ are identical. The boundaries QT and QU are derived from Eq. [26]. If in Fig. 4 one takes θ_*^L towards zero, the whole of the particle becomes

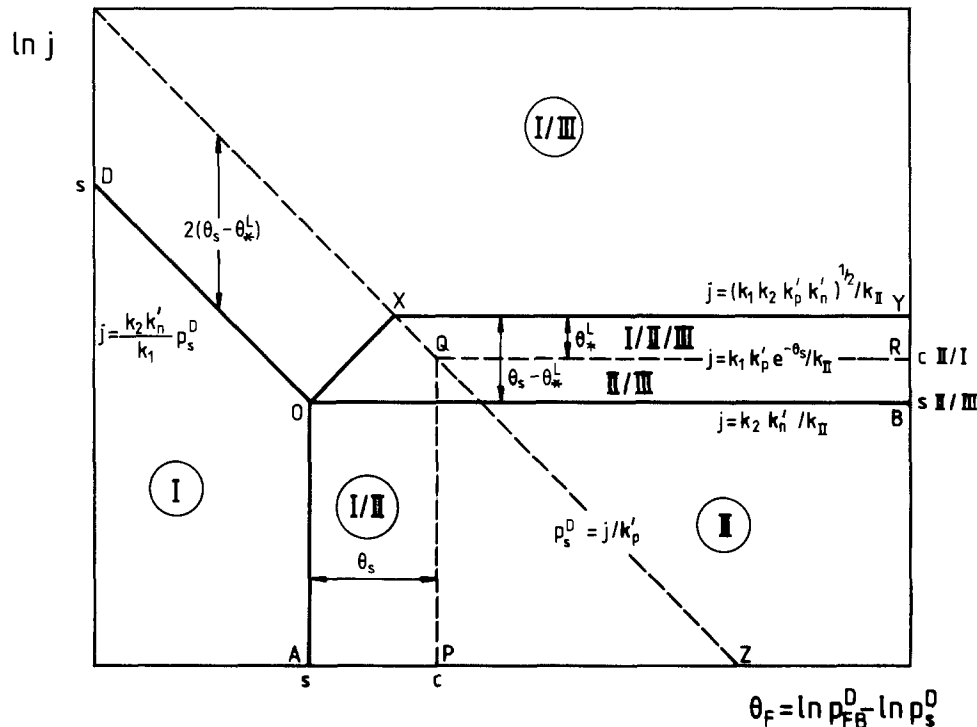


Fig. 4. Kinetic case diagram for case B (see Eq. [28]) and for $\theta_s > 1$. The boundaries AO and PQR are the same as in Fig. 3. The boundary OB now lies lower than the boundary OC in Fig. 3 corresponding to the difference between Eq. [27] and [28].

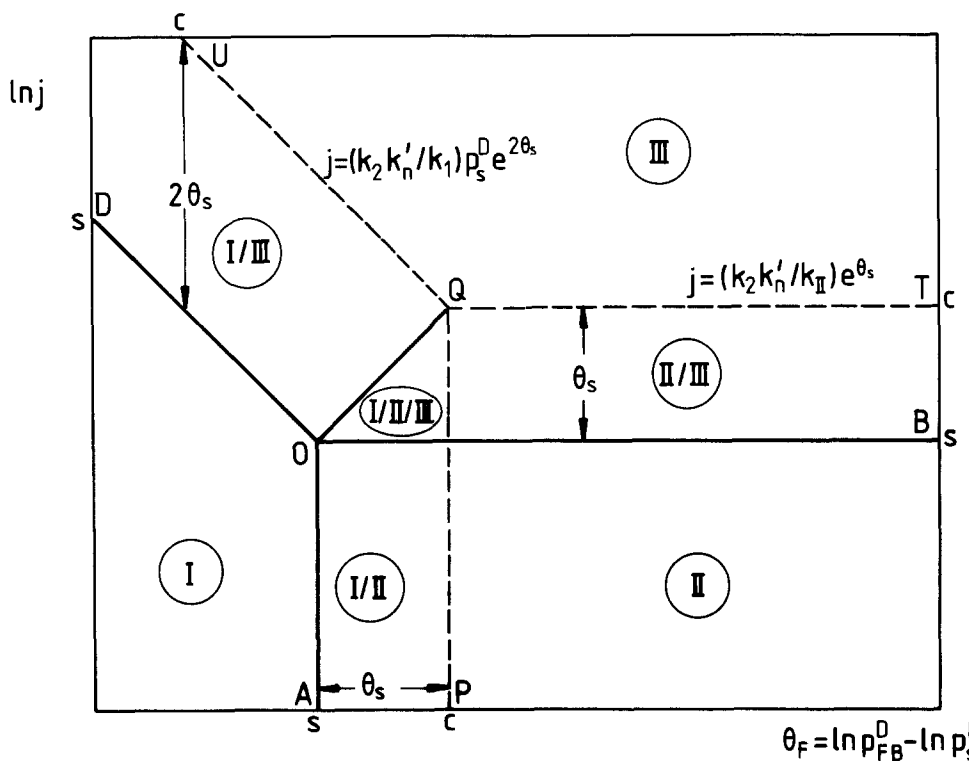


Fig. 5. Kinetic case diagram for case C (see Eq. [29]) and for $\theta_s > 1$. The boundaries OA, OD, OB, and PQ are the same as those in case B in Fig. 4. The boundary QR in Fig. 4 lies above the boundary QT in this figure, corresponding to the difference between Eq. [28] and [29].

case III. The points Q and X become coincident, and Fig. 4 and 5 match. The field-free cases in Table I are discussed below.

Discussion of Kinetic Cases

The kinetic case diagrams show how the different solutions for N in Table I are linked together and how they depend on the photogenerated flux (j) and on θ_F , where θ_F is determined by the redox properties of the solution. Several general conclusions can be drawn. First, the concentrations of the carriers and their fate inside the particle are very dependent on the rate constants for the reactions at the surface k_n' and k_p' . These rate constants will often depend on the concentrations of redox species in the solution and can therefore be varied. Second, since throughout its volume the particle is depleted of majority carriers, the concentration of majority carriers may be very small, and the terms majority and minority may be misleading. For instance, in the case where the concentration of photogenerated holes is significantly larger than the concentration in the dark, from Eq. [3]

$$n_s/p_s \simeq k_p'/k_n'$$

The relative size of the concentrations of holes and electrons depends on the ratio of the surface-rate constants and not at all on how the particle was originally doped. Third, for small particles the amount of band bending as given by θ_s will be much smaller than that found in macroscopic semiconductors. This suggests that the effects of the field are less important and that reasonable estimates of transport and kinetics may be obtained by assuming that the particle is field free. Fourth, the value of p_s^D determines the important parameter θ_F (see Eq. [2]), which plays the same role as the electrode potential for macroscopic electrodes. In any experiment this parameter should be controlled and not left to chance. Finally, which kinetic case is found may depend on the irradiance. Increasing the light intensity increases j , and this is equivalent to moving upwards on the kinetic case diagrams.

Turning now to some more particular points, in Fig. 6 and 7 we have simplified the kinetic case diagrams by ignoring all borderline cases. If θ_s is not too large (corresponding to small particles), then the zones of existence of the borderline cases will be small. The

simplified diagrams give approximate expressions for N from Table I, together with contours which show how N varies in the different zones, provided one assumes for the moment that $N \ll 1$. Decreasing the dark concentration of holes increases N in zones III, 1 and II, 1. It is interesting that in zone II, 2, the flux j will depend on the square root of the irradiance $I^{1/2}$. Zone II, 1 is curious because, if N is small, then one finds that

$$r_s^2 I/L\epsilon \simeq k_2 L_D^3 C p_s^D \exp(\theta_s) \quad [31]$$

This equation matches the photogeneration over the whole spherical particle with the case-III recombination, which is determined by the concentration of holes in the dark recombining at the center of the particle. Equation [31] has to hold all over zone III, 1. Relatively small changes in I or in p_s^D will violate the condition and lead to sharp changes in N and Nl . For instance, an increase in the irradiance (ΔI) where $\Delta I/I \sim N$, will shift the system from case I to case III, 2 giving a steep increase in N and the flux, $j = NI$. For low values of N , case III, 1 is metastable. The tie lines in the inset show how the system will change abruptly from the lower cases to case III, 2. The simplified diagrams in Fig. 6 and 7 also describe the field-free results in Table I.

Finally, it is interesting to note that for most cases a decrease in r_s leads to improvements in N . This is true of case III when one remembers that in the exponential term $\theta_s = r_s^2/6L_D^2$. For this case the advantage of the small particle is that there is no central haven where the holes can congregate before recombining. For case II, where the recombination rate is uniform, the smaller the value of r_s , the greater the area to volume ratio. Hence the surface processes are favored compared to recombination. The one exception is case I with the field. Here N is greater the larger the value of r_s is. This arises because in this case the field is helpful in that it concentrates the minority carriers at the surface. The optimum value of r for efficient solar energy conversion will be discussed below.

To understand these systems and to optimize their design for efficient conversion, it will be necessary to find out to which kinetic case a particular system belongs. The variation of N with variables such as the

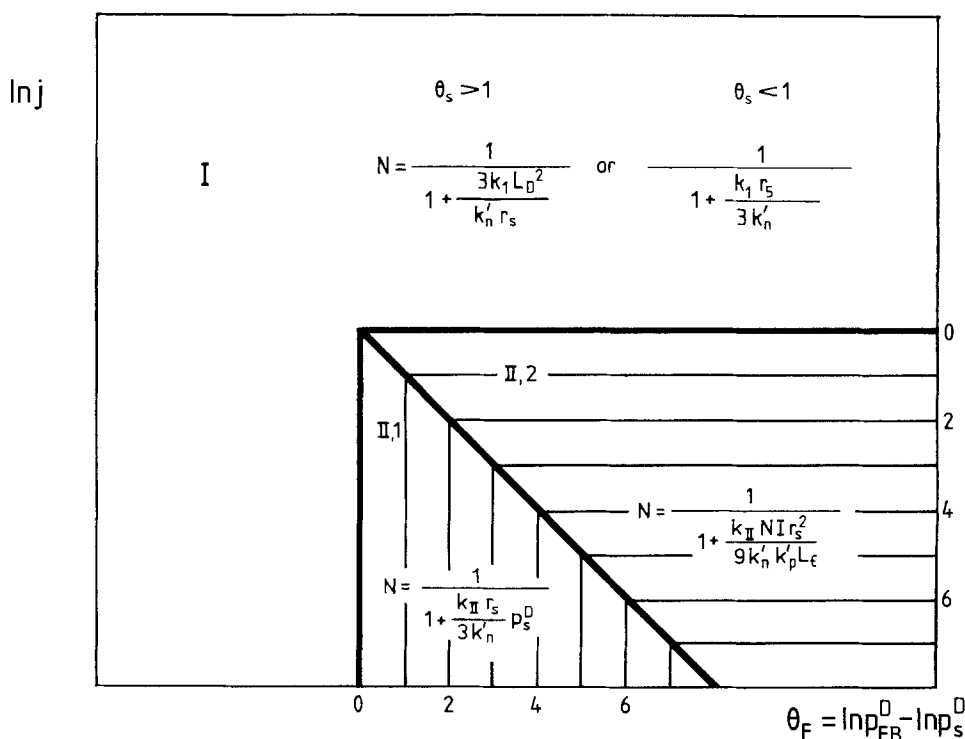


Fig. 6. Simplified kinetic case diagram for case A (Eq. [27]). The schematic contours show that N increases as one moves toward the southeast corner of the diagram.

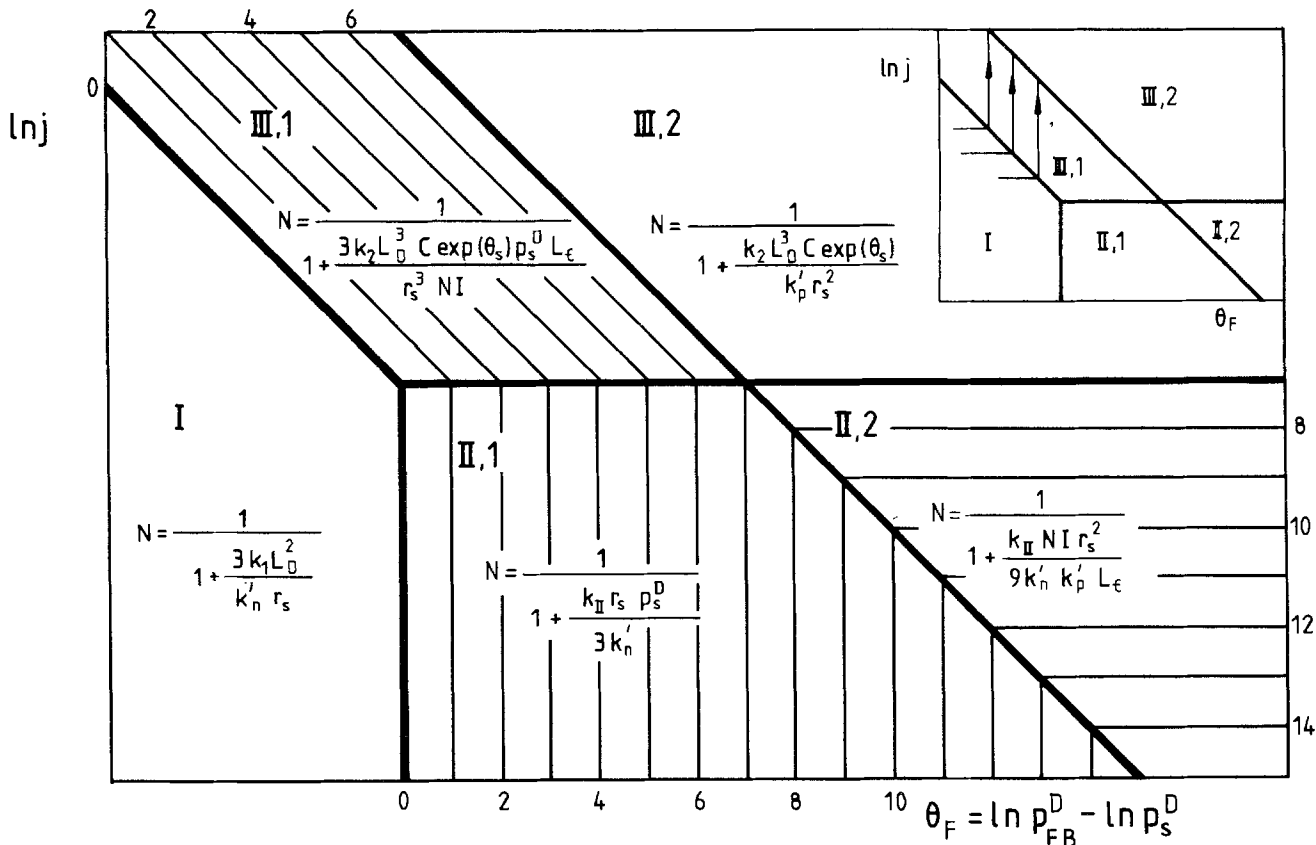
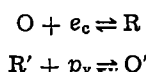


Fig. 7. Simplified kinetic case diagram for case C (Eq. [29]). The expressions given are for $\theta_s > 1$. For a field-free particle the corresponding expressions in Table I should be used for zones I and III. The inset shows how for small values of N , any system will pass rapidly through the III, I zone as the irradiance or θ_F is increased.

irradiance (I), the surface rate constants and their relevant concentrations (k_n' and k_p'), and the concentration of holes in the dark (p_s^D) should enable this to be done.

Solar Energy Conversion Efficiency

While N measures the efficiency of converting the flux of photons to a flux of chemical products, the power conversion efficiency also depends on the difference in free energy of the two products being produced. (For photogalvanic cells the equivalent quantities are current and voltage.) We are interested in this paper in the efficiency of the semiconductor particles, and we will ignore problems that occur after the production of the species in the electrolyte solution, such as concentration polarization or losses by homogeneous back reactions. In this paper we are not concerned with how the products are used. To find the power conversion efficiency, we therefore consider the following artificial system containing two redox couples, one of which reacts with the electrons in the conduction band, and the other of which reacts with the holes in the valence band



We also assume that the back reaction of R is negligible. To tap the energy we then further postulate that we have two wonderful selective electrodes, one of which, X , is reversible to the O/R couple and the other, Y , to the O'/R' couple. It is interesting that we also have to assume that the reaction between R and O' is negligibly slow. If this reaction does take place then there will be efficient recombination in the electrolyte and no current; this situation is the analog of using an unselective metallic electrode in a photogalvanic cell where recombination takes place in the electrode. Now the power produced per unit area of parti-

cle by such an arrangement will be given by the product of the flux (j) and the difference in the electrode potential of the two couples. This difference can conveniently be plotted as a Fermi level in the usual energy diagram, as shown in Fig. 8. In order to prevent the back injection of electrons into the conduction band, we have sacrificed a few kT in the position of the O/R couple. As shown, the O'/R' couple and the electrode Y play the same part in this system as the ohmic contact at the back of a macroscopic semiconductor electrode. It is this couple which determines p_s^D and θ_F . It can be seen that the further E_F' lies above the edge of the valence band, the lower p_s^D is but the more energy is lost. In the case of the macroscopic semiconductor this energy is lost in the semiconductor as the photogenerated carriers are separated by the field. In the case of the particle the free energy is lost in the irreversibility of the $R' \rightarrow O'$ reaction. It must be remembered that the position of the Fermi level for the O'/R' couple includes the $(RT/F) \ln ([O']/[R'])$ term, which arises from the entropy of mixing in the electrolyte solution. This discussion suggests that to obtain the largest possible voltage ΔE , one should locate E_F' so that $\theta_F = \theta_s$. This minimizes the voltage loss but maintains the field throughout the particle. However, as shown in Fig. 6 and 7, in certain cases N is increased if one lowers p_s^D or increases θ_F . The optimum power will be obtained by sacrificing voltage to obtain the maximum current.

We define the power conversion efficiency (γ) for monochromatic light of an energy that matches the bandgap as

$$\gamma = N(1 - \theta_F/\theta_{BG}) \tag{32}$$

where θ_{BG} describes the energy of the bandgap. The optimum value for a device for solar energy conversion (10) is

$$\theta_{BG} = 60 \tag{33}$$

which corresponds to a bandgap of 1.5 eV.

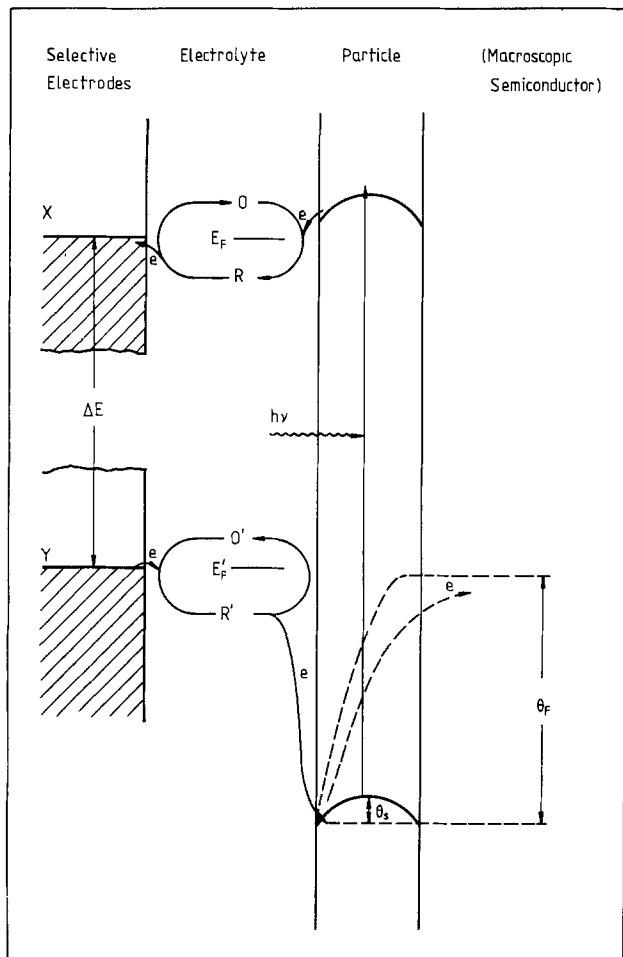


Fig. 8. Diagram showing the conversion of solar energy into electrical energy for a particle and for a macroscopic semiconductor (broken lines). The energy loss is given by θ_F in both cases; in the macroscopic semiconductor this occurs in the bulk of the semiconductor material, while in the case of the particle it occurs at the particle electrolyte interface.

Three Different Strategies for Efficient Conversion

With these considerations, three possible strategies emerge. Optimized devices can be found for cases I, II, 1, and III, 1 in Fig. 6 and 7. We need not consider cases II, 2, and III, 2, because for these cases increasing θ_F will not increase the collection efficiency, but will decrease $(\theta_{BC} - \theta_F)$ and hence γ .

We now discuss each strategy in turn. First we consider the situation where k_n' is large and the photo-generated minority carriers are removed rapidly from the particle. The low value of n then means that the kinetics are case I. Recombination inside the particle is not affected by the concentration of majority carriers. We assume that this concentration is relatively unperturbed from its value in the dark and is given by p_s^D . As discussed above, we can then set p_s^D so that

$$\theta_F = \theta_s = \frac{1}{6} (\tau_s/L_D)^2 = \frac{1}{6} \rho^2 \quad [34]$$

We would like θ_F to be as small as possible. This is achieved with a small value of ρ . The expression for N can be written

$$N = \frac{1}{1 + 3 \frac{k_1 L_D}{k_n' \rho}} \quad [35]$$

The kinetic ratio is smaller the larger the value of ρ . Hence there is an optimum value of ρ , and one does not want a field-free particle.

Substitution from Eq. [33], [34], and [35] in [32] followed by differentiation allows one to find for different values of $(k_1 L_D/k_n')$ these optimum values for ρ together with the corresponding values of N , γ , and θ_F . The results are plotted in Fig. 9. The insets show how, for any particular value of $(k_1 L_D/k_n')$, γ varies with ρ , or, in other words, how critical it is to match the radius of the particle to the Debye length. In the main part of the diagram the broken lines show the values of ρ where γ is 80% of its maximum value. From the results in Fig. 9, we can conclude that, even with the optimum choices of τ_s/L_D and of θ_F , the device will be hopelessly inefficient unless

$$k_n' > k_1 L_D \quad [36]$$

Systems that meet this condition do not require very precise matching of τ_s to L_D ; it is sufficient for the radius to be smaller than 8 times the Debye length.

It is also necessary to remove the holes from the particle, and this requires for $N \approx 1$ that

$$k_p' > J/p_s^D \quad [37]$$

where J is defined in Eq. [2]. If this condition is violated the concentration of holes will build up at the center of the particle. With the condition that $\theta_F = \theta_s$, the center of the particle is close to being field free, and so a significant increase in the concentration of holes will lead to the particle's becoming metallic. In Eq. [37] we can therefore write

$$p_s^D \approx p_{FB}^D \exp(-\theta_F) \quad [38]$$

giving

$$k_p' > J \exp(\theta_F)/p_{FB}^D \quad [39]$$

Turning next to case II, 1, the expression for N from Table I is

$$N = \frac{1}{1 + \frac{1}{3} k_{II} L_D p_{FB}^D \rho_s \exp\left(-\frac{1}{6} \rho_s^2\right) / k_n'} \quad [40]$$

The k_{II} term can be reduced to insignificance ($N \approx 1$) by increasing ρ_s in the exponential term. However, increasing ρ_s increases θ_F , and so once again there is an optimum value of ρ_s . Results for the optimum values of ρ_s , N , γ , θ_F , and k_p' are shown in Fig. 10. Again the insets show how γ varies with ρ_s . The condition for k_p' is the same as that for the strategy given in Eq. [39]. This condition is the same as the boundary between cases II, 1 and II, 2, and makes certain that the system has not crossed this boundary. Turning to k_n' , we find that for $N = 1$

$$k_1 L_D > k_n' > k_{II} J/k_2 \quad [41]$$

The first part of this condition means that N in case I is < 1 and that it is necessary to cross from I into II, 1 to increase N , even though this will reduce γ by reducing $(\theta_{BC} - \theta_F)$. The second part of this condition ensures that the system lies below the horizontal lines in Fig. 6 and 7 and so will cross from case I into case II, 1.

Returning to Fig. 10, it can be seen that in case II, 1, values of θ_F can usually be found which maintain N and γ close to unity. However, a large value of θ_F may violate the condition for k_p' in Eq. [39]. The results in Fig. 10 show that

$$\theta_F \approx \ln(k_{II} L_D p_{FB}^D/k_n') \quad [42]$$

since this is the value required to reduce the k_{II} term in Eq. [40] to insignificance. Substitution of this value in Eq. [39] gives

$$k_p' k_n' > k_{II} J L_D \quad [43]$$

For a successful II, 1 device we require k_n' to satisfy the conditions in Eq. [41] and k_p' to satisfy Eq. [43].

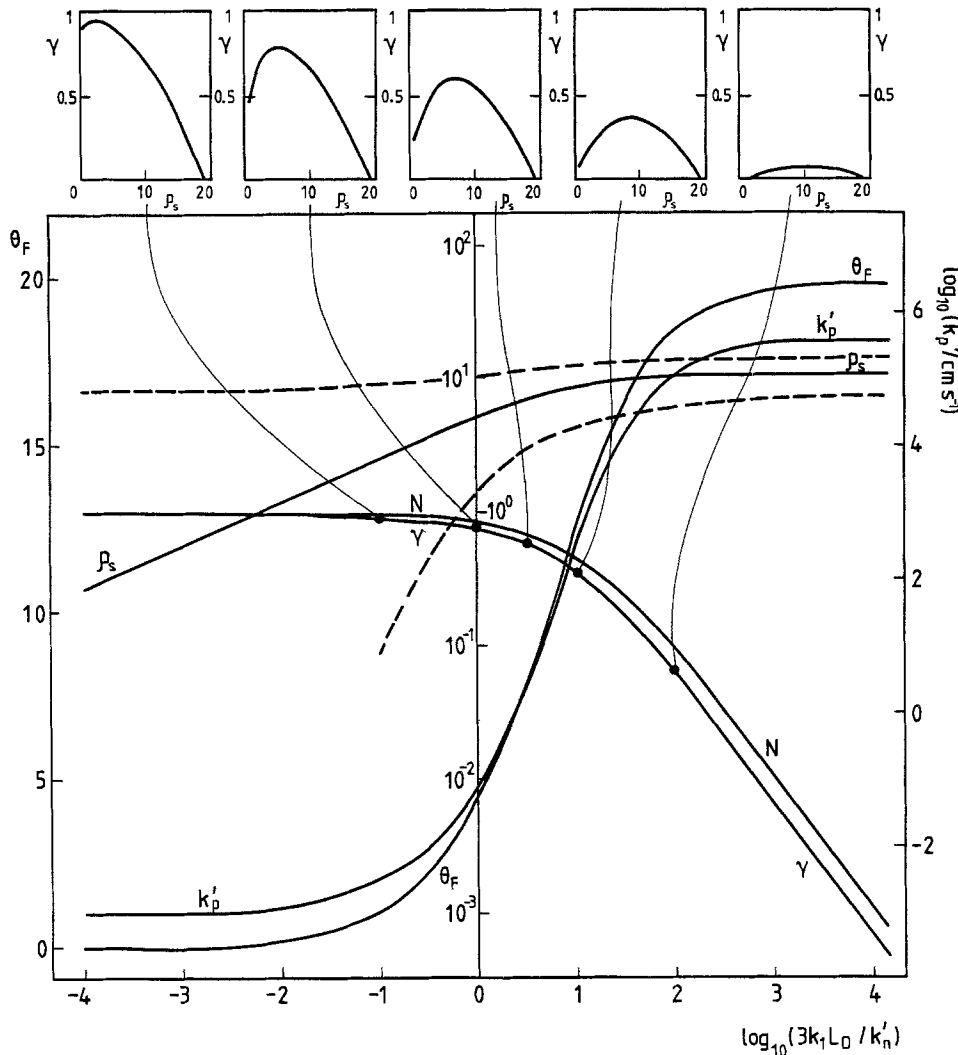


Fig. 9. The conditions for the optimum power production for case I. The diagram shows how the optimum values of N , γ , ρ_s , and θ_F depend upon the case I kinetic parameter ($3 k_1 L_D/k_n'$); k_p' must be greater than the values shown. The insets at each particular value of ($3 k_1 L_D/k_n'$) show how γ , the power conversion efficiency, varies with ρ_s ($= r_s/L_D$). The broken lines show the values of ρ_s , for which γ is 80% of its maximum value.

Furthermore, there has to be a fairly precise matching of the radius of the particle to the Debye length, as shown in Fig. 10.

Finally, for case III, 1 from the results in Table I, we find that with the field

$$N = 1 - \frac{3 C k_2 L_\epsilon \exp\left(\frac{1}{6} \rho_s^2\right) p_s^D}{\rho_s^3 I} \quad [44]$$

Differentiation shows that the kinetic term is minimized with

$$\rho_s = 3 \quad [45]$$

giving a similar result to that for the field-free particle. For this case, as discussed above, we want small particles with θ_s close to unity so as to prevent accumulation and loss of the holes in the center of the particle. The kinetic term is further reduced by reducing p_s^D , but this also increases θ_F . Substitution of Eq. [12], [44], and [45] in Eq. [32] for γ and differentiation shows that the optimum value is

$$p_s^D \simeq \frac{9I}{C \theta_{BG} e^{1.5} k_2 L_\epsilon} \quad [46]$$

giving

$$\gamma \simeq (1 - \theta_F/\theta_{BG}) \quad [47]$$

and

$$\theta_F = \ln [p_{FB}^D / (p_s^D)_m] \quad [48]$$

For these conditions to be possible and for the system to be in case III, 1 we require

$$k_p' > C \theta_{BG} e^{1.5} k_2 L_D/9 \quad [49]$$

$$k_n' < k_{II} J/K_2 \quad [50]$$

and

$$k_n' < C \theta_{BG} e^{1.5} L_D/9 \quad [51]$$

Equations [49], [50], and [51] refer to the III, 2, II, 1, and I boundaries of zone III, 1 in Fig. 7, respectively. A further condition for k_n' is that it must be large enough to prevent a buildup of electrons comparable to the doping density

$$k_n' > J/p_{FB}^D \quad [52]$$

Inspection of the conditions in Eq. [36]-[52] for the three different strategies shows that there are the three characteristic parameters of the system, as given in Table II. To simplify, we have assumed that $k_1 = k_2$. Typical values for each parameter are also given. We can now combine the conditions in Eq. [36]-[52] in a single diagram (Fig. 11), which shows how the strategy to be followed depends upon the vital kinetic parameters k_n' and k_p' .

It is not surprising that case I requires a large value of k_n' ($\sim 10^4 \text{ cm s}^{-1}$) to remove the minority carriers and has a much less severe condition for k_p' . Conversely, case III, 1 requires a large value of k_p' to remove the holes but a much less severe condition for k_n' . The intermediate case II, 1, where recombination is prevented by removing both holes and electrons, has a mixed condition involving both k_n' and k_p' . Figure 11 shows that for efficient conversion at least one of the rate constants k_n' or k_p' has to be rather large ($\sim 10^4 \text{ cm s}^{-1}$) in order to remove the carriers from the particle and thereby prevent recombination in the almost field-free particle. The value of θ_F required for optimization for an efficient device increase from case I ($\theta_F \sim 0$) through case II, 1 (Fig. 10) to case III (Eq.

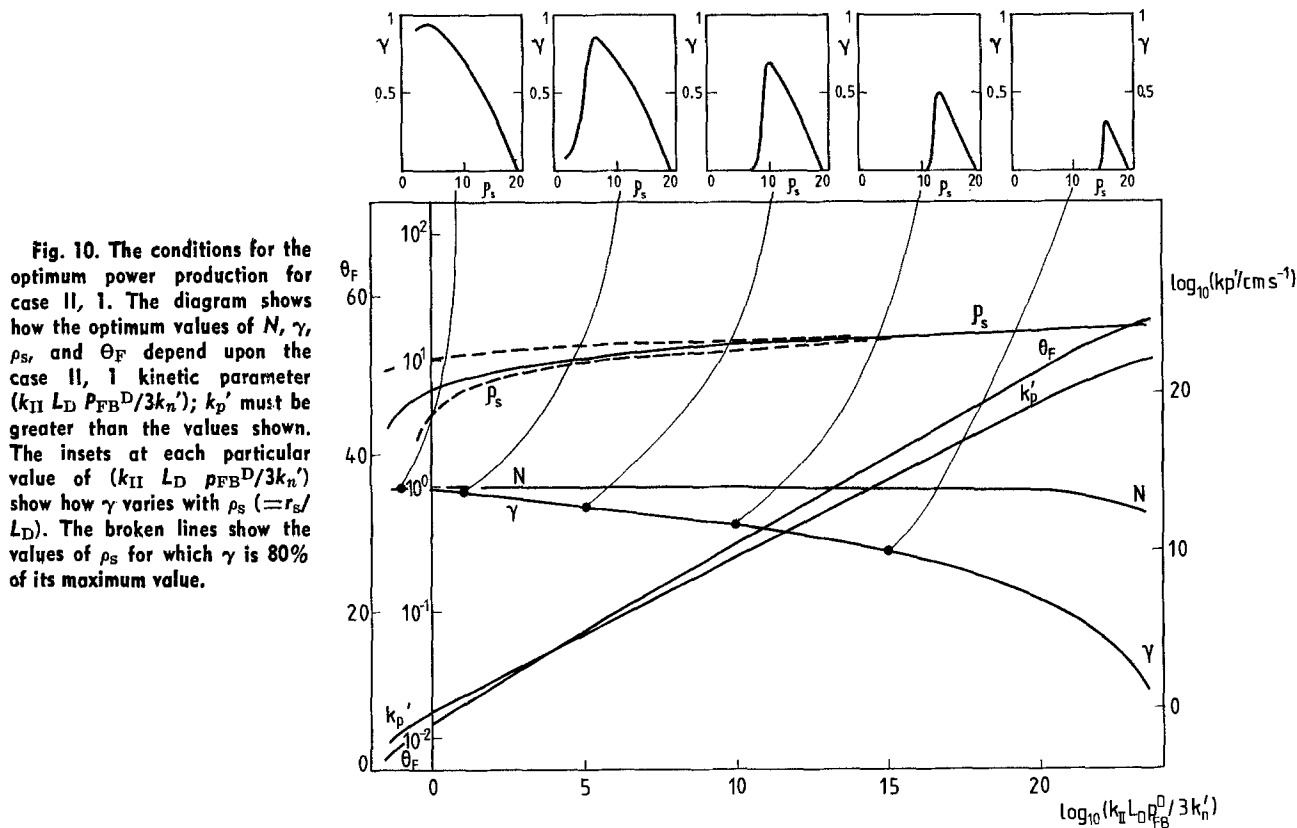


Fig. 10. The conditions for the optimum power production for case II, 1. The diagram shows how the optimum values of N , γ , ρ_{sr} and θ_F depend upon the case II, 1 kinetic parameter ($k_{II} L_D p_{FB}^D / 3k_n'$); k_p' must be greater than the values shown. The insets at each particular value of ($k_{II} L_D p_{FB}^D / 3k_n'$) show how γ varies with $\rho_s (=r_s/L_D)$. The broken lines show the values of ρ_s for which γ is 80% of its maximum value.

[48]). In particular, for case III using the values in Table II we find that $\theta_F \approx 20$ or a third of the value of θ_{BC} . For this reason the natural strategy of removing the minority carriers rapidly (I) is to be preferred to strategy III, where the majority carriers are allowed to accumulate. In the latter case it would be better to change the doping type (n to p or p to n) of the semiconductor and hence convert a case III situation to a case I. Finally, our work shows the importance of matching the radius of the particle to the Debye length. For nearly all of the optimum cases the radius should be a few multiples of the Debye length.

Acknowledgments

We thank the 1851 Commissioners for a Research Fellowship for P.N.B. This is a contribution from the Oxford Imperial Energy Group.

Manuscript submitted Feb. 24, 1983; revised manuscript received Sept. 6, 1983.

APPENDIX

In this Appendix we derive the results in Table I. We start by deriving expressions for the surface concentration n_s and p_s by eliminating j between Eq. [2], [3], and [5]

$$n_s = \frac{1}{3} gr_s N / k_n' \quad [\text{A-1}]$$

and

$$p_s = p_s^D + \frac{1}{3} gr_s N / k_p' \quad [\text{A-2}]$$

Table II. The three parameters in Eq. [36]-[52]

Parameter	Typical value
$k_1 L_D \sim k_2 L_D$	$10^4 \text{ cm s}^{-1} \text{ a}$
$k_{II} J / k_2$	$10^{-1} \text{ cm s}^{-1} \text{ b}$
J / p_{FB}^D	$10^{-3} \text{ cm s}^{-1} \text{ c}$

^a $k_1 \approx 10^{10} \text{ s}^{-1}$ $L_D \sim 10^{-6} \text{ cm}$.
^b $J = 1/3 I (r_s / L_D) I \sim 10^{-7} \text{ mol cm}^{-2} \text{ s}^{-1}$ (10).
 $r_s \sim 3 \times 10^{-7} \text{ cm}$ $L_D \sim 10^{-4}$ giving $J = 10^{-10} \text{ mol cm}^{-2} \text{ s}^{-1}$; $k_{II} / k_2 \sim 10^9 \text{ mol}^{-1} \text{ cm}^3$ corresponding to a shift from term I to term III in Eq. [16] at $p \sim 10^{-9} \text{ mol cm}^{-3}$.
^c Value of J as in note b with $p_{FB}^D \sim 10^{-7} \text{ mol dm}^{-3}$.

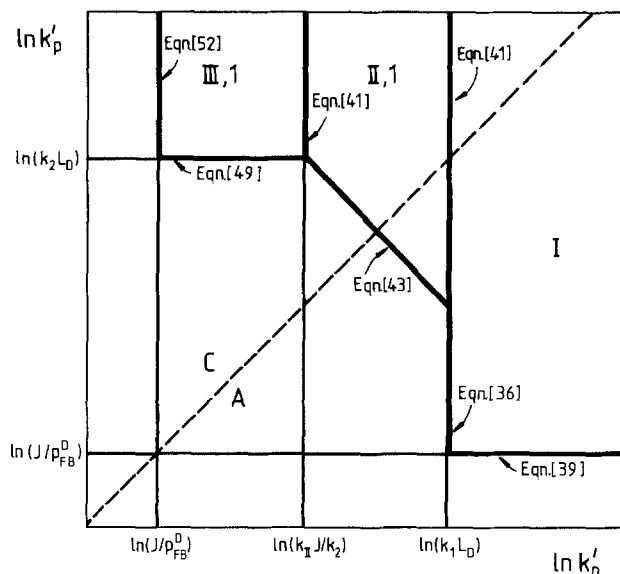


Fig. 11. Diagram showing how the three different optimum strategies depend upon the values of the surface rate constants k_p' and k_n' . For simplicity we have assumed that $k_1 = k_2$. Efficient systems are found towards the northeast corner. The broken line separates case A systems from case C.

For each of the cases in Table I we have to evaluate the integral κ where

$$\kappa = \int_0^{r_s} r^2 v dr \quad [\text{A-3}]$$

and v is given by Eq. [16].

For case I

$$v = k_1 n = k_1 n_s \exp(\theta - \theta_s) \quad [\text{A-4}]$$

where from Eq. [9]

$$\exp(\theta) = \exp(\rho^2/6) = \exp(\lambda^2) \quad [\text{A-5}]$$

Substitution from Eq. [A5] and [A4] in Eq. [A3] gives

$$\kappa = k_1 n_s L_D^3 \exp(-|\theta_s|) 6^{3/2} \int_0^{\rho_s/6^{1/2}} \lambda^2 \exp(\lambda^2) d\lambda$$

where

$$\rho_s = r_s/L_D \quad [\text{A-6}]$$

Assuming that ρ_s is significantly greater than 1, say greater than 8, for there to be significant band bending ($\theta_s > 10$), then we can integrate by parts

$$\begin{aligned} 6^{1/2} \int_0^{\rho_s/6^{1/2}} \lambda^2 \exp(\lambda^2) d\lambda &= \frac{1}{2} \rho_s \exp(\theta_s) \\ &- \frac{1}{2} 6^{1/2} \int_0^{\rho_s/6^{1/2}} \exp(\lambda^2) d\lambda \\ &\simeq \frac{1}{2} \rho_s \exp(\theta_s) \end{aligned}$$

because the second integral is negligible compared to the original integral. Substitution in Eq. [4]-[6] gives

$$\kappa = 3 k_1 n_s r_s L_D^2 \quad [\text{A-7}]$$

Elimination of n_s and κ between Eq. [A-1], [A-7], and [19] gives the result for N in Table I. For n_s itself we obtain

$$n_s = \frac{\frac{1}{3} \rho_s^2 g}{3 k_1 + \rho_s k_{\pi}'/L_D} \quad [\text{A-8}]$$

For case II throughout the sphere

$$v = k_{II} n_s p_s$$

so that

$$\kappa = \frac{1}{3} k_{II} n_s p_s r_s^3 \quad [\text{A-9}]$$

Elimination of n_s , p_s , and κ between Eq. [A-1], [A-2], [A-9], and [19] gives the result for N in Table I.

For case II

$$v = k_2 p = k_2 p_s \exp(\theta_s - \theta) \quad [\text{A-10}]$$

Substitution from Eq. [A-5] and [A-10] in Eq. [A-3] gives

$$\begin{aligned} \kappa &= k_2 p_s L_D^3 \exp(\theta_s) 6^{3/2} \int_0^{\rho_s/6^{1/2}} \lambda^2 \exp(-\lambda^2) d\lambda \\ &\simeq C k_2 p_s L_D^3 \exp(\theta_s) \end{aligned} \quad [\text{A-11}]$$

where

$$C = (3/2) (6\pi)^{1/2} = 6.51$$

and we have assumed that $\rho_s/6^{1/2}$ is greater than 4.

Elimination of p_s and κ between Eq. [A-2], [A-11], and [19] gives the result for N in Table I. The result for p_s is

$$p_s = \frac{p_s^D + \frac{1}{3} g p_s L_D k_p'}{1 + C k_2 L_D \exp(\theta_s)/k_p' \rho_s^2} \quad [\text{A-12}]$$

For the I/III case we follow the approach of Sah *et al.* (11). From Eq. [16]

$$\frac{1}{v} = \frac{1}{k_1 n} + \frac{1}{k_2 p}$$

and there is some value of θ , θ_* ($0 < \theta_* < \theta_s$) where

$$k_1 n_* = k_2 p_* = k_0 \quad [\text{A-13}]$$

Then

$$v = \frac{1}{2} k_0 \operatorname{sech}(\theta - \theta_*) \quad [\text{A-14}]$$

and has its maximum value at $\theta = \theta_*$.

From Eq. [A-3] and [A-14]

$$\begin{aligned} \kappa &= 3(3/2)^{1/2} k_0 L_D^3 \int_0^{\theta_s} \theta^{1/2} \operatorname{sech}(\theta - \theta_*) d\theta \\ &\simeq 3(3/2)^{1/2} k_0 L_D^3 \theta_*^{1/2} \int_{-\infty}^{+\infty} \operatorname{sech}(\lambda) d\lambda \\ &= (3\pi/2) k_0 r_s L_D^2 \end{aligned} \quad [\text{A-15}]$$

where

$$r_s/L_D = (\theta_*/6)^{1/2} \quad [\text{A-16}]$$

Applying the Boltzmann distribution to Eq. [A13]

$$\exp(\theta_* - \theta_s) = (k_2 p_s/k_1 n_s)^{1/2} \quad [\text{A-17}]$$

and

$$k_0 = (k_1 k_2 p_s n_s)^{1/2} \quad [\text{A18}]$$

Elimination of p_s , n_s , k_0 , and κ between Eq. [A-1], [A-2], [A-15], [A-18], and [19] gives the results for N in Table I.

The expression for r_s in Table I is derived by substituting from Eq. [A-1], [A-2], and [A-17] into Eq. [A-15].

REFERENCES

1. K. Kalyanasundaram, E. Borgarello, and M. Grätzel, *Helv. Chim. Acta*, **64**, 362 (1981).
2. D. Duonghong, J. Ramsden, and M. Grätzel, *J. Am. Chem. Soc.*, **104**, 2977 (1982).
3. S. N. Frank and A. J. Bard, *J. Phys. Chem.*, **81**, 1484 (1977).
4. I. Izumi, F. F. Fan, and A. J. Bard, *ibid.*, **85**, 218 (1981).
5. M. Grätzel and A. J. Frank, *ibid.*, **86**, 2964 (1982).
6. W. J. Albery and P. N. Bartlett, *This Journal*, To be published.
7. W. Shockley and W. T. Read, *Phys. Rev.*, **87**, 835 (1952).
8. R. N. Hall, *ibid.*, **87**, 387 (1952).
9. W. J. Albery, P. N. Bartlett, A. Hamnett, and M. P. Dare-Edwards, *This Journal*, **128**, 1492 (1981).
10. M. D. Archer, *J. Appl. Electrochem.*, **5**, 17 (1975).
11. C.-T. Sah, R. N. Noyce, and W. Shockley, *Proc. IRE*, **45**, 1228 (1957).

Mechanisms of Charge Transfer at the Semiconductor-Electrolyte Interface

I. Kinetics of Electroreduction at Dark of $\text{Fe}(\text{CN})_6^{3-}$ and IrCl_6^{2-} in Aqueous Solution on a Sintered Nb-doped n-SrTiO₃ Electrode: Influence of pH

P. Salvador

Instituto de Catálisis y Petroleoquímica, C.S.I.C., Serrano, 119, Madrid (6), Spain

C. Gutiérrez

Instituto de Química-Física "Rocasolano," C.S.I.C., Serrano, 119, Madrid (6), Spain

ABSTRACT

The dark cathodic reduction of $\text{Fe}(\text{CN})_6^{3-}$ and IrCl_6^{2-} in aqueous solution on a sintered Nb-doped SrTiO₃ electrode, at acidic and basic pH, has been studied as a function of the potential and concentration of the oxidized species. With $\text{Fe}(\text{CN})_6^{3-}$, two different regions are observed. At low band bending (high current-density region), the current saturates with increasing concentration of oxidant species, and a pH-independent Tafel slope of ~ 130 mV is found. By contrast, at higher band bending (low current-density region), the current is proportional to the electrolyte concentration, and the Tafel slope increases dramatically at basic pH with respect to that at acidic pH. Ullman's model of isoenergetic electron transfer limited by transport resistance in the semiconductor depletion layer cannot account for this behavior. However, our results are compatible with the two-step kinetic model of charge transfer, involving bandgap surface states, proposed by Vandermolen *et al.* (16). At least two sets of surface states with different energies within the bandgap actively mediate charge transfer through the semiconductor electrolyte interface. Experiments with IrCl_6^{2-} show that these surface states could result from the interaction of the semiconductor surface with H^+ , OH^- , and H_2O solvent species.

Both n-TiO₂ and n-SrTiO₃ are wide-bandgap semiconductors whose behavior as photoanodes in photoelectrochemical cells for water splitting has been intensively studied. However, charge transfer at the interface is still far from being understood. Due to their strong ionic character these oxides have a high ionization potential, and consequently the overlap between the valence band and the filled levels of water molecules is negligible, which makes impossible a direct, isoenergetic transfer of electrons from the water molecules to the valence band during water photo-oxidation.

There is experimental evidence that bandgap surface states can capture holes photogenerated in the valence band (1-7). These surface states could mediate the isoenergetic transfer of electrons from the water molecules. We have recently shown (8, 9) that these surface states could involve surface hydroxyls generated by interaction of the semiconductor with the electrolyte. Both in n-TiO₂ and in n-SrTiO₃ the valence band is made up of filled O:2p orbitals, while the conduction band proceeds from the empty Ti:3d (*t_{2g}*) orbitals. At the surface, in the last atomic layer, the crystal field symmetry of the Ti⁴⁺ and O²⁻ ions is lower than in the bulk, which splits the Ti:3d and O:2p orbitals with formation of new energetic levels in the bandgap. This is supported by the cluster calculations of Kowalski *et al.* (10). Besides, both Ti⁴⁺ and O²⁻ surface ions have a great activity towards solvent OH⁻ and H⁺ ions, respectively, giving rise to different types of chemisorbed OH⁻ groups (surface states) (11), some of them with energies within the bandgap (10). These surface states have been recently used by the authors (12) in a simple model of water photo-oxidation.

Another unknown mechanism is that concerning the dark cathodic reduction of oxidized electrolyte species (13-18). The question arising is whether the transfer of electrons from the conduction band to the empty levels of the electrolyte is direct (isoenergetic) or if it is an inelastic process mediated by surface

states. The study of this process could lead to industrial applications, as the growing importance of electrocatalysis shows (19). We have shown recently (20) that dark reactions can act as back reactions during water photo-oxidation on SrTiO₃ and TiO₂ photoanodes in a photoelectrochemical cell, producing characteristic photocurrent transients responsible for an important decrease of the quantum efficiency.

Neither TiO₂ (15, 16) nor SrTiO₃ (16) follow the simple model for electron transfer from the conduction band to oxidized electrolyte species typical of other well-behaved semiconductor oxides like n-ZnO (21, 22): their Tafel slopes are higher than 60 mV, and the cathodic current tends towards a saturation value upon increasing the concentration of the oxidant. Bard *et al.* (15) were the first to invoke mediation of charge transfer by surface states in order to explain the anomalously high Tafel slopes. More recently, Vandermolen *et al.* (16) found Tafel plots with two different regions: at higher currents the Tafel slope was 60 mV and there was current saturation, while at lower currents the Tafel slope was higher than 60 mV and the current was proportional to the concentration of oxidant. They proposed a two-step kinetic model involving bandgap surface states to explain this phenomenon of current saturation, which had never before been observed in electrochemistry. Later, Ullman (23) attributed current saturation to transport resistance in the space-charge region due to the low carrier mobilities in the wide bandgap semiconductors used.

In the present work, we study the dark cathodic reduction of $\text{Fe}(\text{CN})_6^{3-}$ on a Nb-doped, sintered SrTiO₃ electrode, using as supporting electrolyte 1M Na₂SO₄ at pH 3 and 11. At smaller band bendings (*i.e.*, at higher currents) the cathodic current (*j*⁻) reaches a saturation value at increasing concentration of the oxidized species (*C_{ox}*). In this region, the Tafel slope is ~ 120 mV and pH independent. In the region of higher band bendings (*i.e.*, at lower currents), the current is proportional to the concentration of oxidant, and the Tafel slope is very sensitive to the electrolyte pH.

Key words: semiconductor, interface, electroreduction, kinetics.

These results cannot be explained by Ullman's model. However, they are compatible with the two-step mechanism proposed by Vandermolen *et al.* (16), involving mediation of charge transfer by surface states. We think that these surface states result from the interaction of the semiconductor surface with the different species (OH^- , H^+ , and H_2O) of the solvent (24), and whose energy within the bandgap depends on the pH.

These results are in agreement with our previous findings about the influence of pH on the dark electroreduction of O_2 on n-TiO₂ (18), giving further support to our previous model (8, 9), in which different OH groups covering the semiconductor surface in aqueous medium are active centers for charge transfer between the semiconductor and the electrolyte, not only in water photoelectrolysis, but also in the electroreduction at dark of dissolved oxidized species as well. Finally, we estimate some of the parameters characterizing these surface states and put forward some hypotheses about the influence of pH on their origin.

Experimental

Electrode.—The sintered SrTiO₃ electrode containing 5 weight percent (w/o) Nb₂O₅ was prepared by the Laboratoire de Chimie du Solide, Bordeaux, France, from the single oxides (25). The resistivity was 3 Ω cm, and the geometrical surface in contact with the electrolyte was ~ 0.25 cm². No chemical or mechanical pretreatment of the electrode was effected.

Materials.—All chemicals were reagent grade. The supporting electrolyte was 1M Na₂SO₄, whose pH was adjusted to 3 and 11 with H₂SO₄ and NaOH, respectively. The oxidized species were K₃Fe(CN)₆ and H₂IrCl₆, in concentrations from 10⁻³ to 10⁻¹M. Ultra-pure water was obtained from a Milli-RO+Milli-Q (Millipore, Bedford, Massachusetts) assembly; solutions were previously deoxygenated by N₂ bubbling with vigorous magnetic stirring.

Current measurement.—A simple one-compartment cell was used (18), with a smooth Pt sheet as auxiliary

electrode, and a saturated calomel electrode (SCE) as reference. The potentiostat was a Potentiostat POS 73 from Wenking. Currents were measured with a digital multimeter, Keithley 177 Microvolt DMM. Prior to experiments with each solution, the electrode was left in contact with it for 24h. Stationary currents were measured allowing 13-30 min at each polarization potential to ensure establishment of equilibrium. Fresh electrolyte was used in each measurement.

Capacitance measurement.—Tomkiewicz's method (26) was used in the range 60 Hz-10 kHz. The waveform generator was a Leader LAG-125, and the lock-in amplifier a PAR 5204.

Results

Characterization of the semiconductor; Mott-Schottky plots.—In Fig. 1 we give plots of $1/C^2$ vs. V (C = differential cell capacitance, V = polarization potential vs. SCE) in 1M Na₂SO₄, pH 11 at several frequencies. Each line is the result of a least squares fit to at least 30 points obtained at successively increasing and then decreasing potentials. The slope increased with increasing frequency, although all the lines had a common intersection point (flatband potential V_{FB}) with the abscissa axis. According to Tomkiewicz (26), if this behavior is due to electrode inhomogeneity, then the measurements at the highest frequency most accurately correspond to the space-charge layer. Therefore, in the following we only show measurements at 30 kHz, the maximum frequency we could use.

In Fig. 2 we give the Mott-Schottky plots in 1M Na₂SO₄ at pH 3 and 11. Addition of K₃Fe(CN)₆ or H₂IrCl₆ did not affect the results. Two straight lines with the same slope are obtained in the interval -0.6 to $+1V$ vs. SCE. The shift of V_{FB} with pH is of 63 mV/pH unit, the typical Nernstian behavior of oxides with H^+ and OH^- as potential determining ions (27).

From the slope of the Mott-Schottky equation

$$C_{\text{sc}}^{-2} = (2/q\epsilon\epsilon_0 N_D A^2) (V - V_{\text{FB}} - kT/q) \quad [1]$$

where C_{sc} is the differential capacitance of the semicon-

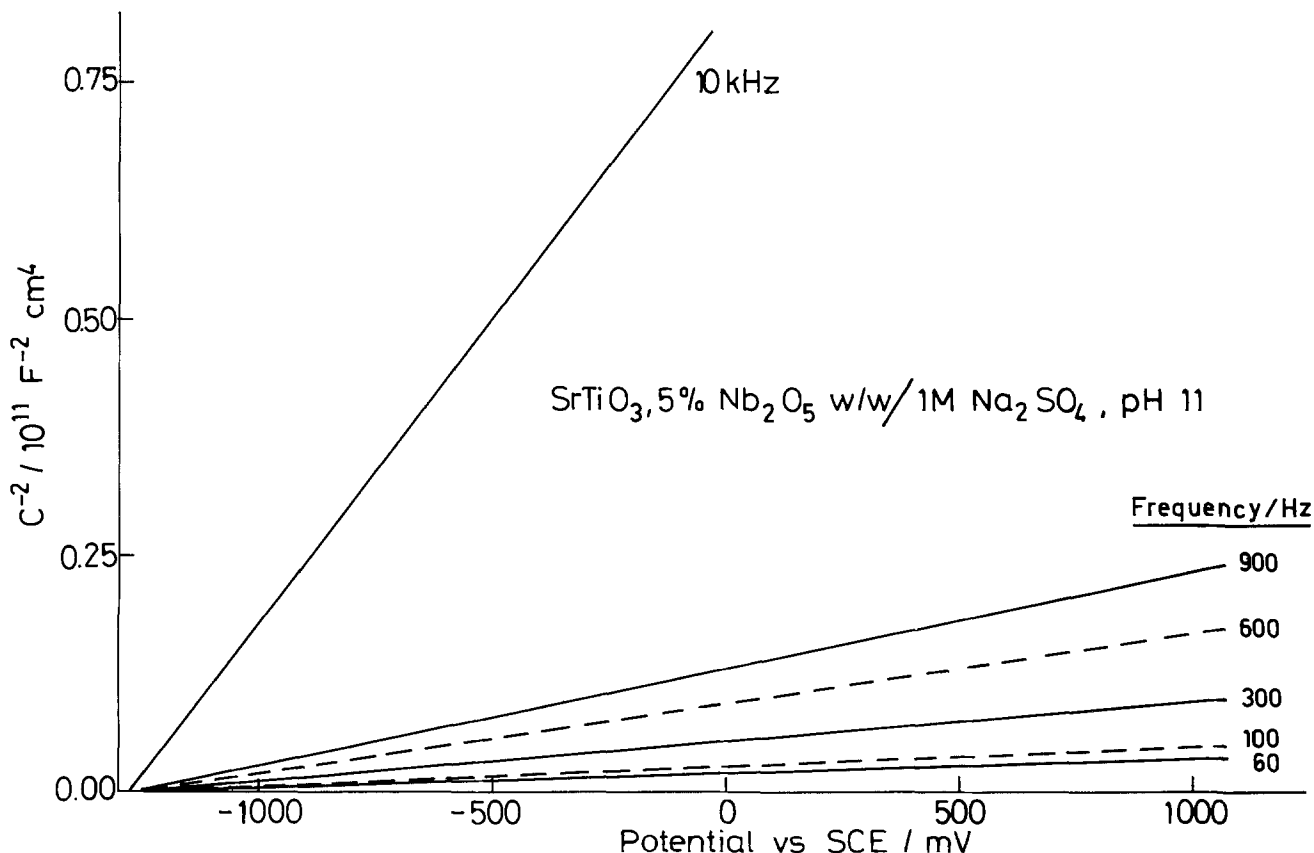


Fig. 1. Mott-Schottky plots of Nb-doped n-SrTiO₃ for several frequencies in 1M Na₂SO₄, pH 11

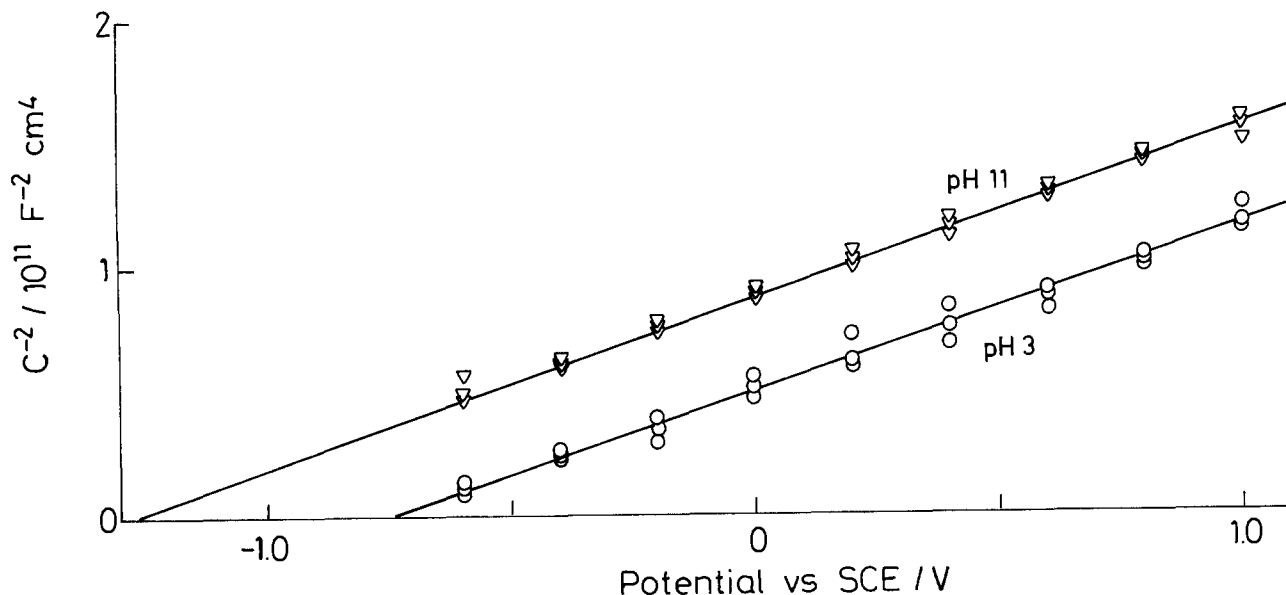


Fig. 2. Mott-Schottky plots of Nb-doped n-SrTiO₃ at 30 kHz in 1M Na₂SO₄, pH 3 and 11

ductor depletion layer, we can obtain the donor concentration N_D , provided we know the semiconductor dielectric constant (ϵ) and the true surface area in contact with the electrolyte (A). (ϵ_0 is the vacuum permittivity). Assuming $\epsilon = 300$ (28) and a roughness coefficient ~ 4 , we obtain from the experimental slope $N_D \approx 10^{19} \text{ cm}^{-3}$. For comparison, N_D can be also calculated from the conductivity σ and the mobility μ through the equation $N_D = \sigma/q\mu$, assuming that most donors are ionized at room temperature, as is the case with Nb-doped TiO₂ (29). The value of the mobility necessary to obtain the same N_D as from Mott-Schottky plots is $\sim 0.1 \text{ cm}^2 \text{ V}^{-1} \text{ s}^{-1}$, about two orders of magnitude lower than that of $6 \text{ cm}^2 \text{ V}^{-1} \text{ s}^{-1}$ measured for monocrystalline SrTiO₃ (30). This large decrease in mobility can be explained by carrier trapping at grain boundaries in the sintered material (31).

Mott-Schottky plots of highly doped semiconductors.

—For Eq. 1 to hold, it is necessary that

$$C_{sc} \ll C_H \quad [2]$$

(C_H = differential capacity of the Helmholtz layer), in which case it is

$$\phi_s \gg \Delta\phi_H \quad [3]$$

where ϕ_s and $\Delta\phi_H$ represent the potential drop in the depletion layer of the semiconductor and the change in the potential drop (ϕ_H) of the Helmholtz layer brought about by polarization, respectively. Linearity of C^{-2} vs. V plots is usually taken to mean that Eq. [2] and [3] apply to the system under study. However, de Gryse *et al.* (32) have shown that in highly doped semiconductors, as is the case here ($N_D \approx 1 \times 10^{19} \text{ cm}^{-3}$), C^{-2} vs. V plots are also linear, although Eq. [1]–[3] do not hold. According to them, under these circumstances, i.e., when the capacity of the depletion region is comparable to that of the Helmholtz layer and therefore a sizable fraction of applied potential drops in the Helmholtz layer, Eq. [1] must be substituted for with

$$C^{-2} = C_H^{-2} [1 + (2C_H^2/\epsilon\epsilon_0 A^2 q N_D) (V - V_{FB} - kT/q)] \quad [4]$$

It is remarkable that Eq. [1] and [4] predict the same slope in C^{-2} vs. V plots, although in Eq. [4] the intercept with the abscissa axis is shifted, relative to that of Eq. [1], towards more negative potentials by the amount

$$\Delta V = q\epsilon\epsilon_0 N_D / 2C_H^2 \quad [5]$$

For $C_H = 2 \times 10^{-5} \text{ F cm}^{-2}$, ΔV becomes already significant at $N_D \approx 10^{19} \text{ cm}^{-3}$.

De Gryse *et al.* (32) also obtained a formula relating $\Delta\phi_H$ to N_D

$$\Delta\phi_H = \left(\frac{2\epsilon\epsilon_0 q N_D}{C_H^2} \right)^{1/2} \left(\phi_s - \frac{kT}{q} \right)^{1/2} \quad [6]$$

This formula, together with the obvious

$$V - V_{FB} = \phi_s + \Delta\phi_H \quad [7]$$

allows us to calculate $\Delta\phi_H/\phi_s$ as a function of polarization potential. Taking $\epsilon = 300$ and $C = 2 \times 10^{-5} \text{ F cm}^{-2}$, we have obtained in this way $\Delta\phi_H$ as a function of $(V - V_{FB})$ (Fig. 3). For the first 0.8V it is $\Delta\phi_H/\phi_s \sim 1$, i.e., about half of the change in applied potential goes to the Helmholtz layer and only the other half to the depletion region

The value of V_{FB} obtained from the Mott-Schottky plot in Fig. 2 should now be corrected by $\Delta V = 0.1V$ according to Eq. [5]. Therefore, V_{FB} is $-1.15V$ at pH 11, and $-0.65V$ at pH 3, about 200 mV negative of E° (H^+/H_2), as usually found for SrTiO₃ (28).

We can now construct with the help of Fig. 3 the diagram of energy levels in Fig. 4, which shows the potential dependence of the semiconductor energy levels with respect to those of the electrolyte. This diagram will be used later on. We have taken E°_{redox} ($Fe[C�]_6^{3-}/Fe[C�]_6^{4-}$) = $+0.25V$ vs. SCE, with a reorganization energy $\lambda = 0.75V$ both at pH 3 and 11. This value of λ is that obtained from measurements on ZnO (22) in the pH range 4.8–12.0 although, according to theoretical calculations (33), λ should change from 0.63V in a strongly basic medium to 1.5V in a strongly acidic medium.

Dark cathodic reduction of $Fe(CN)_6^{3-}$.—Residual currents in the absence of oxidized species were 10^{-7} – $10^{-8}A$. At potentials negative of the H^+/H_2 redox couple, there was a large increase of cathodic current corresponding to H_2 evolution. The residual currents, when significant, were subtracted from the currents of the oxidized species.

In Fig. 5 we give a semilog plot of the reduction current density vs. potential for different concentrations of $K_3Fe(CN)_6$. As mentioned above, the true area of the electrode was taken to be 1 cm^2 . The families of curves on the left- and right-hand sides correspond to pH 11 and 3, respectively. All the current values are free from mass-transport effects, for which purpose strong agitation was needed at the highest currents.

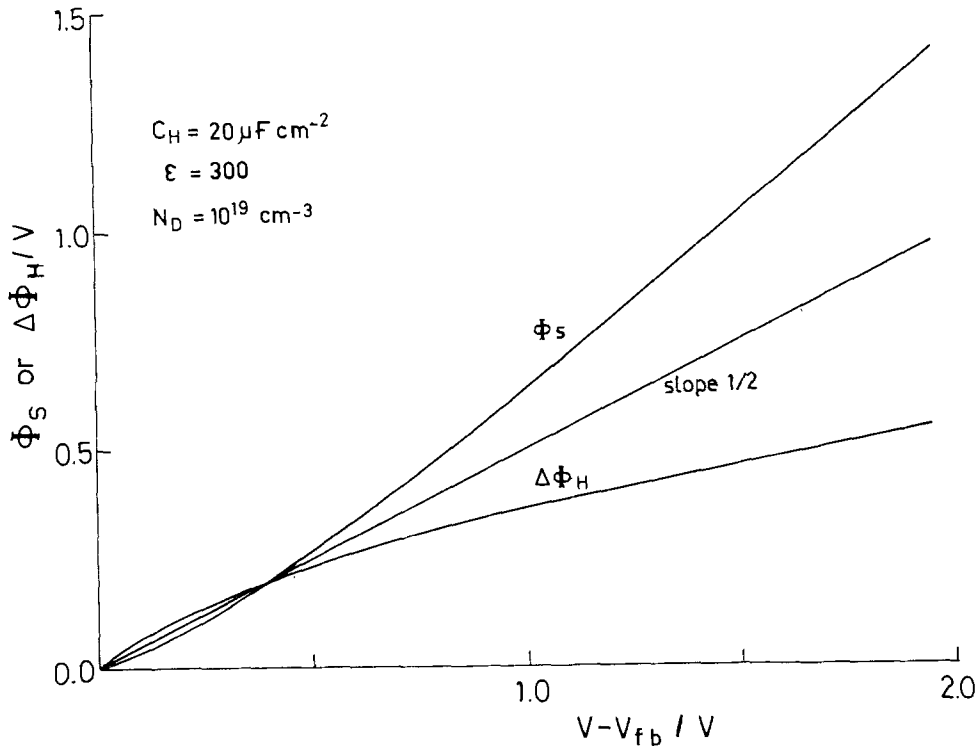


Fig. 3. Dependence of ϕ_s and $\Delta\phi_H$ on the applied polarization ($V - V_{FB}$) according to Eq. [24]. The following parameters were assumed: $\epsilon = 300$, $C_H = 20 \mu F cm^{-2}$, $N_D = 10^{19} cm^{-3}$.

Two segments can be clearly appreciated in each curve. At higher currents there is, both at pH 3 and 11, a segment with a slope of ~ 130 mV at potentials more negative than -0.1 and -0.55 V, respectively. However, at lower currents the behavior at pH 11 is very different from that at pH 3. At pH 11 there is a nearly horizontal plateau, with a slope of ~ 2.2 V, between

-0.5 and $+0.1$ V, while at pH 3 only a short segment with a slope of ~ 320 mV appears between -0.1 and $+0.1$ V. At potentials more positive than $+0.1$ V, the slope decreases drastically at the two pH values.

Dependence of the cathodic current on the concentration of $Fe(CN)_6^{3-}$.—As already found by Vandermolten *et al.* (16), at a given potential current saturation

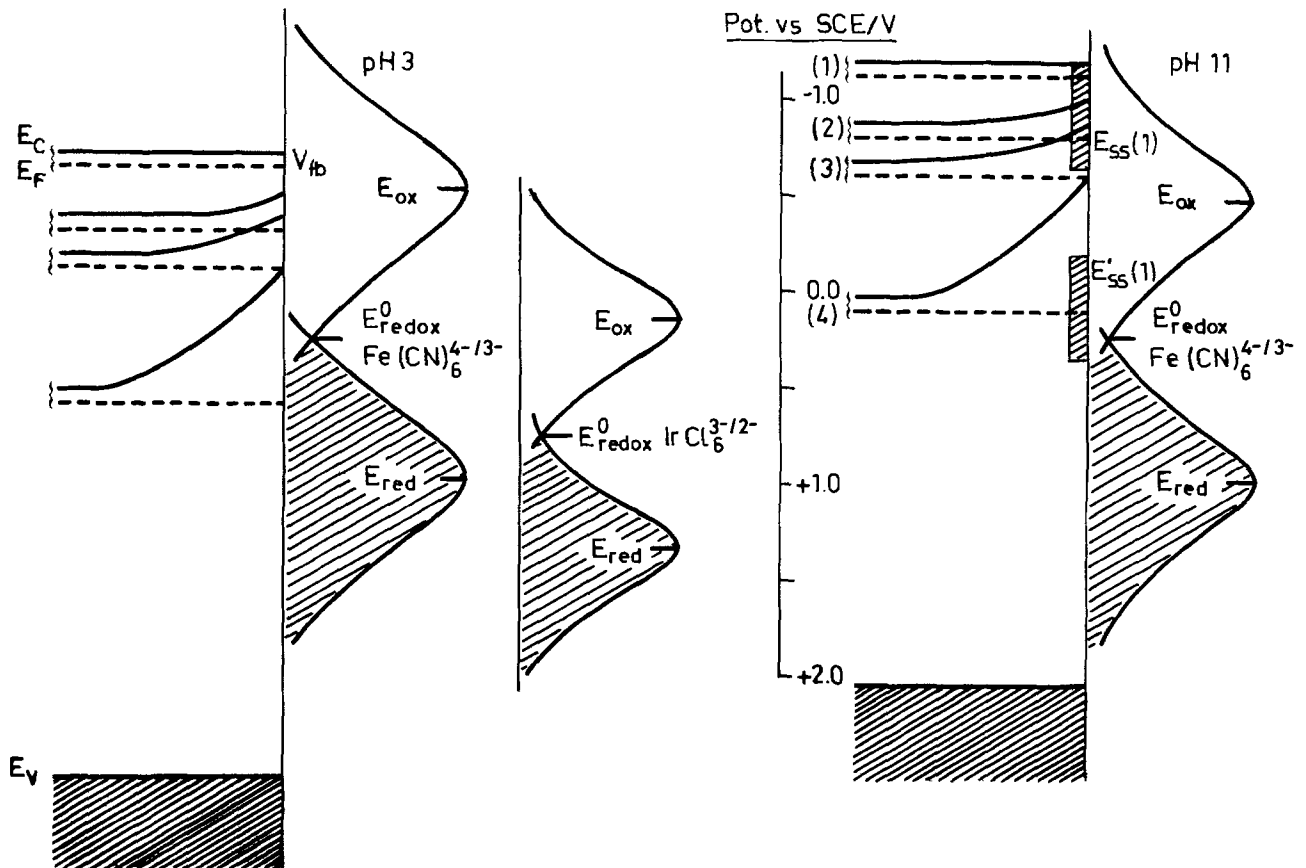


Fig. 4. Diagram of energy levels of n-Sr TiO_3 at pH 3 and 11, and of the empty and filled levels of the $Fe(CN)_6^{3-}/Fe(CN)_6^{4-}$ and $IrCl_6^{2-}/IrCl_6^{3-}$ couples. The shift of E_c (bottom of the conduction band) at the semiconductor surface with increasing positive polarization has been taken from Fig. 3. In the diagram for pH 11 the two sets of surface states have been included; their position is that at the flatband condition. The energetic distribution of the surface states is not known.

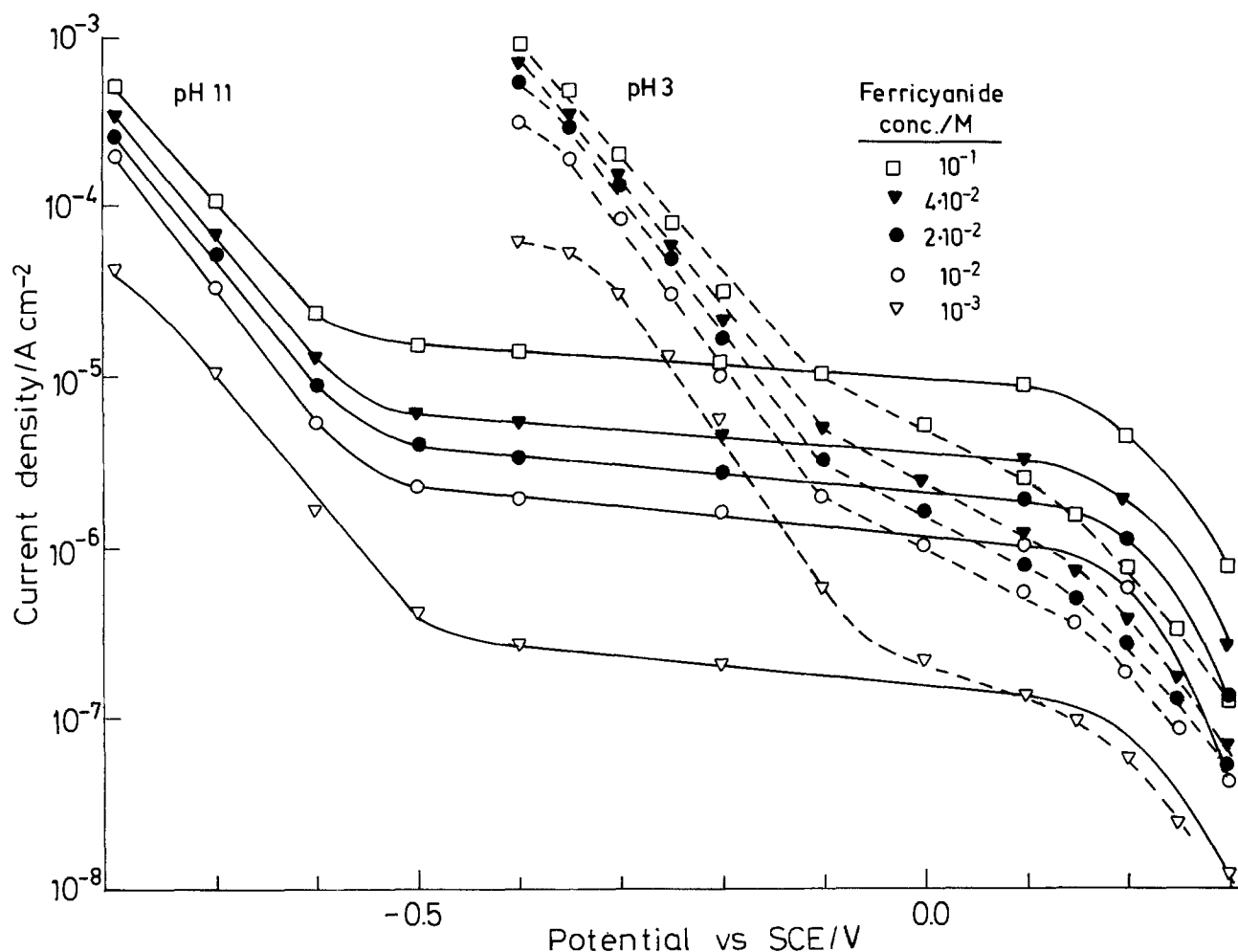


Fig. 5. Tafel plots of the log of the current density vs. potential for different concentrations of $\text{Fe}(\text{CN})_6^{3-}$, at both pH 3 and 11

tion is found only in the segment of higher currents (in our case that with a slope of 130 mV), while the normal behavior (i.e., proportionality between current and concentration) was observed only in the segment of lower currents with a higher Tafel slope.

The empirical relationship between current j^- and concentration C_{ox} in the segment of higher currents was the same found for the first time by Vandermolen *et al.* (16)

$$j^- = \frac{j^-_{\text{sat}} \cdot C_{\text{ox}}}{K + C_{\text{ox}}} \quad [8]$$

In this equation of the Langmuir type, j^-_{sat} is the saturation current reached at high enough concentrations, and K is a constant. We show in Fig. 6 typical curves of j^- vs. C_{ox} at -0.6 and -0.8 V, where the typical saturation behavior can be appreciated. We can rearrange [8] into

$$\frac{1}{j^-} = \frac{K}{j^-_{\text{sat}}} \cdot \frac{1}{C_{\text{ox}}} + \frac{1}{j^-_{\text{sat}}} \quad [9]$$

A plot of $1/j^-$ vs. $1/C_{\text{ox}}$ gives a straight line of intercept $1/j^-_{\text{sat}}$ and slope K/j^-_{sat} . These plots are included in Fig. 6.

In Fig. 7 we have plotted $\log j^-_{\text{sat}}$ vs. V . Two parallel straight lines are obtained at pH 3 and 11, respectively. Their lateral displacement shows practically the same Nernstian behavior as found for V_{FB} (Fig. 2). In the segment of lower currents, the classical proportionality between current and concentration is obeyed at the two pH values, i.e.

$$j^- = K' \cdot C_{\text{ox}} \quad [10]$$

In Fig. 8 we show such behavior at different potentials

for pH = 11. Obviously, K' increases with increasing negative potential.

Dependence of $\log j^-$ on band bending.—With the data of Fig. 3 we can now plot $\log j^-$ vs. ϕ_s , at both pH 3 and 11. The plot for 10^{-2} M $\text{Fe}(\text{CN})_6^{3-}$ is given in Fig. 9. At lower band bendings ($\phi_s < 0.3$ V) and higher currents, the same plot with a Tafel slope of ~ 65 mV is obtained at pH 3 and 11, while at higher band bendings the currents at pH 11 are considerably higher than at pH 3.

Discussion

Models for charge transfer.—Two different mechanisms could be envisaged to account for the transfer of electrons from the conduction band to empty electrolyte levels: (i) isoenergetic transfer of electrons from the bottom of the conduction band at the surface to the empty levels of the oxidized species through the Helmholtz layer at the semiconductor-electrolyte interface. In the following, this will be designated the classical model of fluctuating energy levels. (ii) Inelastic charge transfer through bandgap surface states in a two-step mechanism: filling of surface states with conduction band electrons, and further isoenergetic transfer to empty electrolyte levels (15).

The model to be used must be coherent with the experimental results, which can be summarized by two main features: the current saturation with increasing oxidant concentration in the region of higher currents (i.e., lower band bendings), where the Tafel slope is ~ 130 mV and independent of pH, and the existence of a second region with lower currents (i.e., higher band bendings) where there is proportionality between current and oxidant concentration. In this region the Tafel slope strongly depends on the pH.

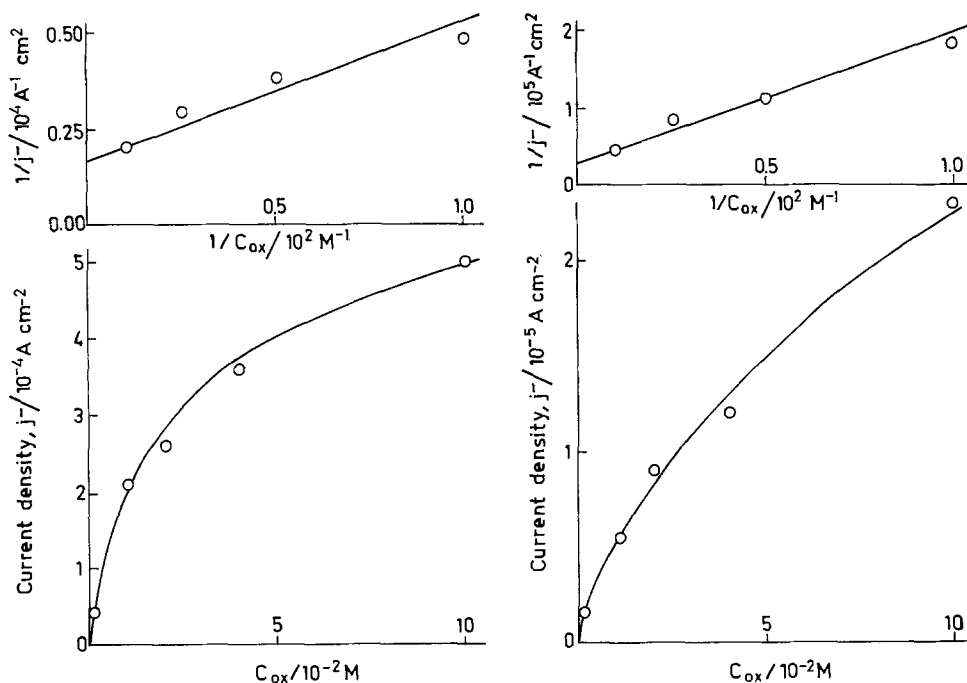


Fig. 6. Plots of the current density, j^- , vs. ferricyanide concentration, C_{ox} , at pH 11, for polarization potentials of $-0.8V$ (left) and $-0.6V$ (right) vs. SCE, which are within the saturation region, with a Tafel slope of 130 mV , in Fig. 5. The same data are also plotted as $1/j^-$ vs. $1/C_{ox}$ in order to show that they obey a Langmuir-type equation (Eq. [8]); the intersection with the vertical axis gives us j^-_{sat} .

Let us try the two models separately.

The classical model is isoenergetic charge transfer.— This model was first developed by Marcus (34) and then by Gerischer (35). Different mathematical approaches based on this fluctuating energy model have been made to find an explicit relationship between current and potential (36-39). Morrison (39) obtained the following simplified formula

$$j^- = qv\sigma_1 n_s d C_{ox} \left(\frac{kT}{\pi\lambda} \right)^{1/2} \exp \frac{-(E_{cs} - E_{ox})^2}{4\lambda kT} \quad [11]$$

In this approximation it is assumed that all ions within a distance d of the surface are active in capturing electrons and have the same capture cross section σ_1 , v is the thermal velocity of electrons in the conduction band, λ the reorganization energy, E_{cs} the bottom of the conduction band at the surface, and E_{ox} the more probable energy level of the oxidized species. n_s is the density of electrons at the surface, and depends on the band bending according to

$$n_s = n_b \cdot \exp -q\phi_s/kT \quad [12]$$

where n_b is the bulk density of conduction band electrons.

This classical model predicts that, provided E_{cs} does not change with polarization, the current is proportional both to n_s and C_{ox} , and therefore cannot give account of the observed current saturation. However, Ullman (23) has recently proposed that current limitation could be due to transport resistance in the space-charge region of low mobility materials, such as TiO_2 , $SrTiO_3$, and $\alpha-Fe_2O_3$, the only semiconductors in which this phenomenon has been observed.

The empirical Eq. [8] is also predicted by Ullman, according to whom it is

$$j^-_{sat} = (qD_n N_D/l) (e^{-\Phi}/Daw(\Phi))^{1/2} \quad [13]$$

and

$$K = D_n/k_c l Daw(\Phi)^{1/2} \quad [14]$$

where $D_n = \mu kT/q$ is the diffusion coefficient of the electrons, l is the Debye length of the space charge region

$$l = (2\epsilon\epsilon_0 kT/q^2 N_D)^{1/2} \quad [15]$$

$\Phi = q\phi_s/kT$ is the barrier height of the depletion layer in adimensional units, and $Daw(\Phi)^{1/2}$ is Daw's function, which, for $\Phi \geq 2.5$, is given with an error lower than 3% by the expression

$$Daw(\Phi)^{1/2} = (0.5 + 0.4/\Phi)(\Phi)^{1/2} \quad [16]$$

In our case, with $N_D = 1 \times 10^{19}\text{ cm}^{-3}$, $D_n = 2.5 \times 10^{-3}\text{ cm}^2\text{ s}^{-1}$ ($\mu = 0.1\text{ cm}^2\text{ V}^{-1}\text{ s}^{-1}$), and $\epsilon = 300$, for $\Phi = 11.7$ ($\phi_s = 0.3V$) the value of j^-_{sat} predicted by Eq. [13] is 0.2 A cm^{-2} , about 4 orders of magnitude higher than the experimental one (Fig. 7). Therefore, Ullman's model does not seem to fit our experimental

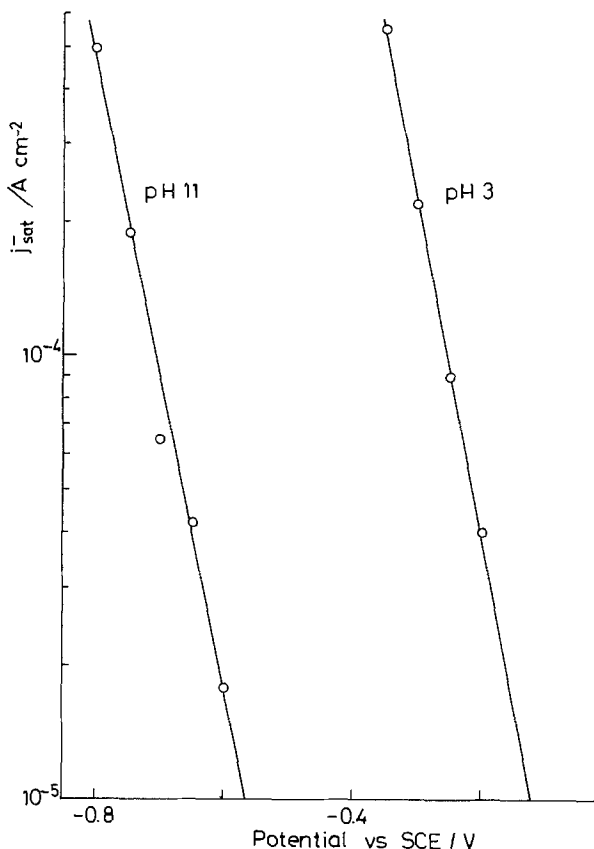
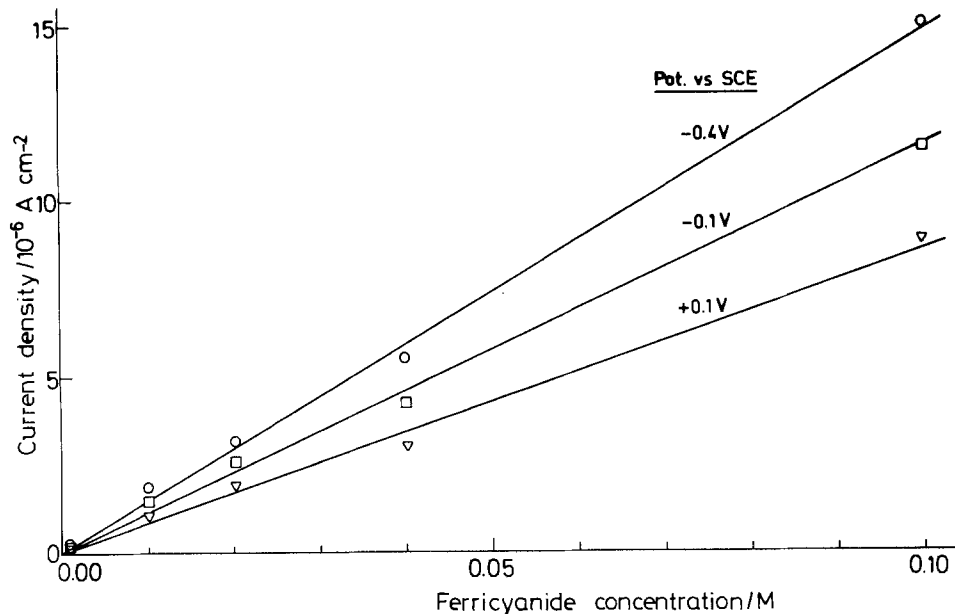


Fig. 7. Tafel plot of the saturation current density, (j^-_{sat}) vs. potential for ferricyanide, both at pH 3 and 11, taken from Fig. 6. Note the parallelism of the two straight lines with a slope of $\sim 130\text{ mV}$.

Fig. 8. Plot of current density vs. ferricyanide concentration at pH 11 in the proportionality region corresponding to the plateau in Fig. 5.



results. Furthermore, it cannot give account of the segments with high Tafel slope in the $\log j^-$ vs. V plots observed both by Vandermolen *et al.* (16) and in this paper.

The surface states trapping kinetic model.—As stated above, Bard *et al.* (15) were the first to invoke mediation of charge transfer by surface states in order

to explain anomalously high Tafel slopes. Later, Vandermolen *et al.* (16) (in the following designated as VGC) were the first to observe current saturation, which they interpreted with a two-step trapping kinetic model also involving surface states.

According to the VGC model, charge transfer is mediated by bandgap surface states overlapping empty

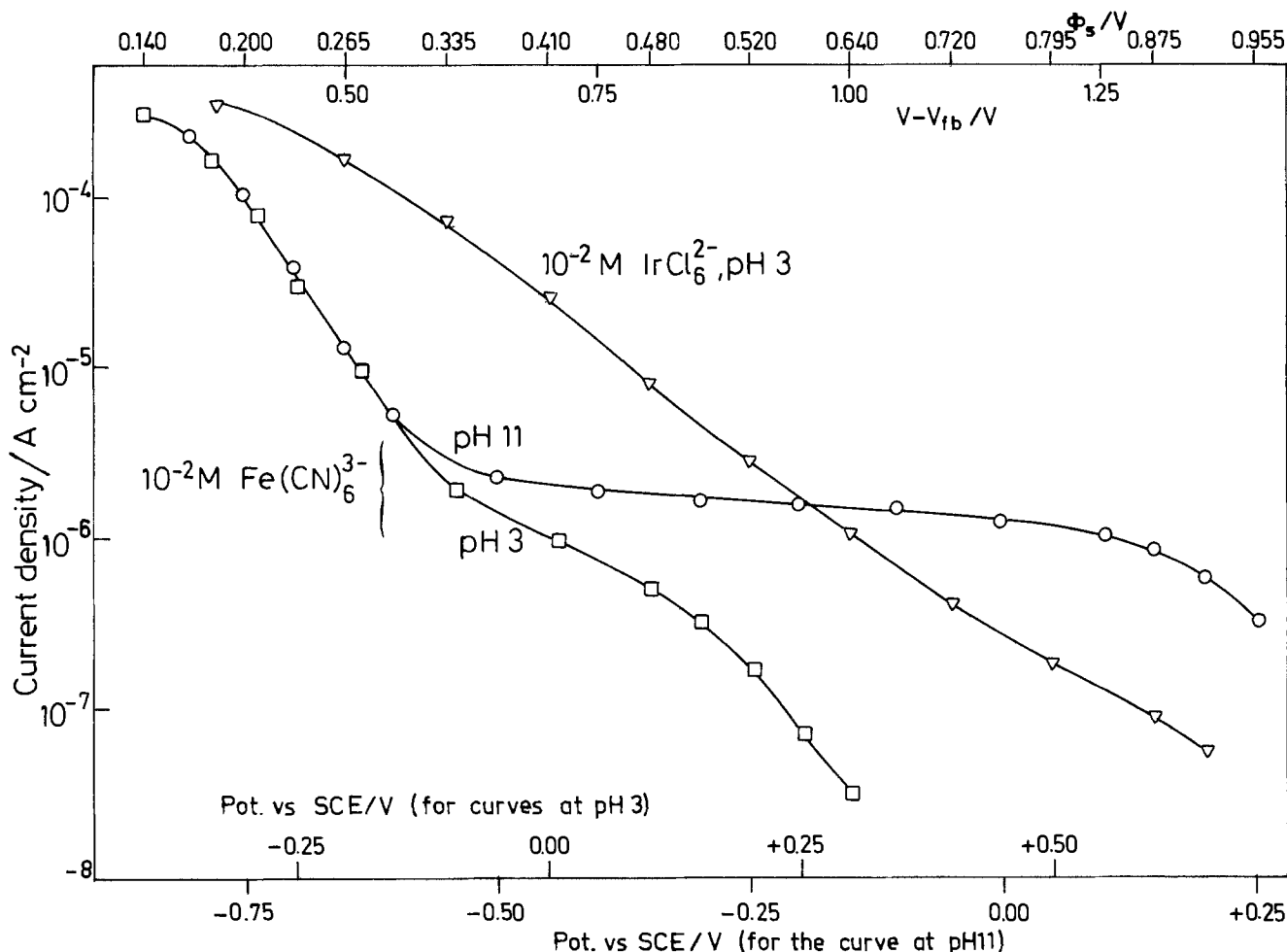


Fig. 9. Plots of current density vs. voltage for $10^{-2}\text{M Fe(CN)}_6^{3-}$ at pH 3 and 11, and for $10^{-2}\text{M IrCl}_6^{2-}$ at pH 3. Note different potential scales for pH 3 and 11; the shift of 0.45V is necessary to make the saturation region of Fe(CN)_6^{3-} at pH 3 coincide with that at pH 11. This shift corresponds to the difference between V_{FB} at pH 3 and 11, so that the three curves have the same horizontal axis of $(V - V_{\text{FB}})$, and therefore the same axis of ϕ_s . Values of $(V - V_{\text{FB}})$ and ϕ_s are given in the upper horizontal axis.

levels of the oxidized species, and therefore involves two steps: transfer of electrons from the conduction band at the surface to the surface states with a rate constant k_1 , and transfer of electrons from the surface states to the empty levels of the oxidized species with a rate constant k_2 . Assuming that the reverse rate constants are negligible, Eq. [7] of VGC (16) can be simplified to

$$j^- = -qN_{ss} \frac{k_1 n_s C_{ox}}{\frac{k_1}{k_2} n_s + C_{ox}} \quad [17]$$

From solid-state theory it is known that $k_1 = v\sigma$, where v is the mean thermal speed of conduction band electrons and σ is the electron-capture cross section of the surface states. k_2 depends on the degree of overlap of the levels of surface states with those of the oxidized species, according to the classical model.

Two limiting situations are readily apparent for the Langmuir-type Eq. [17]. At concentrations of the oxidized species high enough for the first step to be rate limiting, i.e., so high that

$$k_1 \cdot n_s \ll k_2 C_{ox} \quad [18]$$

and consequently all the surface states are practically empty, then the limiting value of the current (saturation current, j^-_{sat}) is given by

$$j^-_{sat} = -q \cdot N_{ss} \cdot k_1 \cdot n_s \quad [19]$$

where N_{ss} is the density of surface states. According to Eq. [19], the voltage dependence of the current is determined by $n_s(V)$ (Eq. [12]), which means that the value of the Tafel slope depends on whether all of the applied voltage changes drop in the semiconductor depletion layer (Tafel slope = 60 mV) or drop partially in the Helmholtz layer (Tafel slope > 60 mV).

The other limiting situation obtains when

$$k_1 n_s \gg k_2 C_{ox} \quad [20]$$

Then the transfer of electrons from the surface states to the electrolyte is rate limiting, and all the surface states are practically filled at the steady state. Under these conditions, the current is proportional to the concentration of oxidized species

$$j^- = qN_{ss}k_2C_{ox} \quad [21]$$

It is evident that in this range the current does not depend on n_s ; therefore, an infinite Tafel slope must be obtained when Eq. [20] holds.

The saturation range.—The VGC model predicts a Tafel slope of 60 mV in this range for the case of an ideal semiconductor where Eq. [2] holds. However, both at pH 3 and 11 we find a Tafel slope mean value of about 130 mV for $10^{-2}M$ ferricyanide, slightly variable with C_{ox} . This discrepancy has a ready explanation in the dependence of V_{FB} on the applied voltage (Eq. [5]). As we have shown in the experimental section, due to the high value of N_D , for $V - V_{FB} \leq 0.8V$, about half of the applied potential drops in the Helmholtz layer (see Fig. 3), which means that a Tafel slope of about 120 mV should be expected in our case. It could be thought that some degree of Fermi level pinning by surface states could produce an additional drop of the applied voltage in the Helmholtz layer. However, this possibility must be discarded, as the Mott-Schottky plots are linear (Fig. 2).

Dependence of the Tafel slope on the polarization. Necessity of postulating at least two sets of surface states.—The dramatic increase of the Tafel slope with increasing band bending (decreasing n_s) in the proportionality region ($j^- \propto C_{ox}$) (Fig. 5), where Eq. [20] holds, is incompatible according to Eq. [17] with a single monoenergetic population of surface states. For a monoenergetic distribution, E_{ss} , with a single k_1 , the

change from the saturation region ($k_1 n_s \ll k_2 C_{ox}$) to the proportionality region ($k_1 n_s \gg k_2 C_{ox}$) with increasing band bending requires, for constant C_{ox} , that k_2 decreases much more rapidly than n_s ; this is only possible if $\phi_s \ll \Delta\phi_H$, i.e., if there is Fermi level pinning, which is not the case here.

To explain this behavior, two sets of surface states mediating electron transfer can be invoked. For the sake of simplicity let us assume that these two sets are monoenergetic, and are characterized by the parameters (E_{ss} , N_{ss} , k_1 , k_2) and (E'_{ss} , N'_{ss} , k'_1 , k'_2), respectively (Fig. 4). Now Eq. [17] should be changed into

$$j^- = j^-_1 + j^-_2 = -qC_{ox}n_s \left[\frac{N_{ss}k_1}{\frac{k_1}{k_2}n_s + C_{ox}} + \frac{N'_{ss}k'_1}{\frac{k'_1}{k'_2}n_s + C_{ox}} \right] \quad [22]$$

where j^-_1 and j^-_2 represent the contribution of both sets of surface states to the total current.

Let us assume that in the potential region $-0.8V < V < +0.1V$ (Fig. 5) it is

$$k_2 C_{ox} \gg k_1 n_s \quad [23]$$

and

$$k'_2 C_{ox} \ll k'_1 n_s \quad [24]$$

Then, the total current can be written

$$j^- = -q(N_{ss}k_1n_s + N'_{ss}k'_2C_{ox}) \quad [25]$$

For large values of n_s , that is, in the more negative potential range of Fig. 5 ($-0.8V < V < -0.6V$), a Tafel slope of 120 mV is observed, which means that

$$\frac{\partial(\log j^-)}{\partial V} = \frac{\partial(\log j^-_1)}{\partial V} = \frac{\partial(\log n_s)}{\partial V} = 120 \text{ mV}$$

for this heavily doped semiconductor, as already discussed. Therefore, in this range the second term in the parenthesis of Eq. [25] can be neglected. As n_s decreases (increasing band bending) the first term in Eq. [25] becomes negligible, and $j^- = j^-_2 = -qN'_{ss}k'_2C_{ox}$. As far as $\partial k'_2/\partial V = 0$, it must be $\partial j^-_2/\partial V = 0$, and an infinite Tafel slope must appear. This situation holds approximately in Fig. 5 for $-0.6V < V < +0.1V$; a true plateau is not obtained in this potential region because of the fact that a fraction of the applied potential does drop in the Helmholtz layer (Fig. 3). At the more positive potentials (i.e., $V > 0.1V$) n_s is so low that Eq. [24] no longer holds; Eq. [25] must then be substituted for by

$$j^- = -qn_s(N_{ss}k_1 + N'_{ss}k'_1) \quad [26]$$

and a dramatic decrease of the Tafel slope is observed again.

Influence of pH on the proportionality (low current-density) region.—It is readily apparent in Fig. 5 that pH markedly affects the proportionality region. A similar, not so marked effect was observed by VGC. They attributed it to a change in the relative position of the energy levels at the semiconductor surface with respect to those in solution, causing a change in k'_2 . Effectively, from Fig. 4 it is evident that upon increasing the pH from 3 to 11, k_2 decreases and k'_2 increases, which explains why the currents in the proportionality range are higher at pH 11 than at pH 3. Actually, an energy distribution of surface states, instead of two separate monoenergetic populations, would explain the results at pH 3, where the increase of the Tafel slope is much lower than at pH 11. A second, separate set of surface states has to be postulated only when the Tafel slope increases dramatically in a

large voltage range, as is the case for pH 11 between -0.5 , and $+0.1V$.

A possible alternative explanation of the influence of pH on the proportionality region is that the states E'_{ss} are mainly present at basic pH, as a consequence of the interaction of the semiconductor surface with the solvent (H^+ , OH^- , and H_2O species). In order to elucidate this point, the dark electroreduction of $IrCl_6^{2-}$ at pH 3 has been compared to that of $Fe(CN)_6^{3-}$ at pH 11 (Fig. 9). The use of $IrCl_6^{2-}$ was dictated because its redox potential is $\sim 0.5V$ more positive than that of the ferro/ferricyanide. This value is approximately equal to the increase in V_{FB} brought about by a decrease of 8 pH units. Therefore, although λ of $IrCl_6^{2-}$ is 0.1-0.2 eV lower than that of $Fe(CN)_6^{3-}$ (33), the degree of overlap (and therefore the currents) should be essentially the same in the two cases, provided that first, the surface states are unaffected by pH changes, and second, neither anion adsorbs specifically, as is apparent from their lack of influence on the capacitance. The absence of a plateau in the Tafel plot of $IrCl_6^{2-}$ at pH 3 (Fig. 9) seems to give evidence that a new set of surface states appears at pH 11 that is not present at pH 3. The position of the higher limit of the new states, E'_{ss} , can be inferred from the positive limit of the plateau in Fig. 5, $+0.1V$ vs. SCE, assuming that the new surface states begin to be emptied at this potential. With the help of Fig. 3 it is readily obtained that the higher limit of E'_{ss} is $\sim 1.0V$ below the bottom of the conduction band, as is depicted in Fig. 4.

Tafel plot with $IrCl_6^{2-}$.—The Tafel plot obtained with $IrCl_6^{2-}$ at pH 3 is shown in Fig. 9. The currents are much higher than those observed with $Fe(CN)_6^{3-}$; they are even higher than the saturation currents depicted in Fig. 7, which runs contrary to the VGC model, according to which the magnitude of the saturation current is independent of the oxidized species. VGC (16) found that, effectively, the saturation current on TiO_2 and $SrTiO_3$ was the same for Fe^{3+} , $Fe(CN)_6^{3-}$, and $IrCl_6^{2-}$. Unfortunately, we could not conduct experiments at higher concentrations of $IrCl_6^{2-}$, as we were reaching diffusion limited currents. A possible explanation for this anomalous behavior is that in our electrode, perhaps because it was polycrystalline and heavily Nb-doped, the interaction of $IrCl_6^{2-}$ with $SrTiO_3$ at pH 3 created new surface states at a concentration low enough for them not to influence the capacitance, but high enough for the saturation current to be much higher than with $Fe(CN)_6^{3-}$.

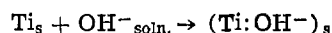
The Tafel plot of $IrCl_6^{2-}$ is approximately a straight line with a slope of ~ 250 mV. The absence of a segment at higher currents with a slope of ~ 130 mV seems to indicate that with $IrCl_6^{2-}$ the rate-limiting step is the transfer of charge from the surface states to the oxidizing species (Eq. [20]), in agreement with the above hypothesis that j^-_{sat} is much higher than with $Fe(CN)_6^{3-}$. The slope of 250 mV is difficult to justify, as it is equal to $(\partial \log [N_{ss} \cdot k_2] / \partial V)^{-1}$ (see Eq. [21]) and both N_{ss} and k_2 change with electrode polarization in an unknown way.

Estimation of some characteristic parameters of the surface states.—The VGC model has been shown to explain qualitatively our experimental results. A quantitative analysis involves a precise knowledge of the actual distribution of surface states, which is far from being known. However, it can be useful to make

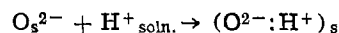
some calculations with the simplest approach of a monoenergetic population of surface states.

The saturation region yields several parameters. From the experimental data of ϕ_s (V) (Fig. 9) and j^-_{sat} (V) (Fig. 7), a combination of Eq. [12] and [19] yields the product $N_{ss}k_1 = j^-_{sat}/qn_s$. Besides, the slope of $1/j^-$ vs. $1/C_{ox}$ plots (Fig. 6) is equal to $k_1 \cdot n_s / k_2 \cdot j_{sat}$, from which k_1/k_2 and $N_{ss}k_2$ are easily obtained. The values of these parameters at pH 11 for two different potentials are given in Table I. It becomes evident that there is a distribution of surface states, as k_1/k_2 increases with increasing ϕ_s . For a monoenergetic population of surface states near the conduction band, k_1/k_2 should decrease, as k_1 must be constant and k_2 should increase with anodic polarization due to a better overlapping of the surface states with empty energy levels of the electrolyte (Fig. 4). It is therefore necessary to assume an energy distribution of surface states in which k_1 increases with decreasing energy.

Origin and nature of the surface states.—The results presented here seem to prove the presence on $SrTiO_3$ of surface states which are present at pH 11 and absent at pH 3, and that therefore would be originated by interaction of n- $SrTiO_3$ with the solvent (H_2O , H^+ , and OH^-). The surfaces of strongly ionic oxides such as TiO_2 or $SrTiO_3$ present two different intrinsic surface states, known as ionic or Tamm surface states which correspond to Ti_s^{4+} cations and O_s anions, respectively. Because of the lower symmetry of both Ti and O^{2-} sites at the semiconductor surface with respect to the bulk, the empty $Ti:3d(t_{2g})$ orbitals responsible for the conduction band should be shifted downwards into the bandgap at the same time that the full $O^{2-}2p$ orbitals responsible for the valence band are shifted upwards. However, it has been established by photoemission experiments that the electronic structure of these surface states is not different from that of the bulk (40), i.e., a decrease of the surface cation coordination seems not to be sufficient to generate bandgap surface states. Surface point defects associated to surface oxygen vacancies ($2Ti^{3+} - V_o$)_s give rise to bandgap surface states in both TiO_2 and $SrTiO_3$ (31). The interaction of these surface states with electrolyte OH^- ions has been thought to give rise to $Ti^{3+}-OH^-$ surface groups, behaving as electron traps, able to mediate electron transfer from the conduction band to electrolyte empty levels (12, 41). Both Ti_s and O_s^{2-} ionic surface states must interact strongly with the electrolyte (39). The Ti_s ionic states act as Lewis acids, taking a couple of electrons from the orbitals of OH^- with a fairly strong interaction that shifts the state nearer the conduction band.



The $O^{2-}:2p$ ionic states behave as Lewis bases, sharing their electron pair with the empty 1s orbitals of H^+ , also with a fairly strong interaction that shifts the state nearer the valence band



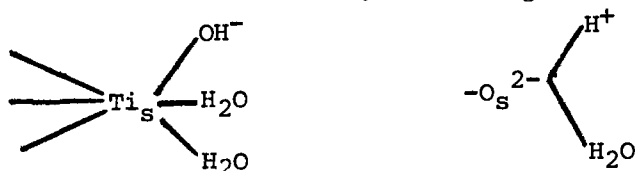
For water molecules contradictory results have been obtained about the dissociative character of their adsorption on TiO_2 and $SrTiO_3$. According to Somorjai *et al.* (42, 43), H_2O adsorbs on TiO_2 without dissociation on single-crystal stoichiometric surfaces, and dissociatively on very heavily Ti^{3+} -doped surfaces. The same authors found that H_2O seemingly adsorbs without

Table I. Parameters characterizing the surface states of the Nb-doped n- $SrTiO_3$ electrode and their charge-transfer characteristics in the saturation range of the cathodic reduction of $Fe(CN)_6^{3-}$

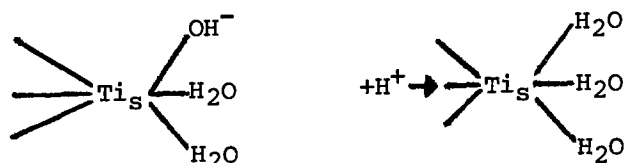
pH	Pot. vs. SCE, V	ϕ_s , V	n_s , cm ⁻³	j^-_{sat} , A cm ⁻²	$N_{ss} \times k_1$, cm s ⁻¹	$N_{ss} \times k_2$, cm s ⁻¹	k_1/k_2
11	-0.8	0.17	1.3×10^{16}	6×10^{-4}	2.9×10^{-1}	2.9×10^{-4}	1.0×10^6
11	-0.6	0.30	8.5×10^{15}	3.6×10^{-3}	2.65	6.3×10^{-6}	4.2×10^6

dissociation on SrTiO₃. More recently, Kurtz and Henrich (44) have shown that the presence of Ti³⁺ surface ions alone is not sufficient to catalyze the dissociative chemisorption of H₂O on either TiO₂ or Ti₂O₃: defect sites, associated with Ti³⁺-O-vacancy complexes, probably catalyze H₂O dissociation.

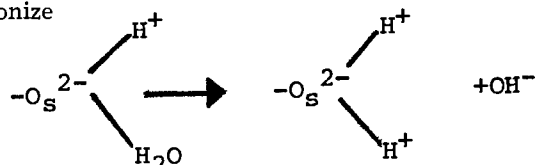
A polycrystalline sample of a given material should show a higher activity than a single crystal of the same material, due to the imperfections (defect sites) of the surface (45). Recent IR studies of anatase powder (46) have shown that TiO₂ in contact with water vapor is covered by a monolayer ($\sim 10^{15}$ mol cm⁻²) of water, half of which is physisorbed molecular water, and the rest is covered, 2/3 by Brönsted acid sites, (O⁻²:H⁺)_s, and 1/3 by Brönsted basic sites, (Ti-OH⁻)_s. The surface concentration of H⁺ and OH⁻ varies with pH, and for most semiconducting oxides this produces a Nernstian dependence of V_{FB} on pH, i.e., $\partial V_{FB}/\partial \text{pH} = 60$ mV (47). The point of zero charge (pzc) is the pH at which the surface concentration of H⁺ ions is equal to that of OH⁻ ions. At the pzc, which is near pH 7 both for TiO₂ and SrTiO₃ (48), the semiconductor surface could be schematized by the following model



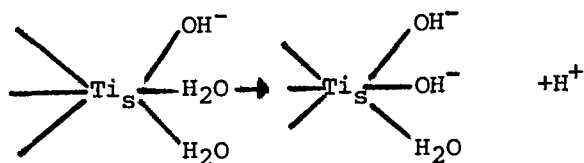
which includes both acid and basic OH surface groups. The amphoteric character of the surface is manifested when the electrolyte pH is different from the pzc. At a pH < pzc, a fraction of OH groups (basic in character) coordinated to Ti surface ions capture protons from the solution



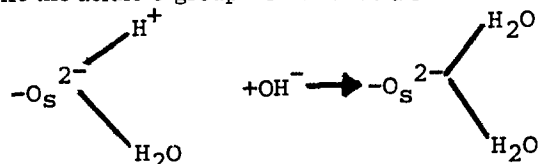
while the acidic O group will either remain unaltered or ionize



The net result will obviously be a decrease of the ratio $[\text{OH}^-]_s/[\text{H}^+]_s$. At pH > pzc water molecules coordinated to Ti_s groups will dissociate giving protons to the solution



while the acidic O group will be neutralized



and consequently the ratio $[\text{OH}^-]_s/[\text{H}^+]_s$ will increase. IR spectra of anatase powder that had been equilibrated with water of different pH values give support to this scheme (49).

Recently, Tomkiewicz (50) detected, by means of subbandgap electroreflectance spectroscopy, what he

believes to be intrinsic surface states at TiO₂ in an aqueous iodide solution, with a maximum 1.3 eV below the conduction band. According to him, in the absence of iodide these intrinsic states interact strongly with OH⁻ ions and/or H₂O molecules and shift towards the conduction band, which makes them undetectable by electroreflectance. It could be possible that these states correspond to surface Ti ions.

Origin of the anomalous electrochemical behavior of SrTiO₃, TiO₂, and α-Fe₂O₃.—Zinc oxide (ZnO) has about the same bandgap and electron affinity (and, therefore, ionization potential) as TiO₂ and SrTiO₃. However, its electrochemical behavior obeys the classical model of direct, isoenergetic charge transfer (22, 51, 52). This difference cannot be attributed to differences in overlap, as the position of the bands is about the same. Its origin, therefore, should be looked for in the difference of the respective intrinsic surface states.

The main difference between the electronic structure of ZnO and those of TiO₂ and SrTiO₃ is the character of the conduction band: it is 4s and 4p for ZnO (53), while for Ti oxides it is Ti: 3d (t_{2g}). Therefore, the interaction of the intrinsic surface states with the solvent should be different in the two cases. Truncation of the crystal lattice at the surface produces a splitting of the Ti⁴⁺:3d (t_{2g}) orbitals so that the Ti-OH⁻ surface groups should be below the conduction band. The ionic surface states associated with Zn²⁺:4s orbitals seem to lie less than 10 mV below E_c (54); therefore, it seems reasonable to assume that the Zn²⁺-OH levels are within the conduction band. This means that conduction band electrons in ZnO must be transferred isoenergetically from the bulk to overlapping electrolyte levels, while in the cases of TiO₂ and SrTiO₃ an electron arriving from the bulk to the surface goes to bandgap energy levels from which it can be transferred to overlapping electrolyte levels.

Current saturation in the dark cathodic reduction of oxidized electrolyte species has also been found with α-Fe₂O₃ (55), another transition metal oxide with 3d-type conduction band. Therefore, of the four wide bandgap semiconducting oxides whose electrochemical behavior has been studied, only ZnO, the only one without d-orbitals in its conduction band, shows the ideal behavior observed with low bandgap covalent semiconductors. This gives some support to the idea that the surface states present in transition-metal oxides and mediating charge transfer to the electrolyte involve 3d orbitals of the metallic cation interacting strongly with OH⁻ and H₂O donor species of the solvent.

Conclusions

The dark electroreduction of Fe(CN)₆³⁻ and IrCl₆²⁻ on a sintered SrTiO₃ electrode at pH 3 and 11, as a function of the concentration of oxidized species, cannot be explained by the classical mechanism of isoenergetic charge transfer, not even when Ullman's model (23) of current control by transport resistance in the space-charge region is used together with the classical mechanism. They can be explained by the two-step mechanism, with mediation of the charge transfer by surface states postulated by VGC (16).

We would like to stress that Ullman's model, although not applicable to our results, could fit other systems in which the charge transfer from the semiconductor to the electrolyte are limited by the charge transport within the space-charge region, and not by the charge transfer from the surface state to the electrolyte. In any case, the observation of saturation currents predicted by Ullman's model for low mobility materials, even in the absence of surface states participating in semiconductor-electrolyte charge transfer, as could be the case for ZnO, would necessitate the use of techniques where the measurements of high currents are not hindered by diffusion limitation.

We have found, as have VGC, that at lower band bendings (i.e., higher currents) the current saturates with increasing concentration of the oxidized species. This anomaly clearly indicates that at least two sets of surface states mediate charge transfer.

We have also found that in the proportionality range the Tafel slope drastically changes with pH, which shows that the set of surface states active in this range results from the interaction of intrinsic ionic surface states of Ti^{4+} :3d (t_{2g}) orbitals with donor species (OH^- and H_2O) of the solvent. This conclusion is reinforced by the fact that the Tafel plot at pH 3 with $IrCl_6^{2-}$, whose empty levels are at about the same energy relative to the semiconductor as those of $Fe(CN)_6^{3-}$ at pH 11, shows no plateau in the proportionality region. However, the electroreduction currents for $IrCl_6^{2-}$ ions reach values considerably higher than the saturation currents for $Fe(CN)_6^{3-}$. This fact is in contradiction with the results of VGC relative to single crystals, and with the prediction of the VGC model that saturation currents should be independent of the nature of the oxidized species. Although we have no proper explanation for this discrepancy, it could be assumed that in the same way that the surface states involved in the transfer of charge are sensitive to pH, they could be also influenced by the nature of the oxidized species, this effect being much more noticeable in sintered, polycrystalline electrodes.

Manuscript submitted March 3, 1983; revised manuscript received Sept. 16, 1983.

El Instituto de Catálisis y Petroleoquímica assisted in meeting the publication costs of this article.

REFERENCES

1. R. Memming in "Semiconductor Liquid-Junction Solar Cells," A. Heller, Editor, p. 38, The Electrochemical Society Softbound Proceedings Series, Princeton, NJ (1977).
2. H. Gerischer, *J. Electroanal. Chem.*, **82**, 133 (1977).
3. H. Morisaki, M. Hariya, and K. Yazawa, *Appl. Phys. Lett.*, **30**, 7 (1977).
4. J. G. Mavroides, V. E. Henrich, H. J. Zeiger, G. Dresselhaus, J. A. Kafalas, and D. F. Kolar, in "Electrode Materials and Processes for Energy Conversion and Storage," J. D. E. McIntyre, S. Srinivasan, and F. G. Will, Editors, p. 45, The Electrochemical Society Softbound Proceedings Series, Princeton, NJ (1978).
5. H. Morisaki and K. Yazawa, *Appl. Phys. Lett.*, **33**, 1013 (1978).
6. D. Laser and S. Gottesfeld, *This Journal*, **126**, 475 (1979).
7. M. Morisaki, H. Kitada, and K. Yazawa, *Jpn. J. Appl. Phys.*, **19**, 679 (1980).
8. P. Salvador, in "Proceedings of the International Conference on Chemical Conversion and Storage of Solar Energy," Boulder, Colorado (1980).
9. P. Salvador, *This Journal*, **128**, 1895 (1981).
10. J. M. Kowalski, K. H. Johnson, and H. L. Tuller, *ibid.*, **127**, 1969 (1980).
11. S. R. Morrison, "Electrochemistry at Semiconductor and Oxidized Metal Electrodes," p. 12, Plenum Press, New York (1980).
12. C. Gutiérrez and P. Salvador, *J. Electroanal. Chem.*, **138**, 457 (1982).
13. E. N. Paleolog and A. Z. Fedotova, *Electrokhimiya*, **5**, 1336 (1969).
14. E. C. Dutoit, F. Cardon, and W. P. Gomes, *Ber. Bunsenges. Phys. Chem.*, **80**, 475 (1976).
15. R. N. Noufi, P. A. Kohl, S. N. Frank, and A. J. Bard, *This Journal*, **125**, 246 (1978).
16. J. Vandermolen, W. P. Gomes, and F. Cardon, *ibid.*, **127**, 324 (1980).
17. B. Parkinson, F. Decker, J. F. Juliao, and M. Abramovich, *Electrochim. Acta*, **25**, 521 (1980).
18. P. Salvador and C. Gutiérrez, *Chem. Phys. Lett.*, **86**, 131 (1982).
19. M. Miyake, H. Yoneyama, and H. Tamura, *J. Catal.*, **58**, 22 (1979).
20. P. Salvador and C. Gutiérrez, *J. Electroanal. Chem.*, To be published.
21. S. R. Morrison, *Surf. Sci.*, **15**, 363 (1969).
22. R. A. L. Vanden Berghe, F. Cardon, and W. P. Gomes, *ibid.*, **39**, 368 (1973).
23. D. L. Ullman, *This Journal*, **128**, 1269 (1981).
24. P. Salvador, *ibid.*, **127**, 2650 (1980).
25. G. Campet, M. P. Dare-Edwards, A. Hamnet, and J. B. Goodenough, *Nouv. J. Chimie*, **4**, 501 (1980).
26. M. Tomkiewicz, *This Journal*, **126**, 3320 (1979).
27. H. Gerischer, in "Advances in Electrochemistry and Electrochemical Engineering," P. Delahay and C. W. Tobias, Editors, Interscience, New York (1961).
28. F. Vanden Kerchove, J. Vandermolen, W. P. Gomes, and F. Cardon, *Ber. Bunsenges. Phys. Chem.*, **83**, 230 (1979).
29. P. Salvador, *Solar Energy Mat.*, **2**, 413 (1980).
30. H. P. R. Frederikse, W. R. Thurber, and W. R. Hosler, *Phys. Rev. A*, **134**, 442 (1964).
31. A. K. Ghosh, A. Rose, H. P. Maruska, T. Feng, and J. Eustace, *J. Electronic. Mat.*, **11**, 237 (1982).
32. R. De Gryse, W. P. Gomes, F. Cardon, and J. Vennik, *This Journal*, **122**, 711 (1975).
33. K. W. Frese, Jr., *J. Phys. Chem.*, **85**, 3911 (1981).
34. R. A. Marcus, *J. Chem. Phys.*, **24**, 966 (1956).
35. H. Gerischer, *Surf. Sci.*, **18**, 97 (1969).
36. H. Gerischer, *Z. Phys. Chem.*, **27**, 48 (1961).
37. R. A. Marcus, *J. Chem. Phys.*, **43**, 697 (1965).
38. R. Memming and F. Möllers, *Ber. Bunsenges. Phys. Chem.*, **76**, 475 (1972).
39. S. R. Morrison, "Electrochemistry at Semiconductor and Oxidized Metal Electrodes," p. 104, Plenum Press, New York (1980).
40. V. E. Henrich and R. L. Kurtz, *Phys. Rev. B*, **23**, 6230 (1981).
41. P. Salvador and C. Gutiérrez, *Surf. Sci.*, **124**, 398 (1983).
42. W. J. Lo, Y. W. Chung, and G. A. Somorjai, *ibid.*, **71**, 199 (1978).
43. S. Ferrer and G. A. Somorjai, *ibid.*, **94**, 41 (1980).
44. R. L. Kurtz and V. E. Henrich, *Phys. Rev. B*, **26**, 6682 (1982).
45. J. M. Thomas, *Adv. Catal.*, **19**, 239 (1969).
46. G. Munuera, V. Rives-Arnau, and A. Sancedo, *J. Chem. Soc., Faraday Trans. I*, **75**, 736 (1979).
47. L. A. Harris and R. H. Wilson, *Ann. Rev. Mater. Sci.*, **8**, 99 (1978), and references therein.
48. M. A. Butler and D. S. Ginley, *This Journal*, **125**, 228 (1978).
49. J. A. Navio Santos, Ph.D. Thesis, University of Sevilla (Spain) (1981).
50. M. Tomkiewicz, *Phys. Rev. Lett.*, **50**, 443 (1983).
51. T. Freund and S. R. Morrison, *Surf. Sci.*, **9**, 119 (1968).
52. S. R. Morrison, *ibid.*, **15**, 363 (1969).
53. W. Göpel, *Ber. Bunsenges. Phys. Chem.*, **82**, 744 (1978).
54. R. K. Swank, *Phys. Rev.*, **153**, 844 (1967).
55. P. Iwanski, J. S. Curran, W. Gissler, and R. Memming, *This Journal*, **128**, 2128 (1981).

Plasma Polymerized Films of Vinylferrocene on Thermally Oxidized Titanium and Single-Crystal Titanium Dioxide

Debra R. Rolison

Naval Research Laboratory, Washington, DC 20375

Royce W. Murray

Department of Chemistry, University of North Carolina, Chapel Hill, North Carolina 27514

ABSTRACT

Titanium, thermally oxidized titanium, and single-crystal TiO_2 have been coated with polyvinylferrocene by an argon-vinylferrocene radio frequency plasma discharge. Voltammetry is observed consistent with the oxidation of ferrocene sites in the polymeric coating at potentials 1.5V positive of the flatband potential for TiO_2 in CH_3CN . As the thickness of the oxide phase is increased, the ease with which ferrocene sites are oxidized decreases. Comparisons are made to TiO_2 substrates coated with polyvinylferrocene by evaporative deposition; these electrodes give a more classical blocking response. The plasma discharge physically alters the semiconductor surface, most likely by generating surface states. In addition, the voltammetric response for plasma-coated TiO_2 /polyvinylferrocene electrodes is improved if conducting materials (e.g., Pt or glassy carbon) are also present in the plasma reactor during plasma deposition. We show that very small minority carrier oxidation currents can be measured by trapping the oxidative charge as ferricenium in the polymer film via potentiostatic experiments at quite positive potentials.

Research on chemical modification of electrode surfaces anticipates the time when an electrode material, a chemical modifier, and a method of modification can be assembled as a package that will predictably perform in electrocatalysis, electrosynthesis, or some other area of electrochemical concern (1). Tailoring electrodes for specific applications relies, in large part, on the predictability of the electrochemical properties of the final product. Predictability may be jeopardized if the modification method unexpectedly alters fundamental characteristics of the electrode material itself. This paper describes such an example for n- TiO_2 .

Some modification methods do appear to affect the substrate, the prime example being radio frequency (RF) plasma treatments. Reactive surfaces, capable of bonding with *in situ* reagents, have been generated for carbon substrates by removal of surface oxides during plasma cleaning (2, 3). Recently, Armstrong reported that exposing a gold metallized-plastic electrode to an oxygen RF plasma created a form of reducible gold oxide that was not observed in the voltammetry of bulk gold or other types of gold films exposed to the plasma (4).

Work in our laboratories shows that RF plasma polymerization can affect changes in the inherent properties of an electrode substrate. The electrochemical response of TiO_2 electrodes plasma coated with polyvinylferrocene differs from that of untreated TiO_2 in a solution of ferrocene. Frank and Bard demonstrated that at potentials positive of -0.8V (SCE), only reductions are possible at single-crystal or polycrystalline TiO_2 in acetonitrile (5). The (dark) oxidation of ferrocene ($E^\circ = +0.4\text{V}$ [SSCE]) in solution at TiO_2 does not occur. By analogy, the oxidation of ferrocene sites immobilized at a TiO_2 surface should not occur. However, for plasma-coated TiO_2 , ferrocene sites are oxidized and in a potential region where n- TiO_2 ($E_{\text{BG}} = 3\text{ eV}$, $E_{\text{FB}} \sim -1.0\text{V}$ [SSCE] in CH_3CN) is normally considered blocked to electron transfer. We shall present evidence that this occurs because the plasma treatment alters the surface energetics of the semiconducting TiO_2 electrode.

Experimental

The vinylferrocene plasma-polymerization procedure has been described previously (3, 6). Plasma reactor geometry B (6, 7) was chosen; this geometry re-

sults in a high rate of polymer film formation and less degradation of ferrocene sites (8). Titanium, thermally oxidized titanium, single-crystal TiO_2 , platinum, and glassy carbon substrates were mounted as electrodes after plasma coating to avoid introduction of other materials into the plasma.

Because subtle changes in the polymer film's characteristics resulted after imbibing solvent from Varian Torr Seal (7), a very high MW epoxy was used to mount and mask the edges of electrodes. The two components (epoxy and versamide resin, 40-60 w/w) cross-link avoiding release of solvent, or any other small molecule, into the polymer. A sample of the hardened epoxy soaked in 0.1M $\text{Et}_4\text{NClO}_4/\text{CH}_3\text{CN}$ for 24h appeared physically unaltered, and the *i*-*E* background of the electrolyte at a Pt working electrode remained unaffected. Mounted electrodes were stored in air for several days before electrochemical use to increase the chemical stability of ferrocene sites in the plasma polymer film (7-9).

Ti disks (punched from 0.67 mm-thick 99.992% Ti foil, Alfa Ventron), 6 mm diam, were polished to a 1 μ finish with diamond paste (Buehler) and degreased with hexane. Titanium samples designated as Ti(0 min) were used without deliberate thermal oxidation, although the native oxide which forms upon exposure of Ti to moisture or air ($\sim 20\text{\AA}$) (10) was unavoidable. Specimens designated as moderately oxidized (Ti/ TiO_2 [*x* min]) were heated on a hot plate in air for *x* min. This mild form of thermal oxidation yielded shiny, golden Ti/ TiO_2 specimens from the polished, silvery Ti. Specimens designated as extensively oxidized (Ti/ TiO_2 [*x* min, 600°C]) were heated in air at 600°C in a muffle furnace for *x* min, colored samples resulted, where the color depended on length of heating. The dull, gray-colored oxide layer which results after heating Ti in a flame (11) was not seen. The depth of the oxide layer, as generated by either form of heating with time, was not measured. Based on color, a Ti sample heated even 1 min at 600°C had a thicker oxide layer than a sample heated for 30 min on a hot plate. Increasing the length of time the Ti was heated was used as a qualitative gauge of oxide depth. These samples were not reduced in hydrogen.

Single-crystal TiO_2 samples (1 \times 2 mm²) were a gift from Professor H. O. Finklea (Virginia Polytechnic Institute and State University). These samples had been reduced in hydrogen at 650°C for 10 min to increase the concentration of charge carriers. The face

Key words: semiconductor, modified electrode, voltammetry, trapping, plasma polymerization.

of the crystal was polished to 1μ , degreased in hexane, and etched for 10 min at 70°C in a solution of 5:1:4 HNO_3 : HF : H_2O . Pt and glassy carbon samples were polished to 1μ and degreased before plasma coating.

Films of conventional polyvinylferrocene [AIBN-initiated polymerization of vinylferrocene in benzene (12)] were deposited on Ti/TiO_2 and single-crystal TiO_2 by evaporating microliter aliquots of a solution of 0.1 mg PVFc/ml toluene (0.47 mM in Fc sites).

Electrochemical experiments were performed in conventional cells and referenced to a sodium-saturated calomel electrode (SSCE). A PAR 173 potentiostat/galvanostat with PAR 179 digital coulometer, PAR 175 universal programmer, and Houston 2000 XY recorder were used. X-ray photoelectron spectra were taken on a du Pont Model 650B electron spectrometer. Peak positions were referenced to C 1s as 285.0 eV. The Pt spectrum of Fig. 7 was obtained on a MacPherson Model 3600 electron spectrometer with positions referenced to Au 4f as 78.0 eV.

Vinylferrocene (Pfaltz and Bauer) was used as received. Bis-2,2'-bipyridine-bis-4-vinylpyridineruthenium(II) hexafluorophosphate was prepared and electropolymerized as previously described (13). Tetraethylammonium perchlorate (Southwestern) was dried at 50°C in a vacuum oven before use. Acetonitrile (MCB) was dried by storing over activated 4A molecular sieves (Linde) or used immediately after reflux and distillation from CaH_2 (Alfa Ventron).

Results and Discussions

XPS.—For uncoated, moderately oxidized Ti/TiO_2 samples, the binding energy difference of the O 1s and Ti $2p_{3/2}$ bands equals 71.5 eV. This value agrees with that reported by Armstrong for TiO_2 (14), demonstrating that our mild thermal oxidation procedure generates the titanium dioxide phase.

A three-minute argon-vinylferrocene plasma discharge produces a polymer film sufficiently thick to block most of the x-ray photoelectrons emitted from the TiO_2 . Compare Fig. 2d and 2b (uncoated *vs.* coated) to see the diminution of the Ti 2p signal after plasma coating moderately oxidized titanium.

The Fe $2p_{3/2}$ region for polyvinylferrocene films plasma deposited on TiO_2 under our RF plasma polymerization conditions shows the predominance of a narrow Fe(II) band at 709 eV. A broad, higher binding energy component due to plasma-damaged Fe(III) sites at 712 eV is always present (Fig. 1a). This general spectrum has been observed for polyvinylferrocene powder harvested from the plasma reactor walls, and for polyvinylferrocene films plasma deposited on Pt, glassy carbon, and RuO_2 (15). By XPS, the type of plasma polymer film that forms is independent of the substrate on which it deposits.

Electrochemistry

Thermally oxidized Ti plasma coated.—The aqueous and nonaqueous electrochemistry of polyvinylferrocene films plasma deposited on conducting substrates has been documented (3, 6, 8, 16, 17). The typical cyclic voltammetric response in CH_3CN is that of a symmetrically shaped wave, with small but nonzero peak separation, at a formal potential characteristic of the ferricenium-ferrocene couple.

Polyvinylferrocene-coated TiO_2 should not exhibit any faradaic response. Instead, Ti/TiO_2 /PPVFc exhibits voltammetry consistent with ferrocene oxidation and ferricenium reduction. The voltammetric response is related to the oxide layer thickness; voltammetric reversibility degrades as oxide thickness increases (see Fig. 2).

Both anodic and cathodic voltammetric peaks are observed for $\text{Ti}(0 \text{ min})$ /PPVFc samples. For the electrode shown in Fig. 2a, anodic peak current decreased 25% by the fifth cycle, faster than the decay of ferricenium sites in a comparably aged film on Pt (9). Cy-

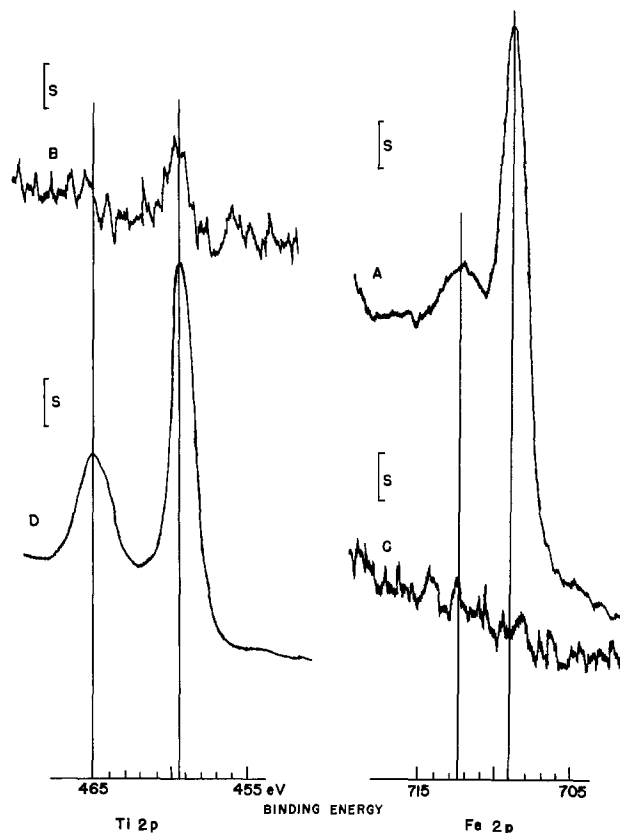


Fig. 1. XPS spectra of the Fe $2p_{3/2}$ and Ti $2p_{3/2,1/2}$ regions for uncoated and plasma-polymerized-vinylferrocene-coated samples of moderately oxidized titanium. A: Fe $2p_{3/2}$ spectrum for Ti/TiO_2 /PPVFc, $S = 1640$ counts/s. B: Ti 2p spectrum for Ti/TiO_2 /PPVFc, $S = 205$ counts/s. C: Fe $2p_{3/2}$ spectrum for Ti/TiO_2 , $S = 680$ counts/s. D: Ti 2p spectrum for Ti/TiO_2 , $S = 5460$ counts/s.

cling $\text{Ti}(0 \text{ min})$ /PPVFc samples to voltages more positive than the ferrocene oxidation wave results in an initial increase in oxidation current that substantially diminishes on subsequent scans as the Ti passivates. The voltammetric response after such a voltage excursion resembles that for moderately oxidized plasma-coated samples, as discussed below. Electrochemical generation of an oxide layer is indicated.

The general response observed after plasma depositing PVFc on moderately oxidized titanium is seen in Fig. 2b and 2c. Well-defined anodic and cathodic peaks are present in the initial scan of the film, but are separated by more than 250 mV. Figure 2c is seen after several subsequent scans. The ferrocene oxidation wave is spread out, but, interestingly, the cathodic wave is still present and well defined, although shifted to more negative potentials. Ferricenium sites are being reduced, so ferrocene sites must continue to be oxidized, although a distinct oxidation wave is absent.

The average surface coverage calculated from the first anodic scan for six moderately heated samples (0, 1, 3, 5, 10, and 20 min), after batch plasma coating, was $8.0 \pm 1.0 \times 10^{-9}$ mol cm^{-2} , a coverage consistent with that observed when Pt, glassy carbon, or RuO_2 are plasma coated under the same experimental conditions (7). The variance in individual surface coverages from the mean is $\sim 12\%$. Thus, moderately reproducible polymeric coverage can be produced on multiple samples coated in a given plasma experiment.

Extensively oxidized titanium, plasma coated with PVFc, exhibits the behavior seen in Fig. 2d. An oxidation wave is never observed, even on the very first anodic scan or for Ti heated for just one minute at 600°C . However, a cathodic peak is still observed, but at a potential shifted to even more negative values, -0.3 to -0.5V (SSCE). This wave is not due to solu-

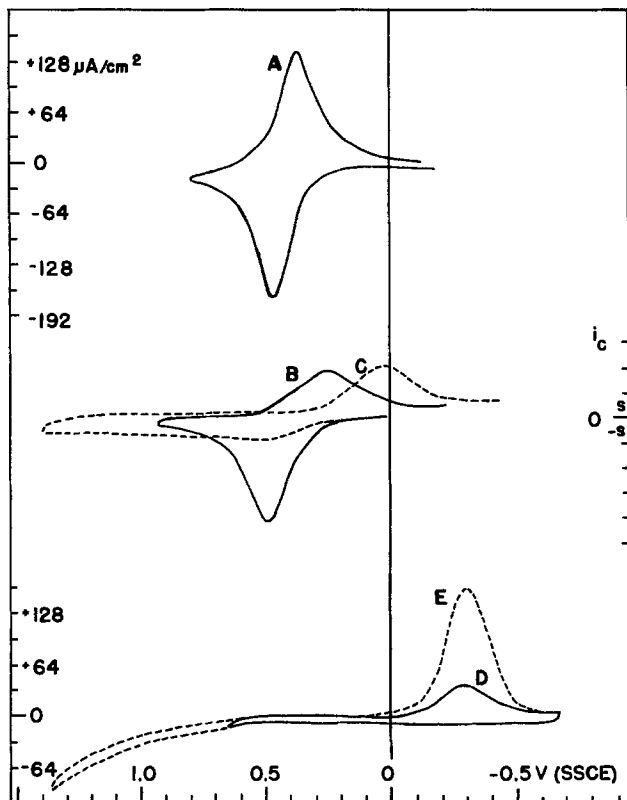


Fig. 2. Variability of the cyclic voltammetric response in 0.1M $\text{Et}_4\text{NClO}_4/\text{CH}_3\text{CN}$ for Ti, moderately oxidized Ti, and extensively oxidized Ti after exposure to a RF argon-vinylferrocene plasma. A: Ti (0 min)/PPVFc, $\nu = 0.2$ V/s. B and C: Ti/TiO₂ (20 min)/PPVFc, $\nu = 0.1$ V/s. B: initial cyclic, $S = 78$ $\mu\text{A}/\text{cm}^2$. C: fifth scan, $S = 32$ $\mu\text{A}/\text{cm}^2$. D and E: Ti/TiO₂ (1 min, 600°C)/PPVFc, $\nu = 0.2$ V/s. E: $E_{\text{SW},a}$ increased to +1.5V.

tion contaminants, as background scans at clean, uncoated Pt, or TiO₂ show no trace of it. Figure 2e demonstrates that the peak current for this cathodic process increases as the anodic potential limit ($E_{\text{SW},a}$) of the cycle is increased to more positive voltages.

We assign this cathodic peak at ~ -0.4 V to reduction of ferricenium. An anodic overvoltage exists; the ferricenium reduction peak is not observed unless the voltage sweep is extended well positive of the formal potential for the ferricenium/ferrocene couple. Roughly, as length of heating at 600°C is increased (and thus as oxide depth increases) the overvoltage for ferrocene oxidation is increased. The cathodic charge measured for the ferricenium reduction wave is, within certain voltage ranges, proportional to the anodic switching potential. Titanium samples heated for 5, 10, or 25 min at 600°C and then plasma coated with polyvinylferrocene have nearly equivalent slopes for the linear portion of their Q_c vs. $E_{\text{SW},a}$ curves, Fig. 3a-3c (281, 255, 287 μF , respectively). A sufficiently thick oxide layer can be prepared, e.g., 100 min at 600°C, to cause the ferricenium reduction peak to vanish, i.e., the originally predicted cyclic voltammetric response of Ti/TiO₂/PPVFc between +2.0 and -1.0V is now observed.

Observing ferrocene oxidation at Ti/TiO₂ is the primary phenomenon. The ferrocene/ferricenium electrochemical process at TiO₂ is not nernstian reversible, even when both anodic and cathodic waves are present in the voltammogram. Oxidation of ferrocene sites in the polymer becomes increasingly more difficult to achieve as the TiO₂ phase deepens. Despite the variability in the voltammetric response for TiO₂/PPVFc, the common factor, regardless of oxide depth, is that ferrocene sites, immobilized in a plasma-deposited polymer at TiO₂, can be oxidized at potentials 1.5V positive of E_{FB} for TiO₂ in CH₃CN.

Thermally oxidized Ti evaporatively coated.—Ferrocene centers can also be placed at the semiconductor surface by evaporation of solutions of polyvinylferrocene prepared by conventional polymerization methods. This less active form of modification was investigated to distinguish between the effects of plasma exposure on TiO₂ and possible Fermi-level pinning of the semiconducting phase (18) due to coating of the surface with a redox polymer.

In the XPS of PVFc films evaporatively deposited from toluene, only the narrow band at 709 eV for Fe(II) is seen; oxidized and/or damaged iron sites are not present in such films, as indicated by the absence of a band at 712 eV (15). Plasma polymerized films are cross-linked and incorporate oxygen upon exposure to air (19). Consequently, the environment surrounding ferrocene sites in a plasma-prepared sample of polyvinylferrocene should differ from that in conventionally prepared polyvinylferrocene. Nonetheless, the ferrocene moiety is known to remain reversibly oxidizable for both types of films deposited on conducting substrates (15-17).

The voltammetry of PVFc evaporatively deposited on Ti/TiO₂ substrates does not mirror that of plasma-deposited polyvinylferrocene films. The results still depend on the oxide thickness, however. Ti/TiO₂ (10 min, 600°C)/PVFc exhibits neither an oxidation wave nor ferricenium reduction peak (Fig. 4a), unlike the plasma-coated analog, where a rereduction peak is observed after sweeping to potentials more positive than 0.8V. An evaporatively coated, moderately oxidized substrate (Ti/TiO₂ [25 min]) also shows no ferrocene oxidation wave, unlike its plasma-coated analog (Fig. 2b), but does show a rereduction wave at negative potentials after sufficiently positive potential sweeps (compare Fig. 4b and 4c).

Evaporating PVFc on freshly polished Ti produces voltammetry as in Fig. 4d and 4e. On the first scan (Fig. 4d) a broad, ill-defined oxidation wave occurs followed upon scan reversal by a reduction peak at -100 mV; by the second scan (Fig. 4e), the Ti has passivated to the extent that no oxidation wave is present at all, but a small cathodic peak at -100 mV persists. For comparison, the voltammetric response of Pt evaporatively coated with PVFc is seen in Fig. 4f. Based on the voltammetry, these evaporatively coated electrodes respond as though a much thicker oxide layer were present than on the plasma-coated Ti/TiO₂ electrodes.

These comparisons show that exposure to the plasma discharge has had a great effect on the appearance and quality of ferrocene/ferricenium electrochemistry at TiO₂. The plasma-coated Ti/TiO₂ is better behaved electrochemically, i.e., it is easier to see the oxidation and re-reduction of ferrocene sites in the polymer overlayer. Based on the similar electrochemistry observed for evaporatively vs. plasma-coated polyvinylferrocene films on metallic and metallic-like substrates (15-17), the polymeric environment can be assumed not to cause these differences for coated Ti/TiO₂.

Single-crystal TiO₂/polyvinylferrocene.—A plasma discharge is a very active means of creating a polymer-coated electrode, unlike solvent evaporation. One reason that Ti/TiO₂/PPVFc reacts electrochemically as though a thinner oxide were present might be due to thinning of the oxide phase during exposure of Ti/TiO₂ to the plasma discharge. Thermal oxidation of Ti produces a more crack-free oxide than one electrochemically generated, but channels still exist (20). A thinner oxide provides more direct access to the underlying Ti through such channels.

To explore the possibility of plasma thinning, we used single-crystal TiO₂ as the substrate in both evaporative and plasma coating experiments. No conducting Ti was present, so plasma thinning should have been of no consequence. Accordingly, we expected little difference between the electrochemistry observed

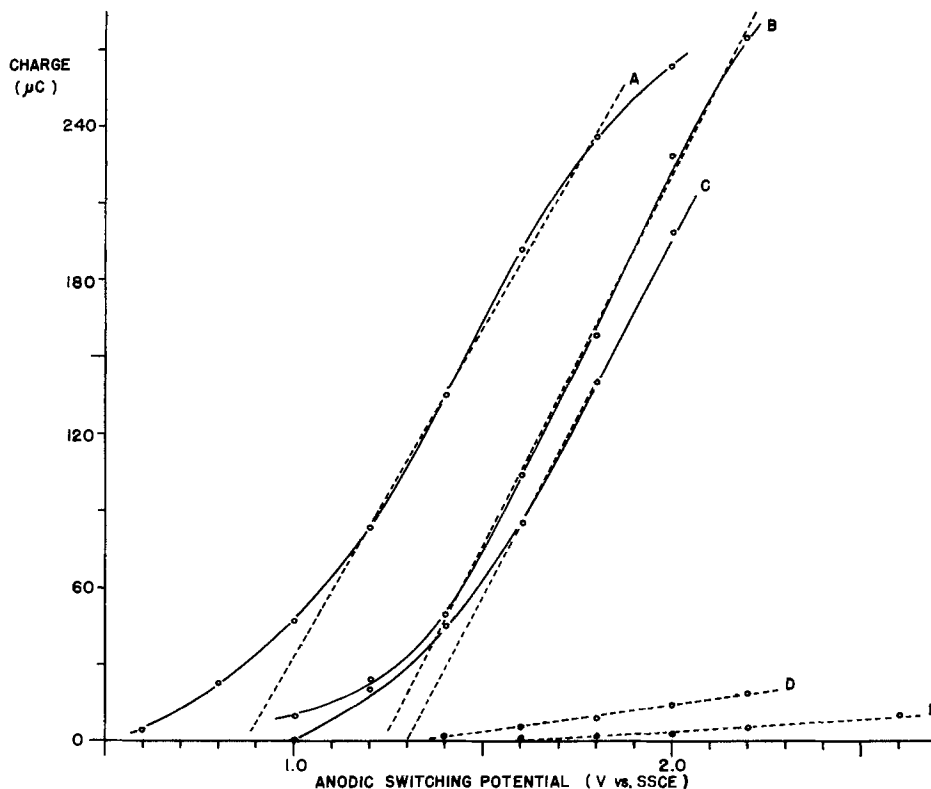


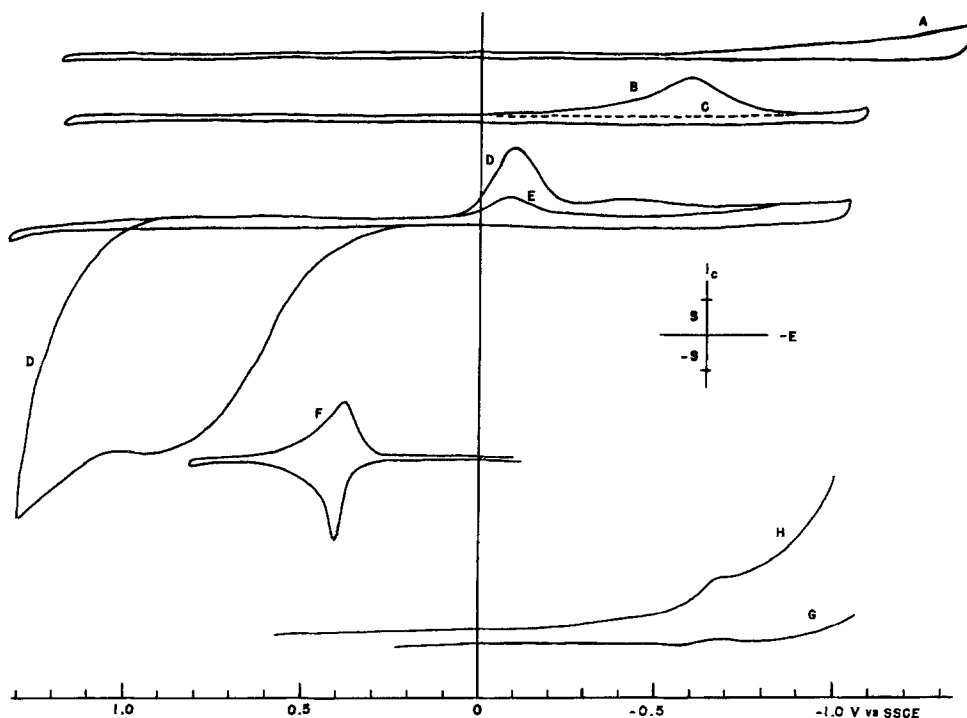
Fig. 3. Cathodic charge measured for the reduction of ferricenium sites in films of plasma-polymerized vinylferrocene deposited on extensively oxidized titanium as a function of the anodic switching potential. $\nu = 0.2$ V/s, $0.1M$ Et_4NClO_4/CH_3CN . A: Ti/TiO₂ (10 min, 600°C)/PPVFc. B: Ti/TiO₂ (25 min, 600°C)/PPVFc. C: Ti/TiO₂ (5 min, 600°C)/PPVFc. D: Ti/TiO₂ (50 min, 600°C)/PPVFc. E: Ti/TiO₂ (100 min, 600°C)/PPVFc.

for plasma- and evaporatively applied coatings; specifically, no ferrocene oxidation should have been observed either directly (an anodic peak or anodic current) or indirectly (a cathodic peak resulting from the reduction of obliquely oxidized ferrocene sites). This result was obtained; cyclic voltammetric scans of both plasma- and evaporatively coated films of polyvinylferrocene on single-crystal TiO₂ in blank electrolyte between +2.0 and -1.0V are identical and indistinguishable from a background scan of uncoated TiO₂ in the same solution. A more forcing voltammetric experiment produced the results described below.

Single-crystal TiO₂ charge trapping.—A reduction peak is not observed when uncoated single-crystal

TiO₂ is potentiostated at very positive potentials in a ferrocene solution and then cycled to negative potentials. If a small oxidation current does flow, and any ferrocene molecules are oxidized, they diffuse away before being detected by their reduction at a potential closer to E_{FB} of the material. Ferrocene embedded in a polymeric film and coated at the electrode surface cannot diffuse away. Any ferrocene centers which do get oxidized are retained as ferricenium centers and can be detected in a negative potential scan. The charge under the cathodic peak is, thus, a measure of the leakage oxidation current. Recognizing this, we briefly explored the charge trapping property of ferrocene polymer layers as a method of detecting ex-

Fig. 4. Voltammetric response for TiO₂ substrates evaporatively coated with conventionally prepared polyvinylferrocene, $0.1M$ Et_4NClO_4/CH_3CN . A: Ti/TiO₂ (10 min, 600°C)/PVFc, $\nu = 0.1$ V/s, $S = 16 \mu A/cm^2$. B and C: Ti/TiO₂ (25 min)/PVFc, $\nu = 0.1$ V/s, $S = 16 \mu A/cm^2$. C: $E_{SW,a} = 0.1V$. D and E: Ti (0 min)/PVFc, $\nu = 0.1$ V/s, $S = 32 \mu A/cm^2$. D: first scan. E: second scan. F: Pt/PVFc, $\nu = 0.1$ V/s, $S = 140 \mu A/cm^2$. G and H: single-crystal TiO₂/PVFc, $\nu = 0.2$ V/s, $S = 4 \mu A/cm^2$. G: potentiostated at 1.56V for 5 min prior to scan to negative potentials. H: potentiostated at 1.73V for min.



tremely small levels of ferrocene oxidation at very positive, normally blocking potentials at single-crystal TiO_2 . These potentiostatic experiments also showed that greater leakage currents flow when the polymer film is applied by plasma deposition.

After potentiostating an evaporatively coated single-crystal TiO_2 electrode at +1.56V for 5 min, a trace of a cathodic wave is observed at -0.66V (see Fig. 4g). By increasing E_{pot} to +1.73V and t to 50 min, the results in Fig. 4h are obtained. The position of the peak remains at -0.66V and, as expected, the peak magnitude has increased. The increase in discharged ferricenium sites is 30% for the 10-fold increase in time. Thus, even for single-crystal, evaporatively coated TiO_2/PVFc , some ferrocene sites become oxidized at very positive potentials with time. We estimate from the accumulated charge that the current flowing to produce these peaks must be of the order of a few hundred picoamperes.

Single-crystal TiO_2 electrodes plasma coated with polyvinylferrocene ($\text{TiO}_2/\text{PPVFc}$) and potentiostated for 5 min at positive voltages produce larger cathodic peaks than evaporatively coated single-crystal TiO_2 electrodes. As with the cyclic experiments at $\text{Ti}/\text{TiO}_2/\text{PPVFc}$, a threshold potential exists. A reduction wave is not seen if the applied E_{pot} is negative of this threshold potential, even though positive of $E^{\circ'}$ for ferrocene oxidation (see Fig. 5). The threshold potential lies between +0.75 and +1.0V (SSCE). As the curves obtained for $E_{\text{pot}} > +1.0\text{V}$ illustrate, once positive of this threshold potential, more positive potentials produce larger reduction peaks; the charges under these cathodic peaks are 0.3, 1.6, and 5.5 μC , respectively.

Increasing the duration of potentiostatic control for $\text{TiO}_2/\text{PPVFc}$ also results in a larger cathodic peak. Two minutes at +1.5V produces the wave seen in Fig. 5a; the wave in Fig. 5b results after increasing the time

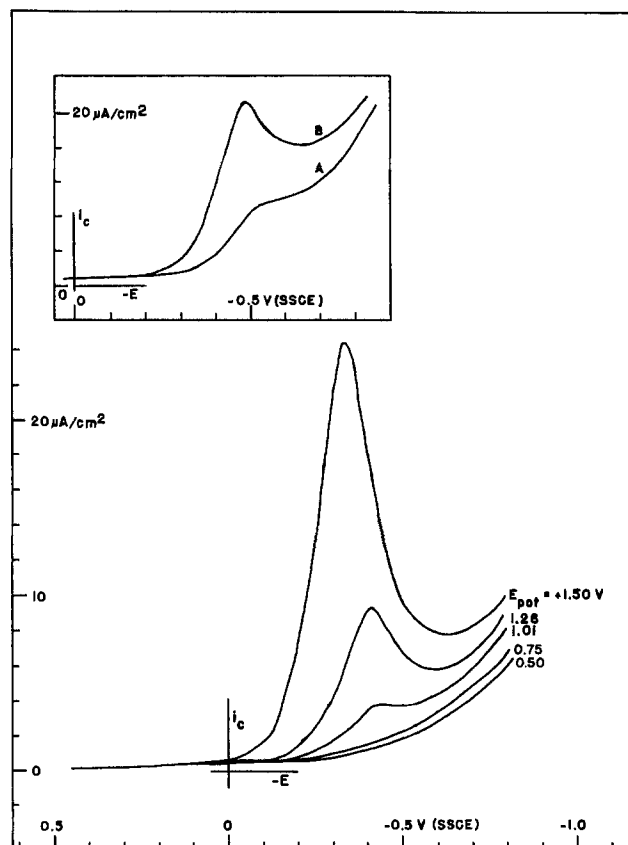


Fig. 5. Linear potential sweep voltammograms for single-crystal TiO_2 plasma coated with polyvinylferrocene after a potentiostatic experiment at positive voltages for 5 min, 0.1M $\text{Et}_4\text{NClO}_4/\text{CH}_3\text{CN}$, $\nu = 0.2\text{ V/s}$. A and B: $\text{TiO}_2/\text{PPVFc}$ held at 1.6V for the stated times. A: 2 min. B: 5 min.

to 5 min. If a constant oxidation leakage current is assumed ($i = q/t$), 4.2 and 4.9 nA anodic currents would produce the cathodic peaks in Fig. 5a and 5b, respectively. At least a 20-fold increase in the observed oxidation leakage current results from exposing single-crystal TiO_2 to the RF plasma. This result is consistent with the above results on Ti/TiO_2 , so that plasma thinning of the TiO_2 film on $\text{Ti}/\text{TiO}_2/\text{PPVFc}$ electrodes can be ruled out as the primary origin of the improved electrochemical behavior of these electrodes.

Unfortunately, ferrocene is a poor candidate as a charge storage medium because ferricenium is chemically unstable. The electrochemical activity of ferrocene-modified metallic electrodes decreases with time poised in the ferricenium state (9, 22). For plasma-polymerized films of polyvinylferrocene on Pt, a ferricenium half-life of approximately 20 min is obtained after curing the film in air for 2 weeks (9). $\text{TiO}_2/\text{PPVFc}$ also exhibits an apparent loss of ferricenium sites. The charge for the curve in Fig. 5 obtained at +1.5V (5.5 μC ; 5 min potentiostating) is 3.7 times greater than that later obtained for Fig. 5b (1.5 μC ; same t , E_{pot}). The electrode had undergone several potentiostatic experiments between the time these curves were recorded; some ferricenium decay undoubtedly occurred. Consequently, we briefly explored an alternative charge storing film.

$\text{TiO}_2/\text{poly}-[\text{Ru}(\text{bpy})_2(\text{vpy})_2]^{2+}$.—Polypyridylruthenium complexes are known for their chemical stability and durability. TiO_2 can be coated by the electropolymerization of vinyl monomers of pyridine or bipyridine coordinated to Ru(II) (13). Electropolymerization occurs after cycling into the ligand-centered reductions, reactions which occur at potentials where TiO_2 is not blocked. The oxidation of the Ru(II) centers ($E^{\circ'} \gg E_{\text{FR}}$) has not been reported for these polymer films on TiO_2 .

$[\text{Ru}(\text{bpy})_2(\text{vpy})_2]^{2+}$ was electropolymerized from CH_3CN onto Ti/TiO_2 (5 min, 600°C) and single-crystal TiO_2 . In monomer-free electrolyte, the ligand-centered reductions are observed at both types of coated specimens, confirming that the polypyridylruthenium polymer is present. Under cycling conditions, no oxidation to Ru(III) or its re-reduction wave is ever seen, for either electrode substrate.

If Ti/TiO_2 (5 min, 600°C/poly- $[\text{Ru}(\text{bpy})_2(\text{vpy})_2]^{2+}$ is potentiostated at potentials positive of the $E^{\circ'}$ for this couple (at metallic electrodes, 1.25V (SSCE)), a cathodic wave appears at 170 mV upon sweeping to negative potentials. Cathodic peak current increases as E_{pot} is increased. A plot of Q_c vs. E_{pot} is linear for $E_{\text{pot}} > 1.8\text{V}$ (SSCE), with a slope of $64 \pm 3\ \mu\text{F}$.

The reproducibility of the amount of cathodic charge accumulated for a Ti/TiO_2 (5 min, 600°C)/poly- $[\text{Ru}(\text{bpy})_2(\text{vpy})_2]^{2+}$ specimen during repetitive potentiostatic/cathodic cycling experiments was investigated briefly. Table I shows that for repetitive scans at a given E_{pot} , the charge measured under the cathodic wave is nearly invariant. This indicates that charge trapping by the polymer film does not rapidly decay with time as it did in the polyvinylferrocene-coated electrodes.

A cathodic wave was, however, never observed for single-crystal $\text{TiO}_2/\text{poly}-[\text{Ru}(\text{bpy})_2(\text{vpy})_2]^{2+}$, even after potentiostating the modified electrode at +2.45V for 30 min. The formal potential of the polypyridylruthenium polymer is 850 mV more positive than that for the ferrocene polymer. Recall that single-crystal TiO_2/PVFc also required extremes in time and E_{pot} (50 min at 1.73V) to achieve a significant and well-defined response. Thus, while increased chemical stability of the electroactive center is necessary for a good charge storage candidate, a low oxidation potential (nearer that of ferrocene) is also important.

Plasma effects.—Gentle modification methods (evaporative deposition of polyvinylferrocene or electro-

Table I.

E_{pot} (V vs. SSCE) ^a	Cathodic charge (μC) ^b	Capacitance (μF) ^c
2.05	33.7	18.5
2.07	38.0	20.9
2.10	39.5	21.4
2.05	36.4	20.2
		Avg. $20.3 \pm 1.2 \mu F$
1.85	16.9	10.6
1.82	16.1	10.2
1.79	14.6	9.5
1.80	15.9	10.3
		Avg. $10.2 \pm 0.5 \mu F$

^a 2 min potentiostatic experiment.

^b Charge measured under cathodic peak with a planimeter.

^c Capacitance calculated as $q/[E_{pot}$ (V vs. NHE)].

polymerization of $[Ru(bpy)_2(vpy)_2]^{2+}$ onto Ti/TiO₂ or single-crystal TiO₂) produce polymer-coated electrodes which behave as classically anticipated based on the blocking behavior of this semiconductor at potentials positive of E_{FB} . As shown, it is only because the electroactive species are immobilized at the electrode surface that the more extreme electrochemical experiment of potentiostating at very positive voltages allows us to detect the production of any oxidized species by its subsequent discharge.

After plasma coating, TiO₂ electrochemically responds as though it were a more conducting material. The plasma discharge probably affects the surface energetics of the semiconductor through surface damage, although both the plasma power (several watts) and temperature (the gas temperature is near ambient) are mild. The relative ease of ferrocene oxidation at moderately and extensively oxidized Ti/TiO₂/PPVFc suggests that the plasma discharge has introduced intermediate levels (surface states) into the bandgap region.

We do not know the chemical identity of these states. We have found, however, that somewhat analogous effects can be produced by the presence of other materials in the Ar plasma discharge, as shown by the following experimental results. Reversible, persistent electron transfer for ferrocene/ferricenium sites is observed when moderately oxidized Ti is exposed to an argon-vinylferrocene plasma discharge in the pres-

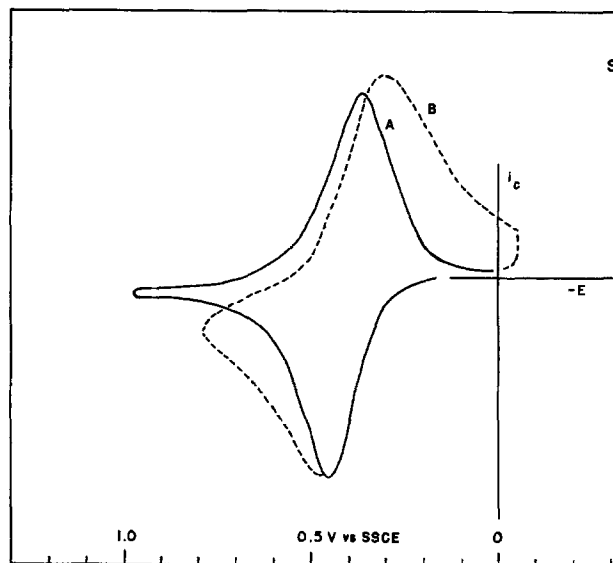


Fig. 6. Cyclic voltammograms for moderately oxidized Ti plasma coated in a RF argon-vinylferrocene discharge with Pt electrode substrates present in the plasma reactor, 0.1M Et₄NClO₄/CH₃CN, $\nu = 0.2$ V/s. A: first scan, $S = 64 \mu A/cm^2$. B: scan after potentiostating at 0.75V for 15 min, $S = 16 \mu A/cm^2$.

ence of small pieces of conducting substrates (Pt, glassy carbon, RuO₂). The characteristic voltammetric response is seen in Fig. 6a. Both anodic and cathodic branches are present, with $\Delta E_p > 90$ mV. This is a smaller ΔE_p than is observed for the initial scan of moderately oxidized Ti plasma coated with PVFc in the absence of conducting substrates ($\Delta E_p > 250$ mV). More importantly, the anodic wave persists beyond five scans. Figure 6b is obtained after potentiostating the electrode of Fig. 6a at 0.75V for 15 min; this is the time equivalent (for $\nu = 0.2$ V/s) to more than 100 cycles without loss of the anodic wave or substantial shifting of $E_{p,c}$ to more negative potentials. Reversible oxidation and re-reduction of ferrocene centers ($q_a = q_c$) at the characteristic E° (0.4V) clearly occurs.

The only new variable in the deposition procedure is the addition of metallic substances into the plasma



Fig. 7. XPS spectrum of the Pt 4f region for a moderately oxidized Ti sample plasma coated in a RF argon-vinylferrocene discharge with Pt foil present in the plasma reactor.

reactor. The electrochemistry now resembles that of a conducting electrode coated with a ferrocene polymer. A possible explanation is that the oxide layer is now doped by atoms of the metallic substance.

The properties of Ti and TiO₂ have been shown to be markedly affected by the addition of trace quantities of noble metals. The presence of ppb Pt ions in a corrosive solution is known to reduce corrosion of Ti to negligible levels and improve its use as an electrode (23). Alloying Ti with <0.1% Pt, other noble metals, or even graphite also provides this protection (24). Deliberate doping of polycrystalline TiO₂ with noble metals has been shown to produce an impurity band in the bandgap region which affects the photoelectrochemical properties of the material, often decreasing the effective bandgap and shifting the photoresponse towards the visible (25).

If in our experiment, the plasma dislodges trace amounts of Pt (or C or Ru) into the plasma gas, introduction of a dopant onto the TiO₂ surface during plasma discharge would appear likely; an enhanced electrochemical response of Ti/TiO₂/PPFVc could then result. To confirm this hypothesis, a 1 min argon-vinylferrocene plasma-coated Ti/TiO₂ sample, prepared in the presence of a strip of Pt foil, was analyzed by XPS. In addition to the usual Fe 2p_{3/2} spectrum, the Pt 4f region clearly shows the Pt 4f doublet (Fig. 7). This confirms that the plasma discharge can transfer material from one substrate in the plasma reactor to another, even under conditions of low power discharge.

Conclusions

The RF plasma argon-vinylferrocene discharge modifies TiO₂ in two respects: first, by coating the electrode with an electroactive species, and second, by altering the surface energetics of the semiconductor, resulting in a less severe blocking response by TiO₂ at potentials positive of E_{FB}. Regardless of the depth of the oxide phase, a TiO₂ electrode plasma coated with polyvinylferrocene exhibits better ferrocene/ferricenium voltammetry than its evaporatively coated analog.

The mechanism for the improvement is the physical interaction of the plasma with the semiconductor surface; this most likely generates surface states in the bandgap region. This manner of introducing surface states/defects may have some utility for the photoelectrochemical and corrosion behavior of TiO₂ and other semiconductors. The plasma discharge may also be used to dope only the outer surface of the semiconductor. This approach is less material intensive than adding a uniform, bulk amount of dopant during the synthesis of the semiconductor, and may offer an alternative to ion implantation.

Immobilized redox sites at n-TiO₂, and presumably other semiconductors, capture and store charge leaked across the space-charge region. This storage is analogous to the preconcentration step in anodic stripping voltammetry where reduced ions amalgamate with the Hg electrode. In this case, holes are concentrated as oxidized sites in the polymer film and stripped from the film during the scan to more negative potentials. This analogy reveals the possibility of using polymer-modified semiconductor electrodes to analytically determine trace amounts of electroactive reactants.

Acknowledgments

The authors wish to thank P. Burgmayer (UNC) for early plasma experiments with thermally oxidized Ti,

Dr. J. M. Calvert (Geo-Centers) for preparation and electropolymerization of [Ru(bpy)₂(vpy)₂]²⁺, and Dr. J. R. Griffith (NRL) for supplying the high MW epoxy. One of the authors (D.R.R.) is especially grateful to Dr. G. G. Rolison (Stockton State College) and Professor H. O. Finklea (VPI) for discussions on the metaphysics of semiconductors.

Manuscript submitted Jan. 14, 1983; revised manuscript received ca. Sept. 12, 1983. This was Paper 679 presented at the Montreal, Quebec, Canada, Meeting of the Society, May 9-14, 1982.

The Naval Research Laboratory assisted in meeting the publication costs of this article.

REFERENCES

1. R. W. Murray, *Acc. Chem. Res.*, **13**, 135 (1980).
2. N. Oyama and F. C. Anson, *J. Electroanal. Chem.*, **87**, 435 (1978); **88**, 289 (1978).
3. R. Nowak, F. A. Schultz, M. Umaña, H. Abruña, and R. W. Murray, *ibid.*, **94**, 219 (1978).
4. N. R. Armstrong and J. R. White, *ibid.*, **131**, 121 (1982).
5. S. N. Frank and A. J. Bard, *J. Am. Chem. Soc.*, **97**, 7427 (1975).
6. R. J. Nowak, F. A. Schultz, M. Umaña, R. Lam, and R. W. Murray, *Anal. Chem.*, **52**, 315 (1980).
7. D. R. Rolison, Ph.D. Thesis, University of North Carolina, Chapel Hill, NC (1980).
8. P. Daum, J. R. Lenhard, D. Rolison, and R. W. Murray, *J. Am. Chem. Soc.*, **102**, 4649 (1980).
9. D. R. Rolison, M. Umaña, P. Burgmayer, and R. W. Murray, *Inorg. Chem.*, **20**, 2996 (1981).
10. V. C. Andreeva, *Corrosion*, **20**, 35t (1964).
11. H. O. Finklea and R. W. Murray, *J. Phys. Chem.*, **83**, 353 (1979).
12. T. W. Smith, J. E. Kuder, and D. Wycheck, *J. Polym. Sci.*, **14**, 2433 (1976).
13. H. D. Abruña, P. Denisevich, M. Umaña, T. J. Meyer and R. W. Murray, *J. Am. Chem. Soc.*, **103**, 1 (1981).
14. C. N. Sayers and N. R. Armstrong, *Surf. Sci.*, **77**, 301 (1978).
15. M. Umaña, D. R. Rolison, R. J. Nowak, P. Daum, and R. W. Murray, *ibid.*, **101**, 295 (1980).
16. P. Daum and R. W. Murray, *J. Electroanal. Chem.*, **103**, 289 (1979).
17. P. Daum and R. W. Murray, *J. Phys. Chem.*, **85**, 389 (1981).
18. A. J. Bard, A. B. Bocarsly, F. R. F. Fan, E. G. Walton, and M. S. Wrighton, *J. Am. Chem. Soc.*, **102**, 3671 (1980).
19. M. Millard, in "Techniques and Applications of Plasma Chemistry," J. R. Hollahan and A. T. Bell, Editors, Chap. 5, John Wiley and Sons, New York (1974).
20. R. W. Schultz and L. C. Covington, *Corrosion*, **37**, 585 (1981).
21. H. Gerischer, in "Physical Chemistry: An Advanced Treatise," Vol. 9A, H. Eyring, D. Henderson, and W. Jost, Editors, pp. 463-542, Academic Press, New York (1970).
22. J. R. Lenhard and R. W. Murray, *J. Am. Chem. Soc.*, **100**, 7870 (1978).
23. W. R. Buck, B. W. Sloope, and H. Leidheiser, *Corrosion*, **15**, 26 (1959).
24. M. Stern and H. Wissenberg, *This Journal*, **106**, 759 (1959).
25. Y. Matsumoto, T. Shimizu, and E. Sato, *Electrochim. Acta*, **27**, 419 (1982).



PAS Testimony to Duplex Structure of Passive Film on Iron

Kotato Ogura*

Department of Applied Chemistry, Yamaguchi University Ube 755, Japan

Akira Fujishima* and Kenichi Honda

Department of Synthetic Chemistry, The University of Tokyo, Hongo, Tokyo 113, Japan

Photoacoustic spectroscopy (PAS) has been employed for the investigation of the solid surface (1-3). This technique has been applied to the examination of electrode surfaces; *e.g.*, to measure the absorption spectra of the electrode surface (4, 5). In these studies, however, the experimental procedure is accompanied by a transfer of an electrode into the PAS cell through the atmosphere. Such procedure is defective in applying PAS to the investigation of thin anodic film like on iron, because air-formed oxide must naturally affect the acoustic signal characteristic of anodic film. Hence, in the application of PAS to the study of thin anodic film, it is requisite that the experiment is performed *in situ* without involving a transfer of a sample to the atmosphere. One of our groups has recently developed an *in situ* PAS technique (6), and this method has been applied to the study of the electrode/solution interface involving the oxide layer on Au (7, 8) and the cathodic decomposition of CdS and ZnO (8).

The present paper describes the use of this method to investigate the passivity of iron. Optical studies of passivity of iron have been carried out extensively (9-18), and the optical thickness of the passive film has been well established. However, there is no agreement on whether the passive film consists of a single layer (9-13) or two layers (14-18) with different composition. Recent optical results seem to support single layer model. Revie *et al.* (11) claim from their data by Auger electron spectroscopy that the passive film is a hydrated ferrous oxide with gel-like structure, and this oxide is degraded to $\gamma\text{Fe}_2\text{O}_3$ during the heating by the beam in the electron diffraction camera. O'Grady (12) refused the existence of Fe_3O_4 from his Mössbauer study. Chen and Cahan (13) have described the passive film as an insulating ferric oxyhydroxide. However, our PAS data obtained here are incompatible with these models and prefer the two-layer model.

The optical evidence presented so far for the two-layer model is not sufficient. The electron diffraction pattern of $\gamma\text{Fe}_2\text{O}_3$ is very close to that of Fe_3O_4 , and the discrimination of Fe_3O_4 from $\gamma\text{Fe}_2\text{O}_3$ by this method is very difficult (19). In a polarizer reading (P)-reduction time plot that was obtained from the ellipsometric experiment by Ho and Ord (16), the inflection corresponding to the transition from $\gamma\text{Fe}_2\text{O}_3$ to Fe_3O_4 is very vague and, hence, is unable to be conclusive evidence for the existence of two layers. Seo *et al.* (17) interpreted their Auger spectra to suggest a duplex structure consisting of $\gamma\text{Fe}_2\text{O}_3$ and Fe_3O_4 . However, as pointed out by Revie *et al.* (11), the sample was transferred through the atmosphere in their experimental technique, and their Auger spectra must involve the spectrum characteristic of air-formed oxide.

* Electrochemical Society Active Member.

Experimental

A one-compartment cell was used with a Pt wire counterelectrode and a saturated calomel reference electrode (SCE). The working electrode was a 0.2 mm thick flat iron (purity: 99.9%) plate of about 1 cm² area. A TDK piezoelectric disk (PZT 51c-C10-2) was attached to the rear of the Fe electrode with epoxy resin. Care was taken to ensure that the Fe electrode was electrically insulated from the piezoelectric disk, and the disk from the solution by the epoxy resin. The Fe electrode surface was polished mechanically with emery papers before use. A Spectra Physics SP164 Ar ion laser was used as the light source. The incident light (wavelength 514.5 nm and its light power 0.2W) was interrupted at 80 Hz by a NF-CH-353 mechanical chopper, and irradiated on the Fe electrode. The signal from the piezoelectric transducer was synchronously detected with a NF-LI-574 lock-in amplifier. External acoustic and electric noise was reduced using a shielding box made of iron and lead.

Electrochemical measurements were carried out with a usual potentiostat together with a potential programmer. The electrolyte was 1.0M potassium phosphate + 0.05M sodium tetraborate buffer solution which was deaerated with nitrogen gas prior to the beginning of an experiment. Before each anodization, the specimen was polarized at -1.0V for 5 min in order to remove the air-formed oxide on iron.

Results and Discussion

Figure 1 shows the current-potential and the photoacoustic signal-potential curves of iron at pH 8.0. The *i*-*E* curves show the typical behavior of an iron electrode in a weak alkaline buffer solution (20) when the potential is scanned between -1.2 and -0.4V (curve a), -1.2 and 0V (curve b), and -1.2 and $+0.8\text{V}$ (curve c). In the acoustic curve a' corresponding to curve a, the signal begins to increase at approximately -0.8V at which anodic current commences to flow. The increase in the photoacoustic signal is due to an increase in the absorption of light at the electrode surface, which reflects the change in the absorptivity of the surface. Hence, this result leads to the conclusion that the iron surface starts to be covered with an oxide at -0.8V . On the reverse scan, the acoustic signal begins to decrease at the same potential; *i.e.*, the oxide starts to disappear. According to the electrochemical experiments combined with a chemical analysis (14), such oxide should be Fe_3O_4 .

In curve c', the acoustic signal continues increasing between -0.8 and $+0.8\text{V}$ on the anodic scan. However, the gradient of the magnitude of the acoustic signal *vs.* potential changes at about -0.4V . This implies that a different type of iron oxide begins to grow on Fe_3O_4 at about -0.4V . This oxide must be $\gamma\text{Fe}_2\text{O}_3$ or γFeOOH .

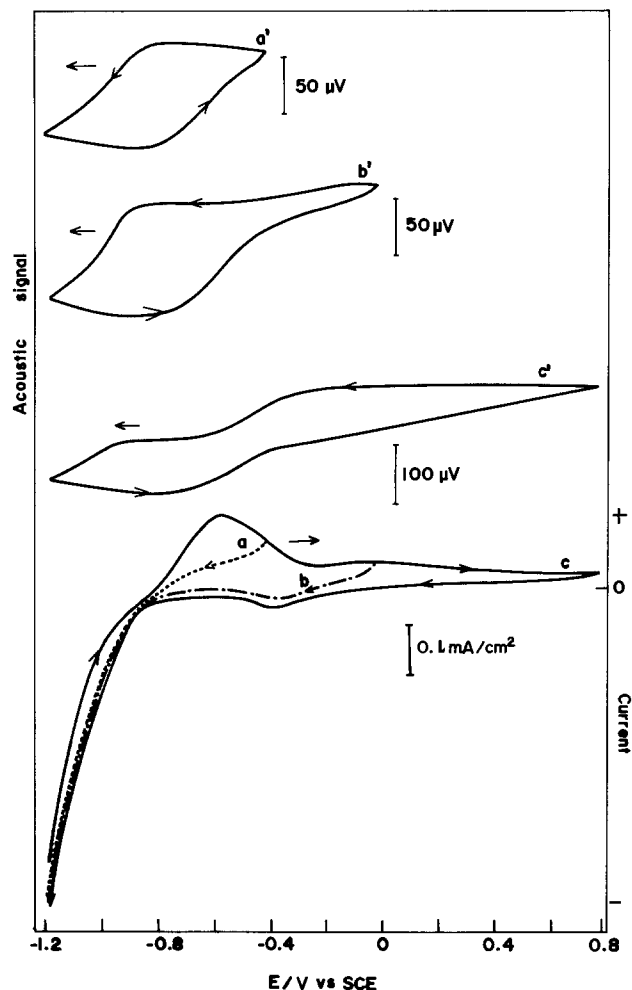


Fig. 1. Photoacoustic signal-potential and current-potential curves of the iron electrode in the 0.1M potassium phosphate + 0.05M sodium borate solution of pH 8.0. Potential scanning rate: 100 s/V; λ : 514.5 nm.

which has been assumed as an outer layer in the two layer model. On the reverse scan, the i - E curve shows a cathodic peak around $-0.4V$. This peak has been investigated in detail by the potentiodynamic or the galvanostatic method, and it is attributed to the reduction of $\gamma\text{Fe}_2\text{O}_3$ (21, 22). The corresponding acoustic signal decreases via two steps: first, at about $-0.4V$ and second, at $-0.9V$. This result therefore supports the existence of two layers on iron, and the reduction of $\gamma\text{Fe}_2\text{O}_3$ and Fe_3O_4 occurring at about -0.4 and

$-0.9V$, respectively. As seen from this figure, and also pointed out previously (22), the current peak corresponding to the reduction of Fe_3O_4 is not observed because of the large cathodic current of hydrogen evolution. This was one of the reasons why the existence of Fe_3O_4 was doubtful. However, these photoacoustic data evidently indicate the simultaneous reduction of Fe_3O_4 with the hydrogen evolution.

Acknowledgment

The authors express their sincere gratitude to Dr. H. Masuda, Mr. S. Morishita, and Y. Nagae for their experimental help.

Manuscript submitted Dec. 4, 1982.

REFERENCES

1. A. Rosencwaig, *Anal. Chem.*, **47**, 592A (1975).
2. M. J. Adams, A. A. King, and G. F. Kirkbright, *Analyst*, **101**, 73 (1976).
3. R. C. Gray, V. A. Fishman, and A. J. Bard, *Anal. Chem.*, **49**, 697 (1977).
4. P. Nordal and S. O. Kanstad, *Opt. Commun.*, **24**, 95 (1978).
5. M. Fujihira, T. Osa, D. Hursh, and T. Kuwana, *J. Electroanal. Chem.*, **88**, 285 (1978).
6. K. Honda, A. Fujishima, and H. Masuda, in "Photoelectrochemistry: Fundamental Process and Measurement Techniques," W. L. Wallace, A. J. Nozik, S. K. Deb, and R. H. Wilson, Editors, p. 622, The Electrochemical Society Softbound Proceedings Series, Pennington, NJ (1981).
7. A. Fujishima, H. Masuda, and K. Honda, *Chem. Lett.*, 1063 (1979).
8. H. Masuda, A. Fujishima, and K. Honda, *Bull. Chem. Soc. Jpn.*, **53**, 1542 (1980); **55**, 672 (1982).
9. N. Sato, K. Kudo, and T. Noda, *Corros. Sci.*, **10**, 785 (1970).
10. N. Sato and K. Kudo, *Electrochim. Acta*, **16**, 447 (1971).
11. R. W. Revie, B. G. Baker, and J. O'M. Bockris, *This Journal*, **122**, 1460 (1975).
12. W. E. O'Grady, *ibid.*, **127**, 555 (1980).
13. C. T. Chen and B. D. Cahan, *ibid.*, **129**, 17 (1982); **129**, 921 (1982).
14. M. Nagayama and M. Cohen, *ibid.*, **109**, 781 (1962).
15. J. Kruger and J. P. Calvert, *ibid.*, **114**, 43 (1967).
16. F. C. Ho and J. L. Ord, *ibid.*, **119**, 139 (1972).
17. M. Seo, J. B. Lumsden, and R. W. Staehle, *Surf. Sci.*, **42**, 337 (1974).
18. M. Cohen, D. Mitchell, and K. Hashimoto, *This Journal*, **126**, 442 (1979).
19. K. Kuroda, B. D. Cahan, Gh. Nazri, E. Yeager, and T. E. Mitchell, *ibid.*, **129**, 2163 (1982).
20. K. Ogura and T. Majima, *Electrochim. Acta*, **23**, 1361 (1978).
21. K. Ogura and K. Sato, *ibid.*, **25**, 857 (1980).
22. K. Ogura and Y. Miwa, *J. Electroanal. Chem.*, **130**, 189 (1981).

Analysis of an Aluminum Plating Bath Using ^{27}Al -NMR Spectroscopy

G. A. R. van Dijk and H. C. A. M. Smoorenburg

Philips Research Laboratories, 5600 JA Eindhoven, The Netherlands

The electrodeposition of aluminum is not possible from an aqueous electrolyte because of the strong electronegativity of the metal. Deposition can be achieved in an ether-based bath, from which water and oxygen are excluded (1-3). It is difficult to determine the exact bath composition of such solutions, which contain AlCl_3 and LiAlH_4 , without interfering with the complex chemistry of the system. In this note, we show that ^{27}Al -NMR spectrometry is a suitable method for analyzing such solutions, and we present

Key words: electrolyte, electrode, spectra, electrodeposition.

results for a plating system based on AlCl_3 , LiAlH_4 , and tetrahydrofuran (THF). To identify possible bath components, we separately synthesized a number of complexes and compared their spectra with those of practical plating solutions.

^{27}Al -NMR Spectroscopy Results

Possible bath constituents.—The most important species which may be present in a plating bath based on $\text{AlCl}_3/\text{LiAlH}_4/\text{THF}$ are listed in Table I. These species were prepared from mixtures of AlCl_3 and

Table I. Possible constituents of an Al-electroplating bath: characteristic ^{27}Al resonance lines

Chemical shift (^{27}Al) (ppm)	Component in THF-solution	Coupling multiplicity	Line-width ^a (Hz)	Coupling constant—JAl-H (Hz)
116	$\text{AlH}_2\text{Cl}_2^-$	singlet ^b (triplet expected)	1500	—
114	AlHCl_2^-	doublet	203	329
108	$\text{AlH}_3 \cdot 2\text{THF}$	singlet ^b (quarter expected)	3000	—
103	AlCl_4^-	singlet	5-20	—
97	AlH_4^-	quintet	54	175
90	$\text{AlH}_2\text{Cl} \cdot 2\text{THF}$	singlet ^b (triplet expected)	2500	—
77	$\text{AlHCl}_2 \cdot 2\text{THF}$	singlet ^b (doublet expected)	1300	—
64	$\text{AlCl}_3 \cdot 2\text{THF}$	singlet	317	—
20	$\text{AlCl}_3 \cdot 4\text{THF}^+$	singlet	broad	—
0	$\text{Al}(\text{H}_2\text{O})_6^{3+}$	singlet	7	—

^a Linewidth as determined in the H-decoupled ^{27}Al -spectra.

^b Quadrupole relaxation dominates.

LiAlH_4 as described in Ref. (4, 5). $\text{Al}(\text{H}_2\text{O})_6^{3+}$ was used as an external chemical shift reference.

For these species, we determined the relevant ^{27}Al -NMR resonance lines (Table I). The measurements were made using a Nicolet NT 200 spectrometer (at $B = 4.7$ T; 52,130 MHz ^{27}Al frequency) with a multi-nuclear broad-band probe. The spectral width was 450 ppm. A 90° pulse with a pulse length of 21 μs was used.

"Fresh" bath.—From the data given in Table I, it is possible to obtain information about the composition of the plating bath. The spectrum of a fresh bath is shown in Fig. 1. The dipolar interaction between the Al and the H-nuclei can be removed by decoupling, which simplifies the spectrum (Fig. 2). From this particular spectrum, we obtained the values given in Table II for the concentration of the various species in a bath containing 14 mol percent (m/o) LiAlH_4 and 86 m/o AlCl_3 in THF (respectively, 0.2 and 1.2 mol liter $^{-1}$).

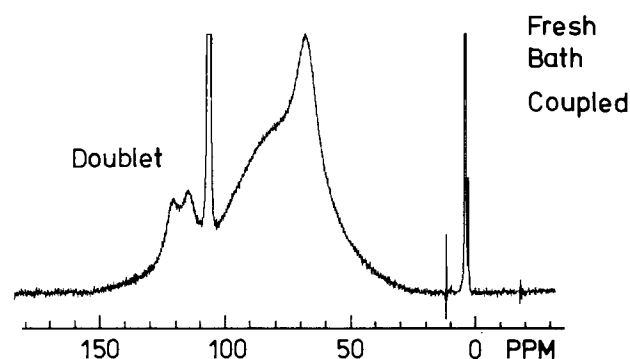


Fig. 1. ^{27}Al -NMR-spectrum of a "fresh" hydride-type Al electroplating bath.

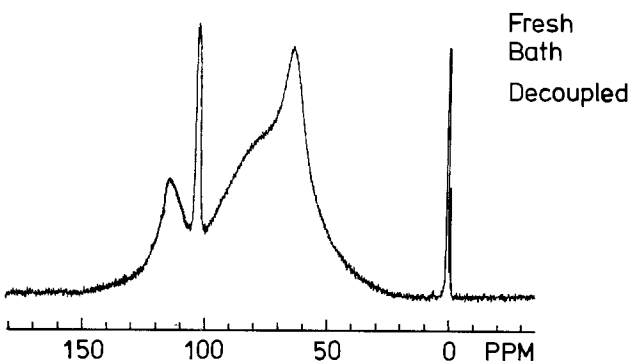


Fig. 2. ^{27}Al -NMR-spectrum of a "fresh" hydride-type Al electroplating bath (decoupled).

Table II. Concentration of species in a "fresh" Al bath

Components	^{27}Al chem. shift (ppm)	Concentration (m/o)
$\text{AlCl}_3 \cdot 2\text{THF}$	64	70 { 36 34 18 12
$\text{AlHCl}_2 \cdot 2\text{THF}$	77	
AlCl_4^-	103	
AlHCl_2^-	114	

"Aged" bath.—With the protracted use of a given plating bath, the quality of the plated Al deteriorates. The NMR-spectrum for such an "aged" bath is shown in Fig. 3. This bath initially contained 1.3 mol liter $^{-1}$ AlCl_3 and 0.3 mol liter $^{-1}$ LiAlH_4 . After nine months operation, it was no longer possible to deposit Al layers of satisfactory quality. The adhesion of the metal to the substrate was poor, and the plated metal, which showed a black surface, reacted with water. In Table III, the composition of this "aged" bath is given.

It is clear that the components which contain hydride ($\text{AlHCl}_2 \cdot 2\text{THF}$ and AlHCl_3^-) are no longer present in the plating solution. Possible causes are leakage of oxygen or water into the plating vessel.

"Replenished" bath.—If the deterioration of the bath described above is caused by the loss of the hydride compounds, it should be possible to restore the original bath quality by adding hydride containing components. One could directly add the missing species or compounds capable of forming the missing hydride containing components by reacting with the remaining chloride. In Fig. 4 we see the effect of the addition of LiAlH_4 to the "aged" bath. Replenishing is also possible with $\text{AlH}_3 \cdot 2\text{THF}$, which can be easily prepared as a crystalline solid (6). This has the great advantage of avoiding the addition of extra lithium ions to the system. The Li is codeposited with the Al at bath concentrations above 0.6 mol liter $^{-1}$ or at high plating rates. The quality of aluminum deposited from the replenished bath was comparable to that obtained from the fresh bath.

Cyclic Voltammograms

To illustrate the effect of bath aging on the electrochemistry, cyclic voltammograms were taken for the

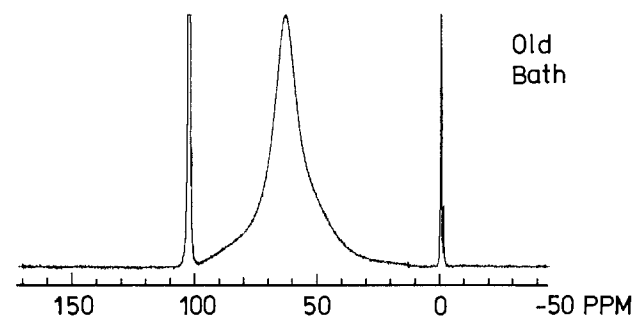


Fig. 3. ^{27}Al -NMR-spectrum of an "aged" hydride-type Al electroplating bath.

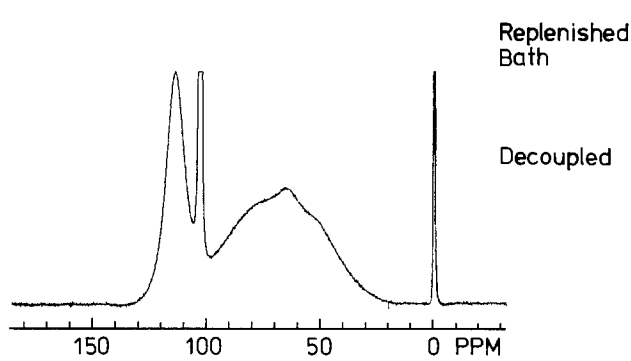


Fig. 4. ^{27}Al -NMR-spectrum of a "replenished" hydride-type Al electroplating bath (decoupled).

Table III. Concentration of species in the "aged" Al bath

Components	²⁷ Al chem. shift (ppm)	Conc (m/o)
AlCl ₃ · 2THF	64	56
AlCl ₄ ⁻	103	44

Original components: 1.3 mol liter⁻¹ AlCl₃ + 0.3 mol liter⁻¹ LiAlH₄ in THF.

Table IV. Concentration of species in the replenished bath

Components	²⁷ Al chem. shift (ppm)	Concentration (m/o)			
AlCl ₃ · 2THF	64	74 { 38			
AlHCl ₂ · 2THF	76		{ 36		
AlCl ₄ ⁻	103			{ 22	
AlHCl ₃ ⁻	114				{ 4

Original components: 1.3 mol liter⁻¹ AlCl₃, 0.3 mol liter⁻¹ LiAlH₄; 0.25 mol liter⁻¹ LiAlH₄ added for replenishing.

The AlCl₃ · 2THF-AlHCl₂ · 2THF-peak has been separated with curve fitting.

three bath compositions described above (Tables II-IV).

Because of the nature of our system, the direct use of a reference is not possible. We used an Al-quasi-reference electrode (99.999% Al wire). This was placed behind the Pt working electrode and connected by a Luggin capillary through the working electrode with the active surface. This was done to decrease the IR drops considerably (7). The counterelectrode was 99.999% Al. Contact between the counter and reference electrode was avoided by placing the reference electrode in a Teflon holder. Prior to the experiment, the working electrode was plated with an Al layer for 30s at 5 mA/cm⁻². The results are shown in Fig. 5. Curve 1 refers to a "new" Al plating bath from which layers of good quality are deposited. The anodic and cathodic waves are clearly recognizable. The peak-peak distance is rather large because of the still considerable IR drop ($R_u \approx 1\Omega$). Curve 2 shows the result of an "aged" bath. No currents above 0.2 mA are observed, indicating that with the depleted solution extreme polarization is required for the electrolytic deposition of metal. In this situation, either coprecipitation of Li and Al or reduction of the solvent is to be expected (8). Curve 3 shows that the anodic and cathodic waves are restored completely after replenishing.

The voltammogram is a clear indication that the hydride containing species are the essential catalytic

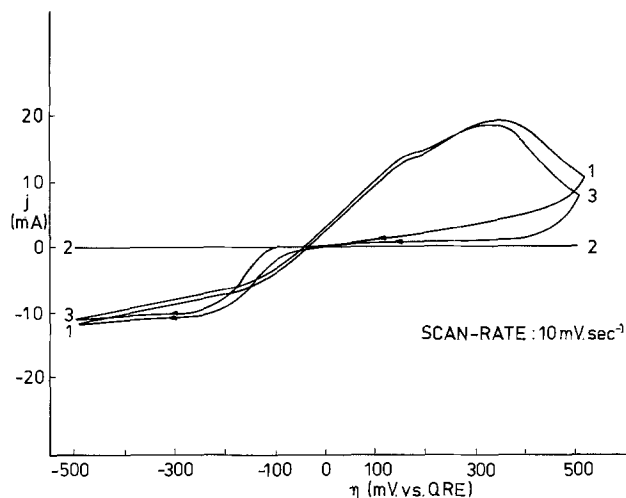


Fig. 5. Cyclic voltammograms of the Al electroplating bath using an Al quasi-reference electrode. Curve 1, "fresh" bath; curve 2, "aged" bath; curve 3, "replenished" bath.

species in the "cyclic" electrode process for Al electroplating (9).

Conclusion

²⁷Al-NMR spectroscopy is very suitable for identifying the constituents of an Al electroplating solution. The essential role of the hydride is clear and it is possible to keep such a plating bath in optimum condition by replenishing species which are lost by "dragged-in" water or oxygen.

Manuscript submitted July 5, 1983; revised manuscript received Aug. 15, 1983.

Philips Research Laboratories assisted in meeting the publication costs of this article.

REFERENCES

1. M. Yoshio and N. Ishibashi, *J. Appl. Electrochem.*, **3**, 321 (1973).
2. J. F. M. v.d. Berg, T. E. G. Daenen, G. Krijl, and R. E. v.d. Leest, *Philips Tech. Rev.*, **39**, No. 3/4, 87 (1980).
3. U.S. Pat. appl. for 8,100,569.
4. K. N. Semenenko, E. A. Lavutad, and A. P. Isaera, *Russ. J. Inorg. Chem.*, **11**, 21 (1976).
5. U.S. Pat. 4,222,827.
6. E. Wiberg and W. Gösele, *Z. Naturforsch., Teil B*, **11**, 485 (1956).
7. C. Yarnitzky and Y. Friedman, *Anal. Chem.*, **47**, 876 (1975).
8. T. E. G. Daenen, *Nature*, **280**, 378 (1979).
9. T. Daenen, G. v. Dijk, and J. v.d. Berg, 68th Ann. Techn. Conf., June 28th, 1981, Boston, First, Int. Symp. Electrodep. of Al (AES) G.1

Electrochemical Deposition of Conducting Ruthenium Oxide Films from Solution

D. P. Anderson and L. F. Warren

Rockwell International Science Center, Thousand Oaks, California 91360

In the last decade, ruthenium oxide, RuO₂ ($x \leq 2$), has been used extensively as the active anode electrocatalyst constituent for Cl₂ and O₂ evolution reactions, in chlorate production, and in metal electrowinning from mixed chloride-sulfate solutions (1-3). More recently, this material has been incorporated in several light-induced water electrolysis schemes (4-8) and

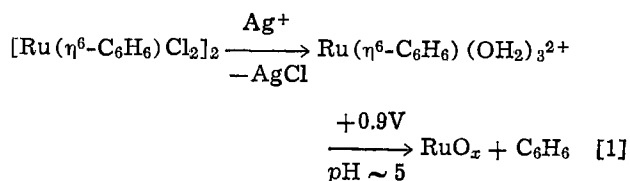
Key words: aqua Ru(II) complex, anodic deposition, oxygen catalyst.

apparently possesses the ability to inhibit CdS photocorrosion by acting as a hole scavenger (6-8). The numerous applications for this catalyst material certainly warrant further studies of its electrochemical properties on a variety of substrates, e.g., semiconductors. The lack of a simple technique for controlled deposition of ruthenium oxide onto conducting substrates prompted us to investigate an electrochemical approach to this problem. We describe here a new

method for electrodepositing conducting hydrated ruthenium oxide films from stable aqueous solutions containing a ruthenium(II) complex.

As with hydrous manganese oxide (MnO_x) (9-10) it was assumed that anodic electrodeposition of RuO_x may take place from an aqueous solution of the corresponding M^{2+} ion. Preparation and isolation of air-sensitive aqua ion $\text{Ru}(\text{OH}_2)_6^{2+}$ salts are, however, tedious procedures involving use of expensive and reactive RuO_4 and ion-exchange chromatography (11). A more accessible aqua ruthenium(II) species is $\text{Ru}(\eta^6\text{-C}_6\text{H}_6)(\text{OH}_2)_3^{2+}$; this is obtained from the very stable organometallic complex $[\text{Ru}(\eta^6\text{-C}_6\text{H}_6)\text{Cl}_2]_2$, which forms in virtually quantitative yield from commercial $\text{RuCl}_3 \cdot 3\text{H}_2\text{O}$ and 1,3- or 1,4-cyclohexadiene (12). Treatment of an aqueous solution of this species with two equivalents of AgBF_4 generated the yellow-aquated $\text{Ru}(\eta^6\text{-C}_6\text{H}_6)(\text{OH}_2)_3^{2+}$ species (12, 13), which appeared to be stable indefinitely over a wide range of pH values. (Although air sensitivity was not apparent, typically, the solutions were stored under an inert atmosphere.) The coordinated benzene stabilizes the ruthenium(II) oxidation state compared with the aqua $\text{Ru}(\text{OH}_2)_6^{2+}$ ion (11).

The anodic electrodeposition of hydrous RuO_x on a rotating Pt disk electrode (400 rpm) took place at a constant potential (+0.9V vs. SCE, corresponding to a current density of ca. 1 mA/cm²) from room temperature aqueous solutions containing the $\text{Ru}(\eta^6\text{-C}_6\text{H}_6)(\text{OH}_2)_3^{2+}$ complex (0.04M), adjusted to pH 5. 0.1M sodium perchlorate was used as supporting electrolyte. No precautions were made to exclude oxygen



Films of thickness corresponding to 20-30 mC/cm² were typically grown, though much thicker films are attainable because the deposits are conducting. Using a cubic approximation of the RuO_2 unit cell of 4.6Å, these charges correspond to nominal thicknesses of 600-1000Å, assuming 100% deposition efficiency.

The resulting smooth brown films were conducting in aqueous electrolytes; this was apparent from the stable anodic-deposition current and from their behavior in the presence of a redox couple. Figure 1 shows the current-potential characteristics of a 600Å film on Pt in a pH 4 buffer (phthalate) electrolyte with and without added $\text{Fe}(\text{CN})_6^{4-}$ ion; the voltammetric behavior of the redox couple is essentially unaffected by the presence of the oxide film. Similar behavior was observed with ferrocene in an acetonitrile/0.1M tetraethylammonium perchlorate electrolyte; however, the voltammetric response of the film itself was greatly suppressed in acetonitrile relative to aqueous electrolytes (14). These results parallel our findings with electrodeposited hydrous MnO_x and other transition metal oxide films (10).

The reversible nature of the electrodeposited ruthenium oxide was further demonstrated by its behavior in 0.1M perchloric acid (pH 1.5, shown in Fig. 2), where at any potential in the sweep an almost reversible behavior was observed as the sweep direction was changed. This was manifested as a rapid current change from anodic to cathodic at a magnitude nearly the same as that on the immediately previous anodic sweeps. The current-potential profiles for our electrodeposited films are qualitatively similar to those of the reversible films generated by anodic/cathodic potential cycling of ruthenized Pt and (oxidized) Ru-on-glass electrodes (15). Differences may be attributed to the particular electrolytes employed; in addition, our

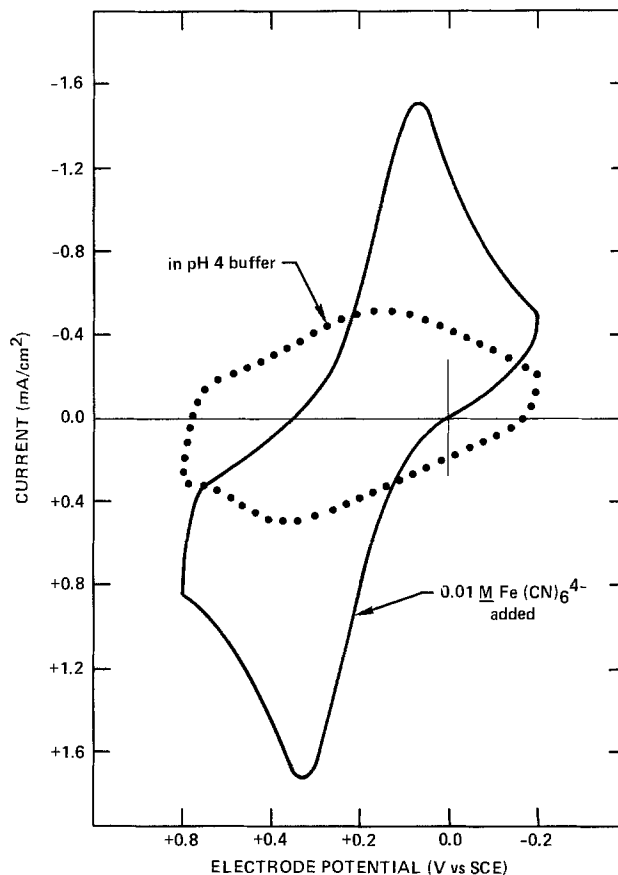


Fig. 1. Cyclic voltammograms at 50 mV/s for an electrodeposited ruthenium oxide film (600Å) on Pt in a room temperature pH 4 buffer (phthalate), with (solid curve) and without (dotted curve) added ferrocyanide (0.01M).

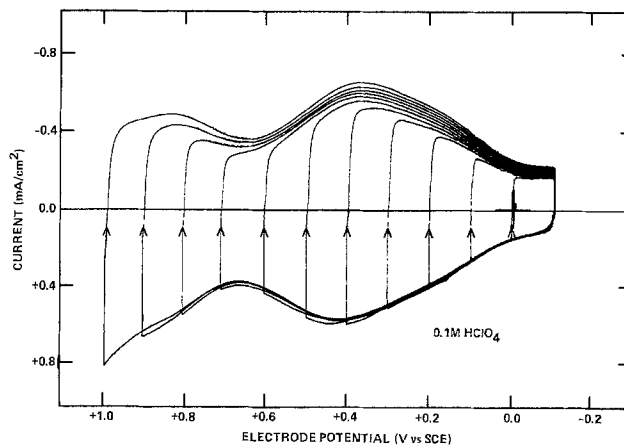


Fig. 2. Cyclic voltammograms of an electrodeposited ruthenium oxide film (1000Å) on Pt in 0.1M HClO_4 (pH 1.5, room temperature); the potential sweep direction was changed (designated by arrows) from anodic to cathodic at increasing 100 mV intervals; sweep rate 50 mV/s. Sweeps start at -0.1V in the direction of more positive potentials.

films appear to be more prone to dissolution; this is perhaps indicative of greater porosity (16). The reversible behavior of these films has been attributed to a mixed valency $\text{Ru}(\text{III-IV})$ oxide/hydroxide in which a rapid redox process (involving protonation) can occur with kinetic facility (15), i.e., formally, $\text{RuO}_2 + \text{H}^+ + e^- \rightleftharpoons \text{RuO}(\text{OH})$.

Slow dissolution of the fresh electrodeposited ruthenium oxide films occurred during potential cycling in aqueous electrolytes. In the pH 4 buffer solution, the films remained intact provided cycling was limited to the range of +0.6 to -0.2V.¹ At more positive

¹The theoretical domain of passivation of ruthenium, corresponding to the formation of $\text{RuO}_2 \cdot 2\text{H}_2\text{O}$ and $\text{Ru}(\text{OH})_3$, is limited to a 600 mV range at pH 4 (17).

potentials in the anodic sweep, an anodic current resulted which was apparently due to both dissolution, involving soluble higher oxidation states, and water oxidation; at high pH's (>10), dissolution predominated, and orange RuO_4^{2-} streamed off the electrode surface. In acidic electrolytes, oxygen evolution was observed at potentials >0.8V; polarization curves in 0.5M H_2SO_4 indicated that the overvoltage for oxygen evolution on the RuO_x films is less by 320 mV than that on Pt (18). Dissolution was also evident, however, and emphasized the importance of stabilizing ruthenium oxide by combination with TiO_2 or other oxides (1, 15, 16, 19).

In conclusion, it is possible to electrochemically deposit conducting films of hydrated ruthenium oxide from an aqueous solution of the benzeneruthenium(II)-aqua complex. The films slowly dissolve in aqueous electrolytes upon potential cycling, yet appear to be catalytic with regards to water oxidation.

Acknowledgments

The authors gratefully acknowledge support of this work by the Department of Energy through contract no. XP-9-8002-1 from the Solar Energy Research Institute, Golden, Colorado.

Manuscript submitted March 25, 1983; revised manuscript received Aug. 22, 1983. This was Paper 80 presented at the Montreal, Quebec, Canada, Meeting of the Society, May 9-14, 1982.

Rockwell International Science Center assisted in meeting the publication costs of this article.

REFERENCES

1. A. Nitola, *Stud. Phys. Theor. Chem.*, **11**, 627 (1981).
2. R. S. Yeo, J. Orehotsky, and S. Srinivasan, *This Journal*, **128**, 1900 (1981).
3. A. J. Scarpellino and G. L. Fisher, Jr., *ibid.*, **129**, 515, 522 (1982).
4. E. Amouyal, P. Keller, and A. Moradpour, *J. Chem. Soc., Chem. Commun.*, 1019 (1980).
5. J. Kiwi, E. Borgarello, E. Pelizzetti, M. Visca, and M. Grätzel, *Angew. Chem. Int. Ed. Engl.*, **19**, 646 (1980); *Nature*, **289**, 158 (1981).
6. K. Kalyznasundaram, E. Borgarello, D. Duanghong, and M. Grätzel, *Angew. Chem. Int. Ed. Engl.*, **20**, 987 (1981).
7. K. Kalyznasundaram, E. Borgarello, and M. Grätzel, *Helv. Chim. Acta*, **64**, 362 (1981).
8. M. Grätzel, *Acc. Chem. Res.*, **14**, 376 (1981), and references therein.
9. E. Barchese, H. C. Chagas, and S. Wolyneec, *An. Acad. Bras. Cienc.*, **53**, 309 (1981), and references therein.
10. D. Tench and L. F. Warren, *This Journal*, **130**, 869 (1983).
11. P. Bernhard, H. Lehmann, and A. Ludi, *J. Chem. Soc., Chem. Commun.*, 1216 (1981).
12. R. A. Zelonka and M. C. Baird, *Can. J. Chem.*, **50**, 3063 (1972); M. A. Bennett and A. K. Smith, *J. Chem. Soc. Dalton Trans.*, 233 (1974).
13. R. O. Gould, C. L. Jones, D. R. Robertson, and T. A. Stephenson, *J. Chem. Soc., Chem. Commun.*, 222 (1977).
14. D. R. Rolison, K. Kuo, M. Umana, D. Brundage, and R. W. Murray, *This Journal*, **126**, 407 (1979).
15. S. Hadzi-Jordanov, H. Angerstein-Kozłowska, M. Yukovic, and B. E. Conway, *ibid.*, **125**, 1471 (1978); M. Yukovic, H. Angerstein-Kozłowska, and B. E. Conway, *J. Appl. Electrochem.*, **12**, 193 (1982).
16. Compare, for example, the RuO_x films on ruthenium of M. Yukovic, H. Angerstein-Kozłowska, and B. E. Conway, *ibid.*, and L. D. Burke and J. K. Mulcahy, *J. Electroanal. Chem.*, **73**, 207 (1976).
17. M. Pourbaix, in "Atlas of Electrochemical Equilibria in Aqueous Solutions," NACE, Houston, Texas (1974).
18. Compare with the results of C. Iwakura, K. Hirao, and H. Tamura, *Electrochim. Acta*, **22**, 329, 335 (1977).
19. A. Mills and M. L. Zeeman, *J. Chem. Soc., Chem. Commun.*, 948 (1981); A. Mills, *J. Chem. Soc., Dalton Trans.*, 1213 (1982).

An Electrochemical Synthesis of Dichlorobutenes from Butadiene as a New Process in the Chloroprene Production System

Yoshio Takasu,* Yoshiharu Matsuda,* Michiko Harada, and Misao Masaki

Faculty of Engineering, Yamaguchi University, Ube, Yamaguchi, Japan

Hiroyuki Watanabe

Toyo Soda Manufacturing Company, Research Laboratory, Shin-nanyo, Japan

Chloroprene ($\text{ClCH}=\text{CHCH}=\text{CH}_2$), an important industrial material, is usually produced by elimination of hydrochloric acid from 3,4-dichloro-1-butene (3,4-DCB) which is synthesized from butadiene and chlorine by chemical reaction at about 300°C. In the latter reaction, trans-1,4-dichlorobutene (trans-1,4-DCB) is also formed, but it is isomerized to 3,4-DCB with a catalyst. The elimination of hydrochloric acid from 3,4-DCB is performed with ethylenediamine (EDA) forming EDA solution of $\text{EDA} \cdot 2\text{HCl}$. The authors have reported in the previous papers (1, 2) that dichlorobutenes (DCB) could be formed by electrolysis of butadiene in an anolyte solution of acetonitrile (MeCN)- CoCl_2 which was separated from

the catholyte ($\text{H}_2\text{O}-\text{NH}_4\text{Cl}$) by an anion-exchange membrane.

This work has been done to develop an electrochemical synthesis process of DCB as a new process in the production of chloroprene from butadiene utilizing the $\text{EDA} \cdot 2\text{HCl}$ solution and $\text{MeCN}-\text{CoCl}_2$ solution as the catholyte and the anolyte, respectively. The advantages of this process are as follows: (i) the elimination process of hydrochloric acid from $\text{EDA} \cdot 2\text{HCl}$ solution is utilized in the electrolytic chlorination process of butadiene; (ii) it does not need the use of expensive and toxic chlorine; and (iii) the chlorination of butadiene is performed at room temperature. Although studies on the electrolytic chlorination of alkenes have been carried out by many investigators (3-5), those of butadiene have scarcely been reported (6).

* Electrochemical Society Active Member.

Key words: butadiene, electrolytic chlorination, ethylenediamine, dichlorobutene.

Experimental

Potentiostatic electrolyses were performed by use of a conventional Pyrex glass H-type cell with a separator of an anion-exchange membrane (Asahi Glass Company, "Selemion-ASV" made of polystyrene; 3 cm diam). A graphite plate of 2 cm diam and a graphite plate of 3 cm diam were used as the anode and the cathode, respectively. Highly purified butadiene was bubbled into the anolyte (MeCN containing 0.5 mol dm⁻³ CoCl₂, 40 ml) during electrolyses in order to keep the concentration of butadiene in the anolyte at a constant value, ca. 2 mol dm⁻³. Tetraalkylammonium chloride was thought to be usable in the solute of the anolyte, but the current efficiency for the formation of DCB in the electrolysis using MeCN-Me₄NCl anolyte was low (ca. 60%). The catholyte (40 ml) was an aqueous solution of NH₄Cl, NaCl, HCl, or an EDA solution containing EDA · 2HCl. Acetonitrile was dried with molecular sieves (5A) and CaH₂, and then distilled twice. Butadiene and its derivatives were determined by gas chromatography (TCD; Silicone Gum SE30-Chromosorb WAW; He). The electrolytic cell was set in a water bath thermostated at 25°C.

Results and Discussion

Table I presents the experimental conditions and the current efficiencies for the formation of DCB. Appreciable amounts of butadiene derivatives other than 3,4-DCB and trans-1,4-DCB (such as cis-1,4-dichloro-2-butene or 4-vinyl-1-cyclohexene) were not detected on the gas chromatograms. The current efficiency for dichlorobutene formation is defined as the percentage of the quantity of electricity that passed through the cell, and was calculated by assuming that the chlorination was a two-electron reaction. The quantity of electricity passed in these runs, 483C, is that required to convert ca. 4% of butadiene initially dissolved in the anolyte into DCB. In the electrolyses using an aqueous solution of such salts as NH₄Cl, NaCl, or HCl as the catholytes, the current efficiencies for the formation of DCB were 96-98%. On the other hand, when EDA solution of EDA · 2HCl (0.5M) was used as the catholyte, the current efficiency attained only 42%. As shown in Fig. 1, the current efficiency in the electrolysis using this catholyte strongly depended on the concentration of EDA · 2HCl, and gave a maximum value at 1.5 mol dm⁻³. The low current efficiency obtained when EDA-EDA · 2HCl is used as the catholyte is most likely due to transport of EDA to the anolyte (solvating Cl⁻) and subsequent oxidation. The oxidation will occur either directly at the anode or mediated since EDA-EDA · 2HCl is likely to be more reactive than butadiene. Figure 2 shows that the addition of a small amount of water to the anolyte improved the current efficiency to nearly 100%. The addition of water might allow water solvation of Cl⁻ and thus less EDA transport across the membrane. The existence of a small amount of water

Table I. Current efficiency for the formation of dichlorobutenes using various compositions of electrolytes

Catholytes	Current efficiency		
	3,4-DCB	trans-1,4-DCB	Total
H ₂ O-NH ₄ Cl (1M)	46	52	98
H ₂ O-NaCl (1M)	44	53	97
H ₂ O-HCl (1M)	37	59	96
EDA-EDA · 2HCl (0.5M)	15	27	42
EDA-EDA · 2HCl (1.5M)	28	57	85
EDA-EDA · 2HCl (0.5M)-H ₂ O (1.7M)	37	61	98

Anolyte: MeCN-CoCl₂ (0.5M)-C₄H₆ (2M); separator: anion-exchange membrane; anode material: carbon plate; cathode material: carbon plate; anode potential: 1.7V vs. Ag/AgCl; amount of anolyte: 40 ml; amount of catholyte: 40 ml; amount of electricity passed: 483C; temperature: 25°C.

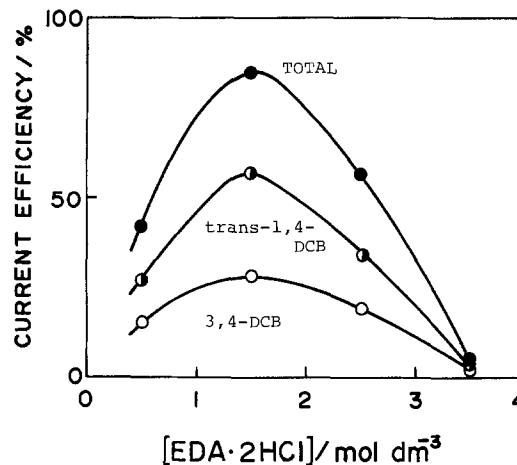


Fig. 1. Effect of EDA · 2HCl concentration in the catholyte on the current efficiency for the formation of dichlorobutenes. Anolyte: MeCN-CoCl₂ (0.5M)-C₄H₆ (2M); catholyte: EDA-EDA · 2HCl; separator: anion-exchange membrane; anode and cathode: carbon plates; anode potential: 1.7V vs. Ag/AgCl; amount of anolyte: 40 ml; amount of catholyte: 40 ml; amount of electricity passed: 483C; temperature: 25°C.

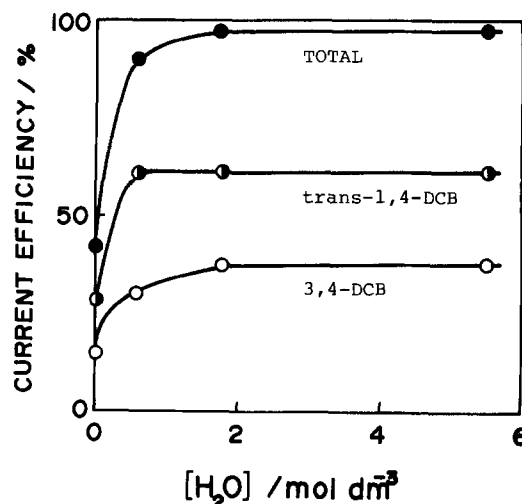


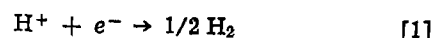
Fig. 2. Effect of H₂O concentration in the catholyte on the current efficiency for the formation of dichlorobutenes. Anolyte: MeCN-CoCl₂ (0.5M)-C₄H₆ (2M); catholyte: EDA-EDA · 2HCl (0.5M)-H₂O; other conditions are shown in the caption in Fig. 1.

in the EDA-EDA · 2HCl solution may be permissible in the recovery of EDA by distillation. It was observed, however, that the membrane was gradually harmed by the catholyte in the duration of the electrolysis when EDA-EDA · 2HCl was used as the catholyte.

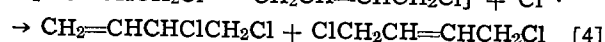
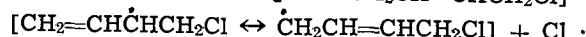
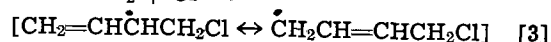
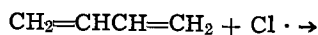
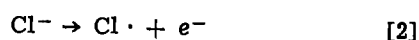
If an anion-exchange membrane which is not harmed by these electrolytes can be obtained, this electrolysis process could be considered for industrialization. Because the current efficiency for the formation of DCB is high, this process can be combined with the elimination process of hydrochloric acid from EDA-EDA · 2HCl solution formed in the production process of chloroprene from DCB by EDA.

The following reaction schemes can be proposed for the reaction.

The cathode reaction is



The anodic reaction is



Acknowledgment

The authors wish to thank Dr. Tatsuro Asawa of the Central Laboratory of Asahi Glass Company for giving us the anion-exchange membrane.

Manuscript submitted Dec. 13, 1982; revised manuscript received Sept. 20, 1983.

REFERENCES

1. Y. Takasu, Y. Matsuda, A. Shimizu, M. Morita, and M. Saito, *Chem. Lett.*, 1685 (1981).
2. Y. Takasu, Y. Matsuda, A. Shimizu, M. Harada, M. Saito, and H. Watanabe, *Denki Kagaku*, **50**, 975 (1982).
3. N. Ibi and A. Selvig, *Chem.-Ing.-Tech.*, **42**, 180 (1970).
4. A. Belanger, G. Belanger, and A. K. Vijn, *This Journal*, **118**, 1543 (1971).
5. D. A. Ashurov, A. M. Akhmedov, Zh. R. Alumyan, Sh. K. Kyazimov, and S. I. Sodykh-zade, *J. Gen. Chem. (USSR)*, **44**, 1810 (1974).
6. A. P. Tomilov, Yu. D. Smilnov, and Yu. I. Rozin, *Zh. Obshch. Khim.*, **44**, 2028 (1974).

Preparation of Vanadium-Tungsten-Oxide Wadsley-Roth Phases by Electrolytic Reduction of Molten Salts

L. F. Schneemeyer and V. Tierney

AT&T Bell Laboratories, Murray Hill, New Jersey 07974

Many framework metal oxides are interesting as materials which can reversibly incorporate lithium atoms into their crystal lattices (1). The extent and rate of the lithium insertion reactions makes some of them candidates for use as positive electrode materials for ambient temperature secondary batteries. Two compounds, $V_2WO_{7.5}$ and $V_{2.4}W_{0.6}O_7$ ¹ (2), both members of a class of compounds known as Wadsley-Roth phases (3), have recently been shown to be particularly suitable for such applications (4).

Wadsley-Roth phases have structures in which blocks of corner-shared MO_6 ($M = V, W$) octahedra are connected through regions of edge sharing, or crystallographic shear. These materials have previously been produced as powders by solid-state synthesis in which appropriate quantities of the starting materials V_2O_5 , VO_2 , and WO_3 are ground together, then heated in evacuated silica tubes until single-phase samples are obtained. Electrolysis of molten salts is an alternative method which has been used in the preparation of oxides containing transition metals in reduced oxidation states. Large well-formed crystals of alkali tungsten bronzes, vanadium spinels, and molybdenum dioxide are among the materials which have been obtained by this technique (5).

An attraction of electrochemical synthesis of materials such as $V_2WO_{7.5}$ and $V_{2.4}W_{0.6}O_7$ Wadsley-Roth phases is the deposition of a film of active material directly onto a conducting substrate to form an electrode for an ambient temperature secondary battery. The current work was undertaken to investigate the feasibility of preparing tungsten-vanadium-oxide Wadsley-Roth phases electrochemically. While no previously unknown phases were found in this study, the electrochemical synthesis of $V_2WO_{7.5}$ and $V_{2.4}W_{0.6}O_7$ from $V_2O_5 + WO_3$ melts at $T = 750^\circ\text{--}800^\circ\text{C}$ was achieved. Furthermore, single crystals of $V_2WO_{7.5}$ of substantial size, suitable for physical property measurements, have been grown.

Experimental

The apparatus used for the electrochemical crystal growth is shown in Fig. 1. The melt was contained in a high-purity recrystallized alumina crucible (Coors). Cracking of the crucible resulting from expansion of the melt upon cooling limited use of a crucible to one run. The crucible was seated in a graphite support. This assembly was contained under N_2 within a quartz vessel itself inside a Lindberg crucible furnace. Melts

were prepared from analytical-grade reagents which were dried before use. A high density, high purity pyrolytic graphite rod, Pt wire and foil, and tungsten foil (Alfa, 99.9%) were variously employed as cathode materials. A Pt-foil electrode served as the anode. No significant attack on the Pt by the melt was observed. Following deposition, traces of V_2O_5 and WO_3 were removed by washing with warm 5% aqueous NH_4OH .

A Princeton Applied Research (PAR) Model 173 potentiostat/galvanostat equipped with a Model 179 digital coulometer was used for crystal growth experiments. Samples were examined by x-ray diffraction on a Rigaku Powder Diffractometer using $CuK\alpha$ radiation and a scan speed of 2°min^{-1} . Scanning electron micrographs were taken with an Autoscan 100 Scanning Electron Microscope (Cambridge Instruments) operated at 25 kV.

Results and Discussion

Wadsley-Roth phase tungsten-vanadium oxides of composition $V_2WO_{7.5}$ and $V_{2.4}W_{0.6}O_7$ were prepared by the electrolysis of fused mixtures of WO_3 and V_2O_5 . Table I lists the experimental conditions for the growth of these materials. Reductions were carried out

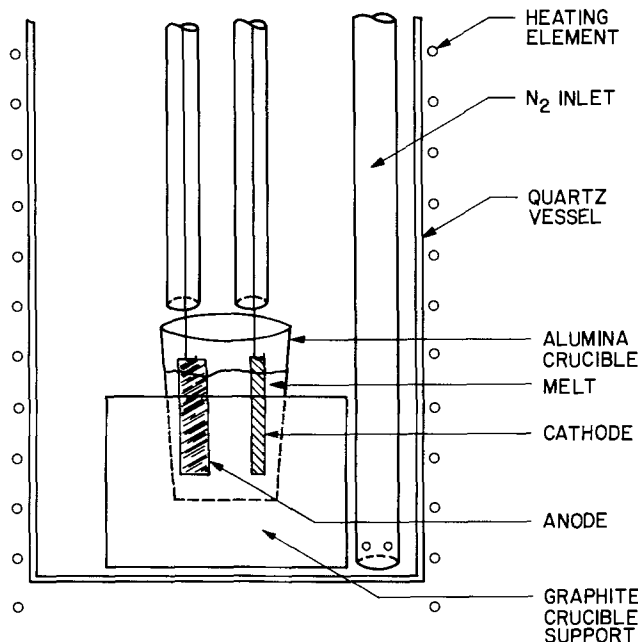


Fig. 1. Schematic representation of molten salt electrolysis system.

¹ The phase reported in the literature and referred to in this paper as having the composition $V_{2.4}W_{0.6}O_7$ has recently been shown to exist over the composition range $V_{2.5}W_{0.5}O_7$ – $V_{2.6}W_{0.4}O_7$.

* Electrochemical Society Active Member.
Key words: inorganic, electrode, synthesis.

Table I. Experimental conditions for the growth of some tungsten-vanadium-oxides by fused-salt electrolysis

Melt composition	Melt temperature	Current density	Cathode	Product
V_2O_5	800°C	100 mA/cm ²	Graphite rod	VO_2
1WO ₃ :12.5V ₂ O ₅	750°C	200 mA/cm ²	Pt foil	$V_2WO_{7.5}$ + $V_{2.4}W_{0.6}O_7$
1WO ₃ :9V ₂ O ₅	770°C	200 mA/cm ²	Pt foil	$V_2WO_{7.5}$ + $V_{2.4}W_{0.6}O_7$
1WO ₃ :4.5V ₂ O ₅	785°-800°C	50-400 mA/cm ²	Pt foil Pt wire Graphite rod	$V_2WO_{7.5}$
1WO ₃ :4V ₂ O ₅ 0.67Na ₂ WO ₄ :0.22V ₂ O ₅ :0.11WO ₃	820°C 700°C	— 20 mA/cm ²	— Graphite rod	— $V_{1-x}W_xO_5$ $x \approx 0.2$

under galvanostatic control. Current densities in the range of at least 50-200 mA/cm² were found to give crystalline deposits. At current densities below 50 mA/cm², little or no product was recovered, presumably because sufficient current must be passed to overcome a competing back reaction. The temperature in most experiments was held just above the melting point of the vanadium pentoxide-tungsten trioxide mixture. The melting point of this mixture increases with increasing proportion of tungsten trioxide. Runs for a given melt carried out at higher temperatures showed no significant variation in the phases produced or, qualitatively, in the product recovered.

The ratio of tungsten to vanadium in the melt is found to control the phase of the product formed. In the absence of WO₃, the electrolysis of molten V₂O₅ yields elongated prismatic crystals of VO₂ (6,7). At the lowest concentration of WO₃ examined in this study (1W: 25V), a mixture of V₂WO_{7.5} and V_{2.4}W_{0.6}O₇ is formed during the electrolysis. From a 1W: 9V melt, V₂WO_{7.5} is formed exclusively. The melting temperatures of mixtures with still higher tungsten trioxide concentration is above the temperature at which V₂WO_{7.5} is known to transform to a V₂O₅ structure type (8). Scanning electron micrographs of V₂WO_{7.5} crystals grown from a 1WO₃:4.5V₂O₅ melt (1W:9V)

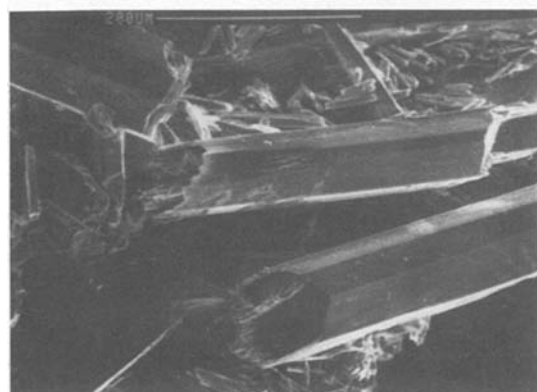
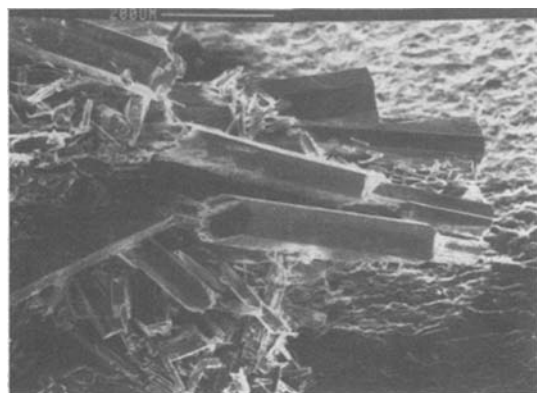


Fig. 2. Scanning electron micrographs at two magnifications of V₂WO_{7.5} crystals deposited on Pt wire at 50 mA/cm² under galvanostatic control. $T_{melt} = 785^\circ C$.

at 785°C at a current density of 50 mA/cm² onto a Pt wire cathode are shown in Fig. 2 at two magnifications. Eight sided rod-shaped crystals ~0.5 mm long are observed. Crystals of up to several millimeters in length have been grown. Precession photographs of one crystal verified the unit cell as that reported for V₂WO_{7.5} and suggested some disorder along the unique axis of the monoclinic unit cell. A scanning electron micrograph of one end of one such V₂WO_{7.5} crystal is shown in Fig. 3. Evident are the well-developed faces of this crystal. The growth of this crystal resulted in a large void in its center. Similar voids were not observed in other crystals.

The electrochemical formation of the Wadsley-Roth phases (V₂WO_{7.5} and V_{2.4}W_{0.6}O₇), rather than W-substituted VO₂ phases, is interesting. The electrolysis of a sodium tungstate melt containing WO₃ and V₂O₅, as listed in Table I, does yield needles of W_xV_{1-x}O₂ with $x \sim 0.2$ as determined from relative peak heights in an x-ray fluorescence experiment. Since electrolyses of V₂O₅-WO₃ melts were carried out at temperatures of 750°-800°C while the Na₂WO₄ + V₂O₅ + WO₃ melt was maintained at 700°C, a difference of only 50°-100°C, temperature is assumed to be of minor importance in the determination of the phase of the resulting material. Of greater importance to the nature of the resulting material may be the relative acidity of the melt. In the preparation of members of the mixed spinel system (Co_{1+x}V_{2-x}O₄) by fused salt electrolysis, it was shown that more reduced products were formed with increasing basicity of the flux (9). Similar behavior is observed in this system. Here, the more basic melt formed from Na₂WO₄ + WO₃ + V₂O₅ yields as its product tungsten-substituted VO₂, while the relatively more acidic WO₃-V₂O₅ melts yield V₂WO_{7.5} and V_{2.4}W_{0.6}O₇. A relationship between melt composition and oxygen activity at the cathode thought to control the composition of the product phase in electrochemical tungsten-bronze syntheses (10) may also be a factor in this system.

Although crystalline samples of the Wadsley-Roth phase metal oxides (V₂WO_{7.5} and V_{2.4}W_{0.6}O₇) have been obtained electrochemically, the present study does not address optimization of product yields. Also,



Fig. 3. Scanning electron micrograph of one end of a V₂WO_{7.5} crystal deposited onto a Pt wire at 50 mA/cm² under galvanostatic control. $T_{melt} = 785^\circ C$.

traces of the melt which cling to the samples following deposition are difficult to preferentially dissolve. The use of alternative melts such as alkali halide-based melts to achieve the deposition of $V_2WO_{7.5}$ and $V_{2.4}W_{0.6}O_7$ or optimization of deposition conditions based on the present melt are possible approaches to countering these limitations.

In summary, the electrochemical synthesis of $V_2WO_{7.5}$ and $V_{2.4}W_{0.6}O_7$ in the form of crystalline deposits on conducting substrates as economical as carbon has been demonstrated, and shows promise for the fabrication of battery electrodes. Growth of single crystals of $V_2WO_{7.5}$ of suitable size and quality for physical property measurements has been achieved.

Acknowledgment

The authors are grateful to Elsa Reichmanis for assistance with scanning electron microscopy, to Robert J. Cava for precession photographs, and to Donald W. Murphy for helpful comments.

Manuscript submitted March 27, 1983; revised manuscript received Sept. 19, 1983.

AT&T Bell Laboratories assisted in meeting the publication costs of this article.

REFERENCES

1. M. S. Whittingham, *Prog. Solid State Chem.*, **12**, 1 (1978).
2. R. J. Cava, D. L. Kleinman, and S. M. Zahurak, *Mater. Res. Bull.*, **18**, 869 (1983).
3. A. D. Wadsley and S. Andersson, in "Perspectives in Structural Chemistry," Vol. 3, J. Dunitz and J. A. Ibers, Editors, John Wiley and Sons, New York (1970).
4. R. J. Cava, D. W. Murphy, and S. M. Zahurak, *This Journal*, **130**, 243 (1983).
5. A. Wold and D. Bellavance, in "Preparative Methods in Solid State Chemistry," P. Hagemuller, Editor, p. 279, Academic Press, New York (1972).
6. D. B. McWhan, M. Marezio, J. P. Remeika, and P. D. Dernier, *Phys. Rev. B*, **10**, 490 (1974).
7. V. N. Andreev, N. E. Timoshchenko, and F. A. Chudnovsky, *J. Cryst. Growth*, **52**, 772 (1981).
8. W. Freundlich, *C.R. Habd. Seances Acad. Sci.*, **260**, 3077 (1965).
9. D. B. Rogers, A. Ferretti, and W. Kunmann, *J. Phys. Chem. Solids*, **27**, 1445 (1966).
10. M. S. Whittingham and R. A. Huggins, in "Solid State Chemistry," NBS Special Publication No. 364, p. 51 (1972).



Oxidation Characteristics and Electrical Properties of Low Pressure Dual TCE Oxides

Y. C. Cheng and B. Y. Liu*

Department of Electrical Engineering, University of Hong Kong, Hong Kong

ABSTRACT

A detailed investigation is conducted on the oxidation characteristics and electrical properties of very thin gate oxides (70-400Å), prepared by a novel two-step trichloroethylene (dual TCE) oxidation process. It is demonstrated that very thin oxide films can be accurately and reproducibly prepared under a variety of oxidation conditions. A reversal of relative oxidation rate of (111) and (100) silicon surfaces is observed at low oxygen partial pressure similar to that reported by earlier researchers. In addition to this observation, we find that the reversal is also strongly dependent on the TCE flow rate. Minima are observed in ΔV_{FB} and V_{FB} as a function of TCE flow rate. While the former results agree with earlier work, the minimum in the latter case is located differently, at a lower flow rate. The breakdown fields on oxides grown by various techniques are compared, and dual TCE oxides are shown to have good breakdown characteristics.

Recently, great interest has been expressed in very thin gate oxide (1). This has been motivated by the requirement of a very thin gate as the key element in the basic circuit device in VLSI circuits, and the application of thin oxide in electrically alterable read-only memory devices. For 1 μm channel length MOSFET's, oxides of the order of 200Å will be used as the dielectric layer under the gate electrode. In order to routinely produce reliable oxides of this thickness, various oxidation techniques have been proposed (2-7). These novel oxidation methods are necessary because the well-established standard dry oxidation at high temperature is not satisfactory, mainly because of (i) difficulty in controlling accurately the thickness of the thin oxide layer because of the fast oxidation rate, and (ii) poor oxide quality as manifested by low electric field breakdown and a large amount of interface charge.

To circumvent the former difficulty, the oxide is usually grown either at low temperature or under low partial pressure (2, 3). The second problem can basically be solved by a two-step process (5-7), which consists of an initial period of low temperature oxidation to provide a high dielectric breakdown strength, and a final phase of high-temperature oxidation to provide a good oxide-silicon interface (8). In order to encompass both of the above advantages and to provide additional beneficial passivation ability against mobile ions, a two-step HCl oxidation technique has been proposed (6). While it has been established that HCl oxidation (9) provides a number of benefits, it does have some practical problems in implementation, as HCl is a highly corrosive and dangerous gas. As a better alternative, a dual TCE process has recently been suggested to grow reliable thin gate oxide (7). It was reported that very thin oxide (70-400Å) with high integrity can be routinely produced with this technique.

However, in order to assess whether or not the dual TCE oxidation technique can be eventually adopted and implemented in any practical manufacturing

process requiring thin oxide layers, the oxidation characteristics and the properties of these oxides must be well understood. This article is a detailed investigation of the dual TCE process.

Experimental Methods and Results on Oxidation Characteristics

For the present studies, p-type <111> oriented silicon wafers with a resistivity of 1-4 $\Omega\text{-cm}$, and n-type <100> oriented wafers with 2-3 $\Omega\text{-cm}$ were used. These were cleaned by a standard cleaning procedure and were subsequently oxidized in a resistance-heated furnace at various temperatures in the presence (or absence) of a small amount of TCE. TCE vapor was added to the oxidizing ambient, which consisted of dry oxygen and dry nitrogen. The partial pressure of oxygen was controlled by adjusting the relative proportion of oxygen and nitrogen. The amount of TCE was controlled by varying the flow rate of another dry nitrogen inlet through a bubbler filled with purified liquid TCE kept at 0°C.

The dual TCE process consists of a low temperature dry oxidation, a low temperature TCE oxidation, and a high temperature TCE oxidation with low oxygen partial pressure. This can be followed by nitrogen annealing if necessary. More detailed information on this

Table I. Summary of two dual TCE oxidation processes and a two-step dry oxidation process

Step	Conditions	Dual A	Dual B	Two-step dry oxide
1	Gas (ml/min) Temp. (°C) Time (min)	O ₂ (500) 850 10	O ₂ (500) 850 10	O ₂ (500) 850 25
2	Gas (ml/min) Temp. (°C) Time (min)	O ₂ :TCE/N ₂ 500:25 850 25	O ₂ :TCE/N ₂ 500:30 850 20	
3	Gas (ml/min) Temp. (°C) Time (min)	N ₂ :O ₂ :TCE/N ₂ 1350:150:25 1050 46	N ₂ :O ₂ :TCE/N ₂ 1350:150:9 1050 74	N ₂ :O ₂ 1350:150 1050 82
4	Gas (ml/min) Temp. (°C) Time (min)	N ₂ (1350) 1050 20	N ₂ (1350) 1050 20	N ₂ (1350) 1050 20

* On leave from South China Institute of Technology, Guangzhou, China.

Key words: thin silicon oxide, oxidation, trichloroethylene.

oxidation technique can be found elsewhere (7). The essential features of two dual TCE processes and a two-step dry oxidation (for comparison) are summarized in Table I.

The oxide film thickness was measured by a Rudolph ellipsometer at a wavelength of 5461Å, taking the silicon refractive index to be 4.040-0.031i (3). Dielectric breakdown measurement was performed with the aluminum dots biased negatively for p-Si, or positively for n-Si, i.e., with n-type or p-type Si in accumulation. The breakdown voltage was measured when the current reached a magnitude of 0.01 mA. Fixed oxide charges and mobile ions were deduced from the flat-band voltages based on the high frequency capacitance measurements.

As indicated in Table I, the dual TCE oxidation technique actually consists of two processes (7). Therefore, the relationship between the overall thickness and time must be accurately determined for a given dual TCE oxidation process. The experimental

plots of oxide thickness as a function of TCE treatment time at P_{O_2} (oxygen partial pressure) = 0.05, 0.1, and 1.0 atm are shown in Fig. 1a-c), respectively.

In Fig. 1a, where the oxygen partial pressure is very low ($P_{O_2} = 0.05$ atm), experimental results from both high and low oxidation temperature show that the oxidation rate is faster on a (100) surface than on a (111) surface. This is consistent with the observation of the occurrence of a reversal of relative oxidation rates of $\langle 111 \rangle$ and $\langle 100 \rangle$ oriented substrates at low oxygen partial pressures (2, 3). However, there is one major difference: earlier observations were made in an atmosphere containing oxygen or water vapor and inert gases, whereas the case in question contained chlorine species in addition to the above gases. However, the same phenomenon of reversal occurs in both situations.

The oxide thickness vs. time characteristics are similar to the generally observed linear-parabolic type of behavior (2). The higher the oxidation temperature, the faster and closer to the parabolic behavior is the

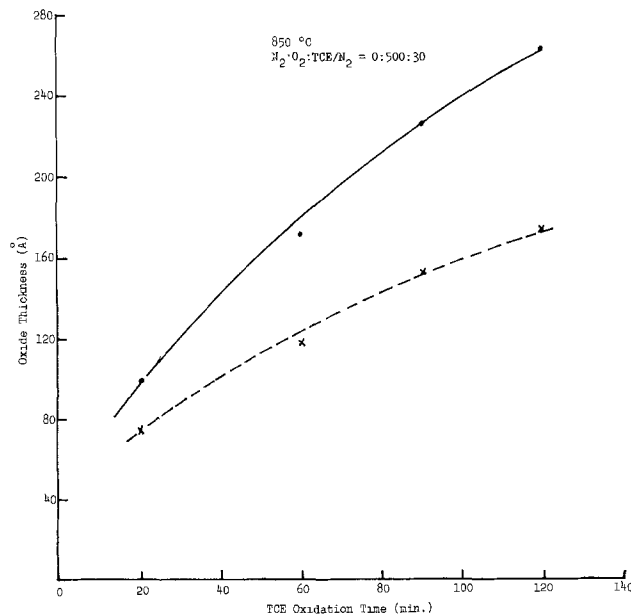
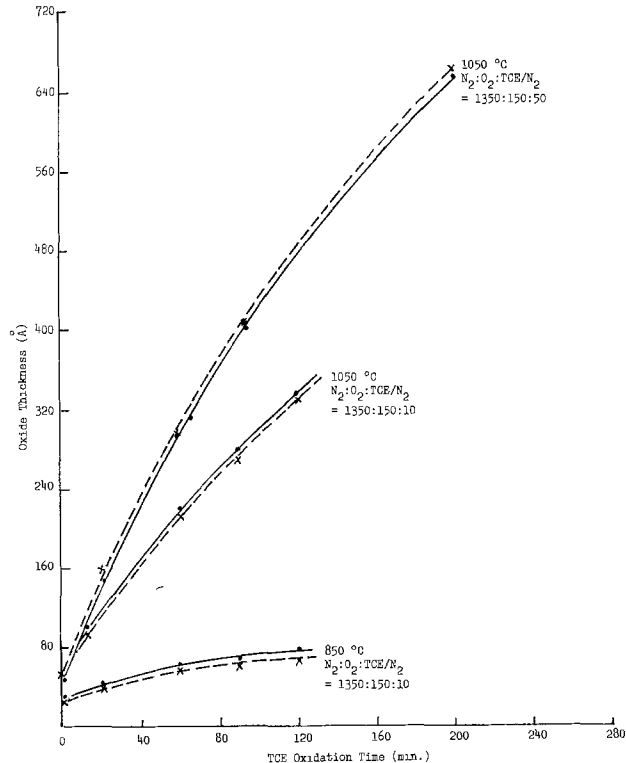
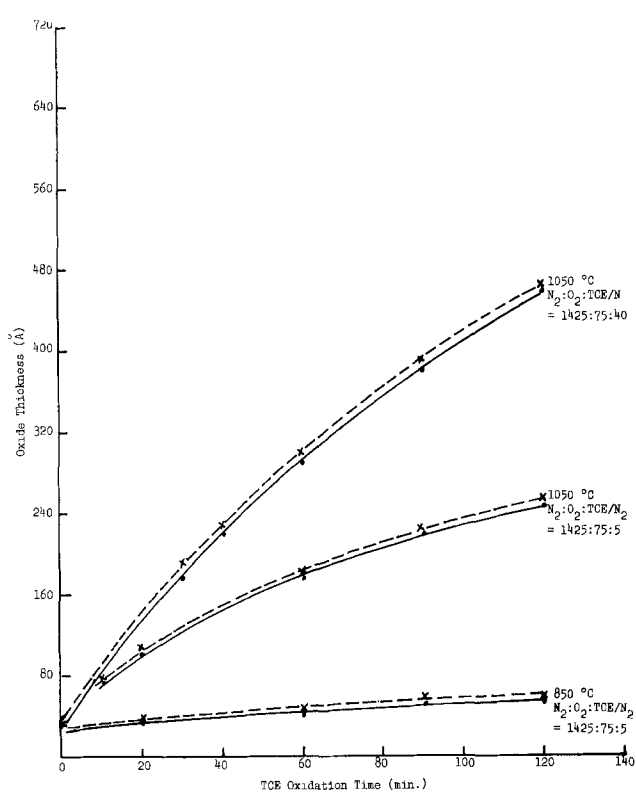


Fig. 1. (a, upper left) Measured oxide thickness vs. TCE oxidation time for p-type (●) and n-type (×) Si at $P_{O_2} = 0.05$ atm. Total oxidation time is 10 min dry oxidation + TCE oxidation time at 850°C, and 5 min dry oxidation + TCE oxidation time at 1050°C. (b, upper right) Same as a, but $P_{O_2} = 0.1$ atm. (c, left) Same as a, but $P_{O_2} = 1.0$ atm.



growth. At a lower temperature, the growth is slow, as expected, and the characteristics are almost a straight line. However, there is another important controlling factor, i.e., the TCE flow rate, which modifies the oxidation rate in a significant manner. In fact, a higher TCE flow rate behaves as if it transforms the oxidation characteristics to that of a higher temperature.

Figure 1b shows similar oxidation characteristics, but at somewhat higher oxygen partial pressure ($P_{O_2} = 0.1$ atm). An interesting observation is found at 1050°C . When the TCE flow rate varies, a reversal of relative oxidation rates of (111) and (100) surfaces occurs. This happens when there is hardly any change of oxygen partial pressure and the temperature is constant. The oxidation characteristics at lower TCE flow rate and at lower temperature are similar to those normally observed, i.e., the oxidation rate at the $\langle 111 \rangle$ oriented surface is faster.

Figure 1c presents results when the oxygen partial pressure is 1 atm. The oxidation characteristics are similar to the case of oxidation in pure oxygen, except that the rate is faster due to the presence of trichloroethylene.

The effect of oxygen partial pressure and TCE/ N_2 flow rate on the oxide thickness of two dual TCE oxidation processes is summarized in Fig. 2. In general, silicon substrates with $\langle 111 \rangle$ oriented surfaces are oxidized more readily than substrates with $\langle 100 \rangle$ orientations at the same oxidation temperature and oxidant pressure. However, at lower P_{O_2} ($P_{O_2} \sim 0.07$ atm at 1050°C and $P_{O_2} \sim 0.04$ atm 850°C), this dependence of oxidation rate on orientation is reversed. As mentioned earlier, this behavior is almost identical to that of oxidation in pure oxygen (2).

Another reversal in the oxidation rate was observed when the TCE/ N_2 flow rate was increased. Typical experimental results are summarized in Fig. 3 to illustrate the effect of TCE flow rates on the oxide growth at different oxygen partial pressures. A comparatively higher TCE flow rate will bring a reversal in the oxidation rate. The higher the oxygen partial pressure,

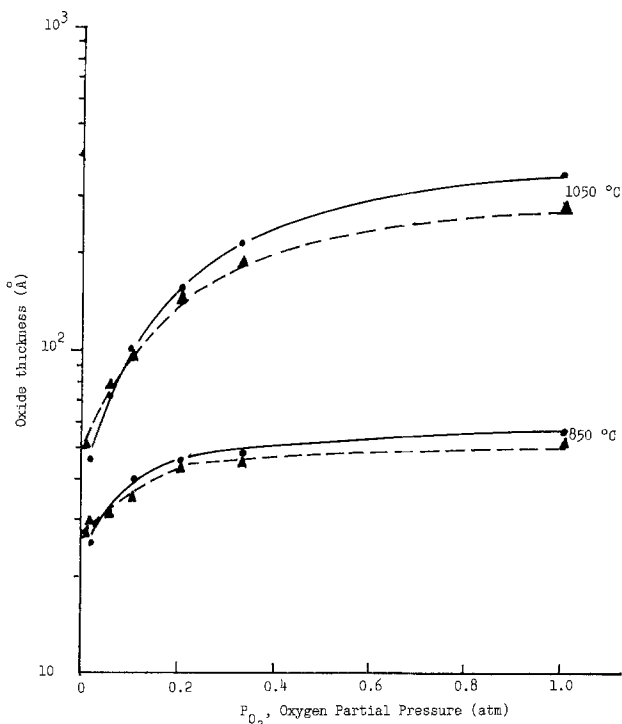


Fig. 2. The effect of O_2 partial pressure on the thickness of p-type (●) and n-type (×) SiO_2 films grown by TCE oxidation process at 850°C and 1050°C . $t_{\text{oxid}} = 10$ min dry oxidation + 10 min TCE oxidation at 850°C , and $t_{\text{oxid}} = 5$ min dry oxidation + 10 min TCE oxidation at 1050°C . $N_2 + O_2 + TCE/N_2 = 1500$ ml/min and $TCE/N_2 = 4.5$ ml/min.

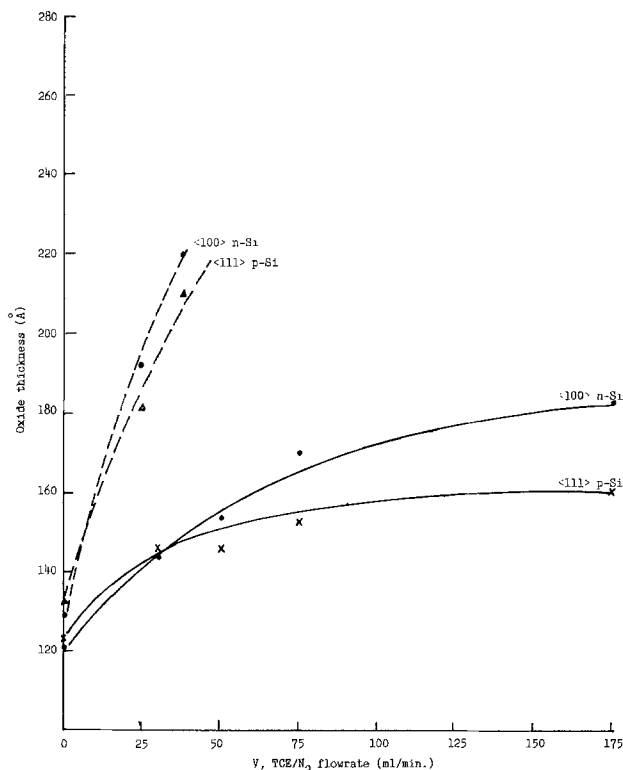


Fig. 3. The effect of TCE/ N_2 flow rate on the thickness of TCE oxides for 1050°C oxidation at different partial oxygen pressure. $t_{\text{oxid}} = 5$ min dry oxidation + 40 min TCE oxidation and N_2 : O_2 :TCE/ $N_2 = 1425$:75:V for $P_{O_2} = 0.05$ (broken line); $t_{\text{oxid}} = 5$ min dry oxidation + 20 min TCE oxidation and N_2 : O_2 :TCE/ $N_2 = 1350$:150:V for $P_{O_2} = 0.1$ (solid line).

the higher the TCE flow rate needed to affect the reversal. In general, the higher the TCE flow rate, the faster will $\langle 100 \rangle$ oriented surfaces be oxidized compared to $\langle 111 \rangle$ oriented surfaces, at both 0.05 and 0.1 atm of oxygen partial pressure.

The experimental data show that the oxide thickness can be accurately and reproducibly controlled by the oxidation time, once a particular set of oxidation conditions is given. The oxidation kinetics are not fully understood at present, and further discussion is deferred to a later section.

Electrical Properties of Dual TCE Oxides

To assess the overall quality of the dual TCE oxides, we have measured the flatband voltages, analyzed the passivation ability, and examined the dielectric breakdown characteristics. Figure 4 summarizes the experimental results of flatband voltages as a function of the TCE flow rate. Similar to earlier results (10), a minimum in flatband voltage is observed. However, the location of the minimum in the present case is different from that of the earlier work; the present minimum occurs when the TCE flow rate is about 10 ml/min, whereas in the other case it occurs when the flow rate is around 50 ml/min. To appreciate the difference, we should note that in the present work the oxide thickness is of the order of 100–200 Å, while in the previous work (10) the oxide thickness varied from 900 to 1650 Å. It has been reported (11) that fixed oxide charge density depends on the thickness of the oxide layer; it increases in magnitude as the oxide thickness decreases. This effect may be related to our observation. Another important difference is that the oxygen partial pressure in the present case is low compared to that of earlier work. However, it remains to be confirmed whether or not the location of the minimum varies with the oxide thickness and/or oxygen partial pressure.

The usual temperature bias stress is applied to the samples to deduce the amount of mobile Na^+ ions from the flatband shift, ΔV_{FB} . Figure 4 shows a typical

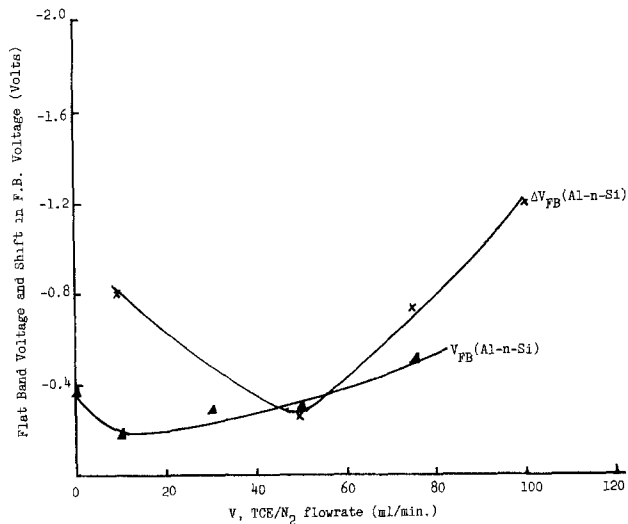


Fig. 4. The effect of TCE/N₂ flow rate on V_{FB} and ΔV_{FB} at $P_{O_2} = 0.1$ atm, $T = 1050^\circ\text{C}$, $t_{\text{oxid}} = 5$ min dry oxidation + 20 min TCE oxidation and $N_2:O_2:TCE/N_2 = 1350:150:V$ for n-type $\langle 100 \rangle$ Si.

set of the experimental data. A minimum is observed in ΔV_{FB} and occurs around the same region as in the earlier work (10) when the TCE flow rate is approximately 50 ml/min. In terms of mobile ion density, the minimum value of ΔV_{FB} corresponds to $2-3 \times 10^9 \text{ cm}^{-2}$, showing the effectiveness of the passivation ability.

Figure 5 summarizes two sets of experimental results for two different dual TCE processes. These curves clearly show that the passivation effect is not achieved abruptly as a function of the oxidation time. This experimental result implies that the usual threshold behavior observed in HCl oxides is not found here. Instead, the passivation ability, i.e., in terms of diminishing the mobile ion density, is acquired gradually, as shown in Fig. 5. In order to achieve a minimum acceptable level of mobile ions, a minimum period of

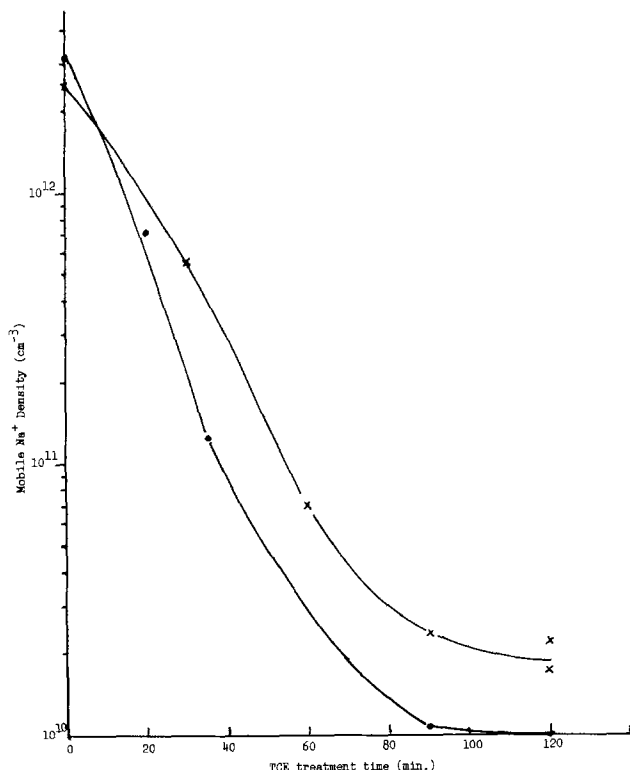


Fig. 5. The effect of TCE treatment time and TCE flow rate on sodium passivation at 1050°C . $t_{\text{oxid}} = 5$ min dry oxidation + TCE + treatment time. $N_2:O_2:TCE/N_2 = 1350:150:50$ (●) and $1425:75:40$ (×).

TCE treatment time is required. This effect may set a limit on the minimum attainable oxide thickness. An optimum process design must be determined from the oxidation characteristics, the effect of TCE flow rate, and the passivation properties, if the dual TCE process is to be implemented as a production process.

Another important electrical property is the breakdown characteristics. In an earlier work (7), we presented an analysis of the dielectric breakdown strength as a function of various TCE oxidation processes. Figure 6 shows typical breakdown characteristics of two-step dry oxides and dual TCE oxides. The dry oxide MOS diode showed a fast transition from an initial high resistive state (Fig. 6a) to a conductive state (Fig. 6b) once the maximum field exceeded the breakdown field strength. However, this type of abrupt transition was not observed in dual TCE oxides (Fig. 6c and 6d) until the current increased to a level of a few hundred microamperes. This breakdown characteristic suggests that the breakdown is nondestructive before maximum equilibrium current is exceeded. This implies that its breakdown voltage is improved somewhat over that of a two-step dry oxide sample.

The breakdown current (i.e., the maximum equilibrium current just prior to breakdown) of various oxides is summarized in Table II. The two-step dry oxidation sample yields a breakdown current only of the order of $10 \mu\text{A}$. The breakdown current in oxide films grown by two different dual TCE oxidation processes is larger by one to two orders of magnitude, at about $150-215 \mu\text{A}$ and $500-800 \mu\text{A}$, respectively. These results suggest that oxide films, obtained by the dual TCE technique, have good oxide integrity and superb dielectric breakdown properties, attributes that are ideally suited as the key element in MOS circuits in very large scale application.

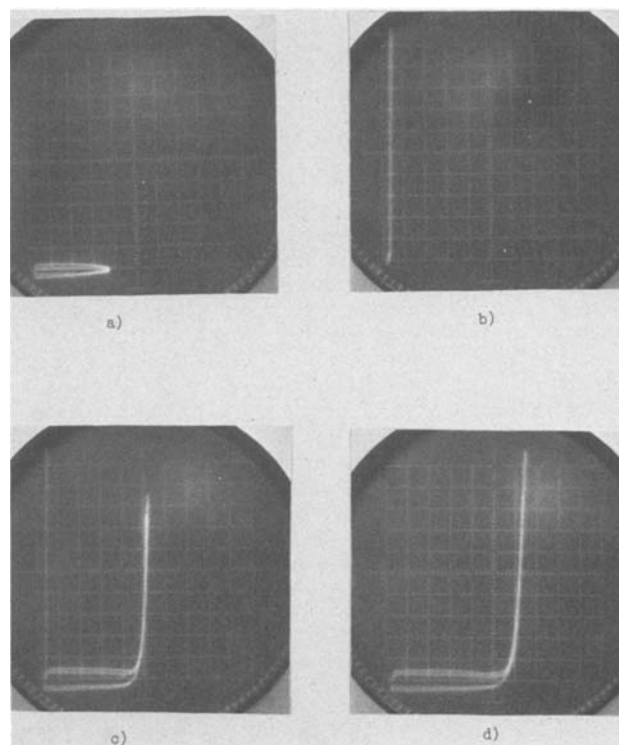


Fig. 6. Typical breakdown characteristics of the different oxides for $\langle 100 \rangle$ n-Si. Positive voltages were applied to $0.6 \times 0.6 \text{ mm}^2$ Al dot electrodes. a) and b) are for two-step dry oxide (260Å) just prior to breakdown (5V per horizontal division) and after breakdown ($10 \mu\text{A}$ per vertical division), respectively. c) is for dual TCE oxide A, where oxide thickness is 240Å with $100 \mu\text{A}$ per vertical division and 5V per horizontal. d) is for dual TCE oxide B, where oxide thickness is 310Å with $50 \mu\text{A}$ per vertical division and 5V per horizontal.

Table II. Comparison of the breakdown properties, fixed charge density, and passivation capability against mobile ions for various oxides

Oxidations cycles	Oxide thickness (Å)	Breakdown field (MV/cm)	Breakdown current (μA)	Fixed charge density, Q_{ss} (cm ⁻²)	Mobile Na ⁺ density (cm ⁻²)
Dual TCE A	240	10.42	150-215	5.38 ~ 6.49 × 10 ¹⁰	3.8 × 10 ¹⁰ ~ 1.9 × 10 ¹¹
Dual TCE B	310	10.32	500-800	5.71 ~ 6.20 × 10 ¹⁰	2 × 10 ⁹ ~ 4.5 × 10 ⁹
Two-step dry oxide	260	7.69	< 10	3.86 ~ 4.31 × 10 ¹⁰	1 × 10 ¹¹ ~ 1.03 × 10 ¹¹

To give an overall comparison of samples prepared from various oxidation processes, Table II summarizes the breakdown properties, charge density, and passivation capability against the mobile ions. From this table, it can be inferred that the dual TCE B oxidation cycle gives an overall superior oxide film in most respects. The improvement in qualities over that of the standard or two-step dry oxidation is remarkable. More investigation could be done to facilitate a practical implementation.

Discussion and Conclusion

In the search for a viable method to routinely grow very thin gate oxides with reliable qualities, we have examined in some detail a novel technique called dual TCE process. It is similar to a two-step dry oxidation method, except that the oxidation atmosphere contains also a small amount of trichloroethylene, and so provides the added benefits of a high dielectric breakdown strength and passivation against mobile sodium ions. It is also analogous to a two-step HCl technique, except that TCE is known to be easier and safer to handle than HCl.

There are a few characteristic properties concerning the dual TCE process. A reversal of relative oxidation rates of <111> and <100> oriented silicon substrates is observed at low oxygen partial pressures and at comparatively fast TCE flow rates. The observed reversal is similar to that reported for dry oxidation at low pressure (2, 3), except it is complicated by the presence of TCE. The oxidation kinetics of the pressure-dependent reversal, with respect to the orientation of the substrate, cannot be satisfactorily explained in terms of the Deal-Grove or Cabrera-Mott mechanisms, even for an atmosphere of only oxygen and inert gas. With the added complication of the active role played by trichloroethylene in oxidation, the kinetics is even more complex than the previous case. In addition to pressure-dependence on oxygen, the observed reversal in the relative oxidation rates is a strong function of TCE flow rate. The mechanism demands a more detailed investigation, and a model is being developed.

The influence of trichloroethylene on flatband voltages of MOS capacitors has been reported by Heald *et al.* (10). Similar observations are also made in the present investigation, with the exception of one major difference in the experimental results and at least two important differences in the experimental conditions. In the earlier work (10), minima were observed in flatband (V_{FB}) and shift in the flatband voltage (ΔV_{FB}) as a function of TCE flow rate, and both minima occur at about 50 ml/min. Our result for ΔV_{FB} agrees with that of Heald *et al.* (10), but our minimum in V_{FB} is at a much lower TCE flow rate. This difference may be due to the fact the oxygen partial pressure is very low in the present case, of the order of 0.1 atm compared to about 1 atm in the other case, and also to the fact our oxide is very thin, on the order of 200Å as compared to about 1600Å of earlier work. As a consequence it is impossible to simultaneously minimize V_{FB} and ΔV_{FB} as a function of the TCE flow rate. This restriction means that we can only locate a range of flow rate, e.g., between 30 and 40 ml/min where both the fixed oxide charge density and the mobile ion density are relatively low, but not at a minimum value.

While the dual TCE oxide possesses a good passivation ability, the acquiring of the capability against mobile ions is rather gradual, not exhibiting the threshold behavior as in the standard HCl oxide (12). This result implies that there is a lower limit on the oxide thickness, since a minimum TCE treatment time is required to obtain the passivation capability. The mechanism of the chlorine atoms' neutralizing the sodium ions has not been investigated in detail. It is not known whether the passivation mechanism is the same in both thin and thick oxide layers. In particular, the dependence on the TCE flow rate requires a very detailed and systematic investigation if the mechanism is to be well understood.

In this paper, we have presented general properties of a novel oxidation process to grow ultrathin but reliable oxide layer. We find that the overall qualities are acceptable for semiconductor application, when compared to the existing two-step dry oxidation and dual HCl process. With its added advantages over HCl oxidation, the dual TCE oxidation technique presents itself as a very promising candidate to become a viable manufacturing process to prepare the necessary thin oxide layers in semiconductor work. In summary, we find that the present oxidation process provides an accurate control of the oxide thickness, good oxide integrity in terms of high breakdown field, low density of interface charges, and passivation ability against mobile ions.

However, we still have occasionally observed hysteresis, especially if the optimum TCE flow rate is not used, in a manner similar to that reported in the earlier TCE work (10). This can be eliminated by applying bias stress cycling a couple of times. This aspect of properties will further be investigated, together with our ongoing work on studies in surface mobility of very thin oxide MOSFET's, analysis of the oxidation kinetics, and experimentation with novel IC structures employing thin oxide layers from dual TCE process.

Acknowledgments

This work was supported in part by the Industrial Development Board of Hong Kong.

Manuscript submitted July 5, 1983; revised manuscript received Oct. 3, 1983.

REFERENCES

1. S. K. Lai, in "Silicon Materials Science and Technology," H. R. Huff, R. J. Kriegler, and Y. Takeishi, Editors, pp. 416-426, The Electrochemical Society Softbound Proceedings Series, Pennington, NJ (1981).
2. Y. Kamigaki and Y. Itoh, *J. Appl. Phys.*, **48**, 2891 (1977).
3. S. I. Raider and L. E. Forget, *This Journal*, **127**, 1783 (1980).
4. A. C. Adams, T. E. Smith, and C. C. Chang, *ibid.*, **127**, 1787 (1980).
5. C. Hashimoto, S. Muramoto, N. Shioni, and O. Nakajima, *ibid.*, **127**, 129 (1980).
6. J. Steinberg, *ibid.*, **129**, 1778 (1982).
7. B. Y. Liu and Y. C. Cheng, Submitted to *This Journal*.
8. Y. C. Cheng, *Prof. Surf. Sci.*, **8**, 218 (1977).
9. R. J. Kriegler, Y. C. Cheng, and D. R. Colton, *This Journal*, **119**, 388 (1972).

10. D. L. Heald, R. M. Das, and R. P. Khosla, *ibid.*, **123**, 302 (1976).
 11. H. P. Vyas, G. D. Kirchner, and S. J. Lee, *ibid.*, **129**, 1757 (1982).
 12. Y. C. Cheng, in "Modern Problems of Surface Physics," I. J. Lalov, Editor, pp. 620-654, Bulgarian Academy of Science, Sofia, Bulgaria (1981).

Surface Charges in a ZnO-B₂O₃-SiO₂ Glass/Silicon System

Y. Misawa, H. Hachino, S. Hara, and M. Hanazono

Hitachi, Limited, Hitachi Research Laboratory, Hitachi, Ibaraki, Japan

ABSTRACT

ZnO-B₂O₃-SiO₂ glasses of different compositions were prepared and the surface charges in glass/silicon systems in which these glasses were used, were studied by measuring the capacitance-voltage curves of metal-glass-silicon capacitors. The effects of glass film thickness, glass composition, and conductivity (n- and p-types) of silicon substrates on surface charges in glass/silicon systems were investigated. The surface charge density of n-type silicon changed in the negative direction with increasing glass film thickness and became constant with a thickness of more than 20 μm . The more negative the glass charge, the lower was its surface-state density. The surface-charge density of glass coated n-type and p-type silicon substrates were found to be linearly related. The surface charge density of mixed glasses with different surface charge density was also investigated.

Glasses which have as principal components ZnO-B₂O₃-SiO₂ are widely used as surface passivants for such silicon power devices as thyristors, transistors, and diodes. Since these glasses are electrically stable at high temperatures and in high electric fields (1, 2), they can readily be applied as a thick film, and they are resistant to humidity and have low ionic mobility. However, in order to allow better designing of glass passivated silicon devices, it is necessary to understand the surface charge configuration in a glass/silicon system. The effects of additives to ZnO-B₂O₃-SiO₂ tertiary glasses on the surface charge density and C-V (capacitance-voltage) shift with B-T (bias-temperature) treatment have already been reported (3). We have described the surface charge configuration of ZnO-B₂O₃-SiO₂ glasses to which PbO, Sb₂O₃, and SnO were added (4) when fired under various conditions.

However, no one has yet reported on the surface charge configuration of the tertiary ZnO-B₂O₃-SiO₂ glass/silicon system. Therefore, we prepared samples of ZnO-B₂O₃-SiO₂ glasses of different compositions and investigated the surface charge configurations in the resultant glass/silicon systems. We also investigated the surface charge configurations in a mixed glass/silicon system.

Experimental

Glass preparation.—The zinc oxide, boron oxide, and silicon oxide components were each weighed considering the weight loss that occurs during the fusion process. The weight loss of each material was computed from the weight change during the fusion process. These materials were then mixed in a revolving mixer. The mixed powder was fused at 1300°C in air. The fused glass was then poured into cold water. The glass frits that were produced were ground in a ball mill to give mean particle sizes of about 4 μm . Table I shows the composition of the glasses produced.

Measurements.—The surface-charge density (N_{FB}) in a glass/silicon system was measured by forming metal-glass-silicon (MGS) capacitors. The MGS capacitors were prepared according to the following procedure. An electrophoretic method was used to deposit the glass powder on a silicon substrate (Table II). Before glass deposition, about 2 μm of the silicon wafer surface was etched off. The deposited glass powder was fired in oxygen at 700°C. Metal electrodes (diameter 2 mm) were formed on the glass film by evaporating aluminum. Deviation of glass film thickness under the electrode of each sample was less than

3 μm . Samples with large bubbles and pin holes in glass films were not used for the C-V measurements. The capacitance of the MGS capacitors was measured with an MIS capacitance meter (Model MI 312F, Sanwa Radio Measurement Works) at a frequency of 1 MHz. Voltage was applied to the sample using a dc voltage source connected to the capacitance meter. Voltage ramping was done manually. The voltage shift, with hysteresis, of the C-V curve was about several volts. This voltage corresponded to a surface charge density of 10^{10} cm^{-2} , which was very small, and hence neglected.

Results and Discussion

Relation between surface-charge density and glass film thickness.—MGS capacitors using glass no. A in films of various thicknesses were prepared by controlling the deposition time. The relationship between surface charge density and glass film thickness is shown in Fig. 1. The sign of the surface-charge density is defined as follows. The positive sign is the direction of accumulation on n-type silicon surfaces, while the negative sign is the direction of inversion on the same surfaces. When a glass film is thin, the surface charge is positive. However, the surface charge shifts rapidly in the negative direction with increasing film thickness and becomes negative with a glass film thickness of 9 μm . The surface charge density is constant with a glass film thickness of more than 20 μm .

This tendency is the same as that of Al₂O₃-Si system (5). Therefore, assuming that the surface-charge dis-

Table I. Glass compositions (w/o)

Glass no.	ZnO	B ₂ O ₃	SiO ₂
A	65.4	24.5	10.1
B	68.0	21.0	11.1
C	62.5	27.5	10.0
D	68.4	20.0	11.6

Table II. Properties of silicon substrates

Conductivity type	n	p
Dopant	Phosphorus	Boron
Resistivity, $\Omega \cdot \text{cm}$	9-15	8-12
Crystal orientation	111	111
Method of production	CZ*	CZ*
Surface finish	Mirror polish	Mirror polish

* CZ: Czochralski.

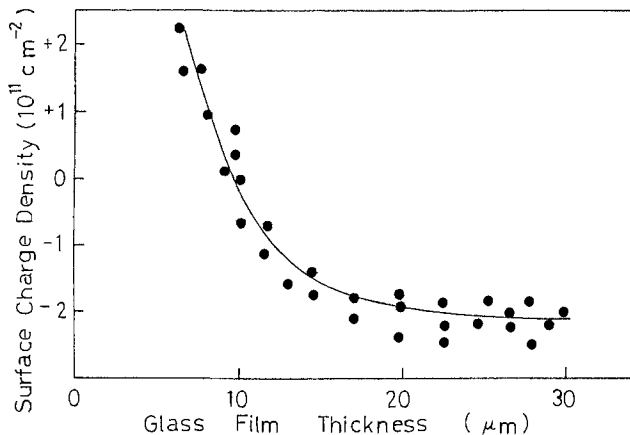


Fig. 1. Relationship between surface-charge density and glass film thickness.

tribution is the same for the same glass film thickness, the relation between surface-charge density (N_{FB}) and glass film thickness can be approximated for the Al_2O_3 -Si system (5) by

$$N_{FB}(X) = -(A - B^{-\alpha x}) \quad [1]$$

where $N_{FB}(X)$ is the surface-charge density of a MGS capacitor with a glass film thickness of x , and A , B , and α are constant values. When A , B , and α are calculated from the experimental values in Fig. 1, $A = 2 \times 10^{11}$, $B = 1.9 \times 10^{12}$, and $\alpha = 2.39 \times 10^3$. The experimental relationship between surface charge density and glass film thickness can be expressed as follows

$$N_{FB}(X) = -(2 \times 10^{11} - 1.9 \times 10^{12} e^{-2.39 \times 10^3 X}) \quad [2]$$

Equation [2] is shown as a solid line in Fig. 1. In Fig. 1 the calculated solid line agrees well with the experimental values. From this curve, it can be deduced that many positive charges exist at the glass-silicon interface and in the glass film near that interface. Negative charges exist deeper in the glass film. It is believed that the positive charges are mainly donor type surface states.

Effect of glass composition on surface charge density.—Four glasses with different compositions were prepared and the surface-charge density and surface-state density of the glass/n-type silicon systems in which these glasses were used, were measured. Table III shows the surface-charge densities obtained by the measurements. The values represent the means for six samples. Surface-charge density depends strongly on glass composition. The surface-charge density shifts in the negative direction with increasing B_2O_3 and decreasing ZnO and SiO_2 content. Figure 2 shows the relationship between surface-state density and energy level for glasses with different surface-charge densities. As can be seen from Fig. 2 and Table III, the more negative the surface-charge density of a glass, the lower is its surface-state density. The energy level of the maximum surface-state density does not depend on glass composition. If surface states are donor type, those which exist above the Fermi level (above 0.3

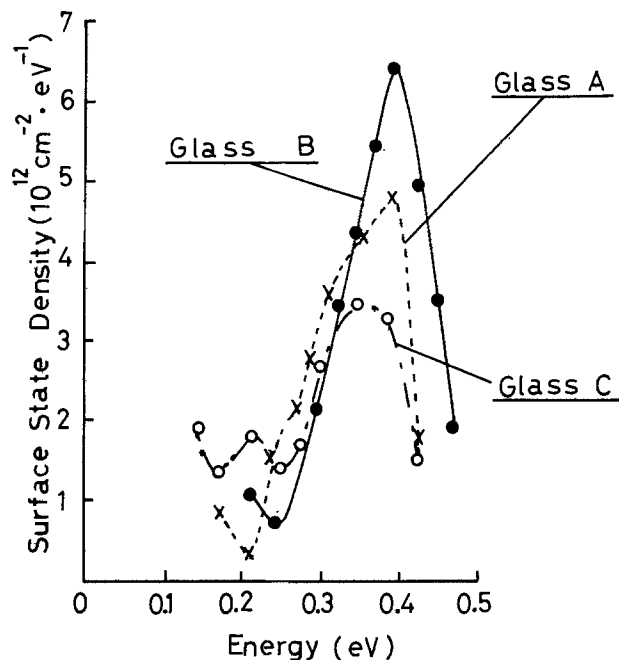


Fig. 2. Surface-state density of glasses with different surface-charge density fired on n-type silicon vs. energy level.

eV) act as positive charges and those which exist below the Fermi level (below 0.3 eV) act as neutral charges. Therefore, the more negative the surface-charge density of a glass, the lower its positive charges due to surface states. On the other hand, if surface states are acceptor type, those which exist above the Fermi level act as neutral charges and those which exist below, act as negative charges. Therefore, as surface-charge density of a glass becomes more negative, there are more negative charges due to surface states. As mentioned above, whether donor or acceptor types, the more negative the surface-charge density of a glass, the more negative charges there are due to surface states. That is, glass composition mainly affects the surface-state density of a glass/silicon system.

Effect of the conductivity type of silicon substrates on surface charge density.—We have already reported briefly on the effect of the conductivity type of silicon substrates on surface charge density (3). In this paper, the relation between the surface-charge density of glass fired on n-type or p-type silicon is described as shown in Fig. 3. The linear relationship indicates that there is no difference in the surface-charge density

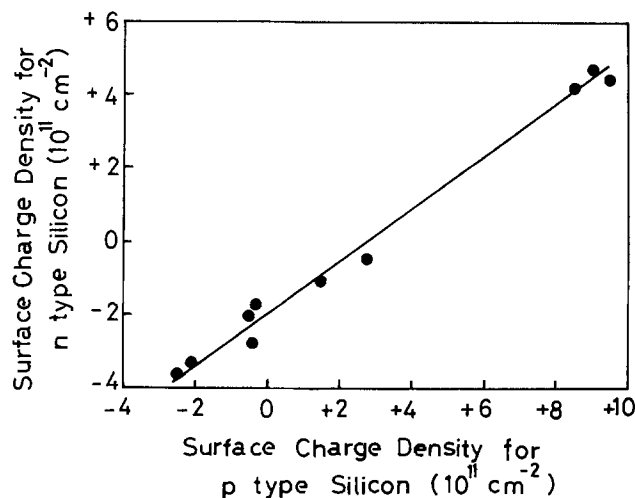


Fig. 3. The relationship between surface-charge density of glasses fired on n-type silicon and p-type silicon.

Table III. Measured surface-charge density for glasses fired on n-type silicon substrates

Glass no.	Surface-charge density (unit/cm ²)
A	-2×10^{11}
B	0
C	-3×10^{11}
D	$+5 \times 10^{11}$

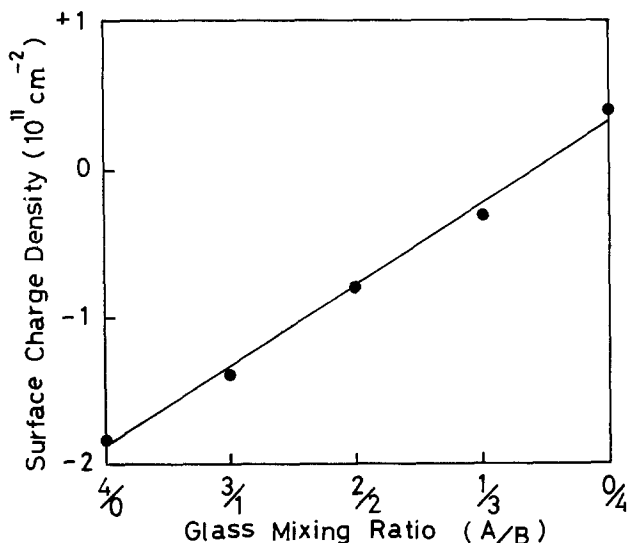


Fig. 4. The relation between surface-charge density of mixed A-B glasses and the mixing ratio.

for glass fired on n-type or on p-type silicon; it is the same regardless of the glass composition. The relationship between the two surface-charge densities can be expressed by the following empirical equation

$$N_{\text{FB}}(n) = \frac{2}{3}N_{\text{FB}}(p) - 2 \times 10^{11} \quad [3]$$

where $N_{\text{FB}}(n)$ is the surface-charge density of the glass fired on n-type silicon and $N_{\text{FB}}(p)$ is the surface-charge density of the glass fired on p-type silicon. Surface-charge density due to fixed charges and mobile charges does not depend on the energy level of silicon, that is, the Fermi level. Therefore, it is believed that the difference in the surface-charge density observed for glass fired on n-type and p-type silicon originates in the surface states that exist between the Fermi levels of n-type and p-type silicon.

Surface-charge density of mixed glass with different surface-charge density.—Glasses A and B with measured surface-charge density of $-1.8 \times 10^{11} \text{ cm}^{-2}$ and $+0.4 \times 10^{11} \text{ cm}^{-2}$, respectively, and with the same particle size distribution were mixed together in different ratios. Figure 4 shows the relationship between

surface-charge density and mixing ratio. The surface-charge density of the mixed A-B glass, which changed in proportion to the mixing ratio, is between the density of the individual glasses. The diameter of the glass powders ($4 \mu\text{m}$) is small compared with that of the electrode (2 mm) on an MGS capacitor. Therefore, it is assumed that the composite surface-charge density is the average of the surface-charge density of glass no. A and glass no. B.

Conclusions

Surface charges in a ZnO-B₂O₃-SiO₂ glass/silicon system were studied by changing the glass film thickness and glass composition. The surface-charge density of the glass/silicon system was observed to shift in a negative direction with increasing glass film thickness, becoming constant at a thickness of more than $20 \mu\text{m}$.

The surface-charge density shifted in a negative direction with increasing B₂O₃ and decreasing ZnO and SiO₂ content. Glasses with a more negative surface charge density had a lower surface-state density. A linear quantitative relation existed between the surface-charge density of glass fired on n-type silicon and that fired on p-type silicon. The surface-charge density of mixed glasses with different surface-charge density changed in proportion to the mixing ratios.

Acknowledgments

The authors wish to thank Messrs. S. Kawai, N. Kawakami, K. Morita, Y. Ikeda, and H. Yagi, and Drs. T. Toda, T. Ogawa, and M. Okamura for their helpful suggestions and encouragement during this study.

Manuscript submitted Oct. 13, 1982; revised manuscript received Sept. 26, 1983.

Hitachi, Limited assisted in meeting the publication costs of this article.

REFERENCES

1. K. Miwa, K. Ikeda, and K. Aoki, *NEC Res. Dev.*, **42**, 1 (1976).
2. C. A. Goodwin, Paper 353 presented at The Electrochemical Society Meeting, Las Vegas, Nevada, Oct. 17-22, 1976.
3. K. Miwa, M. Kanno, S. Kawashima, S. Kawamura, and T. Shibuya, *Denki Kagaku*, **40**, 478 (1972).
4. Y. Miswa, H. Hachino, S. Hara, T. Ogawa, and H. Yagi, *This Journal*, **128**, 614 (1981).
5. Y. Komiya, Y. Tarui, and T. Fujishiro, *Densogihō*, **40**, 58 (1976).

Purification of Optical Waveguide Glass Forming Reagents: Phosphorus Oxychloride

J. W. Mitchell and J. E. Kessler

Bell Laboratories, Murray Hill, New Jersey 07974

ABSTRACT

Low temperature sublimation is shown to significantly reduce the metal and —P—OH containing impurity levels of practical-grade phosphorus oxychloride. Regular distillation and sub-boiling distillation are also effective for removing —P—OH impurities and provide products with 114-119 ppm of residual —P—OH. The purification efficiencies of these physical methods are compared with that resulting from chemical treatment to convert —P—OH impurities into other species. A method based on chemical reaction followed by low temperature sublimation is described for removal of —POH from practical-grade material and reduction of trace materials to low ng/ml levels.

Volatile glass forming reagents of high purity with respect to trace transition elements, —H, and —OH molecular impurities are now widely used for pro-

Key words: trace metal impurities, IR spectra of POCl₃, sublimation, sub-boiling distillation.

duction of optical waveguide glass compositions via vapor-phase oxidation at elevated temperatures. Needs for analytical and purification methods for vapor-phase glass forming chemicals have motivated several previous investigations (1, 2, 3). The advantages and

efficiency of low temperature sublimation for the purification of reagents, which are liquid at ambient conditions, have already been reviewed (2). The potential broad applicability of the method for removing soluble and particulate metal containing species from a variety of fluids was demonstrated by the easily executed sublimation of a variety of reagents and solvents. In particular, several reagent liquids now used as semiconductor dopants or CVD reagents are easily sublimed at low temperature. This paper reports results of investigations of the application of this method to the purification of phosphorus oxychloride (POCl_3), a phosphorus dopant for optical waveguide fabrication.

Experimental

Apparatus and procedures.—The apparatus used for batch scale production of 0.5 liter quantities of purified POCl_3 is shown in Fig. 1. The apparatus, constructed of fused silica and Teflon, was operated inside of a PVC exhaust hood. To minimize container contamination, all parts of the apparatus were leached for several days in 1N HNO_3 , followed by rinsing in distilled water. After a final 12h leaching in 1N HCl at 80°C and soaking in distilled water for several hours, the apparatus was rinsed with distilled, demineralized water and dried in a laminar flow hood. Air admitted to the assembled and evacuated vessel was prefiltered through 0.4 μ Teflon filters.

Sublimation was accomplished by freezing the sample to be purified as a thin shell on the walls of the round-bottom flask by rotating the container and contents continuously in a cryogenic bath. After this flask was attached to the apparatus, the entire system was evacuated to a few mm of Hg pressure. The reagent was sublimed from the round-bottom flask, and the sublimate was collected in the chamber, which was placed in a Dewar filled with a dry-ice-methanol mixture. A source for latent heat of sublimation was provided by room air in contact with the sublimator flask during sublimation. Additional heat was some-

times provided by a heat lamp. Mass flow of vapors from the sublimator to the collector was induced by continuous evacuation of the apparatus.

Following sublimation, the purified sample was recovered from the collection vessel by dismantling the apparatus, crushing the solid with Teflon rods, and then transferring the solid to precleaned and well-dried containers. However, it proved most convenient to allow the sublimate to melt in the assembled apparatus and then to transport the liquid via suction through Teflon tubing connecting the collection vessel to an evacuated container from which transfer to the final storage vessel was made. Samples were then stored as the frozen solid in Teflon bottles.

A standard Pyrex apparatus was used for refluxing or distillation of POCl_3 . A modification of a previously described apparatus (4) was used for sub-boiling distillations under a positive pressure of nitrogen which was dried by passage through a Drierite column.

Reagents and analysis.—Reagent grade POCl_3 (Alfa Ventron) was prefiltered for some studies by vacuum suction through a 0.2 μ FG-fluoropore (Millipore) filter unit.

Aliquots of the original and purified samples were analyzed for trace metals by atomic absorption spectroscopy (AAS) following complete hydrolysis and direct injection of the resulting solution into carbon rod analyzers. Details of the analytical procedure have been reported elsewhere (5). Monitoring of the —P—OH impurity levels was done by infrared spectroscopy. The procedure described by Pasteur provided semiquantitative results on the overall —P—OH levels of starting reagents and purified products (6). All IR spectra were measured in either 3 or 4 mm pathlength cells.

Results and Discussion

Trace metal impurities.—Reagent grade POCl_3 is badly contaminated with trace metals. This is indicated by AAS determinations of a chemical showing 440, 1450, <5, 135, 5, 11, and 23 ng/g of Fe, Ni, Cu, Cr, Co, Mn, and Zn, respectively. Analysis of five lots of POCl_3 for Fe showed 689, 2220, 310, 210, and 253 ng/ml. The levels of Ni, Fe, and Mn are reduced drastically by simply filtering the reagent, as shown by the results in Table I. These data add to a growing body of evidence documenting that metallic impurities present in particulate matter are a primary factor limiting the ultimate state of purity attainable for powdered and liquid reagents. Water, soluble solid reagents Na_2CO_3 , NaCl , NaAc , and KI particulates, separated by filtration and analyzed by x-ray milliprobe fluorescence, showed significant amounts of elemental impurities (7). Unfiltered silicon tetrachloride has been found by analyses to be heavily contaminated with metal impurities (8). However, careful filtration transforms this chemical into an ultrapure reagent. All elements of interest except Fe are below the 1 ng/ml level.

Results in Table I also show significant further improvement in the purity of unfiltered reagent-grade

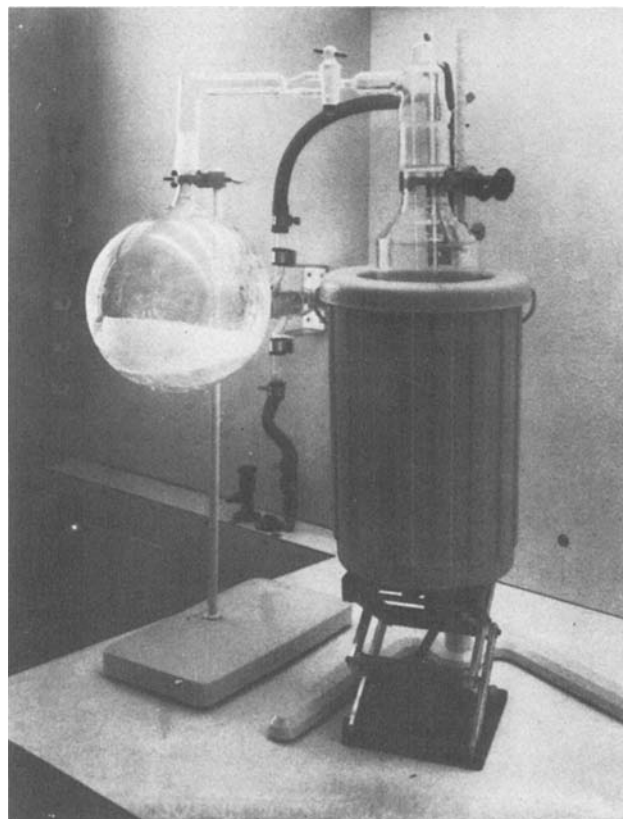


Fig. 1. Sublimation apparatus

Table I. Analysis of POCl_3

Element	Starting material	After filtering	Low temp. sublimation
Ni	1245 ± 70	45	ND ^a
		99	ND
Fe	433 ± 6	151	23 ± 8
Cu	11	64	18
Cr	28	18	ND (< 1)
Zn	12	14	ND
Mn	14	0	2
Co	ND (< 1)	ND	ND

Range of impurities determined by AAS, ng/g.
^a ND is not detected, (Ni), (Cr), (Co), and (Zn) < 1; (Mn) < 0.5 ng/g.

POCl_3 by processing through a single sublimation. The impurity level of the singly sublimed sample (23 ng/g Fe, <1 ng/g Ni) compares well with that of expensive commercially available purified materials, Product 1 (15 ng/g Fe and 19 ng/g Ni) and Product 2 (37 ng/g Fe, <1 ng/g Ni). Further reduction in the iron level of additional POCl_3 samples has occurred, with 15 ng/g being the lowest level achieved for reagent-grade POCl_3 after a single sublimation. This level of purity via low temperature sublimation is not the ultimate with respect to iron. Such is indicated by significantly better results for aqueous hydrazine where a reagent with an initial iron level of 41 ng/ml was reduced to the 2 ng/ml level (9). Using the sublimation method, 1 kg quantities of POCl_3 have been purified and supplied to various investigators.

—*POH impurities.*—Phosphorus oxychloride contains significant levels of —POH impurities, as indicated by the IR spectrum in Fig. 2a. Gas chromatographic-mass spectrometric analytical studies to identify specifically the various P—OH impurities are underway. These impurities may include $(\text{HO})_x\text{—PO}(\text{Cl})_{3-x}$, where $x \leq 3$, HPO_3 , H_3PO_2 , H_3PO_3 , and H_3PO_4 . Because of the higher volatility of POCl_3 in comparison to these various possible —POH containing impurities, badly contaminated POCl_3 (> 1% —OH impurities) is purified significantly during a single sublimation (Fig. 2b). The sublimed material contained ≈ 260 ppm of —POH impurities. Determining whether these residual impurities were originally present in the starting materials and were sublimed simultaneously with POCl_3 or whether they resulted from moisture contamination during the sublimation process is important for further improvement of the purification efficiency with respect to —OH.

Hydroxyl containing impurities in phosphorus oxychloride can also be removed during simple distilla-

tion. Crude reagent-grade material (> 1% —POH) is converted during one distillation into a product containing 110 ppm of P—OH (Fig. 3a). Further careful distillation or reagent-grade material via repetitive sub-boiling distillations yielded a product of similar purity 120 ppm of P—OH (Fig. 3b). In view of the quiescent nature and high separation efficiency of the sub-boiling distillation process, it is not likely that the residual P—OH impurity resulted from entrainment or covaporization of impurities originally present in the starting material. Contamination of the product by residual moisture within the nitrogen-purged distillation system is the more probable source of the residual P—OH. Although either sublimation or controlled distillation may be applied to produce a reasonably high purity product (15 ppb Fe and ≤ 250 ppm —P—OH) from crude, commercially available, reagent-grade POCl_3 , maintenance of the —P—OH purity level over long periods of storage will require the most stringent precautions against contamination by moisture.

In a previous report, chemical reactions between —P—OH and PCl_5 were proposed for the "drying" of phosphorus oxychloride (10). It was also projected that refluxing slightly hydrolyzed POCl_3 to create chlorophosphorus anhydrides would be useful for removal of —P—OH. The P—OH content of practical-grade POCl_3 (> 1% —P—OH) is unchanged by vigorous refluxing with 1% PCl_3 for 2h in a dry nitrogen-purged reflux condenser. Thus reflux reactions of —P—OH such as



appear to be negligible (Fig. 4a). However, under con-

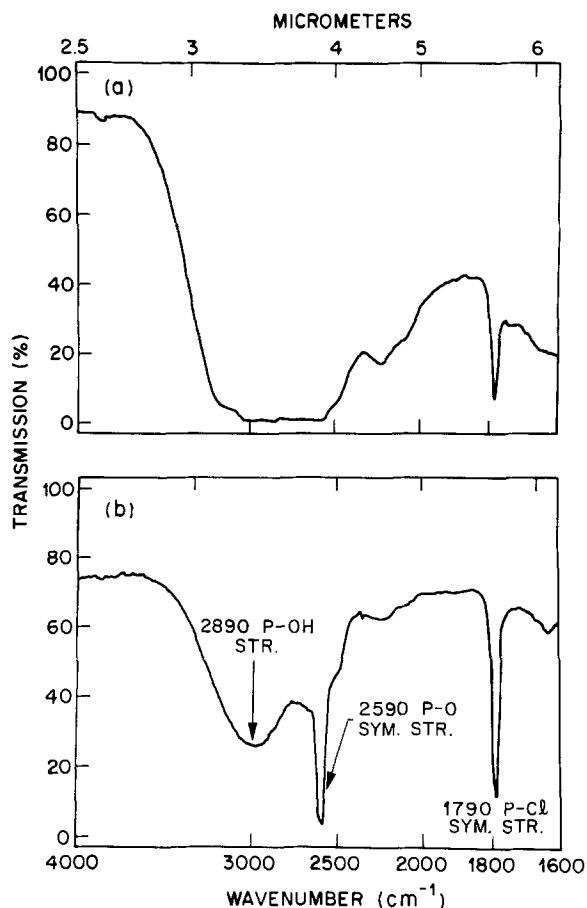


Fig. 2. IR spectra of POCl_3 . a, top: practical-grade POCl_3 . b, bottom: practical-grade POCl_3 after sublimation.

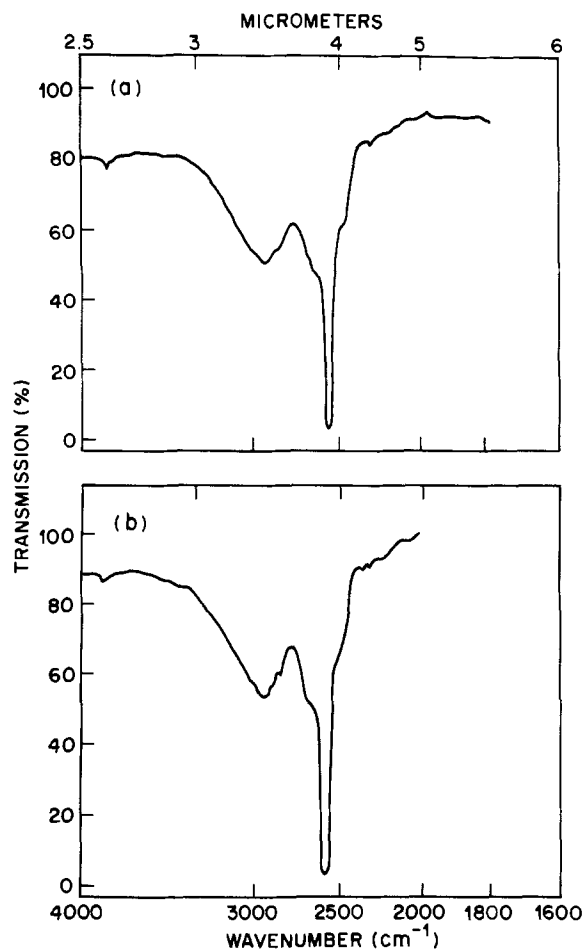


Fig. 3. IR spectra of distilled POCl_3 . a, top: normally distilled product. b, bottom: doubly sub-boiling distilled product.

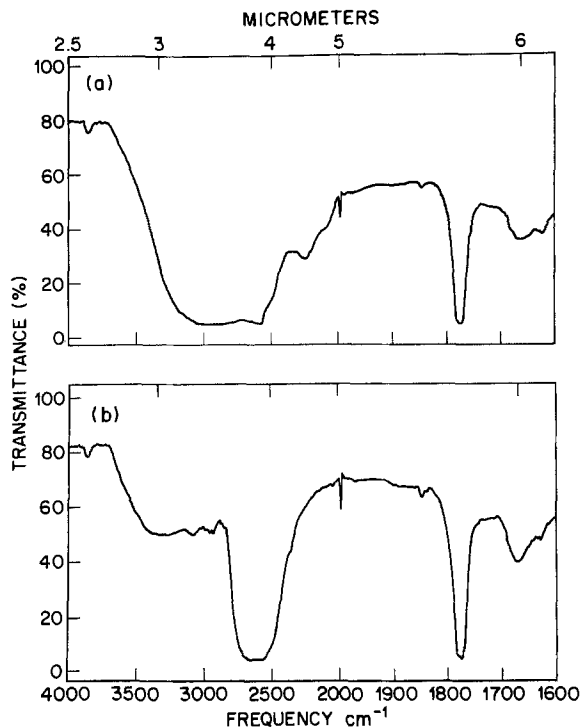


Fig. 4. IR spectra of chemically reacted POCl_3 . A, top: 1% PCl_3 added and refluxed for 2h. B, bottom: 2% PCl_3 added, refluxed for 2 h, saturated with Cl_2 and UV treated, N_2 purged for 1h.

ditions prescribed for the *in situ* generation of PCl_5 , significant chemical reaction of $-\text{POH}$ occurred, as indicated in Fig. 4b. A second 1% (v/v) fraction of PCl_3 was added to the 500 ml sample shown in Fig. 4a, and Cl_2 was added until the solution acquired a distinct yellow coloration. After a 5 min irradiation in a Rayonet Photochemical Reaction, the solution was

purged with dry nitrogen for 1h. Reduction in $\text{P}-\text{OH}$ is clearly evident, while broadening of the 2600 cm^{-1} band could reflect the formation of anhydrides of phosphorus acids. The broad-banded region 3600 to 2900 cm^{-1} indicate the presence of residual amounts of several different types of $-\text{P}-\text{OH}$. Thus, infrared estimates of the residual $-\text{P}-\text{OH}$ content could not be attempted.

Barns (10) found the procedure described above for treatment of the sample in Fig. 4b to remove most of the $-\text{P}-\text{OH}$ from commercially available Ultrex POCl_3 . This product had been preliminarily purified by the supplier to remove trace metals using a fractional freezing process. However, it was grossly contaminated with $-\text{P}-\text{OH}$. The satisfactory chemical conversion of $-\text{P}-\text{OH}$ in the prepurified material indicates that the practical-grade product contained structurally different $-\text{P}-\text{OH}$ containing impurities which are resistant to chemical conversion. Such compounds would have been removed from Ultrex reagents during purification by fractional freezing. The predominant $\text{P}-\text{OH}$ species in this material would then be the expected product resulting from the reaction of POCl_3 with atmospheric moisture according to



This product in turn seems to react readily with PCl_5



while more complex species, for example $(\text{OH})_x-\text{POCl}_{3-x}$ ($x = 2$ or 3), appear to be more chemically resistant.

Practical grade POCl_3 (Fig. 2a) has been decontaminated completely with respect to $-\text{P}-\text{OH}$ impurities by chemically converting sublimable $-\text{P}-\text{OH}$ moieties (reaction 3) into less volatile products via reaction 4. Following treatment of the initial sample (Fig. 2a) with 1% PCl_3 , addition of Cl_2 , UV irradiation (3000Å) for 15 min, and purging with nitrogen, the spectrum in Fig. 5a was obtained. Low temperature sublimation of

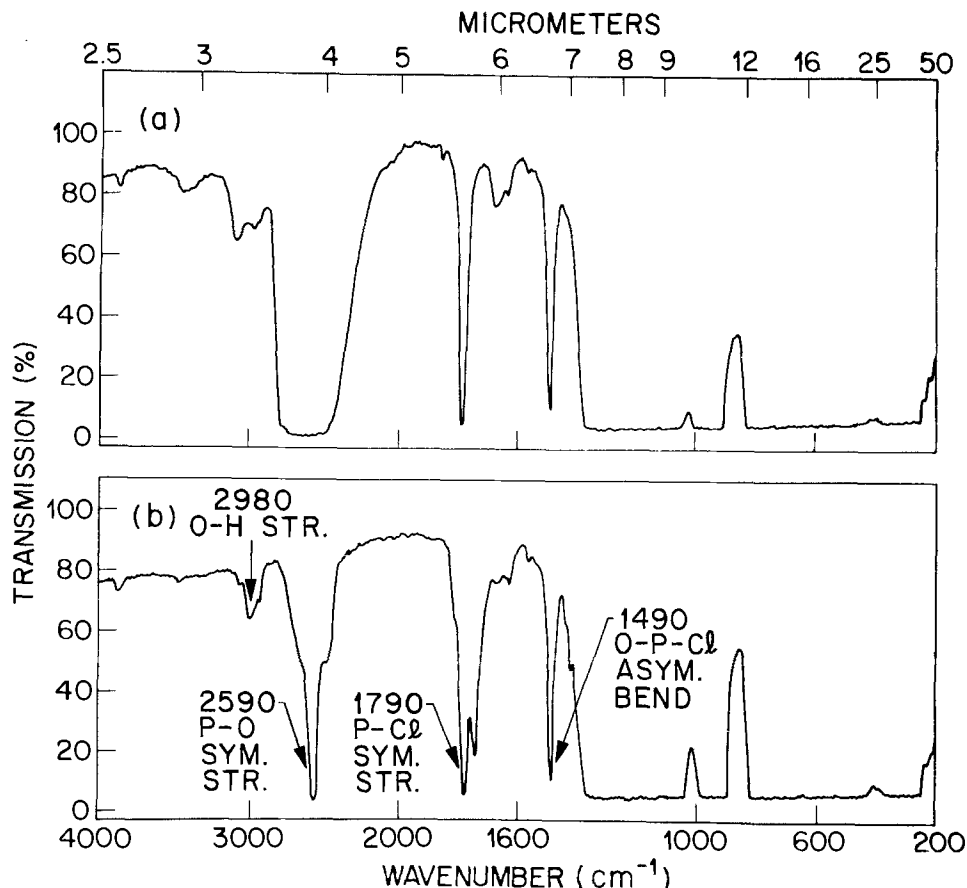


Fig. 5. IR spectra of chemically reacted and sublimed POCl_3 . a, top: 1% PCl_3 added, Cl_2 saturated, UV irradiated, and N_2 purged. b, bottom: sample A sublimed at low temperature.

this product provided the sample with the spectrum shown in Fig. 5b. This essentially complete removal of —P—OH combined with a simultaneous significant reduction of trace elements has converted inexpensive, practical-grade reagents into high purity fiber-optic-grade material. The batchwise sublimation step could in principle be replaced by a continuous distillation with negligible loss in purification efficiency. Substitution of the distillation step would be dependent upon a knowledge of the physical properties of reaction products and those of any remaining impurities. Identification of such impurities are important areas for ongoing analytical investigations.

Acknowledgments

The analytical techniques which supported this study were developed by G. A. Pasteur, T. K. Kometani, and L. D. Blitzer.

Manuscript submitted May 13, 1983; revised manuscript received Oct. 13, 1983.

AT&T Bell Laboratories assisted in meeting the publication costs of this article.

REFERENCES

1. J. W. Mitchell, *J. Pure Appl. Chem.*, **54**, 819 (1982).
2. J. W. Mitchell, *Anal. Chem.*, **50**, 194 (1978).
3. J. W. Mitchell, U.S. Pat. 3,992,159 (1976).
4. M. Zief and J. W. Mitchell, "Contamination Control in Trace Element Analysis," p. 103, John Wiley and Sons, New York (1976).
5. T. Y. Kometani, *Anal. Chem.*, **49**, 289 (1977).
6. G. A. Pasteur, Personal communication.
7. J. W. Mitchell, W. R. Northover, and C. L. Luke, *Anal. Chem.*, **45**, 1503 (1973).
8. T. Y. Kometani, "Chemical Analysis of MCVD Reagents," Unpublished (1979).
9. J. W. Mitchell, T. D. Harris, and L. D. Blitzer, *Anal. Chem.*, **52**, 774 (1980).
10. R. L. Barns, E. A. Chandross, and C. M. Melliar-Smith, Unpublished work.

Computer Simulation of Carbothermic Silica Reduction Processes

Thomas Johansson

KemaNord, Industrial Chemicals, S-840 10 Ljungaverk, Sweden

Gunnar Eriksson

Department of Inorganic Chemistry, University of Umeå, S-901 87 Umeå, Sweden

ABSTRACT

Several types of alternative carbothermic reduction processes for the production of silicon metal were studied by using a model which is applicable to nonequilibrium systems with countercurrently flowing phases. The processes studied include a conventional silicon arc furnace, a silicon arc furnace working at elevated pressures, and a new process called the boot furnace (BF) process. The results indicate that the high pressure alternative cannot compete with the conventional furnace. The BF process should give markedly higher silicon yields as well as a purer product but complicated process equipment is demanded. Many of the alternatives studied might constitute improvements compared with the conventional process, but additional experimental results are required for conclusive evidence.

The conventional carbothermic reduction process of silica to metallic silicon in submerged arc furnaces is very complex. Several gaseous, liquid, and condensed species are involved in chemical reaction because of the high temperatures within the process area. At the same time the chemical environment makes a detailed practical investigation nearly impossible. Additionally, the infeasibility of controlling the internal heat and mass flows implies that the current process yields are far below the theoretically attainable. Practical and theoretical aspects of silicon production have been thoroughly discussed in several previous publications, (e.g., (1-4)).

Consistent mathematical models for the conventional silicon arc furnace process are normally built upon mass and energy balances and the computation of chemical equilibria considering only a limited number of reaction formulas. However, if the aim is to study conceptual, alternative processes, the need to specify a reaction scheme in advance can be a major obstacle. The lack of experimental data may also render the results from such a thermodynamic analysis doubtful. Fortunately, computer programs employing free-energy minimization or any other equivalent sophisticated algorithm for the calculation of chemical equilibria eliminate the need to specify such reaction schemes, and thereby allow the use of a generalized formalism.

Key words: inorganic, plasmas, thermodynamics, reduction.

SOLGASMIX (5) is a free-energy minimizer where the equilibrium mixture may contain a gas phase and condensed phases of invariant or variable composition. Parametrized activity coefficient expressions for species in nonideal phases must be specified by the user. A recently developed extended routine, SOLGASMIX-REACTOR (6), simulates nonequilibrium processes with countercurrently or cocurrently flowing phases. A reactor is conceptually divided into a number of segments, and the SOLGASMIX free-energy minimizer is utilized for computing rates and temperatures of the steady-state flows over the segment boundaries for each species, i.e., for a condition characterized by a total balance in material and enthalpy inputs and outputs. Heat transfer and chemical kinetics are considered indirectly by allowing a portion of the flowing material to bypass some stages of the reactor bed without any reaction. This approach has been successfully applied to several alternative carbothermic reduction processes for silicon or silicon-alloy production (2, 7).

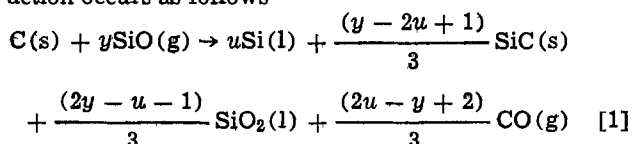
In this paper a model better than those published earlier (2, 6) for the conventional silicon furnace (CSF) process will be described. The new feature is that the model furnace contains a hot part which should depict the arc zone of an operating silicon furnace. Results from SOLGASMIX-REACTOR simulations will also be presented for a new process, the boot furnace (BF) process, and for two modifications of the CSF process, one in which the formation of

metallic silicon in the upper part of the furnace is considered, and one working at elevated pressures.

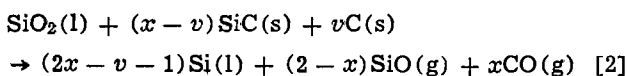
The Silicon Arc Furnace Process

General overview.—The chemical processes taking place inside a silicon arc furnace, where silica is carbothermally reduced to silicon metal, can be outlined by two overall reactions. These reactions are based partly upon results from a previous simulation (2), and partly upon experimental observations of the formation of metallic silicon in the upper parts of the furnace (8).

In the upper parts of the furnace an exothermic reaction occurs as follows



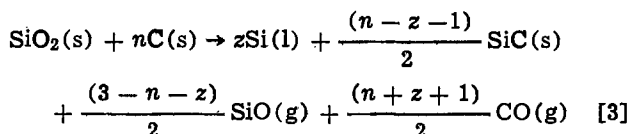
The y value, which is dependent on the amount of available energy, increases with decreasing reaction temperature. The u value is a measure of the amount of silicon metal formed by disproportionation of SiO(g). This is due to the low surface temperature of the silica lumps, which, unlike the carbon supplied, do not take part in any exothermic chemical reactions. Moreover, the further reaction of the condensates Si(l) and SiO₂(s,l) may be hampered by kinetic barriers. A more detailed discussion is given below. The gaseous reaction products, predominantly CO and unreacted SiO, escape from the furnace, whereas the condensed phases descend and react in the lower regions where the main part of the energy is supplied. The overall reaction can be written



The x value, which is determined by the relation between charge consumption and energy supply, increases with increasing reaction temperature. The variable v represents the amount of unreacted carbon originating from the electrodes or from the charge.

The economy of a silicon furnace is strongly dependent on the extent of reaction [2]. An increased value of x , which corresponds to a higher equilibrium temperature and a higher energy consumption per mol silica charged, implies an improved yield of silicon metal and a lower SiO content and thermal potential of the gases leaving the lower regions of the furnace. This has the effect that the amount of SiO lost as top gas is depressed. Thermal potential is used here to denote the energy which can be emitted by the gas by cooling and by chemical reaction during its passage through the charge. The relative influence of x on the metal recovery is much more pronounced than the influence on the energy consumption. By assuming that the partial pressure of SiO is close to constant in the hotter zone of the furnace, an increased value of v results in reduced amounts of SiC reacted and Si produced. The factor u may also be of importance if the silicon metal formed in the upper part of the furnace is inaccessible for reaction until it reaches the lower regions.

The reactions [1] and [2] can be combined to give a total reaction formula for the silicon furnace



where n denotes the carbon-to-silica ratio in the charge. The silica yield (mol Si produced per mol silica charged) is denoted by z and is equal to

$$z = [3u(n - v) + (2x - v - 1)(2ny - nu - n + 3)] / (2vy - vu - v + 3) \quad [4]$$

The following conclusions can be made about the various variables in reaction [3]. z should be as large as possible. n should be as large as possible, but the SiC production, a dirigible factor, must be limited. Higher y values give improved silica yields and an almost unchanged energy consumption, but technical problems with the condensation products arise. Higher u values give improved silica yields, but increased amounts of the condensation products give rise to mechanical problems. x should be as large as possible, but is nearly impossible to control. v should be as low as possible, and has limited dirigibility.

Model description.—In the SOLGASMIX-REACTOR (6) approach, the system is divided into a small number of segments and the program calculates rates and temperatures of the steady-state flows over the segment boundaries. The solution technique employed is one of repetitive substitution, and the iteration process may proceed in either direction throughout the reactor, from top to bottom or from bottom to top. Flows opposite to the iteration direction calculated from a previous iteration (or initial estimate) are used as inputs to the next iteration, whereas flows in the other direction are calculated as the iteration proceeds.

By introducing user-specified distribution coefficients, an approximate means is provided for including chemical kinetic effects and heat transfer in the program. These coefficients were originally designed to reproduce the macro/micro channeling effect in arc furnaces, where gases from the bottom may escape rapidly through the furnace top without the recondensation of volatiles or temperature equalization which equilibrium would predict. In effect, these coefficients give the user a means of preventing some of the gases or condensed phases incoming to a specific segment from entering into reaction and/or heat exchange. Thus, some portion of the raw material input or the intermediate reaction products is allowed to bypass one or several segments. Since the values which these distribution coefficients assume are difficult to predict, they must be determined by empirical comparison between calculation and experiment. They are influenced by the number of segments chosen for the model and the temperature distribution in the segments, but are useful for inclusion of kinetic effects without the additional complexity of calculating individual reaction and/or heat transfer rates.

The thermodynamic data for the chemical system considered (Si, C, O, Al, Ca, Fe) is taken from the JANAF Thermochemical Tables (9), which gives values for temperatures up to 6000 K. In addition to the gas phase containing 28 species, there is a metallic phase assumed not to contain any molecular associations, i.e., the atomic species Si, Al, Ca, and Fe, and a slag phase containing the distinct compounds SiO₂, AlO_{1.5}, CaO, and FeO. The solid phases considered are C, SiO₂, SiC, Al₂O₃, CaO, and FeO. No data in the literature could be found giving activity coefficient expressions in the dilute solution range for the multicomponent liquid phases, which therefore are treated as ideal with activities equal to mol fractions. This simple model for the chemistry of the contaminating metals is thought to be justified at least for qualitative considerations, because of the low concentrations of the impurities and the uncertainties in the thermodynamic data for the constituents of the liquid phases.

The conventional silicon furnace process.—In order to get results as generalized as possible in the modeling, a conventional silicon furnace (CSF) is defined. This does not relate to a specific furnace but is a hypothetical one which behaves similarly to most modern furnaces. The parameters of the model, whose mean-

ing is described elsewhere (2), take values as follows. The reactor is divided into six segments. The raw material (1 mol SiO_2 , $2.5 \cdot 10^{-3}$ mol of the impurities Al_2O_3 , CaO , and FeO , and a calculated amount of carbon, see below) is supplied to the top segment (segment 1). The total energy supply (885 kJ/mol SiO_2 charged) is constrained to the temperature of segment 4, which is determined to be 2340 K in advance, and is distributed so that 80% goes to segment 5, 15% to segment 4, and 5% to segment 3. In addition, 5 kJ is withdrawn from the top segment because of the pyrolysis of the wood chips intermixed with the raw material. The carbon supply is adjusted so that a constant reaction temperature above the boiling point of the reactants (5500 K) is reached in the arc zone of the model (segment 5), which results in no net production/consumption of SiC. Of the total amount of carbon supplied (1.826 mol/mol SiO_2 charged), 0.15 and 0.10 mol reaches the segments 4 and 5, respectively, thereby simulating the low reactivity of the carbon electrodes in the upper parts of the furnace. The enthalpy of this chemically bypassed carbon is changed according to the reaction temperatures in the upper segments. The condensed phases entering one segment react completely in that specific segment, but the intermediate gaseous reaction products are distributed so that 80% reacts in the next upper segment, 15% bypasses one segment before reaction, and 5% bypasses two segments before reaction. Some of the condensed material will probably bypass the high temperature zone of an operating furnace. This is accounted for in the flow scheme by letting the chemical input to segment 6 consist of 1% of the slag produced in segment 3 and 50% of the metal produced in segment 4. The total pressure in segment 1 is 1.01 times the assigned pressure (101.325 kPa), in segment 2 the factor is 1.02, in segment 3 1.04, and in the remaining segments 1.07.

Figure 1 shows the calculated steady-state gaseous and condensed phase flows over the segment boundaries. To illustrate the chemical reactions taking place

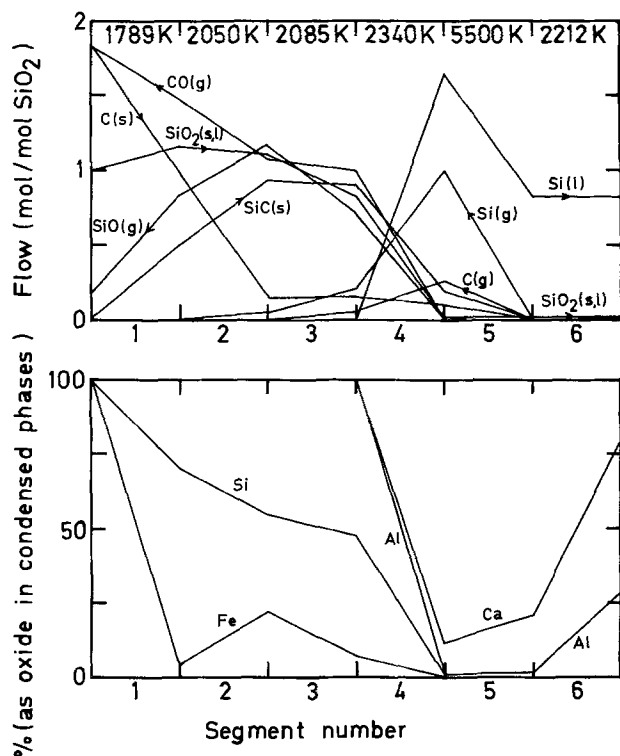


Fig. 1. Calculated flows (mol/mol SiO_2 charged) in the conventional silicon furnace (top) and distribution of silicon and the contaminating metals between slag and other condensed phases (bottom). Parameter values are given in the text.

in the reactor, a linear change in flow is indicated within the segments. The calculated silica yield is 0.819, and the energy yield (mol Si produced per MJ energy supplied) is 0.925. The dependency of some key factors on the silica and energy yields has been investigated earlier (2). It was found that the correlation between the yields and the silica-to-energy feed ratio and the elementary carbon supply to the lower segments is significantly negative. An increased top cooling causes increased silica yields but influences the energy yield only to a minor extent. The impurity content of the raw material has only a marginal effect. However, in the production of silicon containing alloys, the Si activity in the metallic melt is reduced and substantially higher yields can be obtained.

The influence of the variable u in reaction [1] is investigated by cooling 50% of the SiO leaving the reactor to 500 K. The enthalpy produced is supplied to segment 1, and the condensates Si and SiO_2 are recycled either to segment 1 or to segment 4. The remaining parameters are the same as for the CSF process.

The predicted result of this recycling is that the silica yield increases to 0.823 (segment 1) and 0.864 (segment 4), respectively. The silica yield is practically not modified at all for the first case, since the higher SiO activity in segment 1 induces only an enhanced silicon circulation within the reactor. The condensates are excellent reactants and when they are recycled to segment 4, the improved silica yield is obvious. The SiO activity is now determined by the constant temperature of 2340 K in segment 4, and the extra SiO (Si + SiO_2) supplied must react to some extent with SiC to produce Si and CO.

The overall reaction temperature in the part of an operating furnace where Si metal is formed is probably rather constant, and therefore the SiO disproportionation should be beneficial to the process. However, the condensates probably occur in a finely divided and reactive state which has the effect that the major part reacts before it reaches the metal formation zone of the furnace. The assumption that the amount of outgoing SiO is equal to that condensed to Si and SiO_2 within the furnace may be an overestimation, and that therefore the overall effect of the SiO disproportionation is limited. Figure 2 illustrates the flows within a reactor where the condensation products are recycled to segment 4.

At present, a direct quantitative comparison of temperature and composition of the internal flows of intermediate species in an operating furnace with the simulated condition in the model is not possible. However, the directly measurable factors, including carbon and

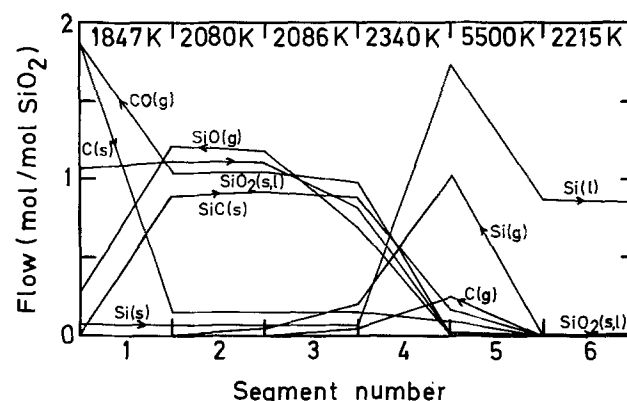


Fig. 2. Calculated flows (mol/mol SiO_2 charged) in a modified conventional silicon furnace where 50% of the SiO leaving the furnace is cooled to 500 K, the enthalpy produced supplied to segment 1, and the condensation products (Si and SiO_2) recycled to segment 4.

silica yields, energy yield after compensation for heat losses, temperature and composition of product and of the gases escaping from different parts of the charge surface, changes in operation when charge composition, energy supply, and furnace geometry is changed, have been shown to be in excellent agreement.

The agreement between simulation results and the real process is not surprising, since the fundamental principles of the algorithm are identical with those used for calculating typical countercurrent distillation processes. This can be exemplified by the term "segment" used here, which has its direct counterpart in theoretical plates. The requirements for using these principles are that the deviation from both enthalpy balance and chemical equilibrium in one point must be more or less proportional to the heat- or mass-transfer rates or the reaction rate, and that at least some phases have opposite flow directions. As is the case in the calculation of distillation processes, equilibria are never assumed or stipulated to be reached in any point. The departure from equilibrium only indicates the direction in which the reaction should proceed and to some extent the reaction rate. A silicon furnace is much more complicated than a distillation process, but SOLGASMIX-REACTOR is developed to cope with these complications.

Alternative Processes

Three alternative processes and one modification of the CSF process for carbothermic reduction of silica have been simulated: the silicon blast furnace (SBF) process (2), the bottom loaded furnace (BLF) process (6, 10, 11), the boot furnace (BF) process (10, 11), and the high pressure silicon furnace (HPSF) process.

Silicon blast furnace process.—In the SBF process, which is discussed in detail elsewhere (2), a mixture of silica and carbon is fed at the top and oxygen gas is injected at the bottom. The feasibility of the process is doubtful because of the high consumption and ensuing high costs of carbon and the large amount of impurities introduced. Combined production of silicon and heat energy by this method is theoretically possible, but the technical problems involved can hardly be solved within the limited economical scope available.

Bottom loaded furnace process.—In the BLF process (6, 10, 11), which seems to have many advantages, silica and energy are fed with a controlled speed into the bottom of the furnace. Compared with the CSF process, there is a reduction in the carbon consumption by 10%, while the silica and energy consumption is reduced by 20%. The economical incentive available for finding new technical solutions is thus great, and despite the fact that problems remain to be solved, the BLF process has a good chance of becoming more profitable than the conventional processes of today. The BLF process will be treated in greater detail in future work.

Boot furnace process.—The principle of the BF process (10, 11) is shown in Fig. 3. A mixture of silica and carbon, with a molar ratio $\text{SiO}_2/\text{C} \cong 1$, is fed to a zone within which the energy supplied is sufficient to cause the formation of an equimolecular gas of SiO and CO. Any surplus of silica which may be introduced after the gas production stage can then extract most of the contaminating metal compounds present in the gas. The purified gas flows into a reactor charged with carbon. Nearly 50% of the SiO reacts with SiC in the lower parts, producing Si and CO; almost all of the remaining SiO reacts with carbon, reproducing the consumed amount of SiC. The extra energy needed for silicon formation from SiO and SiC can be supplied at the sites of gas or silicon production or in between them. If the goal is to make metallurgical qual-

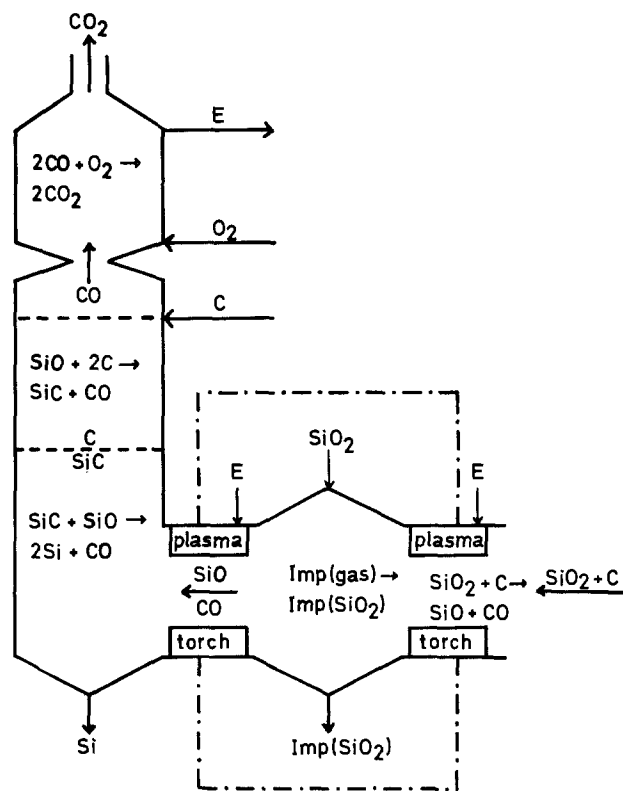


Fig. 3. Overall principle of the BF process

ity or if the feed material is sufficiently pure, the encircled part of Fig. 3 may be omitted.

By using SOLGASMIX-REACTOR, three different alternatives of the BF process have been simulated. In the first, 1 mol of SiO_2 and C, together with impurities and a sufficient amount of energy, is supplied into an arc heater represented by segment 5 (see Fig. 3 with the encircled part omitted). In the second alternative, 1.1 mol SiO_2 , 1 mol C, impurities and a sufficient amount of energy for volatilizing all carbon is supplied into an arc heater (segment 5). The slag and metal melts formed, containing most of the impurities, are discharged, while the gas phase is fed to the reactor proper (segment 4) together with more energy to obtain a maximum silica yield. The third alternative is equal to the second with the exception that the gas phase (from segment 6) reacts with another 0.1 mol SiO_2 (in segment 5) before it reaches the reactor. The input of impurities and the pressure gradient are the same as for the CSF process. The reactor (segments 2 through 4) and the gas burner (segment 1) are identical in the three different alternatives. The other parameters of the reactor model are chosen as described below.

The incoming material to the reactor consists partly of the volatile SiO_2 -C mixture to segment 4 and partly of a sufficient amount of carbon to segment 2 to give optimum yield. The amount of oxygen gas needed to combust CO and SiO completely is injected into segment 1. As mentioned previously, energy is supplied to segment 4, which always contains SiC (alternatives 2 and 3). Segment 1 has a constant temperature of 500 K, and enthalpy is gained by the cooling. No condensation reactions occur, and therefore the intermediary reaction products leaving one segment are assumed to react completely in the adjacent segment.

The predictions from the simulations indicate that this type of reactor produces silicon with a high yield, and with the alternatives 2 and 3 a high purity product is obtained. The carbon consumption lies between 2.065 and 2.094 mol/mol Si produced, but the part of the consumption which exceeds two leads only to SiC and/or SiO production. The variation in silica yield,

which is 0.954, 0.860, and 0.764 for the three cases, respectively, is caused by 9% (case 2) and 17% (case 3) of the silica charged being used only as an impurity extractant or absorbing medium for the gas before it enters the silicon producing reactor. If this fraction of the silica supply is withdrawn from calculation, the yield is over 0.9 for all three alternatives. The energy consumed/mol Si produced is nearly identical and lies between 1000 and 1037 kJ. The impurity content of the silicon metal produced varies in an interesting way. From being 0.5 mol percent (m/o) for the first alternative, it is reduced to only 0.05 m/o for the two other. This latter equality is caused by atomic iron remaining in the gas phase after the first washing stage. This iron will not be oxidized and extracted with the slag because of the low partial pressure of O_2 at the second supply of silica. Most of the iron is instead withdrawn in the metal melt in the gas producing segment. It is important to point out here that accurate activity coefficient expressions describing the nonideal mixing in the slag and metal phases are lacking and all solutions are treated as being ideal. It is thus impossible to draw any far-reaching conclusions concerning the fates of the contaminating metals, but the general trends between different results should give a good illustration of what will happen in an operating process. The enthalpy produced by the combustion in the gas burner is of the same order (757 to 767 kJ/mol Si produced) as the electrical energy supplied to the process.

In Fig. 4 the flow diagram of alternative 1 is presented. The silica and carbon supplied to segment 5 react to a 1:1 mixture of SiO and CO. Because of the surplus energy also supplied to segment 5, SiO reacts in segment 4 with SiC forming Si and CO. Most of the remaining SiO reacts with carbon to CO and SiC in the upper segments. A part of the carbon incoming to segment 2 reaches segment 4 because of the high temperatures in the reactor, which allow a certain pressure of SiO to exist over carbon. In the top segment there is a complete combustion of the incoming gases to CO_2 and SiO_2 .

The possibilities of a technical realization of a BF process are promising because the consumption of raw materials and energy is lower compared to the present-day process; moreover, there is no condensation of silica in the upper part of the furnace. Many technical problems are thereby avoided, for instance, the need for a mechanical treatment of the charge, and the electrodes need not pass through the charge. Since there is no need for connections from the outside to

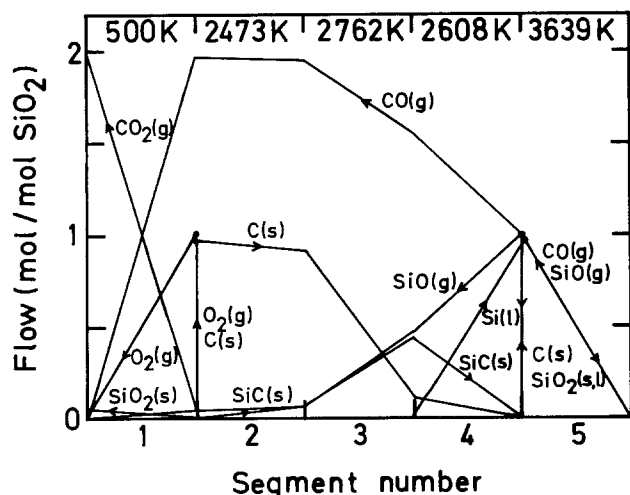


Fig. 4. Calculated flows (mol/mol SiO_2 charged) in a BF process where 954 kJ is supplied to segment 5 and where the charge consists of 1 mol of SiO_2 and C together with impurities to segment 5, 0.97 mol C to segment 2, and 1.01 mol O_2 to segment 1 (see Fig. 3 excluding the encircled part).

the inner parts of the furnace, except for gas supply and outlet, the closing of the furnace is simplified and the energy recovery process, exemplified by segment 1, will be much easier to realize. The process has some drawbacks. The efficiency of an arc heater is not as good as that of a carbon electrode. Also, the predicted temperatures in the reactor are very high, which may cause material problems. On the other hand, temperature may be lowered considerably before the yields drop to the same level as with current arc furnace technology.

The conclusions drawn from the modeling of the BF process indicate that this production method may be a viable alternative when the goal is to produce metallurgical silicon, high purity silicon, or silicon alloys.

High pressure silicon furnace process.—The principle of the HPSF process is merely a conventional silicon furnace working at elevated pressures. The parameter values for the CSF and HPSF processes are all identical, the assigned pressure excepted.

Figure 5 illustrates the consumption of carbon, silica, and energy per mol Si produced in the HPSF process relative to their respective values for the CSF process (Fig. 1) as a function of the assigned pressure. The raw material costs are drastically reduced at a pressure of 0.4 MPa. Between 0.4 and 0.8 MPa the conditions are practically constant. For pressures 0.8 MPa and above, the consumption of silica and energy increases according to the lower enthalpy content of the gases incorporated in the condensation reactions. Larger amounts of gas must then condense in order for the charge material to be heated. Moreover, the equilibrium is displaced to a greater extent towards SiO condensation by increasing pressure. These two factors cause a large flow of SiO_2 which must be compensated by a higher SiC production. Thereby the extra amount of carbon required in the charge would give rise to additional SiO condensation due to the cooling effect. The reactions in segment 4 are only moderately displaced with a slight increase in pressure. In this segment, the gas phase, consisting primarily of SiO and CO, is in equilibrium with the condensed phases SiC and Si, and because of the constant temperature of

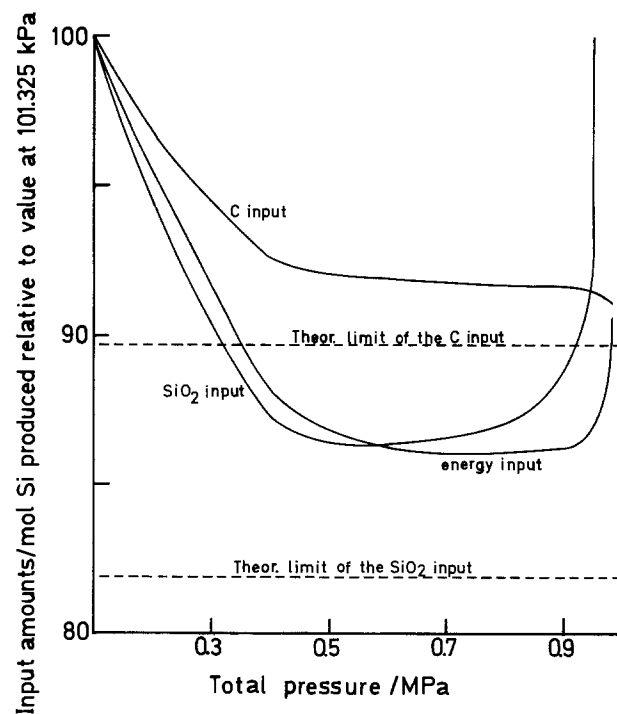


Fig. 5. Carbon, silica, and energy inputs per mol Si produced for the HPSF process relative to their respective values for the CSF process.

2340 K, the quotient $p(\text{SiO})/p(\text{CO})$ is constant. At a total pressure in excess of 0.8 MPa, $p(\text{SiO})$ reaches the value at which SiO_2 can coexist with SiC and Si , causing the silica yield to drop. Since the energy needed for melting this SiO_2 is low below about 0.9 MPa and the energy consumption during gas production is still being reduced, the energy consumption increases later than the silica consumption.

At pressures above 0.9 MPa, the energy consumption for melting the growing amount of SiO_2 is so high that it markedly affects the overall energy consumption. Carbon consumption decreases with increasing pressure in the pressure interval studied because the carbon consumption caused by the SiO production decreases when the condensation becomes more efficient at higher pressures.

Figure 6 shows a flow diagram of an HPSF process with an assigned pressure of 0.6 MPa. It is evident that the condensation of SiO increases and the SiO losses decrease compared with the CSF process in Fig. 1.

The possibilities for a technical realization of an HPSF process are probably limited despite the process' many advantages. There are in principle four different connections to the inner part of the furnace which must be maintained. (i) The gas outflow must pass through a pressure reducing valve. (ii) The silicon melt must be discharged with pressure reduction but without a simultaneous escape of gas. (iii) Energy must be supplied, e.g., electrodes. (iv) The raw material must be entered via a lock system.

These four factors, as well as the greater need for mechanical treatment of the charge caused by the extended condensation, and the safety aspects of having high temperature and pressure inside a furnace, make it hard to believe that such a process will be economically justifiable with the normal size of present-day furnaces. This technique, however, may be utilized in small process units for production of special qualities.

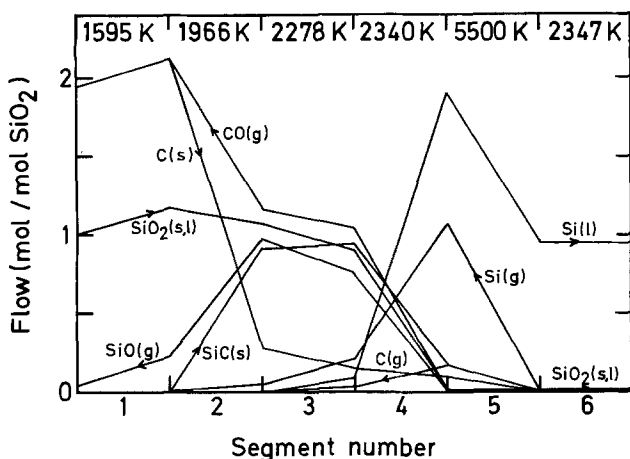


Fig. 6. Calculated flows (mol/mol SiO_2 charged) in a modified conventional silicon furnace working at an assigned pressure of 0.6 MPa.

Future Aspects

The simulation of the six different types of furnace models discussed above indicates the kind of information which can be extracted from the calculations and the limitations of using the SOLGASMIX-REACTOR program. In the future, a detailed investigation of the possibilities of a technical realization of the BLF process will be presented. In a related project, several alternative production methods for ceramic materials, particularly Si_3N_4 , will be presented and evaluated.

Despite the fact that the usefulness of the SOLGAS-MIX-REACTOR model may be limited by the lack of critically assessed thermodynamic data in many systems, there is still at least one important area for program development; namely, treatment of geometric and dynamic information by a finite-element approach to account for static and dynamic effects of inductance, mass and heat transfer, material flow, diffusivity, and kinetics. Again, the drawback is the lack of data required for the calculations. As demonstrated in this work, it seems that the most advantageous way to get quantitative results is to use a method which treats empirical data. Different parameter combinations may then be varied until agreement with a known process is achieved. The parameter values thus found can then be used to simulate similar processes.

Acknowledgment

The authors would like to express their appreciation to Michael E. Hatcher and Walter E. Wahnsiedler for many stimulating discussions and for their support. Financial support for this work by the Swedish Natural Science Research Council and by KemaNord, Industrial Chemicals is gratefully acknowledged.

Manuscript submitted July 14, 1983; revised manuscript received Oct. 3, 1983. This was Paper 242 presented at the Detroit, MI, Meeting of the Society, Oct. 17-21, 1982.

KemaNord assisted in meeting the publication costs of this article.

REFERENCES

1. M. B. Müller, S. E. Olsen, and J. K. Tuset, *Scand. J. Metall.*, **1**, 145 (1972).
2. T. Johansson and G. Eriksson, *ibid.*, **9**, 283 (1980).
3. A. Schei and K. Larsen, *Electr. Furn. Conf. Proc.*, **39**, 301 (1982).
4. S. Selmer-Olsen, *ibid.*, **39**, 310 (1982).
5. G. Eriksson, *Chem. Scr.*, **8**, 100 (1975).
6. G. Eriksson and T. Johansson, *Scand. J. Metall.*, **7**, 264 (1978).
7. W. E. Wahnsiedler, D. T. Stevenson, J. Szekely, G. Eriksson, and T. Johansson, *Light Met.*, **7**, 405 (1982).
8. A. Schei and O. Sandberg, in "Selected Topics in High Temperature Chemistry," T. Førland, K. Grjotheim, K. Motzfeldt, and S. Urnes, Editors, p. 141, Universitetsforlaget, Oslo, Norway (1966).
9. JANAF Thermochemical Tables with Supplements, published by U.S. Department of Commerce (1971, 1974, 1975, 1978).
10. T. Johansson, Brit. Pat. 2,022,069 (1979).
11. T. Johansson, Eur. Pat. Appl. 28, 208 (1981).

Thermal Oxidation of Transition Metal Silicides on Si: Summary

M. Bartur and M-A. Nicolet

California Institute of Technology, Pasadena, California 91125

ABSTRACT

Thin films of almost all transition metal silicides, on a Si substrate, oxidize and form SiO₂ on their surfaces upon annealing in an oxidizing ambient. In applications of these silicides as interconnects in integrated circuits, the oxidation characteristics of a silicide and the SiO₂ growth rate are important. A compilation of the available data concerning silicide oxidation kinetics is presented. Generalization based on the data as presented is difficult. In this summary, we explore the processes controlling the oxidation of metal silicides and point out commonalities and differences between different silicides. We review the four steps controlling silicide oxidation: oxidant transport through the oxide, reaction at the silicide/oxide interface, net transport of Si atoms with respect to metal atoms in the silicide, and reaction at the silicide/Si interface. The diffusing species through the silicide during oxidation correlates with the moving species in silicide formation. A discussion of a mechanism which explains why the oxidation rate of some silicides on a Si substrate is faster than that of bare Si is presented. It is concluded that silicides formed via metal diffusion oxidize faster than silicides formed via Si diffusion.

With the advances in Si technology, scaling of devices to micro size imposes severe requirements for the interconnection lines on the chip. The commonly used poly-Si becomes inadequate because its lowest practical resistivity is ~400 μΩ cm (1). The possibility to use silicides as interconnect material in integrated circuits has generated extensive explorations (2-5). The most important desired properties of an interconnect material are low resistivity and the possibility to form electrically insulating thermal oxide. The reported resistivities of all Si-rich transition metal silicides (6) are at least one order of magnitude lower than highly doped poly-Si. In this paper, we investigate the processes controlling the oxidation of metal silicides.

All metal disilicide films resting on an excess Si substrate investigated so far, except HfSi₂ and NbSi₂, form SiO₂ as a result of thermal annealing in an oxygen environment. Below the grown SiO₂ film, the silicide is preserved morphologically. The oxidation kinetics of different silicides are summarized in Table I. This table shows that different silicides have different oxidation kinetics, which differ from the kinetics of Si oxidation. The reported oxide thickness, which results from oxidation at the low temperature range, for different silicides varies by more than 50%. Also, different authors disagree about the oxidation behavior of a silicide under dry oxidation. For TaSi₂ (14) or WSi₂ (16), it has been reported that there is no oxide

Key words: oxidation, transition metal silicides, mass transport.

growth under dry conditions, but other researchers have shown that these silicides do oxidize in dry O₂. Such variations cannot be attributed solely to the different analytical techniques used by different authors (Tallystep, RBS, AES, and cross-section TEM, multi-beam interferometry). One explanation commonly advanced is that the oxidation behavior depends on the details of the silicide preparation technique. Also, the way the oxidation of the sample is started seems to be very important for some silicides (5, 13).

In this paper, the important processes controlling the oxidation kinetics are summarized, and the commonalities and differences between different silicides are pointed out.

Major Processes

The oxidation process can be separated into four distinct steps:

1. Diffusion of the oxygen containing molecules through the SiO₂ layer.
2. Reaction at the silicide/oxide interface.
3. Net transport of Si atoms relative to the metal atoms in the silicide.
4. Reaction at the Si/silicide interface which releases Si from the substrate.

We comment on these processes in sequence.

1. The transport through the growing oxide is the only diffusion-controlled process which yields a parabolic time dependence in the oxidation kinetics. We

Table I. Kinetics of SiO₂ growth by thermal annealing of silicide films on various substrates in oxidizing ambient

Silicide film	Substrate	Kinetics $x^2 = \text{thickness}$ $t = \text{time}$	Condition	Rate constants at temperature			Activation energy (eV)		Temperature range (°C)	Ref.
				B/A (cm/s)	B (cm ² /s)	(°C)	B/A	B		
Si	Si <?>	$x^2 + Ax = B(t + \tau)$	wet	3.5×10^{-8}	8.0×10^{-18}	1000	1.96	0.71	920-1200	7
		$x^2 + Ax = B(t + \tau)$	dry	2.0×10^{-9}	3.3×10^{-14}	1000	1.99	1.24	650-1200	7
TiSi ₂	Si <?>	$x^2 + Ax = B(t + \tau)$	wet	5.6×10^{-8}	6.4×10^{-18}	1000	2.00	1.39	900-1050	8
TiSi ₂	Si (poly)	$x^2 + Ax = B(t + \tau)$	wet	6.6×10^{-8}	6.4×10^{-18}	1000	2.10	1.51	700-1100	9
CoSi ₂	Si <111>	$x^2 = Bt$	wet		5.1×10^{-18}	1000		1.05	700-1000	10
	<100>	$x^2 = Bt$	dry		3.1×10^{-14}	1000		1.39	650-1100	10
NiSi ₂	Si <111>	$x^2 = Bt$	wet		2.2×10^{-18}	900		1.05	700-900	11
	Si <100>									
	Si (poly)	$x^2 = Bt$	dry		1.1×10^{-14}	900		1.40	700-900	11
	SiO ₂									
MoSi ₂	SiO ₂	$x^2 + Ax = B(t + \tau)$	dry	2.8×10^{-9}	1.9×10^{-14}	1000	1.90	1.60	900-1100	12
MoSi ₂	Si <?>	$x^2 + Ax = Bt$	wet	1.2×10^{-7}	1.0×10^{-12}	1000	0.84	1.10	800-1000	13 ^b
RhSi	Si <?>	$x^2 + Ax = Bt$	wet	1.1×10^{-7}	1.0×10^{-12}	1000	0.92	1.10	800-1000	13
RhSi ₄	Si <?>	$x^2 + Ax = Bt$	wet	1.0×10^{-7}	1.0×10^{-12}	1000	0.99	1.10	800-1000	13
TaSi ₂	Si (poly)	$x^2 = Bt$	wet		1.4×10^{-18}	1000		1.40	900-1050	14
	Si <100>									
	Si <111>	$x^2 = Bt$	dry		2.8×10^{-14}	1000		1.20	800-1200	15
TaSi ₂	Si <?>	$x^2 + Ax = Bt$	wet	8.2×10^{-8}	1.0×10^{-12}	1000	0.93	1.10	800-1000	13
WSi ₂	Si (poly)	$x^{1.82} = B^*t$	wet		$B^* = 4.4 \times 10^{-12}$ a	1000		1.00	1000-1200	16
	SiO ₂	$x^{1.82} = B^*t$	wet		$B^* = 6.9 \times 10^{-12}$ a	1000		0.40	1000-1200	16
WSi ₄	Si <?>	$x^2 + Ax = Bt$	wet	1.3×10^{-7}	6.8×10^{-13}	1000	1.0	1.30	800-1000	13
IrSi _{1.75}	Si <?>	$x^2 + Ax = Bt$	wet	5.8×10^{-8}	8.5×10^{-18}	1000	1.3	1.20	800-1000	13

^a Units of B* are in cm and s with appropriate powers.

^b Data from Ref. (13) was extracted from Fig. 1 and 2 in the temperature range of 800°-1000°C.

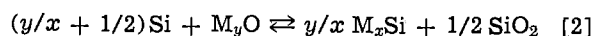
adopt the linear-parabolic oxidation relation (7)

$$x^2 + Ax = B(t + \tau) \quad [1]$$

where x is the oxide thickness, t the oxidation time, B is the parabolic rate constant, B/A is the linear rate constant, and τ is a fitting parameter that takes into account the initial (transient) oxide growth. The value of B is controlled only by the diffusion process of the oxidant in the SiO_2 , while that of A depends on the reactions at the interfaces and the transport through the silicide layer. Figure 1 depicts a comparison of the parabolic rate constant B vs. temperature for oxide growth on Si and different silicides for wet and dry oxidation. For dry oxidation, the data generated by different authors (over a 30-year span) clearly fit one process with one activation energy. Even the data for wet oxidation can be taken as basically indicative of one process only. The data of Murarka *et al.* (14) for TaSi_2 (line 4a) do not agree with other reports (13, 20) nor do they with the general picture. We will ignore those data. Variation in the partial pressure of water vapor can explain some of the other differences there. The first-order conclusion is that the diffusion process through the oxide is the same during oxidation of all silicides. This fact implies that the equilibrium concentration of the oxidant in the oxide and the diffusion coefficient through the oxide are the same regardless of the substrate ($\langle \text{Si} \rangle$, poly-Si, or different silicides). In other words, the physical properties of the oxide are the same. In fact, a recent study (21) has shown that oxides grown on different silicides have similar properties (density, dielectric constant).

2. The reaction at the silicide/oxide interface is the most difficult step to explore. We will not discuss the reaction rate here. We will only elaborate on a first-order thermodynamics argument to predict the oxide formed. The oxidation of thin films does not necessarily follow such equilibrium laws, but the argument gives some general indication about the process. The generalized chemical equilibrium reaction at this interface, assuming limited oxygen supply (in other words, that all oxygen at this interface is reacted), and unlimited

supply of Si from the substrate can be written as

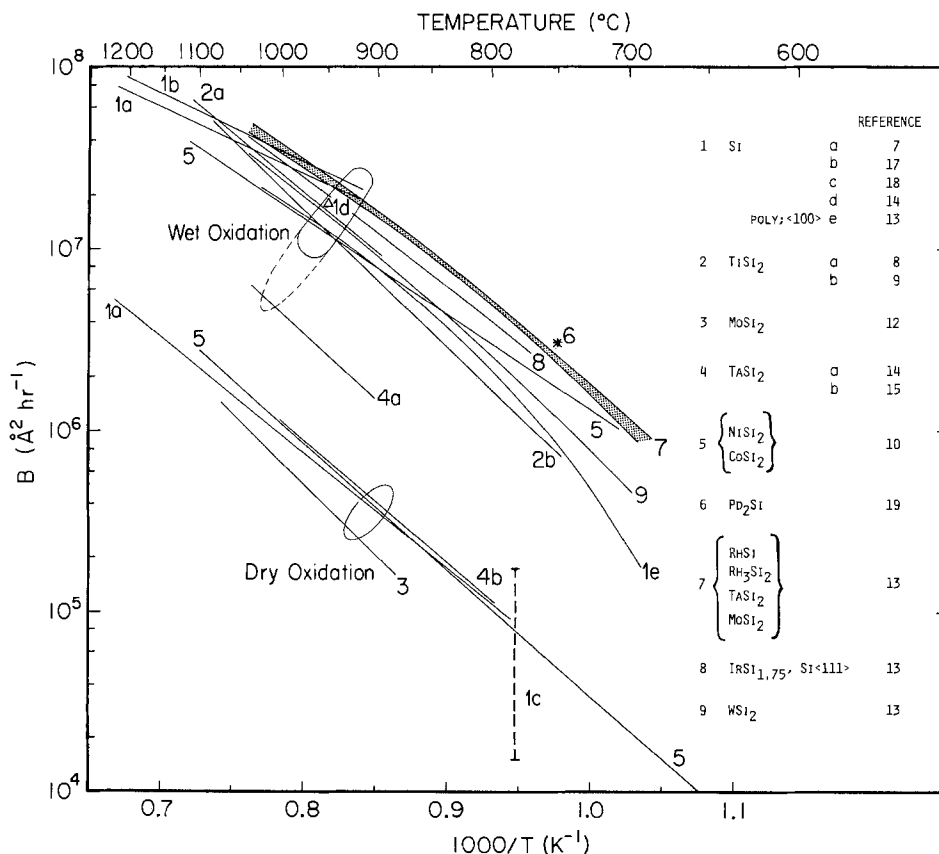


where $M_x\text{Si}$ describes generalized silicide with metal M and M to Si ratio of x , and $M_y\text{O}$ denotes generalized metal oxide with M to O ratio y . This equation expresses a balance between the formation of SiO_2 or the dissociation of the silicide and the formation of a metal oxide. Figure 2 [taken from Bartur (22)] depicts ΔH_R° —the standard heat of the above reaction. Positive ΔH_R° means that metal oxide will form, while negative ΔH_R° predicts SiO_2 formation (22).

From Fig. 2, we conclude that all transition metal silicides, except Zr and Hf, will grow SiO_2 . However, both exceptions, as well as Ti, Nb, and Ta, might be considered marginal cases, because the values used to calculate ΔH_R° are uncertain and apply only to room temperature. Kinetics may play a major role in these cases. Oxidation studies of ZrSi_2 have not been reported. HfSi_2 (23) and NbSi_2 (24) have been reported to disintegrate and to form a mixture of metal and Si oxides. TiSi_2 does form a SiO_2 layer upon oxidation (8, 9), but, according to a recent report (25), it does so only at temperatures above 900°C . Below this temperature, titanium oxide is formed. This observation might also explain the NbSi_2 oxidation results that were obtained at low temperatures. We can conclude that the thermodynamical argument correctly predicts the general oxidation behavior and identifies the marginal cases for which it cannot affirmatively predict the outcome. Thermodynamics, of course, attempts to predict only which oxides may form. The chemical reactions at that interface are not considered. These unexplored reaction rates are a factor in the linear rate constant B/A .

3. The Si transport (relative to the metal atoms in the silicide) during oxidation is a second factor that might affect A . The argument that the method of silicide preparation affects the oxidation kinetics might be attributed to different characteristics of mass transport through the silicide layer. Here, we concentrate on the question of which species moves. The diffusion

Fig. 1. Arrhenius plot of the parabolic rate constant (B) of oxide growth on different silicides and on Si for dry and wet oxidation.



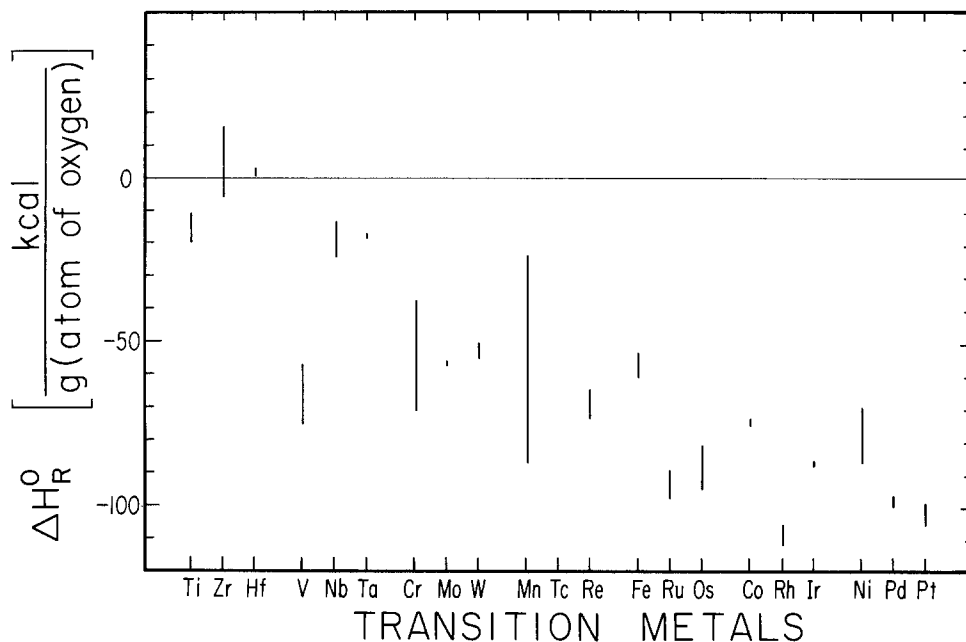


Fig. 2. The difference between the standard heats of reaction ΔH°_R (per oxygen atoms) of the two reactions which preserve the stoichiometry of the silicide layer, forming SiO_2 on the silicide and reconstituting more silicide with the silicon substrate, and forming metal oxide and precipitating out elemental silicon. For metals that have more than one oxide, a range of ΔH°_R values that is determined by the reaction is shown.

mechanism and the diffusion coefficient will not be explored because of the lack of sufficient experimental data.

The possible cases of a diffusion of Si, metal, or both across the silicide are described in Fig. 3. For two independent moving species—moving singly or simultaneously in either direction—there are eight different possible combinations. Three possibilities can be ruled out since they do not preserve the silicide, as is observed experimentally. The fifth case is unlikely, but is retained for the sake of completeness. To resolve the possible cases experimentally, inert marker experiments must be conducted. The results of such experiments performed for silicide oxidation are matched to the proper schematic description and are also depicted in Fig. 3.

4. Reaction at the Si/silicide interface during oxidation is similar in nature to the reaction at that interface during silicide formation. Silicide formation is usually diffusion not reaction controlled (except CrSi_2) at low temperatures at which the reaction can be analyzed. The rates of Si consumption, however, are roughly the same in both the oxidation experiments performed at high temperatures and these silicide formation experiments at the low temperatures. Because at those rates the reaction at the Si/silicide interface is fast, it must be negligible also at high temperature during oxidation.

Discussion

Table I shows that different silicides yield different oxide thicknesses for identical oxidation conditions. However, the data in Fig. 2 demonstrate that the diffusion of the oxidant through the SiO_2 proceeds similarly for all silicides (values of B in Eq. [1] are basically the same). The observed differences in the oxide thickness must be, therefore, caused by dissimilarities in the linear (early) part of the oxidation process (different values of B/A in Eq. [1]). According to Fig. 3, CrSi_2 , CoSi_2 , NiSi_2 , PdSi , and PtSi oxidize by dissociation with metal as the main diffusing species. The dissociation is induced by the reaction of the oxidant with the silicide. The fact that excess Si is generated for some silicides suggests that this reaction proceeds quite readily. The net Si transport through the silicide is much faster than the transport of oxidant through the oxide. If these two processes (reaction and transport) have high rates, the linear rate constant in Eq. [1] (B/A) must be large. As a result, the process is dominated entirely by the parabolic rate constant B , and Eq. [1] simplifies to

$$x^2 = Bt \quad [2]$$

Under this condition, since B is determined by the oxidant diffusion through the oxide, we expect the oxidation rate to be the highest possible, and independent of the substrate on which SiO_2 grows. Indeed, in the silicides that dissociate during oxidation (CoSi_2 , NiSi_2 , PdSi , and PtSi), we find oxidation rates higher than those of Si and the refractory metal silicides, especially at low oxidation temperatures. In effect, these silicides act as catalysts, because they oxidize (and dissociate) more easily than Si, and this promotes high oxidation rates.

To explore a possible connection between the transport across the silicide during oxidation and during silicide formation, we compared the dominant diffusion species during the two processes (Table II). From Fig. 3 and Table II, we find that dissociation during oxidation happens in all the silicides (NiSi_2 , PdSi , PtSi) where the metal is the moving species during silicide formation. For CoSi_2 , one expects, accordingly, that Co is the moving species during silicide formation, but this prediction has yet to be verified experimentally. An exception is CrSi_2 , which also dissociates, while Si moves during silicide formation. But this silicide grows linearly with time [is reaction limited (6)], so that the moving species during silicide formation might be set by the boundary condition and not by diffusivities. The comparison suggests a rule: during oxidation of a silicide that forms by a diffusion-limited process, the dominant moving species is the same as in the silicide formation. In silicide formation or oxidation we deal with the same bulk, and hence the same relative magnitude of diffusivities. If during silicide formation, which usually occurs at lower temperature than oxidation (for comparable Si consumption rates), the

Table II. Dominant diffusion species during silicide formation and oxidation

Silicide	Dominant diffusion species	
	During silicide formation	During silicide oxidation
TiSi_2	Si (6)	Si (26, 27)
CoSi_2	—	Co (28)
NiSi_2	Ni (29)	Ni (28)
Pd_2Si	Si (30); Si and Pd (6)	
PdSi	Pd and Si ^a	Si ? (28)
PtSi	Pt (6)	Pt (27)
CrSi_2	Si (6)	Cr (27)

^a This is an indirect conclusion from sample preparation as described by the authors (28).

Fig. 3. The different possible moving species for mass transport during silicide oxidation. The experimental results are described.

MOVING SPECIES DURING OXIDATION	SCHEMATIC DESCRIPTION	EXPERIMENTAL RESULTS	REFERENCE
Si →		TiSi ₂ Pd ₂ Si (?)	9, 26, 27 28
M ←		CoSi ₂ PdSi	28 28
M ← Si ←		CrSi ₂ NiSi ₂ PtSi	27 28 27
M ← Si →		dissociation + Si supply	
M → Si →		Si supply causes metal release and diffusion	
M → Si ← Si ← M →		These processes do not preserve the silicide.	

process is already diffusion controlled, one expects that the reaction at the Si/silicide interface will not control the process during oxidation either. Hence (assuming similar activation energies), we infer similar boundary conditions generated by the chemical reaction at the interfaces. Therefore, similar bulk and interface properties result in similar atomic fluxes in both cases.

Conclusions

The variation in the oxidation kinetics between Si and silicides, and between the silicides themselves, is due to a different linear rate constant (B/A). In particular, silicides in which the metal is the moving species oxidize more rapidly than bare Si and only a parabolic growth rate is observed experimentally. Silicides in which Si is the moving species are usually formed at high temperatures and the limited Si diffusion through the silicide might impede the oxidation and cause linear rate term change. Enhanced oxidation rates are desirable in IC processing, since dopant diffusion in the Si with the already formed junctions should be minimized. The fact that an enhanced oxidation rate is associated with silicides formed by metal diffusion and can be successfully oxidized at low temperatures gives additional benefits for IC processing. Those silicides are usually formed at relatively low tempera-

tures (less than 450°C) with better control than refractory metal silicides, where Si diffuses during formation. When the metal moves during silicide formation, the Si/silicide interface is expected to be smooth. Kirkendall voids are not expected. Also, from line width considerations and for self-aligned devices, it is preferable (5) that the metal moves during silicide formation.

We thus conclude that, in those respects, silicides formed by metal diffusion have potential for IC interconnects.

Acknowledgments

The work was partially supported by Solid-State Devices, Incorporated.

Manuscript submitted Sept. 15, 1983; revised manuscript received Oct. 24, 1983. This was Paper 285 presented at the Washington, DC, Meeting of the Society, Oct. 9-14, 1983.

The California Institute of Technology assisted in meeting the publication costs of this article.

REFERENCES

1. K. C. Saraswat and F. Mohammadi, *IEEE Trans. Electron Devices*, ed-29, 645 (1982).
2. S. P. Murarka, *J. Vac. Sci. Technol.*, **17**, 775 (1980).
3. K. N. Tu, *ibid.*, **19**, 766 (1981).

4. A. K. Sinha, *ibid.*, **19**, 778 (1981).
5. F. M. d'Heurle, in "VLSI Science and Technology/1982," C. Dell'Oca and W. M. Bullis, Editors, p. 194, The Electrochemical Society Softbound Proceedings Series, Pennington, NJ (1982).
6. M-A. Nicolet and S. S. Lau, in "VLSI Electronics: Microstructure Science," N. Einspruch (Series Editor) and G. Larrabee (Vol. Editor), Chap. 6, Academic Press, New York (1983).
7. B. E. Deal and A. S. Grove, *J. Appl. Phys.*, **36**, 3770 (1965).
8. J. R. Chen, M. P. Houg, S. K. Hsiung, and Y. C. Liu, *Appl. Phys. Lett.*, **37**, 824 (1980).
9. J. R. Chen, Y. C. Liu, and S. D. Chu, *J. Electron. Mater.*, **11**, 355 (1982).
10. M. Bartur and M-A. Nicolet, *Appl. Phys. A*, **29**, 69 (1982).
11. M. Bartur and M-A. Nicolet, *Appl. Phys. Lett.*, **40**, 175 (1982).
12. T. Mochizuki and M. Kashiwagi, *This Journal*, **127**, 1128 (1980).
13. J. E. E. Baglin, F. M. d'Heurle, and C. S. Petersson, *J. Appl. Phys.*, **54**, 1849 (1983).
14. S. P. Murarka, D. B. Fraser, W. S. Lindenberger, and A. K. Sionha, *ibid.*, **51**, 3241 (1980).
15. R. R. Razouk, M. E. Thomas, and S. L. Pressacco, *ibid.*, **53**, 5342 (1982).
16. F. Mohammadi, K. C. Saraswat, and J. D. Meindl, *Appl. Phys. Lett.*, **35**, 529 (1979).
17. W. A. Pliskin, *IBM J. Res. Dev.*, **198** (May 1966).
18. E. A. Irene and P. W. Dong, *This Journal*, **125**, 1146 (1978).
19. M. Bartur and M-A. Nicolet, Unpublished results.
20. D. Pawlik, E. Doering, and H. Oppolzer, Abstract 195, p. 310, The Electrochemical Society Extended Abstracts, Vol. 82-1, San Francisco, CA, May 9-14, 1982.
21. M. Bartur and M-A. Nicolet, *J. Electron. Mater.*, **13**, 81 (1984).
22. M. Bartur, *Thin Solid Films*, **107**, 55 (1983).
23. S. P. Murarka and C. C. Chang, *Appl. Phys. Lett.*, **37**, 639 (1980).
24. T. P. Chow, K. Hamzeh, and A. J. Steckl, *J. Appl. Phys.*, **54**, 2716 (1983).
25. F. d'Heurle, E. A. Irene, and C. Y. Ting, *Appl. Phys. Lett.*, **42**, 361 (1983).
26. J. R. Chen, Yuen-Chung Liu, and Sheng-Deh Chu, *ibid.*, **40**, 263 (1980).
27. C-D Lien, M. Bartur, and M-A. Nicolet, Paper presented at the Materials Research Society Annual Meeting, Boston, Nov. 14-18, 1983.
28. M. Bartur and M-A. Nicolet, *J. Appl. Phys.*, **54**, 5407 (1983).
29. F. M. d'Heurle, C. S. Petersson, L. Stolt, and B. Stritzker, *ibid.*, **53**, 5678 (1982).
30. D. M. Scott, Personal communication (1983).

Ion Beam Etching of Silicon, Refractory Metals, and Refractory Metal Silicides Using a Chemistry Assisted Technique

J. D. Chinn, W. Phillips, I. Adesida, and E. D. Wolf

National Research and Resource Facility for Submicron Structures, School of Electrical Engineering, Cornell University, Ithaca, New York 14853

ABSTRACT

The etching characteristics of silicon and two refractory metals (Ti, Mo) and four refractory metal silicides (TiSi₂, TaSi₂, MoSi₂, PtSi) are described using a technique called chemically assisted ion beam etching (CAIBE). In this technique, reactive Cl₂ gas is introduced into a sample chamber in conjunction with, and relatively independent of, a broad beam of Ar⁺ ions. Incremental increases in the Cl₂ partial pressure caused linearly increasing etch rates for all materials investigated, except for SiO₂. In the case of silicon, correlation between broad beam CAIBE and ultrahigh vacuum (UHV) etching studies was made. The relative etch rate increase of the refractory metals and silicides investigated were found to be related to the vapor pressures of the reaction products. Additional studies have shown that various residual gas contaminants such as hydrogen, oxygen, and H₂O can influence etching mechanisms by reducing the reactive Cl₂ flux or by forming stable oxides. Linewidths with dimensions below 0.6 μm have been obtained in polycide (a stacked silicide/polysilicon) structures with an etch selectivity > 9:1 between the film layers and SiO₂ using CAIBE.

As minimum feature sizes diminish in VLSI silicon gate-MOS devices, the relatively low electrical conductivity of polysilicon interconnects can decrease device performance by increasing RC time delays. Improved characteristics have been obtained by the use of refractory metals-metal silicide/polysilicon composite gate structures, which can significantly increase the conductivity and allow high temperature processing after metallization. However, fine-line patterning of composite structures can pose problems where low volatile metal halides are present. In general, a pattern transfer technique which combines both physical and chemical mechanisms is desired for high selectivity and for anisotropic etched walls. These mechanisms are involved in most dry etching techniques, such as plasma etching (PE) and reactive ion etching (RIE). However, one major drawback of planar plasma processing is in the indirect method of determining the process parameters (RF power, pressure, flow rate, etc.). Furthermore, planar techniques do not allow direct control of the fluxes arriving at the sample surface. Greater control over the fluxes can be achieved through the use of

broad-beam ion sources in which the ion energy and current can be varied independently. However, even in a technique like reactive ion beam etching (RIBE), there is little control over the chemical-etch component which results from the neutrals effusing from the ion source. In the technique used in this work, chemically assisted ion beam etching (CAIBE), a chemically reactive gas is introduced into the sample chamber in conjunction with either inert or reactive ion bombardment. This technique allows for a large range of relatively independent control over the chemical component of the etching process by varying the partial pressure of the reactive gas and the physical component by controlling the ion beam's energy and current. Large increases in selectivity and etch rates over ion milling have been reported for GaAs (1, 2) using this technique. In addition, it has been demonstrated that CAIBE can be used to control etch-wall profiles from directional overcut to undercut sidewalls in Si (3, 4).

For polycide structures, general pattern transfer requirements include anisotropic profiles without undercutting of the polysilicon layer along with a selective etch stop. Most of the work that has been reported on

Key words: plasma, integrated circuits, interconnects.

the patterning of refractory metals and their silicides has been confined to fluorine gas systems using RIE (5-10). Isotropic etching often occurs and undercut profiles can result in high fluorine-content environments. Less undercut in the patterning of polysilicon (11-13) and polycide structures (14) has been reported when chlorinated plasmas are used. In this paper, we report experimental results using the CAIBE technique to etch Si, refractory metals Mo and Ti, and refractory metal silicides $TiSi_2$, $TaSi_2$, $MoSi_2$, and $PtSi$ with Cl_2 as the reactive background gas. This technique has also been used to pattern polycide structures with dimensions below $0.6 \mu m$.

Experimental

The CAIBE experimental apparatus used in this study was a modified, Varian/Extrion RE-580 RIBE system; it is shown schematically in Fig. 1. Several modifications made on the system include a hollow cathode electron emitter within the ion source and a gas tube through which controlled amounts of Cl_2 gas can be admitted into the sample chamber. In a hollow cathode, thermionic ionization of argon occurs. From this small inert-gas plasma, electrons are extracted for impact ionization of either inert or reactive gases within the source. This type of cathode results in stable ion currents with less than 5% fluctuations over hours of operation. The ion source produces a flood beam capable of etching wafers up to 10 cm in diam. The diameter of samples processed in these experiments however did not exceed 2 cm. A Faraday cup is located adjacent to the sample and is connected to a current integrator-ratemeter for measuring the total ionic charge dose and current density.

The reactive chemical component is controlled by varying the flow rate of Cl_2 gas into the sample chamber. At chamber pressures of 10^{-4} torr, the mean free path of a gas molecule is sufficiently long that the chemical flux can have directionality. Etching in the CAIBE mode with directed chemical fluxes (1, 15-18, 29) has shown total etch-yield increases as high as 30 times compared to pure physical sputtering. However, etch uniformity and profile control under these conditions are dependent on the impingement direction of the chemical and ionic fluxes (1). Thus, in order to better utilize the CAIBE technique, etch uniformity was improved using a nondirected chemical flux arriving at the sample surface by diffusion processes.

Samples were mounted on aluminum wafers by mechanical clips and by thermal paste on the back side. Samples of Ti, Mo, $MoSi_2$, and $TaSi_2$ were prepared by sputtering from a pure metal or composite target. $TiSi_2$ and $PtSi$ were prepared by E-beam evaporation of the pure metals, and silicide formation was performed by heating in a vacuum furnace. N^+ polysilicon was grown by LPCVD followed by a phosphorus implant of $5 \times 10^{15}/cm^2$ and drive in. Samples for etch yield and etch rate studies were patterned by photolithography with AZ1350 resist and measured by

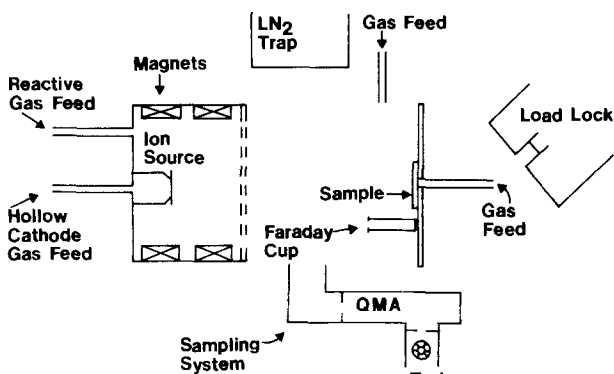


Fig. 1. Schematic of CAIBE system

an Alpha-Step surface profiler. High resolution patterns ($< 0.6 \mu m$) were prepared by E-beam lithography followed by Cr metal liftoff. By using the current integrator, Faraday cup, and load-lock system, samples were exposed to a predetermined charge dose for a fixed ion current density and time. Sample temperature was maintained below $80^\circ C$ under all etch conditions by clamping the sample holder to a freon-cooled stage and by passing argon between the stage and sample.

Results and Discussion

Over the past several years, UHV plasma chemistry studies have provided valuable information and insight into dry etching mechanisms. One such area is in the importance of ion-surface interactions. This has led to rapid development of RIE, and its use instead of the earlier PE technique. However, direct comparisons between ideal UHV environments and etching systems used for semiconductor manufacturing generally cannot be made, because of fundamental differences between the two. In the planar techniques of PE and RIE, the sample is immersed in a plasma and exposed to high fluxes of ions, electrons, and radiation. In the CAIBE technique, experimental conditions are more closely related to UHV environments. In this study, we compared experimental data obtained by Gerlach-Meyer *et al.* (15) in a UHV environment to data obtained in our modified commercially available machine. Good correlation between the two systems is obtained.

In Fig. 2, the etch rate of silicon is shown for various ion energies with incremental increases of Cl_2 gas admitted into the sample chamber. It can be observed that for flow rate increments of 3 sccm of Cl_2 , nearly linear increases in the Si etch rate were measured. Higher etch rates with the same relative etch rate increases were observed with further Cl_2 gas additions until constrained by the pumping speed of system. Etch rates up to five times larger than ion milling rates were obtained. In examining these enhanced etch rates, the Ar^+ -sputter yield was used as a comparative reference. The sputter yields obtained in these experiments show fairly good agreement with other published data (16-17), as shown in Table I. Our slightly higher sputter yields can be attributed to nonideal conditions of a higher residual gas back-

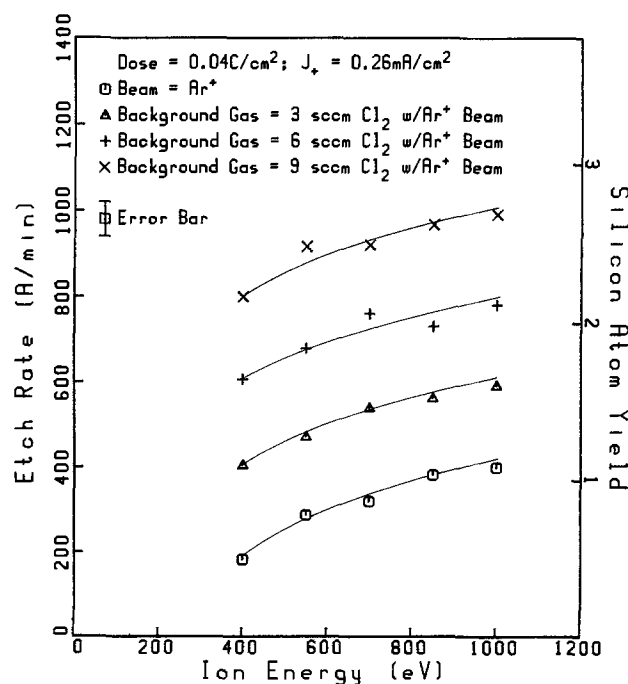


Fig. 2. Etch rates of Si vs. ion energy for incremental increases of Cl_2 gas under Ar^+ ion bombardment.

Table I. Comparison of Ar⁺-etch yields in Si

Si Sputter Yield due to Ar ⁺ Bombardment*			
Ion Energy eV	This work	Ref. 15	Ref. 17
500	.70	—	.66
1000	1.08	.9	.92

* Data for normal incidence ions

ground as compared to the UHV environment. Cl₂ gas was then admitted into the sample chamber, and a partial pressure was estimated using a quadruple mass spectrometer. By using a zero order approximation, we measured a partial pressure increase of $\sim 5.0 \times 10^{-5}$ torr of Cl₂ for each increase of 3 sccm admitted into the sample chamber. The chemical flux of Cl₂ impinging on the sample surface was estimated using statistical mechanics through the following expression

$$\text{Flux} = \frac{nc}{4}$$

where c is the mean velocity and n the particle density for a room temperature gas. This gives an estimated Cl₂ flux on the sample of $\sim 3.6 \times 10^{15}/\text{cm}^2\text{-s}$ at a flow rate of 9 sccm. Using the data of Fig. 2, these etch conditions (1000 eV with 9 sccm Cl₂ flow) gave a total yield of ~ 2.7 Si atoms per incident ion. This is in good agreement with results obtained in a UHV environment (15), as shown in Table II. The slightly lower total yields obtained in our experiments probably results from using a nondirected chemical flux and a rough estimation of the actual Cl₂ partial pressure. In addition, sputter deposited Si was used in the UHV study, and a higher porosity could result in higher etch yields in the presence of Cl₂ under Ar⁺ bombardment than obtained in our studies, in which crystalline Si was used. In the work by Gerlach-Meyer, Cl₂ gas was directed at the Si surface in the presence of low ion currents (~ 0.01 mA/cm²) with a chemical-flux-to-ion-arrival-rate ratio $\sim 160:1$. The total atom yield showed a nearly linear dependence on the Cl₂ flux below some saturation flux. Above a certain saturation flux (high Cl₂ impingement rates), the total Si atom yield was independent of the flux and was determined by the mass and energy of the incident ions.

High chemical-flux-to-ion-arrival-rate ratios comparable to those obtained in the UHV studies could not be obtained in our experimental apparatus, because of vacuum pumping constraints and operation of the ion source. Thus, a Cl₂ impingement rate in which surface saturation is observed in the UHV studies could not be obtained in these experiments. The etch yields at the Cl₂ partial pressures used were thus limited by the availability of Cl₂ for reaction with Si. The etch yields increased linearly with changes in the Cl₂ partial pressure, as indicated in Fig. 2. The ion currents pro-

Table II. Comparison of total silicon atom yields for various Cl₂ gas flux-to-ion-ratios

	Cl ₂ flux rate	CAIBE Yield	Cl ₂ flux/ion ratio
from this work	$3.6 \times 10^{15}/\text{cm}^2 \text{ sec}$	2.7	2.3
ref. 15		3.2	160
from this work	$2.5 \times 10^{15}/\text{cm}^2 \text{ sec}$	2.1	1.55
ref. 15		2.8	40

duced by the broad-beam source were also an order of magnitude greater than from the UHV ion gun. Under our experimental conditions, the chemical-flux-to-Ar⁺-arrival rate ratio was $\sim 2.3:1$ (vs. 160:1), and fairly good agreement in the total yield was still obtained between the ideal UHV and our broad beam results. This suggests that the etch yields are dependent on the energy of the incident ion and the reactive chemical flux, but not on the ion flux below some saturation level of the chemical flux. For a higher ion current, the total atom yield is still the same, but the Si atoms are removed at a faster rate determined by the ion flux. This is an advantage of the CAIBE technique over other planar techniques in finding the desired process parameters. From UHV or CAIBE yield data, the relative etch-rate ratios (the selectivity) for different film layers with the same background gas conditions are only determined by the ion flux. In PE or RIE techniques, various parameters have to be adjusted in order to determine the optimum selectivity.

In the operation of broad-beam ion sources, an order of magnitude pressure difference across the extraction grids usually exists. The transmission of the grid set used in these experiments was approximately 50%. Thus, a portion of the reactive gas background diffuses upstream into the source, where it is ionized and then accelerated back toward the substrate. As the flow of reactive gas into the sample chamber is increased, the higher chamber pressure results in increased currents both within the source and the extracted beam. Hence, Cl₂⁺ and Cl⁺ ions are present in the extracted beam. In order to qualitatively measure the amount of chlorine within the beam, the increase in the beam current for changes in the background gas pressure were measured. In Fig. 3, it can be observed that for large flow rates of Cl₂ gas into the sample chamber, the beam composition approaches nearly 65% Ar⁺ and 35% Cl₂⁺ and Cl⁺. In these experiments, operation of the ion source was adjusted to maintain a constant ion current density. The role of Cl₂⁺- and Cl⁺-ion bombardment in the presence of Cl₂ gas on the total etch yield has not been investigated in UHV environments. Studies are needed in this area to determine if the reactive ions significantly increase the etch yield or behave effectively like Ar⁺ ions in initiating etch reactions. Preliminary etch rate experiments of Si and Cl₂⁺ and Cl⁺ ions with Cl₂ gas impinging on the background gas have indicated that the chlorine ions behave similarly to Ar⁺ ions or that the ion-assisted reaction between the Cl₂ background gas and the Si surface dominates the etching mechanisms.

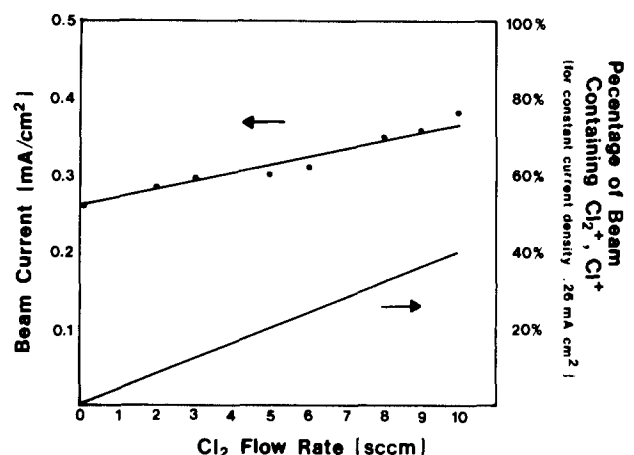


Fig. 3. Total ion beam current for various Cl₂ flow rates. The increase in ion beam current is attributed to the Cl₂ background gas entering the source. The amount of Cl₂⁺ and Cl⁺ is shown as a percentage of the total beam current. It is assumed that the Ar⁺ in the ion beam remains constant.

Table III. Comparison of etch rate increases

Material	Si	Poly-Si	Ti	TiSi ₂	TaSi ₂	MoSi ₂	Mo	PtSi
Relative Etch Rate Increase (Å/min.)	200	177	136	127	75	62	40	35

• Ar⁺ Beam ⊙ Normal Incidence 500 eV
DOSE = 0.04 C/cm² 0.26 mA/cm²
Increments of 3 sccm Cl₂ in Background

Under similar experimental etch conditions, Ti, TiSi₂, TaSi₂, Mo, MoSi₂, and PtSi samples also showed linear incremental etch-rate increases with Cl₂ additions. However, the enhanced etch rates were lower than those of Si. Figure 4 shows the etch rates obtained for TaSi₂ under the same conditions as the Si experiments. Table III lists the relative etch-rate increases caused by adding 3 sccm increments of Cl₂ gas for different materials. By examining the vapor pressures (19-22) of the various chloride reaction products, it can be observed that the relative etch-rate increases of Table III correspond to the relative chloride vapor pressures of Fig. 5. A high vapor pressure implies a high etch-rate increase. Etch rates of other types of materials should be dependent on the vapor pressure of the final reaction products. In Fig. 5, we have listed the downstream mass spectrometry reaction products for the materials etched.

In CAIBE, substrate temperatures have also been reported to add nonlinear effects to the etch rates (18) especially with materials which form low vapor pressure reaction products. Our sample temperatures are assumed to be the same for all materials since the ion dose and current were the same. The substrate temperature effect has been reported in the etching of GaAs with plasmas containing chlorine (23, 24) and bromine (25). This implies that raised sample temperatures in beam processing aid in increasing the etch rates. However, in a beam process, the actual surface temperature

where the ion beam deposits energy with the substrate is unknown. It may be quite high.

Refractory metals often exhibit the property of forming stable and low sputter yield oxides. Thus, background oxygen containing gas contaminants can influence etching mechanisms and etch rates. In most chlorine containing systems, H₂O is a common residual gas, and is known to significantly influence the etch rate of other materials which have a high affinity for oxygen, such as aluminum. In order to investigate the effects of the background gas contaminants, trace amounts of H₂, O₂, HCl, and Cl₂ (with traces of H₂) were added to the sample chamber with the results illustrated in Fig. 6. Additions of H₂ to the sample chamber had no measurable effect on the etch rates. However, when small traces of O₂ were added, etch rates were dramatically reduced on all refractory metals and silicides except for PtSi. In ion milling, Ti is a popular masking material because it has a high affinity for oxygen and low sputter yield. The etch-rate decrease observed with oxygen additions is attributed to the gettering property of the material and the low sputter yield of the oxide.

HCl was the most abundant residual gas in our system. This is a common occurrence even in well-pumped and well-trapped vacuum systems which have been exposed to chlorine containing compounds. When additional amounts of HCl were added to the sample chamber, the etch rates showed little change, as in the case with H₂ additions. When traces of H₂ were

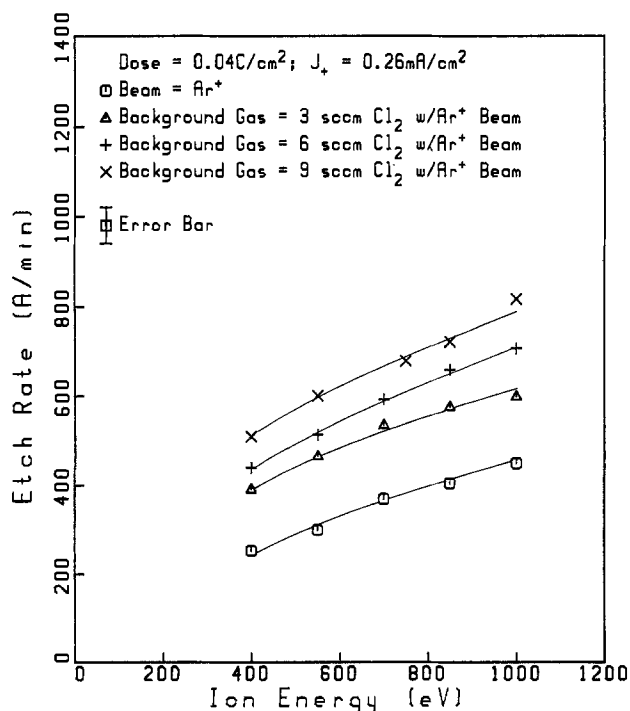
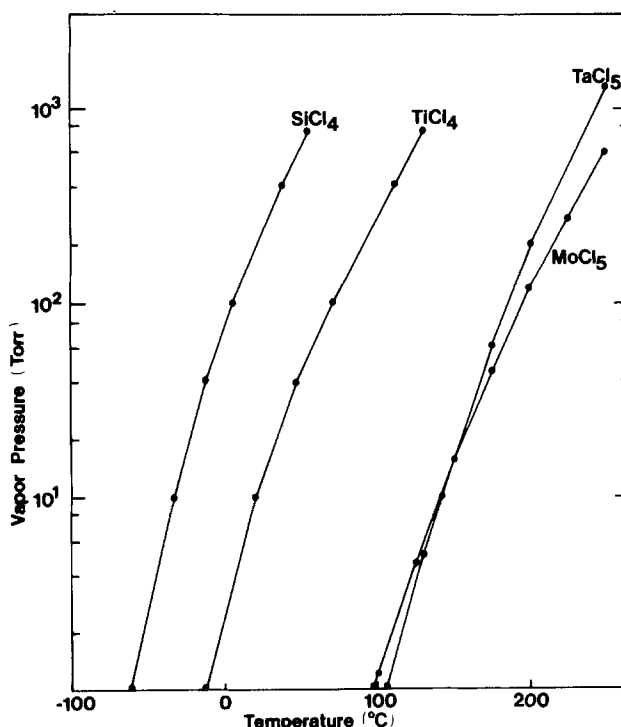
Fig. 4. Etch rates of TaSi₂ using the same conditions as in Fig. 2

Fig. 5. Chloride vapor pressures for various refractory metal chlorides.

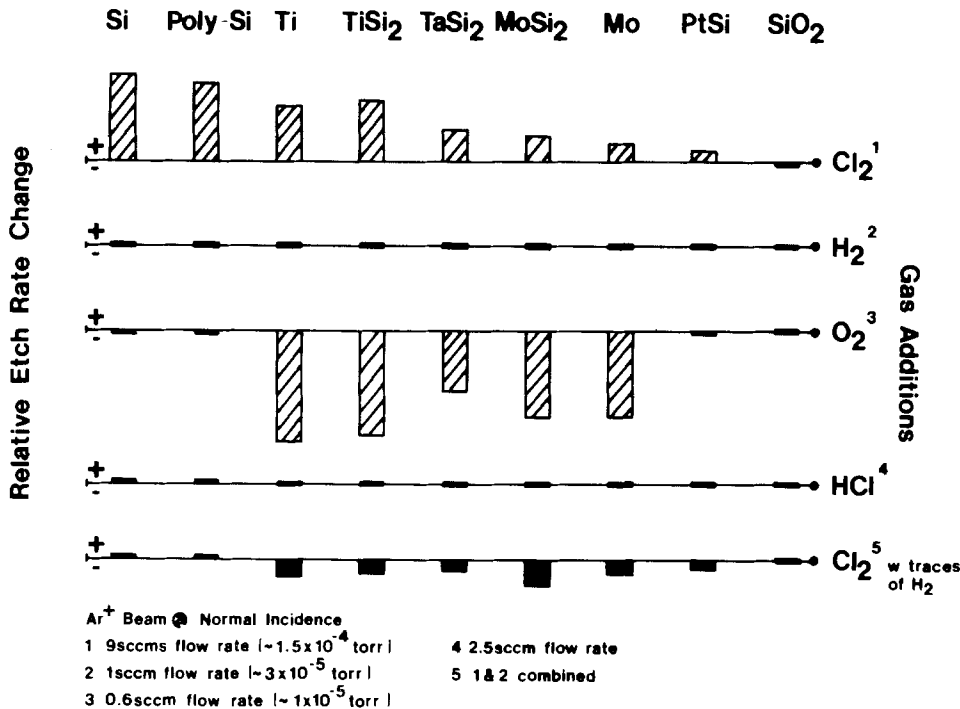


Fig. 6. Relative etch rate changes for gas additions of Cl_2 , H_2 , O_2 , HCl , and Cl_2 with H_2 .

added with Cl_2 additions, a decrease in the etch rates occurred. The reaction of H_2 and Cl_2 to form HCl has presumably occurred. HCl is thought to be a stable molecule that does not contribute to the etching mechanisms. Thus, introducing H_2 is believed to reduce the Cl_2 partial pressure, which reduces the etch rates. Additions of H_2 to fluorocarbon gas systems in PE and RIE reduces the fluorine concentration by forming stable HF (26-27), which does not contribute to the etching mechanisms of Si and SiO_2 . A similar effect is thought to have occurred in these CAIBE experiments.

Oxides are not readily etched in most chlorine gas systems. This property can be utilized to pattern selectively polycide structures. The etch rates of polysilicon and most refractory metals increased over ion milling rates under ion bombardment in the presence of Cl_2 , while the SiO_2 etch rate remained approximately the same. To demonstrate the applicability of the CAIBE technique to device fabrication, we have etched submicron features in a TaSi_2 /polycide stacked structure (Fig. 7). No undercut of the polysilicon was observed, and a selective etch was achieved. Damage to gate oxides is thought to be similar to other etch-

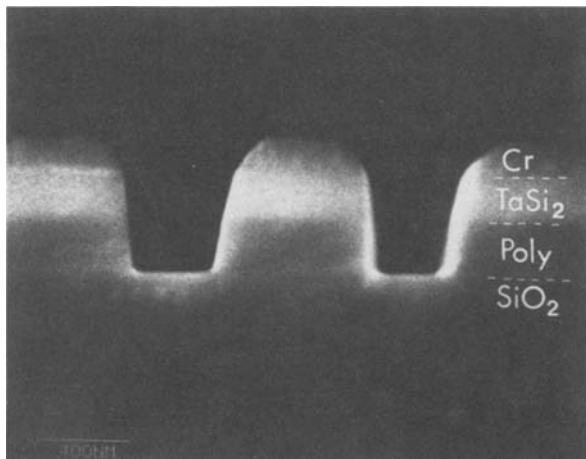


Fig. 7. Scanning electron micrograph of a TaSi_2 polycide structure. Etch conditions: Ar^+ at 570 eV for 180s followed by Ar^+ at 400 eV for 300s with a Cl_2 flow rate of 9 sccm.

ing techniques, such as RIE. In CAIBE, surface damage was shown to be related to the dose of the Cl_2 flux (28) in compound semiconductors. With a high chemical flux, ideality factors of Schottky diodes using current-voltage (I-V) measurements were found to be near unity and increased with lower chemical fluxes. CAIBE should be useful in device fabrication.

Summary

Comparative studies of broad-beam Ar^+ ion processing and UHV studies were made using Cl_2 as the chemical assist component, and good correlation with the etch yields of Si was obtained. The etch rates of various refractory metals and metal silicides have been compared in CAIBE, and the relative etch-rate increases observed are directly related to the vapor pressure of the reaction products. Background gas contaminants, such as oxygen and H_2O , can influence the etch rates by reducing the Cl_2 flux and by forming stable oxides.

Acknowledgments

This article is based on work supported by the National Science Foundation under Grant ECS-8200312. The technical contributions of S. Plimpton are gratefully acknowledged. The authors wish to thank M. J. Harrington and Scott Chang of General Motors Research Laboratories for the polysilicon wafers, and David Scott and Merrick Darley of Texas Instruments for the PtSi wafers.

Manuscript received Sept. 28, 1983.

The National Submicron Facility assisted in meeting the publication costs of this article.

REFERENCES

1. M. W. Geis, G. A. Lincoln, N. Efremow, and W. J. Piacentini *J. Vac. Sci. Technol.*, **19**, 1390 (1981).
2. J. D. Chinn, A. Fernandez, I. Adesida, and E. D. Wolf, *J. Vac. Sci. Technol. A*, **1**, 701 (1983).
3. J. D. Chinn, I. Adesida, and E. D. Wolf, *Appl. Phys. Lett.*, **43**, 185 (1983).
4. J. D. Chinn, I. Adesida, and E. D. Wolf, *J. Vac. Sci. Technol. B*, **1**, 1083 (1983).
5. T. P. Chow and A. J. Steckl, *J. Appl. Phys.*, **53**, 5531 (1982).
6. M. E. Coe and S. H. Rogers, *Solid State Technol.*, **25**, 79 (Aug. 1982).
7. T. P. Chow and A. J. Steckl, *Appl. Phys. Lett.*, **37**, 466 (1980).

8. W. Beinvoogl and H. Mader, *Seimem Forsch u. Entwitel*, **11**, 180 (1982).
9. K. M. Eisele, *This Journal*, **128**, 123 (1981).
10. D. H. Bower, *ibid.*, **129**, 796 (1982).
11. C. M. Horwitz, *IEEE Trans. Electron Devices*, **ed-28**, 1320 (1981).
12. C. S. Korman, *J. Vac. Sci. Technol.*, **20**, 476 (1982).
13. M. Mieth and A. Barker, *J. Vac. Sci. Technol. A*, **1**, 529 (1983).
14. W. Beinvoogl and B. Hasler, *Solid State Technol.*, **26**, 125 (April, 1982).
15. U. Gerlach-Meyer, J. W. Coburn, and E. Kay, *Surf. Sci.*, **103**, 177 (1981).
16. Y. Tu, T. J. Chuang, and H. F. Winters, *Phys. Rev. B*, **2**, 823 (1981).
17. P. C. Zalm, L. J. Beckers, and F. H. M. Sanders, *Nucl. Instr. Methods*, **209**, 561 (1983).
18. M. Geis, G. A. Lincoln, S. Pang, and N. N. Efremow, *J. Vac. Sci. Technol. B*, **1**, 1043 (1983).
19. L. I. Staffanson and P. Enghag, *Scand. J. Metall.*, **2**, 305 (1973).
20. Y. Saeki and R. Matsuzaki, *Denki Kagaku*, **33**, 155 (1965).
21. A. Lansberg and J. L. Schaller, *J. Less-Common Met.*, **23**, 195 (1971).
22. D. R. Stull, *Ind. Eng. Chem.*, **39**, 517 (1947).
23. R. H. Burton and G. Smolinsky, in "Plasma Processing," J. Dieleman, R. G. Frieser, and G. S. Mathad, Editors, p. 250, The Electrochemical Society Softbound Proceedings Series, Pennington, NJ (1982).
24. V. M. Donnelly, D. L. Flamm, and G. J. Collins, Paper 257 presented at the Electrochemical Society Meeting, Denver, CO, Oct. 11-16, 1981.
25. A. Fernandez, Personal communication.
26. L. M. Ephrath, *This Journal*, **126**, 1419 (1979).
27. J. D. Chinn, I. Adesida, E. D. Wolf, and R. C. Tiberio, *J. Vac. Sci. Technol.*, **19**, 1418 (1981).
28. G. A. Lincoln, M. W. Geis, L. J. Mahoney, A. Chu, B. A. Vojak, K. B. Nichols, W. J. Piacentini, N. Efremow, and W. T. Lindley, *J. Vac. Sci. Technol.*, **20**, 786 (1982).
29. R. A. Barker, T. M. Mayer, and W. C. Pearson, *J. Vac. Sci. Technol. B*, **1**, 37 (1983).

Study of the Solubility of Silica in Forsterite by Solid State EMF Measurements

G. Róg

Institut Inżynierii Materiałowej, Akademia Gorniczo-Hutnicza, Al. Mickiewicza 30, Pl-30-059 Kraków, Poland

G. Borchardt*,¹

Laboratoire de Physique du Solide, ENSMIM, Parc de Saurupt, F-54042 Nancy, France

ABSTRACT

By an EMF method, we measured the activity of silica (a_{SiO_2}) as a function of composition in the homogeneity range of forsterite (Mg_2SiO_4) including the compositions in equilibrium with the pure neighboring phases (MgO and MgSiO_3 , respectively) in the phase diagram. The experiments were performed at $1300 \leq T \leq 1780$ K using a solid electrolyte which contained MgF_2 dispersed in a Mg_2SiO_4 matrix. On the basis of the results, published data on the ionic conductivity and the resulting ideas on the dominant defects are critically discussed. Consequences for future transport experiments are investigated.

Magnesiumorthosilicate (Mg_2SiO_4) is a model substance for earth scientists and materials scientists. Despite an increasing number of papers on the physical and chemical properties of this compound and its olivine-type solid solutions, it has not yet been possible to unambiguously identify the lattice defects via which transport of matter occurs in pure Mg_2SiO_4 (forsterite) at high temperatures. Assuming dilute solution theory to be valid, defect equilibria in ternary oxides, including silicates with olivine structure, especially Mg_2SiO_4 , had already been formulated some decades ago. The progress made since those days with regard to the formal aspects of the problem may be gathered from the bibliographies of recent papers published in this field (1-3, 10). (For the sake of brevity we only quote the most recent article on pure forsterite of the respective research groups or a review paper.) The experimental data referred to most frequently are the electrical conductivity measurements of Pluschkell and Engell (4). Recent diffusivity measurements (5-9), which in principle also may be used as a test of the theoretical hypotheses, could not yet be interpreted unambiguously. This seems to be due to an insufficient characterization of the samples used during most of the experiments.

It must be stated that the original questions are not fully answered. This is mainly due to two facts, which are somewhat interrelated: first, the physical proper-

ties (ionic conductivity κ , diffusivities D_i) were measured either as a function of concentration [$\kappa(x_{\text{SiO}_2})$ (4)] or on samples with poorly defined composition [D_i (5-9)]; instead, they should have been measured as a function of the thermodynamic activities of two of the constituent elements in the homogeneity range of the ternary oxide in order to allow a sound thermodynamic treatment. Second, with high defect concentrations the dilute solution approach, usually practiced in defect thermodynamics (2), and the concept of constant mobilities (independent of the composition of the crystal at $P, T = \text{constant}$) (4) are no longer applicable as associations of defects may occur (1, 10).

In this paper, we present experimental results on the activity of a constituent oxide, SiO_2 , in Mg_2SiO_4 as a function of composition and of temperature at a fixed oxygen activity. With the results it is possible to define the silica-rich part of the homogeneity range of Mg_2SiO_4 between 1300 and 1780 K and to reinterpret published data on the ionic conductivity at least qualitatively with respect to the nature of the defects involved. Further, guidelines for planning and performing future diffusivity and deformation experiments can be derived.

Defect Equilibria

For the details on the formulation of defect equilibria within the frame of the dilute solution approach we refer to the literature mentioned above. Summarizing the preliminary results which, strictly speaking,

* Electrochemical Society Active Member.

¹ Present address: Fachbereich Metallurgie und Werkstoffwissenschaften, TU Clausthal, D-3392 Clausthal-Zellerfeld, Germany.

are sophisticated speculations based on crystal chemistry rules, the phase diagram, and only one set of experiments (4), the concept generally accepted until now may be described as follows: (i) pure forsterite, which is stoichiometric with regard to both the cation to anion ratio [$(n_{Mg} + n_{Si})/n_O = 3/4$] and the magnesium to silicon ratio ($n_{Mg}/n_{Si} = 2$), apparently has Frenkel-type defects in the magnesium sublattice as majority defects. (ii) At sufficiently high temperatures up to about 1800 K, Mg_2SiO_4 readily dissolves excess silica (several mol percent [m/o]), but appreciably less excess magnesia ($\lesssim 0.1$ m/o) (4). At still higher temperatures, according to recent results, the solubility of magnesia drastically increases and forsterite incorporates between 0.7 and 2.4 m/o of magnesia (11). In the case of magnesia-rich forsterite, the majority defects might be either $Mg_i^{2\cdot}$ and $V_{Si}^{4\cdot}$ or $V_O^{2\cdot}$ and $V_{Si}^{4\cdot}$ in the Kröger-Vink notation. The incorporation of silica is considered to create either $V_{Mg}^{2\cdot}$ and $V_O^{2\cdot}$ or $V_{Mg}^{2\cdot}$ and $Si_i^{4\cdot}$ as majority defects. Associations of defects are generally neglected (3).

This paper deals with experimental results for $a_{SiO_2} = f(x_{SiO_2})$ in the silica-rich portion of the homogeneity range of Mg_2SiO_4 . We therefore confine ourselves to the theoretical treatment of the corresponding defect equilibria. With the defect concentrations to be expected in this composition range according to the appreciable solubility of silica, dilute solution defect thermodynamics will no longer be applicable. Because of the high concentration of defects, a Debye-Hückel-type calculation of the electrostatic interaction only is not possible either. It will therefore be necessary to adopt a formal treatment including defect complexes.

We shall treat two models, which we shall call A and B. They will be formulated using the Kröger-Vink notation.

Model A.—1 $\hat{=} V_{Mg}^{2\cdot}$, 2 $\hat{=} V_O^{2\cdot}$, 3 $\hat{=} [V_{Mg}, V_O]^x$, 4 $\hat{=} Mg_i^{2\cdot}$, $a_i = x_i \cdot f_i$ being activities, x_i [or also (i)] being a molar fraction, f_i being an activity coefficient

$$SiO_2 \rightleftharpoons Mg_2SiO_4 + 2V_O^{2\cdot} + 2V_{Mg}^{2\cdot}$$

$$K_{2-1} = \frac{(V_O^{2\cdot})^2 (V_{Mg}^{2\cdot})^2}{a_{SiO_2}} \cdot f_{V_O}^2 \cdot f_{V_{Mg}}^2$$

$$= a_1^2 \cdot a_2^2 \cdot a^{-1}_{SiO_2} \quad [1]$$

$$Mg_{Mg}^x \rightleftharpoons V_{Mg}^{2\cdot} + Mg_i^{2\cdot}$$

$$K_{2-2} = (V_{Mg}^{2\cdot}) (Mg_i^{2\cdot}) \cdot f_{V_{Mg}} \cdot f_{Mg} = a_1 \cdot a_4 \quad [2]$$

$$V_O^{2\cdot} + V_{Mg}^{2\cdot} \rightleftharpoons [V_{Mg}, V_O]^x$$

$$K_{2-3} = \frac{[V_{Mg}, V_O]^x}{(V_O^{2\cdot}) (V_{Mg}^{2\cdot})} \cdot f_{[V_{Mg}, V_O]^x} \cdot \frac{1}{f_{V_O} \cdot f_{V_{Mg}}}$$

$$= a_3 \cdot a_2^{-1} \cdot a_1^{-1} \quad [3]$$

with the electroneutrality condition

$$(V_O^{2\cdot}) + (Mg_i^{2\cdot}) = (V_{Mg}^{2\cdot}) \quad [4]$$

and the mass balance with regard to oxygen

$$[V_{Mg}, V_O]^x + (V_O^{2\cdot}) = 2\delta, \quad \delta = x_{SiO_2} - 1/3 \approx 0 \quad [5]$$

where δ is the excess silica concentration ($\delta = 0$ corresponds to the stoichiometric composition of the forsterite).

The equilibrium constants K_{2-i} , $i = 1, 2, 3$ being unknown, the defect concentrations cannot be calculated. In order to get a formal similarity to the well-known relationships of the dilute solution approach, we combine Eq. [1], [2], [3], and [5], wherefrom we obtain upon differentiation

$$\frac{\partial \ln x_1}{\partial \ln a_{SiO_2}} = - \left[\left(\frac{\partial \ln \delta}{\partial \ln a_{SiO_2}} - \frac{1}{2} \right) (K_{2-3} f_1 f_2 f_3^{-1} x_1 + 1) + \frac{\partial \ln f_2}{\partial \ln a_{SiO_2}} + K_{2-3} \cdot f_3^{-1} \frac{\partial \ln f_3}{\partial \ln a_{SiO_2}} \right] \quad [6]$$

This equation reduces to $\partial \ln (V_{Mg}^{2\cdot}) / \partial \ln a_{SiO_2} = 1/4$ for $f_i = \text{constant}$, $K_{2-3} = 0$, and $(V_{Mg}^{2\cdot}) \sim \delta$.

The value of 1/4 for the characteristic slope corresponds to the absence of any defect association. The opposite extreme would be a complete association of the defects, which means $(V_{Mg}^{2\cdot}) \approx 0$, $\partial \ln (V_{Mg}^{2\cdot}) / \partial \ln a_{SiO_2} = 0$.

With $[V_{Mg}, V_O]^x \sim \delta$ and constant and finite values for the activity coefficients f_i , Eq. [6] yields in this limiting case $\partial \ln ([V_{Mg}, V_O]^x) / \partial \ln a_{SiO_2} = 1/2$ as in the dilute solution approach.

$$\text{Model B.}—1 \hat{=} V_{Mg}^{2\cdot}, 2 \hat{=} Si_i^{4\cdot}, 3 \hat{=} Si_{Mg}^{2\cdot}, 4 \hat{=} Mg_i^{2\cdot},$$

$$5 \hat{=} [V_{Mg}^{2\cdot}, Si_{Mg}^{2\cdot}]^x$$

$$2SiO_2 \rightleftharpoons Mg_2SiO_4 + 2V_{Mg}^{2\cdot} + Si_i^{4\cdot}, \quad K_{2-7} = \frac{a_1^2 \cdot a_2}{a_{SiO_2}^2} \quad [7]$$

$$Mg_{Mg}^x \rightleftharpoons V_{Mg}^{2\cdot} + Mg_i^{2\cdot}, \quad K_{2-2} = a_1 \cdot a_4 \quad [2]$$

$$V_{Mg}^{2\cdot} + Si_i^{4\cdot} \rightleftharpoons Si_{Mg}^{2\cdot}, \quad K_{2-8} = \frac{a_3}{a_1 \cdot a_2} \quad [8]$$

$$V_{Mg}^{2\cdot} + Si_{Mg}^{2\cdot} \rightleftharpoons [V_{Mg}^{2\cdot}, Si_{Mg}^{2\cdot}]^x, \quad K_{2-9} = \frac{a_5}{a_1 \cdot a_3} \quad [9]$$

with the electroneutrality condition

$$(Mg_i^{2\cdot}) + (Si_{Mg}^{2\cdot}) + 2(Si_i^{4\cdot}) = (V_{Mg}^{2\cdot}) \quad [10]$$

and the mass balance with regard to silicon

$$[V_{Mg}^{2\cdot}, Si_{Mg}^{2\cdot}]^x + (Si_{Mg}^{2\cdot}) + (Si_i^{4\cdot}) = \frac{\delta}{2} \quad [11]$$

From a procedure analogous to that which yielded Eq. [6], a rather complicated expression results. Simplifying by setting $f_i = \text{constant}$, we get

$$\frac{\partial \ln x_1}{\partial \ln a_{SiO_2}} = - \left(\frac{\partial \ln \delta}{\partial \ln a_{SiO_2}} - 2 \right) \cdot \left[\frac{K_{2-8} K_{2-9} f_5^{-1} x_1^2 + K_{2-8} f_3^{-1} f_1^{-1} x_1 + f_1^{-2} f_2^{-1}}{K_{2-8} f_3^{-1} f_1^{-1} x_1 + 2f_1^{-2} f_2^{-1}} \right] \quad [12]$$

Equation [12] reduces to $\partial \ln (V_{Mg}^{2\cdot}) / \partial \ln a_{SiO_2} = 2/3$ for $f_i = 1$, $K_{2-8} = K_{2-9} = 0$, and $x_1 = (V_{Mg}^{2\cdot}) \sim \delta$. This describes the absence of any defect association. If $(V_{Mg}^{2\cdot}) \approx 0$ and $\partial \ln (V_{Mg}^{2\cdot}) / \partial \ln a_{SiO_2} \approx 0$, which corresponds to the nearly complete association of the point defects (according to Eq. [9]), Eq. [12] reduces to $\partial \ln ([V_{Mg}^{2\cdot}, Si_{Mg}^{2\cdot}]^x) / \partial \ln a_{SiO_2} \approx 2$, which implies $([V_{Mg}^{2\cdot}, Si_{Mg}^{2\cdot}]^x) \sim \delta$, f_i being constant and finite. For partial association (according to Eq. [8]), Eq. [12] would yield $\partial \ln (V_{Mg}^{2\cdot}) / \partial \ln a_{SiO_2} = 1$ with the appropriate general assumptions as mentioned above being valid. Equations [6] and [12] relate the experimentally determined quantity $\partial \ln \delta / \partial \ln a_{SiO_2}$ to the variation of a defect concentration with composition $\partial \ln (V_{Mg}^{2\cdot}) / \partial \ln a_{SiO_2}$.

The (total) ionic conductivity $\kappa(a_{SiO_2})$ can be calculated from $\kappa(x_{SiO_2})$ (4) and $a_{SiO_2}(x_{SiO_2})$ (this work). In special cases (i.e., if the transference number of one defect species is close to 1) we get

$$\frac{\partial \ln \kappa}{\partial \ln a_{\text{SiO}_2}} \approx \frac{\partial \ln \kappa_1}{\partial \ln a_{\text{SiO}_2}} = \frac{\partial \ln x_1}{\partial \ln a_{\text{SiO}_2}} + \frac{\partial \ln u_1}{\partial \ln a_{\text{SiO}_2}},$$

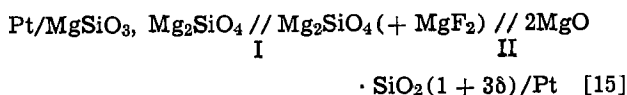
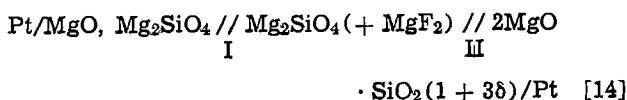
$$t_1 \approx 1 \quad [13]$$

In the dilute solution approach, the mobilities u_i are assumed to be constant. As will be seen below, this is most probably not true for the silica-rich portion of the homogeneity range of forsterite.

Experimental

Preliminary remarks.—For the experimental determination of silica in forsterite, we used an electrochemical method which had been described elsewhere (12) and which is based on the application of a special fluoride electrolyte being present as a second phase in a so-called "inert skeleton."

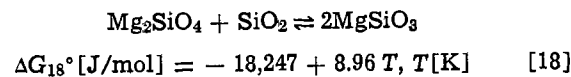
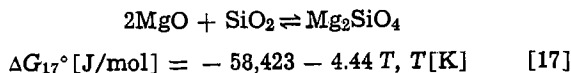
We used the two concentration cells



The measured EMF (E) reflects the difference in the silica activities on both sides of the electrolyte

$$E = \left| \left(\frac{RT}{4F} \ln \frac{a_{\text{SiO}_2}(\text{II})}{a_{\text{SiO}_2}(\text{I})} \right) \right| \quad [16]$$

From our published data (12), standard free enthalpy values for the reactions



are taken for the calculation of the activity values a_{SiO_2} in forsterite.

From cell [14], one obtains

$$a_{\text{SiO}_2}(14\text{-II}) = \exp \left(\frac{4F |E_1| - 58,423 - 4.44 T}{RT} \right) \quad [19]$$

and from cell [15]

$$a_{\text{SiO}_2}(15\text{-II}) = \exp \left(\frac{-4F |E_2| - 18,247 + 8.96 T}{RT} \right) \quad [20]$$

Table I. Composition of the samples and of the electrolyte used in the experiments

Sample no.	x_{SiO_2}	ρ [g/cm ³]	Porosity ($\Delta V/V_m$)	Phases present
1	0.310	3.05	0.051	MgO, Mg ₂ SiO ₄
2	0.336	2.84	0.072	Mg ₂ SiO ₄
3	0.340	2.76	0.094	Mg ₂ SiO ₄
4	0.345	2.92	0.093	Mg ₂ SiO ₄
5	0.350	2.74	0.086	Mg ₂ SiO ₄
6	0.356	2.90	0.095	Mg ₂ SiO ₄
7	0.370	2.94	0.082	Mg ₂ SiO ₄ , (MgSiO ₃)
8	0.395	2.97	0.078	Mg ₂ SiO ₄ , MgSiO ₃
9 (electrolyte)	0.302	3.00	0.039	Mg ₂ SiO ₄ , (MgF ₂) $x_{\text{MgF}_2} = 0.015$ $x_{\text{MgO}} = 0.683$

Sample preparation.—Fine grain powders of reagent-grade MgO and SiO₂ were thermally pretreated, thoroughly mixed with a small amount of binder (oleine acid) and compressed (5×10^8 Pa) before being first sintered in air for 12h at 1200°C. Then, the temperature was increased to 1450°C for another 96h. Afterward, the samples were rapidly cooled to room temperature and controlled by optical microscopy and x-ray diffraction. Densities were determined. The complete set of samples is grouped in Table I together with the electrolyte.

EMF measurements and results.—The measurements were made in air. Up to about 1080°C, quartz glass was used for the construction of the apparatus; above 1080°C alumina was used.

Depending on the temperature, stable EMF values were reached after about 0.5-2h after a change of the measuring temperature. The EMF was measured with a digital vacuum tube voltmeter ($R = 10^{10}\Omega$). Table II shows the measured EMF values for cell [14] together with the a_{SiO_2} data calculated from Eq. [19], as a function of temperature and composition. Table III gives the corresponding information as obtained from cell [15]. With the aid of our data, we calculated the electrical conductivity as a function of temperature and silica activity from published literature values for the conductivity as a function of temperature and composition (4). The results are represented in Table IV.

Discussion

In order to facilitate the interpretation of the numerous data points in the silica-rich part of the homogeneity region, we refer to Fig. 1, 2, and 3. In Fig. 2, the temperature independent characteristic slope in the linear range is $n_\delta = \partial \ln \delta / \partial \ln a_{\text{SiO}_2} \approx 1.42$. Equation [12] shows us that $1 \leq n_\delta \leq 2$ might be tentatively explained by a complex formation involving the equi-

Table II. The EMF values for E as obtained with the experimental setup according to Eq. [14] as a function of composition and temperature (top) and the values for E obtained using Eq. [15] (bottom)

x_{SiO_2}	0.310	0.336	0.340	0.345	0.350	0.356	0.370	0.395
E [mV]								
T [K]								
1300	1.2 (1.6)	103.2 (1.6)	119.9 (2.1)	132.2 (2.3)	139.0 (1.4)	144.8 (1.7)	148.5 (2.1)	149.0 (1.8)
1480	0.7 (1.4)	102.6 (1.9)	122.4 (1.8)	135.3 (1.9)	143.1 (1.6)	151.3 (2.0)	154.2 (2.3)	154.9 (1.6)
1600	1.9 (1.5)	101.5 (1.2)	123.9 (2.5)	137.4 (2.1)	145.9 (2.1)	154.5 (1.7)	159.7 (2.2)	161.0 (1.7)
1780	2.1 (1.7)	103.0 (2.1)	126.3 (1.7)	142.7 (2.0)	152.5 (1.9)	160.2 (2.6)	166.3 (2.0)	165.7 (1.7)
x_{SiO_2}	0.310	0.336	0.340					
E [mV]								
T [K]								
1300	146.2 (4.5)	44.3 (4.5)	30.9 (2.5)					
1480	158.3 (2.7)	54.0 (3.1)	35.7 (3.1)					
1600	161.1 (3.2)	57.2 (2.4)	37.5 (2.2)					
1780	167.0 (1.8)	64.2 (2.0)	40.5 (2.3)					

The data given in parentheses are the absolute values of the experimental error.

Table III. The activity of silica a_{SiO_2} as calculated from the EMF values

x_{SiO_2} 10%	*	0.310	0.336	0.340	0.345	0.350	0.356	0.370	0.395	**
		-23.33	2.67	6.67	11.67	16.67	22.67	36.67	61.67	
T [K]	a_{SiO_2}									
1300	0.0026	0.003	0.105	0.191	0.296	0.377	0.464	0.530	0.539	0.543
1480	0.0051	0.005	0.127	0.236	0.354	0.452	0.586	0.641	0.655	0.666
1600	0.0072	0.008	0.138	0.264	0.391	0.500	0.642	0.747	0.775	0.745
1780	0.011	0.012	0.166	0.305	0.468	0.604	0.738	0.866	0.852	0.857

* a_{SiO_2} for $a_{MgO} = 1$ according to Róg *et al.* (12).
 ** a_{SiO_2} for $a_{MgSiO_3} = 1$ according to Róg *et al.* (12).

Table IV. The ionic conductivity as a function of silica activity and temperature as calculated from the literature (4) with the aid of our activity data

x_{SiO_2}	0.3352		0.3378		0.3424		0.3516		0.3609		n_κ	\tilde{n}_κ
T [K]	a_{SiO_2}	$\kappa \left[\frac{1}{\Omega \text{ cm}} \right]$	a_{SiO_2}	$\kappa \left[\frac{1}{\Omega \text{ cm}} \right]$	a_{SiO_2}	$\kappa \left[\frac{1}{\Omega \text{ cm}} \right]$	a_{SiO_2}	$\kappa \left[\frac{1}{\Omega \text{ cm}} \right]$	a_{SiO_2}	$\kappa \left[\frac{1}{\Omega \text{ cm}} \right]$	$\frac{\Delta \ln \left(\frac{\kappa}{\kappa_0} \right)}{\Delta \ln a_{SiO_2}}$	$\frac{\ln \left(\frac{\kappa(1)}{\kappa(0)} \right)}{\ln \frac{a_{SiO_2}(1)}{a_{SiO_2}(0)}}$
1300	0.081	1.38×10^{-9}	0.149	3.49×10^{-9}	0.243	3.80×10^{-7}	0.399	4.13×10^{-7}	0.533	2.08×10^{-7}	4.885	0.942
1480	0.098	1.39×10^{-7}	0.181	1.35×10^{-6}	0.298	1.52×10^{-5}	0.490	2.68×10^{-5}	0.656	2.35×10^{-5}	4.834	1.090
1600	0.107	1.69×10^{-6}	0.199	9.72×10^{-6}	0.329	1.12×10^{-4}	0.542	2.57×10^{-4}	0.727	3.03×10^{-4}	4.849	1.120
1780	0.128	3.83×10^{-5}	0.236	1.15×10^{-4}	0.389	1.35×10^{-3}	0.637	4.32×10^{-3}	0.851	7.38×10^{-3}	4.954	1.216

The states 0 and 1 in the last column correspond to the compositions with maximum and minimum values of the conductivity for a given temperature (see Fig. 3).

libria described by Eq. [8] and [9]. As absolute values of the defect concentrations are not known, the quantities in the term in brackets in Eq. [12] cannot be further discussed now. Accepting the idea that the

activity coefficients f_i do not vary too much with composition and that their numerical values are more or less close to 1, the numerical value of the term in brackets can be situated between about 0.5 ($K_{2-9}, K_{2-9} \ll 1$) and about 1 ($K_{2-9} \gg 1, K_{2-8} \gg 1$) according to the comments on Eq. [12] above.

With this in mind, we can estimate the dependence of defect mobility on the activity and/or concentration of silica. A general feature of the dependence of conductivity on activity (see Fig. 3) is a high value of the slope $n_\kappa = \Delta \ln \kappa / \Delta \ln a_{SiO_2} \approx 4.9$ in the central part and a region of saturation on both ends of the s-shaped

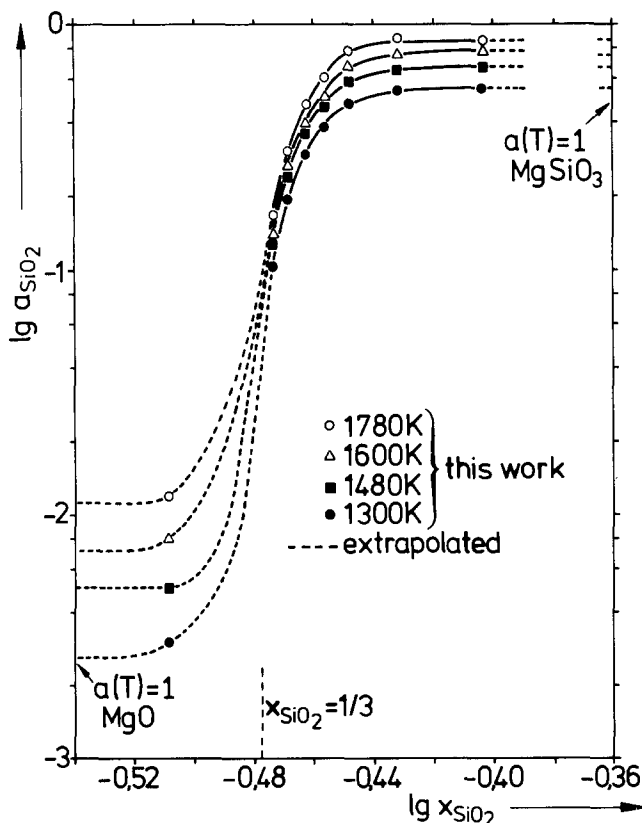


Fig. 1. The homogeneity range of forsterite. (The a_{SiO_2} values for $a_{MgO}(T) = 1$ and $a_{MgSiO_3}(T) = 1$ were calculated from (12), the connection to the experimental curves of this work being represented by broken lines.)

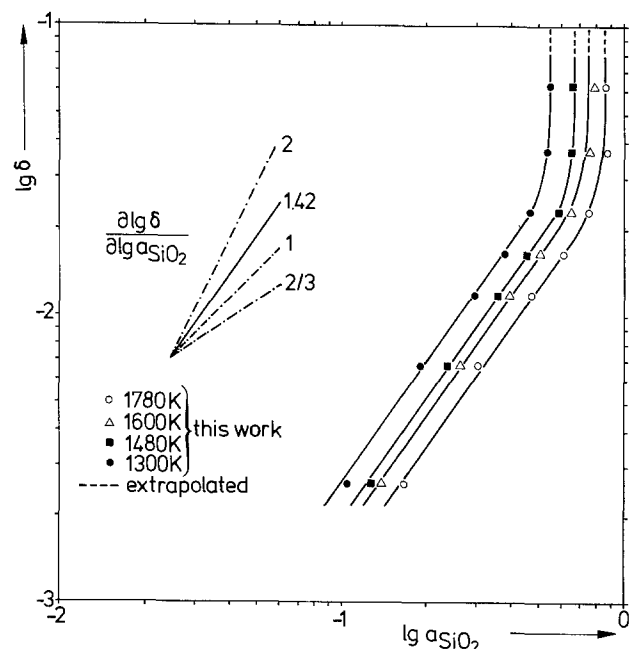


Fig. 2. Excess silica $\delta = x_{SiO_2} - 1/3$ in forsterite as a function of a_{SiO_2} . The extrapolation end points are calculated from (12).

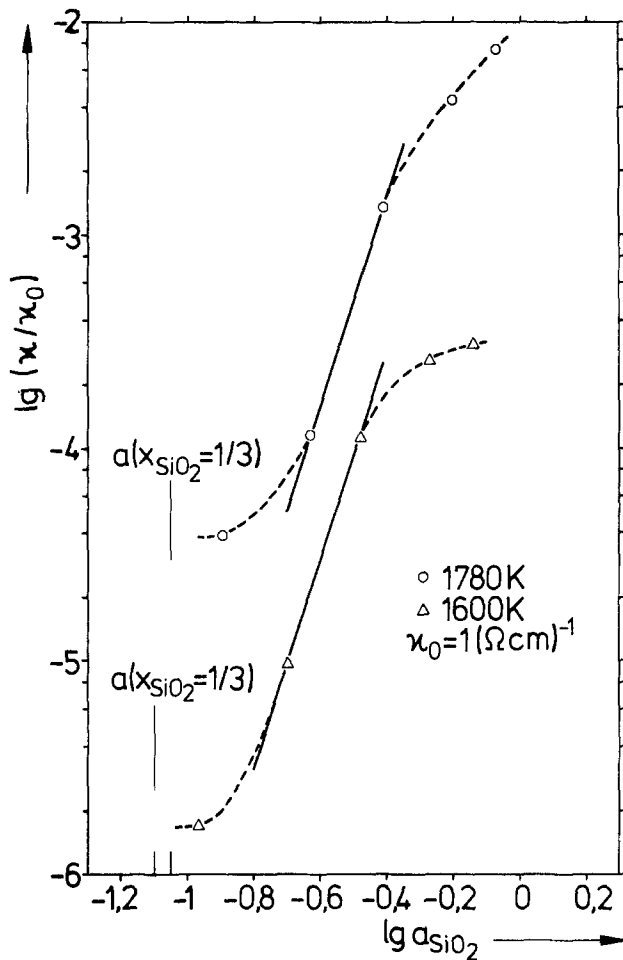


Fig. 3. The ionic conductivity of forsterite as a function of silica activity. (The ionic conductivity data were taken from (4): for a given temperature, $\kappa = \text{constant}$ for $x_{\text{SiO}_2} \lesssim 0.3352$.) The slope of the full line yields $\Delta \ln (\kappa/\kappa_0)/\Delta \ln a_{\text{SiO}_2} = 4.9$ (see text and Table IV). For 1480 and 1300 K the $\lg \kappa$ - $\lg a_{\text{SiO}_2}$ curves show a similar behavior and yield the same slope in the linear part.

curves, which give rise to an apparent slope $\tilde{n}_\kappa \approx 1.1$ (see Table IV).

In the dilute solution approach (1, 2, 4) conductivity or diffusivity measurements are usually evaluated on the basis of constant mobilities u_i . In the case given here, such a procedure would (erroneously) yield the

clear cut answer: $\tilde{n}_\kappa \approx 1.1 \approx 1$; therefore $V_{\text{Mg}^{2+}}$ and $\text{Si}_{\text{Mg}^{2+}}$ should be the majority defects. In reality, the situation is much more complicated: inserting the experimental values in Eq. [12] and [13] and assuming

the simplest case of one mobile species $1 \hat{=} V_{\text{Mg}^{2+}}$, the dependence of the mobility u_1 on the activity of silica can be placed in the interval $4.3 \lesssim \partial \ln u_1 / \partial \ln a_{\text{SiO}_2} \lesssim 4.6$. This indicates a rather strong dependence on concentration. The possible objection that the discrepancy between $\partial \ln \kappa / \partial \ln a_{\text{SiO}_2} \approx 4.9$ and $\partial \ln \delta / \partial \ln a_{\text{SiO}_2} \approx 1.4$ may be entirely due to the term in brackets in Eq. [12] must be rejected because this would require a negative value for K_{2-8} .

Conclusion

From our experimental $a_{\text{SiO}_2}(x_{\text{SiO}_2})$ data and the $\kappa(x_{\text{SiO}_2})$ data of Pluschkell and Engell (4), it must be concluded that magnesium vacancies $V_{\text{Mg}^{2+}}$ and complexes of the type $[V_{\text{Mg}^{2+}}, \text{Si}_i^{4+}]^{2-}$ and $[2V_{\text{Mg}^{2+}}, \text{Si}_i^{4+}]^{\pm}$,

which have already been tentatively discussed by other authors (1, see also (10) for MgSiO_3), are the most probable majority defects in Mg_2SiO_4 , which contains excessive silica. Further, the reinterpretation of the published conductivity data on the basis of our experimental findings reveals a strong dependence of the mobility on the composition of the forsterite in the silica-rich part. As a further consequence, it cannot be excluded that the differences between the published values of silicon and oxygen diffusivities (5-9) may be partially due to the different states of the crystals used with regard to the value of the thermodynamic activity of silicon and magnesium. As the different crystal growth methods may lead to pronounced differences in composition of the single crystals an experimental control by an EMF measurement is strongly advisable prior to further measurements of transport properties or deformation kinetics.

Finally, EMF measurements of the type presented here should be carried out also in the silica-deficient part of the homogeneity range, and, if possible, at more than one value of the oxygen potential and as a function of total pressure at a given temperature. Further lattice dynamics calculations (13) may shed some light on the energetics of the defects postulated above from a more empirical point of view.

Acknowledgments

We are obliged to A. Kozłowska-Róg and to E. Ebeling for their skillful help with the experiments and to Chr. Ebeling, U. Amthor, and E. Voges for their patience in preparing the typescript. One of us (G.B.) is indebted to the French Government and to the Institut National Polytechnique de Lorraine for offering him a temporary position as an associate professor at ENSMIM, Nancy. Financial aid of the Deutsche Akademische Austauschdienst and of the Deutsche Forschungsgemeinschaft made this work possible. G.R. expresses his personal gratitude towards the Technische Universität Clausthal.

Manuscript received May 20, 1983.

Technische Universität Clausthal assisted in meeting the publication costs of this article.

REFERENCES

1. D. M. Smyth and R. L. Stocker, *Phys. Earth Planet. Inter.*, **10**, 183 (1975).
2. H. Schmalzried, *Phys. Chem. Minerals*, **2**, 279 (1978).
3. P. Abélard and J. F. Baumard, *J. Phys. Chem. Solids*, **43**, 617 (1982).
4. W. Pluschkell and H. J. Engell, *Ber. Dtsch. Keram. Ges.*, **45**, 388 (1968).
5. O. Jaoul, B. Houlrier, and F. Abel, *J. Geophys. Res.*, **88**, 613 (1983).
6. M. Poumellec-Badiolle, Thesis, Université de Paris (1979).
7. D. Hallwig, R. Schachtner, and H. G. Sockel, in "Proceedings of the 9th International Symposium on Reactivity of Solids, Cracow 1980," K. Dyrek et al., Editors, Elsevier Scientific Publishing Company, Amsterdam (1982).
8. K. P. R. Reddy, S. M. Oh, L. D. Major, Jr., and A. R. Cooper, Jr., *J. Geophys. Res.*, **85**, 322 (1980).
9. K. Ando, H. Kurokawa, Y. Oishi, and H. Takei, *J. Am. Ceram. Soc.*, **64**, C30 (1981).
10. D. M. Smyth and R. L. Stocker, *Phys. Earth Planet. Inter.*, **16**, 145 (1978).
11. H. Takei and T. Kobayashi, *J. Cryst. Growth*, **23**, 121 (1974).
12. G. Róg, B. Langanke, G. Borchardt, and H. Schmalzried, *J. Chem. Thermodyn.*, **6**, 1113 (1974).
13. Y. Ohashi and L. W. Finger, *Carnegie Inst. Washington, Yearb.*, **72**, 547 (1973).

Defect Luminescence of Thin Films of Cu₂O on Copper

R. Gilbert Kaufman* and R. T. Hawkins

Standard Oil Company (Indiana), Amoco Research Center, Naperville, Illinois 60566

ABSTRACT

Films of Cu₂O, 30 μm thick, have been grown on copper metal foil at 1000°C in 1% O₂/Ar, heat-treated without O₂ present at a number of lower temperatures, and quenched in water. The room temperature emission at 980 nm and its excitation spectrum, attributed to relaxed excitons at copper vacancies, are similar to reported photoluminescence from thick crystals. Apparent quenching of luminescence by interaction among vacancies is observed for sufficiently high copper vacancy concentration. Heat-treatment does not produce copper vacancies, but redistribution of vacancies can increase their photoluminescence by nearly two orders of magnitude. Under the present copper oxidation conditions, the enhanced concentration of copper vacancies near the Cu₂O surface suggests that the rate of oxidation is limited by the diffusion of these vacancies.

The properties of Cu₂O have been studied for decades. This research has been largely confined to bulk crystalline samples. Another approach to the study of the properties of materials is to examine thin films. Such an approach raises the possibility that film properties may be found which are significantly different from bulk properties of the same material, as has, for example, been observed in the case of the luminescence of phosphors. Furthermore, the mechanisms which produce these differences in properties are in themselves of interest. For example, films are not necessarily uniform or in thermodynamic equilibrium, and the choice of conditions of formation of the film, especially the choice of substrate, can control the chemistry and structure of the resulting film. In particular, variations over the thickness of a film can produce gradients in material properties, such as defect structure.

Films of Cu₂O on copper metal constitute an interesting system for the study of such gradients of point defects. Good quality films are relatively easy to prepare, with at least one structure having substantial grain size (1). Such Cu₂O films are nonstoichiometric, with composition a function of oxygen partial pressure during film growth. Characteristic emission and excitation photoluminescence spectra of bulk Cu₂O have been attributed to relaxed excitons at copper and oxygen vacancies (2, 3). However, no analogous studies have heretofore been done for films of Cu₂O on copper, which would be expected to be copper rich in the region next to the metal and copper poor at the exterior surface of the film, nor has any effort been made to use photoluminescence to monitor vacancy concentrations. Since the usual Hall measurements and four point probe conductivity measurements to determine vacancy concentration are not possible with Cu₂O films on copper metal, photoluminescence appears to be a very sensitive, well developed technique to monitor vacancies.

We present here the results of a study of the correlation between the vacancy photoluminescence of films of Cu₂O on copper metal and the conditions of preparation of these films.

Experimental

Copper coupons 1.0 × 1.2 × 0.05 cm of Marz grade copper, nominally five nines purity, from Materials Research Corporation were oxidized at 1000°C in a flowing stream of 1% O₂ in 1 atm of argon to obtain Cu₂O films of 30 μm thickness, as measured by weight gain. The average grain size of the films was generally greater than 100 μm. These films were either left as grown or subjected to a heat-treatment, which consisted of holding the sample in flowing argon at a specific temperature in the 300°-700°C range for 15 min and then manually removing it from the argon

atmosphere and quenching it in water. The films maintained excellent optical quality throughout this preparation and thus required no polishing or etching.

Emission spectra were excited at 633 nm with an unfocused HeNe laser, and were measured using a Rofin 6000 monochromator (with a silicon photodetector) together with a series of prefilters for further wavelength discrimination. Excitation spectra were measured at 10 nm intervals over a 450-690 nm range, using as a source the emission of a 150W xenon arc lamp, filtered by a grating monochromator (Oriel Model 7240) in series with two 11 nm bandpass interference filters (Ditric) to eliminate second-order and scattered light from the grating. These excitation spectra were detected with a silicon photovoltaic and a series of cutoff filters, including a 1 mm thick CdTe crystal. Photoluminescence signals were all corrected to constant excitation intensity.

Results

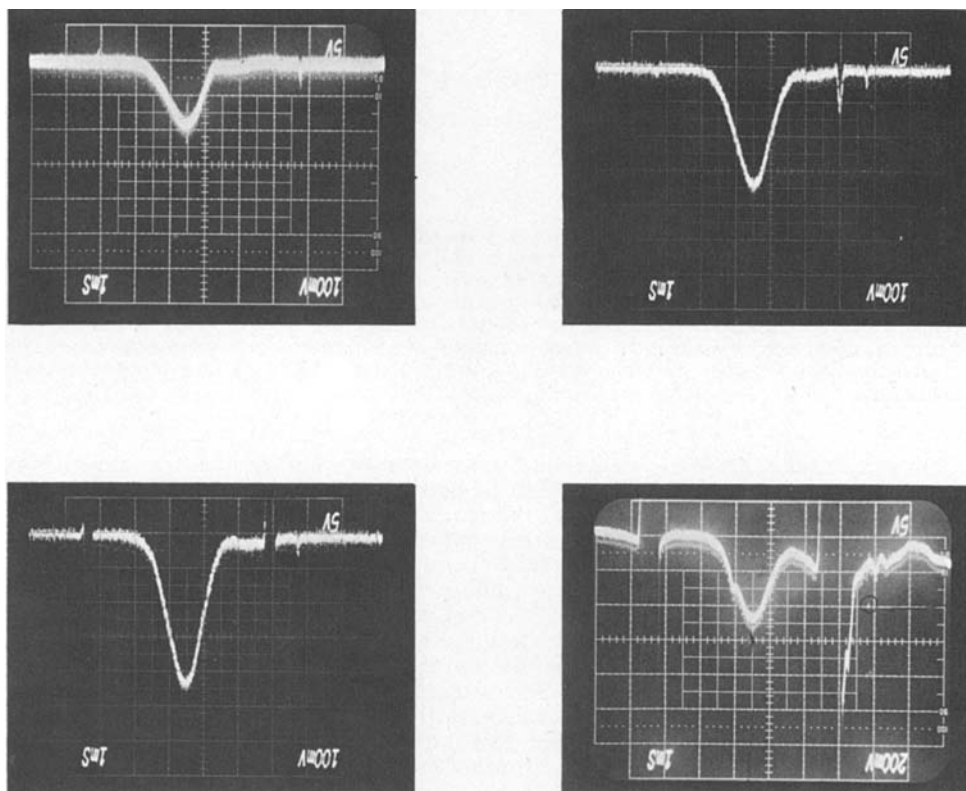
The photoluminescent emission of 30 μm thick Cu₂O films on copper metal at 25°C, excited by the 633 nm HeNe laser line, consists of a single band centered at 980 nm, as shown in Fig. 1. Several cutoff filters were used to remove the exciting light, which appeared in the first and second orders of the monochromator transmission with different intensities, so that any significant intensity of emissions at 700 and 800 nm could be observed. Neither are present at room temperature, although subsequent experiments have shown that they do appear under 633 nm excitation at 77 K. The CdTe filter was found to be the most efficient at removing exciting light while only reducing the 980 nm emission as shown in Fig. 1(d), and was therefore used in the subsequent measurements of excitation spectra.

The excitation spectra for 980 nm emission at 25°C are shown in Fig. 2 for four 30 μm Cu₂O films. Comparison of the spectra of (A) and (B) demonstrates that a 15s etch in 8N HNO₃, which removes 7-8 μm, increases the photoluminescence of as-grown films, while not causing any marked change in the spectral structure. Thus, a nonluminescing "dead" layer is apparently present on the surface. However, the excitation spectrum of (C), which was heat-treated at 500°C, is observed to differ qualitatively from that of (A), and also to be over an order of magnitude more intense. Moreover, etching clearly affects a heat-treated sample significantly more than an as-grown sample, as is shown by the difference between (C) and (D) in Fig. 2. More than half the luminescence is removed with the quarter of the film that was part of a dead layer before heat-treatment. Several features should be noted about these spectra. First, all spectra display excitation peaks at 570 and 620 nm. Second, the ratio of excitation efficiency in the λ > 480 nm region to that in the λ < 480 nm region is significantly greater for the heat-treated samples than for the other ones. Finally, the excitation

* Electrochemical Society Active Member.

Key words: photoluminescence, stoichiometry, spectra, semiconductor.

Fig. 1. Oscilloscope display of emission spectra from 30 μm Cu_2O at 25°C, 20 nm bandpass, 633 nm HeNe excitation: (A) no filter before monochromator; (B) Corning 2-58 (nominally 640 nm high pass) filter; (C) Corning 2-64 (nominally 650 nm high pass) filter; (D) 1.0 mm polished CdTe filter (bandgap at $\lambda \approx 855$ nm). Fine structure on (A) and (D) are the wavelength markers which show the maximum intensity at 980 nm.



at 690 nm, although weak, is well above the background noise in all spectra and appears to be a part of a longer wavelength excitation which is not accessible with the apparatus at hand. This feature at 690 nm is thought (3) to be a direct excitation of a relaxed exciton at a copper vacancy.

Another experiment was performed to measure copper vacancy photoluminescence intensity as a function

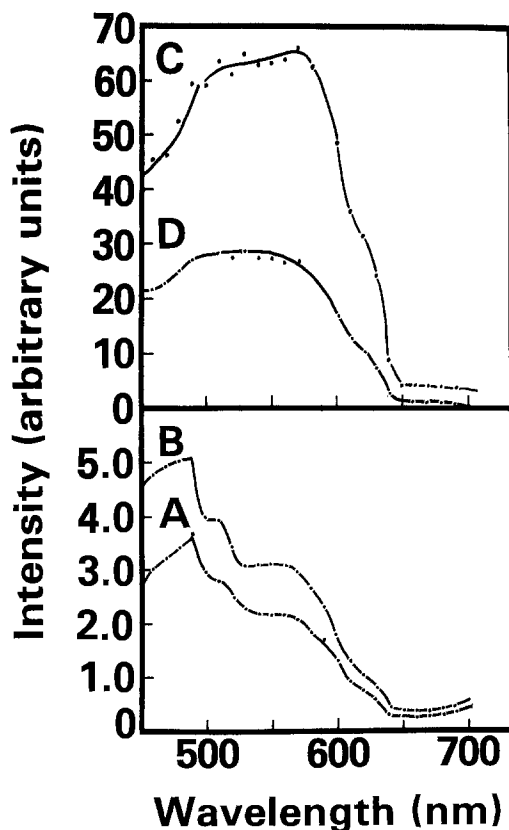


Fig. 2. Excitation spectra for 980 nm emission: (A) as grown; (B) 15s etch in 8N HNO_3 ; (C) heat-treated at 500°C, but not etched; (D) heat-treated at 500°C and etched for 15s in 8N HNO_3 .

of depth in a Cu_2O film. For this purpose, an 80 μm thick film of Cu_2O was grown on copper and heat-treated at 500°C (15 min in argon followed by a water quench, as with the other samples discussed here). The emission intensity, excited at 690 nm and detected at room temperature with a CdTe filter, was repeatedly measured as the film was etched with 8N HNO_3 . The 80 μm thickness was chosen to increase the number of possible etch cycles over what would be the case for a typical 30 μm film. Figure 3 shows the photoluminescence intensity as a function of the thickness of Cu_2O remaining. The fluctuations and otherwise nonlinear behavior of the emission intensity as the first ~ 30 μm of Cu_2O was removed suggests that complex concentration gradients of the luminescing species exist in this surface region. In contrast, the linear behavior of emission intensity with the removal of the remaining 50 μm of Cu_2O suggests that the concentration of luminescing centers is constant in this region adjacent to the copper metal.

The emission intensity was found to have a strong dependence on the temperature used in the heat-

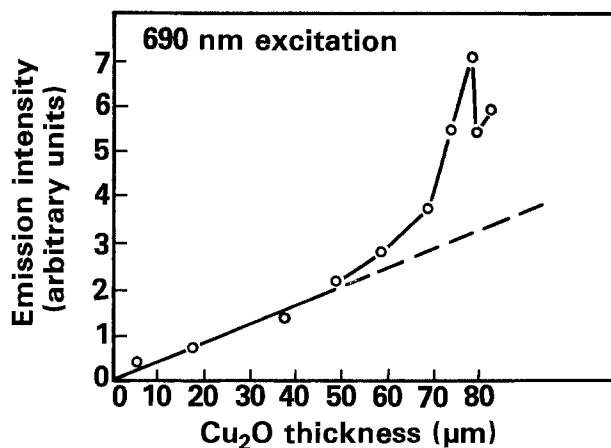


Fig. 3. Emission intensity excited at 690 nm vs. remaining film thickness for 80 μm Cu_2O film, heat-treated at 500°C, etched in steps in 8N HNO_3 .

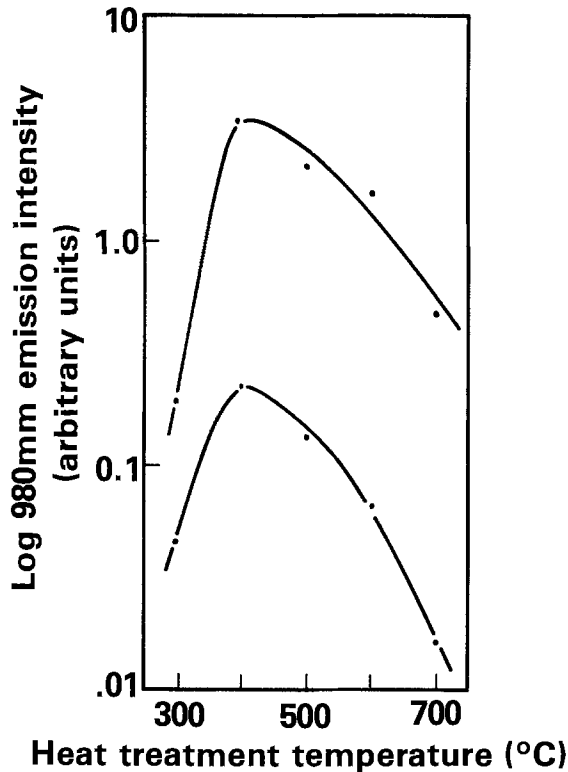


Fig. 4. Semilog plot of emission ($\lambda > 855$ nm) intensity vs. heat-treatment temperature for 570 and 690 nm excitation.

treatment procedure discussed earlier. Figure 4 shows the room temperature emission intensity excited at 570 and 690 nm as a function of heat-treatment temperature. For both excitation wavelengths, a maximum in the photoluminescence occurs in the range between 400° and 500°C. Furthermore, as can be seen in Fig. 4, and as is shown explicitly in Fig. 5, the ratio of the emission intensity excited at 570 nm to that excited at 690 nm increases monotonically with increasing heat-treatment temperature over the range experimentally studied. The causes of these heat-treatment effects will be discussed below.

Discussion

A portion of the stability diagram for the copper-oxygen system is shown in Fig. 6 (4). At 1000°C, Cu_2O

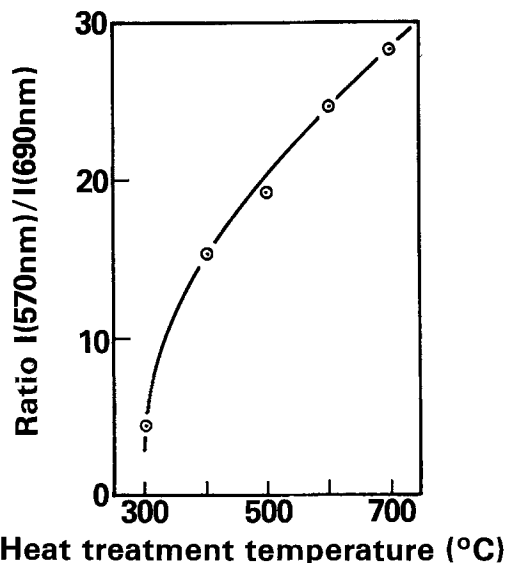


Fig. 5. Ratio of emission ($\lambda > 855$ nm) intensity for 570 nm excitation to that for 690 nm excitation vs. heat-treatment temperature.

is stable for a range of oxygen partial pressures over five orders of magnitude wide. For the experiments reported here, the Cu_2O film growth conditions (1000°C in a 10^{-2} atm oxygen partial pressure) were chosen to lie well within the stable region for Cu_2O in order to ensure that there would be no separate phase of CuO on the surface. Certainly, no Cu_2O film prepared in this work should be expected to have been in thermodynamic equilibrium with the oxidizing atmosphere throughout the film during growth. In fact, if the nonstoichiometry of Cu_2O is viewed as being due either to the solubility of CuO in Cu_2O , or equivalently to the concentration of copper vacancies in Cu_2O , then the layer of Cu_2O near the copper metal should have few copper vacancies, whereas the layer of Cu_2O near the exterior surface should have many copper vacancies, and might possibly have been near equilibrium with the oxidizing atmosphere during growth if the diffusion of copper vacancies away from the surface is slow compared to the oxidation of Cu_2O to CuO . The copper vacancy gradients across Cu_2O films grown in this manner and the modification of these gradients by subsequent heat-treatment strongly affect the photoluminescence properties of Cu_2O on copper, as will be discussed below.

For single-crystal Cu_2O , three broad photoluminescent bands have been reported in the literature (2, 3, 5, 6). Emissions at 720 and 820 nm (both at 77 K) are associated with relaxed excitons at oxygen vacancies, and the emission at 930 nm (also at 77 K) is due to relaxed excitons at copper vacancies. These assignments are supported by the observations that the two short wavelength emissions are completely suppressed by heat-treatment in atmospheres with O_2 partial pressures exceeding 1 torr, and that the long wavelength emission is suppressed by heat-treatment in vacuum. The copper vacancy emission feature has been observed (6) to broaden and shift to longer wavelengths with increasing temperature and remain resolvable at room temperature as a peak at about 960 nm. Therefore, identification of the 980 nm emission observed in this work as being due to relaxed excitons at copper vacancies is straightforward, especially considering the large concentration of copper vacancies expected with the Cu_2O growth procedure used here. Studies of Cu_2O excitation spectra at 77 and 1.6 K have shown that the relaxed exciton emission at copper vacancies is readily observable for all wavelengths from 830 to below 500 nm. The optical absorption of Cu_2O above 640 nm is very weak and an excitation band at ~ 780 nm has been attributed to direct excitation at copper vacancies (3). Below 640 nm, excitation is considered to be indirect with energy transfer from the absorbing host lattice to the luminescing vacancy center. The present observation of 980 nm emission excited from 450 to

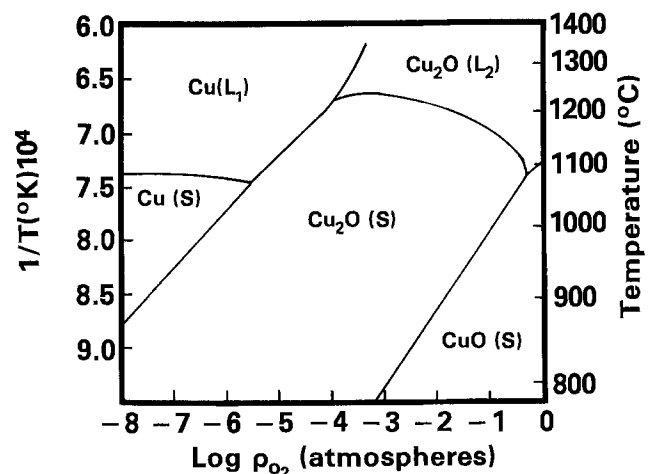


Fig. 6. Stability diagram for the Cu/ Cu_2O /Cu system

690 nm at 25°C is therefore not unexpected and consistent with low temperature measurements.

The strong dependence of the intensity of photoexcited luminescence from relaxed excitons at copper vacancies upon the temperature of a brief heat-treatment of these Cu₂O films in the absence of oxygen is a new and fortunate observation. Copper vacancies are certainly not being produced by a 15 min heat-treatment in argon at 500°C, yet the intensity of the 980 nm emission excited at 690 nm is increased by over an order of magnitude with this procedure, as shown in Fig. 3. Thus, the implication is that the increase in copper vacancy photoluminescence is induced by a thermally assisted redistribution of these vacancies, as is consistently borne out by the experimental results reported here. As was mentioned above, the 1000°C oxidation of Cu₂O to CuO at the surface of a film may be viewed as the creation of copper vacancies there. These vacancies subsequently diffuse toward the copper substrate, so that if the rate of oxidation is faster than the rate of the subsequent diffusion, a layer of vacancies will collect on the surface. The data of Fig. 2 (C) and (D) support this diffusion-limited model of the oxidation process, since the removal of the surface region by etching a 500°C heat-treated sample removes a disproportionate part of the luminescence. Furthermore, the large peak in the luminescence from near the surface region in Fig. 3 also supports this model. In contrast, the rise in luminescence following etching of as-grown samples, as shown in Fig. 2 (A) and (B), as well as the dip in luminescence near the surface shown in Fig. 3, would seem on first inspection to refute a diffusion-limited model. However, these results can be explained with the additional assumption that the luminescence of relaxed excitons at copper vacancies is "concentration quenched" at sufficiently high concentrations, as is known to be the case with luminescence of F centers in alkali halides (7), presumably due to formation of a nonluminescent decay path by the interaction of two or more centers. The slight increase of 980 nm luminescence shown in Fig. 3 at the surface, as compared with the concentration quenched minimum just below the surface, may then be explained by a loss of oxygen, and thus copper vacancies, at the surface by the process



during the heat-treatment of this film, resulting in less concentration quenching at the surface.

Thus, heat-treatment supplies the necessary energy to give sufficient mobility to copper vacancies so that they can diffuse toward the copper metal substrate, thereby breaking up nonluminescent clusters of these vacancies near the surface. The effects of heat-treatment of temperatures up to ~500°C are dominated by the breakup of vacancy clusters, thereby reducing concentration quenching in the surface region and increasing photoluminescence. For heat-treatment temperatures above 500°C, enough vacancies diffuse to (and disappear at) the copper substrate during the 15 min procedure to reduce the luminescence, as is shown in Fig. 4. Figure 5 shows further evidence of the breakup of vacancy clusters by heat-treatment, in that the ratio

of the luminescence excited by the 570 nm light, which is strongly absorbed at the surface of the film, to that of the 690 nm light, which is absorbed weakly and therefore uniformly throughout the Cu₂O film, increases monotonically with increasing heat-treatment temperature. The completely absorbed 570 nm light is preferentially absorbed in the concentration-quenched dead layer on the surface, resulting in reduced photoluminescence efficiency. Heat-treatment removes the concentration quenching by vacancy diffusion, and the apparent efficiency of luminescence excited by 570 nm light increases.

Summary

In summary, this is the first report of room temperature copper vacancy luminescence in thin films of Cu₂O on copper metal. Films of good optical quality were prepared, without etching, which had photoluminescence emission and excitation spectra similar to those reported for much thicker crystals. Furthermore, this is the first demonstration that a brief heat-treatment of such films in the absence of oxygen will allow copper vacancies to diffuse, thereby reducing vacancy concentrations where luminescence is quenched by interactions among vacancies. Finally, this is the first reported use of photoluminescence to study vacancy gradients in films. The results suggest that for Cu₂O films grown on copper at 1000°C in a 1% O₂/Ar atmosphere, the rate-controlling step in copper oxidation is the diffusion of copper vacancies to the copper, since a steep gradient of CuO (or equivalently, copper vacancies) occurs near the Cu₂O surface. Moreover, when the CuO concentration is sufficiently high, the copper vacancies appear not to be luminescent.

Acknowledgments

The authors wish to thank D. Chokshi and R. Rekruciak for their experimental assistance and to D. Lewis and M. Quick for helpful encouragement.

Manuscript submitted July 27, 1983. This was Paper 923 presented at the San Francisco, California, Meeting of the Society, May 8-13, 1983.

Standard Oil Company (Indiana) assisted in meeting the publication costs of this article.

REFERENCES

1. W. J. Tomlinson and J. Yeats, *J. Cryst. Growth*, **38**, 265 (1977); A. Arafa, M. Kenawy, and M. F. El-Daoushy, *An. Fis.*, **69**, 409 (1973); M. Jardinier-Offergeld and F. Bouillon, *J. Vac. Sci. Technol.*, **9**, 770 (1972).
2. J. Bloem, A. J. Van der Houwer van Oordt, and F. A. Kroger, *Physica*, **22**, 1254 (1956); J. Bloem, *Philips Res. Rep.*, **13**, 167 (1958).
3. S. V. Gastev, A. A. Kaplyanskii, and N. S. Sokolov, *Solid State Commun.*, **42**, 389 (1982).
4. J. F. Elliott, *Metall. Trans. B*, **78**, 17 (1976).
5. I. S. Gorban and S. N. Rud'ko *Zh. Prikl. Spektrosk.*, **7**, 249 (1967).
6. C. Duvvury, D. J. Kenway, and F. L. Weichman, *J. Lumin.*, **10**, 415 (1975).
7. See J. H. Schulman and W. D. Compton, "Color Centers in Solids," MacMillan Co., New York (1962), for a general discussion.

A Comparison of HCl- and Trichloroethylene-Grown Oxides on Silicon

M. B. Das, J. Stach,* and R. E. Tressler

Department of Electrical Engineering and Materials Science, The Pennsylvania State University, University Park, Pennsylvania 16802

W. H. Grubbs

Hewlett Packard, Palo Alto, California 94303

ABSTRACT

A comparison of HCl and trichloroethylene (TCE) as chlorine bearing gaseous additives to the oxidizing ambient for growing thermal oxide on silicon at 1150°C was made. According to a thermodynamic analysis of the gas phase species at comparable partial pressures of chlorine in the reactor, the major difference in the gas phase composition is about an order of magnitude lower partial pressure of H₂O and HCl in the TCE system. The parabolic rate constants at 1150°C at approximately the same partial pressures of Cl₂ in both systems over a range of input HCl feed rates of 0-120 cm³/min HCl per liter of dry O₂ (and comparable rates of TCE/N₂ mixture) were similar, being only marginally lower for the TCE system, although the equilibrium HCl and H₂O contents of the TCE reactor were an order of magnitude lower. The addition of HCl and TCE were both found to result in significant increases on inversion times of carriers as determined by capacitance *vs.* time measurements of pulsed MOS capacitors.

With the recent concentration of semiconductor device fabrication in the MOS area, much research has originated to enhance the electrical properties of thermal oxide on silicon. Much of this research has been concerned with the addition of a chlorine bearing species to the oxidizing ambient. Initially work in this area was concerned with the addition of HCl to the oxidizing ambient (1-3). More recent studies indicate that trichloroethylene (TCE) may also be used to enhance the properties of thermal oxide layers (4-5).

Oxidation in the presence of these two halogen containing compounds is reported to increase both the oxide breakdown strength and the minority carrier lifetime in the silicon (6). In addition, the oxide charges associated with thermally oxidized silicon are reportedly reduced. Many of the studies done concerning HCl- and TCE-grown oxides have been done using several oxidation temperatures while maintaining a variety of fabrication constraints.

In this work, the effects of adding similar amounts of HCl and TCE during the oxidation process step while maintaining identical oxidation temperatures and device fabrication constraints in both systems were studied. A comparison of the HCl- and the TCE-oxidation systems was made on three bases. First, the equilibrium partial pressures of the chemical species present in the gas phase in each system were compared at similar additions of HCl and TCE. This comparison was made based on the partial pressure data obtained using the SOLGAS computer program (7). A second comparison of these two systems was made based on the oxide growth kinetics of each system. The final comparison of these two systems dealt with the measured minority carrier lifetime values of carriers in the bulk silicon of MOS test structures fabricated for this study.

Experimental Procedure

The oxidation temperature used in this study was held constant at 1150° ± 2°C in both systems. The gases in the HCl system were first preheated to the oxidation temperature, prior to entering the flat zone of the furnace. This procedure was undertaken in order to ensure that the gaseous reactions were completed prior to impinging on the silicon wafers. The flow rate of gaseous TCE was controlled by varying the flow rate of filtered dry nitrogen through a bubbler filled with liquid TCE. The bubbler temperature was

held constant at 35° ± 0.5°C. In both systems the wafers were first inserted into the oxidation furnace in the presence of nitrogen for 5 min. In the TCE system, a dry O₂ oxide layer was grown for 1 min prior to the addition of TCE/N₂. This process technique was necessary in order to obtain good quality oxides. Wafers which were fabricated without the 1 min dry O₂ oxide layer were found to produce pitted oxides.

For this study, MOS capacitors were fabricated on <100> oriented, n-type silicon wafers, having a bulk resistivity of 7-8 Ωcm. The wafers were chemically cleaned using both high and low pH peroxide solutions. The wafers were then oxidized using the additions of 0, 5, 10, 30, 60, and 120 cm³/min of both HCl and TCE/N₂, while maintaining a constant flow rate of 1.0 l/min of dry O₂ in each system. Oxidation times were varied to result in an oxide thickness of approximately 1000Å for each of the various flow rates of HCl and TCE/N₂. Wafers were given a high temperature anneal in N₂ for 5-10 min, following the oxidation sequence, and a slow pull of the wafers from the furnace tube was used in order to avoid interface and lattice stresses. The aluminum dots were then E-gun evaporated through a metal mask. The oxide was etched from the back of the wafers, and then metallized to ensure a good back-side contact. The MOS test structures were annealed at 500°C for 5 min in nitrogen to remove radiation damage which resulted from the E-gun evaporation technique.

In addition to these test structures, a similar process was used to produce the oxide-growth kinetics in both systems for each flow rate of HCl and TCE/N₂. Wafers were cleaned and inserted into the oxidation system as mentioned previously. Oxide growth times of 10, 20, 30, and 60 min were used at each flow rate of HCl and TCE/N₂, followed by 5 min anneal in N₂. Wafers were then removed from the oxidation furnace for thickness measurements using the ellipsometric technique.

Results and Discussion

Thermodynamic analysis.—The SOLGAS computer program (7) was used to obtain the equilibrium partial pressures of the chemical species present in the HCl and TCE systems at an oxidation temperature of 1150°C. The data input to this program requires the thermodynamic properties of all possible species in the system, as well as the input concentrations of the chemical elements contained in each of these two systems, for each flow rate of both HCl and TCE/N₂. The program is designed to use an iterative procedure to

* Electrochemical Society Active Member.

minimize the Gibbs free energy of the specific system in order to calculate the equilibrium partial pressures of the chemical species.

In the TCE system, the actual concentration of TCE introduced into this system is limited by the vapor pressure of TCE at the bubbler temperature. Using a bubbler temperature of 35°C, the gram-atoms of each element may be determined at each of the various flow rates.

The most significant species to be found in these two systems are shown in Fig. 1 and 2. These two figures represent the partial pressure data of the chemical species in each system, plotted at the various added flow rates of HCl and TCE/N₂. In the HCl system it was found that the partial pressures of H₂O and Cl₂ are equal. A similar plot for the TCE system indicates that the partial pressure of H₂O is more than one order of magnitude lower than the partial pressure of Cl₂.

A further comparison of these two systems, based on the SOLGAS data, indicates that the partial pressure of H₂O in the HCl system is higher than in the TCE/N₂ system, whereas the partial pressure of Cl₂ is nearly the same in each system, when compared at similar flow rates of HCl and TCE/N₂. Note that the HCl partial pressure in the HCl-O₂ system is nearly an order of magnitude larger than the HCl partial pressure in the TCE/N₂-O₂ system at the same input flow rates. Further reference to these curves reveals the presence of HOCl, ClO, and HO at much lower levels in each system.

Oxide growth kinetics.—The oxide-growth curve for the HCl system and the TCE/N₂ system are presented in Fig. 3 and 4, respectively. An analysis of these two sets of curves clearly indicates that the oxidation rate of silicon increases as the input concentration of HCl and TCE in the oxidizing ambient is increased.

The parabolic rate constants for these two systems have been derived from these two sets of curves using the general relationship for the oxidation of silicon (9)

$$x_0^2 + Ax_0 = B(t + r) \quad [1]$$

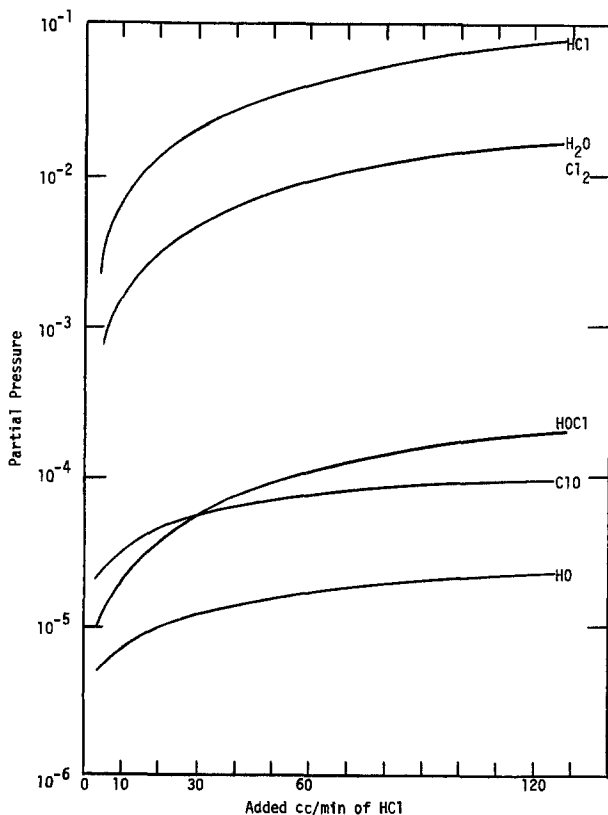


Fig. 1. Partial pressure vs. added cm²/min of HCl for the chemical species of the HCl system.

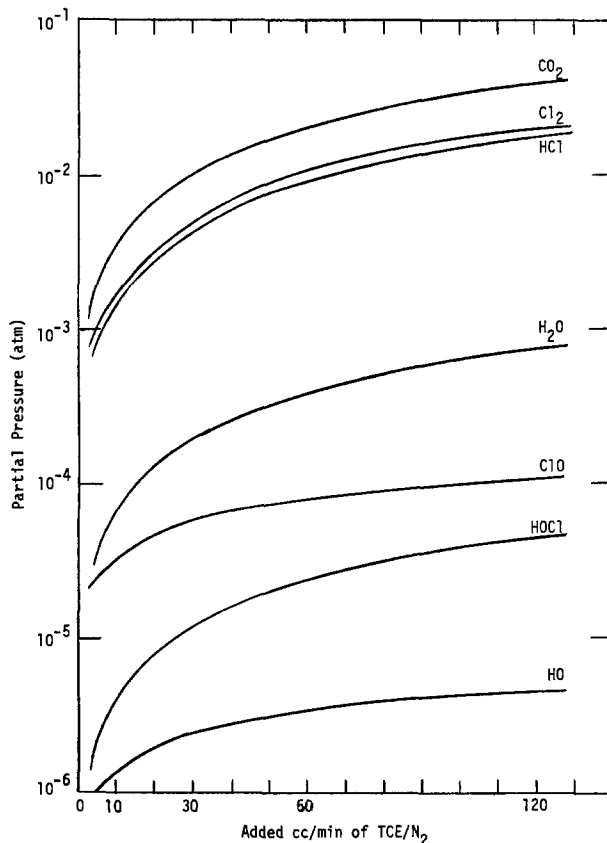


Fig. 2. Partial pressure vs. added cm²/min of TCE/N₂ for the chemical species of the TCE system.

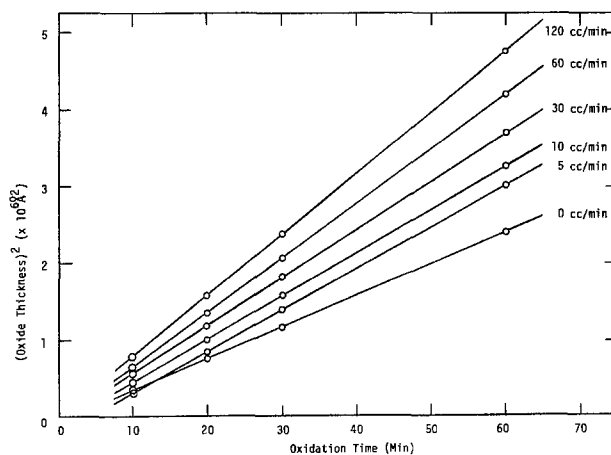


Fig. 3. Oxide growth rate for the HCl system

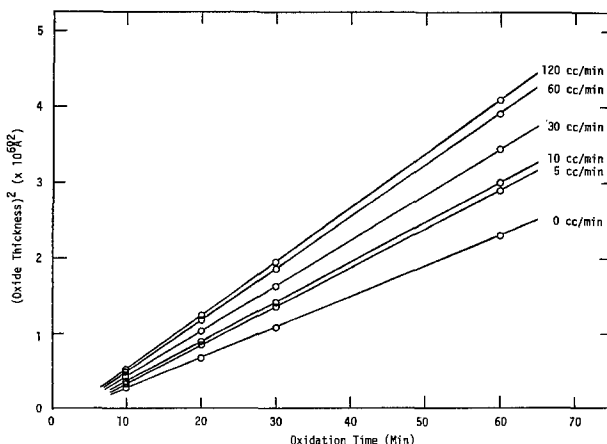


Fig. 4. Oxide growth rate for the TCE system

Table I. The parabolic rate constants of the HCl and TCE systems

Flow rate cm/min	HCl ($\times 10^{-4} \mu^2/\text{min}$)	TCE ($\times 10^{-4} \mu^2/\text{min}$)
0	4.09	4.12
5	5.44	5.19
10	5.74	5.43
30	6.23	6.06
60	7.10	6.64
120	7.98	7.09

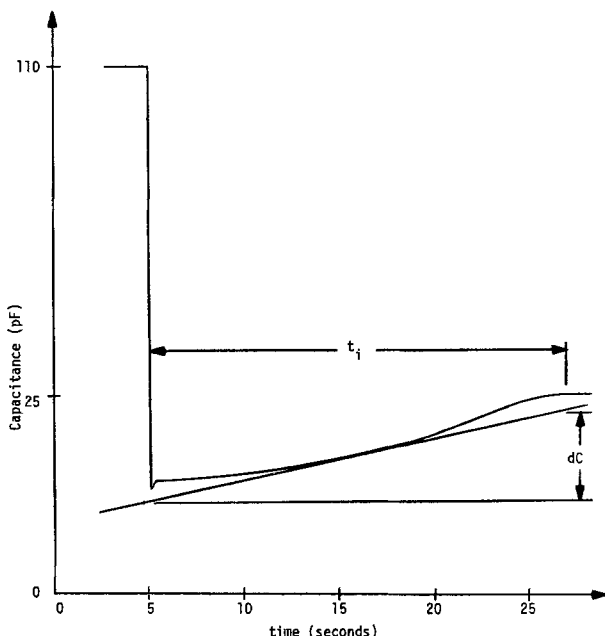
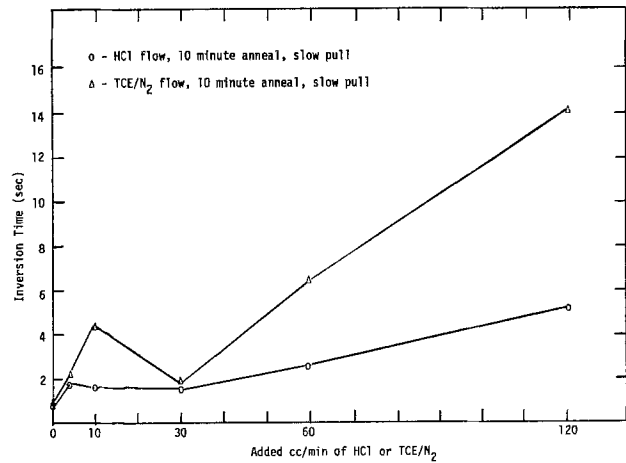
For large times, this equation reduces to the parabolic relationship

$$x_0^2 = Bt \quad [2]$$

where x_0 is the oxide thickness (μm), B is the parabolic rate constant ($\mu\text{m}^2/\text{min}$), and t is the oxide growth time (min). The oxide thickness data was fitted to this equation using the least squares method in order to determine the B constants at each flow rate of HCl and TCE/N₂.

The values of the parabolic rate constants in these two systems are quite comparable at the same input rate of HCl and TCE/N₂, as shown in Table I. Note that of the major species in the oxidizing ambients, the chlorine is the only one which is present in approximately the same composition in both ambients. In the HCl-O₂, ambients both HCl and H₂O are present in levels nearly an order of magnitude greater than in the TCE/N₂ ambients. This result further supports the hypothesis of Tressler *et al.* (10) that the active gaseous species with regard to kinetics of oxidation and passivation in chlorine bearing oxidizing ambients is Cl₂. The slightly lower values of the parabolic rate constants for the TCE/N₂-O₂ ambients may be due to the second-order effect of the reduced H₂O concentration.

Minority carrier lifetime.—In order to determine the effects of HCl and TCE/N₂ on the bulk lifetime of carriers in the MOS test structures, oxides were grown in the presence of various concentrations of these two chlorine species, as mentioned previously. The measurement technique consists of applying a deep depletion voltage step to the metal electrode, after initially biasing the devices into the accumulation mode. A typical capacitance *vs.* time (*C-t*) curve is shown in Fig. 5. The lifetime of carriers may be derived from the slope of this curve using a technique which has been described by Heiman (11). For this study, the inversion time (t_i) (4), defined as the time required for the *C-t* curve to go from the deep depletion to the

Fig. 5. Experimental *C-t* curve of the pulsed MOS capacitorFig. 6. Inversion time vs. HCl and TCE/N₂ flows using a 10 min high temperature anneal and a slow pull in both systems.

inversion mode, has been used to compare the effects of adding various concentrations of HCl or TCE to the oxidizing ambient.

Figure 6 represents a graphic analysis of the data derived from these test structures. It is apparent that the shapes of these two curves are similar and that the addition of 5 cm³/min of HCl or TCE/N₂ results in longer inversion times than the measured values for dry O₂-grown oxides. The largest values of t_i occurred at added flow rates of 60-120 cm³/min of HCl or TCE/N₂. A reduction in inversion time was found at additions of 30 cm³/min of HCl or TCE/N₂. Similar findings have been reported by Declerck *et al.* (4) for the TCE system. A viable explanation for the reduction in t_i at these flow rates has not been determined, but the occurrence of these lower values has been found to be reproducible.

Conclusions

The equilibrium partial pressures of the possible chemical species in the HCl and TCE oxidation systems have been calculated at 1150°C. At nearly equal partial pressures of chlorine in the two systems, for a given flow rate of HCl or TCE/N₂, the partial pressures of H₂O and HCl were found to be approximately an order of magnitude lower in the TCE system.

The kinetics of thermal oxidation at 1150°C in the presence of HCl and TCE are similar at approximately the same partial pressure of Cl₂, although the H₂O and HCl partial pressures are much lower in the TCE system. These results lend support to an earlier hypothesis that Cl₂ is the important active species in the thermal oxidation of silicon with reference to the growth kinetics and passivation.

The measurement of the capacitance *vs.* time curve of the pulsed MOS capacitor has been found to be a convenient method of determining the inversion time of carriers in devices fabricated using various processing constraints. The addition of HCl and TCE were found to result in a significant increase in inversion times (up to a factor of 30 times greater) when compared to values derived from test structures which were fabricated in the presence of dry O₂.

Acknowledgments

This research was funded (in part) by the Advanced Research Projects Agency of the Department of Defense under ARPA Order no. 2397 through the Department of Commerce's National Bureau of Standards' Semiconductor Technology Program under contract no. 5-35717.

Manuscript submitted Jan. 1, 1978; revised manuscript received June 1, 1983. This was Paper 325 presented at the Las Vegas, Nevada, Meeting of the Society, Oct. 17-22, 1976.

The Pennsylvania State University assisted in meeting the publication costs of this article.

REFERENCES

1. G. Baccarani, M. Severi, and G. Soncini, *This Journal*, **120**, 1436 (1973).
2. M. Severi and G. Soncini, *Electron. Lett.*, **9**, 402 (1977).
3. Y. J. van der Meulen, C. M. Osburn, and J. F. Ziegler, *This Journal*, **122**, 284 (1975).
4. G. H. Declerck, T. Hattori, G. A. May, J. Beau-douin, and J. D. Meindl, *ibid.*, **122**, 284 (1975).
5. D. E. Heald, R. M. Das, and R. P. Khosla, *ibid.*, **123**, 302 (1976).
6. P. H. Robinson and F. P. Heiman, *ibid.*, **118**, 141 (1971).
7. G. Eriksson, *Acta Chem. Scand.*, **25**, 2651 (1971).
8. P. M. Ritchey, M.S. Thesis, The Pennsylvania State University, University Park, PA (1976).
9. A. S. Grove, "Physics and Technology of Semiconductor Devices," pp. 23-31, John Wiley and Sons, New York (1967).
10. R. E. Tressler, J. Stach, and D. Metz, *This Journal*, **124**, 607 (1977).
11. F. P. Heiman, *IEEE Trans. Electron. Devices*, **ed-14**, 781 (1967).

The Relation Between Two-Probe and Four-Probe Resistances on Nonuniform Structures

John Albers

National Bureau of Standards, Semiconductor Devices and Circuits Division, Washington, DC 20234

H. L. Berkowitz*

U.S. Army Electronics Technology and Devices Laboratory, ERADCOM, Fort Monmouth, New Jersey 07703

ABSTRACT

A general relation between the two-probe resistance (spreading resistance) and the four-probe resistance on nonuniform resistivity structures is derived. Numerical techniques are presented and discussed for the evaluation of these equations for nonuniform structures. The relation between the four-probe resistance, $Z(x, S)$, and the incremental sheet resistance, $\mathcal{R}(x)$, is shown to arise in the limit as the probe spacing becomes large compared to the distance to an insulating boundary. Specific examples are drawn from calculations on implant-type structures into substrates having insulating boundaries near the end of the implanted region (junction isolation), as well as those where the insulating boundary is far from the implanted region (emulating the back surface of a same conductivity-type substrate). Also presented is a method for the self-consistent calibration of spreading resistance profiles utilizing $Z(x, S)$.

Recently, Dickey (1) has proposed that the two-probe spreading resistance measured on the surface of a thin, nonuniform resistivity, junction-isolated layer is a linear function of the logarithm of the probe spacing (S) with a slope proportional to the four-probe sheet resistance and an intercept which may be related to the probe radius. The basis of the conjecture is an image calculation of the spreading resistance of a thin layer of uniform resistivity over an insulator. For this case, the spreading resistance (R) is of the form

$$R = \frac{\rho}{\pi t} \ln(S/a) \quad [1]$$

where ρ is the resistivity of the layer, t is the thickness of the layer, S is the spacing between the probes, and a is the electrical probe radius. As the sheet resistance of the layer is just ρ/t , Eq. [1] would suggest that the spreading resistance is linear in the logarithm of the probe spacing ($\ln S$) with a slope proportional to the sheet resistance. For layers of nonuniform resistivity formed by junction-isolated boron diffusions with junction depths up to 4.3 μm , this conjecture has been shown to be valid (to within a few percent) when the probe spacing experiment is performed and the results compared with the sheet resistance obtained by means of four-probe measurements (1).

As the applicability of this conjecture to general classes of structures was unknown, several investigations (2, 3) were previously undertaken making use of model spreading resistance data (4). These probe spacing experiment simulations indicated that the probe

spacing experiment would give the correct incremental sheet resistance in the surface region of junction type as well as heavily doped implant and diffusion structures. This conclusion was obtained by comparing the incremental sheet resistance obtained from the probe spacing experiment simulation to that obtained from direct calculation of the resistivity profile. This conclusion was not altered when several forms of the probe-current density (5) were used in the calculations. For lightly to moderately doped layers over substrates of the same conductivity type, the conjecture was found not to hold. In addition, deep layers, typical of power device structures, were found to present what appears to be a breakdown of the conjecture. Also, these investigations showed that the interpretation of the intercept in terms of a probe radius was not well founded. Hence, the use of the probe spacing experiment as a way of obtaining the probe radius is not warranted.

The purpose of this paper is to derive a general relation between the four-probe resistance and the two-probe spreading resistance. It is of utmost importance to emphasize that the four-probe resistance is not necessarily the sheet resistance, but is rather a generalized four-probe resistance. In the discussion which follows, the four-probe resistance refers to the generalized four-probe resistance, the two-probe resistance is the two-probe spreading resistance, and the incremental sheet resistance is referred to as the sheet resistance. All of these quantities are functions of depth. It will be shown that the four-probe resistance is related, in certain well-defined limits, to the sheet resistance. In addition, it will be shown that the four-probe resistance can always be obtained from measurements of the spreading resistance. The latter provides for a simple relation between the two-probe and the four-probe re-

* Electrochemical Society Active Member.

Key words: four-probe resistance, probe-current density, probe radius, probe separation, profile analysis, resistivity, sheet resistance, spreading resistance.

sistances. In addition, the relation between the four-probe resistance and the Dickey conjecture is elucidated. Finally, a self-consistent procedure for determining the probe radius parameter used in spreading resistance profile analysis is developed. Throughout the paper, the symbol "ln" is used to refer to the natural or Naparian logarithm, and the symbol "log" is used for the base-10 logarithm.

Derivation of Relation Between Two-Probe and Four-Probe Resistances

Consider a material of nonuniform resistivity. Four probes are placed on the surface of the material in an in-line configuration with adjacent probes separated by a distance S . The outer two probes are the source-sink combination for the current, while the inner two probes are the voltage sensing probes. It is important to emphasize that value of S is arbitrary and need not be in the range of values usually used for traditional four-probe sheet resistance measurements. Following the general development associated with the Laplace equation multilayer analysis (6, 7), the $\Delta V/I$ or resistance between the inner two probes, denoted by $Z(x, S)$, is given by

$$Z(x, S) = 2\rho(x) \int_0^\infty A(x, \lambda) \{J_0(\lambda S) - J_0(2\lambda S)\} I_\nu(\lambda a) d\lambda \quad [2]$$

where x is the depth, $\rho(x)$ is the nonuniform resistivity, $J_0(\lambda S)$ is the first-order Bessel function, $A(x, \lambda)$ is the kernel of the integral and is related to the details of the underlying resistivity structure, $I_\nu(\lambda a)$ is the Hankel transform of the generalized probe-current density normalized to unit current (5), ν in $I_\nu(\lambda a)$ is an index which refers to the specific form of the current density (3, 5), and λ is the integration variable. As will be shown in the subsequent development, $\pi Z(x, S)/\ln 2$ approaches the sheet resistance as the separation between the probes becomes large compared to the distance to an insulating boundary.

Next, consider the same material contacted by a two-probe configuration typical of spreading resistance measurements. The two-probe spreading resistance at the probe spacing equal to S is given by

$$R(x, S) = 4\rho(x) \int_0^\infty A(x, \lambda) \left\{ \frac{J_1(\lambda a)}{\lambda a} - \frac{J_0(\lambda S)}{2} \right\} I_\nu(\lambda a) d\lambda \quad [3]$$

while the two-probe spreading resistance at the probe spacing equal to $2S$ is given by

$$R(x, 2S) = 4\rho(x) \int_0^\infty A(x, \lambda) \left\{ \frac{J_1(\lambda a)}{\lambda a} - \frac{J_0(2\lambda S)}{2} \right\} I_\nu(\lambda a) d\lambda \quad [4]$$

By subtracting Eq. [3] from Eq. [4], it is easy to show that the four-probe resistance given by Eq. [2] may be simply written as

$$Z(x, S) = R(x, 2S) - R(x, S) \quad [5]$$

Equation [5], which is the desired relation between the two-probe and four-probe resistances, states that the four-probe resistance at a given value of the separation, S , may be simply obtained from the two-probe spreading resistance by taking the difference between the spreading resistance evaluated at $2S$ and the spreading resistance evaluated at S . The central point of the present work is to calculate the four-probe resistance by means of Eq. [2] and to investigate the behavior of the function for various structures and as a function of the probe separation.

In order to complete this section, consider the implications of the Dickey conjecture, *i.e.*, that the spreading resistance is linear in the logarithm of the probe spacing $\ln S$, with a slope proportional to the sheet resistance. If this is the case, the derivative of the spreading resistance with respect to $\ln S$ should under certain well-defined conditions be related to the sheet resistance. Hence, it is quite natural to consider the derivative of the two-probe spreading resistance (as given by Eq. [3]) with respect to $\ln S$. By making use of the chain rule, this derivative, denoted by $D(x, S)$, may be written as

$$D(x, S) = \frac{dR(x, S)}{d \ln S} = S \frac{dR(x, S)}{dS} \quad [6]$$

Substituting Eq. [3] into Eq. [6] and carrying out the derivative of the $J_0(\lambda S)$ Bessel function inside the integral (8) yields

$$D(x, S) = 2\rho(x) \int_0^\infty A(x, \lambda) \lambda S J_1(\lambda S) I_\nu(\lambda a) d\lambda \quad [7]$$

The focal point of the calculations presented here is to consider the functions $Z(x, S)$ and $D(x, S)$ as defined by Eq. [2] and [7], respectively and to show how they are related to the sheet resistance defined as

$$R(x) = \frac{1}{\int_0^x \frac{1}{\rho(x')} dx'} \quad [8]$$

Numerical Evaluation of $Z(x, S)$ and $D(x, S)$

For a particular resistivity structure, the sheet resistance defined by Eq. [8] may be obtained by direct numerical summation or integration. The four-probe resistance and the derivative function were evaluated by making use of the recursion relation for the kernel, *i.e.*

$$A(x, \lambda) = \frac{A(x-d, \lambda)\sigma(x) + \sigma(x-d) \tanh(\lambda d)}{\sigma(x-d) + \sigma(x)A(x-d, \lambda) \tanh(\lambda d)} \quad [9]$$

where d is the sublayer thickness and $\sigma(x)$ is the conductivity. The above form is from Berkowitz and Lux (9) and is fully equivalent to the original form of the recursion relation presented by Choo *et al.* (10). A useful feature of the recursion relation as given by Eq. [9] is that it is easy to obtain the form of $A(x, \lambda)$ for a uniform layer over an insulating boundary, a conducting boundary, or no boundary. By making use of the resistivity structure along with the appropriate boundary condition, it is possible to construct the kernel of the integrals involved in the functions $Z(x, S)$ and $D(x, S)$. Evaluation of the resulting integrals has been accomplished by means of two numerical integration techniques. The first is the trapezoidal-Romberg technique first used by D'Avanzo *et al.* (11, 12) in the evaluation of the arrays of partial integrals involved in the implementation of spreading resistance correction factor integrals. This technique has also been used to generate model spreading resistance data (Eq. [4]). The second technique makes use of a 1250-point integrator.

Extensive testing indicates that the two integration techniques agree well. Because the 1250-point integrator takes far less CPU time than the trapezoidal-Romberg technique, most of the calculations presented here were obtained by means of that technique. For certain situations, a 10,000-point integrator was used. This form allows for evaluation of the integrals over an interval much larger than the one used in the 1250-point scheme. Evaluation of the derivative function, $D(x, S)$, using these latter two techniques sometimes leads to convergence problems. This is due to the large value of the upper limit required in the evaluation of the integral for the case of large probe spacing and thick, same-conductivity type substrates. For these situations, the integrand of $D(x, S)$ decays to zero very

slowly, and the trapezoidal-Romberg technique was used to ensure the convergence of the integrals. For the cases which were investigated, this technique (with an adjustable upper limit) led to convergence. This convergence problem was not seen in the calculation of the four-probe resistance. This is due to the more rapid decay of the integrand of the four-probe resistance integral.

A listing of the Fortran programs used in the 1250-point and 10,000-point schemes may be obtained from either of the authors upon request.

Calculation of $Z(x,S)$ for Two-Layer Structure

These integration techniques were extensively tested on varying thickness uniform layers over an infinite substrate of constant resistivity, and it was found that the four-probe resistance, the derivative function, and the sheet resistance were related by

$$Z(x, S) = \frac{\ln 2}{\pi} R(x) \quad [10]$$

$$D(x, S) = \frac{1}{\pi} R(x) \quad [11]$$

The above results were obtained provided that the substrate resistivity was large compared to the resistivity of the top layer (i.e., for a uniform layer over an insulator), and that x/S is small. For the situation where x/S was comparable to or larger than unity, the relations given by Eq. [10] and [11] did not hold. This is to be expected, since the traditional sheet resistance model (embodied in Eq. [8]) is obtained for the situation where the probes are spaced widely relative to the layer thickness and where the assumption of parallel conduction in the layer holds as a result. For $x/S \geq 1$, $Z(x, S)$ represents the $\Delta V/I$ measured between the two voltage-sensing probes. However, for $x/S \geq 1$, the function $D(x, S)$ cannot be related in a meaningful way to a measurable physical quantity. The behavior of the surface value of $Z(x, S)$ as a function of the ratio of the probe separation and the layer thickness (S/t) is presented in Fig. 1. The specific structure is a variable thickness, $1 \Omega \cdot \text{cm}$, layer over an insulating boundary.

The function $Z(x, S)$ was also evaluated for a general two-layer structure. The behavior of $Z(x, S)$ for a wide range of t/S (for fixed probe spacing) and layer resistivity is presented in Fig. 2. The substrate is infinitely thick and has a resistivity of $1 \Omega \cdot \text{cm}$. The re-

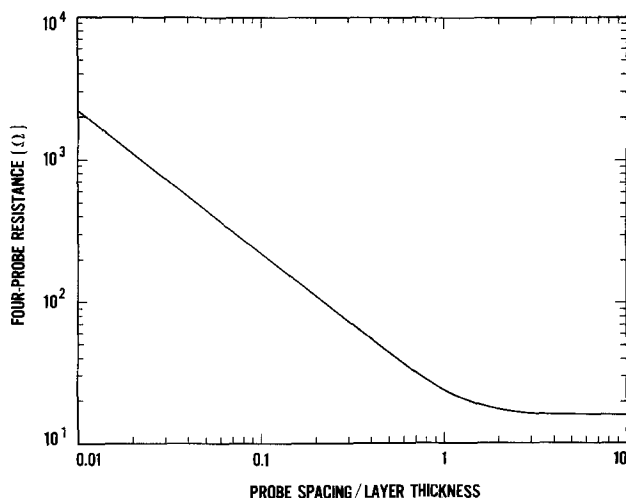


Fig. 1. The behavior of the surface value of $Z(x,S)$ as a function of the ratio of the probe spacing and the layer thickness. The specific structure is that of a varying thickness, $1 \Omega \cdot \text{cm}$, layer over an insulating boundary. If the ratio S/t is greater than 1.67, the four-probe resistance deviates from $\ln(2)/(\pi t)$ by less than 1%.

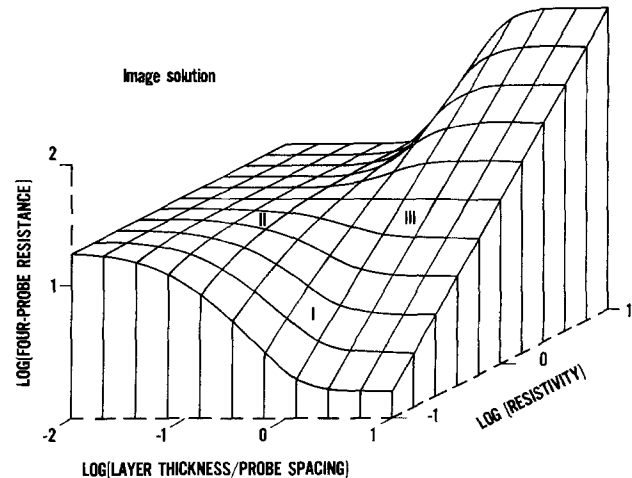


Fig. 2. The four-probe resistance of a uniform layer over an infinitely thick substrate of $1 \Omega \cdot \text{cm}$ resistivity for a wide range of layer resistivity and layer thickness to probe spacing ratio. The data are for a fixed value of probe spacing and represent the dependence of the four-probe resistance on layer thickness and top layer resistivity. The region in which the Dickey conjecture has validity and utility immediately adjoins the square marked I. In this region, the linear dependence of $\log(\Delta V/I)$ on the resistivity indicates that the shorting effects of the substrate are not severe, and the negative slope $\Delta(\log[\Delta V/I])/\Delta \log[t/S]$, indicates that the four-probe resistance varies inversely with layer thickness and that therefore the sheet resistance is a physically meaningful quantity. In the region to the left of II, the four-probe resistance shows too little dependence on the layer resistivity to be of interest. The region marked III is not generally considered for the use of four-probe measurements. However, it is clear from the linear dependence of $\log(\Delta V/I)$ on $\log(\rho)$ that the sensitivity of the four-probe measurement to the layer resistivity is actually greater here than anywhere else on the surface displayed.

sults were also compared with those obtained from a point-source image simulation of the four-probe resistance. A comparison of the results for these two computational schemes is presented in Fig. 3. The calculation of $Z(x, S)$ agreed with the image solution to the full accuracy expected from the integration technique. This is true even though the probe radius and the variable ν in Eq. [2] were varied over wide limits. This confirms the independence of the four-probe resistance to details of the current injection process, i.e.,

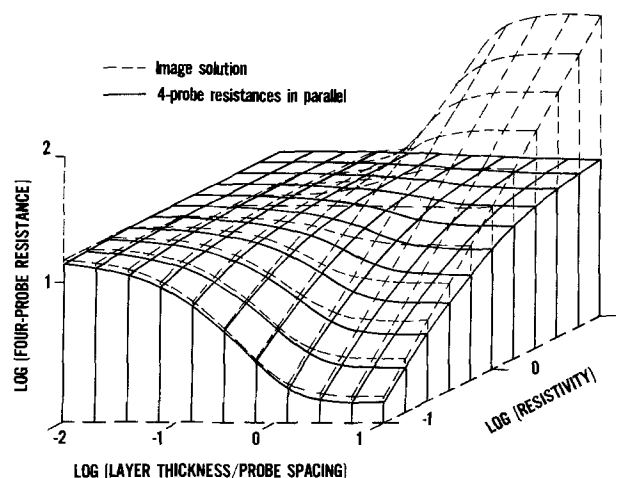


Fig. 3. The results obtained by combining the four-probe resistance shown in Fig. 2 in parallel with $1/(2\pi S)$, the four-probe resistance of an infinite uniform substrate of $1 \Omega \cdot \text{cm}$ resistivity, for $S = 100 \mu\text{m}$. The dashed surface is the one shown in Fig. 2. The relative deviation in the four-probe resistances calculated by the respective methods for the point at the lower right corner is about 10%.

to the probe current density. The surface in Fig. 2 has been subdivided into three regions, denoted by I, II, and III. It is important to note that distinct boundaries of these three regions are not possible, as there is a continuous change from one region to the next. The region denoted by I is that of small top layer resistivity and a large spacing to thickness ratio ($S/t > 1$). In this region, the sheet resistance is a well-defined quantity and the Dickey conjecture is valid. In region II, the probe spacing is still large compared to the top layer thickness ($S/t > 1$), but the top layer resistivity is increasing. Note that the slope of the surface in this region decreases, indicating that the substrate resistivity is dominating the four-probe resistance. Consequently, the four-probe resistance may not be used to obtain information about the layer resistivity. Finally, the region III is that in which the layer thickness is a sizable fraction of, or greater than, the probe spacing. This is a nonstandard region for the operation of a four-point probe in as much as the sheet resistance is not a well-defined quantity here. However, since the $\Delta V/I$ is a linear function of the layer resistivity, the four-probe resistance is a useful measure of layer resistivity.

Calculation of $Z(x,S)$ for Nonuniform Layers

Model resistivity data corresponding to a shallow Gaussian implant into varying resistivity same-conductivity-type substrates were used in these calculations. The substrate resistivities which were used were 126.46, 12.82, and 1.38 $\Omega \cdot \text{cm}$, respectively. These correspond to substrate doping levels of 10^{14} , 10^{15} , and 10^{16} cm^{-3} , respectively. In all cases, the substrate thickness was taken as 350 μm , the approximate thickness of a standard silicon wafer. A typical example of the resistivity data which was used in the calculations is presented in Fig. 4.

The results of these calculations of $Z(x,S)$ and $\mathcal{R}(x)$ are contained in Fig. 5-7. For the case of the 126 $\Omega \cdot \text{cm}$ substrate, the behavior of $Z(x,S)$ as a function of S in the surface region is dominated by the resistivity of the implanted layer. $Z(x,S)$ in this region

is almost independent of the probe spacing, indicating that the sheet resistance is well defined in this region. For substrate resistivities larger than 126 $\Omega \cdot \text{cm}$, the

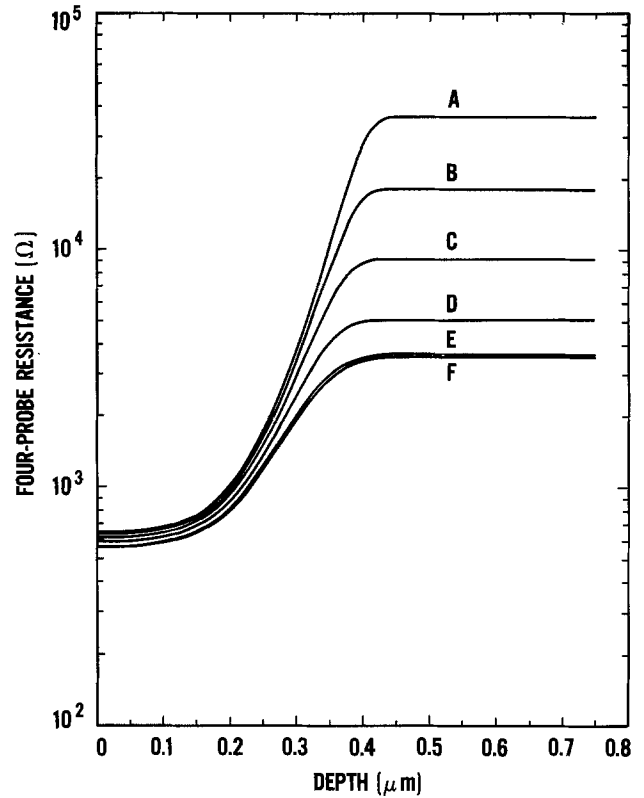


Fig. 5. The behavior of $\pi Z(x,S)/\ln(2)$ for the shallow implant into a 126.46 $\Omega \cdot \text{cm}$ substrate. The substrate is 350 μm thick. The values of S and the corresponding curves are: A = 25 μm , B = 50 μm , C = 100 μm , D = 200 μm , and E = 500 μm . The curve denoted by F is the corresponding four-probe sheet resistance calculated according to Eq. [8].

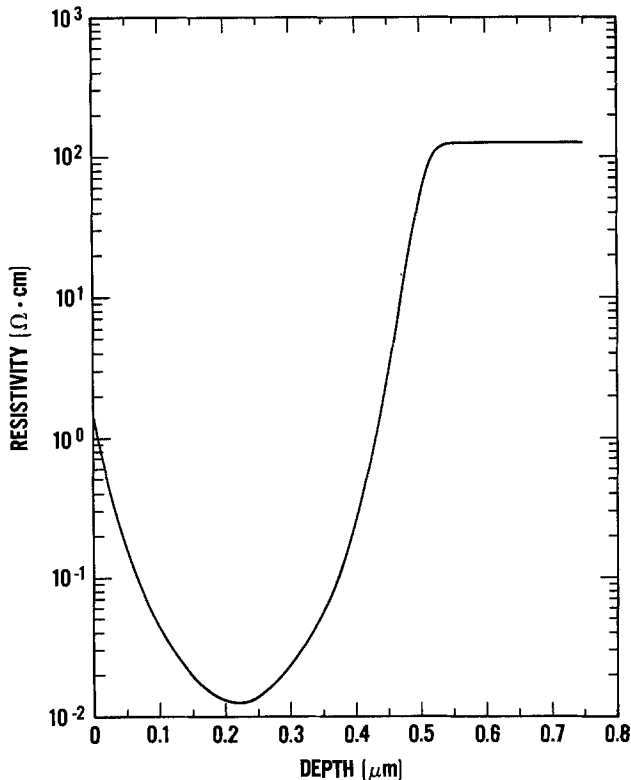


Fig. 4. Typical plot of the resistivity profile used in the calculations of the text. The specific structure is that of a shallow implant into a 126.46 $\Omega \cdot \text{cm}$ substrate.

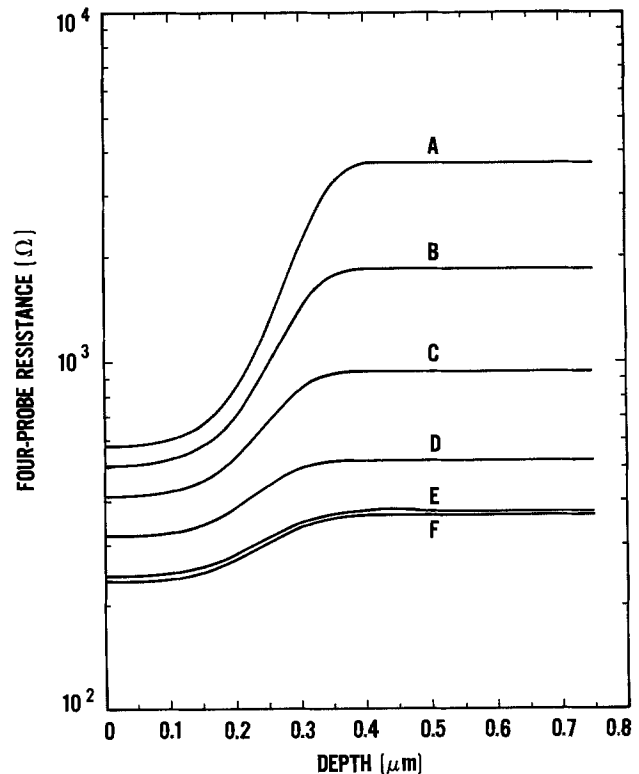


Fig. 6. The S -behavior of $\pi Z(x,S)/\ln(2)$ for a shallow implant into a 12.82 $\Omega \cdot \text{cm}$ substrate. The notation as to the S values and the corresponding curves follows that of Fig. 5.

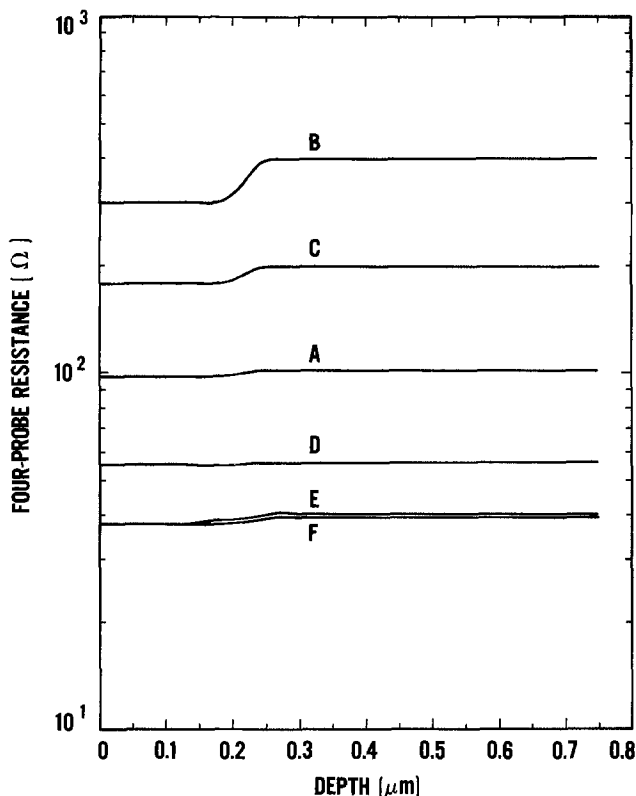


Fig. 7. The S behavior of $\pi Z(x,S)/\ln(2)$ for a shallow implant into a $1.38 \Omega \cdot \text{cm}$ substrate. The notation follows that of Fig. 5 and 6.

Dickey conjecture will hold. As the substrate resistivity decreases from 126 to $12.82 \Omega \cdot \text{cm}$ (from Fig. 5 to Fig. 6), the effects of substrate shorting are clearly evident. In Fig. 6, the dependence of $Z(x,S)$ on S in the surface region has much the same behavior as is observed in the substrate region. There is a distinct advantage in using a small probe spacing; there is more information about the layer in $Z(x,S)$ for small values of S . Finally, as the substrate resistivity is further decreased from 12.82 to $1.38 \Omega \cdot \text{cm}$ (from Fig. 6 to Fig. 7), the effects of substrate shorting are so severe that it is doubtful that even at the smallest spacing that there would be sufficient resolution in $Z(x,S)$ to recover much information about the implanted surface layer.

For the intermediate substrate resistivity case, *i.e.*, for those cases where the substrate value of $Z(x,S)$ minus the surface value of $Z(x,S)$ is significant, the effect of the substrate can be eliminated. This may be done by using the equation

$$Z_{\text{eff}} = \frac{Z_S Z}{Z_S - Z} \quad [12]$$

where Z_{eff} is the value of Z expected at the surface for an insulating substrate and Z_S is the substrate value of $Z(x,S)$. This formula assumes that the layer four-probe resistance can be added in parallel.

For all of the cases considered, the four-probe resistance was found to be independent of the probe-current density and the probe radius used in the calculations. The four-probe resistance was found to depend only upon the resistivity profile. This forms the basis of the calibration procedure presented below.

Calibration of Spreading Resistance Profile Data

A common difficulty associated with the analysis of spreading resistance profile data arises from the fact that the classical relation between the spreading resistance and the resistivity for a uniform material, *i.e.*

$$R = \frac{\rho}{2a} \quad [13]$$

is, in general, not adequate, in that the probe radius (a) may be a function of the resistivity of the material. There are a number of methods which are currently used to account for this difficulty. First, there is the suggestion that a series surface barrier resistance must be included. Second, on purely arbitrary grounds, the empirical formula (11)

$$R = \frac{\rho^m}{2a} \quad [14]$$

is used with the value of a determined from the fit of the curve evaluated at $1 \Omega \cdot \text{cm}$. Third, the probe radius is assumed to be a function of the resistivity, and the form of the function should be obtained from measurements on a series of uniform calibration samples. However, the point of view which is adopted here is that the so-called probe radius (a) is merely a model-dependent parameter to account for the fact that the current density near the pressure contact of a spreading resistance probe is, in general, not known. Inasmuch as the analysis techniques currently used assume a single form of the probe current density, regardless of the details of the resistivity profile in the material, it is clear that the entire idea of a probe radius as a physically measurable quantity must be abandoned. In its place, a self-consistent technique for obtaining the adjustable parameter (a) which makes no assumptions about the physical interpretation of the parameter is proposed. The basis of the technique being proposed is founded in the fact that the function $Z(x,S)$ is independent of the parameter a as well as the details of the current injection process, *i.e.*, the probe-current density. It depends only upon the resistivity profile. The resistivity profile obtained from spreading resistance data analysis is, however, dependent upon the choice of the parameter a . Hence, the four-probe resistance obtained from resistivity profiles interpreted from spreading resistance data will depend indirectly upon the choice of a used in the spreading resistance data analysis.

In this section, the rationale for such a self-consistent calibration scheme and a detailed description of the procedure to be used are presented. It is important to note that this method is based upon the four-probe resistance rather than the sheet resistance. The former quantity has more general significance, and there is no necessity to restrict the application to junction-isolated structures.

An outline of this method is as follows. First, the spreading resistance is measured as a function of the probe spacing on the top surface of the sample being profiled and is fit (using polynomial regression analysis, for example) to a curve representing the spreading resistance as a function of probe spacing. Then, by using a value of the probe spacing which affords maximum sensitivity to the interesting portion of the dopant profile (by choosing the region of Fig. 3 where the function $Z(x,S)$ is proportional to ρ), $Z(x,S)$ is calculated from $R(x,S)$ and $R(x,2S)$ according to Eq. [5]. Second, the sample is beveled, and the spreading resistance is measured as a function of depth (*i.e.*, along the bevelled surface) for the same value of S used to calculate $Z(x,S)$. Third, using a multilayer analysis scheme, the resistivity profile is calculated from the spreading resistance profile for several values of the parameter a . Of course, these should be in a range of values which would be considered to be reasonable. Fifth, these resistivity profiles (which depend parametrically upon the set of a values) are used to determine $Z(S;a)$ according to Eq. [2]. The notation $Z(S;a)$ is used to denote the calculated four-probe resistance which depends indirectly upon a through the interpreted resistivity profiles. Sixth, by interpolation, the calculated $Z(S;a)$ which agrees with the measured four-probe resistance (from the first step) is found. The value of a thus determined represents

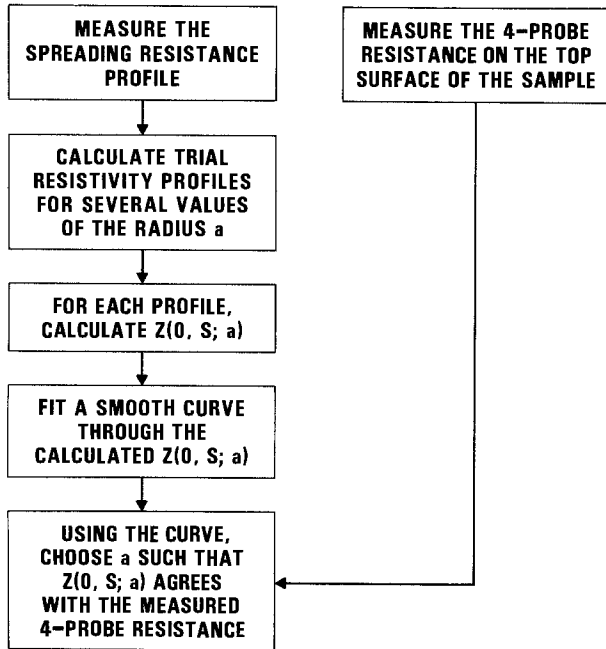


Fig. 8. Schematic diagram of calibration procedure

the self-consistent value of a for the profile in question. This calibration procedure is graphically summarized in Fig. 8.

To determine the sensitivity of this procedure in the evaluation of the probe radius parameter, this method was tested on model spreading resistance data. The model data were generated from the resistivity profiles employed to calculate the $Z(x, S)$ data presented in Fig. 5-7. In all cases, the Choo uniform current density was used along with a probe radius of $a = 2 \mu\text{m}$. The surface values of the spreading resistance, $R(0, S)$, was expressed in terms of a polynomial in S by means of a standard polynomial least-squares fitting routine. A typical plot of $R(0, S)$ vs. S is given in Fig. 9. The spreading resistance as a function of depth and for a fixed value of the probe spacing was then analyzed according to the Berkowitz-Lux correction factor scheme (9) as well as the Dickey local-slope technique (1). This analysis was carried out for a values over the range of 1 to $3 \mu\text{m}$. Typical

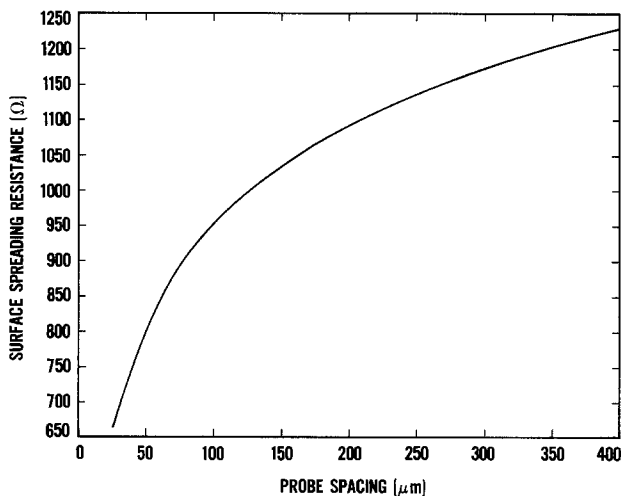


Fig. 9. The surface value of the calculated spreading resistance as a function of the probe separation. The specific structure is that of the shallow implant into a $126.46 \Omega \cdot \text{cm}$ substrate. It is this curve which is fitted by means of a polynomial fit and used to calculate the surface value of $Z(x, S)$ according to Eq. [5].

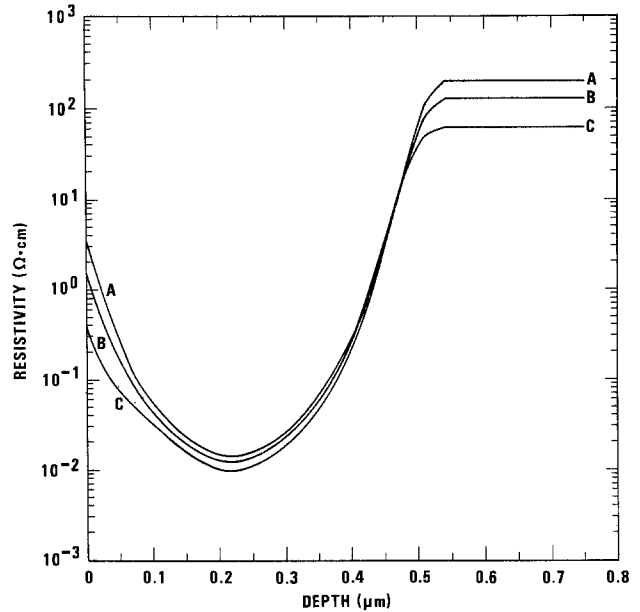


Fig. 10. The effect of the choice of the value of a upon the interpreted resistivity profile. The specific structure is that of the shallow implant into a $126.46 \Omega \cdot \text{cm}$ substrate. The values for a are $A = 3 \mu\text{m}$, $B = 2 \mu\text{m}$, and $C = 1 \mu\text{m}$. The probe spacing is $25 \mu\text{m}$. It should be noted that the qualitative features of the profiles are not sensitive to the choice of a and that variation of a has the effect of shifting the profiles up and/or down. The Berkowitz-Lux correction factor scheme has been used to obtain these resistivity profiles.

resistivity profiles which depend parametrically upon the choice of the value of a are shown in Fig. 10. The corresponding resistivity arrays, $\rho(x; a)$, which depend parametrically upon the choice of a value, were used in the 1250-point integration scheme to obtain the corresponding four-probe resistance denoted by $Z(x, S; \rho[x; a])$. The surface values of these four-probe resistances were then graphically compared with the surface four-probe value determined from the polynomial-fitted $R(0, 2S)$ and $R(0, S)$. Figure 11 contains the results of a typical plot of the surface value of the four-probe resistance against the assumed value of the probe-radius parameter for the case of $S = 25 \mu\text{m}$. From the plot, it is clear that the curvature is

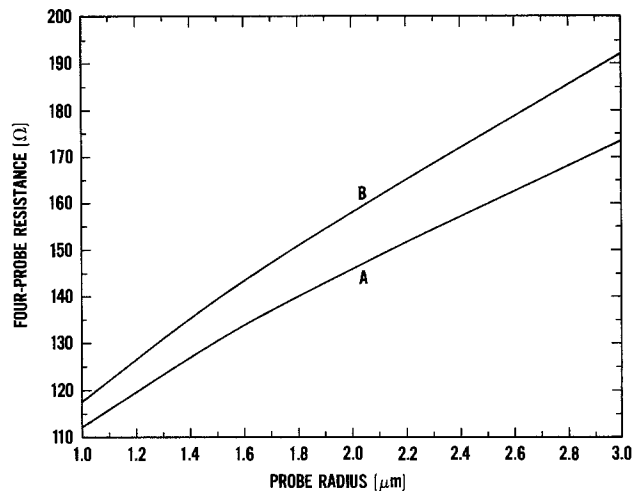


Fig. 11. Typical plot of the dependence of the surface four-probe resistance on the probe radius used in the analysis of the model spreading resistance data. Curve A is that obtained from the Berkowitz-Lux correction factor scheme, while curve B is that obtained from the Dickey local slope technique. The former yields $a = 2 \mu\text{m}$, while the latter yields $a = 1.7 \mu\text{m}$. The value of the probe spacing is $S = 25 \mu\text{m}$.

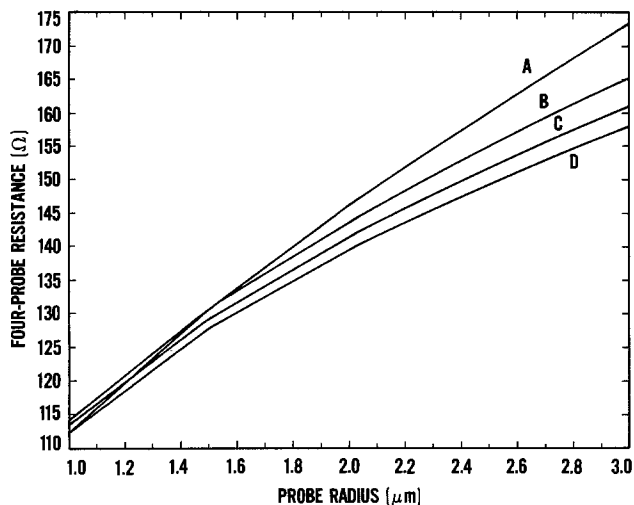


Fig. 12. A series of plots of the results of the calibration investigation for several values of the probe spacing. The values of the probe spacings and the corresponding curves are: $S = 25 \mu\text{m}$ (A), $S = 50 \mu\text{m}$ (B), $S = 75 \mu\text{m}$ (C), and $S = 100 \mu\text{m}$ (D). In all cases, the Berkowitz-Lux correction factor scheme was used.

sufficient to provide sensitivity and yield the value of $a = 2 \mu\text{m}$, which was originally used in the generation of the spreading resistance. In addition, to show that the sensitivity is not degraded by variation of the probe spacing, the results of the analysis for several values of the probe spacing are presented in Fig. 12. It is important to emphasize that the curvature must be sufficient to provide for the evaluation of the value of a . Should the curve be found to be flat, this would preclude the use of this procedure.

Conclusions

A derivation for the four-probe resistance $Z(x, S)$ and its relation to the two-probe spreading resistance $R(x, S)$ has been presented. The calculation of $Z(x, S)$ for a wide range of resistivity structures and probe

separation has been presented and discussed. It was shown that the sheet resistance, $R(x)$, is obtained from $Z(x, S)$ for isolated structures with $S/x > 1$. In addition, it was shown that the function $Z(x, S)$ can be used to self-consistently obtain the probe radius parameter (a) used in spreading resistance profile analysis.

Acknowledgments

The authors would like to thank James R. Ehrstein and R. A. Lux for a number of useful discussions. This research was conducted as part of the NBS Semiconductor Technology Program and the U.S. Army Electronics Technology and Devices Program (ERADCOM).

Manuscript submitted Jan. 11, 1983; revised manuscript received Aug. 1, 1983.

The National Bureau of Standards assisted in meeting the publication costs of this article.

REFERENCES

1. D. H. Dickey and J. R. Ehrstein, NBS Special Publication 400-48, pp. 15-18 (1979).
2. J. Albers, *This Journal*, **129**, 599 (1982).
3. J. Albers, *ibid.*, **129**, 2788 (1982).
4. J. Albers, *Solid-State Electron.*, **23**, 1197 (1980).
5. H. L. Berkowitz and R. A. Lux, *This Journal*, **126**, 1479 (1979).
6. P. A. Schumann and E. E. Gardner, *ibid.*, **116**, 87 (1969).
7. E. E. Gardner and P. A. Schumann, *Solid-State Electron.*, **12**, 371 (1969).
8. Frank Bowman, "Introduction to Bessel Functions," p. 2, Dover, New York (1958).
9. H. L. Berkowitz and R. A. Lux, *This Journal*, **128**, 1137 (1981).
10. S. C. Choo, M. S. Leong, and K. L. Kuan, *Solid-State Electron.*, **19**, 561 (1976).
11. D. C. D'Avanzo, R. D. Rung, and R. W. Dutton, Technical Report 5013-2, Stanford Electronics Laboratory, Stanford University, Stanford, CA (1977).
12. D. C. D'Avanzo, R. D. Rung, A. Gat, and R. W. Dutton, *This Journal*, **125**, 1170 (1977).

Defect Characterization in Monocrystalline Silicon Grown Over SiO_2

J. T. McGinn,* L. Jastrzebski,* and J. F. Corboy

RCA Laboratories, Princeton, New Jersey 08540

ABSTRACT

Crystallographic defect structures in monocrystalline silicon films grown over SiO_2 layers have been characterized by cross-section and planar transmission electron microscopy. Overgrowths of epitaxial silicon films on SiO_2 layers have been seeded from single crystal substrates through openings in the SiO_2 layers. Defect structures have been studied as a function of substrate orientation, seeding procedure, and growth temperature. Defect densities have been dramatically reduced through first-order optimization of the above parameters.

Single crystal growth over amorphous substrates has received considerable attention recently (1-8). Such structures are potentially useful in the area of solid-state device fabrication. Successive overgrowth of silicon above silicon oxide may make possible the fabrication of three-dimensional devices. A number of approaches have been attempted in an effort to achieve a uniform, defect-free overgrowth of monocrystalline silicon above an amorphous insulator such as SiO_2 . These approaches may be divided into the two general categories of seeded (5-8) and unseeded (1-4) growth. In the case of the seeded growth, a single crystal seed

* Electrochemical Society Active Member.

of the desired orientation is in contact with an amorphous or polycrystalline silicon film which has been deposited upon an amorphous, insulating layer. If it is possible to preferentially melt the deposited silicon film in the vicinity of the single crystal seed, crystallization of the melt from the seed can occur via liquid phase epitaxy. Various techniques have been adopted to optimize the crystallization process. The most successful have been the scanning laser technique (5, 6) and the strip heater method (7, 8). Large grains of unseeded silicon have been shown to spontaneously result from the laser annealing of amorphous or polycrystalline films on SiO_2 subbing layers (4). The un-

seeded technique for producing monocrystalline films over amorphous layers is referred to as graphoepitaxy (1-3). In this technique, the surface of the amorphous layer is patterned with a series of grooves. The groove morphology and the pattern geometry are specifically tailored to induce nucleation of a deposited silicon film with a specific orientation (2).

The seeded technique mentioned above requires that the silicon films be elevated to a temperature above their melting point. If it is desired to fabricate three-dimensional device structures, such high temperatures could produce an undesirable redistribution of impurities in those devices which had been buried below the insulating layer. In the unseeded technique, graphoepitaxy, considerable difficulty has been encountered in attempts to produce high-quality silicon films.

Due to the difficulties inherent in the above techniques, an alternative approach of producing single crystal silicon overgrowths via seeded chemical vapor deposition (CVD) has been attempted by Jastrzebski *et al.* (9) and McGinn *et al.* (10). Similar work has been done with GaAs overgrowth by Mellend *et al.* (11). This paper reports the findings of a TEM examination of the microstructure of seeded silicon films grown over SiO₂ strips via a chemical vapor deposition technique.

Experimental

Samples were prepared by thermally oxidizing the surface of either (100) or (111) silicon wafers. Parallel, periodic channels were etched through the oxide exposing the underlying Si surface. The repeat distance of the remaining strips of SiO₂ was 26 μm. Samples with oxide strip widths of either 6 or 20 μm were prepared. The edge of the oxide strip was aligned along either the [01 $\bar{1}$] or [2 $\bar{1}\bar{1}$] directions on the (111) wafers and along either the [001] or [011] directions on the (100) wafers. These structures will be referred to as (hkl)-[uvw] structures indicating the (hkl) plane of the substrate and the [uvw] direction of the edge of the oxide strip. The films were grown in a radiant-heated barrel reactor. The silicon films were deposited in a series of growth-etch steps using a mixture of SiH₂Cl₂, H₂, and HCl. The gas flow rates were 0.75, 82, and 2 liters/min, respectively. Each growth step was followed by an etching step using an HCl, H₂ mixture with the same gas flow as in the growth step (9). These growth conditions were designed to suppress the growth of polycrystalline silicon over the oxide while permitting the growth of single crystal epitaxial silicon. The epitaxial Si grew up through the channel openings and then proceeded to expand laterally across the surface of the SiO₂. Cross sections for TEM studies were cut either normal to the substrate surface or along a {111} plane inclined to both the substrate surface and the oxide strip in order to enhance the visibility of certain crystallographic defects. Shear stress measurements taken in the silicon overgrowth were accomplished by measuring the deviation from orthogonality in a symmetric 001 selected area transmission electron diffraction pattern (14).

Observations

In samples prepared from (111) Si wafers, the channels in the SiO₂ layer were etched along either [01 $\bar{1}$] or [2 $\bar{1}\bar{1}$] directions. Defects in the silicon overgrowth were observed for all strip width and channel orientations. When the channels were etched along [01 $\bar{1}$] directions, an asymmetry in the fault structure about the center of the SiO₂ strips was observed as shown in Fig. 1. In this configuration, the overgrowth above the left side of the oxide strip was twin related to the substrate while the overgrowth above the right side retained the substrate orientation. Beyond the right edge of the oxide strip, irregular twins formed pockets

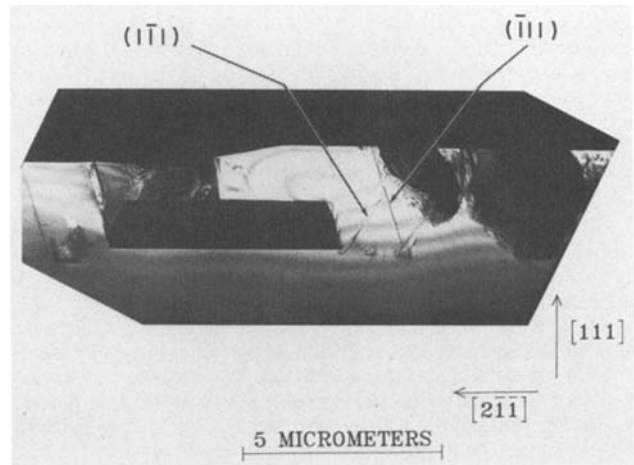


Fig. 1. Lateral overgrowth viewed in cross section above a (111) silicon wafer. The oxide strip runs along the [011] direction. The fault structure is unsymmetrically distributed about the center plane of the oxide strip. A (111)-[01 $\bar{1}$] structure.

in the epitaxial silicon extending from the surface to the substrate overgrowth interface.

When the channels were etched along [2 $\bar{1}\bar{1}$] directions over (111) wafers, the defect structure did not display the asymmetry of the (111)-[01 $\bar{1}$] samples. Figure 2 shows an incomplete overgrowth of a (111)-[2 $\bar{1}\bar{1}$] sample. Here the growth was stopped just as the two growth fronts met above the center of the oxide strip. The overgrowth in this case retained the orientation of the substrate above both sides of the oxide strip. Numerous microtwins are present within the overgrowth as are bands of dislocations, but the asymmetry in twin structures observed in the (111)-[01 $\bar{1}$] sample is absent.

In samples prepared from (100) silicon wafers, the channels in the SiO₂ layer were etched along either [011] or [001] direction. When channels were etched along [011] directions, the silicon which overgrew the SiO₂ was highly defective (Fig. 3). This defect region was bounded below by the oxide strip, above by the free surface, and laterally by the (1 $\bar{1}\bar{1}$) and ($\bar{1}\bar{1}\bar{1}$) planes. The predominant defect feature observed within this volume was macrotwins. Commonly 70-

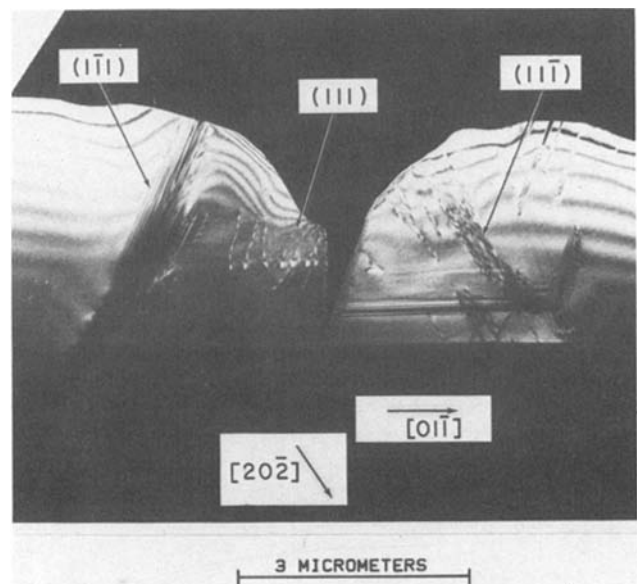


Fig. 2. Lateral overgrowth viewed in cross section above a (111) silicon wafer. The oxide strip runs along a [2 $\bar{1}\bar{1}$] direction. A (111)-[2 $\bar{1}\bar{1}$] structure.

90% of the volume of the defective region was twin related to the substrate. Microtwins over the oxide were also observed. Above the center of the oxide strip, an incoherent grain boundary extended from the sample's surface to the base of the overgrowth. The boundary was presumably formed when the silicon growth fronts emanating from the two edges of the SiO_2 joined above the center of the oxide strip.

When channels in the SiO_2 layer were etched along [001] directions on (100) wafers, a dramatic improvement in the quality of the overgrowth was achieved. Above $6 \mu\text{m}$ wide oxide strips, high quality silicon was grown as in Fig. 4. A void at the base of the overgrowth above the center of the oxide strip was the only commonly observed defect. Occasionally, isolated stacking faults or microtwins were observed in the overgrowth. A grain boundary above the void where the growth fronts joined was not observed.

Silicon (100) overgrowths above $20 \mu\text{m}$ wide, [001] oxide strips displayed a wide variation in defect structures (Fig. 5¹ and 6). In highly defective samples, stacking faults lying along {111} planes, the central void and associated grain boundary and dislocation networks emanating from the edges of the oxide strip (Fig. 5) were all present. In low defect density samples, as seen in Fig. 6, only scattered dislocations and the central void were observed. On a given side of the central boundary, only two of the four possible {111} stacking fault planes were active. Across the boundary, only the remaining two {111} stacking fault planes were active. The normals to the stacking fault planes comprising an active pair are symmetrically disposed about the [001] direction (i.e., the edge of the oxide strip). On a given side of the central grain boundary, only that pair of {111} planes which forms a closed tetrahedron with the central grain boundary and the overgrowth-oxide interface was found to be active. The active pair of stacking faults to one side of the oxide are clearly displayed in Fig. 7 which was cut from a (100)-[001] sample so that the face of the cross section was a {111} plane. By imaging the region of the fault under various diffraction conditions which render the fault invisible (12, 13) it is possible to observe the dislocations in the fault plane. Applying the $\vec{g} \cdot \vec{b} = 0$ invisibility criterion, where \vec{b} is the Burgers

vector of the dislocation and \vec{g} is the diffraction vector, it was determined that the bounding dislocations and therefore the stacking faults were of the $a/6 \langle 211 \rangle$ type. Figure 8 is a planar view of the overgrowth- SiO_2 interface. The stacking faults and microtwins (presumably caused by the formation of $a/6 \langle 211 \rangle$ faults upon successive planes) are seen to have formed in pairs along two intersecting {111} planes. The line of intersection extended from the edge of the oxide through the remaining overgrowth. Each of the stacking faults extended from this line of intersection to the central void along its respective {111} plane. Also in Fig. 8, a periodic set of dislocations is seen edge on along the edges of the oxide strip. Irregularities in the interface between the overgrowth and the oxide were often visible. Occasionally, the center void was absent and an oscillatory interface was observed above the center of the oxide strip, not shown in this work. A second set of oscillations in the Si- SiO_2 interface was observed further away from the central void. These oscillations were observed as parallel contrast bands when a planar sample containing the interface was

¹ Care must be taken in analyzing Fig. 5. The plane of the cross section is a (001). The sample has been rotated in the microscope about the [100] direction to obtain the [011] view shown in Fig. 5. Under these conditions, the pairs of stacking faults to one side of the oxide will intersect the sample's surface in parallel traces. The two members of the right-side pair can be distinguished in Fig. 5 by the narrow, (111), and the broad, (111), projections they make onto the (011) plane of the micrograph. To the left of the figure the stacking faults overlap and are not individually resolvable.

imaged under dynamic conditions as in Fig. 8. These oscillations correspond in number and spacing to the

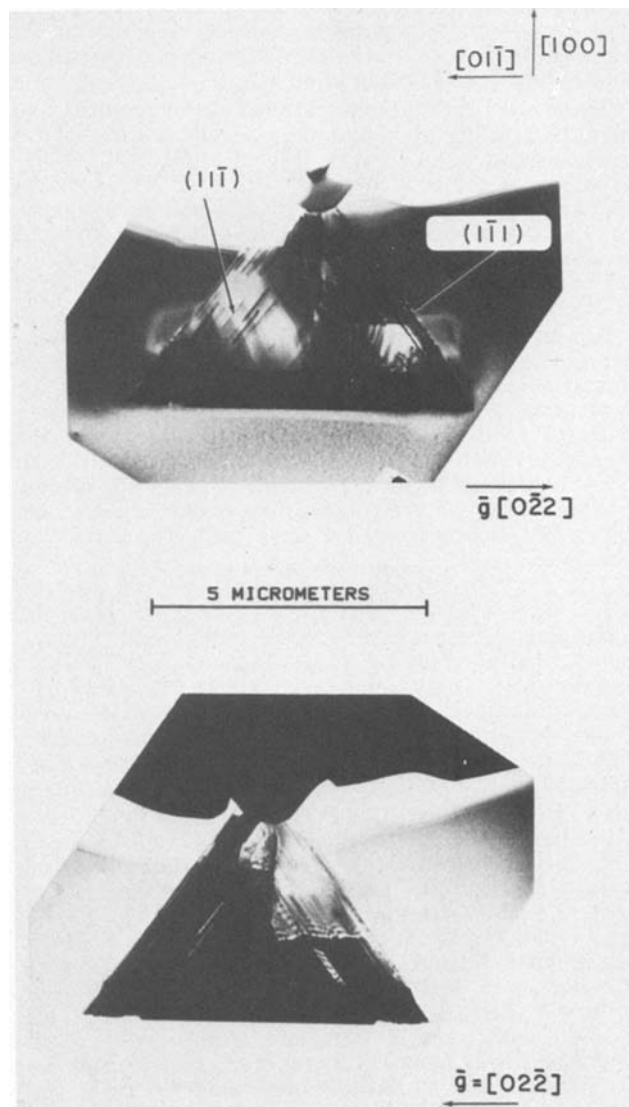


Fig. 3. Darkfield-brightfield pair of micrographs showing a cross-sectional view of a lateral overgrowth above a (100) silicon wafer with the oxide strip running along the [011] direction. A (100)-[011] structure.

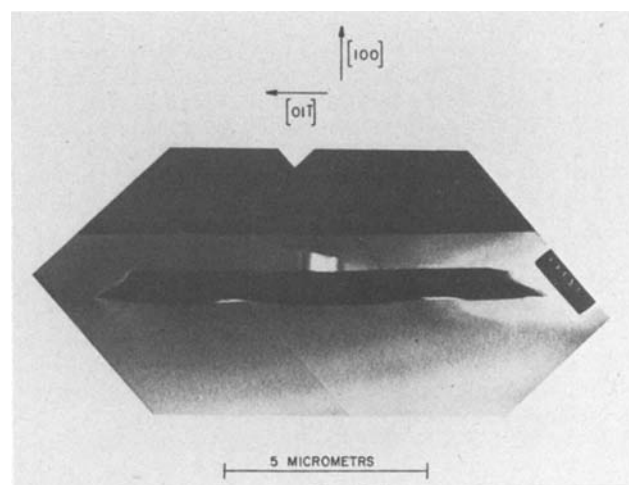


Fig. 4. A micrograph of a (100)-[001] structure above a $6 \mu\text{m}$ wide oxide strip. The faces of the cross section were cut along (011) planes.

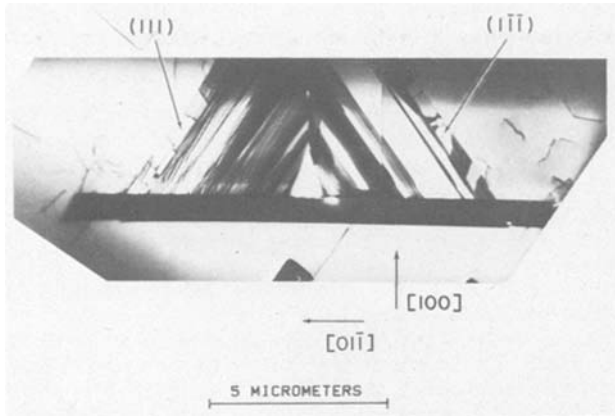


Fig. 5. A micrograph of a (100)-[001] structure above a 20 μm oxide strip. The overgrowth contains a high density of stacking faults, a central void, and grain boundary. The faces of the cross section were cut along (001) planes. The sample was rotated 45° about the [100] to obtain this micrograph.

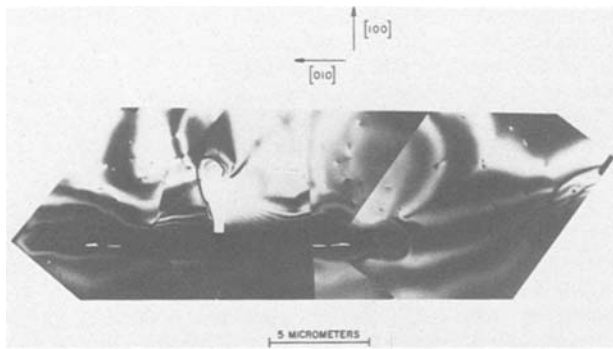


Fig. 6. A cross-sectional micrograph of a low defect density overgrowth on a (100) wafer with the oxide strip running along the [001] direction.

growth-etch cycles which occurred during the ELO deposition.

A void on the underside of the oxide strip approximately 1-3 μm from the edge of the oxide was commonly observed in the (100) samples. The voids were typically irregular in shape, but confined to the bottom of the oxide strip tending not to extend into the single crystal silicon region of the substrate (Fig. 6).

Shear stress measurements (14) were taken along the overgrowth-oxide interface in both high and low defect density samples. In the high defect density samples, the shear stress was below the detectable levels. In the low defect density samples, shear stresses of 3.6×10^9 dyn/cm² which changed sign symmetrically across the center of the oxide strips were measured.

Discussion

The specific nature of the defect generation in the overgrowth film has been shown to be highly sensitive to the crystallographic orientation of both the substrate and the edge of the oxide strip. This may be understood in the case of the ELO films grown on (100) wafers if these orientations are considered relative to the slip planes in silicon as well as the directions in which a dislocation must run in order to be in a minimum energy configuration.

A number of mechanisms may induce stress in the overgrowth: (i) A slight misalignment of the ELO film as it expands over the oxide layer would prevent perfect atomic bonding of the two growth fronts as coalescence occurs. Such misalignments whether leading to distorted atomic bonds or to a low angle grain boundary at the point of coalescence would inevitably result in internal stresses. (ii) Stress may result from

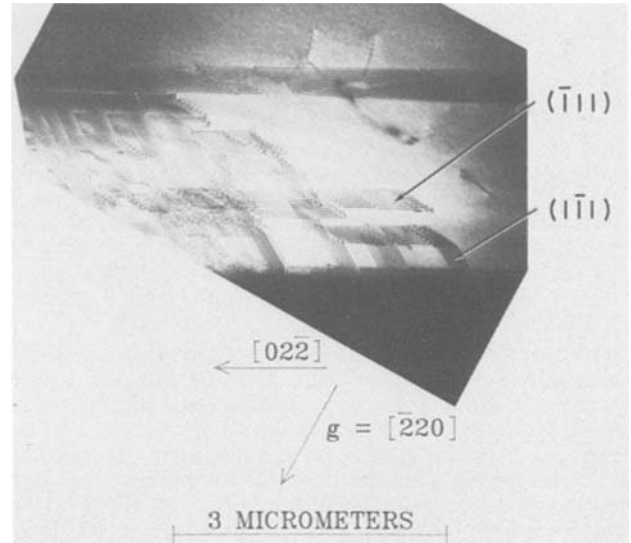


Fig. 7. The two active sets of stacking faults to one side of the oxide strip are observable. This sample is an inclined cross section of a (100)-[001] specimen. The faces of the cross section were cut along the (111) plane,

thermal gradients during cooling, or (iii) to differences in the thermal coefficients of expansion between silicon and SiO₂. The disposition of these internal stresses relative to the {111} slip planes and the <110> directions will strongly influence the deformation mechanisms available for the relaxation of the crystal.

In samples prepared on (111) wafers with the oxide running along a [011̄] direction, the microstructure was asymmetric about the center of the SiO₂ strip. The fabricated structure, consisting of the oxide strip and the neighboring channels, contained a plane of mirror symmetry which is perpendicular to the plane of the substrate and passes through the center line of the

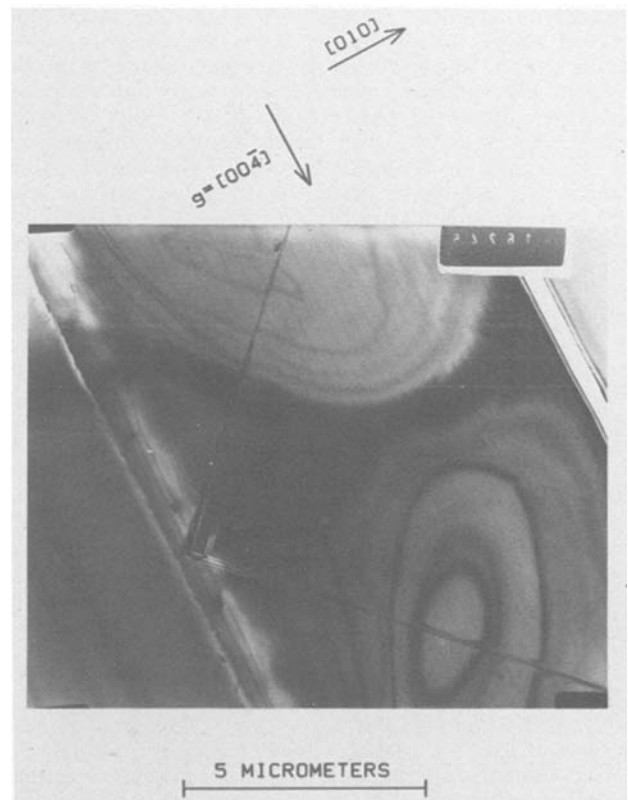


Fig. 8. Planar view of the overgrowth-oxide interface in a (100)-[001] sample.

oxide strip. This is a $(2\bar{1}\bar{1})$ plane in the silicon. Since the $(2\bar{1}\bar{1})$ plane is not crystallographically a mirror plane, symmetric stresses imposed on the two sides of the oxide strip would not be expected to be relieved by identical processes. Extensive evaluation of the ELO films on (111) silicon have not been carried out due to the poor prospects for achieving defect-free material. No attempt has been made to formulate a mechanism for fault formation within the ELO layers grown over (111) substrates. It is simply noted that the observed faults were consistent with the symmetries imposed by the crystallography and the fabricated structures.

In samples grown over (100) wafers with the oxide strips along [011] directions, internal stresses which occurred during growth or subsequent cooling were ideally situated to nucleate dislocations. Internal stress risers, such as the edges of the oxide strip, oscillations in the silicon-SiO₂ interface, the central grain boundary and associated void, all ran along the [011] direction and were possible sites for nucleation of perfect, low-energy dislocations. Once nucleated, these dislocations would have been free to glide along either the $(11\bar{1})$ or $(\bar{1}\bar{1}1)$ planes.

When the oxide strip ran along a [001] direction on a (100) substrate, the lines of high internal stress did not coincide with a direction along which dislocations could be easily nucleated. Any dislocation lying along a [001] direction would have been in a high-energy state and thus would have required a high internal stress for nucleation. In cases where sufficient internal stress existed for dislocation nucleation, along an edge, the experimental results suggest that these dislocations were the source of the active pair of stacking faults which originate at the edge. If these dislocations were to act as a source of the pairs of stacking fault which are shown in Fig. 7 and 8, the Burgers vector of the dislocation would by necessity be limited to that direction which could slip in both of the active stacking fault planes.

The proposed model for stacking fault generation is consistent with the nature of the stacking faults observed above the oxide on (100) samples with [001] oxide strips. Shear strain measurements made in the overgrowth indicated that samples with low stacking fault densities had shear strains of 3.6×10^9 dyn/cm² while the shear strain in highly faulted samples was below detectable limits. This suggests that the stacking faults are generated as a strain relief mechanism. Stacking faults may originate at a number of locations where the local strain would be expected to be high. Namely, the overgrowth-oxide interface and the grain boundary above the center of the oxide strip would be points of high internal strain. The model for stacking fault generation given above has used the edge of the Si/SiO₂ interface as the site of nucleation. At the Si/SiO₂ interface, strain is generated due to the differences in the thermal expansion coefficients across that interface. In addition, the edges of the oxide as well as the undulations in the Si/SiO₂ interface may act as stress risers.

Another possible model is that along the central grain boundary, local atomic rearrangements necessary to accommodate the lattice mismatch between the coalesced growth fronts produced strains sufficient to nucleate stacking faults. If stacking fault nucleation were to occur along the central grain boundary at a height of more than half the width of the oxide, the resulting stacking fault would then be free to extend beyond the edge of the oxide strip. This is a consequence of the fact that the apex formed by the pair of active stacking faults lies along a $\langle 101 \rangle$ direction which is inclined at 45° to the surface of the oxide. It should be noted that a stacking fault extending beyond the edge of the oxide has never been observed. The

major stacking faults emerge from a narrow region near the edge of the oxide strip. In addition, stacking faults have been observed in overgrowths which do not contain central grain boundaries. These observations suggest that a heterogeneous nucleation along a line at the edge of the oxide was the active mechanism for fault formation rather than the homogeneous nucleation of the faults over the face of the central grain boundary. The origin of the grain boundary is unclear. The boundary may have been formed due to a misalignment of the two coalescing growth fronts or as a result of plastic deformation after a continuous overgrowth had formed.

A central void is found above the middle of the oxide strip and coincides with the bottom of the grain boundary discussed above in (100) [001] samples. The origin of the void is presumably related to the inhibition of the transport of the silicon bearing species, in the gas phase, to the surface of the oxide strip just prior to the coalescence of the advancing growth fronts. The shape of the growth fronts will depend upon the growth conditions of the CVD process as well as the crystallographic orientation of the advancing faces. Presumably, the growth fronts in the (100)-[001] samples form almost vertical walls (15) which inhibit the transport of the silicon species to the bottom of the canyon formed by these walls just prior to coalescence. This reduced access of the silicon species, in the gas phase, to the oxide surface may account for the decrease in the separation of the growth striations as the center of the oxide strip is approached in Fig. 8.

Conclusions

The seeded overgrowth of Si via CVD on strips of SiO₂ above single crystal Si substrates has been shown to be a viable process for the production of device grade Si films. The fault structures of the Si overgrowth can be strongly influenced by the choice of a number of crystallographic parameters such as substrate and oxide strip edge orientation.

The stacking faults which are generated in the overgrowth of (100) substrates with the oxide strips along [001] directions appear to arise as mechanisms of strain reduction. The strain is presumably introduced as a result of the differences in the thermal coefficients of expansion between the Si overgrowth and the SiO₂ strips. It is suspected that the faults are generated during the cooling of the structures after the overgrowths are formed. A number of practical steps may be taken in order to further reduce the internal strain experienced by the Si overgrowth. These include the following: (i) use of thinner insulating films, (ii) tailoring the edges of the insulating film to reduce the local strains at those points, (iii) matching the thermal expansion coefficients of the insulating layer more closely to that of the Si overgrowth, and (iv) reduction of the growth temperature to minimize the differences in thermal expansion between the overgrowth and the encapsulated oxide.

Manuscript submitted Sept. 30, 1982; revised manuscript received Oct. 27, 1983.

RCA Laboratories assisted in meeting the publication costs of this article.

REFERENCES

1. M. W. Geis, D. A. Antoniadis, D. J. Silverworth, R. W. Mountain, and H. I. Smith, *Appl. Phys. Lett.*, **37**, 454 (1980).
2. M. W. Geis, D. C. Flanders, H. I. Smith, and D. A. Antoniadis, *J. Vac. Sci. Technol.*, **16**, 1640 (1979).
3. M. W. Geis, D. C. Flanders, and H. I. Smith, *Appl. Phys. Lett.*, **35**, 71 (1979).
4. N. M. Johnson, D. K. Biegelsen, and M. D. Moyer, *ibid.*, **38**, 900 (1981).
5. J. Sakurai, S. Kawamura, H. Muri, and M. Nakano, *Jpn. J. Appl. Phys.*, **20**, L176 (1981).
6. T. I. Kamins, T. R. Cass, C. J. Dell'Oca, K. F. Lee,

- R. F. W. Pease, and J. F. Gibbons, *This Journal*, **128**, 1151 (1981).
7. J. C. C. Fan, M. W. Geis, and B.-Y. Tsaur, *Appl. Phys. Lett.*, **38**, 365 (1981).
 8. J. C. C. Fan, M. W. Geis, and B.-Y. Tsaur, International Electron Device Meeting, Technical Digest, 845 (1980).
 9. L. Jastrzebski, J. F. Corboy, and R. H. Pagliaro, Jr., Abs. 149, p. 242, The Electrochemical Society Extended Abstracts, Vol. 82-1, Montreal, Quebec, Canada, May 9-14, 1982.
 10. J. T. McGinn, L. Jastrzebski, and J. F. Corboy, Abs. 152, p. 246, The Electrochemical Society Extended Abstracts, Vol. 82-1, Montreal, Quebec, Canada, May 9-14, 1982.
 11. A. Mellend, C. Bozler, and J. C. C. Fan, *Appl. Phys. Lett.*, **37**, 560 (1980).
 12. P. B. Hirsch, A. Howie, R. B. Nicholson, D. W. Pashley, and M. J. Whelan, "Electron Microscopy of Thin Crystals," p. 234, Butterworths, London (1965).
 13. J. W. Edington, "Practical Electron Microscopy in Materials Science," p. 145, Van Nostrand Reinhold Co., London (1976).
 14. M. S. Abrahams, J. Blanc, C. J. Buiocchi, and W. E. Ham, *J. Appl. Phys.*, **49**, 652 (1978).
 15. L. Jastrzebski, J. F. Corboy, J. T. McGinn, and R. Pagliaro, Jr., *This Journal*, **130**, 1571 (1983).

Void Formation in Phosphosilicate Glass Film with Heat-Treatment in H₂ Atmosphere

Hideaki Takeuchi and Junichi Murota

Nippon Telegraph and Telephone Public Corporation, Musashino Electrical Communication Laboratory, Musashino, Tokyo, 180 Japan

ABSTRACT

The void formation process and phosphorus behavior in phosphosilicate glass film deposited by chemical vapor deposition techniques were investigated. The films were heat-treated three times, first in N₂ atmosphere for densification, then in H₂ or N₂ atmosphere, and after that in N₂ atmosphere. It was found that (i) void formation takes place with the third heat-treatment in N₂ atmosphere, (ii) with the second heat-treatment in H₂ atmosphere, absorbance of P=O band at 1330 cm⁻¹ decreases and absorbance of band at 1250 cm⁻¹ increases, but further absorbance change does not take place with the third heat-treatment. The gain in absorbance of the band at 1250 cm⁻¹ is proportional to the loss in absorbance of the P=O band at 1330 cm⁻¹. The quantity of phosphorus products formed with heat-treatment in H₂ atmosphere was estimated from the absorbance change of the P=O band at 1330 cm⁻¹. Comparing the quantity of the phosphorus products with the void size and number, it was proposed that the phosphorus products are gaseous species at high temperature, and the quantity of the gaseous species determines the product of the void number in the PSG film and square of the void size.

Phosphosilicate glass (PSG) films deposited by chemical vapor deposition (CVD) techniques are important materials for insulation layers in MOSLSI (1). To design a suitable MOSLSI fabrication process using the PSG film, it is necessary to clarify the structural change of the PSG film with heat-treatment in various kinds of atmosphere, because the PSG films are heat-treated under a variety of conditions for such purposes as glass flow (2), densification of the films (3), or stabilization of MOS devices (4). In a previous work (5), it was found that void formation in the PSG film and decreasing of P=O band absorbance take place simultaneously with heat-treatment in H₂ atmosphere above 1000°C. However, the causes of the void formation and the phosphorus behavior in the PSG film with the heat-treatment in H₂ atmosphere have not been clarified.

In the present work, the PSG films were heat-treated under various conditions three times to obtain an accurate relationship between the void formation and the infrared (IR) spectrum change. It was found that the void formation and IR spectrum change take place separately with sequential heat-treatment in H₂ and N₂ atmospheres. For the PSG film heat-treated in H₂ atmosphere, the void formation takes place under the subsequent heat-treatment in N₂ atmosphere. Absorbance of P=O band at 1330 cm⁻¹ decreases, and absorbance of band at 1250 cm⁻¹ increases, indicating formation of phosphorus products with the heat-treatment in H₂ atmosphere. However, further absorbance change does not take place with the subsequent heat-treatment in N₂ atmosphere. Void size and number are compared with a gain in the phosphorus product

quantity, and the void formation mechanism in the PSG films is discussed.

Experimental

The PSG films were deposited at 420°C in a horizontal reactor using a SiH₄-PH₃-O₂-N₂ gas system and then densified with the first heat-treatment in N₂ atmosphere at 1000°C. The film thickness (T_{PSG}) was about 5600Å after the densification. The substrates used were p-type Si wafers of 30-50 Ω cm with mirror-polished (100) surfaces. The substrates were thermally oxidized before the PSG film deposition in order to prevent phosphorus diffusion into the substrate from the PSG film (6).

After the first heat-treatment in N₂ atmosphere at 1000°C, the PSG films were heat-treated in H₂ or N₂ atmosphere at various temperatures. Then the films were heat-treated in N₂ atmosphere at temperatures higher than that of the second heat-treatment. Under these conditions, it was confirmed using x-ray fluorescence technique that the fraction of phosphorus lost is less than 3% and weight loss of the PSG film is not detected within experimental error. T_{PSG} was measured with a Taylor Hobson Talystep. The normal IR spectrum and the differential IR (DIR) spectrum of the PSG films were measured with a double-beam IR spectrophotometer. To obtain the depth profiles of absorption coefficients due to P=O bonds and Si—O bonds, measurements of the normal IR absorbance and etching of the PSG film in HF solution were repeated. The phosphorus concentration of the PSG film was determined by x-ray fluorescence techniques and neutron activation analysis. The size and the number of the void in the PSG film were obtained from observa-

tion of the PSG film cross section using a scanning electron microscope.

Results and Discussion

T_{PSG} and IR spectrum changes.—The PSG films heat-treated in H₂ or N₂ atmosphere at 900°C were next heat-treated in N₂ atmosphere for 40 min at various temperatures. Figure 1 shows the change of T_{PSG} with the third heat-treatment for the PSG film containing 9.5 weight percent (w/o) phosphorus. T_{PSG} increases with increasing the third heat-treatment temperature for the PSG film second heat-treated in H₂ atmosphere, but does not increase for the PSG film second heat-treated in N₂ atmosphere. From these results, it is expected that the second heat-treatment in H₂ atmosphere contributes to void formation in the PSG film with the third heat-treatment in N₂ atmosphere, because T_{PSG} increase is caused by the void formation (5).

The IR spectra of the PSG films were measured after the second heat-treatment in H₂ or N₂ atmosphere. No IR spectrum change was found for the PSG film heat-treated in N₂ atmosphere. The typical IR spectra of the PSG films before and after the heat-treatment in H₂ atmosphere are shown in Fig. 2. It is found that with the heat-treatment in H₂ atmosphere the absorbance of the P—O band at 1330 cm⁻¹ decreases and the absorbance of the Si—OH band at 3700 cm⁻¹ increases. The DIR spectrum was measured by placing the PSG film second heat-treated in H₂ atmosphere in the sample beam in the spectrophotometer and placing the PSG film second heat-treated in N₂ atmosphere in the reference beam of the spectrophotometer (shown in Fig. 2). Four peaks are found in the DIR spectrum: a concave peak at 1250 cm⁻¹, indicating an appearance of a new band; convex peaks at 1100 cm⁻¹ and 1000 cm⁻¹, indicating a decrease in P—O band vibration absorbance; and convex peak at 1330 cm⁻¹, indicating a decrease in vibration absorbance of P=O bond connected with three bridging oxygen atoms. Further IR spectrum change did not take place with the third heat-treatment in N₂ atmosphere at higher temperature.

From these results, it is suggested that structural change with the second heat-treatment in H₂ atmosphere causes the void formation with third heat-treatment in N₂ atmosphere at higher temperature.

Structural change in the PSG film.—To clarify the structural change in the PSG film with heat-treatment in H₂ atmosphere, a quantitative study was made of the absorbance changes of P=O band at 1330 cm⁻¹,

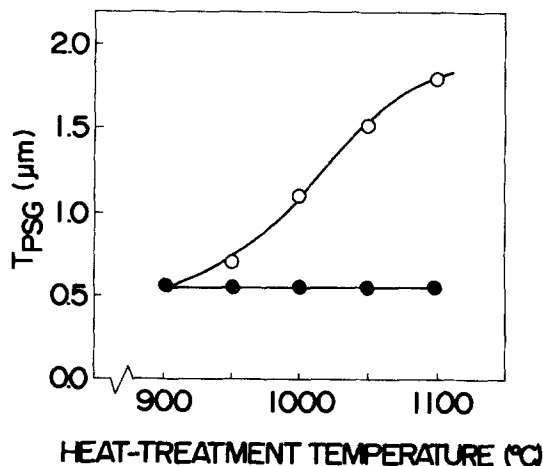


Fig. 1. Change of T_{PSG} with the third heat-treatment in N₂ atmosphere for 40 min. Open circles and closed circles are results for the PSG film second heat-treated in H₂ atmosphere and N₂ atmosphere at 900°C for 160 min, respectively. The PSG film phosphorus concentration is 9.5 w/o.

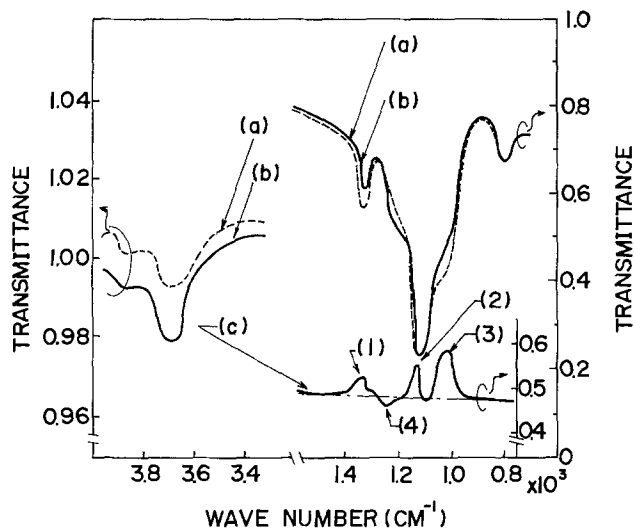


Fig. 2. IR and DIR spectra of the PSG film heat-treated in H₂ atmosphere. (a) and (b) are IR spectra of the PSG film before and after heat-treatment in H₂ atmosphere at 900°C for 160 min, respectively. (c) is DIR spectrum measured by placing the PSG film which is second heat-treated in N₂ atmosphere in the reference beam of the spectrophotometer. (1), (2), and (3) point to convex peaks at 1330, 1100, and 1000 cm⁻¹, respectively. (4) points to concave peak at 1250 cm⁻¹. The PSG film phosphorus concentration is 9.5 w/o.

P—O band at 1000 cm⁻¹, Si—OH band at 3700 cm⁻¹, and band at 1250 cm⁻¹ with heat-treatment in H₂ atmosphere. Figure 3 shows the relationship between P=O band absorbance at 1330 cm⁻¹ (*I_{P=O}*) and P—O band absorbance at 1000 cm⁻¹ (*I_{P-O}*) for the PSG film with heat-treatment in H₂ atmosphere at various temperatures. Here, the plots for the same phosphorus concentration and heat-treatment temperature were obtained for various heat-treatment times. *I_{P-O}* is proportional to *I_{P=O}*. This means that the quantity of phosphorus atoms whose bonding configuration is changed with the heat-treatment in H₂ atmosphere can be evaluated from a change in either *I_{P-O}* or *I_{P=O}*.

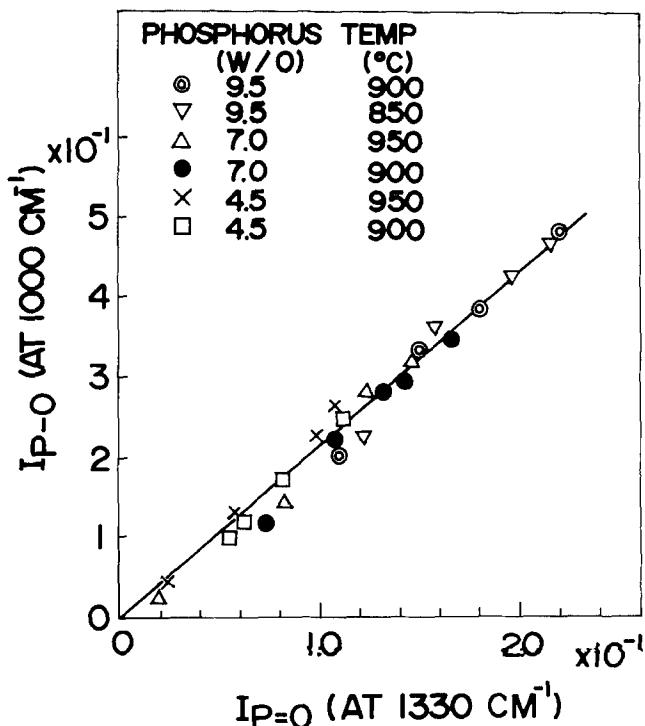


Fig. 3. Relationship between *I_{P=O}* and *I_{P-O}* with heat-treatment at various temperatures in H₂ atmosphere for various phosphorus concentrations.

Figure 4 shows the band absorbance gain at 1250 cm^{-1} (ΔI_{1250}) with heat-treatment in H_2 atmosphere as a function of the P=O band absorbance loss at 1330 cm^{-1} ($-\Delta I_{P=O}$). It is found that ΔI_{1250} is proportional to $-\Delta I_{P=O}$. Figure 4 shows Si-OH band absorbance gain ($\Delta I_{\text{Si-OH}}$) with the heat-treatment in H_2 atmosphere at 850°C for the PSG film containing 9.5 w/o phosphorus. $\Delta I_{\text{Si-OH}}$ increases with increasing $-\Delta I_{P=O}$ and then is saturated. The Si-OH bond numbers per unit volume (N_{OH}) for the PSG film with $-\Delta I_{P=O}$ of 1×10^{-1} , before and after the heat-treatment in H_2 atmosphere, are 3×10^{19} and $6 \times 10^{19} \text{ cm}^{-3}$, respectively. This is calculated from the relationship obtained by Moulson *et al.* (7) between the Si-OH band absorbance at 3700 cm^{-1} and the Si-OH bond concentration. The N_{OH} gain is $3 \times 10^{19} \text{ cm}^{-3}$ with the heat-treatment in H_2 atmosphere. This is negligibly small compared with the quantity of phosphorus atoms whose bonding configuration was changed (about 1×10^{21} , because the $-\Delta I_{P=O}$ change [1×10^{-1}] corresponds to one quarter of total phosphorus atoms [$4 \times 10^{21} \text{ cm}^{-3}$]) with the heat-treatment in H_2 atmosphere.

From these results, it is proposed that the dominant products formed in the PSG film with the heat-treatment in H_2 atmosphere are phosphorus species which have an IR absorption band at 1250 cm^{-1} . The phosphorus species may consist of a P=O bond connected with OH or H atoms, because the absorption band of P=O bond vibration shifts toward a lower frequency from 1330 cm^{-1} when bridging oxygen connected with the phosphorus in the PSG film is replaced by OH or H atoms (8). Further investigation, such as direct analysis of gaseous species in the void, is necessary to clarify the construction of the phosphorus species at high temperature.

Next, the product quantity was estimated from the P=O band absorbance loss at 1330 cm^{-1} in place of using absorption band gain at 1250 cm^{-1} in order to avoid measurement error due to the effect of other bands around the band at 1250 cm^{-1} . Figure 5 shows the heat-treatment time dependence of $I_{P=O}/I_{(P=O)_0}$ with heat-treatment in H_2 atmosphere for various phosphorus concentrations ($I_{(P=O)_0}$ is $I_{P=O}$ for the PSG film before the heat-treatment in H_2 atmosphere).

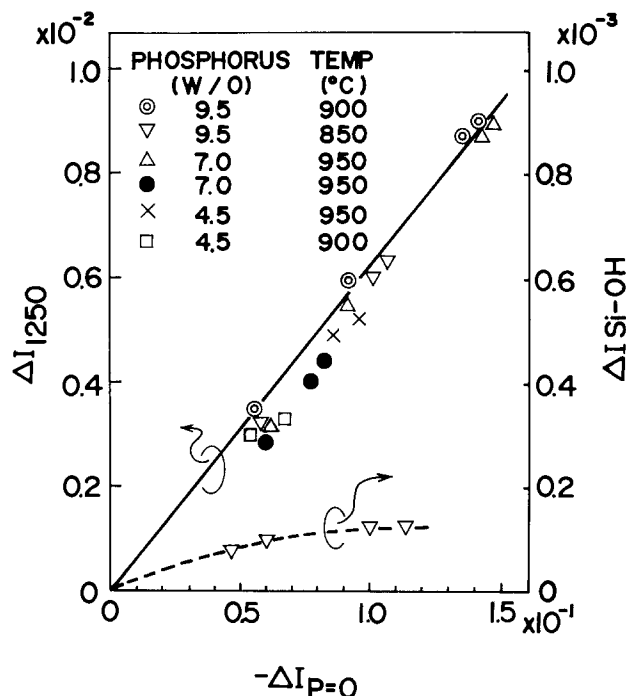


Fig. 4. $-\Delta I_{P=O}$ dependences of ΔI_{1250} and $\Delta I_{\text{Si-OH}}$ with heat-treatment at various temperatures in H_2 atmosphere for various phosphorus concentrations.

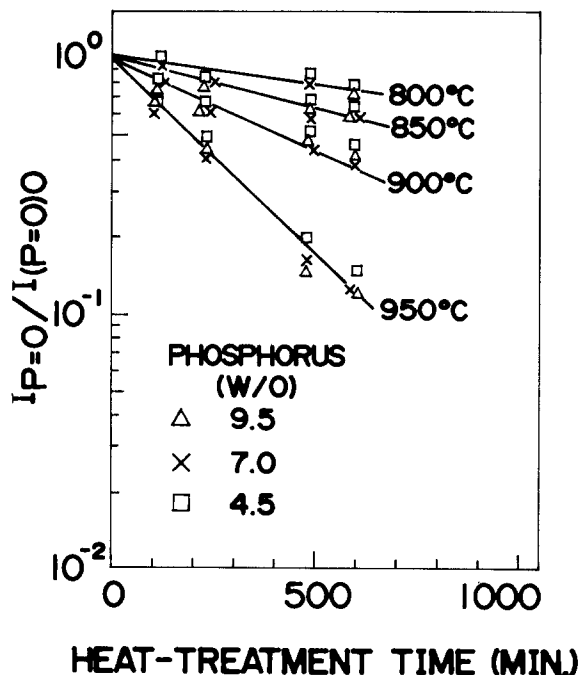


Fig. 5. Heat-treatment time dependence of $I_{P=O}/I_{(P=O)_0}$ in H_2 atmosphere for various temperatures.

$I_{P=O}/I_{(P=O)_0}$ decreases exponentially with an increase in heat-treatment time (t). Disregarding phosphorus concentration, $I_{P=O}/I_{(P=O)_0}$ is approximated by

$$I_{P=O}/I_{(P=O)_0} = \exp(-kt) \quad [1]$$

where $k = 110 \exp(-3.5 \times 10^4 \text{ cal/mol}/RT) \text{ s}^{-1}$. The absorption coefficients of the P=O band are distributed uniformly throughout the PSG film for the film heat-treated in H_2 atmosphere, as shown in Fig. 6. Therefore, the number of the products (N_P) per unit volume in the PSG film which have the absorption band at 1250 cm^{-1} , is expressed by

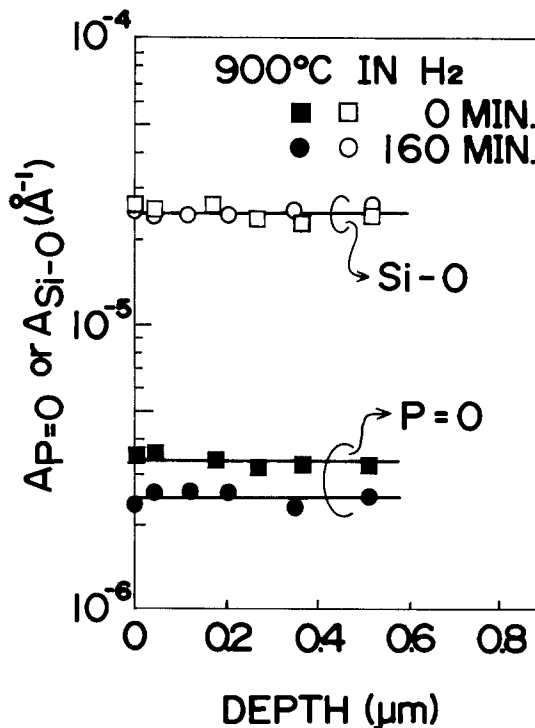


Fig. 6. Depth profiles of P=O band and Si-O band absorption coefficients ($A_{P=O}$ and $A_{\text{Si-O}}$) for the PSG film heat-treated in H_2 atmosphere at 900°C.

$$N_P = M_{(P=O)_0}(1 - \exp[-kt]) \quad [2]$$

where $M_{(P=O)_0}$ is the number of P=O bonds in the unit volume of the PSG film which is not heat-treated in H_2 atmosphere.

Relationship between void size and product quantity.

—From the results described in the previous section, it is obvious that the phosphorus product quantity is proportional to $-\Delta I_{P=O}$. In this section, $-\Delta I_{P=O}$ is compared with the size and number of voids formed with the third heat-treatment in N_2 atmosphere. The void formation mechanism is also discussed.

Figure 7 shows T_{PSG} after the third heat-treatment as a function of $-\Delta I_{P=O}$ for the PSG film containing 4.5–9.5 w/o phosphorus. T_{PSG} increases with an increase in $-\Delta I_{P=O}$ for the PSG film containing 9.5 w/o phosphorus, but T_{PSG} scarcely increases for the PSG film containing less than 7.0 w/o phosphorus. It seems that T_{PSG} increase, i.e., void formation, is inhibited by an increase in PSG-film viscosity due to reduction in phosphorus concentration. Therefore, the dependence of void size and number on $-\Delta I_{P=O}$ was investigated for the PSG film containing 9.5 w/o phosphorus, so that the effect of PSG film viscosity on void size could be neglected.

First, the variations of the void size and number with the heat-treatment in N_2 atmosphere were investigated for the PSG film whose $-\Delta I_{P=O}$ is constant. Figure 8a shows cross-sectional views of the PSG film heat-treated in N_2 atmosphere at $950^\circ C$ for various periods of time after the heat-treatment in H_2 atmosphere at $900^\circ C$ for 240 min. Many small voids are formed at the first step in the heat-treatment in N_2 atmosphere, and the voids tend to gather locally. As a result, they become larger, and T_{PSG} increases. Mean void size (L) and total void number per square centimeter (N_V) in 5600Å-thick PSG film can be obtained from Fig. 8a. The results are shown in Fig. 8b. As heat-treatment time in N_2 atmosphere increases, L increases and is saturated, and N_V decreases and becomes constant. Figure 9 shows the L dependence on N_V . It is found that L is proportional to $N_V^{-1/2}$.

Next, the L and N_V dependences on $-\Delta I_{P=O}$ were obtained for the PSG film with saturated L growth. Figure 10 shows the results with the heat-treatment in N_2 atmosphere at $950^\circ C$ for 360 min for the PSG film second heat-treated for various periods of time in H_2 atmosphere at $900^\circ C$. N_V is proportional to $-\Delta I_{P=O}$, and L is constant in spite of $-\Delta I_{P=O}$.

The relationship between L and pressure in the void

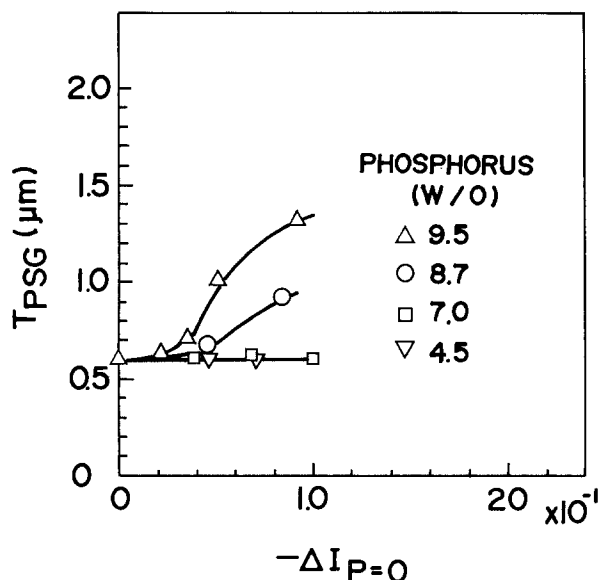


Fig. 7. Change of T_{PSG} with the second heat-treatment in N_2 atmosphere at $1000^\circ C$ for 40 min for various $-\Delta I_{P=O}$. $-\Delta I_{P=O}$ was changed with heat-treatment in H_2 atmosphere at $900^\circ C$ for various periods of time.

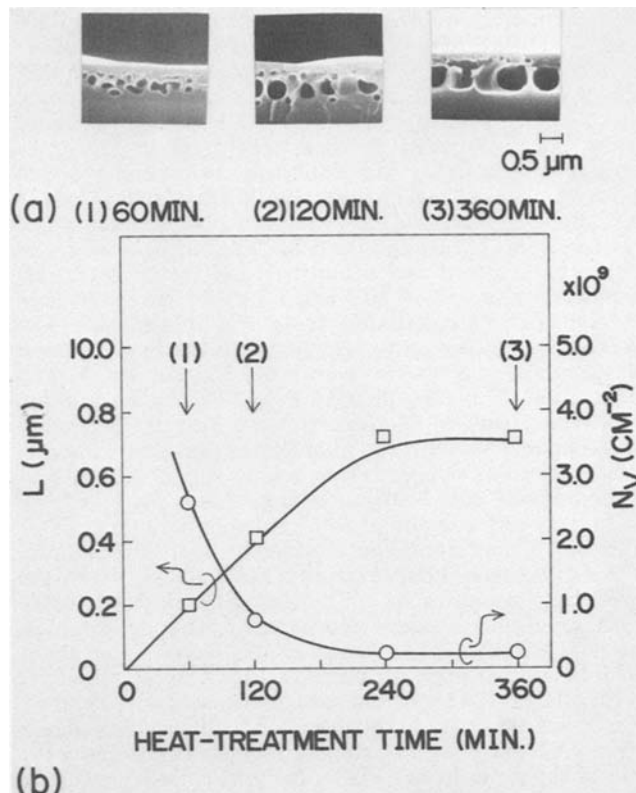


Fig. 8. Change of r and N_V with the third heat-treatment in N_2 atmosphere at $950^\circ C$ for the PSG film heat-treated in H_2 atmosphere at $900^\circ C$ for 240 min. (a) is scanning electron micrograph showing cross sections of the PSG film after the second heat-treatment and (b) is heat-treatment time dependence of r and N_V . The PSG film phosphorus concentration is 9.5 w/o.

is discussed below to explain the effect of the quantity of phosphorus products on void formation. Assuming that the voids are spherical (the radius $[r]$ is defined as $r = L/2$) and L is determined by the pressure in the void and surface energy of the PSG film, the gaseous pressure (P) in a void, the void volume (V) and r can be described by

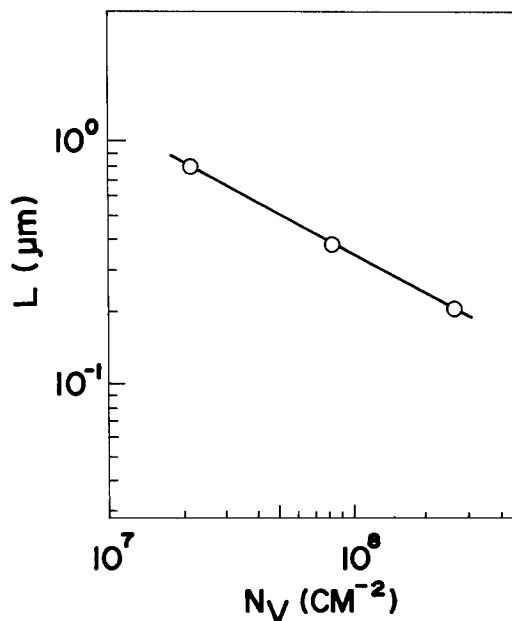


Fig. 9. Relationship between r and N_V for the PSG film second heat-treated in H_2 atmosphere at $900^\circ C$ for 240 min followed by heat-treatment in N_2 atmosphere at $950^\circ C$ for various periods of time. The PSG film phosphorus concentration is 9.5 w/o.

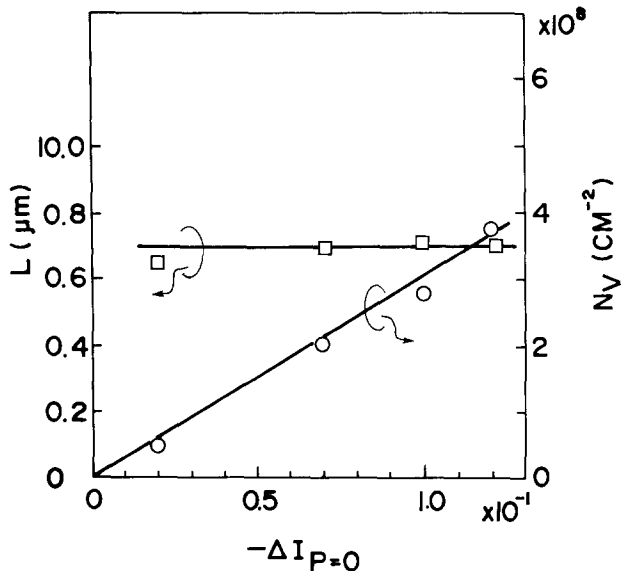


Fig. 10. $-\Delta I_{P=O}$ dependence of r and N_V for the PSG second heat-treated in H_2 atmosphere at $900^\circ C$ for various periods of time and third heat-treated in N_2 atmosphere at $950^\circ C$ for 360 min. The PSG film phosphorus concentration is 9.5 w/o.

$$PV = nRT \quad [3]$$

and

$$P = \frac{2\gamma}{r} \quad [4]$$

where γ is surface energy of the PSG film, R is ideal gas constant, n is the quantity of gaseous species in a void, and T is absolute temperature. Since n is M_P/N_V (M_P is total quantity of the gaseous species per square centimeter in 5600Å-thick PSG film and $V = 4/3 \pi r^3$), M_P can be obtained from Eq. [4] and [3] as follows

$$M_P = r^2 \left(\frac{8\pi\gamma}{3RT} \right) N_V \quad [5]$$

The product of r^2 and N_V is constant under the condition that $-\Delta I_{P=O}$ is constant, as shown in Fig. 9. Therefore, from Eq. [5], it is considered that M_P is constant regardless of the third heat-treatment time in N_2 atmosphere, assuming that γ change is negligibly small. On the other hand, N_V is proportional to $-\Delta I_{P=O}$ when L is independent of $-\Delta I_{P=O}$, as shown in Fig. 10. This means that M_P is proportional to

$-\Delta I_{P=O}$, i.e., the quantity of the phosphorus products formed with the heat-treatment in H_2 atmosphere.

Therefore, it is proposed that the phosphorus products formed with the heat-treatment in H_2 atmosphere are gaseous species at high temperature, and the quantity of the gaseous species determines the product of L^2 and N_V .

Conclusion

The PSG films were heat-treated sequentially three times in N_2 , H_2 , and N_2 atmosphere. It was found that the void formation takes place with the third heat-treatment in N_2 atmosphere. The absorbances of $P=O$ band at 1330 cm^{-1} , and $P-O$ bands at 1100 and 1000 cm^{-1} decrease, and the absorbance of the band at 1250 cm^{-1} increases with the second heat-treatment in H_2 atmosphere. However, no further absorbance change takes place with the third heat-treatment in N_2 atmosphere. The quantity of the phosphorus products formed with the heat-treatment in H_2 atmosphere was estimated from the absorbance change of the $P=O$ band. Comparing the quantity of the phosphorus products formed with the second heat-treatment in H_2 atmosphere with the void size and number, it is proposed that the phosphorus products formed with the second heat-treatment in H_2 atmosphere are gaseous species at high temperature, and the quantity of the gaseous species determines the product of the void number in the PSG film and square of the void size.

Acknowledgments

The authors wish to express their gratitude to Mr. M. Kondo and Dr. E. Arai for encouragement in executing the study.

Manuscript submitted Aug. 3, 1982; revised manuscript received Sept. 19, 1983.

Nippon Telegraph and Telephone Public Corporation assisted in meeting the publication costs of this article.

REFERENCES

1. W. Kern and R. S. Roser, *J. Vac. Sci. Technol.*, **14**, 1082 (1970).
2. W. E. Armstrong and D. L. Tolliver, *This Journal*, **121**, 307 (1974).
3. W. Kern and R. C. Heim, *ibid.*, **117**, 568 (1970).
4. B. E. Deal, *ibid.*, **121**, 198 (1974).
5. H. Takeuchi and J. Murota, *ibid.*, **127**, 752 (1980).
6. J. Wong, *J. Non-Cryst. Solids*, **20**, 83 (1976).
7. A. J. Moulson and J. P. Roberts, *Trans. Faraday Soc.*, **57**, 1208 (1961).
8. J. V. Bell, J. Heister, H. Tannenbaum, and J. Goldenson, *J. Am. Chem. Soc.*, **76**, 5185 (1954).

Passivation and Maskless Processing with Anisotropic Etches in Silicon

D. J. Day, G. W. R. Middleton, T. W. Janes, J. C. White,* and V. J. Mifsud

Royal Signals and Radar Establishment, Great Malvern, Worcestershire, England

ABSTRACT

The passivation of silicon surfaces to anisotropic etches by ion and electron beams is demonstrated. The mechanisms for passivation is attributed to oxide growth induced by lattice damage and strain. Its application as a maskless etch process or etch stop for fabrication of nonplanar microstructures is discussed.

Anisotropic or preferential etching of different crystal planes in silicon has been exploited widely for

* Electrochemical Society Active Member.

Key words: ion and electron beams, etch-stop.

microengineering of mechanical (1) and electrical (2) structures. In such applications conventional masking techniques employing etch-resistant materials are used to define an etch surface with edges aligned to planes

of lower etch rate. By suitable choice of crystal orientation and mask shape, fine geometries of grooves, holes, and points can be obtained.

It has been found that these etches are not only anisotropic but can also be selective in that etching is inhibited in highly doped ($>10^{19} \text{ cm}^{-3}$) silicon (3). This has prompted the use of heavily doped buried layers as etch stops (4, 7), to give self-stopping control on etch depth. An apparently different form of selectivity has been reported employing electrochemical etching (5) where the surface potential is held so that etching occurs for material of one doping level but cause passivation to etching in material of another doping level or type (6). The electrochemical cell employed and pen recorder traces of the cell currents during etching of a p-type crystal and a diode layer of Janes (6) are shown in Fig. 1 and 2. The passivation of the p-type surface was identified with an oxide film since the surface could be restored by a short oxide etch (10:1 buffered HF). This surface passivation by an oxide has also been attributed as the mechanism for etch-stop layers (7). The competition between surface reactions would therefore seem to be the common mechanism for selectivity of these etches, with doping or cell potential as the external means of influence. It is influence rather than control, however, that is usually obtained by these techniques since spontaneous passivation can occur because of a variety of experimental conditions, and an element of nonreproducibility easily arises if surface history is not controlled.

It is the purpose of this paper to report a new passivation process associated with ion implantation that affords far better control over surface etching. The reproducibility obtained with this technique makes it potentially useful in defining a self-aligned mask or etch stop for fabrication of nonplanar microstructures (8).

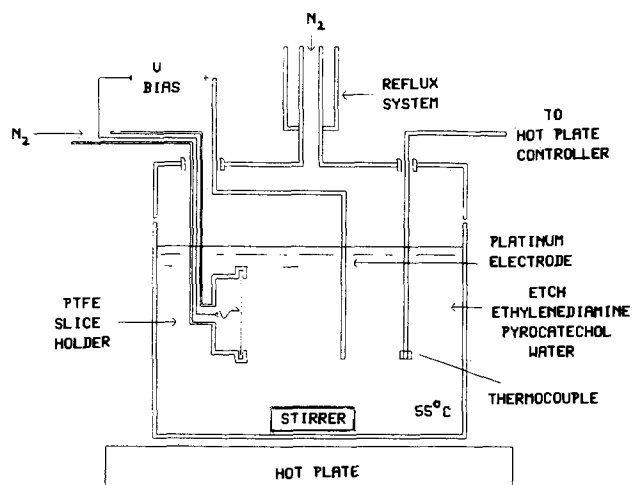


Fig. 1. Anisotropic etching system

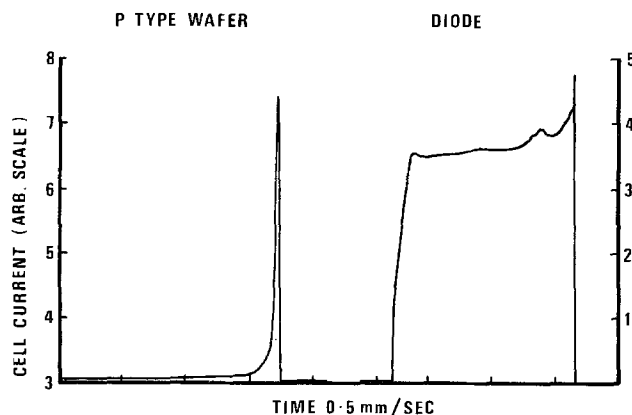


Fig. 2. Cell currents vs. time

Observation

It is observed that ion implanted silicon surfaces are passivated to anisotropic etches, e.g., ethylenediamine or potassium hydroxide. Implanted patterns are therefore left in relief by those etches. This is shown in Fig. 3, which shows an unannealed arsenic implant (10^{14} cm^{-2} at 80 keV) with 1μ line width, relief etched to 0.6μ . This passivation is spontaneous for unannealed implants and persists even after extended annealing, e.g., 1.5h at 1000°C . Its occurrence seems to be determined by the surface concentration of implanted species and can be observed in both directly implanted surfaces as well as those implanted through thin films of oxide or resist, provided a threshold surface concentration is exceeded. The threshold for passivation, however, varies with both implant species and etch conditions, but is generally found to be of the order 10^{17} cm^{-3} . For example, an arsenic-implanted surface of 10^{13} cm^{-2} at 80 keV can be readily relief etched (e.g., 3 min in ethylene diamine at 50°C), while a similar boron implant will etch under the same conditions to a depth of nearly 2000 \AA before passivation is observed. Threshold concentrations for implants are significantly different from that reported for etch stops in bulk silicon ($>10^{19} \text{ cm}^{-3}$).

The threshold for occurrence, however, is less important for device processing than the stability of the passivated surface. It is found that passivation breaks down after prolonged exposure to etches. This breakdown is complicated by a dependence on implanted species, dose, and area, as well as etch temperature and electrode bias. Line widths of 1μ have been relief etched to several microns for an implant dose of 10^{14} cm^{-2} . Freely suspended slices will break down before those held at a surface potential in an electrochemical cell. No electrochemical etching of the unpassivated surface seems to take place; it is found to be a predominantly chemical process. Unimplanted regions, however, can be passivated electrochemically. Moreover, although the stability of the implanted surfaces increases with dose, the differential etch rate of the unimplanted regions is observed to decrease. Typical rates would be $0.25 \mu/\text{min}$ at 10^{13} cm^{-2} down to $0.1 \mu/\text{min}$ at 10^{15} cm^{-2} for ethylenediamine at 50°C .

Discussion

The simplest interpretation of these observations is to regard them as an extension of the etch-stop mechanism for the case of doping by ion implantation. The high peak concentration and finite range of an implanted profile combine with an easily verified requirement for oxide to etch at a slow rate to give a simple model for passivation breakdown and stability. The questions this interpretation raises are then directed toward the differences in the reported behavior of bulk

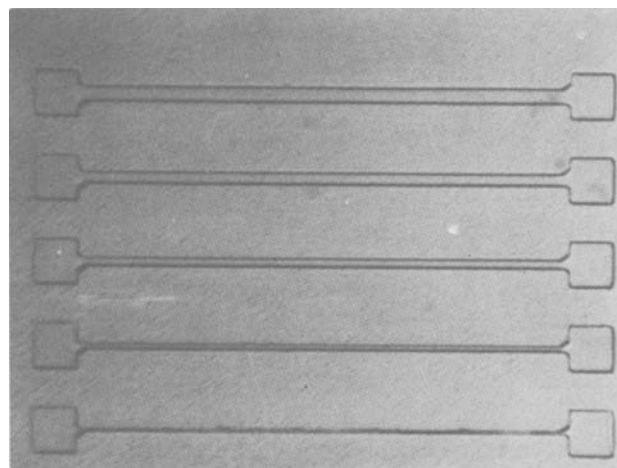


Fig. 3. Unannealed arsenic implant, 0.6μ relief

and implanted surfaces and what new aspects of the mechanism of passivation these illuminate.

It is not only the significant decrease in observed threshold for detectable passivation that is unexpected in this work, but also the fact that these impurities need not be electrically active. To confirm if the electronic or ionic nature of the implanted species made any significant contribution to the surface condition, implantation of silicon in silicon was investigated to emulate the contribution of residual crystal damage and strain. Figure 4 shows a cross section of an unannealed silicon implant (10^{14} cm^{-2} at 80 keV), indicating that no difference could be found in the passivation characteristics of these unannealed implants. In this case, annealing caused passivation to appear preferentially at the periphery of the implant. This suggests that lattice damage or strain makes a considerable contribution to the free energy of the surface. Implanted surfaces having a high free energy due to crystal damage will oxidize more readily under conditions of normal surface oxidation (9). It is reasonable to expect a similar association with passivation. There is one inconsistency with this strain argument: anisotropic etches are used for microfabrication of silicon on sapphire (SOS) wafers with little comment on nonuniformity or passivation, lattice mismatch in this case being a known source of strain in the thin silicon layers. Implantation and relief etching were attempted in both SOS and polysilicon with equal success. Thus lattice strain that has achieved some form of thermodynamic equilibrium or relaxation does not seem to influence surface reactions in the same way as nonequilibrium processes such as implantation.

To pursue this point further, nonequilibrium energy deposition associated with an electron beam was investigated. The different energy-loss mechanisms appropriate to electrons and ions, discernable from their diverse ranges of penetration, will also determine the nature and distribution of crystal damage they produce. It is questionable, therefore, if an electron beam would also induce passivation to these etches and allow direct writing of patterns for relief etching. A lithographic electron beam system with a beam width of 0.2μ at 20 keV and capable of $5 \times 10^{-3} \text{ C/cm}^2$ dose was used to write a test pattern.¹ Only weak images of small relief and poor uniformity could be produced (see Fig. 5). These were readily over etched to leave a persistent silhouette (Fig. 6). The image was enhanced by decreasing the etch temperature (ethylenediamine) from 50°C to room temperature. Local en-

¹ The pattern consisted of 100μ -square fields containing 20 lines varying in width between 0.06 and 1.25μ .

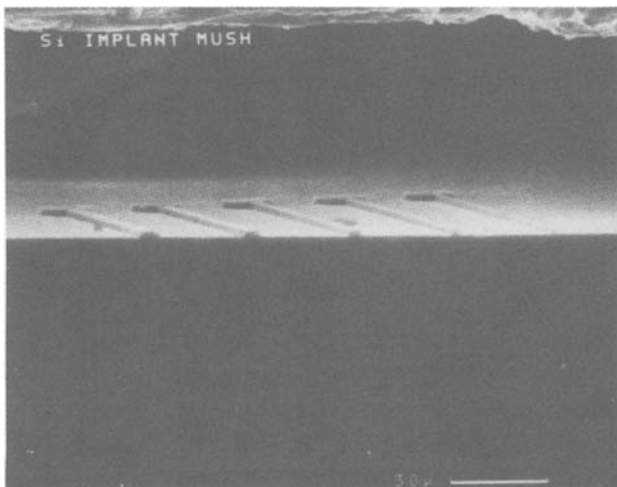


Fig. 4. Unannealed silicon implant 2.5μ relief

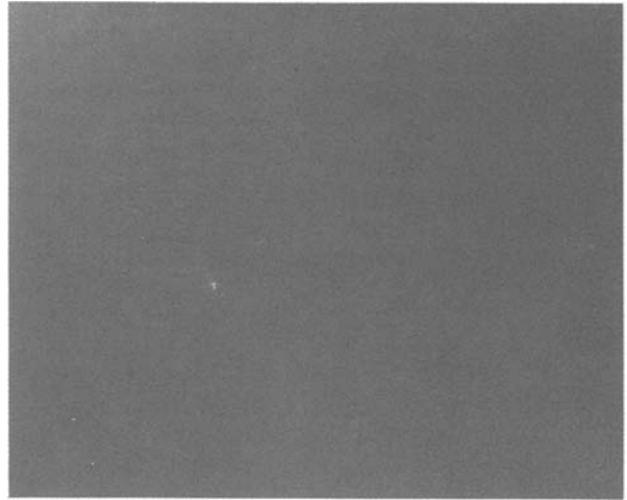


Fig. 5. Etched electron beam test mask

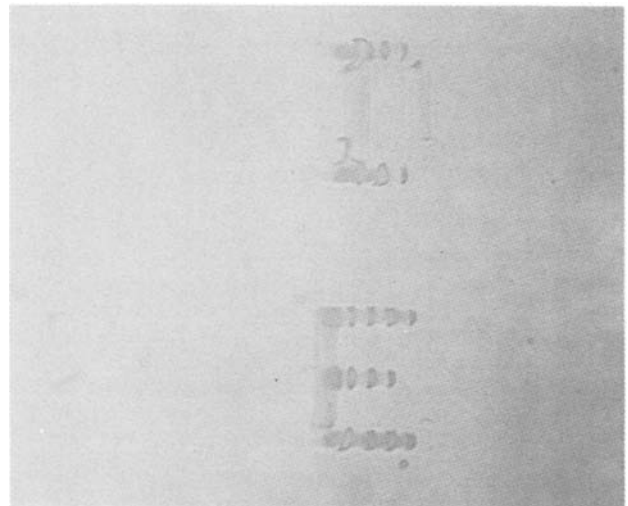


Fig. 6. Overetching of electron beam mask

hancement also occurred at sites where mask overlap occurred giving double exposure (see Fig. 5) or other surface damage occurred, *e.g.*, tweezer marks, as shown in Fig. 7. All of this lends support to the role of lattice damage and strain in favoring passivation.

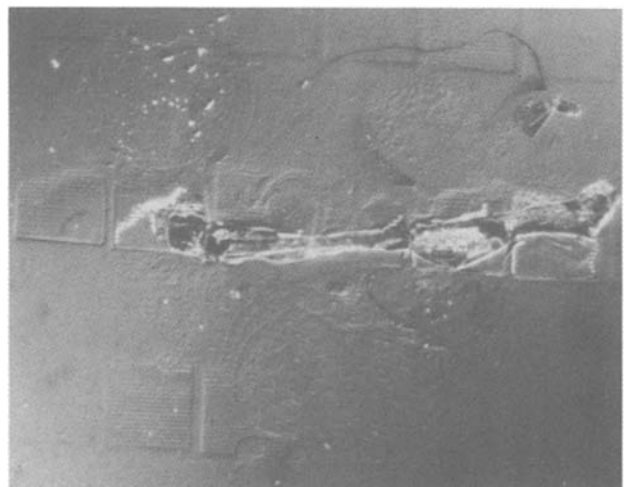
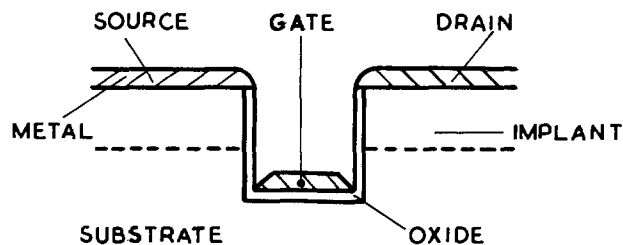
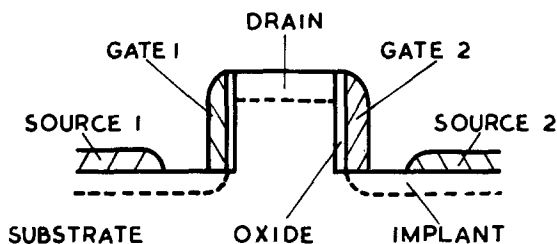


Fig. 7. Etch enhancement at surface damage



(a) GROOVED GATE MOS



(b) VERTICAL MOS

Fig. 8. Novel MOS devices

The weak images make it difficult to comment on the resolution obtainable by electron beam passivation. The line widths, however, appear to be similar and not representative of the lithography. This suggests that the variance of the energy loss distribution function (10) is comparable with the largest lithographic line widths, *i.e.*, $\sim 1\mu$. Maskless processing of relief-etched structures would therefore seem possible employing electron beams at high exposures and/or beam currents and limited resolution.

Conclusions

The passivation of silicon surfaces to anisotropic etches by ion and electron beams has been demonstrated. The observation of this passivation has been shown to be limited by the duration or stability of the passivation rather than its occurrence. It has been argued that the occurrence of this passivation is due to surface conditions favoring the formation of an oxide that itself etches relatively slowly. It has also been argued that such surface conditions are induced by nonequilibrium lattice defects and strain produced by the ion or electron energy loss, while the stability reflects the depth over which this oxide growth is favored.

Finally, exploitation of this passivation for processing microstructures would seem to lie with small-scale nonplanar devices or self-aligned isolation. Figure 8 shows two such novel MOS structures that we are investigating. The grooved gate device allows small self-aligned structures that have improved threshold and punch-through characteristics, while the vertical structures allow submicron channel lengths to be defined by etching to deep implant channel stops. If such nonplanar structures are as successful as ultra-small devices, this technique could prove valuable for maskless processing with ion beam lithography.

Manuscript submitted Feb. 18, 1983; revised manuscript received July 25, 1983.

REFERENCES

1. K. E. Petersen, *Proc. IEEE*, **70**, 420 (1982).
2. K. E. Bean, *IEEE Trans. Electron Devices*, **ed-25**, 1185 (1978).
3. A. Bogh, *This Journal*, **118**, 401 (1971).
4. N. W. Cheung, *Rev. Sci. Instrum.*, **51**, 1212 (1980).
5. H. A. Waggner, *Bell. Syst. Tech. J.*, **49**, 473 (1970).
6. T. W. Janes, J. C. White, and V. F. Mifsud, ESSDERC, Munich (1982).
7. E. D. Palik, J. W. Faust, H. F. Gray, and R. F. Greene, *This Journal*, **129**, 2051 (1982).
8. British Patent application no. 8,235,658 (1982).
9. S. Ferrer, *et al.*, *Philos. Mag.*, **45**, 261 (1982).
10. D. J. Day, *J. Phys. D*, To be published.

Cl Incorporation at the Si/SiO₂ Interface during the Oxidation of Si in HCl/O₂ Ambients

H.L. Tsai,¹ S. R. Butler,* and D. B. Williams

Lehigh University, Bethlehem, Pennsylvania 18015

H. W. Kraner and K. W. Jones

Brookhaven National Laboratory, Upton, Long Island, New York 11973

ABSTRACT

Transmission and analytical electron microscopy, nuclear backscattering, and secondary ion mass spectroscopy have been used to study the incorporation of Cl at the Si/SiO₂ interface during the oxidation of Si. Oxidations were carried out in the range of 1100°-1200°C, for 10-120 min and with HCl additions from 1-13%. It was found that a critical concentration of Cl ($2 \times 10^{15} \text{cm}^{-2}$) is required before a Cl-rich phase is observed. X-ray microanalysis indicates that the matrix in the interfacial region still contains at least about $2 \times 10^{15} \text{cm}^{-2}$ as the Cl-rich phase forms. These two observations suggest that the Cl-rich phase formation takes place in order to reduce the reacted Cl supersaturation in the SiO₂ matrix. Agglomerates, whose growth occurs by thickening and/or coalescence phenomena, are the final morphology observed during the continuing Cl incorporation. Models relating Na-ion passivation to the Cl-rich phase are shown to require modification in terms of the microstructural development.

The oxidation of silicon in chlorine-containing ambients is known to cause chlorine incorporation into the SiO₂ near the Si/SiO₂ interface (1, 2). For several oxidation conditions, phase separated regions have been observed (4-6). It has been asserted that both chlorine incorporation and sodium neutralization are related to the development of the Cl-rich phase formed at the Si/SiO₂ interface (3-5). Recent Cl concentration *vs.* distance profiles through the bulk oxide determined by secondary ion mass spectroscopy (SIMS) were interpreted to be the result of field-aided diffusion (7). The profiles show the chlorine concentration to increase exponentially toward the Si/SiO₂ interface where a peak occurs. Auger analysis-sputter profiles indicate the interface Cl peak is ≤ 3 nm thick (7, 8). This peak is presumably the result of the Si/SiO₂ interface acting as a "sink of the electrochemical potential" for Cl (7). Simple steady-state diffusion models have been proposed to describe the Cl incorporation as a function of oxide thickness (7-9).

To improve the understanding of Cl incorporation, we have carried out detailed determinations of both the Si/SiO₂ interface microstructure and the chlorine concentration and its lateral distribution along the interface. The interface morphology was determined by transmission electron microscopy (TEM). The total Cl content was obtained using nuclear backscattering (NBS) measurements (1, 2). The analytical electron microscope (AEM) [*i.e.* with the microscope operating in scanning transmission (STEM) mode] was used to determine the local Cl concentration at the interface. The Cl concentration profile was investigated in depth on several samples by SIMS. The effect of the initial oxide thickness on the chlorine incorporation process has also been studied. These results will be discussed with the objective of trying to understand the processes controlling chlorine incorporation. The relationship between the Cl-rich phase morphology and the Na-ion passivation models is briefly considered.

Experimental

Samples were prepared by thermal oxidation of (100) silicon (As-doped, 5-10 Ωcm) in ambients containing O₂ and HCl. The oxidation temperature ranged from 1100° to 1200°C and the oxidation time from 10 to 120 min. The HCl volume concentration in the input gas mixture varied from 0 to 13%. Wafers to be oxidized were pushed rapidly into a resistance heated furnace and allowed to stand for 5 min in flowing nitrogen (or argon) for thermal equilibration. Oxidation was started by shutting off the inert

gas and turning on the mixture of HCl and O₂ with a pre-established volume mixing ratio. The total flow rate was kept at 1000 cm³/min. At the end of oxidation, the O₂/HCl flow was stopped, the furnace was purged with nitrogen for 5 min, and the wafers pulled out of the furnace rapidly.

The thickness and refractive index of the oxide films were determined from ellipsometric measurements. For two-step oxidations, the initial dry oxides with thickness ranging from 0 to 80 nm were first grown at 1125°C in the dry O₂ ambient. The subsequent oxidations were carried out at 1125°C with 6% HCl and 1200°C with 3.5% HCl for oxidation times from 10 to 40 min. The thickness of the initial oxide was determined by ellipsometry. The chlorine content of the oxide films was measured by NBS of 2.8 MeV alpha particles using a 3.5 MeV Van de Graaff accelerator. A silicon detector was positioned at a scattering angle of 165°. The Cl content was obtained by comparing the total number of counts above background in the chlorine and oxygen peaks (1, 2). The samples were aligned so that channeling occurred in the (100) Si substrates in order to reduce the background under the Cl peaks.

The chlorine depth profiles were determined by secondary ion mass spectroscopy. The samples were sputtered with an Ne⁺ beam at 5 kV (10). Cl concentrations were determined by use of an ion-implanted standard. The beam was sawtooth-rastered and gated to restrict the detected sample to the central 8% of the sputtered area.

Specimens for examination by electron microscopy were prepared by chemically jet-etching the Si from the back of the wafer using 9HNO₃:1HF solution (6, 11). The etching formed a bowl-shaped depression through the silicon wafer leaving the oxide film supported across a hole in the silicon wafer. Details of the apparatus and methods are given in Ref. (9).

A Philips EM400T TEM/STEM with facilities for x-ray microanalysis was used throughout this study. All micrographs were taken with the microscope operating in the TEM mode at 120 kV. A quantitative metallographic analysis of the microstructures was carried out and the results will be reported in detail elsewhere (16). For x-ray microanalysis, the microscope was operated in the STEM mode using a 10 nm diam electron beam. The x-rays produced by the electron beam-specimen interaction were detected and analyzed by an EDAX energy dispersive spectrometer and a Tracor Northern 2000 minicomputer system. (To avoid blocking the path of the x-rays produced at the Si/SiO₂ interface by the remaining silicon wafer, the oxide layer must face upward after inserting the sample in the microscope.) The chlorine composition averaged through the whole x-ray emitting volume was calculated using the Cliff-Lorimer equation (12).

*Electrochemical Society Active Member.

¹Present address: Center for Solid State Science, Arizona State University, Tempe, Arizona.

Key words: oxidation, impurity, analysis.

$$\frac{\bar{C}_{Cl}}{\bar{C}_{Si}} = k_{ClSi} \frac{I_{Cl}}{I_{Si}} \quad [1]$$

where k_{ClSi} = the Cliff-Lorimer factor, which is 1.05 (15) at the operating voltage (120 kV), \bar{C}_{Si} = the average mass composition of silicon in the analyzed region, C_{Cl} = the average mass composition of chlorine in the analyzed region, I_{Cl} = the net total number of chlorine x-ray counts (above background), and I_{Si} = the net total number of silicon x-ray counts. The mass composition ratio of chlorine in the third phase particle and in the matrix can be obtained by the following equation

$$\frac{\bar{C}_{Cl}^P}{\bar{C}_{Cl}^M} = \frac{(I_{Cl}^P/I_{Si}^P) \bar{C}_{Si}^P}{(I_{Cl}^M/I_{Si}^M) \bar{C}_{Si}^M} \quad [2]$$

where superscripts P and M refer to data taken with the electron beam on the particle and in the matrix nearby. The fact that most of chlorine exists in a very thin layer at the SiO₂/Si interface means that $\bar{C}_{Si}^P = \bar{C}_{Si}^M$, if the electron beam is placed at points with the same specimen thickness (13, 15). This condition can be obtained by moving the beam along a thickness (extinction) fringe, due to the thin crystalline silicon layer below the oxide. Under this condition, the equation for the composition ratio becomes

$$\frac{\bar{C}_{Cl}^P}{\bar{C}_{Cl}^M} = \frac{I_{Cl}^P/I_{Si}^P}{I_{Cl}^M/I_{Si}^M} \quad [3]$$

The silicon composition, \bar{C}_{Si} , is composed of contributions from SiO₂ and Si and is obtained from

$$\bar{C}_{Si} = \frac{C_{SiO_2} V_{SiO_2} + C_{Si} V_{Si}}{V_{SiO_2} + V_{Si}} \quad [4]$$

C_{SiO_2} is the silicon composition in SiO₂, which is 0.467, and C_{Si} is the silicon composition in Si, which is 1. V_{SiO_2} and V_{Si} are the respective x-ray emitting volumes after taking into account the beam spreading. The equation used to calculate these volumes (Eq. [7] below) considers the spread beam to be that volume containing 90% of the transmitted electrons (15). A schematic sketch showing the incident electron-beam size d , beam spreading b_1 at the bottom exit of SiO₂, and beam spreading b_2 at the bottom exit of a thin silicon layer is presented in Fig. 1. After integration, the x-ray emitting volumes in the SiO₂ and the Si are, respectively

$$V_{SiO_2} = \frac{\pi t_{SiO_2}}{4} \left(d^2 + b_1 d + \frac{b_1^2}{3} \right) \quad [5]$$

$$V_{Si} = \frac{\pi t_{Si}}{4} \left[(d + b_1)^2 + (d + b_1)b_2 + \frac{b_2^2}{3} \right] \quad [6]$$

The effective beam spreading b_1 and b_2 in SiO₂ and Si can be calculated using the equation

$$b = 625 \frac{Z}{E_0} (\rho/A)^{1/2} t^{3/2} \quad [7]$$

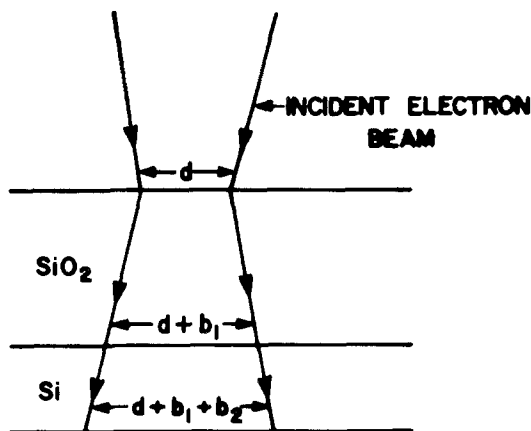


Fig. 1. Schematic representation showing the diameter of the incident electron beam, d , and the beam spreading b_1 and b_2 in the SiO₂ and the Si, respectively.

where b is in cm, Z is the atomic number, A is the atomic weight, E_0 is in keV (=120 keV), ρ is the density in g/cm³, and t is the film thickness in cm. For SiO₂, the average atomic number (10) and atomic weight (20) were used. The oxide thickness is known from the ellipsometry measurements. The silicon layer thickness is either obtained from the known extinction distance in Si or by using contamination spot separation methods (13). The extinction distance for the (220) reflection from Si is 76 nm.

The value of \bar{C}_{Cl} determined using the method described above can be compared with the value calculated independently from NBS. The Cl composition is obtained by averaging the total Cl determined from backscattering measurements throughout the whole x-ray emitting volume. The Cl mass composition is equal to the ratio of the Cl weight to the total weight in the x-ray emitting volume

$$C_{Cl}^{Cal} = \frac{N [\pi(d + b_1)^2/4] w_1}{\rho_1 V_{SiO_2} + \rho_2 V_{Si}} \quad [8]$$

N (Cl/cm²) is the Cl concentration obtained from backscattering measurements, $\pi(d + b_1)^2/4$ is the area excited by the electron beam of size $(d + b_1)$ at the SiO₂/Si interface, w_1 is the weight in grams of one Cl atom. V_{SiO_2} and V_{Si} are the x-ray emitting volumes in SiO₂ and Si. In the above equation, all of the chlorine is assumed to exist in the SiO₂ interface. This is a good approximation as we see from the SIMS profiles presented here and elsewhere (7). Most of the Cl is within 5 nm of the interface for 100-200 nm thick SiO₂ films.

Results

The Si/SiO₂ interfacial morphology was determined as a function of HCl ambient concentration or oxidation time for samples prepared at 1200°, 1170°, 1150°, and 1100°C. We present a few micrographs to show the essential features of the phase development. Detailed studies will be reported separately (16). The line seen in each micrograph corresponds to a length of 0.5 μ m. In agreement with previous work, we have not seen any diffraction effects that would indicate the Cl-rich phase was crystalline.

Figure 2a shows a sample in which no Cl-rich phase could be seen even though it contains Cl. Figures 2b-2d show the phase develop with an increase in number and size of individual particles. The initial stages of agglomeration are seen in Fig. 2d at which point a larger scale lateral nonuniformity appears. Figure 2e shows a typical microstructure of the Cl-rich phase when the agglomeration is more complete. These larger particles are widely spaced, have irregular shape, show increased contrast in the microscope, and are always surrounded by smaller particles.

Figure 3 shows results of the Cl determinations by NBS as a function of the ambient HCl concentration for samples prepared at 1200°, 1150°, and 1100°C with the oxidation times 30, 30, and 60 min, respectively. The three straight lines were drawn to pass through the origin. The Cl contents appear to increase monotonically with increasing HCl concentration. A rapidly increasing region as the third phase particles are developing (2,3) is not obvious in the data presented here. It is possible that this effect may be within the error limits of our data.

Figure 4 is the plot of the chlorine content as a function of the oxidation time for samples prepared at 1200°, 1170°, and 1125°C with various HCl concentrations. All curves appear to follow a similar time-dependent behavior. Again, a rapidly increasing region is not apparent for the oxidation conditions used here, nor has it been reported previously for Cl content as a function of oxidation time.

The Cl concentrations as a function of the initial (dry) oxide thickness are shown in Fig. 5 and 6 for samples prepared at 1125° and 1200°C. The Cl content of the oxide films is seen to decrease as the initial oxide thickness is increased. This decrease is very slight at the lower temperature but becomes more pronounced at higher temperatures and longer times. Figures 7a and 7b are two electron micrographs which indicate that a smaller portion of the interface is covered by the particles (less Cl-incorporated) for a larger initial oxide thickness. TEM observation shows no Cl-rich particles at the SiO₂/Si inter-

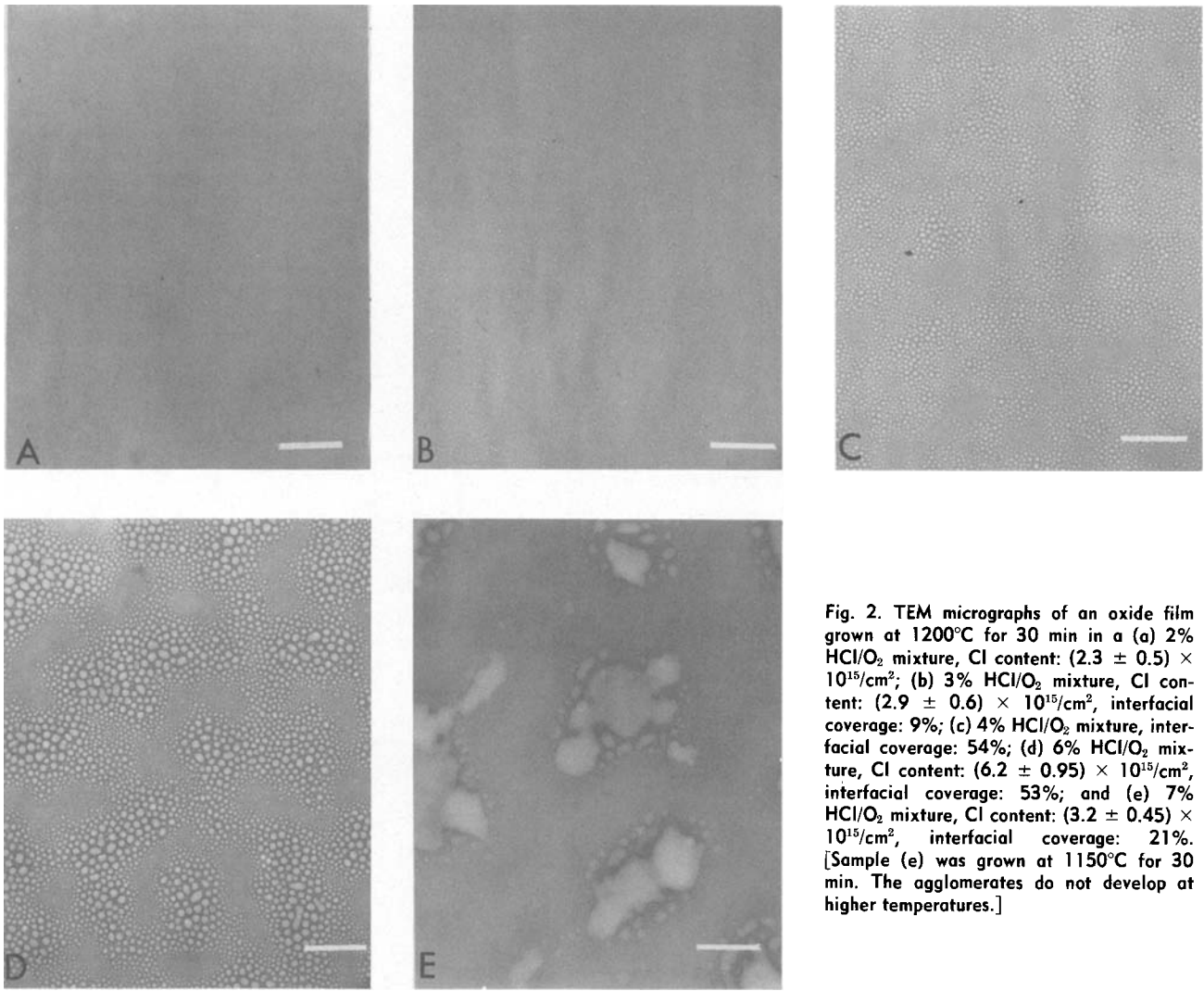


Fig. 2. TEM micrographs of an oxide film grown at 1200°C for 30 min in a (a) 2% HCl/O₂ mixture, Cl content: $(2.3 \pm 0.5) \times 10^{15}/\text{cm}^2$; (b) 3% HCl/O₂ mixture, Cl content: $(2.9 \pm 0.6) \times 10^{15}/\text{cm}^2$, interfacial coverage: 9%; (c) 4% HCl/O₂ mixture, interfacial coverage: 54%; (d) 6% HCl/O₂ mixture, Cl content: $(6.2 \pm 0.95) \times 10^{15}/\text{cm}^2$, interfacial coverage: 53%; and (e) 7% HCl/O₂ mixture, Cl content: $(3.2 \pm 0.45) \times 10^{15}/\text{cm}^2$, interfacial coverage: 21%. [Sample (e) was grown at 1150°C for 30 min. The agglomerates do not develop at higher temperatures.]

face for the samples corresponding to the results shown in Fig. 5. The individual Cl-rich particles were observed (Fig. 7) only for those samples corresponding to the data of Fig. 6 with Cl concentrations $\geq 3.0 \times 10^{15}/\text{cm}^2$.

The local chlorine composition at the SiO₂/Si interface was investigated using x-ray microanalysis with the electron microscope in the STEM mode. Several samples prepared at 1150° and 1200°C were studied. It was found that the electron beam must be focused on the area with a thin silicon layer beneath the oxide, otherwise either very little or no chlorine was detected. Presumably, the HNO₃/HF etchant removes the Cl-containing phase upon contact.

Table I lists the results from x-ray microanalysis. The thicknesses of the SiO₂ film and the silicon layer required for the calculation of the average Si composition in the x-ray emitting volume are shown in Table II. Figure 8 is one example indicating where the x-ray microanalyses were carried out. Before the data acquisition, the specimen was tilted away from the two-beam condition, which eliminates the thickness fringe, makes the particles easier to see, and avoids the possibility of anomalous x-ray generation (14). The specimen was tilted back to the (220) reflection after the data analysis. By observing the carbon contamination spots that form during microanalysis, it was possible to check that the points analyzed were along the same thickness fringe.

For the sample showing no Cl-rich particles, chlorine appears to be uniformly distributed over the interface within the resolution limit of the microscope (Fig. 2a). For oxidation conditions which show isolated particles (Fig. 2b or 2c), the ratio of chlorine concentration in the particle to that in the matrix ranges from 2 to 4. This composition ratio was found to increase slightly with the particle

size. The composition ratio, however, is as high as 7 for a sample showing complex phase-separated regions, *i.e.*, agglomerates (Fig. 2e). SEM observation of the oxide surface of samples with agglomeration are bumpy, presumably due to the thickening of these larger phase-separated regions. The average silicon composition, \bar{C}_{Si} , was determined using Eq. [3]. Equation [1] was then used to calculate the average chlorine composition, \bar{C}_{Cl} . These values of \bar{C}_{Cl} are in reasonable agreement with the nuclear backscattering values of $C_{\text{Cl}}^{\text{cal}}$ calculated in Eq. [8]. Note that the Cl concentration obtained from backscattering measurements is an average value without taking into account the nonuniform distribution of Cl along the SiO₂/Si interface. The beam diameter in the backscattering measurements is 2 mm. The \bar{C}_{Cl} obtained from x-ray microanalysis comes primarily from the chlorine in the interface region. This is due to the fact that the net total number of chlorine x-ray counts from Cl in the bulk oxide (according to the SIMS results) would be below the minimum detectable number of counts calculated by the relation $3(2I_{\text{Cl}}^{\text{b}})^{1/2}$, where I_{Cl}^{b} is the background counts under the chlorine peak (15).

The Cl concentration, after making conversion of \bar{C}_{Cl} weight percent (w/o) to $N(\text{Cl}/\text{cm}^2)$ using Eq. [8], is shown in the last column of Table I. For the three samples with observed Cl-rich phase particles, the matrix contains 2-2.5 $\times 10^{15}$ Cl/cm² independent of the state of agglomeration of the Cl-rich phase.

Figures 9 and 10 show chlorine and hydrogen profiles for samples prepared under conditions where individual particles of the Cl-rich phase are observed (Fig. 2b and 2c). The oxygen data are included to show the uniformity of the ion yield and the sharpness of the Si/SiO₂ interface. Ion implanted standards with Cl in SiO₂ were used to cali-

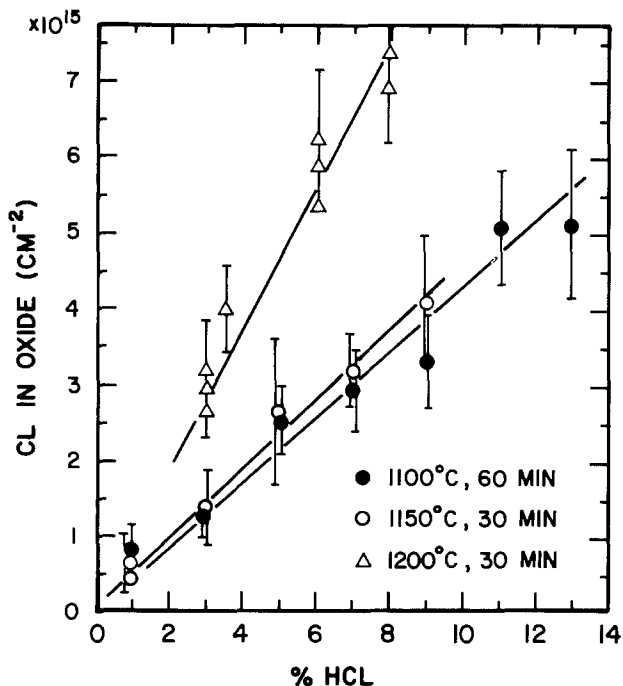


Fig. 3. Cl content of SiO_2 films as a function of the ambient HCl volume fraction at 1100°, 1150°, and 1200°C with oxidation times 60, 30, and 30 min, respectively.

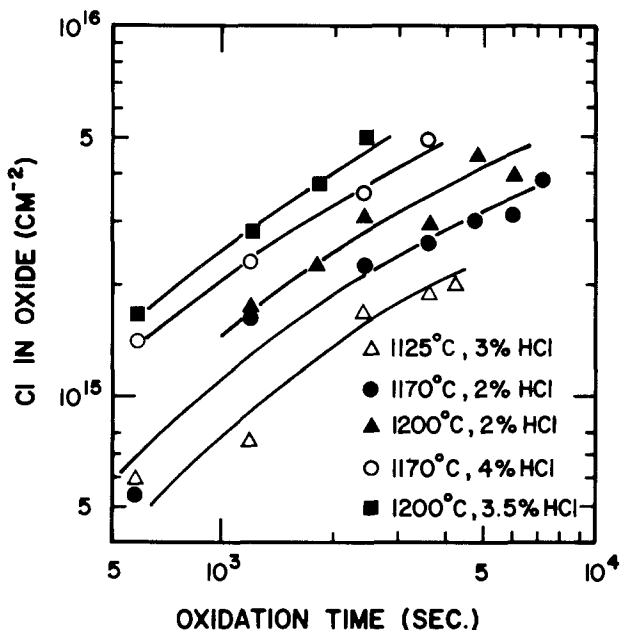


Fig. 4. Cl content of SiO_2 films as a function of the oxidation time at various growth conditions.

brate the Cl concentration scale. The Cl profiles are similar to those reported by Rouse (7). The major difference between the profiles reported by Monkowski *et al.* (17), Rouse (7), and those reported here is the continued de-

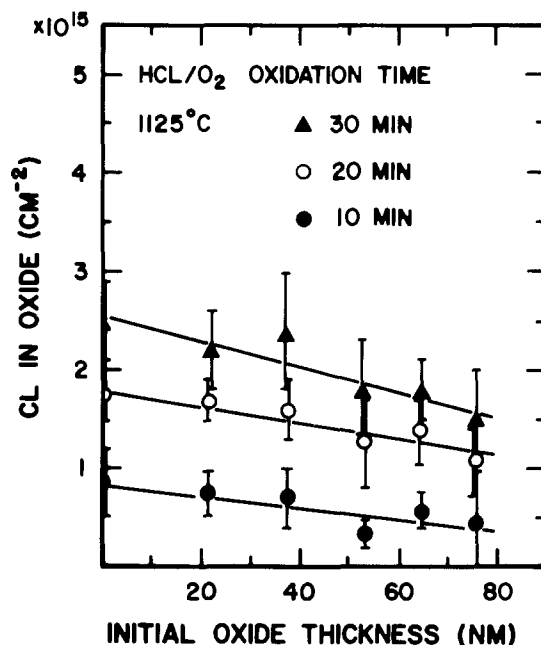


Fig. 5. Cl content of SiO_2 films as a function of initial dry oxide thickness with the second-step oxidation carried out at 1125°C for 10, 20, and 30 min with 6% HCl. The initial oxide was grown at 1125°C in dry O_2 .

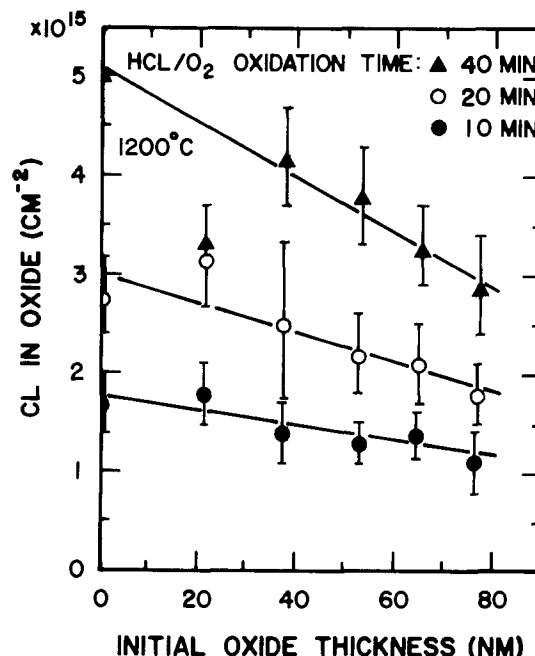


Fig. 6. Cl content of SiO_2 films as a function of initial dry oxide thickness with the second-step oxidation carried out at 1200°C for 10, 20, and 40 min with 3.5% HCl. The initial oxide was grown at 1125°C in dry O_2 .

crease in Cl concentration throughout the bulk of the oxide. This difference appears to be due to their back-

Table I. The chlorine composition ratio and the local chlorine concentration at the SiO_2/Si interface obtained from x-ray microanalysis

Samples	Oxidation conditions	Microstructural characterization	$\bar{C}_{\text{Cl}}^{\text{p}}/\bar{C}_{\text{Cl}}^{\text{m}}$	\bar{C}_{Si} (w/o)	\bar{C}_{Cl} (w/o)	$C_{\text{Cl}}^{\text{cal}}$ (w/o)	N ($\times 10^{15}$ Cl/cm 2)
1	1200°C, 20 min 2% HCl	No third phase particles	0.98 ± 0.11 (a)	66	0.26 ± 0.02	0.35	1.26
2	1200°C, 100 min 2% HCl	Isolated particles	2-4	75	0.30(b) 0.53(c)	0.40	2.0 6.0
3	1150°C, 30 min 5% HCl	Isolated particles	1.75 ± 0.25	75	0.20(b) 0.60(d)	0.36	2.0 3.4
4	1150°C, 30 min 7% HCl	Agglomerated particles	7.2 ± 0.50	75	0.39(b) 2.72(e)	0.61	2.6 17.0

(a) Composition ratio of two points in the matrix; (b) in the matrix; (c) for particle size 40-45 nm; (d) for particle size 30 nm; (e) on an agglomerate.

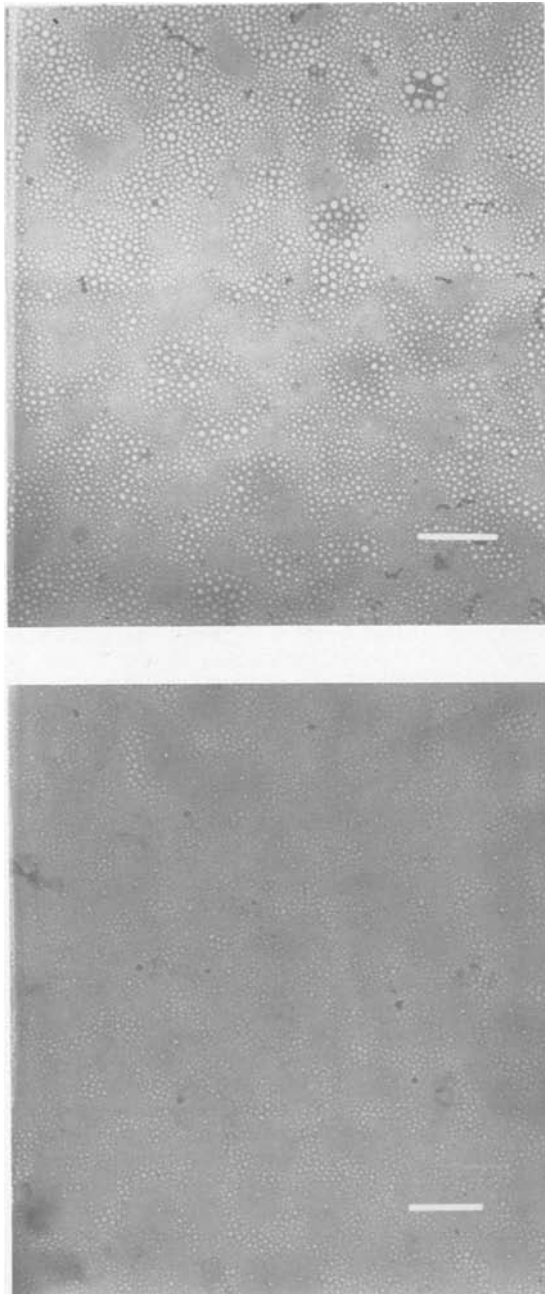


Fig. 7. TEM micrographs of Si/SiO₂ samples prepared at 1200°C for 40 min in a 3.5% HCl/O₂ mixture with the initial oxide thickness (a, top) 77, (b, bottom) 22 nm. The initial oxide was grown at 1125°C in dry O₂ ambient.

ground, which limited the minimum detection level to $10^{19}/\text{cm}^3$ vs. $10^{17}/\text{cm}^3$ for the instrument used in this work. The hydrogen profiles are generally similar to that reported by Burkhardt for a steam-grown oxide (18). The large error bar indicated for the hydrogen concentration is due to the fact that we did not use our ion-implanted standard for hydrogen in SiO₂ during this set of measurements. However, it was used during the overall series of measurements so that we have a reasonably accurate calibration for the hydrogen concentration. The very large concentrations near the interface are uncertain since they would not be consistent with the calibrations for a "minor" impurity in an SiO₂ matrix.

Table II. The SiO₂ and silicon-layer thickness used for x-ray microanalysis

Samples	1	2	3	4
t_{SiO_2} (nm)	126	280	144	147
t_{Si} (nm)	42	85	76	76

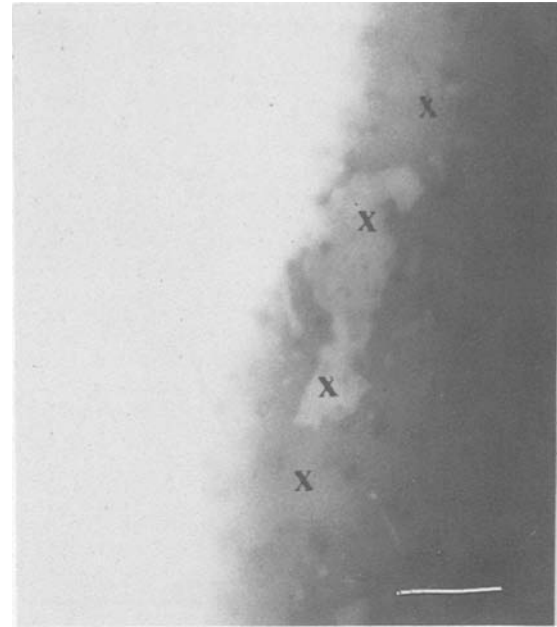


Fig. 8. STEM micrograph of an Si/SiO₂ sample prepared at 1150°C for 30 min in a 7% HCl/O₂ mixture. Positions where Cl analysis were carried out are indicated.

Discussion

Phase Development.—The microstructures may be classified into three types, *i.e.*, microstructures with no Cl-rich phase, with individual Cl-rich phase particles with circular cross section, and those in which the Cl-rich phase has a complex shape which we will simply refer to as agglomerates. Figure 11 summarizes this important characteristic of the microstructure as a function of the average chlorine content and oxidation temperature. We have used the total chlorine content as a variable to classify the microstructure development instead of the time and HCl concentration, which are the experimental parameters. The motivation for this choice is that the microstructure is continually changing during the oxidation process because the Si/SiO₂ interface is moving during

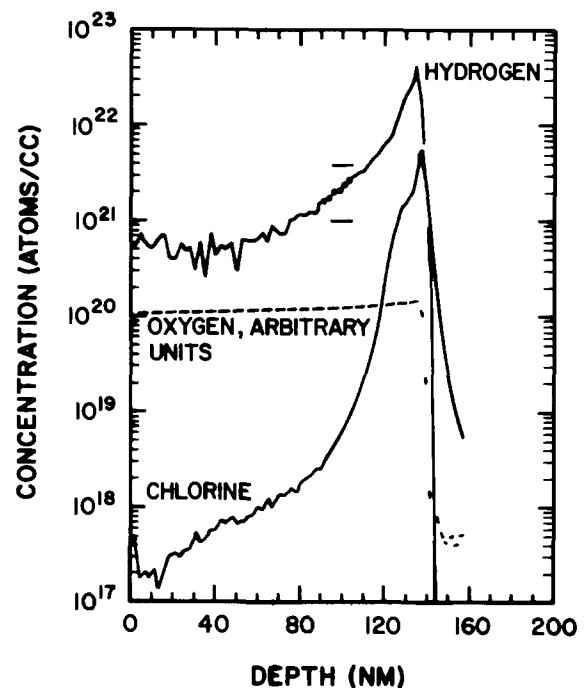


Fig. 9. Hydrogen and chlorine profiles as determined by SIMS. Sample prepared at 1150°C, in 5% HCl-O₂ mixture by a 30 min oxidation. A few of the actual data points are shown in the vicinity of the error bar on the hydrogen profile.

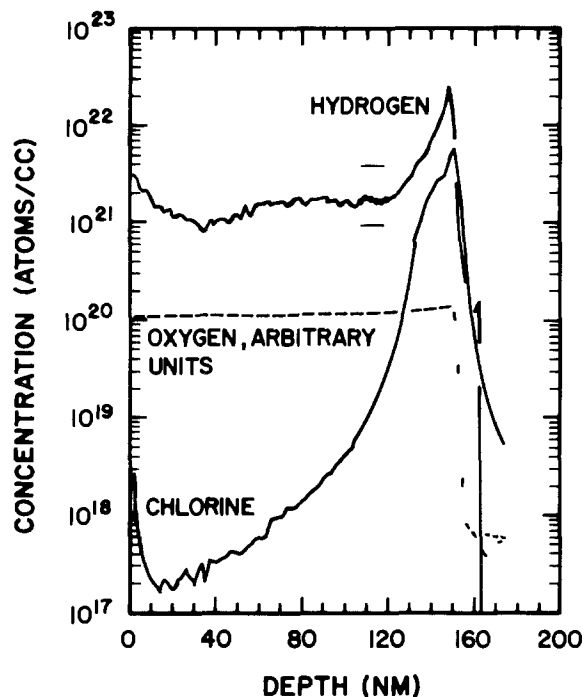


Fig. 10. Hydrogen and chlorine profiles as determined by SIMS. Sample prepared at 1200°C, in 3.5% HCl-O₂ mixture by a 30 min oxidation.

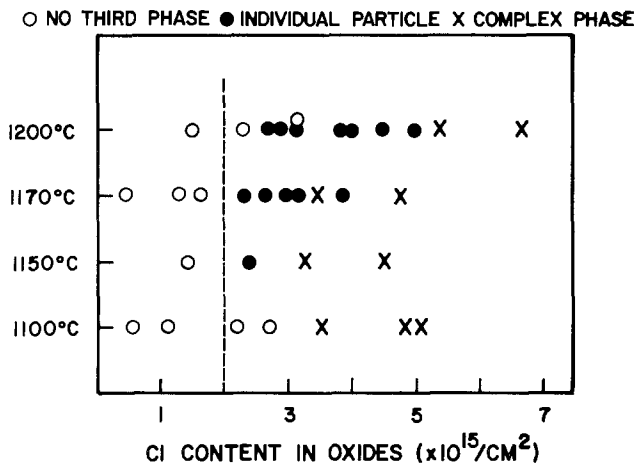


Fig. 11. Characterization of principal features of the morphology as a function of oxide chlorine content at various oxidation temperatures.

the oxidation. Therefore, since the chlorine is always found to be primarily segregated to the interface it must also move, and, thus, the Cl-rich phase particles "move." We specifically do not suggest that this is a macroscopic "dragging" motion but rather the result of continuous formation by chemical reactions (growth) at the Cl-rich phase-silicon (Si/SiO₂) interface and decomposition reactions at the Cl-rich phase-oxide interface. In terms of this variable, the necessary condition for the Cl-rich phase to form is that the total Cl content exceeds 2×10^{15} Cl/cm². However, from Fig. 11 we see that this does not appear to be a sufficient condition. This minimum concentration is similar to the solubility limit of a single-phase region. This is a "quasi-thermodynamic" condition and would not be expected to describe the kinetic aspects of the new phase development (31).

Before discussing the kinetic aspects of this phase development, it is worth inquiring as to the nature of the phase. We have noted that from the electron diffraction information the phase is noncrystalline. The x-ray microanalysis found the Cl areal density in the phase of $\sim 4 \times 10^{15}$ Cl/cm². Cl concentration *vs.* depth profiles using SIMS show an interfacial peak 3×10^{-7} cm wide and average volume concentration of $\sim 10^{21}$ Cl/cm³ (7). Since the

area fractions are $\sim 10\%$, we see this average volume concentration is consistent with what one calculates for the particles, *i.e.*, $4 \times 10^{15}/3 \times 10^{-7} \sim 10^{22}$ Cl/cm³ in the Cl-rich phase. However, the micrographs show that the Cl-rich phase is more transparent to the electron beam than SiO₂. Thus, even with the increased concentration of the higher atomic number element, Cl, the overall electron and/or atomic density is less. Calculations assuming elastic scattering show that to a first approximation even if the 3 nm thick "particle" were a void in a 250 nm Si/SiO₂ layer it would have only $\sim 2\%$ increase in transmission, which is close to the limits of contrast visible to the human eye. Thus, we must conclude that we are dealing with a very low density noncrystalline phase. If the density were about half that of SiO₂, it would mean an Si concentration of $\sim 10^{22}$ /cm³ and an oxygen concentration of $\sim 2 \times 10^{22}$ /cm³. This would be consistent with a molecular composition such as Si₂O₃Cl₂ as suggested by several authors (19, 20). Such compounds have been identified in the gas phase (21). Thus we are dealing with a phase-separation process similar to that found in many silicate glasses (22).

In an extensive study of phase separation of Na₂O-CaO-SiO₂ glasses, the process was found to proceed by nucleation and growth with the critical nucleus radius being ~ 2 to 3 nm (23). This small size resulted even though the interfacial energy was found to be only ~ 4 ergs/cm². This compares with solid/liquid interfacial energies (such as one might consider the crystalline Si/glassy SiO₂ interface) ~ 200 ergs/cm² (24). Therefore, since the particles we see are >10 nm, we are probably observing the growth of the phase following nucleation. Also, such low interfacial energies as found in (23) would be consistent with the large number of particles we see in the individual particle interval of the phase development and with the reluctance of the particles to coarsen and agglomerate. It is also likely that the actual nucleation event occurs on the Si/SiO₂ interface, which has been shown to possess monoatomic steps, etc., that would facilitate the nucleation (25,33). Thus the kinetics we are observing are the result of the growth process of the Cl-rich phase. The observation that Cl can segregate laterally over distances much larger than the oxide thickness, *e.g.*, agglomerate spacings, observed in Fig 2e, implies that the Cl diffusivity is large.¹ We agree with the previous suggestion that the growth process is controlled by the interfacial chemical reactions and not by Cl transport (7). We will discuss these reactions shortly. We point out that in no case was the Cl-rich phase seen to cover the interface. When agglomeration occurred, the interfacial coverage decreased significantly, which is consistent with the ability of Cl to diffuse laterally.

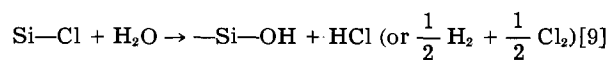
Finally, the lack of conventional coarsening as agglomeration occurs (exemplified by the absence of a Cl-depleted zone around the agglomerates) is consistent with a very low interfacial energy between SiO₂ and the Cl-rich phase as suggested above. Since the Cl-rich phase growth is apparently interface-controlled, we would interpret the clustering and agglomeration as follows: if some Si/SiO₂ interfacial feature resulted in an enhanced Cl reaction rate, the new phase would nucleate and grow rapidly in that region. Thus, particles would contact and agglomerate. Yet, the smaller particles nucleating nearby, but not growing as fast, would still be present, as the micrographs show. The rapid lateral Cl diffusion to these enhanced reaction sites would suppress Cl-rich phase formation in between these regions. Thus, the lateral nonuniformity should be more apparent when the agglomerates are seen. At the lower temperatures of 1150° and 1100 °C, we would expect the interfacial reactions to be more sensitive to interfacial nonuniformities. In agreement with this idea, more clustering and agglomeration phenomena are observed *vs.* uniformly distributed particles (9).

Chlorine incorporation.—The results for the total chlorine incorporated as a function of time or HCl concentration are generally consistent with those previously reported (2, 5, 8). However, a rapid increase in the so-called "threshold" region is not apparent as in our earlier results (2). We believe this is more a matter of experi-

¹At least with respect to the O₂ diffusivity which controls the oxidation process in the range of thicknesses obtained here.

mental conditions than of different phenomena. All of the Cl depth profiles reported here and elsewhere show the chlorine to be segregated to the Si/SiO₂ interface. Thus, the Cl must dissolve in the oxide and diffuse to the interface. The Doremus model of molecular solution and diffusion of gases in SiO₂ appears to explain the Si oxidation kinetics as well as more recent isotope redistribution experiments (26, 27). Therefore, if we apply these ideas to the Cl₂ and HCl transport, the concentration of diffusing species would be $\leq 10^{15}$ cm⁻³ and thus undetected by either SIMS or NBS measurements. As previously suggested by Monkowski *et al.* (4), and demonstrated by Sheu *et al.* (28), Cl₂ appears to be the gas phase species controlling Cl incorporation. We then assume Cl₂ arrives at the Si/SiO₂ interface where it reacts and is incorporated into the SiO₂. In the initial stages of incorporation (Cl $\leq 2 \times 10^{15}$ /cm²), this is a laterally uniform process as indicated by the x-ray analyses and absence of Cl-rich particles. The Cl, and apparently hydrogen, are incorporated into the SiO₂ network as the oxide forms at the interface. These reactions will compete with the oxidation reactions and the outcome will be controlled by the local activities at the interface. One factor which could act to favor the interfacial H and/or Cl incorporation is the lowering of the viscosity of the SiO₂ as a result of the inclusion of these network-modifying species (29). This would enhance the viscous flow which has been suggested as one mechanism of accommodating the volume change (volume per Si) upon oxidation (30). As shown by the x-ray microanalysis, this process occurs throughout the entire range of Cl incorporation studied here (Table I). Thus this process is the incorporation mechanism up to total Cl contents of $\sim 2 \times 10^{15}$ cm⁻². The weak dependence of the total Cl/cm² on initial oxide thickness indicates that the Cl₂ transport is not the rate-limiting step in the incorporation process. Also, as noted above, the large lateral distances (~ 1 μ m) over which the Cl segregation takes place (when agglomerates occur) is consistent with a large diffusivity for Cl. Therefore, it appears that the chemical reaction incorporating Cl into the network is the most important step in the kinetics of incorporation. Thus, fitting the steady-state diffusion models for Cl incorporation to the total Cl/cm² should not be a good method for determining the Cl₂ diffusivity (8).

As the Si/SiO₂ interface moves during oxidation, chlorine incorporated in the SiO₂ at the interface ends up in the "bulk" oxide. This Cl is probably unstable due to the increased O₂ or H₂O activity of these indiffusing oxidants. Diffusing O₂ is not found to exchange with network oxygen nearly as much as H₂O (26, 27). Therefore, the likely displacement reaction is that OH replaces Cl in the network, *i.e.*



This would reduce the Cl concentration as the interface moves, or as oxidation proceeds, and we look at a point fixed with respect to the outer oxide surface. This is qualitatively consistent with the Cl depth profiles. The Cl released in the bulk would diffuse back to the interface where it would react again, resulting in a net accumulation process.

When the Cl concentration reaches a value such that the total Cl $> 2 \times 10^{15}$ cm⁻², the Cl-rich phase becomes stable. As noted above, the nucleation stage was not observed and the growth of the particles beyond ~ 30 -40 nm is limited. Instead of more lateral growth, increased numbers of particles are nucleated. As suggested above, this is consistent with several observations. First, interfacial energies between two amorphous phases (phase separation in silicates) can be very low; second, if the incorporation is reaction-controlled, it should only occur at the Si/SiO₂ interface and not on the "lateral" surfaces of the particles; third, the clustering and lateral nonuniformity of the individual particles may indicate "heterogeneous" nucleation on the Si/SiO₂ interface to be rate controlling (especially at lower temperatures). Since the matrix remains saturated at 2×10^{15} Cl/cm² and the Cl-rich phase has about 4×10^{15} Cl/cm², as the interface

becomes increasingly covered by the particles the additional Cl incorporation is due to the new phase forming. This process will be the principal Cl incorporation process above about 25% interfacial coverage. However, we do not find more than 60% of the interface covered for the conditions studied here. As suggested above, the actual value of interfacial coverage at which agglomeration becomes important is not as well defined as the conditions for individual particle formation. It appears to depend on enhanced local reaction rates for Cl, perhaps due to nonuniformities on the interface. It has been suggested that a gaseous phase may be present under these high chlorine incorporation conditions (31). We will not consider this part of the problem any further.

Returning to the question of the Cl incorporation when the Cl-rich phase is present, we must give further consideration to the moving reaction interface aspect of the process. Since the particles always appear to be "at" the interface, they must effectively "move" with the interface. As we noted previously, this must be the result of the Cl-rich phase being converted to SiO₂ by reactions at its interface with the bulk SiO₂. A similar argument has been suggested by Monkowski *et al.* (19). We suggested a composition for the phase of Si₂O₃Cl₂. Thus this reaction involves replacement of 2 Cl by O or possibly by 2 OH. This latter reaction (involving OH) would again seem more likely due to spatial restraint, *i.e.*, the two silicons bonded to the Cl's would not have to be close enough to bond to the single oxygen. This is consistent with the large hydrogen content of the oxide. Also, the considerable Cl concentration in the oxide away from the interface could imply that, in addition to the Cl incorporation into the matrix between the particles, the SiO₂ formed from the Cl-rich phase also contains Cl in its network. Since the Cl-rich phase is of low mass density, transport of the released Cl within the particle back to the Si interface should be very rapid. Again, reaction at this interface would continue to be the rate-controlling step so that similar kinetics should be observed throughout the complete range of Cl incorporation. However, again we note that the simple steady-state diffusion models with a single "incorporation rate constant" should not be a useful way to try to model the incorporation process. For all conditions, at least two chemical reactions are involved in the net Cl incorporation "reaction." It would appear that modeling studies which try to fit the Cl concentration *vs.* depth profiles, as well as the total Cl, could give the additional information needed to understand the overall Cl-incorporation process.

Sodium neutralization.—The fact that complete sodium neutralization is achieved in the samples containing sufficient incorporated Cl (by increasing the oxidation time or the ambient HCl concentration) is, in general, consistent with the evidence for Cl-rich phase development in the temperature range 1100°-1200°C. The model suggested by Stagg and Boudry for Na⁺ neutralization is that the Na⁺ diffuse laterally to the large agglomerate particles where the charge exchange takes place (32). According to these authors, the samples belonging to the agglomerated phase regime contain Cl higher than 3×10^{15} /cm² for all the oxidation temperatures (5). However, in addition to the agglomerates we have observed individual particle microstructures for samples with Cl content higher than 3.0×10^{15} /cm². These individual particles are also seen in samples with Cl content $< 3.0 \times 10^{15}$ /cm². For these samples with relatively low oxide chlorine content, Stagg and Boudry have demonstrated that the sodium ions at the SiO₂/Si interface can only be partially passivated. However, complete passivation should be achieved more quickly in these samples with the more closely spaced individual particles. This situation contradicts their model for neutralization based on the sodium interface diffusion (32). How the individual particles are correlated with the sodium passivation still needs to be resolved by determining both the microstructure and passivation on the same samples. However, we have shown that the lateral diffusion/agglomerate model needs modification when compared to the trends in the microstructure development.

We next consider the implications of the similar trends in the dependence of the microstructure development and the sodium passivation on the so-called ballistic model for neutralization (3). In this model, only the Na^+ ions arriving at the interface which "hit" a Cl-rich phase particle are neutralized. For oxides grown as a function of the HCl concentration at 1150° and 1200°C with the same oxidation time of 30 min, the individual particle microstructure falls in the so-called "threshold" region of Rohatgi's passivation results (3).² The area fraction generally does increase with the passivation, implying qualitative agreement. But instead of the interface becoming covered by the Cl-rich phase above the "threshold" as required by the ballistic model for 100% passivation, we find the areal fraction to remain approximately constant at ~0.5 or to decrease. Thus in spite of qualitative similarities, this model is also inconsistent with the quantitative features of the microstructure development (as well as with Na^+ lateral diffusion.)

Summary

We have presented data on Cl content and Cl segregation as a function of oxidation conditions. There is good agreement between data obtained by NBS and AEM techniques. This data has led us to conclude that chemical reactions at the interface and in the bulk oxide are the processes controlling chlorine incorporation. When the interfacial Cl concentration and the relative Cl and oxygen incorporation rates reach critical values, a Cl-rich phase forms. The phase is amorphous and contains about twice the Cl of the SiO_2 matrix. The development of this phase controls additional Cl incorporation over a range of oxidation conditions. The upper end of this range is reached when complex shape agglomerate particles of a Cl-rich phase appear. We have not attempted to discuss Cl incorporation in the agglomerate regime other than to note that the x-ray microanalysis tells us that agglomerates act as strong sinks for Cl and are apparently substantially thicker than the initial particles.

The Cl-rich phase appears to nucleate on the Si/SiO₂ interface. The phase develops as individual particles with extensive nucleation and limited lateral growth. This and the lack of conventional coarsening phenomena are consistent with a very low interfacial energy between the Cl-rich phase and SiO₂. Similar low energies have been observed in phase separation in silicate glasses. The agglomeration and clustering that then occurs at higher Cl contents is suggested to be due to locally enhanced Cl reaction rates at the Si/SiO₂ interface. This is consistent with the suggestion that the Cl-rich phase formation is an interface reaction controlled process, not Cl transport controlled. Finally, while the Na-ion neutralization is generally consistent with the phase development, a more careful comparison shows that the currently proposed models of the process are incomplete.

Acknowledgment

We want to thank Professor F. J. Feigl for helpful discussions of this work, and Ms. Carol DalMaso for careful analysis of the microstructures. We also wish to thank Mr. Richard Gale of Lehigh University and Dr. C. W. Magee of RCA for performing the chlorine and hydrogen analysis (SIMS). This work was supported by the NSF Division of Materials Research under grant DMR-8006057.

Manuscript submitted Jan. 13, 1983; revised manuscript received Sept. 20, 1983. This was Papers 198 and 199 pre-

²The oxide Cl content measured in our samples is systematically higher than that reported by Rohatgi *et al.* under the same oxidation conditions (2). In Rohatgi's work an RF-heated cold wall furnace was used. The incoming gases were preheated by passing through narrow passageways in the Si susceptor. It is possible that the HCl and O₂ may not have reacted completely to form the equilibrium concentration of Cl₂. Since Cl₂ is apparently the important gas phase species controlling Cl incorporation, this lack of equilibrium would result in low Cl content samples (2, 3).

sented at the Detroit, Michigan, Meeting of the Society, Oct. 17-21, 1982.

Lehigh University assisted in meeting the publication costs of this article.

REFERENCES

1. Y. S. Van de Meulen, C. N. Osburn, and J. F. Ziegler, *This Journal*, **122**, 284 (1975).
2. A. Rohatgi, S. R. Butler, F. J. Feigl, H. W. Kraner, and K. W. Jones, *ibid.*, **126**, 143 (1979).
3. A. Rohatgi, S. R. Butler, and F. J. Feigl, *ibid.*, **126**, 149 (1979).
4. J. Monkowski, J. Stach, and R. E. Tressler, *ibid.*, **126**, 1129 (1979).
5. J. P. Stagg and M. R. Boudry, *J. Appl. Phys.*, **52**, 885 (1981).
6. J. Monkowski, R. E. Tressler, and J. Stach, *This Journal*, **125**, 1867 (1978).
7. J. W. Rouse, PhD Dissertation, Stanford University, Stanford, CA (1981).
8. J. W. Rouse, C. R. Helms, B. E. Deal, and R. R. Razouk, *J. Vac. Sci. Technol.*, **18**, 971 (1981).
9. H. L. Tsai, PhD Dissertation, Lehigh University, Bethlehem, PA (1982).
10. C. W. Magee, W. L. Harrington, and R. E. Hoenig, *Rev. Sci. Instrum.*, **49**, 477 (1978).
11. H. L. Tsai, D. B. Williams, and S. R. Butler, "Proceedings of the International Symposium on Grain Boundaries and Interfaces in Ceramics," American Ceramic Society, Columbus, OH. In press.
12. G. Cliff and G. W. Lorimer, *J. Microsc.*, **103**, 203 (1975).
13. G. W. Lorimer, G. Cliff, and J. N. Clark, in "Developments in Electron Microscopy and Analysis," J. A. Venables, Editor, p. 153, Academic Press, London (1976).
14. D. Cherns, A. Howie, and M. Jacobs, *Z. Naturforsch.*, **28**, 565 (1973).
15. J. I. Goldstein, in "Introduction to Analytical Electron Microscopy," J. J. Hren, J. I. Goldstein, and D. C. Joy, Editors, p. 83, Plenum Press, New York (1979).
16. H. L. Tsai, D. B. Williams, and S. R. Butler, To be published.
17. I. S. T. Tsong, M. D. Monkowski, J. R. Monkowski, P. D. Miller, C. D. Moak, B. R. Appleton, and A. L. Wintenberg, in "The Physics of MOS Insulators," G. Lucovsky, S. T. Pantelides, and F. L. Galeener, Editors, p. 321, Pergamon Press, New York (1980).
18. P. J. Burkhardt, *This Journal*, **114**, 196 (1967).
19. M. D. Monkowski, J. R. Monkowski, I. S. T. Tsong, and R. E. Tressler, Abstract 370, p. 887, The Electrochemical Society Extended Abstracts, Vol. 81-2, Denver, CO, Oct. 11-16, 1981.
20. S. I. Raider and R. Flitsch, *J. Vac. Sci. Technol.*, **13**, 68 (1976).
21. K. Hirabayashi and I. Iwamura, *This Journal*, **120**, 1595 (1973).
22. R. H. Doremus, "Glass Science," Chap. 4, John Wiley and Sons, New York (1973).
23. J. J. Hammel, *J. Chem. Phys.*, **46**, 2234 (1967).
24. D. Turnbull, *J. Appl. Phys.*, **21**, 1022 (1950).
25. N. Osakake, K. Yagi, and G. Honjo, *Jpn. J. Appl. Phys.*, **19**, L309 (1980).
26. R. Pfeiffer and M. Ohring, *J. Appl. Phys.*, **52**, 777 (1981).
27. S. Rigo, F. Rochet, B. Agius, and A. Straboni, *This Journal*, **129**, 867 (1982).
28. S. R. Butler, H. L. Tsai, D. B. Williams, and Y. D. Sheu, in "Insulating Films on Semiconductors," J. F. Verweij and D. R. Wolters, Editors, p. 47, North Holland, Amsterdam (1983).
29. R. H. Doremus, "Glass Science," p. 105, John Wiley and Sons, New York (1973).
30. E. P. Eernisse, *Appl. Phys. Lett.*, **35**, 8 (1979).
31. M. D. Monkowski, J. Monkowski, R. E. Tressler, and J. Stach, "Materials Science Research," Vol. 14, J. Pask and A. Evans, Editors, p. 361, Plenum, New York (1981).
32. J. P. Stagg and M. R. Boudry, *Inst. Phys. Conf. Ser.*, **50**, 75, The Institute of Physics, Bristol and London (1980).
33. O. L. Krivanek, in "Proceedings of the 37th EMSA Meeting," p. 684, Claitors, Baton Rouge, LA (1979).
34. J. Monkowski, J. Stach, and R. E. Tressler, in "Semiconductor Silicon 1977," H. R. Huff and E. Sirtl, Editors, p. 323, The Electrochemical Society Softbound Proceedings Series, Princeton, NJ (1977).

Planar Interconnection Technology for LSI Fabrication Utilizing Lift-off Process

Kohei Ehara, Takashi Morimoto, Susumu Muramoto, and Seitaro Matsuo

Nippon Telegraph and Telephone Public Corporation, Atsugi Electrical Communication Laboratory, 1839, Ono, Atsugi-shi, Kanagawa 243-01, Japan

ABSTRACT

A surface planarization process for multilevel metallization structure is proposed for higher packing density and higher yields in fabricating LSI's. The technique makes use of the ECR plasma deposition method and a lift-off process. The deposition method is suited for the lift-off process, because of its directional deposition properties and low temperature deposition. The surface planarization process yields a flat surface. Fine patterns in the upper layer are obtained. The potential for using this technology for manufacturing the MOS LSI is verified by the good yield and fine Al patterns for 1 kbyte associative memory fabricated with this process.

For higher packing density in LSI's, a multilevel metallization structure must be improved by miniaturization and by increasing the number of layers. In microfabrication technology, lithographic techniques and dry etching techniques have contributed to the rapid progress in reduction of the lateral dimensions for the patterns. In contrast to such rapid advancement, the thickness of the insulating and conducting films for multilevel interconnection cannot be appreciably reduced, because of wiring resistance and parasitic capacitance. Thus, the LSI surface step height increases compared with the lateral dimensions of the pattern with increasing LSI packing density. In this case, the surface step causes poor step coverage of a deposited thin film, short circuiting, or breakage in conducting lines. In addition, the pattern size uniformity in the lithographic process becomes worse.

In order to solve these problems, planar technology for the interconnection layer has been used. For example, there are several planarization techniques, such as anodic oxidation (1), lift-off (2-4), glass flow (5), surface leveling (6), polymer film coating (7), and etch back employing RIE (8). Anodic oxidation can form completely planar interconnection metallization (1). In this process, the unanodized metal remains in the spaces between the lines, and a reduction in cross-sectional area for the metal line occurs. Thus, it seems that these factors interfere with miniaturizing the LSI's pattern, because it is difficult to further decrease these factors. The lift-off process for surface planarization utilizes Al evaporation on the photoresist without heating the substrate (2, 3). Thus, Al film has a poor step coverage at the sidewall of the through-hole contact or at the surface step of the underlying film pattern edge. Furthermore, the MOS LSI fabrication process utilizes CVD film deposition or H₂ heat-treatment at about 400°C substrate temperature. In these heating processes, hillocks will grow easily for Al film evaporated (9). There is another lift-off process, which can obtain fine-featured smoothly tapered metallization patterns by using a polyimide as the lift-off layer (4). In this process, the remaining surface steps interfere, increasing the number of metallization's levels. The P-glass flow process, which makes the surface smooth (5), requires 1000° to 1200°C heat-treatment and still leaves the surface step. The surface leveling process makes use of organic material flow and its etching, using conditions that etch the photoresist and the underlying P-glass at nearly the same rate (6). Although this process also can obtain a smoothed surface without high temperature heat-treatment, the surface step still remains. There is another process, utilizing a polyimide as an interlevel dielectric (7). Although the film is highly resistant to heat, it seems to be difficult to obtain a uniform miniaturization because of film-thickness variations. The etch-back process, employing RIE, can be used to obtain a smoothed surface (8). In this process also the surface step still remains. There are other planar technologies which have the potential for the application to planar interconnection. For

Key words: multilayer metallization, planar interconnection, lift-off, ECR plasma deposition.

example, there is a technology which employs a low temperature photo-CVD oxide (10) in conjunction with a lift-off. Using this technology, the fabrication of a fully recessed field isolation (11) had been attempted.

This paper introduces a new planar technology for multilevel metallization with a high packing density (12). In this process, surface planarization is carried out employing the lift-off technique. This lift-off utilizes electron cyclotron resonance (ECR) plasma deposition, which has such features as high directionality, high quality, and low temperature deposition (13). Thus, in this lift-off process, the processing ease depends mainly on the deposited film, and not on the stencil. Furthermore, this lift-off utilizes anisotropic dry etching for pattern formation. Therefore, it is suitable for miniaturization and multilevel formation of metallization. In the following sections, a fundamental planar process, ECR plasma deposited film, lift-off yield, and the application to LSI fabrication are described.

Manufacturing Process

The fundamental process steps for making planar interconnections are shown in Fig. 1. Details of these steps are as follows.

Step A.—First Al layer etching with a resist mask using a dry etching technique. Al(Si) film 0.6 μm thick as a first Al layer is deposited by using a magnetron sputter evaporation technique. The substrate temperature is about 300°C. A projection printing technology is used for the photolithography. The photoresist layer is 1.5 μm thick, and the minimum pattern size is a 2 μm lines and spaces. First Al interconnection patterns are etched away in a parallel plate plasma etcher using 0.25 torr CCl₄ gas. All these methods are generally used in the metal interconnection formation.

Step B.—Silicon dioxide (SiO₂) deposition, using the ECR plasma deposition method. The SiO₂ film thickness deposited by the ECR plasma deposition method is the same as in Step A.

Step C.—Sidewall deposited film etching with wet etchant.

Step D.—SiO₂ film lift-off from the resist by resist removing. More details for steps C and D are indicated in Table I. Ammonium fluoride/hydrofluoric acid/ethylene glycol solutions shown in Table I are used to make the SiO₂ and Al etching rate ratio large (14). The lift-off process itself is completed in process 3 of Step D in Table I. But, in case the lifted-off material adheres on the wafer surface again, a high pressure water method is employed, which can remove the adhesive material without giving

Table I. Detail process conditions of Step C and Step D

1. Slight etching, ammonium fluoride/HF/ethylene glycol solutions, 5 min	} Step C
2. Deionized water rinse, 10 min	
3. Ultrasonic cleaning in acetone, 10 min × 2 times	} Step D
4. High pressure water cleaning, 1200 psi, 90s	
5. J-100 cleaning (90°-120°C), trichlorethylene boiling	

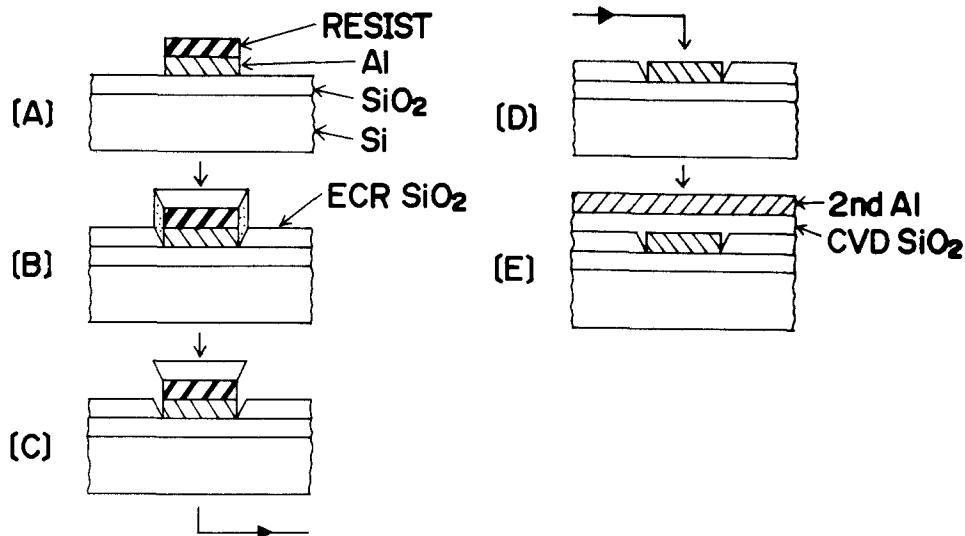


Fig. 1. The lift-off process. A: parallel plate plasma etching. B: ECR plasma deposition. C: slight etching. D: lift-off. E: interlevel insulator and second Al layer formation.

any scratch on the wafer surface. Since the strength of the adhesion is too weak to be removed by the high pressure water method, the removal is completed perfectly. 1200 psi water pressure is used.

Step E.—Filling the remaining groove by interlevel insulator deposition. Second Al layer formation on the substrate. CVD SiO₂ 0.8 μm thick is deposited at 400°C substrate temperature. The second Al interconnection 1.0 μm thick is formed by using the above-mentioned method.

Features of this process are as follows. After a pattern having a steep side wall is formed by using parallel plate plasma etching, the sunken place formed by the etching is buried using the ECR plasma deposition. This process is suitable for miniaturization, because it utilizes anisotropic characteristics both in etching method and deposition method. Next, the processes added to the conventional LSI process are only Steps B, C, and D. With regard to photolithography, generally used process conditions are utilized. Thus, this process can be applied easily to the conventional process by adding Steps B, C, and D.

ECR Plasma Deposited Film Properties

The ECR plasma deposition apparatus allows the performance of high quality thin film deposition at room temperature without the need for thermal reaction (13). It does this by enhancing the plasma excitation efficiency

and the bombardment effect of ions with moderate energies on the deposition reactions through using a microwave ECR plasma generation and a plasma extraction by a divergent magnetic field method. SiO₂ film can be deposited by introducing O₂ and SiH₄ into the plasma and specimen chamber, respectively. The deposition rate increases from about 200 to 400 $\text{\AA}/\text{min}$ at the gas flow rates of O₂ 10 cm^3/min and SiH₄ 10 cm^3/min in the microwave power from 50 to 300W. Table II shows the fundamental characteristics of ECR SiO₂ deposition used in this study.

Step coverage.—Figure 2 shows step height and tapered angle dependence on deposited SiO₂ thickness. CVD SiO₂ is also shown for comparison. The substrate is silicon, which is etched away to form lines and spaces 1 μm deep. For CVD SiO₂, the trench becomes filled when the deposited film thickness becomes greater than 2 μm . However, for ECR SiO₂, the trench is not filled yet to the same deposited thickness. The tapered angle for ECR SiO₂ is constant, even when the ECR SiO₂ thickness is 2 μm , while that for CVD SiO₂ increases after decreasing. For CVD SiO₂, with increasing deposited film thickness, the trench is filled when the tapered angle starts increasing. In this way, in the ECR plasma deposition method, the deposited film surface keeps the substrate shape. Film thickness deposited on the sidewall is about a third of that deposited on the flat surface. The reason that the

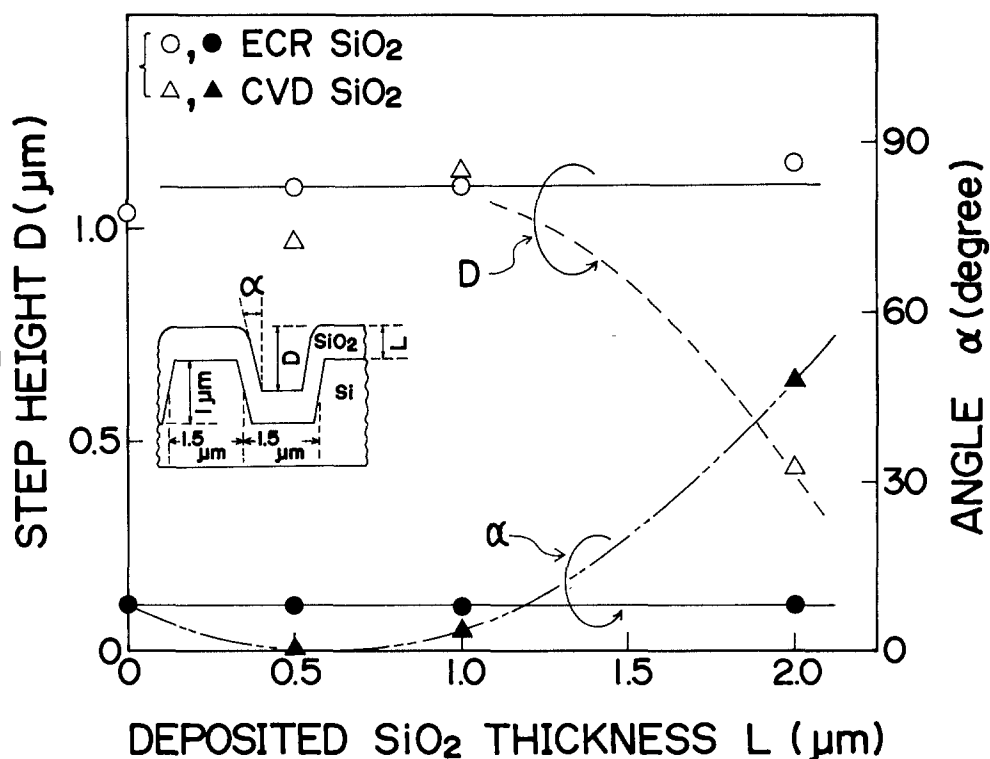


Fig. 2. Step height and tapered angle dependence on deposited SiO₂ thickness.

Table II. Fundamental characteristics of ECR plasma deposited film

Reaction gases	{ SiH ₄ (pure) O ₂	10 cm ³ /min 10 cm ³ /min
Microwave power	100W	
Pressure	2 × 10 ⁻⁴ torr	
Temperature	40°-50°C	
Deposition rate	260 Å/min	
Etching rate by BHF* (25°C)		
{ flat surface	590 Å/min†	
{ sidewall	> ~ 5 μm/min	
Refractive index		1.45-1.47

* (NH₄F 40 weight percent):(HF 50 volume percent) = 10:1 (volume ratio).

† Reference data; thermal oxide (wet 1100°C) 700 Å/min.

step coverage of the ECR SiO₂ becomes a characteristic shape (as mentioned above) is the high directionality of the ECR plasma deposition. The directionality is considered to be produced by the following mechanism. After ions are extracted from the plasma chamber by a magnetic field, they are accelerated towards the substrate by the electric field in the plasma stream. In this process, these ions have no collision for the other gas molecules because of the low gas pressure (mean free path is 20 ~ 30 cm). In addition, the neutral species having no directionality scarcely deposit on the specimen (13).

Film etching rate and other properties.—The etching rate for the ECR SiO₂ deposited on the flat surface was examined using buffered solution containing 10% HF as a function of the solution temperature (10° ~ 35°C). In this temperature range, the etching rates for the ECR SiO₂ are almost the same as those for the thermally grown silicon dioxide film which was etched simultaneously. The refractive index measured by ellipsometry is almost constant at values from 1.45 to 1.47 in wide range of microwave power. In the infrared absorption spectrum for the SiO₂ film deposited at 100W microwave power, the Si-O bond peak is clearly observed at 1065 cm⁻¹ wave number, but no Si-H bond peak is observed. From these results, it is clear that the SiO₂ film deposited on the flat surface has a dense structure. This is because the substrate is bombarded by the ions having an energy (~20 eV) suitable for the deposition reaction. In addition, hydrogen or other impurities are difficult to contain in the film during its growth because of the low gas pressure (13).

Figure 3 is an SEM micrograph of a cross-sectional view, before etching and after etching. During etching with HF, the film on the sidewall is removed, while the film on the flat surface is shallowly etched. As a result, the structure (Step C) shown in Fig. 1 is obtained. Figure 4 shows the change in the cross-sectional view with etching time. The sidewall-deposited film is already removed after 0.2 min. Since the etching rate of the sidewall-

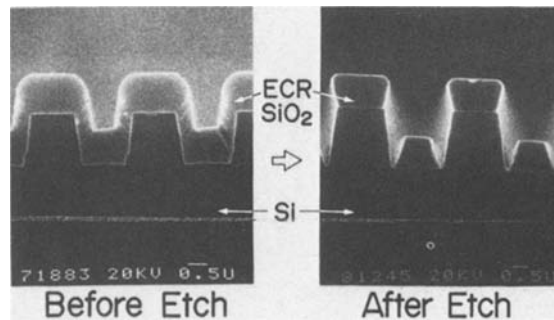


Fig. 3. SEM micrograph showing the cross-sectional view change in step coverage by slight etching

deposited film is markedly large in the wet etchant containing HF, the exact value of the etching rate in the etchant cannot be obtained. However, from the experimental results shown in Fig. 4, the value is roughly estimated to be more than a hundred times that of the flat-surface-deposited film. The differential etch rates for the ECR SiO₂ on the flat surface and the sidewall are explained as follows. Since there is no bombardment of ions on the sidewall, the deposition reaction at the sidewall is not enough; it allows hydrogen and poor molecule bonds to remain in the film. As a result, a loose structure film is deposited on the sidewall. In spite of that, a dense structure film is deposited on the flat surface because of the ion bombardment (13). Space *d*, shown in the cross-sectional view, increases gradually with increasing etching time. The space *d* increasing rate is almost the same as the etching rate for the flat-surface-deposited film. The tapered angle does not change, even if the etching time increases. The tapered angle is determined by the ratio of the thickness between the sidewall-deposited film and the flat-surface-deposited film. From the tapered angle shown in Fig. 4 (~71°), the ratio is about 1:3.

Effect of flatband voltage and mobile ions.—Figure 5 shows the flatband voltage dependence on the SiO₂ thickness. With regard to MOS diode fabrication using ECR plasma deposition, the sample has three layers, namely, from the silicon surface, the thermal oxide, the ECR SiO₂, and Al gate electrode. For comparison, the thermal oxide flatband voltage is also shown. After oxidation or ECR plasma deposition, no heat-treatment is made. The Al electrode is deposited at room temperature by the heat-resistance method in order to prevent other effects on the MOS diode. In this result, the fixed charge density for MOS diode using ECR SiO₂ is less than that using wet SiO₂ (15). It is considered that this difference is due to the fact that the dry SiO₂ is formed between the

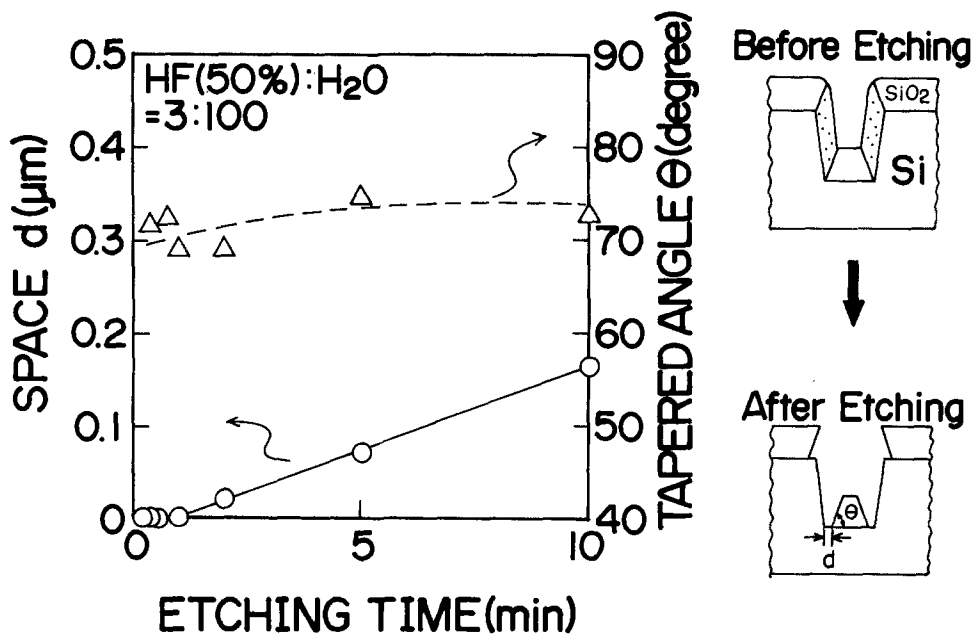


Fig. 4. Change in cross section with etching time.

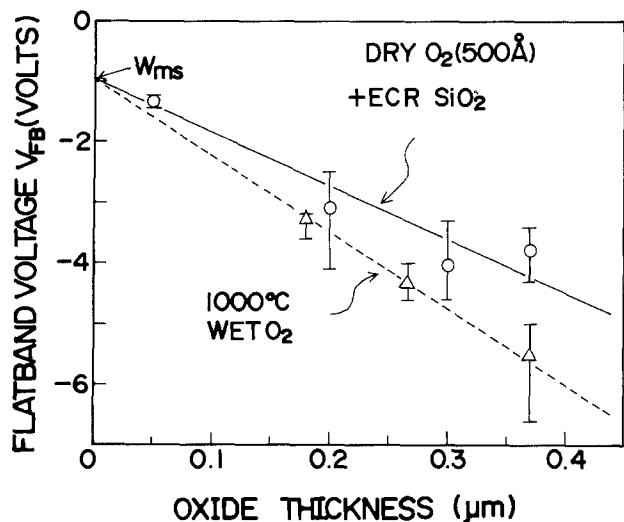


Fig. 5. Flatband voltage shift as a function of oxide thickness

ECR SiO₂ and the silicon surface for the MOS diode using the ECR SiO₂. Because both flatband voltages are almost the same level, no damage is introduced to the fixed charge density by the ECR plasma deposition method.

Furthermore, the mobile ion density for the ECR SiO₂ is evaluated by using the above-mentioned MOS diode in the TVS method (16). The mobile ion density is less than the detectable minimum value (about $5 \times 10^9 \text{ cm}^{-2}$). Thus, it is suggested that no mobile ion contamination is introduced by the ECR plasma deposition method. In this way, with regard to fixed charge density and mobile ions, the ECR plasma deposition has no problems in MOS LSI fabrication.

Lift-off Yield and Surface Flatness

In our lift-off technique, lift-off yield and surface flatness depend on many factors, such as stencil shape, the slight etching amount before lift-off, ECR SiO₂ thickness, etc. Here, among these factors, the Al layer and ECR SiO₂ thicknesses are both fixed at 0.6 μm. Figure 6 shows the dependence of the lift-off yield or the surface flatness on the slight etching amount before lift-off. The interlevel insulator thickness is 0.8 μm. The yield is evaluated by inspection of the wafer surface using an optical microscope. A good evaluation corresponds to the wafer having no lift-off remainder. For the case where the slight etching amount is small, lift-off yield for the line patterns (2 μm wide) is completed easily, but the lift-off for the square patterns (9 μm²) is not completed. The incompleteness of the latter is caused by the photoresist edge shape, which

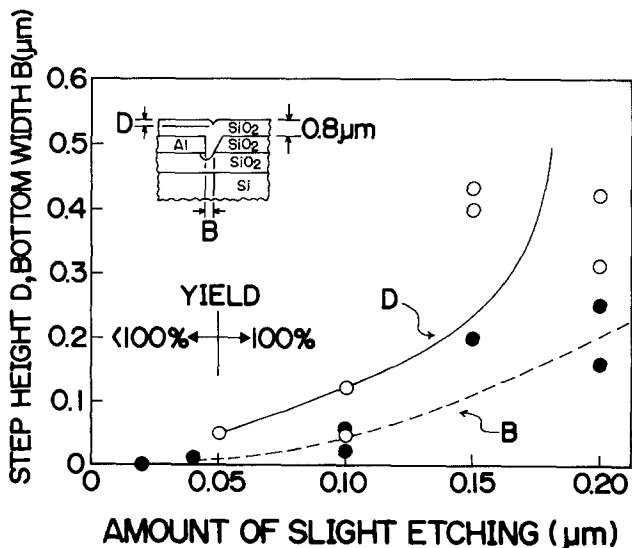


Fig. 6. Step height and bottom width dependence on slight etching amount.

tapered angle is small in the four edges of the square pattern. In this way, the optimum condition for the slight etching amount depends on the photoresist shape in details. Thus, when the tapered angle of the photoresist is small, as mentioned above, by increasing the slight etching amount, the good yield of the lift-off is obtained in good reproducibility, as shown in Fig. 6. However, the greater the slight etching amount is, the worse surface flatness the process offers. With increasing the slight etching amount, bottom width B and step height D, which are shown in the cross-sectional view in Fig. 6, increase gradually. Then, both B and D increase rapidly, as shown in Fig. 6. Thus, taking the lift-off yield and the surface flatness into account, in the present case mentioned above, the slight etching amount is appropriate in the 0.05-0.10 μm range.

Figure 7 shows surface flatness dependence on interlevel insulator thickness. A cross-sectional view of the sample structure is shown in the figure. The slight etching amount before lift-off is about 0.05 μm. After the lift-off process, B defined for the remaining groove shown in Fig. 6 is nearly zero. Width W decreases gradually with increasing interlevel insulator thickness. Step height D diminishes rapidly and becomes less than 0.15 μm when interlevel insulator thickness increases. The remaining groove is filled easily, and the planarized surface is obtained by depositing the interlevel insulator used in the conventional process. An SEM micrograph of a cross-sectional view of this planarized structure is shown in Fig. 8. The buried first Al line is 2 μm wide. The CVD SiO₂ used as the interlevel insulator is 0.8 μm thick. On this planarized structure, a second Al layer is formed.

LSI Fabrication

Test element group fabrication.—Before this technology was applied to LSI fabrication, it was evaluated by applying to a test element group (TEG), which is designed for evaluating the 2 μm rule MOS technology (17). This TEG contains a number of patterns for LSI elements, such as enhancement MOS FET, depletion MOS FET, p-n diode, and multilevel metallization. In most of these characteristics, there is no specific characteristic difference between the element applied by the present technology and a conventional technology. However, for the two-level Al interconnection, resistance and deviations in the second Al wiring are different from those in conventional interconnection. Figure 9 shows the experimental values for the second Al wiring, under which the first Al wiring level is planarized by using the present technology. For comparison, the experimental values for a conventional structure are also shown. These sample structures are drawn in the figure. There are 2006 cross points between the first Al line and the second Al line. Yield for the second Al line is 97-100%. The experimental values for the second Al wiring resistance for the planarized structure can be combined to form a straight line. This line can be

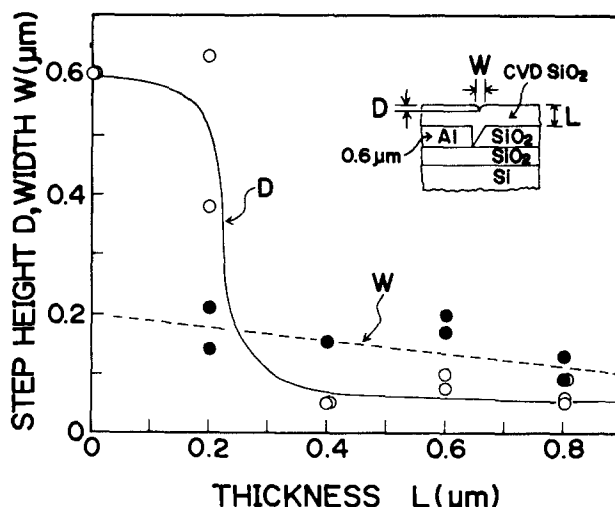


Fig. 7. Surface flatness dependence on interlevel insulator deposited thickness.

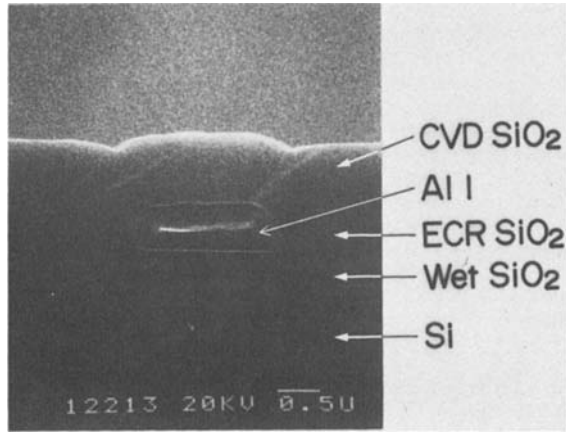


Fig. 8. SEM micrograph of buried Al line. Cross-sectional view

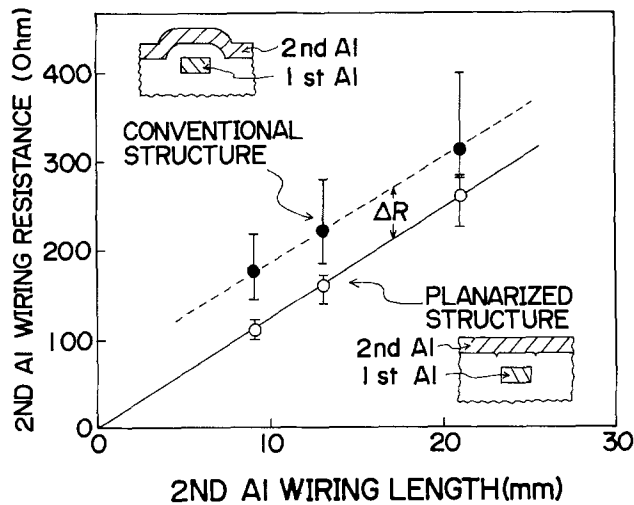


Fig. 9. Second Al wiring resistance comparison. Second Al line width is $4 \mu\text{m}$.

extrapolated to the origin. The straight line, which combines the experimental values for the conventional structure, cannot be extrapolated to the origin. These two straight lines are parallel, and difference ΔR in the figure is the resistance caused by the surface steps of the first Al layer. Thus, the second Al line resistance for the planarized structure is less than that for the conventional structure. As can be seen in the same figure, resistance deviations are also caused by the underlying layer surface flatness.

MOS LSI fabrication.—Evaluation procedure.—Logic LSI's require complicated connections and large areas for the metal interconnections. Thus, the problem of the interconnections has a great effect on the logic LSI's yield. The importance of the problem becomes larger as the LSI's change into VLSI's. In this study, a 1 kbyte associative memory (18) which has a two-level Al interconnection is regarded as TEG for the evaluation of the LSI interconnection. Since the importance of the interconnection fabrication is great in this memory, it is suitable for evaluation of the present technology. As an evaluation procedure for the effectiveness of the present technology, the comparison between the conventional technology and the present technology was carried out in the LSI fabrication process and function testing. The wafers applied to the above technologies were fabricated in the same lot except the planarization of the first Al interconnection. The memory contains about 34,000 MOS transistors. Chip size is $4.1 \text{ mm} \times 4.95 \text{ mm}$. The $2 \mu\text{m}$ n-channel E/D MOS process is used. Table III shows the interconnection scale, such as layout rules, dimensions, numbers, and length for the interconnection in the region where cell areas are arranged.

Evaluation results.—First, observation results about LSI's first Al interconnection fabrication are explained. In the

Table III. Layout rules, dimensions, numbers, and length for the Al two-level interconnections

	First Al layer	Second Al layer
Minimum width	$3.0 \mu\text{m}$	$5.0 \mu\text{m}$
Minimum space	$2.0 \mu\text{m}$	$3.0 \mu\text{m}$
Thickness	$0.6 \mu\text{m}$	$1.0 \mu\text{m}$
Number of interconnections	7550	162
Total wiring length	777 mm	456 mm
Number of through holes	41,500	15,000
Through hole size	$2 \mu\text{m}^2$	$3 \mu\text{m}^2$

present technology, a planarization process is added to the conventional process after etching the first Al. In this case, in spite of the various surface steps in the actual LSI surface, the reason that the present technology is successfully completed is as follows. The factors causing the surface steps, when the first Al layer is etched away and the photoresist on it is not removed yet, are local oxidation of silicon (LOCOS), poly-Si, first through hole, and the first Al line. In this structure, the LOCOS surface step is smooth. The poly-Si surface step becomes smooth, because the glass flow process is carried out for the PSG film covering the poly-Si. Furthermore, steep steps at the first through hole for the contact between the first Al and the diffused layer of Si substrate or between the first Al and the poly-Si gate electrodes are filled by the photoresist coated on the first Al layer. Thus, there are steep steps only at the edges of the first Al interconnection pattern and the photoresist on it. Consequently, the present technology can be applied to the first Al pattern without changing the conventional process, by only adding a few new processes. In the slight etching before the lift-off, the wet etchant mentioned in Table I scarcely attacks the Al layer and has an appropriate etching rate for the slight etching of SiO_2 . Figure 10 shows the LSI surface after the slight etching mentioned above. Only the sidewall of the first Al line and photoresist appear. Surface steps, except for the first Al line, are the ones caused by LOCOS and poly-Si gate electrode. It is suggested that this structure is very suitable for the lift-off.

Next, the observation results regarding LSI's second Al interconnection fabrication is explained. The present technology is different from the conventional technology in the condition of exposure and etching, but the process steps of both technologies are the same. In the conventional technology, since there are surface steps on the wafer surface, photolithography requires a slight overexposure time in order to prevent short-circuiting of the Al lines. Thus, the breakage in the Al lines is apt to occur on the upper part at the surface step. In addition, in the case that the interlevel insulator sidewall on the first Al line is almost vertical, short circuiting is apt to occur. In the present technology, breakage or short-circuiting rarely occurs, because the substrate surface is flat. In this case, since the small surface depression ($< 0.15 \mu\text{m}$) after the interlevel insulator deposition (see above) is completely filled by the second Al film, an appropriate exposure condition, which is almost the same as one for the flat surface, can be applied in order to offer correct lines and spaces. In addition, it is easy to observe the photoresist pattern of the Al lines by the optical microscope, because the underlying layer surface is flat. Figure 10 shows an SEM micrograph of this LSI surface after fabricating the second Al interconnection. This is the same place as that shown in Fig. 10. Since, the first Al line is fully planarized, the steps caused by the first Al line are not shown in the picture. The steps by field isolation and gate electrode are shown.

In this LSI, in order to connect directly the second Al interconnection to the poly-Si gate electrodes or Si-diffused layer, a buffered metallization, formed by the first Al layer ($5 \mu\text{m}^2$) has been used under the second Al layer (17). By using this buffered metallization, it is easy to connect an interconnection with another one lying in a different layer without a specific fabrication process. An SEM micrograph of the through hole where buffered metallization is used is shown in Fig. 11. The conventional through hole is shown in Fig. 11. For the first Al layer's planarization, no surface step caused by the buffered met-

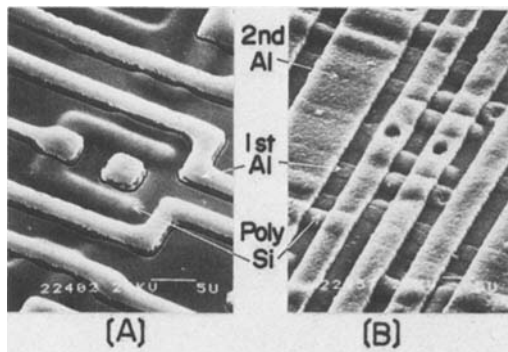


Fig. 10. SEM micrograph of application to LSI fabrication

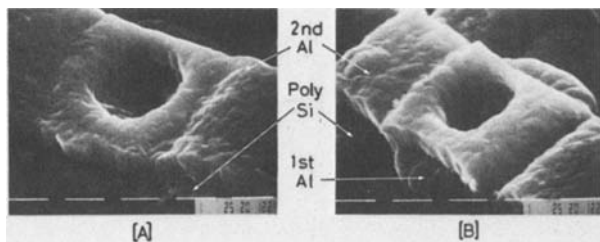


Fig. 11. SEM micrograph of through hole contact between second Al layer, and the diffused silicon layer using a buffered metallization of first Al layer.

alization is observed under the second Al line at the through hole, while a large surface step is observed in the conventional through hole. In the usual LSI fabrication process this structure is not used because it decreases the LSI yield. In the present technology, since the buffered metallization is planarized, the good yield is obtained.

The wafers applied to the present technology and the wafers applied to the conventional technology, which were fabricated in the same lot, were compared by testing 16 function patterns. In the good chip numbers passing the etch test pattern or all test patterns, the wafers applied to the present technology have a better yield than the conventional one. As a result, it was shown that the present planar technology offers a great advantage for LSI fabrication.

Conclusion

Planar interconnection technology, utilizing a lift-off process, which makes use of the ECR plasma deposition method, is presented. The deposition method features high directionality, high quality, and low temperature deposition. These features are suitable for the lift-off process. By using these features, the lift-off is easily completed after etching the sidewall-deposited film on the Al line and the resist film. The remaining groove, which is formed after the lift-off, is completely filled with the interlevel insulator deposition on the substrate. The surface step after planarization is less than $0.15 \mu\text{m}$. The SiO_2 etching amount for the sidewall-deposited film is appropriate in the $0.05\text{--}0.10 \mu\text{m}$ range, taking the surface flatness and the lift-off yield into account.

The present technology has no specific effect on the characteristics of LSI elements, such as a MOS FET. However, the resistance and the deviations in the upper metal interconnections decrease, because of the underly-

ing layer surface's flatness. The technology is applied to the first metallization of the 1 kbyte associative memory, in order to verify its potential for use in MOS LSI fabrication. Since the steep steps are only at the edge of the first Al interconnections, the present technology can be applied to a conventional LSI fabrication process without introducing any serious changes in the process condition. However, several additional processes, such as ECR plasma deposition, slight etching, and lift-off, are introduced to the two-level interconnection fabrication. Finally, it has been shown that this technology offers a great advantage for LSI fabrication, because it leads to a good yield and fine Al interconnections are easily obtained.

Acknowledgments

The authors wish to thank Dr. E. Arai, S. Nakayama, H. Ikawa, and Dr. T. Kitayama for their direction and encouragement. The authors also wish to thank M. Kiuchi for his helpful assistance. The devices were fabricated by the staff members of the High Density Integration Section, the Patterning Technology Section, and the Microfabrication Systems Section at Atsugi Electrical Communication Laboratory, NTT.

Manuscript submitted Feb. 22, 1983; revised manuscript received Sept. 27, 1983.

Nippon Telegraph and Telephone Public Corporation assisted in meeting the publication costs of this article.

REFERENCES

1. G. C. Schwartz and V. Platter, *This Journal*, **122**, 1508 (1975).
2. H. Mutoh, Y. Mizokami, H. Matsui, S. Hagiwara, and M. Ino, *ibid.*, **122**, 987 (1975).
3. B. M. Welch, Y. Shen, R. Zucca, R. C. Eden, and S. I. Long, *IEEE Trans. Electron Devices*, **ed-27**, 1116 (1980).
4. Y. Homma, H. Nozawa, and S. Harada, *ibid.*, **ed-28**, 552 (1981).
5. W. E. Armstrong and D. L. Tolliver, *This Journal*, **121**, 307 (1974).
6. A. C. Adams and C. D. Capio, *ibid.*, **128**, 423 (1981).
7. K. Mukai, A. Saiki, K. Yamamaka, S. Harada, and S. Shoji, *IEEE J. Solid-State Circuits*, **sc-13**, 462 (1978).
8. H. Hazuki, T. Moriya, and M. Kashiwagi, Paper presented at the 1982 Symposium on VLSI Technology.
9. C. J. Santro and D. L. Tolliver, *Proc. IEEE*, **59**, 1403 (1971).
10. J. W. Peters, *IEDM Digest*, p. 240 (1981).
11. J. Y. Chen, R. C. Henderson, J. T. Hall, and E. W. Yee, *ibid.*, p. 233 (1982).
12. K. Ehara, T. Morimoto, S. Muramoto, T. Hosoya, and S. Matsuo, Paper presented at the 1982 Symposium on VLSI Technology.
13. S. Matsuo and M. Kiuchi, in "VLSI Science and Technology," C. J. Dell'Oca and W. M. Bullis, Editors, p. 79, The Electrochemical Society Softbound Proceedings Series, Pennington, NJ (1982).
14. T. A. Shankoff, C. C. Chang, and S. E. Hasszo, *This Journal*, **125**, 467 (1978).
15. E. H. Nicollian and J. R. Brews, "MOS Physics and Technology," p. 469 Wiley-Interscience, New York (1982).
16. N. J. Chou, *This Journal*, **118**, 601 (1971).
17. K. Saito, S. Hamaguchi, and H. Asakawa, *Rev. Electr. Commun. Lab.*, **30**, 649 (1982).
18. T. Nikaido, T. Ogura, S. Hamaguchi, and S. Muramoto, Paper A-2-2 in the 14th Conference on Solid State Devices, Tokyo (1982).

A Mathematical Model of the Coupled Fluid Mechanics and Chemical Kinetics in a Chemical Vapor Deposition Reactor

Michael E. Coltrin

Sandia National Laboratories, Laser and Atomic Physics Division, Albuquerque, New Mexico 87185

Robert J. Kee

Sandia National Laboratories, Applied Mathematics Division, Livermore, California 94550

James A. Miller

Sandia National Laboratories, Combustion Chemistry Division, Livermore, California 94550

ABSTRACT

We describe a numerical model of the coupled gas-phase hydrodynamics and chemical kinetics in a silicon chemical vapor deposition (CVD) reactor. The model, which includes a 20-step elementary reaction mechanism for the thermal decomposition of silane, predicts gas-phase temperature, velocity, and chemical species concentration profiles. It also predicts silicon deposition rates at the heated reactor wall as a function of susceptor temperature, carrier gas, pressure, and flow velocity. We find excellent agreement with experimental deposition rates, with no adjustment of parameters. The model indicates that gas-phase chemical kinetic processes are important in describing silicon CVD.

The chemical vapor deposition (CVD) of solid materials is an important method for producing solid films with high purity and uniformity. Some important applications of CVD include the manufacture of microelectronic devices and silicon solar cells. Even though CVD has widespread use, a fundamental understanding of the interplay among its constituent elements is missing. A unified theoretical picture of CVD requires input from the fields of gas-phase chemical kinetics, fluid mechanics, surface chemistry, and materials science.

In this paper we describe a two-dimensional mathematical model of the coupled gas-phase kinetics and hydrodynamics in a laminar-flow chemical vapor deposition reactor. Specifically, we have studied a reactor in which silicon is deposited as the result of the thermal decomposition of silane. This system was chosen for its relative simplicity and its importance to the microelectronics industry. Nevertheless, our model is quite general, and thus can be applied to other CVD systems if the appropriate gas-phase reaction mechanisms are known.

Our model couples the chemical rate equations with the boundary layer equations describing the hydrodynamics, producing a system of parabolic partial differential equations which are solved numerically. We employ a relatively simple reaction mechanism to describe the inhomogeneous gas-surface chemistry. Ultimately we should include a more detailed model of the surface chemistry, but presently we are primarily interested in a quantitative description of the gas phase. Moreover, as we discuss later, this gas-phase model alone is very successful in describing CVD experimental observables. Our treatment of the gas phase is greatly aided by our earlier work on modeling combustion chemistry (1, 2). Also, our modeling is performed in conjunction with experimental measurements of chemical species concentrations in the gas phase (3).

Our principal purpose in this paper is to present a complete description of the mathematical and numerical formalism of the model. There have been many other theoretical approaches to modeling CVD, however, most of these models have not considered the possibility of gas-phase chemistry. The present model is the most detailed model of the gas phase in CVD to date.

Below we present details of the model, including the set of governing partial differential equations, the reaction mechanism describing SiH_4 pyrolysis, and the numerical solution method. We also present computed temperature, velocity, and chemical species concentration profiles. We compare predicted deposition rates with experimental results.

Key words: CVD, growth, kinetics, transport.

Model Formulation

Transport equations.—We assume in this work that the boundary layer approximations are valid. That is, the Navier-Stokes equations can be reduced to a system of parabolic partial differential equations describing the conservation of mass, momentum, energy, and species composition. The approximation relies on the existence of a principal flow direction in which convective transport is dominant and diffusive effects are negligible. In this approach the pressure is impressed on the flow by the boundary conditions and is uniform in the cross-stream direction. The imposition of pressure replaces the cross-flow momentum equation entirely.

After making the boundary layer approximations, we use the Von Mises transformation (4) to cast the equations in a form in which the stream function replaces the radial coordinate as an independent variable. This transformation eliminates the mass conservation equation, replacing it with an integral. Additionally, it eliminates any explicit reference to the cross-stream convective terms in the resulting system of equations.

The system of equations which form our model are described as follows

Momentum

$$\rho u \frac{\partial u}{\partial x} + \frac{\partial p}{\partial x} = \rho u \frac{\partial}{\partial \psi} (\rho u \mu y^{2\alpha} \frac{\partial u}{\partial \psi}) + \rho g \quad [1]$$

Species

$$\rho u \frac{\partial Y_k}{\partial x} = \dot{\omega}_k W_k - \rho u \frac{\partial}{\partial \psi} (y^\alpha \rho Y_k V_{ky}) \quad (k = 1, K) \quad [2]$$

Energy

$$\rho u c_p \frac{\partial T}{\partial x} = \rho u \frac{\partial}{\partial \psi} (\rho u \lambda y^{2\alpha} \frac{\partial T}{\partial \psi}) - \sum_{k=1}^K \dot{\omega}_k W_k h_k - \rho^2 u y^\alpha \sum_{k=1}^K Y_k V_{ky} c_{pk} \frac{\partial T}{\partial \psi} \quad [3]$$

State

$$p = \rho \frac{R}{\bar{W}} T \quad [4]$$

The diffusion velocity V_{ky} is given in the new coordinates by

$$V_{ky} = - \frac{D_k}{X_k} \rho u y^\alpha \frac{\partial X_k}{\partial \psi} \quad [5]$$

In these equations, the independent variables x and ψ represent the axial coordinate and stream function, re-

spectively. For an axisymmetric flow, the parameter α is 1, and y represents the radius measured from the flow centerline. For $\alpha = 0$ the equations are in planar coordinates. In both cases, the cross-stream coordinate y is a dependent variable and is given in terms of stream function by the following integral

$$\frac{y^{\alpha+1}}{\alpha+1} = \int_0^\psi \frac{d\psi'}{\rho u} \quad [6]$$

or, in the differential equation form that we actually use, by

$$\frac{\partial y^{\alpha+1}}{\partial \psi} = \frac{\alpha+1}{\rho u} \quad [7]$$

Other variables are given by: u , the axial fluid velocity; ρ , the mass density; p , the thermodynamic pressure; T , the temperature; Y_k , the mass fraction of the k th species; X_k , the mol fraction of the k th species; W_k , the molecular weight of the k th species; R , the universal gas constant; g , the acceleration of gravity; D_k , the binary diffusion coefficient of the k th species into the mixture; μ , the mixture viscosity; λ , the mixture conductivity; c_p , the specific heat at constant pressure; h_k , the specific enthalpy of the k th species; ω_k , the rate of production of the k th species by chemical reaction; \bar{W} , the mixture's mean molecular weight.

The transport properties (viscosity, thermal conductivity, and diffusion coefficients) are temperature dependent and are obtained from Lennard-Jones parameters for each of the chemical species using standard techniques (5-8). The specific formulas employed are discussed in detail by Kee and Miller (9).

We compute thermodynamic properties (heat capacities, entropies, and enthalpies) for each of the chemical species from temperature-dependent fits of data [JANAF when available (10)] in the form used by the NASA chemical equilibrium code (11). Thermochemical data were not available for SiH_2 , SiH_3 , Si_2H_2 , Si_2H_3 , Si_2H_4 , Si_2H_5 , and Si_2H_6 . For these species we used the results of an extensive set of electronic structure calculations by Binkley (12) to estimate entropies, energies, and harmonic vibrational frequencies. Standard statistical mechanical techniques (13) were used to convert the frequencies and energies to $c_p(T)$, $h(T)$, and $s(T)$, which were then fit to the polynomial form of Gordon and McBride (11). In the code all chemical production rate terms, thermodynamic properties, and equation of state variables are evaluated by appropriate subroutine calls to CHEMKIN (14), a general-purpose package of chemical kinetics Fortran subroutines.

Boundary conditions.—The two different channel types treated here, axisymmetric and planar, each require slightly different boundary condition formulations. In both cases the equations are parabolic, so boundary conditions are specified for u , T , Y_k , y , and p at the boundary $x = 0$. However, since the x coordinate is time-like for purposes of numerical solution algorithms, the boundary conditions at $x = 0$ may be regarded as initial conditions. In equations of this type (differential/algebraic equations), all of the initial conditions are not independent. Once u , T , Y_k , and p are specified at $x = 0$, the cross-stream velocity v follows as an integral of the mass conservation equation. In stream function coordinates, where v has been eliminated as a variable, it follows that the physical coordinate y must be consistent with the other initial conditions.

The channel walls (or an axis of symmetry and a wall) define the flow boundaries. In stream function coordinates, the walls correspond to streamlines, or lines of constant stream function. By definition, flow is tangent to streamlines; thus, no flow crosses a wall (or axis of symmetry). The boundary condition, corresponding to either the lower wall or the axis of symmetry, is applied at $\psi = 0$. The other boundary condition is applied at ψ_0 , where ψ_0 is determined from Eq. [6] when ψ and u are evaluated at the initial conditions, and an initial mesh in y is specified.

For axisymmetric problems, an axis of symmetry is specified at $\psi = 0$ by

$$\frac{\partial u}{\partial \psi} = \frac{\partial T}{\partial \psi} = \frac{\partial Y_k}{\partial \psi} = 0 \quad [8]$$

In addition, we specify that $y = 0$ at $\psi = 0$.

On solid walls we specify the no-slip boundary, $u = 0$. In some cases we specify T itself, while in others we specify a heat flux, *i.e.*, a temperature gradient. Zero gradients are imposed for the mass fractions of species that do not react at walls (implying no mass flux to the wall). For species that react at the wall, the boundary conditions are more complex, and are discussed below.

Chemical reactions at solid surfaces.—The boundary conditions on chemical species concentrations at a heated surface depend on the extent to which each species undergoes surface reactions. Some species react at the heated surface, depositing silicon. In this model we consider two types of deposition reactions, depending on whether the species is a saturated or unsaturated compound.

Because of the reactive nature of unsaturated chemical species, we assume that they react with the solid surface with unit probability and release molecular hydrogen; in this model these species are SiH , SiH_2 , SiH_3 , Si_2H_2 , Si_2H_3 , Si_2H_4 , and Si_2H_5 . Species that react with unit probability on the surface cannot exist there (because they react instantaneously), and thus the boundary condition for those species is given by

$$Y_{\text{SiH}} = Y_{\text{SiH}_2} = Y_{\text{SiH}_3} = Y_{\text{Si}_2\text{H}_2} = Y_{\text{Si}_2\text{H}_3} = Y_{\text{Si}_2\text{H}_4} = Y_{\text{Si}_2\text{H}_5} = 0 \quad [9]$$

Results of our model are relatively insensitive to this boundary condition. For example, changing the assumed surface-reaction probability from 1 to 0.8 changes the predicted deposition rate by 5% or less.

We assume that the species H , Si_2H_6 , and inert carrier gases do not react at the surface. These species have zero flux to the surface, and thus we enforce the following boundary conditions

$$V_{\text{yH}} = V_{\text{ySi}_2\text{H}_6} = 0 \quad [10]$$

We use the empirical silane surface reaction coefficient of Farrow (15) to describe the deposition due to SiH_4 reacting at the surface. The fraction of silane molecules that decompose upon collision with a heated surface is given by

$$\gamma = 5.45 \exp(-8556/T) \quad [11]$$

However, only a fraction of the silane that decomposes at the surface leads to the formation of solid silicon. According to Farrow's data, this fraction is given by

$$\sigma = 7.6 \times 10^{-3} \exp(3535/T) \quad [12]$$

We assume, as did Farrow, that the rest of the silicon formed by the surface decomposition diffuses away from the surface as gas-phase silicon atoms.

The surface-decomposition fraction (γ) is incorporated into the model as a boundary condition on the SiH_4 concentration. This reaction coefficient is defined as the fraction of the silane flux into the boundary which is decomposed. At steady state, the net flux (incoming minus outgoing flux) at the boundary is equal to the surface reaction rate. The ratio of the flux that would be present for a fractional reaction probability to the flux for a unit reaction probability equals the fraction of the flux which is decomposed. In other words, this ratio is equal to γ of Eq. [11], and the boundary condition derived from this relationship is

$$(V_{\text{ySiH}_4})_{\psi=1} = \gamma (J_{\text{ySiH}_4})_{\psi=1} \quad [13]$$

The notation $(J_{\text{ySiH}_4})_{\psi=1}$ refers to flux which would exist if the concentration of SiH_4 were zero on the boundary, *i.e.*, unit reaction probability.

From Eq. [12] we can calculate the amount of gas-phase Si atoms formed as a fraction $(1 - \sigma)$ of the silane decomposed at the surface. Equation [14] determines the flux of $\text{Si}(g)$ away from the surface

$$-\frac{V_{\text{ySi}} Y_{\text{Si}}}{W_{\text{Si}}} = (1 - \sigma) \frac{V_{\text{ySiH}_4} Y_{\text{SiH}_4}}{W_{\text{SiH}_4}} \quad [14]$$

We now need a relationship between the flux of reactive species into the surface and the flux of hydrogen away from the surface. The hydrogen that was initially tied up in silicon containing species is released when the silicon is deposited. In our model the hydrogen atom flux to the surface is balanced by a flux of molecular hydrogen from the surface. (These incoming hydrogen atoms are contained in the surface reacting species.) This relationship is stated in the following boundary condition

$$-\frac{V_{yH_2}Y_{H_2}}{W_{H_2}} = \frac{V_{ySiH}Y_{SiH}}{2W_{SiH}} + \frac{V_{ySiH_2}Y_{SiH_2}}{W_{SiH_2}} + \frac{3V_{ySiH_3}Y_{SiH_3}}{2W_{SiH_3}} + \frac{2V_{ySiH_4}Y_{SiH_4}}{W_{SiH_4}} + \frac{V_{ySi_2H_2}Y_{Si_2H_2}}{W_{Si_2H_2}} + \frac{3V_{ySi_2H_3}Y_{Si_2H_3}}{2W_{Si_2H_3}} + \frac{2V_{ySi_2H_4}Y_{Si_2H_4}}{W_{Si_2H_4}} + \frac{5V_{ySi_2H_5}Y_{Si_2H_5}}{2W_{Si_2H_5}} \quad [15]$$

The cross-flow velocity must vanish at both the upper and lower boundaries of a channel, *i.e.*, $v = 0$. In stream function coordinates this is accomplished by requiring that the physical coordinate y is zero at the lower surface (or axis of symmetry), and that y equals the channel width (or radius) at the upper streamline ψ_0 . However, since the equation for y [7] is first order, we normally could not require two boundary conditions. We overcome this restriction by retaining the pressure as dependent variable. The extra boundary condition thus allows us to obtain the unique pressure function $p(x)$ (subject to the given value of p at $x = 0$), which is consistent with having two walls (or one wall and an axis of symmetry) in the problem. During the course of the solution we must determine the $p(x)$ which allows the two boundary conditions on $y(\psi)$ to be satisfied simultaneously. In other words, the pressure drop is computed to balance the shear forces exerted by the walls on the fluid.

Chemical reaction mechanism.—The kinetics of SiH_4 thermal decomposition has been the subject of a number of studies (16-20). The reaction mechanism for silane decomposition employed in this work is given in Table I. A further discussion of the reaction mechanism is presented elsewhere (21). Its development was in essentially two stages. First, a large system of 120 elementary reactions was constructed. Using that mechanism, we performed extensive sensitivity analysis (without any transport effects). From this analysis we determined that silane pyrolysis under conditions of interest could be described as a constrained equilibrium process (22). That is, the time evolution of all the species concentrations is determined strictly by the initial silane dissociation step, whose rate coefficient has been experimentally determined (16). Subsequent radical-molecule and radical-radical reac-

tions simply act to shuffle the intermediate species concentrations to their constrained equilibrium values. Therefore, in the interests of simplicity in the boundary layer computations, we reduced the reaction mechanism to the current 20-step mechanism. Over the range of interest this reduced reaction set reproduces the essential features of the full mechanism, *i.e.*, the initiation step is correct and the constrained equilibrium character is preserved.

As part of the analysis of the reaction mechanism we did a formal sensitivity analysis (23), and determined small sensitivities for all rate constants except the initiation step. In addition, in the boundary layer calculations, we did a series of tests in which each of the rate constants of the secondary reactions (R2-R20) were arbitrarily increased and decreased by a factor of 10, and we found that the predicted deposition rates were unaffected. On the other hand, similar tests show a measurable sensitivity to the initiation step. This sensitivity, of course, depends on the particular temperature and flow conditions.

Numerical method.—Method-of-lines formulation.—Our general approach is that of the method-of-lines. After discretization of the spatial derivatives, numerical solution of the resulting system of differential/algebraic equations (DAE's) is accomplished with a code developed by Petzold (24) called DASSL. DASSL solves the equations in a marching fashion, starting from the inflow boundary ($x = 0$) and going toward the outflow boundary. The code implements a variable-order, variable-step algorithm based on the backward differentiation formula (BDF) methods (25). These are stable methods that are particularly well suited for solution of the stiff equations that occur in chemical kinetic models. The DASSL code chooses a sequence of time steps (actually x -coordinate steps) such that the local truncation error in the marching direction is controlled to within a prespecified error tolerance. The general approach in using DASSL is to write a residual function $g(t, y, y')$ at each mesh point, which is zero when the equations are satisfied. DASSL iterates on the solution at each time step until the approximate solution y and y' are sufficiently accurate and so g is zero.

We make the distinction here between standard form ordinary differential equations (ODE's) which are written as $y' = f(t, y)$, and DAE's, which are written in the more general form $g(t, y, y') = 0$. For our purpose, systems of DAE's are distinguished from ordinary systems of parabolic equations by (i) an inability to isolate one time-like derivative per equation (the x derivatives in the boundary layer problem), and/or (ii) coupled equations which have no time-like derivatives. The former situation occurs in our equations when both $\partial u/\partial x$ and $\partial p/\partial x$ appear in the momentum equation. The latter situation occurs in the equations defining the spatial coordinate y in terms of the stream function via Eq. [7], and in specifying a uniform pressure across the channel. The boundary conditions in the y -coordinate are also regarded as algebraic equations.

Approximation of the spatial derivatives is accomplished by finite difference representations on a fixed grid in the stream function. In the momentum, species, and energy equations, we approximate the second derivatives with conventional central difference formulas as

$$\frac{\partial}{\partial \psi} \left(a \frac{\partial f}{\partial \psi} \right) \approx \left(\frac{2}{\psi_{j+1} - \psi_{j-1}} \right) \left[a_{j+1/2} \left(\frac{f_{j+1} - f_j}{\psi_{j+1} - \psi_j} \right) - a_{j-1/2} \left(\frac{f_j - f_{j-1}}{\psi_j - \psi_{j-1}} \right) \right] \quad [16]$$

where the subscript j denotes the j th grid point. We approximate the first derivatives, as needed in Eq. [3], by central differences as

$$\frac{\partial T}{\partial \psi} \approx \frac{T_{j+1} - T_{j-1}}{\psi_{j+1} - \psi_{j-1}} \quad [17]$$

We evaluate terms with no derivatives, such as the chemical production rate in Eq. [2], using the conditions existing at ψ_j . Likewise, the coefficients of derivatives, such as ρu in Eq. [1], are also evaluated at ψ_j .

Table I. Reaction mechanism

Reaction number	Reaction	A^a	E_a^a	Reference
R1	$SiH_4 \rightarrow SiH_3 + H_2$	5.00E12	52.2	(16)
R2	$SiH_4 \rightarrow SiH_3 + H$	3.69E15	93.	(17, 21)
R3	$SiH_4 + SiH_2 \rightarrow Si_2H_6$	5.01E12	1.29	(18)
R4	$Si_2H_6 + H_2 \rightarrow SiH_4 + SiH_2$	6.22E16	2.	(21)
R5	$SiH_4 + H \rightarrow SiH_3 + H_2$	1.04E14	2.5	(19, 20)
R6	$SiH_4 + SiH_3 \rightarrow Si_2H_6 + H_2$	1.77E12	4.4	(21)
R7	$SiH_4 + SiH \rightarrow SiH_3 + SiH_2$	1.38E12	11.2	(21)
R8	$SiH_4 + SiH \rightarrow Si_2H_6$	2.93E12	2.	(21)
R9	$SiH_4 + Si \rightarrow 2SiH_2$	9.31E12	2.	(21)
R10	$Si + H_2 \rightarrow SiH_2$	1.15E14	2.	(21)
R11	$SiH_2 + SiH \rightarrow Si_2H_3$	1.26E13	2.	(21)
R12	$SiH_2 + Si \rightarrow Si_2H_2$	7.24E12	2.	(21)
R13	$SiH_2 + Si_3 \rightarrow Si_2H_2 + Si_2$	1.43E11	18.8	(21)
R14	$H_2 + Si_2H_2 \rightarrow Si_2H_4$	2.45E14	2.	(21)
R15	$H_2 + Si_2H_4 \rightarrow Si_2H_6$	9.31E12	2.	(21)
R16	$H_2 + SiH \rightarrow SiH_3$	3.45E13	2.	(21)
R17	$H_2 + Si_2 \rightarrow Si_2H_2$	1.54E13	2.	(21)
R18	$H_2 + Si_2H_3 \rightarrow Si_2H_5$	2.96E13	2.	(21)
R19	$Si_2H_2 + H \rightarrow Si_2H_3$	8.63E14	2.	(21)
R20	$Si + Si_3 \rightarrow 2Si_2$	2.06E12	24.1	(21)

^a Arrhenius parameters for the rate constants in the form $k_i = A_i \exp(-E_i/RT)$. The units of A_i depend on the reaction order, but are given in terms of mols, cubic centimeters, and seconds. E_a is in kcal/mol.

Integral conditions such as Eq. [6] (or, equivalently, first-order ODE's) are differenced according to the trapezoidal rule as

$$\frac{y_j^{\alpha+1} - y_{j-1}^{\alpha+1}}{\psi_j - \psi_{j-1}} = (\alpha + 1) \frac{2}{\rho_j u_j + \rho_{j-1} u_{j-1}} \quad [18]$$

It is important to represent the integral equations as first-order differential equations and include the variables such as $y^{\alpha+1}$ in the dependent variable vector. The reason for this choice is associated with the structure of the Jacobian matrix which is needed ultimately to solve the problem. When Eq. [18] is used, the number of dependent variables increases, but the Jacobian remains banded (a very desirable feature). On the other hand, if $y^{\alpha+1}$ is considered as a coefficient in the transport equations as defined by the integral Eq. [6], then the Jacobian loses its banded property and the required computer storage increases enormously.

Boundary conditions.—We treat the boundary mesh points the same way logically as we do the interior points. That is, we consider each dependent variable as an unknown on the boundaries and solve a system of equations to determine its value. Since the boundary equations usually do not involve marching derivatives, using such a formalism requires that the full system be solved as a system of DAE's. The procedure may appear inefficient when the boundary values are known exactly and therefore need not be considered as variables. However, its advantage is that all boundary conditions, regardless of complications (e.g., surface reactions involving many species), are treated in the same manner logically. Thus the boundary conditions of a problem can change without changing the logical structure of the dependent variable vector and the Jacobian. Changing from one set of boundary conditions to a completely different set requires very little programming effort. Moreover, with this formalism, boundary conditions on one equation may be functions of variables which would nominally be associated with another equation. For example, a surface reaction boundary condition typically involves several species concentrations and temperature.

As a final note on the numerical method, we discuss application of the uniform pressure condition. Since it is uniform, we could consider the pressure as a single component in the dependent variable vector. However, since the pressure appears in each equation at each mesh point (either directly as $\partial p/\partial x$ or indirectly in transport property

evaluations), using only one variable is undesirable because so doing destroys the block tridiagonal Jacobian structure. We therefore consider the pressure to be an unknown at each mesh point, and solve an equation that forces the pressure at adjacent mesh points to be equal, i.e., $dp/d\psi = 0$. Although we increase the number of dependent variables, we retain the desired Jacobian structure. The finite difference equation at the mesh points states simply that pressure at adjacent nodes is equal

$$p_j - p_{j+1} = 0 \quad [19]$$

The boundary condition applied to Eq. [19] is that y at the outer channel wall is equal to the physical coordinate at the wall. In other words, there is no explicit boundary condition on pressure per se, but the needed boundary condition on y is used implicitly. Note that unlike Eq. [18], which involves nodes j and $j - 1$, Eq. [19] involves nodes j and $j + 1$. This indexing is needed to maintain the block tridiagonal Jacobian structure. We evaluate Eq. [18] at the inner boundary and Eq. [19] at the outer boundary; therefore they are both part of the boundary condition specification at their respective boundaries.

Predictions of Model

The computer model predicts a large number of experimentally observable quantities in the CVD cell; these are discussed individually below. These predictions fall into three broad categories: gas-flow properties, chemical species concentration fields, and deposition rates. Calculated fluid flow quantities include temperature fields, flow streamlines, and velocity fields; these are plotted in Fig. 1.

Two dimensional temperature contours predicted by the model are given in Fig. 1a for a typical run. The incoming gas temperature, at the left of Fig. 1a, is taken as 300 K. The gas is heated from contact with the hot lower surface, causing temperature gradients above the susceptor. Temperature profiles predicted depend on susceptor temperature, flow rate, and carrier gas. As an example, in Fig. 2 we compare temperature profiles under different flow conditions at a fixed susceptor temperature and distance along the susceptor.

Temperature profiles in Fig. 2 for He and H₂ are almost identical because their transport properties are very similar. However, gas-phase chemistry rates and deposition rates are dramatically different in these two carrier gases. The effect of flow velocity on temperature profiles is illustrated in Fig. 2. Increasing the He flow rate by a factor

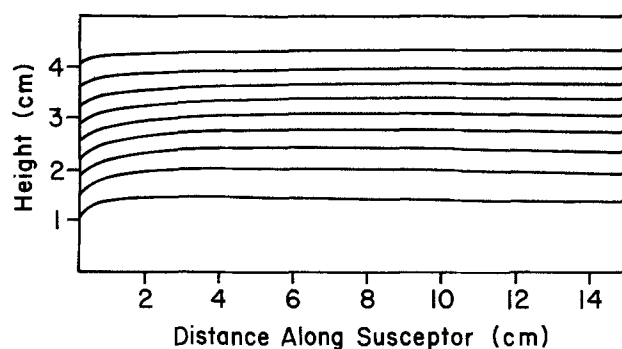
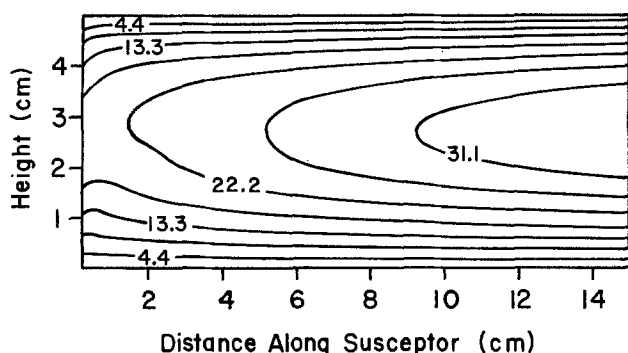
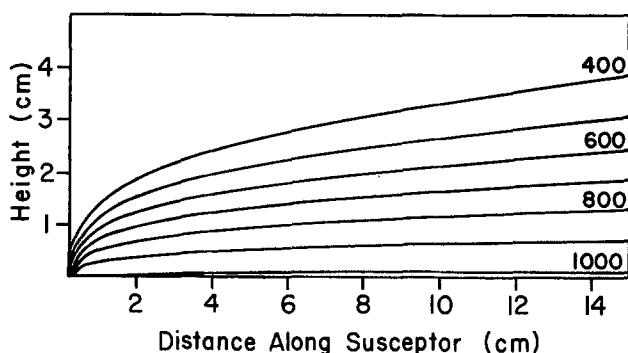


Fig. 1. Fluid flow properties predicted by the numerical model for a typical CVD calculation. Input conditions: susceptor temperature = 1018 K, inlet gas temperature = 300 K, average gas velocity = 15.3 cm/s, 0.6 torr SiH₄ in 640 torr He. A, upper left: temperature contours, labeled in Kelvin. B, upper right: flow streamlines. C, left: gas velocity contours, labeled in cm/s.

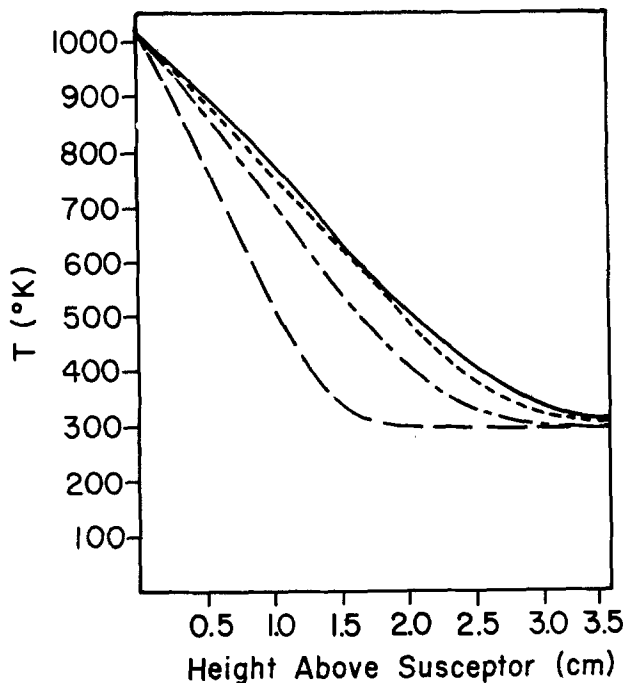


Fig. 2. Temperature profiles as a function of height above the susceptor, calculated for different carrier gases and initial velocities. Input conditions: susceptor temperature = 1018 K, 0.6 torr SiH_4 in 640 torr carrier gas. Profiles are calculated at 4.5 cm from the leading edge of the susceptor. Carrier gases and average velocities are as follows, N_2 : 15.3 cm/s (dashed curve). H_2 : 15.3 cm/s (dotted curve). He: 15.3 cm/s (solid curve). He: 30.6 cm/s (alternating dash-dot curve).

of two creates a sharper temperature gradient; the gas has shorter residence time in the heated region, and therefore higher temperatures cannot extend as far into the gas. Temperature profiles in N_2 carrier are much steeper than in He because nitrogen has a much smaller thermal conductivity. Although N_2 and He are both inert CVD carrier gases, they are not completely interchangeable. The dissimilar temperature profiles will make the extent of gas-phase reactions much different.

Flow streamlines predicted by the model are plotted in Fig. 1b. The streamlines are forced away from the susceptor at its leading edge. The physical explanation for this phenomena is simple. When the gas enters the heated region it expands. Because, by definition, the volume flow rate between two streamlines is constant, the y position of the lower streamline must increase. Most of the expan-

sion of the gas takes place at the leading edge of the susceptor, so the streamlines remain relatively horizontal downstream. Figure 1c shows velocity contours for a typical calculation. We assume the velocity profile at the inlet to be fully developed, *i.e.*, parabolic. The velocity profile remains roughly parabolic further downstream, but the maximum velocity increases due to expansion of the gas.

Chemical species concentrations result from gas-phase chemical reactions in the fluid-flow field. Because the reactions are very temperature sensitive, they exhibit a 2-D spatial variation with the gas-phase temperature. The resulting concentration profiles are thus a sensitive function of susceptor temperature, flow velocity, and carrier gas. Thermal decomposition of silane is rapid in the gas phase close to the hot susceptor. The model predicts the SiH_4 concentration profiles as a function of distance along the susceptor, as illustrated in Fig. 3. At the inlet there is a uniform concentration of room temperature SiH_4 above the susceptor. Downstream, chemical reactions, primarily reaction R1, deplete silane in the gas phase. The depletion is greater and the concentration profile is broader as distance downstream increases.

Figure 4 depicts the sensitivity of predicted silane partial pressure profiles to carrier gas and flow rate. The silane profile in the nitrogen carrier is steeper than in helium, due to the different temperature profile, as discussed above, which results in different decomposition rates. Because the gas-phase temperature is higher in He than in N_2 at a given height above the susceptor, more silane decomposition occurs in He and the silane partial pressure is reduced.

Hydrogen is a product of the SiH_4 decomposition reaction. Thus, an excess of H_2 used as a carrier gas tends to equilibrate the decomposition, resulting in less SiH_4 decomposition. This suppression is reflected in the silane profile in H_2 carrier gas plotted in Fig. 4. At a given temperature, there is much less decomposition of SiH_4 in H_2 than in He. As a result, there is less silane depletion in H_2 , and the deposition rate (discussed in the next section) is much less than in He.

Gas velocity has an important effect on the gas-phase concentration profiles. As gas velocity is increased, the residence time of silane in the heated region is reduced. Therefore, when gas-phase kinetics are slow (at low temperatures), the SiH_4 does not react as extensively, and there is less depletion in the silane partial pressure profile. Figure 4 shows this result when the gas velocity is doubled in He carrier gas.

Because H_2 is a product of the silane decomposition, the H_2 concentration profiles are closely related to those of SiH_4 . Figure 5 is a plot of hydrogen concentration profiles for a calculation in He carrier. The H_2 concentration increases with distance along the susceptor and is at

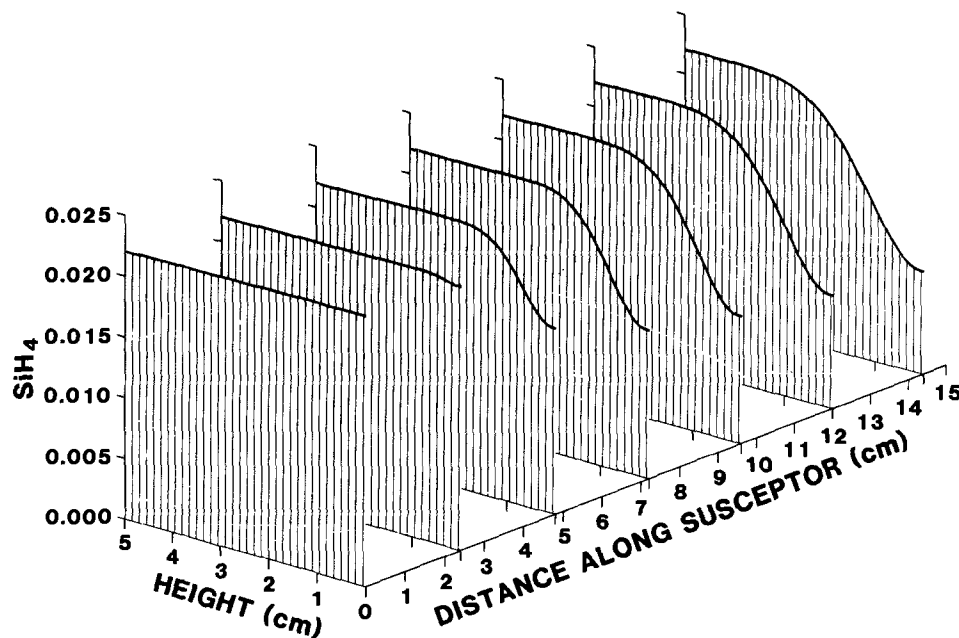


Fig. 3. Silane mass fraction profiles as a function of height above the susceptor and distance along the susceptor for a typical calculation. Input conditions: susceptor temperature = 1000 K, average gas velocity = 12 cm/s, 1.74 torr SiH_4 in 620 torr He.

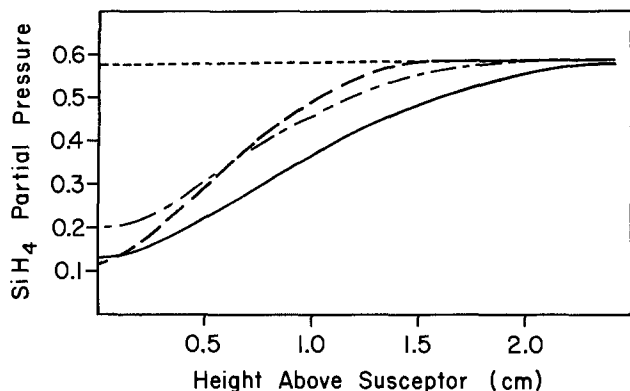


Fig. 4. Silane partial pressure profiles as a function of height above the susceptor, calculated for different carrier gases and initial velocity. Input conditions and identification of curves are the same as in Fig. 2.

maximum near the surface, where silane decomposition is most rapid.

We computed concentration profiles for all chemical species in the reaction scheme (Table I). As an example of

the behavior of a typical intermediate species, we plotted profiles of Si_2H_2 in Fig. 6. The Si_2H_2 profile increases with distance along the susceptor as more chemical reactions take place. However, the Si_2H_2 concentration drops to zero at the surface, due to the boundary condition describing deposition (Eq. [9]). Since it has a large gradient at the surface, Si_2H_2 makes a large contribution to the deposition rate in He carrier gas, as we discuss in the next section.

We observed that a reaction zone begins at the leading edge of the susceptor, and it moves outward and downstream as the silane is depleted and heat diffuses out. In this zone chemical production and depletion takes place; outside the zone only transport processes are active. We also observe that the secondary reactions are all equilibrated in the reaction zone. In high temperature cases, even the initiation step equilibrates in the reaction zone. The position of the reaction zone is determined both by heat transfer away from the heated susceptor and mass transfer processes in the gas phase. The process is quite analogous to what occurs in a diffusion flame [see for example, Miller and Kee (26)].

We picture the process as one in which a reaction zone moves away from the susceptor, eating into the unreacted silane. There is a diffusive flux of silane into the reaction zone from the cold region, and there is little diffusive

Fig. 5. Hydrogen mass fraction profiles as a function of height above the susceptor and distance along the susceptor. Input conditions are the same as in Fig. 3.

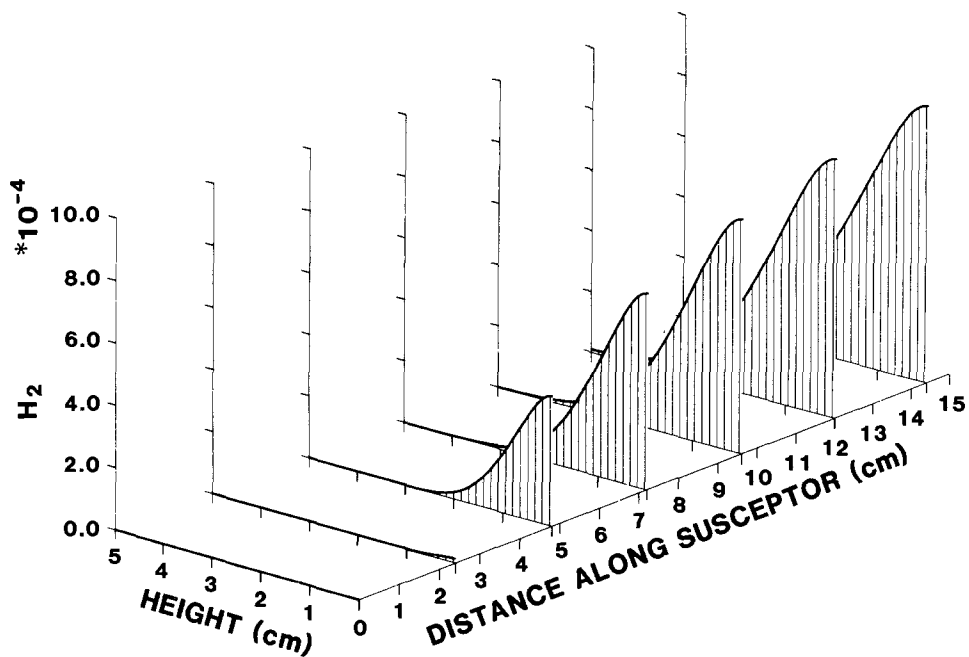
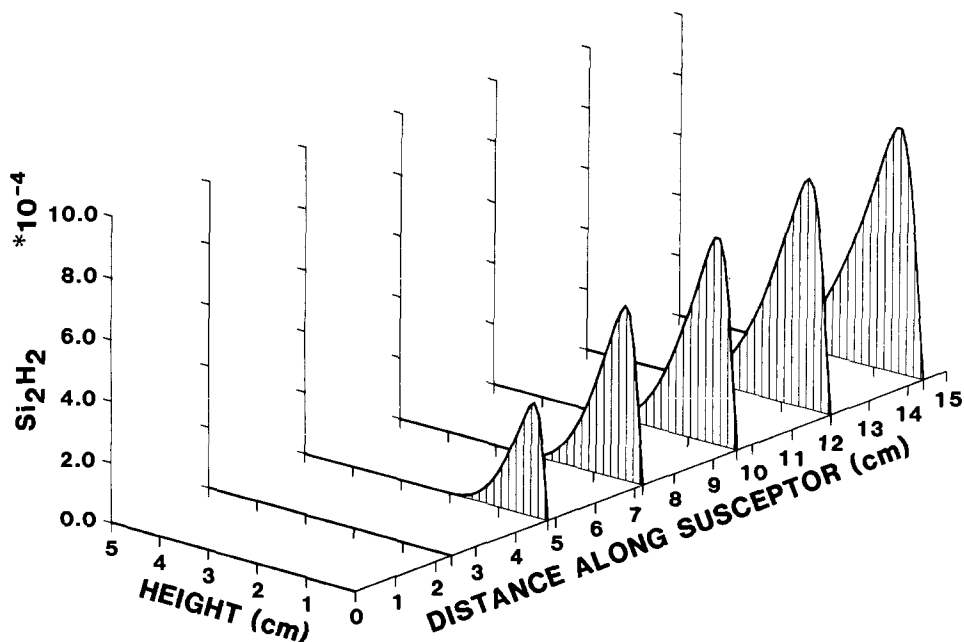


Fig. 6. Si_2H_2 mass fraction profiles as a function of height above the susceptor and distance along the susceptor. Input conditions are the same as in Fig. 3.



flux of silane out of the reaction zone to the susceptor. In high temperature cases, nearly all the silane is depleted in the reaction zone, while in low temperature cases, the silane is not all depleted in the reaction zone because the initiation step is slower. The intermediate species that are chemically produced in the reaction zone diffuse in both directions. The species that diffuse to the susceptor ultimately react on the surface and deposit silicon. The species that diffuse into the cold region remain essentially frozen or unreacted (far from equilibrium) until the reaction zone ultimately reaches them, and reaction occurs.

Within the reaction zone we find a state of "constrained equilibrium" (22). That is, all reactions, except the initiation step, are sufficiently fast that they are essentially in chemical equilibrium. The species production and depletion rates are controlled by diffusive transport and thermodynamic considerations, rather than individual reaction rates. Therefore, we find that the deposition rates and the species profiles are insensitive to the specific rate constants used (except the initiation step). This is fortunate, since there are few measurements of elementary rate constants for the reaction of the silicon intermediate species. However, in many cases the thermodynamic properties that are needed to compute equilibrium constants have been measured, and the others can be estimated from *ab initio* electronic structure computations (12).

Deposition Rate Predictions

A common feature of many CVD systems is that the apparent activation energy for deposition rates at high temperatures is much smaller than at low temperatures. At high temperatures the CVD reactions are very fast. In this case, the deposition rate is limited by the rate at which reactive species can diffuse to the surface, and is not sensitive to temperature. There have been many models for silicon CVD in the high temperature regime (27-46). Usually these models assume that silane does not react in the gas phase, but instead reacts instantaneously at the hot surface. Thus, the SiH_4 concentration at the surface is set to zero as a boundary condition. In many high temperature models, parameters, such as boundary-layer thickness and diffusion constants, are adjusted so that predicted deposition rates match experimental data.

At low temperatures, the apparent activation energy for deposition is much larger than at high temperatures. Because reactions at low temperature are relatively slow, these lower deposition rates have previously been attributed to the kinetics of surface reactions (47-55).

Figure 7 presents a comparison between experimental and theoretical deposition rates as a function of distance along a 1323 K susceptor in H_2 carrier gas. The log of the deposition rate *vs.* distance, from Eversteyn *et al.* (29), was found to be linear, and is represented in Fig. 7 as the solid line. Results of our numerical model are plotted as the square symbols. The agreement between theory and experiment is excellent without adjusting parameters.

At 1323 K, gas-phase decomposition of silane is very fast, and the deposition rate is limited by the rate of diffusion of silicon containing species to the surface. The calculation in Fig. 7 indicates that for these experimental conditions, the radical SiH_2 is primarily responsible for the deposition.

It is useful to compare our model with ones that make the assumptions typically employed in modeling high temperature silicon CVD. These assumptions are that gas-phase decomposition of the SiH_4 does not occur and that SiH_4 reacts instantaneously at the surface, *i.e.*, its concentration is zero there. The results plotted in Fig. 7 as triangles are obtained when our numerical model is used to solve the fluid flow equations with gas-phase chemistry suppressed and the concentration of silane set to zero at the surface, to mimic the previous models. Agreement is very close between the two models, although the mechanisms are dramatically different. This apparent inconsistency is readily explained. The SiH_4 reacts very rapidly in the gas phase close to the susceptor, creating a steep concentration gradient. This silane concentration gradient is nearly equal to that in the second calculation, in which the SiH_4 concentration was set to zero at the surface. In addition, the SiH_2 formed near the surface via re-

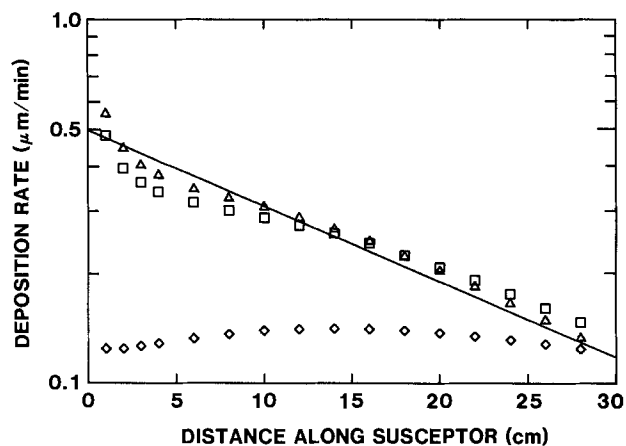


Fig. 7. Comparison of theoretical and experimental deposition rates as a function of distance along the susceptor. Experimental data from Eversteyn *et al.* (29) is well described by the solid line. Points are from model calculations with the following input conditions: susceptor temperature = 1323 K, average gas velocity = 17.5 cm/s, 0.76 torr SiH_4 in 1 atm of H_2 , cell height = 2 cm. Squares are results of the full model. Triangles are results when gas-phase chemistry is omitted and the SiH_4 concentration on the surface is set to zero. Diamonds are results when gas-phase chemistry is omitted and the SiH_4 surface concentration is obtained from Eq. [11].

action R1 diffuses rapidly toward the surface with a diffusion constant close to that of silane. Thus, the rate of diffusion of silicon containing species toward the surface is almost identical in the two calculations.

The assumption that silane reacts with unit probability upon collision with the surface is in variance with experimental results (15, 56-61). Deposition rates calculated when gas-phase chemistry is again suppressed and the surface-reaction probability from Eq. [11] is used as the silane boundary condition are plotted in Fig. 7 as diamonds. This calculation indicates that the measured silane reaction efficiency at the surface is not sufficient to explain the deposition rates of Eversteyn *et al.* (29), and that gas-phase reactions must be included.

Deposition rates predicted by our model as a function of temperature, carrier gas, and total pressure are plotted in Fig. 8. The range of conditions covered in Fig. 8 represents a rigorous test of the model. Experimental deposition rates for a simple cell geometry that can be described well by our two-dimensional model were available only for the case of H_2 carrier gas. The data of van den Brekel (62) are plotted in Fig. 8 as solid triangles. Agreement between experimental and theoretical deposition rates is excellent over the temperature range 700°-1000°C. The model quantitatively predicts the deposition rates, as well as the transition between the high temperature behavior (weak temperature dependence) and low temperature behavior (much higher apparent activation energy). The correct prediction of the low temperature rate is significant because our model includes only the simple surface reaction mechanism described by the boundary conditions, Eq. [9] through [14]. In our model, at low temperatures the apparent activation energy for deposition is principally due to the temperature dependence of the gas-phase reactions in Table I.

The remaining theoretical predictions in Fig. 8 are in qualitative agreement with experimental deposition rate behavior (49, 63, 64). The model predicts two distinct temperature regions, where the apparent activation energies are significantly different. At 1 atm total pressure (APCVD) the low temperature deposition rate in He carrier gas is much higher than in H_2 , while at high temperatures they are almost equal. The activation energy is nearly equal in He and H_2 for low temperature APCVD. The knee in the APCVD plot occurs at a temperature 200 degrees higher in H_2 than in He carrier. For the case of 6 torr total pressure (LPCVD) the deposition rate is much greater than for APCVD, and there is very little dependence of deposition rate on carrier gas. The knee in the He curve is shifted to higher temperature as the total pres-

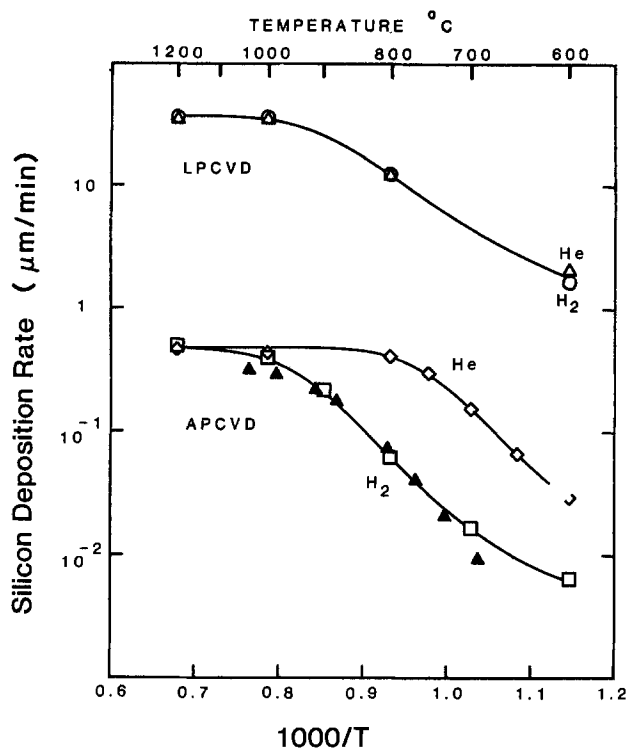


Fig. 8. Deposition rates predicted by the model (open symbols) as a function of temperature, total pressure, and carrier gas. Input conditions for all calculations: average gas velocity = 60 cm/s, 0.76 torr SiH_4 in either 760 torr of carrier gas (APCVD) or 7.6 torr of carrier gas (LPCVD), cell height = 1.25 cm. Deposition rates for APCVD and LPCVD are calculated 15 cm and 1 cm from the leading edge of the susceptor, respectively. Experimental data of van den Brekel (62) is given by the solid triangles. The solid curves have been drawn to distinguish between sets of calculated results.

sure is reduced with the silane partial pressure held fixed.

Many of the reaction rate constants in Table I were estimated. However, all of the calculations represented by

Fig. 1-8 were performed with the same set of rate constants, diffusion coefficients, etc. There has been no adjustment of parameters in the model to obtain agreement with experimental CVD data.

The chemical species that contributes most to the deposition process changes with experimental conditions. Figure 9a gives the percent contribution to the deposition rate of the various silicon containing chemical species in H_2 carrier gas, over the temperature range 600°-1200°C. At low temperatures, the silane surface decomposition reaction described by the boundary conditions in Eq. [11] through [13] contributes most to deposition. Below about 700°C, gas-phase reactions are very slow in H_2 carrier gas. Presence of the excess of H_2 inhibits the rate of decomposition by shifting the equilibrium toward the reactants. At higher temperatures, SiH_2 becomes the most important species contributing to deposition. SiH_2 is the product of the first step in the decomposition mechanism of silane. It is assumed to react at the surface with unit probability to form solid silicon and liberate H_2 gas.

Figure 9b is a similar plot for He carrier gas. Gas-phase chemistry is much faster in He than in H_2 and so, even at 600°C, the surface decomposition of SiH_4 is not nearly as important as in H_2 carrier. At temperatures below about 1000°C, Si_2H_2 is the species that contributes most to the deposition rate. Si_2H_2 is formed primarily because of the series of reactions R1,-R4,-R14. Each of these reactions is suppressed in an excess of H_2 , which is why Si_2H_2 is unimportant in Fig. 9a. At higher temperatures, Si_2 and Si_3 make the largest contribution to the deposition rate. These chemical species are formed in the reaction sequence R1,-R4,-R14,-R17,-R20, and -R13. This reaction sequence is also suppressed in H_2 .

Large concentrations of Si_2 and Si_3 are predicted in the gas phase, close to the susceptor. The model predicts 0.01 torr partial pressure of Si_2 above the susceptor at 1000°C in He carrier gas for the conditions described in Fig. 8. On the basis of these model predictions, Ho and Breiland (65) recently have used laser-excited fluorescence to detect Si_2 above the susceptor in a CVD reactor. This observation of Si_2 is a dramatic confirmation that the gas phase is far from thermodynamic equilibrium [in which Si_2 concentration would be roughly 2×10^{-18} torr, for the conditions of their experiment (65)]. The presence of Si_2 is predicted to turn on very rapidly with temperature, and to be sup-

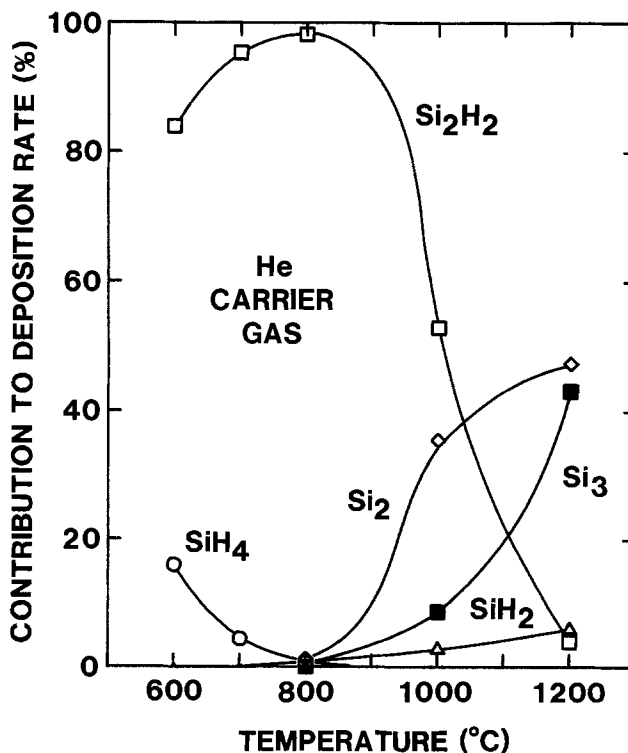
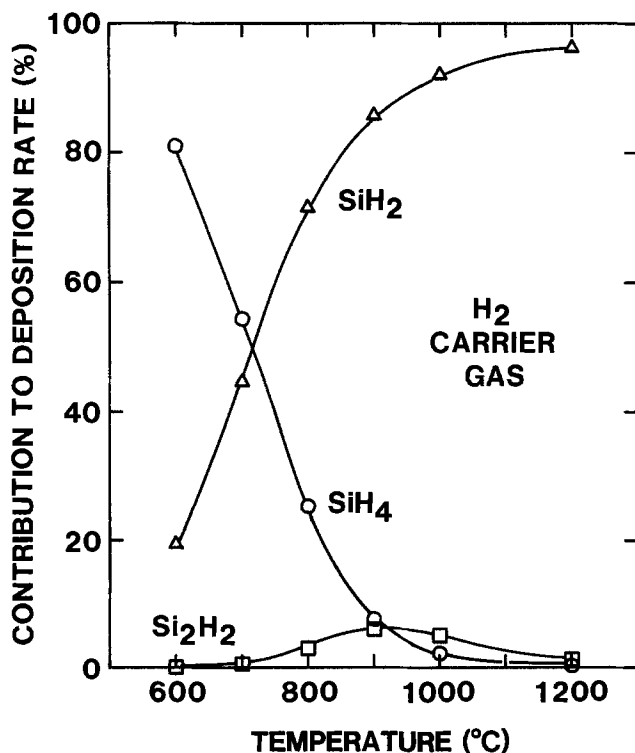


Fig. 9. Percent contributions made to the deposition rate by various chemical species as a function of temperatures in (a, left) H_2 carrier gas, and (b, right) He carrier gas. The chemical species and symbol in each plot are: SiH_4 (open circle), SiH_2 (open triangle), Si_2H_2 (open square), Si_2 (open diamond) and Si_3 (closed square).

pressed by about 5 orders of magnitude in an atmosphere of H₂ carrier. The behavior of the Si₂ and Si₃ concentrations closely mimic experimental observations of gas-phase nucleation of particulates in a CVD reactor. Particulates are observed to form very rapidly above a threshold temperature and are suppressed in H₂ carrier. It is possible that the reaction pathway leading to Si₂ and Si₃ is the precursor to the formation of these nucleation particles.

Summary

We have presented results of a detailed mathematical model of the coupled hydrodynamics and gas-phase chemical kinetics in the CVD of silicon from silane. The model has been used to predict gas-phase temperature, velocity, and chemical species concentration fields. The model also predicts deposition rates as a function of experimental variables, such as susceptor temperature, carrier gas, pressure, and flow velocity. Predicted deposition rates were in excellent agreement with experimental data in Fig. 7 and 8, without use of adjustable parameters.

The model indicates that at high temperatures silane decomposes very rapidly in the gas phase. Radicals formed from this decomposition diffuse to the surface and are primarily responsible for the deposition. The low temperature deposition rate was also described well by our gas-phase kinetics model. The success of the model at low temperature is significant, because the temperature dependence of the deposition rate there has previously been attributed to the rate of reactions on the surface.

These results indicate that the gas phase is very important in silicon CVD. The role of the gas phase merits much more attention than it has previously been given.

Acknowledgments

We would like to thank W. G. Breiland for many helpful discussions about the research presented here. The assistance of L. R. Petzold and J. S. Binkley is also gratefully acknowledged. This work was performed at Sandia National Laboratories and was supported by the U.S. Department of Energy under contract no. DE-AC04-76DP00789 for the Office of Basic Energy Sciences.

Manuscript submitted May 23, 1983; revised manuscript received Sept. 29, 1983. This was Paper 547 RNP presented at the Minneapolis, Minnesota, Meeting of the Society, May 10-15, 1981.

Sandia National Laboratories assisted in meeting the publication costs of this article.

REFERENCES

- M. C. Branch, R. J. Kee, and J. A. Miller, *Combust. Sci. Tech.*, **29**, 147 (1982).
- J. A. Miller, R. E. Mitchell, M. D. Smooke, and R. J. Kee, 19th International Symposium on Combustion, Pittsburgh, p. 181 (1982).
- P. Ho and W. G. Breiland, *Appl. Phys. Lett.*, **43**, 125 (1983).
- See, for example, "Theory of Laminar Flows," Vol. IV, High Speed Aerodynamics and Jet Propulsion," F. K. Moore, Editor, Princeton University Press, Princeton, NJ (1964).
- R. A. Svehla, NASA Technical Report R-132 (1962).
- C. F. Curtiss and J. O. Hirschfelder, *J. Chem. Phys.*, **17**, 550 (1949).
- C. R. Wilke, *ibid.*, **18**, 517 (1950).
- J. O. Hirschfelder, C. F. Curtiss, and R. B. Bird, "Molecular Theory of Gases and Liquids," John Wiley and Sons, New York (1954).
- R. J. Kee and J. A. Miller, Sandia National Laboratories Report, SAND 81-8241 (1981).
- "JANAF Thermochemical Tables," Dow Chemical Company, (1965), and subsequent addenda.
- S. Gordon and B. J. McBride, NASA SP-273 (1971).
- J. S. Binkley, Unpublished.
- S. W. Benson, "Thermochemical Kinetics," 2nd ed., John Wiley and Sons, New York (1976).
- R. J. Kee, J. A. Miller, and T. H. Jefferson, Sandia National Laboratories Report, SAND 80-8003 (1980).
- R. F. C. Farrow, *This Journal*, **121**, 899 (1974).
- H. E. O'Neal, Personal communication. The Arrhenius factors are from an RRKM analysis of data described in (17).
- C. G. Newman, H. E. O'Neal, M. A. Ring, F. Leska, and N. Shipley, *Int. J. Chem. Kinet.*, **11**, 1167 (1979).
- P. John and J. H. Purnell, *J. Chem. Soc.*, **69**, 1455 (1973).
- E. R. Austin and F. W. Lampe, *J. Phys. Chem.*, **81**, 1134 (1977).
- J. A. Confer, K. P. Lynch, and J. V. Michael, *ibid.*, **79**, 1139 (1975).
- M. E. Coltrin and J. S. Binkley, Unpublished.
- J. C. Keck, in "Maximum Entropy Formalism," R. D. Levine and M. Tribus, Editors, MIT Press, Cambridge, MA (1978).
- M. A. Kramer, R. J. Kee, and H. Rabitz, Sandia National Laboratories Report, SAND82-8230 (1982).
- L. R. Petzold, Sandia National Laboratories Report, SAND 82-8637 (1982).
- C. W. Gear, "Numerical Initial Value Problems in Ordinary Differential Equations," Prentice-Hall, Englewood Cliffs, NJ (1971).
- J. A. Miller and R. J. Kee, *J. Phys. Chem.*, **81**, 2534 (1977).
- S. E. Bradshaw, *Int. J. Electron.*, **21**, 205 (1966).
- S. E. Bradshaw, *ibid.*, **23**, 381 (1967).
- F. C. Eversteyn, P. J. W. Severin, C. H. J. van den Brekel, and H. L. Peek, *This Journal*, **117**, 925 (1970).
- F. C. Eversteyn and H. L. Peek, Philips Res. Rep., **25**, 472 (1970).
- F. C. Eversteyn, *ibid.*, **29**, 45 (1974).
- J. Bloem, *This Journal*, **117**, 1397 (1970).
- P. van der Putte, L. J. Giling, and J. Bloem, *J. Cryst. Growth*, **31**, 299 (1975).
- S. Berkman, V. S. Ban, and N. Goldsmith in "Heteroepitaxial Semiconductor Electronic Devices," G. W. Cullen and C. C. Wang, Editors, Chap. 7, Springer, New York (1978).
- W. H. Shepherd, *This Journal*, **112**, 988 (1965).
- R. W. Andrews, D. M. Rynne, and E. G. Wright, *Solid State Technol.*, **61** (Oct. 1969).
- P. C. Rundle, *Int. J. Electron.*, **24**, 405 (1968).
- P. C. Rundle, *J. Cryst. Growth*, **11**, 6 (1971).
- R. Takahashi, K. Sugawara, Y. Nakazawa, and Y. Koga, in "Chemical Vapor Deposition," J. M. Blocher and J. C. Withers, Editors, p. 695, The Electrochemical Society Softbound Proceedings Series, New York (1970).
- K. Sugawara, H. Tochikubo, R. Takahashi, and Y. Koga, *ibid.*, p. 713.
- R. Takahashi, Y. Koga, and K. Sugawara, *This Journal*, **119**, 1406 (1972).
- K. Sugawara, *ibid.*, **119**, 1749 (1972).
- E. Fujii, H. Nakamura, K. Haruna, and Y. Koga, *ibid.*, **119**, 1106 (1972).
- C. W. Manke and L. F. Donaghey, in "Chemical Vapor Deposition," L. F. Donaghey, P. Rai-Choudhury, and R. N. Tauber, Editors, p. 151, The Electrochemical Society Softbound Proceedings Series, Princeton, NJ (1977).
- C. W. Manke and L. F. Donaghey, *This Journal*, **124**, 561 (1977).
- M. L. Hitchman, *J. Cryst. Growth*, **48**, 394 (1980).
- B. A. Joyce and R. R. Bradley, *This Journal*, **110**, 1235 (1963).
- M. J. Duchemin, M. M. Bonnet, and M. F. Koelsch, *ibid.*, **125**, 637 (1978).
- J. Bloem and L. J. Giling, in "Current Topics in Materials Science," E. Kaldis, Editor, Chap. 4, North-Holland (1978).
- M. L. Hitchman, in "Chemical Vapor Deposition," T. O. Sedgwick and H. Lydtin, Editors, p. 59, The Electrochemical Society Softbound Proceedings Series, Princeton, NJ (1979).
- M. L. Hitchman, J. Kane, and A. E. Widmer, *Thin Solid Films*, **59**, 231 (1979).
- F. Hottier and R. Cadoret, *J. Cryst. Growth*, **52**, 199 (1981).
- J. Holleman and T. Aarnink, in "Chemical Vapor Deposition," J. M. Blocher, G. E. Vuillard, and G. Wahl, Editors, p. 307, The Electrochemical Society Softbound Proceedings Series, Pennington, NJ (1981).
- W. A. P. Claassen and J. Bloem, *J. Cryst. Growth*, **51**, 443 (1981).
- W. A. P. Claassen, J. Bloem, W. G. J. N. Valkenburg, and C. H. J. van den Brekel, *ibid.*, **57**, 259 (1982).
- B. A. Joyce and R. R. Bradley, *Philos. Mag.*, **14**, 289 (1966).
- G. R. Booker and R. R. Bradley, *ibid.*, **14**, 301 (1966).
- B. A. Joyce, R. R. Bradley, and G. R. Booker, *ibid.*, **15**, 1167 (1967).
- B. E. Watts, R. R. Bradley, B. A. Joyce, and G. R. Booker, *ibid.*, **17**, 1163 (1967).
- B. A. Joyce, R. R. Bradley, B. E. Watts, and G. R.

- Booker, *ibid.*, **19**, 403 (1968).
61. R. C. Henderson and R. F. Helm, *Surf. Sci.*, **30**, 310 (1972).
62. C. H. J. van den Brekel, Ph.D. Thesis, University of Nijmegen, The Netherlands (1978).
63. W. A. P. Claassen and J. Bloem, *Philips J. Res.*, **36**, 122 (1981).
64. W. A. Bryant, *Thin Solid Films*, **60**, 19 (1979).
65. P. Ho and W. G. Breiland, *Appl. Phys. Lett.*, To be published.

Controlled Reactive Sputter Synthesis of Refractory Oxides

SiO_x, The Silicon-Oxygen System

Troy W. Barbee, Jr., Douglas L. Keith, Lynn Nagel, and William A. Tiller

Department of Materials Science and Engineering, Stanford University, Stanford, California 94305

ABSTRACT

Reactive sputter deposition of refractory oxides, under conditions in which the reaction between the sputtered species and the oxygen is isolated to the deposition surface, has been experimentally investigated, and results have been obtained for the formation of SiO_x (0 < x < 2). It is shown that the dependence of the deposited film stoichiometry on oxygen pressure and the incidence rate of silicon can be correlated with reported results of oxygen adsorption onto single-crystal silicon surfaces and amorphous silicon surfaces. This correlation is made in terms of oxygen exposure and, in our work, a dynamic exposure (L_D) is defined for steady-state synthesis conditions by placing the origin of a moving reference frame at the deposition surface. This correlation shows that the sticking coefficient of oxygen onto room temperature substrates is independent of oxygen coverage (*i.e.*, surface stoichiometry) for coverages less than 0.8. This requires that a mobile precursor adsorption process be operative for oxygen in our experiments. The deduced pressure-independent oxygen sticking coefficient is 1.5 to 4.1 × 10⁻³.

Sputter deposition of refractory compound films of high quality from compound targets is difficult because of the low mechanical integrity of such targets, their low thermal conductivities, inherently low deposition rates, poor stoichiometry control, and the often substantial contamination incurred during the sputter target preparation (1-5). These difficulties may be diminished by reactive sputtering in which the target, consisting of the metal component, is sputtered using a gas mixture consisting of an inert gas (typically argon) and a reactive component, one element of which is active in the formation of the desired compound (1, 2, 6-11). Despite present drawbacks, associated with the difficulty of closely controlling film stoichiometry, reactive sputtering often yields much higher quality films at deposition rates somewhat higher than those attained using compound targets.

The purpose of the work presented in this paper was to develop the reactive sputtering synthesis process so that continuous layers of controllable structure and composition could be formed in a reproducible and routine manner. In this paper we report the results of our studies on the reactive deposition of the oxides of silicon (SiO_x). Films of SiO_x (0 ≤ x ≤ 2) were synthesized at high rates onto substrates held at room temperature. A systematic investigation of the structure-composition-synthesis process variables was conducted for this system, and it was clearly demonstrated that films of controllable stoichiometry, varying over the range SiO_{0.1} to SiO₂, can be reproducibly synthesized at rates (>5 Å/s) equal to or greater than those typically encountered in industry. In addition, the substrate temperature during synthesis was held close to the ambient condition (T_s ≤ 65°C). The low temperature nature of this process is a unique feature of high industrial potential, as it provides a method for forming SiO_x passivating films that does not include time-temperature cycling which could degrade existing device structures.

Experimental Approach and Procedures

The experimental approach was to design experiments so that reaction between the sputtered species (Si in this case) and the reactive gas (O₂) was forced to occur at the deposition surface. It was believed that under such conditions, high deposition rates plus control of structure and stoichiometry would be attainable through control of the relative rates of incidence of the two reactive components

Key words: sputtering, refractories, deposition.

onto this surface. Additionally, if such control were possible, it would facilitate both modeling of the reactive sputtering process and experimental reproducibility in both a given laboratory and between laboratories.

The experimental arrangement (type II) used was designed to isolate the sputter-source plate from the oxygen gas, maintaining it in an inert argon gas atmosphere while introducing an oxygen pressure at the substrate. Two approaches were taken here. In the first (type IIA), argon and oxygen were brought into the chamber separately, with the oxygen inlet surrounding the substrate and the argon introduced as under normal sputtering conditions. In these experiments, the oxygen, though localized at the substrate, was nonuniformly distributed. Also, although higher oxygen concentrations were attainable, source contamination by oxygen still limited the experimental range. A series of experiments was performed using this apparatus, in which the rate of incidence of silicon was held constant and the oxygen pressure at the substrate varied. In this work, the source to substrate distance was 11.5 cm and (100) single-crystal silicon wafers were used as substrates. The silicon incidence rate was 2.9 Å/s (1.45 × 10¹⁵ Si atoms/cm²s). Oxygen incidence rates were varied from 0 to 8 × 10¹⁷ O₂/cm²s (0 ≤ P_{O₂} ≤ 1.6 mtorr).

A second-generation apparatus (type IIB) was designed so that the range of oxygen pressures could be extended and the distribution of oxygen at the deposition surface would be uniform. Two gas ring sources, one for argon and the other for oxygen, were fabricated with the gas inlets in each ring consisting of slits 0.002 in. wide on the inner diameter of two-piece annular structures. For oxygen, the sample was mounted in the ring with the oxygen directed down onto the substrate. For argon, the ring was mounted near the sputter source with the argon stream directed at the sputter-source target. This arrangement is schematically shown in Fig. 1. Improved film uniformity both in thickness and composition was attained with this apparatus. Additionally, oxygen pressures approximately twice those accessible without the argon isolation ring were usable without oxidation of the silicon source plate in the magnetron sputter head. For these experiments, silicon incidence rates were 3.4, 5.9, and 8.2 Å/s or 1.72 × 10¹⁵ Si/cm²s, 2.9 × 10¹⁵ Si/cm²s and 4.1 × 10¹⁵ Si/cm²s, respectively. The general oxygen pressure varied from 0 to 0.6 mtorr (0.08 Pa) in the system. This is considerably lower than the oxygen pressure at the substrate, which was not locally measured in these experiments.

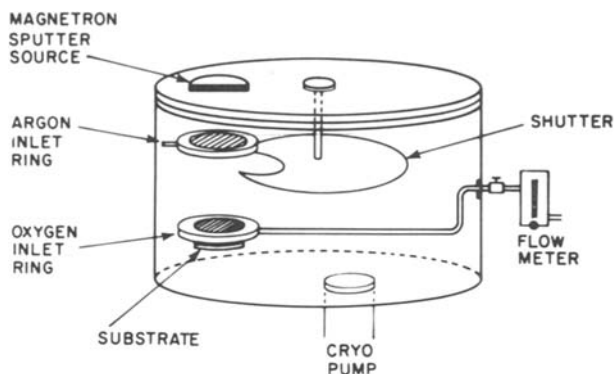


Fig. 1. Experimental apparatus used in type IIA experiments. The center of the sputter source, argon ring, oxygen ring, and substrate were vertically aligned. Deposition was initiated by shutter motion after the flow of argon and oxygen was established.

In summary, experimental apparatus allowing reactive sputter deposition, in which the chemical reaction occurs at the deposition surface, has been developed. In the following, experimental results for SiO_x films synthesized in this manner will be presented. Specific emphasis will be placed on the stoichiometry control and uniformity.

Experimental Results

Type IIA experiments were performed with substrates 11.5 cm away from a 5 cm diam planar magnetron sputter-deposition source. Oxygen was introduced at the substrate; argon was generally introduced into the vacuum chamber. Argon pressure was held constant at 2.1 mtorr, and the total system oxygen pressure varied from 0 to 1.5 mtorr by flow rate control. The silicon source was RF excited with a resulting deposition of 2.9 \AA/s at the substrate onto single-crystal (100)-orientation silicon substrates. Analysis of the film thickness and refractive index by ellipsometry indicated that the oxygen distribution at the substrate was nonuniform. Additionally, oxygen contamination of the sputter source was observed at oxygen pressures greater than 1.5 mtorr.

A second experimental arrangement, type IIB (Fig. 1), was constructed, and experiments similar to those performed above were carried out. A 7.5 cm diam planar magnetron source, a 12 cm source-to-substrate spacing, oxygen pressures from 0 to 0.6 mtorr total system pressure, and silicon deposition rates of 3.4, 5.8, and 8.2 \AA/s were used. The lower range of oxygen pressures necessary here indicates that the partial pressure of oxygen at the deposition surface was at least a factor of 4 to 5 larger than the increase in total system pressure resulting from the introduction of oxygen.

In the following, a systematic presentation of the results obtained with configuration type IIA will be made and then compared to those obtained using configuration type IIB on the basis of the relative rates of incidence of oxygen and silicon. The uniformity of the deposit attained using configuration type IIB will also be demonstrated.

Steady-state synthesis was established by use of a constant flow rate of O_2 into the deposition chamber at the substrate surface and a constant rate of incidence of silicon atoms onto the deposition surface. SiO_x formation was initiated by opening a shutter which isolated the substrate from the silicon sputter source so that both Si and O_2 (at the constant) flux were incident on the substrate and the film was of uniform stoichiometry throughout its thickness. A series of synthesis experiments was performed with constant Si deposition rate, deposition time, source-to-substrate distance, and argon pressure, while the oxygen pressure was varied from 0 to 1.5 mtorr. Film thickness and relative index were determined using ellipsometric techniques ($\lambda = 6328 \text{ \AA}$; angle of incidence = 70°). Film thickness was also measured using mechanical stylus techniques at steps introduced by masking.

The composition of these films was deduced from the refractive index data correlation with results reported for SIPOS material (12) and by electron microprobe analysis of four of our samples. The refractive index has been cor-

related with oxygen concentration in both SIPOS films and our films, as shown in Fig. 2. Oxygen contents were measured using electron microprobe analysis techniques in both cases.

The thickness of our type IIA-deposited SiO_x films, as determined using mechanical stylus techniques and ellipsometry, are presented in Fig. 3 as a function of oxygen pressure during synthesis. The data points represent the average thickness observed at different step positions; the vertical bar provides the range of thickness observed for a given sample. This wide variation results from drift in the oxygen pressure during a given experiment as well as a nonuniform oxygen distribution at the substrate. Since the oxygen incidence rates on the substrate increase linearly with pressure, a linear dependence of t_f with P_{O_2} is expected if a constant fraction of incident oxygen atoms results in the formation of SiO_2 clusters with the specific volume of SiO_2 . Departures from the expected linearity could be related to two primary sources; (i) oxygen contamination of the target which reduces the Si incidence rate, and (ii) the incorporated oxygen does not all form SiO_2 clusters with the expected equilibrium specific volume, but rather takes forms with different specific volumes. At the highest oxygen pressures, the measured thicknesses are smaller than predicted, a result we interpret as being caused by sputter-source contamination with oxygen.

The optical transmission of the films deposited on the masks was indicative of the oxidation state of the films. It is expected that the transmission will increase as the oxygen content increases. Even with the increasing film thickness observed with increasing oxygen pressure, the transparency increases in a nearly monotonic fashion with increased oxygen pressure during synthesis. At the highest oxygen pressures the deposits are transparent, as expected for SiO_2 .

The refractive index for these films was also observed to systematically vary with oxygen pressure from that expected for silicon ($n_f \approx 3.6$ [amorphous] to 3.8 [crystalline]) to that observed for amorphous SiO_2 ($n_f \sim 1.45$). The n_f values were measured on films deposited onto (100) Si substrates using standard ellipsometric techniques ($\lambda = 6238 \text{ \AA}$; angle of incidence = 70°). These results are plotted as a function of oxygen pressure during synthesis in Fig. 4. The extent of the blocks surrounding each data point represents the effect of the variation of P_{O_2} during synthesis as well as the nonuniform distribution of oxygen at the substrate. Oxygen concentration in our films determined using the refractive index-composition relation (Fig. 2) are plotted vs. P_{O_2} during synthesis in Fig. 5. Examination of the samples indicated that nonuniform flow of the oxygen, and therefore, nonuniform oxygen pressure, at the substrate was the primary cause of the variations in composition and film thickness.

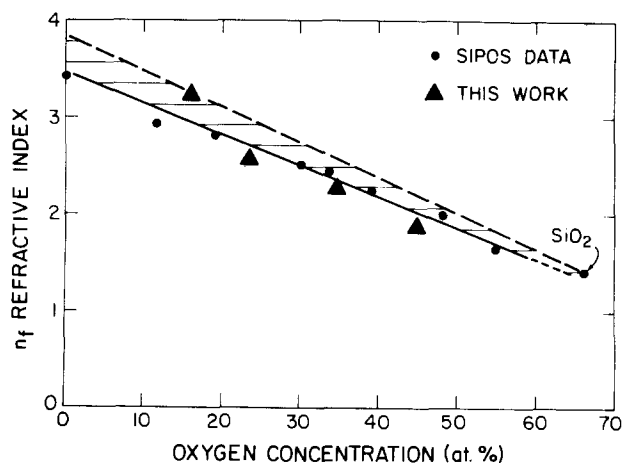


Fig. 2. Refractive index, as determined by ellipsometry, correlated with oxygen concentration as determined by electron microprobe analysis for four SiO_x films formed by reactive sputtering and CVD-synthesized SIPOS films reported in the literature.

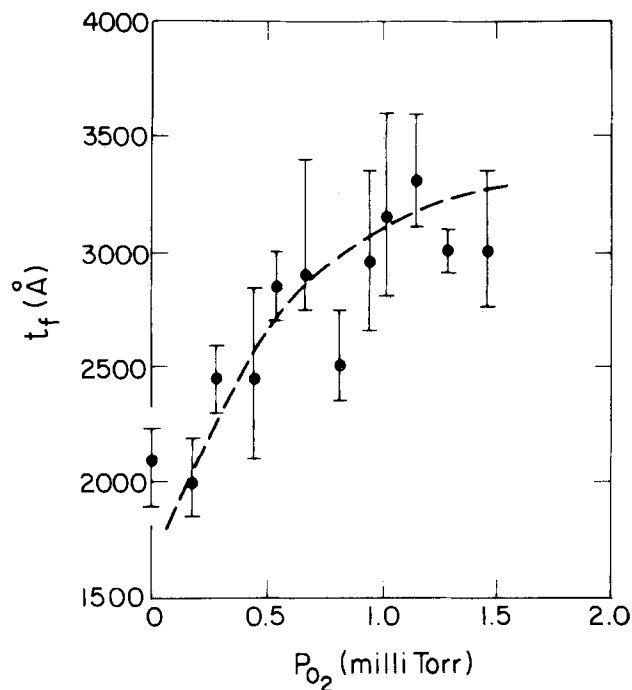


Fig. 3. SiO_x film thicknesses for type IIA experiments as determined by ellipsometry and mechanical stylus techniques ($R_{\text{Si}} = 29 \text{ \AA/s}$) as a function of oxygen pressure.

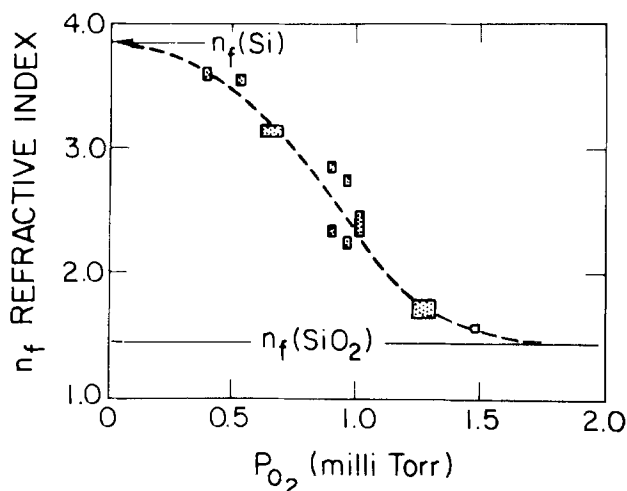


Fig. 4. Refractive index (n_f) as determined by ellipsometry for the films of Fig. 3 (type IIA) as a function of oxygen pressure.

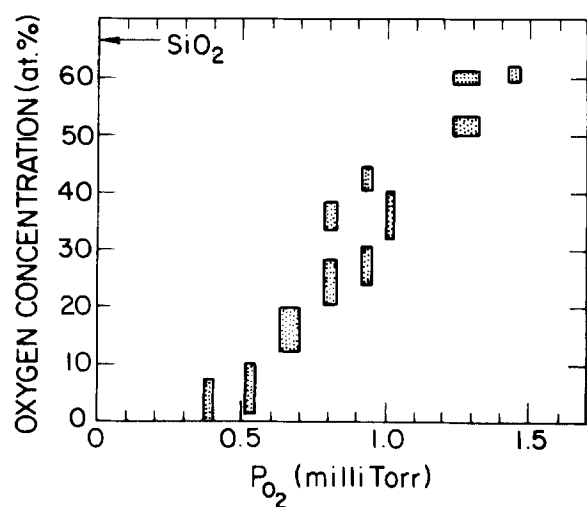


Fig. 5. Oxygen concentration in the films of Fig. 3 (type IIA) as a function of oxygen pressure.

The system was modified (type IIB) as already described (Fig. 1), and a series of depositions made using silicon deposition rates of 3.4, 5.4, and 8.2 \AA/s with total system oxygen pressures of 0 to 0.6 mtorr. Note that these oxygen pressures are approximately a factor of 4 to 5 smaller than those used in the type IIA experiments. This difference is believed to be due to an increased oxygen partial pressure at the deposition surface resulting from the more effective arrangement for introduction of oxygen at the substrate fixture.

The increased homogeneity of the films formed using the type IIB system is shown in Fig. 6, where refractive index and film thickness are plotted as a function of radial distance from the substrate edge to the wafer center. The substrates used were 7.5 cm diam (100) silicon wafers, centered beneath the deposition-source center in the oxygen ring. The decrease in refractive index from the center of the substrate to the edge is very slight, indicating nearly constant stoichiometry. Near the edge, the refractive index drops rapidly because of a slight overpressure of oxygen in that region and shadowing of the incident silicon by masking. The film thickness varies by approximately 16% over a distance of 3.0 cm. This is slightly larger than the expected variation of approximately 12%. The variation is a result of the deposition profile of the sputter source. It is indicative of a composition variation over 3.0 cm of approximately 1 atom percent (a/o). The compositional uniformity of this sample is so demonstrated.

It is useful to compare the results of these type IIB synthesis runs with the type IIA results. This is done in Fig. 7, where oxygen concentration in the films, as determined by the refractive index correlation, is plotted as a function of the relative rates of incidence of O_2 and silicon ($\nu_{\text{O}_2}/\nu_{\text{Si}}$). The silicon rate of incidence was estimated by normalizing the deposition rate to a unit area so that a volume rate was defined, and dividing this by the atomic volume of silicon ($\sim 20 \text{ \AA}^3$) (i.e., $1 \text{ \AA/s} \approx 5 \times 10^{14} \text{ atoms/cm}^2\text{s}$). The incidence rate of oxygen was calculated from the partial pressure of oxygen assuming a temperature of 300 K. Also plotted on this figure for comparison is the data of Ritter (13), where reactive synthesis of SiO_x was carried out using electron-beam evaporation techniques. The general behavior observed is similar for all three sets of data. The lower incidence rate ratios of type IIB as compared to type IIA experiments is believed to be the result of a higher oxygen concentration at the substrate due to a more effective means of oxygen introduction being used. The low oxygen pressures for oxide formation in the work of Ritter (13) will be discussed more fully below.

Mechanism of Reaction

The experimental results presented demonstrate that the synthesis of silicon-oxygen films under controlled conditions, designed so that reaction between silicon and

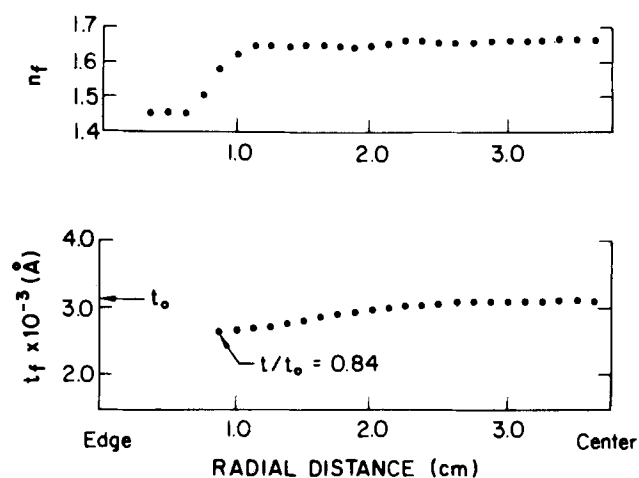


Fig. 6. Film thickness and refractive index plotted as a function of radial distance on a 7.5 cm diam silicon wafer demonstrating both compositional and thickness uniformity in type IIB apparatus synthesized films.

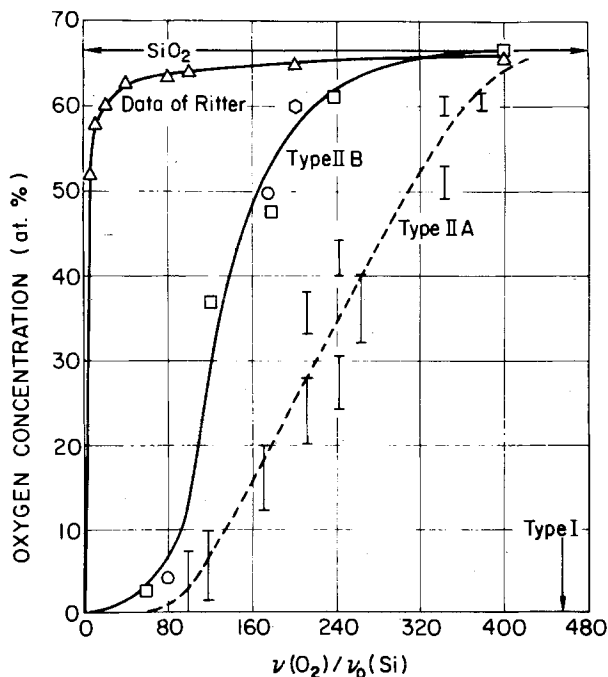


Fig. 7. Oxygen concentration for reactively synthesized films as a function of the ratio of the oxygen (O_2) and silicon incidence rates for types IIA and IIB experiments and for the thermal source results of Ritter (13).

oxygen occurs at the deposition surface, allows formation of films of reproducible stoichiometry and high uniformity onto room temperature substrates. So far we have been discussing our results in terms of the relative rates of incidence of the two reacting species onto the deposition surface. It is important at this point to consider experimental results reported by other investigators concerning the adsorption of oxygen onto surfaces of bulk single crystals and of amorphous silicon. Such surfaces are static in that the number of Si atoms is fixed by the character of the initial surface. In our experiments, a dynamic moving surface, in which both silicon and oxygen are supplied to a moving surface (*i.e.*, where a film is being grown) is studied.

More sophisticated experiments, in which ultrahigh vacuum studies of oxygen absorption on high index silicon planes (14, 15, 16) and amorphous silicon (17), have been reported. In these studies, the oxygen was observed to be absorbed with the coverage being a linear function of oxygen exposure in Langmuirs (torr/s). Sticking probabilities are small (2×10^{-4} to 3×10^{-3}) and strongly affected by the presence of excited oxygen. Additionally, the oxygen is absorbed in an unreacted state. This reaction ($Si + O_2 \rightarrow SiO_2$) is apparently strongly catalyzed by the presence of small amounts of carbon (16). Adsorption on amorphous silicon does not appear to be substantially different from absorption on (111) or (110) silicon surfaces. The sticking coefficient of oxygen on silicon (111) and (110) surfaces were reported to be 2×10^{-4} and 6×10^{-3} , respectively. The higher value on (110) surfaces can be explained by its higher index and the possibility of surface step effects.

In other works (14, 15, 16), the sticking coefficient (S) was determined by analysis of experimental data obtained using Auger electron spectroscopy (AES) (14, 15, 16), High resolution electron spectroscopy (HRES) (14, 15), and ellipsometry (E) (14, 15). It was assumed in all these experiments that the coverage (θ) was directly proportional to the intensity of the signal monitored which was determined as a function of oxygen exposure (L), and that unit coverage was attained when the experimental signal saturated. Under these assumptions, the coverage dependence of the sticking coefficient $S(\theta)$ could be derived as

$$\frac{d}{dt}(\theta) = S(\theta) \frac{\nu P}{N_0} \quad [1]$$

where θ is the fractional coverage, p the pressure, $\nu = 3.48 \times 10^{20}$ molecules/cm²s torr, and N_0 the number of surface sites available for absorption.

The relationship between coverage and exposure is similar to the relationship between composition and relative rates of incidence shown in Fig. 7. A more direct comparison can be made if our data are displayed in terms of the oxygen concentration given as x in SiO_x with $0 \leq x \leq 2$ and a dynamic exposure L_D . The correspondence between coverage and x in SiO_x is clear if we assume that the absorbed species is O_2 and that unit coverage is attained when there is one oxygen molecule absorbed for each silicon surface atom.

Dynamic exposure (L_D) is defined by the time necessary to deposit a monolayer of silicon atoms used in the calculation of oxygen exposure at pressure P_{O_2} . The number of atoms on an exposed (111) silicon surface is calculated to be $\sim 3.96 \times 10^{14}$ /cm². The rate of incidence of silicon atoms (ν_{Si}) has been already given as $\nu_{Si} = R_{Si}/V_{Si}$, where R_{Si} is the deposition rate in $\text{\AA}^3/\text{s}$ and V_{Si} is atomic volume of silicon. The time (τ) to deposit one monolayer (*i.e.*, 3.96×10^{14} atoms/cm²) is then

$$\tau = \frac{3.96 \times 10^{14}}{\nu_{Si}} = \frac{3.96 \times 10^{14} V_{Si}}{R_{Si}} \quad [2]$$

Thus, a dynamic exposure L_D for oxygen can be defined as

$$L_D = P_{O_2} \tau \quad [3]$$

where P_{O_2} is given in torr and τ in seconds. During a steady-state synthesis experiment, static exposure and dynamic exposure are analytically equivalent at small time steps.

Our experimental results are plotted as x in SiO_x vs. dynamic exposure calculated, as outlined above, in Fig. 8. The results of Ritter (13) are also plotted for comparison. The differences are striking. First, the dynamic exposure range, in Langmuirs, over which our data extend is approximately 10^{-4} to 10^{-3} L. In order to gain the same results, Ritter's exposure range was approximately 10^{-8} L to 10^{-2} L. No clear explanation for this appears in the data of either investigation. It is likely, though, that in Ritter's work a substantial amount of excited oxygen was present. The absorption and reaction probability of excited O_2 is orders of magnitude higher than those of unexcited O_2 . Therefore, the reactivity of the oxygen in the evaporation experiment was undoubtedly strongly increased by the experimental arrangement used. In our work, the oxygen was introduced at the substrate in an unexcited state. The substrate-to-sputter-source spacing was large enough to make the coupling between the plasma and the deposition surface minimal (a characteristic of planar magnetron systems). Additionally, substrate heating consistent with the deposition parameters ($T_s < 65^\circ\text{C}$) was observed for extended synthesis experiments (>2h), even with nonwater-cooled substrates, showing that the source-substrate coupling was minimal.

It is useful to compare coverage (14, 15) as determined by E, HRES, and AES with our data for x in SiO_x vs. ex-

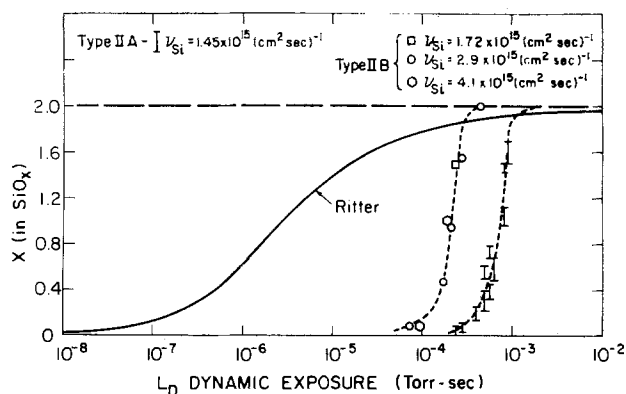


Fig. 8. Oxygen concentration (x in SiO_x) as a function of L_D for films deposited using the type IIA and IIB experimental arrangements and the thermal source data of Ritter (13).

posure (L_D), as shown in Fig. 9. The qualitative behaviors are similar, and quantitative agreement occurs with respect to the exposure range involved (i.e., 10^{-4} to 10^{-3} torr/s). This implies that the rate-controlling step in the synthesis process is identical to that in the absorption process of O_2 on silicon. Hence, our rate-controlling step is the absorption of O_2 with reaction to form SiO_x occurring once the absorption step has taken place.

The slopes of the film stoichiometry curves (x in SiO_x) are steeper than the absorption curves, implying a somewhat larger sticking coefficient. When plotted in a linear manner (Fig. 10), the relationship between it and x in SiO_x is observed to be a linear function of exposure within our experimental scatter. This shows that the sticking coefficient of oxygen is independent of coverage, a condition which can be explained (18, 19, 20) by the presence of a mobile precursor to the chemisorption event. Therefore, it is quite likely that, in our work, a mobile precursor of O_2 adsorbed onto the surface exists and facilitates the chemisorption process.

A sticking coefficient (S) for O_2 onto our moving deposition surface can also be estimated for these data. If we assume unit coverage, when $x = 2$ for x in SiO_x , the coverage can be linearly related to x by $\theta = x/2$. At constant pressure (p) the time rate of change of the coverage (θ) can

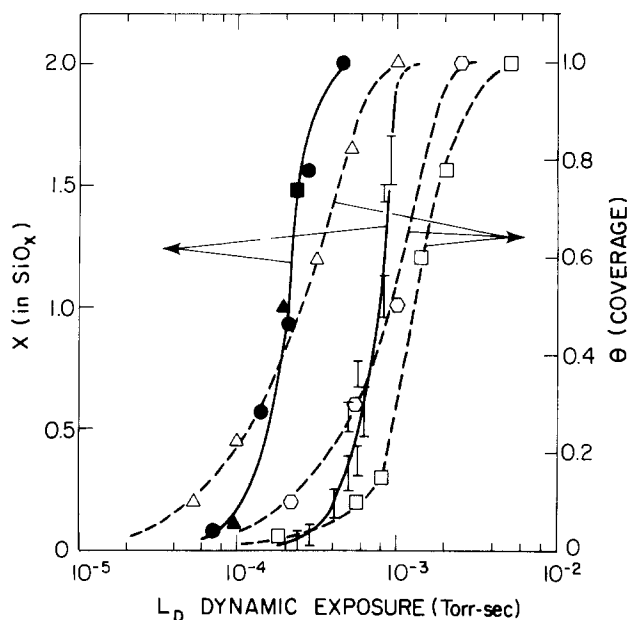


Fig. 9. Experimental results for type IIA (□) and type IIB (●, ■, ▲) compared to the reported results of oxygen coverage on Si(111) surfaces as determined by HRES (□), ellipsometry (○), and Auger analysis (△), assuming that dynamic exposure (L_D) and exposure (L) are equivalent.

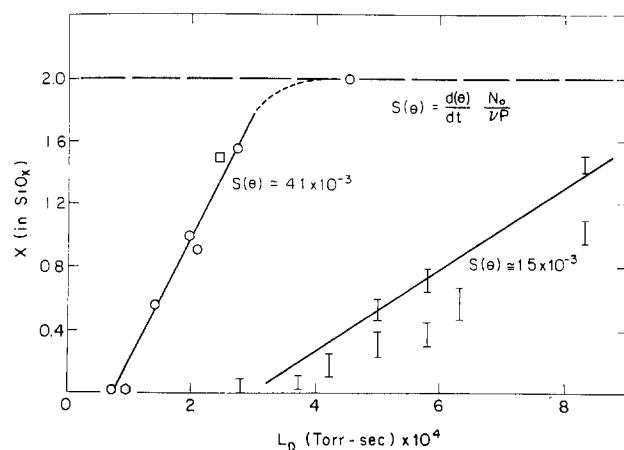


Fig. 10. x in SiO_x as a linear function of L_D (torr/s) allowing estimation of S for oxygen in the type IIA and type IIB experiments (see Eq. [1]).

be related (Eq. [1]) to the sticking coefficient, $S(\theta)$. The sticking coefficients derived on this basis are in the range 1.56×10^{-3} to 4.17×10^{-3} . These numbers are a factor of 5 to 20 larger than the value reported by Ibach (14) ($S = 2.2 \times 10^{-4}$) for an atomically flat (111) surface. This increase in S may be due either to the presence in our work of activated oxygen or to an enhanced reactivity of our amorphous SiO_x surface relative to ideal crystalline surfaces. The latter explanation is consistent with the effects of surface steps on the sticking probability. It would require 6-8% of the surface atoms to be associated with surface steps to achieve sticking probabilities, as we have inferred. Computer simulation studies of amorphous surfaces by Garofolini *et al.* (21) tend to support this interpretation.

The observed independence of the sticking coefficient on θ for O_2 on the silicon surface can be explained by a mechanism in which a physisorbed mobile precursor state for oxygen exists on the sample surface prior to chemisorption. This allows O_2 molecules to move on the surface so that, at substantial coverages ($\theta = 0.5$), the remaining unoccupied chemisorption sites are accessible. A simple model (21) of the combined physisorption-chemisorption process gives the sticking coefficient $S(\theta)$ for the chemisorbed state as

$$S(\theta) = \frac{\alpha(1-\theta)}{(1+r_d/r_c) - \theta(1+r_d/r_m)^{-1}} \quad [4]$$

where θ is the coverage, α the fraction of incident gas molecules entering the precursor state, r_d the rate of desorption, r_m the rate of migration, and r_c the rate of transition from the precursor to the chemisorbed state. In the limit of $\theta \rightarrow 0$, the sticking coefficient S_0 is given by

$$S_0 = \frac{\alpha}{(1+r_d/r_c)} \quad [5]$$

The relationship between r_d and r_c is easily explained in terms of a potential energy diagram, as seen in Fig. 11. There, the potential energy of an adsorbed oxygen molecule is plotted as a function of the molecule's distance from the solid surface. In Fig. 11, q_p represents the heat of physisorption and E_p the activation energy for transition from the physisorbed to the chemisorbed states. If we assume the ratio of the pre-exponential factors of r_d and r_c is K_1 , then

$$r_d/r_c = K_1 \exp[-(q_p - E_p)/RT] \quad [6]$$

where R is the gas constant and T the absolute temperature. Equation [5] then becomes

$$S_0 = \frac{\alpha}{1 + K_1 \exp[-(q_p - E_p)/RT]} \quad [7]$$

In all likelihood $\alpha \approx 1$ at low substrate temperatures, so that the quantity $1 + K_1 \exp[-(q_p - E_p)/RT]$ is equal to

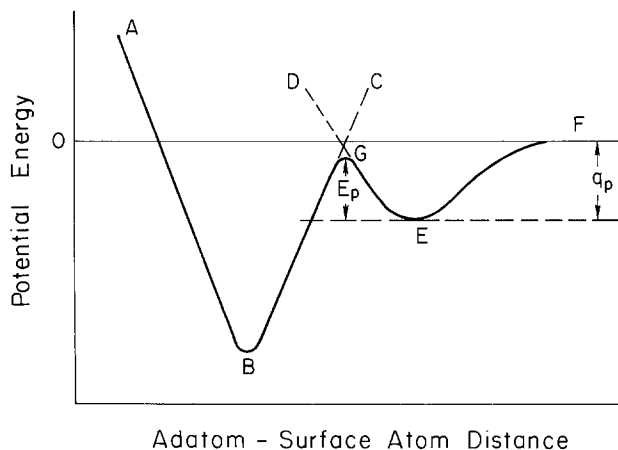


Fig. 11. The intramolecular potential (V_p) vs. distance illustrating the potential wells for both chemisorption and physisorption. The physisorbed state (DEF) represents the mobile precursor with an adsorption energy q_p . If the activation energy E_p for transition from the precursor to the chemisorbed state (ABC) is less than q_p , the activation energy for chemisorption is zero.

approximately 500, since $S = 2 \times 10^{-3}$. Therefore, to a good approximation

$$S_0 = \frac{\alpha}{K_1} \exp [q_p - E_p/RT] \quad [8]$$

indicating that chemisorption occurs with an activation energy close to zero (*i.e.*, $q_p > E_p$), a phenomenon found (22, 23, 24) in the oxidation of many metals.

The result of this interpretation is that the residence time of a physisorbed oxygen molecule on the surface and its migration rate determine the number of chemisorption sites accessible per physisorbed molecule and, therefore, the chemisorption rate. Hence, as the substrate temperature is increased at fixed oxygen pressure and silicon incidence rate, the oxygen concentration in the SiO_x deposit will decrease. This is observed in the reactive deposition of many oxides. The increase is due to the decrease in residence time of physisorbed molecules on the deposition surface relative to the increase in physisorbed oxygen mobility with increasing temperature. Therefore, the reactivity of oxygen and the depositing silicon is decreased by increasing substrate temperature.

Conclusions

A series of experiments, in which the reaction between oxygen and silicon during reactive sputtering is forced to occur at the deposition surface, has been performed and analyzed. A suitable technique was developed for isolating the magnetron sputter source from the ambient oxygen and SiO_x films over the complete range of stoichiometry, $0 < x < 2$, prepared. These films were of excellent uniformity in both thickness and index of refraction. An incidence frequency ratio of O_2 to Si ~ 500 was required for the formation of SiO_2 films.

The present data have been found to correlate well with ultrahigh vacuum oxygen adsorption experiments on clean single-crystal Si surfaces. A sticking coefficient for oxygen of 1.5 to 4×10^{-3} was inferred. The sticking coefficient was found to be independent of coverage (*i.e.*, surface stoichiometry). An appropriate model was deduced to be physisorbed oxygen in a mobile precursor state prior to chemisorption. Such a model yields a consistent explanation of the temperature dependence of the stoichiometry of reactively sputtered oxides in general and SiO_x in particular. These results demonstrate that fundamental information concerning the interaction of oxygen and various elements is accessible through systematic reactive deposition experiments in which the reaction is localized to the deposition surface.

Acknowledgments

This work was supported by the Defense Advanced Research Projects Agency under Contract no. MDA 903-79-C-0484 and benefitted from facilities made available to Stanford University by the NSF-MRL Program through the Center for Materials Research at Stanford University.

Manuscript submitted May 6, 1983; revised manuscript received Sept. 27, 1983.

Stanford University assisted in meeting the publication costs of this article.

REFERENCES

1. L. I. Maissel and R. Glang, Editors, "Handbook of Thin Film Technology," McGraw-Hill, New York (1970).
2. J. L. Vossen and W. Kern, Editors, "Thin Film Processes," Academic Press, New York (1978).
3. J. E. Greene, C. E. Wickersham, J. L. Zilko, L. B. Welsh, and F. R. Szofran, *J. Vac. Sci. Technol.*, **13**, 72 (1976).
4. J. E. Greene, R. E. Klinger, L. B. Welsh, and F. R. Szofran, *ibid.*, **14**, 177 (1977).
5. W. M. Paulson, F. S. Hickerrell, and R. L. Davis, *ibid.*, **16**, 307 (1979).
6. F. B. Fraser and H. D. Cook, *ibid.*, **14**, 147 (1977).
7. J. Joly and J. B. Ranger, *LeVide*, **182**, 34 (1976).
8. R. P. Howson and M. I. Ridge, *Thin Solid Films*, **77**, 119 (1981).
9. M. Miyata, K. Miyake, and S. Nao, *ibid.*, **58**, 385 (1979).
10. S. Schiller, U. Heisig, K. Steinfeld, and J. Struempfel, *ibid.*, **63**, 369 (1979).
11. S. Schiller, G. Beister, S. Schneider, and W. Sieber, *ibid.*, **72**, 475 (1980).
12. K. Seward, Personal communication.
13. E. Ritter, *J. Vac. Sci. Technol.*, **3**, 225 (1966).
14. H. Ibach, K. Horn, R. Dorn, and H. Luth, *Surf. Sci.*, **38**, 433 (1973).
15. R. Dorn, H. Luth, and H. Ibach, *ibid.*, **42**, 583 (1974).
16. P. Morgen, *J. Vac. Sci. Technol.*, **18**, 908 (1981).
17. J. N. Miller, I. Lindau, and W. E. Spicer, *Philos. Mag. B*, **43**, 273 (1981).
18. P. Kisluik, *J. Phys. Chem. Solids*, **3**, 95 (1957).
19. P. Kisluik, *ibid.*, **5**, 78 (1958).
20. D. A. King and M. G. Wells, *Surf. Sci.*, **29**, 454 (1982).
21. S. H. Garofalini, T. Halicioğlu, and G. M. Pound, *J. Non-Cryst. Solids*, **37**, 411 (1980).
22. E. F. Idzak, *Opt. Spektrosk.*, **15**, 54 (1963).
23. C. A. Neugebauer and R. A. Ekvall, *J. Appl. Phys.*, **35**, 547 (1964).
24. C. A. Neugebauer and J. R. Rand, *Proc. IEEE*, **52**, 1234 (1964).

CdS Films Grown by Spray Pyrolysis in an N₂ Ambient

B. F. Shirreffs¹

Thayer School of Engineering, Dartmouth College, Hanover, New Hampshire 03755

C. H. Cheng, K. Geib,* and K. A. Jones*

Department of Electrical Engineering, Colorado State University, Fort Collins, Colorado 80523

ABSTRACT

CdS films were grown by spray pyrolysis in a nitrogen atmosphere in an attempt to reduce the oxygen contamination and therefore the resistivity. This would reduce the loss due to series resistance in solar cells fabricated from them. It was determined that the oxygen contamination could not be reduced in this way due to the fact that a major source of oxygen is the solvent, water. Further, the films were found to contain more chlorine, carbon, and, in some instances, tin than was previously thought. It is suggested that these impurities are responsible for the resistivity of SP films being more strongly affected by oxygen adsorption than are vapor deposited or sintered films, and the resistivity of SP films being extremely sensitive to the deposition temperature of the film.

The spray pyrolysis (SP) (1-3) method for preparing CdS films is an economically attractive method for producing CdS based solar cells (4-8) because it can easily be scaled up for mass production, and the deposition temperature of 320°-450°C is relatively low. However, because the starting materials contain many different elements, the chemicals are in aqueous solution, and the films are grown in air, the potential for film contamination is great.

One of the primary contaminants is thought to be oxygen adsorbed on the surface and at the grain boundaries (2, 3). The oxygen increases the resistivity by decreasing both the carrier concentration and the mobility with the latter effect being more pronounced (2, 3, 9). Further, the effect can be enhanced by heating in air (2, 3), or an oxygen atmosphere (9), and it can be reduced by heating for 5 min at 400°C in H₂ or by heating in a vacuum or a nitrogen ambient. That the SP films do contain a substantial amount of oxygen has been shown by Auger studies (10). Also, the authors concluded that the oxygen contamination was a direct result of growing the films in air.

The larger resistivity of the as-grown films reduces the solar efficiency through a higher series resistance and, therefore, a smaller fill factor. The efficiency can be increased by the hydrogen anneal, but this is a somewhat expensive and dangerous procedure. In this work we investigated the possibility of eliminating this step altogether by growing the films in a nitrogen ambient and thereby removing the source of the oxygen contamination. We did this by comparing the light and dark resistivities, the film composition as determined by XPS measurements, and x-ray diffractometer 2 θ scans of air grown and nitrogen grown films.

Our efforts to eliminate the oxygen contamination were not successful, and we show that this is due to water from the aqueous solution being the primary contamination source. Further, we show that the films contain more chlorine and carbon than was previously thought, and speculate that other compounds form from these elements, and they enhance the sensitivity of the film's resistivity to oxygen adsorption and temperature changes.

Experimental Procedure

The apparatus consisted of a liquid tin bath heated by a hot plate inside a bell jar, a spray system, and a cradle that could be used to raise or lower the substrate. The hot plate was set such that the surface of the glass substrate resting on top of the tin bath was 340°C when there was no spray present. This temperature was chosen because Ma and Bube (3) determined that the conductivity at this substrate temperature is at a local maximum, and other investigators have used a similar deposition temperature (4, 10).

* Electrochemical Society Active Member.

¹ Present address: The Standard Oil Company, Cleveland, Ohio 44115.

Key words: solar cells, oxygen adsorption, impurities, XPS, x-ray diffraction.

The spray solution, which is identical to that used by Ma and Bube, was equimolar 0.1M cadmium chloride (CdCl₂) and thiourea [CS(NH₂)₂]. It was difficult to dissolve the CdCl₂ in the distilled water so it was necessary to heat the solution.

The solution was pumped at 0.5 ml/min by a syringe pump, and it was atomized into a fine spray by air or dry nitrogen flowing through a stainless steel nozzle located 7 in. above the substrate. At this height the spray coated the substrate uniformly. A spray catch was used to protect the substrate until the spray system reached its steady state (~2 min). The polygard plastic tubing carrying the solution was water cooled by a copper coil wrapped around it, and it was further protected from the heat by aluminum foil.

The substrates were squares 1 cm on a side cut from microscope slides. They were thoroughly washed in a glass cleaning solution and then repeatedly rinsed in distilled water.

In a typical run the substrate was loaded into the cradle, the bell jar was lowered, the system was in some instances purged with dry nitrogen (<1 ppm O₂), the power was turned on, the spray was turned on when the substrate reached its steady-state temperature (~20 min), the spray catch was removed after the air bubbles had been purged from the solution line, the film was deposited for 10 min (to a thickness of ~7 μ), the spray catch was set in place, the spray and power were turned off, and the substrate was allowed to cool off either above (fast cool) the tin bath or on (slow cool) it. Some of the films were then annealed in air at 400°C for 30 min or in dry nitrogen for 5 min at 400°C.

Ohmic contacts were made to some films by depositing indium spots 0.7 mm in diameter (*d*) and 1.6 mm apart (*l*), and then annealing the film in a N₂ atmosphere at 225°C for 5 min. It was found that it was easier to make contacts to the air-grown films than it was to the N₂-grown films. The contacts were assessed to be ohmic when the *I-V* curves were linear. The sheet resistance, *R*, in the dark and under room illumination was then determined, and the resistivity, ρ , was calculated using the relationship

$$\rho = Rdt/l$$

where *t* is the film thickness. The thickness was measured using an SEM. The SEM was also used to examine the film morphology. An attempt was also made to measure the carrier concentration and the mobility using a Hall effect apparatus and the van der Pauw technique.

Three XPS profiles of four separate films were taken. One profile was taken at the surface, another after 100Å of material had been sputtered off, and a third after 500Å had been removed. The elements present were identified, and their concentrations were computed from their peak heights using known cross sections. Of the four films examined one was air grown, slow cooled (AS); another was air grown, fast cooled (AF); the third was air

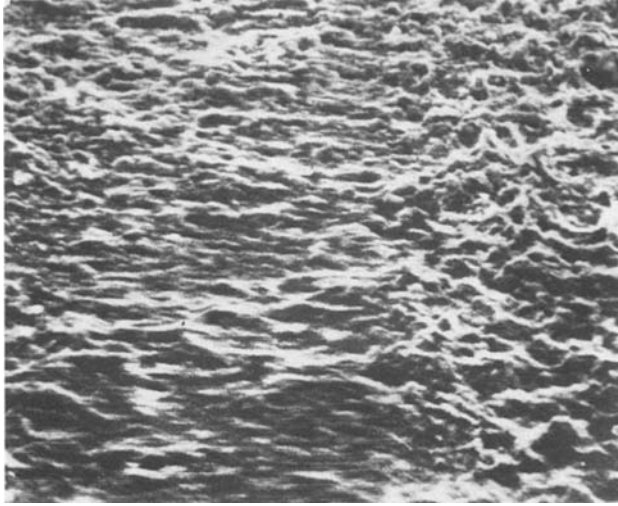


Fig. 1. SEM micrograph of the film morphology (1250 \times)

grown, fast cooled, nitrogen annealed (AFN); and the last was nitrogen grown, slow cooled (NS).

X-ray diffractometer 2θ scans were made to determine if the cubic and the hexagonal phases of CdS were present, and to see if other crystalline materials were present. $\text{CuK}\alpha$ radiation was used in this study. A film was prepared under one of the four conditions (ANF, NS, AF, or AS) examined, annealed in air, and then re-examined. In addition, the AS film was examined after a 2 min wash in distilled water and after a 5 min wash.

Experimental Results

The morphology of the films grown under different conditions was quite similar. A representative example is shown in Fig. 1. This morphology is similar to that seen by Alaei and Rouhani (10).

The resistivities of films grown under similar conditions could vary up to an order of magnitude. However, there were trends, and these are illustrated in Table I where the dark and light resistivities of a sequence of films (NS, AF, AS, and AFN) are listed. There it is seen that the NS resistivity is less than the AF resistivity which, in turn, is less than the AS resistivity. Also, the AFN resistivity is similar to that of the NS sample. The results for the Hall effect measurement on an AS film were that $\mu = 66 \text{ cm}^2/\text{V}\cdot\text{sec}$ and $n = 2.1 \times 10^{14} \text{ cm}^{-3}$. This measurement yields a resistivity of $453 \text{ }\Omega\cdot\text{cm}$ which is larger than the resistivity measurements made on similar films using the other resistivity measurement technique.

The XPS data in Table II, like the Auger data of Alaei and Rouhani (10), show that the films contain large amounts of oxygen, chlorine, and surface carbon. Perhaps the most striking feature is that the nitrogen-grown film contains more, not less, oxygen than the other films. In addition, it contains tin throughout whereas none of the other films do. Another important feature is that all of the films contain surface carbon, but only the annealed film contains carbon at the 500 Å depth.

The diffractometer 2θ scans for $23^\circ < 2\theta < 33^\circ$ are shown in Fig. 2-5. There it is seen that both the cubic phase, represented by the (200) ($2\theta = 31^\circ$) peak, and the hexagonal phase, represented by the (10 $\bar{1}$ 0) ($2\theta = 25^\circ$) and (10 $\bar{1}$ 1) ($2\theta = 28.5^\circ$) peaks, are present. However there are two additional peaks at 24.5° and 30.5° (indicated by the arrows) in

Table I. The light and dark resistivities for nitrogen grown, slow cooled (NS); air grown, fast cooled (AF); air grown, slow cooled (AS); and air grown, fast cooled, nitrogen annealed (AFN) films

	ρ -light $\Omega\cdot\text{cm}$	ρ -dark $\Omega\cdot\text{cm}$
NS	1.5	1.7
AF	26	44
AS	76	190
AFN	3.9	4.8

Table II. The elemental composition of air grown, slow cooled (AS); air grown, fast cooled (AF); air grown, fast cooled, nitrogen annealed (AFN); and nitrogen grown, slow cooled (NS) films as determined by XPS analysis.

Film depth	Element	a/o AS	a/o AF	a/o AFN	a/o NS
Surface	Cd	15.2	19.2	18.8	16.0
	S	13.5	18.3	11.2	1.25
	Cl	11.3	15.4	18.8	14.7
	O	19.3	13.1	20.7	22.6
	C	39.5	34.0	27.7	27.9
100 Å	Sn	1.2	0.0	2.7	6.3
	Cd	33.2	32.7	26.0	22.7
	S	22.8	22.8	14.2	25.2
	Cl	25.4	33.4	28.4	12.7
	O	18.6	9.4	17.4	24.8
500 Å	C	0.0	0.0	14.0	9.3
	Sn	0.0	1.6	0.0	5.3
	Cd	33.1	33.1	23.7	27.8
	S	27.1	28.0	24.1	24.7
	Cl	22.7	31.2	26.9	10.3
	O	17.1	7.6	15.4	31.6
	C	0.0	0.0	9.9	0.0
	Sn	0.0	0.0	0.0	5.5

all of the as-grown films except the NF film, and these peaks are eliminated by the anneal in the NSA and AFA films and are reduced in the ASA. They are further reduced in the latter film by the 2 min wash in distilled water and are eliminated by the 10 min wash. It can also be seen that the anneal increases the peak heights of most of the CdS peaks.

Discussion

Our resistivity data support the suggestion that the resistivity is increased by adsorbed oxygen (9, 11-13). There should be the most adsorbed oxygen in AS films, less in AF films, and the least in NS films. Also, the similarity of the NS and ASN resistivities indicate that at least some of the adsorbed oxygen can be removed by an anneal in nitrogen (9).

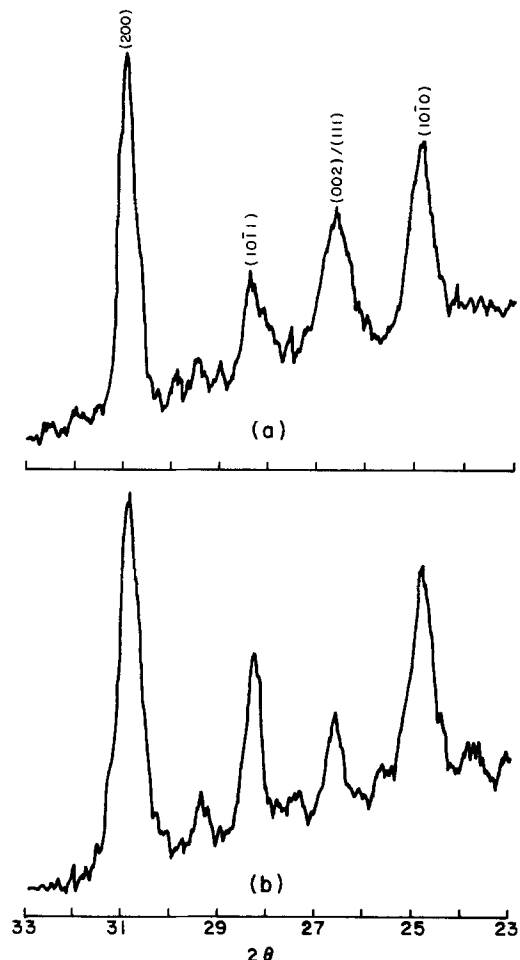


Fig. 2. 2θ diffractometer scans for a nitrogen grown, fast cooled film (a) in the as-grown condition and (b) after a 30 min air anneal.

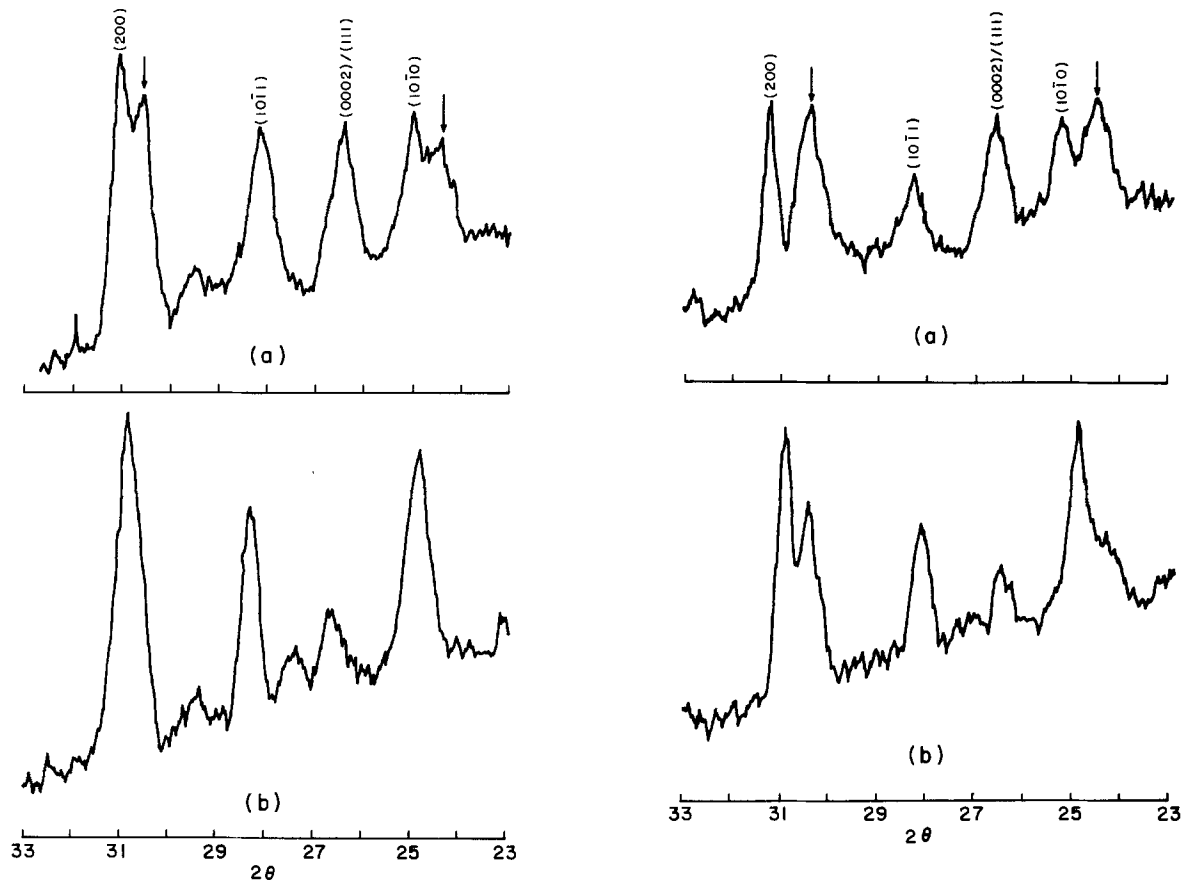


Fig. 3. 2θ diffractometer scans for a nitrogen grown, slow cooled film (a) in the as-grown condition and (b) after a 30 min air anneal.

The mobility calculated from the Hall effect data is comparable, but the carrier concentration is a couple of orders of magnitude less than those of Ma and Bube (3). One possible explanation for our small carrier concentration is that the films are not homogeneous as they must be in order for the van der Pauw method to be applicable.

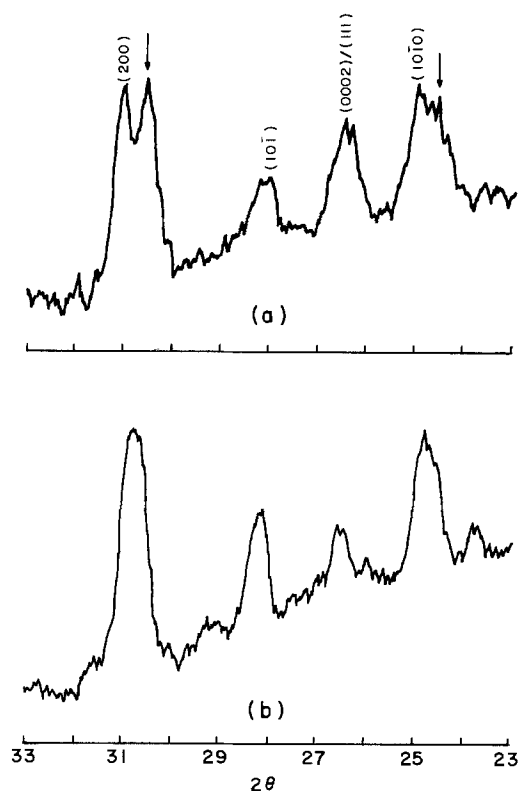


Fig. 4. 2θ diffractometer scans for an air grown, fast cooled film (a) in the as-grown condition and (b) after a 30 min air anneal.

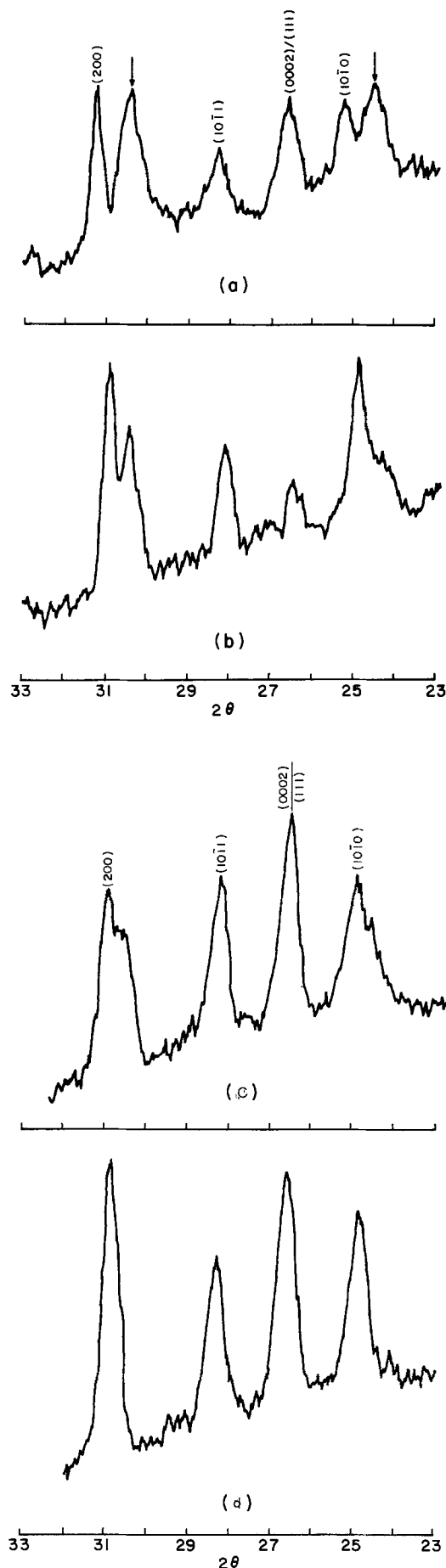


Fig. 5. 2θ diffractometer scans for an air grown, slow cooled film (a) in the as-grown state, (b) after a 30 min anneal in air, (c) after a 30 min air anneal and a 2 min wash in distilled water, and (d) after the film was washed for 10 min.

This could also be why the resistivity measurements made using the van der Pauw technique were larger. This explanation is plausible because the films contain excessive amounts of oxygen and chlorine, and in some instances a second phase is detected.

According to the XPS measurements, there is a substantial amount of oxygen present even when the films are grown in nitrogen. The likely explanation is that a major source of oxygen contamination is the solvent, water. Moreover, the nitrogen-grown film contains more oxygen because it has more tin which is better able to getter the oxygen. It contains more tin since the tin bath is not coated by a protective oxide film. That having a metal present which can getter oxygen increases the oxygen content, was also observed by Alae and Rouhani (10), who found that films containing much indium also contained more oxygen. The tin and the extra oxygen present in the nitrogen grown films could also be responsible for the greater difficulty in making ohmic contacts to them.

Even though the nitrogen-grown films have more oxygen incorporated into them, they have lower resistivities. We speculate that this is due to oxygen being gettered from the CdS film by the extra tin, and also due to less oxygen being adsorbed during the cool down. Most of the resistivity changes caused by oxygen have been attributed to adsorbed oxygen, not oxygen incorporated into the lattice.

Others have also determined that the films contain an excessive amount of chlorine (6, 10). We were unable to determine in what form the chlorine was present. We did look for CdCl₂ diffraction peaks but detected them only when a white film formed when the spray was not a fine mist.

The surface carbon contamination was also observed by others (6, 10). Carbon was found at the 500Å depth only in the annealed sample so it must be removed by the formation of gaseous species. The anneal does drive some of the carbon in, and this could be a factor in the resistivity changes.

The extra x-ray peaks at 24.5° and 30.5° indicate that a phase other than the CdS phases is present. We use the word indicate because the (200) and (10 $\bar{1}$ 0) peaks appear to split. However, the unknown peaks indicated by the arrows do not always appear, and can be reduced or eliminated by an anneal or by rinsing the film in water. We thus attribute these variable peaks to a second phase. This phase is eliminated or its concentration is greatly reduced by the air anneal possibly because it goes into solution at the higher temperature, and it is removed by washing because it is water soluble. An extra x-ray peak was observed by Ma and Bube (3) who attributed it to a (220) reflection of the rock salt CdS phase, and Alae and Rouhani (10) found some extra peaks which they attributed to hydrated CdCl₂. We are not able to compare these results with ours because in neither case did they list the 2θ values.

There are a number of experimental observations that can be explained by these "impurity phases." First, the dark resistivity in the SP films (2, 3, 9) is much more sensitive to oxygen adsorption than either evaporated (3, 14) or sintered CdS (15) films because the impurities greatly enhance the effect. Also, the extreme sensitivity of the dark resistivity to the deposition temperature (3) can be

attributed to the precipitation and dissolution of the "impurity phases." The dependence the resistivity has on the state the impurities are in can also be used to explain the effects the deposition rate has on the resistivity that were observed by Ma and Bube (3).

Other observations made from the x-ray data are, in general, similar to those of others. These include that there is a substantial amount of the cubic phase present in films deposited at 340°C as is evidenced by the existence of the (200) peak (1, 3, 16, 17), there is not a strong preferred orientation in the hexagonal phase as is indicated by the simultaneous appearance of the (10 $\bar{1}$ 0) and (10 $\bar{1}$ 1) peaks (1), and the peak heights are enhanced by an air anneal possibly due to an increase in the film crystallinity (1). There is, however, some preferred orientation as is indicated by the relative peak heights. If the orientation were completely random the 10 $\bar{1}$ 1/10 $\bar{1}$ 0 ratio would be 4/3 and the 111/200 ratio would be 5/2. This, clearly, is not the case as the (10 $\bar{1}$ 0) peak heights are larger than the (10 $\bar{1}$ 1), and the (200) peak heights are larger than the (111).

Acknowledgments

We would like to acknowledge the assistance of V. A. Surprenant for helping us construct the growth apparatus and analyze the x-ray data, R. Kee for helping us analyze the XPS data, and C. W. Wilmsen for the use of his Auger system. We would also like to acknowledge the support of the Research Corporation under grant 7785 and NSF under grant DMR-75-09329. We would also like to thank the reviewers for their thorough review.

Manuscript submitted March 9, 1983; revised manuscript received Aug. 3, 1983.

The Standard Oil Company of Ohio assisted in meeting the publication costs of this article.

REFERENCES

1. R. R. Chamberlin and J. S. Skarman, *The Journal*, **113**, 86 (1966).
2. C. H. Wu and R. H. Bube, *J. Appl. Phys.*, **45**, 648 (1974).
3. Y. Y. Ma and R. H. Bube, *This Journal*, **124**, 1430 (1977).
4. R. R. Chamberlin and J. S. Skarman, *Solid-State Electron.*, **9**, 819 (1966).
5. G. H. Hewig and W. H. Bloss, *Thin Solid Films*, **45**, 1 (1977).
6. Y. Y. Ma, A. L. Fahrenbruch, and R. H. Bube, *Appl. Phys. Lett.*, **30**, 423 (1977).
7. R. S. Feigelson, A. N'Diaye, S. Y. Yin, and R. H. Bube, *J. Appl. Phys.*, **48**, 3162 (1977).
8. S. Y. Yin, A. L. Fahrenbruch, and R. H. Bube, *ibid.*, **49**, 1294 (1978).
9. F. B. Micheletti and P. Mark, *Appl. Phys. Lett.*, **10**, 136 (1967).
10. M. S. Alae and M. D. Rouhani, *J. Electron. Mater.*, **8**, 289 (1979).
11. P. Mark, *J. Phys. Chem. Solids*, **26**, 959 (1965).
12. A. Waxman, *Solid State Electron.*, **9**, 303 (1966).
13. F. B. Micheletti and P. Mark, *J. Appl. Phys.*, **39**, 5274 (1968).
14. P. Mark, *J. Phys. Chem. Solids*, **25**, 911 (1964).
15. A. L. Robinson and R. H. Bube, *This Journal*, **112**, 1002 (1965).
16. B. K. Gupta and O. P. Agnihorti, *Solid State Commun.*, **23**, 295 (1977).
17. B. K. Gupta and O. P. Agnihorti, *Philos. Mag.*, **37**, 631 (1978).

Growth of Fe and FeAs₂ Films on GaAs by Organo-Metal Chemical Vapor Deposition Using Pentacarbonyl Iron and Arsine

P. J. Walsh

Fairleigh Dickinson University, Teaneck, NJ 07666

N. Bottka

Naval Research Laboratory, Washington, DC 20375

ABSTRACT

A number of iron and iron arsenide films have been grown using pentacarbonyl iron and arsine by conventional organo-metal chemical vapor deposition (OM-CVD) on single-crystal GaAs. Auger sputter profile on a 1240Å-thick iron arsenide sample gave a composition consistent with the intended compound, FeAs₂, a narrow-gap semiconductor. Infra-red transmission data on the same film yielded an optical gap of 0.16 ± 0.01 eV, which compares with the known electrical gap of 0.22 eV for bulk FeAs₂. An apparent catalytic action of pentacarbonyl with arsine allows the iron arsenide to form from arsine at low temperatures near 300°C. The low temperature of growth suggests the possibility of forming heterostructures between a narrow-gap semiconductor and a ferromagnetic film. Such a structure was successfully grown on GaAs.

Recent work by Prinz and Krebs (1) has shown that high quality epitaxial Fe can be grown on GaAs surfaces for film thicknesses less than 1 μm. These thin epitaxial films were deposited by the molecular beam epitaxy (MBE) technique using high purity elemental Fe as the source. In those experiments, the optimum growth conditions, as determined by reflection high energy electron diffraction and ferromagnetic resonance occur for substrate temperatures between 175°-225°C.

More recently, Kaplan and Bottka (2) have shown that high quality epitaxial Fe on GaAs surfaces can also be grown using chemical vapor deposition (CVD) by decomposing the organo-metal (CO)₅Fe thermally on the substrate at 200°C in an ultrahigh vacuum chamber. In that UHV-OM-CVD process, *in-situ* Auger electron spectroscopy (AES) and low energy electron diffraction (LEED) analysis was used to characterize the growth process of the Fe film. Those studies showed that Fe growth on GaAs proceeds by layer rather than island formation. The LEED data elucidated the nature of the atomic arrangement of Fe on GaAs for various surface orientations for the first few monolayer coverage.

In the present work, we investigated the growth of films of iron and one of its compounds, the narrow-gap semiconductor FeAs₂, on GaAs by the more conventional technique of OM-CVD, which uses H₂ as a carrier gas to transport the OM species to the substrate. The conventional technique is simple, efficient, and amenable to large scale application.

We have found that with care normal OM-CVD technique does allow the production of Fe and FeAs₂ films on GaAs. Indeed, to our knowledge, this study has produced the first synthesis of FeAs₂ in thin film form. This synthesis is apparently aided by a catalytic enhancement of the decomposition of the arsenic source (AsH₃) in the presence of the iron source, pentacarbonyl iron (CO)₅Fe, which allows FeAs₂ to be formed at a relatively low substrate temperature.

Experimental

The vertical OM-CVD reactor used in these experiments (Fig. 1) is a conventional setup used to grow high quality GaAs and AlGaAs/GaAs on GaAs substrates but with the addition of the (CO)₅Fe source added to the manifold. The reactor gas manifold and mixing system were constructed from passivated stainless steel tubing. Parts were either welded or joined with vacuum-compatible VCR fittings. The system utilizes mass flow controllers for control of the various gaseous flow rates and pneumatically controlled bellow valves for switching all gaseous flows.

The carrier gas used was ultrahigh purity, palladium-purified hydrogen. The arsenic source was ultrahigh pu-

rity arsine contained in a commercially supplied high pressure cylinder. The 99.5%-grade (CO)₅Fe from Alfa Ventron was twice vacuum distilled and transferred into a stainless steel cylinder/bubbler which was held at 24°C during growth. All saturated vapors and gases were mixed and diluted with H₂ in a manifold prior to introduction into the reactor.

The GaAs substrates were undoped liquid-encapsulated Czochralski (100) oriented wafers which were bromine-methanol polished, cleaned, and etched in 1:1 NH₄OH:H₂O prior to loading into the reactor.

The cold-walled growth vessel was a quartz cylinder coupled to the manifold with ultratorr fittings. The sample rested on a silicon carbide-coated graphite susceptor and was RF inductively heated.

Growth of Fe Films

Typical growth conditions for Fe on GaAs are shown in Table I. Iron films grow easily in the temperature range 150°-300°C, and the optimum temperature is at 200°C. This is similar to that found in MBE and in UHV-OM-CVD experiments. The growth rate depends upon the partial pressure of (CO)₅Fe in the reactor. For typical flows of 15 cm³/min of hydrogen through the (CO)₅Fe bubbler and 1 l/min of H₂ dilution, the growth rate was about 200 Å/min, as determined from Dektak measurements.

The sample temperature and its surface IR emissivity was monitored during growth with an Iacon pyrometer¹ operating in the 2-2.6μ spectral range. At 200°C, and just prior to growth, the value of the GaAs substrate emissivity was 0.7. Upon initiation of growth, this value dropped to 0.29, indicating the formation of a metallic, infrared reflecting film. The grown Fe films are highly reflective (Fig. 2), show no indication of tarnishing with time, and are very strongly bonded to the GaAs substrate. A total of 15 Fe/GaAs samples were grown.

Growth of FeAs₂ Films

There are a number of compounds which can be formed between iron and arsenic, including Fe₂As, FeAs, and FeAs₂. The last compound, iron di-arsenide, appears naturally as the mineral loellingite (3), and its growth is favored by an arsenic-rich environment during formation. It is a narrow-gap semiconductor whose properties have been partially studied.

Bulk FeAs₂ has been grown (6) by the vapor transport method in the temperature range 600°-800°C, but, to our knowledge, thin film FeAs₂ had never been previously synthesized. FeAs₂ has the cell dimension (4-7) of $a = 5.300\text{Å}$, $b = 5.983\text{Å}$, and $c = 2.882\text{Å}$, an enthalpy of formation of 10.4 kcal/mol (8, 9), specific gravity of 7.4 (10), and is diamagnetic (11, 12).

¹ Iacon Radiation Thermometer Series 300 C, manufactured by Iacon, Inc., Niles, IL 60648.

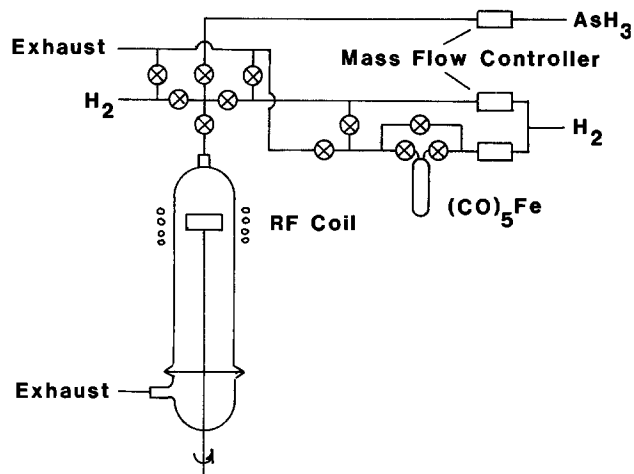


Fig. 1. OM-CVD system used in the growth of Fe and FeAs₂ on GaAs. Arsine and hydrogen enter from tanks located to the right and are exhausted through a bubbler and a burner (neither shown) to the left. The substrate is rotated at approximately 30 rpm.

Table I summarizes the growth conditions of FeAs₂ on GaAs. These films grow in the temperature range 200°-400°C, and the optimum growth temperature seems to be near 300°C, considerably below the vapor transport temperature used for bulk growth (6). We believe that the low temperature growth of FeAs₂ in our OM-CVD system may result from a catalytic action of Fe or (CO)₅Fe on the decomposition rate of AsH₃. Schlyer and Ring (13) have observed pyrolytic decomposition of (CH₃)₃Ga and PH₃ over product-crusted walls at 240° and 270°C. On the basis of their analysis, the authors propose that AsH₃ and (CH₃)₃Ga can catalytically decompose at low temperatures on GaAs surfaces after surface adsorption and formation of complexes. A similar surface catalysis may be operable in our case.

The grown films are highly reflective, and their emissivity during growth is about 0.7, similar to GaAs and distinctly different from the surface emissivity of the growing iron films. The high emissivity is consistent with the low diffuse reflectivity of loellingite (14). The iron di-arsenide films have low surface conductivity, are soft, and show no signs of degradation after nine-month exposure to the atmosphere.

X-ray diffraction measurements at grazing incidence was attempted to obtain crystallographic information about the thin FeAs₂ film. However, results were inconclusive due to the strong background signal of the GaAs substrate.

Figure 3 shows the sputter Auger profile of one of the six FeAs₂-grown films. Atomic concentration estimates from this data indicate that the preferred stoichiometry is nearer FeAs₂ rather than FeAs or Fe₂As, two other possible formations. The interface between the film and the substrate is about 80Å wide. The Ga and carbon peak was monitored but not found in the film. The observed 20% drop in the As atomic concentration in going from FeAs₂ into GaAs is near the 23% atomic concentration difference expected between the two compounds. Interferometric

Table I. Growth condition for Fe and FeAs₂ on GaAs

	Fe	FeAs ₂
Reactor pressure (torr)	760	760
Growth temperature (°C)	150-300	200-400
Optimum growth temperature (°C)	200	300
Total gas flow (l/min)	1.0	1.1
(CO) ₅ Fe source temperature (°C)	24	24
H ₂ /(CO) ₅ Fe bubbler flow (cm ³ /min)	15	10
Arsine flow (cm ³ /min)	—	90
Growth rate (Å/min)	200	80

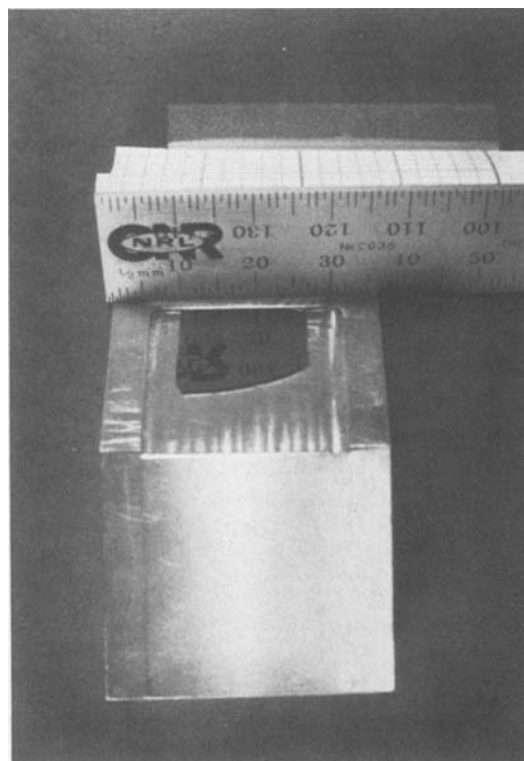


Fig. 2. Typical Fe film grown on single-crystal GaAs

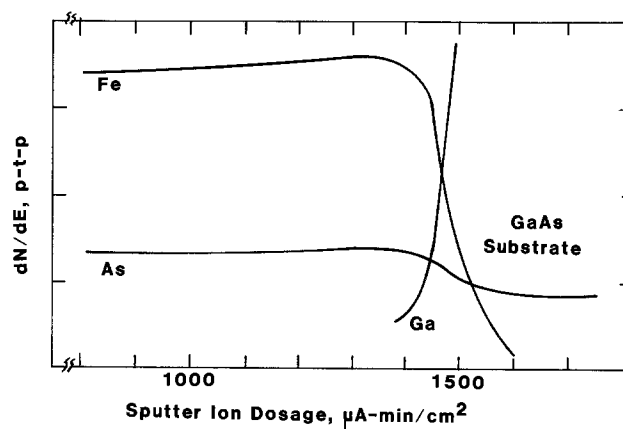


Fig. 3. Sputter Auger profile of FeAs₂-grown film. Variation of Auger elemental sensitivity factors are included. Interferometric measurement on the sputtered crater gave estimate of the film thickness and its growth rate. Film thickness is 1240 ± 50Å.

measurements on the sputtered crater gave estimate of the film thickness and its growth rate. Matrix effects were taken into consideration in presenting the data in Fig. 3. The effect of preferential sputtering in stoichiometric ratio is not known.

Infrared transmission measurements were conducted on the grown 1240Å film sample profiled in Fig. 3 and on a companion GaAs single-crystal substrate. Figure 4 presents the results in terms of the normalized ratio of sample transmittance to that of the substrate over the region from 3.5 to 20 μm. The electrical gap of FeAs₂ determined from the temperature dependence of a bulk sample is 0.22 eV (11) and that energy lies almost exactly at the energy where the normalized transmission has risen half way. If we define the optical gap conventionally as the energy at which the absorption coefficient is 10⁴ cm⁻¹, and neglect interference effects in the optically thin sample, the optical gap of the deposited film is 0.16 ± 0.01 eV. The observed gap energy difference of 0.06 eV between the bulk and our film stems from the different methods of determining gap energies. The bulk conductivity *vs.* temperature measurement gives the extrapolated gap energy at 0 K, whereas our optical data were

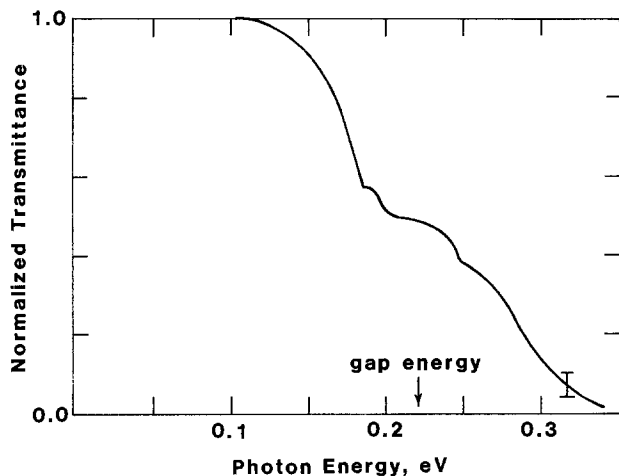


Fig. 4. Normalized ratio of sample transmittance (FeAs_2) to that of the GaAs substrate in the infrared. Arrow indicates the electrical gap energy (11) of FeAs_2 . Uncertainty in the measurement is shown by the bar at the right lower corner.

taken at 300 K. The 2×10^{-4} eV/K gap variation is close to the value observed in most semiconductors. The sample transmission data reveal repeatable optical structures within the measured range which are absent in the GaAs substrate and which appear to be real properties of the film.

Summary

Conventional OM-CVD has been used to grow high quality films of the metal Fe and one of its compounds, FeAs_2 , upon single-crystal GaAs. The successful growth of the narrow-gap semiconductor FeAs_2 raises the possibility that less well-known narrow-gap semiconductors of the type (Fe, Ni, Co)-(P, As, Sb) may be possible. In addition, the growth of compatible Fe and FeAs_2 films within the same OM-CVD system offers promise that heterostructures involving metal and narrow-gap semiconductors may be fabricated in a simple manner by OM-CVD. This possibility is accentuated by the low temperature required at which FeAs_2 grows from arsine in the presence

of pentacarbonyl iron. Because of this relatively low growth temperature, attempts were made to deposit alternate thin layers of FeAs_2/Fe on GaAs. We were successful in a preliminary growth of a $\text{FeAs}_2/\text{Fe}/\text{FeAs}_2/\text{Fe}$ heterostructure, whose overall thickness was approximately 150Å, on single-crystal GaAs. The resulting heterostructure has a brilliant luster, and is strongly bonded and lasting. Further work is needed to characterize its properties.

Acknowledgments

We would like to thank the kind assistance of R. Colton and E. Shafrin in the Auger analysis, and R. Kaplan, G. Prinz, A. Berry, and E. Swiggard for their helpful discussion.

Manuscript submitted July 29, 1983; revised manuscript received Oct. 14, 1983.

The Naval Research Laboratory assisted in meeting the publication costs of this article.

REFERENCES

1. G. A. Prinz and J. J. Krebs, *Appl. Phys. Lett.*, **39**, 397 (1981).
2. R. Kaplan and N. Bottka, *ibid.* **41**, 972 (1982).
3. C. J. Smithells, "Metals Reference Handbook," p. 193 ff, Interscience, New York (1955).
4. H. Holseth and A. Kjekshus, *Acta Chem. Scand.*, **22**, 3284 (1968).
5. E. H. Roseboom, *Am. Mineral.*, **48**, 271 (1963).
6. G. Rosenthal, R. Kershaw, and A. Wold, *Mater. Res. Bull.*, **7**, 479 (1972).
7. A. Kjekshus and T. Rakke, *Acta. Chem. Scand.*, **A31**, 517 (1977).
8. L. P. Ruzinow and B. S. Gulvanitskii, "Equilibrium Transformations of Metallurgical Reactions," p. 416, Izd. Metallurgiya, Moscow (1975).
9. P. A. Ioffe, N. S. Rudashevskii, and L. Sh. Tsemekhan, *Russ. J. Inorg. Chem.*, **23**, 1126 (1978).
10. "Chemical Rubber Company Handbook," 48th Edition, Table B183.
11. A. K. L. Fan, G. H. Rosenthal, H. L. McKinzie, and A. Wold, *J. Solid State Chem.*, **5**, 136 (1972).
12. A. Kjekshus and T. Rakke, *Acta Chem. Scand.*, **A33**, 469 (1979).
13. D. J. Schlyer and M. A. Ring, *This Journal*, **124**, 569 (1977).
14. B. J. Wood and R. G. J. Strens, *Mineral. Mag.*, **43**, 509 (1979).

Oxygen-Doped Molybdenum Films for MOS Gate Application

Shin-ichi Ohfuji, Chisato Hashimoto, Takao Amazawa, and Junichi Murota

Nippon Telegraph and Telephone Public Corporation, Atsugi Electrical Communications Laboratory, 1839, Ono, Atsugi-shi, Kanagawa Pref., 243-01 Japan

ABSTRACT

Intentionally oxygen-doped Mo films (MoO_x) for MOS gate electrodes are investigated to eliminate the penetration of implanted As ions into the silicon substrate through the gate electrodes and gate oxides. The MoO_x films are prepared by reactive sputtering of Mo in a mixture of Ar and O_2 gases. Depth profiles of As ions and MOS C-V curves are measured to estimate stopping properties. For as-deposited MoO_x films, whose oxygen concentrations are higher than 20 atom percent (a/o), As ion penetration depth is within 0.15 μm under 100 keV As ion implantation. This depth is about one third of that in normal Mo films. This excellent stopping property can be attributed to the nearly amorphous structure, which suppresses As ion channeling in the films resulting from oxygen doping. The resistivity of MoO_x films with 39 a/o oxygen after annealing at 1000°C for 30 min is 25 $\mu\Omega\text{-cm}$, which is only three times as large as that for normal Mo films. In MoO_x gate MOS structures, MOS characteristics are independent of oxygen concentrations in the films, and are almost the same as the characteristics for normal Mo gate electrodes.

Thin molybdenum (Mo) films have been attracting much attention as self-aligned gate electrodes and interconnections for highly packed MOSFET integrated circuits (1, 2). The reason for this is their low resistivity, high temperature resistance, and high density (10.3 g cm^{-3}), which is beneficial for ion implantation masking materi-

Key words: metals, integrated circuits, ion implantation, sputtering.

als. Nozaki, however, has reported that unwanted depletion modes have been observed in Mo gate MOSFET characteristics when arsenic (As) ion implantation is carried out using Mo gates as masks (3). Fujinaga has pointed out that the main cause of this phenomenon is the anomalous penetration of As ions into the silicon substrate caused by As ion channeling in some columnar Mo grains (4). To improve stopping properties, silicon nitride (5) and molybdenum nitride (6) coatings on Mo films, as

well as a direct nitridation technique for Mo gate electrodes (4, 7), have been proposed.

The authors propose the adoption of oxygen-doped Mo (MoO_x) gate electrodes having a simple formation process for a powerful masking material against ion implantation. Degradation in conductivity and MOS characteristics is shown to be low compared with normal Mo gate electrodes. MoO_x films were prepared by the reactive sputtering of Mo in an Ar and O₂ gas mixture. The electrical and structural properties of these films were investigated, and the effect of oxygen doping into Mo films on MOS characteristics was examined using MoO_x-gate MOS capacitors.

Experimental Procedures

MoO_x films (0.2-0.6 μm thick) were deposited on oxidized silicon wafers at room temperature in a mixture of Ar and O₂ gases using an RF planar magnetron sputtering apparatus. A pure Mo target, with nominal purity of 99.95%, was used. Prior to deposition, the deposition chamber was evacuated to 3×10^{-7} torr by a turbo molecular pump. The oxygen concentration (C_o) in the MoO_x films was controlled within the range of 3-39 atom percent (a/o), by varying the partial pressure of the O₂ gas introduced into the chamber between 0 (undoped) and 2.5×10^{-4} torr. A 3 a/o concentration was observed as a background value when no O₂ gas was introduced, at which the partial pressure of residual O₂ gas in the Ar-introduced chamber was less than 5×10^{-8} torr, as measured by a quadrupole mass analyzer. The partial pressure of Ar gas and RF deposition power were 7.5×10^{-3} torr and 1.5 kW, respectively. After deposition, several of the samples were annealed in the temperature range of 600°-1000°C for 30 min in an N₂ ambient.

The C_o was measured by Auger electron spectroscopy (AES) for the as-deposited state using sensitivity corrections for the constitutional elements (8). The measurement error in this method was at most several atom percent; the measurement accuracy of the relative concentration among samples was better. The depth distribution of oxygen in the films was uniform and changed very little even after annealing at 1000°C for 30 min.

Arsenic ions were implanted at room temperature into the MoO_x films and gate electrodes of MOS capacitors at 100 keV energy to a dose of 1×10^{16} ions-cm⁻². The implantation angle was 6° from the normal to the sample surface. The arsenic depth profiles were measured by SIMS (Cameca, IMS-3F).

The film structure was investigated using an x-ray diffractometer. The average grain size for Mo and molybdenum oxide (in this experiment, only MoO₂) was determined from the broadening of the diffraction peaks of Mo(211) and MoO₂(110)(111), respectively, using Scherrer's equation (9). The morphology of the surfaces and cleaved sections of the films were observed by a scanning electron microscope (SEM).

The electrical resistivity of the films was determined by a four-point probe method in conjunction with thickness measurements using a Talystep (Rank Taylor Hobson).

To clarify the effects of oxygen doping into Mo gate electrodes on MOS characteristics, basic MOS capacitor structures were fabricated on p-type (5 Ωcm) (100) silicon wafers. The gate oxide was grown in dry O₂ at 950°C to 40 and 140 nm thick. Step etching was carried out on the 140 nm thick oxide to have four oxide steps. After the deposition 0.2 μm-thick MoO_x films onto the oxide, gate electrode areas 500 μm square were defined by photolithography and wet chemical etching in a mixed solution of H₃PO₄, HNO₃, and CH₃COOH. Several wafers were implanted with As ions, and both the implanted and unimplanted samples were annealed in N₂ at 1000°C for 30 min. Next, low temperature annealing in a mixture of H₂ and N₂ at 450°C was carried out for 30 min to reduce both interface trap density and fixed oxide charge density in the MOS structures. Under these annealing conditions, the molybdenum oxide in the films was not reduced.

The work function of MoO_x gate electrodes was obtained by measuring 1 MHz C-V flatband voltages as a function of gate oxide thickness. In addition, interface trap densities were estimated by quasistatic C-V measurement.

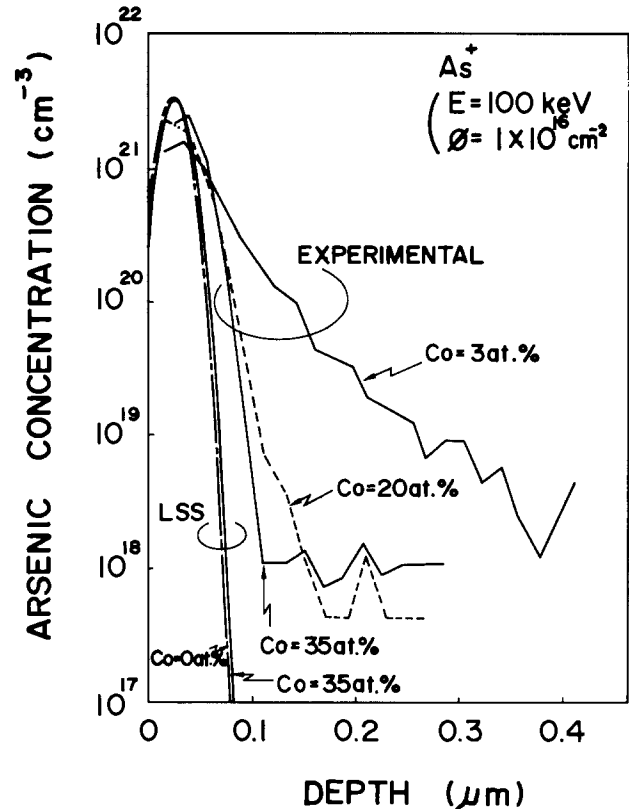


Fig. 1. Depth distribution profiles of implanted As ions in 0.6 μm thick MoO_x films. Smooth curves represent LSS theoretical distributions for C_o = 0 and 35 a/o.

Results and Discussion

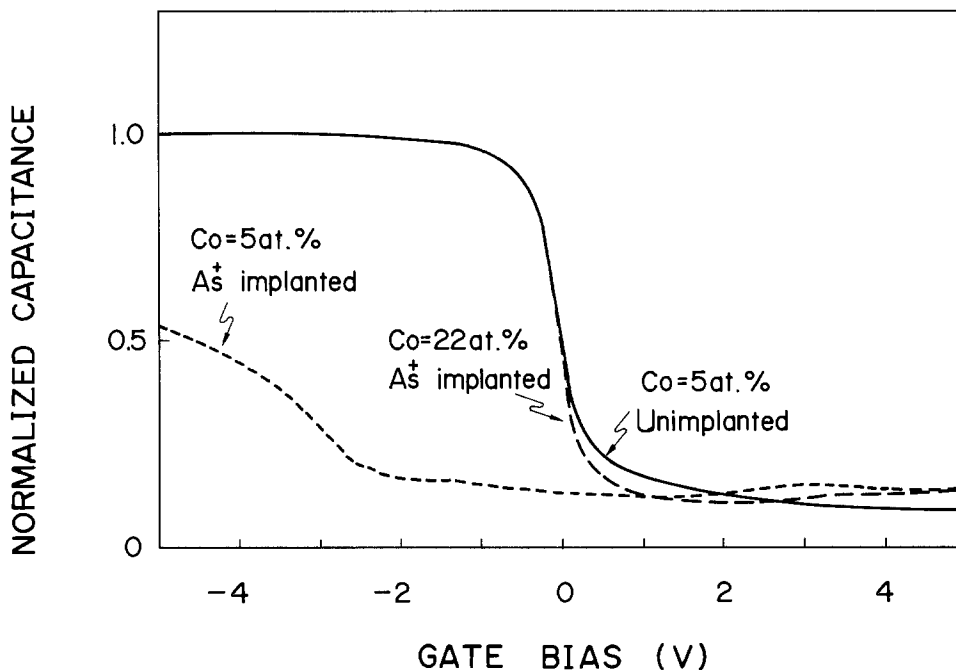
Arsenic ion stopping properties.—Figure 1 shows depth distribution profiles for the As ions implanted into 0.6 μm thick MoO_x films. For comparison, two calculated profiles are shown as smooth curves. These profiles represent LSS theoretical distributions in samples with C_o = 0 and 35 a/o. Here, it is assumed that (i) film structures are amorphous, (ii) ion distribution profiles in the films are Gaussian, and (iii) the density for MoO_x films, d_{MoO_x} (g cm⁻³), is calculated from the bulk densities of Mo ($d_{\text{Mo}} = 10.3$ g cm⁻³) and MoO₂ ($d_{\text{MoO}_2} = 6.44$ g cm⁻³) in accordance with C_o (a/o), and is expressed as

$$d_{\text{MoO}_x} = \frac{(100 - \frac{3}{2} C_o) A_{\text{Mo}} + \frac{C_o}{2} A_{\text{MoO}_2}}{(100 - \frac{3}{2} C_o) \frac{A_{\text{Mo}}}{d_{\text{Mo}}} + \frac{C_o}{2} \cdot \frac{A_{\text{MoO}_2}}{d_{\text{MoO}_2}}} \quad [1]$$

where A_{Mo} is the atomic weight of Mo (95.9), and A_{MoO_2} is the molecular weight of MoO₂ (127.9). For MoO_x films with C_o = 3 a/o, the deep penetration of As ions is observed. At the depth of 0.3 μm, which is a typical gate electrode thickness in refractory metal gate MOS devices (10), As ions are still detected and an exponentially distributed tail is shown. This tail is probably caused by As ion channeling in columnar Mo grains in the films (4). With an increase in C_o from 3 to 35 a/o, the As concentration near the film surface increases, and the penetration depth becomes shallower. Here, the As concentration below 2×10^{18} cm⁻³ is due to background noises in the SIMS measurements. For films with C_o = 35 a/o, the experimentally determined distribution comes closer to the LSS theoretical distribution for a density of 8.6 g cm⁻³, calculated from Eq. [1].

The excellent stopping properties of MoO_x films were also confirmed by the MOS C-V measurement of MOS capacitors, as shown in Fig. 2. For examples with C_o = 5 a/o, the C-V curve for implanted capacitors shifts remarkably to the negative direction of gate bias from that for unimplanted capacitors. For comparison, the C-V curve for implanted capacitors with C_o = 22 a/o is also shown in Fig. 2. The C-V curve roughly agrees with that for unimplanted capacitors with C_o = 5 a/o. When C_o was higher

Fig. 2. 1 MHz C-V curves for $\text{MoO}_x(0.2 \mu\text{m})/\text{SiO}_2(40 \text{ nm})/\text{Si}$ capacitors surrounded by a $0.85 \mu\text{m}$ -thick oxide guard band. Several samples were implanted with As ions at 100 keV energy to a dose of $1 \times 10^{16} \text{ ions-cm}^{-2}$.



than 20 a/o and the MoO_x films were thicker than $0.2 \mu\text{m}$, no large shift in the C-V curves was observed after As ion implantation. The C-V shift in the samples with $C_o = 5 \text{ a/o}$ is probably caused by interface traps at the SiO_2/Si interface, as well as changes in carrier concentration at the silicon substrate surface resulting from the penetration of As ions into the substrate (11). Therefore, it is suggested that oxygen doping ($C_o = 20\text{-}35 \text{ a/o}$) into Mo films in the film preparation process is very effective for preventing the penetration of implanted As ions into the silicon substrate.

Film structure.—The remarkable improvement in the stopping properties of MoO_x films is presumed to be due to the structural change caused by the doped oxygen. Figure 3 shows x-ray diffractometer traces for as-deposited MoO_x films with $C_o = 3, 22,$ and 35 a/o . It is found that the film with $C_o = 3 \text{ a/o}$ (Fig. 3a) consists of preferentially oriented $\langle 110 \rangle$ Mo grains perpendicular to the film surface. The intensities of the (110) peak and other diffraction peaks from Mo become lower with an increase in C_o (Fig.

3b) and almost disappear at $C_o = 35 \text{ a/o}$ (Fig. 3). This suggests that the doped oxygen suppresses Mo grain growth during deposition, and makes the films nearly amorphous. Therefore, the high stopping properties of MoO_x gate electrodes can be attributed to the amorphous structure which suppresses the ion channeling effect in Mo grains.

Next, annealing effects on film structures were investigated for normal process temperatures. Figure 4 shows x-ray diffractometer traces for films with $C_o = 22 \text{ a/o}$ annealed at 1000°C . Both MoO_2 and Mo are found to be structural components, and the Mo(110) reflection intensity is higher than that for as-deposited films (Fig. 3b). The diffraction peaks for MoO_2 were also observed when C_o was above 7 a/o . Figure 5 shows the reflection intensities for Mo and MoO_2 as a function of annealing temperature for films with $C_o = 3$ and 39 a/o . For films with $C_o = 39 \text{ a/o}$, abrupt increases in both $\text{MoO}_2(110)(111)$ and Mo(110) peak intensities are observed in the temperature range of $600^\circ\text{-}800^\circ\text{C}$. This result indicates that the doped oxygen in the films, which may exist as a Mo-O solid solution at the boundaries of fine Mo grains before annealing, crystallizes into a MoO_2 accompanied with Mo grain growth in the range between 600° and 800°C . Above 800°C , the $\text{MoO}_2(110)(111)$ peak intensity almost reaches saturation. The Mo(110) peak intensity increases slightly in the same manner as for films with $C_o = 3 \text{ a/o}$. These results show that MoO_2 crystallization is almost completed in annealing below 800°C , whereas Mo grain growth continues at temperatures of over 800°C . Figure 6 shows directly observed SEM images of MoO_x films. The as-deposited films have flat surfaces and very fine grains (Fig. 6a and 6b), whereas an increase in grain sizes is observed after annealing at 1000°C (Fig. 6c and 6d). In these images, no difference can be seen between the samples with $C_o = 3 \text{ a/o}$ and those with $C_o = 39 \text{ a/o}$. Grain size for both Mo and MoO_2 after annealing at 1000°C , measured by x-ray diffraction, was about $0.15 \mu\text{m}$ diam for all samples. This is responsible for the lack of difference observed between the samples with $C_o = 3 \text{ a/o}$ and those with $C_o = 39 \text{ a/o}$.

From these results, it is concluded that by annealing at 1000°C , nearly amorphous MoO_x films become polycrystalline films composed of Mo and MoO_2 grains having almost the same diameters.

Electrical resistivity.—Figure 7 shows electrical resistivity for $0.33 \mu\text{m}$ thick MoO_x films as a function of annealing temperature. The resistivity, which increases as a result of oxygen doping for as-deposited films, decreases slightly after annealing up to 600°C . However, it decreases abruptly in the temperature range between 600° and 800°C , and saturates above 800°C . After annealing at 1000°C , a resistivity of $25 \mu\Omega \text{ cm}$ can be obtained for films

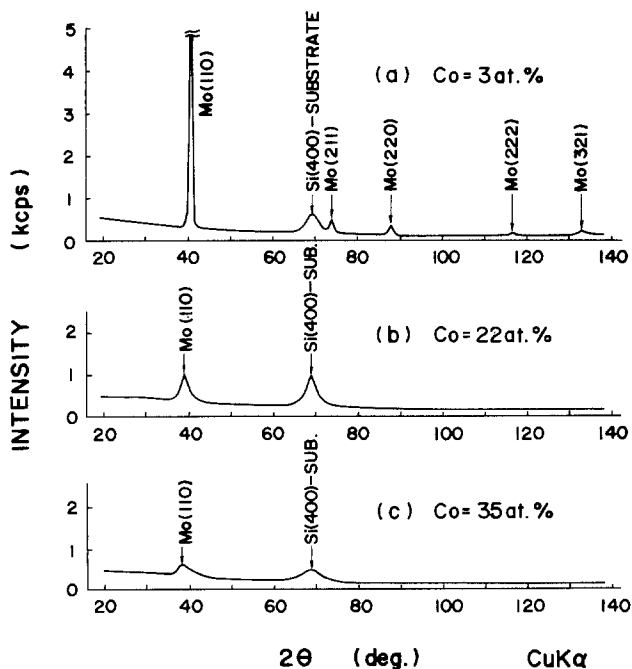


Fig. 3. X-ray diffractometer traces for as-deposited MoO_x films with (a) $C_o = 3 \text{ a/o}$, (b) $C_o = 22 \text{ a/o}$, and (c) $C_o = 35 \text{ a/o}$.

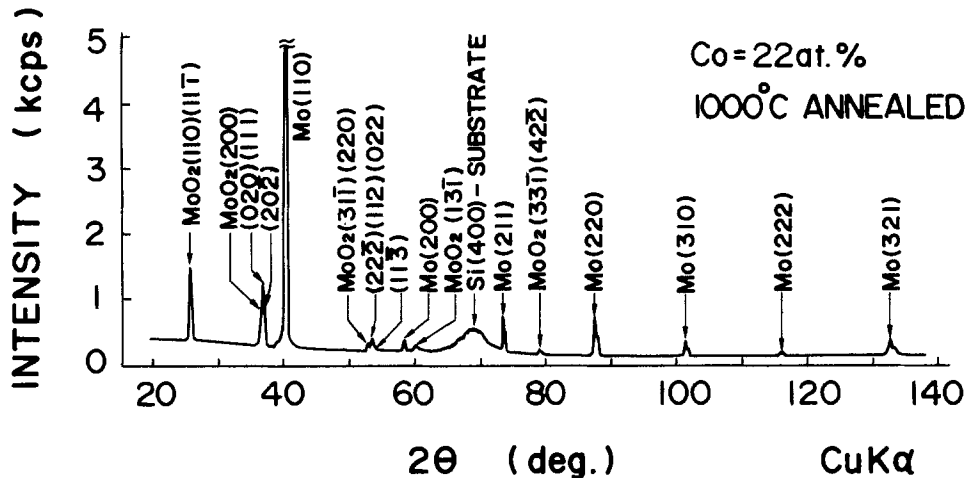


Fig. 4. X-ray diffractometer traces for C_o = 22 a/o films annealed in N₂ ambient at 1000°C for 30 min.

with C_o = 39 a/o, which is only 3 times as large as that for normal Mo films (C_o = 3 a/o, 9-10 μΩ cm). The resistivity of the MoO_x films can further be decreased close to that for pure Mo film by a high temperature annealing in either H₂ or a mixture of H₂ and N₂ (12). Indeed, a resistivity of 10 μΩ cm was obtained for C_o = 39 a/o by annealing at 1000°C in a mixture of H₂ (10%) and N₂ for 5 min.

The abrupt decreases in resistivity in the temperature range between 600° and 800°C (Fig. 7) agree well with the MoO₂ and Mo grain growth characteristics as shown in Fig. 5. On the other hand, the bulk resistivity for MoO₂ (90 μΩ cm) (13) is much higher than that for pure Mo (5.3 μΩ cm). Thus it is thought that the abrupt decreases in resistivity are attributed to the occurrence of electron conduction through the highly conductive Mo grains which grow in accordance with the conversion of doped oxygen into crystallized MoO₂.

For the resistivity of MoO_x films (C_o = 3-39 a/o) annealed above 800°C, it was found that it was nearly a linear function of the number of Mo grain boundaries per

unit length (reciprocal of average Mo grain size <D> in MoO_x films), when electron conduction through the highly resistive MoO₂ grains was eliminated. This elimination procedure was performed by subtracting an equivalent MoO₂ layer thickness, calculated from the C_o and bulk densities for Mo and MoO₂, from the total MoO_x film thickness. Furthermore, the extrapolated resistivity at 1/<D> = 0, which approximately represented the intrinsic resistivity of Mo grains in the films (14), was less than 8 μΩ cm for C_o = 3-39 a/o. This value is only 1.5 times as large as the bulk resistivity for pure Mo. From these results, it is suggested that, in addition to the highly resistive MoO₂ grains, the contribution of electron scattering at the Mo grain boundaries to film resistivity is relatively large compared with that due to lattice defects or impurity scattering in Mo grains. This is similar to the conduction mechanism in undoped Mo films (15).

Characteristics of MoO_x gate MOS structures.—An important parameter for MOS characteristics in new gate materials is the work function, which is obtained from the

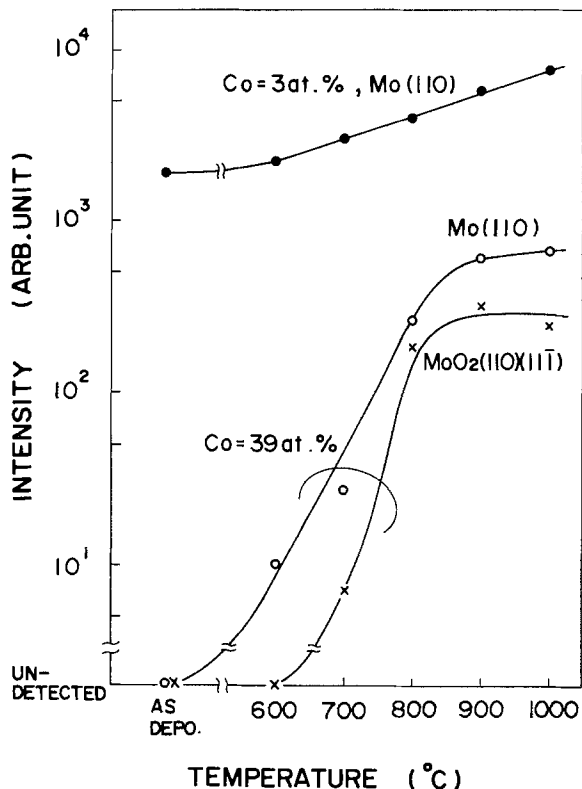


Fig. 5. Variations in x-ray reflection intensities for Mo(110) peaks (C_o = 3 and 39 a/o) and MoO₂(110)(11T) peaks (C_o = 39 a/o) as a function of annealing temperature in N₂ ambient for 30 min.

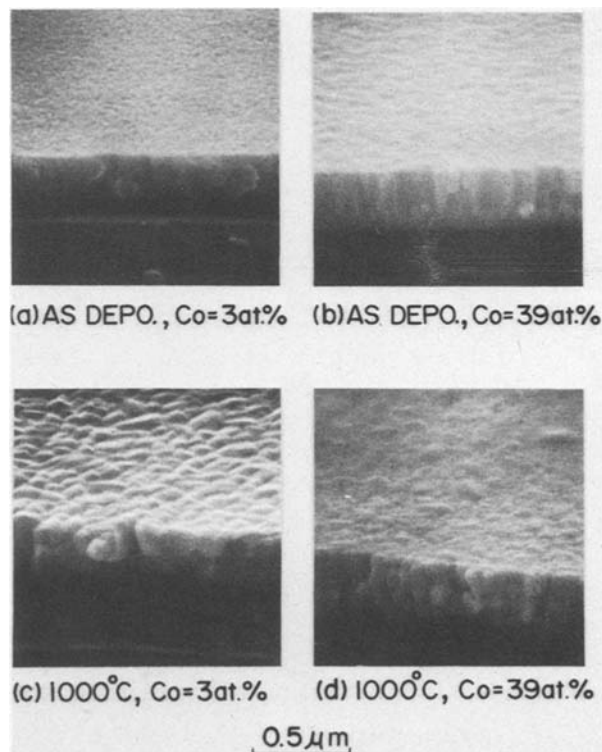


Fig. 6. SEM images showing surfaces and cleaved sections of (a) and (b) as-deposited, and (c) and (d) 1000°C annealed MoO_x films with C_o = 3 and 39 a/o.

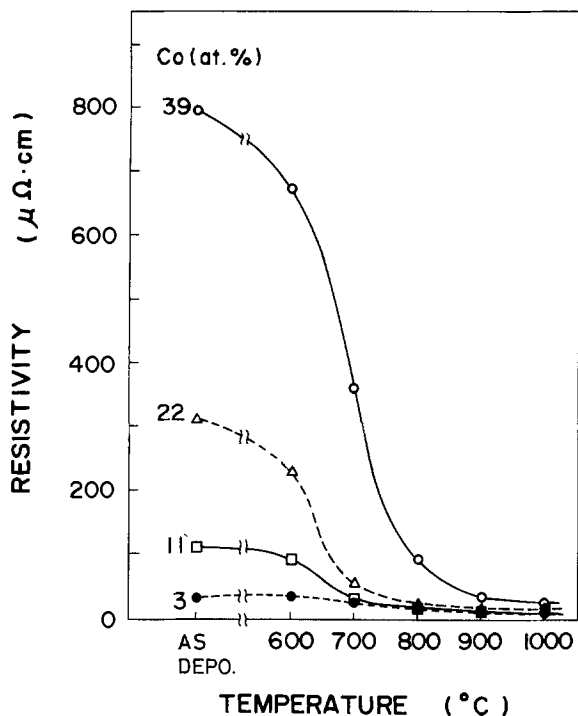


Fig. 7. Variations in the electrical resistivity of MoO_x films with C_o , = 3, 11, 22, and 39 a/o as a function of annealing temperature in N_2 for 30 min.

metal-semiconductor work function difference, ϕ_{MS} , given as an intercept of flatband voltage vs. oxide thickness, shown in Fig. 8. Prior to flatband voltage measurements, samples were annealed at 1000°C in N_2 for 30 min followed by low temperature annealing in a mixture of H_2 and N_2 at 450°C for 30 min. The difference in ϕ_{MS} values for MoO_x films with $C_o = 5$ -30 a/o is only 0.03V, which is within the experimental error. Therefore, the work function ($4.8 \pm 0.03\text{V}$) obtained from the ϕ_{MS} is almost independent of C_o . This result is comparable with the Mo and Mo nitride work function of $4.69 \pm 0.03\text{V}$, which is independent of the nitrogen concentration (16). Furthermore, this result suggests that $\text{MoO}_x/\text{SiO}_2$ interfaces in the MOS structures continue to be dominated by the contact between Mo grains and SiO_2 in spite of the existence of large MoO_2 grains in the gate electrodes. In addition, fixed oxide charge density (N_f) calculated from the slope of flatband voltage vs. oxide thickness relation, is as low as $2.3 \times 10^{10} \text{ cm}^{-2}$, and interface trap density (D_{it}) is less

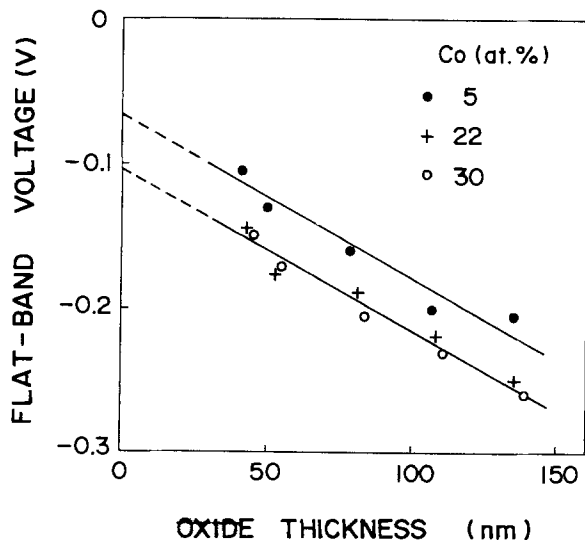


Fig. 8. Variations in flatband voltages as a function of oxide thickness for MoO_x gate MOS capacitors with $C_o = 5, 22,$ and 30 a/o.

than $5 \times 10^{10} \text{ cm}^{-2} \text{ eV}^{-1}$. These results are also independent of C_o .

From these results, it is concluded that the effect of oxygen doping into the Mo films on MOS characteristics is negligible and that the good MOS characteristics of MoO_x gate MOS structures are confirmed.

Conclusion

The effects of oxygen doping on Mo films has been investigated from the viewpoints of As ion stopping properties, film structure, electrical resistivity, and MOS characteristics.

The penetration depth of implanted 100 keV As ions in MoO_x films decreases from $0.4 \mu\text{m}$ (in normal Mo films) to $0.15 \mu\text{m}$, with an increase in oxygen concentration (C_o) to higher than 20 a/o. This remarkable improvement can be attributed to the amorphous film structure, which suppresses the ion channeling effect in Mo grains.

The resistivity, which increased as a result of oxygen doping in as-deposited films, decreases abruptly after annealing above 600°C . After annealing at 1000°C , a value of $25 \mu\Omega \text{ cm}$ is obtained for $C_o = 39$ a/o, which is sufficiently low for MOS gate electrodes. The abrupt decrease in resistivity in the 600°C - 800°C range can be explained by the electron conduction through highly conductive Mo grains, which grow in size because of the conversion of doped oxygen into crystallized MoO_2 .

The work function of MoO_x gate electrodes in MOS structures is independent of C_o . The fixed oxide charge density and interface trap density are also sufficiently low. Therefore, it is concluded that MoO_x film is a possible metal gate material for overcoming As ion penetration observed in normal Mo gate structures. Moreover, this material is compatible with the polysilicon gate process.

Acknowledgments

The authors wish to thank T. Matsumoto, E. Arai, and N. Shiono for their advice and encouragement. They would also like to thank M. Oshima and I. Kawashima for their work on SIMS.

Manuscript submitted June 26, 1983; revised manuscript received Oct. 3, 1983.

Nippon Telegraph and Telephone Public Corporation assisted in meeting the publication costs of this article.

REFERENCES

1. D. M. Brown, W. E. Engeler, M. Garfinkel, and P. V. Gray, *This Journal*, **115**, 874 (1968).
2. T. Mano, K. Takeya, T. Watanabe, N. Ieda, K. Kiuchi, E. Arai, T. Ogawa, and K. Hirata, *IEEE J. Solid-State State Circuits*, **sc-15**, 865 (1980).
3. T. Nozaki, H. Okabayashi, and K. Higuchi, *Jpn. J. Appl. Phys.*, **20**, 1121 (1981).
4. K. Fujinaga and H. Harada, *ibid.*, **21**, 373 (1982).
5. Y. Murao, K. Kudoh, and K. Kobayashi, Abstract 527, p. 1318, The Electrochemical Society Extended Abstracts, Vol. 80-2, Hollywood, FL, October 5-10, 1980.
6. H. Okabayashi, K. Higuchi, and T. Nozaki, Abstract 302, p. 753, The Electrochemical Society Extended Abstracts, Vol. 81-1, Minneapolis, MN, May 10-15, 1981.
7. M. J. Kim and D. M. Brown, in "International Electron Devices Meeting Technical Digest," p. 560 (1982); M. J. Kim, D. M. Brown, and W. Katz, *This Journal*, **130**, 1196 (1983).
8. P. W. Palmberg, *Anal. Chem.*, **45**, 549A (1973).
9. See, for example, B. D. Cullity, "Elements of X-Ray Diffraction," Chap. 3, Addison-Wesley, Reading, MA (1956).
10. F. Yanagawa, T. Amazawa, and H. Oikawa, *Jpn. J. Appl. Phys.*, **18**, Suppl. 18-1, 237 (1979).
11. Y. Wada, S. Nishimatsu, and N. Hashimoto, *This Journal*, **127**, 206 (1980).
12. M. J. Kim and D. M. Brown, Abstract 364, p. 564, The Electrochemical Society Extended Abstracts, Vol. 83-1, San Francisco, CA, May 8-13, 1983.
13. D. B. Rogers, R. D. Shannon, A. W. Sleight, and J. L. Gillson, *Inorg. Chem.*, **8**, 841 (1969).
14. A. F. Mayadas and M. Shatzkes, *Phys. Rev. B*, **1**, 1382 (1970).
15. H. Oikawa and T. Tsuchiya, *J. Vac. Sci. Technol.*, **15**, 1117 (1978).
16. M. J. Kim and D. M. Brown, *IEEE Trans. Electron Devices*, **ed-30**, 598 (1983).

Photoresist Adhesion Promoters for Gold Metallization Processing

J. N. Helbert

Motorola, Incorporated, Semiconductor Products Sector, Process Technology Laboratory, Phoenix, Arizona 85008

The final step in the fabrication of integrated circuits requiring lithographic pattern delineation is usually metallization. In this step, a metal film is deposited, lithographically patterned using a polymeric resist, then selectively etched, either wet chemically or dry, using the resist pattern mask (1). The result is an intricate metal line network connecting the appropriate transistors, resistors, and other devices of the integrated circuit (IC).

Two metals are widely used in IC metallization processes—aluminum and gold. While aluminum is attractive from a cost point of view, gold is very resistant to chemical corrosion and is also much less prone to the electromigration effect which becomes very important when metallization lines become very small, as is the case for very large-scaled IC's (1).

When using gold as the metallization layer, where metal patterns $2-3\ \mu\text{m}$ wide are concerned, it becomes imperative that the polymeric resist has excellent adhesion to that surface. Various (and sometimes intermittent) degrees of resist pattern adhesion failure to gold have been observed at Motorola in the fabrication of advanced bipolar circuits and RF modules. As a result, an extensive amount of work has been expended to find silane adhesion promoting agents for gold, and the results of this search are reported in this note.

Silane coupling agents for mineral surfaces are well known (2), but silane promoters for gold are virtually unknown for IC resist metallization processes. These agents promote polymer adhesion to mineral surfaces through the chemical interaction with surface silanol moieties encountered at the surfaces of these systems (2-4). Gold has a surface drastically different in that it does not possess these surface adhesion promoting sites because it is a noble metal and is essentially corrosion resistant (5). As an example for comparison, the surface of aluminum metal is known to be easily chemically oxidized, while gold does not oxidize even under O_2 plasma conditions (6). Therefore, coupling agents for which a different adhesion promoting mechanism is operative are needed more for gold than for oxidizing metals, minerals, and the synthetic dielectric layers encountered in electronic device fabrication.

A practical experimental approach for testing polymeric resist (*i.e.*, positive photoresist) adhesion during pattern development has been adopted. The test pattern (or metal etch mask) is one that yields a series of unexposed resist islands of varying dimensions from 0.5 to 5 μm wide and 4 to 20 μm long, surrounded by larger exposed and developed areas. Prior to resist spinning by conventional spinning techniques, the gold substrates were water rinsed and dried 30 min to 1 h at 200°C. Gold wafers, utilized for simulated wafer rework testing, were cleaned with acetone, followed by 10-30 min of O_2 plasma cleaning at 300W. The commercially available promoters (Petrarch Systems, Incorporated) were applied as dilute solutions 0.3-7% by weight in acetone. The promoter coated substrates were not thermally cured prior to photoresist (PC-129-SF or Allied P-2025) application. The photoresist, however, was cured 30 min at 90°C in air. Control substrates were not treated with promoters and usually exhibited 50-90% island image "lifting" when adhesion failure occurred (see Fig. 1). In some control tests no "lifting" occurred, but inferior adhesion was observed at pattern edges. Adhesion failure in control samples

occurred most frequently when the lithographic exposure was E-beam (Cambridge EBMF-II), but adhesion failure was also observed on optically (Cobilt 2020H) exposed control substrates.

When the gold testing substrates were primed with promoter solutions of silanes containing phosphorus (DPETS), carbonyl (TMSA), or sulfur (BTPTS) or (MPTS), no adhesion failure was ever observed (*i.e.*, 0% resist island loss) as is depicted in Fig. 2. Test wafers for all four systems were capable of withstanding 30-40% overdevelopment without incurring any test pattern island "lifting," and adhesion promotion on both new and reworked gold test wafers was achieved. Control samples, on the other hand, often failed even when the control substrates were underdeveloped, as is the case for the substrate pictured on the left-hand side of Fig. 1. Underdevelopment is indicated by resist nonclearing around the edges of the written outer squares.

Similarly dramatic adhesion enhancement has been demonstrated and reported for silane promoted silicon dioxide substrates (2-4, 7, 8). These results were achieved due to the chemical interaction of organosilane promoters with the surface silanols of that particular substrate system. Analogous surface moieties, aluminols ($-\text{Al}-\text{OH}$), are also present on oxidized aluminum samples, and good adhesion has been observed for this substrate due to chemical interactions between adhering polymeric films and these surface groups (6, 9). In contrast, gold surfaces are free of surface adhesion promoting groups like silanols as pointed out earlier; therefore, any photoresist adhesion enhancement observed for it must be attributed to a different and unique promotion enhancement mechanism. In fact, tests carried out with the halogenated, alkoxy or amino silanes successfully tested for improving resist adhesion to SiO_2 surfaces of Ref. (2-4, 8) failed to demonstrate improved

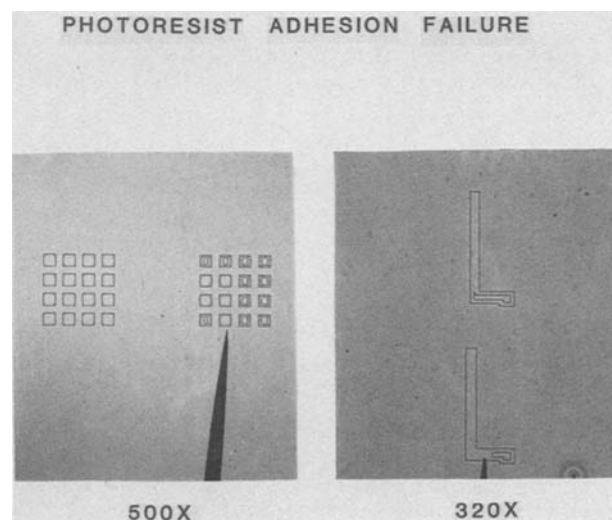


Fig. 1. Optical micrographs of "lifted" photoresist test images. The pointers mark areas where island images or parts of them are missing due to adhesion failure following exposure and development.

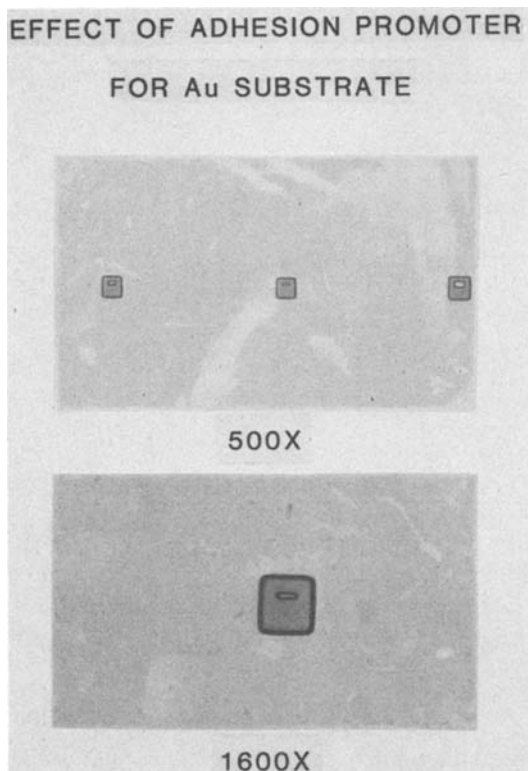


Fig. 2. Optical micrographs of gold test island images where photoresist adhesion has been promoted with TMSA. The areas around the gold island images have been ion-milled to the substrate and the photoresist has been removed by O_2 plasma etching.

adhesion to gold test wafers. Definitive improved resist image adhesion to gold was observed only with the four silane adhesion promoters listed above.

The improved lithographic resist adhesion to gold, observed for test wafers primed with the four silanes of this work, is attributed to a complexation or chemisorption mechanism. The $-C=O$ of TMSA, $-S-$ of BTPTS and MPTS, and $=P-$ of DPTS are moieties capable of acting as chelating or chemisorption sites for the molecular silanes; thus, creating layer to layer bonding with greater strength than that observed where just van der Waals interactions occur to the gold surface atoms. Polymeric adhesion of oxygen containing poly-

mers (e.g., $+CH_2-C(CH_3)-\overset{O}{\parallel}C-OCH_3$) to metal surfaces

has been recently attributed to metal-oxygen-polymer complexation, as evidenced by observed x-ray photo-

emission and infrared spectroscopic results which were consistent with a chelation-like interlayer bonding mechanism (9, 10). Although these studies do not deal with adhesion promoters per se, they do illustrate the principle of a weak chemical bonding mechanism at the interface between metal and organic and/or polymeric layers. There is no inherent reason why a silane containing oxygen would not interact similarly to yield a more organic-like and resist adhering gold metal substrate from one of less adhering. As for the silanes containing phosphorus and sulfur, it is well-known that stable gold complexes involving ligands containing these elements have been synthesized (5). Thus, gold has an affinity for chemical interaction with these elements and most probably with silanes containing them.

In conclusion, it is felt that the improved resist adhesion of this work is due to the chemical interaction of the chelating silanes to the gold surface-atoms, which creates an improved and adhering substrate to resist from one previously more chemically inert or non-adhering.

Acknowledgments

The author thanks C. Walker for her diligent experimental support and P-C. Liu for helpful discussions.

Manuscript submitted Aug. 26, 1983; revised manuscript received Oct. 12, 1983.

Motorola, Incorporated, Semiconductor Product Sector assisted in meeting the publication costs of this article.

REFERENCES

1. D. W. Hess, *Chem Technol.*, 432 (July 1979).
2. E. P. Plueddemann, *J. Adhesion*, 2, 184 (1970); "Silane Coupling Agents," Plenum Press, New York (1982).
3. K. L. Mittal, *Solid State Technol.*, 89 (May 1979).
4. J. N. Helbert and H. G. Hughes, Abstract 118, p. 306, The Electrochemical Society Extended Abstracts, Vol. 81-1, Minneapolis, MN, May 10-15, 1981; B. E. Wagner, J. N. Helbert, E. H. Poindexter, and R. D. Bates, *Surf. Sci.*, 67, 251 (1977); J. N. Helbert and H. G. Hughes, in "Adhesion Aspects of Polymeric Coatings," K. L. Mittal, Editor, pp. 499-509, Plenum Press, New York (1983).
5. E. S. Gould, in "Inorganic Reactions and Structures," Chap. 11, Holt, Rinehart and Winston, New York (1963).
6. A. K. Hays and D. A. Haaland, *Org. Coatings and Appl. Polymer Sci. Proc.*, 47, 383 (1982).
7. R. A. Conture, R. T. Gleason, and J. J. Lajza, Jr., U. S. Pat. 3,586,554 (1971).
8. R. H. Collins and F. T. Deverse, U. S. Pat. 3,549,368 (1970).
9. W. Suétaka, Abstract 112, p. 292, The Electrochemical Society Extended Abstracts, Vol. 81-1, Minneapolis, MN, May 10-15, 1981; in "Adhesion Aspects of Polymeric Coatings," K. L. Mittal, Editor, pp. 225-235, Plenum Press, New York (1983).
10. J. M. Burkstrand, *Org. Coatings and Plastics Chem. Preprints*, 45, 820 (1981); in "Physicochemical Aspects of Polymer Surfaces," Vol. 2, K. L. Mittal, Editor, pp. 1093-1100, Plenum Press, New York (1983).

A 3.8 μm Period Sawtooth Grating in InP by Anisotropic Etching

C. J. Keavney¹ and Henry I. Smith

Massachusetts Institute of Technology, Research Laboratory of Electronics, Cambridge, Massachusetts 02139

Anisotropic etching has often been used to create unusual structures in crystals. The technology is highly developed in the case of silicon, and many useful devices and applications have been realized (1-5). While many reagents are known which will etch the (100) planes of InP faster than the (111)A planes (6-8), there is no known etchant which is as highly selective for InP as KOH is for Si. Accordingly, the production of sawtooth and square-wave profile structures on a fine scale in InP is problematical. We describe here a procedure which has been used to

make 3.8 μm period gratings with sawtooth profiles on the (100) surfaces of InP wafers.

Hydrobromic acid (HBr) was selected as the etchant in this experiment, because it was shown by Adachi and Kawaguchi (6) to reveal (111)A planes in InP, and because it is compatible with photoresist masking. The ratio between (100) and (111)A etch rates was not high enough at room temperature to achieve useful sawtooth profiles, but it was found that this ratio increased at lower temperatures. This increase is expected from the assumption that the etch rate is activation limited and follows a simple Arrhenius rate equation, and that the anisotropy results from a higher activation energy for the (111)A plane

¹ Present address: Spire Corporation, Patriots Park, Bedford, Massachusetts 01730.

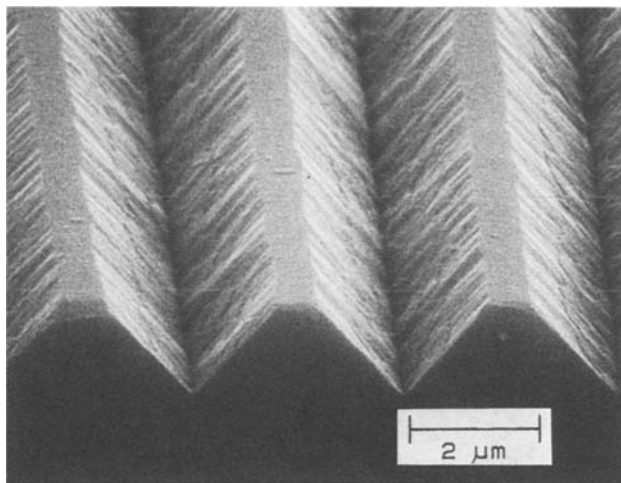


Fig. 1. Scanning electron micrograph of a sawtooth profile grating etched in InP with HBr. The grating period is $3.8 \mu\text{m}$.

than for the (100) plane. A temperature of -15°C was found to give a sufficiently high anisotropy.

The samples used in this work were cleaved from commercially available (100) Sn-doped InP wafers. After polishing, a corner of each wafer was etched with 1:1 HCl (12N) and H_2O_2 (30%) solution for 30s at room temperature. This etch produced elongated pits on the (100) surface. Because it also etches the (111)B planes faster than the (111)A planes, the long directions of these pits indicate the line of intersection of the (111)A planes with the surface. These pits are useful for aligning the grating mask.

The wafers were then cleaned by ultrasonic agitation in a sequence of solvents: trichloroethylene, acetone, and methanol. They were immersed in 60% KOH in water at 50°C for 20 min, then washed in detergent (with ultrasonic agitation) and rinsed in deionized water. An adhesion promoter, octadecyl dimethyl [3-(trimethoxysilyl) propyl] ammonium chloride, known as DMOAP, was applied (other adhesion promoters are expected to work as well), and then $0.5 \mu\text{m}$ of Shipley² AZ1350B positive resist was spin-coated onto the wafers and prebaked according to the manufacturer's recommendations.

A photomask with a $3.8 \mu\text{m}$ period grating was placed in contact with the wafer. The lines on the grating were aligned manually with a cleaved edge of the wafer, in the same direction as the long axes of the pits which were

²Shipley Corporation, Newton, MA 02158.

etched into the wafer corner beforehand. This ensured that the (111)A planes would form a sawtooth grating. The resist was exposed, developed, and postbaked according to the manufacturer's recommendations. After development, the grating lines were about $1.4 \mu\text{m}$ wide.

The etching was carried out in a glass beaker at -15°C with agitation. The etchant was 9N (48% by weight) HBr. The etch was stopped when undercutting of the resist lines caused them to begin to lift off of the wafer; this took about 10 min. The resist was stripped, and the sample was examined in an optical microscope and a scanning electron microscope (Fig. 1). As can be seen in the electron micrograph, the remaining (100) portion of the top of each sawtooth is about $0.4 \mu\text{m}$ wide. The bottoms of the grooves, where two (111)A planes meet, appear sharp at the resolution of the micrograph. The origin of the ripple on the (111)A facets is not known.

Assuming that the resist mask will lift off when the flat tops of the sawtooth structure reach $0.4 \mu\text{m}$ in width, a ratio of (100) etch rate to (111)A etch rate of at least 8.3 is needed in order for the grooves to be completely etched before the resist mask fails. Our result shows that HBr at -15°C meets this requirement. We have made other measurements which indicate that HBr at 4°C has a ratio of about 7.7.

In summary, HBr at -15°C has been used to etch a $3.8 \mu\text{m}$ period sawtooth grating in (100) InP through a photoresist mask. The observation that reducing the temperature of the etch increases the anisotropy indicates that the activation energy (as described by an Arrhenius rate law) for the (111)A surface is greater than that for the (100) surface.

Acknowledgments

This work was sponsored by the Naval Ocean Systems Center. The authors thank C. Fonstad and R. Markunas for many helpful discussions.

Manuscript submitted July 5, 1983; revised manuscript received Sept. 23, 1983.

The Massachusetts Institute of Technology assisted in meeting the publication costs of this article.

REFERENCES

1. K. E. Bean, *IEE Trans. Electron. Devices*, **ed-25**, 1185 (1978).
2. D. L. Kendall, *Ann. Rev. Mater. Sci.*, **9**, 373 (1979).
3. J. B. Angell, S. C. Terry, and P. W. Barth, *Sci. Am.*, **248**, 44 (1983).
4. D. C. Flanders, *J. Vac. Sci. Tech.*, **16**, 1615 (1979).
5. N. Tsumita, J. Melngailis, A. M. Hawryluk, and Henry I. Smith, *ibid.*, **19**, 1211 (1981).
6. S. Adachi and H. Kawaguchi, *This Journal*, **128**, 1342 (1981).
7. H. C. Gatos and M. C. Lavine, *ibid.*, **107**, 427 (1960).
8. B. Tuck and A. J. Baker, *J. Mater. Sci.*, **8**, 1559 (1973).

Deep Donor Levels in He Implanted n-Type Silicon

Masahiro Yoshizawa, Masayasu Miyake, and Hiroyuki Harada

Nippon Telegraph and Telephone Public Corporation, Atsugi Electrical Communication Laboratory, 1839, Ono, Atsugi-shi, Kanagawa, 243-01 Japan

In VLSI fabrication, ion beam technology using light ions (H, He) has many applications, such as ion beam lithography (1, 2) and FIPOS technology (3). In these technologies, it is important to investigate the energy level, concentration profile, and annealing behavior of damage produced by ion implantation. There have been many works on damage produced by proton implantation (4-6). However, there have been only a few studies on damage produced by He implantation (7). Energy levels and concentration profiles of deep levels in He-implanted Si have been studied for a $5 \times 10^8 \text{ cm}^{-2}$ implantation dose without annealing by using the DLTS method (7). For applying He implantation to the preceding technologies,

Key words: Schottky C-V method, implantation damage, energy level, annealing behavior.

however, it is necessary to study the properties of the damage in a higher dose range.

In the present study, energy levels and the concentration profiles of deep levels in n-type Si produced by He implantation with doses of $10^{14} \sim 10^{15} \text{ cm}^{-2}$ are investigated by the Schottky contact C-V measurement method. The implantation energy dependence of the peak depth and the annealing behavior in an N_2 atmosphere between 500° and 700°C are also reported.

CZ n-type $\langle 100 \rangle$ silicon wafers with $0.83 \sim 0.92 \Omega\text{-cm}$ resistivity were used. Arsenic was implanted into the back side of the wafers at 100 keV with a 10^{15} cm^{-2} dose, and the wafers were annealed at 900°C for 30 min to obtain an ohmic contact. Helium ions were implanted into the wafers at $40 \sim 150 \text{ keV}$ with a $10^{14} \sim 10^{15} \text{ cm}^{-2}$ dose.

After annealing in an N_2 atmosphere at $500^\circ \sim 700^\circ\text{C}$ for 30 min, Au electrodes (0.155 mm diam) were evaporated on the wafers in order to obtain Schottky contacts, and Al back contacts were evaporated.

In the C-V measurement (8), the concentration profile is given by the width of the space charge layer (x_m) and the concentration of the level (N_m). For the deep level, the observed profile obtained by using $x_m - N_m$ is an apparent profile, and is not equal to the actual profile of the deep level. For the deep level produced by implantation, donor and acceptor levels can be identified from the shape of the observed peaks. The number of peaks equals the number of levels. The C-V measurements having temperature variations separate the deep and shallow levels.

Figure 1 shows the apparent concentration profile measured by the Schottky C-V method at different measurement temperatures. Helium implantation was performed at 60 keV with a dose of 10^{15} cm^{-2} . The annealing temperature was 600°C . A flat concentration profile deeper than $0.9 \mu\text{m}$ shows the substrate impurity concentration, which is $6 \times 10^{15} \text{ cm}^{-3}$. Two donor peaks are observed. We call the smaller x_m peak level 1, and the other level 2. Figure 2 shows the temperature dependence of the apparent peak depths of the two levels. Level 2 is a deep level, since the apparent peak depth decreases with an increase in temperature. The apparent peak depth of level 1 decreases with an increase in temperature below 30°C , and does not shift above 30°C . This indicates that the energy of level 1 (E_1) is nearly equal to the Fermi level at 30°C , which is $E_c - E_1 = 0.21 \text{ eV}$, and level 1 is a deep level below 30°C . The energy of level 2 (E_2) is deeper than E_1 , because the apparent peak depth of level 2 changes in the higher temperature range; that of level 1 does not change. The measured profile above 30°C equals the actual profile of level 1. The peak depth of level 1 at 60 keV is determined to be $0.48 \mu\text{m}$.

Since level 2 is a deep level and level 1 is shallower than the Fermi level above 30°C , E_2 and the concentration of level 2 (N_2) are expressed as the following equations (8)

$$\frac{\epsilon(E_F - E_2)}{q^2} = \frac{N_0(x_m - x_2)^2}{2} + \int_{x_m}^{x_2} \int_{x_m}^{x'} N_1(x) dx dx' \quad [1]$$

$$N_2(x_2) = (N_m - N_0 - N_1[x_m]) \frac{x_m}{x_2} \frac{\partial x_m}{\partial x_2} \quad [2]$$

$$\frac{\partial x_m}{\partial x_2} = \frac{N_0(x_m - x_2) + \int_{x_2}^{x_m} N_1(x) dx}{N_0(x_m - x_2) + N_1(x_m)(x_m - x_2)} \quad [3]$$

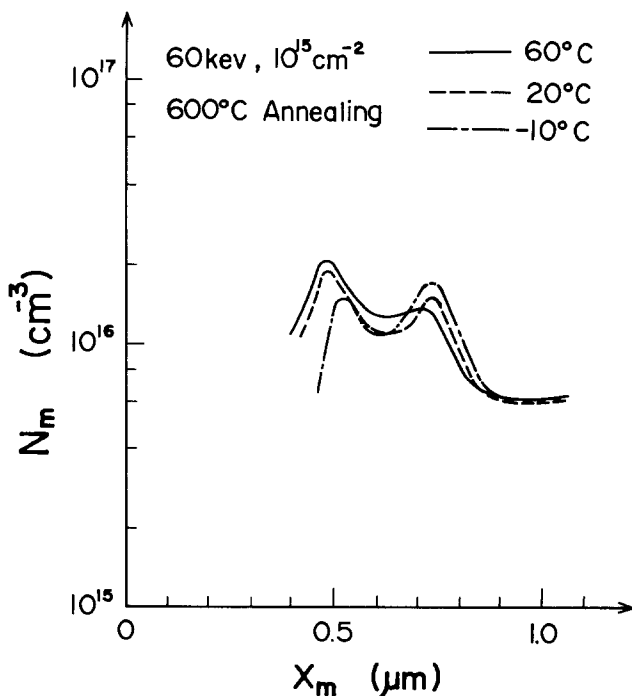


Fig. 1. Apparent concentration profiles measured by the Schottky C-V method at different measurement temperatures.

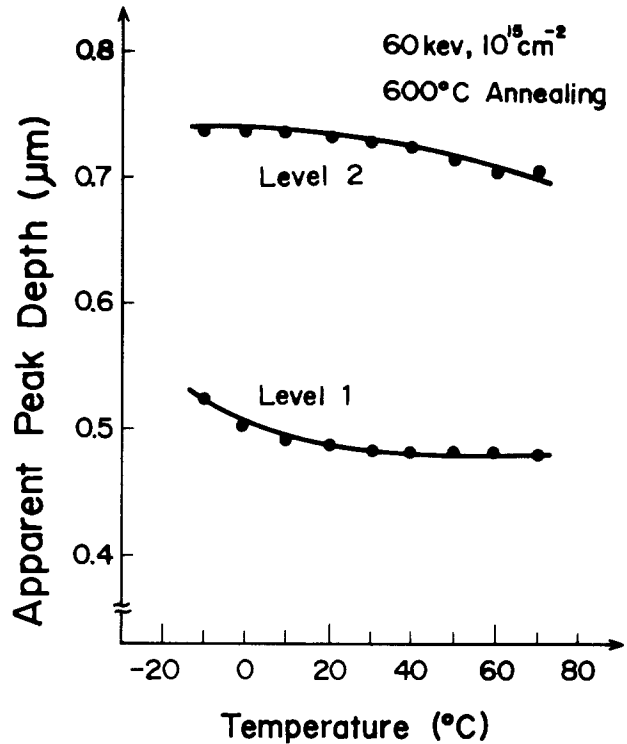


Fig. 2. Temperature dependence of the apparent peak depth of levels.

where N_0 is the substrate impurity concentration, $N_1(x)$ is the concentration of level 1 at depth x , and x_m and x_2 are the depths at which the levels 1 and 2 cross the Fermi level, respectively.

It is thought that level 1 and level 2 are related to the damage produced by He implantation. Thus it is relevant to assume that the actual peak depth of level 2 is equal to that of level 1. Under this assumption, energy level E_2 is calculated to be $E_c - E_2 = 0.52 \text{ eV}$ from Eq. [1] in the temperature range of above 30°C . The peak concentration of level 2 is determined to be $1.5 \times 10^{16} \text{ cm}^{-3}$, using Eq. [2] and [3] and the concentration profile of level 1. The obtained peak concentration of level 2 is equal to that of level 1.

Figure 3 shows the implantation energy dependence of the actual peak depth of the levels. The points represent experimental data in the present study. The solid line is the calculated curve of the peak depth of the energy transfer rate into atomic displacements from the extended LSS theory (9). This corresponds to the peak depth of the vacancy concentration. Both are in good agreement. The concentration profile obtained in the present study is nearly Gaussian. It was confirmed that these two levels have the same annealing behavior in the $500^\circ \sim 700^\circ\text{C}$ range, and have the same peak concentration in the dose range of $10^{14} \sim 10^{15} \text{ cm}^{-2}$. The peak concentration decreases as the annealing temperature increases. Both peaks disappear after a 30 min annealing at 700°C when the dose is 10^{15} cm^{-2} , and disappear after a 30 min annealing at 600°C when the dose is 10^{14} cm^{-2} .

Three levels have been observed in He implanted n-type Si at $E_c - 0.18$, $E_c - 0.23$, and $E_c - 0.41 \text{ eV}$ using the DLTS method (7) for a dose of $5 \times 10^8 \text{ cm}^{-2}$ when annealing is not performed. The $E_c - 0.18$, $E_c - 0.23$, and $E_c - 0.41 \text{ eV}$ energy levels have been identified as the A center (O-V), the divacancy center, and the phosphorus vacancy center (P-V), respectively. The P-V center cannot be observed in the present study, because the concentration of the center is less than the substrate concentration. The A center and the divacancy center have been also observed in a proton-implanted Si (6) or an electron-irradiated Si (7). The $E_c - 0.21 \text{ eV}$ energy level obtained in the present study is tentatively identified as a divacancy from its annealing threshold (6). In the previous studies, the $E_c - 0.52 \text{ eV}$ energy level has not been observed, because the range of the measuring temperature is not high enough. For the electron-irradiated Si, the $E_c - 0.54 \text{ eV}$ energy

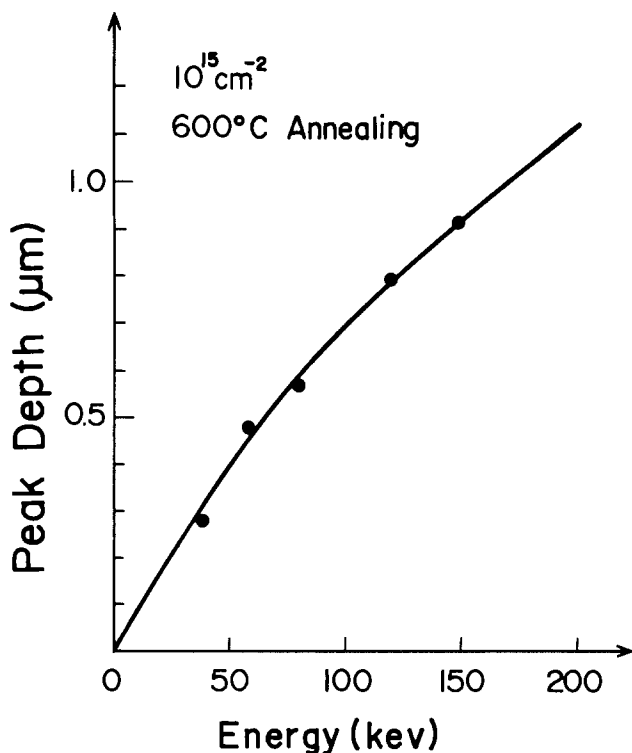


Fig. 3. Implantation energy dependence of the peak depth of the levels. The solid line is the peak depth of the vacancy concentration profile calculated from the extended LSS theory.

level, which is identified as a divacancy center, has been observed in the photoconductivity measurement (10). The $E_c - 0.52$ eV energy level in the present study is close to this level, and is identified as a divacancy. Both levels observed in the present study are considered to be divacancy centers. This is consistent with the results that both levels have the same peak depth, concentration, and annealing behavior.

In summary, the deep levels produced by He implantation were studied in a dose range of $10^{14} \sim 10^{15} \text{ cm}^{-2}$ by the Schottky contact C-V measurement method. Two deep donor levels having the same peak depth and concentration were observed. Energy levels are located at $E_c - E_1 = 0.21$ eV, and $E_c - E_2 = 0.52$ eV. Implantation energy dependence of the peak depth of the levels is in good agreement with the calculated peak depth of vacancy concentration profile from the extended LSS theory. These two levels have the same annealing behavior between 500° and 700°C . It is thought that the levels can be identified because of divacancies.

Acknowledgments

The authors wish to express their thanks to Dr. Arai for his advice and encouragement.

Manuscript submitted Jan. 24, 1983; revised manuscript received Oct. 10, 1983.

Nippon Telegraph and Telephone Public Corporation assisted in meeting the publication costs of this article.

REFERENCES

1. G. Stengl, R. Kaitna, H. Loschner, P. Wolf, and R. Sacher, *J. Vac. Sci. Technol.*, **16**, 1883 (1979).
2. D. B. Rensch, R. L. Seliger, G. Csanky, R. D. Olney, and H. L. Stover, *ibid.*, **16**, 1897 (1979).
3. K. Imai and S. Nakajima, in "Technical Digest of the IEEE International Electron Devices Meeting," p. 376, Washington, DC (1981).
4. E. Ligeon and A. Guivarc'h, *Radiat. Eff.*, **27**, 129 (1976).
5. W. K. Chu, R. H. Kastel, R. F. Lever, S. Mader, and B. J. Masters, *Phys. Rev. B*, **16**, 3851 (1977).
6. L. C. Kimering, P. Blood, and W. M. Gibson, in "Defects and Radiation Effects in Semiconductors 1978," (Inst. Phys. Conf. Ser. 46) p. 273 (1979).
7. K. L. Wang, *J. Appl. Phys.*, **53**, 449 (1982).
8. M. Schulz, *Appl. Phys. Lett.*, **23**, 31 (1973); *Appl. Phys.*, **4**, 225 (1974).
9. T. Tsurushima and H. Tanoue, *J. Phys. Soc. Jpn.*, **31**, 1695 (1971).
10. A. H. Kalma and J. C. Corelli, *Phys. Rev.*, **173**, 734 (1968).

Equilibrium Calculations for the Si-H-Cl System from 300 to 3000 K

Carlyle S. Herrick* and Rony A. Sanchez-Martinez

General Electric Company, Corporate Research and Development, Schenectady, New York 12345

The Si-H-Cl system is an important concern to semiconductor technology since at least four different compounds belonging to that system have been used as starting materials in the manufacture of merchant silicon for the semiconductor trade, or for the deposit of solid epitaxial layers in silicon device fabrication. These activities are supported by a considerable amount of available information on equilibrium compositions at temperatures below 1700 K, approximately the melting point of solid silicon (1-10). Exploratory experiments or surveys at those higher temperatures comprising the liquid range of silicon find no comparable support in the literature. Only fragmentary and sometimes conflicting equilibrium data are available (1, 2). To fill that need, this note describes the results of equilibrium calculations covering the temperature range from room temperature to 3000 K. The term silane homolog as used here may refer to any compound in the series SiH_4 , SiH_3Cl , SiH_2Cl_2 , SiHCl_3 , and SiCl_4 .

A number of authors have employed a variety of computer codes to solve the equilibrium calculation problem (1, 2, 8, 10). We used a modified version of the system free energy minimizing code prepared by Gordon and McBride (11). It routinely performed a second equilibrium calcu-

lation using the output of the first calculation as input for the second. Checking the code in this way proved to be necessary for reliable results. Twenty chemical species were considered in each calculation, more than in prior studies. Heat capacity, enthalpy, and entropy data

Table 1. Equilibrium partial pressures in atmospheres calculated for total $P = 1.0$ atm and $\text{Cl}/\text{H} = 0.1$

	1000 K	1600 K	2200 K	2800 K
H_2	0.938	0.875	0.848	0.742
SiCl_4	2.43×10^{-2}	1.43×10^{-3}	6.45×10^{-6}	1.64×10^{-7}
SiHCl_3	2.76×10^{-2}	2.46×10^{-3}	3.07×10^{-5}	1.50×10^{-6}
SiH_2Cl_2	8.87×10^{-4}	3.07×10^{-4}	1.63×10^{-5}	1.94×10^{-6}
SiH_3Cl	1.80×10^{-5}	2.01×10^{-5}	4.16×10^{-6}	1.16×10^{-6}
SiH_4	3.72×10^{-7}	9.00×10^{-7}	6.11×10^{-7}	3.61×10^{-7}
HCl	8.19×10^{-3}	9.02×10^{-2}	1.16×10^{-1}	1.11×10^{-1}
SiCl_3	3.53×10^{-4}	4.38×10^{-3}	4.82×10^{-4}	8.26×10^{-5}
SiCl_2	1.23×10^{-4}	3.30×10^{-2}	3.12×10^{-2}	2.00×10^{-2}
SiCl	6.45×10^{-13}	3.14×10^{-6}	5.80×10^{-4}	8.53×10^{-3}
Si_2Cl_6	7.97×10^{-8}	1.76×10^{-9}	4.68×10^{-13}	1.78×10^{-15}
Cl_2	2.11×10^{-15}	1.43×10^{-9}	1.22×10^{-7}	1.21×10^{-6}
Cl	1.85×10^{-11}	4.14×10^{-6}	5.14×10^{-4}	7.23×10^{-3}
H	2.18×10^{-9}	5.03×10^{-5}	5.15×10^{-3}	7.00×10^{-2}
SiH	2.88×10^{-14}	2.02×10^{-7}	1.52×10^{-4}	5.38×10^{-3}
Si	1.64×10^{-18}	9.36×10^{-8}	3.56×10^{-4}	3.42×10^{-2}
Si_2	1.01×10^{-21}	2.49×10^{-10}	5.17×10^{-6}	1.41×10^{-3}
Si_3	4.71×10^{-23}	5.53×10^{-11}	1.18×10^{-6}	2.72×10^{-4}

* Electrochemical Society Active Member

Key words: silanes, chlorosilanes, conversion, yield.

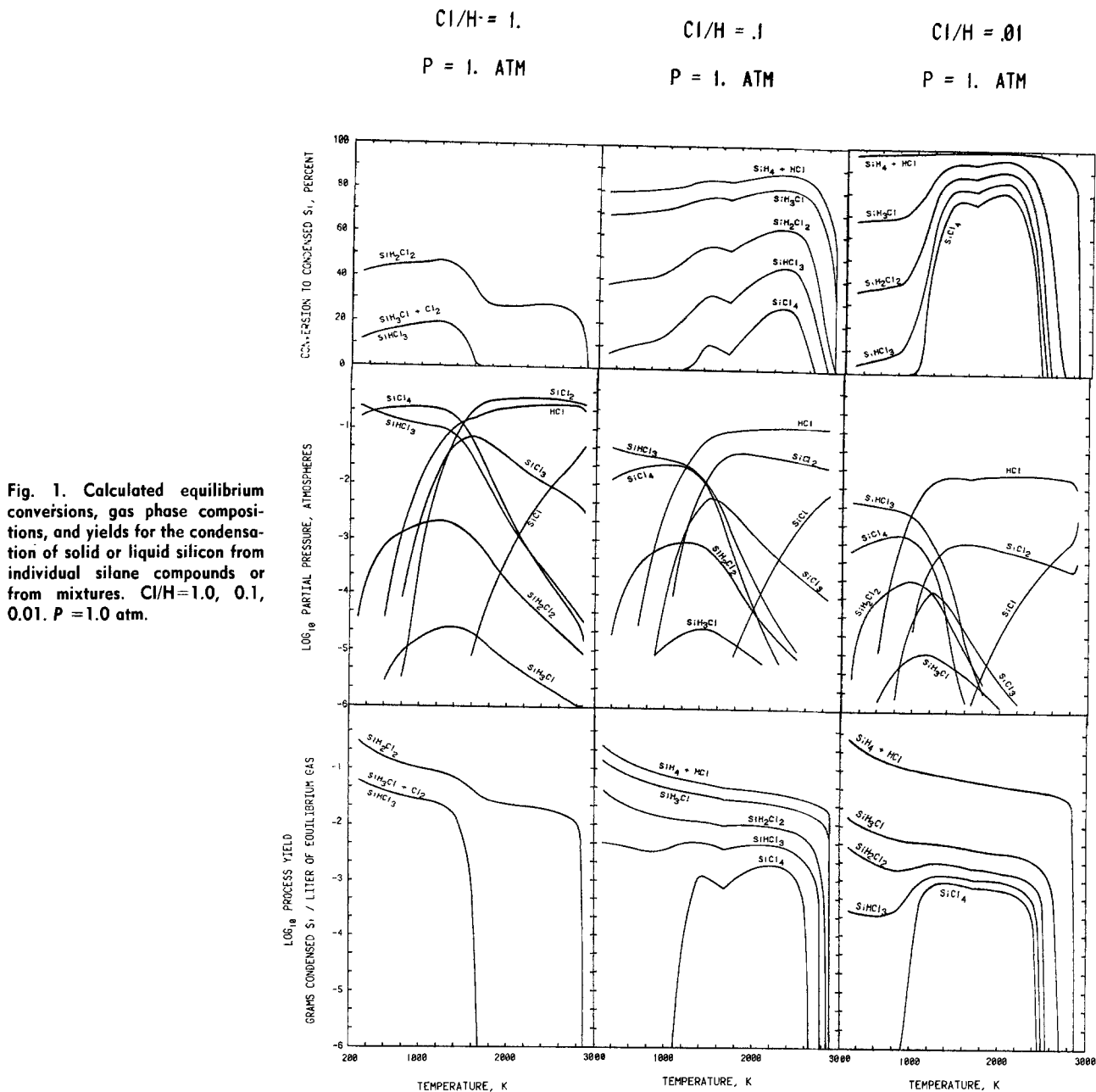


Fig. 1. Calculated equilibrium conversions, gas phase compositions, and yields for the condensation of solid or liquid silicon from individual silane compounds or from mixtures. $Cl/H=1.0, 0.1, 0.01$. $P=1.0 \text{ atm}$.

were obtained from JANAF tables (12) in combination with the most recently reported values of heat of formation (8, 13).

Calculations included the entire range of temperatures at which elemental silicon might be condensed from equilibrium gas from room temperature up to the boiling point of silicon at about 3500 K. In no case did silicon vapor saturate equilibrium gas at a temperature above 3000 K. Since thermally ionized species occur only to a very minor extent below the boiling point of silicon, they were not considered in this work. Also omitted was consideration of possible unfavorable kinetics at temperatures near ambient.

Equilibrium vapor phase composition values calculated at four widely separated temperatures are listed in Table I. The data for the two lower temperatures, and others, have been compared with published data from four separate sources (3, 5-7). All major constituents and most minor ones agree well. $SiCl_3$ values are an exception, being two orders of magnitude greater than previously reported (6, 7). This small difference is thought to be due to more recent thermodynamic data and the larger number of chemical species considered.

The results of many equilibrium calculations are correlated in Fig. 1 and 2. In both figures, the three graphs comprising each vertical column all relate to the pressure and composition conditions listed at the top of the

column. In each case, the topmost graph shows equilibrium conversion data, the middle graph shows equilibrium composition data, and the bottom graph has equilibrium yield data. Conversion refers to the degree of completion of the reaction to form condensed phase elemental silicon, while yield refers to the amount of such silicon formed in unit volume of equilibrium gas.

Figure 2 illustrates one novel way in which equilibrium data can be arranged to give a broad view of condensed phase elemental silicon availability. Comparisons made in a horizontal direction show the effects of changing relative compositions, (Fig. 1) and of changing system total pressure (Fig. 2). Comparisons made in a vertical direction show the effects of choosing various silane homologs or intermediate mixtures thereof. Note that vertical lines are isotherms and due to system invariance a single gas phase composition describes the equilibrium behavior of all of the different starting compounds.

Along any isotherm, both conversions and yields of mixtures of neighboring silane homologs may be found by a linear interpolation between the two curves on Fig. 1 and 2 based on relative proportions of the constituents. Of course the input relative proportions of silane homolog and hydrogen must change for different silane compounds or mixtures in order to maintain Cl/H constant.

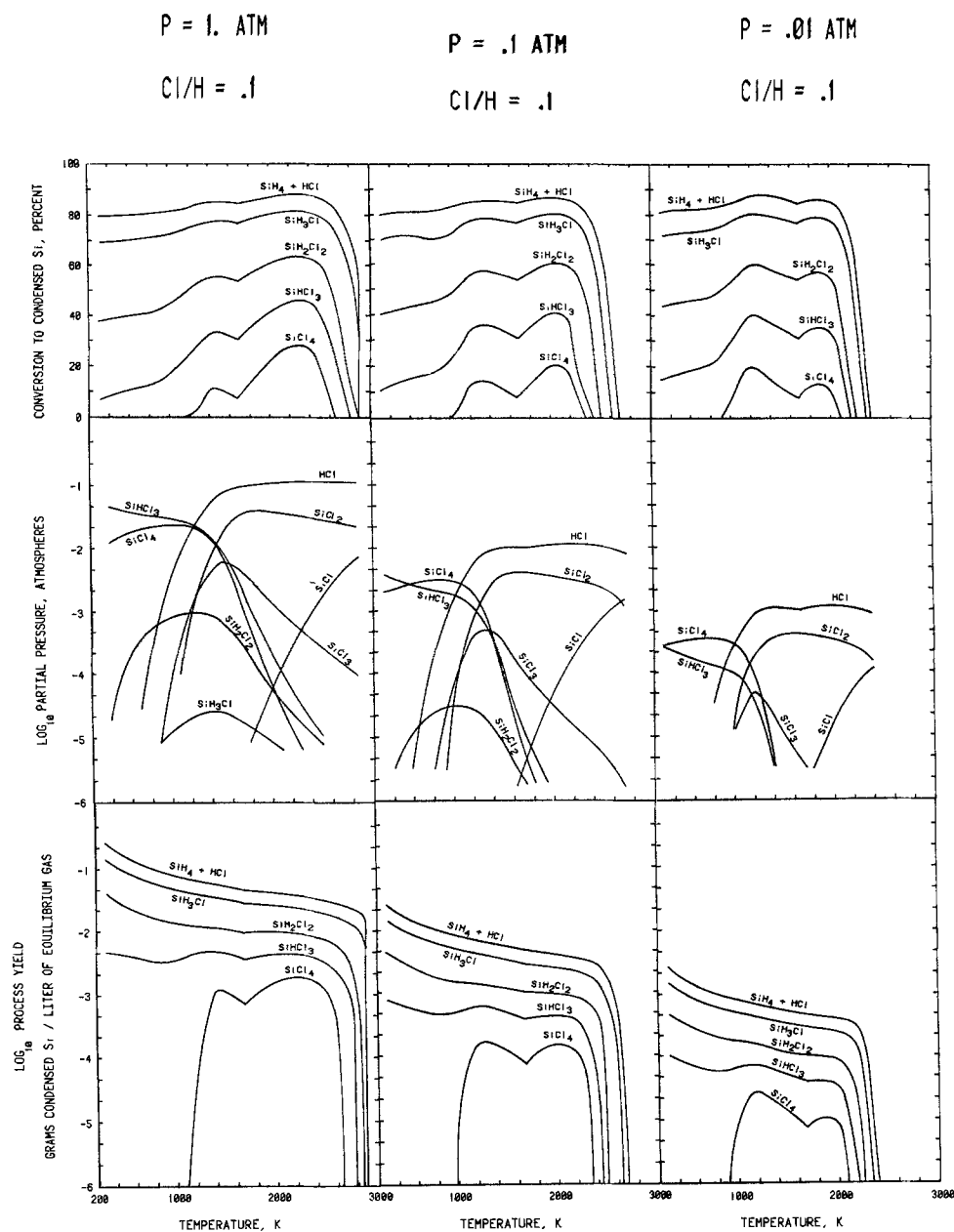


Fig. 2. Calculated equilibrium conversions, gas phase compositions, and yields for the condensation of solid or liquid silicon from individual silane compounds or from mixtures. $P=1.0, 0.1, 0.01$ atm. $\text{Cl/H} = 0.1$.

There are a number of special cases for mixtures. For example, 1-1 molar mixtures of silanes which differ in constitution by two hydrogen atoms will normally have the same atomic composition (add HCl to SiH_4) as the pure silane compound of intermediate constitution and will therefore give identical results at equilibrium. Similarly, 2-1 or 1-2 mixtures of silanes which differ by three hydrogen atoms will have the same atomic composition and give identical equilibrium results as one of the two intermediate silanes. Additional special cases exist for mixtures of silane differing by four hydrogen atoms.

Additions of HCl or Cl_2 produce equilibrium changes which are proportional to the changes they create in the atomic composition of the feed in exactly the same manner as for mixtures. Special cases also occur in the same way. See the left-hand column of Fig. 1 for an example.

Figure 2 can provide preliminary answers to a number of questions related to increasing silicon production. For example, in some instances the conversion and yield curves are bimodal, with a minimum occurring at the melting temperature of silicon and maxima at both lower and higher temperatures. In column 2 of Fig. 1, it is apparent that silicon processes operating near the left-hand peak (solid silicon region) for the conversion of SiCl_4 , SiHCl_3 , or SiH_2Cl_2 would enjoy substantially higher conversions and the same yield if operated near the right-hand peak (liquid silicon region).

A second example in column 2 of Fig. 1 originates from the near equality of conversion of SiCl_4 at the right-hand peak maximum (liquid silicon) and the conversion of SiHCl_3 at the silicon melting temperature. Any process using SiHCl_3 near the melting temperature could maintain the same conversion but change to SiCl_4 as the feed material by raising the operating temperature to attain the right-hand peak. The bottom graph in column 2 of Fig. 1 suggests a yield decrease of about one-half for that exchange. The overall result is that an operator who could double reactor space velocity or reactor volume or an equivalent combination, could also enjoy whatever price differential existed between the two feed materials.

Many other factors enter into silicon processing decisions, particularly those relating to silicon purity. It is possible, therefore, that advantages suggested by equilibrium data such as the examples above may not be compatible with some other process requirement in a particular situation.

Manuscript submitted Nov. 22, 1982; revised manuscript received ca. Aug. 17, 1983.

General Electric Company assisted in meeting the publication costs of this article.

REFERENCES

1. K. R. Sarma and M. J. Rice Jr., *This Journal*, **128**, 2647 (1981).
2. M. Diana, L. DeMarino, L. Mastrantuono, and R. Rossi, *Rev. Int. Hautes. Temp. Refract.*, **18**, 203 (1981).
3. J. Nishizawa and H. Nihira, *J. Cryst. Growth*, **45**, 82 (1978).
4. V. S. Ban and S. L. Gilbert, *This Journal*, **122**, 1382 (1975).
5. V. S. Ban, *ibid.*, **122**, 1389 (1975).
6. P. Van Der Putte, L. J. Giling, and J. Bloem, *J. Cryst. Growth*, **31**, 299 (1975).
7. E. Sirtl, L. P. Hunt, and D. H. Sawyer, *This Journal*, **121**, 919 (1974).
8. L. P. Hunt and E. Sirtl, *ibid.*, **119**, 1741 (1972).
9. L. P. Hunt and E. Sirtl, in "Chemical Vapor Deposition, Second International Conference," J. M. Blocher and J. C. Withers, Editors, The Electrochemical Society Softbound Proceedings Series, Princeton, NJ (1970).
10. R. F. Lever, *IBM J. Res. Develop.*, **8**, 460 (1964).
11. S. Gordon and B. J. McBride, Report NASA SP-273, NTIS (March 1976).
12. JANAF Thermochemical Tables, IFI/Plenum, New York (1977).
13. M. Farber and R. D. Srivastava, *J. Chem. Thermodyn.*, **11**, 939 (1979).



Patterning of Tantalum Polycide Films

R. W. Light* and H. B. Bell*

Sandia National Laboratories, Albuquerque, New Mexico 87185

Gate level interconnect composed of a layer of doped polysilicon covered by a refractory metal silicide (polycide structure) is becoming an important feature of some integrated circuit technologies (1). These composite structures retain the relatively well characterized polysilicon/SiO₂ interface while permitting a lower resistivity than possible with polysilicon alone. Dry etching chemistries used for patterning polysilicon are not generally compatible with these composite materials, often producing an undesirable etched line profile or other complications. For example, a fluorine based plasma will typically etch the polysilicon out from under the silicide resulting in an overhang that will reduce step coverage by subsequent depositions. It has been recently shown that by adding Cl₂ to an SF₆ plasma, a continuous profile can be formed on Ta polycide lines (2). In this paper we discuss the etching behavior of TaSi₂/polysilicon films in a BCl₃/Cl₂ based reactive ion etching process. Control of the etched line profile by variation of the process parameters will be emphasized.

EXPERIMENTAL

TaSi₂/polysilicon (polycide) samples are prepared by depositing 3000 Å of LPCVD polysilicon on thermally oxidized 100mm diameter silicon wafers, phosphorus doping the polysilicon to 30 Ω/□, cleaning the polysilicon surface in 50:1 HF, and sputtering 3000 Å of TaSi₂ onto the polysilicon from a composite target.

Key words: semiconductor, plasmas, etching.

The wafers are coated with 1.8 μm of KTI 820 photoresist and patterned with 2, 3, 4, and 5 μm lines and spaces. Single film samples of TaSi₂ and polysilicon films are prepared in a similar fashion on oxidized silicon wafers. SiO₂ etch rates are determined from oxidized wafers patterned with a photoresist grid pattern.

A Plasma Therm, Inc., Hexetch 640 reactive ion etching system with a 3000 W, 13.56 MHz rf power supply is used for this study. This reactor holds 24, 100 mm diameter wafers on a central, vertically configured, hexagonal cathode enclosed in a bell jar. RF power is applied to the cathode and is regulated to maintain a preset dc self bias voltage on the cathode. The wafer holding cathode and the bell jar are temperature regulated at 30°C. SiO₂ coated wafers are placed in wafer locations not containing sample wafers. The system pressure is fixed at 10 mT and the total gas flow at 40 sccm. Endpoint is determined by monitoring the intensity of the 451 nm Cl₂ emission signal. Profile data are obtained by SEM.

RESULTS AND DISCUSSION

The etched line profile of the polycide structure is a function of the dc self bias voltage, the BCl₃/Cl₂ ratio and the number of wafers in the reactor (loading). A slightly sloped, continuous profile is desired to give adequate step coverage by later deposition processes. The effect of the dc self bias voltage and the percentage of Cl₂ in BCl₃ on the character of the etched profile is illustrated in Fig. 1 for polycide wafers (one wafer load) etched to endpoint. As the dc self bias volt-

age increases (more negative) and/or the Cl_2 percentage in BCl_3 decreases, the lateral etch rate of the TaSi_2 layer decreases relative to the vertical etch rate. While a fluorine based process often produces lateral etching of the polysilicon layer, lateral etching of the TaSi_2 layer dominates with this application of BCl_3/Cl_2 chemistry. Loading also affects the line profile with the relative lateral etch rate of TaSi_2 decreasing with an increase in the number of wafers. For example, in Fig. 1, the profile obtained at 60% Cl_2 , -300 V, and one wafer in the reactor displays a lateral etching of the TaSi_2 layer. If the number of wafers is increased to 6 or more, the profile no longer appears undercut. At voltages less than -300 V (more positive), TaSi_2 undercut can be reduced with increased reactor loading but cannot be totally eliminated. These profile dependencies are similar to those found for reactive ion etching of Al/Si with BCl_3/Cl_2 mixtures (3).

The profile dependence on BCl_3/Cl_2 composition and load is consistent with a sidewall passivation model in which the boron species limit the lateral etching reaction by recombining with the Cl etching species in the absence of ion bombardment (4). In this description of etch directionality decreasing the percentage of Cl_2 in BCl_3 or consuming Cl_2 by using larger wafer loads at constant dc bias voltage increases the relative concentration of boron type recombinants. The dependence of line profile on dc self bias voltage is consistent with positive ion assisted chemistry occurring on the bombarded surfaces. Lateral etching of the polysilicon layer was not detected under any of the experimental conditions.

A significant loading effect is observed for both the polycide and photoresist films with the etch rates decreasing as the number of wafers in the reactor is increased. Both the TaSi_2 and the polysilicon components of the polycide composite contribute to the observed loading effect as shown in Fig. 2 for 20% Cl_2 in BCl_3 and -300 V dc bias. A slightly

sloped continuous polycide profile is obtained when the etch rates of polysilicon, TaSi_2 , and photoresist are similar. A 3.0 μm wide polycide line etched with 20% Cl_2 in BCl_3 , -300 V, and a 12 wafer load is shown in Fig. 3. The original photoresist line profile must have a slope to obtain this degree of taper on the etched line. Sloped photoresist profiles may be formed by a judicious choice of photolithographic parameters and/or postdevelopment bake temperatures. Linewidth variation of 3.0 μm lines wafer to wafer and within a wafer etched under these conditions is typically +5% ($+\sigma$). The combined loading effect observed for polycide films is shown in Fig. 4 for 20% and 60% Cl_2 in BCl_3 and -300 V dc bias. SiO_2 etch rates range between 40 and 70 $\text{\AA}/\text{min}$ with a dc self bias voltage of -300 V, 20% to 60% Cl_2 in BCl_3 , and 1 to 18 wafers in the reactor.

CONCLUSION

Fine line patterning of Ta polycide interconnect can be achieved with a BCl_3/Cl_2 reactive ion etching process. The etched line profile is a function of the BCl_3/Cl_2 composition, the dc bias voltage, and the wafer load. A continuous, tapered line profile can be obtained by using wafer loading conditions in which the TaSi_2 , polysilicon, and photoresist etch rates are similar. This type of profile is often necessary to insure adequate step coverage by later deposition steps.

REFERENCES

1. F. Mohammadi, Solid State Technology, 24, 65 (1981).
2. H. J. Mattausch, P. Hasler, and W. Beinvoogl, J. Vac. Sci. Technol. B, 1, 15 (1983).
3. R. W. Light, H. B. Bell, and H. Macro, Electrochemical Society Extended Abstracts, Abstract No. 169, 83-1 (1983).
4. C. J. Mogab and H. J. Levinstein, J. Vac. Sci. Technology, 17, 721 (1980).

Acknowledgments

We wish to thank Bruce Draper for the TaSi₂ samples and helpful discussions, and Kathy Rogers for the SEM data. We are grateful to Dr. R. E. Anderson, Dr. P. V. Dressendorfer, and Dr. T. V. Nordstrom for reviewing this manuscript. This work was performed at Sandia National Laboratories and was supported by the U. S. Department of Energy under contract no. DE-AC04-76DP00789.

Manuscript submitted Oct. 7, 1983; revised manuscript received Nov. 18, 1983.

Sandia National Laboratories assisted in meeting the publication costs of this article.

*Electrochemical Society Active Member.

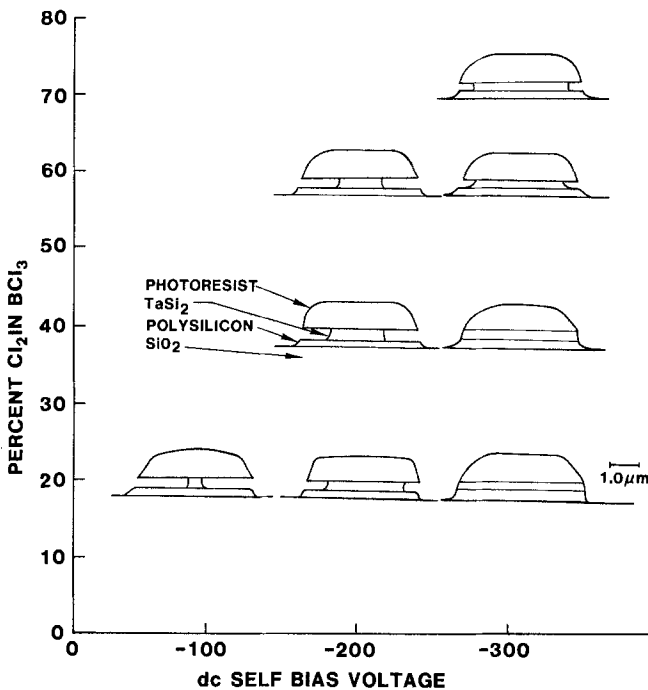


Fig. 1. The effect of percentage Cl₂ in BCl₃ and dc self bias voltage on the profiles of polycide lines.

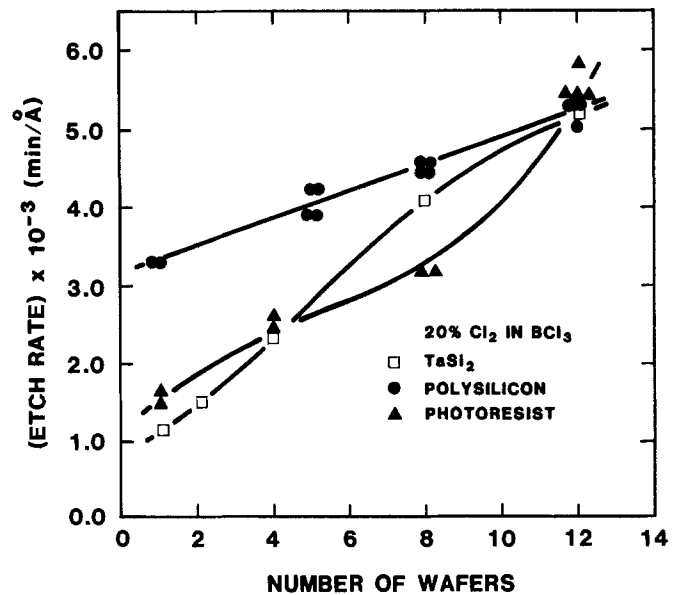


Fig. 2. The loading effect for TaSi₂, polysilicon, and photoresist (data from single film samples).

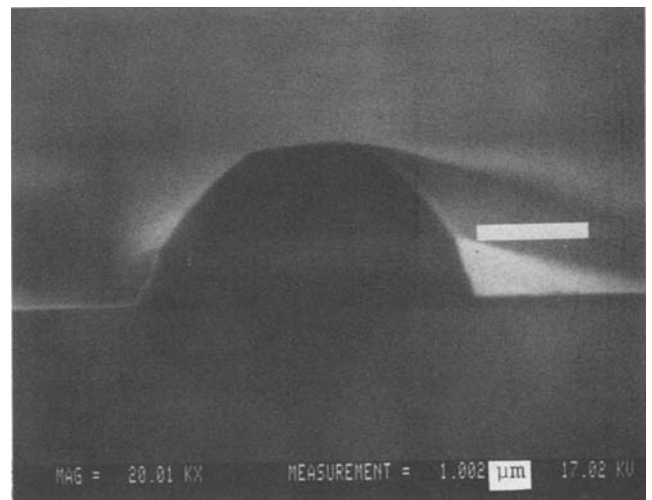


Fig. 3. An etched 3.0 μm polycide line with photoresist.

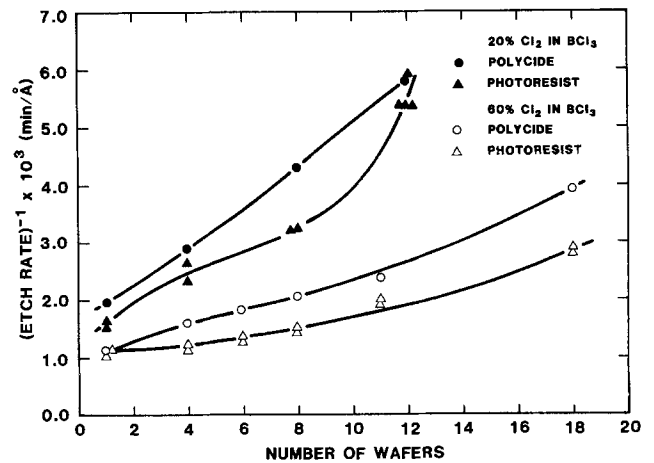


Fig. 4. The loading effect for polycide films.

Conformal Step Coverage of Electron Beam-Assisted CVD of SiO₂ and Si₃N₄ Films

L. R. Thompson,* L. Gobis,** D. Bishop, J. J. Rocca, K. Emery, and G. J. Collins

Department of Electrical Engineering, Colorado State University, Fort Collins, Colorado 80523

We have recently reported electron beam assisted chemical vapor deposition (CVD) of silicon dioxide (SiO₂) and silicon nitride (Si₃N₄) films at low (200°C) substrate temperatures (1,2,3). Herein, we examine the ability of the electron beam deposition technique to conformally cover patterned aluminum and polysilicon steps.

Conformal coverage of such uneven features by deposited dielectric layers without thinning and cusping is important in multilayer metal devices. Thinning of dielectric sidewalls lowers interlayer breakdown voltages and cusping causes step coverage problems in subsequent metallization steps.

Details of the experimental arrangement and the electrical, physical and chemical properties of both SiO₂ and Si₃N₄ films deposited using the electron beam assisted CVD technique have been presented elsewhere (1, 2, 3). Reactant gases used for the deposition of SiO₂ and Si₃N₄ films include nitrous oxide and ammonia as respective oxygen and nitrogen donors. The silicon donor was 5% silane in nitrogen.

The deposition technique uses an electron beam to generate a spatially confined plasma reaction volume. To a first approximation the plasma region is a planar sheet with cross sectional area 1 x 25 mm. Deposition occurs at rates up to 500 Å/min on a heated substrate (150-500°C) located directly beneath the planar region defined by the electron beam generated plasma.

To study the step coverage properties of the electron beam deposition technique aluminum was sputter deposited (8000Å thick) upon a thermal SiO₂ (1000Å thick) covered silicon wafer. The wafer was masked using conventional photolithography and wet chemically etched to achieve aluminum lines 10 to 20 μm wide. Separately a polysilicon layer (4000Å thick) was deposited over another thermal SiO₂ (1000Å thick) covered silicon wafer. The polysilicon

was also masked and standard dry processing techniques were used to achieve polysilicon lines 10 to 20 μm wide.

SiO₂ layers were then electron beam deposited on both aluminum and polysilicon patterned silicon wafers. The SiO₂ films were deposited at a substrate temperature of 350°C, with a N₂O/SiH₄ mass flow ratio of 20 and a chamber pressure of 0.3 Torr. The electron beam discharge current and voltage were 50 mA and 4 kV, respectively.

Separately Si₃N₄ films were electron beam deposited at substrate temperatures of 350°C, with a NH₃/SiH₄ mass flow ratio of 60 and a total chamber pressure of 0.35 Torr. The electron beam current and voltage were 25 mA and 4.2 kV, respectively.

After electron beam SiO₂ and Si₃N₄ deposition the silicon wafers were cleaved revealing the coverage over aluminum and polysilicon steps using a SEM. For the case of polysilicon steps the wafer was etched in a 1 M KOH solution in order to distinguish the polysilicon and SiO₂ or Si₃N₄ interface while aluminum covered wafers were cleaved at 77 K to obtain sharp metal lines.

Figure 1 (a,b,c,d,) shows electron beam deposited SiO₂ and Si₃N₄ films conformally covering both aluminum and polysilicon patterns. A slight cusping of the 0.5 μm SiO₂ film in figure 1b at the base of the polysilicon step is evident. Optimization of the deposition conditions to reduce cusping has not been undertaken. Figure 1d depicts smooth Si₃N₄ coverage to the right of the polysilicon step while coverage on the surface of the step is rough due to the uneven polysilicon. Likewise the electron beam deposited SiO₂ and Si₃N₄ films conformally cover the surface of aluminum steps as in figure 1a and 1c. Film thinning over step sidewalls is less than 10 percent as measured by inspection of the SEM micrographs. Also, no film cracking was visible for all of the SiO₂ and Si₃N₄ layers investigated (0.4 μm to 5 μm thick).

Acknowledgement

This work was supported by the National Science Foundation, the Office of Naval Research, and NASA-Lewis. We thank Hewlett Packard, Loveland, CO for providing the patterned wafers and access to the SEM.

REFERENCES

1. L. R. Thompson, J. J. Rocca, K. Emery, P. K. Boyer, and G. J. Collins, *Appl. Phys. Lett.*, **43**, 777, 1983.
2. D. Bishop, J. J. Rocca, K. Emery, L. Thompson, and G. J. Collins, to be published, *Appl. Phys. Lett.*
3. K. Emery, L. R. Thompson, D. Bishop, P. K. Boyer, H. Zarnani, J. J. Rocca, C. A. Moore, and G. J. Collins, *Materials Research Society*, November 14-16, 1983, Boston, MA.

*Electrochemical Society Student Member.

**Present address: Hewlett-Packard, Loveland, CO.

Colorado State University assisted in meeting the publication costs of this article.

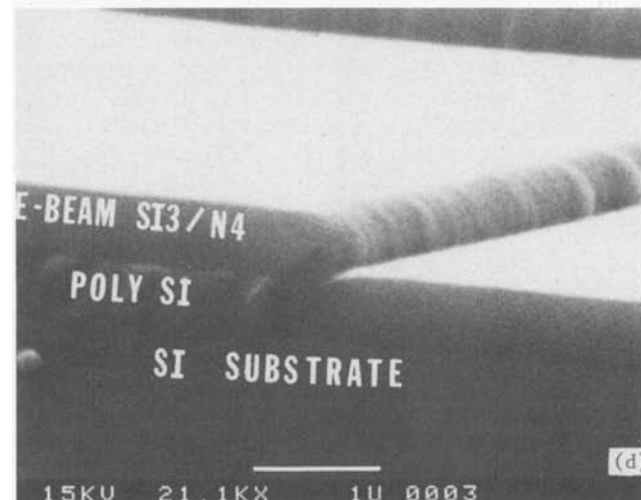
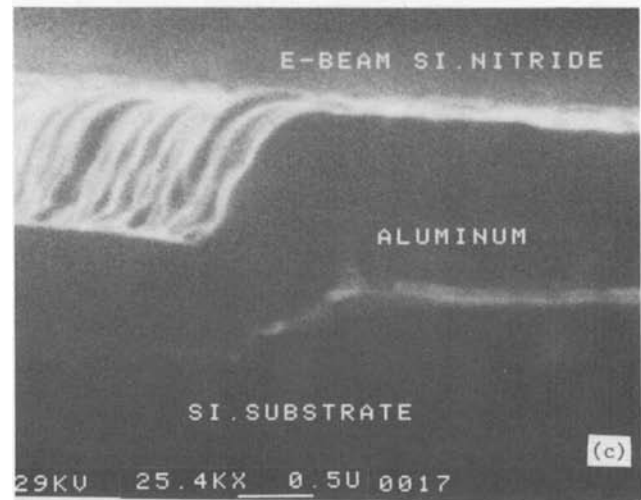
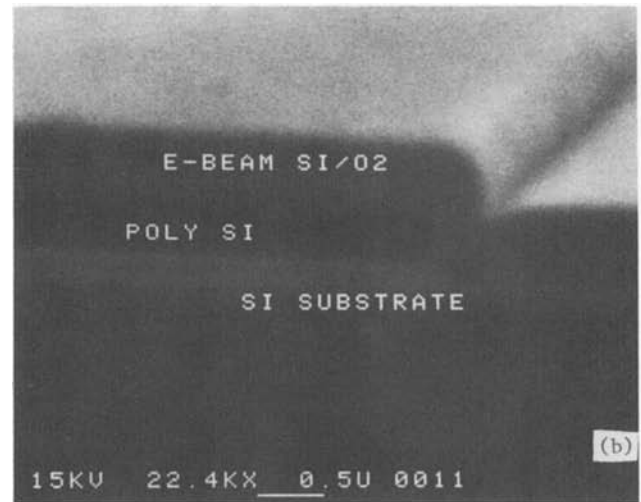
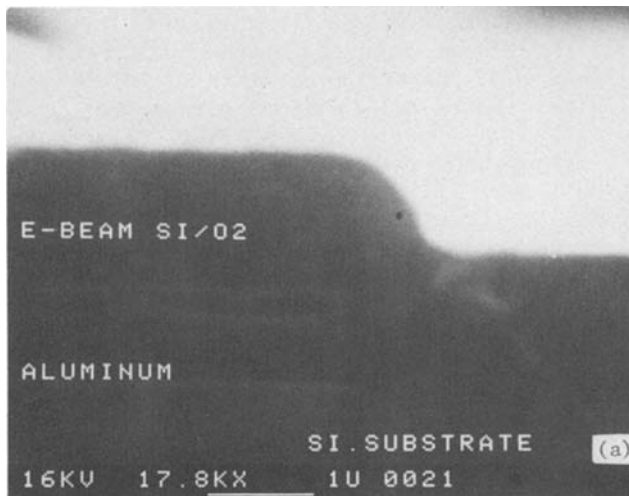


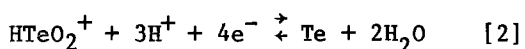
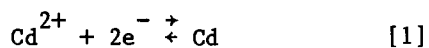
Fig. 1. SEM photographs of electron beam deposited SiO_2 and Si_3N_4 over 8000 \AA Al and 4000 \AA poly-Si steps. A, above: $1 \mu\text{m}$ SiO_2 over Al. B, top right: $0.5 \mu\text{m}$ SiO_2 over poly-Si. C, center right: $1 \mu\text{m}$ Si_3N_4 over Al. D, bottom right: $1 \mu\text{m}$ Si_3N_4 over Al.

In Situ Preparation of Undoped p-Type CdTe by Cathodic Electrochemical Deposition

Juan Llabres†

Solar Energy Research Institute, Solid State Research Branch, Golden, Colorado 80401

Recently, photovoltaic materials researchers have been investigating the use of several II-VI semiconductor compounds (e.g., CdS, CdTe, CdSe) in a new technique—electrochemical deposition (1). Low-cost preparation of polycrystalline CdTe as an absorber material has also been investigated for p-CdTe/n-CdS heterojunction solar cells (2). This paper presents details about the in-situ preparation of p-type CdTe deposited on polished stainless steel and low-sheet-resistance indium-tin oxide (ITO). The deposition process was carried out in an aqueous solution (18 MΩ-cm deionized water) containing CdSO₄ (1M) and saturated TeO₂. The solution pH, a parameter that mainly regulates the deposition rate in the potentiostatic mode, was adjusted by adding more H₂SO₄ to a previously chosen value. The pH range that produces uniform thin films is 2.0–3.5 (3). Several material combinations have been tested for the counter-electrode. The best, most reproducible results were obtained by using a platinum foil with an area similar to that of the cathode in combination with a short rod of tellurium (99.9999) acting as an auxiliary anode. The reduction reactions at the electrode,



lead to the compound formation at the cathode, under stoichiometric conditions that are controlled by the cathodic potential (4). Therefore, at potentials more positive than a certain value [−660 mV vs. standard calomel electrode (SCE)] reaction [2] is more favorable than reaction [1], resulting in an undoped semiconductor material with a p-type majority carriers intrinsic conduction caused by excess Te atoms placed interstitially (5).

Manuscript submitted Oct. 4, 1983; revised manuscript received Nov. 11, 1983.

†Permanent address: Solid State Physics Institute C.S.I.C. Spain.

Key Words: semiconductor, film, deposition.

Special emphasis has been given to preventing electrolyte poisoning by undesired neutral or ionized impurities. Small amounts of chlorine atoms, which may come from the reference calomel, have been observed by Auger electron spectroscopy in a few samples deposited from aged electrolytes. A mechanism of impurification could be the Cl₂ molecule formation at the anode, its diffusion through the liquid, and a subsequent reduction to Cl[−] at the cathode and immediate incorporation in the film. In any case, the chloride ions lead to a compensation of acceptor centers, resulting either in an increase in resistivity or in a change in majority carriers type (6). The electrolytic cell was operated potentiostatically by means of a PAR Potentiostat-Galvanostat Model 173. A PAR Digital Coulometer Model 179 was used to determine film thickness during deposition. Cell temperature was kept at 82° ± 3° C, and a low-speed magnetic stirrer aided in solution convection. The CdTe zincblende structure appears clearly in the X-ray diffraction diagrams of samples grown at potentials ranging from −620 to −660 mV (vs. SCE). A second phase of tellurium is observed with materials grown at more positive potentials. The preferred orientation found in single-phase samples grown on stainless steel, the only kind analyzed by the X-ray diffraction, is [111]. Scanning electron microscopy has revealed an average grain size of about 5 μm. For samples grown on ITO substrates, the grain size appears to be significantly smaller (<1 μm).

As we already pointed out about reactions [1] and [2], one can conclude that the electrical resistivity depends upon material stoichiometry. In order to find out the Cd/Te ratio, compositional measurements by electron probe for microanalysis measurements were performed. Results showed that the Te and Cd atomic percentages decrease and increase, respectively, as the cathodic potential is made more negative, and that both atomic percentages equal unity for a

potential of about -660 mV (vs. SCE). These results are in agreement with those obtained from X-ray diffraction diagrams.

Electric properties of thin films (with a thickness of 0.7-1.3 μm) prepared by in-situ electrochemical deposition have been examined in devices consisting of a conductive substrate, a CdTe thin film, and metallic dots. Since the CdTe/Au contact behaves differently whether the semiconductor is p- or n-type (7), and p-CdTe/In is a Schottky barrier (8), the behavior of these two contacts becomes a criterion for determining the material majority carrier type. Therefore, several gold and indium dot contacts $1.1 \times 10^{-2} \text{cm}^2$ in area were evaporated (pressure $\approx 10^{-6}$ torr) on each sample through a metallic mask. Before any evaporation occurred, samples were etched in a hot KOH solution to remove any remaining superficial Te that would either shunt the evaporated contacts or distort the results, due to a TeO_x isolant thin layer in series with the device. A method has been described (9) that enables us to measure the bulk resistivity as well as the specific contact resistivity.

Fig. 1 shows the dependence of the bulk resistivity on cathodic potential in devices formed by a stainless steel substrate, an undoped p-CdTe junction, and an ohmic gold contact. The base stainless steel/p-CdTe contact is made ohmic by depositing a few atomic monolayers of Te before CdTe deposition begins. In Figure 1, the vertical bars represent the resistivity variation found at different dots located along the two dimensions of the sample surface (with an area of $\approx 2 \text{cm}^2$). The CdTe/Au contact behaves ohmically in a wide range of applied voltages; in contrast, the CdTe/In presents a Schottky barrier characteristic. These results demonstrate the p-type property of the reported material. Figure 1 also shows that bulk resistivity is notably decreased by the incorporation of excess Te into the materials crystal lattice. Note that the range for single-phase CdTe preparation is quite short (40 mV, approximately). In fact, high infrared transmission values demonstrate that there is not a Te second phase in films grown in this range. Specific p-CdTe/Au contact resistivity values depending on bulk resistivity range from 2 to $2 \times 10^{-2} \Omega\text{-cm}^2$.

Acknowledgment

The author is indebted to Dr. S.K. Deb and Dr. R. Noufi for providing support and stimulating discussions.

The Solar Energy Research Institute assisted in meeting the publication costs of this article.

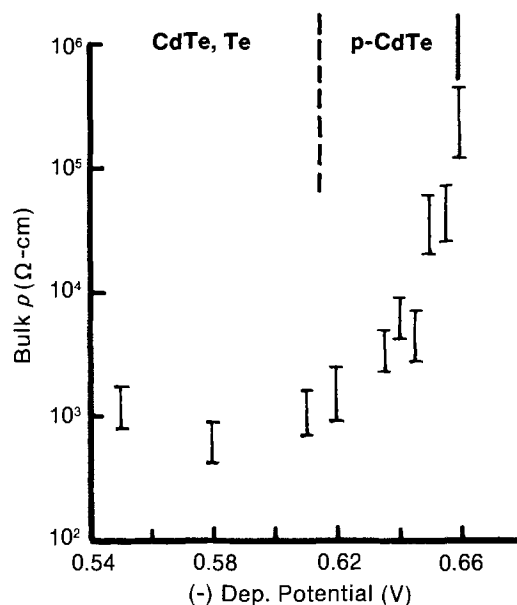


Fig. 1 p-type cadmium telluride bulk resistivity as a function of cathodic potential. The region of single-phase p-CdTe deposition is also shown.

References

1. G. Hodes, J. Manasen, S. Neagu, D. Cahen and Y. Mirovsky, *Thin Solid Films*, **90**, 433 (1982), and references therein.
2. Y. S. Tyan and E. A. Perez-Albuerne, 16th IEEE PV Specialist Conf. 1982 p. 794.
3. J. Llabres, Polycrystalline Thin Film Review Meeting, 16-18 May 1983, Golden Colo., p. 193.
4. M. P. R. Panicker, M. Knaster, and F. A. Kröger, *this Journal*, **125**, 566 (1978).
5. D. de Nobel, *Philips Res. Repts.* **14**, 430 (1959).
6. K. Zanio, "Semiconductors and Semimetals", v. 13, p. 134, Academic Press, New York (1978).
7. K. W. Mitchell, Ph.D. Thesis, Stanford University (1976).
8. F. G. Courreges, Ph.D. Thesis, Stanford University (1979).
9. A. L. Fahrenbruch, and R. H. Bube, "Fundamentals of Solar Cells" p. 198, Academic Press, New York (1983).

Anodic Dissolution of Iron Phthalocyanine Film Electrodes

Carlos A. Melendres*

Argonne National Laboratory, Materials Science and Technology Division, Argonne, Illinois 60439

Shu Qian-Xu

Department of Chemistry, University of Science and Technology of China, Hefei, Anhwei, China

In a recent presentation (1), we showed the existence of an anodic wave at about 0.6V vs. Hg/Hg₂SO₄ in the cyclic voltammogram of iron phthalocyanine (FePc) film electrodes in 0.05 M H₂SO₄ solution. We now present results of investigations by rotating ring-disc electrode and Raman spectroscopic techniques which indicate that this wave is associated with the anodic dissolution of the FePc film. This observation is relevant to the problem of stability of phthalocyanine electrodes for O₂ reduction.

Experimental.--FePc films supported on gold electrodes were prepared by (1) evaporation of 0.2-0.25 wt.% FePc/pyridine solutions on the Au surface and (2) by vapor deposition under high vacuum. Further experimental details and instrumentation are the same as described in previous publications (2,3). All potentials were measured against a Hg/Hg₂SO₄ reference.

Results and Discussion.--The anodic behavior of FePc films in 0.05 M H₂SO₄ solution is exemplified in the cyclic voltammogram at a rotating disc (with ring) electrode as shown in Fig. 1a. Both peak current and peak potential appear to vary with film thickness but are independent of the presence of oxygen in the solution. Integration of the area under the wave indicates that the charge passed corresponds to multiple layers of material being involved in the oxidation process. At low scan rates, (<5mv/sec) the integrated charge is directly proportional to the weight of FePc film taken for evaporation, and hence also to the film thickness. Complete quantitative oxidation of the film can be accomplished coulometrically by holding the potential at about 0.75V. Fig. 2 shows the relation between the weight of the FePc film (W) and the charge (Q) passed during controlled potential oxidation. From the slope of the line in Fig. 2, we calculate the number of electrons involved in the oxidation process to be 1.2±0.2.

Measurements of current at the Au ring were also made as a function of ring potential

while simultaneously scanning the disc potential. A typical result is shown in Fig. 1b. Significant ring current is measured with the ring potential set at about -0.2V and at more negative values. Thus the anodic oxidation process results in the production of a soluble species which is reducible on a Au electrode. Cyclic voltammetry shows that the reduced species is not re-oxidizable at a Au electrode. Following excursion of the potential to +0.75V and beyond, we find by microscopic examination that the electrode surface is as smooth and clear as before the FePc film was laid on it.

To determine whether the film is indeed dissolving anodically or whether the iron center is coming off the macrocycle as is commonly believed, laser Raman spectroscopic examination of the film "in-situ" was undertaken. If the FePc were dissolving, we expect the Raman bands due to the whole molecule to disappear following the anodic oxidation. If only the iron center were removed, the phthalocyanine framework should remain and give a spectrum somewhat different from that of the original FePc (3,4). Results showed that on scanning the potential very slowly to +0.8V, the whole FePc spectrum disappeared completely. We also followed the intensity of a prominent band, e.g. at 1520 cm⁻¹, in the Raman spectrum of FePc as a function of potential. Our normal coordinate analysis (5) shows this band to be a mixture of normal modes due to C-N and C-C stretches as well as C-N-C angle deformation. A typical result is shown in Fig. 3. Disappearance of this band and the whole spectrum at 0.8V indicates removal of the FePc from the electrode surface. Since we find no greenish blue particles in solution that would indicate a spalling-off of the FePc film, we are lead to conclude that the film is irreversibly anodically oxidized and passes into solution either as a solvated cation or other soluble entity.

While the results described above were obtained with films prepared by solution evaporation, we observed the same anodic dissolution behavior with films prepared by vapor

deposition on Au substrates under high vacuum. This is in contrast with observations made by Green and Faulkner (6) who claim to have found that FePc undergoes an irreversible electrochromic change on oxidation. They, however, used a different electrolyte and electrode substrate.

Acknowledgment

This investigation was carried out at Argonne National Laboratory with financial support from the Materials Science Division, Office of Basic Energy Sciences, Department of Energy.

*Electrochemical Society Active Member.

Manuscript submitted June 26, 1983; revised manuscript received Nov. 9, 1983.

REFERENCES

1. C.A. Melendres and X. Feng, Abstract 876, The Electrochemical Society Extended Abstracts Vol. 82-1, Montreal, Quebec, Canada, May 9-14, 1982.
2. C.A. Melendres and X. Feng, *This Journal*, 130, 811 (1983).
3. C.A. Melendres and F.A. Cafasso, *ibid.*, 128, 755 (1981).
4. R. Arco and R.O. Loutfy, *J. Raman Spec.*, 12, 262 (1982).
5. C.A. Melendres and V.A. Maroni, to be published.
6. J.M. Green and L.R. Faulkner, *J. Am. Chem. Soc.*, 105, 2950 (1983).

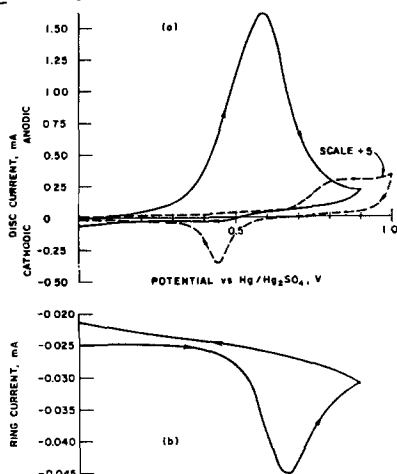


Fig. 1a. Cyclic Voltammograms at a Gold Rotating Disc (with ring) Electrode
 ---- Pure Gold
 ——— FePc-Film-on Gold. (film thickness $\approx 4500 \text{ \AA}$)
 0.05 M H₂SO₄ in ambient air
 scan rate = 17 mV/sec
 rotation rate = 1000 rpm

Fig. 1b. Variation of Current at Au Ring with Disc Potential
 $E_{\text{Ring}} = -0.5\text{V}$

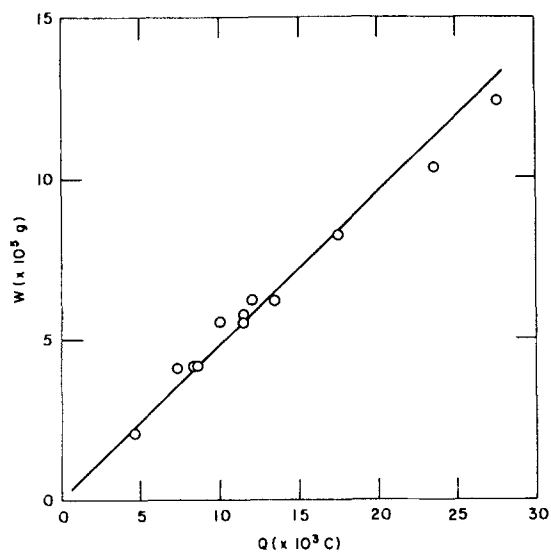


Fig. 2. Coulometric Charge as a Function of Quantity of FePc Film
 $E = +0.75\text{V}$
 Electrode area = 0.454 cm^2

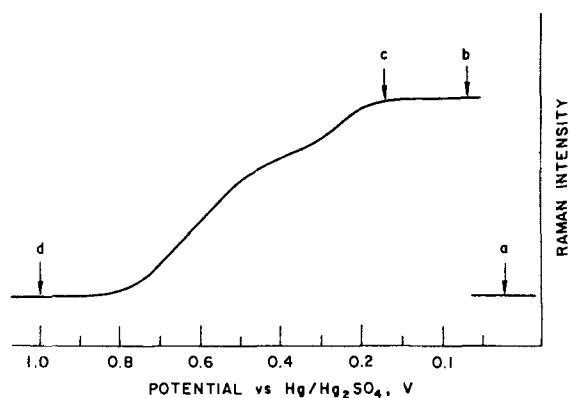


Fig. 3. Intensity of Raman Signal at 1520 cm^{-1} as Function of Potential
 a - background signal level
 b to c - steady state signal at open circuit before scanning electrode potential
 d - background signal after scanning potential past 0.8V

Potential scan rate = 5 mV/sec
 Film thickness $\sim 5000 \text{ \AA}$
 Kr⁺ Laser, 6471 \AA exciting line
 P = 100 mW



Reports on the Energy Research Summer Fellowship Awards



Jesús A. del Alamo



Jean-Noël Gorce



D. B. Graves



Leslie C. Hardy



James A. Osborn

During the summer of 1983, the following students were awarded Energy Research Summer Fellowships. Each award carried with it a grant of \$2000.

- Mr. Jesús A. del Alamo, of Stanford University, Stanford, California.
- Mr. Jean-Noël Gorce, of the Georgia Institute of Technology, Atlanta, Georgia.
- Mr. D. B. Graves, of the University of Minnesota, Minneapolis, Minnesota.
- Mr. Leslie C. Hardy, of Northwestern University, Evanston, Illinois.
- Mr. James A. Osborn, of Rutgers University, Piscataway, New Jersey.

The Energy Research Summer Fellowship Awards are made "without regard to sex, citizenship, race, or financial need. They are made to graduate students pursuing work between the degrees of B.S. and Ph.D., in a college or university in the United States or Canada." The recipients' projects are in fields relating to energy research or of interest to The Electrochemical Society. The Awards were sponsored by the Department of Energy and made by the Summer Fellowship Committee of the Electrochemical Society.

Jesús A. del Alamo was born in Soria, Spain. He received his Ingeniero de Telecomunicación degree from the Universidad Politécnica de Madrid, Spain, in 1980, and his M. S. degree from Stanford University, Stanford, California, in 1983. He is working on his Ph. D. degree at Stanford.

Mr. del Alamo has received numerous awards, and has been a visiting student at Katholieke Universiteit Leuven in Belgium, and the University of Edinburgh in Scotland.

Mr. del Alamo's report is given below.

Epitaxial Growth of Heavily Phosphorus-Doped Silicon

Material problems have so far precluded a systematic characterization of heavily doped Si. The intrinsic and technological limitations of as-grown crystal, diffused or implanted layers have permitted only partial knowledge of the band structure and minority carrier properties of heavily doped Si. An understanding of the physics of heavily doped Si is of enormous importance for VLSI bipolar transistors, high concentration solar cells, and low temperature CMOS.

Epitaxially grown heavily doped Si is a good candidate for carrying out this fundamental study because of its ability to fabricate flat and very abrupt impurity profiles, lack of limitations in layer thickness, and technological simplicity. The problems to solve are the incorporation of dopant species in the growing Si layer to obtain the high doping levels of interest and the control of the density of defects to allow the fabrication of test devices.

Epitaxial heavily doped Si by itself may be of interest as a material for VLSI bipolar base regions if grown under low pressure, low temperature conditions, because of the tight control of impurity profiles it allows and the lack of compensation of impurities. Its use has already been reported in the fabrication of hyperabrupt IMPATT Si diodes (1).

Experimental

In this work epitaxial heavily phosphorus doped Si has been grown on <100> B-doped 0.1-0.2 Ω -cm substrates. All the ex-

periments were carried out in a horizontal, RF-heated epitaxial reactor (Hugle Model HIER II) operating at atmospheric pressure. The quartz reactor tube had an effective cross section of 27 cm² above the susceptor. The silicon carbide-coated graphite susceptor was tilted at an angle of 2°. Hydrogen was used as the carrier gas at a flux of 79 l/min. Silane was the source of silicon at a partial pressure of 10⁻³ atm in all cases. Phosphine was delivered as the dopant source through a double-dilution system. With PH₃ tanks of 1 and 5% (in H₂), partial pressures ranging from 1.2 × 10⁻⁶ to 3.3 × 10⁻³ atm were reached in the reaction chamber. All depositions herein reported were done during 10 min at 1050°C. Prior to growth, all wafers were vapor etched in 5 × 10⁻³ atm HCl for 4 min at 1200°C.

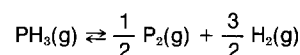
One quarter of a 3 in. wafer was processed at a time. After epitaxy, it was sawn into 7 × 7 mm² chips. On these chips the characterization of the layers was carried out by a combination of techniques: spreading resistance, groove and stain, van der Pauw measurements, and Secco etch for defect count.

Characterization and Discussion

Figure 1 shows a typical spreading resistance profile. The carrier distribution throughout the layer is very flat, and an abrupt transition occurs at the interface. The small bump near the junction and the slightly lower surface concentration are artifacts of the spreading resistance numerical algorithm.

Figure 2 collects the resulting electron concentration in the epitaxial layer vs. the partial pressure of PH₃ in the reaction tube. Electron concentrations as high as 1.5 × 10²⁰ cm⁻³ were obtained. In the lower concentration range, from 1.7 × 10¹⁹ to approximately 6 × 10¹⁹ cm⁻³, the electron concentration is proportional to a power of the PH₃ partial pressure with an exponent of \approx 0.3, in good agreement with theoretical predictions of Bloem *et al.* (2) of 0.25. At higher concentrations, the electron concentration rolls off.

The physical origin of this power-law dependence of the P concentration in the epitaxial layer is based on the following reactions (2)



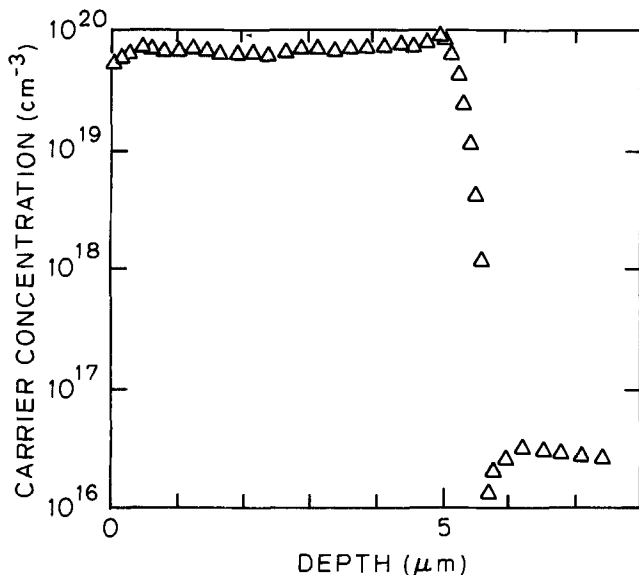


Fig. 1. Spreading resistance profile of a typical heavily doped epitaxial region.

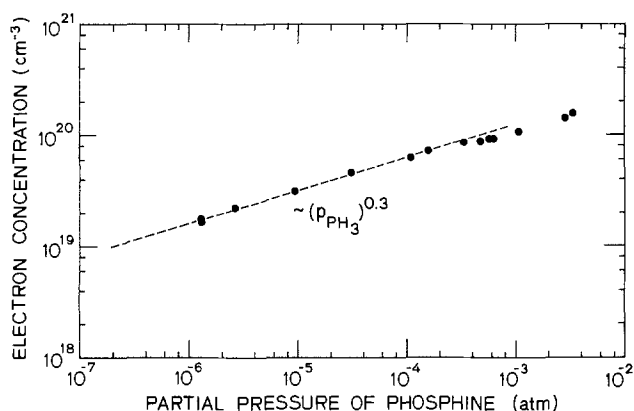
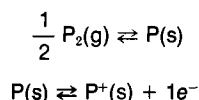


Fig. 2. Epitaxial layer electron concentration vs. initial partial pressure of PH_3 in the reactor (temp = 1050°C , $p_{\text{SiH}_4} = 10^{-3}$ atm).



We have in this case the following equilibrium constants as defined by Bloem *et al.* (2)

$$K_1 = \frac{(\rho_{\text{P}_2})^{1/2} (\rho_{\text{H}_2})^{3/2}}{\rho_{\text{PH}_3}} \approx \frac{(\rho_{\text{P}_2})^{1/2}}{\rho_{\text{PH}_3}} \quad [1]$$

$$K_a = \frac{[\text{P}]}{(\rho_{\text{P}_2})^{1/2}} \quad [2]$$

$$K_b = \frac{[\text{P}^+] \cdot n}{[\text{P}]} \quad [3]$$

which gives

$$[\text{P}^+] = K_a K_b \frac{(\rho_{\text{P}_2})^{1/2}}{n} = K_1 K_a K_b \frac{(\rho_{\text{PH}_3})}{n} \quad [4]$$

Bloem *et al.* computed the equilibrium concentration in H_2 of P , P_2 , P_4 , PH , PH_2 , and PH_3 as a function of the input concentration of PH_3 at several temperatures. A thermodynamical approach was used by assuming that equilibrium in the gas phase is attained near the silicon surface. The result of their calculation showed that at high partial pressures of PH_3

$$\rho_{\text{PH}_3} \approx K (\rho_{\text{PH}_3}^0)^{1/2} \quad [5]$$

where $\rho_{\text{PH}_3}^0$ represents the initial partial pressure of PH_3 .

In Eq. [4] we therefore have

$$[\text{P}^+] = K K_1 K_a K_b \frac{(\rho_{\text{PH}_3}^0)^{1/2}}{n} \quad [6]$$

If the semiconductor is intrinsic, $n = n_i(T)$, and

$$[\text{P}^+] \sim (\rho_{\text{PH}_3}^0)^{1/2} \quad [7]$$

If it is extrinsic

$$n = [\text{P}^+] \quad [8]$$

and

$$[\text{P}^+] \sim (\rho_{\text{PH}_3}^0)^{1/4} \quad [9]$$

The intrinsic carrier concentration in Si at 1050°C is between 10^{18} and 10^{19} cm^{-3} ; its value is not well known (3, 4). In any case, at the levels of doping obtained in the present experimental work, the growing Si layer is definitely extrinsic, and Eq. [9] applies.

Our exponent of 0.3 rather than 0.25 as indicated by Eq. [9] may be due to small divergences in the computer result (5).

The deviation from this power law at higher partial pressures of PH_3 may lie in the failure of Eq. [8] because of incorporation of inactive P in the growing layer, or the failure of the Henry's law ($k = \rho_{\text{P}}/[\text{P}]_{\text{Si}}$) as solid solubility is approached. Total P activation in epitaxial Si layers have been demonstrated up to a concentration of $3 \times 10^{19} \text{ cm}^{-3}$ (5). SIMS analysis of our samples will reveal the reason for the lower electron concentration at the higher PH_3 levels.

Figure 3 shows the growth rate vs. partial pressure of PH_3 . The growth rate is fairly constant up to a level of $\approx 4 \cdot 10^{-4}$ atm, above which it decreases abruptly. Similar results have been found by Gupta (6) in the $\text{AsH}_3/\text{SiH}_4$ and $\text{B}_2\text{H}_6/\text{SiH}_4$ systems. It is interesting to note that the deviation of the power-law dependence of the electron concentration vs. the PH_3 partial pressure occurs at approximately the same point as the decay in the growth rate. This coincidence suggests that both effects may be related to the reaction kinetics, rather than the dopant incorporation in the Si.

Figure 4 shows electron mobility vs. electron concentration in the layer. Both measurements were obtained by measuring resistivity and Hall mobility in a van der Pauw setup, with a magnetic field of 1.12 kG at 23°C . The Hall coefficient was assumed to be equal to unity, as the work of Nakanuma (5) suggests. Each data point represents an average of five measurements carried out at five different current levels. The data here reported closely follow the NBS data (7) and extend the range beyond their maximum concentration. Their analytical fitting significantly diverges at the high doping range. The fitting to the experiments of Massetti *et al.* (8) is lower at the very high concentration regime, probably due to the large scattering of their experimental data.

Figure 5 collects the density of etch pits defined by Secco etch in 5 min. The defects seem to be perfect or misfit dislocations. There appears to be a strong correlation between doping level and defect density. The values here reported are compatible with the fabrication of test devices for the characterization of minority carrier behavior.

Summary

Heavily doped epitaxial silicon has been grown in a PH_3/SiH_4 system. Electron concentrations as high as $1.5 \times 10^{20} \text{ cm}^{-3}$ have been obtained. At the highest doping range the electron concentration diverges from theoretical expectations. The origin of

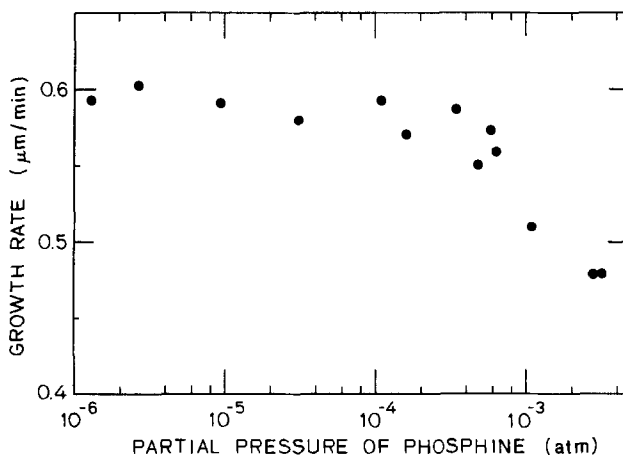


Fig. 3. Epitaxial layer growth rate vs. initial partial pressure of PH_3 . (1050°C , $p_{\text{SiH}_4} = 10^{-3}$ atm).

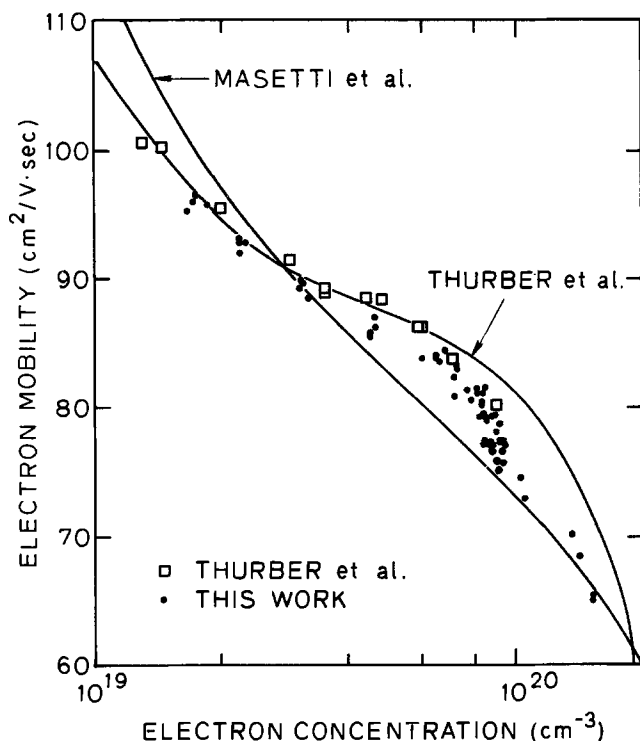


Fig. 4. Electron mobility vs. electron concentration at 23°C. The continuous lines represent fittings to experimental data of the indicated authors.

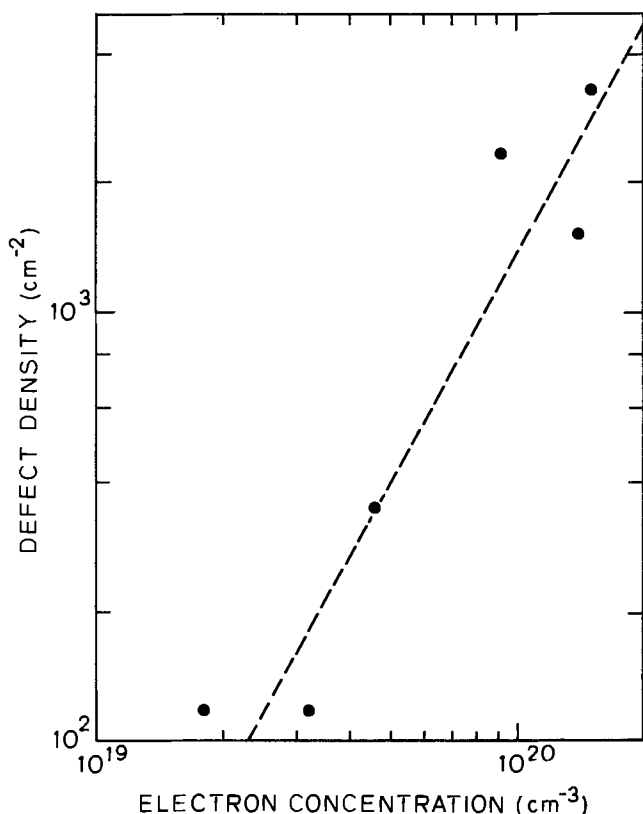


Fig. 5. Density of etch pits defined by Secco etch vs. electron concentration.

this discrepancy is not clear. Electron mobilities have been measured. The obtained values agree very well with previous measurements on bulk and thermally diffused silicon. The defect density in the epitaxial layers allow the fabrication of test devices for the characterization of heavily doped silicon.

Acknowledgment

The support of The Electrochemical Society through The Electrochemical Society Energy Research Summer Fellowship

funded by the Department of Energy is gratefully acknowledged. I am deeply indebted to my advisor, Richard M. Swanson, for his interest and guidance throughout the course of this work. I also wish to thank the staff of the Integrated Circuits Laboratory, where all experimental work was performed.

REFERENCES

1. M. Heitzmann and M. Boudot, *IEEE Trans. Electron. Devices*, **ed-30**, 759 (1983).
2. J. Bloem, L. J. Giling, and M. W. M. Graef, *This Journal*, **121**, 1354 (1974).
3. C. D. Thurmond, *ibid.*, **122**, 1133 (1975).
4. R. Colclaser, "Microelectronics: Processing and Device Design," p. 126, John Wiley & Sons, New York (1980).
5. S. Nakanuma, *This Journal*, **111**, 1199 (1964).
6. D. C. Gupta, *J. Electron. Mater.*, **1**, 371 (1972).
7. W. R. Thurber, R. L. Mattis, Y. M. Liu, and J. J. Filliben, *This Journal*, **127**, 1807 (1980).
8. G. Masetti, M. Severi, and S. Solmi, *IEEE Trans. Electron. Devices*, **ed-30**, 764 (1983).

Jean-Noel Gorce received his B. S. degree in Chemistry from the University of Georgia, Athens, Georgia, in 1981. He is currently working on his Ph. D. at the Georgia Institute of Technology, Atlanta, Georgia.

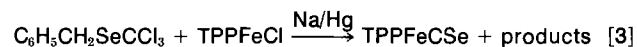
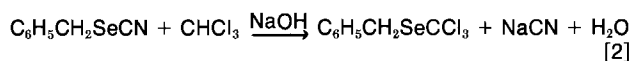
Mr. Gorce has had his work published in *Inorganic Chemistry*. From 1981 to 1983, he worked as a teaching assistant at Florida State University.

Mr. Gorce's report is given below.

Voltammetric Investigation of a Selenocarbonyl-Iron Porphyrin

The discovery of cytochrome P450 possessing a biochemically active iron-carbene bond (1) prompted us to investigate related model compounds. The iron-carbene bond in the cytochrome P450 hemoprotein was generated during the metabolic reduction of polyhalogenated compounds. Knowledge of carbene-iron porphyrin redox stabilities is essential for comprehending the role played by this moiety in cytochrome P450. A series of synthetic, isoelectronic carbene-iron porphyrin compounds are presently under investigation in this laboratory. These include the carbonyl, thiocarbonyl, and selenocarbonyl complexes of 5,10,15,20-tetraphenylporphyrinatoiron(II). Of present interest is the selenocarbonyl iron porphyrin, TPPFeCSe. This complex is one of just a few complexes containing a Fe-C=Se bonding arrangement. The paucity of metalloselenocarbonyl complexes is a result of the lack of stable precursors such as CSeCl₂ or CSe₂.

The preparation of TPPFeCSe was accomplished via a modification of the procedure presented by Battioni *et al.* (2). The synthesis requires three consecutive reactions.



The reductive electrochemistry of carbene-iron porphyrins has been investigated (3, 4). The initial injection of one electron occurs reversibly while the injection of a second electron is succeeded by chemical complications. The electro-oxidation of TPPFeCSe has been extensively investigated (5). This complex underwent two discrete one-electron quasireversible oxidations. This is unlike the C=O complex of Fe-porphyrins, in which the oxidation resulted in the dissociation of the Fe-C bond (6, 7).

The purpose of this report is to provide a detailed description of the synthesis and the oxidative electrochemistry of the only known selenocarbonyl iron porphyrin.

Experimental

The chemicals used were or were presumed to be highly toxic. Selenium containing compounds gave off a noxious odor. All reactions were carried out under a well-ventilated hood. Selenium containing waste products were disposed of by treatment with sodium hypochlorite solution.

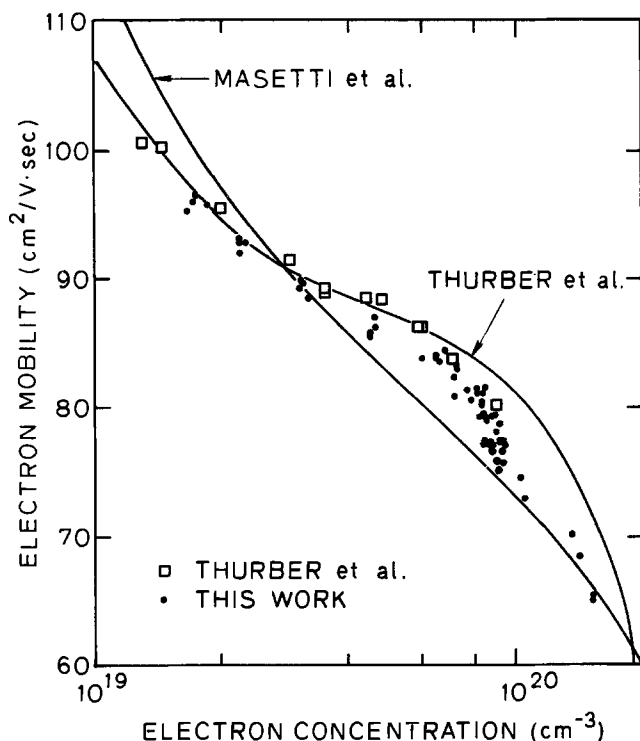


Fig. 4. Electron mobility vs. electron concentration at 23°C. The continuous lines represent fittings to experimental data of the indicated authors.

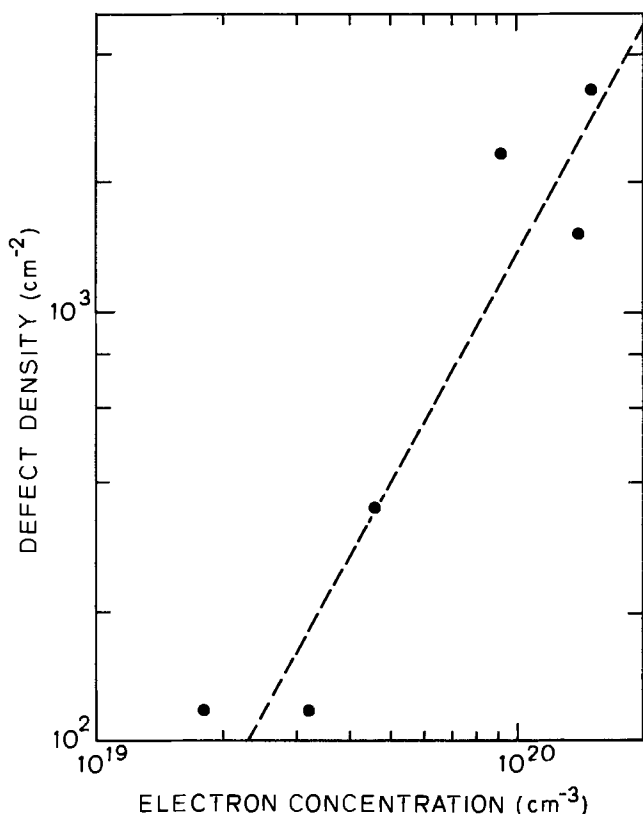


Fig. 5. Density of etch pits defined by Secco etch vs. electron concentration.

this discrepancy is not clear. Electron mobilities have been measured. The obtained values agree very well with previous measurements on bulk and thermally diffused silicon. The defect density in the epitaxial layers allow the fabrication of test devices for the characterization of heavily doped silicon.

Acknowledgment

The support of The Electrochemical Society through The Electrochemical Society Energy Research Summer Fellowship

funded by the Department of Energy is gratefully acknowledged. I am deeply indebted to my advisor, Richard M. Swanson, for his interest and guidance throughout the course of this work. I also wish to thank the staff of the Integrated Circuits Laboratory, where all experimental work was performed.

REFERENCES

1. M. Heitzmann and M. Boudot, *IEEE Trans. Electron. Devices*, **ed-30**, 759 (1983).
2. J. Bloem, L. J. Giling, and M. W. M. Graef, *This Journal*, **121**, 1354 (1974).
3. C. D. Thurmond, *ibid.*, **122**, 1133 (1975).
4. R. Colclaser, "Microelectronics: Processing and Device Design," p. 126, John Wiley & Sons, New York (1980).
5. S. Nakanuma, *This Journal*, **111**, 1199 (1964).
6. D. C. Gupta, *J. Electron. Mater.*, **1**, 371 (1972).
7. W. R. Thurber, R. L. Mattis, Y. M. Liu, and J. J. Filliben, *This Journal*, **127**, 1807 (1980).
8. G. Masetti, M. Severi, and S. Solmi, *IEEE Trans. Electron. Devices*, **ed-30**, 764 (1983).

Jean-Noel Gorce received his B. S. degree in Chemistry from the University of Georgia, Athens, Georgia, in 1981. He is currently working on his Ph. D. at the Georgia Institute of Technology, Atlanta, Georgia.

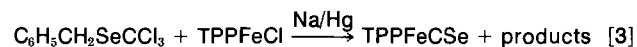
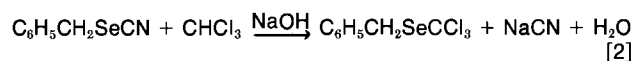
Mr. Gorce has had his work published in *Inorganic Chemistry*. From 1981 to 1983, he worked as a teaching assistant at Florida State University.

Mr. Gorce's report is given below.

Voltammetric Investigation of a Selenocarbonyl-Iron Porphyrin

The discovery of cytochrome P450 possessing a biochemically active iron-carbene bond (1) prompted us to investigate related model compounds. The iron-carbene bond in the cytochrome P450 hemoprotein was generated during the metabolic reduction of polyhalogenated compounds. Knowledge of carbene-iron porphyrin redox stabilities is essential for comprehending the role played by this moiety in cytochrome P450. A series of synthetic, isoelectronic carbene-iron porphyrin compounds are presently under investigation in this laboratory. These include the carbonyl, thiocarbonyl, and selenocarbonyl complexes of 5,10,15,20-tetraphenylporphyrinatoiron(II). Of present interest is the selenocarbonyl iron porphyrin, TPPFeCSe. This complex is one of just a few complexes containing a Fe-C=Se bonding arrangement. The paucity of metallo-selenocarbonyl complexes is a result of the lack of stable precursors such as CSeCl₂ or CSe₂.

The preparation of TPPFeCSe was accomplished via a modification of the procedure presented by Battioni *et al.* (2). The synthesis requires three consecutive reactions.



The reductive electrochemistry of carbene-iron porphyrins has been investigated (3, 4). The initial injection of one electron occurs reversibly while the injection of a second electron is succeeded by chemical complications. The electro-oxidation of TPPFeCSe has been extensively investigated (5). This complex underwent two discrete one-electron quasireversible oxidations. This is unlike the C=O complex of Fe-porphyrins, in which the oxidation resulted in the dissociation of the Fe-C bond (6, 7).

The purpose of this report is to provide a detailed description of the synthesis and the oxidative electrochemistry of the only known selenocarbonyl iron porphyrin.

Experimental

The chemicals used were or were presumed to be highly toxic. Selenium containing compounds gave off a noxious odor. All reactions were carried out under a well-ventilated hood. Selenium containing waste products were disposed of by treatment with sodium hypochlorite solution.

Material.—Benzylselenocyanate ($C_6H_5CH_2SeCN$) was obtained via modification of the procedure used by Jackson (8). To 100 ml of acetone, 10.0g of potassium selenocyanate was added. This mixture was stirred for 15 min until all of the potassium salt dissolved. To this solution was added a slight excess, (10.0g) of benzylchloride. The solution was vigorously stirred for 1h at room temperature, at which time a white precipitate developed. The KCl precipitate was removed by filtration. The filtrate was cooled to $10^\circ \pm 2^\circ C$ and left to stand for 30 min. A second crop of solid KCl was removed by filtration. The remaining solution was reduced to approximately 30 ml and set aside to permit crystallization of the desired product. Over a 2h period, white crystals grew. They were filtered and twice recrystallized from acetone. A melting point of $72^\circ-73^\circ C$ was obtained (literature value (8) was $71.5^\circ C$). This product was obtained in a 74% yield based on potassium selenocyanate.

Benzyl trichloromethyl selenoether ($C_6H_5CH_2SeCCl_3$) was obtained using the procedure used by Makosza and Fedorynski (9) for their synthesis of the analogous sulfur compound. 4.40g of benzyl selenocyanate and 70 mg of the phase-transfer agent triethylbenzylammonium chloride (TEBA) were dissolved in 8.00g of chloroform. This mixture was stirred at room temperature for 30 min. To this solution, 4.5 ml of 50% NaOH was added dropwise over a period of 10 min. The reaction was maintained at a temperature of $40^\circ \pm 2^\circ C$ for a period of 4h and allowed to cool to room temperature. 20 ml of water was added to the mixture, and then the organic and aqueous layers were separated. The aqueous layer was extracted with three 15 ml portions of $CHCl_3$. These extracts were combined with the initial organic phase. This solution was washed thrice with water, dried, and the solution volume was reduced by evaporation *in vacuo* at $50^\circ C$. The remaining liquid was vacuum distilled. A transparent, light-yellow liquid was collected at $67^\circ \pm 2^\circ C$ and 5 ± 5 mm Hg. An NMR spectrum obtained on the distillate was comparable to that reported by Battioni *et al.* (1). Based on the benzyl selenocyanate, the yield of benzyl trichloromethyl selenoether was 69%.

150 mg of $TPPFcCl$ was obtained by twice extracting a dichloromethane solution of $(TPPFc)_2O$ with 20 ml portions of 2M aqueous HCl, drying the organic layer over anhydrous Na_2SO_4 , and reducing to dryness on a rotary evaporator. The u-oxo iron porphyrin dimer had been prepared previously by the method of Adler *et al.* (10). The porphyrin monomer was dissolved in 45 ml of freshly distilled benzene and placed in the central compartment of a three-compartment Schlenk pot. In the two remaining compartments were placed 80 mg of benzyl trichloromethyl selenoether and 2 ml of a 1.5% Na/Hg amalgam, respectively. The entire system was taken through five freeze-pump-thaw cycles to remove all oxygen and then maintained under an atmosphere of N_2 . At this point, the reducing agent was introduced to the porphyrin solution, and this mixture was stirred for 15 min. Benzyl trichloromethyl selenoether was then added, and the mixture was vigorously stirred for 1h. Consequently, the porphyrin solution changed from a dark brown to a blood red. The mixture was filtered and evaporated to dryness. The remaining purple solid was dissolved in dichloromethane and applied to a column of neutral alumina. With dichloromethane as the eluting solvent, a fast moving red band separated from a slower moving dark brown-green band and a stationary black one. The first band gave a visible spectrum characteristic of $TPPFcSe$ (2). Based on $TPPFcCl$, the yield was calculated at 38%.

The supporting electrolyte, tetrabutylammonium perchlorate (TBAP) was obtained from the Eastman Chemical Company. Prior to use, TBAP was recrystallized three times from absolute ethanol and vacuum dried for 24h. 1,2-dichloroethane was extracted successively from concentrated sulfuric acid and distilled water. The resultant organic phase was dried over anhydrous $MgSO_4$, filtered, fractionally distilled over phosphorous pentoxide in a nitrogen atmosphere, and stored in the dark over 4Å molecular sieves.

Instrumentation.—Cyclic voltammetric experiments were carried out on an EG&G Princeton Applied Research Model 174A Polarographic Analyzer. A conventional three-electrode setup was used with a Pt button working electrode, a Pt wire counterelectrode and a saturated calomel electrode (SCE) as reference. Aqueous contamination of the electrochemical solution was minimized by isolating the reference electrode via a fritte. Voltammograms were recorded on a Houston Omni-graphic 2000 X-Y recorder. To compensate for solution resist-

ance, positive feedback was employed using the accessory 174-50 Polarographic Analyzer Interface.

Differential pulse voltammetry was performed using the instrument mentioned above except that the mainframe polarographic analyzer was modified to allow user selection of the pulse direction independent of the potential sweep direction. For the differential pulse experiments, a potential scan rate of 10 mV/s was employed. The pulse interval was maintained at 0.5s while the pulse amplitude varied between 5 and 100 mV.

Coulometric and chronocoulometric experiments were carried out using an EG&G Princeton Applied Research Model 173 Potentiostat/Galvanostat. Coulometry was executed in a specially designed microvolume sealed cell. Large surface working and counter Pt electrodes were substituted for those used in the voltammetric experiments. Visible spectral measurements were taken using a Tracor Northern Optical Multichannel Analysis System.

All solutions were deoxygenated by passing a stream of solvent-saturated prepurified N_2 into the solution for at least 10 min prior to acquiring voltammetric data. To maintain an O_2 -free environment, the solution was blanketed with N_2 during all experiments. All potentials reported herein were referenced to the SCE and were uncorrected for liquid-junction potentials.

Results and Discussion

A solution of $TPPFcSe$ in 0.10M TBAP/1,2-dichloroethane gave a visible spectrum with a predominant Soret band at 408 nm and a corresponding extinction coefficient of 2.24×10^5 . Alpha and beta bands were located at 551 ($\epsilon = 9 \times 10^3$) and 524 nm ($\epsilon = 17 \times 10^3$), respectively. These values are similar to those reported by Battioni *et al.* (2) for the pentacoordinated $TPPFcSe$ complex in benzene. A comparable visible spectrum was reported for the analogous $TPPFcS$ complex (5); however, it had a less intense Soret band.

In the 1,2-dichloroethane solution, $TPPFcSe$ underwent two consecutive electro-oxidations. Typical cyclic voltammograms depict these events in Fig. 1. Cyclic voltammograms studies from 20 to 500 mV/s were carried out on the first oxidative process. In this range of potential-sweep rates, the ratio of anodic to cathodic peak currents were all near unity. Calculated $E_{1/2}$ values remained constantly at 0.83V. The ratio of the anodic peak current to the square root of the scan rate was found to be

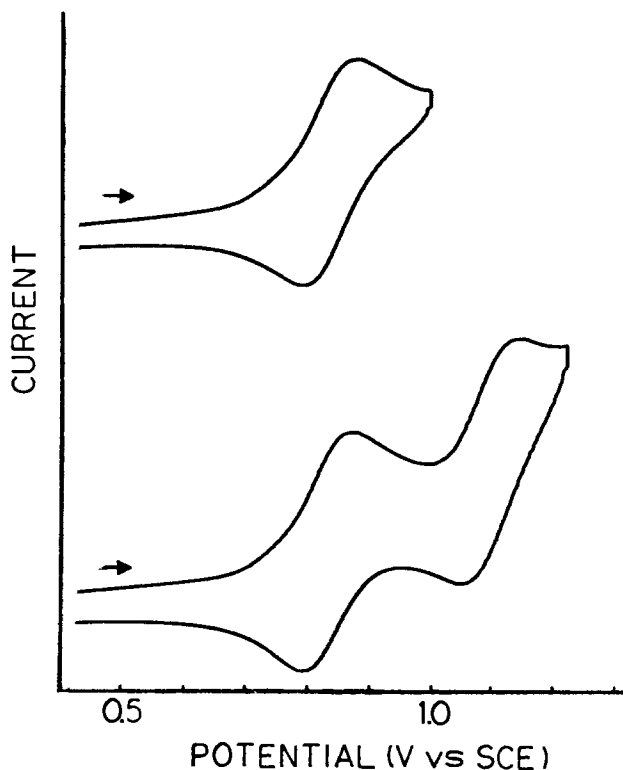


Fig. 1. Cyclic voltammograms obtained for the electro-oxidation of $TPPFcSe$ in 0.1M TBAP/1,2-dichloroethane. The upper trace depicts the first oxidation of $TPPFcSe$, and the lower trace depicts both the first and the second oxidations of $TPPFcSe$. Both cyclic voltammograms were obtained at a potential-scan rate of 200 mV/s.

Table I. Cyclic voltammetry study of TPPFeCSe¹

Scan rate	$\frac{i_{pc}}{i_{pa}}$	$E_{p,a}$	$E_{p,c}$	ΔE	$E_{p/2}$	$E_{1/2}$	$\frac{i_{pa}}{v^{1/2}}$	$\frac{E_{p,a}^-}{E_{p/2}^-}$	$\frac{E_{p/2}^-}{E_{1/2}^-}$	$\frac{E_{p,a}^-}{E_{1/2}^-}$
TPPFcCSe \rightleftharpoons [TPPFcCSe] ⁺ + e										
0.500	0.98	881	784	96	802	832	31.3	79	30	49
0.200	1.01	872	793	79	801	832	32.9	71	31	40
0.100	0.97	867	796	71	800	832	31.6	67	32	35
0.050	0.98	865	799	67	800	832	33.1	65	32	33
0.020	1.00	863	801	62	800	832	33.2	62	31	31
[TPPFcCSe] ⁺ \rightleftharpoons [TPPFcCSe] ²⁺ + e										
0.500	—	1155	1059	96	—	1107	—	—	—	48
0.200	—	1149	1067	82	—	1108	—	—	—	41
0.100	—	1141	1069	72	—	1105	—	—	—	36
0.050	—	1139	1072	67	—	1106	—	—	—	33
0.020	—	1138	1074	64	—	1106	—	—	—	32

¹Complex was dissolved in 0.1M TBAP/1,2-dichloroethane. Potentials are given in mV. Scan rates are in V/s. Currents are in μ A.

Table II. Differential pulse voltammetry study of TPPFeCSe¹

Pulse amplitude	$E_{p(+)}$	$W_{1/2(+)}$ ²	$E_{p(-)}$	$W_{1/2(-)}$ ²	$E_{1/2}$	$\frac{E_{p(-)}}{E_{p(+)}}$	$\frac{i_{p(-)}}{i_{p(+)}}$
TPPFcCSe \rightleftharpoons [TPPFcCSe] ⁺ + e							
5	837	105	842	103	840	5	1.05
10	837	118	848	120	842	11	1.02
25	828	125	854	125	841	26	1.04
50	817	134	868	132	842	51	1.04
100	792	158	892	157	842	100	1.00
[TPPFcCSe] ⁺ \rightleftharpoons [TPPFcCSe] ²⁺ + e							
5	1112	102	1117	102	1114	5	1.06
10	1110	116	1121	119	1116	11	1.01
25	1102	123	1127	123	1114	25	1.02
50	1093	136	1141	130	1117	48	1.02
100	1070	160	1168	155	1119	98	1.00

¹Complex was dissolved in 0.1M TBAP/1,2-dichloroethane. Potential are given in mv. Pulse amplitudes are in mV.

² $W_{1/2}$ = peak width at half height.

independent of scan rate. The separation between anodic and cathodic peak currents decreased from 96 mV at 500 mV/s to 62 mV at 20 mV/s. A separation of 59 mV would be expected for a totally reversible one-electron transfer. Furthermore, at a scan rate of 20 mV/s, $E_{p,a} - E_{p/2,a}$ and $E_{p,a} - E_{1/2}$ values were calculated to be 62 and 31 mV, respectively. Theoretical values for a totally reversible one-electron transfer are 56.5 and 28 mV, respectively. A summary of the cyclic voltammetry studies of TPPFeCSe is given in Table I.

Typical differential pulse voltammograms of TPPFeCSe in solution are shown in Fig. 2. A series of differential pulse voltammograms with pulse amplitudes ranging from 5 to 100 mV were carried out on the first oxidation. At a pulse amplitude of 5 mV, the peak width at half height gave a value of 104 ± 2 mV

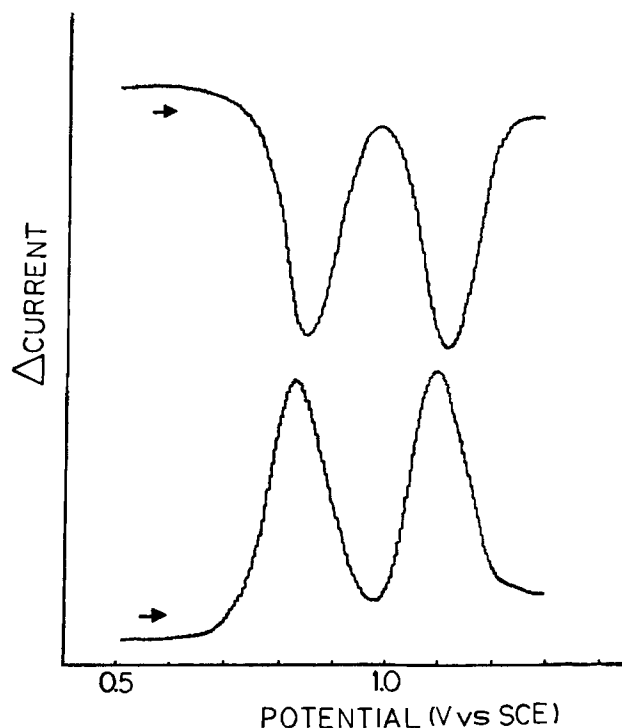


Fig. 2. Differential pulse voltammograms of the electro-oxidations of TPPFeCSe in 0.1M TBAP/1,2-dichloroethane. The upper trace was obtained by superimposing negative potential pulses on a linear-potential ramp. The lower trace was obtained by superimposing positive potential pulses on a linear-potential ramp. The pulse amplitude was set of 25 mV.

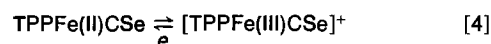
and increased to 157 ± 2 mV at a pulse amplitude of 100 mV. For a reversible one-electron transfer the peak width at half height is expected to approach 90.4 mV as the pulse amplitude approaches zero. Differential pulse voltammograms were obtained by imposing first positive and then negative potential pulses on linear-potential ramp. This permitted analysis of data with the Birke's method (11). Separation between potential peaks [$E_{p(-)} - E_{p(+)}$] were within 1 mV of the pulse amplitude. Current ratios were about unity. The $E_{1/2}$ value of 0.84V was independent of the pulse amplitude but slightly more positive than the value obtained via cyclic voltammetry. A summary of the differential pulse voltammetric data of TPPFeCSe is given in Table II.

Cyclic and differential pulse voltammograms were also obtained in the characterization of the second charge-transfer event. Cyclic voltammetry yields a $E_{1/2}$ value of 1.11V regardless of scan rate. At a scan rate of 20 mV/s, the separation between anodic and cathodic peak was measured at 64 mV while $E_{p,a} - E_{1/2}$ gave a value of 32 mV. Both these values increased with increasing scan rate. Via inspection of the differential pulse voltammograms, $E_{1/2}$ was calculated at 1.12V with no apparent dependency on pulse amplitudes. Peak current values for this second electro-oxidation resembled that of the first. The peak width at half height was measured at 102 ± 2 mV. In considering Birke's criteria, the ratio of the current peaks resulting from the positive and negative application of potential pulses on a linear ramp were again essentially unity. The potential separation between these current peaks were all within 2 mV of the applied potential pulses.

Taken collectively, the voltammetric results indicate that the electro-oxidation of TPPFeCSe in 1,2-dichloroethane is best described as taking place in two discrete one-electron quasireversible charge transfers. Exhaustive electrolysis at 0.97V resulted in a charge transfer of 1.02 electron per equivalent. Subsequent electrolysis at 1.35V resulted in a charge transfer of 1.08 electrons per equivalent. Reversal of the potential to the initial potential of zero charge (0.12V) gave a charge transfer of 2.21 electrons per equivalent.

Chronocoulometric experiments were employed to deduce the diffusion coefficient of TPPFeCSe in solution. A value of $9.7 \pm 0.3 \times 10^{-6}$ cm²/s was obtained. From this value and cyclic voltammetry results, the heterogeneous rate of electron transfer was computed (12) as $4.6 \pm 0.4 \times 10^{-2}$ cm/s. This value resides just within the boundary zone suggested by Matsuda and Ayabe (13) for a quasireversible electron transfer.

By analogy to TPPFeCS (5), the following reaction pathway is proposed for the electro-oxidation of TPPFeCSe.





The first oxidation process involves a metal-centered reaction. The abstraction of the first electron occurs from a metal orbital. The second oxidation process involves the production of a porphyrin cation radical. The second electron is removed from a porphyrin π orbital.

Future research will consider the electroreduction of TPPFeCSe and investigate the redox mechanism of TPPFeCSe in the presence of the nucleophiles.

Acknowledgments

Acknowledgment is made to The Electrochemical Society for an Energy Research Summer Fellowship sponsored by the Department of Energy. Acknowledgment is also made to the donors of the Petroleum Research Fund, administered by the ACS, and to the Cottrell Grants Program of the Research Corporation for the support of this research. Special thanks are made to Dr. L. A. Bottomley for his advice and support on this project.

REFERENCES

1. C. R. Wolf, D. Mansuy, N. Nastainczyk, G. Deutschmann, and V. Ullrich, *Mol. Pharmacol.*, **13**, 698 (1977).
2. J-P. Battioni, D. Mansuy, and J-C. Chottard, *Inorg. Chem.*, **19**, 791 (1980).
3. D. Lexa, J-M. Saveant, J-P. Battioni, M. Lange, and D. Mansuy, *Angew. Chem. Int. Ed. Engl.*, **20**, 578 (1981).
4. J-P. Battioni, D. Lexa, D. Mansuy, and J-M. Saveant, *J. Am. Chem. Soc.*, **105**, 207 (1983).
5. L. A. Bottomley, M. R. Deakin, and J-N. Gorce, *Inorg. Chem.*, Accepted for publication
6. G. M. Brown, F. R. Hopf, T. J. Meyer, and D. G. Whitten, *J. Am. Chem. Soc.*, **97**, 5385 (1975).
7. R. C. Gurira and J. Jordan, *Anal. Chem.*, **53**, 864 (1981).
8. C. L. Jackson, *Annalen der Chemie*, **179**, 1 (1875).
9. M. Makosza and M. Fedorynski, *Synthesis*, 274 (1974).
10. A. D. Adler, F. R. Longo, F. Kampas, and K. Kim, *J. Inorg. Nucl. Chem.*, **32**, 2443, (1970).
11. R. L. Birke, M-H. Kim, and M. Strassfeld, *Anal. Chem.*, **53**, 852 (1981).
12. R. S. Nicholson, *ibid.*, **37**, 1351 (1965).
13. H. Matsuda and Y. Ayabe, *Z. Electrochem.*, **59**, 494 (1955).

D. B. Graves was born in Daytona Beach, Florida. He received his B. S. degree from the University of Arizona, Tucson, Arizona, in 1978. He also received his M. S. degree from the University of Arizona. He is working on his Ph. D. degree at the University of Minnesota, Minneapolis, Minnesota.

Mr. Graves has worked as a computer process control engineer for Standard Oil of California.

Mr. Graves' report is given below.

Plasma Enhanced Chemical Vapor Deposition

My work is aimed towards a more quantitative treatment of plasma-enhanced chemical vapor deposition (PCVD) primarily as used in microelectronics manufacturing processes. The specific objective of the research is to predict the behavior of PCVD reactors given operating conditions or changes in operating conditions. This will be possible only if the roles of physical transport and chemical kinetics in the overall deposition process, including in particular the role of the highly nonequilibrium gas discharge plasma, are understood.

The strategy for achieving this goal is to combine measurements from a carefully designed experimental reactor with results from a mathematical model of the reactor. The experiment and model are complementary tools: the model results, validated by comparison to experimental measurements, can be used to extend and generalize experimental results.

The reactor is designed with parallel-plate electrodes (RF at 13.56 MHz). The lower electrode is powered. It is porous, so that the reactant gas may pass through and impinge on the heated, grounded upper electrode upon which film deposition takes place. The flow is always laminar, since PCVD reactors are operated at pressures around 1 torr, which keeps the Reynolds number, typically, at less than 10. The stagnation-point flow configuration is one of the easiest flows to model, since a transformation of the equations of motion results in a single nonlinear ordinary-differential equation describing axial and radial velocities. This configuration will give a radially uniform rate of deposition over a significant portion of the deposition

plate. Besides the equation of motion, additional model equations include chemical species balances, an energy balance, and equations describing the behavior of the discharge. The fluid mechanics, heat, and mass transfer equations have been solved for this configuration.

Another key feature of the experimental reactor is the use of the quartz crystal microbalance to measure, *in situ* and in real time, the rate of film deposition. This deposition-rate measurement is based on the change in resonant frequency of a thin slice of piezoelectric quartz crystal as a thin, solid, adherent film is deposited on the surface of the crystal. This technique is well recognized and several commercial devices are available for room temperature processes. We are extending the technique to higher temperatures (200°-300°C) by using dual crystals, one exposed to film deposition, the other shielded, both experiencing the same temperature. The temperature problem arises because crystal resonant frequency is a very sensitive function of temperature as well as film thickness.

The stagnation-point flow parallel-electrode reactor is simple and relatively easy to model. The well-defined flow field and *in situ* film deposition measurement could make this configuration as popular in the study of CVD as the rotating disk electrode is in the study of liquid phase electrochemical systems. Naturally, any CVD system of interest can be studied using this configuration: we concentrate on deposition of transition metals and silicides, because these films are currently of considerable practical interest.

Leslie C. Hardy received his B. A. degree from Oberlin College, Oberlin, Ohio, in 1979. He is working for his Ph. D. at Northwestern University, Evanston, Illinois.

Mr. Hardy has studied at the University of Akron. He has worked as an Associate Research Chemist for the A. E. Staley Manufacturing Company.

Solid Polymer Electrolytes

Solid electrolytes are currently the subject of intensive research, and solid-state rechargeable batteries are one of their principal potential uses. Most solid electrolytes are ceramic or glassy inorganic materials in which one charged species is mobile and the countercharge is held in a fixed lattice position. Thus the electrical properties displayed by these conductors may be attributed to a known charge carrier. Unlike solvent-swollen ion exchange resins, solid-polymer electrolytes are solvent free. In poly(ethylene oxide) complexed with sodium iodide, for example, the salt is dissociated so that either ion may be mobile. Knowledge of relative mobilities of the oppositely charged ions is important for fundamental studies as well as various applications. To date, determination of the transport numbers for ions in solid-polymer electrolytes has been difficult and experimentally inconsistent from one laboratory to another. Here we report the study of chloride conduction in anhydrous films of poly(diallyldimethylammonium chloride) plasticized with poly(ethylene glycol) (average MW = 300). In this polymer electrolyte, the positive countercharge is anchored in the polymer backbone where its mobility is limited to backbone fluctuations and not diffusion of the polymer chain, since the time scale of experimental measurements is short (alternating current measurements from 10 Hz - 500 kHz).

Variable temperature conductivity of the chloride ion in the amorphous polymer matrix yields curved plots of $\ln(\sigma T)$ vs. $1/T$. This behavior, which is similar to that of diffusion of small molecules through polymers, has been seen previously for other amorphous polymer electrolytes. Transport of ions in these materials may be described by equations similar to the WLF equation rather than the Arrhenius law.

An important reason for the use of poly(diallyldimethylammonium chloride) is that the positive charge on the nitrogen is surrounded by four aliphatic groups, thus separating opposite charges somewhat to allow for possible mobility. Tight ion pairing has been shown to significantly reduce the mobility of charge carriers in solid-polymer electrolytes.

Use of plasticizers is known to increase polymer chain flexibility and free volume, and decrease the glass-transition temperature. These changes are also known to increase ionic conductivity in solid-polymer electrolytes. The conductivity of brittle pure polymer at 25°C was not measurable on our instruments, while the flexible plasticized polymer has conductivities on the order of 10^{-8} ($\Omega^{-1} \text{ cm}^{-1}$) at 25°C to 10^{-5} at 100°C. Prelimi-

nary results indicate that increasing the plasticizer level from 0.32 to 0.65 weight fraction (mole ratios of chloride to hydroxyl of 2 and 0.67, respectively) increases conductivity by about 100 times at room temperature.

AC complex impedance data collected over the frequency range of 10 Hz – 500 kHz with platinum ion blocking electrodes were used to calculate bulk conductivity of samples. Complex impedance plots are typical of those seen for ionic conductors with blocking electrodes. Although calomel electrodes are normally used with liquid electrolytes, their use with the solid chloride conductor was found to be successful. Complex impedance data collected using the ion-reversible electrodes indicate that chloride ions are mobile and may be transferred across the electrode-electrolyte interface. The spur due to double-layer capacitance seen for ion blocking electrodes is converted to an arc for charge-transfer resistance, as predicted by impedance/frequency response theory, and as has been seen for other solid-polymer electrolyte systems.

In addition to the conductivity data discussed above, these polymer electrolytes have been characterized by IR spectroscopy, differential scanning calorimetry, hot-staged polarized microscopy, and x-ray diffraction.

Further work will include dc polarization studies with ion blocking and ion-reversible electrodes. Conductivity of different anions of varying size and geometry along with different quaternary ammonium polymers may also yield useful information on the nature of charge transport in solid-polymer electrolytes. In addition, extending variable frequency measurements down to 10^{-1} Hz should facilitate interpretation of complex impedance plots since the relative mobilities of the charged species are known. This situation is different from other cases, where techniques have been used in which either charged species may be mobile.

James A. Osborn was born in Salem, New Jersey. He received his B. A. degree in chemistry from Rutgers College, New Brunswick, New Jersey, in 1981. He is working on his Ph. D. degree at Rutgers University Graduate School in Piscataway, New Jersey.

Mr. Osborn's current interest in immobilized enzyme chemically modified electrodes.

Mr. Osborn's report is given below.

Mr. Osborn's research has centered around the use of chemically modified carbonaceous supports for the immobilization of enzymes and coenzymes, their use as analytical sensors, and the characterization of the modified surfaces.

The area of immobilized enzymes in analytical chemistry has received widespread attention over the past ten years. The immobilization of enzymes onto various electrode materials has been motivated by several factors, including the provision of convenient and straightforward measurement of species of biological and clinical interest. As the use of immobilized enzymes in analysis continues to be developed, research dealing with effects of immobilization on biological molecules has also kept pace.

His interest in immobilized enzymes was motivated through his work on a project involving the use of activated carbon as a support for the immobilization of enzymes. Activated carbon was ground and sifted to a uniform size with subsequent modification involving the well-known linking agent, cyanuric chloride. Steps were also taken to increase the surface hydroxyl functionality concentration with which the cyanuric chloride presumably reacts specifically. The cyanuric chloride activated surface was then used to react with the enzyme chymotrypsino-

gen through its lysine residues. It was shown that samples prepared this way retained a higher specific activity than on samples that were prepared by physical adsorption of the enzyme. Activated carbon was chosen due to its high surface area and electrical conductivity among other things.

Characterization of the cyanuric chloride modified activated carbon was accomplished by the potentiometric titration of the hydrolysis product: chloride ion. This helped to evaluate the effects of various surface pretreatments on the eventual loading of cyanuric chloride. These results were also correlated with the results of thermal analysis of the samples.

The enzymes, alcohol dehydrogenase and glycerol dehydrogenase, were both investigated by attachment to spectroscopic grade graphite rods through a procedure similar to the above in an attempt to sense for ethanol and glycerol amperometrically. The inability to oxidize the NADH reaction product cleanly and reproducibly led to further investigation of the electrochemistry of both free and immobilized NADH.

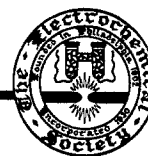
The electrocatalytic and electrochemical properties of thin films of the coenzymes FMN and FAD irreversibly adsorbed on highly ordered pyrolytic graphite were examined in buffer solutions which contained ferricyanide, NADH, and dissolved oxygen. The latter gave the most pronounced effect on voltammograms of the thin films with the other two giving irreproducible or no effects indicating an interaction.

Currently, his work centers around attaching the enzymes chymotrypsin and trypsin to spectroscopic grade graphite electrodes and attempting to observe a change in activity with change in surface potential. Since it has been shown that an immobilized enzyme is greatly affected by its microenvironment, the change in potential might then conceivably have an effect.

Attempts to observe the above effects were at first hampered by preparations of low overall activity, making observation of small changes difficult. In an attempt to increase the binding sites for covalent attachment of the enzymes, a poly(acrylic acid) film was first adsorbed from aqueous solution by the electrode. The next step involved the activation of the carboxylic acid groups with a water soluble carbodiimide. The electrodes were then reacted with the appropriate enzyme. Such preparations have demonstrated both increased activity and stability. The properties of the preparations have been investigated with regard to the effect on activity of pH, ionic strength, metal ions in solution, temperature dependence, and certain other comparisons between the free and immobilized preparation, including the effects of several inhibitors.

The activity of the preparations was determined by a spectroscopic technique. A closed flowing system which allowed for continuous mixing and monitoring of the absorbance of the substrate solution was used in conjunction with a three electrode system in order to observe the effects of surface potential change on the activity. The reference electrode was a miniature SCE, the auxiliary electrode a coiled Pt wire, and the working electrode made up of the enzyme immobilized graphite rod. The coiled Pt wire was placed concentrically around the working electrode in a system designed to minimize the volume of substrate solution. At this point, applied potentials have been observed to have a pronounced effect on the apparent activity of the rods.

The need for a uniform surface for subsequent modification was also motivated by a project involved in observing the potentiometric response of peptidase electrodes to various substrates and inhibitors. Thus far, chymotrypsin and trypsin have been immobilized via the previous procedure. These electrodes have responded to substrates and an inhibitor thus far. The dependence of response on concentration has also been observed. The effects of inhibitors on further response to substrates is also being investigated.



EST

Ionic Conductivity and Phase Transition of the Spinel System $\text{Li}_{2-2x}\text{M}_{1+x}\text{Cl}_4$ ($\text{M} = \text{Mg, Mn, Cd}$)

Ryoji Kanno, Yasuo Takeda, Kazuaki Takada,* and Osamu Yamamoto*

Department of Chemistry, Faculty of Engineering, Mie University, Tsu 514, Japan

ABSTRACT

The spinel systems $\text{Li}_{2-2x}\text{M}_{1+x}\text{Cl}_4$ ($\text{M} = \text{Mg, Mn, Cd}$) with $0 \leq x \leq 0.33$ has been studied by means of impedance measurement, differential thermal analysis, and x-ray diffraction analysis. The ionic conductivity increases and the activation energy for conduction decreases with increasing x within the solid solution range, $0 \leq x \leq 0.20$ in $\text{Li}_{2-2x}\text{Mg}_{1+x}\text{Cl}_4$, $0 \leq x \leq 0.24$ in $\text{Li}_{2-2x}\text{Mn}_{1+x}\text{Cl}_4$, and $0 \leq x \leq 0.05$ in $\text{Li}_{2-2x}\text{Cd}_{1+x}\text{Cl}_4$. The highest conductivity is found to be $1.5 \times 10^{-5} \text{Scm}^{-1}$ in $\text{Li}_{1.52}\text{Mn}_{1.24}\text{Cl}_4$ at room temperature and 0.35Scm^{-1} in $\text{Li}_{1.9}\text{Cd}_{1.05}\text{Cl}_4$ at 400°C . The three chloride spinels exhibit a first-order phase transition and a diffuse transition. The diffuse transition temperatures decrease with increasing x .

Solid lithium ion conductors having high ionic conductivity are of particular interest for the Li-based high energy density batteries. Many systems have been studied to search high lithium ion conductivity solids (1-10). Recently, a new class of lithium ion conductors, Li_2MCl_4 ($\text{M} = \text{Mg, Mn, Fe, Cd}$), has been reported by Kanno *et al.* (11) and Lutz *et al.* (12), which has a high ionic conductivity at elevated temperatures. The compound Li_2MCl_4 has been determined by the neutron diffraction method to have the inverse spinel structure (13); half of the lithium ions are tetrahedrally surrounded by chloride ions, and the other half of them, together with the M ions, are distributed statistically over the octahedral sites. Lutz *et al.* (14) found the reversible phase transition from the spinel structure to a cubic defect structure at a high temperature with the help of differential thermal analysis and high temperature x-ray diffraction analysis. Of these compounds, Li_2CdCl_4 has the highest conductivity of 0.35Scm^{-1} at 400°C , the value of which is comparable or more than that of the high lithium ion conductors reported previously.

A solid solution $\text{Li}_{2-2x}\text{M}_{1+x}\text{Cl}_4$ may be expected to have higher ionic conductivity than the stoichiometric compound because the substitution of M^{2+} ion for Li^+ ion could produce the lithium ion vacancy which leads to high Li^+ ion conductivity. The solid solution $\text{Li}_{2-2x}\text{Cd}_{1+x}\text{Cl}_4$ has been examined briefly by Kanno *et al.* (11). $\text{Li}_{1.9}\text{Cd}_{1.05}\text{Cl}_4$ was found to have higher conductivity than Li_2CdCl_4 .

In this study, the electrical properties of the solid solution systems $\text{Li}_{2-2x}\text{M}_{1+x}\text{Cl}_4$ ($\text{M} = \text{Mg, Mn, Cd}$) are examined. Further, the phase transition in these systems is discussed on the basis of the results of electrical conductivity measurement, differential thermal analysis, and high temperature x-ray diffraction technique.

Experimental

Reagent grade LiCl , CdCl_2 , and MnCl_2 dried under vacuum at elevated temperatures were used as starting materials. Dehydrated MgCl_2 was prepared by heating $\text{MgCl}_2 \cdot \text{NH}_4\text{Cl} \cdot 6\text{H}_2\text{O}$ under vacuum at 400°C .

* Electrochemical Society Active Member.

Key words: solid electrolyte, lithium ion conductor, lithium chloride, spinel structure.

The melting points of these chlorides were in good agreement with the reported values. The appropriate quantities of LiCl and MCl_2 ($\text{M} = \text{Mg, Mn, Cd}$) were ground together and were pressed into pellets under 90 MPa in an argon-filled glove box. Then the pellets were heated in an evacuated Pyrex tube for one week at a temperature just below the corresponding melting points. X-ray powder photographs were taken by a Debye-Scherrer camera using nickel-filtered $\text{CuK}\alpha$ radiation. The powder samples were encapsulated in glass capillaries. Silicon powder was used as an internal standard. Differential thermal analysis (DTA) was carried out for the sample sealed in a Vycor tube under vacuum; $\alpha\text{-Al}_2\text{O}_3$ powder sealed in a Vycor tube of the same size was used as a standard. The electrical conductivities were measured in the temperature range between room temperature and 500°C in a dry argon gas flow. A sample of about 0.7g was pressed under a pressure of 60 MPa into a pellet of 10 mm diam. The densities of the pellets were about 80% of the theoretical densities calculated from the lattice parameters. Ionically blocking electrodes were obtained by evaporating gold on both sides of the pellets. The conductivity was measured at frequencies between 5 Hz and 500 kHz using an HP 4800A vector impedance meter. The resistances were derived by interpretation of complex impedance plane diagrams of the data. The EMF of the cell, $\text{LiTiS}_2/\text{Li}_2\text{MCl}_4/\text{TiS}_2$, was measured to determine the ionic transport number. Commercial grade titanium disulfide was used without further purification. The lithium intercalation compound LiTiS_2 was prepared by the reaction of n-butyl lithium with TiS_2 (15).

Results and Discussion

X-ray measurement.—X-ray powder diffraction patterns of the samples obtained at room temperature showed the cubic spinel structure reported previously (11-14). The observed lattice parameter of the stoichiometric compound Li_2CdCl_4 at room temperature (10.635Å) is in good agreement with the value reported by Lutz *et al.* (10.635Å) (14) and by van Loon and de Jong (10.637Å) (13), while those of Li_2MgCl_4 (10.426Å) and Li_2MnCl_4 (10.491Å) are slightly different from the reported values. The lattice parameters for the systems $\text{Li}_{2-2x}\text{Mg}_{1+x}\text{Cl}_4$, $\text{Li}_{2-2x}\text{Mn}_{1+x}\text{Cl}_4$, and

$\text{Li}_{2-2x}\text{Cd}_{1+x}\text{Cl}_4$ are shown in Fig. 1 as a function of x . The lattice parameters decrease linearly with increasing x for $0 \leq x \leq 0.20$ in $\text{Li}_{2-2x}\text{Mg}_{1+x}\text{Cl}_4$, for $0 \leq x \leq 0.24$ in $\text{Li}_{2-2x}\text{Mn}_{1+x}\text{Cl}_4$ and for $0 \leq x \leq 0.05$ in $\text{Li}_{2-2x}\text{Cd}_{1+x}\text{Cl}_4$. The solid solution range in $\text{Li}_{2-2x}\text{Cd}_{1+x}\text{Cl}_4$ is rather small compared with the other systems because the ionic radius of cadmium is rather larger than that of lithium. The x-ray powder diffraction patterns of the samples with $x < 0$ showed the lines due to LiCl and those of the samples with a higher x value than the solubility limit showed the lines due to MCl_2 . The decrease in the lattice parameters by substitution of Li^+ for M^{2+} ion in $\text{Li}_{2-2x}\text{M}_{1+x}\text{Cl}_4$ could be explained by assuming that one lithium ion vacancy is produced by each divalent cation substituted into lithium ion sites to keep the charge neutral. Hanebali *et al.* (16) reported that $\text{Li}_{2-2x}\text{V}_{1+x}\text{Cl}_4$ with spinel structure showed the decrease in the lattice parameter with increasing x . They also suggested the formation of lithium ion vacancies by substitution of lithium ions by divalent metal ions. $\text{Li}_{1.60}\text{Mg}_{1.20}\text{Cl}_4$, $\text{Li}_{1.52}\text{Mn}_{1.24}\text{Cl}_4$, and $\text{Li}_{1.90}\text{Cd}_{1.05}\text{Cl}_4$ should have 10%, 12.5%, and 2.5% lithium ion vacancies, respectively. The radius of magnesium ion for tetrahedral coordination (CN4), 0.58 Å, and for octahedral coordination (CN6), 0.67 Å (17), is very close to lithium ion for the corresponding coordination, 0.59 and 0.67 Å. In view of the ionic radius, excess magnesium ion in $\text{Li}_{2-2x}\text{Mg}_{1+x}\text{Cl}_4$ could occupy both the octahedral and tetrahedral sites. On the other hand, the radii of manganese ion (0.83 Å for CN6) and cadmium ion (0.95 Å for CN6) are larger than that of lithium ion. Therefore, it could be considered that the excess divalent ions occupy only the octahedral sites, which are more open compared to the tetrahedral sites. Hanebali *et al.* (16) suggested that vacancies were pro-

duced on the octahedral sites in $\text{Li}_{2-2x}\text{V}_{1+x}\text{Cl}_4$ from analogy to oxide spinel such as $\text{A}^{2+}\text{M}^{2+}\text{O}_3$ (A = Mn, Co, Zn and M = Ti, Mo). However, a more detailed structure determination will be necessary to discuss the sites of vacancy.

Magnetic susceptibilities χ were measured to determine the spin state of Mn^{2+} ion in Li_2MnCl_4 with the help of a Faraday balance from 78 K to room temperature. The sample was contained in evacuated silica tube. The susceptibilities are well described by the Curie-Weiss law. The magnetic moment 5.42 BM obtained from the paramagnetic susceptibility is close to the calculated value, 5.92 BM, which corresponds to the value of high spin Mn^{2+} ions in the octahedral environment.

Electrical conductivity.—The electrical conductivities were measured in the temperature range between room temperature and 500°C. The conductivities of the samples with ionically blocking electrodes showed a frequency dependence over the temperatures examined. In order to estimate the bulk resistance, the data were plotted in the complex impedance planes, X (imaginary component) vs. R (real component). The typical results of Li_2MnCl_4 at 27° and 304°C are shown in Fig. 2. The high frequency semicircle in the impedance diagram at room temperature is due to a parallel combination of the bulk electrolyte resistance with the bulk capacity. The bulk resistance was obtained by the extrapolated real-axis intercepts of the semicircle at a lower frequency. The impedance diagram at 304°C appears to consist of a straight line, and no semicircle due to bulk capacity is observed. The electrolyte resistances are obtained by extrapolation to the real axis. The temperature dependence and the composition de-

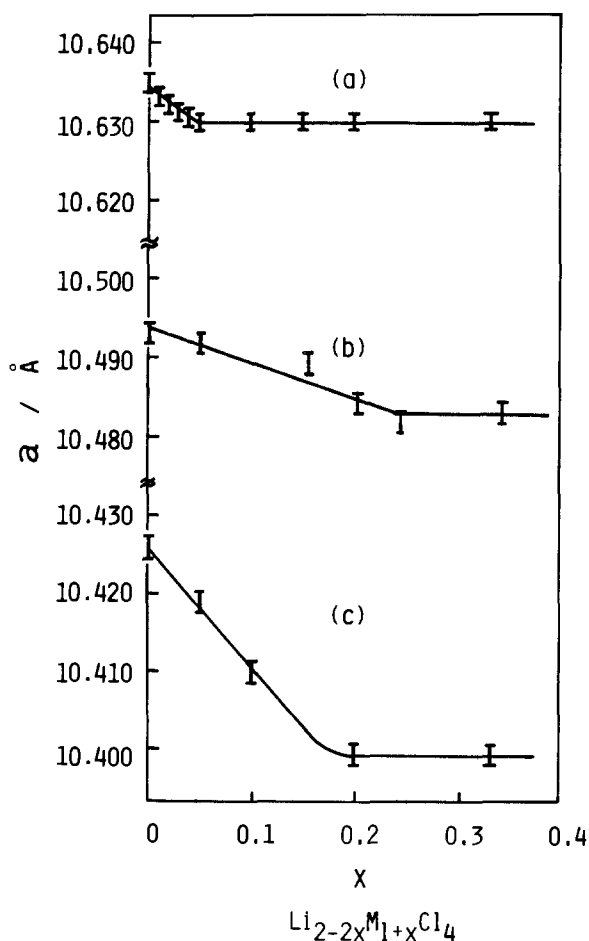


Fig. 1. The lattice parameters of $\text{Li}_{2-2x}\text{Cd}_{1+x}\text{Cl}_4$ (a), $\text{Li}_{2-2x}\text{Mn}_{1+x}\text{Cl}_4$ (b), and $\text{Li}_{2-2x}\text{Mg}_{1+x}\text{Cl}_4$ (c) at room temperature.

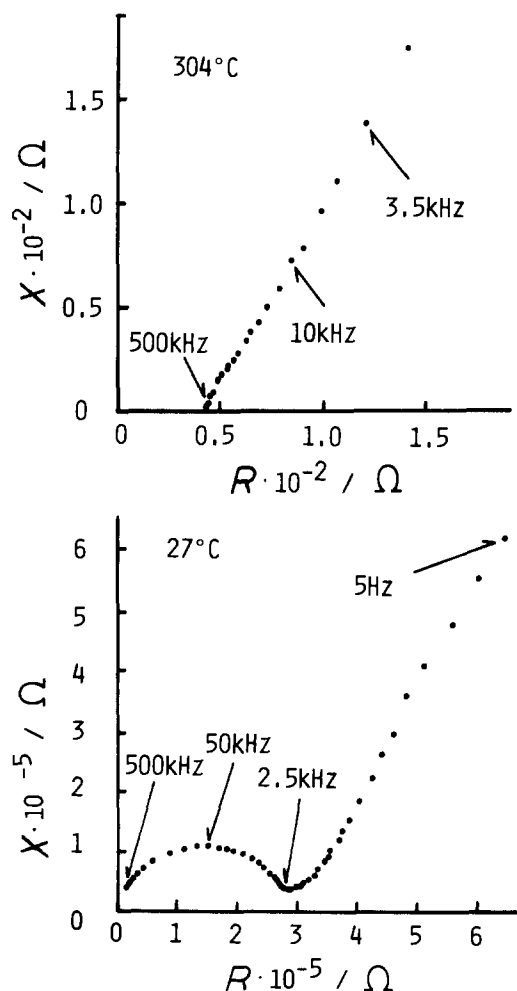


Fig. 2. Complex impedance plane plots for Li_2MnCl_4

pendence of the conductivity, σ , of $\text{Li}_{2-2x}\text{M}_{1+x}\text{Cl}_4$ ($\text{M} = \text{Mn, Mg, Cd}$) are shown in Fig. 3, 4, and 5, where dotted lines indicate two-phase structures as described later. The Arrhenius plots showed a change in slope at a high temperature. The temperatures of the conductivity knee decrease with increasing x in $\text{Li}_{2-2x}\text{M}_{1+x}\text{Cl}_4$. The conductivity knee will be discussed in the later section. At room temperature, the conductivity vs. composition curves show a maximum conductivity of $1.5 \times 10^{-5} \text{ Scm}^{-1}$ at $x = 0.24$ for $\text{Li}_{2-2x}\text{Mn}_{1+x}\text{Cl}_4$, $3.4 \times 10^{-5} \text{ Scm}^{-1}$ at $x = 0.20$ for $\text{Li}_{2-2x}\text{Mg}_{1+x}\text{Cl}_4$, and $2.9 \times 10^{-6} \text{ Scm}^{-1}$ at $x = 0.05$ for $\text{Li}_{2-2x}\text{Cd}_{1+x}\text{Cl}_4$. The compositions that exhibit the maximum conductivity correspond to the phase boundary of the solid solution $\text{Li}_{2-2x}\text{M}_{1+x}\text{Cl}_4$. At a higher temperature, such as 400°C , no significant composition dependence of the conductivity is found. The composition dependence of the activation energy for conduction calculated from the logarithm of the conductivity vs. reciprocal of the absolute temperature curve is observed in $\text{Li}_{2-2x}\text{M}_{1+x}\text{Cl}_4$ both above and below the conductivity knee. At lower temperatures, the samples that show the maximum conductivity have the lowest activation energy: 48 kJmol^{-1} for $\text{Li}_{1.52}\text{Mn}_{1.24}\text{Cl}_4$ and $\text{Li}_{1.6}\text{Mg}_{1.2}\text{Cl}_4$, and 54 kJmol^{-1} for $\text{Li}_{1.9}\text{Cd}_{1.05}\text{Cl}_4$. The maximum conductivity and lowest activation energy of the samples of the phase boundary in the solid solution $\text{Li}_{2-2x}\text{M}_{1+x}\text{Cl}_4$, which may have the highest mol fraction of lithium ion vacancy, suggest that the conduction of the lithium ion seems to be affected by the number of lithium ion vacancies produced by substitution of Li^+ ion for M^{2+} ion. Li_2MCl_4 transforms to a cubic defect structure at high temperatures, which has a structural lithium ion vacancy. No composition dependence of the conductivity at high temperatures may indicate that trans-

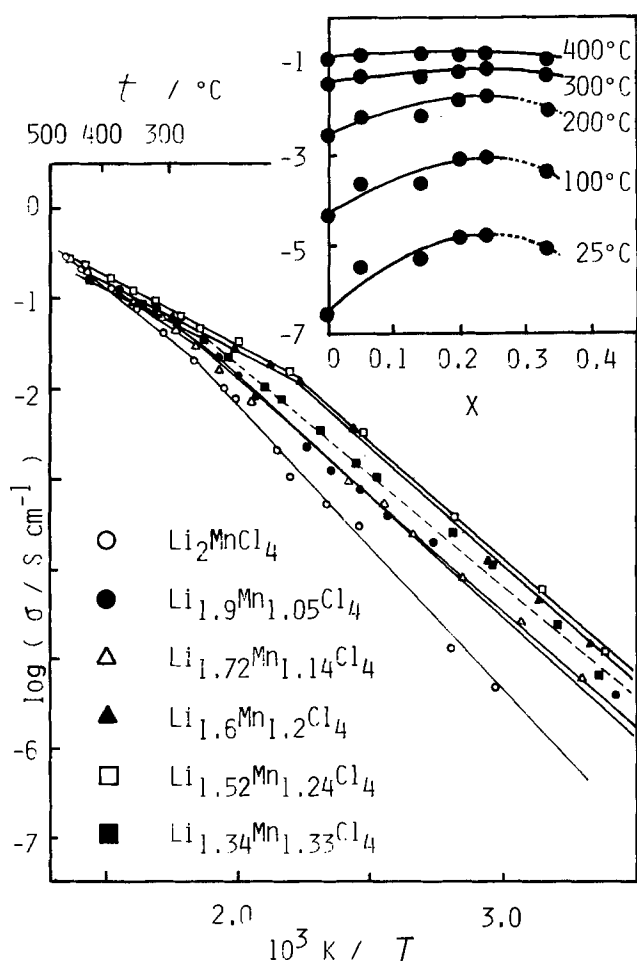


Fig. 3. Temperature dependence and composition dependence of the conductivity, σ , of $\text{Li}_{2-2x}\text{Mn}_{1+x}\text{Cl}_4$.

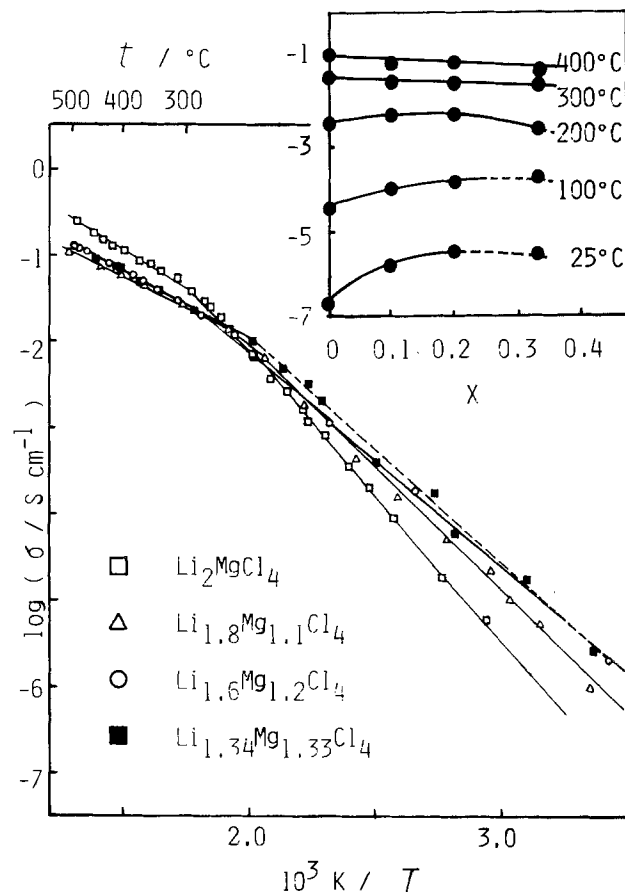


Fig. 4. Temperature dependence and composition dependence of the conductivity, σ , of $\text{Li}_{2-2x}\text{Mg}_{1+x}\text{Cl}_4$.

port via lithium ion vacancies is not the proper way to understand the phenomenon.

The EMF of the cell $\text{LiTiS}_2/\text{Li}_2\text{MnCl}_4/\text{TiS}_2$ was measured to determine the ionic transport number, where LiTiS_2 was prepared chemically by using *n*-butyllithium, and the EMF of the cell Li/LiClO_4 in propylen carbonate/ LiTiS_2 , 1.8V, agreed very closely with that reported previously (18). The open-circuit voltage of 0.58V at room temperature was in good agreement with 0.59V calculated from free enthalpy change of the reaction $\text{TiS}_2 + \text{Li} = \text{LiTiS}_2$ (18). This result suggests that the ionic transport number is nearly unity at room temperature.

Decomposition potential.—The decomposition potential was measured with the help of the cell $\text{Pt}/\text{Li}_2\text{MCl}_4/\text{Pt}$ under vacuum at 400°C for Li_2MnCl_4 and Li_2CdCl_4 , and at 480°C for Li_2MgCl_4 . A dc current was applied across the cell. The current vs. applied voltage curves are shown in Fig. 6. The decomposition potentials were estimated to be 1.2, 1.1, and 1.3V for Li_2MgCl_4 , Li_2MnCl_4 , and Li_2CdCl_4 , respectively. The decomposition potentials are not well-defined, since the chemical potentials at neither electrode were defined. They do, however, give an indication of the stability of these phases.

Phase transition of the systems $\text{Li}_{2-2x}\text{M}_{1+x}\text{Cl}_4$.—Figures 7, 8, and 9 show the temperatures of the conductivity knees and the phase transition temperatures obtained by DTA together with the results of high temperature x-ray diffraction photographs of $\text{Li}_{2-2x}\text{Mn}_{1+x}\text{Cl}_4$, $\text{Li}_{2-2x}\text{Mg}_{1+x}\text{Cl}_4$, and $\text{Li}_{2-2x}\text{Cd}_{1+x}\text{Cl}_4$, respectively.

In $\text{Li}_{2-2x}\text{Mn}_{1+x}\text{Cl}_4$, solid-state transition temperatures, T_1 , obtained by DTA increase with x from 417°C at the stoichiometric composition to 537°C at $x = 0.33$. The temperatures of the conductivity knees, T_{cond} , obtained by the electrical conductivity measurement, decrease with x . No peak in DTA curves corresponding

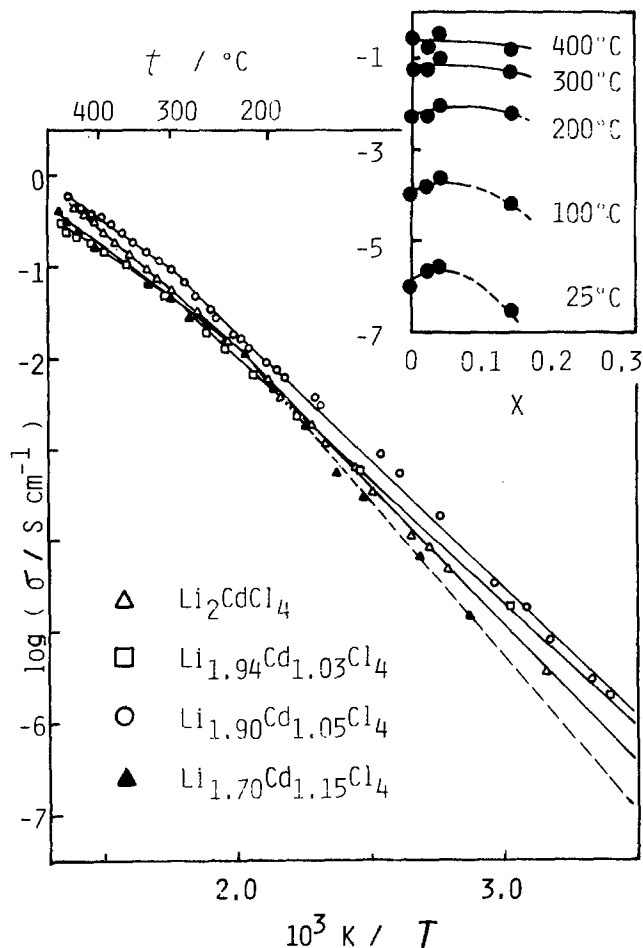


Fig. 5. Temperature dependence and composition dependence of the conductivity, σ , of $\text{Li}_{2-2x}\text{Mg}_{1+x}\text{Cl}_4$.

to the conductivity knees was observed. The high temperature x-ray photographs of the samples with $x = 0.24$ and 0.33 above T_1 showed the patterns with NaCl type cubic structure, which was reported by Lutz *et al.* (14) in the stoichiometric compound. Therefore, the transition temperatures in the solid solution system obtained by DTA correspond to a transition from the spinel structure to NaCl type cubic phase. No significant difference between x-ray photographs was found below and above T_{cond} .

In $\text{Li}_{2-2x}\text{Mg}_{1+x}\text{Cl}_4$, the solid-state transition temperatures obtained by DTA also increase with x from 518°C at $x = 0.0$ to 541°C at $x = 0.1$. For the samples with $x > 0.1$, no solid-state transition was observed in

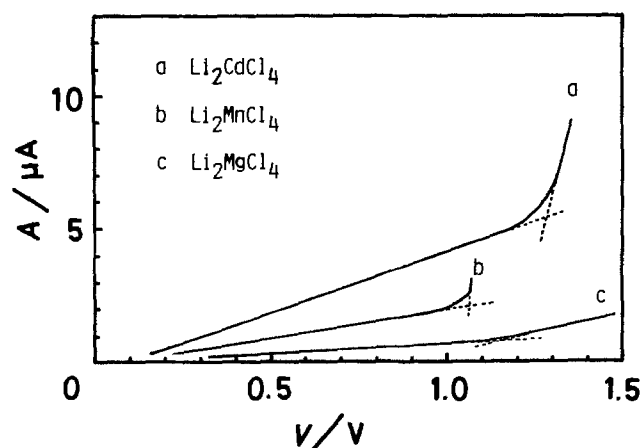


Fig. 6. The current, A , vs. voltage, V , curves for the cell $\text{Pt}/\text{Li}_2\text{MCl}_4/\text{Pt}$.

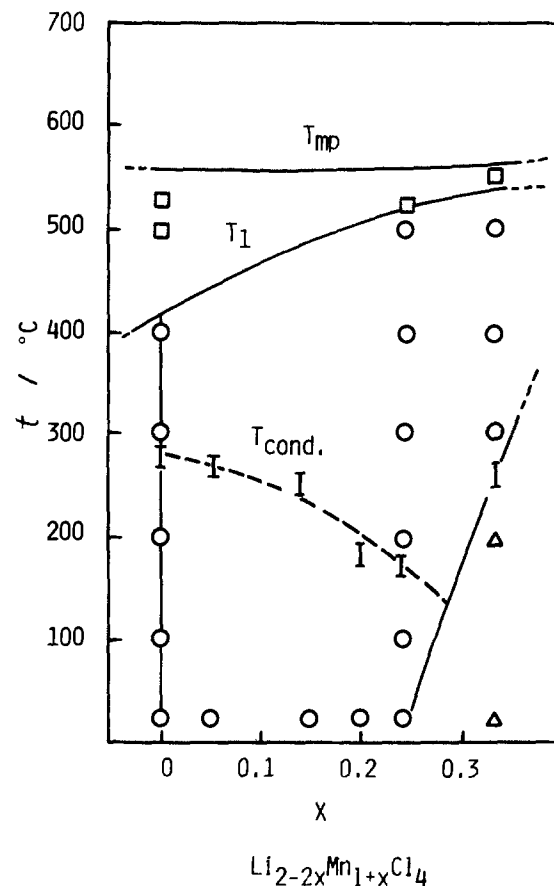


Fig. 7. Phase relation in the $\text{Li}_{2-2x}\text{Mn}_{1+x}\text{Cl}_4$ system. (○) Spinel phase; (□) defect NaCl structure phase; (△) spinel phase + MnCl_2 .

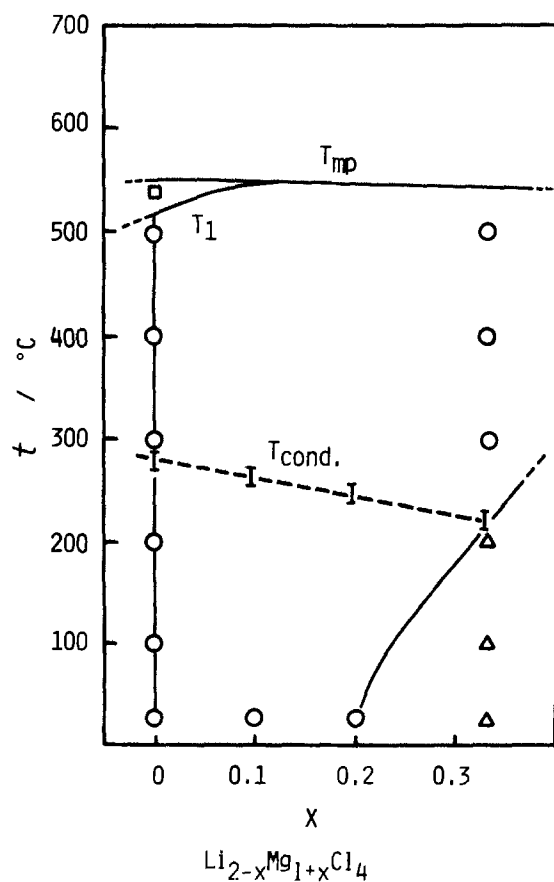


Fig. 8. Phase relation in the $\text{Li}_{2-2x}\text{Mg}_{1+x}\text{Cl}_4$ system. (○) Spinel phase; (□) defect NaCl structure phase; (△) spinel phase + MgCl_2 .

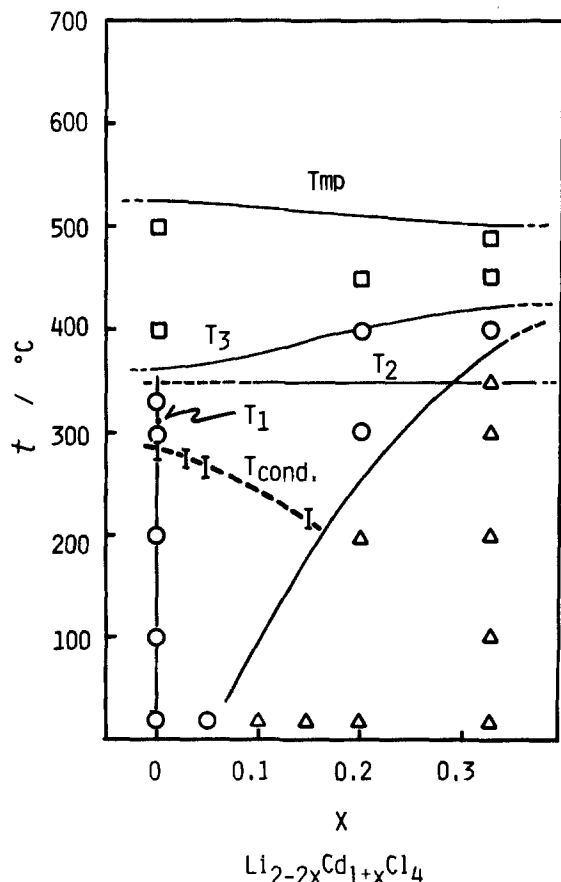


Fig. 9. Phase relation in the $\text{Li}_{2-2x}\text{Cd}_{1+x}\text{Cl}_4$ system. (○) Spinel phase; (□) defect NaCl structure phase; (△) spinel phase + CdCl_2 .

the DTA curves. The x-ray diffraction photograph of the sample with $x = 0$ at 540°C showed the pattern with cubic defect NaCl structure. The solid-state transition is related to the transition from the spinel structure to the cubic defect NaCl structure. The temperatures of the conductivity knees decrease with increasing x as in $\text{Li}_{2-2x}\text{Mn}_{1+x}\text{Cl}_4$. There is no peak in DTA curves corresponding to the temperature of the conductivity knees. The x-ray photograph of the sample with $x = 0.33$ at 200°C showed mixed spinel phase and MgCl_2 . The photograph at 300°C , however, showed no extra lines due to MgCl_2 . The composition of the phase boundary of the solid solution $\text{Li}_{2-2x}\text{Mg}_{1+x}\text{Cl}_4$ at 300°C is $x = 0.33$ or more.

In $\text{Li}_{2-2x}\text{Cd}_{1+x}\text{Cl}_4$, phase transitions obtained by DTA are rather complicated compared with those in $\text{Li}_{2-2x}\text{Mn}_{1+x}\text{Cl}_4$ and $\text{Li}_{2-2x}\text{Mg}_{1+x}\text{Cl}_4$. Three solid-state phase transitions were observed; T_1 was observed only in the stoichiometric compound at 305°C , T_2 was observed for the samples with $x > 0.1$, and T_3 observed for all the samples with $x > 0$. Lutz *et al.* (14) reported the transition T_1 and T_3 for the stoichiometric compound. X-ray diffraction photographs below the transition temperature T_3 showed the pattern with the spinel structure and those above T_3 the pattern with a cubic NaCl structure. These results suggest that the transition temperature T_3 is related to the phase transition from the spinel phase to a cubic defect NaCl structure. No clear difference was observed in x-ray diffraction photographs below and above the transition temperatures T_1 and T_2 . The temperatures of the conductivity knees decrease with increasing x . There is no peak in DTA curves corresponding to the temperatures of the conductivity knees. Further, x-ray diffraction photographs showed that the solid solution range of the system $\text{Li}_{2-2x}\text{Cd}_{1+x}\text{Cl}_4$ broadens with increasing temperature.

In all the systems $\text{Li}_{2-2x}\text{M}_1+x\text{Cl}_4$, the conductivity knees were observed between 300° and 200°C . Lutz *et al.* (12) suggested that the lithium lattice deformation occurred gradually below the phase transition temperature from a spinel structure to a defect cubic structure, and that the conductivity knee was related to an order-disorder type phase transition.

O'Keefe (19) empirically classified ionic solids into three categories with respect to fast ionic conduction. Class I solids do not undergo "nonconducting-conducting transformation" in the solid state but become highly conducting only upon melting. Class II solids, such as notably Ag^+ and Cu^+ salts, exhibit a first-order phase transition to the high conducting state. There are also a number of salts in which the nonconducting-conducting transformation is not a first-order transition as in class II solids but is spread out over a substantial temperature range. Such salts are classified as class III. The transition was named the Faraday (diffuse) transformation. The diffuse phase transitions were found in CaF_2 (20) and PyAg_5I_7 (Py: pyridinium ion) (21). CaF_2 shows a conductivity knee at about 1160°C . The diffuse phase transition is associated with disorder of the anion sublattice. The cation lattice retains the fcc structure through the phase transition. The activation energy changes from 200 to 140 kJmol^{-1} below and above the conductivity knee. PyAg_5I_7 also has diffuse phase transition associated with disorder of the cation sublattice, and a conductivity knee was found at around 52°C . In the lower temperature phase, not all the Ag^+ ions are completely mobile, while in the higher temperature phase, all are mobile. The transition in the system $\text{Li}_{2-2x}\text{M}_1+x\text{Cl}_4$ obtained by the electrical conductivity measurement also seems to be classified as a diffuse type transition. The decrease of transition temperatures with x in $\text{Li}_{2-2x}\text{M}_1+x\text{Cl}_4$ suggests that the order-disorder transition temperature is decreased with the incorporation of lithium ion vacancies. In $\text{Li}_{2-2x}\text{Mn}_{1+x}\text{Cl}_4$, the transition temperature at the composition $x = 0.33$ obtained by conductivity measurements was higher than the transition temperature at $x = 0.24$. X-ray diffraction photographs at 20° and 200°C of $\text{Li}_{1.34}\text{Mn}_{1.33}\text{Cl}_4$ showed the diffraction lines due to a mixture of the spinel phase and MnCl_2 , while those at 300°C showed only lines due to a spinel phase. Therefore, the change in slope at 280°C does not correspond to an order-disorder transition. Further comment on an order-disorder transition must await studies based on heat capacity measurement and more detailed high temperature x-ray experiments.

Conclusion

The solid solution with spinel structure, $\text{Li}_{2-2x}\text{M}_1+x\text{Cl}_4$, has been examined and found to have high ionic conductivity. $\text{Li}_{1.9}\text{Cd}_{1.05}\text{Cl}_4$ shows the highest conductivity of $3.5 \times 10^{-1}\text{ Scm}^{-1}$ at 400°C , which is higher than that of $\text{Li}_{14}\text{Zn}(\text{GeO}_4)_4$, reported previously with the highest conductivity in the temperature range $300^\circ\text{--}400^\circ\text{C}$. At room temperature, $\text{Li}_{1.52}\text{Mn}_{1.24}\text{Cl}_4$ exhibits the highest conductivity of $1.5 \times 10^{-5}\text{ Scm}^{-1}$. In spite of the high conductivity, the solid solutions show the low decomposition potential of about 1.1–1.3V. Because of this value, the utilization of this electrolyte in batteries will be limited.

Acknowledgments

This research was supported financially in part by Grant-in-Aid for Scientific Research from the Ministry of Education, and also in part by TOTO Limited.

Manuscript submitted July 6, 1983; revised manuscript received Oct. 27, 1983.

REFERENCES

- G. C. Farrington and W. L. Roth, *Electrochim. Acta*, **22**, 767 (1977).
- U. v. Alpen, G. H. Talat, and A. Rabenau, *Appl. Phys. Lett.*, **30**, 621 (1977).

3. A. Rabenau, *Solid State Ionics*, **6**, 277 (1982).
4. Y-W. Hu, I. D. Raistrick, and R. A. Huggins, *This Journal*, **124**, 1240 (1977).
5. H. Y-P. Hong, *Mater. Res. Bull.*, **13**, 117 (1978).
6. P. Hartwig, W. Weppner, W. Wichelhaus, and A. Rabenau, *ibid.*, **14**, 493 (1979).
7. P. Hartwig, W. Weppner, and W. Wichelhaus, in "Fast Ion Transport in Solids, Electrodes and Electrolytes," P. Vashishta, J. N. Mundy, and G. K. Shenoy, Editors, p. 487, North-Holland, Amsterdam (1979).
8. P. Hartwig, W. Weppner, W. Wichelhaus, and A. Rabenau, *Solid State Commun.*, **30**, 601 (1979).
9. J. Schoonman and P. H. Bottelberghs, in "Solid Electrolyte," P. Hagenmuller and W. van Gool, Editors, p. 354, Academic Press, New York (1978).
10. W. Weppner and R. A. Huggins, *This Journal*, **124**, 35 (1977).
11. R. Kanno, Y. Takeda, and O. Yamamoto, *Mater. Res. Bull.*, **16**, 999 (1981).
12. H. D. Lutz, W. Schmidt, and H. Haeuseler, *J. Phys. Chem. Solids*, **42**, 287 (1981).
13. C. J. J. van Loon and J. de Jong, *Acta Crystallogr. Sect. B*, **31**, 2549 (1975).
14. Von H. D. Lutz, W. Schmidt, and H. Haeuseler, *Z. Anorg. Allg. Chem.*, **453**, 121 (1979).
15. M. B. Dines, *Mater. Res. Bull.*, **10**, 287 (1975).
16. L. Hanebali, T. Machej, C. Cros, and P. Hagenmuller, *ibid.*, **16**, 887 (1981).
17. R. D. Schannon and C. T. Prewitt, *Acta Crystallogr. Sect. B*, **25**, 925 (1969); *ibid.*, **26**, 1046 (1970).
18. M. S. Whittingham, *Prog. Solid State Chem.*, **12**, 41 (1978).
19. M. O'Keefe and B. G. Hyde, *Philos. Mag.*, **33**, 219 (1976).
20. C. E. Derrington, A. Lindner, and M. O'Keefe, *J. Solid State Chem.*, **15**, 171 (1975).
21. S. Geller and B. B. Owens, *J. Phys. Chem. Solids*, **33**, 1241 (1972).

Quantitative Phase Analysis of Crystalline and Amorphous Components of Positive Plates in Lead-Acid Batteries Operated under Simulated Electric-Vehicle Service

K. Harris, R. J. Hill, and D. A. J. Rand

Institute of Energy and Earth Resources, CSIRO Division of Mineral Chemistry, Port Melbourne, Victoria 3207, Australia

ABSTRACT

The crystalline and amorphous component phases of positive plates taken from lead-acid batteries in simulated electric-vehicle service were examined by quantitative XRD analysis. They were compared with independent determinations from electrical measurements and wet chemical analysis. Changes in temperature, discharge current, the ratio of α -PbO₂: β -PbO₂, and the amount of amorphous material are correlated with the capacity and cycle life of the batteries.

The ability of a lead-acid battery to supply and store energy depends on the initial electrochemical activity of the material in the positive plate and the rate at which this activity is lost during cycling. Utilization of the active mass at the beginning of service is a function of the discharge current density, the rate of electrolyte diffusion into the plate, the total surface area of the active material, the degree of electrical contact between the particles of material in the plate and between the particles and the current collector (grid), and the intrinsic electrochemical activity of the particles themselves. These factors are found to change both during a given discharge cycle and between subsequent discharge cycles, so that the battery is eventually unable to supply a useful discharge rate and/or amount of energy.

The relationship between the composition of the formed positive-plate material and some of its performance characteristics has been a subject of continuing interest for almost fifty years (1-21). In the charged condition, the positive plate consists of a lead-alloy grid supporting variable amounts of the polymorphs α -PbO₂ and β -PbO₂, both of which are converted to PbSO₄ during discharge (22). The relative proportions of the two forms of PbO₂ have been found to influence the discharge capacity (4-6, 8, 9), mechanical strength (6, 7), oxygen overvoltage characteristics (9), particle- and pore-size distribution (8, 9, 12), and surface area (8, 12) of the active material. In addition, measurements of the amount of PbSO₄ produced on discharge and/or left unconverted at the end of charging can provide information about the

efficiency of the charge/discharge process and the nature and whereabouts of any material which is not participating in the cell reaction. Changes in the relative proportions of the PbO₂ and PbSO₄ phases, and quantitative measurements of the utilization of the active material are, therefore, of particular importance in attempts to understand and improve the performance characteristics and cycle life of lead-acid batteries.

In addition to these crystalline phases, numerous studies have documented the presence of poorly crystalline, or "amorphous," material¹ in battery plates, and changes in its abundance according to the method of plate preparation and cycling history have been reported (11, 12, 16, 17, 19, 20, 23-26). Indeed, Caulder and Simon (23) have suggested that there is an inverse relationship between the degree of structural order of PbO₂ and its electrochemical activity, and that the amount of the inactive (ordered) variety increases during charge/discharge cycling (23, 24, 27, 28). However, since these observations have been disputed (29), the need for more quantitative estimates of the active and inactive components is apparent (22, 29).

The application of an XRD method to the analysis of positive plates of lead-acid batteries has already been reported (21). However, that study involved analysis of only the crystalline component phases. In the present work, we have further developed this technique for determining both the crystalline and the amorphous components of large numbers of samples taken from the positive plates of lead-acid batteries operated under simulated electric-vehicle service. In

Key words: amorphous, cell, energy conversion, phase transformation.

¹The term "amorphous," as used in this paper, refers to material which does not give rise to normal x-ray diffraction peaks, either because it is truly structureless, or because the particle size is very small (*i.e.*, < 100Å).

order to assess the performance of such plates, the XRD phase analysis results have been compared with independent measurements obtained from electrical parameters and wet chemical analysis, with particular emphasis being placed on the role of the amorphous component in the cell reaction.

X-Ray Diffraction Method for Positive-Plate Phase Analysis

The method that we have selected for the analysis of the positive-plate material is a version of the internal standard technique (30-37) specifically designed to (i) minimize the diffraction problems associated with the particular phases under study, and (ii) address questions relating to battery performance. The amount of amorphous material present in battery plate samples is determined accurately by the use of CaF_2 as the reference phase.

As discussed by Chung (32, 33) and others (34-37), the fundamental equation relating phase concentration (W) and diffracted peak intensity (I) in the internal standard method is

$$W_i = (I_i/I_s) (W_s/RI_i) \quad [1]$$

where RI_i , the so-called reference intensity ratio, is a constant for a given phase i in the presence of an internal standard s (in the present case, CaF_2) added in the weight proportion W_s . The weight fraction of the phase i (W_i) is obtained simply by measuring the intensity ratio I_i/I_s , given that W_s is known and RI_i has been determined previously for a mixture containing the same weight fraction of s .

For reasons outlined previously (21), we have chosen not to obtain values of RI_i from measurements of I_i/I_s in synthetic samples of known W_i/W_s , that is, from calibration curves corresponding to the rearrangement of Eq. [1]: $RI_i = (I_i/I_s) (W_s/W_i)$. Instead, we have decided to calculate RI_i from first principles using the known structural and x-ray scattering properties of the individual phases, that is, from the expression

$$RI_i = (Q_i/Q_s) (D_s/D_i) \quad [2]$$

where Q is the calculated powder diffraction intensity, and D is the product of the unit-cell volume and mass of the unit-cell contents (in atomic mass units) for each phase (21, 38).

The weight percentages (w/o) of the different phases are determined using Eq. [1]. Any difference between the sum of the determined weight percentages and 100% is assigned to the amount of amorphous material present in the sample. A complete description of the method, including details of the preparation of samples, the regions of diffraction record scanned, the treatment of backgrounds, and the calculation logic, has been presented elsewhere (21, 39).

Test Batteries and Operational Procedure

The XRD phase analysis method was applied to samples taken from the positive plates of test lead-acid batteries subjected to charge/discharge cycles that simulated electric-vehicle service in an urban environment. Details of test station design and charging procedure have been reported previously (21, 39-46). The batteries themselves consisted of six 2V cells joined in series, with each cell containing four positive and five negative flat plates and having a nominal capacity of 60 Ah (20h rate). Positive plates were wrapped in fiberglass cloth. The cell containers had detachable lids and the intercell connectors were specially designed to allow the batteries to be disassembled easily for collecting plate specimens at various stages of cycle life.

All of the batteries were operated under the Australian Electric Vehicle Association (AEVA) standard driving schedule (47) shown in Fig. 1. The current profiles of two vehicles operating over the AEVA driving schedule were obtained. The vehicles involved were a

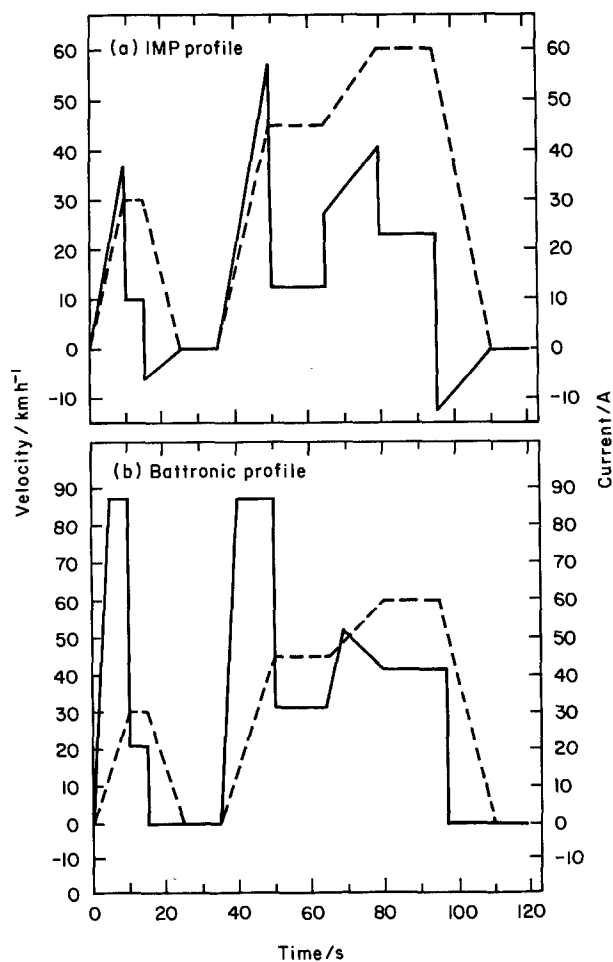


Fig. 1. AEVA driving schedule (---) and battery current approximation (—) for (a) IMP electric van, and (b) Batronic electric van.

Batronic electric van on loan from the Australian Lead Development Association, and an Induction Motor Propulsion (IMP) van developed by Gosden (48) under the sponsorship of the Australian National Energy Research, Development and Demonstration Council. The Batronic van has a ten-year-old design, whereas the IMP van is representative of present-day electric vehicle design, having ac motor drive and microprocessor-controlled operation with a regenerative braking facility.

The current profiles of the two vans were scaled down from those experienced by the vehicle battery packs to equivalent rates for the test batteries used in the laboratory simulated studies (Fig. 1). The scaling factor was equal to the ratio of the test-battery capacity to the vehicle-battery capacity. After scaling down, test batteries operating under the simulated Batronic van profile experienced an average discharge current of 30.5A, whereas those under the IMP van profile drew only 12.4A (Table I). As a result, test batteries with the same nominal capacity at the 20h rate have different capacities in the simulated service of the IMP and Batronic vehicles, and have markedly different initial ranges over the AEVA schedule (Table I). A comparison of the performance of batteries under simulated driving of the two vans therefore enables an assessment to be made of the advantages gained by the introduction of advanced vehicle design. For all batteries tested, smooth-current discharge was used and terminated at 9.6V. The end of useful battery life was taken as the point at which the discharge capacity, converted to the 20h rate, had fallen to 75% of the nominal value at 25°C.

Table I. Characteristics and performance summary of test batteries

Parameter	Battery				
	T1	T2	T3	T4	T5
Simulated driving profile	IMP	← Batronic →			
Sb content of grid (w/o)	6.	5.3	5.3	5.3	5.3
Average AEVA ¹ discharge current (A)	12.4 ²	30.5	30.5	30.5	30.5
Operating temperature (°C)	25.	25.	40.	50.	60.
Capacity at the average AEVA rate at 25°C (Ah) ³	38.1	28.5	28.5	28.5	28.5
Initial range of vehicle over the AEVA schedule (km)	92.	28.	28.	28.	28.
Battery life ⁴ (charge/discharge cycles)	157.	116.	157.	245.	341.
Distance traveled during battery life (km)	13,225.	2621.	3692.	7690.	10,337.
Initial α -PbO ₂ : β -PbO ₂ ratio (charged)	0.868	0.819	0.378	0.975	0.369
Failure α -PbO ₂ : β -PbO ₂ ratio (charged)	0.124	0.165	0.113	0.165	0.184
Weight shed material (g cycle ⁻¹)	3.29	0.97	1.92	1.30	1.30
Water added (ml cycle ⁻¹)	8.9	3.4	8.0	21.7	51.6

¹ Australian Electric Vehicle Association standard driving schedule (47).

² Incorporates the effects of regenerative braking.

³ All batteries have a nominal capacity of 60 Ah at the 20h rate at 25°C and a positive-plate active-material density of 4.58 kg liter⁻¹.

⁴ Defined as the point at which the battery capacity has fallen to 75% of its nominal value at the AEVA rate at 25°C.

More than 60 batteries of various types have now been cycled under simulated electric-vehicle service in our laboratories. We report herein the detailed quantitative XRD phase analysis results obtained from five of these batteries, spanning a range of operating temperatures (25°-60°C), two different initial α -PbO₂: β -PbO₂ ratios (~0.4 and ~0.9), and two different discharge currents (for Batronic and IMP vans). These and other characteristics of the five test batteries are summarized in Table I.

The five batteries were operated at 25° (two batteries), 40°, 50°, and 60°C in thermostatically controlled water baths. At various stages of cycle life, the batteries were disassembled and specimens (1 cm²) of charged and discharged grid/active material were collected from the plates with a specially designed set of cutters. Sampling was rotated between plates and cells so that all plates were treated equally. During the sampling procedure, care was taken to preserve the fiberglass wrapping around the plates, and to minimize plate separation and disturbance. Earlier studies (42-44) have shown that periodic sampling of this kind has no deleterious effect on battery capacity or cycle life. However, heavier sampling (*e.g.*, samples from all 24 positive plates at one time) can severely diminish battery performance.

Results and Discussion

XRD analyses of "single-phase" samples.—Before applying the XRD method of phase analysis to samples taken from batteries, studies were made on several commercially available samples of chemically prepared CaF₂, β -PbO₂, and PbSO₄, together with α -PbO₂ prepared by oxidation of β -PbO at 340°C (11), and α -PbO₂ and β -PbO₂ prepared by electroformation of positive battery plates in 1M NaOH and 4M H₂SO₄ (49), respectively. The results are given in Table II.

For all samples analyzed, the integrated observed peak intensities for each scan region agreed closely with the calculated values. Compared to the diffraction patterns from chemically prepared α -PbO₂, the patterns from α -PbO₂ prepared by electroformation in 1M NaOH had much higher backgrounds and broad tails on

the peaks. Both of these factors indicate that a significant proportion of the crystallites have sizes less than about 0.2 μ m, and give rise to the possibility that many of these particles are too small to diffract at all and may therefore contribute to an amorphous component. This was confirmed by analysis; *e.g.*, in Table II the electroformed α -PbO₂ sample is seen to contain about 48% of its mass as amorphous material.

Chemically prepared α -PbO₂ is also poorly crystalline (Table II) with a variable amorphous content between about 20 and 35 w/o, but both electroformed and chemically prepared β -PbO₂ usually contain less than 15 w/o of noncrystalline material. In addition, both α -PbO₂ and β -PbO₂ usually contain small amounts of the other polymorph. In contrast, PbSO₄ was found (Table II) to be essentially 100% crystalline and very pure.

Kordes (12) used a combination of x-ray and neutron diffraction methods to determine the proportions of amorphous and crystalline material in various samples of PbO₂. It was found that the amorphous content of α -PbO₂ was in the range 40-70 w/o and that of β -PbO₂ in the range 18-50 w/o. As found in our studies (Table II), the amount of amorphous material was dependent on the method of preparation of the lead dioxide.

The ranges of values shown in Table II for each sample were obtained from repeated analyses of samples prepared by different operators, using different sample thicknesses, grinding times, and weights. Values suggest that the results are conservatively reproducible to within about 5% by weight for all four components. As discussed below, XRD analyses were also performed on various synthetic mixtures of PbSO₄ and β -PbO₂ (and α -PbO₂ in other studies not reported here) in order to check the accuracy and precision of the method. In all cases, the XRD results were well within 5 w/o of the known compositions of the mixtures.

XRD analyses of positive plate material.—Figure 2 shows the progressive changes in the α -PbO₂, β -PbO₂, PbSO₄, and amorphous material contents for both the charged [plots (a)] and the discharged [plots (b)] state

Table II. Results of XRD phase analyses of "single-phase" materials (w/o)

Sample	α -PbO ₂		β -PbO ₂		PbSO ₄		Amorphous	
	Min.	Max.	Min.	Max.	Min.	Max.	Min.	Max.
α -PbO ₂ : chem. prep. ¹	77.7	82.1	0.0	2.4	0.0		19.4	23.2
chem. prep. ¹	65.3	70.8	2.4	2.9	0.0		28.2	33.5
electroformed	44.4	46.0	6.5	6.9	0.0		47.0	49.9
β -PbO ₂ : Univar AR	1.6	3.3	91.1	98.1	0.0	0.9	-0.4	7.0
electroformed	4.0	5.2	83.1	86.2	0.0		10.9	14.1
PbSO ₄ : Unilab LR		0.0	0.0		98.1	101.1	-1.1	1.9

¹ Different samples prepared using the same chemical method.

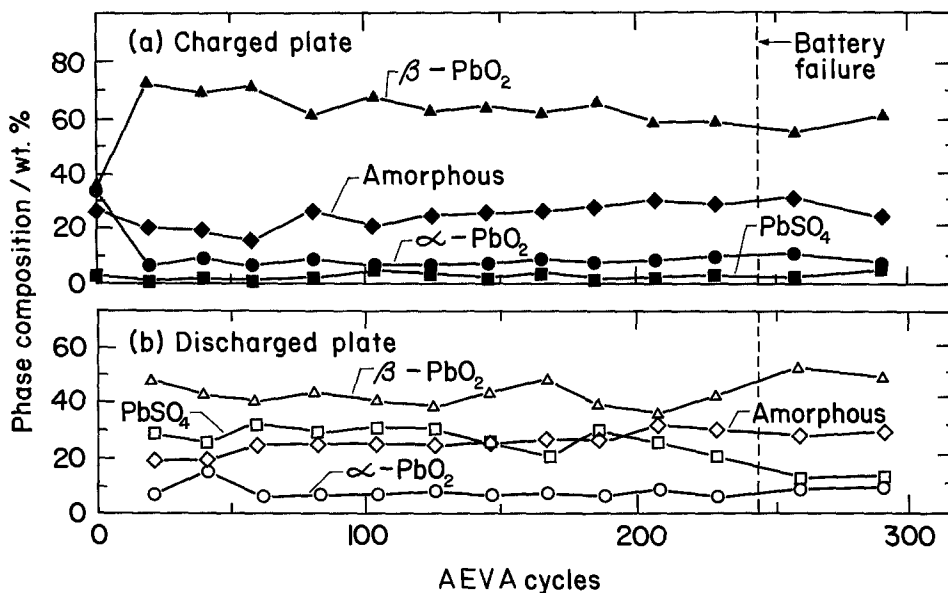


Fig. 2. Phase composition (w/o) of (a) charged and (b) discharged positive plates from test battery T4 after AEVA cycling at 50°C; discharge under the Batronic profile.

of battery T4 as a function of the number of cycles of simulated electric-vehicle operation. These plots for battery T4 are typical of those found for the other four batteries tested. In order to discuss trends in plate composition with cycle life, groups of analyses typical of the early, middle, and late stages of operation have been averaged and presented in numerical form in Table III. Also included in Table III are the amounts of active material (crystalline plus amorphous) discharged to PbSO₄ at each of these three stages of cycle life.

Inspection of the phase analysis results summarized in Table III shows that:

(i) Utilization of the positive-plate active material during the early and middle stages of battery operation was about 50% higher with the IMP than with the Batronic van driving profile (cf. batteries T1 and T2 operated at 25°C). This difference is due to the lower average discharge current required by the IMP profile and leads to a much greater initial driving range for this vehicle (Table I).

(ii) For a given vehicle current-profile, utilization of active material during the early stages of battery operation increased more or less uniformly with temperature from a value of ~18 w/o for battery T2 at 25°C to ~36 w/o for T5 at 60°C. A similar observation has been reported by Asai *et al.* (50). Active material utilization remained fairly constant during the early and middle stages of battery life, and declined sharply during the final stage of operation. These utilization rates are typical for batteries operated under the high rates of discharge experienced in electric vehicles.

(iii) The five test batteries began service with α -PbO₂: β -PbO₂ ratios between 0.37 and 0.98, and subsequent charge/discharge cycling reduced this ratio to 0.11-0.18 at failure (Table I). This decline in the oxide ratio was found to be more rapid with increase in temperature and decrease in discharge rate. This can be explained by the fact that both of these operating conditions promote penetration of the electrolyte into the active material and hence decrease the pH in the interior of the plates. This leads to an environment more favorable to the formation of β -PbO₂ from α -PbO₂ (through PbSO₄) on recharging.

(iv) At all stages of battery operation, the conversion of α -PbO₂ to PbSO₄ was less than that of β -PbO₂ to PbSO₄, e.g., for battery T2, the maximum conversion rates of α -PbO₂ and β -PbO₂ were 5 and 30%, respectively. Both rates increased with temperatures, e.g., for battery T5, the maximum conversion rates of α -PbO₂ and β -PbO₂ were 20 and 45%, respectively. However, whereas the conversion of α -PbO₂ remained approximately the same throughout the life of each battery,

the conversion of β -PbO₂ dropped significantly (to values around 20%) as battery failure was approached. Since analysis showed that the α -PbO₂ resided predominantly in the interior of the plates during the middle and late stages of battery operation, it is concluded that the loss of PbO₂ activity is primarily associated with the lead dioxide present in the external portions of the plates, i.e., those areas most affected by loss of interparticle contact through active material "softening."

(v) Throughout battery life, the PbSO₄ content of the charged plates remained fairly constant, especially at high temperature. The amount of PbSO₄ produced during battery discharge was significantly reduced in the final stages of operation. These results, and those of others (51), suggest that the decline in battery capacity is due not to sulfation of the positives in the charged state, but to an inability of the PbO₂ to be reduced during discharge. Electrical isolation of the active material by grid corrosion, therefore, does not appear to be a major cause of failure, since decreased reactivity would then be observable during both the charge and discharge processes. A more likely explanation for the decline in battery performance is the electrical isolation of unconverted PbO₂ particles by the growth of PbSO₄ particles or films during discharge (8, 52-55).

(vi) The amount of amorphous material in the positive plates varied between 10 and 29 w/o for the batteries studied and may be compared to a value of 34 w/o determined by Kordes (12). Within a given battery, there is a tendency for the amount of amorphous material to increase as cycling proceeds (Fig. 2), and for the material in inner portions of the plate to be less crystalline than in the outer parts.

(vii) The variability of phase composition between adjacent plates in any one battery was higher in the discharged than in the charged state. This again suggests that it is the reduction of PbO₂ to PbSO₄ which is the life limiting factor in battery performance, rather than the oxidation of PbSO₄ to PbO₂. In other studies reported both below, and previously (21, 39, 43, 44), we have observed that individual plates within a battery do indeed develop their own unique phase compositions as cycling proceeds and that this nonuniformity can lead to severe loss of capacity and cycle life. It was found that plate uniformity was maintained for longer periods of time at higher temperatures of operation.

*Comparison of XRD analyses with alternative measurements of battery performance.—Electrical measurements.—*From a knowledge of the weight of the

Table III. Average XRD phase composition (w/o), amount of active material discharged (w/o), and selected PbSO₄ chemical analyses for positive plates during the early, middle, and late stages of operation of the five test batteries listed in Table I

Battery	Stage of operation ¹	Battery condition ²	Cycle number of each sample contributing to average phase compositions	Average phase composition (w/o)				Amount of active material discharged ³ (w/o)	Total S converted to PbSO ₄ (w/o)
				α-PbO ₂	β-PbO ₂	PbSO ₄	Amorphous		
T1 (IMP, 25°C)	E	C	24, 43, 63	9.87	59.10	8.33	22.73	27.94	} Not determined
		D		9.07	37.23	36.27	17.43		
	M	C	82, 103	10.55	65.45	11.35	12.65	30.25	
		D		8.80	37.00	34.65	19.60		
	L	C	139, 181, 222	7.20	57.87	9.47	25.47	10.17	
		D		6.73	50.63	18.93	23.67		
T2 (Batronic, 25°C)	E	C	19, 44	21.30	52.70	3.60	22.35	18.05	8.75 30.78
		D		20.15	35.90	21.65	22.25		
	M	C	67, 90	14.65	64.25	3.05	18.10	17.90	8.33 28.42 12.06 30.78
		D		14.65	46.35	20.70	18.35		
	L	C	118, 145	10.70	64.80	7.70	16.85	16.35	
		D		10.10	50.30	24.05	15.55		
T3 (Batronic, 40°C)	E	C	26	9.9	70.2	9.0	10.9	24.0	} Not determined
		D		9.0	47.1	24.0	19.9		
	M	C	63	8.8	78.3	2.4	10.5	26.4	
		D		8.8	53.6	28.8	8.8		
	L	C	109	8.2	72.8	3.3	15.7	20.9	
		D		7.5	53.1	24.2	15.1		
T4 (Batronic, 50°C)	E	C	19, 39, 59, 80, 101	8.14	69.22	2.51	20.10	27.32	7.02 40.08
		D		7.99	42.05	28.11	21.82		
	M	C	122, 143, 164, 185	7.83	63.78	2.38	26.00	23.67	6.02 36.55
		D		6.45	42.00	26.05	25.55		
	L	C	206, 228, 258, 290	9.65	58.55	3.09	28.76	15.20	9.57 26.86
		D		7.69	45.25	17.80	29.25		
T5 (Batronic, 60°C)	E	C	20, 42, 62, 85	9.93	76.28	3.83	9.98	36.37	} Not determined
		D		7.78	42.03	31.45	18.73		
	M	C	127, 168	12.10	74.65	2.10	11.20	29.45	
		D		9.85	47.50	28.95	13.80		
	L	C	208, 251, 300	12.30	66.83	3.20	17.67	15.60	
		D		10.97	52.57	15.70	20.77		

¹ E = early, M = middle, L = late.

² C = charged, D = discharged.

³ Amount = Σ(net positive changes (D-C) in PbSO₄ and amorphous material).

active material in the positive plates (~590g per cell), it is possible to calculate the weight percentage of PbSO₄ produced by the passage of a given amount of electricity during discharge. The weight percentages of PbSO₄ so calculated (assuming no shedding of material) for each of the cycles at which the battery was sampled for XRD analysis are plotted for batteries T2 and T4 in Fig. 3. Also shown are the corresponding values of the weight percentages of PbSO₄ (and amorphous material) produced during discharge of the batteries (as determined by XRD analysis), together with the values of PbSO₄ content obtained from chemical analysis (LECO method) of the total sulfur content of the same samples (Table III).

Despite the fact that the PbSO₄ contents calculated from capacity measurements are averages over all six cells in the battery, whereas the XRD and chemical analysis values are single-sample estimates from a quantity of material approximately equal to 0.6% of the mass of only one of the four positive plates in one of the cells, there is good agreement between the three PbSO₄ curves for each battery in Fig. 3. Why the XRD-derived values should, on average, be slightly lower than the electrical and chemical values is unclear, but it could be related to the fact that the discharge of amorphous PbO₂ to amorphous PbSO₄ cannot be de-

tected by XRD phase analysis alone; the parallelism of the XRD and chemically determined values suggests that this is indeed the case.

Chemical measurements.—Attempts to determine the overall composition of the bulk active material by chemical analysis for lead are limited by the uncertainty associated with the assumption of a valence state for lead, the level of nonstoichiometry, and/or the presence of intermediate oxides, water molecules, hydroxyl groups, etc. (11, 22, 56). However, the sulfur present in cycled plates is unambiguously present as PbSO₄ (no basic lead sulfates were visible in the diffraction patterns), and this material is not affected by any of the problems associated with the oxide phases. Any excess in the sulfur content of the charged or discharged bulk material (determined by chemical means) over that measured in the crystalline fraction (by XRD phase analysis) must therefore represent the sulfur contained within the amorphous material.

Samples of positive-plate active material from battery T4 in both the charged and discharged states, and also samples from two other test batteries after slow discharge at the 20h rate, were subjected to total sulfur analysis. The results are plotted in Fig. 4 against the corresponding XRD estimates of the crystalline PbSO₄

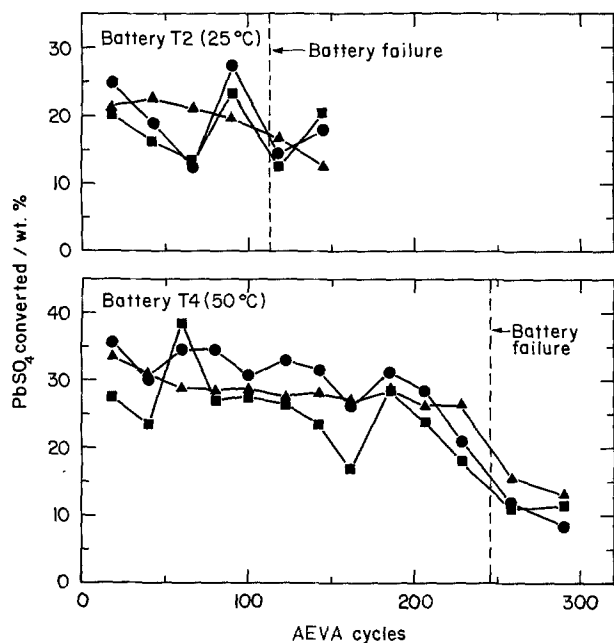


Fig. 3. Comparison of XRD-determined utilization of positive material in test batteries T2 and T4 with the corresponding amount determined either coulometrically or chemically. (▲) Ah converted to equivalent PbSO_4 (w/o). (■) XRD determination of active material discharged (w/o). (●) Total S content converted to equivalent PbSO_4 (w/o).

content of other portions of the same samples. The least squares linear regression line through all the data points for T4 is indicated by the dashed line (correlation coefficient = 0.991), and the 1:1 relationship between total S and PbSO_4 content is drawn as a solid line (labeled as 100% crystalline). The error in each total S measurement is estimated to be about 1% (relative to the amount determined); the error bars for total S have been omitted from the low-value data points (<2 w/o) since they are within the width of the data point itself. A uniform error of about ± 2 w/o (absolute) is estimated to apply to all the values obtained from XRD analysis.

The most obvious feature of the data plotted in Fig. 4 is that the amount of crystalline sulfate in battery

plates, when obtained from XRD measurements, is always significantly less than the amount calculated from determination of the total S content. Assuming that the total S values are not in doubt, this feature could be due to: (i) the presence of a systematic error in the XRD method of analysis whereby the amount of PbSO_4 is consistently underestimated, or (ii) the presence of noncrystalline PbSO_4 , which is measured by the total S analysis, but is not detected by XRD analysis.

As a check on the accuracy and precision of the XRD method in the context of this experiment, five synthetic samples were prepared containing a 1:1 by weight mixture of CaF_2 (internal standard) with Unilab PbSO_4 and Univar $\beta\text{-PbO}_2$; the latter compounds were in the ratios 0:100, 10:90, 20:80, 40:60, and 60:40, respectively. Unilab PbSO_4 and Univar $\beta\text{-PbO}_2$ are known to consist of 100 and 95 w/o crystalline material, respectively (Table II). The five mixtures were then subjected to XRD phase analysis, and the resultant crystalline PbSO_4 contents were plotted against the total S weight percentage (Fig. 4). For all five synthetic samples, the theoretical 1:1 line lies well within the estimated error of the XRD determination, adding further credence both to the accuracy and to the estimated precision of the XRD phase analysis method. The deviation of the T4 test battery analyses from the theoretical 1:1 (i.e., 100% crystalline) relationship in Fig. 4 is therefore considered to be real and to be due to the presence of amorphous PbSO_4 in the plates.

Chemical and XRD analyses of samples taken from battery T2 operated at 25°C exhibited the same relationship between the crystalline PbSO_4 and the total S content as that observed in Fig. 4 for battery T4 at 50°C. This suggests that the temperature of operation has little, if any, effect on the partitioning of the PbSO_4 between the crystalline and amorphous components.

Role of the amorphous component in positive-plate material.—Of particular interest is the fact that not only is there PbSO_4 in the amorphous fraction, but that the amount of this noncrystalline sulfate increases with the amount of crystalline PbSO_4 . For example, for a T4 battery sample ostensibly containing no crystalline sulfate, the intersect of the regression line in Fig. 4 suggests that there is actually 0.4 w/o total S present, corresponding to 4.1 w/o amorphous PbSO_4 , whereas

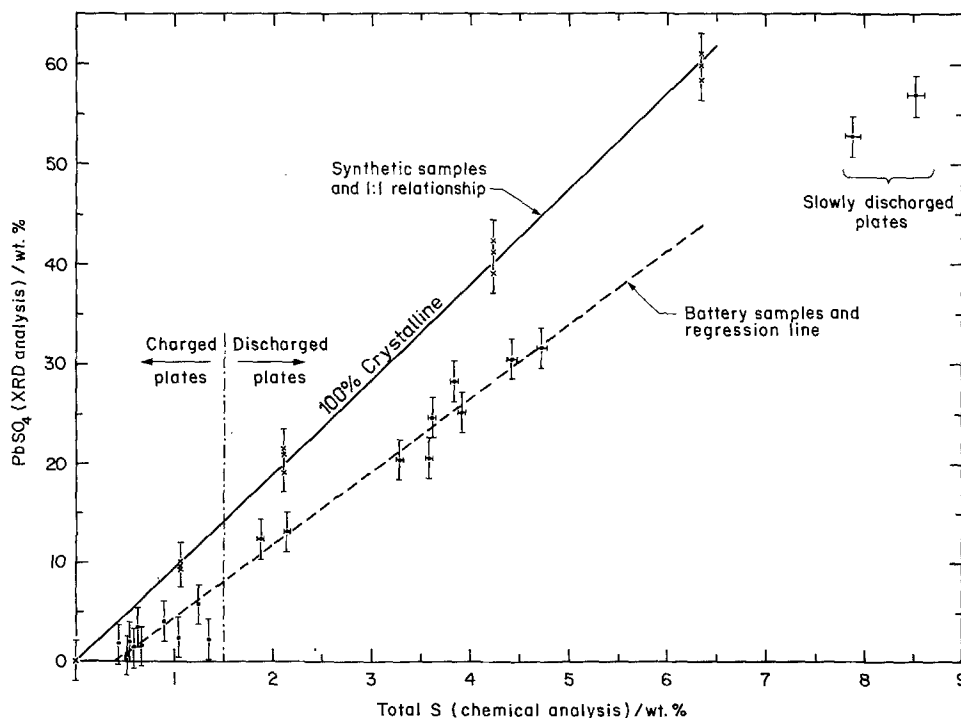


Fig. 4. Comparison of PbSO_4 content (XRD analysis, w/o) in synthetic samples and in charged/discharged positive plates of test battery T4 operated at 50°C under the AEVA driving schedule, with total S content determined by chemical analysis. (---) Least squares regression line through battery data. (—) Theoretical 1:1 relationship between plotted parameters. Also included are corresponding results obtained for two other test batteries subjected to a slow discharge at the 20h rate. The estimated precision of the determinations are indicated by error bars.

for a sample containing 30.0 w/o crystalline PbSO_4 there is an additional 12.1 w/o of amorphous PbSO_4 .

Taking battery T4 as a case in point, the amount of amorphous material increased from 20 to 29 w/o during cycle life (Table III). However, there was no significant change in the amorphous content between the charged and discharged states at any stage of cycle life. The increase in the deviation of the experimental PbSO_4 line from the 100% crystalline line in Fig. 4 as the sulfate content increased cannot, therefore, be related to a corresponding increase in the total amount of amorphous material in the plates as they were discharged. Instead, the proportion of PbSO_4 in the amorphous fraction must be increasing, i.e., amorphous dioxide (either $\alpha\text{-PbO}_2$ or $\beta\text{-PbO}_2$) must be discharging to amorphous PbSO_4 . Behavior of this kind was typical of all five test batteries. In only three cases in Table III (T1, middle life; T3, early life; T5, early life) was a significant change in the amount of amorphous material observed during discharge. This suggests that the processes of charge and discharge generally take place between particles of broadly equivalent size during the operation of the batteries, i.e., crystalline material converts to crystalline material, and amorphous to amorphous.

Table IV presents calculations of the relative utilization of the amorphous and crystalline fractions of the positive-plate active material of batteries T2 and T4, together with corresponding results for another test battery subjected to a slow discharge at the 20h rate (top right-hand corner of Fig. 4). For a given battery, the results show that, within the accuracy of the determinations, there is little difference in the degree of utilization of the two forms (i.e., crystalline and amorphous) of lead dioxide in batteries operated under either simulated-electric-vehicle or slow-discharge conditions. Thus, it appears that particle size (as delineated in the present study) has little, if any, effect on the activity of the positive-plate material. As discussed above, the utilization of both forms of lead dioxide increases both with increase in temperature and with decrease in discharge rate.

The indication that amorphous lead dioxide has the same electrochemical activity as crystalline lead dioxide is somewhat surprising when it is noted that neutron diffraction studies (25, 39) have shown that part of the amorphous component is a lead-rich intermediate oxide with $\sim 40\%$ lead atoms in the Pb(II) valency state. It can only be concluded at this stage, therefore, that this intermediate oxide has a similar electrochemical activity to near-stoichiometric PbO_2 .

Battery cycle life and equivalent distance traveled.—Of the three parameters tested in the present study, namely, operating temperature, discharge current, and initial $\alpha\text{-PbO}_2\text{:}\beta\text{-PbO}_2$ ratio, the former two exert by

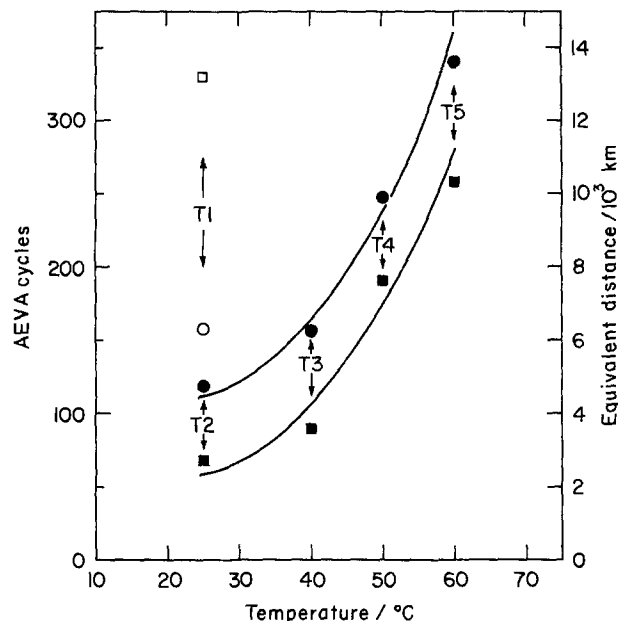


Fig. 5. Number of charge/discharge cycles (○ IMP, ● Batronic) and equivalent kilometers traveled (□ IMP, ■ Batronic) plotted as a function of operating temperature for batteries T1-T5.

far the greatest influence on overall battery performance (Table I).

In Fig. 5, the number of charge/discharge cycles and equivalent kilometers traveled for each of the five test batteries have been plotted against the operating temperature. For the four batteries, T2-T5, subjected to the Batronic van discharge profile, the improvement in battery performance with temperature, as given by both cycle life and equivalent kilometers traveled, is dramatic (see also Table I); both measures of performance are improved by more than a factor of three on raising the temperature from 25° to 60°C.

Although the increase in battery performance with temperature appears to be relatively uniform, it is interesting to note that the two batteries (T2 and T4) with initial $\alpha\text{-PbO}_2\text{:}\beta\text{-PbO}_2$ ratios around 0.9 (Table I) lie above the smooth curves in Fig. 5, whereas the two batteries (T3 and T5) with a low initial oxide ratio (i.e., around 0.4) lie below the curves. A high value for the initial $\alpha\text{-PbO}_2$ content of the formed plates therefore appears to be advantageous to battery performance, albeit to an extent less than that effected by increasing the operating temperature. The fact that even a modest correlation obtains between the $\alpha\text{-PbO}_2\text{:}\beta\text{-PbO}_2$ ratio and cycle life is somewhat surprising, since for most of the batteries (especially T4 and T5 operated at higher temperatures) the lead-

Table IV. Calculation of relative utilization rate of amorphous and crystalline lead dioxide in test batteries T2 (25°C) and T4 (50°C) in the early (E), middle (M), and late (L) stages of battery life, and in another test battery subjected to a slow discharge at the 20h rate at 25°C†

Quantity	Process	T2			T4			Slow discharge
		E	M	L	E	M	L	E
Crystalline PbO_2 (charged state), A	(w/o) $\alpha\text{-PbO}_2 + \beta\text{-PbO}_2$	74.0	78.9	75.5	77.4	71.6	68.2	71.4
Crystalline PbSO_4 produced, B	(w/o) Discharge-charge	18.1	17.7	16.4	25.6	23.7	14.7	56.5
Equivalent crystalline PbO_2 produced, C	(w/o) $B \times 0.789^*$	14.3	14.0	12.9	20.2	18.7	11.6	44.6
Utilization of crystalline PbO_2	(%) $100 \times (C/A)$	19.3	17.7	17.1	26.1	26.1	17.0	62.5
Amorphous PbSO_4 (charged state), D	(w/o) Total S-crystalline	5.2	5.3	4.4	4.5	3.6	6.5	3.7
Amorphous PbSO_4 (discharged state), E	(w/o) Total S-crystalline	9.1	7.7	6.7	12.0	10.5	9.1	23.7
Amorphous PbSO_4 produced, F	(w/o) E - D	3.9	2.4	2.3	7.5	6.9	2.6	20.0
Equivalent amorphous PbO_2 produced, G	(w/o) $F \times 0.789^*$	3.1	1.9	1.8	5.9	5.4	2.1	15.8
Amorphous PbO_2 (charged state), H	(w/o) Total amorphous D	17.2	12.8	12.5	15.6	22.4	22.3	24.6
Utilization of amorphous PbO_2	(%) $100 \times (G/H)$	18.0	14.8	14.4	37.8	24.1	9.4	64.2

† Data for T2 and T4 obtained from Table III; data for slow discharge battery not given in detail.

* Ratio factor = (molecular weight PbO_2) / (molecular weight PbSO_4).

dioxide ratio was lowered to a value around 0.15 early in the service life. This suggests that the ratio itself is not important, but that it is the conditions of curing and/or formation of the plates (giving rise to an initially high ratio) that determine the final performance level.

A comparison of the performance of battery T1, operated at the same temperature (25°C) as T2 but under the IMP driving profile, shows that the lower average discharge current (12.4 compared to 30.5A, Table I) results in a 35% improvement in cycle life and a five-fold increase in equivalent kilometers traveled. It can be seen from Fig. 5 that a similar improvement in vehicle range under the Batronic profile would only be achieved by operating the same battery above 60°C. The advantages of advanced vehicle design are obvious.

Mode of battery failure.—Detailed examination of the XRD phase analysis results presented in Fig. 2 and Tables III and IV reveals that the onset of battery failure is associated with several factors.

(i) An accelerating decline in the conversion rate of β -PbO₂ to PbSO₄, both in the crystalline and amorphous components, despite the fact that the overall PbO₂ content of the charged plate remains relatively constant (especially at low temperatures). Neutron diffraction, structural, and electrochemical activity studies discussed elsewhere (25, 39) suggest that β -PbO₂ particles in battery plates remain intrinsically electrochemically active and that the inability of bulk β -PbO₂ to discharge is probably a consequence of the individual particles becoming electrically isolated from each other in the active mass and from the current collecting grid itself. Similar conclusions have been drawn by other workers (8, 53-55), although the possibility of a loss in electrochemical activity of the PbO₂ itself has received support (23, 24, 27, 28, 52, 57, 58). Since the majority of the PbSO₄ produced on discharge continues to be converted back to PbO₂ on charge, progressive encapsulation of the PbO₂ by insulating particles or films of PbSO₄ would appear to be the more likely mechanism for this electrical isolation (as opposed to passivation of the grid by PbSO₄ films). The former mechanism is eminently feasible, since PbSO₄ particles grow at the expense of PbO₂ particles and are able to convert back to PbO₂ since they remain in contact with the electrolyte.

(ii) An increase in the amount of amorphous material. The amorphous material displays a somewhat more rapid decline in utilization with battery cycling than the crystalline component (Table IV). A rise in temperature may be expected to increase the amount of fine-grained material with cycling, and we note (Table III) that batteries T3, T4, and T5 do indeed display the greatest relative increases in the amorphous component over their service life.

(iii) An increase in the variability of positive-plate phase composition and active material utilization (see particularly batteries T1-T3 operated at lower temperatures). The occurrence of an occasional sulfated plate has been accepted in the past as a consequence of variability in plate manufacture, but this has not been considered to be a major cause of failure (44). However, measurements of the potentials of positive- and negative-plate groups in individual cells of batteries monitored during charge/discharge cycling have shown that catastrophic declines in battery capacity can be related to the failure (*i.e.*, sharp drop in discharge voltage) of a positive-plate group in only one of the cells (39). Subsequent XRD phase analysis of the positive plates in the failed cells has often revealed that one or more of the plates are heavily sulfated in the charged state. The heavy sulfation has therefore contributed to a sharp decrease in the electrical conductivity of the active material and thus to a rapid decline in its discharged voltage (8, 54, 55). Why only

certain plates are sulfated when the majority of the others in the battery, and indeed in the same cell, are not, remains to be determined. Whatever the cause of sulfation, it is clear from Fig. 2 that the operation of a battery at high temperature promotes the maintenance of a more uniform distribution of phases between the plates and prevents the early formation of "hard" sulfate.

(iv) An increased rate of shedding in the cell observed (by potential measurements) to fail first. Nonetheless, the amount of material shed was not sufficient by itself to cause cell failure. No marked increase in the rate of material shedding from the plates was observed on raising the operating temperature from 25° to 60°C (Table I).

(v) Negative plate degradation at high temperatures. For example, autopsies conducted on T5 operated at 60°C revealed that swelling and mossiering of the negative plates took place. This led to internal shorting of the battery. In addition, the grids of the positive plates were found to be in a badly corroded state and extremely fragile. Since this battery was observed to maintain a relatively uniform plate composition during its considerable period of service, it is likely that batteries operated at high temperature fail by a different mechanism (namely, positive-plate grid corrosion and/or negative-plate mossiering) from those operated at lower temperatures (namely, plate inhomogeneity/sulfation of the charged plates).

Summary and Conclusions

Application of the XRD phase analysis procedure to single-phase samples of various chemically and electrochemically prepared varieties of PbO₂ and PbSO₄, and to synthetic mixtures of these compounds, has demonstrated the viability of the method for phase analysis of positive plates of lead-acid batteries. This conclusion has been confirmed by comparisons of XRD results for real battery plates with those for independent estimates of composition obtained from electrical measurements and wet chemical analysis.

Studies of batteries operated under simulated electric-vehicle service at four temperatures, two ratios of the PbO₂ dimorphs, and two mean discharge currents have indicated that the overall utilization of active material increases substantially with increasing temperature and decreasing current. The utilization of β -PbO₂ is observed to be higher than that of α -PbO₂ under all conditions. The amount of α -PbO₂ declines rapidly during the early stages of battery operation due to an irreversible conversion to β -PbO₂, but the utilization of this oxide remains fairly constant, whereas that of β -PbO₂ declines. This observation may explain why batteries with higher initial values of the α -PbO₂: β -PbO₂ ratio appear to have longer cycle lives.

Decline in battery capacity at all temperatures is brought about by the failure of the β -PbO₂ particles to be reduced to PbSO₄ on discharge, rather than a failure of the PbSO₄ to be oxidized on charge. This suggests that electrical isolation of the β -PbO₂ particles is the cause of capacity loss rather than the development of extensive grid corrosion. However, at low temperatures of operation, variability in phase composition between individual positive plates can be quite large, and the occasional development of a few heavily sulfated charged plates can lead to the failure of the entire battery, even though the majority of the plates are not sulfated.

At higher temperatures of operation, the positive plates are more uniform in composition and failure of the battery does not result from heavy sulfation of a few individual plates. Instead, the battery fails due to negative-plate swelling and mossiering, and/or the presence of substantial positive-plate grid corrosion. Nevertheless, as at lower temperatures, the capacity of the battery slowly declines throughout the middle and

later stages of operation as the conversion efficiency of β -PbO₂ to PbSO₄ decreases.

Comparison of XRD results with wet chemical analysis results shows that the amorphous PbO₂ component of the positive plates discharges at a similar rate to that of the crystalline component, but that the amorphous material utilization declines somewhat more rapidly with cycling. Since the amorphous content of plates varies from only 10 to 29 w/o, and increases slightly during cycling, the presence of amorphous material has only a small adverse effect on overall battery performance. Nevertheless, the results suggest that the amorphous content should be kept to a minimum during plate manufacture.

Acknowledgments

We are indebted to the Australian Lead Development Association for the loan of their Battronic van, to Mr. D. Gosden for technical information on the IMP van, to Dunlop Batteries Australia, Limited, for supplying materials for the test batteries, to the International Lead Zinc Research Organization for their joint support and for permission to publish this work, and to our colleagues D. C. Constable, J. R. Gardner, J. A. Hamilton, P. R. Strode, S. Swan, R. G. Whiteley, and L. B. Zalzman for their assistance with the technical work.

Manuscript submitted May 20, 1983; revised manuscript received Oct. 5, 1983.

The CSIRO Division of Mineral Chemistry assisted in meeting the publication costs of this article.

REFERENCES

- J. E. Hatfield and O. W. Brown, *Trans. Electrochem. Soc.*, **72**, 361 (1937).
- R. H. Greenburg and B. P. Caldwell, *ibid.*, **80**, 71 (1941).
- H. Bode and E. Voss, *Z. Electrochem.*, **60**, 1053 (1956).
- S. Ikari, S. Yoshizawa, and S. Okada, *J. Electrochem. Soc. Jpn.*, **27**, E-186, E-223 (1959).
- V. H. Dodson, *This Journal*, **108**, 401 (1961).
- V. H. Dodson, *ibid.*, **108**, 406 (1961).
- A. C. Simon and E. L. Jones, *ibid.*, **109**, 760 (1962).
- E. Voss and J. Freundlich, in "Batteries," D. H. Collins, Editor, p. 73, Pergamon Press, Oxford (1963).
- P. Ruetschi, J. Sklarchuk, and R. T. Angstadt, in "Batteries," D. H. Collins, Editor, p. 89, Pergamon Press, Oxford (1963).
- N. N. Federova, I. A. Aguf, L. M. Levinzon, and M. A. Dasoyan, *Ind. Lab.*, **30**, 914 (1964).
- N. E. Bagshaw, R. L. Clark, and B. Halliwell, *J. Appl. Chem.*, **16**, 180 (1966).
- D. Kordes, *Chem.-Ing.-Tech.*, **38**, 638 (1966).
- W. C. M. Carey, British Railways Research Department Report C.R.21 (July 1965).
- P. Ness, *Electrochim. Acta*, **12**, 161 (1967).
- T. Chiku, *This Journal*, **115**, 982 (1968).
- K. Weisener, W. Hoffman, and O. Rademacher, *Electrochim. Acta*, **18**, 913 (1973).
- K. Weisener and P. Reinhardt, *Z. Phys. Chem.*, **256**, 285 (1975).
- A. A. Abdul Azim and A. A. Ismail, *J. Appl. Electrochem.*, **7**, 119 (1977).
- P. R. Skidmore and R. R. Schwarz, *Analyst*, **104**, 952 (1979).
- H. Nguyen Cong, A. Ejjenne, J. Brenet, and P. Faber, *J. Appl. Electrochem.*, **11**, 373 (1981).
- K. Harris, R. J. Hill, and D. A. J. Rand, *J. Power Sources*, **8**, 175 (1982).
- J. Burbank, A. C. Simon, and E. Willihnganz, in "Advances in Electrochemistry and Electrochemical Engineering," P. Delahay and C. W. Tobias, Editors, p. 157, Wiley-Interscience, New York (1971).
- S. M. Caulder and A. C. Simon, *This Journal*, **121**, 1546 (1974).
- A. C. Simon and S. M. Caulder, in "Power Sources 5," D. H. Collins, Editor, p. 109, Academic Press, London (1975).
- R. J. Hill, *Mater. Res. Bull.*, **17**, 769 (1982).
- P. T. Moseley, J. L. Hutchison, and M. A. M. Bourke, *This Journal*, **129**, 876 (1982).
- S. M. Caulder, J. S. Murday, and A. C. Simon, *ibid.*, **120**, 1515 (1973).
- A. C. Simon, S. M. Caulder, and J. T. Stemmler, *ibid.*, **122**, 461 (1975).
- B. Burrows and H. Giess, *ibid.*, **122**, 1640 (1975).
- L. E. Alexander and H. P. Klug, *Anal. Chem.*, **20**, 886 (1948).
- H. P. Klug and L. E. Alexander, "X-Ray Diffraction Procedures," 2nd. ed., Wiley-Interscience, New York (1974).
- F. H. Chung, *Adv. X-Ray Anal.*, **17**, 106 (1974).
- F. H. Chung, *J. Appl. Crystallogr.*, **8**, 17 (1975).
- S. Altree-Williams, J. G. Byrnes, and B. Jordan, *Analyst*, **106**, 69 (1980).
- C. R. Hubbard, E. H. Evans, and D. K. Smith, *J. Appl. Crystallogr.*, **9**, 169 (1976).
- C. R. Hubbard and D. K. Smith, *Adv. X-Ray Anal.*, **20**, 27 (1977).
- S. Altree-Williams, *Anal. Chem.*, **50**, 1272 (1978).
- R. J. Hill, *J. Power Sources*, **9**, 55 (1983).
- D. C. Constable, J. R. Gardner, J. A. Hamilton, K. Harris, R. J. Hill, D. A. J. Rand, S. Swan, and L. B. Zalzman, ILZRO Project no. LE-290, Progress Rpt. 6 (January-June 1982).
- J. A. Hamilton, K. Harris, J. F. Moresby, and D. A. J. Rand, ILZRO Project no. LE-290, Progress Rpt. 1 (July 1, 1979-December 1, 1979).
- D. Barrett, M. T. Frost, J. A. Hamilton, K. Harris, I. R. Harrowfield, J. F. Moresby, and D. A. J. Rand, ILZRO Project no. LE-290, Progress Rpt. 2 (December 1, 1979-June 15, 1980).
- M. T. Frost, J. A. Hamilton, K. Harris, I. R. Harrowfield, R. J. Hill, J. F. Moresby, and D. A. J. Rand, ILZRO Project no. LE-290, Progress Rpt. 3 (July-December 1980).
- J. R. Gardner, J. A. Hamilton, K. Harris, R. J. Hill, J. F. Moresby, and D. A. J. Rand, ILZRO Project no. LE-290, Progress Rpt. 4 (January-June 1981).
- M. T. Frost, J. R. Gardner, J. A. Hamilton, K. Harris, I. R. Harrowfield, R. J. Hill, J. F. Moresby, D. A. J. Rand, S. Swan, and L. B. Zalzman, ILZRO Project no. LE-290, Progress Rpt. 5 (July-December 1981).
- D. A. J. Rand, S. Swan, R. Woods, and L. Zalzman, NERDDC Project 79/9317, Progress Report no. 2, CSIRO Division of Mineral Chemistry Communication MCC 333 (June 1981).
- J. R. Gardner, K. Harris, R. J. Hill, D. A. J. Rand, S. Swan, R. Woods, and L. B. Zalzman, NERDDC Project 79/9317, Progress Report no. 3, CSIRO Division of Mineral Chemistry, Communication MCC 396 (June 1982).
- "Interim Procedure for Testing Electric Road Vehicles," Australian Electric Vehicle Association, Melbourne (1976).
- D. Gosden, in "EVE 80, Electric Vehicle Exposition Conference Papers," K. King, Editor, p. 409, South Australian Energy Council, Adelaide (1980).
- A. B. Gancy, *This Journal*, **116**, 1496 (1969).
- K. Asai, M. Tsubota, K. Yonezu, and K. Ando, *J. Power Sources*, **7** (1981).
- C. P. Wales and A. C. Simon, *This Journal*, **128**, 2512 (1981).
- A. C. Simon and S. M. Caulder, *ibid.*, **118**, 659 (1971).
- P. Casson, N. A. Hampson, K. Peters, and P. Whyatt, *J. Appl. Electrochem.*, **7**, 257 (1977).
- J. Bouet and J. P. Pompon, *Electrochim. Acta*, **26**, 1477 (1981).
- H. Metzendorf, *J. Power Sources*, **8**, 281 (1982).
- J. A. Duisman and W. F. Giauque, *J. Phys. Chem.*, **72**, 562 (1968).
- J. L. Dawson, M. E. Rana, B. Munasiri, and J. McWhinnie, in "Power Sources," Vol. 7, J. Thompson, Editor, p. 1, Academic Press, London (1979).
- P. Faber, *Electrochim. Acta*, **26**, 1435 (1981).

A "Precharged" Positive Plate for the Lead-Acid Automotive Battery

I. Positive Plate Allowing Direct Incorporation of PbO_2

E. J. Taylor*

Giner Incorporated, Waltham, Massachusetts 02154

G. A. Shia*

Allied Corporation, Buffalo Research Laboratory, Buffalo, New York 14210

D. T. Peters*

Inco Alloy Products Company Research Center, Inco-Sterling Forest, Suffern, New York 10901

ABSTRACT

A process to manufacture the positive plate of the lead-acid battery that eliminates conventional curing and formation steps via the direct incorporation of PbO_2 active material into the grid is described. "Precharged" plates made from a mixture of tetrabasic lead sulfate, PbO_2 , and water were found to be strong and capable of delivering first cycle (*i.e.*, with no formation) cranking rate capacity which was 35% of conventionally produced plates tested in the same format. Full capacity is obtainable within three to five charge-discharge cycles. At this point, the precharged plates were found to be structurally indistinguishable from conventionally processed plates. To ensure in these initial studies that the PbO_2 was electrochemically active, the material was obtained from electrochemically formed conventional positive plates. The successful use of chemically prepared PbO_2 is demonstrated in the following paper. This new process is simple and will allow the manufacture of ready-to-use plates on modern automated expanded metal platemaking equipment.

The work described in this paper addresses a radical approach to lead-acid battery manufacture which would result in a simpler processing technology more amenable to modern automated expanded metal plate making equipment and would offer the marketing advantage of a truly dry charged battery with an "infinite" shelf life. To aid in the understanding of the significance of this work, a brief description of current lead-acid battery processing technology is required (1, 2).

Conventional battery plates are made from a starting material consisting of an incompletely oxidized Pb powder (Pb, PbO orthogonal and tetragonal forms), sometimes mixed with Pb_3O_4 in various ratios. This powder is mixed with H_2SO_4 and water to form a paste which is then applied to a lead alloy grid. Subtle differences exist between the positive and negative pastes, but the reactive paste chemistry is not different. Numerous complex chemical reactions occur during the mixing of this reactive paste leading to PbSO_4 , $\text{PbO} \cdot \text{PbSO}_4$, $3\text{PbO} \cdot \text{PbSO}_4 \cdot \text{H}_2\text{O}$, $4\text{PbO} \cdot \text{PbSO}_4$, and Pb_3O_4 in various relative concentrations depending on: (i) starting material composition; (ii) relative amount of acid and water added; and (iii) mixing rate and mixing temperature. The pasted plates are allowed to cure, usually for several days. During curing, the water is removed from the plates in a manner such that dissolved compounds are deposited at paste particle contact points in a manner analogous to cement setting (1). Additional chemical reactions occur during curing which can change the relative concentrations of the species in the pasted plate. Additionally, shrinkage of the paste from the grid members may occur during curing. This shrinkage can deleteriously affect the resulting battery plate, particularly when nonantimonial alloys are used in the battery grids. The variables influencing the curing process are time, temperature, and humidity. After curing, the plates are immersed in acid and a formation current which anodically forms lead dioxide at the positive and cathodically forms sponge lead at the negative is applied to the plates for an extended period up to about 24h. This formation current generates a conductive network of positive and negative active materials and an integral grid/active mass interface. Both phenomena

aid in the subsequent discharge of the battery plates by forming a conductive network between the grid and the active mass. Additionally, much speculation regarding the production of a lead dioxide (in the positive plate) of intrinsic electrochemical activity exists in the literature and is discussed in the following paper (3). The variables to be considered during formation are: (i) current density; (ii) acid concentration; (iii) time; and (iv) the composition of the cured plate. The above-mentioned process variables are considered critical to the formation of a good positive plate and this topic has been the subject of numerous technical papers (4-6). The numerous variables involved in conventional lead-acid battery manufacture and their concomitant effect on battery performance make a simpler more controllable manufacturing scheme highly desirable.

Consequently, the goal of this work was the direct incorporation of the active masses (*i.e.*, lead dioxide and sponge lead) into a grid, thus eliminating the process steps of curing and formation. In eventual application, it would be desirable for these "precharged" electrodes when incorporated in an automotive starting, lighting, and ignition (SLI) battery to be capable of delivering sufficient cranking rate capacity to start an automobile with subsequent charging by the automobile's electrical system generating the additional reserve capacity. In addition to providing a simpler, more controllable automated process, this envisioned manufacturing scheme would offer a type of dry-charged product with an extended shelf life. Since these battery plates need not come in contact with sulfuric acid prior to their use, the sulfation of the active masses which limits conventionally manufactured battery shelf life would not occur.

Work on the precharged positive electrode process has been divided into two areas: (i) development of a technique to incorporate PbO_2 into a grid in a dischargeable form, and (ii) identifying a chemically produced but electrochemically active form of PbO_2 which may be incorporated into the above process. The first topic is covered in this paper. The second is the subject of a subsequent paper (3). The method of preparation, performance, and characteristics of positive electrodes produced via this novel process have been described in two patent applications (7, 8). A

* Electrochemical Society Active Member.

process for manufacturing a precharged negative electrode will be reported at a later date.

Experimental

Experimental evaluation of the precharged active mass formulations was conducted on $40 \times 68 \times 2$ mm grids cast in a Pb-0.065% Ca-0.50% Sn alloy as shown in Fig. 1. The test cell consisted of one test positive between two conventionally manufactured negative plates from the Exide 10 A-h small rechargeable battery separated by microporous rubber separators. Positive polarization was recorded vs. a Hg/Hg₂SO₄ reference electrode in the same solution. The electrochemical evaluation was conducted in 100 ml of 1.280 sp gr sulfuric acid electrolyte. Cells were discharged (without any prior "boost" charging) at a 10A (200 mA/cm²) cranking rate at room temperature. Capacity was measured as the time in seconds to reach 500 mV positive polarization. Capacity is also expressed in this work as utilization efficiency; i.e., the percentage of the theoretical ampere-hour capacity based on the weight of active material delivered by the experimental plate. The cells were then recharged to a potential limit of 2.5V with initial current density limited to 60-80 mA, and the process was repeated until five cranking rate discharge capacities were recorded.

The general processing scheme involved applying a water paste of the precharged active mass to the grid followed by hot-pressing the pasted grids between two stainless steel platens at 130°C for 30-60s at about 36 MPa (5200 psi). The precharged electrode performance was compared to that of conventionally produced positive electrodes tested in the same format.

Results

To separate the intrinsic activity consideration of electrochemically produced lead dioxide from precharged formulations, initial experiments were conducted with lead dioxide obtained by crushing pellets from well formed positive plates. The initial approach to binding the lead dioxide into the grid was to thoroughly mix lead dioxide and 0.5 w/o (weight percent) Teflon¹ (du Pont K-10) powder in a mechanical mixer with substantial shearing action. The mass was

¹ Registered trademark of the E. I. du Pont de Nemours and Company.

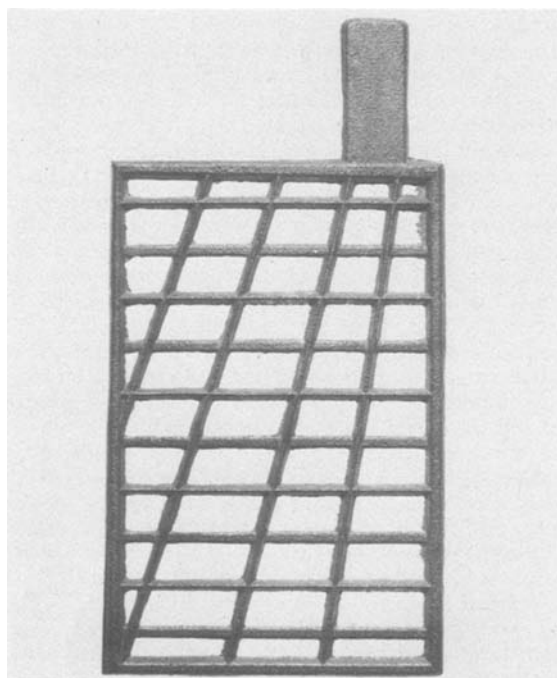


Fig. 1. The small Pb-0.065% Ca-0.50% Sn cast grid used in this study. Dimensions are $40 \times 68 \times 2$ mm.

then wet with water, pasted, and pressed into grids as described above. One batch of plates made in this manner was overpasted by 0.8 mm (0.030 in) to determine if any benefit was incurred from the additional compacting action. Teflon-bonded plates and the laboratory standard plates made by conventional paste technology are described in Table I, and the discharge characteristics are presented in Table II. No capacity at the cranking rate was observed with Teflon-bonded electrodes, and during charge, the active mass was observed to mechanically disintegrate from the grids. Some electrodes from these two batches were then tested at a 10 mA/cm² rate. The flush-pasted electrodes exhibited poor first cycle capacity and could not mechanically tolerate the subsequent charging. The overpasted electrodes could withstand subsequent charging but still were far inferior to the standard plates even after a third cycle low rate conditioning discharge.

At this point it was concluded that material which could add mechanical support to the precharged active mass and could additionally be converted to lead dioxide on charging would be beneficial. Tetrabasic lead sulfate (TTB) was identified as a possible material which could serve this purpose. TTB has a fibrillar, needle-like morphology as shown in Fig. 2. TTB is used in place of a conventional paste by Western Electric to manufacture the round cell for stationary float service applications (9). The advantages of a TTB paste are: (i) it may be prepared from water, (ii) shrinkage during curing is eliminated, and (iii) increased cycle life performance has been reported (9, 10). The improved cycle life performance of plates formed from a TTB paste appears due to its metasomatic conversion to PbO₂ (9, 10) in which the initial TTB morphology is maintained. Metasomes are generally characterized as hard, dense materials due to their diffusional growth mechanism, analogous to zone refining (9). Apparently the resultant interlocking prismatic needles of PbO₂ act to delay the active mass shedding. The presence of needles of PbO₂ in conventional pastes (presumably resulting from the TTB in the cured mass) has additionally been correlated to improved cycle life behavior (11). One drawback of positive plates produced from a TTB paste is the longer formation time required and the necessity to form in low gravity acid (1.001-1.005) to prevent sulfation of the TTB (12). TTB is oxidized to PbO₂ via the following reaction (5)

Table I. Active mass weight, porosity, and theoretical capacity of Teflon-bonded precharged electrodes and lab standard positive electrodes

	Active mass weight (g)	Porosity, %	Theoretical capacity (A · h)
Flush-pasted	31.3 ± 0.57	40	7.01 ± 0.128
0.8 mm (30 mil) overpasted	40.9 ± 1.9	38	9.16 ± 0.426
Lab standard	25.9 ± 1.1	41	5.80 ± 0.246

Table II. Discharge times of Teflon-bonded and lab standard positives at a 10 mA/cm² rate to a 1.75V cutoff

Cycle	Average data from four electrodes		Lab standard positives
	Discharge time (s) Teflon-bonded positives		
	Flush-pasted	Overpasted	
1	16.1	32.2	203
2	0	39.3	203
3	0	126.9*	203
4	0	52.2	203

* 2 mA/cm² conditioning discharge.

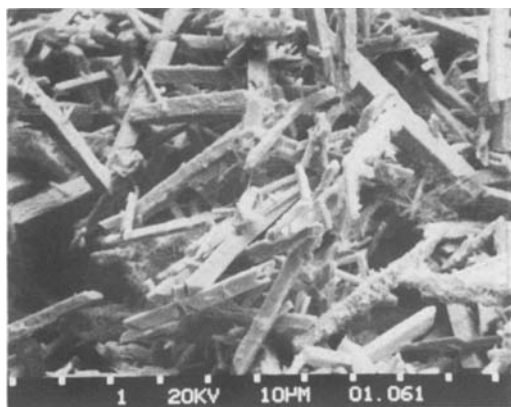


Fig. 2. Scanning electron micrograph of tetrabasic lead sulfate (TTB) as received from the Eagle-Picher Company.



1g of TTB converts to 1g of PbO_2 , and a 15% volume reduction accompanies the conversion.

A mix of 30 w/o TTB and 70 w/o PbO_2 obtained from battery plates was thoroughly blended in a wire mill, and 29 ml of water was added per 100g of mix. Grids were then hand-pasted and hot-pressed. A scanning electron micrograph of a pellet of this active mass after hot-pressing is shown in Fig. 3. In this particular micrograph, the PbO_2 is a chemically prepared material from Eagle-Picher. The characteristics of these plates along with their first and second cycle performance are shown in Table III. Note that included in the 25.9g of precharged active mass is 30% of material (TTB) which is incapable of delivering capacity. These plates were able to deliver first discharge capacity at the cranking rate (200 mA/cm^2), and exhibited improved discharge capacity after their first charge. Note the initial polarization (IP) characteristic in Table III. This is the voltage drop just after the discharge current is applied to the plate and is attributed to IR losses in the grid/active mass and at the grid/active mass interface. In the first cycle, the IP for the precharged plates is somewhat larger than for standard plates and may be rationalized by insufficient interparticle and grid/active mass contact resulting in larger "IR" losses relative to the standard plates. The decrease in IP with subsequent cycling indicates the development of a more integral active mass and grid/active mass interface. The bulk porosity of these plates is somewhat lower than one would encounter in automotive plates (~45%) but porosity could perhaps be increased later by judicious choice of PbO_2 particle



Fig. 3. Scanning electron micrograph of "precharged" positive plate made with 30% TTB and 70% Eagle-Picher (medium cure) lead dioxide prior to exposure to sulfuric acid.

Table III. Performance of TTB-bound precharged positives using battery plate PbO_2 at two degrees of overpasting at 200 mA/cm^2 cranking rate

	Average of six electrodes		
	TTB-bound precharged positives		Lab standard positives*
	0.8 mm (30 mil) Over-pasted	0.25 mm (10 mil) Over-pasted	
Active mass weight (g)	29.6 ± 0.71	25.9 ± 0.87	25.9 ± 1.1
Porosity (%)	39	40	41
IP (mV)			
1st discharge	346 ± 4	332 ± 18	264 ± 9
2nd discharge	273 ± 9	273 ± 6	
Discharge time (s)			
1st discharge	59.9 ± 5.4	57.6 ± 6.5	160 ± 15
2nd discharge	114 ± 15	123 ± 3	
Utilization efficiency (%)			
1st discharge	2.51 ± 0.23	2.76 ± 0.31	7.61 ± 0.75
2nd discharge	4.78 ± 0.63	5.89 ± 0.14	

* Conventional well-formed plates after 10 charge-discharge cycles.

size and size distribution or even with the use of pore formers if necessary.

Some overpasting of the grid to enhance the effectiveness of the pressing operation was found to be beneficial. The data of Table III shows, however, that an overpaste as large as 0.8 mm (30 mil) is not necessary and that somewhat higher utilization efficiencies are obtained with the 0.25 mm (10 mil) overpaste.

The active mass after three discharge and two charge regimes is shown in Fig. 4. No evidence of TTB is observed, indicating its nearly total conversion to PbO_2 . This active mass appears more integral and it is apparent that the conversion of TTB to PbO_2 has acted to cement the structure together. The cranking rate performance of these precharged plates expressed as utilization efficiency during the first five cycles is shown in Fig. 5. By the third cycle, the cranking rate performance of the precharged plates is within the error range of the conventional positives.

Discussion

A limited amount of work was done to better understand the role of tetrabasic lead sulfate as a binder in the active material. Study of a number of scanning electron micrographs of the active material after hot-pressing but before immersion in acid (similar to Fig. 3) seemed to indicate little if any mechanical interaction of the PbO_2 particles with the needle-shaped TTB fibers. To determine if the morphology of the TTB had any effect on the initial performance of the plate, a mix of PbO_2 and 30 w/o TTB was prepared from TTB that had been ground in a mortar and pestle. The TTB before and after grinding is shown in the SEM's of

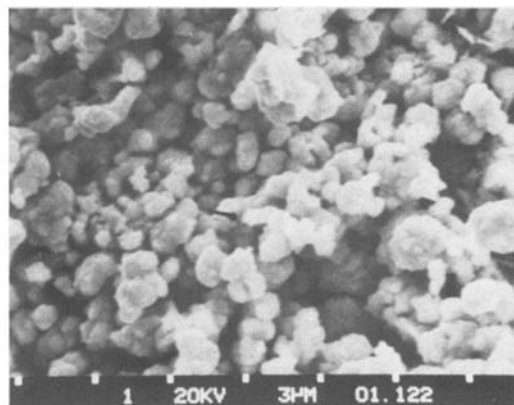


Fig. 4. Scanning electron micrograph of "precharged" positive material in the charged state after three discharge-recharge cycles.

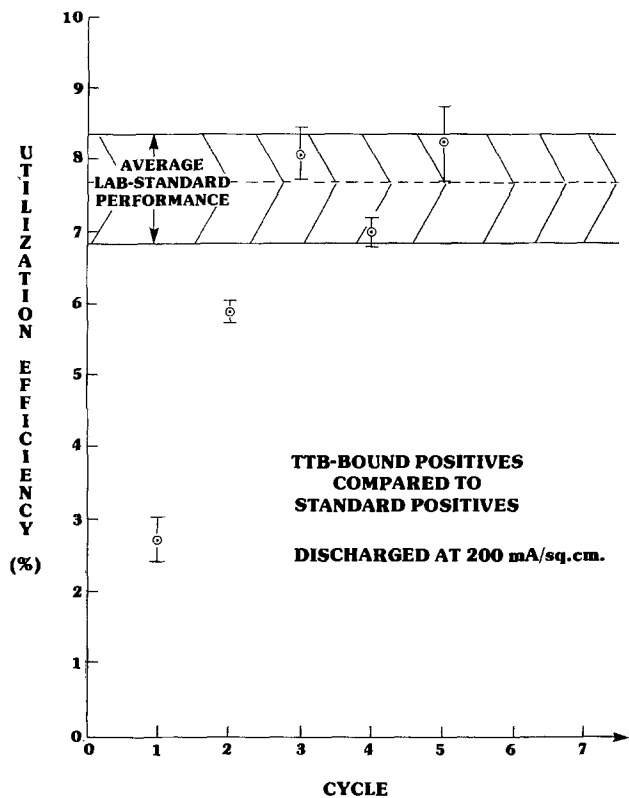


Fig. 5. Utilization efficiency at cranking rate (200 mA/cm^2) vs. cycle number for TTB-bound positives compared to standard positives. PbO_2 obtained from formed SRB positives. 0.25 mm (10 mil) overpasting of a 30% TTB-70% PbO_2 mix.

Fig. 6. After assembling these plates into cells, the capacity on the initial discharge was very similar to plates made with "as-received" TTB. It was noted, however, that the plates with ground TTB seemed to charge more rapidly and by the third discharge-recharge cycle, the capacity was in the range of conventional plates having similar density and pore size distribution characteristics. Plates were also made using no binder of any kind. After hot-pressing, these plates are reasonably strong and on initial discharge, they exhibit capacity and utilization efficiency greater than precharged plates made with TTB. But on subsequent cycles these plates deteriorated rapidly due to severe shedding of the PbO_2 .

From these experiments, it is concluded that the TTB makes no contribution to the mechanical properties of the plate in the hot-pressed condition and that a hot-press operation in itself results in a plate able to withstand handling. The TTB does, however, provide effective binding action on charge and through subsequent discharge-recharge cycles. Further, the morphology of the TTB is not important. In fact, binding of the plate is accelerated if the characteristic needle shape of the TTB is destroyed by grinding to effectively decrease the particle size of the TTB in the mix. Apparently, binding or cementing action on cycling results from local dissolution and reprecipitation and is markedly promoted by the presence of the tetrabasic lead sulfate.

Conclusion

These initial studies have shown that using TTB and battery plate PbO_2 , a "precharged" positive plate may be manufactured by a scheme which eliminates the conventional process steps of curing and formation. In the initial discharge with no prior formation, these "precharged" electrodes deliver ~35% of the cranking rate capacity at room temperature relative to conventionally prepared positives. Additional capacity is then generated from the "cycle up" capability of these

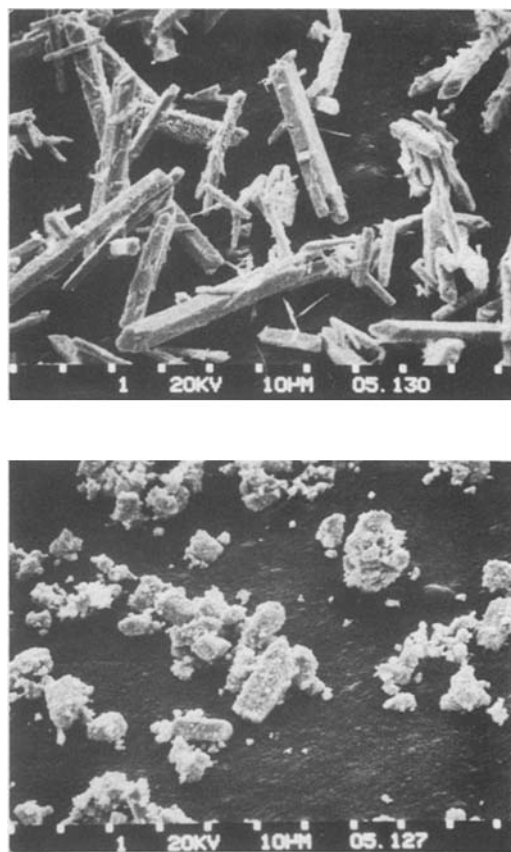


Fig. 6. Scanning electron micrographs of tetrabasic lead sulfate before (A, top) and after (B, bottom) grinding.

plates during subsequent charge or discharge-recharge cycles.

Clearly, a manufacturing process of this type offers the advantages of a process more amenable to automated continuous battery plate manufacture. Additionally, as with all dry-charged batteries, these batteries could be shipped at 1/3 less weight since they need not come in contact with acid until ready for sale, and the limited shelf-life problems resulting from a reactive paste would not be encountered.

This work addressed the problem of incorporating battery PbO_2 into a dischargeable structure. Clearly, an economical way of preparing an electrochemically active form of PbO_2 to be incorporated into this process is required. The following paper addresses the effect of various PbO_2 samples on precharged performance and plate morphology, and presents cycle life data results.

It is recognized that much work remains to be done to prove and to optimize the proposed new process. The critical effects of low temperatures on discharge performance, among many factors, had not been evaluated at the time work on the concept was discontinued.

Acknowledgments

This work was conducted under the auspices of Inco Research and Development Center at Sterling Forest. Initial discussions and encouragement from J. C. Duddy are gratefully acknowledged. The skillful assistance of D. Ropp in performing the laboratory testing is also acknowledged.

Manuscript submitted Aug. 19, 1983. This was Paper 36 presented at the San Francisco, California, Meeting of the Society, May 8-13, 1983.

Inco Alloy Products Company Research Center assisted in meeting the publication costs of this article.

REFERENCES

1. H. Bode, "Lead-Acid Batteries," John Wiley & Sons, New York (1977).
2. U. S. Bagotzky and A. M. Shundin, "Chemical Power Sources," Academic Press, New York (1980).
3. E. J. Taylor, G. A. Shia, and D. T. Peters, *This Journal*, **131**, 487 (1984).
4. A. C. Simon and E. L. Jones, *ibid.*, **109**, 760 (1962).
5. J. Burbank, *ibid.*, **111**, 765 (1964).
6. J. Burbank and E. J. Ritchie, *ibid.*, **116**, 125 (1969).
7. G. A. Shia and E. J. Taylor, U.S. Patent Application 385,507 (1982).
8. G. A. Shia and E. J. Taylor, U.S. Patent Application 385,508 (1982).
9. R. V. Biagetti and M. C. Weeks, *Bell Syst. Tech. J.*, **1305** (1970).
10. J. Burbank, *This Journal*, **113**, 10 (1966).
11. J. Burbank, in "Proceedings of the 3rd International Battery Symposium," pp. 43-60, Bourne-mouth (1962).
12. C. F. Yarnell and M. C. Weeks, *This Journal*, **126**, 7 (1979).

A "Precharged" Positive Plate for the Lead-Acid Automotive Battery

II. Effect of Various PbO₂ Types and Paste Formulations on "Precharged" Positive Plate Performance

E. J. Taylor*

Giner Incorporated, Waltham, Massachusetts 02154

G. A. Shia*

Allied Corporation, Buffalo Research Laboratory, Buffalo, New York 14210

D. T. Peters*

Inco Alloy Products Company Research Center, Inco-Sterling Forest, Suffern, New York 10901

ABSTRACT

A positive lead-acid battery electrode made by the direct incorporation of PbO₂ and a binder into the grid was described in the previous paper (1). The performance of "precharged" PbO₂ electrodes formulated with PbO₂ from various sources is reported in this paper. The PbO₂ samples were first characterized by x-ray diffraction, wet chemical analysis, differential scanning calorimetry, thermogravimetric analysis, BET surface area, and particle size distribution. Positive plates made from these PbO₂ samples were constructed using tetrabasic lead sulfate and other materials as binders according to the "precharged" plate concept previously described (1). Performance of these plates correlates with active material morphology and PbO₂ particle size rather than any intrinsic PbO₂ activity. Tetrabasic lead sulfate (TTB) and lead sulfate were shown to be the preferred binding materials for the "precharged" positive plate. Plates made with about 30% TTB and strengthened for early cycle performance with dynel fiber and Teflon¹ for green strength exhibited superior cycle life performance on a simulated automotive cycle life test relative to conventionally prepared positive electrodes.

A previous paper (1) described a novel lead-acid battery manufacturing process using tetrabasic lead sulfate (TTB) and lead dioxide to form a "precharged" positive plate which could be discharged at the automotive cranking rate. The lead dioxide used in that work was obtained from well formed conventionally processed battery plates to eliminate the effect of any intrinsic activity differences between battery and chemically produced lead dioxides. Clearly, for such a plate-making process to be economical, a relatively inexpensive chemically prepared PbO₂ would have to be suitable.

Numerous studies have been reported in the literature concentrating on the differences between chemically and electrochemically prepared lead dioxide. Chemical analysis indicated that, in general, electrochemically prepared lead dioxide was nonstoichiometric, whereas chemically prepared lead dioxide was nearly stoichiometric (2, 3). Using differential thermal analysis (DTA) and x-ray diffraction (XRD), it was shown that battery plate lead dioxide exhibited a considerable defect structure compared to chemically produced lead dioxide (4). Using nuclear magnetic resonance, other workers detected the presence of two types of combined hydrogen in battery plate lead dioxide compared to one form of combined hydrogen in chemically prepared samples (5). In addition, more combined hydrogen was observed in battery lead dioxide than in the chemical lead dioxide. The battery

positive capacity loss was attributed solely to the gradual conversion of the active form of lead dioxide to the inactive form during cycling. This inactive form of lead dioxide was indistinguishable from the reagent grade chemically prepared material. Using DTA, these workers identified an exothermic peak near 200°C in battery lead dioxide which was not present in chemically prepared samples (6). This peak was associated with the presence of combined hydrogen and attributed to the reordering of the lead dioxide lattice with the evolution of oxygen and combined water. During cycling, this peak area decreased (along with the battery plate capacity) and eventually disappeared with the thermogram becoming indistinguishable from that obtained from reagent grade lead dioxide. Other researchers, using neutron powder diffraction were able to show that battery lead dioxide contained hydrogen in the lattice along with an associated lead deficiency (7). Finally, other workers studying chemically and electrochemically prepared lead dioxide found amorphous material in the electrochemically prepared sample (8). The decrease in positive plate performance was attributed to the conversion of the "intrinsically" active amorphous lead dioxide to the nonactive crystalline form during cycling. Inelastic neutron scattering has also been used to attempt to distinguish between chemical and electrochemical forms of PbO₂. Moseley *et al.* found that both forms contained hydrogen probably in the form of water (9). Varma and co-workers found PbO₂ from battery plates to be associated with water molecules (10). Much evidence and speculation in the literature suggest that the intrinsic electro-

* Electrochemical Society Active Member.

¹ Registered trademark of the E. I. du Pont de Nemours and Company.

chemical inactivity of chemical lead dioxides would be a major barrier to its use in a positive electrode.

Consequently, this work focuses on the effect of various lead dioxide samples on "precharged" positive performance. In addition, the influence of active material particle size, porosity, and pore size distribution, as well as alternate binding materials in place of TTB, and cycle life performance of the "precharged" positives are reported. The binding material must convert to lead dioxide during the first few cycles of plate life.

Experimental

The processing and evaluation of "precharged" positive electrodes is as described in the preceding paper (1). Various lead dioxide samples were obtained from commercial sources for evaluation in the precharged positive format. These samples along with lead dioxide from battery plates were characterized by thermal gravimetric analysis (TGA), differential scanning calorimetry (DSC), XRD, wet chemical analysis, BET surface area, and particle size distribution. Bulk porosity and pore size distribution of the precharged electrodes and three conventionally cured and formed lab standard batches of varying bulk porosity were characterized by mercury porosimetry.

Tribasic lead sulfate and simple lead sulfate were substituted for TTB in the precharged format and evaluated. Finally, one precharged electrode batch was cycle life tested using an accelerated test regime having relatively high discharge rate and considerable overcharge. The test consisted of discharge at 3A for 4 min, followed by a 5A-2.5V per cell charge for 10 min, followed by 1 min at open circuit. Discharge and charge currents were adjusted to account for slight weight differences in the various electrode groups tested. The test is characterized by a shallow discharge at a reasonably high rate (20 min rate for the standard electrodes) followed by substantial overcharge. This is the type of regime encountered in automotive applications. The test was terminated when the cell polarization was greater than 625 mV prior to completing 4 min of discharge. This test is nonstandard but would be expected to yield a valid comparison between the experimental electrodes and conventionally prepared plates of the same size.

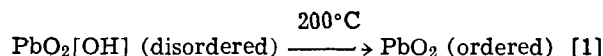
Results

PbO₂ characterization.—A number of lead dioxide samples were incorporated into the "precharged" positive format and evaluated. The oxides used, their BET surface area, and wet chemical analysis are shown in Table I. The reagent grade samples (Baker, Mallinckrodt, and Eagle-Picher ASC) were all characterized by a high PbO₂ content and a BET surface area in the range of 0.7-1.0 m²/g. Eagle-Picher also produces lead dioxide samples of increasing surface area for use as curing agents to promote polymer cross-linking. The Eagle-Picher high surface area samples were all pro-

duced in the same basic manner as the reagent grade samples; i.e., chemical oxidation of a divalent lead compound. The chemical analysis of these materials was ~90% PbO₂ with XRD indicating the presence of Pb₃O₄. The β-PbO₂ polymorph was the only form indicated by XRD in all the above samples. The battery plate lead dioxide obtained from a conventionally cured and formed positive plate contained 93% PbO₂ and exhibited a BET surface area of 9 m²/g. XRD indicated the presence of a small amount of the α-PbO₂ polymorph in addition to the β-PbO₂ polymorph.

The particle size distributions of the various lead dioxide samples are given in Fig. 1. The battery PbO₂ Sample A consisted of particles in the 1-3.0μ range. The Eagle-Picher ASC Sample B was typical of the reagent grade samples with a relatively broad particle size distribution. The Eagle-Picher high surface area samples all exhibited relatively sharp particle size distributions which become shifted to the submicron range as the BET surface area increased. The higher surface area of the chemical lead dioxides results from particles of smaller and smaller diameter, whereas the relatively high surface area of the battery sample results from its roughened irregular structure.

Thermogravimetric analysis (TGA) was obtained for the various PbO₂ samples after oven drying them overnight at 130°C to remove surface water. The TGA weight loss of the battery PbO₂ was 2% up to 300°C under argon at 10 psig and 10°C/min heating. The weight loss of all the other samples under the same conditions was less than 0.05%. DSC for these lead dioxide samples are shown in Fig. 2. The region of specific interest is the vicinity of 200°C, where various workers have attributed an exothermic peak observed in battery PbO₂ to the reaction (6)



This exothermic peak was observed in the battery lead dioxide Sample A and no evidence of the peak was seen in the chemically prepared samples, consistent with the reports in the literature and noted above.

Active material characterization.—The active material porosity characteristics as determined by mercury intrusion, and performance on a room temperature cranking rate (200 mA/cm²) discharge test of three

Table I. Chemical analysis and BET surface area of various PbO₂ samples

Sample	Source	Chemical analysis %PbO ₂	%SO ₄	BET (m ² /g)
A	Battery PbO ₂ *	93.0	2.3	9.0
B	Eagle-Picher (ASC)	98.9	—	0.7
C	Eagle-Picher (slow cure)	90.0	—	6.0
D	Eagle-Picher (medium cure)	88.8	—	8.0
E	Eagle-Picher (fast cure)	91.5	—	12.0
F	Eagle-Picher ("faster" cure)	83.5	—	27.0
G	Baker reagent	98.9	—	0.7
H	Mallinckrodt	100.2	—	0.8

* Obtained from well formed battery positive plates.

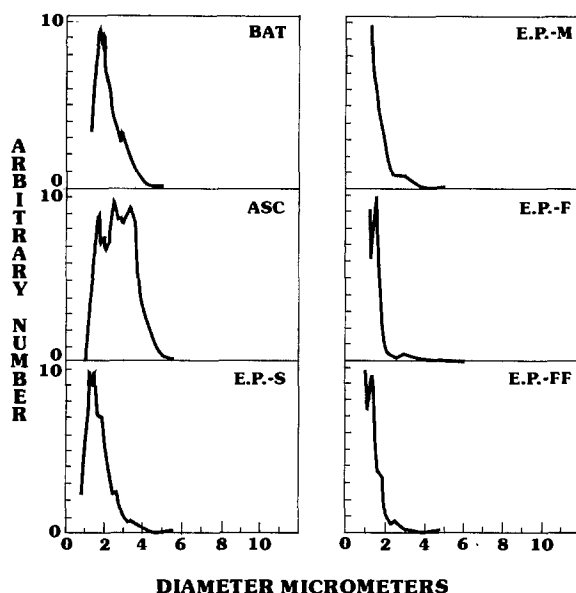


Fig. 1. Particle size distribution of various lead dioxide samples: BAT-PbO₂ obtained from battery plates; ASC-Eagle-Picher reagent grade PbO₂; E.P.-S Eagle-Picher (slow cure) PbO₂; E.P.-M Eagle-Picher (medium cure) PbO₂; E.P.-F Eagle-Picher (fast cure) PbO₂; E.P.-FF Eagle-Picher ("faster" cure) PbO₂.

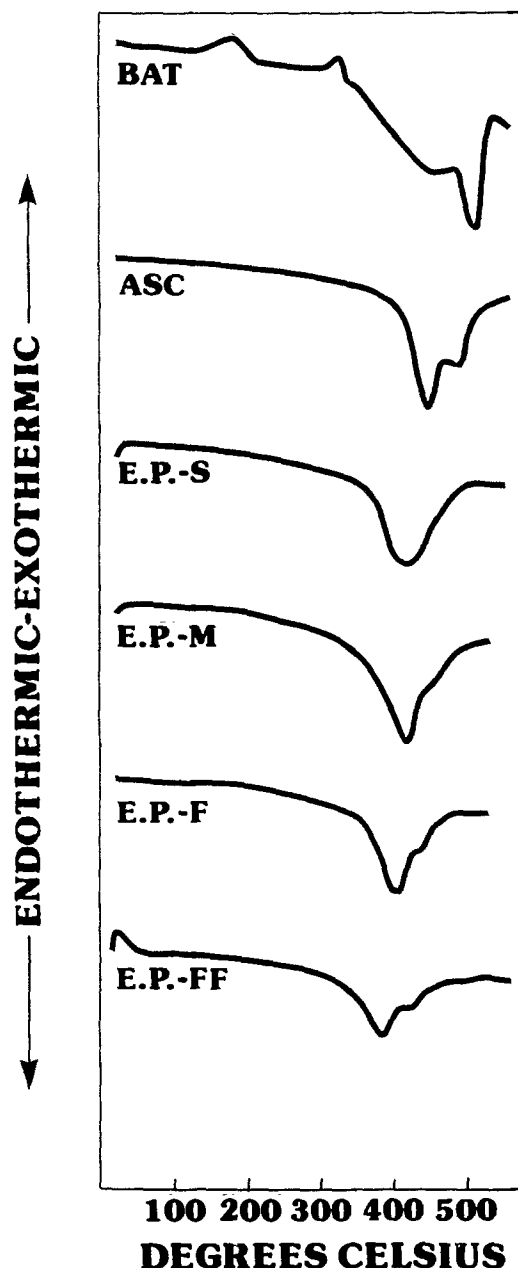


Fig. 2. Differential scanning calorimetry for various lead dioxide samples. As identified in Fig. 1.

conventionally prepared positive electrodes of different bulk porosity are shown in Table II. Note that while the active mass weights remain roughly the same, the bulk porosity range is $\sim 10\%$. A measure of pore size distribution is the pore radii at which 50, 80, 90, and 95% of the pore volume is intruded. In all three batches, 95% intrusion occurs by the time the pore radii have decreased to $0.03\text{--}0.06\mu$. In going from a bulk porosity of 35 to 45%, the pore radii at which 50% intrusion occurs increases from 0.562 to 1.52μ . In other words, bigger pores become apparent as the bulk porosity increases. The high rate discharge time increases with increasing porosity.

In Table III, the characteristics of "precharged" positive electrodes made with 30% TTB and 70% of the various PbO_2 samples and processed as described previously (1) are given. Water was added to these mixes so as to obtain pastes of similar plasticity. Larger amounts of water were required for the higher surface area lead dioxide samples. The mercury intrusion data may be classified into three groups for comparison with the standard electrodes. Precharged plates made with Sample A battery PbO_2 exhibit similar intrusion data

to the lab standards. Plates made with high surface area PbO_2 exhibit 50% intrusion at $\sim 0.1\mu$ and 95% intrusion at $\sim 0.03\mu$. Conversely, plates made with low surface area reagent grade PbO_2 exhibit 50% intrusion at $>1.0\mu$ and 95% intrusion at $>0.4\mu$. The significance of these data is exemplified by considering the pore volume distribution *vs.* pore radii shown in Fig. 3. The lab standard and precharged plates made with battery PbO_2 have a relatively large range of pore sizes. The precharged electrodes made with large particle reagent grade PbO_2 (Sample B), consists of large pores. Those made with high surface area PbO_2 (12 and $27\text{ m}^2/\text{g}$) (not shown in Fig. 3) consist of pores less than 0.1μ radii. A reasonable compromise is found in the medium cure PbO_2 Sample D.

Performance

The performance of the precharged plates to five high rate discharges ($200\text{ mA}/\text{cm}^2$) with no charge prior to the first discharges is shown in Fig. 4. Capacity is expressed here as utilization efficiency; *i.e.*, the percentage of the theoretical ampere hour capacity based on the weight of the active material delivered by the

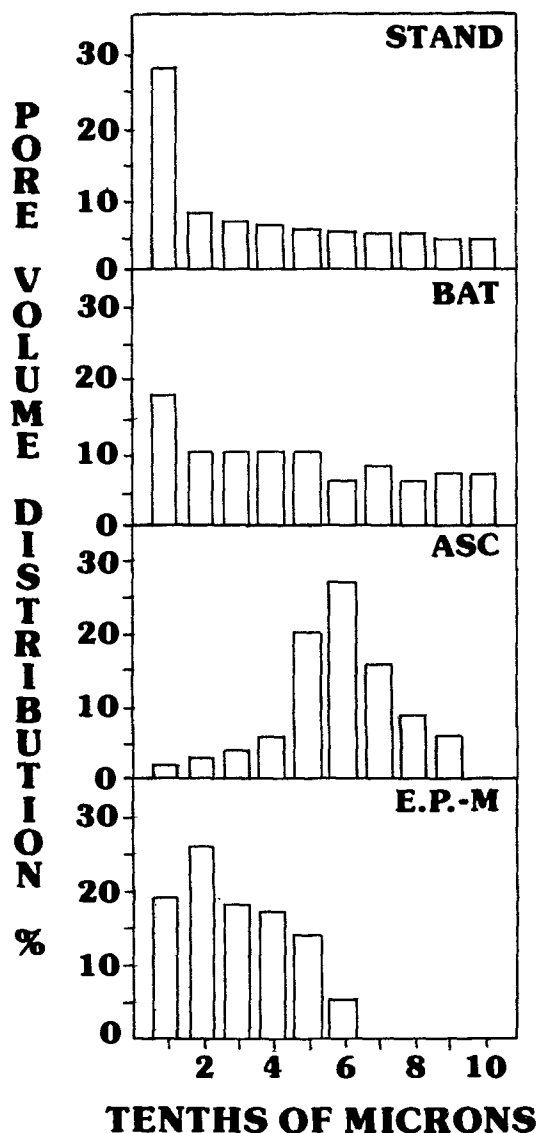


Fig. 3. Plates characterized by pore volume distribution: STAND—lab standard positive plate from Batch 10; BAT—precharged positive plate made from battery PbO_2 ; ASC—precharged positive plate made from Sample B Eagle-Picher reagent grade PbO_2 ; E.P.-M—precharged positive plate made from Sample D Eagle-Picher (medium cure) PbO_2 .

Table II. Plate characteristics and cranking rate discharge of lab standard positives

Electrode ID	Active mass weight (g)	Bulk porosity (%)	Hg porosimetry intrusion (μ)				Cranking rate (200 mA/cm ²) discharge time (s)	Utilization efficiency (%)
			50%	80%	90%	95%		
Batch 10	25.3 \pm 1.08	35.3	0.562	0.112	0.052	0.0328	164.0 \pm 16.9	8.03 \pm 1.10
Batch 11	25.0 \pm 0.12	38.5	0.889	0.217	0.0647	0.0350	249.0 \pm 35.6	12.02 \pm 0.89
Batch 12	24.0 \pm 0.39	45.6	1.52	0.562	0.198	0.0610	263.4 \pm 24.0	13.58 \pm 1.28

Table III. Precharged plate characteristics

Mix	Active mass weight (g)	Bulk porosity (%)	Hg porosimetry intrusion (μ)			
			50%	80%	90%	95%
70% Battery PbO ₂ -(Sample A)-30% TTB	26.4 \pm 0.86	40.7	0.464	0.126	0.0497	0.0319
70% Eagle-Picher (ASC)-(Sample B)-30% TTB	23.3 \pm 0.76	47.8	1.07	0.736	0.711	0.464
70% Eagle-Picher-(Sample E)-30% TTB-95 ml H ₂ O	24.5 \pm 0.99	42.6	0.0667	0.0427	0.0344	0.0281
70% Eagle-Picher-(Sample D)-30% TTB 100 ml H ₂ O	27.1 \pm 1.94	40.8	0.123	0.0762	0.0533	0.0381
70% Eagle-Picher-(Sample F)-30% TTB-115 ml H ₂ O	21.4 \pm 0.97	49.0	0.0649	0.0418	0.0309	0.0242

Table IV. Plate characteristics of a precharged positive batch using Eagle-Picher (fast cure) sample E PbO₂ at various conditions

Electrode state	Chemical analysis		BET, m ² /g	Bulk porosity	Intrusion volume (μ)			
	%PbO ₂	%SO ₄			50%	80%	90%	95%
After pressing	62.5	2.7	7	42.6	0.0667	0.0427	0.0344	0.028
After 1h in acid	58.6	7.8	4	38.0	0.0577	0.0381	0.0296	0.0242
After 1st charge	76.1	6.7	21	39.7	0.0628	0.0381	0.0293	0.0237

experimental plate. No first cycle capacity was obtained at this rate from precharged electrodes made with reagent grade lead dioxide (Sample B), although these electrodes did "cycle up" after subsequent charge. The first cycle performance of the precharged electrodes made with the 27 m²/g PbO₂ (Sample F) was remarkable, especially when one considers the presence of 30% inactive material in the active mass weight. These electrodes were not able to withstand subsequent charging, and it is suspected that this deterioration is related to the active material pore size distribution. The Eagle-Picher (Sample E-fast cure) precharged plate exhibited reasonable first discharge performance with subsequent "cycle up" capability. However, the Eagle-Picher (Sample D-medium cure) precharged plate seemed to offer the best compromise between first cycle performance and "cycle up" capability which approached that of the Batch 11 lab standard positive electrodes (Table II).

The physical plate characteristics of a batch of precharged positives made from Eagle-Picher Sample E

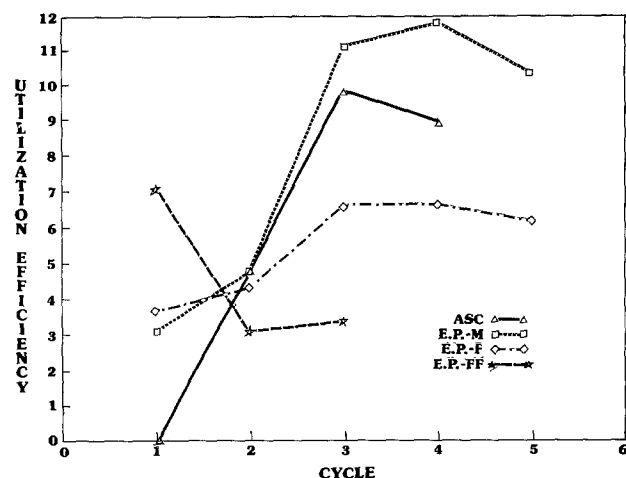
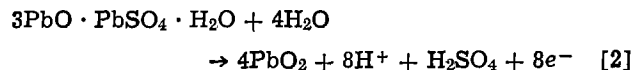


Fig. 4. High rate discharge (200 mA/cm²) utilization efficiency vs. cycle number of various precharged positive plates made with 30% TTB-70% PbO: ASC-Eagle-Picher reagent grade PbO₂; E.P.-M Eagle-Picher (medium cure) PbO₂; E.P.-F Eagle-Picher (fast cure) PbO₂; E.P.-FF Eagle-Picher (faster cure) PbO₂.

PbO₂ were characterized at three times; (i) after pressing, (ii) after soaking in acid for 1h but not discharged, and (iii) after discharge followed by the first charge. The data are presented in Table IV. The plates show a decrease in PbO₂ and an increase in SO₄ after soaking in acid for 1h. The data correlate with the fact that the acid specific gravity was also observed to drop during this soak along with the porosity decrease. A 15% volume increase is associated with PbO₂ → PbSO₄. The 3.9% drop in PbO₂ would account for a 1.58% SO₄ increase, whereas we observe a 5.1% increase in SO₄. Presumably, the TTB or an impurity therein is sulfating. A certain amount of sulfation may be beneficial by acting to hold the PbO₂ particles in contact. After charging, the pore size distribution remains the same, but the BET surface area and the PbO₂ content increase. This data would seem to indicate that the bulk porosity and pore size distribution of these precharged plates do not change significantly on putting them in acid and on charging, whereas the BET surface increases to that of a standard plate, apparently by nucleation of an array of extremely small particles on the surfaces of the structure present.

Tribasic lead sulfate as a binder.—A batch of precharged plates was made with 30 w/o (weight percent) tribasic lead sulfate-70% Eagle-Picher medium cure PbO₂ (Sample D). Tribase also has a needle-like morphology and should convert to PbO₂ via



These plates exhibited extensive sulfation after submersion in acid and no first discharge capacity was derived from them. They did, however, exhibit good capacity after four or five 200 mA/cm² discharges and recharge cycles. The extensive sulfation of the tribase precharged plates apparently severely decreased the plate porosity and limited its initial discharge capability. Therefore tribasic lead sulfate is not a suitable "binder" for these plates.

PbSO₄ as a binder with dynel and Teflon.—Neutral lead sulfate, PbSO₄, was also tried as a binder for the PbO₂. Because prior work had shown that in the hot-pressed condition, the sulfates do not contribute to

the mechanical strength of the plate, additions of 1 w/o dynel fiber and 0.5 w/o Teflon were also made to the mix to improve the "green" strength. Dynel fiber is commonly used in positive plates to strengthen the active material. The Teflon was added to the dry powder mix as an emulsion, and dried over night. Sufficient water was then added to provide the desired consistency for pasting. In these experiments, 75 w/o Eagle-Picher medium cure PbO_2 (Sample D-Table I) was mixed with 25 w/o of either TTB or $PbSO_4$. The performance of these plates in the 200 mA/cm² discharge test at room temperature is shown in Fig. 5. The initial performance was very good for both batches with capacity increasing markedly in the first few cycles. The better initial discharge performance of the plates made with $PbSO_4$ may be attributed to the absence of sulfation. The initial performance of the batch of plates made with TTB is somewhat lower than those made with $PbSO_4$, however these plates also "cycled up." These plates were cycle life tested with the rather severe test described above. After 3000 cycles these electrodes showed 20% failure (2 out of 10) compared to 40% failure after 1500 cycles (4 out of 10) for lab standard electrodes (Batch 11 of Table II).

Conclusion

A process for making positive battery plates not requiring curing or formation and using high surface area chemically prepared lead dioxide mixed with TTB or lead sulfate has been described. During their first discharge, these plates deliver roughly 40% of the cranking rate capacity of conventionally prepared positive electrodes. In the first few discharge-recharge cells, the TTB or lead sulfate is converted to lead dioxide and acts to cement the structure together and increase the capacity to that of standard conventionally produced plates.

The precharged plate bulk porosity and pore size distribution is controlled by the particle size distribu-

tion and morphology of the lead dioxide used to make the plates. The plate porosity characteristics and lead dioxide morphology and size, rather than intrinsic lead dioxide activity, are apparently the critical parameters dictating the precharged positive performance. Tetrabasic lead sulfate and neutral lead sulfate appear to be suitable "binder" additives at about the 25 w/o level. Although a material such as tribasic lead sulfate which sulfates heavily and blocks the plate porosity is not acceptable, a certain amount of sulfation may be beneficial to precharged electrode performance.

Plates made from TTB with 1 w/o addition of dynel fiber and 0.5 w/o Teflon significantly out-performed standard positive electrodes on a cycle life test which simulated but was more severe than the SAE J-240 test used to characterize automotive starting, lighting, and ignition (SLI) batteries.

This envisioned process for manufacturing positive battery plates (a process for making negative battery plates will be reported later) would appear simpler and more amenable to continuous automated manufacture than the conventional process. Additionally, the marketing advantage of a truly dry-charged SLI battery with extended shelf life enhances the attractiveness of this scheme.

Acknowledgments

This work was conducted under the auspices of Inco Research and Development Center at Sterling Forest, NY. The authors would like to acknowledge the work of J. T. Arms in the formulation studies using Teflon and dynel fiber. The authors acknowledge the support of the Exide Corporation and also the contribution of the Inco Alloy Products Company Research Center in providing both the time and support required for the preparation of this paper after the decision by Inco to leave the battery business.

Manuscript submitted Aug. 19, 1983. This was Paper 37 presented at the San Francisco, California, Meeting of the Society, May 8-13, 1983.

Inco Alloy Products Company Research Center assisted in meeting the publication costs of this article.

REFERENCES

1. E. J. Taylor, G. A. Shia, and D. T. Peters, *This Journal*, **131**, 483 (1984).
2. N. E. Bagshaw, R. L. Clarke, and B. Halliwell, *J. Appl. Chem.*, **16**, 180 (1966).
3. J. A. Duisman and W. F. Giaugue, *J. Phys. Chem.*, **72**, 562 (1968).
4. M. J. Gillibrand and B. Halliwell, *J. Inorg. Nucl. Chem.*, **34**, 1143 (1972).
5. S. M. Caulder, J. S. Murday, and A. C. Simon, *This Journal*, **120**, 1515 (1973).
6. S. M. Caulder and A. C. Simon, *ibid.*, **121**, 1546 (1974).
7. J. D. Jorgensen, R. Varma, F. J. Rotella, and N. P. Yao, *ibid.*, **129**, 1678 (1982).
8. R. J. Hill, *Mater. Res. Bull.*, **17**, 769 (1982).
9. P. T. Moseley, J. L. Hutchison, C. J. Wright, and M. A. M. Bourke, *This Journal*, **130**, 829 (1983).
10. R. Varma, J. Eckert, J. A. Goldstone, A. D. Taylor, and J. Jorgensen, Paper 883 presented at The Electrochemical Society Meeting, San Francisco, California, May 8-13, 1983.

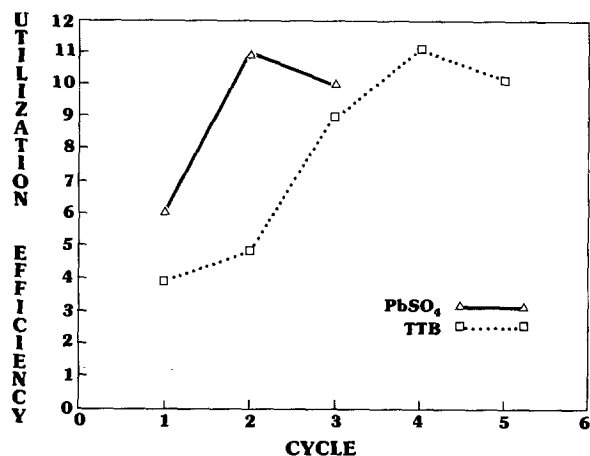


Fig. 5. High rate discharge (200 mA/cm²) utilization efficiency of precharged positive plates made with 75% Sample D Eagle-Picher (medium cure) PbO_2 and strengthened with 1 w/o dynel fiber, 0.5 w/o Teflon, and either $PbSO_4$ or TTB as "binder" material.

The Lithium/Sulfuryl Chloride Electrochemical Cell

K. A. Klinedinst*

GTE Laboratories, Incorporated, Waltham, Massachusetts 02254

ABSTRACT

The development of a practical sulfuryl chloride-based lithium/oxyhalide cell technology has been delayed by anode corrosion and cathode polarization problems encountered when the standard oxyhalide cell electrolyte and cathode formulations are used. The anode stability problem can be significantly alleviated by the use of a reverse polarity cell design, the substitution of $\text{Li}_2\text{B}_{10}\text{Cl}_{10}$ for LiAlCl_4 as the electrolyte salt, and the addition of a suitable cosolvent (SO_2 or SOCl_2). Further, at least under ambient temperature storage and discharge conditions, anode passivation is completely absent with hermetically sealed $\text{Li}/\text{SO}_2\text{Cl}_2$ cells of this type. Cathode polarization can be reduced most effectively by the use of a supported platinum cathode material. This cathode material also results in substantially increased discharge capacities, although the overall reaction stoichiometry is unaffected by the catalyst. Finally, SO_2Cl_2 thermal decomposition measurements indicate that, as the temperature of the SO_2Cl_2 electrolyte in a hermetic cell is increased from 25° to 80°C, the pressure differential across the cell case will rise to about 3.5 atm. Then, as the temperature is decreased to a lower value, the pressure differential will also decrease to the equilibrium value characteristic of that lower temperature, indicating a thermally stable, reversible system.

Soon after the discovery of the lithium/thionyl chloride electrochemical cell, optimization studies led to the development of storable, high performance cells suitable for a variety of applications (1, 2). It was realized, however, that cells with sulfuryl chloride (SO_2Cl_2) rather than thionyl chloride (SOCl_2) as the oxyhalide might offer some advantages. In particular, the higher OCV of the $\text{Li}/\text{SO}_2\text{Cl}_2$ system (3.90V for $\text{Li}/\text{SO}_2\text{Cl}_2$ vs. 3.65V for Li/SOCl_2) should translate into higher load voltages. Further, the absence of elemental sulfur as a discharge product with SO_2Cl_2 might lead to improved capacities and to improved safety characteristics (3). However, even though the expected load voltage and capacity advantage was observed at low current densities with cells containing PTFE-bonded carbon cathodes, it was lost at higher rates (this was apparently a cathode performance problem) (4). Further, $\text{Li}/\text{SO}_2\text{Cl}_2$ cells were found to undergo self-discharge at a rate at least twice that experienced with Li/SOCl_2 cells (5). Another source of concern has been the tendency of SO_2Cl_2 to undergo thermal decomposition to SO_2 and Cl_2 , leading to higher internal cell pressures and to possible effects upon cell chemistry (3, 6).

Several techniques have been suggested for the alleviation of the cathode polarization and anode corrosion problems. Among the techniques proposed for the reduction of cathodic polarization are the use of a very high surface area carbon black in place of the standard Shawinigan black cathode material (3), the addition of halogens to the SO_2Cl_2 electrolyte (7, 8, 9), and the use of supported platinum to catalyze the electroreduction of the oxyhalide (5, 10, 11, 20). The only suggested technique for reducing the severity of the anode corrosion problem has been the traditional one of employing a cell design which minimizes the amount of metallic cell hardware that is both in contact with the anode and exposed to the oxyhalide electrolyte (12).

Reported here are the results of an investigation designed to find optimal solutions to the anode corrosion and cathode polarization problems. Additionally, the thermal decomposition of the oxyhalide has been investigated.

Experimental

Electrolytes.—The SOCl_2 and SO_2Cl_2 were obtained from Hooker Chemical Company and Aldrich Chemical Company, respectively. They were distilled over lithium before use. Fluka aluminum chloride was used without further purification. Lithium chloride (Baker Chemical) was ground in a mortar and dried *in vacuo*

* Electrochemical Society Active Member.

Key words: sulfuryl chloride, lithium battery, oxyhalide cathodes.

at 160°C for 30h prior to use. Solutions of LiAlCl_4 were prepared by dissolving the required amount of AlCl_3 in the oxyhalide followed by the addition of excess LiCl . These electrolytes were purified by refluxing over lithium for 15-20h. The preparation and purification of the $\text{Li}_2\text{B}_{10}\text{Cl}_{10}$ has been described previously (13). A 0.25M $\text{Li}_2\text{B}_{10}\text{Cl}_{10}$ in SO_2Cl_2 electrolyte was prepared by directly dissolving the required amount of $\text{Li}_2\text{B}_{10}\text{Cl}_{10}$ in purified SO_2Cl_2 . In some cases, a quantity of purified SOCl_2 or SO_2 was also added to the $\text{Li}_2\text{B}_{10}\text{Cl}_{10}/\text{SO}_2\text{Cl}_2$ electrolyte.

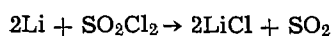
Lithium/oxyhalide cells.—AA-size Li/SOCl_2 and $\text{Li}/\text{SO}_2\text{Cl}_2$ cells were used in much of the experimental work. Standard bobbin-design cells with lithium anodes and PTFE-bonded Shawinigan black cathodes were used for much of the work (1, 4). Additionally, a reverse polarity AA cell design was employed (5). In cells of this type, the 8.3 cm² PTFE-bonded Shawinigan black cathode is pressed against the inside wall of the 304 stainless steel can, and the central cylindrical lithium anode is connected to the insulated terminal. The standard and reverse polarity cells contained glass-fiber separator paper and were filled with about 4 cm³ of the oxyhalide electrolyte. They all contained pre-weighed 0.65g lithium anodes and were hermetically sealed via TIG welding. Finally, some experiments were performed using planar geometry cells in Pyrex containers with ground-glass joints and glass-to-metal feed throughs for the lead wires (14). The cathodes employed in these cells were formed from PTFE-bonded Shawinigan black with or without the addition of 10% supported platinum.

Cell discharge, self-discharge, and voltage delay.—Sets of twelve identically constructed hermetically sealed AA cells were stored for one month at ambient temperature before being examined. During the one-month storage period, microcalorimetric measurements were performed using a Tronac Model 350 calorimeter. The stored cells were discharged briefly through 50Ω loads to determine the degree of anode passivation (voltage delay) resulting from the open-circuit stand. Then, two-thirds of the stored cells were discharged to termination through 200Ω loads. The resulting discharge curves were analyzed to yield the average plateau voltages and capacities (to a 2.0V cutoff). Next, the self-discharge characteristics of the discharged and undischarged stored cells were determined in the following way. The cells were cut open in an inert atmosphere, and the remaining metallic lithium was removed, washed with purified THF, and allowed to dry. The amount of remaining lithium was then determined by an acid-base titration procedure to obtain the amount of lithium consumed by self-discharge dur-

ing storage or during the combined periods of storage and discharge.

Sets of identically constructed hermetic and non-hermetic cells were also discharged to termination across a series of constant loads to yield average current densities ranging between 2 and 200 mA/cm². The load voltages were recorded as a function of time, and the discharge characteristics were obtained from analyses of the resulting discharge curves.

Product analysis.—A number of cathode-limited Li/SO₂Cl₂ cells in Pyrex containers and with Shawinigan black and 10% platinum on Shawinigan black as cathode materials were discharged to termination at a 2 mA/cm² rate. The fully discharged cathodes were removed from the cells and leached with pure SO₂Cl₂ to remove most of the residual LiAlCl₄ electrolyte salt. (The amount of LiAlCl₄ remaining after the SO₂Cl₂ leach was determined by atomic absorption analysis.) After vacuum drying, the cathode materials were weighed and leached with distilled water to remove the LiCl discharge product. Then, potentiometric chloride ion titrations were performed using a 0.1M AgNO₃ solution with a Ag/AgCl ion-sensitive electrode. The titration results, adjusted for the amount of residual LiAlCl₄ not removed by the SO₂Cl₂ leach, were compared with the amount of Cl⁻ that would be contained within each cathode assuming the overall discharge reaction to be



Microscopic analysis.—Lithium foil samples were prepared for scanning electron microscopic (SEM) analysis by the following procedure. Strips of freshly exposed lithium (Foote Mineral Company) were sealed in glass ampuls filled with purified SO₂Cl₂, 1.8M LiAlCl₄ in SO₂Cl₂, and 0.25M Li₂B₁₀Cl₁₀ in SO₂Cl₂. The samples were stored at ambient temperature for one or two month intervals. The ampuls were then opened in an argon-filled dry box and the lithium samples were removed, washed with purified THF, and mounted for analysis. The mounted samples were transferred to a JEOL Model JSM-U3 SEM without exposure to air.

Gas pressure measurements.—Five milliliter quantities of purified SO₂Cl₂ containing 1.8M LiAlCl₄, 0.1M AlCl₃, or 0.01M AlCl₃ were sealed within a Monel tube fitted with a Monel pressure gauge. In some cases, the tube also contained 20 mg of Shawinigan black with or without the presence of 10% supported platinum. These samples were stored in a thermostatically controlled oven. With each sample, the equilibrium pressure within the sealed tube was recorded as a function of increasing and decreasing temperature for temperatures between 50° and 80°C.

Results and Discussion

Li/oxyhalide cells with SOCl₂ and SO₂Cl₂ electrolytes.—Standard configuration (case negative) hermetically sealed AA-size Li/SOCl₂ and Li/SO₂Cl₂ cells were discharged to termination at ambient temperature through constant loads ranging between 2 and 100Ω. These cells contained as electrolytes 1.8M solutions of LiAlCl₄ in the two oxyhalides. Typical discharge curves obtained with SOCl₂ cells discharged through 20Ω loads are compared in Fig. 1. The average load voltages and the discharge capacities obtained from such discharge curves are plotted vs. the log of the average discharge rate in Fig. 2 and 3, respectively. (Each plotted point in Fig. 2 was obtained by averaging over the plateau portion of the complete constant load discharge curve of a separate Li/SOCl₂ or Li/SO₂Cl₂ cell. The discharge capacities were obtained by integrating the discharge curves to a 2.0V cutoff.)

At discharge rates no higher than a few milliamperes per square centimeter of geometric surface area, the average load voltages obtained with the two oxyhalides

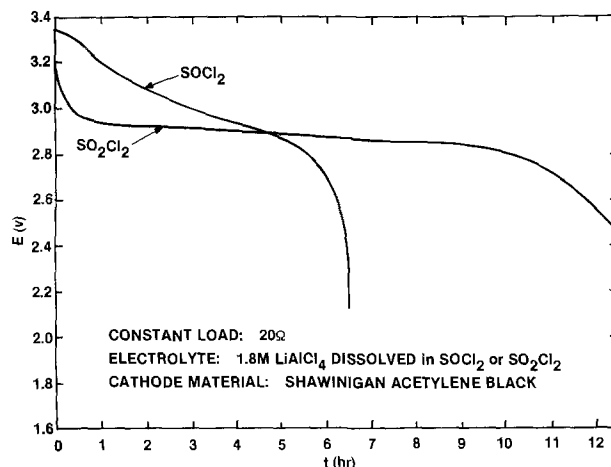


Fig. 1. AA size Li/oxyhalide cell discharge curves

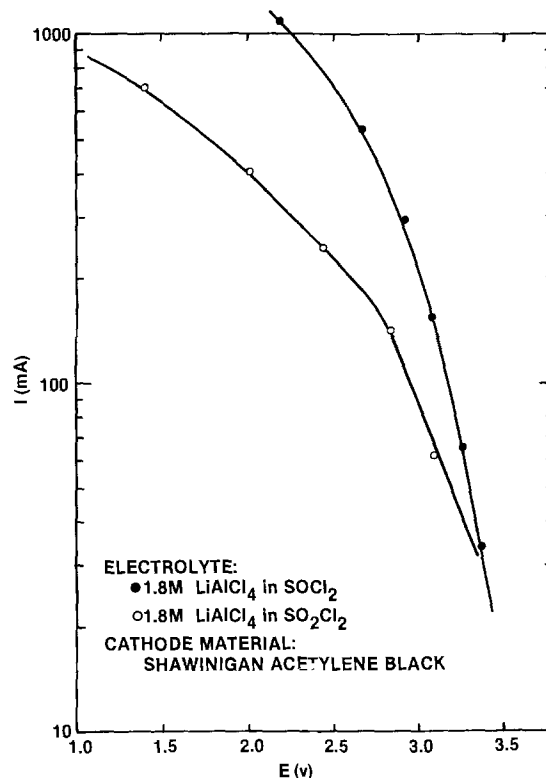


Fig. 2. AA size Li/oxyhalide cell polarization data

are similar. However, the higher the discharge rate, the lower the load voltage obtained with the SO₂Cl₂ electrolyte relative to that obtained with the SOCl₂ electrolyte. In contrast, as shown in Fig. 3, the Li/SO₂Cl₂ cells yielded capacities far greater than those obtained with the SOCl₂ electrolyte. In fact, for discharge rates above 15 mA/cm², the use of the SO₂Cl₂ electrolyte produced capacities between 2 and 3 times those obtained with the standard SOCl₂ electrolyte.

Typical lithium corrosion, voltage delay, and performance results obtained with standard configuration SOCl₂ and SO₂Cl₂ AA cells stored for one month at ambient temperature are compared in Table I.

Listed first in Table I are the average amounts of lithium consumed by self-discharge during storage (expressed as ampere-hour equivalents). As indicated, about twice as much lithium was lost through self-discharge with SO₂Cl₂ as with SOCl₂.

Listed next are the average voltage delay characteristics obtained with the two electrolytes. The initial load voltage and the plateau voltage measured when the stored cells were briefly discharged through 50Ω

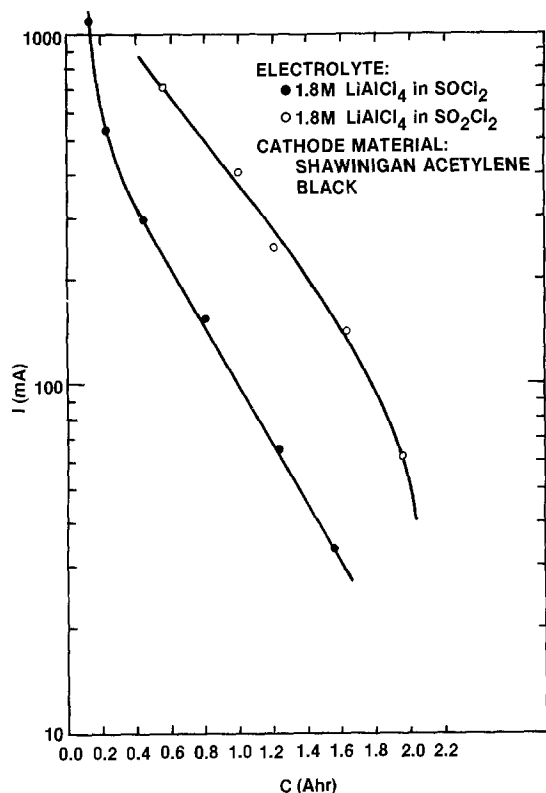


Fig. 3. AA size Li/oxyhalide cell capacity data

loads are both indicated, as is the time required for the load voltage to reach 90% of the plateau value. Clearly, the anode passivation incurred with the SO_2Cl_2 electrolyte is much less severe than is that with SOCl_2 .

Listed next are the average plateau voltages, the average discharge rates, and the capacities (to a 2.0V cutoff) characteristic of the two groups of stored cells when discharged through 200 Ω loads. In keeping with the fresh cell polarization data, there was no significant difference between the average load voltages obtained with the two oxyhalides. Moreover, the SO_2Cl_2 cells yielded discharge capacities that were, on average, about 15% below those obtained with SOCl_2 .

The final entry in the table is the amount of lithium anode material lost through self-discharge during the combined periods of storage and discharge. With the SOCl_2 electrolyte, no significant lithium corrosion occurred while the cells were being discharged. In contrast, with SO_2Cl_2 nearly as much lithium was lost during discharge as was lost on storage.

With the exception of the improved voltage delay characteristics, the AA cells containing the SO_2Cl_2 electrolyte apparently offer no advantages over those containing SOCl_2 . On the contrary, the severe cathodic polarization and anode corrosion problems encountered with SO_2Cl_2 would seem to make its use highly impractical.

Table I. Standard configuration Li/oxyhalide AA cells stored one month at ambient temperature—1.8M LiAlCl_4 electrolytes

	SOCl_2	SO_2Cl_2
Li lost during storage	0.12 Ah	0.23 Ah
50 Ω discharge Init E \rightarrow load E t to 0.9 load E	1.45 \rightarrow 3.00V 6.0s	2.45 \rightarrow 3.20V 1.0s
200 Ω discharge E avg I avg C (to 2.0V) Li lost during storage and discharge	3.34V 16.7 mA 2.15 Ah 0.13 Ah	3.35V 16.8 mA 1.84 Ah 0.42 Ah

Anode passivation and corrosion.—In the standard configuration (case negative) cylindrical cell, a substantial amount of metallic cell hardware is both in electrical contact with the anode and exposed to the electrolyte. On the assumption that the high self-discharge rates observed with SO_2Cl_2 -based electrolytes are at least partly due to the reduction of SO_2Cl_2 upon this exposed hardware (with the simultaneous oxidation of the lithium anode material), a so-called reverse polarity (case positive) cell design was developed. With cells of this type, the lithium anode is connected to the insulated terminal so that there is much less exposed metal hardware in electrical contact with the anode. The averaged anode corrosion, voltage delay, and performance results obtained with standard and reverse polarity Li/ SO_2Cl_2 cells stored for one month at ambient temperature are compared in Table II. As indicated, the polarity reversal technique resulted in an approximate 50% reduction in the self-discharge rate during both storage and discharge. However, polarity reversal had no effect upon the voltage delay characteristics of the stored cells. Finally, the case positive cells exhibited slightly higher load voltages. So, except for a small loss of capacity, polarity reversal has an overall beneficial effect upon the characteristics of the stored cells. Nevertheless, the corrosion rates experienced with the reverse polarity cells are still much higher than could be tolerated in most applications.

It is known that, with Li/ SOCl_2 cells, the substitution of lithium closoboranes, e.g., $\text{Li}_2\text{B}_{10}\text{Cl}_{10}$, for LiAlCl_4 in the electrolyte significantly alters the nature of the passivating LiCl film (13, 15, 16). Further, SOCl_2 cells with the $\text{Li}_2\text{B}_{10}\text{Cl}_{10}$ electrolyte salt often exhibit improved voltage delay and self-discharge characteristics. So, experiments were performed in order to determine whether similar performance improvements might also result from the use of the $\text{Li}_2\text{B}_{10}\text{Cl}_{10}$ salt in SO_2Cl_2 electrolytes.

That the electrolyte salt may play a decisive role in determining the Li/ SO_2Cl_2 self-discharge rate is certainly suggested by the microcalorimetric data listed in Table III. The table compares the heat outputs measured on the twentieth day of ambient temperature storage with reverse polarity SO_2Cl_2 cells as a function of the molar concentration of LiAlCl_4 . (The tabulated values are the averages of data obtained with several identical cells.) As indicated, the higher the salt concentration, the greater the rate of heat evolution.

Table II. Standard and reverse polarity Li/ SO_2Cl_2 AA cells stored one month at ambient temperature—1.8M LiAlCl_4 electrolytes

	Standard configuration	Reverse polarity
Li lost during storage	0.23 Ah	0.10 Ah
50 Ω discharge Init E \rightarrow load E t to 0.9 load E	2.45 \rightarrow 3.20V 1.0s	2.45 \rightarrow 3.20V 1.0s
200 Ω discharge E avg I avg C (to 2.0V) Li lost during storage and discharge	3.35V 16.8 mA 1.84 Ah 0.42 Ah	3.40V 17.0 mA 1.74 Ah 0.26 Ah

Table III. Heat output measured on the twentieth day of ambient temperature storage with reverse polarity Li/ SO_2Cl_2 AA cells as a function of LiAlCl_4 concentration

LiAlCl_4	Heat output (μW)
0.00	210
0.25	328
1.80	1003

The performance results obtained with reverse polarity AA cells containing 1.8M LiAlCl₄ and 0.25M Li₂B₁₀Cl₁₀ in SO₂Cl₂ as electrolytes after being stored for one month at ambient temperature are compared in Table IV. As indicated, the salt substitution reduced the rate of lithium corrosion to a value within the standard error limit for this experiment, both during storage and discharge through a 200Ω load. Further, the use of the alternate electrolyte salt resulted in a 150 mV rise in average load voltage, and in the virtual elimination of anode passivation. (In fact, the voltage delay incurred when the stored cells were discharged through a 50Ω load was so slight as to be undetectable on a sensitive high speed recorder.) The only negative result of the salt substitution was a further loss of capacity.

The use of the Li₂B₁₀Cl₁₀ salt to form the SO₂Cl₂ electrolyte is at least as effective in the elimination of anode passivation and corrosion as the corresponding salt substitution with SOCl₂. To investigate this phenomenon SEM analyses were performed upon lithium samples stored at ambient temperature for one and two month intervals in pure SO₂Cl₂, in SO₂Cl₂ containing 1.8M LiAlCl₄, and in SO₂Cl₂ containing 0.25M Li₂B₁₀Cl₁₀. The surfaces of the lithium samples stored in the pure oxyhalide, after one month storage, give no indication of the formation of surface films (see Fig. 4a). However, the surfaces of the samples stored in the two electrolyte solutions were all found to be covered by films of LiCl. With the LiAlCl₄ electrolyte, the LiCl films were composed of closely packed, well-formed crystallites ranging in size between 2.5 and 25 μm (see Fig. 4b). In contrast, with the Li₂B₁₀Cl₁₀ electrolyte, the LiCl films were generally amorphous in appearance, with the largest recognizable crystallites being about 2 μm in size (see Fig. 4c). (In general, the surfaces of the samples stored in the electrolytes for two months were very similar in appearance to the surfaces of the samples stored for only one month.)

The performance improvements achieved by the use of a reverse polarity cell configuration and by salt substitution are listed in Tables II and IV. As indicated, the combination of these two techniques resulted in a reduction in the rate of anode corrosion to a value almost below the level of detectability, the virtual elimination of voltage delay, and in a 200 mV increase in load voltage at a 1.6 mA/cm² current density. Unfortunately, these performance improvements were accompanied by a 10% reduction in average discharge capacity.

This capacity limitation can be overcome by the addition of a cosolvent (SO₂ or SOCl₂) to the SO₂Cl₂ electrolyte. Typical results achieved by the addition of 25% SOCl₂ to the 0.25M Li₂B₁₀Cl₁₀ in SO₂Cl₂ electrolyte are presented in Table V. (Comparable results have been obtained by the addition of 7.5% SO₂ to the electrolyte.) As indicated, the use of the cosolvent increased the average discharge capacity from 1.66 to 1.94 Ah. Furthermore, this was accomplished without a reduction in average load voltage, without initiating

Table IV. Reverse polarity Li/SO₂Cl₂ AA cells stored one month at ambient temperature—1.8M LiAlCl₄ and 0.25M Li₂B₁₀Cl₁₀ electrolytes

	1.8M LiAlCl ₄	0.25M Li ₂ B ₁₀ Cl ₁₀
Li lost during storage	0.10 Ah	0.00 Ah
50Ω discharge Init E → load E	2.45 → 3.20V	No detectable voltage delay (Load E = 3.47V)
t to 0.9 load E	1.0s	
200Ω discharge E avg	3.40V	3.55V
I avg	17.0 mA	17.8 mA
C (to 2.0V)	1.74 Ah	1.66 Ah
Li lost during storage and discharge	0.26 Ah	0.01 Ah

Table V. Reverse polarity Li/SO₂Cl₂ AA cells stored one month at ambient temperature—0.25M Li₂B₁₀Cl₁₀ electrolyte

	Without cosolvent	With 25% SOCl ₂
Li lost during storage	0.00 Ah	0.01 Ah
50Ω discharge Init E → load E	No voltage delay (Load E = 3.47V)	No voltage delay (Load E = 3.44V)
t to 0.9 load E		
200Ω discharge E avg	3.55V	3.56V
I avg	17.8 mA	17.8 mA
C (to 2.0V)	1.66 Ah	1.94 Ah
Li lost during storage and discharge	0.01 Ah	0.01 Ah

Table VI. Heat output measured on the twentieth day of ambient temperature storage with reverse polarity Li/SO₂Cl₂ AA cells as a function of electrolyte composition (all cells contained 0.25M Li₂B₁₀Cl₁₀)

Cosolvent	Heat output (μW)
none	666
7.5% SO ₂	160
25% SOCl ₂	172

anode corrosion, and without causing any detectable voltage delay. (The cosolvent apparently improves the cathode utilization efficiency, perhaps by modifying the nature of the crystalline LiCl deposited within the porous cathode.)

In Table VI are listed the microcalorimetry results obtained with reverse polarity SO₂Cl₂ cells on the twentieth day of ambient temperature storage. These cells contained as electrolytes 0.25M solutions of Li₂B₁₀Cl₁₀ in SO₂Cl₂ without a cosolvent, with the addition of 7.5% SO₂, and with the addition of 25% SOCl₂. As indicated, the use of a cosolvent also reduces the rate of heat evolution by a factor of four, suggesting that, in addition to improving the cathode utilization efficiency, the cosolvent may also further reduce self-discharge.

In Fig. 5 is shown a typical discharge curve for a reverse polarity AA cell with 0.25M Li₂B₁₀Cl₁₀ in SO₂Cl₂ containing 25% SOCl₂ as electrolyte and stored for one month at ambient temperature before being discharged through a 200Ω load. A 3.57 average plateau voltage was achieved at a 2 mA/cm² discharge rate. The capacity was approximately 2.1 Ah. In Fig. 6 is a typical initial load voltage vs. time (voltage delay) curve achieved with a reverse polarity AA cell with the electrolyte stored for one month at ambient temperature before being discharged through a 50Ω load. This curve demonstrates that, even with the use of a sensitive high speed recorder, no anode passivation was detected with any of the stored cells containing the closoborane electrolyte salt.

Cathode performance.—It is apparent from the Li/SOCl₂ and Li/SO₂Cl₂ AA cell polarization data (see Fig. 2) that the standard acetylene black Li/oxyhalide cell cathode material is not a particularly good catalyst for the electroreduction of SO₂Cl₂. This fact becomes more and more apparent the higher the discharge rate. As indicated above, several techniques have been suggested for the alleviation of the cathode polarization problem, including the use of an alternate high surface area carbon black as the cathode material (3), the addition of halogens to the SO₂Cl₂ electrolyte (7, 8, 9), and the doping of the acetylene black cathode material with substances that catalyze the electroreduction of the SO₂Cl₂ (5, 10, 11, 17). Of the known catalytic cathode additives, supported platinum is the most efficient, particularly at high discharge rates. (It has been suggested that the platinum facilitates the decomposition of SO₂Cl₂ at the electrode surface so that

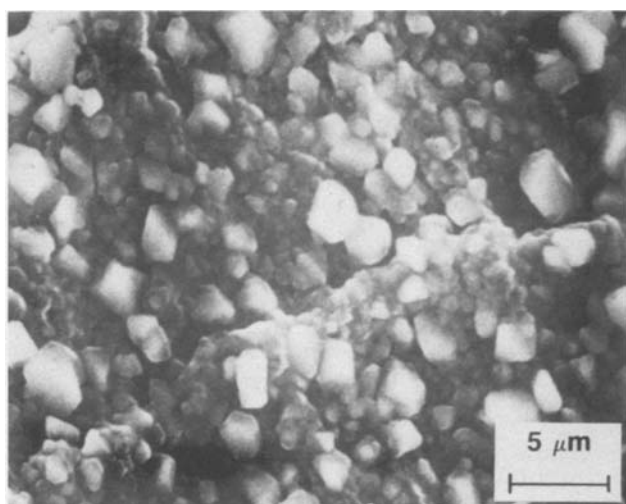
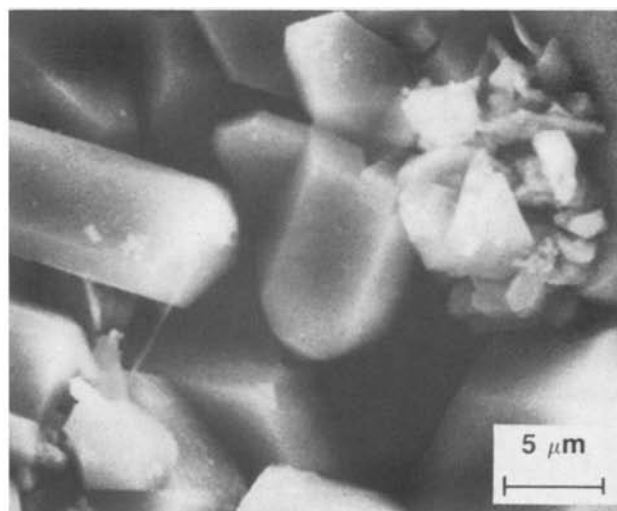
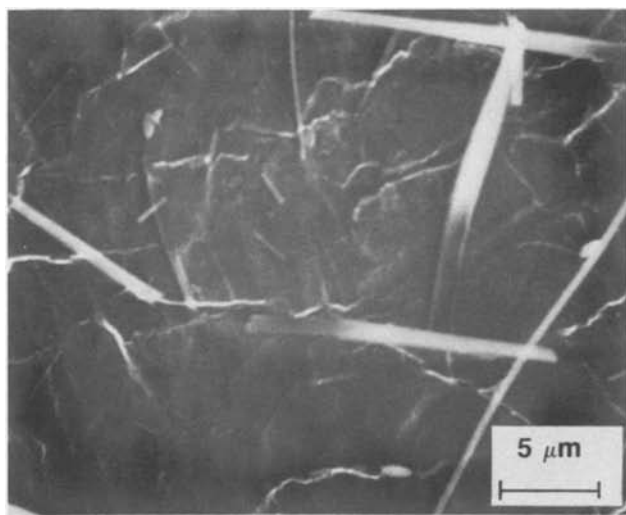


Fig. 4. Micrographs of lithium surfaces stored in SO_2Cl_2 for one month at 25°C . A, upper left: pure SO_2Cl_2 . B, upper right: 1.8M LiAlCl_4 in SO_2Cl_2 . C, left: 0.25M $\text{Li}_2\text{B}_{10}\text{Cl}_{10}$ in SO_2Cl_2 .

the reduction of SO_2Cl_2 proceeds through chlorine, even with a SO_2 -saturated electrolyte (19).

Cathode limited $\text{Li}/\text{SO}_2\text{Cl}_2$ cells with planar electrode geometry and with 1.8M LiAlCl_4 in SO_2Cl_2 as electrolyte were discharged at ambient temperature across a series of constant loads so as to produce average discharge rates ranging between 10 and $200\text{ mA}/\text{cm}^2$. Duplicate tests were run with cells containing $1\text{ cm}^2 \times 1\text{ mm}$ PTFE-bonded Shawinigan acetylene black cathodes with and without the presence of 10% supported platinum. The resulting discharge curves were analyzed to yield the polarization and discharge

capacity data shown in Fig. 7 and 8, respectively. (Figure 7 is a semilogarithmic plot of the average current density vs. the average plateau load voltage. Figure 8 is a semilogarithmic plot of the average current density vs. the discharge capacity to a 2.0V cutoff.)

As shown in Fig. 7, the higher the discharge rate, the greater the decrease in polarization that results from the use of the supported platinum electrocatalyst. For instance, at a $200\text{ mA}/\text{cm}^2$ current density, an average load voltage of about 3.0V is obtained with the supported platinum cathode material vs. 2.15V in the absence of the supported platinum. As shown in Fig. 8,

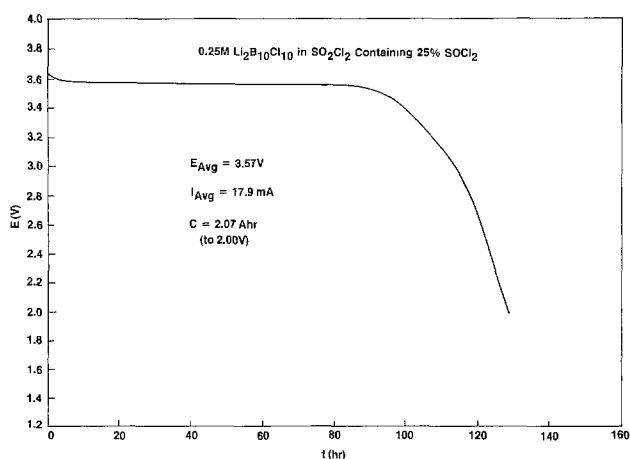


Fig. 5. 200Ω discharge curve for reverse polarity $\text{Li}/\text{SO}_2\text{Cl}_2$ AA cell stored for one month at ambient temperature.

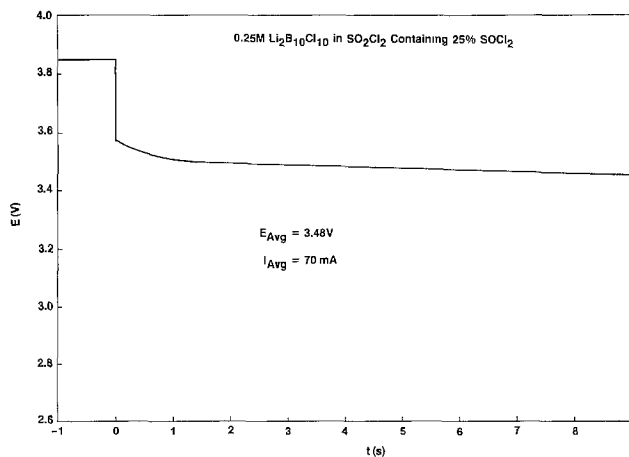
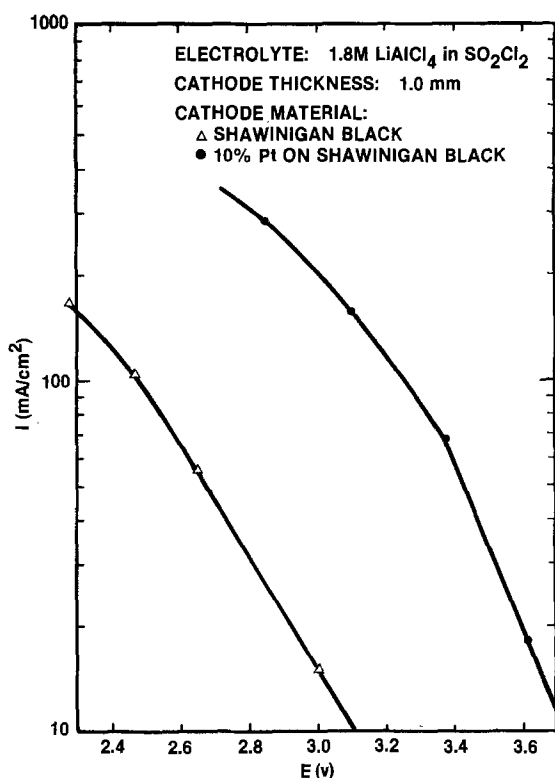
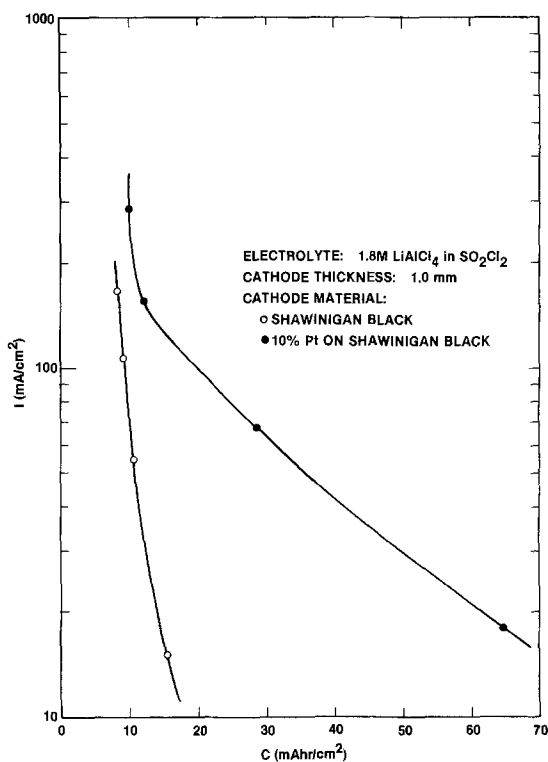


Fig. 6. 50Ω discharge curve for reverse polarity $\text{Li}/\text{SO}_2\text{Cl}_2$ AA cell stored for one month at ambient temperature.

Fig. 7. Li/SO₂Cl₂ cell polarization dataFig. 8. Li/SO₂Cl₂ cell capacity data

the use of the supported platinum cathode material also results in much-improved cathode utilization efficiency over the entire range of discharge rates. For instance, at 20 mA/cm² a four-fold increase in cathode utilization efficiency is accomplished by the addition of 10% metallic platinum to the cathode. Typical 20Ω constant load Li/SO₂Cl₂ discharge curves obtained with and without the catalyst are compared in Fig. 9.

In Fig. 10 are compared polarization curves characteristic of Li/SOCl₂ and Li/SO₂Cl₂ cells with 10% Pt on Shawinigan black cathode and with 1.8M LiAlCl₄ electrolytes. It is apparent that, with this cathode ma-

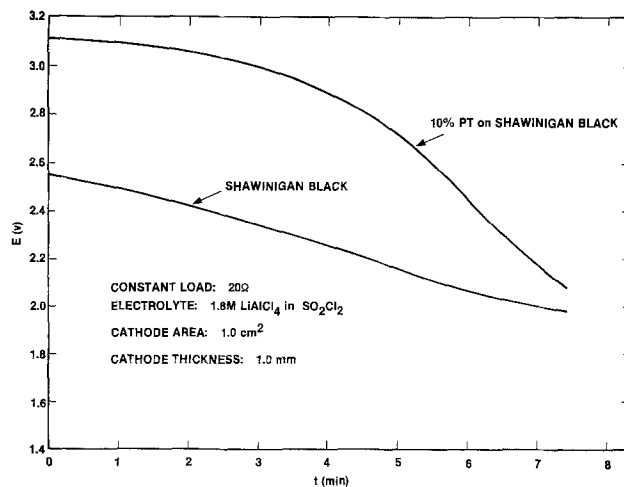
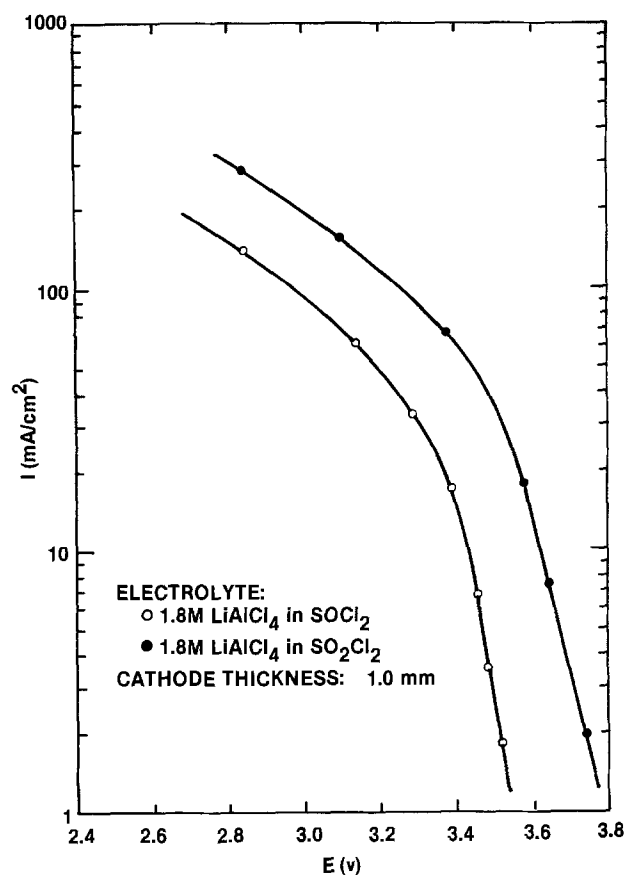
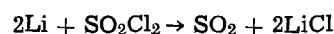
Fig. 9. Li/SO₂Cl₂ cell discharge curves

Fig. 10. Li/oxyhalide cell polarization data with 10% Pt on Shawinigan black cathodes.

terial, the approximately 300 mV difference in OCV experienced with the two oxyhalides is maintained even at current densities in the 100-200 mA/cm² range. The corresponding Li/SOCl₂ and Li/SO₂Cl₂ cell discharge capacities (to a 2.0V cutoff) are compared as a function of log *I* in Fig. 11. As shown, the capacities obtained with the SO₂Cl₂ electrolyte are far superior to those obtained with SOCl₂ for current densities ranging over two orders of magnitude.

The overall Li/SO₂Cl₂ cell reaction has been demonstrated to be



According to this reaction, one mol of LiCl is produced per mol of discharged lithium. Experiments (described above) were performed to determine if a change in the overall reaction stoichiometry might

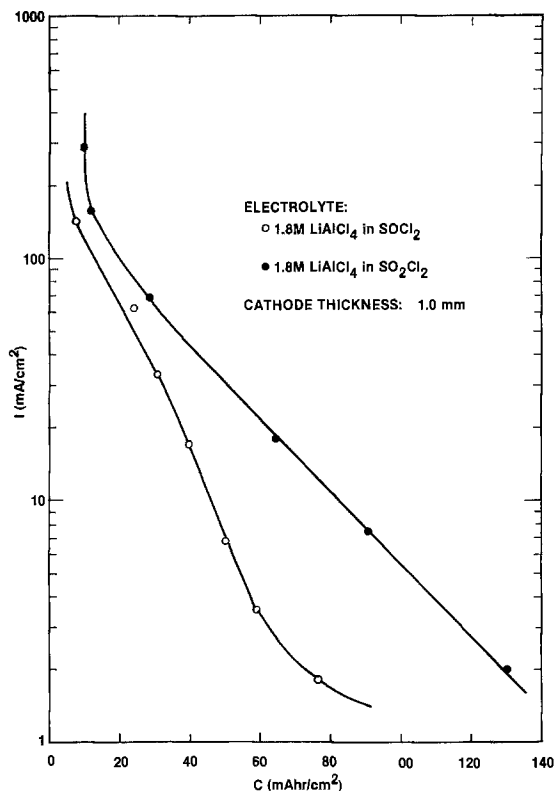


Fig. 11. Li/oxyhalide cell capacity data with 10% Pt on Shawinigan black cathodes.

result from the addition of supported platinum to the acetylene black cathode material. With the cathodes not containing any supported platinum, the titration results predicted discharge capacities 1.3% greater than the measured capacities [in agreement with the earlier results of Gilman and Wade (3)]. With the cathodes containing 10% supported platinum, the titration results predicted discharge capacities 6.0% greater than were actually measured. Thus, it was concluded that, for both cathode materials, the discharge of a Li/SO₂Cl₂ cell at a moderate rate results in the formation of one mol of LiCl for every mol of oxidized lithium anode material. To further substantiate this conclusion, the discharged cathode materials were subjected to a battery of qualitative analytical tests designed to indicate the presence of any other discharge product that might be insoluble in the SO₂Cl₂ electrolyte (18). No indication of the presence of any other product was found, save for a trace of SO₄⁼ possibly produced by the hydrolysis of a small amount of residual SO₂Cl₂ that might not have been removed during the vacuum drying step.

SO₂Cl₂ decomposition.—The relative thermal instability of SO₂Cl₂ (compared to SOCl₂) is well recognized (3, 5, 10, 19). It is well established that, in the presence of a suitable catalyst, SO₂Cl₂ decomposes to SO₂ and Cl₂



The extent of decomposition increases with increasing temperature. From a practical point of view, therefore, the usefulness of SO₂Cl₂-based electrolytes will be partly determined by the thermal stability of the SO₂Cl₂ and by the reversibility of the decomposition reaction. As described above, the equilibrium decomposition pressure has been measured as a function of temperature (for temperatures between 50° and 80°C). Five milliliter quantities of purified SO₂Cl₂ containing 1.8M LiAlCl₄, 0.1M AlCl₃, or 0.01M AlCl₃ were used. In some cases, the SO₂Cl₂ solutions were in contact with 20 mg portions of Shawinigan black with or without the presence of 10% supported platinum. The experi-

mental results are compared in the log pressure vs. reciprocal temperature plot shown in Fig. 12.

As indicated, the equilibrium pressures are independent of the identity and concentration of the dissolved compound and of the presence and identity of the high surface area material. Moreover, no evidence of any hysteresis was observed with increasing and decreasing temperatures. However, the equilibrium pressures were attained much more slowly with the 0.01M AlCl₃ solution than with 0.1M AlCl₃ and 1.8M LiAlCl₄ solutions. Finally, the absence of any dissolved AlCl₃ or LiAlCl₄, much lower final pressures were obtained (even after more than 24h at temperature). This suggests that the dissolved material functions as a catalyst for the decomposition, presumably by a chloride exchange mechanism. Thus, as the temperature of the SO₂Cl₂ electrolyte in a hermetically sealed cell is increased from 25° to 80°C, the pressure differential across the metal case will rise to about 3.5 atm. Then, as the temperature is decreased to a lower value, the pressure differential will also decrease to the equilibrium value characteristic of that lower temperature, indicating a reversible dissociation for SO₂Cl₂.

Summary and Conclusions

Traditional Li/SOCl₂ cell technology is based upon the use of an acetylene black cathode material coupled with LiAlCl₄ dissolved in the oxyhalide as an electrolyte. However, when this approach is taken with SO₂Cl₂ rather than SOCl₂ as the oxyhalide, anode corrosion and cathode polarization problems are encountered, which have discouraged the development of a practical Li/SO₂Cl₂ cell technology.

It has been found that, by the use of a reverse polarity cell design, the substitution of Li₂B₁₀Cl₁₀ for LiAlCl₄ as the electrolyte salt, and the addition of a suitable cosolvent (SO₂ or SOCl₂), a hermetic Li/SO₂Cl₂ cell is achieved by which can be realized the recognized potential advantages of SO₂Cl₂-based electrolytes (high load voltages and capacities with the absence of elemental sulfur as a discharge product), coupled with a low self-discharge rate and (at least under ambient temperature storage and discharge conditions) the complete absence of voltage delay.

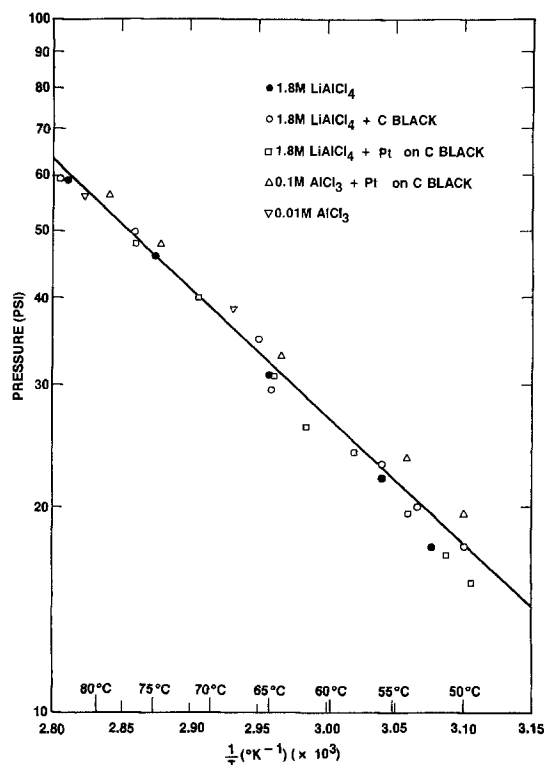


Fig. 12. SO₂Cl₂ decomposition pressure vs. reciprocal temperature.

Cathode polarization can be reduced most effectively by the use of a supported platinum cathode material. For instance, at a 200 mA/cm² discharge rate, polarization is reduced by 0.85V through the addition of 10% metallic platinum to the acetylene black cathode material. Further, with this cathode material, the approximately 300 mV difference in OCV experienced with SOCl₂ and SO₂Cl₂ electrolytes is maintained on load, even at current densities in the 100 to 200 mA/cm² range. Increased cathode utilization efficiencies also result from the use of this catalytic additive. However, the increased capacities do not result from a change in the overall reaction stoichiometry. The use of supported platinum cathode materials in hermetic cells with electrolytes selected primarily for their effects upon anode stability and passivation will be the subject of a later report.

Finally, the thermal decomposition of SO₂Cl₂ has been studied for temperatures between 50° and 80°C as a function of the presence and concentration of dissolved AlCl₃ or LiAlCl₄. The dissolved material apparently functions as a catalyst for the decomposition reaction. However, the equilibrium decomposition pressures are independent of the presence or absence of acetylene black cathode materials. With SO₂Cl₂ electrolyte solutions, no hysteresis is observed with increasing and decreasing temperatures, indicating a reversible thermal dissociation.

Manuscript submitted Aug. 4, 1983; revised manuscript received Oct. 21, 1983. This was Paper 76 presented at the Denver, Colorado, Meeting of the Society, Oct. 11-16, 1981, and Paper 52 presented at the San Francisco, California, Meeting of the Society, May 8-13, 1983.

GTE Laboratories, Incorporated, assisted in meeting the publication costs of this article.

REFERENCES

1. D. Morley and R. J. Solar, in "Proceedings of the 28th Power Sources Conference," Atlantic City, NJ, June 12-15, 1978, The Electrochemical Society, Inc., p. 222 (1979).
2. N. Marincic and F. Goebel, in *ibid.*, p. 224.

3. S. Gilman and W. Wade, Jr., *This Journal*, **127**, 1427 (1980).
4. J. J. Auburn and N. Marincic, in "Power Sources 5," D. H. Collins, Editor, p. 683, Academic Press, London (1975).
5. K. A. Klinedinst, in "Proceedings of the 30th Power Sources Conference," Atlantic City, NJ, June 7-12, 1982, The Electrochemical Society, Inc., p. 157 (1983).
6. P. Pascal, "Nouveau Traite de Chimie Minerale," Vol. XIII, pp. 1539-1550, Masson et Cie, Paris (1956).
7. C. C. Liang, M. E. Bolster, and R. M. Murphy, *This Journal*, **128**, 1631 (1981).
8. C. C. Liang, M. E. Bolster, and R. M. Murphy, in "Proceedings of the 29th Power Sources Conference," Atlantic City, NJ, June 9-12, 1980, The Electrochemical Society, Inc., p. 144 (1981).
9. J. C. Hall and M. Koch, DELET-TR-81-0420-2, Grant no. DAAK20-81-C-0420 (1982).
10. K. A. Klinedinst, Abstract 76, p. 190, The Electrochemical Society Extended Abstracts, Vol. 81-2, Denver, Colorado, Oct. 11-16, 1981.
11. N. Doddapaneni, Abstract 582, p. 1395, The Electrochemical Society Extended Abstracts, Vol. 81-2, Denver, Colorado, Oct. 11-16, 1981.
12. F. Marikar, J. Phillips, J. C. Hall, and H. F. Gibbard, Abstract 91, p. 226, The Electrochemical Society Extended Abstracts, Vol. 81-2, Denver, Colorado, Oct. 11-16, 1981.
13. C. Schlaikjer, C. A. Young, and M. Dobrusin, DELET-TR-78-0558.1F, Grant no. DAAB07-78-C-0558 (1980).
14. K. A. Klinedinst and M. J. Domeniconi, *This Journal*, **127**, 539 (1980).
15. C. R. Schlaikjer, U.S. Pat. 4,020,240 (1977).
16. A. N. Dey and J. Miller, *This Journal*, **126**, 1445 (1979).
17. N. Doddapaneni, Abstract 583, p. 1398, The Electrochemical Society Extended Abstracts, Vol. 81-2, Denver, Colorado, Oct. 11-16, 1981.
18. C. R. Schlaikjer, F. Goebel, and N. Marincic, *This Journal*, **126**, 513 (1979).
19. W. K. Behl, *ibid.*, **127**, 1444 (1980).
20. S. Gilman and W. Wade, Jr., Abstract 33, p. 91, The Electrochemical Society Extended Abstracts, Vol. 79-2, Los Angeles, California, Oct. 14-19, 1979.

Electrochemical and Ellipsometric Investigations of Passive Films on Iron in Borate Solutions

II. Cathodic Reduction of Passive Films on Iron

Z. Szklarska-Smialowska* and W. Kozlowski

Institute of Physical Chemistry, Polish Academy of Sciences, Warsaw, Poland

ABSTRACT

Passive films formed under strictly controlled conditions during anodic polarization of iron in borate buffer solution were reduced in the same solution with a constant cathodic current. The cathodic charge consumed for the reduction of passive film was greater than the theoretical value calculated under the assumption that Fe₂O₃ was reduced to Fe²⁺. The higher the oxidation potential was and the longer oxidation time was employed, the greater was the consumed charge found experimentally. At certain characteristic thicknesses of the passive film associated with changes in film growth during its formation, inflections of the E_{red} vs. time and E_{red} vs. film thickness were observed.

Investigations of passive films on iron have usually been performed by measuring either the film growth during the anodic oxidation of metal or the cathodic reduction of the oxide film. No detailed studies aimed at elucidating mechanisms of both these processes on the same specimen and in the same electrolyte have been carried out so far. The purpose of the present work was to undertake such studies in continuation of our previous investigation of passive film formation

(1). This approach was thought to be useful in providing a better understanding of the nature of several consecutive passivation stages found by Kruger and Calvert (2) and in our work (1). The set of Armco iron specimens and the two borate buffer solutions of pH 8.45 differing in H₃BO₃ and Na₂B₄O₇ content were the same as those used in the first part of this work (1).

If a low constant cathodic current density is applied, two plateaus appear in the graph of consumed charge as a function of potential. The first plateau is commonly attributed to the reduction of the external film layer,

* Present address: Department of Metallurgical Engineering, The Ohio State University, Columbus, Ohio 43201.

and the second plateau to the reduction of the internal layer of Fe_3O_4 (3-7). According to others (8-10), the anodic film contains a single layer of $\gamma\text{-Fe}_2\text{O}_3$ which is reduced to Fe^{2+} and Fe^0 . It has also been assumed that the reductive dissolution of the film is accompanied by other reduction processes occurring in the solid phase. For example, such mechanisms have been proposed by Sato *et al.* (11), and Chen and Cahen (12) for galvanostatic and potentiostatic reduction, respectively. The following expression is used to calculate film thickness (d)

$$d = \frac{QMw}{zF\rho r}$$

where Q is the cathodic charge consumed, Mw = molecular weight of the compound undergoing reduction, z = number of electrons used, F = Faraday constant, ρ = density of the compound, r = roughness coefficient. Because neither the exact chemical composition of the reduced compound nor the roughness coefficient is known, arbitrary values are commonly assumed for Mw , z , ρ , and r . Therefore, the results obtained are uncertain and must be treated with caution. Even if the chemical composition is well defined, the density of a very thin film may well differ from that attributed to the bulk phase. Moreover, water molecules and anions present in the electrolyte can be incorporated into the film. Roughness coefficients, particularly in the case of passive films, are unknown.

Experimental

The measurements were carried out with the same Armco iron which was used to study the anodic oxidation process (1). In fact, the cathodic reduction was commenced in the same electrolyte solution immediately after the passivation experiment was completed. A constant current of $17 \mu\text{A} \cdot \text{cm}^{-2}$ was used. During reduction, the potential, cathodic charge, and changes in optical constants were recorded. This procedure was chosen because during the time required to change the electrolyte, taking into consideration that the cell had a volume of 0.5 liter, the exposure of the electrode to the argon atmosphere could result in modification of the surface film. However, the procedure employed had also some potential disadvantage, namely, that if ferric ions passed into solution during oxidation, they could be reduced to ferrous, which would lead to an excessive consumption of cathodic charge. Calculations showed, however, that this factor would give rise to a negligible error in the cathodic charge consumed during film dissolution.

Another process which can occur during the cathodic reduction of anodic films should be taken into consideration. Ferrucous ions formed in the reduction process would precipitate as $\text{Fe}(\text{OH})_2$ on the film surface if the solubility product of this compound in the electrolyte were exceeded.

The time dependence of Fe^{2+} concentration during cathodic reduction of the passive film at different current densities is shown in Fig. 1. These values were calculated from the formula

$$C_{(0,t)} = \frac{2i}{nF\pi D} \sqrt{t}$$

Fick's second law and the Laplace transform method were used, with initial and final boundary taken as $t = 0$, $x \cong 0$, $C = 0$, and $t \cong 0$, $x \rightarrow \infty$, $C \rightarrow 0$. The following equation was also used

$$i = nFD \left[\frac{\partial c}{\partial x} \right]_{x=0}$$

for $x = 0$ and $t > 0$, and following values were taken for calculations: $i = 0.17$, 0.1 , and $0.05 \text{ A} \cdot \text{m}^{-2}$; $n = 1$, and $D = 10^{-5} \text{ cm}^2 \cdot \text{s}^{-1}$. The concentration of $\text{Fe}(\text{OH})_2$, $1.26 \times 10^{-7} \text{ mol} \cdot \text{cm}^{-3}$, at which the solubility product

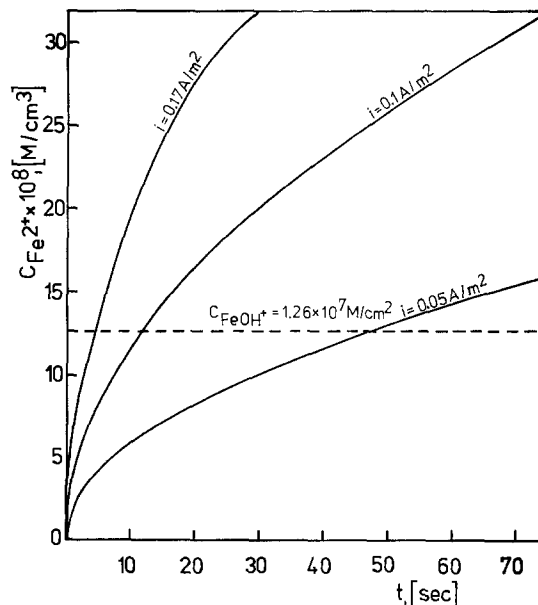


Fig. 1. Concentration of Fe^{2+} at the electrode as a function of reduction time. Reduction currents 0.17, 0.1, and 0.05 A/m^2 .

is exceeded at pH 8.45, is marked in Fig. 1. This value was calculated from the solubility product ($K_{so} = [\text{FeOH}^+][\text{OH}^-] = 10^{-9.4}$) established by Misawa (13). It is seen that at $i = 0.17 \text{ A} \cdot \text{cm}^{-2}$, the solubility product is exceeded already after 4s of the cathodic reduction. At $i = 0.05 \text{ A} \cdot \text{cm}^{-2}$, this time period is 46s.

Some evidence that $\text{Fe}(\text{OH})_2$ precipitates during reduction on the film surface and hampers exit of Fe^{2+} can be gathered from the difference observed in the $\delta\psi$ vs. $\delta\Delta$ curves obtained in solution 1 in the course of the oxidation and reduction processes (Fig. 2). At the beginning of the reduction process, ψ increases for an almost constant value of Δ , while the $\delta\psi$ vs. $\delta\Delta$ curve obtained during reduction was higher than that obtained during oxidation. So, values of n and k are slightly decreased during reduction. This seems to indicate that the presence of hydroxide affects the average optical properties of the film. These effects were evident only in solution 1 for films formed at high anodic potentials and for oxidation times longer than 10 min.

Results

Variations in potential and film thickness with time during the cathodic reduction process have been measured for films grown in solution 1 for 1.5, 10, 30, 600, and 3600s, and for those grown in solution 2 for 1.5,

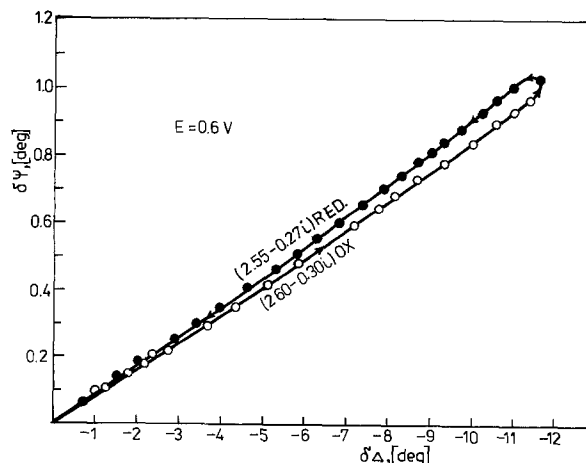


Fig. 2. $\delta\psi$ vs. $\psi\Delta$ measured during oxidation of iron and reduction of iron oxide in solution 1.

10, 30, 1200, and 3600s. Only some of the results obtained will be presented here, because the character of relationships recorded for times longer than 1.5s were similar. Typical examples of potential *vs.* cathodic charge curves obtained for films formed at various anodic potentials and for different time periods are

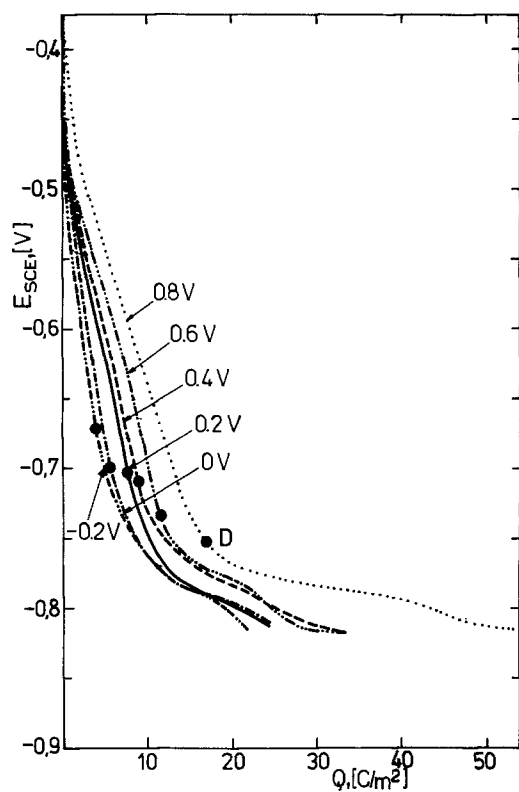


Fig. 3. Dependence between potential and cathodic charge during the reduction of films formed in 1.5s at different anodic potentials in solution 1.

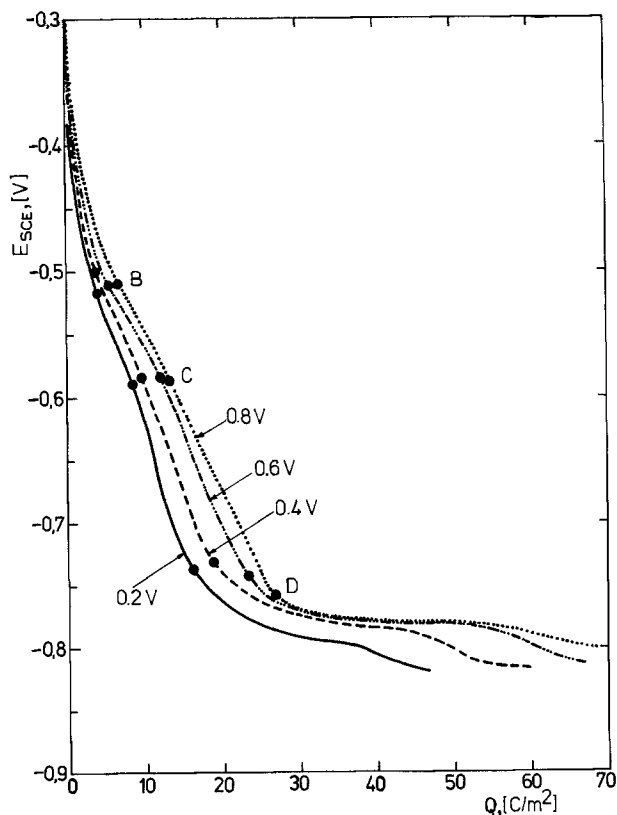


Fig. 4. Dependence between potential and cathodic charge during the reduction of films formed in 30s at different anodic potentials in solution 1.

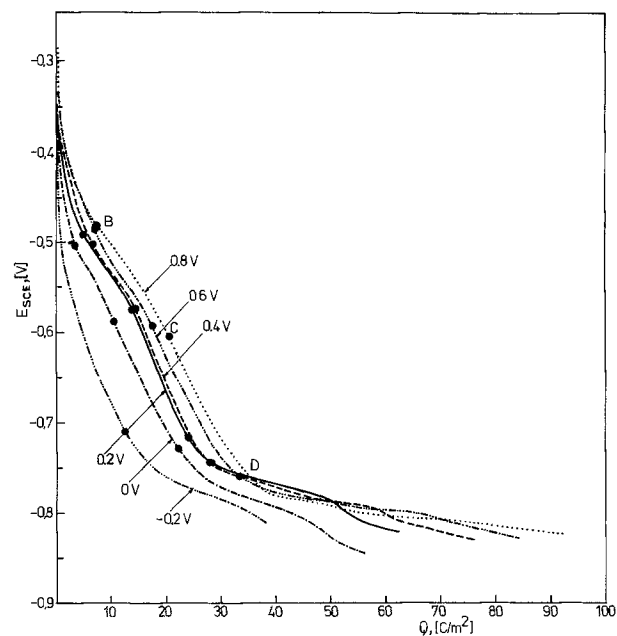


Fig. 5. Dependence between potential and cathodic charge during the reduction of films formed in 1h in solution 1.

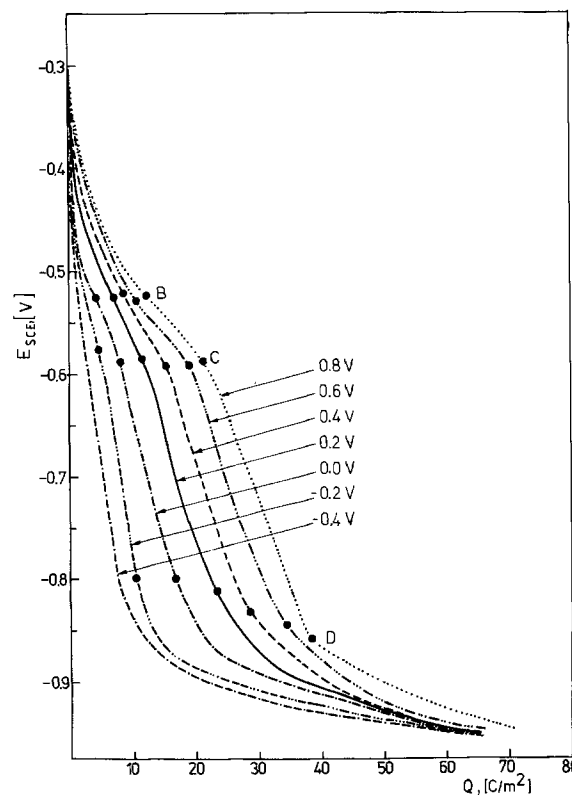


Fig. 6. Dependence between potential and cathodic charge during the reduction of films formed in 1h in solution 2.

given in Fig. 3-6. In these graphs, characteristic points based on ellipsometric measurements of film thickness *vs.* reduction potential at constant current density are marked by the letters "A," "B," "C," and "D;" their meaning will be discussed later.

During reduction of times formed in short oxidation times, i.e., 1.5s, a rapid drop of potential to about -0.76 and -0.95 V occurred in solutions 1 and 2, respectively. After these potentials were attained, further changes were insignificant. Specimens oxidized for $t \geq 10$ s in both solutions showed potential plateaus (or bends) which were more pronounced for films grown for a longer time at higher anodic potentials, especially in solution 2.

Comparison of the curves obtained leads to the conclusion that the cathodic charge necessary to reach the potential plateau (about -0.8 and -0.95 V in solutions 1 and 2, respectively) increases with both anodization time and oxidation potential.

Figures 7, 8 (solution 1), and 9 (solution 2) compare changes in film thickness with cathodic charge density. Thicknesses were determined ellipsometrically for films formed at different oxidation potentials as marked on the respective curves.

During reduction of films grown for 1.5s in both solutions, a linear dependence initially exists between film thickness and charge density. Later, the reduction rate and film thickness diminish, and the d vs. Q relationship becomes nonlinear. During reduction of films grown for $t \cong 10$ s, the linear segment of the d vs. Q curve is preceded and followed by nonlinear segments.

Hence, for passivation times longer than 10s, and passivation potentials higher than about -0.1 V in solution 1 and -0.3 V in solution 2, the relationship between film thickness and cathodic charge density indicates that reduction occurs in three stages characterized by different reduction rates of the film.

The following conclusions can be reached on the basis of the results obtained for both solutions:

1. The longer the passivation time of iron at the given potential, and the higher the anodic potential for the given passivation time, the higher the charge consumed in film reduction is.

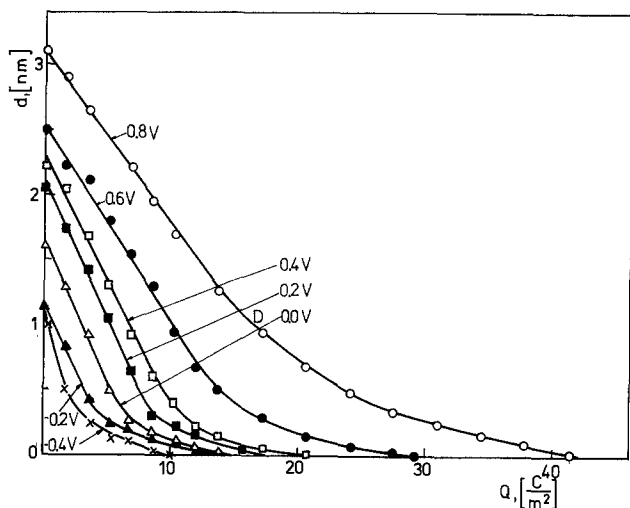


Fig. 7. Dependence between film thickness determined ellipsometrically and cathodic charge for specimens passivated for 1.5s in solution 1 at different potentials.

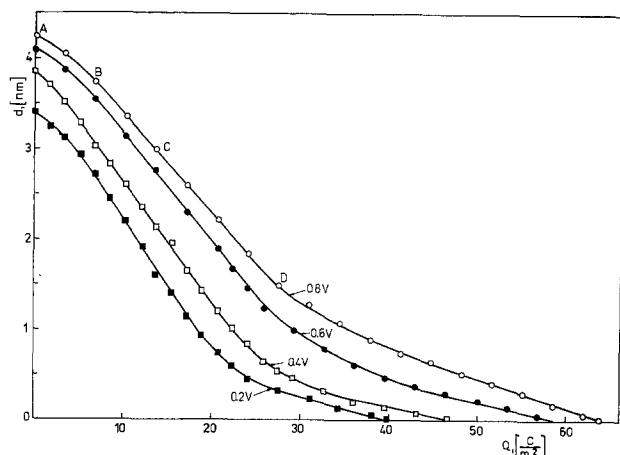


Fig. 8. Dependence between film thickness determined ellipsometrically and cathodic charge for specimens passivated for 30s in solution 1.

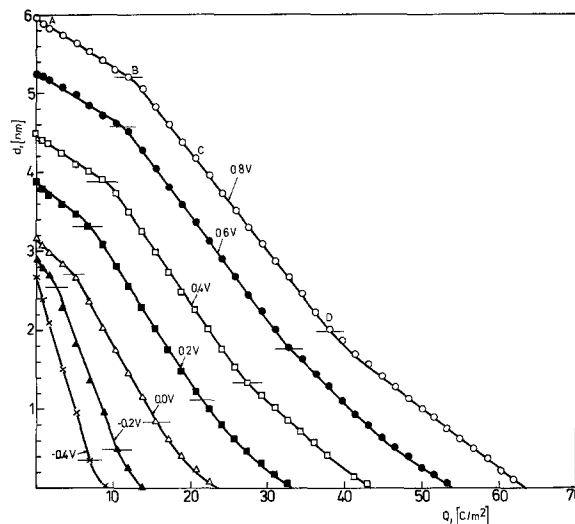


Fig. 9. Dependence between film thickness determined ellipsometrically and cathodic charge for specimens passivated 1h in solution 2.

2. The higher the passivation potential and the longer the passivation time, the greater the thickness of the film reduced in the final stage of reduction is.

3. The charges consumed for the reduction of films formed at the same potential and time are higher for films grown in the dilute solution 1 than in the more concentrated solution 2.

The last observation appears to suggest that less dense films are formed in solution 2 relative to solution 1.

Figures 10-14 show typical examples of changes in potential vs. film thickness during galvanostatic reduction of films formed at different passivation potentials and times. Results obtained in solution 1 are plotted in Fig. 10-12, and those in solution 2 are given in Fig. 13.

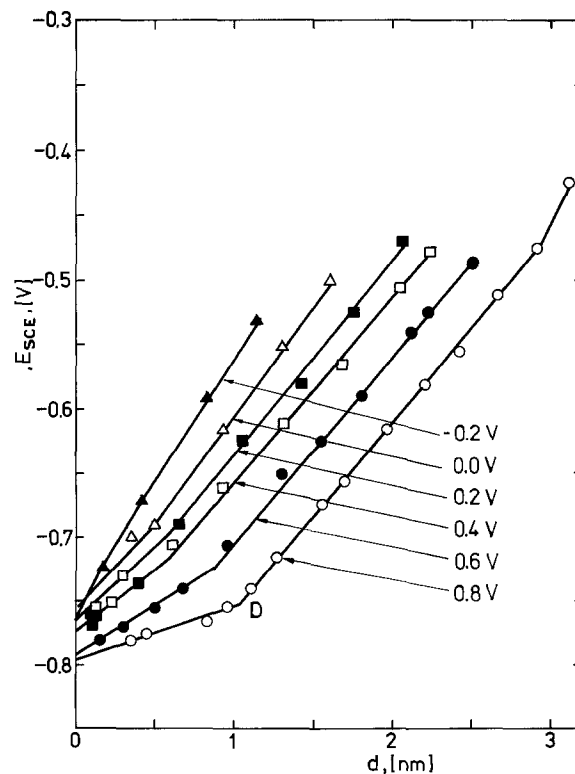


Fig. 10. Dependence between reduction potential and film thickness determined ellipsometrically for specimens passivated for 1.5s in solution 1 at different potentials.

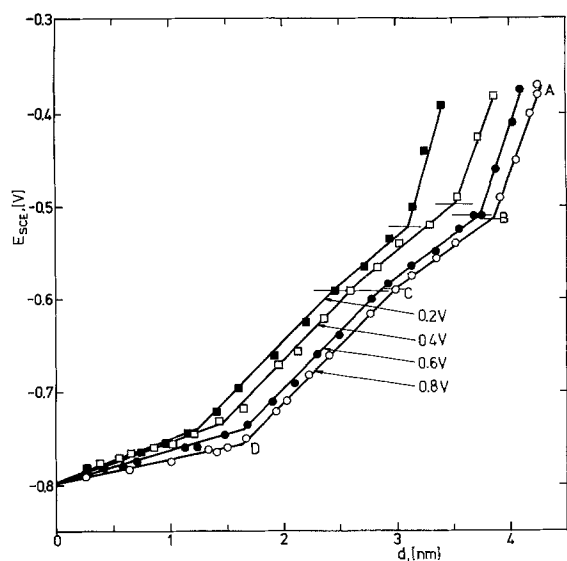


Fig. 11. Dependence between reduction potential and film thickness determined ellipsometrically for specimens passivated for 30s in solution 1.

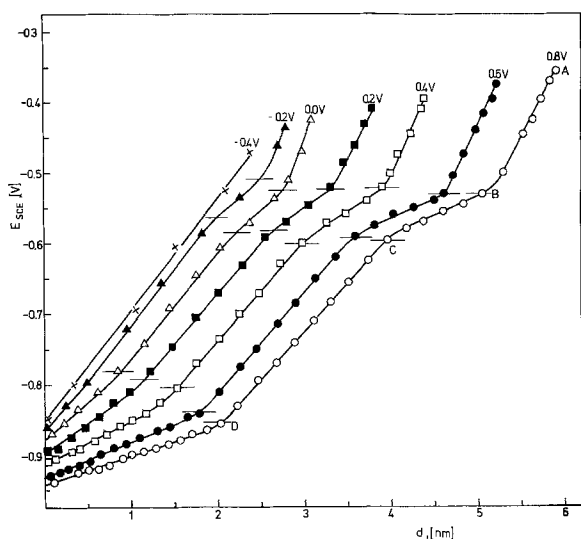


Fig. 12. Dependence between reduction potential and film thickness determined ellipsometrically for specimens passivated for 1h in solution 1.

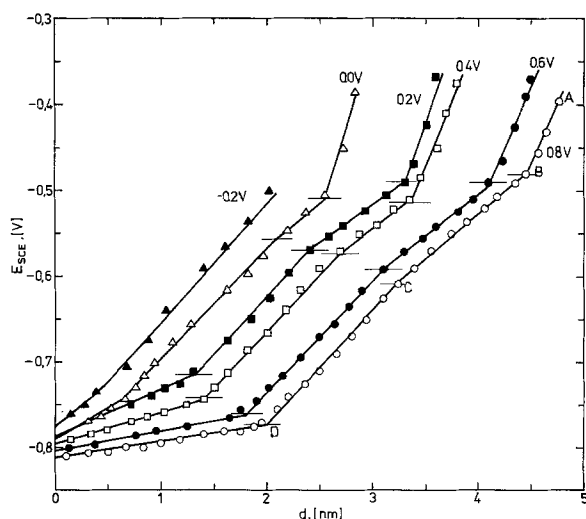


Fig. 13. Dependence between reduction potential and film thickness determined ellipsometrically for specimens passivated for 1h in solution 2.

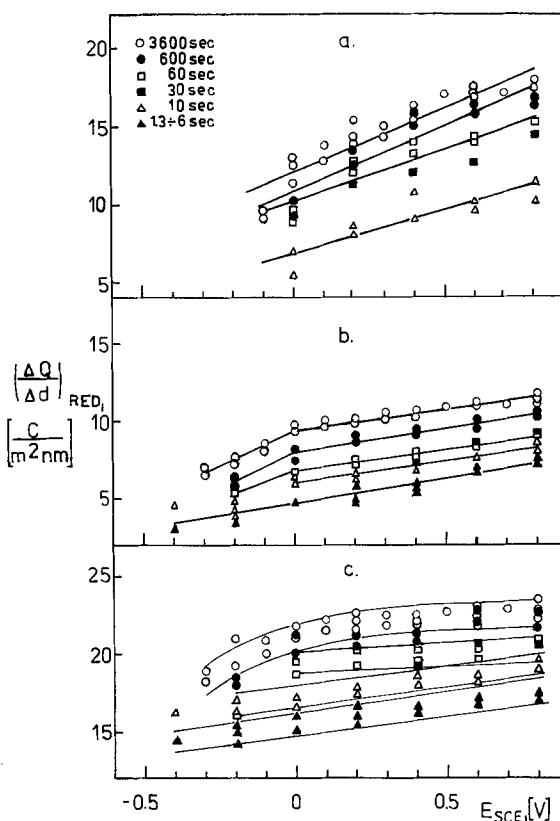


Fig. 14. Cathodic charge consumed for the reduction of film formed in Stages A-B (a), B-D (b), and D-Me (c) in different periods of time and at different anodic potentials; solution 1.

For films formed over about 1.5s, the relationship between cathodic potential and film thickness shows two linear segments at higher anodic potentials. The initial decrease of potential with thickness is faster than the final decrease. However, during reduction of films formed over 10s, and at $E \approx -0.1V$ in solution 1, and at $E \approx -0.2V$ in solution 2, the potential vs. d curves exhibit four linear segments, which are more pronounced for films oxidized for a longer time at higher anodic potentials.

In Fig. 10-13, points at which changes in slope of the E vs. d curves occur are marked "B," "C," and "D," while "A" indicates a film formed over 60 min. The same letters are marked in certain plots of d vs. Q and E vs. Q . It is seen that points B and D in the E vs. d plot also appear in E vs. Q and d vs. Q plots, while point C is clearly noticeable in the E vs. d relationship but is absent in the d vs. Q plot.

The individual reduction steps that appear in the E vs. d and E vs. Q relationships correspond to the four oxidation stages discussed in the first part of our work (1). Specifically, the A-B step showing reduction of the outermost film layer corresponds to the oxidation Stage IV; B-C corresponds to Stage III, C-D to Stage II, and D-Me (reduction of the metal-adhering layer) to the oxidation Stage I. However, film thicknesses at potentials corresponding to the point D are higher during reduction than during oxidation.

It follows from the experimental results that:

1. The potential values corresponding to point B range from -0.50 to $-0.53V$ in solution 1 and from -0.51 to $-0.53V$ in solution 2. These potentials are independent of both passivation potential and time.
2. Potential values corresponding to point C range from -0.57 to $-0.60V$ in both solutions and are independent of passivation potential and time.
3. Potential values corresponding to point D range from -0.7 to $-0.77V$ in solution 1 and from -0.8 to $-0.86V$ in solution 2. These values become lower for greater thicknesses of films to be reduced during the

D-Me step. Reduction of the film ended at potentials ranging from -0.76 to -0.86 V in solution 1 and from -0.85 to -0.95 V in solution 2.

Calculated values of the cathodic charge (Q) consumed for the reduction of the anodic film of $d = 1$ nm and an area of 1 m^2 in three consecutive steps A-B, B-D, and D-Me are collected in Fig. 15 and 16 for solution 1 and 2, respectively. These graphs correlate values of $(\Delta Q/\Delta d)_{\text{red}}$ with passivation potentials and time.

The $(\Delta Q/\Delta d)_{\text{red}}$ values for the B-D step apply to all potentials studied because a linear dependence exists between film thickness and charge. For the A-B and D-Me steps, average values were considered for each individual step, in accordance with the fact that no linear dependence exists between d and Q .

It follows from Fig. 14 that:

1. The $\Delta Q/\Delta d$ ratios during the D-Me step are greater in solution 1 compared with those in solution 2, but the opposite is true for the B-D step. For the A-B step, both solutions give rise to similar values of $\Delta Q/\Delta d$.

2. For all the reduction steps, the $\Delta Q/\Delta d$ ratios increase with increasing oxidation potential and passivation time. The influence of potential is most prominent in step A-B. At constant oxidation time, $\Delta Q/\Delta d$, for both steps A-B and B-D, is a linear function of potential starting from about 0.0 V in solution 1 and about -0.2 V in solution 2. The difference in $\Delta Q/\Delta d$ obtained for specimens oxidized in solution 2 for 30 and 60 min are insignificant.

Discussion

In Table I, calculated values are given for the cathodic charge necessary to reduce a unit volume of film containing a definite compound of iron. Charges consumed for reduction from Fe^{3+} to Fe^{2+} and from Fe^{3+} to Fe^0 are listed in the upper and lower part of the table, respectively.

Since it is possible that at potentials more negative than those corresponding to point D, Fe^{3+} could be reduced to Fe^0 and the fraction of the cathodic charge could be consumed in the reduction of hydrogen ions, only steps A-B and B-D, during which the above two reactions could not occur, will be discussed here.

Comparison of the theoretical charges given in the upper part of Table I with those found experimentally (Fig. 14) indicates that in most cases the latter are much greater than the former. Only for low oxidation potentials and short oxidation times are the experimental results close to the theoretical data. There are two likely reasons for this difference in charges: (i) during film growth and reduction, roughening of the surface takes place, and (ii) reduction to Fe^{2+} proceeds from an oxidation degree higher than Fe^{3+} .

Considerations based on the results of ellipsometric measurements and on tentative calculations of the most probable variations in the roughness coefficient have led to the conclusion that surface roughening alone could not be responsible for the observed excess

of cathodic charge consumed. For example, increased passivation potential has been found to increase the refraction index slightly, while surface roughening produces an opposite effect. Although surface roughening can probably occur during both anodic and cathodic reduction (3), this fact is expected to have an insignificant effect on the cathodic charge consumed.

Much more important effects might be expected if reduction from an oxidation degree higher than Fe^{3+} occurs.

The occurrence of highly oxidized iron compound in passive films was presumed by several authors (3, 14, 15). According to Nagayama and Cohen (3), the internal (i.e., iron-adherent) layer of the film is composed of Fe_3O_4 , while the external layer is composed of Fe_2O_3 , but contains iron oxidized to Fe^{6+} on the surface. Konno and Nagayama (13) claim that in the outermost film layer the average oxidation degree significantly exceeds that of Fe^{3+} . Using XPS method, they found an average valence of iron in the film equal to 3.59. Higher oxidation degrees have also been assumed by Chen *et al.* (15), and others.

Taking into consideration the occurrence of higher oxidized iron (above Fe^{3+}) in the external part of film, average oxidation degrees (v) were calculated assuming different values of the roughness coefficient (r). For $r = 1$, high, unrealistic values were obtained. If $r = 1.5$ was assumed, the computed v value was slightly higher than $3+$ for the reduction step and slightly lower than $3+$ for the B-D step. At longer oxidation times, and higher anodic potentials, higher v values were obtained. The v values obtained for $r = 1.5$ seem probable and are lower than those found by Konno and Nagayama (14).

As mentioned before, four distinct stages are observed during both the anodic oxidation and the cathodic reduction of oxide film. In addition, at film thicknesses corresponding to the characteristic points B and C, the reduction potentials are independent of both oxidation potential and time. Since, at the characteristic points B and C, the film thicknesses obtained from measurements of the change in d vs. t during anodic oxidation, and from the changes in d vs. E during cathodic reduction, are the same, it can be deduced that during oxidation Stages II, III, and IV at a given anodic potential, no substantial change in film composition occurs, irrespective of time of oxidation and reduction.

There is no agreement in the pertinent literature regarding electrochemical reactions responsible for two waves on the E vs. t curve during cathodic reduction of passive films at constant current density.

It seems reasonable to assume that a bend appears in the E vs. t plot when a characteristic potential is reached at which the film adopts certain specific properties (composition, conductivity, density) leading to a substantial change in the mechanism and rate of the further process of oxidation or reduction. It would be premature to speculate on the actual composition and

Table I. Calculated cathodic charge necessary to reduce a unit volume of film containing a definite compound of iron

Compound	$\left(\frac{\Delta Q}{\Delta d}\right)_{\text{red}} \left[\frac{C}{\text{m}^2\text{nm}}\right]$	$d \left[\frac{\text{g}}{\text{cm}^3}\right]$	Mw	Type of reaction
Fe_2O_3	6.34	5.24	159.70	$\text{Fe}_2\text{O}_3 \rightarrow 2\text{Fe}^{2+}$
Fe_3O_4	6.04	5.00	159.70	$\text{Fe}_3\text{O}_4 \rightarrow 2\text{Fe}^{2+}$
Fe_2O_4	4.32	5.18	231.50	$\text{Fe}_2\text{O}_4 \rightarrow 3\text{Fe}^{2+}$
FeOOH	4.44	4.09	88.63	$\text{FeOOH} \rightarrow \text{Fe}^{2+}$
$\text{Fe}_2\text{O}_2.5\text{OH}$	5.33	4.66	168.70	$\text{Fe}_2\text{O}_2.5\text{OH} \rightarrow 2\text{Fe}^{2+}$
$\text{Fe}_2\text{O}_3.5\text{OH}$	5.72	5.00	168.70	$\text{Fe}_2\text{O}_3.5\text{OH} \rightarrow 2\text{Fe}^{2+}$
$\text{Fe}(\text{OH})_2$	3.25	3.60	106.87	$\text{Fe}(\text{OH})_2 \rightarrow \text{Fe}^{2+}$
$\text{Fe}(\text{OH})_3$	2.20	2.44	106.87	$\text{Fe}(\text{OH})_3 \rightarrow \text{Fe}^{2+}$
Fe_2O_3	12.68	5.24	159.70	$\text{Fe}_2\text{O}_3 \rightarrow \text{Fe}^{2+} + \text{Fe}^0$
Fe_3O_4	8.64	5.18	231.50	$\text{Fe}_3\text{O}_4 \rightarrow 2\text{Fe}^{2+} + \text{Fe}^0$
Fe_2O_4	12.96	5.18	231.50	$\text{Fe}_2\text{O}_4 \rightarrow \text{Fe}^{2+} + 2\text{Fe}^0$
Fe_3O_4	17.28	5.18	231.50	$\text{Fe}_3\text{O}_4 \rightarrow 3\text{Fe}^0$

structure of the film having these characteristic properties.

Conclusions

1. In borate solution of pH 8.45, the cathodic charge consumed for the reduction of passive film is greater than the theoretical, calculated charge.

2. The charge consumed for reduction of passive film is greater for higher oxidation potentials and longer oxidation times.

3. The charge consumed for reduction of passive film in borate buffer solution of pH 8.45 depends on the concentration of H_3BO_3 and $Na_2B_4O_7$ and is less in the more concentrated solution 2 than in the dilute solution 1.

4. At certain characteristic thicknesses of the passive film, which correspond to changes in the growth of the film during its formation, inflections of the E_{red} vs. t and E_{red} vs. d curves are observed. These characteristic film thicknesses occur at constant potentials independent of either the oxidation potential or time.

Manuscript submitted Jan. 11, 1983; revised manuscript received Sept. 23, 1983.

REFERENCES

1. Z. Szklarska-Smialowska and W. Kozłowski, *This Journal*, **131**, 234 (1984).
2. J. Kruger and J. P. Calvert, *ibid.*, **114**, 43 (1967).
3. M. Nagayama and M. Cohen, *ibid.*, **109**, 781 (1962).
4. S. Haruyama and T. Tsuru, *Corros. Sci.*, **13**, 275 (1973).
5. T. Tsuru and S. Haruyama, *ibid.*, **16**, 623 (1976).
6. D. Rahner and W. Forker, *Z. Phys. Chem.*, **18**, 344 (1978).
7. A. Rauscher, H. Konno, and M. Nagayama, *Electrochim. Acta*, **22**, 823 (1977).
8. K. Ogura and T. Majima, *ibid.*, **23**, 1361 (1978).
9. K. Ogura and K. Sato, *ibid.*, **25**, 857 (1980).
10. K. Ogura and T. Ohama, *Corrosion*, **37**, 569 (1981).
11. N. Sato, K. Kudo, and T. Noda, *Corros. Sci.*, **10**, 785 (1970).
12. C. T. Chen and B. D. Cahan, *This Journal*, **129**, 17 (1982).
13. T. Misawa, *Corros. Sci.*, **13**, 659 (1973).
14. H. Konno and M. Nagayama, in "Passivity of Metals," R. P. Frankenthal and J. Kruger, Editors, p. 585, The Electrochemical Society Monograph Series, Princeton, NJ (1978).
15. C. T. Chen, B. D. Cahan, and E. Yeager, Technical Report no. 48, Case Western Reserve University, Cleveland, OH (1979).

Atmospheric Sulfidation of Copper Alloys

I. Brasses and Bronzes

G. W. Kammlott, J. P. Franey, and T. E. Graedel

AT&T Bell Laboratories, Murray Hill, New Jersey 07974

ABSTRACT

Although it is widely recognized that copper alloys are subject to sulfidation upon exposure to the atmosphere, the information available on the sulfidation rates of these alloys has come largely from field exposures under uncontrolled conditions. To gain more definitive information on the rates and processes involved in atmospheric sulfidation of copper alloys, we exposed nine copper alloys (brasses, nickel-substituted brasses, and other common compositions) to low concentrations of hydrogen sulfide in humidified air. Among the specific results are the following. (i) The resistance to sulfidation of the brasses was 50-100 times better than that of pure copper. (ii) The substitution of nickel for part or all of the zinc produces alloys even more resistant to sulfidation for low to moderate exposures; at longer exposures their behavior is mixed. (iii) Beryllium copper and phosphor bronze are somewhat more resistant to sulfidation than copper except for long exposures, when all three behave similarly. (iv) A silicon bronze sulfidized more rapidly than copper for most exposure periods. (v) Alloying copper with 10% aluminum yields an alloy with a sulfidation resistance nearly as good as the brasses. These results are discussed in conjunction with the information available on oxide growth on these alloys, and it is demonstrated that the sulfidation resistance of the alloys is quite similar to their resistance to oxidation, once an initial oxide film has formed. The degree to which the surface oxide film inhibits copper diffusion is thus reflected in the oxidation and sulfidation behavior of a given alloy. The results indicate that the performance in sulfidizing environments of equipment containing copper alloy components or parts can thus be markedly influenced by the particular alloys selected by the physical designer.

Unalloyed copper is valued highly as a metal because of its high electrical conductivity and ease of fabrication. Among the disadvantages for certain applications are its relative softness and its susceptibility to certain forms of atmospheric corrosion. These disadvantages can be minimized, however, by alloying the copper with other metals to form harder, more corrosion-resistant alloys while retaining much of copper's good workability properties.

Among the trace gases present in the atmosphere, those containing sulfur in a reduced chemical state are often the most detrimental to copper. The cuprous sulfide that forms under atmospheric conditions degrades its electrical and mechanical surface properties, as well as its appearance. Although the rates of sulfidation of the copper alloys are generally considered less rapid than that of pure copper (1, 2), few quantitative data are available. In a related paper (3), we report on studies of the sulfidation of copper-nickel-tin alloys by hydrogen sulfide (H_2S), one of the most reactive of atmospheric corrodants. In this paper, we describe similar studies dealing with several brasses and related nickel alloys, together with common alloys of copper containing the elements aluminum, beryllium, phos-

phorus, and silicon. Taken together, the studies provide quantitative information on the sulfidation characteristics of virtually all the copper alloy families, including most of the common materials in industrial use.

Experimental Technique

Sample characteristics.—Nine different alloys were selected for this study; their characteristics are presented in Table I. Five of the alloys form a group composed of brasses (copper-zinc alloys), alloyed brasses (alloys of copper, zinc, and <4% additional elements), and alloys in which nickel has been substituted for part or all of the zinc (nickel silver, copper nickel). The remaining four alloys were chosen to explore the sulfidation behavior of copper alloyed with other metals. In addition to the elements shown in Table I, small (<1%) amounts of other metals (Pb, Fe, etc.) are typical constituents of some of these alloys.

The alloys were procured in a variety of commercially available forms. Alloys 17200, 46400, 51000, 63000, and 65500 were received as 2.5 cm diam rods. Alloys 44300 and 71500 were received as 2.4 cm diam tubes with wall thicknesses of ~0.2 cm. Alloys 26000 and 75200 were received in sheet form. Wafers were cut

Table I. Characteristics of samples

Designation		Composition (w/o)					Properties		
							Rockwell Hardness \ddagger		Corrosion resistance*
CDA Code \dagger	Common name	Cu	Zn	Ni	Sn	Other	Typical	This work	
46400	Naval brass	60	39		1.0		B55-95	B69	F-E
75200	Nickel silver	65	17	18		0.5 Mn, 0.3 Fe	B40-90	B26	E
71500	Copper nickel	65	1	32		1.0 Mn, 1.0 Fe	B35-80	B85	E
26000	Cartridge brass	70	30				B11-93	B93	F-E
44300	Admiralty brass	71	27		1.0	0.8 As	B37-73	B88	G-E
17200	Beryllium copper	98				2.0 Be	B58-99	B98	G-E
51000	Phosphor bronze	94	0.3		5.0	0.3 P	B26-97	B79	G-E
65500	Silicon bronze	95	1	0.6		3.2 Si, 1.0 Mn	B40-95	B93	G-E
63000	Aluminum bronze	85	0.3		0.2	10 Al, 3.0 Fe, 1.5 Mn	B96-98	B97	G-E

* From Smith (4): F = fair, G = good, E = excellent. In the discussion section, the differences and similarities between these ratings and our results are described. \dagger Designation system administered by the Copper Development Association. \ddagger Typical values are from Ref. (31). Values of samples used in this work were determined following the complete surface preparation and polishing sequence.

from the rods and sectioned, producing wedge-shaped samples of radius 1.2 cm. The tubes were opened by a single cut along their axes, rolled flat, and cut to produce samples of dimension 1.0 cm \times 1.0 cm. The sheet samples were cut to sizes similar to those of the tube samples.

The sample hardness was measured with a Wilson Hardness Tester, Model no. 3JR-PL, using a 100K Rockwell B scale. Alloy 75200, which had the lowest hardness value, was further examined with a Wilson Superficial Hardness Tester, Model no. 3JS, using a 15T scale. The resulting values are given in Table I.

Although little quantitative information on the sulfidation rates of any of these alloys is available, qualitative assessments of their corrosion resistance have been presented by Smith (4). These assessments, reproduced in the last column of Table I, suggest that the corrosion resistance of most of the materials is satisfactory, although alloys 46400 (naval brass) and 26000 (cartridge brass) rank below the other materials. Smith's ratings apply, of course, to general field service rather than to exposure to a single corrosive species (as we study). We compare his assessments with our own results later in this paper.

Sample preparation.—The reproducibility of atmospheric corrosion is influenced markedly by the surface preparation of the samples (5, 6). Careful and consistent sample preparation is thus vital if corrosion experiments are to be of maximum usefulness. Our approach to sample preparation was to cut the samples to the desired size, anneal them if desired, and then prepare the surfaces by mechanical polishing techniques. The first step in the polishing process was wet smoothing on 600 grit Al_2O_3 paper. This was followed by sequential wet polishing with Al_2O_3 powders (7). This polishing sequence yielded a surface with mean roughness $<0.3 \mu\text{m}$. Replicate samples produced by this technique showed variations in sulfidation rate of $<2\%$, much less than that of replicate samples prepared by etching techniques (8).

Sample exposure.—Nine samples of each of the nine alloys were exposed to hydrogen sulfide in wet air for periods ranging from 1-170h. The thicknesses of the sulfide films which formed were then determined. In several cases, sulfidation behavior that was particularly interesting led us to expose additional samples to study that behavior in more detail. As a result, this analysis is based on results from a total of 100 samples.

The corrosive environment to which the samples were exposed consisted of 3.0 ± 0.2 parts per million (ppm) of hydrogen sulfide gas in humidified air (RH = $93 \pm 3\%$) at room temperatures ($20^\circ \pm 1^\circ\text{C}$). H_2S concentrations higher than a small fraction of a ppm are rare in field environments (9). It has been reported, however, that the sulfidation of pure copper is a linear

function of total H_2S exposure (10). If we assume this dependence to hold also for copper alloys, we can use H_2S concentrations higher than ambient levels to accelerate the rate of sulfidation (i.e., to shorten the exposure time) of the alloys.

The details of the multiport corrosion exposure chamber and its accessories are described elsewhere (11); we summarize them briefly here for convenience. Each of the samples was attached to a flexible insert sized to fit one of the ports of the exposure chamber; this permitted samples to be inserted and withdrawn rapidly and without noticeably altering the corrosive environment. Control of the H_2S concentration in the chamber was achieved by using polymer permeation techniques. The water content of the air was varied by adjusting the portion of the air supply that passes through the humidifier. A dew point hygrometer and hot wire anemometer monitored the dew point and flow rate continuously. Each sensor was sampled periodically throughout the exposure period by a dedicated desktop computer system; the resulting values for the exposure conditions were derived from statistical analyses of these data.

Sample examination and analysis.—The morphology of the copper sulfide films was studied with a Kent-Cambridge 2A scanning electron microscope equipped with a solid-state x-ray detector and a multichannel analyzer. The thicknesses of the corrosion films were determined by energy-dispersive x-ray analysis (EDXA). The preparation of thickness standards necessary for this method is discussed elsewhere (12). The calibration curve that resulted related the ratio of intensities of sulfur and copper x-rays to the thickness of the Cu_2S sulfidation film. The thickness values were accurate to $\pm 20\%$ or $\pm 8 \text{ nm}$, whichever was smaller.

Results

The sulfidation of the three brasses is shown in Fig. 1, together with data previously acquired (8) on the sulfidation of "oxygen-free, high conductivity" copper (99.99% pure). It is apparent that the sulfidation rates of the brasses are all lower than that of copper, and that the rates of the brasses are rather closely grouped. The highest of the three, cartridge brass (alloy 26000), has a sulfidation rate about 1/50 that of copper. This performance is significantly better than that of cartridge brass on a long-term field-exposure test (13). Since both sulfidation and chloridation of samples are common in field exposures, this result may suggest that the resistance of alloy 26000 to sulfidation is better than its resistance to chloridation. Admiralty brass (alloy 44300), which differs from cartridge brass chiefly in the substitution of $\sim 1\%$ tin and $\sim 1\%$ arsenic for $\sim 2\%$ zinc, shows essentially the same sulfidation rate. The best resistance to sulfidation is displayed by naval brass (alloy 46400), in which the copper is alloyed with zinc to a higher percentage than

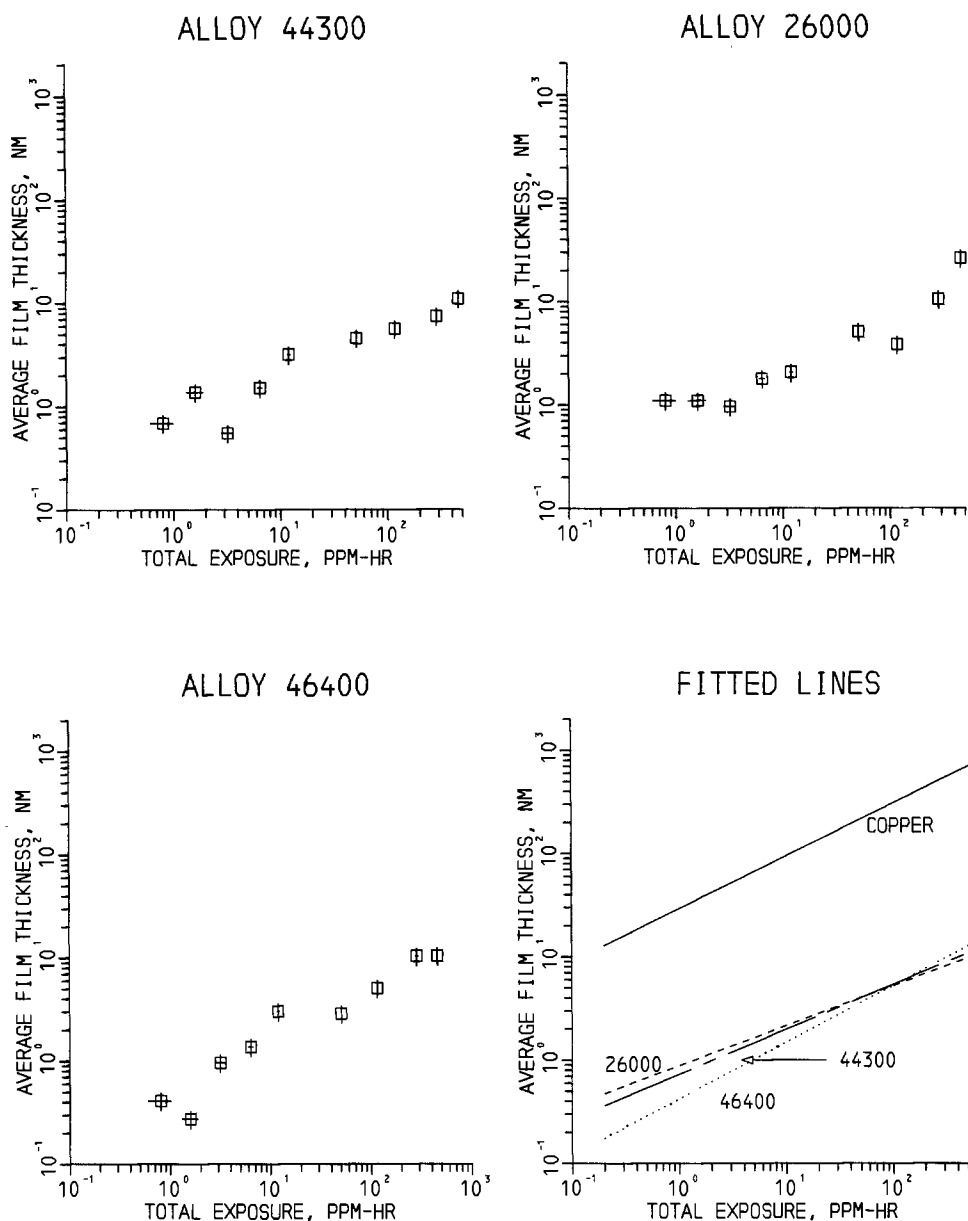


Fig. 1. Cu_2S film thickness as a function of total exposure (the product of exposure time and H_2S concentration) for pure copper and for three common brasses: cartridge brass (alloy 26000), admiralty brass (alloy 44300), and naval brass (alloy 46400). The estimated error bars are shown for each data point. The linear and quadratic lines on this and the following graphs are least squares fits to the data points, except that the final alloy 26000 point is eliminated from the fit (see text). Alloy samples receive a total H_2S exposure of $10 \text{ ppm} \cdot \text{h}$ in about a year's time at the average urban location (8).

in any other alloy in these experiments.

The sulfidation of copper is known to be markedly reduced by alloying the copper with nickel (13). In Fig. 2, we explore the sulfidation of alloys similar to naval brass in degree of alloying, but with nickel substituted for half (nickel silver, alloy 75200) or nearly all (copper nickel, alloy 71500) of the zinc. At the shorter exposures, the addition of nickel reduces the sulfidation rate below even that of naval brass. The low hardness of alloy 75200 (Table I) is consistent with its measured average grain size of 0.09 mm , a size that is characteristic of a fully annealed material. Thus, the sulfidation resistance may be somewhat enhanced by annealing. At longer times, the sulfidation rate of alloy 75200 becomes equal to that of naval brass. For the longest exposure, the rate of alloy 75200 sulfidation exceeds that of naval brass. Similar poor performance at long exposure times has been seen in a similar alloy exposed to field environments (14). Alloy 71500 shows superior sulfidation resistance at low and moderate exposures, but the sulfide film thickness increases rapidly near $E = 70 \text{ ppm} \cdot \text{h}$ to nearly that of copper. Our data provide quantitative support for LaQue and Copson's statement (13) that "the high-zinc brasses and the nickel silvers are more resistant to tarnishing than copper," at least for low and moderate exposures.

The samples with smaller fractions of alloying com-

ponents showed considerable variation in their sulfidation behavior. In Fig. 3, the sulfidation of copper is compared with those of two alloys containing about 95% copper: phosphor bronze (alloy 51000) and silicon bronze (alloy 65500). The sulfidation rates of all three materials are rather high. That of silicon bronze is very similar to that of copper, both showing a steady increase in sulfidation followed by transition to a limiting sulfide thickness of $\sim 250 \text{ nm Cu}_2\text{S}$ under our exposure conditions. These results are consistent with field exposure results for this alloy (13). The sulfidation behavior of phosphor bronze is quite different. At low to moderate exposures it is significantly more resistant to sulfidation than are the other two materials. At $E \sim 20 \text{ ppm} \cdot \text{h}$, its sulfidation rate increases suddenly to that of copper, which it follows thereafter.

Figure 4 compares copper sulfidation with that of beryllium copper (alloy 17200) and aluminum bronze (alloy 63000). The resistance to sulfidation of the aluminum bronze is much better than that of copper, rather close to that of the brasses, and monotonic throughout, as has been seen for similar alloys in field tests (13). The beryllium copper sulfidizes at a rate about a factor of five below that of copper for low and moderate exposures, but at $E = \sim 10 \text{ ppm} \cdot \text{h}$, the rate suddenly increases to that of copper, which it follows thereafter. Although alloys 51000 and 71500, and possibly 26000 and 75200, exhibit somewhat the

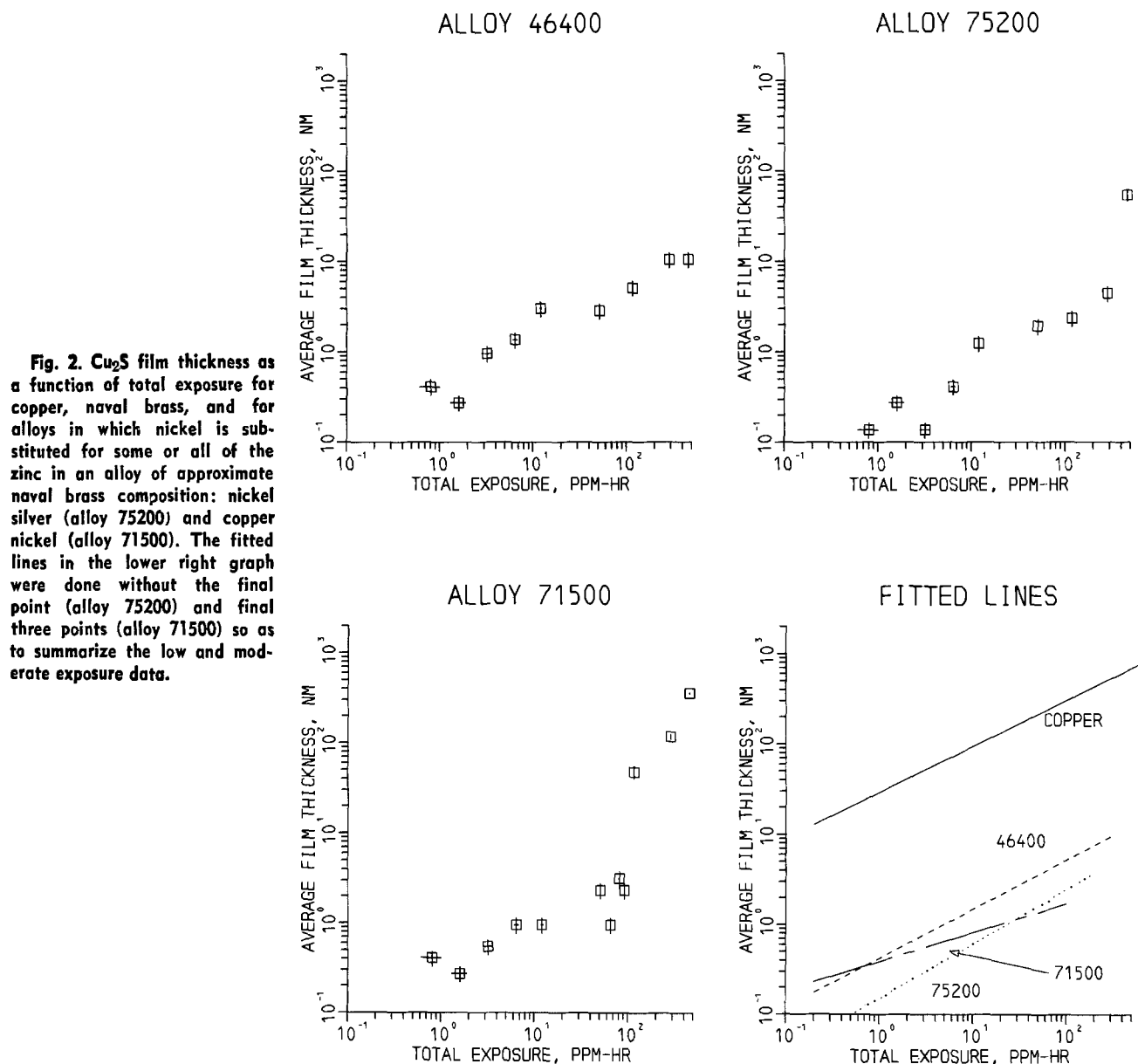


Fig. 2. Cu_2S film thickness as a function of total exposure for copper, naval brass, and for alloys in which nickel is substituted for some or all of the zinc in an alloy of approximate naval brass composition: nickel silver (alloy 75200) and copper nickel (alloy 71500). The fitted lines in the lower right graph were done without the final point (alloy 75200) and final three points (alloy 71500) so as to summarize the low and moderate exposure data.

same characteristics in their sulfidation rates, the rate behavior of alloy 17200 is the most clearly defined sigmoid in our data.

To summarize the data, of the nine alloy samples tested, five (26000, 44300, 46400, 63000, and 75200) are markedly superior to copper in resistance to sulfidation, one (65500) is similar to copper in that respect, and three (17200, 51000, and 71500) exhibit behavior superior to copper at low and moderate exposures and essentially equal to that of copper for higher exposures.

Discussion

The results of this work demonstrate that the common brasses are one to two orders of magnitude more resistant to H_2S sulfidation than is pure copper. The substitution of nickel for a portion of the zinc produces an alloy at least as resistant to sulfidation as are the brasses. Aluminum also forms sulfidation resistant alloys with copper. The relative merits of copper nickel (alloy 71500), phosphor bronze (alloy 51000), and beryllium copper (alloy 17200) from the standpoint of resistance to sulfidation depend largely on the use to which they are put. This is a consequence of the sigmoidal behavior of their sulfidation curves. Generally satisfactory performance at low exposures gives way to performance similar to that of copper at higher exposures. These sigmoidal curves, apparently the first to be observed for sulfidation, are perhaps the

most intriguing feature of our data. They indicate the existence of at least three different regimes of sulfidation behavior. The first, at low exposures, is characterized by moderate increases in sulfidation with exposure. The second, at intermediate exposures, shows a rapid increase in the sulfidation rate with exposure, perhaps reflecting a breakdown in the protective oxide layer. The third, at long exposures, shows a transition to a regime in which a limiting film thickness is approached. Sigmoidal corrosion curves have occasionally been seen in oxidation studies (15-18). The explanation given is that the initial stage of oxide adsorption on the metal surface is followed by the growth of oxide nuclei (16, 19-20). This growth is rapid, since the initial resistance to nucleation has been overcome. Once the nuclei have grown enough to coalesce, new oxide must form atop an oxide layer, and the diffusion rate through that layer becomes the rate-limiting step (16, 20).

The situation in the present case differs in that the sulfide layer must be grown atop the existing oxide layer. [Auger analysis (21) shows that there is very little growth of sulfide within the oxide layer or of additional oxide growth during sulfidation.] Diffusion of metal ions through the oxide layer will thus provide a relatively uniform damping of the sulfidation rate in all regimes. We envision the sequential picture as follows. In the first stage, individual H_2S molecules are adsorbed randomly onto the oxide layer. When Cu_2S

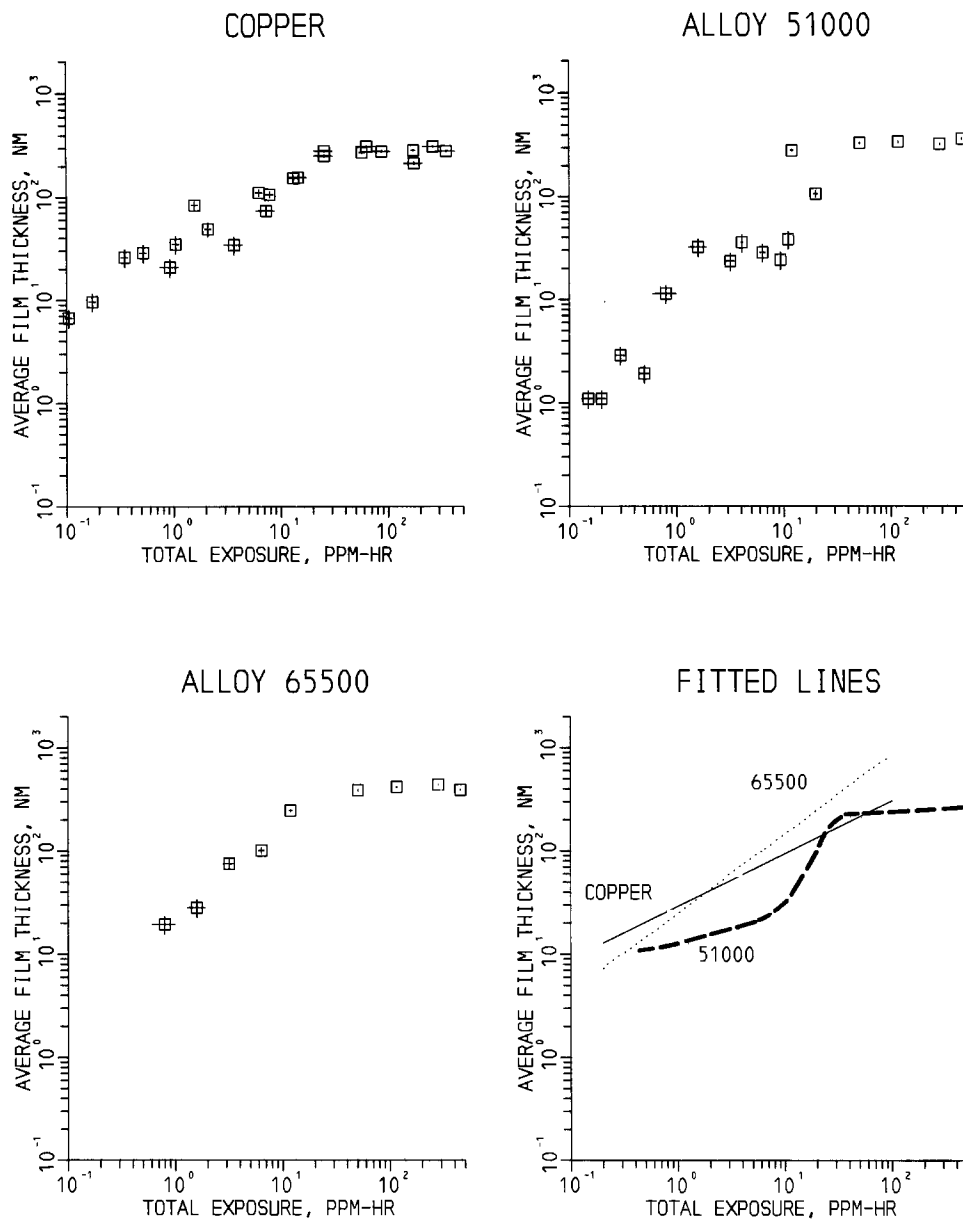


Fig. 3. Cu_2S film thickness as a function of total exposure for copper, phosphor bronze (alloy 51000), and silicon bronze (alloy 65500), two alloys that contain approximately the same percentage ($\sim 95\%$) of copper. For ease in comparison, the two groups of data for alloy 51000 close to the transition region are given separate linear fits and joined by eye.

nuclei become sufficiently well formed [probably at defect sites in the oxide lattice or at surface imperfections (8)], more rapid lateral growth occurs. This stage ends when a coalesced sulfide layer is formed by the intersecting, growing Cu_2S islands. The requirement for Cu^+ diffusion through both the oxide and sulfide layers then produces an exponential approach to the surface film thickness produced after long exposures.

A remaining item of discussion is the relationship between the sulfidation rate behavior of the different alloys and their composition. Little sulfidation research on these alloys is available, but their oxidation has been investigated fairly extensively. The success of an alloying constituent in minimizing oxidation is strongly related to the strength and permeability of the initial oxide film that forms on the alloy (22). In the case of a brass, a zinc-rich oxide layer is formed (23, 24); this layer is relatively impervious to diffusing copper ions and thus inhibits both oxidation and sulfidation (24, 25). Nickel forms a mixed oxide when alloyed with copper (26-28) and is a good oxidation inhibitor only at relatively high ($>10\%$) concentrations (27, 29). Copper rich alloys with aluminum form films of $\gamma\text{-Al}_2\text{O}_3$ which allow moderate Cu^+ diffusion (30). The effect of beryllium is to form a thin protective film of BeO which partially inhibits oxidation (23). When silicon is alloyed with copper, the surface film

is largely SiO_2 (18), but it is both permeable to copper ions and subject to rupture (18) and thus provides little oxidation protection (30).

The data we have presented indicate that the sulfidation resistance of the copper alloys is quite similar to their resistance to oxidation following the formation of the initial surface oxide film. Since each process involves the diffusion of copper ions from the bulk material through the oxide layer, it is clear that this diffusion is rate limiting for most of the sulfidation exposures in our work. Some of the influences of alloy composition on corrosion may reflect their individual reaction and diffusion characteristics. For example, brasses are known to lose zinc from surface layers as part of the corrosion process (2, 25, 32), a process which changes both the morphology and composition of the surface layers. In a subsequent study, we will examine the relationships of sulfide layer growth to localized forms of corrosion and dealloying of samples exposed to controlled corrosive atmospheres in the laboratory.

A final topic of interest is the comparison of our results with the "corrosion resistance" assessments of Smith which appear in Table I. His qualitative ratings suggest that the nickel alloys 71500 and 75200 have the highest resistance, that cartridge brass (alloy 26000) and naval brass (alloy 46400) are sometimes only fair, and that the others are roughly equivalent and of high

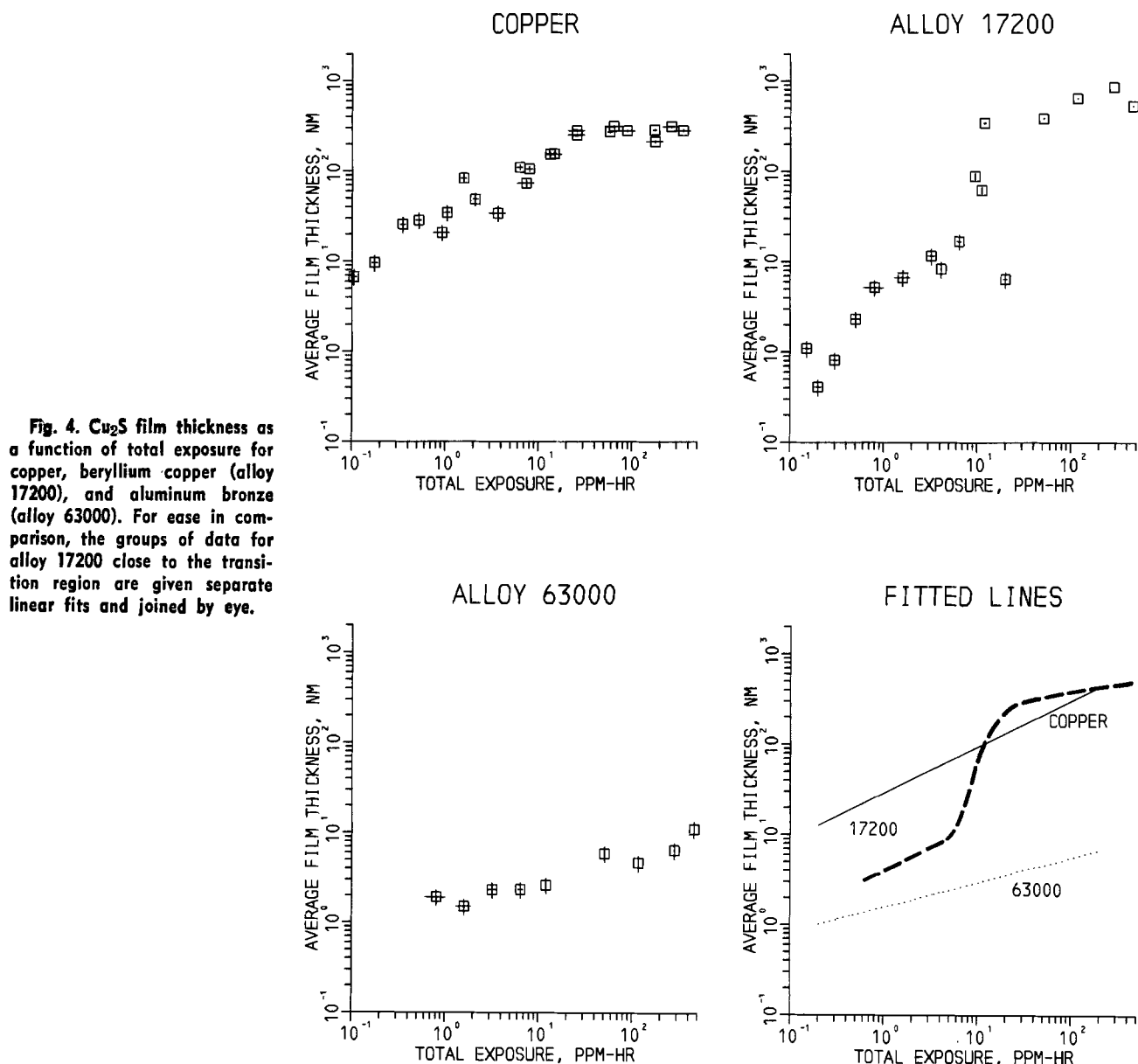


Fig. 4. Cu_2S film thickness as a function of total exposure for copper, beryllium copper (alloy 17200), and aluminum bronze (alloy 63000). For ease in comparison, the groups of data for alloy 17200 close to the transition region are given separate linear fits and joined by eye.

corrosion resistance. For sulfidation, at least, our quantitative results (for sulfidation only, rather than for the more general field corrosion to which Smith's assessment applies) differ with some of Smith's ratings and permit more precise comparisons in all cases. At high exposures, the brasses are superior. Alloying with nickel in place of zinc produces mixed behavior. Aluminum bronze is quite resistant to sulfidation, as is beryllium copper at low and moderate exposures. Phosphor bronze is relatively poor except for low exposures. Alloying with silicon appears to be of no advantage from a sulfidation resistance standpoint.

It is apparent that there are wide differences in sulfidation susceptibility among the common industrial alloys of copper, and that physical designers concerned with such susceptibility can greatly improve the sulfidation resistance of their designs by careful selection of the appropriate copper alloy.

Manuscript submitted Dec. 10, 1982; revised manuscript received June 6, 1983.

AT&T Bell Laboratories assisted in meeting the publication costs of this article.

REFERENCES

- H. Leidheiser, Jr., "The Corrosion of Copper, Tin, and Their Alloys," p. 7 ff, John Wiley and Sons, New York (1971).
- E. Mattsson and R. Holm, in "Proceedings of the International Symposium on Atmospheric Corrosion," W. H. Ailor, Editor, pp. 365-381, John Wiley and Sons, New York (1982).
- G. W. Kammlott, J. P. Franey, and T. E. Graedel, *This Journal*, **131**, 511 (1984).
- W. F. Smith, "Structure and Properties of Engineering Alloys," p. 215 ff, McGraw-Hill, New York (1981).
- W. E. Campbell and U. B. Thomas, *Trans. Electrochem. Soc.*, **76**, 303 (1939).
- G. Oelsner, *Galvanotechnik*, **64**, 460 (1973).
- M. E. Davis and T. J. Louzon, *Metallography*, **13**, 195 (1980).
- T. E. Graedel, J. P. Franey, and G. W. Kammlott, *Corros. Sci.*, **23**, 1141 (1983).
- T. E. Graedel, in "Handbook of Environmental Chemistry," Vol. 2A, O. Hutzinger, Editor, pp. 107-143, Springer, Heidelberg (1980).
- J. P. Franey, T. E. Graedel, and G. W. Kammlott, in "Proceedings of the International Symposium on Atmospheric Corrosion," W. H. Ailor, Editor, pp. 383-392, John Wiley and Sons, New York (1982).
- J. P. Franey, *Corros. Sci.*, **23**, 1 (1983).
- G. W. Kammlott, *Appl. Spectrosc.*, **35**, 324 (1981).
- F. L. LaQue and H. R. Copson, "Corrosion Resistance of Metals and Alloys," 2nd Ed., p. 592 ff, Reinhold Publishing Corp., New York (1963).
- R. S. Herman and A. P. Castillo, in "Corrosion in Natural Environments," pp. 82-96, ASTM STP-558, American Society for Testing and Materials, Philadelphia (1974).

15. U. R. Evans, *Trans. Faraday Soc.*, **41**, 365 (1945).
16. A. Rönquist, *J. Inst. Met.*, **91**, 89 (1962-1963).
17. P. Kofstad, *This Journal*, **110**, 491 (1963).
18. W. J. Tomlinson and J. Yates, *Oxid. Met.*, **12**, 323 (1978).
19. U. R. Evans, "The Corrosion and Oxidation of Metals," pp. 837-838, 939-941, Edward Arnold Ltd., London (1960).
20. R. W. Bartlett, *This Journal*, **111**, 903 (1964).
21. S. P. Sharma, *ibid.*, **127**, 21 (1980).
22. O. Kubaschewski and B. E. Hopkins, "Oxidation of Metals and Alloys," pp. 249-253, Butterworths, London (1962).
23. F. N. Rhines and B. J. Nelson, *Trans. Am. Inst. Min. Met. Pet. Eng.*, **156**, 171 (1944).
24. W. J. Van Ooij, *Surf. Technol.*, **6**, 1 (1977).
25. J.-F. Nowak, M. Lambertin, and J.-C. Colson, *Corros. Sci.*, **17**, 603 (1977).
26. D. P. Whittle and G. C. Wood, *ibid.*, **8**, 295 (1968).
27. D. P. Whittle and G. C. Wood, *J. Inst. Met.*, **96**, 115 (1968).
28. R. F. North and M. J. Pryor, *Corros. Sci.*, **10**, 297 (1970).
29. N. B. Pilling and R. E. Bedworth, *Ind. Eng. Chem.*, **17**, 372 (1925).
30. M. D. Sanderson and J. C. Scully, *Corros. Sci.*, **10**, 165 (1970).
31. Standards Handbook of Wrought Copper and Copper Alloy Mill Products, 7th Ed., Copper Development Assn., Inc., New York (1973).
32. T. L. Barr and J. J. Hackenberg, *J. Am. Chem. Soc.*, **104**, 5390 (1982).

Atmospheric Sulfidation of Copper Alloys

II. Alloys with Nickel and Tin

G. W. Kammlott, J. P. Franey, and T. E. Graedel

AT&T Bell Laboratories, Murray Hill, New Jersey 07974

ABSTRACT

In order to assess quantitatively the sulfidation characteristics of industrially used alloys of copper, we have exposed a variety of copper-nickel-tin alloys as well as the pure metals to hydrogen sulfide in humidified air. The thicknesses of the resulting sulfide films were then determined. Nickel and tin were very resistant to sulfidation and copper alloys containing at least a combined total of 8% of these metals were resistant as well. The rate of sulfidation for the 92 Cu/4 Ni/4 Sn alloy is decreased with respect to copper by a factor of about four for moderate exposures. The rate continues to decrease as more alloying metal is added to the copper, reaching an equivalent rate of $<0.2 \text{ nm Cu}_2\text{S yr}^{-1}$ for an alloy of 78 Cu/15 Ni/8 Sn in a typical field environment. The content of nickel in the alloy appears to be more important to the inhibition of sulfidation than the tin content. A spinodal alloy after heat-treatment is less resistant to sulfidation than the same alloy as cold-worked. Annealed 725 alloy (89 Cu/9 Ni/2 Sn) is more prone to initial sulfidation than is the same alloy when work hardened. The results of this and earlier work demonstrate that alloys of copper containing at least 10% of any of the common alloying metals are some thirty times more resistant to sulfidation than pure copper.

Pure copper is subject to progressive sulfidation upon exposure to atmospheric environments containing reactive sulfur compounds. Some of its alloys are much more corrosion resistant. Experience has demonstrated that alloys containing more than a few percent of nickel are relatively tarnish-free under normal use conditions. This qualitative knowledge is often insufficient, however, as when a materials scientist attempts to predict an alloy's behavior in a severe corrosive environment or when new alloys are prepared for which no field experience exists.

The object of the present work is to provide quantitative information on the atmospheric sulfidation of several ternary alloys of copper, together with the base metals. Because of their industrial utility, especially for electrical and electronic applications, we have performed corrosion experiments on copper, nickel, and tin, and on copper/nickel/tin ternary alloys of varying composition, spinodal structure, and hardness. The results of those experiments are described here. In a companion paper (1), we describe the results of similar experiments on alloys of copper with zinc, silicon, beryllium, and aluminum.

Experimental Technique

The metals and alloys selected for these experiments are representative of a variety of spinodal and non-spinodal materials in common industrial use. Their properties are summarized in Table I. Our experiments included simultaneous exposure of copper metal to provide a base line against which the sulfidation of the samples could be compared. The copper was of the "oxygen-free, high conductivity" type of 99.99% purity. Nickel and tin metals were also exposed in-

dividually so that their sulfidation sensitivities could be assessed; both were 99.99% pure. The alloys were taken from manufactured stock. Their compositions are accurate to ½%.

The samples used in the experiments had surface dimensions of about $1 \times 2 \text{ cm}$ and were about 2 mm thick. Surface preparation of the samples, exposure to corrosive environments, and post-exposure examination and analysis followed techniques previously described (1).

Table I. Properties of samples

CDA code†	Common name	Nominal composition (w/o)				Percent cold-work‡	Hardness*
		Cu	Ni	Sn	Other		
11000	Copper	100	—	—	—	35-40	52 R _B
—	Nickel	—	100	—	—	0	5.3 Brinnell
—	Tin	—	—	100	—	0	70 Vickers
72600	4/4	92	4	4	—	75-78	84 R _B
72700	9/6	85	9	6	—	75-78	31 R _C
72800	10/8	82	10	8	—	75-78	38 R _C
72900	15/8	77	15	8	—	75-78	37 R _C
51000	Phosphor bronze	95	—	5	0.2P	50-60	93 R _B
72500	Work-hardened	89	9	2	—	21	85 R _B
72500	Annealed	89	9	2	—	0	27 R _B
72700	9/6 Spinodal	85	9	6	—	75-78	43 R _C

† Designation system administered by Copper Development Association.

‡ From Ref. (16).

* R_B and R_C values refer to the Rockwell B and C scales, and were measured as part of this work. The Brinnell and Vickers values are from Ref. (15).

Results

Sulfidation of nickel and tin metals.—The susceptibilities of unalloyed nickel and tin to sulfidation were examined by exposing samples of the metals to the corrosive environment for periods of as long as 3 weeks, i.e., to a total exposure of ≈ 1500 ppm · h. Such an exposure is equivalent to approximately a century of reduced sulfur exposure in a typical environment or to approximately 10 yr in an extremely corrosive environment (2). The surfaces of these samples did not undergo degradation visible to the naked eye during that period, nor was any sulfur detectable by SEM/EDXA techniques. These results set upper limits of ≈ 0.2 nm to the amount of sulfide film present on the samples. Since less than 5 min in such an environment is sufficient to grow 1 nm of sulfide film on copper, the sulfidation rates of nickel and tin under our conditions are less than 10^{-4} that of copper and may be disregarded in our subsequent analyses. Such low sulfidation rates for nickel and tin are qualitatively consistent with the results of other investigators (3-6).

Sulfidation of Cu/Ni/Sn alloys of different composition.—Ternary alloys of copper, nickel, and tin customarily consist of ≈ 75 weight percent (w/o) copper. The nickel to tin ratio is generally between one and two. For our tests, we selected four alloys in commercial use, as shown in Table I. The nickel content of the alloys ranged from 4 to 15 w/o, and the total alloying metals content from 8 to 23 w/o. The sulfidation of these alloys upon exposure to the H_2S atmosphere is shown in Fig. 1. It is evident that the resistance to sulfidation increases with decreasing copper content. The vertical line labeled E_1 is the total exposure received in a 10 yr period at a typical field H_2S concentration of 1 ppb (2). Although clearly a crude approximation of a lifetime exposure, the intercepts of the fitted curves with this exposure line suggest that for alloys containing at least 15% of the alloying metals, < 10 nm of sulfide film can be expected during a 10 yr exposure to a field environment with typical concentration of reduced sulfur gases. (In general, of course, other

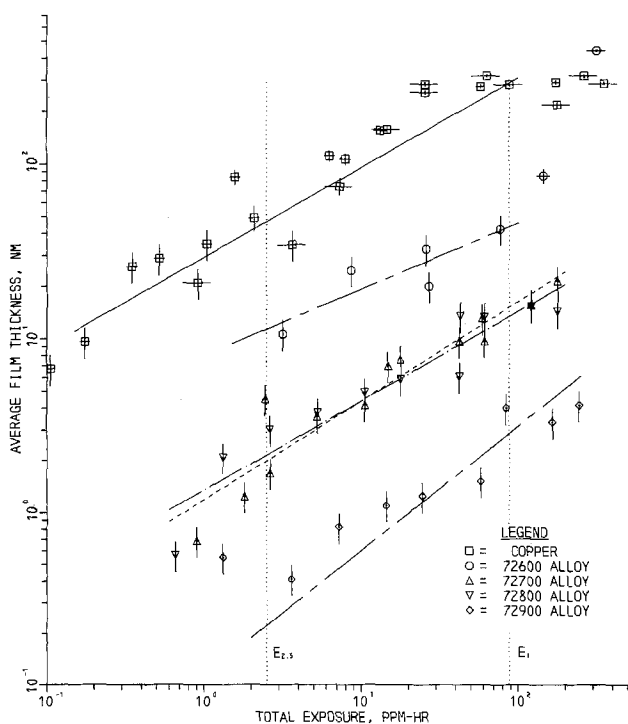


Fig. 1. Film thickness as a function of total exposure for Cu/Ni/Sn ternary alloys. The lines on this and most of the following graphs are least squares fits to the logarithms of the data points. That for the 72600 alloy is fit only to the first five data points (see discussion of Fig. 3 in text).

corrosive agents are present as well, so our results are probably lower limits to the corrosion anticipated in field service.)

To show the dependence of sulfidation on alloy composition in more detail, and for comparison of the results with those for pure copper, Fig. 1 also includes a vertical line at a total exposure of 2.5 ppm · h. (At this exposure, the ternary alloy sulfidation has proceeded far enough for the differences to be distinguished, while that for copper has not yet reached the exponential fall-off region). Using the intercepts of the fitted curves with the $E_{2.5}$ line, we then proceed to plot in Fig. 2 the film thickness (ψ) as a function of nickel content. The data have the form

$$\log(\psi_{2.5}) = 1.70 - 0.15f \quad [1]$$

where (f) is the nickel content in weight percent. The sulfidation rate is decreased by about a factor of four from that of pure copper for the 72600 alloy; this factor becomes approximately two hundred as the content of alloying metals is increased to 15 Ni/8 Sn.

Effect of individual alloy constituents on sulfidation.—To examine in more detail the effects on sulfidation of the nickel content of the alloy, exposures were conducted with samples of phosphor bronze, an alloy containing ≈ 5 w/o tin, a very small amount of phosphorus, and no nickel. In Fig. 3, the results of these exposures are compared with those of the 72600 alloy, which has nearly the same tin content as phosphor bronze, in addition to ≈ 4 w/o nickel. We have noted previously (1) that phosphor bronze shows sigmoidal behavior, as seen also in Fig. 3. Figure 3 shows that sigmoidal behavior appears to be a property of the 72600 alloy as well, but the rapid increase in the sulfidation rate occurs at about twice the exposure required to produce the same effect in phosphor bronze. Thus it appears that the presence of the nickel reduces sulfidation sig-

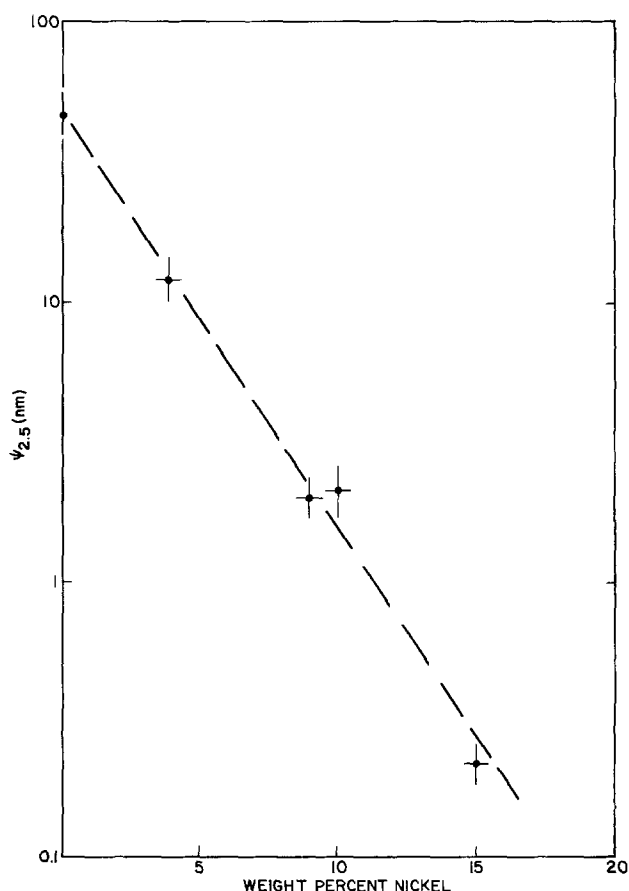


Fig. 2. Film thickness (ψ) as a function of weight percent nickel for $E = 2.5$ ppm/h.

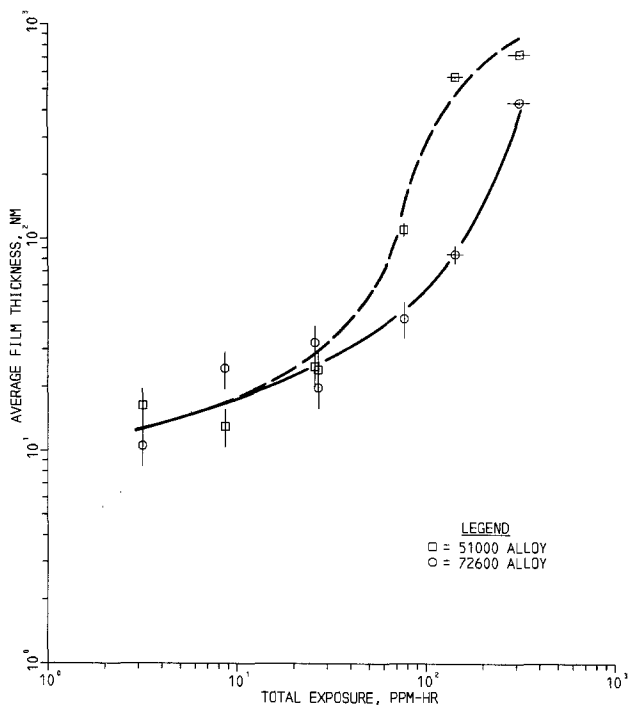


Fig. 3. Film thickness as a function of total exposure for the 72600 alloy (solid line) and for the 51000 alloy (dashed line). The sigmoidal curves are fit by eye.

nificantly at the longer exposure times, a result in qualitative agreement with experiments on high-temperature corrosion of copper-nickel alloys by sulfur vapor (5).

A similar approach was used to examine the effects of tin content on sulfidation. The comparison was made between the 72800 alloy (85 Cu/9 Ni/6 Sn) and the 72500 alloy (89 Cu/9 Ni/2 Sn). The elimination of 4 w/o of alloying tin has little effect on the sulfidation rate (Fig. 4).

We conclude from Fig. 3 and Fig. 4 that the presence of nickel in these ternary alloys is more important for

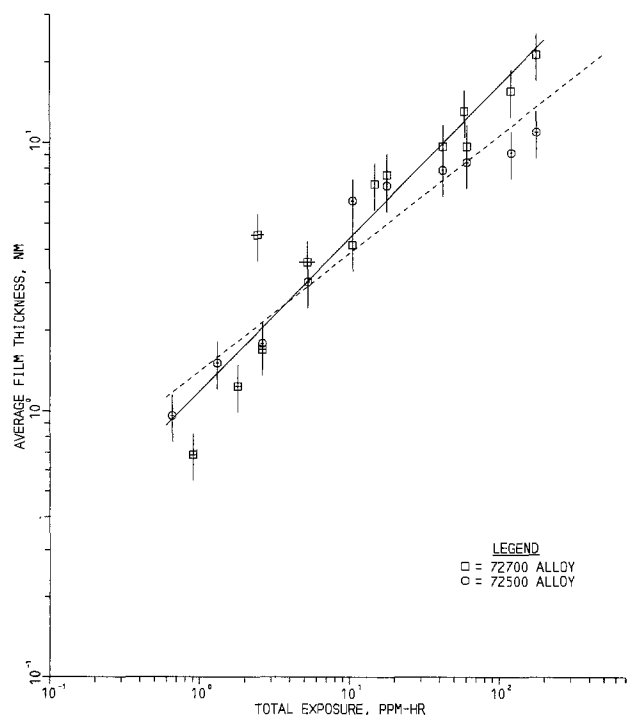


Fig. 4. Film thickness as a function of total exposure for the 72700 alloy (solid line) and for the 72500 alloy (dashed line).

their corrosion resistance than is the presence of tin. Additional evidence is provided by studies of a high-tin bronze (70-75 Cu/20-25 Sn/1-5 Pb) described in more detail elsewhere (7). Its sulfidation rate proved to be between that of pure copper and of phosphor bronze, i.e., relatively susceptible to sulfidation.

Effect of spinodal structure on sulfidation.—Ternary alloys of copper, nickel, and tin may be heat-treated to develop an extremely fine modulated structure which provides a substantial increase in mechanical yield strength (8, 9). The structure so developed is characterized by a wavelength of approximately 10 nm and a compositional amplitude of ≈ 1 w/o Sn. The data discussed above would suggest that a variation of this magnitude should not noticeably influence sulfidation kinetics. To investigate this prediction, we performed parallel exposure tests on samples of the 9/6 alloy prior to and following a heat-treatment to develop the spinodal structure (10). The results are presented in Fig. 5. Although both alloys are relatively resistant to sulfidation, the segregation produced by the spinodal heat-treatment is seen to have increased the tendency of the alloy to sulfidize. The effect is approximately equivalent to reducing the quantity of alloying nickel from 9 to 4% (see Fig. 1). The apparent anomaly in these data may be explained by the fact that coincident with spinodal decomposition in the matrix, equilibrium precipitation occurs at the grain boundaries. Corrosion reactions are favored at such boundaries (11).

Effect of work hardening on sulfidation.—Corrosion of various types is often influenced by cold-working (12). To examine this phenomenon for copper alloys, we annealed samples of the 72500 alloy in air at 100°C. Metallographs of the annealed and work-hardened (i.e., as-received) samples are shown in Fig. 6. Matched samples of the annealed and work-hardened samples were then exposed to the corrosive atmosphere. The results are plotted in Fig. 7. It is apparent that the work-hardened material was more resistant to initial sulfidation (by a factor of two to three). The result appears contradictory to that for the spinodal alloy, in which grain boundaries seem to play a central role in

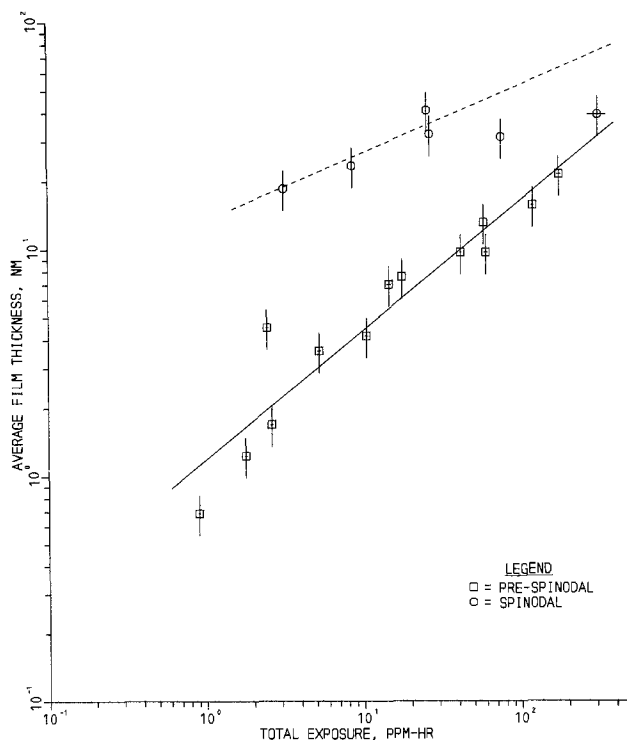


Fig. 5. Film thickness as a function of total exposure for the 72700 alloy prior to and following heat-treatment to produce spinodal structure.

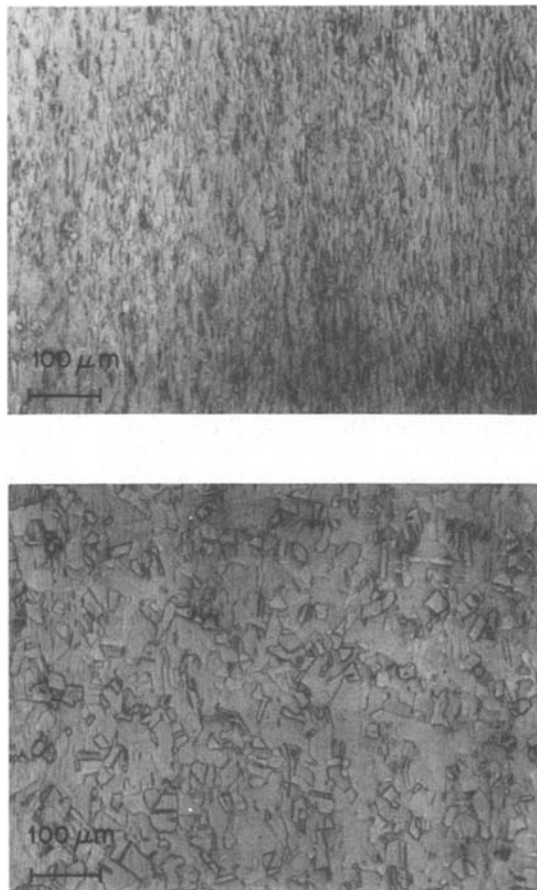


Fig. 6. Metallographs of the 72500 alloy in the work-hardened condition: as-received (a, top); after annealing (b, bottom).

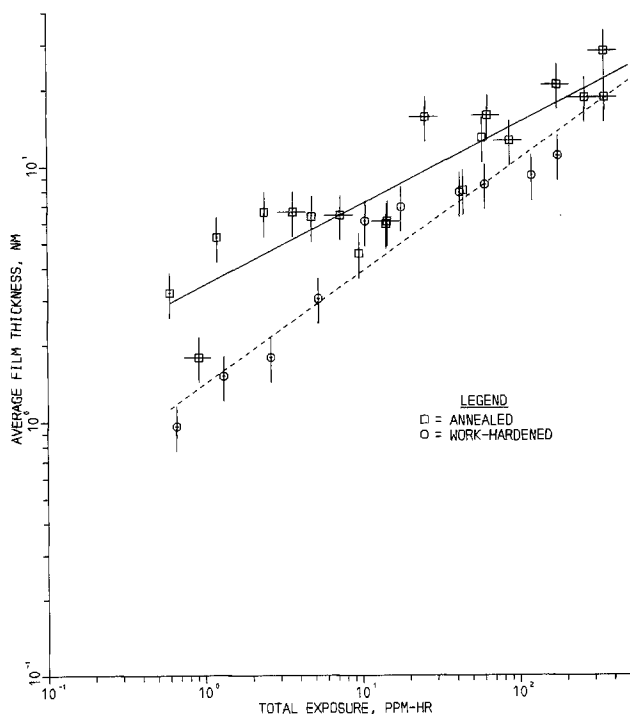


Fig. 7. Film thickness as a function of total exposure for annealed (solid line) and work-hardened (dashed line) samples of 72500 alloy.

sulfidation. We note, however, that heavily cold-rolled copper develops a preferred texture different from that of the fully annealed form (13), and that the oxidation rate of copper differs with the crystal face that is exposed (4). We suggest that sample texture may have been an important cause of these results. The results

are consistent with those obtained by other workers on binary alloys of copper and nickel at temperatures of 320°-500°C (14). We will report subsequently on experiments to determine whether the effect is restricted to copper-nickel alloys or is somewhat more general.

Discussion and Summary

Sulfidation rate testing of pure metals has quantified previous observations that nickel and tin are quite sulfidation resistant, while copper sulfidizes readily. The addition of nickel and tin to pure copper decreases sulfidation at a rate exponentially dependent on the amount of alloying nickel. Thus, 92 Cu/4 Ni/4 Sn sulfides much less rapidly than pure copper, and increasing the nickel content to 9 w/o lowers the rate such that little formation of sulfide film may be expected in a typical field environment.

To investigate the relative merits of nickel and tin as sulfidizing inhibitors in alloys, commercial alloys having similar concentrations of one metal and dissimilar concentrations of the other were exposed to corrosive environments. At 9 w/o Ni, the removal of 4 w/o Sn (from 6 to 2) had little effect on sulfidation. At 4-5 w/o Sn, the removal of 4 w/o Ni (from 4 to 0) resulted in formation of thick sulfidation films at lower exposure. Such a result is consistent with an interpretation that sulfidation is inversely related to nickel content, a result supported by corrosion studies of bronzes (copper-tin alloys not containing nickel).

Comparative sulfidation tests of an 85 Cu/9 Ni/6 Sn alloy prior to and subsequent to spinodal heat-treatment demonstrated that the spinodal structure tends to sulfidize more rapidly, although the rate is still moderate. This result must be related to the structure of the spinodal alloy, perhaps involving modification of the composition at grain boundaries.

Comparative sulfidation tests of 72500 alloy (89 Cu/9 Ni/2 Sn) in annealed and work-hardened states demonstrated that the latter was the more resistant to sulfidation. This result may reflect the influence of texture on sulfidation and is consistent with work by others on copper-nickel binary alloys, but is in contrast with the conventional picture that the cold-working of materials increases their tendency to corrode (12). We are now engaged in detailed metallographic analyses in conjunction with corrosion experiments to explore in detail the relationship between corrosion and cold-working of copper alloys. The results will be reported separately.

When the sulfidation results of this work and of our work on brasses and bronzes (1) are compared with the alloy compositions, it can be seen that the sulfidation rate reflects the percentage of alloying constituents. In Fig. 8, this relationship is displayed. To construct the figure, the sulfide film thickness at a moderate total exposure of 10 ppm-h is plotted as a function of alloying percentage. It can be seen that the percentage of alloying metal is a reasonably successful ordering parameter. Obviously, the behavior of the individual alloying metals is responsible for deviations from the general pattern. Several of these deviations deserve comment. Beryllium-copper (alloy 17200) is significantly more resistant to sulfidation at this moderate exposure than would be suggested by its alloying percentage. Silicon-bronze (alloy 65500) is less resistant to sulfidation than might be anticipated. In general, it appears that alloys of copper containing at least ten percent of any of the common high-percentage alloying metals (Zn, Ni, Sn, Al) are some thirty times as resistant to sulfidation as is pure copper, and that no major improvement in sulfidation resistance results from alloying copper to a degree higher than about 10 percent.

Acknowledgments

We thank P. R. White for providing most of the samples, J. T. Plewes for numerous discussions, and R. C.

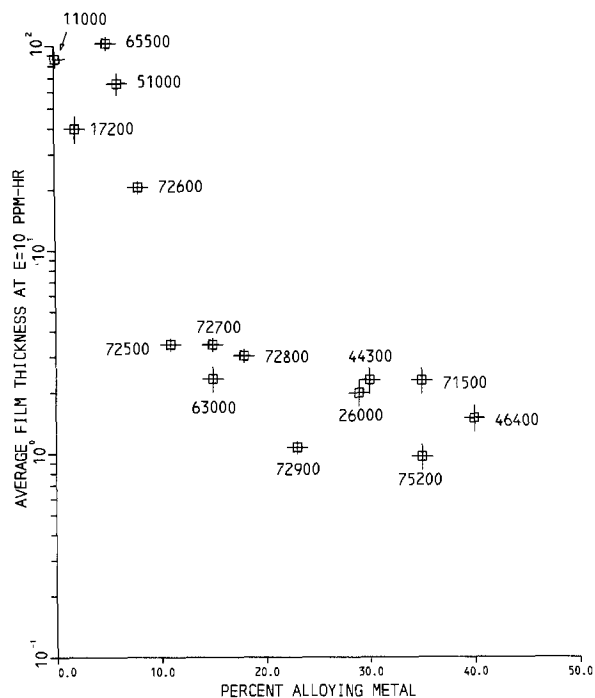


Fig. 8. Cu_2S film thickness at a total exposure of 10 ppm · h as a function of the weight percent of metals with which the copper is alloyed. The CDA number of each alloy is given beside its data point. The group of points at upper left is for pure and lightly alloyed copper. The points near the center are those for an alloy of aluminum and for the Cu/Ni/Sn ternary alloys. The points at the right are those of the brasses and nickel silvers.

Stoffers for performing the heat-treatment and work-hardening.

Manuscript submitted Dec. 10, 1982; revised manuscript received June 6, 1983.

AT&T Bell Laboratories assisted in meeting the publication costs of this article.

REFERENCES

1. G. W. Kammlott, J. P. Franey, and T. E. Graedel, *This Journal*, **131**, 505 (1984).
2. T. E. Graedel, in "Handbook of Environmental Chemistry," Vol. 2A, O. Hutzinger, Editor, pp. 107-143, Springer, Heidelberg (1980).
3. D. W. Rice, P. B. P. Phipps, and R. Tremoureaux, *This Journal*, **127**, 563 (1980).
4. H. Leidheiser, Jr., "The Corrosion of Copper, Tin, and Their Alloys," p. 7ff, John Wiley, New York (1971).
5. B. D. Lichter and C. Wagner, *This Journal*, **107**, 168 (1960).
6. S. C. Britton, "The Corrosion Resistance of Tin and Tin Alloys," pp. 13-16, Tin Research Institute, Greenford, Middlesex, England (1952).
7. L. Soto, J. P. Franey, T. E. Graedel, and G. W. Kammlott, *Corros. Sci.*, **23**, 241 (1983).
8. J. W. Cahn, *Trans. Met. Soc. AIME*, **242**, 166 (1968).
9. K. B. Rundman, in "ASM Metals Handbook, 8th Ed.," Vol. 8, pp. 184-185, American Soc. for Metals, Metals Park, OH (1973).
10. T. J. Louzon, in "ASM Metals Handbook, 9th Ed.," Vol. 4, pp. 734-738, American Soc. for Metals, Metals Park, OH (1981).
11. V. Phillips, *J. Appl. Phys.*, **23**, 712 (1962).
12. H. W. Hayden, W. G. Moffatt, and J. Wulff, "The Structure and Properties of Materials," Vol. III, p. 169, John Wiley, New York (1965).
13. A. Rönnquist, *J. Inst. Metals*, **91**, 89 (1962-1963).
14. B. Chattopadhyey and S. Sadigh-Esfandiary, *Corros. Sci.*, **13**, 747 (1973).
15. T. Lyman, Editor, "ASM Metals Handbook," 1st Ed., p. 1046, 1071, American Soc. for Metals, Metals Park, OH (1948).
16. R. A. Wilkins and E. S. Bunn, "Copper and Copper Base Alloys," McGraw-Hill, New York (1943).

Inhibition of Low Temperature Hot Corrosion by Zn, Na Mixed Sulfates

Relation Between Sulfation and Corrosion Reactions

James G. Foggo, III, Douglas B. Nordman, and R. L. Jones*

Naval Research Laboratory, Chemistry Division, Washington, DC 20375

ABSTRACT

Zinc effects in low temperature hot corrosion (LTHC) were investigated by examining the sulfation of Co_3O_4 and NiO by SO_3 in 50 mol percent (m/o) $\text{ZnSO}_4\text{-Na}_2\text{SO}_4$ melts at 700°C. Sulfation was substantially reduced as compared to sulfation in pure Na_2SO_4 , especially for Co_3O_4 . Corrosion tests with $\text{ZnSO}_4\text{-Na}_2\text{SO}_4$ deposited on BC-21 composition CoCrAlY, showed LTHC to be inhibited under SO_3 concentrations up to 500 ppm. The results demonstrate that the corrosive properties of Na_2SO_4 melts are significantly affected by ZnSO_4 . LTHC inhibition is postulated to result from reduced solubility of CoSO_4 in the $\text{ZnSO}_4\text{-Na}_2\text{SO}_4$ melt, and/or formation of "barrier" films on the oxide and metal surfaces.

Zinc anodes, and occasionally Zn-containing coatings, are used to protect sea water ballasted fuel tanks on ships. With gas turbine powered ships, the possibility of zinc contamination of the fuel causes concern, since zinc has been reported to produce intergranular corrosion in nickel-based superalloy turbine blades (1). However, Canadian Navy ship gas turbines have burned zinc-contaminated fuel, with ZnSO_4 being formed on the hot section blades, with apparently little harm (2). Canadian studies indicate, in fact, that 2.5-5.0 weight percent (w/o) additions of ZnSO_4 inhibit hot corrosion in aggressive 90 w/o $\text{Na}_2\text{SO}_4\text{-10 w/o NaCl}$ melts at 900°C (2). Only cobalt-based superalloys were tested, but nickel-based blades withstood

corrosion in the ship engines apparently as well as cobalt-based vanes, indicating that ZnSO_4 may protect both metals under some circumstances.

Other tests also suggest Zn may have inhibitive effects. In 900°C burner rig trials, Zn was more effective as an inhibitor additive than Cr for Mar M-509, IN-792, and IN-738, but not for corrosion susceptible IN-100 (3). In addition, early NRL low temperature hot corrosion (LTHC) experiments showed that 50 mol percent (m/o) deposits of $\text{ZnSO}_4\text{-Na}_2\text{SO}_4$ (eutectic mp 470°C) gave essentially no corrosion of BC-21 CoCrAlY (a Co-based gas turbine blade coating used in Navy shipboard engines) at 700°C, whereas severe corrosion was produced by molten Co-, Ni-, Fe-, or Cu-Na mixed sulfate deposits (4).

These instances of apparent hot corrosion inhibition

* Electrochemical Society Active Member.

Key words: corrosion, fused salts, coatings, sulfidation, metals.

by zinc have not been explained. For 700°C hot corrosion, the sulfation of cobalt and nickel oxides in the presence of Na₂SO₄ to form low-melting mixed Co,Na- or Ni,Na-sulfates on the blade surface is known to be crucial (5-7). Conceivably therefore, ZnSO₄ could inhibit LTHC by interfering with the sulfation of Co or Ni oxides, or by affecting other reactions in the mixed sulfate formation.

Accordingly, experiments were undertaken (i) to investigate mixed sulfate formation and decomposition reactions in the presence of ZnO/ZnSO₄, and (ii) to determine whether ZnSO₄ can inhibit 700°C hot corrosion of BC-21 CoCrAlY blade coating under SO₃ concentrations relevant to Navy marine gas turbine operation.

Experimental

The general procedures and apparatus have been described previously (6, 8). The experiments were conducted at 700 ± 5°C in multizone constant temperature tube furnaces fitted with a catalytically inert (quartz) combined furnace tube and analytic trap system which allowed determination of the SO₂ and SO₃ concentrations in the exhaust gas. Filtered laboratory air at 200 ml/min was used as the furnace gas, with electronic controllers providing input of controlled concentrations of SO₂ or equilibrated SO₂-SO₃ (obtained by placing a platinum catalyst upstream in the 700°C temperature zone). The concentrations ranged from approximately 100-3000 ppm (1 × 10⁻⁴-3 × 10⁻³ atm) SO_x, where SO_x = SO₂ + SO₃, and were controlled to ±10% as verified by gas analysis. Since SO₃ appears to be the critical species, our discussions will refer principally to SO₃ concentrations, although the SO₃, in fact, is present in an SO₂-SO₃ mixture.

The metal oxides studied were fine powders of 99.998% purity (Puritronic grade, Johnson Matthey Chemicals). The sodium sulfate was ACS certified reagent grade (Fisher) and the anhydrous SO₂ of 99.98% purity (Matheson). For the mixed metal oxide-sodium sulfate experiments, a stock of each mixture was prepared, with thorough mixing and grinding, and then samples (usually 250 mg) were taken from this stock for each individual experiment. The powder specimens were spread evenly (without compaction) over the bottom of glazed porcelain boats (Coors 6A, 97 × 16 × 10 mm od) in a layer 1-2 mm thick. The sample size and arrangement were chosen to facilitate equilibration with the furnace gas, and to simulate (to some degree) the thin sulfate films occurring on turbine blades.

Two different CoCrAlY specimens were employed in the corrosion experiments. One was a 5 mil PVD coating of CoCrAlY [20.9Cr, 12.9Al, 0.32Y, bal Co (w/o)] on Rene 80, and the other a bulk casting of CoCrAlY alloy [22Cr, 11Al, 0.5Y, bal Co (w/o)]. The compositions, listed here as provided by the suppliers, are within BC-21 specifications. No difference in corrosion behavior between the two specimens was noted. No analysis was made of the Rene 80, which was assumed to be within alloy specifications. The corrosion specimens were mounted in epoxy and metallurgically cross-sectioned (with dry polishing) and then examined by scanning electron microscopy/energy dispersive x-ray analysis (SEM/EDXA) using a 20° specimen tilt angle and palladium anticharging coating.

Results and Discussion

ZnO catalysis.—The sulfation of Co₃O₄ and NiO appears to involve SO₃ specifically (6, 8). However, this fact has been obscured because these oxides catalyze the reaction, SO₂ + ½ O₂ = SO₃, and sulfation can be obtained even when the furnace gas contains only SO₂. To understand the sulfation of ZnO, it is important to know, therefore, whether ZnO is catalytic for the SO₂-SO₃ equilibrium reaction. Accordingly, tests

were made where air containing 500 ppm SO₂ was passed at 200 ml/min over 100 mg samples of ZnO or Co₃O₄ powders maintained at 700°C in porcelain boats. Zinc oxide produced SO₃/SO₂ ratios of 0.03-0.05 (very near the "blank" obtained without any oxide present) whereas Co₃O₄ consistently produced SO₃/SO₂ ratios of about 0.4.

Zinc oxide thus evidently has low catalytic activity for the SO₂-SO₃ reaction. There was no weight gain for either ZnO or Co₃O₄, indicating that neither oxide is directly sulfated under these conditions.

Evolved SO₃/SO₂ ratios from mixed sulfate decomposition.—Zinc sulfate has been reported to evolve SO₂ upon decomposition, while nickel sulfate and cobalt sulfate were found to yield SO₃ (9). Since SO₃ is more corrosive than SO₂ in mixed sulfate corrosion (10), sulfate mixtures containing ZnSO₄ might, if they produce SO₂ rather than SO₃, be less corrosive than pure NiSO₄-Na₂SO₄ or CoSO₄-Na₂SO₄ deposits. The thermal decomposition of 50 m/o mixes of CoSO₄-Na₂SO₄ and ZnSO₄-Na₂SO₄ under air alone (200 ml/min) at 700°C was therefore compared. The decompositions were carried out under two conditions: in porcelain boats where no substrate effect would be expected, and on CoCrAlY surfaces where corrosion reactions can enter. Both sulfate mixtures melted and flowed initially, giving sulfate layers of less than 1 mm thickness. As found in previous research (4), there was extensive corrosion of the CoCrAlY under the CoSO₄-Na₂SO₄ deposits, but very little apparent corrosion under the ZnSO₄-Na₂SO₄ deposits.

The data from the decomposition experiments are presented in Table I. Although the SO₃/SO₂ ratios showed considerable variation between individual experiments, clear trends in behavior are nonetheless evident.

In particular, we note that, except for Co,Na sulfate on CoCrAlY, the ratios obtained were generally well above the equilibrium ratio of 1.1 for SO₃/SO₂ for the SO₂-SO₃-air system at 700°C (11). Both Zn,Na- and Co,Na-mixed sulfates must therefore evolve SO₃ as the major decomposition gas, and differences in corrosivity of the two mixed sulfates cannot be explained on the basis that one emits SO₂ and the other SO₃.

The origin of the SO₂ in the decomposition gas has not been established, but presumably some SO₃ could be converted to SO₂ by catalysis by the oxide produced during decomposition. Mass spectrometric studies of the thermal decomposition of pure sulfates have shown that catalysis by oxides within the sulfate powder affects the SO₃/SO₂ ratio, tending to move it toward equilibrium (12). This possibility would be consistent also with Co,Na sulfate (Co₃O₄ being a better catalyst than ZnO) showing lower SO₃/SO₂ ratios than Zn,Na sulfate for decomposition on porcelain. The very low SO₃/SO₂ ratios (0.6-0.3) measured for decomposition of Co,Na sulfate on CoCrAlY suggest, on the other hand, that SO₃ is being consumed, or reduced to SO₂, by corrosion reactions with the CoCrAlY.

Single sulfate formation.—As a basis for study of mixed sulfate formation, the equilibrium SO₃ partial pressures required for formation of the pure sulfate (or oxysulfate) from ZnO, Co₃O₄, and NiO were determined. In these determinations, the SO₃ concentra-

Table I. Evolved SO₃/SO₂ ratios in 700°C decomposition of mixed sulfates in air flowing at 200 ml/min

Mixed sulfate	Substrate	Range of observed SO ₃ /SO ₂ ratios
50 m/o ZnSO ₄ -Na ₂ SO ₄	Porcelain	8.7-2.0
50 m/o ZnSO ₄ -Na ₂ SO ₄	CoCrAlY	3.6-0.9
50 m/o CoSO ₄ -Na ₂ SO ₄	Porcelain	4.0-0.8
50 m/o CoSO ₄ -Na ₂ SO ₄	CoCrAlY	0.8-0.3

tion in the air flowing over 100 mg samples of the respective oxides in porcelain boats at 700°C was increased at 24h intervals until a weight gain was obtained which indicated formation of the sulfate or oxysulfate. The SO₃ concentration was subsequently increased for two or more tests (using fresh oxide samples each time) and the 24h weight gains then extrapolated to zero (as indicated in Fig. 1) to define the SO₃ equilibrium pressure. The species formed were identified by x-ray diffraction and confirmed to be CoSO₄ and NiSO₄ for the cobalt and nickel oxides, but ZnO · 2ZnSO₄ for ZnO. From Fig. 1, the equilibrium SO₃ concentrations at 700°C are indicated to be 250 ppm (2.5 × 10⁻⁴ atm) for ZnO-ZnO · 2ZnSO₄, 600 ppm (6.0 × 10⁻⁴ atm) for Co₃O₄-CoSO₄, and 1250 ppm (1.25 × 10⁻³ atm) for NiO-NiSO₄.

For the treatment in Fig. 1 to be valid, it is necessary that the oxides react only with SO₃. This was shown previously for Co₃O₄ (8) and NiO (6). Two observations from the present work indicate that ZnO also reacts specifically with SO₃. This was shown first in experiments in the sulfation of ZnO where the platinum catalyst was removed at two concentrations which had given sulfation. No sulfation then occurred in either case (Fig. 1), even though the total SO_x concentration (SO_x = SO₂ + SO₃) remained unchanged. The second observation was in the sulfation of 50 m/o ZnO-Na₂SO₄ (see below). In this case, in the early time periods when the rate of ZnSO₄ formation was high, the exhaust gas was found to be depleted in SO₃ (but not SO₂), giving SO₃/SO₂ ratios of the order of 0.5-0.7. As the ZnSO₄ formation became completed, the SO₃ levels increased, and the exhaust SO₃/SO₂ ratios returned to the equilibrium value of 1.1. Thus sulfation of ZnO appears clearly to occur via reaction with SO₃, and not SO₂.

The validity of the sulfation experiments was verified by calculating the standard free energies for the sulfation reactions as written below, using the relationship $\Delta G^\circ = -RT \ln K$ and the equilibrium SO₃ partial pressures determined in Fig. 1, and then comparing these energies with the standard free energies from the literature

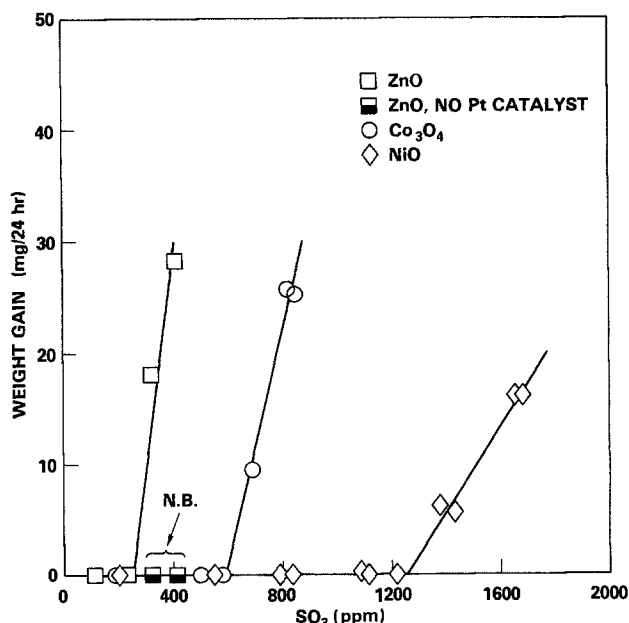
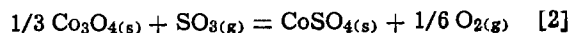


Fig. 1. Equilibrium SO₃ concentrations for sulfation of metal oxides at 700°C. (Note: the "ZnO, no Pt catalyst" results are plotted for comparison at the SO₃ concentrations achieved with equilibrated SO_x; the actual SO₃ levels in the absence of Pt were below 50 ppm in both cases.)

Table II. Free energy of formation (kcal/mol) at 700°C

Sulfate	Present work	Turkdogan (13)	Barin-Knacke (14)
ZnO · 2ZnSO ₄	-32 ± 1	-30.6 ± 0.7	-28.7
CoSO ₄	-13.8 ± 0.6	-16 ± 5	-11.9
NiSO ₄	-12.9 ± 0.6	-12.9 ± 0.6	-18.1



These energies, along with their expected uncertainties which were calculated assuming the SO₃ concentrations to be within ±20% and the temperature within ±5°, are compared in Table II with data from the literature. There is good agreement except perhaps for the CoSO₄ value which, according to Turkdogan, has a high uncertainty. The equilibrium SO₃ partial pressures determined here can therefore be taken as being of good accuracy.

The kinetics of sulfation for the different oxides were also studied to a limited extent. Representative data are shown in Fig. 2 where the SO₃ concentrations used were 500 ppm (2× equilibrium) with ZnO, 800 ppm (1.3× equilibrium) with Co₃O₄, and 1600 ppm (1.3× equilibrium) with NiO. The difference in yield is most likely inherent with the oxides, and not caused by the slight differences in relative SO₃ sulfation pressures. Notice also that the high yield for ZnO is to the oxysulfate, and not the sulfate which comes at a higher P_{SO₃}. Studies of NiO vs. CoO sulfation have shown CoO to sulfate significantly more rapidly and to a greater extent than NiO as the result of the formation of a Co₃O₄ layer on the CoO surface (15).

Most to be noted in Fig. 2 are the low yields of both CoSO₄ (~50%) and NiSO₄ (~40%), even though thermodynamics predicts that there should be complete conversion to the sulfate. The failure to obtain 100% yields is not unusual, however, since the problem of achieving complete sulfation even under highly favorable thermodynamic conditions is well known. Generally it is thought that sulfate films form on the oxide particles and act as "barrier" layers which reduce access of SO₃ to the remaining oxide in the particle interior (16).

Mixed sulfate formation.—As pointed out in the introduction, the sulfation of Co and Ni oxides to form low melting mixed Co,Na and Ni,Na sulfates is a criti-

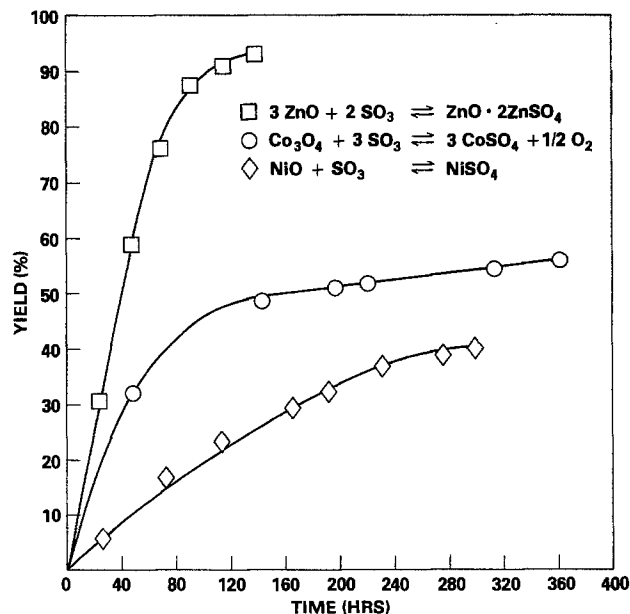


Fig. 2. Sulfation kinetics of metal oxides at 700°C

cal step in low temperature hot corrosion (5-7), and we are interested therefore in determining what effect ZnO/ZnSO₄ might have in these processes. Pure zinc sulfate is highly hydrophilic and difficult to keep dry. Consequently, our experimental procedure was to generate ZnSO₄ *in situ* by bringing 250 mg specimens of 50 m/o ZnO-Na₂SO₄ to equilibrium under different SO₃ partial pressures at 700°C. Weighed quantities of Co₃O₄ (90 mg) or NiO (84 mg) were then added to the ZnSO₄-Na₂SO₄ melt, with the subsequent sulfation of the Co₃O₄ or NiO (at the same temperature and SO₃ level) being followed by monitoring of the weight gain. The quantities of reagents were selected so that, if all the oxides were completely sulfated, the final solution would be 33 m/o each in ZnSO₄, NaSO₄, and Co or Ni sulfate. Complete sulfation would correspond to 90 mg weight gain with ZnO, and to 84 or 90 mg gain with Co₃O₄ or NiO, respectively.

A liquid phase occurs in the ZnSO₄-Na₂SO₄ system at 700°C once the ZnSO₄ concentration exceeds ~20 m/o (17), and there was a question as to whether this liquid phase would interfere with sulfation of the remaining ZnO. However, nearly complete conversion (i.e., 50 m/o ZnSO₄ formation) was achieved within 48-72h in each experiment (cf. Fig. 3 and 4), which indicates that access of SO₃ to the ZnO was not significantly hindered by the presence of the intervening liquid ZnSO₄-Na₂SO₄ film. Similarly, it is assumed that sulfation of the added oxides, which were wetted by and incorporated into the ZnSO₄-Na₂SO₄ melt at temperature, was not significantly affected by reduced transport of SO₃ through the liquid ZnSO₄-Na₂SO₄ phase.

A second set of experiments was run for comparison using Co₃O₄ (90 mg)-Na₂SO₄ (320 mg) and NiO (84 mg)-Na₂SO₄ (320 mg) mixtures which would lead to 33 m/o Co (or Ni)SO₄-67 m/o Na₂SO₄ if completely sulfated. Thus, the same amount of "solvent" sulfate was available in each set of experiments, with the only difference being that the cations are Na⁺ only in the one case, but mixtures of Zn²⁺ and Na⁺ in the other. This direct comparison allows the influence of Zn to be the most clearly seen.

The weight gain data for representative ZnO-Na₂SO₄-Co₃O₄ experiments are given in Fig. 3. Notice that 95% conversion to ZnSO₄ is achieved even at 175 ppm SO₃, which is below the 250 ppm SO₃ concentration shown earlier to be required for Zn oxysulfate formation. Evidently ZnSO₄ formation is promoted by solution in

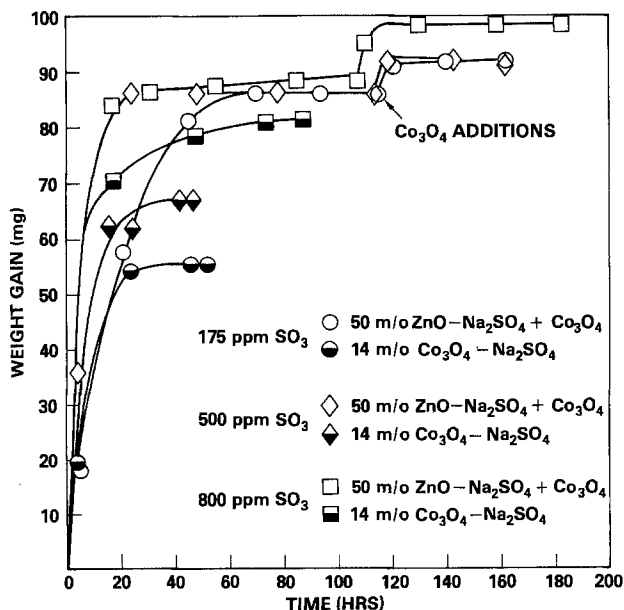


Fig. 3. Effect of ZnO on sulfation of Co₃O₄-Na₂SO₄ at 700°C

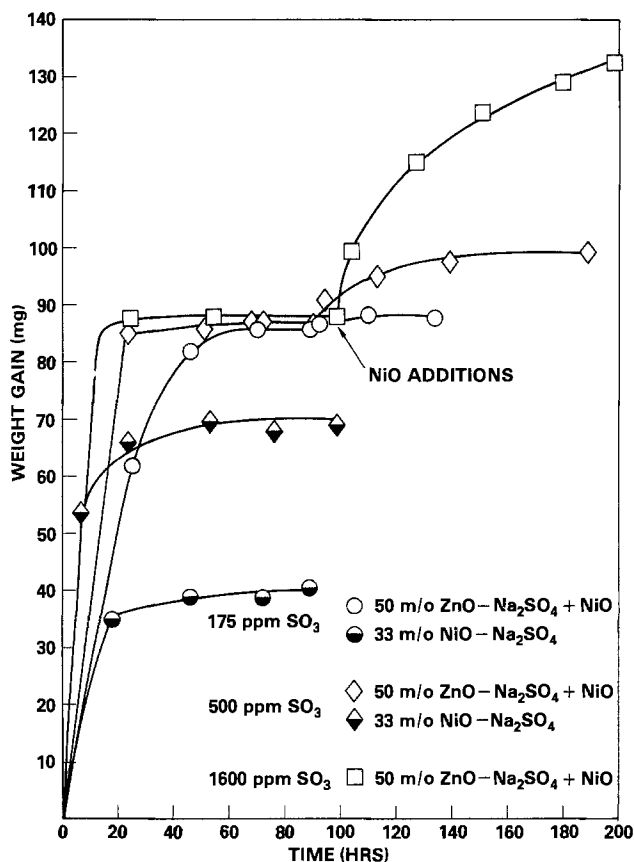


Fig. 4. Effect of ZnO on sulfation of NiO-Na₂SO₄ at 700°C

Na₂SO₄; the same effect has been seen earlier where the formation of CuSO₄-MnSO₄ solid solution caused CuSO₄ to be generated at SO₃ concentrations normally producing the oxysulfate (18). Conversely, the weight gains indicate that conversion is not totally complete even at 1600 ppm SO₃ (Fig. 4), and traces of ZnO could in fact be found by analysis (see below). The ZnSO₄ was very near 50 m/o, however, and the sulfate was fully molten as predicted by the phase diagram.

When the Co₃O₄ was added, surprisingly little further sulfation occurred, with the apparent weight gains deriving from the sulfation of Co₃O₄ ranging from only ~5 mg at 175 ppm SO₃ to ~10 mg at 800 ppm SO₃. This contrasts to the behavior for Co₃O₄ in Na₂SO₄ (also shown in Fig. 3) where, for the same total amount of "solvent" sulfate and SO₃ concentration, weight gains corresponding to nearly ten times greater sulfation of Co₃O₄ were obtained. Thus, the presence of the Zn cation appears to very strongly inhibit the sulfation of Co₃O₄.

Note that substantial sulfation of Co₃O₄ occurs in the presence of Na₂SO₄ at SO₃ levels, e.g., 175 ppm, well below the 600 ppm SO₃ equilibrium concentration found here for the sulfation of pure solid Co₃O₄ at 700°C. This is possible because the CoSO₄ activity is lowered by dissolution in Na₂SO₄. Lowering of the CoSO₄ activity occurs also in Zn,Na sulfate, but evidently to a lesser extent. Advantage of this solution behavior has been taken in industry where, e.g., the use of Na₂SO₄ has been proposed to improve yields in the sulfate roasting of Co, Cu, Ni, and Zn ferrites (19). On the other hand, complete sulfation of the Co₃O₄ did not occur, with the Zn,Na sulfate melts, even at 800 ppm SO₃ which exceeds the 600 ppm SO₃ level required for direct sulfation of Co₃O₄. This point will be discussed in a later section.

Essentially the same sulfation behavior was seen at the 175 and 500 ppm SO₃ concentration levels for ZnO-

Na_2SO_4 -NiO (Fig. 4), with only very limited sulfation of NiO appearing to occur in contrast to the NiO- Na_2SO_4 system (also Fig. 4). At 1600 ppm SO_3 , however, (i.e., above the 1250 ppm equilibrium concentration level for direct sulfation of NiO), there was substantial sulfation of NiO in the Zn,Na sulfate melt, with sulfation proceeding at a finite rate even after 100h at temperature.

Mixed sulfate analysis.—At the end of the sulfation runs, selected specimens of the residual mixed sulfate/oxide masses were analyzed by dc argon plasma atomic emission spectrometry to verify the amounts of sulfate formed. The specimens were taken up in dilute acid (0.01N H_2SO_4) to prevent possible precipitation of $\text{Zn}(\text{OH})_2$ or $\text{Co}(\text{OH})_2$, with the solutions filtered through 0.47 μ Millipore filters to remove the insoluble oxide residue. Care was taken to ensure that the sulfates were completely dissolved and that the filtered oxides were well rinsed. Control tests were also made which indicated that there should be little (<10%) dissolution of the residual oxide by the dilute acid wash solution with the techniques used. The filtered oxides were not quantitatively analyzed, but they were examined by EDXA in the SEM which confirmed that a trace of ZnO remained unsulfated even at 1600 ppm SO_3 .

The results in Table III show good agreement between the expected and found quantities of ZnSO_4 and NiSO_4 in the sulfation of ZnO- Na_2SO_4 -NiO (Sample 2). However, the values for CoSO_4 in sulfated ZnO- Na_2SO_4 - Co_3O_4 (Samples 1 and 3) were more than twice as high as expected, while the ZnSO_4 results were low. A check of the analytical procedure using a solution containing a known amount of CoSO_4 (Sample 4) gave moderately high results, but analytical inaccuracy is not likely the cause of the Samples 1 and 3 discrepancies. Rather, it appears that ZnSO_4 may be partially displaced as ZnO from the ZnSO_4 - Na_2SO_4 melt as the added Co_3O_4 is sulfated and goes into solution. The observed weight gain for " Co_3O_4 sulfation" then would be the net difference between the weight loss resulting from ZnSO_4 going to ZnO, and the weight gain for Co_3O_4 going to CoSO_4 . Recalculating the data in Table III on this basis gives expected weights for CoSO_4 of 20 mg for Sample 1 and 28 mg for Sample 3. The substantially better agreement of these values with the analytical results suggests that ZnSO_4 is in fact displaced from the melt as Co_3O_4 is sulfated.

Solution behavior.—It is well known, e.g., from metallurgy, that the solubility of a species in a melt can be strongly affected by the introduction of a second species into the melt. The effect, which is often characterized through "interaction" parameters (20), may be either to increase or reduce solubility. In the study at hand, the presence of ZnSO_4 in the Na_2SO_4 melt clearly appears to reduce the solubility of CoSO_4 .

Table III. Mixed sulfate analysis by dc argon plasma atomic emission spectrometry

Sample	Expected sulfates from weight gain	Analytic results ($\pm 5\%$)		
		Co	Ni	Zn
1 (500 ppm SO_3 , Fig. 3)	11 mg CoSO_4 , 175 mg ZnSO_4	28 mg CoSO_4	—	166 mg ZnSO_4
2 (500 ppm SO_3 , Fig. 4)	25 mg NiSO_4 , 175 mg ZnSO_4	—	27 mg NiSO_4	175 mg ZnSO_4
3 (175 ppm SO_3 , Fig. 3)	12 mg CoSO_4 , 173 mg ZnSO_4	27 mg CoSO_4	—	157 mg ZnSO_4
4 (Test standard)	27 mg CoSO_4 (from 50 mg $\text{CoSO}_4 \cdot 7\text{H}_2\text{O}$)	33 mg CoSO_4	—	—

Beyond this, however, there may also be barrier film formation, as suggested by the following line of reasoning. Several experiments were run using SO_3 levels which exceeded the equilibrium SO_3 concentration determined here for 700°C sulfation of solid Co_3O_4 (600 ppm) and NiO (1250 ppm) in air. When the mixtures were only the metal oxide and Na_2SO_4 , the result was essentially complete sulfation of the metal oxide (e.g., 14 m/o Co_3O_4 - Na_2SO_4 in Fig. 3). However, when the mixture contained ZnO/ ZnSO_4 , only limited sulfation of the metal oxide occurred, particularly for Co_3O_4 (cf. Fig. 3). From a thermodynamic basis, complete sulfation would be expected even in this case. Given free access of SO_3 , the Co_3O_4 should sulfate and dissolve in the melt until its solubility is exceeded, and then solid CoSO_4 should be produced until the remainder of Co_3O_4 is consumed. This is the behavior seen with the SO_3 - Co_3O_4 - Na_2SO_4 system (7). The lack of complete sulfation under higher than equilibrium SO_3 partial pressures is therefore indirect evidence that a compound or barrier layer is forming on the Co_3O_4 surface which interferes with further sulfation of the oxide.

The reaction kinetics indicated in Fig. 3 are also consistent with this theory; i.e., there is a quick weight gain after Co_3O_4 addition (corresponding to barrier film formation) and then little further reaction (because of barrier film stifling of the sulfation reaction). The barrier film could be precipitated CoSO_4 itself, displaced ZnO, or a combination of both. The slow, continued sulfation of NiO at 1600 ppm SO_3 (Fig. 4) suggests that the barrier film formed in this case is not as protective as that formed with ZnSO_4 - Na_2SO_4 - Co_3O_4 , perhaps because ZnO is not being displaced from the melt (cf. Table III).

Corrosion tests with ZnSO_4 - Na_2SO_4 .—The 700°C corrosion of BC-21 CoCrAlY was studied using (i) deposits of 50 m/o ZnSO_4 - Na_2SO_4 under air, or (ii) deposits of 50 m/o ZnSO_4 - Na_2SO_4 or ZnO- Na_2SO_4 under 175 and 500 ppm concentrations of SO_3 in air. In the latter case, the ZnO- Na_2SO_4 was found to be quickly converted to ZnSO_4 - Na_2SO_4 , with no discernible difference then seen in the corrosion behavior. The majority of work therefore was simply with ZnSO_4 - Na_2SO_4 deposits. The deposits melted and flowed at temperature, giving final sulfate layers of generally less than 0.5 mm thickness.

The residual salts on the corroded specimens were not analyzed because very small quantities were involved. However, analyses of the sulfate salts on low temperature corroded turbine blades routinely show water soluble Ni and Co, but not (presumably because the SO_3 partial pressure is not high enough) Cr or Al. Mixed sulfate formation involving Co and Ni, but not Cr or Al, would therefore be expected in the present experiments (see below).

As in our earlier observations (4), little corrosion was found with 50 m/o ZnSO_4 - Na_2SO_4 under air; i.e., where simply the thermal decomposition of ZnSO_4 - Na_2SO_4 is involved. This contrasts to thermal decomposition of 50 m/o CoSO_4 - Na_2SO_4 on CoCrAlY which produces severe corrosion (4). Typical results are shown in Fig. 5 which is for rather thick deposits of ZnSO_4 - Na_2SO_4 on a section of bulk CoCrAlY. No corrosion is visible under the heavy ZnSO_3 - Na_2SO_4 layer, but there are small pits on the bottom of the section which probably result from a thin film of sulfate creeping to the underneath of the section. These pits display the morphology which is characteristic of low temperature hot corrosion (7). Figure 5 shows also that as the sulfate decomposes, ZnO is deposited out both at the air-sulfate and sulfate-metal interfaces. Presumably therefore, the SO_3 partial pressure within the sulfate layer is less than 1.75×10^{-4} atm, since this pressure was shown sufficient to maintain >45 m/o ZnSO_4 in Na_2SO_4 in our sulfation studies (Fig. 3 and

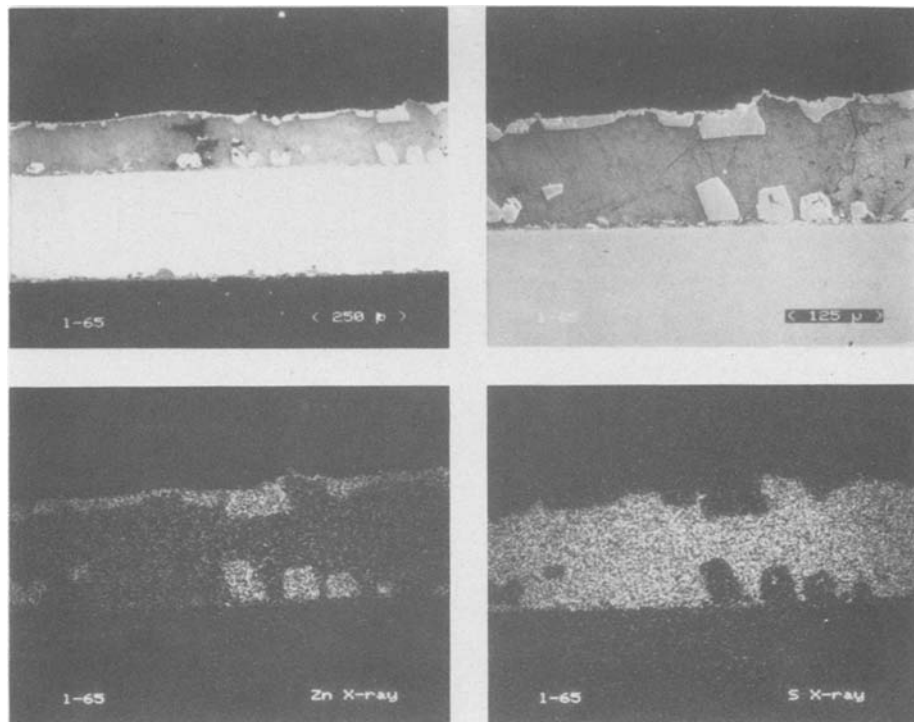


Fig. 5. $\text{ZnSO}_4\text{-Na}_2\text{SO}_4$ (50 m/o) on bulk BC-21 composition CoCrAlY after 24h in air at 700°C . The characteristic two-phase structure of the alloy is visible in the metal.

4). Thus, one explanation for $\text{ZnSO}_4\text{-Na}_2\text{SO}_4$ deposits not corroding CoCrAlY may be that the SO_3 partial pressure within the deposit is too low for significant cobalt sulfation to occur.

Corrosion of CoCrAlY by mixtures of $\text{ZnSO}_4\text{-CoSO}_4\text{-Na}_2\text{SO}_4$ was also studied, and it was found that as long as the ZnSO_4 concentration exceeded the CoSO_4 concentration, corrosion was inhibited, but when the CoSO_4 concentration was larger by, e.g., two to one or more, the CoCrAlY was corroded.

When tests were made under SO_3 , little corrosion was generally seen for specimens exposed up to 150h under 175 ppm SO_3 . A representative test specimen cross section is shown in Fig. 6 where x-ray mapping identifies the $\text{ZnSO}_4\text{-Na}_2\text{SO}_4$ surface layer and shows that the sulfate film contains essentially no cobalt. Some typical LTHC pitting corrosion did occur in the

175 ppm SO_3 tests, especially in thin areas of the sulfate deposits. However, the total corrosion was always much less than occurred with equivalent Na_2SO_4 or $\text{CoSO}_4\text{-Na}_2\text{SO}_4$ deposits for the same P_{SO_3} and time of exposure, so ZnSO_4 clearly inhibits LTHC in this sense.

Corrosion experiments were also conducted using 500 ppm SO_3 . More attack was noted than with 175 ppm SO_3 , but corrosion was still substantially less with $\text{ZnSO}_4\text{-Na}_2\text{SO}_4$ than for equivalent times of exposure with Na_2SO_4 alone.

The corrosion pits formed under 175 and 500 ppm SO_3 were found almost invariably at the thin edge rather than under the thicker portion of the $\text{ZnSO}_4\text{-Na}_2\text{SO}_4$ deposit. The $\text{ZnSO}_4\text{-Na}_2\text{SO}_4$ mixture was molten at 700°C , but not totally fluid. Thus the sulfate at the deposit edge may not be 50 m/o $\text{ZnSO}_4\text{-Na}_2\text{SO}_4$, but may contain less ZnSO_4 which would make the edge sites

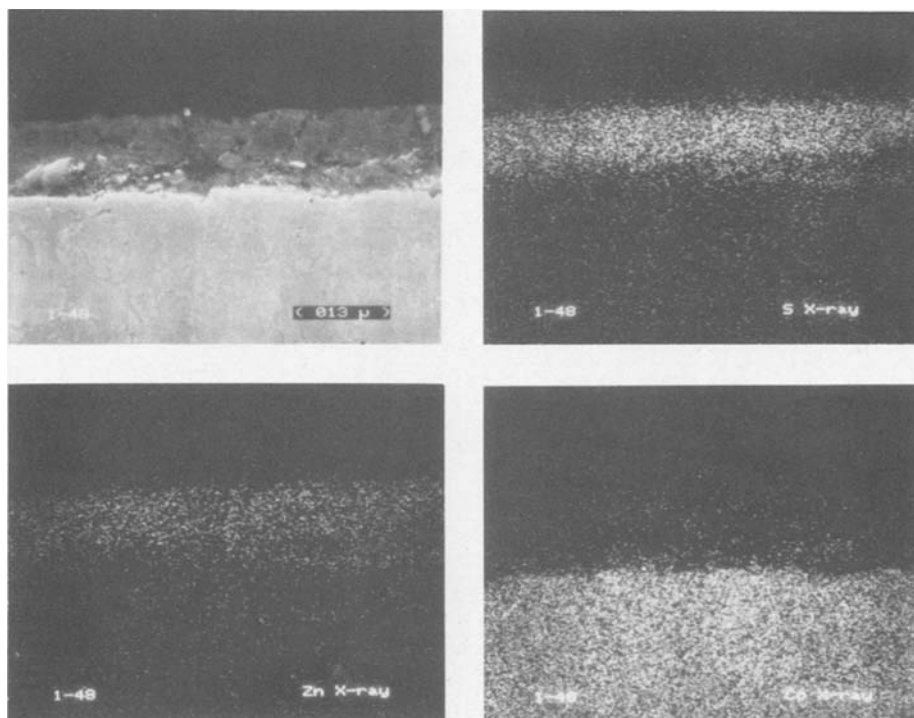


Fig. 6. $\text{ZnSO}_4\text{-Na}_2\text{SO}_4$ interface with BC-21 composition CoCrAlY coating after 146h under 175 ppm SO_3 in air at 700°C .

more corrosion susceptible. When the sulfate deposits on corroded specimens were examined by low power light microscopy, color micrographs were obtained which clearly showed localized reddish (rich in CoSO_4) regions in the greenish-white ZnSO_4 - Na_2SO_4 surface film. This shows that the sulfate deposits are only sluggishly miscible at 700°C , and gives reason to expect that the wetting and mixing properties of the sulfates, as well as the specific sulfate concentration, will be critical in determining the effectiveness (and reproducibility) of ZnSO_4 inhibition of 700°C hot corrosion of CoCrAlY .

The corrosion of the Rene 80 blade metal was not studied explicitly, since the CoCrAlY coating is meant to provide the principal protection of the blade against hot corrosion. However, several instances were observed where the specimen was corroded severely at its cut edge (*i.e.*, where both the coating and blade metal are exposed to sulfate and SO_3) even though the CoCrAlY coating over the body of the specimen was essentially unattacked. A representative example is shown in Fig. 7.

The x-ray maps in Fig. 7 indicate (i) that there is a sulfur concentration near the corrosion front, and (ii) that Ni and Co are intermingled throughout the corrosion phase which is evidence of substantial intertransport of cobalt and nickel in the corrosion process. This corrosion may be similar to "cut-edge" attack of CoCrAlY -coated Rene 80 by pure Na_2SO_4 (no SO_3 overpressure) at 885°C , which appears to involve an internal liquid nickel sulfide (21). In the present case, examination at high magnification did not reveal the large sulfide phases found with 885°C corrosion. At 700°C under 175 ppm SO_3 , it may well be (although it cannot be proved here) that the morphology in Fig. 7 results from formation of mixed Co,Ni,Na sulfates, with sulfides not being principally involved.

In either event, it is possible that accelerated corrosion could occur if the CoCrAlY coating on a Ni-based blade were penetrated, even in the presence of "inhibitive" Zn,Na sulfate. Also, Ni-based alloys may be more susceptible to Zn,Na sulfate corrosion than cobalt alloys, especially at higher SO_3 concentrations, as indicated by the substantial NiO sulfation shown in Fig. 4. The degree of corrosion may differ depending on the inherent corrosion resistance of the Ni alloy, as seems to be the case in the 900°C burner rig testings cited (3).

Conclusions

The sulfation of Co_3O_4 and NiO in molten eutectic 50 m/o ZnSO_4 - Na_2SO_4 is substantially reduced as compared to their sulfation in the presence of an equivalent amount of Na_2SO_4 . The reduced sulfation appears to be caused by decreased solubility of CoSO_4 and NiSO_4 in ZnSO_4 - Na_2SO_4 as a result of solute-solute interactions with ZnSO_4 , and/or formation of a barrier film (perhaps displaced ZnO or precipitated CoSO_4 or NiSO_4) on the metal oxide surface which inhibits further sulfation of the remaining oxide.

Although corrosion is not totally halted, the low temperature hot corrosion of CoCrAlY is inhibited by deposits of ZnSO_4 - Na_2SO_4 for SO_3 concentrations up to 500 ppm. The post-test morphologies are consistent with inhibition being caused by reduced CoSO_4 solubility in the sulfate surface film.

In particular, the present investigation demonstrates that the chemical and corrosive properties of sulfate melts can be significantly affected by addition of secondary sulfates. The methodology should be applicable for the study of other potential hot corrosion inhibitor additives.

Acknowledgments

This research was sponsored under the NAVSEA Program for Development of Advanced Marine Gas Turbine Materials, and the support is gratefully acknowledged. Thanks are due also to Dr. J. A. Goebel of Pratt and Whitney Aircraft and Professor G. H. Meier of the University of Pittsburgh, who furnished the CoCrAlY specimens, and to Dr. Rm. Panayappan of NRL for the atomic emission spectroscopy analyses.

Manuscript submitted Jan. 24, 1983; revised manuscript received Oct. 6, 1983. This was Paper 123 presented at the Detroit, Michigan, Meeting of the Society, Oct. 17-21, 1982.

Naval Research Laboratory assisted in meeting the publication costs of this article.

REFERENCES

1. J. J. MacFarlane, in "The Mechanism of Corrosion by Fuel Impurities," H. R. Johnson and D. J. Littler, Editors, p. 270, Butterworths, London (1963).
2. R. S. Hollingshead, D.R.E.A. Report 80/2.

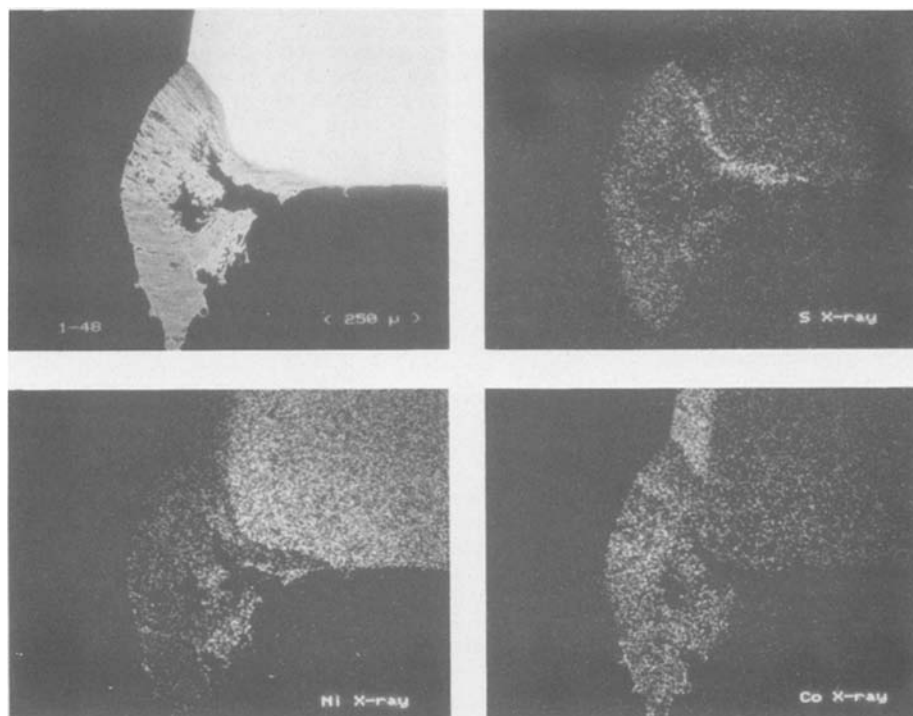


Fig. 7. Corrosion at cut edge on BC-21 composition CoCrAlY -coated Rene 80 deposited with 50 m/o ZnSO_4 - Na_2SO_4 and exposed to 175 ppm SO_3 in air at 700°C for 146h.

3. D. L. Deadmore and C. E. Lowell, NASA Tech. Memo TM-78966, NASA Lewis Research Center, Cleveland, OH (July 1978).
4. R. L. Jones, NRL Memorandum Report 4072 (Sept. 1979).
5. K. L. Luthra and D. A. Shores, *This Journal*, **127**, 2202 (1980).
6. R. L. Jones and S. T. Gadomski, *ibid.*, **129**, 1613 (1982).
7. K. L. Luthra, *Metall. Trans.*, **13A**, 1843 (1982).
8. R. L. Jones, in International Conference on High Temperature Corrosion, NACE, San Diego, CA, 1981, To be published.
9. B. Lorant, *Zh. Anal. Khim.*, **219**, 256 (1966).
10. H. H. Krause, A. Levy, and W. T. Reid, *Trans. ASME, Ser. A*, **90**, 38 (1968).
11. K. H. Stern and E. L. Weise, Natl. Stand. Ref. Data Ser., National Bureau of Standards, No. 7 (Sulfates) (1966).
12. D. R. Knittel, K. H. Lau, and D. L. Hildenbrand, *J. Phys. Chem.*, **84**, 1890 (1980).
13. E. T. Turkdogan, "Physical Chemistry of High Temperature Technology," Academic Press, New York (1980).
14. I. Barin and O. Knacke, "Thermochemical Properties of Inorganic Substances," Springer-Verlag, New York (1973, 1977).
15. L. E. K. Holappa and M. H. Tikkanen, in "React. Solids," J. Wood et al., Editors, p. 635, Plenum, New York (1977).
16. P. Marier and T. R. Ingraham, *Can. Metall. Q.*, **11**, 617 (1972).
17. E. M. Levin, C. R. Robbins, and H. W. McMurdie, "Phase Diagrams for Ceramists," 2nd ed., Fig. 1123, The American Ceramic Society, Columbus, OH (1969).
18. E. T. Turkdogan and J. V. Vinters, *Inst. Min. Metall., Trans., Sect. C*, **86**, 59 (1977).
19. F. T. Bumazhnov, *Izv. Vyssh. Uchebn. Zaved., Tsvet. Metall.*, **15**, 56 (1972).
20. O. Kubaschewski and C. B. Alcock, "Metallurgical Thermochemistry," 5th ed., p. 57, Pergamon Press, New York (1979).
21. R. L. Jones and S. T. Gadomski, in "Properties of High Temperature Alloys," Z. A. Foroulis and F. S. Pettit, Editors, p. 824, The Electrochemical Society Softbound Proceedings Series, Princeton, NJ (1977).

Breakdown of Passivity of Nickel by Fluoride

I. Electrochemical Studies

B. Löchel

Institut für Physikalische Chemie, Freie Universität Berlin, D-1000 Berlin 33, Germany

H.-H. Strehblow*

Institut für Physikalische Chemie, Universität Düsseldorf, D-4000 Düsseldorf, Germany

M. Sakashita

Faculty of Engineering, Hokkaido University, Sapporo, Japan

ABSTRACT

The attack of fluoride on passive nickel has been studied in strongly acidic solutions (1M HClO₄) and weakly acidic and alkaline buffers. Two main potential ranges with different kinetics of metal dissolution were found. In the whole passive range, the corrosion current density is increased. Up to 1.1V, the transfer of the Ni²⁺ ions from the oxide into the electrolyte is catalyzed by HF with an electrochemical reaction order of 1.63. This leads to a thinning of the oxide film to a higher electrical field strength and consequently to the increased stationary corrosion current density. At potentials $\epsilon \geq 1.2V$, an NiF₂ overlayer is formed on the rest of the passivating oxide. This leads to an electrochemical reaction order of -0.79 for HF. The kinetics of the two potential ranges are explained with appropriate mechanisms involving the formation of a Ni²⁺F⁻ surface complex or the presence of a passivating fluoride film. Fluoride may be seen as a simpler model system for the other halides which cause a localized breakdown of passivity.

The action of aggressive anions on passive metals like iron and nickel leads to a locally or generally increased dissolution rate. Among the halides, fluoride is of special interest. Its presence yields only a general increase of the corrosion rate in strongly acidic solutions, which facilitates the interpretation of the results (1). Consequently, it can aid in deeper insight into the processes occurring during the breakdown of passivity. Passive nickel and iron in fluoride containing electrolytes may thus be seen as model systems for localized corrosion in the presence of other aggressive anions, especially chloride. In this work, we examine the influence of fluoride on the passivity of nickel in acidic solutions. In a second part, we study the thickness and composition of the films formed before and after the fluoride attack by surface analysis like x-ray photoelectron spectroscopy (XPS) and low energy ion scattering spectroscopy (ISS). These results helped to interpret the electrochemical findings.

* Electrochemical Society Active Member.

Key words: passivity, breakdown of passivity, corrosion of nickel in HF solutions.

Experimental

For the nickel electrodes a 99.95% material of Vakuumschmelze Hanau was used. Small flag-shaped electrodes of 1.7 cm² surface area were electropolished in an H₂SO₄-H₂O mixture (2), soldered to a copper wire, and fixed to a glass tube. The contact area was covered with epoxy resin. For surface analysis, the pretreated specimens were rinsed with triply distilled water and cut close to the epoxy covered part. Rotating disk electrodes were prepared from a 5 mm diam cylindrical material embedded in epoxy resin. Details about the specimen preparation and the experimental setup were briefly described previously (3). All solutions were prepared from chemically pure substances (*pro analysi*) and triply distilled water. Most experiments were performed in 1M HClO₄ and some in phthalate buffer pH 4.9 (0.05M KH phthalate plus 0.023M KOH) and borate buffer pH 8.0 (0.05M H₃BO₃ plus 0.039M KOH). After prepassivation of the specimen at appropriate electrode potentials for typically 1 and 2h, fluoride was added by 1 cm³ of a concentrated HF solution

or by solid KF. All experiments were performed at $25^\circ \pm 0.2^\circ\text{C}$. $\text{Hg}/\text{Hg}_2\text{SO}_4/0.5\text{M H}_2\text{SO}_4$ served as a reference electrode. All potential values are given in reference to the standard hydrogen electrode and are corrected for liquid junction potentials.

Results

The current density potential curve in fluoride containing electrolytes has been described previously (1, 4) and is given again in Fig. 1. In 1M HClO_4 , nickel has a large passive range of $>1\text{V}$, with a transpassive increase at $\epsilon > 1.5\text{V}$. A step at $\text{ca. } \epsilon = 1.8\text{V}$ is due to the overlap of the decrease of the dissolution current by the formation of a nickel III oxide layer and an increase of the current of oxygen evolution. This behavior is similar to $1\text{M H}_2\text{SO}_4$ (5). The addition of fluoride causes a generally increased current density (Fig. 1). The maximum current of active dissolution, however, is decreased by one order of magnitude. The step in the transpassive region is still observed; however, all features of the polarization curve are shifted by about 0.1V in the anodic direction. A broad current peak with its maximum at $\epsilon = 1.15\text{V}$ is obtained in the passive range. The HF concentration does not influence the peak position, and the maximum current increases only slightly with HF concentration (Fig. 2). The two current minima (I and II), however, are markedly affected. Minimum I increases and minimum II decreases with HF concentration. During the action of HF, a general attack of the surface is obtained. In addition many small pits are formed on the grains, particularly at the grain boundaries (1). However, the diameter of these hemispheric pits does not grow larger than $2\ \mu\text{m}$ in more than 1h. Therefore, they cannot be related to the increase of the current density to several mAcm^{-2} .¹ The metal surface appears unchanged and bright or roughened, depending on the achieved current density and time of exposure. No current density at the minima depends on the stirring of the electrolyte or the rotation of the disk electrode up to $\leq 2000\ \text{rpm}$. Therefore, these processes are not controlled by diffusion processes. At the current maximum at 1.1V , a visible dark blue film is formed. It has a good adhesion to the metallic substrate and cannot be washed off in a jet of water. A sufficiently vigorous stirring of the electrolyte, e.g., $\geq 400\ \text{rpm}$ for the rotating disk, leads to a removal of the visible film at the current maximum and an increase of the current to a new nontransport-controlled level. At the falling edge of the maximum at $\epsilon = 1.2\text{--}1.3\text{V}$, current oscillations are observed for rotated and nonrotated electrodes, and only a temporary partly covering visible film is formed. These oscillations are also found in fluoride containing sulfuric acid (4).

¹ No covered pits were found after careful *in situ* and *ex situ* inspection with an optical and scanning electron microscope of high resolution. Therefore, localized corrosion can be excluded.

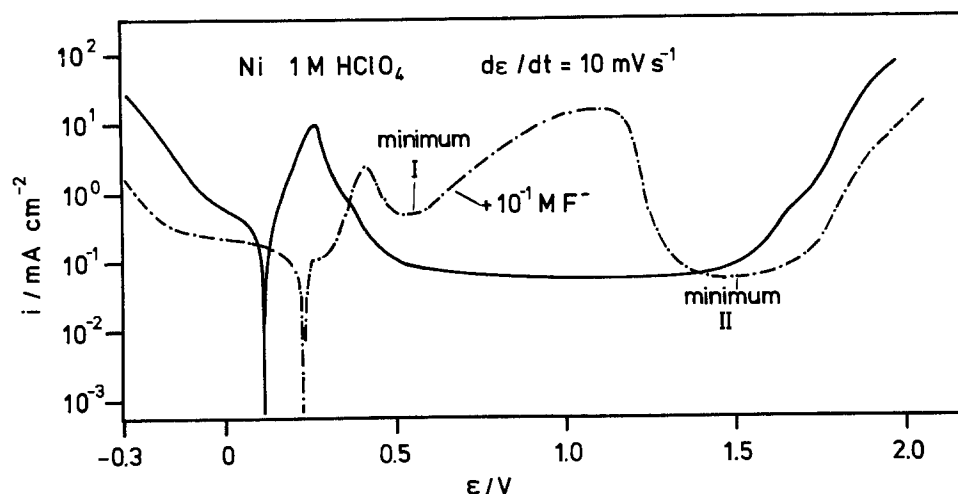


Fig. 1. Potentiodynamic polarization curve of nickel in 1M HClO_4 (solid line), and in 1M HClO_4 plus 0.1M HF (dashed line). $d\epsilon/dt = 10\ \text{mVs}^{-1}$.

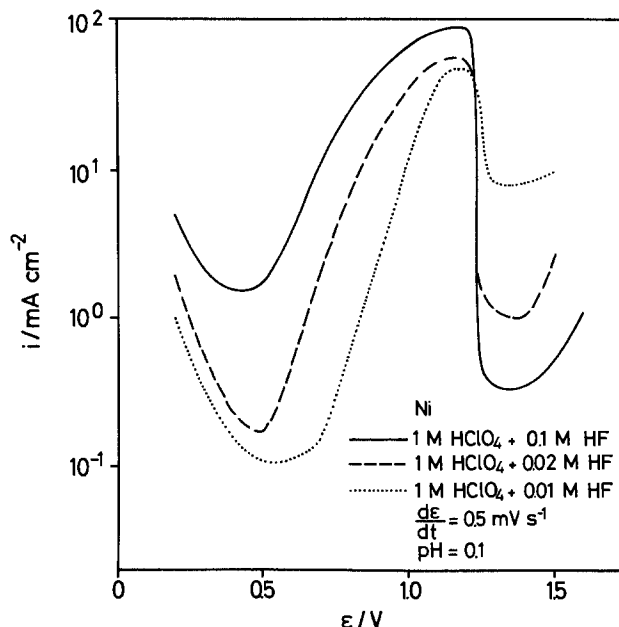


Fig. 2. Potentiodynamic polarization curves of nickel in 1M HClO_4 with different concentrations of HF.

For a prepassivated specimen, the corrosion current density in 1M HClO_4 shows a pronounced change with time after the fluoride addition. The results for the two characteristic potentials at the minima of Fig. 1 are shown in Fig. 3a and 3b for different HF concentrations. For minimum I, the current increases faster with higher HF content and achieves a plateau in every case. This final stationary value increases with the HF concentration. At minimum II, a peak is obtained, especially for high HF contents, with a final approach to a stationary plateau value. The current peak gets smaller with decreasing HF and vanishes for $[\text{HF}] = 0.001\text{M}$, whereas the plateau value increases. This completely different behavior suggests that the corrosion mechanisms are different for the two parts of the passive range. Figure 4 compares the stationary values of the polarization curve in 0.1M HF containing 1M HClO_4 with potentiodynamic results. The change of the current density from the active dissolution to the minimum I is less pronounced when stationary conditions have been achieved.

A double logarithmic plot of the stationary current densities and the HF concentration for the two representative potentials (minima I and II) shows a linear relationship (Fig. 5)

$$\epsilon = 0.5\text{V}: \quad \log i = 1.75 + 1.63 \log [\text{HF}] \quad [1]$$

$$\epsilon = 1.4\text{V}: \quad \log i = -1.4 - 0.79 \log [\text{HF}] \quad [2]$$

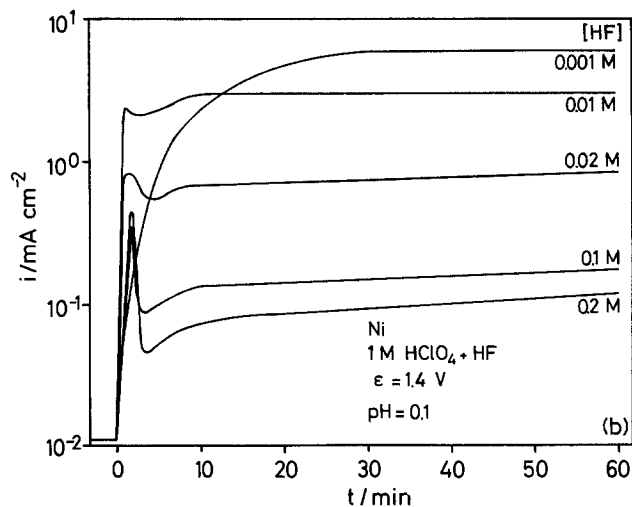
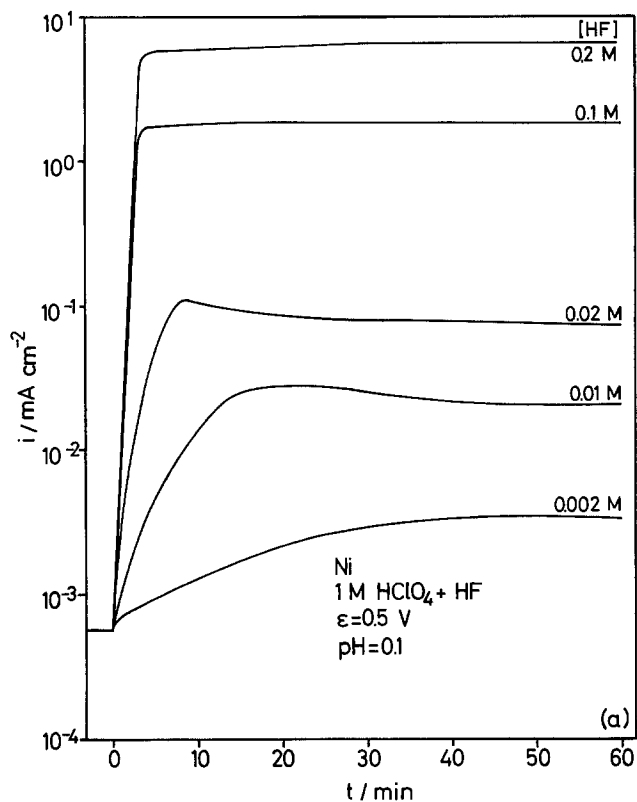


Fig. 3. Increase of the current density with time on nickel specimen prepassivated for 2h in 1M HClO_4 , after the addition of different concentrations of HF. a, left: $\epsilon = 0.5\text{V}$, minimum I, above: $\epsilon = 1.4\text{V}$, minimum II.

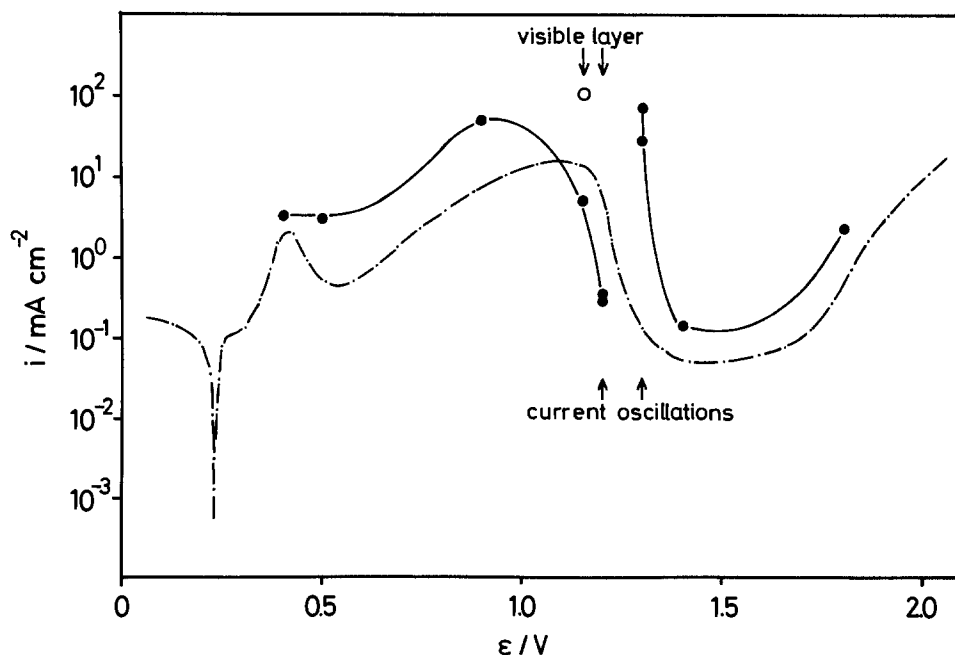
Galvanostatic transients of specimen after reaching potentiostatic stationary conditions reflect the characteristics of the potentiodynamic polarization curve. If the galvanostatic current is higher than the stationary potentiostatic value at $\epsilon = 0.5\text{V}$, slightly more positive electrode potentials are achieved after an intermediate maximum. If smaller values are chosen, the potential falls in the region of active dissolution after a plateau near 0.5V (Fig. 6a). Its length decreases with the given current density. The time is used apparently for the removal of the remaining passive film.

For a specimen pretreated at $\epsilon = 1.4\text{V}$, the potential falls in two steps (Fig. 6b). The length of the first step at $\epsilon \approx 1.4\text{V}$ decreases linearly with the current density. Apparently, the deviation of the stationary current corresponds to the removal rate of a surface layer. The second step is of equal length for all applied current densities, indicating that the surface of the electrode is

in the same situation when the first step is finished. Apparently, the same surface layer has to be moved. If higher current densities than $i_{c,s} = 0.06\text{mAcm}^{-2}$ are chosen, potential oscillations within the range of the second minimum are found. For sufficiently high current densities, the amplitude of these oscillations may cause the potential to drop to $\epsilon \approx 0.5\text{V}$ and finally into the active potential range (curve 5 in Fig. 6b). These galvanostatic transients suggest that passivating films are removed.

In F^- -free $1\text{M H}_2\text{SO}_4$, a change from potentiostatic to galvanostatic conditions causes damped potential oscillation with a final constant value in the transpassive range or negatively damped oscillation with a final constant amplitude (4). When this amplitude is high enough, a change to the higher values of oxygen evolution is observed rather than a drop to the potential range of active dissolution, which might be a conse-

Fig. 4. Stationary polarization curve of nickel in 1M HClO_4 plus 0.1M HF (solid line), values 30 min after HF addition, prepassivated for 2h in 1M HClO_4 , compared to the potentiodynamic polarization curve (dashed line). \circ : stationary current density at $\epsilon = 1.15\text{V}$ with vigorous stirring (RDE) without fluoride layer.



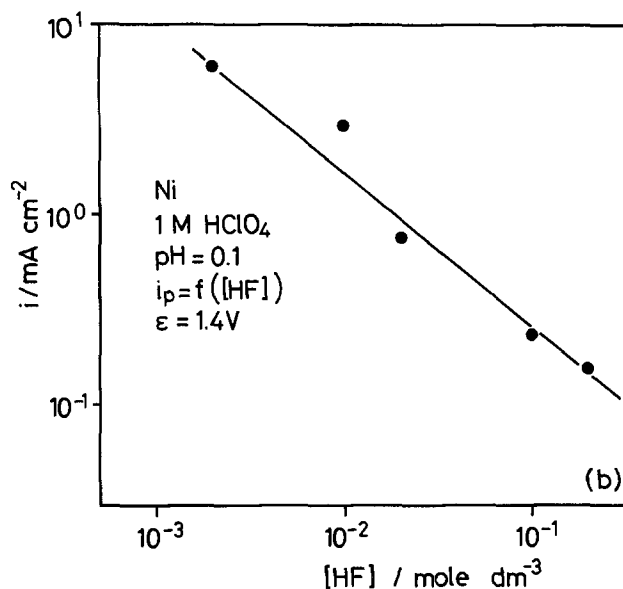
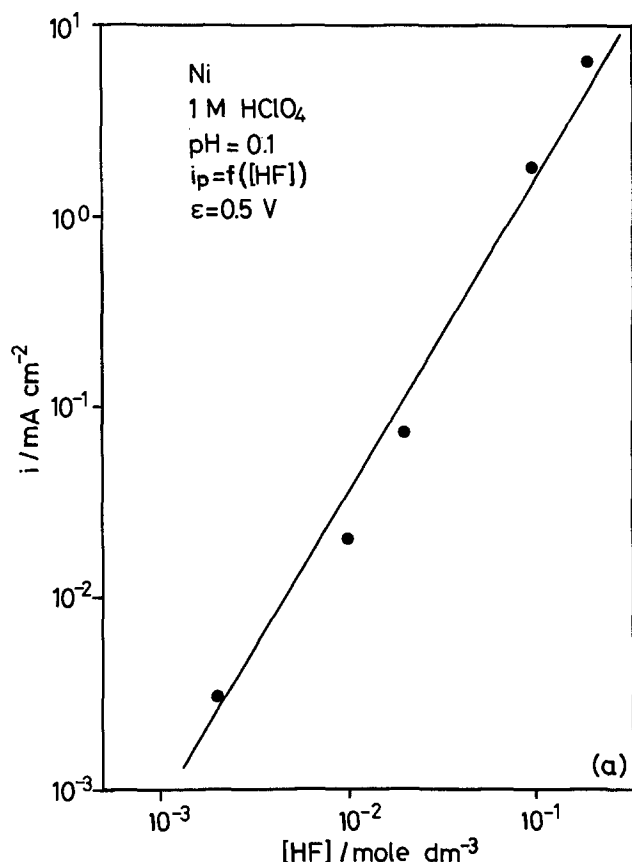


Fig. 5. Increase of stationary current density in 1M HClO₄ plus HF as a function of the HF concentration. a, left: $\epsilon = 0.5V$, minimum I, b, above: $\epsilon = 1.4V$, minimum II.

quence of the smaller current densities within the passive range of F⁻-free solutions. No potential oscillations are reported for pure perchlorate solutions but they are found in F⁻ containing electrolytes (4).

The nature and composition of these films cannot be deduced only from electrochemical experiments. For this purpose, surface analytical methods, such as XPS and ISS, have been applied (6). They show a pronounced difference of the surfaces for the two characteristic ranges of the polarization curve. At minimum I up to the maximum at $\epsilon = 1.1V$, a passivating oxide film is found with a reduced thickness compared to the HF-free solution. About 6Å of the remaining oxide (NiO) are covered by 8Å of nickel hydroxide [Ni(OH)₂]. At $\epsilon > 1.2V$ (minimum II), thick films of NiF₂ cover the thinned oxide layer (4A). The thickness of these fluoride films decreases with increasing electrode potential from several thousand angstroms at the current maximum (visible layer) to a few nanometers at minimum II. They apparently reduce the corrosion process to the small values at minimum II.

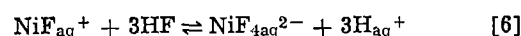
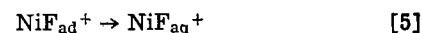
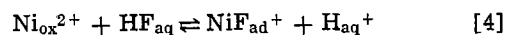
For higher pH values (phthalic acid pH 4.0, phthalate buffer pH 4.9) similar features are found for the polarization curves (Fig. 7a). The current densities are smaller, and the peak of the maximum is shifted by -60 mV/pH. In borate buffer pH 8.0, no peak is found in the passive range, and the current density is increased only slightly by the fluoride addition (Fig. 7b).

Discussion

The different electrochemical behavior of nickel in the two characteristic potential regions of minimum I and II is interpreted as a consequence of two different passivity mechanisms. Figure 8 shows a phase diagram of a passive film on nickel with the related processes. A high electrical field strength within the passive layer causes the migration of Ni²⁺ ions for compensation of the dissolution reaction and a possible layer formation at the oxide electrolyte interface. The potential drop $e_{2,3}$ determines the charge transfer reaction of Ni²⁺ or its complexes with F⁻, i.e., the corrosion reaction [4] (see below). For stationary conditions, when the layer

is neither growing nor getting thinner, this potential drop is determined by the equilibrium [3] of the formation of anions at the layer surface, i.e., O²⁻ for an oxide and F⁻ for a fluoride. In the case of passive iron, this leads to a characteristic pH dependence of the logarithm of the stationary corrosion current density (7). For unstationary conditions, $e_{2,3}$ may contain an overpotential because reaction [3] will occur in either direction and the equilibrium might be distorted. For nickel, the stationary dissolution current density is potential dependent (5). Therefore, one has to assume that $e_{2,3,s}$ is changing with the electrode potential ϵ . This, in turn, requires a change of the composition of the oxide surface or, in other words, of its oxidation state (8). In this regard, the situation of passive nickel is more complicated than that of iron. The small potential dependence of the current density depicted in Fig. 1 in HF-free HClO₄ should be seen as a consequence of the applied potentiodynamic condition when compared to the stationary values in 1M H₂SO₄ of Ref. (5).

The transfer of Ni²⁺ ions from the oxide into the electrolyte is catalyzed by fluoride. This process is similar to the catalysis of the corrosion of passive iron in sulfate (7), chloride (9), or fluoride (10) containing electrolytes. We assume that the Ni²⁺ ions at the oxide surface are first complexed after reaction [4]. This surface complex is transferred into the electrolyte by the ion transfer reaction [5] and finally transformed to a higher complexed anion by reaction [6].



Assuming equilibrium for reaction [4] and taking reaction [5] as the rate-determining step, one gets for the stationary corrosion current density $i_{c,s}$

$$i_{c,s} = 2kF[NiF_{ad}^+] \exp\left(\frac{\alpha F}{RT} e_{2,3,s}\right) \quad [7]$$

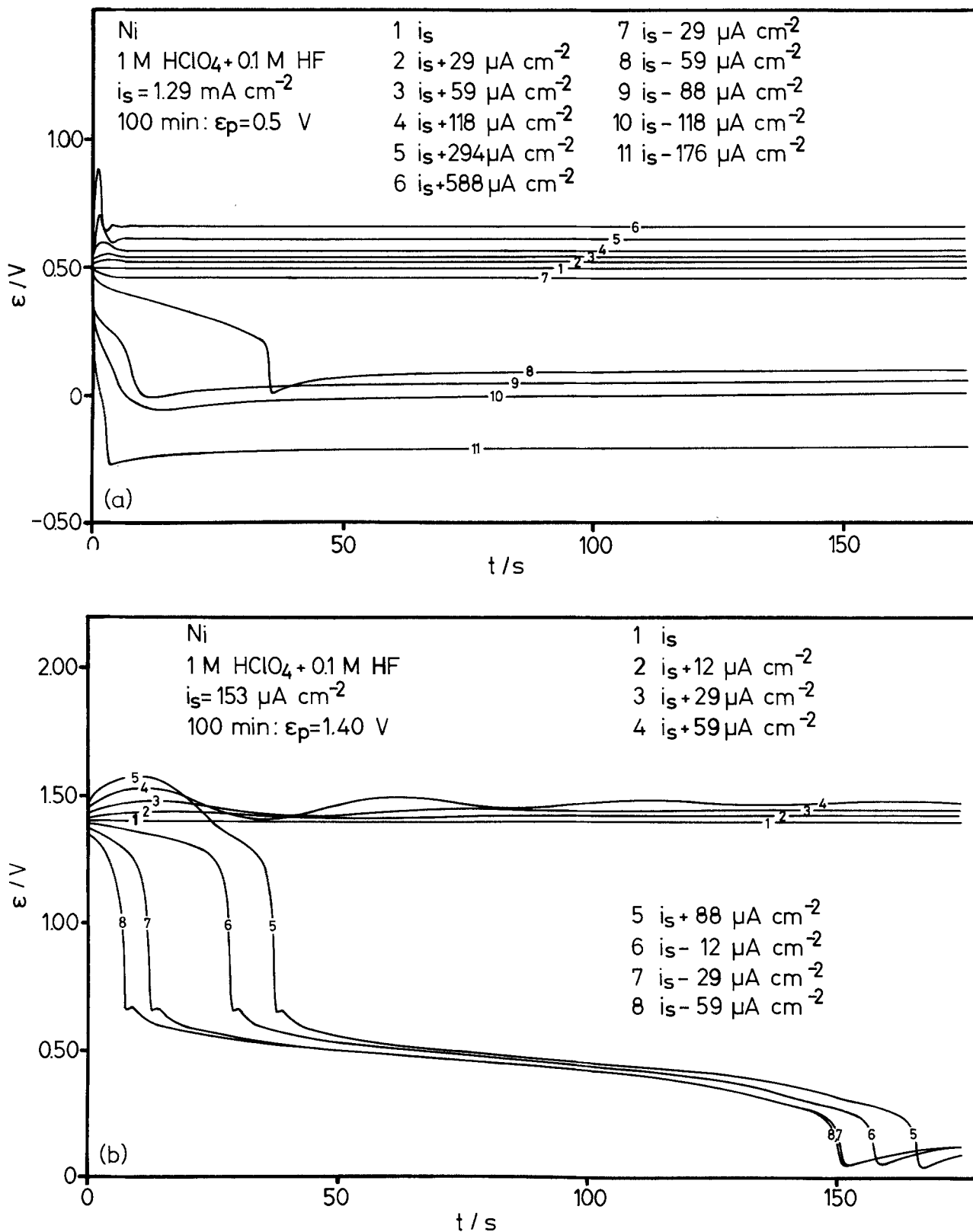


Fig. 6. Galvanostatic transients of nickel electrodes, prepassivated for 2h at ϵ in 1M HClO₄, in 1M HClO₄ plus 0.1M HF with currents higher or smaller than the stationary potentiostatic values. a, top: $\epsilon = 0.5\text{V}$, minimum I. b, bottom: $\epsilon = 1.4\text{V}$, minimum II.

with $[\text{NiF}_{\text{ad}}^+]$ being the surface concentration of the intermediate complex.

From the equilibrium for the electroadsorption [4] follows

$$[\text{NiF}_{\text{ad}}^+] = \frac{[\text{Ni}_{\text{ox}}^{2+}][\text{HF}_{\text{aq}}]}{[\text{H}_{\text{aq}}^+]} \exp\left(-\frac{\Delta G^\circ}{RT}\right) \exp\left(\frac{\gamma F}{RT} \epsilon_{2,3,s}\right) \quad [8]$$

The electroadsorption valency (γ) takes into account that only part of the total potential drop $\epsilon_{2,3,s}$ is effective because of the own dimensions of the anion. γ may also include a possible partial electron exchange between adsorbens and adsorbate (11).

Equation [8] is a Langmuir isotherm for the electroadsorption equilibrium [4], as is shown more clearly by introducing the surface coverage (θ) of the fluoride

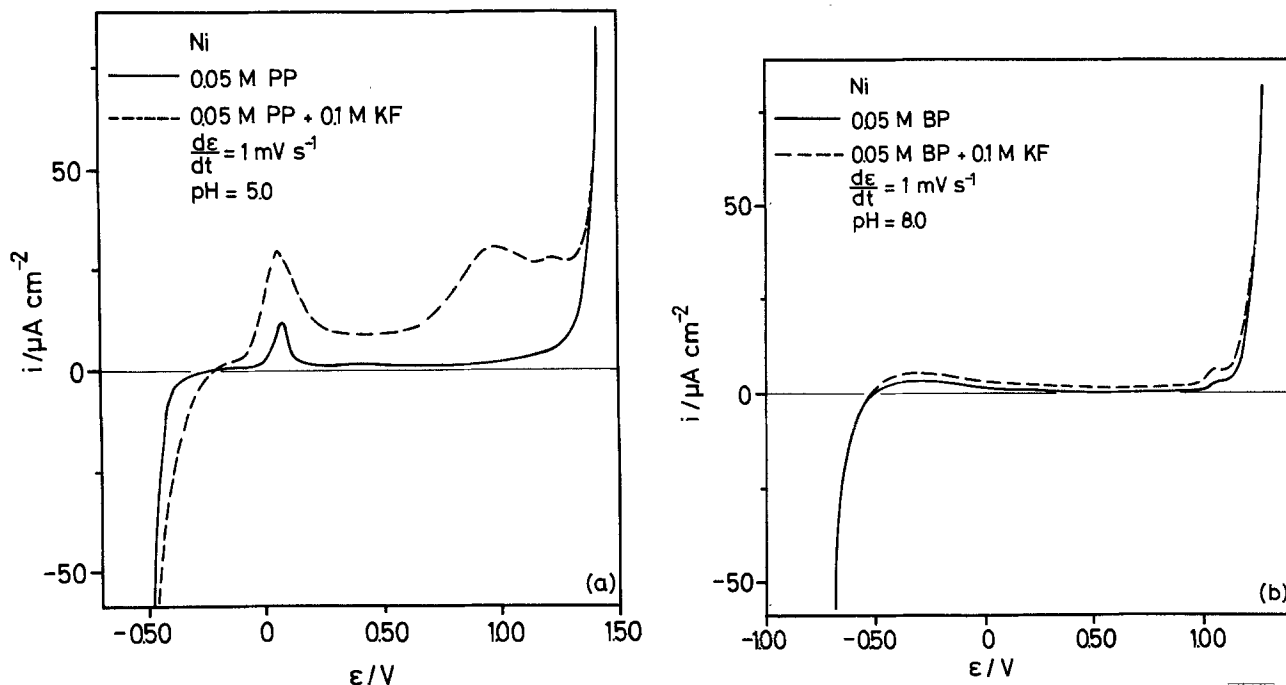


Fig. 7. Potentiodynamic polarization curve of nickel, $d\epsilon/dt = 1 \text{ mVs}^{-1}$. a, left: phthalate buffer plus 0.1M KF, $\text{pH} = 4.9$. b, right: borate buffer plus 0.1M KF, $\text{pH} = 8.0$.

complex

$$\frac{[\text{NiF}_{\text{ad}}^+]}{[\text{Ni}_{\text{ox}}^{2+}]} = \frac{\theta}{1 - \theta} = \frac{[\text{HF}_{\text{aq}}]}{[\text{H}_{\text{aq}}^+]} \exp\left(-\frac{\Delta G^\circ}{RT}\right)$$

$$\exp\left(\frac{\gamma F}{RT} \epsilon_{2,3,s}\right) = a[\text{HF}_{\text{aq}}] \quad [9]$$

$[\text{Ni}_{\text{ox}}^{2+}]$ is the surface concentration of those nickel ions not transformed into a surface complex, or, in other words, it is the concentration of the free adsorption places. The adsorption constant a depends on the pH and the potential drop $\epsilon_{2,3,s}$ at the oxide elec-

trolyte interface. θ is the concentration ratio of the surface complex and the sum of the free and occupied adsorption places $[\text{Ni}_{\text{ox}}^{2+}]_t = [\text{NiF}_{\text{ad}}^+] + [\text{Ni}_{\text{ox}}^{2+}]$

$$\theta = \frac{[\text{NiF}_{\text{ad}}^+]}{[\text{Ni}_{\text{ox}}^{2+}]_t} = \frac{a[\text{HF}_{\text{aq}}]}{1 + a[\text{HF}_{\text{aq}}]} \quad [10]$$

Introducing θ in Eq. [7] yields

$$i_{c,s} = 2kF\theta [\text{Ni}_{\text{ox}}^{2+}]_t \exp\left(\frac{\alpha F}{RT} \epsilon_{2,3,s}\right) \quad [11]$$

From the equilibrium of reaction [3], one gets the pH dependence of $\epsilon_{2,3,s}$

$$\epsilon_{2,3,s} = \epsilon_{2,3,s}^\circ - 0.059 \text{ pH} \quad [12]$$

Introducing Eq. [10] and [12] in [11] and assuming a small surface coverage $\theta \ll 1$ with $a[\text{HF}_{\text{aq}}] \ll 1$ so that Henry's adsorption isotherm is valid with $\theta = a[\text{HF}_{\text{aq}}]$, one gets

$$i_{c,s} = i_{c,s}^\circ [\text{HF}_{\text{aq}}] \exp\{-2.303 \text{ pH} (\alpha + \gamma - 1)\} \quad [13]$$

$$i_{c,s}^\circ = 2kF \exp\left(-\frac{\Delta G^\circ}{RT}\right) \exp\left\{\frac{(\alpha + \gamma)F}{RT} \epsilon_{2,3,s}^\circ\right\} \quad [14]$$

This mechanism yields the following electrochemical reaction orders for HF and H^+

$$\frac{d \log i_{c,s}}{d \log [\text{HF}_{\text{aq}}]} = 1; \quad \frac{d \log i_{c,s}}{d \text{ pH}} = 1 - \alpha - \gamma \quad [15]$$

Assuming a higher Ni^{2+} - F^- complex for the corrosion mechanism, a higher reaction order is obtained for HF as follows

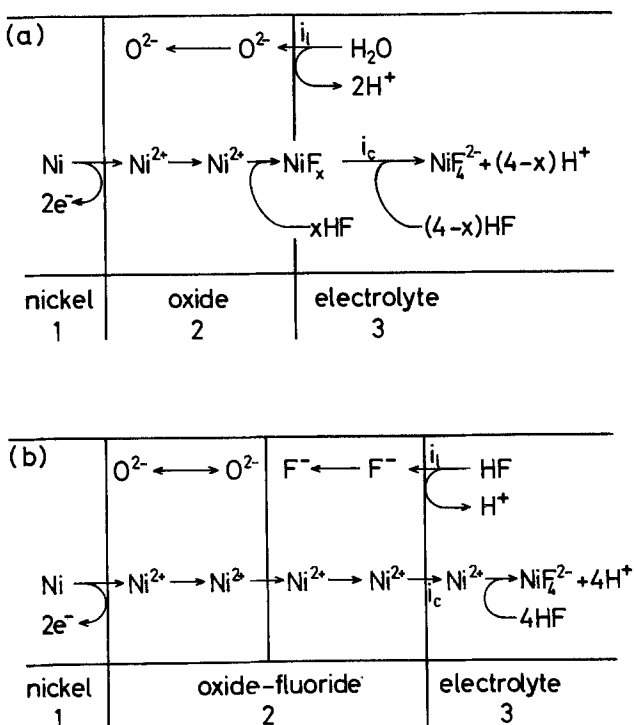
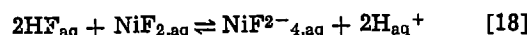
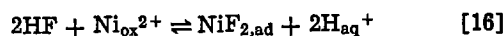


Fig. 8. Phase diagram for a passivated nickel electrode in HF containing electrolyte with the related electrode reactions. a: Surface catalytic mechanism of the minimum I. b: Mechanism in presence of a fluoride layer, minimum II.

The electroadsorption equilibrium of Eq. [16] leads to a Langmuir isotherm similar to the case of the association of two adsorbed species. This equilibrium yields

the following equation

$$\frac{\theta}{1-\theta} = \frac{[\text{NiF}_{2,\text{ad}}]}{[\text{Ni}_{\text{ox}}^{2+}]} = \frac{[\text{HF}_{\text{aq}}]}{[\text{H}_{\text{aq}}^+]^2} \exp\left(-\frac{\Delta G^{\circ}}{RT}\right) \exp\left(\frac{2\gamma F}{RT} \epsilon_{2,3,s}\right) \quad [19]$$

Applying Eq. [12] for the equilibrium of O^{2-} formation yields

$$\frac{\theta}{1-\theta} = a' [\text{HF}_{\text{aq}}] = [\text{HF}_{\text{aq}}] \exp\left(-\frac{\Delta G^{\circ}}{RT}\right) \exp\left(\frac{2\gamma F}{RT} \epsilon_{2,3,s}\right) \exp\{4.606(1-\gamma)\text{pH}\} \quad [20]$$

$$\theta = \frac{[\text{NiF}_{2,\text{ad}}]}{[\text{Ni}_{\text{ox}}^{2+}]_t} = \frac{a'[\text{HF}_{\text{aq}}]^2}{1+a'[\text{HF}_{\text{aq}}]^2} \quad [21]$$

For the rate-determining step [17], one obtains

$$i_{c,s} = 2k'F[\text{NiF}_{2,\text{ad}}] = 2k'F\theta[\text{Ni}_{\text{ox}}^{2+}]_t \quad [22]$$

Introducing Eq. [20] and [21] in [22] and applying Henry's law with $a'[\text{HF}_{\text{aq}}] \ll 1$ for Eq. [21], one gets

$$i_{c,s} = i_{c,s}^{\circ} [\text{HF}_{\text{aq}}]^2 \exp\{4.606(1-\gamma)\text{pH}\} \quad [23]$$

$$i_{c,s}^{\circ} = 2k'F[\text{Ni}_{\text{ox}}^{2+}]_t \exp\left(-\frac{\Delta G^{\circ}}{RT}\right) \exp\left(-\frac{2\gamma F}{RT} \epsilon_{2,3,s}\right) \quad [24]$$

$$\frac{d \log i_{c,s}}{d \log [\text{HF}]} = 2; \quad \frac{d \log i_{c,s}}{d \text{pH}} = 2 - 2\gamma \quad [25]$$

The experimental value for the reaction order of HF (1.63) is between those of the two discussed mechanisms. If the simplification of Henry's law is no longer valid, reaction orders < 2 will result for HF also for the second mechanism (Eq. [16]-[18]). After Eq. [21] and [22], θ will vary with [HF], causing a change from a second-order law to no dependence for high surface coverages when saturation is achieved. With the experimental result of 1.63 for the HF reaction order, we favor the second mechanism (Eq. [16]-[18]). After the first mechanism (Eq. [4]-[6]), only a reaction order ≤ 1.0 is expected (Eq. [10], [11], [15]).

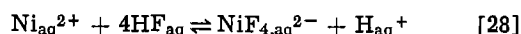
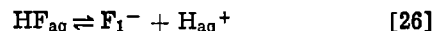
$i_{c,s}$ decreases with increasing pH after the experiments. After Eq. [25], this cannot be understood for $\gamma \leq 1$ with the second mechanism (Eq. [16]-[18]), but it would not contradict Eq. [15] of the first one. However, one has to take into account that hydrogen fluoride ($\text{pK} = 3.45$) is fully dissociated at pH 5 and that the fluoride anion might be involved in the dissolution process instead of HF. Thus the H^+ ion no longer participates in the electroadsorption reactions [4] and [16], which in turn changes the pH dependence of the stationary current to $d \log i_{c,s}/d \text{pH} = -(\alpha + \gamma)$ for the first mechanism (Eq. [4]-[6]), and to $d \log i_{c,s}/d \text{pH} = -2\gamma$ for the second one (Eq. [16]-[18]). These circumstances explain the high decrease of $i_{c,s}$ with increasing pH and complicate the interpretation, especially in alkaline solutions where small $i_{c,s}$ values are found.

The fluoride-induced dissolution mechanism leads to a thinning of the oxide film in the potential range of minimum I, as has been found by XPS analysis (6). About 2 min after the addition of HF, the thinning of the passive layer is finished, and a new stationary state for $i_{c,s}$ is achieved (Fig. 3a). The thinner oxide layer results in a higher electrical field strength, providing a sufficient ion transport to compensate the increased stationary dissolution current density at the oxide-electrolyte interface. No fluoride was found by

XPS at the surface of the specimen after HF exposure at minimum I after carefully rinsing with triply distilled water (6). These findings support further the surface catalytic mechanism and make impossible explanation by a chemical change of the passive layer.

With increasing electrode potential (ϵ), the current density rises to its maximum. Apparently, the potential drop $\epsilon_{2,3}$ increases, which leads to a higher concentration of fluoride complexes or surface coverage of F^- via the electroadsorption equilibrium of reaction [16]. These effects are in favor of the anodic dissolution process. a' increases exponentially with the potential drop $\epsilon_{2,3,s}$ (Eq. [19], [20]), which causes a decrease of the reaction order of HF after Eq. [21] and [22]. When a monolayer of NiF_2 is obtained, $i_{c,s}$ should no longer increase with $[\text{HF}_{\text{aq}}]$. This is apparently the situation when a continuous NiF_2 layer is formed at the current maximum ($\epsilon = 1.1\text{V}$). The current values of the potentiodynamic polarization curve show a very reduced dependence of the HF concentration at these potentials (Fig. 2).

The high current densities at the maximum lead to the formation of a visible NiF_2 layer, presumably by precipitation. The composition of this layer has been determined by XPS analysis and by comparison with standards (6). This passivating NiF_2 layer reduces the corrosion current density. The change from an oxide to a fluoride layer has pronounced consequences for the mechanism at minimum II. The potential drop $\epsilon_{2,3,s}$ for stationary conditions is now determined by the equilibrium of F^- formation [26] on a fluoride layer



With the ion transfer of Eq. [27] as the rate-determining step, one obtains

$$i_{c,s} = 2k''F[\text{Ni}_1^{2+}] \exp\left(\frac{2\alpha''F}{RT} \epsilon''_{2,3}\right) \quad [29]$$

The electrochemical equilibrium [26] leads to the following dependence of the potential difference $\epsilon''_{2,3}$ at the fluoride-electrolyte interface

$$\mu_{\text{F}^-} + \mu_{\text{H}^+} - \mu_{\text{HF}} - F\epsilon''_2 + F\epsilon''_3 = 0$$

Inserting the concentration dependence of the chemical potentials $\mu_i = \mu_i^{\circ} + RT \ln a_i$ and introducing $\epsilon''_{2,3} =$

$$\epsilon''_2 - \epsilon''_3 \text{ and } \epsilon''_{2,3} = \frac{1}{F} \sum \mu_i^{\circ} \text{ for the sum of the stan-}$$

dard potentials μ_i° , one gets

$$\epsilon''_{2,3} = \epsilon''_{2,3}^{\circ} - 0.059 \text{pH} - 0.059 \log [\text{HF}_{\text{aq}}] \quad [30]$$

Inserting Eq. [30] in [29] yields

$$i_{c,s} = i_{c,s}^{\circ} [\text{HF}]^{-2\alpha''} \exp(-4.606\alpha'' \text{pH}) \quad [31]$$

$$i_{c,s}^{\circ} = 2k''F[\text{Ni}_1^{2+}] \exp\left(\frac{2\alpha''F}{RT} \epsilon''_{2,3}\right) \quad [32]$$

This results in the following electrochemical reaction order for HF and pH

$$\frac{d \log i_{c,s}}{d \log [\text{HF}]} = -2\alpha''; \quad \frac{d \log i_{c,s}}{d \text{pH}} = -2\alpha'' \quad [33]$$

With the measured value of -0.79 for the HF reaction order at minimum II, one obtains $\alpha'' \approx 0.4$ for the charge transfer coefficient. This is a reasonable value for the ion transfer step.

The approach to the new stationary condition for $i_{c,s}$ at minimum II with time after the HF addition (Fig. 3b) is caused by the thinning of the passivating oxide and the formation of the NiF_2 overlayer. The current-

time behavior corresponds closely to the results of the surface analysis. The thinning of the oxide layer is completed after 1 min (6) when the current achieves its intermediate maximum (Fig. 3b). The following current decrease occurs in close relation to the formation of the NiF₂ overlayer. Stationary conditions are achieved after ca. 10 min.

The removal of the visible nickel fluoride film at the current maximum of Fig. 1 by vigorous stirring with >400 rpm goes along with a complete removal of any fluoride at the surface as has been found by XPS analysis (6). This shows that the surface catalytical mechanism of minimum I is still effective at the current maximum.

The potential oscillations of Fig. 6b should be seen as a consequence of the form of the current-density potential curve and of changes within the surface layers with time. These processes are not fully understood, although they have been already reported for similar conditions for this system (4). Apparently, damped oscillation occurs in both directions of minimum II if $i > i_s$. However, if the potential drops below the value of the current maximum, it does not recover and moves to minimum I with the related changes of the surface layer. As i is too small to maintain the potential at minimum I (cf. Fig. 1), ϵ has to drop to the active region with a complete removal of the passive film. If $i < i_s$, a final stable situation is achieved only with an active electrode potential in any case.

Conclusions

The presence of aggressive anions affects decisively the passive corrosion current density. In a lower potential range the passive layer of nickel is thinned by the action of HF (minimum I). This causes a higher electrical field strength and an increased corrosion current density. The transfer of the nickel ions from the oxide to the electrolyte is catalyzed by the formation of a fluoride complex at the surface. The electrochemical reaction order for HF is 1.63. In the second minimum, the corrosion current is decreased by the formation of an NiF₂ overlayer with a thinned oxide still present underneath. According to the changed chemistry of the surface, a different mechanism is effective. The reaction order of HF is -0.79. This is a consequence of the equilibrium of F⁻ formation on the surface, which determines the potential difference $\epsilon_{2,3}$ at the fluoride layer-electrolyte interface.

The effect of anions on the dissolution kinetics of passive metals is rather common. In many cases, a localized attack is observed, i.e., as for iron and nickel in solutions of the other halides. In these cases, the increased current density leads to a local accumulation of the corrosion products and hence of the halides. This, in turn, increases the catalytic activity with a severe thinning of the passive film and its complete removal. The high halide concentration thus prevents a repassivation of the growing pits autocatalytically. Simi-

larly, a high bulk concentration of chlorides ($\cong 1M$) may prevent the formation of a passive film completely (12, 13).

The general attack of the passive oxide by acidic HF solutions in comparison to the local effects of the other halides may be a consequence of the stronger complexing ability of fluoride. Therefore, it might not be necessary to accumulate corrosion products and thereby fluoride by an intense local or general metal dissolution. HF adsorbs most readily at the total passive surface, so that the formation of two-dimensional salt nuclei does not dominate the breakdown, as in the case of iron in chloride solutions (9). The more general attack of fluoride on passive nickel or iron (10) simplifies the complicated process of localized corrosion. In this regard, fluoride is a model system for the breakdown of passivity. The complexing and catalytical capability of the halides should be seen as the main source of breakdown of passivity and localized corrosion. A further support by ohmic drops in large pits, especially when they are occluded, and acidification by hydrolysis which, however, is not effective in already strongly acidic solutions, may help to stabilize the pit growth.

Acknowledgment

For one of us, M. Sakashita, we acknowledge a fellowship of the Alexander von Humboldt Stiftung and the hospitality at the Freie Universität Berlin, which enabled him to participate in this project.

Manuscript submitted July 9, 1982; revised manuscript received Sept. 22, 1983.

The Alexander von Humboldt Stiftung assisted in meeting the publication costs of this article.

REFERENCES

1. H.-H. Strehblow, B. Titze, and B. Löchel, *Corros. Sci.*, **19**, 1047 (1979).
2. H.-H. Strehblow, *Prakt. Metallogr.*, **12**, 283 (1975).
3. B. Löchel and H.-H. Strehblow, *Werkst. Korros.*, **31**, 353 (1980).
4. J. Osterwald and H. Trunk, *ibid.*, **28**, 321 (1977).
5. K. Arnold and K. J. Vetter, *Z. Electrochem.*, **64**, 244 (1960).
6. B. Löchel and H.-H. Strehblow, *This Journal*, To be published.
7. K. J. Vetter and F. Gorn, *Electrochim. Acta*, **18**, 321 (1973).
8. K. J. Vetter, *This Journal*, **110**, 597 (1963).
9. K. E. Heusler and L. Fischer, *Werkst. Korros.*, **27**, 697 (1976).
10. B. Löchel and H.-H. Strehblow, *Electrochim. Acta*, **28**, 565 (1983).
11. J. W. Schultze and K. J. Vetter, *J. Electroanal. Chem.*, **44**, 63 (1973).
12. H.-H. Strehblow and J. Wonnors, *Z. Phys. Chem., N.F.*, **98**, 199 (1975).
13. H.-H. Strehblow and J. Wonnors, *Electrochim. Acta*, **22**, 421 (1977).

Corrosion Properties of Amorphous Iron-Zirconium Films in 1N Sulfuric Acid

L. D. McCormick, N. S. Wheeler,* and C. R. Molock*

U.S. Department of the Interior, Bureau of Mines, Avondale Research Center, Avondale, Maryland 20782

C. L. Chien

Department of Physics, The Johns Hopkins University, Baltimore, Maryland 21218

ABSTRACT

Amorphous iron-zirconium alloys, ranging in composition from $\text{Fe}_{90}\text{Zr}_{10}$ to $\text{Fe}_{33}\text{Zr}_{67}$, have been studied by anodic polarization and passivation decay in 1N sulfuric acid. The results showed a compositional enhancement of corrosion resistance with increasing zirconium concentration. Auger electron spectroscopy indicated that exposure to the sulfuric acid solution enhances the surface zirconium concentration with respect to the bulk of the exposed alloy and also with respect to the as-deposited surface composition. X-ray photoemission spectroscopy shows that the passive film is a mixture of zirconium oxides and hydroxides and iron oxides and hydroxides.

As part of its mission to conserve resources, the Bureau of Mines is studying the factors leading to the corrosive degradation of materials from exposure to reactive species, especially in mining and metallurgical processing environments. Metallic glasses, because of their amorphous character, which eliminates crystalline defects, and because they can be formed over wide ranges of compositions, have significant potential for materials applications in environments susceptible to corrosion. This potential was demonstrated initially by Hashimoto *et al.* (1), who discovered that several iron-based amorphous alloys have corrosion properties superior to those of crystalline alloys of stainless steel. Subsequently, several amorphous alloys have been studied to determine their corrosion properties. For a recent review, see Waseda and Aust (2).

There are two major groups of alloy systems which form amorphous structures: metal-metal and metal-metalloid. Results of Hashimoto *et al.* indicate that the incorporation of a metalloid, *e.g.*, phosphorus, carbon, or boron, into a metal to form an amorphous alloy results in a chemically unstable alloy and does not anodically passivate in acidic solutions (3). However, the inclusion of a second metal to form a ternary system often results in anodic passivation and greatly improves corrosion resistance.

Metal-metal amorphous alloys have not been as extensively studied. Naka *et al.* (4) examined the corrosion behavior of amorphous $\text{Cu}_{50}\text{Zr}_{50}$ and $\text{Cu}_{50}\text{Ti}_{50}$ and compared their results with Cu, Zr, and Ti polycrystalline metals and with Cu-Zr and Cu-Ti polycrystalline alloys. Their data indicate that these metal-metal amorphous alloys have superior corrosion resistance compared to crystalline alloys of similar composition. However, based upon available data, Waseda and Aust (2) and Hashimoto (5) conclude that the enhancement in corrosion behavior due to amorphicity is much greater in metal-metalloid systems than in metal-metal systems. Waseda and Aust (2) and Hashimoto (5) concluded that in metal-metal systems the corrosion properties of the alloy are principally determined by the most corrosion resistant metal. If such is the case, an amorphous metal-metal alloy can be produced for a specific corrosion environment based on the corrosion behavior of the individual components.

Subsequent work by Walmsley (6) indicated that perhaps metal-metal amorphous systems are not superior to crystalline materials if crystalline defects can be eliminated. Walmsley studied the Cu-Zr amorphous system ranging from $\text{Cu}_{85}\text{Zr}_{15}$ to $\text{Cu}_{20}\text{Zr}_{80}$. The corrosion resistance of amorphous Cu-Zr is better than

that of crystalline systems at low concentrations of Zr. This is because of the presence of alpha-Cu, which does not passivate in the crystalline system. However, at high Zr compositions, all phases contain Zr, and the amorphous and crystalline materials display comparable corrosion properties. Therefore, the author concludes that any enhancement in corrosion resistance is due to lack of crystalline defects instead of the amorphicity of the films.

Based upon these limited studies of metal-metal amorphous alloys, the effect of crystallinity *vs.* composition is not clear. This study is concerned with the compositional effect on the electrochemistry of iron-zirconium amorphous alloys formed by ion sputtering onto a vitreous carbon substrate. Anodic polarization and passivation decay tests were conducted in 1N H_2SO_4 to study corrosion properties. After electrochemical testing, the surface films were characterized by Auger electron spectroscopy (AES) and x-ray photoemission spectroscopy (XPS).

Experimental

Zirconium samples were cut from Alpha¹ high purity (99.9%) 0.25 mm foil into 1.9 cm squares, chemically polished with a solution of nitric and hydrofluoric acids in high-purity (HP) water (resistivity of 18 $\text{M}\Omega\text{-cm}$), rinsed in HP water, and dried in a stream of dry nitrogen.

High purity (99.5%) 0.25 mm Materials Research Corporation iron foil was cut into 1.9 \times 1.3 cm samples, degreased sequentially in acetone and methanol, and rinsed with HP water. Polycrystalline Fe12Cr and Fe18Cr were cut into 1.9 cm squares from sheet stock, ground with 180 through 600 grit silicon carbide paper, annealed for 2h at 600°C under an argon atmosphere, pickled in a 20% nitric acid solution with a few drops of HF added, and rinsed with HP water. The iron, Fe12Cr, and Fe18Cr samples were then electropolished in a 9:1 volume ratio of glacial acetic acid and 70% perchloric acid solution, rinsed with HP water, and dried in a stream of dry nitrogen.

Vitreous carbon was used as a substrate for the amorphous Fe-Zr films because it is not expected to form a good galvanic couple with the Fe-Zr film nor react with 1N H_2SO_4 . Vitreous carbon sheet stock, 2 mm thick, was cut into 1.9 cm squares, ground with 320 through 600 grit silicon carbide paper, and polished with 5 and 0.05 μm gamma alumina powders. After polishing, a few small pits could be seen in an otherwise highly polished surface. Polished samples were sequentially degreased with acetone and methanol,

¹ Reference to specific trade names or manufacturers is for identification only and does not imply endorsement by the Bureau of Mines.

* Electrochemical Society Active Member.
Key words: alloy, ESCA, passivity, AES.

rinsed with HP water, and dried in a stream of dry nitrogen.

Amorphous Fe₉₀Zr₁₀, Fe₈₀Zr₂₀, Fe₆₀Zr₄₀, Fe₅₀Zr₅₀, and Fe₃₃Zr₆₇ samples were produced by argon ion sputtering from a pellet of desired composition onto a vitreous carbon substrate. The substrate was cooled by either liquid nitrogen or water during sputtering. Prior to sputtering, the chamber vacuum was in the 10⁻⁶ Pa range. Deposition rates were between 50 and 100 nm/min utilizing argon ions. In order to verify that the deposited films were amorphous, we utilized Mossbauer spectroscopy with a 57 Co in Rh source. The magnetic and hyperfine interactions of thick amorphous and polycrystalline Fe-Zr films have been previously studied by Mossbauer spectroscopy and correlated with x-ray diffraction studies (7, 8). Films which were amorphous based upon x-ray diffraction demonstrated significantly different Mossbauer spectra compared to polycrystalline films. Therefore, we were able to verify amorphicity of films which were too thin for x-ray analysis and were deposited on vitreous carbon substrates. Composition of selected alloys was verified by proton-induced x-ray emission.

All electrochemical tests were run in a 1 liter modified Greene cell (9) equipped with a nitrogen gas bubbler, a platinum sheet counterelectrode, and a glass Luggin probe connected by a solution bridge to a saturated calomel electrode (SCE). All potential measurements were with respect to the SCE and converted to the normal hydrogen electrode (NHE). The samples were held in a polycarbonate sample holder with a FETFE Teflon O-ring sealing the exposed region from the remainder of the sample. Depending on the O-ring size, 1/3 to 1/2 cm² of the sample surface was exposed. The test solution was 1N H₂SO₄ which had been deaerated by bubbling nitrogen gas through the solution 12h prior to the test. The nitrogen purity was 99.998% with <10 ppm oxygen, <2 ppm hydrogen, and <1 ppm methane.

After electrochemical testing, Fe-Zr amorphous samples were analyzed with Auger electron spectroscopy (AES). One analysis was performed on an untested portion of the film and another on the region which had been exposed to 1N H₂SO₄. Base pressure of the AES system prior to use was 1 × 10⁻⁶ Pa. A primary beam of 4 μA, 5 keV electrons was used to excite Auger electrons, which were then detected by a cylindrical mirror analyzer. The analyzer was modulated at 1300 Hz with 2V peak to peak. To obtain depth profiles, inert gas sputtering was used. An argon ion beam was obtained at 2.5 keV utilizing a pressure of 5 × 10⁻³ Pa. The ion beam was rastered over an area of approximately 2 × 3 mm. The electron beam had a diameter (full width at half maximum) of approximately 150 μm and was aligned in the center of the rastered area. The ion sputter rate was calibrated against a 100 nm thick Ta₂O₅ film. No correction was made for variation in sputtering due to different matrices.

X-ray photoemission spectroscopy (XPS) was used to determine the chemical nature of the as-sputtered amorphous films and the passive films formed in 1N H₂SO₄. Passive films were formed by placing samples into solution at a selected potential (the "hold-release potential" shown in Table I) and holding them at this potential until the current reached steady state. Then the samples were withdrawn from the solution, rinsed in HP water, and dried in dry nitrogen. XPS analyses were performed by Perkin-Elmer, Edison, New Jersey, utilizing a Mg K_α source and a Physical Electronics Model 560 system. All spectra were charge corrected to the 284.6 eV peak of carbon. Each sample was analyzed in two areas: inside and outside the exposed region. Initially a survey scan was done in each region to determine film composition. This was followed by high resolution scans of each peak to determine chemical structure.

Table I. Passivation decay times and potentials and corrosion potentials for Fe-Zr amorphous alloys and for polycrystalline Fe-Cr alloys, Fe, and Zr

Metal or alloy	t _d (mean, min)	No. samples	E _{hold-release} (V _{NHE})	E _{corr} (V _{NHE})
Fe	0.23 ± 0.04	2	1.492	-0.29
Fe ₉₀ Zr ₁₀	2.8 ± 0.8	2	0.592	-0.19
Fe ₆₀ Zr ₄₀	•	2	0.592	-0.20
Fe ₅₀ Zr ₅₀	•	1	0.592	-0.23
Fe ₃₃ Zr ₆₇	•	1	0.592	-0.26
Zr	•	1	0.592	-0.24
Fe12Cr	20 ± 17	6	0.742	-0.25
Fe18Cr	2130	1	0.842	-0.26

* Samples were still passive at the end of the 2.5 day test.

Two electrochemical tests were used for evaluating the corrosion properties of the amorphous alloys, polycrystalline Fe, Zr, Fe12Cr, and Fe18Cr in deaerated 1N H₂SO₄. Anodic polarization was used to indicate whether a particular metal would passivate in the test environment and to compare its passivation ability with those of other metals tested. Prior to anodic polarization, the Fe12Cr and Fe18Cr alloys were cathodically reduced at -17 μA/cm² until the potential dropped discontinuously, indicating that the air-formed oxide had been reduced. Cathodic reduction was not done on the amorphous Fe-Zr alloys, polycrystalline iron, or polycrystalline zirconium. The oxide film on iron dissolved readily upon being placed in solution. Zirconium was not reduced to eliminate the possibility of introducing hydrogen into the matrix. Instead of cathodic reduction, zirconium samples were placed in solution at open circuit and allowed to reach a steady potential before testing was begun. Amorphous Fe-Zr alloys were not cathodically reduced, since AES showed that the air-formed oxides were only tens of nanometers thick. Polarization scans were run potentiodynamically in the anodic direction at 60 V/h, beginning at potentials negative to the corrosion potential (E_{corr}). [See Ref. (10) for a definition of the corrosion potential.] However, for zirconium scans, the current in the region of the corrosion potential was so low that it could not be recorded potentiodynamically. Instead, the region between ±100 mV of E_{corr} was obtained galvanostatically and incorporated with the potentiodynamic results into Fig. 1. Passivation decay tests were conducted by placing the sample in the test cell at or near the passive potential having the lowest current density as determined from the anodic polarization curve, holding the selected potential until a quasi-steady-state current was achieved, and then releasing potential control and monitoring open-circuit potential (E_{oc}) vs. time. A sample was determined to have lost passivity when E_{oc} reached the corrosion potential, the latter having been determined from anodic polarization (see Fig. 1). If the sample had not reached the corrosion potential after 2.5 days, the test was terminated in order to avoid leakage of solution into the sample holder. An active-passive metal will remain passive as long as its potential is anodic to the primary passive potential (E_{pp}) defined in Ref. (10). However, few active-passive metals remain passive at open circuit; most drift back to the corrosion potential. The passivation decay time (t_d) defined in Fig. 2, is a measure of the metal's ability to remain passive and allows comparisons to be made between samples in a given test environment.

Results and Discussion

Polarization curves for Fe-Zr alloys are shown in Fig. 3. The cathodic portion of the scan is shown only for Fe₃₃Zr₆₇ since it is similar for all the amorphous Fe-Zr alloys tested. Increasing the zirconium concentration decreases the critical anodic current density until the active-passive current peak is not found in

Fig. 1. Polarization curves in deaerated 1N H₂SO₄ at 60 V/h. A: Zr. B: Fe₃₃Zr₆₇ amorphous alloy. C: Fe18Cr. D: Fe.

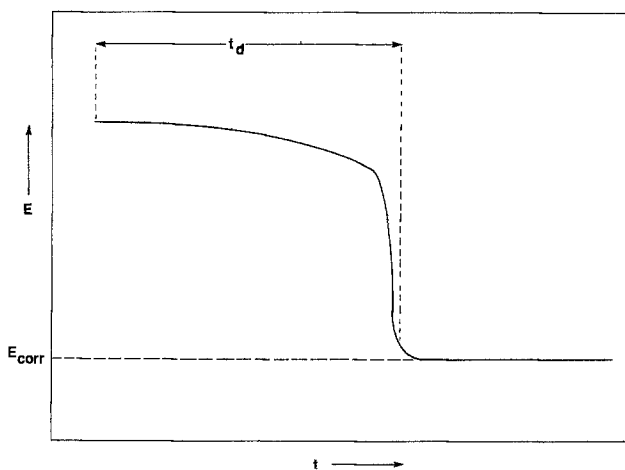
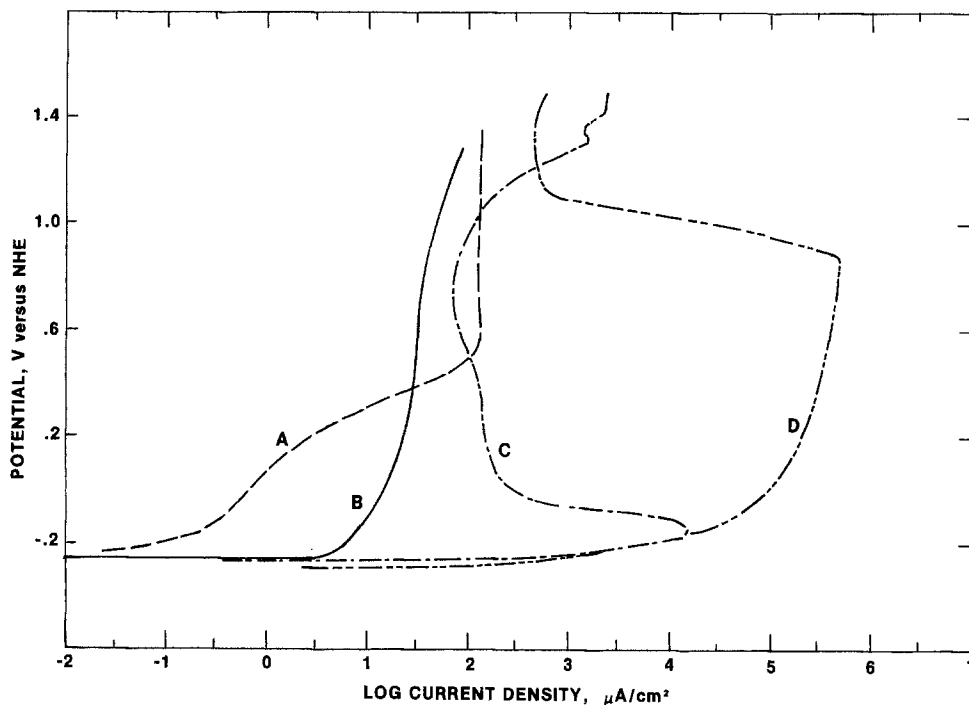


Fig. 2. Passivation decay test

the Fe₆₀Zr₄₀ or Fe₃₃Zr₆₇ curves. The polarization curve for Fe₅₀Zr₅₀ (not shown) fits between those of Fe₆₀Zr₄₀ and Fe₃₃Zr₆₇ and also lacks the active-passive current peak. The absence of an active-passive peak seems to indicate that the hydrogen reduction curve intersects the metal oxidation curve only in the passive region (11).

A comparison of the polarization scans for polycrystalline Fe, Zr, Fe18Cr, and amorphous Fe₃₃Zr₆₇ in Fig. 1 shows that Fe₃₃Zr₆₇ has a significantly lower current density than Fe18Cr or iron. In addition, amorphous Fe₃₃Zr₆₇ compares favorably to zirconium above 0.4V NHE, but zirconium exhibits significantly lower current densities between the corrosion potential and approximately 0.4V NHE. The corrosion potentials listed in Table I are the crossover potentials for the potentiodynamic polarization scans. Table I shows that the corrosion potential of the amorphous iron-zirconium alloys becomes more negative as the zirconium concentration is increased. This trend suggests that increasing the zirconium concentration may decrease the hydrogen exchange current density (i_0) as defined in Ref. (10). Extrapolation of the cathodic branches of the curves shown in Fig. 3 indicates that the amorphous Fe-Zr alloys trend toward lower i_0 values as the Zr concentration increases. However, this could also be due to alterations in the anodic partial

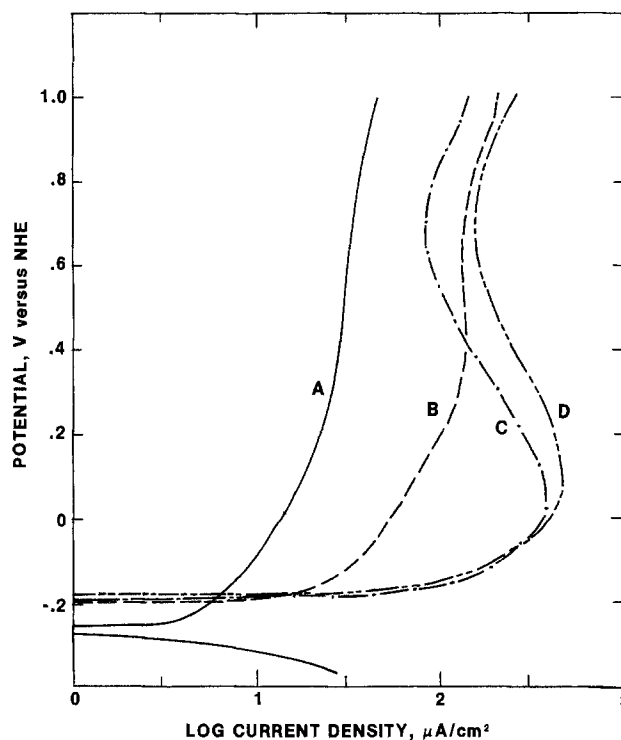


Fig. 3. Polarization curves of Fe-Zr amorphous alloys in deaerated 1N H₂SO₄ at 60 V/h. A: Fe₃₃Zr₆₇. B: Fe₆₀Zr₄₀. C: Fe₈₀Zr₂₀. D: Fe₉₀Zr₁₀.

process or a combination of alterations in both anodic and cathodic processes. It should be noted that polycrystalline iron does not fit this trend, since E_{corr} of iron is more negative than for any of the amorphous alloys.

The corrosion current density as defined in Ref. (10) was also determined. Owing to the relatively fast polarization scan rate used, these values are not reported. However, the trend observed was that increasing the zirconium concentration lowered the corrosion current density for the amorphous iron-zirconium alloys.

The potentials used to passivate each sample prior to passivation decay are given in Table I. The potential of 0.592V NHE, which is the potential where the mini-

imum passive current density of $\text{Fe}_{90}\text{Zr}_{10}$ occurs, was selected as the hold-release potential for the passivation decay test on zirconium and iron-zirconium alloys. As Fig. 3 shows, this is in the passive region for each of the samples which has an identifiable active-passive region. Polycrystalline Fe and Fe12Cr samples were held at the potential determined from their polarization curves to yield the minimum passive current.

The results from Table I show that a significant increase in passivation decay time can be gained by increasing the zirconium concentration of an iron-based amorphous alloy. It should be noted that $\text{Fe}_{80}\text{Zr}_{20}$, $\text{Fe}_{50}\text{Zr}_{50}$, and $\text{Fe}_{33}\text{Zr}_{67}$, which are above the critical composition for loss of active-passive peaks, maintained passivity for the maximum duration of the test.

These data compare favorably with the results of Walmsley (6) on amorphous Cu-Zr alloys in 0.1N H_2SO_4 . His data also show a continuous decrease in the active-passive peak with increasing zirconium concentration until at $\text{Cu}_{32}\text{Zr}_{68}$ it disappears completely. Direct comparisons are not possible due to different solution concentrations and different scan rates.

Linear polarization was performed on an $\text{Fe}_{50}\text{Zr}_{50}$ amorphous alloy after a 2.5 day passivation test in which the potential had remained at 0.274V NHE for the previous 1.5 days. The corrosion rate was determined from linear polarization to be $0.8 \mu\text{m}$ per year, indicating the alloy is probably passive at this potential. As a test of the stability of this passive potential, the sample was potentiostated to the corrosion potential of $\text{Fe}_{50}\text{Zr}_{50}$ (-0.23V NHE) and released. The potential drifted back to 0.274V. This implies that the passive film is not easily reduced. For this film reduction to occur, the potential may have to be held to -0.23V for some time or at an even more negative potential.

Even though Hashimoto (5) concluded that metal-metal systems generally do not possess extremely high corrosion resistance compared to metal-metalloid systems, the effect of alloying with a metal can yield a much more corrosion resistant material than a metal-metalloid system if the alloying metal is chosen to have good corrosion properties. This is demonstrated by comparing the data for $\text{Fe}_{80}\text{Zr}_{20}$ with those of Hashimoto *et al.* (3) for amorphous alloys with 20% metalloid. The critical current density (10) for $\text{Fe}_{80}\text{Zr}_{20}$ is more than two orders of magnitude lower than that for Fe-1Zr-13P-7C.

The results of four AES analyses are shown in Fig. 4-7 for $\text{Fe}_{80}\text{Zr}_{20}$ and $\text{Fe}_{60}\text{Zr}_{40}$ amorphous alloys. From these the effects of both composition and exposure to the test solution can be seen. The deposited low zirconium alloy ($\text{Fe}_{80}\text{Zr}_{20}$) shows zirconium depletion and high oxygen levels in the surface region ($<5 \text{ nm}$ deep). A comparison of Fig. 4 and 5 demonstrates the effect of exposure to 1N H_2SO_4 on the surface film. As can be seen, the near surface region ($<2 \text{ nm}$) of the sample exposed to 1N H_2SO_4 is significantly enhanced in zirconium and depleted in iron with respect to their relative concentrations in the bulk. The higher

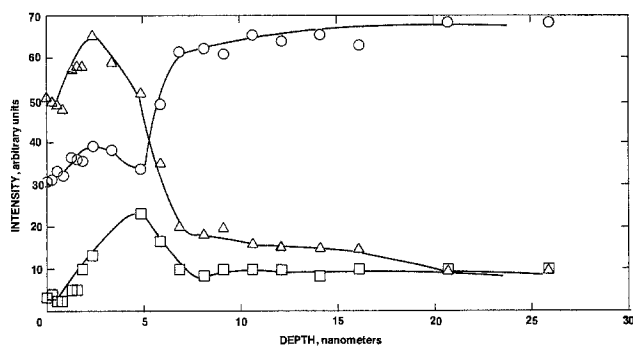


Fig. 4. AES depth profile of $\text{Fe}_{80}\text{Zr}_{20}$ as deposited amorphous alloy. Δ : oxygen. \circ : iron. \square : zirconium.

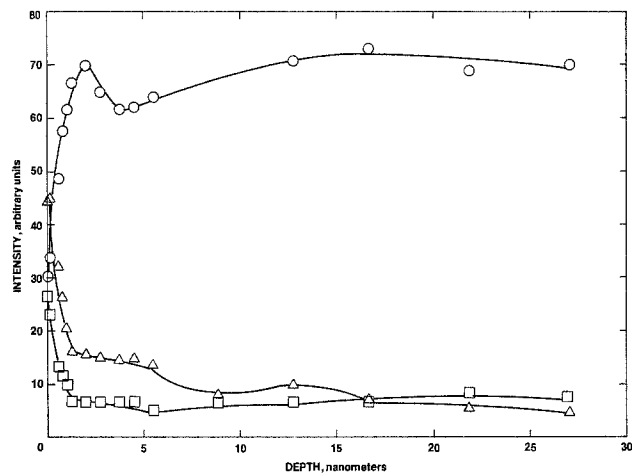


Fig. 5. AES depth profile of $\text{Fe}_{80}\text{Zr}_{20}$ amorphous alloy after passivation in 1N H_2SO_4 . Δ : oxygen. \circ : iron. \square : zirconium.

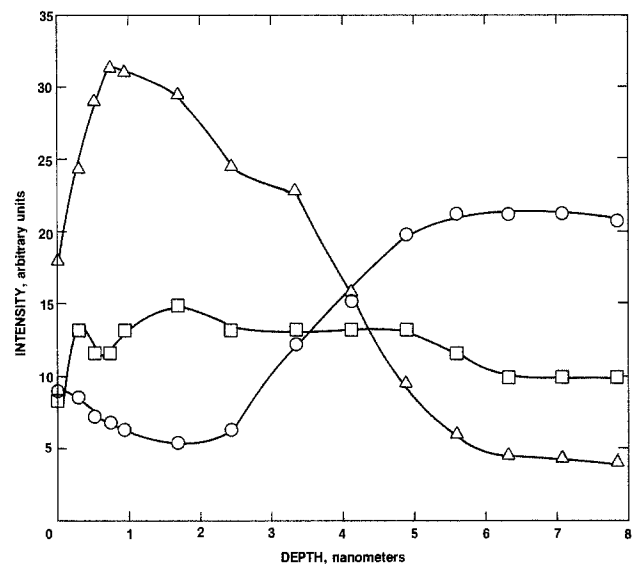


Fig. 6. AES depth profile of $\text{Fe}_{60}\text{Zr}_{40}$ as deposited amorphous alloy. Δ : oxygen. \circ : iron. \square : zirconium.

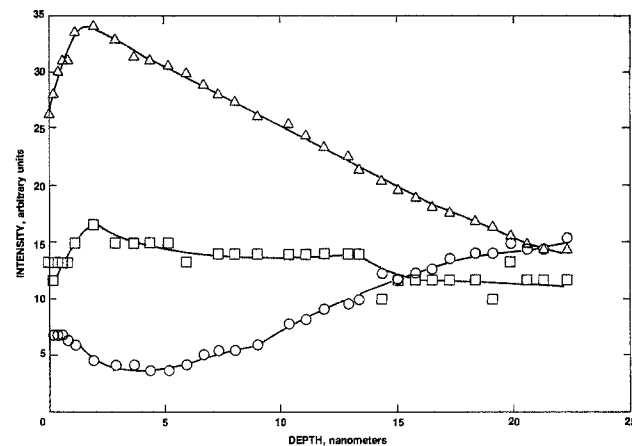


Fig. 7. AES depth profile of $\text{Fe}_{60}\text{Zr}_{40}$ amorphous alloy after passivation in 1N H_2SO_4 . Δ : oxygen. \circ : iron. \square : zirconium.

zirconium alloy ($\text{Fe}_{60}\text{Zr}_{40}$) shows the same effect, but because of higher initial zirconium concentration, the zirconium enhancement in the passive film is not as pronounced (Fig. 6 and 7). Other compositions tested demonstrate the same phenomenon with increasing zirconium composition of the as-deposited alloy, until $\text{Fe}_{33}\text{Zr}_{67}$, at which the enhancement of surface zirconium is not detected.

XPS data agreed well with previously determined AES data. Surface films on as-deposited amorphous alloys consisted of iron, zirconium, oxygen, and carbon. After exposure, sulfur was present, and the iron to zirconium ratio had changed to indicate significant surface enhancement of zirconium. High resolution scans revealed that surface carbon was present as graphitic carbon. Oxygen scans indicated a mixture of metal oxide and hydroxide with a larger hydroxide contribution in the exposed region. High resolution scans of iron and zirconium peaks verified the presence of both oxides and hydroxides and that hydroxides were enriched after exposure to the test solution. Iron oxides were determined to be a mixture of Fe_2O_3 and Fe_3O_4 . High resolution scans of sulfur showed that all sulfur was present as sulfate.

These AES and XPS results indicate that the improvement in corrosion properties of amorphous Fe-Zr alloys in 1N H_2SO_4 is partially due to a compositional effect in the surface region, probably caused by the loss of iron into solution. Therefore, this system's corrosion properties would be determined more by the effect of zirconium than by that of iron. This agrees with the idea expressed by Hashimoto (5) that the corrosion properties of amorphous metal-metal alloys are mainly determined by the content of the element having the higher corrosion resistance. This raises the possibility that amorphous metal-metal alloys can be selected based upon the high corrosion resistance of one member but having mechanical, physical, or other properties of the base metal.

Conclusions

The alloying of zirconium to form amorphous iron-base alloys results in significant enhancement of corrosion properties in 1N H_2SO_4 , compared to polycrystalline iron and iron-chromium alloys, as demonstrated by both anodic polarization and passivation decay. AES and XPS results show that the passivation of the amorphous alloys is due to surface enrichment of zirconium. XPS data demonstrate that the passive film is a mixture of iron and zirconium oxides and hydroxides.

The corrosion data agree with previous studies showing that the corrosion properties of metal-metal amorphous alloys are determined by the metal with the highest corrosion resistance. This is in contrast to metal-metalloid amorphous alloys, which can display significantly better corrosion resistance than any of the component elements. However, it is important to note that this does not imply that metal-metalloid amorphous alloys have superior corrosion properties compared to metal-metal amorphous alloys. The data obtained in this study showed that the amorphous Fe-Zr system has better corrosion resistance than many metal-metalloid amorphous alloys.

Manuscript submitted March 30, 1983; revised manuscript received Sept. 30, 1983.

The U.S. Department of the Interior assisted in meeting the publication costs of this article.

REFERENCES

1. M. Naka, K. Hashimoto, and T. Masumoto, *J. Jpn. Inst. Met.*, **38**, 835 (1974).
2. Y. Waseda and K. T. Aust, *J. Mater. Sci.*, **16**, 2337 (1981).
3. K. Hashimoto, K. Asami, M. Naka, and T. Masumoto, *Corros. Sci.*, **19**, 857 (1979).
4. M. Naka, K. Hashimoto, and T. Masumoto, *J. Non-Cryst. Solids*, **30**, 29 (1978).
5. K. Hashimoto, *Sci. Rep. Res. Inst. Tohoku Univ., Series A, Suppl.*, **28**, 201 (1980).
6. R. G. Walmsley, Ph.D. Dissertation, Stanford University, Stanford, CA (1981).
7. C. L. Chien and K. M. Unruh, *J. Magn. & Magn. Mater.*, **31-34**, 1587 (1983).
8. M. Ghafari, U. Gonser, H. G. Wagner, and N. Naka, *Nucl. Instrum. Methods*, **199**, 197 (1982).
9. N. D. Greene, NASA report no. AD 609718 (1965).
10. "Conventions Applicable to Electrochemical Measurements in Corrosion Testing," Section G-3, p. 884, and "Standard Reference Method for Making Potentiostatic and Potentiodynamic Anodic Polarization Measurements," Section G-10, p. 906, Part 10, American Society for Testing and Materials, Philadelphia, PA (1982).
11. N. D. Greene, *Corrosion*, **18**, 136t (1962).

Multivalent Ions in the Electrical Double Layer: The Extended Mean Spherical Approximation

C. J. McClanahan and D. A. McQuarrie

Department of Chemistry, University of California, Davis, California 95616

ABSTRACT

An extension of the mean spherical approximation, MSA, is used to study the restricted primitive model of the electrical double layer involving multivalent ions. Comparisons are made between this approximation, the MSA, and the Poisson-Boltzmann approximation.

The electrical double layer is prevalent in a large variety of systems of interest in chemistry and biology. It also plays an important role in many technological processes. In many instances, the ionic solutions contain multivalent ions which very significantly effect the behavior of these systems. Of these multivalent ion solutions, those containing a mixture of divalent and monovalent ions are the most commonly found in double layer systems.

Recently, the statistical mechanical integral equations used to describe bulk ionic fluids have been applied to the planar electrical double layer. This has been done in an effort to consistently account for ion size which is not done in the simpler Poisson-Boltzmann approxi-

mation, PBA (1-3). Many of these integral equation approaches have not yet been used to study the effects of multivalent ions on the structure and thermodynamics of the double layer. There is, however, a limited amount of Monte Carlo data available (4). Here we use an extension of the mean spherical approximation, MSA, to investigate multivalent systems and compare the results with the MSA and the PBA.

Development

The wall is considered to be hard, of uniform charge density, $eE/4\pi$, and of dielectric constant ϵ . The ionic solution is modeled as a neutral mixture of charged hard spheres in a uniform medium of dielectric constant

ϵ . Note that no image or specific solvent effects are accounted for. Ions of type i are of diameter σ_i , have a valence z_i , and are of number density, ρ_i , in the bulk fluid. The wall-particle Ornstein-Zernike equation for this system is (5)

$$h_{w1}(x) = c_{w1}(x) + 2\pi \sum_j \rho_j \int_0^\infty dt c_{ij}(t) \int_{x-t}^{x+t} ds h_{wj}(s) \quad [1]$$

where $h_{w1}(x)$ is the wall-particle indirect correlation function, in which x is the distance from the wall to the particle. $h_{w1}(x)$ is related to the wall particle correlation function, $g_{w1}(x)$, by

$$h_{w1}(x) = g_{w1}(x) - 1 \quad [2]$$

The function $c_{ij}(t)$ is the bulk direct correlation function for ion pairs i, j . A closure relation and specification of $c_{ij}(t)$ is required before Eq. [1] can be solved for $h_{w1}(x)$. In the approximations considered here, the bulk MSA direct correlation function is used for $c_{ij}(t)$. The MSA for the wall particle correlation functions involves setting

$$h_{wj}(x) = -1 \quad x < \sigma_j/2 \quad [3]$$

$$c_{wj}(x) = -z_j \beta e E x \quad x > \sigma_j/2 \quad [4]$$

where e is the magnitude of elementary charge and $\beta = 1/kT$ with k being the Boltzmann constant and T the temperature. Blum has solved Eq. [1] in this approximation using the Wiener-Hopf technique as applied by Baxter (5, 6). The solution is in terms of the factor-correlation functions for the corresponding bulk problem. It leads to analytic expressions for both the correlation functions and the potential drop across the interface. The MSA is a linearized theory and is only applicable at small electric fields. It is very desirable to develop a theory which would describe the interface at higher electric fields yet would not have to be solved numerically. One possibility is to try to improve the wall-particle direct correlation function by adding to it a sum of parameterized exponentials, i.e., setting

$$c_{wj}(x) = -z_j \beta e E x + \sum_n A_{nj} \exp(-\mu_{nj} x) \quad [5]$$

where the A_{nj} and μ_{nj} are parameters to be determined by some means. We now turn to solving Eq. [1] using Eq. [3] and [5] as closure relations and return to the problem of determining the A_{nj} and μ_{nj} .

The method of solving the extended mean spherical approximation, EMSA, has been briefly given by Blum and Henderson (7). It is quite similar to Blum's solution of the MSA. For completeness and to aid in understanding the application of the MSA to multivalent ionic solutions, we present a condensed derivation of the solution.

To aid in the analysis, we introduce the short range functions $c_{ij}^o(r)$ and $c_{w1}^o(x)$ defined by

$$c_{ij}(r) = c_{ij}^o(r) - \beta \frac{z_i z_j e^2}{\epsilon r} \quad [6]$$

and

$$c_{w1}(x) = c_{w1}^o(x) - \phi_{w1}(x) \quad [7]$$

where in the EMSA

$$\phi_{w1}(x) = -z_1 \beta e E x + \sum_n A_{n1} \exp(-\mu_{n1} x) \quad [8]$$

Multiplying Eq. [1] by $\sqrt{\rho_1}$, taking the Fourier transform, and using Eq. [6] and [7] gives

$$\tilde{h}_w(k) [I - \tilde{c}(k)] = \tilde{c}_w^o(k) - \tilde{\phi}(k) \quad [9]$$

where the matrices are defined by the components

$$\tilde{h}_{w1}(k) = \sqrt{\rho_1} \int_{-\infty}^{\infty} dx e^{ikx} h_{w1}(x) \quad [10]$$

$$\tilde{c}_{w1}^o(k) = \sqrt{\rho_1} \int_{-\infty}^{\sigma_1/2} dx e^{ikx} c_{w1}^o(x) \quad [11]$$

$$\phi_{w1}(k) = \sqrt{\rho_1} \int_{\sigma_1/2}^{\infty} dx e^{ikx} \phi_{w1}(x) \quad [12]$$

$$\tilde{c}_{ij}(k) = \lim_{\mu \rightarrow 0} \frac{4\pi\sqrt{\rho_i\rho_j}}{k} \int_{-\infty}^{\infty} dr r (\sin kr) c_{ij}^o(r) - D_{ij}/(k^2 + \mu^2) \quad [13]$$

where

$$D_{ij} = z_i z_j \alpha^2 \quad [14]$$

and

$$\alpha^2 = 4\pi\beta e^2/\epsilon \quad [15]$$

Blum has argued that via the Weiner-Hopf technique the bracketed term in Eq. [9] can be factored, i.e.

$$[I - \tilde{c}(k)] = Q(k) Q^T(-k) \quad [16]$$

where the superscript T denotes transpose. The factor correlation functions are defined by

$$Q_{ij}(k) = \delta_{ij} - \sqrt{\rho_i\rho_j} \int_{\lambda_{ij}}^{\infty} dr e^{ikr} Q_{ij}(r) \quad [17]$$

where

$$\lambda_{ij} = (\sigma_i - \sigma_j)/2 \quad [19]$$

By combining Eq. [9] and [16], we obtain

$$\tilde{h}_w(k) \tilde{Q}(k) = [\tilde{c}_w^o(k) - \tilde{\phi}_w(k)] \{\tilde{Q}^T(-k)\}^{-1} \quad [20]$$

Fourier inverting Eq. [20] for $x > \sigma_1/2$ yields

$$\begin{aligned} \sqrt{\rho_1} h_{w1}(x) - \sum_k \sqrt{\rho_k\rho_1} \int_{\lambda_{k1}}^{\infty} dr h_{wk}(x-r) Q_{k1}(r) \\ = - \sum_k \sqrt{\rho_1} \int_{\sigma_k/2}^{\infty} dr \phi_{wh} P_{kj}(r-x) \end{aligned} \quad [21]$$

where

$$P_{kj}(z) = \frac{1}{2\pi} \sqrt{\frac{\rho_k}{\rho_1}} \int_{-\infty}^{\infty} dk e^{-ikz} \{\tilde{Q}^T(-k)\}_{kj}^{-1} \quad [22]$$

The $c_{wk}^o(k)$ term gives no contribution to this inverse since it is a bounded function without singularities in

the complex half-plane, $Imk < \delta$, where $\tilde{Q}^T(-k)$ is also nonsingular. A contour around the lower complex plane may be used to show that the term vanishes. Dividing Eq. [21] by $\sqrt{\rho_1}$ and using Eq. [2] and [3] it may be rewritten as

$$\begin{aligned} g_{w1}(x) - \sum_k \rho_k \int_{\lambda_{k1}}^{x-\sigma_k/2} dr g_{wk}(x-r) Q_{k1}(r) = 1 \\ - \sum_k \rho_k \int_{\lambda_{k1}}^{\infty} Q_{k1}(r) dr \\ - \sum \sqrt{\frac{\rho_k}{\rho_1}} \int_{\sigma_1/2}^{\infty} dr \phi_{wk} P_{k1}(r-x) \end{aligned} \quad [23]$$

The Laplace transform of Eq. [23] is

$$\begin{aligned} \tilde{g}_{w1}(s) = \sum_{jk} e^{-s\sigma_j/2} \tilde{Q}_{kj}(0) \tilde{Q}_{j1}(s)/s \\ - \sum_j e^{-s\sigma_j/2} F_j(s) \tilde{Q}_{j1}^{-1}(s) \end{aligned} \quad [24]$$

where

$$\tilde{F}_j(s) = \int_0^{\infty} dx e^{-sx} \int_{\sigma_1/2}^{\infty} dr \phi_{wh}(r) P_{kj}(r-x) \quad [25]$$

and

$$\tilde{Q}(s)_{ij} = \delta_{ij} - \rho_i \int dx e^{-sx} Q_{ij}(r) \quad [26]$$

In his careful analysis of the solution of the MSA for the bulk system (8, 9), Blum has derived explicit expressions for $\tilde{Q}(s)_{ij}$ and its inverse. For the case of similar size ions

$$\tilde{Q}_{ij}^{-1}(s) = \delta_{ij} + \frac{\rho_i}{\rho} \tilde{P}^o(s) + \frac{z_i \rho_i z_j}{\xi} \tilde{P}^\pm(s) \quad [27]$$

where $\rho = \sum \rho_i$ and $\xi = \sum z_i^2 \rho_i$. $\tilde{P}^o(s)$ is the hard core portion given by

$$1 + \tilde{P}^o(s) = \frac{(1 - \eta)^2 s^3 e^{s\sigma}}{12\eta L(s) + S(s) e^{s\sigma}} \quad [28]$$

with

$$L(s) = \left(1 + \frac{1}{2}\eta\right)s + 1 + 2\eta \quad [29]$$

$$S(s) = (1 - \eta)^2 s^3 + 6\eta(1 - \eta)s^2 + 18\eta^2 s - 12\eta(1 + 2\eta) \quad [30]$$

and $\eta = \rho\sigma^3/6$. The charge portion is defined by

$$1 + \tilde{P}^\pm(s) = \frac{s^2}{s^2 + 2\Gamma s + 2\Gamma^2(1 - e^{-s\sigma})} \quad [31]$$

where

$$2\sigma\Gamma = \sqrt{1 + 2\sigma\kappa} - 1 \quad [32]$$

and

$$\kappa^2 = \alpha^2 \xi \quad [33]$$

Before we can invert Eq. [24] to obtain $g_{wi}(x)$, a suitable expression for $\tilde{F}_j(s)$ (Eq. [25]) is needed. This in turn requires an expression for $\tilde{P}_{ij}(k) = \sqrt{\rho_i/\rho_j} \{\tilde{Q}^T(-k)\}_{ij}^{-1}$ where $\tilde{Q}_{ij}(k)$ is given in Eq. [17]. Noting that

$$\tilde{Q}_{ij}(-is) = \sqrt{\frac{1}{\rho_i}} \tilde{Q}_{ij}(s) \sqrt{\rho_j} \quad [34]$$

where $\tilde{Q}(s)$ is given in Eq. [27], we have

$$\begin{aligned} \tilde{P}(-is)_{ij} &= \sqrt{\frac{\rho_i}{\rho_j}} \{\tilde{Q}^T(-is)\}_{ij}^{-1} \\ &= \sqrt{\frac{\rho_i}{\rho_j}} \left\{ \sqrt{\frac{1}{\rho_i}} \tilde{Q}_{ij}^{-1}(s) \sqrt{\rho_j} \right\}^T \\ &= \delta_{ij} + \frac{\rho_i}{\rho} \tilde{P}^o(s) + \frac{z_i \rho_i z_j}{\xi} \tilde{P}^\pm(s) \quad [35] \end{aligned}$$

Now since $P_{ij}(x) = 0$ for $x < \sigma/2$, inverting Eq. [25] and changing variables gives

$$F_j(x) = \sqrt{\frac{\rho_k}{\rho_j}} \int_0^\infty dr' \phi_{wk}(x+r') P_{kj}(r') \quad [36]$$

Using Eq. [8] in [36] yields

$$\begin{aligned} F_j(x) &= \sum_k \sqrt{\frac{\rho_k}{\rho_j}} z_k \beta e E \int_0^\infty dr' (x+r') P_{kj}(r') \\ &+ \sum_{k,n} \sqrt{\frac{\rho_k}{\rho_j}} A_{nk} \int_0^\infty dr' e^{-\mu_{nk}(x+r')} P_{kj}(r') \\ &= -\lim_{s \rightarrow 0} \beta e E \sum_k \sqrt{\frac{\rho_k}{\rho_j}} z_k \left(x - \frac{\partial}{\partial s} \right) \tilde{P}_{kj}(s) \\ &+ \sum_{k,n} \sqrt{\frac{\rho_k}{\rho_j}} A_{nk} e^{-\mu_{nk}x} P_{kj}(\mu_{nk}) \quad [37] \end{aligned}$$

where

$$\tilde{P}_{kj}(s) = \int_0^\infty dr e^{-sr} P_{kj}(r) \quad [38]$$

With the use of Eq. [35] and [28]-[33], it can be shown that

$$\lim_{s \rightarrow 0} \sum_k z_k \tilde{P}_{kj}(s) = 0 \quad [39]$$

and

$$\lim_{s \rightarrow 0} -\frac{\partial}{\partial s} \sum_k z_k \tilde{P}_{kj}(s) = -z_j/\kappa \quad [40]$$

Thus

$$\begin{aligned} F_j(x) &= -z_j \beta e E x / \kappa \\ &+ \sum_{k,n} \sqrt{\frac{\rho_k}{\rho_j}} A_{nk} \tilde{P}_{kj}(\mu_{nk}) e^{-\sigma/2/(s + \mu_{nk})} \quad [41] \end{aligned}$$

or

$$\begin{aligned} \tilde{F}_j(s) &= -z_j \beta e E e^{-s\sigma/2} / \kappa s \\ &+ \sqrt{\frac{\rho_k}{\rho_j}} A_{nk} \tilde{P}_{kj}(\mu_{nk}) e^{-\sigma/2(s + \mu_{nk})} / (s + \mu_{nk}) \quad [42] \end{aligned}$$

Equation [42] combined with Eq. [24] is essentially the solution to the problem. All that is required is the Laplace inverse of this expression. Analytic expressions have been derived for the inverses of $\tilde{P}^o(s)$ and $\tilde{P}^\pm(s)$ (10). The EMSA solution simply involves these expressions and their convolutions with an exponential function.

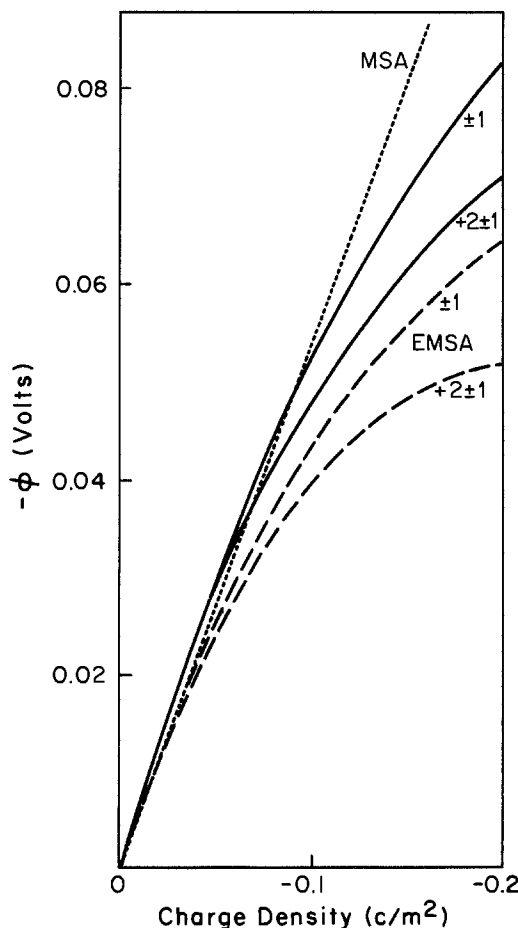


Fig. 1. Diffuse layer potential as a function of charge density on the wall for ± 1 and $+2 \pm 1$ electrolyte solutions of the same ionic strength with $\sigma = 0.425$ nm, $T = 298$ K, $\epsilon = 78.5$, and $\sigma\kappa = 0.9877$. The concentration of the ± 1 solution is 0.5M. The solid curves mark the PBA results and the broken curves mark the MSA and EMSA results as labeled.

By choosing the parameters in Eq. [8] such that

$$\sum_i z_i \rho_i \phi_{wi}(x) = -\xi \beta e E x + \xi \sum_n B_n e^{-\nu_n x} \quad [43]$$

and

$$\sum_i \rho_i \phi_{wi}(x) = \rho \sum_n A_n e^{-\mu_n x} \quad [44]$$

where A_n, B_n, μ_n, ν_n are the EMSA parameters, the solution is greatly simplified. In this instance, the local net charge density is given by

$$\sum_i z_i \rho_i g_{wi}(x) = \xi \left[b + \sum_n B'_n \right] F(x) - \sum_n \nu_n B'_n \int_0^x \exp[-\nu_n(x-t)] F(t) dt \quad [45]$$

where $F(x)$ is the Laplace inverse of $[1 + \tilde{P}(s)]/s$, $B'_n = B_n[1 + \tilde{P}^\pm(\nu_n)]$, and $b = \beta e E/k$. The total local number density is

$$\sum_i \rho_i g_{wi}(x) = \rho \left[1 + \frac{(1-\eta)^2}{1+2\eta} A'_n \right] g_o(x) - \frac{(1-\eta)^2}{1+2\eta} \sum_n \mu_n A'_n \int_0^x \exp[-\mu_n(x-t)] g_o(t) dt \quad [46]$$

where $g_o(t)$ is the inverse of $(1+2\eta)[1 + \tilde{P}^o(s)]/s(1-\eta)^2$; that is, the distribution function for hard

spheres near a hard wall and $A'_n = A_n[1 + \tilde{P}^o(\mu_n)]$. For Eq. [45] and [46] the values at contact are

$$\sum_i z_i \rho_i g_{wi}(\sigma/2) = \xi \left[b + \sum_n B_n \right] \quad [47]$$

$$\sum_i \rho_i g_{wi}(\sigma/2) = \rho \left[\frac{1+2\eta}{(1-\eta)^2} + \sum_n A_n \right] \quad [48]$$

The diffuse layer potential is

$$\phi = \frac{4\pi e}{\epsilon} \sum_i z_i \rho_i \int_0^\infty g_{wi}(x) dx \quad [49]$$

$$= \frac{b(1-\sigma^2\Gamma^2)}{\kappa^2} - \frac{4\pi\xi}{\epsilon\kappa} \sum_n \frac{B_n}{\nu_n} \quad [50]$$

Note that the first term in each of these expressions corresponds to the MSA solution of this problem.

Now we can return to the question of how to determine the parameters used in the EMSA. Several different approaches have been used for the symmetric electrolyte case. These can roughly be grouped into two categories; one in which the parameters are used to cause the results to agree with theoretical constraints or with specific results from other approximations and the other in which Eq. [8] is fitted to a reasonable approximation for the direct correlation function. In the case of a mixture of divalent and monovalent ions, there are usually too many parameters for the first type approach to be used. The second approach is actually an adaptation of the EMSA used in describing bulk ionic systems. An approximate $\phi_{wi}(x)$ is obtained by using a hypernetted chain, HNC, type closure relation

$$\phi_{wi}(x) = -\beta e E x + g_{wi}(x) - 1 - \ln [g_{wi}(x)] \quad [51]$$

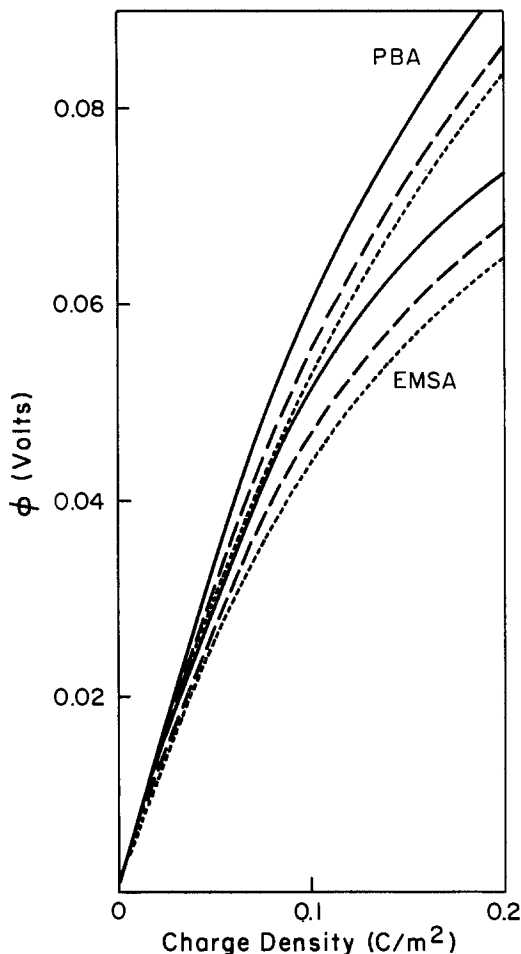


Fig. 2. Diffuse layer potential as a function of charge density for a positively charged wall. The results for the ± 1 (dotted line), $+2-1$ (solid line), and $+2\pm 1$ (dashed line) cases are given. The PBA and EMSA results are the upper and lower set of curves as labeled. The model parameters are listed in Fig. 1.

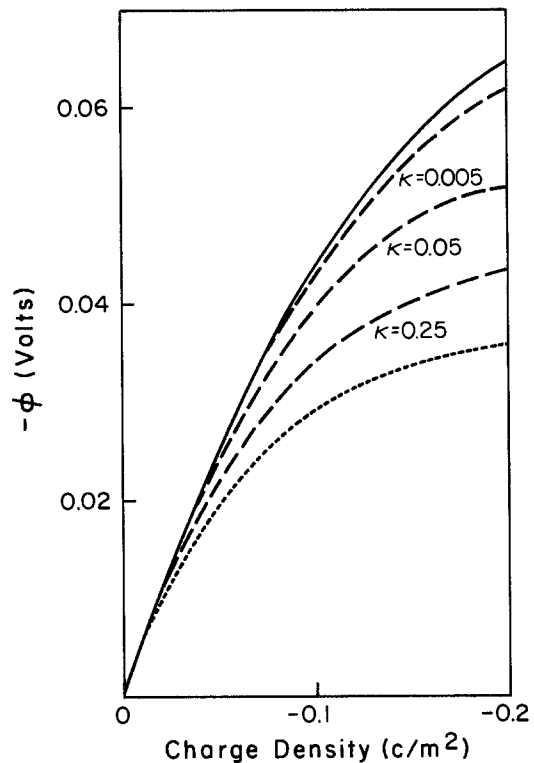


Fig. 3. Diffuse layer potential as a function of charge density on the wall demonstrating how it varies with the amount of divalent cations present. These results are for the EMSA. The solutions have the same ionic strength. The curves for $+2\pm 1$ cases are labeled by the ratio of $+2$ to $+1$ ions, $k = 0.005$, $k = 0.05$, and $k = 0.25$. ± 1 case (solid line), $\pm 2-1$ case (dotted line). The model parameters are listed in Fig. 1.

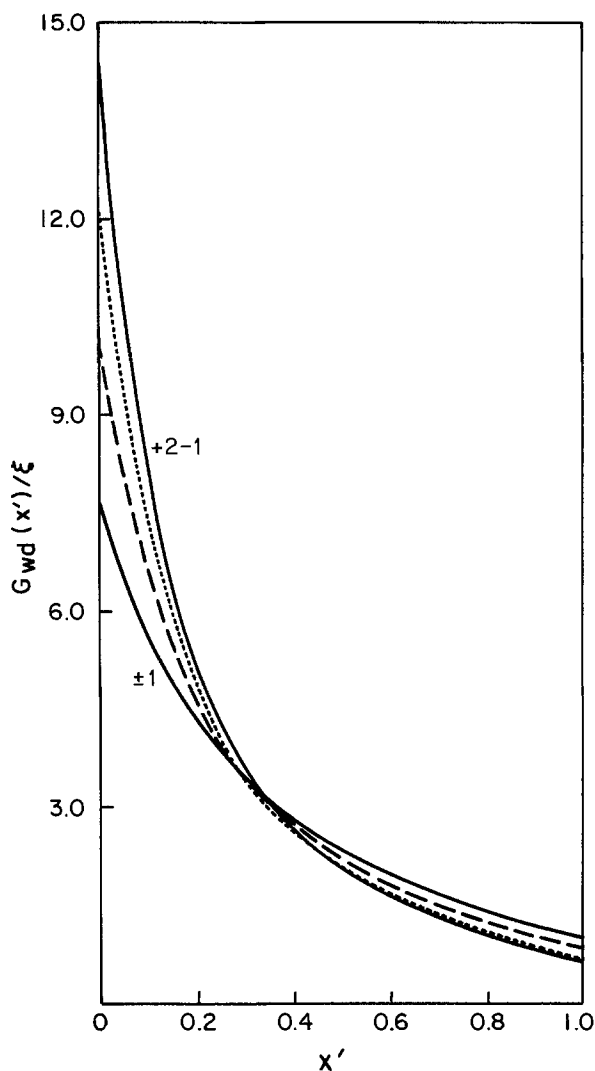


Fig. 4. Reduced net charge density as a function of distance demonstrating how it varies with the amount of divalent cations present. In all cases, $\sigma\kappa = 0.9877$, and the other model parameters are listed in Fig. 1. The wall has a charge density of -0.15 C/m^2 . $G_{wd}(x')$ and x' are defined in Fig. 5 and $\xi = \sum z_i^2 \rho_i$. The solid curves give the results for the ± 1 and $+2-1$ cases as labeled. The results for the $+2\pm 1$ case with divalent to monovalent cation density ratios of $k = 0.25$ (dotted line) and $k = 0.05$ (dashed line) are given.

with an approximate $g_{wi}(x)$. The analogy to the method of Medina-Noyola *et al.* (11) would be to use

$$g_{wi}(x) = \exp(-z_i b e^{-\kappa x}) \quad [52]$$

Another possibility, in hopes of obtaining better results at higher electric fields, would be to use the appropriate $g_{wi}(x)$ from the PBA using a Stern type layer to account for ion size (12). With the $g_{wi}(x)$ chosen, the parameters of the EMSA can easily be determined by a curve fitting procedure.

Results

One of the most important quantities associated with the electrical double layer is the potential drop across the interface. It was found that use of Eq. [52] in Eq. [51] leads to unrealistic results for the diffuse layer potential except at low surface charge densities. Therefore, the appropriate PBA $g_{wi}(x)$ was used in Eq. [51] and much more reasonable results were obtained. Figures 1-3 show these results. In most instances, only two exponential terms or four parameters were used in Eq. [8]. The general trend is for the EMSA to predict a diffuse layer potential of lower

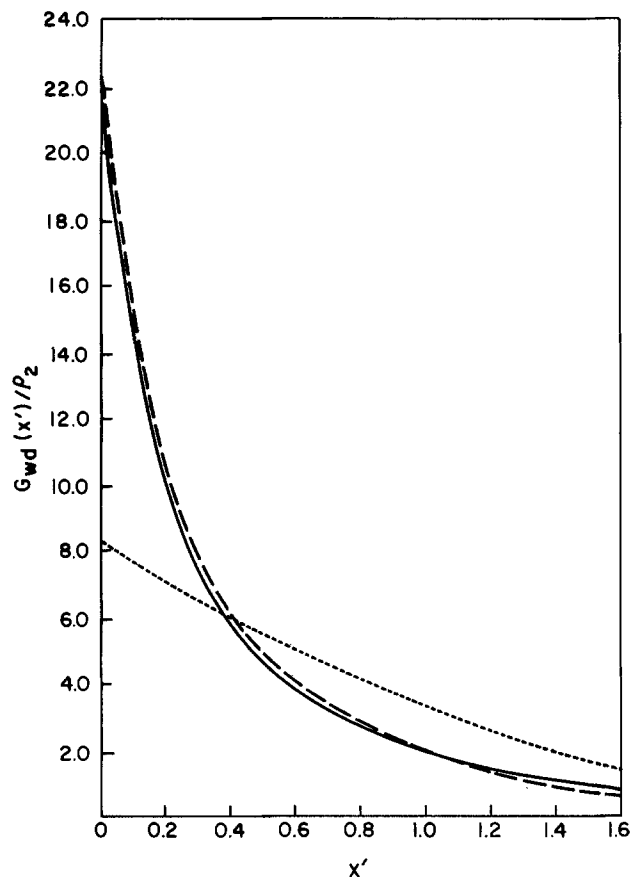


Fig. 5. Plot of the reduced net charge density vs. distance for the $+2\pm 1$ case. Here $x' = x/\sigma - 0.5$ where x is the distance measured from the wall. $G_{wd}(x')/\rho_2 = \sum g_{wi}(x')/\rho_2$ where ρ_2 is the bulk density of the $+1$ ion. The ratio of $+2$ to $+1$ ions is 0.05 and $\sigma\kappa = 0.9877$. The model parameters are listed in Fig. 1. The wall has a charge density of -0.15 C/m^2 . PBA (solid line), EMSA (dashed line), and MSA (dotted line).

magnitude than the PBA, the difference increasing with the absolute value of the charge density. This trend is consistent with the Monte Carlo and HNC results for the ± 1 ion case (12, 13). The relative positioning of the curves in the EMSA for the different cases such as ± 1 , $+2-1$, and $+2\pm 1$ is the same as in the PBA. Note that the EMSA diffuse layer potential is much more realistic than the linear MSA result. Figure 3 shows that the magnitude of the diffuse layer potential decreases with an increase in the relative amount of divalent cations at constant ionic strength. This is due to the ability of the divalent ions to screen the charged wall more effectively than the monovalent ions.

The structure of the interface appears to be similar to that predicted by the PBA. Figures 4 and 5 show typical distributions of reduced net charge densities. The EMSA can be seen to be a great improvement over the MSA in this regard.

Although not shown in Fig. 1-5 the agreement of EMSA and PB with Monte Carlo data is quite good (13). There are no MC data for 2-1-1 systems, but Fig. 6 shows the reduced electrostatic potential $e\phi/kT$ as a function of distance from the wall for a 2-1 electrolyte for a negatively charged wall. This system has been shown to have a great discrepancy between PB and Monte Carlo data (14). Most unusual is the dip in the potential near the wall as predicted by the Monte Carlo data; the potential actually becomes negative. The EMSA demonstrates this same behavior even though the Poisson-Boltzmann wall particle correlation functions are used for input in the direct

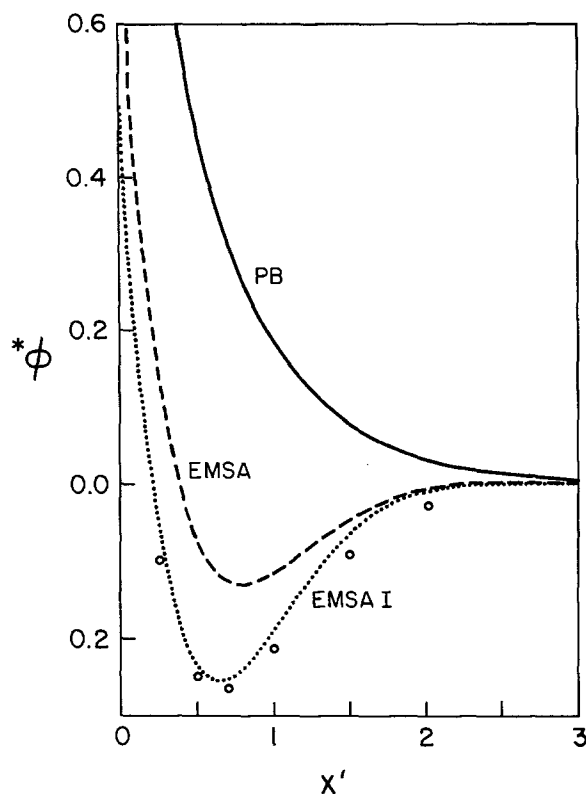


Fig. 6. Reduced electrostatic potential as a function of distance from the wall for a +2-1 electrolyte. The divalent ion has a concentration of 0.5M and the surface charge density is -0.1512 C/m^2 .

correlation function. In an effort to try to improve the EMSA results, the $g_{wi}(x)$ obtained from the EMSA were used in Eq. [51] in place of the Poisson-Boltzmann distribution functions. This new direct correlation function was then used to obtain new $g_{wi}(x)$. The procedure was carried out twice and the results are labeled EMSAI in Fig. 6. This demonstrates a possible way of improving the EMSA.

The explanation for the dip in the $\phi(x)$ curves is pictured in Fig. 7. Here the EMSAI ion distributions are seen to oscillate about their bulk value of 1, causing the potential to change signs. This prediction of a counterion concentration less than the bulk value is very unusual. Such oscillations cannot be predicted by the PBA. The EMSAI ion distributions are nearly identical to the Monte Carlo data for this case.

Summary

The EMSA is a convenient analytic approximation which describes the electrical double layer much more accurately than the MSA. Also, it can easily be applied to multivalent ionic solutions. These results demonstrate the versatility of the EMSA. However, it is difficult at the moment to assess their accuracy. The EMSA is an improvement of the MSA and appears to be quite useful in studying the electrical double layer. The procedure used here, while easy to implement, is restrictive since no size dependence is accounted for

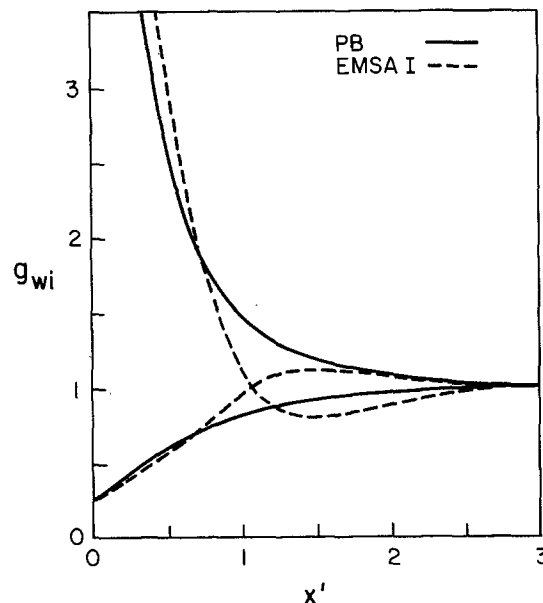


Fig. 7. The ion distributions as a function of distance from the wall a +2-1 electrolyte. The electrolyte concentration and the surface charge density are the same as in Fig. 6.

in the direct correlation function. It is very desirable to adapt approaches similar to those used for the ± 1 case (7) to these multivalent electrolyte cases or to develop new procedures which could account more consistently for size effects.

Acknowledgment

This work was supported by a grant from the National Institutes of Health, GM 26864-05.

Manuscript submitted Sept. 3, 1982; revised manuscript received June 16, 1983. This was Paper 639 presented at the Montreal, Quebec, Canada, Meeting of the Society, May 9-14, 1982.

University of California at Davis assisted in meeting the publication costs of this article.

REFERENCES

1. G. Gouy, *J. Phys.*, **9**, 457 (1910); D. L. Chapman, *Philos. Mag.*, **25**, 475 (1913).
2. D. C. Grahame, *J. Chem. Phys.*, **21**, 1054 (1953).
3. B. Abraham-Shrauner, *J. Math. Biol.*, **2**, 333 (1975).
4. I. Snook and W. van Meegen, *J. Chem. Phys.*, **74** (1981).
5. L. Blum and G. Stell, *J. Stat. Phys.*, **15**, 439 (1976).
6. L. Blum, *J. Chem. Phys.*, **70**, 136 (1977).
7. L. Blum and D. Henderson, *J. Can. Chem.*, **59**, 1906 (1981).
8. L. Blum, *Mol. Phys.*, **30**, 1529 (1975).
9. L. Blum and J. S. Høye, *J. Phys. Chem.*, **81**, 1311 (1977).
10. D. Henderson and W. R. Smith, *J. Stat. Phys.*, **19**, 191 (1978).
11. M. Medina-Noyola and D. A. McQuarrie, *J. Chem. Phys.*, **74**, 3025 (1981).
12. L. Blum, D. Henderson, D. A. McQuarrie, and W. Olivares, *Chem. Phys. Lett.*, **71**, 569 (1980).
13. G. M. Torrie and J. P. Valleau, *J. Chem. Phys.*, **73**, 5807 (1980).
14. G. M. Torrie and J. P. Valleau, *J. Phys. Chem.*, **86**, 3251 (1983).

Film Thickness Determination of PMMA on InP by Ellipsometry

Richard Scheps¹

Department of Electrical Engineering, Colorado State University, Fort Collins, Colorado 80523

ABSTRACT

The thickness of polymethylmethacrylate (PMMA) films deposited in solution on InP is measured by ellipsometry to determine its dependence on terminal spin speed. The PMMA solution behaves as a steady-state Newtonian fluid. Film thickness in excess of the periodic thickness is measured by combining data taken at three angles of incidence; a procedure for applying this technique is discussed. The main feature consists of assigning the film index from data taken at the incident angle where the ellipsometer readings are most sensitive to film index, and using this index in determining the film thickness at the other two angles. The basis supporting this procedure is presented, and the dependence of the ellipsometric model on uncertainties in the assignment of film and substrate optical constants is discussed specifically in terms of its effect on the three-angle technique.

It was recently shown (1) that the thickness of polymethylmethacrylate (PMMA) films on GaAs can be measured ellipsometrically for films as thick as 2.7μ . The sensitivity of the ellipsometric data to film index and film thickness is angle dependent, and in the course of performing film measurements on GaAs it was found that certain measurements were highly imprecise and led to large uncertainties in the film thickness. In the present work, the three sets of data are treated somewhat differently. The data set from the incident angle most sensitive to film index is used to assign the film index. This index is then used in the analysis of the other data points to obtain the film thickness. This procedure considerably simplifies the data generation and analysis tasks and results in more precise film thickness determinations.

The work that follows presents the basis for treating the data in this manner. The angle dependence of the ellipsometric sensitivity is presented for a range of dielectric films on InP, and the method for selecting the data set that determines the film index is described. The influence of uncertainties in the substrate optical constants on the accuracy of the film index and thickness is addressed, and results of film thickness ellipsometry of PMMA on InP are presented.

Theory

The model used for the representation of elliptically polarized light and the interpretation of the ellipsometric data was described in detail by McCrackin *et al.* (2). The Fortran program used in the data analysis is that described by them (2) (referred to below as MPSS) and was provided by McCrackin (3). The MPSS equations show that the ellipsometer readings are periodic in film thickness. The ellipsometer used in this work allows incident angles (ϕ) of 30° , 50° , or 70° . Using a film index of 1.49 [the index of PMMA at 632.8 nm (4)] the periodic film thicknesses (T_ϕ) are

$$\begin{aligned} T_{30} &= 225.42 \text{ nm} \\ T_{50} &= 247.58 \text{ nm} \\ T_{70} &= 273.63 \text{ nm} \end{aligned} \quad [1]$$

The film thickness d can be written as

$$d = t_\phi + n_\phi T_\phi \quad [2]$$

where t_ϕ is the "residual" thickness, that is, the film thickness less an integral multiple of T_ϕ , and n_ϕ is an integer ≥ 0 .

It has been shown for the film measurements on GaAs (1) that ellipsometric data taken at three angles of incidence uniquely determine the n_ϕ and d for thickness as great as 2.7μ . The method relies on the fact that the T_ϕ are different at each angle, and the relative magnitudes of the residual thicknesses t_ϕ are used to select the appropriate quantitative expression

to calculate the n_ϕ . A table relating the magnitudes of the residual film thickness to the expressions for n_ϕ was presented by the author (1) for films of index 1.49.

To obtain accurate film thickness values, one needs to measure the PMMA film index after deposition. However, the ellipsometer is not equally sensitive to the index at all three angles of incidence. For example, at a given angle the residual film thickness may be close to T_ϕ . In such a case the coordinates are determined by the substrate optical constants, and one could not expect to obtain film index data near T_ϕ with reasonable accuracy without an ellipsometer having high angular resolution capabilities. This suggests that a more appropriate method would be to assign the film index from data taken at the angle of incidence where the ellipsometer is most sensitive to film index. This index is then inserted into the Fortran program, and the other two data points are analyzed to determine the film thickness only. The film thickness determination is then made from the residual thicknesses using the method of the author (1) with the assigned film index. The method for determining which data set is most sensitive to film index is straightforward; it requires mapping the data points on grids where the ellipsometer readings and film optical constants are parameters. This method is illustrated below.

Experiment and Results

The ellipsometer used in the present work is a Gaertner Model L117 with a compensator fixed at $+45^\circ$. Two sets of polarizer and analyzer readings are taken at each angle of incidence, and the computer program uses the average of these two readings. The relationship between the two sets of data is

$$\begin{aligned} P1 &= P2 + 90^\circ \\ A1 &= 180^\circ - A2 \end{aligned} \quad [3]$$

where $A1$, $P1$ and $A2$, $P2$ are the first and second set of analyzer and polarizer readings, respectively. These readings are related to Δ and ψ by

$$\begin{aligned} \Delta &= 270^\circ - 2P1 \\ \psi &= A1 \end{aligned} \quad [4]$$

The ellipsometer angular resolution is 0.1° , and the re-settability was found to range from 0.1° for the 30° angle of incidence measurements to 0.5° for the 70° angle of incidence.

Prior to performing the film thickness measurements, a number of InP substrates were examined ellipsometrically to assign the optical constants. Substrates were iron doped, cut in the (100) plane, and chemomechanically polished. The surface treatment consisted of a light scrub, a 3 min etch in 10 weight percent (w/o) HIO_3 , followed by a rinse in deionized distilled water and blowing dry with dry nitrogen. Substrates treated in this manner gave reproducible optical constants.

¹ Present address: Naval Ocean Systems Center, Code 8113, San Diego, California 92152.

Key words: PMMA, InP, ellipsometry, E-beam writing.

Data on the bare substrates were taken at three angles of incidence, but the 70° data were considered the most accurate. Determination of the substrate optical constants resulted from the average of many measurements on a number of substrates taken at 70°. Figure 1 illustrates the sensitivity of Δ and ψ to changes in the optical constants at the different angles of incidence. The complex refractive index can be written as

$$n = N - ik = N(1 - iK) \quad [5]$$

where $K = k/N$. The instrumental resolution is shown in the figure, as well as the literature value (5) and experimentally determined value for the optical constants. These values are $N = 3.42$, $K = 0.0813$, and $N = 3.47 \pm 0.02$, $K = 0.13 \pm 0.01$ for the literature and experimentally determined optical constants, respectively. The figure illustrates the reason for preferring the 70° data, and also indicates that resolution or re-settability limits cannot account for the discrepancy between measured and literature values. (Note that while these limits are the same for both the polarizer and analyzer readings, the factor of 2 in Eq. [4] makes Δ twice as uncertain as ψ .)

A similar discrepancy was observed for GaAs (1), and its source remains unknown. One possible source is instrumental misalignment, which MPSS indicates is critical for accurate substrate optical constant determination (but not critical for accurate film thickness measurements). No special alignment procedures were followed in this work. A native film on the substrate is another likely possibility. InP is known (6) to develop oxide films, and no exceptional precautions

were taken to inhibit film growth. For reasons mentioned in the Theory section, the ellipsometer could not be expected to provide accurate thickness and index data for a thin native film. However, analyzing the "bare substrate" experimental data as if it were a film-covered substrate, using the literature values for the substrate optical constants, and assigning the film index arbitrarily to 1.5 results in a film thickness determination of 2.8 nm. For the subsequent film analysis, the experimentally determined optical constants were used.

Substrates prepared as above had films deposited by spinning a solution of 9 w/o 496 K PMMA in chlorobenzene for 60s. Films were then baked for 75 min at 160°C. Film thickness was generally uniform within 5% up to 0.5 nm from the sample edge.

The central issue in this work is the minimization of film thickness errors when simultaneously using data taken at different incident angles and, hence, different sensitivities. Figures 2 and 3 illustrate the variation of Δ and ψ with film thickness for the three incident angles and for a series of film indexes. The curves are shown for a complete cycle of film thickness: the Δ and ψ values repeat for films in excess of the periodic film thickness T_ϕ . The origin of each curve is given by the Δ and ψ for the bare substrate ($N = 3.47$, $K = 0.13$) and for films of thickness $n_\phi T_\phi$, as in Eq. [2].

When the film index is unknown, the steep slopes near the origin for the curves translate the uncertainty in the analyzer reading to uncertainty in the film index, and hence uncertainty in the film thickness. This thickness uncertainty is particularly large for Δ , ψ points just above the origin, where adjacent index curves have film thicknesses close to the appropriate T_ϕ . Figure 4 presents the origin region for the 50° curves in greater detail. The method used in this work to determine the film index and thickness was to map the Δ , ψ points for a given sample on curves such as those shown in Fig. 2 and 3. The film index was then assigned using the data at that incident angle where the adjacent film index curves showed the greatest separation. The other two data points were analyzed with the assigned film index, and the resulting t_ϕ give

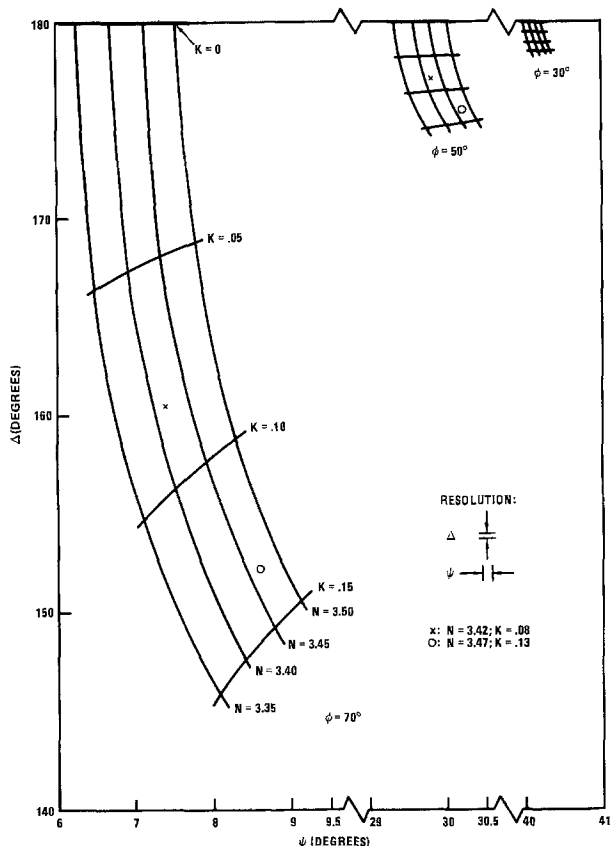


Fig. 1. Bare substrate ellipsometry coordinates for incident angles of 30°, 50°, and 70°. For each angle of incidence, a grid of substrate N and K values is used to generate corresponding Δ and ψ coordinates. The locus of Δ , ψ points for fixed N or fixed K is drawn in the figure as a vertical or horizontal line, respectively. The instrumental resolution in Δ and ψ units is shown, and the literature (x) and present work (o) values for N and K are indicated. Note breaks in horizontal scale. Grid lines at 50° and 30° are unlabeled but correspond to the 70° grid lines.

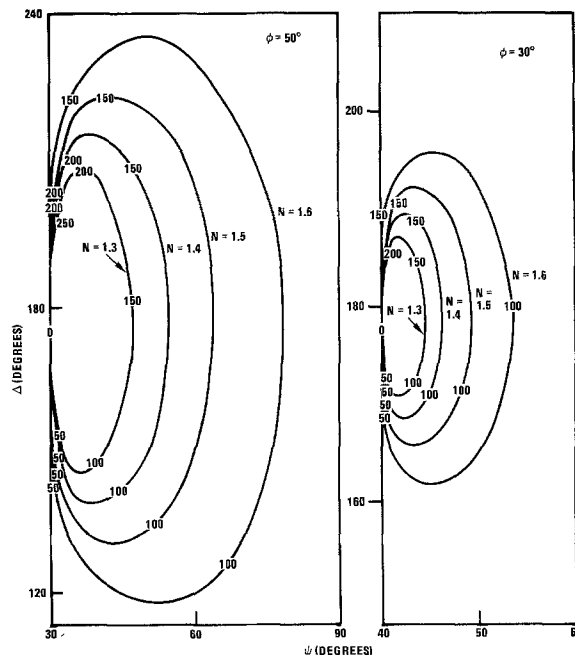


Fig. 2. Locus of Δ , ψ points for films of index N and thickness d as shown, for incident angles of 50° and 30°. Film thickness is shown directly on curves in nm. Note scale expansions for 30° curve relative to 50° (factor of 2 for both horizontal and vertical axes).

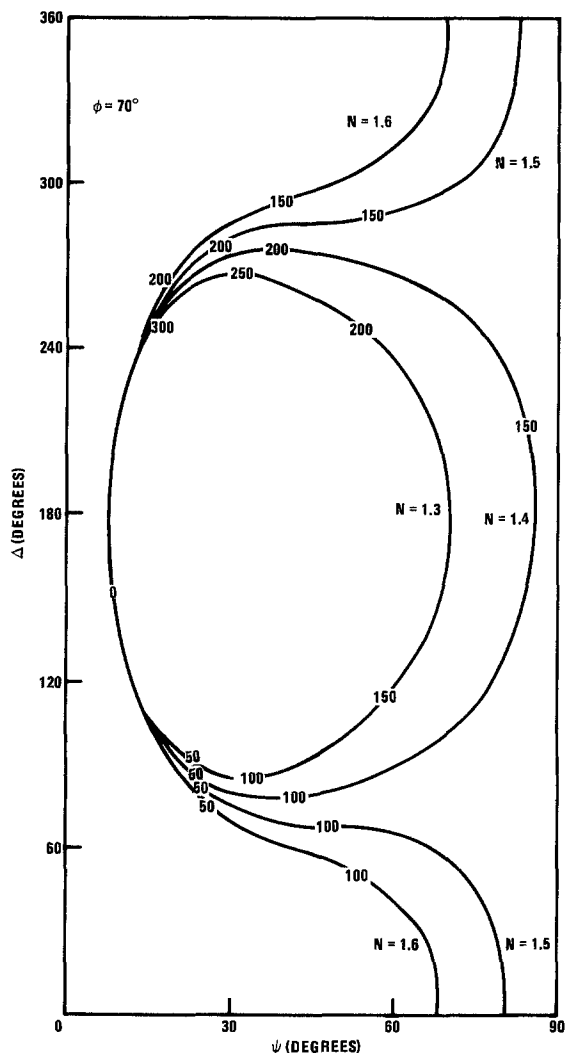


Fig. 3. Locus of Δ, ψ coordinates for films of index N and thickness d as shown, for a 70° angle of incidence. Film thickness in nm written directly on curve.

the total film thickness using the three-angle technique as described by the author (1).

The results of the film thickness vs. spin rate measurements are shown in Fig. 5. Points were taken at spin rates ranging from 2800 to 8000 rpm. The characteristic spin curve is very similar to that found for GaAs. An earlier study of the dependence of photoresist film thickness on final spin velocity (7) attempted to fit the data to an equation of the form

$$d = b\omega^n \quad [6]$$

where d is the film thickness in nm and ω is the angular velocity in 1000 rpm. The photoresists examined by O'Hagen and Daughton (7) gave angular velocity exponents in the range of -0.4 to -0.7 . The exponent for a steady-state Newtonian fluid is predicted (8) to be $-2/3$. The data for PMMA was fitted to Eq. [6] using a linear regression least squares fit and resulted in the curve

$$d = 2549.7 \omega^{-0.663} \quad [7]$$

The close agreement between the angular velocity dependent exponent in Eq. [7] and the steady-state Newtonian exponent indicate that transient effects due to solvent volatility are unimportant. Substrate type and topography also appear to have little effect on the "Newtonian-mess" of the 9% PMMA solution.

The variation in calculated film thickness as a function of substrate optical constants was measured for a range of N and K chosen to be symmetric about the value used in this work and include the literature

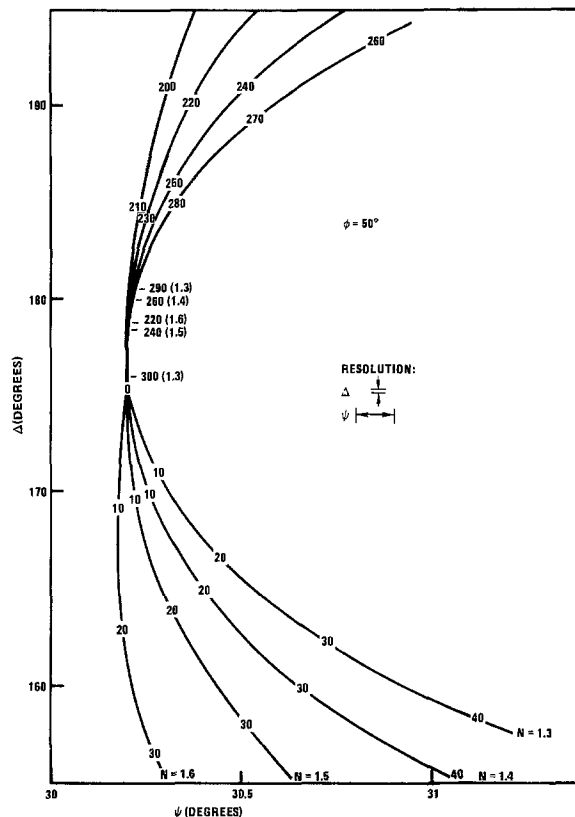


Fig. 4. Detail of 50° curves in Fig. 2; d in nm and N as labeled. Near $\Delta = 180^\circ$ film thickness points are labeled with the corresponding film index in parentheses. Note scale difference between ordinate and abscissa.

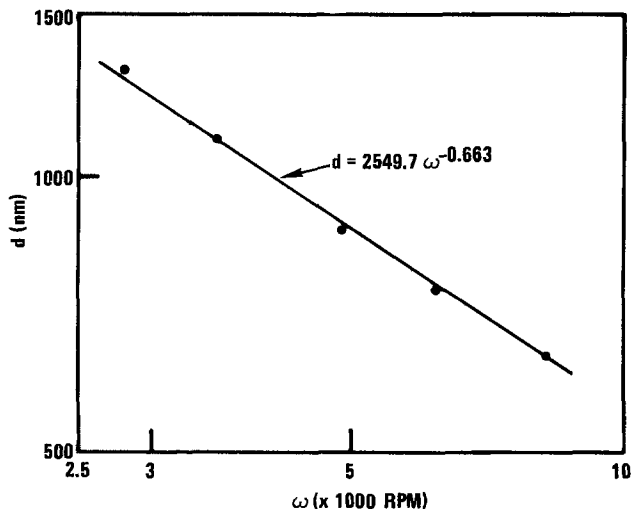


Fig. 5. Film thickness as a function of terminal spin speed for a solution of 9% PMMA in chlorobenzene. Dots are data points, line is least squares fit to data.

value at the limit. Calculations at all three angles of incidence showed the range of film thickness to lie between 1 and 3 nm of the value obtained with $N = 3.47, K = 0.13$ when the film index was fixed at 1.49. In cases where the film index is unknown, the film thickness uncertainty for the same range of substrate optical constants is generally larger. A variational computation was performed in which the Fortran program was required to find both the film thickness and index as the substrate parameters were varied. For Δ, ψ coordinates near $t_\phi = 100$ nm, the range of substrate parameters produced film indexes of 1.49 ± 0.1 . Film thickness variations were similar in magnitude to those found when the film index was fixed. Over the thick-

ness range $50 \text{ nm} \leq t_{\phi} \leq (T_{\phi} - 50 \text{ nm})$ and the same range of substrate optical constants, the film index variation is larger and ranged from between 1.45 and 1.53 at 30° to between 1.44 and 1.55 at 70° . The corresponding film thickness variations were within $\pm 5 \text{ nm}$ in all cases, except for the 70° point at 200 nm , which showed a variation of 15 nm . In evaluating the effects of substrate optical constants on film thickness accuracy, it should be recognized that the range of substrate parameters used for the variational calculations is much greater than the experimental uncertainty of the bare substrate ellipsometry, and for the results presented for PMMA on InP there is little impact of the substrate parameter uncertainty on film index and thickness.

Conclusion

The technique of assigning the film index from ellipsometric data taken at one angle of incidence reduces the inaccuracies involved in using the three-angle technique for measuring film thickness. The ellipsometric sensitivity to film thickness at three angles of incidence is discussed for the case where the film index is known, as well as for the case where the film index must be determined. This leads to a graphical evaluative technique to assess the most favorable data with which to assign the film index, and allows one to assess the expected accuracy of the results. Uncertainties in assigning the substrate optical constants are seen to have only a small effect on the film thickness accuracy when the film index is known, but may be larger when the substrate parameter uncertainty is large and the film index is unknown. Results of the

film thickness dependence on spin rate are given for PMMA on InP, and it is concluded that the film thickness varies inversely as the $2/3$ power of the terminal spin speed.

Acknowledgment

The author wishes to acknowledge the support of Professors Ferry and Wilmsen at Colorado State University, and to thank Dr. A. K. Nedoluha at the Naval Ocean Systems Center for providing the facilities required to conduct this investigation. This work was funded by the Office of Naval Research.

Manuscript submitted April 13, 1983; revised manuscript received Sept. 9, 1983.

REFERENCES

1. R. Scheps, *This Journal*, **129**, 2273 (1982).
2. F. L. McCrackin, E. Passaglia, R. R. Stromberg, and H. L. Steinberg, *J. Res. Nat. Bur. Stand. Sect. A*, **67**, 363 (1963).
3. F. L. McCrackin, Personal communication.
4. L. Levi, "Applied Optics," Vol. 2, p. 918, John Wiley and Sons, New York (1980).
5. B. O. Seraphin and H. E. Bennet, in "Semiconductors and Semimetals," Vol. 3, R. K. Willardson and A. C. Beer, Editors, p. 530, Academic Press, New York (1967).
6. J. F. Wager, C. W. Wilmsen, and L. L. Kazmerski, Results presented at the 10th Annual Conference on Physics and Chemistry of Semiconductor Interfaces (PCSI-10), Santa Fe, NM (January 1983).
7. P. O'Hagan and W. J. Daughton, Kodak Publication No. G-48, Rochester, NY (1978).
8. B. D. Washo, *IBM J. Res. Dev.*, **21**, 190 (1977).

Relationships among Electrochemical, Thermodynamic, and Oxygen Potential Quantities in Lithium-Transition Metal-Oxygen Molten Salt Cells

N. A. Godshall,^{*,1} I. D. Raistrick,* and R. A. Huggins*

Department of Materials Science and Engineering, Stanford University, Stanford, California 94305

ABSTRACT

The interdependence of thermodynamic parameters, phase equilibria, and electrochemical measurements can be used as a powerful tool in the development of high specific energy cells. These principles were used in the analysis of electrochemical experiments performed on ternary lithium-transition metal-oxide ($M = \text{Mn, Fe, and Co}$) positive electrodes. The free energies of formation of LiMnO_2 , Li_2FeO_4 , LiFeO_2 , and LiCoO_2 were found to be -178.21 , -399.88 , -154.18 , and -131.62 kcal/mol at 400°C . The electrochemical displacement reactions were found to be reversible in LiCl/KCl molten salt cells over a range of 0.0 - 3.0 Li equivalents per mol at current densities of 5 - 15 mA/cm^2 . The equilibrium potential vs. Li was found to be a logarithmic function of the calculated oxygen partial pressure for any tie triangle in which Li_2O is present, or for any tie triangle containing ternary oxide phases Li_xMO_y , which are only marginally stable with respect to Li_2O and the relevant binary oxides MO_y . Compounds with oxygen partial pressures above 10^{-25} atm were found to be unstable in LiCl/KCl electrolyte at 400°C .

The reversible work ΔG_r of a secondary electrochemical cell is directly related to its equilibrium potential-composition (E - x) curve

$$\Delta G_r = -zF \int_0^x E dx \quad [1]$$

The total free energy change in the electrochemical reaction therefore represents the integral of the equilibrium potential curve (1, 2). That is, the computed ΔG_r of a given reaction represents the area under the curve, but by itself, says nothing of the shape of the curve.

The free energy change of the electrochemical reaction can be written as

$$\Delta G_r = \Delta G^{\circ}_f(\text{Products}) - \Delta G^{\circ}_f(\text{Reactants}) \quad [2]$$

That is, the available energy stored in a cell is limited by the difference between the free energy of formation ΔG°_f of reactants and products. Therefore a high energy cell is the result of formation of very stable products from very unstable reactants. Furthermore since the ultimate choice of stable products is limited (e.g., Li_2O in the case of lithium-based systems, and elements such as Fe), the search for high energy cells must focus primarily on the search for relatively unstable reactant materials.

* Electrochemical Society Active Member.

¹ Present address: Altus Corporation, San Jose, California 95112.

Key words: ternary, lithium, oxides, phases, equilibria.

Phase equilibria within a multicomponent system are determined by the thermodynamic state of lowest free energy. This thermodynamic state can be monitored by reversible (open-circuit) electrochemical measurements, which thereby yield phase equilibria information. Conversely, a knowledge of the phase equilibria in a system affords a direct means of calculation of electrode capacity (number of equivalents per mol of reactant) in an electrochemical system, while thermodynamic data can be used to predict the reversible voltage.

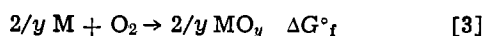
The overall composition of a ternary positive electrode material Li_xMO_y will, in general, pass through one-, two-, and three-phase regions of a ternary phase diagram as lithium is added to it in an electrochemical cell. One-phase and two-phase equilibrium in a ternary system at constant temperature and pressure have nonzero degrees of freedom ($F = 2$ and $F = 1$, respectively), so that both the composition of one or more phases, and the reversible potential of the cell vary with Li composition (x). Solid-solution electrodes such as TiS_2 and NbSe_2 are examples of single-phase electrodes (3).

Not until three phases coexist in equilibrium at constant temperature and pressure, is a ternary system truly invariant ($F = 0$). The resulting region of phase equilibrium in a ternary phase diagram must have the shape of a triangle. The Gibbs phase rule for an isothermal isobaric ternary system dictates that an area bounded by four or more sides violates thermodynamic equilibrium. The reversible potential vs. Li will be the same for any composition lying within a three-phase tie triangle. An electrochemical titration resulting in a change in the overall composition within the same tie triangle involves only changes in the amounts of the three phases present, not in their compositions, and is known as a displacement reaction. In general, displacement-reaction electrodes contain as many phases (P) as they contain components (C), so that electrochemical cells containing them yield constant voltage plateaus. This is different from solid-solution electrodes, where the potential varies with composition, even under conditions of zero current flow.

Equilibrium Oxygen Partial Pressure Calculations

Free energy calculations based on Eq. [1] and [2] predict that many binary and ternary transition metal oxides should yield quite high cell voltages vs. lithium. In particular, the higher oxides should yield the highest cell potentials because of their larger free energy of reaction ΔG_r upon reduction by lithium. Unfortunately, this principle is somewhat offset by the fact that many of these higher oxides have been found to reduce to lower oxides when in contact with some electrolytes, such as the common LiCl/KCl molten salt. For this reason, it was determined that an analysis of the equilibrium oxygen partial pressures of these transition metal oxides was necessary.

An Ellingham diagram (4) is a common means of graphically representing ΔG°_f vs. temperature data, as illustrated in Fig. 1 for the case of several manganese oxides. Each (solid) line represents the Gibbs free energy of formation of an oxide phase from its elements M and O_2



Each formation reaction is usually written on a "per mol O_2 " basis so that lines in an Ellingham diagram are generally parallel, since the gaseous O_2 accounts for most of the entropy change of the reaction ΔS_r , which is manifested in the slope of the $\Delta G^\circ_f - T$ lines.

An equilibrium oxygen partial pressure scale was later added to the standard Ellingham diagram to permit a graphical means of determining the p_{O_2} above these oxides (5). It is important to note, however, that

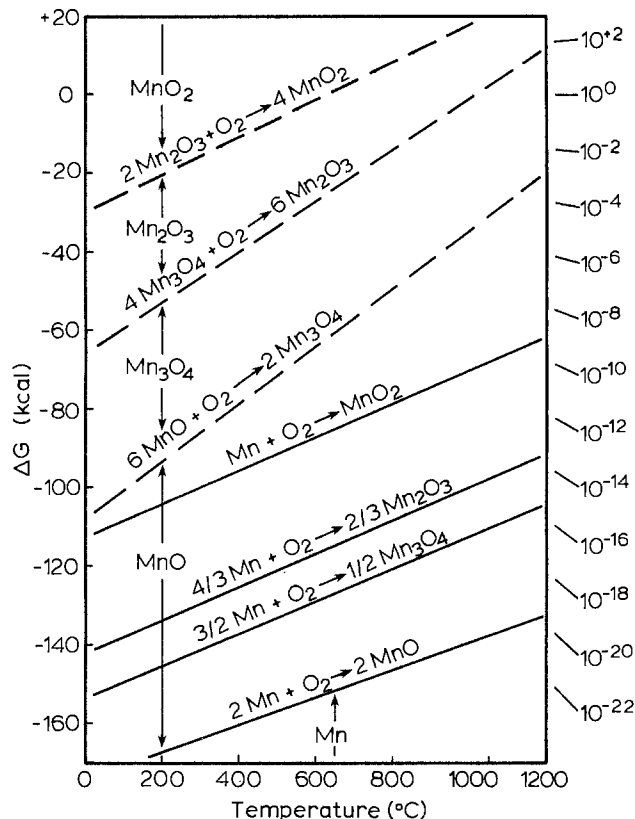
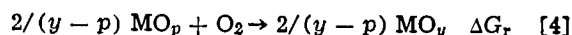


Fig. 1. Ellingham diagram illustrating "integral" (solid line) and "difference" (dashed line) formation reaction lines for manganese oxides.

this is valid only for reactions where reactants and products are at equilibrium, and is not generally true for reactions describing the formation of a compound from its elements. Only the lowest line in Fig. 1 (MnO) represents both a "formation" and "equilibrium" reaction. Higher oxide lines (solid lines Mn_3O_4 , Mn_2O_3 , and MnO_2) represent "formation" reactions of these products, but are not true "equilibrium" lines since elemental Mn would not be stable in contact with these higher oxides.

The equilibrium oxygen partial pressure p_{O_2} above two oxides in equilibrium at a given temperature and total pressure depends, therefore, not on the free energies of formation ΔG°_f of these oxides from their elements; but rather on the free energy of reaction ΔG_r of the higher oxide MO_y from its next lower oxide MO_p



This free energy of reaction is given by

$$\Delta G_r = 2/(y-p) [\Delta G^\circ_f(\text{MO}_y) - \Delta G^\circ_f(\text{MO}_p)] \quad [5]$$

The free energies of reaction between neighboring manganese oxides (again on a "per mol O_2 " basis) are illustrated by the dashed lines of Fig. 1. They represent the differences between the formation reaction (solid) lines after adjustment for the stoichiometric numbers. They also lie higher in the diagram since the ΔG values of these "difference" reactions are smaller in magnitude than those for the formation, or "integral" reactions. Furthermore, the "difference" lines represent the true stability regions of each oxide, as illustrated in Fig. 1. They also yield proper oxygen partial pressure information when used in conjunction with the p_{O_2} scale of Fig. 1.

The oxygen partial pressure when the two oxides are in equilibrium may be found analytically through the use of

$$\Delta G_r = -RT \ln K \quad [6]$$

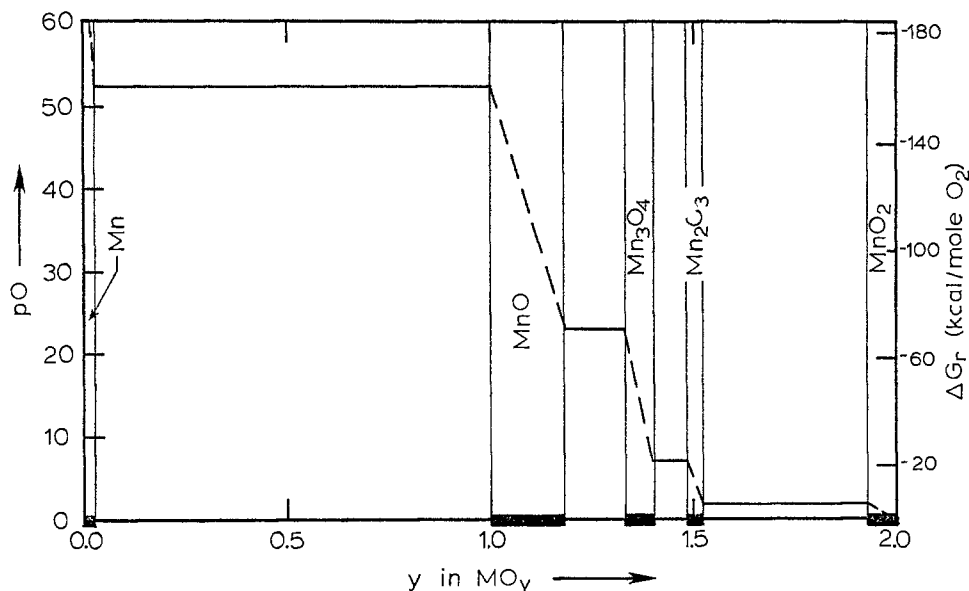


Fig. 2. Equilibrium oxygen partial pressures exhibited by manganese oxides as a function of composition at 400°C.

since the equilibrium constant K for reaction [4] is given by $1/p_{O_2}$ if both oxides remain pure and in their standard states. That is

$$\Delta G_r = +RT \ln p_{O_2} \quad [7]$$

so that this specific value of oxygen partial pressure is given by

$$p_{O_2} = \exp(\Delta G_r/RT) \quad [8]$$

It is useful to define a logarithmic parameter p_0 analogous to the hydrogen ion concentration parameter pH

$$p_0 = -\log p_{O_2} \quad [9]$$

This oxygen potential parameter may therefore be calculated directly from the free energy of reaction [4] and the absolute temperature

$$p_0 = -\Delta G_r/(2.303 RT) \quad [10]$$

The variation of oxygen partial pressure with overall composition in the manganese-oxygen system is illustrated in Fig. 2. This system is used as an example because it contains several binary oxide phases. In this case, the composition parameter was chosen as the oxygen/manganese ratio, or "y" in MO_y . The variable stoichiometry of single-phase regions is illustrated on the abscissa through the use of heavy dark lines. The oxygen potential p_0 is plotted on the ordinate, but may also be given by the free energy of reaction ΔG_r at fixed temperature (Eq. [10]). As discussed above, the range of p_{O_2} over which a phase is stable is determined by the equilibrium with its two neighboring phases; one stable at lower oxygen pressures, and the other stable at higher oxygen pressures.

The oxygen partial pressure is seen to remain constant in two-phase regions ($F = 0$), but may vary over many orders of magnitude in single-phase regions ($F = 1$). This is a direct result of the Gibbs phase rule at constant temperature and total pressure. The dashed lines shown within single-phase regions are schematic only; they are not typically linear functions of composition. The equilibrium oxygen partial pressures at 400°C of all first-row transition metal binary oxides were calculated from Eq. [4]-[10] and are illustrated in Fig. 3.

The expected high voltages of some lithium cells with transition metal oxides as positive electrodes cannot be realized with LiCl-KCl molten salt electrolytes because it has been found that the highest oxides reduce to lower oxides in this electrolyte at 400°C. This is because their equilibrium oxygen partial pressures are higher than the p_{O_2} present in the LiCl-KCl salt. For instance, MnO_2 and $LiMn_2O_4$ yield very high theo-

retical voltages vs. lithium, but were found to reduce when placed in this molten salt.

In order to determine the limit of p_{O_2} for which no reduction will occur in this electrolyte, many binary and ternary transition metal oxides were individually mixed with solid LiCl/KCl powder and placed in molybdenum tubes. They were then immersed in molten LiCl/KCl at 400°C for approximately 18h. This was followed by ambient temperature x-ray analysis under Kapton film. It was found that all oxides with calculated oxygen partial pressures above 10^{-25} atm either reduced to well-defined lower oxides (e.g., Fe_2O_3 reduced to Fe_3O_4) or yielded amorphous x-ray patterns (e.g., MnO_2). Below 10^{-25} atm (solid line in Fig. 3), all binary oxides were found to be stable in the LiCl/KCl molten salt. The stability ranges of the binary oxides were then used to project the approxi-

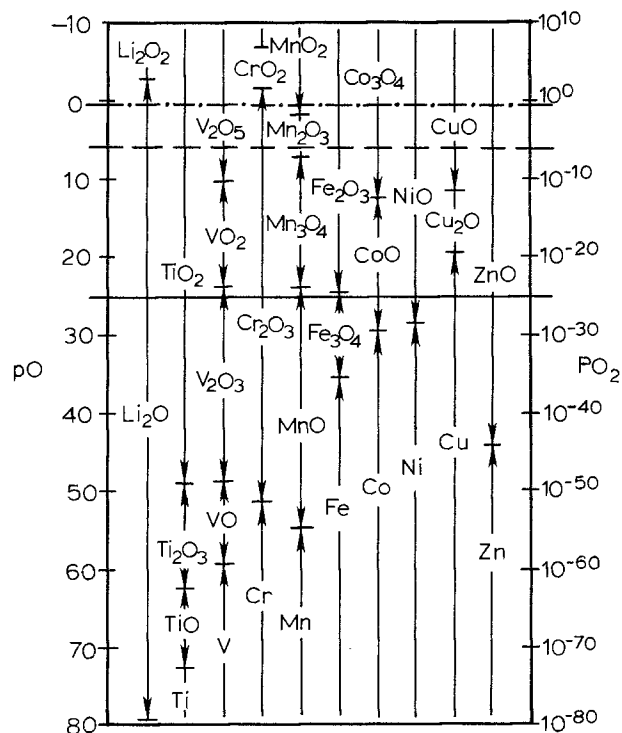
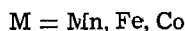
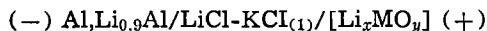


Fig. 3. Equilibrium oxygen partial pressures of binary first-row transition metal oxides at 400°C. Also illustrated are isobaric O_2 lines (1 atm total pressure): air, $p_{O_2} = 0.21$ atm (dash-dot line); helium glove box, $p_{O_2} = 10^{-6}$ atm (dashed line); LiCl/KCl electrolyte, $p_{O_2} = 10^{-25}$ atm (solid line).

mate positions of isobaric O_2 lines within a ternary phase diagram, since the constant partial pressures above two neighboring binary oxides provide an estimation of where ternary O_2 isobars intersect the legs of a Gibbs composition triangle.

Equilibrium Potential-Composition Curves

The electrochemical reduction of Li_xMO_y cathodes by reaction with lithium was studied in cells of the type



The cathode material (positive electrode) was a ternary compound composed of lithium, oxygen, and the first-row transition metals Mn, Fe, or Co (1, 2). The electrochemical reactions were found to be reversible at 400°C. Electrochemical reduction and oxidation was performed at current densities of 5-15 mA/cm². The current was repeatedly interrupted so that the equilibrium, or open-circuit, cell potential was obtained as a function of Li composition (6). The changes in composition were calculated from the integrated current and Faraday's law. Two equilibrium potential-composition curves are illustrated in Fig. 4 and 5 for the initial electrode compositions of Fe_3O_4 and $LiFe_5O_8$, respectively.

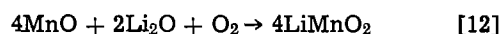
The tie triangles in each ternary system were thus determined by plotting the extent of the various constant voltage plateaus, determined by reacting lithium with several different initial compositions, on each respective Gibbs composition triangle, Fig. 6. Tie lines exist where steps occur between plateau voltages, Fig. 7. The three phases present in each tie triangle were confirmed by x-ray diffraction analyses of samples taken from the positive electrodes.

This technique also permits a determination of the thermodynamic properties of these intermediate ternary compounds where little or no literature data existed thus far (7). The integral free energy of formation (ΔG_f°) of each initial compound was calculated by integration of its respective equilibrium potential curve according to the equation

$$\Delta G_f^\circ (Li_xMO_y) = zF \int_x^{2y} E dx + y\Delta G_f^\circ (Li_2O) \quad [11]$$

The free energies of formation at 400°C of $LiMnO_2$, Li_3FeO_4 , $LiFeO_2$, and $LiCoO_2$ were calculated this way and found to be -178.21, -399.88, -154.18, and -131.62 kcal/mol, respectively.

The activities of all species are constant in any three-phase region of a ternary system at constant temperature and pressure. Furthermore, the activities of all species, not just the electroactive one (Li), may be calculated within each tie triangle, so long as the free energy of formation of each of the three equilibrium phases is known. Oxygen partial pressures may be calculated for each tie triangle by writing an equilibrium reaction between O_2 gas and the three phases of which the tie triangle is composed. For example, in the case of the MnO , Li_2O , $LiMnO_2$ tie triangle



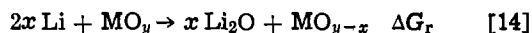
for which, at 400°C

$$\Delta G_r = -146.68 \text{ kcal/mol } O_2 \quad p_{O_2} = 2.37 \times 10^{-48} \text{ atm} \quad [13]$$

Analytical Relation Between Tie Triangle Voltages and Oxygen Partial Pressures

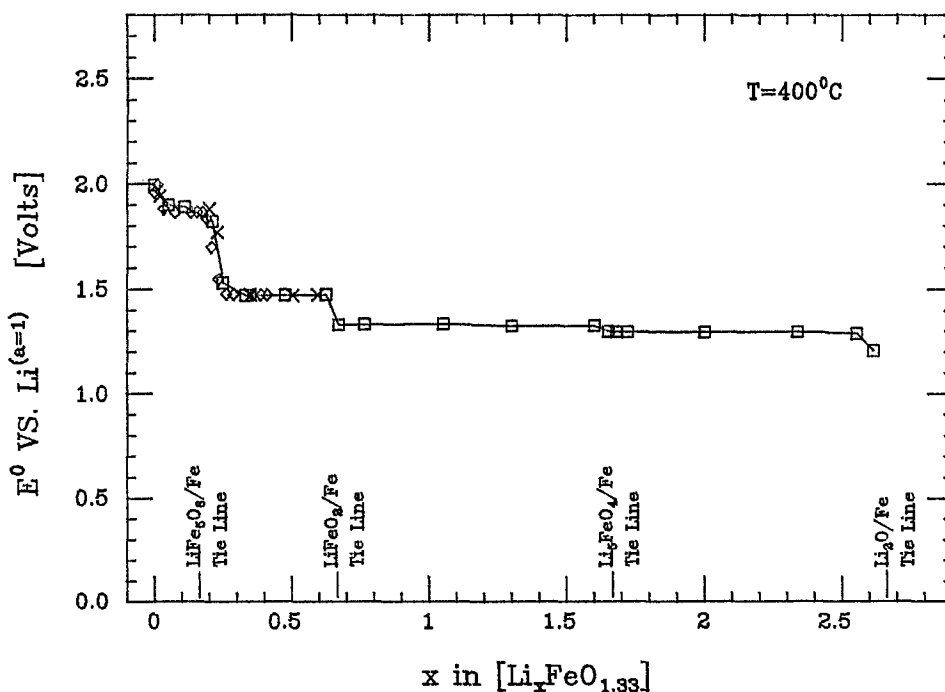
Any relationship between the voltage vs. lithium E and the oxygen partial pressure p_{O_2} would be of fundamental importance, for it would allow oxygen partial pressure calculations to be used to predict equilibrium voltages of lithium electrochemical cells. It is also possible to extend such a relation to other alkali metal (Na, K, etc.) cells, and other cathode materials (e.g., sulfides). However, such a relation would be expected to carry a constraint, since a ternary system ($C = 3$) would not, in general, have the activity of one component vary directly as a function of only a second component.

It was therefore desired to analytically derive the relation between E and p_{O_2} in a ternary system to better understand any voltage limitation imposed by the p_{O_2} limitation (10^{-25} atm) of the $LiCl/KCl$ electrolyte. The general equilibrium equation for a ternary tie triangle composed of two binary transition metal oxides (MO_y and MO_{y-x}) and lithium oxide (Li_2O) may be written as



where the free energy of this reaction is given by

Fig. 4. Equilibrium potential-composition curve for the initial composition Fe_3O_4 .



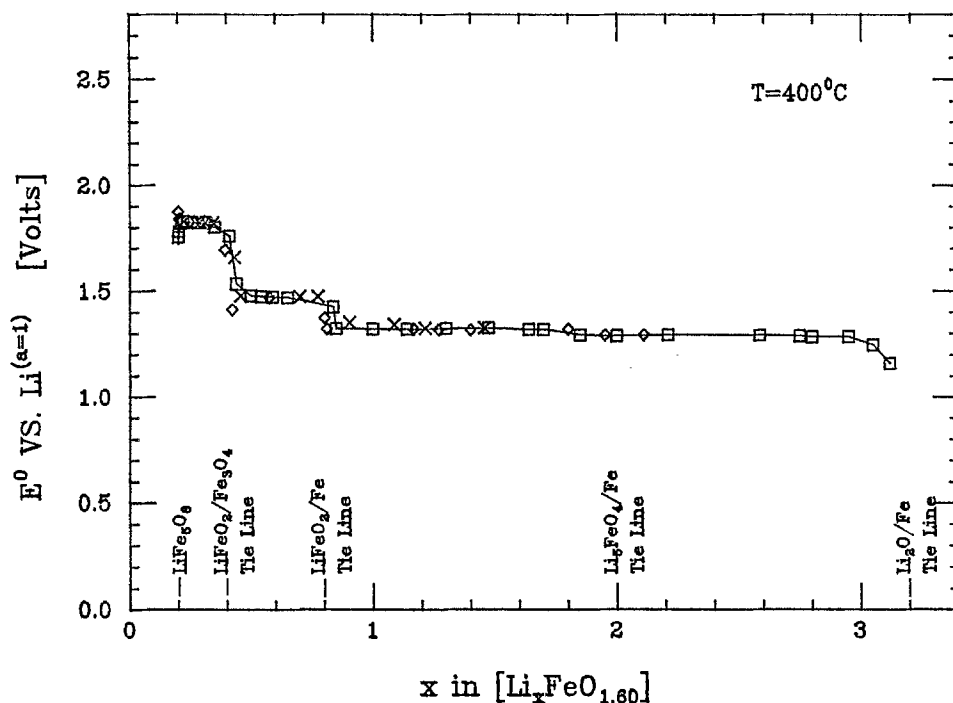
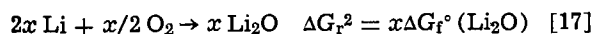
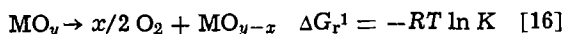


Fig. 5. Equilibrium potential-composition curve for the initial composition LiFe_5O_8 .

$$\Delta G_r = \Delta G_r^1 + \Delta G_r^2 \quad [15]$$

when the ternary reaction [14] is written as the summation of two binary reactions according to Hess's law



Reaction [16] specifies the equilibrium oxygen partial pressure above two adjacent binary transition metal oxides, and reaction [17] represents the formation of Li_2O . Substitution into Eq. [15] yields

$$E = -\Delta G_r/zF = -\Delta G_r^1/zF - \Delta G_r^2/zF \quad [18]$$

The charge number z of reaction [14] is given by $[2x]$. So long as both binary transition metal oxides of reaction [16] remain pure and in their standard states, their activities may be taken as unity, resulting in

$$E = RT/(2xF) \ln(p_{\text{O}_2})^{x/2} - \Delta G_f^\circ(\text{Li}_2\text{O})/(2F) \quad [19]$$

Simplification results in a linear relation between E and $\ln p_{\text{O}_2}$ with a slope of $RT/(4F)$ and a Y-intercept of 2.654V.

$$E = RT/(4F) \ln(p_{\text{O}_2}) - \Delta G_f^\circ(\text{Li}_2\text{O})/(2F) \quad [20]$$

This, of course, may alternately be expressed in terms of $\log p_{\text{O}_2}$ and p_0

$$E = -2.303 RT/(4F) \log(p_{\text{O}_2}) - \Delta G_f^\circ(\text{Li}_2\text{O})/(2F) \quad [21]$$

and

$$E = -2.303 RT/(4F) p_0 - \Delta G_f^\circ(\text{Li}_2\text{O})/(2F) \quad [22]$$

Experimental Relation Between Tie Triangle Voltages and Oxygen Partial Pressures

The electrochemical titrations of lithium into Li_xMO_y cathodes were used to experimentally determine the equilibrium potentials E of tie triangles in the ternary systems containing manganese, iron, and cobalt. In addition, the free energies of formation ΔG_f° of intermediate ternary compounds were then calculated by integration of the equilibrium potential-composition curves. This, in turn, permitted the calculation of equilibrium oxygen partial pressures p_{O_2} of the same tie triangles for which E values were determined experimentally. Both values are listed in the tie triangles of Fig. 7. An uncertainty remains in the Li-Fe-O ter-

nary system regarding the relative stability of the $\text{LiFeO}_2/\text{Fe}_3\text{O}_4$ tie line vs. the $\text{LiFe}_5\text{O}_8/\text{Fe}$ tie line, illustrated by the dash-dot lines in Fig. 7(b).

The equilibrium voltage vs. Li of each three-phase region is plotted as a function of the equilibrium oxygen partial pressure of that region in Fig. 8. The result is a linear relationship between E and the logarithm of p_{O_2} of the form

$$E = m \log p_{\text{O}_2} + b \quad [23]$$

The equation for the experimental line of Fig. 8 was found to be

$$E = 1.45 \times 10^{-2} \ln p_{\text{O}_2} + 2.65V \quad [24]$$

Extrapolation of this line results in X- and Y-intercepts of

$$E = 0.0V \quad p_0 = 80$$

$$p_0 = 0 \quad E = 2.65V$$

Like the analytical derivation leading to Eq. [20], these experimental data indicate that Li_2O is a primary factor in this relation, since the X-intercept is the same as the equilibrium oxygen partial pressure above a mixture of Li and Li_2O at 400°C, and the Y-intercept is the theoretical voltage of a lithium/oxygen cell at 400°C. Furthermore, the slope of this line was found to be $(RT/4F)$, where the factor of 4 is the number of Li equivalents required to react with 1 mol of O_2 to form Li_2O .

Equation [20] was derived for tie triangles containing Li_2O , such as the $\text{Mn}, \text{Li}_2\text{O}, \text{MnO}$ tie triangle included in Fig. 8. In addition, it was found that the potentials of binary first-row transition metal monoxides, when compared with their equilibrium oxygen partial pressures, also follow the relation of Fig. 8. This relation is therefore generally valid for any tie triangle containing Li_2O and two binary oxides as constituents.

Although most tie triangles in these ternary Li-M-O systems are not composed of Li_2O and binary transition metal oxides, they were experimentally found to also follow the linear relation between E and $\ln p_{\text{O}_2}$ of Fig. 8 and Eq. [20]. Specifically, all tie triangles studied in the lithium-manganese-oxygen ternary system have Li_2O present as one phase, but the two higher voltage triangles have ternary oxide phases present—not just binary oxides as used in the analytical derivation shown

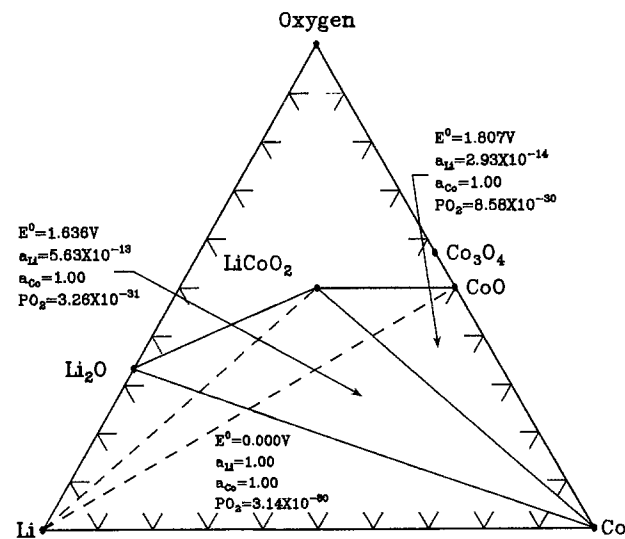
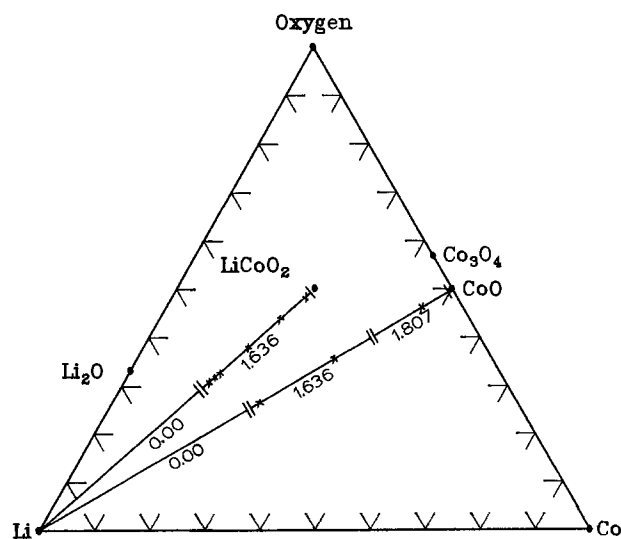
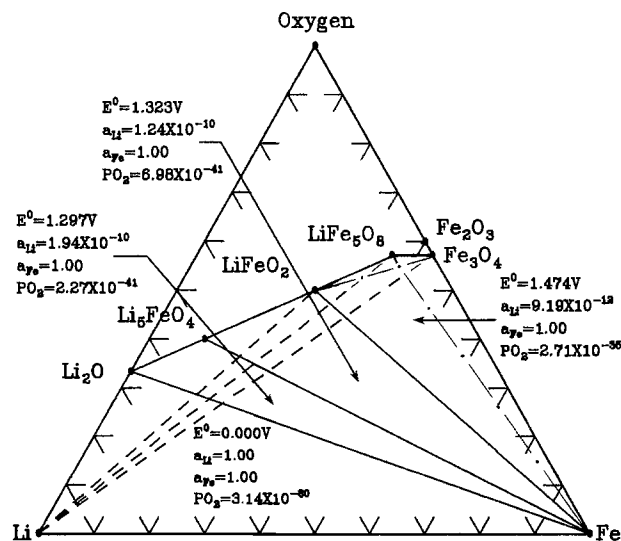
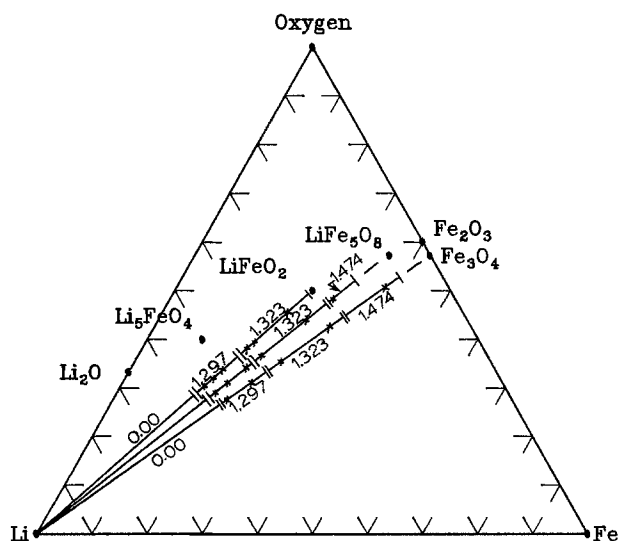
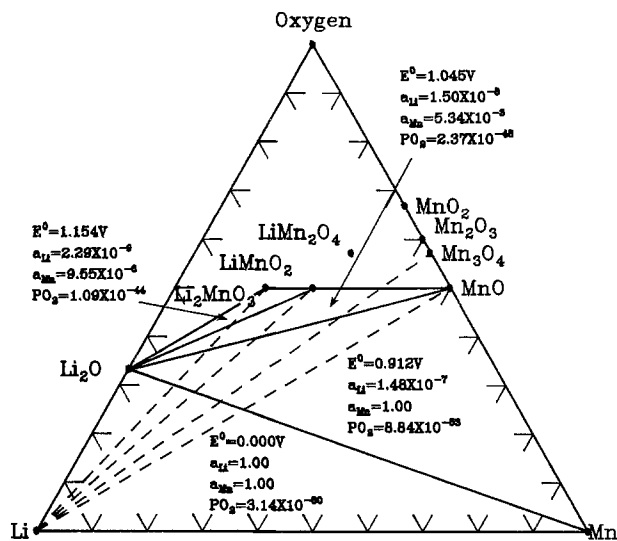
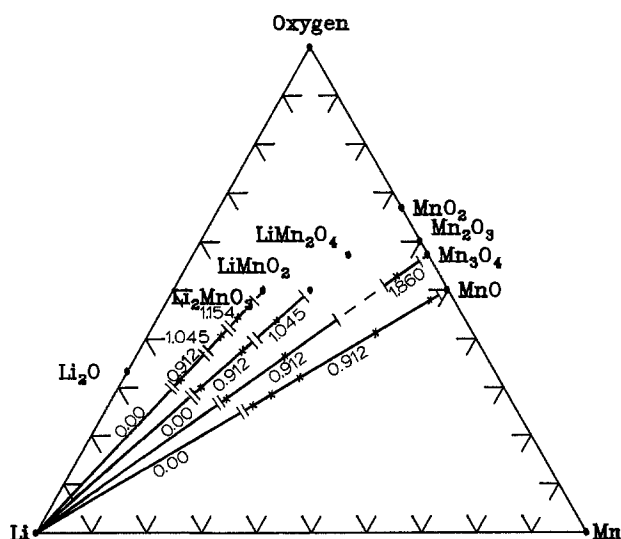


Fig. 6. Constant voltage plateaus found in the (a, top) Li-Mn-O, (b, middle) Li-Fe-O, and (c, bottom) Li-Co-O ternary systems at 400°C.

Fig. 7. Phase equilibria in the (a, top) Li-Mn-O, (b, middle) Li-Fe-O, and (c, bottom) Li-Co-O ternary systems at 400°C.

above. However, their lithium and oxygen activities were still found to obey Eq. [20]. Conversely, two tie triangles studied in the lithium-iron-oxygen system have binary oxides, yet contain no Li₂O. They, too, were found to follow this relation.

This correlation may be extended to tie triangles not containing Li₂O, so long as the ternary oxide phases of

which the tie triangles are composed are only marginally stable with respect to Li₂O and their neighboring binary oxides. The marginal stabilities of most ternary oxides studied in this work explain why the tie triangles cited above in the manganese and iron systems correspond closely to this relation, although it is strictly valid only for tie triangles containing Li₂O and binary transition metal oxides. That is, a ternary oxide

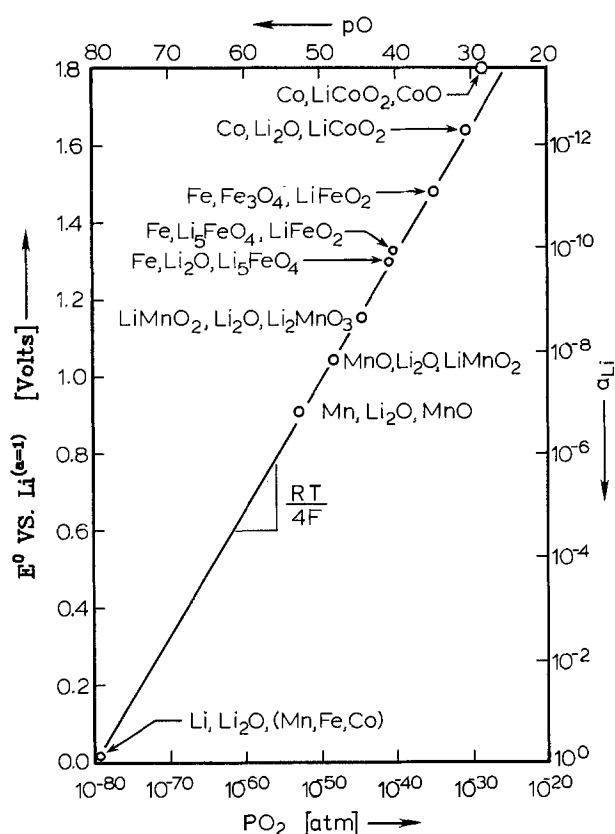


Fig. 8. Relation between tie triangle voltages and equilibrium oxygen partial pressures in Li-M-O systems at 400°C.

which is only marginally stable with respect to other oxides behaves as though it were composed of the proper amounts of Li₂O and binary oxide MO_y, for which the E vs. p_{O_2} derivation is exact.

Furthermore, tie triangles with phases much more thermodynamically stable than their "weighted averages" will deviate from this relation in a predictable manner. Tie triangles with reactant phases significantly more stable than their "weighted averages" will have voltages lower than those predicted by this relation. Conversely, triangles with product phases significantly more stable than their "weighted averages" will have voltages higher than those predicted by this relation.

An example of the latter is given by the LiCoO₂, CoO, Co tie triangle, which has an equilibrium oxygen partial pressure of 10⁻³⁰ atm (the same as that between CoO and Co). The voltage vs. Li predicted by Fig. 8 is 1.684V, but was found experimentally to be 1.807V. The voltage of 1.684V would have been observed had the ternary compound LiCoO₂ not existed. The fact that it is considerably more stable (14.9%) than the "weighted average" increases the voltage to 1.807V, since in this triangle, LiCoO₂ is a product phase.

Conclusions

The free energies of formation of four intermediate ternary oxides (LiMnO₂, Li₅FeO₄, LiFeO₂, and LiCoO₂) were determined from electrochemical experiments,

and found to be -178.21, -399.88, -154.18, and -131.62 kcal/mol, respectively, at 400°C. Lithium could be reversibly reacted with these oxides at current densities of 5-15 mA/cm² over a range of 0.0-3.0 eq/mol at voltages of 1.0-1.8V vs. Li. Compounds lying closer to the oxygen corner of these ternary lithium-metal-oxygen systems yield higher cell voltages, because these higher oxides represent less stable compounds. They therefore yield greater energy when reduced to more stable compounds during the electrochemical reactions which occur within the cell. This effect, unfortunately, is somewhat limited by the fact that the highest oxides of each system have been found to reduce to lower oxides when placed in the molten salt electrolyte. That is, their equilibrium oxygen partial pressure is too high when in contact with the LiCl-KCl salt. For instance, MnO₂, LiMn₂O₄, V₂O₅, CuO, and Cu₂O yield very high theoretical voltages vs. lithium, but were found to reduce when placed in molten LiCl/KCl salt. The linear relationship between cell voltage (E) and oxygen potential ($\ln p_{O_2}$) imposes a maximum cell voltage of 1.820V vs. Li on cells utilizing oxide cathode materials in contact with LiCl/KCl molten salt electrolyte at 400°C. For a limit of 10⁻²⁵ atm, the $[RT/(4F) \ln p_{O_2}]$ term of Eq. [20] represents a loss of 0.835V from an idealized lithium/oxygen (1 atm) cell, which would have an equilibrium voltage of 2.654V.

The oxygen partial pressure limit of 10⁻²⁵ atm ($E = 1.820V$) imposed by the LiCl/KCl electrolyte or its surroundings represents, perhaps, the largest impediment to the development of even more desirable oxide cells. So long as an alloy of lithium (e.g., Li-Al or Li-Si) is required in the anode compartment, the specific energy of a cell cannot be increased significantly by simply finding longer plateau materials. This is because the additional energy of reaction obtained from longer plateau materials is offset by the weight of the additional allowing element required. Therefore, the specific energy of these cells can be significantly increased only by increasing their operating voltages, which requires that the oxygen partial pressure limit be increased.

Acknowledgment

This work was supported by the United States Department of Energy under Contract EC-77-S-02-4506 and LBL Subcontract 4503110.

Manuscript submitted April 4, 1983; revised manuscript received Aug. 29, 1983.

REFERENCES

1. N. A. Godshall, I. D. Raistrick, and R. A. Huggins, *Mater. Res. Bull.*, **15**, 561 (1980).
2. N. A. Godshall, I. D. Raistrick, and R. A. Huggins, Paper presented at the 16th Intersociety Energy Conversion Engineering Conference, Atlanta, Georgia, Vol. 1, p. 769, 1981.
3. M. S. Whittingham, *Prog. Solid State Chem.*, **12**, 41 (1978).
4. H. T. Ellingham, *J. Soc. Chem. Ind., London*, **63**, 125 (1944).
5. F. D. Richardson and J. H. E. Jeffes, *J. Iron Steel Inst.*, **160**, 261 (1948).
6. W. Weppner and R. A. Huggins, *This Journal*, **124**, 1569 (1977).
7. W. Weppner and R. A. Huggins, *ibid.*, **125**, 7 (1978).

Influence of Mechanical Polishing on the Photoelectrochemical Properties of SrTiO₃ Polycrystalline Anodes

P. Salvador

Instituto de Catálisis y Petroleoquímica, C.S.I.C., Serrano, 119 Madrid -6, Spain

C. Gutiérrez

Instituto de Química-Física "Rocasolano," C.S.I.C., Serrano, 119 Madrid -6, Spain

G. Campet and P. Hagenmüller

Laboratoire de Chimie du Solide du CNRS, Université de Bordeaux I, 33405 Talence Cédex, France

ABSTRACT

The influence of lattice defects produced by mechanical polishing of the surface upon the photoelectrochemical properties of polycrystalline SrTiO₃ anodes was investigated. The lattice defects were correlated to various subbandgap energy levels. Part of them were attributed to local Ti-O bond weakening; they should lie close to the bandedges thus causing a tailing of the bandgap absorption and a shift of the flatband potential towards more positive values. Deeper subbandgap states resulting from Ti-O bond breaking should render the semiconductor strongly sensitive to visible light. However, these lattice defects should also act as recombination centers causing a decrease of the hole diffusion length and therefore a decrease of the photocurrent efficiency.

Suitable semiconducting anodes for photoelectrolysis of water must satisfy the following main conditions: (i) chemical stability against photocorrosion; (ii) a bandgap small enough (~ 2.3 eV) for maximum efficiency; (iii) ability to spontaneously drive the photodecomposition of water. This last condition requires that the conduction bandedge is well above the H⁺/H₂ redox potential in the aqueous electrolyte.

n-type SrTiO₃ has attracted widespread attention because of its chemical stability. Besides, it requires no biasing to generate H₂ and O₂: its low electron affinity fixes the bottom of its empty Ti⁴⁺:3d conduction bandedge above the H⁺/H₂ redox level (1). Unfortunately, the very large bandgap energy, $E_g = 3.2$ eV for the intrinsic material (2), precludes its use for solar energy conversion. A strategy to partially eliminate this above inconvenience consists of doping the semiconductor with Cr³⁺, either homogeneously (1, 3) or by diffusion from the surface at high temperature (4). Thus, a new cathodic Cr³⁺:3d³ valence band is formed inside the bandgap, giving rise to an impressive photosensitization at high anodic bias due to Cr³⁺ to Ti⁴⁺ charge transfer. However, under the normal working conditions required for a photocell, i.e., no bias and steady illumination, the quantum efficiency both for visible and UV light is too low because the chromium levels also act as recombination centers which lower the photoresponse (3).

Some of us have also reported that SrTiO₃ electrodes become strongly sensitive to visible light by appropriate surface pretreatments such as mechanical polishing (5, 6). As shown in Fig. 1, the visible response was related to the existence of [O:2p]_{bb} and [Ti:3d(t_{2g})]_{bb} subbandgap states [bb is the bond-breaking associated with broken Ti-O bonds produced by the abrasion of the surface (6)]. On the other hand, it is well known that lattice defects produced by mechanical polishing of ZnO (7), GaAs (8), or TiO₂ electrodes (9, 10) act as traps for electrons and holes, leading to an increased recombination and so to a significant diminution of the photocurrent.

In the present work, the photoelectrochemical behavior of polished SrTiO₃ polycrystalline anodes, designated as [pol-SrTiO₃], is compared with that of unpolished samples symbolized by [o-SrTiO₃]. This comparative study is based upon the determination, from

voltage and wavelength dependences of the quantum efficiency, of the physical parameters determining the behavior of the electrodes.

Experimental

Details concerning the anode fabrication and the surface treatment have already been reported (5). The

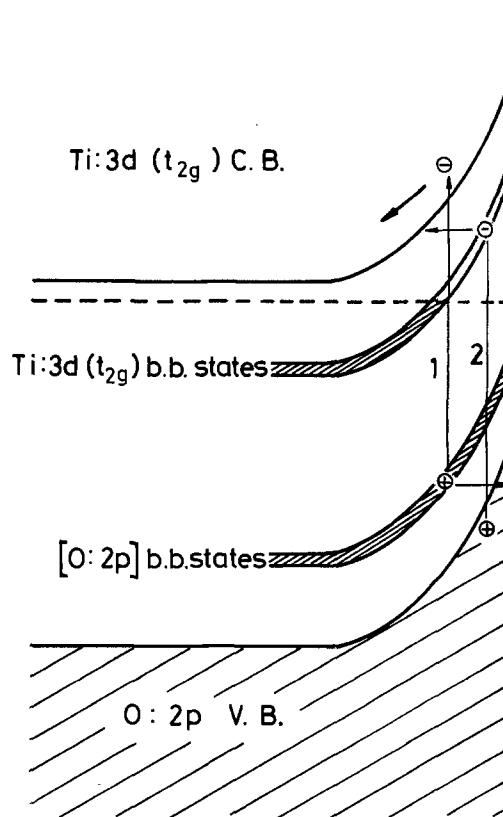


Fig. 1. Schematic illustration of the visible photoconduction mechanisms giving rise to a visible photocurrent: electrons can be photoexcited from the occupied [O:2p]_{bb} states to the conduction band (process 1) or from the valence band to empty [Ti:3d(t_{2g})]_{bb} states (process 2).

Key words: junctions, semiconductor, energy conversion.

experimental apparatus used for the electrochemical measurements has also been described previously (11). The electrolyte was a 1M Na₂SO₄ solution; the pH = 3 was adjusted by addition of H₂SO₄. The electrode potentials are quoted relative to the saturated calomel electrode (SCE). The photoelectrode was illuminated with a 150W Xe lamp followed by a Bausch & Lomb grating monochromator. Photocurrent efficiencies were measured with a high impedance HP 3478 A programmable multimeter coupled to a 4032 Commodore computer. The photon flux reaching the electrode surface was determined by means of a calibrated EG&G 4000 B silicon photovoltaic detector.

The real part of the relative permittivity (ϵ_r) of the sample was deduced from capacitance measurements using a 1680 General Radio capacitance bridge.

A Keithley high impedance multimeter allowed accurate determination of the sample conductivity.

Results

Emphasis was given to the photocurrent efficiency η calculated from

$$\eta = \frac{i_{(\text{light})} - i_{(\text{dark})}}{qI_0} \quad [1]$$

where $i_{(\text{light})}$ and $i_{(\text{dark})}$ are current densities under illumination and at dark, respectively, I_0 represents the photon flux absorbed by the photoelectrode, and q is the electronic charge.

Reflectivity of the samples was measured with a Cary 17 spectrophotometer. Polishing produced no noticeable change in reflectivity in the UV region ($\lambda < 370$ nm), while it decreased the reflectivity in the visible region (Fig. 2).

Photocurrent efficiency-voltage (η -V) and photocurrent efficiency-wavelength (η - λ) characteristics.—Figures 3a and 3b show typical η -V curves at 370 nm (bandgap illumination) and at 470 nm (subbandgap illumination). The η - λ dependences are given in Fig. 4 at 1V vs. SCE.

A substantial increase of the pol-SrTiO₃ photoreponse to visible light can be observed. However, a substantial decrease of the efficiency in the UV region is also observed. These effects were observed in all of the samples studied.

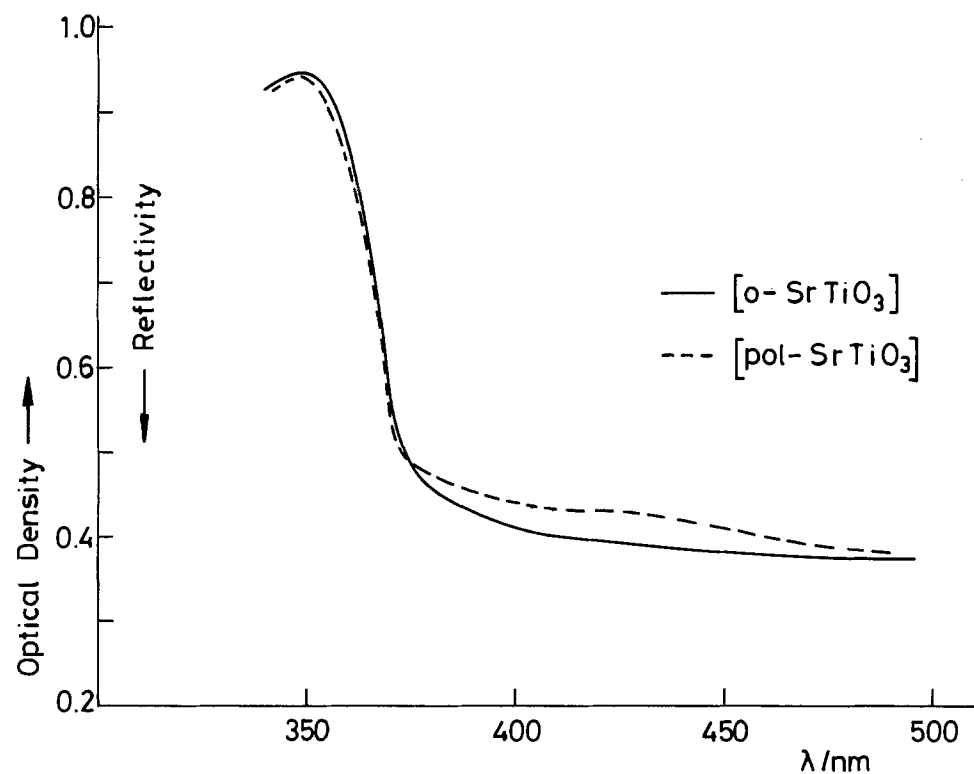


Fig. 2. Influence of polishing on the diffuse reflectance spectrum of sintered polycrystalline SrTiO₃.

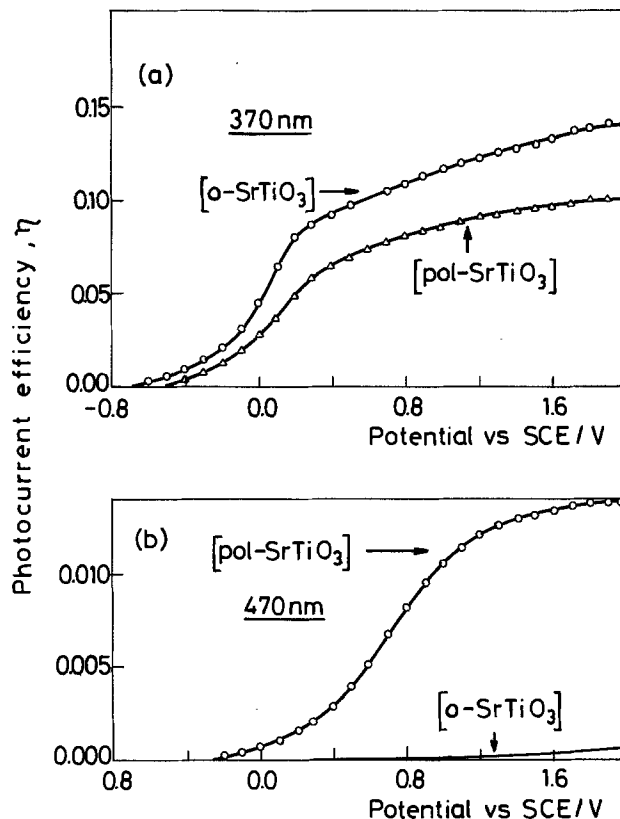


Fig. 3. Photocurrent efficiency vs. potential: (a, top) $\lambda = 370$ nm; (b, bottom) $\lambda = 470$ nm.

Flatband potential V_{FB} and ionized donor density concentration, N_D .—These parameters can be reasonably estimated from the theory of depletion layer photoeffects developed by Gärtner (12) and discussed by several authors (13-16). Using this model, Kennedy and Frese (13) calculated that

$$\ln(1 - \eta) = -\alpha W - \ln(1 + L_p) \quad [2]$$

where α is the semiconductor absorption coefficient, L_p is the hole diffusion length in the bulk (outside the

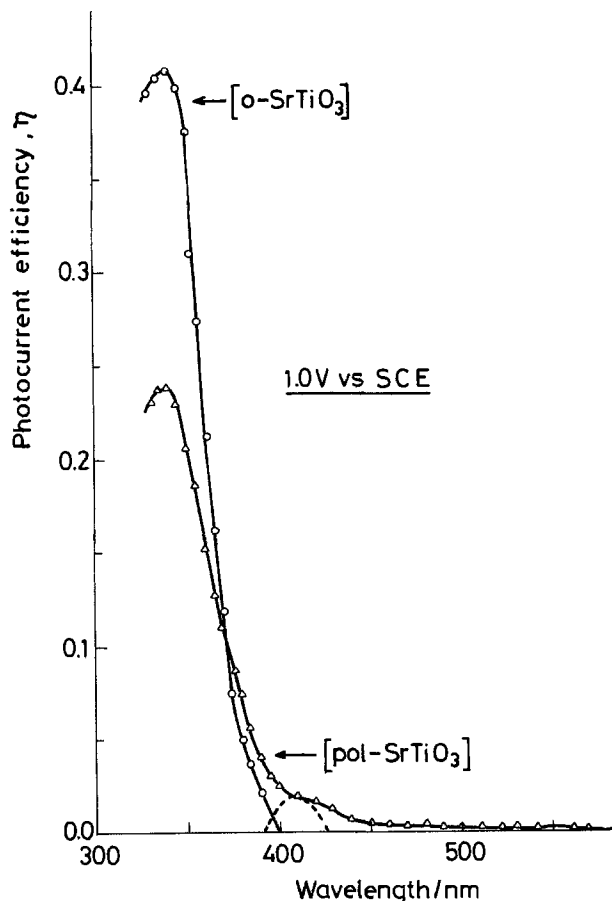


Fig. 4. Photocurrent efficiency-wavelength dependence at 1V (vs. SCE).

depletion layer), and W is the depletion layer width given by

$$W = \left(\frac{2\epsilon_r\epsilon_0}{qN_D} \right)^{1/2} (V - V_{FB})^{1/2} \quad [3]$$

where ϵ_r and ϵ_0 have the usual meaning and $(V - V_{FB})$ is the band bending with V_{FB} being the flatband potential.

Implicit in Eq. [2] is also the absence of carrier recombination at the semiconductor-electrolyte interface, i.e., that the transfer of holes from the semiconductor to the electrolyte is not the limiting step (17). This has been proved to be valid at sufficiently large voltages [$(V - V_{FB}) > 1V$] for several sintered semiconducting electrodes including undoped TiO_2 (11), Al- and Nb-doped TiO_2 (18, 19), and $BaTiO_3$ (13). We have recently shown (20) that a source of surface electron-hole recombination at low band bending is the reduction by conduction band electrons of species photogenerated during water photoelectrolysis, such as O_2 and H_2O_2 . This recombination process, with rates depending on $(V - V_{FB})$, is independent of the physical bulk properties of the semiconductor and represents a general limitation of Eq. [2] for most oxide photoanodes.

Provided that $\alpha L_p \ll 1$, i.e., $1 + \alpha L_p \approx \alpha L_p$, Eq. [2] can be written

$$\ln(1 - \eta) = -\alpha(W + L_p) \quad [4]$$

Besides, if $W \gg L_p$ one gets

$$\ln(1 - \eta) = -\alpha W \quad [5]$$

These two assumptions are generally valid for penetrating radiations ($\alpha > 10^4 \text{ cm}^{-1}$) and for not heavily doped semiconducting oxides ($N_D \leq 10^{18} \text{ cm}^{-3}$) (21).

Combination of Eq. [3] with Eq. [5] leads after squaring to

$$[\ln(1 - \eta)]^2 = \frac{2\alpha^2\epsilon_r\epsilon_0}{qN_D} (V - V_{FB}) \quad [6]$$

According to Eq. [6], the plot of $[\ln(1 - \eta)]^2$ vs. potential should be linear, the intersection with the abscissa giving V_{FB} .

Figure 5, deduced from Fig. 3a, shows $[\ln(1 - \eta)]^2$ vs. potential curves at 370 nm. They present a good linearity above 0.5V (SCE), i.e., for $V - V_{FB} \geq 1.1V$. Gärtner's model does not apply at lower band bendings because of electron-hole recombination at the electrode surface (20) and also at the depletion layer for the polished sample (see Discussion).

The flatband potentials obtained by extrapolation are given in Table I. These values are in good agreement with those obtained from the UV photocurrent onset potential (Fig. 3a). Besides, the donor density concentration, N_D , can be calculated from the slope of the plots, provided the real part of the relative permittivity, ϵ_r , and the absorption coefficient at 370 nm are known. A frequency-independent value of 200 was obtained for ϵ_r in the range from 0.1 to 100 kHz, and α (370 nm) is $2.6 \times 10^3 \text{ cm}^{-1}$ (22). The calculated N_D values are included in Table I. It is to be remarked that the difference in N_D between the polished and the unpolished samples is a real effect and not an apparent one due to changes in reflectivity, as polishing has nearly no effect on the diffuse reflectivity in the UV range (see Fig. 2).

Bandgap energy, E_g .—This parameter is contained, together with the incident photon flux $h\nu$, in the following expression valid for indirect bandgap semiconductors, as is the case for $SrTiO_3$ (23)

$$\alpha = A \frac{(h\nu - E_g)^2}{h\nu} \quad [7]$$

where A is a constant.

Algebraic manipulation of Eq. [4] and [7] leads to

$$[-h\nu \ln(1 - \eta)]^{1/2} = A^{1/2} (W + L_p)^{1/2} (h\nu - E_g) \quad [8]$$

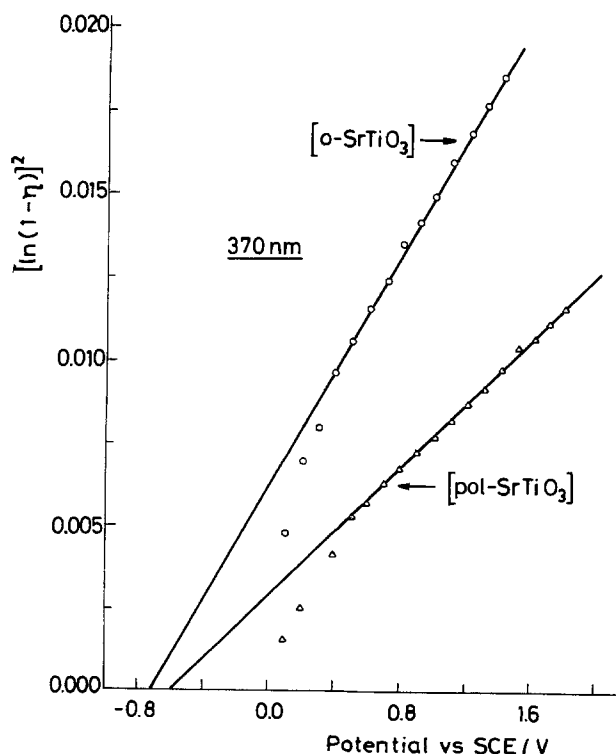


Fig. 5. Determination of V_{FB} and N_D from $[\ln(1 - \eta)]^2$ vs. potential plots at $\lambda = 370 \text{ nm}$.

Table I. Experimental physical parameters at room temperature for the samples studied

	$\sigma/0^{-1} \cdot \text{cm}^{-1}$	V_{FB} (V)	N_{D} (10^{17}cm^{-3})	E_{g} (eV)	L_{p} (cm)	W (10^{-5}cm) at 1V vs. SCE
o-SrTiO ₃	10 ⁻³	-0.70	1.7	3.15	3.1×10^{-6} (370 nm)	4.7
pol-SrTiO ₃	10 ⁻³	-0.60	3.1	2.95	9.6×10^{-7} (370 nm) 6×10^{-7} (470 nm)	3.4

Therefore, a plot of $[-h\nu \ln(1-\eta)]^{1/2}$ against $h\nu$ allows the determination of E_{g} .

Figure 6, obtained from Fig. 4, shows a linear variation of $[-h\nu \ln(1-\eta)]^{1/2}$ vs. $h\nu$ (for $h\nu > 3.3$ eV). The intercept with the $h\nu$ axis gives the E_{g} value (Table I).

Hole diffusion length, L_{p} .—Equation [2] allows L_{p} to be estimated. By introducing the value of W in Eq. [2] it can be written

$$-\ln(1-\eta) = \alpha W_0 (V - V_{\text{FB}})^{1/2} + \ln(1 + \alpha L_{\text{p}}) \quad [9]$$

where, for the sake of clarity, the ratio $(2\epsilon_r \epsilon_0 / q N_{\text{D}})^{1/2}$, whose parameters are now known, is designated as W_0 .

According to Eq. [8], the plot of $-\ln(1-\eta)$ vs. $(V - V_{\text{FB}})^{1/2}$ should be linear with a slope $S = \alpha W_0$ and an intercept

$$\ln(1 + \alpha L_{\text{p}}) = \ln \left(1 + \frac{S}{W_0} L_{\text{p}} \right)$$

from which L_{p} is obtained without needing to know the value of α .

Figures 7a and 7b are the corresponding plots at 370 nm for both samples and at 470 nm for [pol. SrTiO₃]. They are deduced from Fig. 3a and 3b and from the previously determined V_{FB} . Straight lines are obtained at high anodic bias where recombination does not exist and Gärtner's model applies. From extrapolation of the straight line obtained by minimum least squares fitting, reliable L_{p} values can be obtained. They are included in Table I. As can be seen, the assumption $W \gg L_{\text{p}}$, which allowed V_{FB} and N_{D} to be determined through Eq. [5], is now justified. The error in V_{FB} which is incurred by neglecting L_{p} in Eq. [9] is 0.09V which is not significant because the accuracy in η is not better than $\pm 10\%$, at the most.

Discussion

The two main effects of polishing on the photoelectrochemical properties of sintered n-SrTiO₃ electrodes are sensitization to visible light and decrease of the photoresponse to UV radiation. This qualitative behavior has been found to be general for the different samples studied, and has been discussed elsewhere (6). On the other hand, in an attempt to correlate this behavior with the physical properties of the electrodes, we have shown that Gärtner's model holds for the sc-electrolyte junction in the band bending region ($V - V_{\text{FB}} > 1.1\text{V}$) of negligible electron-hole recombination, both in the sc surface and in the depletion region. The experimental data shown in Table I should not be considered as reproducible to the last significant figure for different n-SrTiO₃ samples, but as typical of the effect of polishing on the physical parameters of n-SrTiO₃. A more precise study should compare measurements on several samples and probably should take into account additional information about the polishing effects; however, this exceeds the aim of the present work.

The main features observed in Table I, that polishing brings about, are a shift of V_{FB} towards positive values, an apparent increase of N_{D} , and a noticeable decrease of both E_{g} and L_{p} . The increase of N_{D} upon polishing has also been reported to occur with TiO₂ (24) and ZnO (25). This result is not surprising since lattice defects can behave as hole traps at the illuminated electrode, giving rise to an accumulation of positive charge in the depletion layer and to an apparent increase of the donor concentration. The decrease of E_{g} , as well as the positive shift of V_{FB} , could reasonably be related to a tailing of the band gap absorption due to energy states near the bandedges. These states are very likely associated with Ti—O bonds whose co-

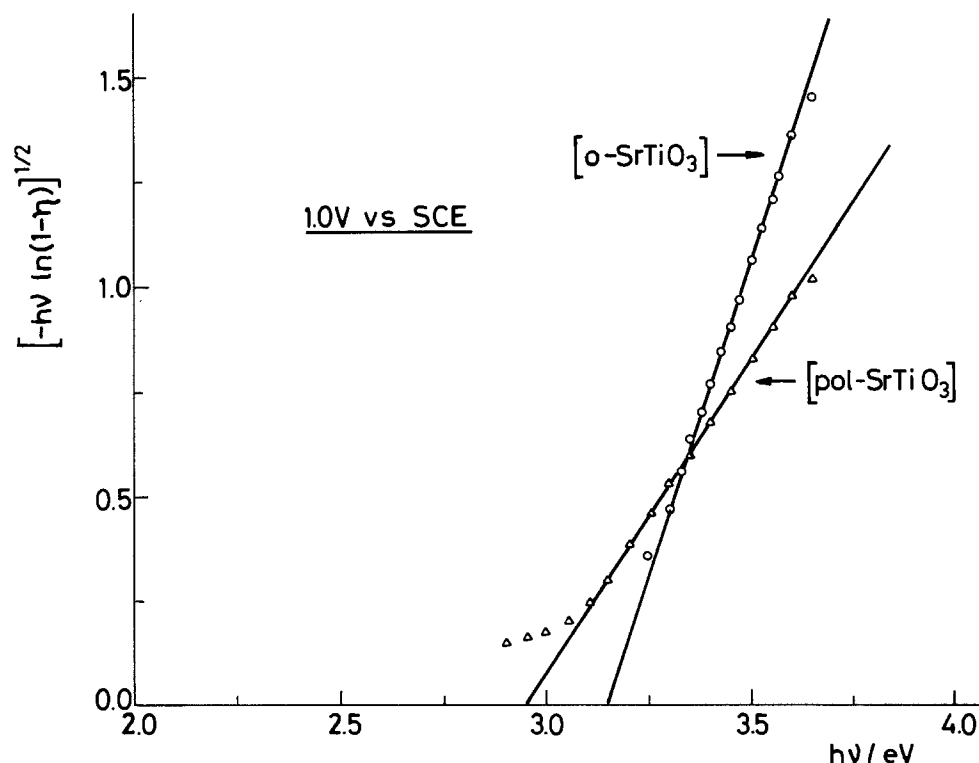


Fig. 6. Determination of E_{g} from the variation of $[-h\nu \ln(1-\eta)]^{1/2}$ as a function of $h\nu$ at 1V (vs. SCE).

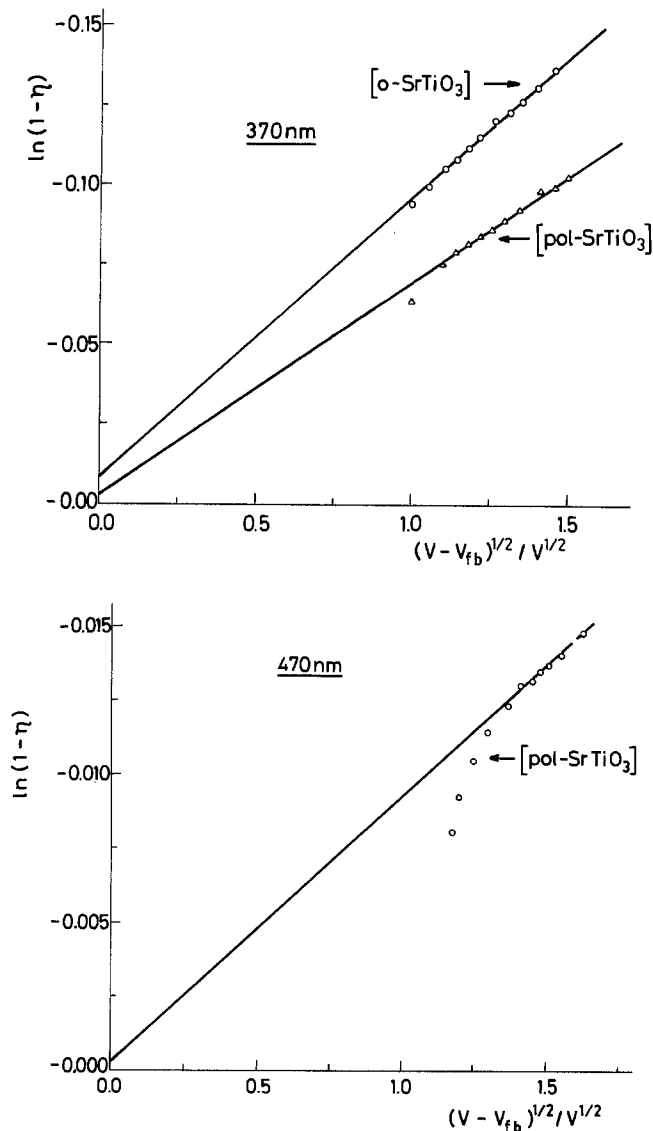


Fig. 7. Determination of L_p from $\ln(1-\eta)$ vs. $(V - V_{FB})^{1/2}$ plots. The straight lines were obtained by minimum least squares fitting of the experimental points with the following correlation factors: (a, top) 0.999 for $[o\text{-SrTiO}_3]$ and 0.997 for $[\text{pol-SrTiO}_3]$ ($\lambda = 370$ nm); (b, bottom) 0.998 for $[\text{pol-SrTiO}_3]$ ($\lambda = 470$ nm).

valency is weakened in the disordered lattice. A Ti—O bond weakening means that locally the splitting between the oxygen: 2p orbitals and the titanium: 3d (t_{2g}) orbitals is reduced. This originates $[O:2p]_{bw}$ and $[Ti:3d(t_{2g})]_{bw}$ subbandgap states (bw meaning bond weakening) close to the valence and conduction bands, respectively. As the flatband potential of the polished sample is 0.1V less negative than that of the unpolished electrode, the $[Ti:3d(t_{2g})]_{bw}$ centers should approximately lie within 0–0.1 eV below the conduction band of the unpolished sample. Besides, $E_g[o\text{-SrTiO}_3] - E_g[\text{pol-SrTiO}_3] \approx 0.2$ eV; thus, the $[O:2p]_{bw}$ levels lie within 0.1 eV above the unperturbed valence band. The shoulder in the η - λ action spectrum observed at 410 nm (3.0 eV) can be attributed to these levels (dashed line of Fig. 4). As illustrated in Fig. 8, the Ti—O bond weakening must not be misunderstood with the Ti—O bond breaking that introduces the above mentioned $[O:2p]_{bb}$ and $[Ti:3d]_{bb}$ centers.

Finally, we must remark that the charging of the tailing surface-state band generated by polishing, which is accompanied by a decrease of the net negative surface charge, could also contribute to the observed shift of V_{FB} in the anodic direction.

Figure 4 clearly shows that bandgap states generated during polishing have a deleterious effect on the

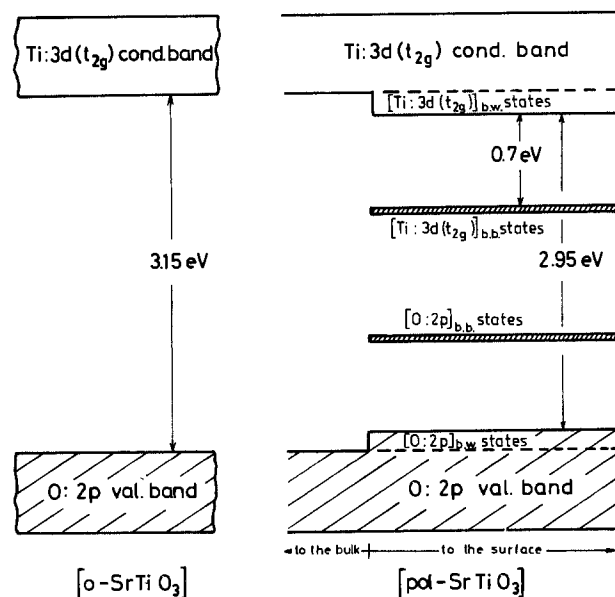


Fig. 8. Schematic of the modification of the band structure near the surface of $[\text{pol-SrTiO}_3]$.

UV photocurrent efficiency. Their influence can be described as follows.

In Eq. [2], absence of recombination at the depletion layer was assumed. However, this assumption cannot apply in the presence of a high density of recombination centers, as has been recently treated by Jarrett (26). In fact, for a hole to reach the interface with the electrolyte, its lifetime τ_r must be equal to or greater than its transit time τ_t across the electric field. Introducing the concept of "gain" used in photoconductivity experiments, it must be $Q \equiv \tau_r/\tau_t \approx 1$.

Q can be written (27)

$$Q = \frac{L_p^2 q^2 N_D}{2\epsilon_r \epsilon_0 kT} \quad [10]$$

where we distinguish the hole diffusion length in the depletion layer, L'_p , from L_p in the bulk. Then the condition for efficient electron-hole separation in the electric field region becomes (27)

$$L_p'^2 \cdot N_D \geq \frac{2\epsilon_r \epsilon_0 kT}{q^2} \quad [11]$$

For $Q < 1$, Eq. [5] (which applies to electron hole pairs generated within the depletion layer) must be written

$$\eta = Q[1 - e^{-\alpha W}] \quad [12]$$

According to Eq. [2], all the electron-hole pairs photo-generated within a $(L_p + W)$ distance from the surface must participate efficiently in the photocurrent, provided that $Q \geq 1$. A simple calculation making use of the data of Table I shows this to be the case for the unpolished sample. So, applying Eq. [11], it can be shown that $L'_p \geq 7.5 \times 10^{-6}$ cm and therefore $L'_p \geq 2.4 L_p$.

On the other hand, the net decrease in the quantum efficiency in the UV region for the polished electrode (Fig. 4) cannot be explained by a simple decrease of W and L_p (Table I). In fact, let us compare for instance η_{max} in Fig. 3 at 340 nm for the two samples. Since $Q \geq 1$ for the unpolished electrode, we can write according to Eq. [4]

$$\begin{aligned} \ln(1 - 0.41) &= -\alpha_{340 \text{ nm}}(W + L_p) \\ &= -\alpha_{340 \text{ nm}} \times 5.01 \times 10^{-5} \quad [13] \end{aligned}$$

Hence, $\alpha_{340 \text{ nm}} = 1.05 \times 10^4 \text{ cm}^{-1}$. Using the same reasoning for the polished sample, and assuming the

same $\alpha_{340 \text{ nm}}$, it should be for $Q \leq 1$ and $(L_p + W) = 3.5 \times 10^{-5}$ (Table I)

$$\eta = 1 - e^{-(L_p + W)} = 0.31 \quad [14]$$

This value is higher than the experimental one of 0.24. Obviously this discrepancy in η must result from partial recombination inside the depletion layer.

The actual value of Q can be given by the relation between both values of η , i.e., $Q = 0.24/0.31 = 0.78$, which upon insertion in Eq. [10] gives us: $L'_p = 3.7 \times 10^{-6}$ cm.

The influence of polishing on the recombination process could therefore be summarized in the following way: $[0:2p]_{bb}$ and $[\text{Ti}:3d(t_{2g})]_{bb}$ levels generated in the bandgap act as hole and electron traps, respectively, producing a measurable decrease of the carrier lifetime. In the perturbed layer, but outside the depletion layer, L_p decreases by a factor of ~ 3 ; this decrease does not affect η , as $W \gg L_p$. This factor cannot be calculated in the depletion layer (i.e., for L'_p), but it is expected to be considerably greater than that obtained for L_p , since for the unpolished sample it has been shown that $L'_p > 2.4 L_p$ (probably $L'_p \gg L_p$), while for the polished one it is only $L'_p \sim 5 L_p$. Consequently, the decrease of the quantum efficiency in the UV region after polishing is mainly due to increasing electron-hole recombination inside the electric field region. These results are in agreement with the model proposed recently by Lam and Franceschetti (28) for undoped and transition metal-doped sintered semiconducting oxide photoanodes, which took into account recombination of carriers within the depletion layer.

Recently, Praet *et al.* (10), working with TiO₂ single-crystal electrodes, arrived at the conclusion that polishing reduces L_p by a factor ranging from 3 to 183. Only the lowest value is comparable to that found in this work for polycrystalline SrTiO₃.

It becomes apparent that the optimum photoresponse is not necessarily achieved by enhancing the polishing effect in order to create a larger density of subbandgap states, but by balancing the losses due to recombination against the increase of the photoresponse in the visible region. It must also be pointed out that the holes photogenerated in the polished sample by visible ($\lambda = 470$ nm) and UV ($\lambda = 370$ nm) light have quite similar L_p values (Table I). If the visible response observed for $[\text{pol-SrTiO}_3]$ electrode was mainly due to carrier excitation from the $[0:2p]_{bb}$ states to the conduction band (Fig. 1, mechanism 1), much lower values of L_p would then have been obtained for $\lambda = 470$ nm than for $\lambda = 370$ nm, due to a partial localization of the photogenerated holes into the $[0:2p]_{bb}$ centers (small

polarons). As this does not occur, most of the holes are photogenerated in the valence band of $[\text{pol-SrTiO}_3]$ electrode. Consequently, the visible photocurrent should be mainly due to electron excitation from the valence band to the empty $[\text{Ti}:3d]_{bb}$ subbandgap states, followed by tunneling to the conduction band (Fig. 1, mechanism 2).

Manuscript submitted June 6, 1983; revised manuscript received Oct. 31, 1983.

REFERENCES

1. H. P. Maruska and A. K. Ghosh, *Sol. En. Mater.*, **1**, 237 (1979).
2. D. Redfield and W. J. Burke, *Phys. Rev. B*, **6**, 3104 (1972).
3. G. Campet, M. P. Dare-Edwards, A. Hamnett, and J. B. Goodenough, *Nouv. J. Chim.*, **4**, 501 (1980).
4. A. Mackor and G. Blasse, *Chem. Phys. Lett.*, **77**, 6 (1981).
5. B. T. Chang, G. Campet, J. Claverie, and P. Hagemüller, *Solid State Commun.*, **43**, 335 (1982).
6. B. T. Chang, G. Campet, J. Claverie, P. Hagemüller, and J. B. Goodenough, *J. Solid State Chem.*, **49**, 247 (1983).
7. H. Gerischer, F. Heim, M. Lübke, E. Meyer, B. Pettinger, and H. R. Schöppel, *Ber. Bunsenges. Phys. Chem.*, **77**, 284 (1973).
8. R. L. Van Meirhaeghe, F. Cardon, and W. P. Gomes, *ibid.*, **83**, 236 (1979).
9. R. H. Wilson, L. A. Harris, and M. E. Gerstner, *This Journal*, **126**, 844 (1979).
10. A. Praet, F. Vanden Kerchove, W. P. Gomes, and F. Cardon, *Solar Energy Mat.*, **7**, 481 (1983).
11. P. Salvador, *Solid State Commun.*, **34**, 1 (1980).
12. W. W. Gärtner, *Phys. Rev.*, **116**, 84 (1959).
13. J. H. Kennedy and K. W. Frese, *This Journal*, **123**, 1683 (1976).
14. M. A. Butler, *J. Appl. Phys.*, **18**, 1 (1979).
15. H. Reiss, *This Journal*, **125**, 937 (1978).
16. R. H. Wilson, *J. Appl. Phys.*, **48**, 4292 (1977).
17. P. Salvador, *This Journal*, **123**, 1895 (1981).
18. P. Salvador, *Mater. Res. Bull.*, **15**, 1287 (1980).
19. P. Salvador, *Solar Energy Mat.*, **2**, 413 (1980).
20. P. Salvador and C. Gutiérrez, *J. Electroanal. Chem.*, In press.
21. A. A. Soliman and H. J. J. Seguin, *Solar Energy Mat.*, **6**, 201 (1982).
22. H. A. Weakliem, W. J. Burke, D. Redfield, and V. Korsum, *R.C.A. Rev.*, **36**, 149 (1975).
23. M. A. Butler, *This Journal*, **128**, 200 (1981).
24. K. Vos and H. J. Krusemeyer, *J. Phys. C*, **10**, 3893 (1977).
25. S. R. Morrison and T. Freund, *NBS Spec. Publ.* **455**, 139 (1976).
26. H. S. Jarrett, *J. Appl. Phys.*, **52**, 4681 (1981).
27. P. Salvador, *ibid.*, In press.
28. R. U. E. 't Lam and D. R. Franceschetti, *Mater. Res. Bull.*, **17**, 1081 (1982).

Vacuum Evaporated CdSe_{1-x}Te_x Thin Films for Electrochemical Photovoltaic Cells

Michael A. Russak and Charles Creter

Grumman Aerospace Corporation, Research and Development Center, Bethpage, New York 11714

ABSTRACT

CdSe_{1-x}Te_x thin films have been produced over a wide range of x values by concurrent vacuum evaporation of the constituent elements. The most consistent results in terms of producing single-phase material were obtained when substrate temperatures were in the range of 350°-450°C. Photoelectrochemical evaluation of the resultant thin films indicated postdeposition heat-treatment and surface etching were necessary to maximize photovoltaic outputs. A dependence of photoelectrochemical behavior, bandgap, and efficiency on x value was also found. The maximum efficiency recorded was 7.4% for a CdSe_{0.8}Te_{0.2} composition under simulated AM2 conditions.

The thin film CdSe/aqueous sulfide-polysulfide photoelectrochemical system has received a great deal of attention in recent years as a potentially practical, low-cost system for photovoltaic applications (1-6). However, even though CdSe electrodes with sunlight conversion efficiencies (η) of over 6% have already been reported (7), the bandgap of CdSe (1.72 eV) is not ideally matched to the solar spectrum. This may be ultimately a limitation on obtaining conversion efficiencies in excess of 10% when counterelectrode polarization losses are encountered in actual cell structures. Ideally, a semiconductor with a bandgap of 1.45 eV, such as CdTe, would provide the maximum photovoltaic efficiency for terrestrial applications (*i.e.*, AM1 to AM2 conditions) (8, 9). However, CdTe has been reported to be stable in selenide and telluride containing electrolytes, but only partially stable in sulfide containing electrolytes. The highly colored nature of the former electrolytes diminishes the advantage of the more favorable bandgap by increasing the short wavelength photocurrent losses. As a result, no significant improvement in efficiency of the CdTe/Se_n⁻² system compared to the CdSe/S_n⁻² system has been reported (10). Also, the extreme air sensitivity of the selenide and telluride containing electrolytes presents a problem for practical devices.

Fortunately, a promising compromise has been identified where polycrystalline electrodes have been produced from mixtures of CdSe and CdTe that have a bandgap of ~1.45 eV and the photovoltaic output stability of CdSe alone in sulfide-polysulfide electrolyte (11, 12). In particular, an electrode of CdSe_{0.65}Te_{0.35} composition prepared by sintering a mixture of CdSe and CdTe has been produced with η ~8% (11).

We have found that CdSe_{1-x}Te_x alloy films for photoelectrochemical solar cells can also be produced by a concurrent elemental vacuum evaporation technique. This paper presents our findings on the evaluation of these thin film electrodes in aqueous sulfide-polysulfide electrolyte.

Experimental

CdSe_{1-x}Te_x thin films were deposited by the concurrent vacuum evaporation of the constituent elements from three independently controlled resistive heated sources arranged in a parallel geometry. Each source was controlled by a microprocessor-driven feedback controller activated by an oscillating quartz crystal monitor. The actual vacuum system used is shown in Fig. 1, with the three automatic deposition controllers (Sloan Technology Corporation, Santa Barbara, California) in the background. The key feature of this system is the tubular shielding arrangement of the crystal monitors by which no interference between deposition

sources is registered. The vertical baffles between sources minimize extraneous heating of one source by the adjacent one, which could otherwise be a problem due to the low power level required to evaporate the elements used. High purity (5N⁺ or 6N) elements in 1-5 mm shot form were used as the source materials (Alpha Division, Ventron Corporation, Danvers, Massachusetts, or Atomergic, Incorporated, Plainview, New York).

Individual depositions of each element indicated that there was approximately a 10% thickness gradient for Se in going from left to right across the 12 cm substrate holder. The Te gradient is also about 10% in the opposite direction. The thickness of Cd was found to vary by less than 5% in going from the center to the edges of the substrate holder. To minimize the effect of these gradients, the substrates were placed in a 5 × 5 cm area in the center of the substrate holder for the ternary evaporations. The source to substrate distance was 45 cm. The substrates were titanium sheet (0.25 mm) that had been carefully cleaned and then etched in a dilute HCl:HF etchant to provide a slight surface roughness, which promoted good film adherence. The substrates were clamped to the copper-block substrate holder, into which cartridge-type heaters and a thermocouple were inserted to provide substrate temperature control during the deposition. Tantalum

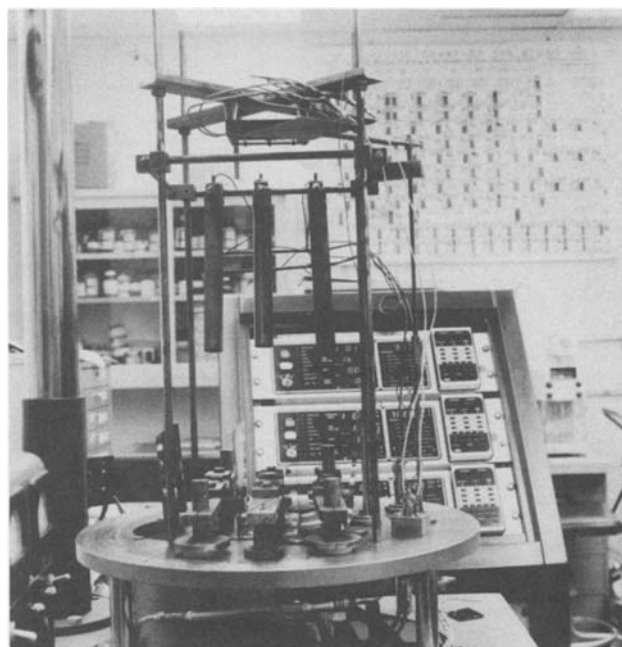


Fig. 1. Triple source vacuum deposition system used to produce CdSe_{1-x}Te_x thin film.

Key words: semiconductor, thin films, electrolyte, energy conversion.

buffed evaporation boats, the type commonly used for silicon monoxide evaporation, were used for the Cd and Se, but the Te reacted with the tantalum boats and an Al₂O₃ crucible was used.

Qualitative chemical analysis of the thin films was done by energy dispersive analysis of x-rays (EDAX) at Grumman, and quantitative compositional data were generated using a wavelength dispersive electron microprobe (EPMA) at the Solar Energy Research Institute (SERI, Golden, Colorado). X-ray diffraction analysis was done using a diffractometer with CuK α radiation.

The thin film electrode mounting procedures and photoelectrochemical test fixturing employed have been described previously (3). I-V characteristics were measured in aqueous 2.5M Na₂S-1M S-1M KOH electrolyte using a platinum counterelectrode and a saturated calomel reference electrode in a standard potentiostatic arrangement. White light measurements were done using a simulated AM2 spectrum provided by a W-I ELH lamp mounted in a dichroic parabolic reflector (13). A 0.25m grating monochromator with a 1000W Xe light source was used to generate monochromatic I-V curves and spectral response data. All light intensities were measured with a calibrated thermopile detector.

Results and Discussion

Thin film deposition.—Several deposition parameter-variation studies were conducted in order to establish the relationships among deposition conditions, resultant film composition and structure, optical and electronic properties, and current-voltage behavior. Three critical deposition parameters for producing single-phase, crystalline ternary thin films of a specific composition were found: substrate temperature (T_s), the Se to Cd atomic vapor stream ratio, and the total Se + Te to Cd atomic vapor stream ratio. The most critical steps in optimizing the photovoltaic output of the ternary thin film electrodes were postdeposition heat-treatment and chemical surface treatment (etching) of the heat-treated electrodes.

Based on previous experience with producing CdSe thin film electrodes by vacuum evaporation, two deposition regimes were investigated in the most detail (3, 5, 14). Initially, a series of ternary depositions was done, during which T_s was held at 100°C, the total Se + Te to Cd atomic ratio was set at three, and the ratio of Se to Te was varied. This general approach was analogous to that taken in producing the CdSe films deposited with excess Se, which have produced the highest efficiencies reported to date (3, 6). The composition and associated EDAX spectra (after firing at 500°C for 15 min) for this series of depositions are shown in Fig. 2. The variation of I-V performance for these films, which were only partially crystalline as deposited, was found to depend on postdeposition heat-treatment temperature, time, and atmosphere. Heat-treatment in the range of 400°-500°C in air produced the electrodes with the best photovoltaic output ($\eta \sim 5\%$, AM2), which is similar to the results obtained in the CdSe system. However, measurement of the action spectra of these electrodes showed very little extension of response into the near IR, as would be expected with the addition of increasing amounts of Te into this alloy system. X-ray diffraction analysis revealed the films were a mixture of CdSe and TeO₂ rather than a CdSe expanded lattice as would be expected with the addition of up to 0.22 mol fraction Te (15, 16). So, even though the presence of Te was maintained in these films throughout their processing, as indicated by EDAX, it was incorporated in a nonphotoactive manner in the final processed electrode. Post-deposition processing in vacuum or inert gas atmosphere was not successful in producing good photovoltaic quality CdSe_{1-x}Te_x material from films deposited under these conditions.

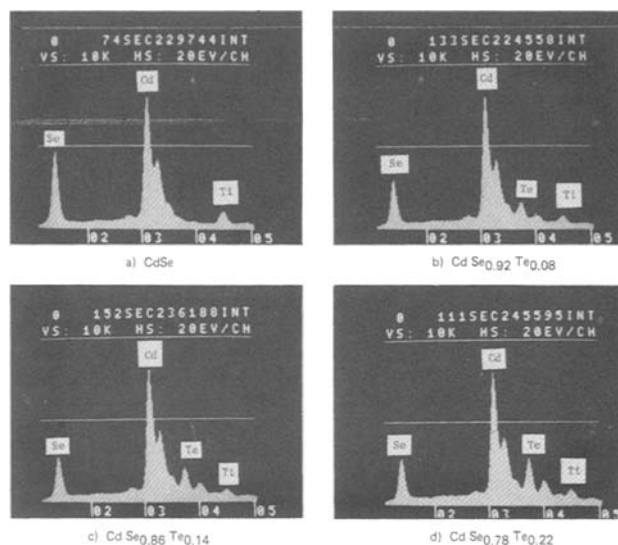


Fig. 2. EDAX spectra showing variation in relative amounts of Se and Te in alloy films deposited at 100°C and heat-treated at 500°C in air.

As a result of these findings, it was concluded that a better approach to producing single-phase CdSe_{1-x}Te_x films would be to insure the selected compound formation by deposition at high T_s followed by subsequent heat-treatment to optimize I-V output. It was found that a full range of single-phase crystalline CdSe_{1-x}Te_x films ($0 \leq x \leq 0.53$) could be produced by the direct reaction of the elements on substrates held at 300°-450°C. At temperatures below 300°C, the films were generally only partially crystallized, whereas at $T_s > 450^\circ\text{C}$, even though the films were crystalline, film adherence was poor and Te could not always be put in the film. The actual x value in the as-deposited ternary film was found to depend on the Se to Cd ratio during deposition and T_s . This is shown in Table I, where the dependence of alloy composition on this ratio is presented for $T_s = 400^\circ\text{C}$. X-ray diffraction analysis indicated that all these films were single-phase material with a strong texture. Films A through E had hexagonal wurtzite structures, with lattice parameters increasing with increased Te content, whereas film F had a cubic sphalerite structure. These findings are in agreement with those already reported for this alloy system (15, 16). The columnar microstructure of these films was quite evident, as shown in Fig. 3, which is a scanning electron micrograph of film C. Another trend in the ternary films was that at a constant Se to Cd ratio and fixed Te rate, less Te was incorporated into the film as T_s was increased. This behavior is shown in Table II for atomic vapor stream ratios of 0.63 to 1 to 0.9 for Se, Cd, and Te, respectively. The data trends summarized in Tables I and II indicate that thermodynamically it is easier to form CdSe than to

Table I. Dependence of thin film composition* on Se to Cd atomic vapor stream ratio at $T_s = 400^\circ\text{C}$

Sample	Atomic ratio (calculated) Se: Cd**	Composition (a/o)			Atomic ratio (measured) Se: Cd
		Cd	Se	Te	
A	0.90	51.06 ± 1.42	48.38 ± 1.35	0.56 ± 0.07	0.95
B	0.80	51.10 ± 1.93	46.22 ± 1.74	2.67 ± 0.88	0.90
C	0.63	51.53 ± 2.57	39.76 ± 1.98	8.72 ± 0.43	0.77
D	0.58	50.86 ± 2.73	36.59 ± 1.31	12.55 ± 0.85	0.72
E	0.51	50.38 ± 3.28	32.54 ± 1.14	17.08 ± 2.09	0.65
F	0.31	49.61 ± 1.34	23.80 ± 0.64	26.60 ± 0.72	0.48

* Chemical composition done using an electron microprobe with CdSe and CdTe single-crystal standards.

** The Te deposition rate was constant.

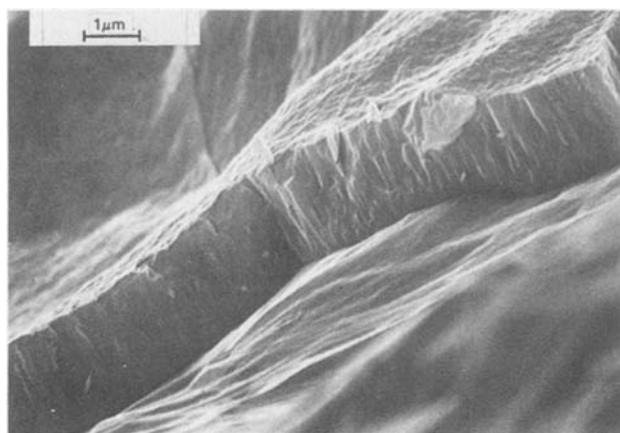


Fig. 3. SEM micrograph of film C (Table I) showing roughened titanium substrate and columnar microstructure of thin film.

form the $\text{CdSe}_{1-x}\text{Te}_x$ ternary when sufficient Se is present. This is consistent with the difference in heats of formation for CdSe and CdTe (17).

The compositional uniformity of the thin films produced by the elemental evaporation method was checked using the electron microprobe. Figures 4-6 show the composition variation found in a CdSe, a CdTe, and a $\text{CdSe}_{0.8}\text{Te}_{0.2}$ (film C, Table I) film all deposited at $T_s = 400^\circ\text{C}$. As can be seen from these results, there is very little compositional variation.

Photoelectrochemical evaluation.—As found with CdSe thin films produced by elemental evaporation, the as-deposited $\text{CdSe}_{1-x}\text{Te}_x$ films exhibited very poor photovoltaic response. It was therefore necessary to heat-treat them to optimize their I-V performances (5). Postdeposition heat-treatment in air in the range of 400°C – 450°C provided the best photovoltaic performance. The relationship between optical bandgap and ternary composition was determined by noting the longest wavelength of light for which a photocurrent was observed for each electrode. In these experiments, a polysulfide electrolyte was used for junction formation. The electrodes were photoetched before testing (18, 19), then held in reverse bias to insure prompt photogenerated carrier separation. Lock in detection was used to measure the photoresponse. The results

Table II. Variation in Se and Te content of $\text{CdSe}_{1-x}\text{Te}_x$ thin films with T_s for Se: Cd: Te ratio of 0.63:1:0.9

T_s ($^\circ\text{C}$)	Composition (a/o)		
	Cd	Se	Te
350	51.22 ± 0.60	35.62 ± 0.42	13.16 ± 0.04
375	51.02 ± 2.04	37.43 ± 1.79	11.55 ± 0.55
400	51.53 ± 2.57	39.76 ± 1.98	8.72 ± 0.43
425	51.10 ± 1.52	47.22 ± 1.30	2.30 ± 0.21
450	50.58 ± 1.01	49.42 ± 0.98	< 1

are summarized in Fig. 7. The E_g values used for CdSe and CdTe in this figure were determined for thin film electrodes deposited by coevaporation of Cd + Se and Cd + Te, respectively, at $T_s = 400^\circ\text{C}$. There is a decrease in bandgap with increasing Te content to a minimum at an x value of ~ 0.5 , after which it increased up to the value of 1.45 eV for CdTe. It should be noted that the minimum of 1.36 eV occurs for a film that is of the cubic structure, which is in agreement with previously reported results (15, 16). The cubic phase is, however, photoelectrochemically less stable than the hexagonal phase in sulfide-polysulfide electrolyte and therefore of less interest for actual photovoltaic cell applications (16).

Photoelectrochemical performance of thin film electrodes in this alloy system was also investigated. The significant findings were that as x was increased up to 0.53, the resultant spectral response extended further into the near IR, as shown in Fig. 7. However, only for $x < 0.25$ did J_{sc} increase with the addition of Te. The flatband potential (V_{FB}), measured by determining the high intensity photocurrent onset potential, became more positive. There was less band bending in the electrode, and the open-circuit voltage (V_{oc}) decreased. Also, as the Te content increased, the light I-V curve developed a "foot" characteristic near the V_{oc} , which is indicative of a recombination-dominated behavior rather than one dictated by dark current (20). In addition, for $x > 0.25$, the photoetching treatment was less effective in improving the I-V performance. Table III summarizes the variation of V_{FB} , V_{oc} , λ_{to} (maximum wavelength of photoresponse), and maximum AM2 conversion efficiency (η_{max}) as a function of Te content. Figures 8-10 show the effect of photoetching treatment on the I-V performance of CdSe, $\text{CdSe}_{0.8}\text{Te}_{0.2}$ (film C), and $\text{CdSe}_{0.47}\text{Te}_{0.53}$ (film F) electrodes.

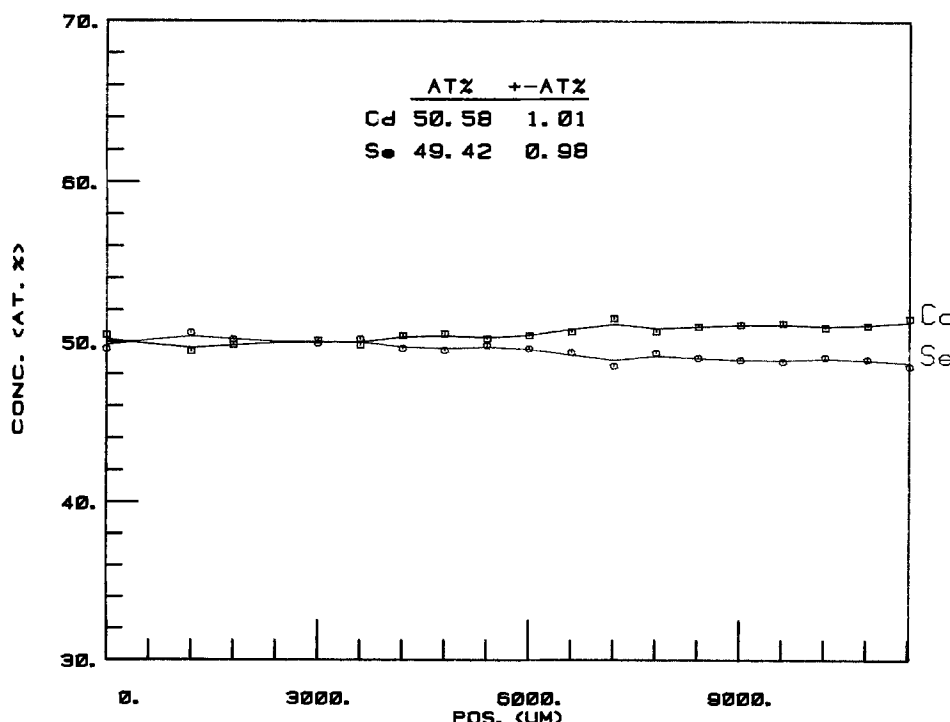


Fig. 4. Compositional uniformity of a CdSe film deposited by coevaporation of Cd and Se at $T_s = 400^\circ\text{C}$.

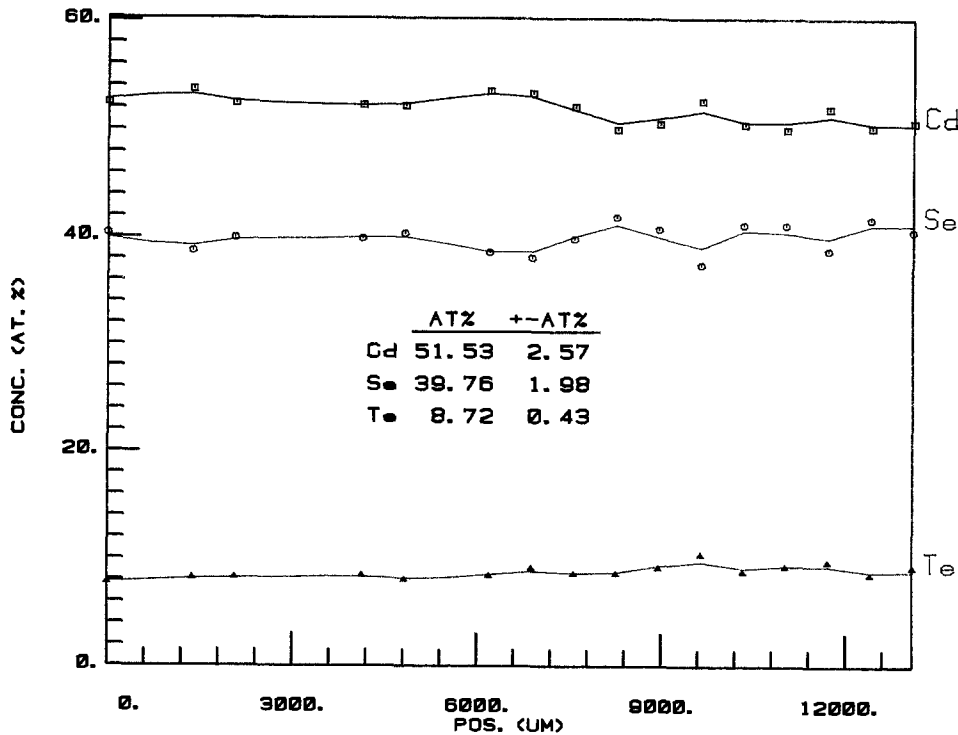


Fig. 5. Compositional uniformity of a CdTe film deposited by coevaporation of Cd and Te at $T_s = 400^\circ\text{C}$.

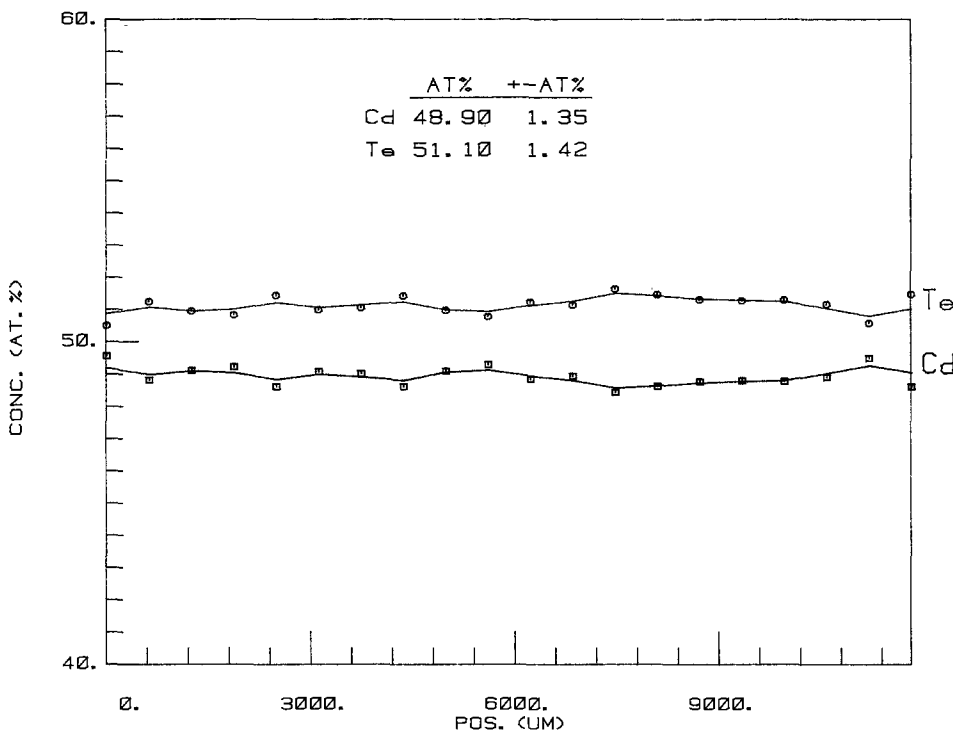


Fig. 6. Compositional uniformity of a CdSe_{0.8}Te_{0.2} (film C) deposited by simultaneous evaporation of Cd, Se, and Te at $T_s = 400^\circ\text{C}$.

The data in Table III indicate there is a minimum in the V_{FB} vs. composition relationship, which correlates with the minimum in the bandgap of the alloy films. The minimum also corresponds to the maximum in spectral response. This trend is contrary to that reported in the CdSe_{1-x}S_x thin film system, where a maximum in V_{FB} was found with alloy composition (21). These results are also unexpected, based on reported values of electron affinity for CdSe (4.95 eV) and CdTe (4.28 eV) (22). Since the electron affinity of the ternary should be between these two values, a more negative V_{FB} should result for the alloy film compared with CdSe. Yet, the V_{FB} of n-CdTe (single crystal) has been measured to be somewhat positive of CdSe (single crystal) (23). Although, in some cases, the conduction-band energy level of CdTe has been placed below that of CdSe on a composite redox

couple-semiconductor energy diagram, implying a more positive V_{FB} (24). There is obviously some disagreement here, and the observed variation of V_{FB} (and V_{oc}) with Te content cannot be explained solely by consideration of the electron affinities of CdSe and CdTe. It is possible that the surface condition of these electrodes changes with increasing Te content in such a manner that a change in the Helmholtz layer potential drop occurs. This drop could then shift the V_{FB} to more positive values (20). This would be consistent with the persistence of the "foot" characteristic in the I-V curves shown in Fig. 8-10 with increasing x value, even after photoetching.

Further investigation of the CdSe_{1-x}Te_x thin film characteristics was carried out by applying a Gartner model analysis, in which, if the junction is assumed to be a Schottky barrier and recombinations can be ne-

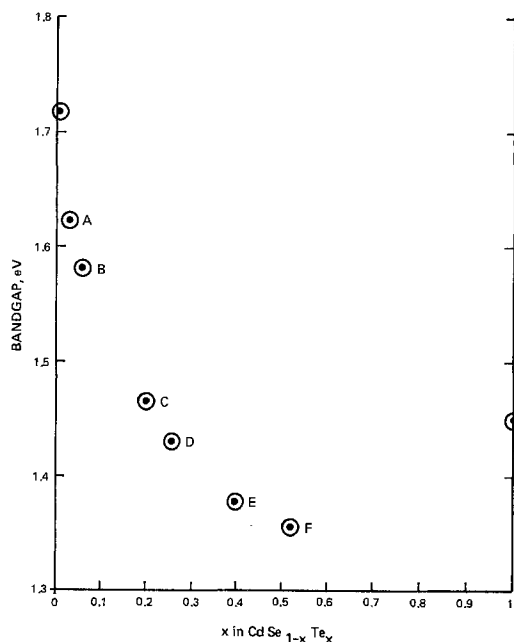


Fig. 7. Dependence of bandgap on composition in $\text{CdSe}_{1-x}\text{Te}_x$ alloy system.

glected in the space charge layer, with sufficient reverse bias the monochromatic quantum yield (ψ_m) is given by (25)

$$\psi_m = 1 - e^{-\alpha W_0} / (1 + \alpha L_p) \quad [1]$$

where α is the absorption coefficient at a particular wavelength, L_p is the minority carrier diffusion length, and W_0 is the depletion width given by

$$W_0 = (\epsilon_0 \epsilon \Delta V / 2qN)^{1/2} \quad [2]$$

where ϵ_0 is the permittivity of free space, ϵ is the semiconductor dielectric constant, ΔV is the barrier height, which has a maximum value of $[V_{\text{FB}} - V_{\text{redox}}]$, q is the elementary charge, and N the majority carrier density. If Eq. [2] is substituted into Eq. [1], then the relationship between ψ_m and the applied reverse bias voltage (V_a) can be written as

$$\ln(1 - \psi_m) = \alpha (\epsilon_0 \epsilon / 2qN)^{1/2} (V_{\text{FB}} - V_a)^{1/2} - \ln(1 + \alpha L_p) \quad [3]$$

Then a plot of $\ln(1 - \psi_m)$ vs. $(V_{\text{FB}} - V_a)^{1/2}$ should yield a straight line (at high enough reverse bias) with a slope of $-\alpha (\epsilon_0 \epsilon / 2qN)^{1/2}$ and intercept of $-\ln(1 + \alpha L_p)$, from which N and L_p can be obtained, provided α is known.

Table III. Variation of flatband potential, open-circuit voltage, spectral response, and efficiency of $\text{CdSe}_{1-x}\text{Te}_x$ thin film electrodes^a

Sample	Composition	V_{FB} (V)	V_{oc} (V)	λ_{to} (nm)	η_{max} (%)
	CdSe	-1.60	0.67	730	4.7
A	$\text{CdSe}_{0.99}\text{Te}_{0.01}$	-1.59	0.60	770	4.8
B	$\text{CdSe}_{0.93}\text{Te}_{0.05}$	-1.55	0.58	785	5.1
	$\text{CdSe}_{0.89}\text{Te}_{0.11}^b$	-1.53	0.55	810	5.8
C	$\text{CdSe}_{0.81}\text{Te}_{0.19}$	-1.50	0.53	840	7.4
D	$\text{CdSe}_{0.75}\text{Te}_{0.25}$	-1.45	0.49	850	5.0
E	$\text{CdSe}_{0.67}\text{Te}_{0.33}$	-1.38	0.44	862	4.2
F	$\text{CdSe}_{0.47}\text{Te}_{0.53}$	-1.25	0.37	910	2.6
	CdTe	-1.45 ^c	—	845 ^d	< 1

^a All values taken after chemical etch in 25% HNO_3 and photoetch treatments.

^b This is a calculated composition based on deposition parameters and not actually measured.

^c Literature value for n-CdTe single crystal (23).

^d Determined with p-type CdTe thin film electrode produced by coevaporation of Cd and Te.

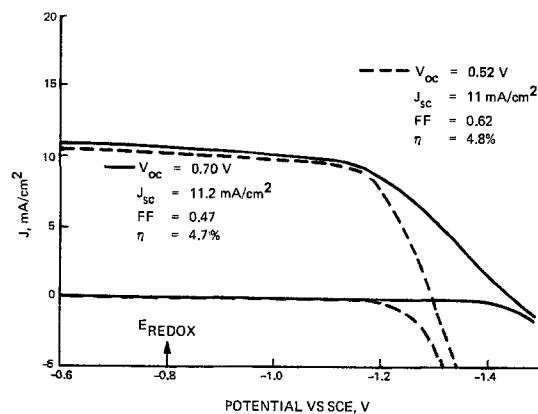


Fig. 8. I-V curves for CdSe/thin film electrode before (—) and after (---) photoetching treatment.

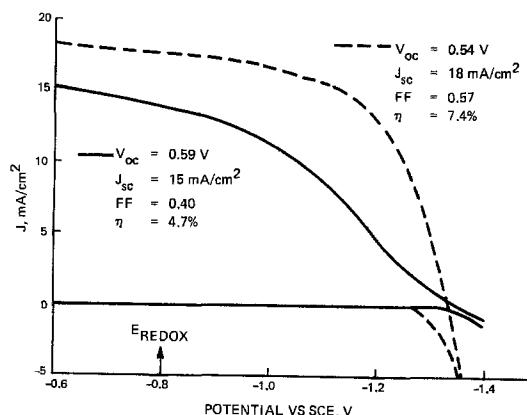


Fig. 9. I-V curves for $\text{CdSe}_{0.8}\text{Te}_{0.2}$ (film C) electrode before (—) and after (---) photoetching treatment.

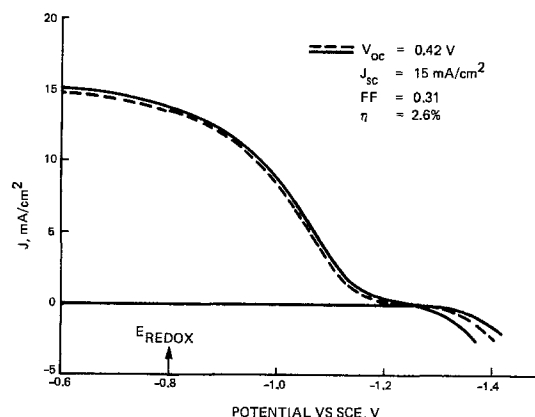


Fig. 10. I-V curves for $\text{CdSe}_{0.47}\text{Te}_{0.51}$ (film F) electrode before (—) and after (---) photoetching treatment.

The analysis was carried out using 700 nm radiation, a wavelength where absorption occurs in the bulk of the material, thereby eliminating surface effects, and α values determined in our laboratory for the CdSe and $\text{CdSe}_{1-x}\text{Te}_x$ films in Table III. The results of this analysis indicated that the N levels were fairly constant. However, the L_p and quantum yield (ψ_m) values decreased significantly as x increased beyond 0.2. These results are summarized in Table IV. They support the explanation that, for this type of film, recombination dominates the I-V performance as x increases.

The maximum photovoltaic performance for these films was recorded for the $\text{CdSe}_{0.8}\text{Te}_{0.2}$ composition (Fig. 9); $\eta = 7.4\%$ was obtained. In this case, the photoetching treatment had a significant effect on the light

Table IV. Variation of N , L_p , and Φ_m with x for CdSe_{1-x}Te_x thin film electrodes

Sample	x value	N (cm ⁻³)	L_p (μ m)	Φ_m (at 700 nm)
A	0.00	8×10^{16}	0.38	0.62
B	0.01	3×10^{16}	0.20	0.68
C	0.05	4×10^{16}	0.22	0.72
D	0.19	5×10^{16}	0.18	0.61
E	0.25	8×10^{16}	0.11	0.49
F	0.33	1×10^{17}	0.01	0.39
F	0.53	7×10^{16}	0.08	0.40

and dark I-V curves. SEM micrographs of the film before and after etching (Fig. 11) reveal a selective etch pattern that increases the electrode surface area and thereby improves light collection and electrode kinetics. But the etching also improves the long wavelength photoresponse of the electrode. This is evidenced by the change in the action spectrum of this electrode shown in Fig. 12. Photoetching significantly flattens out the action spectrum at longer wavelengths where absorption is occurring outside the space charge layer. This indicates that the bulk properties of the film have improved. However, the absorption edge itself is still rather broad, indicating that there are transitions occurring with less than full bandgap light due to energy levels within the bandgap. Any changes at shorter wavelengths are obscured by the electrolyte absorption below about 520 nm. The reasons for the decrease in effectiveness of the photoetching treatment at $x > 0.20$ are not known at present. However, based on the results shown in Table IV, the decreasing L_p found at $x > 0.20$ indicates that the electronic transport properties of the films are poor in this composition range and

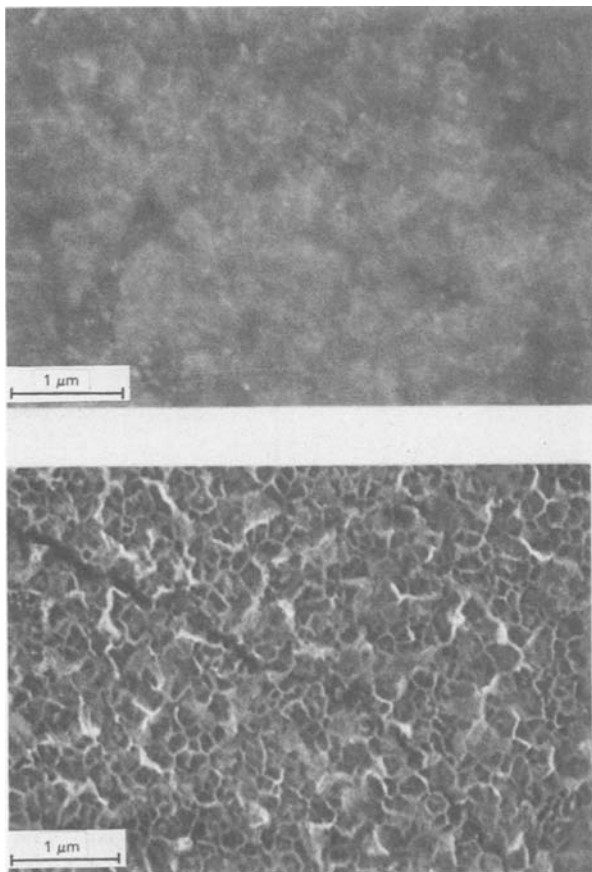


Fig. 11. SEM pictures showing surface of film C before and after photoetching treatment.

may be the most dominant factor controlling the I-V behavior, regardless of the condition of the near surface region.

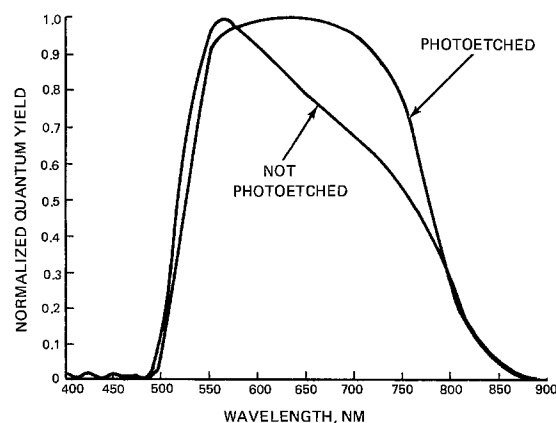


Fig. 12. Effect of photoetching on spectral response characteristics of CdSe_{0.8}Te_{0.2} electrode with 7.4% conversion efficiency after photoetching.

The output stability of these electrodes was found to follow a trend similar to that already reported for slurry painted CdSe_{1-x}Te_x material (16, 26). Films A to C have been run for several weeks at the maximum power point under constant illumination (~ 100 mW/cm², IR-filtered Xe arc) with less than 5% decrease in efficiency. Films D, E, and F showed decreases in power output of 15%, 40%, and 75%, respectively, after two weeks of constant illumination.

Summary

The concurrent elemental evaporation technique has been shown to be a suitable method for the deposition of alloy films in the CdSe_{1-x}Te_x system. The critical deposition parameters were found to be the substrate temperature and the Cd to Se vapor stream ratio. The compositional uniformity of the films was excellent, and the photovoltaic output improved with increasing x value up to $x = 0.20$, above which it decreased. In general, as the Te content in the films increased (over the range of $0 \leq x \leq 0.53$) the spectral response of the film was shifted to longer wavelengths, but the quantum efficiency and the minority carrier diffusion length decreased. As a result, the I-V curves took on a recombination dominated shape, rather than one dictated by dark current. However, an optimum combination of spectral response, electrode band bending, and transport properties occurred for the CdSe_{0.81}Te_{0.19} composition, resulting in a power conversion efficiency of 7.4% under simulated AM2 conditions.

Acknowledgments

Funding for this work was provided by the Solar Energy Research Institute (SERI), Golden, Colorado. The authors gratefully acknowledge the contribution of Chuck Herrington of SERI in providing the quantitative chemical data using electron microprobe analysis. Technical discussions with Joseph Reichman of Grumman are also acknowledged, as is the technical assistance of Joseph Havranek.

Manuscript submitted June 21, 1983; revised manuscript received Sept. 21, 1983.

Grumman Aerospace Corporation assisted in meeting the publication costs of this article.

REFERENCES

- G. Hodes, J. Manassen, and D. Cahen, *Nature*, **261**, 406 (1976).
- J. Manassen, G. Hodes, and D. Cahen, *This Journal*, **124**, 532 (1977).
- M. A. Russak, J. Reichman, H. Witzke, S. K. Deb, and S. N. Chen, *ibid.*, **127**, 725 (1980).
- G. Hodes, D. Cahen, J. Manassen, and M. David, *ibid.*, **127**, 2252 (1980).
- J. Reichman and M. A. Russak, *ibid.*, **128**, 2025 (1981).

6. M. A. Russak and J. Reichman, *ibid.*, **129**, 542 (1982).
7. J. Reichman and M. A. Russak, *J. Appl. Phys.*, **53**, 708 (1982).
8. J. Loferski, *ibid.*, **27**, 777 (1956).
9. H. Hovel, "Semiconductors and Semimetals: Vol. 11, Solar Cells," p. 75, Academic Press, New York (1975).
10. A. Heller, K. C. Chang, and B. Miller, in "Semiconductor Liquid-Junction Solar Cells," A. Heller, Editor, p. 54, The Electrochemical Society Softbound Proceedings Series, Princeton, NJ (1977).
11. G. Hodes, *Nature*, **285**, 29 (1980).
12. G. Hodes, J. Manassen, S. Neagu, D. Cahen, and Y. Mirovsky, *Thin Solid Films*, **90**, 433 (1982).
13. K. Yaas and H. B. Curtis, NASA Report no. NASA TM-X-3059, Springfield, VA (1968).
14. D. Bonnet and E. Rickus, in "Proceedings of the 14th PV Specialists Conference," p. 629, IEEE, New York (1980).
15. A. D. Stuckes and G. Farrell, *J. Phys. Chem. Solids*, **25**, 477 (1964).
16. D. Cahen, G. Hodes, and J. Manassen, "Photoeffects at Semiconductor Electrolyte Interfaces," p. 369, ACS Symposium Series 146 (1980).
17. M. R. Lorenz, in "II-VI Semiconducting Compounds," D. G. Thomas, Editor, p. 215, W. A. Benjamin, Inc., New York (1967).
18. R. Tenne and G. Hodes, *Appl. Phys. Lett.*, **37**, 4, 428 (1980).
19. C. J. Lui, J. Olsen, D. R. Saunders, and J. H. Wang, *This Journal*, **128**, 1224 (1981).
20. J. Gobrecht and H. Gerischer, *Solar Energy Mater.*, **2**, 131 (1979).
21. R. Noufi, P. Kohl, and A. Bard, *This Journal*, **125**, 375 (1978).
22. A. Milnes and D. Feucht, "Heterojunctions and Metal-Semiconductor Junctions," p. 8, Academic Press, New York (1972).
23. M. S. Wrighton, A. B. Bocarsly, J. M. Bolts, A. B. Ellis, and K. D. Legg, in "Semiconductor Liquid-Junction Solar Cells," A. Heller, Editor, p. 138, The Electrochemical Society Softbound Proceedings Series, Princeton, NJ (1977).
24. A. Heller and B. Miller, *Electrochim. Acta*, **25**, 29 (1980).
25. W. W. Gartner, *Phys. Rev.*, **116**, 84 (1959).
26. G. Hodes, J. Manassen, and D. Cahen, *J. Am. Chem. Soc.*, **102**, 5962 (1980).

Electrochemical Removal and Concentration of Hydrogen Sulfide from Coal Gas

Hyun S. Lim*† and Jack Winnick*

Georgia Institute of Technology, Atlanta, Georgia 30332

ABSTRACT

An electrochemical membrane concentration cell was demonstrated as an effective means of removing and concentrating H₂S from a hot gas stream. The device consists of a high temperature molten sulfide electrolyte with porous carbon electrodes. The process-gas is passed through the cathode chamber, where H₂S is selectively removed. With passage of current, the anion migrates to the anode, where elemental sulfur is evolved. Removal rates and cell overpotentials are reported as functions of current densities, gas flow rates and composition, and temperature.

The product gas from advanced coal gasifiers will likely be utilized in combined-cycle or molten carbonate-based energy conversion systems. Whether used in this or similar manner for electric power generation or converted to SNG for direct use, nearly all the sulfur must be removed. Hydrodesulfurization converts the complex sulfur species primarily to H₂S.

Current processes for H₂S removal are based on aqueous scrubbing (e.g., Selexol, Rectisol). Regeneration of the scrubbing liquor can provide a concentrated stream of H₂S, which can then be converted to elemental sulfur in the Claus process. Alternative processes produce SO₂, which must then be reduced to yield sulfur. There is a need for a simpler process which would operate at or near gasifier temperatures (700°-1000°C).

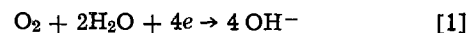
Electrochemical membrane concentrators have been used to remove dilute levels of contaminant gases and to concentrate them into by-product streams. Electrochemical concentration involves an electrochemical reaction at one electrode and the reverse reaction at the other electrode. Thus, there is no net cell reaction, but there is a net transfer of mass from a region of low concentration to a region of high concentration.

We here examine the application of an electrochemical concentrator to remove H₂S from coal gas and concentrate it into usable form. In concept, the contaminated coal gas is fed to the cathodes of a multi-cell stack of electrochemical concentrators operating at the gasifier temperature and pressure. Elemental

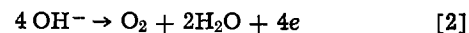
sulfur is emitted from the anodes. The clean-up process, as envisioned, would not involve scrubbing and concomitant loss of sensible heat and pressure head. Transfer of the H₂S is effected by diffusion through porous electrodes, migration of sulfide ions through the membrane, and evolution of sulfur at the other electrode.

Theory

Electrochemical membrane cells have been used to purify gaseous components. For example, oxygen has been extracted from air or other gaseous mixtures (1). The O₂ is selectively removed from the gas mixture at one electrode, transported ionically, and emitted at the other electrode. Oxygen is reduced at the cathode to form hydroxide ions

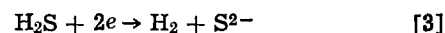


Four hydroxide ions are transported through the membrane to the anode where oxygen is liberated



Oxygen purities greater than 97% are obtained.

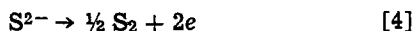
In principle, the gas from a coal gasifier containing H₂S could be similarly fed to the cathode of an electrochemical cell where the H₂S is reduced to form sulfide ion



With passage of current, the sulfide ion would migrate to the anode through the membrane. At the anode, elemental sulfur vapor would be generated

*Electrochemical Society Active Member.

† Present address: E. I. du Pont de Nemours Company, Martinsville, Virginia 24112.



The driving force is supplied by an external dc power source. The minimum potential required to drive the concentration cell can be calculated from the Nernst equation

$$E = E_0 - \frac{RT}{nF} \ln \left[\frac{(a_{\text{H}_2})_{\text{ca}} (a_{\text{S}_2})_{\text{an}}^{1/2}}{(a_{\text{H}_2\text{S}})_{\text{ca}}} \right] \quad [5]$$

where

$$-nFE_0 = \Delta G^\circ_{\text{H}_2\text{S}} \quad [5a]$$

$$(a_{\text{H}_2})_{\text{ca}} = P \cdot (C_{\text{H}_2})_{\text{ca}} \quad [5b]$$

$$(a_{\text{H}_2\text{S}})_{\text{ca}} = P \cdot (C_{\text{H}_2\text{S}})_{\text{ca}} \quad [5c]$$

$$(a_{\text{S}_2})_{\text{an}} = P \cdot (C_{\text{S}_2})_{\text{an}} \quad [5d]$$

a , P , C are activity of gaseous species, pressure, and concentration, respectively.

At 927°C, E_0 is about -162.2 mV based on two-electron transfer and 7.48 kcal for the Gibbs free energy of formation of H_2S (2). The equilibrium voltage for 90% removal and concentration to 90% S_2 from 0.65% H_2S is about 437 mV at 1 atm. For operation of the entire process at 10 atm, the equilibrium voltage is about 497 mV.

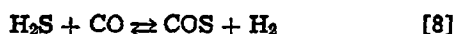
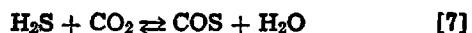
The success of electrochemical concentration depends first on the selection of proper electrode materials and the stability of the electrolyte at the operating conditions. The criteria for electrode selection are primarily stability and conductivity in the hot sulfide environment. Thermodynamic analysis has indicated that gold, platinum, and carbon are the most stable materials. However, gold and platinum are so expensive that their use in a full-scale cell is not feasible. Carbon electrodes were therefore evaluated as both anode and cathode.

It is necessary to identify an electrolyte which is stable and whose melting point is compatible with coal gasification processes (700°-1000°C). No data exist for alkali sulfides, but the eutectic temperature of a binary alkali sulfide (xz - yz) can be predicted from the model proposed by Lumsden (3). The eutectic temperature is given as

$$T = \frac{KN_y^2 + \Delta H_{f,x}}{(\Delta S_{f,x} - R \ln N_x)} \quad [6]$$

where N_x , N_y , $\Delta H_{f,x}$, and $\Delta S_{f,x}$ are mol fractions of xz and yz in the mixture, and enthalpy, and entropy of pure xz , respectively. K , the interaction parameter, includes the London and polarization forces. The eutectic temperatures of $\text{Na}_2\text{S}/\text{K}_2\text{S}$ and $\text{Na}_2\text{S}/\text{Li}_2\text{S}$ were estimated with $K = 0$. Sharma (4) estimated the heat of fusion based on Temkin's model of the phase equilibrium between lithium sulfide and iron sulfide. Eutectics are predicted at 920 and 1125 K with 40 mol percent (m/o) Na_2S , 60% K_2S and 63% Na_2S , and 37% Li_2S , respectively. These mixtures appeared to be reasonable choices for preliminary experiments.

Other reactions are possible besides those desired



Reactions [7] and [8] indicate the amount of COS formed at equilibrium. At 927°C, [7] and [8] both show a maximum of 10^{-4} mol fraction COS in equilibrium with the inlet H_2S in the gas from an advanced gasifier (see Table I). Several species in the process gas may also react with the electrolyte

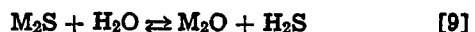


Table I. Typical gas composition from advanced air-blown gasifier (6)

Component	m/o
H_2	14.0
N_2	48.0
CO	29.0
CO_2	3.0
CH_4	3.3
H_2S	0.7
COS	Trace
H_2O	2.0

The reactions show the tendency of the electrolyte anion to be converted from sulfide to some other species. Thermodynamic tables (5) were used to estimate the equilibrium for each reaction based on lithium as the cation. At 927°C, reactions [9], [10], and [11] are negligible; their equilibrium constants are 2.966×10^{-4} , 3.96×10^{-4} , and 7.11×10^{-7} , respectively. Reaction [12] is the only one of consequence. Therefore, for this reaction, the thermodynamic analysis is made based on each of lithium, sodium, and potassium as the cation in the electrolyte. Their equilibrium constants are 0.058, 0.053, and 0.008, respectively, at 927°C. The equilibrium is driven to the left with increasing temperature. The electrolyte containing potassium as the cation is the most resistant to conversion from sulfide to carbonate. The equilibrium constant of 0.008 would limit the outlet H_2S to about $5 \times 10^{-4}\%$. This is equivalent to 99.9% removal of H_2S using the gas composition from advanced gasifiers (6).

Experimental

To test the concept, a small cell similar to a molten carbonate fuel cell was constructed. A schematic of the cell housing is shown as Fig. 1, and the assembled cell is shown in Fig. 2. The cell housings are made of dense graphite; the process gas was introduced and removed through 0.635 cm Al_2O_3 tubes. A thermocouple was inserted close to the gas flow channel with a 316 stainless steel tube, which also acted to transmit current from the potentiostat/galvanostat.

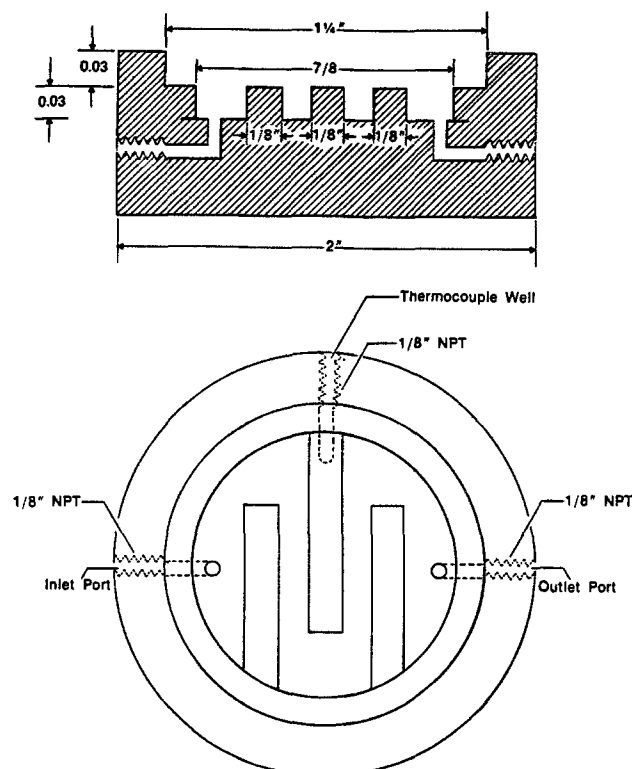


Fig. 1. Schematic diagram for cell housing

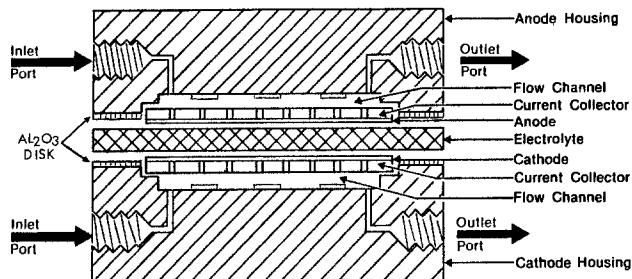


Fig. 2. Schematic diagram for assembled cell with Al_2O_3 ring

The process gas is prevented from leaking out by wet sealing, which is produced by contact with the electrolyte-filled membrane. Direct contact between the molten electrolyte and graphite housing produces degradation, which was prevented by thin, dense alumina shims. The face seal between shim and housing was sufficiently leak free.

Carbon electrodes having a porosity of 52%, thickness of 4.5 mm, and 3.175 cm diam were purchased from Ultra Carbon Company. They are used as both anode and cathode.

The electrolyte mixture was retained in a membrane composed of a porous inert matrix material (MgO), so that the electrolyte mass remained in a semisolid state at the operating condition. Hot pressing and impregnation were the two techniques employed to manufacture the membrane. The hot pressing involved electrolyte and matrix material compression at 6000 psi at temperatures just below the electrolyte melting point. Impregnation involved melting of electrolyte into the partially sintered matrix material in a vacuum furnace.

The process gas is a simulated syn-gas purchased from Matheson Gas Products. Condensing water vapor caused severe problems with the gas chromatograph; absorption of the water upstream altered the H_2S content. For this reason, most tests were run with a gas composed of 50% H_2 , 0.65% H_2S , and the balance N_2 . A few tests were run with CO_2 present (CO formed *in situ* due to the water-gas shift reaction) to test the effect of reaction [12].

The gases were analyzed with a Hewlett-Packard 5840 Gas Chromatograph with a thermal conductivity detector. Most of these tests were conducted with hydrogen in the anode. This allowed simple analysis of the anode effluent as H_2S rather than S_2 .

Electrochemical measurements were made using a PAR-371 Potentiostat/Galvanostat. Most data were taken in the galvanostatic mode. The ohmic resistance of the cell was estimated using the current interruption technique. Figure 3 shows the apparatus and flow system.

Results and Discussion

Electrochemical measurement made in a cell such as this, that is, with porous electrodes and an immobilized electrolyte, are subject to experimental uncertainties larger than those typical of measurements with planar electrodes in free electrolyte. This is due, for the most part, to the uncertain and variable active area and the possibility for voids within the tile. Furthermore, the electrolyte is subject to varying polysulfide content.

Although anhydrous Na_2S and Li_2S were purchased, the initial large amounts of polysulfide lowered the melting point. A slow lowering of cell impedance was observed as the temperature climbed to 785°C . Simultaneously, large quantities of H_2S were seen in both anode (H_2) and cathode (fuel-gas) exit gas streams due to reaction between H_2 and sulfur species which emitted from the polysulfides. At about 840°C , a sharp further decrease in impedance occurred, indicating melting of the stable electrolyte. The temperature corresponded closely to the temperature (852°C) predicted by the Lumsden equation.

The open-circuit potentials were measured as functions of temperature and H_2S and H_2 concentrations in cathode and anode streams. The open-circuit potential predicted by the Nernst equation was calculated using the outlet concentration of gas species. Table II shows measured and calculated open-circuit potentials, H_2S outlet concentration from cathode and anode streams, and temperature. The discrepancies between calculated and measured open-circuit potentials are probably due to concentration differences between the electrode interfaces and bulk streams.

The polarizations were lowered with the hot-pressed membrane; current densities above 30 mA/cm^2 were attained at cell overpotentials below 540 mV. A large ohmic drop prevented the cell with the impregnated membranes from operating at current densities above 15 mA/cm^2 . This can be attributed to discontinuities within the matrix material and poor wetting between the electrode and membrane. However, the impreg-

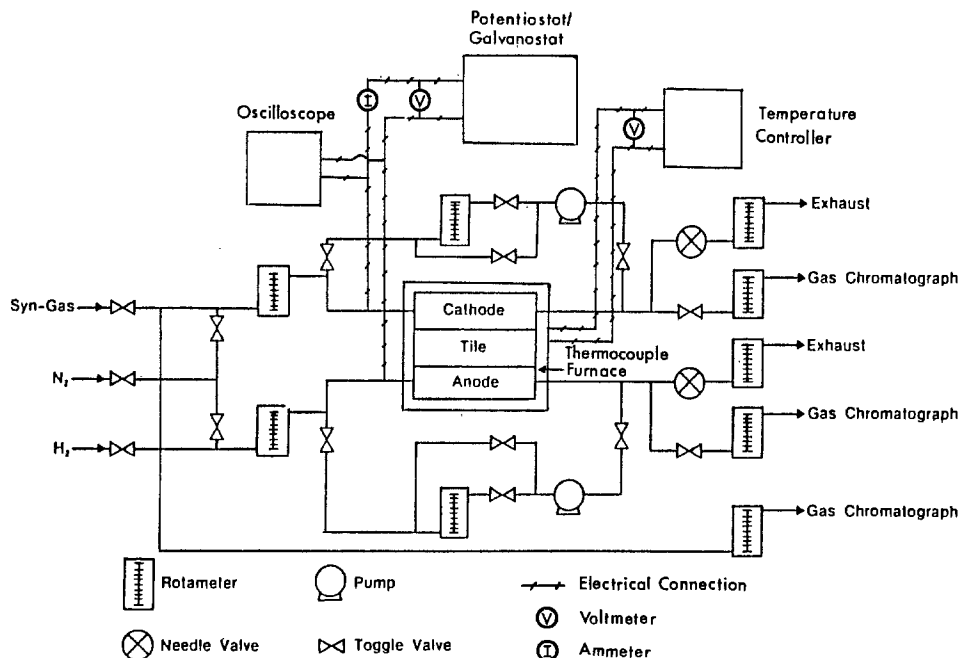


Fig. 3. Experimental apparatus

Table II. Observed and calculated open-circuit potential

OCP _{obs} (mV)	OCP _{cal} (mV)	(H ₂ S) ca (%)	(H ₂ S) an (%)	Temp (°C)
-80	-88	0.50	0.15	791
-75	-50	0.46	0.31	805
-78	-100	0.49	0.11	795

nation method produced a high residual strength so that extended cell operation was possible.

The dependence of the overpotential on the flow rate, H₂S inlet concentrations, and temperature was investigated with the impregnated membrane. The effect on overpotential of cathode flow rate is shown in Fig. 4. The overpotential at constant current density decreases with increased flow rate. Increasing the gas flow rate in the cathode cavity increases the mass transfer coefficient of the reactants from the bulk of the gas phase to the electrode reaction area. As the mass transfer coefficient increases the gas-phase limiting current increases and the concentration overpotential drops. The overpotential at constant current density decreases with increasing temperature. This is due to lowered electrolyte resistance and increased solubility of H₂S gas, as well as enhanced kinetics. At low temperature (710°C), the overpotential increased steeply as the current density increased, indicating a limiting current density. Lowering of overpotential with increasing H₂S inlet concentration is shown in Fig. 5. As the inlet H₂S concentration increases the limiting current increases pro-

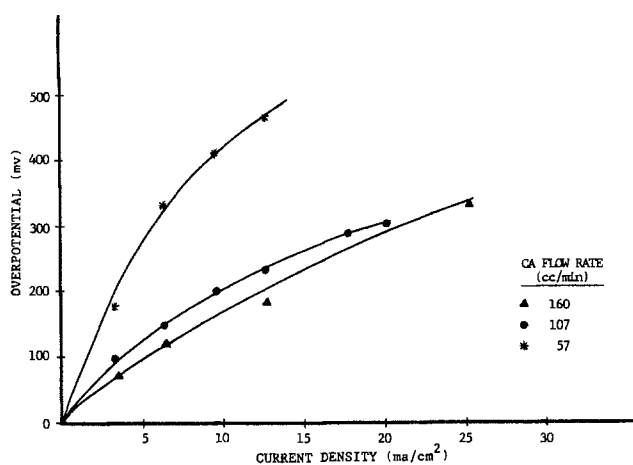


Fig. 4. Overpotential vs. current density at 840°C, 0.65% H₂S concentration.

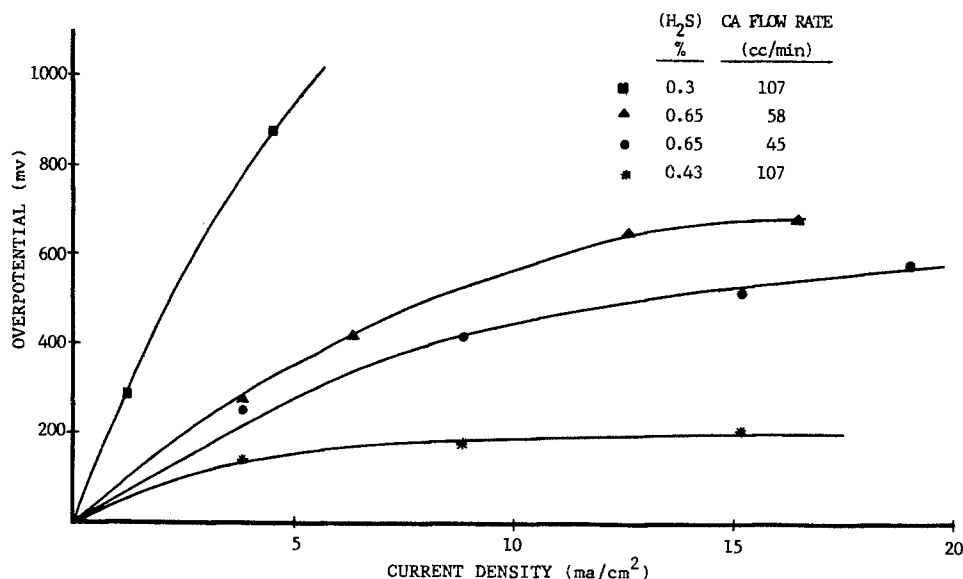


Fig. 5. Overpotential vs. current density at 918°C.

portionally, consequently lowering the concentration overpotential.

It should be emphasized that the quantitative results are highly dependent on the physical construction of the electrodes and membrane (for reasons stated earlier). Performance must improve with materials optimization. The trends found, however, are considered significant.

The results for removal efficiency as a function of current density with an inlet gas containing 0.43% H₂S, 50% H₂, and the balance N₂ are shown in Fig. 6. The removal efficiency is increased by increasing the current density. Removal efficiencies of 98.8% were achieved at flow rates as high as 260 cm³/min. The H₂S concentration was reduced to as low as 50 ppm at the cathode, and 3.2% of H₂S was achieved at the anode. This anodic value is not viewed as a real limit for the process but merely as a result of the minimum flow needed to transmit samples to the analyzer.

H₂S removals at open circuit were observed during these runs. Removal at open circuit may be due to diffusion of H₂S from the cathode chamber through the electrolyte tile to the anode. An effective diffusion coefficient of 9×10^{-4} cm²/s was obtained based on the H₂S molar flux through the membrane from the cathode to anode at open circuit. This high diffusional flux is not seen in well-manufactured membranes; it is probably due to gas channels in our crude ones. Back diffusion of H₂S from anode to cathode became significant when the H₂S concentration at the anode was high. The removal efficiencies, as adjusted for the diffusion of H₂S through the membrane, are shown in Fig. 6.

The current efficiency as a function of current density is shown in Fig. 7. The current efficiency is the ratio of the mols of H₂S removed to the theoretical mols that could be removed by 2F of electricity. High current efficiencies were achieved at low current density. Observed current efficiencies greater than 100% were due to diffusion of H₂S from cathode to anode at very low currents (and hence very low removals). A steady hydrogen flow was necessary for the anode to deliver its effluent to the chromatograph. At these conditions, the exiting anode H₂S concentrations were lower than those exiting the cathode. This would never be the case in a commercial device. A gradual decrease in the current efficiency with increasing current density was observed. The low current efficiency at high current density is apparently due in part to back diffusion of H₂S from anode to cathode. The adjusted current efficiencies are also shown in Fig. 7.

A preliminary attempt was made to assess the relative importance of activation and concentration over-

Fig. 6. Removal efficiency as a function of current density.

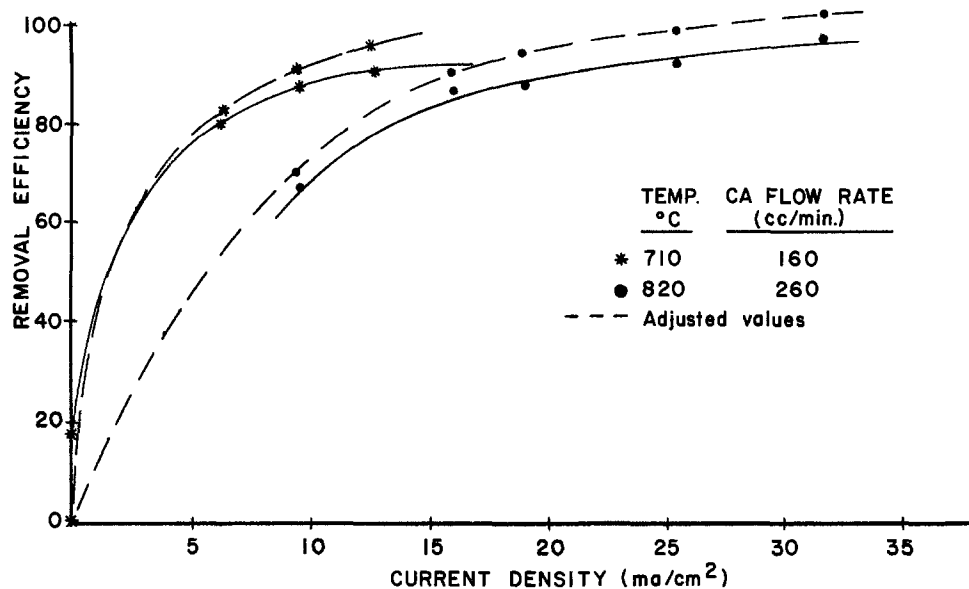
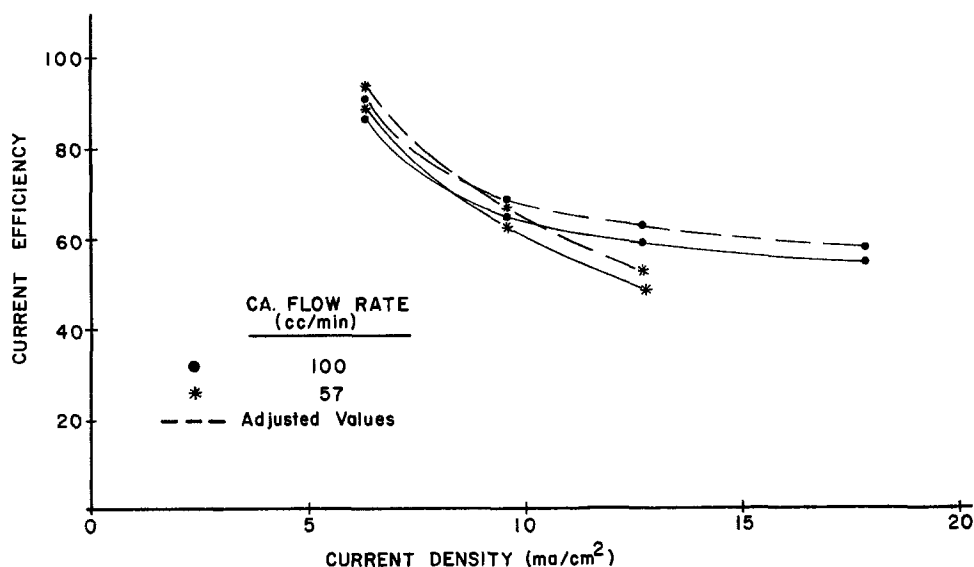


Fig. 7. Current efficiency as a function of current density at 840°C and 65% H₂S cathode inlet.



potential. This attempt was hindered, perhaps crucially, by the absence of a reference electrode. However, a large flow of pure hydrogen was maintained at the anode to depolarize it as much as possible. A transient galvanostatic pulse technique was used. The ohmic polarization is presumed to appear in less than 1 μ s. On planar electrodes, activation polarization is expected to occur in 10^{-6} to 10^{-4} s (7). Concentration polarization decays in the range of 10^{-4} to 10^{-3} s (7). The porous carbon electrodes in use here have slower decay response because the gas concentration in the pores changes more slowly than that at a planar electrode.

There was a distinct difference in the shape of the decay curves for runs at different temperatures (8). The response at 805°C was considerably slower than those at 840° and 896°C. If one assumes that the activation polarization decays primarily from 10^{-3} to 10^{-2} s and concentration polarization from 10^{-2} s on, some relative measure can be made. A rough Allen-Hickling plot was made, based on galvanostatic pulses made at five currents. The exchange current densities (presumed at the cathode) were found to be 4.6 and 3.3 mA/cm² at the higher temperatures. Yet, at the lower temperature, an exchange current density of 9.0 mA/cm² was calculated. Lowering of the true interfacial area with increased temperature may be the cause of this, possibly through increased electrode flooding. The concentration polarization, however, was much more severe at the lower temperature, showing typically six times that for the higher temperature runs. This effect

may be due to the solubility of the H₂S, which increases in the melt with increasing temperature. With the low concentrations of H₂S in the cathode gas, the dissolved H₂S or one of its products is likely the limiting reactant.

The effect of electrode thickness was also explored. Increasing thickness of porous graphite had no deleterious effect on cell performance. The usual thickness used was 0.762 mm. However, electrodes up to 4.5 mm were tested. These results indicate gas-phase pore diffusion is not controlling.

Most tests were performed with the anode depolarized with hydrogen. No effect on H₂S removal efficiency at the cathode was observed when the H₂ was replaced with N₂. In nondepolarized tests, an increase of 50 mV at 15 mA/cm² was needed over the depolarized voltage to maintain galvanostatic conditions. However, plugging of the anode outlet tube with condensed sulfur was observed. The tube was unplugged by purging with hydrogen, which converts the condensed sulfur to hydrogen sulfide.

When simulated syn-gas (SSG) containing 0.3% H₂S, 30% H₂, 20% CO₂, and balance N₂ was fed into the cathode, a gas composition of 12.8% CO, 7.2% CO₂, 12.8% H₂O, 17.2% H₂, 0.3% H₂S, and balance N₂ is predicted from the water-gas shift reaction equilibrium calculation at 927°C.

The water-gas shift reaction was studied by passing SSG through a stainless-steel loop inside the furnace. The CO₂ concentration at inlet and outlet were com-

pared. Conversion of 44.4% and 54% CO₂ was observed at 927° and 1027°C, respectively. Thermodynamic analysis indicated that 45% and 64% of the CO₂ should be converted to CO at 927° and 1027°C, respectively, with SSG containing 30% H₂ and 20% CO₂. Thus, the water-gas shift reaction has a fast rate of reaction and is close to equilibrium.

With CO₂ and H₂O from the water-gas shift reactions, the electrolyte anion may be converted from sulfide to carbonate by reaction [12]. The CO₂ concentrations at the exit from the loop and cathode were compared at 936 K and found to be similar. This indicated that there is little or no CO₂ removal by the molten Na₂S-Li₂S mixture. X-ray powder diffraction analysis indicated that there was no displacement of sulfide ions by carbonate ions in the electrolyte. The effect of potassium sulfide in the electrolyte was not explored experimentally due to problems with K₂S purification. However, K₂S is most favored thermodynamically. There was no effect seen on H₂S removal efficiency of the CO₂, and no CO₂ was evident in the anode exhaust.

The cell potential responded sharply to cathode gas composition. When mixtures similar to the SSG, but without H₂S, were introduced, the cell potential increased steadily at about 100 mV/min. Adding CO₂ to the gas had no effect. Reinserting the H₂S brought the potential back to its original level.

Current was held constant for several hours at a time. It was changed in steps of 5 or 10 mA/cm². The outlet gas concentrations responded immediately¹ and remained within 10% of their new values over the steady state. Gas samples were taken every 30 min or every hour. Some steps in current were positive and some negative, so that replication occurred. There was no noticeable hysteresis.

Most of the results reported here came from an experiment which ran continuously for 100h. Some other experiments ran over 500h each. Upon disassembly, the carbon electrodes were partially wetted by electrolyte. The electrodes were conductive, and no structural damage was observed even under scanning electron microscopy.

Economic Analysis

The concept of electrochemical concentration must be shown to be an economically viable method for removing H₂S from the process stream of a coal gasifier. A preliminary economic feasibility study was based on a capacity of 10,000 TPD of Illinois no. 6 coal using a Texaco air-blown gasifier.

The power needed to drive the electrochemical cell can be estimated from voltage and current demand. The theoretical potential is calculated to be about 0.5V. However, various overpotentials associated with the real process will probably bring the total required voltage to near 1V. The current needed to remove 100% of the H₂S is directly calculated from Faraday's law to be 21.5 × 10⁶A based on two-electron transfer. On this basis, the power demand is 21.5 MW, or about 1.5% of the output of the plant. This value compares favorably with the utility demand by the Selexol process, which is about 4.7% of the plant output (9). Capital costs are estimated based on the design of a battery similar to NASA's "Energy Conversion Alternatives Study for Molten Carbonate Fuel Cells" (ECAS) (10). The total area requirement to remove H₂S completely was based on a limiting current density of 50 mA/cm², which is a conservative estimate at high temperature. Current densities of 160 mA/cm² are regularly achieved in molten carbonate fuel cells (MCFC) with total overpotential of about 300 mV. A major difference between the MCFC and our device is the composition of the oxidant. The MCFC operates with up to 30% CO₂, while

our H₂S cell will have exit H₂S concentrations of a few hundred parts per million.

A closer experimental analog is the molten carbonate CO₂ concentrator, under development for NASA applications (11). Here, the oxidant typically contains 0.4% CO₂ (in air) and can be purified to about 200 ppm. The cathodic overpotential at 50 mA/cm² is typically a few hundred millivolts (11). This cell uses optimized hardware; the electrolyte tiles and porous electrodes have been developed for the MCFC over the past twenty years.

The limiting current density due to gaseous diffusion of the H₂S from the bulk gas has been calculated from standard mass transfer correlations (8). With a gas flow of 350 cm/s, this limit is about 150 mA/cm², assuming that the bulk H₂S concentration is 10% of the inlet (90% removal). Pore diffusion in a properly designed electrode has been found to be unimportant (11). Further, since we have already achieved 35 mA/cm², we feel 50 mA/cm² is realizable.

A total superficial area is then calculated at 4.3 × 10⁴ m² with a capital investment of \$24 million. The cost is estimated based on the ECAS value for a MCFC plant of about \$140/m² (1976 dollars), which was then arbitrarily scaled up by a factor of four to \$560/m². There is clearly a great deal of uncertainty in this figure. However, a Selexol plant of the same H₂S capacity is estimated to cost over \$200 million, an order higher than the concentrator estimate.

Conclusions

The feasibility of electrochemical concentration for removal of H₂S from coal gas at high temperatures was demonstrated. The concept was tested with a binary mixture of Na₂S and Li₂S as the electrolyte, and porous carbon as electrodes. The graphite electrode housings were assembled with Al₂O₃ gas tubes and found to be inert at the operating conditions. The molten sulfide is very stable in the reducing environment, and carbon electrodes were stable even at a total cell potential of 1.8V.

A 98.8% removal efficiency of H₂S has been achieved with the SSG containing no CO₂ with reasonable levels of polarization. Current densities above 35 mA/cm² were attained during tests using a cell of 7.92 cm² superficial area.

A preliminary experiment with gas containing CO₂ indicated that the removal efficiency of H₂S does not depend on CO₂. X-ray powder diffraction analysis indicated that there was no measurable displacement of sulfide by carbonate ions in the electrolyte.

Preliminary economic analysis indicates that the capital and operational costs for the electrochemical concentrator are favorable at this early stage of development.

Acknowledgment

This work was partially supported by the Energy and Environment Division of the Argonne National Laboratory (DOE).

Manuscript submitted Dec. 17, 1982; revised manuscript received ca. Sept. 16, 1983.

REFERENCES

1. S. H. Langer and R. G. Haldeman, *J. Phys. Chem.*, **68**, 962 (1964).
2. I. Barin and O. Knacke, "Thermochemical Properties of Inorganic Substances," Springer-Verlag, Berlin (1973).
3. J. Lumsden, *Disc. Faraday Soc.*, **32**, 138 (1961).
4. R. A. Sharma, *This Journal*, **123**, 448 (1970).
5. I. Barin, O. Knacke, and Kubaschewski, "Thermochemical Properties of Inorganic Substances-Supplement," Springer-Verlag, Berlin (1977).
6. Private Communication, Energy and Environment Division, Argonne National Lab., Argonne, IL (1981).
7. I. Trachtenberg, *This Journal*, **111**, 110 (1964).

¹ Some 15 min were needed to deliver a gas sample from the cell to the chromatograph.

8. H. S. Lim, Ph.D. Thesis, Georgia Institute of Technology, Atlanta, GA (1982).
9. EPRI, EM-1333, "Assessment of Sulfur Removal Processes for Advanced Fuel Cell Systems," Final Report, prepared by C. F. Baraun & Co., Alhambra, CA (Jan. 1980).
10. NASA, CR 134955, "Energy Conversion Alternative Study," United Technologies Phase II Final Report, Integrated Coal Gasifier/Molten Carbonate Fuel Cell Power Plant Conceptual Design and Implementation Assessment (1976).
11. J. Weaver, M.S. Thesis, Georgia Institute of Technology, Atlanta, GA (1982); J. Weaver and J. Winnick, *This Journal* **131**, 20 (1984).

A Quantitative Examination of the Mixed Potential Mechanism in Mineral Flotation

K. C. Pillai and J. O'M. Bockris*

Department of Chemistry, Texas A&M University, College Station, Texas 77843

ABSTRACT

The origin of the present work lies in a suggestion by Salamy and Nixon, which was implemented by Tolun and Kitchener, and has become the principal theory of some types of flotation. However, it has never been subject to quantitative verification. The electrochemical kinetics of oxygen reduction and those of the anodic oxidation of potassium ethyl xanthate were examined first individually and then together. The mineral substrates used were iron pyrites and galena. The cathodic Tafel slope on pyrites was 110 mV, and the order of reaction 1.2. On galena, the slope was 120 mV. In anodic reactions, the Tafel slope on pyrites was 95 mV, and the order 0.7. On galena, the slope was 240 mV. Results obtained with O₂ alone and xanthate alone verified the theory. Results obtained when the components were mixed gave agreement only if the excess of the adsorbed xanthate on the oxygen kinetics was taken into account.

In mechanisms suggested for flotation of sulfide minerals in the presence of xanthate collectors, one may distinguish early views, e.g., chemical (xanthate \rightleftharpoons xanthic acid \rightleftharpoons adsorbed acid) (1), and ion exchange theories (replacement of sulfide ions of the mineral by xanthate) (2, 3). However, these were not consistent with Plaksin's discovery of the dependence of the flotation process on an oxygen content in the solution (4).

This discovery was consistent with a suggestion of Salamy and Nixon (5) (which they, however, had applied experimentally only to a mercury surface): that the donation of electrons by the oxidation of xanthate was coupled to the supply of electrons to reduce oxygen. Plaksin (4) himself, however, suggested that the part played by the O₂ was to cause galena (PbS) to change from a surface of n-type to p-type, and thus facilitate anion (i.e., xanthate) adsorption [cf. Plaksin and Shafeev (6), Guarnaschelli (7), Dixon *et al.* (8), and Richardson (9)].

Tolun and Kitchener (10) are generally credited with having originated the mixed potential theory, though they themselves attribute it to Salamy and Nixon (5). By making polarographic measurements on PbS in the presence of xanthate, Tolun and Kitchener found that the potential of flotation (i.e., the open-circuit potential of PbS in the presence of both xanthate and O₂) was between the initial anodic current for xanthate oxidation and the corresponding cathodic current for oxygen reduction. This was qualitatively consistent with their model. Woods (11, 12), showed that, by using a bed of sulfide mineral particles, flotation could be achieved without oxygen by changing the potential to the more positive region, which would arise were a mixed potential mechanism with O₂ allowed to occur on the same electrode. However, later studies by Biegler *et al.* (13) of O₂ reduction on different samples of pyrite (FeS₂) failed to show any correlation between the characteristics of O₂ reduction and the semiconducting properties of the sulfide used.

Several parallel works of importance have appeared. Fuerstenau *et al.* have reported the electrochemical oxidation of xanthate on FeS₂ (14); and the oxidation

of potassium diethylthiophosphate on Cu₂S has been studied by Chander and Fuerstenau (15). In particular, *ex situ* IR studies have been made by the former (14) of the surface species (by mixing the xanthate-treated FeS₂ with a mineral oil as a mull for the IR), which they found to be dixanthogen. Quite similar studies were carried out independently by Majima and Takeda (16). However, Granville *et al.* (17) have shown evidence from IR studies that on PbS the dominating species is lead xanthate.

An interesting contribution was made by Ahmed (18), who set up connected electrochemical cells consisting, e.g., of two electrodes of PbS, one in deaerated xanthate solution and the other in deaerated solution of the same kind but lacking in xanthate. When O₂ was bubbled over the latter electrode, a current was observed between the two electrodes in qualitative agreement with a mixed potential concept.

Somasundaran [cf. Healy (19, 20), Fuerstenau (20), and Goddard (21)] made electrochemical contributions of a different kind. They are well summarized in a recent review of Somasundaran and Goddard (21). However, the systems treated here were largely oxide minerals, and the models used for the interpretation of the data do not involve electrode kinetics, since there is no evidence that O₂ reduction is a vital part of the mechanism of flotation. Here, the crux of the discussion is the degree to which it is possible to regard the interfaces concerned as being subject to potential determining absorbing ions (Nernstian) or polarizable and hence subject to double layer theory (Sternian). Charge generations (22), electrostatic adsorption (23), and some evidence for the role of ion-molecular complexes (24) have been studied.

In summary, for the sulfide minerals, there is qualitative evidence for a mixed potential view of the mechanism by which the collector comes onto the surface prior to flotation. However, many of the facts are subject to the Plaksin-originated type of interpretation, in which changes in the semiconducting properties of the interface dominate electrode kinetic features. There has been no quantitative proof of the mixed potential theory. Further, if the mixed potential theory is valid, the implication for the structure of the collector is that it must not only have a struc-

* Electrochemical Society Active Member.

Key words: mixed potential, mineral flotation, pyrite, galena, xanthate.

ture which adsorbs on the mineral and oxidizes as well in the appropriate potential range, but it should also have suitable catalytic property for the O_2 reduction reaction. The present work is aimed at the elucidation of these matters.

Experimental Details

Materials

Specimens of the minerals pyrite and galena (6.5 cm^3) were obtained from Wards Natural Science Establishment, Incorporated. The pyrite was of Spanish origin and galena was from Sweetwater Mines, Missouri.

Kodak potassium ethyl xanthate (KEX) was purified by dissolving in acetone and recrystallizing three times by addition of ether. The crystals were then stored in a dry nitrogen atmosphere. Prior to the experiment, a fresh KEX solution in the electrolyte was prepared.

Measurements of Semiconductor Properties

The resistivities and Hall mobilities for the surface of mineral disks were obtained by the method of Van der Pauw (25), developed for samples of arbitrary shape. The experimental details are similar to those reported elsewhere (26).

Electrode Preparation

About 2-3 mm thick and $0.5\text{-}1 \text{ cm}^2$ surface area specimens were cut from the massive materials using a diamond saw. Contact to the electrode was made by attaching a copper lead to one surface of the electrode with a conducting silver epoxy cement. The exposed copper lead and the back side of the electrode were then coated with a nonconducting epoxy and the hardened-capsule tight-fitted into a Teflon holder. This arrangement proofed the electrode against the effects of possible leaks. The ohmic nature of the electrical contact was checked by measuring the current-voltage characteristics of the electrode.

The electrode surface was prepared before each electrochemical run by hand polishing for about 5 min each with a succession of finer grades of silicon carbide paper, down to 600 grade. The electrode was then degreased with spectropure trichloroethylene, and washed thoroughly with deoxygenated triple-distilled water prior to immersion into the experimental solution.

Electrochemical Measurements

A conventional three-compartment glass cell with a three-electrode system was used. A saturated calomel electrode was the reference electrode; however, the potentials are expressed on the normal hydrogen scale.

To obtain $E\text{-log } i$ data, the steady-state potentiostatic polarization technique was used. The steady-state current was read at each applied potential. It was found that this was established after 3-4 min. The potential was controlled by a PAR potentiostat (Model 173), and the current-time curves were recorded with a $y\text{-t}$ (Industrial Scientific, Incorporated) recorder.

Cyclic voltammograms were recorded as preliminary measurements, using the above setup coupled with a programmer PAR Model 175.

The experiments were carried out in borate buffer of pH 9.1 (a pH near to that of the flotation process). The electrolyte was pre-electrolyzed at a current density of 1 mA/cm^2 for 15h. Experimental solutions of KEX were prepared by adding small volumes ($0.2\text{-}0.3 \text{ cm}^3$) of a concentrated solution of KEX, prepared freshly each day, to a pre-electrolyzed base electrolyte. All operations were carried out in an all-glass assembly under an N_2 atmosphere.

Measurements with different partial pressures of O_2 were achieved by mixing O_2 and N_2 under controlled-flow conditions using flowmeters (Flowrater, Fischer and Porter Company).

XPS measurements of the electrode surface before and after contact with the collector were carried out and will be reported elsewhere (27).

Methodology

Three methods of surface treatment of the mineral electrodes were tried to find out which method would give the most reproducible results. The first method involved the procedure as described in the Electrode preparation section. The second method consisted of the same procedure followed by etching in $HCl:H_2O$ (1:3) solution for 15 min, and then by thorough washing in deoxygenated conductivity water prior to introduction into the experimental solution. In the final set of experiments, the electrode surface was prepared as given in the Electrode preparation section, followed by electropolishing for 3 min at 0.375 A cm^{-2} in a mixture of conc H_3PO_4 and $HCl:H_2O$ (1:4) solution saturated with CrO_3 (28). The last method resulted in the formation of a thick oxide film on the electrode surface, giving high Tafel slopes, e.g., of $250 \text{ mV decade}^{-1}$, for O_2 reduction at $p_{O_2} = 1$ in pH 9.1.

Although the first and second methods gave similar results, the most reproducible results and those with the most linear Tafel plots for O_2 reduction were obtained by following the first method of surface preparation (see Electrode preparation), followed by a cycling of the electrode potential at a scan rate of 1 mV s^{-1} , starting from the open-circuit potential (E_{open}) and going towards more negative potentials until the cathodic reduction of FeS_2 started (in the absence of O_2 and xanthate). Then, the reverse scan was carried out in more positive regions until the anodic oxidation of FeS_2 began in the absence of xanthate. Such a scan (with return to E_{open}) was carried out only once. This approach was followed because it was the most reproducible of those examined. After scanning between about 0.0 and $-0.4V \cdot NHE$, the electrodes was disconnected from the potentiostat. The potential was then observed to change over about 30 mV until reaching, after about 30 min, a rate of variation of around 1 mV in 5 min. Potentiostatic transients were then commenced.

While the above sequence of potential cycling was adopted for O_2 reduction studies, for xanthate oxidation under an N_2 atmosphere, the electrode was scanned first in the more positive, rather than the more negative, direction. This ensured that the oxidized product of xanthate formed on the electrode in the anodic cycling step was reduced and did not exert any influence on the subsequent $i\text{-t}$ measurements.

Results

Pyrite

Semiconductor parameters.—The FeS_2 was found to be an n-type material; the charge carrier density was $3.9 \times 10^{18} \text{ cm}^{-3}$, and the resistivity was $4 \times 10^{-2} \Omega \text{ cm}$. The Hall mobility was around $4.5 \times 10^1 \text{ cm}^2 V^{-1} s^{-1}$.

Current-voltage curves.— O_2 reduction on FeS_2 .—The Tafel plots for O_2 reduction obtained on an FeS_2 electrode in pH 9.1 borate buffer at $p_{O_2} = 1$ and 0.33 are shown in Fig. 1. The number of experiments at each pressure was 5-10.

The cathodic Tafel slope ($-b_c$) for O_2 reduction is $110 \pm 5 \text{ mV decade}^{-1}$ for both $p_{O_2} = 1$ and 0.33. The exchange current density ($i_{o,c}$) was calculated by extrapolating the linear portion of the Tafel line to the theoretical equilibrium potential ($E_{e,c}$). The $E_{e,c}$ values for O_2 reduction in pH 9.1 are $+0.690V$ (NHE) for $p_{O_2} = 1$ and $+0.683V$ (NHE) for $p_{O_2} = 0.33$. The respective extrapolated $i_{o,c}$ values are $4.6 \pm 0.3 \times 10^{-12} \text{ A cm}^{-2}$ and $1.0 \pm 0.3 \times 10^{-12} \text{ A cm}^{-2}$ of apparent electrode area.

The cathodic reaction order with respect to O_2 partial pressure is

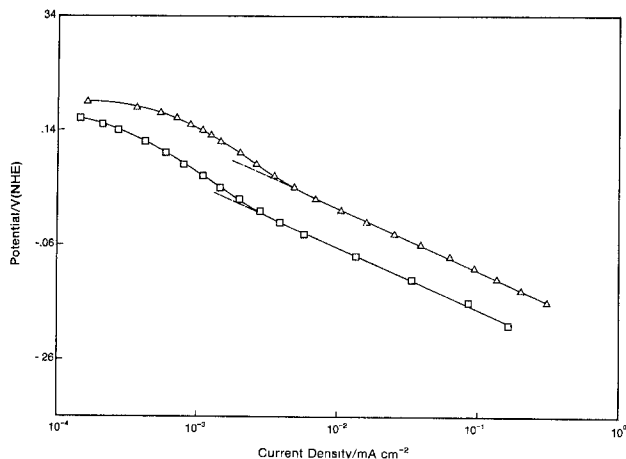
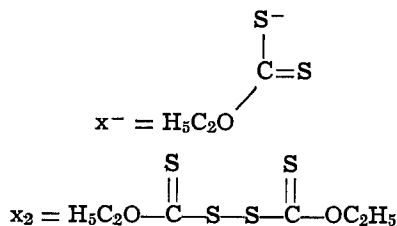


Fig. 1. E -log i plots for O_2 reduction at FeS_2 electrode in borate buffer pH 9.1. $-\Delta-\Delta-$: $p_{O_2} = 1$. $-\square-\square-$: $p_{O_2} = 0.33$.

$$\left[\frac{\partial \ln i_c}{\partial \ln p_{O_2}} \right]_{E,pH} = 1.2$$

KEX oxidation of FeS_2 .—The E -log data for the anodic oxidation of KEX studied at $10^{-2}M$ and $10^{-3}M$ concentrations under a N_2 atmosphere are given in Fig. 2. The anodic Tafel slope (b_a) for xanthate oxidation is 95 ± 5 mV decade $^{-1}$ at both concentrations of KEX studied.

In xanthate oxidation, one has to calculate a reversible redox potential necessary for the computation of the exchange current density, but one has to meet the difficulty that the components of the redox couple



where x^- is the ethyl xanthate anion and x_2 is the diethyldixanthogen, are not sufficiently soluble to be used at ratios corresponding to unit molarity or activity for each component. To calculate, therefore, a reversible redox potential, it is necessary to choose some arbitrary concentration of the KEX, and assume that an equilibrium is set up with diethyldixanthogen, the solubility of which is small. According to Fuerstenau *et al.* (14), the solubility of x_2 at 25°C.

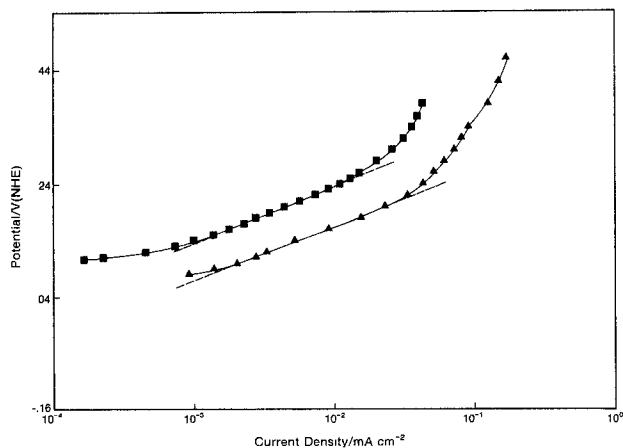


Fig. 2. E -log i plots for KEX oxidation at FeS_2 electrode in borate buffer pH 9.1. $-\Delta-\Delta-$: $C_{KEX} = 10^{-2}M$. $-\square-\square-$: $C_{KEX} = 10^{-3}M$.

pH 9.4, and KEX concentration of $2 \times 10^{-5}M$ is $5.0 \times 10^{-6}M$. The experimental work of Majima and Takeda (16) gives the redox potentials, determined on Pt electrodes, for several homologues of xanthate in solution in equilibrium with the corresponding dixanthogens at saturation. For KEX at $10^{-3}M$, the determined redox potential is 0.13V (NHE), and at $10^{-2}M$ is 0.07V (NHE). The values of Majima and Takeda (16) are reasonably in agreement with the data of Fuerstenau *et al.* (14), *e.g.*, at KEX $10^{-2}M$ and the corresponding x_2 at $5 \times 10^{-6}M$ for pH 9.4 (the Majima and Takeda values were at pH = 9), the Fuerstenau *et al.* value is 0.087V (NHE), and the Majima and Takeda value is 0.07V (NHE) (activity coefficients neglected). Correspondingly, on an FeS_2 electrode, the resting potential attained in the presence of $10^{-2}M$ of KEX was 0.062V (NHE). It was thought appropriate, therefore, to calculate the exchange current density ($i_{o,a}$) for the xanthate oxidation at the determined reversible potential 0.07V (NHE).

The $i_{o,a}$ value at this condition is $1.0 \times 10^{-6} A cm^{-2}$ (*i.e.*, at $10^{-2}M$ concentration of KEX). At $10^{-3}M$ KEX [$E_{e,a} = +0.13V$ (NHE)], the $i_{o,a}$ value is $9.0 \times 10^{-7} A cm^{-2}$.

The anodic reaction order with respect to KEX is

$$\left[\frac{\partial \ln i_a}{\partial \ln [x^-]} \right]_E = 0.71$$

Mixture of O_2 and KEX.—The Tafel plots recorded for the O_2 reduction and xanthate oxidation when both O_2 and KEX are present together are given in Fig. 3. This corresponds to the system in which $p_{O_2} = 1$ and $C_{KEX} = 10^{-2}M$, and we designate this system A. The Tafel lines for the corresponding concentration of O_2 reduction and xanthate oxidation, taken in the absence of each other, are superimposed onto Fig. 3 for a comparison. It is evident that the anodic oxidation of xanthate remains unaffected within the experimental error in the presence of O_2 . The O_2 reduction is, however, catalyzed about 40 times in the presence of xanthate, without any indication in change of the reduction mechanism. The $i_{o,c}$ measured for the O_2 reduction reaction in the presence of $10^{-2}M$ KEX is $2.7 \pm 0.3 \times 10^{-11} A cm^{-2}$. The mixed potential (E_m) and the open-circuit current (i_m , the rate at which the collector is being used up) were calculated by the extrapolation of the linear portions of the Tafel lines. However, since the xanthate oxidation process does not show a linear Tafel region in the mixture, a tangent with a slope of 95 mV was drawn to the anodic polarization curve to

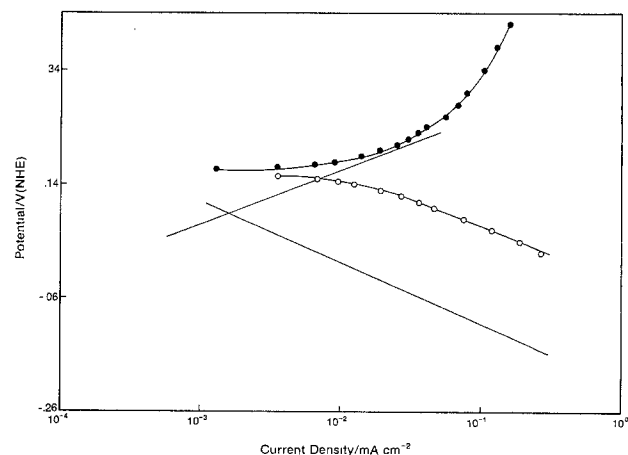


Fig. 3. E -log i plots at FeS_2 electrode in borate buffer pH 9.1. $-\circ-\circ-$: O_2 reduction ($p_{O_2} = 1$) in the presence of $10^{-2}M$ KEX. $-\bullet-\bullet-$: KEX oxidation ($C_{KEX} = 10^{-2}M$) in the presence of O_2 of $p_{O_2} = 1$. —: Measurements in the absence of other component.

calculate these parameters.¹ The E_m and i_m values of the mixtures are 0.167V (NHE) and 9×10^{-8} A cm⁻², respectively.

The Tafel plots for O₂ reduction and xanthate oxidation when both O₂ and xanthate were present were recorded for different combinations of p_{O_2} and xanthate concentrations, as follows. B: $p_{O_2} = 1$ and $C_{KEX} = 10^{-3}M$. C: $p_{O_2} = 0.33$ and $C_{KEX} = 10^{-2}M$. D: $p_{O_2} = 0.33$ and $C_{KEX} = 10^{-3}M$. These are shown in Fig. 4-6. These graphs are drawn in a way similar to that of Fig. 3, in which the individually measured anodic and cathodic curves are superimposed for comparison. In all these systems, the general behavior is similar to that shown in Fig. 3 for system A (i.e., $p_{O_2} = 1$ and $C_{KEX} = 10^{-2}M$), except that in systems with $p_{O_2} = 0.33$, the $-b_c$ is decreased to 70-75 mV by KEX (from 110 mV without it). The E_m and i_m values of the mixture are given in Table I.

With these experimental values of E_m and i_m obtained for the mixtures, the coefficients of the variation of E_m and i_m with reactant concentration were calculated. These are given in Table II.

Galena

Electrode pretreatment.—The surface treatment procedure, as described in the Electrode preparation section,

¹The choice of a potential at which to take this tangent is arbitrary. This one has the advantage that it agrees with the slope in the absence of oxygen.

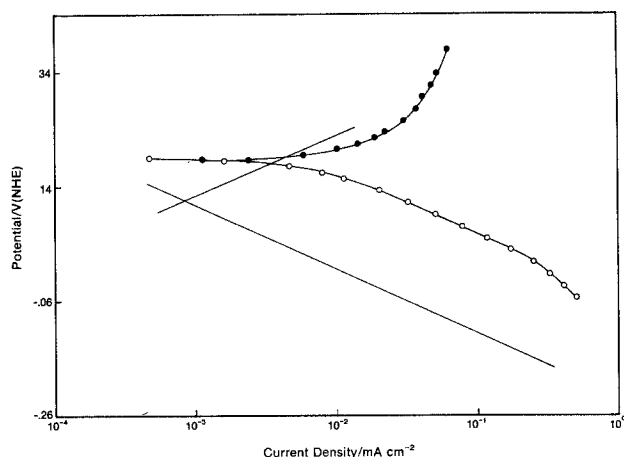


Fig. 4. E -log i plots at FeS₂ electrode in borate buffer pH 9.1. —○—○—: O₂ reduction ($p_{O_2} = 1$) in the presence of $10^{-3}M$ KEX. —●—●—: KEX oxidation ($C_{KEX} = 10^{-3}M$) in the presence of O₂ of $p_{O_2} = 1$. —: Measurements in the absence of other component.

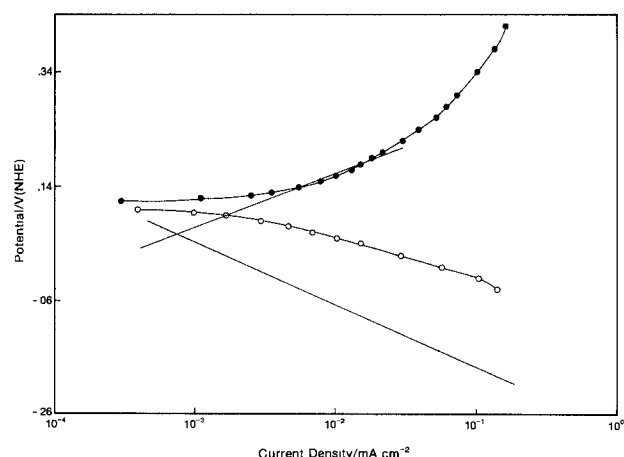


Fig. 5. E -log i plots at FeS₂ electrode in borate buffer pH 9.1. —○—○—: O₂ reduction ($p_{O_2} = 0.33$) in the presence of $10^{-2}M$ KEX. —●—●—: KEX oxidation ($C_{KEX} = 10^{-2}M$) in the presence of O₂ of $p_{O_2} = 0.33$. —: Measurements in the absence of other component.

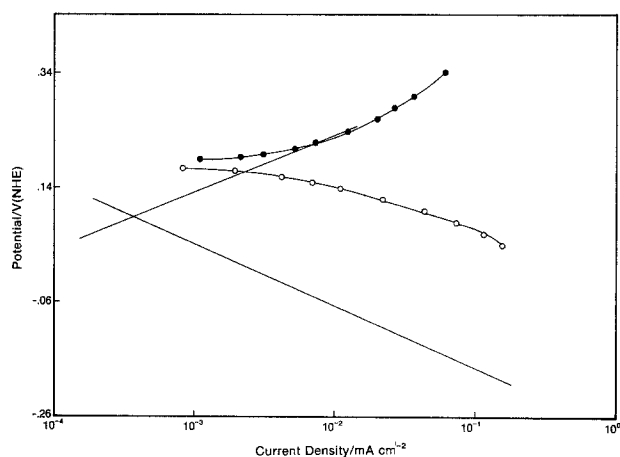


Fig. 6. E -log i plots at FeS₂ electrode in borate buffer pH 9.1. —○—○—: O₂ reduction ($p_{O_2} = 0.33$) in the presence of $10^{-3}M$ KEX. —●—●—: KEX oxidation ($C_{KEX} = 10^{-3}M$) in the presence of O₂ of $p_{O_2} = 0.33$. —: Measurements in the absence of other component.

tion, was found to give reproducible results. The other two methods (cf. Methodology section, above), namely, the one involving etching in HCl:H₂O (1:3) solution for 15 min prior to introduction into the experimental solution, and the one in which the electrode was chemically polished (28), gave irreproducible results for O₂ reduction. Hence, the surface preparation by polishing with different grades of emery paper, degreasing with trichloroethylene, and ending with a thorough water wash, was adopted in the further studies with PbS electrodes.

Even with this method of surface preparation, the cycling of the electrode potential was found to affect the subsequent i - t measurements. Thus, the anodic polarization of PbS was found to affect the cathodic current, probably because of electrode dissolution in the anodic region. Hence, the electrode potential was not cycled prior to the i - t measurements. The electrode was introduced into solution, the rest potential was established, and the i - t measurements were then carried out.

Semiconductor parameters.—The PbS was found to be an n-type material; the charge carrier density was 9.8×10^{16} cm⁻³, and the resistivity was 7×10^{-1} Ω cm. The Hall mobility was around 9.0×10^1 cm² V⁻¹ s⁻¹.

Current-voltage curves.—The Tafel plots for the cathodic O₂ reduction alone and the anodic xanthate oxidation alone, on PbS, are shown in Fig. 7. The $-b_c$ for $p_{O_2} = 1$ is 120 ± 10 mV decade⁻¹, and $i_{o,c}$ at $E_{e,c}$ of +0.690 (NHE) is $2.8 \pm 0.3 \times 10^{-12}$ A cm⁻².

The E -log i plot for xanthate oxidation (conc = $10^{-2}M$) is linear over a small current density region, and the b_a has a high value, i.e., 240-260 mV decade⁻¹. The $i_{o,a}$ at $E_{o,a}$ of 0.07V (NHE) is 2.4×10^{-7} A cm⁻². The E -log i plot shows a depolarization at higher current densities (slope = 45-50 mV), and this is followed by a region in which the current decreases with increasingly positive potential. This indicates an inhibition of the electrode processes. Similar behavior was not observed with FeS₂.

The measurement of O₂ reduction and xanthate oxidation, carried out in the presence of O₂ ($p_{O_2} = 1$) and

Table I. Experimental E_m and i_m values obtained in solutions containing O₂ and KEX

	Systems			
	(A)	(B)	(C)	(D)
E_m V	0.17	0.19	0.10	0.18
$i_m \times 10^8$ A cm ⁻²	9.00	7.30	2.20	3.30

Table II. Experimental coefficients pertinent to the mixed potential situation

	C_{KEX} constant		p_{O_2} constant	
	Systems (A)/(C) ($C_{KEX} = 10^{-2}M$)	Systems (B)/(D) ($C_{KEX} = 10^{-3}M$)	Systems (A)/(B) ($p_{O_2} = 1$)	Systems (C)/(D) ($p_{O_2} = 0.33$)
$[\partial E_m / \partial \log p_{O_2}]_{x^-}, \text{pH}$	0.150	0.002	—	—
$[\partial \log i_m / \partial \log p_{O_2}]_{x^-}, \text{pH}$	1.300	0.700	—	—
$[\partial E_m / \partial \log [x^-]]_{p_{O_2}}, \text{pH}$	—	—	-0.023	-0.085
$[\partial \log i_m / \partial \log [x^-]]_{p_{O_2}}, \text{pH}$	—	—	0.100	-0.180

KEX (conc = $10^{-2}M$) together, are given in Fig. 8. When O_2 is added to the xanthate in solution, the b_a for xanthate oxidation has a higher value, i.e., 240-260 mV decade $^{-1}$. However, the rate of oxidation of xanthate is increased by about 2.5 times in the presence of O_2 . The O_2 reduction is inhibited by about 10 times in the presence of xanthate, although the $-b_c$ remains the same. The $i_{0,a}$ and $i_{0,c}$, correspondingly, are 5.6×10^{-7} A cm $^{-2}$ and 1.4×10^{-14} A cm $^{-2}$, respectively. The E_m and i_m values in the mixture are $-0.065V$ (NHE) and 1.6×10^{-7} A cm $^{-2}$, respectively.

Discussion

Pyrite

Oxygen reduction kinetics.—To elucidate the mechanism of reduction of O_2 and FeS_2 , some seventeen reaction schemes for O_2 reduction have been considered, and these are given in Appendix 1.

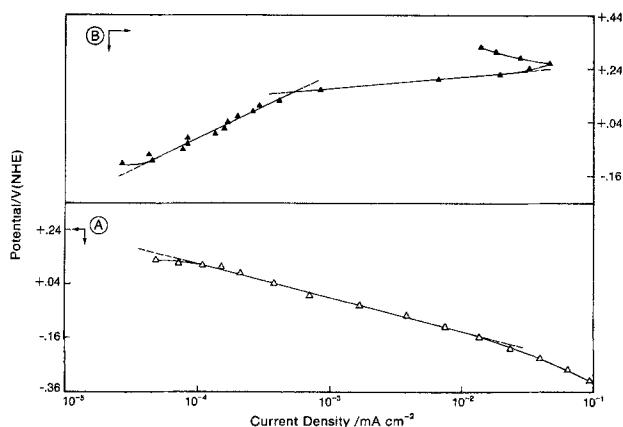


Fig. 7. E -log i plots at PbS electrode in borate buffer pH 9.1. A: O_2 reduction ($p_{O_2} = 1$) in the absence of KEX. B: KEX oxidation ($C_{KEX} = 10^{-2}M$) in the absence of O_2 .

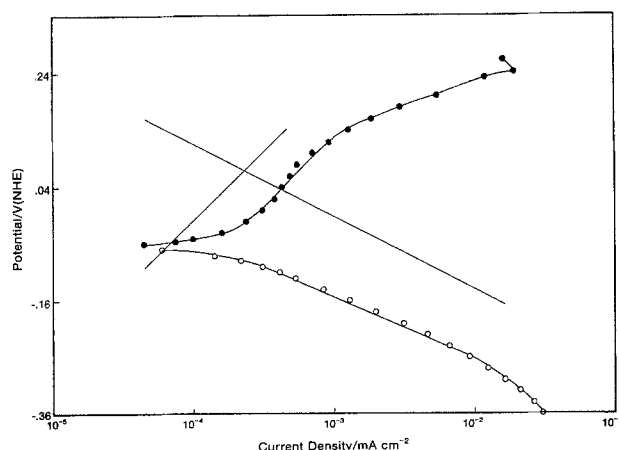


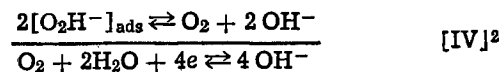
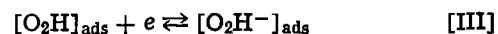
Fig. 8. E -log i plots at PbS electrode in borate buffer pH 9.1. —○—○—: O_2 reduction ($p_{O_2} = 1$) in the presence of $10^{-2}M$ KEX. —●—●—: KEX oxidation ($C_{KEX} = 10^{-2}M$) in the presence of O_2 of $p_{O_2} = 1$. —: Measurements in the absence of other component.

Mechanisms C9, C12, C14, and C16 are the only ones of the mechanism in Table A-I which give a $[\partial E / \partial \ln i]$ of $2RT/F$ and $[\partial \ln i_c / \partial \ln p_{O_2}]$ of unity, with the first step rate determining (rds). These four mechanisms proceed through H_2O_2 (HO_2^- in alkaline solution) as an intermediate. H_2O_2 was identified in the O_2 reduction at the FeS_2 electrode, in $HClO_4$ acid solution (13), and in alkaline solutions (32). However, these above four mechanisms with the first step as rds also predict that

$$\left[\frac{\partial \ln i_c}{\partial (2.3pH)} \right]_{E,T} = 0$$

The available experimental data indicate that O_2 reduction at noble metals (33, 34) and at FeS_2 (13, 32) is pH dependent at $pH > 4$. These four mechanisms can be regarded as not applicable in the present studies, since they were carried out at $pH 9.1$.

The present experimental results are, however, consistent with mechanism C17, which involves H_2O_2 as an intermediate. The reaction scheme is



With step II as rds, and with the condition that the intermediates $[O_2H^+]_{ads}$ and $[O_2H]_{ads}$ are present at limitingly low coverages, it is evident that this mechanism does predict finite values for the pH dependence of i_c (cf. Table A-I).

The solvent displacement mechanism has not been considered here (see below) because, studying reactions involving H_2 and O_2 evolution or their dissolution, one is concerned either with zero water displacement [as with H_3O^+ discharge (40)], or with the displacement of one (as, probably, when direct electron transfer to O_2 occurs).

Xanthate oxidation mechanism.—Various reaction schemes for xanthate oxidation have been worked out and are compiled in Table III. The anodic mechanisms 3 and 4 are similar to 1 and 2, respectively, but they have the desorption of dioxanthogen as an additional reaction step. Table III indicates that none of the kinetic parameters for the mechanisms listed are in agreement with the values reported here for b_a and $[d \ln i_a / d \ln C_{KEX}]_E$.

In organoelectrochemical reactions, the competition between adsorbed intermediates and water molecules may be important (41). Further, in flotation mechanisms, water displacement by the collector has an effect on hydrophobicity. Accordingly, kinetic parameters have been calculated in terms of solvent displacement

² Step [IV] is often quoted in the oxygen reduction literature (29, 31, 33). However, it involves the difficulty of surface anion recombination. This may be diminished in two ways. Thus, image forces reduce the repulsion (35); and also, it seems reasonable to suppose that charge transfer adsorption occurs, i.e., the surface charge on the anion must be < 1 . For example, anion adsorption on perovskites (36) shows full coverage with respect to OH^- in alkaline solution, and this would not be possible unless partial charge transfer had occurred.

Table III. Proposed mechanisms and related kinetic parameters for xanthate oxidation

Rate-determining step	Langmuir				Temkin (0.2 < θ < 0.8)*	
	$\partial E/\partial \ln i$		$[\partial \ln i/\partial \ln C_{\text{KEX}}]_E$		$\partial E/\partial \ln i$	$[\partial \ln i/\partial \ln C_{\text{KEX}}]_E$
	$\theta \rightarrow 0$	$\theta \rightarrow 1$	$\theta \rightarrow 0$	$\theta \rightarrow 1$		
1. $X^- \rightleftharpoons X_{\text{ads}} + e$ $X_{\text{ads}} + X_{\text{ads}} \rightleftharpoons X_2$	$2RT/F$ $RT/2F$	— ∞	1 2	— 0	$2RT/F$ RT/F	1.0 1.0
2. $X^- \rightleftharpoons X_{\text{ads}} + e$ $X_{\text{ads}} + X^- \rightleftharpoons X_2 + e$	$2RT/F$ $2RT/3F$	— $2RT/F$	1 2	— 1	$2RT/F$ RT/F	1.0 1.5
3. $X^- \rightleftharpoons X_{\text{ads}} + e$ $X_{\text{ads}} + X_{\text{ads}} \rightleftharpoons X_{2_{\text{ads}}}$ $X_{2_{\text{ads}}} \rightleftharpoons X_2$	$2RT/F$ $RT/2F$ $RT/2F$	— ∞ ∞	1 2 2	— 0 0	$2RT/F$ $2RT/F$ $2RT/F$	1.0 0.5 0.5
4. $X^- \rightleftharpoons X_{\text{ads}} + e$ $X_{\text{ads}} + X^- \rightleftharpoons X_{2_{\text{ads}}} + e$ $X_{2_{\text{ads}}} \rightleftharpoons X_2$	$2RT/F$ $2RT/3F$ $RT/2F$	— $2RT/F$ ∞	1 2 2	— 1 0	$2RT/F$ $2RT/F$ $2RT/F$	1.0 1.0 0.5

* Temkin interaction parameter for the intermediates is assumed to be equal.

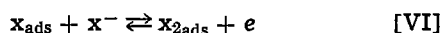
Table IV. Solvent displacement mechanisms for xanthate oxidation*

Rate-determining step	Langmuir				Temkin (0.2 < θ < 0.8)	
	$\partial E/\partial (2.3 \ln i)$		$[\partial \ln i/\partial \ln C_{\text{KEX}}]_E$		$\partial E/\partial (2.3 \ln i)$	$[\partial \ln i/\partial \ln C_{\text{KEX}}]_E$
	$\theta \rightarrow 0$	$\theta \rightarrow 1$	$\theta \rightarrow 0$	$\theta \rightarrow 1$		
1. $X^- \rightleftharpoons X_{\text{ads}} + e$ $X_{\text{ads}} + X_{\text{ads}} \rightleftharpoons X_2$	152 ($m = 1.5$) 34 ($m = 1.5$)	— 285 ($m = 1.5$)	1 2	— 0	152 ($m = 1.5$) 60 (independent of m)	1.00 1.00
2. $X^- \rightleftharpoons X_{\text{ads}} + e$ $X_{\text{ads}} + X^- \rightleftharpoons X_2 + e$	152 ($m = 1.5$) 43 ($m = 1.5$)	— 99 ($m = 1.5$)	1 2	— 1	152 ($m = 1.5$) 60 (independent of m)	1.00 1.50
3. $X^- \rightleftharpoons X_{\text{ads}} + e$ $X_{\text{ads}} + X_{\text{ads}} \rightleftharpoons X_{2_{\text{ads}}}$ $X_{2_{\text{ads}}} \rightleftharpoons X_2$	152 ($m = 1.5$) 44 ($m = 1.5, l = 6$) 46 ($m = 1.5, l = 6$) 38 ($l = 6$) 40 ($l = 7$)	— -20 ($m = 1.5, l = 6$) -15 ($m = 1.5, l = 6$) 143 ($l = 6$) 122 ($l = 7$)	1 2 2 2	— 0 0 0	152 ($m = 1.5$) -60 ($m = 1.5, l = 6$) -45 ($m = 1.5, l = 7$) ∞	1.00 -1.00 -1.30 0.00
4. $X^- \rightleftharpoons X_{\text{ads}} + e$ $X_{\text{ads}} + X^- \rightleftharpoons X_{2_{\text{ads}}} + e$ $X_{2_{\text{ads}}} \rightleftharpoons X_2$	152 ($m = 1.5$) 62 ($m = 1.5, l = 6$) 66 ($m = 1.5, l = 7$) 38 ($l = 6$) 40 ($l = 7$)	— 324 ($m = 1.5, l = 6$) 522 ($m = 1.5, l = 7$) 143 ($l = 6$) 122 ($m = 7$)	1 2 2 2	— 1 0 0	152 ($m = 1.5$) -60 ($m = 1.5, l = 6$) -45 ($m = 1.5, l = 7$) 90 ($m = 1.5, l = 7$) 94 ($m = 1.5, l = 7$) 95 \pm 5	1.00 -0.50 -0.83 0.67 0.64 0.71
Experimental						

* m and l are the number of water molecules replaced by one molecule of x_{ads} and $x_{2_{\text{ads}}}$, respectively. $m = 1.5$ and $l = 6-7$ (see text).

mechanisms (41), and the results are given in Table IV. The mechanism 4 with step 3 as the rds, and with the intermediates following the Temkin adsorption isotherm, predicts b_a of 90-95 mV³ and $[\partial \ln i_a/\partial \ln C_{\text{KEX}}]_E = 0.67-0.64$, which are in good agreement with the experimental values of 95 \pm 5 mV and 0.71.

The reaction scheme is, therefore



with step VII as rds, and $x_{2_{\text{ads}}}$ following a Temkin adsorption isotherm. The corresponding current density is (41)

³The range arises because of uncertainty in the number of water molecules displaced by dioxanthogen. This has been taken, on the basis of space filling models, as 6-7.

$$i^+_{\text{VII}} = 2Fk^+_{\text{VII},0} \theta_{X_2} \exp \left[(1 - \gamma) \frac{l\mu FE}{e_0 \delta RT} \right] \cdot \exp[(1 - \epsilon) l r \theta] \quad \text{[14]}$$

where l = the number of water molecules replaced by one molecule of $x_{2_{\text{ads}}}$, μ and δ are the dipole moment and the diameter of water molecule, respectively; e_0 = unit electronic charge; $r\theta$ is a function of the surface coverage θ of the adsorbed intermediates. The symbols γ and ϵ are symmetry factors.

⁴In taking m and r to be the Temkin parameters for the interaction of x_{ads} with $x_{2_{\text{ads}}}$, we follow Gileadi and Stoner (41). In fact, there is no precise justification for assuming that the interaction parameters in a Temkin formulation should be proportional to the number of water molecules which an adsorbent displaces, i.e., to the adsorbent's size. Conversely, this treatment is at least better than the previous treatments which assume identity of all the Temkin r values. In fact, r will tend to increase with the size of the adsorbent.

The quantity $r\theta$ can be calculated from the equilibrium step [VI]⁵

$$r\theta = \ln \left\{ [K_{VI,0}]^{\frac{1}{l-m}} \cdot [x^-]^{l-m} \cdot \exp \left[-\frac{\mu}{e_0\delta} \frac{FE}{RT} \right] \cdot \exp \left[\frac{1}{l-m} \frac{FE}{RT} \right] \right\} \quad [2]$$

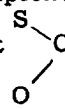
where m is the number of water molecules replaced by one molecule of x_{ads} .

Therefore

$$i^+_{VII} = K[x^-]^{0.51} \exp \left[\frac{l}{l-m} (1-\gamma) F \frac{E}{RT} \right] \quad [3]$$

Hence

$$b_a = \left[\frac{\partial E}{\partial \log i^+_{VII}} \right]_{x^-} = \frac{1}{(l/l-m)} \frac{1}{(1-\gamma)} \frac{2.303RT}{F} \left[\frac{\partial \ln i^+_{VII}}{\partial \ln [x^-]} \right]_E = \frac{0.5l}{(l-m)}$$

The parameters m and l require the area occupied by the adsorbed species x and x_2 . The projected surface areas for the discharged radical are 16.0 Å² and 62.6 Å², respectively, for the orientation in which the planar part  lies on the surface with the alkyl

group pointing into the solution. These values were calculated considering molecules as spherical and arranged in hexagonal close packing. With a value of 10.2 Å² for water,⁶ m and l are 1.5 and 6-7, respectively. The kinetic parameters are thus 90-94 mV, and 0.67-0.64.

These considerations are based on a model in which there are no multilayers. In the flotation region for FeS₂, there is evidence for their absence (42-44). The findings of recent XPS measurements (27) also indicated that the mineral surface contains less than a monolayer of the collector. Gardner and Woods (12) have interpreted sweep measurements in a more anodic region to indicate multilayer formation of dixanthogen on FeS₂. However, (i) if multilayer formation were uniform, steady-state xanthate oxidation partnered by oxygen reduction would be difficult to conceive (45), (ii) the $i-t$ transients do not increase their rate of decline with time at more anodic potentials where the suspected multilayers would be thicker, (iii) in Ahmed's results (18), hydrophobicity could be rapidly (i.e., < 100-200 ms) turned on and off by closing and opening the circuit, which would be improbable if dixanthogen were present in multilayers, and (iv) it is possible that the calculations by Gardner and Woods (12) of the coulombs in the sweep regions were increased by solute readsorption.

Mixed potential model.—The rate equations for the O₂ reduction and xanthate oxidation can be written as

$$i_c = -4F\theta_c k_c^0 p_{O_2} [H^+] \exp [-\beta FE/RT] \quad [4]$$

and

$$i_a = 2F\theta_a k_a^0 [x^-]^{0.51} \exp \left[\frac{l}{(l-m)} (1-\gamma) FE/RT \right] \quad [5]$$

⁵ It is correct to consider only step [VI] (and not [V]) when evolving $r\theta$ in the Temkin mode. Thus, applying the Temkin conditions to [V], one obtains $r\theta_{x_{ads}} = -EF + \ln|x^-| + \text{const.}$, i.e., $\theta_{x_{ads}}$ is linear with potential. In the deduction of Eq. [2], were $\theta_{x_{ads}}$ expressed in terms of [V], no change in the exponential terms of [2] would occur.

⁶ This value was calculated by assuming hexagonal close packing of H₂O on the electrode surface and no dimer formation.

where θ_c and θ_a are the areas over which the cathodic and anodic reactions, respectively, take place, and k_c^0 and k_a^0 are the respective rate constants under zero-field conditions.

Equations [4] and [5] can be expressed, in terms of the exchange current density as

$$i_c = i_{o,c} \exp [-\beta F(E - E_{e,c})/RT] \quad [4']$$

$$i_a = i_{o,a} \exp \left[\frac{l}{l-m} (1-\gamma) F(E - E_{e,a})/RT \right] \quad [5']$$

For the mixed potential theory to be applicable to a system, in which the above two are the partial reactions which determine the open-circuit mixed potential E_m and the corresponding current i_m , the following conditions should be satisfied

$$|i_c| = i_a = i_m \quad [6]$$

and

$$E = E_m \quad [7]$$

The applicability of the mixed potential model can be tested by two methods.

Method 1: Calculation of E_m and i_m .—Combining Eq. [4'] and [5'] to get E_m and i_m

$$E_m = \frac{RT}{(\alpha_a + \alpha_c)F} \ln \left[\frac{i_{o,c}}{i_{o,a}} \right] + \frac{\alpha_c}{\alpha_a + \alpha_c} E_{e,c} + \frac{\alpha_a}{\alpha_a + \alpha_c} E_{e,a} \quad [8]$$

and

$$i_m = [i_{o,a}]^{\frac{\alpha_c}{\alpha_a + \alpha_c}} [i_{o,c}]^{\frac{\alpha_a}{\alpha_a + \alpha_c}} \exp \left[\frac{\alpha_a \alpha_c}{\alpha_a + \alpha_c} \cdot \frac{F}{RT} E_{e,cell} \right] \quad [9]$$

where

$$\alpha_a = \frac{(1-\gamma)l}{l-m}$$

$$\alpha_c = \beta$$

and

$$E_{e,cell} = E_{e,c} - E_{e,a}$$

By knowing $i_{o,a}$ and $i_{o,c}$ values in the mixture (from Fig. 3-6), E_m and i_m can be calculated, since α_c and α_a are known. These calculated values of E_m and i_m can be compared with experimentally obtained values in the mixture.

The degree of agreement is high, as shown in Table V.

Method 2: Test of differentials.—Equating Eq. [4] and [5], we get

$$\left[\frac{\partial E_m}{\partial \log p_{O_2}} \right]_{x^-,pH} = \frac{b_a |b_c|}{b_a + |b_c|} \left\{ 1 + \left[\frac{\partial \log (\theta_c/\theta_a)}{\partial \log p_{O_2}} \right]_{x^-,pH} + \left[\frac{\partial \log (k_c^0/k_a^0)}{\partial \log p_{O_2}} \right]_{x^-,pH} \right\} \quad [10]$$

and

$$\left[\frac{\partial \log i_m}{\partial \log p_{O_2}} \right]_{x^-,pH} = -\frac{b_a}{b_a + |b_c|} \left\{ 1 + \left[\frac{\partial \log (\theta_c/\theta_a)}{\partial \log p_{O_2}} \right]_{x^-,pH} + \left[\frac{\partial \log (k_c^0/k_a^0)}{\partial \log p_{O_2}} \right]_{x^-,pH} \right\} + \left[\frac{\partial \log \theta_c}{\partial \log p_{O_2}} \right]_{x^-,pH} + \left[\frac{\partial \log k_c^0}{\partial \log p_{O_2}} \right]_{x^-,pH} \quad [11]$$

Table V. A comparison of experimental and calculated E_m and i_m

Systems	E_m V		$i_m \times 10^6$ A cm ⁻²	
	Experimental	Calculated	Experimental	Calculated
(A) $p_{O_2} = 1$ and $C_{KEX} = 10^{-2}$	0.17	0.16	9.00	7.20
(B) $p_{O_2} = 1$ and $C_{KEX} = 10^{-3}$	0.19	0.19	7.30	7.80
(C) $p_{O_2} = 0.33$ and $C_{KEX} = 10^{-2}$	0.10	0.08	2.20	1.40
(D) $p_{O_2} = 0.33$ and $C_{KEX} = 10^{-3}$	0.18	0.17	3.30	2.40

As a "zeroeth" approximation, let it be assumed that the pressure terms in the parentheses are zero. A comparison of the calculated values with the experimental values is then as follows (Table VI).

The results of Table VI show poor consistency between fact and model. In reconsidering Eq. [10] and [11], it seems reasonable to continue to accept a negligible variation of rate constant with pressure, but to admit that the relative occupancy of cathodic and anodic sites (θ_c/θ_a) may depend upon oxygen pressure. One can then calculate the change of θ_c/θ_a caused by a change of oxygen pressure (the assumption is that the discrepancies of Table VI are due entirely to this variation).

Considering the system (A)/(C), one finds, thus, the value of 1.3 for

$$\left[\frac{\partial \log i_m}{\partial \log p_{O_2}} \right]_{x^-, pH}$$

i.e., a change of 10 times in p_{O_2} causes a change of 19.9 times in i_m . From Eq. [4] and the values of Table VI

$$\frac{(i_c)_{p_{O_2}=1}}{(i_c)_{p_{O_2}=0.1}} = \frac{(\theta_c)_{p_{O_2}=1}}{(\theta_c)_{p_{O_2}=0.1}} \exp \left[-\frac{\beta F}{RT} (0.150) \right]$$

where 0.150 is the corresponding change of the mixed potential. Hence

$$\frac{(\theta_c)_{p_{O_2}=1}}{(\theta_c)_{p_{O_2}=0.1}} \approx 677 \quad [12]$$

Similar reasoning, applied to the anodic reaction, shows that

$$\frac{(\theta_a)_{p_{O_2}=1}}{(\theta_a)_{p_{O_2}=0.1}} = 0.53 \quad [13]$$

The sum of θ_c and θ_a at each pressure may be taken as unity for each pressure, respectively. The resulting two equations, together with Eq. [12] and [13], yield the values of Table VII. The same approach can be applied to the systems (B)/(D).

⁷ The large change is not irrational in view of the attractive interaction between xanthate and radicals from oxygen reduction (see Fig. 3 and Fig. 5).

Table VI. Experimental and calculated coefficients (with the assumption of cathodic/anodic area ratio independent of O_2 pressure)

	Systems (A)/(C) (i.e., at a constant $C_{KEX} = 10^{-2}M$)		Systems (B)/(D) (i.e., at a constant $C_{KEX} = 10^{-3}M$)	
	Experimental	Calculated	Experimental	Calculated
$\left[\frac{\partial E_m}{\partial \log p_{O_2}} \right]_{x^-, pH}$ V decade ⁻¹	0.150	0.044	0.002	0.048
$\left[\frac{\partial \log i_m}{\partial \log p_{O_2}} \right]_{x^-, pH}$	1.300	0.500	0.700	0.500

Table VII. Calculation of degree of occupancy of FeS_2 surface with cathodic and anodic sites

Systems (A)/(C)	$p_{O_2} = 0.1$		$p_{O_2} = 1$	
	θ_c	θ_a	θ_c	θ_a
Systems (A)/(C)	0.613	0.990	0.480	0.520
Systems (B)/(D)	0.890	0.110	0.460	0.540

It can be seen (Table VII) that the model used (mixed potential hypothesis; negligible pressure dependence of rate constant but pressure dependence of cathodic/anodic site ratio) gives a reasonable order of changes for the system (A)/(C), in which KEX is at $10^{-2}M$ and the oxygen pressure varies by ten times. However, for the systems (B)/(D) ($KEX = 10^{-3}M$), the results are unfavorable, θ_c decreasing anomalously with increase of oxygen pressure. It is possible that this discrepancy arises because, in the systems (B)/(D), there is a competing oxidation of the substrate. Some evidence for this can be seen by the increased deviation (from Tafel relation) of the i-V curves in Fig. 4 and 6.

Galena

The O_2 reduction on PbS will be assumed to occur through a mechanism similar to that on FeS_2 . The only evidence available is that $-b_c$ on PbS has the same slope as on FeS_2 , i.e., 120 mV decade⁻¹.

The high b_a value (>240 mV) observed for xanthate oxidation on PbS can be explained in terms of the anodic mechanism 4 (Table IV) is operative on PbS (solvent displacement mechanism) with the step II as the rds, and the intermediate following a Langmuir adsorption isotherm with $\theta \rightarrow 1$. At more positive potentials (see Fig. 7), the slope changes to one of 40 mV and this would be consistent with mechanism 4, although step III would now be the rds.

The decrease of the xanthate oxidation rate observed at higher potentials (Fig. 7) indicates that the surface compound formed on PbS in the presence of KEX is chemically different from that on FeS_2 , where the current increases continuously with potential. In the case of PbS, it is possible that step III of the mechanism 4 (Table IV) may be the rds, as long as the surface coverage of x_{2ads} is small. With increase in $\theta_{x_{2ads}}$, there is a possibility that x_{2ads} is converted to surface compounds such as lead ethyl xanthate and elemental sulfur (17), which can inhibit the further electron transfer reaction at the interface.

Coming to the mixed potential model, as applicable to PbS in the mixture of O_2 and KEX (Fig. 8), the experimental values of E_m and i_m [$-0.065V$ (NHE) and $1.6 \times 10^{-7}A$ cm⁻²] are in good agreement with the calculated values from Eq. [8] and [9] [$-0.078V$ (NHE) and $1.35 \times 10^{-7}A$ cm⁻²].

Comparison of the Behavior of FeS_2 and PbS

O_2 reduction.—The $i_{o,c}$ values for O_2 reduction at $p_{O_2} = 1$, of $4.6 \pm 0.3 \times 10^{-12}A$ cm⁻² and $2.8 \pm 0.3 \times 10^{-12}A$ cm⁻² at FeS_2 and PbS electrodes, respectively, indicate a higher catalytic activity of FeS_2 for this reaction. This is in accordance with studies (46, 47) on electrocatalytic reduction with thiospinels of the transition elements.

Both FeS_2 and PbS are semiconductors (see Experimental section). A value of 0.5 for the transfer coefficient (α) for the O_2 reduction at both FeS_2 and PbS indicates the absence of a Schottky barrier within the sulfides (48) and that the semiconductor-solution interphase properties predominate over the semiconductor properties. Surface states are evidently present.

Xanthate oxidation.— FeS_2 shows a higher $i_{o,a}$ value for xanthate oxidation ($1 \times 10^{-6}A$ cm⁻² for $C_{KEX} = 10^{-2}M$) than PbS ($2.4 \times 10^{-7}A$ cm⁻²). These values

APPENDIX

Table A-1. Proposed mechanisms and related kinetic parameters for O₂ reduction

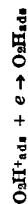
Rate-determining step	Langmuir			Temkin (0.2 < θ < 0.8)*		
	∂E/∂ ln i		∂ ln i/∂ ln pO ₂ ^{1/2} p _H		∂E/∂ ln i	
	θ → 0	θ → 1	θ → 0	θ → 1	∞	2RT/F 2RT/F
C-1. Bockris' electrochemical oxide path						
O ₂ ⇌ 2 O _{ads}	∞	∞	1.00	0	∞	1.00
O _{ads} + H ₂ O + e ⇌ OH _{ads} + OH ⁻	2RT/F 2RT/F	2RT/F 2RT/F	0.50 0.50	0 -1	2RT/F 2RT/F	0.00 0.25
OH _{ads} + e ⇌ OH ⁻	∞	∞	1.00	0	∞	1.00
C-2. Oxide path						
O ₂ ⇌ 2 O _{ads}	∞	∞	1.00	0	∞	1.00
O _{ads} + H ₂ O ⇌ 2 OH _{ads}	2RT/F	2RT/F	0.50	0	2RT/F	-0.50
OH _{ads} + e ⇌ OH ⁻	∞	∞	1.00	0	∞	-0.50
C-3. Hydrogen peroxide path						
O ₂ + H ₂ O ⇌ O ₂ H ₂ + OH _{ads}	∞	∞	1.00	0	∞	1.00
O ₂ H ₂ + H ₂ O ⇌ O ₂ H ₂ + OH _{ads}	RT/F	∞	1.00	-1	∞	-0.25
O ₂ H ₂ + e ⇌ 2 OH _{ads}	RT/2F	∞	1.00	-2	∞	0.25
OH _{ads} + e ⇌ OH ⁻	2RT/F	2RT/F	0.25	0	2RT/F	0.25
C-4. Metal peroxide path						
O ₂ + H ₂ O ⇌ O ₂ H ₂ + OH _{ads}	∞	∞	1.00	0	∞	1.00
O ₂ H ₂ + e ⇌ O ₂ H ₂ + OH _{ads}	RT/F	∞	1.00	-1	∞	-0.25
O ₂ H ₂ + H ₂ O ⇌ 2 OH _{ads}	RT/2F	∞	1.00	-2	∞	0.25
OH _{ads} + e ⇌ OH ⁻	2RT/F	2RT/F	0.25	0	2RT/F	0.25
C-5. Electrochemical metal peroxide path						
O ₂ + H ₂ O ⇌ O ₂ H ₂ + OH _{ads}	∞	∞	1.00	0	∞	1.00
O ₂ H ₂ + e ⇌ O ₂ H ₂ + OH ⁻	2RT/3F	2RT/F	1.00	-1	∞	0.00
O ₂ H ₂ + H ₂ O ⇌ 2 OH _{ads}	RT/2F	∞	1.00	-2	∞	0.25
OH _{ads} + e ⇌ OH ⁻	6RT/5F	2RT/F	0.33	0	2RT/F	0.25
C-6. Hoar' path						
O ₂ + 2e ⇌ O ²⁻ _{ads}	RT/F	∞	1.00	0	RT/F	1.00
O ²⁻ _{ads} + 2H ₂ O ⇌ 2HO ⁻ ₂ + OH ⁻	RT/F	∞	1.00	0	-RT/F	-0.50
HO ⁻ ₂ + OH _{ads} + e ⇌ OH ⁻	RT/F	∞	0.50	0	∞	0.00
OH _{ads} + e ⇌ OH ⁻	2RT/3F	2RT/F	0.50	-1	2RT/3F	0.50
C-7. Conway and Bourgault's path						
O ₂ + H ₂ O ⇌ O ₂ H ₂ + OH _{ads}	∞	∞	1.00	0	∞	1.00
O ₂ H ₂ + e ⇌ O ₂ H ₂ + OH _{ads}	RT/F	∞	1.00	-1	∞	-0.25
O ₂ H ₂ + H ₂ O + e ⇌ OH _{ads} + OH ⁻	2RT/5F	2RT/F	1.00	-2	2RT/F	0.00
OH _{ads} + e ⇌ OH ⁻	6RT/5F	2RT/F	0.33	-0.33	2RT/F	0.25
C-8. Electrochemical O₂H desorption path						
O ₂ + H ₂ O ⇌ O ₂ H ₂ + OH _{ads}	∞	∞	1.00	0	∞	1.00
O ₂ H ₂ + e ⇌ O ₂ H ₂ + OH ⁻	2RT/3F	2RT/F	1.00	-1	∞	0.00
O ₂ H ₂ + H ₂ O + e ⇌ OH _{ads} + OH ⁻	2RT/5F	2RT/F	1.00	-2	2RT/F	0.00
OH _{ads} + e ⇌ OH ⁻	6RT/5F	2RT/F	0.33	-0.33	2RT/F	0.25
C-9. Riddiford's path						
O ₂ + H ₂ O + e ⇌ O ₂ H ₂ + OH ⁻	∞	∞	1.00	0	∞	1.00
O ₂ H ₂ + e ⇌ O ₂ H ₂ + OH ⁻	2RT/3F	2RT/F	1.00	-1	∞	0.00
O ₂ H ₂ + H ₂ O + e ⇌ 2 OH _{ads}	2RT/5F	2RT/F	1.00	-2	2RT/F	0.00
2 OH _{ads} + e ⇌ OH ⁻	2RT/3F	2RT/F	0.50	-1	RT/F	-0.50
C-10. Krasil'shchikov's path						
O ₂ ⇌ 2 O _{ads}	∞	∞	1.00	0	∞	1.00
O _{ads} + e ⇌ O ⁻ _{ads}	2RT/F	2RT/F	0.50	0	2RT/F	0.00
O ⁻ _{ads} + H ₂ O ⇌ OH _{ads} + OH ⁻	RT/F	∞	0.50	0	∞	0.00
OH _{ads} + e ⇌ OH ⁻	2RT/3F	2RT/F	0.50	-1	2RT/F	0.25
C-11. Wade and Hackerman's path						
O ₂ + H ₂ O + 2e ⇌ 2 OH ⁻ _{ads} + 2 O _{ads}	RT/F	∞	1.00	0	RT/F	1.00
O _{ads} + H ₂ O + 2e ⇌ 2 OH ⁻ _{ads}	RT/3F	∞	1.00	-2	3RT/4F	0.17
2 OH ⁻ _{ads} ⇌ 2 OH ⁻	RT/4F	∞	1.00	-2	2RT/3F	0.33

C-12. Oxygen-water discharge path									
$O_2 + H_2O + e \rightleftharpoons O_2H_{ads} + OH^-$	$2RT/F$	$2RT/F$	1.00	0	0	$2RT/F$	1.00	0	0
$O_2H_{ads} + e \rightleftharpoons O_{ads} + OH^-$	$2RT/3F$	$2RT/F$	1.00	0	-1	$2RT/F$	0.00	0	0
$O_{ads} + H_2O + e \rightleftharpoons OH_{ads} + OH^-$	$2RT/5F$	$2RT/F$	1.00	0	-2	$2RT/F$	0.00	0	0
$OH_{ads} + e \rightleftharpoons OH^-$	$2RT/7F$	$2RT/F$	1.00	0	-3	RT/F	0.50	0	-0.5
C-13. Damjanovic's path									
$O_2 \rightleftharpoons 2 O_{ads}$	∞	∞	1.00	0	0	∞	1.00	0	0
$O_{ads} + H_2O \rightleftharpoons (O-H-OH)_{ads}$	$2RT/F$	$2RT/F$	0.50	0	0	$2RT/F$	0.00	0	0
$(O-H-OH)_{ads} + e \rightleftharpoons (O-H-OH)^-_{ads}$	RT/F	$2RT/F$	0.50	0	0	∞	0.00	0	0
$(O-H-OH)^-_{ads} \rightleftharpoons OH_{ads} + OH^-$	$2RT/3F$	$2RT/F$	0.50	0	-1	$2RT/F$	0.00	0	0
C-14. Electrochemical hydrogen peroxide desorption path									
$O_2 + H_2O + e \rightleftharpoons O_2H_{ads} + OH^-$	$2RT/F$	$2RT/F$	1.00	0	0	$2RT/F$	1.00	0	0
$O_2H_{ads} + e \rightleftharpoons O_{ads} + OH^-$	$2RT/3F$	$2RT/F$	1.00	0	-1	$2RT/F$	0.00	0	0
$O_{ads} + H_2O \rightleftharpoons (O-H-OH)_{ads}$	$RT/2F$	∞	1.00	0	-2	∞	0.00	0	0
$(O-H-OH)_{ads} + e \rightleftharpoons (O-H-OH)^-_{ads}$	$2RT/5F$	$2RT/F$	1.00	0	-2	$2RT/F$	0.00	0	0
$(O-H-OH)^-_{ads} \rightleftharpoons OH_{ads} + OH^-$	$RT/3F$	∞	1.00	0	-2	∞	0.00	0	0
$OH_{ads} + e \rightleftharpoons OH^-$	$2RT/7F$	$2RT/F$	1.00	0	-3	RT/F	0.50	0	-0.5
C-15. O'Grady's path									
$O_2 + 2H_2O \rightleftharpoons 2 OH^+_{ads} + 2 OH^-$	∞	$2RT/F$	1.00	0	0	∞	1.00	0	0
$OH^+_{ads} + e \rightleftharpoons OH_{ads}$	$2RT/3F$	$2RT/F$	0.50	0	-1	$2RT/F$	0.00	0	0
$OH_{ads} + e \rightleftharpoons OH^-$	$2RT/3F$	$2RT/F$	0.50	0	-1	$2RT/F$	0.25	0	-0.5
C-16. Bagotskii's path									
$O_2 + e \rightleftharpoons O_{2,ads}$	$2RT/F$	RT/F	1.00	0	0	$2RT/F$	1.00	0	0
$O_{2,ads} + H_2O \rightleftharpoons O_2H_{ads} + OH^-$	RT/F	∞	1.00	0	0	∞	0.00	0	0
$O_2H_{ads} + e \rightleftharpoons O_2H^-_{ads}$	$2RT/3F$	$2RT/F$	1.00	0	-1	$2RT/F$	0.00	0	0
$2 O_2H^-_{ads} \rightleftharpoons O_2 + 2 OH^-$	$RT/4F$	∞	2.00	0	-2	RT/F	1.00	0	0
C-17. O ₂ H ⁺ Electrochemical desorption path									
$O_2 + H_2O \rightleftharpoons O_2H^+_{ads} + OH^-$	∞	$2RT/F$	1.00	0	0	∞	1.00	0	0
$O_2H^+_{ads} + e \rightleftharpoons O_2H_{ads}$	$2RT/3F$	$2RT/F$	1.00	0	$-1(-0.5)^b$	$2RT/F$	0.00	0	0
$O_2H_{ads} + e \rightleftharpoons O_2H^-_{ads}$	$RT/4F$	∞	2.00	0	-2	∞	0.00	0	0
$2 O_2H^-_{ads} \rightleftharpoons O_2 + 2 OH^-$	$2RT/F$	$2RT/F$	1.20	0	-0.2^c	∞	1.00	0	-1
Experimental									

* τ is the p.d. between outer Helmholtz plane and the bulk of the solution.

^a Temkin interaction parameter for all intermediates is taken as equal.

^b Value for the coefficient, when ξ is not constant. Thus, with the step



as rds

$$[\partial \ln i / \partial (2.3 \text{ pH})]_{1F} = -1 + (\beta - 1)(F/2.303RT) [\partial (\delta \text{ pH}) / \partial \text{ pH}]_{1F}$$

The ξ potential may be related approximately to Cor^- by an equilibrium equation (37-39)

$$\xi = \xi_0 - (RT/F) \ln \text{Cor}^-$$

Hence

$$[\partial \ln i / \partial (2.3 \text{ pH})]_{1F} = -0.5$$

^c Value extrapolated from experimental i-V plots of Ref. (13b) (pH range 9.1-12.1).

differ by too small a degree to justify significant theoretical interpretation.

The consistence found with a Temkin isotherm for xanthate oxidation of FeS₂ (but Langmuir for PbS) may be related to the Fe-Fe distance (3.82Å) compared with the Pb-Pb distance in PbS (4.18Å). The adsorbed organics are probably orthogonal to the electrode surface (see Xanthate oxidation section, above), and may adsorb on the metal sites (49). The lateral interaction between the same organic molecules apart at these two distances would be in a ratio of around 1.5:1 (FeS₂ to PbS).

Mixture of O₂ and KEX.—The oxidized xanthate present on the surface accelerates O₂ reduction of FeS₂; it inhibits it on PbS. This is in accordance with the literature that the hydrophobic species that forms on FeS₂ is different from that on PbS (14, 16, 17).

Conclusions

1. The mechanism of O₂ reduction on both FeS₂ and PbS involves the rds of O₂H⁺_{ads} + e → O₂H_{ads}. H₂O₂ is an intermediate.

2. The mechanism of the oxidation of xanthate occurs through a solvent displacement mechanism. The rds is the desorption of dixanthogen for FeS₂; and x_{ads} + x⁻ → x_{2ads} + e for PbS.

3. The mixed potential theory is consistent with the measured electrode kinetics with respect to the comparison of E_m and i_m values. The measured differential coefficients [∂E_m/∂ log pO₂]_{x⁻,pH} and [∂ log i_m/∂ log pO₂]_{x⁻,pH} are, however, different from the values predicted by the simple model, in which the cathodic to anodic area ratio (θ_c/θ_a) is assumed independent of O₂ partial pressure. By considering the variation of θ_c/θ_a with O₂ partial pressure,⁸ it is possible to bring a consistency between the theory and experiment, in systems containing high concentrations of KEX in solution. When KEX concentration is low, theory and experiment are not in good agreement. This may be due to partial oxidation of the substrate.

4. Within this situation, the mixed potential theory is consistent with the available data.

Acknowledgment

The authors are grateful to Dr. Ron Woods of the CSIRO, Melbourne, Australia for discussion and to the National Science Foundation, Washington, D.C. for financial support under grant No. CPE-8006977.

Manuscript submitted March 14, 1983; revised manuscript received Sept. 15, 1983.

⁸The origin of such a variation may arise from reaction of the adsorbed xanthate intermediate and a possible peroxide. Enhancement of the oxygen kinetics could come as a result of bubble adhesion.

REFERENCES

- A. M. Cook and J. C. Nixon, *J. Phys. Colloid Chem.*, **54**, 445 (1950).
- A. M. Gaudin, "Flotation," 2nd ed., p. 131, McGraw-Hill, New York (1957).
- K. L. Sutherland and I. W. Wark, "Principles of Flotation," p. 67, Australian Institute of Mineral Metallurgy, Melbourne (1955).
- I. Plaksin, *Trans. Am. Inst. Min. Engrs.*, **214**, 319 (1959); (*Min. Engrg.*, **11**, March 1959).
- S. G. Salamy and J. C. Nixon, *Aust. J. Chem.*, **7**, 146 (1954).
- I. N. Plaksin and R. Sh. Shafeev, *Trans. Instn. Min. Metall.*, **72**, 715 (1963).
- C. Guarnaschelli, *Trans. AIME*, **247**, 324 (1970).
- D. R. Dixon, R. O. James, and T. W. Healy, *ibid.*, **258**, 81 (1975).
- P. E. Richardson and D. L. Edelstein, in "The Physical Chemistry of Mineral-Reagent Interactions in Sulfide Flotations," P. E. Richardson, G. R. Hyde, and M. S. Ojalvo, Editors, p. 72, U.S. Bureau of Mines, Information Circular 8818 (1978).
- R. Tolun and J. A. Kitchener, *Trans. Inst. Min. Metall.*, **73**, 313 (1964).
- R. Woods, *J. Phys. Chem.*, **75**, 354 (1971).
- J. R. Gardner and R. Woods, *Aust. J. Chem.*, **30**, 981 (1977).
- (a) T. Biegler, D. A. J. Rand, and R. Woods, in "Trends in Electrochemistry," J. O'M. Bockris, D. A. J. Rand, and B. J. Welch, Editors, p. 291, Plenum Press, New York (1977); (b) T. Biegler, D. A. J. Rand, and R. Woods, *J. Electroanal. Chem.*, **60**, 151 (1975).
- M. C. Fuerstenau, M. C. Kuhn, and D. A. Elgillani, *Trans. Soc. Min. Eng./AIME*, **241**, 148 (1968).
- S. Chander and D. W. Fuerstenau, *J. Electroanal. Chem.*, **56**, 217 (1974).
- H. Majima and M. Takeda, *Trans. Soc. Min. Eng./AIME*, **241**, 431 (1968).
- A. Granville, N. P. Finkelstein, and S. A. Allison, *Trans. Inst. Min. Metall.*, **81**, C 1 (1972).
- S. M. Ahmed, *Int. J. Miner. Process.*, **5**, 175 (1978).
- T. W. Healy, in "Electrochemistry," H. Bloom and F. Gutman, Editors, p. 285, Plenum Press, New York (1977).
- D. W. Fuerstenau and T. W. Healy, in "Adsorptive Bubble Separation Technology," R. Lemlich, Editor, p. 91, Academic Press, New York (1972).
- P. Somasundaran and E. D. Goddard, in "Modern Aspects of Electrochemistry," Vol. 13, B. E. Conway and J. O'M. Bockris, Editors, p. 207, Plenum Press, New York (1979).
- P. Somasundaran, *J. Colloid Interface Sci.*, **27**, 659 (1968).
- P. Somasundaran, *Trans. AIME*, **255**, 64 (1974).
- P. Somasundaran, *Int. J. Miner. Process.*, **3**, 35 (1976).
- L. J. Van der Pauw, *Philips Res. Rep.*, **13**, 1 (1958).
- J. O'M. Bockris and T. Otagawa, Submitted to *Surf. Sci.*
- K. C. Pillai, V. Y. Young, and J. O'M. Bockris, Submitted to *Surf. Sci.*
- R. B. Heimann, "Auflosung Von Kristallen: Theorie und technische Anwendung," Springer Verlag, New York (1975).
- A. Damjanovic, in "Modern Aspects of Electrochemistry," Vol. 5, J. O'M. Bockris and B. E. Conway, Editors, p. 369, Plenum Press, New York (1969).
- W. O'Grady, C. Iwakuna, J. Huang, and E. Yeager, in "Electrocatalysis," M. W. Breiter, Editor, p. 286, The Electrochemical Society Softbound Proceedings Series, Princeton, NJ (1974).
- V. S. Bagotskii, L. N. Nedrasov, and N. A. Shumilova, *Russ. Chem. Rev.*, **34**, 717 (1965).
- R. Woods, Personal communication (1982).
- J. P. Hoare, "The Electrochemistry of Oxygen," p. 128, Interscience, New York (1968).
- M. A. Genshaw, Ph.D. Dissertation, University of Pennsylvania, Philadelphia, PA (1966).
- J. O'M. Bockris, M. A. V. Devanathan, and K. Muller, *Proc. R. Soc. London, Ser. A*, **274**, 55 (1963).
- T. Otagawa, Ph.D. Dissertation, Texas A&M University, College Station, TX (1983).
- J. F. Wolf, R. Yeh, and A. Damjanovic, *Electrochim. Acta*, **26**, 811 (1981).
- B. E. Conway, "Theory and Principles of Electrode Processes," p. 94, Ronald, New York (1964).
- J. O'M. Bockris and B. E. Conway, *Trans. Faraday Soc.*, **48**, 724 (1952).
- D. M. Matthews and J. O'M. Bockris, in "Modern Aspects of Electrochemistry," Vol. 6, J. O'M. Bockris and B. E. Conway, Editors, p. 243, Plenum Press, New York (1971).
- E. Gileadi and G. E. Stoner, *This Journal*, **118**, 1316 (1971).
- A. M. Gaudin, P. L. de Bruyn, and O. Mellgren, *Min. Eng.*, **8**, 65 (1956).
- P. Siedler, G. Sandstede, and H. Franz, *Z. Erzbergu Metallhüttenwes.*, **15**, 293 (1962).
- P. F. Wells and A. B. Van Cleave, *Can. J. Chem. Eng.*, **53**, 641 (1975).
- P. J. Harris and N. P. Finkelstein, *Int. J. Miner. Proc.*, **2**, 77 (1975).
- A. Alt, H. Binder, and G. Sandstede, *J. Catal.*, **28**, 8 (1973).

47. H. Behret and H. Binder, *Chem.-Ztg.*, **97**, 378 (1973).
 48. M. Green, in "Modern Aspects of Electrochemistry," Vol. 2, J. O'M. Bockris, Editor, p. 343, Butterworths, London (1959).
 49. R. Woods, in "Flotation, A. M. Gaudin Memorial Volume," Vol. 1, M. C. Fuerstenau, Editor, p. 298, Am. Inst. Min. Metall. Pet. Eng., New York (1976).

Use of the Junction Between Two Solid Electrolytes for the Potentiometric Measurement of Gaseous Oxides

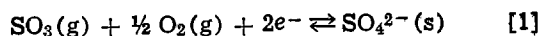
A. Bélanger,* M. Gauthier,* and D. Fauteux*

Institut de recherche d'Hydro-Québec, Varennes, Québec, J0L 2P0, Canada

ABSTRACT

The contact between two solid electrolytes such as a stabilized zirconia and potassium sulfate can be used to measure the activity of volatile oxides, SO₂ or SO₃ for instance. On this basis, a new type of sensor has been designed which produces stable voltages logarithmically dependent on the concentration of the gas to be measured. This principle was extended to the measurement of other gaseous oxides, namely carbon oxides, using K₂CO₃ as the electrolyte. The range of these sensors covers a few parts per million to several thousand parts per million and their operating temperature varies from 600° to 900°C.

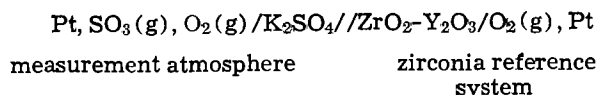
The last years have witnessed many publications on the application of solid electrolytes for analytical purposes, the best known being the oxygen sensor in which a stabilized zirconia is used as the electrolyte (1, 2). More recently, the operating principle of the oxygen sensor has been applied to other types of potentiometric devices, especially for the measurement of gases containing halogen and volatile oxides (3, 4). In the latter category, a new type of solid-electrolyte sensor has been developed and patented at IREQ for measuring the activity of gaseous oxides in air or in combustion gases; it has proven particularly suitable for measuring carbon and sulfur oxides (3-5). In these applications, the solid electrolyte contains an alkaline or alkaline earth salt of the oxyanion corresponding to the oxide whose activity is to be measured. For SO₂ and SO₃, potassium sulfate is used for example, whereas for CO and CO₂ the electrolyte will consist basically of K₂CO₃. In the case of the sulfur oxide sensors, the electrode reaction may be written as follows (6)



In the sulfur oxide sensor, the metal electrodes are comprised of platinum or gold, according to whether the total sulfur content is to be measured or just the SO₃ without modifying the gas phase equilibrium (7, 8).

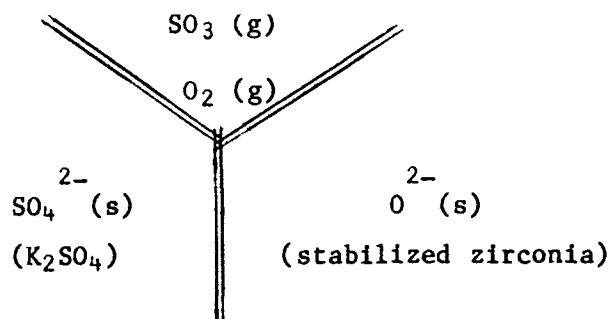
The development of the new sensor involved studying different types of reference electrodes, of which the most important so far as sulfur oxides are concerned are (i) gas reference electrodes based on circulation of a known mixture of SO₂ and air (6), (ii) gas reference electrodes obtained by the thermal decomposition of a sulfate (7), (iii) Ag/Ag⁺ type of reference electrode [1% Ag₂SO₄ added to the K₂SO₄ of the electrode (6)], and (iv) zirconia reference electrodes where two solid electrolytes are brought into contact, one containing the oxyanion of the oxide to be measured, e.g., K₂SO₄, the other being stabilized zirconia (7).

The stabilized zirconia reference electrode enters into the following electrochemical chain



During the development, the stabilized zirconia reference was found to be far less stable than the other three, despite its practical advantages. For example, if used discontinuously on a daily basis, the cell EMF may vary by several tens of millivolts for no apparent reason. The nature of the atmosphere surrounding the zirconia-sulfate junction had a considerable influence on the EMF stability. This was easily solved by sealing the zirconia-sulfate junction with a suitable ceramic product, whereupon the reference signal became far more stable (7).

The foregoing observations led to a study of the mechanism involved in the influence of the junction atmosphere on the signal. The first step in this study was to examine the equilibria at the triple junction between the solid sulfate, the stabilized zirconia, and the gas phase



A first treatment of these equilibria and some preliminary results were presented recently (9, 10). For these studies, an experimental device was designed which would optimize the contact between the gas phase and the electrolyte junction by means of a very small zirconia tip slightly embedded in the K₂SO₄ (or K₂CO₃) electrolyte. The device comprises three totally independent atmospheres, so that the junction atmosphere can be changed without modifying the other two (see Experimental).

The aim of this paper is to discuss the mechanism operating at these junctions and to present detailed experimental results which demonstrate the potential interest of the triple junction for analytical purposes, especially for monitoring trace gaseous constituents such as SO₂, SO₃, CO, and CO₂. Electrolytic junction sensors are the product of technologies very similar to

* Electrochemical Society Active Member.

those employed for detectors with metallic electrodes. A detailed insight into the different models and the variety of measuring instruments that exist may be gained from the literature (3-7), so that only the section of the sensor where the various electrochemical equilibria are established will be described here (see Fig. 1 and 2a).

Experimental Materials and Procedures

The techniques used for the preparation of the gas mixtures and of the electrolytes, as well as the experimental setups, were reported in previous papers (4, 5, 7). Briefly, three similar setups were used, as schematized in Fig. 2. The three-atmosphere sulfur oxide sensor (Fig. 2a) comprises an airtight alumina crucible containing a mixture of powdered MgSO_4 and MgO which determines the partial pressures of SO_3 , SO_2 , and O_2 in the crucible through thermal decomposition of MgSO_4 at the temperature of measurement. For this atmosphere (referred to as S) the electrode is made of platinum. The second atmosphere (O) is similarly generated by the equilibrium between Pd , PdO , and O_2 , which are sealed inside the zirconia-doped ($\text{ZrO}_2\text{-Y}_2\text{O}_3$) oxygen minisensor (11, 12); again, the electrode is made of platinum. Finally, the third atmosphere (J) is established by circulating gas mixtures of SO_2 and O_2 through the sensor. A platinum catalyst is placed in the inlet tube of the sensor to ensure that the equilibrium between SO_3 , SO_2 , and O_2 is reached.

The two-atmosphere sulfur oxide sensor (Fig. 2b) is similar to that of Fig. 2a, except that the oxygen sensor was unsealed and the Pd-PdO mixture withdrawn so that the atmosphere (O) is replaced by the circulating atmosphere (J), which serves at the reference gas.

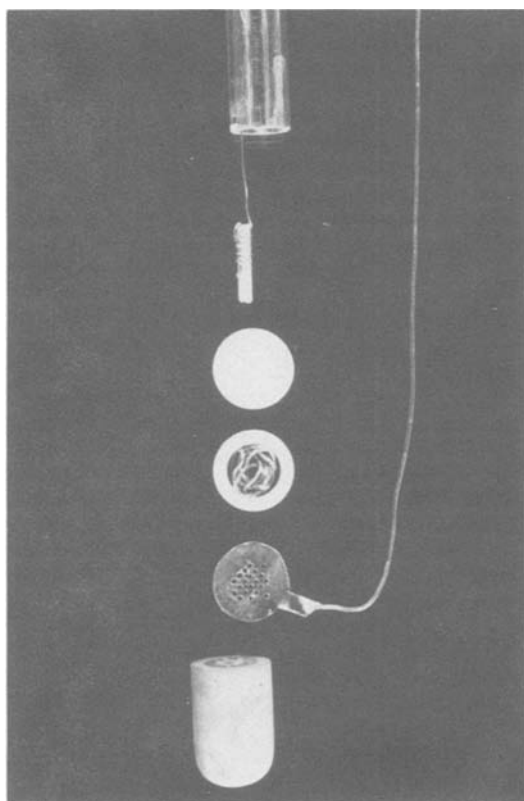


Fig. 1. Photograph showing details of the tip of the sensing element of the sulfur oxide 2-compartment sensor. The components from top to bottom are: (1) dual-port quartz tube (ϕ in ≈ 3 mm); (2) oxygen minigauge ($\phi = 2$ mm; $l = 10$ mm) and platinum wire ($\phi = 0.2$ mm); (3) K_2SO_4 electrolyte pellet ($\phi = 7$ mm; $l = 3$ mm); (4) alumina spacer with platinum wire; (5) perforated platinum grid with platinum wire forming the electrode; and (6) alumina crucible containing powdered MgO and MgSO_4 .

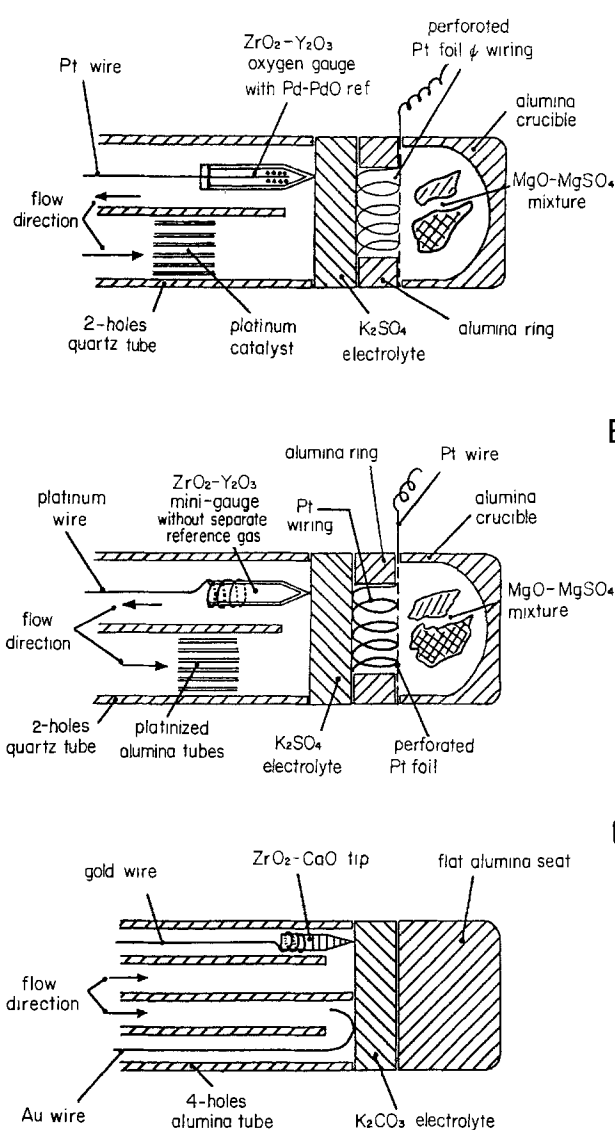
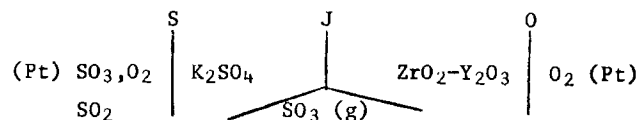


Fig. 2. Schematic of sulfur oxide (A) 3-compartment sensor, (B) sulfur oxide 2-compartment sensor, and (c) carbon oxide 2-compartment sensor.

For the two-atmosphere carbon oxide sensor (Fig. 2c), the $\text{ZrO}_2\text{-Y}_2\text{O}_3$ oxygen minisensor was replaced by calcia-stabilized zirconia ($\text{ZrO}_2\text{-CaO}$). As in Fig. 2b, atmosphere (O) is the same as atmosphere (J). The reference atmosphere (C) is defined by circulating a gas mixture consisting of a known concentration of CO_2 in air.

Results and Discussion

General expression for the electromotive force (EMF).—The electrochemical cell of the measurement junction may be described as (3)



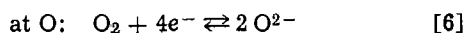
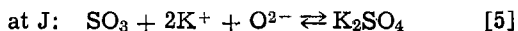
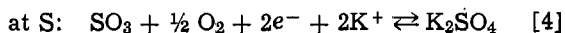
The EMF resulting from this electrochemical chain may be expressed as follows if the electrochemical potential of the majority carriers is assumed to be constant within each electrolyte

$$\tilde{\mu}_{\text{O}_2}^{\text{S}} = \tilde{\mu}_{\text{O}_2}^{\text{J}} \quad [2]$$

and

$$\tilde{\mu}_{\text{K}^+}^{\text{S}} = \tilde{\mu}_{\text{K}^+}^{\text{J}} \quad [3]$$

where the indexes O²⁻ and K⁺ identify the majority carriers while J, O, and S denote the interface. Assuming also that equilibrium is reached at the different interfaces, then



from which the following expressions can be derived

$$\mu^{\text{S}}_{\text{SO}_3} + \frac{1}{2} \mu^{\text{S}}_{\text{O}_2} + 2\tilde{\mu}^{\text{S}}_{\text{K}^+} + 2\tilde{\mu}^{\text{S}}_{e^-} = \mu^{\text{S}}_{\text{K}_2\text{SO}_4} \quad [7]$$

$$\mu^{\text{J}}_{\text{SO}_3} + 2\tilde{\mu}^{\text{J}}_{\text{K}^+} + \tilde{\mu}^{\text{J}}_{\text{O}^{2-}} = \mu^{\text{J}}_{\text{K}_2\text{SO}_4} \quad [8]$$

$$\mu^{\text{O}}_{\text{O}_2} + 4\mu^{\text{O}}_{e^-} = 2\mu^{\text{O}}_{\text{O}^{2-}} \quad [9]$$

The last three equations yield the difference in the electrochemical potential of the electrons

$$\tilde{\mu}^{\text{S}}_{e^-} - \tilde{\mu}^{\text{O}}_{e^-} = -\frac{1}{2} \mu^{\text{S}}_{\text{SO}_3} - \frac{1}{4} \mu^{\text{S}}_{\text{O}_2} + \frac{1}{4} \mu^{\text{O}}_{\text{O}_2} + \mu^{\text{J}}_{\text{SO}_3} \quad [10]$$

The difference in internal electrical potential is

$$\Delta\phi = -\frac{1}{2F} \mu^{\text{S}}_{\text{SO}_3} - \frac{1}{4F} \mu^{\text{S}}_{\text{O}_2} + \frac{1}{4F} \mu^{\text{O}}_{\text{O}_2} + \frac{1}{2F} \mu^{\text{J}}_{\text{SO}_3} \quad [11]$$

From which the EMF is obtained by expressing the chemical potential of the different species

$$E = -\frac{RT}{2F} \ln p^{\text{S}}_{\text{SO}_3} - \frac{RT}{4F} \ln p^{\text{S}}_{\text{O}_2} + \frac{RT}{4F} \ln p^{\text{O}}_{\text{O}_2} + \frac{RT}{2F} \ln p^{\text{J}}_{\text{SO}_3} \quad [12]$$

The general expression of the cell EMF becomes

$$E = \frac{RT}{2F} \ln \frac{p^{\text{J}}_{\text{SO}_3}}{p^{\text{S}}_{\text{SO}_3}} \cdot \frac{(p^{\text{O}}_{\text{O}_2})^{1/2}}{(p^{\text{S}}_{\text{O}_2})^{1/2}} \quad [13]$$

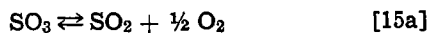
The sensor EMF depends only on the SO₃ partial pressure at the junction whenever the reference atmospheres (O) and (S) are fixed; the junction then acts as a specific SO₃ detector. Experimentally, there are a number of situations which can be described by Eq. [13]. On the one hand, for sulfur oxide references of the circulation or decomposition type, Fig. 2b and 2c, we can experimentally fix $p^{\text{S}}_{\text{O}_2} = 0.21$ in air. On the other hand, when the sensor includes only two independent atmospheres, $p^{\text{O}}_{\text{O}_2}$ can be replaced by $p^{\text{J}}_{\text{O}_2}$. Finally, as previously shown (4), $p^{\text{J}}_{\text{SO}_2}$ and $p^{\text{J}}_{\text{SO}_3}$ can be expressed in terms of $(p^{\text{J}}_{\text{SO}_2})_{\text{in}}$, which is the SO₂ concentration of the gas mixture prepared at room temperature in the laboratory for circulating past the electrolytic junction (4, 6)

$$p^{\text{J}}_{\text{SO}_2\text{in}} = p^{\text{J}}_{\text{SO}_2} + p^{\text{J}}_{\text{SO}_3} \quad [14]$$

If fully catalyzed, the different species are related by the equilibrium constant

$$K = \frac{p^{\text{J}}_{\text{SO}_2} \cdot (p^{\text{J}}_{\text{O}_2})^{1/2}}{p^{\text{J}}_{\text{SO}_3}} \quad [15]$$

of the reaction



On the basis of Eq. [14] and [15], Eq. [13] becomes

$$E = \frac{\left[\frac{(p^{\text{J}}_{\text{SO}_2})_{\text{in}}}{1 + \frac{K}{(p^{\text{J}}_{\text{O}_2})^{1/2}}} \right] \cdot (p^{\text{O}}_{\text{O}_2})^{1/2}}{p^{\text{S}}_{\text{SO}_3} \cdot (p^{\text{S}}_{\text{O}_2})^{1/2}} \quad [16]$$

For a two-atmosphere sensor, the index O merely has

to be replaced by (J), since the atmosphere becomes common. Then

$$E = C + \frac{RT}{2F} \ln (p^{\text{J}}_{\text{SO}_2})_{\text{in}} + \frac{RT}{2F} \ln p^{\text{J}}_{\text{O}_2} - \frac{RT}{2F} \ln [K + (p^{\text{J}}_{\text{O}_2})] \quad [16a]$$

where C is a constant that includes the sulfate reference signal. This expression is identical in all aspects to the one derived for sensors with metallic electrodes (7). Relations [16] and [16a] are valid only if the gases reaching the junction have been suitably catalyzed to respect relation [15].

Two-atmosphere sulfur oxide sensor.—The variation in the EMF for a two-atmosphere quartz device sketched in Fig. 2b as a function of $\ln p^{\text{J}}_{\text{SO}_2\text{in}}$ is given in Fig. 3. These results agree with the theoretical behavior predicted by Eq. [16] and [16a] for a two-atmosphere sensor using a reference sulfur oxide atmosphere obtained by decomposing an equimolar mixture of MgO and MgSO₄. The $p^{\text{S}}_{\text{SO}_3}$ value resulting from this decomposition reaction may be obtained from the literature. The decomposition equilibrium of sulfates has been studied using many analytical techniques. Mention may be made, among others, of the work by Marchal (14) (total pressure measurement), Dewing and Richardson (15) (differential thermal analysis), Skeaff and Espelund (16) (p_{O_2} measurements) and, finally, Kellogg (17) (review article). For the purpose of this study, Skeaff and Espelund's data (16) were used because they were obtained under experimental conditions similar to ours and are in fairly good agree-

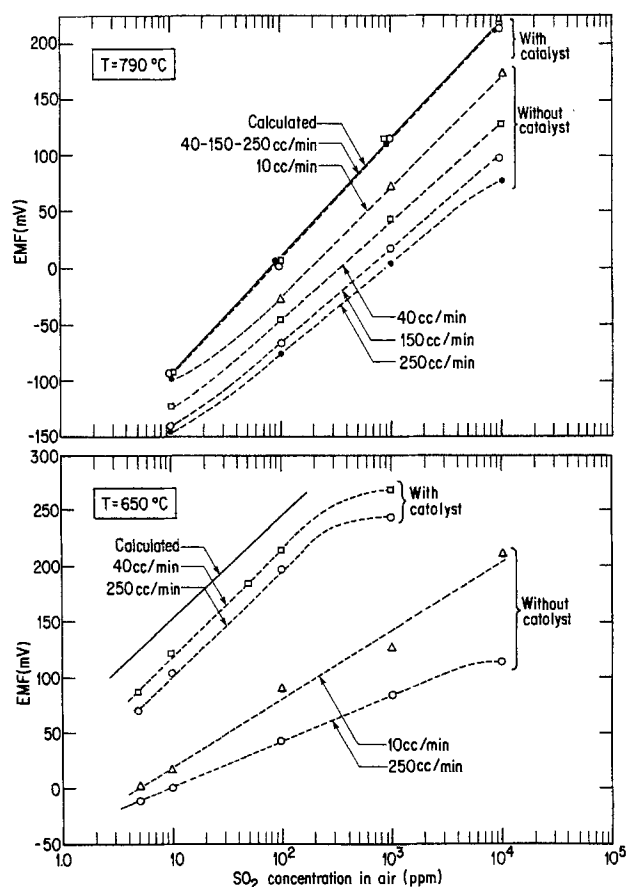


Fig. 3. EMF of a sulfur oxide 2-compartment sensor (Fig. 2b) plotted vs. SO₂/air gas mixtures circulating at the junction. These results show the influence of the flow rate with and without a catalyst at two temperatures; 790° and 650°C. Solid lines show calculated values by Eq. [16] while the dotted lines describe the experimental results.

ment with ours. The latter authors proposed the following thermodynamic data for the decomposition of magnesium sulfate according to the reaction (valid between 940 and 1230 K)



$$\Delta H^\circ = 69.73 \text{ kcal mol}^{-1}$$

$$\Delta S^\circ = 44.27 \text{ cal K}^{-1} \text{ mol}^{-1}$$

These values can then be used to calculate ΔG° and, therefore, p_{SO_3} in Eq. [13] and [16] since

$$K_{\text{decomp.}} = \exp(-\Delta G^\circ/RT) = \frac{[\text{MgO}]p_{\text{SO}_3}^{\text{S}}}{[\text{MgSO}_4]} = p_{\text{SO}_3}^{\text{S}} \quad [18]$$

assuming that the activities of the two pure solids equal unity.

On the other hand, to calculate the equilibrium constant K [15], the expression put forward by Kellogg (17) was slightly modified to take account of the more recent results compiled by Stern and Weise (18)

$$\log_{10} K = 8.987 - \frac{5590}{T} - 1.2157 \log_{10} T \quad [19]$$

where T is in Kelvin.

Combining relations [18] and [19] with [16], the value of the EMF of a two-compartment sensor can be determined for all values of $p_{\text{SO}_2}^{\text{J}}$ in. The calculated curves are shown as continuous lines for two temperatures in Fig. 3. At 790°C, the curve runs through the experimental points for the entire range of $p_{\text{SO}_2}^{\text{J}}$ in for all flow rates shown, provided that the gas passes over a suitable catalyst maintained at the sensor operating temperature before it reaches the zirconia-sulfate junction. For lower temperatures, the calculated curve deviates from the experimental points even when the gases are circulating slowly over the catalyst, probably because of incomplete catalysis of the reaction [16]. Actually, even with catalysis, the flow rate always has a considerable influence on the signal, which was not the case at the higher temperature. Catalysis is even more noticeably incomplete at higher concentrations, so much so that above 1000 ppm, the EMF

reaches a maximum and can even drop again slightly if the concentration is further increased, which is indicative of a serious poisoning of the catalyst.

Figure 4 illustrates the performance of the sulfate-zirconia sensor (two atmosphere device, Fig. 2b) as a function of the variation in the oxygen content of the gas circulating at the junction. When Eq. [16a] was used to calculate the theoretical values, the curves obtained often differed from the experimental results. This behavior is believed to result from the difficulty in maintaining a constant temperature throughout the sensor, particularly when one or more atmospheres are circulating. For this reason, it was felt that for comparative purposes an analytical expression describing only the expected trends of the results would be preferable. In Eq. [16], $p_{\text{SO}_2}^{\text{J}}$ in and $p_{\text{SO}_3}^{\text{S}}$ can be considered constant and the relation becomes

$$E = C + \frac{RT}{2F} \ln (p_{\text{O}_2}^{\text{J}})^{1/2} - \frac{RT}{2F} \ln \left[1 + \frac{K}{(p_{\text{O}_2}^{\text{J}})^{1/2}} \right] \quad [20]$$

and eliminating the constant C

$$E' = \frac{RT}{2F} \ln p_{\text{O}_2}^{\text{J}} - \frac{RT}{2F} \ln [K + (p_{\text{O}_2}^{\text{J}})^{1/2}] \quad [21]$$

The calculated values of the two terms in Eq. [21] are given in Table I at three temperatures. Since the value of C in Eq. [20] is unknown, the values of E' have no absolute meaning; therefore it was deliberately decided to have the calculated and experimental points meet at one point, at $p_{\text{O}_2} = 20.8\%$ in air (numbers in parentheses in Table I). For instance, at $T = 583^\circ\text{C}$ and $p_{\text{O}_2} = 20.8\%$, the experimental EMF is 170 mV. Using Eq. [21], the calculated value of E' is -35 mV. Since the experimental and calculated curves are to meet at $p_{\text{O}_2} = 20.8\%$, the correction will be zero at this particular point. Thus in Fig. 4, the EMF is 170 mV in air. For $p_{\text{O}_2} = 10.18\%$, $E' = -50$ mV, the correction will be $[-50 - (-35)] = -15$ mV, as in Fig. 4, at $p_{\text{O}_2} = 10.18\%$ EMF = 170 - 15 = 155 mV, and so on.

The agreement between the calculated values of Fig. 4 (continuous line) and experimental points is

Fig. 4. EMF of a sulfur oxide 2-atmosphere sensor (Fig. 2b) plotted vs. oxygen content of the gas circulating at the junction at different temperatures. The sulfur dioxide concentration used for each curve is shown in parentheses. The continuous lines describe the theoretical profile calculated from Eq. [21]. The dotted lines show the slope of $RT/2F$ and $RT/4F$, respectively, at low and high p_{O_2} (see text).

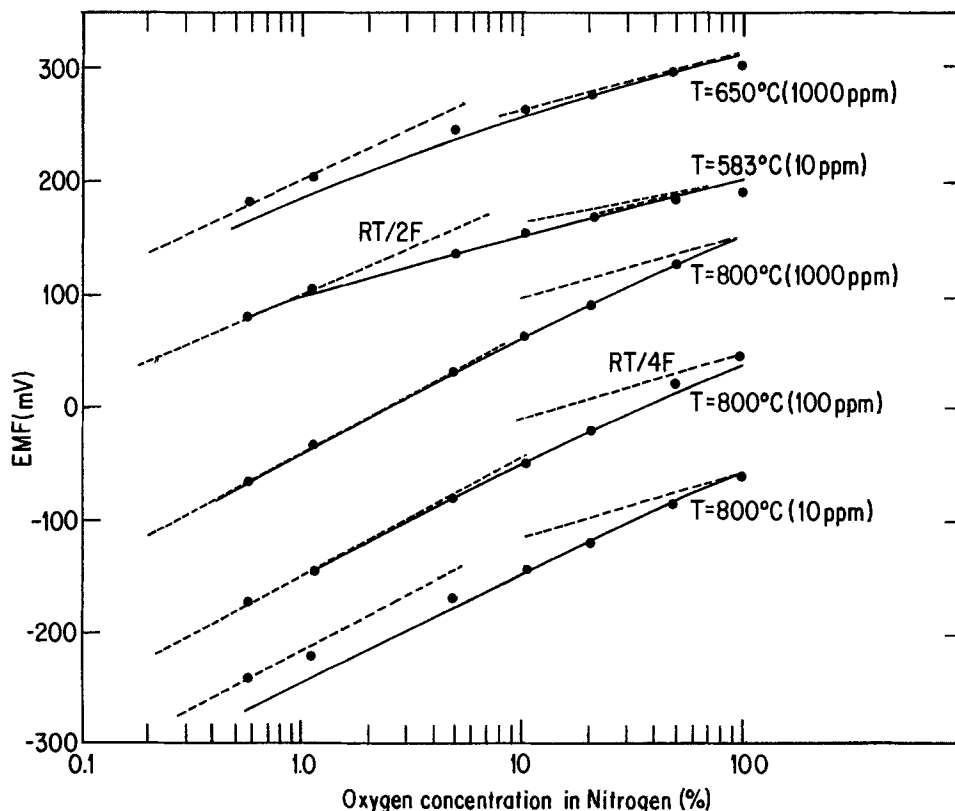


Table I. Calculated data using Eq. [21] to obtain the dotted profiles described in Fig. 4

O ₂ (%)	E' (Eq. [21])		
	T = 583°C (mV)	T = 650°C (mV)	T = 800°C (mV)
0.58	-121	-155	-251
1.13	-103	-133	-221
4.8	-67	-87	-158
10.18	-50	-66	-126 (92)
20.8	-35 (170)	-44 (279)	-97 (-20)
48.8	-17	-25	-64 (-118)
100.0	-3	-8	-37
RT			
2F	84.9	91.6	106.5
K	0.78	0.21	1.24

generally satisfactory, except at extreme temperatures and concentrations [e.g., (p_{SO_2})_{in} = 10 ppm at 800°C and (p_{SO_2})_{in} = 1000 ppm at 600°C] when catalysis effects or detection limits can have an influence. This will be discussed later.

Furthermore, two borderline cases exist which simplify Eq. [21], as shown by the dotted lines in Fig. 4. In accordance with Eq. [21], the signal varies with a slope of $RT/4F$ at low temperatures for high p_{O_2} ($K \ll p_{\text{O}_2}$) and a slope of $RT/2F$ at high temperatures for low p_{O_2} ($K \gg p_{\text{O}_2}$). These two limiting conditions at high and low p_{O_2} are interesting because they allow elimination of the signal dependence on p_{O_2} by simple electronic subtraction of the EMF of a zirconia oxygen sensor, which is a function of $RT/4F$ [see Ref. (4)].

Three-atmosphere sulfur oxide sensor.—The results presented in Fig. 5 were obtained with a three-atmosphere quartz arrangement (Fig. 2a) using the University of Grenoble minisensor (see Experimental). The figure shows plots of the sensor EMF vs. ($p^{\text{J}}_{\text{SO}_2}$)_{in} for three operating temperatures.

As with the two-atmosphere sulfur oxide sensor, gas phase equilibrium is not achieved at low temperatures (SO₃ favored), particularly when the sulfur oxide concentration is high; this produces a clearly visible deviation in the curve. At higher temperatures, e.g., 780°C, catalysis is excellent and the curve is linear up to ($p^{\text{J}}_{\text{SO}_2}$)_{in} = 10,000 ppm (≈1%). However, the detection threshold for sulfur oxides is better at lower temperature (0.3 ppm) whereas the sensor response ceases to be linear at 800°C for ($p^{\text{J}}_{\text{SO}_2}$)_{in} ≤ 10 ppm. The theoretical slope of the curves in Fig. 5 was drawn through the mean of the experimental points (continuous line).

In order to calculate the theoretical position of the curve exactly, it is essential to refer to the general expression of the EMF, i.e., Eq. [16], in which the temperature dependence of the two reference electrodes

Table II. Data used to calculate the expected position of the experimental curve in Fig. 5 by Eq. [16]

Parameter	600°C (873 K)	648°C (921 K)	705°C (978 K)	780°C (1053 K)
RT 2F (mV)	86.6	91.4	97.0	104.5
K (atm) ^{1/2}	0.1019	0.2427	0.4324	1.0091
K _{atm} = p^S_{SO₃} (atm)}	1.65 × 10 ⁻⁸	1.34 × 10 ⁻⁷	1.24 × 10 ⁻⁶	3.12 × 10 ⁻⁵
(p ^S _{O₂}) ^{1/2} (atm) ^{1/2}	0.458	0.458	0.458	0.458
(p ^O _{O₂}) ^{1/2} Pd- PdO (10) (atm) ^{1/2}	2.47 × 10 ⁻³	5.67 × 10 ⁻³	1.35 × 10 ⁻¹	3.61 × 10 ⁻¹
E at (p ^J _{SO₂}) _{in} = 10 ⁻⁴ atm (mV)	+210	+163	+105	+20

is taken into account: $p^{\text{S}}_{\text{SO}_3} = \int (\text{MgO-MgSO}_4)$ and $p_{\text{O}_2} = \int (\text{Pd-PdO})$. When ($p^{\text{J}}_{\text{SO}_2}$)_{in} is equal to 10⁻⁴ atm (100 ppm), for example, the calculated EMF's are respectively 210 mV (at 600°C), 105 mV (at 705°C) and 20 mV (at 780°C). The corresponding curves are shown by short dotted lines in Fig. 5. The data used for the calculation are summarized in Table II.

Considering all experimental errors and, in particular, the inevitable temperature gradient inside the sensor, the agreement between calculated and experimental curves may be considered satisfactory. In fact, a temperature difference of 20°C between the measured temperature and the crucible temperature can account for a 20 mV shift in the experimental EMF ($\Delta E/\Delta t \approx 1$ mV/°C), while an equivalent temperature difference between the measured temperature and that of the platinum catalyst at the inlet can be responsible for an additional 6 mV shift in the EMF ($\Delta E/\Delta t \approx 0.3$ mV/°C).

Figure 6 shows the dependence of the signal of the three-atmosphere sensor on the oxygen content of the gas circulating at the junction. Again the experimental curves show very good agreement with the calculated values. In fact, the p_{O_2} dependence of Eq. [16] can be expressed very simply if ($p^{\text{J}}_{\text{SO}_2}$)_{in}, ($p^{\text{O}}_{\text{O}_2}$)^{1/2}, $p^{\text{S}}_{\text{SO}_3}$, and $p^{\text{S}}_{\text{O}_2}$ are constants. Thus, the following equation is obtained

$$E'' = \frac{RT}{2F} \ln \left[1 + \frac{K}{(p^{\text{J}}_{\text{O}_2})^{1/2}} \right] \quad [22]$$

or

$$E'' = \frac{RT}{2F} \ln [K + (p^{\text{J}}_{\text{O}_2})^{1/2}] - \frac{RT}{2F} \ln (p^{\text{J}}_{\text{O}_2})^{1/2} \quad [23]$$

The latter expression shows that the EMF of the sensor will be independent of p_{O_2} when the temperature is

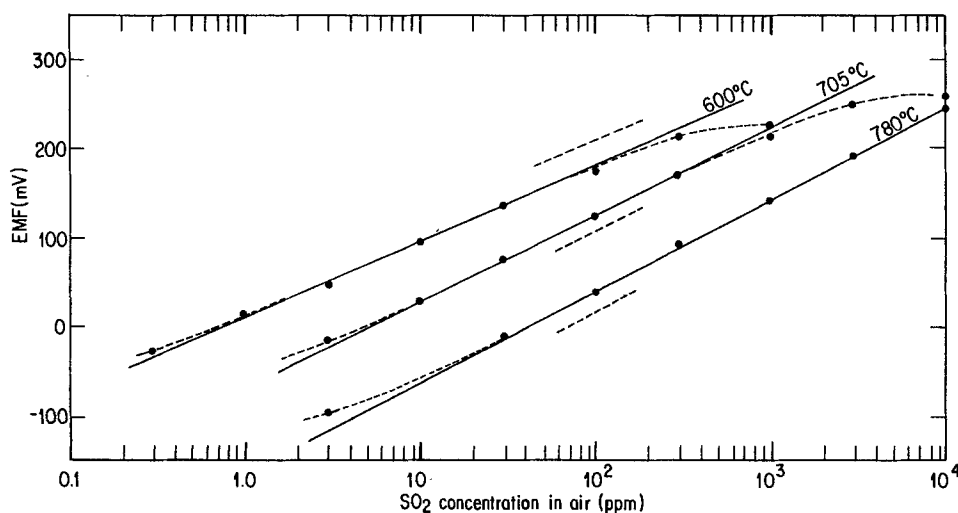
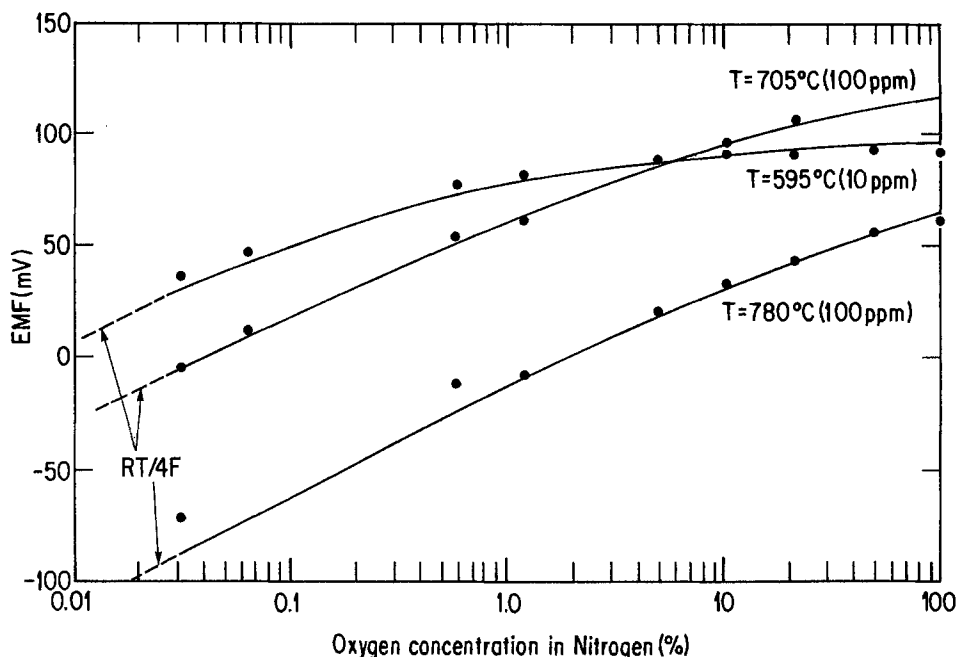


Fig. 5. EMF of sulfur oxide 3-compartment sensor (Fig. 2a) plotted vs. SO₂ concentration in air for three temperatures. The dotted lines describe the experimental performance of the sensors compared to theoretical prediction (continuous line). Short dotted lines indicate the calculated position of the curves using Eq. [16] (see text).

Fig. 6. EMF of sulfur oxide 3-compartment sensor (Fig. 2a) plotted vs. p_{O_2} of the gas circulating at the junction. The results were obtained at three temperatures: 595°C (10 ppm), 705°C (100 ppm), and 780°C (1000 ppm). The sulfur dioxide concentration used for each curve is shown in parentheses. The continuous line describes the calculated behavior of the EMF. At low concentrations, the three dotted lines correspond to the $RT/4F$ values predicted by relation [23] at low p_{O_2} .



low at high levels of $p_{O_2}^J$; in other words, for $K \ll (p_{O_2}^J)^{1/2}$. On the other hand, at high temperatures and low $p_{O_2}^J$, the slope of the curve E vs. $\ln p_{O_2}^J$ will be $RT/4F$, i.e., when $K \gg (p_{O_2}^J)^{1/2}$. This dependence of the signal on p_{O_2} is summarized in Table III. For easier comparison of the results, the calculated curve was made to fit the experimental values for $p_{O_2}^J = 0.21$ atm (continuous line in Fig. 6). The general agreement between the two curves may be considered quite satisfactory considering the inevitable catalysis and thermal-gradient problems encountered with this type of device.

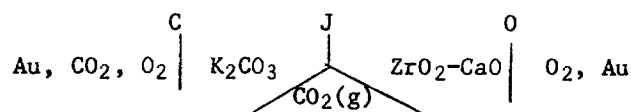
Interference study.—Finally in this study, an attempt was made to determine the sensitivity of this type of sensor to the presence of other gases normally found in stack effluents. A two-atmosphere sulfur oxide sensor was used for these tests. The results may be found in Table IV.

These results appear to confirm that sulfate-stabilized zirconia junctions are virtually insensitive to the pres-

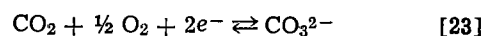
ence of interferants, as already shown for sulfur oxide sensors with metallic electrodes (4).

Two-atmosphere carbon oxide sensors.—The following test (Fig. 7) was performed on a setup adapted for use with a reference electrode obtained by circulating a known concentration of CO_2 in air (Fig. 2c). The sensor consists of an alumina cylinder comprising two pairs of tubes that serve as gas inlets and outlets. The pointed zirconia rod is located at the outlet of one of the pairs. The first tests were performed using the ZrO_2 - Y_2O_3 minisensor, as in the case of the sulfur oxides but, it was soon realized that this material was being chemically attacked by the K_2CO_3 pellet, making the EMF very unstable. This problem was solved by replacing the yttria-doped zirconia by calcia-doped zirconia. For similar reasons, the platinum electrodes in contact with the K_2CO_3 electrolyte had to be replaced by gold.

The expression for this sensor EMF is similar to the one used for sulfur oxides except that the gaseous species detected, in this case CO_2 , is the same as the one used to prepare the gas mixture at room temperature. Furthermore, at the sensor operating temperature, the thermodynamic equilibrium between CO , CO_2 , and O_2 is totally shifted towards CO_2 ($K_{eq} \approx 10^{10}$ in air at $700^\circ C$). For these two reasons, it is unnecessary to use the notation $(p_{CO_2}^J)_in$ as in the case of SO_2 . The electrochemical cell describing the carbon oxide sensor is



The half-reaction corresponding to the carbon oxide electrode is



which yields the expression for the EMF of a two-atmosphere sensor

$$E = \frac{RT}{2F} \ln \frac{p_{CO_2}^J \cdot (p_{O_2}^O)^{1/2}}{p_{CO_2}^C \cdot (p_{O_2}^O)^{1/2}} \quad [24]$$

where (C) refers to the carbonate reference interface. In Eq. [24] the indexes (O) and (J) are the same since they correspond to a common atmosphere.

As illustrated in Fig. 7, the plot of the potential vs. the log of the concentration of the gaseous oxide circulating at the junction produces straight lines with slopes of $RT/2F$ as a function of $\ln p_{CO_2}$ and $RT/4F$ as

Table III. Calculated data from Eq. [23] to obtain the theoretical profile described in Fig. 6

p_{O_2} in nitrogen (%)	E^* (Eq. [23])		
	$T = 595^\circ C$ (mV)	$T = 705^\circ C$ (mV)	$T = 780^\circ C$ (mV)
0.032	-69	-136	-184
0.062	-59	-132	-169
0.58	-30	-80	-121
1.13	-24	-68	-107
1.2	-23	-67	-105
4.8	-13	-46	-78
5.0	-12	-45	-77
10.18	-10	-36	-65
20.8	-7	-28	-53
48.8	-5	-20	-41
100.0	-3	-15	-32
$\frac{RT}{4F}$ (mV)	43.1	48.5	52.2
K (atm) ^{1/2}	0.094	0.432	1.01

Table IV. Sensitivity of the sulfur oxide sensor to some other gaseous species

10, 100, or 1000 ppm SO_2 -air	+ 1000 ppm NO_2	no influence
10, 100, or 1000 ppm SO_2 -air	+ 10% CO_2	no influence
100 ppm SO_2 -air	+ 100 ppm HCl	no influence (after 10 min)

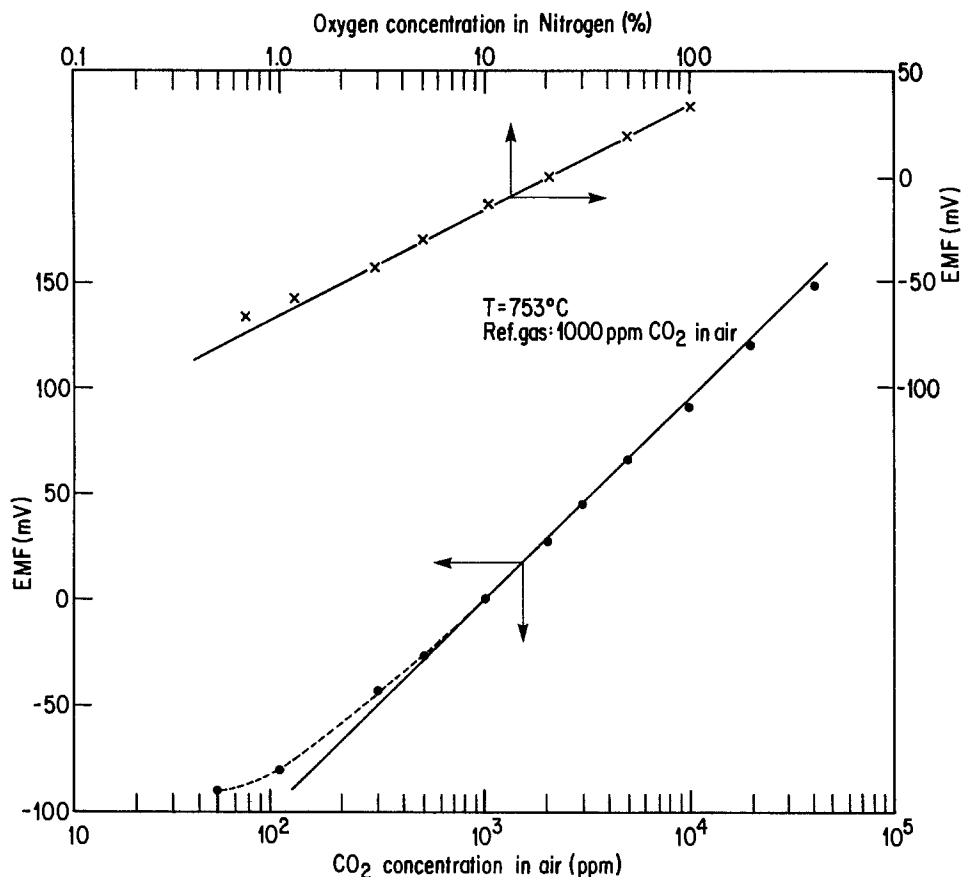


Fig. 7. EMF of a carbon oxide 2-compartment sensor (Fig. 2c) plotted vs. CO_2 concentration in air (lower curve) and vs. p_{O_2} when the carbon oxide content ($p_{\text{CO}_2}^j$)_{in} is constant (upper curve).

a function of $\ln p_{\text{O}_2}^j$. The calculated slopes appear as the continuous lines in the same figure. Curve *E* vs. $\ln p_{\text{CO}_2}^j$, as expected, crosses zero when the atmosphere circulating at the junction and in the carbonate reference compartment is the same. Contrary to the sulfur oxide sensor, in which one or two reference atmospheres, namely (S) and (O), are established by thermal decomposition of solid powder mixtures, carbon oxide sensors have a single reference atmosphere (C) which is obtained by circulating a gas mixture of a known composition of CO_2 in air. As mentioned earlier, at the sensor operating temperature, the thermodynamic equilibrium shifts towards CO_2 , and the kinetics of the gas-phase reaction are sufficiently rapid, making the use of a catalyst unnecessary. Furthermore, in the design of the carbon oxide sensor, the reference atmosphere (C) and the junction atmosphere (J) are so close to each other that little thermal gradient could exist. This is not true for the sulfur oxide sensor, for which the theoretical values of the EMF calculated by Eq. [16] and the experimental values have to be corrected to take into account the effect of thermal gradients (see Fig. 5). For the carbon oxide sensor, since there are no thermal gradients, the experimental and theoretical values of the EMF are close, which eliminates the need for any correction term.

At concentrations below 500 ppm, the same curve shows a deviation corresponding to a lower detection threshold, apparently characteristic of the electrolyte, in this case K_2CO_3 (19). The lower detection level could be associated with the dissociation of CO_3^{2-} to give K_2O and CO_2 , a process which can be quite important, especially if the solubility of the K_2O in K_2CO_3 is high. The detection threshold always increases with the temperature: in the case of K_2SO_4 , for example, the deviation starts at ≈ 10 ppm at 800°C whereas at 600°C , the curve is still linear at concentrations as low as 0.3 ppm (see Fig. 5). It is also worthwhile mentioning that the lower detection level is of the same order of magnitude for gaseous oxide sensors using metallic electrodes. It may thus be concluded

that this phenomenon is not related to partial solubility of the zirconium oxides in K_2CO_3 or in K_2SO_4 .

The study of the sensor with a carbonate-zirconia junction was completed by examining the device response for mixtures of combustible gases and/or interferants in air. These results, listed in Table V, are expressed in terms of deviations from the response of the sensor to a gas mixture containing 1000 ppm of CO_2 in air. Because complete oxidation of most gases is reached in those tests, the value of +29 mV for C_2H_4 is not surprising, since two molecules of CO_2 are formed for each C_2H_4 that enters the sensor. In the case of CH_4 , the device would need to incorporate a catalyst in the inlet port to reach total oxidation of the molecule, especially at high flow rates.

Conclusion

The results obtained from various tests on a sensor with an electrolytic junction demonstrate advantages for analyzing gaseous effluents containing sulfur or carbon oxides, especially for stack monitoring. Its operating principle is the same as that of a gaseous-oxide sensor using metallic electrodes; in particular, in the case of the two-atmosphere sensor, the EMF expression is identical to that of an equivalent sensor with metallic electrodes.

Table V. The effect of some gases on the signal of the carbon oxide sensor

Gas mixture	Δ EMF's at different flow rates (reference atm: 1000 ppm CO_2 in air)		
	1 cm^3/min (mV)	10 cm^3/min (mV)	50 cm^3/min (mV)
1000 ppm CH_4 -air	-5	-15	-39
1000 ppm C_2H_4 -air	+29	+29	+25
1000 ppm CO -air	0	0	+3
1000 ppm CO_2 /air + 10% H_2O	—	—	≈ 0 (after 5 min)
1000 ppm CO_2 /air + 10 ppm HCl	—	—	≈ 0 (after 5 min)

Both types of sensor produce a stable potentiometric signal that can be measured with a modicum of electronic equipment. When the gases are not catalyzed, the sulfur oxide sensor can act as a SO₃-specific sensor; otherwise, the total sulfur content is measured. For continuous use on a long-term basis, particularly at high SO₂ values, junction-type devices will probably have a better lifespan because they do not comprise metallic electrodes, which are susceptible to aging and can consequently induce malfunctions of the probe.

The EMF of the sensor is sometimes independent of p_{O₂} at the junction (Eq. [13]), or the dependence on p_{O₂} can be eliminated through a signal compensation device. This is easily achieved by attaching a metallic electrode to the minisensor of a three-atmosphere sensor and subtracting the signal from this complementary oxygen sensor electronically from the sulfur oxide signal (4), thus obtaining an oxygen-independent signal. In this particular case though, care should be taken in the choice of the complementary metallic electrode to minimize aging problems associated with the aggressive conditions normally encountered in chimney stacks.

Acknowledgments

The authors would like to express their appreciation to Dr. M. Kleitz of the Laboratoire d'Énergétique Electrochimique (LEE) of Grenoble, France, for valuable discussions on the equilibria involved and on the operating principles of the electrolytic junctions. Many thanks are also due to Dr. G. Vitter, also from the LEE, who kindly supplied the oxygen minisensor. The assistance of R. Bellemare in the experimental work is likewise acknowledged.

Manuscript submitted April 25, 1983; revised manuscript received Sept. 10, 1983. This was Paper 737 presented at the Montreal, Quebec, Canada, Meeting of the Society, May 9-14, 1982.

Institut de recherche d'Hydro-Quebec assisted in meeting the publication costs of this article.

REFERENCES

1. J. Weissbart and R. Ruka, *Rev. Sci. Instrum.*, **32**, 593 (1961).

2. J. Fouletier, H. Seiner, and M. Kleitz, *J. Appl. Electrochem.*, **4**, 305 (1974).
3. M. Gauthier, A. Bélanger, Y. Meas, and M. Kleitz, in "Solid Electrolytes," P. Hagenmuller and W. van Gool, Editors, p. 497, Academic Press, New York (1978).
4. M. Gauthier, A. Chamberland, A. Bélanger, and M. Poirier, *This Journal*, **124**, 1584 (1977); M. Poirier, M. Gauthier, and A. Bélanger, U.S. Pat. 4,295,935.
5. A. Chamberland, M. Gauthier, and A. Bélanger, in "4th Proceedings of the International Clean Air Congress, Conference 108," International Union of Air Pollution Prevention Association, Tokyo (1977); M. Gauthier and A. Chamberland, Canada Pat. 1,002,599.
6. M. Gauthier and A. Chamberland *This Journal*, **124**, 1579 (1977).
7. M. Gauthier, R. Bellemare, and A. Bélanger, *ibid.*, **128**, 371 (1981).
8. A. Bélanger and A. Chamberland, Environment Canada, Report APCD 79-1 (June 1979), Available from the authors.
9. M. Kleitz, A. Pelloux, and M. Gauthier, in "Fast Ion Transport in Solids," P. Vashishta, J. N. Mundy, and G. K. Shenoy, Editors, p. 69, Elsevier North Holland Inc., (1979).
10. M. Gauthier, D. Fauteux, and A. Bélanger, Abstract 737 presented at The Electrochemical Society Meeting, Montreal, Québec, Canada, May 9-14, 1982.
11. C. Deports, M. Henault, F. Tasset, and G. Vitter, French Pat. 73,32671 (1973).
12. J. S. Warner, Ph.D. Thesis, Columbia University, New York (1964).
13. P. Gervais, A. Chamberland, and M. Gauthier, Internal report, IREQ-1475 (October 5, 1976), Available from the authors.
14. G. Marchal, *J. Chim. Phys.*, **22**, 493 (1925).
15. E. W. Dewing and F. D. Richardson, *Trans. Faraday Soc.*, **55**, 611 (1959).
16. J. M. Skeaff and A. W. Espelund, *Can. Metall. Q.*, **12**, 445 (1973).
17. H. H. Kellogg, *Trans. Metall. Soc. AIME*, **230**, 1622 (1964).
18. K. H. Stern and E. L. Weise, NSRDS-NBS 7, U.S. Dept. of Commerce, Washington, DC (1966).
19. A. Bélanger and D. Fauteux, Unpublished results.

Ion Transport in the Polymer Electrolytes Formed Between Poly(ethylene succinate) and Lithium Tetrafluoroborate

R. Dupon,* B. L. Papke, M. A. Ratner, and D. F. Shriver*

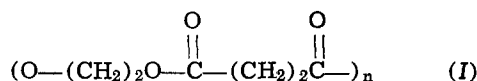
Department of Chemistry and Materials Research Center, Northwestern University, Evanston, Illinois 60201

ABSTRACT

Solid electrolyte complexes of poly(ethylene succinate), PESc, and LiBF₄ were prepared by heating the salt with the molten polymer. The complexes were completely amorphous over the concentration range 1:1 to 3:1 polymer repeat units:metal cation. At salt concentrations above the 1:1 composition, a salt phase was present, and at salt concentrations less than 3:1, free crystalline polymer was observed. Within the 1:1 to 3:1 concentration range, increasing salt concentration was accompanied by decreasing conductivity, and increasing glass transition temperatures. This behavior is discussed in terms of free-volume theory, with dynamical corrections.

Recent studies reveal an interesting and potentially useful class of solid polymer electrolytes formed by the interaction of polyethers with alkali metal salts (1-3). The formation of these polymer salt complexes appears to be facilitated by a high concentration of polar groups in the polymer, high polymer chain flexibility which permits polymer reorientation for the effective sol-

vation of a salt, small lattice energy for the salt, and low cohesive energy density of the polymer (4). With these ideas in mind, we have studied the interaction of poly(ethylene succinate), I, with alkali



metal salts. This host polymer has the requisite high

* Electrochemical Society Active Member.

concentration of polar groups and judging from the relatively low glass transition temperature, T_g (-1°C), the polymer chain is fairly flexible. Also the value of T_g and mechanical properties suggest that the cohesive energy density is low.

We report here the first preparation and characterization of the polymer salt complexes formed between PESc and alkali metal salts, along with information on the electrical properties of these materials. A very brief preliminary description of this system has appeared (3).

Experimental

Poly(ethylene succinate) (Aldrich) was dissolved in chloroform, filtered, precipitated with hexane, air dried, and then dried under high vacuum. Reagent grade LiBF_4 (Pfaltz and Bauer) was dried by heating under vacuum at 125°C for 12h. Infrared spectra were used to check for the presence of water in the purified salt, polymer, and polymer electrolytes. Only anhydrous materials were used for electrical measurements. Starting materials and complexes were manipulated in a nitrogen-filled glove box or air-free apparatus. Poly(ethylene succinate) $\cdot \text{LiBF}_4$ complexes were prepared by heating above the polymer melting point on intimately ground stoichiometric mixtures of anhydrous polymer and salt contained in a Teflon dish. Temperatures on the order of 125°C were typically used. The samples were then cooled slowly over a period of 2h.

Infrared spectra were recorded using a Perkin-Elmer 399 grating infrared spectrophotometer for samples in the following form: LiBF_4 as a Nujol mull and PESc as a cast film from chloroform solution. The IR spectra of pure PESc were obtained using the cast sample contained in an evacuable cell and PESc $\cdot \text{LiBF}_4$ complexes as heat-pressed films between KBr plates.

The pure polymer and the respective complexes between sealed glass plates were examined at 12.5 power magnification using a Leitz Wetzlar polarizing microscope equipped with a Mettler FP52 hot stage. The heating rate was typically $10^\circ/\text{min}$.

Differential scanning calorimetry measurements were performed on samples sealed in Perkin-Elmer aluminum volatile sample pans using a Perkin-Elmer DSC-2 instrument equipped with a liquid nitrogen cooling system. A dry helium atmosphere was maintained over the sample chamber, and transition temperatures were obtained by extrapolation of a plot of observed transition temperature *vs.* (heating rate) $^{1/2}$ to zero heating rate.

X-ray diffraction patterns were determined using $\text{CuK}\alpha$ radiation on pressed samples protected from the atmosphere. Scattering and receiving slits were adjusted to optimize sample illumination. Slit widths were changed at the same 2θ locations for all samples and the scans at different slit widths were overlapped in order to estimate relative peak intensities.

Conductivities were measured using complex admittance/impedance techniques over the frequency range 5 Hz to 500 kHz. Samples were pressed (under an inert atmosphere) at 10,000 psi into 0.5 in. diam pellets. Samples which were relatively noncompliant were

pressed at 50°C . Electrical measurements were made in a specially designed two-electrode Kel-F cell, which permitted exclusion of the atmosphere. Ion blocking platinum disks 0.5 in. diam, 0.005 in. thick, were used as electrodes. Variable temperature measurements were performed in a thermostated forced-air heating chamber which was controlled by a Bruker B-ST 100/700 temperature control unit. Temperatures were monitored to within $\pm 0.1^\circ\text{C}$ by an iron-constantan thermocouple. All connecting leads were coaxial cable. The data was collected using a Hewlett Packard 4800A vector impedance meter, which is accurate to $\pm 5\%$ under our conditions.

Results

The average molecular weight of the PESc was determined to be 1700 from the sharp melting endotherm of this polymer using the empirical melting point (T_m)-molecular weight relationship (5)

$$1/T_m = 2.59 \times 10^{-3} + 0.179/\bar{M} \quad [1]$$

The limiting stoichiometry of the poly(ethylene succinate)- LiBF_4 complex formation was determined by physical measurements on materials prepared with various polymer to metal salt ratios. The x-ray diffraction patterns of pure polymer, salt, and unreacted mixtures agreed well with the published data (6, 7). In contrast to the highly crystalline parent PESc, all of the PESc- LiBF_4 complexes were found to be amorphous. Crystalline phases which were observed in the PESc- LiBF_4 materials always matched with the pure polymer or pure salt. The maximum salt concentration in the complex was thus established as one polymer repeat unit per salt formula unit, $\pm 10\%$. As judged by x-ray diffraction and optical microscopy, the PESc $\cdot \text{LiBF}_4$ complexes remain completely amorphous as the salt concentration is progressively decreased to a value of 3:1 polymer repeat units per LiBF_4 . These amorphous materials range from a hard plastic-like material at 1:1 concentration to compliant rubbery species at 3:1 stoichiometry.

Below salt concentrations corresponding to the ratio 3:1 PESc: LiBF_4 , crystalline regions of uncomplexed PESc appeared. These were observed as spherulites when viewed through the polarizing microscope, and their identity was confirmed by the presence of x-ray diffraction peaks at $d = 3.80\text{\AA}$ and 4.39\AA . The infrared spectra of the pure polymer (Fig. 1) showed sharp, well-defined bands over the spectral range 700-4000 cm^{-1} , whereas the spectra of the complexes are broad and diffuse, especially in the 1500-1000 cm^{-1} region, which is characteristic of amorphous polyester systems (8). Comparison of the spectra before and after complex formation revealed no detectable shifts for any of the polymer band positions. Spectra obtained for amorphous samples cooled to 77 K displayed no significant improvement in resolution. Judging from the published kinetics of crystallization of poly(ethylene succinate) (7, 9-11) and various annealing experiments which we performed on the complexes, the amorphous phases do not arise from supercooled glassy PESc.

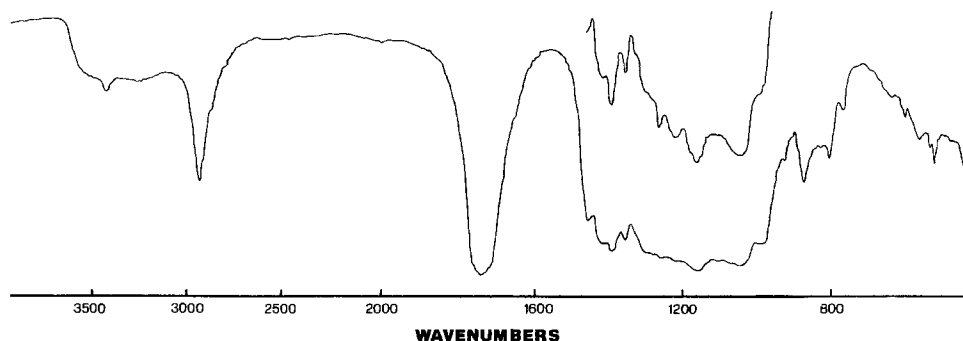


Fig. 1. Infrared spectrum of PESc $\cdot \text{LiBF}_4$, 2:1.

Table I. Comparison of glass transition temperatures and conductivities for PESc · LiBF₄ complexes at various stoichiometries

Ratio of PESc to LiBF ₄	T _g , K	Conductivity at 65°C, (Ω cm) ⁻¹
(Pure PESc)	272.1	—
3:1	288.2	3.4 × 10 ⁻⁶
2:1	288.4	1.8 × 10 ⁻⁶
1.5:1	295.8	4.9 × 10 ⁻⁷
1:1	299.7	2.0 × 10 ⁻⁷

The observed change in mechanical rigidity and in electrical conductivity (see below) over the 1:1 to 3:1 range prompted an investigation of the glass transition temperatures. The values of T_g were found to increase with increasing salt concentration, Table I. The trend in glass transition temperatures thus parallels qualitative changes in mechanical properties.

Complex admittance plots of the conductivity response in these systems, using ion-blocking electrodes, were consistent with a model equivalent circuit containing a capacitance (geometric) in parallel with both a resistance (bulk) and a second capacitance (double layer). Such a combination should result in a single arc followed by a spur when plotted in the complex plane. A representative plot is shown in Fig. 2 for a PESc · LiBF₄ sample at 70°C. Within the 1:1 to 3:1 stoichiometry range, the conductivity decreases dramatically as the salt concentration increases, Fig. 3. In addition, a gentle curve is obtained when the conductivity data are plotted in Arrhenius coordinates, Fig. 4, which agree with expectations for amorphous conductors. It should be noted that samples of pure PESc exhibited a conductivity response outside of the measuring capability of the vector impedance meter over the temperature range 25°–90°C. The uncomplexed polymer thus has a conductivity less than 10⁻⁹ (Ω cm)⁻¹ over this temperature range.

As stated above, at salt concentrations lower than the 3:1 stoichiometry, uncomplexed crystalline polymer appeared in the x-ray diffraction patterns. In the 3:1 to 4:1 stoichiometry range, a large decrease in conductivity is observed as a second phase of crystalline PESc appears. Between 4:1 and 5:1 stoichiometry, the amount of crystalline PESc continues to increase but the conductivity remains nearly constant and low, Fig. 3.

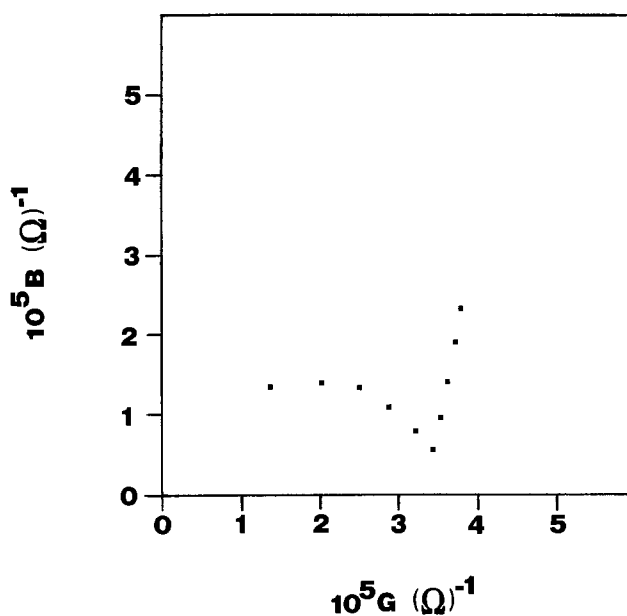


Fig. 2. Representative complex admittance plot for PESc · LiBF₄, 3:1, complex at 70° using ion-blocking electrodes.

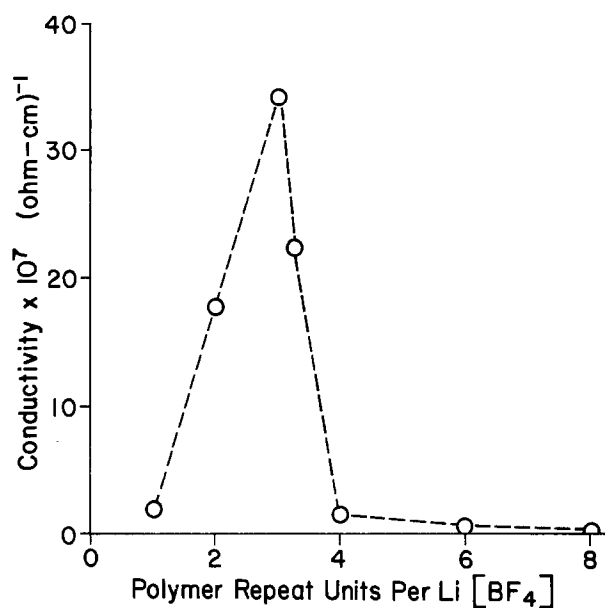


Fig. 3. Conductivity vs. composition for PESc · LiBF₄

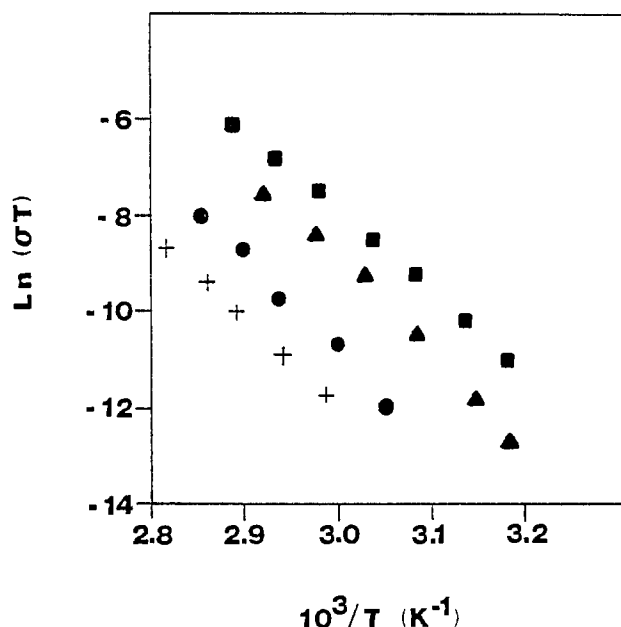


Fig. 4. Variable temperature conductivity for PESc · LiBF₄: 1:1 (●); 2:1 (▲); 3:1 (■); 6:1 (+).

Discussion

The identity of the charge carrier in PESc · alkali metal salt complexes has not been determined unambiguously, however, several lines of evidence suggest that both cation and anion mobility are important. The absence of an obvious electronic conduction mechanism in pure PESc and the observed low conductivity of this material suggest that the conductivity of the complex is ionic in nature. The similarity in the observed magnitudes of the conductivity for a variety of Li⁺ salts (LiCF₃SO₃, LiCF₃COO, LiBF₄) implicates the Li⁺ ion as a charge carrier (3).

To further clarify the nature of the mobile species, the conductivity responses of PESc · NaCF₃SO₃ complexes were investigated using both ion-blocking Pt electrodes and sodium ion-reversible amalgam electrodes. The complex admittance spectrum of PESc · NaCF₃SO₃ using ion-blocking Pt electrodes consists of an arc followed by a spur. This behavior may be effectively modeled with an equivalent circuit containing a capacitance (apparently geometric) in parallel with both a resistance (apparently bulk electrolyte) and a

second capacitance (apparently electrical double layer). The admittance plots obtained using sodium ion-reversible Na-Hg electrodes consisted of a single vertical line, a result which may be modeled by an equivalent circuit containing a capacitance (geometric) in parallel with a resistance (bulk). Since the magnitude of the double layer capacitance was greatly reduced by the use of sodium ion-reversible electrodes, the cation is implicated as a charge carrier. However, it appears from preliminary measurements, performed with a polarization cell, that the transference number for Na⁺ is on the order of 0.1 at 60°C; therefore the bulk of the current is carried by the anion (12).

The conductivity behavior observed in the PESC · LiBF₄ stoichiometry range 1:1 to 3:1 demonstrates that effects other than that of charge carrier concentration dominate the ion mobility. The temperature dependent conductivity, whether of Arrhenius form or in a form related to amorphous behavior, contain a prefactor which predicts increasing conductivity with increasing carrier concentration. The observation of the opposite behavior indicates that changes in the physical characteristics of the PESC · LiBF₄ complexes dominate the conductivity response.

Decrease of conductivity with increasing carrier concentration is well known in framework solid electrolytes, where it is associated with strong correlation of the charge carriers (13). It has also been observed previously for polymeric solid electrolytes such as cross-linked poly(ethylene oxide) (14) and poly(propylene oxide) (15).

Large amplitude polymer segmental motion is thought to be important in the ion transport process in polymer electrolytes (3, 14-16). The variation in ionic conductivity with carrier concentration in the PESC · LiBF₄ complexes may be attributed to the relative freedom of mobility of polymer chain segments. The 3:1 PESC · LiBF₄ stoichiometry represents the lowest salt concentration for which complex formation is complete, *i.e.*, no crystalline regions of uncomplexed polymer remain. As salt concentration is increased above the 3:1 ratio, the rigidity is observed to increase, and higher glass transition temperatures and diminished conductivity result, apparently due to the progressive immobilization of polymer chains. It is, however, noteworthy that in the present case the variations in conductivity (and in apparent fluidity) are so sizable, given the very small change in glass transition temperatures. Table I shows only small changes in glass transition temperature over the same stoichiometry range for which Fig. 3 shows large conductivity variation, and over which the apparent viscosity rises sharply. The inverse viscosity, or the fluidity, is given, using simple free-volume type arguments (14, 17)

$$\eta^{-1} = C \exp \left[-\frac{E_a}{kT} - \frac{\gamma V^*}{V_{Fg} + \alpha(T - T_g)} \right] \quad [2]$$

Here C is a constant, E_a an activation energy for polymer rearrangement, and γ a geometric factor accounting for free-volume overlap; V^* and V_{Fg} are, respectively, the minimum hole size to accommodate the moving chain segment and the free volume at T_g ; and α is the derivative of free volume with temperature. Upon changing from 1:1 to 3:1 salt concentration, only α and T_g in Eq. [2] will change very much. But the very small T_g change (17° out of 300) substituted into Eq. [2] will not lead to substantial changes in η^{-1} unless α is very large.

Again using free-volume theory, the ionic conductivity can be written (14)

$$\sigma T = \sigma_0 \exp \left[-\frac{\gamma V_2^*}{V_{Fg} + \alpha(T - T_g)} - \frac{E_a + E_b + W/2e}{kT} \right] \quad [3]$$

where σ_0 is temperature-independent, V_2^* is the minimum hole size for an ionic hopper, and the second activation-energy term in the exponent characterizes the ion-pair dissociation and activated jumping. The simple point to be made is that the observed sharp peak in Fig. 3 appears to go beyond the free-volume result, Eq. [3]. The essential behavior of the σT product should, from comparison of Eq. [3] with Eq. [2], follow the sample fluidity if free-volume ideas hold. This is reasonable in a free-volume context: as T is increased above T_g , the volume available for motion, either of polymer chains or of solvent, should increase proportionally to $T - T_g$. As T_g increases, with increased salt concentration, the free volume should drop, decreasing both σT and η^{-1} . What is not expected is the very sharp drop of Fig. 3, given the small change in T_g . A possible explanation for this lies in the kinetic behavior of the free volume: if the polymer motions occur slowly (high viscosity), the ions may not be able to take advantage of the free volume for transport. This possibility was alluded to by Cohen and Grest (17), and forms the basis of a dynamic percolation theory being developed in this laboratory (18).

Acknowledgment

This research was partially supported by the Office of Naval Research. Early work on the system was sponsored by the Northwestern Materials Research Center which is funded by the NSF MRL program. We are grateful to A. Nitzan for incisive remarks.

Manuscript submitted June 1, 1983; revised manuscript received Sept. 26, 1983.

REFERENCES

1. D. E. Fenton, J. M. Parker, and D. V. Wright, *Polymer*, **14**, 589 (1973).
2. M. Armand, J. M. Chabagno, and M. Duclot, in "Proceedings of the 2nd International Conference on Solid Electrolytes," St. Andrews (1978).
3. D. F. Shriver, B. L. Papke, M. A. Ratner, R. Dupon, T. Wong, and M. Brodwin, *Solid State Ionics*, **5**, 83 (1981).
4. B. L. Papke, M. A. Ratner, and D. F. Shriver, *J. Phys. Chem. Solids*, **42**, 493 (1981).
5. K. Ueberreiter, G. Kanig, and A. S. Brenner, *J. Polym. Sci.*, **16**, 53 (1955).
6. A. S. Ueda, Y. Chatani, and H. Tadokoro, *Polym. J.*, **2**, 387 (1971).
7. I. Shapiro and H. G. Weiss, *J. Am. Chem. Soc.*, **75**, 1753 (1953).
8. K. Molland-Moritz and D. O. Hummel, *J. Mol. Struct.*, **19**, 289 (1973).
9. K. Ueberreiter and K. Jander, *Kolloid Z. Z. Polym.*, **222**, 97 (1968).
10. K. Ueberreiter, *ibid.*, **234**, 1083 (1969).
11. K. Ueberreiter and K. J. Lucas, *Makromol. Chem.*, **140**, 65 (1970).
12. Shaun Clancy, Northwestern University, Personal communication.
13. J. B. Bates, H. Engstrom, J.-C. Wang, B. C. Larson, N. J. Dudney, and W. E. Brundage, in "Fast-Ion Transport in Solids," J. B. Bates and G. C. Farrington, Editors, North Holland, Amsterdam (1981).
14. H. Cheradame, in "IUPAC Macromolecules," H. Benoit and P. Rempp, Editors, pp. 251-264, Pergamon Press, New York (1982); H. Cheradame, J. L. Souquet, and J. M. Latour, *Mater. Res. Bull.*, **15**, 1173 (1980).
15. M. B. Armand, J. M. Chabagno, and M. J. Duclot, in "Fast-Ion Transport in Solids," P. Vashishta, J. N. Mundy, and G. K. Shenoy, Editors, p. 131, Elsevier, North Holland, Amsterdam (1979).
16. B. L. Papke, M. A. Ratner, and D. F. Shriver, *This Journal*, **129**, 1694 (1982).
17. M. H. Cohen and G. S. Grest, *Phys. Rev. B*, **20**, 1077 (1979).
18. S. Druger, A. Nitzan, and M. A. Ratner, *J. Chem. Phys.*, **79**, 3133 (1983).

An X-Ray Radiography-Densitometry Technique for the Quantitative Determination of Metal Deposit Profiles

Fritz G. Will* and Charles D. Iacovangelo*

General Electric Company, Corporate Research and Development, Schenectady, New York 12301

ABSTRACT

The application of x-ray radiography in conjunction with high resolution optical densitometry for the quantitative determination of metal deposit profiles parallel and perpendicular to the substrate surface is described. The principles of the technique and the range of its applicability are discussed. The technique is applied to the study of zinc deposition on highly porous carbon foams from circulating aqueous zinc bromide solutions. The effect of substrate pore size on the zinc distribution is explored. Zinc is found to deposit predominantly on the porous substrate/electrolyte and substrate/current collector interfaces. Smaller pore size favors smoother and more uniform deposits throughout the substrate.

Battery electrodes often contain the active material distributed within a porous conducting substrate. Examples are Zn electrodes utilizing porous carbon substrates, as employed in Zn-Cl₂ (1, 2), Zn-Br₂ (3-5), and Ni-Zn (6) batteries. Repeated charge and discharge sometimes leads to a redistribution of the active material and concomitant changes in electrode performance. Thus, techniques that allow a study of the effect of various electrode and process parameters on the metal distribution across and within the porous substrate are of interest. X-ray radiography is one such technique.

In the past, x-ray radiography has mainly been used in battery studies to determine the porosity of separators (7) and electrodes (8), or to establish the position of a liquid electrolyte or reactant in capillaries (9, 10).

In this paper, the application of x-ray radiography in conjunction with high resolution optical densitometry for the quantitative determination of the depth and surface profile of metal deposits in porous substrates (11) is discussed. The technique yields quantitative information with excellent spatial resolution in cases where the x-ray absorption coefficient of the metal deposit is considerably larger than that of the substrate. Depending on the magnitude of the absorption coefficient and the theoretical density, the metal deposit may be a few millimeters thick; in that case, sufficient x-ray intensity is transmitted to the film. These conditions are met for electrodes which employ porous carbon substrates and active materials such as Zn. Results on the deposition of Zn on a highly porous carbon substrate in Zn-Br₂ cells with electrolyte flow parallel to the electrode surface are described. The effect of substrate pore size on the Zn distribution in the substrate and on its surface is examined.

The technique is readily applicable to studying the effect of a variety of electrode and process parameters on metal deposit morphology. Furthermore, the changes in deposit morphology as a function of plating time can be investigated.

Experimental

Zn was deposited in Zn-Br₂ cells on porous reticulated vitreous carbon (RVC) foams¹ cemented to graphite current collector plate² with a conductive adhesive.³ The dimensions of the foam and the graphite plate are 10 × 10 × 0.2 cm and 13 × 12 × 0.64 cm, respectively. A Nafion 120 cation exchange membrane (E. I. du Pont de Nemours and Company) was spaced 0.2 cm from the carbon foam, separating the bromine electrode from the foam. A schematic diagram of the cell design is shown in Fig. 1.

* Electrochemical Society Active Member.

¹ Produced by Chemotronics, Incorporated, now Franklin Engineering, Ann Arbor, Michigan.

² Union Carbide, Grade CGW.

³ Dylon Industries, Incorporated, Grade GC.

A peristaltic pump was used to circulate the electrolyte at a flow rate of 160 cm³/min, equivalent to a Reynolds number of 2500. The electrolyte entered into a free electrolyte gap at the bottom of the cell and exited through another free electrolyte space at the top. This aided attaining uniform electrolyte flow across the electrode surface. A rubber gasket around the edges of the foam prevented the electrolyte from flowing through the foam. Foams of two different average pore diameters, namely, 0.22 and 0.45 mm, were employed. These foams are designated by the manufacturer as 100-pore and 45-pore foam, based upon an average number of 100 and 45 pores per inch, respectively. The open cellular structure of these foams is shown in the scanning electron micrographs (SEM's) of Fig. 2a and b, taken at a magnification of 30×. The void volume of both foams is about 97%. The values for surface area/volume ratio and resistivity are 26.2 cm²/cm³ and 0.5 Ω · cm for the 45-pore foam and 65.6 cm²/cm³ and 0.3 Ω · cm for the 100-pore foam, respectively (11). Zn deposition, corresponding to battery charging, was performed at room temperature at a constant current density of 25 mA/cm² for 4h in 30 weight percent (w/o) aqueous ZnBr₂ solution. Reagent grade chemicals and double-distilled water were used in preparing the solution. After Zn deposition and prior to obtaining x-ray radiographs, the cell electrolyte was removed, and distilled water was circulated through the cell at 160 cm³/min for 10 min.

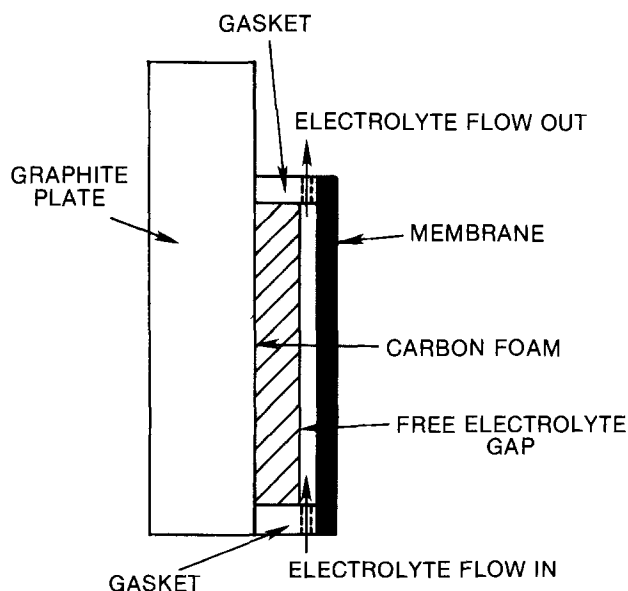


Fig. 1. Half-cell schematic showing vitreous carbon foam substrate on graphite plate with electrolyte flow parallel to surface.

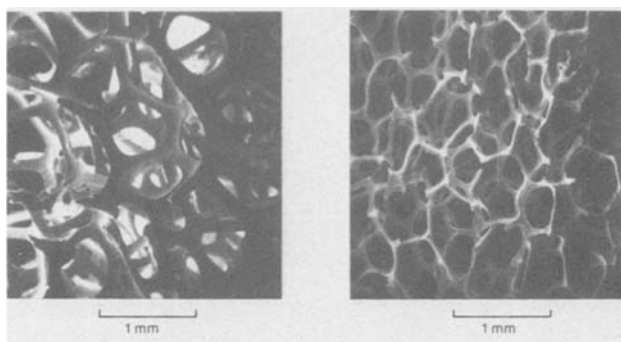


Fig. 2. SEM's of vitreous carbon foams at 30 \times magnification. A, left: 45-pore foam. B, right: 100-pore foam.

X-ray radiographs were taken of the face and cross sections of the electrodes with a Hewlett Packard Faxitron series x-ray system. Polaroid 55 positive/negative film was employed. A quantitative measure of the zinc density profile perpendicular to the foam surface was obtained through densitometer measurements of the radiograph film negatives at a magnification of 20 \times . An automatic recording microdensitometer (Joyce-Loebel Model MKIIC) with slit dimensions 8 \times 0.04 mm was employed for this purpose. The quantitative results, obtained with the densitometer, were compared with SEM's of electrode surfaces and cross sections. In order to examine the Zn profile perpendicular to the foam, three 6 mm-wide segments were cut from the top to the bottom of the electrode. The location of these segments is shown in Fig. 3, a photomicrograph of the foam face.

Principle of Measurement Technique

The measurement principle is shown in the three schematic drawings of Fig. 4. A segment of height H (10 cm), width W (6 mm), and total thickness $L + L_p$ (foam 2 mm; plate 6.4 mm) is cut from the electrode and placed on x-ray film with x-rays penetrating the width W . The largest attenuation of the incident x-ray beam intensity occurs in regions of high metal density; the beam is essentially unattenuated in areas where only carbon foam is present. The transmitted x-ray intensity thus produces an image on the film negative, in which the lightest areas correspond to areas of highest metal density in the electrode cross section. The radiographs shown in this paper are film positives for which the opposite is true.

In the densitometer evaluation of the film negatives, visible light, confined by a slit, penetrates a 0.04 mm-wide section of the negative at a time, and the transmitted light intensity is measured with a photomultiplier tube; the highest light intensity corresponds to areas with the densest metal deposit on the electrode segment. This is indicated schematically in the lower part of Fig. 4.

Actually, the densitometer records the optical density of the film negative by comparison with the density of an optical attenuator or gray wedge. The principle of operation of the densitometer is based on a true double-beam light system, in which two beams from a single light source, one of which passes through the sample film negative, are switched alternately to a single photomultiplier. If the two beams are of different intensity, a signal is produced by the photomultiplier, which, after amplification, causes a servo motor to move the optical attenuator which reduces the intensity difference to zero. In this way, a continuously null balancing system is obtained, in which the position of the optical attenuator is made to record the optical density at any particular part of the film negative.

The quantitative relationship between the apparent metal density in the carbon foam and the recorded optical density is readily obtained. When a beam of

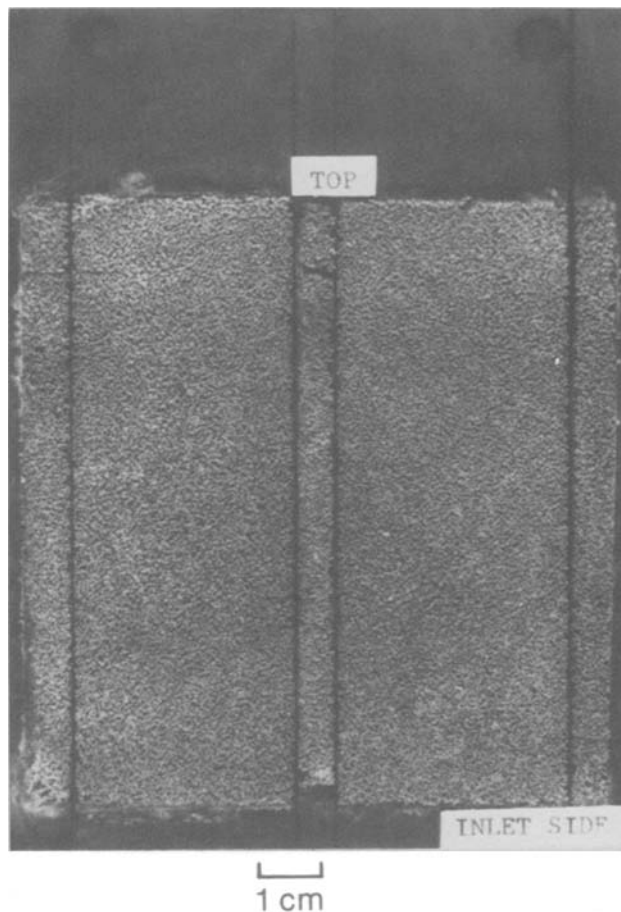


Fig. 3. Photomicrograph of carbon foam (10 by 10 cm) at 1 \times , showing three segments used for radiography.

x-rays penetrates a material of known width W , its intensity is attenuated according to

$$J_{XR} = {}_0J_{XR} \exp[-\mu W] \quad [1a]$$

where ${}_0J_{XR}$ is the incident beam intensity, J_{XR} the transmitted intensity, and μ the linear x-ray absorption coefficient of the material. In cases where the density of the material is different from the theoretical bulk density of the solid, it is more convenient to write Eq. [1a] in terms of the mass absorption coefficient μ/ρ and the apparent density ρ_{app}

$$J_{XR} = {}_0J_{XR} \exp[-(\mu/\rho) \rho_{app} W] \quad [1b]$$

μ/ρ is related to the x-ray wavelength λ according to

$$\mu/\rho = Kz^4\lambda^3 \quad [2]$$

where K is a constant, and z is the atomic number. Thus, the absorption coefficient increases strongly with increasing wavelength.

In the present study, the continuous x-ray spectrum or white radiation of a tungsten tube at 30 keV was employed (12). The shortest wavelength at which radiation is emitted is 0.413 \AA , and the peak intensity occurs at 0.54 \AA . Toward longer wavelengths, the intensity decreases, attaining a value of 18% of peak intensity at 1 \AA .

The x-ray mass absorption coefficients for a number of elements of interest in battery research are summarized in Table I as a function of the x-ray wavelength (13). At the K and L absorption edges of the heavier elements, the absorption coefficients show a discontinuity. This is indicated in the table by lines leading through the table.

At the peak intensity of 30 keV tungsten radiation at 0.54 \AA , C has a mass absorption coefficient of only 0.31 cm^2/g . Therefore, with the exception of Al, the x-ray

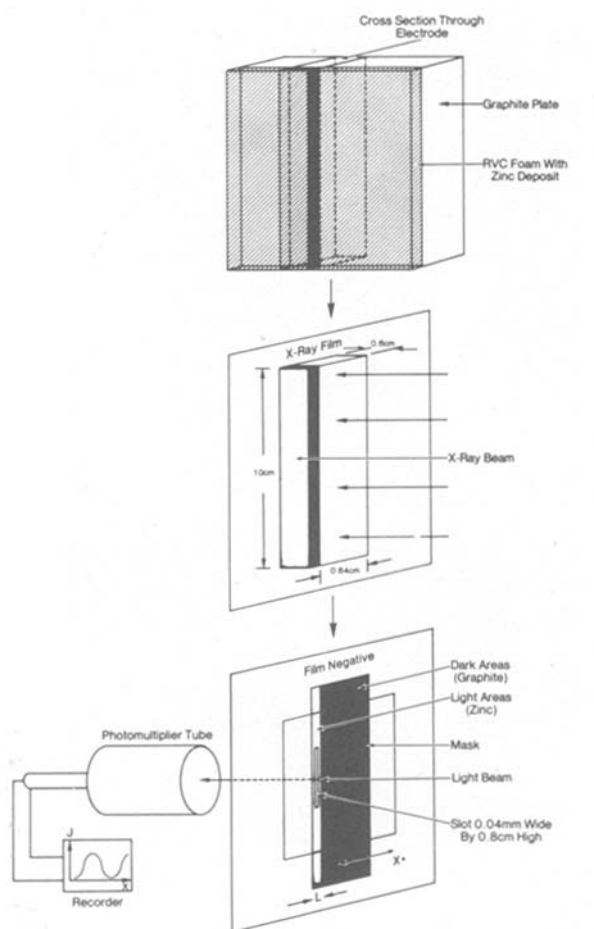


Fig. 4. Schematic diagram of radiography-densitometry procedure.

absorption of C is negligible compared to that of the elements listed in Table I. In the present case of Zn deposited on a carbon foam of 3% theoretical density, the effect of the carbon foam is not detectable.

The optical density (degree of darkening) of the developed film negative, D , is related to the logarithm of the exposure in a "characteristic curve." In the normal working range of the film, the relationship is expressed by⁴

$$D = \gamma \log E \quad [3]$$

where γ is the development factor and

⁴ Many industrial x-ray films yield a linear density-exposure relationship and, hence, result in a different form of Eq. [5].

Table I. X-ray mass absorption coefficients for selected elements, μ/ρ (cm^2/g)

λ (Å)	C	Al	Ni	Zn	Br	Ag	Cd	Pb
0.1	0.14	0.15	0.30	0.35	0.50	1.05	1.10	3.41
0.2	0.15	0.26	1.25	1.51	2.31	5.19	5.51	3.86
0.3	0.17	0.50	3.88	4.69	7.15	16.07	17.03	11.9
0.4	0.23	1.03	8.68	10.47	15.97	35.89	38.04	26.6
0.5	0.31	1.93	16.19	19.54	29.78	9.4	10.0	49.7
0.6	0.42	3.22	27.00	32.58	49.66	15.7	16.8	82.9
0.8	0.83	7.21	60.38	72.88	111.07	35.3	37.6	176.5
1.0	1.54	13.50	113.04	136.44	27.29	66.1	70.3	66.6

$$E = J_{\text{XR}} \cdot t \quad [4]$$

the exposure of the negative to the constant x-ray intensity, J_{XR} , for time t . Combining Eq. [1b] and [4] results in

$$D = \gamma \log {}_0J_{\text{XR}t} - (\gamma/2.3) (\mu/\rho) W\rho_{\text{app}} \quad [5]$$

The optical density is thus linearly related to the apparent metal density in the foam, and the radiograph is a true map of the metal density distribution parallel or perpendicular to the foam face as long as the exposure range of the film is not exceeded. Calibration of the optical density curve in terms of apparent metal density is obtained by determining the total area under the D vs. x curve, which corresponds to the total known amount of metal deposited into a given electrode volume.

The requirement to stay in the linear exposure range of the film places inherent limitations on the applicability of the technique. For x-rays, the density range from $D = 0.1$ to 4 is feasible. The incident beam exposure, ${}_0J_{\text{XR}t}$, must be chosen such that $D = 4$ is not exceeded for the minimum value of ρ_{app} present in the electrode. The largest possible value of ρ_{app} that still results in discernible film darkening is then fixed by Eq. [5] with $D = 0.1$ for specified film properties, mass absorption coefficient, and material width W . In the case of Zn with $\mu/\rho = 10.5 \text{ cm}^2/\text{g}$ for the short wavelength limit of the spectrum and $W = 6 \text{ mm}$, this leads to a maximum value of $\rho_{\text{app}} = 1.8 \text{ g/cm}^3$ or 26% of theoretical density.

Results and Discussion

Scanning electron microscopy.—SEM's of the surface and a cross section of 45-pore foam after Zn plating with 25 mA/cm^2 for 4h at $N_{\text{Re}} = 2500$ are presented in Fig. 5. The SEM's relate to the center segment of the electrode (cf. Fig. 3) and were taken at a magnification of $30\times$ from the surface and $14\times$ from the cross section. The major features of the Zn deposit evident from the SEM's are a nodular Zn growth at and near the surface of the foam, no discernible Zn deposit in most of the interior, and some Zn particles near the foam/graphite plate interface. Not evident from the SEM's, but clearly visible in the optical microscope, is a continuous Zn coating on the foam strands in the interior and on the graphite plate surface.

For comparison, Fig. 6a and b show the equivalent SEM's of the Zn deposit on the 100-pore foam, demonstrating the effect of smaller pore size. The deposit on the foam surface consists of a larger number of smaller Zn nodules, and they are more evenly distributed across the surface. A somewhat larger number of small Zn particles is also visible in the interior and at the plate interface of the foam.

The observed differences in Zn morphology between 45- and 100-pore foam are most likely due to the larger surface area and lower resistivity of the latter. This results in a larger number of nucleation sites for Zn growth and in more uniform current density.

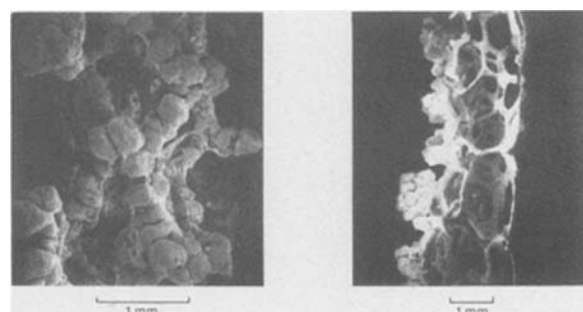


Fig. 5. SEM's of 45-pore foam after Zn plating from 30% ZnBr_2 solution with 25 mA/cm^2 for 4h at $N_{\text{Re}} = 2500$. A, left: electrode face at $30\times$. B, right: electrode cross section at $14\times$.

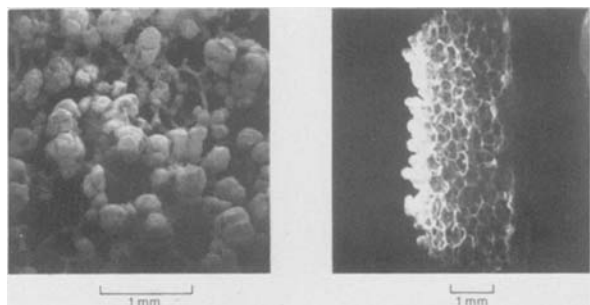


Fig. 6. SEM's of 100-pore foam with Zn deposited for 4h at 25 mA/cm². A, left: electrode face at 30 \times . B, right: electrode cross section at 14 \times .

The characteristic bimodal Zn distribution, with maxima in apparent Zn density occurring at the two C foam interfaces, corresponds to long plating times. It is to be expected that the Zn distribution in the initial stages of plating is different and changes with time as the Zn deposit alters the conductance of the foam substrate.

Radiography.—Figures 7a and b show x-ray radiographs of the surface and center cross section of the 45-pore foam after Zn plating. The dark areas correspond to Zn, the light areas to voids or carbon foam. In contrast to the SEM's, Fig. 7a and b show essentially the complete objects in actual size. Therefore, the uniformity of Zn plating parallel and perpendicular to the entire foam surface can immediately be judged. The Zn deposit is relatively uniform across the surface, with a slightly denser deposit on the far side of the electrolyte inlet (left side of Fig. 7a). The radiograph of the cross section reveals a dense Zn deposit at and near the foam/electrolyte interface, only isolated Zn aggregates in the interior, and a thin dense Zn coating at the foam/plate interface.

The corresponding radiographs of 100-pore foam, shown in Fig. 8a and b, display generally similar features, except that smaller Zn particle size and smoother, more uniform Zn plating is evident.

Densitometry.—The cross-sectional radiographs of 45- and 100-pore foam, shown in Fig. 7b and 8b, were evaluated with the densitometer, and the results are shown in Fig. 9. In the graph, $x = 0$ corresponds to the

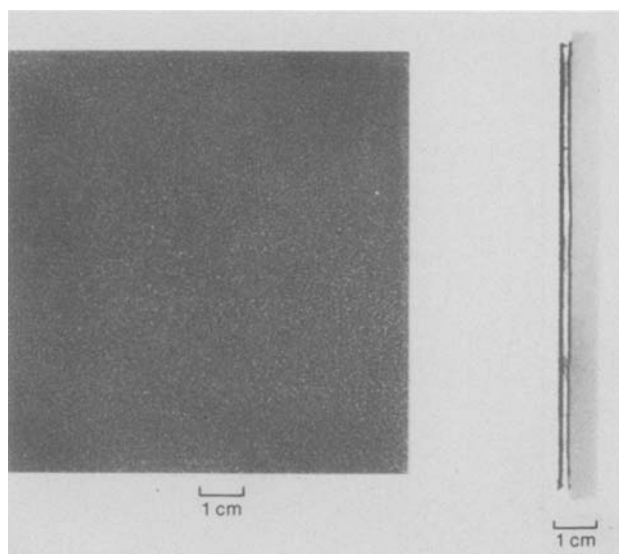


Fig. 7. X-ray radiographs of Zn deposit on 45-pore foam after 4h at 25 mA/cm². A, left: electrode face at 1 \times . B, right: cross section at 1 \times .

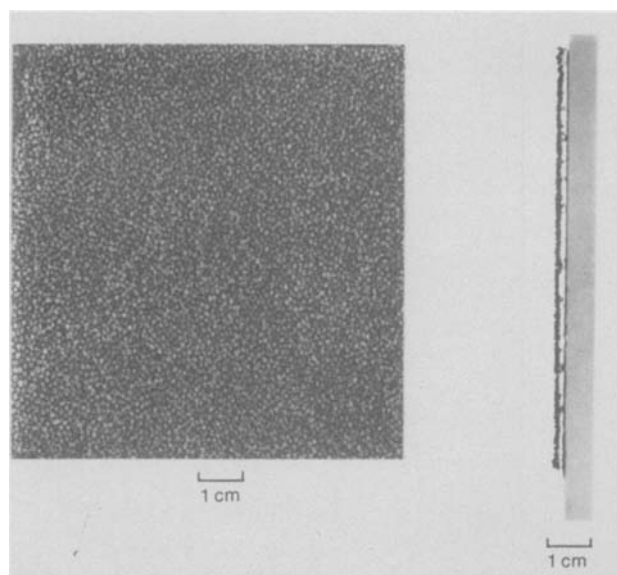


Fig. 8. X-ray radiographs of Zn deposit on 100-pore foam after 4h at 25 mA/cm². A, left: electrode face at 1 \times . B, right: cross section at 1 \times .

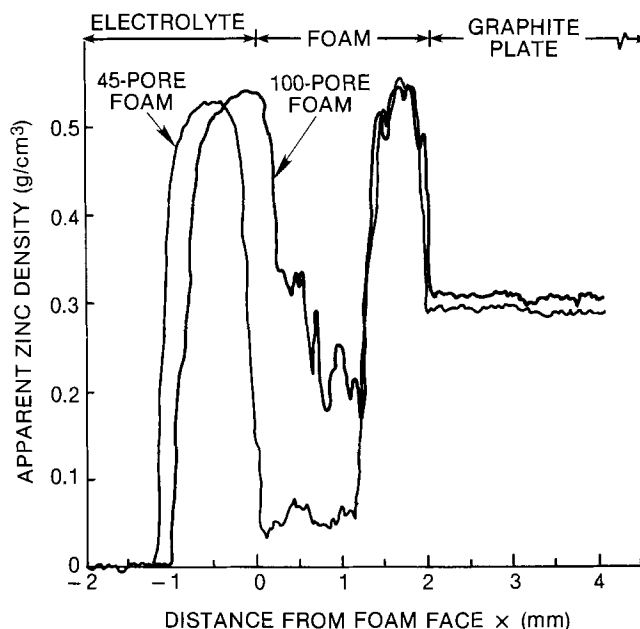
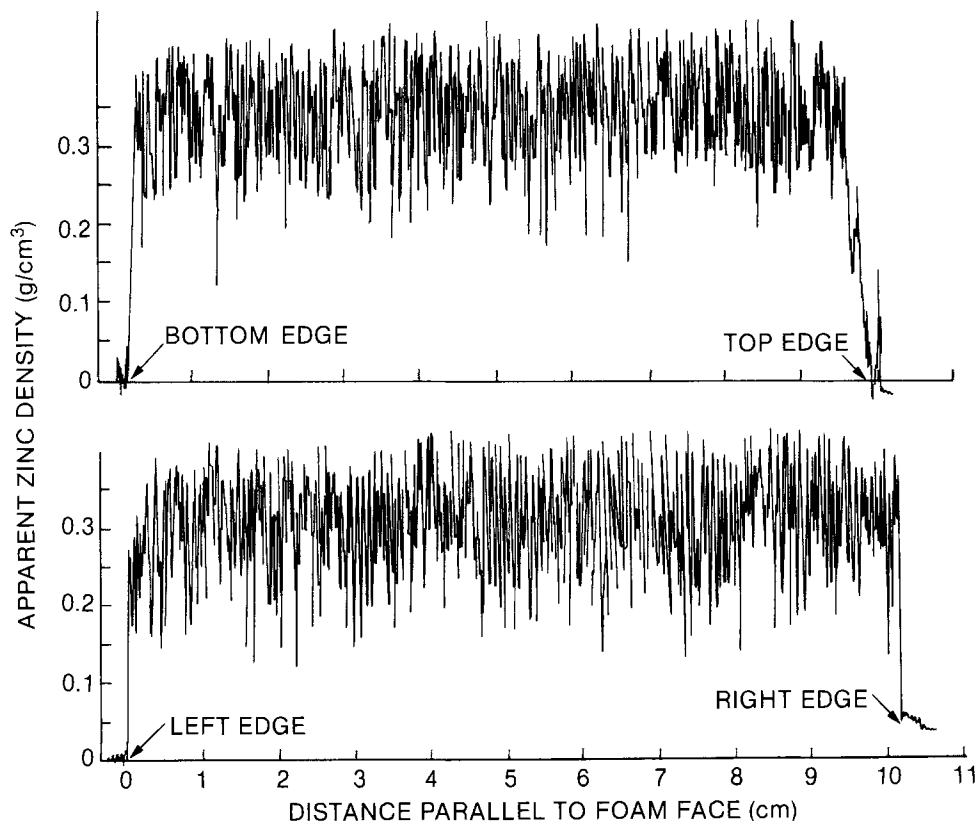


Fig. 9. Densitometer traces of Zn deposit profiles perpendicular to surface on 45- and 100-pore carbon foam, plated for 4h at 25 mA/cm² in 30% ZnBr₂ solution circulating at $N_{Re} = 2500$.

foam/electrolyte interface and $x = 2$ mm to the foam/graphite plate interface. The graph shows that significant amounts of Zn have been plated on the surface of the foam, extending approximately 1 mm into the electrolyte. Furthermore, considerable Zn plating has occurred within 0.6 mm of the foam/graphite plate interface. The apparent densities of the Zn deposits near the foam face and the plate are both between 0.5 and 0.6 g/cm³ or 7 to 9% of the theoretical density. Considerably less Zn was deposited in the interior of the 45-pore foam. This small amount of Zn corresponds to the thin continuous Zn coating of the carbon strands, clearly discernible in the optical microscope.

Use of 100-pore instead of the coarser 45-pore foam results in less Zn deposit on the surface and comparatively more Zn plating within the foam interior. Also, the Zn deposit on the 100-pore foam protrudes less into the electrolyte. The fractions of Zn deposited on the foam surface, in its interior, and near the graphite plate for both foams are summarized in Table II.

Fig. 10. Densitometer traces of Zn distribution parallel to electrode surface on 10×10 cm 100-pore carbon foam along centerlines from left to right (lower trace) and bottom to top (upper trace).



As a result of the uniform electrolyte flow across the surface, applicable to our study, the Zn distribution across the surface is also quite uniform. Such uniform electrolyte flow is produced by the use of a rectangular cavity, spanning the whole width of the electrode at the bottom and the top. This "free electrolyte space" has a very small flow resistance compared to that of the electrode/membrane gap. Densitometry of the x-ray radiograph of the electrode face of 100-pore foam (see Fig. 8) demonstrates the uniformity of the Zn deposit. Figure 10 shows densitometer traces across the electrode surface along the centerlines from left to right (lower trace) and from bottom to top. The mean apparent Zn density is seen to be fairly constant along both centerlines. The large, almost periodic fluctuations in actual Zn density demonstrate the spatial resolution of the technique: with a slit width of only 0.04 mm and an average pore diameter of 100-pore foam of 0.22 mm, the densitometer resolves the relatively higher Zn density on C strands as compared to the lower density in the voids between strands.

The uniform Zn distribution across the surface leads one to expect Zn deposit profiles which are rather invariant with location across the surface. This was actually observed on cross sections taken from various parts of the electrode surface, as shown in Fig. 3.

Conclusions

X-ray radiography in conjunction with optical microdensitometry can be used as a quantitative tool in the study of various parameters affecting metal deposit profiles on porous substrates. The technique yields apparent metal density with a spatial resolution of 0.04 mm. Applicability of the technique requires (i) that the x-ray absorption of metal and substrate be

different enough to produce sufficient contrast and (ii) working in the linear exposure range of the film. For a given material, the second criterion can often be met by suitable choice of the sample thickness and x-ray wavelength.

The technique has been applied to the case of zinc deposited on a high porosity carbon foam. A study of the effect of pore size on the zinc distribution in the foam yields the finding that smaller pore size favors more uniform zinc distribution throughout the foam. This is most likely due to the higher surface area and lower resistivity of the fine-porous foam, resulting in a larger number of nucleation sites and more uniform current distribution than in the coarse foam.

Acknowledgment

This work was supported in part by the U.S. Department of Energy under Contract no. EY-76-C-02-2950. The help of Mrs. A. M. Davies in performing the densitometry is gratefully acknowledged.

Manuscript submitted July 15, 1983; revised manuscript received Oct. 10, 1983.

General Electric Company assisted in meeting the publication costs of this article.

REFERENCES

1. P. C. Symons, International Conference on Power Sources, Brighton, England (1973).
2. C. H. Chi, P. Carr, and P. C. Symons, *Intersoc. Energy Convers. Eng. Conf. Rec.*, **14**, 692 (1979).
3. F. G. Will, *ibid.*, **12**, 250 (1977).
4. R. A. Putt, *ibid.*, **16**, 793 (1981).
5. R. J. Bellows, P. Grimes, H. Einstein, E. Kantner, T. Malachuk, and K. Newby, *IEEE Trans. Veh. Technol.*, **vt-32**, 26 (1983).
6. A. Charkey, *Intersoc. Energy Convers. Eng. Conf. Rec.*, **11**, 452 (1976).
7. G. L. Clark and C. H. Liu, *Anal. Chem.*, **29**, 1539 (1957).
8. K. Appelt and A. Nowacki, *Electrochim. Acta*, **11**, 137 (1966).
9. M. Bonnemay, G. Bronoel, and E. Lavart, *ibid.*, **9**, 727 (1964).
10. A. Gibson, "Power Sources 6," p. 673, Academic Press, London (1977).

Table II. Fractions of zinc deposited on and in carbon foam substrate

Foam type	On surface $x \leq 0$	In interior $0 \leq x \leq 1.3$ mm	Near plate $1.3 \leq x \leq 2$ mm
45-pore	0.52	0.12	0.36
100-pore	0.37	0.33	0.30

11. F. G. Will, C. D. Iacovangelo, J. S. Jackowski, and F. W. Secor, U.S. Department of Energy, Final Report C00-2950-1 (1978).
12. A. H. Compton and S. K. Allison, "X-Rays in Theory and Experiment," p. 38, D. Van Nostrand Co., Inc., New York (1940).
13. H. A. Liebhafsky, H. G. Pfeiffer, E. H. Winslow, and P. Zemany, "X-Rays, Electrons, and Analytical Chemistry," pp. 525-528, Wiley-Interscience, New York (1972).

Shifts in Redox Formal Potentials Accompanying the Incorporation of Cationic Complexes in Perfluoro Polycarboxylate and Polysulfonate Coatings on Graphite Electrodes

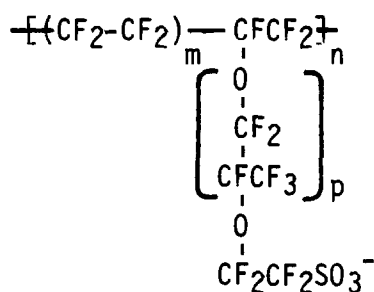
Yu-Min Tsou and Fred C. Anson*

California Institute of Technology, Arthur Amos Noyes Laboratories, Division of Chemistry and Chemical Engineering, Pasadena, California 91125

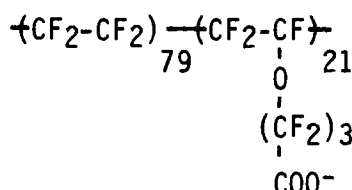
ABSTRACT

The formal potentials of several redox couples incorporated in coatings of a perfluoropolycarboxylate on graphite electrodes were measured and compared with the formal potentials of the same couples in homogeneous solution. The differences observed agreed with those calculated from the Nernst equation with the independently measured incorporation coefficients for both halves of the redox couples. The dependences of the shifts in formal potentials on the nature of the incorporating complex ion, the ionic strength, and the temperature were determined and indicated that the incorporation equilibrium is governed by electrostatic and hydrophobic interactions that act in opposite directions. The incorporation of most cations examined was driven by large increases in entropy which overcame the usually unfavorable enthalpy changes.

Redox reactants incorporated in polyelectrolyte coatings on electrode surfaces will exhibit formal potentials that are shifted from their values in solution whenever the two oxidation states of the reactant have different equilibrium constants for incorporation by the polyelectrolyte. This situation has been recognized in earlier reports (1, 2) and in a recent study this aspect of the electrochemistry of redox polymer coatings was examined in detail (3). In continuing studies of the electrochemical responses obtained from redox reactants at electrodes coated with Nafion, I, and the related polyelectrolyte, II,



Nafion



Polyelectrolyte II

we noted unusually large shifts in the formal potentials of certain redox couples upon incorporation into these

coatings. Both the magnitude of the shift in formal potential and its sign were influenced strongly by the nature of the ligands coordinated to the metal center of the redox couples. It was the purpose of the experiments described here to document the behavioral differences observed with several redox couples in both polyelectrolytes and to attempt to understand their origins. The results indicate that both electrostatic and hydrophobic interactions of incorporated electroactive ions with the polyelectrolyte combine to determine the direction of shifts in formal potentials. The temperature dependences of the shifts in formal potential were also measured. They pointed to large entropic contributions to the differences in the equilibrium incorporation of the oxidized and reduced halves of the redox couples.

Experimental

Materials.—Nafion¹ coatings were prepared as previously described (4) by evaporation of aliquots of a solution of the polymer supplied by E. I. du Pont de Nemours and Company several years ago. Polymer II was supplied in the form of a fine suspension of the methyl ester by Asahi Glass Company, Tokyo. To prepare coatings, aliquots of the suspension were evaporated on freshly cleaved electrodes. The resulting deposit was exposed to 1M NaOH for 5 min to convert the ester to the carboxylate, and the electrode was then washed thoroughly with water. The extent and uniformity of the de-esterification were not examined in detail, but it was established that increasing the time that the coatings were exposed to the 1M NaOH produced no changes in their behavior. Electrodes were prepared from pyrolytic graphite (Union Carbide Company, Chicago) and mounted according to previously described procedures (5). Ru(NH₃)₆Cl₃ (Mathey-Bishop Company) was recrystallized before use.

[CpFeCp-CH₂-N⁺(CH₃)₃]Br⁻ (Cp = cyclopentadienide) (Research Organic/Inorganic Company) was used as received. Ru(NH₃)₅isonicotinamide(ClO₄)₂ (6) and Os(bpy)₃ClO₄ (7) were synthesized according to the cited references. Solutions were prepared with distilled water, which was further treated by passage through a purification train (Barnstead Nanopure).

* Electrochemical Society Active Member.

Key words: Nafion, redox polymer, enthalpy, entropy.

¹ Nafion is a trademark of E. I. du Pont de Nemours and Company.

Procedures.—Conventional two-compartment cells and apparatus were employed to obtain cyclic voltammograms. To evaluate formal potentials for reactants incorporated in electrode coatings, the cyclic voltammograms were recorded at scan rates low enough (e.g., a few mV s^{-1}) to obtain symmetrical waves with almost equal peak potentials. The quantities of the oxidized and reduced halves of redox couples incorporated by coatings were measured chronopotentiometrically (8) to avoid possible alterations in the equilibrium ratio of oxidant to reductant by insufficiently precise potentiostatic control of the electrode potential. Potentials were measured and are quoted with respect to a calomel reference electrode saturated with sodium chloride, SSCE.

Temperature dependences of formal potentials were evaluated from cyclic voltammograms recorded in a nonisothermal cell having a thermally jacketed compartment for the working and auxiliary electrodes and a separate compartment for the reference electrode. The reference electrode was maintained at a fixed temperature. The principles and assumptions involved in the use of such cells have been examined in detail (9) and several recent experimental examples of their successful applications are available (10). Exposure of the polyelectrolyte coatings to solutions at 50°C caused the measured formal potentials of incorporated redox couples to drift slightly before new stable potentials resulted. We believe this behavior is the result of reproducible structural changes in the coatings. For this reason, the temperature dependences of formal potentials were measured with coatings that had been exposed to a solution at 50°C long enough for the cyclic voltammetric response to stabilize (ca. 30 min). Thereafter, reproducible peak potentials were obtained at all temperatures.

Results

Cyclic voltammograms for the $\text{Ru}(\text{NH}_3)_6^{3+/2+}$ couple at a graphite electrode coated with the carboxylate polyelectrolyte, II, are shown in Fig. 1. The effects of changes in scan rate on the response are the subject of Fig. 1a, while 1b is concerned with the effects of changes in the coating thickness at a fixed scan rate. With thinner coatings or lower scan rates, the voltammograms exhibit two peaks. These are more clearly separated in the anodic half of the voltammograms.

The anodic peak at -0.15V is quite close to the corresponding peak obtained at an uncoated electrode, and it is this peak that disappears when the electrode used to record the voltammograms in Fig. 1 is transferred to a pure supporting electrolyte solution. Similar behavior was reported earlier for the voltammetry of $\text{Ru}(\text{NH}_3)_6^{3+/2+}$ at electrodes coated with polyvinylsulfate (1). The peak that is present only in solutions containing $\text{Ru}(\text{NH}_3)_6^{3+/2+}$ is believed to arise from the diffusive penetration of the polymer coating by the complex so that it is reduced and reoxidized directly at the electrode surface. That the peak does not arise from reaction at bare patches of the electrode exposed by imperfections in the coating was indicated by tests of coated electrodes with nonincorporating anions, such as $\text{Fe}(\text{CN})_6^{4-}$, which exhibited much smaller peak currents and much greater peak potential separations at coated than at bare electrodes. In any case, the present study was devoted to comparisons between the voltammetric responses of redox couples at bare electrodes and those taken after their incorporation into coatings on electrodes which are subsequently transferred to a pure supporting electrolyte solution. Thus, the second peak evident in Fig. 1 presented no problems.

In Fig. 2 the cyclic voltammogram for $\text{Ru}(\text{NH}_3)_6^{3+/2+}$ at a bare graphite electrode is compared with that for the same couple incorporated in a coating of the carboxylate polyelectrolyte, II. The large difference in the average of anodic and cathodic peak potentials (i.e., the formal potentials) of the couple in the two cases is evident. This difference in formal potentials should reflect the difference in the strength of the binding of each half of the redox couple to the polyelectrolyte coating. For example, if $[\text{O}]_s/[\text{R}]_s$ and $[\text{O}]_p/[\text{R}]_p$ are the equilibrium ratios of the concentrations of the oxidized and reduced forms of a couple in the solution (s) and polyelectrolyte (p) phases, respectively, the difference in the formal potentials observed in the two phases should be given by Eq. [1]

$$E_p^f - E_s^f = \frac{RT}{F} \left(\ln \frac{[\text{O}]_s}{[\text{R}]_s} - \ln \frac{[\text{O}]_p}{[\text{R}]_p} \right) \quad [1]$$

Experimental values of E_p^f and E_s^f were obtained from the average of the peak potentials of voltammograms, such as those in Fig. 2. The voltammograms obtained

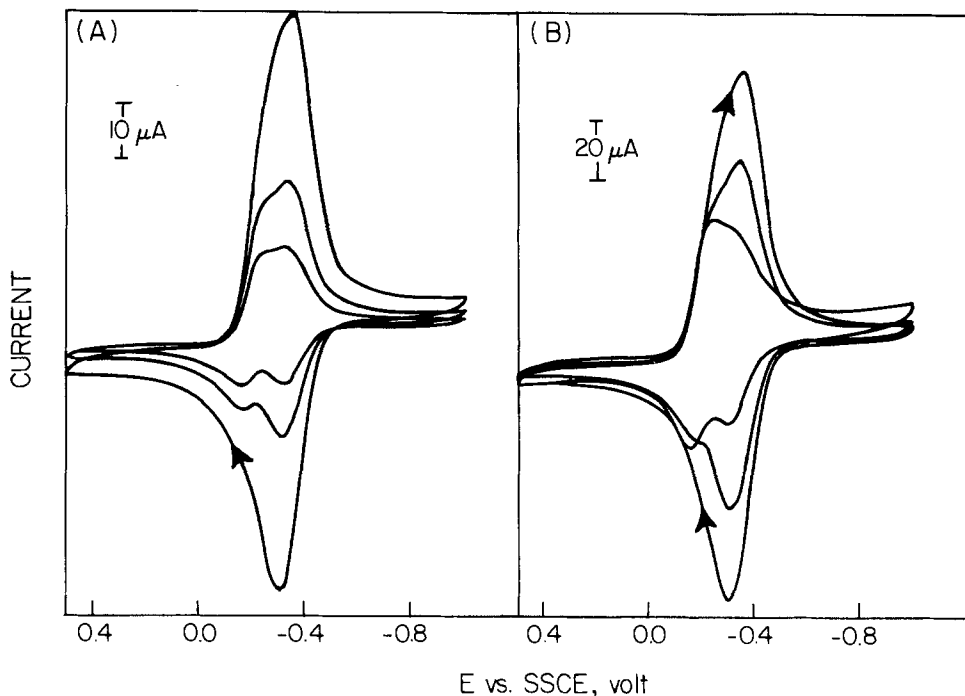


Fig. 1. Steady-state cyclic voltammograms for $1.0 \text{ mM Ru}(\text{NH}_3)_6^{3+}$ solution at a graphite electrode coated with polyelectrolyte II. Supporting electrolyte: 0.2M KCl at $\text{pH } 5.5$. (A) Coating contained $2.1 \times 10^{-7} \text{ mol cm}^{-2}$ of carboxylate groups. Scan rate: $10, 20, 50 \text{ mV s}^{-1}$. (B) Scan rate: 100 mV s^{-1} . Coatings contained $4.2, 8.4,$ and $21 \times 10^{-8} \text{ mol cm}^{-2}$ of carboxylate groups.

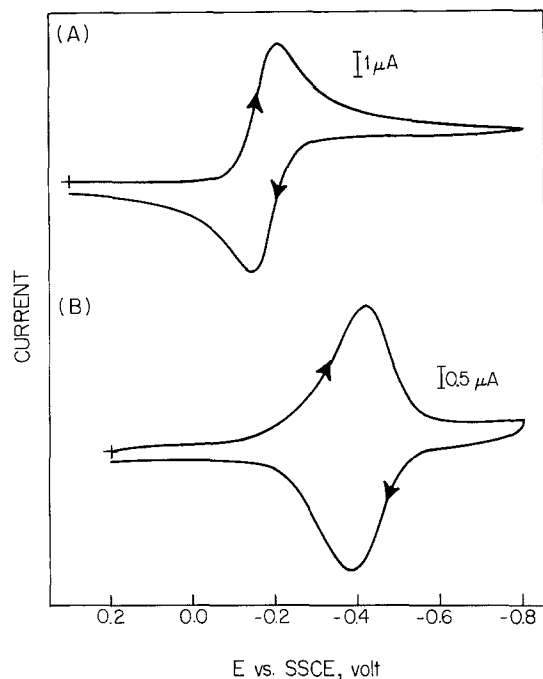


Fig. 2. (A) Cyclic voltammograms for 0.5 mM $\text{Ru}(\text{NH}_3)_6^{3+}$ at a bare graphite electrode. (B) Repeat after the electrode was coated with polyelectrolyte II (8.4×10^{-8} mol cm^{-2} of carboxylate groups), soaked in the $\text{Ru}(\text{NH}_3)_6^{3+}$ solution for 5 min and transferred to pure supporting electrolyte (0.02M CH_3COONa at pH 5.5). Scan rate: 5 mV s^{-1} for both curves.

with the polyelectrolyte coatings were recorded at scan rates sufficiently small ($< 5 \text{ mV s}^{-1}$) so that all of incorporated complex was reduced or oxidized during each half-cycle. The peak currents were proportional to scan rate, as expected under these conditions (11), and the formal potential was taken as the simple average of the peak potentials, which were typically separated by 10 to 30 mV by residual ohmic potentials present in the cell and coating. At bare electrodes, the peak potentials were usually separated by 60-70 mV, as expected (12). The formal potential (E_s^f) was obtained from the average of the peak potentials corrected for the difference in the solution diffusion coefficients of the two halves of the redox couple (12). This correction typically amounted to 1 to 2 mV.

The open-circuit equilibrium potential assumed by bare (or coated) electrodes in solutions containing both O and R is given by

$$E_{\text{eq}} = E_s^f - \frac{RT}{F} \ln \frac{[\text{R}]_s}{[\text{O}]_s} \quad [2]$$

Thus, Eq. [1] can be rewritten as

$$E_p^f = E_{\text{eq}} + \frac{RT}{F} \ln \frac{[\text{R}]_p}{[\text{O}]_p} \quad [3]$$

where E_{eq} is the equilibrium potential of the coated (or bare) electrode in an incorporation solution which leads to the concentration ratio $[\text{R}]_p/[\text{O}]_p$ in the polyelectrolyte phase. Thus, to test Eq. [1], coated electrodes were equilibrated in incorporation solutions containing various ratios of the oxidized to reduced form of the redox couple. The formal potentials of the redox couple in the coating (E_p^f) were then compared with the sum $E_{\text{eq}} + RT/F \ln [\text{R}]_p/[\text{O}]_p$ calculated from the observed values of E_{eq} and the measured concentrations of R and O in the polyelectrolyte phase. The latter were determined chronopotentiometrically (8) after the equilibrated electrode was transferred to a pure supporting electrolyte solution. The constant current densities (i) utilized in the chronopotentiometric measurements were kept small enough to be sure that all of the incorporated reactant in the coatings had

been oxidized or reduced at the transition time (τ), so that the quantity of reactant could be calculated as $i\tau/nF$.

At the transition time, a constant current in the opposite direction was passed through the coating until a second transition corresponding to the sum of the oxidized and reduced reactant initially present in the coatings resulted. Thus, if the first transition time (τ_1) was obtained with an anodic current (i_1), and the second, (τ_2) resulted from a subsequent cathodic current (i_2)

$$\frac{[\text{O}]_p}{[\text{R}]_p} = \frac{i_2\tau_2 - i_1\tau_1}{i_1\tau_1} \quad [4]$$

Figure 3 shows two representative chronopotentiograms for coatings in which the $\text{Ru}(\text{NH}_3)_6^{3+/2+}$ or $\text{Os}(\text{bpy})_3^{3+/2+}$ redox couples had been incorporated. Table I summarizes the results of a series of such experiments with three redox couples to test whether Eq. [1] and [3] provide an adequate description of the behavior of the coated electrodes. The agreement between the calculated and observed potentials in the last two columns of Table I is, in most cases, within the experimental precision of $\pm 5 \text{ mV}$, so that Eq. [1] and [3] appear to be obeyed over a reasonably wide range of $[\text{R}]_p/[\text{O}]_p$ ratios. Thus, it may be concluded that the difference in measured formal potentials of redox couples in solution and incorporated within poly-

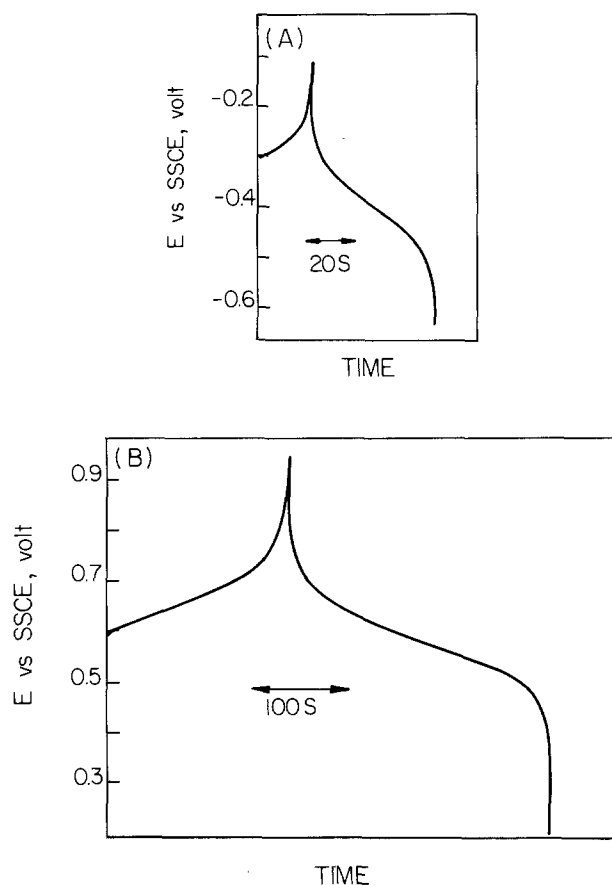


Fig. 3. Chronopotentiograms for the $\text{Ru}(\text{NH}_3)_6^{3+/2+}$ and $\text{Os}(\text{bpy})_3^{3+/2+}$ couples in coatings of polyelectrolyte II. (A) Electrode coated with 2.1×10^{-7} mol cm^{-2} of carboxylate group equilibrated with a solution containing $\text{Ru}(\text{NH}_3)_6^{3+}$ and $\text{Ru}(\text{NH}_3)_6^{2+}$ ($E_{\text{eq}} = 312 \text{ mV}$; $[\text{Ru}(\text{NH}_3)_6^{3+}] + [\text{Ru}(\text{NH}_3)_6^{2+}] = 1.0 \text{ mM}$) before transfer to pure supporting electrolyte solution (0.02M CH_3COONa at pH 5.5). Constant current density = $1.15 \mu\text{A cm}^{-2}$ for oxidation of Ru(II) and $23.0 \mu\text{A cm}^{-2}$ for reduction of Ru(III). (B) Electrode coated with 8.4×10^{-8} mol cm^{-2} of carboxylate groups equilibrated with a solution of $\text{Os}(\text{bpy})_3^{3+}$ and $\text{Os}(\text{bpy})_3^{2+}$ ($E_{\text{eq}} = 602 \text{ mV}$; $[\text{Os}(\text{bpy})_3^{3+}] + [\text{Os}(\text{bpy})_3^{2+}] = 0.5 \text{ mM}$). Constant current density = $2.87 \mu\text{A cm}^{-2}$ throughout.

Table I. Calculated and observed shifts in formal potentials of redox couples incorporated in coating of polyelectrolyte II^a

Redox couple	E_{eq}^b (mV)	$\frac{[R]_p^c}{[O]_p}$	$E_{eq} + \frac{RT}{F} \ln \left(\frac{[R]_p}{[O]_p} \right)$ (mV)	E_p^f (mV)
Ru(NH ₃) ₆ ^{3+/2+}	-312.0	0.024	-408.0	-402.0
Ru(NH ₃) ₅ isn ^{3+/2+} *	-60.0	5.000	-20.0	-21.0
	-43.0	2.570	-20.0	-21.0
	-40.0	2.450	-17.0	-21.0
	-37.0	1.800	-22.0	-21.0
	-24.0	0.900	-23.0	-21.0
	-19.0	0.900	-20.0	-21.0
	0.0	0.630	-12.0	-21.0
	+10.0	0.420	-12.0	-21.0
Os(bpy) ₃ ^{3+/2+}	602.0	2.380	624.0	609.0
	605.0	2.210	625.0	609.0

^a The coatings contained 8.4×10^{-8} mol cm⁻² of carboxyl groups in every case, except Ru(NH₃)₆^{3+/2+}, where the coating contained 2.1×10^{-7} mol cm⁻². Supporting electrolyte for both the incorporation and chronopotentiometric assay was 0.02M CH₃COONa at pH 5.5.

^b Open-circuit equilibrium potential (vs. SSCE) of the electrode in the solution from where the incorporation was carried out.

^c Ratio of the reduced to the oxidized form of the redox couple in the polyelectrolyte phase. Determined by chronopotentiometric assay using Eq. [4].

^d Formal potential (vs. SSCE) of the redox couple within the polyelectrolyte coating.

* isn = isonicotinamide.

electrolyte II reliably reflects the difference between the free energy changes associated with the incorporation of the two halves of the redox couple by the polyelectrolyte.

Effect of changes in ionic strength.—The incorporation of cationic redox couples by polyelectrolyte II is an ion exchange process involving displacement of equivalent quantities of the unipositive counterions initially present in the polyelectrolyte. For this reason, the extent of incorporation for each half of a redox couple would be expected to exhibit a dependence on the ionic strength of the incorporation solution. This expectation was tested by measuring the differences between the formal potentials of several redox couples in solution and within the polyelectrolyte coating as a function of ionic strength. The results, summarized in Table II, show that the difference in formal potentials measured inside and outside of the polyelectrolyte coatings is strongly dependent on ionic strength and on the nature of the redox couple.

Temperature dependence of the formal potential.—To obtain additional insight into the factors responsible

Table II. Ionic strength dependence of the difference between redox formal potentials in solution and within coatings of polyelectrolyte II^a

Redox couple	Supporting electrolyte conc ^b M	E_s^f ^c vs. SSCE mV	E_p^f ^d vs. SSCE mV	$E_p^f - E_s^f = \Delta E^f$ mV
Ru(NH ₃) ₆ ^{3+/2+}	0.02	-169.0	-402.0	-233.0
	0.20	-185.0	-347.0	-162.0
	2.00	-220.0	-290.0	-70.0
Ru(NH ₃) ₅ isn ^{3+/2+}	0.02	158.0	-21.0	-179.0
	0.02	619.0	609.0	-10.0
Os(bpy) ₃ ^{3+/2+}	0.02	608.0	632.0	24.0
	2.00	607.0	683.0	76.0
CpFeCpCH ₂ N-(CH ₃) ₂ ^{2+/+} *	0.20	388.0	381.0	-7.0

^a All coatings contained 8.4×10^{-8} mol cm⁻² of carboxyl groups.

^b The supporting electrolyte was CH₃COONa, and all solutions were adjusted to pH 5.5.

^c Formal potential of the couple in homogeneous solution, obtained from the average of cyclic voltammetric peak potentials and corrected for differences in diffusion coefficients (12).

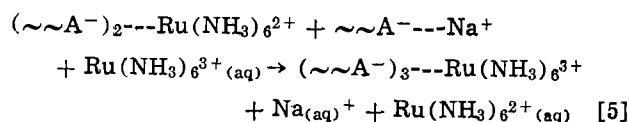
^d Formal potential of the redox couple with the polyelectrolyte coating as obtained from cyclic voltammograms recorded at low scan rate.

* Cp = cyclopentadienide.

for the opposite shifts in formal potential of the Ru(NH₃)₆^{3+/2+} and Os(bpy)₃^{3+/2+} couples upon their incorporation in the polyelectrolyte coatings, the temperature dependences of the formal potentials of the two couples were measured within the coatings and at a bare electrode. The results, plotted in Fig. 4, show that increases in temperature cause the formal potentials for both couples to shift to more negative values within coatings of polyelectrolyte II but in the opposite direction in homogeneous solutions.

The formalism of Weaver *et al.* (9) can be used to evaluate half-reaction entropies for redox couples (ΔS_{rc}°) from the slopes of the lines in Fig. 4. The resulting values are listed in Table III. For Ru(NH₃)₆^{3+/2+}, the value of ΔS_{rc}° at the bare electrode agrees well with that reported by Weaver *et al.* (9), and the value for Os(bpy)₃^{3+/2+} is not far from their value for the isostructural Fe(bpy)₃^{3+/2+} couple (9).

The difference between the values of ΔS_{rc}° at bare and coated electrodes ($\Delta \Delta S_{rc}^\circ$) (Table III) represents the entropy change associated with an overall reaction such as



where $\sim\sim A^-$ represents one of the anionic fixed charge groups of the polyelectrolyte, and (aq) denotes the hydrated ion in the bulk of the solution. The ionic aggregates inside the polyelectrolyte, denoted by $(\sim\sim A^-)_n \text{---Ru(NH}_3)_6^{n+}$, may also be hydrated to an extent that is great enough to affect both their entropies and enthalpies significantly.

The positive values of $\Delta \Delta S_{rc}^\circ$ in Table III show that the substitution for one incorporated cationic complex of its redox partner with the higher charge leads to a net increase in entropy in each case. The corresponding enthalpic differences, $\Delta \Delta H_{298}^\circ$, are positive, strikingly so in the case of polyelectrolyte II. Thus, the preferential incorporation of the more highly charged cations is driven by the large release of entropy.

pH dependence of the incorporation.—The effective pK_a of the carboxylic acid groups in polyelectrolyte II can be inspected by measuring the effect of pH on the incorporation of cations by the polyelectrolyte. Experiments of this type were performed by exposing a coating of polyelectrolyte II to a solution of Ru(NH₃)₆³⁺ which was adjusted to pH values between 1.5 and 5.5. After the incorporation equilibrium had been attained (30 min of exposure proved adequate), the coated electrode was transferred to a pure supporting electrolyte solution at the same pH, and the amount of Ru(NH₃)₆³⁺ retained by the coating was determined by stepping the electrode potential to -0.6V and measuring the total cathodic charge that passed before the current decreased to background levels. The results are shown in Fig. 5. The pH at which the incorporation reaches one-half of its maximum value [only ca. 36% of the total carboxylate groups in the coating bound Ru(NH₃)₆³⁺ cations that were in electronic contact with the electrode] is 2.2. This value is close to the pK_a of 1.9 measured more directly for a similar perfluorocarboxylate polyelectrolyte (13). However, the shape of the plot in Fig. 5 does not match that of a typical pH titration curve. This is presumably because of interactions among the high concentration of carboxylate groups within the polyelectrolyte. Similar behavior was reported recently in coatings of protonated polyvinylpyridine (14). Thus, it is not accurate to identify the pH corresponding to half-maximum incorporation in Fig. 5 with a single pK_a of the functional group. The "effective pK_a " (14) varies with the degree of protonation and with the ionic strength. Nevertheless, it is clear that at pH values as low as 1, protons compete

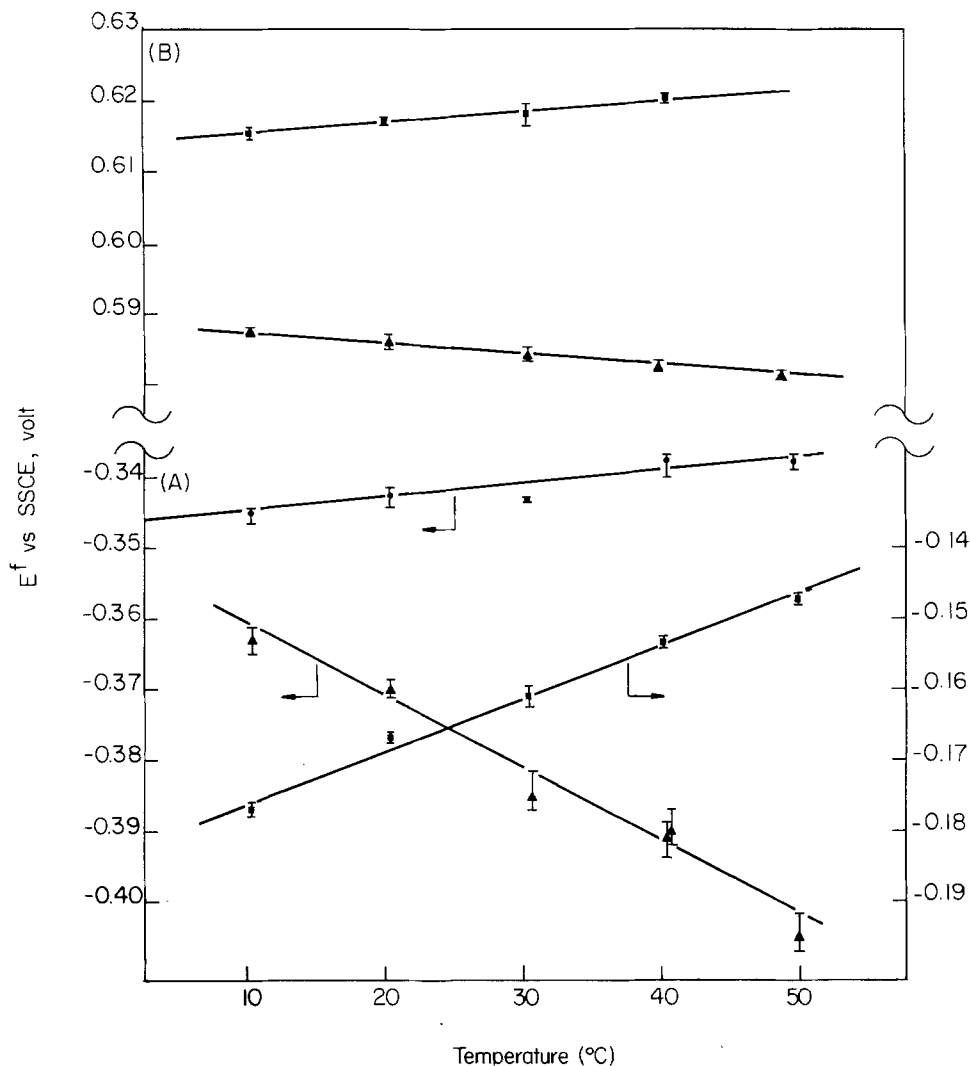


Fig. 4. Temperature dependences of the formal potentials of the $\text{Ru}(\text{NH}_3)_6^{3+/2+}$ and $\text{Os}(\text{bpy})_3^{3+/2+}$ couples. (A) $\text{Ru}(\text{NH}_3)_6^{3+/2+}$. (B) $\text{Os}(\text{bpy})_3^{3+/2+}$. (■) Bare electrode. (▲) Electrode coated with polyelectrolyte (II). (●) Electrode coated with Nafion. Supporting electrolyte: 0.02M CH_3COONa at pH 5.5.

quite successfully with $\text{Ru}(\text{NH}_3)_6^{3+}$ ions for counter-ionic sites within the polyelectrolyte.

Discussion

The combination of data in Tables I and II shows that the equilibrium constants governing the incorporation of cations by coatings of polyelectrolyte II control the changes in the formal potentials of redox couples extracted into the coatings. The trends in the values of $E_p^f - E_s^f (= \Delta E^f)$ in Table II demonstrate that the relative equilibrium binding constants for two halves of a redox couple are not determined solely by the magnitudes of their positive charges. Thus, the $\text{Ru}(\text{NH}_3)_6^{3+/2+}$ and $\text{Os}(\text{bpy})_3^{3+/2+}$ couples involve the same pair of charge types but, at ionic strengths above ca. 0.05M, the formal potentials of the two couples are shifted in opposite directions by incorporation.

The additional factor affecting the incorporation equilibria seems likely to be hydrophobic interactions

between the large fluorocarbon component of the polyelectrolyte coating and the incorporating cations. Previously cited evidence of such hydrophobic interactions has included the blue shift in the fluorescence of $\text{Ru}(\text{bpy})_3^{2+}$ incorporated in Nafion membranes compared with the red shift observed with other, less hydrophobic, polyelectrolytes (15). In addition, the much smaller diffusion coefficients within Nafion coatings of cations surrounded by hydrophobic ligands has been interpreted in terms of a strong interaction between the diffusing ions and the hydrophobic fluorocarbon portions of the interior of the polyelectrolyte (16).

The trends evident in the data of Table II can be rationalized in terms of the relative importance of hydrophobic and electrostatic interactions between the incorporated cations and the polyelectrolyte. For example, at an ionic strength of 0.2M, ΔE^f is positive for $\text{Os}(\text{bpy})_3^{3+/2+}$, near zero for $\text{CpFeCpCH}_2\text{N}(\text{CH}_3)_3^{2+/+}$ and negative for $\text{Ru}(\text{NH}_3)_6^{3+/2+}$. The less highly

Table III. Differences in half-reaction entropies and enthalpies for the $\text{Ru}(\text{NH}_3)_6^{3+/2+}$ and $\text{Os}(\text{bpy})_3^{3+/2+}$ couples in coatings of Nafion and polyelectrolyte II^a

Redox couple	Electrode coating	$\Delta S_{rc}^{\circ b}$ cal/K · mol	$\Delta \Delta S_{rc}^{\circ c}$ cal/K · mol	$\Delta \Delta H_{298}^{\circ d}$ kcal mol ⁻¹	$\Delta \Delta G_{298}^{\circ e}$ kcal mol ⁻¹
$\text{Ru}(\text{NH}_3)_6^{3+/2+}$	Bare	+17.1 (0.99)			
	Nafion II	+4.6 (0.90) -23.5 (0.98)	+12.5 +40.6	-0.36 +7.22	-4.09 -4.88
$\text{Os}(\text{bpy})_3^{3+/2+}$	Bare	+3.5 (0.90)			
	II	-3.8 (0.95)	+7.30	+1.42	-0.75

^a Supporting electrolyte: 0.02M CH_3COONa at pH 5.5.

^b The entropy change for the half-reaction: $\text{M}^{2+} + e^- \rightleftharpoons \text{M}^{3+}$. Calculated from the slopes of the lines in Fig. 4. Linear correlation coefficients are given in parentheses.

^c, ^d, ^e Differences between ΔS_{rc}° , ΔH_{298}° , and ΔG_{298}° at coated and bare electrodes. Calculated from $\Delta \Delta H^{\circ} = \Delta \Delta G^{\circ} - T \Delta \Delta S_{rc}^{\circ}$; $\Delta \Delta G_{298}^{\circ} = -nF \Delta E^f$.

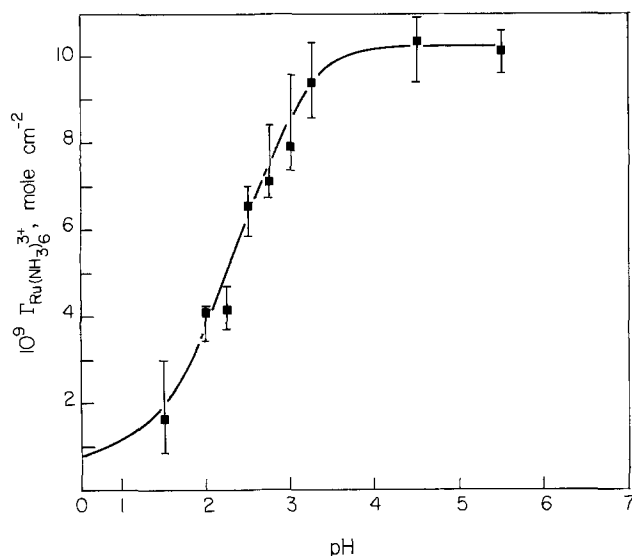


Fig. 5. Incorporation of $\text{Ru}(\text{NH}_3)_6^{3+}$ by polyelectrolyte II as a function of pH. Electrode coating contained 8.4×10^{-8} mol cm^{-2} of carboxylate groups. Electrode was equilibrated for 30 min with a 5 mM solution of $\text{Ru}(\text{NH}_3)_6^{3+}$ at each pH before transfer to pure supporting electrolyte for measurement of the quantity incorporated. Supporting electrolyte: pH ≥ 4.5 : acetate buffer; $2.25 \leq \text{pH} \leq 3.25$: phosphate buffer; pH ≤ 2 : HCl + NaCl. The ionic strength was maintained at 0.2M.

charged (i.e., reduced) form of each couple would be more hydrophobic and therefore would be expected to be preferentially stabilized by hydrophobic interaction compared with its more highly charged (oxidized) partner. By contrast, purely electrostatic stabilizing interactions would act in the opposite direction. Thus, the values of ΔE^f for the three couples listed above indicate the dominance of hydrophobic interactions for $\text{Os}(\text{bpy})_3^{3+/2+}$ and hydrophilic interactions for $\text{Ru}(\text{NH}_3)_6^{3+/2+}$, with the two factors exerting approximately equal and opposite influences in the case of $\text{CpFeCpCH}_2\text{N}(\text{CH}_3)_3^{2+/+}$. This seems chemically reasonable because the order of increasing hydrophobicity of the three redox couples is very likely to be $\text{Os}(\text{bpy})_3^{3+/2+} > \text{CpFeCpCH}_2\text{N}(\text{CH}_3)_3^{2+/+} > \text{Ru}(\text{NH}_3)_6^{3+/2+}$.

The effects of changes in ionic strength on the values of ΔE^f in Table II for the $\text{Ru}(\text{NH}_3)_6^{3+/2+}$ and $\text{Os}(\text{bpy})_3^{3+/2+}$ couples can be understood on the same basis. Alterations in the intensity of hydrophobic interactions produced by changes in ionic strength are not likely to be as large as the expected (17) decreases in electrostatic interaction as the ionic strength increases. The latter changes can be substantial as the behavior of the $\text{Os}(\text{bpy})_3^{3+/2+}$ couple indicates. In 2M supporting electrolyte, ΔE^f is most positive, pointing to the strongest hydrophobic stabilization, while in 0.02M solutions ΔE^f becomes slightly negative, suggesting that under these conditions the strength of the electrostatic interaction has increased sufficiently to overcome the hydrophobic factors that act in the opposite direction. The much more hydrophilic $\text{Ru}(\text{NH}_3)_6^{3+/2+}$ couple exhibits ΔE^f values that reflect dominance by electrostatic interactions at all ionic strengths. The intensity of these interactions is evidently quite large for this couple, as indicated by the unusually large value of ΔE^f in the 0.02M electrolyte.

ΔE^f was also measured for the $\text{Ru}(\text{NH}_3)_6^{3+/2+}$ couple at 0.2M ionic strength in Nafion coatings. The value observed was -100 mV, compared with -164 mV for polyelectrolyte II under the same conditions. Similar differences exist between the strength of the binding of alkali cations by ion-exchange resins based on sulfonate and carboxylate groups (18). The behavioral difference has been ascribed to differences in the struc-

ture of the primary hydration spheres of the cations induced by the two types of anionic binding groups (18). In the present case, where hydrophobic and electrostatic factors are also believed to influence the strength of cation binding, the difference in ΔE^f for Nafion and polyelectrolyte II for the $\text{Ru}(\text{NH}_3)_6^{3+/2+}$ couple may reflect a greater control by electrostatic binding in the latter coating.

The entropic control of the incorporation equilibria revealed in the data of Table III suggests a primary role for water molecules in the overall incorporation process. This accords with several previous studies of cation binding by polyanionic electrolytes (19), in which evidence was presented for the release of water molecules from both the charged binding sites and the hydration spheres of the bound cations. The large negative value of ΔS_{rc}° for the $\text{Ru}(\text{NH}_3)_6^{3+/2+}$ couple in polyelectrolyte II signals an unusual ionic and solvation environment for the couple in this polyelectrolyte. The binding of the $\text{Ru}(\text{NH}_3)_6^{3+/2+}$ couple by Nafion produces much smaller value of $\Delta \Delta S_{rc}^\circ$ than for binding to the polycarboxylate, II. This may be a reflection of a higher charge density on the fixed anionic sites in II compared with Nafion. This could produce tighter ion pairing with multiply charged cations within polyelectrolyte II and greater loss of water molecules from the outer coordination spheres of the incorporated complexes. Differences in the partial molar volumes of sulfonate and carboxylate bearing polyelectrolytes upon incorporation of cations were explained in similar terms by Tondre and Zana (19d).

The positive value of $\Delta \Delta H^\circ$ for incorporation of the $\text{Ru}(\text{NH}_3)_6^{3+/2+}$ couple by polyelectrolyte II (Table III) represents the net result of a variety of coulombic and dipolar interactions whose individual contribution to the measured values of $\Delta \Delta H_{298}^\circ$ it would be extremely difficult to disentangle. However, it may be worth noting that the behavior we have observed is similar to that reported for the incorporation from aqueous solution of an organic sulfonate (8-anilino-1-naphthalene sulfonate) by the hydrophobic portion of a block copolymer of polyethylene oxide and poly(2-hydroxyethyl methacrylate) (20). The incorporation, which is free of direct electrostatic binding between fixed charge groups and the incorporating ions, is also governed by a positive entropy change that overcomes a corresponding increase in enthalpy. Differences in the ion-dipole interaction energies between the incorporating ion and water molecules inside and outside the polymer may make important contributions to the enthalpy changes in both this instance and the incorporation of the $\text{Ru}(\text{NH}_3)_6^{3+/2+}$ couple by polyelectrolyte II. In any case, the point to be derived from the present study is that the factors governing the relative binding interactions of polyelectrolytes and complex ions can involve much more than the relative charge densities of the latter.

Acknowledgments

This work was supported by the U.S. Army Research Office. Dr. H. Zumbrennen offered many helpful suggestions during early stages of this work. We thank Asahi Glass Company, Tokyo, for a sample of polyelectrolyte II.

Manuscript submitted May 20, 1983; revised manuscript received Sept. 23, 1983.

REFERENCES

1. N. Oyama, T. Shimomura, K. Shigehara, and F. C. Anson, *J. Electroanal. Chem. Interfacial Electrochem.*, **112**, 271 (1980).
2. K.-N. Kuo and R. W. Murray, *ibid.*, **131**, 37 (1982).
3. H. Braun, W. Storck, and K. Doblhofer, *This Journal*, **130**, 807 (1983).
4. D. A. Buttry and F. C. Anson, *J. Am. Chem. Soc.*, **104**, 4824 (1982).
5. N. Oyama and F. C. Anson, *ibid.*, **101**, 3450 (1979).

6. R. G. Gaunter and H. Taube, *Inorg. Chem.*, **9**, 2627 (1970).
7. C. Creutz, M. Chou, T. L. Netzel, M. Okumura, and N. J. Sutin, *J. Am. Chem. Soc.*, **102**, 1309 (1980).
8. A. J. Bard and L. R. Faulkner, "Electrochemical Methods," p. 536, John Wiley and Sons, Inc., New York (1980).
9. E. L. Yee, R. J. Cave, K. L. Guyer, P. D. Tyma, and M. J. Weaver, *J. Am. Chem. Soc.*, **101**, 1131 (1979).
10. (a) N. Sutin, M. J. Weaver, and E. L. Yee, *Inorg. Chem.*, **19**, 1096 (1980); (b) E. L. Yee and M. J. Weaver, *ibid.*, **19**, 1077 (1980); (c) M. J. Weaver and S. M. Nettles, *ibid.*, **19**, 1641 (1980); (d) S. Sahami and M. J. Weaver, *J. Electroanal. Chem. Interfacial Electrochem.*, **122**, 155, 171 (1981); (e) V. T. Taniguchi, W. R. Ellis, Jr., V. Cammarata, J. Webb, F. C. Anson, and H. B. Gray, *Adv. Chem. Ser.*, **201**, 51 (1982).
11. N. Oyama and F. C. Anson, *This Journal*, **127**, 640 (1980).
12. A. J. Bard and L. R. Faulkner, "Electrochemical Methods," Chap. 6, John Wiley and Sons, New York (1980).
13. Z. Twardowski, H. L. Yeager, and B. O'Dell, *This Journal*, **129**, 328 (1982).
14. H. Zumbrennen and F. C. Anson, *J. Electroanal. Chem. Interfacial Electrochem.*, **152**, 111 (1983).
15. P. C. Lee and D. Meisel, *J. Am. Chem. Soc.*, **102**, 5477 (1980).
16. D. A. Buttry and F. C. Anson, *ibid.*, **105**, 685 (1983).
17. F. G. Helfferich, "Ion Exchangers," Chap. 4, McGraw-Hill, New York (1962).
18. (a) H. Morawetz, "Macromolecules in Solution," 2nd ed., p. 369, John Wiley and Sons, New York (1975); (b) L. Lazare, B. R. Sundheim, and H. P. Gregor, *J. Phys. Chem.*, **60**, 641 (1956); (c) I. Michalei and A. Katchalsky, *J. Polym. Sci.*, **23**, 683 (1957); (d) F. Nelson and K. A. Kraus, *J. Am. Chem. Soc.*, **80**, 4154 (1958); (e) M. H. Gottlieb and H. P. Gregor, *ibid.*, **76**, 4639 (1954).
19. (a) G. E. Boyd and D. P. Wilson, *Macromolecules*, **15**, 78 (1982); (b) M. Finaudo and M. Milas, *ibid.*, **6**, 879 (1973); (c) J. Hen and U. P. Strauss, *J. Phys. Chem.*, **78**, 1013 (1974); (d) C. Tondre and R. Zana, *ibid.*, **76**, 3451 (1972).
20. M. Ikemi, N. Odagiri, and I. Shinohara, *Polymer J.*, **12**, 777 (1980).

Measurements of the Steady-State Activation Overpotential of Chlorine Evolving Electrodes

I. V. Kadija

Olin Corporation, Metals Research Laboratories, New Haven, Connecticut 06511

ABSTRACT

Detailed measurements of interfacial concentration and concentration overpotential of chlorine evolving platinized platinum electrodes were performed in 4.9M NaCl, at 25°C and 1 atm chlorine or 1 atm nitrogen in the cell. Based on these and electrode polarization measurements, steady-state activation overpotential curves were obtained. The applied method enabled for the first time in this field, development of true steady-state activation overpotential curves. Our findings indicated that 30-40 mV/decade slopes typically obtained in nitrogen atmosphere were essentially a sequence of quasi equilibria at the electrode interface. Also, micropolarization data obtained near the open circuit with chlorine atmosphere in the cell were found to be a concentration overpotential phenomenon. The true activation overpotential was found to become a significant part of the electrode polarization only after it exceeded several millivolts in chlorine saturated brine. In nitrogen saturated brine, where the open circuit was undefined, the activation overpotential became significant for polarizations that exceeded two decades of steady-state low current density polarization. In this case, the activation overpotential was observable as a departure from a 32 mV/decade slope. The obtained activation overpotential curves can be used as a base for developing kinetic parameters, however, a considerably greater emphasis than in the past must be given to the corresponding interfacial conditions.

A steady-state electrochemical reaction brings about a concentration gradient across the interface. Assuming a charge transfer reaction virtually at equilibrium, the concentration overpotential is defined (1) as the difference between the steady-state potential and the potential across the interface obtained at the open circuit (equilibrium potential). Using activity terms rather than concentration in the Nernst equation, the concentration overpotential (η_c) for an electronation reaction can be expressed in the following form

$$\eta_c = \frac{RT}{nF} \ln \frac{a_{x=0}}{a^0} \quad [1]$$

where $a_{x=0}$ is the activity of the reacting species at the interface in g ions/l, and a^0 is the activity of the same species in the bulk in g ions/l. According to the Fick's law of steady-state diffusion, assuming a known and virtually constant activity coefficient, $a^0 - a_{x=0}$ is proportional to the current density

$$a^0 - a_{x=0} = - \frac{i\delta}{nFD} \times 10^3 \quad [2]$$

where i is the current density in A/cm², δ is the diffusion layer thickness in cm, and D is the diffusion co-

efficient of the reacting species in cm²/s. By introducing Eq. [2] in Eq. [1], one obtains

$$\eta_c = \frac{RT}{nF} \ln \left(1 + \frac{10^3 i \delta}{nFD a^0} \right) \quad [3]$$

An inherent property¹ of expression [3] is the η_c 's linear dependence on current density for small values of $10^3 \frac{i\delta}{nFD} / a^0$. For such operating conditions, Eq. [3] may be written as

$$\eta_c = i \frac{RT\delta 10^3}{n^2 F^2 D a^0} \quad [4]$$

or

$$\eta_c = K \cdot i$$

where

$$K = \frac{RT\delta 10^3}{n^2 F^2 D a^0}$$

For example, for a single electron charge transfer reaction for $a^0 = 1$ g ion/l, $F = 9.65 \times 10^4$ As/g ion, $D = 10^{-5}$ cm²/s at current density of 10^{-3} A/cm², and

¹ $\ln(1 \pm x) = \pm x$
 $x \rightarrow 0$

$\delta = 10^{-2}$ cm, one obtains $\eta_c = 0.61$ mV. The linear dependence exists up to seven times higher current density giving 4.2 mV. The given example corresponds to a situation frequently encountered in electrochemical investigations, i.e., 1 g ion/l concentration of reacting species, current density of several mA/cm², and depending on the stirring rate, diffusion layer thickness of 50–200 μ . Hence, concentration polarization is present throughout the experiment. Its true value, however, may be determined only by means of retrofitting the necessary information into Eq. [4] or even more accurately, since Fick's law is an approximation, by applying the true value of $a_{x=0}$ in Eq. [1].

In a similar approach, the low field approximation of the Butler-Volmer equation is frequently being used for establishing the kinetic parameters of electrochemical reactions (1)

$$i = \frac{i_0 F \eta_A}{RT} \quad [5]$$

($-0.01 < \eta_A < +0.01$) where η_A is the activation overpotential. Equation [5] expresses the linear relationship between the activation overpotential and the current density if the electrode potential is close to the equilibrium potential established in the particular electrode/electrolyte system.

Now, both Eq. [4] and [5] are applicable to the same system and in the same polarization range. In the presence of both, concentration and activation polarization, there is a linear relationship between the current and the polarization. Clearly, the overall polarization will be the arithmetic sum of the two overpotentials. Eventually, one may make use of Eq. [5] if η_c is measured and its relevance determined.

The role of the concentration overpotential becomes even more important for the investigation of the kinetics of reversible reactions with electrode potential depending on both reactant and product species activity. For example, for a redox couple $A^{n+}/A^{(n-1)+}$ one can write the concentration overpotential expression as

$$\eta_c = \frac{RT}{nF} \left[\ln \frac{a_{A^{(n-1)+}}}{a_{A^{(n-1)+, x=0}}} + \ln \frac{a_{A^{n+}, x=0}}{a_{A^{n+}}} \right] \quad [6]$$

Since in this case the same applied current generates interfacial activity changes for both species, it is necessary to be very accurate in identifying these changes at the instant of taking polarization data. In an example analogous to the one above with both species having a bulk activity of 1 g ion/l, a current of 7×10^{-3} A/cm² will generate 8.4 mV of concentration overpotential. If, however, one of the species is one order of magnitude lower in bulk activity, its interfacial activity change becomes considerable. In that case, we must use Eq. [3] to describe concentration overpotential which in turn follows the logarithmic dependence. For example, by doubling the one species' interfacial activity, one obtains $RT/F \ln 2 = 20$ mV for concentration overpotential. Hence, the species with the lower bulk activity becomes the predominant factor in establishing the concentration overpotential.

Since its measurement introduces considerable complexity to the logistics of the electrochemical investigation, the interfacial activity change of the reacting species is typically presumed to be negligible in the literature. "Sufficient stirring" with a rotating disk, fast flowing electrolytes, or other means is regularly introduced as an *a priori* method to eliminate the concentration gradient. Also typical is the transient method approach where the current-voltage measurements are made prior to the establishment of the steady-state concentration gradient.

However, the above-mentioned methods are usually overestimated concerning their effectiveness in eliminating the concentration polarization. In essence, the interfacial activity deviation from the bulk values is

always present and its relevance to the experimenter's conclusions can be determined only upon detailed measurements of the changes or at least upon a thorough investigation of the mass transport conditions at the interface. Recently, the International Union of Pure and Applied Chemistry, Commission on Electrochemistry, has issued a set of recommendations concerning publishing of the information obtained in investigations of electrode reaction values, transfer coefficients, and rate constants (2). "In view of the complications and confusion which exist in the literature," several suggested basic recommendations put the emphasis on having mass transport and interfacial concentration rigorously controlled and defined.

In the chlor-alkali industry, noble metal-coated titanium anodes provide an excellent substrate for a reversible chlorine/chloride reaction. In such cases, the concentration overpotential can be described with an expression similar to Eq. [6]

$$\eta_c = \frac{RT}{F} \ln \frac{a_{Cl^-}}{a_{Cl^-, x=0}} + \frac{RT}{2F} \ln \frac{a_{Cl_2, x=0}}{a_{Cl_2}} \quad [7]$$

Throughout the existing literature dealing with this subject, in interpreting the current/voltage curves, the electrode equilibrium potential is typically expressed through the chlorine partial pressure, Eq. [8]. By this means, the interfacial chlorine activity $a_{Cl_2, x=0}$ had forever lost its identity being locked into a presumed chlorine equilibrium between the gaseous and the liquid phase. Since the partial pressure over the electrolyzer stays virtually constant throughout the experiment, one may be easily brought to the conclusion that $a_{Cl_2, x=0}$ is always equal to the bulk activity, a_{Cl_2} .

In reality, on a chlorine or any other gas producing surface, one cannot identify the charge transfer sites with gas phase nucleating sites. Typically, the catalytic electrode surface, on an atom scale level, has a density of 10^6 – 10^{12} /cm² of charge transfer sites while the number of gas nucleating sites, on a macroscale, is considerably smaller and ranges from 10^2 to 10^5 /cm². The separation between the two brings up mass transport limitation leading to considerable chlorine supersaturation at the interface (3–8). Clearly, the brine saturation by sparging 1 atm Cl₂ through the electrolyte will have no bearing on the chlorine transport phenomena at the interface in a steady state. Moreover, considerable supersaturation at the interface can cause minor but measurable supersaturation in the bulk since measurably large flux of supersaturated chlorine can diffuse into the bulk without being disengaged by bubbles at the interface. Examples of this mechanism are well demonstrated with high speed movie camera and double ring disk measurements of other gas evolving reactions (4).

In our first contribution (11) we have measured chlorine interfacial concentration in three different sets of chlorine partial pressure and bulk pH conditions; Cl₂ sparged chlor-alkali cell (Cl₂ partial pressure 0.96 atm), N₂ sparged chlor-alkali cell (Cl₂ partial pressure 0.0 atm), and in chlorate cell conditions at pH 7 (Cl₂ partial pressure 0.01 atm). With fixed thickness of diffusion layer at 23 μ , we have shown that the chlorine interfacial concentration follows linearly the current density regardless of the chlorine partial pressure. Furthermore, in the case of a chlorine-saturated chlor-alkali cell, we have measured chlorine bulk activity which exceeded gas/liquid equilibrium. Hence, it was demonstrated that one may not use chlorine partial pressure but only the interfacial chlorine activity as information relevant to the concentration polarization.

This manuscript deals with the chlorine concentration overpotential as a function of the diffusion layer thickness. It also establishes experimentally verified constants applicable to the concentration overpotential measurements for chlorine evolution investiga-

tion at 25°C in 4.9M brine. This information has practical value in establishing the actual activation overpotential if the diffusion layer thickness is known.

Experimental Method

Janssen and Hoogland (9) have shown that diffusion layer thickness is a function of current density that is evidently a result of the varying bubble dynamics. In order to measure the concentration polarization dependence on diffusion layer thickness, one must have a current independent means for controlling the magnitude of the latter. Based on the previous findings (4, 10, 11), we have selected the rotating double ring disk system. Here diffusion layer thickness can be varied independently from the rate of the gas producing reaction. In this perspective, the information given throughout the manuscript is different from the one that may be obtained at a stationary electrode. A diminishing diffusion layer thickness with increasing current density with a stationary system would require diffusion layer thickness analysis from one to another steady state (9).

The experimental method was described earlier (11) in detail. Briefly, it contains the following steps: First, the required diffusion layer thickness was established by fixing the rotating ring disk system at a constant rotation speed. Secondly, from a power supply, an anodic and constant current density was established at the inner ring which served as the operating electrode. Typically, the electrode potential was reached within 1s or less. However, the potential reading was made after at least 3 min have elapsed since the polarographic measurement at the outer ring required 2-3 min to be performed. We have polarographically analyzed the molecular chlorine interfacial concentration by means of the outer ring's independent circuit. The limiting currents for molecular chlorine reduction at the outer ring were proportional to the concentration of molecular chlorine at the operating inner ring's interface (11). An accuracy of $\pm 2\%$ enabled a detailed measurement of the interfacial changes. By means of the activity coefficient and the interfacial concentration, we have calculated the actual steady-state concentration overpotential and used it for establishing the activation overpotential under various hydrodynamic conditions at two rotating ring electrodes.

In experiments performed with the outer ring as an operating electrode, there were no simultaneous measurements of interfacial concentration due to the logistics of the rotating double ring system operation. Presented data are based on the measured polarization and the concentration changes calculated from our previously verified equation [Eq. [7], Ref. (11)].

Since a tenfold increase in chlorine activity gives only 29.5 mV change in the operating electrode potential, we have increased our accuracy by having sets of three Ag/AgCl and three SCE reference electrodes. IR drop corrections were made by current interruption methods. The apparatus was thermostated at $25.0 \pm 0.5^\circ\text{C}$. Special care was taken to avoid supersaturation in the bulk since the analytical outer ring measures the total concentration (11). We restricted our currents to less than 100 mA. We introduced Cl_2 or N_2 bubblers to increase the chlorine disengagement from the bulk. Frequent checks of the limiting current for molecular chlorine reduction at the outer ring at no current from the inner ring was used as a measure of the bulk saturation level (11). Chlorine and nitrogen partial pressure above the solution were 0.95-0.97 atm. All the curves have been reproduced at least three times. Increasing and decreasing current steady-state polarization measurements were within ± 0.7 mV.

Diffusion layer thickness selection.—Janssen and Hoogland (9) have shown that for a range of current densities between 0.1-1.0 A/cm² diffusion layer thick-

ness of a chlorine producing anode at 25°C varies within 60-10 μ , respectively. Hence, we have selected the range of diffusion layer thickness between 15-50 μ since it reflects most accurately the ones obtainable in industrial practice or in experiments with rotating disks.

pH range selection.—In the majority of chlor-alkali operations, the steady-state anolyte pH varies from pH 4.5 to 2.0. Operating with a 95-99% efficiency for chlorine reaction, the interface is typically more acidic than the bulk anolyte due to the 1% to 5% current efficiency in oxygen evolution from water. In view of the potentially variable bulk pH, we have conducted the majority of our chlor-alkali experiments within a pH range of 0.5-2.0. Yokoyama *et al.* (22) have reasonably used a similar range to avoid significant hypochlorite formation. Based on our previous findings (11), however, this change does not introduce any measurable variation in the interfacial saturation phenomena.

Results

The solid N_2 curves in Fig. 1 and 2 are the polarization curves obtained at various rotation speeds on the inner and outer rings, respectively, with N_2 atmosphere in the anolyte. At lower current densities (less than 20 mA/cm²), we have obtained parallel lines with both rings. The average slope of the lines was 32 ± 1 mV/decade.

Solid Cl_2 curves shown in Fig. 1 and 2 describe the polarization curves on the inner and outer rings, respectively, with Cl_2 atmosphere in the anolyte. At higher current densities, these coincide with the N_2 atmosphere curves at corresponding rotation speeds. We have obtained an open-circuit potential of 1.073 ± 0.001 (V) vs. SCE.

Figure 3 shows the change in electrode polarization in N_2 atmosphere as a function of diffusion layer thick-

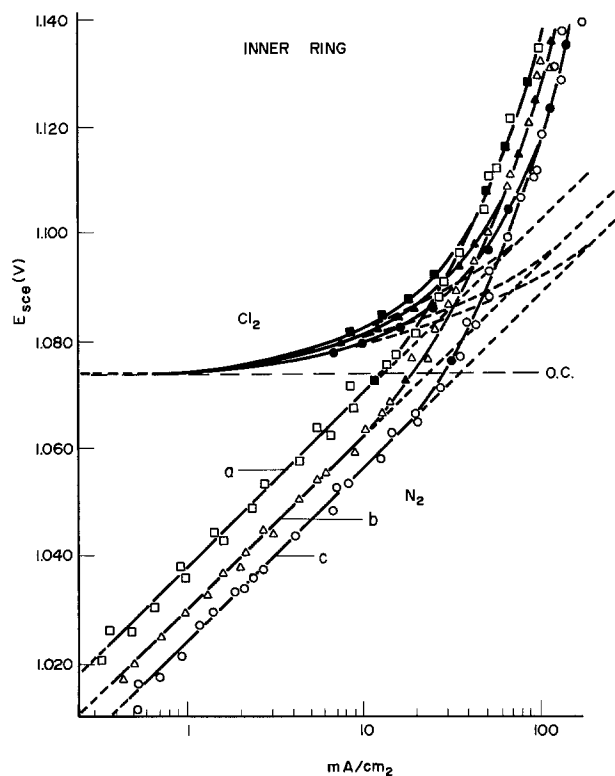


Fig. 1. Inner ring: steady-state polarization curves. Electrolyte saturated with, N_2 -nitrogen, Cl_2 -chlorine, 0.95-0.97 atm. Full lines are experimental curves, dashed lines are theoretical curves for concentration polarization based on measured interfacial concentration of molecular chlorine for N_2 (Eq. [15]), Cl_2 (Eq. [21]), (a) 518, (b) 1770, and (c) 4628 rpm.

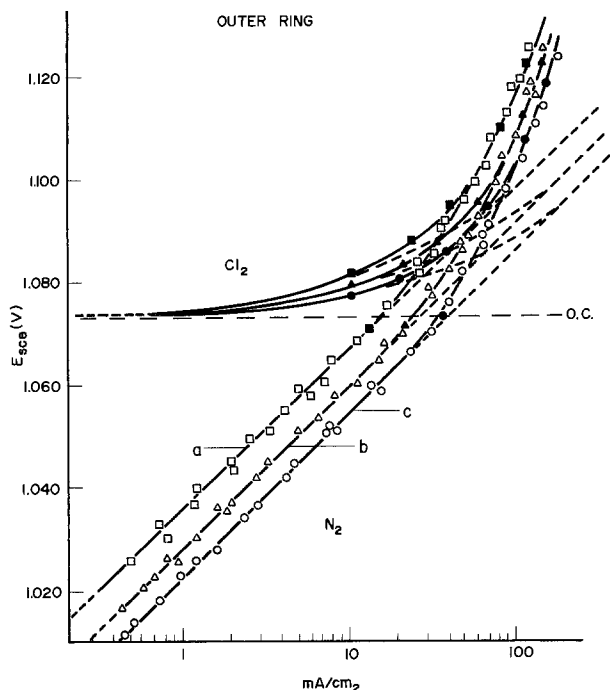


Fig. 2. Outer ring: steady-state polarization curves. Electrolyte saturated with, N_2 -nitrogen, Cl_2 -chlorine, 0.95-0.97 atm. Full lines are experimental curves, dashed lines are theoretical curves based on calculated interfacial concentration of molecular chlorine for N_2 (Eq. [15]), Cl_2 (Eq. [21]), (a) 518, (b) 1770, and (c) 4625 rpm.

ness at constant current density. We have chosen three current densities: 0.7, 2.4, and 9.6 mA/cm^2 .

For the inner ring as an operating anode in both Cl_2 and N_2 saturated anolytes, our measurements of interfacial chlorine concentration have reproduced our previously reported findings and confirmed Eq. [7], Ref. (11).

Discussion

Open-circuit conditions.—The equilibrium potential of a chlorine/chloride electrode can be described by means of the chlorine partial pressure, Eq. [8], as well as by means of the chlorine activity, Eq. [9]

$$E_{Cl_2/Cl^-} = E^{\circ}_{Cl_2 g/Cl^-} + \frac{RT}{2F} \ln P_{Cl_2} - \frac{RT}{F} \ln (m_{Cl^-} \gamma_{Cl^-}) \quad [8]$$

where $E^{\circ}_{Cl_2 g/Cl^-} = 1.3583V$ (12, 13), and

$$E_{Cl_2/Cl^-} = E^{\circ}_{Cl_2 aq/Cl^-} + \frac{RT}{2F} \ln (m_{Cl_2} \gamma_{Cl_2}) - \frac{RT}{F} \ln (m_{Cl^-} \gamma_{Cl^-}) \quad [9]$$

where $E^{\circ}_{Cl_2 aq/Cl^-} = 1.395$ (12)

At the open circuit in a nitrogen-saturated cell, since there is no molecular chlorine, the potential is not defined. The electrode potential fluctuates depending on the electrochemical activity of platinum oxides. However, in a chlorine-saturated cell the reversible chlorine/chloride system is established. By introducing numerical values into Eq. [8], one obtains

$$E_{Cl_2/Cl^-} = 1.3583 + 0.0295 \log (0.96 \pm 0.01) - 0.059 \log (5.45 \times 0.92) \quad [10]$$

$$E_{Cl_2/Cl^-} = 1.317 \pm 0.0005V$$

or,

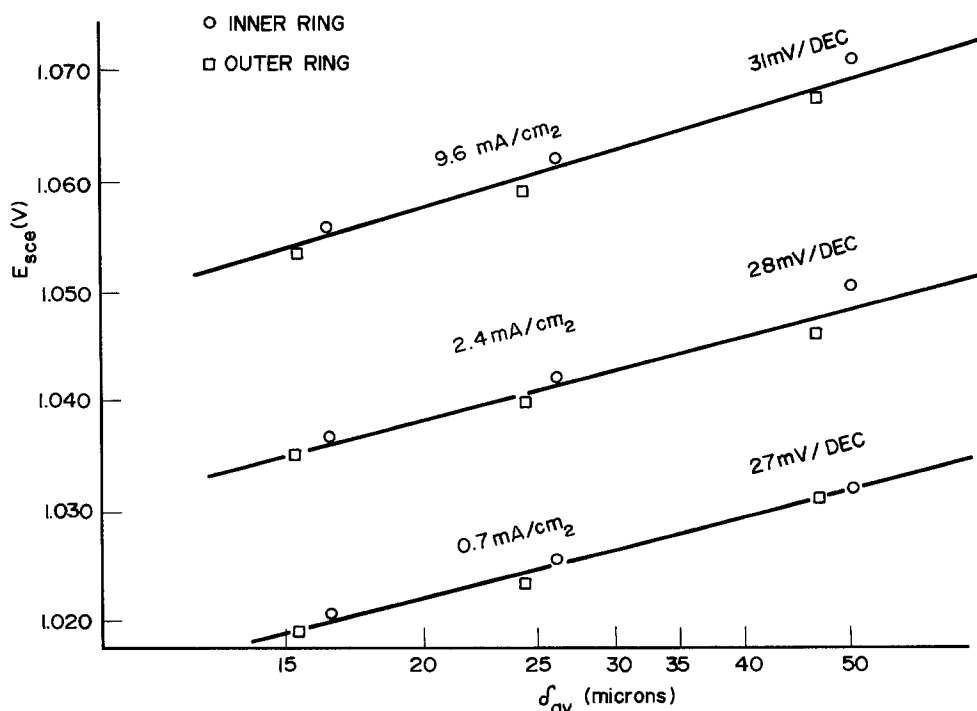
$$E_{Cl_2/Cl^-} = 1.073 \pm 0.0005V \text{ vs. SCE}$$

where 5.45 is the molality of brine and 0.92 is the coefficient of activity of the chloride ion (14). The experimental value of $1.073 \pm 0.001V$ is in good agreement with the theoretically calculated one based on Cl_2 partial pressure.

Equation [9], however, requires the measurement of the molecular chlorine activity in solution. Three species are conceivably coexisting in a solution where chlorine is being dissolved. These are Cl_2 , $HClO$, and Cl_3^- . Following Sherrill's and Izard's (15) and Yokota's (16) measurements, the $HClO$ concentration presents only 1% or less of the total Cl_2 dissolved in our operating conditions. Concerning Cl_3^- we have given the same treatment as if it were active Cl_2 . This approximation has been made previously by Yokota (16).

We have calculated the activity coefficient from the ratio of chlorine solubility in pure water and brine

Fig. 3. N_2 saturated electrolyte, inner and outer ring. Experimental data of electrode polarization at constant current density and variable diffusion layer thickness, $(dE_c/d \ln \delta)_i$.



assuming the 1.0 atm pressure of chlorine, as recommended by Sherrill and Izard (15)

$$\gamma_{\text{Cl}_2} = \frac{m^w_{\text{Cl}_2}}{m^1_{\text{Cl}_2}} = \frac{0.0592(15)}{0.0256} = 2.31 \quad [11]$$

By introducing numerical values in Eq. [9] one obtains

$$E_{\text{Cl}_2/\text{Cl}^-} = 1.3950 + 0.0295 \log \frac{(0.022 \times 2.31)}{0.894} - 0.059 \log (5.45 \times 0.92) \quad [12]$$

$$E_{\text{Cl}_2/\text{Cl}^-} = 1.3175 \pm 0.0005\text{V} \\ = 1.0735 \pm 0.0005\text{V vs. SCE}$$

The above value is also in a good agreement with the experimentally obtained value, $1.073 \pm 0.001\text{V vs. SCE}$.

Operating conditions.—Once the chlorine production starts in a nitrogen saturated anolyte, the reversible chlorine/chloride reaction can occur even though the bulk chlorine activity and chlorine partial pressure are virtually zero. At any given steady state, the interfacial electrolyte has a certain chlorine activity defined by current density and mass transport conditions. Assuming the bulk chlorine activity to be zero, the interfacial concentration is described by Eq. [7] of Ref. (11) with the first term of the equation equal to zero

$$C_{\text{Cl}_2, x=0} = 4.3 \times 10^2 \cdot i \cdot \delta \quad [13]$$

where i is the current density in A/cm^2 and δ is the diffusion layer thickness in centimeters. Equation [13] is analogous to Eq. [2] with bulk chlorine concentration being zero. To obtain molality of the concentration, one must divide Eq. [13] by 0.894. Furthermore, to calculate the activity of the interfacial chlorine one must apply the activity coefficient that may be applicable for the investigated range of chlorine concentrations. Yokota (16), Smirnov and Aliev (17), and Hine and Inuta (18) have shown for concentrated solutions that the linear dependence between pressure and solubility is preserved for pressure ranging from 0.1 to 6.0 atm. Also, by simulating partial pressure/liquid phase equilibria, we have conducted several calculations with the commercially available computer program (14) and found that the activity coefficient stays within $\pm 1\%$ of 2.11 for our measured range of C_{Cl_2} . Although value 2.11 would not introduce any significant departure in our calculation, we have used our value of activity coefficient $\gamma_{\text{Cl}_2} = 2.31$. Hence, Eq. [13] can be converted to describe chlorine activity change as a function of current density and diffusion layer thickness at the interface

$$m_{\text{Cl}_2} \cdot \gamma_{\text{Cl}_2} = \frac{C_{\text{Cl}_2, x=0}}{0.894} \times 2.31 = (1.11 \pm 0.03) \times 10^3 \cdot i \cdot \delta \left(\frac{M}{1000 \text{ g H}_2\text{O}} \right) \quad [14]$$

In Fig. 1 and 2, the N_2 solid curves show experimental polarization curves on two rings at three different rotation speeds. Dashed lines are drawn based on Eq. [15] obtained by combining Eq. [14] with Eq. [9]

$$E_C = 1.3537 + \frac{RT}{2F} \ln [(1.11 \pm 0.03) \times 10^3 \cdot i \cdot \delta] \quad [15]$$

where E_C is the electrode steady-state potential due to the chlorine activity² at the interface. Dashed lines, Eq. [15], and experimental N_2 curves coincide for each rotation speed indicating that our polarization is essentially a result of an interfacial chlorine activity change with current density and diffusion layer thickness. One may notice, however, that the expression [9] used

² Chloride ion activity term is assumed constant as discussed previously (11). Therefore, $1.395 - 0.041 = 1.354\text{V}$ is the electrode potential for the unit molecular chlorine activity.

in deriving Eq. [15] represents the equilibrium potential dependence on chlorine and chloride species activity. Naturally, since our open circuit is undefined, expression [15] represents the quasi-equilibrium steady-state polarization curves which, in the absence of activation overpotential, can have and indeed have virtually the same values as the ones obtainable in a set of equilibrium conditions with bulk activities identical to the ones at the interface during the steady-state operation. Furthermore, in Table I, we have listed the calculated currents that would, following Eq. [13], give 0.022 M/l chlorine saturation in the adjacent electrolyte. Such concentration exists in the bulk electrolyte if we saturate the solution with chlorine at partial pressure of 0.96 ± 0.01 atm. A dashed vertical line from our open-circuit conditions ($0.96 \pm 0.01 \text{ Cl}_2$, 1.073 vs. SCE) intercepts the polarization curves obtained in N_2 atmosphere with a considerable accuracy at current densities listed in Table I.

In addition, our experimental curves, Fig. 1 and 2 (N_2 lines), and Fig. 3 show polarization slopes of 32 mV/decade and 28.5 mV/decade, respectively. From Eq. [15] one obtains theoretical slopes of 29.5 mV/decade for each

$$\left(\frac{dE_C}{d \ln i} \right) = 29.5 \text{ mV/decade} \quad [16]$$

$$\left(\frac{dE_C}{d \ln \delta} \right) = 29.5 \text{ mV/decade} \quad [17]$$

In a cell equilibrated with the 0.95–0.97 atm Cl_2 , the steady-state interfacial activity is the sum of the bulk chlorine activity and the interfacial activity increment resulting from the electrochemical chlorine generation

$$a_{\text{Cl}_2, x=0} = a^0_{\text{Cl}_2} + (1.11 \pm 0.03) \times 10^3 \cdot i \cdot \delta \quad [18]$$

where $a^0_{\text{Cl}_2} = \frac{0.022 \times 2.31}{0.894}$ from Eq. [12]. Eq. [18] is analogous to Eq. [2].

In this case, expression [7] describes the concentration overpotential. By replacing $a^0_{\text{Cl}^-}/a_{\text{Cl}^-, x=0} = 1$, and

$$\frac{a_{\text{Cl}_2, x=0}}{a_{\text{Cl}_2}} = \frac{a^0_{\text{Cl}_2} + (1.11 \pm 0.03) \times 10^3 \cdot i \cdot \delta}{a_{\text{Cl}_2}} \quad [19]$$

one obtains

$$\eta_c = \frac{RT}{2F} \ln \left[1 + \frac{(1.11 \pm 0.03) \times 10^3 \cdot i \cdot \delta}{0.0568} \right] \quad [20]$$

For the purpose of comparison with the nitrogen-saturated brine data we have plotted the experimental current voltage curves on the same graph (Cl_2 solid curves). The corresponding concentration polarization curve is described with Eq. [21] which is the sum of Eq. [9] and [20]

$$E_C = E_{\text{Cl}_2/\text{Cl}^-} + \eta_c \\ = 1.354 + \frac{RT}{2F} \ln [0.0568 + (1.11 \pm 0.03) \times 10^3 \cdot i \cdot \delta] \quad [21]$$

Up to a polarization of 6–8 mV, the dashed lines, based on Eq. [21], and the full lines (Cl_2 curves) from

Table I. Currents that generate 0.022 M/l molecular chlorine saturation in the anode adjacent electrolyte (N_2 in bulk)

	RPM	Avg δ	i Calculated	i Experimental	% Accuracy
Inner ring	4625	16.3	31.6	28.9 ± 1	92
	1770	26.4	19.4	17.1 ± 0.5	88
	518	49.6	10.3	11.0 ± 0.5	94
Outer ring	4625	15.2	33.6	33.6 ± 1	100
	1770	24.7	20.7	23.1 ± 0.5	90
	518	46.1	11.1	12.4 ± 0.5	90

our experimental measurements are virtually identical. Hence, up to 6-8 mV our polarization is essentially a result of the concentration gradient generated by chlorine evolution from the electrode surface. Furthermore, Table II shows the experimentally obtained polarizations from the open circuit at the same current densities as in Table I. These currents generate a supersaturation of 0.022 M/l of molecular chlorine in the adjacent electrolyte. Theoretically, from Eq. [20], one can calculate a polarization of 8.9 mV due to the interfacial concentration gradient from 0.022 to 0.044 M/l.

At lower rotation speeds and thicker diffusion layers, supersaturation can be reached with lower current densities. Consequently, the activation overpotential is negligible and all of the polarization can be attributed to the excess concentration at the interface. Therefore, at 518 rpm there is a good agreement with 8.9 mV as predicted. At 1770 rpm there is an activation overpotential of 2-3 mV, at 4625 rpm, 3-5 mV.

Clearly, our polarization curves obtained with the platinized platinum electrodes in essence reflect the concentration overpotential for current densities up to 20 mA/cm². For such conditions, a direct application of the low field approximation, Eq. [5], to the micropolarization measurements near the open circuit would evidently be erroneous since the activation overpotential appears only at higher current densities. The situation may be different with electrodes of lower catalytic activity. Activation polarization may become significant at current densities low enough to cause any measurable concentration overpotential. This, however, must be established in each case remembering Eq. [13] and its contribution to the interfacial chlorine activity expressed through Eq. [15] and [20].

Measurements of activation overpotential.—Figure 4 shows the actual activation overpotential curves for both rings. Each data point is obtained by graphical subtraction of the concentration overpotential points on the curves represented by Eq. [21] from the experimental polarization curve obtained in Cl₂-saturated brine. These curves represent the actual activation overpotential free of any remnants of the concentration overpotential.

Surface absorption/desorption, exchange currents, Tafel slopes, and other parameters still bear a strong mark of varying interfacial activity of molecular chlorine. Absorption/desorption phenomena can depend in this case, not only on the chloride ion or Cl radical surface kinetics, but a consideration must be given to the role of molecular chlorine and its absorption/desorption mechanism. Low field approximation, for example, does not follow Eq. [5] predictions for overvoltages higher than 3 mV, suggesting changes in electrode kinetics with increasing current density. In a similar manner, apparent Tafel slopes reflect the surface kinetics parameters as well as interfacial changes. In order to apply these in the mechanism studies of the reaction, one must take into account the molecular chlorine interfacial activity changes occurring in the range of currents used for establishing the slope.

Furthermore, i_0 is a product of the concentration independent rate constant k and the interfacial concentration of the reacting species C_{Cl^-} or $C_{Cl_2, x=0}$ (1)

$$i_0 = Fk C_{Cl_2, x=0} e^{-\beta FE^0/RT} = Fk C_{Cl^-} e^{-(1-\beta)FE^0/RT} \quad [22]$$

Table II. Overpotentials of ring anode in chlorine-saturated solution at 0.022 M/l supersaturation at the interface at respective rotation speed

Ring	4625	1770	518
Inner	14 mV	12 mV	9 mV
Outer	12 mV	11 mV	10 mV

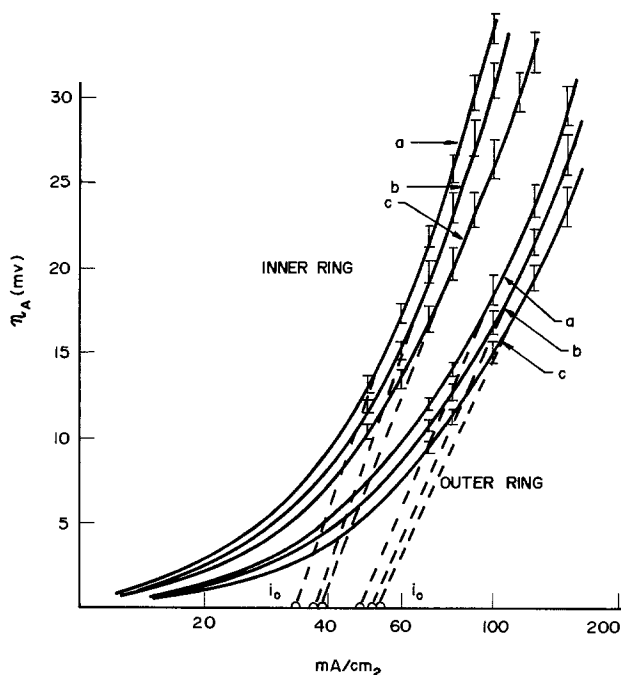


Fig. 4. Cl₂ saturated electrolyte—activation overpotential curves for inner and outer ring. Concentration polarization measured and eliminated. (a) 518, (b) 1770, and (c) 4625 rpm.

In our experiments, however, the measurable activation overpotential falls in the range of $C_{Cl_2, x=0} > 2C_{Cl_2}^0$. Hence, an extrapolation of the curves to the zero η_A gives information pertinent only for particular interfacial conditions. Consequently, it would be erroneous to make comparisons between different catalytic surfaces without considering the interfacial conditions for which extrapolated values were determined. The lower catalytic activity surfaces, of course, may show a predominant charge transfer resistance near the open circuit thus permitting a correlation between the i_0 and the $C_{Cl_2}^0$.

Our activation overpotential curves, Fig. 4, show two distinctive sets of polarization curves for the two rings. This result indicates that the two rings have different catalytic activity.

Distinction in activation polarization within one set of curves can be attributed only to the interfacial concentration variation with rotation since all three curves are obtained on the same ring of identical surface activity but at different mass transport conditions. Table I shows that mass transport conditions, although not identical at the two rings, overlap considerably, i.e., diffusion layer thicknesses for both rings fit in the range of 15.2-49.6 μ with small differentiation in magnitudes for identical rotation speeds. Under operating conditions with a negligibly small difference in surface catalytic activity between the two rings, or, in the absence of an activation overpotential, the polarization curves for both rings should line up in the sequence as expected by mass transport variations (well demonstrated in N₂ curves for lower current densities, Fig. 1, 2, and 3). At higher current densities, where activation overpotential becomes significant, by subtracting the concentration overpotential from our polarization curves, we were able to identify the difference between the surface activities of the two rings.

The outer ring is more active and we attribute this phenomenon to the platinized platinum formation process described in our earlier work (19). Platinum deposition is performed from a chloroplatinic solution under higher than limiting current conditions. This method was developed to provide an active surface with submicronic dendrites which do not interfere with mass transport conditions at the interface. With a

fixed rotation speed, chloroplatinic acid concentration, and deposition time, a larger amount of platinum will be deposited on the outer ring. Hence, a better catalytic activity can be attributed to it. A coulometric oxidation of adsorbed hydrogen, for example, indicates a 12-15% larger adsorption capacity in the outer compared to the inner ring.

We are presently proceeding in establishing the mechanism of chlorine evolution from these surfaces, however, with much greater emphasis on interfacial saturation than encountered in the literature dealing with this subject. Conway and Novak (20), for example, attribute a 42 mV/decade polarization slope in N_2 atmosphere to a Tafel region entirely disregarding the interfacial saturation phenomena. In a similar approach, they make a thorough mechanistic interpretation based on specific adsorption of chloride species assuming an undisturbed interfacial equilibrium of 1 atm Cl_2 with brine. In our opinion, their experiments presented in their Fig. 2 show strong evidence of specific adsorption. However, this may not be only a result of Cl^- ion specific adsorption, as stated by the authors. Other adsorbed intermediate species like Cl_2 , $Cl_2(H_2O)_x$, etc., may as well be in a quasi equilibrium with dissolved molecular chlorine at the interface. At the corresponding current density range, the interfacial chlorine concentration is closer to a several atmosphere supersaturation level rather than to 1 atm as assumed by the authors. Under such conditions, desorption of molecular chlorine or even chlorine hydrate may become the rate-determining step. In a similar fashion, micropolarization data obtained by Tilak (21) and Yokoyama *et al.* (22) on several substrates reflect predominantly the linearity of concentration overpotential with small interfacial chlorine concentration changes as indicated by Eq. [3]. Thus, the extrapolated information about the reaction mechanisms bears an inherent factual error. Furthermore, Fajta *et al.* (23) discussed Tafel slopes assuming interfacial equilibrium of molecular chlorine throughout their experiments. Nevertheless, the current densities they applied were carried well over 100 mA/cm². Krishtalik *et al.* (24), for example, assume interfacial equilibrium of molecular chlorine with 0.057 atm Cl_2 partial pressure in cell atmosphere despite a rate of 1 A/cm² of chlorine evolution. Under such conditions with diffusion layer thickness of approximately 15-20 μ (9), the interfacial chlorine saturation is over an order of magnitude higher than one would expect based on liquid/gas phase equilibrium.

In conclusion, we think that far too much work was done in the past in this field entirely neglecting the interfacial chlorine saturation phenomena. This manuscript points out the potentially erroneous approach and indicates the routes to avoid misleading conclusions. In a well-defined system by means of Eq. [13], (21), or analogous equations, it is possible to establish a sound base for investigation of mechanistic phenomena.

Acknowledgments

The author wishes to acknowledge the cooperation and support by Olin Chemicals Research Center in Charleston, Tennessee. Especially appreciated is the help provided by W. M. Clarke in performing computer-simulated calculations of activity coefficients. Dr. Ron Datson, Dr. Ron Miles, Dr. David Justice, and Mr. James Ford contributed with their discussions.

Manuscript submitted May 13, 1982; revised manuscript received Aug. 1, 1983.

Olin Corporation assisted in meeting the publication costs of this article.

LIST OF SYMBOLS

a° bulk activity of the electrochemically active species ($m^\circ\gamma^\circ$)

$a_{x=0}$	interfacial activity of the electrochemically active species ($m\gamma$)
$A^{n+}/A^{(n-1)+}$	single electron redox couple
$a^\circ Cl^-$	bulk activity of chloride ions ($m^\circ Cl^- \gamma^\circ Cl^-$)
$a^\circ Cl_2$	bulk activity of molecular chlorine ($m^\circ Cl_2 \gamma^\circ Cl_2$)
$a_{Cl^-, x=0}$	interfacial activity of chloride ions, in this manuscript assumed to be the same as $a^\circ Cl^-$, $m^\circ Cl^- \gamma^\circ Cl^- = m_{Cl^-} \gamma_{Cl^-}$
$a_{Cl_2, x=0}$	interfacial activity of molecular chlorine ($m_{Cl_2} \gamma_{Cl_2}$), in this manuscript $m_{Cl_2} \gamma_{Cl_2} \cong m^\circ Cl_2 \gamma^\circ Cl_2$
$C^\circ Cl_2$	bulk concentration of molecular chlorine M/l at the open circuit $C^\circ Cl_2 = C_{Cl_2, x=0}$
$C^\circ Cl^-$	bulk concentration of chloride ions M/l, at the open circuit and concentrated brine solutions $C^\circ Cl^- = C_{Cl^-, x=0}$, Ref. (11)
$C^\circ Cl_2, x=0$	interfacial concentration of molecular chlorine M/l, in nitrogen purged anolite $C_{Cl_2, x=0}$ defined by Eq. [13]
D	diffusion coefficient of the species 10^{-5} cm ² /s
E_{Cl_2/Cl^-}	equilibrium potential of a chlorine/chloride electrode
$E^\circ Cl_2 \text{ g}/Cl^-$	standard potential of chlorine/chloride electrode. Chlorine activity expressed through partial pressure, for 1 atm 1.358V (12, 13)
$E^\circ Cl_2 \text{ aq}/Cl^-$	standard potential of chlorine/chloride electrode for unit chlorine activity 1.395V (12)
E_c	electrode quasi equilibrium or steady-state concentration overpotential, both due to the chlorine activity at the interface $E_c = E_{Cl_2/Cl^-}$ when $\eta_c = 0$ or $E_c = \eta_c$ when E_{Cl_2/Cl^-} is undefined, Eq. [21]
i	average current density on the anode (A/cm ²)
i_0	exchange current density for the couple Cl_2/Cl^-
k	rate constant, cm/s
K	$RT\delta 10^3/n^2F^2Da^\circ$
$m^\circ Cl^-$	molality of Cl^- in the bulk, M/1000 g H_2O
$m^\circ Cl_2$	molality of Cl_2 in the bulk, M/1000 g H_2O
m_{Cl^-}	molality of Cl^- at the interface, M/1000 g H_2O
m_{Cl_2}	molality of Cl_2 at the interface, M/1000 g H_2O
$m^w Cl_2$	molality of Cl_2 in water at 25°C and 1 at Cl_2 , 0.0592 M/1000 g H_2O (15)
$m^l Cl_2$	molality of Cl_2 in brine, 285 g/l NaCl, 25°C and 1 at Cl_2 , 0.0256 M/1000 g H_2O (11)
Greek Symbols	
γ	activity coefficients of the species
$\gamma_{Cl_2} = \gamma^\circ Cl_2$	activity coefficient of Cl_2 , defined as $m^w Cl_2/m^l Cl_2 = 2.31$ or 2.11 by computer program (14)
γ_{Cl^-}	activity coefficient of Cl^- , 0.92 ± 0.015 (14)
δ	average diffusion layer thickness at the anode surface, cm
η_A	anode activation overpotential, V
η_c	anode concentration overpotential, V

REFERENCES

- J. O'M. Bockris and A. K. N. Reddy, "Modern Electrochemistry," Plenum, New York, NY (1970).
- International Union of Pure and Applied Chemistry, Physical Chemistry Division, Commission on Electrochemistry, *Electrochim. Acta*, **26**, 1867 (1981).
- B. N. Kabanov, "Electrochemistry of Metals and Adsorption," Freund Publishing House, Holon, Israel (1969).
- I. V. Kadija, B. Z. Nikolić, and A. R. Despić, *J. Electroanal. Chem. Interfacial Electrochem.*, **57**, 35 (1974).
- N. Ibl, *Oberfläche-Surf.*, **13**, 1 (1972).
- B. Kabanov and A. Frumkin, *Z. Phys. Chem.*, **4**, 539 (1933).
- V. V. Skorchelletti, "Theory of Metal Corrosion-Khimiya," Leningrad (1973), Keter Publishing

- House Ltd., Jerusalem (1975). Trans. from Russian.
8. E. Barendrecht, L. J. J. Janssen, and R. M. deJonge, Paper 250 presented at The Electrochemical Society Meeting, Boston, MA, May 6-11, 1979.
 9. L. J. J. Janssen and J. G. Hoogland, *Electrochim. Acta*, **18**, 543 (1973).
 10. I. V. Kadija, *Electrochim. Acta*, **23**, 149 (1977).
 11. I. V. Kadija, *This Journal*, **127**, 599 (1980).
 12. M. Pourbaix, "Atlas D'Equilibres Electrochimiques a '25°C'," Ganthier-Villars GCIE, Paris (1963).
 13. T. Mussini and G. Faita, in "Encyclopedia of Electrochemistry of the Elements," Vol. 1, A. J. Bard, Editor, Chap. 1, Marcel Dekker Inc., New York (1973).
 14. ECES: Equilibrium Composition of Electrolyte Solutions, Computer Program, Oli Systems Inc., New York, Morristown, NJ (1975).
 15. M. S. Sherrill and E. F. Izard, *J. Am. Chem. Soc.*, **53**, 1667 (1931).
 16. N. Yokota, *Kagaku Kagaku*, **22**, 476 (1958).
 17. V. A. Smirnov and Z. M. Aliev, *Zh. Fiz. Khim.*, **50**, 1/32 (1976).
 18. F. Hine and S. Inuta, *Bull. Chem. Soc. Jpn.*, **41**, 71 (1968).
 19. I. V. Kadija and V. M. Nakić, *J. Electroanal. Chem. Interfacial Electrochem.*, **34**, 15 (1972).
 20. B. E. Conway and D. M. Novak, *J. Chem. Soc. Faraday Trans.*, **1**, **75**, 2454 (1979).
 21. B. V. Tilak, *This Journal*, **126**, 1343 (1979).
 22. T. Yokoyama and M. Enyo, *Electrochim. Acta*, **15**, 1921 (1970).
 23. G. Faita, G. Fiori, and A. Nidola, *This Journal*, **116**, 92 (1969).
 24. V. E. Kazarinov, L. I. Krishtakik, and Yu. V. Pleskov, *Trans. SAEST*, **12**, 287 (1977).

Technical Notes



Lead-Acid Battery Cathodes Incorporating Chemically Prepared PbO₂

P. T. Moséley* and N. J. Bridger

AERE Harwell, Materials Development Division, Oxfordshire, OX11 0RA, England

The positive plates of lead-acid starting, lighting, and ignition (SLI) batteries are manufactured according to a time-honored industrial process in which a mixture of finely divided lead, lead oxides, basic lead sulfates, water, and sulfuric acid is pressed, in the form of a paste, into a grid of a lead alloy. The pasted grid is held in an environment of controlled humidity and temperature for a recrystallization process akin to cement curing to take place. The plate is then electrochemically "formed" in a dilute sulfuric acid electrolyte to convert the active material to PbO₂. The forming process involves a complicated sequence of reactions, and it is necessary to carry out the formation in two stages separated by a hold time in order for most of the active mass to be converted. The details of the curing and formation procedures employed may vary from one manufacturer to another, but the whole operation, which is performed on batches of batteries, usually takes about a week.

The manufacture of positive plates for traction batteries differs only in detail: a dry mixture of lead, PbO, and Pb₃O₄ is poured into long thin separator bags which each contain a central lead current collector projecting down from the top of the plate. The formation operation proceeds in a similar way to that for SLI batteries.

These manufacturing processes are rather inefficient, and it would appear that a far less costly product could be obtained through the use of a continuous process in which lead dioxide would be injected directly into the interstices of the lead grid.

Aside from the cost of replacing established plants, one reason why the industry has not yet replaced the batch process with a continuous one is likely to be the published claims that lead dioxide prepared by a chemical method yields little (1) or no (2) capacity as a cathode material in a lead-acid cell. It has been demonstrated by nuclear magnetic resonance (NMR) measurements (3) that there is a difference in the

hydrogen content between chemically prepared and electrochemically prepared PbO₂, and neutron transmission measurements (4) appear to confirm this difference. It has even been suggested (3) that the loss of the hydrogen component is a factor contributing to the progressive loss of capacity observed during the battery life.

High resolution electron microscopy (5) has brought to light a tendency for defect structure and structural intergrowth in PbO₂, but these properties seem to be characteristic of the material regardless of the means adopted to prepare it (4).

It is characteristic of presently available lead-acid positive plates that they generally yield only 1/4-1/3 of the theoretical capacity which would be expected on the basis of the mass of PbO₂ present. It is also found that SLI batteries, which have an energy density much nearer electric vehicle target figures than do tubular batteries, lose capacity after an unacceptably short cycle life.

The published literature is short on evidence to support the claim that chemically prepared PbO₂ cannot be used in a lead-acid cell, and a recent attempt to quantify the effect led to the contrary result (6): that there was no less capacity available from a plate prepared with chemically prepared PbO₂ than from a commercially available plate. Lead dioxide prepared by the action of nitric acid on Pb₃O₄ was mixed with dry polytetrafluoroethylene (PTFE) powder (1 weight percent [w/o]), and pressed into a battery grid from which the commercial product had been removed (6). Capacity measurements were made by low rate discharge through a resistor.

The experiments reported here were designed to extend the testing of chemical PbO₂ capacity to constant current discharge, to explore the range of binder content necessary to perform the function of the conventional curing process in retaining the active material in the grid, and to try to discover at what stage the difference in hydrogen content between chemical and electrochemical PbO₂ develops.

* Electrochemical Society Active Member.
Key words: discharge, cathode.

Lead dioxide was prepared by suspending Pb_3O_4 in hot nitric acid, according to a procedure given in the literature (7). The product varied slightly in color between dark brown and black, but always yielded the x-ray powder diffraction pattern of beta PbO_2 (tetragonal).

A commercial battery was dismantled to provide a hard rubber case to hold plates for charge/discharge cycling. One positive plate from the battery was used to provide benchmark capacity data with which the experimental plates could be compared, and others were stripped of their active material and repasted with mixes based on chemical PbO_2 .

Positive plates were charge/discharge cycled one at a time at constant current against a commercial negative plate. The two plates were kept apart by a perforated sheet of perspex. The mean plate separation was about 5 cm. No other separator was used.

The active material was mixed with varying proportions of PTFE and, in some cases, graphite powder. This mixture was then pressed into the commercial plate and placed into the cell in the battery case for cycling and capacity tests.

Initially, a commercial positive plate was discharged at 30 A/m² to a cutoff limit of 1.0V. The plate, which contained 130g PbO_2 , afforded a discharge capacity of 7 Ah, which corresponds to a utilization of 25%.

Three mixtures of chemical PbO_2 , PTFE, and graphite were tested under similar conditions for initial discharge capacity and polarization characteristics, as shown in Table I.

All three mixtures adhered to the lead grid well, but mixture 3 was drier and stiffer than the other two, polarized badly at the outset, and swelled in thickness during use by a factor of about three. All three compositions were much richer in the highly resistive PTFE component than the mixtures that had been made earlier (6) with dry PTFE powder. So, it is scarcely surprising that the utilization, which in the earlier case was similar to that for commercial plates (25%), was rather less (up to 15%) in the present work.

The highest utilization was demonstrated by plate 1. The active material mix was insufficient to cover the whole plate, but no material appeared to be shed, and the capacity was steady through 40 deep discharge/charge cycles until the plate was removed to make way for tests on other mixtures. A typical discharge/charge cycle for plate 1 is shown in Fig. 1.

Table I also shows that the neutron scattering cross sections of two of the mixtures after drying for 24h at 120°C are much greater than that for the dry beta PbO_2 (4) with which they were prepared. This difference signifies a greater hydrogen content, but may be due to an increase in moisture retention caused by the presence of the PTFE. No neutron scattering measurements had been made on the material mixed with dry PTFE during the earlier work (6).

The influence on the ultimate capacity of variation in the details of the preparation of lead dioxide was investigated. As shown in Table II, variation in acid

Table I. Composition, initial discharge characteristics, and neutron cross-sections of synthetic active masses made using chemically prepared PbO_2

Plate	Composition (g)			Utilization (% of theoretical)	Neutron cross section (b)
	PbO_2	PTFE	Graphite powder		
1	24	8	7	15	30.4
2	24	5	0	12	9.6
3	48	10	18	4	Not measured

Neutron cross section of dry PbO_2 [Ref. (4)] = 2.5b.

¹ Materials dried 24h at 120°C.

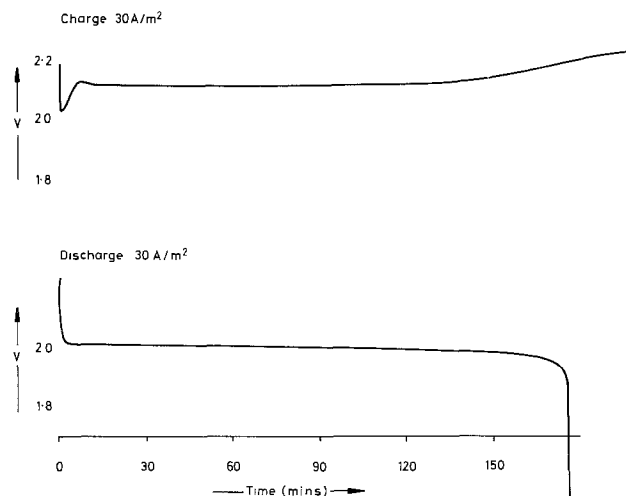


Fig. 1. Typical discharge/charge cycle from plate 1 (see text)

strength did not alter the utilization. However, the temperature may be important.

The grain size of the PbO_2 product in all cases (measured by x-ray diffraction line breadth) was of the order of 500Å. Mixtures for measurement of capacity of materials shown in Table II were composed of 17g PbO_2 , 7g graphite, and 10g PTFE.

In a further experiment, there was shown to be little variation in utilization over a wide range of PTFE content, as shown in Table III.

The mixture made without PTFE showed that capacity does not depend on the presence of the polymer. The material was completely shed from the plate after one cycle. It is clear from the rest of Table III that even a rather small quantity of PTFE in the mixture is sufficient to overcome this problem.

The present experiments, carried out at constant current, confirm the earlier report (6) that chemical PbO_2 can be used to obtain electrochemical capacity. The range of PTFE content that has been successfully used to prepare battery positives with chemical PbO_2 is now quite wide. Further, it has been shown (Table III) that neither of the additives (PTFE, graphite) is essential for electrochemical capacity to be obtained from chemically prepared PbO_2 .

The grids used in these tests were all partly corroded, and x-ray diffraction showed a substantial layer

Table II. Variation of conditions of preparation of PbO_2

Nitric acid strength	Temperature of prep'n (°C)	Time at temp (min)	Utilization (% theoretical capacity)
5m	95	15	15
6m	95	15	16
3m	95	15	18
5m	80	15	8
5m	100	15	14

Table III. Variation of utilization (% of theoretical capacity) with PTFE content of test mixture

w/o PTFE	w/o graphite	Utilization
0.2	0.0	25 Ref. (6)
0.0	19.0	19 ^a
2.0	20.0	19
3.0	20.0	12
5.0	20.0	9
10.0	20.0	13
20.0	20.0	15

^a All the active material was shed from this plate after one complete discharge.

of PbSO_4 on the surface of the grid members. This layer probably constituted an unnecessary impediment to the achievement of high utilization figures so that there may be prospects for improvement.

The achievement of greater utilizations will depend on the availability of a grid in which (i) regions of active material are not eliminated from participating in the discharge reaction by an insulating layer of PbSO_4 , and (ii) acid access to the active material is maintained at all states of charge.

These are the only ultimate limitations on the utilization of electrochemical or chemical PbO_2 which are imposed by the plate itself.

The key as to whether or not chemical PbO_2 electrodes can be developed to give longer lived batteries may lie in the possible microstructures that can be developed. Recently, it was observed (8) that capacity loss is largely due to resistance increase of intergranular contact.

The demonstration that chemically prepared PbO_2 can be used for the manufacture of positive plates for lead-acid batteries opens the way to the development of continuous processes for commercial manufacture. In the case of flat plates, the function of the curing process will need to be replaced by a binder to hold the active material in place, but for tubular cells it should be possible to pour neat PbO_2 powder into the separator bags, which will retain the active material in position (9). In each case, the curing and formation stages can be omitted from the production time, and after a few discharge/charge cycles the strength of the plates will be decided by the morphology developed by the recrystallization of a large part of the active mass.

After the present work was carried out, a note was published from another lab (10) which appears to support the central contention of this paper.

Acknowledgments

The authors are grateful to Mr. M. A. M. Bourke for experimental assistance and to Dr. C. J. Wright for neutron scattering cross-section measurements.

Manuscript submitted Jan. 31, 1983; revised manuscript received Oct. 24, 1983.

AERE Harwell assisted in meeting the publication costs of this article.

REFERENCES

1. A. C. Simon and S. M. Caulder, ILZRO project LE-255, Paper presented at ILZRO Battery Research Meeting, Munich (1980).
2. J. Perkins, *Mater. Sci. Eng.*, **28**, 167 (1977).
3. S. M. Caulder, J. S. Murday, and A. C. Simon, *This Journal*, **120**, 1515 (1973).
4. P. T. Moseley, J. L. Hutchison, C. J. Wright, M. A. M. Bourke, R. I. Hill, and V. S. Rainey, Submitted to *This Journal*.
5. P. T. Moseley, J. L. Hutchison, and M. A. M. Bourke, *This Journal*, **129**, 876 (1982).
6. P. T. Moseley and M. R. H. Hill, Br. Pat. Appl. no. 8,208,326 (1982).
7. N. E. Bagshaw, R. L. Clarke, and B. Halliwell, *J. Appl. Chem.*, **16**, 180 (1966).
8. J. Bouet and J. J. Pompon, *Electrochim. Acta*, **26**, 1477 (1981).
9. P. T. Moseley and N. J. Bridger, Br. Pat. Appl. no. 8,222,739 (1982).
10. R. J. Hill, *Mater. Res. Bull.*, **17**, 769 (1982).

Lithium-Copper Molybdate Voltage Compatible Battery

F. Bonino and M. Lazzari

Polytechnic of Milan, Centro Studio Processi Elettrodici del CNR, Milano, Italy

B. Scrosati*

University of Rome, Dipartimento di Chimica, Rome, Italy

Because of the popularity of portable microelectronic devices, interest has risen in high energy, long-life power sources having working voltages around 1.5V. These improved systems are usually termed "compatible" batteries, since they may directly be interchanged with conventional zinc and mercury dry cells, with great advantages in terms of reliability and longevity.

Among the most promising compatible high energy power sources of this type are the lithium organic-electrolyte batteries with copper-based (1), lead-based (2), or bismuth-based (3) cathodes.

As alternative cathode material, we have considered copper molybdate (CuMoO_4), which offers good characteristics of specific capacity and specific energy. The performance of this material in a typical lithium-organic electrolyte cell is described and discussed here.

Experimental

The preparation of CuMoO_4 was reported in detail in a previous paper (4). Basically, the compound was obtained by direct reaction between reagent-grade MoO_3 and CuO . The structure of CuMoO_4 prepared in

this way was characterized by x-ray analysis (see Table I).

Copper sulfide, Cu_2S (chalcocite), used here for comparison purposes, was prepared by annealing for 24h at 475°C a stoichiometric Cu and S mixture, maintained in an evacuated two-chamber glass envelope. The structure of the final compound was again char-

Table I. X-ray analysis of copper molybdate cathode material

CuMoO_4 ASTM card 22/242		CuMoO_4 Our sample	
2θ	I/I ₀	2θ	I/I ₀
9.58	40	9.60	35
15.98	60	16.00	40
19.12	40	19.15	38
19.55	40	19.40	48
22.42	60	22.40	30
23.28	60	23.35	20
23.90	100	24.00	100
24.94	40	25.00	26
26.52	80	26.50	75
26.84	60	26.85	40
27.06	60	27.10	40
27.70	40	27.90	32
28.68	40	28.65	32
29.68	60	29.90	40
30.02	60	30.10	40
33.01	70	33.10	48

* Electrochemical Society Active Member.

Key words: lithium batteries, voltage compatible, microelectronics.

acterized by x-ray analysis: the reflections obtained matched those listed in the ASTM card 23-961.

The solvents used, *i.e.*, propylene carbonate (PC) and butyrolactone (BL) were purified by fractional distillation, followed by treatment with molecular sieves (4Å).

All the lithium salts, LiAsF₆ (USS Agri-Chemicals), LiCF₃SO₃ (3M), and LiClO₄ (Merck), were pure products. The latter was dried at 240°C under vacuum.

Typical laboratory cells were used for the discharge tests. These cells consisted of a lithium pellet, a glass-wool separator soaked with the electrolyte, and a cathode pellet (supported on a copper substrate), housed in a plastic container having stainless-steel terminals.

Results and Discussion

The basic electrochemical characteristics of the Li/CuMoO₄ couple in typical organic electrolytes were originally studied, and the results were reported in previous papers (4, 5). Here, attention is given to the discharge behavior in relation to the power requirements of portable microelectronic devices.

Initially, the influence of the type of lithium salt dissolved in the organic solvent (here propylene carbonate) was evaluated. Figure 1 shows typical discharge curves at 0.5 mA/cm² for the Li/CuMoO₄ couple in the LiClO₄-PC and LiCF₃SO₃-PC electrolytes. Both the electrolytes behave satisfactorily, showing flat discharges with working plateaus around 1.5V. The initial spike between 2 and 1.5V could be due to residual traces of unreacted MoO₃ in the CuMoO₄ cathodic material. However, since these traces could

not be detected by x-ray analysis, other explanations (*e.g.*, unknown impurities, surface effects, etc.) could also apply. In any case, the spike is completely eliminated by a predischARGE in all the cells using the CuMoO₄ cathodic material.

The role of the electrolyte is illustrated in Fig. 2, where two discharge curves at 0.5 mA/cm² for LiClO₄-PC and LiAsF₆-BL are compared. The test clearly indicates that LiClO₄-PC is more effective in terms of average voltage and overall performance. This result points out the superior characteristics of the LiClO₄-PC solution as an electrolyte in lithium power sources. Indeed, these characteristics, which follow from a favorable compromise between conductivity and stability, make the LiClO₄-PC the preferred electrolyte medium in various established lithium primary batteries. Therefore, this electrolyte has been also selected for the final evaluation of the Li/CuMoO₄ system discussed here.

Typical discharge curves of the Li/LiClO₄-PC/CuMoO₄ cell at various rates are shown in Fig. 3. The promising behavior of this cell is further indicated by the trend of the discharge plateaus, which remain flat even at currents much higher than those usually required for microelectronic applications.

The discharge mechanism of the cell was investigated by x-ray analysis. Spectra taken on cathodes discharged to a 1V cutoff revealed the presence of metallic copper. Therefore, one can propose that the discharge reaction, which involves 2F per mol of CuMoO₄, results in the displacement of copper by lithium, that is

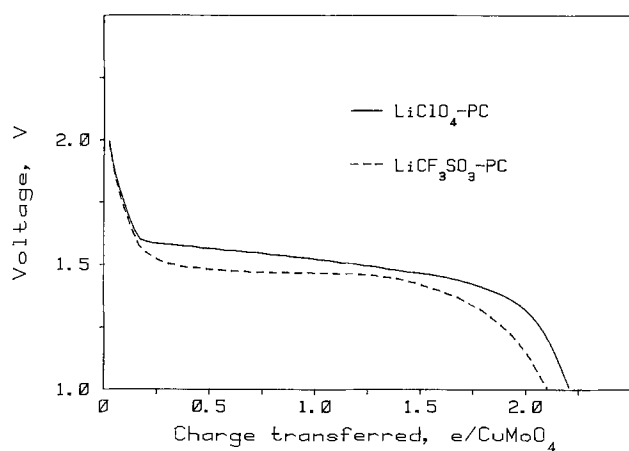


Fig. 1. Typical discharge curves at room temperature and at 0.5 mA/cm² of the Li/CuMoO₄ couple in two electrolytes.

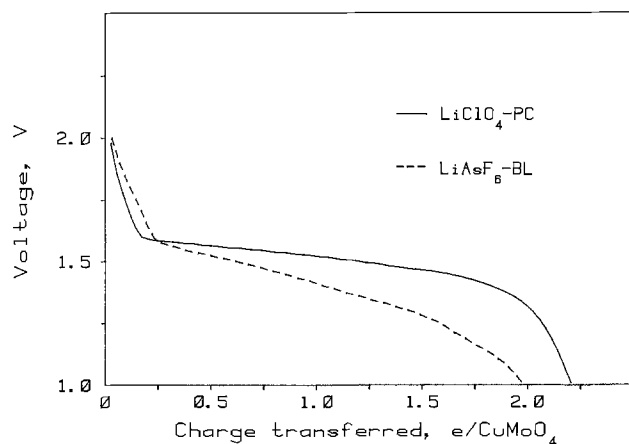


Fig. 2. Typical discharge curves at room temperature and at 0.5 mA/cm² of the Li/CuMoO₄ couple in two electrolytes.

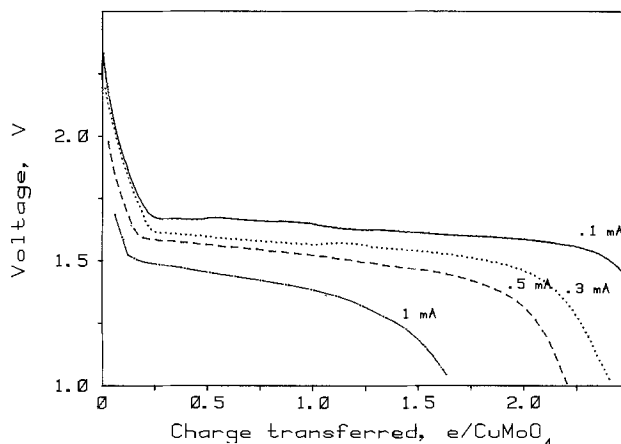


Fig. 3. Typical discharge curves of the Li/LiClO₄-PC/CuMoO₄ cell at room temperature and at various rates.

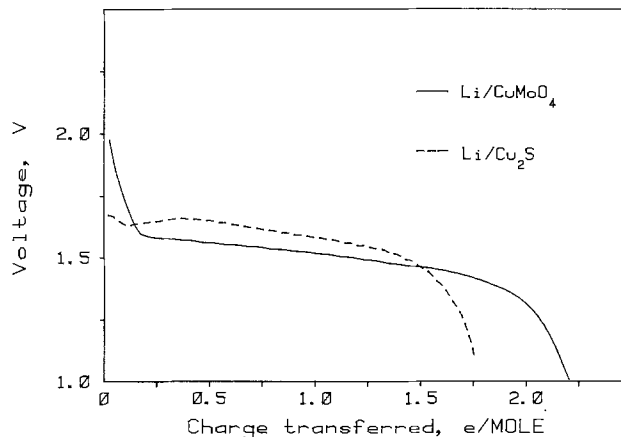


Fig. 4. Typical discharge curves at room temperature and at 0.5 mA/cm² of the Li/LiClO₄-PC/CuMoO₄ and the Li/LiClO₄-PC/Cu₂S cells.



The formation of copper during discharge is a desirable event, since it gives the cathode sufficient electronic conductivity to be used without additives (graphite). This result is beneficial in terms of overall energy density.

In Fig. 4 the performance of the CuMoO_4 cathode is compared in the same type of Li cell with that of Cu_2S , i.e., a cathodic material proposed for the commercial production of compatible batteries (1). The result indicates that the performances of the two cathodes are comparable, thus showing that copper molybdate may indeed be considered as a valid candidate for 1.5V lithium batteries. The energy density of this material, when discharged at 0.3 mA/cm² to a 1V cutoff, is 440 Wh/kg. Work is progressing in our laboratories on the Li/CuMoO₄ couple in button cells having a size more commonly used in popular portable devices, such as electronic watches and pocket calculators.

Gas Evolution in Aluminum Electrolytic Capacitors

C. Gómez-Aleixandre, J. M. Albella,* and J. M. Martínez-Duart

Universidad Autónoma, Instituto de Física del Estado Sólido, CSIC, and Departamento de Física Aplicada, Cantoblanco, Madrid-34, Spain

Gas evolution in aluminum electrolytic capacitors constitutes one of their main drawbacks in comparison to other types of capacitors lacking a liquid electrolyte. In this respect, one of the most common causes of failure shown by liquid electrolyte capacitors is electrolyte leakage through the seal or even explosions produced by internal pressure buildup. In order to prevent these hazards, some substances, known as depolarizers, are usually added to the capacitor electrolyte with the purpose of absorbing the hydrogen evolved at the cathode (1, 2). Although the gas evolution problem in electrolytic capacitors has been known for a long time, there is a lack of literature on both direct measurements of the gas evolved and assessments of the amount of depolarizer active for the hydrogen absorption process.

Aluminum electrolytic capacitors of 100 μF and 40V nominal voltage, miniature type (diam 8 mm, height 18.5 mm), were manufactured under standard specifications. The capacitors were filled with about 0.5 ml of an electrolyte consisting essentially of a solution of boric, adipic, and phosphoric acids in ethylene glycol. Picric acid and p-benzoquinone in molar concentrations of 0.01M and 0.05M, respectively, were added as depolarizers, yielding an electrolyte with a resistivity of about 80 $\Omega\text{-cm}$ and a pH of 5.1. The pressure inside the capacitors was monitored by a conventional U-shaped manometer made from a capillary glass tube filled with distilled water. The number of mols of gas generated in the capacitor (n_g) was calculated from the measured pressure (sensitivity 0.1 mm Hg) and the value of the internal volume of the manometer-capacitor system.

The gas evolution processes can be better interpreted if a constant current is applied to the capacitor. The magnitude of the current, provided by an operational power supply (Kepco-OPS-2000), was varied in the range from 100 to 1000 μA . The reason for using currents larger than the capacitor leakage current (28 μA) was to accelerate the generation of gas and therefore carry out the experiments in a reasonable time (2-3h for each constant current run). Under these circumstances, the voltage developed across the

Acknowledgments

The authors wish to thank Dr. G. Pistoia of the University of Rome for the helpful discussion, and the Consiglio Nazionale delle Ricerche for financial support.

Manuscript submitted May 24, 1983; revised manuscript received Sept. 8, 1983. This was Paper 527 presented at the San Francisco, California, Meeting of the Society, May 8-13, 1983.

REFERENCES

1. Ray-o-Vac Bulletin XR 2016-1 (1980).
2. M. Broussely, Y. Jumel, and J. P. Gabano, *J. Power Sources*, **5**, 83 (1980).
3. P. Fiordiponti, G. Pistoia, and C. Temperoni, *This Journal*, **125**, 14 (1978).
4. F. Bonino, B. DiPietro, B. Rivolta, and B. Scrosati, *J. Power Sources*, **2**, 265 (1977).
5. B. DiPietro, B. Scrosati, F. Bonino, and M. Lazzari, *This Journal*, **126**, 729 (1979).

capacitor increased to about 60V for the highest currents employed. Between each run, the capacitor dielectric properties (capacitance and loss factor) remained essentially unaltered, as shown in a previous paper (3). Simultaneously, no pressure drops were detected after each run with the capacitors in open circuit.

Figure 1 shows the variation of the mol number of gas generated as a function of the polarization time (t) for different values of the current (I) through the capacitor. Two linear stages are observed for each curve, the slopes in every stage increasing as the currents increase. Besides, for currents below a certain critical value I_c , the amount of gas evolved is practically zero even after long polarization times (see the 100 μA curve in Fig. 1).

To get further information on the gas evolution process, experiments were carried out for each constant current at different temperatures in the range 20°-80°C. Figure 2 shows the variation of n_g with time for a current $I = 500 \mu\text{A}$ and several temperatures. It can be appreciated that, as the temperature increases, the slope of the first linear stage of the curves gets successively smaller until, for $T \sim 35^\circ\text{C}$, it becomes zero. Simultaneously, the slopes of the second linear stages, and therefore the corresponding gas evolution rates, slightly increase with the temperature.

For the interpretation of the results of Fig. 1 and 2, we can assume that the only gas that contributes significantly to the pressure buildup is hydrogen electrochemically generated at the cathode following Faraday's law, i.e., $n_g = Kit$, where K is the gas mol number generated per unit charge. This assumption is based on the experiments of Burger and Wiswanathan carried out in an open cell with an electrolyte similar to the one employed in this work (1). Furthermore, the presence of other gasses in large quantities would not be consistent with the zero slope observed in the first part of the curves of Fig. 2 for $T \sim 35^\circ\text{C}$.

The linear dependence of n_g on the polarization time, shown in the curves of Fig. 1, and the change in the slopes at some definite times t_e , suggest that, in the first stage of the curves, the gas evolution rate is diminished by the absorption of hydrogen by the depolarizer.

* Electrochemical Society Active Member.

Key words: dielectrics, capacitance, electrolysis.

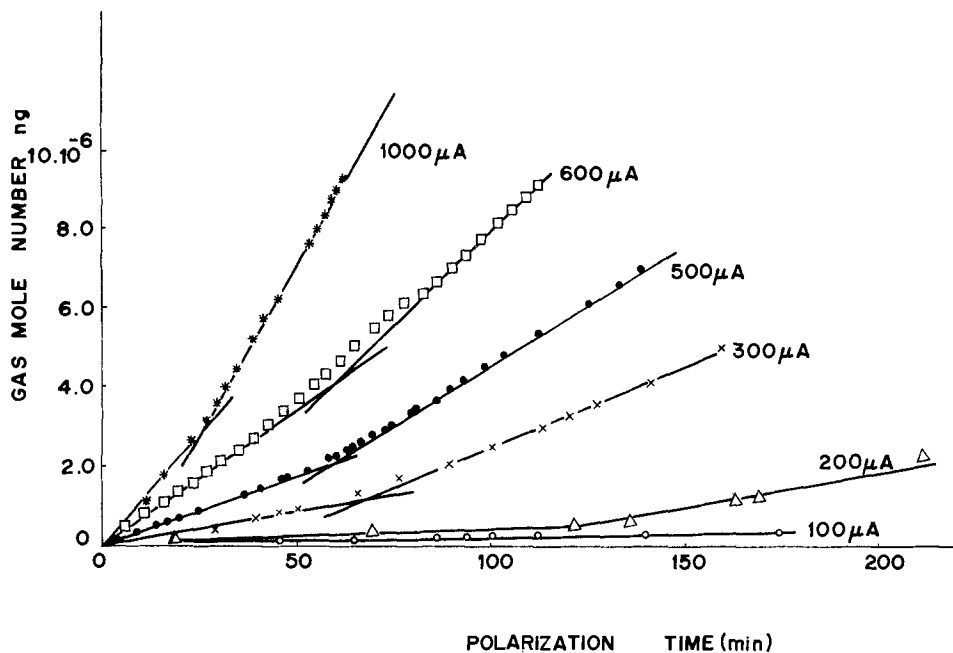


Fig. 1. Mol number of generated gas as a function of polarization time, for different currents through the capacitors.

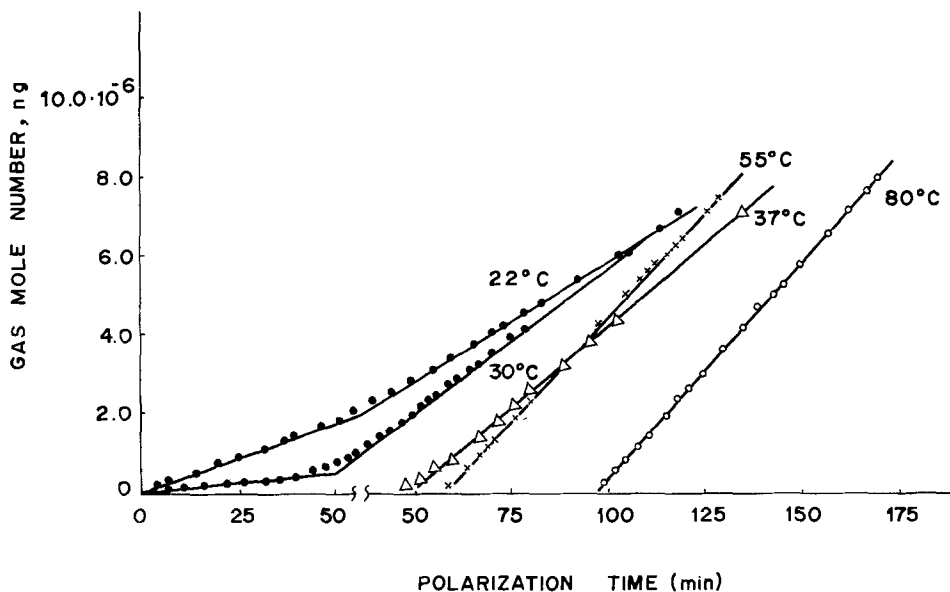


Fig. 2. Mol number of generated gas as a function of time for a current of 500 μA and several temperatures.

The hydrogen absorption, assumed to proceed at a constant rate v , is carried out through a reduction reaction of the quinone and the picric acid, this last compound undergoing a multistage reduction of the nitro radicals (4, 5). The slope changes observed at time t_e in the curves of Fig. 1 and 2 could then be associated with a diminution of the reaction rate v due to the exhaustion, at a given temperature, of that portion of the depolarizer in contact with the surface of the cathode.

Within the above simple model, one can assume that for $t > t_e$, $v \approx 0$, and therefore write: $n_g = Kit - n_d$, where n_d represents the number of hydrogen mols which have reacted with the depolarizer during the time t_e . The value of n_d can then be directly obtained from the intersect of the second linear part of the curves of Fig. 1 with the ordinate axis. As expected from our model, all the curves converge to the same point, yielding a value of $n_d = (1.56 \pm 0.15) \cdot 10^{-6}$ mol. The variation of n_d with temperature can also be obtained by applying the same procedure to the curves of Fig. 2. It is then found that n_d varies from a value of 1.45×10^{-6} mols at 22°C to a value of 10.5×10^{-6} mols at 80°C (see Table I).

The large increase in the number of hydrogen mols reacting with the depolarizer as the temperature is raised implies, in the first place, that at low temperatures (about 20°C), the reduction reaction is strongly inhibited, probably because of the slow diffusion mechanism of the reactants towards the surface of the cathode. In addition, it is also suggested that we are dealing with a thermally activated reaction mechanism. An Arrhenius plot of the values of n_d gives an activation energy $\Delta E = 6.1$ kcal/mol, which is similar to the 7.0 kcal/mol reported in the literature for another typical depolarizer, p-nitrobenzoic acid (1). In this context, ΔE can be considered as the activation

Table I. Number of mols of hydrogen reacting with the depolarizer as a function of temperature

T (°C)	n_d (mols)
22	1.45×10^{-6}
30	3.31×10^{-6}
37	4.23×10^{-6}
55	6.21×10^{-6}
80	10.50×10^{-6}

energy for the slowest step controlling the reduction reaction, e.g., diffusion of the reactants to the cathode, adsorption of hydrogen, etc.

From the results of this work we can conclude that the internal gas generation, observed in aluminum miniature electrolytic capacitors subjected to stressed electrical conditions, is controlled by two competitive processes: (i) gas generation at the cathode following Faraday's laws, and (ii) hydrogen absorption by the depolarizer following a thermally activated reaction mechanism. Both reactions are favored by the temperature, especially the second one. As a consequence, the internal gas evolution might get smaller when the electrolytic capacitors operate at moderate temperatures. Since the nominal leakage current of a capacitor is well below the value of the critical current I_c found in this work, it can also be concluded that the efficiency of the depolarizer is high in preventing the evolution of gas in a capacitor operating under normal working conditions.

Identification of Electrolyte Salts in Thionyl Chloride Relevant to Voltage Delay

James M. Chen, David R. Damian, Jr., Richard M. Stepnowski, and Clifton A. Young*

The University of Dallas, Chemistry Department, Irving Texas 75061

Thionyl chloride is used as the electrolyte solvent in lithium/thionyl chloride batteries. The thionyl chloride in the battery is also reduced at the catalytic carbon cathode of the battery. The standard electrolyte salt for this battery is LiAlCl_4 (1). One of the problems with this battery is the so-called voltage delay phenomenon. After storage there will be a delay before these batteries deliver their full voltage when put on load (2, 3). Two proposals have been made to alleviate or solve this problem by replacing the standard electrolyte salt with another different salt (4, 5). However, in both cases, subsequent workers have questioned whether the described salts were the actual species in solution (6, 7). Clearly, a technique for isolating and identifying the salts in these solutions is desirable. The importance of analyzing thionyl chloride electrolytes has been shown before by others (8, 9).

We report here on the development of a technique for isolating lithium salts from solution and on its application to systems of significance to thionyl chloride batteries. This technique entails addition of dimethoxyethane to the solution to precipitate the salt. It eliminates the possible use of rigorous conditions, such as evaporation of the solvent, which leaves an intractable, amorphous material.

LiAlCl_4 electrolyte is frequently made *in situ* by reacting LiCl , a Lewis base, with AlCl_3 , a Lewis acid, dissolved in thionyl chloride. One of the proposals was to replace the Lewis base LiCl with an alternative Lewis base Li_2O (4). It was proposed that the electrolyte salt was $\text{Li}_2\text{O} \cdot 2\text{AlCl}_3$ (4). Subsequently, this claim was modified, and it was proposed that the salt was a mixture of LiAlCl_4 and $\text{AlCl} \cdot \text{SO}_2$ (6). Interest in this electrolyte has continued (10). Li_2S has also been proposed as an alternative Lewis base (11).

Carbonates have been used as sources for oxides in chloroaluminate melts (12, 13). Sulfite ion might be expected to behave in a similar manner; however, it has been found to slowly react with chloroaluminate melts to produce thionyl chloride and sulfur dioxide

Acknowledgments

We wish to thank S. A. Bianchi (Spain), and the Comisión Asesora de Investigación Científica y Técnica for financial support of this work. One of us (C. G. A.), acknowledges the Consejo Superior de Investigaciones Científicas for the grant awarded while working in this project.

Manuscript submitted Dec. 29, 1982; revised manuscript received Oct. 21, 1983.

REFERENCES

1. F. J. Burger and S. Wiswanathan, *Electrochem. Technol.*, **6**, 189 (1968).
2. M. Hagihara and S. Takimoto, U.S. Pat. 3,454,840 (1969).
3. J. M. Albella, C. Gomez-Aleixandre, and J. M. Martinez-Duart, *J. Appl. Electrochem.*, **14**, 9 (1984).
4. A. A. Darchen and D. Peltier, *Bull. Soc. Chim. Fr.*, 401 (1972).
5. I. L. Finar, "Organic Chemistry," 6th ed., p. 649, Longman Group, Ltd., London (1973).

(14). There has also been an attempt to form Lewis acid adducts with a whole series of oxoanions using BF_3 (15). In the course of that work, it was found that both carbonate and sulfite reacted with BF_3 (15). By analogy with Li_2O , we examined possible Lewis acid-base interactions with these sources of oxide, namely, sulfite and carbonate.

Halogen exchange in thionyl chloride is well known (16). AlCl_3 has been observed to exchange with COCl_2 when AlCl_3 is dissolved in that solvent (17). Halogen exchange by tetrahaloaluminate ions with methylene chloride has also been observed to occur (18). This exchange was observed to be catalyzed by AlCl_3 (18). It is therefore to be expected that AlCl_4^- ion exchanges halogen when dissolved in thionyl chloride (19). Using our technique, we tested this expectation.

Experimental

Preparation of $\text{LiAlCl}_4/\text{SOCl}_2$ electrolyte.—Anhydrous AlCl_3 was dissolved in 50 ml SOCl_2 . This solution was stirred with excess LiCl for 3h. The solution was filtered through an enclosed glass frit (Kontes K-956250) to remove unreacted LiCl . We had some difficulty with preparing this known electrolyte. We attributed the difficulty to unpredictable reaction between two phases (solid and liquid). We recommend that the reaction mixture be refluxed, as our other preparations were, and that careful analytical quality control be exercised over electrolytes used in actual batteries.

Preparation of other electrolytes.—All remaining electrolytes were made in an analogous manner. Aluminum chloride was the limiting reagent. The salt being used as a Lewis base was added in excess to the AlCl_3 in about 50 ml of thionyl chloride. The mixture was refluxed for 3h and filtered as described above.

Isolation of electrolytes and preparation of analytical samples.—Equimolar (to Al) amounts of dimethoxyethane (measured by volume) were added to the electrolyte solutions. The precipitate was isolated by filtering in the enclosed glass frit described above using a

* Electrochemical Society Active Member.

Key words: battery, electrolyte, analysis, chelation.

mechanical vacuum pump. The precipitate was washed once with thionyl chloride. The sidearm flask into which the filtrate and thionyl chloride had drained was replaced with a sealed tube, and the precipitate was pumped dry through a stopcock at the top of the enclosed frit for 0.5h. The extremely hygroscopic salt, while still under vacuum, was immediately hydrolyzed by adding water through the stopcock. To minimize loss of HCl, the water was added from a trap. The water solution of the salt was diluted to a measured volume.

Standard taper glassware gasketed with Teflon sleeves was used for all the above manipulations. When the remaining thionyl chloride was pumped off, the sleeves were supplemented by vacuum grease applied to the outsides of the joints. Teflon sleeves were necessary because of the reactivity of thionyl chloride. The grease prevented a slow leak from destroying the hygroscopic solid. Unfortunately, it also prevented us from obtaining a total weight of the precipitate. The drying is the most critical step of the procedure, at all other times the thionyl chloride protects the salt from moisture. All manipulations should be done in a hood.

Isolation of AlCl₃ from thionyl chloride.—Equimolar amounts of dimethoxyethane were added to these solutions. The precipitates were treated exactly as described above.

Analysis of the hydrolyzed salt.—All analyses were carried out on aliquots of the volumetric solution. Aluminum was determined gravimetrically by the method of Howick and Jones (20). We found it essential to distill the acetone used in this procedure, as suggested by those authors (20). Chloride was determined by argentimetric titration (21). This technique will determine any bromide at the same time. The cation (usually lithium) was determined from an ion exchange total cation determination (22), from which the aluminum determination was subtracted. The titration was carried out using a pH meter, so that if the thionyl chloride had not been completely removed in drying, endpoints due to SO₂ titration would also be observed. All of these literature techniques were verified on control samples of LiCl and anhydrous AlCl₃ and their combinations dissolved in water. The aluminum gravimetric method was further verified on primary standard aluminum wire dissolved in HCl.

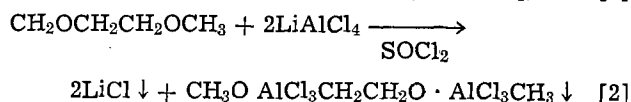
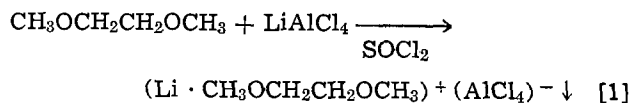
Tetrabromoaluminate exchange.—Tetramethylammonium tetrabromoaluminate was made by the method of Bradley *et al.* (23). Their synthesis was verified by analysis. This salt was dissolved in thionyl chloride. The thionyl chloride immediately turned brown. The solvent was removed by vacuum distillation to a dry ice-acetone trap. The solid salt was hydrolyzed and

analyzed as above. SOCl₂ which had exchanged with bromide was hydrolyzed immediately and discarded, since thionyl bromide had been implicated in an unexplained explosion (24).

Results and Discussion

The results of our analyses of a number of electrolytes of interest either chemically or in batteries are presented in Table I.

Identification of the precipitate.—Notwithstanding the fact that aluminum chloride is also precipitated by dimethoxyethane (second item in Table I), we believe that the precipitates of the lithium salts are chelates of lithium, and not the result of chloride displacement from the aluminum by the dimethoxyethane. The two possible reactions in their expected stoichiometries are as follows



The evidence in the literature indicates very strongly that the stoichiometry of reaction [2] would be two aluminum chlorides to one dimethoxyethane (25). In an experiment where dimethoxyethane was the limiting reagent, the yield would indicate that the stoichiometry was one to one (first item in Table I).

In order to resolve the question of which reaction took place, we added dimethoxyethane to a solution of tetramethylammonium tetrachloroaluminate in thionyl chloride. Dimethoxyethane would not be expected to interact with tetramethylammonium. The solution was made by adding a two-to-one excess of tetramethylammonium chloride to aluminum chloride in thionyl chloride. The excess was to insure that there was no uncombined aluminum chloride present. Addition of 60% excess of dimethoxyethane to this solution gave a precipitate, which redissolved upon mixing. Addition of a 200% excess gave a permanent precipitate. We conclude that formation of the aluminum chloride-ether complex is reversible, and, clearly, excess chloride will suppress the reaction. When sufficient dimethoxyethane is added to force the reaction, a permanent precipitate is formed, and this precipitate is insoluble in a solution containing excess dimethoxyethane. However, we had already observed that when twice as many mols of dimethoxyethane as salt were added to a solution of a lithium salt, the precipitate

Table I. Analyses of thionyl chloride electrolyte salts

Sample number	Experiment		Analytical results				Molar ratios		Yield based on Al ³⁺ *
	Mols AlCl ₃	Salt	Mols Al ³⁺	Mols Cl ⁻	Total cation	Cation by difference	Cl ⁻ Al ³⁺	Cation Al ³⁺	
S3-62A	0.0227	LiCl	0.00976	0.0385	0.0397	0.0104 ^b	3.94	1.07	43% ^c
S2-73A	0.161	—	0.0128	0.0404	—	—	3.16	—	80%
S1-131A	0.0228	Li ₂ O	0.0213	0.0839	0.0851	0.0212 ^b	3.94	0.99	94%
S2-96A	0.0132	Na ₂ SO ₃	0.00900	0.0351	0.0357	0.0087 ^d	3.90	0.97	68%
S1-150A	0.0215	Li ₂ CO ₃	0.0189	0.0768	0.0761	0.0194 ^b	4.06	1.03	88%
S2-89A ^e	0.0133	Li ₂ S	—	—	—	—	—	—	—
S3-73A ^f	—	N(CH ₃) ₄ AlBr ₄ ^g	0.645 × 10 ⁻⁴	2.54 × 10 ^{-3 h}	2.77 × 10 ⁻³	0.835 × 10 ^{-3 i}	3.94	1.29	—
S3-68A	0.0183 ^j	—	0.0149	0.0494 ^b	—	—	3.32	—	81%

* Dimethoxyethane was measured by volume and a one-to-one molar ratio to AlCl₃ was used except where noted.

^b Li⁺.

^c 88% of dimethoxyethane, known from its volume and density to be the limiting reagent in this experiment.

^d Na⁺.

^e Sulfur, identified by its melting point [observed: 108°-113°C, literature: 112.8°C, (35)], was isolated from this sample. No further work was done on this system.

^f Dimethoxyethane was not used in this sample, see Experimental.

^g Prepared by the method in Ref. (23).

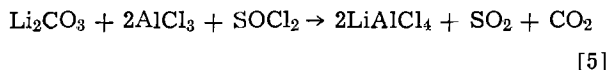
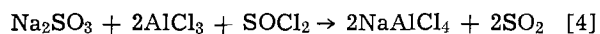
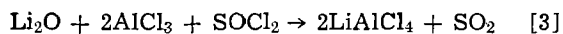
^h No Br⁻ was detected.

ⁱ N(CH₃)₄⁺.

^j AlBr₄⁻.

redissolved. We conclude that there are two different precipitates and that the precipitate of lithium tetrachloroaluminate is probably a salt of an ether chelate of the lithium ion which is soluble in a solution containing excess dimethoxyethane.

Analysis of the electrolytes.—We found that when oxide or a source of oxide (third, fourth, and fifth items in Table I) were refluxed with aluminum chloride and thionyl chloride, they reacted completely to form tetrachloroaluminate ion. This is not surprising, since thionyl chloride is a strong inorganic as well as organic chlorinating reagent (26). The probable reactions are



AlCl_3 has been observed to catalyze reactions of thionyl chloride with a variety of metals (27) and it might also catalyze the already observed reaction of SOCl_2 with oxides (28).

Our results on the electrolyte based on Li_2O are in agreement with those reported by J. P. Gabano. He found, as we did, that when Li_2O was refluxed it reacted completely to form LiAlCl_4 and presumably SO_2 (third item in Table I) (29). We did not attempt to characterize the products of the reaction of Li_2O with AlCl_3 and SOCl_2 at room temperature because our isolation technique does not work on a mixture. In our opinion, the results obtained by Gabano in this reaction at room temperature (6) can be ascribed to incompleteness of reaction. While AlCl_3 forms complexes with both SO_2 (30) and SOCl_2 (31), the complexes formed with SOCl_2 have been isolated from mixtures (31), while that formed with SO_2 was made from an equimolar mixture of AlCl_3 and SO_2 (30). Also, AlCl_4^- can be isolated from solution in sulfur dioxide (32). Therefore, we do not feel $\text{AlCl}_3 \cdot \text{SO}_2$ is an important constituent of this system.

Our results when Li_2S is used as a Lewis base are in agreement with a suggestion made by Abraham *et al.* (11) that elemental sulfur might be formed (sixth item in the Table I). AlCl_3 catalyzes reaction between thionyl chloride (containing oxidized sulfur) and lithium sulfide (containing reduced sulfur), a possibility clearly recognized by those who originally worked on this system (11).

Our observation of halogen exchange on both AlBr_3 and AlBr_4^- is not surprising in view of the well-known halogen lability of thionyl chloride (16) and the previously observed lability of halogen on aluminum (18) (items seven and eight in Table I).

Conclusions

This isolation technique can be and here has been used to isolate and characterize the anions of salts in solution in thionyl chloride. It is not limited to lithium; we found that sodium worked also (fourth item in Table I). There are definite limitations to this technique. It cannot be used on mixtures, and it cannot be used quantitatively to establish the total concentration of salt in the electrolyte. Nonetheless, it may be possible that this kind of technique is usable in other solvents also.

Finally, our work shows that it is important that the reactivity of thionyl chloride be considered when attempts are made to synthesize or dissolve new salts in this solvent. Both the Li_2O -based (6) electrolyte and $\text{Li}_2\text{B}_{10}\text{Cl}_{10}$ (5) have been proposed as solutions to the voltage delay problem in lithium/thionyl chloride batteries. The evidence above and elsewhere (6, 7, 29) now indicates that both of these salts react with thionyl chloride to produce SO_2 . SO_2 has already been shown to alleviate voltage delay (33). This means that every

publicly proposed solution to this problem of which we are aware inadvertently or advertently adds SO_2 to the electrolyte except where reserve cell configurations are used (34), and SO_2 may be the cause of improved battery performance observed with these electrolytes. Clearly there needs to be a thoughtful reevaluation of research on this problem.

Acknowledgment

We thank the John B. O'Hara Chemical Sciences Institute of the University of Dallas for financial support. We thank Amalia R. Cipolla for her assistance with the qualitative experiments on the identity of the precipitate.

Manuscript submitted June 1, 1983; revised manuscript received Oct. 10, 1983.

REFERENCES

- W. K. Behl, in "Proceedings of the 28th Power Sources Conference," Atlantic City, NJ, June 12-15, 1978, The Electrochemical Society, Inc., p. 30 (1979).
- N. Marincic, A. Lombardi, and C. Schlaikjer, in "Proceedings of the 27th Power Sources Conference," Atlantic City, NJ, June 21-24, 1976, p. 37 (1977).
- A. Leef and A. Gilmour, *J. Appl. Electrochem.*, **9**, 663 (1979).
- J. P. Gabano and P. Lenfant, in "Battery Design and Optimization," S. Gross, Editor, p. 348, The Electrochemical Society Softbound Proceedings Series, Princeton, NJ (1979).
- C. R. Schlaikjer, U.S. Pat. 4,020,240 (1977).
- J. P. Gabano and G. Gelin, *Power Sources*, **8**, 3 (1980).
- C. A. Young, H. Van Willigen, and R. F. Lee, *Inorg. Chim. Acta*, **65**, L241 (1982).
- R. J. Staniewicz and R. A. Gary, *This Journal*, **126**, 981 (1979).
- K. French, P. Cukor, C. Persiani, and J. Aubourn, *ibid.*, **121**, 1045 (1974).
- J. Bressan, G. Feuillade, and R. Wiart, *ibid.*, **129**, 2649 (1982).
- K. M. Abraham, R. M. Mank, and G. L. Holleck, Report to U.S. Army Electronics Research and Development Command, DELET-TR-78-0564-F, pp. 68-87, Fort Monmouth, NJ (1980).
- B. Gilbert and R. A. Osteryoung, *J. Am. Chem. Soc.*, **100**, 2725 (1978).
- B. Tremillon, A. Bermond, and R. Molina, *J. Electroanal. Chem.*, **74**, 53 (1976).
- K. W. Fung and D. A. Aikens, *Inorg. Nucl. Chem. Lett.*, **11**, 669 (1975).
- V. Gutman, U. Mayer, and R. Kristi, *Synth. React. Inorg. Met.-Org. Chem.*, **4**, 523 (1974).
- L. F. Johnson, Jr. and T. H. Norris, *J. Am. Chem. Soc.*, **79**, 1584 (1957).
- J. L. Huston, *J. Inorg. Nucl. Chem.*, **2**, 128 (1956).
- R. G. Kidd and D. R. Truax, *J. Am. Chem. Soc.*, **90**, 6867 (1968).
- See also J. C. Lockhart, *Chem. Rev.*, **65**, 131 (1965).
- L. C. Howick and J. O. Jones, *Talanta*, **9**, 1037 (1962).
- H. H. Willard, L. L. Merritt, Jr., J. A. Dean, and F. A. Settle, Jr., "Instrumental Methods of Analysis," 6th ed., pp. 681, 955, D. Van Nostrand, New York (1981).
- H. Kratochvil, "Chemical Analysis," pp. 103-107, Barnes and Noble, New York (1970).
- R. H. Bradley, P. N. Brier, and D. E. H. Jones, *J. Chem. Soc. A*, 1397 (1971).
- T. R. Bettle, *Chem. Eng. News*, p. 5, July 12, 1982.
- G. B. Frankforter and E. A. Daniels, *J. Am. Chem. Soc.*, **37**, 2560 (1915); H. Gilman and L. D. Apperson, *J. Org. Chem.*, **4**, 168 (1939); P. Hagenmuller and J. Rouxel, *C.R. Acad. Sci.*, **247**, 1623 (1958); J. L. Atwood, D. C. Hrncir, R. Shakir, M. S. Dalton, R. D. Priestler, and R. D. Rogers, *Organometallics*, **1**, 1021 (1982); but see also R. E. Van Dyke and H. E. Crawford, *J. Am. Chem. Soc.*, **72**, 2829 (1950).
- M. Davis, H. Szkuta, and A. J. Krubsack, *React. Mech. of Sulfur Compounds*, **5**, 1 (1970).
- R. A. Hubbard and W. F. Luder, *J. Am. Chem. Soc.*, **73**, 1327 (1951).

28. H. B. North and A. M. Hageman, *ibid.*, **35**, 352 (1913).
29. J. P. Gabano, in "Lithium Nonaqueous Battery Electrochemistry," E. B. Yeager, B. Schumm, Jr., G. Blomgren, D. R. Blankenship, V. Leger, and J. Akridge, Editors, p. 71, The Electrochemical Society Softbound Proceedings Series, Pennington, NJ (1980).
30. H. Gerding and E. Smit, *Z. Phys. Chem. B*, **51**, 200 (1942).
31. D. A. Long and R. T. Bailey, *Trans. Faraday Soc.*, **59**, 594 (1963).
32. P. Barbier and G. Mairesse, *C.R. Acad. Sci., Ser. C*, **272**, 66 (1971).
33. D. L. Chua, W. C. Merz, and W. S. Bishop, in "Proceedings of the 27th Power Sources Conference," Atlantic City, NJ, June 21-24, 1976, p. 33 (1976).
34. N. Marincic and A. Lombardi, U.S. Pat. 4,087,594 (1978); see also N. Marincic and A. Lombardi, Research and Development Report for U.S. Army Electronics, ECOM-74-0108-F, pp. 145-147 (1977).
35. "CRC Handbook of Chemistry and Physics," R. C. Weast, Editor, p. B143, The Chemical Rubber Co., Cleveland, OH (1971).

Photoelectrochemical Investigation of a Poly(Ethylene Oxide) Cell

Anthony F. Sammells* and Peter G. P. Ang*

Eltron Research, Incorporated, Naperville, Illinois 60540

The modification of poly(ethylene oxide) (PEO) into an alkali ion conducting polymer solid electrolyte by its formation of solid solutions with several alkali metal salts has been well documented over the last few years (1-5). Although the ionic conductivities of such materials are quite low ($\approx 10^{-5} \Omega^{-1} \text{cm}^{-1}$ at ambient temperature), particularly in comparison to aqueous electrolytes, this in part can be compensated for by their fabrication into thin electrolyte samples. Such solid polymer electrolyte materials can conveniently be prepared by evaporation of methanol from solutions containing PEO and an appropriate alkali ion salt onto a suitable substrate. Formation of a thin solid polymer electrolyte layer is then achieved typically by annealing under vacuum at temperatures below 120°C. Transference number (t) measurements for PEO/NaSCN-based solid polymer electrolytes have shown predominantly alkali ion conductivity.

Recently, some preliminary photocurrent/voltage data were reported (7) on a solid-state photoelectrochemical (PEC) cell consisting of PEO/KI, I_2 as a solid polymer redox electrolyte prepared on a tin oxide conducting substrate in intimate contact with an n-Si photoanode. This photoanode was initially coated with platinum and subsequently protected from photoanodic corrosion effects by a layer of polypyrrole. The substitution of alternate redox electrolytes for the aqueous systems predominantly pursued in photoelectrochemical cells is one approach to address photoanodic corrosion effects at the illuminated photoelectrode/electrolyte interface. Alternative redox electrolytes have included organic nonaqueous (8) ambient-temperature molten salts (9) and inorganic solid electrolytes (10). These latter electrolytes have been previously discussed by us at the solid-state interface of n-CdSe with the silver-ion conducting solid electrolyte RbAg_4I_5 . With this solid electrolyte, however, photoactivity was detected even in the absence of a semiconductor junction, a probable consequence of the spontaneous photoreduction of Ag^+ and/or the presence of a Demer-type photovoltage (11). Because of this interfering photoeffect with silver-ion conducting solid electrolytes, there is an obvious incentive to investigate PEC phenomena using alternative redox solid electrolytes where the opportunity for photoeffects by the solid electrolyte is less likely to occur.

In work discussed here, PEC measurements have been made on the solid polymer electrolyte PEO/NaSCN, containing $\text{Na}_2\text{S}/\text{S}$ as an introduced redox species. The fact that various redox couples can be incorporated into these alkali-ion conducting poly-

meric materials may give us the opportunity to use such modified materials in photoelectrochemically rechargeable cells where the stored energy, via oxidized or reduced species within the electrolyte and close to the photoelectrode, could be later electrochemically discharged. This would require that the redox species incorporated within the polymer be essentially immobile. In mainly crystalline PEO electrolyte, ionic conduction is predominantly via an alkali ion transport mechanism along polymer helical chains; for more amorphous PEO materials, a configurational entropy-dominated transport process is likely (12).

Aqueous liquid-junction PEC cells with storage, having the general configuration p-InP/ S^{2-} , $\text{S}_n^{2-}/\text{I}^-$, $\text{I}_2/\text{n-WSe}_2$ have previously been investigated (13). Here the relatively high ionic conductivity of the aqueous electrolytes used allowed large interelectrode distances to be tolerated. For PEO-based cells, however, small interelectrode distances are essential to minimize internal resistance losses. To identify an analogous two-photoelectrode solid-state cell based upon PEO requires that one of the photoelectrodes be transparent, to ensure illumination of both electrode/redox electrolyte interfaces. The use of p-InP as a photocathode in such devices would, consequently, preclude the use of n-WSe₂ as the second photoelectrode.

The PEO-based redox electrolyte was prepared by introducing PEO (Aldrich Chemical Company, MW 600,000) and NaSCN into anhydrous methanol in a 4.5:1 molar ratio of the polymer repeat unit, as discussed by others (6). With continuous stirring an equimolar (0.1M) solution of Na_2S and S up to a sulfide concentration corresponding to 1/10 that of NaSCN was slowly added. During addition of the sulfide species to the PEO · NaSCN solution, the mixture was initially yellow, but became colorless after stirring for 30 min. Upon standing for several weeks, some precipitation became evident in this solution. A PEC cell was prepared by initially placing a drop of freshly prepared PEO · NaSCN/ Na_2S solution onto the surface of a Nesatron tin-doped indium oxide conducting glass electrode and allowed to dry in the atmosphere. This was then treated under vacuum at 75°C for 1h. The p-InP photocathode was obtained from Crysta Communications, Incorporated, (Zn-doped $6 \times 10^{16} \text{cm}^{-3}$, $\langle 111 \rangle$ surface used) and had a resistivity of 0.6 Ωcm . Ohmic contact was made by first sputtering a thin layer of gold, followed by electrodeposited Zn, and later another layer of sputtered gold. The electrode was annealed at 465°C for 1 min. Initial attempts to make contact of this photoelectrode to the solid polymer redox electrolyte on the conducting glass met with mixed results. Reproducible

* Electrochemical Society Active Member.

Key words: poly(ethylene oxide), indium phosphide, solid-state photoelectrochemical cell.

contact was made by introducing a drop of the PEO containing methanol solution onto the photocathode, and after drying, lightly pressing onto the already cured polymer electrolyte present on the conducting glass surface. Final curing of this cell was performed under vacuum for 2h at 75°C.

The initial photoelectrochemical performance of the cell p-InP/PEO · NaSCN, Na₂S, S/cond. glass at 25°C is shown in Fig. 1 under 100 mW/cm² quartz iodine illumination. Positive photopotentials of 200 mV were observed. Upon potentiostating, the p-InP at -1.2V vs. its dark potential, cathodic photocurrents of ≈10 μA/cm² were observed. The rather high photoelectrode bias voltage required to achieve such photocurrents and poor fill factor are in part symptomatic of the highly resistant polymer electrolyte used. Cell resistances could be significantly reduced by increasing temperature, thereby resulting in higher currents. Cells prepared, however, were mechanically stabilized by the use of a wax support between the photoelectrode current collector and a glass substrate. Because of this, cell temperature excursions were avoided.

The photoelectrochemical oxidation of the Na₂S/S couple incorporated into PEO was also investigated on n-GaAs. The n-GaAs single crystal was obtained from Crystal Specialties Incorporated, and had a carrier density of 10¹⁶/cm³ after silicon doping. Ohmic contact to the semiconductor was made by thin-film evaporation of an 88Au/12Ge alloy. The <111> face was used in these experiments after initially etching in H₂SO₄/H₂O₂ before drying and coating with PEO · NaSCN, Na₂S, S. This photoanode was contacted to a Nesatron conducting glass electrode and annealed in an analogous manner to that discussed previously for p-InP. A photocurrent/potential curve for this cell is shown in Fig. 2. Here the initial photopotential obtained was -150 mV using 100 mW/cm² quartz iodine illumination. Anodic photocurrents of 9 μA/cm² were obtained after subjecting the cell to a 1.5V positive bias. Because of the opaque nature of gallium arsenide, however, this photoanode cannot be used in a two-photoelectrode cell where p-InP is used as a photocathode. Similar cells prepared using single-crystal n-CdS typically gave negative photopotentials in the -200 to -250 mV range.

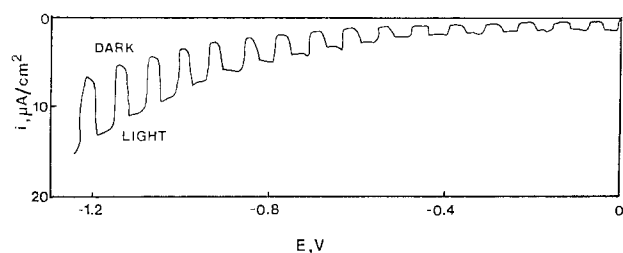


Fig. 1. Current-voltage curve for the cell p-InP/PEO.NaSCN, Na₂S,S/cond. Glass with and without 100 mW/cm² quartz iodine illumination.

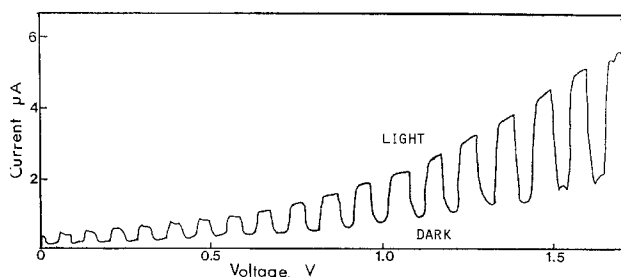


Fig. 2. Current-voltage curve for the cell n-GaAs/PEO.NaSCN, Na₂S,S/cond. Glass with and without 100 mW/cm² quartz iodine illumination.

It is necessary for a two-photoelectrode solid-state PEC cell using a solid polymer electrolyte not only that one of the photoelectrodes be transparent, but also that the redox species incorporated into the PEO not corrode the photoelectrodes during illumination. Although we have found the redox kinetics of halogens introduced into PEO, in general, higher than for the Na₂S/S couple, we have not yet been able to fabricate a two-photoelectrode cell which fulfills the above requirements using a halogen as one of the redox couples.

As a result, we have fabricated the solid-state two-photoelectrode cell p-InP/PEO · NaSCN, Na₂S, S/n-CdS using single-crystal photoelectrodes. The n-CdS single crystal was obtained from Cleveland Crystal. Ohmic contact to the material was made by initially contacting with a gallium-indium eutectic followed by silver epoxy and curing at 150°C for 1h. The two-photoelectrode cell was prepared by placing a drop of the PEO redox electrolyte onto the surface of each electrode, allowing to dry in the atmosphere, and partially curing at 60°C under vacuum for 1h. The two electrodes were lightly pressed together to make effective contact and then finally cured at 75°C for 1h. The cell is shown schematically in Fig. 3. The dark open-circuit voltage was 560 mV, presumably due to some nonequilibrium effects between the photoelectrodes and PEO. Upon illumination through the n-CdS photoanode to the solid-state junctions of the redox PEO with both these photoelectrodes under 100 mW/cm² quartz iodine illumination, photopotentials up to 540 mV could be initially generated. Hence initial overall cell voltages in excess of 1000 mV could be achieved between the two photoelectrodes. After several hours, the photopotential realized with this cell reduced to ≈400 mV. The photoresponse of this cell is shown in Fig. 4. Potentiostating the cell to 0.0V in the dark resulted in the passage of insignificant currents. Even when this cell was potentiostated at 0.0V under illumination, currents only in the 0.3 μA range were observed as a result of the high resistivity of the electrolyte under ambient conditions.

We conclude that although PEO-based redox electrolytes offer the opportunity to fabricate solid-state PEC cells, their eventual practicality into small devices is contingent upon increasing PEO ionic conductivity. Compensation of this present limitation by the use of small interelectrode spacing greatly increases the susceptibility to cell shorting during fabrication.

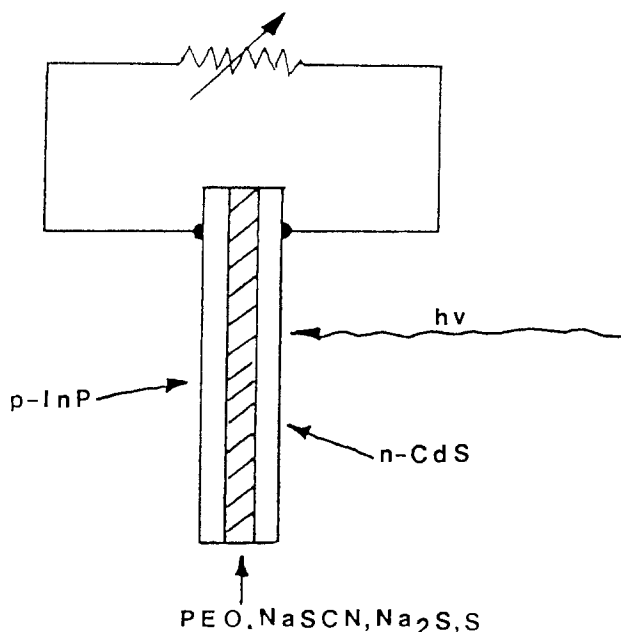


Fig. 3. Schematic diagram of cell p-InP/PEO · NaSCN, Na₂S, S/n-CdS.

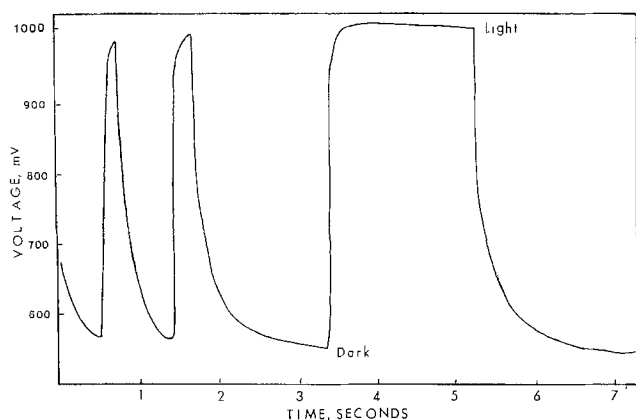


Fig. 4. Variation of voltage with time for cell p-InP/PEO-NaSCN. Na₂S, S/n-CdS with and without 100 mW/cm² quartz iodine illumination.

Acknowledgment

This work was supported by the Office of Naval Research under contract no. N00014-83-C-0108.

Manuscript submitted May 13, 1983; revised manuscript received ca. Oct. 12, 1983.

REFERENCES

1. D. E. Fenton, S. M. Parker, and P. V. Wright, *Polymer*, **14**, 589 (1973).
2. P. V. Wright, *Br. Polymer J.*, **7**, 319 (1975).
3. C. C. Lee and P. V. Wright, *Polymer*, **23**, 681 (1982).
4. B. L. Papke, M. A. Ratner, and D. F. Shriver, *J. Phys. Chem. Solids*, **42**, 493 (1981).
5. D. R. Payne and P. V. Wright, *Polymer*, **23**, 690 (1982).
6. R. DuPon, D. H. Whitmore, and D. F. Shriver, *This Journal*, **128**, 715 (1981).
7. T. Skotheim and I. Lundstrom, *ibid.*, **129**, 894 (1982).
8. M. E. Langmuir, P. Hoening, and R. D. Rauh, *ibid.*, **128**, 2357 (1981).
9. P. Singh, R. Singh, K. Rajeshwar, and J. DuBow, *ibid.*, **128**, 1145 (1981).
10. P. G. P. Ang and A. F. Sammells, in "Photoeffects at Semiconductor/Electrolyte Interfaces," A. J. Nozik, Editor, pp. 287-299, ACS Symp. Series 146, Washington, DC (1981).
11. H. Dember, *Physik Z.*, **33**, 207 (1932).
12. B. L. Papke, M. A. Ratner, and D. F. Shriver, *This Journal*, **129**, 1694 (1982).
13. P. G. P. Ang, C. J. Liu, A. A. Rossignuolo, A. J. Tiller, and A. F. Sammells, in "Measurement Techniques for Photoelectrochemical Solar Cells," W. L. Wallace, A. G. Nozik, S. K. Deb, and R. H. Wilson, Editors, p. 697, The Electrochemical Society Softbound Proceedings Series, Pennington, NJ (1982).

Utility of Surface Reaction Entropies for Examining Reactant-Solvent Interactions at Electrochemical Interfaces. Ferricinium-Ferrocene Attached to Platinum Electrodes

Joseph T. Hupp and Michael J. Weaver*

Department of Chemistry, Purdue University, West Lafayette, Indiana 47907

Reactant-solvent interactions are of prime importance to both the kinetics and thermodynamics of electrode processes. Since electrochemical reactions inevitably occur within the interfacial region, it is desirable to gain information on the nature of reactant solvation at the electrode surface as well as in bulk solution. We have demonstrated that useful information on the latter for simple redox couples can be obtained from the so-called reaction entropy (ΔS°_{rc}) determined from the temperature dependence of the formal potential (E^f) using a nonisothermal cell arrangement (1)

$$\Delta S^{\circ}_{rc} = F(dE^f/dT)_{ni} \quad [1]$$

Since the temperature dependence of the thermal liquid junction potential in such a cell can be arranged to be negligibly small, ΔS°_{rc} essentially equals the difference ($\bar{S}^{\circ}_{red} - \bar{S}^{\circ}_{ox}$) between the ionic entropies of the reduced and oxidized forms of the redox couple in the bulk solution. The reaction entropies of simple transition-metal redox couples have been found to be extremely sensitive to the chemical nature of the coordinated ligands and the surrounding solvent, illustrating the importance of specific ligand-solvent interactions to the overall redox thermodynamics (1-5).

It would clearly be desirable additionally to determine reaction entropies for redox couples residing in the interfacial region. Such surface reaction entropies ($\Delta S^{\circ}_{rc,s}$) would yield insight into the solvation changes accompanying the elementary electron-transfer step

for the redox couple in a particular interfacial environment. For redox couples present at sufficiently high concentrations at the interface to enable the formal potential for the interfacial (adsorbed) redox couple (E_a^f) to be measured, values of $\Delta S^{\circ}_{rc,s}$ can be obtained directly from (cf. Eq. [1])

$$\Delta S^{\circ}_{rc,s} = F(dE_a^f/dT)_{ni} \quad [2]$$

Whereas ΔS°_{rc} corresponds to the overall entropy driving force for transforming the bulk-solution reactant to product, $\Delta S^{\circ}_{rc,s}$ equals the thermodynamic entropy change for the heterogeneous electron-transfer step itself (6). Thus $\Delta S^{\circ}_{rc,s}$ and ΔS°_{rc} are related by

$$\Delta S^{\circ}_{rc,s} = \Delta S^{\circ}_{rc} + \Delta S^{\circ}_p - \Delta S^{\circ}_s \quad [3]$$

where ΔS°_p and ΔS°_s are the entropic work terms associated with forming the "precursor" state for electron transfer from the bulk reactant, and the "successor" state from the bulk product, respectively (6). We report here values of $\Delta S^{\circ}_{rc,s}$ for a surface-attached ferricinium-ferrocene couple in several solvents in order to illustrate the virtues of such measurements for elucidating the nature of reactant-solvent interactions at electrochemical interfaces.

For surface redox couples where the redox center lies within the inner layer, ΔS°_p and ΔS°_s are expected to be both nonzero and different, so that $\Delta S^{\circ}_{rc,s} \neq \Delta S^{\circ}_{rc}$. Indeed, we have recently obtained such a result for a specifically adsorbed Co(III)/(II) sepulchrate couple vs. the corresponding bulk solution couple (7). For electrode reactions where the redox center is present in the diffuse layer or at the outer Helmholtz plane, it

* Electrochemical Society Active Member.

is conventional to assume that the work terms are purely coulombic in nature (8) so that $\Delta S_p \approx \Delta S_s \approx 0$ and hence $\Delta S_{rc,s} \approx \Delta S_{rc}$. This assumption is required in order to extract true frequency factors for electron transfer from the temperature dependence of electrochemical kinetics (6, 9). However, in actuality even $\Delta S_{rc,s}$ for an outer-sphere reaction might be expected to differ significantly from ΔS_{rc} in a given solvent medium, bearing in mind the structure sensitivity of ionic entropies (1-5) and the possibility that the solvating environment in the vicinity of the surface may differ significantly from that in the bulk solution. Indeed, one reason for pursuing the present study was to discover whether differences which we have recently observed between the energetics of structurally similar electrochemical reactions involving surface-bound and solution-phase redox couples (10) could be rationalized in terms of differences between the bulk and interfacial solvation environments.

Measurement of Surface Reaction Entropies

Although it is not feasible to evaluate $\Delta S_{rc,s}$ for outer-sphere (*i.e.*, unadsorbed) redox couples, a suitably high interfacial concentration of normally unadsorbed, and, presumably, fully solvated, reactant can be achieved by attaching the redox center to the electrode surface via an inert covalent linkage. As a model system, we studied the ferricinium-ferrocene redox couple attached to a platinum electrode, as shown in Fig. 1. We prepared the surface-bound ferrocene by using the chemical modification procedure described by Sharp *et al.* (11). This system was selected since both the bond to the platinum surface and the electroactive center itself are exceptionally stable, placing the redox center about 6-8Å from the electrode surface (11). In addition, it was anticipated that the surface-attached couple would exhibit reversible behavior in a variety of solvents.

Efforts to prepare the same ferrocene derivative in solution were unsuccessful. Nevertheless, *n*-ferrocenemethylene-*p*-toluidine (Alfred Bader Chemicals), shown in Fig. 2, was selected as a reasonably close analog of the surface-attached complex, since in the vicinity of the redox center the structures of the two substituents are closely similar. Formal potentials for either the surface-attached or bulk-solution redox couples were obtained from the average peak potentials of the cyclic voltammograms. [Quasi-reversible, rather than reversible, behavior was typically observed for the surface-attached, as well as bulk-solution, couples, with anodic-cathodic peak separations up to *ca.* 50 mV even in the presence of IR compensation; cf. Ref. (11)]. Values of E_a^f for the reduction of the surface-bound ferricinium derivative could be measured with sufficient accuracy to enable $\Delta S_{rc,s}$ to be determined to within about $6 \text{ J} \cdot \text{deg}^{-1} \cdot \text{mol}^{-1}$. Representative E_a^f data obtained in aqueous solution are plotted against temperature in Fig. 3. Data also were obtained in methanol, acetonitrile, dimethylsulfoxide, and sulfolane. Attempts were made to measure $\Delta S_{rc,s}$ in

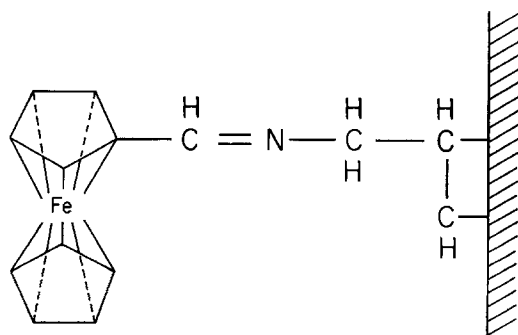


Fig. 1. Mode of attachment of ferrocene to platinum surface

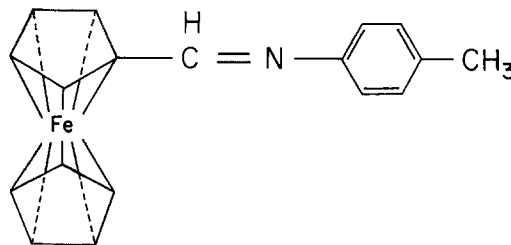


Fig. 2. Ferrocene derivative (*n*-ferrocenemethylene-*p*-toluidine) used as solution analog of surface-attached ferrocene in Fig. 1.

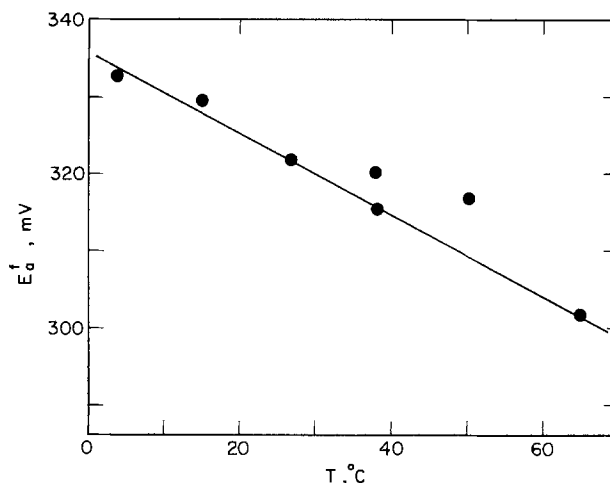


Fig. 3. Representative plot of E_a^f vs. temperature in aqueous 0.1M TEAP. Potentials vs. saturated calomel electrode at 24°C, using nonisothermal cell arrangement (1).

formamide, nitromethane, and acetone, but were unsuccessful with the first solvent due to instability of the surface complex, and with the other two because of irreproducible behavior. Either 0.1M tetraethylammonium perchlorate or 0.2M LiClO₄ was used as the supporting electrolyte. Additional experimental details are given in Ref. (3).

The resulting values of $\Delta S_{rc,s}$ and E_a^f are summarized in Table I, together with ΔS_{rc} data for the ferrocene and *n*-ferrocenemethylene-*p*-toluidine couples in bulk solution. Contrary to our initial expectations, the reaction entropies for the surface couple and its solution analog were found to be in reasonable agreement in each solvent. Evidently, the solvent interactions experienced by the surface-attached couple are not noticeably different from the reactant-solvent interactions occurring in bulk solution. At least for this couple, therefore, it appears that differences between solvent structure in bulk solution and in the double layer where the surface redox site is located do not greatly influence the electron-transfer energetics.

Interpretation of Surface Reaction Entropy Values

Although the two derivatized ferrocene couples (Fig. 1 and 2) yield similar reaction entropies, these tend to be less positive than the ΔS_{rc} values for the unsubstituted ferricinium-ferrocene couple (Table I). Furthermore, the formal potentials for the surface-attached couple in various solvents are positive of those for ferrocene itself, while the E^f values for the *n*-ferrocenemethylene-*p*-toluidine couple are still more positive (Table I; note that the E^f values quoted are *vs.* that for ferrocene itself in the same solvent). The differences in formal potentials between ferrocene and its derivatives are probably manifestations of the greater electron withdrawing capabilities of carbon-nitrogen double bonds as compared to hydrogen (12). Thus, such an electron withdrawing substituent would tend to stabilize the relatively electron-rich ferrocene re-

Table I. Formal potentials (mV) and reaction entropies (J deg⁻¹ mol⁻¹) for surface-attached and bulk-solution ferricinium-ferrocene couples

Solvent	ΔT_{bp}^a	Surface-attached ferrocene		n-Ferrocenemethylene-p-toluidine		Ferrocene ^c	$(\Delta S^{\circ}_{rc,s})_{Born}^d$	Ref.
		$\Delta S^{\circ}_{rc,s}$	E_{a1}^f	ΔS°_{rc}	E_{r1}^f	ΔS°_{rc}		
Water	174	-50	201	<i>e</i>	<i>e</i>	-21	10.5	(18)
Methanol	117	-1	48	-12	172	13	27.0	(19)
Dimethylsulfoxide	135	13	122	<i>f</i>	~180	52	14.0	(20)
Sulfolane	—	25	74	33	140	31	14.0	(21)
Acetonitrile	105	25	92	25	146	48	20.5	(20)
Acetone	62	—	—	54	225	67	40.0	(22)

^a From Ref. (15).

^b Formal potential vs. solution ferrocene/ferricinium couple in the same medium at 25°C, except for sulfolane at 30°C. Supporting electrolyte was 0.1M tetraethylammonium perchlorate; 0.2M LiClO₄ used in dimethylsulfoxide.

^c From Ref. (3).

^d $\Delta S^{\circ}_{rc,s}$ at 25°C predicted from the Born model; calculated from Eq. [4] using dielectric constant data from literature indicated.

^e Measurements precluded because of insolubility of complex.

^f Irreproducibility of E^f prevented accurate determination of ΔS°_{rc} .

dox center to a greater extent than for ferricinium, leaving the former more difficult to oxidize, and thereby yielding a positive shift in the formal potential. The systematic differences in reaction entropies seen between ferrocene and the derivatized couples can also be rationalized on this basis. Whether the differences in formal potentials between the adsorbed couple and its solution analog result from surface attachment or from differences in substituent properties is not entirely clear. A detailed study of substituent effects on the redox thermodynamics and kinetics of several solution ferrocene derivatives is in progress.

A curious aspect of the results is the marked solvent dependence of both the $\Delta S^{\circ}_{rc,s}$ and ΔS°_{rc} values. The magnitude of these quantities expected from purely continuum electrostatic considerations is given by (3)

$$\Delta S^{\circ}_{rc,s} (= \Delta S^{\circ}_{rc}) = - (e^2 N / 2r\epsilon T) (d \ln \epsilon / d \ln T) \quad [4]$$

where e is the electronic charge, N is Avogadro's number, ϵ is the dielectric constant of the solvent, and r is the radius of the ferricinium cation. The $\Delta S^{\circ}_{rc,s}$ values listed in the last column of Table I are obtained from Eq. [4] using literature values of ϵ and assuming that $r = 3.8\text{\AA}$ (13). There is clearly no general pattern of agreement between the experimental and these calculated quantities, the Born treatment predicting a much milder solvent dependence of $\Delta S^{\circ}_{rc,s}$ than is observed. Similar breakdowns of the dielectric continuum model in predicting reaction entropies have

been found for several bulk solution couples in a number of solvents (1-5).

A probable reason for the failure of Eq. [4] is that the major property determining the entropy of charge-induced solvent reorientation is the degree of "internal order" of the solvent (i.e., self-association and long-range structuring induced by hydrogen bonding), rather than the macroscopic dielectric properties (14, 15). Thus, a solvent having a high degree of internal order would be relatively unperturbed by a charged molecule, whereas considerable solvent ordering around the ion would occur in a medium having little intermolecular structure. Since such charge-dipole interactions will be absent for neutral ferrocene, a positive contribution to the reaction entropy ($\bar{S}^{\circ}_{red} - \bar{S}^{\circ}_{ox}$) would be anticipated for the present redox couples, especially in relatively nonassociated solvents. Criss *et al.* (14, 15) have suggested estimating the degree of internal order of a solvent from the difference in boiling point (ΔT_{bp}) compared to that for a structurally analogous hydrocarbon. These values of ΔT_{bp} are also listed in Table I. Indeed, the $\Delta S^{\circ}_{rc,s}$ values for the surface-attached ferrocene couple do for the most part vary as expected with the corresponding values of ΔT_{bp} .

An unusual result which merits comment is the large negative value of $\Delta S^{\circ}_{rc,s}$ ($-50 \text{ J deg}^{-1} \text{ mol}^{-1}$) found in water (Table I). A small negative value of ΔS°_{rc} has previously been observed for the bulk-solu-

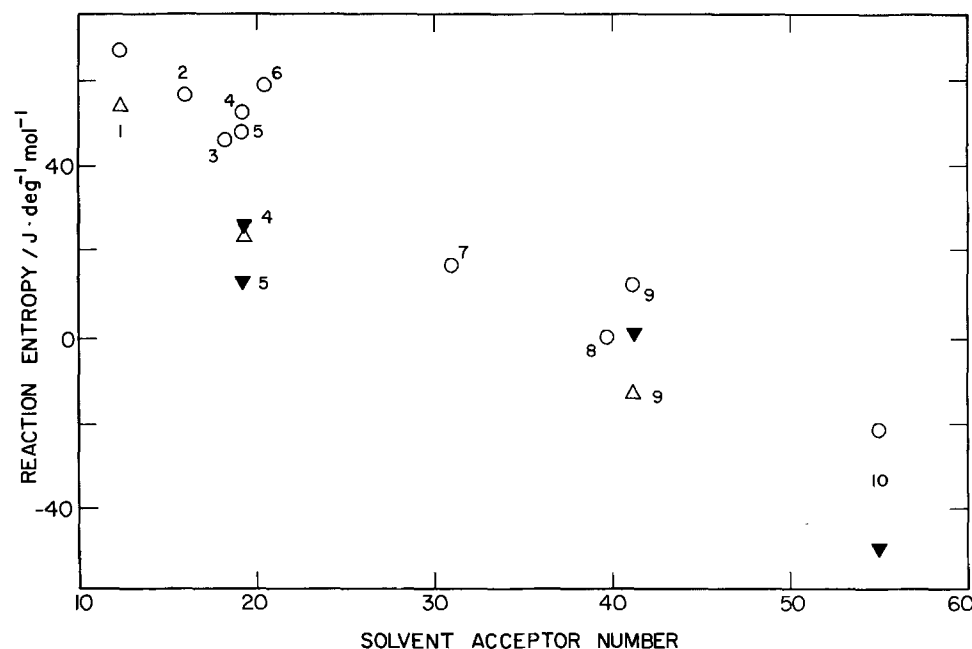


Fig. 4. Plot of reaction entropies for surface-attached and solution-phase ferricinium-ferrocene couples in various solvents vs. solvent Acceptor Number (16). Filled triangles: surface-attached ferrocene (Fig. 1). Open triangles: bulk-solution derivatized ferrocene (Fig. 2). Open circles: bulk-solution ferrocene. Key to solvents: 1: acetone. 2: dimethylformamide. 3: propylene carbonate. 4: acetonitrile. 5: dimethylsulfoxide. 6: nitromethane. 7: N-methylformamide. 8: formamide. 9: methanol. 10: water.

tion ferrocene couple, also in water (3). This suggests that the net solvent ordering in the vicinity of the surface-attached redox center is less extensive in the cationic than in the neutral state, in qualitative disagreement with the expectations from an electrostatic treatment. These negative reaction entropy values possibly result from donor-acceptor interactions between the cyclopentadienyl rings and the acidic water hydrogens (3). Since the electron density on the cyclopentadienyl rings will be greater in the reduced state, such specific solvent interactions should be enhanced, leading to increased solvent ordering and a decrease in entropy compared with that for the oxidized state. If such an explanation were correct a correlation between $\Delta S^{\circ}_{rc,s}$ and the acidity of the solvent might be expected. Figure 4 shows a plot of the reaction entropies for the adsorbed couple and its solution analog as well, as for unsubstituted ferrocene vs. the solvent "acceptor number," which is an empirical measure of the electron accepting capabilities of the solvent (16). A reasonable correlation is indeed observed. Alternatively, both the negative reaction entropies in water and methanol and the dependence upon the solvent acceptor numbers can be rationalized in terms of a negative contribution to ΔS°_{rc} arising from disruption of the surrounding solvent structure by the charged solute (17). Regardless of the detailed explanations, similar solvation factors are clearly important in determining the redox properties of the surface-attached and solution ferrocene couples.

The present work demonstrates the feasibility of determining surface reaction entropies and illustrates the utility of these measurements for elucidating the various elements of interfacial reactant-solvent interactions. Given the sensitivity of $\Delta S^{\circ}_{rc,s}$ measurements to the solvent structure, we suggest that this approach might also usefully be employed to gain insight into reactant solvation in polymer film electrodes, for which the question of solvent penetration within the film is of current interest.

Acknowledgments

This work was supported in part by the Office of Naval Research and the Air Force Office of Scientific Research.

Manuscript received June 6, 1983.

REFERENCES

1. E. L. Yee, R. J. Cave, K. L. Guyer, P. D. Tyma, and M. J. Weaver, *J. Am. Chem. Soc.*, **101**, 1131 (1979).
2. E. L. Yee and M. J. Weaver, *Inorg. Chem.*, **19**, 1077 (1980).
3. S. Sahami and M. J. Weaver, *J. Solution Chem.*, **10**, 199 (1981).
4. S. Sahami and M. J. Weaver, *J. Electroanal. Chem.*, **122**, 155 (1981).
5. S. Sahami and M. J. Weaver, *ibid.*, **122**, 171 (1981).
6. J. T. Hupp and M. J. Weaver, *ibid.*, **143**, 43 (1983).
7. J. T. Hupp, P. A. Lay, H. Y. Liu, W. H. F. Petri, A. M. Sargeson, and M. J. Weaver, *J. Electroanal. Chem.*, In press.
8. P. Delahay, "Double Layer and Electrode Kinetics," Chap. 7, 9, Interscience, New York (1965).
9. M. J. Weaver, *J. Phys. Chem.*, **80**, 2645 (1976); *ibid.*, **83**, 1748 (1979).
10. S. W. Barr and M. J. Weaver, *Inorg. Chem.*, In press; K. L. Guyer and M. J. Weaver, In press.
11. M. Sharp, M. Petersson, and K. Edstrom, *J. Electroanal. Chem.*, **95**, 123 (1979).
12. P. Zuman, "Substituent Effects in Organic Polarography," p. 76, Plenum Press, New York (1967).
13. D. R. Stranks, *Discuss. Faraday Soc.*, **29**, 73 (1960).
14. C. M. Criss, R. P. Held, and E. Luksha, *J. Phys. Chem.*, **72**, 2970 (1968).
15. C. M. Criss, *ibid.*, **78**, 1000 (1974).
16. V. Gutmann, "The Donor-Acceptor Approach to Molecular Interactions," Plenum Press, New York (1978); *Electrochim. Acta*, **21**, 661 (1976).
17. J. T. Hupp and M. J. Weaver, Submitted to *Inorg. Chem.*
18. "CRC Handbook of Chemistry and Physics," 56th Edition, p. E61 (1975-1976).
19. P. G. Sears, R. Holmes, and L. R. Dawson, *This Journal*, **102**, 145 (1955).
20. G. J. Janz and R. P. T. Tomkins, "Nonaqueous Electrolyte Handbook," Vol. I, Academic Press, New York (1972).
21. J. W. Vaughan and C. F. Hawkins, *J. Chem. Eng. Data*, **9**, 140 (1964).
22. P. Dobos, "Electrochemical Data," p. 105, Elsevier Scientific Publishing Co., Amsterdam (1975).



SSST

Structural Analysis of Silicon-Implanted Polymethyl Methacrylate Films on Glass

Carl E. Bleil and Bernard A. MacIver

General Motors Research Laboratories, Electronics Department, Warren, Michigan 48090-9055

ABSTRACT

Electron diffraction and microscopic analyses of silicon-implanted polymethyl methacrylate (PMMA) films deposited on glass substrates have been carried out with the aid of differential etching. Results show the films to consist of amorphous and polycrystalline graphite structures incorporating diamond-like structure in the bulk of the film and silicon carbide crystallites near the film-glass interface. Particle size is typically less than 50 nm with some crystallites as large as 0.5 μm .

The preparation of thin films with diamond-like properties has intrigued investigators for many years. Such properties as chemical inertness, hardness, and high electrical resistance are only a few of commercial interest. In the past, many attempts to thermally deposit films with diamond-like properties met with only limited success. However, extensive research over the past decade shows considerable promise for diamond-like carbon coatings for a wide variety of applications (1).

Recent developments in our laboratory (2) to produce special films for photolithography which were harder and more chemically inert than chromium, the standard hard surface photomask material of the semiconductor industry, led to processed films of polymethyl methacrylate (PMMA). Interestingly, these films showed properties similar to those reported by Aisenberg and Chabot (3) who used a beam of positively charged carbon ions to prepare their films. In 1976, Spencer *et al.* (4) analyzed films prepared in a manner similar to that of Aisenberg and reported them to contain polycrystalline diamond-like structures. Similarly, the earlier analysis of our films (2) showed that the composition was mainly carbon and suggested that diamond-like structures might exist but the results were not conclusive. Indeed, it is very likely that the silicon-implanted PMMA simply represents one class of the so-called diamond-like carbon, or i-C films (5).

In this paper, we present a detailed analysis of the structure of Si⁺-implanted PMMA films on glass. This was accomplished through the use of differential etching, scanning electron microscopy (SEM), and reflection electron diffraction (RED).

Experimental

Samples of processed PMMA films were prepared by first spinning PMMA dissolved in chlorobenzene onto a glass substrate and baking the film for 30 min at 180°C to remove solvent, leaving a 0.5 μm thick film of PMMA. The PMMA films were then implanted with silicon in two steps. In the first implant step, the dose was 3×10^{15} ions/cm² at 200 keV to ensure a good bond with the glass substrate and to break down C—O—H bonds, leaving mainly carbon. A second im-

Key words: hard carbon films, silicon carbide, differential etching.

plant of silicon, this time with a dose of 5×10^{15} ions/cm² at 150 keV, was used to alter the bonding of the residual carbon and to continue implanting near the film glass interface to improve adhesion. The dose rate was 2 $\mu\text{A}/\text{cm}^2$ for both implants. During this total processing, the film thickness was reduced from 0.5 μm to about 0.1 μm . The substrate temperature was assumed to be about 600 K (6). The resulting films appeared quite opaque, and when subjected to various solvents, including acids, bases, and organics, were found to be chemically inert. Similarly, scratch tests showed the films to be at least as hard as chromium films normally used for photolithography.

Transmission electron diffraction of films removed from the glass substrates with hydrofluoric acid showed only very diffuse rings normally ascribed to amorphous materials. X-ray diffraction was not tried because of the very low absorption coefficient of carbon and the fact that the films were only about 0.1 μm thick. However, reflection electron diffraction provided interesting clues to the film structure. In the earliest attempts to do RED, both spotty rings and spot patterns were observed, which suggested the presence of both polycrystalline graphite and the hexagonal diamond structure.

Based on these early results it was proposed that, if the diamond phase existed, it should exhibit an etch rate in an oxygen plasma somewhat different from the graphite structure. Such differential etching should allow RED to delineate the composition of the film with depth. Additional samples were prepared by oxygen plasma etching for various times and both SEM and RED were used to analyze the resulting samples.

Results

Typical SEM observations of the prepared samples are shown in Fig. 1. From the resulting relief patterns, it is quite clear that as the etch time increases, the concentration and the size of the particles in relief have generally increased. In a few instances, as shown in Fig. 2, these particles exhibited geometric structure, characteristic of single crystals. The largest of these appears to be greater than 0.5 μm in breadth and as thick as the residual film.

The optical density of the films is also observed to decrease with increasing etch time, which would be

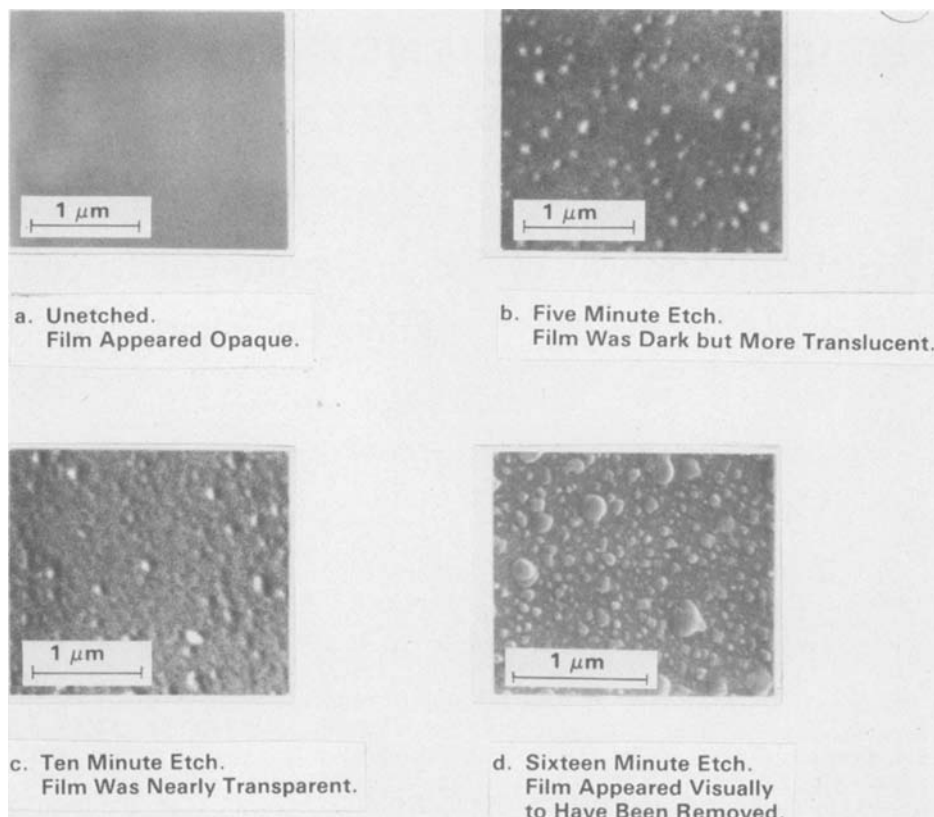


Fig. 1. Scanning electron micrographs of silicon-implanted PMMA films etched in an oxygen plasma for various times.

expected if the graphite structure were preferentially removed. Moreover, while the films were very hard and scratch resistant before etching, rubbing them against smooth glass was not observed to scratch the glass. After etching, the surface could be made to scratch smooth glass by a simple rubbing operation. Thus, the relief structure is not simply etched glass but is somewhat harder.

Reflection electron diffraction of the oxygen plasma etched samples produced numerous patterns, some of which were different from those found earlier (see Fig. 3a). As we analyzed the many diffraction patterns obtained, we observed that the unetched samples were mostly of amorphous carbon. Better defined patterns of both graphite and diamond-like structures were obtained in the lightly and moderately etched films but no silicon carbide patterns were observed except for the heavily etched samples (i.e., near the film-glass interface). While all three structures were possibly present near the interface, the frequency of clearly defined silicon carbide structure overwhelmingly

dominated the patterns observed. The patterns were analyzed using an independent gold film as a standard (Fig. 3b), and the corresponding lattice spacing (*d*-values) are listed in Table I. The accepted *d*-values for graphite, diamond, and silicon carbide are also listed (7). Initially, for many samples, charging by the electron beam produced "blooming" and resulted in unacceptable distortion of the diffraction pattern. This problem was almost completely removed with a thin conductive palladium film deposited on the sample. It was noted that the samples that had not been etched showed significantly less charging than the etched samples. We presume that the incorporated graphite in the unetched samples served to discharge the surface because the graphite is fairly conductive. No blooming occurred with the gold standard.

The general agreement between the observed and the accepted *d*-values for the gold standard provides a measure of the precision of these results. The internal consistency of the patterns from our test specimens is sufficient so that, even with some distortion due to charging, the several patterns can be identified and the result provides clear evidence for the presence of SiC, graphite, and diamond-like phases.

Discussion

The shrinkage of the PMMA film during implantation is clear evidence of material loss which, from Auger analysis (2), appears to have been primarily the oxygen and hydrogen from the polymer. The bulk of the remaining film is carbon except in the region of the interface where the concentration of silicon increases significantly. Nevertheless, the observation of silicon carbide only at the interface is particularly interesting since the total silicon implant is sufficiently small that it cannot reasonably account for the silicon carbide formation directly unless all the silicon is deposited at the interface. Therefore, we propose that the high energy implant into the interface actually induces decomposition of the glass, producing a silicon-rich layer. The process leads to significant atomic mixing in the manner described by Liau and Mayer (8). The

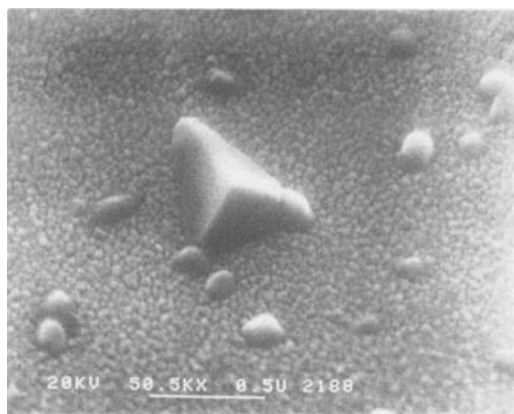


Fig. 2. Scanning electron micrograph of a large crystallite near the film-glass interface.

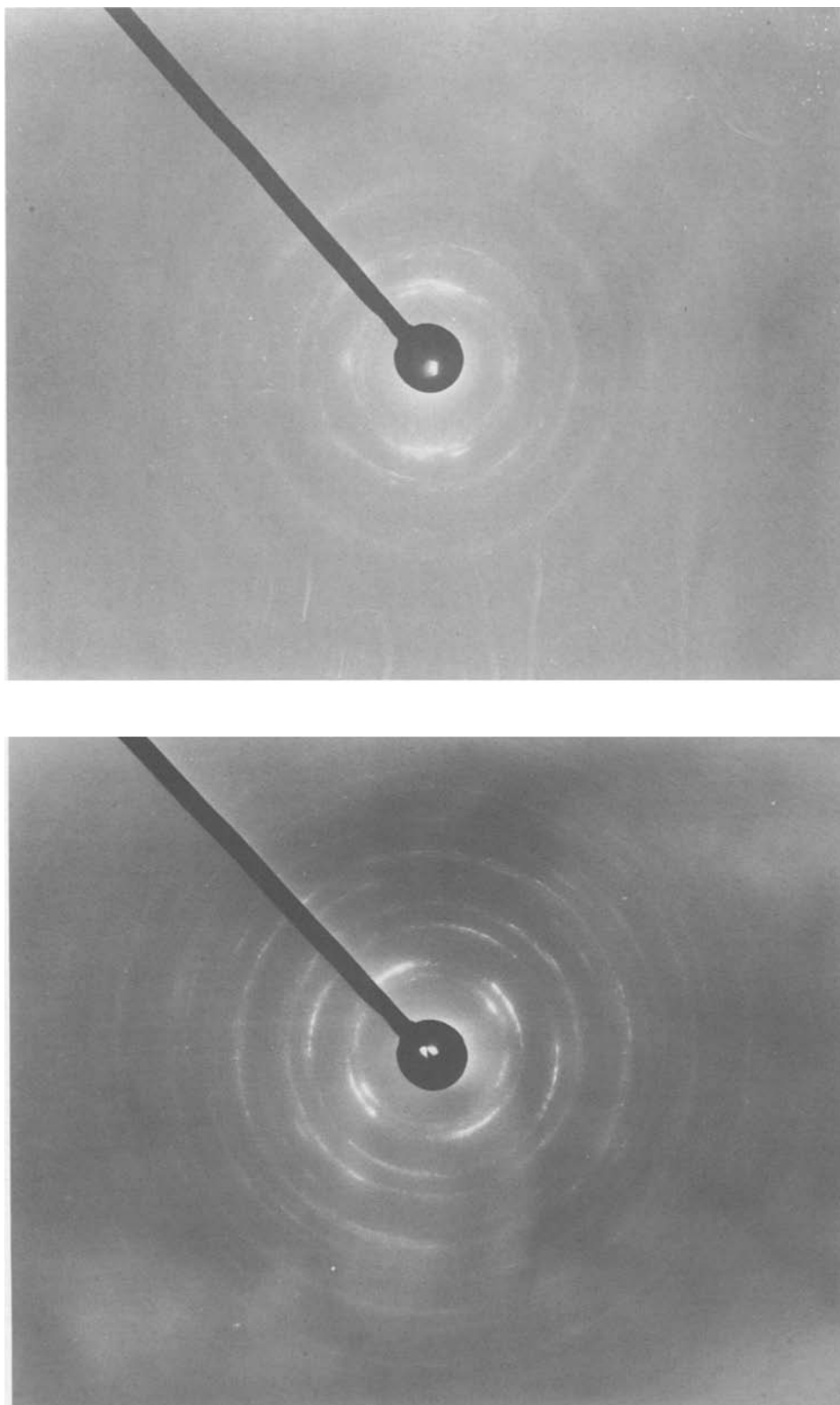


Fig. 3. Typical electron diffraction patterns of (a, top) silicon carbide and (b, bottom) gold standard.

recrystallization of this layer could then produce the silicon carbide we observe and undoubtedly accounts for the very strong bond to the substrate.

One might expect, as suggested by Spencer *et al* (4), that during the reordering of the carbon bonds after the disruption by an adsorbed ion, any of the possible carbon bonding configurations might occur. Even if this were the case, it is most likely that the strongest bonds would form first. Moreover, in subsequent absorption events, the weakest bonds would be removed preferentially. Thus, the allotropes of carbon which

form weakest bonds, would most likely be absent or appear only on the top surface of the film. Hexagonal graphite would be formed at greater film depth because of the stronger planar bonding. Cubic and hexagonal diamond with tetrahedral bonding would also most likely form in the bulk film or near the interface.

To account for the formation of the silicon carbide at the interface or perhaps even the diamond structure in the bulk film, a brief description of the expected energy transfer is probably adequate. The energy of an individual silicon ion entering the film is from 150 to

Table I. Comparison of experimentally observed d-values obtained from RED of silicon-implanted PMMA and gold with tabulated values

Part A

Observed d-values	Graphite hexagonal 4H			Graphite rhombohedral 6B			Diamond hexagonal 8H			Diamond cubic		
	d	hkl	I/I ₀	d	hkl	I/I ₀	d	hkl	I/I ₀	d	hkl	I/I ₀
3.33	3.348	002	100	3.348	003	100	2.184	100	29			
2.20							2.111	101	100			
2.13	2.127	100	3	2.08	101	11	2.059	004	57	2.060	111	100
2.06												
2.03	2.027	101	15				1.930	102	43			
1.87							1.315	105	15			
1.66	1.674	004	6	1.674	006	6	1.261	110	33	1.26	220	27
1.26												
1.23	1.228	110	4	1.228	110	4						
1.22												
1.21												
1.20				1.190	107	1						
1.16	1.153	112	6	1.153	113, 113̄	6	1.162	106	23			
1.13	1.133	105	1	1.116	009	1	1.07	114	18	1.07	311	16
0.99	0.990	114	4	0.990	116, 116̄	4	0.855	206	14			
	0.862	116	4									
0.82				0.8259	119, 119̄	4	0.8214	211	8	0.818	331	15

Part B

Observed d-values	Silicon carbide hexagonal 12H			Silicon carbide cubic 8F			Observed d-values	Gold (standard pattern)			
	d	hkl	I/I ₀	d	hkl	I/I ₀		d	hkl	I/I ₀	K
2.63	2.628	101	35				2.36	2.355	111	100	10.13
2.51	2.516	102, 006	100	2.520	111	100	2.038	2.039	200	52	10.19
2.37	2.357	103	35				1.435	1.442	220	32	10.23
2.18	2.179	104	14	2.180	200	20	1.213	1.230	311	36	10.27
	1.999	105	5				1.157	1.1774	222	12	10.36
1.67	1.679	107	6				1.029	1.0196	400	6	10.09
1.54	1.541	110, 108	43	1.5411	220	35	0.935	0.9358	331	23	10.20
	1.419	109	12				0.910	0.9120	420	22	10.21
	1.329	201	2				0.835	0.8325	422	23	10.15
1.32	1.314	116, 202	28	1.314	311	25					Average 10.20 ± 0.05
	1.290	203	4								
	1.258	204, 0012	3	1.258	222	5					
1.069	1.080	208	3	1.089	400	5					
	1.044	209	3								
1.009	0.9998	212 +	5	0.9999	331	10					
	0.989	213	2								
	0.974	1112, 214	3	0.9748	420	5					
	0.941	1015	2								
0.870	0.889	218, 300 +	6	0.8895	422	5					
	0.864	219	3								
0.782	0.839	306 +	5	0.8387	511, 333	5					

200 keV and this energy is transferred to the film in less than 10^{-11} s. The volume in which this energy is deposited, assuming a 10 nm diam, is of the order of 10^{-23} m³. Even though there is undoubtedly extensive ionization in this volume, the electron cloud loses its energy to the lattice according to Liu *et al.* (9) in about 10^{-11} s. Based on the spontaneous recrystallization rate of silicon (10), for example, it would require about 10^{-9} s for a crystallite of some 20 nm to grow. It seems reasonable to expect the thermal and pressure spikes produced by the absorption of a single ion to exist for as long as 10^{-10} s or longer (11). Hence, even at this rate of energy dispersal a seed crystal encompassing some 5-10 unit cells could be produced in the time available. For longer dwell times, larger crystallites could be produced, even without postulating secondary epitaxial growth from a nearby ion absorption. Since, for the implant dose used here, there are, on the average, several absorbed ions for each 0.1 nm², the probability of producing 50 nm crystallites by secondary epitaxial growth is reasonably high. Increased implant dose should increase the probability of occurrence of large crystallites and/or produce a higher density of crystallites.

Based on the observations of composition with film thickness and the above-generalized picture, one might explain the material properties. For example, the weakly bonded graphite at the surface would provide good opacity while the film hardness is provided by the planar or tetrahedral bonding in the bulk form.

The adhesion to the glass substrate is very likely related to the strong SiC bonding to the surface.

Conclusions

We believe our results clearly show that etching prepared films in an oxygen plasma reveals a differential etching structure with the concentration of slowly etching particles increasing with film depth.

Moreover, under our conditions for preparation, scanning electron microscopy shows the typical particle size of the slower etching species to be less than 50 nm with some crystallites as large as 0.5 μm.

Reflection electron diffraction with depth shows the following. (i) At the surface, the film is mainly amorphous carbon and fine grain polycrystalline graphite. (ii) In the bulk, there is evidence of polycrystalline graphite and diamond-life structure. (iii) Silicon carbide dominates in the region of the film-glass interface. Thus, all of these observations are consistent with our hypothesis of film formation.

Finally, the bonding observed in the structures of silicon-implanted PMMA films could account for their opacity, extreme hardness, and adhesion.

Acknowledgments

The authors would like especially to thank Don Betner of Detroit Diesel Allison-Indianapolis for his kind and expert assistance and for the use of the electron diffraction and photographic equipment. We also gratefully acknowledge the patient efforts of Walter

Lange of the Analytical Chemistry Department for the SEM micrographs.

Manuscript submitted June 3, 1983; revised manuscript received Nov. 8, 1983. This was Paper 398 presented at the San Francisco, California, Meeting of the Society, May 8-13, 1983.

General Motors Research Laboratories assisted in meeting the publication costs of this article.

REFERENCES

1. B. Bendow, Summary of the Workshop on Diamond-Like Coatings, Albuquerque, NM, April 1982.
2. B. A. MacIver, *This Journal*, **129**, 827 (1982).
3. S. Aisenberg and R. W. Chabot, *J. Vac. Sci. Technol.*, **10**, 104 (1973).
4. E. G. Spencer, P. H. Schmidt, D. C. Joy, and F. J. Sansalone, *Appl. Phys. Lett.*, **29**, 118 (1976).
5. L.-P. Andersson, *Thin Solid Films*, **86**, 193 (1981).
6. G. Ryding, *Electronic Packaging and Production*, p. 68 (March 1975).
7. Reference data taken from the Powder Diffraction File of the JCPDS International Center for Diffraction Data 1981.
8. Z. L. Liao and J. W. Mayer, in "Treatise on Materials Science and Technology," Vol. 18, J. K. Hirvonen, Editor, p. 19, Academic Press, New York (1980).
9. J. M. Liu, H. Kurz, and N. Bloembergen, *Mater. Res. Soc. Symp. Proc.*, **13**, 3 (1983).
10. G. Auvert, A. Perio, and F. Morin, p. 48, Materials Research Society Meeting Abstracts, Boston, MA, Nov. 16, 1981.
11. F. P. Incropera and D. P. DeWitt, in "Fundamentals of Heat Transfer," John Wiley & Sons, New York (1981).

Tolpography Modeling in Dry Etching Processes

Yoshio Sakai,^{*1} John L. Reynolds,^{*2} and Andrew R. Neureuther*

Department of Electrical Engineering and Computer Sciences, and the Electronics Research Laboratory, University of California, Berkeley, California 94720

ABSTRACT

Some aspects of the interaction among wafer topography and the thin film processes of directional dry etching and deposition are presented in experiment and simulation. The anisotropy of dry etching, which has helped make VLSI possible, increases the interdependence of processing steps and opens the possibility of creative uses of topographical effects in fabricating devices. Examples illustrate the importance of these effects and the basic mechanisms involved. Simulation is particularly well suited for systematically examining the trade-offs among processing steps. Design graphs characterize the effect of anisotropy on line-width loss and oxide removal in polysilicon gate etching, and on thin film resistance in tapered oxide etching. Guidelines for planarization by isotropic deposition and anisotropic etching are suggested. Comparisons with experiments show that the reported planarizing effect is better than expected.

The advent of dry etching and new deposition techniques helps make possible the reduced size and increased complexity in integrated circuit devices. The directionality of dry etching allows feature sizes in devices down to 1 μm (1, 2), and provides a flexible medium for creative processing solutions to device performance problems (3, 4). Novel deposition techniques contribute to higher packing densities (5-7). Simulation (8-10) is useful in characterizing and optimizing the individual deposition and etching processing steps. This paper extends simulation to several new topography control techniques and explains several situations which involve optimization of the interaction between processing steps.

The interaction between process steps is important in anisotropic dry etching. Simple directional etching forms steep, fine patterns which lead to poor coverage in the subsequent deposition of thin films. When followed by deposition and a second directional etch, a residue remains in the vicinity of the abrupt topographic steps. This unetched residue can lead to detrimental effects such as electrical shorts when it is a conductor, but when it is an insulator, it also serves to planarize the topography and can be used in a creative manner as a temporary ion implantation mask (4). Many of these topography creation and interaction problems can be effectively characterized through simulation. The process simulator, simulation and modelling of profiles in lithography and etching (SAMPLE) (9), models the time evolution of an etched line-edge profile. The program uses weighted rate

components and topographical information to produce a two-dimensional line graph of the expected cross section. This paper uses SAMPLE and scanning electron micrographs (SEM's) of laboratory test structures to study these wafer topography issues.

Anisotropic Etching at Steps

Figure 1 illustrates how the underlying topography in a double-level polycrystalline silicon process affects the percentage of electrical shorts in the second-level

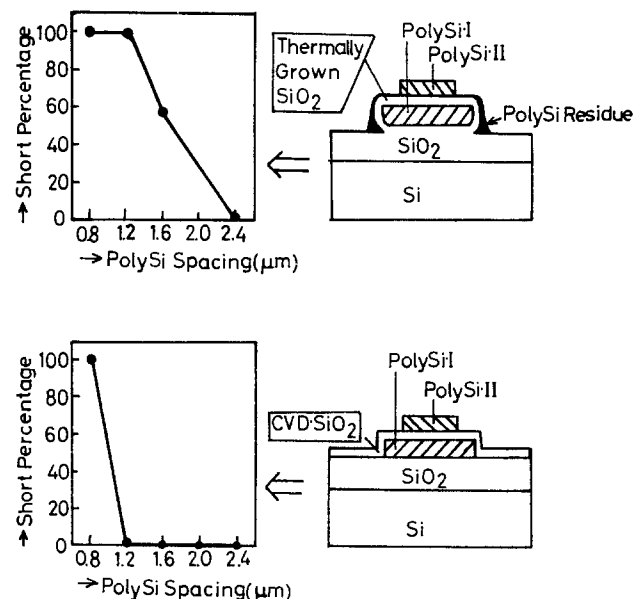


Fig. 1. Percentage of electrical shorts between parallel lines of polysilicon vs. line spacing.

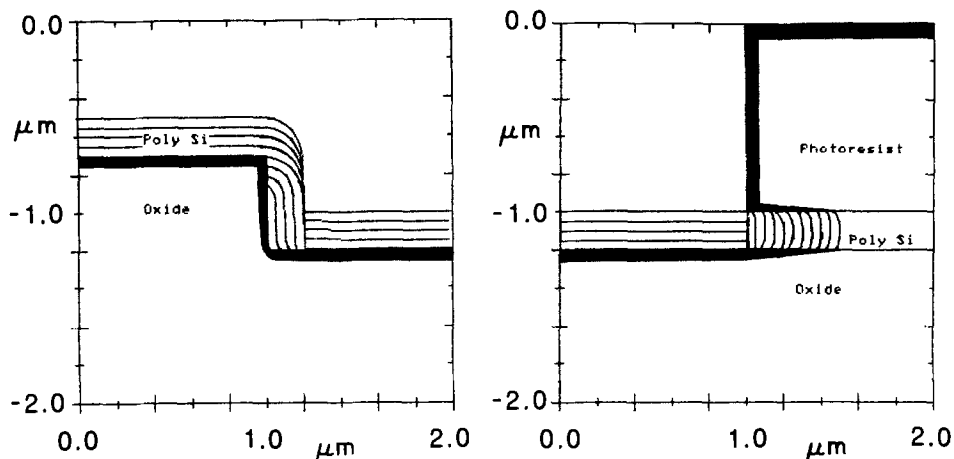
¹ Present address: Hitachi Central Research Laboratory, Tokyo, Japan.

² Present address: Microelectronics Center of North Carolina, Research Triangle Park, North Carolina 27709.

* Electrochemical Society Active Member.

Key words: plasma etching, anisotropic etching, deposition, computer simulation.

Fig. 2. Simulation of residue removal and gate definition using directional etching and isotropic overetching.



polysilicon lines. In Fig. 1a, a thermally oxidized insulating layer produces a topography undesirable because of its indented structure at the base. After anisotropic etching of the second level of polysilicon, the indentation remains full of unetched polysilicon. The residue causes the electrical shorts in parallel lines of a second layer of silicon. The percentage of shorts increases rapidly for parallel lines separated by less than $2 \mu\text{m}$ because the filaments can form continuous bridges at close spacing. Changing the method of applying the insulator provides a more suitable topography for the dry etching of the second conductor level. As shown in the second part of Fig. 1, silicon dioxide chemically vapor deposited (CVD) at a high temperature makes a better step without indentation. In this case, the percentage of shorts in the second level of polysilicon lines is almost zero above $1 \mu\text{m}$ spacing.

A problem related to the unetched residue at steps also occurs in patterning the first level of polysilicon. The gate electrode material is undercut, while the residue is being etched, as shown in the simulation of Fig. 2. Here, the overlying layer is etched directionally to an end point, and the residue is then removed by introducing an isotropic component during overetching. Simultaneously, in the gate mask region the isotropic overetching undercuts the line, as on the right in Fig. 2. The line width lost depends on the residue thickness and the amount of isotropy in the second etching step. In addition to this undercutting problem, the underlying film, such as the gate oxide, is also attacked during the overetching residue removal process.

An alternative to this double-step process is the use of mixture etching in which a directional and an isotropic component are used throughout a single step.

With this mixed process, the undercutting can be reduced, but the residue thickness remains larger and longer overetching is required. Unfortunately, the anisotropic conditions which reduce the line-width loss have lower selectivity (etch-rate ratio) between the polysilicon and the oxide underneath. Anisotropy thus results in more oxide thickness loss. An example of the relationship between the etch-rate ratio of polysilicon to oxide and anisotropy is shown in Fig. 3a [from Ref. (11)]. The etching selectivity is drastically reduced as the anisotropic ratio increases to the more directional extreme. The relationship between selectivity and anisotropy can be used to explore the basic trade-off between line-width loss and underlying oxide thickness loss. The graph in Fig. 3b compares the polysilicon line-width loss and the oxide etched during the overetching process as a function of anisotropy. The assumed step height is $0.5 \mu\text{m}$, and the deposited thickness of polysilicon is 200 nm . The broken curve corresponds to a single-step etching process where a mixture of isotropic and directional components are used throughout. The solid curve corresponds to a two-step etching process where the first step uses directional etching to an end point, then uses a mixture etching during the overetch time. In both processes, the line-width loss is large in the isotropic region, while the oxide attacked is large in the anisotropic region. The oxide gets etched more in the two-step process because of the need for a longer overetching time. However, the polysilicon line-width loss is less in the double-step process. These curves aid as design guides for determining the optimal etching conditions. A process can be chosen depending upon how much line-width or oxide loss can be tolerated. For instance, if the maximum allowable polysilicon undercut and oxide etched

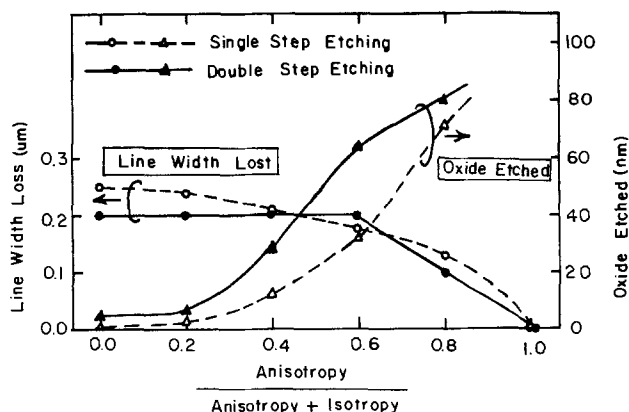
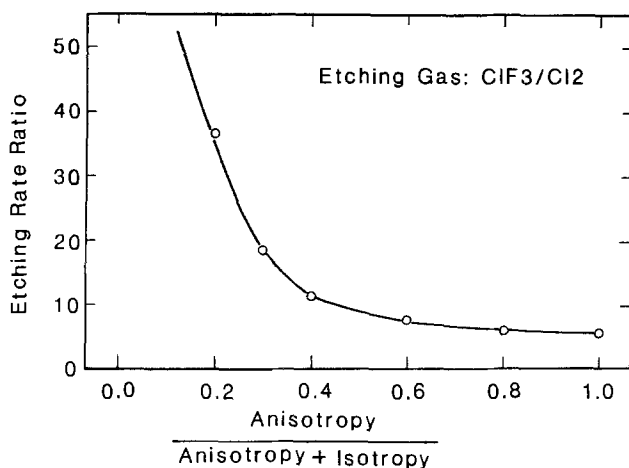


Fig. 3. (a) Etch rate ratio of poly-Si to SiO_2 [from Ref. (11)]. (b) Line-width lost and oxide etched during over etching time to remove residue at a $0.5 \mu\text{m}$ step.

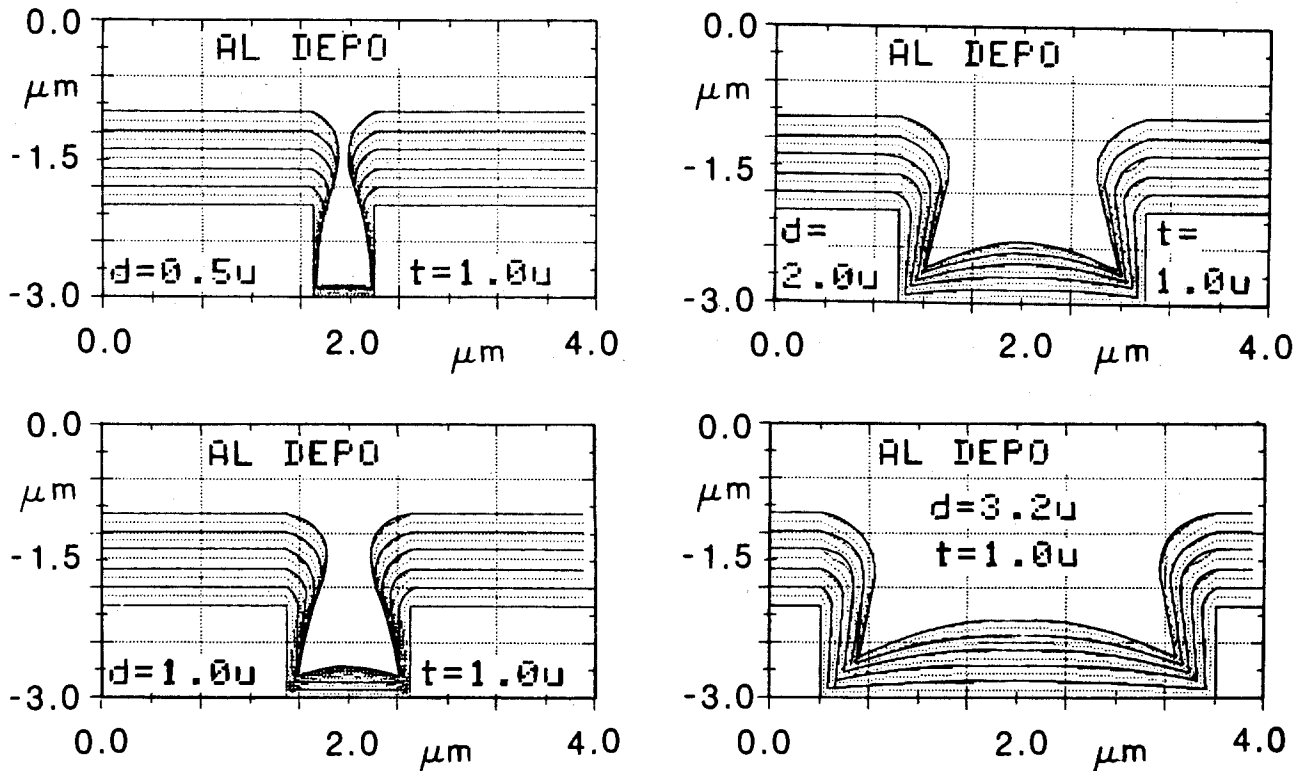


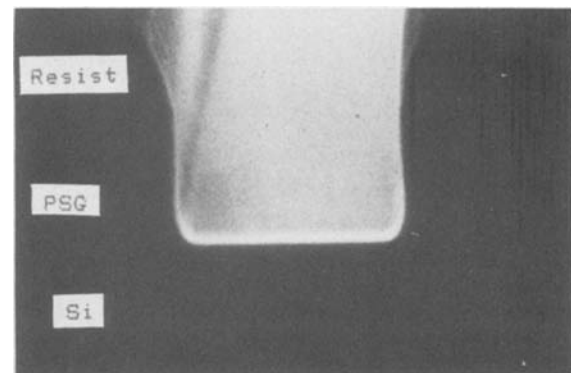
Fig. 4. Simulation of Al deposition in varying window sizes

are $0.2\ \mu\text{m}$ and $30\ \text{nm}$, respectively, the etching condition would fall into the 0%-40% anisotropy ratio for two-step processing. In this case, a good single-step process cannot be found, since such results in large line-width loss.

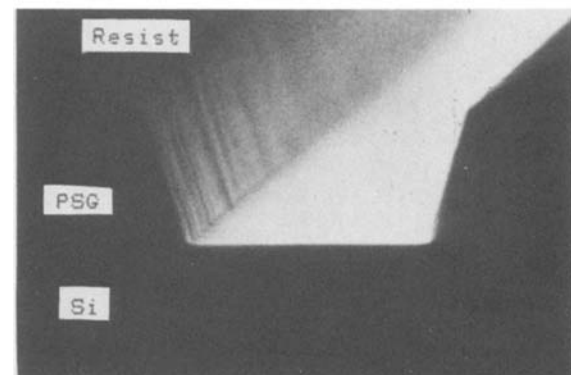
Step Coverage

Another topography problem is depositional film coverage of dry etched steps. The directional dry etching provides good line-width control and tight layout tolerances, but it results in profiles with steep edges and high aspect ratios, which cause poor coverage when thin films are later deposited. The trade-offs in depositing over dry-etched steps are easily explored using simulation. Figure 4 shows the sputtered aluminum film coverage in contact windows and narrow gaps. Due to the two-dimensional shadowing effect during Al deposition (8), the Al thickness at the bottom corner is much less than the nominal thickness. The shadowing effect becomes more pronounced as the gap dimension is reduced. The Al thickness in a $1\ \mu\text{m}$ wide contact with $1\ \mu\text{m}$ tall vertical walls is only 10% of that of the deposited-film thickness. Even though dry etching would allow reduction to submicron size contact holes, the conventional deposition techniques could not be used to form contact electrodes.

To improve the aluminum coverage of steps with conventional sputter deposition, the contact hole may be tapered (15). A sloped edge provides good coverage, but unnecessarily gradual slopes reduce the tight layout tolerance. Therefore, a compromise in slope and coverage is desirable. Figure 5 demonstrates how photoresist erosion during the etching process can be utilized to give a sloped edge profile. When the photoresist with a steep edge is used as an etching mask in conventional etching steps, the contact window reflects the steepness, because the horizontal resist erosion rate is small. A slightly tapered edge profile can be obtained when tapered photoresist is used as the etching mask. The thinner edge of the mask erodes away, transferring a slope to the contact window edge in the etching process. Postbaking the resist after development is commonly used to taper the resist edge, as shown in the bottom of Fig. 5. Figure 6 illustrates



(a)



(b)

Fig. 5. Profiles of dry etched silicon dioxide using nonreflow and reflow (angled) resist masks.

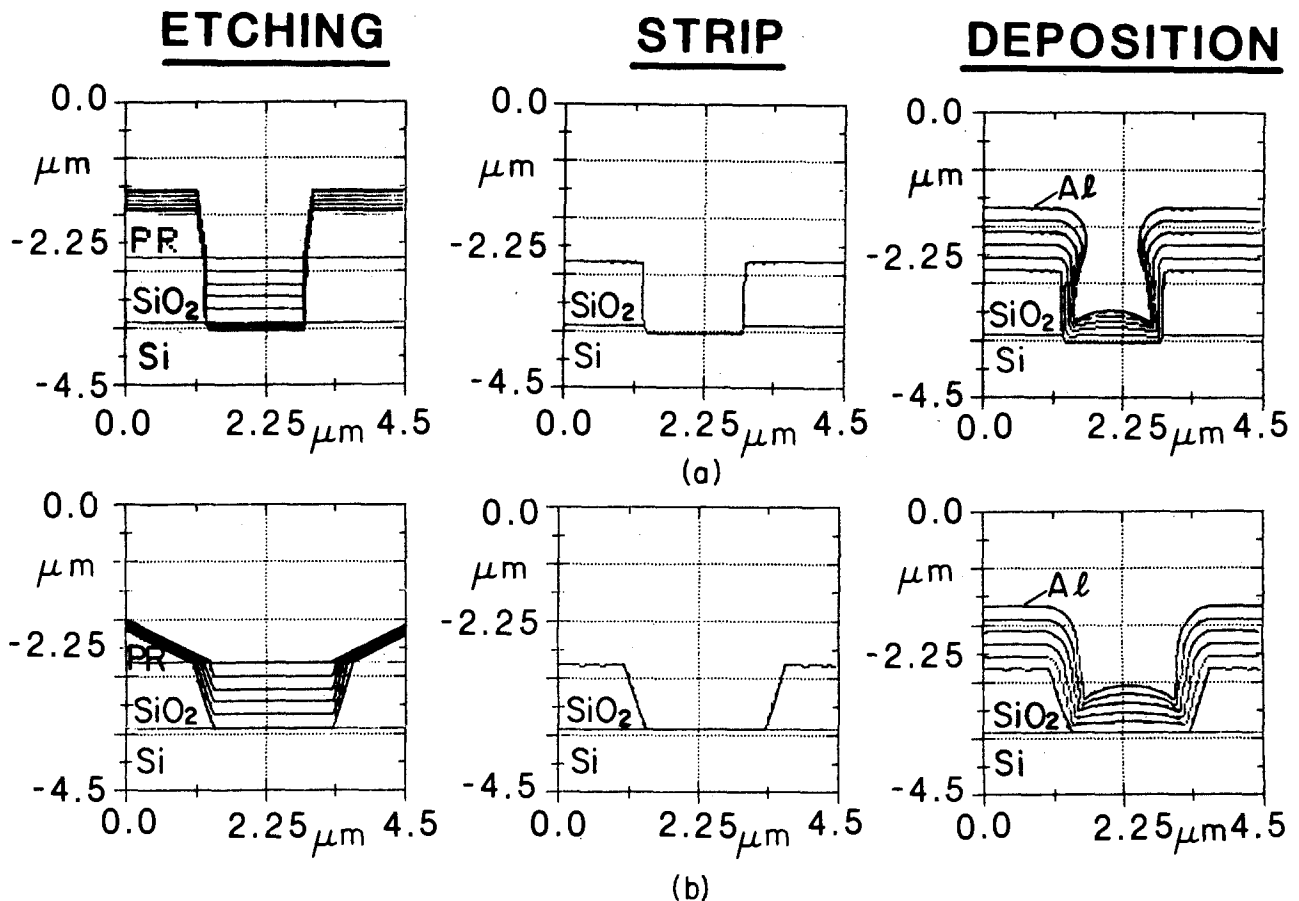


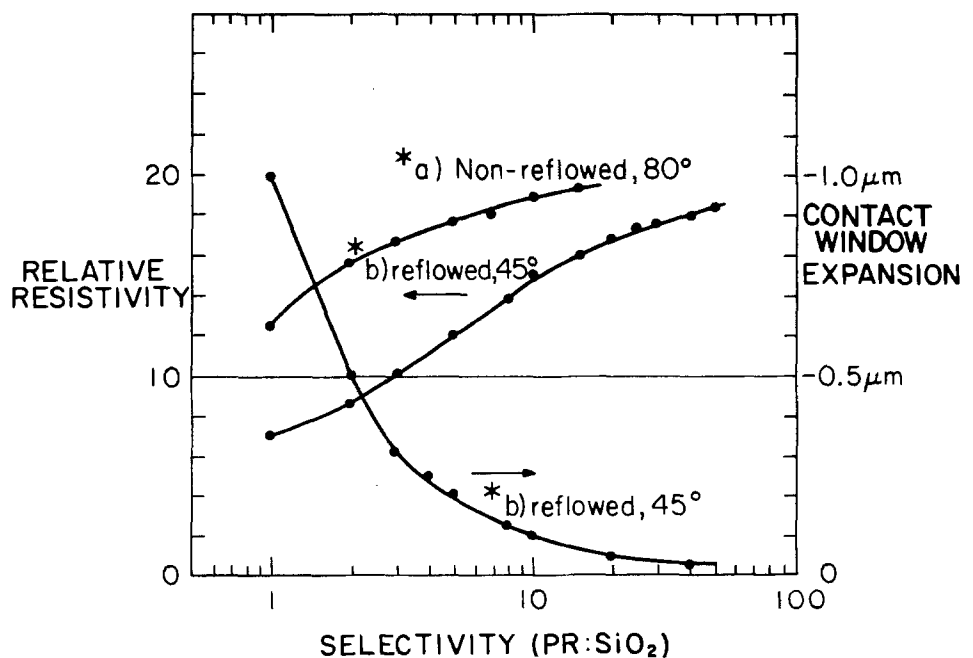
Fig. 6. Simulation of the dry etching of SiO₂ followed by Al deposition using straight and angled masks

the corresponding simulated sequential processing steps. The steep photoresist profile coupled with the vertical etching makes a steep profile that it is difficult for the aluminum to cover. The tapered photoresist with some lateral expansion of the contact hole produces a slightly sloped edge, which provides better step coverage.

The effect of the resist-to-oxide selectivity on the resulting contact-hole size and on the depositional film resistivity can be characterized. A photoresist mask with an initial sidewall taper angle that is etched anisotropically produces a tapered opening in the sili-

con dioxide layer. The oxide sidewall angle depends on the initial resist profile angle and the etch selectivity between the resist and the oxide. The taper in the oxide results in an expansion of the contact hole size, though. This is shown in Fig. 7 for nonreflowed resist of 80° and reflowed resist of 45° as a function of selectivity. The oxide taper angle also affects the subsequent metal coverage. The relative resistivity of the metal line crossing the gap is used to specify the quality of the deposited line. A relationship between resistance and sidewall taper has been generated for a 1 μm gap in a 1 μm thickness of oxide with a 1 μm of sputtered

Fig. 7. Relative resistance of aluminum across gaps and contact window expansion vs. selectivity for two mask angles. (a) 80°, nonreflowed. (b) 45°, reflowed.



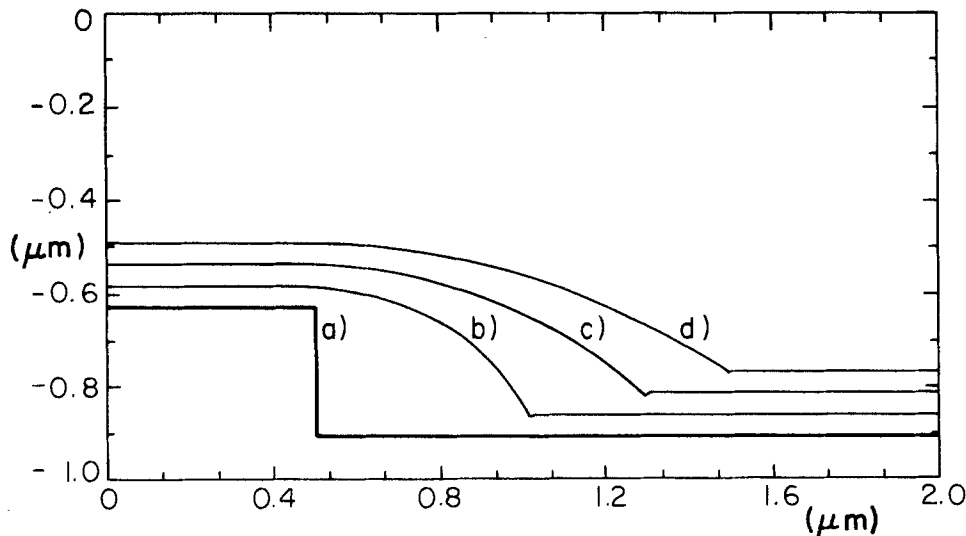


Fig. 8. Simulation of a multi-step process planarizing an edge by successively leaving residue. (a) Initial profile, a 0.3 μm rectangular step. (b) Profile after the initial deposition/anisotropic etch cycle. (c) Profile after the second deposition/anisotropic etch cycle. (d) Profile after the third deposition/anisotropic etch cycle.

Al in Ref. (12). This relation between angle and resistance is used for the relative resistance vs. selectivity plotted in Fig. 7. The graph shows how the combination of reflow angle and selectivity can be chosen for the trade-off between resistance and contact window expansion. An oxide sidewall angle of about 60° is a reasonable compromise for sputter deposition without bias. For reflow resist, initially tapered to 45°, a process with 2:1 oxide selectivity achieves the 60° oxide sidewall angle. The use of reflow produced a profile of 63° in Fig. 5, while without reflow, the sidewall angle was steeper than 85°.

Planarization

Now we examine the constructive use of dry etching in planarizing nonuniform surfaces. If a residue is left at steps intentionally, it can be used to ease step coverage in later processing steps. One way is to deposit a thick oxide by CVD at high temperature or at low pressures to obtain a completely isotropic covering of the nonuniform topography. This deposited oxide is then etched back anisotropically to leave a rounded residue at every vertical step. Several isotropic depo-

sition/anisotropic etch steps will leave a larger and larger amount of residue at the concave edge, giving a gradual slope to the edge, as shown in the simulation in Fig. 8. This residue is the basis for the lowly doped drain and offset gate technologies (4).

If, however, the deposited oxide film thickness exceeds one-half the gap spacing, as in Fig. 9, the oxide fills the gap and tends to planarize the surface. The nonplanar dip remaining in the oxide surface decreases as the thickness-to-gap-width ratio is increased. From simulation it can be seen that the oxide surface dip in a 2 μm gap with 2 μm of deposited and etched oxide amounts to only 0.1 μm. This eliminates the problem of sputtering over narrow, deep channels.

Figure 10 illustrates experimentally the isotropic deposition/anisotropic etching method for several test structures. Gaps were directionally etched in silicon. A thin layer of oxide was grown before deposition for later underetching to distinguish between the layers. Then a layer of CVD polysilicon was deposited and etched anisotropically in a sulfur hexafluoride and oxygen mixture (SF₆/10% O₂). After dry etching each layer of the polysilicon, a new distinguishing layer of

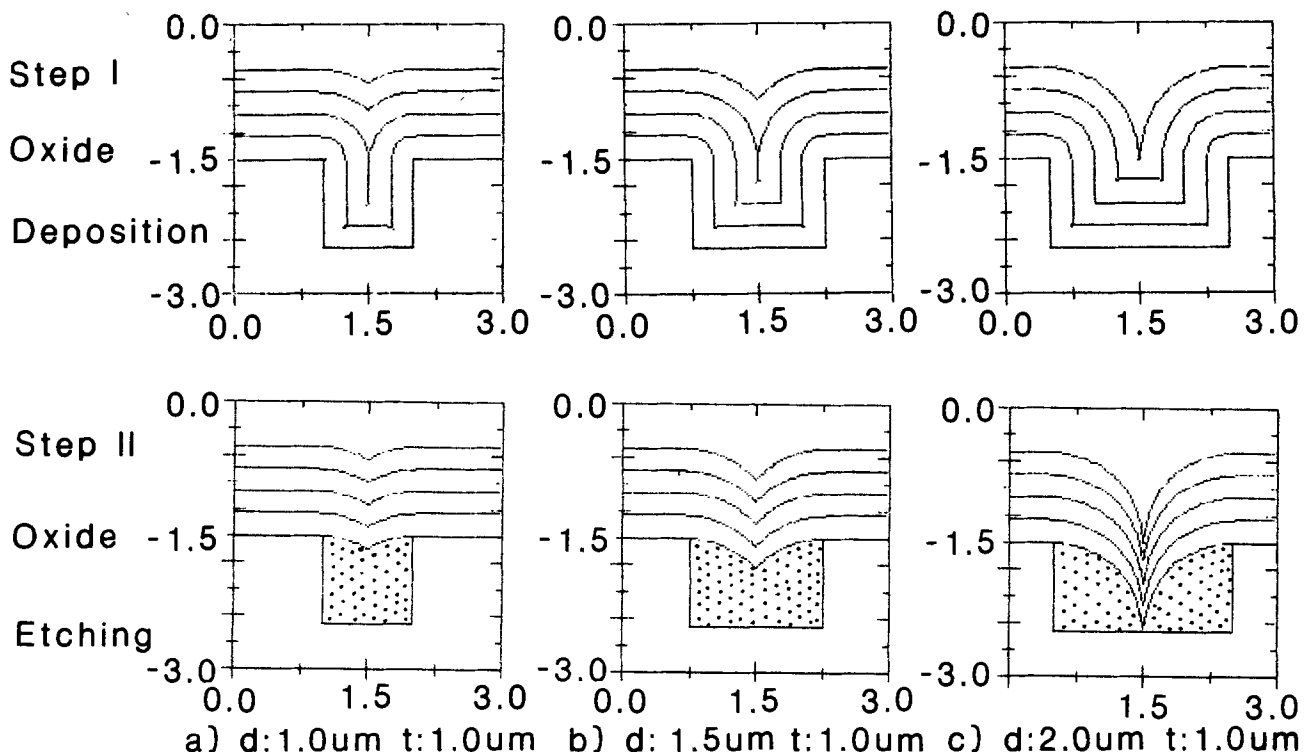


Fig. 9. Simulations of planarization by filling gaps with isotropically deposited material and then anisotropically back-etching

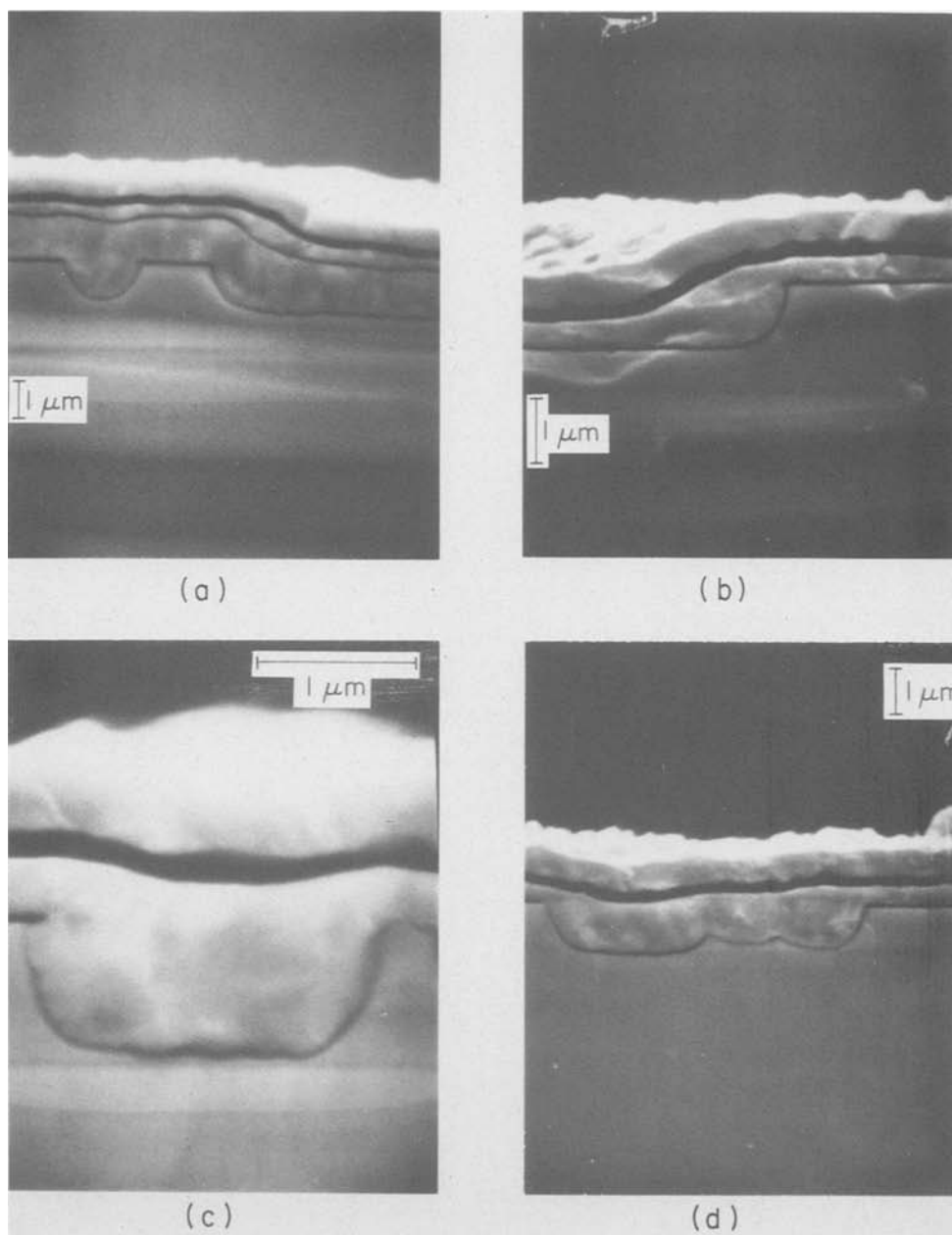


Fig. 10. SEM's of planarization processes using successive isotropic deposition and anisotropic etching. (a) A space and an edge. (b) An edge. (c) A $2 \mu\text{m}$ space. (d) A $7 \mu\text{m}$ space.

oxide was grown. This process was repeated several times. The back-etching of these thin oxide layers reveals the history of the surface shape at various steps (13, 14). The first two micrographs show that isotropical deposition followed by anisotropic etching preferentially leaves a smoothing residue at step edges. These correspond well to the simulation in Fig. 8. The third photo demonstrates how a narrow ($2 \mu\text{m}$) gap is planarized by filling with CVD material and etching. The final photo in Fig. 10 shows that the same effect occurs in a wider $7 \mu\text{m}$ space. This structure has the dip predicted by simulation in Fig. 9, but shows experimentally that the planarization effect is greater than expected.

The simulated aluminum deposition across the top of planarized structures is shown in Fig. 11. Planarization remarkably improves the Al film coverage. The aluminum line resistance is estimated to be almost one order of magnitude less than that of the nonplanarized structure. Therefore, the planarization process for gaps and steps can be useful in reducing interconnection resistance in VLSI technology.

Conclusion

Experiment and simulation are used to explore topographical interaction between etching and deposi-

tion processing steps. Experimental data are included to document the importance of these process interactions and to illustrate the physical mechanisms producing the topographic effects. Design graphs have been generated to illustrate the process options in several current thin film processing technologies.

Simulation and experimental verification lead to several important conclusions. A single-step mixture of isotropic and anisotropic etching removes less gate oxide while removing residue than a double-step process for the same amount of undercut at the polysilicon gate. When considering the resistance of sputtered Al lines into contact windows, tapering the oxide sidewall to 60° by resist reflow and appropriate etching selectivity is a reasonable compromise of layout tolerances. For planarization, an isotropic deposition of material of thickness one-half the narrow gap widths is adequate, but further experimentation shows that the smoothing is better than expected.

Acknowledgments

The authors wish to thank Mr. Kiyuji Ikeda and Mr. Yoshifumi for the SEM photographs of the tapered gaps. We also appreciate the help of Mr. S. N. Nandgaonkar in using the computer. Research is sup-

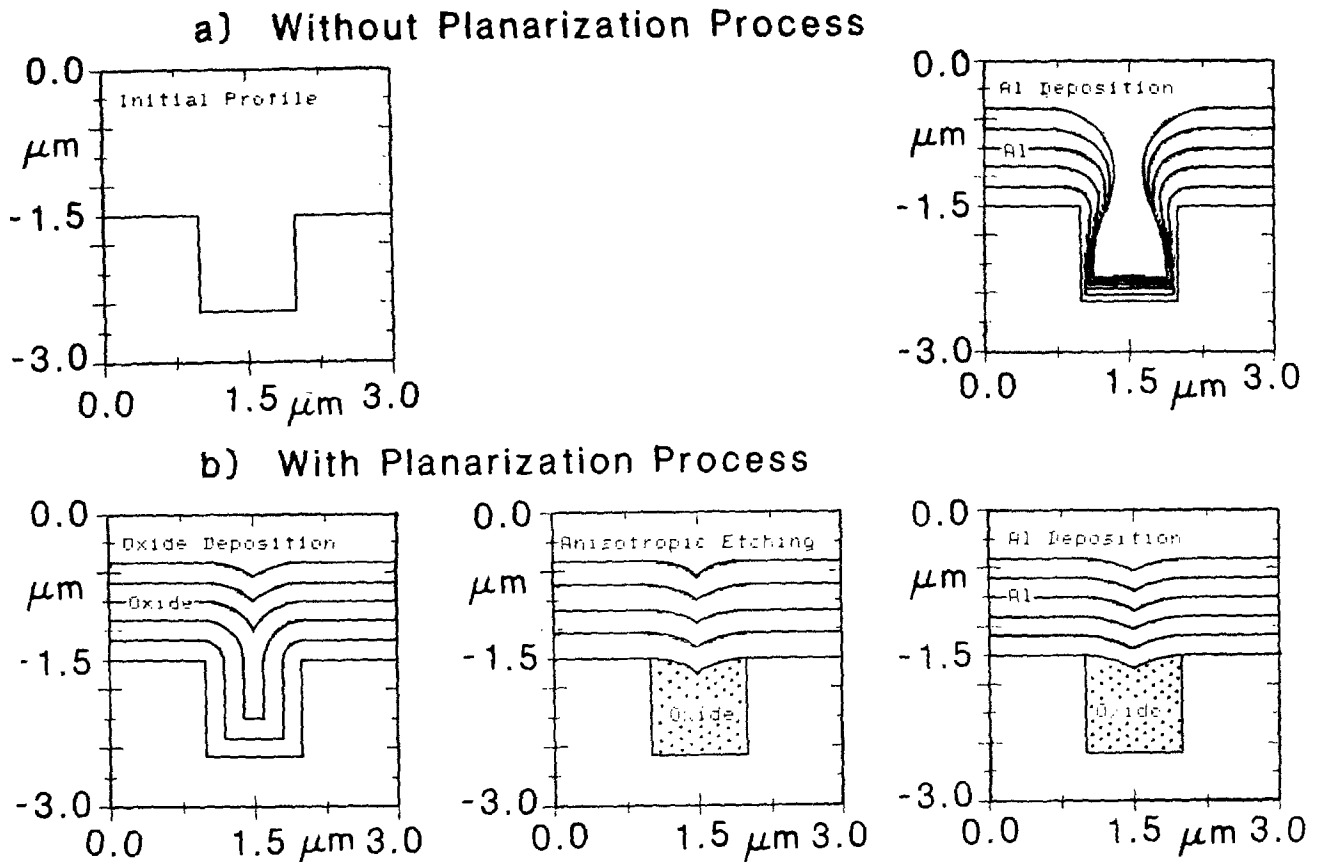


Fig. 11. Comparison of Al application over planarized and nonplanarized surfaces

ported in part by Hitachi Corporation, Sandia National Laboratories, and NSF ECS-8106234.

Manuscript submitted Oct. 25, 1982; revised manuscript received July 18, 1983.

REFERENCES

1. L. M. Ephrath, *IEEE Trans. Electron Devices*, ed-28, 1315 (1981).
2. T. Shibata, K. Hieda, M. Sato, M. Konaka, R. L. M. Dang, and H. Zizukai, *IEDM Tech. Dig.*, 647 (1981).
3. W. R. Hunter, T. C. Holloway, P. K. Chatterjee, and A. F. Tasch, Jr., *ibid.*, 764 (1980).
4. S. Ogura, P. T. Tsang, W. W. Walker, D. L. Critchlow, and J. F. Shepard, *ibid.*, 651 (1981).
5. C. Y. Ting, V. J. Vivalda, and H. G. Schaefer, *J. Vac. Sci. Technol.*, 15, 1105 (1978).
6. Y. Homma, A. Yajima, and S. Harada, *IEDM Tech. Dig.*, 570 (1981).
7. T. Batchelder, in "SPIE Proceedings," Vol. 275, pp. 143-149, (1981); *Solid State Technol.*, 25, 111, (February 1982).
8. I. A. Blech, *Thin Solid Films*, 6, 113 (1970); I. A. Blech, D. B. Fraser, and S. E. Hasyko, *J. Vac. Sci. Technol.*, 15, 13019 (1978).
9. W. G. Oldham, A. R. Neureuther, C. Sung, J. L. Reynolds, and S. N. Nandgaonkar, *IEEE Trans. Electron Devices*, ed-27, 1455 (1980).
10. A. R. Neureuther, C. H. Ting, and C. Y. Liu, *ibid.*, ed-27, 1449 (1980).
11. D. L. Flamm, D. N. K. Wang, and D. Maydan, Paper 270 presented at The Electrochemical Society Meeting, Denver, Colorado, Oct. 11-16, 1981.
12. K. Lee, Y. Sakai, and A. R. Neureuther, Paper presented at 1982 Symposium on VLSI Technology, Oiso, Japan, September 1982.
13. N. Rovedo, M.S. Thesis, University of California, Berkeley, California (1979).
14. C. Y. Ting, V. J. Vivalda, and H. G. Schaefer, *J. Vac. Sci. Technol.*, 15, 1105 (1978).
15. N. S. Viswanathan, *ibid.*, 16, 388 (1979).

The Characterization of Heteroepitaxial Silicon by Surface Photovoltage Technique

Improved Properties in SOS Films Resulting from Implant Damage and Solid-State Regrowth

J. Lagowski,^{*1} L. Jastrzebski,^{*} M. T. Duffy,^{*} C. Magee, and G. W. Cullen^{*}

RCA Laboratories, Princeton, New Jersey 08540

ABSTRACT

Electronic properties of ion implanted and recrystallized silicon-on-sapphire films were studied by surface photovoltage as a function of implantation dose (varied from 10^{15} to 10^{16} cm^{-2}). It has been found that all essential characteristics of SOS films undergo a pronounced improvement as a result of high dose (4.8×10^{15} cm^{-2}) implantation with Si ions followed by a brief annealing (4h at 600°C). The most important improvement has been found with respect to reduction (about two orders of magnitude) in deep-level concentration situated at the middle of the energy gap, and a significant increase in the minority carrier lifetime.

Ion implantation and subsequent thermal annealing have recently been used as processing steps leading to solid-state recrystallization of heteroepitaxial silicon films on sapphire (1). It has been demonstrated that such processing can improve the crystalline perfection of the films, particularly in the vicinity of the silicon-sapphire interface (2). In the present study, we examine the effects of solid-state recrystallization on the electrical properties of SOS films implanted with Si ions. The films were $\sim 5000\text{\AA}$ thick. Implantation was carried out at 380 keV with a dose ranging from 1 to 8×10^{15} Si^{++} cm^{-2} . Implanted films were annealed at 600°C for 4h. As verified by x-ray measurements, the amorphous-like damage of SOS wafers caused by implantation was effectively removed during annealing, evidently as a result of the solid-state recrystallization process.

X-ray pole-figure measurements (3) were made on the films before implantation, after implantation, and after annealing. The volume percent (v/o) concentrations of (100) and {221} were determined after each processing step relative to the initial concentrations of the (100) parent and {221} twins. The extent of amorphization by implantation and the extent of recrystallization after annealing were deduced from these measurements.

The distribution of Al in the implanted SOS films was measured by SIMS. The electrical properties of the SOS films were measured using photovoltage spectroscopy for macroscale characterization and laser scanning photovoltage microprofiling for the determination of electrical inhomogeneities (4-7). The metal-semiconductor (MS) structures employed in the photovoltage spectroscopy measurements were prepared by evaporation of a semitransparent Al layer on freshly etched (30s in HF) epilayer surfaces. Measurements were carried out at temperatures of 100-300 K utilizing chopped monochromatic light and phase-sensitive detection or signal averaging for spectral response and relaxation time measurements, respectively. Four samples with Si implant doses of 1, 2, 4, and 8×10^{15} ions- cm^{-2} were prepared and measured simultaneously to assure the reliability of this comparative study.

The effect of solid-state recrystallization on the photovoltage spectra of SOS is shown in Fig. 1, where photovoltages of Si-implanted and annealed films are plotted for different implantation doses. These spectra are normalized to the photovoltage value at $h\nu = 2$ eV. In the subbandgap region ($h\nu < E_g$) where the most significant differences are seen, the photovoltage is due to photoionization transitions involving deep

levels (4). The low energy photovoltage threshold can be considered to be a typical feature of heteroepitaxial silicon. According to our recent study, the deep levels E_{t1} located in the vicinity of midgap are involved in these photoionization transitions. They apparently originate from dangling bonds of structural defects

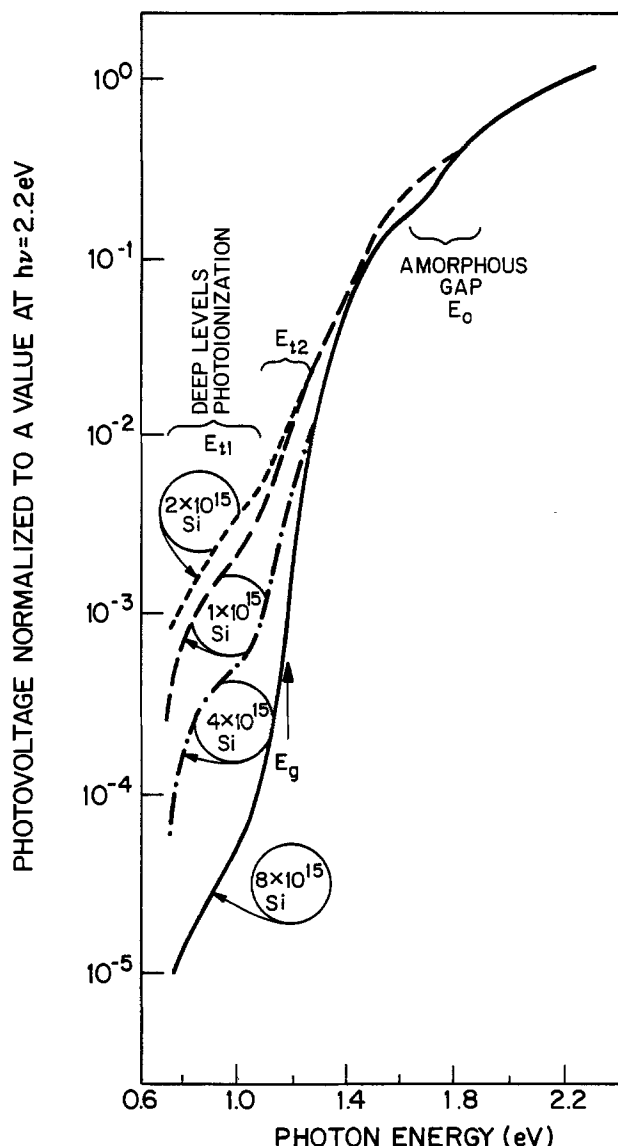


Fig. 1. Photovoltage spectra of SOS films implanted with various doses of silicon (after annealing).

^{*} Electrochemical Society Active Member.
¹ Present address: Massachusetts Institute of Technology, Cambridge, Massachusetts 02139.

(5, 6), providing a sensitive electronic measure of the crystalline perfection of SOS films.

For photon energy in the range 0.9-1.0 eV, a second photovoltage threshold is observed, indicating the presence of E_{t2} levels (4). In the region $h\nu \gtrsim 1.1$ the band-to-band generation of excess carrier takes place and the photovoltage becomes sensitive to interband optical transitions. A typical feature of these transitions is the presence of a high energy shoulder around $h\nu \simeq E_0$, not observed for bulk single crystalline Si, but an inherent characteristic of amorphous Si. In our previous study (4), we have assigned the structure around $h\nu \simeq E_0$ to a slight amorphization of the SOS films, most likely originating from a region of inferior crystalline quality in the vicinity of the silicon-sapphire interface. For thin SOS films (typically 0.6 μm), the photovoltage exhibits a series of interference maxima-minima (4). In the spectra of Fig. 1, the interference maxima-minima were averaged, since they are of no interest in the present study.

It is seen from Fig. 1 that the subbandgap photoionization transitions are reduced by as much as two orders of magnitude in the SOS films which received a high implantation dose. This effect is clearly seen in Fig. 2, in which the deep level (E_{t1}) concentration is plotted vs. the Si-implantation dose [the deep level concentration in arbitrary units was determined from the values of $V(h\nu = 0.8 \text{ eV})/V(h\nu = 2 \text{ eV})$ (5)]. The results in Fig. 2 indicate that a threshold Si-implant concentration greater than $2 \times 10^{15} \text{ ions-cm}^{-2}$ is required to suppress deep levels in SOS films. The improvement in electronic properties caused by Si-implantation and subsequent annealing was also observed in photovoltage relaxation measurements at low temperatures ($\sim 200 \text{ K}$). As discussed previously (4), the photovoltage transient, caused by interrupting the illumination, exhibits an exponential time dependence with a time constant which is inversely proportional to the concentration of minority carrier traps. The time constant in films annealed after an Si-dose of

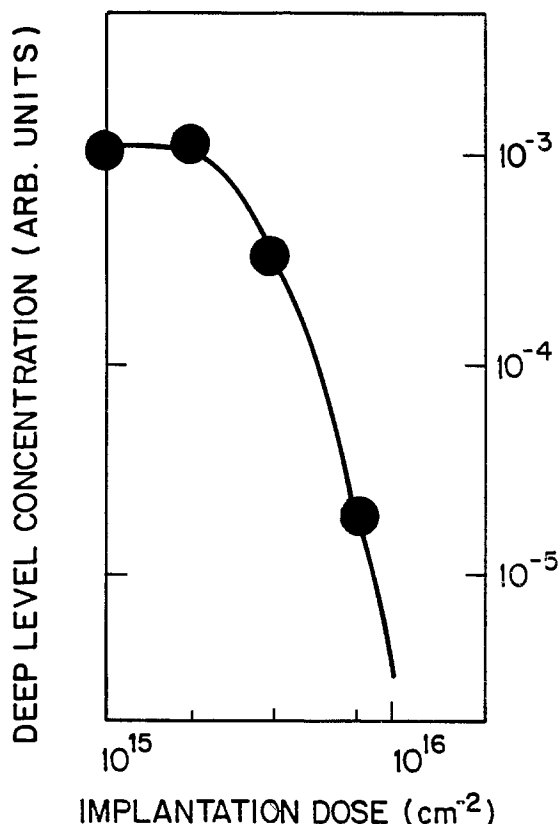


Fig. 2. Concentration of deep levels as a function of the implantation dose.

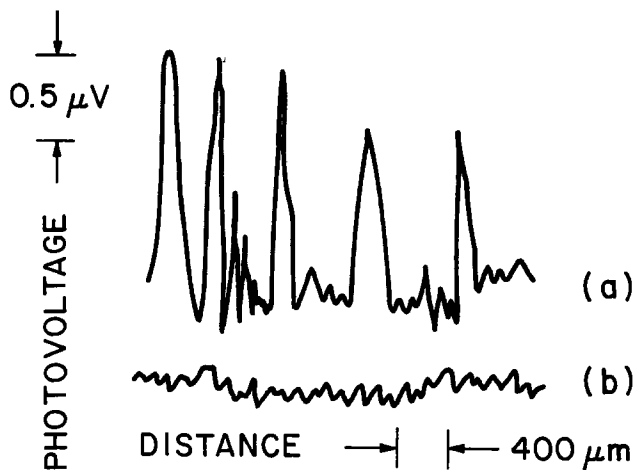


Fig. 3. Photovoltage scans of deposits exposed to (a) 1×10^{15} and (b) $8 \times 10^{15} \text{ ions-cm}^{-2}$ Si implantation.

$8 \times 10^{15} \text{ ions-cm}^{-2}$ was higher by as much as a factor of four than for a low implantation dose of $1 \times 10^{15} \text{ ions-cm}^{-2}$. Accordingly, it can be concluded that solid-state recrystallization reduces the concentration of minority carrier trapping centers.

The above results show the effects of recrystallization on the average (macroscopic) properties of silicon-on-sapphire. Improvement in the electrical homogeneity of heteroepitaxial silicon is observed with photovoltage measurements carried out with a very small focused light spot (15 μm diam). These types of measurements constitute a powerful technique for detection of inhomogeneities in semiconductors (7). In this technique, localized excitation of excess carriers by a focused He-Ne laser beam generates a differential photovoltage between two contacts which are located away from the excitation point and kept in the dark (7). The photovoltage signal is due to the presence of a horizontal gradient in carrier concentration, diffusion length, or the concentration of trapping centers. A localized potential barrier (e.g., an electrically active grain boundary) constitutes a typical example of an inhomogeneity that leads to pronounced photovoltaic signals. In a perfectly homogeneous material, no photovoltage signal is observed.

Typical high resolution photovoltage scans of the central portion of SOS wafers with the lowest ($1 \times 10^{15} \text{ ions-cm}^{-2}$) and the highest ($8 \times 10^{15} \text{ ions-cm}^{-2}$) Si-implantation doses are shown in Fig. 3a and 3b, respec-

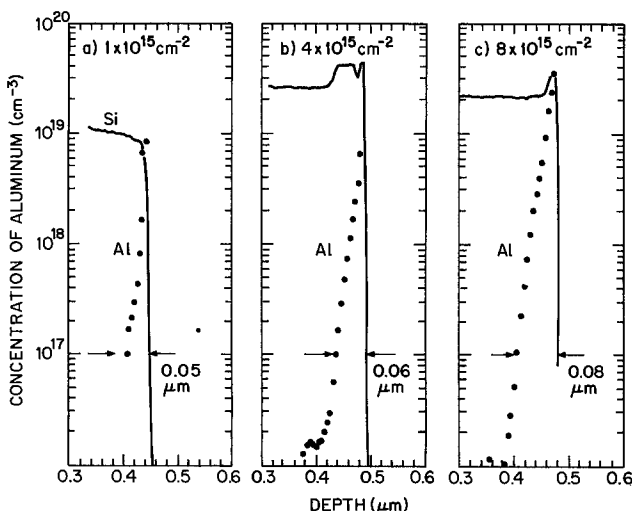


Fig. 4. Distribution of Al in the vicinity of sapphire interface for various doses of implantation: (a) $1 \times 10^{15} \text{ cm}^{-2}$, (b) $4 \times 10^{15} \text{ cm}^{-2}$, and (c) $8 \times 10^{15} \text{ cm}^{-2}$. The distance on which Al concentration is reduced to 10^{17} cm^{-3} is marked on the figures.

Table I. Result of x-ray pole-figure analysis of ion-implanted and annealed heteroepitaxial silicon

Dose (ions-cm ⁻²)	Amorphization of (100) (% by vol)	Recrystallization of (100) (% by vol)
1 × 10 ¹⁵	20	100
2 × 10 ¹⁵	55	100
4 × 10 ¹⁵	90	105
8 × 10 ¹⁵	95	105

tively. It is evident that the film which received the high implantation dose was much more homogeneous than the film which received the low implantation dose.

The results of x-ray pole-figure analysis on silicon films implanted and annealed simultaneously with the samples used in the photovoltage measurements are given in Table I.

It can be seen from Table I that at the higher implant doses, more (100)-oriented silicon was present after the recrystallization process than had been present initially. This results from the conversion of {221} twin material, initially present in the films mostly in the interfacial region, to the (100) orientation as a result of amorphization and recrystallization. A corresponding decrease in the {221} concentration of the films was simultaneously observed. It should be noted, however, that these measurements are reproducible to no better than about 5%. Consequently, it is not possible to state conclusively that recrystallization is complete. Some small amount of amorphous material, not detectable by x-ray analysis, may still remain after annealing.

SIMS profiles of the Al distribution in the implanted SOS films are shown in Fig. 4. It is evident that the amount of aluminum which has been displaced into the silicon from the sapphire increases with increasing implantation dose. The aluminum concentration drops to a value of 10¹⁷ atoms-cm⁻³ in the distance of 0.05, 0.06, and 0.08 μm from the sapphire interface in the samples implanted with silicon doses of 1, 4, and 8 × 10¹⁵ ions-cm⁻², respectively. It is evident from the above results that the chemical nature of the interfacial region is significantly changed by ion implantation.

It has been shown recently that the density of electrically active defects is related to the concentration of {221} twins in heteroepitaxial silicon (5). TEM cross-section micrographs indicate that the highest concentration of crystallographic defects is in the interfacial region (8). Therefore, it should not be surprising that the largest reduction in the concentration of electrically

active defects has been observed in the samples with the largest changes in the interfacial region. The reduction observed in the concentration of electrical inhomogeneities probably results from the homogenization of the interfacial region by ion implantation and recrystallization.

It is of interest to note that improvements caused by the solid-state recrystallization are similar to those caused by the hydrogenation of SOS films. As we have recently shown, (6) atomic hydrogen introduced into SOS films suppresses the concentration of E_{t1} levels, reduces trapping effects, and decreases the magnitude of microscopic inhomogeneities. These beneficial effects of atomic hydrogen were attributed to saturation of the dangling bonds of structural defects located mostly at the interface by hydrogen. This led to passivation of their electrical activity.

We believe that the effects reported here are related to reduction of the concentration of structural defects, especially in the interfacial region, as a result of the recrystallization process and/or their passivation by interaction with point defects or impurities, e.g., aluminum. Further study is needed to assess the effect of lower energy implants (which would reduce damage of sapphire) on the electronic properties of SOS films subjected to the solid-state regrowth procedure.

Manuscript submitted May 18, 1983; revised manuscript received Aug. 17, 1983.

RCA Laboratories assisted in meeting the publication costs of this article.

REFERENCES

1. See, for example, I. Golecki and M. A. Nicolet, *Solid-State Electron.*, **23**, 803 (1980); T. Inoue and T. Yoshii, *Appl. Phys. Lett.*, **36**, 64 (1980).
2. I. Golecki, G. Kinoshita, A. Gat, and B. M. Paine, *Appl. Phys. Lett.*, **37**, 919 (1980); S. S. Lau, S. Matteson, J. W. Mayer, P. Revesz, J. Gyulai, J. Roth, T. W. Sigmon, and T. Cass, *ibid.*, **34**, 76 (1979).
3. R. T. Smith and C. W. Weitzel, *J. Cryst. Growth*, **58**, 61 (1982).
4. J. Lagowski, L. Jastrzebski, and G. W. Cullen, *This Journal*, **128**, 2665 (1981).
5. L. Jastrzebski, M. T. Duffy, J. F. Corboy, G. W. Cullen, and J. Lagowski, *J. Cryst. Growth*, **58**, 37 (1982).
6. L. Jastrzebski, J. Lagowski, G. W. Cullen, and J. I. Pankove, *Appl. Phys. Lett.*, **40**, 713 (1982).
7. J. Lagowski, L. Jastrzebski, and G. W. Cullen, *This Journal*, **129**, 2609 (1982).
8. M. S. Abrahams, C. J. Buiocchi, J. F. Corboy, and G. W. Cullen, *Appl. Phys. Lett.*, **33**, 773 (1978).

Effect of Nitridation of Silicon Dioxide on Its Infrared Spectrum

M. L. Naiman, C. T. Kirk, R. J. Aucoin, F. L. Terry, and P. W. Wyatt

MIT Lincoln Laboratory, Lexington, Massachusetts 02173

S. D. Senturia

MIT, Cambridge, Massachusetts 02139

ABSTRACT

Thick oxide films (≈ 220 nm) have been nitrided heavily in ammonia. Dispersion analysis was performed on infrared transmission spectra of oxide, nitrided oxide, and CVD nitride films. The following conclusions may be drawn from the spectra: nitrided oxide is not the same material as CVD silicon nitride; nitridation results in significant loss of Si-O asymmetric stretch intensity; and nitridation leads to the appearance of a spectral peak for planar triply bonded N-Si asymmetric stretch analogous to that in trisilylamine. About 43% of the oxygen was replaced by nitrogen.

The high temperature nitridation of thermal silicon dioxide films in ammonia has been shown to have a profound effect on the radiation resistance of thin (10-20 nm) oxides (1, 2). The primary locus of failure due to radiation in NMOS circuitry is the field oxide, and recent studies have shown that the radiation resistance of thick (200-400 nm) oxides is also affected by nitridation (3). Thick nitrided oxides have been shown by Auger spectroscopy to have incorporated significant amounts of nitrogen in their outer layers and smaller amounts at their silicon interfaces (4-7). In this study, infrared spectroscopy was used to evaluate the nature of the incorporated nitrogen. We find that it is planar trigonally bonded, and we show quantitatively the degree of conversion to nitride.

Experimental

Lightly doped silicon wafers, 5 cm diam, were lapped and polished on both sides to provide a taper of 0.0025-0.020 cm; this taper is required to prevent interference effects in the silicon from obscuring the results. A set of wafers were oxidized at 1000°C using a cycle consisting of 10 min of oxygen, 30 min of steam, and 20 min of nitrogen, to provide oxide films about 220 nm thick on each side. Some of these oxidized wafers were then nitrided in ammonia at 1 atm pressure for 6h at 1100°C. A second set of wafers were coated with 200 nm of LPCVD silicon nitride. The pertinent characteristics of these films are given in Table I.

Infrared transmission spectra of the various samples were measured in the spectral range of 1400-800 inverse centimeters using a Beckman 4250 infrared spectrophotometer. The slit width, under program control, varied from 0.5 mm at 1400 cm^{-1} to 2.1 mm at 800 cm^{-1} . The period was 1s, and the scan speed 50 $\text{cm}^{-1}/\text{min}$. The indicated resolution is a few inverse centimeters, and the photometric error is less than 1%. The spectra were measured using uncoated but tapered silicon wafers as references. The data for each spectrum were digitized and normalized (9). The higher energy portions (asymmetric stretch modes) of each spectrum were decomposed into their constituents; the lower energy peaks (symmetric stretch and rocking modes around 850 cm^{-1} and below for oxide and nitrided oxide, and around 600 cm^{-1} and below for CVD nitride) were ignored.

Dispersion Analysis

Dispersion analysis is a process wherein a set of oscillators is specified which will allow the synthesis of curves having reasonable agreement with the optical data. It has been applied in the past to bulk quartz (10) and crystalline Si_3N_4 (11), but has not to our knowledge been used for films of either silicon oxide or nitride. SiO_2 films have been studied by Kramers-

Kronig analysis (12), which yields values for the optical constants n and k . Dispersion analysis provides information not only on the optical constants n and k , but also on the oscillators which induce changes in these constants. The oscillators can be related, in turn, to the molecular structure of the material.

Our analysis follows that used by Spitzer and Kleinman (10). Following Seitz (13), the classical dispersion theory of crystals leads to these equations for the refractive index n and the extinction coefficient k at optical frequency ν

$$n^2 - k^2 = \epsilon_0 + \sum_j 4\pi\rho_j\nu_j^2 \frac{\nu_j^2 - \nu^2}{(\nu_j^2 - \nu^2)^2 + \gamma_j^2 \nu_j^2 \nu^2} \quad [1]$$

$$nk = \sum_j 2\pi\rho_j\nu_j^2 \frac{\gamma_j\nu\nu_j}{(\nu_j^2 - \nu^2)^2 + \gamma_j^2 \nu_j^2 \nu^2}$$

where the summation is over the lattice oscillators and each oscillator is characterized by its polarization ρ_j , width $\gamma_j\nu_j$, and frequency ν_j .

The quantity ρ_j is related to the oscillator strength f_j by

$$\rho_j = (Ne^2/4\pi^2m\nu_j^2)f_j$$

where N is the oscillator concentration and e and m are the charge and mass of the electron. The long wavelength dielectric constant is given by

$$\epsilon = \epsilon_0 + \sum_j 4\pi\rho_j$$

where ϵ_0 is the short wavelength dielectric constant.

The accommodation required to change from a crystalline to an amorphous structure introduces a distribution in bond strengths and thereby a distribution in oscillator frequencies. We take this distribution to be gaussian and hence replace ρ_j in Eq. [1] by

$$\rho_j \rightarrow \rho_j \frac{1}{1.201 \delta_j \sqrt{\pi}} \int \{\exp - [(\nu_i - \nu_j)/1.201 \delta_j]^2\} d\nu_i \quad [2]$$

where δ_j is the gaussian half width at half maximum for the j -th oscillator distribution ($1.201\delta_j = \sqrt{2} \sigma_j$).

Table I. Ellipsometric characteristics of films
 $\lambda = 632.8$ nm

	Index of refraction	Thickness, nm
Thermal oxide	1.465	240.4
Nitrided oxide	1.443	239.4
CVD nitride	1.925*	212.5

* An index of 1.925 indicates an atomic percent composition $\text{N}_a/(\text{N}_a + \text{O}_a) = 0.9$ (8).

Key words: dielectrics, transmittance, optics, growth.

where σ_j is the standard deviation). Equations [1] now become

$$n^2 - k^2 = \epsilon_0 + \sum_j \frac{4\sqrt{\pi}}{1.201\delta_j} \rho_j \nu_j^2 \int \frac{\{\exp - [(\nu_1 - \nu_j)/1.201\delta_j]^2\} (\nu_1^2 - \nu^2)}{(\nu_1^2 - \nu^2)^2 + (\gamma_j \nu \nu_1)^2} d\nu_1$$

$$nk = \sum_j \frac{2\sqrt{\pi}}{1.201\delta_j} \rho_j \nu_j^2 \int \frac{\{\exp - [(\nu_1 - \nu_j)/1.201\delta_j]^2\} \gamma_j \nu \nu_1}{(\nu_1^2 - \nu^2)^2 + (\gamma_j \nu \nu_1)^2} d\nu_1 \quad [3]$$

Analysis of a film consists of tentatively identifying a set of oscillators, each characterized by parameters ρ_j , δ_j , ν_j , γ_j , which, when inserted into Eq. [3], and then into the equations for optical transmission through the sample (see below), yield a best fit to the experimental data.

For a film on a supporting wafer the effective transmission is mediated by the silicon layer. The equations for transmission rapidly become intractable as the number of films increases; however, because of symmetry, they can be somewhat simplified by having films on both sides of the substrate, and by treating the wafer as lossless. All our results are for wafers with films on both sides.

Heavens (14) gives for the transmission of a single film on an absorbing substrate

$$T_1 = \frac{n_2}{n_0} \frac{[(1 + g_1)^2 + h_1^2] [(1 + g_2)^2 + h_2^2]}{[\exp(2\alpha)] + (g_1^2 + h_1^2)(g_2^2 + h_2^2) [\exp(-2\alpha)] + C \cos 2\theta + D \sin 2\theta}$$

where

$$g_1 = \frac{n_0^2 - n_1^2 - k_1^2}{(n_0 + n_1)^2 + k_1^2} \quad h_1 = \frac{2n_0k_1}{(n_0 + n_1)^2 + k_1^2}$$

$$g_2 = \frac{n_1^2 - n_2^2 + k_1^2 - k_2^2}{(n_1 + n_2)^2 + (k_1 + k_2)^2} \quad h_2 = \frac{2(n_1k_2 - n_2k_1)}{(n_1 + n_2)^2 + (k_1 + k_2)^2}$$

$$\alpha = \frac{2\pi k_1 d_1}{\lambda} \quad \theta = \frac{2\pi n_1 d_1}{\lambda}$$

$$C = 2(g_1g_2 - h_1h_2) \quad D = 2(g_1h_2 + g_2h_1)$$

and n_0 is the index of air, $n_1 = n_1 - ik_1$ and d_1 are the index and thickness of the film, and $n_2 = n_2 - ik_2$ is the index of the silicon wafer.

For a tapered wafer, all phases of the light reflected inside the wafer are added, thereby canceling the resonance effects. If the silicon is perfectly lossless, i.e., $k_2 = 0$, then the transmission of the structure with films on both sides is, with the correction for the change of n on exit, simply the square of the above

$$T_2 = \left(\frac{[(1 + g_1)^2 + h_1^2] [(1 + g_2)^2 + h_2^2]}{[\exp(2\alpha)] + (g_1^2 + h_1^2)(g_2^2 + h_2^2) [\exp(-2\alpha)] + C \cos 2\theta + D \sin 2\theta} \right)^2 \quad [4]$$

We take the index of silicon to be $n_2 = 3.42 + i0$ (15). The dispersion in this frequency range is negligible. The small absorption actually present in the silicon is partially compensated by the reference wafer and by the normalization procedure. The effect of the oxygen content of the silicon, which is measurable both in its dissolved and cristobalite forms, is discussed below.

Results

The spectra for oxide, nitrided oxide, and CVD nitride are shown as the top traces in Fig. 1, 2, and 3, respectively. The fit is achieved iteratively by choosing values for ν_j , ρ_j , γ_j , and δ_j for the several peaks, computing $n^2 - k^2$ and nk from Eq. [3], and then T_2 from Eq. [4]. Each measured curve was normalized at the high and low frequency ends to the computed values.

The results of the spectral analysis of the data are presented in Table II, together with selected literature data from the crystalline compounds and trisilylamine

(vapor) (16), the latter being the simplest trigonally bonded N—Si₃ compound. The bottom traces of Fig.

1, 2, and 3 show the difference between the experimental spectra and the spectra computed from the oscillators of Table II.

The main peak, at 1065 cm⁻¹ in oxide and nitrided oxide, is discussed in detail below. The line at about 1090 inverse centimeters may be attributed to interstitial oxygen in the wafer (17). The line disappears when the films are etched off and reappears when the spectra are recorded without a reference wafer. The appearance is due to the interaction of the lossy wafer and the lossy film in this frequency range, which is not taken into account in our calculations. Note that this is the only sharp line in the spectra; it is similarly sharp in the bare wafers. The presence of this line leads to an uncertainty of 1 or 2 cm⁻¹ in the width and position and a small fraction in the height of the main

(1065) peak. The 1220 line is presumed due to cristobalite in the wafer (17); the 1165 line has been variously attributed to mixed and longitudinal modes (10).

The other lines are presumed to be due to asymmetric stretch of the O—Si or N—Si bonds. The strong line about 1070 cm⁻¹ attributed to the TO mode is dominant in α -quartz, thermal oxide, and nitrided thermal oxide. The width of this line more than

quadruples in going from α -quartz to thermal oxide because bond strengths are altered in forcing the Si—O tetrahedra to accommodate to more random orientations in the vitreous structure.

A new peak at 1000 cm⁻¹ has appeared in the nitrided oxide spectrum, while the main Si—O peak has been reduced and broadened. We attribute this new peak to planar, trigonally bonded nitrogen, because it is close in frequency to the peak for trisilylamine (16).

If the number of silicon bonds is constant during nitridation, then the supplanting of doubly coordinated oxygen by triply coordinated nitrogen should reduce the concentration of oscillators N by a factor of 2/3. However, if the nitrogen is trigonally bonded, the in-plane asymmetric stretch mode is doubly degenerate, doubling the oscillator strength f_j in that mode. Hence, nitridation should result in a factor of $2 \times 2/3 = 1.33$ increase in the product of density and oscillator strength Nf_j for the nitrogen oscillators compared to the loss in Nf_j for the oxygen oscillators. The product

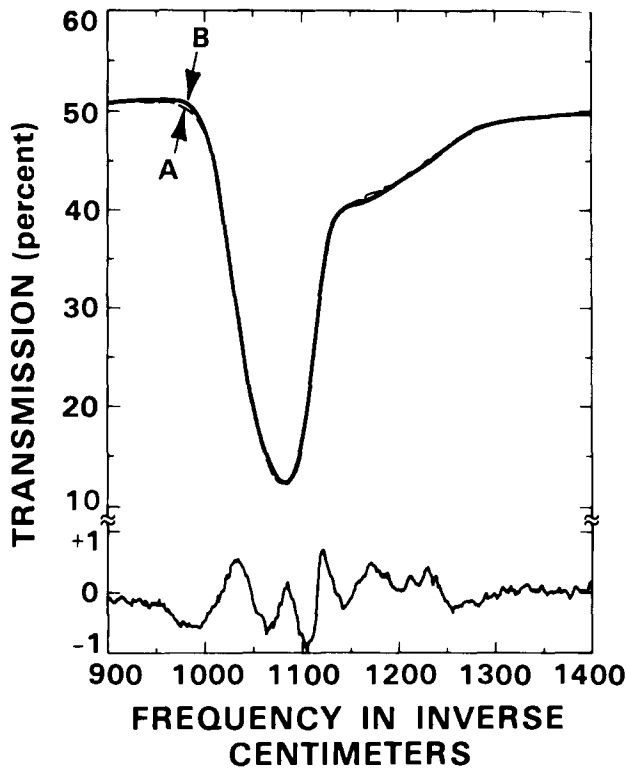


Fig. 1. Infrared spectra of thermal oxide. Top curve: A = Experimental, B = Calculated. Bottom curve: A minus B.

Nf_j is proportional to the polarization $\rho_j \nu_j^2$, so we would expect that the ratio $\rho_{N\nu N^2} / \rho_{O\nu O^2} = 1.33$. As shown in Table II, the scaled polarization for the oxide line decreased by $32,000 - 18,000 = 14,000$, while the mea-

Table II. Principal spectral peaks*

	This Work			Previous Work		
	Thermal oxide	Nitrided oxide	CVD Si ₃ N ₄	α -SiO ₂ (10)	Si ₃ N ₄ (11)	N(SiH) ₃ (16)
ν_j	1220	1222		1227		
$\rho_j \nu_j^2$	1300	1240		1078		
$\gamma_j \nu_j$	8	8		135		
δ_j	26	34		—		
ν_j	1165	1146	1164	1163		
$\rho_j \nu_j^2$	3100	5000	1200	1076		
$\gamma_j \nu_j$	7	8	8	7		
δ_j	32	49	50	—		
ν_j	1088.5	1088.5				
$\rho_j \nu_j^2$	9000	3050				
$\gamma_j \nu_j$	2.5	2.5				
δ_j	17	22				
ν_j	1064.5	1064.5	1076	1072		
$\rho_j \nu_j^2$	32,000	18,000	2,600	61,000		
$\gamma_j \nu_j$	8	8	8	7.6		
δ_j	28.5	30	44	—		
ν_j		1000	1000		1051	996
$\rho_j \nu_j^2$		18,700	6,200		11,000	—
$\gamma_j \nu_j$		8	8		26	—
δ_j		80	42		—	—
ν_j			937.5		980	
$\rho_j \nu_j^2$			12,000		29,000	
$\gamma_j \nu_j$			8		15	
δ_j			40		—	
ν_j			891		900	
$\rho_j \nu_j^2$			10,000		32,000	
$\gamma_j \nu_j$			8		19	
δ_j			35.5		—	
ν_j			818		854	
$\rho_j \nu_j^2$			53,000		51,000	
$\gamma_j \nu_j$			8		25	
δ_j			54		—	

* ν_j = oscillator width. $\rho_j \nu_j^2$ = scaled polarization. $\gamma_j \nu_j$ = Lorentzian width. δ_j = Gaussian width.

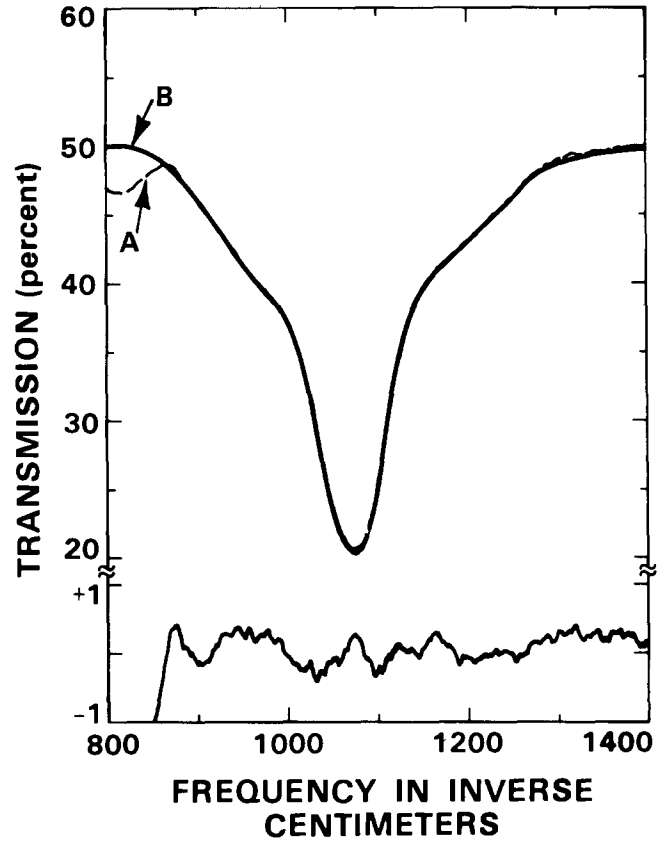


Fig. 2. Infrared spectra of nitrided oxide. Top curve: A = Experimental, B = Calculated. Bottom curve: A minus B.

sured value for the nitride line was 18,700; the ratio $18,700 / 14,000 = 1.34$, which represents excellent agreement. The indicated composition for the nitride film is about SiO_{1.14}N_{0.57}.

The CVD nitride spectrum is quite distinct from the nitrided oxide spectrum. The CVD spectrum has been

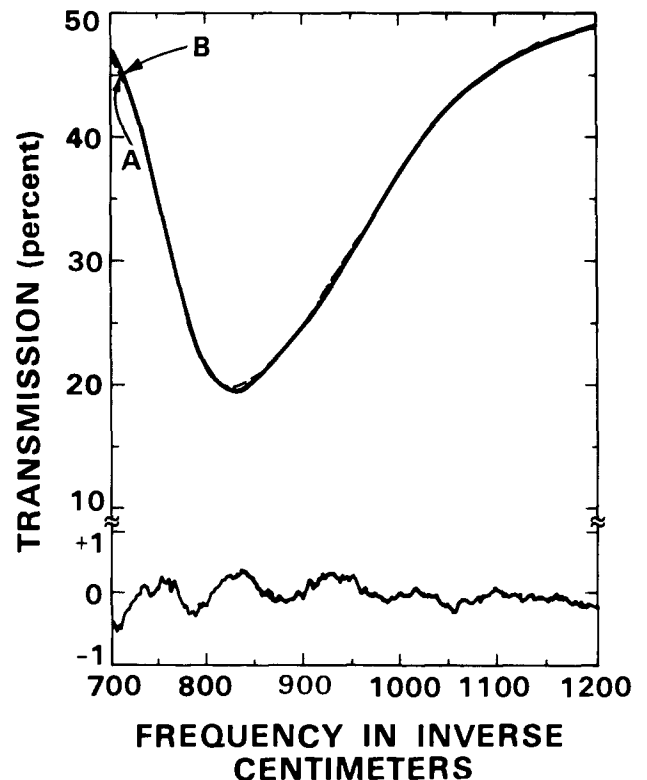


Fig. 3. Infrared spectra of CVD nitride. Top curve: A = Experimental, B = Calculated. Bottom curve: A minus B.

decomposed into oscillators that correspond to α - Si_3N_4 , except for a general shift to lower frequency by 1-5%.

Conclusions

We find, as did Habraken *et al.* (7), that nitridation decreases the amplitude and increases the width of the main thermal oxide peak. Decomposing the peaks shows a new line at 1000 cm^{-1} in the nitrated oxide; about 43% of the oscillators have been converted to the new peak. The near coincidence in frequency to the trisilylamine peak, which has been shown to be due to planar trigonal N—Si₃ bonds, leads us to ascribe the new peak to planar trigonally bonded nitrogen. Note that this peak does not occupy a dominant position in either the crystalline or amorphous (CVD) silicon nitride spectrum. The line width of the new peak again increases as the nitride structure is made compatible to the oxide matrix.

Manuscript received June 1, 1983. This was Paper 124 presented at the San Francisco, California, Meeting of the Society, May 8-13, 1983.

Massachusetts Institute of Technology assisted in meeting the publication costs of this article.

REFERENCES

1. M. L. Naiman, F. L. Terry, J. A. Burns, J. I. Raffel, and R. J. Aucoin, *IEDM*, 562 (1980).
2. F. L. Terry, M. L. Naiman, R. J. Aucoin, and S. D. Senturia, *IEEE Trans. Nuc. Sci.*, **ns-28**, 4389 (1981).
3. F. L. Terry, R. J. Aucoin, M. L. Naiman, P. W. Wyatt, and S. D. Senturia, *IEEE Electron Dev. Lett.*, **ed-4**, 191 (1983).
4. T. Ito, T. Nozaki, and H. Isikawa, *This Journal*, **127**, 2053 (1980).
5. R. J. Aucoin, M. L. Naiman, F. L. Terry, and R. Reif, *ibid.*, **128**, 364C (1981).
6. Y. Hayafuji and K. Kajiwara, *ibid.*, **129**, 2102 (1982).
7. F. M. P. Habraken, A. E. T. Kuiper, Y. Tamminaga, and J. B. Theeten, *J. Appl. Phys.*, **53**, 6996 (1982).
8. A. K. Gaid, G. K. Ackermann, V. J. Lucarini, and R. C. Bratter, *This Journal*, **124**, 599 (1977).
9. J. E. Dial, R. E. Gong, and J. N. Fordemwalt, *ibid.*, **115**, 326 (1968).
10. W. G. Spitzer and D. A. Kleinman, *Phys. Rev.*, **121**, 1324 (1961).
11. Yu. N. Volgin, G. P. Dubrovskii, and Yu. I. Ukhonov, *Sov. Phys. Solid State*, **17**, 1088 (1975).
12. H. R. Phillip, *J. Appl. Phys.*, **50**, 1053 (1953).
13. F. Seitz, "Modern Theory of Solids," Chap. 17, McGraw Hill Book Co., Inc., New York (1940).
14. O. S. Heavens, "Optical Properties of Thin Solid Films," pp. 76-77, Academic Press, Inc., New York (1955).
15. F. A. Johnson, *Proc. Phys. Soc.*, **73**, 265 (1959).
16. E. A. V. Ebsworth, J. R. Hall, M. J. Mackillop, D. C. McKean, N. Sheppard, and L. A. Woodward, *Spectrochim. Acta*, **13**, 202 (1958).
17. F. Shimura, H. Tsuya, and T. Kawamura, *Appl. Phys. Lett.*, **37**, 483 (1980).

Photointercalation and Optical Information Storage Using $\text{Cu}_{6-x}\text{PS}_5\text{I}$

G. Betz and H. Tributsch

Hahn-Meitner-Institut für Kernforschung Berlin GmbH, Bereich Strahlenchemie, D-1000 Berlin 39, Germany

S. Fiechter

Albert-Ludwigs-Universität, Kristallographisches Institut, D-7800 Freiburg, Germany

ABSTRACT

The agyrodite $\text{Cu}_6-x\text{PS}_5\text{I}$ is simultaneously a copper ion conductor and a p-type electronic semiconductor. With an energy gap of $\Delta E_G = 2.05\text{ eV}$, the compound intercalates copper upon illumination as demonstrated in photoelectrochemical experiments. The intercalation of copper is accompanied by a color change which is believed to be due to an annihilation of I_2^- color centers. In experiments in which Cu was partially replaced by Ag, photointercalation was verified by means of x-ray fluorescence measurements. It is shown how such a photointercalation reaction could be used to store optical information.

Since the proposal of light-induced intercalation and deintercalation as a possible mechanism for solar energy and optical information storage, several semiconducting host materials have been investigated. Light-induced topotactical reactions have been investigated on p-ZrSe₂ [intercalation of metal ions (1)], n-HfSe₂ [deintercalation of metal ions (2)], and TiO₂(B) [deintercalation of protons (3)]. In the last case, the studies could be made using aqueous electrolytes because of the high stability of the material. In all other cases, organic electrolytes were required to avoid rapid corrosion as a consequence of an intercalation of aqueous species. Preliminary experiments with other materials such as p-ZrS₂ (4), p-FePS₃ (5), and n-InSe (6) have shown that semiconducting host materials of good photocurrent efficiency, corrosion stability, reversibility, and high ionic conductivity are not abundant. Also crucial is the question where the electronic energy levels of the guest atoms have to be placed in an energy scheme. Only those systems are of practical interest which maintain semiconducting properties during intercalation at high concentrations of intercalated guest atoms. Therefore, it appears reasonable to select systems which are semiconducting when fully intercalated. Such a system is $\text{Cu}_6\text{PS}_5\text{I}$ ($\Delta E_G =$

2.05 eV) which can be deintercalated to become a $\text{Cu}_{6-x}\text{PS}_5\text{I}$ compound.

Experimental

Material.—Crystals of $\text{Cu}_6\text{PS}_5\text{I}$ grown by chemical vapor transport in the presence of liquid CuI (7) have a cubic high temperature structure (SG: $F\bar{4}3m$; $Z = 4$) with a disordered Cu-cation sublattice. The idealized anion sublattice, consisting of S and I, forms a framework of interpenetrating centered icosahedra providing ideal and distorted tetrahedral cation sites (Fig. 1) (8). The P atoms reside in the perfect tetrahedral sites surrounded by four S atoms.

The 24 Cu atoms are distributed on a 48-fold split position in distorted anion tetrahedra. Two of these tetrahedra always have a common face. In Fig. 1, a double tetrahedron is outlined and the possible positions which are normally occupied by one Cu atom are marked (9). One Cu position is situated near the common tetrahedral face and exhibits a trigonal planar coordination, while the other is within the tetrahedron (7, 9). Since the resulting double tetrahedra (24 per unit cell) are interconnected by cornersharing and edgesharing to a three-dimensional framework, the observed copper ion conduction (10) can be under-

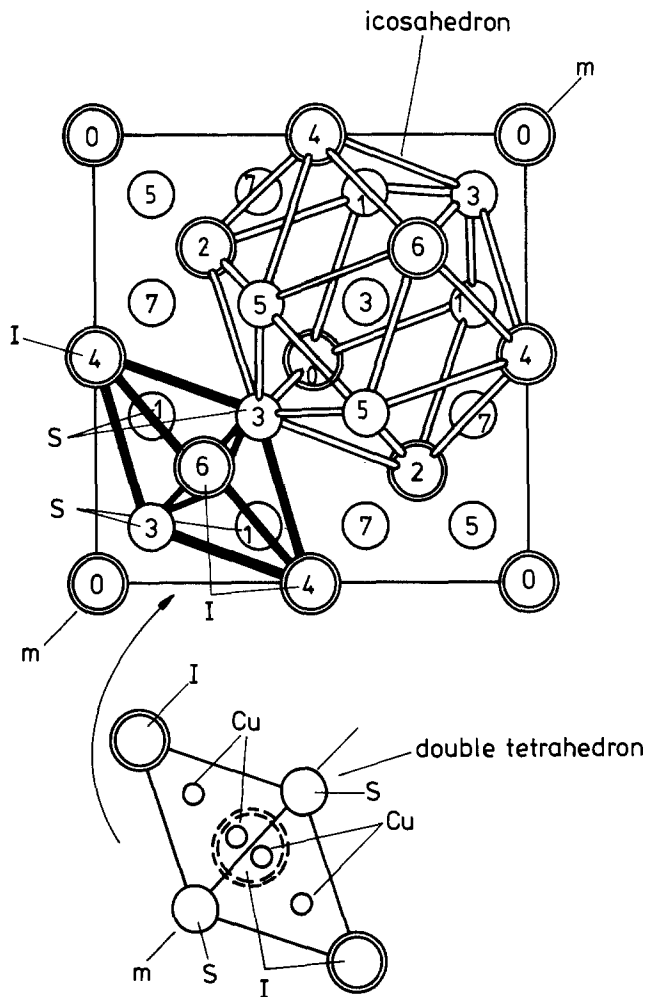


Fig. 1. Projection of the idealized anion sublattice of $\text{Cu}_6\text{PS}_5\text{I}$ along $[100]$ with an anion icosahedron outlined (7). The crystal structure of $\text{Cu}_6\text{PS}_5\text{I}$ can also be built up with double tetrahedra as building units. The numbers are heights in eighths of the unit cell. One of the 24 double tetrahedra which contains one Cu atom is also outlined. The Cu atom is able to migrate between the marked positions.

stood as a hopping process of Cu atoms from one double tetrahedron to a neighboring one. It is assumed that during the Cu migration one double tetrahedron can contain two copper atoms in the tetrahedral positions.

The $\text{Cu}_6\text{PS}_5\text{I}$ crystals were red and transparent. With a Seebeck effect device (GCA Solid State Measurements) the material was identified as a p-type semiconductor. The bandgap is 2.05 eV (11).

Sample preparation.—The crystals used in the experiments were plates with an area of 2–3 mm². Some of the crystals were treated in concentrated nitric acid at 50°C for 20 min to partially remove copper from the $\text{Cu}_6\text{PS}_5\text{I}$ lattice. The nitric acid oxidizes the $\text{Cu}_6\text{PS}_5\text{I}$ by forming $\text{Cu}(\text{NO}_3)_2$ (12). As a consequence of this treatment, the surface is etched and cracks may occur.

A 500Å gold layer was evaporated onto the back face of both the treated and the untreated crystals. The back contact was made by gluing the contacted crystal with Ag epoxy onto a brass electrode holder which was electrically isolated with silicon rubber.

Experimental setup.—Photoelectrochemical experiments were performed in a standard three-electrode cell with an Ag/AgNO₃ electrode as a reference electrode and a copper or silver wire as counterelectrode. The experiments were done in a 0.1M tetraethylammonium perchlorate (TEAPC) acetonitrile solution

containing either 0.01M CuCl or 0.02M AgNO₃. Oxygen and water were removed from the acetonitrile with Cr-HMDS (hexamethyldisiloxane) bound to the surface of silicagel (13).

The CuCl was dried by chemical transport with HCl and N₂ at 600°C. The AgNO₃ and the TEAPC were dried by heating under vacuum. The experiments were carried out in a glove box.

Cyclic voltammograms were obtained with a potentiostat (PAR 179) equipped with a coulometer and a scanning device (PAR 175). A 450W Xe lamp (Oriel) served as a light source. Photocurrent spectra were obtained with a high intensity monochromator (Bausch and Lomb) equipped with a grating blazed at 700 nm.

Results

Figure 2 shows that if the electrolyte contains merely TEAPC as a conducting salt there is only a negligibly small cathodic photocurrent in the negative potential region (probably due to traces of copper). Adding 0.01M CuCl, the cathodic photocurrent is increased by an order of magnitude. Both the cathodic photocurrent and the cathodic dark current decrease when the electrode potential is kept at a constant negative potential. This causes the hysteresis in the cyclic voltammogram of Fig. 3a. When the scan direction is reversed at negative potential values, an anodic discharge current starts to flow which also decreases with time. When the potential is again swept into the negative direction, the onset of the cathodic photocurrent occurs more positive (Fig. 3a). Figure 3b shows the photo- and dark-current after an anodic charge of 16.5 mC/cm² had passed through the electrode at a potential of +0.4V vs. Ag/AgNO₃. In this case, there is clearly an additional increase of cathodic photocurrents. The onset of photocurrents is shifted further towards positive potential values. There is a similar increase in the photocurrent density when the crystal is pretreated with concentrated nitric acid to remove copper.

Color changes from red to black have been attributed to differences of the Cu content in the material (12). An electrode that had been treated before in concentrated nitric acid was illuminated to reintercalate copper with light. The surface of the crystal, which had turned opaque after treatment in concentrated nitric acid ($\text{Cu}_{6-x}\text{PS}_5\text{I}$), regained its red color and transparency ($\text{Cu}_6\text{PS}_5\text{I}$) in the neighborhood of the

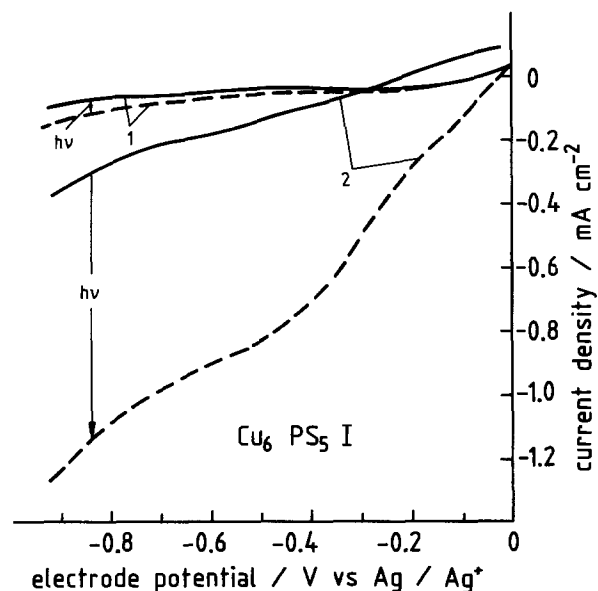


Fig. 2. Photocurrent and dark current density as a function of the electrode potential applied on $\text{Cu}_{6-x}\text{PS}_5\text{I}$ (sweep rate: 20 mV sec⁻¹). (1) 0.01M TEAPC-acetonitrile, (2) after addition of 0.01M CuCl.

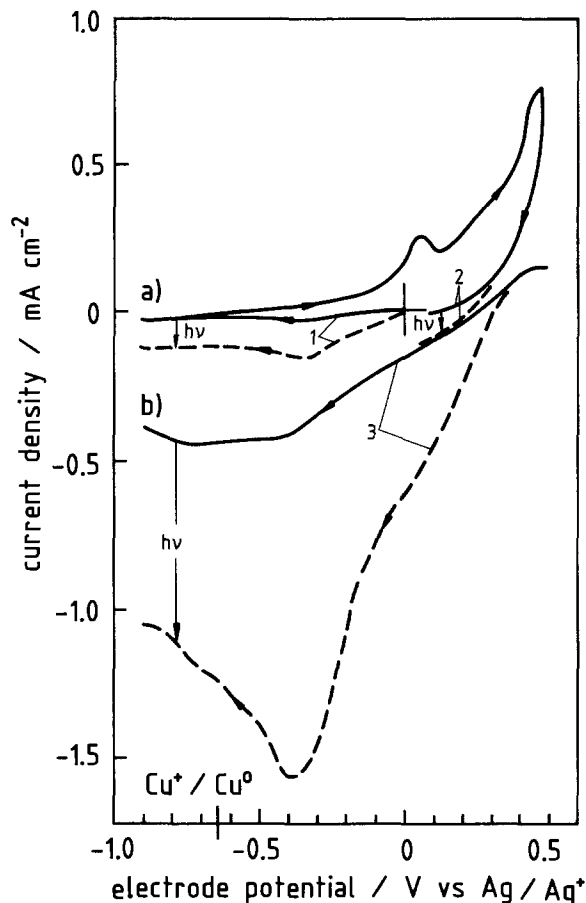


Fig. 3. Photocurrent and dark current density as a function of the electrode potential (sweep rate: 20 mV sec^{-1}). The electrolyte is $0.01\text{M CuCl}/0.01\text{M TEAPC}/\text{acetonitrile}$. (a) $\text{Cu}_6\text{PS}_5\text{I}$ (first sweep), (b) after complete sweep and anodic polarization, and (c) after passage of 23.5 mC/cm^2 of anodic charge.

cracks in the surface. These places are in general more favorable for intercalation than the smooth surface. The surface of the originally black electrode after illumination and passage of 54 mC/cm^2 photocurrent is shown in Fig. 4.

The intercalation of foreign guest ions can be conveniently monitored by x-ray fluorescence. Because of restrictions in lattice parameters, we tried to intercalate the small guest ion Ag^+ into a $\text{Cu}_{6-x}\text{PS}_5\text{I}$ electrode. The experiment was performed in a 0.02M AgNO_3 solution with a silver foil as counterelectrode. The potential was fixed at $E = -0.1\text{V vs. Ag/AgNO}_3$. A cathodic charge of 24 mC/cm^2 passed through the electrode which had been pretreated in HNO_3 . The outer part of the electrode broke away as a consequence

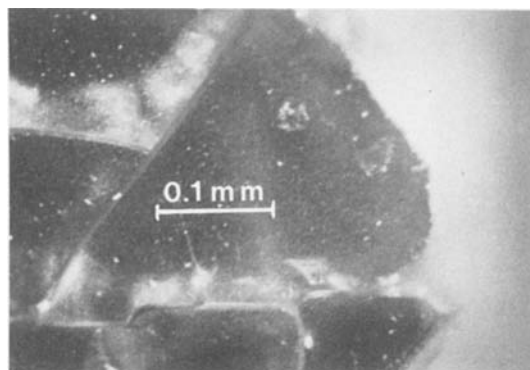


Fig. 4. Brightening up of regions along fracture lines ($\text{Cu}_6\text{PS}_5\text{I}$) of a copper-depleted material ($\text{Cu}_{6-x}\text{PS}_5\text{I}$) as a result of photo-intercalation.

of excessive intercalation far away from equilibrium. It contained 70% Ag. Within a layer of $25\text{-}30\mu$ beneath the surface of the electrode, the silver content was up to 20%. Figure 5 shows the distribution of silver perpendicular to the electrode surface.

To check whether this photointercalation mechanism allows the conversion of light energy into electrical energy we built a photoelectrochemical cell with a $\text{Cu}_{6-x}\text{PS}_5\text{I}$ crystal as the photoactive electrode and a silver foil as counterelectrode. No external potential was applied in this experiment. When illuminating the $\text{Cu}_{6-x}\text{PS}_5\text{I}$ electrode, there was a cathodic current flow as shown in Fig. 6. In the dark, the direction of the current did not reverse as it should have if the discharge reaction would have taken place. Also in the corresponding setup with copper, no discharge current was found in the dark.

Photocurrent spectra were recorded to prove whether the color change by chemical and electrochemical treatment is accompanied by a change in the bandgap of the material. Figure 7 shows the photocurrent spectra before, 1, and after treatment, 2, with HNO_3 . As a comparison, we show the absorption spectra before (b) and after (a) treatment with Br_2 , which also leads to the removal of copper from the $\text{Cu}_6\text{PS}_5\text{I}$ crystals (12).

Figure 8 shows the photocurrent spectra before, 1, and after, 2, passing an anodic charge of 10.6 C/cm^2 through the electrode at a potential of $E = 0.4\text{V vs. Ag/AgNO}_3$. The surface of the electrode turned black as a consequence of this electrochemical treatment.

Discussion

The mixed Cu ion conducting and electronic p-type semiconducting properties of $\text{Cu}_6\text{PS}_5\text{I}$ suggest photo-

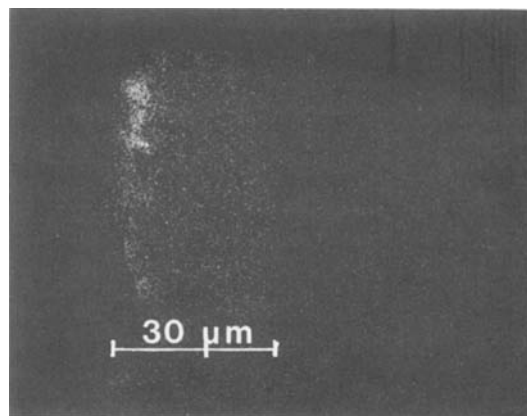


Fig. 5. Quantitative x-ray fluorescence of Ag concentration profile of photointercalated $\text{Cu}_{6-x}\text{Ag}_y\text{PS}_5\text{I}$ perpendicular to the $\text{Cu}_{6-x}\text{PS}_5\text{I}$ electrode surface.

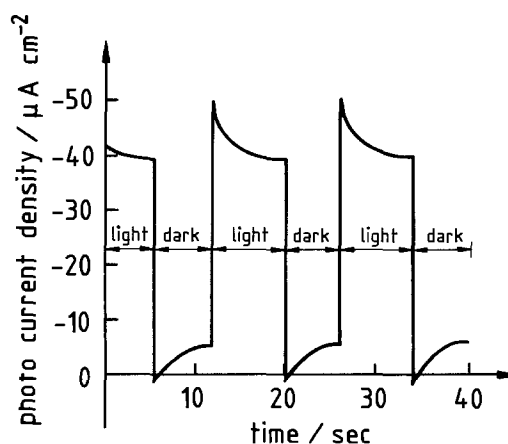


Fig. 6. $\text{Cu}_{6-x}\text{PS}_5\text{I}/0.1\text{M TEAPC}/\text{acetonitrile}$ (0.02M AgNO_3)/Ag photoelectrochemical cell during intermittent illumination.

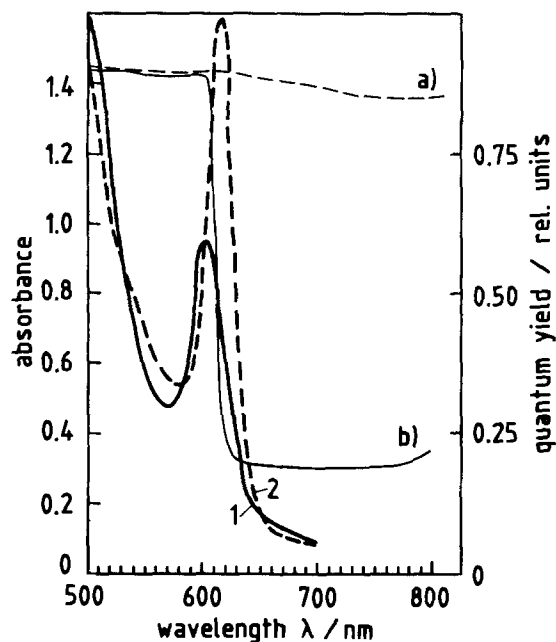


Fig. 7. Photocurrent spectra (1, 2) and absorption spectra (a,b) of untreated $\text{Cu}_6\text{PS}_5\text{I}$ (1, b) and after passage of anodic charge ($10, 5 \text{ Ccm}^{-2}$) (2, a).

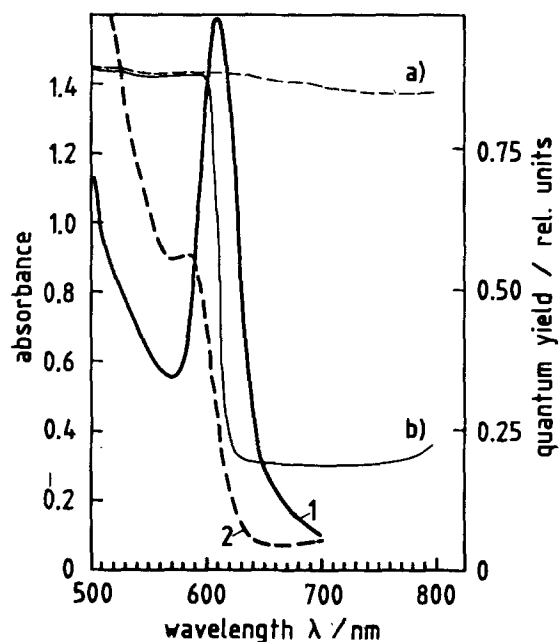


Fig. 8. Photocurrent spectra (1, 2) and absorption spectra (a, b) of untreated $\text{Cu}_6\text{PS}_5\text{I}$ (1, b) and after chemical deintercalation (2, a) (HNO_3 20 min at 50°C).

intercalation of Cu^+ ions as a possible photoreaction in the presence of Cu^+ ions. Figure 2 demonstrates that the presence of Cu^+ ions is responsible for the photocurrents observed in the $\text{Cu}_{6-x}\text{PS}_5\text{I}/0.1\text{M TEAPC-acetonitrile}$ (0.01M CuCl)/ Cu cell. Since in the potential region of this experiment Cu^{2+} does not exist (14), the only possible redox reactions of $\text{Cu}_{6-x}\text{PS}_5\text{I}$ with copper are plating of copper on the surface or intercalation of copper. We excluded the possibility that Cu is plated in this potential region in a separate experiment. At an electrode potential of $-0.65 \text{ vs. Ag/Ag}^+$, we passed a cathodic charge of 0.1 C/cm^2 through the electrode. This corresponds to about 300 monolayers of copper. But no copper layer could be observed on the electrode surface. Correspondingly, the x-ray fluorescence measurements show that in a photoreaction with Ag as a foreign guest atom, silver

is not plated on the surface of $\text{Cu}_{6-x}\text{PS}_5\text{I}$, but is incorporated into the bulk (Fig. 5). The fact that a black copper-deficient electrode regains the color and transparency of the copper-rich material upon illumination (Fig. 4) demonstrates that the removed copper is again inserted by light. The current-voltage behavior of Fig. 3 can be interpreted in terms of intercalation and deintercalation of Cu^+ ions. At positive electrode potential values, copper is deintercalated from the $\text{Cu}_6\text{PS}_5\text{I}$ lattice to give $\text{Cu}_{6-x}\text{PS}_5\text{I}$. Thus, the photocurrent density at a negative electrode potential increases because there are more unoccupied positions for the photointercalation of Cu^+ ions. The shift of the onset of cathodic currents after sweeping to positive potential values is also typical for an electrochemical charging/discharging reaction (15).

We think that our experiments demonstrate that intercalation of copper is the actual light reaction. A description of the photointercalation mechanism of Cu in terms of an energy band scheme is presented in Fig. 9. The electron created upon optical excitation within the space charge layer reduces the copper ion for intercalation into the $\text{Cu}_{6-x}\text{PS}_5\text{I}$ host lattice. The color change of $\text{Cu}_6\text{PS}_5\text{I}$ which is connected with the removal of Cu^+ ions from the $\text{Cu}_6\text{PS}_5\text{I}$ host lattice is not due to a change in the bandgap of the material. This can be concluded from the photocurrent spectra shown in Fig. 7 and 8. In both cases, there is no significant change in the bandgap that could explain the color change.

We assume that the creation of I_2^- color centers by the removal of Cu atoms is responsible for the in-

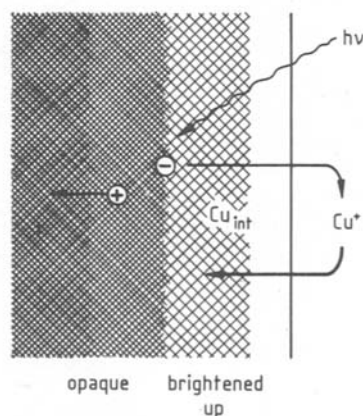
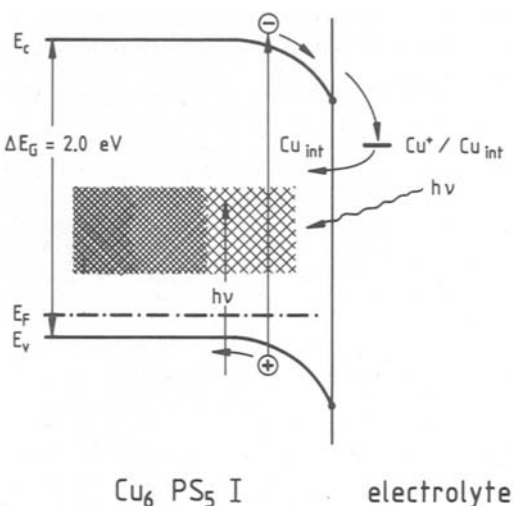
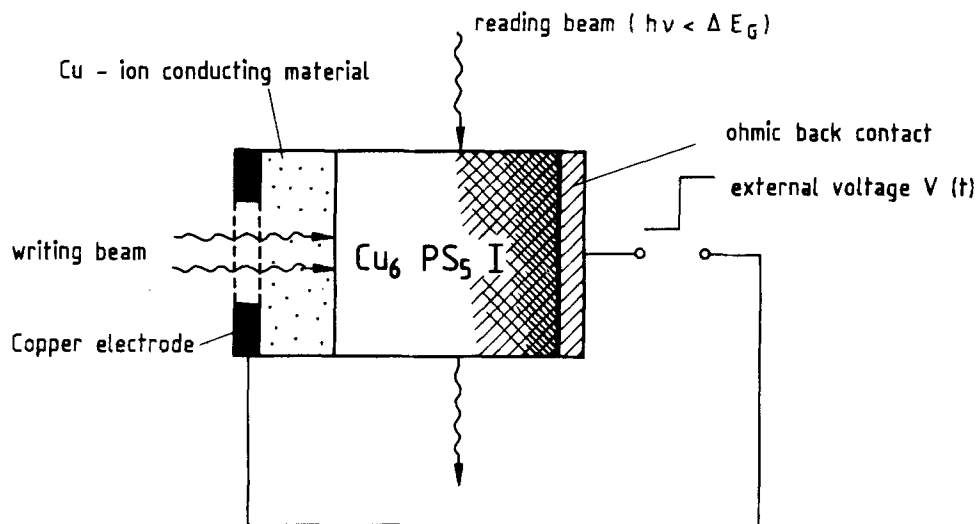


Fig. 9. Energy scheme of $\text{Cu}_{6-x}\text{PS}_5\text{I}$ showing electronic states of color centers (shaded area within the energy gap) and their annihilation as a consequence of photointercalation of copper (above).

Fig. 10. Principle of optical information storage device based on color center annihilation in $\text{Cu}_{6-x}\text{PS}_5\text{I}$ through photointercalation of Cu.



creased optical absorption in $\text{Cu}_{6-x}\text{PS}_5\text{I}$. When copper atoms are removed from the lattice iodine atoms are left behind. These atoms together with normal I^- ions form I_2^- color centers. Similar color centers can also be found in LiF crystals (16). The energetic positions of the electrons that can be excited optically from these color centers are shown in Fig. 9a as a shaded area. When copper is intercalated into $\text{Cu}_{6-x}\text{PS}_5\text{I}$, the color centers disappear. The opaque crystal brightens to a red color.

Though photointercalation reaction with suitable materials provide, in principle, means to convert and store light energy as chemical energy, the photointercalation reactions studied are not suited for energy conversion because there is little tendency for a discharge reaction in the dark (Fig. 6). The color change associated with the photointercalation of copper could, however, in principle, be used to store optical information. Such an optical storage element for one bit is shown in Fig. 10. It consists of a grain of $\text{Cu}_6\text{PS}_5\text{I}$ in contact with a Cu ion conducting material which has to be transparent in the region of interest. At the front there is a ring-shaped copper counterelectrode. An external voltage can be applied between the copper electrode and the ohmic back contact.

The red transparent copper-rich crystal symbolizes a logical "1" the opaque crystal a logical "0". When this element is illuminated with light of an energy $h\nu > \Delta E_G$, copper can be photointercalated into the $\text{Cu}_6\text{PS}_5\text{I}$ lattice. Since the opaque crystal regains its transparency in this way, one has written a "1" into the element. The information can be read out with light of an energy $h\nu < \Delta E_G$.

To delete the stored "1," one has to apply a positive voltage at the $\text{Cu}_6\text{PS}_5\text{I}$ electrode. The crystal becomes opaque when the copper ions are released from the crystal into the electrolyte. This element has the advantage of the stored information not being lost when the external voltage is switched off.

To make such an element technologically applicable further studies concerning the reversibility and stability of such a device are necessary.

Acknowledgments

The authors would like to thank Mrs. Siegmann, Free University of Berlin, for SEMQ measurements. We

also thank our colleagues in the laboratory for valuable discussions.

Manuscript submitted Sept. 29, 1983; revised manuscript received Nov. 2, 1983.

Hahn-Meitner-Institut für Kernforschung Berlin GmbH assisted in meeting the publication costs of this article.

REFERENCES

1. H. Tributsch, *Appl. Phys.*, **23**, 61 (1980).
2. M. Abramovich, O. Gorochoy, and H. Tributsch, *J. Electroanal. Chem.*, In press.
3. G. Betz, H. Tributsch, and R. Marchand, *J. Appl. Electrochem.*, Submitted for publication.
4. B. Fotouhi, O. Gorochoy, A. Katty, N. Le Nagard, C. Levy-Clement, D. Schleich, B. Tehy, and H. Tributsch, *Sol. Energy R&D Eur. Community, Ser. D*, p. 78-85, 2 (1983).
5. Unpublished results, this laboratory.
6. H.-M. Kühne, D. Schleich, and H. Tributsch, Unpublished results.
7. W. F. Kuhs, R. Nitsche, K. Scheunemann, *Mater. Res. Bull.*, **11**, 1115 (1976).
8. W. F. Kuhs, R. Nitsche, and K. Scheunemann, *Acta Crystallogr. Sect. B*, **34**, 64 (1978).
9. W. Konz, Thesis, Albert-Ludwigs-University, Freiburg, 1983.
10. W. F. Kuhs, R. Nitsche, and K. Scheunemann, *Mater. Res. Bull.*, **14**, 241 (1979).
11. T. M. Batirov, V. M. Fridkin, R. Nitsche, and K. A. Verkhovskaya, *Phys. Status Solidi A*, **72**, 105 (1980).
12. S. Fiechter, Thesis, Albert-Ludwigs-University, Freiburg, 1982.
13. Geyer-Lippmann, Thesis, Free University of Berlin, Berlin, 1981.
14. M. E. Langmuir, M. A. Parker, and R. D. Rauh, in "Photoelectrochemistry: Fundamental Processes and Measurement Techniques," W. L. Wallace, A. J. Nozik, S. K. Deb, and R. H. Wilson, Editors, p. 315, The Electrochemical Society Softbound Proceedings Series, Pennington, NJ (1982).
15. U. Armand, Thesis, University of Grenoble, Grenoble, 1978.
16. W. Känzig, *Phys. Rev. Lett.*, **4**, 117 (1960).

Arsenic Dopant Influence upon the Sintering Behavior of the Aluminum-Polysilicon Interface

Nicole Herbots, Fernand Van de Wiele, and Maurice Lobet*

Laboratoire de Microelectronique, Universite Catholique de Louvain, Louvain-la-Neuve, Belgium

Robert G. Elliman

Department of Communication and Electronic Engineering, Royal Melbourne Institute of Technology, Melbourne, Australia

ABSTRACT

Interdiffusion between thin films of aluminum (Al) and polycrystalline silicon (poly-Si) has been studied with the purpose of obtaining a stable interface upon sintering for IC metallization. The solid-phase crystal regrowth of Si due to this low temperature interdiffusion has also been investigated. Dopant segregation towards the interfaces and the grain boundaries of arsenic-implanted poly-Si was used successfully to control the kinetics of Al-poly-Si interactions. The correlation between the arsenic depth profiles, the Si-layer microstructure, and the sintering behavior of the Al-poly-Si interface was measured by RBS, (scanning) AES, SEM, TEM, and grazing incidence x-rays. Quantitative results and discussion of the diffusion mechanisms at work are presented. It is shown that the presence of an arsenic segregation peak on top of the poly-Si layer stabilizes Al/poly-Si interface. A concentration of 10^{19} atom/cm³ appears to be a minimum threshold for sintering at 465°C.

The aluminum-silicon (Al-Si) contact, which is extensively used in semiconductor technology, is a limiting factor in scaling down integrated circuit components. The sintering of the Al-Si interface, necessary to obtain good ohmic contacts, introduces reliability problems due to interdiffusion between Al and Si and crystal regrowth of the dissolved material. These interactions may appear for any structural morphology of the Si substrate: single-crystal Si (1, 2), polycrystalline Si (poly-Si) (3), or amorphous Si (4, 5). The low temperature enhancement of Si crystal regrowth, due to the diffusion of Al atoms, presents interesting prospects for solid-phase epitaxy (6, 7).

Because of the extensive use of LPCVD poly-Si in integrated circuits, poly-Si-Al interfaces command particular attention. Forming contacts by means of Al-poly-Si structures has been shown to reduce diode reverse current by a factor of 10 and enhances bipolar transistor gain (8). In addition, MOS circuit density might be increased if the Al-contact were made directly on the poly-Si gate.

Such Al-poly-Si structures require well-defined, stable interfaces. This requirement is not fulfilled by classical Al-metallization, justifying the use of sophisticated technologies to create diffusion barriers between Al and Si. In the present work, a good stability of the Al-poly-Si contact has been brought about by taking advantage of the presence of arsenic, which segregates to the grain boundaries (GB's) and to the interfaces of the poly-Si film. Indeed, Al diffuses mainly along the GB's in the poly-Si layer (9, 11), while Si atoms are mainly extracted from the poly-Si GB's (10, 11), and solute atoms within the GB's of polycrystalline films are known to decrease the diffusivities within the layers involved (12) both for self-diffusion and impurity diffusion.

This paper shows that Al-poly-Si interdiffusion strongly depends upon the dose of dopant in Al-poly-Si and the location of this dopant within the microstructure; it gives evidence that dopant segregation can reduce Al diffusivity in poly-Si, and that this segregation effect, if present at the Al-poly-Si interface, can totally inhibit interdiffusion between the two films at usual sintering temperatures (465°C in this work). In the present work, ion implantation and thermal annealing were used to introduce the arsenic

into the desired sites, while several solid surface analysis techniques were combined to study the interface behavior. The results show that an arsenic segregation peak on top of the poly-Si layer must be preserved to obtain interface stability. A peak concentration of 10^{19} atom/cm³ appears to be a minimum threshold. Since interconnection stripes of poly-Si must always be heavily doped, this condition can be fulfilled in any standard technology, if special attention is paid to the treatment of the poly-Si surface layer before metallization.

Experimental Procedure

From among the standard dopants of Si, arsenic was chosen because of its attractive features: high solid solubility in Si, low thermal diffusivity, and easy detectability in solid surface analysis. To enhance the arsenic influence upon the Al-poly-Si contact, a peak concentration was created in the top region of the poly-Si layers by using low energy ion implantation or adjusted thermal annealing schedules.

Identification of key parameters.—Several parameters influence thin film interfaces during thermal treatment. These are layer thickness, grain size, crystalline defect density, interface quality, and the presence of a native oxide between the layers. Their roles are usually linked together in technological processes. Consequently, five sets of samples were prepared to set apart the influence of the dopant from the other factors (Fig. 1). In each set of samples, the influence from the single-crystal substrate was avoided by growing a SiO₂ layer on it before poly-Si deposition. Such an Al/poly-Si/SiO₂/Si structure appears in MOSFET circuits when an Al contact is made on the poly-Si gate.

In the samples of set I, no implantation was made to provide comparison with doped samples and previous works using intrinsic poly-Si (3). The next four sets of samples were As implanted, but various poly-Si microstructures were created in order to analyze effects related to crystallinity. In the samples of set II, the implantation damage was not removed; a thin amorphous layer, (0.035 μ) containing most of the As, was formed near the poly-Si/Al interface. A high As concentration was thus present near the contact, but without segregation within the Si structure. In set III, a totally amorphous layer of Si was used, to compare the behavior of these samples with the one having a poly-Si layer amorphous only within a thin surface

* Electrochemical Society Active Member.
Key words: polysilicon, aluminum, arsenic doping, metal-semiconductor interface, ohmic contact.

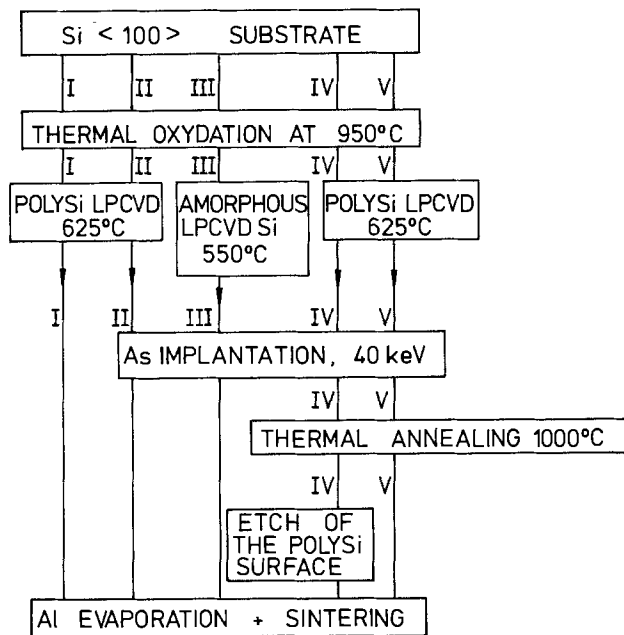


Fig. 1. Flowchart of the technological steps undergone by the samples.

region (set II). In the samples of set IV and V, the polycrystalline structure of the Si layer was restored after implantation, by annealing. In the two sets of samples, the As was expected to have segregated to the interfaces and the GB's (13, 14). A fraction of the implanted dose, thus accumulated at the poly-Si surface, was removed before Al deposition in the samples of set IV, while it was kept in the samples of set V to study its effect upon an interdiffusion at the Al/poly-Si contact independently of the influence of the segregation at the GB's.

Sintering duration ranged between a few minutes and tens of hours. In those cases where interdiffusion takes place, a characteristic duration of interaction can thus be determined.

Sample preparation.—Wafers of N-type <100> single-crystal Si were thermally oxidized and divided into five sets. The oxide thickness was $0.1 \pm 0.005 \mu$, and the substrate resistivity 11–18 Ω cm. Sets I, II, IV, and V were capped with a poly-Si film deposition in an LPCVD reactor at 180 mtorr, at 625°C, with thicknesses ranging between 0.1 and $0.45 \pm 0.01 \mu$. Set I consisted of intrinsic poly-Si layers to reproduce Nakamura's experiment (3) in order to provide a reference for comparison with doped samples. Sets II, IV, and V received a shallow implantation of As (40 keV), at three different doses: $5 \cdot 10^{15}$ atom/cm², $5 \cdot 10^{14}$ atom/cm², and $5 \cdot 10^{13}$ atom/cm². In sets IV and V, the implantation damage was removed by a 1000°C¹ annealing under a N₂ ambient for 45 min, resulting in both As diffusion within the grains of the films and As segregation towards the GB's. The grain size at the poly-Si surface increased from 0.04 μ , which is the usual size for a 625°C deposit (15), to 0.1 μ for doses of $5 \cdot 10^{15}$ atom/cm² and $5 \cdot 10^{13}$ atom/cm², and to 0.15 μ for $5 \cdot 10^{14}$ atom/cm². The wafers of set IV were etched in a diluted solution of hydrofluoric acid (2%) for 5 min to remove the accumulated As at the surface. Tests showed that several minutes are necessary to completely remove the accumulated As. Amorphous Si was deposited on set III (550°C LPCVD) and implanted like the previous samples (but without any further high temperature annealing step). Al layers with thickness ranging between 0.3 and 1.1 μ were then

¹ The temperature chosen constitutes a practical compromise to obtain high electrical activation, to remove implantation damage, and to induce As segregation.

evaporated by electron gun at a rate of 0.0025 μ /s under a working pressure of 10^{-6} torr. Figure 1 summarizes the characteristics of the five sets of samples. Every set of samples was sintered at 465°C in both forming gas (90% N₂ and 10% H₂) and N₂ ambient.

Analytical techniques.—RBS measurements were made on each sample, since this technique provides a quick diagnosis of compositional changes, layer thickness, and interface modifications. A 2 MeV helium beam, delivered by the University of Louvain Van der Graaff accelerator and having a cross-sectional area of approximately 1 mm², impinged upon the targets under working pressure of 10^{-6} torr. Backscattered particles were counted by a solid-state detector having a 15 keV resolution. Measurements were laterally averaged over the dimensions of the spot.

Auger electron spectroscopy (AES), performed with a 3 keV electron beam, was used under a working pressure lower than 10^{-9} torr to study more accurately the compositional changes at the surface and resolve some ambiguities in the RBS spectra. Scanning and transmission electron micrographs (SEM and TEM) provided further information, such as grain size and surface topology. X-rays at grazing incidence were used to verify the composition and crystallinity of the layers.

Experimental Results

Table I summarizes the results obtained in the present work by specifying the annealing time at which interdiffusion takes place for each set, and thus each microstructure, for each dose and for Al and Si thicknesses of 0.3 μ .

Similar results were obtained for the Al/poly-Si interface stability for the next combination: 1.1 μ Al on 0.3 μ poly-Si, 0.5 μ Al on 0.3 μ poly-Si, 0.3 μ Al on 0.5 μ poly-Si, and 0.3 μ Al on 0.1 μ poly-Si (see Fig. 4 below).

For each sample, the figures showing the corresponding RBS spectrum and micrographs are given in cases where the measurements are specifically presented in the paper. Otherwise, samples having features identical to those already illustrated are not shown, but are specified by "as in Fig. . . ."

Microstructural effects.—As previous work has shown (5), increasing the grain size of the poly-Si layer reduces interdiffusion between Al and poly-Si. In the present study, it was found that the structure of the poly-Si layer near the Al-poly-Si interface can have an effect upon the interdiffusion kinetics stronger than that of the average microstructure. This becomes obvious when comparing the sintering behavior of the samples of sets II and III. In the samples of set II, the top of the 0.3 μ poly-Si layer is highly amorphized by ion implantation within a thickness of 0.04 μ .² In the samples of set III, the whole Si layer is amorphous. Even after the shortest annealing time (5 min), both sets of samples exhibited the same level of strong interdiffusion; RBS analysis (Fig. 2a) show that the original Al/poly-Si interface completely disappears, and that a new interface is formed at the same place. This fact shows that most of the Si migrates towards the free surface, while the Al goes down towards the oxide. AES confirms that Si is present in concentration as high as 75 atomic percent (a/o) (Fig. 2b) within the first monolayers of the sample surface, for both sets. Since more than 50 a/o of the original Al layer has been replaced by Si, such an interdiffusion may be called "layer inversion."

Most of the implanted arsenic appears to be trapped at the new interface region, while a fraction of it

² The dose threshold making mono-Si amorphous at 40 keV is $2 \cdot 10^{14}$ atom/cm² for P (mass = 29 amu) and $8 \cdot 10^{13}$ atom/cm² for Ga (mass = 70 amu) (16). Since poly-Si layers contain already much more disorder than mono-Si, a dose of $5 \cdot 10^{13}$ atom/cm² of As (mass 75 amu) is enough to amorphize the region being implanted.

Table I. Initial microstructure, sintering time inducing interdiffusion, for each As dose, for samples, where Al and poly-Si thickness are 0.3μ for each set of samples.

Parameters	I	II	III	IV	V
Initial grain size	Intrinsic poly-Si 0.04μ	(Intrinsic poly-Si) 0.04μ + 0.04μ amorphous Si on top of the layer	Totally amorphous Si	(As-doped poly-Si) 0.10μ 0.15μ 0.10μ	(As-doped poly-Si) 0.10μ 0.15μ 0.10μ
As location	(no As)	Within the amor- phous 0.04μ top layer	Within the first 0.04μ of the layer	Within the grains and GB's	Within the grains GB's and at the interface
As profiles	1 — 2 — 3 —	Fig. 2a, II Fig. 2a, II as in Fig. 2a, II	Fig. 2a, III Fig. 2a, III as in Fig. 2a, III	Fig. 5, IV as in Fig. 5, IV as in Fig. 5, IV	Fig. 5, V as in Fig. 5, V as in Fig. 5, V
Sintering times in FG and N ₂ for interdiffusion	Extensive interdif- fusion $t < 10h$ as in Fig. 4, top	Dose independent, fast interdiffusion	Dose independent, fast interdiffusion	Dose dependent in- terdiffusion	Dose dependent stability
1	—	$t < 5s$ Fig. 2a, II	$t < 5s$ Fig. 2a, III	$30s \ll t < 65h$ Fig. 7, IV	$t > 65h$ Fig. 7, V
2	—	$t < 5s$ Fig. 2a, II	$t < 5s$ Fig. 2a, III	$30s \ll t < 65h$ as in Fig. 7, IV	$t > 65h$ as in Fig. 7, V
3	—	$t < 5s$ as in Fig. 2a, II	$t < 5s$ as in Fig. 2a, III	$t = 30s$ as in Fig. 6	$t = 30s$ as in Fig. 6
Final microstruc- ture: grain size	Large Si crystal- lites on the surface 10μ , Fig. 3b	Si crystallites on the surface	Si crystallites on the surface	Si crystallites on the surface	Stable
1	—	10μ Fig. 3b	1μ Fig. 3c	10μ Fig. 3b	Except 3
2	—	10μ as in Fig. 3b	1μ as in Fig. 3c	10μ as in Fig. 3b	
3	—	10μ as in Fig. 3b	1μ as in Fig. 3c	10μ as in Fig. 3b	10μ as in Fig. 3b

segregates at the new Si surface, this fraction being independent of the original dose, as is clearly seen for the profile ϕ_2 (As dose = $5 \cdot 10^{14}$ atom/cm²), at $50\times$ in Fig. 2a. No measurable concentration of arsenic appears near the oxide.³ Thus, comparable compositional changes occur at the same rate in both sets of samples, although 90 a/o of the Si-layer of samples of set II (shallow implanted poly-Si) is polycrystalline. In addition, the presence of an amorphized top region enhances by at least two orders of magnitude the rate of interdiffusion between Al and poly-Si, as compared to undamaged poly-Si layers. The sintering time needed to get the same level of interdiffusion with intrinsic poly-Si (set I) appears to be 10h at 465°C. These results for intrinsic poly-Si (set I) are consistent with Nakamura's work (3).

The difference in microstructure between set I (intrinsic poly-Si), set II (implanted poly-Si), and set III (amorphous Si) determines the morphology of the inverted layers (Fig. 3). Intrinsic poly-Si (set I) and implanted poly-Si (set II), in spite of different sintering durations, evolve to the same microstructure (Fig. 3c) when reaching "inversion." The new Si layer, formed on the top of the structure, consists of large, flat crystallites, several microns wide, for poly-Si layers 0.3μ thick and Al layers 0.3μ , 0.5μ , and 1.1μ thick. Segregated Al is found between the crystallites, in quantities corresponding to the concentration measured by AES when averaged on 1 mm² spot (between 25 and 30 a/o). Spatially resolved AES (Fig. 3a) shows that the Al concentration within the Si crystallites falls below the detectability limit (0.1%), and that the Si concentration within the Al region does also.

Micrographs also reveal certain aspects of the interdiffusion mechanisms. Some of the largest grains (0.1μ) of the original poly-Si layer are left undissolved under the new crystallites. TEM and SEM photographs show that the Si layers have evolved a step further than in Nakamura's work (3). The original state of the layers is depicted in Fig. 4a. Figure 4b shows Nakamura's results (3). In the present case, the original Si layers

³The original measurable dose of arsenic is found by adding the interface and surface signals in the RBS spectra.

have been nearly consumed. The reaction scheme can thus be completed (Fig. 4c). New crystallites reach the surface and can grow up to 60μ wide. The thickness of both films affects the final microstructure of the reacted films, as Nakamura has previously shown for intrinsic poly-Si (3), and as depicted in Fig. 4b. Figure 4c of the present work shows that the relative thickness of the layers fixes the final microstructure of the inverted layers, but does not affect the interdiffusion at the interface. Since this fact was observed for each set of samples, only results for Al and Si layers 0.3μ thick are presented. When the Al layer dissolves in the Si, a coalescence effect appears, due to the surface tension within the Al film, so that flattened Al globules are formed on the new Si surface (Fig. 3b, 3c).

The persistent coloration of the sintered Al layers is due to the effective dielectric constant of the inverted layers. A characteristic resonance appears at a given wavelength, depending on the distribution and the geometrical factors of the Al globules (16), so that different colors were observed for samples having different microstructures.

If Si crystallites formed from an amorphous layer (set III) are compared with those formed from poly-Si (sets I and II), they appear to be smaller (1μ) for the same level of inversion (Fig. 3c). As compared to samples of set II, they are smaller by one order of magnitude for the same sintering time. They are regular, hexagonal, and interconnected in chain, which is not the case for the large islands of Si formed in samples of sets I and II. Hence, the state of the Si top region is responsible for a sudden interdiffusion, but the morphology of the whole layer fixes the microstructure of the new Si crystallites.

Effect of dopant location in the microstructure.—As can be inferred from Fig. 2a and Table I, (columns II and III), dopants introduced in the Si layer do not affect interdiffusion if they do not interact with the microstructure. The samples of sets II and III are not found to be dose dependent. Arsenic in concentrations as high as 10^{21} atom/cm³ near the surface has no effect upon the interdiffusion kinetics in an amorphous environment at the sintering temperature used

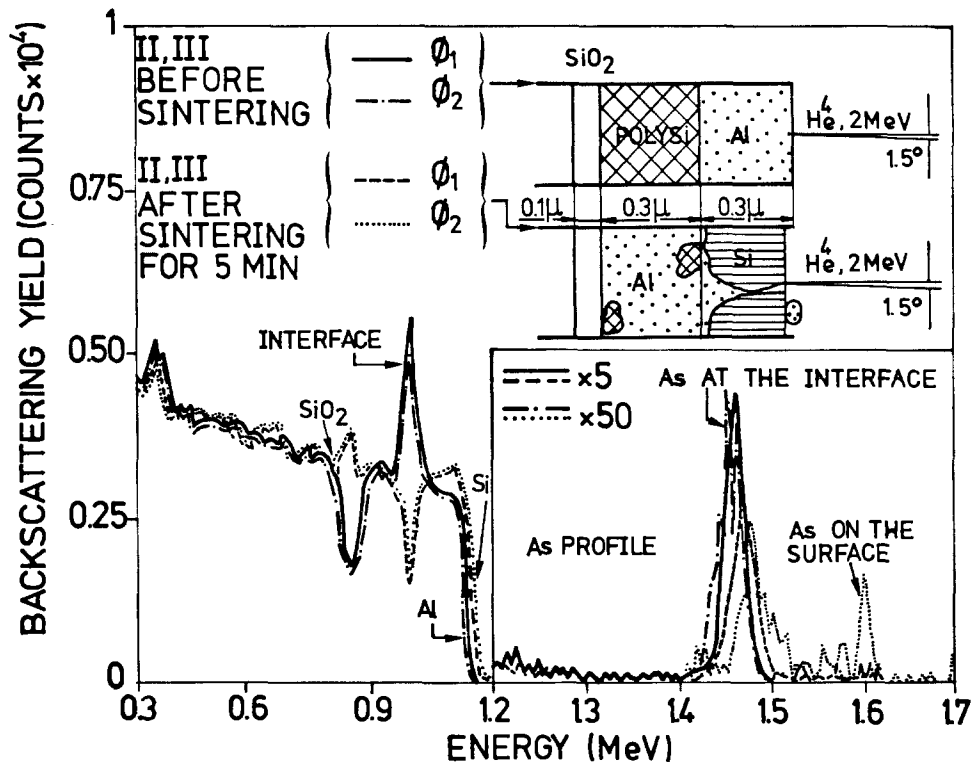
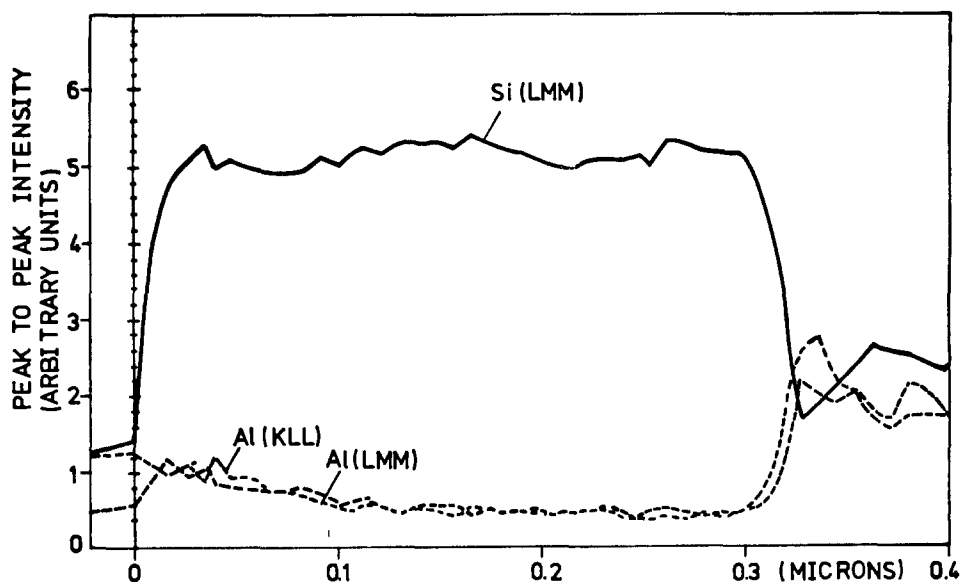


Fig. 2. A, top: RBS spectra of samples of set II and III, before and after 5 min of sintering at 465°C in forming gas, for a dose of $5 \cdot 10^{15}$ atom/cm² (ϕ_1) and of $5 \cdot 10^{14}$ atom/cm² (ϕ_2). (Structure of sample depicted in upper corner, $t_{Al} = t_{poly-Si} = 0.3\mu$). After annealing, Si and arsenic are detected on the surface, while the Al/poly-Si interface is inverted. B, bottom: Typical AES spectra of the sintered samples of (a), shown here for the case $\phi_1 = 5 \cdot 10^{15}$ atom/cm², set II.



here (465°C). In the samples of sets IV and V, where the polycrystalline structure of Si is restored by thermal annealing after ion implantation, the dopant diffused within the whole layer. The As profile is flat except at the poly-Si/Al and at the poly-Si/SiO₂ interfaces, where accumulation of the dopant due to segregation occurred during annealing. As can be seen from Fig. 5, curve V, for an As dose of $5 \cdot 10^{15}$ atom/cm² implanted in a 0.3- μ -thick poly-Si layer, As concentration at both interfaces is $1.4 \cdot 10^{20}$ atom/cm³, while the mean concentration within the film is $6.8 \cdot 10^{19}$ atom/cm³. Grazing angle RBS measurements with a depth resolution of 40Å showed that As pile-up is confined within a 150Å region. After etching (curve IV, Fig. 5), the segregation peak at the poly-Si surface disappears, and the As concentration appears to be less in this region than within the film, showing clearly that the poly-Si surface has been depleted in As. Thus, in samples of set IV, where the surface peak is removed (Fig. 5b, IV), only the As diffused within the grains and the As segregated at the GB's play a role.

During sintering tests, the Al/poly-Si interface evolution is strongly dose dependent. After 30 min of sintering, only the samples implanted with the lowest dose ($5 \cdot 10^{13}$ atom/cm²) lose their interface definition (Fig. 6). Hence, the annealing treatment after ion implantation has increased the interdiffusion time by one order of magnitude, as compared to samples of sets II and III. The dose dependence is not related to a large increase of the grain size following the enhancement of poly-Si grain growth rate by As doping. Indeed, at concentrations above 10^{19} atom/cm³, the presence of As decreases this rate (14), and it is precisely above this level that As segregation at the GB's inhibits interdiffusion in this experiment (Fig. 6). Moreover, SEM micrographs show that grain size increase was about the same for both the lowest and the highest dose used (0.1 μ).

In the samples of set V, the As has segregated at the poly-Si surface before Al deposition. Due to the presence of As, samples could withstand 65h of sintering without significant interdiffusion at the Al/poly-Si

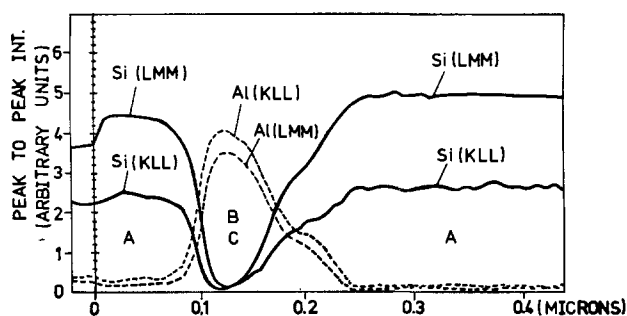
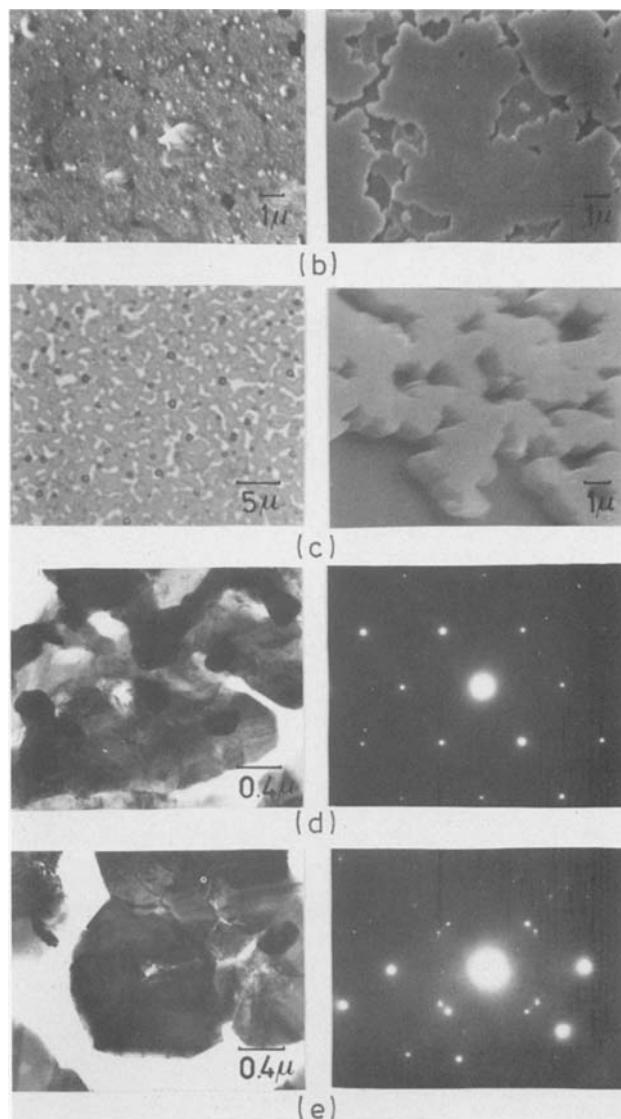


Fig. 3. A, above: Scanning AES spectra of the sample of Fig. 2b, $t_{Al} = t_{Si} = 0.3\mu$, $\phi_1 = 5 \cdot 10^{15}$ atom/cm², $t = 5$ min, $T = 465^\circ\text{C}$, in forming gas (set II). This distribution is typical for inverted layers. B, right: Typical SEM micrograph of the surface of inverted poly-Si; on the left for the same sample in Fig. 3a; on the right for an undoped sample of set I, with $0.3\mu = 0.3\mu$ for $t = 10$ h, $T = 465^\circ\text{C}$ in forming gas, after Al was etched to put in evidence the grain structure. Comparison of both pictures shows that the grain size is the same. The right one shows some undissolved poly-Si under the new crystallites. C, right: Typical optical micrograph of the surface of inverted layers, obtained from amorphous Si (set III), here for the case $5 \cdot 10^{15}$ atom/cm², $t_{Al} = t_{poly-Si} = 0.3\mu$, $t = 5$ min, $T = 465^\circ\text{C}$ in forming gas, before (left) Al was etched. Right: SEM micrograph of the same layer after Al etch. D, right: TEM micrographs of the Si crystallites as in B, after Al etch. The electron diffraction pattern shows that they consist of single-crystal Si. E, right: TEM micrographs of the Si crystallites as in C after Al etch. The electron diffraction pattern shows that they consist of small-sized Si crystals.



interface (Fig. 7, V) while the samples of set IV (etched poly-Si) experienced interdiffusion for the same annealing time. The inversion effect decreased as dose increased in this last set of samples, in contrast with the unannealed samples of sets II and III, which did not show dose dependence (Fig. 2). However, the inverted layers of samples of set IV had the same microstructure as the other poly-Si samples of sets I and II (Fig. 3b). For the highest dose, the As profile moved from a flat line (Fig. 5, IV) to an exponential decay (Fig. 7, IV), with an identical accumulation on the surface, as in the case of samples of sets II and III (Fig. 2).

Discussion

According to the present results, the interdiffusion between thin films of Al and poly-Si appears to reach thermodynamic equilibrium under annealing by a complex mechanism, the kinetics of which can be controlled. During the establishment of thermodynamic equilibrium, the extent to which Al and poly-Si dissolve into each other cannot be predicted from the Al-Si phase diagram for bulk material (19). Moreover, this dissolution is accompanied by two complex phenomena: the segregation of a significant amount of Si to the free surface of the layered structure and the enhancement of Si crystal regrowth at low temperatures.

Kinetics of the interdiffusion between Al and poly-Si layers.—The extensive interdiffusion between Al and

poly-Si is consistent with some of their properties affecting the kinetics of the Al-Si system. Al and Si have about the same atomic radius, 1.43 and 1.32Å, respectively.

The Al is a p-dopant for Si. The radius of a positively ionized Si atom decreases down to 0.41Å and diffuses more easily in Al. This effect will especially be important in poly-Si, because GB's offer additional Al-Si contact sites. Since Al penetrates extensively within the disordered structure of the poly-Si GB's (9, 11), more Si atoms will tend to be ionized in poly-Si than in mono-Si.

In the case of amorphous Si (sets II, III) the diffusion of Al is enhanced by the higher density of defects. On average, many more Si atoms will be in contact with Al atoms, so that the interdiffusion rate will be increased.

An As-rich poly-Si/Al contact and As-rich GB's will induce an increase of the size of the Si atoms, radius (2.71Å), implying a slowing down of the diffusion, as observed for sets IV and V (Fig. 6 and 7, curve V).

The modification of the electronic environment of semiconductor atoms by a metallic contact has also been proposed by Hiraki to explain the migration of Si atoms from a mono-Si substrate through a metal layer towards the free surface, in ultrahigh vacuum, under low temperature annealing. He proposed that Si atoms turn to a metallic state, where they form bonds with the metal atoms at the interface (20). In

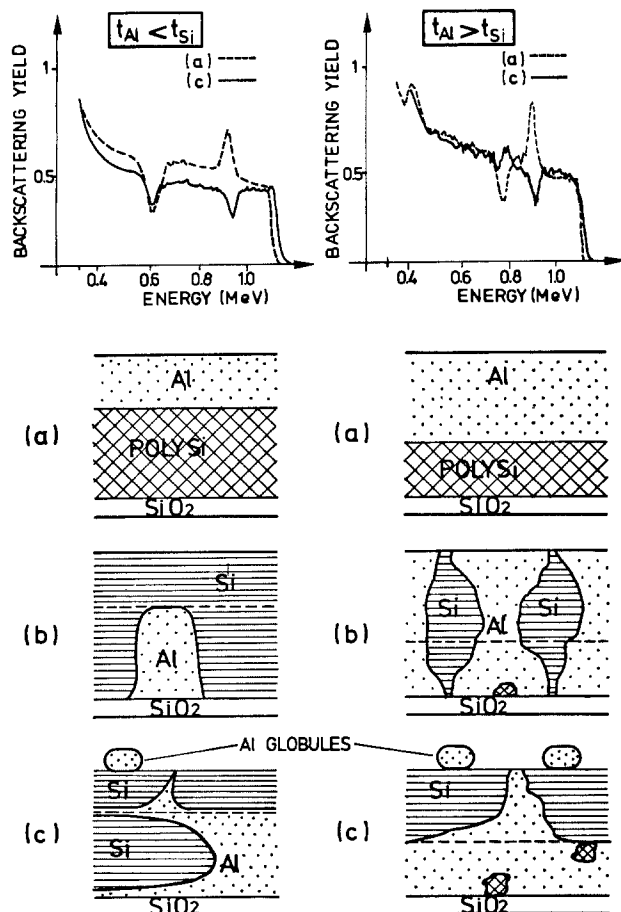


Fig. 4. Scheme of the interdiffusion phenomenon between Al and poly-Si, with corresponding RBS spectra, in the case of a thicker (left) and a thinner (right) Al layer. Diagram (b) is from Ref. (3) and shows mixing between Al and poly-Si. Diagram (c) is more detailed because more analyses were made in the present work.

the present work, we propose further that this effect induces a decrease of the size of the Si atoms, and thus facilitates the Si diffusion within the Al film.

Moreover, the presence in poly-Si and in amorphous Si layers of more Si atoms in a metallic state explains the extensive interdiffusion observed in those disordered microstructures.

We extend Hiraki's results obtained in UHV to real processing conditions for non-monocrystalline Si. Indeed, Hiraki's metal-deposition, annealing, and AES measurements in UHV lead to a final surface composition with Si present in the first monolayer. In the present work, AES measurements depict the surface as contaminated by a first monolayer of carbon, under which an oxygen layer was found chemically bonded to a third monolayer of Al, thus forming Al_2O_3 . Si was detected under this native oxide, which probably inhibits the last step of segregation.⁴

On the other hand, we have shown that by saturating with As the interface and GB's of poly-Si, the interdiffusion mechanisms could be inhibited in agreement with the proposed model.

Thermodynamics of the Al/poly-Si system.—The diffusion mechanism induced by the modification of the electronic environment of Si atoms is thermodynamically favored by the following properties of Al and Si.

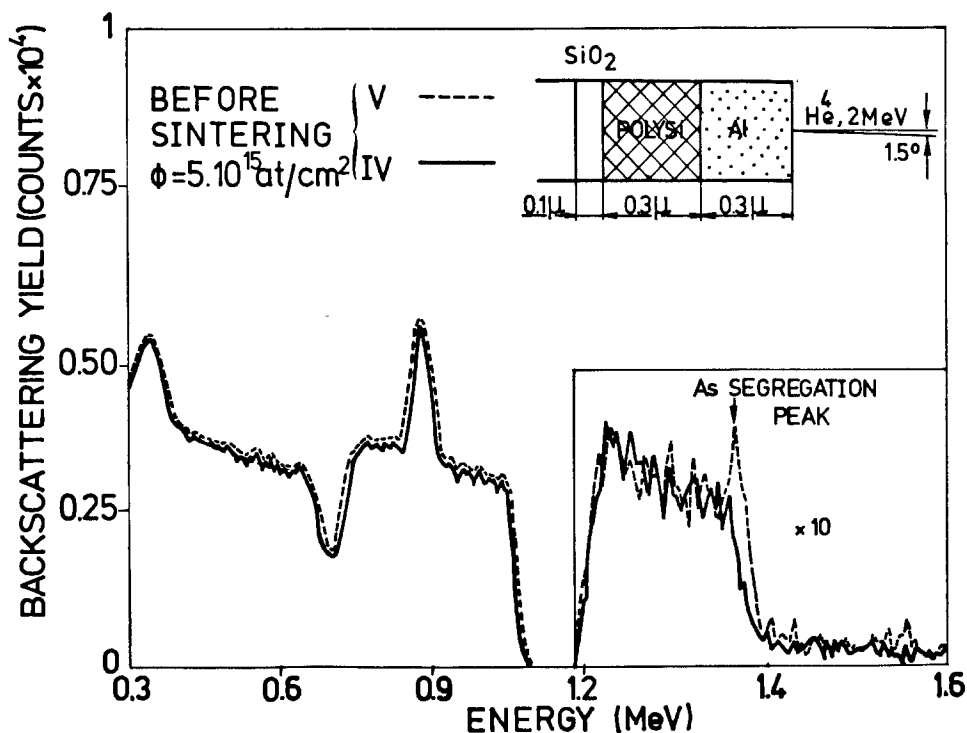
1. The bonding energy of an Al-Si atomic pair is lower than that of an Al-Al or of a Si-Si pair, implying that the formation of Al-Si pairs is actually promoted at the Al/Si contact sites.

2. The segregation of the liberated Si atoms at the surface is then induced by the lower free surface energy of Si (0.6 J/m^2) (21), as compared to that of Al (1.2 J/m^2) (22).

3. The enhancement of Si crystal regrowth on an amorphous substrate (SiO_2) depends on the original crystalline state of the layer. In the case of amorphous Si (set III), crystallites appear on the sample surface, but are smaller than in the case of poly-Si (sets I, II, IV). Since the larger crystallites of the original layer are the last to disappear, it can be assumed that Si first dissolves in Al, then segregates to the surface and crystallizes. The dependence on the original state of the layer may be explained by a transfer of the dissolution energy into crystallization energy, since for equally

⁴This may explain the results obtained by Faith who stabilized Al/Si contacts by an alternate deposition of Al and Al_2O_3 (23).

Fig. 5. RBS spectra of samples of sets IV and V before sintering for a dose of $5 \cdot 10^{15} \text{ atom/cm}^2$. $t_{\text{Al}} = t_{\text{poly-Si}} = 0.3 \mu$. The arsenic profile of V reveals segregation to both interfaces of the poly-Si layer. In the case of IV, the segregation peak at the Al/poly-Si interface has been etched and the poly-Si surface is depleted in As. Otherwise, both spectra are identical.



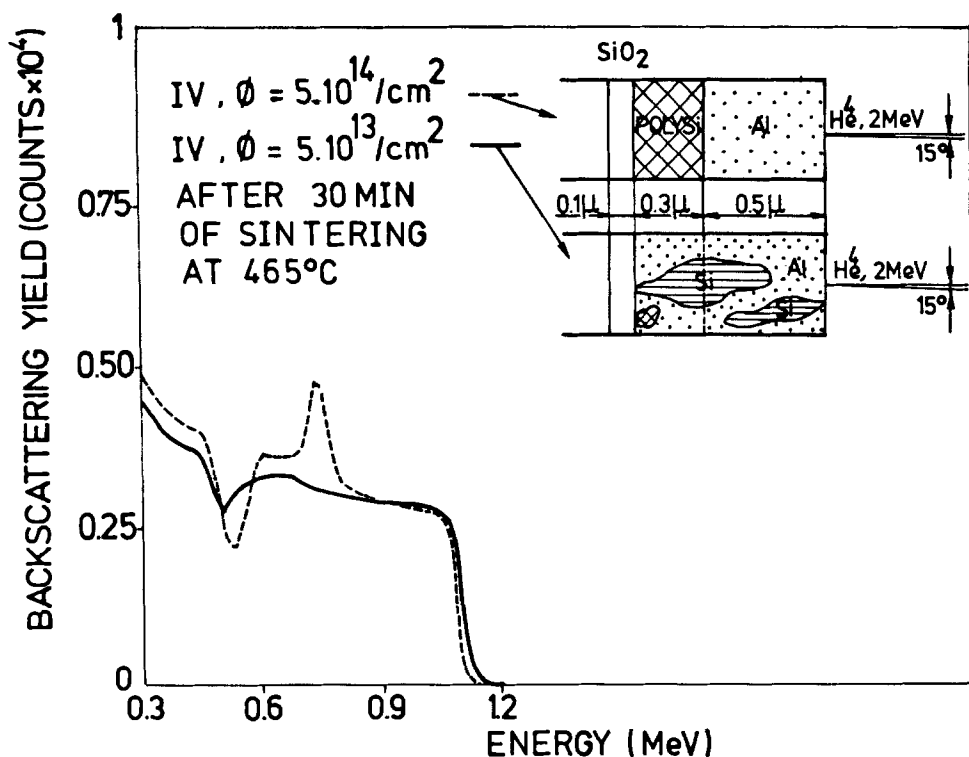


Fig. 6. RBS spectra of samples of set IV, $t_{\text{poly-Si}} = 0.3\mu$, $t_{\text{Al}} = 0.5\mu$, after 30 min of sintering in forming gas showing the dose dependence of the interface stability. The sample which is arsenic implanted with a dose of $5 \cdot 10^{13}$ atom/cm² has lost its interface definition and intermixing of the layers has occurred, while the samples implanted with a higher dose show a good stability.

fast diffusing layers (set II and III, Table I), there is a difference of one order of magnitude between the size of the resulting crystallites.

Inhibiting As concentration.—The threshold concentration of 10^{19} atom/cm³ found here to inhibit interdiffusion appears in other diffusion-in-poly-Si effects (18).

In order to explain the dependence of the poly-Si grain growth on the dose and nature of dopants, Mei assumed a diffusion controlled process (18). In the case of As, he quantitatively accounted for the fact that the poly-Si grain growth, enhanced at low doses, decreases for concentrations above 10^{19} atom/cm³. Therefore, he used a diffusion model including segregation. The Al diffusion in poly-Si studied here is in-

hibited by the same dopant at the same threshold concentration, but only if segregation has occurred in the poly-Si.

Thus, we may conclude that the steric configuration of negatively ionized Si atoms at the GB's and interfaces in As-doped poly-Si slows down both the Si diffusion and the Al diffusion in the layer.

An additional reason for Al-Si bonds not to be formed may be the saturation by As of the dangling bonds (DB) at the interface and GB's, under thermal annealing (set IV and V). A concentration of 10^{19} atom/cm³ should then be enough to passivate the majority of DB at the poly-Si surface, an estimate which is difficult to ascertain by measurement of the poly-Si surface structure and its concentration of DB.

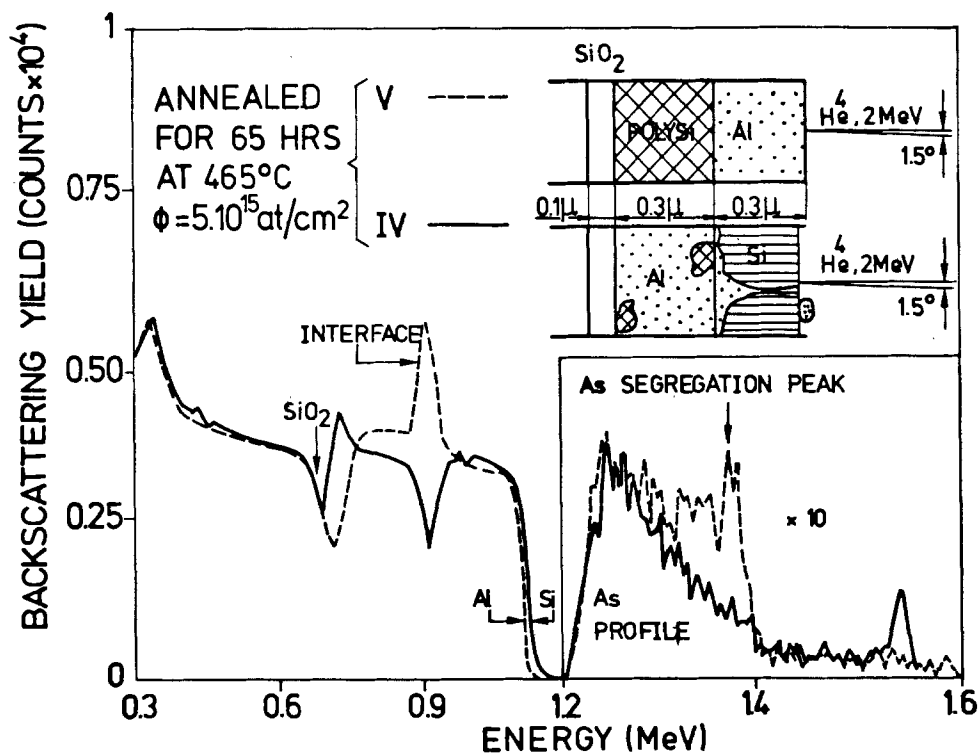


Fig. 7. RBS spectra of the samples of sets IV and V, $t_{\text{Al}} = t_{\text{poly-Si}} = 0.3\mu$ for a dose of $5 \cdot 10^{15}$ atom/cm² after 65h of sintering, showing the correlation between the poly-Si-Al interface stability and the arsenic depth profiles within the poly-Si layers. Sample V has kept a good interface definition because of the presence of the As segregation peak, while sample IV is inverted.

Conclusions

The sintering behavior of the poly-Si/Al interface has been investigated. Our aim was to stabilize this interface. Since solute atoms within GB's of polycrystalline films can decrease the diffusivity within the layer, advantage has been taken from the fact that poly-Si must be heavily doped to obtain a high conductivity, as it is the case in a standard IC fabrication. A systematic procedure was conceived to observe the mechanisms at work. Several solid-state surface analysis techniques were combined to obtain a detailed picture of the sintered layers. Results may be summarized as follow.

1. Dopant segregation is effective in reducing the Al diffusivity within the poly-Si film (set IV, V).

2. The microstructure at the top of the poly-Si layer appears to have more influence upon the interface behavior than the morphology of the whole layer (set II).

3. The top region of the poly-Si layer also plays a basic role when a dopant is present. Segregation of the dopant to this surface has a greater inhibition effect upon the Al/poly-Si interdiffusion than the segregation to GB's.

4. Both the microstructure of the poly-Si surface and the dopant segregation within the first monolayers appear to control the diffusion to such an extent that they can inhibit diffusion through layers as thick as 1μ , (set V). Generally, this fact shows that interface and surface properties can totally determine the behavior of thin films.

5. Understanding the mechanisms at work allows controlling the kinetics of thin film interaction by inhibiting the initiating phenomenon at a monolayer scale.

6. The effects observed in this work could be explained by several physical considerations, which were shown to complete existing models.

Further electrical measurements are presently being made upon stabilized contacts and will be published shortly. The entire experiment will be repeated with other segregating dopants.

Acknowledgments

The authors wish to thank Jean-Pierre Colinge of the CNET (Meylan, France) and Mr. John Virzi of the Laboratoire de Microélectronique of U.C.L. for critically reading this paper. They would like to thank all the members of the Laboratoire de Microélectronique U.C.L., of the Electrical Engineering Department of Salford University, of the Unité de Physique Nucléaire U.C.L., of the Département de Métallurgie Physique U.C.L., of the Instituut voor Industriële Scheikunde K.U.L., and of the Unité de Physico-Chimie de l'Etat Solide U.C.L., for lending their facilities and their kind support to this work. They would also like to thank Dr. R. Van den Berghe of Bell Telephone Manufactur-

ing Company, Surface Analysis Department for making the scanning AES analysis. The work of N. Herbots was supported by a grant of the Institut pour l'Encouragement de la Recherche Scientifique dans l'Industrie et l'Agriculture (I.R.S.I.A.).

Manuscript submitted Feb. 1, 1983; revised manuscript received ca. Oct. 26, 1983.

The Univerite Catholique de Louvain assisted in meeting the publication costs of this article.

REFERENCES

1. T. M. Reith and J. D. Schik, *Appl. Phys. Lett.*, **25**, 524 (1974).
2. H. Sankur, J. O. Mc Caldin, and J. Devaney, *ibid.*, **22**, 64 (1973).
3. K. Nakamura, M. A. Nicolet, J. W. Mayer, R. J. Blattner, and C. A. Evans, Jr., *J. Appl. Phys.*, **46**, 4678 (1975).
4. D. H. Lee, R. R. Hart, and O. J. Marsh, *Appl. Phys. Lett.*, **20**, 73 (1972).
5. J. M. Harris, R. J. Blattner, I. D. Ward, C. A. Evans, Jr., H. L. Fraser, M. A. Nicolet, and C. C. Ramliller, *J. Appl. Phys.*, **48**, 2897 (1977).
6. S. S. Lau, "Handbook on Semiconductors," Vol. 3, p. 532, North Holl. Ed., (1980).
7. G. Ottaviani and G. Majni, *J. Appl. Phys.*, **50**, 6865 (1979).
8. H. T. Ning and R. Isaac, *IEEE Trans. Electron Devices*, ed-27, 2051 (1981).
9. J. C. Hwang, P. S. Ho, J. E. Lewis, and D. R. Campbell, *J. Appl. Phys.*, **51**, 1576 (1980).
10. A. J. Learn and R. S. Nowicki, *Appl. Phys. Lett.*, **35**, 611 (1979).
11. K. Nakamura and M. Kamoshida, *J. Appl. Phys.*, **48**, 5349 (1977).
12. D. Gupta, D. R. Campbell, and P. S. Ho, in "Thin Films," P. M. Poate, K. N. Tu, and J. W. Mayer, Editors, p. 161 (1978).
13. M. M. Mandurah, K. C. Sarawat, C. R. Helms, and T. I. Kamins, *J. Appl. Phys.*, **51**, 5755 (1980).
14. B. Swaninathan, E. Demoulin, T. W. Sigmon, R. W. Dutton, and R. Reif, *This Journal*, **127**, 2227 (1980).
15. T. I. Kamins, M. M. Mandurah, and K. C. Saraswat, *ibid.*, **125**, 929 (1978).
16. Rouard and A. Messen, in "Progress in Optics," E. Wolf, Editor, p. 79, North Holland (1977).
17. G. Carter and W. A. Grant, in "Ion Implantation in Semiconductors," Arnold, Editor, p. 164 (1976).
18. L. Mei, M. Rivier, Y. Kuvart, and R. W. Dutton, in "Semiconductor Silicon 1981," H. R. Huff, R. J. Kriegler, and Y. Takeishi, Editors, p. 1007, The Electrochemical Society Softbound Proceedings Series, Pennington, NJ (1981).
19. M. Hansen, *Constit. of Bin. Alloys*, 2nd Ed., McGraw Hill, p. 133 (1958).
20. A. Hiraki, in "Jap. An. Rev. in Elec.," Niskizawa, Editor, p. 36, North Holland (1982).
21. W. R. Tyson and W. A. Miller, *Surf. Sci.*, **62**, 267 (1971).
22. J. O. Mc Caldin and T. C. Mc Gill, *An. Rev. Mater. Sci.*, **10**, 65 (1980).
23. T. J. Faith, *J. Appl. Phys.*, **52**, 4630 (1981).

Dry Developable Multilayer Resist Using Direct Pattern Formation by Electron Beam-Induced Vapor-Phase Polymerization

Masao Morita, Saburo Imamura, Toshiaki Tamamura, Osamu Kogure, and Kei Murase

Nippon Telegraph and Telephone Public Corporation, Ibaraki Electrical Communication Laboratory, Polymer Section, Tokai, Ibaraki, 319-11, Japan

ABSTRACT

A new technique for high resolution lithography with a dry-developed multilayer resist system is demonstrated. The technique involves a direct pattern fabrication by electron beam-induced vapor-phase graft-polymerization. No wet process was included in the pattern fabrication. The use of a double-layer base film consisting of a thin silicone resin as a top layer and a thick AZ-1350J film as a bottom layer enabled the transfer of graft-polymerized polystyrene patterns on the silicone resin to thick resist with submicron-sized feature.

As the minimum feature of semiconductor devices becomes smaller, the fabrication process becomes more difficult when achieving high resolution lithography. Recently, two kinds of approaches were extensively studied to solve the difficulties. One is the dry development of resists, which can eliminate various problems involved in wet development, such as a resolution loss by resist swelling (particularly in negative-type resists), the treatment of large volumes of organic or inorganic solvents, and poor adaptability to automatic line fabrication processes (1, 2). However, it is not easy to obtain sufficiently large differences in dry etching rates for dry developable resist systems. This often causes the serious reduction in patterned resist thickness.

Another is the multilayer resist system, which realizes submicron resist patterns with a high aspect ratio. This method is extremely effective and becomes inevitable for high resolution lithography on uneven substrates (3-6). However, almost all multilayer resist systems reported so far employ the wet development to define the exposed patterns in top thin resist (7). In this paper we report a novel technique for a dry-developed multilayer resist.

Our principle for dry development is direct pattern formation by electron-beam-induced polymerization. In polymer chemistry, this process is called graft polymerization. When polymer films are subjected to an organic monomer gas after or during high energy beam exposure, polymeric materials are deposited on exposed areas of film (8-10). If a significant difference in dry etching characteristics between deposited graft-polymer and the base polymer film obtains, dry development is possible by etching the base film using the patterned graft-polymer as a mask. We have found that a class of silicone resins can initiate electron-beam-induced graftpolymerization with a reasonable sensitivity and can be applied to this multilayer resist system.

Figure 1 shows our process for dry-developed multilayer resist. A thick organic polymer layer, 1.0 μm of AZ-1350J photoresist (Shipley), was coated on a silicon wafer and baked at 230°C for 1h. The baking makes the film insoluble in organic solvents. The room temperature vulcanizing silicone varnish (Toray Silicone) was spun at 2000 rpm on the AZ layer. The varnish is instantly cured by moisture in the air during the spinning and makes about 0.5 μm thick film.

The wafer was then exposed with an electron beam exposure machine ESM-301 (Elionix) operating at 20 kV, which was modified to allow the exposed wafer to be subjected to vapor-phase graft polymerization. The exposed wafer was transferred from the exposure chamber to the grafting chamber through a gate valve without contacting the air. The grafting chamber was in vacuum so that the graft monomer could be easily vaporized and introduced to the grafting chamber

when the valve connecting the chamber and monomer vessel was opened. The temperature of the wafer was controlled at a slightly higher temperature than that of the monomer in the vessel, in order to prevent the monomer gas from condensing on the wafer. Grafting time was 60 min, and monomer pressure was 3 torr. Styrene was selected as a graft monomer because it is known to have a relatively high dry-etch resistance. The monomer was purified by fractional distillation and degassed to remove dissolved oxygen. After grafting, the wafer was removed from the grafting chamber.

The graft-polymerized patterns were transferred to the silicone layer by means of reactive ion etching using CF_4/H_2 gas with a parallel-plate etching machine DEM-451 (ANELVA). The etch rate of the silicone layer was 100 nm/min, whereas that of the graft polymerized polystyrene was less than 70 nm/min. Using the obtained silicone patterns as a mask, the AZ-1350J layer was reactive ion etched with oxygen

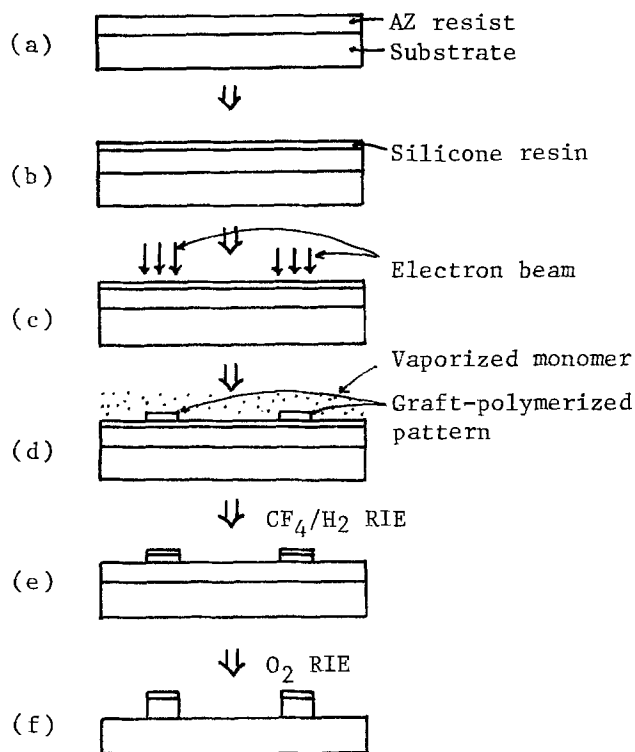


Fig. 1. Processing sequence schematic for direct pattern formation by electron-beam-induced vapor-phase polymerization. (a) Bottom layer coating. (b) Top layer coating. (c) Electron beam exposure. (d) Vapor phase polymerization. (e) Transfer of graft-polymerized pattern to silicone. (f) Transfer of silicone pattern to AZ.

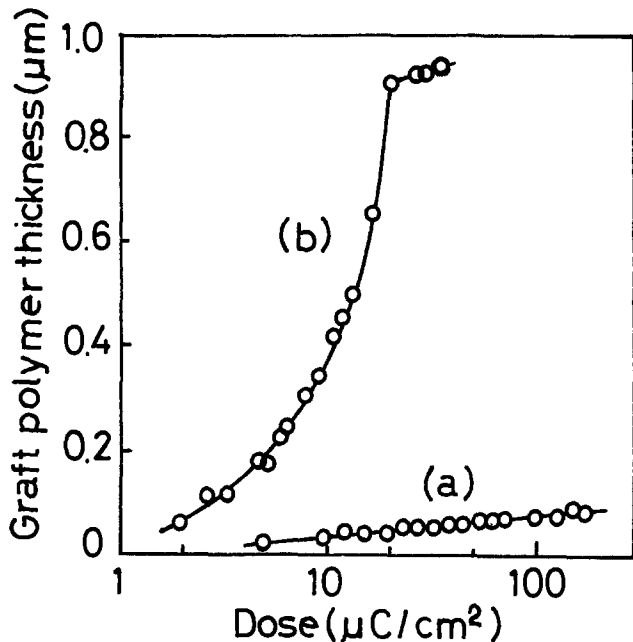


Fig. 2. Sensitivity curves of silicone resin grafted with styrene for 60 min. (a) Silicone varnish (polydimethylsiloxane). (b) Silicone varnish containing 7% vinyl groups.

gas. The oxygen ion etching rate of AZ-1350J at 200 mtorr is 110 nm/min. As the silicone layer does not show any thickness reduction by O_2 gas etching, thick resist patterns can be fabricated without any wet process in our system.

A typical sensitivity curve is given for an electron-beam-initiated graft polymerization in Fig. 2a, where styrene monomer was grafted on $0.5 \mu\text{m}$ silicone resin for 60 min. The Y-axis of Fig. 2 indicates the observed thickness increase in the exposed areas.

Figure 3 shows an SEM picture of thick resist patterns fabricated by our method, where $0.5 \mu\text{m}$ wide lines were obtained with $1.0 \mu\text{m}$ spaces. The resulting resist patterns have vertical walls with a linewidth loss less than $0.1 \mu\text{m}$ in a sidewall. The surface residue resulting from unetched silicone resin in the unexposed region would be removed if the silicone resin was slightly overetched.

The electron beam sensitivity can be significantly improved by introducing vinyl groups into silicone resin, as shown in Fig. 2b. In the lower dose region, the sensitivity curve has a rather long tail, but shows a substantial thickness rise beyond $10 \mu\text{C}/\text{cm}^2$. This long tail does not affect the resolution of this system, because a slight overetching of the silicone layer can easily remove the thinly grafted polystyrene in the tailing region. This means that the steep rise in the sensitivity curve beyond $10 \mu\text{C}/\text{cm}^2$ defines the high resolution of the system.

The use of multilayer system is essential with respect to the resolution. As the film deposition by graft polymerization has no anisotropic characteristics, the grafted polymer should be as thin as possible to minimize a pattern broadening. This means that the base film thickness to be directly etched with the mask of graft-polymerized film is severely limited by the resolution to be achieved. The combination of thin silicone resin as a directly etched layer using graft-polymerized film and thick organic polymer as the bottom layer can resolve the conflict between resolution and the overall resist thickness with this new technique.

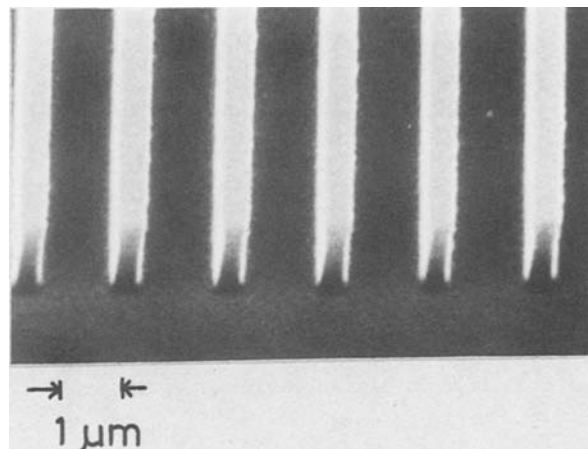


Fig. 3. SEM of reactive-ion-etched AZ pattern showing a $1.0 \mu\text{m}$ wide line in $1.0 \mu\text{m}$ thickness using direct pattern formation by electron-beam-induced vapor-phase polymerization. Upper resist: polydimethylsiloxane. Dose: $80 \mu\text{C}/\text{cm}^2$. Grafting time: 60 min.

In summary, a new technique for high resolution lithography with a dry-developed multilayer resist system was demonstrated. The technique involves a direct pattern formation by electron-beam-induced vapor-phase polymerization. The use of a double-layer base film consisting of a thin silicone resin as a top layer and thick AZ-1350J film as a bottom layer enables the transfer of graft-polymerized polystyrene patterns to thick resist patterns with submicron-sized feature. No wet process is included in the pattern fabrication. Furthermore, our processes suggest the possibility of the use of very low energy electron beam or ion beam, which can diminish the device damage caused by the high energy beam exposure, because only the surface layer of base film could be involved with film deposition by graft polymerization.

Acknowledgment

The authors wish to thank K. Harada for his helpful discussion.

Manuscript submitted March 23, 1983; revised manuscript received Sept. 15, 1983.

Nippon Telegraph and Telephone Public Corporation assisted in meeting the publication costs of this article.

REFERENCES

- G. N. Taylor and T. M. Wolf, *This Journal*, **127**, 2665 (1980).
- M. Tsuda, S. Oikawa, W. Kanai, K. Hashimoto, A. Yokota, K. Nuino, I. Hijikata, A. Uehara, and H. Nakane, *J. Vac. Sci. Technol.*, **19**, 1351 (1981).
- J. M. Moran and D. Maydan, *ibid.*, **16**, 1620 (1979).
- M. Hatzakis, D. Hoffer, and T. H. P. Chang, *ibid.*, **16**, 1631 (1979).
- M. Hatzakis, *ibid.*, **16**, 1984 (1979).
- B. J. Lin and T. H. P. Chang, *ibid.*, **16**, 1669 (1979).
- G. N. Taylor, T. M. Wolf, and J. M. Moran, *ibid.*, **19**, 872 (1981).
- A. N. Broers, W. W. Molzen, J. J. Cuomo, and N. D. Wittels, *Appl. Phys. Lett.*, **29**, 569 (1976).
- M. Gazard C. Duchesne, J. C. Dubois, and A. Chapiro, *Polym. Eng. Sci.*, **20**, 1069 (1980).
- S. Hattori, S. Morita, M. Yamada, J. Tamano, and M. Ieda, Proc. Regional Technical Conf. Mid-Hudson Sect., Soc. Plastics Eng., Ellenville, NY, Nov. 8-10, 1982, pp. 311-328; M. Yamada, J. Tamano, K. Yaneda, S. Morita, and S. Hattori, Proc. Sym. on Dry Processes, Tokyo, Japan, Nov. 18-19, 1982, pp. 90-93.

Carrier Lifetime Reduction by Argon Implantation into Silicon

A. Mogro-Campero* and R. P. Love

General Electric Research and Development Center, Schenectady, New York 12301

ABSTRACT

The reduction of carrier generation lifetime caused by argon implantation into silicon has been studied as a function of argon dose and annealing treatments. The capacitance transient technique was used to deduce that: (i) carrier generation lifetime in the depletion region decreases by four orders of magnitude with doses up to 10^{14} cm⁻², and varies inversely with dose; (ii) the separable contribution to capacitance relaxation due to surface generation and diffusion varies as the square of the dose. The region of low lifetime appears to remain localized within 1 μ m from the surface even after annealing for 1h at 1200°C. Partial recovery of generation lifetime occurs after annealing for 1h at 1100° or 1200°C. Complete recovery was observed only after several hours at 1200°C, and slow cooling (2°C min⁻¹). The resistance to high temperature treatment implies that regions of low lifetime can be incorporated with three-dimensional control into device structures.

Carrier recombination and generation in silicon occurs by various processes. Because silicon is an indirect gap semiconductor, band-to-band recombination and generation are very improbable, and at low carrier-injection levels the dominant mechanism is phonon-assisted events via deep level defects. These defects can be crystalline imperfections such as those induced by radiation damage, impurities such as gold atoms, and/or a combination of both, such as the oxygen-vacancy complex. At large carrier concentrations, other processes may dominate recombination, and these may be important in devices handling large currents. For example, in a p-i-n structure, such as in a p-i-n diode or thyristor, recombination involving three carriers (Auger events) becomes significant at carrier densities in excess of 10^{17} cm⁻³ (1). We will not be concerned here with this recombination mechanism. In such devices, a decrease in the recombination lifetime results in an increase in forward voltage drop and a decrease in the reverse recovery time. Since low values of these device parameters are usually desirable, a compromise must be achieved. In addition, the leakage current is also a function of lifetime. Thus, adjustment of device parameter values requires tailoring the carrier lifetime.

The values of recombination and generation lifetimes are determined by the temperature and properties of the deep levels (their energy, concentration, and electron and hole capture cross sections). In addition, recombination lifetime depends on the doping and injection levels. The relative values of the high level injection recombination lifetime, the low level injection recombination lifetime, and the generation lifetime will be different for different deep levels, and will thus lead to a variety of possible device parameter adjustments. This reason alone serves as justification for the search of new methods of lifetime control. In addition to the differences in deep level properties, the techniques currently in use (electron irradiation, gold and platinum diffusion) have distinct advantages and disadvantages which we shall not discuss. One property which they share in practice is that with them lifetime reduction is achieved throughout the silicon, with very limited spatial localization allowed. Localized lifetime control would offer the device designer an additional degree of freedom, and becomes imperative in high voltage integrated circuitry.

We have been investigating ion implantation as a lifetime-control technique. In a general case, deep levels are provided both by the damage produced by the implantation process, and by the implanted species itself. A distinct advantage of this method is that localized lifetime control on a very small scale is made possible. The shallow range of implanted ions provides the simple solution to spatial planar control by the usual masking procedures. It is, of course, necessary

that lifetime reduction persist after the ensuing high temperature treatments used in device processing. If three-dimensional spatial localization is desired, lifetime reduction must survive the high temperature epitaxial growth process.

We report here on the use of argon implantation for lifetime reduction. A deep level has been reported at 0.5 eV below the conduction band for samples of silicon implanted with argon (2). It seems that this may be a true impurity level rather than one associated with implantation damage, since no similar deep level was found for neon or xenon. In addition, in a study of the relative effectiveness of argon and silicon implantation into silicon (3), it was found that whereas silicon implantation had no effect on the lifetime at doses $< 10^{14}$ cm⁻², argon implantation produced lifetime reduction at doses $> 10^{11}$ cm⁻². This result for argon is consistent with the work to be presented here.

Procedure

n-Type CZ silicon wafers of (111) orientation and doping density 2×10^{15} cm⁻³ were used. The backs of the wafers were implanted with 10^{15} cm⁻² phosphorus of 100 keV to ensure a low resistance contact to aluminum. The front surfaces were implanted with 200 keV argon. A portion of the top surface of each wafer remained unimplanted for control measurements. 60 nm of dry oxide were grown at 1000°C for 50 min with subsequent anneals in nitrogen. A multidiameter set of aluminum dots was then evaporated to form MOS capacitors and sintered at 450°C in nitrogen for 30 min. The range of 200 keV argon ions in silicon is 203 ± 82 nm (4). The sputtering coefficient at this energy is unity (5), so that only about one monolayer is removed by an argon dose of 10^{15} cm⁻².

Ghandhi's definition of generation lifetime (1) was used. This differs from the definition used by some authors by a factor of two. The carrier generation rate (carriers per unit volume per unit time) is given by $n_i/(2\tau_g)$, where τ_g is the generation lifetime and n_i is the intrinsic carrier concentration. Lifetime measurements at room temperature were carried out by a capacitance transient technique (the Zerbst method). The voltage is suddenly changed into the deep depletion regime, and the formation of the inversion layer by carrier generation is observed via the capacitance transient (6). Capacitance was measured at 1 MHz.

Although this method is relatively laborious, it is possible to deduce separately the generation lifetime in the depleted zone (τ_g) and the parameter s due to the combined effect of near-surface generation and minority carrier diffusion into the depletion region from the quasi-neutral bulk. The separation is essentially achieved by dividing carrier generation into two components: those that are independent of the time varying depletion depth are lumped into the parameter s , and generation within the time varying depletion

* Electrochemical Society Active Member

zone is associated with the generation lifetime τ_g . For samples of doping density 10^{15} cm^{-3} , the shallow boundary of the generation volume within the depletion region sweeps by the implant range ($0.2 \mu\text{m}$) during the time period of validity of the Zerbst analysis (7). Therefore, at least some of the implant-related defects contribute to the effective generation lifetime deduced by the Zerbst technique. The parameter s consists of the sum of the surface generation velocity under inversion, near-surface generation which is independent of depletion depth, and the diffusion component $(n_i/N)(D/\tau)^{1/2}$ (8), where N is the shallow donor or acceptor doping density, and D and τ are the minority carrier diffusion coefficient and carrier lifetime in the quasi-neutral bulk. A typical variation of generation lifetime and parameter s of a factor of two was found on a single wafer.

The surface contribution can result from two components: the surface generation velocity under the inversion layer (included in the parameter s), and the surface generation velocity in the uninverted region at the dot perimeter (s_0). The contribution of s_0 was estimated by following the analysis in (6), where it is shown that $\tau_Z^{-1} = \tau_g^{-1} + 8s_0/d$, where τ_Z is the generation lifetime given by the Zerbst analysis, τ_g is the corrected generation lifetime, and d is the diameter of the test dot. Therefore, a plot of τ_Z^{-1} vs. d^{-1} should be linear, and an extrapolation to $d^{-1} = 0$ gives the value of τ_g . In attempting to implement this technique, the main difficulty found was scatter in the data. An example is given in Fig. 1. From such data we estimate that the use of a 1 mm dot results in a finite diameter correction factor $1.0 < C < 1.7$. For simplicity, we assume henceforth that $C = 1$.

Results

The generation lifetime deduced from the capacitance transient analysis is its average value over a portion of the depletion volume (7) which we call the sampling volume. The sampling volume increases with increasing depletion voltage, so that if the generation lifetime τ_g is constant with depth, one expects it to be constant as a function of depletion voltage. This is seen to be true for an unimplanted area (top of Fig. 2). If a region of low lifetime lies below the sampling volume, the measured lifetime should decrease as the sampling depth is increased and penetrates the low lifetime region. Once the sampling depth is such that the entire region of low lifetime is contained within the sampling depth, the measured lifetime should increase with a further increase in sampling

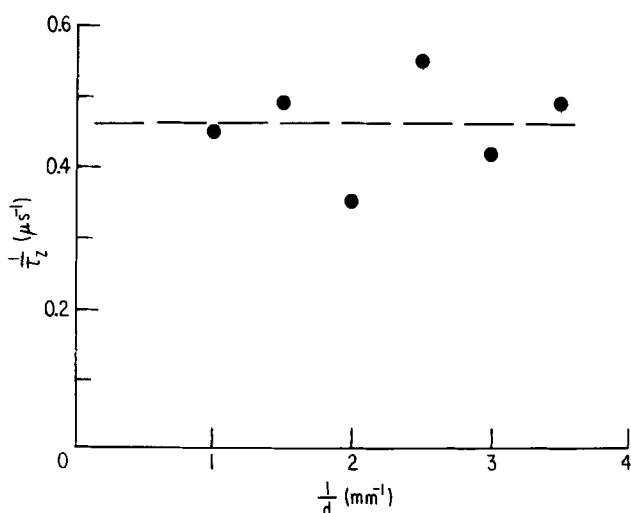


Fig. 1. τ_Z is the generation lifetime measured by the Zerbst technique on a dot of diameter d . The silicon sample was implanted with $10^{14} \text{ Ar cm}^{-2}$ and annealed at 1200°C for 50 min.

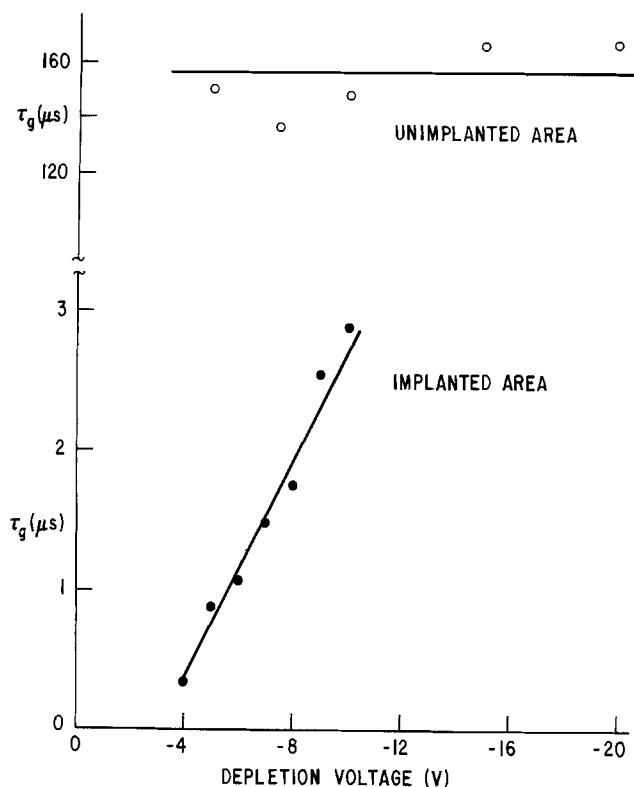


Fig. 2. Generation lifetime τ_g vs. depletion voltage for a sample implanted with $10^{14} \text{ Ar cm}^{-2}$ and annealed at 1200°C for 50 min.

depth. The behavior observed for τ_g vs. depletion voltage is shown in the lower portion of Fig. 2. For this sample, the maximum depletion depths at depletion voltages of -5 and -10V are $1.5 \mu\text{m}$ and $2.3 \mu\text{m}$, respectively. The increase of τ_g with depletion voltage in the implanted region means that the region of reduced lifetime is entirely contained within $1 \mu\text{m}$ from the surface. Therefore, depth localization has been preserved even after an annealing treatment of 1200°C for 50 min. Since τ_g in the implanted regions is a function of depletion voltage, we adopt standard pulsing voltages for lifetime determination ($+10$ to -10V). However, it must be kept in mind that the actual value of τ_g within the region of reduced lifetime is at least a factor of ten lower (as can be seen from the lower portion of Fig. 2).

Generation lifetime as a function of argon dose is shown in Fig. 3; τ_g can be decreased by four orders of magnitude. These results are consistent with a study using similar experimental conditions (3). An inverse dose relationship is apparent; this can be understood by noting that lifetime is inversely proportional to the density of deep levels (1), which in this case are introduced by implantation. The parameter s derived from the capacitance transient analysis is shown in Fig. 4 as a function of argon dose, and is seen to increase as the square of the dose. As mentioned previously, the parameter s contains contributions due to near-surface generation and diffusion. The diffusion component can become important when a region of low lifetime lies within a diffusion length of the depletion region; specific cases related to denuded zones and intrinsic gettering have been recently discussed (9, 10). The diffusion contribution may be important in our case due to the low lifetime region which extends beyond the depletion zone in the lateral direction. The strongest dependence on implant dose in this diffusion term is probably via the lifetime, which leads to $s \propto (\text{DOSE})^{0.5}$. The contribution due to surface generation may be important in the present case because of a radiation-related increase in near-surface deep levels, whose density is

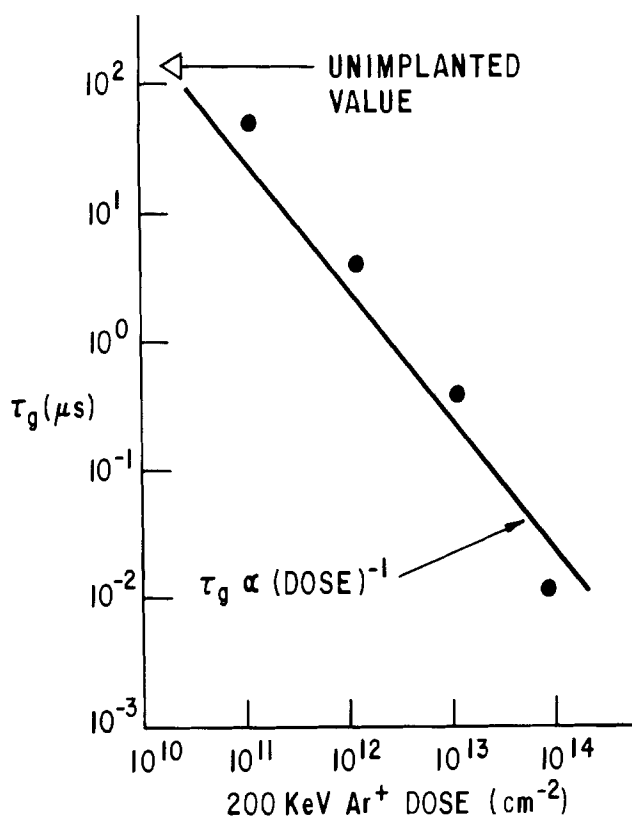


Fig. 3. Generation lifetime τ_g vs. argon dose for samples subjected to 1000°C for 50 min to grow 60 nm of oxide after implantation into the silicon.

proportional to the surface generation velocity (11). The dominance of the surface contribution thus leads to $s \propto \text{DOSE}$. In our case the observed dependence $s \propto (\text{DOSE})^2$ could be due to a combination of two irradiation-related defects which have subsequently become paired.

The rapid increase of the parameters s with dose prompts the question of the relative contributions of generation mechanisms to inversion layer charge during the capacitance transient. Using the standard expression (6) for the rate of change of inversion layer charge, it follows that the ratio of the contributions from s to that from generation within the sampling volume in the depletion region is $R \cong 2s\tau_g/(W - W_F)$, where W is the time-dependent depletion depth of final value W_F . The maximum contribution from the depleted zone occurs during the early portions of the capacitance transient. For the experimental conditions here, the contributions due to s will be dominant for $\tau_g s \gtrsim 1 \mu\text{m}$. From Fig. 5, this is satisfied for argon doses $\gtrsim 4 \cdot 10^{12} \text{ cm}^{-2}$. For the purposes of the next figure, let τ_z be the generation lifetime determined by the Zerbst technique. By neglecting the surface and diffusion contributions, a simpler analysis of the capacitance transient (12) has been used in the literature to obtain the generation lifetime; let τ_H be the generation lifetime determined by this method. In our case, this method becomes inadequate with increasing dose, as shown in Fig. 6. The discrepancy becomes larger than a factor of 2 for doses in the 10^{12} cm^{-2} range, which corresponds to a dominant contribution from s as deduced above from examining Fig. 5. The total charge density associated with the oxide which was grown after implantation was evaluated from flatband voltage shift of C-V curves. The measured charge density of 10^{11} cm^{-2} was independent of argon dose.

The ionized doping density was determined by the maximum-minimum capacitance method (13). This method gives an average doping density up to the

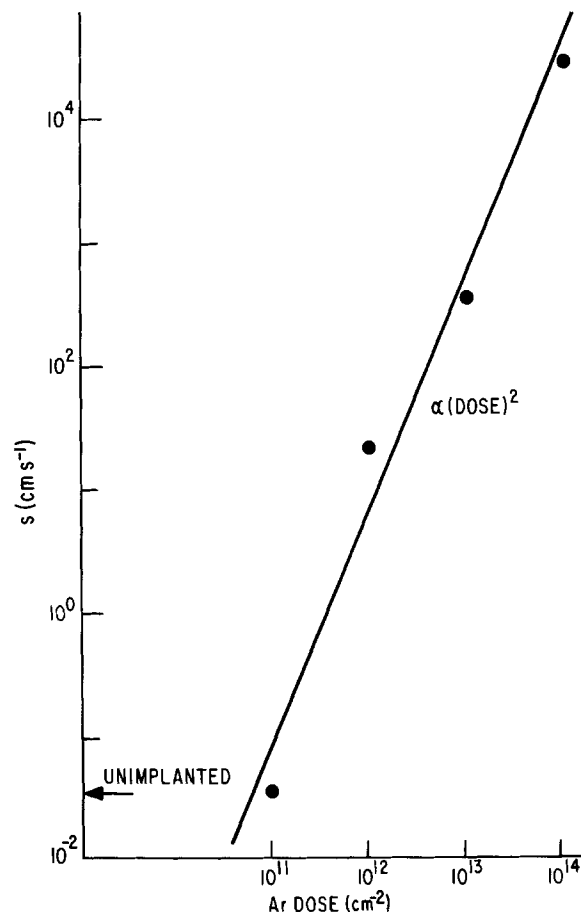


Fig. 4. Parameter s vs. argon dose for samples subjected to 1000°C for 50 min to grow 60 nm of oxide after implantation into silicon.

equilibrium depletion depth under inversion ($0.6 \mu\text{m}$ in our case), so that the results should be sensitive to possible doping changes introduced by the argon implantation (range of $0.2 \mu\text{m}$). No changes in doping density were observed up to at least $10^{13} \text{ Ar cm}^{-2}$.

Of the three energy levels associated with argon implantation (2), two are donors (at 0.22 and 0.5 eV from the conduction band), and one is an acceptor state (at 0.18 eV from the valence band). Thus, one might expect doping density changes due to strong compensation to be significant when the density of the electrically active fraction of argon-related deep levels approaches the shallow donor level density. Within a standard deviation from the peak of the

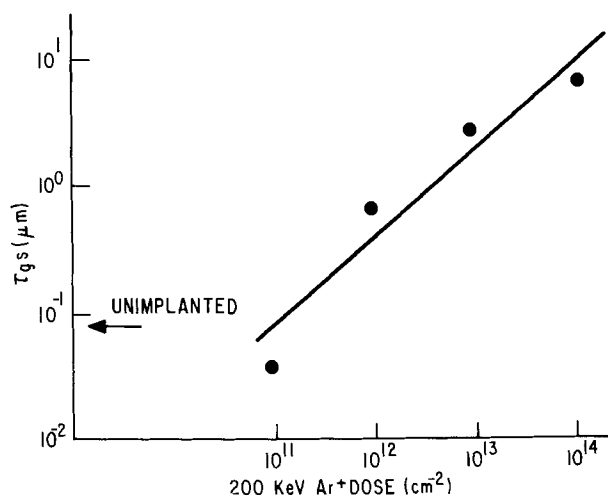


Fig. 5. $\tau_g s$ vs. argon dose from the data in Fig. 3 and 4

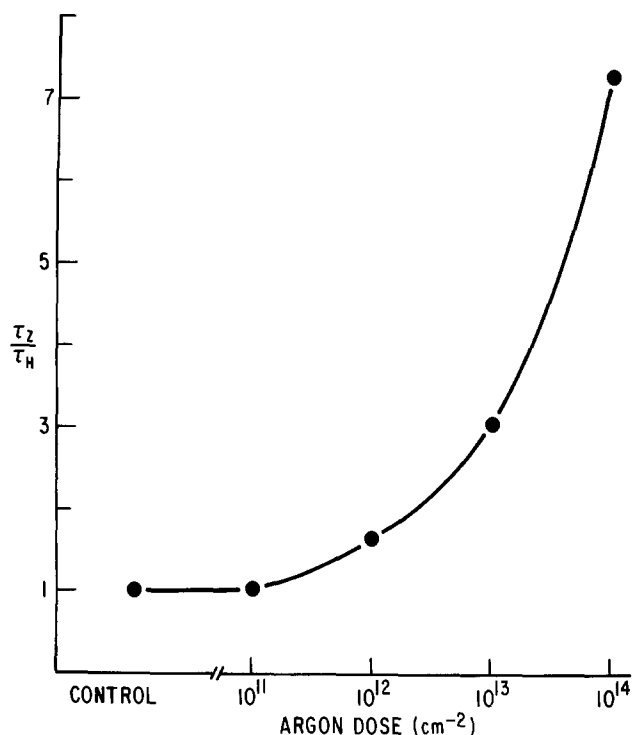


Fig. 6. The ratio of generation lifetimes determined by capacitance transient analysis. τ_z and τ_H are defined in the text.

implanted argon, its average density for a dose of 10^{13} cm^{-2} is $4 \cdot 10^{17}$ cm^{-3} , far in excess of the shallow doping density of 10^{15} cm^{-3} . Thus, the effective electrically active fraction of argon atoms seems to be low. This may be related to the aggregation of argon atoms, which produce detectable bubbles of 3 nm diam at a dose of 10^{14} cm^{-2} under similar experimental conditions (3). Other contributions to effective recombination-generation centers as well as donor and acceptor levels may be provided by implantation-induced defects and resident impurities (such as oxygen, which is present at levels of about 10^{18} cm^{-3} in CZ crystals). Interactions between the argon and such defects may be important, particularly since it is known that implanted argon is an effective gettering agent in silicon (14).

We now turn our attention to the effects of higher temperature annealing. The generation lifetime as a function of annealing temperature is shown in Fig. 7; the lifetime recovers to within a factor of about 100. The behavior of the parameter s for these samples is shown in Fig. 8. The value of s decreases, but even at 1200°C, it is still a factor of about 1000 higher than in the unimplanted areas.

The highest annealing temperature tested (1200°C) is close to the highest processing temperature used. These high temperatures are used, for example, to grow thick oxide layers and thick epitaxial layers of Si on Si by chemical vapor deposition (CVD). The behavior of generation lifetime as a function of annealing time at 1200°C is shown in Fig. 9. The sharp decrease of τ_g in the implanted area at 2h, before proceeding to recover, is interesting. A corresponding maximum in the parameter s was also found. This behavior may indicate the predominance of a different type of deep level produced by high temperature annealing, perhaps involving defect interactions as discussed above. All the annealing experiments discussed so far were terminated by relatively rapid cooling (the wafers are pulled out from the hot zone to an ambient at 300°C within a few seconds). To investigate the effect of slow cooling, some samples were cooled at a controlled rate of 2°min^{-1} . The results are shown in Fig. 10. Cooling rate is seen to have a

noticeable effect. The decrease in lifetime at 2h is again present, but at a reduced magnitude. After 5h,

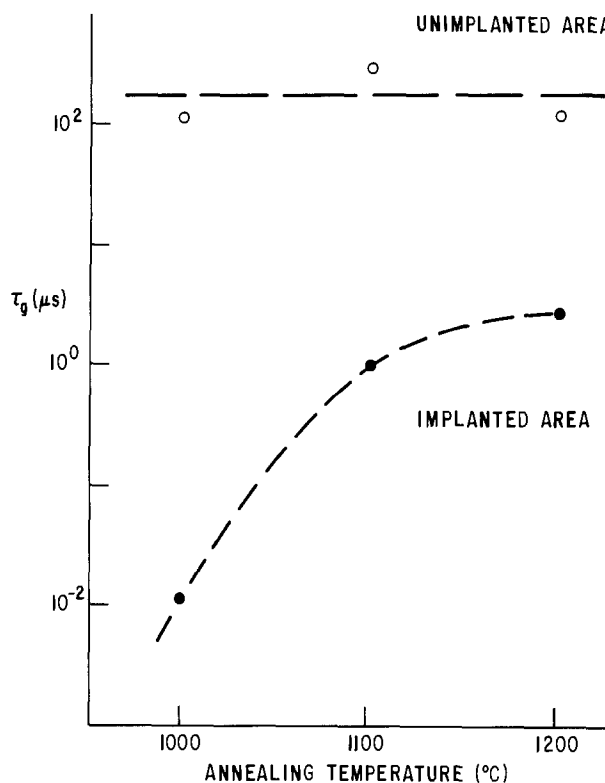


Fig. 7. Generation lifetime as a function of annealing temperature. Annealing time is 50 min in all cases. The argon dose was 10^{14} cm^{-2} .

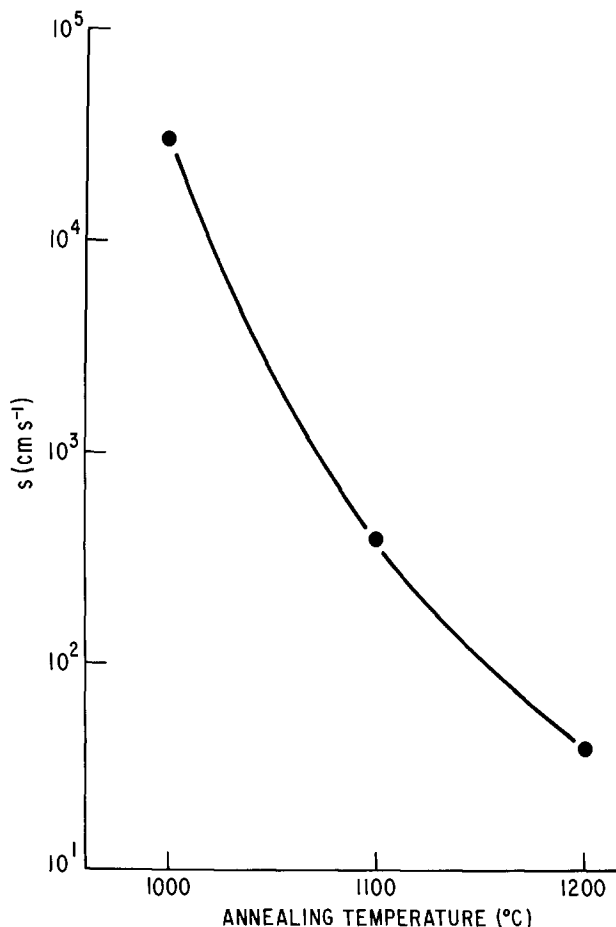


Fig. 8. Parameter s as a function of annealing temperature for conditions as in Fig. 7.

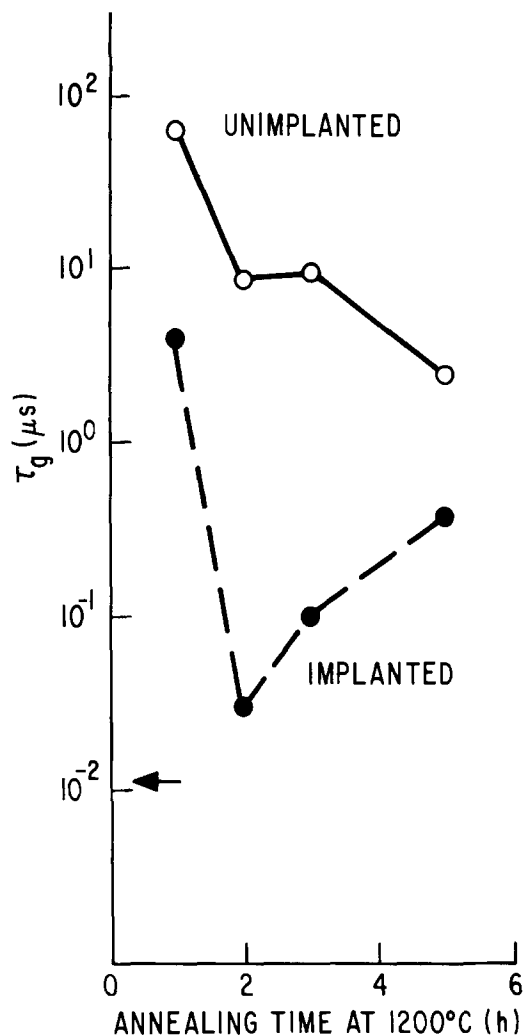


Fig. 9. τ_g vs. annealing time at 1200°C. Implanted areas contain 10^{14} Ar cm^{-2} . The arrow indicates the lifetime for a sample with minimum heat-treatment (1000°C for 50 min). The samples were cooled rapidly (hundreds of degrees s^{-1}).

the lifetimes in the implanted and unimplanted areas are indistinguishable, which was also found to be true for s .

The work reported here includes argon doses of $\leq 10^{14}$ cm^{-2} . In order to make detection of argon by the SIMS technique possible, some samples were implanted with higher doses (10^{15} - 10^{16} cm^{-2}). The depth profiles of mass 40 from these samples showed an erratic behavior of unknown origin, *i.e.*, the shapes of depth profiles were sometimes inconsistent with tabulated values.

Conclusions

The perimeter effect in the measurement of lifetime by the Zerbst method was shown to be small when using 1 mm diam capacitors. A more simplified treatment of the capacitance transient which neglects the surface and diffusion contributions (12), has been found to be inadequate for the samples with higher argon doses studied here. We have found that values of generation lifetime can be controlled over several orders of magnitude by argon doses up to 10^{14} cm^{-2} followed by a thermal treatment at 1000°C for 1h. The reported values of τ_g are conservative, since we have shown that the actual localized minimum values of τ_g are at least a factor of ten lower. The bulk generation rate within the sampling volume in the depletion region varies as the argon dose, but generation due to the combined effect of the surface and diffusion varies as dose squared. This latter dependence suggests that generation-recombination centers near the surface in-

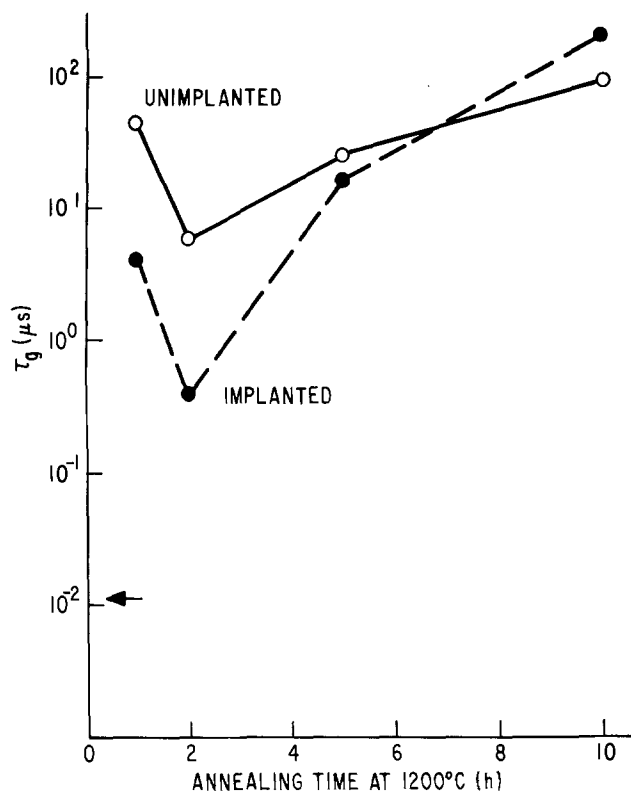


Fig. 10. Same as Fig. 9, but with a controlled cooling rate of 2°min^{-1} .

volve a pairing of two irradiation-related defects. Doping density was found to be unaffected by argon implantation at least up to a dose of 10^{13} cm^{-2} . Higher temperature annealing (up to 1h at 1200°C) induces partial recovery of the generation lifetime. The region of low lifetime appears to remain localized within 1 μm from the surface even after annealing for 1h at 1200°C. Complete lifetime recovery was observed after several hours at 1200°C followed by slow cooling.

These results show that argon implantation can be used to decrease carrier lifetime substantially in silicon. Localization in the x-y plane can be easily implemented by selective oxide masking. Si on Si epitaxial growth by CVD can be used to effectively bury the argon, and therefore to achieve three-dimensional localization of low lifetime regions, thus allowing these to be introduced into device structures (*e.g.*, into fast switching devices).

Acknowledgments

We thank P. Cerniglia, G. Gidley, B. Hatch, and M. Lazzeri for ably carrying out various wafer processing steps; ion implantations were performed by R. Reihl and W. Whitney. We are grateful to D. Schroder for pointing out the possible importance of the lateral diffusion contribution to the relaxation of the capacitance transient in this experiment, and to W. Katz for the SIMS runs. We are indebted to A. Sears for information on the equipment for measuring capacitance, and to S. Ashok for making us aware of Ref. (2). Discussions on radiation damage with W. Johnston, C. Bean, and R. Fleischer are gratefully acknowledged.

Manuscript received Sept. 12, 1983. This was Paper 319 presented at the San Francisco, California, Meeting of the Society, May 8-13, 1983.

General Electric Company assisted in meeting the publication costs of this article.

REFERENCES

1. S. K. Ghandhi, "Semiconductor Power Devices," John Wiley and Sons, Inc., New York (1977).

2. J.-W. Chen and A. G. Milnes, *Ann. Rev. Mater. Sci.*, **10**, 157 (1980).
3. H. F. Kappert, G. Sixt, and G. H. Schwuttke, *Phys. Status Solidi A*, **52**, 463 (1979).
4. B. Smith, "Ion Implantation Range Data for Silicon and Germanium Device Technologies," Research Studies Press, Inc., Forest Grove, Oregon (1977).
5. H. H. Andersen, in "Physics of Ionized Gases 1974," V. Vujovic, Editor, Institute of Physics, University of Zagreb, Zagreb, Yugoslavia (1974).
6. D. K. Schroder and J. Guldborg, *Solid-State Electron.*, **14**, 1285 (1971).
7. T. W. Collins and J. N. Churchill, *IEEE Trans. Electron Devices*, **ed-22**, 90 (1975).
8. D. K. Schroder, *ibid.*, **ed-19**, 1018 (1972).
9. S. N. Chakravarti, P. L. Garbarino, and K. Murty, *Appl. Phys. Lett.*, **40**, 581 (1982).
10. D. N. Nichols, Abstract 279, p. 430, The Electrochemical Society Extended Abstracts, Vol. 83-1, San Francisco, California, May 8-13, 1983.
11. D. J. Fitzgerald and A. S. Grove, *Surf. Sci.*, **9**, 347 (1968).
12. F. P. Heiman, *IEEE Trans. Electron Devices*, **ed-14**, 781 (1967).
13. B. E. Deal, A. S. Grove, E. H. Snow, and C. T. Sah, *This Journal*, **112**, 308 (1965).
14. A. G. Nassibian and B. Golja, *J. Appl. Phys.*, **53**, 6168 (1982).

Fines in Fluidized Bed Silane Pyrolysis

G. Hsu, R. Hogle,¹ N. Rohatgi, and A. Morrison*

Jet Propulsion Laboratory, California Institute of Technology, Pasadena, California 91109

ABSTRACT

Silicon deposition on silicon seed particles by silane pyrolysis in a fluidized bed reactor is being investigated as a low cost, high throughput method to produce high purity polysilicon for solar cell applications. Studies of fines, particles 0.1-10 μ diam, initiated from homogeneous decomposition in the reactor were conducted using 2 and 6 in. diam fluidized beds. The studies show functional dependences of fines elutriation on operating parameters such as silane feed concentration, temperature, gas velocity, and bubble size. The observation that the fines elutriation is generally below 10% of the silicon-in-silane feed is explained using a concept of scavenging by large particles in an environment of less free space for homogeneous nucleation. Preliminary results suggest that, with proper conditions and distributor design, high silane concentration (>50% SiH₄ in H₂) feed may be used for silicon production in fluidized bed reactors.

Silicon deposition in a fluidized bed reactor (FBR) was first tested in the early 1960's (1) using chlorosilane for producing semiconductor purity polysilicon. However, the success of the alternative Siemens process (2, 3) led to its universal utilization for commercial production and the de-emphasis of FBR process development. Since 1975, the new potential market for semiconductor grade silicon for photovoltaic applications made a production reactor like the FBR, with the capabilities of continuous high throughput operation and low energy cost, very attractive. Silane is used in this FBR process because of its advantages in low deposition temperature, complete conversion in the irreversible reaction, noncorrosive atmosphere, and the ease of recycling the by-product hydrogen.

In a conventional chemical vapor deposition type of reactor using silane for silicon production, there is a limit of silane concentration in hydrogen [the "critical silane concentration" (4, 5)] beyond which unwanted fines are homogeneously nucleated. In addition to the desirable chemical vapor deposition on the substrate, silicon powders or fines, in the size from submicron to ~10 μ , form in the gas phase. These fines present mechanical problems to the operation of the reactor, and are difficult to transport. They are considered losses to the process. The major reason the chemical vapor deposition type of reactor is operated at low silane concentration is to prevent excessive fines formation; thus, this type of operation is limited in throughput. In a fluidized bed reactor, less fines are generated because (i) less free space is available for homogeneous nucleation and (ii) the silicon seed particles scavenge the homogeneously nucleated fines and incorporate them into the deposition growth (6). Consequently, the net amount of fines becomes much less than that in a chemical vapor deposition reactor at the same silane concentration. A fluidized bed reactor, therefore, can be operated at a much higher silane concentration and the FBR process economics are greatly improved, relative to the Siemens type of chemical vapor deposition process.

In a forthcoming paper, we shall discuss the overall deposition growth mechanism and the details of the phe-

nomena involved in the operation of a silane-fluidized bed reactor. In this study, we shall concentrate on the experimental results of fines elutriation and the functional dependence of fines elutriation on operation parameters.

Experimental

Apparatus.—The experimental data on fines elutriation were collected from both 2 and 6 in. diam fluidized bed reactors. The 2 in. reactor was designed for establishing basic feasibility in the fluidized bed approach, while 6 in. FBR represents the smallest size of a practical engineering reactor to remove the wall effect. Experiments using these two FBR systems provided a means for testing of fines elutriation behavior in a fluidized bed silane pyrolysis system over a wide range of conditions.

The schematic diagram of a fluidized bed reactor is depicted in Fig. 1. The 2 in. id reactor is 36 in. high with an expanded head of 4 in. id \times 6 in. high. The reactor is externally heated with three zones of clamshell-type electrical resistance heaters with an overall height of 18 in. and a total output of 2.2 kW. The temperature was monitored by iron-constantan type K thermocouples located at various heights both outside and inside the reactor wall as well as at the distributor plate. The flows of hydrogen and silane were measured by rotameters. The gases were premixed and preheated to 300°-350°C before being injected into the reactor. The bottom of the reactor was a 30° cone with a 1/2 in. orifice gas distributor or a distributor fabricated from a 200 mesh stainless steel screen supported by a 1/8 in. stainless steel plate perforated with multiple 1/32 in. holes. The temperature of the distributor was kept below 400°C by blowing room temperature nitrogen onto the distributor. The compositions of the inlet and outlet silane-hydrogen gas mixtures were analyzed by a Hewlett Packard Model 5710A gas chromatograph.

The exit gas from the reactor was passed through MICROPORE filters (porosity 0.1 μ m) before being flared off. The pressure in the reactor was maintained at 5 psig with the help of a back pressure regulator. The pressure drop fluctuation across the bed was continuously monitored by a differential pressure transducer. The pressure difference signal was used to indicate the fluidization behavior of the bed.

* Electrochemical Society Active Member.

¹ Present address: C. F. Braun Company, Alhambra, California.

Key words: silicon production, fluidized bed reactor, silane pyrolysis, homogeneous nucleation.

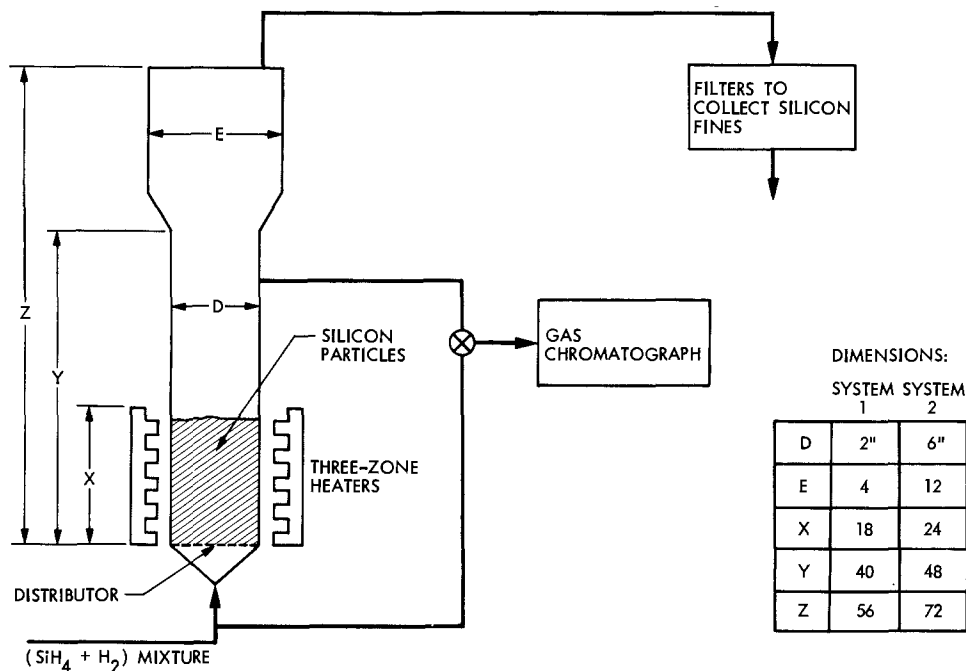


Fig. 1. Fluidized bed reactor systems for fines studies.

The 6 in. diam reactor was fabricated from a 6 in. Schedule 40 type 316 stainless steel pipe. The reactor dimensions are 6 in. id \times 48 in. high with an expanded head of 12 in. id \times 24 in. high. The reactor is externally heated with three independently controlled heaters. The bottom two heaters are made of silicon carbide heating rods, and the top one is a clamshell-type electrical resistance heater with total output of 18 kW. With proper heating, no deposition on the reactor wall is observed. The reactor was fluidized with a multilayer screen (trade name DYNAPORE) gas distributor, or a distributor fabricated from no. 325 mesh screen supported by the 1/20 in. thick plate perforated with 1/8 in. holes. In order to keep the distributor temperature less than 400°C and to avoid premature silane decomposition and plugging of the distributor screen, water cooling was employed both at the periphery of the distributor and beneath the distributor screen.

In all of the experiments, the silicon fines were collected in filters located at the exit line of the reactor expanded head (Fig. 1). For the 2 in. reactor, a 5 in. diam MICROPORE filter was used, and a submicron size cartridge-type of filter was used for the 6 in. reactor.

Procedure.—The silicon dust was collected for at least 15 min after steady-state operation was achieved for a selected bed temperature, silane concentration, and fluidization velocity. The silicon fines collected on the filter were weighed and transferred into a polyethylene bag and sealed in order to avoid oxidation of silicon. The percent of fines elutriated was defined as the ratio of fines collected in the filter to the corresponding silicon-silane feed during that period.

Seed particle sizes of 150-300 μm were used. For the 2 in. diam FBR, a typical bed height of 6 in. was used, whereas a 2 ft height was used for the 6 in. FBR. The fluidization gas velocity ratio, u/u_{mf} (where u is the superficial gas velocity and u_{mf} is the minimum fluidization velocity) was varied from 1 to 10, with a typical number of 5. Seed particles were prepared by crushing and grinding semiconductor grade polysilicon, screening to the specific mesh sizes, and leaching with a mixture of HF, H₂O₂, and deionized water to remove oxide and metal impurities.

Discussion of Results

The fine particles formed by the pyrolysis of silane in a fluidized bed are clusters of submicron size nuclei formed from homogeneous gas phase decomposition, nucleation, and coagulation; this is depicted in Fig. 2. The size range for the clusters is about 1-10 μm . The x-ray diffraction analysis showed that the silicon fines are of crystalline structure. Under the conditions employed, no significant attrition of particles was observed.

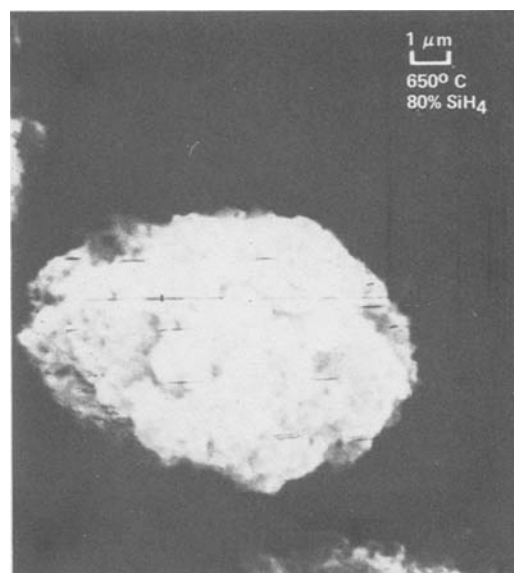


Fig. 2. SEM examination of FBR fines

Silane concentration.—Since the first step in fines formation is gas phase decomposition, the maximum fines level can be estimated from the percentage of homogeneous decomposition in the overall reaction scheme. The following simplified calculation of the maximum expected fines is based on the assumption that homogeneous decomposition leads to fines formation at all concentration levels. Since, generally, homogeneous decomposition and heterogeneous deposition are first order with respect to silane concentration, the percentage of fines formation in terms of the feed silicon content is the ratio of the homogeneous rate constant to the sum of the homogeneous and heterogeneous rate constants. In the literature, an expression for the homogeneous first-order rate constant was approximated by (7)

$$k_r = 2.0 \times 10^{13} \exp(-51,700/RT) \quad [1]$$

whereas the heterogeneous rate constant for a fixed particle bed operated under conditions similar to those used in this work was given as (8)

$$K_s = 5.14 \times 10^9 \exp(-38,800/RT) \quad [2]$$

Thus, at 650°-700°C, the maximum calculated percentages of fines formation are 77-83%. In a fluidized bed, the fines are less to begin with because of less free space

available for homogeneous nucleation; and they are further scavenged and incorporated into the deposition. These combined phenomena result in a very low residual fines level, generally less than 10% of the silicon in silane feed as shown in Fig. 3. For a feed silane concentration below 10%, the fines elutriation level is almost negligible.

Temperature.—As the temperature is increased, calculations using the Arrhenius rate constant dependence show that the rate of the homogeneous reaction rises faster than that of heterogeneous deposition. Figure 4 shows the difference between the theoretical fines formation calculated from the assumption that homogeneous decomposition produces fines and the experimental level measured from the effluent filter. These data indicate substantial reduction in fines elutriation. The concept of scavenging is involved to explain the decrease.

There is an optimum temperature range for FBR reactor operation. The effect of the temperature is illustrated in the scanning electron microscope (SEM) pictures presented in Fig. 5. There is a lower limit of operation temperature set by the deposition quality. At $\sim 550^\circ\text{C}$, the product appears to adhere loosely and to be granular in nature. As the temperature is increased past 600°C to 650°C ,

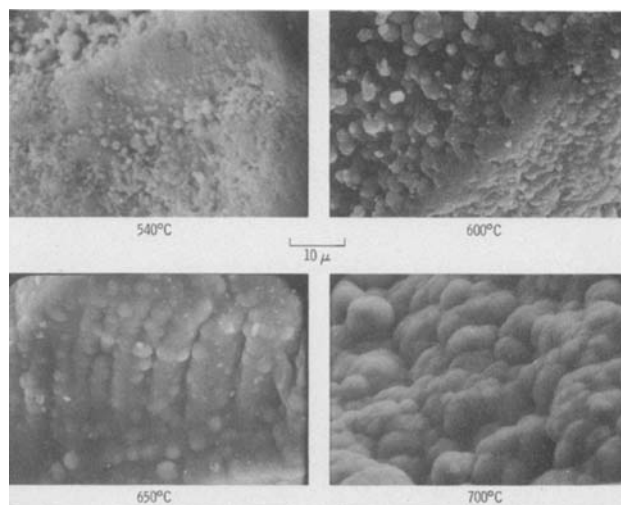


Fig. 5. Deposit surface quality (SEM) vs. temperature

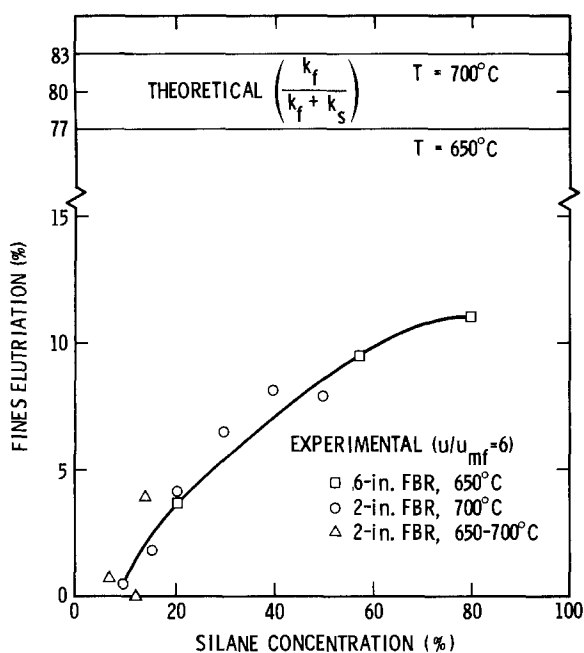


Fig. 3. Fines elutriation vs. silane feed concentration

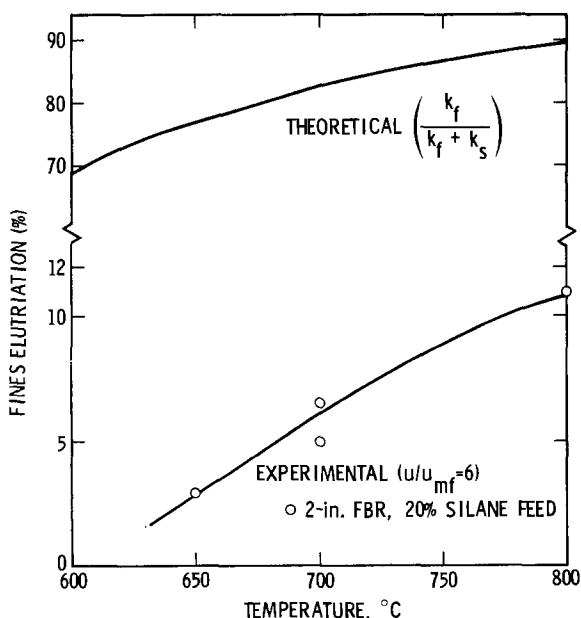


Fig. 4. Fines elutriation vs. temperature

the deposit appears to be more coherent and dense. At 700°C , the deposit is very coherent and dense. It is evident from the SEM pictures that the silicon deposits have a nodular shape. It is believed that these nodules are formed as a result of the combined actions of the collection of the very small particles (created by homogeneous gas phase decomposition and nucleation) on the surface of seed particles and of heterogeneous CVD-type deposition. The morphology was found to be dependent on the deposition rate and the particle surface temperature. Based on the product morphology, the lower limit for operating the fluidized bed reactor in silane pyrolysis is 600°C and the optimal temperature region is $\sim 700^\circ\text{C}$. Above $\sim 800^\circ\text{C}$, economically intolerable levels of fines are formed.

Gas bubble size.—In a fluidized bed reactor, the gas void space between the fluidized solid particles directly influences the ratio of the fines formation to the heterogeneous deposition. When large gas bubbles occur at the grid of the distributor plate, large amounts of fines are generated in the bubbles.

The data which demonstrates this effect of gas bubble size is shown in Table I in terms of the distributor effect on fines elutriation. Thus, it is essential in fluidized bed design to maintain the gas distribution so as to produce uniform tiny bubbles. This can be achieved either by using a distributor with small openings or a multilayer screen. A very poor situation is one in which the fluidized bed operates in a slugging mode to favor a large amount of homogeneous decomposition and thus high fines production.

Gas velocity.—Other parameters that affect the fines elutriation in a fluidized bed are the bed height and the gas velocity. Bed height affects the residence time for the fines in the bed and thus influences the efficiency of trapping the fines. Gas velocity or retention time can be translated into the retention time of the gas in the bed; as this factor is increased the time for incorporating the fines onto the seed particles increases.

The dependence of elutriation on gas velocity was illustrated, for example, in the data: the dust level of $u/u_{mf} = 3$

Table I. Distributor effect on fines elutriation

Silane concentration (C%)	Temperature (T, °C)	Opening of distributor to bed diameter ratio (d/D)	Fines elutriation (%)
20	700	2.00×10^{-4} **	4.6
20	700	0.25**	6.5
60	650	2.83×10^{-4}	9.5
65***	650	1.45×10^{-3}	12.2

* Estimated equivalent ratio of a multilayer screen distributor.

** Nozzle type of distributor.

*** Note that silane concentration increases from 60 to 65%, which may also increase the level of fines.

was 6% and the level for $u/u_{mf}=6$ was 10% at a bed temperature of 700°C and a 65% silane concentration. However, care must be taken to avoid the use of gas velocities below the limit at which the reaction region spread out by the fluidizing gas will be too narrow. In this case, the resulting high reaction density causes undesirable bed agglomeration. In an earlier study (6), the lower limit for gas velocity, expressed by the parameter u/u_{mf} , was experimentally determined to be 3. The upper limit for velocity was reached when the bed slugged in an uncontrollable mode; this was found to be at $u/u_{mf}=8$.

Conclusions

Key operating guidelines for fluidized bed silicon production from silane have been defined. A scavenging mechanism has been proposed to account for the low fines elutriation in the temperature range of 600°-800°C. Below 600°C, the deposits are relatively poor and loosely adhered to the particle surface. Above 800°C, fines level starts to increase rapidly. Bed agglomeration appears to be avoidable by keeping $u/u_{mf}>3$. Beds have been operated at velocities as high as $u/u_{mf}=8$ without problems, such as excessive dust entrainment and erratic bed behavior.

Based on the above empirical guidelines for temperature and fluidization velocity, the operating envelope for fluidized bed silane pyrolysis systems is thus identified as follows

$$\begin{aligned} 600^{\circ}\text{C} \leq T \leq 800^{\circ}\text{C} \\ 3 \leq u/u_{mf} \leq 8 \end{aligned} \quad [3]$$

The optimal operating condition from fines elutriation and morphology point of view is $T=700^{\circ}\text{C}$ and $u/u_{mf}=5$. Within the identified operating envelope, the fines elutriation percentage is generally below 10% of the silicon-in-silane feed. The preliminary results suggest that high silane concentration (>50%) feed can be used with-

out excessive fines generation if this set of operating conditions can be maintained.

Acknowledgment

The authors would like to thank D. Feller and J. Lloyd for their valuable laboratory assistance. This paper presents the results of one phase of research carried out by the Jet Propulsion Laboratory, California Institute of Technology, sponsored by the U.S. Department of Energy through an agreement with National Aeronautics and Space Administration.

Manuscript submitted July 11, 1983; revised manuscript received Nov. 11, 1983.

Jet Propulsion Laboratory assisted in meeting the publication costs of this article.

REFERENCES

1. H. W. Ling, U.S. Pat. 3,012,861 (1961).
2. M. S. Bawa, R. C. Goodman, and J. K. Truitt, in "Chemical Vapor Deposition, Fourth International Conference," G. F. Wakefield and J. M. Blocher, Jr., Editors, p. 63, The Electrochemical Society Softbound Proceedings Series, Princeton, NJ (1973).
3. D. Laskafeld and T. Roznov, *Int. Chem. Eng.*, **9**, 440 (1969).
4. J. U. M. S. Murthy, N. Miyamoto, M. Shimbo, and J. Nishizawa, *J. Cryst. Growth*, **33**, 1 (1976).
5. F. C. Eversteijn, *Philips Res. Rep.*, **26**, 134 (1971).
6. N. K. Rohatgi, G. C. Hsu, and R. Lutwack, in "Materials and New Processing Technologies for Photovoltaics," J. A. Amick, V. K. Kapur, and J. Dietl, Editors, p. 477, The Electrochemical Society, Softbound Proceedings Series, Pennington, NJ (1982).
7. T. Hogness, T. L. Wilson, and W. C. Johnson, *J. Am. Chem. Soc.*, **58**, 108 (1936).
8. S. K. Iya, R. N. Flagella, and F. S. DiPaolo, *This Journal*, **129**, 1531 (1982).

Plasma Anodic Nitridation of Silicon in N₂-H₂ System

M. Hirayama, T. Matsukawa, H. Arima, Y. Ohno, N. Tsubouchi, and H. Nakata

Mitsubishi Electric Corporation, LSI Research and Development Laboratory, Itami, Hyogo 664 Japan

ABSTRACT

Silicon nitride films were directly formed on silicon by plasma anodic nitridation within nitrogen and hydrogen. The nitridation pressure ranged from 0.5 to 2.0 torr, at temperatures from 700° to 900°C. The growth rate of silicon nitride increased with an increase of the dc bias voltage to the silicon wafers. The refractive index of the films was measured to be about 2.00-2.30 by ellipsometry. Film composition was analyzed with Auger electron spectroscopy. Dielectric breakdown strength of the silicon nitride films was about 6.0 MV/cm after oxygen heat-treatment.

Direct nitridation of silicon has been an attractive technique for VLSI device fabrications for the last few years. The dielectric constant of the silicon nitride film is larger than that of the oxide film, and impurities in the gate poly-Si are prevented from diffusing through the silicon nitride film to the channel region. Unfortunately, the silicon nitride deposited on silicon wafers by LPCVD has interfacial instabilities between the silicon nitride and the silicon substrate. Many efforts have tried to obtain the silicon nitride film by direct reaction of silicon in a nitrogen ambient. Although thermal nitridation and plasma-enhanced thermal nitridation were previously reported, the film thickness is only about 100Å even at high reaction temperatures (1, 2). Using nitrogen ambient and pure ammonia for the thermal nitridation (3), the films were very thin because of the slow diffusion of nitridant species through the nitride film. The growth kinetics of thermal nitridation for films below a thickness of 100Å has been analyzed (4). From previous works, the process limitations of thermal nitridation prevent using it for formation gate films for MOSFET's. The nitridation technique was used to form thin gate dielectric films such as nitrided oxide or oxy-nitride films (5). In fact, VLSI devices such as high density single-transistor dynamic

Key words: plasma nitridation, anodization, silicon nitride gate insulator film.

RAM's or electrical erasable and programable ROM's use these nitrided films as a gate insulator film.

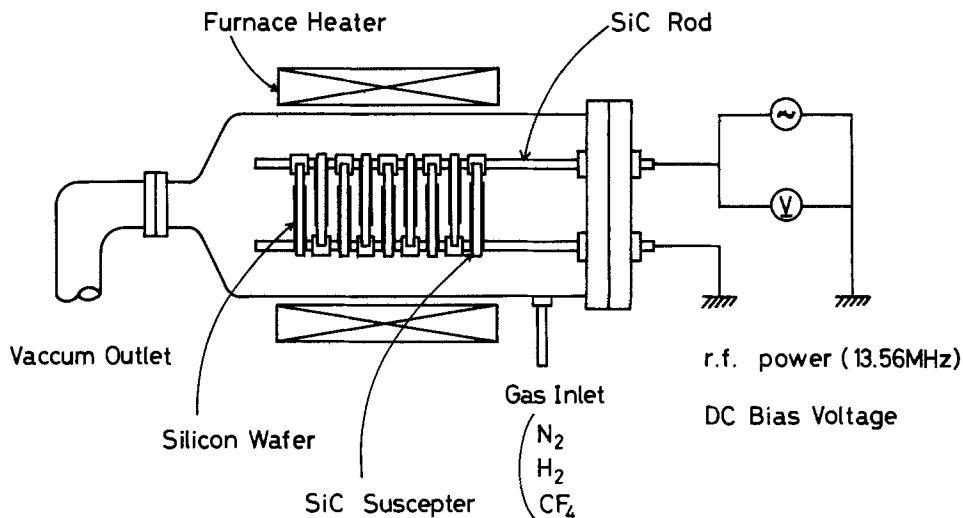
Attempts to improve the growth rate and the electrical properties of nitrided films was made using plasma anodic nitridation. Anodization of silicon or anodic oxidation of silicon is a promising approach to accelerate the oxidation rate in semiconductor processing (6). Similarly, plasma anodic nitridation is expected to be useful for nitridation of silicon. The method has the advantage of lower temperature in fabrication of VLSI devices and is expected to improve the interfacial characteristics and electrical properties of the nitride films.

This paper reports some nitridation characteristics of silicon using only nitrogen and hydrogen and a new plasma anodization technique. Some properties of the silicon nitride film obtained by this new technique are also described. We studied plasma anodic nitridation of silicon in the temperature range of 700°-900°C, instead of the conventional thermal nitridation process requiring temperatures above 1000°C.

Experimental Procedure

The starting material was (100) oriented CZ silicon wafers with n-type resistivity of 1-5 Ω-cm. Wafers were chemically cleaned in sulfuric acid and hydrochloric acid and rinsed with deionized water. They were then dipped

Fig. 1. Schematic diagram of experimental apparatus for plasma anodic nitridation.



in 2% hydrofluoric acid for 30s, rinsed with deionized water, and dried in flowing nitrogen gas. The experimental apparatus, shown schematically in Fig. 1, was a horizontal 150 mm diam quartz tube heated to temperatures between 700°-900°C. Cleaned wafers were loaded onto a silicon carbide (SiC) susceptor in the cold zone. After the insertion of the boat, the reaction tube was capped and evacuated with a mechanical booster pump. High purity hydrogen and nitrogen gases were used for the nitridation and flow rates controlled with a mass flow controller. Carbon fluoride (CF_4) and hydrogen were used for pre-etching of silicon surface at a pressure of 0.05 torr for 1 min to remove the native oxide on the silicon surface. Before nitridation in hydrogen and nitrogen plasma, the system was pumped down to 1×10^{-4} torr with a turbo molecular pump to minimize the residual gases. The gas mixture was admitted to vacuum tube through a variable leak valve while a mechanical pump kept the pressure in the reaction tube at 0.5-2.0 torr under flow condition. Once the pressure became stable, a 13.56 MHz RF power was supplied to the silicon carbide rods so that a plasma discharge was excited between the alternate susceptors. In addition, dc bias was applied to the anode (maximum voltage was 250V). This method differs significantly from the previous works.

The thickness and refractive index of as-grown films were determined by the ellipsometry. These were consistently calculated by a computer. The chemical compositions of the films were measured using Auger electron spectroscopy (AES) with a cylindrical mirror analyzer. To measure the dielectric breakdown voltages, polycrystalline silicon electrodes were formed onto the film to make MOS capacitors.

Results

Growth conditions.—Figure 2 shows the relation between film thickness and reaction time at 900°C, 1:1 nitrogen:hydrogen, 1.00 torr, and 150V dc bias voltage on the SiC electrodes. Silicon wafers loaded on the positive electrode nitrided faster than those on the negative electrode. Typical growth rate on the positive electrode was about 1.5 Å/min, and the nitride film was 623Å thick after 7 hr nitridation. Previously, silicon nitride films were limited to about 100Å for thermal nitridation or the plasma-enhanced nitridation (1-3), due to slow diffusion of the nitridant species across the thermal nitride film below 1100°C. These experimental results suggest that the film growth kinetics of the plasma anodic nitridation is different from those of thermal nitridation systems.

Under the same nitridation conditions, film thickness increases with temperature as shown in Fig. 3. The growth rate of the nitride film on silicon loaded onto the negative electrode was smaller. Below 200°C, the nitride film was scarcely visible. Dependence of film thickness on nitridation pressure was minimal in the range from 0.5 to 2.0 torr as shown in Fig. 4. At a nitridation pressure below 0.1 torr, the growth rate of the nitride film abruptly decreased.

The most interesting experimental result is the dependence of film thickness on dc bias voltage as shown in Fig. 5. The nitridation temperature and pressure were 900°C and 1.0 torr, respectively, for 150 min. It is clear that the film thickness increases linearly with the increase of the applied dc bias voltage. On the negative electrode SiC rods, the nitridation was slightly accelerated by the bias voltage. The dc bias voltage was limited at any specific pressure, and the maximum voltage value was 178V at 2.0 torr. Even though the silicon wafers and the SiC disk susceptors were isolated by quartz insulators on SiC rods, at a low bias voltage, the plasma anomalous discharge occurred unexpectedly at low pressures.

Film composition.—The refractive index, as measured by ellipsometry, ranged from 2.0 to 2.3, which was slightly larger than silicon nitride films formed by LPCVD. This may be due to deviation of stoichiometry of silicon nitride. For films below 100Å thick, it is difficult to determine both the refractive index and the film thickness by ellipsometry.

The as-grown film composition was analyzed by Auger electron spectroscopy. The films contained only silicon, nitrogen, and oxygen, and the compositions were consistent with mixtures of Si_3N_4 and SiO_2 . Since hydrogen is not detectable with Auger spectroscopy, the hydrogen

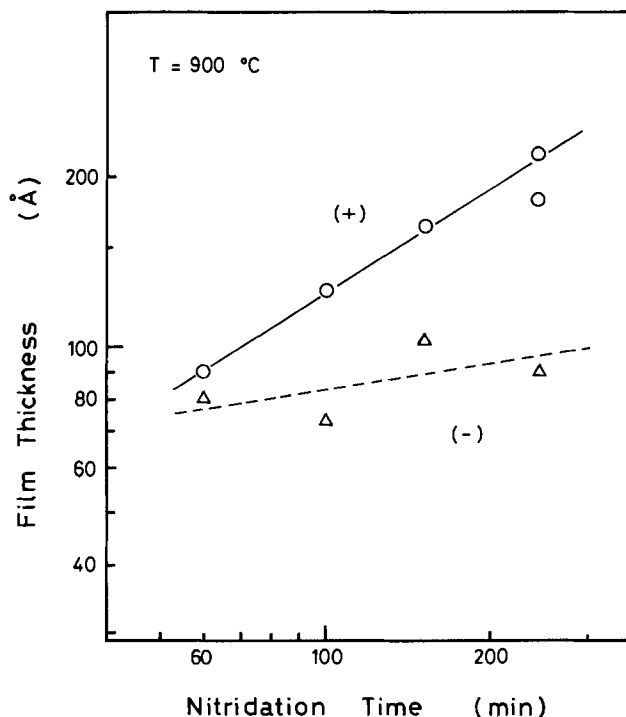


Fig. 2. Relation between film thickness and nitridation time

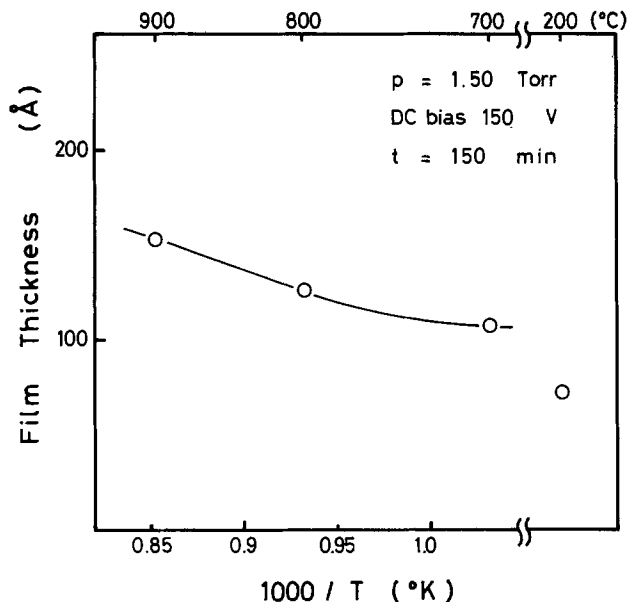


Fig. 3. Dependence of nitridation temperature on film thickness

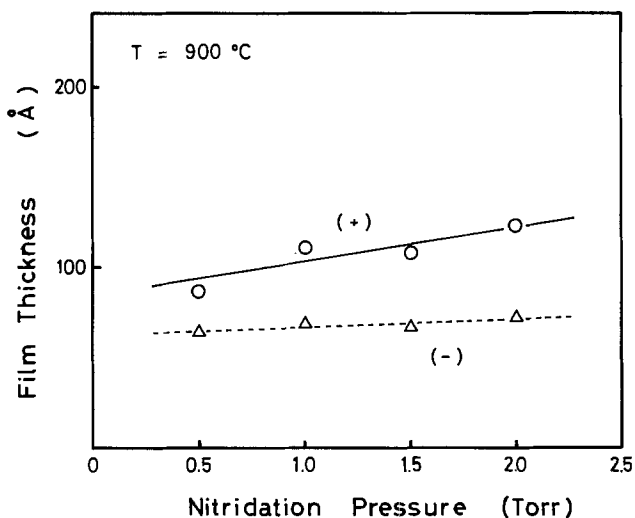


Fig. 4. Dependence of film thickness on nitridation pressure

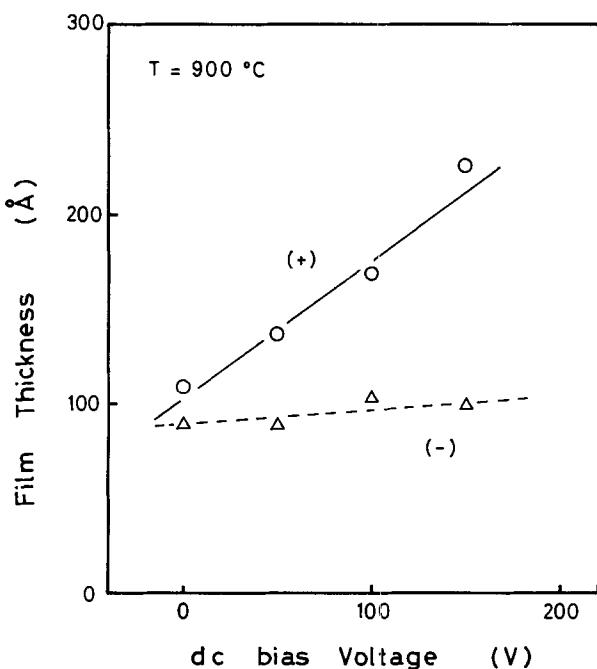


Fig. 5. Dependence of film thickness of the dc bias voltage

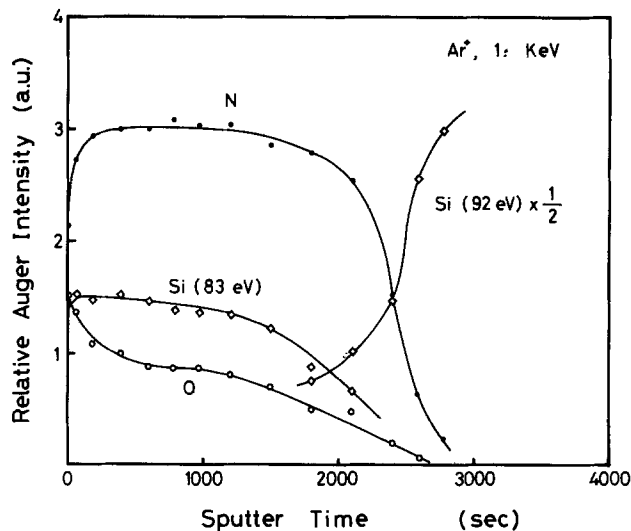


Fig. 6. Typical Auger depth profiles of plasma anodic nitridation film

content of these films is not known. Sputter etching was accomplished with a 1.0 keV argon beam to obtain depth profiles. Depth profiles of components of films grown at 150 min, 1 torr hydrogen and nitrogen, and 900°C are shown in Fig. 6. Thickness of this sample was 120Å. Nitrogen and oxygen concentrations (closed and open circles, respectively) were calculated from the peak height of the KLL transition spectrum. The relatively flat nitrogen and oxygen profiles show that the film was a silicon oxynitride. The most striking feature of Fig. 6 is the nitrogen profile in silicon substrate beyond the interface. Nitrogen apparently diffused into silicon more easily than oxygen even though it is said that the nitriding species diffuses slower through nitride compared to oxygen through oxide. However, reaction of nitrogen on the silicon surface seems to have occurred more easily than oxygen.

Dielectric breakdown strength.—To measure the dielectric breakdown strength of the nitride films, MOS capacitors were fabricated by Si gate MOS technology. A thick oxide film was formed at the field region by conventional photolithography and etching. The gate area was 1 mm². After the nitridation, phosphorus-doped polycrystalline silicon was deposited in an LPCVD system in electrodes and interconnection regions. The breakdown strength of the gate dielectric was measured by the voltage ramping at 100 V/s, and breakdown identified when the gate leakage current exceeded 1 μA. The average breakdown of as-grown nitrided films occurred at about 3.2 MV/cm. The value is rather low in comparison with that of the oxide films obtained at the same temperature, 900°C. Shown in Fig. 7 are typical distributions of the dielectric breakdown strength of the nitride films after heat-treatment in nitrogen and oxygen. The nitride film was formed at 900°C, dc bias of 150V in nitrogen and hydrogen at 1.5 torr. The oxygen ambient was more effective in improving the dielectric breakdown strength. The average dielectric breakdown strength was 6.5 MV/cm after

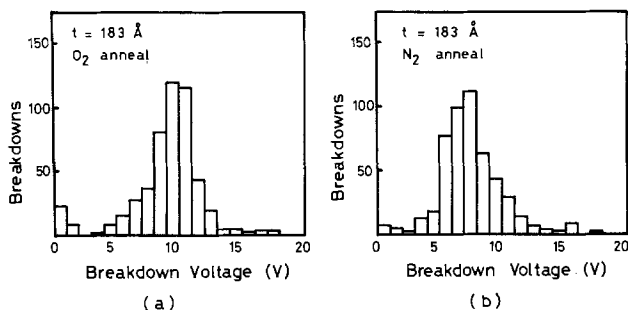


Fig. 7. Typical dielectric breakdown strength distributions. (a) Annealed in oxygen (b) annealed in nitrogen.

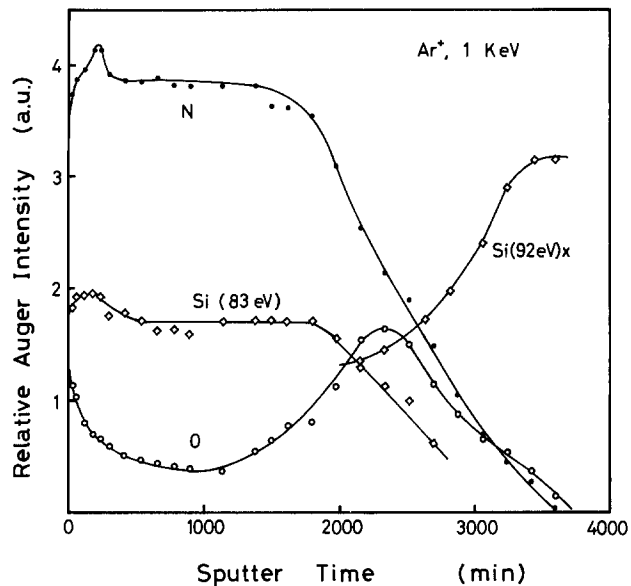


Fig. 8. Auger depth profiles of LPCVD silicon nitride film

postannealing in oxygen for 20 min at 1000°C, and 5.1 MV/cm in nitrogen ambient for 30 min at 1000°C.

Discussion

The object of this work is to obtain thick silicon nitride films by direct nitridation of silicon. The nitride film must be stable and reliable for VLSI devices. According to the previous reports about thermal nitridation or plasma-enhanced nitridation, the growth rate of silicon nitride was low and a maximum film thickness was 120Å. The reason is believed to be the presence of oxidant species such as oxygen and water in reaction ambient apparently prevents the nitridation of silicon surface. The nitridation rate of silicon is limited by diffusion of the nitridant species across the nitride film, and is further inhibited by diffusion through the oxide film. It is necessary to reduce the amount of oxidant species to less than 1 ppm water and 0.1 ppm oxygen.

To reduce the oxidant species in the nitridation ambient, the background pressure before nitridation was reduced to below 1×10^{-4} torr by a 500 liter/s turbo molecular pump in our experimental apparatus. Furthermore, ultrahigh purity hydrogen and nitrogen gases flowed to the quartz reaction tube through stainless piping using Swedgelock connectors. Ammonia was not used in the nitridation process because it was difficult to purify it to the semiconductor grade. It may be useful to etch the silicon surface for a few minutes with $\text{CF}_4\text{-H}_2$ plasma prior to the nitridation, since the native oxide on the silicon could obstruct nitridation. To confirm the above expectation, a silicon nitride film of 100Å thick was deposited by LPCVD on the silicon surface. From the Auger depth profile of LPCVD film shown in Fig. 8, oxygen was detected in the silicon nitride region and a strong oxygen pile up at the interface between the silicon nitride and the silicon substrate. The pile up may indicate a native oxide layer on the initial silicon. Also, the oxygen profile extends into the silicon substrate beyond the nitrogen

profile. This film is composed of three elements; silicon (29%), nitrogen (65%), and oxygen (6%). It also has about a one third oxygen content compared with the plasma nitride film. From these results, the pre-etching process before nitridation is necessary and effective in excluding the native oxide. The oxygen level was lower in the LPCVD film than in the plasma anodic nitridation film. It is possible that the origin of the oxygen is from the wall of the quartz reaction tube at the plasma nitridation. In plasma nitridation, oxygen is sputtered by ions to a higher level than that of the LPCVD, even though the background pressure was lower than that of the LPCVD.

In spite of limited diffusion of the nitridant species, the growth rate was kept constant during the thick nitride film formation when the dc bias voltage was applied to the silicon wafers. The nitridation mechanism can be analogized with the anodic oxidation of Si (6). Similar to oxidation, nitridation proceeds at both plasma/nitride and nitride/silicon interfaces. Ions of N and Si and/or their vacancies move across the nitride film with an electric field, and nitridation proceeds linearly with growth time, as observed. The nitridation process was also considered as the results of the ion drift process (7). In fact, the growth rate of the nitride film was linearly increased with the increase of the dc bias voltage and the film thickness up to about 630Å in 390 min nitridation was obtained.

Conclusions

Formation of thick silicon nitride films was possible by direct plasma anodic nitridation of silicon. A nitrogen and hydrogen mixture gas was effective for nitridation without an ammonia ambient. The growth rate of the nitride films depended on the nitridation temperature, pressure, and dc bias voltage on the silicon wafers. In 390 min nitridation of silicon at 900°C, a nitride film thickness over 630Å was obtained with a dc bias voltage of 150V. The index of the refraction of films ranged from 2.00 to 2.30, slightly smaller than films by LPCVD because of higher oxygen content. The dielectric breakdown strength of the nitride film was 6.0 MV/cm after annealing in oxygen.

Acknowledgments

The authors wish to acknowledge the encouragement of Dr. H. Oka and Dr. H. Abe. They also thank Professor T. Sugano of the University of Tokyo for his useful discussions and kind suggestions.

Manuscript submitted Sept. 14, 1983; revised manuscript received Nov. 7, 1983.

Mitsubishi Electric Corporation assisted in meeting the publication costs of this article.

REFERENCES

1. R. G. Frieser, *This Journal*, **115**, 1092 (1968).
2. T. Ito, S. Hijiya, T. Nozaki, H. Arakawa, M. Shinoda, and F. Fukukawa, *ibid.*, **125**, 448 (1978).
3. S. P. Murarka, C. C. Chang, and A. C. Adams, *ibid.*, **126**, 994 (1979).
4. C. Y. Wu, C. W. King, M. H. Lee, and C. T. Chen, *ibid.*, **129**, 1559 (1982).
5. S. S. Wong, C. G. Sodini, T. W. Ekstedt, H. R. Grinolds, K. H. Jackson, and S. H. Kwan, *ibid.*, **130**, 1139 (1983).
6. V. Q. Ho and T. Sugano, *IEEE Trans. Electron Devices*, **ed-27**, 1436 (1980).
7. D. L. Pufrey, F. G. M. Hathorn, and L. Young, *This Journal*, **120**, 1529 (1973).



A New Defect Etch for Polycrystalline Silicon

B. L. Sopori

Solavolt International,¹ Phoenix, Arizona 85062

Currently, there is considerable interest in using polycrystalline silicon for solar cells. Several techniques are being developed for growing polycrystalline silicon at high speeds, in particular, as thin ribbons (or sheets). Characterization of defects in these materials is essential. Chemical etching has been applied extensively for defect delineation in single-crystal silicon. Several etchants, such as the Dash, Sirtl, Secco, Wright, and Schimmel etchants, have been developed for revealing defects in single-crystal silicon wafers (1-5). Although these etches have also been used, with some success, for defect delineation in polycrystalline silicon, the general requirements of a defect etch for polycrystalline silicon are somewhat different than those for single-crystalline silicon. The requirements are: (i) Etching characteristics should be isotropic, *i.e.*, defects in all orientations should be delineated and the size of etch pits should be nearly the same. (ii) The etch pits should indicate the direction of defect propagation. This is an important property which permits one to determine if defects, such as dislocations, follow crystallographic slip planes or form networks crossing the slip planes. These features can help determine the mechanisms causing defect generation. (iii) The etch rate should be rapid. (iv) The etchant should not leave a residue of metallic ions. This last requirement allows device fabrication in regions adjacent to defect-etched regions, thus permitting one to correlate device performance with crystal characteristics. Furthermore, because of contamination, it is undesirable to have etchants containing metals in clean processing areas.

Clearly, many defect etchants developed for single-crystal wafers do not satisfy the first two requirements. This is because the quality of defect delineation depends on surface orientation. For example, Sirtl etch works well on (111) surfaces, but leads to the formation of an ambiguous morphology on (100) surfaces. Wright etch appears to work well on many orientations; however, because of the preferential nature of the etch, difficulties arise in defect delineation due to the formation of different size etch pits on different grain orientations. Furthermore, the shapes of the etch pits are strongly controlled by grain orientations rather than by the direction of the defect. Although Dash etch reveals dislocations in all orientations, it requires long etch times. In many applications Secco etch is suitable for polycrystalline silicon etching; however, it does not meet the last requirement indicated above. Schimmel etch has shown only limited success, mainly because the etch leaves a heavy stain on the samples.

This paper describes an optimized isotropic etch designed for revealing defects in polycrystalline silicon. Additional features of the etch are that it does not contain metallic ions and is compatible with photoresist masking. Variations in the etch composition may be used for better delineation in high defect density regions.

Etch Composition

The etch (hereafter called Sopori etch) consists of a mixture of 36 parts HF (49%), 20 parts CH₃COOH (glacial), and α parts HNO₃ (70%), where α may be varied between 1 and 2. Detailed kinetics of HF:CH₃COOH:HNO₃ etches

¹ Solavolt International is a partnership of Motorola Solar Energy, Incorporated (a subsidiary of Motorola, Incorporated) and SES, Incorporated (a subsidiary of Shell Oil Company).

Key word: polycrystalline silicon, crystal defects, dislocations, defect delineation, defect etch.

have been discussed by Schwartz and Robbins (6, 7). They have divided these etches into two groups based on the rate-controlling mechanisms. According to their classification, this etch is in the regime of high HF concentration where the etch rate is limited by the concentration of the oxidizing species, *i.e.*, HNO₃. Isotropic etching characteristics of high HF concentration etches have also been observed previously (6) and applied to etching mesa diodes in polycrystalline silicon (8, 9).

Experimental

The substrate material consisted of 0.1-16 Ω -cm n- and p-type RTR² ribbons grown by laser or electron beam melting, 1 Ω -cm p-type Wacker Silso³, and Czochralski-grown (Cz) single-crystal wafers. Cz and Wacker Silso were chemically/mechanically polished on one side, whereas RTR ribbons were used with as-grown surfaces. All samples were cleaned in H₂SO₄:H₂O₂ (3:1) at 90°C, followed by a DI water rinse, and dried with nitrogen. Etch solutions were freshly mixed, and etching was done with samples held vertically in a Teflon⁴ holder while the samples were mechanically agitated. Etched samples were rinsed in DI water, dried with nitrogen, and examined under optical (VIS/IR) microscopes. It should be pointed out that etching in 36:20:1, to obtain low etch rates and/or small etch pits, may cause a light bluish stain on the sample. This stain does not interfere with defect inspection and identification, and may be readily dissolved in H₂SO₄:H₂O₂ solutions.

To determine the bulk etch rate, samples were partly masked by photoresist (Waycoat 450)⁵ using conventional photolithography and etched for different times. After removing the photoresist, the step heights were measured using a surface profilometer.

To study defect delineation characteristics for different orientations, single-crystal Cz wafers of different orientations, *viz.*, (100), (110), (111), and polycrystalline substrates whose grain orientations were determined by an optical diffraction technique (10) were used.

Results

The photograph in Figure 1 shows the defect distribution in various grains of a section of RTR ribbon that has been etched for 30s in 36:20:2. The sample was etched without any surface preparation. Various twins and grain boundaries delineated by the etch are marked in the figure.

Figure 2 shows magnified photographs of several regions of the same sample. Etch pits seen in this figure are mostly either circular or elliptical in shape and are due to dislocations propagating along (or at small angles away from) the normal to the surface. Various defects are identified. The grating-like pattern seen in these pictures is a characteristic of the as-grown ribbon surface.

Figures 1 and 2 clearly show delineation of dislocations in a variety of grain orientations in RTR ribbons.

² RTR (Ribbon-to-Ribbon) growth is a technique developed by Motorola where by large-grain silicon ribbons are grown from fine-grain polycrystalline ribbons by laser or electron beam melting.

³ Wacker Silso is polycrystalline silicon manufactured by Wacker, Germany.

⁴ Teflon is du Pont's registered trademark for its fluorocarbon plastic.

⁵ Waycoat 450 is a negative photoresist manufactured by L. P. Hunt Chemicals.

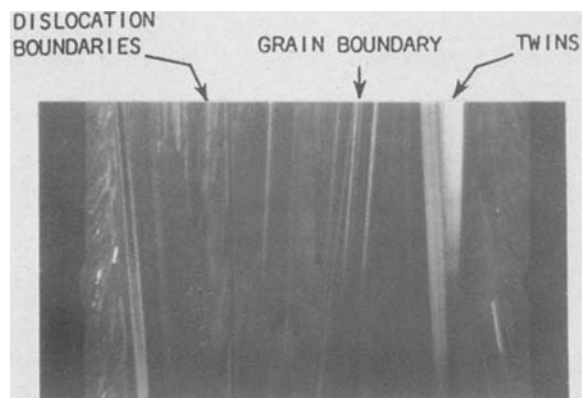


Fig. 1. Photograph of a section of an RTR ribbon etched for 30s in Sopori etch [36:20:2 (HF:CH₃COOH:HNO₃)].

To demonstrate defect delineation on a wide variety of orientations, Fig. 3 shows photographs of two adjacent samples from an RTR ribbon. One of the samples was texture etched to show different grain orientations by reflection contrast, and the other etched in Sopori etch. The large grains were found to be misoriented with respect to the (110) plane by $\pm 15^\circ$ about the x -axis and $\pm 11^\circ$ about the Y -axis. Small grains (not identified in the

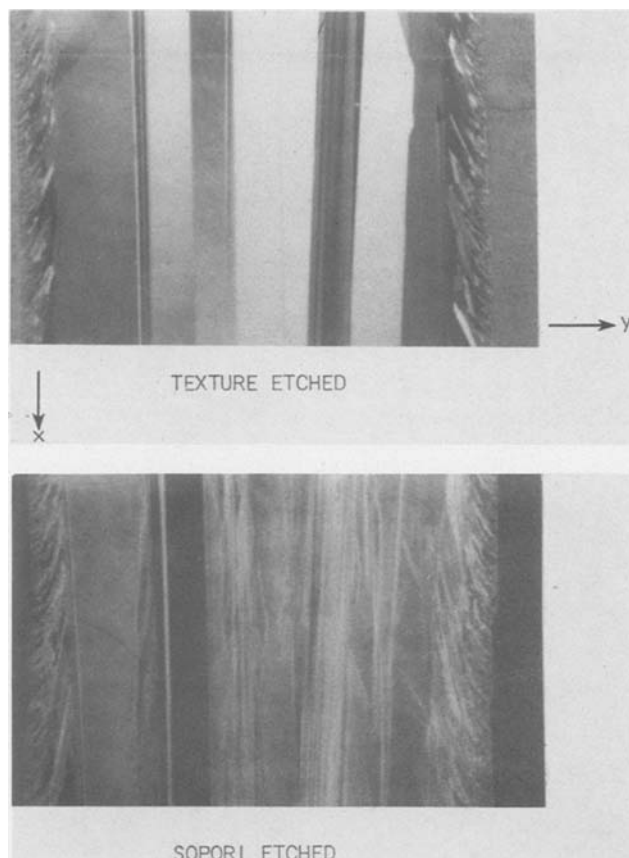


Fig. 3. Adjacent samples from an RTR ribbon. A(top): texture etched to show different grains by reflection contrast. misorientation angles are referred to the axes shown. B(bottom): defect orientation by Sopori etch.

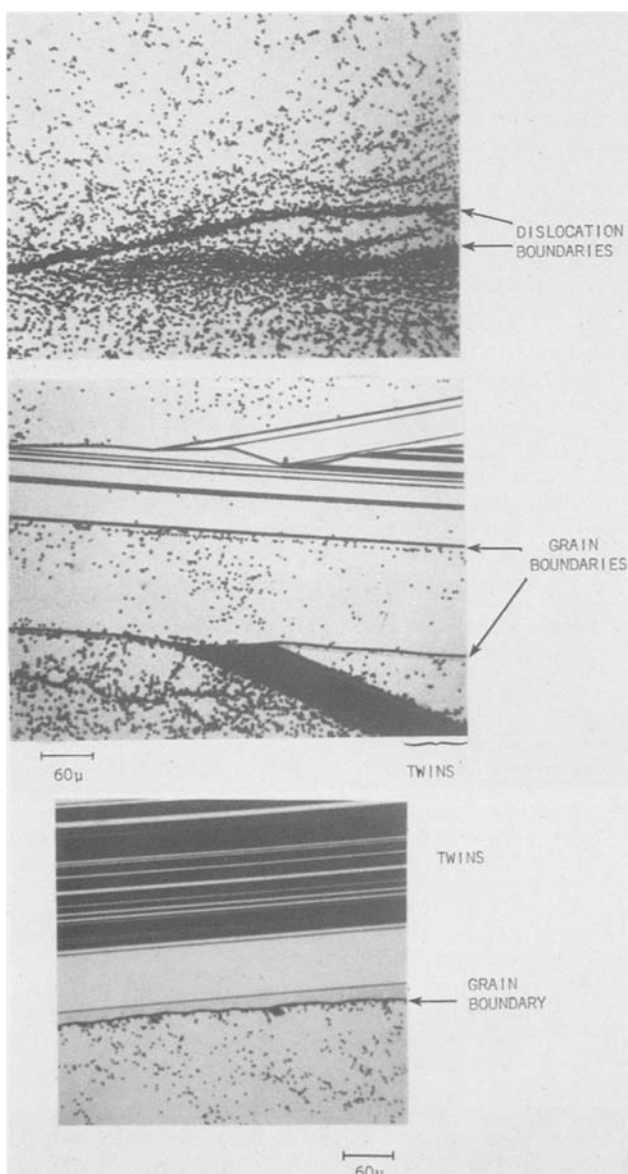


Fig. 2. Several typical regions of a defect-etched ribbon

figure) possess other orientations, such as (111) and (100). Defect delineation is clearly seen from the accompanying photograph. The effectiveness of defect delineation on different orientation samples was further confirmed by (i) the use of single-crystal Cz wafers of (100), (110), and (111) orientation into which defects were introduced by nonisothermal heating, and (ii) the use of polycrystalline substrates of other preferred grain orientations, e.g., Wacker Silso, which was found to have most grains close to (111). This extensive study did not reveal any difficulties in delineating crystallographic defects on any grain orientations. Furthermore, the etch pit size does not vary significantly for different orientations.

Defect delineation characteristics of this etch were compared with several other etches. To permit a direct comparison of the effect of these etches on different grain orientations, polycrystalline ribbons, which have nearly longitudinal grains, were scribed into samples such that they possessed many common grains. Figure 4 shows typical examples of etch pits formed by different etchants on the same grain. These samples were cleaned in the manner previously described.

A detailed comparison of different etches for polycrystalline silicon will be given elsewhere (11). Here we may briefly summarize the results as seen in Fig. 4 as follows: (i) The etching characteristics of Sopori etch are very similar to that of Secco etch (which is isotropic). (ii) Although Schimmel etch also produces etch pits similar to Sopori etch, it results in excessive stains and, additionally, delineates defects only in p-type substrates, Schimmel etch also generates different etch-pit sizes on different orientations and has been reported to have defect delineation characteristics which are dependent on the ambient light level. (iii) The post-etch surface quality of samples etched in Sopori etch is similar to that of Secco etch. However, the best surface quality is obtained from the Wright etch.

It is of particular interest to compare the advantages of Sopori etch with a preferential etch such as Wright etch,

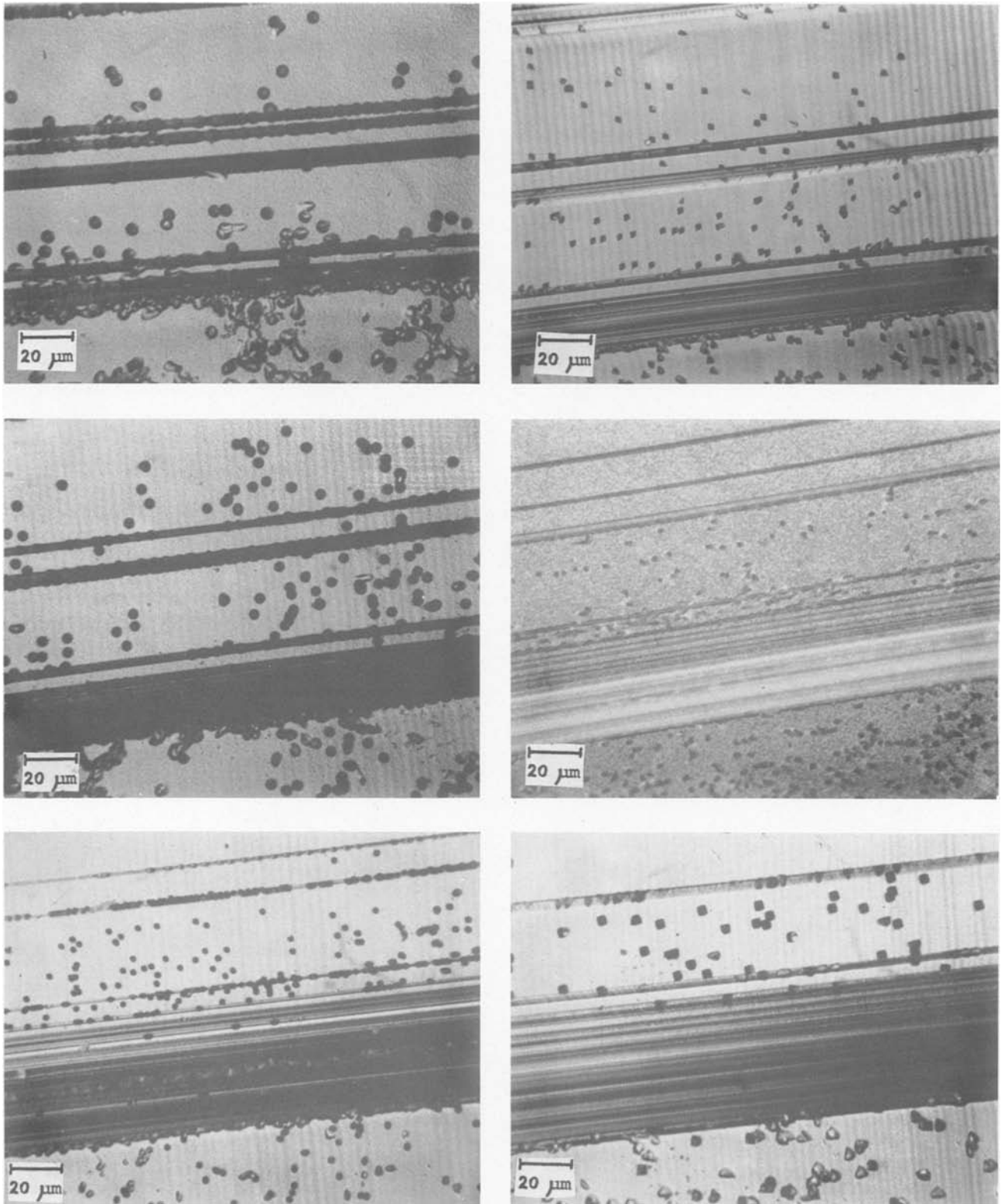


Fig. 4. Etch pits formed by different etchants on the same grain. All samples $0.4 \Omega\text{-cm}$, p-type. A (top left): 30s Sopori etch. B (top right): 2 min Sirtl etch. C (middle left): 2 min Secco etch. D (middle right): 5 min Schimmel etch. E (bottom left): 15 min Dash etch. F (bottom right): 5 min Wright etch.

which has recently been used quite extensively for polycrystalline silicon. For this purpose, two adjacent samples having the same grain structure were laser scribed from a ribbon. One of the samples was etched in Sopori etch for 30s, and the other in Wright etch for 5 min. Figure 5 shows a comparison of dislocation configurations revealed by the Wright and Sopori etches. The etch pit shapes of simple slip dislocations in a grain whose surface orientation is (110) are shown in Fig. 5a and 5b. The etch pits due to Wright etch are square, indicative of the

two-fold symmetry of (110), and do not indicate directly the direction of defect propagation. From Fig. 5a, the elliptical etch pits clearly indicate that the dislocations are at an angle to the surface and parallel to the twin boundary, *i.e.*, the (111) plane. Some other regions having dislocation loops and networks are shown in Fig. 5c and 5d. The comet shapes of individual etch pits and interconnected etch pits seen in the Sopori-etched sample are indicative of dislocation loops and networks, respectively. However, looking at the Wright etched section, it is not, in

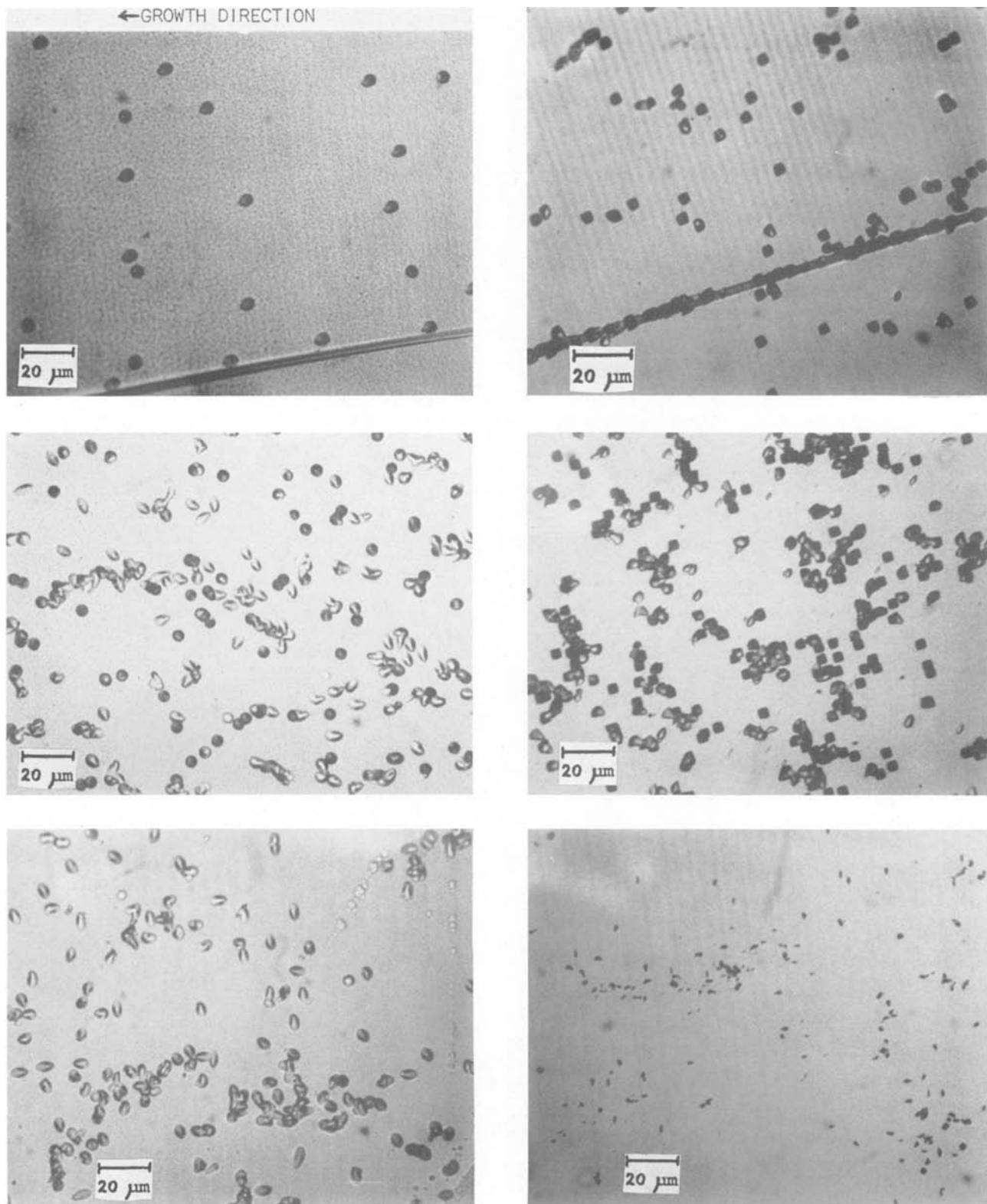


Fig. 5. Comparison of defect delineation by 30s Sopori etch and 5 min Wright etch. A (top left) and B (top right): (100) grain orientation with simple slip dislocations for Sopori etch and Wright etch, respectively. C (middle left) and D (middle right): grain with dislocation networks for Sopori etch and Wright etch, respectively. E (bottom left) and F (bottom right): dislocation delineation on a (100)-oriented grain for Sopori etch and Wright etch, respectively.

general, possible to determine the nature and direction of dislocations, although the presence of different pit shapes in the same grain (as seen in Fig. 5d) would imply dislocation propagation at different angles. Another disadvantage of a preferential etch is that the etch-pit size varies with grain orientation. This is seen by comparing the etch pit sizes of Fig. 5c and 5f, which show dislocations on a (100) grain revealed by the Sopori and Wright etches, respectively, with those of Fig. 5a-5d. Clearly, the etch pit

size on (100) due to Wright etch is much smaller than that on (110). Consequently, we believe that the advantages of using a preferential defect etch for generating well-defined geometric etch-pit shapes on single-crystal substrates (for easy identification of the nature of the defect and the crystal orientation) are diminished for polycrystalline substrates.

The relationship between the shape of the etch pit and the direction of defect propagation can be demonstrated

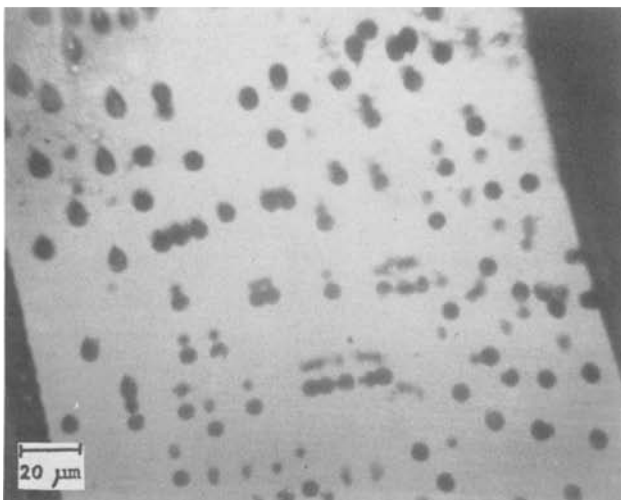
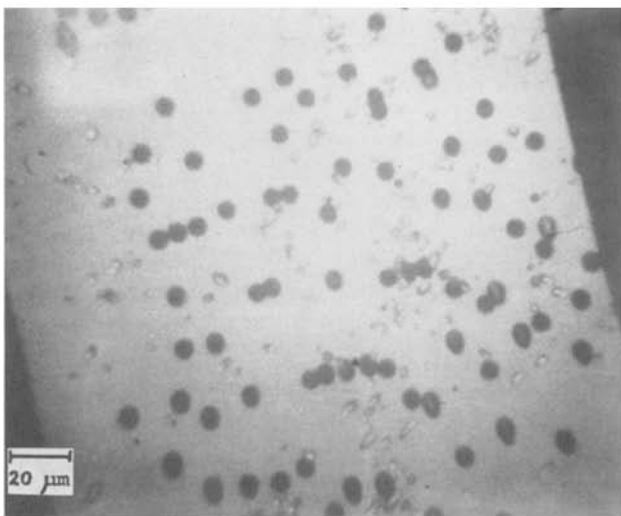
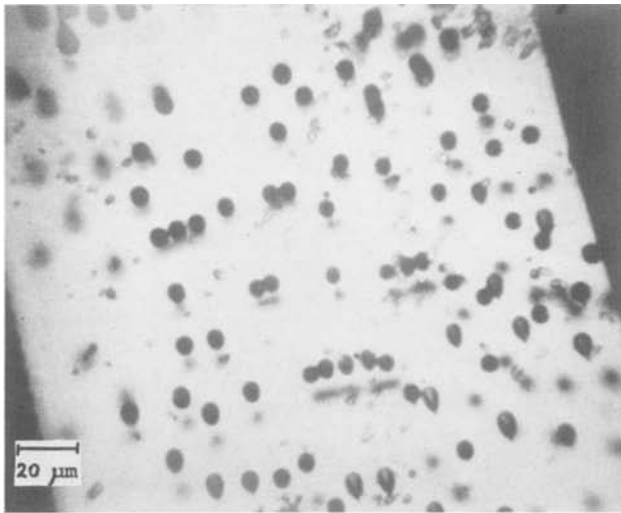


Fig. 6. IR photographs of a ribbon etched in 36:20:2 showing a correspondence between etch pits on the top and bottom surfaces due to each dislocation. Ellipticity of each etch pit is related to angle at which dislocation propagates. A (top): transmission mode, top surface focused. B (middle); reflection mode. C (bottom): transmission mode, bottom surface focused.

by viewing a sample, etched with Sopori etch, under an infrared (IR) microscope. Figure 6 shows IR photographs of a sample taken under different viewing conditions. In Fig. 6a, the well-defined dark images are due to etch pits on the top surface, and the blurred images are due to etch

pits on the back surface (away from the objective). To help identify the top surface etch pits in Fig. 6a, a photograph of the same region taken in reflection is shown in Fig. 6b. A correspondence between the top and the bottom etch pits of the same dislocation can be easily recognized for most cases. It is obvious from the photos in Fig. 6 that an increase in the ellipticity of an etch pit is accompanied by an increase in the separation between the top and the bottom etch pits of the same dislocation. For ease in recognition of etch pits on the bottom side, a photograph of the back side (focused in transmission mode) is given in Fig. 6c.

Sopori etch also works well for delineation of stacking faults, as shown in Fig. 7.

Discussion

Sopori etch shows excellent delineation characteristics with etch rates that are the same for all orientations. Figure 8 shows bulk etch rates using two compositions de-

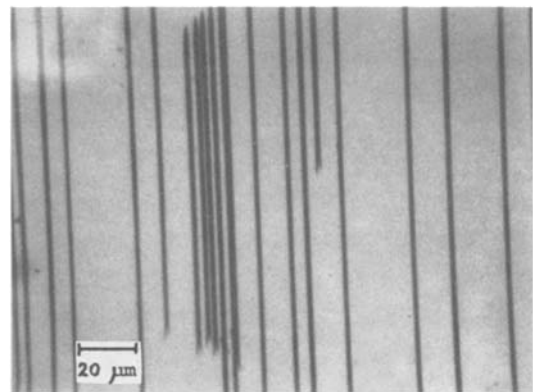
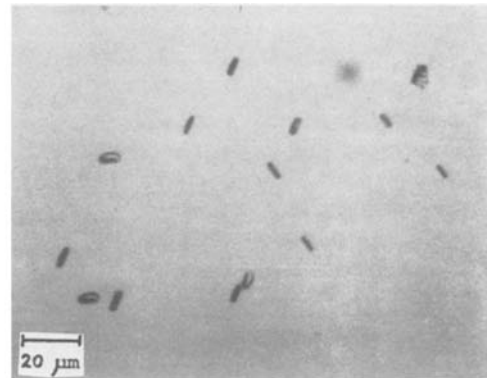


Fig. 7. Sopori etch delineations of stacking faults. A (top): oxidation-induced faults on a (111)-oriented Cz wafer. B (bottom): bulk stacking faults in an oxygen-rich RTR ribbon.

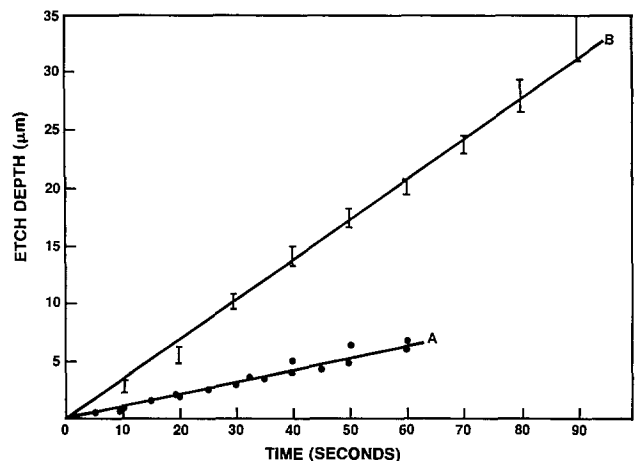


Fig. 8. Bulk etch rates for (A) 36:20:1 and (B) 36:20:2

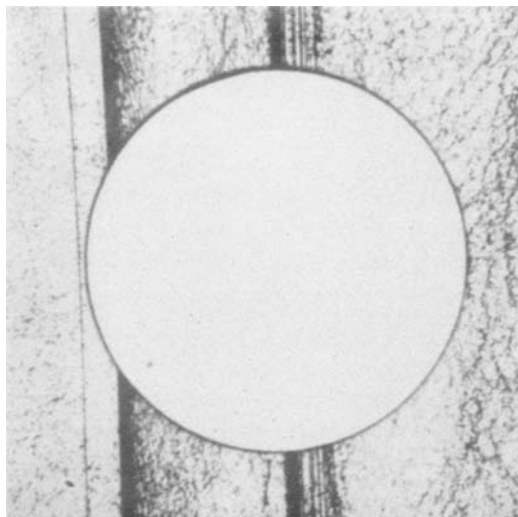


Fig. 9. 50 mil mesa diode formed by Sopori etch, with underlying defect structure. Diode width = 1270 nm.

scribed in this paper. Although etch rates are higher than for other defect etches, we have found that no appreciable degradation of surface quality occurs, and the etch rates are quite controllable. These features of the etch, along with the capability of masking with conventional photoresists, have been used to fabricate mesa devices. The advantage of using this etch is that substrate structure is revealed during mesa etching. This offers a convenient way of correlating device performance with substrate structure. The underlying defect structure of a 1270 mm diam. mesa diode, formed by the 36:15:1 etch, is shown in Fig. 9. Etch rates can be adjusted between the two cases shown in Fig. 8 by further dilution of 36:20:2 by CH_3COOH up to 36:25:2 without affecting the quality of defect delineation.

Alternatively, by cooling the etch (to 10°C), the etching time was increased to 2 min. The cooled etch also improves surface quality and eliminates the formation of any occasional stains. For everyday purposes, the etch (36:20:2) is premixed in the desired quantities (10 to 50 gal) and stored in 1 gal containers for use over a period of up to a few months. The etch is routinely used for defect delineation in a variety of polycrystalline silicon substrates of different grain sizes and grown by different techniques.

Acknowledgments

The author would like to thank Dr. F. Secco and Ms. M. Wright Jenkins for many helpful suggestions regarding this work and for critical reading of the manuscript. I would also like to thank the reviewers for pointing out Ref. 5. Technical help from Tom Nilsson, Marge McClure, and Jan Markham is greatly appreciated.

Manuscript submitted Aug. 17, 1982; revised manuscript received Oct. 5, 1983.

Motorola, Incorporated, assisted in meeting the publication costs of this article.

REFERENCES

1. W. C. Dash, *J. Appl. Phys.*, **27**, 1193 (1956).
2. E. Sirtl and A. Adler, *Z. Metallkd.*, **52**, 529 (1961).
3. D. F. Secco, *This Journal*, **119**, 948 (1972).
4. M. W. Jenkins, *ibid.*, **124**, 757 (1977).
5. D. G. Schimmel, *ibid.*, **123**, 734 (1976).
6. H. Robbins and B. Schwartz, *ibid.*, **107**, 108 (1960).
7. H. Robbins and B. Schwartz, *ibid.*, **108**, 365 (1961).
8. B. L. Sopori, in "Electronic and Optical Properties of Polycrystalline or Impure Semiconductors, and Novel Silicon Growth Methods," K. V. Ravi and B. O'Mara, Editors, p. 66, The Electrochemical Society Proceedings Series, Pennington, NJ (1980).
9. B. L. Sopori, DOE contract AC-01-79ET-23104, Final Report (1980).
10. B. L. Sopori, *J. Appl. Optics*, **20**, 1758 (1981).
11. B. L. Sopori and T. Nilsson, To be published.

Amorphous Silicon Produced by Ion Implantation

Etching Rate in HF Solution and Effect of Annealing

L. Liou and W. G. Spitzer

Departments of Materials Science and Physics, University of Southern California, Los Angeles, California 90089-0241

S. Prussin*

TRW Electronics Systems Group, Redondo Beach, California 90278

This study is an investigation of the effect of the state of amorphous Si on the etching rates in HF acid. Recently, two different metastable amorphous states have been identified for Si (1). Measurements of several different physical properties of amorphous Si produced by high fluence ion implantation have indicated that the as-implanted state, called a-I, is essentially unique in that the properties have nearly the same values for a wide range of implantation parameters (1, 2). The second state, called a-II, is produced by thermal annealing an a-I sample for a short time in the temperature range 400°-600°C. After reaching the a-II state, further annealing does not significantly change any of the measured properties until the material recrystallizes (1-3). The properties which change for a-I → a-II have values in the a-II state which are between those for a-I and crystalline Si.

One of the properties used to characterize the a-I and a-II states was the "dangling bond density" as determined from an ESR measurement (total number of unpaired spins) and the infrared reflection interference spectrum (layer thickness). The dangling bond density was ob-

served to decrease (1, 2) by a factor of about two for a-I → a-II, which suggests that one might observe a difference in chemical behavior for the two states. It is known that crystalline Si is not etched by a 48% HF solution (4, 5) while amorphous Si is etched. However, two different reports place the near-room-temperature rate at about 600 Å/h in one case (6) and 32 Å/h in the other (7). The thermal histories of the amorphous Si in these prior studies is uncertain.

In the present work, two sets of ion-implanted Si samples were used. In one set, the samples were cut from a wafer section having a polished (100) surface which was implanted at room temperature with 5×10^{14} As⁺ ions/cm² having an incident energy of 100 keV. The Si was cut from a p-type ingot having a resistivity between 20 and 40 Ωcm. The second set was taken from another section of the same wafer in which the implantation was done with 5×10^{15} ions/cm² of 200 keV Si⁺ ions. During the implantation, a retaining ring shielded a portion of the wafer section from the implantation beam. In each case, samples were cut so that a small portion of the surface area at one end was nonimplanted material. The thickness of the layer removed in the etching was determined in two

* Electrochemical Society Active Member.

Key words: amorphous, semiconductors, etching, anneal.

ways: (i) infrared reflection as a function of frequency shows interference fringes which can be used to measure the thickness of the amorphous layer before and after etching, and (ii) the step height on the surface, introduced by the etching at the amorphous-crystalline (a-c) interface as measured by a Sloan Dektak Profilometer. The use of infrared reflection measurements to characterize implantation-produced amorphous Si layers has been discussed in detail in the literature (1-3, 8). The infrared measurements indicated that the amorphous layers extended from the top surface to a uniformly deep a-c interface.

The as-implanted samples were all cleaned carefully by washing sequentially in DI water, trichloroethylene, acetone, methanol, and DI water. All containers were similarly cleaned after a preliminary wash with detergent solution. In one case, the sample surface was also cleaned by an oxygen plasma etch which removed $<50\text{\AA}$ of material. In this case, the surface was rinsed in HF to remove residual oxide, and photoemission (XPS) measurements indicated only traces of residual carbon, oxygen, and fluorine on the surface.¹

Three methods were used to etch the samples in 48% HF solution: (i) quiescent (the sample simply immersed in the etchant), (ii) the sample plus etchant in an ultrasonic bath, and (iii) stirring of the etching solution (stirring rod rotating at approximately 200 rpm).

The etching of the a-I material was nonuniform; so, meaningful etching rates cannot be given. This was the result for all samples and all etching techniques. The pre-etching thickness of the a-I layer was determined from the infrared measurements to be $0.128 \pm 0.004\ \mu\text{m}$ for the As⁺-implanted samples, hereafter called group 1, and $0.395 \pm 0.003\ \mu\text{m}$ for the group 2 (Si⁺-implanted samples). An example of the etching of a-I material is given in Fig. 1a, which is a photograph of surface of a group 1 sample after quiescent etching for 3h. The gross nonuniformity is apparent. The Dektak profile shown in Fig. 1b shows substantial portions of the path are close to the crystalline substrate in depth. The plateau regions, where a-I material still remains, indicate a removal rate of $>100\ \text{\AA}/\text{h}$. Since the area of the infrared beam spans the inhomogeneities, the infrared measurements are not meaningful in such a case. Increasing the etching time to 5h results in the a-I material being largely gone, and after 7h, it is

¹ R. P. Vesquez of Jet Propulsion Laboratories performed the plasma etch and made the photoemission measurement.

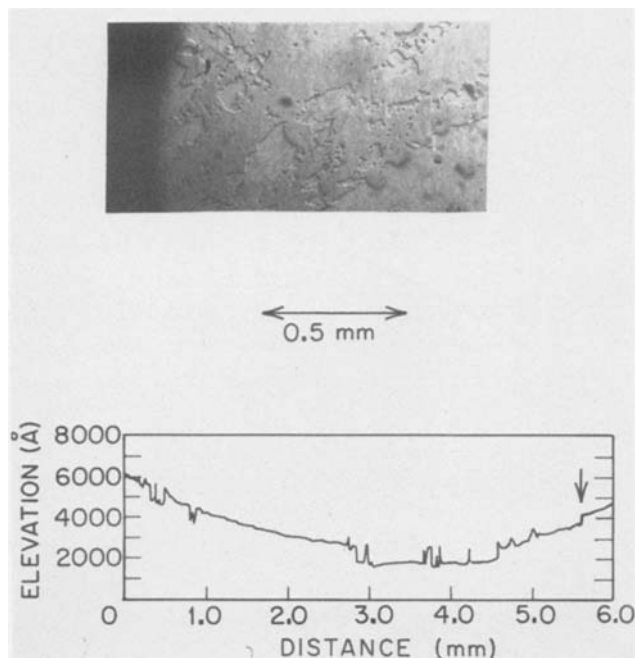


Fig. 1. Top: a (100) Si surface implanted with $100\ \text{keV}$, $5 \times 10^{14}\ \text{As}^+/\text{cm}^2$ ions and in o-l (as-implanted) state after quiescent etching for 3h in 48% HF. Bottom: a Dektak profilometer recording for traverse of a section of a sample similar to that shown at top. Arrow indicates the amorphous and crystalline interface step.

totally removed. The measured step height after 7h is 1240\AA . Since the density change produced by the implantation-induced $c \rightarrow a$ transition results in a $\sim 2\%$ swelling of the amorphous layer (1, 2), the step height anticipated from the initial infrared measurement is $0.98\ (0.128\ \mu\text{m})$ or $0.125 \pm 0.004\ \mu\text{m}$, which is in good agreement with the Dektak result.

The a-II material showed a very different etching behavior than that just described for the a-I material. The a-I \rightarrow a-II transition was produced by annealing several samples from both groups at 400° and 500°C in a quartz tube furnace at diffusion pump vacuum. The infrared reflection spectrum verified that the annealing was sufficient to produce a change in the refractive index of the amorphous layer (1-3); which indicated a-I \rightarrow a-II, i.e., $n(c) = 3.44$, $n(a-I) = 3.84$, and $n(a-II) = 3.70$; all at a frequency of $\nu = 4000\ \text{cm}^{-1}$. The cleaning procedures were the same as those described above. An example of some of the results are shown for two samples in Fig. 2, where one observes uniform etching for as long as 6h and the infrared and Dektak measurements give similar removal rates. The nonuniformity is increasing at the longer times, as indicated by the increasing error bars for the step-height measurements. For still longer etching times, the measurements indicated progressively more inhomogeneous removal, and frequently staining was observed.

The results of all the etching measurements are summarized in Table I. It is worthwhile to make several observations concerning the information in the table.

1. The etching characteristics are completely different for a-I and a-II materials, but appear to be largely inde-

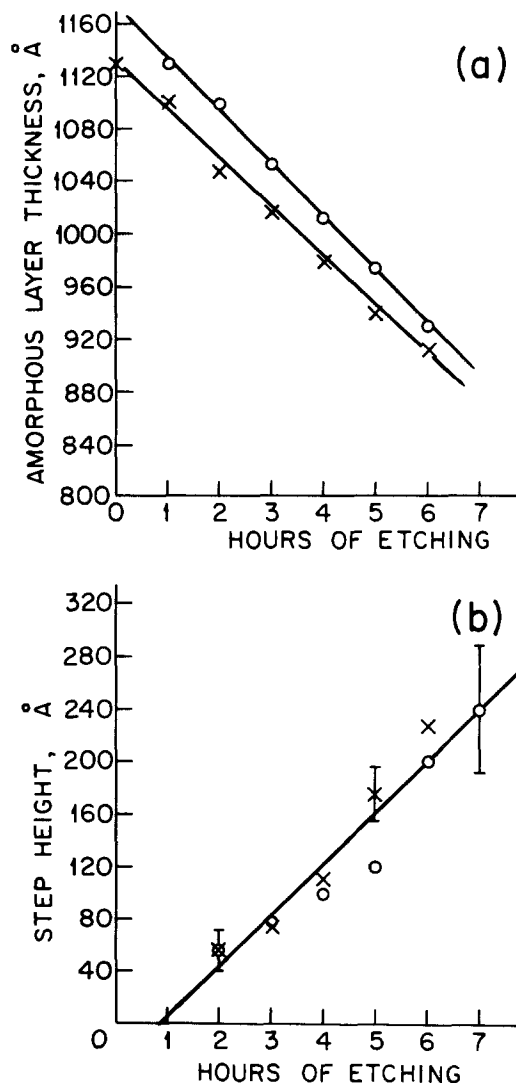


Fig. 2. Quiescent etching results for two group 1 samples (As⁺-implanted) in the a-II state. A, top: Infrared measurements of the a-II layer thickness. o, see Table I, sample 7. x, see Table I, sample 8. B, bottom: Step height measurements for the same samples in Fig. 2a.

Table I. Summary of etching results for a-Si samples

Sample no.	Group	Amorphous Si state	Anneal condition	Etching procedure	Rate (Å/h)	Comments
1	1	a-I	none	quiescent	$\approx 1 \times 10^2$ (sh)	Highly nonuniform. Rate specified is for plateau of a-I material (see text). Surface cleaned by rinsing in HF and methanol, before and after plasma etching. Surface is nonuniform but not as much as sample 1.
2						
3	2	a-I	none	quiescent	$\approx 1 \times 10^2$ (sh)	
4	1	a-I	none	ultrasonic bath	$\approx 1 \times 10^2$ (sh)	Highly nonuniform, rate larger than that for quiescent case.
5						
6	1	a-I	none	stirring	~ 3 to 4×10^2 (sh)	Not so nonuniform as other a-I etching methods but rate not constant in time.
7	1	a-II	400°C/2h	quiescent	41 (ir)* 40 (sh)	Uniform, measurements in 1h intervals for 7h.
8	1	a-II	400°C/2h	quiescent	38 (ir) 40 (sh)	Uniform, measurements in 1h intervals for 7h.
9	1	a-II	400°C/2h	quiescent	40 (sh)	Less uniform than samples 7 and 8.
10	2	a-II	400°C/2h	quiescent	40 (ir)	
11	2	a-II	400°C/2h	quiescent	~ 50 (ir) ~ 60 (sh)	Surface layer etched at a more rapid rate than material at depths $>200\text{Å}$. Same procedure as sample 9, but with initial plasma etch and HF and methanol rinse.
12	2	a-II	400°C/2h	quiescent	36 (ir)	
13	2	a-II	500°C/1h	quiescent	~ 50 (ir) ~ 50 (sh)	Pronounced stain develops after 2h.
14	1	a-II	400°C/1h	ultrasonic bath	~ 70 (sh) ~ 67 (ir)	
15	1	a-II	400°C/2h	ultrasonic bath	~ 70 (sh) ~ 67 (ir)	Uniform, measurements in 1h intervals for 7h.
16	1	a-II	400°C/2h	stirring	~ 80 (ir) ~ 77 (sh)	

*(sh) means step height measured value; (ir) means infrared interference determined value.

pendent of whether the sample is from group 1 (As⁺-implanted) or group 2 (Si⁺-implanted).

2. While the etching of the a-I material is grossly nonuniform, the rates for the plateaus are substantially larger than those observed for the a-II material. This result is qualitatively consistent with the anticipated difference in behavior based on the change observed in the dangling bond density.

3. While there is some spread in the experimental removal rates for the a-II material, there is an indication that the rate is lowest for quiescent and largest for stirring, not an unexpected result. The average value for the quiescent rate is 42.5 Å/h with a standard deviation of ± 8.5 Å/h, while the rate for stirring is almost twice as large. In many cases the surfaces show some staining during the prolonged etching procedures.

4. Comparison with previously reported rates indicates that the 33 Å/h value given by Tsai *et al.* (7) is close to that observed here for a-II material (quiescent). The approximately 600 Å/h value reported by Gerasimko *et al.* (6) would indicate they were etching a-I material, even though they did not indicate the nonuniformity observed here.

Gibbons *et al.* (9) observed that quiescent etching rates can be highly variable, and Tsai *et al.* indicated that surface contamination may be responsible in part for nonuniform etching. If the amorphous layers contain microvoids, a common occurrence in deposited layers, or if the implantation leaves a thin crystalline surface layer, then one may also observe highly variable etch rates. However, it is clear from the above measurements that the state of the amorphous Si also influences the etch rate. Recently, Prussin (11) indicated that dynamic annealing may occur during ion implantation of the specimen if high beam current densities are used and the samples are not in good contact with a heat sink. Our preliminary measurements of the IR reflection spectrum show that when dynamic annealing occurs, the amorphous material still remaining

has a refractive index between those of state a-I and a-II. Therefore, one might expect different etching rates of the ion-implanted material with different cooling arrangements and ion beam currents.

Acknowledgment

Two of the authors (L.L. and W.G.S.) were supported in part by the Joint Services Electronics Program under Contract no. F49620-81-C-0070 monitored by the Air Force Office of Scientific Research.

Manuscript received Sept. 12, 1983.

REFERENCES

- J. E. Fredrickson, C. N. Waddell, W. G. Spitzer, and G. K. Hubler, *Appl. Phys. Lett.*, **40**, 172 (1982); W. G. Spitzer, G. K. Hubler, and T. A. Kennedy, *Nucl. Instrum. Methods*, **209/210**, 309 (1983).
- C. N. Waddell, W. G. Spitzer, J. E. Fredrickson, G. K. Hubler, and T. A. Kennedy, *Submitted to J. Appl. Phys.*
- C. N. Waddell, W. G. Spitzer, G. K. Hubler, and J. E. Fredrickson, *J. Appl. Phys.*, **53**, 5851 (1982).
- D. J. Mazey, R. S. Nelson, and R. S. Barnes, *Philos. Mag.*, **17**, 1145 (1968).
- V. F. Gianola, *J. Appl. Phys.*, **28**, 868 (1957).
- N. N. Gerasimenko, A. V. Drurechemskii, S. I. Romanov, and L. S. Smirnov, *Sov. Phys. Semicond.*, **7**, 1461 (1974).
- M. Y. Tsai and B. G. Streetman, *J. Appl. Phys.*, **50**, 183 (1979).
- G. K. Hubler, C. N. Waddell, W. G. Spitzer, J. E. Fredrickson, S. Prussin, and R. G. Wilson, *ibid.*, **50**, 3294 (1979); G. K. Hubler, R. P. Malmberg, C. N. Waddell, W. G. Spitzer, and J. E. Fredrickson, *Radiat. Eff.*, **60**, 35 (1982).
- J. F. Gibbons, E. O. Hechtel, and Tsurushima, *Appl. Phys. Lett.*, **15**, 117 (1969).
- M. Y. Tsai, B. G. Streetman, R. J. Blattner, and C. A. Evans, Jr., *This Journal*, **126**, 98 (1979).
- S. Prussin, D. I. Margolese, and R. N. Tauber, *J. Appl. Phys.*, **54**, 2316 (1983).

Growth and Physical Properties of LPCVD Polycrystalline Silicon Films

G. Harbeke, L. Krausbauer, E. F. Steigmeier, and A. E. Widmer

Laboratories RCA Limited, Zurich, Switzerland

H. F. Kappert¹ and G. Neugebauer²

Institute of Physics, University of Dortmund, Germany

ABSTRACT

Undoped LPCVD silicon films have been deposited at five temperatures between 560° and 620°C. The films were characterized as grown and after thermal annealing at 900°, 950°, and 1000°C. We used x-ray diffraction, TEM, SEM, Raman and elastic light scattering, optical absorption and reflection, and other techniques in order to obtain information on the grain size, structure, structural perfection, and surface roughness. We found that polysilicon films of good structural perfection, low strain, and small surface roughness are obtained when the films are deposited in the amorphous phase and subsequently crystallized at 900°-1000°C. Such films are superior in all investigated material aspects to films grown in the crystalline phase.

The quality of polycrystalline silicon layers used as MOS gates, load resistors in memory cells, and various other applications in the IC technology is of paramount importance for the device performance. Within the last several years, the technique of low pressure chemical vapor deposition (LPCVD) has become the standard preparation method for polysilicon films in IC manufacturing. A few studies on the structure, morphology, and electrical properties of LPCVD polysilicon films have been reported (1, 2). It was concluded that polycrystalline films formed above 600°C are more stable than the amorphous films deposited at lower temperatures. Amorphous films seemed undesirable because of uncontrolled crystallization in postdeposition heat-treatments. We have reinvestigated this question by a systematic variation of the growth conditions and a comprehensive characterization by x-ray diffraction, electron microscopy, and electrical techniques, and also by several optical methods. The main conclusion from the results presented in this paper is that in contradiction to the previous belief, only films deposited in the amorphous phase and subsequently crystallized have the high quality in terms of structural perfection and surface roughness which is required for critical applications.

Film Deposition and Thermal Annealing

The growth experiments were carried out in a conventional hot wall LPCVD reactor equipped with a 124 mm id quartz tube and a 1 m³min⁻¹ Alcatel double-stage rotary pump. The deposition temperature was measured inside the deposition tube during the film growth. Substrates with a 2 in. diam and placed perpendicularly to the tube axis with a spacing of ¼ in. were used. Sapphire {1102} substrates were chosen for measuring the film thickness. {100} silicon substrates covered with a 300 nm thick thermally grown SiO₂ were chosen for all the electrical, optical, x-ray, and TEM characterization methods, and some quartz substrates were chosen for optical absorption measurements. Films of 0.5 μm thickness were deposited from undiluted silane at temperatures of 560°, 570°, 580°, 600°, and 620°C. Silane gas flow rates from 50 to 200 cm³ min⁻¹ and deposition pressures of 120-350 mtorr were used. The growth rate at 600° and 620°C was limited to 10 nm min⁻¹ by reducing the deposition pressure from 350 to 120 mtorr. The film thickness was measured after growth with a "Dektak" surface profilometer on the films deposited on sapphire substrates. For this purpose, a small window of about 3 × 3 mm was etched in the center of the wafer. The masking was done with Apiezon wax, and the film was etched with an etchant consisting of HF-acetic-HNO₃ with a ratio of 1:1:10 by volume. The growth rate as

a function of deposition temperatures is shown in Fig. 1. The calculated apparent activation energies of 32-39.9 kcal/mol agree well with 32 kcal/mol reported for LPCVD by Gieske and McMullen (3).

After the initial characterization with some of the methods, the Si/SiO₂ substrates were cleaved into four equal parts prior to thermal recrystallization. One part was kept in the as-grown state for further reference while the others were annealed at 900°, 950°, and 1000°C, respectively. The annealing treatments were done in N₂ + 0.5 volume percent (v/o) O₂ for 30 min. The thin SiO₂ film which grows during annealing was not removed before characterization.

X-Ray Diffraction

X-ray diffraction was used to examine the degree of crystallinity and crystallite size and texture of the as-grown and annealed layers. For each layer, the three most intense reflections from the {111}, {220}, and {311} planes were recorded with a Siemens Type F diffractometer (Cu-radiation, 40 kV). The crystallite size was determined from the linewidth (full width at half maximum) by applying the Scherrer formula (4): $D = 0.9\lambda / (B \cos \Theta_B)$ where $\lambda = 1.5405 \text{ \AA}$, Θ_B is the Bragg angle, and B the linewidth corrected for the $K\alpha_1 - K\alpha_2$ line splitting (5) and instrumental broadening (6); the latter had been determined by using an Au standard. Thus, the corrected halfwidth was interpreted as being fully due to a crystallite size effect, neglecting strain influences. The line intensities were corrected for the film thickness and normalized for the strength of the signal expected from a randomly oriented signal (7, 8).

The grain size accuracy and reproducibility expected from this method is about 10-20%. However, with this procedure a single grain size is determined from each diffraction line while in reality there is a wide distribution of grain sizes present (see TEM measurements). Nevertheless, one obtains from x-rays an order of magnitude grain size and relative trends for the polysilicon layers.

The layer properties deduced from the x-ray measurements are given in Table I and Fig. 2. The layers deposited at 560° and 570°C are x-ray amorphous (no line intensities); note the fact, however, that a few small crystallites are observed by TEM (see next section). Layers deposited at 580°C are partly amorphous/partly crystalline as deduced from low line intensities. The high temperature layers appear to be fully crystalline (since for these layers the line intensities do not increase any more with annealing). After annealing ($T_a = 900^\circ\text{-}1000^\circ\text{C}$), all layers are fully polycrystalline.

The grain sizes of the as-grown layers range between 100 and 770 Å and differ because they were obtained from different diffraction lines. A <311> preferred orientation (texture) is found for as-grown layers deposited at 580° and 600°C, while a strong <110> texture is exhibited by the 620°C layers. In the 620°C films, a very pronounced

¹Present address: Klinikum, University of Freiburg, Germany.

²Present address: Fachbereich Physik, University of Essen, Germany.

Key words: semiconductor, films, CVD.

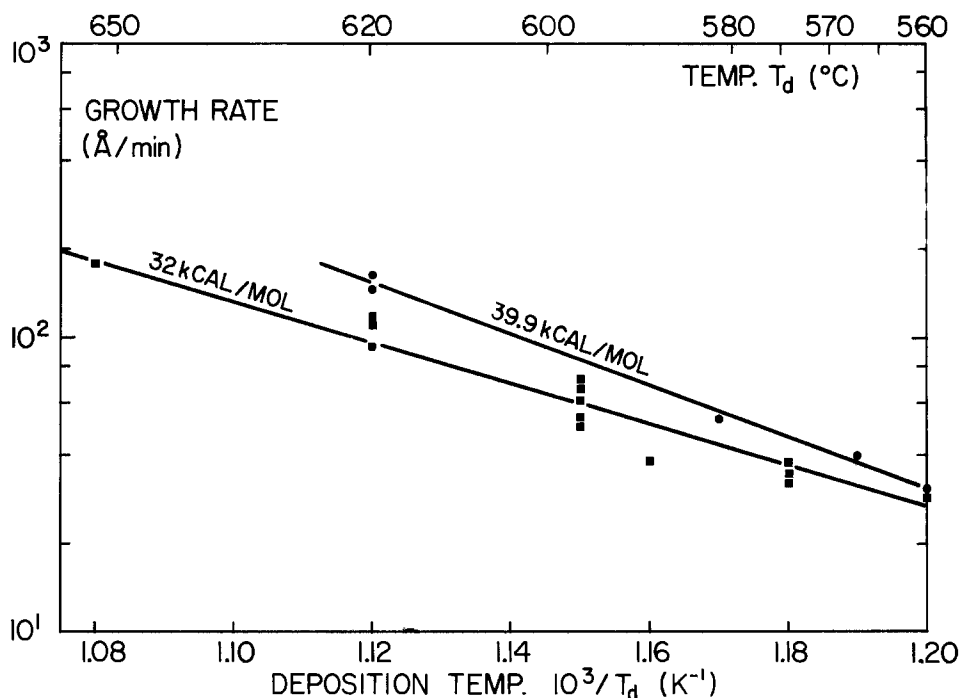


Fig. 1. Growth rate as a function of deposition temperature T_d for two different deposition conditions. ● 350 torr, $\text{SiH}_4 = 200 \text{ cm}^3 \text{ min}^{-1}$. ■ 120 torr, $\text{SiH}_4 = 50 \text{ cm}^3 \text{ min}^{-1}$.

columnar structure was observed by cross-sectional TEM (9) and the grain dimension D_{220} is by far the largest. A columnar structure similar to our 620°C layers has been reported by Falckenberg *et al.* (10) for poly-Si films deposited by LPCVD at 625°C.

Grain growth seems to take place in a different way when the layers are deposited in the amorphous phase and annealed at 900°-1000°C. It appears that nucleation takes place in randomly oriented grains, but the largest grain dimensions and texture develop in <111> direction. This trend overcomes the original weak <311> texture in the layers deposited at 580°C so that <111> texture becomes dominant by annealing. The structure and morphology of the originally polycrystalline layers is preserved during annealing except for a slight grain growth.

We conclude from the x-ray diffraction that the crystallization of amorphous layers does not lead to unreproducible structures (1). Texture and grain size are remarkably reproducible in the entire deposition temperature range from 560° to 580°C. The average grain size is somewhat larger than in originally polycrystalline films but still small compared to present design rule dimensions and even future submicron scales.

Transmission Electron Microscopy

For TEM investigations, the following sample preparation was performed: a 3 mm diam disk was cut out of the original wafer by ultrasonic techniques. An angle lap of

Table I. Texture and grain size

T_d (°C)	D_{111} (Å)	D_{220} (Å)	D_{311} (Å)	Texture
As-grown				
560	X-ray amorphous			—
570	X-ray amorphous			—
580	770	290	240	Weak <311>
600	110	340	180	<311>
620	140	770	180	<110>
Annealed at 1000°C				
560	870	530	390	<111>
570	890	640	510	<111>
580	910	570	530	<111>
600	180	490	310	<311>
620	190	750	380	<110>

D_{hkl} = grain size evaluated from the x-ray diffraction line (hkl) according to the Scherrer formula (see text).

about 1° was performed at the surface of this disk, the sample was then thinned by ion etching (HF-HNO_3) starting from the substrate side. The oxide layer was removed by a 1 min etch in HF and finally the poly layer jet-etched until a small hole occurred. This preparation technique permits an examination of the polysilicon layers at various depths. The samples were investigated by bright and dark field techniques and by selected area electron diffraction.

The TEM results for as-grown layers show that the low temperature layers all are found to be partly crystalline (differing partly from x-ray and Raman results due to the testing method) while the high temperature group is fully crystalline (11). The average crystallite size \bar{S} and size distribution was determined by measuring 30-100 crystallites

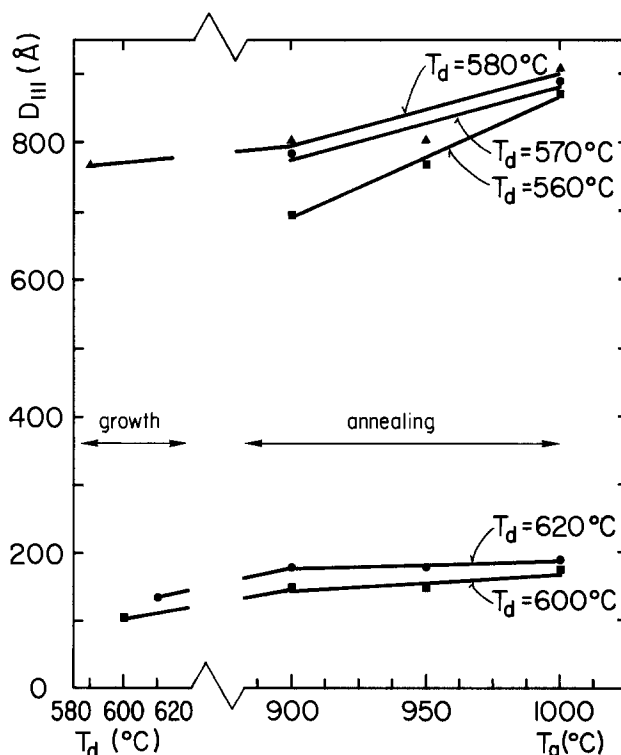


Fig. 2. X-ray grain size D_{111} as a function of annealing temperature T_a for various deposition temperatures T_d .

from the bright and dark field micrographs (Fig. 3a, b) for relative large grains and from the diffraction micrographs (Fig. 3c) for small particles. The average crystallite size \bar{S} increases approximately linearly with T_d (see Fig. 4) from 50 to 300Å, (neglecting large irregularly shaped crystallites at the 580°C layer surface).

However, there is a wide distribution of grain sizes present in all layers. This is illustrated in Fig. 5, where the distribution of the grain sizes is plotted for a 620°C layer. Many grains are smaller or larger than \bar{S} . Slightly different grain size distributions are found at the substrate-layer interface (I) and at the layer surface (S), indicating a higher crystalline volume fraction at the substrate-layer interface for the 560° and 570°C layers (11).

Annealed layers were studied by TEM exclusively for 1000°C annealing, since x-ray had shown little annealing temperature dependence. The low temperature layers, after annealing, exhibit grain sizes \bar{S} around 800Å while the high temperature layers group around 300Å (Fig. 4). Annealing thus has a large effect on the crystallite size of the low temperature group which is to be expected since these layers are mainly amorphous in the as-grown state. The grain size of the high temperature group, however, increased very little, since the original deposition in crystalline form imposes some constraints on further grain growth. These results, in general, compare well with x-ray and in particular with the grouping for the D_{111} values (see Fig. 2). As already pointed out, the agreement between x-ray and TEM average crystallite size determination is quite satisfactory (11). It should be noted, however, that our TEM technique yields only grain dimensions in the plane of the film. Cross-sectional TEM work (9) has shown that, e.g., our $T_d = 620^\circ\text{C}$ films have a pronounced

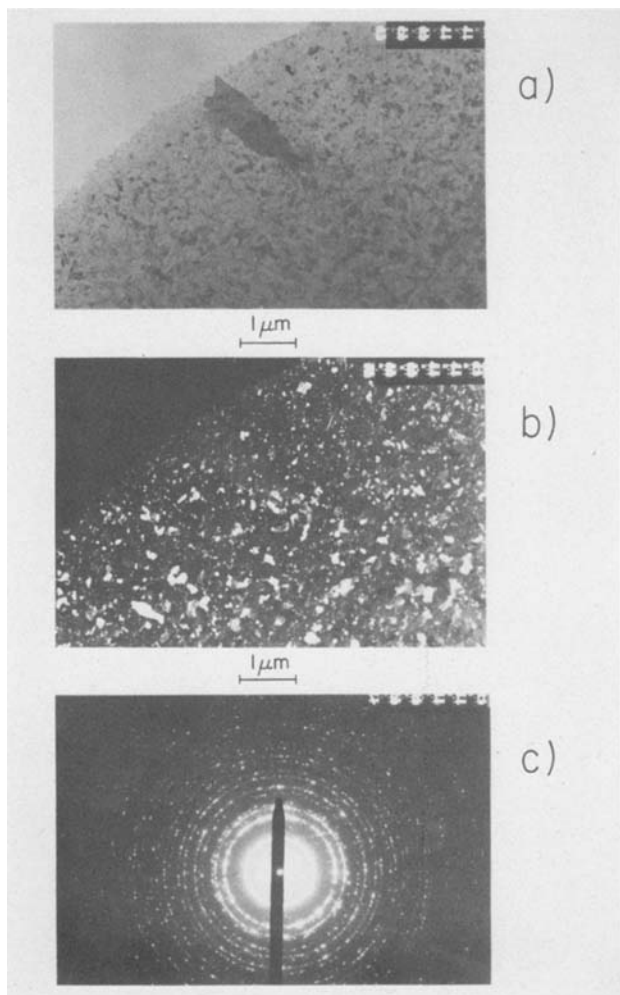


Fig. 3. Bright field (a, top), dark field (b, middle), and selected area diffraction (c, bottom) micrographs for an LPCVD layer deposited at $T_d = 560^\circ\text{C}$ and annealed at $T_a = 1000^\circ\text{C}$, taken at the SiO_2 -Si interface.

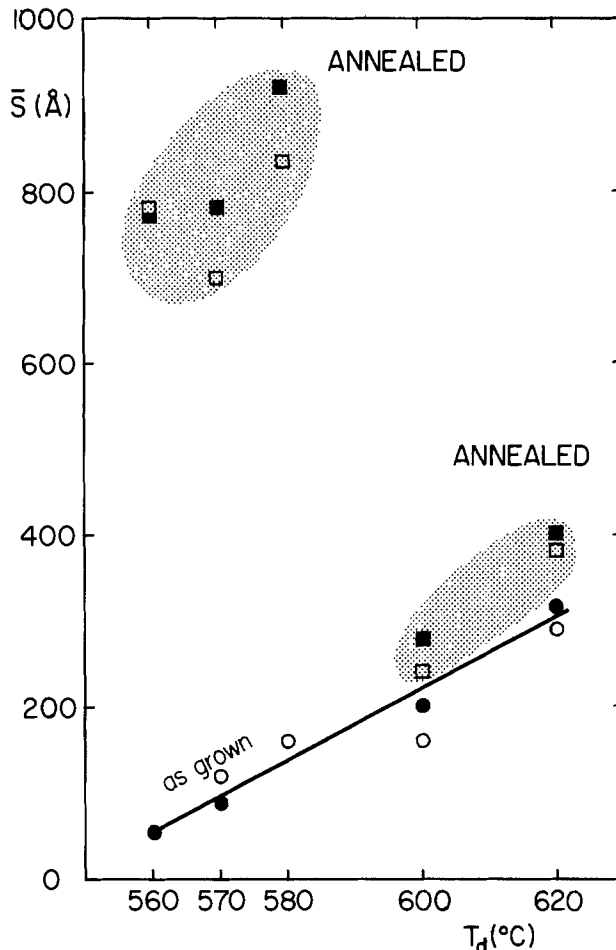


Fig. 4. Average crystallite size \bar{S} for LPCVD Si-layers, as-grown (\circ : interface, \bullet surface) and annealed at 1000°C (\square : interface, \blacksquare surface) as a function of T_d .

columnar structure such that many grains extend vertically through the entire film.

The grain size distribution of annealed $T_d = 620^\circ\text{C}$ layers is shown in Fig. 5 (note that there is a very small probability for sizes larger than 700Å). It can be seen from Fig. 6 that the annealed low T_d layers, in particular those grown at 560° and 570°C, show a smooth grain size distribution. The distribution is shifted to larger sizes as compared to $T_d = 620^\circ\text{C}$ (Fig. 5) but there are very few grains of a few thousand angstroms in diameter. So the TEM results show in even greater detail than x-ray diffraction that the crystallization of amorphous layers yields a well-defined morphology.

Brown *et al.* (1, 2, 7) have reported on the structure of LPCVD films grown at $T_d \geq 525^\circ\text{C}$ on silicon wafers covered with 1000Å of thermally grown oxide. Their results agree with ours in the sense that polycrystalline films are formed for $T_d \geq 600^\circ\text{C}$. However, average crystallite sizes determined by these authors using TEM were 550-870Å for as-grown layers, nearly three times our values. This may be due to the detailed deposition conditions which, as mentioned elsewhere in this paper, play an important role in this transition temperature region (600°-620°C). For annealed layers, no grain sizes were quoted by Brown *et al.* In terms of texture, the $\langle 110 \rangle$ texture for high temperature as-grown and annealed layers is confirmed by us, while there is a difference for annealed 580°C layers for which Kamins *et al.* find $\langle 311 \rangle$ while we find $\langle 111 \rangle$ texture. Moreover, we have to emphasize again that originally amorphous films can be thermally converted into reproducible stable polycrystalline structures.

Light Scattering

Raman scattering.—Raman scattering can provide the following useful information on the films in the as-grown and annealed state:

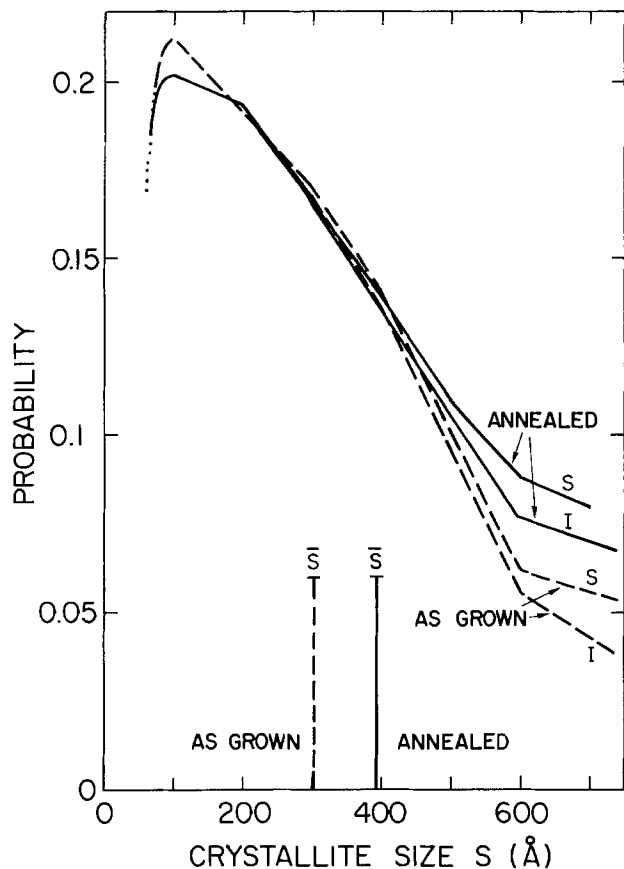


Fig. 5. Grain size distribution for an LPCVD layer, deposited at $T_d = 620^\circ\text{C}$, as-grown and annealed at 1000°C . I = interface, S = surface.

1. From the frequency of the line, the degree of crystallization (amorphous, crystalline, or mixed) can be determined in a short time. This makes use of the fact

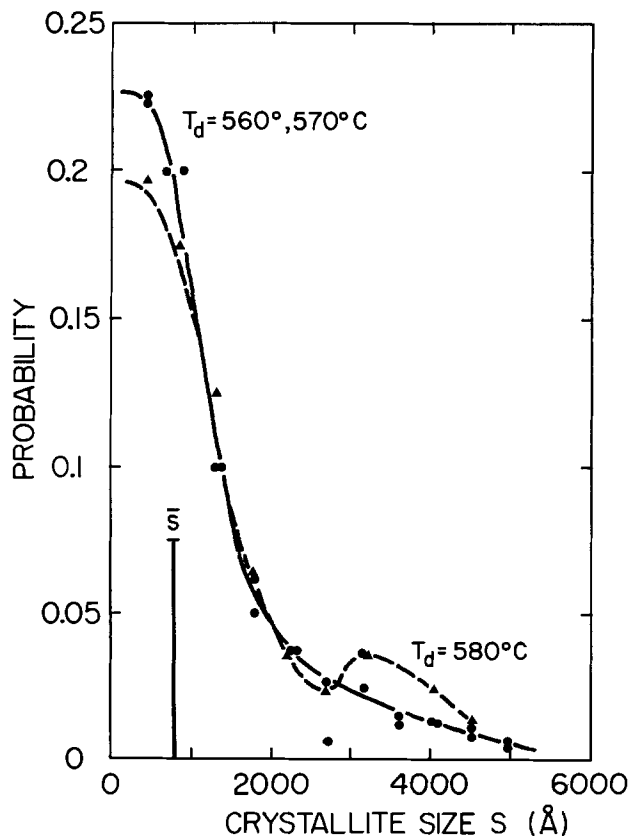


Fig. 6. Grain size distribution for low T_d LPCVD Si layers annealed at 1000°C . (\bullet) $T_d = 560^\circ, 570^\circ\text{C}$; (\blacktriangle) $T_d = 580^\circ\text{C}$.

that in crystalline silicon the lattice vibration line is observed as a sharp line at 522 cm^{-1} as seen, e.g., in Fig. 7 (top), while in the amorphous state the breakdown of lattice periodicity relaxes the symmetry restrictions and permits scattering from all vibrational modes resulting in a broad line centered at 483 cm^{-1} , as seen, e.g., in Fig. 7 (bottom). Intermediate states between the two forms (i.e., partly crystalline, partly amorphous) are easily recognizable as a superposition as found, e.g., in Fig. 7 (center). One should note that the terms Raman, x-ray, and TEM amorphous are not equivalent due to a different response by the different techniques.

2. From the intensity of the Raman line, after annealing, the crystalline perfection can be judged.
3. From the Raman line shape (or width), after annealing, one can determine the amount of lattice perturbation and internal strain remaining in the layers.

We have made use of the standard Raman scattering technique (12), with a 100 mW laser light of 5145Å focused to a spot of $50\text{ }\mu\text{m} \times 2\text{ mm}$ on the film. We have verified that these conditions are sufficient for avoiding thermal crystallization by the beam. The scattered light is dispersed in a double monochromator and detected by photon counting. Using a fast scanning technique with suitable averaging can provide the results in a few minutes. The light penetration depth amounts to the reciprocal absorption coefficient which is discussed in the next chapter.

The results are presented in Fig. 8 for as-grown and annealed films vs. deposition temperature. For convenience, we have plotted the maximum Raman intensity; any intensity above the 20-25 counts/s amorphous maximum intensity is therefore due to the crystalline contributions. The predominant crystallization state (amorphous, crystalline) is denoted by the appropriate symbol. The as-grown low temperature group ($T_d \leq 580^\circ\text{C}$) is found to be completely Raman amorphous, while the high temperature group ($T_d \geq 600^\circ\text{C}$) is observed to be partly to fully crystalline with a more or less strong amorphous tail in the spectrum. Upon an-

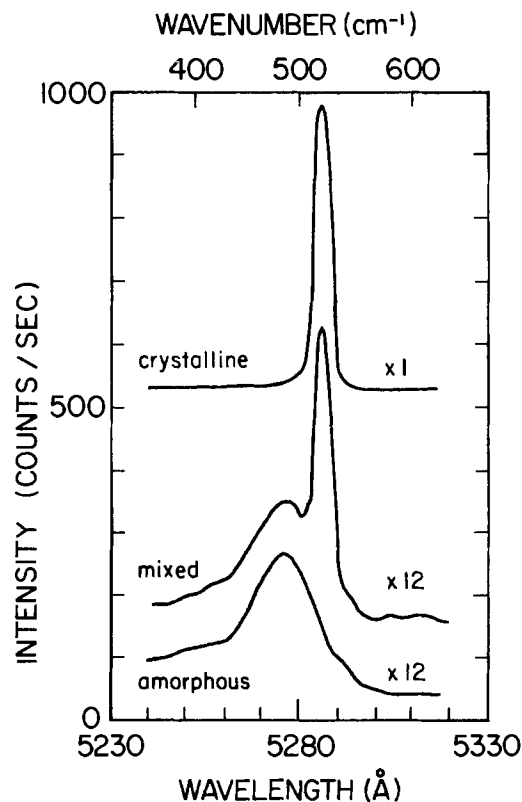


Fig. 7. (Bottom) Raman spectrum of amorphous layer, as deposited at 570°C . (Middle) mixed amorphous-crystalline layer deposited at $590^\circ\text{--}600^\circ\text{C}$. (Top) crystalline layer, deposited at 570°C with subsequent annealing at 900°C .

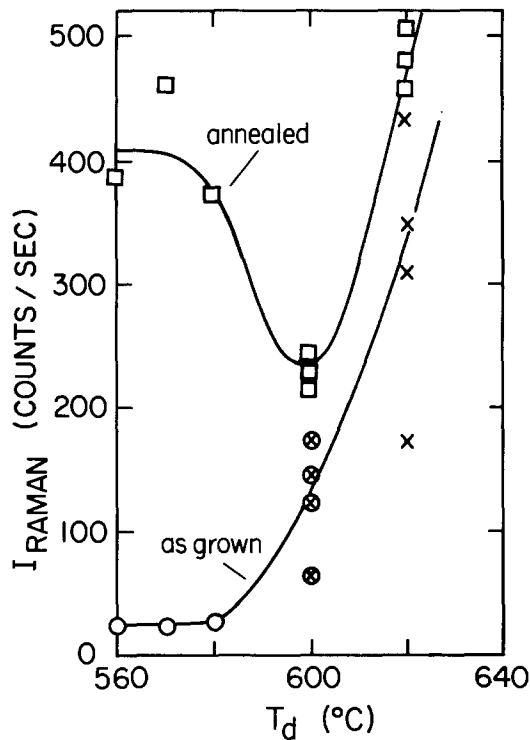


Fig. 8. Raman peak intensity for as-grown and annealed layers vs. deposition temperature. \circ = amorphous; \times , \square = crystalline, \otimes = mixed.

nealing, we find no particular dependence on temperature within the range 900°-1000°C. However, of interest is the very strong dip observed in the annealed curve of Fig. 8 for $T_d = 600^\circ\text{C}$ for which the strongly deposition temperature-dependent texture of the crystalline grains might be responsible (see under x-ray).

Some more subtle differences between the low ($T_d \leq 580^\circ\text{C}$) and the high ($T_d \geq 600^\circ\text{C}$) group layers can be found by studying the Raman line shape of annealed films. Preliminary results on this have been reported (11) and are considered to be of importance for device applications. It is found [see Fig. 2 of Ref. (11)] that the Raman line of the low temperature grown polysilicon films quite closely resembles the Raman line of bulk single-crystal silicon while the high temperature grown films exhibit a strong line shape distortion, evident mostly as a low frequency tail. This tail, when integrated, exceeds the bulk silicon integrated intensity by as much as 26%. In a different manner, this can be seen in Fig. 9 where the full Raman linewidth at one-tenth peak height is plotted vs. deposition temperature. The difference between the low and the high temperature group films is indeed very striking. An interpretation of this behavior can easily be given, and is in line with the other findings by light scattering (*i.e.*, elastic scattering to be discussed below). Any contributions to Raman scattering in silicon from modes of lower frequency than the first-order Raman line are possible only if the lattice periodicity of the material is seriously disturbed (of which the limit would be a fully noncrystalline structure). Thus, as judging from Fig. 9 [or Fig. 2 of Ref. (11)], there is little or no disturbance for the annealed low temperature group films which can be considered to be excellent. On the contrary, the high temperature group layers ($T_d \geq 600^\circ\text{C}$) after annealing remain in a highly disturbed state of partly well and partly (maybe up to 26 v/o) poorly crystallized material. It is the latter which is highly undesirable for some device applications since it is internally highly strained (dislocations, stacking faults, *etc.*), and this can produce unwanted defects in an active device area.

Elastic scattering.—The technique of elastic light scattering can be used to determine the structural perfection of polysilicon layers. Every material exhibits an intrinsic elastic scattering which is given by temperature or en-

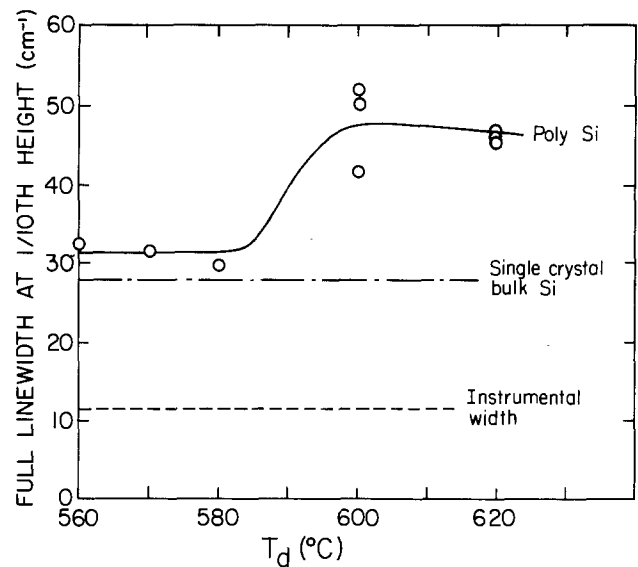


Fig. 9. Raman linewidth of annealed layers (900°-1000°C) vs. deposition temperature. The low temperature group is close to bulk single crystal while the high temperature group exhibits large linewidth distortions.

trophy fluctuations. In addition, extrinsic elastic scattering is produced by all kinds of structural imperfections of the bulk such as mosaic misorientation, twinning, strain, grain boundaries, stacking faults, dislocations (in general all effects resulting in changes in refractive index), as well as local defects. In terms of surface to volume, the elastic scattering can in principle originate (*i*) from the surface roughness, and (*ii*) from the volume structural imperfection to within the light penetration depth (see section on Raman scattering) in the layer.

For cases where the surface is not exceedingly poor, we have found that the second source dominates since the surface represents only a small portion of the scattering volume. We have, *e.g.*, been able to show (13) that the elastic light scattering on SOS (silicon on sapphire) wafers is strongly correlated with UV reflectivity which again has been shown to be correlated (14) with the twinning density and the SOS device yield.

Elastic light scattering measurements on polysilicon layers were performed by means of two methods: the spectrometer and the scanner for dust and defect detection (15) used in the quality control mode (13). In the former, the same arrangement and the same power and spot size was used, as given above for Raman scattering, except for an additional 10^6 - 10^8 attenuation filter inserted in front of the photomultiplier; the scattered elastic intensity is then recorded for the various wafers. In the latter, by using the laser scanner in the quality control mode, laser light is falling onto the spinning wafer while being translated. The scattered elastic light originating from the bulk (*i.e.*, not from dust or individual defects) is used as a measure for the crystalline perfection. Both methods correlate extremely well.

The elastic scattering results from the spectrometer method for as-grown and annealed layers have been published previously (11). As grown, the elastic light scattering intensity of the low temperature group is very low, in fact it is found to be very close to good single-crystal silicon, and it remains that way upon annealing. Therefore, this material is of very good structural perfection. In contrast, the high temperature group exhibits a very high elastic scattering intensity. Also, the variations (scatter of the data) within the high temperature group are considerable, due to the transition regime. This additional scattering observed for the high temperature group must be interpreted as extrinsic in nature, and caused by the very large volume portions of imperfect and poorly crystallized material in this group, as described above, in connection with the linewidth in the Raman scattering section.

A correlation of these elastic scattering results with Raman scattering is presented in Fig. 10 for as-grown

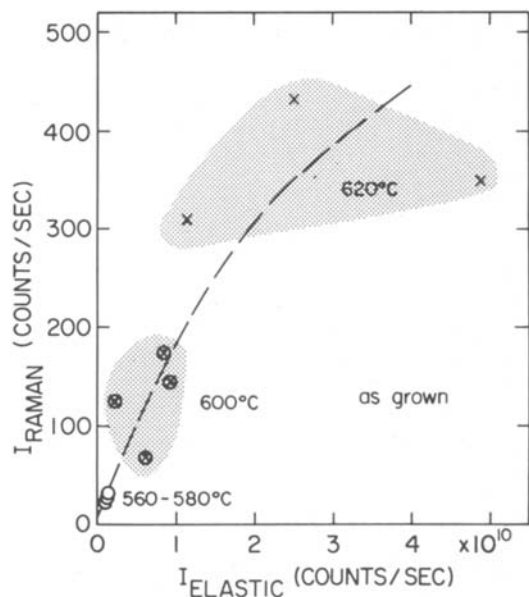


Fig. 10. Correlation between Raman and elastic intensity for different deposition temperatures, as grown. \circ = amorphous, \times = crystalline, and \otimes = mixed.

layers, from where it is seen that these data correlate quite well in the sense that low temperature amorphous grown films are of high structural perfection while high temperature crystalline films are of rather poor structural perfection. It should be mentioned here that the results of the scanner method, which will be published elsewhere (13), are in full agreement with these findings. In fact, this second method, which is very convenient, lends itself to a rapid characterization (in a matter of seconds) of as-grown material in terms of quality.

Optical Absorption and Refractive Index

Optical absorption.—The optical absorption coefficient has been measured in order to determine the light scattering volume involved in Raman and elastic scattering. For convenience, we have grown polysilicon layers on quartz glass substrates concurrent with the layers grown on silicon/silicon oxide substrates. They have been used to determine the absorption coefficient, as-grown and annealed, from the transmitted and reflected laser intensities at 5145 and 4416Å.

The resulting absorption coefficient is given in Fig. 11 for 4416Å vs. the layer deposition temperatures. It is seen that the absorption coefficient of the low temperature group ($T_d \leq 580^\circ\text{C}$) after annealing at 900°C is very close to the absorption coefficient of single-crystal bulk silicon (16). This provides further support for the findings of Raman scattering intensity, in particular linewidth (see above), and of elastic intensity (see above) that the low temperature growth provides material which after annealing closely resembles the single-crystal silicon material properties. The absorption coefficient of the high temperature group ($T_d \geq 600^\circ\text{C}$), on the other hand, is very different from the single-crystal absorption coefficient (Fig. 11) This can easily be understood in terms of the large distorted volume portion discussed in the context of light scattering. The distorted regions of structural imperfection in the high temperature group give rise to a great deal of internal scattering which seemingly reduces the transmitted light and thus increases the apparent absorption coefficient.

Refractive index.—The refractive index is important for routine thickness measurements with the optical thickness monitor described by Sandercock (17). The effective refractive index was measured as a function of the film deposition temperature by relating the optical thickness t_{opt} for $n = 1$ as measured with the optical monitor to the thickness reading with the "Dektak" surface profilometer t_{eff} , according to $n_{eff} = t_{opt}/t_{eff}$. The results in Fig. 12 show two distinct regions with $n_{eff} \approx 3.9 - 4$ for amorphous material deposited at $T_d \leq 580^\circ\text{C}$ and a transition region

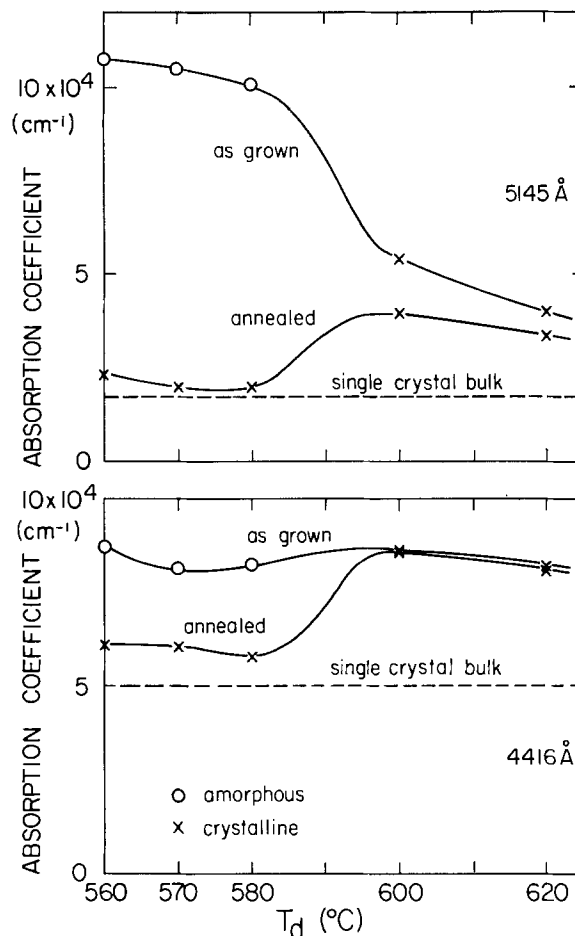


Fig. 11. Absorption coefficient of polysilicon vs. deposition temperature, as-grown and annealed (900°C - 1000°C), at 5145Å (top) as pertinent for Raman and elastic using spectrometer method and at 4416Å (bottom) as pertinent for scanner method.

for $T_d > 580^\circ\text{C}$ where the material is deposited with a mixed amorphous/crystalline structure. The anomalous data points around $n \approx 3.23$ (denoted by *) appear to be the result of excessive surface roughness at this deposition temperature. The error originates from the surface profilometer reading as the stylus cannot follow the full

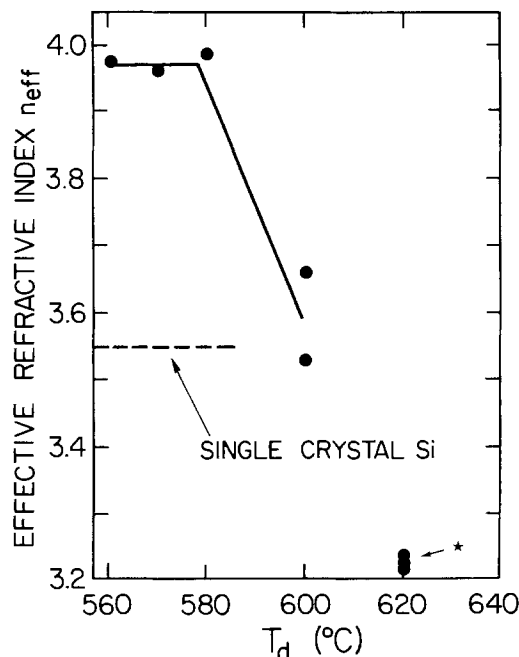


Fig. 12. Effective refractive index n_{eff} for measurements with the thickness monitor as a function of T_d . * See text.

depth contour of the microscopic surface roughness in contrast to the optical thickness monitor. This was independently confirmed by evaluating a 5400Å thick SiO₂ film with a 1600Å thick deep grating on the surface. It is obvious that the large change in refractive index can be used to get rapid information on whether the deposited material is amorphous or polycrystalline.

Surface Roughness

A slightly rough surface is one in which the surface irregularities are small but not negligible compared to the wavelength of the incident radiation. It has been shown (18) that the optical properties of such a surface are determined by two statistical functions, *i.e.*, the probability distribution of height $D(z)$ and the autocorrelation function $A(s)$ connecting two points on the surface. Because of the continuity of the surface, both functions are mutually dependent. They are characterized by the root mean square (rms) roughness σ defined by $\sigma^2 = \langle z^2 \rangle$ relative to the mean surface level, $z = 0$, and by the correlation length, a , respectively. If $D(z)$ is assumed to be a Gaussian distribution function, the peak to peak surface roughness σ_{pp} is in first approximation given by $\sigma_{pp} = 2 \cdot \sqrt{2} \sigma$.

We determined the surface roughness σ of as-grown and annealed films using a technique developed by Cunningham and Braundmeier (19). A silver layer of 700-1000Å thickness is evaporated onto the silicon surface and then the reflectance of the silvered surface is measured in the wavelength region of surface plasmon excitation, *i.e.*, $\lambda = 3500\text{Å}$. Normally, incident light couples to surface plasmons only through surface irregularities such that the loss of reflectance ΔR , compared to that of a smooth silver surface, is a direct measure of σ . Quantitative σ values are based on a correlation between ΔR and σ values obtained by an interferometric method (19).

We found [see Ref. (11)] σ values of less than 15Å for films in the amorphous phase, *i.e.*, at $T_d \leq 580^\circ\text{C}$. Deposition at 620°C yields reproducible values between 50 and 60Å whereas $T_d = 600^\circ\text{C}$ occasionally gives a smooth surface when other runs produce rough films. Similar results have been obtained by Aspnes *et al.* (20) using ellipsometry to characterize the surface quality of LPCVD films deposited at 575° , 740° and 870°C . σ values in excess of 100Å have been reported for deposition temperatures of 880° - 980°C (21).

It is very remarkable that our σ values are not changed by the annealing treatment at 900° - 1000°C (11). The main conclusion to be drawn here is that the surface roughness is not parallel to the average grain size (see Table I). The annealed low temperature films have an average grain size of about 800Å and $\sigma < 15\text{Å}$ whereas the annealed high temperature films have average grain sizes of 200-400Å and $50\text{Å} < \sigma < 60\text{Å}$. This important fact results from the growth history. If the films are grown in the amorphous state, their surface is smooth, and this smoothness is preserved during recrystallization. The crystallites which are formed in this process do not "stick out" from the surface. It seems possible that a crystallization near the surface leads to a distribution and arrangement of grains such that they can be accommodated within the given contour. If, on the other hand, the films grow in the crystalline state, the surface structure results from the shapes of individual grains which can grow fairly uninhibited. Differences within the group of high temperature films may be due to the different type of texture occurring from $T_d = 600^\circ$ or 620°C . It is obvious that for all those critical applications which rely on an extremely smooth polysilicon surface, one has to avoid growth temperatures of 600°C or higher. In terms of surface roughness, they are either irreproducible (600°C) or unacceptable (620°C).

It was also shown that rapid characterization of the surface roughness is possible by measuring the reflectance of the untreated surface at two fixed wavelengths ($\lambda = 280$ and 400 nm). This technique has been used before to measure the near-surface crystallinity of silicon on sapphire (14). Results obtained on the as-grown and annealed silicon films have been published elsewhere (22).

TEM micrographs of surface replica of the polysilicon films have been taken. Shadowing techniques have been used for evaporation of a 10-20Å thick Pt film under 45°

incidence. Figure 12a shows that a film grown at 570°C and annealed at 1000°C has a lateral structure with a typical dimension of about 200Å but a peak to peak surface roughness σ_{pp} smaller than 50Å. The film grown at 620°C in Fig. 13b has a typical lateral dimension from peak to peak or valley to valley corresponding to the correlation length a of the order of 1000Å. The value for σ_{pp} , deduced from the width of the shadow contours visible in Fig. 13b, is about 200-300Å. Keeping in mind that σ_{pp} is a few times σ_{rms} , these values are in good agreement with the roughness values deduced from the optical measurements.

SEM micrographs have been taken directly of the uncoated surface in order to make sure that no artifacts are introduced by the metallization applied in either of the other two techniques. Indeed, the same lateral dimensions have been found as in TEM. Also, when the samples are tilted, the pronounced differences in the surface height distribution between the low temperature group and the high temperature group become clearly visible. It is also worth noting that in the TEM and SEM studies, no increase of the surface roughness by annealing was observed. In conclusion, electron microscopy confirms the optical roughness values and, in addition, gives insight into the lateral structure.

Conclusions

In this detailed investigation, we have shown that the properties and device quality of polysilicon films depend most sensitively on the deposition temperature and, hence, on the structure in the as-grown state. If polysilicon films of high structural perfection, low strain, and small surface roughness are required, then the deposition temperature should not exceed 580°C .

The reason for the high quality of such films seems to lie in the fact that they condense in the amorphous structure. This type of structure leads to a better grain formation in subsequent annealing processes as compared to direct deposition in the crystalline structure. In the postcrystallized, originally amorphous, films, we observe less strain and higher perfection than in growth-crystallized films. Also, the original small surface roughness of less than 20Å (root mean square value) is preserved in the crystallization process although a grain size distribution with an average size of about 800Å develops.

The growth rate increases with increasing temperature and is higher than 50 Å/min at 580°C . Somewhat higher

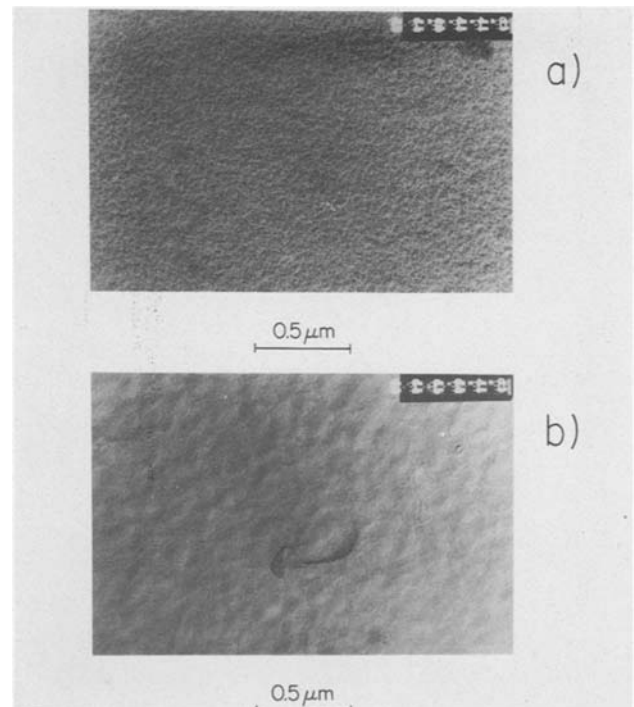


Fig. 13. TEM micrographs of shadowed surface replica of polysilicon films annealed at 1000°C . (a, top) $T_d = 570^\circ\text{C}$; and (b, bottom) $T_d = 620^\circ\text{C}$.

growth rates can be obtained at $T_d \geq 600^\circ\text{C}$ but only at the cost of lower structural and surface perfection.

The results of our investigation on *in situ* phosphorus-doped LPCVD polysilicon films will be described in a forthcoming publication (23).

Acknowledgments

We thank H. Auderset, H. Fehlmann, and E. Meier for their important contributions to this work. We are also indebted to M. Duffy and R. Smith for helpful discussions and close collaboration.

Manuscript submitted Jan. 31, 1983; revised manuscript received June 30, 1983. This was Paper 415 presented at the San Francisco, California, Meeting of the Society, May 8-13, 1983.

Laboratories RCA Limited assisted in meeting the publication costs of this article.

REFERENCES

- W. A. Brown and T. I. Kamins, *Solid State Technol.*, **22**, 51 (July 1979).
- T. I. Kamins, *This Journal*, **127**, 686 (1980).
- R. J. Gieske and J. J. McMullen, in "Chemical Vapor Deposition," L. F. Donaghey, P. Rai-Choudhury, and R. N. Tauber, Editors, p. 183, The Electrochemical Society Softbound Proceedings Series, Princeton, NJ (1977).
- B. D. Cullity, "Elements of X-ray Diffraction," p. 99, Addison-Wesley, Reading, MA (1967).
- R. Brill, *Z. Kristallogr.*, **68**, 387 (1928).
- L. V. Azaroff, "Elements of X-ray Crystallography," p. 556, McGraw-Hill, New York (1968); B. E. Warren, "X-ray Diffraction," p. 257, Addison-Wesley, Reading, MA (1969).
- T. I. Kamins, M. Mandurah, and K. C. Saraswat, *This Journal*, **125**, 927 (1978).
- J. V. Smith, Editor, X-ray Powder Data File Card 5-0565, American Society for Testing and Materials, Philadelphia (1960).
- J. T. McGinn, Abstract 414, p. 647, The Electrochemical Society Extended Abstracts, Vol. 83-1, San Francisco, CA, May 8-13, 1983.
- R. Falckenberg, E. Doering, and H. Oppolzer, Abstract 570, p. 1429, The Electrochemical Society Extended Abstracts, Vol. 79-2, Los Angeles, CA, Oct. 14-19, 1979.
- G. Harbeke, L. Krausbauer, E. F. Steigmeier, A. E. Widmer, H. F. Kappert, and G. Neugebauer, *Appl. Phys. Lett.*, **42**, 249 (1983).
- G. Harbeke and E. F. Steigmeier, *RCA Engineer*, **15**, 82 (1970).
- E. F. Steigmeier and H. Auderset, *This Journal*, To be published.
- M. T. Duffy, J. F. Corboy, G. W. Cullen, R. T. Smith, R. A. Soltis, G. Harbeke, J. R. Sandercock, and M. Blumenfeld, *J. Cryst. Growth*, **58**, 10 (1982).
- E. F. Steigmeier and H. Auderset, *RCA Rev.*, **44**, 5 (1983).
- Landolt-Börnstein, in "Numerical Data and Functional Relationships in Science and Technology," Group III, Vol. 17a, p. 387, Springer (1982); R. Hulthén, *Phys. Scr.*, **12**, 342, Berlin (1975).
- J. R. Sandercock, *J. Phys. E*, **16**, 866 (Sept. 1983).
- H. Davies, *Proc. Inst. Elec. Eng. Part 4*, **101**, 209 (1954).
- L. J. Cunningham and A. J. Braundmeier, Jr., *Phys. Rev. B*, **14**, 479 (1976).
- D. E. Aspnes, J. B. Theeten, and F. Hottier, *Phys. Rev. B*, **20**, 3292 (1979).
- K. L. Chiang, C. J. Dell'Oca, and F. N. Schwettmann, *This Journal*, **128**, 2267 (1979).
- G. Harbeke, E. Meier, J. R. Sandercock, M. Tgetgel, M. T. Duffy, and R. A. Soltis, *RCA Rev.*, **44**, 19 (1983).
- G. Harbeke, L. Krausbauer, E. F. Steigmeier, A. E. Widmer, H. F. Kappert, and G. Neugebauer, *RCA Rev.*, **44**, 287 (1983).



Growth and Characterization of Thin Gate Oxides by Dual TCE Process

B. Y. Liu* and Y. C. Cheng

Department of Electrical Engineering, University of Hong Kong, Hong Kong

ABSTRACT

A novel Dual TCE (two step trichloroethylene) oxidation process has been developed to grow thin and highly reliable gate oxides for very large scale MOS application. The main features consist of an initial low temperature oxidation providing a low-defect-density oxide structure and a subsequent high temperature oxidation providing a good interface with passivation ability against mobile ions. Combinations of various percentages of TCE and different oxidation conditions are examined. It is found that thin oxides obtained by Dual TCE process have high dielectric break-down fields and good oxide-silicon interface, similar to those obtained by two step HCl oxidation, but without their associated disadvantages.

INTRODUCTION

The trend of VLSI strategy is to pack as many devices as possible on a single chip. One of the ways to achieve this goal is to shrink the dimensions of the device structure. In MOS technology, the miniaturization procedure calls for scaling down all physical dimensions, among which an important one is the gate oxide. To realize a sub-micron MOS channel, the dimension of the gate oxide must be scaled down to the order of 100 Å or less¹. Therefore, techniques to routinely form very thin and highly reliable oxides must be established, in order to fully exploit the potential of VLSI technology.

Several groups of workers have reported different methods² to grow thin gate oxides. Kamigaki and Itoh² employed low oxygen partial pressures to obtain thin oxides. Raider and Forget³ and Adams et al.⁴ examined the growth kinetics and properties of very thin oxides. More recently, an HCl oxidation technique⁵ has been applied to form thin and highly reliable gate oxides^{6,7}. In both studies, a two-step HCl oxidation process at different temperatures was invoked.

The idea of a two-step⁶ or dual cycle⁷

HCl oxidation to grow reliable thin gate oxides evolves quite naturally from several experimental observations. It has been reported⁸ that oxides grown at a high temperature have a higher defect density than those grown at lower temperatures. Oxides obtained by HCl oxidation show a significant decrease in defect density when grown at lower temperatures around 900 °C. However, on the other hand, it is known⁹ that below 1060 °C the passivation ability of HCl oxides is not effective. Furthermore, charges at the oxide-silicon interface are not at a minimum if the oxides are grown at lower temperatures¹⁰.

Taking the above facts into consideration and noting that the condition of the oxide-silicon interface is primarily dictated by the final stage of oxidation, a two-step oxidation scheme is an obvious strategy to obtain high-quality thin oxides. The first stage of growth at low temperature is to obtain a low-defect-density oxide structure. The second stage is to perform the HCl oxidation at higher temperature so that a good oxide-silicon interface is obtained, in addition to the beneficial properties of the passivation effect.

The two-step HCl oxidation appears to be a good technique to form reliable thin gate oxides. Besides the good quality mentioned above, the thin oxides thus obtained should possess all the other benefits of HCl oxides, such as elimination of stacking faults¹¹ and improved low-frequency noise performance¹². However, the HCl oxidation technique has, after all, several drawbacks due to its insidious side effects. HCl is a very dangerous acid and cannot be handled easily. Furthermore, it is very corrosive and causes the oxide to have a rough surface if the concentration of HCl is too high. The use of trichloroethylene (TCE) has been reported¹³ to be just as effective as HCl, but without its disadvantages.

Indeed, TCE has some distinct advantages over HCl in that it is much easier to handle,

contains sufficient chlorine and is far less corrosive. However, the technique of TCE oxidation has not been reported to apply to grow thin and reliable gate oxides. In the present work, we report the successful application of TCE oxidation to form very thin and reliable gate oxides. Thin oxides ranging from 90 Å to 500 Å were obtained by different TCE oxidation cycles. Relevant properties of these SiO₂ films were compared to those obtained by the standard dry oxidation process in order to determine the most appropriate TCE conditions to grow thin oxides for VLSI application.

TCE OXIDATION CYCLES

For the present studies, p-type, <111> oriented silicon wafers with a resistivity of 2 to 4 Ω-cm were used, and these were cleaned in H₂O₂-NH₄OH-H₂O (2:1:5, volume) and H₂O₂-HCl-H₂O (2:1:7, volume), followed by DI water rinse. After standard cleaning procedure, these were oxidized in a resistance-heated furnace at various temperatures in the presence (or absence) of a small amount of TCE. TCE vapor was added to the oxidizing ambient which consisted of dry oxygen and dry nitrogen. The partial pressure of oxygen was controlled by adjusting the relative proportion of oxygen and nitrogen. The amount of TCE was controlled by varying the flow rate of another dry nitrogen inlet through a bubbler filled with purified liquid TCE kept at 0 °C. Details of quantitative data regarding the oxidation ambients can be found in Table I.

Several TCE oxidation cycles were performed, and resulting oxides were compared with those obtained by the standard dry oxidation procedure. We call the first one 'total TCE process' in which the entire oxidation takes place in an ambient of oxygen and TCE (other than a small amount of nitrogen as the carrier gas) at a high temperature of 1060 °C. Then the oxide was annealed in nitrogen at the same temperature. The second one is called 'partial TCE process' which differs from the total TCE process in having an initial low temperature (900 °C) dry oxidation and a subsequent high temperature TCE oxidation and nitrogen annealing. The last one is the 'dual TCE process' which consists of a low temperature dry oxidation, a low temperature TCE oxidation and a high temperature TCE oxidation with low oxygen partial pressure. This can be followed by nitrogen annealing, which has not been performed in the present studies. The essential features of these processes are summarized in Table I.

Table I : Summary of various oxidation cycles

Steps	Conditions	Total	Partial	Dual	Standard
1	Gas (ml/min)	-	O ₂ :500	O ₂ :500	O ₂ :500
	Temp. (°C)	-	900	900	1060
	Time (min)	-	10	8	13
2	Gas (ml/min)	O ₂ :500	O ₂ :500	O ₂ :500	-
		TCE/N ₂ :40	TCE/N ₂ :40	TCE/N ₂ :40	-
	Temp. (°C)	1060	1060	900	-
	Time (min)	12	11	15	-
3	Gas (ml/min)	N ₂ :500	N ₂ :500	N ₂ :500	N ₂ :500
				O ₂ :50	
				TCE/N ₂ :25	
	Temp. (°C)	1060	1060	1060	1060
	Time (min)	40	40	40	40

Note. TCE/N₂ denotes the flowrate of dry nitrogen bubbling through liquid TCE, and by varying this rate, the amount of TCE can be controlled.

The oxide film thickness was measured by a Rudolph ellipsometer, Model 43603-200E at a wavelength of 5461 Å, taking the silicon refractive index to be 4.040 - 0.031 i⁴. SiO₂ films on the back sides of wafers were carefully etched by HF. Aluminum electrodes were evaporated from a tungsten boat. Al dot electrodes with 0.51 mm, 0.76 mm, 1.02 mm and 1.52 mm diameters were patterned photolithographically, and the back sides of wafers were evaporated with thick Al films. Dielectric breakdown measurement was performed with the aluminum dots biased negatively, i.e., with the p-type silicon in accumulation. The breakdown voltage was measured on these aluminum dots with four different sizes when the current density reached a magnitude of 0.049, 0.022, 0.012 and 0.008 mA/mm² respectively. For each sample, the mean value of breakdown voltages was obtained from one hundred measurements, and the corresponding breakdown field was computed from the breakdown voltage and oxide film thickness. Fixed oxide charges and mobile ions were deduced from the flat band voltages, based on the high frequency capacitance-voltage measurements using MSI Electronics Model 868 C-V plotter.

RESULTS AND DISCUSSIONS

Typical statistical distributions of the average breakdown field for both TCE and standard oxides are summarized in Figure 1.

It is noted that most breakdown occurs at high fields, within a very narrow range for various TCE oxides. The spread in the breakdown field is large in standard oxides. Table II classifies the breakdown strength for various oxides.

Table II : Comparison of percentage of capacitors for various oxidation cycles
(Area of capacitor = 0.204 mm²)

	Standard Oxide (352 Å)	Total TCE Oxide (477 Å)	Partial TCE Oxide (408 Å)	Dual TCE Oxide (499 Å)
> 6 MV/cm	71.6%	89.5%	95.8%	96.1%
> 8 MV/cm	58.9%	82.9%	90.7%	90.3%
< 4 MV/cm (Low Field Breakdown)	14.7%	4.8%	1%	0%

For total TCE oxide, more than 82% of the breakdown field occurs at fields between 8 to 11 MV/cm, while more than 90% of the breakdown field occurs at the same range for partial TCE and dual TCE oxides. These should be contrasted with the standard oxide which has only 58.9% breakdown field larger than 8 MV/cm. Furthermore, 14.7% of low field breakdowns (< 4 MV/cm) is found in the standard oxides, in contrast to the observation that there is practically no occurrence of low field breakdown in dual TCE oxides.

Figure 2 shows the mean value of electric field breakdown versus capacitor area for the various groups of oxides. The breakdown field drops as the electrode area increases, and levels off as the area increases, and reaches a constant value as the area exceeds about 1.5 mm². The slopes of decrease in the breakdown field are less steep in TCE oxides than that of standard oxide. The mean value of breakdown field in dual TCE oxides and partial TCE oxides is higher than that based on other oxidation condition. The value of the dual TCE breakdown is comparable to the published results of breakdown field in two-step HCl oxides^{6,7}. However, it should be pointed out that exhaustive attempts have not been made in the present work to optimize the dual TCE oxidation conditions in order to obtain the best overall oxide quality.

The fixed oxide charge of dual TCE oxide is significantly lower than that in other samples, as shown in Table III. These values are typical of thin oxides¹⁴. Once again, it should be mentioned here, no attempts have been made to minimize the charge density because no

Table III : Q_{ss} of various oxidation cycles

Sample	Standard Oxide (352 Å)	Oxide TCE Oxide (477 Å)	Partial TCE Oxide (408 Å)	Dual TCE Oxide (499 Å)
Q_{ss} (cm ⁻²)	2.6×10^{11}	1.9×10^{11}	1.75×10^{11}	1.4×10^{11}

N₂ annealing was performed in the dual TCE oxide.

For the effect of protection against mobile ions contamination, bias-temperature-stress had been performed, and the shifts in flat-band voltages in dual TCE oxides are at least ten times smaller than those of our standard oxide samples. More detailed information on the fixed oxide charge density, passivation capability against the mobile ions, and dielectric breakdown properties can be found in a separate publication¹⁵.

CONCLUSION

In our search for techniques to grow thin and highly reliable oxides, we have demonstrated that the dual TCE oxidation cycle is a viable method. Samples obtained show all the good qualities as found in the two-step HCl oxidation technique, but without the inherent difficulties and disadvantages associated with HCl. While we have shown the feasibility of the dual TCE oxidation technique, more work is needed to fully characterize and understand this method, in order that an optimal process can be found. The fixed charge density might be minimized if a conscientious effort is made in annealing the sample, and in adjusting the proper percentage of incorporation of chlorine atoms. Attempts should also be made to render the passivation ability more effective by finding the optimum combination of temperature, TCE percentage and time of duration. In conclusion, we believe the dual TCE oxidation technique will provide a reliable but simple method to grow ultra thin gate oxides for VLSI application.

REFERENCES

1. S.S. Liu et al., IEEE J. Solid-St. Circuits SC-17, 810 (1982).
2. Y. Kamigaki and Y. Itoh, J. Appl. Phys. 48, 2891 (1977).
3. S.I. Raider and L.E. Forget, J. Electrochem. Soc. 127, 1783 (1980).

4. A.C. Adams, T.E. Smith, and C.C. Chang, J. Electrochem. Soc. 127, 1787 (1980).
5. R.J. Kriegler, Y.C. Cheng, and D.R. Colton, J. Electrochem. Soc. 119, 388 (1972).
6. C. Hashimoto, S. Muramoto, N. Shiono, and O. Nakajima, J. Electrochem. Soc. 127, 129 (1980).
7. J. Steinberg, J. Electrochem. Soc. 129, 1778 (1982).
8. C. Osburn, J. Electrochem. Soc. 121, 809 (1974).
9. K. Kobayashi, K. Tanabashi, K. Ohta, and T. Kubota, Denki Kagaku 42, 294 (1974).
10. Y.C. Cheng, Prog. in Surface Sci. 8, 181 (1977).
11. H. Shiraki, Jpn. J. Appl. Phys. 15, 1 (1976).
12. Y.C. Cheng, J.W. Haslett, E.J.M. Kendall, R.J. Kriegler, and F.J. Scholz, Proc. IEEE 62, 859 (1974).
13. G.J. Declerck, T. Hattori, G.A. May, J. Beaudouin, and J.D. Meindl, J. Electrochem. Soc. 122, 436 (1975).
14. H.P. Vyas, G.D. Kirchner, and S.J. Lee, J. Electrochem. Soc. 129, 1757 (1984).
15. Y.C. Cheng and B.Y. Liu, This Journal, submitted.

Acknowledgment

This work was supported in part by the Industrial Development Board of Hong Kong.

*On leave from South China Institute of Technology, Guangzhou, China.

Manuscript submitted May 17, 1983; revised manuscript received Dec. 15, 1983.

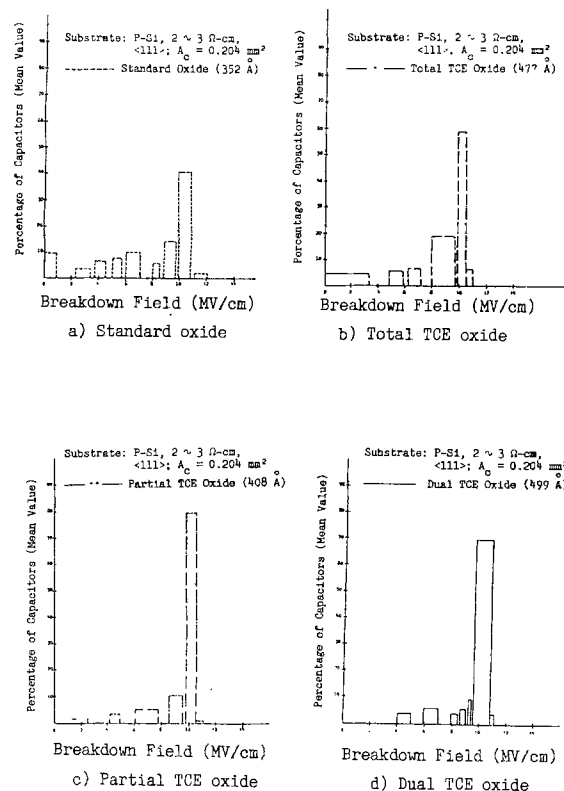


Figure 1 Typical statistical distributions of breakdown fields for various oxidation process: a) Standard oxide, b) Total TCE oxide, c) Partial TCE oxide, and d) Dual TCE oxide.

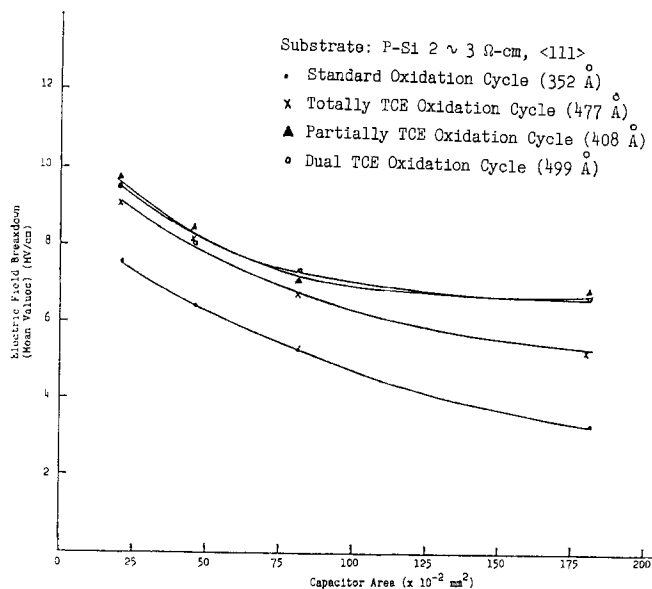


Figure 2 Electric breakdown vs. capacitor area for TCE and standard oxidation process.

Polymer Films on Electrodes

13. Incorporation of Catalysts into Electronically Conductive Polymers: Iron Phthalocyanine in Polypyrrole

R. A. Bull, F.-R. Fan, and A. J. Bard*

Department of Chemistry, University of Texas at Austin, Austin, Texas 78722

Abstract

Tetrasulfonated iron phthalocyanines (FePcS) can be incorporated into electronically conducting polypyrrole by electrochemical polymerization of pyrrole in the presence of FePcS. The FePcS modified glassy carbon electrodes catalyzed the reduction of O_2 at potentials 250 to 800 mV less negative than at bare glassy carbon or at polypyrrole-coated glassy carbon not containing FePcS. Rotating ring-disk experiments indicated some hydrogen peroxide formation at most pH's. However, at high pH essentially exclusive reduction of O_2 to H_2O was observed at potentials 250 mV less negative than at a non-catalyzed electrode.

(end of abstract)

One of the main motivations for the preparation of modified electrodes, including those covered with polymer films, is the incorporation of electrocatalysts onto the electrode surface. For example, catalysts have been covalently attached to the substrate, irreversibly adsorbed, and introduced into polymer films via electrostatic binding (1). Of particular interest have been electrocatalysts for the reduction of oxygen (2-5); these often are based on metal porphyrins and phthalocyanines. Among the problems arising in the utilization of catalytic modified electrodes are the limited effectiveness on monolayers (6), instability of the attached or adsorbed materials, and low rate of charge transport through non-electronically conductive films. We suggest here the incorporation of a catalyst into a conductive polymer layer by electrochemical polymerization in the presence of catalyst and briefly describe the characteristics of such an electrode for the reduction of oxygen.

Electrochemical Society Active Member *

Key Words: catalysis, polymers, voltammetry, electrodes

The conductive polymer chosen was polypyrrole (PP); a number of electrochemical studies of this material have demonstrated that this can be readily deposited by electrochemical oxidation of pyrrole from nonaqueous or aqueous solutions (7-10). The catalyst was tetrasulfonated phthalocyanine incorporating iron (FePcS) and the substrate was glassy carbon (GC). The advantages of this system include ease of preparation, and both high conductivity and high porosity of the PP film (11), leading to rapid transport of both charge and solution substrate within the electrode structure.

Polypyrrole films were deposited from aqueous 0.05 M sodium trifluoroacetate solutions (NaTFA) (pH 1-7) that were 0.1 M in pyrrole by anodic oxidation at +0.7 V vs. SCE at GC. Polymer film thicknesses were estimated by taking 24 mC/cm² of charge to be equivalent to a 1 μ m film (8c). GC/PP/FePcS films were prepared by an identical procedure except that the solution contained only 1 mM FePcS and 0.1 M pyrrole. Oxidation of pyrrole in the presence of FePcS was necessary for catalyst incorporation. Control experiments in which a GC electrode was held at +0.7 V vs. SCE in a FePcS solution not containing pyrrole showed no O_2 - reduction catalysis. PP films deposited in the absence FePcS and then cycled through the PP redox waves in a solution containing FePcS also showed no catalytic activity.

CV Experiments.--A typical cyclic voltammogram (CV) of a FePcS/PP film (0.1 μ m thick) is shown in Fig. 1a for a 0.1 M NaTFA electrolyte (pH 1.7) saturated with N_2 . The small waves for FePcS reduction and re-oxidation are superimposed on the large PP background; the large background currents have been ascribed to capacitive charging of the highly porous PP film (11). An estimate of the amount of electroactive FePcS in the polymer from the CV, assuming n=1 for Fe(III)/Fe(II) couple

Manuscript submitted Feb. 22, 1983.

is 2 to 6×10^{-11} moles/cm² geometric area. The FePcS redox waves were stable to cycling within the potential limits imposed by PP. Scanning to potentials sufficiently negative for PP reduction (i.e. out to -0.3 to -0.5 V vs. SSCE) resulted in a decrease in the peak currents (i_p) for the FePcS waves. Potentials positive enough for irreversible PP oxidation ($+0.8$ V vs. SSCE at pH 1 to $+0.4$ V at pH 13) also decreased i_p for the FePcS redox waves, although the film still remained on the electrode surface.

In O₂-saturated solutions the current at the FePcS² wave was greatly increased (Fig. 1b); this is attributed to the catalyzed reduction of O₂. In all cases significantly higher reduction currents were found at more positive potentials at GC/PP/FePcS than at GC/PP or bare GC electrodes. For example, under the conditions of Fig. 1b, O₂ reduction at GC/PP occurs at about -0.8 V vs. SSCE. The effect of pH on the potentials for catalyzed O₂-reduction was similar to that found for the FePcS waves themselves. At pH < 3, the shift of E_d was 45 mV/pH unit. As with the FePcS redox waves themselves, the waves attributed to O₂ reduction disappeared upon irreversible PP oxidation.

RRDE Experiments.--Reduction of O₂ at bare and modified GC disk electrodes with detection of products (e.g. H₂O₂) via oxidation at a Pt ring electrode provided additional information about catalysis by incorporated FePcS (Fig. 2). At a bare GC electrode O₂-reduction occurred to produce a mass transfer-controlled wave, with the limiting current, i_L , increasing with angular rotation velocity, ω . For GC/PP electrodes a wave at similar potentials was observed, but i_L reached a limiting value at about 1000 rpm. The collection efficiencies, N, found for GC and GC/PP electrodes (for O₂ reduction at the disk and H₂O₂ oxidation at the ring) were generally 0.26-0.30; this is less than the collection efficiency found with this electrode and a soluble redox couple such as Fe(CN)₆^{3-/4-}, where N = 0.39. For a GC/PP/FePcS disk electrode, the reduction of O₂ essentially coincided with the FePcS reduction wave and occurred at less negative potentials compared to GC and GC/PP electrodes, similar to the CV results. At most pH's anodic ring currents were observed when O₂ was reduced at the disk (e.g. at pH = 6.5, E_d = -0.6 V; E_r = $+1.0$ V vs. SSCE), demonstrating that some H₂O₂ is produced. Typical results for a 0.12 μm PP/FePcS film in O₂-saturated 0.1M NaTFA (pH 6.5) are given in

Fig. 2a. Strict correspondence to the Levich equation (i_p vs. $\omega^{1/2}$) was not found with this electrode, perhaps because of interference from the background processes of PP. The reduction of O₂ at GC/PP/FePcS in 0.1 M NaOH did not lead to anodic ring currents until the disk potential attained values where direct O₂ reduction of GC/PP occurs. Typical RRDE voltammograms are given in Fig. 2b. After an initial "break-in period" during which the reduction current decreased, the current between -0.1 and -0.3 V was independent of ω . No ring currents were observed at these values of E_d. When E_d reached -0.35 V, the onset potential for O₂ reduction at bare GC, anodic current became apparent. Note, however, that even at these potentials the anodic currents were very small, so that N-values in this region were two orders-of-magnitude smaller than for catalyzed O₂ reduction at lower pH. These results suggest that FePcS catalyzes the decomposition of H₂O₂ in 0.1 M NaOH solution.

In general, over the pH range of 1.7 to 13, N-values for GC/PP/FePcS electrodes were always smaller than those for bare GC electrodes at the same pH. However, at lower pH, N was nearly the same as that for the bare electrode. At pH 13, N was two orders of magnitude less than at a bare GC electrode, even at potentials where peroxide is produced at GC.

The stability of FePcS-PP films depended on the pH and the cathodic scan limits. If the PP films were reduced, O₂-reduction activity decreased. As a result, limiting currents and i_p vs. $\omega^{1/2}$ data could not be obtained. This was particularly so at low pH, where PP reduction began at only slightly negative potentials. The stability of the catalyst-film during O₂ reduction and in the presence of reduction products, e.g. H₂O₂, is also of interest. Successive O₂-reduction scans, especially at low pH, resulted in a gradual decrease in the disk current. After prolonged O₂ reduction the initially shiny blue-black FePcS-PP film changed to a gray particulate deposit that was easily removed from the electrode. At this point, little O₂ reduction activity was observed and, after N₂ saturation, no FePcS redox activity was found. The addition of H₂O₂ to the electrolyte also brought about rapid delay of catalytic activity.

In conclusion, this method of incorporation of catalysts via conductive polymers onto an electrode surface appears to be a promising one. For the GC/PP/FePcS electrodes we have observed significant

catalytic activity for O_2 reduction at potentials 250 to 800 mV² less negative (depending on pH) than at bare GC or GC/PP electrodes. Moreover, the observed current densities for O_2 reduction based on the geometric area of the electrode appear to be larger than those reported for similar catalysts adsorbed on electrodes (2,5). This can probably be attributed to the high conductivity and porosity of the PP matrix, making a larger number of catalyst centers accessible per unit area of electrode to dissolved O_2 .

The PP background often hindered the collection of precise peak and limiting current data for quantitative kinetic analysis. As a result, only qualitative aspects of O_2 reduction mechanisms can be discussed. The similarity of the FePcS and catalyzed O_2 reduction potentials suggests a redox-type mechanism (12). However, the voltammetric behavior and the change of N with pH suggest at least two simultaneous O_2 reduction processes. At low pH the reduction is predominantly to peroxide and N is nearly that found for an unmodified GC electrode. As the pH is raised the Tafel slopes increased and N decreased from that at an unmodified electrode. At intermediate pH, the 2e and 4e processes are competitive, but at high pH no peroxide was detected at potentials positive of O_2 reduction at GC, suggesting a direct 4e reduction to H_2O . The 4 electron process probably involves the dismutation of H_2O_2 by FePcS, as suggested for iron porphyrins in methylacrylate polymers (13). Direct reduction of H_2O_2 is also possible; however, H_2O_2 contributes to instability of PP and loss of catalytic activity. The stability of PP/FePcS catalyst increased at higher pH.

The catalytic behavior found here is qualitatively similar to those observed by Zagel et. al. (2) and perhaps involve similar mechanisms. This suggests that incorporation of FePcS into PP has essentially no effect on the mechanism or catalytic behavior. However, the conductive support enhances the effectiveness of the catalyst by providing more surface area and a larger percentage of active centers than are present in adsorbed films or catalysts in non-conducting polymers and provides a convenient method of attaching the catalyst to the substrate (14).

References

1. R. W. Murray in "Electroanalytical Chemistry," A. J. Bard, ed., Marcel Dekker, Inc., New York, Vol. 13, 1983 (in press).

2. J. Zagel, P. Bindra, E. Yeager, This Journal, 127, 1506 (1980).
3. J. P. Collman, M. Marrullo, P. Denisevich, C. Koval, F. C. Ansoh, J. Electroanal. Chem., 101 117 (1978).
4. R. R. Durand, Jr., F. C. Anson, J. Electroanal. Chem. (in press).
5. A. Bettelheim, R. J. H. Chan, T. Kuwana, J. Electroanal. Chem., 99, 391 (1979).
6. C. P. Andrieux, J. M. Dumas-Bouchiat and J. M. Saveant, J. Electroanal. Chem., 123, 171-178 (1981).
7. A. Dall'Olivo, G. Dascola, V. Varacca and V. Bocchi, Comp. Rend., 433, 267c (1968).
8. (a) A. F. Diaz and K. K. Kanazawa, J. Chem. Soc., Chem. Commun. 635 (1979); (b) K. K. Kanazawa, A. F. Diaz, R. H. Geiss, W. D. Gill, J. F. Kwak, J. A. Logan, J. F. Rabolt and G. B. Street, ibid., 854 (1979); (c) A. F. Diaz and J. T. Castillo, ibid., 397 (1980); (d) K. K. Kanazawa, A. F. Diaz, W. D. Gill, P. M. Grant, G. B. Street and G. P. Gardini, Synthetic Metals, 1, 329 (1979/80); (e) A. Diaz, J. M. Vasquez Vallejo and A. Martinez Duran, IBM J. Res. Develop., 25, 42 (1981).
9. (a) R. Noufi, A. J. Frank and A. J. Nozik, J. Am. Chem. Soc., 103, 1849 (1981); (b) R. Noufi, D. Tench and L. F. Warren, This Journal, 127, 2310 (1980); (c) T. Skotheim, I. Lundstrom, and J. Prejza, This Journal, 128, 1625 (1981).
10. F.-R. F. Fan, B. Wheeler, A. J. Bard and R. Noufi, ibid., 128, 2042 (1981).
11. R. A. Bull, F.-R. F. Fan, A. J. Bard, ibid., 129, 1009 (1982).
12. F. Beck, J. Appl. Electrochem., 7, 239 (1977).
13. A. Bettelheim, R. J. H. Chan, T. Kuwana, J. Electroanal. Chem., 110, 93 (1980).
14. Support of this research, a joint project with Prof. A. B. Lever, by the Office of Naval Research and by the National Science Foundation (CHE 7903729) is gratefully acknowledged.

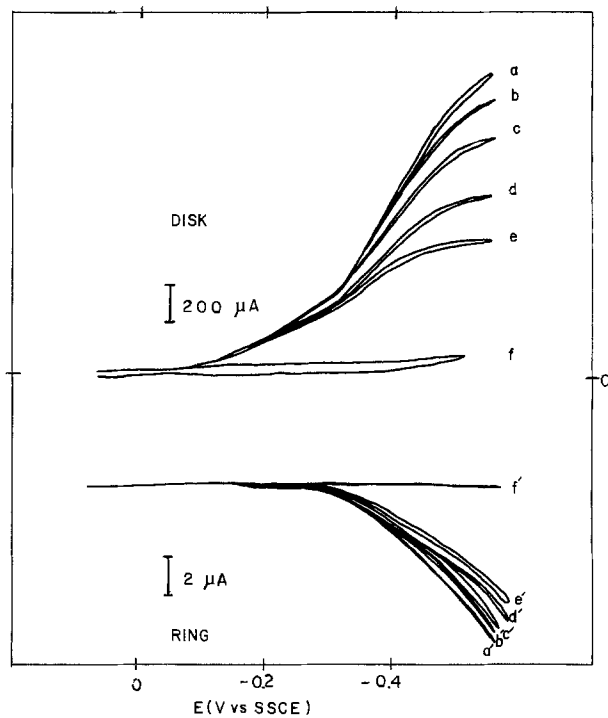
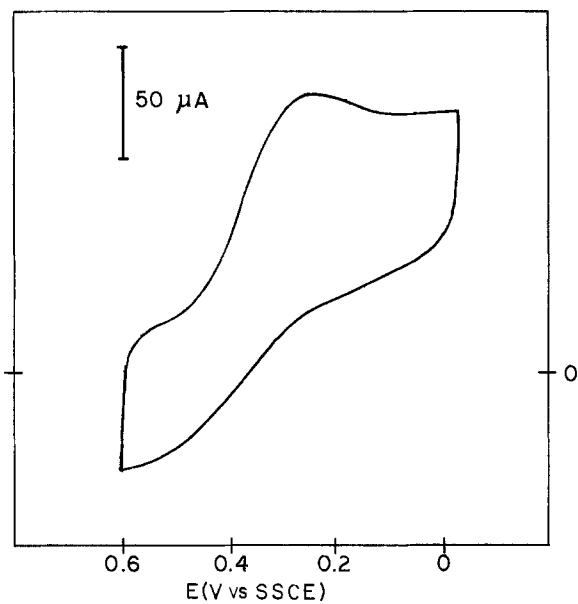
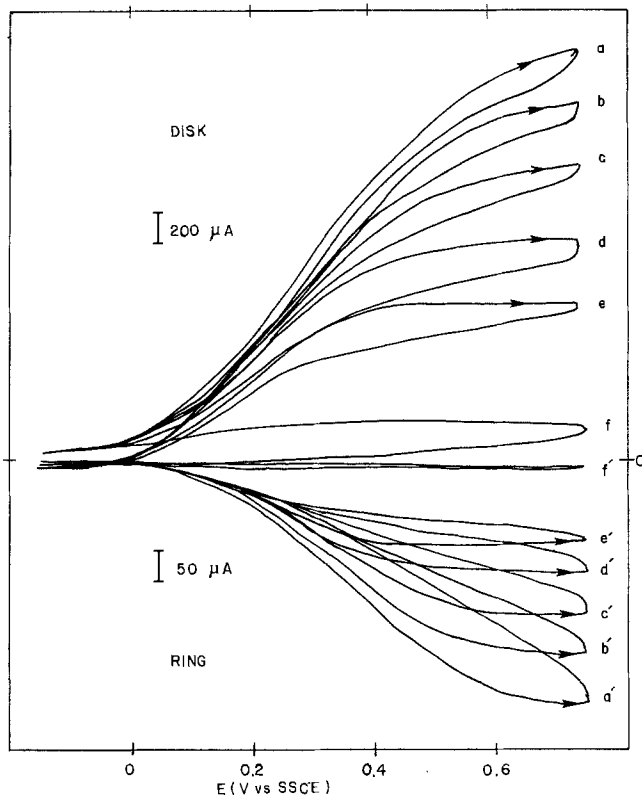
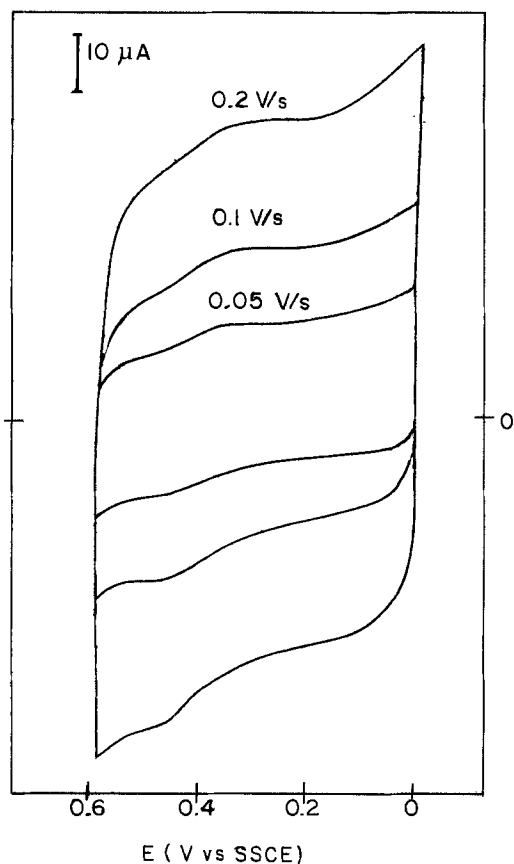


Fig. 1. Cyclic voltammetry of a $0.1 \mu\text{m}$ FePcS/PP film in 0.1M NaTFA ($\text{pH} = 1.7$); (a, top) N_2 -saturated; (b, bottom) O_2 -saturated, $V = 0.1 \text{ V/s}$.

Fig. 2. Rotating ring-disk electrode voltammograms of a $0.1 \mu\text{m}$ FePcS/PP film in O_2 -saturated electrolyte at $\omega(\text{rpm})$, (a, a') 2000; (b, b') 1500; (c, c') 1000; (d, d') 500; (e, e') 250; (f, f') 2000 in N_2 -saturated electrolyte (a, top) 0.1M NaTFA ($\text{pH} = 6.5$) and (b, bottom) 0.1M NaOH.



An Admittance Study of the Lead Electrode

S. H. Glarum* and J. H. Marshall

AT&T Bell Laboratories, Murray Hill, New Jersey 07974

ABSTRACT

Although impedance measurements are recognized as a valuable adjunct to electrochemical studies, the full realization of the power of the technique has been limited by the need for the expeditious creation and interpretation of a large data base involving impedance, frequency, and potential. Complex-plane plots or analogous representations are often used to deduce and parametrize equivalent circuit descriptions. Mathematically these parameters can be described within the context of rather generalized models by partial derivative functions involving current, potential, and concentrations. Fixed potential measurements evaluate these functions at the selected potentials, but often it is the functions themselves rather than their values which are of prime interest. This study endeavors to obtain such partial derivative functions for the electrodeposition of Pb from perchloric acid solutions, using a microcomputer to analyze a large data base gathered with coordinated measuring apparatus. Complex-plane plots suggest a relatively simple model, with the current being an arbitrary function of potential and the local surface concentration of Pb^{++} ions. From this assumption, it has been possible to extract and plot the partial functions directly. A variety of plating additives were also examined. Each revealed distinctive effects in its partial derivative function plots.

Fundamental studies of electrochemical deposition and dissolution are essential for a scientific comprehension of many important technological processes. Quasi-static current-voltage measurements have been widely applied, but their utility is largely restricted to observing the slowest rate-limiting step. Often this step is solute mass transport and uninteresting from the viewpoint of understanding the true surface reaction. Impedance measurements have been often used to probe electrode behavior on shorter time scales. Because of the time consumed in ac measurements, however, such studies have nearly always been restricted to zero current conditions. Exchange currents may be deduced from such data, but the behavior at other potentials can only be inferred through the assumption of an explicit functional relationship.

In more recent years, automated impedance measuring apparatus has extended the state of the art, making possible considerably more sophisticated studies (1-5). Results are normally plotted in the complex admittance or impedance plane. From the shapes of these plots, equivalent circuits may be deduced and parameters evaluated for the circuit elements. Formally, these elements can be expressed in terms of partial derivatives involving parameters such as current, potential, and concentration. Ideally one would like simultaneous impedance measurements at all frequencies and all potentials. Then, instead of measuring numbers, one would be able to extract the functions themselves rather than their values for a single potential. In earlier work, we have found plots of the real and imaginary admittance components useful for studying the variations of electrode reactions with potential (5). These components, however, are themselves nonlinear functions of underlying partial derivative functions, and are most useful when dominated by a single element. For a more complete analysis, one would like to extract the partial derivative functions themselves from the admittance data.

This study attempts such an analysis for lead dissolution and deposition. Several impedance studies

have been previously reported, but all have been restricted to zero current conditions, yielding only an exchange current density (6-10). The lead electrode has proved especially convenient, for over a wide potential range its behavior can be expressed in terms of a double layer capacitance, a Warburg impedance, and a surface resistance. From impedance measurements *vs.* potential at multiple frequencies, we have found it possible to obtain the partial derivatives as continuous functions of potential. Although certain assumptions are still required, they are of a quite general nature, requiring that the current be a function only of potential and the surface concentration of Pb^{++} ions.

These procedures have also been applied to lead solutions containing the additives thiourea, phenolphthalein, and polypropylene glycol. Each turns out to have a quite distinctive effect when analyzed in terms of its partial derivative functions.

Experimental

The majority of experiments used a 10 mM $\text{Pb}(\text{ClO}_4)_2$ (Alfa Products) solution in 1N HClO_4 (Baker Ultrex). The solution was vigorously degassed with argon, and was thermostated at 25°C.

A 1/16 in. diam platinum rotating disk electrode provided the substrate for lead deposition. The surface was polished immediately prior to each experiment. Lead wire fused within glass capillary tubing served as the reference electrode. Open-circuit potential measurements between the reference and fresh lead deposits were always within 1 mV, our measurable limit.

Sweep frequency measurements, 200 kHz-100 Hz, were made at the open-circuit potential for each series of runs to measure electrolyte resistance and check on the double layer capacitance. The results of prime interest in this paper, however, are derived from admittance-potential measurements at fixed frequencies. As described previously, phase detector outputs were first signal-averaged, and then converted to admit-

* Electrochemical Society Active Member.

tance values by a Texas Instrument 960A minicomputer (5).

In a major experimental enhancement, the 500+ points accumulated for each run were then stored on floppy disks through the intervention of an additional microcomputer. Rather than having to process and plot results between runs, the time between successive measurements became minimal, and this proved important for the comparisons between runs required for data reduction to partial derivative functions. Stored data files were accessible to either computer. Existing minicomputer programs did the heavy number crunching involved in current distribution corrections and the separation of electrolyte resistance. These results were then processed by microcomputer BASIC programs to find the partial functions, and results were plotted semilogarithmically on an X-Y recorder. Thus, the full set of data could be analyzed and displayed with a minimum of human intervention. BASIC programs were also used to construct plots for explicit model functions.

Analysis

Formally, the current flowing in an electrodeposition process, $I(\eta, c, q_i)$, may be expressed as a function of potential, η , the concentration of metal ions, c , and a set of other possible parameters, q_i . When the potential is modulated, $\eta = \bar{\eta} + \eta^* \exp(i\omega t)$, the remaining parameters may also be modulated, i.e., $c = \bar{c} + c^* \exp(i\omega t)$, where η^* , c^* , etc., are complex, time-independent variables. Thus

$$I^* = \left(\frac{\partial I}{\partial \eta} \right)_{c, q_i} \eta^* + \left(\frac{\partial I}{\partial c} \right)_{\eta, q_i} c^* + \left(\frac{\partial I}{\partial q_i} \right)_{\eta, c} q_i^* \quad [1]$$

The information to be obtained from modulation experiments can therefore be represented by a set of partial functions.

If we define $c^*(b)$ as the concentration modulation at a plane a distance b from the electrode, beyond which concentration gradients lie normal to the plane, the high frequency Warburg solution is (19)

$$I_s^*(b) = zFA(i\omega D)^{1/2} c^*(b) \quad [2]$$

where $I_s^*(b)$ is the current modulation at this plane due to the solute species represented by c , z , and D are the charge diffusion coefficient of the solute ion, and A is the planar area. For a hypothetically smooth and uniform electrode surface, $b \rightarrow 0$ and $I^* = I_s^*$ if all current is initially transferred from the electrode to a single solute species.

Admittance measurements yield the ratio I^*/η^* , and, with the assumption that $b = 0$, Eq. [1] may be written as

$$I^* = \left(\frac{\partial I}{\partial \eta} \right)_c \eta^* + [(i\omega D)^{1/2} zFA]^{-1} \left(\frac{\partial I}{\partial c} \right)_\eta I^* \quad [3]$$

where the "hidden" variables are incorporated in the modified pair of partial derivative functions. These functions will be frequency independent if these variables are unimportant or not modulated. Should their frequency dependence parallel I^* or η^* , their detection will depend upon a quantitative examination of the derived functions.

Equation [3] constitutes the basis for the analyses in this study and our objective is to extract from experimental data the two partial derivatives and their ratio, $(\partial c/\partial \eta)_I$, as functions of potential. The electrode impedance is given by the ratio η^*/I^* , and Eq. [3] leads to a simple series equivalent circuit composed of a resistance and a Warburg element, i.e., $Z^* = 1/Y^* = A + B/(i\omega)^{1/2}$. Given A and B , the partial derivatives in Eq. [3] can be evaluated. Unfortunately, the double layer capacitance, C_{dl} , introduces a complication, and a single admittance measurement was found to be

insufficient for the evaluation of these parameters. Instead, measurements for at least two frequencies were required.

Results will only be independent of the solution algorithm if the partial functions are frequency independent, and this proves not always to be the case. We therefore sketch the procedure used. Let ω_1 and ω_2 be the two frequencies ($\omega_1 < \omega_2$) and Y_1^* and Y_2^* the associated experimental admittances. We define

$$\begin{aligned} R' &= Y_1' \\ R'' &= Y_1'' - (\omega_1/\omega_2) Y_2'' \end{aligned} \quad [4]$$

thereby eliminating C_{dl} from R^* . Now let

$$\begin{aligned} Q' &= R' \\ Q'' &= R'' + (\omega_1/\omega_2) S(\omega_2, A, B) \end{aligned} \quad [5]$$

and solve $1/Q^* = A + B/(i\omega_1)^{1/2}$ for A and B . Finally let

$$S(\omega_2, A, B) = \text{Im} [A + B/(i\omega_2)^{1/2}]^{-1} \quad [6]$$

and iterate to Eq. [5] until convergence is achieved. In practice, a 4:1 frequency ratio was satisfactory and the 500+ points could be handled by a BASIC program within 2 min. Values for A and B reflect primarily the lower frequency data, while C_{dl} is found from $Y_2'' - S$, and is largely determined by the higher frequency data. A is inversely proportional to $\partial I/\partial \eta$, and B to $\partial c/\partial \eta$. Thus, when current is primarily limited by concentration polarization, the latter partial is more accurately determined, while the former function becomes noise prone. The converse applies when surface resistance dominates. For 10 mM Pb^{++} solutions, both effects are commensurate, hence our attention to this concentration level.

Equation [3] offers a more general basis for the analysis of admittance data than does the assumption of an explicit model function $I(\eta, c)$. Still, one should understand that this equation entails some assumptions regarding additional parameters, and its usefulness depends upon deriving frequency-independent functions which exhibit "reasonable" behavior. By way of illustration, let us consider the hypothetical function

$$\begin{aligned} I &= I_0 [\exp(\beta e \eta / kT) - x \exp(-\alpha e \eta / kT)] \\ x &= 1 + I/I_{lim} \end{aligned} \quad [7]$$

x being the surface concentration normalized to the bulk concentration and I_{lim} the magnitude of the rotating disk limiting current. The function $\partial I/\partial x$ will then have a linear semilog plot vs. potential, with intercept and slope giving I_0 and α . The function $\partial I/\partial \eta$ has a more interesting shape, with a limiting cathodic value of $\alpha e I_{lim} / kT$, exponential anodic behavior, and a possible minimum depending upon the ratio I_0/I_{lim} . Figure 1 depicts a family of plots for this function for different ratios. Note that the experimental partial derivative functions provide several independent means for evaluation of the three parameters.

Results

The experimental procedure for this study paralleled that previously used for tin (11). Plating took place during a cathodic sweep beginning at an anodic overpotential of +80 mV and running to a lower potential of -250 mV. Admittance measurements were made on the anodic retrace to the starting potential. There the electrode was stripped and the cycle repeated four to eight times for signal averaging. Various combinations of sweep rates between 10 and 200 mV/s were explored to establish a reproducibility window for deposit thickness. A sweep rate of 30 mV/s was chosen for the cathodic trace, leading to a nominal 700Å deposit at the start of data acquisition. A 150 mV/s rate was selected for the anodic trace to minimize morphological changes during measurement.

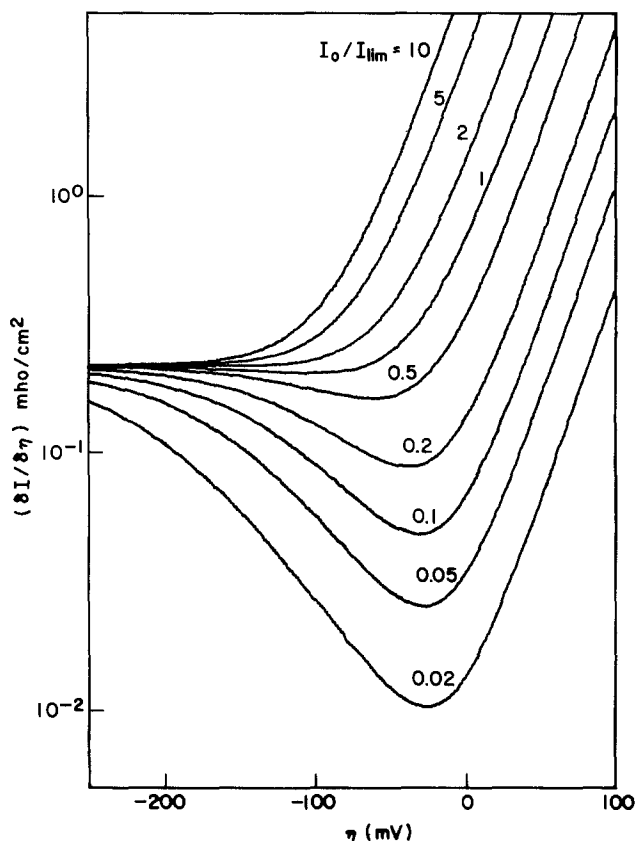


Fig. 1. Theoretical plots for the function $(\partial I/\partial \eta)_c$ given by Eq. [7] with parameters $\alpha = 0.5$, $\beta = 1.0$, $i_{lim} = 11 \text{ mA/cm}^2$, and indicated ratios for I_0/i_{lim} .

With thicknesses greater than 2000 Å, irregular behavior attributable to dendritic growths could be seen in current-voltage curves (12).

A significant hydrogen evolution current was observed for the first two to three sweeps following introduction of the electrode into the bath. This current soon abated and a flat limiting current region was established down to -250 mV . Underpotential deposition of a lead monolayer not removed under the stripping conditions employed is presumed responsible. At the lowest potential, -250 mV , no further evidence for H_2 formation was apparent after the first few cycles. To avoid the formation of higher valence lead species, the overpotential was not allowed to exceed $+80 \text{ mV}$.

A diffusion coefficient of $9.4 \pm 0.4 \times 10^{-6} \text{ cm}^2/\text{s}$ was found from limiting current measurements for disk rotational speeds of 25–400 rad/s. This value agrees satisfactorily with the literature, 9.8×10^{-6} (13) and was used for subsequent analyses.

Upon completion of a series of experiments and after final stripping of bulk lead at $+80 \text{ mV}$, the electrode was removed, quickly dried, and examined under a microscope. Inevitably, there were indications of a film masking the fine platinum polishing scratches normally visible with oblique illumination. Dramatic color changes ensued when a drop of deionized water was added to the surface. In addition to development of an overall yellow cast, we witnessed red, green, and blue sections from optical interferences. After the electrode had been returned to the acid bath and rotated for a minute under open-circuit conditions, all traces of the film and the discoloration disappeared and surface detail returned to that of a freshly polished platinum surface.

Atmospheric oxidation was suspected, for when the bath was saturated with oxygen, the electrode emerged from plating and stripping cycles with no indications of a film residue. Evidently, the film re-

tains a Pb species other than the bulk metal which oxidizes to yellow acid-soluble PbO . The interference colors would seem to rule out the adatom monolayer not removed at the stripping potential. The film and its attendant colorations were also seen with all the addition agents to be discussed presently.

Figures 2a and 2b plot the real and imaginary components of the surface admittance for a $10 \text{ mM Pb}(\text{ClO}_4)_2/1\text{N HClO}_4$ solution after a current distribution correction and the subtraction of the electrolyte resistance (ca. 10Ω). These data constitute the input for the partial derivative analysis. Figures 3a and 3b show the results of this analysis for the three partial derivative functions and the double layer capacitance. All functions were frequency independent above -150 mV , but below this potential both $\partial I/\partial \eta$ and $\partial I/\partial x$, where x is the reduced surface concentration $c(0)/c_0$, showed a definite dispersion.

Qualitatively, above -150 mV these plots conform to the predictions of a model described by Eq. [7]. Both $\partial I/\partial x$ and $\partial x/\partial \eta$ show exponential behavior, while $\partial I/\partial \eta$ exhibits a cathodic plateau. Note that this feature, not evident in the 40 Hz data in Fig. 2a, is clearly extracted at this frequency by the analysis. Further experiments confirmed the plateau level varied as the square root of disk rotational speed varied and thus also as the limiting current varied.

The dispersion below -150 mV reveals an inadequacy of the three parameter equivalent circuit: surface resistance, Warburg impedance, and double layer capacitance. As no dispersion was seen in plots of $\partial x/\partial \eta$, the source of the dispersion appears to lie in $\partial I/\partial \eta$, which is inversely proportional to the surface resistance. In the dispersion region, the Warburg impedance exceeds the plateau resistance by more than an order of magnitude. Empirically, $\partial I/\partial \eta$ appears to vary as $\omega^{1/2}$.

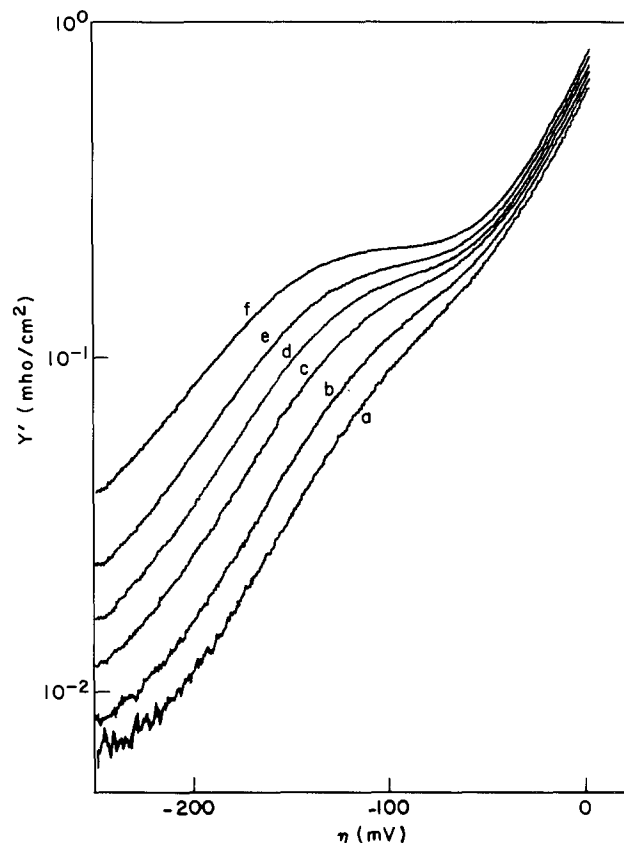


Fig. 2a. Dependence of the real part of the surface admittance, Y' , for a $10 \text{ mM Pb}(\text{ClO}_4)_2$ solution in 1N HClO_4 after current distribution corrections and the subtraction of electrolyte resistance. Curves a-f correspond to measurements at 40, 80, 200, 400, 800, and 2000 Hz.

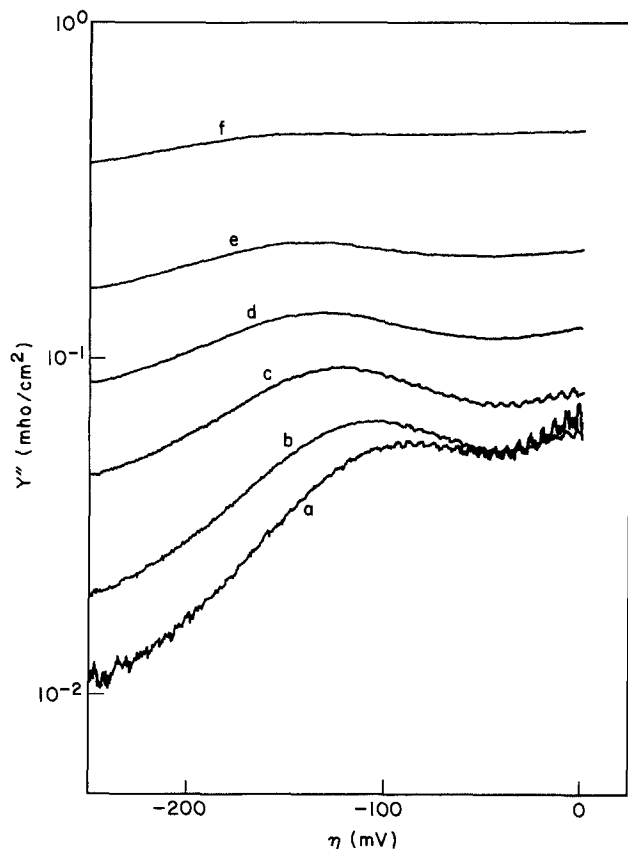


Fig. 2b. As for Fig. 2a, but for the imaginary part of the surface admittance, Y'' .

Marked changes were observed when phenolphthalein (0.2 mM) was added to the 10 mM solution. Figures 4a and 4b show the results for the partial derivative analysis. An order of magnitude reduction in the exchange current is evident from the functions $\partial I/\partial \eta$ and $\partial I/\partial x$ at $\eta = 0$. The former now has a prominent minimum near -20 mV, which follows from Eq. [7] when $I_0 \ll I_{lim}$. The cathodic plateau remains, however, at nearly the same level. This function was independent of frequency over the range 40–800 Hz, including the slight drop seen below -200 mV.

The remaining partial functions, however, show large dispersions near $\eta = 0$ which increase as the first power of frequency and suggest errors in the evaluation of $\partial x/\partial \eta$, which is inversely proportional to the Warburg impedance. Surface resistance dominates the impedance in this region. In contrast to the results for the additive-free solution, all functions were frequency independent below -150 mV.

Because of the limited solubility of phenolphthalein in water, additions of a 10 mM solution in ethanol were made to the bath. Measurements using an equivalent volume of pure ethanol established that the changes were not due to the alcohol. Moreover, no differences were found when measurements were made immediately after additive addition or following several hours of degassing which might have removed some of the ethanol.

Figure 5 plots analysis results for a 10 mM $Pb(ClO_4)_2/1N$ $HClO_4$ solution with 0.5 mM (monomer) polypropylene glycol (PPG) added. The average molecular weight, 425, leads to an actual polymer concentration of 0.07 mM. Although similar in appearance to the phenolphthalein results (Fig. 4), there are distinctive differences. The minimum for the function $\partial I/\partial \eta$ has shifted to -50 mV, and this function does not approach the previous cathodic plateau level. Plots using 40–800 Hz data showed no dispersion at any potential. Dispersions in the functions $\partial I/\partial x$ and $\partial x/\partial \eta$ appeared above -100 mV, but their magnitudes were

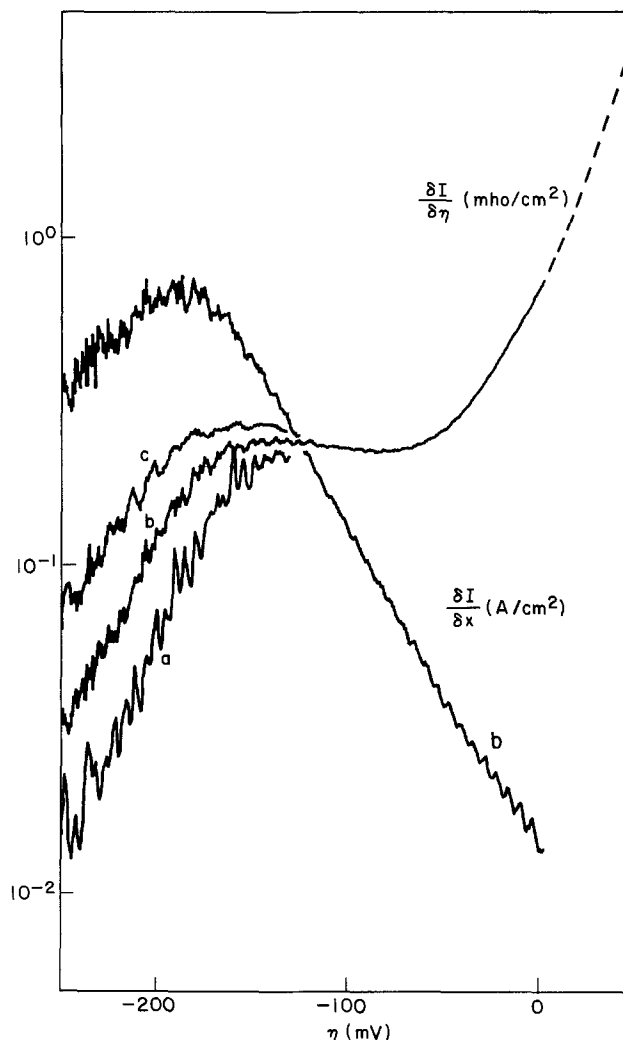


Fig. 3a. The potential dependence of the functions $(\partial I/\partial \eta)_x$ and $(\partial I/\partial x)_\eta$ obtained from the data in Fig. 2. Curves a, b, and c were obtained, respectively, through analysis of 40, 200, and 800 Hz data with 2000 Hz data. (The extension above $+5$ mV is taken from separate measurements.)

somewhat less than in the case of phenolphthalein. The double layer capacitance was reproducibly greater over most of the potential range, 30–48 $\mu F/cm^2$.

The final additive examined in this study was thiourea. Analysis results for a 10 mM $Pb(ClO_4)_2/1N$ $HClO_4$ solution containing 0.5 mM thiourea are shown in Fig. 6a and 6b. The partial functions reflect an order of magnitude increase in the exchange current density. The resistive portion of the surface impedance is now so small that $\partial I/\partial \eta$ and $\partial I/\partial x$ plots are quite noisy below -100 mV. The surface impedance is dominated by the Warburg contribution, and it can be seen that it is the function $\partial x/\partial \eta$ which is most accurately evaluated.

No plateau for $\partial I/\partial \eta$ is evident, although there are indications of an incipient inflection before this function continues to drop off exponentially in a manner similar to the extreme cathodic behavior seen in Fig. 3a. The function $\partial I/\partial x$ also peaks at about the same level in this region, and exponential behavior is only evident over a 100 mV potential range.

Discussion

Our analysis, predicated upon Eq. [3], presumes an equivalent circuit of series-connected resistive and Warburg elements in parallel with the double layer capacitance. The Warburg admittance is directly proportional to the function $\partial x/\partial \eta$, while the resistive admittance is directly proportional to $\partial I/\partial \eta$. The former function characterizes concentration gradients

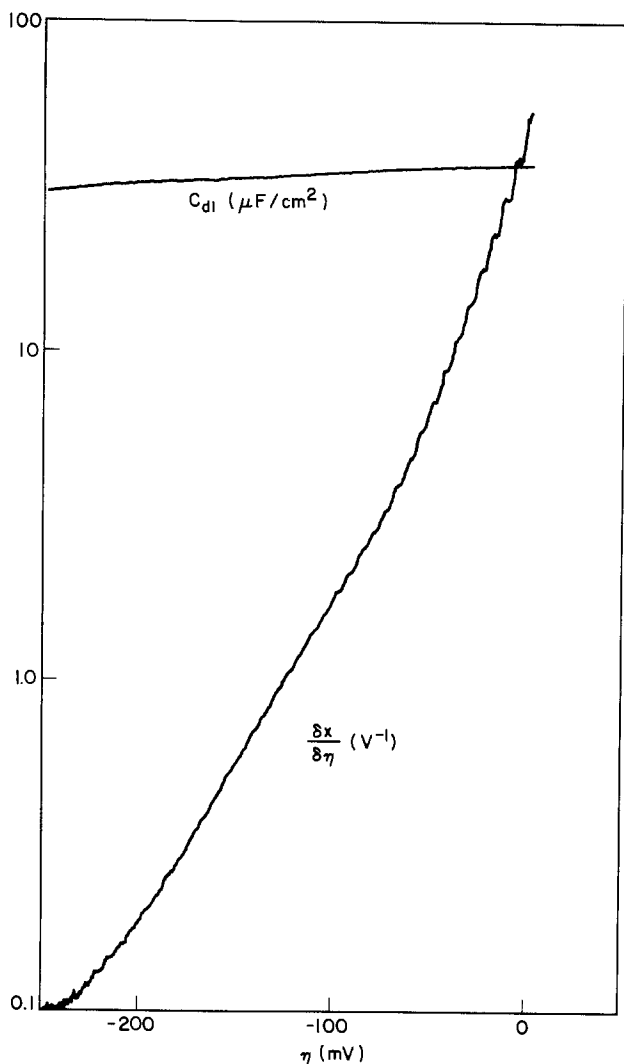


Fig. 3b. The potential dependence of the functions $(\partial x/\partial \eta)_I$ and C_{dl} obtained from the data in Fig. 2. These functions are frequency independent.

within the Nernst layer, which is about 15μ thick under the prevailing rotating disk conditions. The parameter x represents the Pb^{++} concentration, normalized to its bulk value, at an inner Nernst layer plane. Formally, this plane is a hypothetical surface parallel to the electrode beyond which concentration gradients lie normal to the surface and concentration changes can be described by one-dimensional diffusion kinetics. The Warburg admittance is frequency dependent because, as the frequency decreases, an increasing portion of the Nernst layer is sampled by ions diffusing from the electrode surface. For frequencies 40-1000 Hz, this thickness ranges from 0.2-4.0 μ . At still lower frequencies, which allow sufficient time for a concentration perturbation to propagate through the Nernst layer (ca. 1 Hz), the frequency dependence shifts from a $(i\omega)^{1/2}$ dependence to resistive behavior. At higher frequencies deviations from ideal $(i\omega)^{1/2}$ behavior may be anticipated when the size of the sampled region reduces to the scale of surface roughness.

The resistive contribution to the electrode impedance represents the net result of all kinetic processes occurring between the metal surface and the inner Nernst layer boundary. Lower values for $\partial I/\partial \eta$ reflect increased surface inhibition of the electrode reaction, whereas lower values for $\partial x/\partial \eta$ indicate increased retardation by solute concentration gradients. The ratio of these functions, $\partial I/\partial x$, measures the relative contributions of surface and solute effects, and for a 10 mM solution at 200 Hz, both are of the same magnitude for $\partial I/\partial x \approx 0.2$ A/cm².

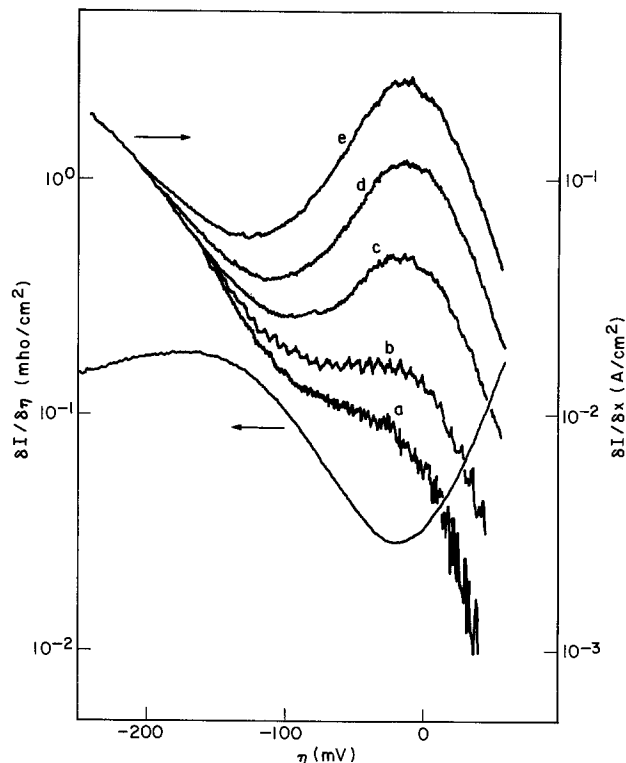


Fig. 4a. The potential dependence of $(\partial I/\partial \eta)_x$ and $(\partial I/\partial x)_\eta$ after a 0.2 mM phenolphthalein addition. The former function is frequency independent. Curves a-e were obtained using 40, 80, 200, 400, and 800 Hz data in combination with 2000 Hz data.

The first surface characteristic we consider is the apparent double layer capacitance. For additive-free solutions this function varies from 30 $\mu F/cm^2$ at -250 mV to 37 $\mu F/cm^2$ at 0 mV. With phenolphthalein added, values range from 24 to 29 $\mu F/cm^2$, and for PPG, 30 to 48 $\mu F/cm^2$. Thiourea solutions show a constant 44 $\mu F/cm^2$ value over most of the cathodic potential range with a drop near 0 mV (Fig. 6b). This decrease was atypical, and all other studies involving this additive gave increases above 0 mV to frequency-dependent values ca., 75 $\mu F/cm^2$.

The range of the capacitances for all solutions is characteristic of the metal-electrolyte interface and reveals no untoward behavior. In particular, there is neither a decrease indicative of a surface film blocking ionic migration to the metal surface nor an enhancement due to reversibly adsorbed surface species. The gradual rise with potential may be rationalized by an increase in surface roughness as deposition progresses. The atypical behavior of thiourea solutions suits this interpretation because of the much larger anodic currents encountered with this additive.

Of the partial derivative functions, let us first examine $\partial x/\partial \eta$. As previously mentioned, this function is determined by changes within the Nernst layer and may therefore be less sensitive to surface complications. Additionally, we have established experimentally that this function is frequency independent with well-defined potential regions of log-linear behavior for the additive-free and thiourea solutions. Consider the nature of this function as given by Eq. [7], bearing in mind that it is not our objective to obtain a "best" fit to this equation, but rather to use it as a guide for discussion. From Eq. [7] we obtain

$$\left(\frac{\partial x}{\partial \eta}\right)_I = (e/kT) (\beta \exp[(\alpha + \beta)e\eta/kT] + \alpha x) \quad [8]$$

and note contributions from two terms corresponding to cathodic and anodic partial currents. At sufficiently

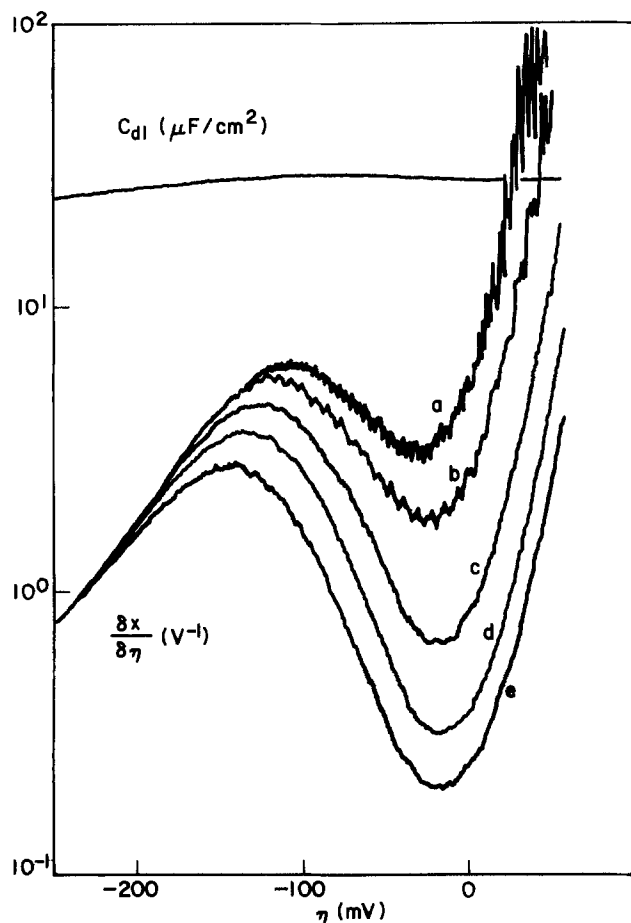


Fig. 4b. The potential dependence of $(\partial x/\partial \eta)_I$ and C_{dl} after phenolphthalein addition (cf. Fig. 4a).

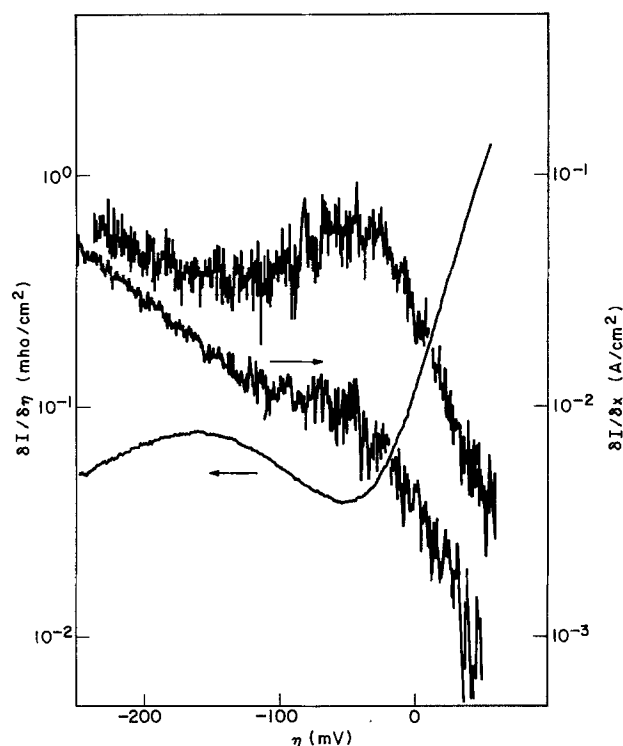


Fig. 5. The potential dependence of $(\partial I/\partial \eta)_x$ and $(\partial I/\partial x)_\eta$ after a 0.5 mM (monomer) addition of polypropylene glycol (PPG). The two plots for the latter function are for 80 and 800 Hz data in combination with 2000 Hz data.

cathodic potentials, this function may be anticipated to be proportional to the inner Nernst plane concentration, x . In the limiting current region in the absence

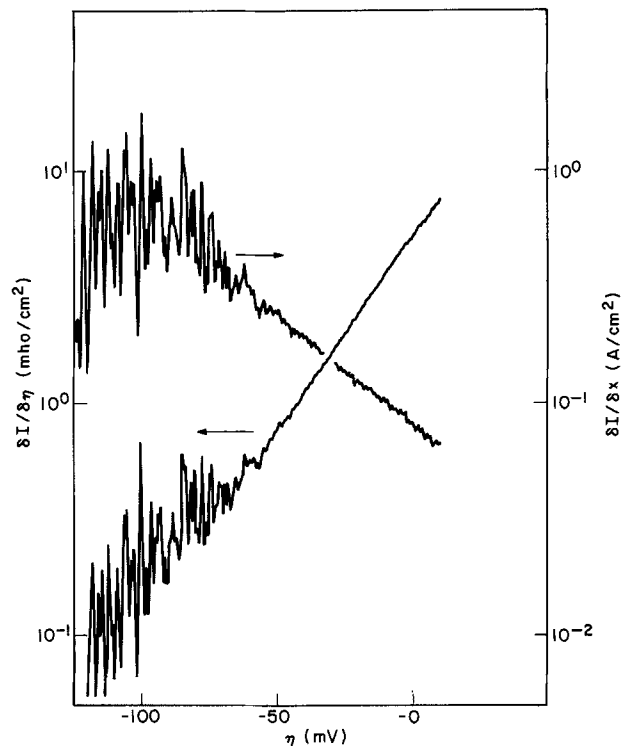


Fig. 6a. The potential dependence of $(\partial I/\partial \eta)_x$ and $(\partial I/\partial x)_\eta$ after a 0.5 mM thiourea addition. These functions are frequency independent.

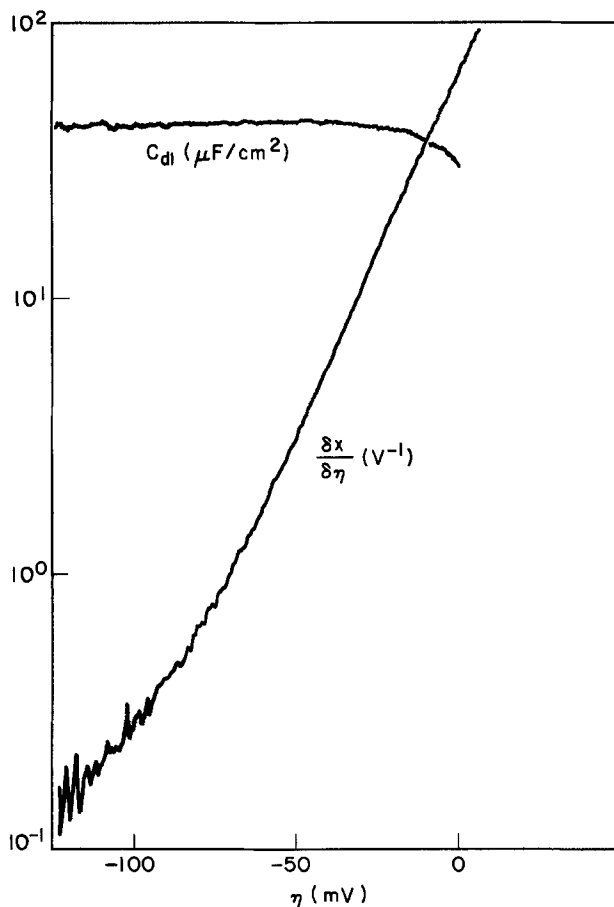


Fig. 6b. The potential dependence of $(\partial x/\partial \eta)_I$ and C_{dl} after thiourea addition (cf. Fig. 6a). The behavior of the latter function is atypical of other measurements on this system.

of additives, we observe log-linear behavior with a 103 mV/decade slope corresponding to $\alpha = 0.58$. It is noteworthy that experimentally this function is frequency

independent and log-linear over a potential range where the other partial functions show a more complex potential and frequency dependence. Between -75 and -50 mV, an increase in slope to 42 mV/decade occurs. Then, according to Eq. [8], $\alpha + \beta = 1.40$. We note that the function's value at $\eta = 0$ independently also gives a value for $\alpha + \beta$, and from this intercept we obtain 1.35.

In the presence of thiourea, log-linear functional behavior is seen down to -75 mV, beyond which a decrease in slope occurs. Signal-to-noise limitations unfortunately obscure an accurate slope evaluation at the lower potentials. Assuming that the extensive linear portion of Fig. 6b reflects the contribution of the anodic partial current, we find from the slope that $\alpha + \beta = 1.53$, while from the $\eta = 0$ intercept, $\alpha + \beta = 1.55$.

Corresponding analyses for $\partial x/\partial \eta$ with phenolphthalein and PPG present are hampered by the frequency dispersion above -150 mV. Below this potential, a frequency-independent log-linear region with a 120 mV/decade slope ($\alpha = 0.5_0$) is found for the former additive, while a more tenuous 130 mV/decade slope ($\alpha = 0.4_6$) can be ascertained for the latter. Separate PPG experiments at 20 Hz and extending to lower potentials gave 115-125 mV/decade slopes over a full decade. Steeper slopes were also observed with these additives at anodic potentials. Although function values were frequency dependent because of the adjacent dispersion region, slopes were less affected. For PPG, Fig. 5 shows 33-36 mV/decade slopes extending over two decades ($\alpha + \beta \approx 1.6-1.8$). With phenolphthalein present, no distinctly linear region was observed, although the slope increased to values within this range at the upper potentials of measurement. In both cases, function values at $\eta = 0$ were too low, by factors of 4 or more, to be self-consistent with the slopes.

To summarize the information garnered from the experimental $\partial x/\partial \eta$ functions, values for α of 0.5-0.6 and for $\alpha + \beta$ of 1.4-1.7 appear consistent with the potential dependence of this function for all three additives studied as well as for the additive-free case. This function also provides a measure of the actual surface concentration of Pb^{++} ions in the limiting current region. At the minimum potentials examined, this concentration was about 0.5% of its bulk value for the additive-free and thiourea solutions, and 3-5% for the phenolphthalein solutions.

The second function of interest is $(\partial I/\partial x)_\eta$, and from Eq. [7]

$$\left(\frac{\partial I}{\partial x}\right)_\eta = -I_0 \exp(-\alpha e\eta/kT) \quad [9]$$

Provided Eq. [7] is relevant, semilog plots for this function should be linear with a slope giving α and an intercept at $\eta = 0$ yielding the exchange current density, I_0 . Note that the previous function discussed is not explicitly dependent upon this parameter.

For additive-free solutions, linear semilog behavior is found above -150 mV, and for thiourea solutions above -125 mV. In the former case, we deduce $\alpha = 0.63$ and $I_0 = 11$ mA/cm², whereas for the latter, $\alpha = 0.61$ and $I_0 = 86$ mA/cm². At lower potentials, this function, particularly in the former instance, appears to peak at a value ca. 1 A/cm² and then decrease in a frequency-dependent manner. This behavior is not predicted by Eq. [7].

For the phenolphthalein and PPG solutions, a frequency-dependent dispersion hinders an equivalent interpretation. A linear and frequency-independent section for this function is observed in the former case between -200 and -125 mV, giving $\alpha = 0.57$ and $I_0 = 1.6$ mA/cm². Below -125 mV, linear plots also appear for the PPG solutions corresponding to $\alpha = 0.30$ and $I_0 = 3.3$ mA/cm². Although both additives have sub-

stantially lowered the exchange current, their differential influences are evident in α values.

In both of these instances, a dispersion leading to a maximum can be seen at higher frequencies. The position of this maximum is correlated with the minimum of $\partial I/\partial \eta$ and, for frequencies in the range 40-1000 Hz, the maximum value increases linearly with frequency. Discussion of possible sources for this dispersion will be deferred, but we note that as $\omega \rightarrow 0$ the experimental behavior of $\partial I/\partial x$ also appears consistent with Eq. [7].

Except in the case of PPG solutions, α values are also in agreement with those given independently by analysis of the function $\partial x/\partial \eta$. The plots of $\partial I/\partial x$ reveal the major influence of additives upon the exchange current density. Thiourea leads to an 8-fold increase, while phenolphthalein gives an equivalent decrease at the concentrations employed.

The third partial function which can be derived from the analysis of impedance data, $\partial I/\partial \eta$, is given by the ratio of the two functions previously discussed. For the model described by Eq. [7]

$$\left(\frac{\partial I}{\partial \eta}\right)_x = (eI_0/kT) [\beta e\beta e\eta/kT + \alpha x e^{-\alpha e\eta/kT}] \quad [10]$$

We note contributions from both anodic and cathodic partial currents. At anodic potentials, a linear semilog plot is expected with a slope yielding β . In the cathodic limiting current region

$$-I \approx I_{\text{lim}} \approx I_0 x \exp(-\alpha e\eta/kT) \quad [11]$$

and a constant value for the function, $\alpha eI_{\text{lim}}/kT$ is predicted. At $\eta = 0$ the function's value reduces to $(\alpha + \beta)(eI_0/kT)$. The traditional ac determination of exchange currents measures this point of the function and generally assumes that $(\alpha + \beta) = z$.

For the thiourea solutions, plots show anodic slopes of 59 mV/decade or $\beta = 1.01$. Measurements using additive-free solutions consistently also gave linear plots corresponding to $\beta = 0.9-1.0$. For the 10 mM limiting current density of 11 mA/cm² and $\alpha = 0.6$, the expected plateau value is 0.26 mho/cm² and is independent of the exchange current. The function derived for the additive-free solution does exhibit a constant value region near this level, but results for thiourea solutions are ambiguous because of a higher noise level.

The general shape of this partial function is complex and shows a distinct minimum for the phenolphthalein and PPG solutions. Rather than relying upon asymptotic behaviors to evaluate parameters, we prefer to simulate function plots based on Eq. [7]. This lets us examine in greater detail information contained in the shape of the curve without approximation. Four parameters are required for a simulation: the limiting current, the exchange current, and α and β . The first has been determined independently and the second was selected to reproduce the value of the function at $\eta = 0$. Plots were then made for various combinations of α and β . Finally a nominal "best" β value was used to construct a family of cathodic curves for different α . These were then complemented by a family of anodic curves for different β values and a "best" α .

Such a simulation is shown in Fig. 8 for phenolphthalein together with the experimental function. On the anodic side, a β value of 0.90-0.95 seems appropriate. At cathodic potentials the experimental function ranges between the simulations for α equal 0.60 and 0.65, but no single value appears adequate to describe the function's shape. Below -150 mV, the experimental function peaks and then slowly declines. This behavior lies beyond the predictions of Eq. [7] and appears to be frequency independent between 40 and 1000 Hz.

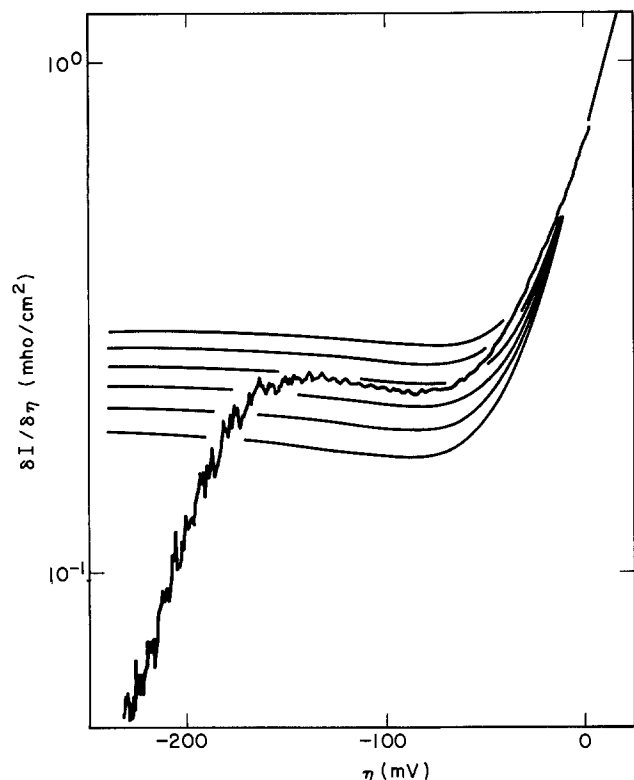


Fig. 7. A comparison of the experimental $(\partial I / \partial \eta)_x$ function in Fig. 3a with theoretical plots based on Eq. [7] for $\alpha = 0.45(0.05)0.70$ and $\beta = 120$.

Corresponding plots for PPG solutions. Fig. 9, suggest $\beta = 1.3$, and in the cathodic region the experimental function lies between simulations for α equals 0.30 and 0.35, with no single value correctly describ-

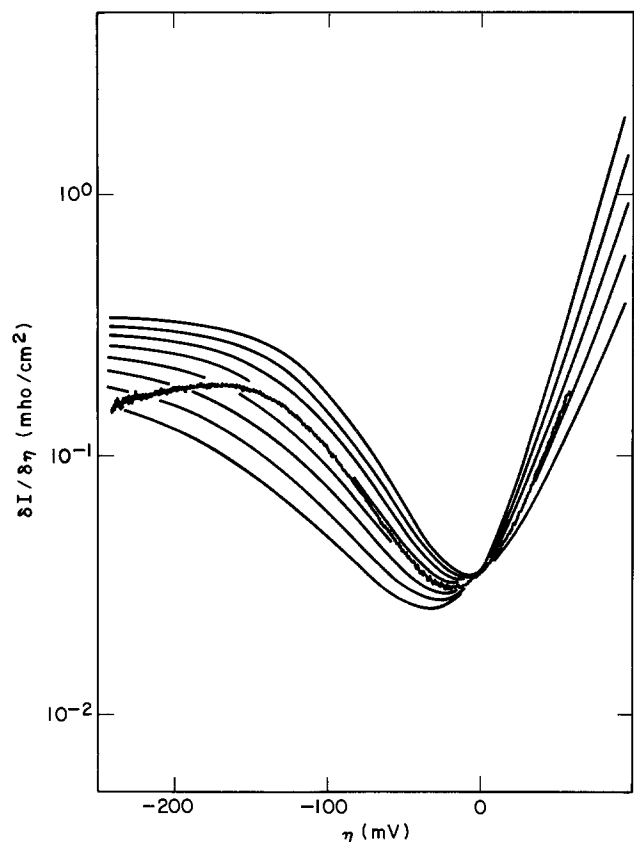


Fig. 8. A comparison of the experimental $(\partial I / \partial \eta)_x$ function in Fig. 4a (phenolphthalein) with theoretical plots based on Eq. [7] for $\alpha = 0.45(0.05)0.80$ and $\beta = 0.8(0.1)1.2$.

ing its shape. Deviations below -150 mV resemble those for the phenolphthalein solutions.

Simulations for additive-free solutions are shown in Fig. 7. The experimental function lies between the curves for α equals 0.55 and 0.60, but as in the preceding cases, no single value suffices to fit the data. Below -150 mV, a more drastic deviation from model behavior is evident, and the function is proportional to $\omega^{1/2}$ for frequencies between 40 and 1000 Hz.

With the exception of the PPG solutions, the general behavior for all functions is consistent with parameters for Eq. [7] of $\alpha \sim 0.6$ and $\beta \sim 1.0$. These values have been derived from a variety of independent features of the partial functions. The exchange current density is strongly dependent upon the additives present.

Previous work has reported values based on the concentration dependence of the exchange current as measured at equilibrium. For the model represented by Eq. [7]

$$I_0 \propto [c]^{\beta/(\alpha+\beta)} \quad [12]$$

Reported values for the exponent vary substantially, 0.15-0.20 (8), 0.37 (7), and 0.5 (10), all of which imply $\alpha \cong \beta$. The position of the minimum for the function $\partial I / \partial \eta$ also depends upon this ratio. Experimentally, this minimum always lies at cathodic potentials and necessarily we require $\alpha < \beta$. We thus see little chance for reconciling previous reports with our studies of variations with potential. (An identical situation exists results for copper deposition (14).) Exchange current densities from previous work range from 10 to 50 mA/cm² for 10 mM solutions, and agree somewhat better with our 11 mA/cm² value for additive-free solutions.

The value $\alpha = 0.6$ strongly suggests a limiting one-electron cathodic process, implying a Pb(I) surface intermediate. If we surmise

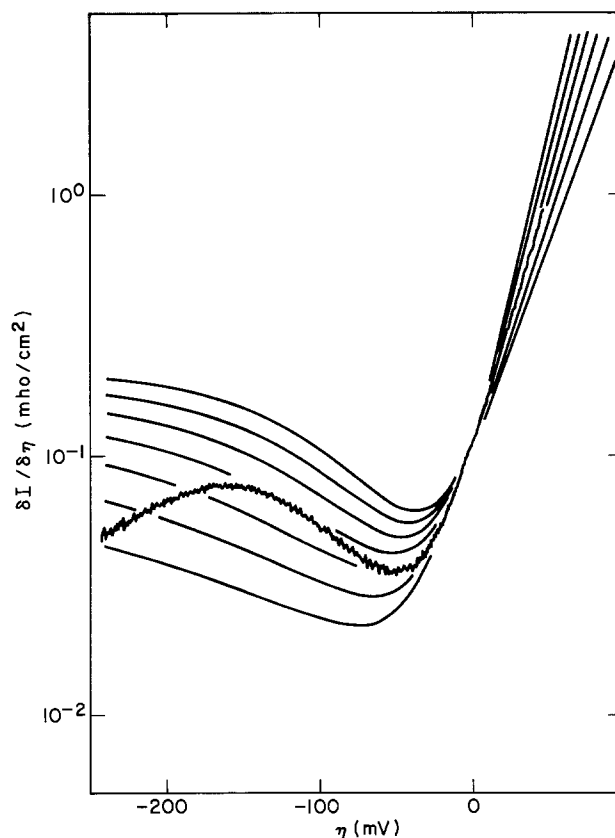
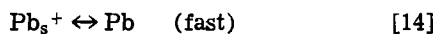


Fig. 9. A comparison of the experimental $(\partial I / \partial \eta)_x$ function in Fig. 5 (PPG) with theoretical plots based on Eq. [7] for $\alpha = 0.2(0.05)0.5$ and $\beta = 1.0(0.1)1.5$.

followed by a rapid second electron transfer



the mechanism would be similar to the Mattson-Bockris interpretation of copper deposition, the primary distinction being in the solubility of the intermediate (14). For this mechanism, the concentration, c_1 , of the surface species will be

$$c_1 = c_{10} \exp(e\eta/kT) \quad [15]$$

and

$$I_2 = I_1 + AF(dc_1/dt) \quad [16]$$

The ac response is therefore given by

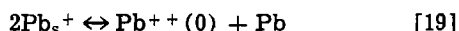
$$I^* = I_1^* + I_2^* = i\omega(eAF/kT)c_1\eta^* + 2I_1^* \quad [17]$$

and

$$I_1^* = \left(\frac{\partial I_1}{\partial \eta} + (ex_1/kT) \frac{\partial I_1}{\partial x_1} \right) \eta^* + \left(\frac{\partial I_1}{\partial x_2} \right) x_2^* \quad [18]$$

This two-step model predicts an additional capacitance of $eAFc_1/kT$ in parallel with the double layer capacitance, and this capacitance should increase exponentially with potential. The expected form of $\partial I/\partial \eta$ is also modified. No anomalous behavior was found for the double layer capacitance and, assuming a maximum contribution of order $10 \mu\text{F}/\text{cm}^2$, the maximum surface concentration would be of order $10^{12}/\text{cm}^2$ (0.1%) at any potential. This model further requires that $\alpha + \beta = 2$, somewhat at variance with our results.

An alternative path might involve a rapid surface disproportionation reaction for the second step, *i.e.*



in which case $x_2 = x_1^2$. In this instance

$$I^* = \left(\frac{\partial I}{\partial \eta} \right) \eta^* + \left[\frac{\partial I}{\partial x_2} + (1/2x_1) \left(\frac{\partial I}{\partial x_1} \right) \right] x_2^* \quad [20]$$

and we find the function $\partial I/\partial x$ to be now affected. Simulations show that instead of being log-linear, this function will bend downwards with increasing potential. All experimental deviations lie in the opposite direction. Although a value $\alpha + \beta = 1.5$ can be deduced for this model from slopes, at $\eta = 0$ a value of 2 should still be given by $\partial x/\partial \eta$.

The dispersions observed in plots for phenolphthalein and PPG appear in regions where the resistive surface impedance substantially exceeds the diffusional impedance, whereas the cathodic dispersion for additive-free solutions occurs where the converse situation prevails. Both may be empirically explained by a Warburg-like admittance, $Y = (i\omega)^{1/2}W_x$, in parallel with both the double layer capacitance and the electro-deposition admittance.

Such an element couples the apparent partial functions because of the method of analysis. In the former instance, as a limiting case.

$$\left(\frac{\partial I}{\partial x} \right)_{\text{app}} \simeq \omega zFA\sqrt{D}c_0W_x \left(\frac{\partial I}{\partial \eta} \right)^{-1} \quad [21]$$

The proportionality to frequency and the inverse variation with $\partial I/\partial \eta$ seen in Fig. 4a and 4b are accounted for, as well as the absence of a significant dispersion for $\partial I/\partial \eta$. From Fig. 4, we estimate $W_x = 3 \times 10^{-6}$ mho-s^{1/2} for the true electrode area. In the converse situation, it is $(\partial I/\partial \eta)$ which is most sensitive to W_x and

$$\left(\frac{\partial I}{\partial \eta} \right)_{\text{app}} \simeq \left(\frac{\partial I}{\partial \eta} \right) \left[1 - (2\omega)^{1/2}W_x \left(\frac{\partial I}{\partial \eta} \right)^{-1} \right]^{-1} \quad [22]$$

From the 800 Hz plot in Fig. 3a, we obtain $W_x = 2 \times 10^{-6}$ mho-s^{1/2}. The magnitude of this empirical admittance is a fraction of that of the double layer ca-

pacitance, even at the lowest frequencies, typically 10%. Since similar magnitudes for W_x account for both dispersions, we will not associate it with the deposition process. The dispersions may reflect nonideal double layer capacitance behavior at low frequencies, possibly related to the observed surface film. Electrode imperfections, particularly at the metal-epoxy interface, might also be involved. Although a correction for this effect would increase the value of $\partial x/\partial \eta$, it amounts to only 2% for 40 Hz additive-free data at $\eta = 0$ and does not significantly raise the reported value for $\alpha + \beta$ of 1.35.

The value for $(\partial x/\partial \eta)_{I=0}$ should correspond to the slope of a plot of $(\ln c)$ vs. the equilibrium electrode potential, and for a reversible two-electron process the Nernst equation gives $78 \text{ V}^{-1} = ez/kT$. Experimentally however, we find values ca. 55 V^{-1} . Open-circuit potentials were therefore measured for concentrations between 1 and 50 mM $\text{Pb}(\text{ClO}_4)_2$ in 1N HClO_4 . Plots for both bulk lead electrodes and thin film deposits on platinum gave canonical 30 mV/decade slopes.

Additional experiments were attempted to resolve the difference between ac results and the open-circuit potential measurements. One possibility was that the freshly formed surfaces studied might not be near a state of thermodynamic equilibrium. Changes in ac response were therefore monitored at several frequencies after a plating cycle was halted at -1 mV. Results were subjected to a partial derivative analysis and are shown in Fig. 10.

Over the first several minutes there is a 40% drop in $\partial I/\partial \eta$, and a 15% drop in the double layer capacitance, but $\partial x/\partial \eta$ remains constant at $52 \pm 2 \text{ V}^{-1}$ during the decay period. The capacitance drop probably reflects a roughness decrease by dissolution, while the larger decrease in $\partial I/\partial \eta$ corresponds to a reduction in the exchange current, possibly through a reduction in the

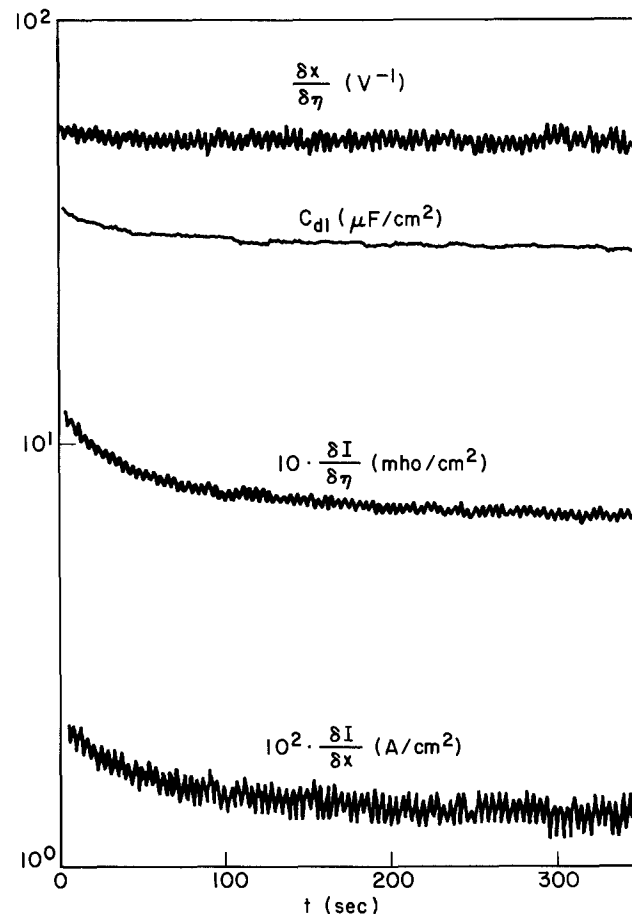


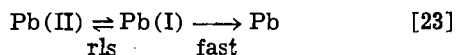
Fig. 10. The decay of partial functions when the potential sweep was halted at -1 mV.

surface density of growth sites. The behavior of $\partial x/\partial \eta$, however, fails to show a relaxation towards its equilibrium value.

Complex plane measurements to a lower frequency of 0.5 Hz were also made using a nonrotating electrode after a 5 min waiting period. Impedance diagrams showed a linear 45° plot below 50 Hz, and from Z'' values below 5 Hz we obtained $\partial x/\partial \eta = 52 \pm 4 \text{ V}^{-1}$, agreeing with fixed frequency measurements.

The ac results appear to be internally self-consistent, but suggest no explanation for their divergence from equilibrium expectations. Evaluation of $\partial x/\partial \eta$ does require known values for the diffusion coefficient, electrode area, and concentration, and does presume that all current crossing the metal/electrolyte interface is initially carried by diffusing Pb^{++} ions. We might speculate among these possibilities, but the fact remains that the $\partial x/\partial \eta$ functions also give values for $\alpha + \beta$ which concur with values obtained independently from the slopes of the various functions.

If we forsake a detailed balance representation for equilibrium electrode behavior at the frequencies employed, the simplest interpretation is a two-step reduction path: the first being a rate-determining charge transfer step, the second a rapid and irreversible step



One interpretation could be electron transfer to a solvated Pb(II) ion followed by the rapid decay of an unstable Pb(I) species. The irreversibility of the second step insures the absence of a detectable capacitance due to the intermediate.

Anodic behavior, characterized by $\beta \simeq 1$, has as its simplest interpretation the direct dissolution of a doubly charged lead ion which acquires its solvation shell within the Helmholtz layer



The drop in $\partial I/\partial \eta$ from its plateau at extreme cathodic potentials is reminiscent of the behavior of tin (11). There we proposed an explanation based on three-dimensional concentration gradients focused upon discrete deposition sites. The essential distinction between one- and three-dimensional diffusion processes is that the latter lead to a resistive or frequency independent contribution to the impedance, whereas the former have a $(i\omega)^{1/2}$ dependence.

To translate this effect into the present formulation, we shall split the diffusion process into two spatial regions, with r being the distance from the electrode. For $a < r < b$ hemispherical diffusion predominates, while for $b < r$ the linear model will be assumed. Solution of the diffusion equation

$$i\omega c^*(r) = D\nabla^2 c^*(r) \quad [25]$$

with fixed boundary conditions for $c^*(r)$ at $r = a$ and $r = b$ leads to

$$\begin{aligned} a < r < b \quad c^*(r) &= c^*(a) \frac{a \sinh[\gamma(b-r)]}{r \sinh[\gamma(b-a)]} \\ &+ c^*(b) \frac{b \sinh[\gamma(r-a)]}{r \sinh[\gamma(b-a)]} \\ b < r \quad c^*(r) &= c^*(b) \exp[-\gamma(r-b)] \end{aligned} \quad [26]$$

where $\gamma = (i\omega/D)^{1/2}$.

Renormalization by equating the hemispherical and planar fluxes at $r = b$ lets us solve for $c^*(a)$ in terms of the current or flux at $r = a$. Omitting a lengthy exercise, we obtain in the low frequency limit, $i\omega b^2 \ll D$.

$$c^*(a) = I^*[(2\pi N a z F A D)^{-1} + (z F A / i\omega D)^{-1}] \quad [27]$$

where N is the density of deposition sites with effective radius a . Substitution into Eq. [1] gives

$$\begin{aligned} Z^* &= \left(\frac{\partial I}{\partial \eta} \right) + \left(2\pi N a z F A D c_0 \frac{\partial x}{\partial \eta} \right)^{-1} \\ &+ \left(\sqrt{i\omega D} z F A c_0 \frac{\partial x}{\partial \eta} \right)^{-1} \end{aligned} \quad [28]$$

The second rhs term is a resistive addition due to constrictive diffusion. When this term dominates the contribution from $\partial I/\partial \eta$

$$\left(\frac{\partial I}{\partial \eta} \right)_{\text{app}} = 2\pi N a z F A D c_0 \left(\frac{\partial x}{\partial \eta} \right) \quad [29]$$

and

$$- \left(\frac{\partial I}{\partial x} \right)_{\text{app}} = 2\pi N a z F A D c_0 \quad [30]$$

Thus, the latter function, as evaluated by our analysis, should show limiting cathodic behavior proportional to the density of deposition sites. For additive-free lead solutions, the experimental function attains a maximum value ca. 0.5 A/cm², corresponding to $N a = 4000$, or estimating $a \simeq 5 \times 10^{-8}$ cm, $N \simeq 8 \times 10^{10}$ /cm². For PPG and phenolphthalein solutions, only minor deviations from linearity for this function were found, but the maximum value reached was but 0.05 A/cm² over the potential range studied. Thiourea solutions show some indications of also limiting at the 0.5 A/cm². Given the thickness of these deposits, this number density may be correlated with grain size, implying that only a small number of growth sites are concurrently active per grain.

Our findings also offer some insights into the manner by which additives influence lead plating. One might postulate their role is either to modify the density of growth sites or the rate-limiting step, or both. Thiourea and phenolphthalein were found to change the exchange current density in opposite directions, but α and β values remained similar to those for additive-free solutions. This suggests that these additives function primarily by altering growth site densities, but not kinetics at these sites. The behavior of PPG, however, differs significantly. Apart from reducing the exchange current density, it markedly reduces α and increases β . Interestingly, $\alpha + \beta$ remains about the same as for the other cases, suggesting a common rate-limiting step, but with the limiting barrier relocated in the Helmholtz region. The shift to a lower α value indicates a greater portion of the bias potential appears between the metal surface and the barrier, as would be the case if an intervening layer of low polarizability were present.

Kohl has examined the morphological and voltammetric effects of phenolphthalein and Triton X-100 on Sn/Pb plating from HBF_4 (12). The latter additive, like PPG a polyglycol, was found to suppress dendritic growth without appreciably changing the surface resistance, whereas phenolphthalein significantly increased this resistance without inhibiting dendrite formation. For the systems we have examined, both additive types increased surface resistance at $\eta = 0$, as indicated by reductions in exchange current densities. However, because of a lower α value, the polyglycol is more effective in maintaining a high surface resistance at cathodic deposition potentials.

Finally, we should comment briefly on the surface film mentioned among our results. The interpretation of impedance measurements has not invoked this film, and were it not for a visual microscopic inspection, its presence would have gone undetected. Normal double layer behavior indicates the film must be quite porous and permeable to the electrolyte. Possibly the film is buried during deposition and only surfaces upon stripping. At the completion of stripping, we have always observed abrupt changes in ac and dc currents, with no lingering tail to indicate slowly oxidizing lead.

We anticipate such behavior should the film contain metallic lead residues.

The visual changes seen during oxidation of the wet film might suggest a Pb(I) species. This, however, runs counter to established lead chemistry, and Pb⁺ ions have only been observed in the gas phase and matrices subjected to ionizing radiation (17). The reported suboxide, Pb₂O, is believed to be a nonstoichiometric mixture of Pb and Pb(II) (18). Our conclusion that Pb⁺⁺ reduction is limited by a one-electron transfer step requires only a transient Pb⁺ state. Indeed, no pseudocapacitance was found which would reveal an equilibrium surface concentration. If the film is related to the suboxide mixture, then why it is not oxidized to PbO during stripping remains an unanswered question.

Manuscript submitted May 19, 1983; revised manuscript received Nov. 11, 1983.

AT&T Bell Laboratories assisted in meeting the publication costs of this article.

REFERENCES

1. C. Gabrielli and M. Keddam, *Electrochim. Acta*, **19**, 355 (1975).
2. R. D. Armstrong, M. F. Bell, and A. H. Metcalfe, *J. Electroanal. Chem.*, **77**, 287 (1977).
3. R. J. Schwall, A. M. Bond, R. J. Loyd, J. G. Larson,

- and D. E. Smith, *Anal. Chem.*, **49**, 1797 (1977).
4. B. D. Cahan and C. T. Chen, *This Journal*, **129**, 474 (1982).
5. S. H. Glarum and J. H. Marshall, *ibid.*, **128**, 968 (1981).
6. W. Lorenz, *Z. Phys. Chem.*, **19**, 377 (1959).
7. S. Haruyama, *J. Electrochem. Soc. Jpn.*, **35**, 62 (1967).
8. N. A. Hampson and D. Larkin, *Trans. Faraday Soc.*, **65**, 1660 (1969).
9. E. M. Strochkova, K. V. Rybalka, and D. I. Leikis, *Elektrokhimiya*, **11**, 336 (1975).
10. V. I. Chernenko and Yu. E. Udovenko, *ibid.*, **13**, 1311 (1977).
11. S. H. Glarum and J. H. Marshall, *This Journal*, In press.
12. P. A. Kohl, *ibid.*, **129**, 1196 (1982).
13. R. Parsons, "Handbook of Electrochemical Constants," Butterworth, London (1959).
14. E. Mattson and J. O'M. Bockris, *Trans. Faraday Soc.*, **55**, 1586 (1959).
15. J. Newman, "Electrochemical Systems," p. 177, Prentice-Hall, Englewood Cliffs, NJ (1973).
16. O. R. Brown and H. R. Thirsk, *Electrochim. Acta*, **10**, 383 (1965).
17. T. Tsuboi, *Phys. Rev. B*, **21**, 2635 (1980).
18. M. C. Sneed and R. C. Brasted, "Comprehensive Inorganic Chemistry," Vol. VII, p. 236, Van Nostrand, New York (1967).
19. K. J. Vetter, "Electrochemical Kinetics," section 62, Academic Press, New York (1967).

A Mathematical Model for the Iron/Chromium Redox Battery

Peter S. Fedkiw* and Rick W. Watts

Department of Chemical Engineering, North Carolina State University, Raleigh, North Carolina 27695

ABSTRACT

A mathematical model has been developed to describe the isothermal operation of a single anode-separator-cathode unit cell in a redox-flow battery and has been applied to the NASA iron/chromium system. The model, based on porous electrode theory, incorporates redox kinetics, mass transfer, and ohmic effects as well as the parasitic hydrogen reaction which occurs in the chromium electrode. A numerical parameter study was carried out to predict cell performance to aid in the rational design, scale-up, and operation of the flow battery. The calculations demonstrate: (i) an optimum electrode thickness and electrolyte flow rate exist; (ii) the amount of hydrogen evolved and, hence, cycle faradaic efficiency, can be affected by cell geometry, flow rate, and charging procedure; (iii) countercurrent flow results in enhanced cell performance over cocurrent flow; and (iv) elevated temperature operation enhances cell performance.

A redox cell stores energy in the change of the oxidation state of a fully soluble redox couple. The use of redox reactions in a battery was pointed out by Thaller (1) and the developmental effort has been mainly carried out at NASA-Lewis (2). Cost studies (3, 4) have projected that the redox battery is a promising energy storage system for load leveling. An extensive search by NASA for possible redox couples and electrode materials has led to the present acidified Fe(II)/Fe(III) and Cr(II)/Cr(III) couples carried out on a catalyzed graphite felt electrode. Other redox battery systems have been examined (5-7) as well as hybrid batteries in which one electrode involves a soluble redox couple and the other uses a reactant with a phase change (8-10). The Zn/Cl₂ and Zn/Br₂ cells may be classified as a hybrid redox cell.

The design of the Cr/Fe cell has proceeded mainly by an experimentally guided effort. The technology has progressed to the point where pilot plant evaluations of the battery system are now feasible. The scale up from the laboratory could proceed more efficiently if a predictive mathematical model was available to guide quantitatively the work and aid in the correlation and extrapolation of experimental data. This report discusses such a model which is generated by ap-

plying porous electrode theory to a single iron electrode-separator-chromium electrode unit cell. Optimization of the battery design and operation may be rationally guided with the model, and examples of such results are given. The calculations presented here use parameters which are characteristic of the Fe/Cr system, but the discussion presents guidelines which may be applied to other flow battery systems.

Newman and Trainham have presented a model for the Fe/Ti redox flow cell (11). They compared the flow-through to the flow-by electrode configuration and concluded that the flow-by configuration, as utilized in the NASA cell, was inherently the better of the two. Several assumptions were made in their analysis which limits its utility. They assumed: (i) linear kinetics; (ii) a single electrode reaction in each compartment; and (iii) potential variations in the current flow direction and concentration variations in the streamwise flow direction only. These assumptions were not made in the present analysis and, hence, the effect of geometrical and operational parameters on faradaic efficiency and cell performance can be better examined.

Model Development

Figure 1 shows a schematic diagram of a single anode-separator-cathode unit in the redox battery. In

* Electrochemical Society Active Member.
Key words: battery, energy storage.

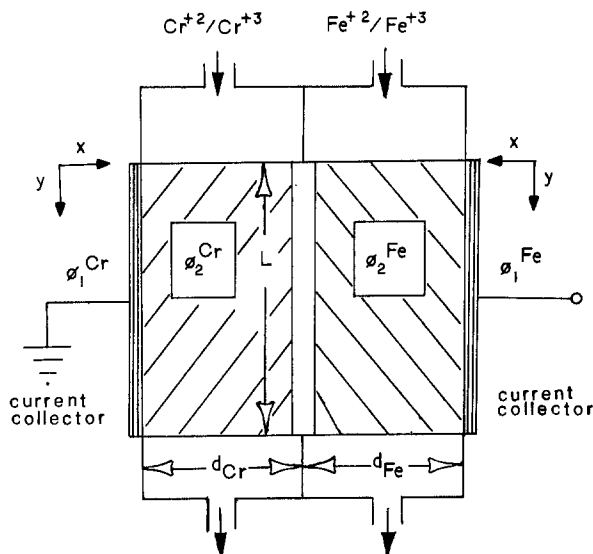


Fig. 1. Schematic diagram of the Fe-Cr redox cell

an actual battery, a number of these cells are arranged in series in a cell stack. The electrode is a porous graphite felt which is compressed by the bipolar current collectors. The felt in the chromium compartment is coated with an Au/Pb catalyst. The potential and concentration of reactant and product are assumed to vary in both the X and Y coordinate within each electrode. Variations along the cell width are neglected. The fluid enters the cell through a manifold, flows through the electrode, and exits through another manifold. The individual cells in a cell stack share a common inlet and outlet manifold for each electrolyte. The anolyte and catholyte solutions are acidified with HCl and are isotonic to prevent the swelling of the membrane separator. Not shown in the figure are the two storage tanks from which the solutions are recirculated and the potential sensing open-circuit cell and a rebalance cell which are an integral part of a fully functional cell stack (2).

The volume-averaged conservation of charge and mass equations, porous electrode theory, are applied within each electrode under isothermal operating conditions (12). The reaction distribution within the chromium compartment depends upon the reaction distribution within the iron compartment since the charge transferred from one flows to the other across the separator. Consequently, the equations are coupled by the continuity conditions imposed at the separator. The following effects are accounted for: (i) the kinetics of each redox reaction; (ii) the parasitic hydrogen reaction which occurs in the chromium compartment. (Since the Cr(III)/Cr(II) couple is electro-negative, there normally exists a cathodic overpotential for proton reduction which is particularly an acute problem on charge near full state-of-charge conditions. No secondary reactions occur in the Fe electrode.); (iii) cell geometry; (iv) mass-transfer effects; (v) state-of-charge; (vi) separator resistance; and (vii) solution physical properties. The governing equations for each electrode compartment are discussed below.

Conservation

$$\text{of charge: } \kappa_j \nabla^2 \phi_j^l = a_i i_{n,\text{total}} \quad [1]$$

The conservation of charge equation has been written assuming Ohm's law is valid; since the solutions are well supported, the migration flux is neglected. The right side of the balance represents the total charge density per unit electrode volume leaving the matrix phase. In the iron compartment only one reaction occurs, but in the chromium compartment the redox reaction and proton reduction both contribute to this term. The effective solution conductivity in the

electrode is calculated from that of the electrolyte by $\kappa = \epsilon^{1.5} \kappa_0$ (13).

Conservation

$$\text{of mass: } v_j \nabla C^j = \epsilon D_j \nabla^2 C^j + \frac{\alpha_i i_{n,j} s_{R^j}}{n_j F} \quad [2]$$

Dispersion is neglected in the y direction but diffusion is accounted for. Convective transport only occurs in the y direction; it is assumed that there is no fluid velocity in the x direction, but rather diffuse transport of material occurs along this coordinate. A similar equation as used for κ is applied to calculate the effective diffusivity ϵD from the bulk value. It was assumed in the analysis that the diffusivity of the (II) oxidation state of a species was the same as that of the (III) species; consequently, only one differential mass balance was required in each compartment since an algebraic expression gave the concentration of the other redox species. In this work, a balance was written for Fe^{+2} and Cr^{+3} , the reactants in a charge cycle.

$$\text{Surface flux: } \frac{s_{R^j} i_{n,j}}{n_j F} = k_{mj} (C^j - C_s^j) \quad [3]$$

A mass transfer coefficient is used with Faraday's law to relate the local electrochemical reaction rate to the local surface-to-bulk concentration difference of the reactant. The Wilson-Geankoplis correlation for k_m was used (14).

$$\begin{aligned} \text{Kinetics: } i^{\text{Fe}_{n,\text{total}}} = i_{n,\text{Fe}} = i^{\text{Fe}_{o,f}} \left\{ (\text{Fe}_{s^{+2}}/\text{Fe}_{t^{+2}}) \right. \\ \left. \exp \left[\frac{F}{RT} \alpha_{\text{A}^{\text{Fe}}} (\phi_1^{\text{Fe}} - \phi_2^{\text{Fe}}) \right] - (\text{Fe}_{s^{+3}}/\text{Fe}_{t^{+3}}) \right. \\ \left. \exp \left[-\frac{F}{RT} \alpha_{\text{C}^{\text{Fe}}} (\phi_1^{\text{Fe}} - \phi_2^{\text{Fe}}) \right] \right\} \quad [4] \end{aligned}$$

$$\begin{aligned} i^{\text{Cr}_{n,\text{total}}} = i_{n,\text{Cr}} + i_{n,\text{H}_2} = i^{\text{Cr}_{o,f}} \left\{ (\text{Cr}_{s^{+2}}/\text{Cr}_{t^{+2}}) \right. \\ \left. \exp \left[\frac{F}{RT} \alpha_{\text{A}^{\text{Cr}}} (\phi_1^{\text{Cr}} - \phi_2^{\text{Cr}}) \right] - (\text{Cr}_{s^{+3}}/\text{Cr}_{t^{+3}}) \right. \\ \left. \exp \left[-\frac{F}{RT} \alpha_{\text{C}^{\text{Cr}}} (\phi_1^{\text{Cr}} - \phi_2^{\text{Cr}}) \right] \right\} \\ + i_{o,\text{H}_2} \left\{ \exp \left[\frac{F}{RT} \alpha_{\text{A}^{\text{H}}} (\phi_1^{\text{Cr}} - \phi_2^{\text{Cr}} - U_{\text{AH}}) \right] \right. \\ \left. - \exp \left[-\frac{F}{RT} \alpha_{\text{C}^{\text{H}}} (\phi_1^{\text{Cr}} - \phi_2^{\text{Cr}} - U_{\text{AH}}) \right] \right\} \quad [5] \end{aligned}$$

The redox reactions are assumed to occur by simple elementary steps which are characterized by a Butler-Volmer type expression. The chromium redox reaction is actually somewhat more complicated. The Cr(II) and Cr(III) species form complexes with Cl^- ions which effect their reactivity (15). In particular, the monochloride-pentahydrate complex of Cr(III) is easier to reduce than the hexahydrate complex. Both species exist in solution but higher temperature favors the monochloride species.

The electrode potential, ϕ_1^l , is assumed uniform because of the high conductivity of the matrix. The solution potential, ϕ_2^l , is measured with a reference electrode of the same kind as the main reaction in electrode j. The concentrations of reactant and product in this hypothetical reference electrode are at the feed conditions. The exchange current density for the redox reaction is, consequently, evaluated at the feed condition which is dependent upon the state-of-charge as shown below

$$i^{\text{Fe}_{o,f}} = i^{\text{Fe}_{o,\text{ref}}} \left[\frac{\text{Fe}_{t^{+2}}}{\text{Fe}_{\text{ref}^{+2}}} \right]^{\alpha_{\text{C}^{\text{Fe}}}} \left[\frac{\text{Fe}_{t^{+3}}}{\text{Fe}_{\text{ref}^{+3}}} \right]^{\alpha_{\text{A}^{\text{Fe}}}} \quad [6]$$

$$i_{Cr_{o,f}} = i_{Cr_{o,ref}} \left[\frac{Cr_f^{+2}}{Cr_{ref}^{+2}} \right]^{\alpha_{O^{Cr}}} \left[\frac{Cr_f^{+3}}{Cr_{ref}^{+3}} \right]^{\alpha_{A^{Cr}}} \quad [7]$$

The hydrogen reaction occurs in the chromium compartment because of the large driving force for proton reduction. The term U^{AH} in the hydrogen kinetic expression is dependent upon the state-of-charge and accounts for the open-circuit potential difference between the Cr(III) and the proton reduction; it was calculated assuming Nernstein behavior. It was assumed that the proton reduction is kinetically controlled, and since the H^+ concentration is approximately one order of magnitude greater than the total Cr species, a mass balance for H^+ was not required.

The boundary conditions on the potential for each electrolyte were specified as follows

$$y = 0 \quad \frac{\partial \phi_2^j}{\partial y} = 0 \quad [8]$$

$$y = L \quad \frac{\partial \phi_2^j}{\partial y} = 0 \quad [9]$$

$$x = 0 \quad \frac{\partial \phi_2^j}{\partial x} = 0 \quad [10]$$

$$x = d_{Cr} \quad R_{s^{Cr}} \frac{\partial \phi_2^{Cr}}{\partial x} = \phi_2^{Cr} - \phi_2^{Fe} - V_{oc} \quad [11]$$

$$x = d_{Fe} \quad -R_{s^{Fe}} \frac{\partial \phi_2^{Fe}}{\partial x} = \phi_2^{Cr} - \phi_2^{Fe} - V_{oc} \quad [12]$$

Equations [8] and [9] assume no shunt current in the manifold. In a cell stack, a potential difference between electrolytes in adjacent compartments will cause a shunt current. Proper design of the manifold system can reduce the shunt current but not eliminate it. The results presented here can be thought of as a best case where the parasitic loss of shunt current has been totally eliminated. Equation [10] states that all the current is carried by the matrix at the current collector. Equations [11] and [12] express the continuity of current and potential across the electrolyte-separator interface in the chromium and iron electrode, respectively. The separator resistance R_s is assumed to be constant.

The boundary conditions on Cr^{+3} and Fe^{+2} depend upon the electrolyte flow orientation: cocurrent or countercurrent

$$y = 0 \quad \begin{array}{c} \text{Fe} \\ -\epsilon D_{Fe} \frac{\partial C^{+2}}{\partial y} + vC^{+2} = vC_f^{+2} \end{array}$$

$$y = L \quad \frac{\partial C^{+2}}{\partial y} = 0$$

$$x = 0 \quad \frac{\partial C^{+2}}{\partial x} = 0$$

$$x = d \quad \frac{\partial C^{+2}}{\partial x} = 0$$

feed ratio of Fe^{+2} and Cr^{+3} , respectively. Four coupled nonlinear elliptic partial differential equations were generated and made dimensionless, and thereby generating nine dimensionless terms characteristic of each electrode. A finite-difference-collocation numerical procedure (16) was used to solve this nonlinear system by iteration until a relative difference of 10^{-5} was obtained between each iteration for all dependent variables at all points on the solution grid. As a check of the validity of the numerical integration, the cell current was calculated three independent ways: (i) concentration change of Fe^{+2} from inlet to outlet; (ii) integrated membrane current density; and (iii) volumetric integration of local Fe reaction rate or Cr plus H_2 reaction rate. In the worst case, the largest deviation of a current from the average value of the above three methods was 0.2%. The detailed nondimensional equations and parameters and further discussion of the numerical solution scheme are given by Watts (17).

Results and Discussion

It was beyond the scope of this work to optimize the cell design and operation. However, an endeavor has been made to illustrate that optimum design and operational parameters and charge/discharge protocols exist, and the model is a useful aid in finding these optima.

The numerical solution to the model equations has been used to: (i) calculate the cell performance map (current-voltage-flow rate relationship); (ii) investigate the effect of countercurrent and cocurrent arrangement of reactant streams; (iii) study the effect of electrode thickness and length; (iv) study the effect of higher temperature operation; and (v) investigate two different charge/discharge protocols.

The open-circuit voltage varied with the depth of discharge and was calculated by

$$V_{oc} = V_{formal} - (RT/F) \ln [(Cr_f^{+3}Fe_f^{+2}) / (Cr_f^{+2}Fe_f^{+3})] \quad [17]$$

The voltage V_{formal} was set at 1.05V (2). The depth of discharge, f , defines the reactant and product concentrations at any given time and is defined by the following

$$\begin{aligned} Cr_f^{+3} &= fCr_1^{+3} \\ Cr_f^{+2} &= (1-f)Cr_1^{+3} \\ Fe_f^{+2} &= (Fe_1^{+2} - Cr_1^{+3}) + fCr_1^{+3} \\ Fe_f^{+3} &= Fe_1^{+3} + (1-f)Cr_1^{+3} \end{aligned} \quad [18]$$

$$\begin{array}{c} \text{Cr} \\ \text{cocurrent:} \quad -\epsilon D_{Cr} \frac{\partial C^{+3}}{\partial y} + vC^{+3} = vC_f^{+3} \end{array}$$

$$\text{countercurrent:} \quad \frac{\partial C^{+3}}{\partial y} = 0$$

[13]

$$\text{cocurrent:} \quad \frac{\partial C^{+3}}{\partial y} = 0$$

$$\text{countercurrent:} \quad -\epsilon D_{Cr} \frac{\partial C^{+3}}{\partial y} + vC^{+3} = vC_f^{+3}$$

[14]

$$\frac{\partial C^{+3}}{\partial x} = 0 \quad [15]$$

$$\frac{\partial C^{+3}}{\partial x} = 0 \quad [16]$$

Equation [3] was combined with the kinetic expression for $i_{n,Fe}$ or $i_{n,Cr}$ to eliminate the surface-to-

It was assumed that Cr was the limiting reactant as would occur with isotonic electrolytes. The subscript 1

Table I. Parameters used in calculations

Parameter	Cr	Fe	H ₂
$i_{0, \text{ref}}$ (mA/cm ²) (at $f = 0.5$)	50 (25°C) 100 (65°C)	7.5 (25°C) 15 (65°C)	5×10^{-5} (25°C) 10^{-4} (65°C)
α_A	0.65	0.5	0.5
α_C	0.35	0.5	0.5
κ_0 ($\Omega^{-2}\text{cm}^{-1}$)	0.5 (25°C) 1.0 (60°C)	0.5 (25°C) 1.0 (60°C)	—
D_0 (cm ² /s)	6×10^{-6}	6×10^{-6}	—
a (cm ⁻¹)	280	280	—
d (cm)	0.1-0.25	0.1-0.25	—
L (cm)	15-122	15-122	—

at $f = 0.5$: $\text{Cr}^{+3} = \text{Cr}^{+2} = 0.45M$ and $\text{Fe}^{+2} = \text{Fe}^{+3} = 0.55M$
 f : 0.1-0.9
 Q : 80-800 ml/min
 R_s : $2 \Omega \cdot \text{cm}^2$ (65°C)
 $4 \Omega \cdot \text{cm}^2$ (25°C)
 U^{AB} : 0.33V at $f = 0.5$
 W : 30.48 cm

signifies the concentration is evaluated at fully discharged conditions ($f = 1$).

Net power calculations are reported here and represent the gross power from the cell minus the parasitic pumping loss. The pumping loss was calculated by applying the Ergun equation (18) to find the pressure drop across the felt electrode and adding that loss to the pressure drop in the inlet and outlet manifold. The latter was calculated by using an empirical correlation to fit the available hydraulic data (19).

Parameter values used in this study.—The geometric, operational, and physical parameters used in the calculations are presented in Table I. An effort was made to choose values as physically reasonable as possible; however, certain parameters, such as the kinetic constants for the reactions at elevated temperatures, are not yet available. Clearly, the dominant cell resistance is the separator ohmic resistance with the electrolyte resistance of next importance followed by kinetic and mass-transfer resistance. It should be emphasized, however, that these conclusions are valid at the feed conditions, which may not, under all operating conditions, be characteristic of the entire electrode.

Cell performance map.—Figure 2 shows a calculated, so-called, cell performance map for both charge and discharge at three cell polarizations with a countercurrent flow arrangement. The cell current I_c asymptotically approaches a limit at high flow rates at which the intrinsic reaction kinetics and ohmic resistances limit the reaction. At low flow rates, the current is controlled by the supply of reactant. This mass-transfer limited current, indicated by the dashed line labeled Q_{SF} on the figure, is that current which could

be obtained from the cell if all available reactant was consumed. The NASA literature implies that very little can be gained by operating the cell at a flow rate greater than twice the stoichiometric requirement. It can be seen from Fig. 2 that at $2 \times Q_{\text{SF}}$, indicated by the dashed line labeled Q_2 , the cell is indeed operating on the nearly flat portion of the curve. However, it has been predicted in this work, as will be discussed in a following section, that maximizing the net discharge power requires a larger stoichiometric flow multiple which is dependent upon the state-of-charge. In the parameter range studied in this report, this multiple varied from 1.3 to 10.6.

Figure 2 illustrates that mass-transfer resistance apparently is not important except at low unpractical flow rates. However, the kinetic and electrolyte resistance at high flow rates add a small and calculable contribution to the total cell resistance. The separator resistance was set at $4 \Omega \cdot \text{cm}^2$ for Fig. 2. At the high flow rates, the total cell resistance is calculated to be $4.44 \Omega \cdot \text{cm}^2$. As the separator resistance is lowered, the relative importance of the other contributing terms to the total cell resistance will increase.

Electrolyte flow arrangement.—The effect of the electrolyte flow arrangement, cocurrent as compared to countercurrent, has not been experimentally examined. By analogy to heat exchangers and mass-transfer separation devices, it is anticipated that the electrical driving force can be more uniformly distributed with a countercurrent flow arrangement than with cocurrent flow. Consequently, a more effective utilization of the membrane and electrode would result.

The model does indeed predict a more uniform distribution with countercurrent flow. Figure 3 shows the current density at the separator as a function of streamwise position for cocurrent and countercurrent flow at two flow rates. At $Q = 600$ ml/min the membrane current density variation from the inlet to outlet is 2.3 times greater for cocurrent than for countercurrent flow. Similarly, at $Q = 400$ ml/min, the same ratio is 2.8. For both flow rates, the result of countercurrent flow is a smoother current distribution.

Table II compares cell performance under cocurrent and countercurrent flow at various flow rates under charge at a 90% state-of-charge condition. The conversion of Cr^{+3} or Fe^{+2} at any flow rate is always greater with countercurrent flow, but the faradaic efficiency is greater at the low flow rates with cocurrent flow. More H_2 is evolved at the low flow rates with countercurrent flow, which causes the drop in faradaic efficiency. The cause of this seemingly anomalous behavior is due to the excess of Fe^{+2} (in comparison to Cr^{+3}) with isotonic solutions. Since the

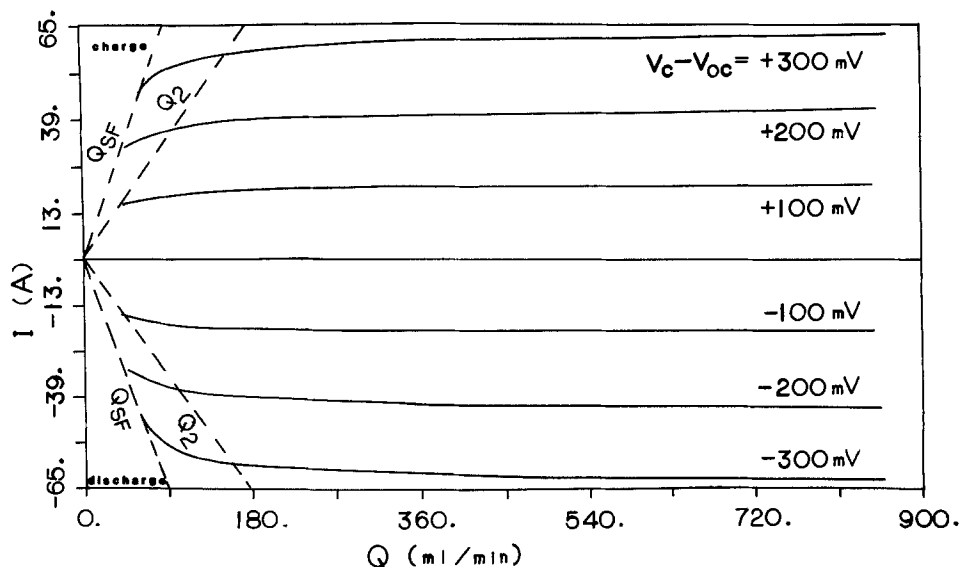


Fig. 2. Cell performance map at selected polarizations. Parameter values listed in Table I and $f = 0.5$, $d_{\text{Cr}} = d_{\text{Fe}} = 0.25$ cm, $L = 30.5$ cm, $T = 25^\circ\text{C}$. Q_{SF} indicates the stoichiometric flow and Q_2 indicates twice the stoichiometric flow.

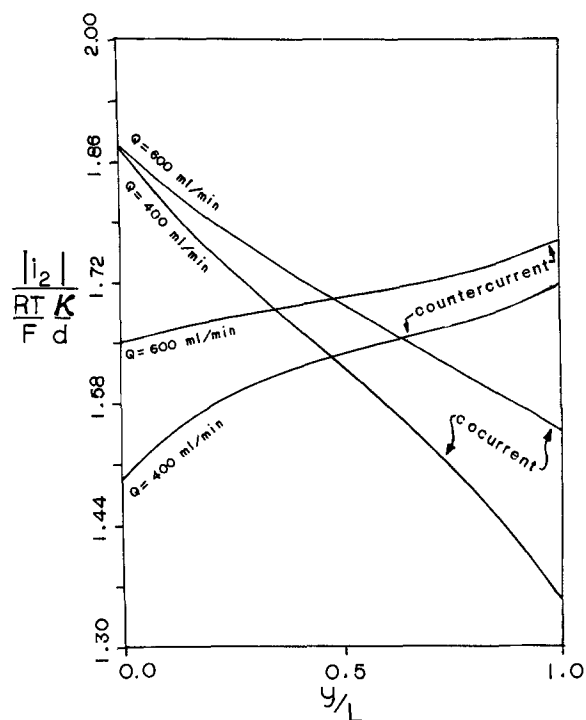


Fig. 3. Separator current density at -300 mV discharge polarization. Parameter values listed in Table I and $f = 0.1$, $d_{Cr} = d_{Fe} = 0.25$ cm, $L = 30.48$ cm, $T = 25^\circ\text{C}$.

countercurrent flow mode is more efficient in reducing Cr^{+3} , the charge which is passed when the excess Fe^{+2} is oxidized is directed to H^+ reduction. The flow rate at which this transition occurs is too low for practical use, but this clearly points out a potential operational problem if unbalanced reactant solutions are used.

Electrode thickness and flow rate.—If the electrode thickness is increased, more surface area is made available and, hence, one might expect a larger reaction rate at any given cell polarization. The increase in chromium conversion and hydrogen production should be asymptotic with increasing thickness. Predicted currents at 25°C for three electrode thicknesses are shown on Fig. 4. The calculations have shown that the cell current ($I_c = I_{Cr} + I_{H_2}$) actually increases with decreasing electrode thickness at a fixed flow rate. For a given flow rate, decreasing the electrode thickness will result in an increase in velocity with an attenuation of the mass-transfer resistance and a consequential increase in current. Eventually, however, as the electrode thickness is decreased below the penetration depth, a drop in cell current will result.

Table II. Comparison of cell performance for cocurrent and countercurrent flow*

min) Q (ml/	Cr^{+3} < Cr^{+3} > _L	Fe^{+2} < Fe^{+2} > _L	I_c (A)	I_{H_2} (A)	I_{Cr} (A)	η_{Far}
Cocurrent						
800	0.529	0.757	59.44	-4.85	-54.58	0.918
600	0.392	0.683	58.12	-5.22	-52.89	0.910
400	0.156	0.548	55.34	-6.37	-48.97	0.885
200	0.017	0.259	45.33	-16.90	-28.50	0.629
150	0.022	0.100	41.32	-20.10	-21.31	0.516
Countercurrent						
800	0.529	0.757	59.51	-4.84	-54.66	0.919
600	0.390	0.683	58.24	-5.20	-53.03	0.911
400	0.150	0.546	55.59	-6.32	-49.27	0.896
200	0.020	0.245	46.25	-17.65	-28.65	0.620
150	0.012	0.073	42.60	-21.15	-21.50	0.505

* $d_{Cr} = d_{Fe} = 0.25$ cm, $L = 30.48$ cm, $V_o - V_{oc} = 300$ mV, $f = 0.1$, $T = 25^\circ\text{C}$.

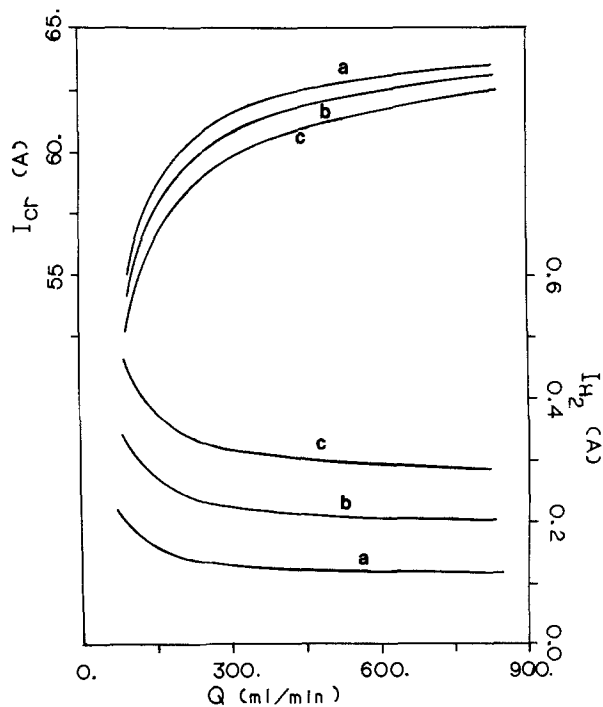


Fig. 4. Current due to chromium and hydrogen reactions at 300 mV charge polarization. Parameter values listed in Table I and $f = 0.5$, $L = 30.48$ cm, $T = 25^\circ\text{C}$. (a) $d_{Cr} = d_{Fe} = 0.1$ cm; (b) $d_{Cr} = d_{Fe} = 0.175$ cm; (c) $d_{Cr} = d_{Fe} = 0.25$ cm.

The penetration depth is defined by the following equation for infinite matrix conductivity (20)

$$d_{j,pen} = \left\{ \frac{RT}{F} \kappa_j / [(\alpha_A^j + \alpha_C^j) a_i^{j_{o,t}}] \right\}^{1/2} \quad [19]$$

The reaction rate decreases by approximately a factor of e for each penetration layer into the electrode. If $d_j \gg d_{j,pen}$, a decrease in electrode thickness initially removes an electrode which is largely unavailable to the main reaction. As $d_j \sim d_{j,pen}$, a further decrease in electrode thickness results in less electrodes available to the main reaction with a subsequent decrease in cell current. For the parameter values used in Fig. 4, the penetration depth at the inlet is 0.026 and 0.066 cm for the chromium and iron electrode, respectively. This indicates the need for a thinner electrode in the chromium than in the iron compartment. For illustrative purposes, the electrode thickness in both compartments was kept identical for all calculations.

In order to examine the effect of electrode thickness alone on cell performance while holding the variation in all other effects to a minimum, it is necessary to vary the flow rate. Table III presents calculations in which the electrode thickness is varied but the flow rate is adjusted to maintain a constant velocity. It can be seen that providing more electrode surface by increasing the cell thickness does result in a higher cell current if the velocity is held constant.

If the flow rate is held constant and the electrode thickness is increased, the pumping loss is decreased and the net power output from the cell, under certain conditions, may be increased. Because of the combination of pumping losses, kinetic, and mass-transfer effects, an optimum electrode thickness exists which maximizes the net power output on discharge. Figures

Table III. Effect of electrode thickness at constant velocity*

d (cm)	Q (ml/min)	I_{Cr} (A)	I_{Fe} (A)	I_{H_2} (A)	η_{Far}
0.25	400	-60.90	61.04	-0.297	0.995
0.175	280	-60.46	60.69	-0.228	0.998
0.10	160	-58.77	58.92	-0.153	0.997

* $V_c - V_{oc} = 300$ mV, $f = 0.5$, $L = 30.48$ cm, $v = 0.879$ cm/s, countercurrent flow, $T = 25^\circ\text{C}$.

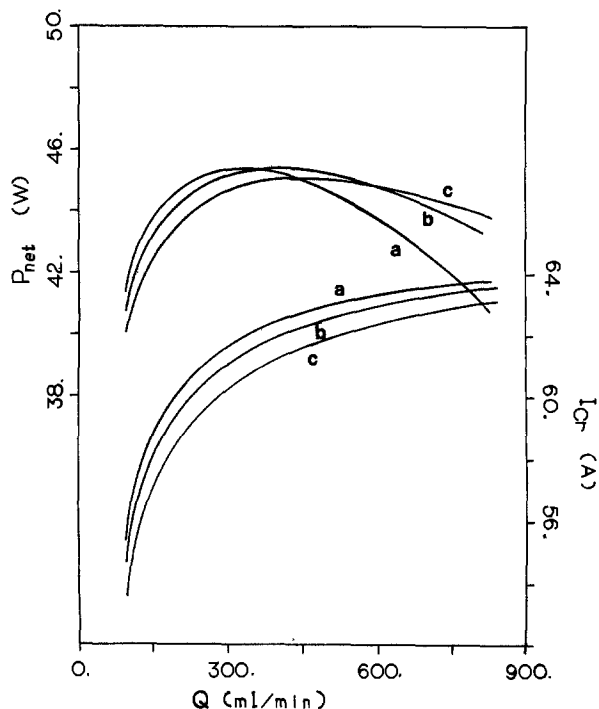


Fig. 5. Net cell power and current due to chromium conversion at -300 mV discharge polarization. Parameter values listed in Table I and $f = 0.5$, $L = 30.48$ cm, $T = 25^\circ\text{C}$. (a) $d_{\text{Cr}} = d_{\text{Fe}} = 0.1$ cm; (b) $d_{\text{Cr}} = d_{\text{Fe}} = 0.175$ cm; (c) $d_{\text{Cr}} = d_{\text{Fe}} = 0.25$ cm.

4 and 5 illustrate the effect of varying electrode thickness and flow rate on cell performance for charge and discharge, respectively. An electrode thickness of 0.1 cm is the best of the three shown. Under charge, a cell with 0.1 cm electrodes delivers the greatest chromium conversion and the least hydrogen evolution. Under discharge, the net cell power is nearly maximized

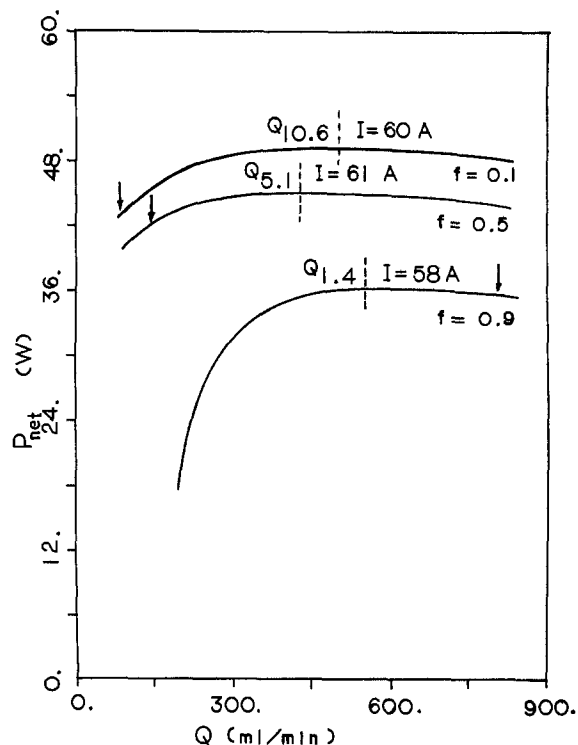


Fig. 6. Net cell power vs. flow rate at various depths of discharge for a -300 mV discharge polarization. Manifold losses included. Stoichiometric flow multiple and cell current at the optimal flow-rate indicated. Parameter values listed in Table I and $d_{\text{Cr}} = d_{\text{Fe}} = 0.25$ cm, $L = 30.48$ cm, $T = 25^\circ\text{C}$. Manifold dimension: 0.2 cm \times 0.4 cm. Arrows indicate twice the stoichiometric flowrate.

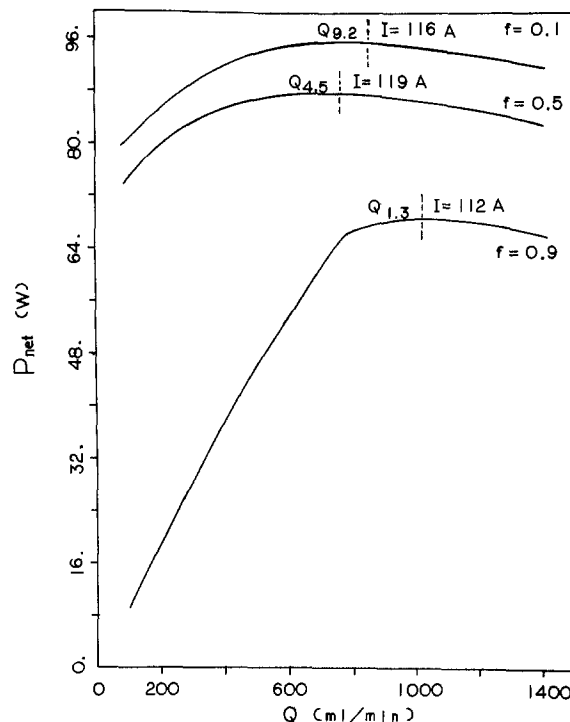


Fig. 7. Same as Fig. 6 except $T = 65^\circ\text{C}$

and chromium conversion is the greatest with 0.1 cm thick electrodes. Thinner electrodes would not be of any further advantage because of larger parasitic pumping losses.

Figures 6 and 7 illustrate the net power output as a function of flow rate at three depths of discharge for a -300 mV discharge polarization at low and high temperature, respectively. The current at the power optimum is indicated on the figure as well as the flow rate expressed as a multiple of the stoichiometric flow rate. The optimum flow rate varies with the depth of discharge. At $f = 0.5$, the optimum flow rate is less than that at $f = 0.1$ or $f = 0.9$. The explanation for this trend lies in the nonconstant nature of the chromium and iron exchange current densities. On discharge, at low values of f , the exchange current densities are less than their maximum due to product poisoning. At high values of f , reactant starvation causes the exchange current densities to decrease. Therefore, at extremes of depth of discharge, higher flow rates are needed to overcome the effects of reactant starvation or product poisoning in order to produce the power maximum. At sufficiently high flow rates at any depth of discharge, the reaction is limited by kinetics, and further increase in flow rate will not result in increased cell current and gross power. The decrease in the P_{net} vs. Q curves to the right of the maximum is attributed to the parasitic pumping losses.

It is apparent from the figures that any rule of thumb, such as the optimum flow rate being a multiple of 1.5-2 times the stoichiometric flow rate, does not rigorously apply; however, the power maximums are broad for the parameters used in these calculations. The maximum becomes better defined as the pumping loss increases with longer cells, thinner electrodes, or smaller manifolds. The latter is a particularly important consideration because the smaller the manifold, the lower will be the shunt currents, but with a consequential increase in pumping loss.

Electrode length.—Predictions of cell performance at a fixed polarization and flow rate of a lengthened electrode show that the cell current also increases, but in a diminishing manner. Because of reactant consumption in the inlet region of the cell, more of the electrical driving force is expended near the outlet in

overcoming concentration polarization as the cell length is increased. Therefore, the longer the cell, the more the reactant-starved condition exists over the cell length and, eventually, no increase in reactant conversion will result from increased cell length. The cell polarization may not, in sufficiently long cells, be great enough to overcome the concentration polarization, and the reverse redox reaction may occur. Furthermore, at cell lengths in which the chromium electrode becomes reactant-starved, the hydrogen evolution increases drastically, thereby lowering the faradaic efficiency. These effects are illustrated in Table IV. The advantage of countercurrent flow arrangement is seen for the shorter length cells but not for the longer cells because of the inherent reactant imbalance with the isotonic solutions.

Charge/discharge cycles.—The amount of hydrogen which is produced in an entire cycle will depend on the charge/discharge procedure used. If the cell polarization is varied and all other conditions held constant, both the cell current and the rate of hydrogen evolution will also vary. This is especially true when the cell is nearly charged. An infinite number of charge/discharge protocols can be proposed; in this work only two are examined: (i) a constant cell voltage of 1.35V under charge and 0.75V under discharge, and (ii) a constant cell polarization of +300 mV under charge and -300 mV under discharge. At $f = 0.5$, these two protocols are identical. Figure 8 shows how the cell and hydrogen current vary over a charge cycle for the two polarization protocols. Figure 9 shows the same result but at a higher temperature.

In order to calculate charge and discharge times and energy stored or used, a storage tank volume of 1820 liters/electrolyte was used based on recommendations of a cost study (4). Table V summarizes these results. The cycle energy efficiency is low because of the large polarization used in the calculation. It is seen, however, that less time is required to charge the cell at constant polarization than with a constant cell voltage. There is little difference in the faradaic efficiency at the lower temperature in the two protocols; however, at the higher temperature, the constant cell voltage charge has a higher efficiency because of the dramatic increase of H_2 production near fully charged conditions under constant polarization.

Conclusions

1. A mathematical model of an isothermal redox flow battery has been developed which incorporates redox reaction kinetics and the parasitic H_2 reaction, mass-transfer effects, and ohmic losses in the separator and electrolyte.
2. Optima exist in the design and operation of the redox flow cell. Specifically, the electrode thickness, cell voltage, and electrolyte flow rate can be optimized to maximize the cell current or faradaic efficiency. The model is a useful aid in locating these optima.
3. The separator ohmic resistance is the dominant cell resistance followed by the electrolyte ohmic resistance. Kinetic resistances are much less than separator or electrolyte resistances and mass-transfer resistance is almost negligible at reasonable flow rates.

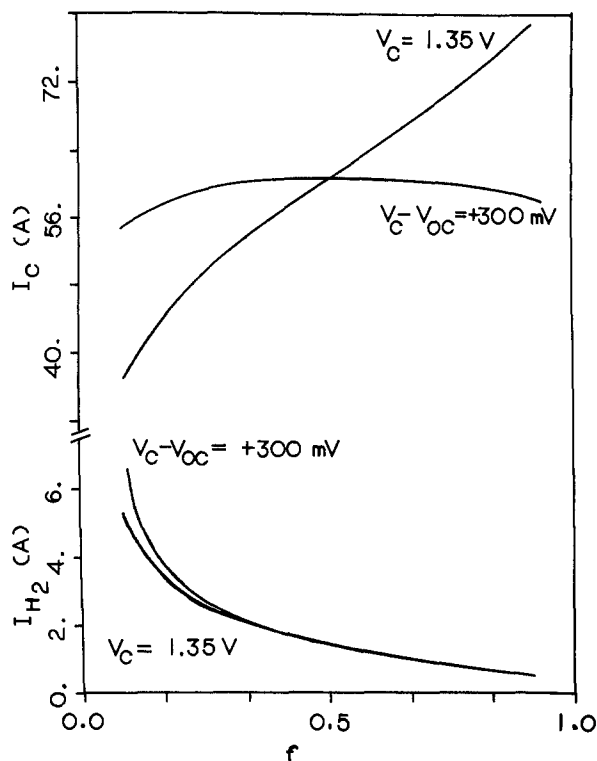


Fig. 8. Cell and hydrogen current vs. depth of discharge over a charge cycle for constant cell voltage and constant cell polarization. Parameter values listed in Table I and $Q = 400$ ml/min, $d_{Cr} = d_{Fe} = 0.25$ cm, $L = 30.48$ cm, $T = 25^\circ\text{C}$.

4. The cell current approaches the limiting current at low electrolyte flow rates and asymptotes at high flow rates to an upper limit determined by kinetic and ohmic constraints. At $2 \times Q_{SF}$, for the parameters

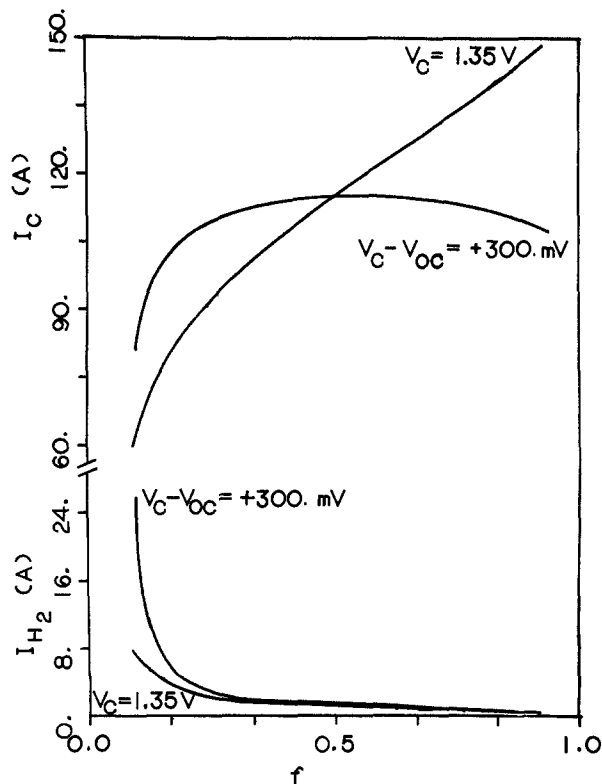


Fig. 9. Cell and hydrogen current vs. depth of discharge over a charge cycle for constant cell voltage and constant cell polarization. Parameter values listed in Table I and $d_{Cr} = d_{Fe} = 0.25$ cm, $L = 30.48$ cm, $T = 65^\circ\text{C}$.

Table IV. Effect of electrode length on cell performance on charge*

L (cm)	$\langle Cr^{+3} \rangle_L$		$\langle Fe^{+2} \rangle_L$		I_C (A)	I_{H_2} (A)	I_{Fe} (A)	η_{Far}
	Cr^{+3}	Fe^{+2}	Cr^{+3}	Fe^{+2}				
Cocurrent								
15.24	0.660	0.835	-19.69	-0.47	20.16	0.978		
30.48	0.364	0.690	-36.82	-1.08	37.90	0.972		
60.96	0.008	0.493	-57.44	-4.58	62.02	0.926		
121.90	0.000	0.000	-57.43	-24.02	81.45	0.705		
Countercurrent								
15.24	0.656	0.835	-19.76	-0.45	20.21	0.978		
30.48	0.361	0.689	-37.07	-1.04	38.10	0.973		
60.96	0.004	0.486	-57.63	-5.20	62.82	0.917		
121.90	0.004	0.299	-57.63	-28.15	85.82	0.673		

* $Q = 400$ ml/min, $V_c = 1.35$ V, $f = 0.1$, $T = 25^\circ\text{C}$.

Table V. Charge/discharge cycle study*

Protocol	25°C		
	Energy stored/ withdrawn (Wh)	η_{Far}	t (hr) ch/ds
Charge: $V_c = 1.35V$	2010	0.965	25.4
Discharge: $V_c = 0.75V$	1030	0.980	24.0
Charge: $V_c - V_{oc} = 0.3V$	2010	0.968	24.5
Discharge: $V_c - V_{oc} = -0.3V$	1030	0.979	23.3
65°C			
Charge: $V_c = 1.35V$	1980	0.978	13.5
Discharge: $V_c = 0.75V$	1050	0.991	13.4
Charge: $V_c - V_{oc} = 0.3V$	2010	0.966	13.4
Discharge: $V_c - V_{oc} = -0.3V$	1050	0.991	13.1

* $d_{cr} = d_{Fe} = 0.25$ cm, $L = 30.48$ cm, $Q = 400$ ml/min, counter-current flow.

used in this study, the cell is operating on the nearly flat portion of the current-flow rate curve.

5. Countercurrent electrolyte flow is predicted to improve cell performance in comparison to cocurrent flow at all practical flow rates. This increased performance can be attributed to the result of more uniform current distribution.

6. For the range of parameters used in this study, the cell current increased with decreasing electrode thickness at a fixed flow rate. Actually, the decreased electrode surface area tends to decrease the cell current; however, the decreased area of flow results in a higher velocity and enhanced mass transfer within the penetration thickness and, therefore, increases cell current. If the electrode thickness and electrolyte flow rate are simultaneously varied in such a manner as to maintain a constant velocity, the cell current decreases as the electrode becomes thinner.

7. On the discharge cycle, the electrolyte flow rate which results in maximum net power output is lowest at midcycle ($f = 0.5$) and increases at either extreme of depth of discharge as the effects of reactant starvation or product poisoning become more important. A simple rule of thumb such as the optimum flow rate being 1.5 or 2 times the stoichiometric flow rate does not rigorously apply across an entire cycle. The maximum is shallow at $R_s = 4 \Omega \cdot \text{cm}^2$ but becomes better defined as R_s decreases.

8. Increasing the cell length at constant flow rate results in a larger cell current but in a diminishing returns manner. Faradaic efficiency decreases with increasing length, and, eventually, added length supports only the hydrogen reduction with no improvement in chromium conversion.

9. The chromium conversion and cell energy efficiency are functions of the charge/discharge protocol employed. The model provides a means of finding a charge/discharge protocol that gives the maximum chromium conversion while, at the same time, results in minimum hydrogen evolution.

10. An increase in the cell operating temperature from 25° to 65°C results in greater reaction rates, improved electrolyte and membrane conductivities, increased cycle energy efficiency, and reduced charging times.

Acknowledgments

This work was partially supported by the NASA-Lewis Research Center. Computational funds were provided by the School of Engineering. Mr. Allan Hauser assisted in the early stages of the work.

Manuscript submitted March 14, 1983; revised manuscript received Nov. 15, 1983.

LIST OF SYMBOLS

a	specific surface area, cm^2/cm^3
C^{+2} or C^{+3}	bulk concentration of iron or chromium, mol/cm^3
Cr_f^{+3}	feed concentration, mol/cm^3
Cr_1^{+3}	concentration at fully discharged state, mol/cm^3
$\langle Cr^{+3} \rangle_L$	average concentration leaving electrode, mol/cm^3
ϵD	effective diffusivity, $D_0 \epsilon^{1.5}$, cm^2/s
D_0	intrinsic diffusivity, cm^2/s
d	electrode thickness, cm
F	Faraday's constant, 96,485 C/eq
Fe_f^{+2}	electrode feed concentration, mol/cm^3
Fe_1^{+2}	concentration at fully discharged state, mol/cm^3
$\langle Fe^{+2} \rangle_L$	average concentration leaving electrode, mol/cm^3
f	depth of discharge
I_c	cell current, A
I_{Fe}	current due to iron conversion ($= I_c$), A
$i_{n,j}$	normal current density at pore wall from reaction j , A/cm^2
I_{Cr}	current due to chromium conversion, A
I_{H_2}	current due to H_2 formation, A
i_0^j	exchange current density of reaction j , A/cm^2
k_m	mass-transfer coefficient, cm/s
L	electrode length, cm
n_j	number of electrons in reaction j
Q	electrolyte flow rate, cm^3/s
R	gas constant
R_s	separator resistance, $\Omega \cdot \text{cm}^2$
sR^j	stoichiometric coefficient of reactant
T	temperature, K
U_{AH}	open-circuit potential difference between H_2 and Cr reaction, V
V_{oc}	open-circuit cell voltage, V
V_c	cell voltage, V
v	velocity in electrode, cm/s
W	electrode width, cm

Greek Symbols

α_A^j	anodic transfer coefficient of reaction j
α_C^j	cathodic transfer coefficient of reaction j
ϵ	porosity
κ	effective conductivity, $\kappa_0 \epsilon^{1.5}$, $\Omega^{-1}\text{cm}^{-1}$
κ_0	intrinsic solution conductivity, $\Omega^{-1}\text{cm}^{-1}$
ϕ_1^j	matrix potential in electrode j , V
ϕ_2^j	solution potential in electrode j , V

Subscripts

f	feed condition
s	pore wall surface

REFERENCES

1. L. Thaller, *Proc. 9th IECEC* (1974).
2. Pertinent NASA-Lewis technical memos: TMX-7154; TM-79143; TM-79186; TM-81632; TM-81464; TM-82702; TM-82607; TM-82707; TM-82854; TM-82720; TM-82686.
3. M. Warshay and L. O. Wright, *This Journal*, **124**, 173 (1979).
4. K. Michaels and G. Hall, NASA CR-165260, final report (1980).
5. C. C. Liu, R. T. Galasco, and R. F. Savinell, *This Journal*, **128**, 1755 (1981).
6. C. C. Liu, R. T. Galasco, and R. F. Savinell, *ibid.*, **129**, 2502 (1982).
7. R. J. Remick, P. G. P. Ang, and A. F. Sammells, Abstract 151, p. 413, The Electrochemical Society Extended Abstracts, Vol. 80-2, Hollywood, FL, Oct. 5-10, 1980.
8. G. B. Adams, R. P. Hollandsworth, and E. L. Littauer, *Proc. 16th IECEC*, **1**, 812 (1981).
9. R. F. Savinell and D. A. Polaski, *Proc. 16th IECEC*, **1**, 817 (1981).
10. L. W. Hruska and R. F. Savinell, *This Journal*, **128**, 18 (1981).
11. J. A. Trainham and J. Newman, *Electrochim. Acta*, **26**, 455 (1981).
12. J. S. Newman and W. Tiedemann, in "Advanced Electrochemistry Electrochemical Engineering," Vol. 11, John Wiley and Sons, New York (1981).
13. R. E. de la Rue and C. W. Tobias, *This Journal*, **106**, 827 (1959).
14. E. J. Wilson and C. J. Geankopolis, *Ind. Engr. Chem. Fundam.*, **5**, 9 (1966).

15. D. A. Johnson and M. A. Reid, Abstract 252, p. 405, The Electrochemical Society Extended Abstracts, Vol. 82-2,
 16. P. S. Fedkiw, *Comp. Chem. Engr.*, **6**, 327 (1982).
 17. R. W. Watts, M.S. Thesis, North Carolina State University, Raleigh, NC (1983).
 18. R. B. Bird, W. E. Stewart, and E. N. Lightfoot, in "Transport Phenomena," John Wiley and Sons, New York (1960).
 19. M. A. Hoberecht, NASA TM-82598 (1981).
 20. J. Newman and W. Tiedemann, *AIChE J.*, **21**, 25 (1975).

Discharge Kinetics of the Nickel Electrode

A. H. Zimmerman* and P. K. Effa

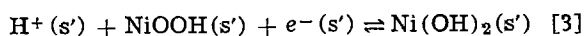
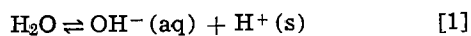
The Aerospace Corporation, Chemistry and Physics Laboratory, El Segundo, California 90245

ABSTRACT

The kinetics of nickel electrode discharge are found to be controlled by solid-state proton diffusion under normal high rate discharge conditions. As the nickel electrode is discharged, the conductivity of the active material decreases until eventually mixed kinetics are observed where the electrode impedance has significant contributions from both proton diffusion and charge transfer resistance. Further discharge results in the formation of a semiconductor layer at the metal-active material interface that is depleted in charge carriers and has a relatively high electronic resistance. The depletion layer is responsible for the secondary discharge plateau of the nickel electrode at 0.0 to -0.5 V vs. Hg/HgO. Changes in electrode capacitance during depletion layer formation appear to provide a sensitive measure of the uniformity of electrode discharge. The effects of cobalt additives on the kinetics have been experimentally measured, and while cobalt does not change the discharge mechanism, it does increase the ionic and electronic conductivity of the active material allowing a greater depth of discharge before depletion layer formation.

The oxidation/reduction reactions at the nickel electrode have been the subject of a number of studies during recent years. As more experimental studies have been reported, it has become clear that the electrochemistry of the nickel electrode is quite complex. The early work of Bode *et al.* (1), and the later work of Schrebler-Guzman *et al.* (2) indicated the existence of both α and β phases of Ni(OH)₂. These two phases may be oxidized to γ and β phases of nickel oxyhydroxide, respectively, and may also undergo chemical interconversion. Additional energetically discernible phases have been found in the work of Schrebler-Guzman *et al.* (3) and Barnard *et al.* (4). In light of the growing number of possible phase structures, it is anticipated that the kinetics of the nickel electrode oxidation/reduction processes will be difficult to unravel, particularly in sintered nickel electrodes, where the effects of additives and phase nonuniformities are expected to provide additional kinetic and thermodynamic complexity.

Nickel electrode reduction has been found to follow diffusion kinetics in a number of previous studies (5-8). The limiting diffusion process in the voltage range above 0.2V (vs. Hg/HgO) is the diffusion of protons formed at the electrode/electrolyte interface to the charge transfer site. The reduction process may be represented as



Reaction [1] represents the formation of a proton at catalytic site *s* at the electrode/electrolyte interface; reaction [2] involves diffusion of the proton from site *s* into the electrode to the charge transfer site *s'*; and reaction [3] is the charge transfer process involving the reduction of one of the higher valency species of active material in the lattice, represented here as simply NiOOH. Reactions [1] and [3] are not generally believed to be rate limiting under the operating conditions of the nickel electrode because they would not account for the observed diffusion kinetics. A recent report (9) that reaction [1] may be rate limiting appears to be more consistent with diffusion of OH⁻

between the bulk electrolyte and the active material surface as the rate-limiting step for high rate electrode operation, particularly at reduced concentrations of OH⁻. Reaction [2], proton diffusion, is generally regarded as controlling the rate of nickel electrode discharge at the potential and current densities normally used in battery operation. Barnard (10) has obtained electrochemical evidence that the protons involved in processes [1]-[3] are delocalized throughout the active material lattice, a result that is consistent with spectroscopic data in which the lack of IR absorption bands due to OH in the oxidized active material is reported (11). The proton diffusion rate and proton concentration are expected to depend on the phase composition of the NiOOH, as well as on the presence of additives in the lattice structure (8).

During normal discharge of the nickel electrode in a battery cell, the diffusion process indicated by reaction [2] is rate limiting. However, for some conditions of electrode structure (13) or operation (12), the electrode voltage can prematurely drop to a plateau at 0.0 to -0.5 V (vs. Hg/HgO), and the electrode can discharge a substantial portion of its capacity at the lower potential. The lower voltage discharge has been attributed to effects such as adsorbed oxygen (14-17), lower energy nickel oxides (18-22), and conductivity changes (13, 23). Measurements of the electrode kinetics in the low state of charge region should allow the process(es) causing the low discharge voltage plateau to be identified. Such measurements of the electrochemical kinetics of the nickel electrode are reported here. The kinetics are measured over a wide range of electrode potential for electrodes of flat plate and sintered construction, with and without cobalt additives. The work described here provides evidence indicating that conductivity changes coupled with the formation of an interfacial loss layer are responsible for the premature depletion of nickel electrode capacity at voltages sufficient for battery operation.

Experimental

Nickel electrodes were made by electrochemical deposition (24) of Ni(OH)₂ on either 4 cm² flat nickel plates or 1 cm² sintered nickel substrates. The nickel sinter substrate used was 0.076 cm thick and had a porosity of 79.5%. Cathodic deposition at 4 and 35 mA/cm² was used for the flat plate and sintered elec-

* Electrochemical Society Active Member.

Key words: kinetics, impedance, electrode, battery.

trodes, respectively, using a boiling solution 60% in 2M Ni(NO₃)₂ and 40% in ethanol. Cobalt nitrate was added to the solution to give the desired Ni/Co ratio for studying the effects of cobalt additives. Chemical deposition in a sintered electrode was done by repetitively evacuating the air from the sinter while dipped in a 2M Ni(NO₃)₂ solution and then dipping in a 20% KOH solution. Typically, about 0.1 g/cm² of Ni(OH)₂ was deposited on the sintered electrode (1.60 g/cm³ void), and about 6 mg/cm² was deposited on the flat plate electrodes. All electrodes were cycled prior to experimental use until the capacity stabilized, which was typically five complete charge/discharge cycles. Rated capacities which will be referred to were 20 and 0.14 mAh/cm² for sintered and flat plate electrodes, respectively.

Electrode charge and discharge, impedance measurements, and capacitance monitoring were done automatically using a computer which continuously monitored electrode voltage and controlled the current passing through the electrode. An operational amplifier power supply having a 10 kHz frequency response was used to charge and discharge the electrodes. The electrodes were monitored in a nitrogen-purged, polystyrene test cell that incorporated a nickel sheet counterelectrode, a Hg/HgO reference electrode, and 31% KOH electrolyte. Electrode capacitance could be monitored by the computer through the application of a current step, the capacitance being obtained from the ratio of the magnitude of the current step to the initial slope of the electrode voltage response. Electrode capacitance was only measured at potentials where the initial voltage response to a current step was exponential in time; in potential regions where diffusion dominates the electrode kinetics, capacitance measurements are meaningless. The computer similarly measured the electrode impedance by monitoring the time dependence of the voltage response to a small current step. The method for obtaining the impedance from such transient data has been previously described (25). The time resolution for such transient acquisition was 1 ms. All transient voltage responses for both capacitance and impedance measurements were less than 5 mV in amplitude. Digital filtering of the amplified voltage response gave a typical noise level of less than 25 μ V in the electrode voltage. Capacitance measurements could be automatically done during electrode discharge with a typical precision of $\pm 0.5\%$; the accuracy was generally less than this because the electrode did not act as an ideal RC equivalent circuit. All capacitance measurements reported here are at potentials where the nickel electrode exhibited a nearly exponential time response, and have an accuracy of about $\pm 5\%$. All experiments were done at room temperature, 23 \pm 2 $^{\circ}$ C.

Nickel Electrode Discharge Kinetics

Results.—The Ni electrode voltage typically follows the curve indicated in Fig. 1 when it is discharged first at C/10, then at a lower rate (C/100). The points, a, b, and c indicated in Fig. 1 are the points during discharge at which the measurements in Fig. 2 were made. Figure 2 indicates the kinetic response of this electrode to a small current step at the upper voltage plateau during high rate discharge (point a), during low rate discharge (point b), and on the lower voltage plateau (point c). Also included in Fig. 2 are the electrode impedances calculated from the data at points, a, b, and c during discharge. As has been found by other workers (6-8), the kinetics are diffusion controlled during discharge on the upper voltage plateau at point a. Diffusion control is indicated by the linear region in the plot of transient voltage vs. \sqrt{t} in Fig. 2 at point a, or similarly by the linear dependence rising from the origin with a 45 $^{\circ}$ slope in the impedance plot of Fig. 2 at point a. The electrode at point b, while

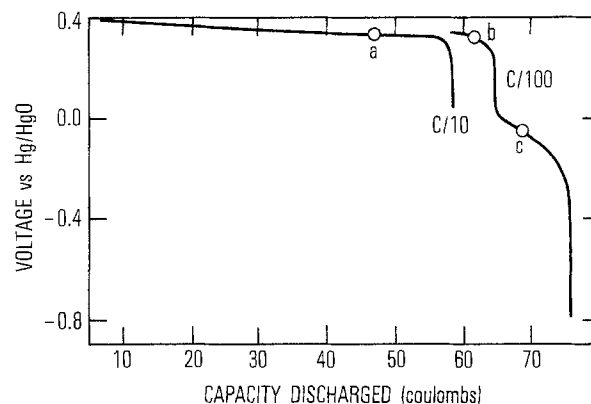


Fig. 1. Discharge voltage of a sintered nickel electrode at C/10 rate followed by a C/100 discharge of residual capacity. The points a, b, and c refer to measurement points in Fig. 2.

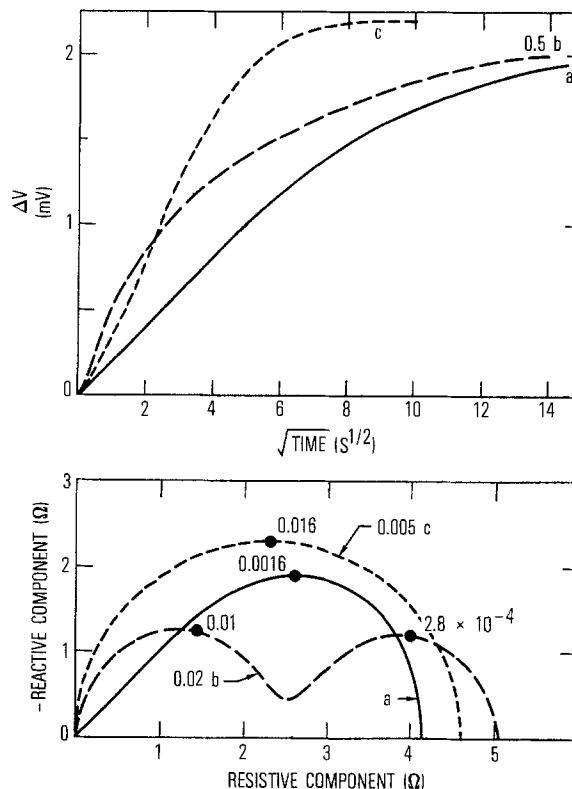


Fig. 2. Transient impedance measurements at points a, b, and c during the discharge of Fig. 1. The upper curves are the transient responses to current changes, and the lower curves are the impedances calculated from the time transients. The numbers indicate the frequencies of the reactive extremes in Hz. The multipliers indicated have been applied to both coordinates.

still discharging on the upper voltage plateau, exhibits mixed kinetics suggestive of both activation and diffusion-controlled processes influencing the discharge. At point c on the lower plateau, the discharge kinetics are dominated by an activation-controlled process. Activation kinetics are characterized by an exponential transient response in time, which gives a semicircular impedance plot as shown in Fig. 2 for point c. In the discussion that follows, the resistance and capacitance associated with the activation controlled processes at points b and c will be labeled R and C, respectively. The diffusion resistance associated with the diffusion-controlled process at points a and b in Fig. 1 will be referred to as R_d.

Both R and C were measured during constant current discharge as a function of potential and state of charge. These results are indicated in Fig. 3 and 4, respectively. In Fig. 3 log R is plotted vs. potential during the course of a C/100 discharge. Also, at various

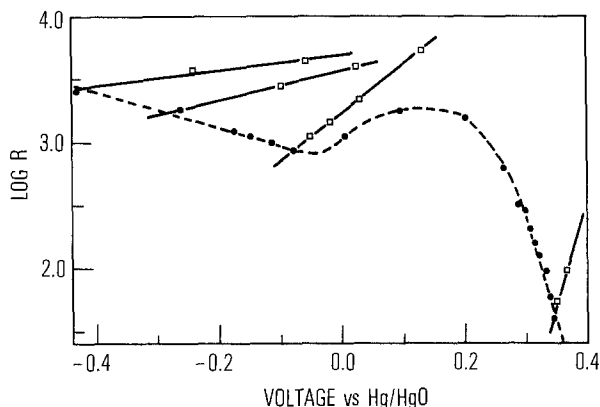


Fig. 3. Resistance R , as a function of voltage (solid circles) during $C/100$ discharge of the residual capacity in a sintered nickel electrode. At various times during the $C/100$ discharge the resistance was measured as a function of potential, as indicated by the solid lines.

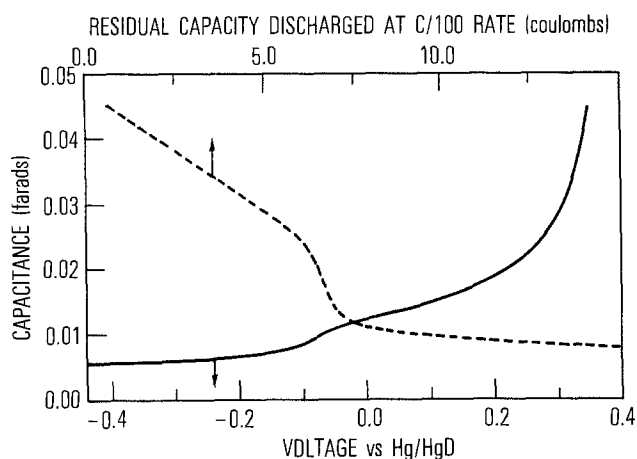


Fig. 4. Sintered nickel electrode capacitance as a function of voltage (solid line) and capacity discharged (dashed line) during discharges of residual capacity at $C/100$ rate.

times during the discharge in Fig. 3, the current was varied so as to allow measurement of R as a function of voltage at a constant oxidation state. The capacitance of the sintered nickel electrode is indicated as a function of residual capacity Q , and also as a function of electrode voltage in Fig. 4. The capacitance decreases linearly with Q until the lower voltage plateau is reached, after which the capacitance is relatively constant during further discharge. While the capacitance does appear to vary with state of charge in Fig. 4, the variation in the capacitance actually appears to depend only on the electrode voltage in the range -0.3 to 0.25 V. Essentially the same voltage/capacitance curve as in Fig. 4 is obtained at all states of charge if the voltage of the nickel electrode is varied from about -0.3 to 0.25 V vs. Hg/HgO, suggesting that the capacitance may be controlled by a thin surface layer rather than by the properties of the bulk active material.

The results indicated in Fig. 1-4 are for an electrochemically impregnated sintered nickel electrode. Similar results were obtained for chemically deposited active material. Flat plate electrodes also gave similar behavior in that diffusion-controlled kinetics changed into mixed kinetics, and then finally into activation-controlled kinetics as the electrode was discharged. For the flat plate electrodes the current density was scaled down to realize a $C/10$ or a $C/100$ rate.

Discussion of nickel electrode kinetics.—Three processes have been observed that can control reduction

rates at the nickel electrode. The diffusion kinetics that are observed above 0.3 V are consistent with previous results attributed to proton diffusion in Ni electrodes (6-8) and in the NiCd cell (25). For a flat plate electrode, proton diffusion coefficients of about 10^{-10} cm^2s^{-1} are obtained from the measured diffusion times, assuming a film thickness proportional to capacity (about 10^{-4} cm). Deviations from ideal diffusion-controlled behavior are observed at high currents ($> C/2$) and also above about 70% state of charge. It is possible that these deviations are due to nonuniform ionic conduction within the active material; for example, proton diffusion should be predominantly along grain boundaries at the beginning of discharge when reaction is largely at the grain surfaces. The impedance arising from electrolyte diffusion in the pore structure of the sintered electrodes was not significant relative to the solid-state proton diffusion impedance at the discharge rates employed here, but did become significant at higher rates. This conclusion is supported by the similar impedance characteristics measured for flat plate and porous electrodes.

While still on the upper voltage plateau, but at low states of charge, a second process begins to control the kinetics, as indicated by the mixed kinetics at point b in Fig. 1 and 2. This process is activation controlled, and as shown in Fig. 3 has a Tafel slope of about 60 mV/decade. The same slope was observed for all electrodes studied: flat plate electrodes, sintered electrodes, and electrodes in commercial NiCd cells. The slope is consistent with the single-electron transfer process given by reaction [3] becoming rate limiting. Also, since the capacitance decreases linearly with charge transfer site density or electrode state of charge in the region above 0.2 V, reaction [3] appears most likely to control the rate. Therefore, in the region having about a 60 mV/decade Tafel slope, the density of charge transfer sites appears to have decreased to the level where charge transfer has become rate limiting. Discharge in this region continuously decreases the density of higher valency sites and thereby increases the charge transfer resistance of the active material. It should also be noted that the open-circuit voltage of the active material continuously decreases as the density of higher valency sites diminishes.

As the Ni electrode is discharged towards the divalent state, a third process can cause the electrochemical kinetics to change dramatically in the potential range between 0.1 and 0.2 V. While the active material above 0.2 V acts as an electronic conductor, below 0.2 V a layer of active material begins to behave like a semiconductor, exhibiting Tafel slopes (Fig. 3) that continuously increase as the material is reduced. The sudden decrease in capacitance that accompanies the transition to the lower voltage plateau (Fig. 4) is consistent with the formation of a layer of carrier-depleted material at the metal current-collector/active material interface, such that the resistance and capacitance of this layer now dominate the discharge kinetics. Continued discharge on the lower voltage plateau causes the depletion layer to grow in thickness (and resistance) towards the solution interface.

The model presented above is similar to models put forth qualitatively by Klapste *et al.* (13) and somewhat more quantitatively by Barnard *et al.* (23), in that changes in the conductivity of the active material cause the lower voltage plateau. The model of Barnard *et al.* (23) fits the Tafel slope reported here on the upper voltage plateau. However, the Tafel slopes observed on the lower voltage plateau suggest that a poorly conducting semiconductor layer has formed and that the electrode overpotential arises from the space charge voltage across the layer. The layer is kinetically maintained by current flow, and it is therefore expected that both its thickness and its conductivity at a given state of charge will depend on current den-

sity. The kinetics on the lower plateau are clearly activation controlled, indicating that conduction through the depleted layer does not occur through ionic migration.

While it is technically true that a secondary plateau in the voltage is not observed during recharge of a Ni electrode, the increased resistance associated with the depletion layer can be clearly seen in the early stages of Ni electrode oxidation. After generation of a depletion layer by a low rate discharge to low potentials, the electrode voltage goes through an initial high voltage peak when recharge is initiated. It has been well established that after shorting NiCd cells down for long periods, recharge must be initiated at quite a low rate to keep the voltage from initially rising to unacceptably high levels. Such a voltage peak is likely to arise from the ohmic contribution of the depletion layer, which can become quite thick in instances of long-term cell short down.

Electrode capacitance and nonuniformities.—The model described above for the kinetics of the nickel electrode suggests that above about 0.25V the capacitance of the electrode is controlled by the density of higher valency sites available for reduction, giving the linear relationship between capacitance and residual capacity in Fig. 4 below 6C (above 0.25V). Continued discharge to the lower voltage plateau causes a drop in capacitance as it becomes controlled by the space charge capacitance across the depleted layer at the active material/current collector interface. The drop in capacitance should be sensitive to the structure of the active material at this interface. A low interfacial contact area (high interfacial current density) should give a greater drop in capacitance, and any energetic differences in active material at the current collector interface should spread the capacitance drop over a range of discharge capacity and thereby decrease the sharpness of the drop. The manner in which the capacitance varies during discharge of residual capacity can therefore indicate the causes for changes or differences in electrode performance. In Fig. 5, plots of electrode capacitance as a function of residual capacity are shown for a sintered nickel electrode after being cycled 32 times, after being reconditioned, and for a flat plate nickel electrode. The most striking difference between the electrodes is the degree of sharpness of the capacitance drop as electrode voltage drops to the lower discharge plateau. For the sintered electrode that has been cycled many times, the active material at the current collector interface has developed significant nonuniformities, which are likely to be associated with energetic variations between different phases

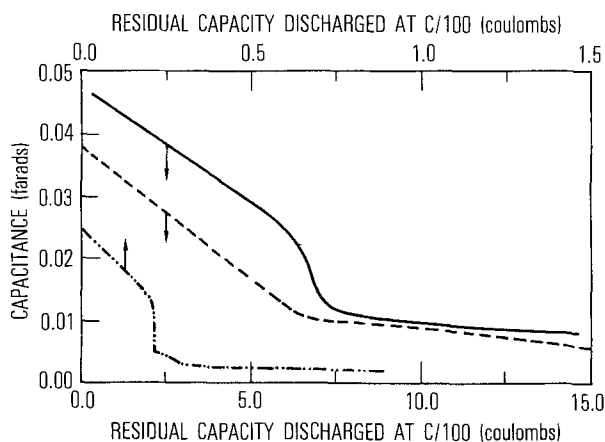


Fig. 5. Capacitance of nickel electrodes during a C/100 discharge of residual capacity. The solid curve is for an uncycled 1 cm² sintered electrode after formation, dashed curve for a 1 cm² sintered electrode after 32 cycles, and the dash-dot curve is for an uncycled 4 cm² flat plate nickel electrode.

or structures of the active material at the interface. The flat plate electrode, however, has an extremely sharp drop in capacitance in Fig. 5, suggesting a highly uniform active material/current collector interface. The greater relative drop in capacitance for the flat plate electrode is likely to be due to a somewhat higher interfacial current density.

The capacitance on the lower plateau, if due to a perfectly uniform semiconductor layer, would be expected to exhibit a Mott-Schottky dependence on voltage. This relationship is plotted in Fig. 6 for differing amounts of residual capacity discharged for both sintered and flat plate electrodes. At all states of discharge, the relationship is essentially linear above 0.0V for the flat plate electrode, and above 0.05V for the sintered electrodes. The linear ranges are not large because data only extend up to about 0.15V, since the depleted layer cannot be maintained above this voltage under galvanostatic conditions. It is interesting to note that for all states of discharge for both the flat plate and the sintered electrodes, the higher voltage data extrapolate to 0.32V vs. Hg/HgO. A possible explanation for the linear behavior at higher voltages and the pronounced curvature at lower voltages is that at lower voltages the depleted layer becomes quite thick relative to grain sizes and active material nonuniformities, thus giving a highly inhomogeneous space charge region. At high voltages, the depleted layer is extremely thin, and is therefore less likely to exhibit Mott-Schottky deviations.

Cobalt additive effect.—Additives such as cobalt are generally considered to significantly improve nickel electrode performance. Although the effects of additives of this kind on the mechanisms of nickel electrode operation are not completely understood, it is expected that the additives can affect both ionic and electronic conductivity of the active material. The effects of a 10% cobalt additive on the kinetics of the sintered nickel electrode were evaluated, and are given in Fig. 7. The data in Fig. 7 clearly show that the overall discharge mechanisms on the upper and lower voltage plateaus are unchanged by the Co additive. However, the Co additive decreased the diffusion resistance during the C/100 discharge by about an order of magnitude, indicating substantially increased ionic conductivity. The electronic conductivity of the active material is also increased by the higher defect concentration provided by the cobalt. As has been previously reported (26), the increased defect concentration decreases the equilibrium electrode voltage

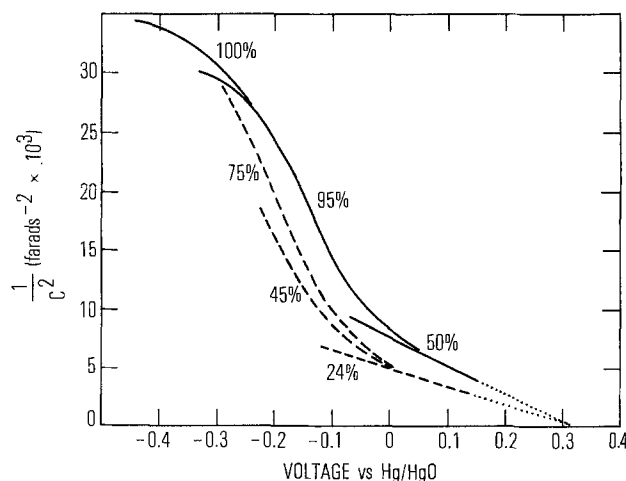


Fig. 6. Mott-Schottky plots for sintered (solid lines) and flat plate (dashed lines) nickel electrodes at various points of discharge of residual capacity. The percentages of residual capacity discharged are indicated. For flat electrode $1/C^2$ has been scaled down by 10.

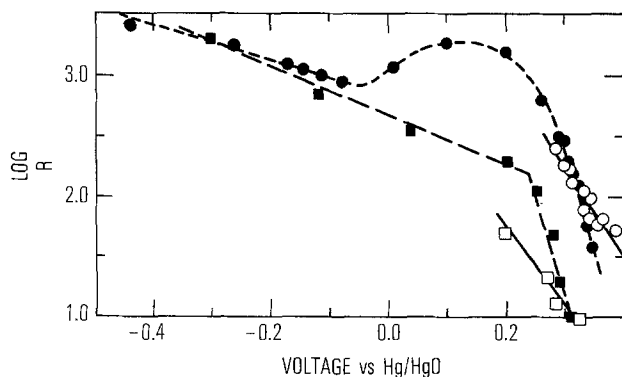


Fig. 7. Resistance R , as a function of voltage for a sintered nickel electrode (closed circles) and a sintered nickel electrode with 10% cobalt additive (closed squares) during a C/100 discharge of residual capacity. The open symbols indicate the diffusion resistances R_d , that were also measured at the higher voltages.

about 70 mV. This has significant effects on the rechargeability of the nickel electrode. The high peak in the resistance during the transition from the upper to the lower voltage plateau appears to be eliminated by the cobalt additive. The peak and how cobalt additives act to eliminate it are the subject of continuing study.

Acknowledgments

The support of the Space Division of the United States Air Force is gratefully acknowledged (contract no. F04701-81-C-0082). We also wish to thank P. Riley for invaluable technical assistance in the chemical analysis of the electrodes.

Manuscript submitted March 7, 1983; revised manuscript received Nov. 7, 1983. This was Paper 40 presented at the San Francisco, California, Meeting of the Society, May 8-13, 1983.

The Aerospace Corporation assisted in meeting the publication costs of this article.

REFERENCES

- H. Bode, K. Dehmelt, and J. Witte, *Electrochim. Acta*, **11**, 1079 (1966).
- R. S. Schrebler Guzman, J. R. Vilche, and A. J. Arvia, *J. Appl. Electrochem.*, **9**, 183 (1979).

- R. S. Schrebler Guzman, J. R. Vilche, and A. J. Arvia, *This Journal*, **125**, 1578 (1978).
- R. Barnard, C. F. Randell, and F. L. Tye, *J. Appl. Electrochem.*, **10**, 109 (1980).
- D. Tuomi, *This Journal*, **112**, 371 (1965).
- D. M. MacArthur, *ibid.*, **117**, 422 (1970).
- D. M. MacArthur, *ibid.*, **117**, 729 (1970).
- Z. Takehara, M. Kato, and S. Yoshizawa, *Electrochim. Acta*, **16**, 833 (1971).
- R. E. Carbonio, V. A. Macagno, M. C. Giordano, J. R. Vilche, and A. J. Arvia, *This Journal*, **129**, 983 (1982).
- R. Barnard, C. F. Randell, and F. L. Tye, *J. Electroanal. Chem.*, **119**, 17 (1981).
- J. F. Jackowitz, in "The Nickel Electrode," R. Gunther and S. Gross, Editors, p. 48, The Electrochemical Society Softbound Proceedings Series, Pennington, NJ (1982).
- R. Barnard, G. T. Crickmore, J. A. Lee, and F. L. Tye, *J. Appl. Electrochem.*, **10**, 61 (1980).
- B. Kalpste, J. Mrha, K. Micka, J. Jindra, and V. Marecek, *J. Power Sources*, **4**, 349 (1979).
- J. Zedner, *Z. Elektrochem.*, **11**, 809 (1905); **12**, 463 (1906); **13**, 752 (1907).
- S. U. Falk, *This Journal*, **107**, 662 (1960).
- H. Bode, K. Dehmelt, and H. V. Dohren, Abstract 6, in "Proceedings of the Second International Symposium on Batteries," D. H. Collins, Editor, Oriol Press, Brighton (1966).
- I. A. Dibrov, *Elektrokhimiya*, **14**, 114 (1978).
- F. Foerster, *Z. Elektrochem.*, **13**, 414 (1907); **14**, 17 (1908); **14**, 285 (1908).
- O. Glemser and J. Einerhand, *Z. Elektrochem.*, **54**, 302 (1950).
- O. Glemser and J. Einerhand, *Z. Anorg. Allg. Chem.*, **261**, 26 (1950).
- J. A. Cherepkova, V. A. Kasyan, V. V. Sysoeva, N. N. Milyutin, and A. L. Rotinyan, *Elektrokhimiya*, **11**, 443 (1975).
- V. A. Kasyan, V. V. Sysoeva, N. N. Milyutin, and A. L. Rotinyan, *Elektrokhimiya*, **11**, 1427 (1975).
- R. Barnard, C. F. Randell, and F. L. Tye, *J. Appl. Electrochem.*, **10**, 127 (1980).
- D. F. Pickett and J. T. Maloy, *This Journal*, **125**, 1026 (1978).
- A. H. Zimmerman, M. R. Martinelli, M. C. Janecki, and C. C. Badcock, *ibid.*, **129**, 289 (1982).
- R. Sabapathy, P. V. Vasudeva Rao, and H. V. K. Udupa, *J. Electrochem. Soc. India*, **16**, 135 (1967).

Breakdown of Passivity of Nickel by Fluoride

II. Surface Analytical Studies

B. P. Löchel

Institut für Physikalische Chemie, Freie Universität Berlin, D-1000 Berlin 33, Germany

H.-H. Strehblow*

Institut für Physikalische Chemie, Universität Düsseldorf, D-4000 Düsseldorf 1, Germany

ABSTRACT

Passive layers on nickel and their change by the action of fluoride have been studied by surface analyses such as x-ray photoelectron spectroscopy (XPS) and low energy ion scattering (ISS). The thickness of the layers is deduced from the height of the XPS signals Ni2p3/2, O1s, and F1s and their attenuation by covering layers. Argon sputtering gives information on the in-depth structure of the passivating films in combination with XPS and the higher depth resolution of ISS. Their thickness and chemical composition change with the electrode potential and the time of exposure to HF. A multilayer structure is found with an inner oxide and outer hydroxide film and, in a higher potential range, a fluoride layer in between. The layer structure shows a close correspondence to the results of the electrochemical examination.

The thickness and composition of surface layers are of decisive importance for processes at the solid-

electrolyte interface. Especially in the field of corrosion, the analysis of the metal surface is necessary to gain a deeper insight into the phenomena and a better interpretation of the electrochemical results. Therefore, we started a combined study of x-ray photoelec-

* Electrochemical Society Active Member.
Key words: passivating layers, breakdown of passivity, nickel, fluoride, XPS, ISS, layer thickness.

tron spectroscopy (XPS), ion scattering spectroscopy (ISS), and electrochemical examinations. In a previous paper, the influence of fluoride on the passive behavior of nickel was studied (1). A profound explanation of the findings was only possible on the basis of the surface analytical results. We examined the films of passivated nickel and those which have been attacked by fluoride. For this purpose, the specimens are prepared under well-defined electrochemical conditions.

Experimental

The specimen preparation was described in detail previously (1). After the individual pretreatment, the specimens were rinsed with triply distilled water and transferred into the vacuum chamber as quickly as possible, typically within 1 min. For the analysis, we used an ESCALAB 5 system (Vacuum Generators, Limited) with a fast entry airlock, a preparation chamber, a main analytical vessel with an optimum pressure of $5 \cdot 10^{-11}$ mbar and an operating pressure of some few 10^{-10} mbar after sample induct. The XPS analysis was run with a Mg $K\alpha$ source with 300 W power. For sputtering and ISS analysis, a fine focusing scanning ion gun was used. For depth profiling, an argon beam with 3 keV primary energy and a controlled specimen current of 0.7 μ A was scanned over an area of 8×8 mm. ISS was performed with a helium beam of 1 keV primary energy and 10 nA current to avoid any changes during analysis. A gas inlet system facilitated the rapid change of gases for the ion gun. Phases of argon sputtering and analysis with helium followed alternatively, thus providing an ISS depth profile. After each sputter period, an XPS analysis of the most relevant peaks was taken. The sputter area was large enough to get only contributions of equally etched parts of the surface. For ISS, the signal was taken from a small part of the sputtered area in the center.

With the ISS spectrum, one may distinguish between the three main elements, Ni, O, and F present at the surface. This method has an in-depth resolution of a monolayer. However, depth profiles are affected by the different changes caused by argon ion sputtering. Therefore, we used ISS only to determine qualitatively the sequence of multilayer structures.

For XPS analysis, we used the O1s signal at the binding energies $E_B = 529.3$ and 531.5 eV to distinguish between oxide and hydroxide, the F1s signal at $E_B = 685$ eV, and the Ni2p3/2 peaks in the range $E_B = 852$ – 868 eV. At $E_B = 852.8$ eV, the metallic Ni peak is found. The peak at 856.5 eV is an overlap of several signals, Ni(OH)₂, NiO, and the "shake up" of the metallic nickel. NiO is found at 853.4 and 855.4 eV and Ni(OH)₂ at 855.8 eV. In the presence of fluoride, a peak at 857.2 eV is attributed to NiF₂ after comparison with standards. The related "shake up" is found at 863.5 eV. As nickel is present simultaneously at the surface in different valence states, the peaks and their satellites overlap to a complicated structure with a base line not well defined. Unfolding this structure is affected with a large error. Therefore, we did not use

this part of the Ni2p3/2 signal for quantitative analysis. The main qualitative and quantitative information was taken from the metallic Ni2p3/2, the O1s, and the F1s peak.

As references, we used a sputter-cleaned Ni specimen, NiO, Ni(OH)₂, and NiF₂ powder pressed in a tin foil to reduce surface charging (2) and a Ni sample oxidized in air at 700°C and so covered with a visible NiO film thick enough to prevent any contribution of the metallic Ni peak. Table I shows the relevant peak positions of different nickel compounds. In cases where surface charging was a problem, the signals were corrected by referring them to the Cls position with $E_B = 284.6$ eV. Carbon was always present in traces because of the inevitable contaminants from the electrolyte and the exposure to the environment. The results of Table I show a good agreement with those from the literature (3–9) and helped in identification of the nature of the surface films. The Ni2p3/2 peak of the Ni₂O₃ specimen is close to the positions of NiO and Ni(OH)₂. The distinction between Ni₂O₃ and NiO in the absence of Ni(OH)₂ is possible by using the different O1s peak positions (7). In presence of Ni(OH)₂ this distinction is impossible on the basis of ESCA measurements. Therefore, we could not find small amounts of Ni₂O₃ in a NiO matrix as postulated for the transpassive potential range for Ni. However, the presence of Ni₂O₃ cannot be ruled out.

Results and Discussion

The XPS spectra of electropolished nickel rinsed with triply distilled water show qualitatively the presence of a NiO film with a Ni(OH)₂ overlayer (Fig. 1). The Ni2p3/2 shows a metallic Ni peak ($E_B = 852.8$ eV) attenuated by the surface film and a peak at $E_B = 856.5$ eV with its origin from NiO, Ni(OH)₂, and a "shake up" contribution. The O1s signal demonstrates the presence of hydroxide ($E_B = 531.5$ eV) and a shoulder at $E_B = 529.9$ eV of oxide. Argon sputtering enlarges the shoulder at lower binding energy with a simultaneously vanishing hydroxylic signal. A change from nickel hydroxide to oxide or even its reduction to nickel metal by preferential sputtering during argon ion bombardment may be excluded by the results of other authors (6, 7) and own tests with Ni(OH)₂ specimens. Consequently, the surface film has a double structure with an inner oxide and an outer hydroxide layer. Sputtering enlarges the metallic Ni2p3/2 signal as a consequence of the thinning of the surface film and, contrary to Ni(OH)₂, by a partial reduction of NiO to Ni metal by preferential sputtering.

ISS shows only a Ni and O peak. Both signals appear after a short argon sputtering of some few minutes corresponding to a removal of less than one monolayer. This is a typical effect of all ISS spectra when water or OH groups are present at the surface. Backscattering of helium at the lighter hydrogen atoms does not occur.

The nickel specimen passivated in 1M HClO₄ ($\epsilon = 1.4V$) showed a similar XPS spectrum (Fig. 2). The Ni metal peak is less pronounced, and at $E_B = 855$ eV

Table I. Binding energies of XPS peaks and satellites of different nickel standards referred to Cls with $E_B = 284.6$ eV

Specimen	Ni2p3/2			O1s			F1s
				O ²⁻	OH ⁻	O ^{ads}	
Ni metal	852.8		858.6 ^b				
NiO	853.4	855.4 ^a	860.5 ^b	529.3	531.2		
Ni(OH) ₂	855.8		861.7 ^b		531.0		
NiF ₂	857.2		863.5 ^b		531.4		
Ni ₂ O ₃ (4)	855.7		861.4 ^b	531.7			684.5
Ni, mech. polished	852.8			529.3	531.2	532.8	
Ni, electropolished	852.5	856.0		529.3	531.5		
Ni, heated in air to 700°C	853.6	855.3 ^a	860.9 ^b	529.3	531.2		

^a Multiplet splitting 141.

^b Satellite (shake up).

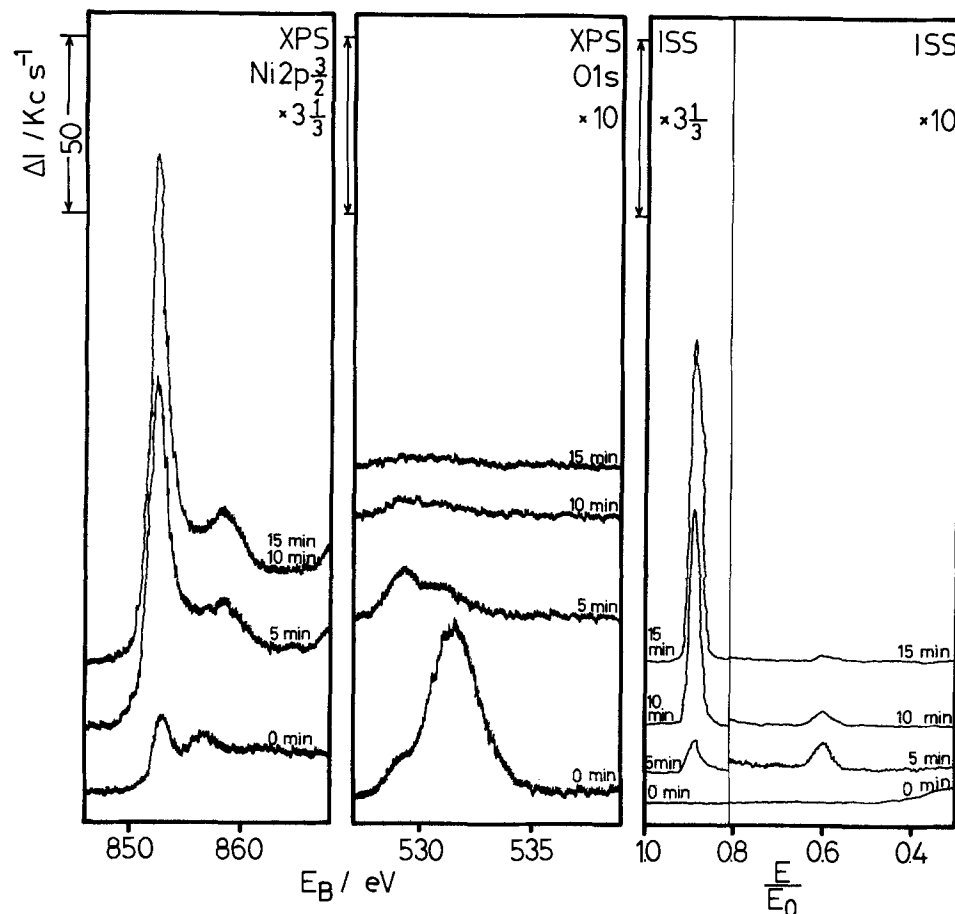


Fig. 1. XPS and ISS depth profile of a nickel specimen electroplated in a 57% H_2SO_4 + 43% H_2O mixture.

a larger $\text{Ni}2p_{3/2}$ signal is found. This is a consequence of a thicker oxide film. Two distinct $\text{O}1s$ signals indicate the presence of an oxide and hydroxide layer.

Sputtering with argon ions again enlarges the Ni metal peak and reduces the oxide shoulder at $E_B = 855$ eV. The $\text{O}1s$ hydroxide signal also vanishes first within

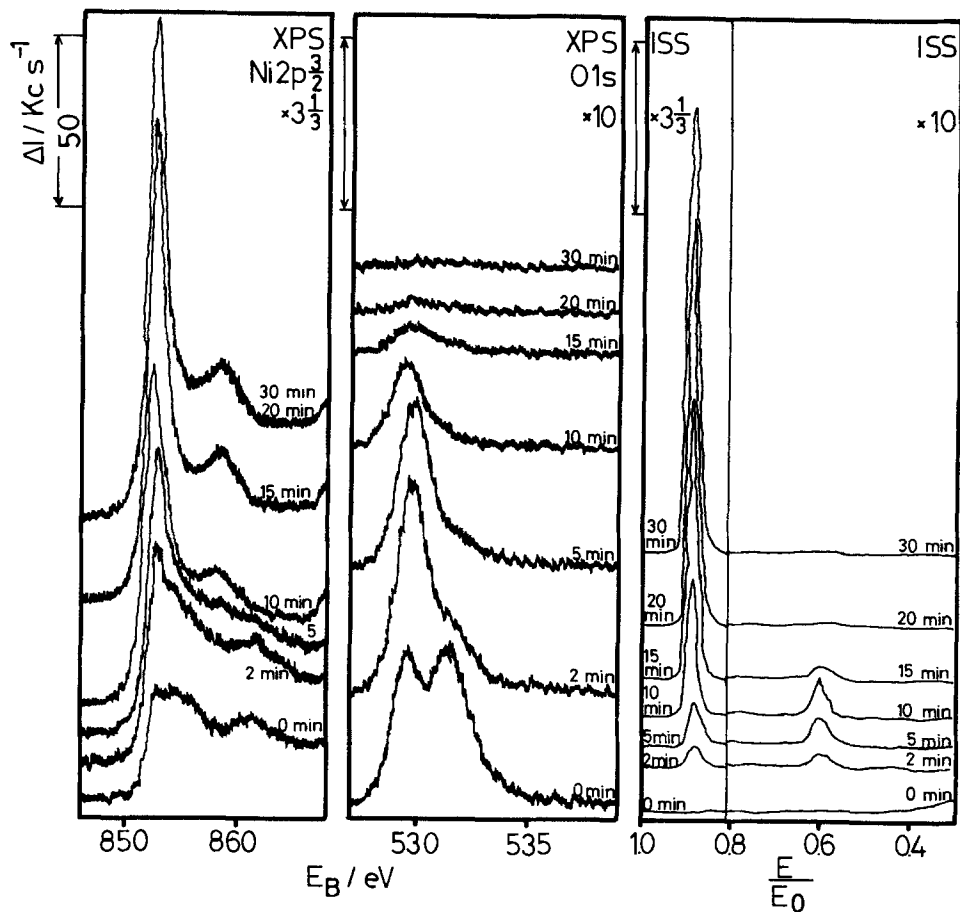


Fig. 2. XPS and ISS depth profile of a passive film on nickel formed in 1M HClO_4 at $e = 1.4\text{V}$ for 3h.

about 5 min; the O1s oxide signal vanishes within 20 min. The ISS signal does not contain further information. The oxygen signal also disappears within 20 min of sputtering. A comparison with the electropolished Ni specimen shows a hydroxide layer of similar thickness by both the size of the O1s hydroxide signal and its disappearance within the same sputtering time. However, the oxide thickness has doubled after the results for the O1s signal. The XPS depth profile shows again an outer hydroxide and an inner oxide layer for passivated nickel electrodes. Similar results are obtained within the whole passive range of $\epsilon = 0.5$ -1.8V. In the transpassive region for $\epsilon > 1.5$ V, an increase of the oxide thickness is found. A higher valent oxide, i.e., Ni₂O₃, which is postulated from electrochemical results could not be detected. A clear indication of its presence is not possible because of the small chemical shift of the Ni2p3/2 peak (Table I).

To obtain quantitative results, the thickness of the surface layers was calculated from the XPS signals. For base line subtraction the background at both sides of a signal was connected at the peak position (10). With sufficient accuracy the peak heights between the maximum and the base line were taken for a quantitative evaluation instead of the peak areas which were controlled in several cases. The calculation was performed on a relative basis with peak height ratios, which minimized the error. Any changes by unfolding the overlapping peaks causes a larger inaccuracy. The structure of the Ni2p3/2 signal is complicated by the overlapping peaks of the different nickel compounds and their satellites. An unfolding for quantitative evaluation would give rather uncertain results. Therefore, we used only the Ni metal peak at $E_B = 852.8$ eV, and in addition the much simpler O1s signal ($E_B = 829.3$ and 531.5 eV). For the unfolding we assume a symmetrical peak shape with identical leading and tailing edges.

The attenuation of the Ni2p3/2 metal signal is used to get a value for the thickness of the total layer. If y is the thickness of the oxide, x of the hydroxide, and δ of the total layer (Fig. 3), one obtains for the attenuated Ni metal signal

$$I_1^{Me} = KF\sigma^{Me}[\text{Ni}]\lambda_{Me}^{Me} \exp(-\delta/\lambda_o^{Me}) \quad [1]$$

$$\delta = x + y \quad [1a]$$

where F is the intensity of the x-ray source and K a characteristic constant of the spectrometer containing the transmission characteristic of the energy analyzer and the detector and the angular acceptance of the analyzer. σ^{Me} is the photoionization cross section for the Ni2p3/2 signal after Scofield (11), corrected for the anisotropy of the photoelectron emission including the angle between the x-ray source and the energy analyzer (12, 13). $[\text{Ni}] = 0.1516$ mol cm⁻³ is the concentration of the nickel atoms in the metal (14), and λ_{ox}^{Me} the escape depth of the Ni2p3/2 photoelectrons from a NiO matrix. In a first approximation, the escape depth depends only on the kinetic energy after the relation

$$\lambda = B\sqrt{E_{kin}} \quad [2]$$

for kinetic energies $E_{kin} > 100$ eV (15) so that the values of NiO and Ni(OH)₂ do not differ ($\lambda_{ox}^{Me} \approx \lambda_{OH}^{Me}$). λ_{Me}^{Me} is the escape depth for the metal matrix, which is different from that of the oxides when considering the matrix effect to a first approximation (15).

For a clean sputtered nickel surface, one obtains for the Ni metal signal

$$I^{Me} = KF\sigma^{Me}[\text{Ni}]\lambda_{Me}^{Me} \quad [3]$$

Dividing Eq. [1] and [3] yields the following relations for identical experimental conditions for the spectrometer (K, F)

$$\frac{I_1^{Me}}{I^{Me}} = \exp(-\delta/\lambda_o^{Me}) \quad [4]$$

With the measured intensity of the Ni2p3/2 metal signal of the passivated specimen I_1^{Me} and the clean and uncovered standard I^{Me} , one obtains the total thickness $\delta = x + y$ of the double layer after relation [4]. For the subdivision in the two parts x and y , one may use the ratio of the peak heights of the O1s hydroxide and oxide peak

$$\frac{I_{OH}^o}{I_{ox}^o} = \frac{[\text{OH}^-][1 - \exp(-x/\lambda_{OH}^o)]}{[\text{O}^{2-}] \exp(-x/\lambda_{OH}^o)[1 - \exp(-y/\lambda_{ox}^o)]} \quad [5]$$

$[\text{OH}^-] = 0.0896$ mol cm⁻³ and $[\text{O}^{2-}] = 0.0839$ mol cm⁻³ are the molar concentrations of the OH⁻ and O²⁻ ions of NiO and Ni(OH)₂, respectively (14). The factor in brackets takes account of the self-attenuation of the signal with increasing thickness of the hydroxide and oxide layer, respectively. The additional exponential factor in the lower part reflects the attenuation of the O1s oxide signal by the hydroxide overlayer. Equation [5] requires identical experimental conditions for the spectrometer again.

Neglecting the matrix effects on the escape depth with $\lambda_{ox}^o = \lambda_{OH}^o = \lambda^o$, one obtains the relation for the thickness x of the hydroxide layer

$$x = -\lambda^o \ln \frac{I_{ox}^o[\text{OH}^-] + I_{OH}^o[\text{O}^{2-}] \exp(-d/\lambda^o)}{I_{OH}^o[\text{O}^{2-}] + I_{ox}^o[\text{OH}^-]} \quad [6]$$

Equations [4] and [6] permit one to calculate the thickness $\delta = x + y$ of the total layer, and the parts x for the hydroxide and y for the oxide.

The results of this evaluation are depicted in Fig. 4. For a better understanding, the potentiodynamic polarization curve of nickel in 1M HClO₄ is represented together with the total thickness δ and the oxide thickness y . The hydroxide thickness x equals the distance between both curves. The error of these results is most affected by the uncertainty of the escape depth λ of the electrons. This may be estimated to be $\pm 20\%$, thus leading to a similar error for the thickness values after Eq. [4] and [6] with $\delta \sim \lambda$ and $x \sim \lambda$.

Weakly acidic and alkaline solutions.—The passive layer in phthalate (pH 5.0) and borate buffer (pH 8.0) has the same double layer structure and only slight changes in thickness are found. Table II compares some results of the three electrolytes. Marcus *et al.* found the same structure but half the thickness for nickel passivated at $\epsilon = 0.54$ V in 0.1M H₂SO₄ (3). They used, however, the complex Ni2p3/2 signal for their evaluation and did not take into account the attenuation by the covering layers. Ohtsuka and Heusler determined similar values in 1M H₂SO₄ ($\epsilon = 0.6$ -1.6V, $\delta = 14$ -20Å) for the total layer (16) by *in situ* ellipsometry, and Sato in borate buffer pH 8.4 (17).

The thickness of the hydroxide layer does not change with potential and pH and does not seem to have a pronounced influence on the passive behavior. Its constant thickness for all electrolytes suggests that it is

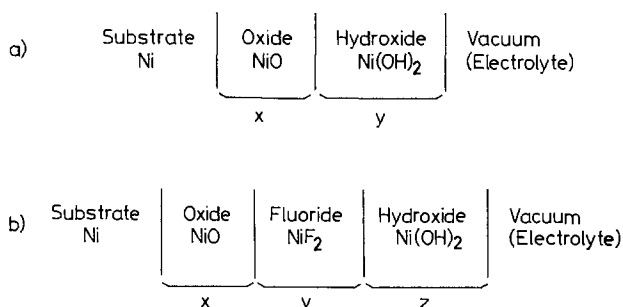


Fig. 3. Model of the passive layer on nickel. a: without fluoride. b: with an intermediate fluoride layer.

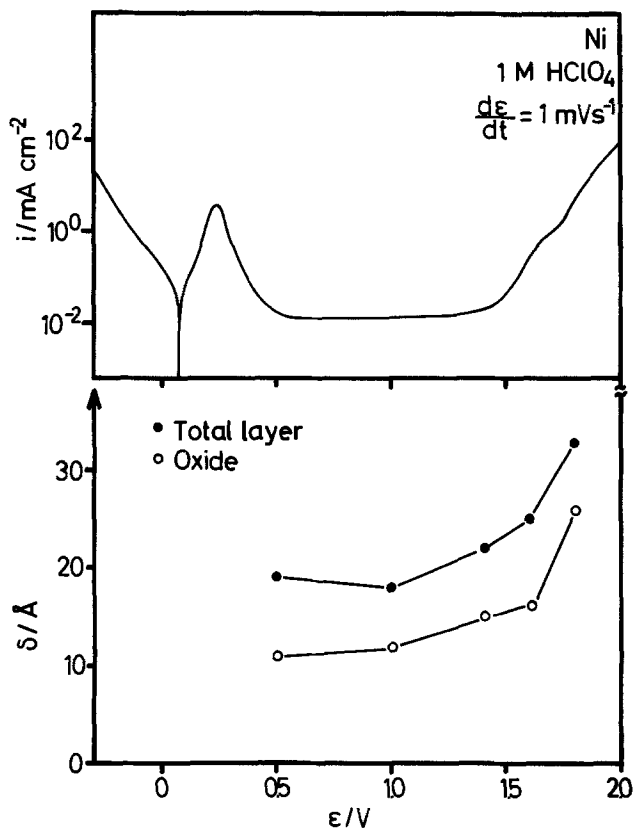


Fig. 4. Polarization curve of nickel and layer thickness after 2h prepassivation in 1M HClO₄ at different electrode potentials ϵ calculated from the XPS results. ●: total layer. ○: oxide layer. Difference refers to hydroxide layer.

not formed by secondary processes (*i.e.*, by precipitation from the adherent solution during the removal of the samples from the electrolyte or during rinsing with water). Small amounts of Ni²⁺ (passive current density < 1 μ A cm⁻²), especially within an adherent acidic electrolyte are expected to be washed off much more readily than in alkaline buffers with a lesser

Table II. Layer thickness of passivated nickel at different potentials ϵ in 1M HClO₄, phthalate buffer pH 4.9 and borate buffer pH 8.0 and of electropolished nickel

Electrolyte	ϵ/V	Time of passivation min	δ/A	Thickness/ δ of	
				Oxide	Hydroxide
1M HClO ₄	0.5	140	19	11	8
	1.0	120	18	12	6
	1.4	200	22	15	7
	1.6	120	25	16	9
	1.8	120	33	26	7
Phthalate buffer	1.1	160	19	14	5
Borate buffer	0.5	170	24	17	7
Nickel electropolished	—	—	29	7	22

tendency to form precipitates. The oxide layer determines the passivating properties, as shown by its change with potential especially in the transpassive region, where a reduced dissolution, besides the evolution of oxygen, is found (18). The thinner oxide layer on electropolished nickel also supports this conclusion. These specimens are much better protected against aggressive electrolytes when they are prepassivated additionally for a sufficiently long period (19, 20), and achieve smaller stationary current densities with time.

Passive films after fluoride attack.—The addition of HF to 1M HClO₄ causes a pronounced increase of the corrosion current density of a passivated nickel electrode. The current density potential curve has a maximum and two characteristic minima (Fig. 6) (21, 22). To get an explanation for these features of the polarization curve and the effective corrosion mechanisms, we examined the nickel specimen after fluoride attack by surface analysis.

Figure 5 shows a depth profile by XPS and ISS of a nickel electrode prepassivated in 1M HClO₄ for 2h after the attack by 0.1M HF for 30 min at minimum I ($\epsilon = 0.5V$). Before the specimen was transferred from the electrolyte into the UHV chamber, stationary conditions with a constant current density had been achieved. The spectra were qualitatively the same as those without the fluoride addition. No fluoride was

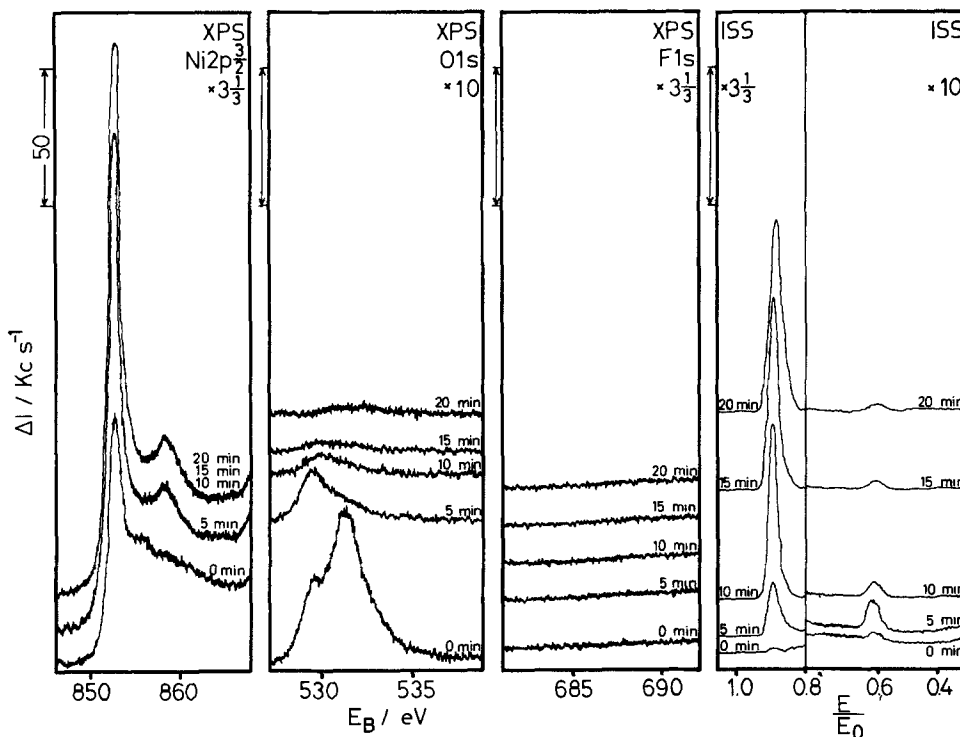


Fig. 5. XPS and ISS depth profile of 2h in 1M HClO₄ prepassivated nickel after 30 min of exposure to 1M HClO₄ + 0.1M HF at $\epsilon = 0.5V$ (minimum I).

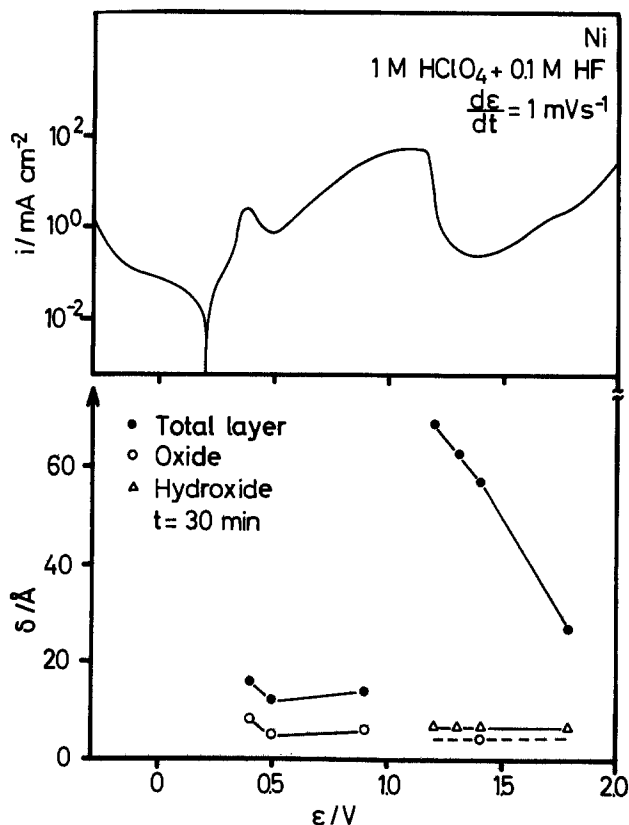


Fig. 6. Polarization curve of nickel and layer thickness at different electrode potentials ϵ after 30 min of exposure in 1M HClO_4 + 0.1M HF. \bullet : total layer. \circ : oxide layer. \triangle : hydroxide layer. Difference refers to fluoride layer.

found in the surface layer by XPS and ISS after the fluoride attack (1% NiF_2 detection limit). The $\text{O}1s$ signal indicates the double layer structure. The OH signal disappears first during argon sputtering, demonstrating the outside position of the hydroxide. It takes about half the time to remove the passive layer compared to the specimen without fluoride attack, indicating its severe thinning. This is confirmed by the quantita-

tive evaluation of the $\text{Ni}2p_{3/2}$ metal peak and the two $\text{O}1s$ signals with Eq. [4] and [6] (Fig. 6). The thickness of the hydroxide layer is unchanged. These findings demonstrate the importance of the oxide layer and its changes for the passive behavior. Similar results are obtained in the whole potential range of minimum I up to the intermediate maximum ($\epsilon = 0.4$ – 0.9V) (Fig. 6).

More pronounced differences were found for those electrodes which had been exposed to HF containing HClO_4 at potentials of minimum II. At $\epsilon = 1.4\text{V}$, a large $\text{F}1s$ signal indicates the presence of fluoride in the surface film (Fig. 7). The $\text{O}1s$ signal shows the presence of hydroxide; however, oxide cannot be detected on the unspattered specimen. A very small $\text{Ni}2p_{3/2}$ metal signal is caused by a much thicker surface film than on a passive electrode in HClO_4 without HF (see Fig. 2). The signal at $E_B = 857.4\text{ eV}$ refers to NiF_2 , as is seen by comparison with a NiF_2 standard (Table I). This peak is at the position of the Ni metal satellite. However, the Ni shake-up peak is much too small to give any appreciable contribution with the vanishing main Ni metal peak of the unspattered specimen. The height of the satellite is generally about 17% of the total (main peak plus satellite).

During sputtering, a small $\text{O}1s$ oxide signal appears when the hydroxide peak is vanishing (Fig. 7). The fluoride disappears within ca. 1h when the oxide is still present.

ISS gives further information about the structure of the surface film. The increasing peak at $E/E_0 = 0.65$ is attributed to fluoride (Fig. 7). When the fluoride layer disappears after ca. 1h, an oxide signal is found at $E/E_0 = 0.60$, indicating a NiO sublayer. The preferential sputtering of the lighter elements oxygen and fluorine is accompanied by a partial reduction of the nickel compounds NiO and NiF_2 (7), which causes an early increase of the $\text{Ni}2p_{3/2}$ metal signal. This is overcome by its normal increase in later stages as a consequence of the removal of the surface layer.

The XPS and ISS examinations (Fig. 7) suggest a triple-layer structure for nickel electrodes in the range of minimum II. A very thin NiO layer at the metal surface is covered by a much thicker NiF_2 superimposed by a thin Ni(OH)_2 layer. The hydroxide layer is found by the $\text{O}1s$ signal on a non- or short-time (< 15 min) sputtered specimen (Fig. 7). A good ISS

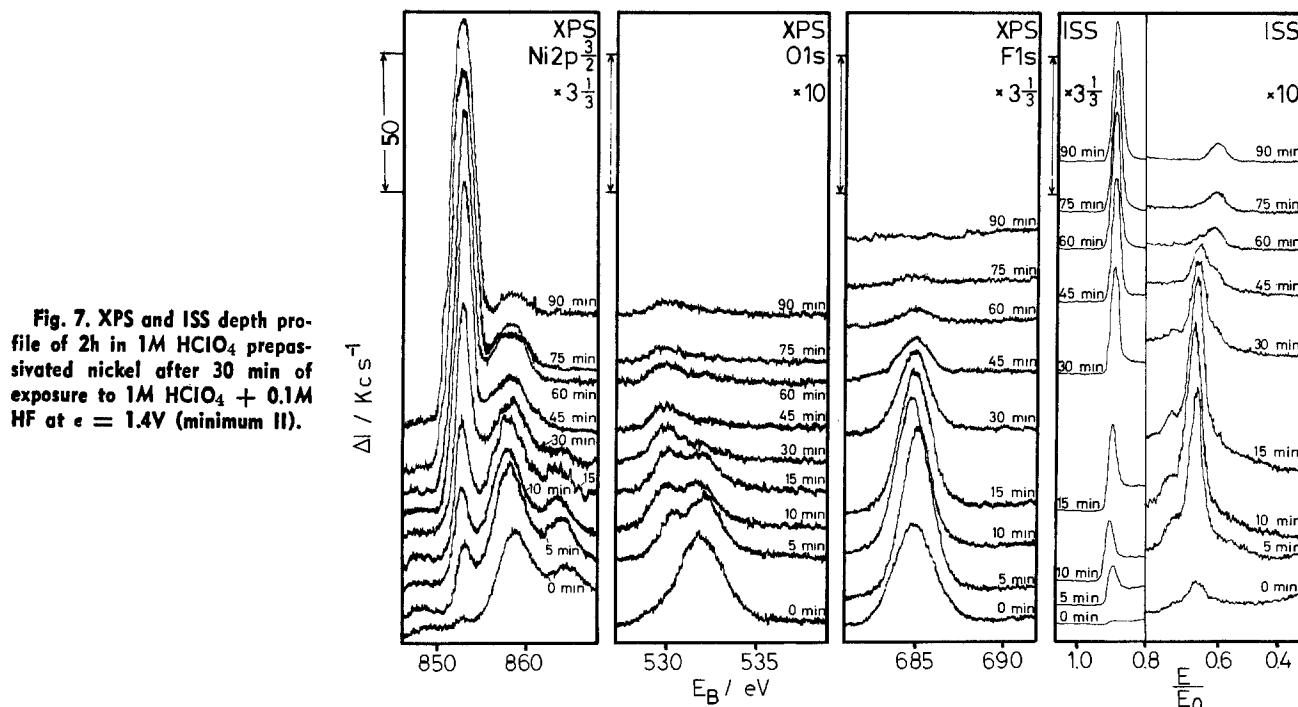


Fig. 7. XPS and ISS depth profile of 2h in 1M HClO_4 prepassivated nickel after 30 min of exposure to 1M HClO_4 + 0.1M HF at $\epsilon = 1.4\text{V}$ (minimum II).

signal is obtained only after some sputtering when hydrogen is removed.

Besides the position of the Ni2p_{3/2} peak at $E_B = 857.4$ eV, the quantitative evaluation of the XPS signals gives information about the chemical nature of the fluoride containing layer. For this purpose the peak heights of F1s and Ni2p_{3/2} are divided by the corrected photoionization cross sections (11-13) $\sigma_F = 5.46$ and $\sigma_{Ni} = 17.03$. The molar ratio is obtained after relation [7]. The energy dependence of the escape depth Eq. [2] cancels with that of the transmission function $T \sim (E_{Kin})^{-1/2}$ of the ESCALAB 5 (10).

$$\frac{n_F}{n_{Ni}} = \frac{I_{F\sigma_{Ni}\lambda_{Ni}T_{Ni}}}{I_{Ni\sigma_F\lambda_F T_F}} = \frac{I_{F\sigma_{Ni}}}{I_{Ni\sigma_F}} \quad [7]$$

Table III gives the molar ratio of fluorine to nickel for prepassivated specimens exposed to 1M HClO₄ + 0.1M HF for 30 min in the potential range of minimum II. The results show sufficient coincidence with those for a NiF₂ standard. The Ni2p_{3/2} fluoride signal is not corrected for the small peak of the nickel hydroxide. However, its contribution is estimated to be less than 5%. Its consideration would enlarge only slightly the n_F/n_{Ni} ratio.

From the position and height of the XPS peaks, we have to conclude that a NiF₂ layer is present at the surface in the potential range $\epsilon = 1.1$ to $<1.8V$; however, small amounts of higher valent nickel compounds (i.e., NiF₃) cannot be excluded. Very small amounts of oxide and hydroxide are also seen in the depth profiles so that some contaminations of the fluoride film seems reasonable. This holds especially for the visible blue-black layers formed at the peak maximum ($\epsilon = 1.15V$) (1). They are apparently much too thick to permit a contribution of the thin NiO sublayer to the O1s signal. Even after 30 min of sputtering a very small O1s is still detected (Fig. 8). Also in this case, the increase of the Ni2p_{3/2} metal signal demonstrates the partial reduction of the surface film (NiO, NiF₂) by preferential sputtering of the lighter elements (O and F). The nickel substrate cannot give any contribution when it is covered by the visible coherent film which only might contain some pores. Appreciable amounts of complexes with a high F content within the film such as [NiF₆]⁴⁻ may be excluded. They would cause a pronounced chemical shift of the Ni2p_{3/2} and

Table III. Molar ratio n_F/n_{Ni} after Eq. [10] from XPS peak heights for surface layers prepared by 30 min exposure to 1M HClO₄ + 0.1M HF at different potentials and NiF₂ standard, $\epsilon = 1.15V \triangleq$ visible fluoride film

ϵ/V	n_F/n_{Ni}
1.15	2.21
1.20	2.13
1.30	2.29
1.40	2.43
1.80	2.12
NiF ₂ standard	2.25

F1s signal to $E_B = 861.2$ eV and $E_B = 687.8$ eV as compared to K₂NiF₆ (23), which is not found experimentally.

The thickness of the triple layer may be calculated from the peak heights of the XPS signals similar to the case of an ordinary passive film on nickel. For this more complicated situation, the F1s peak is used as well, leading to the following equation for the peak height ratios

$$\frac{I_{O_{OH}}}{I_F} = \frac{\sigma_o[OH^-] [1 - \exp(-x/\lambda^o)]}{\sigma_F[F^-] \exp(-x/\lambda^o) [1 - \exp(-y/\lambda^F)]} \quad [8]$$

$$\frac{I_{O_{ox}}}{I_F} = \frac{\sigma_o[O^{2-}] \exp(-(x+y)/\lambda^o) [1 - \exp(-z/\lambda^o)]}{\sigma_F[F^-] \exp(-x/\lambda^o) [1 - \exp(-y/\lambda^F)]} \quad [9]$$

where x is the thickness of the hydroxide, y of the fluoride, and z of the oxide layer. The escape depths of the electrons originated at F and O atoms are only slightly different, $\lambda^o = 12\text{\AA}$ and $\lambda^F = 11\text{\AA}$, when the matrix effect is neglected and Eq. [2] is applied. With the approximation $\lambda^o \approx \lambda^F = \lambda$, one obtains the following relations

$$x = -\lambda \ln \left[\frac{b/c + (f/h) \exp(-\delta/\lambda)}{a/c + g/h} \right] \quad [10]$$

$$y = -\lambda \ln [(g/h) + (f/h) \exp(-[\delta - x]/\lambda)] \quad [11]$$

with the following expressions

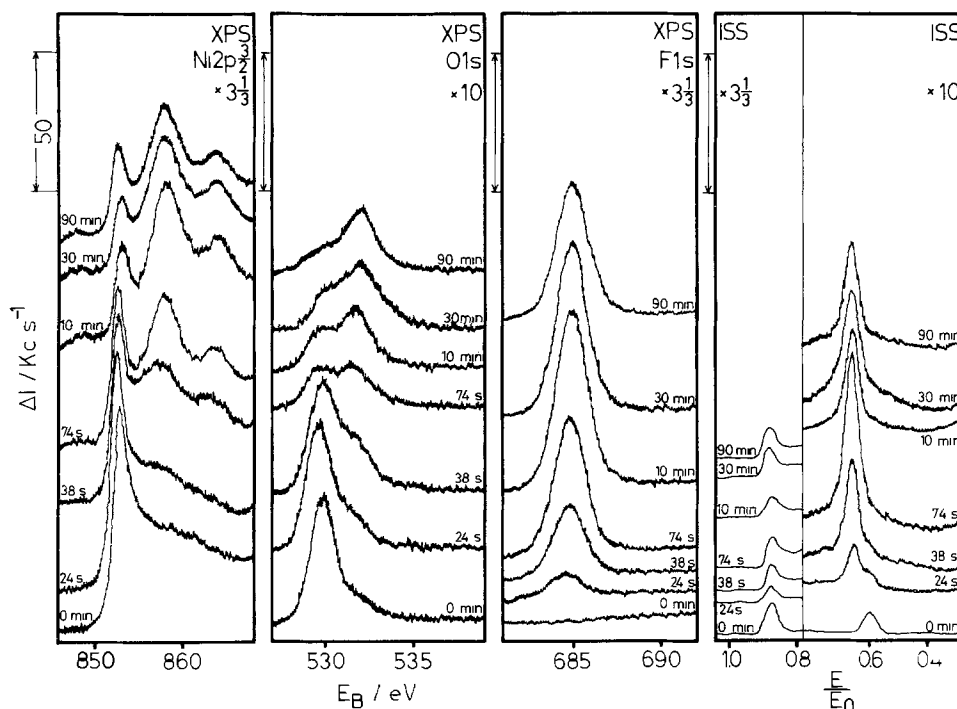


Fig. 8. XPS and ISS spectra of 2h in 1M HClO₄ prepassivated nickel after different times of exposure to 1M HClO₄ + 0.1M HF at $\epsilon = 1.4V$ (minimum II) after 5 min of argon sputtering (0.7 μA , 3 kV).

$$\begin{aligned}
 a &= I_{\text{OH}\sigma\text{F}}[\text{F}^-] + I_{\text{F}\sigma\text{O}}[\text{OH}^-] \\
 b &= I_{\text{F}\sigma\text{O}}[\text{OH}^-] \\
 c &= I_{\text{OH}\sigma\text{F}}[\text{F}^-] \\
 f &= I_{\text{F}\sigma\text{O}}[\text{O}^{2-}] \\
 g &= I_{\text{Ox}\sigma\text{F}}[\text{F}^-] \\
 h &= I_{\text{F}\sigma\text{O}}[\text{O}^{2-}] + I_{\text{Ox}\sigma\text{F}}[\text{F}^-] \\
 \delta &= x + y + z \text{ (total layer thickness)}
 \end{aligned}
 \quad [12]$$

For the concentrations of the anions, the previously mentioned values of the bulk materials NiO, Ni(OH)₂, or NiF₂ are applied [$[\text{F}^-] = 0.0958 \text{ mol cm}^{-3}$ (14)]. The total layer thickness δ is calculated again from the attenuation of the Ni2p3/2 metal signal. The relatively thick fluoride layer causes problems in the determination of the thickness of the oxide (z) and the total layer thickness (δ). The nickel metal and nickel oxide signals are attenuated to a large extent, so that δ may be determined only with a relatively large error of $\pm 20\%$. After the depth profiles, a small oxygen content within the fluoride was taken into account. This situation enlarges the nickel oxide peak and leads to much too high values for the oxide thickness x . Table IV shows the thickness of the triple layer after exposure to HClO₄ + 0.1M HF for different times at potentials in the range of the minimum II ($\epsilon = 1.2$ -1.8V), where transparent films are formed. The values in the brackets are obtained by direct application of Eq. [4], [10], and [11]. The other more correct values are obtained from the time dependence of the fluoride attack, especially for short-time exposures. This is described below.

Change of the surface layer with time.—The changes of the thickness and composition of the surface layers occur in close coincidence with the features of the current density-time curves (1). Figure 8 depicts the XPS and ISS spectra after different times of attack by 0.1M HF in 1M HClO₄. The specimens are all sputtered for 5 min with identical conditions to get a well-developed ISS spectrum, which is not suppressed by the presence of H atoms at the surface. Consequently, the O1s hydroxide signal is reduced to only a small shoulder close to the oxide peak for a nonattacked sample. With increasing time of HF exposure, the O1s oxide signal gets smaller because the NiO is covered by an increasing fluoride layer and the oxide itself is thinned. The increase of the O1s hydroxide signal for long times of HF exposure is presumably caused by an OH⁻ contamination of the fluoride layer. The HF attack increases the Ni2p3/2 fluoride and the F1s signal and decreases the Ni2p3/2 metal signal.

Similarly, the ISS spectrum reflects the growth of the fluoride layer on NiO. After 24s of attack, a small oxide shoulder is still seen besides the fluoride peak. After 38s, the fluoride film is already thick enough to

cover the oxide completely after 5 min of sputtering. Consequently, a large F peak is found without an oxide shoulder for > 38s of HF exposure. The depth profiles of specimens with increasing fluoride attack are consistent with an increasing intermediate fluoride layer. The sputter time for the detection of the rest of the oxide at the metal surface by ISS increases with the exposure to HF. Similarly it takes more time to remove the fluoride from the surface.

The F1s and the Ni2p3/2 fluoride peaks increase, and the O1s oxide signal decreases with the time of exposure. At 75s of HF attack, the maximum of the F1s and Ni2p3/2 fluoride signal and a minimum of the O1s oxide peak are achieved, and no pronounced change occurs within the following 90 min.

For short times of HF exposure up to 74s, the calculation of the thicknesses x , y , and z of the triple surface layer does not cause major problems. The attenuation of the Ni2p3/2 metal and O1s oxide signal still permits determination of reliable values. After several minutes, however, both peaks are too small to be measured with a large overlapping Ni2p3/2 fluoride and O1s hydroxide signal. A 10 min sputtering, however, gives an estimate of the layer thickness applying relations [4] and [10]-[12]. The hydroxide signal was taken from the unspattered, whereas the oxide and the fluoride signals were taken from the sputtered specimen. During the sputtering process, the hydroxide is mainly removed. To some extent the fluoride is also. This increases the F1s signal because only the self-attenuation of the layer is effective now. The partial reduction of the surface by preferential sputtering leads to a somewhat too small total thickness δ so that these values for 10-90 min should be seen as an estimate.

The results for $\epsilon = 1.4\text{V}$ are depicted in Fig. 9. The changes occur in close relation to the polarization curve. The thinning of the oxide layer occurs during the first 1.5 min. At the same time the fluoride layer is formed. During the first 30s, the oxide thinning is responsible for the current increase; in the following minute, the growth of the fluoride layer reduces its value. After 1.5 min, only minor changes in the layer structure and the current density are found.

The thickness of the three layers are also inserted in the diagram in Fig. 6. The decrease of the current for $\epsilon > 1.0\text{V}$ coincides with the formation of a fluoride film. At the current maximum its protecting properties are still not sufficient. Although a visible film is observed, the corrosion of nickel is not effectively suppressed. This should be seen as a consequence of the layer structure, which presumably is porous or not dense enough to reduce effectively the transfer of the metal ions from the metal into the electrolyte. At the falling edge of the current density up to $\epsilon < 1.2\text{V}$, the surface is covered only partially by a visible film. Current oscillations indicate the instability of this

Table IV. Layer thickness of prepassivated nickel after exposure to HF or KF containing 1M HClO₄, phthalate buffer pH 4.9 and borate buffer pH 8.0 for different times and potentials

Electrolyte	ϵ/V	Time/min Passivation + 0.1M F ⁻		$\delta/\text{\AA}$	Thickness/ \AA of		
					Oxide	Fluoride	Hydroxide
1M HClO ₄ + 0.1M HF	0.40	120	30	16	8	—	8
	0.50	120	30	12	5	—	7
	0.90	120	30	14	6	—	8
	1.20	240	30	69	4 (28)	60 (36)	5
	1.30	250	30	63	4 (25)	54 (33)	5
	1.40	190	30	57	4 (10)	48 (42)	5
	1.80	200	30	27	4 (8)	18 (14)	5
Phthalate buffer + 0.1M KF	0.50	120	120	22	13	1	8
	0.50	190	10	19	11	—	8
	0.95	190	150	20	11	2	7
	1.20	180	30	21	12	1	8
	1.20	170	90	27	15	3	9
Borate buffer + 0.1M KF	0	190	10	37	18	—	19
	1.00	200	30	29	19	—	10

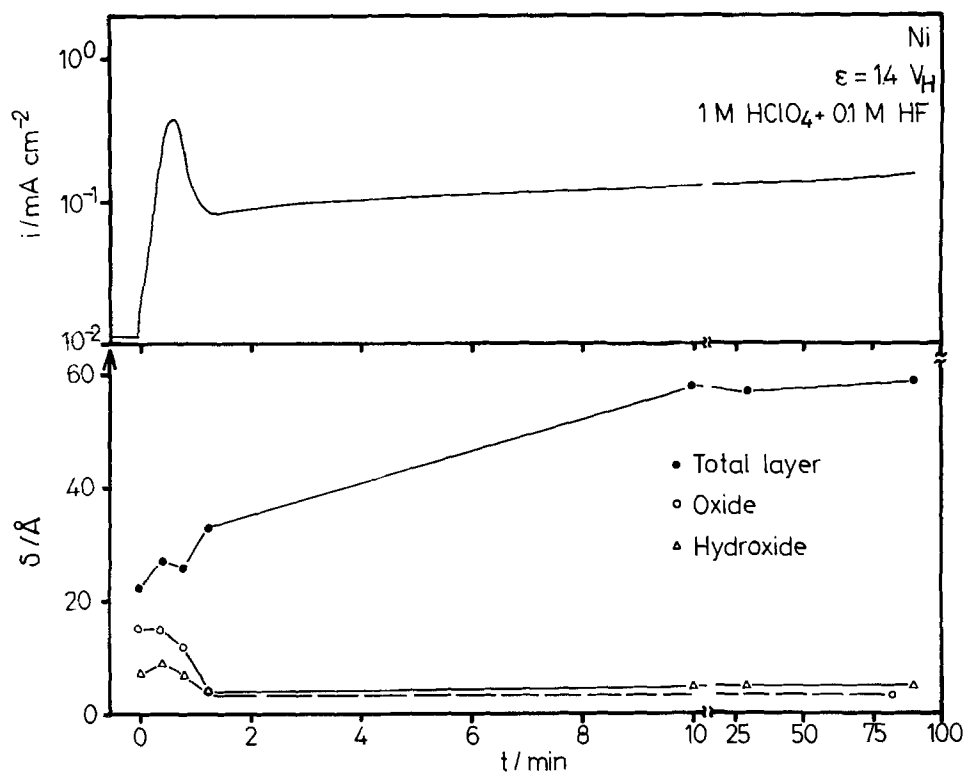


Fig. 9. Current density time curve of 2h prepassivated nickel after exposure to 1M HClO₄ + 0.1M HF and the related change of the layer thickness at $\epsilon = 1.4V$ (minimum I1). ●: total layer. ○: oxide layer. △: hydroxide layer. Difference refers to fluoride layer.

layer which may be even removed completely by sufficient stirring (i.e., by rotation of a Ni disk electrode at > 400 rpm). At $\epsilon \geq 1.2V$ the nonvisible, nonporous protecting fluoride films are formed. The change of their physical structure may explain why the current density decreases with the thickness in the range $\epsilon = 1.2-1.4V$, because in most cases of passivity the opposite behavior is found.

Weakly acidic and alkaline solutions.—The effect of HF and F⁻ on the passive current density in more alkaline solutions is less pronounced, as has been described already in detail (1, 19). In phthalate buffer pH 4.9 with 0.1M KF, an intermediate maximum is found in the polarization curve, whereas in borate buffer pH 8.0 with 0.1M KF, the same results are ob-

tained as in fluoride-free solution. In minimum I in phthalate buffer even after more than 120 min of KF exposure, only a very weak F1s signal is found just above the background. This disappears during 10 min of sputtering (Fig. 10). From comparison with the fluoride-covered specimen of Fig. 7, this corresponds to much less than 1 monolayer and should be seen as a quantity adsorbed at the surface of the passive film. This result would support the catalytic effect of HF for the passive current density by the formation of a surface complex at the oxide-electrolyte interface (1). The depth profile for $\epsilon = 0.5V$ shows again an inner oxide and outer hydroxide layer. The quantitative evaluation of the XPS signals (Eq. [4] and [6]) leads to similar results as in 1M HClO₄ (Table IV). At $\epsilon \geq$

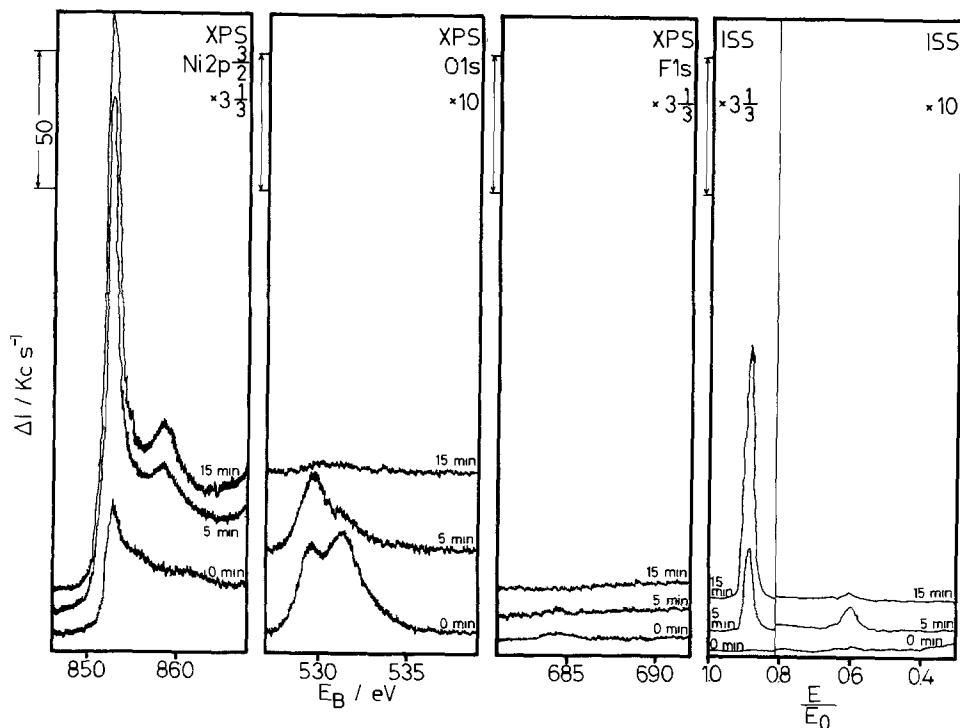
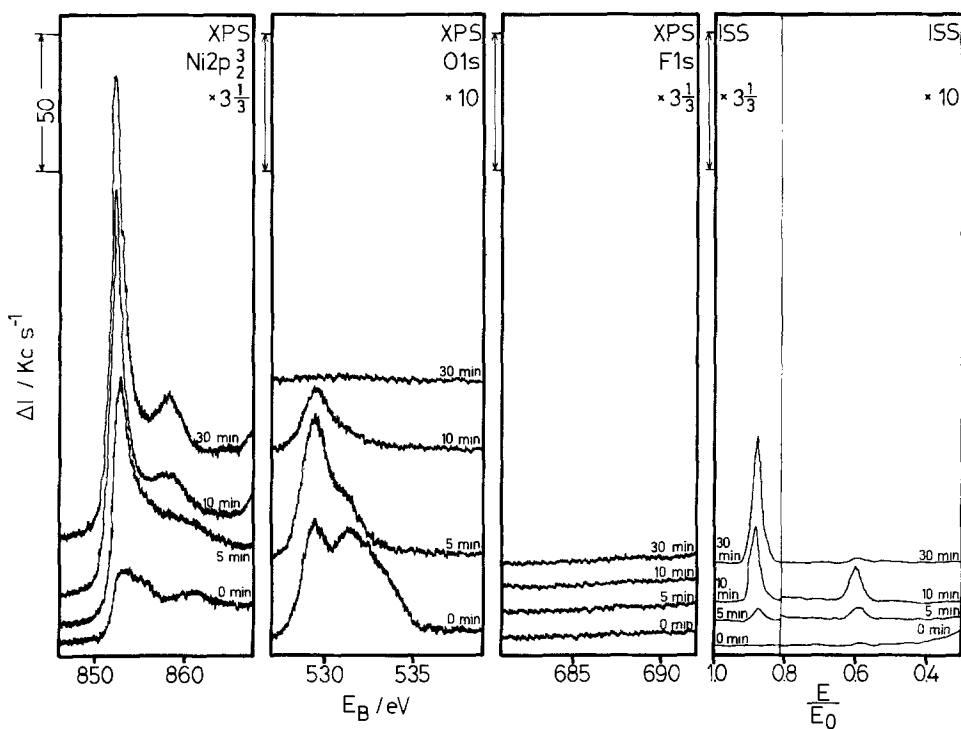


Fig. 10. XPS and ISS depth profile of 2h in phthalate buffer pH 4.9 prepassivated nickel after 120 min exposure to additional 0.1M KF at $\epsilon = 0.5V$ (minimum I).

Fig. 11. XPS and ISS depth profile of 2h in 0.1M phthalate buffer pH 4.9 prepassivated nickel after 150 min exposure to additional 0.1M KF at $\epsilon = 0.95V$.



0.95V (maximum and minimum II), a more pronounced F1s signal is found which should be attributed to a fluoride layer (Fig. 11). It is, however, much thinner than in 1M HClO₄ despite the longer exposure to KF (150 min). Its intermediate position is demonstrated again by the depth profile with the O1s signal and the ISS oxygen and fluorine peaks. No visible layer is found at any potential in the weakly acidic fluoride solution.

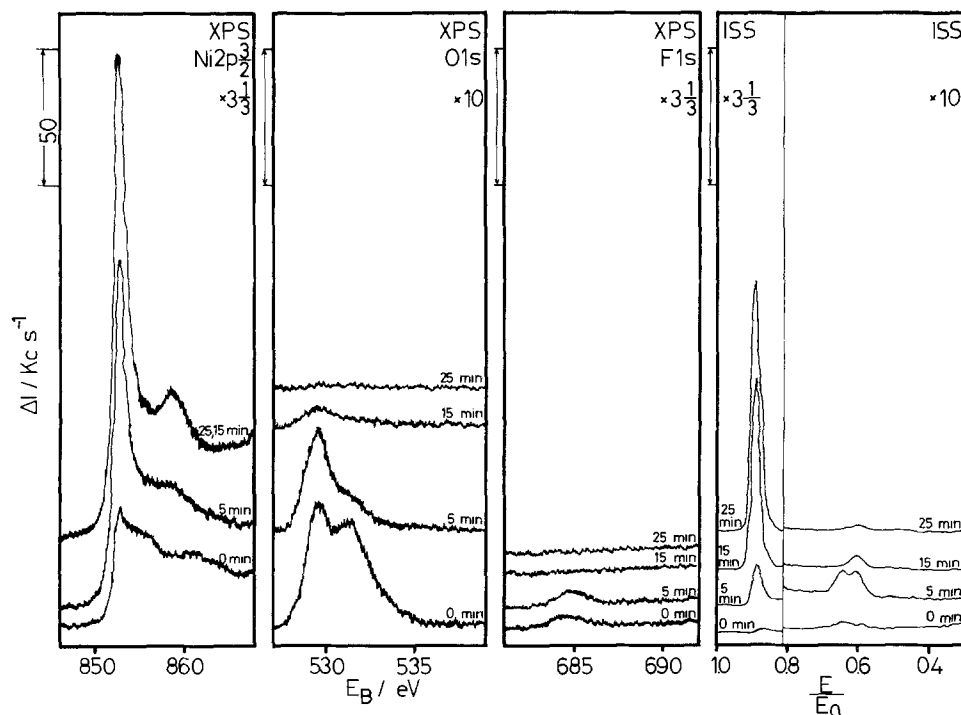
In borate buffer pH 8.0 no fluoride is detected at the surface within the whole passive range. The layer structure and thickness do not show any major changes. Only the outer hydroxide layer increases (Fig. 12). These results confirm the electrochemical findings that fluoride does not affect appreciably the passive behavior of nickel at pH 8.0 (1).

Conclusion

The application of XPS and ISS is well suited to obtaining information about the chemical and physical structure of passivating layers on metals. The quantitative evaluation of the XPS results permits the calculation of the thickness of surface layers up to 60Å.

The passive layer in fluoride-free solutions of pH 0.0-8.0 consists of an inner oxide and an outer hydroxide layer of 8Å, which does not change with potential and pH, and therefore should not be responsible for the passive behavior. The oxide layer grows, however, with potential, especially in the transpassive range. Its thickness is similar for the solutions of different pH and close to the values of other authors ob-

Fig. 12. XPS and ISS depth profile of 2h in 0.1M borate buffer pH 8.0 prepassivated nickel after 30 min exposure to additional 0.1M KF at $\epsilon = 1.0V$.



tained by other methods. It represents the main barrier for the passive behavior.

In the case of nickel in HF or fluoride containing solutions, a close correlation between the electrochemical and surface analytical results was obtained which helped in interpretation of the mechanism of fluoride attack. In a lower potential range (minimum I), a surface catalytically enhanced dissolution is found which assumes for the mechanism the formation of an intermediate Ni^{2+} fluoride complex at the surface (1). Therefore, no F^- is found for specimens prepared in HClO_4 and rinsed with water. Only in phthalate buffer a very weak F1s signal indicates the presence of adsorbed fluoride, less than one monolayer. The hydroxide layer is unaffected. However, the oxide is thinned.

In the higher potential range (minimum II), a thick fluoride layer is found in $1M \text{HClO}_4 + 0.1M \text{HF}$. It grows with the time of HF exposure and gets thinner with increasing electrode potential. The oxide is thinned to ca. 4Å. It is situated at the metal surface covered by 20-70Å of fluoride followed by 8Å of hydroxide at the outmost position. The fluoride has passivating properties and compensates partly for the thinning of the barrier type of oxide.

In phthalate buffer pH 4.9, the oxide layer is thinned to a smaller extent and less fluoride is formed. This corresponds to a much smaller current increase for this electrolyte.

In borate buffer pH 8.0, no current increase, no fluoride at the surface, and no thinning of the oxide layer is found.

The quantitative evaluation of the XPS peaks shows that the fluoride layer has a composition similar to NiF_2 with some contamination by oxide and hydroxide. Any Ni-F complexes or higher valent nickel compounds could not be detected by XPS. The chemical shift between NiO and Ni_2O_3 is too small to find small amounts of three valent nickel ions in a two valent matrix.

These examinations show that a combined study with electrochemical and surface analytical methods gives a good insight into the processes occurring at the solid-electrolyte interface and is especially suited for the study of surface films passivity and corrosion phenomena.

Manuscript submitted July 9, 1982; revised manuscript received Sept. 22, 1983.

Freie Universität Berlin assisted in meeting the publication costs of this article.

REFERENCES

1. B. Löchel, H.-H. Strehblow, and M. Sakashita, *This Journal*, **131**, 522 (1984).
2. G. E. Theriault, T. L. Barry, and M. J. B. Thomas, *Anal. Chem.*, **47**, 1492 (1975).
3. P. Marcus, J. Oudar, and I. Olefjord, *J. Microscop. Spectr. Electron.*, **4**, 63 (1979).
4. T. Dickinson, A. F. Povey, and P. M. A. Sherwood, *J. Chem. Soc. Faraday Trans. 1*, **73**, 327 (1977).
5. C. D. Wagner, L. H. Gale, and R. H. Raymond, *Anal. Chem.*, **51**, 466 (1979).
6. K. S. Kim and N. Winograd, *Surf. Sci.*, **43**, 625 (1974).
7. K. S. Kim, W. E. Baitinger, J. W. Amy, and N. Winograd, *J. Electron. Spectrosc. Relat. Phenom.*, **5**, 351 (1974).
8. K. S. Kim and R. E. Davis, *ibid.*, **1**, 251 (1972/1973).
9. L. J. Mantienzo, Lo I. Yin, S. O. Grim, and W. E. Swartz, *Inorg. Chem.*, **12**, 2762 (1973).
10. M. P. Seah, *Surf. Interf. Anal.*, **2**, 222 (1980).
11. J. H. Scofield, *J. Electron. Spectrosc. Relat. Phenom.*, **8**, 129 (1976).
12. D. J. Kennedy and S. T. Manson, *Phys. Rev. A*, **5**, 227 (1972).
13. R. F. Railman, A. Mseseane, and S. T. Manson, *J. Electron. Spectrosc. Relat. Phenom.*, **8**, 389 (1976).
14. "Handbook of Chemistry and Physics," p. B135, The Chemical Rubber Co., Cleveland, OH (1977).
15. M. P. Seah and W. A. Dench, *Surf. Interf. Anal.*, **1**, 2 (1979).
16. T. Ohtsuka and K. E. Heusler, *J. Electroanal. Chem.*, **100**, 319 (1979).
17. N. Sato, *Denki Kagaku*, **46**, 584 (1978).
18. K. J. Vetter and K. Arnold, *Z. Elektrochem.*, **64**, 244 (1960).
19. H.-H. Strehblow, *Werkst. Korros.*, **27**, 792 (1976).
20. B. P. Löchel and H.-H. Strehblow, *ibid.*, **31**, 353 (1980).
21. H.-H. Strehblow, B. Titze, and B. P. Löchel, *Corros. Sci.*, **19**, 1047 (1979).
22. J. Osterwald and H. Trunk, *Werkst. Korros.*, **28**, 321 (1977).
23. C. A. Tollman, W. M. Riggs, W. J. Linn, C. M. King, and R. C. Wendt, *Inorg. Chem.*, **12**, 2770 (1973).

Electrochemical and Ellipsometric Investigations of Passive Films on Iron in Borate Solutions

III. The Kinetics of Film Growth on Iron at Transpassive Potentials

W. Kozłowski and A. Szklarska-Smiałowska

Institute of Physical Chemistry, Polish Academy of Sciences, Warsaw, Poland

ABSTRACT

Ellipsometric technique has been used to study the oxide film formation on iron in two borate buffer solutions of pH 8.4 in the transpassive region of potentials. At the potential of oxygen evolution ($\sim 1.0 V_{\text{SCE}}$), a slight decrease of the refractive index with respect to its value in the passive region was observed, indicating some changes in the composition or structure of the film. Above $1.4 V_{\text{SCE}}$, a second thicker film grows on the top of the passive film. This outer film, which is probably composed of corrosion products, exhibits a low refractive index. At high anodic potentials (above $1.5 V_{\text{SCE}}$), pitting occurs.

There have been very few studies of the film formation on iron in borate solutions at potentials corresponding to the oxygen evolution reaction or above. Sato *et al.* (1) measured the thickness of films formed in borate solutions of pH 7.45, 8.42, and 9.37 by galvanostatic reduction. The films were reduced in a bo-

rate solution of pH 6.35 containing As_2O_3 as inhibitor. Based on these measurements and analyses of the Fe^{2+} content in solution, it was concluded that in the region of O_2 evolution, up to the potential where transpassive dissolution of iron began to occur ($\sim 1.3 V_{\text{SCE}}$), the thickness of the film increased with increasing

potential. On the other hand, the film thickness was potential independent above 1.3V. Also, the potential for the transpassive iron dissolution was found to be independent of pH. A mechanistic model for film breakdown was developed to interpret these results (2). According to that model, when a certain critical film thickness is attained, mechanical breakdown of the film occurs as a result of the high electrostrictional pressure. This pressure can produce compressive stresses exceeding a critical breakdown stress in the oxide film.

Ellipsometric investigations performed by Sato *et al.* (3) supported the above results and conclusions. The film was found to be composed of two layers: an inner barrier layer of γ -Fe₂O₃, and a deposited outer layer of hydrated iron III oxide. The complex indexes of refraction for the barrier layer were (2.50-0.30i) and (2.50-0.22i) within the potential range of 0.5-1.3V and above 1.3V, respectively. The complex index of refraction of the outer layer was found to be the same in both potential ranges: 2.20-0.10i. The same authors (3) claim that from 0.5V to 1.3 V_{SCE} the state of oxidation of iron in both the barrier and the deposited layer is +3, but above 1.3V, a small amount of Fe²⁺ is also present in the barrier layer. Hence, the composition of the film is probably close to Fe₃O₄. However, in the deposited layer only Fe³⁺ is present. At the boundary between these oxide layers, an excess of iron or iron vacancies occurs.

Electron diffraction studies of the oxide film formed in borate solution of pH 8.5 at 1.25 V_{SCE} indicated that the film is composed of Fe₃O₄ (4). The same film structure was found (4) in NaOH (pH 11.4) and in H₂SO₄ (pH 1.1) solutions.

There are also several papers dealing with the composition and properties of films formed on iron in the transpassive region of potentials, but in solutions other than borate. These studies were conducted to explain the processes occurring during electrochemical machining (ECM) of steel parts. The film formed on mild steel after ECM in NaClO₃ was γ -Fe₂O₃, as determined by reflection electron diffraction (RHEED) and electron probe analysis (5). However, in NaNO₃ solution, it was assumed (6, 7) that electronically conductive Fe₃O₄ is formed because most of the current was consumed by the O₂ evolution reaction instead of metal dissolution.

Cohen *et al.* (8), using RHEED and x-ray emission analysis (XRE), have established that the film formed during electropolishing in a mixture of HClO₄ and CH₃COOH is composed of a mixture of anhydrous Fe₃O₄ and γ -Fe₂O₃.

According to some authors, anodic films may undergo changes at the potential of oxygen evolution. For example, Oshe *et al.* (9), suggested that in the transpassive region of potential, an increase of current that occurs in the Fe-Na₂SO₄ system at the beginning of oxygen evolution is connected with the removal O²⁻ and OH⁻ from the almost stoichiometric γ -Fe₂O₃. The decrease in concentration of O²⁻ and OH⁻ in the film results in an increased current associated with iron dissolution.

Also, Vetter (10) takes into consideration the possibility of oxide film participation in the oxygen evolution reaction. It is worthwhile noting that some experimental evidence obtained for platinum suggests that the anodic film takes part in the oxygen evolution reaction (11). However, the results of studies (12) on anodic oxygen evolution on α -Fe₂O₃ in H₂SO₄ solution seem to exclude any possibility of withdrawal of oxygen from the oxide lattice.

The existing models for breakdown of the passive film in the transpassive region of potentials (3, 6, 13, 14), suggest that the first step consists of anion adsorption on the metal surface. With increasing anion concentration, the efficiency of metal dissolution should

increase. In agreement with this conclusion, Mao and Chin (7) obtained higher current efficiencies for iron dissolution in NaClO₃ with increasing concentration of ClO₃⁻.

The aims of the present work were as follows: (i) to compare the optical properties of film formed in the passive and transpassive state; (ii) to establish the kinetics of film growth in the transpassive region of potentials; (iii) to determine whether the optical parameters or film thickness change before film breakdown occurs; and (iv) to compare the properties of films formed in two borate buffer solutions of the same pH (8.42) but differing in borate concentration.

Experimental

The material, preparation of specimens, and ellipsometric methods have been described in Part I (15) of this series of papers. In this case, the bubbles of oxygen evolving at high anodic potentials were removed from the electrode surface by a stream of argon in order to facilitate the measurements.

Results

The anodic polarization curves obtained for both solutions, with the transpassive region of potentials included, have been given in Part I of this study. These curves show that at high anodic potentials (above 1.2-1.3V) the current densities are higher in the more concentrated solution 2 than in the dilute solution 1.

The changes in current density at constant potentials recorded as a function of time in solution 2 for potentials in the oxygen evolution region are plotted in Fig. 1. It is seen that within the time period examined, the current density continues to decrease only at an applied potential of 1.0V. At higher anodic potentials the current density, after decreasing during the first few minutes, increases until a steady-state value is reached. An increase in the applied potential decreases the time in which a minimum current density is observed. At very high anodic potentials (above 2.0V), a minimum does not appear. Similar results were obtained for solution 1, but the current density minima were less pronounced than for solution 2.

The effects of applied potential on the optical parameters n and k are shown in Fig. 2 for both solutions 1 and 2. A small decrease in n with increasing anodic potential occurs in both solutions at potentials above 1.0V, this effect being more pronounced in solution 2. Figure 2 also includes values of n and k obtained in the passive range of potentials from 0.5 to 0.8V. The real part of refractive index, n , is only slightly lower in the oxygen evolution range than in the passive region of potentials. The absorption coefficient k increases a

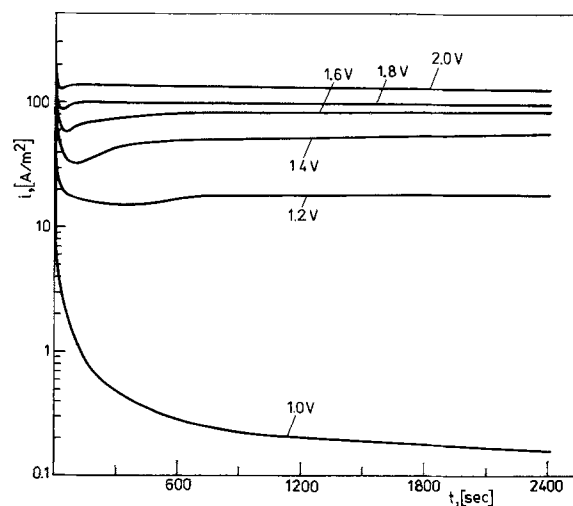


Fig. 1. Changes in current density with time at constant potentials in solution 2 (0.15M H₃BO₃ + 0.375M Na₂B₄O₇ · 10 H₂O).

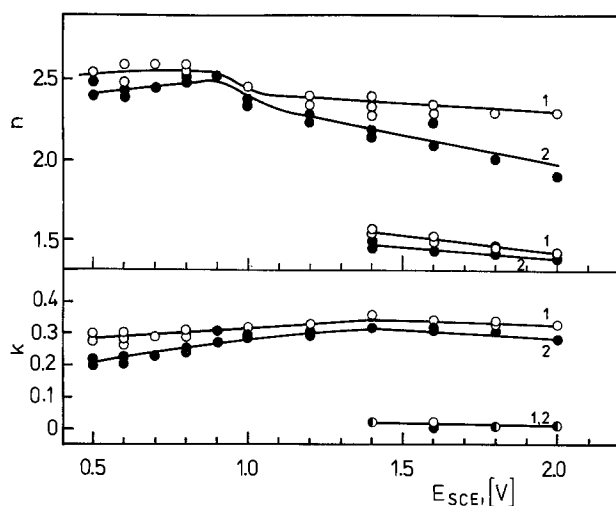


Fig. 2. Dependence of optical parameters (n and k) on potential for films formed during 1h of polarization in both solutions. Optical parameters of the outer layer formed above 1.4V are also given.

little from 0.8 to 1.1V, and at still higher potentials attains a steady-state value. In the lower part of Fig. 2, values of n and k are given for films that form on the outer layer at potentials higher than 1.4V. The optical parameters of these outer layer films are very low and do not exceed 1.57 and 0.27 for n and k , respectively.

It seems that the values of n and k found for the outer layer are potential independent. These parameters have been evaluated assuming that the first (inner) layer does not undergo any change during the outer layer formation, which is a simplification in the data analysis. At these potentials, transpassive dissolution of iron occurs, which can lead to surface roughening. Moreover, pitting takes place in solution 2 at potentials higher than 1.55V, while in solution 1, pitting was only sporadically observed. Therefore, the values of n and k for the outer film layer are affected by some undefined error.

Figures 3 and 4 show the film thickness as a function of time for solution 1 and 2, respectively.

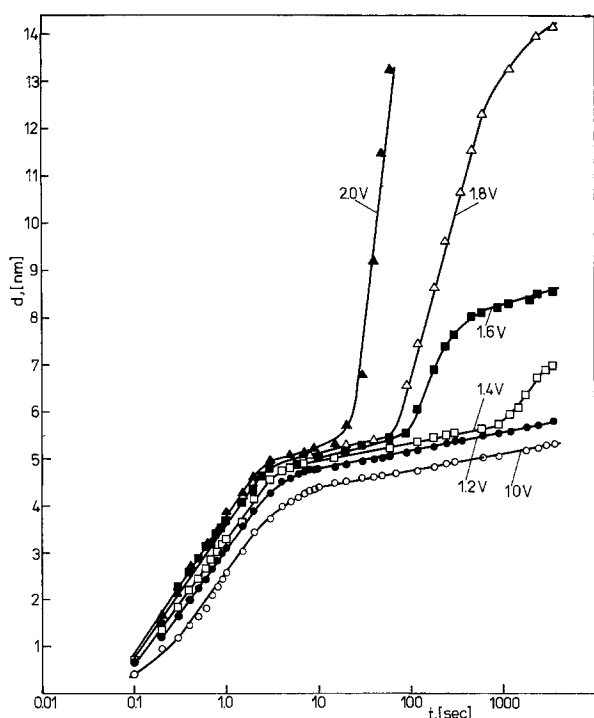


Fig. 3. Thickness of film as a function of time for films formed at different potentials in solution 1.

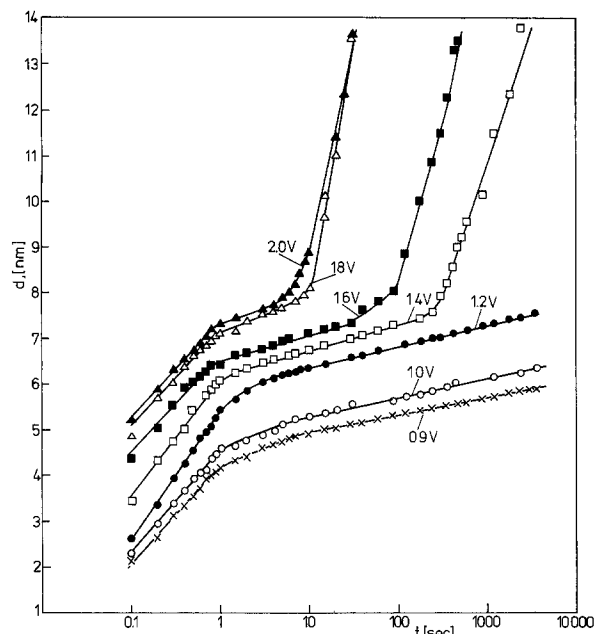


Fig. 4. Thickness of film as a function of time for films formed at different potentials in solution 2.

At high anodic potentials, the films grow in several stages, similar to films formed in the lower potential range as discussed in Part I of this work. However, the first stage identified previously as stage I appeared only at a potential of 1V in solution 1. Evidently, at higher potentials, stage I lasted for less than 0.1s. Therefore, the first segments of the dependence of film thickness on log time correspond to stage II of film growth. Further stages of film growth identified in Part I of this study as stages III and IV also appear at some definite potentials.

In contrast with the behavior observed in the passive region, above 1.4V a second layer grows rapidly on the top of the passive film. This outer layer, which exhibits low n and k values, is a result of the breakdown of the passive film and consists of corrosion products probably containing borate anions.

As the applied anodic potential increases, the rate of the outer layer growth increases, and the time necessary to start formation of that layer becomes less.

The thicknesses of films formed under the same experimental conditions in solution 2 are always greater compared with films formed in solution 1. On the other hand, by comparing the time at which the outer layer formation becomes significant in solution 2 (Fig. 4) with the minimum current density (i) obtained from the i vs. time relationship (Fig. 1), it can be concluded that the higher is the anodic potential, the shorter is the time of inner layer formation, and that the formation of the outer film begins as the current density increases after attaining its minimum.

Figure 5 gives the results of measurements of film thickness (inner and outer layers) as a function of potential. The film thicknesses are computed after 1h polarization. Here again, thicker films form in solution 2 compared with solution 1.

Discussion

As shown in Fig. 2, at about $-1.0V$, which corresponds to the potential of oxygen evolution, the real part of the index of refraction suddenly decreases and continues to diminish slowly as the anodic potential is increased. These effects are more pronounced in solution 2 compared with solution 1. Sudden changes do not, however, occur in the case of the absorption coefficient k . This suggests that at potentials above that, corresponding to oxygen evolution, the structure of the film tends to be less dense. The above results appear to

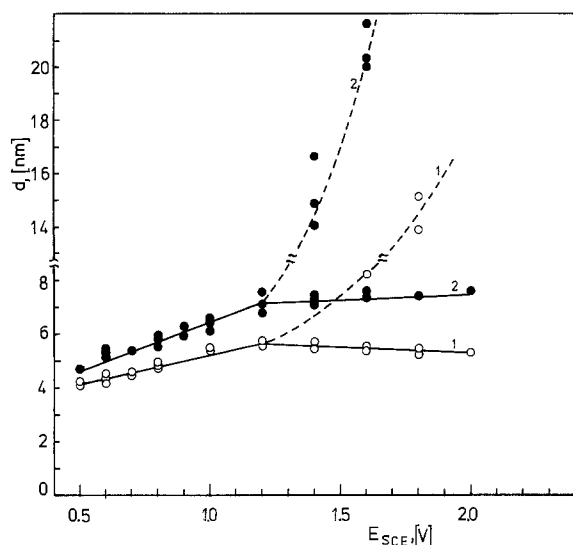


Fig. 5. Film thicknesses (inner and outer layer) obtained in both solutions after 1h of polarization at various potentials.

indicate that when the oxygen evolution reaction occurs on the surface of film, the latter undergoes some reconstruction and probably suffers local damage due to the action of the high electric field. Consequently, oxygen begins to be evolved on the metal surface as well, and this leads to further damage of film and to iron dissolution at higher potentials. If a constant potential higher than 1.4V is applied over 1h, a second layer starts to grow on the top of the weakened passive film. This outer layer, which forms by precipitation of corrosion products on the surface of the partially damaged passive film, exhibits a very low n value coupled with a k value close to zero. Corrosion products are probably composed of iron hydroxides and borates, for example, $\text{FeO}(\text{OH})_2$. It should be emphasized that in the 1.4-2.0V potential range, the increment of thickness of the I and II layers of passive film per potential unit is less than at potentials lower than 1.4V, and consequently, the field strength is higher.

From Fig. 3 and 4 it is evident that in the more concentrated solution 2 the layer of corrosion products forms more rapidly and at lower potentials than in solution 1. Presumably, this is due to the less protective character of the film grown in solution 2 (15, 16) and to the larger content of borate anions occluded by this film compared with that formed in solution 1. As a result, the film formed in solution 2 is much more susceptible to localized corrosion. So, in solution 2, pitting was observed to occur within 1h at 1.55V, while in solution 1 pitting was absent at this potential.

These results indicate that pitting of iron may occur in the absence of aggressive anions in the electrolyte if conditions leading to the interruption of passive film

exist, and repassivation is prevented. In the system considered, these conditions were provided by the high electric field which determined the localized breakdown of the film and the concurrent deposition of non-protective corrosion products. These corrosion products seem to be formed by dissolution of the metal substrate, precisely at those locations where the localized breakdown took place.

Conclusions

1. At the potential of oxygen evolution (about 1.0V), the passive film formed in stage I and II exhibits small changes in its optical properties. These changes are more pronounced in the more concentrated boric buffer solution 2 compared with the dilute solution 1.
2. In both solutions, at 1.0 and 1.2V, the film grows in several stages as described in Part I of this work. Because of the high oxidation rate, the first stage can be revealed only in solution 1 at a potential of 1V. Above 1-1.2V, the breakdown of passive film occurs in stages III and IV of film formation, depending on the potential.
3. At potentials higher than 1.4V, an outer layer of corrosion products with a low refractive index grows on the surface of the passive film.
4. Significant pitting commences when the potential reaches 1.5V in the more concentrated solution 2. In solution 1, slight pitting takes place above 1.5V.

Manuscript submitted Jan. 11, 1983; revised manuscript received Sept. 23, 1983.

REFERENCES

1. N. Sato, K. Kudo, and T. Noda, *Electrochim. Acta*, **16**, 1909 (1971).
2. N. Sato, *ibid.*, **16**, 1683 (1971).
3. N. Sato, K. Kudo, and R. Nishimura, *This Journal*, **123**, 1419 (1976).
4. C. L. Foley, J. Kruger, and C. J. Bechtoldt, *ibid.*, **114**, 994 (1967).
5. J. P. Hoare, M. A. La Boda, M. L. McMillan, and A. J. Wallace, Jr., *ibid.*, **116**, 199 (1969).
6. K. W. Mao, M. A. La Boda, and J. P. Hoare, *ibid.*, **119**, 419 (1972).
7. K. W. Mao and D. T. Chin, *ibid.*, **121**, 191 (1974).
8. M. Cohen, D. Mitchell, and K. Hashimoto, *ibid.*, **126**, 442 (1979).
9. E. K. Oshe, J. L. Rosenfeld, and V. G. Doroshenko, *Zashch. Met.*, **13**, 410 (1977).
10. K. J. Vetter, "Electrochemical Kinetics, Theoretical and Experimental Aspects," p. 615, Academic Press, New York (1967).
11. K. J. Rozental and V. J. Veselovskii, *Dokl. Acad. Nauk SSSR*, **111**, 637 (1956).
12. A. J. Khentov, A. M. Sukhotin, and E. A. Gankin, *Zashch. Met.*, **13**, 326 (1977).
13. T. P. Hoar, D. C. Mears, and G. P. Rothwell, *Corros. Sci.*, **5**, 279 (1965).
14. T. P. Hoar, *ibid.*, **7**, 341 (1967).
15. W. Kozlowski and A. Szklarska-Smialowska, *This Journal*, **131**, 234 (1984).
16. W. Kozlowski and A. Szklarska-Smialowska, *ibid.*, **131**, 499 (1984).

Influence of Incorporated Cl^- in NiO on the Pitting Susceptibility of Nickel

B. MacDougall* and M. J. Graham

National Research Council of Canada, Division of Chemistry, Ottawa, Ontario, K1A 0R9, Canada

ABSTRACT

The pitting susceptibility of nickel in 0.08M Cl^- solutions (pH 4.0 Na_2SO_4) has been determined by both potentiodynamic and potentiostatic techniques, the former giving a pitting potential and the latter an induction time, τ_{ind} , for pit initiation. The potentiostatic approach is preferred because of the good reproducibility of results. Samples were prepassivated in non- Cl^- or Cl^- containing solutions and then potentiostatically polarized in 0.08M Cl^- at different potentials and τ_{ind} measured. For either pretreatment, τ_{ind} decreased exponentially as the potential of pitting increased, i.e., $\log 1/\tau \propto V$. Oxides on samples prepassivated in Cl^- solution contain incorporated Cl^- and are significantly more resistant to pitting than those formed in Cl^- -free solutions. This increase in pitting resistance for the Cl^- -treated samples is in contrast to their decreased resistance to open-circuit breakdown. Cl^- incorporation results in $\sim 2\%$ expansion of the NiO lattice leading to a more defective and thus less stable film towards open-circuit breakdown. The τ_{ind} results strongly suggest that Cl^- incorporated in the oxide lattice (as distinct from Cl^- in the electrolyte) is not a precursor to pit initiation since it actually increases the resistance to pitting.

In a previous paper (1), it was shown that formation of the passive oxide film on nickel in a Cl^- containing electrolyte resulted in the incorporation of Cl^- into the oxide lattice. While Auger sputter profiles indicated that the Cl^- was mainly distributed in the outer layers of the oxide film, the results were not compatible with a simple adsorption of Cl^- on the oxide surface (cf. 2-7). Indeed, the Cl^- signal increased substantially as the first oxide layer was sputtered away, and there appeared to be approximately twice as much Cl^- in the second layer as in the first. The amount of chloride in the film was highly dependent on the $[\text{Cl}^-]$ in solution and the potential of anodization. The maximum homogeneous atomic concentration of Cl^- which could be achieved was $\sim 5\%$. (This concentration is determined assuming a uniform layer-by-layer distribution of Cl^- .) The concentration of incorporated Cl^- quickly reached a steady-state value ($\leq 15\text{s}$) if the films were formed in a Cl^- containing solution. On the other hand, incorporation into an initially Cl^- -free NiO film, achieved by subsequent anodization in a Cl^- containing solution, was dependent on the state of perfection of the passive film. The results suggested that Cl^- incorporation into an existing passive film occurred via local breakdown-repair events. These breakdown events were not induced by the presence of Cl^- , but were simply due to chemical dissolution of the oxide at local defects, i.e., the process that gives rise to the corrosion current even in the absence of Cl^- . Local reformation of the film in the Cl^- containing solution therefore resulted in a local Cl^- incorporation. A more perfect oxide film has fewer defects and therefore a slower rate of Cl^- uptake.

While the previous paper (1) indicated that Cl^- can incorporate into the NiO lattice, it did not address the question of the influence of this Cl^- on the pitting susceptibility of nickel. It is known that Cl^- in solution plays a major role in pit initiation [by virtue of its ability to interfere with passive film formation (8)], but the role of Cl^- incorporated in the oxide is not so clear. In the present paper, the influence of previously incorporated Cl^- on the induction time for potentiostatic pit initiation is studied with a view to determining whether Cl^- in the oxide lattice is a precursor to pit initiation.

Experimental

Polycrystalline nickel specimens, 1×2.5 cm, were prepared as described previously (9). All potentials are referred to the saturated calomel electrode, $\text{Hg}/\text{Hg}_2\text{Cl}_2$. Experiments were conducted at 25°C in de-

aerated solutions of pH 4.0 Na_2SO_4 . Chloride was incorporated into passive NiO films by forming the films in pH 4.0 $\text{Na}_2\text{SO}_4 + 1.0\text{M Cl}^-$. Pitting experiments were conducted in pH 4.0 $\text{Na}_2\text{SO}_4 + 0.08\text{M Cl}^-$.

Results and Discussion

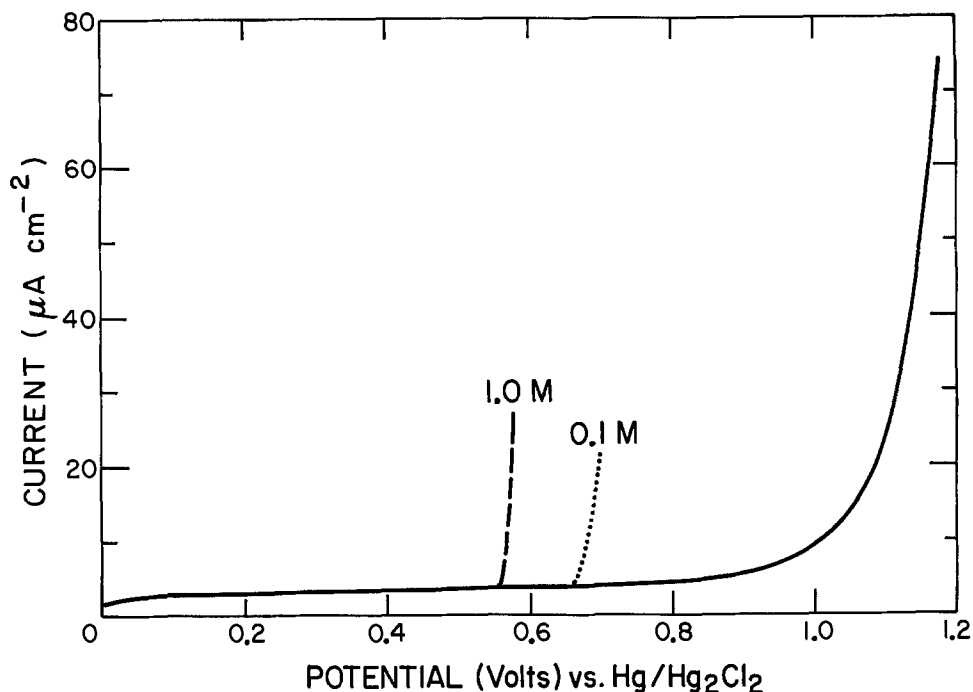
Potentiodynamic vs. potentiostatic pitting experiments.—Pitting susceptibility can be determined either potentiodynamically or potentiostatically. The former gives a pitting potential which is usually a function of sweep rate (8), while the latter gives an induction time for pit initiation at a specific potential. The potentiodynamic approach is illustrated in Fig. 1 for a solution without Cl^- and for solutions with 0.1 and 1.0M Cl^- . The profile obtained in the absence of Cl^- is a background sweep showing the passive potential range and the potential region where oxygen evolution begins, the latter giving rise to a gradual increase in anodic current. In the presence of Cl^- (added after the samples were prepassivated), the anodic current abruptly increases at potentials cathodic to oxygen evolution with the pitting potential decreasing with increasing $[\text{Cl}^-]$.

While the pitting potential obtained during a sweep experiment is quite distinct (Fig. 1), the scatter of results from experiment to experiment is too large (± 25 mV) for the technique to be used to quantitatively assess the role of incorporated Cl^- in the pitting process. The considerable scatter of results may possibly be associated with the simultaneous variation during a sweep of both potential and time, these being the two parameters which play key roles in pit initiation. Consequently, small variations in the induction time for pitting (e.g., see Fig. 2) can show up as quite large changes in the pitting potential even at slow sweep rates. Because of this, pitting susceptibilities were determined by holding the potential constant and measuring the induction time for pit initiation, τ_{ind} .

Influence of electrode pretreatment on pitting susceptibility.—The details of the experimental determination of τ_{ind} can be understood by reference to Fig. 3, where nickel electrodes were prepassivated at 0.3V for 15s in pH 4.0 Na_2SO_4 solutions containing either no Cl^- or 1.0M Cl^- . The pretreated electrodes were removed from solution, flushed with doubly distilled water and then reimmersed in a fresh pH 4.0 Na_2SO_4 solution (containing no Cl^-) at 0.3V for 30s. The potential was then increased to the value at which τ_{ind} was to be measured, and after 90s sufficient Cl^- was added (from a 2M NaCl stock solution) to give a $[\text{Cl}^-] = 0.08\text{M}$. Nitrogen bubbling was continued for 30s after adding the Cl^- to ensure complete mixing. τ_{ind} is the time

* Electrochemical Society Active Member.
Key words: corrosion, films, passivity.

Fig. 1. Potentiodynamic current-potential profiles for nickel electrodes at 2 mV s^{-1} in pH 4.0 Na_2SO_4 with different $[\text{Cl}^-]$: 0 (solid line); 0.1 (dotted line); and 1.0M (dashed line) Cl^- . In each case, electro-polished nickel was cathodically reduced in pH 4.0 Na_2SO_4 at $20 \mu\text{A cm}^{-2}$ and the potential then stepped to 0V for 60s before initiating the sweep. Cl^- was immediately added to the solution prior to starting the sweep so that the film was always formed in a non- Cl^- solution.



between the addition of Cl^- and the abrupt increase in current indicative of pit initiation. As seen in Fig. 3, the sharp increase of anodic current upon pit initiation, together with the virtual absence of breakdown-repair events prior to sustained pitting, makes it easy to determine τ_{ind} .

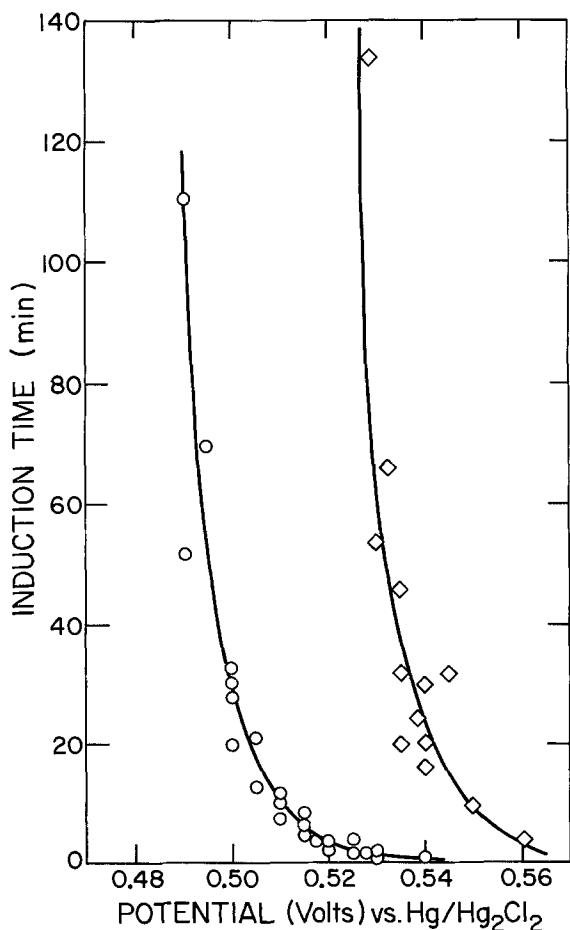


Fig. 2. Induction time for pitting, τ_{ind} , vs. potential of anodization for nickel samples pretreated at 0.3V in pH 4.0 Na_2SO_4 either with (—◇—) or without (—○—) 1M Cl^- in solution, and pitted in a 0.08M Cl^- solution. (Details of the induction time measurements are given in Fig. 3).

Figure 2 is a plot of τ_{ind} vs. anodic potential for samples prepassivated in non- Cl^- and Cl^- containing solutions. (The data were obtained from a large number of nickel specimens.) In each case, the induction time for pitting decreases exponentially as the potential of the pitting experiment is increased. The good linearity between $\log(1/\tau)$ and potential is shown in Fig. 4. This type of relationship has been noted by others for the pitting of stainless steel (10, 11) and is taken to indicate that the pitting process involves a step such as the adsorption of Cl^- under electrochemical control. It has been shown previously (8) that Cl^- in solution interferes with oxide formation on nickel, probably because of competitive adsorption and interference with the development of the protective oxide film, and so the exponential relationship between induction time and potential is not surprising. What is surprising, however, is the fact that nickel samples pretreated in 1.0M Cl^- at 0.3V, and thus having ~ 4.0 atom percent (a/o) Cl^- incorporated in the oxide lattice (1), are substantially more resistant to pit initiation than those samples which were pretreated in a non- Cl^- solution. The presence of 4 a/o Cl^- in the oxide lattice as seen in Fig. 2 increases the pitting potential for a particular induction time by ~ 40 mV. Besides the data points shown in Fig. 2, pitting experiments were also performed on Cl^- -treated electrodes at potentials of 0.50, 0.51, and 0.52V, and in all cases the τ_{ind} was $> 5\text{h}$, i.e., the Cl^- -treated samples are resistant to pitting under conditions where the Cl^- -free samples pit anywhere from 2 to 30 min. For some reason, the presence of Cl^- in the oxide film actually increases the resistance to Cl^- -induced pitting.

A possible explanation for the observed behavior in Fig. 2 is that the nickel electrodes passivated in 1.0M Cl^- solution have a substantially rougher surface because of the large amount of nickel dissolution during prepassivation [see Fig. 3 and Ref. (8)]. To determine if surface roughness is the reason for the increased pitting resistance, samples passivated in 1.0M Cl^- were cathodically reduced at $20 \mu\text{A cm}^{-2}$ for 30 min in a fresh pH 4.0 Na_2SO_4 solution prior to the pitting experiment. Auger analysis of the surface oxide indicated that cathodic reduction effectively removed the previously incorporated Cl^- . Table I shows the induction time at three different potentials for samples treated in three different ways: (i) passivated in a Cl^- containing solution, (ii) passivated in a Cl^- containing solution and then cathodically reduced to remove the

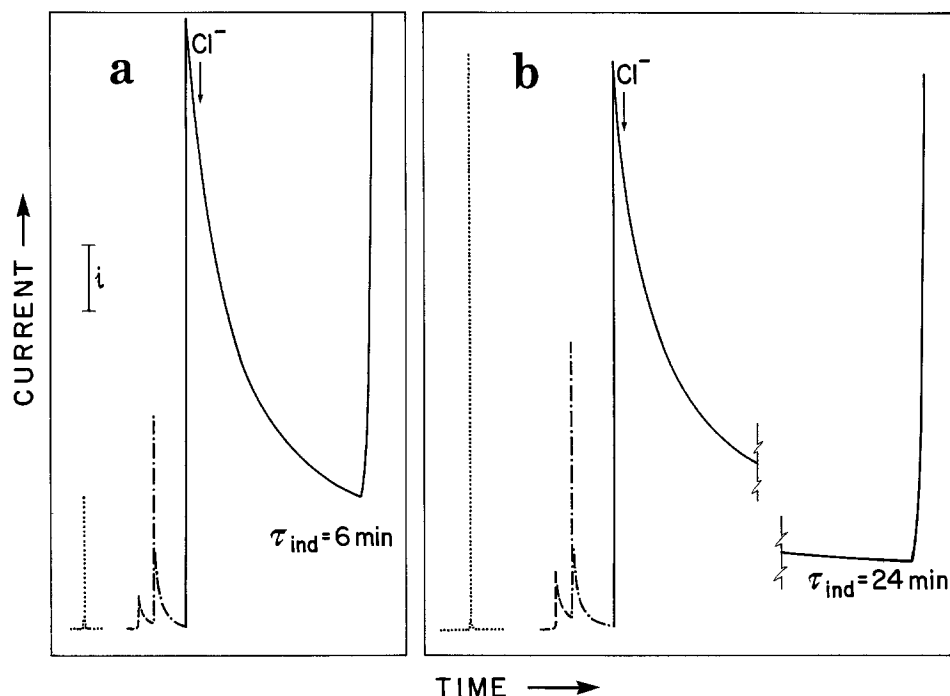


Fig. 3. (a) Current-time profile (dotted line) for electro-polished and cathodically reduced nickel upon stepping the potential to 0.3V in pH 4.0 Na₂SO₄ for 15s. The electrode was then removed and re-immersed in a fresh pH 4.0 Na₂SO₄ solution at 0.3V (dashed line) for 30s, after which time the potential was increased to 0.515V (dash-dot line); 90s later, sufficient Cl⁻ was added to give a concentration of 0.08M. τ_{ind} indicates the induction time for pitting after the addition of Cl⁻. The current sensitivity, in relation to the current marker *i*, is 5 mA cm⁻² (dotted line), 50 μA cm⁻² (dashed line) and (dash-dot line), and 0.5 μA cm⁻² (solid line), i.e., the sensitivity was increased at 0.515V just before Cl⁻ was added. (b) Similar to (a) except the pretreatment was in 1.0M Cl⁻ (dotted line) and the potential at which the induction time was measured was 0.54V [(dash-dot line) and (solid line)].

Cl⁻, and (iii) passivated in a non-Cl⁻ solution. The Cl⁻-treated specimens which were cathodically reduced behave similarly to those treated in non-Cl⁻ solution, suggesting that the increase in τ_{ind} after prior Cl⁻ treatment is not simply due to surface roughening but rather to the presence of Cl⁻ in the film.

Influence of incorporated Cl⁻ on film properties.— To determine the influence of incorporated Cl⁻ on the dissolution stability of oxide films, open-circuit decay profiles were obtained for films formed both in the presence and absence of Cl⁻ in solution. Figure 5 shows the results for oxides formed at 0.4V for 15s with different solution [Cl⁻] and then immersed on

open circuit in a fresh Cl⁻-free pH 4.0 Na₂SO₄ solution. The presence of Cl⁻ in the oxide film does not alter the overall shape of the potential decay profile, but resistance of the film to breakdown does decrease with increasing amounts of Cl⁻ in the film, i.e., the oxide film is more defective with incorporated Cl⁻ (12-17). This is in contrast to the beneficial effect that incorporated Cl⁻ has on pitting resistance.

To determine the structure of the oxide, reflection high energy electron diffraction patterns were obtained from a Ni(111) crystal passivated in 1.0M Cl⁻ at 0.3V. The oxide contained ~4 a/o Cl⁻. The patterns indicated the presence of a thin single-crystal NiO film with a lattice parameter ~2% larger than that expected for stoichiometric NiO. The mean oxide particle size was ~20Å. In contrast, a similar passivation treatment in a Cl⁻-free pH 4.0 Na₂SO₄ solution produced a film of almost stoichiometric NiO, again with a mean particle size of 20Å (9, 12). The lattice expansion for the film containing Cl⁻ is not surprising since the Cl⁻ ion is ~50% larger than the O²⁻ ion and the expansion is similar to that observed for the oxide on electro-polished nickel (9). There appears to be a correlation between lattice expansion and susceptibility to open-

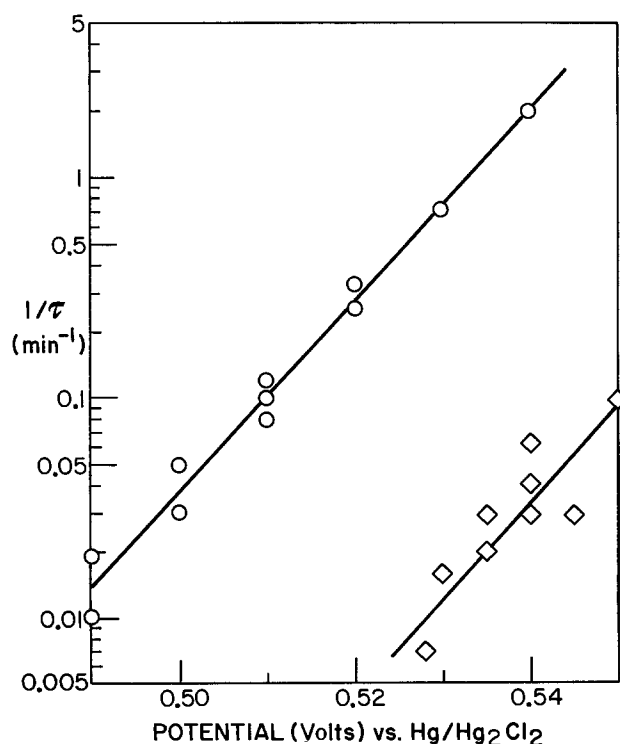
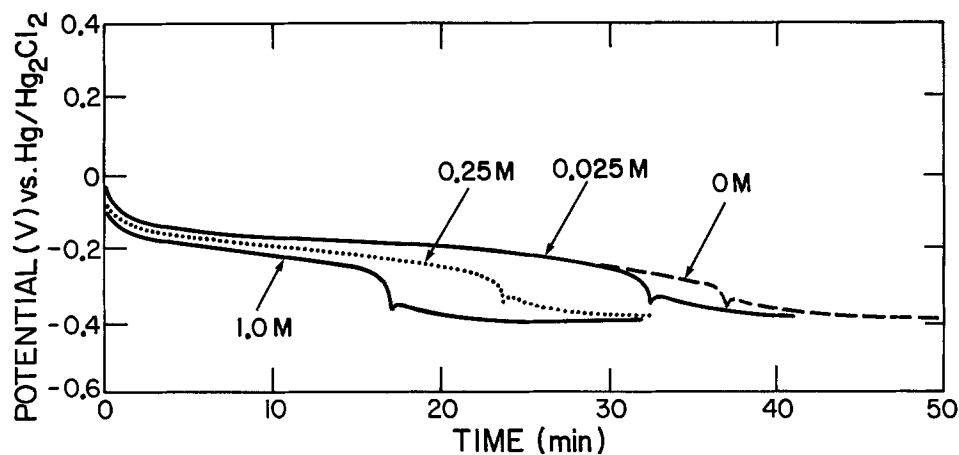


Fig. 4. Plot of log τ_{ind} vs. potential using data from Fig. 2

Table I. Influence of electrode pretreatment on induction time, τ_{ind}, for pitting in pH 4.0 Na₂SO₄ + 0.08M Cl⁻ at different potentials. Pretreatment was at 0.3V for 15s in pH 4.0 Na₂SO₄ either with 1.0M Cl⁻ (i.e., oxide loaded with Cl⁻) or without Cl⁻ (i.e., no loading). Also given are the induction times obtained after loading with Cl⁻ followed by cathodic reduction (CR) in fresh pH 4.0 Na₂SO₄ at 20 μA cm⁻² for 30 min to remove Cl⁻ from the film

Potential	Pretreatment	τ _{ind}
0.52V	Loaded with Cl ⁻ Loaded + CR No loading	> 2 hr 6 min 2 min
0.525V	Loaded with Cl ⁻ Loaded + CR No loading	5 hr; > 6 hr; > 4 hr 3 min 2 min
0.53V	Loaded with Cl ⁻ Loaded + CR No loading	55 min; > 90 min 2 min 1 min

Fig. 5. Open-circuit decay profiles, in Cl^- -free pH 4.0 Na_2SO_4 , for electropolished and cathodically reduced nickel pre-passivated at 0.4V for 15s in solutions containing 0, 0.025, 0.25, and 1.0M Cl^- .



circuit breakdown, with both the film on electropolished Ni and that containing Cl^- breaking down more rapidly on open circuit than the passive film.

The role of incorporated Cl^- in pit initiation.—The fact that incorporated Cl^- simultaneously makes the oxide film more defective and more resistant to pitting suggests that the beneficial effects associated with incorporation overcome the negative influence on film stability. Perhaps incorporated Cl^- changes the conductivity of the film which would result in a shift of the pitting potential in order to achieve the same driving force for pitting. Alternatively, it has been suggested that pitting occurs at islands of adsorbed Cl^- (3, 18-20). The presence of Cl^- incorporated in the oxide could conceivably make it more difficult to achieve these high local surface concentrations so that higher anodic potentials are needed to achieve the critical values for pitting. At this stage, we can only speculate as to the key process(es) in pit initiation on previously passivated nickel surfaces and the mechanism by which incorporated Cl^- influences this initiation. However, the present results clearly indicate that Cl^- incorporation into the oxide increases the resistance to pit initiation and this suggests that such incorporation is not a precursor to initiation. While it may be attractive to propose that Cl^- incorporation into a preformed passive film is the event that triggers local passivity breakdown and subsequent pit initiation, the results of this investigation suggest otherwise.

Acknowledgment

This work was supported under National Research Council of Canada grant no. 23097.

Manuscript submitted April 4, 1983; revised manuscript received Oct. 7, 1983.

National Research Council of Canada assisted in meeting the publication costs of this article.

REFERENCES

1. B. MacDougall, D. F. Mitchell, G. I. Sproule, and M. J. Graham, *This Journal*, **130**, 543 (1983).
2. Z. Szklarska-Smialowska, H. Veifhaus, and M. Janik-Czachor, *Corros. Sci.*, **16**, 649 (1976).
3. M. Janik-Czachor, A. Szummer, and Z. Szklarska-Smialowska, *ibid.*, **15**, 775 (1975).
4. M. Janik-Czachor, *Werkst. Korr.*, **30**, 225 (1979).
5. M. Janik-Czachor, *Corrosion*, **35**, 360 (1979).
6. M. de Cunha Belo, B. Rondot, F. Pons, J. Le Hérycy, and J. P. Langeron, *This Journal*, **124**, 1317 (1977).
7. A. E. Yaniv, J. B. Lumsden, and R. W. Staehle, in "Passivity and its Breakdown on Iron and Iron Base Alloys," R. W. Staehle and H. Okada, Editors, p. 72, NACE, Houston (1976).
8. B. MacDougall, *This Journal*, **126**, 919 (1979).
9. B. MacDougall and M. Cohen, *ibid.*, **121**, 1152 (1974).
10. T. Shibata and T. Takeyama, *Corrosion*, **33**, 243 (1977).
11. N. Sato, T. Nakagawa, K. Kudo, and M. Sakashita, *Trans. Jpn. Inst. Met.*, **13**, 103 (1972).
12. B. MacDougall and M. Cohen, *This Journal*, **124**, 1185 (1977).
13. B. MacDougall and M. Cohen, in "Passivity of Metals," R. P. Frankenthal and J. Kruger, Editors, p. 827, The Electrochemical Society Softbound Proceedings Series, Princeton, NJ (1978).
14. B. MacDougall, *This Journal*, **125**, 1883 (1978).
15. B. MacDougall, *ibid.*, **127**, 789 (1980).
16. B. MacDougall and M. Cohen, *Electrochim. Acta*, **23**, 145 (1978).
17. B. MacDougall, D. F. Mitchell, and M. J. Graham, *Corrosion*, **38**, 85 (1982).
18. K. E. Heusler and L. Fischer, *Werkst. Korr.*, **27**, 551 (1976).
19. M. Janik-Czachor and S. Kaszczyszyn, *ibid.*, **33**, 500 (1982).
20. M. Janik-Czachor, *This Journal*, **128**, 513C (1981).

Electrodeposition of Nickel and Cobalt Oxides onto Platinum and Graphite Electrodes for Alkaline Water Electrolysis

Yih-Wen D. Chen and Rommel N. Noufi*

Solar Energy Research Institute, Golden, Colorado 80401

ABSTRACT

Smooth, compact, and bright films of nickel and cobalt oxides were prepared from 0.5M acetate aqueous solutions and electrodeposited onto platinum and graphite electrodes. Oxygen evolution potentials in 1M NaOH at room temperature were about 150-170 mV lower on nickel(III) oxide [NiO(OH)] and cobalt(III) oxide (Co₂O₃)-coated anodes than on bare anodes. Scanning electron micrographs of NiO(OH) deposits showed no morphological change after extensive electrolysis, and electrocatalytic activity was stable in long-term controlled-potential coulometric electrolysis. However, the electrocatalytic activity of Co₂O₃ showed initial decay followed by a fairly constant behavior. No visible change in the surface of the Co₂O₃ deposit was observed after extensive electrolysis.

The electrochemical properties of metal oxide electrodes have attracted interest over several decades. Early work was oriented toward understanding thick films relevant to battery development (1). The objective of more recent studies has been to develop a fundamental understanding of the redox processes in these films (2, 3). Since hydrogen has recently been considered one of the clean fuels for energy storage (4-6), its production by various methods (7-9) has been proposed. Splitting water to hydrogen and oxygen by electrolysis remains the simplest and most economical method. One drawback in alkaline water electrolysis is the high overvoltage of the oxygen evolution on anodes.

Although metal anodes have been conventionally used for water electrolysis (10-12), their use is not feasible because these anodes [especially nickel anodes (13)] tend to form a nonconducting oxide film, causing oxygen evolution to deteriorate with time. Metal oxides that can provide a catalytic path for oxygen evolution have been recognized (2). Most of the anodic metal oxides studied were formed by anodization of the bare substrates in alkaline solution (14-17). In this paper, we investigate electrodeposition of thin films of nickel and cobalt oxides on platinum and graphite to study an inexpensive method to prepare and characterize these very thin film electrocatalysts. The objective of the above task is to apply the results to semiconductor photoelectrodes in order to bring about or facilitate the photoelectrolysis of water.

Experimental

Reagents.—Sodium acetate and sodium hydroxide are Baker-analyzed reagents. Nickel(II) sulfate was obtained from Johnson Matthey Chemical, Limited, and cobalt(II) acetate was obtained from Alfa Products. All of the reagents were reagent grade and were used without further treatment.

Electrodes.—Rotating platinum disk and graphite disk electrodes (area = 0.20 cm²) were obtained from Pine Instrument Company. The electrodes were polished with 1, 0.3, and finally with 0.05 μm aluminum oxide.

Cells.—All measurements and electrodeposition were performed in a three-electrode cell and are compared with the saturated calomel electrode (SCE) results. The cell assembly is simply a beaker with 250 ml capacity and a Teflon cap with four holes for the rotating disk electrode, reference electrode, counterelectrode, and gas dispersing tube. To keep the reference electrode from contaminating the electrolyte, a Beckman junction tube (no. 531041) was used to fill the support-

ing electrolyte. All experiments were conducted at room temperature and under argon atmosphere.

Apparatus.—A PAR Model 173 potentiostat with Model 175 Universal programmer and Model 179 Digital coulometer was used to control potential electrodeposition, cyclic voltammetric measurements, and potential coulometric electrolysis of water. A Houston Model 200 X-Y recorder registered the data.

Analysis of the film.—The nickel and cobalt contents in the film were determined by dissolving the metal oxides in 1% HNO₃ and measuring by atomic absorption.

Results and Discussion

Electrodeposition of nickel(III) oxide on platinum and graphite electrodes.—The nickel(III) oxide, NiO(OH), was previously formed when nickel(II) oxide was electrochemically oxidized to the +3 oxidation state (14-16). In this investigation, NiO(OH) was prepared directly from 0.5M sodium acetate aqueous solution with 0.05M NiSO₄. Figure 1 illustrates the cyclic voltammogram for the oxidation of nickel(II) ion onto platinum. On the first anodic scan, no obvious anodic peak was observed; however, on the subsequent cycles, anodic peaks were easily identified. Upon scan reversal, reduction waves of the oxide were observed. The increase in redox peaks with each cycle indicates the

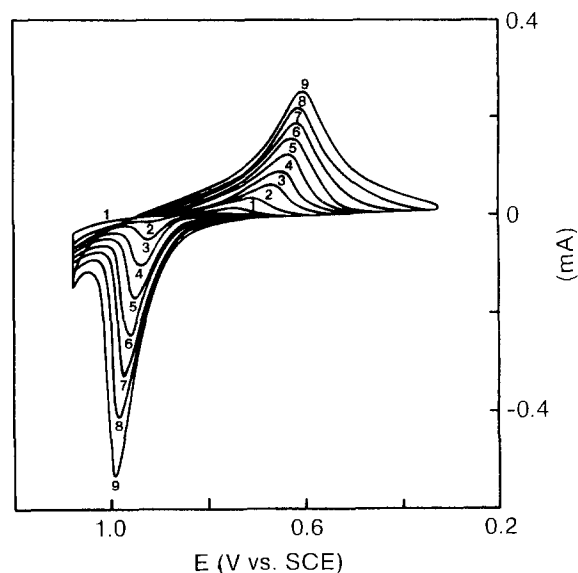


Fig. 1. Cyclic voltammograms at 50 mV/s for a rotating (900 rpm) platinum disk electrode (0.20 cm²) in an aqueous solution containing 0.05M NiSO₄ and 0.5M sodium acetate.

* Electrochemical Society Active Member.

Key words: electrocatalytic activity, morphology, stability.

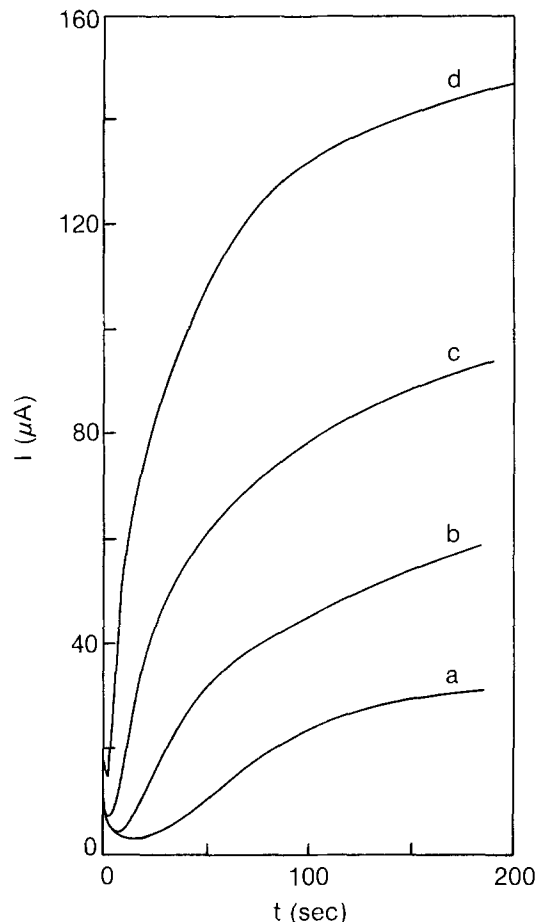


Fig. 2. Controlled potential coulometric electrodeposition of NiO(OH) on rotating (900 rpm) platinum disk electrode (0.20 cm^2) in aqueous solution containing 0.05 M NiSO_4 and 0.5 M sodium acetate at (a) 1.025 V , (b) 1.050 V , (c) 1.075 V , and (d) 1.100 V vs. SCE.

growth of the deposit. At potentials $>1.0 \text{ V}$, anodic currents [the result of electrocatalytic evolution of oxygen at the NiO(OH) film] increase with each cycle. This increase is seen again in Fig. 2, which illustrates controlled potential coulometric electrodeposition at different anodic limits. At each anodic limit, the anodic current decreases initially until $\sim 0.06 \text{ mC}$ had passed, which is the estimated quantity needed for monolayer deposition ($\sim 0.30 \text{ mC/cm}^2$) (18). After monolayer formation, the current density increases during the extensive electrodeposition because of electrocatalytic

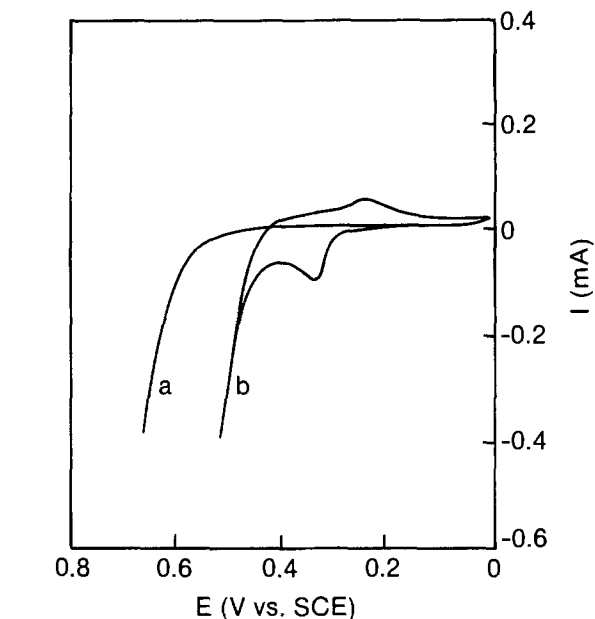
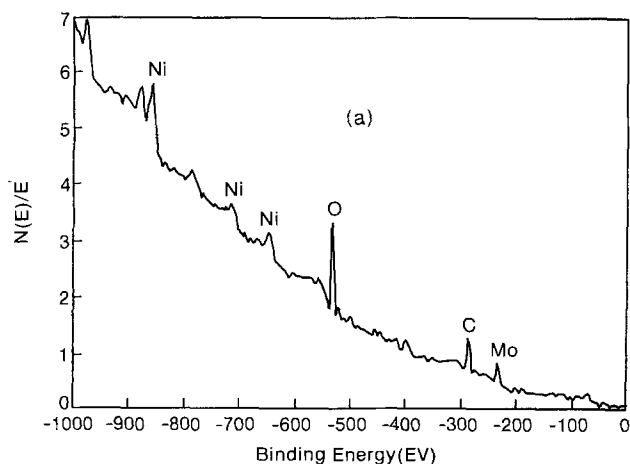


Fig. 4. Cyclic voltammograms at 50 mV/s for a rotating (900 rpm) platinum disk electrode (0.20 cm^2) in 1 M NaOH aqueous solution. Curve a: uncoated platinum electrode. Curve b: NiO(OH)-coated platinum electrode electrodeposited at $+1.10 \text{ V}$ with 15 mC passed, on rotating (900 rpm) platinum disk electrode, in an aqueous solution containing 0.05 M NiSO_4 and 0.5 M sodium acetate.

oxidation of water. Through x-ray photoelectron spectroscopy (XPS), the deposition product was identified as predominantly NiO(OH) (see Fig. 3), which is similar to the results obtained from the anodic oxidation of the Ni(OH)₂ film (14-16). Therefore, the NiO(OH) species seems essentially responsible for the catalyzed oxygen evolution. The oxygen evolution occurring with the anodic electrodeposition of NiO(OH) film is also evident from the analysis of the nickel content in the film (measured by atomic absorption, as shown in Table I). The coulometric efficiency of the deposition decreases with increase in applied potential.

The controlled potential coulometric electrodeposition of NiO(OH) on platinum and graphite electrodes yields reproducible, compact, and smooth films. With this method, thick conducting films can be deposited over 1 C/cm^2 . In comparison, passive oxide films were normally grown on nickel electrodes with limited thickness (19-21).

The electrocatalytic evolution of oxygen was also observed in 1 M NaOH aqueous solution, where the

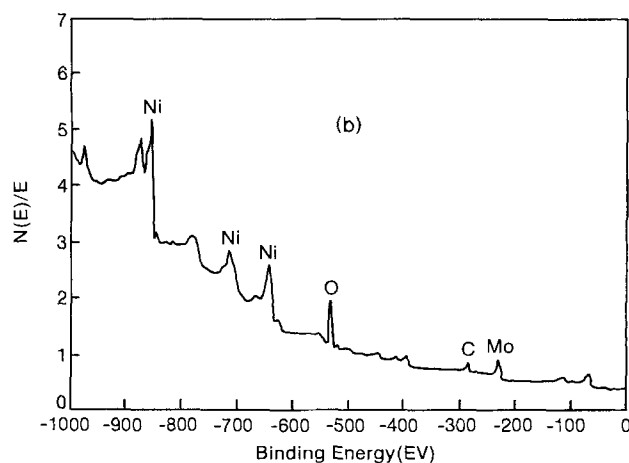


Fig. 3. XPS spectra of NiO(OH) electrodeposited on platinum (0.25 cm^2) at a potential, $E_a = 1.10 \text{ V}$ with $Q = 3.7 \text{ mC}$ in an aqueous solution containing 0.5 M sodium acetate and 0.05 M NiSO_4 . A, left: XPS spectrum of the immediate surface. B, right: XPS spectrum of the bulk.

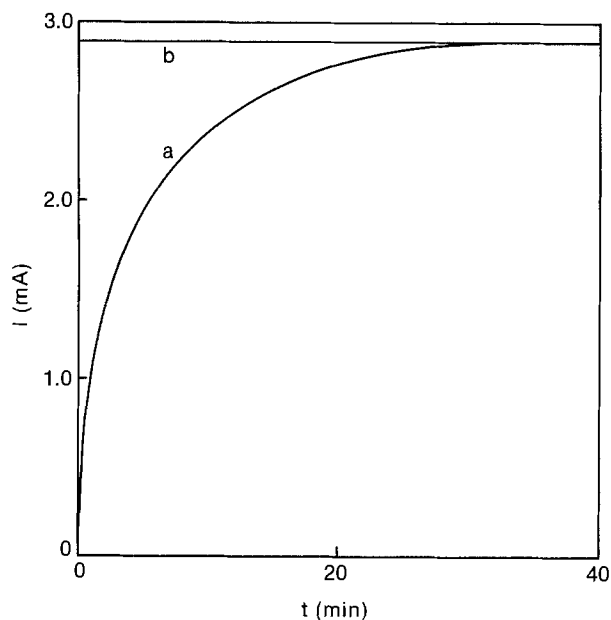


Fig. 5. Oxygen evolution at NiO(OH)-coated platinum electrode (0.20 cm^2) at $+0.55 \text{ V}$ in 1 M NaOH aqueous solution. Curve a: current-time curve for initial electrolysis. Curve b: current-time curve for continuous electrolysis after 3 days. The NiO(OH)-coated anode was prepared by electrodeposition on rotating (900 rpm) platinum disk electrode (0.20 cm^2) at $+1.0 \text{ V}$ with 10 mC passed in an aqueous solution containing 0.05 M NiSO_4 and 0.5 M sodium acetate.

oxygen evolution potential was about 150 mV lower on the NiO(OH) electrode than on the platinum anode (as shown in Fig. 4). The long-term stability of oxygen evolution on NiO(OH) film was tested in 1 M NaOH , and the film showed good stability. Initially, the catalytic current increased sharply, and then reached steady state after a few minutes (Fig. 5). The electrolysis continued for 3 days with no decay in current. Therefore, no passive oxide film formed, and there was also no morphological change in the NiO(OH) film (Fig. 6).

Electrodeposition of cobalt(III) oxide onto platinum and graphite electrodes.—Cobalt(III) oxide films were prepared by electrodeposition onto platinum and

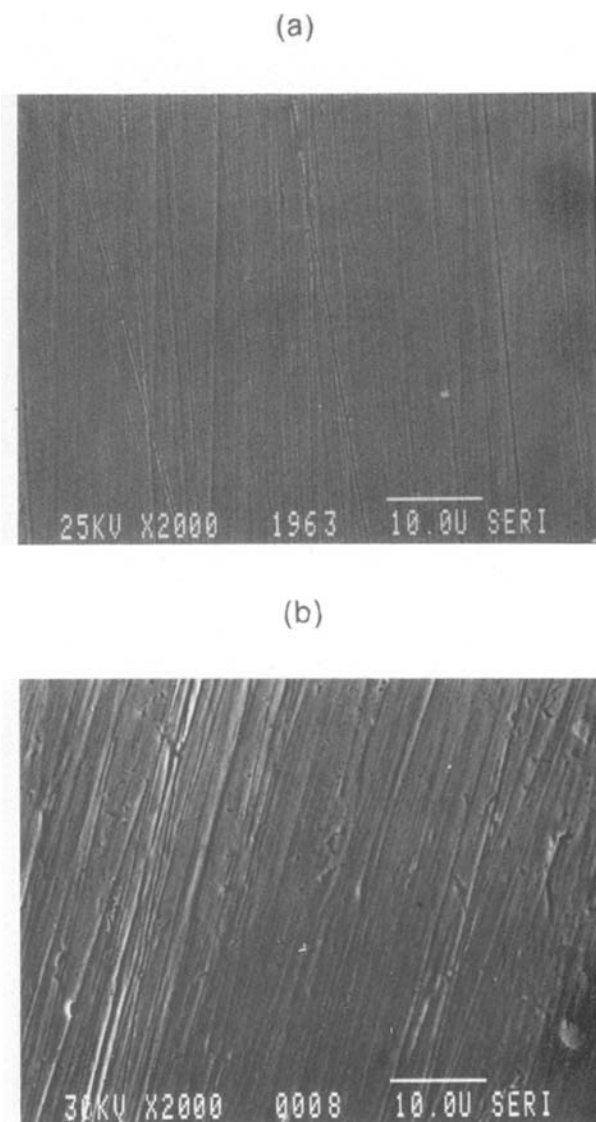


Fig. 6. Scanning electron micrographs of NiO(OH)-coated platinum electrode (times 2000) for (a, top) before and (b, bottom) after oxygen evolution in 1 M NaOH aqueous solution.

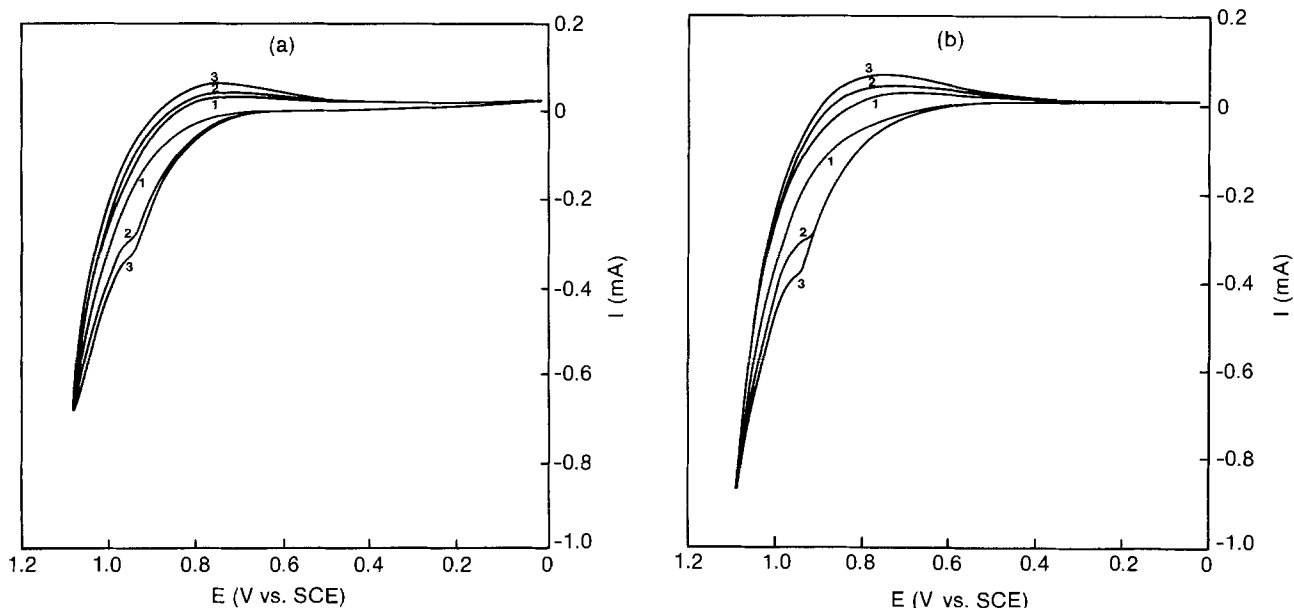


Fig. 7. Cyclic voltammograms at 50 mV/s for a (a, left) rotating (900 rpm) platinum disk electrode (0.20 cm^2) and (b, right) rotating (900 rpm) graphite disk electrode (0.20 cm^2) in aqueous solution containing 0.05 M Co(OAc)_2 and 0.5 M sodium acetate.

graphite electrodes in essentially the same way as the NiO(OH)-coated electrodes. Cyclic voltammograms of the oxidation of cobalt(II) ion onto platinum and graphite electrodes were basically the same for both electrodes (Fig. 7). On the first anodic scan, no obvious anodic peak was observed; however, on the subsequent cycles, anodic peaks were observed. On the scan reversal, broad and relatively small reduction waves were observed. The increase in peak height with each cycle indicates the growth of the film. The oxidation currents at the anodic limit increase while the film is continuously deposited, indicating the electrocatalytic evolution of oxygen. However, the catalytic effect by the cobalt oxide is not as clear as it is with NiO(OH); a more complicated film growth behavior is observed (Fig. 8). At each anodic limit, the oxidation current decreases initially until ~ 0.10 mC had passed, which is the estimated quantity (~ 0.5 mC/cm²) required for

monolayer deposition (21). After the monolayer formation, the current density increases and then decreases during bulk electrodeposition. The increase in the current density might indicate catalytic oxygen evolution, followed by a decrease in current density due to the less conducting character of the film. The electrodeposited film was not stable in air. The orange film gradually changes to green on the surface and becomes soluble in 1M NaOH. However, the underlayer of the green film stays orange and stable in 1M NaOH. XPS measurements were not sensitive enough to distinguish between the binding energies of Co₂O₃, Co₃O₄, and CoO (Fig. 9). However, Co₂O₃ is most likely the cobalt oxide deposited because the stoichiometry fits the analytical results of coulometric efficiency of the electrodeposition at lower applied anodic potential (Table I). At the lower potential, over 90% coulometric efficiency based on Co₂O₃ film formation is observed.

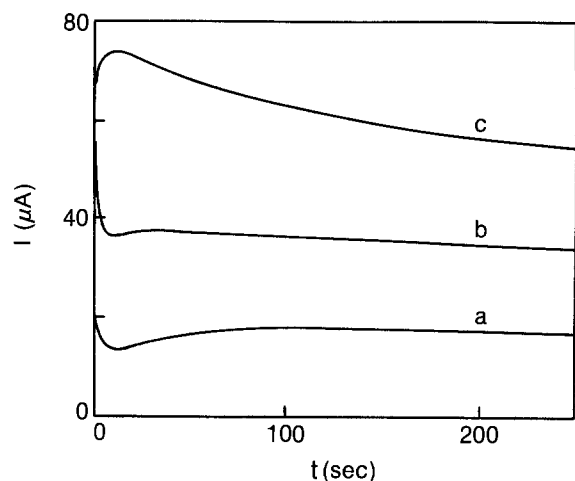


Fig. 8. Controlled potential coulometric electrodeposition of cobalt(III) oxide on rotating (900 rpm) platinum disk electrode (0.20 cm²) in an aqueous solution containing 0.05M Co(OAc)₂ and 0.5M sodium acetate at (a) 0.80V, (b) 0.85V, and (c) 0.90V vs. SCE.

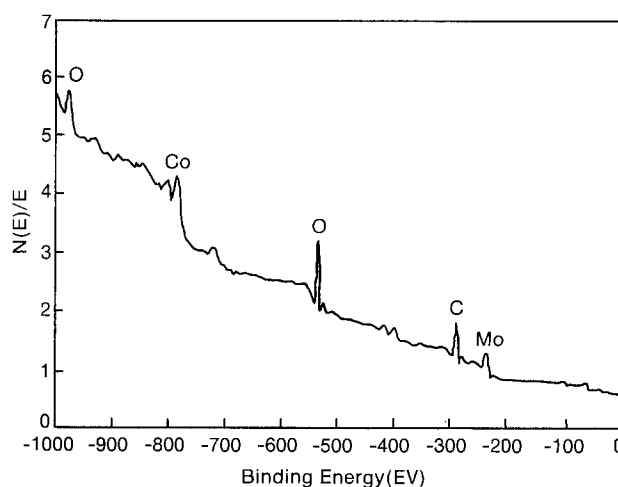


Fig. 9. XPS spectrum of cobalt oxide electrodeposited on platinum (0.25 cm²) at +0.80V with 2 mC passed in an aqueous solution containing 0.05M Co(OAc)₂ and 0.5M sodium acetate.

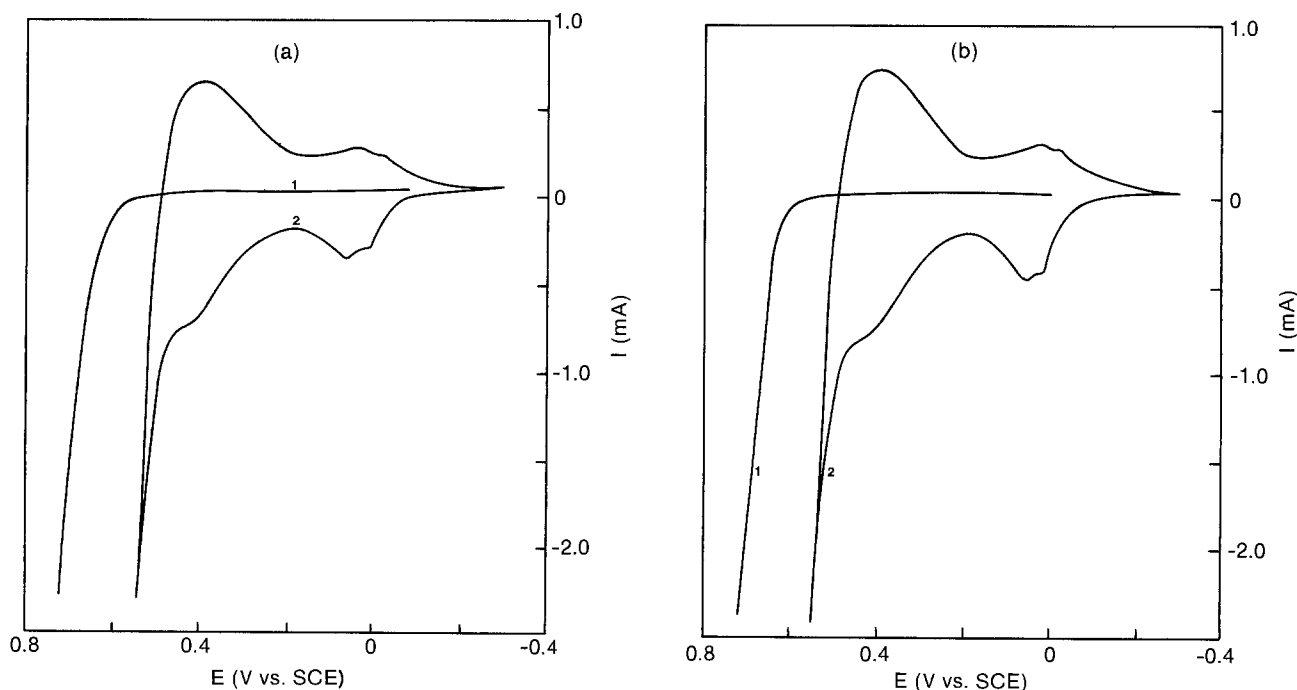


Fig. 10. Cyclic voltammograms at 50 mV/s for a (a, left) rotating (900 rpm) platinum disk electrode (0.20 cm²), and (b, right) rotating (900 rpm) graphite disk electrode (0.20 cm²), in 1M NaOH aqueous solution. Curves 1: uncoated platinum or graphite electrode. Curves 2: cobalt(III) oxide-coated platinum or graphite electrode at +0.80V with 10 mC passed from an aqueous solution containing 0.05M Co(OAc)₂ and 0.50M sodium acetate.

Table I. Coulometric efficiency of electrodeposition of nickel(III) and cobalt(III) oxides^a

Sample number	Metal analyzed	Q _a ^b (mC)	E _a ^c (V)	C ^d (ppm)	Coulometric efficiency (%)
1	Ni	30	1.10	0.47	28
2	Ni	30	1.07	0.55	32
3	Ni	30	1.00	0.62	36
4	Co	30	0.80	1.65	93
5	Co	30	0.90	1.55	88
6	Co	30	1.05	1.32	75
7	Co	30	1.10	1.12	63

^a An aqueous solution of 0.5M sodium acetate and 0.05M NiSO₄ was used to electrodeposit NiO(OH) on a rotating (900 rpm) platinum disk electrode. An aqueous solution of 0.5M sodium acetate and 0.05M Co(OAc)₂ was used to electrodeposit cobalt(III) oxide on a rotating (900 rpm) graphite disk electrode.

^b The number of coulombs applied for electrodeposition.

^c The constant anodic potential applied for electrodeposition.

^d Metal oxides were dissolved in 10 ml 1% HNO₃ and were measured by atomic absorption.

^e Coulometric efficiency is based on NiO(OH) and Co₂O₃ formation.

The electrocatalytic evolution of oxygen was evident in 1M NaOH aqueous solution where the oxygen evolution potential was about 170 mV lower on Co₂O₃ than uncoated anodes (see Fig. 10). The long-term stability of oxygen evolution on Co₂O₃ film was tested in 1M NaOH, and this film also showed good stability (Fig. 11). Contrary to NiO(OH), the catalytic current initially decreases sharply and stays fairly constant during extensive electrolysis. Initially, the catalytic current of Co₂O₃ is larger than that of NiO(OH). However, after extensive electrolysis, the catalytic current of Co₂O₃ becomes less than that of NiO(OH). Essentially, no visible change in the cobalt(III) oxide film was observed after long-term oxygen evolution experiment.

Acknowledgments

The authors wish to thank Rick Matson for preparing the scanning electron micrographs, and Bob Fischer for performing XPS. This work was carried out under a grant from the Director's Development Fund program at the Solar Energy Research Institute under Contract EG-77-C01-4042 to the Department of Energy.

Manuscript submitted July 11, 1983; revised manuscript received Dec. 5, 1983.

The Solar Energy Research Institute assisted in meeting the publication costs of this article.

REFERENCES

- P. C. Milner and U. B. Thomas, in "Advances in Electrochemistry and Electrochemical Engineering," C. W. Tobias, Editor, Vol. 5, p. 1, John Wiley and Sons, New York (1967).
- G. W. D. Briggs, "Electrochemistry: Specialist Periodical Reports," Vol. 4, Chemical Society, Washington, DC (1974).
- A. Damjanovic and A. J. Ward, in "International Reviews of Science, Electrochemistry, Physical Chemistry Series Two," Vol. 6, J. O'M. Bockris, Editor, Butterworths, London (1976).
- A. J. Bard, *J. Photochem.*, **10**, 59 (1979); *Science*, **207**, 139 (1980); *J. Phys. Chem.*, **86**, 172 (1982).
- J. O'M. Bockris, in "Environmental Chemistry," J. O'M. Bockris, Editor, Plenum Press, New York (1977).
- T. N. Vizioglu and W. Seifritz, Editors, "Hydrogen Energy Systems," Proceedings of the 2nd World Hydrogen Energy Conference, International Association of Hydrogen Energy (1978).
- J. Kiwi, K. Kalyanasundaram, and M. Gratzel, *Struct. Bonding*, **49**, 37 (1982).
- J. O'M. Bockris, in "Trends in Electrochemistry," J. O'M. Bockris, D. A. J. Rand, and B. J. Welch, Editors, p. 79, Plenum Press, New York (1977).
- B. D. McNicol, *Catalysis*, **2**, 243 (1978).
- P. H. Smith, in "Industrial Electrochemical Processes," A. J. Kuhn, Editor, Elsevier, New York (1971).
- E. A. Chapman, *Chem. Process Eng.*, **46**, 387 (1965).
- R. L. Costa and P. G. Grimes, *Chem. Eng. Prog.*, **63**, 56 (1967).
- H. Vandebore and R. Leysen, in "International Society of Electrochemistry, 31st Meeting Proceedings," E. Vecchi, Editor, p. 315, Venice, Italy (1980).
- B. MacDougall and M. J. Graham, *This Journal*, **128**, 2321 (1981).
- J. L. Ord, J. C. Clayton, and D. J. DeSmet, *ibid.*, **124**, 1714 (1977).
- P. W. T. Lu and S. Srinivasan, *ibid.*, **125**, 1416 (1978).
- G. Bronoel and J. Reby, *Electrochim. Acta*, **25**, 973 (1979).
- D. M. Kolb, *Adv. Electrochem. and Electrochem. Eng.*, **11**, 125 (1978).
- T. Dickinson, A. T. Povey, and P. M. A. Sherwood, *J. Chem. Soc., Faraday Trans. 1*, **73**, 327 (1977).
- B. MacDougall, D. F. Mitchell, and M. J. Graham, *Isr. J. Chem.*, **18**, 125 (1979).
- B. MacDougall and M. Cohen, *This Journal*, **124**, 1185 (1977).

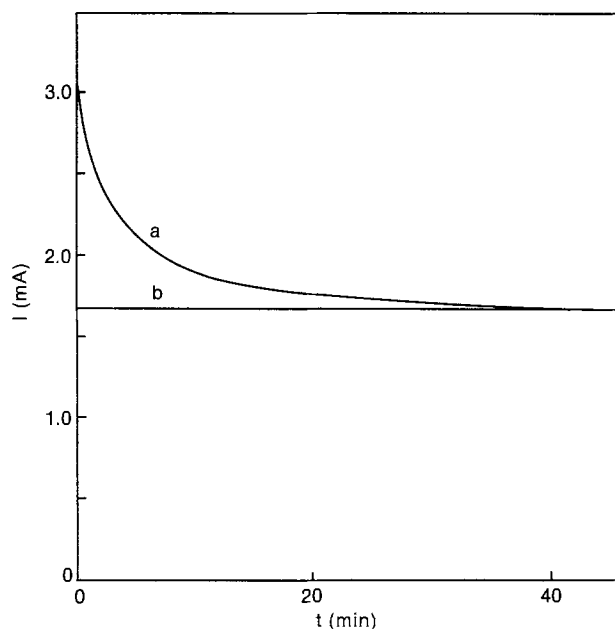


Fig. 11. Oxygen evolution at cobalt(III) oxide-coated graphite electrode (0.20 cm²) at +0.55V in 1M NaOH aqueous solution. Curve a: current-time curve for initial electrolysis. Curve b: current-time curve after electrolysis for 3 days. The cobalt(III) oxide-coated anode was prepared by electrodeposition on rotating (900 rpm) graphite disk electrode (0.20 cm²) at +0.80V with 10 mC passed from an aqueous solution containing 0.05M Co(OAc)₂ and 0.5M sodium acetate.

Electrolyte Electroreflectance of Single-Crystal CdIn₂Se₄ in a Photoelectrochemical Solar Cell

Micha Tomkiewicz* and Withana Siripala

Department of Physics, Brooklyn College of CUNY, Brooklyn, New York 11210

Reshef Tenne

Department of Plastics Research and Structural Chemistry, The Weismann Institute of Science, Rehovot 76100, Israel

ABSTRACT

Electroreflectance was used to evaluate the optical properties of CdIn₂Se₄ in polysulfide solution, before and after photoetching. The variations of signal intensity with electrode potential were used to trace the band position as a function of potential. It was found that the optical transition fits a three-dimensional parabolic model of the density of states, with direct transition at 1.825 eV. When the crystal is photoetched, there is a shift of 98° in the phase factor and a decrease in the broadening parameter from 0.42 to 0.32 eV. By monitoring the signal intensity with potential, it was shown that, irrespective of photoetching, the Fermi level is pinned as reverse bias conditions are approached. The pinning is ascribed to surface states that most likely originate from the adsorption of the electrolyte. The variation of the flatband potential with electrode potentials was calculated and was determined to occur because of the changes in the potential of the Helmholtz layer; the energy distribution and the density of states, which are responsible for those changes in potential of the Helmholtz layer, were also calculated.

II-VI materials, especially Cd-chalcogenides, are among the most often-considered photoelectrodes for use in photoelectrochemical solar cells (1). Because the electropositive constituent can be cross-substituted to obtain better optical and electrical properties, ternary chalcogenides are particularly attractive as electrodes in photoelectrochemical devices. These considerations led to a study of single-crystal CdIn₂Se₄ as an electrode in photoelectrochemical solar cell; the study results were not promising (2). It was clear from that study that although the bandgap of CdIn₂Se₄ is high making suitability as a photoelectrode questionable, that deficiency can be modified easily by controlling the In-to-Cd ratio (3). The low photovoltaic response of CdIn₂Se₄ was attributed primarily to poor surface conditions, which give rise to surface recombination and excessive dark currents under forward bias and reverse bias conditions. In an effort to alleviate some of these problems, various chemical etching methods were attempted, but with little effect. Photoetching proved to be more successful and resulted in a significant increase in the performance of the electrode.

In view of the significant improvements in the performance of binary chalcogenides such as CdSe and CdTe due to photoetching (4), it became increasingly important to understand the mechanisms by which this kind of "surface" treatment can improve the photoresponse of the electrode. In an effort to understand the photoresponse of CdIn₂Se₄ and the effect of photoetching on its response, differentiation between static, energetic factors (such as composition, potential distribution, etc.), and kinetic factors (such as recombination mechanisms) was attempted.

The use of electrolyte electroreflectance (EER) to determine some of the optical properties that are of key importance in determining the photoelectrochemical activity of the crystal is made. The changes in some of these parameters due to photoetching and the variations of the position of the bandedges with electrode potential are determined. The use of EER is then quantified to determine the degree of Fermi level pinning (5). The Fermi level pinning is correlated with a quantitative description of the surface states that give rise to the pinning, and those findings are correlated with some of the dynamic performance characteristics of CdIn₂Se₄ crystals.

* Electrochemical Society Active Member.

Key words: semiconductor, reflectance, solar, interfaces.

Experimental

A CdIn₂Se₄ crystal, synthesized from the constituent elements,¹ was polished to a 1 μm finish and etched with fresh aqua regia (1:4 HNO₃:HCl mixture). Ohmic contact was made by rubbing In-Ga alloy on the back surface of the crystal, and a copper wire was attached to the crystal with silver epoxy. The electrode was sealed with an insulating epoxy, with the front surface exposed, and mounted in a N₂-purged solution of Na₂S:S:NaOH 1/1/1M within a sealed plastic cell. A Pt foil was used as the counterelectrode. Photoetching was carried out in ten times diluted aqua regia by connecting the photoelectrode, a Pt foil as the reference electrode, and a carbon electrode to a potentiostat, and illuminating the photoelectrode with a W/X light source at an intensity of ~ AM1. The electrode was photoetched potentiostatically at 1V vs. Pt for 30s.

The EER spectra were measured *in situ* in the PEC cell configuration using apparatus described elsewhere (5). A PAR Model 173 potentiostat was used to operate the cell in the potentiostatic mode during photoetching.

Only one small wafer was available for the experiments that are described here. This was unfortunate, because at the conclusion of the theoretical treatment additional parameters were necessary to make complete measurements. The crystal, which was kept in the polysulfide solution for a few months, suffered severe dark corrosion, probably because of leaching of In and dissolutions of In₂S₃. The corrosion relates to the short-term stability (few hours) reported with regard to the photocorrosion of this material (2).

Results and Discussion

The spectra.—Figure 1 shows the EER spectra for CdIn₂Se₄ in aqueous polysulfide, at a dc bias of -0.2V vs. Pt and a modulating voltage of 0.2V P.P. at a frequency of 70 Hz. Figure 1a and 1b are the spectra before and after photoetching, respectively.

The lineshape of the electroreflectance signal sharpens considerably due to photoetching, and the characteristic third derivative (6) lineshape appears after the surface treatment. The intensity of the EER signal is enhanced due to the KCN washing, but there is very little effect on the lineshape, and this was not analyzed further.

¹The crystal was grown and doped by W. Girit, Centro de Física, Instituto Venezuela de Investigación Cient., Caracas, Venezuela.

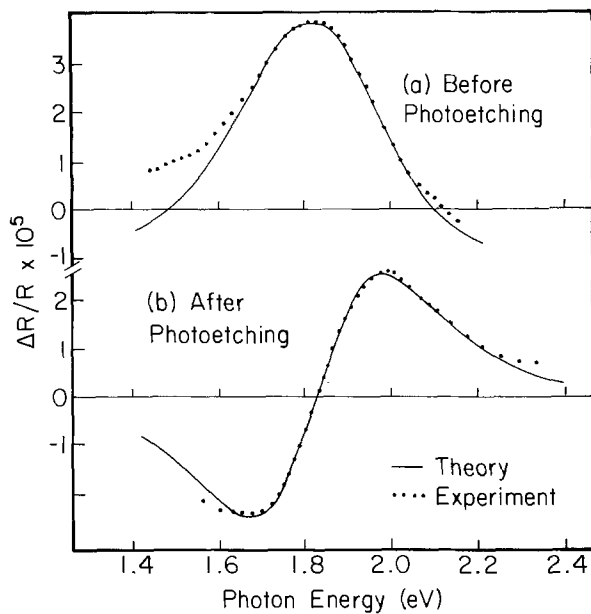


Fig. 1. EER spectra for CdIn₂Se₄ in aqueous polysulfide, at a dc bias of $-0.2V$ vs. Pt and a modulating voltage of $0.2V$ (peak to peak). a: before photoetching. Experiment (dotted curve) and theory (solid curve) with the following parameters: $n = 2.5$, $E_g = 1.825$ eV, $\theta = 217.5^\circ$, and $\Gamma = 0.416$ eV. b: after photoetching. Experiment (dotted curve) and theory (solid curve) with the following parameters: $n = 2.5$, $E_g = 1.825$ eV, $\theta = 315.5^\circ$, and $\Gamma = 0.316$ eV.

In view of the gross differences between the lineshape of the EER before and after photoetching and the apparent shift in the position of the peak, the main question was whether chemical changes occur during the photoetching process. Such changes occur due to selective photoetching and give rise to different band structure parameters. Changes in electroreflectance might be accounted for by selective photoetching of defects. These will manifest in terms of changes in the field distribution at the surface and the intrinsic linewidth of the EER signal. Electroreflectance spectra exhibit one positive and one negative extremum for each critical point. This can be expressed in terms of a general lineshape function of the form (6)

$$\frac{\Delta R}{R} = \text{Re} [C e^{i\theta} (E - E_g + i\Gamma)^{-n}] \quad [1]$$

where C and θ are amplitude and phase factors; $n \geq 2$ is characteristic of the critical points such that for simple parabolic models, $n = 3$ for a two-dimensional model, $n = 5/2$ for a three-dimensional model, and $n = 2$ for exciton; E_g is the energy gap; and Γ is a broadening parameter related to the lifetime. The phase factor θ , in addition to a contribution from the Seraphin coefficients (7), will contain contributions from electron-hole coulomb interaction and from inhomogeneities in the electric field distribution in depth determined by the penetration depth of the light (8). If photoetching does not alter the chemical composition of the surface through selective etching but does change drastically the defect concentration, θ will probably be the most sensitive parameter that will be modified by the treatment, and n and E_g will remain unchanged.

The four parameters that determine the lineshape were fitted to the spectra of the samples after the photoetching. The best fit of the experimental data to the theoretical lineshape function is shown in Fig. 1b with the following parameters: $n = 2.5$, $E_g = 1.825$ eV, $\theta = 315.5^\circ$, and $\Gamma = 0.316$ eV.

The fitting of Eq. [1] to the spectrum of the sample before photoetching was done by keeping E_g and n constant and changing only θ and Γ . The experimental

and the theoretical curves for this sample are shown in Fig. 1a. A shift of 98° - 217.5° is shown in θ , while the broadening parameter increases by about 30%, to 0.416 eV. Because the Seraphin coefficients and the electron-hole coulombic interactions normally do not change with surface treatment, it is believed that this large change in θ is due entirely to changes in the inhomogeneities in the electric field distribution due to the surface treatment. This conclusion is supported by the drastic improvement in the performance characteristics being achieved by photoetching (2). The energy gap found here is on the high energy side of previously reported values, which were evaluated by photoresponse (2), absorption measurements (9), and thermoreflectance (9).

Fermi level pinning.—Figure 2 shows the variation of the intensity of the electroreflectance signals with electrode potential. In both cases, the signal decreases dramatically toward the reverse bias. This behavior was found to occur in polycrystalline CdSe (5) and was interpreted to be due to Fermi-level pinning due to surface states that are fast enough to equilibrate at the modulation frequency. This causes part of the potential drop to fall across the Helmholtz layer, thus modulating the position of the bandedges relative to the reference electrode, resulting in a decreased modulation amplitude on the space charge layer and, hence, a decreased electroreflectance signal.

In the "low field" regime, the electroreflectance signal is given by (6)

$$\frac{\Delta R}{R} = - \left(\frac{2eN_D V_{sc}}{\epsilon_s} \right) L(\hbar\omega) \quad [2]$$

where $L(\hbar\omega)$ is a spectral lineshape function, which was discussed previously; V_{sc} is the modulated voltage across the space charge layer; N_D is the density of the

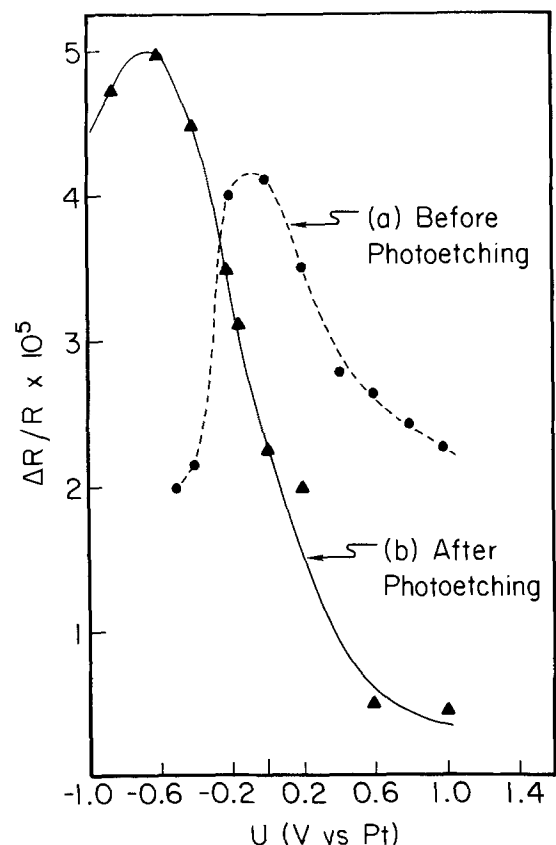


Fig. 2. Variation of the EER signal with the potential for CdIn₂Se₄ in aqueous polysulfide. A: before photoetching (photon energy = 1.8 eV). B: after photoetching (photon energy = 2.0 eV). Modulating voltage = $0.2V$ (peak to peak).

ionized donors; ϵ_s is the static permittivity; and e is the electronic charge. The potential drop across the space charge layer can be expressed as

$$\Delta\phi_s = U - U_{FB} \quad [3]$$

where U is the electrode potential, and U_{FB} is the flatband potential. Assuming no IR drop, the change in electrode potential due to the modulation will be divided between the space charge layer and the Helmholtz layer according to (10)

$$\delta U = \delta\Delta\phi_s + \delta\phi_o = V_{sc} + \delta\phi_o \quad [4]$$

where ϕ_o is the potential drop across the Helmholtz layer. The change in the potential of the Helmholtz layer due to a change in the number of ionized surface states is given by (11)

$$\delta\phi_o = \frac{e}{C_H} \delta N_{ss}^+ \quad [5]$$

where C_H is the capacitance of the Helmholtz layer, and N_{ss}^+ is the area concentration of the ionized surface states. Combining Eq. [2], [3], [4], and [5] results in

$$\frac{\Delta R}{R} = K \left(1 - \frac{e}{C_H} \frac{dN_{ss}^+}{dU} \right) dU \quad [6]$$

where

$$K = -\frac{2eN_D}{\epsilon_s} L(\hbar\omega) \quad [7]$$

and dU is the modulating potential (taken here to be a small displacement of the dc electrode potential). Within the low field regime, $\Delta R/R$ should be independent of the dc potential, which will decrease for $dN_{ss}^+/dU > 0$, namely, for an n-type semiconductor anodic shift of the electrode potential will result in incremental ionization of the surface states. Within this regime, $\Delta R/R$ will be maximum for $dN_{ss}^+/dU = 0$ and will decrease when dN_{ss}^+/dU increases. This can be expressed in close form as

$$\Gamma = \frac{e}{C_H} \frac{dN_{ss}^+}{dU} = 1 - \frac{\Delta R/R}{(\Delta R/R)_{\max}} \quad [8]$$

Equation [8] is valid provided that $(\Delta R/R)_{\max}$ occurs when $dN_{ss}^+/dU = 0$, still within the low field regime. If this condition is satisfied, the electroreflectance will provide direct measurement of $\frac{1}{C_H} \frac{dN_{ss}^+}{dU}$, which facilitates capacitance measurement by providing direct differential measurement, in contrast to the total system response of the impedance measurements.

Quantitative correlations between the two techniques have been described (5). Because changes in the flatband potential originate from changes in the potential drop across the Helmholtz layer, i.e., $\delta\phi_o = \delta U_{FB}$, it follows from Eq. [5] and [8] that

$$\Gamma = \frac{dU_{FB}}{dU} \quad [9]$$

$$U_{FB} = U_{FB}^0 + \int_{U_{\max}}^U \Gamma dU \quad [10]$$

where U_{\max} is the potential at which $\Delta R/R$ is maximum.

Equation [10] is valid within the assumptions that led to Eq. [8]: in terms of U_{FB} , at $U = U_{\max}$ the flatband potential is still U_{FB}^0 because $dN_{ss}^+/dU = 0$. Because $\int_{U_{\max}}^U \Gamma dU$ can be directly evaluated from the electroreflectance data, Eq. [10] provides an experimentally accessible way to determine U_{FB} as a function of electrode potential.

Because in all cases of interest here the Fermi level is not pinned when U is close to U_{FB}^0 , the latter can be determined independently either from the forward

bias portion of the electroreflectance [not a low field regime (12)] or by an alternative technique such as capacitance (13) or modulated light-induced current voltage response, which will determine the turn-on potential of the system. The Fermi level is completely pinned when $\Gamma = 1$. The potential drop across the space charge layer at this potential can be measured directly by using the same methodology as previously described. The potential drop will remain constant upon further increase in the potential in the reverse bias direction. A parameter that might prove to be useful in describing the pinning process is defined in Eq. [11]

$$\gamma = \frac{U_{FB} - U_{FB}^0}{U_{FB}^P - U_{FB}^0} \quad [11]$$

where U_{FB}^P is the flatband potential at the electrode potential in which the Fermi level is completely pinned, i.e., when $\Gamma = 1$. By definition, γ will vary from 0 to 1 and will provide direct measure of the pinning process. γ is a function of the electrode potential and the density and rate of the surface states.

Figure 3 shows the shift in the flatband potential of CdIn₂Se₄ before and after the photoetching experiment. Consistent with Fig. 2, the photoetching increased the Fermi level pinning. Before photoetching, the Fermi level pinning appears only in reverse bias; thus, it has no effect on the performance of the electrode in a photovoltaic device. The breakdown at 0.4V reverse bias, for both the chemically etched and the photoetched samples (2), which results in enhanced anodic dark current, can be a manifestation of this phenomena. The Fermi level pinning increase upon photoetching is surprising. No satisfactory explanation can be made of this phenomenon. This interpretation is based on the assumption that the potential, U_{\max} in which $\Delta R/R$ is maximum, $U_{FB} = U_{FB}^0$, no Fermi-level pinning occurs under these conditions. If this assumption is incorrect, and at $U = U_{\max}$ the Fermi-level pinning has already occurred—to different degrees with the two samples—then Fig. 3 must be modified and the conclusions derived from this figure, reevaluated.

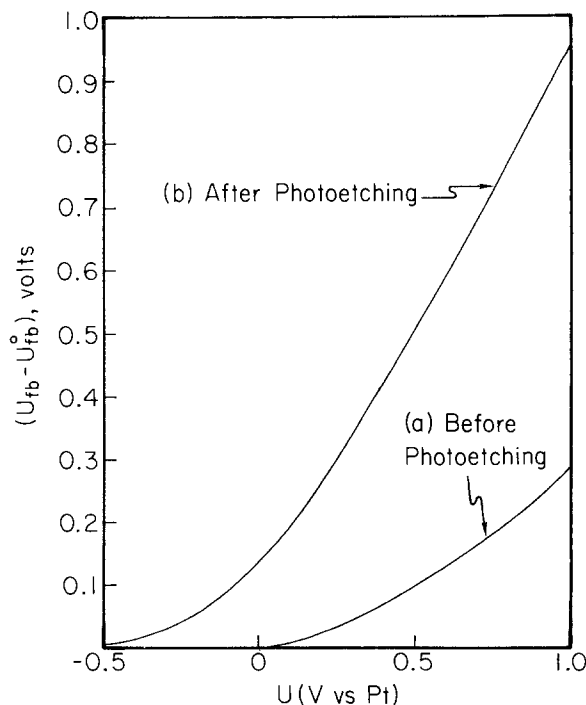


Fig. 3. Shift in the flatband potential with the potential for CdIn₂Se₄ in aqueous polysulfide, before (a) and after (b) photoetching.

Characterization of the surface states responsible for the pinning.—Assuming Gaussian energy density distribution for the surface states (13)

$$N_{ss}(E) = \frac{N_t}{\sigma e (2\pi)^{1/2}} \exp[-(E_t - E)^2 / 2(\sigma e)^2] \quad [12]$$

where σe is the standard deviation in energy, E is the energy of the surface states, E_t is the energy at maximum density, and N_t is the total concentration. The number of ionized states is given by (13)

$$N_{ss}^+(E_F) = \frac{N_t}{2} \left[\operatorname{erf} \left(\frac{E_t - E_F}{\sigma\sqrt{2}} \right) - \operatorname{erf} \left(\frac{E_t - E_c}{\sigma\sqrt{2}} \right) \right] \quad [13]$$

Neglecting the energy difference between the Fermi level and the bottom of the conduction band in the bulk of the semiconductor and using Eq. [10], the variables in Eq. [13] can be transformed to electrochemical potentials by using the following identities

$$\begin{aligned} E_F &= -eU \\ E_c &= -eU_{FB} = -eU_{FB}^0 - e \int_{U_{max}}^U \Gamma dU \\ E_t - E_c &= E_t^0 - E_c^0 = -eU_t^0 + eU_{FB}^0 \end{aligned} \quad [14]$$

This will lead to

$$N_{ss}^+(U) = \frac{N_t}{2} \left[\operatorname{erf} \left(\frac{-U_t^0 + U - \int_{U_{max}}^U \Gamma dU}{\sigma\sqrt{2}} \right) - \operatorname{erf} \left(\frac{-U_t^0 + U_{FB}^0}{\sigma\sqrt{2}} \right) \right] \quad [15]$$

Differentiation of Eq. [15] with respect to U and application of Eq. [8] and [9] yields

$$\frac{\Gamma}{1 - \Gamma} = \frac{eN_t}{C_H \sigma (2\pi)^{1/2}} \left[\exp \frac{-1}{2\sigma^2} \left(U_t^0 - U + \int_{U_{max}}^U \Gamma dU \right)^2 \right] \quad [16]$$

The three unknown parameters in Eq. [16] are U_t^0 , σ , and N_t/C_H . The solid lines in Fig. 4 are the best fit of Eq. [16] to the experimental results, which were cal-

culated based on the data in Fig. 2. The parameters which were evaluated from this fit are Before photoetching:

$$U_t^0 = 0.823V \text{ vs. Pt}$$

$$\sigma = 0.4V$$

$$\frac{eN_t}{C_H} = 0.88V$$

After photoetching:

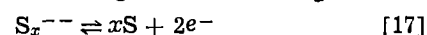
$$U_t^0 = 0.172V \text{ vs. Pt}$$

$$\sigma = 0.1V$$

$$\frac{eN_t}{C_H} = 6.88V$$

The fit is good in both cases for the reverse bias conditions. The fit is not good under forward bias conditions, where the degree of pinning is small because $\Gamma/1 - \Gamma$ is less sensitive to $[(\Delta R/R)_{max}]$ as it approaches reverse bias, and the low field regime assumption breaks as it approaches bias when the penetration depth of the light exceeds the penetration of the electric field. Assuming $C_H = 30 \mu\text{F}/\text{cm}^2$ (13), then $N_t = 1.7 \times 10^{14}/\text{cm}^2$ for the chemically etched surface and $N_t = 1.3 \times 10^{15}/\text{cm}^2$ for the photoetched surface. Because this analysis is based on the data used in Fig. 3, it is not surprising that the coverage of surface states has increased upon photoetching. For the chemically etched surface the total coverage is smaller but the width is considerably greater than the coverage and width of the photoetched surface. This suggests that the origin of the width of the surface state band is not due to overlap (14) or reorganization of the solvent (15) but more likely due to surface heterogeneity, which is more pronounced on the chemically etched surface than on the photoetched one. This is consistent with the lineshape parameters described in the discussion of spectra.

Because surface heterogeneity plays a minor role in the photoetched sample, identifying the nature of the surface states from that sample is easier. U_t^0 in that case agrees well with the rest potential of the electrode, which is determined by oxidation-reduction of the adsorbed ions according to the following reaction



which is also the potential of counterelectrode.

If the adsorbed polysulfide constitutes the surface states responsible for the Fermi-level pinning, it will be impossible to remove them and retain the photovoltaic properties of the cell. Thus, the only way to remove Fermi-level pinning is to slow down the dark reaction responsible for ionization of these states. It was demonstrated, in the case of CdSe, that this is possible because single-crystal CdSe in the same electrolyte does not have a tendency toward Fermi-level pinning; however, strong pinning effects, similar to those observed in this analysis, were demonstrated with polycrystalline CdSe (5) in the same solution.

Conclusions

Electroreflectance was used to evaluate the optical properties of CdIn₂Se₄ in polysulfide solution before and after photoetching. The variations of the signal intensity with electrode potential were used to trace the band position as a function of potential.

It was found that the optical transition fits a three-dimension parabolic model of the density of states with direct transition at 1.825 eV. There is a shift of $\sim 100^\circ$ in the phase factor and a decrease of 25% in the broadening parameter, from 0.42 to 0.32 eV, when the sample is photoetched. This result indicates that the photoetching does not alter the chemical composition of the surface through selective photoetching but strongly affects the potential distribution at depths character-

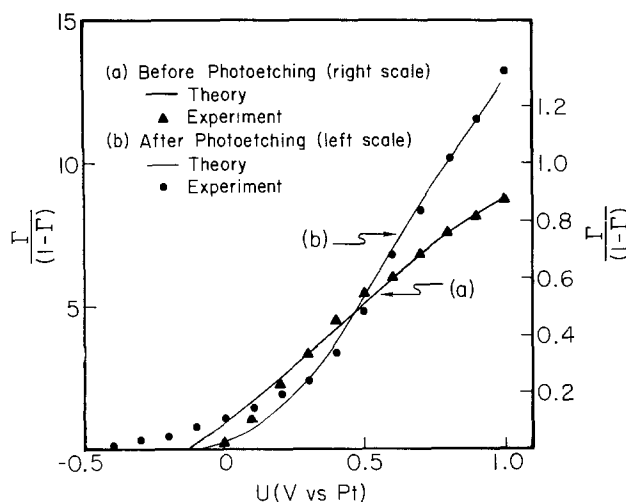


Fig. 4. $\Gamma/(1 - \Gamma)$ vs. potential. A: before photoetching. Experiment ($\blacktriangle\blacktriangle\blacktriangle$) and theory (—) with the following parameters: $U_t^0 = 0.823V$ vs. Pt, $\sigma = 0.4V$, and $eN_t/C_H = 0.88V$. B: after photoetching. Experiment ($\bullet\bullet\bullet$) and theory (—) with the following parameters: $U_t^0 = 0.172V$ vs. Pt, $\sigma = 0.1V$, and $eN_t/C_H = 6.88V$. For more details see Eq. [16].

ized by the penetration depth of the light. The effects on the potential distribution probably originate from selective etching defects.

It was shown that by monitoring the variation of the signal intensity with potential, irrespective of photoetching, the Fermi level starts to be pinned as reverse bias conditions are approached. Photoetching apparently enhances the pinning, due to the increased number of surface states. The energy and density of the surface state most likely originate from the absorbed polysulfide ions.

The experimental results presented here suffer from deficiencies that make some of the conclusions conditional. The quantitative evaluation of the shift in the bandedges with the electrode potential is based on comparison to conditions in which the Fermi level is not pinned. There is no direct evidence to support the contention that the Fermi level of CdIn₂Se₄ in polysulfide solutions unpins at any potential. The potential of reference used was where the electroreflectance signal is maximum. In addition to the uncertainty in whether the Fermi level is unpinned at this potential, there is uncertainty in whether the electroreflectance is in the low field regime at this potential, although the signal does fit the third derivative lineshape.

To clarify whether the Fermi level is unpinned at the potential of maximum electroreflectance signal, where and under what conditions Fermi level is unpinned throughout the potential regime must be determined. In addition, an independent evaluation of U_{FB}^0 and the doping level will have to be made, and the variations in those parameters with photoetching evaluated. Such data are necessary for the determination of the absolute position of the bandedges as a function of potential and not just the shift in position, as occurred in this analysis. As noted, it was impossible to carry out further required experiments.

Acknowledgment

This work was partially supported by SERI through Contract no. ZE-2-02098-01. W. S. acknowledges the support of the Exxon Education Fellowship for new research initiatives. R. T. acknowledges the partial

support of the Ministry of Science and Technology of Germany.

Manuscript submitted Feb. 7, 1983; revised manuscript received Aug. 30, 1983.

REFERENCES

1. For a recent review, see "Photoelectrochemistry: Fundamental Processes and Measurement Techniques," W. L. Wallace, A. J. Nozik, S. K. Deb, and R. H. Wilson, Editors, The Electrochemical Society Softbound Proceedings Series, Pennington, NJ (1982).
2. R. Tenne, Y. Mirovsky, Y. Greenstein, and D. Cahen, *This Journal*, **129**, 1506 (1982).
3. L. S. Koval, S. I. Radautsan, and V. V. Sobolev, *Inorg. Mater., Eng. Transl.*, **8**, 1776 (1972).
4. R. Tenne and G. Hodes, *Appl. Phys. Lett.*, **37**, 428 (1980); R. Tenne, *Appl. Phys.*, **25**, 13 (1981); N. Muller and R. Tenne, *Appl. Phys. Lett.*, **39**, 283 (1981).
5. R. P. Silberstein, J. K. Lyden, M. Tomkiewicz, and F. H. Pollak, *J. Vac. Sci. Technol.*, **19**, 406 (1981); R. P. Silberstein, F. H. Pollak, J. K. Lyden, and M. Tomkiewicz, *Phys. Rev. B*, **24**, 7397 (1981).
6. D. E. Aspnes, *Surf. Sci.*, **37**, 418 (1973).
7. B. O. Seraphin and N. Bottka, *Phys. Rev. A*, **139**, 560 (1965).
8. D. E. Aspnes, in "Handbook on Semiconductors," Vol. 2, T. S. Noss and M. Bulkanski, Editors, Chap. 4A, North Holland (1980).
9. R. Trykozko, in "Proceedings of the Third International Conference on Ternary Compounds, Edinburgh, April 1977," p. 249, (1977).
10. B. Pettinger, H. R. Schoppel, T. Yokoyama, and H. Gerischer, *Ber. Bungen. Phys. Chem.*, **78**, 1024 (1974).
11. V. A. Myamlin and Y. V. Pleskov, "Electrochemistry of Semiconductors," Chap. 1, Plenum Press, New York (1967).
12. M. Tomkiewicz, J. K. Lyden, R. P. Silberstein, and F. H. Pollak, in "Photoeffects at Semiconductor-Electrolyte Interfaces," A. J. Nozik, Editor, American Chemical Society Symposium Series, Vol. 146 (1981).
13. M. Tomkiewicz, *This Journal*, **126**, 1505 (1979).
14. M. Tomkiewicz, *Surf. Sci.*, **101**, 286 (1980).
15. S. R. Morrison, "The Chemical Physics of Surfaces," Chap. 2, Plenum Press, New York (1977).

Electroactive Properties of Polyaromatic Molecules

Robert J. Waltman, A. F. Diaz,* and Joachim Bargon¹

IBM Research Laboratory, San Jose, California 95193

ABSTRACT

Electroactive and electrochromic films of electropolymerized polyazulene and polythiophene have been found to be surprisingly insensitive to common solvents and temperature. As electrodes in all-organic batteries these thin polymeric films allow current densities of 2 mA/cm² at open-circuit voltages of 2.3V. The electrochromic properties suggest application in electro-optical displays.

The variety of compounds which have been found to undergo electrochemical polymerization have demonstrated the facility of the electrochemical approach to synthesis of electrically conducting polymeric films. Such films have been prepared from molecules which represent all pertinent classes of aromatic compounds. They include the heterocyclic pyrroles (1, 2), thiophenes (3-5), furan (5), carbazoles (6, 7), the polynuclear aromatic hydrocarbons pyrene or fluorene (8), and even the nonbenzenoid aromatic hydrocarbon azulene (9). When in the oxidized form, all of these polymers are semiconducting (10^{-6} - $10^2 \Omega^{-1}$

cm⁻¹), with polypyrrole exhibiting the highest conductivities of $10^2 \Omega^{-1} \text{ cm}^{-1}$. Thin films from polypyrrole, polythiophene, and polyazulene which are supported by a Pt surface are also attractive, because they exhibit electroactive and electrochromic properties. Thus, electrically conducting polymers become suitable for application in electro-optic display devices (10) or as electrode materials (11). Successful application in the latter has been demonstrated by the fabrication of a lightweight, rechargeable battery employing a polyacetylene electrode, whereby large power and energy densities were obtained (12). The fact that electrochemically prepared polymers, such as polythiophene or polyazulene, have similar properties, points to their potential application in energy tech-

* Electrochemical Society Active Member.

¹ Institut für Physikalische Chemie, Bonn-1, Germany.

nology as well. Accordingly, we report herein some properties of these materials relevant to their applications in battery technology.

Experimental

All compounds were obtained from commercial sources. Polythiophene and poly- β -substituted thiophenes were prepared by the electrochemical oxidation of the appropriate thiophene monomers in a three-electrode, single- or two-compartment cell. Platinum, gold, and sodium chloride calomel (SSCE) were used as the working, counter, and reference electrodes, respectively. The solutions were typically 10^{-4} - 10^{-3} M in monomer, in a 0.1M electrolyte/acetonitrile solution. The electrolyte, usually tetraethylammonium tetrafluoroborate (TEAFB), was recrystallized from alcohol-ethyl acetate and dried under vacuum. The acetonitrile (Burdick and Jackson, spectrometric grade) was used directly without further purification. The solutions were bubbled with argon for 5-10 min, and protected by an argon blanket. Cyclic voltammograms of polymer films were measured in electrolyte solutions containing no other electroactive species. All electrochemical measurements were performed with an IBM EC225 Voltammeter Analyzer.

Results and Discussion

Electrochemical data.—Cyclic voltammetric data for some thiophene monomers and their corresponding polymers are given in Table I. All of the monomers show irreversible oxidation peaks and give rise to colored solutions upon electro-oxidation. The value of n for the oxidation reaction was estimated from the Nicholson and Shain treatment for a totally irreversible electron-transfer process which provides $n^{3/2}D^{1/2}$, where D was assumed equal to 10^{-5} cm² s⁻¹. In general, the reaction of compounds which produce polymer films occurs on the electrode surface and has n values between 2 and 3, as estimated from cyclic voltammetry. From elemental analysis, n values between 2.07 and 2.17 are obtained for some of these polymers. The reaction of compounds which produce soluble products and, therefore, occur away from the electrode, has n values between 1 and 2, depending upon whether monomeric ($n = 2$) or dimeric ($n = 1$) products are formed (13). Accordingly, the α,α' -blocked 2,5-dimethylthiophene has an n value of 1.2, similar to 2,5-dimethylpyrrole (13).

Whereas low molecular weight products are obtained from α -substituted heterocycles, polymeric films are indeed obtained from certain β -substituted monomers. The cyclic voltammogram of a typical 60 nm thin film of polythiophene on a Pt surface obtained from the electropolymerization of 2,2'-bithiophene is shown in Fig. 1.

The details of the electroactive properties of these films have been previously considered (4), and no reiteration is necessary here. However, it is important to

Table I. Cyclic voltammetric data for thiophenes: monomer concentration 8.9-23.0 $\mu\text{mol cm}^{-3}$ in 0.1M TEAFB/CH₃CN with sweep rate 50 mV s⁻¹

Compound	Monomer				Polymer E _{pa} (V)
	E _{pa} (V)	$i/AC\nu^{1/2}$ (A cm mol ⁻¹ s ^{1/2})	$10^{2n^{3/2}}D^{1/2}$ (cm s ^{1/2})	n	
thiophene	2.06	3791	1.4	2.7	0.96
3-methylthiophene	1.86	3203	1.2	2.4	0.72
3-iodothiophene	2.03	2362	0.9	2.0	
3-bromothiophene	2.10	3085	1.1	2.3	1.06
3-thiopheneacetonitrile	2.22	2725	1.0	2.2	1.12
3-thiophenecarboxylic acid	2.28	1031	0.4	1.2	
3-cyanothiophene	2.46	2260	0.8	1.9	
3-nitrothiophene	2.69	2476	0.9	2.0	
2,5-dimethylthiophene	1.77	1134	0.4	1.2	

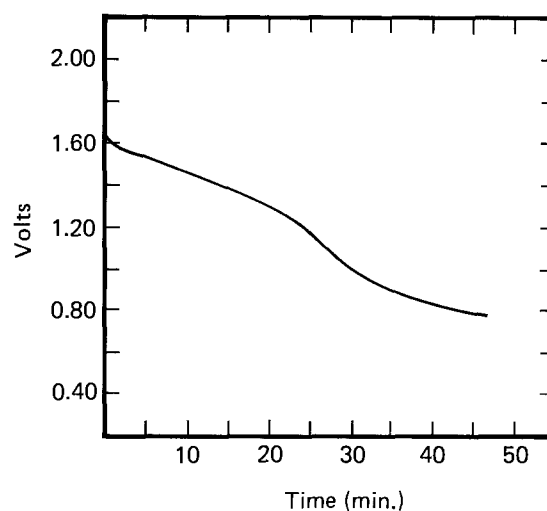


Fig. 1. Cyclic voltammogram of [Pt]-polythiophene-BF₄ film in 0.1M TEAFB/CH₃CN solution.

point out that these films can be cycled repeatedly between the oxidized, conducting state and the neutral, nonconducting state, an event which is accompanied by a reversible color change from green-back to a pale-copper color, respectively. The cycling behavior is observed for polythiophene films derived from either the monomer or the 2,2'-dimer. The anodic peaks obtained from the dimer derived polymer films, however, are noticeably sharper with peak widths at half height (PWHH) of ca. 90 mV for 60 nm films, while monomer derived films of the same thickness have PWHH of ca. 300-350 mV. Since it is known that the oxidation and reduction reaction is controlled by the diffusion of counteranions into and out of the surface-localized film, diffusion of ions through the dimer-derived film is less limiting. This may also reflect the more regularly α,α' -linked monomer units in the dimer-derived film. The sensitivity of the electrical properties of polythiophene to linkages between monomer units other than α,α' -bonds has been pointed out by Sanechika *et al.* (14). In particular, they found that the electrical conductivity of polythiophene decreases with increasing β -linkages introduced between monomer units.

Figure 1 also shows that the peak oxidation potential of polythiophene occurs at +1.0V. This is far anodic of the peak oxidation potential of polypyrrole (-0.15V), with the important consequence that polythiophene films are much more stable, especially to the presence of oxygen. Thus, unlike polypyrrole, neutral or electrochemically oxidized polythiophene films can be exposed to air, or even passed under a stream of oxygen, yet when put back into an electrolyte solution and cycled electrochemically, they retain their switching capabilities. However, ESCA studies of the neutral films reveal the presence of bonded oxygen at the surface of these materials. For neutral polythiophene films exposed to air for 24h, the C:S:O ratio is 4.0:0.55:1.0, respectively, while a 14 day exposure reveals a C:S:O ratio of 4.0:0.5:1, respectively (15). However, the surface properties are not representative of the bulk properties of the film, as is evidenced by its ability to retain electrochemical switching.

The electrochemical behavior of polyazulene films is similar to that of polythiophene films insofar that they too are electroactive and electrochromic (Fig. 2). The peak oxidation potential of the polymer film occurs at +0.650V, *i.e.*, lower than the polythiophene counterpart but still anodic of polypyrrole.

Stability of films.—For successful performance of these materials in various applications, such as in batteries, apart from the desirable electroactivity of the films, their stability under different conditions be-

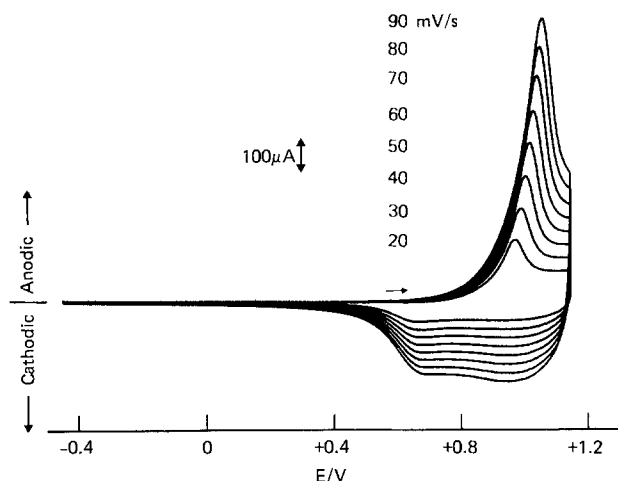


Fig. 2. Cyclic voltammogram of [Pt]-polyazulene- BF_4 film in 0.1M TEAFB/ CH_3CN solution.

comes of paramount importance. Thus, thicker films from polythiophene and polyazulene can be peeled off from the Pt anode. These are flexible, continuous, free standing films which are electrically conducting to the extent of $1 \Omega^{-1} \text{cm}^{-1}$. The oxidized, conducting forms of these polymer films are also remarkably stable

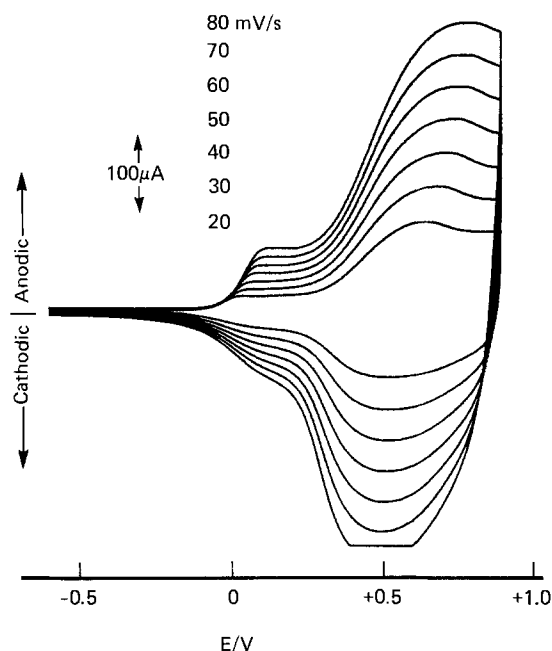


Fig. 4. The shift in the peak oxidation potential of polythiophene as a function of temperature.

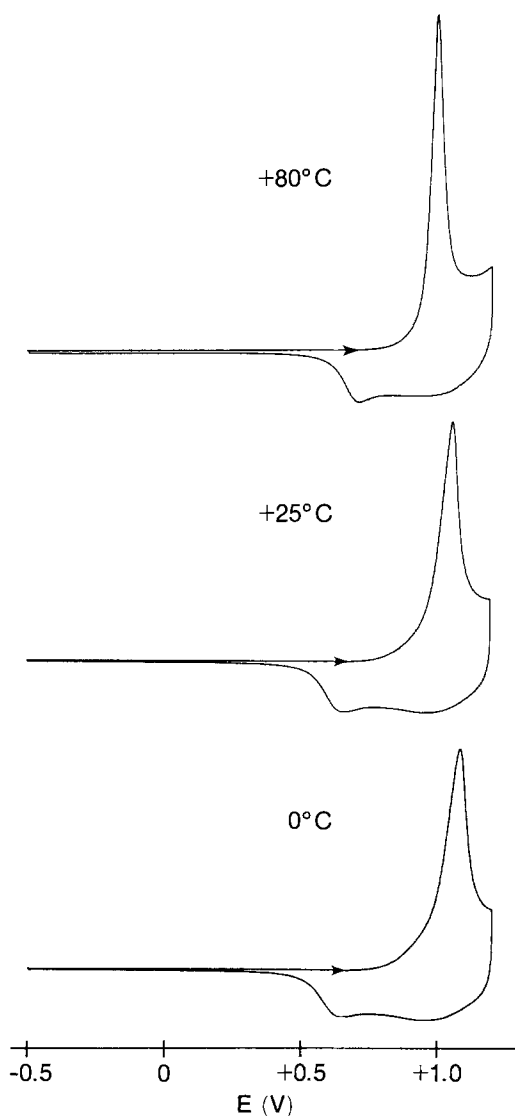


Fig. 3. Cyclic voltammograms of [Pt]-polythiophene- BF_4 as a function of temperature in 0.1M TEAFB/ CH_3CN .

under different conditions. They are insoluble in strong acids, bases, or common organic solvents. For example, when oxidized films are placed in 6M HCl or NaOH, or in a solvent such as dichloromethane for 1h, they retain their electroactive properties when subsequently electrochemically cycled. The thicker films are also thermally stable to heating at 80°C for several hours. When kept for 3h at this temperature, polyazulene and polythiophene show a decrease in conductivity from 0.4 to $0.2 \Omega^{-1} \text{cm}^{-1}$, and from 0.1 to $0.04 \Omega^{-1} \text{cm}^{-1}$, respectively, while heating for 20h results in a ten-fold decrease in their conductivities. Whereas the thick films show moderate stability to heating, the thin films display a sensitivity of the switching behavior to changes in temperature. Thin films were cycled repeatedly in the temperature range between 0.0° and 80°C , and were found to be stable under these conditions for at least several hours. The electroactive properties are still retained (Fig. 3), and the peak oxidation potential shifts cathodically by 0.88 mV deg^{-1} with increasing temperature (Fig. 4). The 70 mV shift in the oxidation potential is reversible in this range, and a noticeable sharpening of the anodic peak is observed at higher temperatures (Fig. 3).

Apart from the demonstrated temperature stability, these data also allow information concerning the energetics of the switching reaction in this temperature range. The reaction is electrochemically irreversible and thus the relation $dG = -nFE$ cannot be applied. However, the dE/dT dependence is real and can be related to $d(dG)/dT$, which provides $-dS$. Thus, $dS = nF(dE/dT) = -3.4 \text{ cal deg}^{-1}$, whereby $n = 0.17$, i.e., the amount of charge consumed in the partial oxidation of the film, as can be derived from elemental analysis data. This change of state also involves a change in composition where anions are incorporated into the film in order to balance the positive charges along the polymer chain. The sign and magnitude for the entropy term dS is consistent with what is characteristic for molecular complex formation (16). The sign for dS suggests that as the film switches from the neutral to the oxidized state, accommodation of counter-anions (which is necessary to balance the positive charge induced in the polymer chain) results in a structure more rigid than in the neutral state of the film.

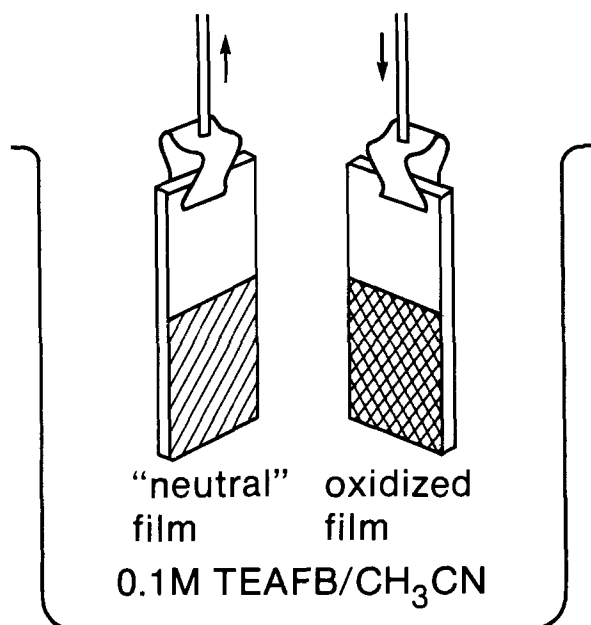


Fig. 5. Electrochemical peak oxidation potential of thiophene monomers vs. their respective Hammett substituent constants.

Substituent effects.—The eventual application of these materials in energy technology or in other fields will demand some chemical modifications in order to meet particular criteria. For example, we have demonstrated previously that the conductivity of polythiophene can be increased 100-fold with the introduction of a single β substituent (4). The fraction of counteranions in the film can also vary depending on which substituent is introduced into the parent polymer. Correspondingly, an investigation of polythiophene films with appropriate β substituents showed that when the peak oxidation potential of some β -substituted monomers are plotted against their respective Hammett substituent constants, a linear correlation is obtained (Fig. 5). The shift in the peak oxidation potentials of the series of β -substituted thiophenes is dependent on three parameters: namely, their polar, steric, and mesomeric effects, which are exerted by the substituents (17). This behavior can be described by the usual Hammett-Taft

$$E = \rho_{\pi\sigma} + S$$

equation where $\rho_{\pi\sigma}$ describes the polar-mesomeric parameters, and S accounts for the steric factor (17). Accordingly, Fig. 5 allows three conclusions to be drawn. First, the straight-line fit indicates that all of the monomers are oxidized by the same mechanism, *i.e.*, electro-oxidation results in the removal of a π electron from the thiophene ring. Second, the positive sign for the substituent constant ρ_{π} reveals that as the substituents take on more electrophilic character, the oxidation of the corresponding thiophenes proceed more difficultly. Finally, the steric term S appears to be minimal since for the substituents chosen here, a straight-line fit is obtained. Thus, the primary effect exerted by the β substituents is electronic and described by the $\rho_{\pi\sigma}$ term. One possible interpretation of these facts (Fig. 5) suggests that there is an optimum potential range, *i.e.*, reactivity of the radical cation intermediate, which favors radical cation coupling in the follow-up reaction to yield polymeric films. Thus, under these conditions, polymerization occurs only for the parent thiophene, and the methyl-, bromo-, and iodo-substituted thiophenes. The latter two monomers yield poorly conducting films, while the other two polymers, polythiophene and poly(3-methylthiophene), have conductivities of *ca.* 10^{-2} – 10^{-1} , and $1 \Omega^{-1} \text{ cm}^{-1}$, respectively. 3-Thiophene carboxylic acid,

3-cyano-, and 3-nitro-thiophene yield no polymers on electro-oxidation under these conditions. Several reasons may be attributed to the lack of polymers obtained from the latter three monomers. One interpretation postulates that the stability (or reactivity) of these monomers is affected by the β substituents. Thus, as the reactivity of the radical cation intermediates increases, as reflected in their increasing oxidation potentials (Fig. 5), the more reactive these intermediates become with respect to nucleophiles, or they undergo other "escape" reactions, *e.g.*, with the solvent or other nucleophilic species in the vicinity of the Pt surface. Thus, one possible effect of these strongly electron withdrawing groups is to destabilize the radical cation intermediate to the extent that radical cation coupling reactions become unfavorable when compared with other reaction pathways. Another reason for their failure to promote electropolymerization may be due to a breakdown of the solvent, since the anodic potentials applied become rather high for the nitro- and cyano-substituted monomers (Table I).

While steric factors do not seem to play any appreciable role in the primary electro-oxidation of the monomer (Fig. 5), their subsequent follow-up reactions (radical cation polymerization) are more susceptible to steric effects, which, therefore, may well play a role in deciding whether polymerization can compete favorably with other potential follow-up reactions, such as with nucleophiles. This may explain the overall inferior quality of the polymer films derived from the 3-bromo- and 3-iodo-thiophenes, even though their oxidation potentials do not differ greatly from that of the parent thiophene monomer. It is, however, interesting to note that while a bulky substituent, such as iodo, allows polymerization (albeit of poor quality), a sterically smaller cyano group does not.

Another example of a property-structure correlation between thiophene monomers and their corresponding polymers is reflected in Fig. 6, where the peak oxidation potentials of some thiophene monomers are plotted against their respective polymers. The straight-line fit suggests that β -substituted monomers and their respective polymers are made up of a related system of π electrons, *i.e.*, the electronic structures of the monomers and their corresponding polymers must be alike. This is consistent with the fact that polythiophene (and polypyrrole) consists primarily of α,α' -linked monomer units (3, 4).

Battery applications.—The stability of polythiophene and polyazulene films as described above suggests application of these materials as battery electrodes. Of particular importance is the high extent of

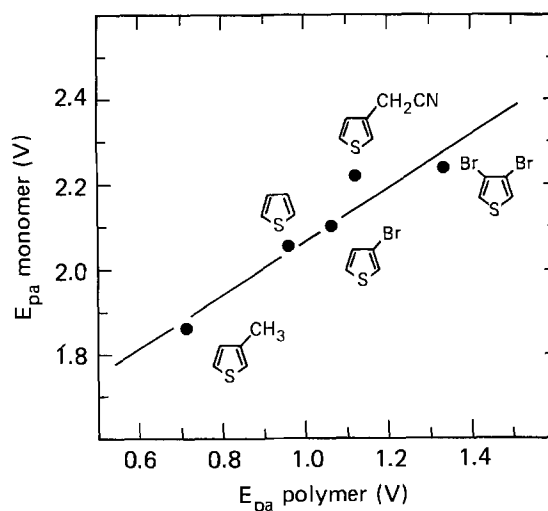


Fig. 6. Peak oxidation potential of thiophene monomers vs. their respective polymers in 0.1M TEAFB/CH₃CN.

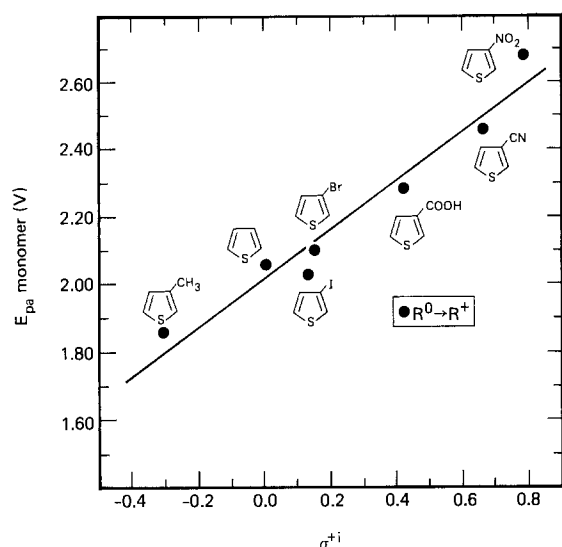


Fig. 7. A simple "all polymer" battery cell

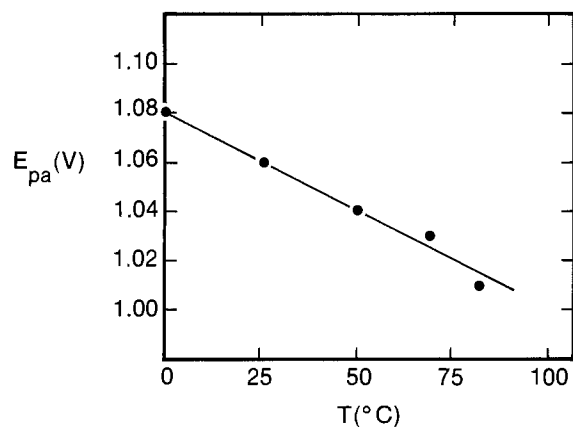


Fig. 8. A typical voltage change during 0.15 mA constant-current discharge of a polyazulene battery cell.

counteranions which can be incorporated into these polymer films, especially into polyazulene, whereby one counteranion is shared by four azulene monomer units (Table II). Polythiophenes are additionally attractive from the standpoint that their film properties are readily altered via substituent groups. Thus, a simple battery cell (as shown in Fig. 7) was assembled utilizing oxidized and neutral polymer films adhered onto Pt as the two terminals. The films were typically $1 \times 2 \text{ cm}^2$ with a thickness of ca. 10^{-3} cm , corresponding to a film weight of about 1-2 mg. These were immersed into a 0.1M TEAFB acetonitrile solution containing no other electroactive species. The arrows in Fig. 7 indicate the direction of electron flow. A polyazulene battery yielded a maximal open-circuit voltage of ca. 2.3V and an optimal initial short-circuit current of 4 mA. These data are summarized in Table II for both polyazulene and polythiophene batteries. These preliminary results for polyazulene are taken from

Table II. Batteries from polyazulene and polythiophene

	Polyazulene	Polythiophene
Elemental composition	(AZ) $_{14}^+$ · BF $_4^-$	(TH) $_{14}^+$ · BF $_4^-$
Current density	0.4-2.2 mA/cm 2	0.02 mA/cm 2
Voltage	0.5-2.3V	0.5V

five such batteries, while those for polythiophene (monomer derived) are based upon a single battery test. Polythiophene batteries derived from the dimer may conceivably yield higher values since they can store more charge (six monomer units share one charge) than the monomer-derived films. The batteries tested so far could be recharged at constant current, e.g., at 1 mA, to yield similar values in the regenerated cells.

Our values are actually quite similar to the "all polymer" polyacetylene batteries of MacDiarmid *et al.* (18). However, unlike polyacetylene, which is known to be air sensitive, polyazulene batteries can be open to the air, at least short-term (days) tests revealed no apparent effect of air on the stability of the batteries. However, the long-term effect of oxygen on the re-chargeability of polyazulene batteries has not been investigated thus far. Figure 8 shows the voltage change during a constant current discharge of 0.15 mA for a polyazulene cell in 0.1M TEAFB acetonitrile. More work is in progress.¹

Manuscript received Aug. 25, 1983. This was Paper 546 presented at the San Francisco, California, Meeting of the Society, May 8-13, 1983.

IBM Corporation assisted in meeting the publication costs of this article.

¹After this work was completed, data characterizing the electrochromic behavior of polythiophenes was reported by Garnier *et al.* (19).

REFERENCES

1. A. Dall'Olio, Y. Dascola, V. Varacca, and V. Bocchi, *Acad. Sci. Ser. C*, **267**, 433 (1968).
2. A. F. Diaz, K. K. Kanazawa, and G. P. Gardini, *J. Chem. Soc., Chem. Commun.*, 635 (1979); A. F. Diaz and J. I. Castillo, *ibid.*, 397 (1980); K. K. Kanazawa, A. F. Diaz, W. D. Gill, P. M. Grant, G. B. Street, G. P. Gardini, and J. F. Kwak, *Synthetic Metals*, **1**, 329 (1979/1980).
3. A. F. Diaz, *Chem. Scr.*, **17**, 145 (1981).
4. R. J. Waltman, J. Bargon, and A. F. Diaz, *J. Phys. Chem.*, **87**, 1459 (1983).
5. G. Tourillon and F. Garnier, *J. Electroanal. Chem.*, **135**, 173 (1982).
6. J. F. Ambrose and R. F. Nelson, *This Journal*, **115**, 1159 (1968).
7. J. Bargon, M. Mohmand, and R. J. Waltman, *IBM J. Res. Develop.*, **27**, 330 (1983).
8. R. J. Waltman and J. Bargon, Unpublished results.
9. J. Bargon, S. Mohmand, and R. J. Waltman, *Mol. Cryst. Liq. Cryst.*, **93**, 279 (1983).
10. A. F. Diaz and K. K. Kanazawa, in "Extended Linear Chain Compounds," Vol. 3, J. S. Miller, Editor, p. 417, Plenum Press, New York (1982).
11. A. F. Diaz, J. M. Vasquez Vallejo, and A. Martinez Duran, *IBM J. Res. Develop.*, **25**, 42 (1981).
12. P. J. Nigrey, A. G. MacDiarmid, and A. J. Heeger, *Mol. Cryst. Liq. Cryst.*, **83**, 309 (1982).
13. A. F. Diaz, A. Martinez, K. K. Kanazawa, and M. Salmon, *J. Electroanal. Chem.*, **130**, 181 (1981).
14. K. Sanechika, T. Yamamoto, and A. Yamamoto, *J. Polym. Sci., Polym. Lett. Ed.*, **20**, 365 (1982).
15. A. F. Diaz, R. Hernandez, R. J. Waltman, and J. Bargon, *J. Phys. Chem.*, To be published.
16. J. E. Leffler and E. Grunwald, "Rates and Equilibria of Organic Reactions," John Wiley and Sons, Inc., New York (1963).
17. P. Zuman, "Substituent Effects in Organic Polarography," Plenum Press, New York (1967), and references therein.
18. A. G. MacDiarmid, M. Aldissi, R. B. Kaner, M. Maxfield, and R. J. Mammone, Abstract 558, p. 843, The Electrochemical Society Extended Abstracts, Vol. 83-1, Washington, DC, Oct. 9-14, 1983.
19. F. Garnier, G. Tourillon, M. Gazard, and J. C. DuBois, *J. Electroanal. Chem.*, **148**, 299 (1983).

Electrocatalysis of the Cathodic Reduction of Carbon Dioxide on Platinized Titanium Dioxide Film Electrodes

Milena Koudelka, Alain Monnier, and Jan Augustynski*

Département de Chimie Minérale, Analytique et Appliquée, Université de Genève, 1211 Genève 4, Switzerland

ABSTRACT

Cyclic voltammetric measurements on the electrochemical reduction of CO₂ at platinized and nonplatinized TiO₂ film electrodes are reported. It is shown that carbon dioxide, dissolved in aqueous solution or present in a mixture with water vapor, undergoes strong, irreversible adsorption on the Pt-TiO₂ surface. The adsorption of CO₂, taking place at open circuit, results in the formation of electrochemically detectable species. The reduction of the adsorbed carbon dioxide at the Pt-TiO₂ electrode starts at even lower cathodic potentials than in the case of unsupported Pt electrode and produces two kinds of reduced species revealed by anodic peaks on the cyclic voltammograms. The existence of two electrochemically detectable reduced-CO₂ species is explained in terms of the surface diffusion of the reaction intermediates and/or products between adsorption sites at the metal, Pt, and at the oxide, TiO₂.

Among various oxide-supported noble metal catalysts, the platinum-titanium dioxide system has recently attracted particular attention because of its potential applications in the field of photocatalysis and/or gas-phase heterogeneous catalysis. Thus, a suspension of platinized TiO₂ in an acidic aqueous solution, irradiated with the UV light, has been shown (1) to induce the photodecomposition of water into hydrogen and oxygen. Another example of a photocatalytic reaction (which, contrary to the previous one, is characterized by a negative Gibbs free energy change) is the photodecomposition of acetic and other carboxylic acids into corresponding alkanes and carbon dioxide (2, 3). In these processes, platinum particles are believed to act as local cathodes for the formation of adsorbed hydrogen atoms and for the H₂ evolution which accompany various photoanodic reactions involving positive holes photogenerated at the surface of n-type TiO₂.

In the related field of water photolysis, Grätzel and co-workers (4, 5), using RuO₂ and Pt cosupported on colloidal TiO₂ particles as redox catalyst in the presence of Ru(bipy)₃²⁺ sensitizer, have succeeded in improving considerably the efficiency of water cleavage by visible light. The above results have been explained (5) in terms of adsorption of the sensitizer at the surface of TiO₂ particles as being a crucial step of the overall process.

In addition, various transition metal catalysts supported on TiO₂, including the Pt-TiO₂ system, have recently been investigated (6) with special regard to their activity for CO-H₂ Fischer-Tropsch synthesis.

Following a preliminary study in this laboratory (7) on the cathodic reduction of dissolved CO₂ at polycrystalline TiO₂ and RuO₂-TiO₂ film cathodes, we have undertaken a systematic characterization of different activated-TiO₂ electrodes. In this paper, the electrochemical characteristics of TiO₂ and platinized TiO₂ film electrodes are discussed in connection with the hydrogen evolution and carbon dioxide reduction reactions.

Experimental

TiO₂ and platinized TiO₂ film electrodes were prepared by a thermal decomposition method using cross sections (~0.3 cm²) of 99.8% titanium rods (Kobe Steel, Limited) as a support. The TiO₂ films were obtained by applying onto the previously etched Ti substrates, layer by layer, a solution of TiCl₄ (puriss. from Fluka) in a mixture of analytical-grade methanol and ethanol. Each layer of the solution was decomposed by heating in air at ~450°C. In the case of platinized electrodes, one or two final layers of an aqueous solution of H₂PtCl₆ (Fluka) were applied before submitting them,

for about 40 min, to a final thermal treatment in argon at ~550°C. Thus formed, TiO₂ films were 10-15 μm thick and consisted of anatase. The amount of platinum present on the surface of platinized TiO₂ samples was checked by means of x-ray induced photoelectron spectroscopy (XPS) (8). For different samples analyzed by XPS the platinum content in the outermost surface layer ranged from 10 to 13 atom percent (a/o) (given with respect to Ti(IV) from TiO₂, taken as 100 a/o). Since the mean escape depth for the photoelectrons with a kinetic energy close to 1200 eV is usually considered to reach 15-20 Å, the above result indicates that the coverage of the TiO₂ surface with Pt was in all cases distinctly less than a monolayer. This is additionally supported by the evidence, based on the observed decrease of the amount of Pt on the surface following the activation of the electrode at 550°C, that platinum diffuses to a significant extent into the TiO₂ substrate.

All solutions employed in electrochemical experiments were made up with analytical-grade chemicals and twice-distilled water. For most experiments, a calomel reference electrode in 0.1N KCl solution was used. Potentials on this scale are referred to as *E* (V vs. 0.1 NCE). Carbon dioxide or argon, both under 1 atm, were continuously bubbled through the solution; the bubbling was interrupted only for the duration of a cyclic voltammetry experiment. All measurements were effected at 40°C.

Results and Discussion

The choice of a suitable electrolyte for the study of CO₂ reduction at TiO₂ and Pt-TiO₂ electrodes was quite a complex question because of the known tendency of a number of ions (especially anions) to adsorb irreversibly on the surface of TiO₂ (9). Thus, for example, the nature of the second anion present in the solution has been shown (10) to strongly affect the cathodic reduction of Fe(CN)₆³⁻ ions at the TiO₂ film electrodes similar to those used in the present study. Among various nearly neutral solutions, chloride solutions appear to influence least the cathodic behavior of TiO₂. Therefore, after a series of preliminary cyclic voltammetry experiments, a 0.5M KCl solution was chosen as a supporting electrolyte. In addition, most of the electrochemical measurements were repeated using a 0.5M K₂SO₄ solution; no significant differences were observed.

Figure 1 shows typical cyclic voltammetry *i*-*E* profiles for Pt, Pt-TiO₂, and TiO₂ electrodes, recorded in an argon-saturated 0.5M KCl solution. For comparison purposes, similar experiments were also performed in a deaerated 0.5M KHCO₃ solution, which was chosen in order to minimize the possible influence of anion adsorption on the surface of platinum (11). They en-

* Electrochemical Society Active Member.

Key words: cyclic voltammetry, adsorption, film electrode.

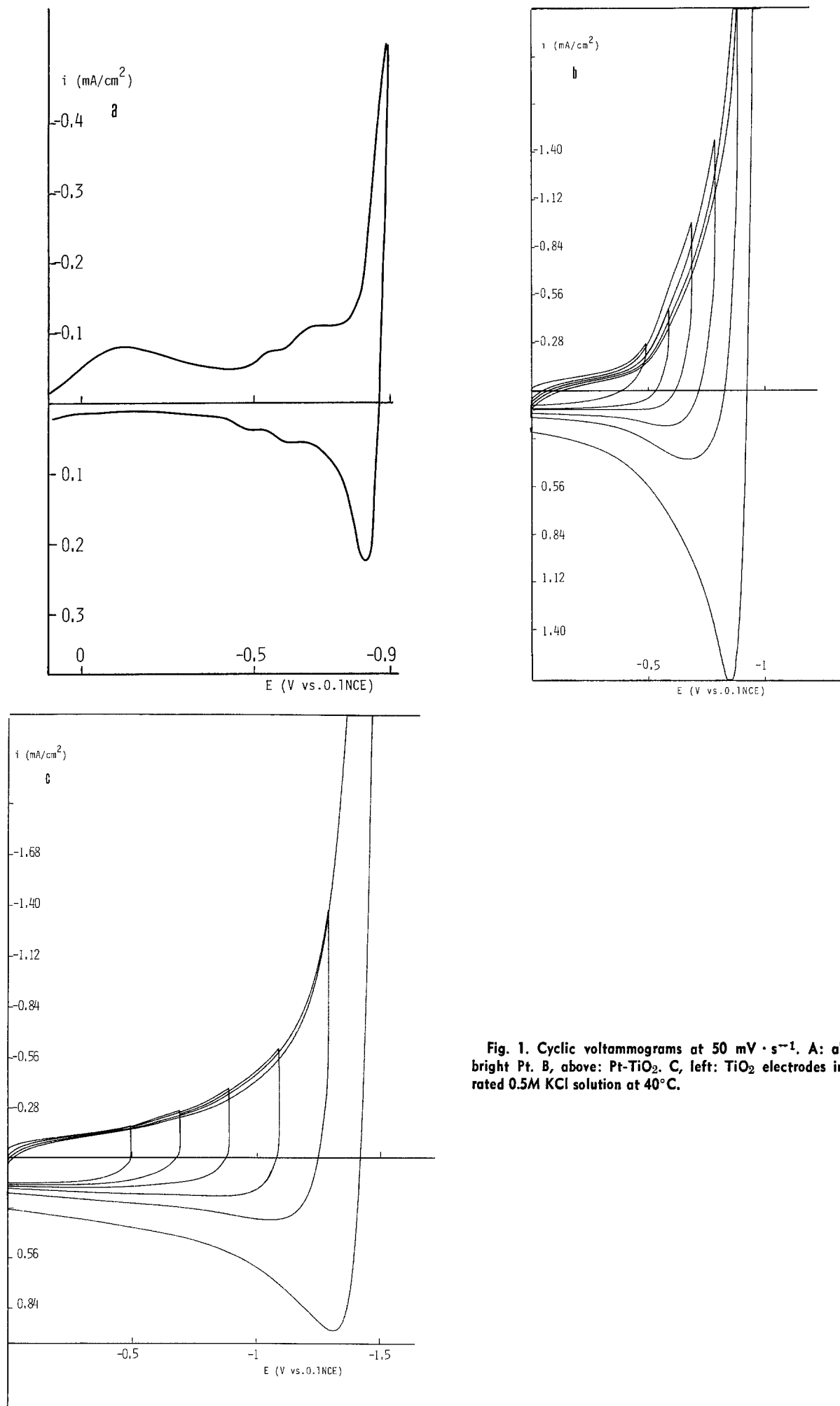


Fig. 1. Cyclic voltammograms at $50 \text{ mV} \cdot \text{s}^{-1}$. A: above, left: bright Pt. B, above: Pt-TiO₂. C, left: TiO₂ electrodes in Ar-saturated 0.5 M KCl solution at 40°C .

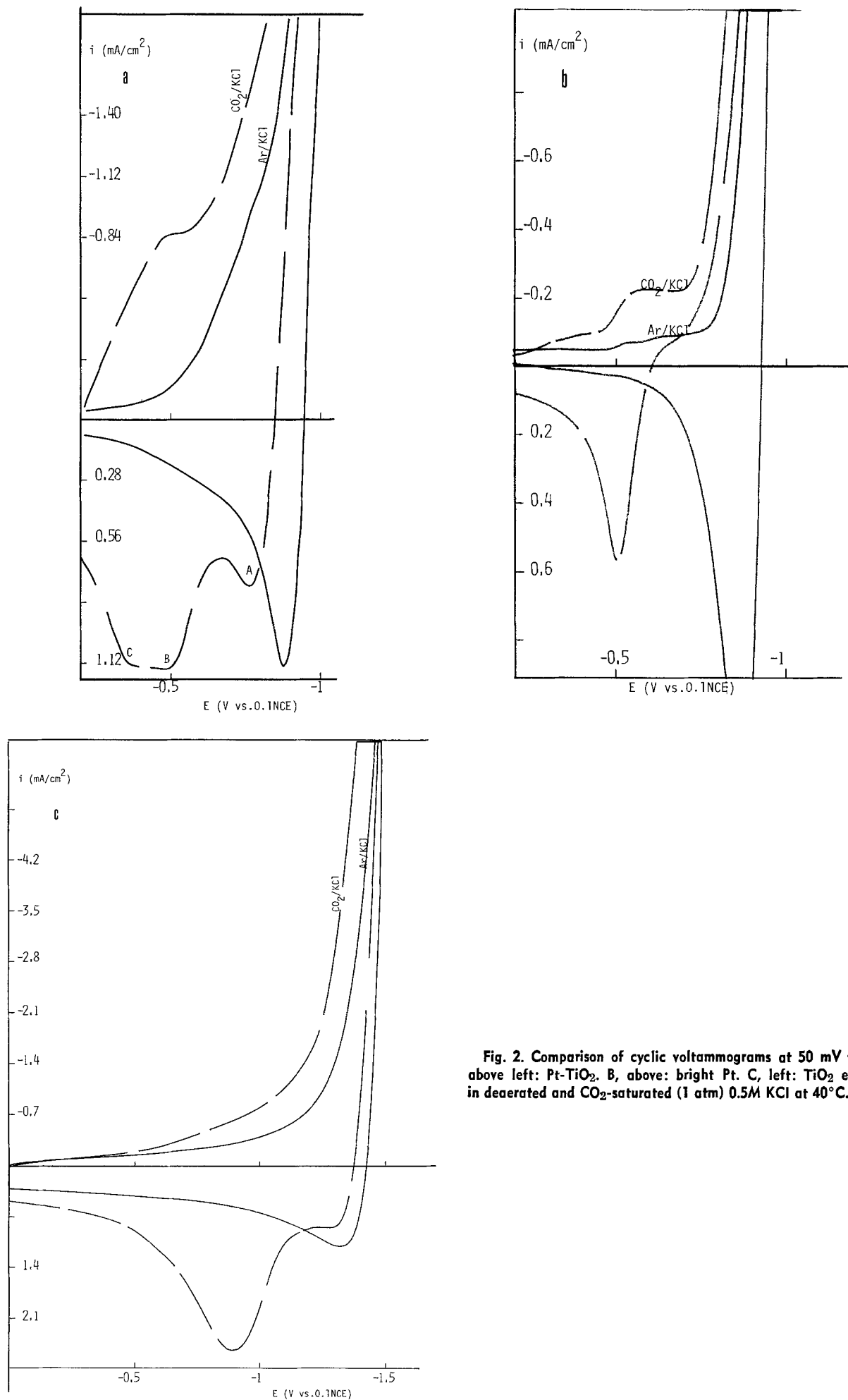
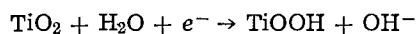


Fig. 2. Comparison of cyclic voltammograms at $50 \text{ mV} \cdot \text{s}^{-1}$. A, above left: Pt-TiO₂. B, above: bright Pt. C, left: TiO₂ electrodes in deaerated and CO₂-saturated (1 atm) 0.5M KCl at 40°C.

able us to conclude that, if in the case of bright Pt the presence in the solution of Cl^- ions affects the amount of charge corresponding to H deposition, no such effect is perceptible for the Pt-TiO₂ electrode.

The hydrogen evolution at the bright platinum and Pt-TiO₂ electrodes started in the same (within 100 mV) potential region, -0.8 to -0.9V vs. 0.1 NCE, while it was shifted about 0.7V to more cathodic potentials in the case of the nonplatinized TiO₂ electrode. However, similar shapes of the *i*-E curves observed for the platinized and nonplatinized TiO₂ suggest that, in spite of a much larger hydrogen overvoltage exhibited by the latter electrode, the sequence of cathodic reactions at both kinds of surfaces is probably the same. In particular, the initial increase of the cathodic current, occurring at potentials preceding the hydrogen region, is likely to be consistent with a partial-surface-reduction of TiO₂



which must involve the proton transfer from the adsorbed molecule of water (7). At more cathodic potentials (i.e., at about -0.8V for Pt-TiO₂ and -1.6V vs. 0.1 NCE for TiO₂), the electrode surface is supposed to become covered with adsorbed hydrogen atoms, giving rise to an anodic current maximum on the reverse sweep. Cyclic voltammograms obtained in 0.5M KCl solution saturated with CO₂ (Fig. 2) showed a number of features differentiating them from the curves in Fig. 1. The most significant one was a distinct increase of the cathodic current at the Pt-TiO₂ electrode, occurring already at about -0.2V (Fig. 2a), i.e., at the potentials less negative than in the case of the bright Pt electrode

(Fig. 2b). On the reverse (anodic) sweep, up to three distinct peaks, corresponding, in order of increasing potentials, to the oxidation of hydrogen (peak A) and of two reduced forms (or reduction products) of CO₂ (peaks B, C) electrodeposited at the Pt-TiO₂ electrode, were observed. This constitutes an important difference with respect to the behavior of bright platinum for which a single peak, usually associated (12) with the oxidation of "reduced carbon dioxide", occurred on the anodic sweep (Fig. 2b).

When the potential of the Pt-TiO₂ electrode was repetitively cycled, extending each time the cathodic limit by an additional 0.1V while holding the anodic limit the same, the oxidation charge increased, and peaks C, B, and finally A appeared successively (Fig. 3a). The fact that peak C was already clearly visible when the cycle was limited cathodically at -0.5V is to be connected with a marked affinity for CO₂ exhibited by the hydrated Pt-TiO₂ surface. Experiments consisting in simply exposing a Pt-TiO₂ electrode¹ to 0.5M KCl solution saturated with CO₂ and transferring it, after thorough washing, to an Ar-saturated 0.5M KCl solution, have revealed only a small difference between the cyclic voltammetry *i*-E profiles obtained in the latter solution and those usually observed in solutions saturated with CO₂. A prolonged cycling of the potential between extended limits, corresponding, to the H₂ and O₂ evolution reactions, respectively, was

* Before being submitted to the adsorption experiments, freshly prepared Pt-TiO₂ and TiO₂ electrodes were repetitively cycled (within the utmost potential limits shown in Fig. 1b and 1c) in 0.5M KCl solution saturated with argon. About ten cycles usually sufficed for the electrodes to reach a reproducible voltammetric behavior.

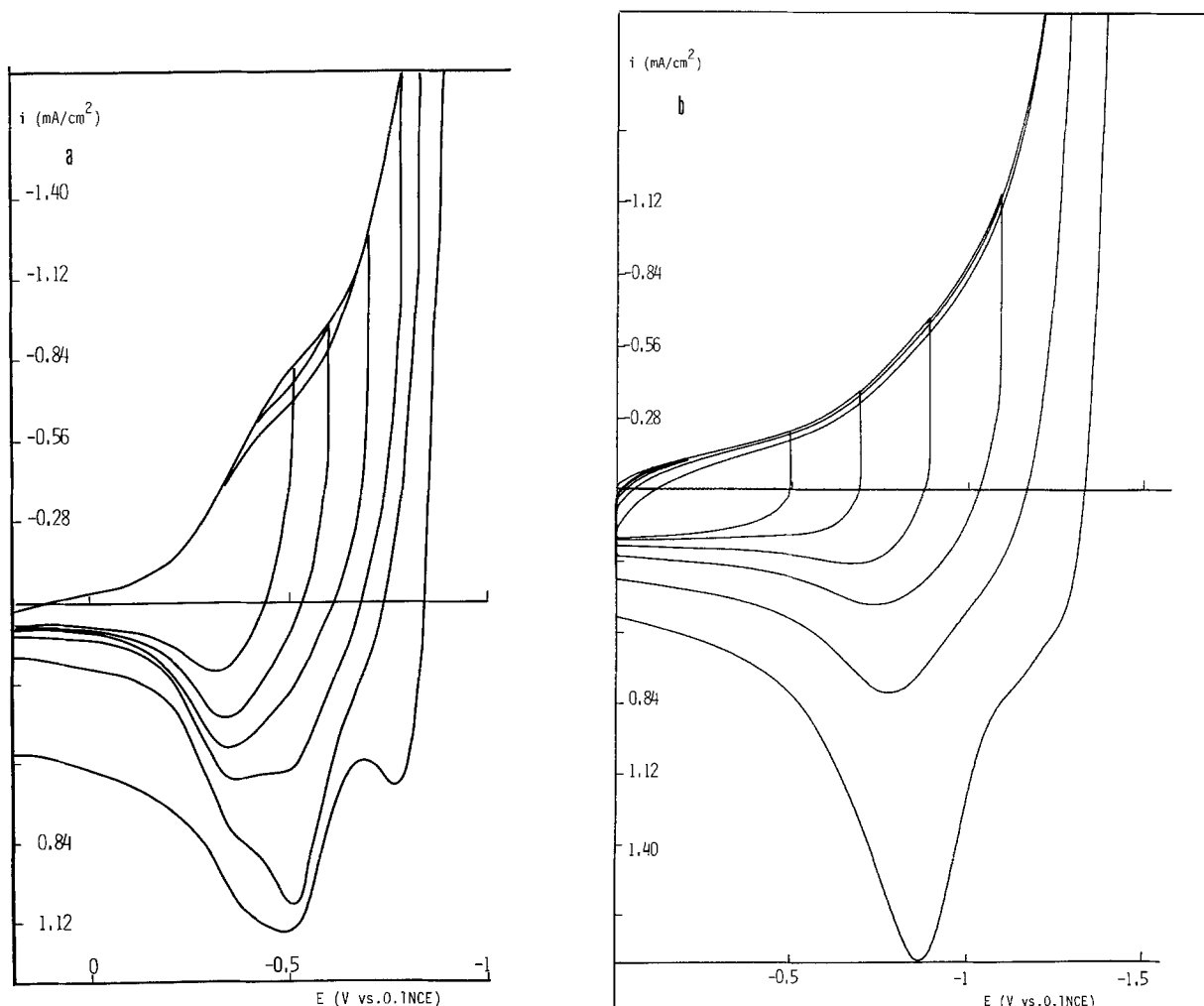


Fig. 3. Cyclic voltammetry *i*-E profiles at $50 \text{ mV} \cdot \text{s}^{-1}$, corresponding to various cathodic limits. A, left: Pt-TiO₂. B, right: TiO₂ electrodes in CO₂-saturated (1 atm) 0.5M KCl at 40°C.

necessary in order to remove most of the chemisorbed CO₂ from the Pt-TiO₂ surface. No such behavior was observed in the case of nonplatinized TiO₂ film electrodes; furthermore, the corresponding cyclic voltammetry *i*-*E* profiles obtained in CO₂/0.5M KCl solution showed only two anodic peaks (Fig. 3b). This indicates that the Pt-TiO₂ film electrodes exhibit actually a quite specific activity for CO₂ reduction which cannot be simply explained, for example, in terms of enhanced surface conductivity, but is probably the result of a profound modification of the energetics of CO₂ adsorption.

In this connection, it seems interesting to mention recent results concerning the gas-phase adsorption of CO₂ on platinized TiO₂ powder, reported by Tanaka and White (13). According to these authors, the Pt-TiO₂ catalyst induces, at room temperature, a decomposition of carbon dioxide into chemisorbed oxygen atoms and carbon monoxide. The decomposition rate of CO₂ has been significantly higher on reduced Pt-TiO₂ samples than on the oxidized ones. In order to check whether the dissociative adsorption of CO₂ from aqueous KCl solution could be responsible for the presence of an additional anodic peak (peak B or peak C) observed on the reverse sweep in our cyclic voltammograms (Fig. 2a), a few experiments were also performed in a 0.5M KCl solution saturated with carbon monoxide. As appears from the latter measurements, the thermally formed Pt-TiO₂ electrodes behave with regard to the CO adsorption in quite a different manner than smooth or platinized platinum. In fact, cyclic voltammograms of Pt recorded in solutions saturated with CO usually exhibit a sharp peak during anodic sweep, placed at about 0.9V (RHE), assigned (14) to the oxidation of adsorbed carbon monoxide to carbon dioxide. In addition, as a consequence of a repulsive interaction between the coadsorbed hydrogen atoms and carbon monoxide molecules, the potential at which hydrogen starts to be evolved at platinum is substantially shifted in the negative direction with respect to that observed in the absence of CO from the solution. Both of these features, typical of the CO adsorption on

platinum, were absent from the cyclic voltammograms of the Pt-TiO₂ electrodes, the only indication of the presence of CO in the solution being a slight increase of the cathodic current in the region of potentials corresponding to the formation of H_{ad} atoms together with a broadening of the related anodic peak. These results do not allow, therefore, any definitive conclusion about the nature of the interaction (dissociative or not) between CO₂ and the hydrated Pt-TiO₂ surface. The existence of two distinct species, formed as a result of the cathodic reduction of CO₂ adsorbed on the Pt-TiO₂ surface, has been confirmed by the experiments carried out with a rotating disk Pt-TiO₂ electrode. As shown in Fig. 4, the rotation of the electrode leads to a disappearance from the *i*-*E* curve of peak B, while peak C, placed at more anodic potentials, remains practically unchanged (Fig. 4b). This suggests that one of the above species (that associated with peak B) undergoes an easy desorption into the solution, while the second one (associated with peak C) remains strongly adsorbed on the Pt-TiO₂ surface. A similar conclusion can be drawn from the changes in the shape of cyclic voltammograms as a function of the sweep rate. As shown in Fig. 5, an increase of the sweep rate from 20 to 50 mV · s⁻¹ produces an enhancement of peak B, and, in addition, a shoulder, placed nearly at the same potential as peak C, appears on the cathodic side of the voltammogram. For still higher sweep rates (100 and 200 mV · s⁻¹), peak C increases more rapidly than peak B, and the above-mentioned shoulder is slightly shifted in the direction of more cathodic potentials. Such behavior is consistent with the height of peak B's being controlled by the rate of diffusion of the related species from the surface of the electrode and the height of peak C increasing proportionally to ν , the sweep rate (rather than to $\nu^{1/2}$).

Conclusions

We have shown that the behavior of the Pt-TiO₂ film electrode with regard to the reduction of aqueous CO₂ differs markedly from those exhibited by both the unsupported Pt and the nonplatinized TiO₂. Two most

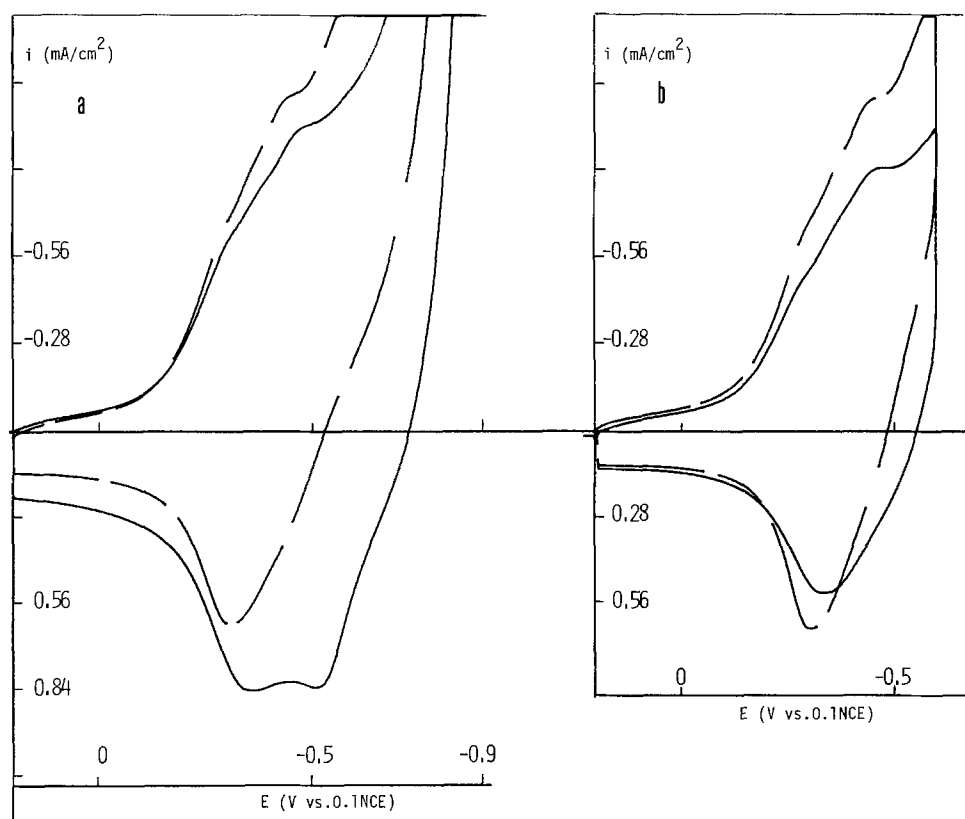


Fig. 4. Potentiodynamic *i*-*E* profiles at 50 mV · s⁻¹ for a stationary (continuous lines) Pt-TiO₂ and a rotating disk (at 1800 rpm) Pt-TiO₂ electrode in CO₂-saturated 0.5M KCl at 40°C. Cathodic limits: -0.9V for (a, left) and -0.6V for (b, right).

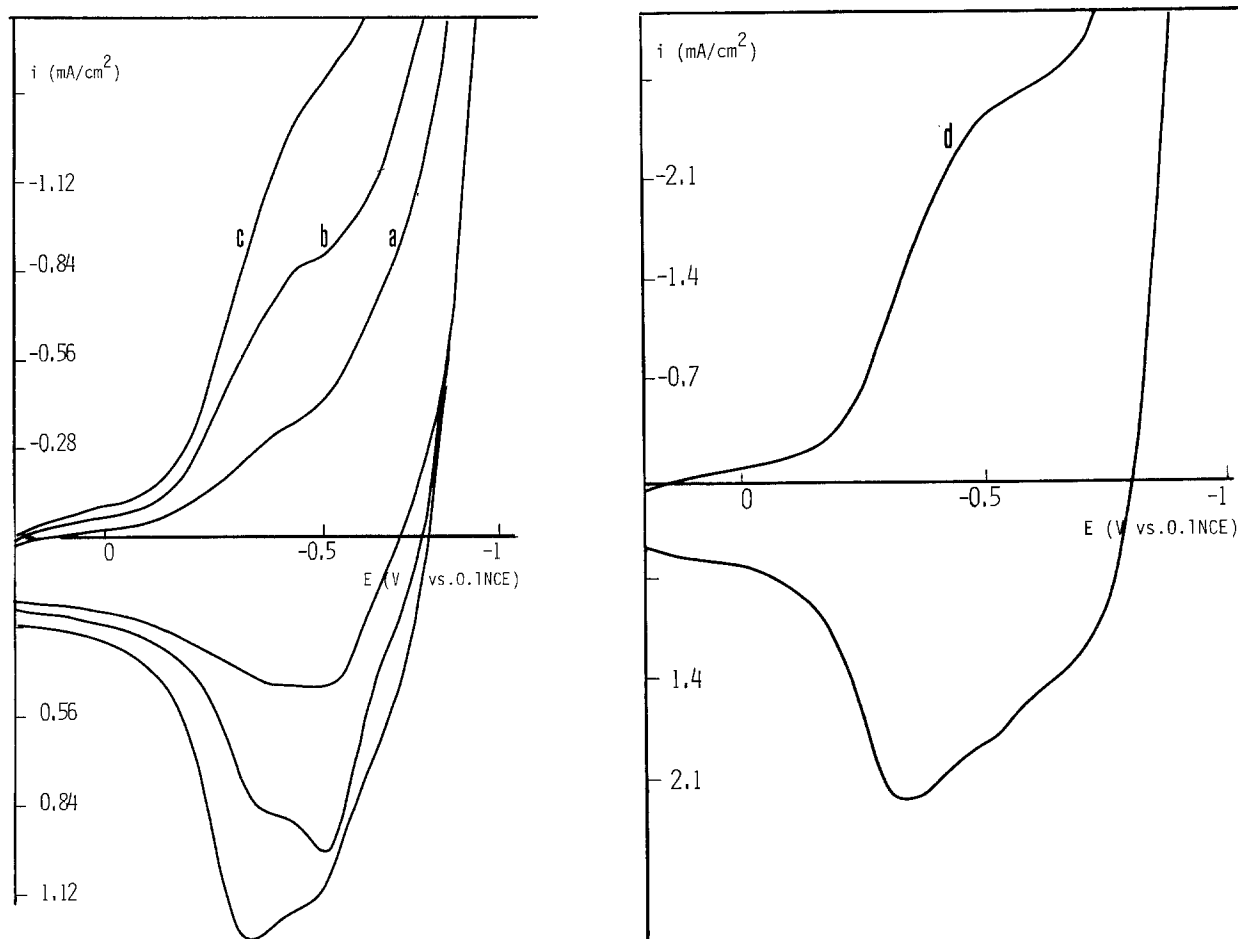


Fig. 5. Cyclic voltammetry i - E profiles, obtained at 20 (curve a), 50 (curve b), 100 (curve c) and 200 $\text{mV} \cdot \text{s}^{-1}$ (curve d) for Pt-TiO₂ in CO₂-saturated (1 atm) 0.5M KCl at 40°C.

significant features of this behavior are the strong, irreversible adsorption undergone by CO₂ at open circuit (i.e., at quite positive potentials, between 0.1 and 0.0V vs. 0.1 NCE or about 0.75–0.65V vs. RHE) and the existence of two distinct intermediates and/or products of the CO₂ reduction at the Pt-TiO₂ electrode. Both the Pt metal and the oxide TiO₂ are apparently needed to observe the chemisorption of CO₂ which takes place in the presence of H₂O adsorbed dissociatively on the oxide surface. It is to be noted, in this connection, that only exposure of the Pt-TiO₂ surface to a mixture of CO₂ and H₂O vapor, but not to dry CO₂, results in the formation of electrochemically detectable chemisorbed species. In the case of metallic (unsupported) Pt, the chemisorption of CO₂ is observed only at cathodic potentials preceding hydrogen evolution: in the presence of the H_{ad} atoms.

In addition to its capability to dissociate water, the role of the TiO₂ support in the cathodic reduction of CO₂ can be to provide acceptor sites for the reduced species formed on the adjacent metal sites. For instance, Solymosi *et al.* (15), in their infrared study of the surface interaction between H₂ and CO₂ (in gas phase) over a TiO₂-supported rhodium catalyst, found that the formed formate ions are preferentially adsorbed on the TiO₂ support. Thus, the likely existence of two kinds of adsorption sites on the Pt-TiO₂ surface and the possibility of the desorption of the reaction products via the TiO₂ support would explain the presence of multiple anodic peaks on the reverse sweep of cyclic voltammograms in Fig. 2a and 3a.

Acknowledgments

The authors would like to acknowledge Professor B. E. Conway of the University of Ottawa for helpful comments. The support of this research by the Swiss

National Science Foundation is gratefully acknowledged.

Manuscript submitted June 14, 1982; revised manuscript received March 19, 1983. This was Paper 357 presented at the Montreal, Quebec, Canada, Meeting of the Society, May 9–14, 1982.

The Université de Genève assisted in meeting the publication costs of this article.

REFERENCES

1. A. V. Bulatov and M. L. Khidekel, *Izv. Akad. Nauk SSSR, Ser. Khim*, **8**, 1902 (1976).
2. B. Krautler and A. J. Bard, *J. Am. Chem. Soc.*, **100**, 2239, 5985 (1978).
3. A. J. Bard, *Science*, **207**, 139 (1980).
4. J. Kiwi, E. Borgarello, E. Pelizzetti, M. Visca, and M. Grätzel, *Angew. Chem.*, **92**, 663 (1980).
5. E. Borgarello, J. Kiwi, E. Pelizzetti, M. Visca, and M. Grätzel, *Nature (London)*, **289**, 158 (1981).
6. S. J. Tauster, S. C. Fung, R. T. K. Baker, and J. A. Horsley, *Science*, **211**, 1121 (1981).
7. A. Monnier, J. Augustynski, and C. Stalder, *J. Electroanal. Chem.*, **112**, 383 (1980).
8. J. Sanchez, M. Koudelka, and J. Augustynski, *ibid.*, **140**, 161 (1982).
9. J. Sanchez and J. Augustynski, *ibid.*, **103**, 423 (1979).
10. J. Augustynski, M. Koudelka, and J. Sanchez, Paper no. A24 presented at the 31st meeting of the International Society of Engineers, Venice, Sept. 22–26, 1980.
11. H. Angerstein-Kozłowska, B. E. Conway, B. Barnett, and J. Mozota, *J. Electroanal. Chem.* **100**, 417 (1979).
12. J. Giner, *Electrochim. Acta*, **8**, 857 (1963).
13. K. Tanaka and J. M. White, *J. Phys. Chem.*, **86**, 3977 (1982).
14. S. Gilman, *ibid.*, **66**, 2657 (1962).
15. F. Solymosi, A. Erdöhelyi, and T. Bánsági, *J. Chem. Soc. Faraday Trans. 1*, **77**, 2645 (1981).

Luminescence Probe Studies of Nafion Polyelectrolytes

N. E. Prieto and C. R. Martin*

Department of Chemistry, Texas A&M University, College Station, Texas 77843

ABSTRACT

Results of luminescence probe studies of solutions of the polyelectrolytes obtained upon dissolving Nafion are reported. The primary objective of this work was to study the nature of the interactions between these anionic polyelectrolytes and their counterions. Both 1100 and 1200 equivalent weight Nafion were studied; solutions of these Nafions were prepared using a procedure developed in this laboratory. These luminescence probe studies have shown that strong binding to the Nafion polyelectrolytes occurs when both hydrophobic and electrostatic interactions are possible. Hence, Nafion preferentially binds hydrophobic cations such as $\text{Ru}(\text{bpy})_3^{2+}$ (bpy = 2,2'-bipyridine), methylviologen, and auramine O over simple inorganic cations such as H^+ , Na^+ , and Mg^{2+} . The implications of this unusual ion exchange selectivity to transport properties of Nafion films and membranes are discussed.

Perfluorinated ionomers (1) have been used in a variety of electrochemical applications, including use in chlor-alkali cells (2, 3), water electrolyzers (4), zinc-bromine cells (5), hydrogen-halogen cells (6), hydrogen-oxygen fuel cells (7), and as agents for the preparation of chemically modified electrodes (8). These ionomers also have a number of nonelectrochemical uses (9, 10). Because of their remarkable versatility, much current research effort is being devoted to studying the morphological and chemical properties of these ionomers (1). We have recently described a procedure for dissolving perfluorinated ionomer membranes (11). This allows, for the first time, for a study of the intrinsic chemical properties of the poly(perfluorosulfonate) (PFS) molecule itself. Such studies should allow for a more thorough understanding of the chemical features, and perhaps of the morphological features, of ionomer membranes. We report at this time results of various luminescence probe studies of the polyelectrolytes obtained by dissolving the 1100 and 1200 equivalent weight versions of du Pont's Nafion (1). The primary objective of this work is to study the interactions between these anionic polyelectrolytes and their counterions.

Experimental

Materials.—Samples of 1100 and 1200 equivalent weight Nafion were kindly donated by E. I. du Pont de Nemours and Company. These were dissolved using the procedure of Martin *et al.* (11), which uses 50:50 ethanol-water as the solvent. The alcohol was removed from these solutions, immediately before use, by heating. The Na^+ form of the polyelectrolytes (Na-PFS's) were obtained by adding carefully measured quantities of NaOH to the polymer solutions. $\text{Ru}(\text{bpy})_3\text{Cl}_2 \cdot 6\text{H}_2\text{O}$ (bpy = 2,2'-bipyridine) (G. F. Smith), 1,1'-dimethyl-4,4'-bipyridinium dichloride hydrate (methylviologen) (Aldrich), and 1,1'-diheptyl-4,4'-bipyridinium dibromide (heptylviologen) (Aldrich) were used without further purification. Tris(2,4-pentanedione)cobalt(III), $\text{Co}(\text{acac})_3$, (Alfa) was recrystallized from benzene, washed with diethyl ether, and dried at 60°C (12). Auramine O [4,4'-(imidocarbonyl)bis(N,N'-dimethylaniline) monohydrochloride] (the cation is abbreviated AO^+ (Sigma) was recrystallized from NaCl (13). 11-(3-hexyl-1-indolyl)undecyltrimethylammonium bromide [the cation is abbreviated (6-In-11⁺) (14)] was donated by N. J. Turro. All other reagents were ACS reagent grade and were used without further purification. Triply distilled water was used throughout this work. The 1100 and 1200 equivalent weight versions of Nafion gave essentially identical results. Only the 1100 data are reported.

Emission intensity and absorbance measurements.—Emission spectra were obtained using a Spex Fluorolog

2 spectrofluorometer. $\text{Ru}(\text{bpy})_3^{2+}$, AO^+ , and 6-In-11⁺ were excited at 455, 435, and 290 nm, respectively. Emission intensity was monitored at 600 nm for the $\text{Ru}(\text{bpy})_3^{2+}$ quenching studies. Absorption spectra were taken using a Beckman Model 26 photometer.

The solutions for the luminescence intensity measurements were prepared by adding aliquots of stock solutions of the polymer (1% weight volume [w/v]) to $\text{Ru}(\text{bpy})_3^{2+}$ ($2 \times 10^{-5}\text{M}$), AO^+ ($5 \times 10^{-5}\text{M}$), or 6-In-11⁺ ($2 \times 10^{-5}\text{M}$) solutions in quartz cuvettes. Hamilton microliter syringes were used. The cuvette solution was mixed thoroughly after each addition of polymer solution, and intensities were corrected for dilution. The addition of salt solution or quencher to a PFS/ $\text{Ru}(\text{bpy})_3^{2+}$ or PFS/ AO^+ solution followed a similar procedure.

Lifetime measurements.— $\text{Ru}(\text{bpy})_3^{2+}$ lifetime measurements were done at the Center for Fast Kinetics Research at the University of Texas at Austin. Lifetimes for $\text{Ru}(\text{bpy})_3^{2+}$ in pure water, in a solution 0.01% in H-PFS (proton form of the polyelectrolyte) and in a solution of 0.01% Na-PFS were obtained [all solutions were $2 \times 10^{-5}\text{M}$ in $\text{Ru}(\text{bpy})_3^{2+}$]. Solutions were degassed with prepurified nitrogen. A Quantrel YG 481 Nd:YAG Q-switched dye laser (535 nm, ca. 10 ns pulse) was used as the excitation source. Luminescence emission was monitored at 650 nm with an RCA R928 photomultiplier tube and processed with a Biomation (Gould) multichannel analyzer and a PDP-11/70 minicomputer. Metal screens were used to attenuate the incident laser intensity.

Results and Discussion

The luminescence probe studies.—As noted above, the primary objective of this work is to study the nature of the interactions between the Nafion polyelectrolytes and their counterions. Clearly, an electrostatic interaction (15a) will be present, but because hydrophobic interactions (15b) have been implicated in various studies of Nafion membranes (8, 16, 17), it was of interest to see if evidence for such interactions could be observed in solutions of the polyelectrolytes. Luminescence probe studies have been shown to be quite effective at characterizing polyion-counterion interactions in other polyelectrolyte systems (18-24). Two types of luminescence probe experiments were used here. The first involved studies of the effect of addition of the PFS's on the luminescence emission intensities of various cationic probes in aqueous solution. Three structurally diverse probes, 6-In-11⁺ (14, 22, 23), $\text{Ru}(\text{bpy})_3^{2+}$, and AO^+ (24) were chosen for these studies. 6-In-11⁺ was chosen because the effect of solvent polarity on its emission characteristics are dramatic and well characterized (14, 22, 23), and because it has been used to study polyion-counterion interactions in poly(styrene-sulfonate) (PSS) (23). $\text{Ru}(\text{bpy})_3^{2+}$ was chosen because Lee and Meisel have

* Electrochemical Society Active Member.

suggested that hydrophobic interactions between this ion and the fluorocarbon chain material occur in 1200 equivalent weight Nafion membranes (16). AO^+ was chosen because it has proved to be ideally suited for studying polymer-probe interactions (24).

The second set of luminescence probe experiments involved studies of the effect of the PFS's on the rates of quenching of $\text{Ru}(\text{bpy})_3^{2+*}$ by various electron transfer quenching agents. $\text{Ru}(\text{bpy})_3^{2+}$ was chosen for these studies because it strongly binds to the PFS's (*vide infra*) and because its luminescence in aqueous solution has been well characterized (25).

Luminescence intensity studies.—Figure 1 shows the effect of addition of an aqueous solution of Na-PFS (1 w/v) on the emission spectra of 6-In-11⁺. A pronounced blueshift in the position of the emission spectrum is observed (wavelength of maximum emission intensity, λ_{max} , in water is 374 nm, λ_{max} in Nafion solution is 356 nm). A blueshift in the emission of a probe (relative to water) is often indicative of a more hydrophobic environment for the probe (26). [The photochemical mechanism for such a shift is discussed by Brand and Gohlke (26).] The observed blueshift, then, suggests that Nafion is engaging in hydrophobic interactions with 6-In-11⁺. In this type of luminescence probe study, however, it is desirable to compare the emission of the probe from the unknown environment with its emission spectrum from some well-characterized environment. It is known that PSS can engage in strong hydrophobic interactions with its counterions (18, 23). Turro and Okubo observed a pronounced blueshift in the emission of 6-In-11⁺ from aqueous solutions of PSS, which they attributed to hydrophobic binding of this probe by PSS (23). The similarity in the responses of this probe to the unknown (Nafion) and standard (PSS) environments adds further evidence for hydrophobic interactions between 6-In-11⁺ and Nafion.

In addition to the shift in λ_{max} , a decrease in emission intensity, with the initial additions of Na-PFS, is observed (Fig. 1b), followed by a gradual increase in intensity with further additions (Fig. 1c). Similar results were obtained by Turro and Okubo in their investigations of Na-PSS (23). They suggest that quenching by trace impurities present in the polymer solution may account for the initial decrease in emission intensity (23).

Further evidence for a strong hydrophobic component to the interaction between 6-In-11⁺ and PFS is obtained from studies of 6-In-11⁺ absorption spectra. As shown in Fig. 2, the absorbance at 290

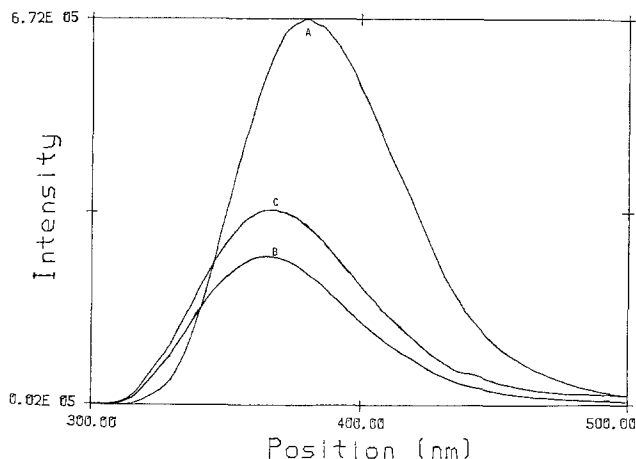


Fig. 1. Effect of addition of Na-PFS on fluorescence spectra for 6-In-11⁺ ($2 \times 10^{-5} \text{M}$). A: no Nafion added. B: after addition of Na-PFS solution, 3.79×10^{-8} mols of $-\text{SO}_3^-$ sites added. C: after addition of more Na-PFS solution, 5.05×10^{-7} mols of $-\text{SO}_3^-$ sites added.

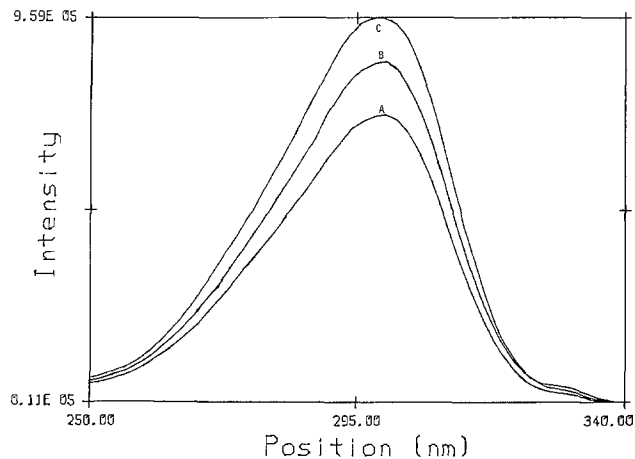


Fig. 2. Excitation spectra of 6-In-11⁺ ($2 \times 10^{-5} \text{M}$, monitored at 374 nm). A: no Nafion added. B: after addition of Na-PFS solution, 7.26×10^{-8} mols of $-\text{SO}_3^-$ sites added. C: after addition of more Na-PFS solution, 1.99×10^{-7} mols of $-\text{SO}_3^-$ sites added.

nm increases as Na-PFS is added to a solution of 6-In-11⁺. Turro has shown that the absorbance for this probe increases as the polarity of the environment around the probe decreases (22, 23); furthermore, a similar increase in absorbance was observed with PSS (23). Figure 2 shows excitation spectra obtained with the fluorometer, but true absorbance spectra (obtained with the spectrophotometer) gave identical results. Finally, it is important to note that while the data shown in Fig. 1 and 2 refer specifically to the Na⁺ form of PFS, essentially identical results were obtained with the proton form. These studies clearly show that 6-In-11⁺ engages in strong hydrophobic interactions with the PFS's.

Figure 3 shows the effect of concentration of Na-PFS (expressed as the molarity of $-\text{SO}_3^-$ sites) on the intensity of emission by $\text{Ru}(\text{bpy})_3^{2+*}$. Emission intensity is expressed as the ratio I/I^0 , where I^0 is the intensity in pure water, and I is the intensity after addition of an increment of the Na-PFS solution (21). Emission intensity increases with increasing concentration of PFS until a stoichiometrically equivalent amount of $-\text{SO}_3^-$ sites have been added to the solution (i.e., until $2 \times [-\text{SO}_3^-] = [\text{Ru}(\text{bpy})_3^{2+}]$). This increase in intensity is not due to some polymer-induced change in bulk concentration of the $\text{Ru}(\text{bpy})_3^{2+}$, because the absorption spectrum (corrected for dilution) is unaffected by the presence of PFS, nor is it due merely to a change in the shape of the emission

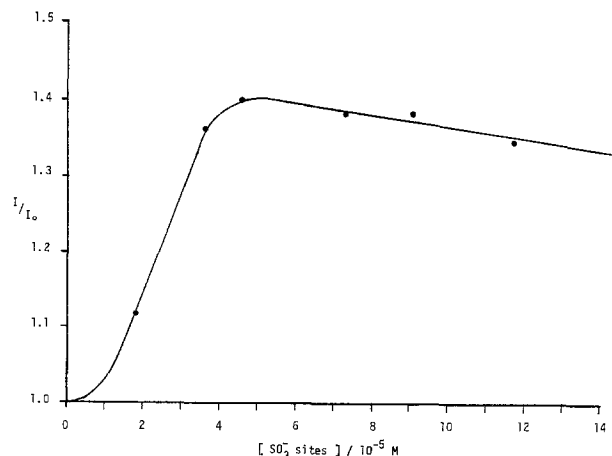


Fig. 3. Dependence of $\text{Ru}(\text{bpy})_3^{2+*}$ luminescence emission intensity on concentration of Na-PFS. $[\text{Ru}(\text{bpy})_3^{2+}] = 2 \times 10^{-5} \text{M}$. $\lambda_{\text{EX}} = 455 \text{ nm}$, $\lambda_{\text{EM}} = 610 \text{ nm}$.

band, because an analogous plot of the areas under the emission bands gives an identical curve. When greater than stoichiometric amounts of PFS are added, a leveling in emission intensity is observed (Fig. 3).

The leveling of the emission intensity at the stoichiometric equivalence point implicates a role for electrostatic interactions in the observed increase in emission intensity. However, if a hydrophilic, divalent metal ion (e.g., Mg^{2+}) is added to a $Ru(bpy)_3^{2+}$ /PFS solution, a huge excess of the hydrophilic ion is required to return I/I° back to 1 (Fig. 4, the ratio (mols Mg^{2+} /mols $Ru(bpy)_3^{2+}$) to make $I/I^\circ = 1$ is ca. 1000). If the increase in emission intensity (Fig. 3) resulted from purely electrostatic interactions, the ability of Mg^{2+} to replace $Ru(bpy)_3^{2+}$ as the counterion of the polyelectrolyte would not be so severely retarded, that is, one might expect the ratio (mols Mg^{2+} /mols $Ru(bpy)_3^{2+}$) required to make I/I° ca. 1 to be close to unity. Given the hydrophobic nature of $Ru(bpy)_3^{2+}$, the results in Fig. 4 indicate that there is also a strong hydrophobic interaction between this counterion and the PFS's. The binding of $Ru(bpy)_3^{2+}$ to the PFS's is via a concerted hydrophobic/electrostatic interaction.

When $Ru(bpy)_3^{2+}$ is used as a luminescence probe of hydrophilic polyions, where only electrostatic interactions are extant, emission intensity does not change with the concentration of the polyion (27). This suggests that the increase in emission intensity in Fig. 3 is caused by the hydrophobic part of the interaction. Kurimura *et al.* saw a similar increase in emission intensity when PSS was added to a $Ru(bpy)_3^{2+}$ solution and also concluded that this increase was due to hydrophobic interactions (21). A consideration of the effect of water on the nonradiative rate constant provides a possible explanation for the observed increases in $Ru(bpy)_3^{2+}$ emission intensity. As recently noted by Casper and Meyer (28), water is particularly effective at promoting nonradiative decay in $Ru(bpy)_3^{2+}$. It seems likely, then, that any interaction which shields $Ru(bpy)_3^{2+}$ from water will increase its quantum yield [the radiative rate constant is relatively insensitive to solvent (28)]. Since it is the incompatibility of water and the hydrophobic solute which promotes hydrophobic bonding (15b), it is reasonable to assume that when bound to PFS, $Ru(bpy)_3^{2+}$ minimizes

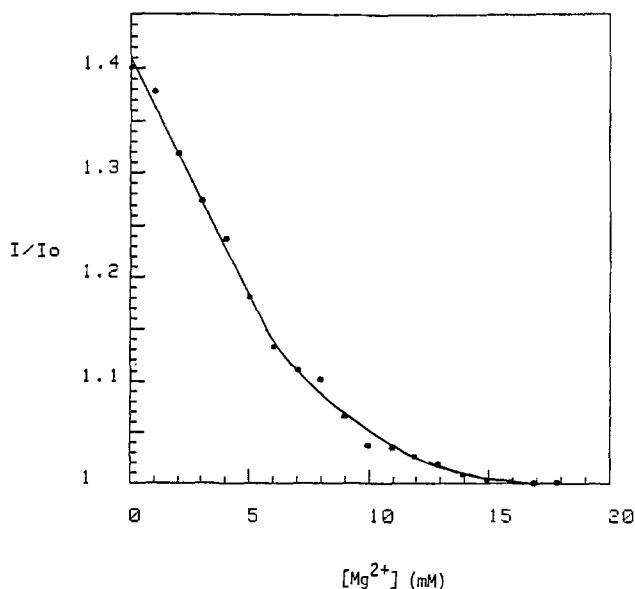


Fig. 4. Effect of addition of $MgSO_4$ on emission intensity of $Ru(bpy)_3^{2+}$ from a $Ru(bpy)_3^{2+}$ /Na-PFS solution. 2×10^{-8} mols $Ru(bpy)_3^{2+}$, 6×10^{-8} mols Nafion $-SO_3^-$ sites (see Fig. 3).

its contact with water. Therefore, a quantum yield increase would be expected.

The final luminescence probe used was AO^+ . In nonviscous solvents, electronic excitation energy in AO^+ is dissipated as heat via rotation of its phenyl rings (24). For this reason, AO^+ does not fluoresce in water (Fig. 5) or other nonviscous solvents (24). Binding of AO^+ to polyanions hinders phenyl ring rotation, and fluorescence can be observed (24). Figure 5 shows that Na-PFS can induce fluorescence in AO^+ . As was the case with $Ru(bpy)_3^{2+}$, fluorescence intensity is proportional to $[-SO_3^-]$ until a stoichiometrically equivalent quantity of polymer is added. Furthermore, huge excesses (ca. 1000-fold) of Na^+ are required to return the emission intensity to background levels, indicating that AO^+ also binds via a concerted hydrophobic/electrostatic interaction.

Quenching studies.—It is well known that quenching reactions between an electronically excited cation and a cationic quencher are accelerated in the presence of a polyanion (19, 27, 29). This acceleration is due to the concentration of the cations in the domain around

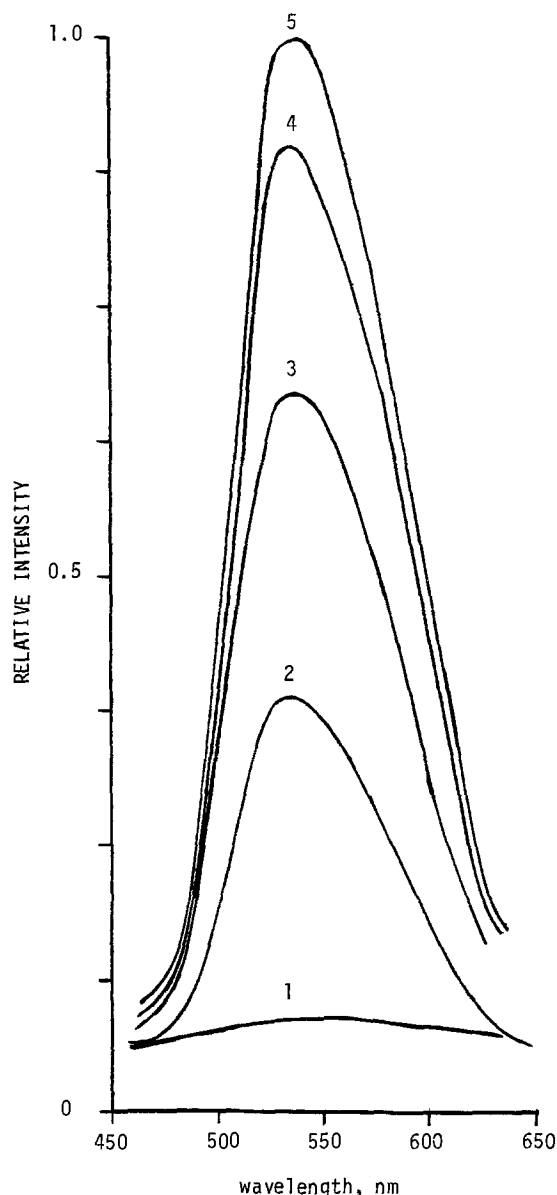


Fig. 5. Fluorescence spectra of AO^+ as a function of concentration of Na-PFS ($[AO^+] = 5 \times 10^{-5} M$, $\lambda_{EX} = 435$ nm). 1: no Na-PFS. 2: 9×10^{-9} mols of $-SO_3^-$ sites. 3: 1.8×10^{-8} mols $-SO_3^-$ sites. 4: 2.7×10^{-8} mols $-SO_3^-$ sites. 5: 3.6×10^{-8} mols $-SO_3^-$ sites.

the polyion chains (*i.e.*, the local concentrations of both emitter and quencher are higher than the bulk concentrations) (19, 27, 29). It was of interest to see if acceleration of quenching reactions between cationic quenchers and $\text{Ru}(\text{bpy})_3^{2+}$ could be observed in the presence of the PFS's. Furthermore, given the strongly hydrophobic nature of the PFS's (*vide supra*), it was of particular interest to see if a contribution from hydrophobic interactions (18) could be discerned in any acceleration observed.

Quenching rate constants were determined using the emission intensity form of the Stern-Volmer equation (30). Typical Stern-Volmer plots are shown in Fig. 6. We have obtained apparent quenching rate constants from such plots for hydrophilic cation, hydrophobic cation, and neutral quenchers in the presence of both Na-PFS and H-PFS's (Table I). Measured $\text{Ru}(\text{bpy})_3^{2+}$ lifetimes of 640 ± 10 ns (Na-PFS) and 590 ± 10 ns (H-PFS) were used for calculation of these rate constants. They are called apparent quenching rate constants because they have been calculated assuming the bulk quencher concentrations. To obtain real quenching rate constants, the values shown in Table I would have to be normalized, as described by Meisel *et al.* (19). Since it is the magnitude of the rate constant enhancement which is of interest here, normalization was not attempted.

Table I shows that quenching rate constants are enhanced for all of the cationic quenchers. The amount of enhancement can be described quantitatively by the enhancement factor (α), which is the ratio of the apparent rate constant in the presence of the polymer to the rate constant observed in pure water. Enhancement factors (Table II) for the hydrophobic cations (methylviologen and heptylviologen) are seven to ten times larger than the enhancement factors for the hydrophilic cations. As in the previous set of experiments, these data show that hydrophobic interactions can play an important role in the binding of counterions to the PFS's. Again, however, the importance of the electrostatic component of the interaction is demonstrated because quenching by neutral $\text{Co}(\text{acac})_3$ is not changed appreciably by the presence of the polyanion.

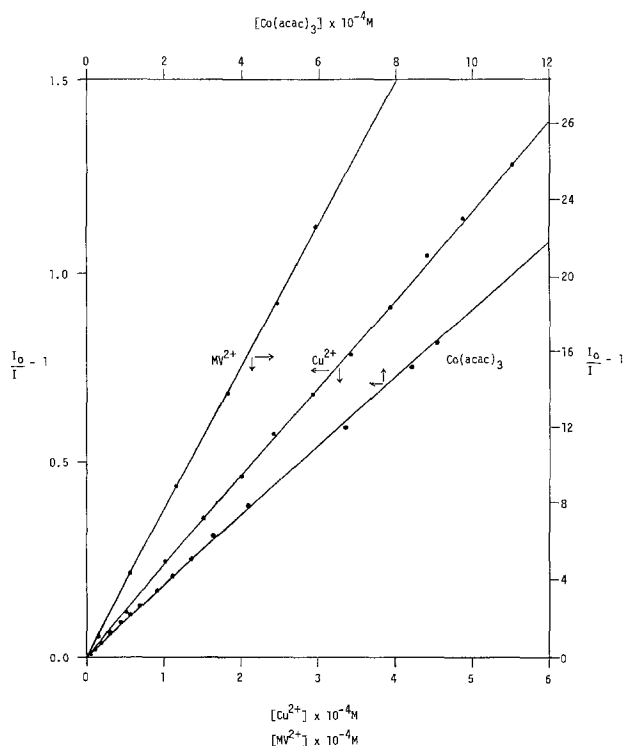


Fig. 6. Typical Stern-Volmer plots for quenching of PFS-bound $\text{Ru}(\text{bpy})_3^{2+}$ by various quenchers. $[\text{Ru}(\text{bpy})_3^{2+}] = 2 \times 10^{-5} \text{ M}$, $[\text{Na-PFS}] = 0.05\%$.

Table I. Apparent second-order rate constants ($\text{M}^{-1}\text{S}^{-1}$) for quenching of $\text{Ru}(\text{bpy})_3^{2+}$ emission by various quenchers. Effect of the PFS's on the rate constants

Medium	Quenchers				
	Cu^{2+}	Fe^{2+}	MV^{2+} ^a	HV^{2+} ^b	$\text{Co}(\text{acac})_3$ ^c
Water	7.7×10^{7d}	2.1×10^{6e}	4.5×10^{8f}	4.2×10^{8g}	1.1×10^{9h}
H-PFS ⁱ	2.4×10^8	2.2×10^9	1.5×10^{11}	9.7×10^{10}	1.5×10^9
Na-PFS ⁱ	3.9×10^9		4.5×10^{11}		

^a Methylviologen.

^b Heptylviologen.

^c acac = acetylacetonate.

^d Ref. (33).

^e Ref. (19).

^f Ref. (16).

^g Ref. (34).

^h Ref. (12).

ⁱ Solution was $2 \times 10^{-5} \text{ M}$ in $\text{Ru}(\text{bpy})_3^{2+}$ and 0.05% in polymer.

Table II. H-PFS induced enhancement factors, α ($\alpha =$ apparent rate constant in the presence of polymer divided by pure water rate constant) for various quenchers*

Quencher	Cu^{2+}	Fe^{2+}	MV^{2+}	HV^{2+}	$\text{Co}(\text{acac})_3$
α	31	10	330	230	1.4

* See Table I.

As was indicated by the data obtained in the intensity studies, a concerted hydrophobic/electrostatic interaction is required to produce strong binding.

Conclusions

This work has shown that strong binding to the Nafion polyelectrolytes occurs when both electrostatic and hydrophobic interactions are possible. This helps to explain why a Nafion film on an electrode surface retains hydrophobic counterions (*e.g.*, $\text{Ru}(\text{bpy})_3^{2+}$, MV^{2+}) (8) when the film is immersed in a solution containing high (*e.g.*, 0.1M) salt concentrations and none of the hydrophobic ion. Nafion shows very different selectivity than the polyelectrolytes investigated by Anson (31), which apparently bind only via electrostatic interactions. We are currently investigating ion exchange selectivity in cationic analogs of Nafion to see if hydrophobically driven ion exchange is a general phenomenon.

This work raises important points concerning the transport properties of Nafion. The permeability of a material to a solute species is proportional to the product of the partition constant and the diffusion coefficient for that species in the material. In most of the electrochemical applications of Nafion, high permeability to cations is desired. Because of the affinity of the polymer for hydrophobic cations (*i.e.*, high partition constant), these ions could show higher permeabilities than smaller alkali metal ions, if the membrane is in contact with a solution containing both types of cations. Finally, these data corroborate results obtained previously in this laboratory, which showed that rates of ionic diffusion through Nafion films can be affected by hydrophobic interactions (32).

Acknowledgments

This work was supported in part by the Office of Naval Research and the Robert A. Welch Foundation. The authors would like to thank M. A. J. Rodgers and S. Atherton of the Center for Fast Kinetics Research, University of Texas at Austin, for assisting with the lifetime measurements and for valuable discussions.

Manuscript submitted March 11, 1983; revised manuscript received Oct. 26, 1983. This was Paper 566 presented at the San Francisco, California, Meeting of the Society, May 8-13, 1983.

The Office of Naval Research assisted in meeting the publication costs of this article.

REFERENCES

1. A. Eisenberg and H. L. Yeager, Editors, "Perfluorinated Ionomer Membranes," ACS Symposium Series No. 180, ACS, Washington, DC (1982), and references therein.
2. W. Grot, *Chem.-Ing.-Tech.*, **50**, 299 (1978).
3. W. Grot, G. E. Munn, and P. M. Walmsley, Paper 154 presented at the Meeting of the Electrochemical Society, Houston, TX, May 7-11, 1972.
4. R. S. Yeo, J. McBreen, G. Kissel, F. Kulesa, and S. Srinivasan, *J. Appl. Electrochem.*, **10**, 741 (1980).
5. F. G. Will, *This Journal*, **126**, 36 (1979).
6. R. S. Yeo and D.-T. Chin, *ibid.*, **127**, 549 (1980).
7. A. B. LaConti, A. R. Fragala, and J. R. Boyack, in "Electrode Materials and Processes for Energy Conversion and Storage," J. D. E. McIntyre, S. Srinivasan, and F. G. Will, Editors, p. 354, The Electrochemical Society Softbound Proceedings Series, Princeton, NJ (1977).
8. C. R. Martin, I. Rubinstein, and A. J. Bard, *J. Am. Chem. Soc.*, **104**, 4817 (1982), and references therein.
9. G. A. Olah, G. K. S. Prakash, and J. Sommer, *Science*, **206**, 13 (1979).
10. H. L. Yeager and A. Steck, *Anal. Chem.*, **51**, 862 (1979).
11. C. R. Martin, T. A. Rhoades, and J. A. Ferguson, *ibid.*, **54**, 1639 (1982).
12. D. Meyerstein, J. Rabani, M. S. Matheson, and D. Meisel, *J. Phys. Chem.*, **82**, 1879 (1978).
13. R. H. Conrad, J. Heitz, and L. Brand, *Biochem.*, **9**, 1540 (1970).
14. N. E. Schore and N. J. Turro, *J. Am. Chem. Soc.*, **97**, 2488 (1975).
15. a. A review of polyelectrolyte/counterion interactions is given in G. S. Manning, *Ann. Rev. Phys. Chem.*, **23**, 117 (1972); b. A brief review of hydrophobic interactions is given by J. Fietelson in "Ion Exchange and Solvent Extraction," Vol. 2, J. A. Marinsky and Y. Marcus, Editors, Marcel Dekker, New York (1969).
16. P. C. Lee and D. Meisel, *J. Am. Chem. Soc.*, **102**, 5477 (1980).
17. C. R. Martin and H. Freiser, *Anal. Chem.*, **53**, 902 (1981).
18. N. J. Turro and T. Okubo, *J. Phys. Chem.*, **86**, 1535 (1982).
19. D. Meisel, J. Rabani, D. Meyerstein, and M. S. Matheson, *ibid.*, **82**, 985 (1978).
20. T. Okubo and N. J. Turro, *J. Phys. Chem. Soc.*, **85**, 4034 (1981).
21. Y. Kurimura, H. Yokota, K. Shigehara, and E. Tsuchida, *Bull. Chem. Soc. Jpn.*, **55**, 55 (1982).
22. N. J. Turro, Y. Tanimoto, and G. Gabor, *Photochem. Photobiol.*, **31**, 527 (1980).
23. N. J. Turro and T. Okubo, *J. Am. Chem. Soc.*, **104**, 2985 (1982).
24. G. Oster and Y. Nishijima *Fortschr. Hochpolym. Forsch.*, **3**, 313 (1964).
25. K. Kalyanasundaram, *Coord. Chem. Rev.*, **46**, 159 (1982).
26. L. Brand and J. R. Gohlke, *Ann. Rev. Biochem.*, **41**, 843 (1972).
27. D. Meisel and M. S. Matheson, *J. Am. Chem. Soc.*, **99**, 6577 (1977).
28. J. V. Casper and T. J. Meyer, *ibid.*, **105**, 5583 (1983).
29. H. Morawetz, *Acc. Chem. Res.*, **3**, 354 (1970).
30. C. A. Parker, "Photoluminescence of Solutions," pp. 71-74, Elsevier Publishing Co., Amsterdam (1968).
31. N. Oyama and F. C. Anson, *This Journal*, **127**, 247 (1980).
32. C. R. Martin and K. A. Dollard, *J. Electroanal. Chem.*, **159**, 127 (1983).
33. D. Meisel, M. Matheson, and J. Robin, *J. Am. Chem. Soc.*, **100**, 117 (1978).
34. M. A. J. Rodgers and J. C. Becker, *J. Phys. Chem.*, **84**, 2762 (1980).

The Effect of Reactive Gases on Oxygen Sensor Responses

J. I. Federer

Oak Ridge National Laboratory, Metals and Ceramics Division, Oak Ridge, Tennessee 37830

ABSTRACT

Ceramic electrolyte oxygen sensors consisting of stabilized zirconia with platinum electrodes were compared in flowing gases in a laboratory apparatus. The oxygen partial pressures indicated by these sensors in reactive gases were substantially different. Gases containing CO produced a greater difference than gases containing H₂. The responses of these sensors were attributed to their relative catalytic behavior.

Commercially available oxygen measuring devices include those based on ceramic electrolytes, paramagnetism, and electrometry. An important use of oxygen sensors is measurement of oxygen concentrations in the combustion environments of industrial furnaces and automobile exhausts. In these applications, the sensors measure the oxygen concentration and, if coupled with auxiliary instrumentation, control the air/fuel ratio being burned. A potential application for oxygen sensors is in fluidized bed combustors (FBC's) burning coal. The need for an oxygen sensor was demonstrated during corrosion testing of candidate steam-tube materials in a test bed. Severe oxidation-sulfidation corrosion of type 316 stainless steel occurred in one location of the bed, but the same alloy corroded little at similar temperatures in other locations (1, 2). This behavior suggested that the corrosiveness of the environment varied significantly within the bed. Corrosion of stainless steels by an oxidation-sulfidation mechanism is governed by the thermodynamic stability

Key words: ceramics, electrolyte, cell, catalysis.

of the oxides and sulfides of the elements involved (3, 4). Fluctuations in oxygen and sulfur concentrations that result in combinations of low oxygen and high sulfur might increase corrosion. An oxygen measuring system (OMS) was needed, therefore, to study and control corrosion behavior in fluidized beds. Several movable devices might systematically reveal oxygen concentrations within the bed, thereby aiding interpretation of corrosion results. Subsequently, stationary devices at strategic locations could monitor and control oxygen concentrations at levels consistent with efficient combustion and acceptable corrosion.

Commercially available oxygen sensors were investigated to determine the type most suitable for FBC use. This investigation focused on the mode of operation, temperature capability, and measuring range of ceramic electrolyte, paramagnetic, and electrometric devices. Paramagnetic devices use the paramagnetic property of oxygen (most other gases are diamagnetic) to produce a flow of oxygen, a constituent of a gas mixture, over a thermistor in contact with the gas.

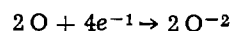
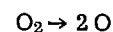
Current flow in the thermistor is proportional to the oxygen content of the gas. In electrometric devices, oxygen in a gas is reduced to hydroxyl ions at the cathode of an electrochemical cell. Migration of the ions to the anode under the influence of an imposed voltage constitutes an electric current, which is proportional to the oxygen content of the gas. This investigation revealed that paramagnetic and electrometric devices can measure oxygen concentrations in samples only at approximately ambient temperature. Since the typical operating temperature of an FBC is 875°C, samples would have to be extracted and cooled for measurement. Possible problems with extracted samples include clogging of sampling lines with particulate matter and change in composition of the gas sample caused by shift in equilibria during cooling or by mixing. These potential problems and limited measuring range eliminated paramagnetic and electrometric devices in favor of those based on ceramic electrolytes. The latter have several apparent advantages over the other types: high temperature capability, which allows *in situ* measurements; wider measuring range; and faster response to changes in oxygen concentrations. Possible problems with ceramic electrolyte sensors include breakage by thermal shock or impact by bed material, corrosion and erosion, and sluggish response due to deposition of bed materials. Although these problems might be minimized by design or mode of operation, the serious nature of another problem identified during laboratory testing requires understanding for maximum usefulness of these devices in FBC's. This problem concerns the difficulty of measuring oxygen concentrations in reactive gas mixtures using commercially available ceramic electrolyte probes. This paper concerns the large differences in response that were obtained during comparison of commercially available oxygen probes in a laboratory apparatus.

Oxygen Probes Evaluated

Two Corning *in situ* probes (Model 8081) were tested. Their construction is similar to that shown in Fig. 1. The alumina protection tube was 22.2 mm od by 0.6m long. The two probes were similar except for a porous ceramic layer over the sensor of one probe. Layers of this type protect the sensor against erosion. Two Bosch automobile exhaust sensors, modified as shown in Fig. 2, were also tested. The original housing and electri-

cal lead (neither shown in Fig. 2) were replaced with two stainless steel tubes and a Teflon insulator. An extracted-sample (off-line) oxygen sensor served as a reference sensor. All sensors had stabilized zirconia ceramic electrolytes with platinum electrodes.

The zirconia is typically in the form of a closed-end tube (Fig. 1). The closed end is coated inside and outside with a thin porous layer of platinum. The platinum coatings form the electrodes of a solid-state electrochemical cell, and platinum wires attached to the electrodes permit the cell voltage to be measured. In the normal mode of operation, a gas of known oxygen concentration (usually air) is in contact with the inner surface (cathode) of the sensor, and the outer surface is in contact with a gas of lower oxygen content to be measured. At the cathode, where the oxygen concentration is high, oxygen molecules dissociate and acquire electrons to become ions as shown



At the anode, where the oxygen concentration is low relative to the cathode, the reverse reactions occur. The net result is an open-circuit cell voltage, which is related to the unknown oxygen concentration through the Nernst equation

$$E = (RT/nF) \ln(p_{\text{O}_2})_r / (p_{\text{O}_2})_x$$

where n is the number of gram equivalents per mol (here four, from the oxygen ionization reaction), F is Faraday, or 96,500 coulombs per gram equivalent, R is the gas constant, or 8.314 J/(mol · K), T is the absolute temperature in degrees kelvin, $(p_{\text{O}_2})_r$ is the reference oxygen partial pressure,¹ and $(p_{\text{O}_2})_x$ is the partial pressure to be determined. The cell voltage depends directly on T and inversely on $\ln(p_{\text{O}_2})_x$. As will be shown, apparent values of $(p_{\text{O}_2})_x$ in dynamic reactive gases can vary between the actual value and the thermodynamic equilibrium value. The platinum coating on the sensor tends to catalyze reactions in reactive gases. The indicated $(p_{\text{O}_2})_x$ in a dynamic system of flowing reactive gases, therefore, represents a local approach to equilibrium at the surface of the sensor.

¹ Throughout this paper p_{O_2} represents the partial pressure of molecular oxygen.

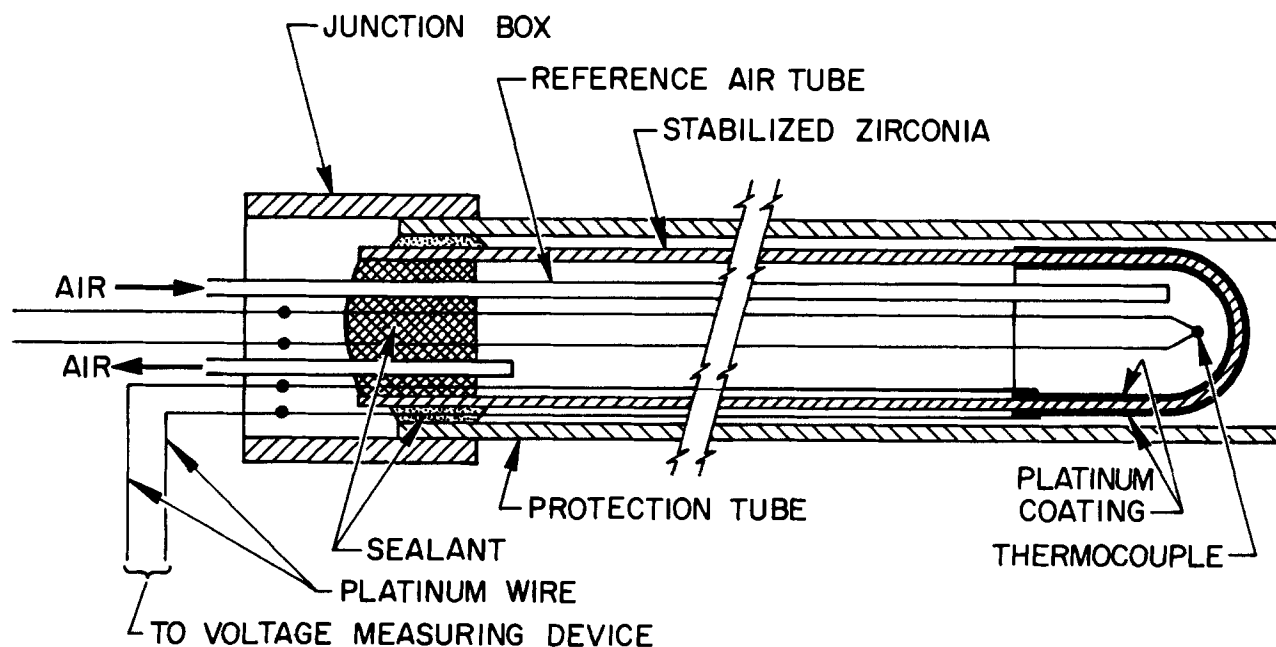


Fig. 1. Ceramic electrolyte oxygen sensor

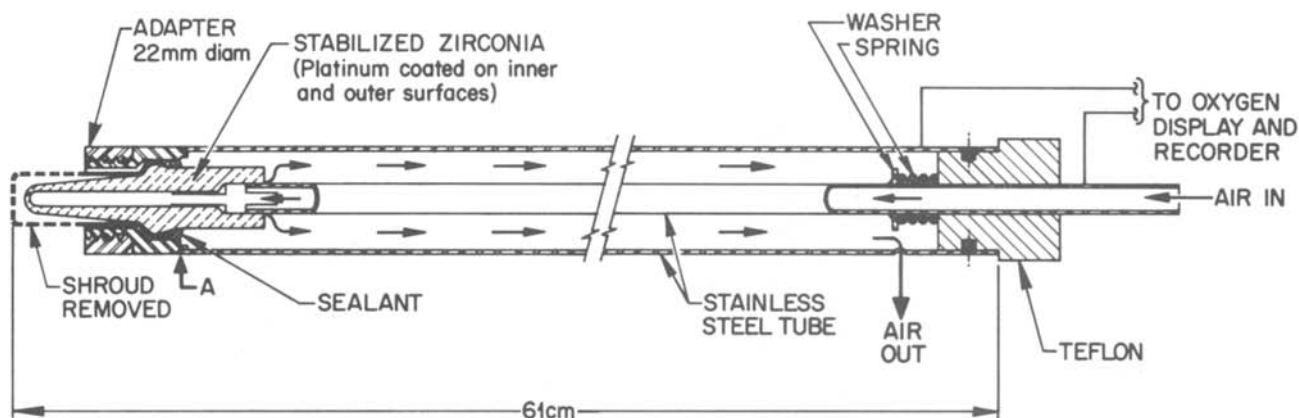


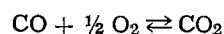
Fig. 2. Modified Bosch oxygen sensor

Apparatus

The apparatus for comparing the Corning and Bosch probes is shown schematically in Fig. 3. Gas mixtures with selected oxygen contents were metered into the two lines leading to the oxygen probe furnace. The gases were first heated by contact with extended surfaces in the preheat furnace and then passed through insulated tubing into the probe furnace. Although the time required to respond to sudden changes in oxygen concentration was also measured in this apparatus (5), only the results of comparing probes under steady-state flow conditions will be described here. During these comparisons, gas of the desired p_{O_2} followed the crossover path indicated in Fig. 3. The two Corning probes were placed in the apparatus, as depicted in Fig. 3. Two Bosch probes were similarly located in a subsequent experiment.

An extracted-sample oxygen sensor manufactured by Applied Electrochemistry, Incorporated, (AEI) served as the reference sensor. The AEI instrument was also used to display the output from the probes being tested. Unlike instruments provided with most commercially available oxygen probes, which typically display oxygen content ranging from 0 to 25% with a minimum resolution of 0.01%, the AEI instrument displays the cell output in millivolts (0-1000 mV), oxygen content in percent (1×10^{-6} to 100%), and $\log p_{O_2}$ [atm] (0 to -20).

Comparison tests required gas mixtures containing different concentrations of oxygen. Mixtures were prepared from air, Ar, Ar-80% CO, Ar-0.5% CO, CO, Ar-4% H₂, and CO₂. The AEI system was calibrated with air, argon (for which the oxygen content was determined independently), and CO₂-CO mixtures, for which the oxygen content was calculated from the expression for the equilibrium constant K of the reaction



$$K = p_{CO_2}/p_{CO}p_{O_2}^{1/2} \text{ or } p_{O_2} = (p_{CO_2}/Kp_{CO})^2$$

where p_{CO_2} , p_{CO} , and p_{O_2} are the partial pressures of CO₂, CO, and O₂, respectively. The p_{O_2} of air, the p_{O_2} of argon determined by mass spectrometric analysis, and the calculated p_{O_2} of Ar-CO-CO₂ mixtures at equilibrium at 750°C are shown in Fig. 4, a plot of p_{O_2} values measured by the reference sensor against calculated or analytically determined p_{O_2} values. No data are shown between about 1 Pa and 2 pPa because the required small flow rates of CO could not be accurately measured. Nevertheless, agreement appears to be satisfactory over 19 orders of magnitude.

With the knowledge that the reference oxygen sensor accurately measured p_{O_2} , mixtures of various p_{O_2} could be prepared by simply mixing gases until the desired p_{O_2} was indicated by the reference sensor, that is, without accurately metering the gas components. The accuracy

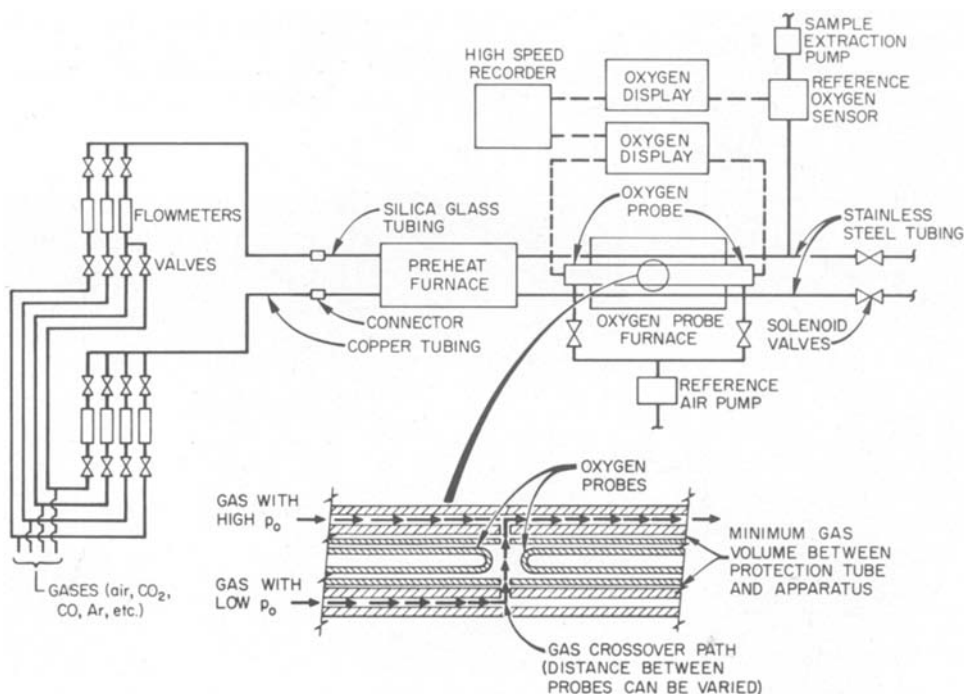


Fig. 3. Apparatus for testing the performance of oxygen probes.

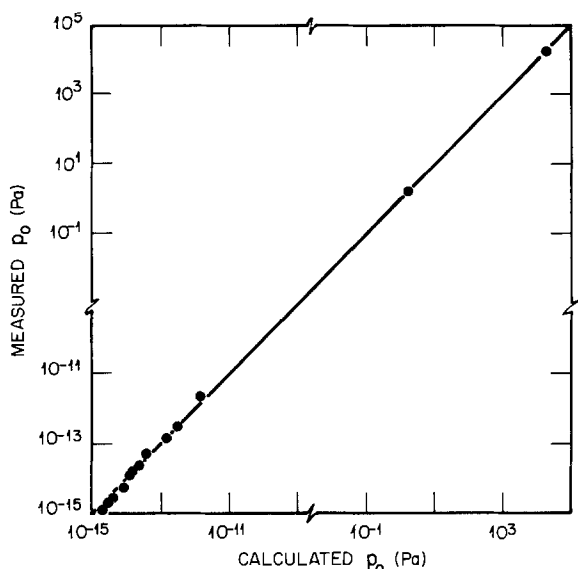


Fig. 4. Calculated p_0 values vs. values measured with the reference oxygen sensor.

of the device was checked periodically, however, with mixtures of known compositions.

Results

The Corning probes were compared with the reference sensor at 750°C by use of steady flows of gases of different p_0 . The results are shown in Fig. 5, wherein p_0 indicated by the reference is plotted against that indicated by the Corning probes. Because the values depended on gas flow rate and exposure time, the data in Fig. 5 represent steady values after 3-6h of steady flow. During these tests, the probe with the porous ceramic layer required much longer times to attain a steady p_0 , apparently because the porous layer restricted access of gas to the sensor. Nevertheless, both probes eventually reached substantial agreement with the reference sensor.

The Bosch probes are compared with the reference sensor at 750°C in Fig. 6, wherein the cell voltage of the Bosch probes is plotted against the reference from 0 to about 800 mV (21 kPa-0.31 nPa). The dashed line in Fig. 6 indicates the desired agreement between the Bosch and reference sensor, and the data points show the actual agreement. At the higher oxygen concen-

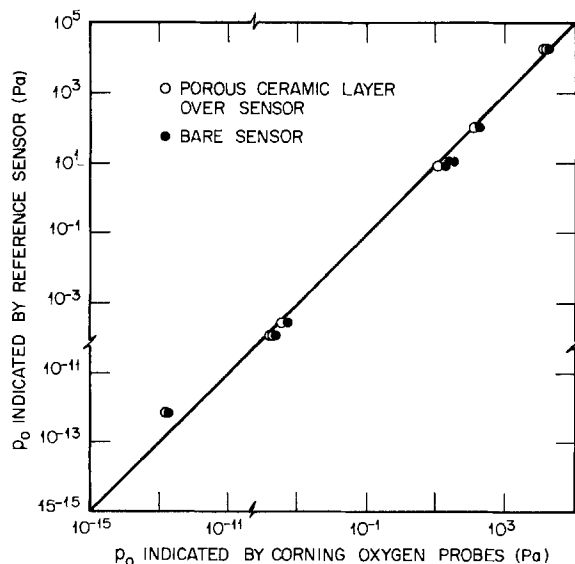


Fig. 5. Comparison of Corning probes with reference sensor

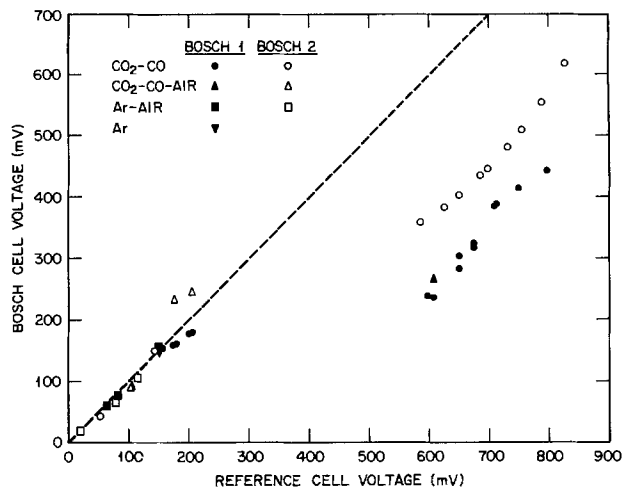


Fig. 6. Comparison of Bosch probes with reference sensor

trations, represented by cell voltages of 0-200 mV, the agreement is satisfactory, but at higher cell voltages (lower oxygen concentrations) agreement is poor. The points for the Bosch sensors at cell voltages greater than about 200 mV could be represented by straight lines intersecting the reference sensor axis at about 225 mV (Bosch 2) or 350 mV (Bosch 1). The shift away from the line of perfect agreement occurred when the gas mixtures contained substantial amounts of CO.

The Bosch and reference sensors are both ceramic electrolyte cells consisting of stabilized zirconia closed-end tubes coated inside and outside with platinum. A possibly important difference between the cells, however, is an additional coating of metal oxide on the outer platinum coating of the Bosch cell. A cross section of the Bosch sensor in Fig. 7 shows the platinum and metal oxide coatings on the zirconia. The porous platinum coating is about 3 μm thick, and the oxide coating (also porous) varies from 35 to 100 μm in thickness. X-ray diffraction revealed that the oxide is a spinel or a mixture of spinels. X-ray fluorescence revealed the presence of Al, Fe, Mg, Ti, V, Cr, Mn, and Ni. This doubly coated outside surface is in contact with the atmosphere being measured, and the other surface (inside) is always in contact with air, the reference gas for both sensors. A possible explanation for the difference in behavior between the two sensors is the presence of this extra coating. Although the platinum coating on the reference sensor can catalyze the oxidation of CO to CO₂, which reduces p_0 at the sensor surface, the metal oxide coating on the Bosch sensor

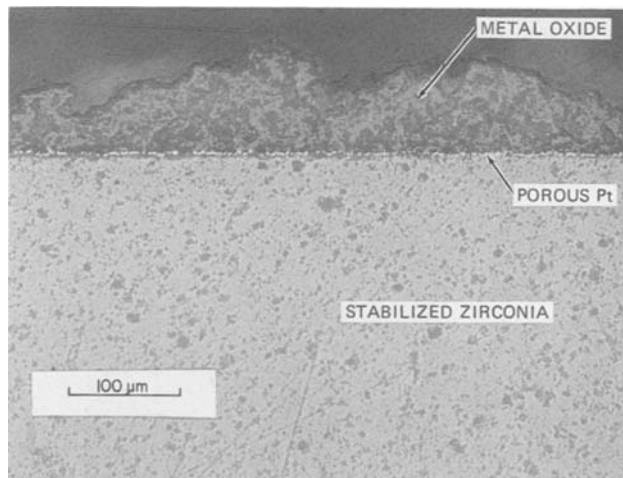


Fig. 7. Coatings on the outer surface of the Bosch sensor

partially prevents catalysis by the platinum. Consequently, when both sensors are in contact with a reactive gas mixture such as CO₂-CO, the reference sensor indicates a lower p_0 because of a more complete reaction at the sensor surface. The Bosch sensor, being less catalytically active, measures p_0 nearer to the actual (unreacted) value in the gas mixture.

Additional comparisons were obtained with mixtures of air with Ar-4% H₂ and with Ar-0.5% CO. The concentration of either H₂ or CO was gradually increased in the mixtures, as shown in Table I, to cause p_0 to decrease by formation of H₂O or CO₂, respectively. The resulting p_0 was calculated from the final gas composition, assuming that all H₂ or CO had reacted with oxygen to form H₂O or CO₂. Table I shows that p_0 indicated by the Bosch and reference sensors, in agreement with calculated values, gradually decreased as available oxygen was consumed. When the gas reached compositions that allowed all available oxygen to be converted to either H₂O or CO₂, the reference sensor indicated lower p_0 values by many orders of magnitude. The indicated values approached thermodynamic equilibrium values that can be calculated from the final gas composition and the equilibrium constants. Lack of better agreement between calculated values and those indicated by the reference sensor can be explained in part by an estimated accuracy of only $\pm 10\%$ in initial gas flow rate. Also, flow rates may have been too high to allow attainment of equilibrium at the surface of the sensor.

The Bosch sensor also indicated much lower p_0 values when all available oxygen was consumed; however, in a manner similar to that in Fig. 6, the Bosch sensor indicated higher p_0 than did the reference. The indicated difference in p_0 between the Bosch and reference sensors was about a factor of 10⁴ for gases containing excess hydrogen and about 10¹³ for gases containing excess CO. These results show not only that the Bosch and reference sensors have different catalytic behavior, but that the Bosch sensor is more catalytic to gases containing excess H₂ than it is to gases containing excess CO.

Discussion

The results of this work revealed that the design of ceramic electrolyte sensors significantly affects performance. Although consisting basically of stabilized

zirconia with platinum electrodes, the Corning and Bosch sensors performed differently. The two Corning sensors agreed with the reference oxygen sensor over a wide range of p_0 values. When contacted with a reactive gas mixture (CO₂-CO), the platinum catalyzed the oxidation of CO resulting in p_0 values predicted by thermodynamic equilibrium between CO and CO₂. Manifestation of the same effect was observed during measurements in an FBC when a large concentration of CO was present in the combustion environment (6). In this latter case, a gas chromatograph and a paramagnetic device indicated p_0 values approximately 12 orders of magnitude higher than did a ceramic electrolyte sensor. The anomaly was attributed to the catalytic behavior of the ceramic electrolyte sensor.

The Bosch sensors indicated much higher p_0 than the reference when exposed to reactive gas mixtures in which the equilibrium oxygen concentration is very low. In this case, the reference sensor indicated p_0 values near to calculated equilibrium values. At the same time, the Bosch sensor indicated p_0 values 4 and 13 orders of magnitude higher than the reference for gas mixtures containing H₂ and CO, respectively. The catalytic behavior of the Bosch sensor evidently is quite different from that of the reference and Corning sensors. A possible explanation for the difference in catalytic behavior is the nature of the ceramic layers. Whereas the porous ceramic layer on the Corning sensor was fabricated separately and then placed in contact with the sensor, the oxide layer on the Bosch sensor was evidently applied as a coating by flame spraying or by a similar method. Although the coating on the Bosch sensor was quite porous (see Fig. 7), the method of application may have produced intimate contact between the oxide and platinum layers, thereby greatly reducing the surface area and associated catalytic effect of the platinum layer. Haaland (7) searched for noncatalytic electrodes for measuring nonequilibrium oxygen concentrations associated with combustibles (CH₄, C₃H₈, CO, and H₂). He found that platinum electrodes were catalytic in mixtures of oxygen and each of the combustibles. Silver and gold catalyzed CO, even though both were only slightly catalytic to CH₄. Platinum electrodes poisoned with lead were the least catalytic to nonequilibrium gas mixtures of the electrodes investigated.

Table I. Comparison of Bosch and reference sensor indications with calculated oxygen pressures

Gas flow rates (cm ³ /min)			Initial gases (mol/min)					Final gases (mol/min) ^a			p_0 (kPa)		
Air	Ar-4% H ₂	Ar-0.5% CO	H ₂	CO	O ₂	N ₂	Ar	H ₂ O	CO ₂	O ₂	Calculated ^b	Bosch	Reference
500	12	0	<0.0001		0.0051	0.0190	0.0008	<0.0001		0.0051	20.5	20.4	20.0
500	100	0	0.0002		0.0051	0.0190	0.0049	0.0003		0.0050	17.1	17.0	17.0
500	200	0	0.0004		0.0051	0.0190	0.0096	0.0006		0.0049	14.3	14.6	14.6
500	235	0	0.0005		0.0051	0.0190	0.0113	0.0010		0.0049	13.5	13.5	13.5
500	300	0	0.0006		0.0051	0.0190	0.0143	0.0012		0.0048	12.2	12.3	12.3
300	500	0	0.0010		0.0031	0.0114	0.0235	0.0015		0.0026	6.7	6.5	6.4
300	1000	0	0.0020		0.0031	0.0114	0.0469	0.0030		0.0021	3.3	3.3	3.1
300	1500	0	0.0030		0.0031	0.0114	0.0703	0.0045		0.0016	1.8	1.9	1.7
300	2000	0	0.0040		0.0031	0.0114	0.0937	0.0060		0.0011	0.98	1.3	1.0
300	2500	0	0.0050		0.0031	0.0114	0.1171	0.0075		0.0006	0.44	0.65	0.48
300	3000	0	0.0060		0.0031	0.0114	0.1405	0.0090		0.0001	0.06	0.30	0.19
300 ^c	3500 ^c	0	0.0070		0.0031	0.0114	0.1639	0.0093		<0.0001	2 E-15 ^d	1 E-11	1 E-15
500	0	100	<0.0001	0.0051	0.0190	0.0051		<0.0001	0.0051		17.5	17.2	16.9
500	0	200	0.0001	0.0051	0.0190	0.0099		0.0001	0.0051		15.0	15.0	14.8
500	0	300	0.0001	0.0051	0.0190	0.0148		0.0002	0.0050		13.1	12.7	12.6
400	0	300	0.0001	0.0041	0.0152	0.0147		0.0002	0.0040		12.0	11.7	11.6
300	0	300	0.0001	0.0031	0.0114	0.0146		0.0002	0.0030		10.6	10.0	10.1
200	0	300	0.0001	0.0020	0.0076	0.0144		0.0002	0.0019		8.2	8.2	8.5
100	0	300	0.0001	0.0010	0.0038	0.0144		0.0003	0.0009		5.1	5.1	5.8
25	0	500	0.0002	0.0003	0.0010	0.0242		0.0006	0.0002		0.78	0.90	0.70
25	0	1000	0.0004	0.0003	0.0010	0.0485		0.0008	0.0001		0.20	0.35	0.23
25	0	1500	0.0005	0.0003	0.0010	0.0727		0.0009	0.0001		0.13	0.11	0.06
25 ^c	0	2000 ^c	0.0007	0.0003	0.0010	0.0970		0.0009	<0.0001		2 E-15 ^d	1 E-02	2 E-14
25 ^c	0	2500 ^c	0.0009	0.0003	0.0010	0.1212		0.0009	<0.0001		1 E-16 ^d	2 E-03	4 E-16
25 ^c	0	3000 ^c	0.0011	0.0003	0.0010	0.1454		0.0009	<0.0001		4 E-17 ^d	4 E-04	2 E-16

^a Plus inlet N₂ and argon and any remaining H₂ or CO after all O₂ is consumed. ^b Calculated from final gas composition assuming that all H₂ and CO react with O₂ (if available) to produce H₂O and CO₂, respectively. ^c Gas composition that allows all O₂ to be converted to H₂O or CO₂. ^d Calculated from final gas composition and equilibrium constants at 750°C: 5.75 E+09 for H₂-O₂-H₂O and 7.25 E+09 for CO-O₂-CO₂.

If all gases within the FBC atmosphere were at equilibrium, the catalytic behavior of the sensor would not be important, and the sensor would accurately display p_{O_2} . Intuitively, equilibrium would not be expected in an FBC because of complex reaction kinetics associated with numerous gaseous species and because of imperfect mixing of air, powdered coal and limestone, and reaction products. The previously mentioned discrepancy between a ceramic electrolyte, paramagnetic sensor, and gas chromatograph indicate a state of nonequilibrium (6). Thus, in reactive gas mixtures, the response of a ceramic electrolyte sensor will depend to some extent on its catalytic behavior. In an FBC, the sensor would probably be influenced by several factors, including the actual p_{O_2} of the gas, gas composition, gas flow rate, catalytic behavior, and deposits on the sensor. The sensor probably would become coated with a material consisting mostly of $CaSO_4$, unless protected by a filter. If the sensor initially had a bare platinum electrode, the coating might decrease the catalytic behavior in a manner similar to the oxide coating on the Bosch sensor.

In spite of the data presented herein showing different behavior by ceramic electrolyte sensors, and discussion of reasons why these devices will not accurately measure p_{O_2} in reactive gases, they might still be useful diagnostic tools in FBC's. Rocazella *et al.* demonstrated the ability of a Bosch probe to differentiate combustion products resulting from stoichiometric and air-rich mixtures (8). Furthermore, they showed that corrosion characteristics in several alloys correlated well with p_{O_2} values indicated by the probe.

Acknowledgment

This research was sponsored by the Morgantown Energy Technology Center, U.S. Department of Energy, under Contract W-7405-eng-26 with the Union Carbide Corporation.

Manuscript submitted July 7, 1983; revised manuscript received Nov. 14, 1983.

Oak Ridge National Laboratory assisted in meeting the publication costs of this article.

REFERENCES

1. R. H. Cooper, T. G. Godfrey, and J. H. DeVan, Report ORNL/TM-7734/P1, Oak Ridge National Laboratory, Oak Ridge, TN (1981).
2. T. G. Godfrey and J. H. DeVan, Report ORNL/TM-7734/P2, Oak Ridge National Laboratory, Oak Ridge, TN (1981).
3. John Stringer and D. P. Whittle, Paper presented at the Technische Vereinigung der Grosskraftwerksbetreiber Conference on Corrosion and Deposition in Power Plants, Essen, Germany, June 1-2, 1977.
4. E. A. Gulbransen and G. H. Meier, Report DOE/FE/13547-01, U.S. Department of Energy, Washington, DC (1980).
5. J. I. Federer, Report ORNL/TM-8520, Oak Ridge National Laboratory, Oak Ridge, TN (1983).
6. M. J. Cooke, A. J. B. Cutler, and E. Raask, *J. Inst. Fuel*, **65**, 153 (1972).
7. D. M. Haaland, *This Journal*, **127**, 796 (1980).
8. M. A. Rocazella, I. G. Wright, and C. F. Holt, Paper 83-GT-249, presented at the 28th International Gas Turbine Conference and Exhibit, ASME, Phoenix, AZ, March 27-31, 1983.

A Potentiodynamic Study of Metals Affecting Precious Metal Recovery from Alkaline Cyanide Solutions

D. W. Kirk* and F. R. Foulkes*

Department of Chemical Engineering and Applied Chemistry, University of Toronto, Toronto, Ontario, M5S 1A4, Canada

ABSTRACT

A potentiodynamic study was carried out to determine the effects of various ions on the electrorecovery of precious metals from an industrial cyanide leaching solution. Synthetic solutions were prepared and studied to determine the effects of Cu, Ni, and Pb individually and in combination on the recovery of gold and silver. Lead, known to be electrochemically active, was studied at a low concentration (1 ppm), whereas copper and nickel were studied at high concentrations (250 ppm), corresponding to levels found in an industrial solution. Both copper and lead were found to enhance silver and gold reduction reactions in the potential sweep measurements. Separation of the two reactions was also improved. In addition, these two metals inhibited the onset of hydrogen evolution. Nickel had the opposite effect. Separation and initiation of the gold and silver plating peaks was inhibited, and the hydrogen evolution reaction was depolarized. The influence of nickel predominated over the effects of copper and lead. The data, obtained from synthetic electrolyte solutions, were compared with those obtained from the industrial leach solution.

The purpose of this study was to investigate the effects of interactions between various metals dissolved in an aqueous alkaline cyanide solution. The results of this work will be used to help explain the behavior of industrial leach solutions in electrowinning operations. The particular industrial solution considered in this case was an alkaline cyanide electrolyte used for precious metal recovery from a gold bearing ore from Pamour Mines, Porcupine, Ontario. As a result of the leaching operation, a number of metals were dissolved. Gold and silver, together with a substantial amount of copper, were recovered by precipitation with zinc. Although gold and silver recovery by electrolysis could be an attractive alternative because of the possibility of selective metal re-

covery, the effect of the interaction of the various metals in solution on the electrowinning operation is not known.

Studies using porous flow through reactors for metal electrorecovery have shown that both industrial and multicomponent synthetic electrolytes yield much poorer metal recovery and current efficiency than the corresponding single-component electrolytes (1-5). The difficulties with multicomponent electrolytes result in part from polarization and depolarization effects, codeposition, underpotential deposition, and catalytic effects. Even trace amounts of some metals can cause substantial changes in plating rates. McIntyre and Peck (6) showed that trace amounts of Hg, Tl, Pb, and Bi could greatly enhance gold plating rates in alkaline phosphate electrolytes. The metals were reported to remain in the electric double layer and act as catalysts

* Electrochemical Society Active Member.

Key words: electrodeposition, voltammetry, precious metals, alkaline cyanide.

for the plating reaction. In the case of multicomponent solutions, there is little evidence whether all, or only certain plating reduction reactions, would be accelerated.

The behavior of metal ions also is affected by the electrolyte. Cyanide complexes with metals to form stable anions. Gold, for example, is found almost exclusively as $\text{Au}(\text{CN})_2^-$. Electromigration forces acting near the electrode surface in cyanide solutions are therefore different than those in chloride solutions. In chloride solutions, more negative electrode potentials increase the electromigration force towards the electrode, whereas in cyanide solutions, more negative potentials increase the repulsion of the complexed metal from the electrode. The reduction potential of some metals is affected by cyanide electrolytes and metals such as copper and nickel can form a variety of complexes so that the plating behavior of a complex mixture of metals is not easily predictable.

Before a study of precious metal electrowinning was carried out, linear potential sweep profiles of various metals singly and in combination were measured. The metals studied were those found in significant concentrations in the industrial leach solution or those thought to have catalytic properties (Au, Ag, Cu, Ni, Pb). In order to have the results applicable to porous bed work, a porous graphite felt was used in the linear sweep voltammetry work.

Experimental

The electrochemical cell used for linear sweep voltammetry (LSV) measurements consisted of a 50 ml Pyrex glass cell sealed using a rubber stopper with ports for electrodes and gas sparging. The working electrode consisted of porous graphite felt (Carborundum Corporation, Niagara Falls, New York) $0.6 \times 0.6 \times 1.9$ cm with a specific surface area¹ of 3.45×10^3 cm^{-1} and porosity 0.88. Contact was made by means of a Pt wire (0.08 cm diam) imbedded 1.6 cm into the felt and sealed in a glass tube to isolate it from the solution. The electrode appears to partially utilize both internal and external surface area, since metal deposits were found throughout the electrode. A total resistance of the carbon felt of $7 \times 10^{-3} \Omega$ was calculated from a measured specific conductivity of $5.0 \times 10^3 \text{S}$. The electrode was soaked for 24h in KOH solution and then well rinsed in double-distilled water before use.

A saturated calomel reference electrode² was housed in a Luggin capillary with the capillary tip 2 mm from the graphite surface. The counterelectrode was a platinum disk (1 cm diam) set 2 cm from the working electrode. Tank nitrogen gas was bubbled through the solutions for 5 min before each run using a glass frit for good gas dispersion. During a run, nitrogen gas was passed over the solutions to maintain a low dissolved-oxygen content.

The industrial leach solution was supplied courtesy of Pamour Mines, Porcupine, Ontario. The synthetic electrolytes were prepared from analytical-grade KOH and KCN and double-distilled water. Gold solutions were obtained by dissolving gold powder (99.9%) in alkaline cyanide; solutions of other metals (Cu, Ag, Ni, Pb) were prepared from their nitrate salts. pH and cyanide determinations were obtained using an Orion Digital pH meter Model 401 with glass pH and cyanide specific electrodes, respectively.

A PAR potentiostat Model 371, programmer Model 175, and coulometer Model 379, and a Houston Instruments Omnigraphic 2000 XY recorder were used for the LSV and reactor measurements. A sweep rate of $10 \text{ mV} \cdot \text{s}^{-1}$ was used. A rotating disk electrode (Astra Scientific International, Incorporated) was also used. The glassy carbon electrode for the rotating disk had a diameter of 2 mm.

¹ Manufacturer's data based on total volume.

² All potentials are reported vs. the SHE.

A porous flow-through electrochemical reactor was used to compare actual metal recoveries at various potentials with potential sweep measurements. The cell shown in Fig. 1 was constructed of Pyrex and contained a platinum current feeder and anode. The cathode bed, consisting of the porous graphite felt previously described, was 3.1 cm diam and 2.3 cm deep. A saturated calomel reference electrode, housed in a Luggin capillary with the tip 2 mm from the bed, was placed upstream of the carbon fiber electrode. This arrangement restricted the maximum bed potential to prevent hydrogen evolution.

The electrolyte flow rate was controlled by gravity feed and was monitored at the cell outlet. A flow rate of $15 \text{ ml} \cdot \text{min}^{-1}$ was used, and no channeling was observed at this rate. Gold, silver, and copper were determined by neutron activation analysis, and nickel was determined by polarography.

Results and Discussion

Effect of oxygen.—A steady-state linear potential sweep of a 0.025M KOH solution is shown in Fig. 2a. Curve a is the potential profile of the solution after purging the solution with nitrogen for 5 min. There is evidence of two small cathodic peaks at -0.22 and -0.8V . Curve b is the potential profile of the first scan after the solution had been oxygenated for 5 min. The two peaks are much more prominent in curve b and were thought to belong to the reduction of residual oxygen. The first peak at -0.2V in the deoxygenated solution and -0.34V in the oxygenated solution most likely corresponds to the reaction (7, 8)



The shift in the start of the peak from about -0.075 to $+0.13 \text{V}$ would correspond to a 2.9×10^3 change in oxygen concentration. Gordienko and Antropov (9) found the first peak at -0.24V on Fe electrodes and identified it as HO_2^- formation. The second peak has been noted by a number of workers (11-13) and identified as the reduction of the $\text{O}_{2\text{-ads}}$ species or direct O_2 reduction.

Reactions involving either two or four electron pathways have been suggested in the literature (9, 10, 14, 16-18) to account for the reaction.

Effect of cyanide.—In Fig. 2b, steady-state potentiodynamic profiles are shown for cyanide and cyanate

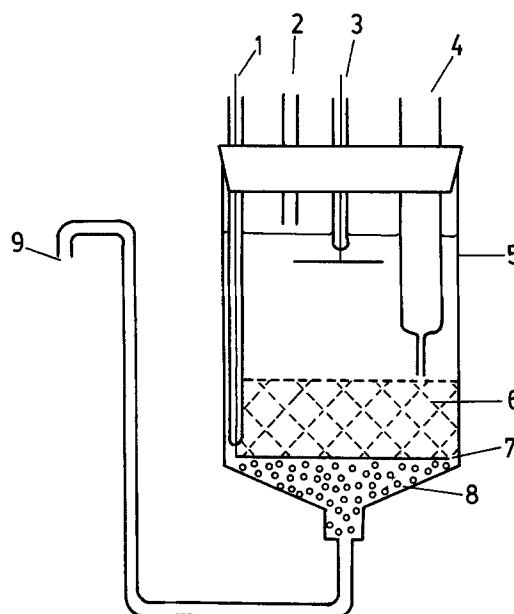


Fig. 1. Schematic diagram of cell. 1: cathode feeder. 2: electrolyte inlet. 3: Pt anode. 4: Luggin capillary for SCE reference electrode. 5: Pyrex cell, 3.1 cm diam. 6: porous carbon felt cathode. 7: Pt screen feeder. 8: glass beads. 9: electrolyte outlet.

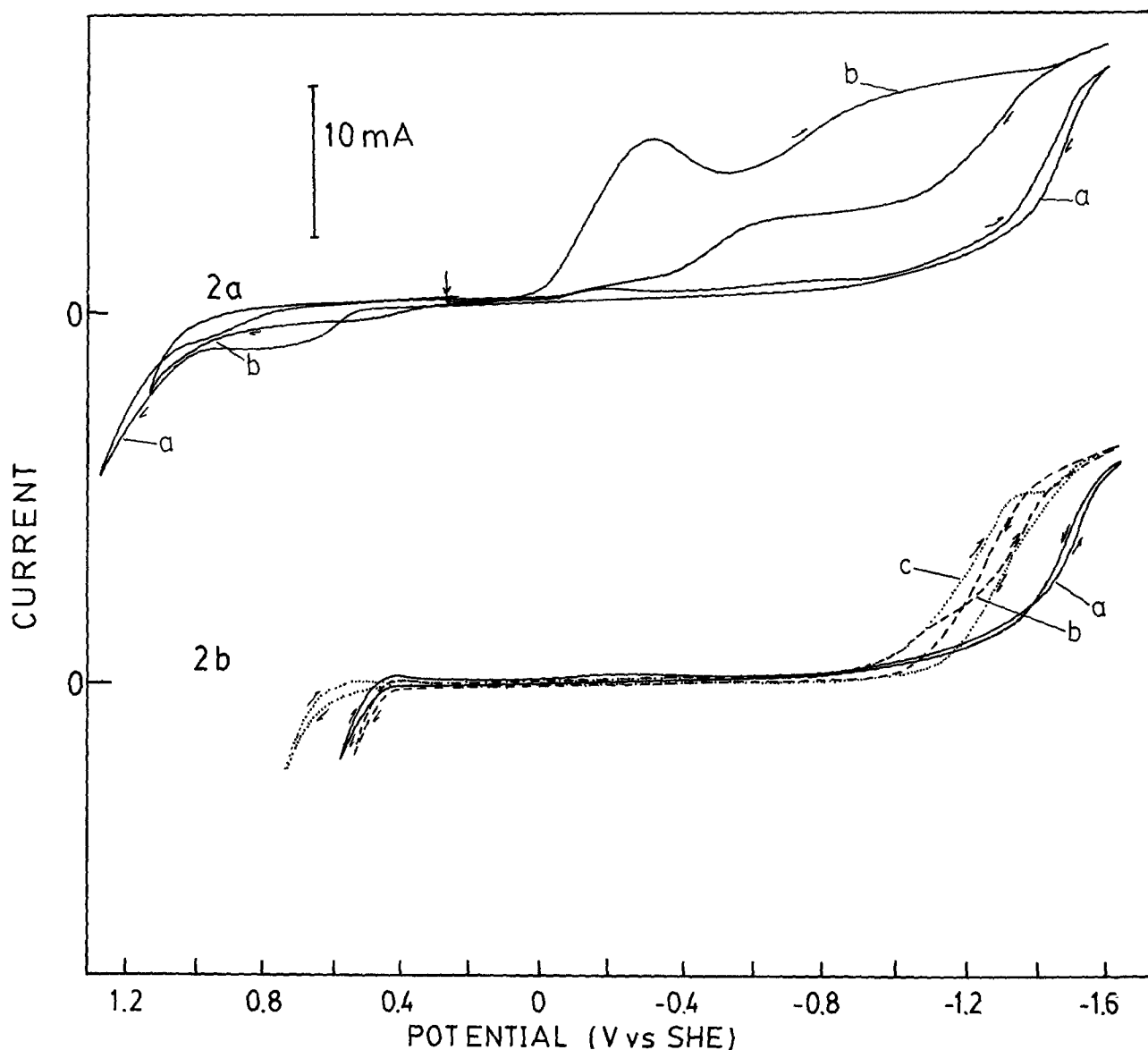
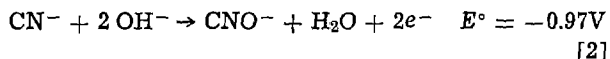
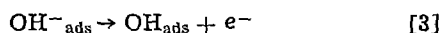


Fig. 2. 2a: linear potential sweep profile of a 0.025M KOH solution at 22°C. Sweep rate: $10 \text{ mV} \cdot \text{s}^{-1}$. Effect of dissolved oxygen. a: steady-state profile, electrolyte deoxygenated with N_2 . b: first sweep profile after saturating solution with O_2 for 5 min. Arrow indicates initial potential. 2b: steady-state potential sweep profile of a 0.025M KOH solution at 22°C. Sweep rate: $10 \text{ mV} \cdot \text{s}^{-1}$. Effect of cyanide and cyanate. a: 0.01M KCN. b: 0.10M KCN. c: 0.1M KCN + 0.1M KOcN.

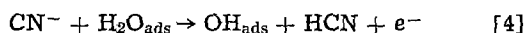
additions to the alkaline electrolyte. At 0.01M KCN, little change is noted in the cathodic portion of the sweep. The anodic portion of the sweep shows an oxidation reaction which begins at less positive potentials (0.49V) than in the cyanide-free solution (Fig. 2a, curve a). The reaction normally proposed for cyanide oxidation is that via (19)



This reaction has a reversible potential of $\approx -0.99\text{V}$ for 0.01M KCN + 0.025M KOH + $\approx 10^{-6}\text{M}$ CNO⁻ and would therefore have an unusually large overpotential. Another possibility is that the cyanide depolarizes the oxygen evolution reaction. The rate-determining step for oxygen evolution without cyanide present is



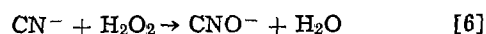
with a transfer coefficient (α_A) of 0.5 (31). One reaction that could depolarize the reaction is



Oxidation of cyanide would then take place by chemical reaction with oxygen or peroxide via



or



The ratio of CN⁻ oxidized to oxygen used still would be 2:1, and the apparent ratio of Faradays of electrons per mol of CN⁻ oxidized would be 2:1, as reported in the literature (20). In Table I, the experimentally measured numbers of faradays per mol of CN⁻ oxidized are presented at various potentials. Since no

Table I

Potential (V)	ΔCN^- (mol)	Coulombs (c)	\bar{n}
+0.542	5.10×10^{-5}	3.42	0.73 ± 0.5
+0.742	6.53×10^{-5}	8.89	1.42 ± 0.2
+0.942	1.07×10^{-4}	15.29	1.68 ± 0.3
+1.142	9.04×10^{-5}	14.47	1.80 ± 0.5

* 95% confidence limits.

Each value represents the average of four measurements taken in a sequence of 15 min periods in solutions without deoxygenation. From a 50 ml solution of 0.01M KCN + 0.025M KOH, 2 ml were removed every 15 min. After addition of 1 ml of 10M KOH, the sample was diluted to 50 ml and the CN⁻ concentration recorded.

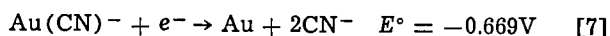
one-electron reactions could be found to account for the oxidation, the low values of n (i.e., ≤ 2) apparently indicate that some oxidation may be caused by residual oxygen. In order to accommodate the cyanide-specific ion electrode, these measurements had been carried out in an open cell without deoxygenation. If the data are corrected for oxygen solubility ($8.5 \text{ mg} \cdot \text{dm}^{-3}$ at 22°C) (32) assuming that $8.5 \text{ mg} \cdot \text{dm}^{-3} \text{ O}_2$ is available for the decomposition of cyanide in each measurement, then the values of n become 1.40 ± 0.5 , 2.38 ± 0.2 , 1.97 ± 0.8 , and 2.35 ± 0.5 for the potentials 0.542, 0.742, 0.942 and, 1.142V vs. SHE, respectively. These values indicate that the number of faradays per mol of cyanide oxidized by electrolysis is two, as should be expected.

An increase in the cyanide concentration to 0.1M (Fig. 2b, curve b) causes the oxidation reaction to initiate at less positive potentials, as would be predicted from reaction [2]. The increase in cyanide concentration causes the cathodic portion of the sweep to shift $\approx 150 \text{ mV}$ more positive. Depolarization of the hydrogen evolution reaction or reduction of the cyanate ion formed from the previous oxidation cycle could cause this shift. Addition of cyanate (0.1M) to the electrolyte (Fig. 2b, curve c) does show a more pronounced reduction reaction starting at about -0.9V . The reversible potential for reaction [2] in 0.1M $\text{CN}^- + 0.1\text{M CNO}^- + 0.025\text{M OH}^-$ is -0.875V .

The cyanate addition causes the suppression of the oxidation reaction to more positive potentials, which is consistent with the predicted behavior if reaction [2] is operative.

It can be seen that the exponential current rise at the end of the cathodic scans is apparently terminated with the start of a plateau. This feature is apparently the result of gas bubble formation in the porous bed and subsequent blockage of electrode surface area. Depletion of the reactants within the porous bed could also contribute to this behavior.

Effect of gold.—Potential scans for an alkaline cyanide electrolyte (0.1M KCN + 0.025M KOH) with the addition of gold cyanide are shown in Fig. 3a. At a gold concentration of 17.5 ppm (curve a), there is a small shoulder on the curve at about -1.2V . With a more concentrated solution (175 ppm Au), a peak develops. The reversible potentials for the gold plating reaction [7] are -0.796 and -0.737V for 17.5 ppm and 175 ppm Au, respectively (19)



A series of oxidation reactions can be seen in the anodic portions of the scans, indicating the dissolution of gold plated during the cathodic scans. The nature of the dissolution reactions has been discussed elsewhere (21-26). With the addition of 1.0 ppm Pb to the solution (Fig. 3a, curve c), there is a shift in the gold plating reaction to less negative potentials. A large oxidation peak at -0.35V is seen in the scan. This peak is at a potential at which gold dissolution has been found (21, 25, 26). The magnitude of the oxidation peak is greater than the reduction peak, so that additional plating also must occur at potentials more negative than the reduction peak. A potential scan with only Pb (1 ppm) present in the alkaline cyanide solution (0.1M KCN + 0.025M KOH) is shown in Fig. 3b. No major peaks are noted, but in the anodic scan there are two small oxidation peaks, presumably from lead dissolution. Some of the complex behavior of the gold oxidation peak seen in Fig. 3a, curve c is apparently due to the lead oxidation reactions, since evidence of the two lead peaks can be seen in the large oxidation peak (Fig. 3a, curve c).

The reversible potential for lead ion reduction (1 ppm) in uncomplexed form is about -0.3V . Therefore,

the inhibition of the hydrogen evolution reaction is probably the result of plated lead which has a large hydrogen overvoltage. In contrast, the overpotential for cyanide oxidation or oxygen evolution seen in Fig. 3b is slightly reduced with the presence of Pb.

The effect of Pb additions on gold plating in alkaline phosphate solutions has been studied by McIntyre and Peck (6), who reported that Pb and other metals (Hg, Tl, and Bi) caused depolarization of the gold plating reaction by acting as a catalyst in the electrical double layer at the cathode surface. Of these metals with catalytic activity, only Pb was found in the industrial leach solution. An analysis of the industrial solution is given in Appendix 1.

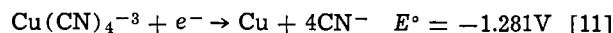
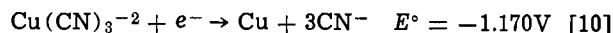
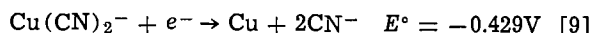
Effect of silver.—Potential scans in alkaline cyanide solution (0.1M KCN + 0.025M KOH), with the addition of Ag, are shown in Fig. 3c. Curve a is the potential scan with a 2.3 ppm Ag content. The plating reaction is not readily distinguished from the background reduction reactions (Fig. 2b, curve b). However, the anodic scan shows the presence of two small oxidation reactions at -0.45 and -0.3V , presumably from the dissolution of Ag plated during the cathodic scan. A tenfold increase in the Ag concentration to 23 ppm (Fig. 3c, curve b) results in the appearance of a distinct reduction peak at -1.05V . Since the silver cyanide reduction reaction has a reversible potential of -0.409V for $\text{CN}^- = 0.1\text{M}$ and $\text{Ag}^+ = 23 \text{ ppm}$, there is a substantial overpotential for the reaction



With the appearance of a silver reduction peak for the larger silver concentration, an increase in the two oxidation peaks would be expected. This is observed in Fig. 3c, curve b. The two peaks merge, forming a larger peak with a maximum at -0.32V .

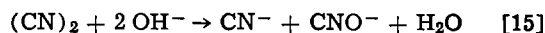
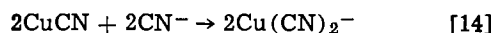
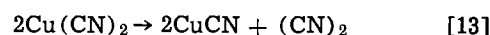
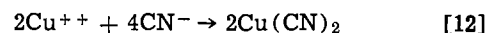
The addition of 1 ppm Pb to the electrolyte (Fig. 3c, curve c) results in a substantial drop in the overpotential for silver deposition. The plating reaction now begins at about -0.75V . A much larger peak also can be seen in the anodic scan, indicating that more silver is plated in the cathodic scan. It is interesting to note that the silver oxidation reaction also is depolarized by the lead addition and begins at more negative potentials (-0.55V) than the apparent reversible potential (-0.409V). This is probably the consequence of the depletion of the $\text{Ag}(\text{CN})^-$ species during the cathodic scan. There is evidence of a lead oxidation peak (Fig. 3b) in the silver oxidation peak (Fig. 3c, curve c).

Effect of copper.—Copper is found in the industrial leach solution. The possible reduction reactions are



From equilibrium data, $\text{Cu}(\text{CN})_2^-$ should predominate.

At a copper concentration of 600 ppm, the reversible potentials for reactions [9], [10], and [11] are -0.430 , -1.11 , and -1.16V , respectively. In order to check the coordination number for the copper in the cyanide complex, copper nitrate solution was added to a 0.01M KCN solution and the remaining free cyanide determined. The results indicated that 3.9 ± 0.2 mols of cyanide were lost per mol of copper added. This would suggest that the $\text{Cu}(\text{CN})_4^{-3}$ predominates. However, the mechanism for copper cyanide formation given by Miller (27) is



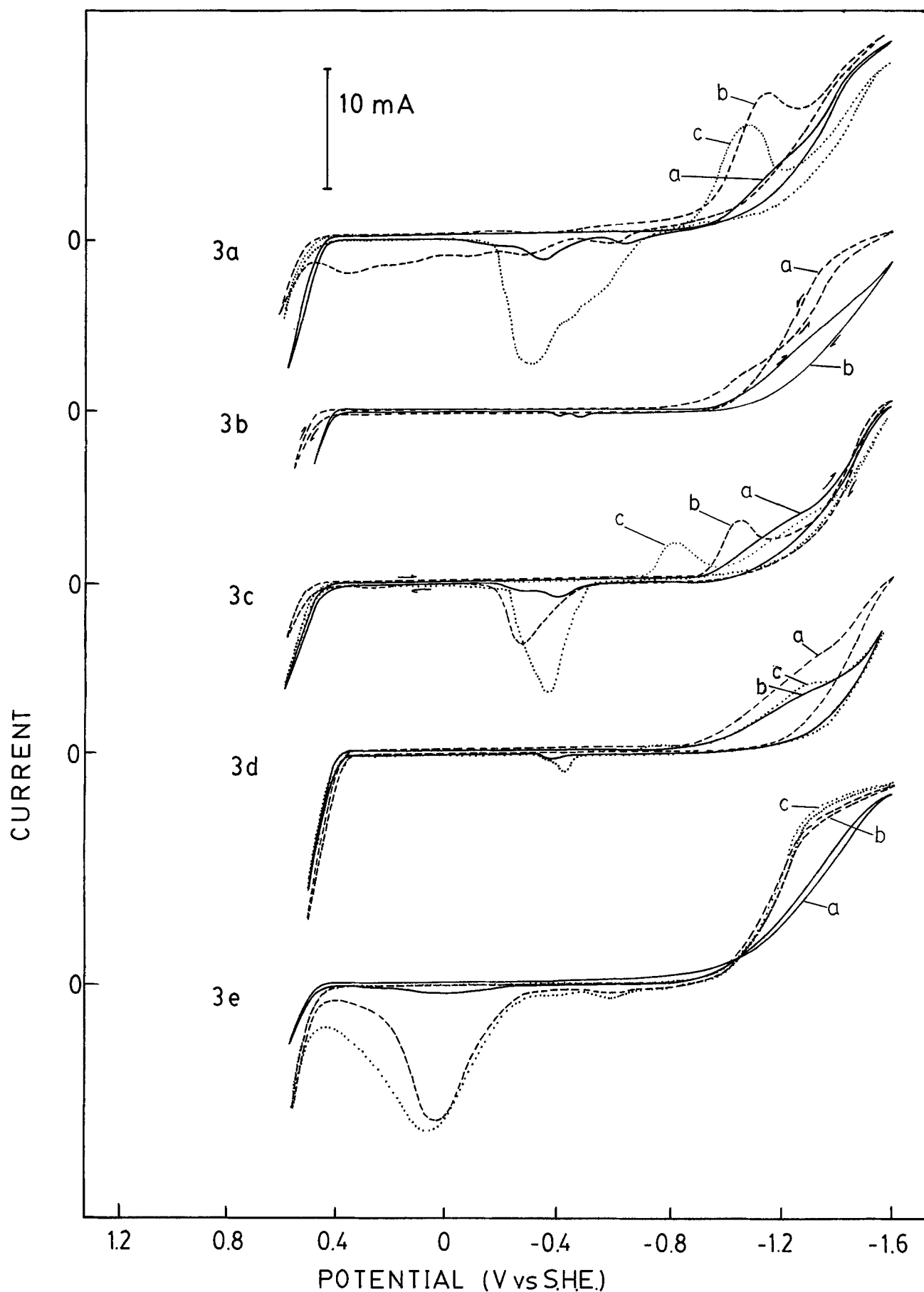
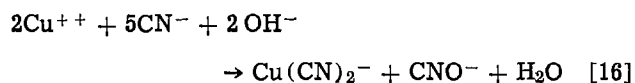


Fig. 3. Steady-state potential sweep profiles of a 0.025M KOH + 0.1M KCN solution at 22°C. Sweep rate: $10 \text{ mV} \cdot \text{s}^{-1}$. 3a: effect of gold. a: 17.5 ppm Au. b: 175 ppm Au. c: 175 ppm Au + 1 ppm Pb. 3b: effect of lead. a: no Pb. b: 1 ppm Pb. 3c: effect of silver. a: 2.3 ppm Ag. b: 23 ppm Ag. c: 23 ppm Ag + 1 ppm Pb. 3d: effect of copper. a: 300 ppm Cu. b: 600 ppm Cu. c: 600 ppm Cu + 1 ppm Pb. 3e: effect of nickel. a: 250 ppm Ni. b: 500 ppm Ni. c: 500 ppm Ni + 1 ppm Pb.



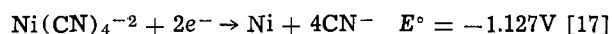
From this reaction sequence, 2.5 mols of free cyanide would be lost per mol of copper added. Since a value of 3.9 was determined, some of the copper must be in a higher oxidation state than $\text{Cu}(\text{CN})_2^-$. Penneman and Jones reported (28) that the principal complex in alkaline cyanide is $\text{Cu}(\text{CN})_3^{2-}$.

Figure 3d, curve a shows the steady-state potential sweep profile for copper containing alkaline cyanide electrolyte (0.025M KOH + 0.1M KCN + 300 ppm Cu). Comparison with Fig. 2a, curve b with the absence of copper reveals that the shoulder observed at -1.4V is smaller with the 300 ppm Cu addition. No oxidation peak is apparent in the anodic scan with the copper present. Both features indicate that copper does not plate under these conditions. In the anodic portion of the scan there is a noticeable depolarization of the anodic oxidation reaction. The reaction begins at about +0.25V, compared with +0.4V with no copper present (Fig. 2a, curve b).

With a copper concentration of 600 ppm (Fig. 3d, curve b), the current in the cathodic portion of the sweep is lowered to a greater extent than with 300 ppm Cu. In this case, however, there is evidence of an oxidation peak at -0.45V, indicating that some plating may have taken place. Only a slight further decrease in the anodic depolarization can be seen with the larger Cu concentration. From these measurements it can be seen that copper inhibits the hydrogen evolution reaction and accelerates the anodic oxidation of cyanide and oxygen evolution. The addition of 1 ppm of Pb to the electrolyte (Fig. 3d, curve c) results in the appearance of a small peak in the cathodic scan at -1.38V. The corresponding anodic scan has an oxidation peak at -0.5V, which overlaps the peak found without the lead addition (-0.45V). With only lead present (Fig. 3b) there is also an oxidation peak at -0.5V, although this smaller than with the copper present. It is not clear to what extent the oxidation peak is due to copper or lead oxidation.

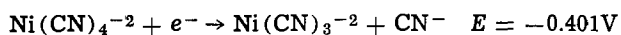
Effect of nickel.—Nickel also is found in the industrial leach solution at a concentration of 250 ppm. A steady-state potential sweep profile is shown in Fig. 3a, curve a for a solution 0.025M KOH + 0.1M KCN + 250 ppm Ni. The Ni addition does not change the current measured at either end of the anodic or cathodic sweeps from the solution without Ni present (Fig. 2a, curve b). However, with nickel present, there is less hysteresis shown at the cathodic end, and there is a small, broad oxidation peak at about 0.0V. This peak is enhanced when the nickel concentration is increased to 500 ppm (curve b). In addition, this peak was observed to be caused by a reduction reaction beginning at about -1.2V. (The cathodic scan limit was terminated at successively less negative potentials until the oxidation peak could no longer be detected.)

If the nickel is assumed to be complexed as $\text{Ni}(\text{CN})_4^{2-}$, then the reversible reduction potential can be calculated from thermodynamic data (30)



For the conditions 0.1M KCN + $8.516 \times 10^{-3}\text{M}$ $\text{Ni}(\text{CN})_4^{2-}$ (600 ppm Ni) $E = -1.07\text{V}$. Therefore, the oxidation peak found at -0.05V could be the oxidation of nickel plated in the previous cathodic scan.

Alternatively, nickel can form an oxidation/reduction couple involving nickel cyanide complexes (19)



The addition of 1 ppm of Pb to the solution (Fig. 3e, curve c) results in only a slight increase in the nickel oxidation peak at -0.05V.

Effect of metal combinations.—A steady-state potential sweep profile is shown in Fig. 4a for a solution 0.025M KOH + 0.1M KCN with 17.5 ppm Au + 2.3 ppm Ag (curve a). Only a single plating peak is observed at about -1.15V, but two overlapping oxidation peaks are at -0.25 and -0.30V. Comparison with the profiles with Au and Ag present individually (Fig. 3a, curve a and Fig. 3c, curve a) reveals that only a few changes occur. The complex nature of the oxidation peak at potentials $\geq -0.4\text{V}$ is enhanced with both Au and Ag present, and the gold oxidation peak at -0.67V (Fig. 3a, curve a) is not observed. These effects could be the result of the sensitivity of the dissolution reactions to changes in surface structure with both Au and Ag plated.

With the addition of 1 ppm Pb to the solution (Fig. 4a, curve b), two reduction peaks now can be found at -0.82 and -1.0V, and the hydrogen evolution reaction is inhibited. The gold and silver plating reactions apparently are independently depolarized and enhanced by the presence of Pb. The first peak at -0.82V corresponds to the silver plating peak in Fig. 3c, curve c, and the second peak at -1.0V corresponds to the gold plating peak in Fig. 3a, curve c. Only a single oxidation peak is found with Pb present.

The effect of copper (300 ppm) on the steady-state potential sweep profile with both silver and gold present in the solution is shown in Fig. 4b, curve a. When compared with Fig. 4a, curve a, this profile reveals that copper also causes the silver and gold plating reactions to be separated and shifted to less negative (less cathodic) potentials. Copper also suppresses the onset of the hydrogen evolution reaction; a shoulder at -1.3V can be seen. The inhibiting effect of copper on the hydrogen evolution reaction was not expected, since without gold and silver present little effect was found (Fig. 3d, curve a). McIntyre and Peck (26) reported that in alkaline phosphate solutions copper did not depolarize gold plating. In contrast, in the alkaline cyanide solution in this study, copper did depolarize both the gold and silver plating reactions. In the anodic scan there is evidence of greater metal plating from the large complex anodic peak at -0.32V. In addition to the gold and silver oxidation, this peak also may contain a contribution from a copper oxidation reaction (Fig. 3c, curve b).

The effect of Ni addition to the steady-state potential sweep profile of the solution with Au, Ag, and Cu present is shown in Fig. 4b, curve b. In this case, some of the depolarizing effect of copper is lost. A single plating peak is seen at -0.88V, and the corresponding oxidation peak at $\sim -0.42\text{V}$ is reduced in magnitude. In addition, the hydrogen evolution reaction is depolarized. In the anodic scan there is an additional oxidation peak at $\sim 0.0\text{V}$, which is found when only nickel is present (Fig. 3e, curve a).

With the addition of 1 ppm of Pb to the combination of Ag + Au + Cu + Ni (Fig. 4c, curve b), the depolarizing effects of Pb on gold and silver plating no longer appear to be present. The hydrogen evolution reactions are only marginally inhibited with nickel present in the solution. There is no evidence that the amount of Au and Ag plated increases with lead addition, as it did in the solution without Ni present (Fig. 4a, curve b).

Thus it appears that the presence of nickel has the most detrimental effect on the recovery of gold and silver of any of the metals studied. There does not appear to be any separation of the gold and silver plating reactions, and the hydrogen evolution reaction is depolarized, increasing the likelihood of low current efficiency. Copper addition, on the other hand, appears to

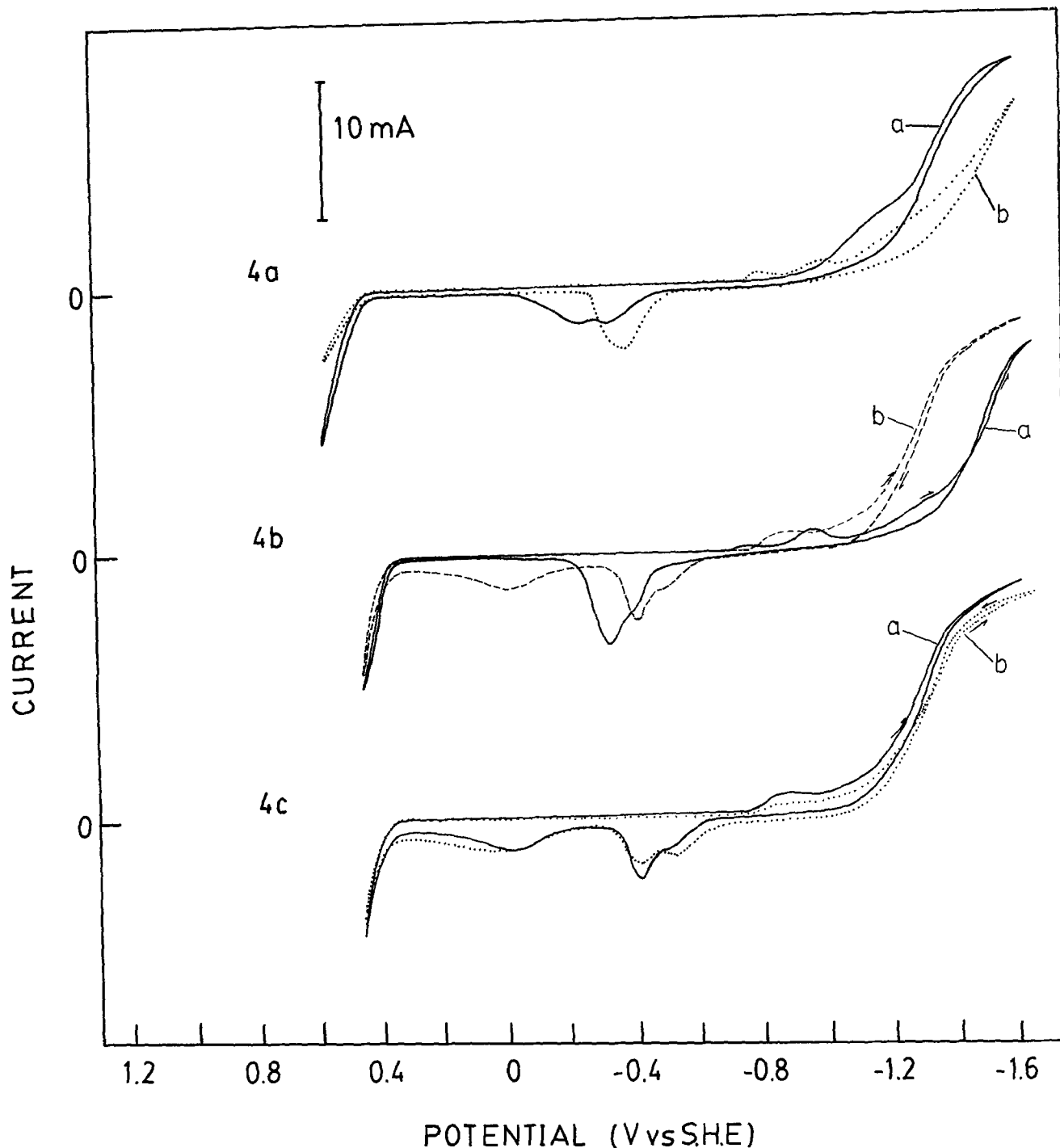


Fig. 4. Steady-state potential sweep profile of a 0.025M KOH + 0.1M KCN solution at 22°C. Sweep rate: $10 \text{ mV} \cdot \text{s}^{-1}$. 4a: effect of gold and silver. a: 17.5 ppm Au + 2.3 ppm Ag. b: 17.5 ppm Au + 2.3 ppm Ag + 1 ppm Pb. 4b: effect of gold and silver with copper and nickel. a: 17.5 ppm Au + 2.3 ppm Au + 300 ppm Cu. b: solution a + 250 ppm Ni. 4c: effect of metal combinations with and without lead. a: 17.5 ppm Au + 2.3 ppm Ag + 300 ppm Cu + 250 ppm Ni. b: solution a + 1 ppm Pb.

allow separation of the gold and silver plating peaks while inhibiting the hydrogen evolution reaction. The copper effects are masked by the presence of nickel. Lead has been shown to depolarize gold and silver plating reactions in alkaline cyanide as well as inhibit hydrogen evolution. Lead also enhances the separation of gold and silver plating peaks in potential scan measurements. The presence of nickel, however, eliminates the catalytic effects of lead.

Industrial solutions.—A steady-state potential sweep profile for an industrial leach solution is shown in Fig. 5. The solution composition is given in Appendix 1. The profile shows a single reduction peak at about -0.95V , which is most likely a mixed gold and silver plating reaction. The reaction begins at more negative

potentials than in the synthetic solution (Fig. 4c, curve b), and hydrogen evolution begins at less negative potentials. Thus, separation difficulties or poor current efficiencies might be expected for gold and silver recovery with potentials more negative than -1.0V . An anodic peak is seen at about -0.38V , and is characteristic of the gold and silver dissolution reaction found in the synthetic solutions. Another oxidation reaction is found beginning at about 0.0V . This corresponds to the nickel oxidation reaction observed in Fig. 3c starting at potentials near 0.0V . The reaction is irreversible, since no corresponding reduction peak could be found. A rotating glassy carbon disk electrode (2 mm diam) was also used to test the industrial leach solution. A single reduction wave was found beginning at -0.72

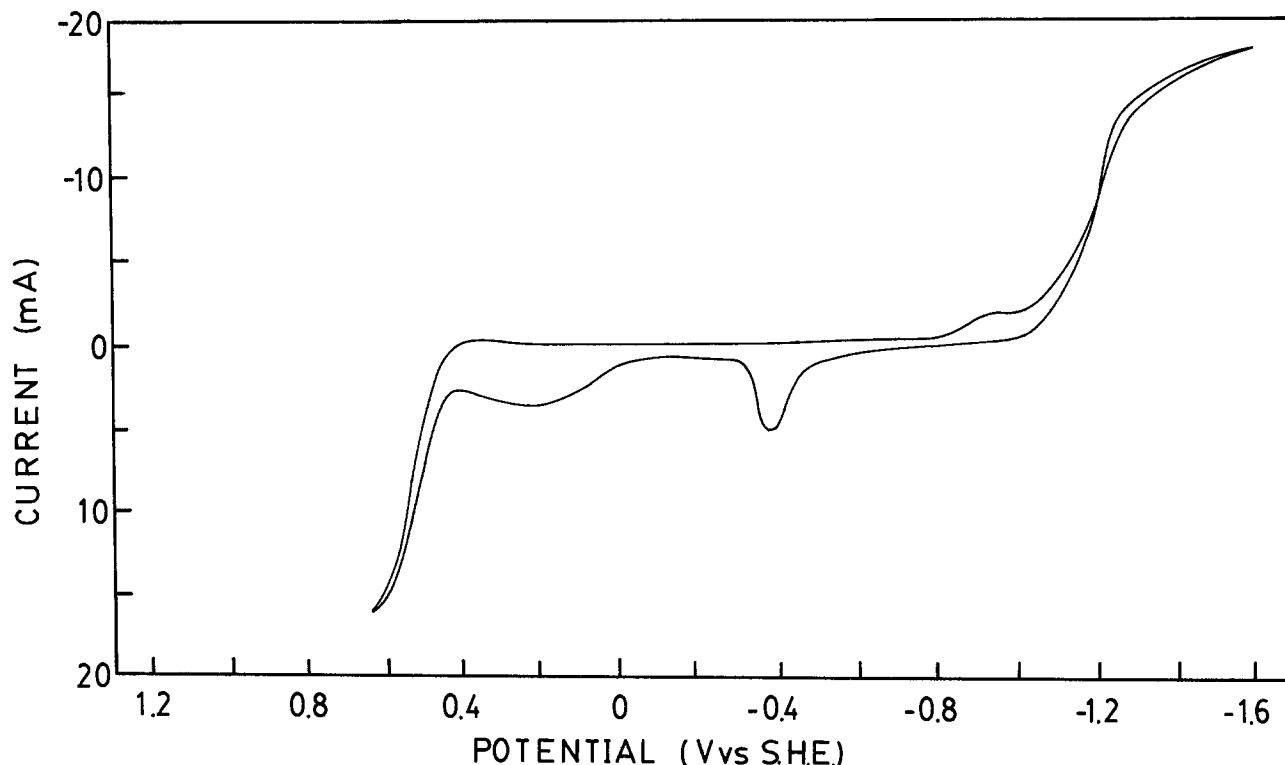


Fig. 5. Steady-state potential sweep profile of an industrial leach solution at 22°C. Sweep rate: $10 \text{ mV} \cdot \text{s}^{-1}$. Composition given in Appendix 1, cyanide concentration adjusted to 0.1M.

and leveling off at -0.86 V for a sweep rate of $10 \text{ mV} \cdot \text{s}^{-1}$.

At a sweep rate of $20 \text{ mV} \cdot \text{s}^{-1}$ and a rotation speed of 1000 rpm, the first sweep potential profiles were recorded with successive increments of gold (11 ppm units). The current measured at -0.76 V in the rotating disk measurements (corresponding to the plateau seen in Fig. 5) increased linearly with gold concentration.

The same procedure was followed with silver doping of the industrial leach solution with 10 ppm Ag increments. A shoulder, which was slightly better resolved at slower sweep rates ($5 \text{ mV} \cdot \text{s}^{-1}$), was found at -0.66 V in the potential sweep measurements. Although the currents at -0.66 V increased linearly with silver concentration, there was no well-defined limiting current region.

With copper additions of 200 ppm increments to the leach solution, the currents at potentials $\leq -1.36 \text{ V}$ increased with copper concentration, but there was no evidence of a peak or shoulder for copper plating. However, in the anodic scans, an oxidation peak was found at $+0.22 \text{ V}$, which increased with copper concentration.

The rotating disk measurements have better mass-transfer rates and more uniform potentials at the working electrode surface than do the graphite felt electrodes, so that the peak potentials tend to be closer to the reversible values. Thus, the plating peak found using the industrial leach solution is at -0.95 V for the porous carbon electrode and -0.86 V for the rotating disk electrode. Measurements using porous flow-through electrodes should correspond more closely to measurements using the porous carbon electrode.

Experiments also were conducted to determine the composition and extent of recovery at various potentials. These measurements were undertaken as a preliminary investigation of the behavior of the use of a porous flow-through reactor for metal recovery. Although the conditions for metal recovery were different than the conditions used in potential sweep measurements, the reactor used the graphite felt as a porous flow-through cathode. Diffusional limitations did not appear to be a significant factor in the work. A de-

scription of the reactor has been given in the experimental section.

The percentage of copper, gold, nickel, and silver recovered from the industrial leach solution is shown as a function of cathode potential in Fig. 6. It is clear from Fig. 6 that silver is efficiently recovered at potentials $\leq -0.66 \text{ V}$. The reduction peak found for silver in the potential scans is the result of silver deposition. The single reduction peak in the potential sweep measurements for the industrial leach solution indicates that the gold and silver reduction reactions were not well separated. This behavior is supported by the results of Fig. 6. Although not efficiently recovered, gold is partially removed from the electrolyte at -0.66 V .

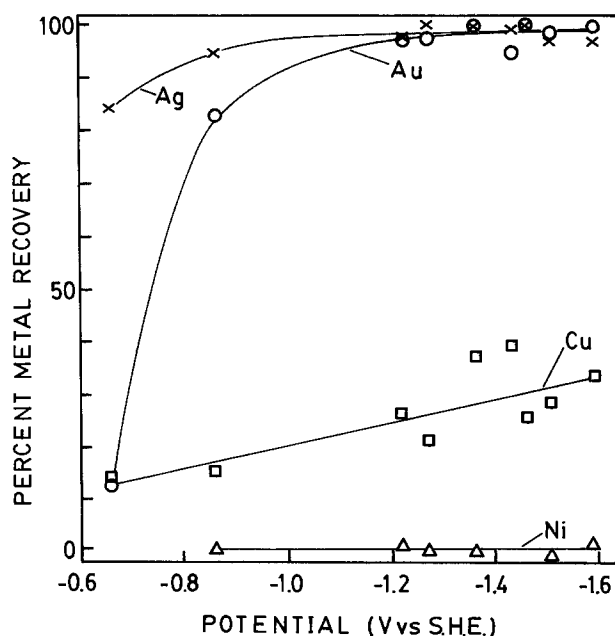


Fig. 6. Percent metal recovery from industrial leach solutions at various potentials. Flow rate: $15 \text{ ml} \cdot \text{min}^{-1}$, $T = 22.5^\circ \pm 1.5^\circ \text{C}$.

Some copper (14.5%) was also removed, although there is little evidence for copper ion reduction at potentials $\leq -1.36\text{V}$ in the potential scan measurements.

There are two possibilities for the unexpected copper recovery. One is that the metals codeposit and that the earlier evidence for copper deposition was hidden in the silver and gold peaks. It is known that copper contamination in gold plating baths results in codeposition Andreeva *et al.* (33) showed that with copper present in gold cyanide solutions, the gold overpotential increases and at the same time the copper overpotential decreases. Zur and Ariel (34) reported that the presence of copper in acid chloride solutions caused a lowering of gold recovery efficiency from 90% to $\leq 60\%$ with their porous electrode reactor. In our work, both gold and silver were recovered efficiently over a large potential region, but the recovered metal contained a large copper content. The mass ratio of Cu: Au in the industrial electrolyte is so great (10:1) that codeposition might be expected. The other possibility is that chemical adsorption might account for some of the recovery. Although the effect of chemical adsorption was reduced by allowing the solution to flow through the reactor for a minimum of 5 min before the experiment was commenced, and by operating the reactor at steady state for 30 min, chemical adsorption cannot be ruled out because of the large surface area of the porous electrode. Chemical adsorption might be expected to cause a fairly uniform utilization of the porous bed. However, this was not observed, since the metal distribution in the bed indicated that only the entrance region of the bed had a significant copper content. From Fig. 6, it can be seen that the copper recovery was at best 39.6% and showed only a small increase with potential. The cause of the large variation of percent recovery of copper has not been determined. The gold recovery is high at potentials $\leq -0.86\text{V}$. Thus, the gold reduction peak found in the potential sweep experiments corresponds to a gold plating reaction. The presence of nickel has a pronounced effect on synthetic solutions containing copper, silver, and gold. Although no reduction peak was found in the potential sweep work, an oxidation peak resulting from the prior reduction of nickel at potentials more negative than -1.2V was found. From Fig. 6, it can be seen that even at the most negative potentials (-1.59V) no nickel plating was found. Thus, it would appear that the nickel oxidation peak at -0.05V in the potential sweep work was not from deposited nickel; most likely it was from a reduced nickel cyanide species. It is not clear whether the effect of nickel in polarizing the gold and silver plating reactions and depolarizing the hydrogen evolution reaction is due to monolayer deposition or modification of the double layer. (The analysis for nickel was not sufficiently sensitive to detect monolayer deposition.) However, bulk deposition of nickel can be ruled out.

It was found that potential variation within the bed did not cause the codeposition of copper and gold with silver. The upstream position of the reference electrode caused the largest electrode/solution potential difference to occur in the upstream portion of the bed where 90% of the metal deposition took place. A decreasing potential difference was found with bed depth, so that the potentials shown in Fig. 6 represent the greatest driving force available for plating.

Conclusions

1. Linear scan voltammetry measurements show that metal ion interactions play a significant role in the behavior of alkaline cyanide solutions.

2. Lead in low concentrations (1 ppm) acts as a depolarizer for both silver and gold plating in alkaline cyanide. Lead also inhibits hydrogen evolution. The catalytic action of lead is not effective with nickel in the solution (250 ppm).

3. Copper (300 ppm) can act as a depolarizer for both silver and gold plating reactions in alkaline cyanide solutions. Hydrogen evolution is inhibited by copper if gold and silver are also present in the solution. The copper catalytic activity is inhibited by the presence of nickel (250 ppm).

4. Nickel (250 ppm) inhibits both silver and gold plating and depolarizes the hydrogen evolution reaction in alkaline cyanide solutions.

5. Gold and silver can be efficiently recovered from the industrial leach solution even in the presence of nickel. However, copper also codeposits.

Acknowledgments

The authors would like to thank R. Lenki for some of the measurements in this work and the Natural Sciences and Engineering Research Council of Canada for the financial support for this work.

Manuscript submitted Nov. 12, 1982; revised manuscript received Sept. 26, 1983.

APPENDIX 1

Analysis of the Industrial Leach Solution

Species	Concentration ppm
Au	17.5
Ag	2.3
Cu	300.0
Ni	250.0
Zn	30.0
Fe	0.5
Pb	1.3
As	1.0
Co	2.0
Al	0.4
Mg	2.0
Na,K	320.0
CN ⁻ total	700.0
CN ⁻ free	300.0
CNO ⁻	20.0
CNS ⁻	1800.0
S ₂ O ₈ ²⁻	1800.0
SO ₄ ²⁻	1020.0
S ²⁻	0.1
pH = 11.4.	

Analysis and solution courtesy of Pamour Mines, Porcupine, Ontario, Canada.

REFERENCES

- J. M. Williams and M. C. Olson, in "Water," G. F. Bennett, Editor, p. 119, AIChE Symp. Ser., New York (1976).
- K. B. Keating and J. M. Williams, *Resource Recov. Conserv.*, **2**, 39 (1976).
- A. W. Byrson and K. A. Dardis, *J. Chem. Technol. Biotech.*, **30**, 14 (1980).
- Ch. Yarnitzky, M. Ariel, and C. Zur, *J. Appl. Electrochem.*, **10**, 473 (1980).
- G. A. Carlson and E. E. Estep, *This Journal*, **119**, 114C (1972).
- J. D. E. McIntyre and W. F. Peck, *ibid.*, **123**, 1800 (1976).
- J. Divisek and B. Kastening, *J. Electroanal. Chem.*, **65**, 603 (1975).
- R. W. Zurilla, R. K. Sen, and E. Yeager, *This Journal*, **125**, 1103 (1978).
- N. A. Gordienko and L. I. Antropov, *Teor. Eksp. Khim.*, **6**, 708 (1970).
- I. Morcos, *This Journal*, **112**, 1008 (1975).
- S. Palous and R. Buvet, *Bull. Soc. Chim. Fr.*, 1602, 1606 (1962).
- Yu. A. Mazitov, K. I. Rozental, and V. I. Vevelovskii, *Elektrokhimiya*, **36** (1965).
- F. van den Brink, E. Barendrecht, and W. Visscher, *This Journal*, **127**, 2003 (1980).
- M. R. Tarasevich, G. I. Zakharkin, and R. M. Smirnova, *Elektrokhimiya*, **7**, 1293 (1971).
- G. Magner, M. Savy, and G. Scarbeck, *This Journal*, **127**, 1077 (1980).
- N. E. Khomutov and U. S. Stamkulov, *Zh. Vses. Khim. O-va.*, **15**, 459 (1970).

17. L. N. Nekrasov, *Electrochimica*, **4**, 362 (1968).
18. E. Yeager, N.T.I.S. AD-A Report AD-A011905 (1975).
19. W. M. Latimer, "The Oxidation States of the Elements and Their Potentials in Aqueous Solutions," 2nd ed., p. 201, Prentice-Hall, New York (1959).
20. H. Tamura, T. Arikado, H. Yoneyama, and Y. Matsuda, *Electrochim. Acta*, **19**, 273 (1974).
21. D. W. Kirk, F. R. Foulkes, and W. F. Graydon, *This Journal*, **125**, 1436 (1978).
22. D. W. Kirk, F. R. Foulkes, and W. F. Graydon, *ibid.*, **126**, 2287 (1979).
23. D. W. Kirk and F. R. Foulkes, *ibid.*, **127**, 1993 (1980).
24. D. W. Kirk, F. R. Foulkes, and W. F. Graydon, *ibid.*, **127**, 1962 (1980).
25. T. P. Pan and C. C. Wan, *J. Appl. Electrochem.*, **9**, 653 (1979).
26. D. M. MacArthur, *This Journal*, **119**, 672 (1972).
27. G. D. Parkes and J. W. Mellor, "Mellor's Modern Inorganic Chemistry," p. 593, Longmans, Green and Co., New York (1946).
28. R. A. Penneman and L. H. Jones, *J. Phys. Chem.*, **24**, 293 (1956).
29. D. N. Hume and I. M. Koltoff, *J. Am. Chem. Soc.*, **72**, 4423 (1950).
30. H. E. Barner and R. V. Scheuerman, "Handbook of Thermochemical Data for Compounds and Aqueous Species," p. 72, John Wiley and Sons, New York (1978).
31. J. O'M. Bockris and A. K. N. Reddy, "Modern Electrochemistry," p. 1103, Plenum, New York (1970).
32. G. A. Truesdale, A. L. Downing, and G. F. Lowden *J. Appl. Chem. (London)*, **5**, 53 (1955).
33. G. P. Andreeva, N. P. Fedot'ov, and P. M. Vyacheslavov *J. Appl. Chem. (USSR)*, **37**, 1465 (1964).
34. C. Zur and M. Ariel, *J. Appl. Electrochem.*, **11**, 639 (1981).

Gas Permeation in SPE Method

I. Oxygen Permeation Through Nafion and NEOSEPTA

Z. Ogumi,* Z. Takehara,* and S. Yoshizawa*

Department of Industrial Chemistry, Faculty of Engineering, Kyoto University, Kyoto, Japan

ABSTRACT

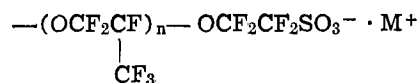
The permeation of oxygen at atmospheric pressure through Nafion® 120 and NEOSEPTA® ACH-45T ion-exchange membranes was investigated by an electrochemical monitoring technique, which utilizes SPE composite electrodes prepared by an electroless plating method. The oxygen diffusion coefficients were almost the same ($\sim 10^{-7} \text{cm}^2 \cdot \text{s}^{-1}$) for each material, but the oxygen solubility was much higher in Nafion than in NEOSEPTA. The oxygen solubility in NEOSEPTA could be explained in terms of dissolution in the aqueous component of the membrane, but the oxygen solubility in Nafion was too high for such an explanation, and was postulated to involve the role of the polytetrafluoroethylene backbone.

Recently, electrolyzers employing solid polymer electrolyte (SPE) have undergone extensive investigation for applications such as water electrolysis (1), brine electrolysis (2), and electro-organic synthesis (3-5). With these SPE methods, the permeation of electrochemically reactive species through the SPE material results in decreases in current efficiency and unwanted side reactions. This has been observed, for example, in electro-organic syntheses using "both-sides" SPE methods (5), in which anodic and cathodic reactions take place on electrodes deposited on both sides of the SPE membrane. Permeation by electrically neutral gases is easier than by ionic species bearing the same charge as the fixed ion of the SPE material because of the smaller size and absence of appreciable electrostatic repulsion in the case of the former. The permeation of diffusant depends strongly on the properties of the ion exchange membrane and on the conditions encountered.

Recent solid-polymer electrolyte fuel cells have received considerable interest as electrochemically regenerative energy storage systems (6). As encountered in electrolyzers, gas permeation through the solid-polymer materials (usually ion-exchange membranes) decreases efficiency of fuel cells.

Because of its high chemical and thermal stability, a perfluorinated sulfonic acid membrane such as Nafion® usually is employed in a solid-polymer electrolyte fuel cell. Perfluorinated ion-exchange membranes also are desirable for use with SPE electrolyzers, although conventional ion-exchange membranes based on a styrene-divinylbenzene copolymer may be applicable to some systems (3).

Nafion is based on a polytetrafluoroethylene backbone with pendant side chains of the form



The structure of Nafion has attracted the interest of many workers and has been the subject of considerable investigation (7). Using low angle x-ray measurements, Yeo and Eisenberg (8, 9) have inferred an ionic cluster model with a Bragg distance of 51Å. This model recently has been improved by Yeager and Steck (10). As mentioned above, permeation through Nafion is important both in fuel cells and in SPE electrolyzers. It is also of interest from the viewpoint of elucidating the peculiar structure of Nafion (7). In this regard, the permeation parameters of hydrogen (11), chlorine (11), and bromine (11, 12) have been investigated. In the present work, the diffusion coefficients and the solubilities of oxygen through Nafion 120 and NEOSEPTA® ACH-45T have been investigated by electrochemical monitoring of diffusion transients using SPE composite electrodes prepared by an electroless plating method (3). The values for the two different membranes are compared and discussed with reference to reported permeation parameter data.

Experimental

Membrane.—Nafion 120, a cation exchange membrane, and NEOSEPTA ACH-45T, an anion exchange membrane, were chosen for this study. These membranes have exchange capacities of 0.83 meq/g and 1.3-2.0 meq/g and thickness of 0.025 cm (unreinforced) and 0.014-0.020 cm (reinforced), respectively. The former is widely used as a chemically and thermally stable membrane with a perfluorosulfonic group and is the product of E. I. du Pont de Nemours and Company (Wilmington, Delaware), and the latter is a typical hydrocarbon anion exchange membrane with a quater-

* Electrochemical Society Active Member.

Key words: gas, diffusion, ion exchange, membrane.

nary ammonium group and the product of Tokuyama Soda Company (Yamaguchi, Japan).

The Nafion 120 membranes were pretreated by soaking in boiling water in the Na^+ form for 30 min. The NEOSEPTA membranes, supplied in the Cl^- form, were converted to the NO_3^- or OH^- form by immersion for more than 12h in 1M NaNO_3 or 0.5M NaOH .

Chemicals.—All chemicals except hydrazine were of reagent grade. Hydrazine was of chemical pure grade. All chemicals were used without further purification. Solutions were prepared with distilled water. Nitrogen was of 99.99% purity and oxygen of 99.6% purity.

Deposition of Pt or Ag on the membranes.—Platinum was deposited on one or both sides of the Nafion using an electroless plating method described previously from chloroplatinic acid solution using hydrazine as a reductant (3). In this method, the reductant diffuses through the membrane, which is set to separate a deposition cell into two compartments of a metal ion solution and of a reductant solution. The reductant diffusing through the membrane reduces the metal ion on the surface of the membrane facing the metal ion solution. NEOSEPTA in the NO_3^- or OH^- form was deposited with Ag by the same method, but on only one side. These prepared SPE composite electrodes are referred to as Pt-Nafion and Ag-NEOSEPTA, respectively.

Electrolysis cell.—The SPE composite electrode was mounted in the cell described schematically in Fig. 1. This cell was separated by the composite into two compartments. The right-hand compartment facing the deposited metal on the composite was filled with 0.5M K_2SO_4 , whereas the left-hand compartment contained prehumidified gas. The electrodes were connected to a potentiostat (Hokuto Denko Model HA-301). The electrode potential was measured against a Ag/AgCl (3.3M KCl) reference electrode positioned in a Luggin capillary. For linear potential sweep voltammetry, a function generator (Hokuto Denko Model HB-104) was connected to the potentiostat, and nitrogen was bubbled through the right-hand compartment throughout the experiment. The temperature of the solution in the right-hand compartment was kept constant by circulating the solution between the cell and the stock tank, which was located in a thermostated bath. The gas temperature was kept constant by flowing the gas through a long copper tube immersed in the constant temperature bath.

Permeation measurements.—The permeation of oxygen through the membrane was monitored using the electrochemical technique used by Yeo *et al.* (11) to

measure the permeation of hydrogen and halogens through Nafion and by Nanis *et al.* (13) and Yoshizawa *et al.* (14) to measure hydrogen permeation through iron.

When oxygen was introduced into the left-hand compartment of the cell in Fig. 1, which was previously filled with nitrogen, oxygen permeated the membrane separating the two compartments. The oxygen permeation rate was monitored electrochemically by the SPE composite electrode bonded to the side of the membrane away from the gas compartment. This was achieved by setting the potential of the bonded electrode at a value at which the incoming oxygen was reduced under mass-transfer-limited conditions. All measurements were carried out at atmospheric pressure.

Results

E-i relationships.—Figure 2 shows the results from a set of linear potential sweep experiments on Pt-Nafion. Curve a was obtained using 100% nitrogen and curve b using 100% oxygen. Despite the very slow sweep rate of $5 \text{ mV} \cdot \text{s}^{-1}$, at $-0.1 \text{ V vs. Ag}/\text{AgCl}$, a small current peak is observed that corresponds to the reduction of the oxygen permeating through the membrane. A comparison of curve b with curve a shows that oxygen is reduced under mass-transfer limiting conditions below $-0.05 \text{ V vs. Ag}/\text{AgCl}$. The mass transfer is here controlled by the diffusion through the membrane. Similar E-i curves were obtained using Ag-NEOSEPTA.

Although the actual mechanism of oxygen reduction on SPE composite electrodes is a complex problem, it has been assumed that the overall reduction on Pt-Nafion and on Ag-NEOSEPTA takes place according to the four-electron reduction process. It is reasonable to assume that oxygen ultimately is reduced to water on Pt and Ag electrodes on SPE composites since the metals are deposited in a manner similar to that of Pt blacks (3) and are known to be very active catalysts for the decomposition of any peroxides that might be formed as intermediates (15). This will be discussed in more detail in a subsequent paper (16). In all the experiments of the present work, therefore, the potential of the SPE composite electrode was set at $-0.25 \text{ V vs. Ag}/\text{AgCl}$ in order to reduce oxygen under diffusion limiting conditions. The steady-state reduction current was assumed to be proportional to the oxygen content of the gas in the left-hand compartment of the cell.

Oxygen permeation results.—The oxygen permeation transients observed as reduction currents reflect diffusion under a well-defined set of initial and boundary conditions. These conditions can be described in terms of the variation with time (t) of the oxygen concentration (c) at any distance (x) from the left-hand side

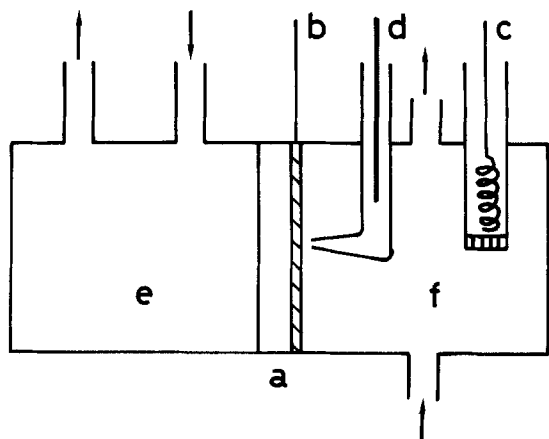


Fig. 1. Schematic diagram of an electrolysis cell fitted with a one-side SPE composite. a: SPE composite. b: working electrode on SPE composite. c: counterelectrode. d: Ag/AgCl reference electrode. e: gas compartment. f: 0.5M K_2SO_4 .

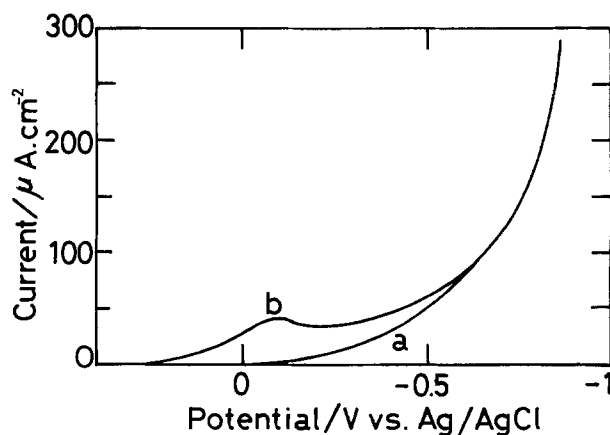


Fig. 2. E-i curves on Pt-Nafion. Sweep rate: $5 \text{ mV} \cdot \text{s}^{-1}$. Curve a: nitrogen. Curve b: oxygen in the gas compartment, 0.5M K_2SO_4 in the right compartment.

of the membrane, which has a thickness (l). Assuming the stepwise introduction of oxygen into the left-hand compartment at time $t = 0$ and that the dissolved oxygen concentration at the input side of the membrane instantaneously achieves and maintains the constant value (c_0), then

$$c = c_0; x = 0; t \geq 0 \quad [1]$$

Since oxygen arriving at the right-hand side (*i.e.*, at the electrode on the SPE composite) is reduced quantitatively to water, then

$$c = 0; x = l; t \geq 0 \quad [2]$$

Prior to the introduction of oxygen, the membrane contacts 100% pure nitrogen gas and nitrogen-saturated 0.5M K_2SO_4 , so that the initial condition is

$$c = 0; 0 < x < l; t = 0 \quad [3]$$

Fick's second law (Eq. [4]) is applicable and can be solved under the conditions set by Eq. [1]-[3] by the use of Laplace and Fourier transformations

$$\frac{\partial c}{\partial t} = D \frac{\partial^2 c}{\partial x^2} \quad [4]$$

The oxygen diffusion flux (J) is described by Fick's first law

$$J = -D \frac{\partial c}{\partial x} \quad [5]$$

Solving the above equations yields the flux (J_t) at $x = l$ and time t in terms of the dimensionless form (J_t/J_∞) *vs.* τ , the reduced dimensionless time

$$J_t/J_\infty = (2/\sqrt{\pi\tau}) \cdot \exp(-1/4\tau) \quad [6]$$

where

$$\tau = Dt/l^2 \quad [7]$$

D is the diffusion coefficient, and J_∞ is the steady-state flux at $t \rightarrow \infty$. The numerically obtained theoretical curve of (J_t/J_∞) *vs.* τ is plotted as the solid line in Fig. 3.

Under steady-state diffusion conditions, a linear concentration gradient is established through the membrane and the flux can be expressed in terms of the steady-state current density i_∞

$$i_\infty = \frac{nFDc_0}{l} \quad [8]$$

where n assumed to be 4, is the number of mols of electrons consumed per mol of oxygen reduced at the monitoring electrode on the SPE. A plot of J_t/J_∞ ($=i_t/i_\infty$) against time (t) should fit with the theoretical curve of Fig. 3. The selection arbitrarily of one point from the curve leads directly to the value of D through Eq. [7]. For example, $J_t/J_\infty = i_t/i_\infty = 1/2$ corresponds to $\tau = 0.138$ from Eq. [6] or from the theoretical curve of Fig. 3. Using Eq. [7]

$$D = 0.138 \cdot l^2/t_{1/2} \quad [9]$$

where $t_{1/2}$ is the time at which (i_t/i_∞) becomes 1/2 on the experimentally obtained plot of (i_t/i_∞) *vs.* t . The closeness of the fit of the experimental transient curve with the theoretical curve is a measure of the extent to which the diffusional behavior of the system agrees with the postulated model. The fit also tests the experimental results. As an example, the broken "build-up" curve in Fig. 3 shows one set of experimental results obtained for the transient permeation behavior of oxygen through Pt-Nafion at 25°C.

The steady-state permeation rate (i_∞) can be directly measured, and c_0 can be calculated from Eq. [8] using the D value obtained from the transient measurement.

An analogous theoretical analysis can be made for the stepwise change of the gas composition in the left-hand compartment from oxygen to nitrogen. Since in this case the current decreases with time, the curve is called a "decay" curve (as opposed to the previous case, in which the curve resulting from the introduction of oxygen was termed a "buildup" curve). The theoretical decay curve also was calculated and is shown in Fig. 3. The experimental results show good agreement with both the buildup and decay curves. The current was corrected for the inevitable residual current ($\sim 10 \mu A$) shown in Fig. 2, which was measured before and after all experiments and stayed small and almost constant during each measurement.

Table I summarizes the results of permeation measurements on Pt-Nafion and Ag-NEOSEPTA. It can be seen that the oxygen diffusion coefficients are almost identical in both membranes. The oxygen solubility, however, is remarkably higher in Pt-Nafion than in Ag-NEOSEPTA. Figure 4 shows the Arrhenius plot for the oxygen diffusion coefficient in Pt-Nafion when the right-hand compartment contained 0.5M K_2SO_4 solution and the left-hand compartment contained prehumidified oxygen gas. Analysis of the re-

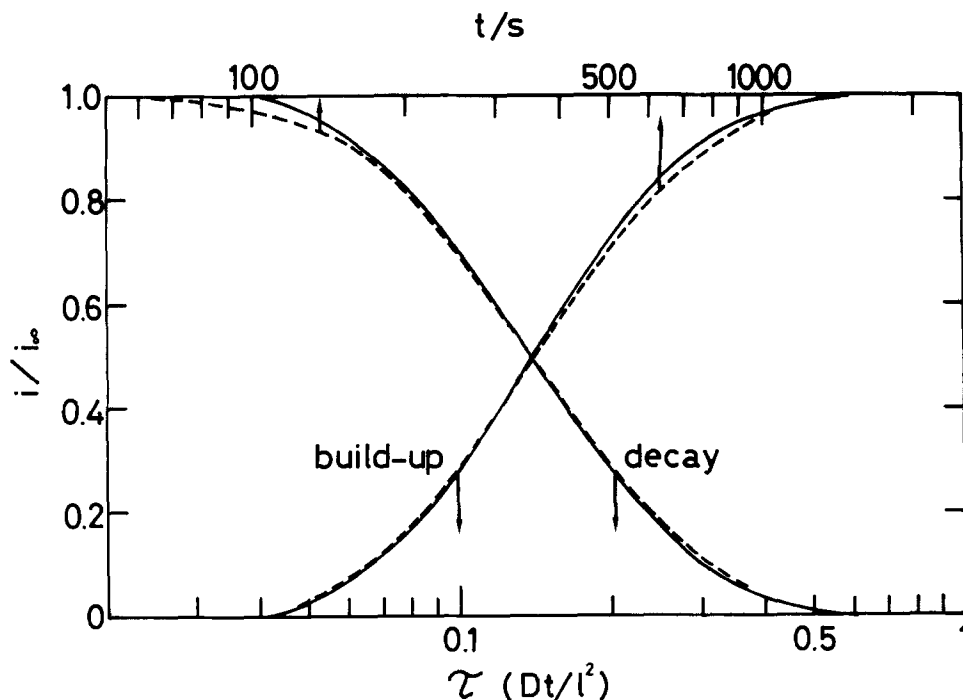


Fig. 3. Oxygen permeation transient currents. Solid line: theoretical curves from Eq. [6]. Broken line: experimental results through Pt-Nafion at 25°C in 0.5M K_2SO_4 .

Table I. Permeation parameter of oxygen through Nafion and NEOSEPTA ACH-45T

Membrane	Temp °C	$J_{\infty} \times 10^6$ A · cm ⁻²	$t_{1/2}$ s	$D \times 10^7$ cm ² · s ⁻¹	$c_0 \times 10^8$ M
Nafion	20	26.7	355	2.4	7.20
	30	28.6	295	2.9	6.50
	40	36.7	193	4.4	5.30
	50	46.8	197	5.2	5.90
NEOSEPTA	25	4.7	131	2.4	0.77

sults shows that

$$D = 3.1 \times 10^{-3} \exp(-5500 \pm 120/RT) \text{ cm}^2 \cdot \text{s}^{-1} \quad [10]$$

where $R = 1.987 \text{ cal} \cdot \text{mol}^{-1} \cdot \text{deg}^{-1}$ and T is absolute temperature. The diffusion coefficient was found to be dependent on the sample number and pretreatment history of the Nafion, which will be discussed in detail in a subsequent paper; the oxygen solubility was almost independent of the sample and pretreatment.

Discussion

E-i relationships.—Even at the very slow sweep rate of $5 \text{ mV} \cdot \text{s}^{-1}$, a small peak was observed in the oxygen voltammogram in Fig. 2. This reflects the very small diffusion coefficient of $10^{-7} \text{ cm}^2 \cdot \text{s}^{-1}$ (discussed below) and the formation of a stable diffusion layer that must be inside the membrane. At faster sweep rates, very large double layer charging currents were observed that can be ascribed to very large active surface areas of the SPE composite electrodes. Ag-NEOSEPTA was stable for more than 50h during the permeation measurements. Since stable peroxides would very readily attack NEOSEPTA ACH-45T membranes, this supports the assumption that peroxides are not formed as intermediates during the oxygen reduction, or, if formed, are rapidly decomposed. This confirms that oxygen is totally reduced on the electrode to water by the four-electron process.

Oxygen permeation.—The good agreement of the experimental curves with the theoretical curves over the complete range of values confirms that the permeation obeys the postulated ideal diffusion behavior and that the deposition of metals on the membrane does not disturb the ideal diffusional conditions.

Table II summarizes some diffusion coefficients and solubilities of oxygen and a number of other species in

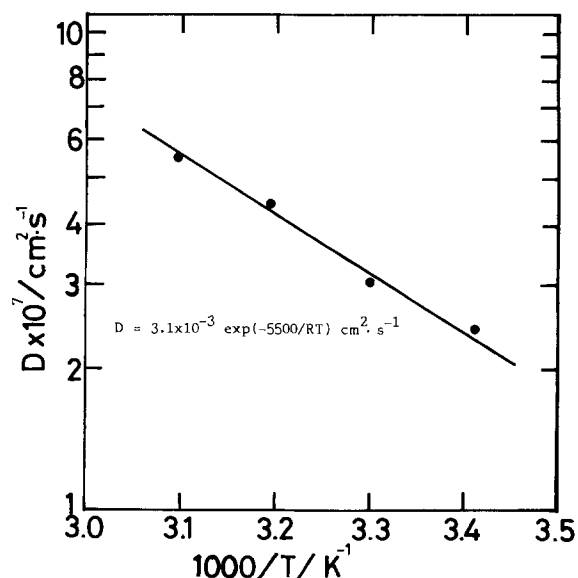


Fig. 4. Arrhenius plot for oxygen diffusion coefficient through Pt-Nafion in $0.5M \text{ K}_2\text{SO}_4$.

Table II. Diffusion coefficients and solubilities of oxygen and others in several media

Diffusant	Medium	Temp °C	$D \times 10^7$ cm ² · s ⁻¹	$c \times 10^8$ M	Ref.
O ₂	H ₂ O	25	295.00	1.30	(17)
	0.5M K ₂ SO ₄	25	—	0.85	(17)
	0.5M H ₂ SO ₄	25	—	1.13	(17)
	n-C ₇ F ₁₆ PTFE	25	—	26.80	(18)
H ₂	Nafion 120	25	1.40	26.80	(19, 20)
	14% HCl aq	25	6.60	24.50	(11)
Cl ₂	Nafion 120	25	2.40	110.00	(11)
	14% HCl aq	25	—	—	—
Br ₂	Nafion 120	25	1.17	—	(12)
	4M NaBr	25	—	—	—
Na ⁺	Nafion 120	60	1.96	—	(21)
	9.5M NaOH	60	—	—	—

several media that are relevant to Nafion and NEOSEPTA ACH-45T. The oxygen diffusion coefficients shown in Table I for Pt-Nafion and Ag-NEOSEPTA, which are almost equal in value, are reasonable when compared with the values in Table II for chlorine (11) and bromine (12) through Nafion, although the values are two orders of magnitude smaller than the corresponding values in water (17).

The activation energy for the diffusion of oxygen through Nafion has been determined to be about $5500 \text{ cal} \cdot \text{mol}^{-1}$ (see Fig. 4). This value appears reasonable in view of the values of $5170 \text{ cal} \cdot \text{mol}^{-1}$ for hydrogen through Nafion and $5560 \text{ cal} \cdot \text{mol}^{-1}$ for chlorine through Nafion determined by Yeo and McBreen (11).

The relatively low oxygen solubility in Ag-NEOSEPTA is easily explained by the dissolution of the gas in the aqueous portion of the membrane when the volume of the hydrocarbon backbone and the high concentration of the electrolyte in the membrane are taken into consideration. However, the oxygen solubility in Pt-Nafion was found to be much higher than in Ag-NEOSEPTA. The structure of Nafion is much different from NEOSEPTA, a usual hydrocarbon ion exchange membrane. In their model, Yeager and Steck divided Nafion into three regions, a hydrophobic PTFE backbone region, a hydrophilic aqueous region, and an intermediate region (10). They concluded the aqueous region as almost the same as an aqueous solution of high concentration. Adopting their model, we see that this high solubility cannot be borne by the aqueous part of the Nafion on account of the very low solubility of oxygen in water or in aqueous solution (17). Additionally, changing cation from K^+ to Na^+ scarcely caused the change of the solubility. As indicated in Table II, oxygen is, however, highly soluble in some hydrophobic solvent, e.g., benzene or fluorinated solvents (18). The solubilities and permeabilities of several gases through polytetrafluoroethylene (PTFE) have been investigated using gold and platinum metallized thin PTFE membranes (19, 20). The data for oxygen are included in Table II. Yeo *et al.* (11) and Will (12) seem to have considered that the diffusants dissolve in the aqueous portion of Nafion. Although this explanation is sufficient to explain the solubilities of chlorine and bromine in Nafion, the solubilities of hydrogen, determined by Yeo *et al.* and of oxygen, from the present work, are too high to be explained on this basis. The high solubilities indicate a specific interaction between the PTFE backbone of Nafion and the hydrogen and oxygen, thus resulting in some special influence of the PTFE backbone on the gas permeation characteristics of Nafion. The influence of the PTFE backbone should appear in both hydrophobic and intermediate regions of Nafion in the model by Yeager and Yeo. The details of these effects are being investigated.

Summary

The permeation of oxygen through Nafion 120, a cation-exchange membrane of the perfluorinated sul-

ionic acid type, and through NEOSEPTA ACH-45T, an anion-exchange membrane of styrene-divinylbenzene copolymer, was investigated by an electrochemical monitoring technique using SPE composite electrodes. While the oxygen diffusion coefficients of both membranes were quite similar, the oxygen solubility was much higher in Nafion than in NEOSEPTA. The higher value in Nafion cannot be explained in terms of dissolution of the gas in the aqueous part of the membrane. Instead, specific interaction between oxygen and hydrophobic backbone in Nafion is inferred.

Acknowledgments

Special thanks are due to Professor F. Foulkes, visiting professor from the University of Toronto, for his helpful discussions. The authors also wish to thank E. I. du Pont de Nemours and Company and the Tokuyama Soda Company for providing membrane samples.

Manuscript submitted Aug. 15, 1983; revised manuscript received Nov. 16, 1983.

Kyoto University assisted in meeting the publication costs of this article.

REFERENCES

1. P. W. T. Lu and S. Srinivasan, *J. Appl. Electrochem.*, **9**, 269 (1979).
2. A. P. Laconti, Japan Tokkyo Kokai, 54-112398 (1979).
3. Z. Ogumi, K. Nishio, and S. Yoshizawa, *Denki Kagaku*, **49**, 212 (1981).
4. Z. Ogumi, K. Nishio, and S. Yoshizawa, *Electrochim. Acta*, **26**, 1779 (1981).
5. Z. Ogumi, H. Yamashita, K. Nishio, and S. Yoshizawa, *Electrochim. Acta*, **28**, 1687 (1983).
6. E. Gileadi, S. Srinivasan, F. J. Salzano, C. Brun, A. Beaufriere, S. Gottesfeld, L. J. Nuttall, and A. B. Laconti, *J. Power Sources*, **2**, 191 (1977).
7. "Perfluorinated Ionomer Membranes," Chap. 7-13, A. Eisenberg and H. L. Yeager, Editors, ACS Symposium Series 180, American Chemical Society, Washington, DC (1982).
8. R. S. Yeo and A. Eisenberg, *Polymer Prepr.*, **16**, 104 (1975).
9. R. S. Yeo and A. Eisenberg, *J. Appl. Polym. Sci.*, **21**, 875 (1977).
10. H. L. Yeager and A. Steck, *This Journal*, **128**, 1880 (1981).
11. R. S. Yeo and J. McBreen, *ibid.*, **126**, 1682 (1979).
12. F. G. Will, *ibid.*, **126**, 36 (1979).
13. J. McBreen, L. Nanis, and W. Beck, *ibid.*, **113**, 1218 (1966).
14. S. Yoshizawa and K. Yamakawa, *Boshoku Gijutsu*, **24**, 365, 511 (1975).
15. J. P. Hoare, "The Electrochemistry of Oxygen," p. 117, Interscience, New York (1968).
16. Z. Ogumi, N. Yoshida, K. Nishio, Z. Takehara, and S. Yoshizawa, In preparation.
17. Chemical Society of Japan, "Kagaku Binran," Maruzen, Tokyo (1975).
18. M. H. A. Hamza, G. Serratrice, M. J. Sebe, and J. J. Delpuechy, *J. Am. Chem. Soc.*, **103**, 3733 (1981).
19. T. K. Gibbs and D. Pletcher, *Electrochim. Acta*, **25**, 1105 (1980).
20. C. McCallum and D. Pletcher, *ibid.*, **20**, 811 (1975).
21. H. L. Yeager, B. Kipling, and R. D. Dotson, *This Journal*, **127**, 303 (1980).

Kolbe Electrolysis of Mixtures of Aliphatic Organic Acids

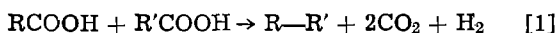
P. F. Levy, J. E. Sanderson, and L. K. Cheng

Dynatech R/D Company, Cambridge, Massachusetts 02139

ABSTRACT

Kolbe electrolysis of mixtures of n-butanoic with n-hexanoic acid and propanoic with n-hexanoic acid have been performed in aqueous solution at a smooth platinum anode. Typically, hexane production by the oxidation of butanoic acid, or butane production from propanoic acid, in aqueous solution is not observed to exceed a few percent. In the current work, significant increases of these products were observed. In addition, a substantial fraction of the remaining C₃ or C₄ acids reacted were converted to mixed alkane dimers with hexanoic acid. These results are interpreted by a model in which n-hexanoic acid and its various oxidation products form a lipophilic layer at the anode surface which provides an environment where further oxidation to carbonium ions is disfavored. This model has been suggested previously to explain pressure effects on Kolbe electrolysis (1). This observation supports the feasibility of producing mixed linear alkanes for use as fuels and chemicals from mixed organic acids which may be produced by anaerobic fermentation of organic matter.

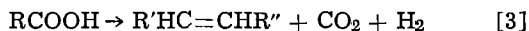
The Kolbe reaction, decarboxylation and dimerization of aliphatic carboxylic acids, has been observed to occur at smooth platinum anodes (2, 3) following the stoichiometry



Hofer and Moest (4) described the electrolytic oxidation of organic acids to produce alcohols



a reaction which is prevalent at carbon anodes (5). Production of side products has been observed to accompany alcohol and dimer formation. The primary side product is usually olefin



where R' and R'' are either hydrogen or organic radicals. Other side products include esters, nondimerized alkanes, and cyclopropane derivatives (3, 6). Oxygen can also be produced when the reactant is carried out in aqueous solution, particularly at low current densities.

The production of dimeric alkane (Kolbe) product predominates when the reaction is carried out at smooth platinum anodes with acetic and fatty acids containing at least six carbon atoms. Reported yields of Kolbe product from propanoic acid are only a few percent and n-butanoic only slightly higher (5, 7). This paper reports increased yields of dimer product from propanoic and n-butanoic acids in mixtures with n-hexanoic acid. A model is suggested to explain these results. Effects seen due to changing current density, temperature, liquid flow rate, and reactant concentration are consistent with the suggested model.

Experimental

The details of the experimental electrolysis system used in this study are described in a previous paper (1). Briefly, the system shown in Fig. 1 consists of a flow-through electrolytic cell (ECO, Incorporated) modified and reinforced to allow it to be operated at elevated pressure, a 1 liter liquid reservoir, pump, power supply, and condenser. Product gas collection

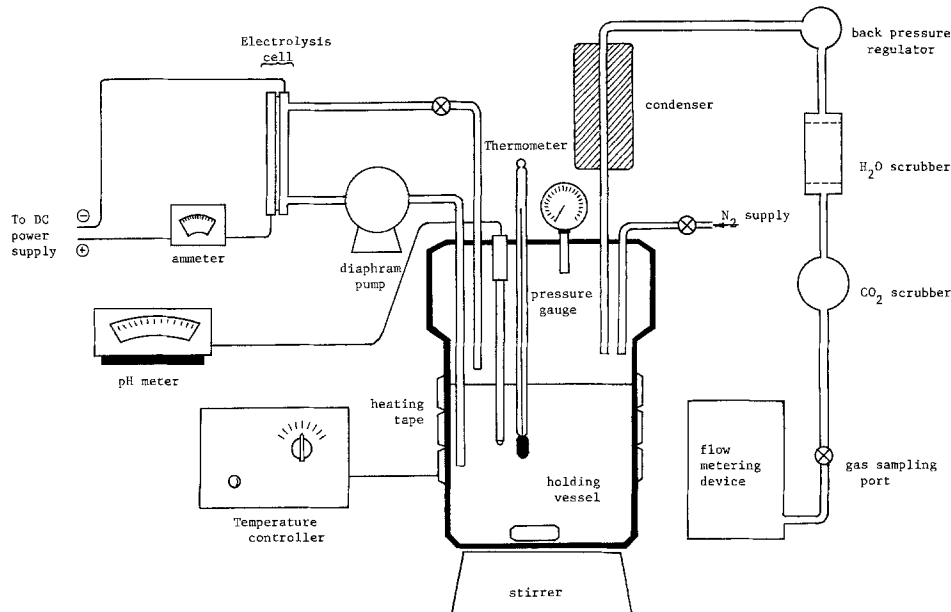


Fig. 1. Diagram of integrated electrolysis system.

is accomplished by liquid displacement. The anode is a platinum foil sheet and cathode is stainless steel. The electrodes are separated by a pressed fiber gasket giving an electrode spacing of approximately 0.15 mm. The exposed internal surface area of the electrodes is either 36.0 or 7.33 cm².

All products (gaseous, water immiscible, and water soluble) are separated and quantified by gas chromatography. All reagents were reagent-grade materials obtained from major supply houses and were used without purification. In all experiments, 0.5M sodium sulfate was used as a supporting electrolyte. The pH of the solution was adjusted to 7.0 with sodium hydroxide at the start of each experiment.

Results

Experiments were run in which mixtures of various concentrations of butanoic and hexanoic or propanoic and hexanoic acids were reacted, temperature was varied in the reaction of butanoic or pentanoic acid, and flow rate, concentration, or current density was varied in the reaction of pentanoic acid.

In the tabulation of the results of these experiments, the product distributions are reported as percent of organic acid reactant converted to each product based on the total amount of that organic acid reacted in the experiment. In each experiment reported, hydrogen is recovered accounting for the total current supplied. Material balances indicated in the results show the percentage of anode product recovered compared to the total current supplied.

Mixtures of butanoic and hexanoic acids were electrolytically oxidized on a platinum anode. The initial pH in all these experiments was 7.0 and the final pH was 9.0 (± 0.3). The yield of butanoic acid products

is shown in Table I. The yield of coupled products formed entirely or partially from 0.7M butanoic acid (n-hexane and n-octane) increases as the initial concentration of hexanoic acid increases, up to 0.35M, as seen in Fig. 2. The ratio of butanoic to hexanoic acid reacted in these experiments is observed to decrease as hexanoic acid concentration is increased (Fig. 3). This ratio can be normalized as indicated in the figure, and the normalized ratio of acids reacted is approximately 1/3 (butanoic/hexanoic) at all hexanoic acid concentrations above 0.35M. In the same set of experiments, the formation of coupled products from hexanoic acid (n-octane and n-decane) in the presence of 0.7M butanoic acid follows a similar pattern to that observed for butanoic acid when examined as a function of hexanoic acid concentration (Fig. 4).

An analogous increase in the formation of coupled products (butane and heptane) from propanoic acid was seen when hexanoic acid was added to the electrolysis solution (Table II). In these experiments the normalized ratio of propanoic/hexanoic acid reacted is 1/6.25.

The effects of temperature, current density, concentration, and liquid flow rate were observed in electrolysis solutions containing a single reacting organic acid (butanoic or pentanoic). The results in general are consistent with other studies of these variables (6). Table III shows an increase in alcohol formation at increased temperature. Table IV shows a decrease in dimer formation with decreasing flow rate (Runs 158, 164, and 166). At a relatively low flow rate, an increase in organic acid concentration restores dimer formation to that seen at high flow rates (Runs 166, 167, and 168). An effect on the product distribution is observed for current densities below 0.27 A/cm² (Fig.

Table I. Percent yields of butanoic acid products from electrolytic oxidation of mixtures of butanoic and hexanoic acids on platinum anode* (current density 0.28 A/cm²; pH 7-9; atmospheric pressure)

Run	Reacting organic acids	Propanols	Esters	Olefins	Paraffins	Material balance	C ₄ /C ₆ Reacted
118	1.4M butanoic	45.7	4.0	31.1	17.1	93.0%	—
130	1.4M butanoic	42.6	1.7	33.6	20.5	89.0%	—
134	0.7M butanoic/0.1M hexanoic	40.0	4.3	35.6	17.5	82.3%	5.14
133	0.7M butanoic/0.2M hexanoic	25.6	11.5	28.7	31.2	84.7%	1.90
136	0.7M butanoic/0.3M hexanoic	19.5	14.7	16.5	46.7	82.2%	0.75
132	0.7M butanoic/0.35M hexanoic	13.9	12.5	14.1	56.4	93.6%	0.66
122	1.4M butanoic/0.7M hexanoic	2.9	3.7	10.7	76.8	88.7%	0.59
137	0.7M butanoic/0.5M hexanoic	7.8	14.5	13.1	62.1	81.5%	0.47
119	0.7M butanoic/0.7M hexanoic	15.6	6.3	15.6	53.2	86.0%	0.30
131	0.7M butanoic/0.7M hexanoic	1.7	20.6	12.3	62.2	84.2%	0.32
135	0.7M butanoic/1.0M hexanoic	2.0	28.1	10.2	57.1	89.2%	0.23

* Yields based on mol percent of total butanoic acid consumed to form measured quantities of each product.

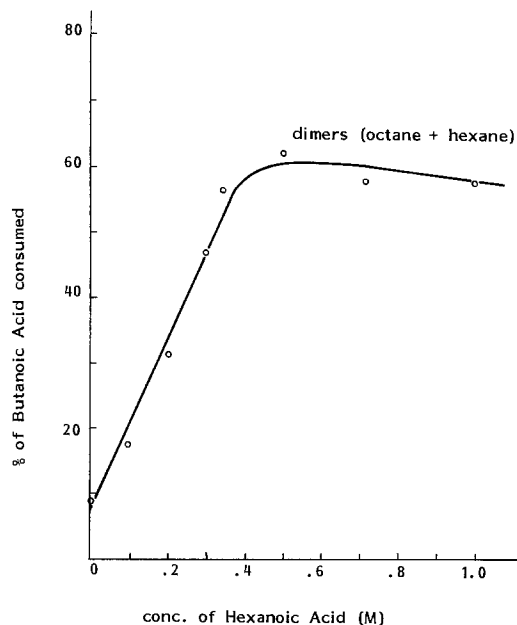


Fig. 2. Yield of dimeric alkane products from butanoic acid in mixtures with varying concentrations of hexanoic acid.

5). As the current density decreases, products requiring a two-electron oxidation are favored. At current densities below 0.13 A/cm^2 a significant increase in production of O_2 from water is observed.

Discussion and Conclusions

Conditions favoring production of coupled products from propanoic, butanoic, and pentanoic acids have been reported. These conditions include the presence of hexanoic acid, current densities above 0.27 A/cm^2 , low temperature, high liquid flow rate, and high reacting organic acid concentrations. Earlier work demonstrated increased yields of coupled products at elevated reactor pressures (1).

The hypothesis suggested in our earlier paper (1), that coupled product yield is increased by improving the integrity of a lipophilic layer at the electrode surface, is further supported by the experimental results presented in this paper. The influence of hexanoic acid on the products formed from butanoic acid is interpreted to be caused by the formation of a lipophilic layer comprised of hexanoic acid, its electrolysis prod-

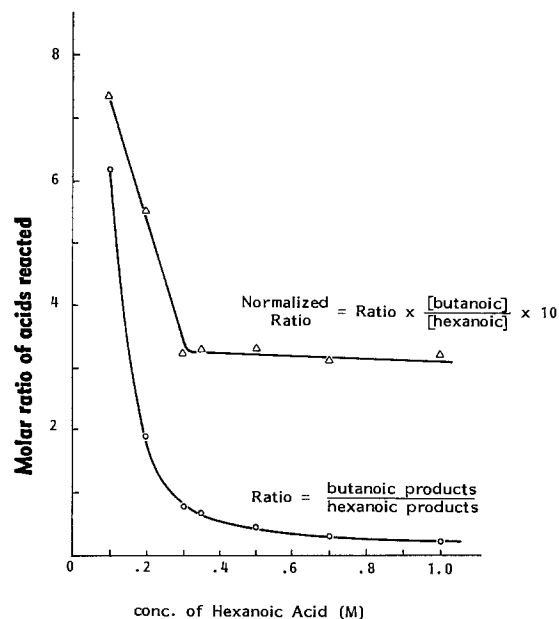


Fig. 3. Ratio of butanoic to hexanoic acid reacted as a function of hexanoic acid concentration in the mixture.

ucts, and intermediates. The existence of this layer is most strongly supported by the ratio of butanoic/hexanoic acid reacted in the mixed acid experiments. The normalized ratio of 1/3 (Fig. 3) suggests a higher partition coefficient for hexanoic acid than butanoic acid into the lipophilic layer. Observation of a lower normalized ratio between propanoic and hexanoic acids is consistent with the relative partition coefficients of these acids between aqueous and organic solvents.

If it is the influence of the lipophilic layer that primarily controls the product distribution rather than properties of the reacting acids themselves, then the formation of coupled products in the mixed acid runs should be governed by a mass action statistical distribution. The formation of coupled products from two reacting organic acids can be represented by the general equation

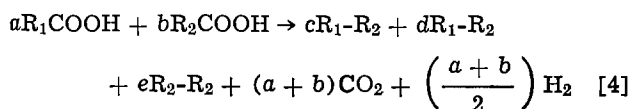


Table II. Percent yields of propanoic acid products from electrolytic oxidation of mixtures of propanoic and hexanoic acid on platinum anode* (current density 0.28 A/cm^2 ; pH 7-9; atmospheric pressure)

Run	Reacting organic acids	Ethene	Butane	Heptane	Ethanol	Esters	Material balance	Cs/Ca
147	2.0M propanoic	60.9	0.0	—	30.8	8.6	94.3	—
151	2.0M propanoic/1.0M hexanoic	43.1	33.5	15.1	3.6	4.6	90.0	0.32
152	1.4M propanoic/1.0M hexanoic	28.8	14.8	44.0	2.2	10.3	101.1	0.24
153	1.4M propanoic/0.7M hexanoic	25.7	9.2	42.0	5.6	5.3	81.0	0.30

* Yields based on mol percent of total propanoic acid consumed to form measured quantities of each product.

Table III. Effect of temperature on yield of products* (current density 0.28 A/cm^2 ; pH 7-9; atmospheric pressure)

Run	Reacting organic acid	Temperature ($^{\circ}\text{C}$)	Alcohols	Esters	Dimers	Olefins	Other**	Current to O_2	Material balance
130	1.4M butanoic	22	42.6	1.7	20.5	33.6	1.6	—	89.0
141	0.7M butanoic	22	65.6	0.0	8.9	24.4	1.0	3.4	100.0
138	0.7M butanoic	80	73.1	<1	4.9	21.3	0.7	13.3	98.3
140	0.7M pentanoic	22	25.3	9.7	36.1	25.4	3.4	3.4	100.0
139	0.7M pentanoic	80	44.7	6.1	29.5	16.1	3.6	9.1	100.0

* Product yields calculated as mol percent acid reacted to form product compared to total mols acid reacted in run. Current forming O_2 expressed as percent of current supplied in run.

** Refers to disproportionation products such as butane from pentanoic acid.

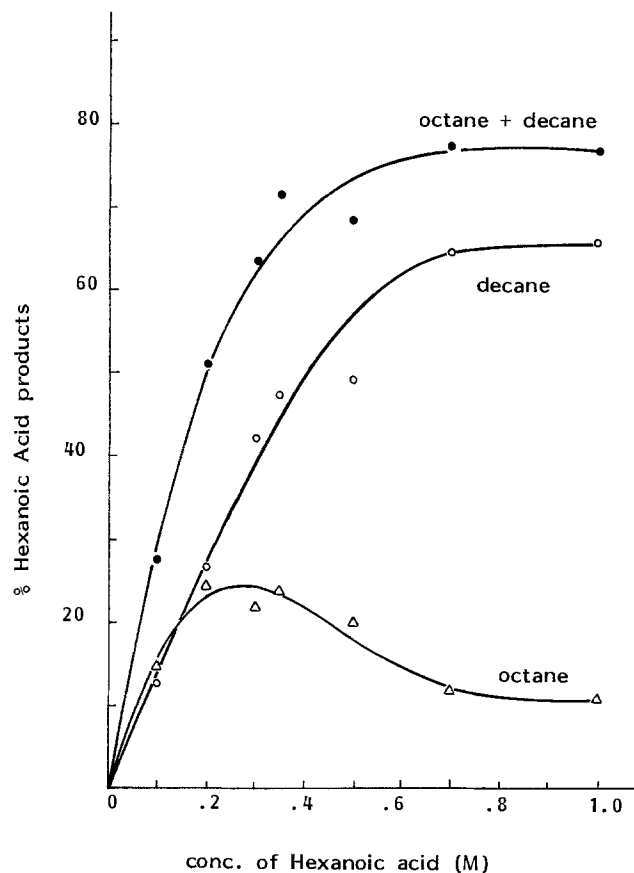


Fig. 4. Yield of dimeric alkane products from hexanoic acid in mixtures with butanoic acid.

If " r " is defined as the ratio of the organic acids reacted (a/b), then the statistical distribution of coupled products formed is

$$R_1 - R_1 = r^2$$

$$R_1 - R_2 = 2r \quad [5]$$

and

$$R_2 - R_2 = 1$$

This interpretation is applied to results from the mixed acid experiments in Table V. Expected product distributions are calculated from the ratio of butanoic to

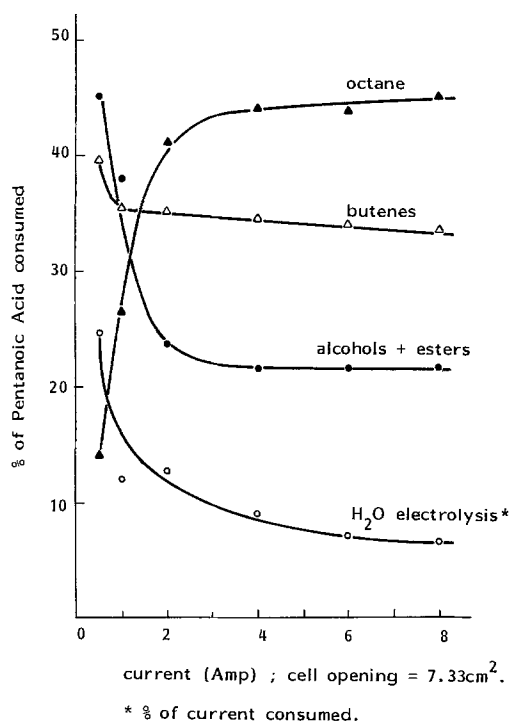


Fig. 5. Yield of products from pentanoic acid as a function of current density.

hexanoic acid reacted and compared with experimentally observed product distributions. In the presence of greater than 0.3M hexanoic acid, reasonably good agreement is seen between the expected and observed distribution of coupled products. Over a thirty-six fold range of observed ratios, all calculated values agree to within better than a factor of two. Variations from the expected and observed distribution may be due to factors not considered by this simple model such as differences in diffusivity and competing reactions leading to formation of other products.

The extent to which the ratios of dimeric products to cross-coupled products can be explained by a simple statistical model argues against electrochemical control of the product distribution. Perhaps a more powerful argument may be made based on the effect of the mere presence of hexanoic acid, and presumably other

Table IV. Effect of liquid flow rate and organic acid concentration on product distribution* (current density 0.28 A/cm²; cross-sectional area for flow 0.016 cm²; exposed anode area 7.33 cm²)

Run	Reacting organic acid	Butenes	Octane	Alcohols	Esters	Current to O ₂	Material balance	Flow rate (ml/s)
158	1.0M pentanoic	35.2	41.1	15.5	8.2	12.7	98.4	8.0
164	1.0M pentanoic	32.5	38.3	20.3	8.9	10.1	100.8	2.8
166	1.0M pentanoic	32.3	25.8	36.6	5.3	17.4	104.6	1.4
167	1.5M pentanoic	32.0	42.7	18.3	7.0	12.7	98.7	1.8
168	0.6M pentanoic	34.4	21.1	37.5	6.9	14.3	105.4	1.8

* Product yields calculated as mol percent acid reacted to form product compared to total mols acid reacted in run. Current forming O₂ expressed as percent of current supplied in run.

Table V. Expected and observed ratios of alkane dimer formation from butanoic-hexanoic mixed runs

Run	Reacting organic acids	Butanoic Hexanoic Reacted (r)	Hexane		Octane		Hexane	
			Expected ($r^2/2r$)	Observed	Expected ($2r$)	Observed	Expected (r^2)	Observed
122	1.4M butanoic/0.7M hexanoic	0.59	0.30	0.35	1.18	1.08	0.35	0.38
131	0.7M butanoic/0.7M hexanoic	0.32	0.16	0.16	0.64	0.47	0.10	0.07
132	0.7M butanoic/0.35M hexanoic	0.66	0.33	0.26	1.32	1.04	0.44	0.27
135	0.7M butanoic/1.0M hexanoic	0.23	0.11	0.10	0.46	0.33	0.05	0.03
136	0.7M butanoic/0.3M hexanoic	0.75	0.38	0.30	1.50	1.04	0.56	0.31
137	0.7M butanoic/0.5M hexanoic	0.47	0.24	0.21	0.94	0.83	0.22	0.17

longer chain fatty acids, on the degree of coupling of the short chain acids, which have generally been observed to give very low yields of coupled product. The clearest illustration of the effect may be seen by comparing the results of Runs 147 and 151 listed in Table II. In these experiments, the addition of 1.0M hexanoic acid to the electrolyte solution resulted in an increase in the conversion of propanoic acid to butane from a negligible amount to approximately one-third of the acid reacted, probably the highest butane yield ever observed in aqueous Kolbe electrolysis. One could argue that any increased yields of the cross-coupled products could be a result of the electrochemical behavior of the longer chain acid, but it is difficult to explain the increased yields of short chain dimer by anything but a physical effect of the longer chain acid and its electrolysis products.

Results from the experiments which varied temperature, current density, flow rate, and concentration may be interpreted as being supportive of the hypothesis of control of product distribution by a lipophilic layer. As the integrity of the layer is disrupted by increased temperature (volatilization of olefin products), local depletion of reacting organic acid (seen at low flow rate and low bulk concentration), or lowered current density allowing infiltration of water, the formation of dimeric (noncarbonium ion) products is decreased. This explanation is consistent with the effect of reactor pressure on the product distribution reported previously (1).

The ability to improve alkane (coupled product) yields for C₃ to C₅ acids in Kolbe electrolysis has potential practical applications in conversion of dilute

aqueous solutions of organic acids to hydrocarbons. Particularly in the conversion of mixed organic acids obtained from the fermentation of polysaccharides, substantial yields of coupled alkane products can be obtained from C₃ to C₆ acids, providing a sufficient concentration (0.35M) of hexanoic acid is maintained or, as previously shown (1), if the reaction is carried out under pressure.

Acknowledgment

This work was carried out through the sponsorship of the Department of Energy, Division of Advanced Energy Projects, Office of Basic Energy Sciences under Contract no. DE-AC02-81ER10914 and the direction of Dr. Ryszard Gajewski.

Manuscript submitted June 12, 1983; revised manuscript received Nov. 1, 1983.

REFERENCES

1. J. E. Sanderson, P. F. Levy, L. K. Cheng, and G. W. Barnard, *This Journal*, **130**, 1844 (1983).
2. H. Kolbe, *Ann. Chim.*, **69**, 257 (1849).
3. B. C. L. Weedon, *Q. Rev. Chem. Soc.*, **6**, 380 (1952).
4. H. Hofer and M. Moest, *Ann. Chim.*, **323**, 284 (1902).
5. L. Ebersson, in "Organic Electrochemistry," M. Baizer, Editor, p. 469, Marcel Dekker, New York (1973).
6. J. H. P. Utley, in "Techniques of Chemistry," Vol. 5, Part 1, N. L. Weinberg, Editor, p. 793, Wiley, New York (1974).
7. M. J. Allen, in "Organic Electrode Processes," Reinhold, New York (1958).

Voltammetric and XPS Analysis of Metal-Complexed Polytyramine Films : Geometry-Dependent Electron Transfer Therein

Minh-Chau Pham, Pierre-Camille Lacaze, and Jacques-Emile Dubois

Institut de Topologie et de Dynamique des Systèmes de l'Université Paris VII, associé au CNRS, 75005 Paris, France

ABSTRACT

Electrodes coated with redox polymers are prepared by coordinating various metal ions with ligands from polytyramine films. The nature of the cation determines the geometry of the metal-polymer complex and hence the voltammetric behavior of the coatings. Electron transfer between adjacent pairs of redox centers inside the film can occur with a four-coordinate structure, but not with a penta- or hexacoordinate structure.

Various methods have been used to bind transition metal complexes to ligand containing polymers (1-8). Recent studies in this field deal with the variations in the electrochemical responses of electrodes coated with metal-complexed films (9-12).

Our previous study on the preparation and analysis of polyquinolinol films coordinated with Cu(II) or Co(II) ions indicates that the electrical and electrochemical properties of these electroactive electrodes depend on the geometry of these metal-complexed films (12). We report herein the XPS and voltammetric analysis of metal complexed films formed by coordinating Cu(II), Co(II), Fe(II), Zn(II), or Mn(II) ions with ligands from polytyramine films. Like our results for metal complexed polyquinolinol films (12), our results on metal-complexed polytyramine films indicate that their electrochemical behavior, as well as the electron transfer mechanism therein, depends on the nature of the cation which determines the complex geometry.

Experimental

Only commercial reagents were used. The tyramine was from Aldrich. All of the chlorides (CuCl₂, 2H₂O;

CoCl₂, 6H₂O; ZnCl₂, MnCl₂, 4H₂O; FeCl₂, 4H₂O) were from Prolabo (R. P. Normapur); CH₃COOH and CF₃COONa from Aldrich; and LiClO₄ from Fluka. The methanol was a Baker analyzed reagent. The de-ionized water was distilled twice in a quartz apparatus.

Electrochemical experiments were performed with a PAR 173 potentiostat connected to a PAR 175 programmer. The electrodes were bulk or thin layer Pt, deposited on glass plates by sputtering.

Film identification by x-ray photoelectron spectroscopy (XPS) was conducted on a Vacuum Generators Escalab MKI instrument using unmonochromated MgK_α x-rays.

Multiple reflection IR spectra were recorded on a Model 9 Wilks Scientific Corporation device mounted on a Nicolet 60 SX spectrometer.

Results

Polytyramine film formation.—The preparation and characterization of polytyramine films with a thickness of ca. 50 nm formed by electrochemical oxidation on platinum or iron electrodes is described in a previous

study on polyphenylene oxide films with amino group substituents (13).

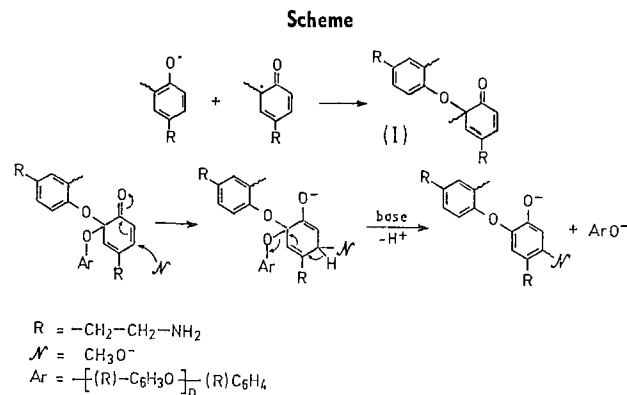
For the present study, different thicknesses of these polytyramine films were prepared by electrochemically oxidizing tyramine (0.1M) in 0.3M NaOH-MeOH and subjecting the electrode to different potential sweep cycles at 50 mV s⁻¹. A thickness of ca. 50 nm was obtained after ten successive sweep cycles between 0.0 and 2.0V (SCE); a thickness of ca. 120 nm was obtained by two sweep cycles between 0.0 and 3.0V (SCE) followed by eight sweep cycles between 0.0 and 2.0V (SCE); a thickness of 150 nm was obtained by four sweep cycles between 0.0 and 3.0V (SCE) followed by eight sweep cycles between 0.0 and 2.0V (SCE).

The multiple-reflection IR spectrum of the polytyramine film (Fig. 1) displays an absorption band at 1255 cm⁻¹ ascribable to the C—O—C polyoxide groups. There are two other characteristic bands at 3364 and 3268 cm⁻¹ attributed to the —NH₂ group (N—H stretching), and another band at 1080 cm⁻¹ attributed to the C—N bond (C—N stretching). These vibrations are also observed with the tyramine monomer (in KBr pellet) at 3334, 3282, and 1042 cm⁻¹ (14).

XPS analysis confirms that the films of different thicknesses are indeed polymer films (Fig. 2a).

Calculating the intensity of the XPS signals emitted by the various elements while taking into account the sensitivity of each gives C₈O_{2.2}N_{1.09} as the approximate formula for the polytyramine film. The same type of calculation for a simple tyramine film obtained by evaporating a methanol solution with tyramine onto a Pt electrode gives C₈O_{0.96}N_{0.9} as the formula for tyramine. The oxygen index of ca. 2.2 in the polytyramine film might be accounted for by a side reaction occurring during the electrochemical polymerization. With tyramine, which is a *para*-substituted phenol, coupling of the phenate radicals can occur at the *ortho* position of the phenol group (15); during anodic coupling of the phenol, a nucleophilic agent such as CH₃O⁻ can attack the quinol-ether polymer intermediate (I) at the *meta* position (see Scheme). This interpretation resembles that advanced by Mengoli *et al.* (16) for the grafting of amine moieties onto polyphenylene oxide during the electropolymerization

of phenol in the presence of amines. Such a side-reaction mechanism indicates that C₈O_{2.2}N_{1.09} might be the formula for polytyramine.



Metal complexed polytyramine film formation.—Cu(II) ions can be coordinated with ligands from a polytyramine film by immersing the film for 15 min in a boiling 5 × 10⁻¹M aqueous medium of CuCl₂. The polytyramine-Cu(II) film is then rinsed ultrasonically in distilled water and is air-dried.

For complexation with Co(II), Fe(II), Mn(II), or Zn(II) ions, an organic medium is required. After dissolving 10⁻¹M MCl₂ [M is Fe(II), Zn(II), Co(II), or Mn(II)] in DMF and bringing this solution to boiling point, a polytyramine film immersed therein for 15 min forms a complex with the metal ions M. After complexation, the treated sample is first rinsed in DMF by ultrasonic stirring to eliminate MCl₂ traces; it is then again rinsed ultrasonically in methanol to eliminate DMF traces. Thereafter, it is air-dried before use in experiments.

XPS analysis of a polytyramine-Co(II) complex.—XPS analysis of a polytyramine film before and after the treatment with CoCl₂ indicates that the treatment indeed results in the formation of a complex between cobalt ions and ligands of the polytyramine film.

Six samples of polytyramine films of various thickness treated with CoCl₂, 6H₂O were analyzed by XPS (Fig. 2b). Averaged binding energies, averaged com-

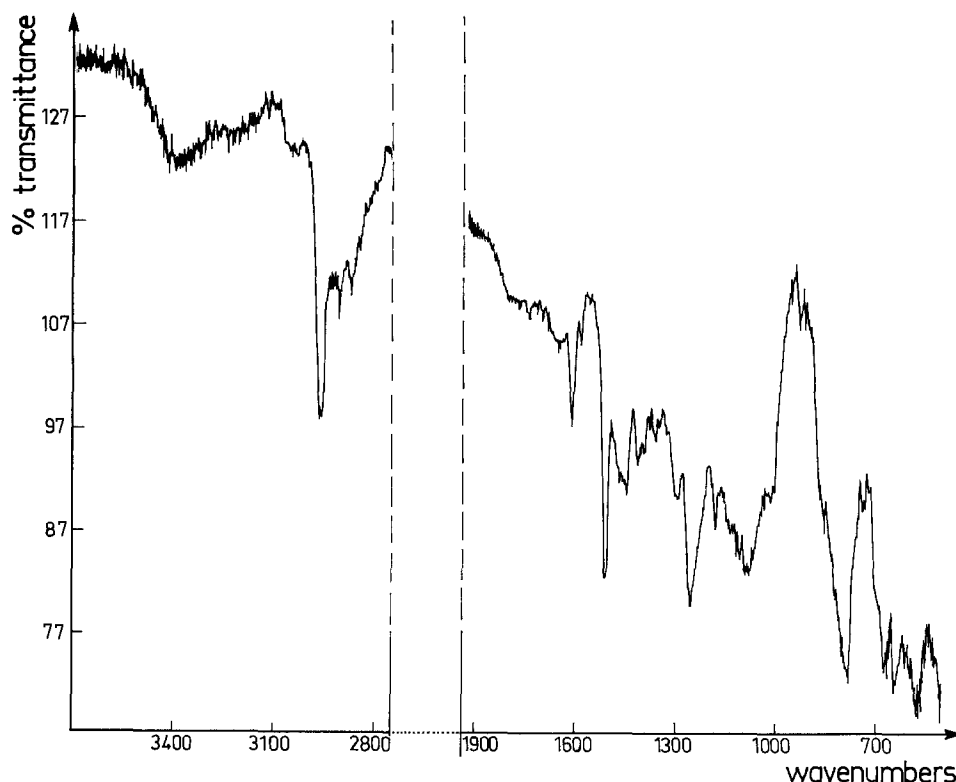


Fig. 1. IR spectrum of the polytyramine film obtained on Pt.

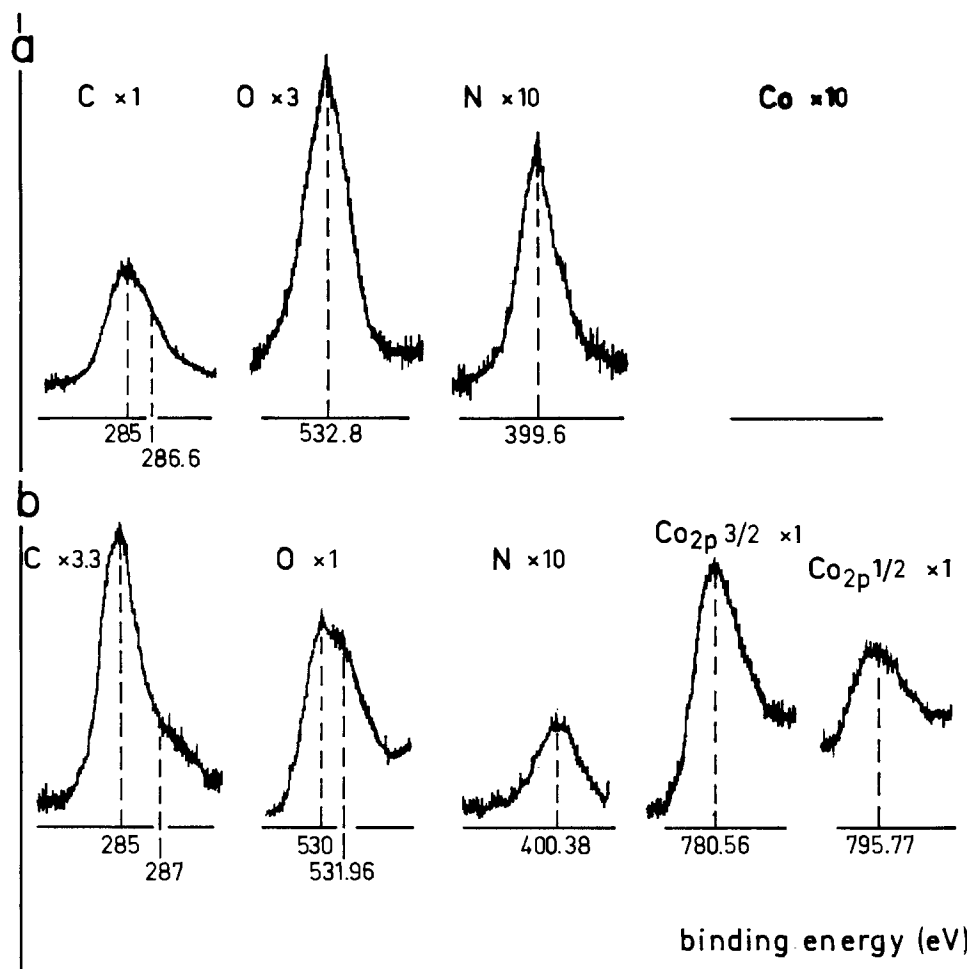


Fig. 2. XPS spectra of (a) a polytyramine film, and (b) a polytyramine-Co(II) film.

plexed film formulas, and bond types are given in Table I (17, 18).

A comparison of the spectra of a polytyramine film (Fig. 2a) with the spectra of a polytyramine-Co(II) (Fig. 2b) shows that in the N_{1s} spectrum, the nitrogen binding energy increases from 399.6 eV in the untreated sample to 400.38 eV in the treated sample (thereby indicating that the partial charge from the N atoms increases, in accordance with actual coordination between Co(II) ions and N). The treated film also displays two O_{1s} signals (one at 530.57 eV that might arise from interaction between H_2O molecules and Co(II) ions, and one at 531.96 eV ascribable to C—O—C bonds in interaction with Co(II) ions, plus a $Co_{2p_{3/2}}$ and a $Co_{2p_{1/2}}$ signal (at 780.56 and 795.77 eV).

Quantitative analysis of the six samples gives $C_3O_{3.58 \pm 0.82}N_{1.12 \pm 0.03}Co_{0.88 \pm 0.33}$ as the average formula of the polytyramine-Co(II) complex. The rather large standard deviations for the oxygen and cobalt in this

formula might be due to incomplete metalation between the polymer ligands and the Co(II) ions.

Plotting the oxygen index vs. the cobalt index using six data points gives an approximate straight line with a slope of ca. 2 and an ordinate origin of 2. This indicates the presence of ca. two additional oxygen atoms (aside from the two oxygen ligands in the untreated polytyramine film) per cobalt ion when complexation occurs.

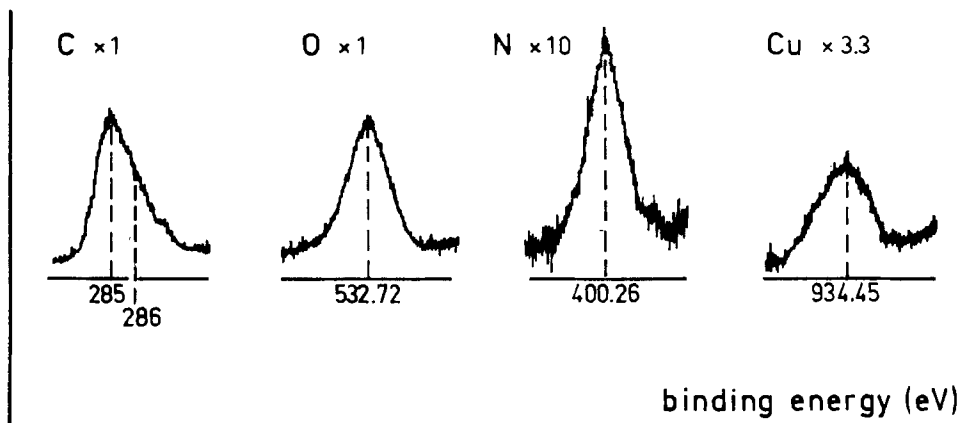
XPS analysis of a polytyramine-Cu(II) complex.—Results of XPS analysis of a polytyramine film before and after complexation with $CuCl_2 \cdot 2H_2O$ are given in Table II.

The XPS spectra of a polytyramine-Cu(II) complex are given in Fig. 3. Like for the previously studied polyquinolinol films, before and after complexation with Cu(II) ions (12b), the increase in the N_{1s} binding energy of the complexed film is indicative of coordina-

Table I. XPS analysis of a polytyramine film and a polytyramine-Co(II) film

Spectra	Polytyramine film		Polytyramine-Co(II) film	
	Binding energy (eV)	Bond types	Binding energy (eV)	Bond types
C_{1s}	286.6 285	C—O—C blended with C—N C—O—C	287 285	C—O—C blended with C—N reference C
O_{1s}	532.8	C—O—C	531.96 ± 0.89 530.57 ± 0.33	$\begin{array}{c} C \\ \\ O \rightarrow Co \\ \\ C \\ \\ Co-OH_2 \end{array}$
N_{1s}	399.6	$\begin{array}{c} H \\ \\ -N-H \end{array}$	400.38 ± 0.3	$\begin{array}{c} H \\ \\ -N \rightarrow Co(II) \\ \\ H \end{array}$
$Co_{2p_{3/2}}$ $Co_{2p_{1/2}}$			780.56 ± 0.15 795.77 ± 0.29	— Co(II)

Fig. 3. XPS spectra of a polytyramine-Cu(II) film.



tion between the Cu(II) ions and nitrogen ligands. The complexed film emits a Cu(II)_{2p_{3/2}} signal at 934.4 eV (19, 20). Unlike the polyquinolinol- and polytyramine-Co(II) complexes, the polytyramine-Cu(II) spectra display only one O_{1s} signal, thereby indicating that oxygenated ligands in the polytyramine-Cu(II) film come from the polytyramine; this is confirmed by quantitative analysis which gives C₈O_{2.3±0.3}N_{0.86±0.03}Cu_{0.01±0.01} as the formula for this complex. The oxygen index in this formula is about the same as in the formula of an untreated polytyramine film: C₈O_{2.2}N_{1.09}. This likeness indicates that, unlike what occurs with polyquinolinol- and polytyramine-Co(II) complexes, no oxygenated ligands from the salt participate in polytyramine-Cu(II) complexation.

XPS analysis of polytyramine-Fe(II), -Mn(II), and -Zn(II) complexes.—Results of XPS analysis of a polytyramine film after complexation with FeCl₂, 4H₂O, or MnCl₂, 4H₂O, or ZnCl₂, 4H₂O, are summarized in Table III.

Electrochemical responses of electrodes coated with metal-complexed polytyramine films.—Polytyramine-Cu(II) films were studied by cyclic voltammetry in an aqueous medium with 0.2M LiClO₄-HClO₄ or 0.2M CF₃COONa-CF₃COOH. A "forming" period similar to

that observed previously with poly(2-methyl-8-quinolinol)-Cu(II) complexes (12b) is observed, i.e., the peak current increases during the first potential scan cycles and then stabilizes. This phenomenon lasts much longer at pH 4 than at pH 2 (Fig. 4). In LiClO₄-HClO₄-H₂O (pH 2), at a scan rate of 200 mV s⁻¹, there is an oxidation and a reduction peak for the polytyramine-Cu(II)/polytyramine-Cu(I) couple at + 0.54 and + 0.4V (SCE), respectively.

Electrochemical data obtained by cyclic voltammetry for various polytyramine-Cu(II) films in various electrolytic media are given in Table IV.

The pH of the supporting electrolytes clearly affects the electroactivity of Cu(II) sites. Voltammograms recorded at pH 2 and 1 are more symmetrical and have shorter peak potential separations than voltammograms at pH 4. The above-reported XPS results showing inhomogeneous and incomplete complexation between Cu(II) ions and the polymer ligands of the film could mean that the remaining number of uncomplexed NH₂ groups which can be protonated increases as the pH becomes lower, thereby increasing the swelling and the flexibility of the polymer chain and lending it a more open texture. This in turn would facilitate counterion entry into the films and could thereby account for the significant pH-dependent difference in the forming periods and in the shapes of the voltam-

Table II. XPS analysis of a polytyramine film and a polytyramine-Cu(II) film

Spectra	Polytyramine film		Polytyramine-Cu(II) film	
	Binding energy (eV)	Bond types	Binding energy (eV)	Bond types
C _{1s}	286.6 285	C—O—C blended with C—N reference c	286 285	C—O—C blended with C—N reference c
O _{1s}	532.8	C—O—C	532.72 ± 0.28	C—O—C
N _{1s}	399.6	—N—H	400.26 ± 0.13	Cu(II) ↑ —N—H
Cu _{2p_{3/2}}			934.45 ± 0.4	Cu(II)

Table III. XPS analysis of polytyramine-Fe(II), -Mn(II), and -Zn(II) films

Spectra	Polytyramine-Fe(II) film		Polytyramine-Mn(II) film		Polytyramine-Zn(II) film	
	Binding energy (eV)	Bond types	Binding energy (eV)	Bond types	Binding energy (eV)	Bond types
C _{1s}	287.16 285	C—O—C blended with C—N reference C	287.28 285.00	C—O—C blended with C—N reference C	287.40 285.00	C—O—C blended with C—N reference C
O _{1s}	531.96 530.76	C—O—C H ₂ O—Fe(II)	532.40	broad peak	530.60	broad peak
N _{1s}	400.08	H —N—H ↓ Fe(II)	400.20	H —N—H ↓ Mn(II)	400.20	H —N—H ↓ Zn(II)
Metal ions	711.44 724.96	Fe _{2p_{3/2}} Fe _{2p_{1/2}}	642.30 654.00	Mn _{2p_{3/2}} Mn _{2p_{1/2}}	1023.10 1046.20	Zn _{2p_{3/2}} Zn _{2p_{1/2}}
Cl	198.40 199.70	Cl _{2p_{3/2}} Cl _{2p_{1/2}}		not detected	198.88 200.20	Cl _{2p_{3/2}} Cl _{2p_{1/2}}
Complex formula	C ₈ O _{2.51} N _{0.71} Fe _{0.42} Cl _{0.15}		C ₈ O _{2.4} N _{0.55} Mn _{0.30} Cl ₀		C ₈ O _{2.16} N _{1.05} Zn _{0.2} Cl _{0.05}	

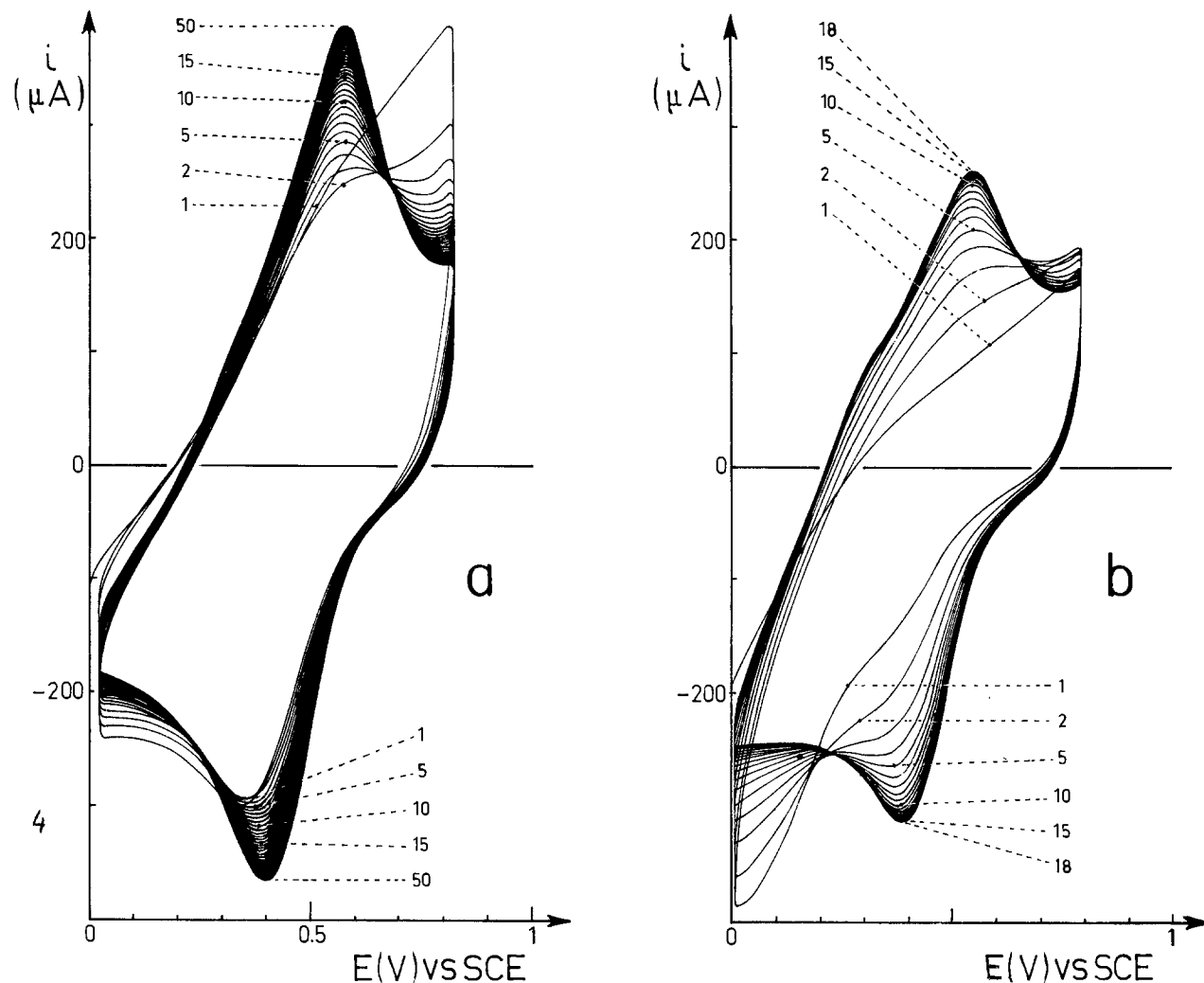


Fig. 4. Voltammograms recorded at 100 mV s^{-1} with a Pt electrode coated with a polytyramine-Cu(II) film during successive sweeps (the sweep number is given for each curve). A: $\text{LiClO}_4\text{-HClO}_4$ (pH 4) medium. B: $\text{LiClO}_4\text{-HClO}_4$ (pH 2) medium.

mograms for polytyramine-Cu(II) films. Anson *et al.* have also noticed that pH levels affect the electrochemical responses of electroactive polymer-coated electrodes (9).

The electrolyte-dependent variation in the voltammetric responses of the polytyramine-Cu(II) films bolsters this interpretation. The voltammograms of these same polytyramine-Cu(II) films display much greater peak potential separations in a CF_3COONa

electrolyte than in a NaClO_4 electrolyte at the same pH. Up to 200 mV s^{-1} , peak current intensities increase linearly with the scan rate; they increase less rapidly at faster scan rates.

Overall results indicate that with polytyramine-Cu(II) films the rate of the redox reaction of the films is controlled by the electrochemical charge diffusion rate through the film. Integration of the voltammogram gives $6.4 \times 10^{-9} \text{ mol cm}^{-2}$ as the concentration of

Table IV. Electrochemical data for cyclic voltammetric curves of a polytyramine-Cu(II) film

Electrode	Medium	pH	mV s^{-1}	E_{pc} V (SCE)	E_{pa} V (SCE)	ΔE_p mV
1. Polytyramine (ca. 100 nm) treated with $5 \times 10^{-2} \text{ M CuCl}_2$	0.2M CF_3COONa + CF_3COOH	4	100	0.33	0.56	230
		1	100	0.37	0.56	190
2. Polytyramine (ca. 100 nm) treated with $5 \times 10^{-2} \text{ M CuCl}_2$	0.2M LiClO_4 + HClO_4	1	100	0.38	0.52	140
		4	100	0.39	0.55	140
3. Polytyramine (ca. 100 nm) treated with $5 \times 10^{-2} \text{ M CuCl}_2$	0.2M LiClO_4 + HClO_4	2	100	0.43	0.55	120
		1	100	0.43	0.52	90
4. Polytyramine (ca. 100 nm) treated with 10^{-2} M CuCl_2	0.2M LiClO_4 + HClO_4	2	20	0.41	0.50	100
		2	50	0.40	0.52	120
		2	100	0.40	0.54	140
		2	200	0.40	0.56	160
		2	500	0.40	0.65	250
5. Polytyramine (ca. 100 nm) treated with 10^{-2} M CuCl_2	0.2M LiClO_4 + HClO_4	2	100			no couple detected
		2	200			no couple detected
6. Polytyramine (<50 nm) treated with $5 \times 10^{-2} \text{ M CuCl}_2$	0.2M LiClO_4 + HClO_4	2	50			weak peak currents
		2	100			weak peak currents
			200			

electroactive sites in the complex; *i.e.*, the equivalent of *ca.* six layers participate in the redox process.

The same type of electroactivity is observed with polytyramine films treated with 5×10^{-1} or $10^{-1}M$ $CuCl_2$ solutions. However, when a polytyramine film

is treated with a $5 \times 10^{-2}M$ $CuCl_2$ solution, there is almost no cyclic voltammetry response, even though a weak $Cu(II)$ signal is detected by XPS. This might be explained by a smaller density of $Cu(II)$ ions within the film, which would mean that the electroactive

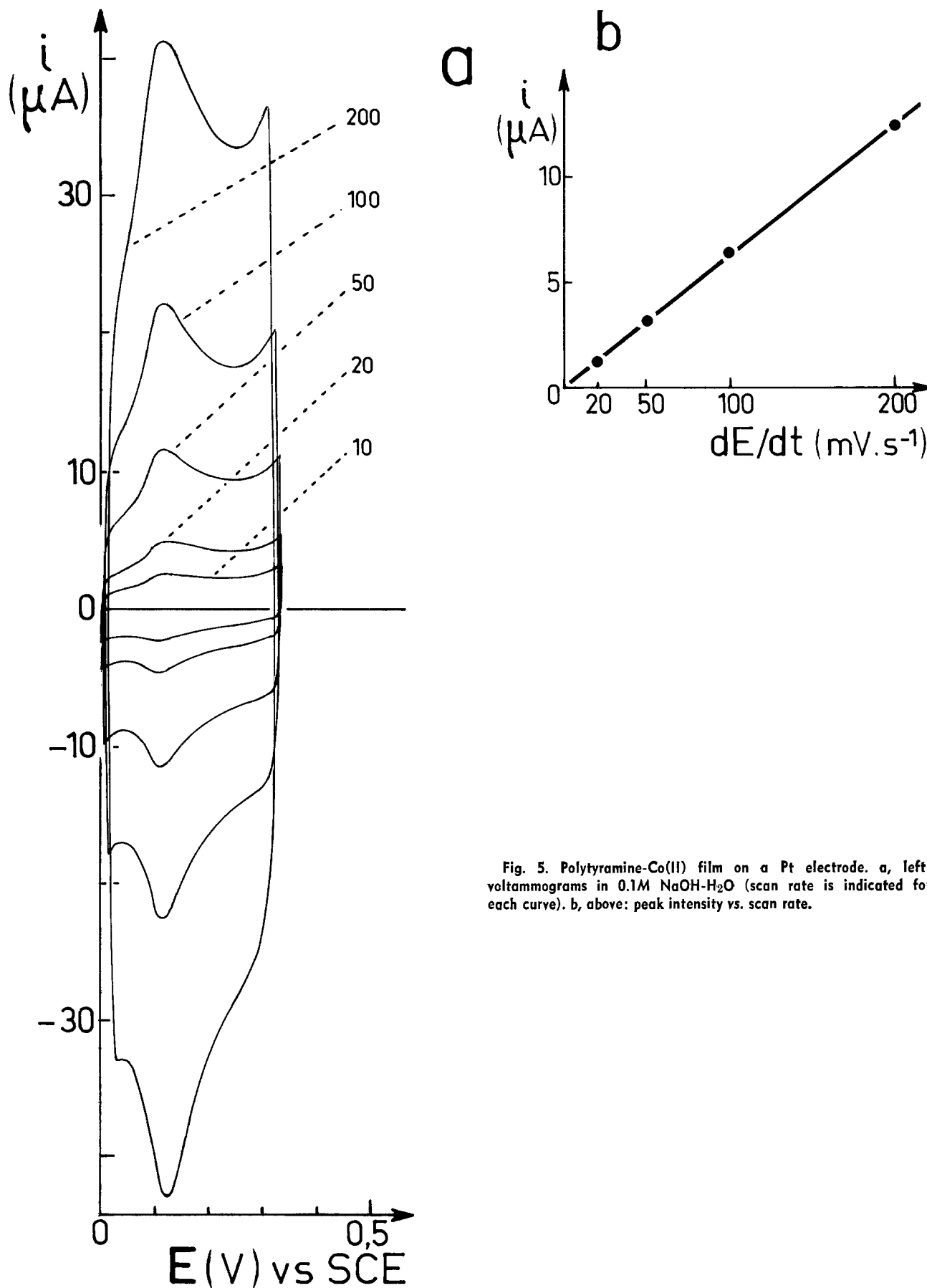


Fig. 5. Polytyramine-Co(II) film on a Pt electrode. a, left: voltammograms in 0.1M NaOH-H₂O (scan rate is indicated for each curve). b, above: peak intensity vs. scan rate.

sites are not close together enough for electron hopping transfer to be able to occur.

As the voltammogram of a thin polytyramine film (50 nm) treated with a $5 \times 10^{-1} M$ $CuCl_2$ solution (electrode 6, Table IV) also displays low peak currents, the current observed for a thick film can be considered to represent the integration of electroactive sites throughout the film thickness.

Polytyramine-Co(II) films on a Pt electrode subjected to cyclic voltammetry in 0.1M NaOH-H₂O display an electrochemical behavior totally unlike that of polytyramine-Cu(II) films. A perfectly reversible redox system is detected from the start, and no "forming" is observed; *i.e.*, as of the first potential scan between 0.0 and 0.4V (SCE), the polytyramine-Co(II)/polytyramine-Co(III) couple is observed at 0.10V (SCE) with ΔE_p equal to zero, and the peak current varies linearly with the sweep speed (Fig. 5). A concentration of cationic sites of only *ca.* 7×10^{-11} mol cm⁻² (the equivalent of a tenth of the layer at the metal-film interface) participates in the redox process. It is noteworthy that the voltammograms of two Pt electrodes coated with polytyramine-Co(II) films of unequal thickness (50 and 120 nm) are identical ($\Delta E_p = 0$) and have the same peak current intensity. The redox couple is very stable, as attested to by the fact that the peak current intensity remains unchanged even after hundreds of scan cycles between 0.0 and 0.4V (SCE) at 100 mV s⁻¹.

Polytyramine-Fe(II) films on a Pt electrode subjected to cyclic voltammetry in an aqueous medium containing 0.1M KCl-0.1M HCl behave like polytyramine-Co(II) films. The voltammogram displays reversible redox peaks at 0.47V (SCE) without a preliminary forming period, and the low concentration of electroactive sites is about the same as in polytyramine-Co(II) films (Fig. 6). The low concentration of electroactive sites and the good reversibility of the redox couple indicate that only cationic sites in the vicinity of the metal-film interface participate in the redox process. This would mean that the complex structure does not lend itself to electron hopping transfer within the film. It is more likely that the polytyramine-Fe(II) film is a penta- or hexacoordinate structure (as in the case of the cobalt-complexed polymer films), rather than a four-coordinate structure (as are the copper complexed polymer films).

It should be noted that, unlike copper or cobalt redox couples, the iron redox couple is not very stable. Peak current intensity diminishes after *ca.* 50 potential scan cycles.

Polytyramine-Mn(II) or polytyramine-Zn(II) films subjected to cyclic voltammetry elicit no response whatsoever, regardless of the medium.

Conclusion

Ligands from polytyramine films form complexes with Cu(II) or Co(II) ions less readily and less quickly than ligands from previously studied (12b) polyquinolinol films. However, the difference between the electrochemical responses of copper- and cobalt-complexed polytyramine films resembles the difference between the electrochemical responses of copper- and cobalt-complexed polyquinolinol films (12b).

This difference between copper and cobalt films might be explained by the fact that, in redox polymer films, communication between electroactive metals involves physical diffusion of the metal ions (from ligand site to ligand site) (21, 22) and/or electron self-exchange (2a, 2b, 22-24). In both oxidation states, copper would be more labile, whereas Co(III) would not physically diffuse through the coating to the electrode surface. Because the concentration of redox sites in the polymer cannot be measured, there is no way to measure the diffusion constant to distinguish contributions from the two mechanisms, electron hopping

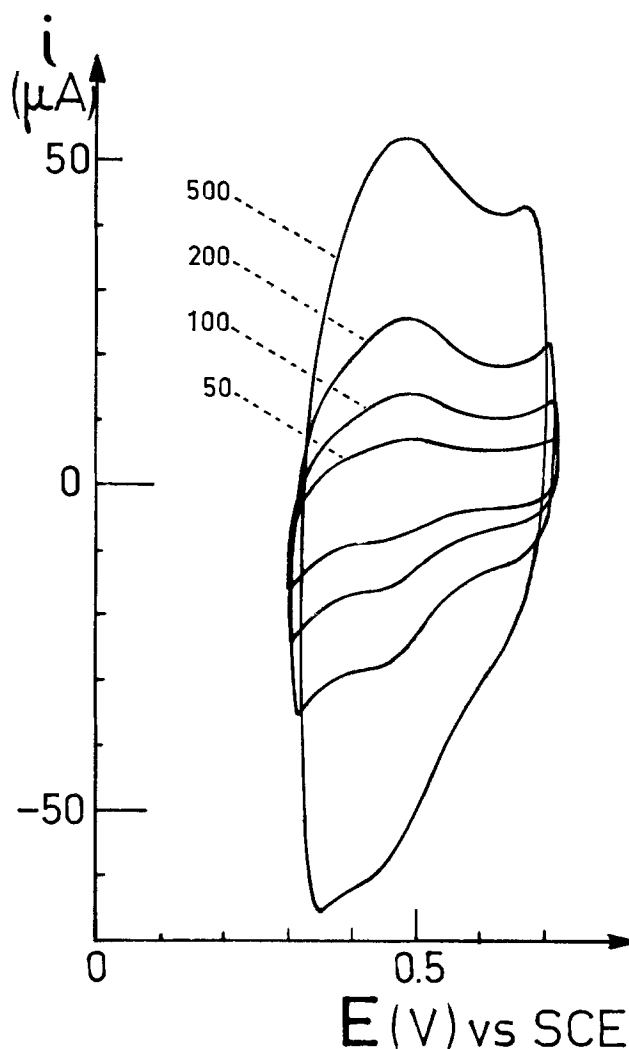


Fig. 6. Voltammograms recorded in 0.1M KCl-0.1M HCl, H₂O with a Pt electrode coated with a polytyramine-Fe(II) film. The scan rate is indicated for each curve.

and molecular diffusion. However, in the study at hand, electron hopping seems to be the prevalent charge-transport mechanism. The four-coordinate structure of the copper complexes would enhance electron hopping transfer between electroactive sites, whereas the penta- or hexacoordinate structure of cobalt-complexed films would enable only the cationic sites at the metal-film interface to participate in the redox process.

Cobalt complex redox couples are perfectly reversible with either polymer (in both cases $\Delta E_p = 0$); only a fifth of the polyquinolinol-Co(II) film layer or a tenth of the polytyramine-Co(II) layer is electroactive. In contrast, polymer films with copper-complex redox couples have high ΔE_p values; *ca.* 12 layers of a poly(2-methyl-8-quinolinol)-Cu(II) film or six layers of a polytyramine-Cu(II) film take part in the redox process. These high values demonstrate that most of the cationic sites throughout the copper-complexed polymers are indeed involved in the redox process.

Voltammetry results for an iron-complexed film resemble those for a cobalt-complexed film. This behavior is typical of a penta- or hexacoordinate complex.

Acknowledgments

We thank Professor J. P. Doucet for use of the Nicolet 60 SX spectrometer, Dr. Mir-Hedayatullah for many helpful discussions, Dr. M. Delamar for help in XPS interpretation. Mr. M. Leclerc for XPS technical assist-

ance, and Mrs. N. Pedrono for valuable aid in recording multiple reflection IR spectra.

Manuscript submitted April 18, 1983; revised manuscript received ca. Nov. 4, 1983. This was Paper 624 presented at the Montreal, Quebec, Canada, Meeting of the Society, May 9-14, 1983.

The Institut de Topologie et de Dynamique des Systemes assisted in meeting the publication costs of this article.

REFERENCES

- (a) N. Oyama and F. C. Anson, *J. Am. Chem. Soc.*, **101**, 739 (1979); (b) *ibid.*, **101**, 3450 (1979).
- (a) N. Oyama and F. C. Anson, *This Journal*, **127**, 247 (1980); (b) *ibid.*, **127**, 640 (1980); (c) *Anal. Chem.*, **52**, 1192 (1980).
- N. Oyama, T. Shimomura, K. Shigehara, and F. C. Anson, *J. Electroanal. Chem.*, **112**, 271 (1980).
- O. Haas and J. G. Vos, *ibid.*, **113**, 139 (1980).
- P. J. Peerce and A. J. Bard, *ibid.*, **114**, 89 (1980).
- J. Calvert and T. J. Meyer, *Inorg. Chem.*, **20**, 27 (1981).
- G. J. Samuels and T. J. Meyer, *J. Am. Chem. Soc.*, **103**, 307 (1981).
- H. D. Abruna, P. Denisevich, M. Umana, T. J. Meyer, and R. W. Murray, *ibid.*, **103**, 1 (1981).
- K. Shigehara, N. Oyama, and F. C. Anson, *ibid.*, **103**, 2552 (1981).
- P. Denisevich, H. D. Abruna, C. R. Leidner, T. J. Meyer, and R. W. Murray, *Inorg. Chem.*, **21**, 2153 (1982).
- C. R. Martin, I. Rubinstein, and A. J. Bard, *J. Am. Chem. Soc.*, **104**, 4817 (1982).
- (a) M. C. Pham, G. Tourillon, P. C. Lacaze, and J. E. Dubois, *J. Electroanal. Chem.*, **111**, 385 (1980); (b) M. C. Pham, J. E. Dubois, and P. C. Lacaze, *This Journal*, **130**, 346 (1983).
- J. E. Dubois, P. C. Lacaze, and M. C. Pham, *J. Electroanal. Chem.*, **117**, 233 (1981).
- C. N. R. Rao, "Chemical Applications of Infrared Spectroscopy," New York and London (1963).
- F. Bruno, M. C. Pham, and J. E. Dubois, *Electrochim. Acta*, **22**, 451 (1977).
- G. Mengoli, S. Daolio, and M. M. Musiani, *J. Appl. Electrochem.*, **10**, 459 (1980).
- U. Gelius, P. F. Haden, J. Hedman, B. J. Lindberg, R. Manne, R. Nordberg, C. Nordling, and K. Siegbahn, *Phys. Scr.*, **2**, 70 (1970).
- R. Nordberg, R. G. Albridge, T. Bergmark, U. Ericson, J. Hedman, C. Nordling, K. Siegbahn, and B. J. Lindberg, *Ark. Kemi.*, **18**, 257 (1967).
- D. Briggs, "Heyden Handbook of X-Ray and Ultraviolet Photoelectron Spectroscopy," London (1978).
- R. R. Gagne, J. L. Allison, C. A. Koval, W. S. Mialki, T. J. Smith, and R. A. Walton, *J. Am. Chem. Soc.*, **102**, 1905 (1980).
- F. C. Anson, T. Ohsaka, and J. M. Savéant, *J. Phys. Chem.*, **87**, 640 (1983).
- D. A. Buttry and F. C. Anson, *J. Electroanal. Chem.*, **130**, 333 (1981).
- N. Oyama, K. Sato, and H. Matsuda, *ibid.*, **115**, 149 (1980).
- F. B. Kaufman and E. M. Engler, *J. Am. Chem. Soc.*, **101**, 547 (1979).

Stoichiometry of Formation and Conductivity Response of Amorphous and Crystalline Complexes Formed Between Poly(ethylene oxide) and Ammonium Salts: $\text{PEO}_x \cdot \text{NH}_4\text{SCN}$ and $\text{PEO}_x \cdot \text{NH}_4\text{SO}_3\text{CF}_3$

Matthew Stainer, L. Charles Hardy,* D. H. Whitmore,* and D. F. Shriver*

Departments of Chemistry and Material Science and Materials Research Center, Northwestern University, Evanston, Illinois 60201

ABSTRACT

Stoichiometries have been studied for the interaction between poly(ethylene oxide) and the ammonium salts NH_4SCN and $\text{NH}_4\text{SO}_3\text{CF}_3$ in the polymer to salt composition range 10:1 to 2:1. A single crystalline phase having the approximate composition 4:1 $\text{PEO} \cdot \text{NH}_4\text{SCN}$ was identified, and an approximate phase diagram was constructed. The $\text{PEO} \cdot \text{NH}_4\text{SO}_3\text{CF}_3$ system is more complex, and a phase diagram was not obtained; however, at least two compounds of 8:1 and 4:1 stoichiometry are indicated. Conductivity plots indicate that the metastable amorphous phase of the various materials has a conductivity approximately $10^3 \Omega^{-1} \text{cm}^{-1}$ higher than that of the crystalline phase at room temperature. The NH_4^+ ion rather than H^+ is implicated as a charge carrier. We were not successful in determining transference numbers for anions and cations.

Recently, solvent-free polymer electrolytes have attracted considerable attention because of their potential application in high energy density batteries and because of the many unanswered fundamental questions on ion transport in polymers (1-4). The temperature-dependent conductivity of amorphous polyether-salt complexes reveals curved plots of $\ln(\sigma T)$ vs. $1/T$, which are linear when the temperature variable $1/(T - T_0)$ is employed. This functional dependence of the ion transport has previously been observed for small molecule diffusion through polymers, and one possible interpretation is that cooperative polymer conformation fluctuations are responsible for the transport process. The empirical constant T_0 represents the temperature below which the polymer motions responsible for ion transport are frozen out, and therefore it is approximately equal to the glass transition tem-

perature, T_g . The $1/(T - T_0)$ dependence is reproduced by the configurational entropy model of Gibbs and co-workers, which gives Eq. [1] for the conductivity

$$\sigma = AT^{-1/2} \exp \{-K/T - T_0\} \quad [1]$$

where

$$K = T_0 \Delta \mu S_c^* / B k_B \quad [2]$$

A , T_0 , and B are constant, S_c^* is the minimum configurational entropy required for rearrangement, and k_B is the Boltzmann constant. The pre-exponential term, A , is proportional to the carrier concentration (5). The related Fulcher equation was applied to the amorphous solid electrolytes, alkali metal salts in poly(propylene oxide), by Armand and co-workers (6).

Most of the research to date has focused on lithium and sodium ion conductors, where the respective metals may be used as reversible electrodes (7-9). In the present work, ammonium ion has been chosen for

* Electrochemical Society Active Member.

study because little is known about the transport of proton containing species in polymer electrolytes. Also, the ammonium containing poly(ethylene oxide) (PEO) systems provide metastable amorphous phases, which are useful for testing theories on ion transport. This research has focused on the stoichiometry of interaction between NH_4SCN or $\text{NH}_4\text{SO}_3\text{CF}_3$ and PEO, and a comparison of ion transport in the crystalline and amorphous states of these polymer electrolytes.

The size of the NH_4^+ ion is interesting in its relationship to structural models for PEO-salt complexes which have been presented to date. The most convincing model indicates that cations Li^+ , Na^+ , or K^+ reside in a helical tunnel and are coordinated to oxygen atoms in a fashion very similar to cations in an 18-crown-6 complex (10), where the cavity size for each is essentially the same (diam $\sim 2.6\text{\AA}$ for PEO complex and for 18-crown-6). Until recently, x-ray crystal structures of many 18-crown-6 complexes of ammonium and rubidium salts have indicated that these cations, both with a radius of 1.48\AA , are too large to fit in the cavity, but sit on top of it. Recent structures of 18-crown-6 with ammonium ions indicate that this assertion is incorrect and instead the depth of penetration of the crown ether by an ammonium ion depends on the relative strength of interaction of the ion surrounding groups (11). Hydrogen bonding is an important interaction here.

Complexes of PEO with rubidium and cesium salts have been reported to be amorphous, unlike the crystalline complexes obtained when using the smaller alkali metal cations Na^+ and K^+ (10). An explanation for this behavior might be that since the cations do not fit inside the helical cavity, the structure is not regular and therefore not crystalline. Also, irregular crosslinking of the polyether backbone through interactions with cations may induce the amorphous structure. But RbI has been shown to form a crystalline complex with an eight-oxygen polyether capped by aromatic end groups; the polyether is wrapped around the cation in a helical fashion. This complex is originally obtained as an oil which slowly recrystallizes. Under similar conditions with NH_4SCN substituted for RbI as the complexing salt, crystals were not obtained (12).

The evidence indicates that size and hydrogen bonding ability play important roles in interactions of NH_4^+ with short chain polyethers and possibly with PEO. From the previous information, it would be difficult to predict the exact stoichiometry of interaction of ammonium salts with PEO. Anion differences, which would affect crystal packing, might also be expected to play an important role. For example, the complex $\text{PEO} \cdot \text{Na}[\text{B}(\text{C}_6\text{H}_5)_4]$ has a maximum ratio of ether oxygens to Na^+ of about 7:1 due to the bulky anion (13).

Experimental

Materials.—Poly(ethylene oxide) (PEO) with an average molecular weight 600,000 (Aldrich) was purified and dried as described previously (10). Reagent grade NH_4SCN was dried under vacuum at 100°C for 19h. $\text{NH}_4\text{SO}_3\text{CF}_3$ was prepared by neutralization of freshly distilled HSO_3CF_3 to pH 6 with ammonium hydroxide, recrystallization from THF/hexane, and drying under vacuum for 24h. $\text{ND}_4\text{SO}_3\text{CF}_3$ was prepared from $\text{NH}_4\text{SO}_3\text{CF}_3$ and D_2O . Due to the hygroscopic nature of these salts and purified PEO, all operations were carried out in a nitrogen atmosphere dry box or using standard Schlenk techniques. Anhydrous salts were checked for signs of water by IR prior to use. Reagent grade methanol (MCB) was dried by refluxing over iodine-activated magnesium for 1 day followed by distillation under a nitrogen atmosphere. Tungsten bronze, $(\text{NH}_4)_x\text{WO}_3$ ($x \approx 0.25$), was prepared by reduction of ammonium paratungstate in hydrogen at-

mosphere (300 torr) at $\sim 500^\circ\text{C}$ by the method of Dickens *et al.* (14).

The polymer electrolytes were prepared typically on a 0.5g scale by combining stoichiometric quantities of the polymer and salt and addition of 15 ml anhydrous methanol. The mixture was stirred until all solids dissolved. Dissolution indicates complexation, since PEO is not soluble in methanol. The solvent was removed by evaporation under vacuum and dried under high vacuum (10^{-3} torr) for 24h.

Differential scanning calorimetry (DSC).—Thermal analysis of PEO-ammonium salt electrolytes was carried out using a Perkin Elmer DSC-2 differential scanning calorimeter on a range of 1 mcals with a heating rate of 10 K/min unless otherwise noted. Endothermic transition temperatures were determined by the intersection of a line drawn through the leading edge of the fusion peak with an extrapolated base line. Samples were typically 1-4 mg and loaded under a nitrogen atmosphere in hermetically sealed aluminum pans. Peak shape and location depend somewhat on packing, geometry, and size of sample, which could not be well controlled since samples were either films or cut from chunks.

An iridium standard was used to calibrate the DSC-2 temperature scale and for heat of fusion calculations. After each scan, samples were quenched at 320 K/min down to 300 K. The samples were then rescanned using the original conditions. After recrystallization from the melt (time dependent on stoichiometry and salt) samples were scanned again.

Optical polarized microscopy.—Crystalline-amorphous state changes were observed using optical polarized microscopy. A Leitz Wetzlar polarizing microscope equipped with a Mettler FP52 hot stage was used to observe the disappearance of birefringence. Samples were prepared by hot pressing electrolyte material between a microscope slide and cover slip and sealing with epoxy in a nitrogen atmosphere.

X-ray diffraction measurements.—X-ray diffraction measurements were obtained with a Rigaku automated diffractometer and radiation analyzer using $\text{CuK}\alpha$ radiation. Symmetrical reflection was used on pressed pellets which were held in place and protected from atmospheric moisture by Scotch-brand transparent tape. A beryllium window was used for the sample side exposed to x-rays.

Conductivity measurements.—AC impedance measurements over the frequency range 20 Hz-500 kHz were made using a Hewlett Packard 4800A vector impedance meter. Polymer samples were pressed at 10,000 psi in a $\frac{1}{2}$ in. diam die (thickness 1-2 mm) and loaded in a sealed sample holder between either 0.2 mm-thick Pt disks or $(\text{NH}_4)_{0.25}\text{WO}_3$ electrodes which were $\frac{1}{2}$ in. diam pellets (~ 2 mm thick) pressed from finely ground powder. Variable temperature measurements between 25° and 100°C were carried out with the sample in a thermostated heating chamber controlled by a Bruker B-ST temperature control unit.

Results and Discussion

Polymer-salt phases.—The x-ray diffraction patterns of various stoichiometries of $\text{PEO} \cdot \text{NH}_4\text{SCN}$ mixtures are shown in Fig. 1. Comparison of the pattern of the 8:1 composition with that of pure PEO indicates the presence of uncomplexed crystalline PEO in addition to crystalline polymer salt complex. At high salt concentrations, 3:1 and 2:1 compositions, reflections arising from the presence of free salt are seen. The pattern for $\text{PEO}_{4.0}\text{NH}_4\text{SCN}$ does not contain reflections of either free salt or uncomplexed polymer. Differential scanning calorimetry experiments confirm the conclusion, drawn from the x-ray results, that a crystalline complex is formed between salt and polymer with the approximate stoichiometry of $\text{PEO}_{4.0}\text{NH}_4\text{SCN}$. The DSC

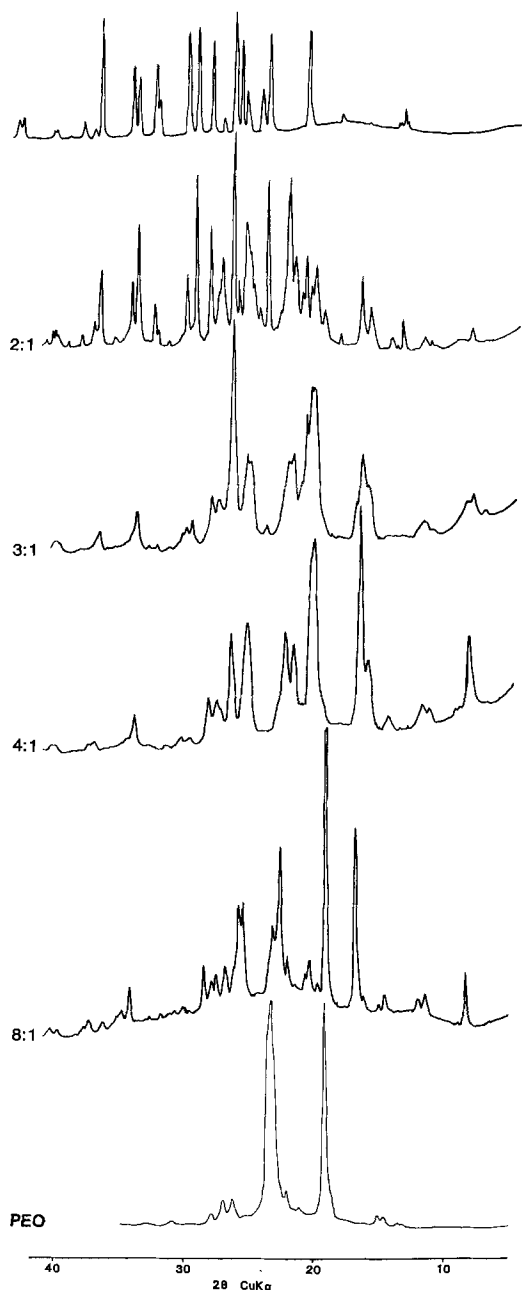


Fig. 1. X-ray diffraction patterns for NH_4SCN (upper trace), poly(ethylene oxide) (lower trace), and complexes between poly(ethylene oxide) and NH_4SCN (center traces). The ratios of PEO to NH_4SCN are indicated.

thermograms are shown in Fig 2. A single sharp endotherm at 68°C is found for $\text{PEO}_{4.0}\text{NH}_4\text{SCN}$. Optical microscopy experiments show that this endotherm corresponds to the melting of the crystalline complex. Decreasing the salt concentration successively to the 5:1 and 6:1 compositions gives a relative decrease in the magnitude of the 68°C endotherm and the appearance of an endotherm at $\sim 42^\circ\text{C}$. The latter can be assigned to the eutectic melting of a mixture of $\text{PEO}_{4.0}\text{NH}_4\text{SCN}$ and PEO. Optical microscopy also shows that this represents the transition from a crystalline to an amorphous phase. The phase diagram for the PEO- NH_4SCN system is shown in Fig. 3. The melting points of NH_4SCN and PEO 600,000 are 149° and 65°C , respectively. The complex $\text{PEO}_{4.0}\text{NH}_4\text{SCN}$ melts at 68°C , and the temperature of the eutectic melt is 42°C . The endotherm at $\sim 95^\circ\text{C}$ in the DSC thermogram of the 3:1 composition does not arise from the polymer-salt interaction, but is assigned on the basis

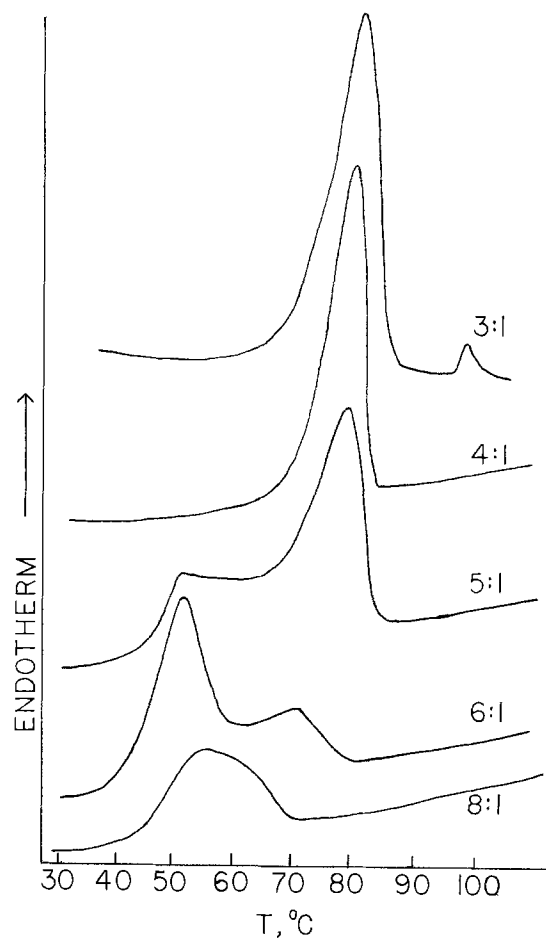


Fig. 2. Differential scanning calorimetric scans of the poly(ethylene oxide)-ammonium thiocyanate system. The ratio of polymer to salt is indicated. The heating rate was $10^\circ\text{C}/\text{min}$ in each scan.

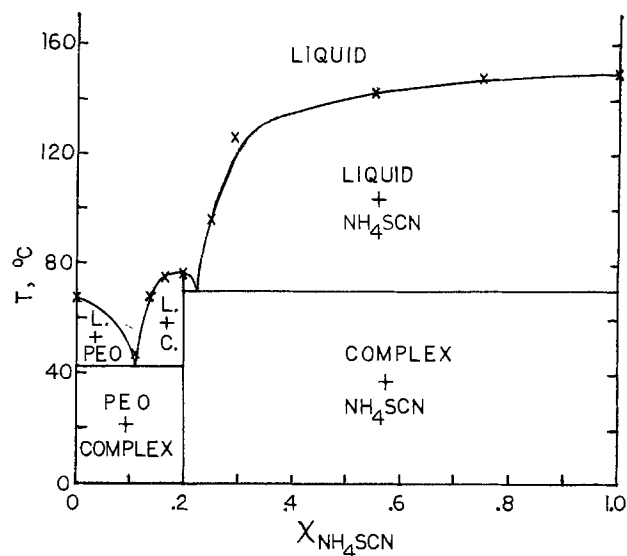


Fig. 3. Approximate phase diagram for the PEO · NH_4SCN system. The 4:1 (PEO · NH_4SCN) complex, shown at 0.2 mol fraction of salt, may exist over a range of stoichiometry, but this was not readily established.

of optical microscopy to a phase transition in crystalline NH_4SCN (15).

In contrast to the data for 8:1 PEO · NH_4SCN , the x-ray diffraction pattern of 8:1 PEO · $\text{NH}_4\text{SO}_3\text{CF}_3$ does not contain reflections assignable to free PEO. The DSC thermogram for this complex (Fig. 5) shows a single endotherm at 41°C . The failure to detect un-

complexed PEO by x-ray powder diffraction suggests that the thermal event observed at 41°C is not a eutectic melting, as was found for the NH_4SCN case, but corresponds to the crystalline-amorphous phase transition of a polymer-salt complex. Increasing the salt concentration to the 4:1 composition gives a second higher temperature endotherm in the DSC traces at 60°C (Fig. 5). This is assigned to the crystalline melt of a second polymer salt complex phase corresponding roughly to 4:1 polymer to salt stoichiometry similar to that found in the PEO- NH_4SCN system. Although a single endotherm is seen in the DSC at a composition of 10:1, evidence for the presence of small amounts of PEO is seen in optical microscopy and x-ray diffraction. The diffraction pattern (Fig. 4) is essentially identical to that of 8:1 PEO · $\text{NH}_4\text{SO}_3\text{CF}_3$ with the exception of an additional reflection which corresponds to one of the two strong reflections found for PEO. Comparison of the x-ray diffraction patterns of the 8:1 and the 5:1 stoichiometries reveals a close similarity with additional strong reflections being

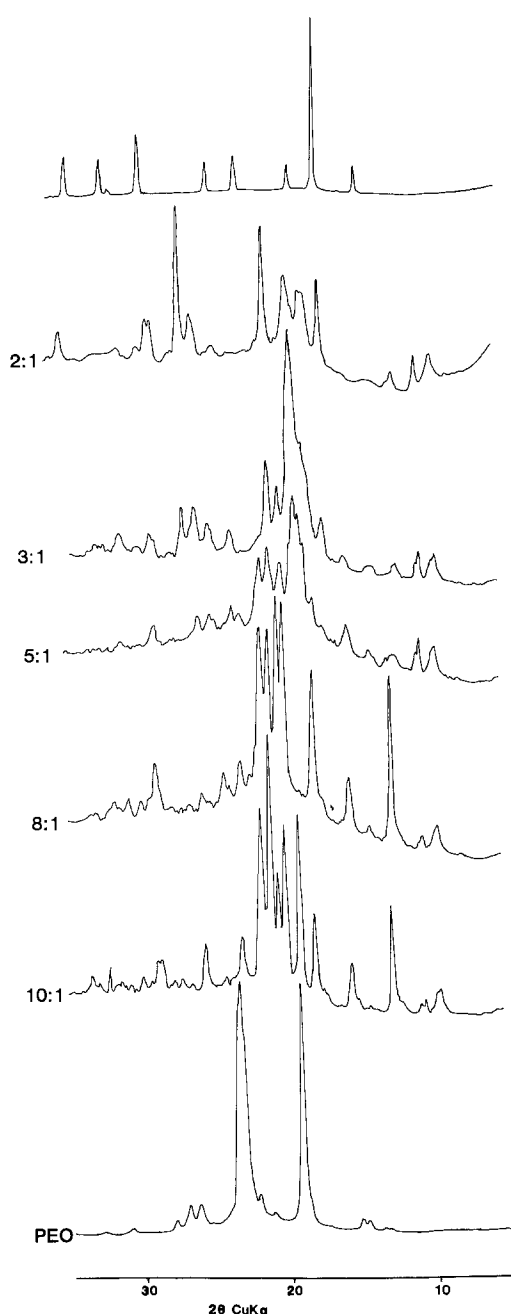


Fig. 4. X-ray diffraction patterns for $\text{NH}_4\text{SO}_3\text{CF}_3$ (upper trace), PEO (lower trace), and complexes formed between these constituents (center traces). The ratios of PEO to $\text{NH}_4\text{SO}_3\text{CF}_3$ are indicated.

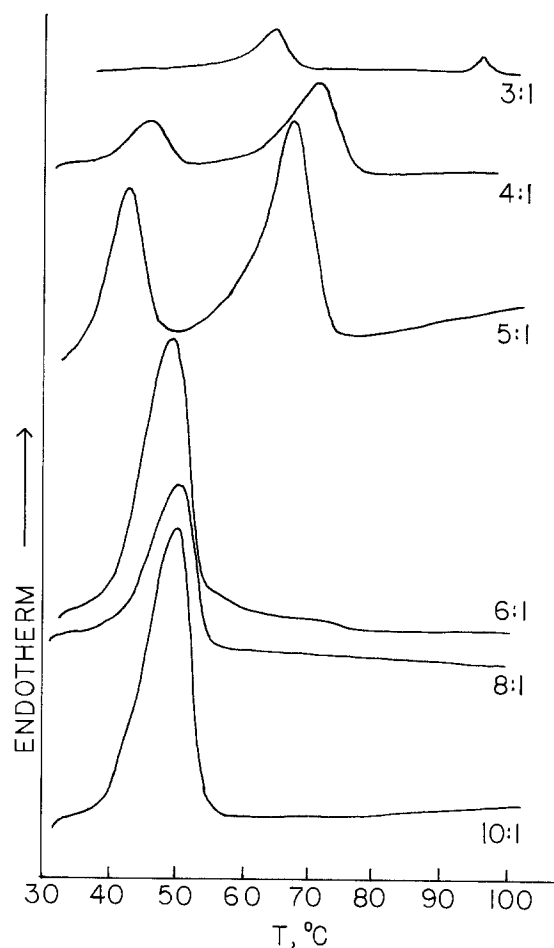


Fig. 5. Differential scanning calorimetric thermograms of the PEO- $\text{NH}_4\text{SO}_3\text{CF}_3$ system. The ratio of polymer to salt are indicated. The heating rate was $10^\circ\text{C min}^{-1}$ in each scan.

found for the latter. This is consistent with the DSC results, which indicate that both of the crystalline complex phases are present at the 5:1 stoichiometry. Similarly, the diffraction pattern of the 3:1 stoichiometry is much different from that of the 8:1 supporting the DSC result, which shows that the low salt concentration complex phase is absent at the 3:1 stoichiometry. Interestingly, the 3:1 and 2:1 compositions do not appear, from the x-ray data, to contain free uncomplexed salt. This behavior contrasts with the NH_4SCN system, and thus the endotherm at 94°C seen in the DSC traces at high concentrations of $\text{NH}_4\text{SO}_3\text{CF}_4$ may possibly arise from a further polymer · salt complex phase.

The rates of crystallization of the polymer · salt phases are slow. Rescanning of the DSC samples, after quenching and equilibration at room temperature, gives thermograms in which the 41° and 60°C endotherms are absent. The rates of crystallization vary with polymer:salt stoichiometry and anion. For the $\text{NH}_4\text{SO}_3\text{CF}_3$ complexes, crystallization from the melt is complete after 24h; the low salt stoichiometry phase crystallizes more slowly. In the case of NH_4SCN , the rates are slower on the order of weeks for the 8:1 and 6:1 stoichiometries and a few days for 4:1. For $\text{PEO}_{3.0}\text{NH}_4\text{SO}_3\text{CF}_3$, the endotherm at $\sim 94^\circ\text{C}$ is seen on immediate rescanning, while the endotherm at 57°C is absent.

Conductivity measurements.—Measurements of the conductivity of the PEO ammonium ion complexes were carried out at temperatures between 25° and 100°C. Plots of $\ln(\sigma T)$ vs. $1/T$ for NH_4SCN and $\text{NH}_4\text{SO}_3\text{CF}_3$ complexes of various stoichiometries are shown in Fig. 6 and 7, respectively. Perhaps the most

striking features are the steep rises in conductivity over relatively small temperature intervals, which occur when the crystalline complexes are heated. For $\text{PEO}_{8.0}\text{NH}_4\text{SCN}$, this sharp rise occurs at about 45°C . Similarly, for the 5:1 complex there is a pronounced rise at $\sim 45^\circ\text{C}$ with a smaller inflection at $\sim 72^\circ\text{C}$, while for the 4:1 only a single sharp rise in conductivity is observed at $\sim 72^\circ\text{C}$. This latter transition has been observed previously for the 4:1 complex (16), but no conductivity was reported for the amorphous state. For the 3:1 stoichiometry, the inflection is slightly elevated to $\sim 80^\circ\text{C}$ due to the presence of excess salt. This behavior parallels the endothermic events seen in the DSC measurements which correspond to the crystalline to amorphous phase transitions. Conductivity plots of the $\text{PEO} \cdot \text{NH}_4\text{SO}_3\text{CF}_3$ complexes (Fig. 7) show the same features with sharp rises or inflections corresponding to features in the DSC traces (Fig. 5).

The slow recrystallization of the complexes from the amorphous melt facilitates the measurement of the conductivity in that phase below the crystalline melting temperature. Cooling to room temperature and remeasuring the conductivities between 25° and 100°C gives the curves in Fig. 6b and 7b. Notable is the large enhancement in conductivity in the amorphous phase over that in the crystalline material, about a factor of $10^3 \Omega^{-1} \text{cm}^{-1}$ at room temperature. Also, for the amorphous phase the curve is not strictly linear but is slightly bowed; thus the system does not exhibit true Arrhenius behavior. The transitions seen in the conductivity plots are reproducible after recrystallization.

Conductivity in PEO-salt complexes has been shown to be essentially ionic in nature (7). The relative mobilities of cation and anion, however, are of particular importance, especially in relation to the practical ap-

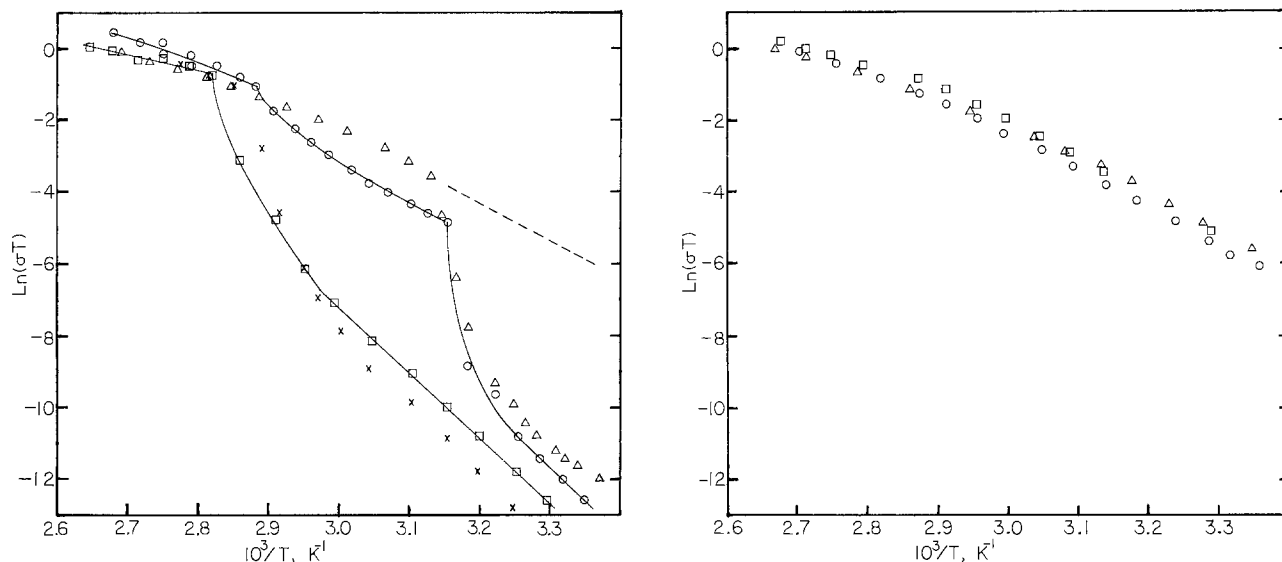


Fig. 6. Electrical conductivity, σ ($\Omega^{-1} \text{cm}^{-1}$), vs. temperature plotted as $\ln(\sigma T)$ vs. $1000/T$, for crystalline and amorphous phases of $\text{PEO} \cdot \text{NH}_4\text{SCN}$ at various ratios of polymer to salt: Δ , 8:1; \circ , 5:1; \times , 4:1; \square , 3:1. A, left: crystalline material. Measurements made starting at room temperature ($\sigma \sim 1 \times 10^{-8}$) and heating to 100°C ($\sigma \sim 2 \times 10^{-3}$). Dashed line indicates conductivities in the amorphous phase shown in B. B, right: amorphous material. After quenching the sample from 100°C to room temperature, conductivities were measured starting at room temperature ($\sigma \sim 1 \times 10^{-5}$) and heating to 100°C ($\sigma \sim 2 \times 10^{-3}$).

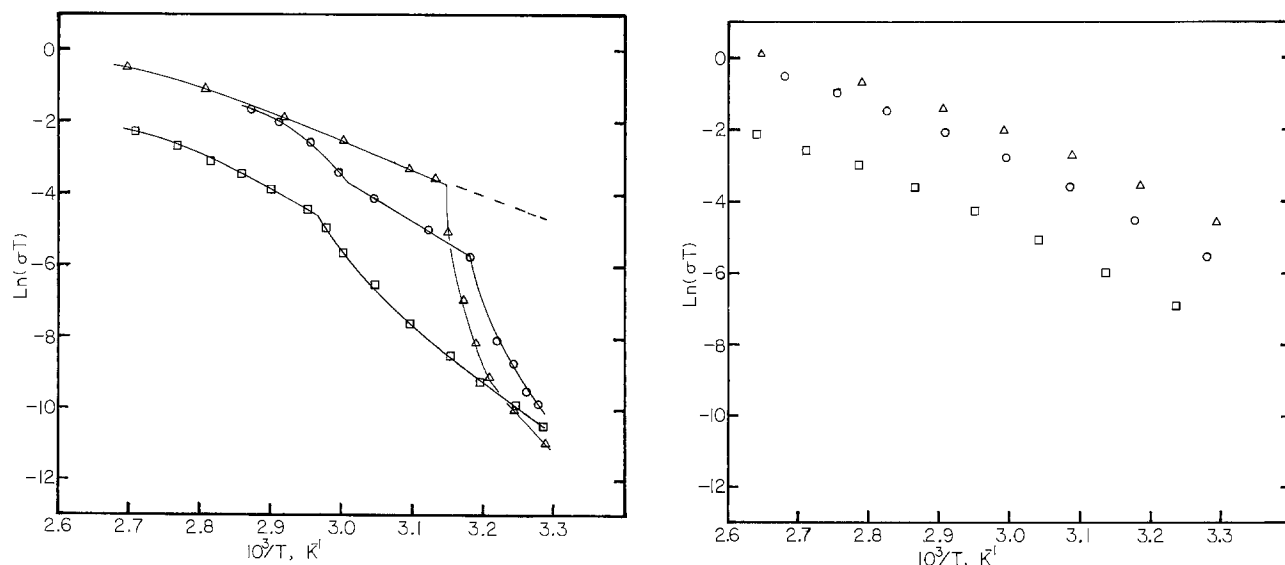


Fig. 7. Electrical conductivity, σ ($\Omega^{-1} \text{cm}^{-1}$), vs. temperature plotted as $\ln(\sigma T)$ vs. $1000/T$, for crystalline and amorphous phases of $\text{PEO} \cdot \text{NH}_4\text{SO}_3\text{CF}_3$ at various ratios of polymer to salt: Δ , 8:1; \circ , 5:1; \square , 3:1. A, left: crystalline material. Measurements made starting at 35°C ($\sigma \sim 5 \times 10^{-8}$) and heating to 100°C ($\sigma \sim 1 \times 10^{-3}$ for 8:1, $\sim 3 \times 10^{-4}$ for 3:1). Dashed line indicates conductivity in the amorphous phase shown in more detail in B. B, right: amorphous material. After quenching the sample from 100° to 35°C , conductivities were measured starting at 35°C and heating to 100°C . For the 8:1 electrolyte, σ increases from $\sim 2 \times 10^{-5}$ to $\sim 1 \times 10^{-3}$ and is about a factor of 2.5 less for the 3:1 electrolyte.

plications of polymer electrolytes in energy storage devices. Weston and Steele have shown that in 8:1 PEO · LiClO₄ complexes the transport number for the lithium ions is less than 0.5 (8), and Sorensen and Jacobsen have found a cation transport number of 0.54 in PEO_{4.5}LiSCN (9).

As indicated below, ionic motion in PEO · NH₄X probably does not involve proton transfer from NH₄⁺ to the polyether polymer backbone. The conductivity behavior of PEO_{4.0}ND₄SO₃CF₃ is essentially identical to that for the normal isotopic ammonium complex, and there is no increase in the slope of the Arrhenius plots due to an isotope effect. Therefore, a transport mechanism involving proton transfer seems unlikely.

An experiment was performed in which a polymer complex was doped with ammonia, because the presence of free NH₃ might provide a mechanism for proton transport. The polymer salt complex absorbs ammonia readily and swells and exhibits mechanical properties similar to those of an undoped polymer salt complex in the amorphous phase. No enhancement of conductivity was observed. The ammonia-doped polymer has roughly the same conductivity as the undoped material in the amorphous phase, again indicating that H⁺ conductivity does not occur. Finally, evidence for the mobility of NH₄⁺ was obtained using ion reversible and ion blocking electrodes. Figure 8 shows the ac complex admittance plots for 5:1 PEO · NH₄SO₃CF₃ in the frequency range 50 × 10⁴ to 20 Hz with Pt (blocking) and (NH₄)_{0.25}WO₃ (reversible) electrodes. The latter electrode material is reversible to NH₄⁺ ions and shows the "spur" typical of an arrangement where the double-layer capacitance at the electrode-electrolyte interface is removed by reversible transfer of NH₄⁺ ions. The ammonium ions are thus clearly

implicated as a mobile species in these polymer electrolytes. However, we were unsuccessful in determining the transport number with a polarization cell having ammonium tungsten bronze electrodes, so it is possible that the anion contributes substantially to the conductivity.

Conclusion

Although determining the stoichiometry of interaction has been an important segment of this work, the most significant aspect has been determining the conductivity behavior of these materials in their crystalline and metastable, amorphous states. In the amorphous state, conductivity enhancement at room temperature is roughly 10³ Ω⁻¹ cm⁻¹ greater than for the corresponding crystalline state of these electrolytes. This behavior strengthens the assumption that cooperative polymer conformation fluctuations are responsible, at least in part, for the transport process in these conductors. Such a large conductivity enhancement indicates that other amorphous solid electrolytes above their T_g's might be very promising as fast ionic conductors.

Other comparisons of crystalline vs. amorphous conductivity in the same electrolyte have been reported (8, 16). But in the PEO · LiClO₄ 8:1 comparison (8), the amorphous state was induced by the addition of water, so the true comparison of conductivities may be difficult to make, since water is known to increase conductivity. In another report (16), slightly higher conductivities due to annealing above the melting point of the electrolyte PEO · LiClO₄ 8:1 or PEO · LiSO₃CF₃ 8:1:1 are suggested to be due to slow recrystallization, but this conclusion is not confirmed by other means.

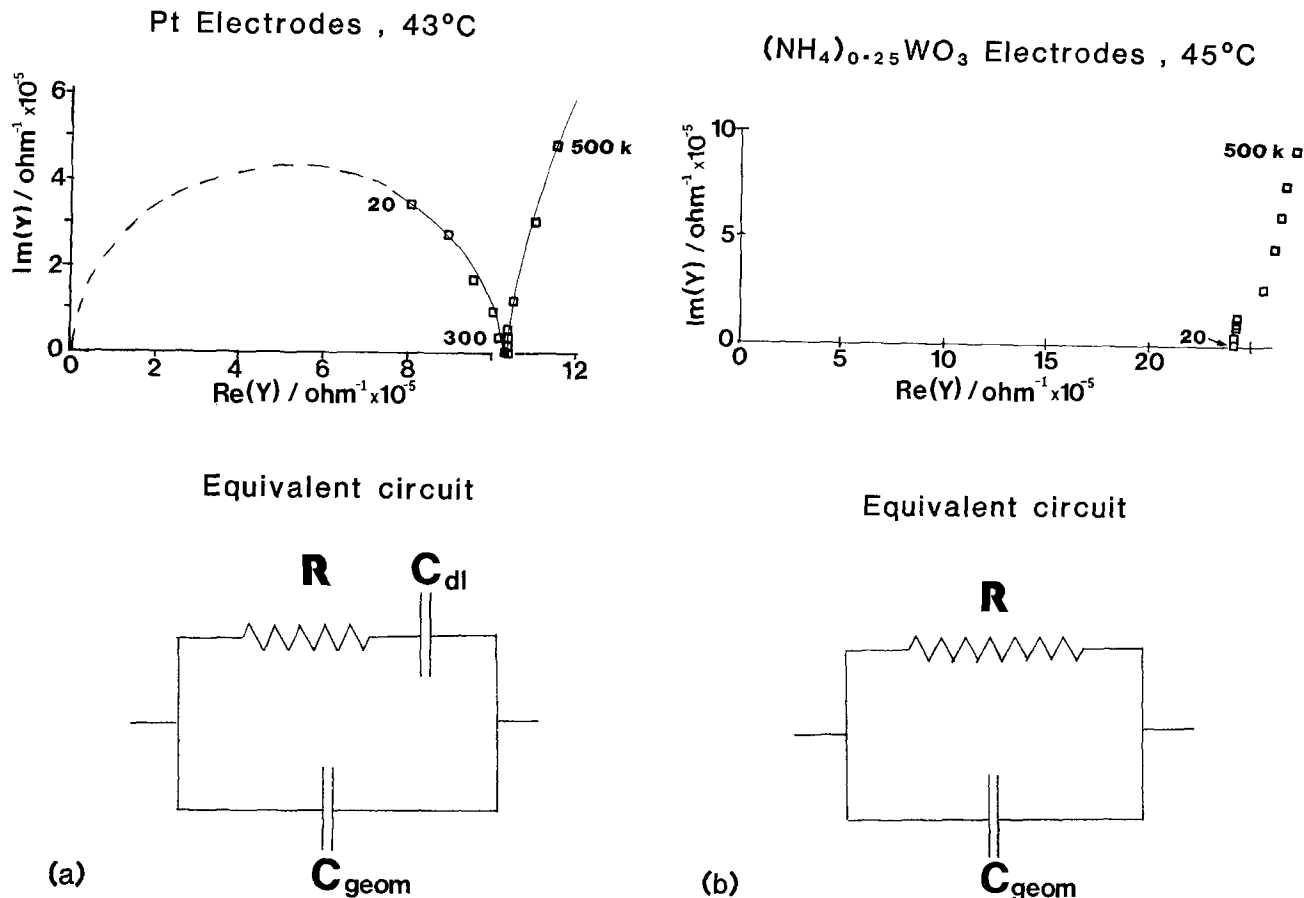


Fig. 8. Plot of the imaginary part vs. the real part of the admittance (Y) for PEO · NH₄SO₃CF₃ 5:1. a, left: with Pt electrodes at 43°C. b, right: with ammonium tungsten bronze electrodes at 45°C. The equivalent circuits corresponding to cases A and B are shown with circuit elements: bulk resistance, R ; geometric capacitance, C_{geom} ; double layer capacitance C_{dl} . Frequencies (20 Hz-500 kHz) are listed next to data points.

Acknowledgments

This research was supported by the NSF Materials Research Laboratory Program through the Northwestern University Materials Research Center and by the Office of Naval Research. We appreciate helpful conversations with Professors Mark Ratner and Buckley Crist.

Manuscript submitted April 25, 1983; revised manuscript received Nov. 7, 1983.

REFERENCES

1. R. W. Dupon, B. L. Papke, M. A. Ratner, D. H. Whitmore, and D. F. Shriver, *J. Am. Chem. Soc.*, **104**, 6247 (1982).
2. C. C. Lee and P. V. Wright, *Polymer*, **23**, 681 (1982).
3. M. B. Armand, in "Lithium Nonaqueous Battery Electrochemistry," E. B. Yeager, B. Schumm, Jr., G. Blomgren, D. R. Blankenship, V. Leger, and J. Akridge, Editors, p. 261, The Electrochemical Society Softbound Proceedings Series, Pennington, NJ (1980).
4. J. E. Weston and B. C. H. Steele, *Solid State Ionics*, **7**, 75 (1982).
5. B. L. Papke, M. A. Ratner, and D. F. Shriver, *This Journal*, **129**, 1694 (1982).
6. M. B. Armand, J. M. Chabagno, and M. J. Duclot, in "Fast Ion Transport in Solids," P. Vashishta, N. J. Mundy, and J. N. Shenoy, Editors, p. 131, North Holland, New York (1979).
7. R. W. Dupon, D. H. Whitmore, and D. F. Shriver, *This Journal*, **128**, 715 (1981).
8. J. E. Weston and B. C. H. Steele, *Solid State Ionics*, **7**, 81 (1982).
9. P. R. Sorensen and T. Jacobsen, *Electrochim. Acta*, **27**, 1671 (1982).
10. B. L. Papke, M. A. Ratner, and D. F. Shriver, *J. Phys. Chem. Solids*, **42**, 493 (1981).
11. K. N. Trueblood, C. B. Knobler, D. S. Lawrence, and R. V. Stevens, *J. Am. Chem. Soc.*, **104**, 1355 (1982), and references therein.
12. G. Weber, W. Saenger, F. Vögtle, and H. Sieger, *Angew. Chem., Int. Ed. Engl.*, **18**, 227 (1979).
13. B. L. Papke, Ph.D. Thesis, Northwestern University, Evanston, IL (1982).
14. P. G. Dickens, A. C. Halliwell, D. J. Murphy, and M. S. Whittingham, *Trans. Faraday Soc.*, **67**, 794 (1971).
15. Y. Kinsho, N. Onodera, M. Sakiyama, and S. Seki, *Bull. Chem. Soc. Jpn.*, **52**, 395 (1979).
16. P. V. Wright, *Br. Polym. J.*, **7**, 319 (1975).
17. J. E. Weston and B. C. H. Steele, *Solid State Ionics*, **2**, 347 (1981).

Photoelectrochemistry of Lamellar n- and p-Type InSe in Aqueous Solution

Claude Levy-Clement,* Nicole Le Nagard, and Ouri Gorochov

Laboratoire de Physique des Solides, CNRS, 92195 Meudon Principal Cedex, France

Alain Chevy

Laboratoire de Physique des Milieux très condensés, associé au CNRS, 75230 Paris Cédex 05, France

ABSTRACT

n- and p-type InSe single crystals have been grown by the Bridgman-Stockbarger method and characterized by their electronic transport properties. A photoelectrochemical study in aqueous media using the cleavage surface shows rectifying behavior in the dark, confirming diode behavior for both. InSe electrodes exhibit anodic and cathodic photocurrents. These photocurrents are related to a photoelectrochemical effect when a positive bias is applied to n-type InSe and when a negative bias is applied to p-type InSe, whereas the cathodic photocurrent for the n-type and the anodic photocurrent for the p-type are due to a photoconductive effect. Flatband potentials in acidic solution have been determined from the change of sign of the photocurrent and from Mott-Schottky plots of the capacitance (-0.6V vs. SCE for n-type and $+0.2\text{V}$ vs. SCE for p-type). The flatband potential is not pH dependent. Photocurrent spectra indicate a 1.2 eV bandgap. The behavior of InSe electrodes is explained in terms of the location of the valence and conduction bands on the electrochemical scale.

The photoelectrochemical properties of lamellar transition-metal dichalcogenides have recently received a great amount of attention as electrodes in photoelectrochemical cells. The group VIA (W and Mo) chalcogenides have been studied most often (1), as these materials have bandgap between 1.0 and 1.6 eV (2). Another layered-type semiconductor with an adequate bandgap (1.3 eV) for solar energy conversion is indium selenide (InSe); however, its photoelectrochemical properties are not well characterized. This material exhibits n- or p-type conductivity depending on the growth conditions (3-4). InSe belongs to the III-VI semiconductor group, which includes GaS, GaSe, and GaTe (2). Among these compounds, only the photoelectrochemical behavior of p-type GaSe electrodes has been studied (5). This material has a bandgap of 2 eV.

The lamellar structure of InSe is strongly anisotropic and shows covalently bonded units (Se-In-In-Se) held

together by van der Waals forces (Fig. 1). The cleavage plane, that is the van der Waals surface, is made of selenium atoms bonded together with covalent forces. With the Bridgman growth method, the rhombohedral γ -3 R polytype is formed (6). The optical properties and the band structure are fairly well known in the ordinary configuration $\vec{E} \perp \vec{C}$ (7-8), \vec{C} being the crystallographic direction perpendicular to the van der Waals surface, and \vec{E} being the electric vector of in-

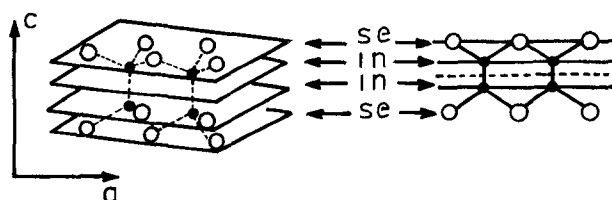


Fig. 1. Crystal structure of InSe

* Electrochemical Society Active Member.

Key words: n- and p-type InSe, layered semiconductor, photoelectrochemistry, photoconductivity.

cident light. The energy gap in InSe is "quasidirect," that is to say that the direct gap is at 1.3 eV, and the optical transition is only weakly allowed by spin-orbit coupling in the valence band. A parabolic exciton is bound to this gap ($n = 1$, $E = 1.257$ eV). The indirect gap, some 50 meV below the energy of the direct gap, is weak enough not to be observable in optical absorption. Two direct transitions at 2.4 and 2.78 eV are also permitted in this direction. In the solar spectrum region, the absorption coefficient values vary from 10^{-3} cm $^{-1}$ at the absorption edge to 10^{-4} cm $^{-1}$ at 2.5 eV. A remarkable photoconductivity behavior with the occurrence in InSe of negative photoconductivity and photomemory effects has led to the proposal of complex schemes of recombination centers (9). Photovoltaic properties have been studied on single crystals (9f-10).

InSe can be obtained as large crystals using the Bridgman technique, and this material can be used as a model for the photoelectrochemical behavior of lamellar materials, especially for studying the influence of structural effects on the performance in electrochemical cells. Crystals can easily be cleaved in planes

perpendicular to the c axis and only little lattice damage should result from surface preparation. Thus

the $\perp c$ face exhibits quite ideal properties for interfacial studies. As the first part of this study, we report the photoelectrochemical behavior of n- and p-type InSe samples in aqueous solution when the exposed

surface is parallel to the layers ($\perp c$ face).

Experimental

Crystal growth.—The InSe crystals were grown by the Bridgman-Stockbarger method from the high purity elements, 6N In and 5N Se, using an excess of In (11). The phase diagram of InSe indicates an incongruent melting of InSe (12), and $In_{1+x}Se$ compositions have been used in order to avoid the peritectic reaction. n-Type compounds have been obtained when chlorine or gallium were the doping agents, whereas for p-type compounds the doping agent was zinc (3).

Electrical characteristics.—The transport properties were determined from the resistivity and Hall voltage measurements of these crystals. Ohmic electrical contacts were made by ultrasonically soldering with pure indium metal for the n-type material and with conductive silver paint for the p-type crystals. The resistivity was measured using the four-probe direct current van der Pauw technique. The activation energy of the impurity levels was obtained from the variation of the resistivity with temperature from liquid nitrogen to room temperature. The number and sign of current carriers were determined by alternating current Hall measurements.

Experimental procedure.—The layer planes of the cleaved single crystal were used without pretreatment. Ohmic contacts to the back of the crystals were made as described above. The crystals were encapsulated in epoxy resin (EPOXI-PATCH) exposing only the layer planes to the electrolyte. Electrolytes were prepared from reagent-grade chemicals and distilled water. Photoelectrochemistry studies were done in 0.1M H_2SO_4 . In addition, 1M KCl and 0.1M NaOH electrolytes were used in order to find the effect of pH on the photoelectrochemical properties. I_3^-/I^- and $Fe^{2+}/$

Table II

Nature of the electrodes	Initial photovoltages values	
	0.1M H_2SO_4	0.1M NaOH
n-type sample 1	-330 mV	-230 mV
p-type sample 3	+280 mV	+230 mV

Fe^{3+} redox couples were also examined. The reference electrode was saturated calomel and the counterelectrode a platinum wire. Several procedures were used: dark current/voltage characteristics [$I(V)$], capacitance/voltage characteristics [$C(V)$], and photocurrent I_{ph} as a function of the electrode potential V and incident light wavelength. Since the optical range of interest was the near infrared and visible region of the spectrum, a simple Pyrex optical flat window was used. The capacitance of the semiconductor space-charge region was determined by measuring that part of a small (10 mV) ac signal at 1 kHz and 500 Hz, which was in quadrature with the initial reference phase. The exact value of the capacitance was obtained by comparing the observed signal with the values obtained for capacitors of known value. The detection of the in phase and quadrature signals was performed using an ADS-1 ATNE lock-in detector. The illumination of the electrodes was performed by a 70W tungsten-iodine lamp. The intensity of the white light focalized on the semiconductor was close to 100 mW/cm 2 . Either direct or chopped white light or monochromatic chopped light (Jobin Yvon H-20 Spectrometer) was used. The frequency of the chopper was approximately 100 Hz, and the modulated photocurrent was detected with the lock-in amplifier. The spectral distribution of the combination of the tungsten-iodine lamp and the monochromator was determined using a thermocouple detector (2M Dexter) in the infrared region and a calibrated silicon diode (P V 215-EGG) in the visible region.

Results

Transport properties.—The transport properties are reported in Table I for the three samples used as photoelectrodes. These values should be considered as average ones, because, due to the nonstoichiometric Bridgman growth method used, there is some discrepancy between the electrical results across the crystal ingot.

For the experimental value of the carrier density determined from the Hall voltage measurements, assuming a one-electron band model, the width of the depletion layer was estimated (last column of Table I). The formula used is $w = [2 \epsilon \epsilon_0 (V - V_B)/e N_0]^{1/2}$, where ϵ , the dielectric constant of InSe, is 9.74 (7d), and the band bending $V - V_B$ has been chosen to be 1V.

Photovoltages.—The initial photovoltage values obtained in 0.1M H_2SO_4 and in 0.1M NaOH are reported in Table II. After several voltammetric sweeps under light, these values decrease to less than 60 mV.

Voltammetric behavior in the dark.—In 0.1M H_2SO_4 in the dark, the interfaces of samples 1 (n-type) and 3 (p-type) are rectifying, i.e., they have a diode-like voltammogram (Fig. 2a and 2b). However, the character of a given interface is found to change with time after several voltammetric sweeps under light. A deterioration of the diode behavior in the dark is found.

Table I

Sample number	Type	Doping agent	Resistivity Ω cm $^{-1}$	Mobility cm $^2/V$ s	Carriers number/cm 3	Impurity level activation energy	Depletion layer $\mu V^{-1/2}$
1	n	100 ppm Cl $_2$	5	1000	$1.7 \cdot 10^{15}$	0.1 eV	0.8
2	n	10 ppm Ga	42	400	$1.0 \cdot 10^{15}$		1.0
3	p	500 ppm Zn	240	40	$6.8 \cdot 10^{14}$	0.27 eV	1.6

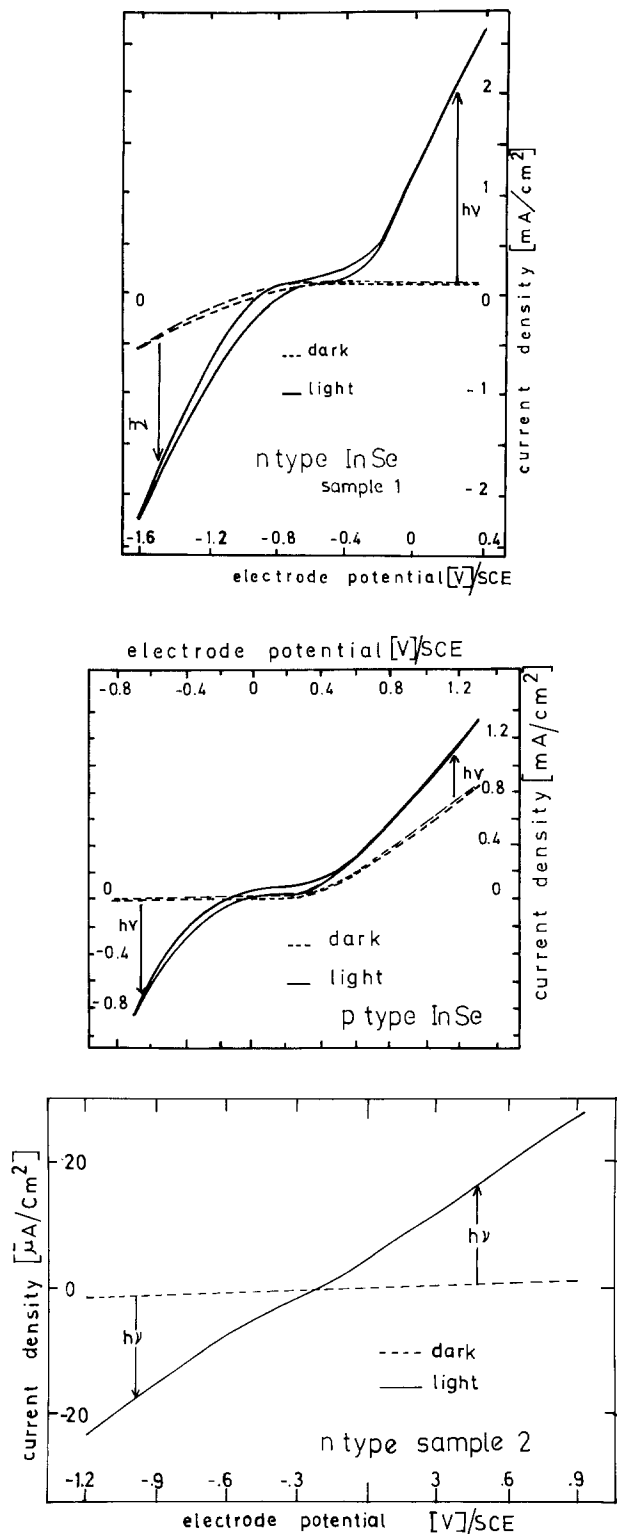


Fig. 2. I-V curves of three InSe samples in the presence of 0.1M H_2SO_4 . A, top: Sample 1. ----: in the dark. —: under direct white light (70W tungsten-iodine lamp). B, middle: Sample 3. ----: in the dark. —: under direct white light (70W tungsten-iodine lamp). C, bottom: sample 2. ----: in the dark. —: under direct white light (70W tungsten-iodine lamp).

For sample 2 (n-type), the initial current varies linearly with the applied potential and at $\pm 1V$ vs. SCE it is equal to $1 \mu A$ (Fig. 2c).

Voltammetric behavior under illumination in 0.1M H_2SO_4 .—The current voltage characteristics under white light for samples number 1, 3, and 2 are represented in Fig. 2a, 2b, and 2c. respectively. All samples show both anodic and cathodic photocurrents. For

sample 1 (n-type), the photocurrent changes sign at $-0.7V$ and at $\pm 1V$ from this value the intensity of the anodic photocurrent is twice the cathodic one. For sample 3 (p-type) at $\pm 1V$ from the change of sign of the photocurrent occurring at $+0.2V$, the cathodic photocurrent is ten times greater than the anodic one. Sample 2 shows a linear photocurrent curve of several $\mu A/cm^2$ and the current changes sign at $-0.2V$.

The shapes of the current-voltage curves change when the wavelength of the light varies. For sample 1, the cathodic photocurrent decreases when the wavelength decreases. For example, between 1040 and 990 nm it is two times larger than the anodic photocurrent (at $\pm 1V$ from the change of sign), while at 680 nm it becomes ten times weaker than the anodic photocurrent (Fig. 3a). The contrary is observed for the p-type sample 3, and the ratio of the cathodic to the anodic photocurrent equals 2 at 1000 nm and 12 at 640 nm (Fig. 3b). The variation of the photocurrent was measured as a function of the variation of the light wavelength. The semiconductor electrodes were polarized for all samples at $+1V$ and $-1V$ from the change of the sign of the photocurrent. The results are presented for samples 1, 3, and 2 in Fig. 4a, 4b, and 4c, respectively.

To observe the effect of pH on the current-voltage characteristics of InSe, new electrode samples were tested in contact with solution of 1M KCl and 0.1M NaOH. Photocurrent voltage characteristics show that there is no real change in the value of the intercept of the photocurrent curves with the potential axis when the pH changes. For the p-type InSe, the cath-

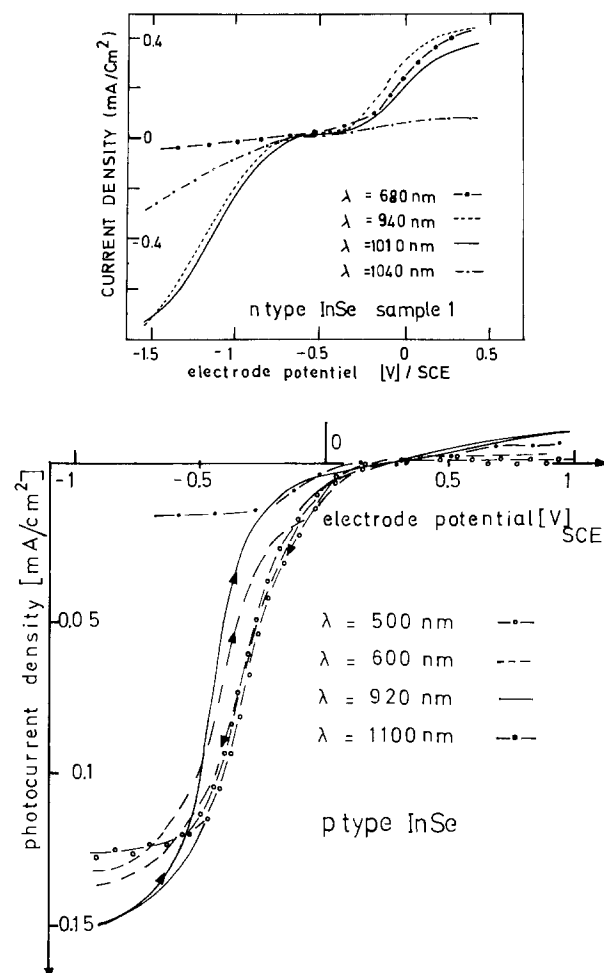


Fig. 3. Current vs. potential characteristics of two samples at various photon energies. A, top: n-type sample 1 in 0.1M H_2SO_4 . ----: 1040 nm. —: 1010 nm. ----: 940 nm. —○—○—○: 680 nm. B, bottom: p-type sample 3 in 0.1M H_2SO_4 . ----: 1100 nm. —: 920 nm. ----: 600 nm. —○—○—○: 500 nm.

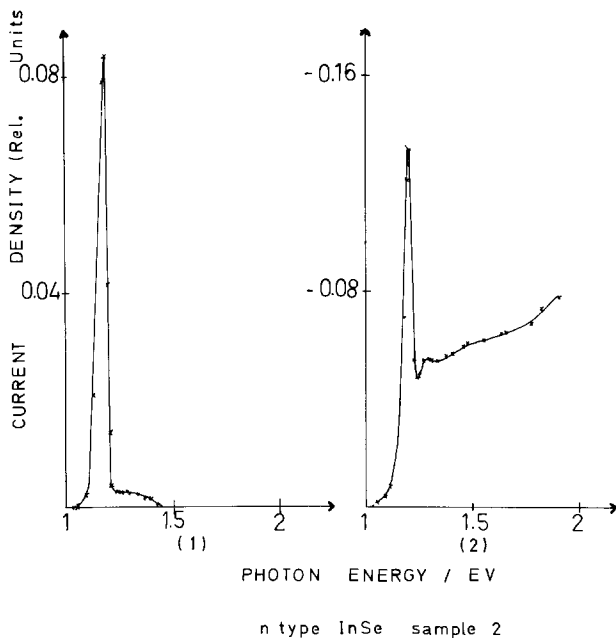
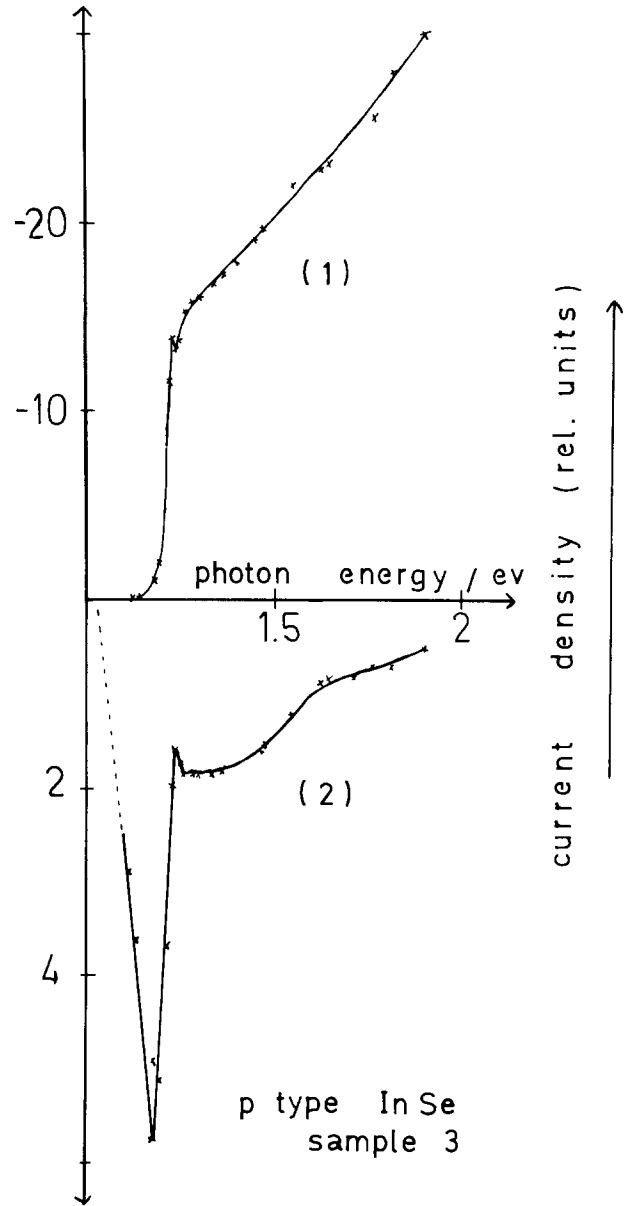
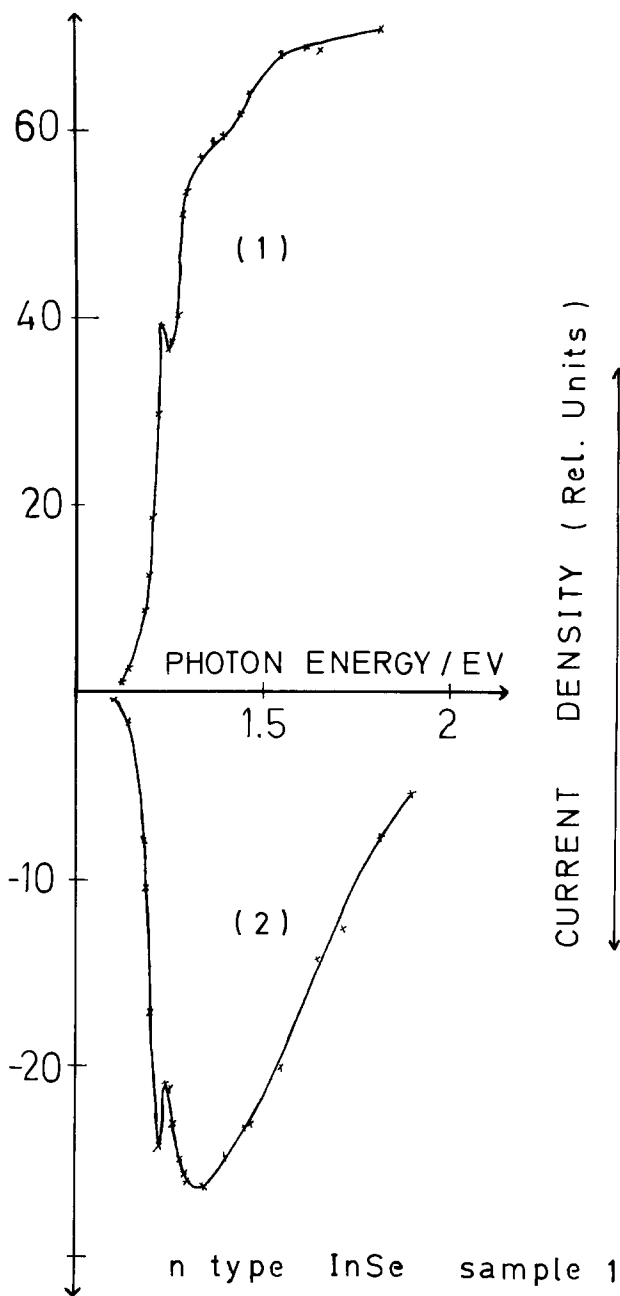


Fig. 4. Spectral responses of three samples when illuminated with monochromatic beam in 0.1M H₂SO₄. A, top left: n-type sample 1. Curve 1: photocurrent spectrum when a +0.4V is applied. Curve 2: photoconductivity spectrum when a -1.6V is applied. B, top right: p-type sample 3. Curve 1: photocurrent spectrum when a -0.8V is applied. Curve 2: photoconductivity spectrum when a +1.2V is applied. C, left: n-type sample 2. Photoconductivity spectra when a +0.8V is applied (curve 1), and when a -1.2V is applied (curve 2).

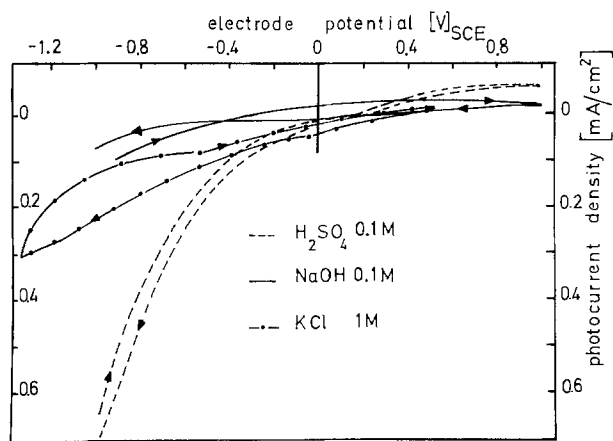


Fig. 5 I-V curve of p-InSe (sample 3) under chopped white light (70W tungsten-iodine lamp) in solutions containing 0.1M H_2SO_4 (---), 0.1M KCl (-.-.-), and 0.1M NaOH (—).

odic photocurrent decreases from H_2SO_4 to KCl and to NaOH (Fig. 5) and for the n-type InSe the anodic photocurrent changes in a similar way. A strong hysteresis of the curves, depending on whether the values are obtained as the potential is increasing or decreasing, is observed in the presence of KCl or NaOH. Since previous experimenters had reported the stabilization of electrodes in aqueous solution by the addition of I_3^-/I^- , electrodes of InSe were placed in a solution of 1M KI dissolved in 0.5M H_2SO_4 . For both p- and n-type samples, no change was observed in the shape of the photocurrent, but only a large decrease of the intensity. The electrodes were no longer shiny and started to turn brown. The same result was observed in presence of $\text{Fe}^{2+}/\text{Fe}^{3+}$.

In the presence of 0.1M H_2SO_4 , InSe photoelectrodes were reasonably stable, but after an exposure of several hours under white light (70W tungsten lamp) the crystals were photocorroded and a thin red layer of selenium appeared which could easily be removed by adhesive tape.

Capacitance measurements.—Capacitance measurements were undertaken to determine the flatband potentials. New crystals were used so that the measurement could be performed on a surface which had not yet been corroded. Figures 6a and 6b show the plot of capacitance vs. potential and the curves of $1/C^2$ vs. V (Mott-Schottky plot) for sample 1 (n-type) and sample 3 (p-type), respectively. For both n- and p-type samples, we obtained linear Mott-Schottky plots over a potential range of 300-500 mV in 0.1M H_2SO_4 . From

the intercept, values of -0.6V for sample 1 (n-type) and $+0.2\text{V}$ vs. SCE for sample 3 (p-type) were estimated for the flatband potentials. It was not possible to calculate flatband potentials from a sample after substantial photocorrosion had occurred as the capacitance curves were no longer regular.

Discussion

The sign of the photopotentials and the shape of the dark current are in agreement with the transport properties determined for the n- or p-type electrodes. Contrarily, the current voltage characteristics under illumination do not clearly indicate the carrier type of the electrodes because all samples show both anodic and cathodic photocurrents. From the transport properties measurements, it appears that the majority carrier density is low for InSe and the hypothesis of a photoconductive effect responsible for the unexpected anodic and cathodic photocurrents could be invoked. This photoconductive effect corresponds to an increase in carriers or of their mobility by the absorption of light. The decrease of the intensity of these photocurrents under forward bias when the wavelength decreases (Fig. 3a and 3b) is an indication that they are due to an effect not at the junction but in the bulk, which is the case for the photoconductivity. To prove the existence of a large photoconductivity in InSe, we did the following experiment with a p-type crystal in contact with the air. Two electrical contacts were made with one on the front of the crystal at one end and the other contact on the back at the other end. A controlled bias between $+1\text{V}$ and -1V across the front and back contacts was applied. When the sample was illuminated by a small spot of light (1mm^2) not striking the electrical contact, a several microamperes photocurrent appeared, proportional to the applied voltage, and with direction changing with the sign of the bias. The curve obtained under this condition is similar to the curve number 2c obtained for sample 2 in contact with 0.1M H_2SO_4 , and the photocurrents are thus only photoconductive currents. When we did the same experiment lighting only the front contact, we got a large photocurrent under cathodic bias and a smaller one in the other direction under opposite bias. The curve obtained is similar to that shown in Fig. 2b for the p-type sample in contact with H_2SO_4 , the Schottky barrier being established by the metallic electrical contact. The anodic photocurrent for the n-type sample 1 and the cathodic photocurrent for the p-type sample 3 in contact with an electrolyte is consistent with the presence of the Schottky barrier at the semiconductor/electrolyte interface. From the diminution of the intensity of the cathodic photocur-

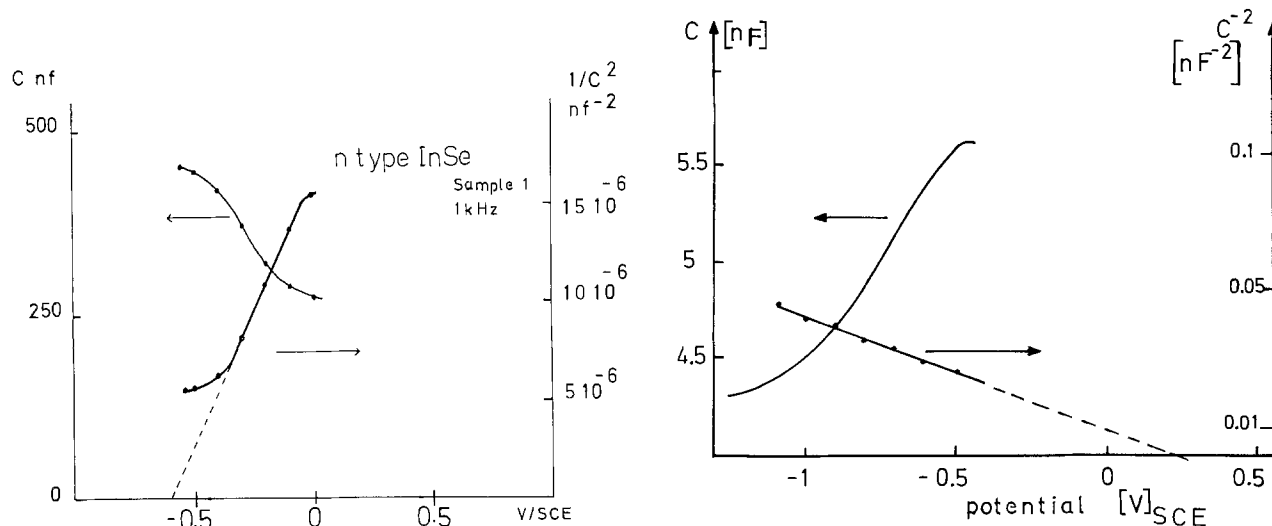


Fig. 6. Capacitance-voltage curve and Mott-Schottky plot ($1/C^2$ vs. V) for two samples in 0.1M H_2SO_4 . Frequency: 1 kHz. A, left: n-type sample 1. B, right: p-type sample 3.

rents obtained for the p-type sample 3 when the electrolyte changes from H_2SO_4 to KCl to NaOH , it is obvious that this cathodic photocurrent is due to the hydrogen evolution (Fig. 5). The anodic photocurrent for the n-type sample 1 may be due to a photocorrosion reaction; the intensity of the anodic photocurrent is higher in presence of H_2SO_4 than in presence of NaOH . From these results, we can deduce that the current curves under illumination *vs.* potential represented in Fig. 2a and 2b for samples 1 and 3 show the presence of two effects: photoelectrochemical and photoconductive. For sample 2 (n-type), there was no formation of a Schottky barrier, and only the photoconductivity was observed. The reasons for this are not clear. Figures 4a and 4b represent for n- and p-type materials the spectral response due to the photoelectrochemical process (curve 1) and the photoconductivity spectrum (curve 2). The spectral response determined in the region where the primary photocurrent is due to a photoelectrochemical reaction between the semiconductor and the solution is in good agreement with published optical absorption spectra (3, 7d). For the photocurrent spectra shown in curve 1, the $I_{\text{ph}} \sim (E_g - h\nu)^{n/2}$ law was not verified for either $n = 1$ or $n = 4$. From Fig. 4a curve 1 and 4b curve 1, we can see that the bandgap energy is around 1.2 eV; however, the small peak at 1.24 eV may be due to the exciton bonded to the direct transition at 1.35 eV (7d). The particular shape of the photoconductivity spectra shows again that the current decreases when the energy of the light increases (Fig. 4a, curve 2, 4b, curve 2, 4c) as expected due to the photoconductive effect (9f).

Flatband potentials from the Mott-Schottky plots and photocurrent curves are in agreement. They are estimated as -0.6V for the n-type and $+0.2\text{V}$ for the p-type. The resistivity measurements at low temperatures give the activation energy of the impurity levels—the difference between the Fermi level and the edge of the conduction band ($E_C - E_F$) for an n-type—as 0.1 eV. The difference between the Fermi level and the edge of the valence band ($E_V - E_F$) for the p-type (*i.e.*, the activation energy) equals 0.27 eV. From these results presented above and with the 1.2 eV value for the bandgap energy, the position of the bandedges for n- and p-type InSe can be estimated as -0.45V *vs.* NHE for the conduction band and as $+0.75\text{V}$ *vs.* NHE for the valence band. From these values reported in Fig. 7, it appears that InSe could be a good hydrogen evolving semiconductor photocathode if a suitable metal catalyst is plated at the surface. As a p-type lamellar semiconductor, InSe could be used to study photointercalation, the principle of which was described by Tributsch (13). The position of the bandedges authorizes one to predict that, among the cations that could be intercalated, copper (I) would be the most promising because the copper redox potential is situated between the band energy levels of InSe.

Conclusion

The photoelectrochemical behavior of the van der Waals surfaces of n- and p-type InSe have been studied in 0.1M H_2SO_4 . Under white light, voltammetric study shows the presence of photocurrents of two origins: photoelectrochemical reactions and photoconductivity. The behavior of InSe electrode has been characterized in terms of the location of the valence and conduction bands. These results permitted us to choose copper as a suitable cation to be used to demonstrate that the photoinduced intercalation is possible in a p-type layered compound (14). Since previous results from band structure calculation (8), optical data, and transport measurements (7a-7d, 15) show the existence of a large anisotropy in the physical properties of InSe between the direction of the van der Waals surfaces and the direction perpendicular to the layers, the photo-

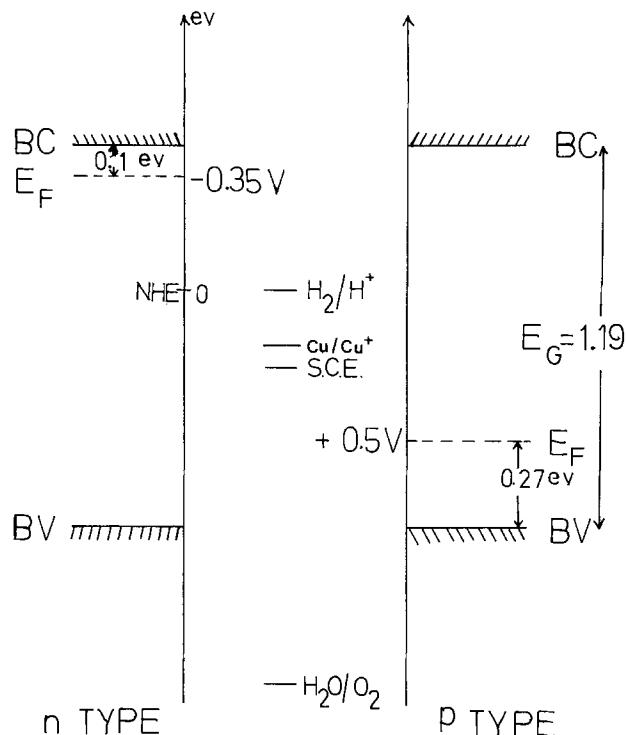


Fig. 7. Schematic representation of the energetics at the n-type and p-type InSe electrode/solution interface.

effect should reflect this anisotropy. The results of these experiments will be reported subsequently.

Acknowledgment

The authors would like to thank B. Theys and M. Etman for measuring the capacitance-voltage curves.

Manuscript submitted May 12, 1983; revised manuscript received Nov. 28, 1983.

REFERENCES

- (a) H. Tributsch and J. C. Benett, *J. Electroanal. Chem. Interfacial Electrochem.*, **81**, 97 (1977); (b) H. Tributsch, *This Journal*, **125**, 1086 (1978); F. Kwai, H. Tributsch, and T. Sakata, *Chem. Phys. Lett.*, **69**, 336 (1980); (c) L. F. Schneemeyer and M. S. Wrighton, *J. Am. Chem. Soc.*, **101**, 6496 (1979); (d) H. J. Lewerenz, A. Heller, and F. J. Disalvo, *ibid.*, **102**, 1877 (1980); (e) F.-R. F. Fan, H. S. White, B. Wheeler, and A. J. Bard, *ibid.*, **102**, 5142 (1980); (f) H. S. White, F.-R. F. Fan, and A. J. Bard, *This Journal*, **128**, 1045 (1981); (g) B. A. Parkinson, T. R. Furtak, D. Canfield, K. K. Kam, and G. Kline, *Discuss. Faraday Soc.*, **70**, 233 (1980); (h) G. Kline, K. K. Kam, D. Canfield, and B. A. Parkinson, *Solar Energy Mater.*, **4**, 301 (1981); (i) F.-R. F. Fan and A. J. Bard, *This Journal*, **128**, 948 (1981).
- "Physics and Chemistry of Materials with Layered Structures," Vol. 4, P. A. Lee, Editor, D. Reidel Publishing Company (1976).
- F. Bertrand, Thèse de 3ème cycle, Paris (1979).
- A. Chevy, Thèse d'Etat, Paris (1981).
- (a) H. Gerischer, J. Gobrecht, and J. Turner, *Ber. Bunsenges. Phys. Chem.*, **59**, 601 (1980); (b) H. Gerischer and M. Lübke, *ibid.*, **85**, 709 (1981).
- (a) K. Schubert, E. Dörre, and E. Günzel, *Nature*, **41**, 448 (1954); (b) A. Likforman, D. Carre, J. Etienne, and B. Bachet, *Acta. Cryst. B*, **31**, 1252 (1975); (c) K. C. Magpal and S. Z. Ali, *Indian J. Pure and Appl. Phys.*, **13**, 258 (1975); (d) J. Rigoult, A. Rimsky, and A. Kuhn, *Acta. Cryst. B*, **36**, 916 (1980).
- (a) R. W. Damon and R. W. Redington, *Phys. Rev.*, **96**, 1498 (1954); (b) M. V. Andriyashik, M. Y. Sakhnoski, V. B. Timofeev, and A. S. Yakimova, *Phys. Status Solidi*, **28**, 277 (1968); (c) J. C. Merle, R. Bartiromo, E. Borsella, M. Piacentini,

- and A. Savoia, *Solid State Commun.*, **28**, 251 (1978); (d) N. Piccioli, R. Le Toullec, F. Bertrand, and J. C. Chervin, *J. Phys. (Paris)*, **42**, 1129 (1981).
8. (a) R. H. Williams, J. V. McCanny, R. B. Murray, L. Ley, and P. C. Kemeny, *J. Phys. C*, **10**, 1223 (1977); (b) Y. Depeursinge, E. Doni, R. Girlanda, A. Baldereschi, and K. Maschke, *Solid State Commun.*, **27**, 1449 (1978); (c) J. Robertson, *J. Phys. C*, **12**, 4777 (1979).
 9. (a) E. N. Kaziev, M. K. Sheinkman, I. B. Ermdovich, and G. A. Akhundov, *Phys. Status Solidi*, **31**, K.39 (1969); (b) G. B. Abdullaev, M. KH. Alieva, and A. Z. Mamedoua, *ibid.*, **25**, 75 (1968); (c) A. Sh. Abdinov and A. G. Kyazym-Zade, *Sov. Phys. Semicond.*, **9**, 1113; (d) *ibid.*, **9**, 1290; (e) *ibid.*, **9**, 1537 (1976); (f) A. Segura, J. P. Guesdon, J. M. Besson, and A. Chevy, *J. Appl. Phys.*, **54**, 877 (1983).
 10. (a) P. I. Voronyuk, A. S. Yakimova, and Z. D. Kovalyuk, *Izv. Fiz.*, **7**, 120 (1970); (b) V. L. Bakumenko, Z. D. Kovalyuk, L. N. Kurbatov, U. G. Tagaev, and V. F. Chishko, *Sov. Phys. Semicond.*, **12**, 216 (1977); (c) A. Segura, A. Chevy, J. P. Guesdon, and J. M. Besson, *Solar Energy Mater.*, **2**, 159 (1980); (d) A. I. Malik, V. B. Baranyuk, and Z. D. Kovalyuk, *Sov. Phys. Semicond.*, **14**, 241 (1980).
 11. A. Chevy, A. Kuhn, and M. S. Martin, *J. Cryst. Growth*, **38**, 118 (1977).
 12. (a) A. Likforman and M. Guittard, *CR Acad. Sci.*, **279c**, 33 (1974); (b) K. Imai, K. Suzuki, Y. Hasegawa, and Y. Abe, *J. Cryst. Growth*, **54**, 501 (1981).
 13. H. Tributsch, *Appl. Phys.*, **23**, 61 (1980).
 14. C. Levy-Clement and B. Theys, *This Journal*, To be published.
 15. S. M. Atakishiev and G. A. Akhundov, *Phys. Status Solidi*, **32**, K33 (1969).

I-V Behavior of the CdSe/Sulfide-Polysulfide and CdSe/Ferro-Ferricyanide Photoelectrochemical Systems

Joseph Reichman and Michael A. Russak

Grumman Aerospace Corporation, Research and Development Center, Bethpage, New York 11714

ABSTRACT

The initial results of a comparison study of the I-V behavior in the n-CdSe/sulfide-polysulfide and the n-CdSe/ferro-ferricyanide photoelectrochemical systems are reported. The greatly enhanced power conversion efficiency of the latter system (14.2% at 52 mW/cm², AM2) compared to the former (7.2%) is attributed to the greater band bending induced in the electrode by the more positive redox potential of the ferro-ferricyanide couple, as well as the enhanced minority carrier transfer kinetics due to a better match between the CdSe valence band and the energy level of the reduced redox species. Energy band diagrams of both systems are presented, and an analysis of monochromatic and dark I-V behavior discussed.

CdSe electrochemical photovoltaic systems have been under investigation for several years, with the CdSe-aqueous sulfide-polysulfide (SPS) electrolyte receiving the most attention (1-4). Some work has also been reported for the CdSe-ferro-ferricyanide (FFC) electrolyte (5-7). However, only recently have efficiencies higher than those found in SPS electrolyte and reasonable stabilities been reported for CdSe in aqueous alkaline FFC electrolyte (8). The key to achieving those improvements is coating the CdSe with a protective layer of Se (8) or a conducting polymer such as polypyrrole (9).

The purpose of this paper is to report results of a comparison study between the CdSe-aqueous SPS and FFC electrolytes. This study was initiated to investigate the origins of very significant differences in I-V behavior that we found in these cells, which resulted in an efficiency of 14.2% for the FFC electrolyte compared to 7.2% for the SPS electrolyte.

Experimental

The experiments reported here were done with an n-CdSe (1120) single-crystal (Cleveland Crystal Corporation) electrode which was back contacted using a copper wire and silver-filled epoxy on an evaporated indium (~5000Å thick) layer. The back and sides of the electrode were covered with insulating epoxy. The electrode was polished with 0.05 μm Al₂O₃, and then etched in 4:1 (volume) HCl:HNO₃. The exposed CdSe area was 0.18 cm². A sulfide-polysulfide electrolyte composition of 2.5M Na₂S, 1M S, 1M KOH, and a ferro-ferricyanide electrolyte composition of 0.5M K₄Fe(CN)₆, 0.5M Na₂Fe(CN)₆, 1M KOH were used for the photoelectrochemical measurements. Before being

tested in the FFC electrolyte, the electrode was anodized in 1M Na₂SO₄, as described by Frese (10, 11), to provide an Se layer of about 1500Å to inhibit photo-corrosion. Dried N₂ was bubbled through the electrolytes during the evaluations to minimize electrolyte oxidation and provide agitation. The white light source was a W-I ELH lamp mounted in a dichroic reflector, which provided a good AM2 spectral simulation (12). Monochromatic I-V curves were obtained using a 0.25m grating monochromator and a 1 kW xenon arc lamp. All light intensities were measured with a calibrated thermopile detector.

Results and Discussion

The I-V curves for the CdSe electrode in the SPS and FFC electrolytes are shown in Fig. 1. The incident light intensity was 52 mW/cm². The superior performance of the electrode in FFC is quite evident in this figure; in particular, the improved fill factor (FF) and increased open-circuit voltage (V_{oc}) are most notable. The short-circuit current densities (J_{sc}) differ only slightly in this case. In general, the J_{sc} for the FFC will depend on the concentration of the redox ions in solution, the thickness of the selenium layer (10, 12), and the optical path length of the incident radiation through the electrolyte. The significant increase in FF and V_{oc} is general, however, and has been observed for a number of single-crystal and thin film CdSe samples. The intensity dependence of the J_{sc} was also measured up to 200 mW/cm², and was found to be linear up to 52 mA/cm² for the SPS electrolyte and linear up to 18-20 mA/cm² for the FFC electrolyte at ~100 mW/cm². The saturation in the FFC electrolyte is probably due to the onset of the diffusion-limited current (12). The output of the CdSe/Se/FFC system was stable for several hours at white light intensities

Key words: energy conversion, semiconductor, electrolyte, junction.

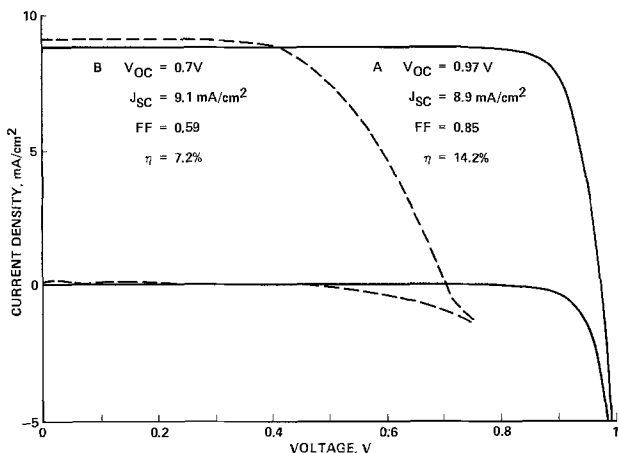


Fig. 1. I-V traces of CdSe in (a) SPS and (b) FFC electrolytes at 52 mW/cm² light intensity.

between 50 and 100 mW/cm², after which a slow decrease in photocurrent was noted. There was no measurable decrease in output observed in the experiments done at 600 nm with intensities of ~1 mW/cm² from which the kinetic analysis was done.

To gain an understanding of the causes of the observed differences in V_{oc} and FF, additional measurements were made to determine some of the basic parameters of the two systems. The flatband potential (V_{FB}) was measured in each electrolyte by noting the potential at which the photogenerated current became zero using phase-sensitive detection and 150 mW/cm² chopped-light illumination.

Values of -1.62 and -0.96V were determined for SPS and FFC, respectively, and these are in agreement with those determined by extrapolation of Mott-Schottky plots for these electrolytes (8, 13). The ionized donor density of $1 \times 10^{17} \text{ cm}^{-3}$ derived from the C-V data agreed with the value obtained by Hall measurements. In addition, the equilibrium redox potentials of the electrolytes were measured on Pt using SCE as the reference and found to be -0.8 and +0.26V for the SPS and FFC, respectively.

Based on these measurements, potential diagrams for the two junctions were constructed. These are shown in Fig. 2. The flatband potential corresponds to the Fermi potential of the CdSe when the bands are flat. The conduction band edge potential was calculated from the measured donor density assuming a conduction-band density of states of 10^{19} . The valence band edge potential was determined using the bandgap energy of 1.7 eV. As indicated in Fig. 2, the equilibrium band bending of the FFC system is 1.22V, as compared to only 0.8V for SPS system. This makes the maximum attainable V_{oc} of the FFC system 0.42V greater than that of the SPS system. The measured open-circuit

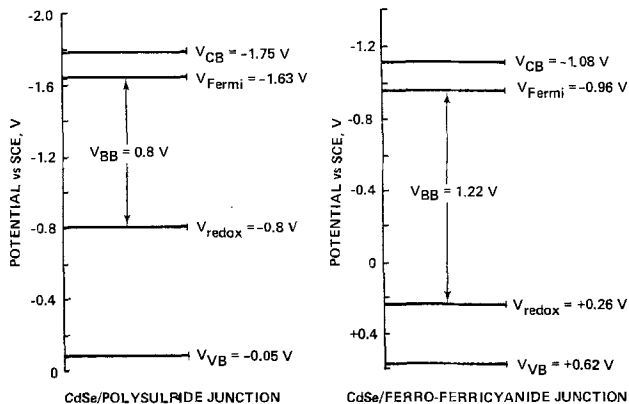


Fig. 2. Potential diagrams for CdSe/SPS and CdSe/FFC junctions

voltage difference of 0.3V at 52 mW/cm² light intensity is somewhat less than this maximum attainable difference. The deviation is due to the increased dark current of the FFC system as will be shown. The greater band bending of the FFC system can also account in part for the improved fill factor.

Measurements of quantum efficiencies and dark currents as a function of potential were made to determine if the difference in band bending is the only cause for the change in performance characteristics. Figure 3 shows the quantum efficiency of the CdSe electrode in the two electrolytes as a function of band bending (i.e., 0.0V corresponds to the V_{FB} for each system). These data were obtained using chopped (25 Hz) 600 nm light and lock-in detection. 600 nm was selected because there is no electrolyte absorption in SPS or FFC and the transmission of the Se overlayer is >95% (11).

If the difference in the I-V characteristics shown in Fig. 1 were caused only by the difference in equilibrium band bending, then the quantum efficiency curves of Fig. 3 would superimpose. However, the FFC electrolyte system shows a higher quantum efficiency at smaller values of band bending than the SPS electrolyte. In this region of band bending, space-charge region recombinations become an important photocurrent limiting mechanism (13, 14). These results then indicate that for the FFC system charge transfer kinetics are faster than for SPS, and so reduce the minority carrier density in the space-charge region which reduces recombination losses.

Calculations of the monochromatic I-V data at 600 nm were made using a model that has space-charge region and bulk recombination as the photocurrent loss mechanisms (14) and has provided consistent results for the CdSe/SPS system (13). However, before the model was applied to the CdSe/FFC data, some additional measurements were done to insure that the CdSe/Se (corrosion layer)/FFC system was not a buried p-n junction/ohmic electrolyte interface similar to that reported for metal-filmed semiconductors (15). The CdSe electrode was etched and then anodized in 1M Na₂SO₄ to develop a Se corrosion layer of ~3000Å. The electrode was briefly run in the FFC electrolyte, after which it was washed thoroughly with deionized water and dried. The front face was then coated with an evaporated layer of In about 5000Å thick, which was carefully contacted with Ag epoxy to make an In/CdSe/Se/In structure. The I-V trace for this showed ohmic behavior, as seen in Fig. 4, indicating that the Se corrosion layer was not providing a buried junction. These findings are consistent with the

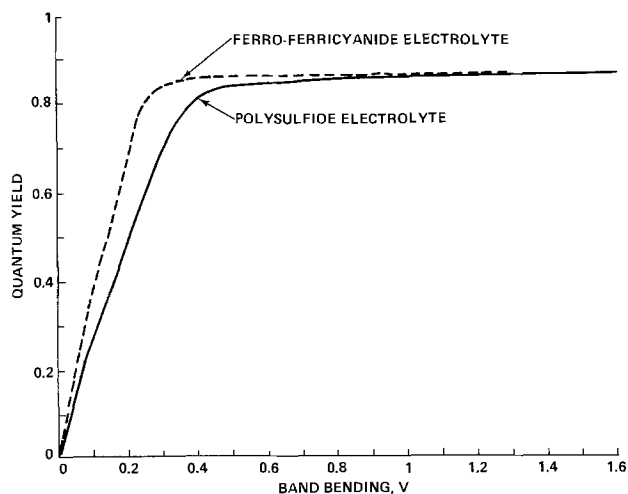


Fig. 3. Quantum yield as a function of band bending of CdSe electrode in the two redox electrolytes at 1.24 mW/cm², 600 nm incident radiation.

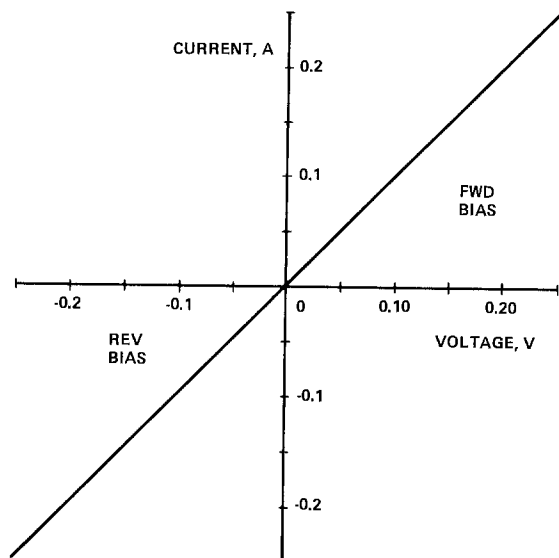


Fig. 4 I-V trace for In/CdSe/Se/In structure showing ohmic behavior.

kinetic analysis done by Frese establishing the good hole conduction of the Se corrosion layer (11).

Reasonably good fits to the I-V data were obtained with the model using minority carrier hole charge transfer velocities of 1000 and 400 cm/s for the FFC and SPS electrolytes, respectively. This was the only adjustable parameter considered. For an equal concentration of redox couples, this would make the rate constant of the FFC couple about five times faster than the SPS couple. This improvement in charge transfer of the FFC system is consistent with its one-electron charge transfer compared to more complex electron transfer for the SPS system. Additionally, the greater overlap of the FFC reduced ion energy states with the CdSe valence band states also would favor higher charge transfer rates (8).

To compare charge transfer rates for the majority carrier electrons in the FFC and SPS electrolytes, measurements were made of the dark currents as a function of potential. The results are presented in Fig. 5, where the dark current is given as a function of band bending using the obtained values of V_{FB} . As previously discussed for the photocurrent, if the charge transfer rates were equal, the two curves would superimpose. For the same amount of band bending, however, the FFC system shows considerably higher dark currents. In addition, the slope of the I-V curve for the FFC displays ideal diode behavior with a slope of 60 mV/decade at band bending greater than 0.3V. The SPS system, on the other hand, displays nonideal diode behavior over the entire potential range. The greater dark current in the FFC electrolyte is attributed to a greater charge transfer rate for majority carriers. As the band bending gets smaller, greater differences in the dark currents of the two systems are observed. This is due to the increasing nonideal behavior of the SPS electrolyte and is attributed to charging of surface states. This shifts the flatband potential to more negative values with increasing voltage. Changes in voltage appear across the Helmholtz region, as well as the space charge region, thereby making the change in current less sensitive to changes in voltage. This surface-state charging effect also appears in the FFC electrolyte; however, it occurs only at potentials closer to flatband.

Conclusions

The improved performance characteristics of CdSe electrodes in FFC electrolyte compared to SPS electrolyte are attributed not only to enhanced minority carrier charge transfer kinetics, but also to greater equilibrium band bending induced by the more positive

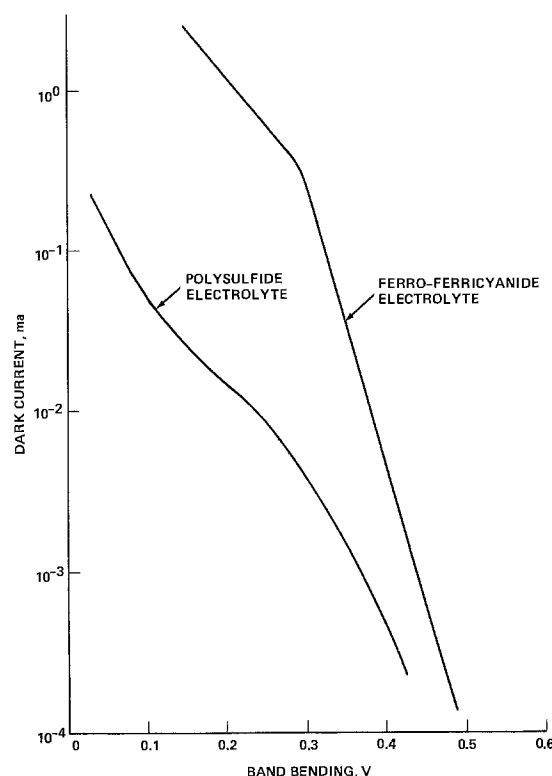


Fig. 5. Dark current as a function of band bending of CdSe electrode in the two redox electrolytes.

redox potential of the FFC. The increased dark current in the FFC electrolyte compared to the SPS electrolyte is due to enhanced charge transfer kinetics for majority carriers, and it acts to reduce the difference in the open-circuit voltage of the two systems that might be expected from differences in equilibrium band bending.

Manuscript submitted June 6, 1983; revised manuscript received Oct. 26, 1983.

Grumman Aerospace Corporation assisted in meeting the publication costs of this article.

REFERENCES

1. A. B. Ellis, S. W. Kaiser, and M. S. Wrighton, *J. Am. Chem. Soc.*, **98**, 1635 (1976).
2. G. Hodes, J. Manassen, and D. Cahen, *Nature*, **261**, 403 (1976).
3. A. Heller, K. C. Chang, and B. Miller, *This Journal*, **124**, 697 (1977).
4. M. A. Russak, J. Reichman, H. Witzke, S. K. Deb, and S. N. Chen, *ibid.*, **127**, 725 (1980).
5. R. Vanden Berghe, W. P. Gomes, and F. Cardon, *Z. Phys. Chem.*, **92**, 91 (1974).
6. J. Gobrecht and H. Gerischer, *Solar Energy Mater.*, **2**, 131 (1979).
7. R. Noufi, D. Tench, and L. F. Warren, *This Journal*, **127**, 2709 (1980).
8. K. W. Frese, Jr., *Appl. Phys. Lett.*, **40**, 3, 275 (1982).
9. L. Warren and D. Tench, Results reported at 4th EPC Contractor's Review Meeting, Denver, CO, October 1981.
10. K. W. Frese, Jr., in "Photoelectrochemistry: Fundamental Processes and Measurement Techniques," W. L. Wallace, A. J. Nozik, S. K. Deb, and R. H. Wilson, Editors, p. 157, The Electrochemical Society Softbound Proceedings Series, Pennington, NJ (1982).
11. K. W. Frese, Jr., *This Journal*, **130**, 28 (1983).
12. K. Yass and H. B. Curtiss, NASA RN NASA TM-X-3059, NTIS, Springfield, VA (1974).
13. J. Reichman and M. A. Russak, in "Photoeffects at Semiconductor-Electrolyte Interfaces," A. J. Nozik, Editor, pp. 359-368, ACS Symposium Series 146, Washington, DC (1981).
14. J. Reichman, *Appl. Phys. Lett.*, **36**, 574 (1980).
15. S. Menezes, A. Heller, and B. Miller, *This Journal*, **127**, 1268 (1980).

The Stability of Silane Layers on Titanium Dioxide Electrodes

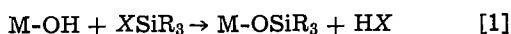
R. Vithanage and H. O. Finklea*

Department of Chemistry, Virginia Polytechnic Institute and State University, Blacksburg, Virginia 24061

ABSTRACT

Silane monolayers were synthesized on TiO₂ electrodes and examined for their stability during the photoelectrolysis of water at various pH's. X-ray photoelectron spectroscopy was used to monitor the silane layer; correction was required for the frequent presence of a contaminant layer after the electrochemical treatment. In general, silane layers suffered noticeable losses after ca. 3 C/cm² of charge was passed. Considerable improvements in stability could be obtained by cross-linking the silane layer during synthesis and by reacting the electrode a second time. The most stable silane layer was synthesized from SiCl₄ "capped" with Me₂SiCl₂.

Silanization is one of the most versatile methods of generating modified electrode surfaces (1). It is based on the reaction between a hydrolytically sensitive Si-X bond (X = Cl, OR, NHR) and a surface OH group (Eq. [1]). The latter function can be found on any wet oxide surface. The list of



successfully silanized electrode substrates includes metals (Au, Pt), quasimetals (highly doped SnO₂, In₂O₃), and semiconductors (Si, Ge, TiO₂, GaAs) (1-3).

With respect to semiconductor electrodes, two applications of silanization have been sought: inhibition of photoactivated corrosion (3a-3d, 4) and catalysis of electrochemical processes, e.g., hydrogen evolution (3d-3f, 3h, 1, 5). Two questions of interest with respect to silanized electrodes are (i) the effects of the silanization on the semiconductor electrode properties, and (ii) the durability of the silane layer. On the former question, the published evidence indicates that there is little, if any, effect on electron transfer properties, provided that the redox molecule either is bound close to the semiconductor surface or has access to the surface. The latter question is likewise important; a durable modified electrode is essential for any practical applications.

We wish to address the question of durability of nonelectroactive silane layers on semiconductor electrodes. To avoid complications due to the concomitant corrosion of the electrode, TiO₂ is chosen as a model substrate. A strenuous test for silane stability is the photoelectrochemical oxidation of water at the TiO₂ anode. Gas evolution tends to disrupt surface films. Likewise, very reactive intermediates (hydroxy radicals) are generated at the surface. Except for fairly acidic electrolytes (6), TiO₂ is stable during photoelectrolysis.

An earlier report (7) indicated that silane layers survived photoelectrolysis at intermediate pH's. We have extended our test to longer photoelectrolysis times and a wider pH range, and have found evidence for partial loss of the silane layer under these conditions. To increase the durability of the silane layer, attempts were made to internally cross-link the silane moieties.

The history of the silane layers was monitored by x-ray photoelectron spectroscopy (XPS).

Experimental

Electrode preparation.—Disk electrodes (6 mm diam) were cut from a single-crystal boule of rutile (Commercial Crystal Laboratories), exposing the (001) face. The disks were initially polished, doped in hydrogen (600°C), and etched in hot concentrated sulfuric acid (250°C), as previously described (8). Prior to silanization, the electrodes were steamed for 2-3h to ensure hydration. After their first use, the electrodes were hand polished using 5 μm alumina, etched, and steamed before each experiment.

* Electrochemical Society Active Member.

Silanization.—Using a procedure developed for silanizing TiO₂ powders (9), the TiO₂ electrodes were dried under vacuum at 150°C for 2h, and then exposed without cooling to a controlled pressure of silane vapor (liquid silane at 15°C). After 1h, excess vapor was pumped away.

A cross-linking reaction scheme was devised to improve silane layer stability. Following the silanization reaction, the electrodes were exposed to water vapor (liquid at 15°C) for 1h, pumped down for 20 min, and then heated (150°C) under vacuum for 2h.

A double cross-linking reaction refers to the silanization and cross-linking procedure being repeated a second time.

Electrochemistry.—Photocurrent generation was performed in four different electrolytes of varying pH: 0.5M H₂SO₄ (pH 0.5), H₃PO₄/KH₂PO₄ buffer, ionic strength 0.2M (pH 2.0), KH₂PO₄/Na₂HPO₄ buffer, ionic strength 0.2M (pH 6.0), and 0.1M NaHCO₃/0.1M Na₂CO₃ (pH 10.0). The TiO₂ electrode was irradiated with the water-filtered output of a 150W Xe arc lamp. At ca. 1V vs. SCE photocurrent densities of 0.7-2 mA/cm² were obtained. Photocurrent generation was terminated after approximately 1C of charge (3.5 C/cm²) had passed. No significant changes in the photocurrent level were observed during this test; photocurrent densities of silanized electrodes were comparable to that of clean electrodes. As noted previously (7), the photocurrent-voltage curves were not noticeably affected by any of the silanizations.

XPS.—All XPS spectra were recorded on a du Pont 650B spectrometer with a magnesium anode. Titanium, oxygen, carbon, and silicon were monitored before and after each photoelectrochemical experiment. Peak areas of the Ti(2p_{3/2}) and Si(2p) peaks were calculated by triangular approximation. Peak energies are referred to C(1s) at 285.0 eV.

Results

TiO₂ is readily modified by a variety of silanes. Successful silanizations yield characteristic changes in the XPS spectra (7): (i) the Ti(2p) peaks are reduced in intensity, (ii) the O(1s) spectrum changes from a single peak at 530 eV to a doublet, the second peak being at 532 eV, and (iii) the Si(2s) and Si(2p) peaks appear above background signal. An estimation of average thickness for the silane layer can be obtained from the comparison of the Ti peak intensity to that of a blank electrode (see below) (10, 11). In general, the synthetic procedure yields silane layer thicknesses consistent with one or two monolayers. Occasionally low silanization yields, i.e., very small Si peaks, are observed. Such instances we attribute to poorly hydroxylated surfaces (9). As a consequence, electrodes are steamed over a beaker of boiling water to promote maximum hydration of the surface. However, uncontrolled polymer formation is undesirable. The synthetic procedure is designed to maintain strictly anhydrous conditions to prevent the silane from reacting

with any species other than the surface O-H groups. Such precautions usually work, but in a few experiments polymer coatings did form (strong Si peak, no visible Ti peak), most notably with SiCl_4 .

The diagnostic criteria for silane stability is based on the Si and Ti peaks. While the higher binding energy peak in the O(1s) spectrum is characteristic of silanized electrodes, organic contamination of the electrodes produces a similar peak. In order to avoid large uncertainties introduced by day-to-day variations in the spectrometer sensitivity, the Si(2p) peak area is normalized by the Ti(2p_{3/2}) peak area for each sample. The Si-to-Ti peak ratio is monitored as a function of electrochemical treatment. Qualitatively, a stable silane layer should exhibit no change in the ratio after photocurrent generation. Loss of the silane layer should cause the Si peak to decrease, the Ti peak to increase, and the Si-to-Ti peak ratio to decrease sharply. These criteria were used to establish that the silane layers are stable to soaking in the four electrolytes for 12h (but they are rapidly stripped in 1M NaOH).

However, both the Si and Ti peak areas often decrease after the electrochemical treatment, and the C(1s) peak increases. Such an effect can be explained by the deposition of a contaminant layer (probably organic) upon the electrode surface. The coating reduces peak intensities of all underlying elements due to inelastic scattering of the photoelectrons. A possible source of the contamination is the epoxy (Shell Epon 828 + du Pont PACM-20) used to insulate the TiO_2 disk edges. The presence of the coating prevents the simple interpretation of silane stability given above.

Electrode contamination should in fact cause an increase in the Si-to-Ti peak ratio for a stable silane layer. This prediction is based on the exponential decrease of photoelectron intensity with the thickness of the scattering layer (10)

$$I_{\text{coated}}/I_{\text{clean}} = \exp(-d/\lambda) \quad [2]$$

In Eq. [2], d is the thickness of the coating and λ is the characteristic scattering length of the substrate photoelectron. The appropriate values for λ are estimated to be 1.7 nm for the Ti(2p_{3/2}) photoelectrons and 2.2 nm for the Si(2p) photoelectrons (10). Applying Eq. [2] to the Si-to-Ti peak ratio, one obtains

$$\frac{I_{\text{Si}}}{I_{\text{Ti}}}(\text{coated}) = \frac{\exp(-d/\lambda_{\text{Si}})}{\exp(-d/\lambda_{\text{Ti}})} \frac{I_{\text{Si}}}{I_{\text{Ti}}}(\text{uncoated}) \quad [3]$$

where d is now the thickness of the organic coating overlying both the silane and the TiO_2 . When the values for λ_{Si} and λ_{Ti} are substituted into Eq. [3], one gets

$$\frac{I_{\text{Si}}}{I_{\text{Ti}}}(\text{coated}) = \exp(+d/7.5 \text{ nm}) \frac{I_{\text{Si}}}{I_{\text{Ti}}}(\text{uncoated}) \quad [4]$$

Consequently, the Si-to-Ti peak ratio appears larger as a result of the organic contaminant layer. Equation [4] also predicts that the Si-to-Ti peak ratio should be less sensitive to the thickness of the contaminant layer than either the Si or Ti peaks.

With this in mind, we present our results in the form of stacked bar graphs, shown as a function of pH. One TiO_2 electrode was used at each pH. The upper bar graphs illustrate the Ti(2p_{3/2}) peak area; loss of Ti peak intensity after photocurrent generation indicates contamination of the electrode. The lower bar graphs are the Si-to-Ti ratios. For reference, a monolayer of silane corresponds to a Si-to-Ti peak ratio of 0.05-0.10. Figures 1, 2, and 3 contain the results for the single "normal" silanization, the cross-linking reaction, and the double cross-linking reaction, respectively.

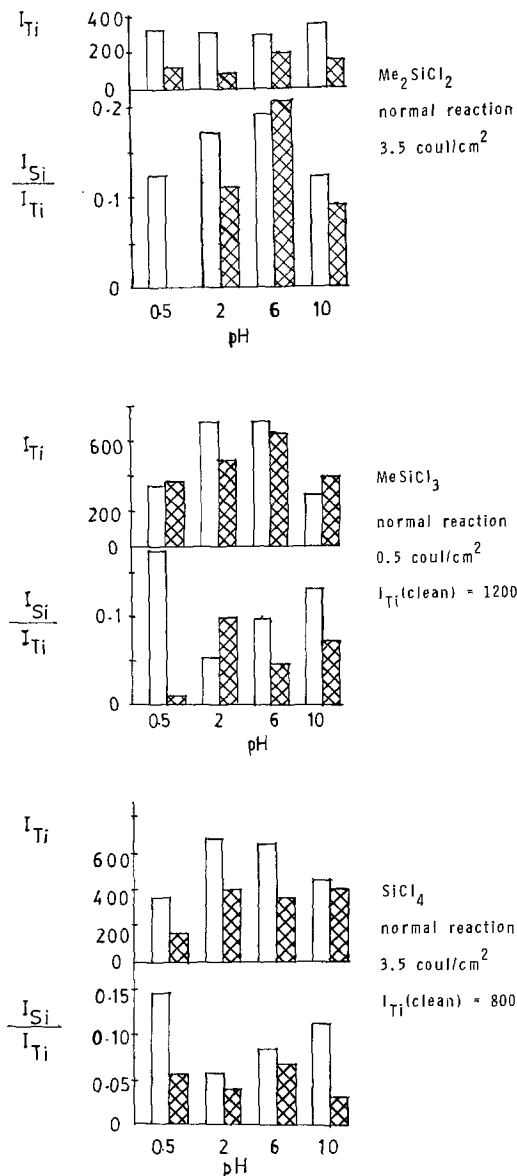


Fig. 1. Normal reaction conditions (see text). Open bars: after silanization. Cross-hatched bars: after photocurrent generation. A, top: Me_2SiCl_2 . B, middle: MeSiCl_3 . C, bottom: SiCl_4 .

Discussion

In earlier papers, we reported that silane layers on TiO_2 electrodes survived photocurrent generation in water (7) and in acetonitrile (12). Both the photocurrent density and the total coulombs of charge passed were over a factor of ten lower than in the present work. Consequently, we attribute the loss of silane

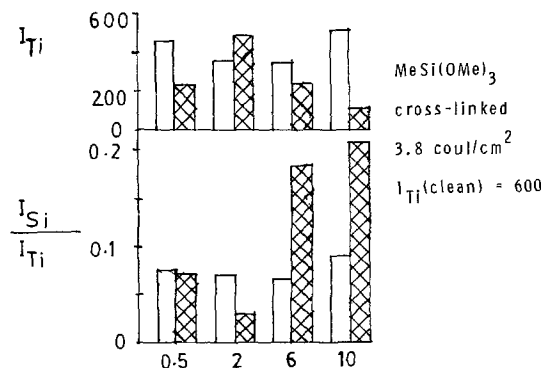


Fig. 2. Cross-linked once. $\text{MeSi}(\text{OMe})_3$. Same convention as in Fig. 1.

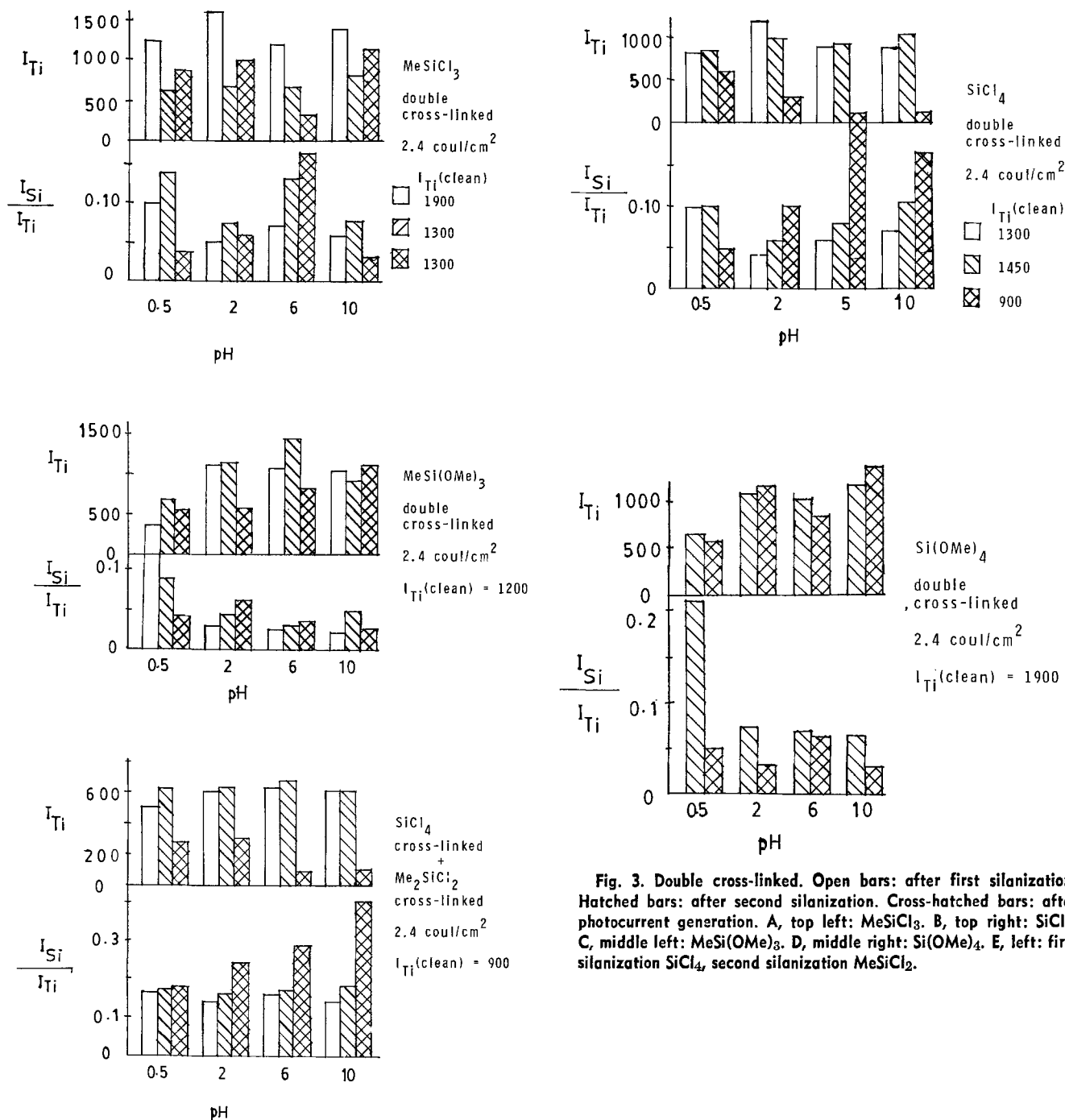


Fig. 3. Double cross-linked. Open bars: after first silanization. Hatched bars: after second silanization. Cross-hatched bars: after photocurrent generation. A, top left: MeSiCl₃. B, top right: SiCl₄. C, middle left: MeSi(OMe)₃. D, middle right: Si(OMe)₄. E, left: first silanization SiCl₄, second silanization MeSiCl₂.

layers shown here to the more severe test conditions. Figure 1 illustrates the point for Me₂SiCl₂, MeSiCl₃, and SiCl₄. In nearly every case, the Si-to-Ti ratio decreases concurrently with a decrease in the Ti peak area. The loss is particularly noticeable in 0.5M H₂SO₄ (pH 0.5). Given the prediction that the Si-to-Ti ratio should increase when electrode coating is observed, it is apparent that a sizable fraction of silane has been removed. Not shown are the data for a monofunctional silane, hexamethyldisilazane. Complete loss of silicon results from the photocurrent generation for that silane.

The cross-linking reaction was devised as a means of improving the silane layer stability. The proposed reaction sequence is shown in Fig. 4. A trifunctional (or tetrafunctional) silane is reacted with surface O-H groups, as in the "normal" reaction. With the assumption that an average of two bonds are formed between the silicon and the surface (9, 11), one or more unreacted Si-X (X = Cl, OMe) bonds exist on each silane. Added water vapor converts these bonds to silanols. In the final step, the silanols are condensed to form a lateral linkage between silicons. The expecta-

tion of greater stability is based on the lateral cross-links. Silane loss most likely proceeds via hydrolysis of the M-O-Si linkage. If this connection is severed, then lateral cross-links would prevent the silicon atom from leaving the surface. Eventually the broken linkage may "heal," *i.e.*, recondense.

These expectations are supported by the data (Fig. 2). MeSi(OMe)₃ generates surface layers that appear stable at pH 6 and 10. The apparent loss at pH 2 may be anomalous (in fact, results for individual electrodes must be treated with caution; the overall pattern of a given experiment is more reliable).

As a further effort for extra stability, we proceeded to the double cross-linking scheme. The objective of the second silanization is to block any holes existing in the first silane layer and to tie up any free surface OH groups. Another objective is to construct a second silane layer on top of the first one. This is predicated on the knowledge that free silanols exist after the cross-linking reaction with tetrafunctional silanes (9).

The results are summarized in Fig. 3. The Ti peak areas and Si-to-Ti peak ratios are shown after each silanization step (Fig. 3d excepted) as well as after

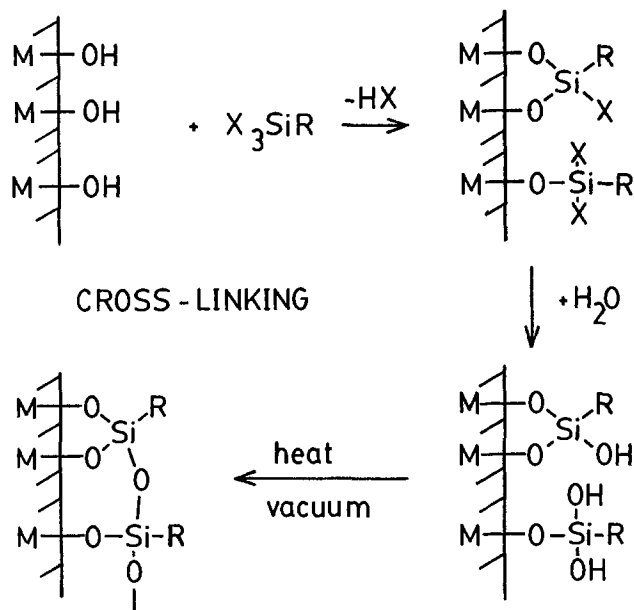


Fig. 4. The cross-linking reaction scheme

the electrochemical treatment. It is evident that the silane coverage increases following the second silanization; however, the net increase is small. When Ti peak areas are normalized for variations in the spectrometer sensitivity (given by the area of a "clean" Ti peak), no significant change in the Ti peak areas is visible. Likewise, the Si-to-Ti peak ratios show slight increases. We interpret this result as indicating (i) that there are few "holes" in the first silane layer, i.e., monolayer saturation is achieved in the course of the reaction (9), and (ii) that in the case of the tetrafunctional silanes, the density of free silanols on the modified surface is considerably lower than that of the original surface.

Surface layer stability varies from silane to silane in a nonsystematic fashion. MeSiCl_3 (Fig. 3a) exhibits noticeable loss of silane except at pH 6. $\text{Si}(\text{OMe})_4$ (Fig. 3d) presents the same pattern: a decrease in the Si-to-Ti peak ratios along with a slight gain in the Ti peak ratios. However, SiCl_4 (Fig. 3b) and $\text{MeSi}(\text{OMe})_3$ (Fig. 3c) show the pattern expected for a stable silane layer coated with a contaminant layer: loss of Ti signal, gain of Si-to-Ti peak ratios. In all of these experiments, loss of the silane layer is most evident at pH 0.5. Silane loss is probably associated with TiO_2 corrosion. Whether the silane layer inhibits corrosion is not apparent from these experiments.

A final experimental variation reveals a promising direction for stable surface layers (Fig. 3e). When TiO_2 electrodes are first modified with SiCl_4 and then Me_2SiCl_2 (both cross-linked), the surface layer thus formed exhibits the best stability observed so far, even at pH 0.5. It is possible that the bonded dimethylsilyl moieties impart a hydrophobic character to the surface layer. We suggest that hydrophobicity may be another key to surface layer stability on electrodes.

With the assumption of silane layer stability, Eq. [2] and [4] can be used to estimate the thickness of the contaminant layer for the data in Fig. 3e. From the diminution of Ti peak areas with respect to that of a clean electrode, coating thicknesses of 1.2, 3.6, and 3.0 nm are calculated at pH 2, 6, and 10, respectively. Based on increases in the Si-to-Ti peak ratio, the corresponding numbers are 3.1, 3.8, and 5.8 nm. The agreement is only approximate. The larger values obtained using the Si-to-Ti ratios suggest that the 7.4 nm coefficient in Eq. [4] may be too large, which in turn would indicate a greater difference in the scattering lengths of Ti and Si photoelectrons than the theoretical values suggest. For example, a scattering

length of 2.7 nm for Si(2p) photoelectrons would change the coefficient of Eq. [4] to 4.6 nm, and would give values of 1.9, 2.4, and 3.6 nm for the coating thicknesses. Another problem is the hidden assumption that silane and contaminant layers are uniform in thickness across the electrode surface. This assumption seems unlikely in view of the facile water oxidation at the TiO_2 anode. Access of reagents to the electrode and products from the electrode appears to be unhindered. Also, rearrangements of the silane morphology may be occurring. For these reasons, we have not presented quantitative estimations of silane layer thickness before and after photoelectrolysis for most of the data.

A comparison of Fig. 2 with Fig. 3c highlights a major problem with surface syntheses. For the same silane [$\text{MeSi}(\text{OMe})_3$] and nominally the same synthesis procedure, a considerable difference (factor of two) is seen in the Si-to-Ti peak ratio on newly silanized electrodes. A similar wide variation in coverage is implied by the different Si-to-Ti peak ratios obtained with all the different silanes and for a given silane on the four electrodes. The factors affecting silane coverage are still poorly understood. However, the changes observed in the Si-to-Ti ratio for a single electrode are more certain. Repetitive measurements of that ratio on a single electrode over a 2 week period show a standard deviation of only 18% about the mean (seven measurements) and no systematic trend, despite a considerable change in spectrometer sensitivity.

Conclusions

The stability of thin silane layers on TiO_2 during the photoelectrolysis of water can be markedly improved by cross-linking the silane layers during synthesis, and also perhaps by adding a hydrophobic "capping" layer. Very long-term stability is not known; even the most stable silane layers may eventually degrade. When possible, pH extremes should be avoided. The silane layers do not affect the photoelectrolysis current density.

Acknowledgment

This work was supported by a grant from the Diamond Shamrock Corporation.

Manuscript submitted May 6, 1983; revised manuscript received Nov. 7, 1983.

REFERENCES

1. R. W. Murray, *Acc. Chem. Res.*, **13**, 135 (1980), and references therein.
2. R. W. Murray, *Phil. Trans. R. Soc. London*, **A302**, 253 (1981).
3. (a) M. S. Wrighton, R. G. Austin, A. B. Bocarsly, J. M. Bolts, G. Haas, K. D. Legg, L. Nadjo, and M. C. Palazotto, *J. Am. Chem. Soc.*, **100**, 1602 (1978); (b) J. M. Bolts and M. S. Wrighton, *ibid.*, **100**, 5257 (1978); (c) *ibid.*, **101**, 6179 (1979); (d) J. M. Bolts, A. B. Bocarsly, M. C. Palazotto, E. G. Walton, N. S. Lewis, and M. S. Wrighton, *ibid.*, **101**, 1378 (1979); (e) A. B. Bocarsly, E. C. Walton, M. G. Bradley, and M. S. Wrighton, *J. Electroanal. Chem.*, **100**, 283 (1979); (f) A. B. Bocarsly, E. G. Walton, and M. S. Wrighton, *J. Am. Chem. Soc.*, **102**, 3390 (1980); (g) D. C. Bookbinder and M. S. Wrighton, *ibid.*, **102**, 5123 (1980); (h) N. S. Lewis, A. B. Bocarsly, and M. S. Wrighton, *J. Phys. Chem.*, **84**, 2033 (1980); (i) J. A. Bruce and M. S. Wrighton, *J. Electroanal. Chem.*, **122**, 93 (1981); (j) A. B. Fischer, J. A. Bruce, D. R. McKay, G. E. Maciel, and M. S. Wrighton, *Inorg. Chem.*, **21**, 1766 (1982); (k) J. A. Bruce and M. S. Wrighton, *J. Am. Chem. Soc.*, **104**, 74 (1982); (l) R. N. Dominey, N. S. Lewis, J. A. Bruce, D. C. Bookbinder, and M. S. Wrighton, *ibid.*, **104**, 467 (1982); (m) R. A. Simon, A. J. Ricco, and M. S. Wrighton, *ibid.*, **104**, 2031 (1982).
4. H. Yoneyama, Y. Murao, and H. Tamura, *J. Electroanal. Chem.*, **108**, 87 (1980).
5. H. D. Abruna and A. J. Bard, *J. Am. Chem. Soc.*, **103**, 6898 (1981).

6. L. A. Harris and R. H. Wilson, *This Journal*, **123**, 1010 (1976); L. A. Harris, D. R. Cross, and M. E. Gerstner, *ibid.*, **124**, 839 (1977).
7. H. O. Finklea and R. W. Murray, *J. Phys. Chem.*, **83**, 353 (1979).
8. H. O. Finklea, *This Journal*, **129**, 2003 (1982).
9. H. O. Finklea and R. Vithanage, *J. Phys. Chem.*, **86**, 3621 (1981).
10. D. F. Untereker, J. C. Lennox, L. M. Wier, P. R. Moses, and R. W. Murray, *J. Electroanal. Chem.*, **81**, 309 (1977).
11. P. R. Moses, L. M. Wier, J. C. Lennox, H. O. Finklea, J. R. Lenhard, and R. W. Murray, *Anal. Chem.*, **50**, 576 (1978).
12. H. O. Finklea, H. Abruna, and R. W. Murray, in "Interfacial Photoprocesses: Energy Conservation and Synthesis," M. S. Wrighton, Editor, p. 253, *Advances in Chemistry Series*, no. 184 The American Chemical Society, Washington, DC (1980).

The Role of the Lower Metal Oxide/Higher Metal Oxide Couple in Oxygen Evolution Reactions

P. Rasiyah* and A. C. C. Tseung*

Department of Chemistry, The City University, London EC1V OHB, England

ABSTRACT

The minimum potential for the evolution of oxygen on six oxides (RuO₂Li_{0.1}Ni_{0.9}O, Li_{0.3}Co_{2.7}O₄, IrO₂, PbO₂, and PtO₂) in 5N KOH has been studied by potentiostatic steady-state and galvanostatic charging experiments. The results show that there is an excellent correlation between the minimum potential for oxygen evolution on the first three oxides and their lower oxide/higher oxide couples (RuO₂/RuO₄ = 1.387V; Ni₂O₃/NiO₂ = 1.43V; Co₂O₃/CoO₂ = 1.447V) listed in Pourbaix diagrams. For IrO₂, there was good agreement between the lower oxide/higher oxide couple (IrO₂/IrO₃ = 1.35V) determined in this work by galvanostatic charging. Galvanostatic charging on PbO₂ and PtO₂ indicates that oxygen evolution takes place at 1.76 and 1.71V, respectively. However, these two values do not correlate with their lower oxide/higher oxide couple values. It is therefore suggested that oxygen evolution on such oxides proceeds via the OH⁻/HO₂⁻ couple (1.77V), where the reaction intermediates are physisorbed. We also discuss the stability of the lower and higher oxides of the six metals considered from the point of view of the crystal field concept.

Although oxygen evolution has been studied on numerous metals and oxides and many mechanisms have been put forward to explain the oxygen evolution reactions on these substrates, no satisfactory explanation has yet been given for the different voltage values on different substrates at a particular current density. It is of great fundamental interest to determine the factors responsible for the differences. Up to now few investigations (1-3) have been directed at ascertaining these factors.

Ruetschi and Delahay (1) carried out a theoretical investigation and concluded that different overvoltages on metals arise because of the difference in the magnitude of the M—OH bond energies. They assumed the rate-determining step to be the initial discharge of the OH⁻ ion. The M—OH bond energies were estimated in three ways and then plotted against the values of the overpotential for oxygen evolution at 1 A/cm² in 1N KOH at room temperature. The slope of the plot was taken to indicate the difference in overvoltages and the heats of activation and was accounted for by the changes in the M—OH energy that occur from metal to metal. The authors did not choose to plot all the bond energy values, since some of them showed marked departures from the correlation. Co metal showed the lowest overpotential and the highest M—OH bond energy.

Tseung and Jasem (2), in a recent investigation of oxygen evolution on semiconducting oxides, emphasized the role of the metal/metal oxide couple or the lower metal oxide/higher metal oxide couple in determining the minimum potential required for oxygen evolution, together with other essential factors such as electrical resistivity, electrode microstructure, and corrosion properties. Based on these criteria, they suggest that NiCo₂O₄ is of interest as an oxygen evolution electrocatalyst. Teflon-bonded NiCo₂O₄ gave an oxygen evolution current density of 1 A/cm² at 1.6V vs. the dynamic hydrogen electrode (DHE) at 70°C in 5N KOH.

The work carried out by Vijh (4), although not directly pertaining to oxygen evolution, warrants mention. He found an empirical correlation between the

two quantities, the metal/metal oxide standard electrode potential and the electronic conductivity, which have been postulated to govern oxygen evolution. Vijh also correlated the bandgap of the oxides to the metal/metal oxide standard electrode potential, thus linking the two solid-state properties to the electrode potential.

Hickling and Hill (3) carried out oxygen evolution measurements on ten different metal anodes in alkaline solution over a current density range of 10⁻⁵ to 1 A/cm², in 1N KOH at 20°C. They also studied the variation of the oxygen overvoltage on the different metals with time. Table I gives the oxygen evolution potential obtained by Hickling and Hill on ten metals at a current density of 1 A/cm² in 1N KOH. Also included in Table I are the lower oxide/higher oxide couples of the ten metals. These values were obtained from literature (5), except for lead, whose value was obtained by galvanostatic charging (Fig. 1). Figure 1 gives the plot of oxygen evolution potential obtained by Hickling and Hill on ten metals at a current density of 1 A/cm² vs. the lower oxide/higher oxide couple, showing a very good correlation. The metal Cd was not included in the correlation since its lower oxide/higher oxide couple was not available in literature. The results presented in Table I suggest that the oxygen evolution

Table I. The oxygen evolution potentials at 1 A/cm², 25°C in 5N KOH and the potentials of the lower oxide/higher oxide couple of ten metals

Metal	Oxygen evolution potential (3) (Volts vs. RHE)	Couple governing oxygen evolution	Potential of couple governing oxygen evolution (5) (V)
Co	1.84	Co ₂ O ₃ /CoO ₂	1.477
Cu	2.00	Cu ₂ O/CuO	0.669
Au	2.86	Au ₂ O ₃ /AuO ₂	2.630
Pb	2.27	*	
Fe	1.86	FeO/Fe ₂ O ₃	0.271†
Ni	2.27	Ni ₂ O ₃ /NiO ₂	1.434
Pd	2.51	PdO ₂ /PdO ₃	2.030
Pt‡	2.14	*	
Ag	2.29	AgO/Ag ₂ O ₃	1.569
Cd	—	—	—

* Electrochemical Society Active Member.

Key words: oxygen evolution, lower metal oxide/higher metal oxide, semiconducting oxides.

† Possibly governed by the OH⁻/HO₂⁻ couple for which E₀⁰ = 1.76V. ‡ Value of hydrated oxide used. § Platinized Pt.

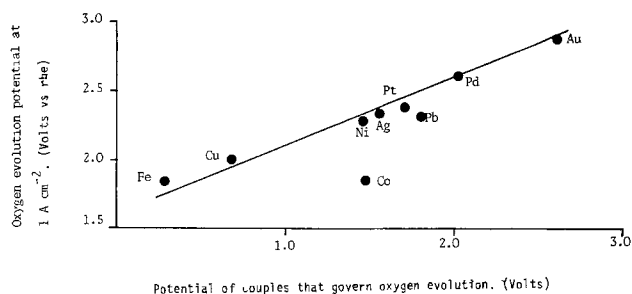


Fig. 1. Correlation of the oxygen evolution potential at 1 A/cm² in 5N KOH at 25°C of nine metals and the respective couples that govern oxygen evolution.

potential at high current densities (e.g., 1 A/cm²) on metals is governed by the lower oxide/higher oxide couple of the metal.

This paper describes the oxygen evolution studies carried out on six oxides to ascertain the role of the lower oxide/higher oxide couple in relation to the oxygen evolution performance.

Choice of Oxides

An oxide should possess two important properties to be considered for this study: corrosion resistance and fairly low electrical resistivity. Six oxides were chosen for this study: PtO₂, Li_{0.1}Ni_{0.9}O, Li_{0.3}Co_{2.7}O₄, IrO₂, PbO₂, and RuO₂. Although the corrosion resistance of the latter three oxides is doubtful, initial polarization studies carried out proved that these oxides have adequate corrosion resistance for the purpose of this study.

Materials and Methods

IrO₂ and PtO₂ were prepared by thermal treatment of IrCl₃ and H₂PtCl₆ · H₂O, respectively. Li_{0.1}Ni_{0.9}O and Li_{0.3}Co_{2.7}O₄ were prepared by freeze drying. These two oxides were doped with Li⁺ to lower their electrical resistivity. RuO₂ and PbO₂ were obtained commercially. The room temperature, compressed, powder resistivities of the six oxide powders were measured using a Teflon die. The Brunauer, Emmett, and Teller (BET) specific surface areas of the six oxides were also measured. Table II gives the electrical resistivities and the BET specific areas of the six powders.

Electrode preparation.—Since this investigation involves a comparative study of six oxides, it is necessary to normalize the oxide loading of the electrodes. Furthermore, the electrode preparation has to be carried out under uniform conditions. The electrocatalyst loadings of each of the six oxide electrodes were controlled as far as possible to contain approximately 1 m² of BET specific surface area of oxide per cm² of electrode. The oxide loading was kept at such high values so that oxygen evolution potentials would be the lowest possible for all six electrodes and a comparative study would be possible. Initial exploratory work based on different oxide loading confirmed the validity of this approach. For example, a preanodized FEP- (fluorinated ethylene propylene) bonded Li-doped Co₃O₄ electrode

of electrocatalyst loading 27.8 mg/cm² gave an oxygen evolution performance of 1.562V vs. the DHE in 5N KOH at a current density of 5 mA/cm². Changing the electrocatalyst loading from 27.8 mg/cm² to 32.1 mg/cm² gave approximately the same oxygen evolution potential under similar conditions. Similar observations were made for PtO₂. Preanodized PtO₂ electrodes consisting of 44 and 63 mg of PtO₂ per cm² gave oxygen evolution potentials of 1.771 and 1.774V for a current density of 5 mA/cm² under similar conditions. Furthermore, for each oxide, initial optimization studies were carried out by preparing electrodes containing different FEP-to-oxide ratio and then subjecting them to oxygen evolution studies.

Electrochemical evaluation.—All electrodes were preanodized to obtain a stable electrocatalytic surface and to reduce the oxygen bubble size. Electrodes of different oxides required different preanodization conditions. A three-compartment glass cell was used for all electrochemical measurements. A DHE was used as the reference electrode. When calibrated against a reversible hydrogen electrode in 5N KOH at 25°C, the potential of the DHE was found to be -18 mV. The interrupter technique was used to measure the ohmic drop between the Luggin capillary and the working electrode.

Anodic charging curves were used to determine the couple that determines the potential at which oxygen evolution begins in 5N KOH at 25°C. The curves for the oxides of Ir, Pb, and Pt were obtained by passing a small anodic current on cathodized electrodes (10 mA/cm² for 5h) which were previously anodized. The charging curves on the oxides of Ru, Ni, and Co were carried out on freshly prepared electrodes.

Results and Discussion

The charging curve on reduced IrO₂ (Fig. 2) shows two peaks at potentials less than 0.5V. This region has been related to adsorption of atomic hydrogen (6, 7) on Ir. At higher potentials, there are two points of inflection, at 0.84 and 0.94V, and a peak at 1.35V. The points of inflection at potentials 0.84 and 0.94V could be related to Ir/IrO and Ir/IrO₂ couples, which have values (8) of 0.81 and 0.93V, respectively. Since the ratio of the charges between the potential range 0.84-0.94V and 0.94-1.35V is approximately 1:1, it could be concluded that Ir ion attains an oxidation state of six, i.e., forms IrO₃ before evolving oxygen. Thus, for IrO₂, the lower oxide/higher oxide couple that governs oxygen evolution is IrO₂/IrO₃, which has the value of 1.35V. The charging curves on the oxides of Ru, Ni, and Co (not given) suggested that the potentials of couples that govern oxygen evolution are 1.39, 1.44, and 1.47V, respectively. These values are in good agreement with the lower oxide/higher oxide couple values of 1.387 (RuO₂/RuO₄), 1.434 (Ni₂O₃/NiO₂), and 1.447V (Co₂O₃/CoO₂) reported by Pourbaix (5). The study of oxygen evolution on PbO₂ and PtO₂ is interesting in that in the case of the former the cation is of oxidation state four, which is the highest that is possible for Pb. In the latter case, the next highest oxidation state is six determined by the couple PtO₂/PtO₃ of value 2.0V. Charging curves on reduced PbO₂ and PtO₂ (Fig. 3 and 4) show peaks at potentials of 1.76 and 1.71V, respectively, before oxygen evolution takes place. These two values cannot be assigned to a higher oxidation state in either case. However, the values are very close to the potential of the OH⁻/HO₂⁻ of 1.77V, thus, having the possibility of oxygen evolution taking place via the formation of the peroxide intermediate. If this is the case, these two oxides behave as an inert surface on which the reaction intermediates are physisorbed (ps), as opposed to the active surfaces where chemisorbed intermediates are formed on the other four oxides. A mechanism with (HO₂⁻)_{ps} intermediate could be

Table II. BET specific surface areas and the electrical resistivities of six oxides

Oxide	BET specific surface area (m ² g ⁻¹)	Room temperature electrical resistivity (Ω-cm)
PtO ₂	14	140.0
IrO ₂	14	<0.1
RuO ₂	17	<0.1
PbO ₂	15	<0.1
Li _{0.3} Co _{2.7} O ₄	38	5.0
Li _{0.1} Ni _{0.9} O	47	60.0

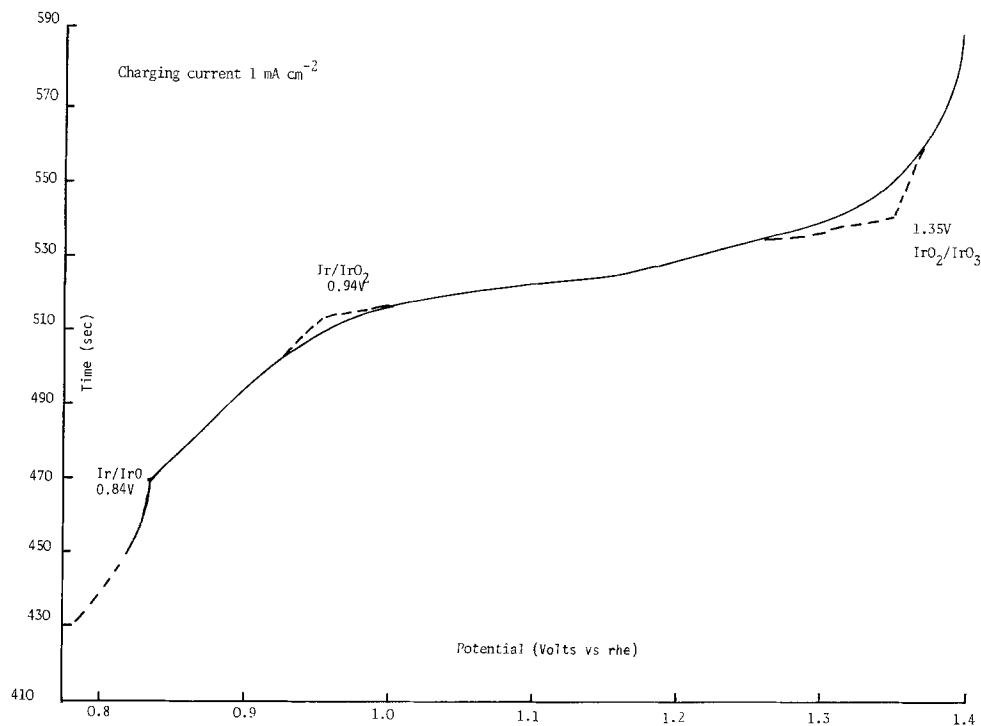


Fig. 2. Anodic charging curve on reduced IrO_2 at 25°C in $5N$ KOH .

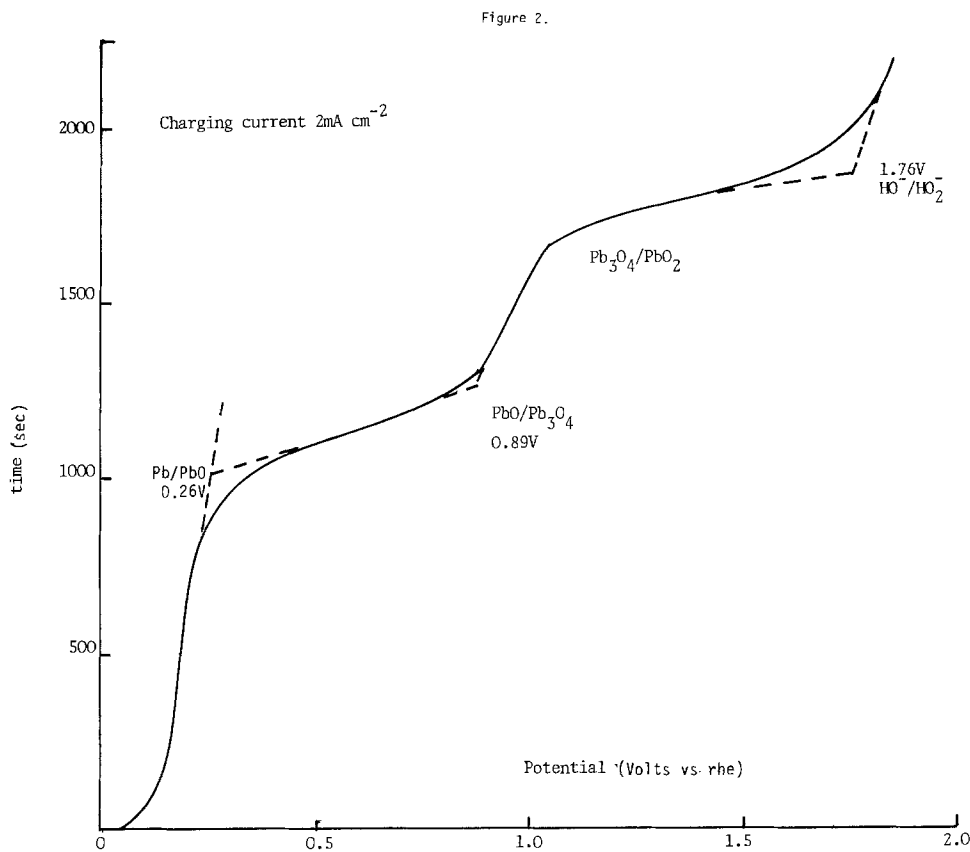
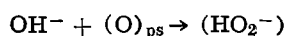
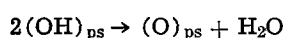
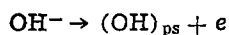


Fig. 3. Anodic charging curve on reduced PbO_2 at 25°C in $5N$ KOH .



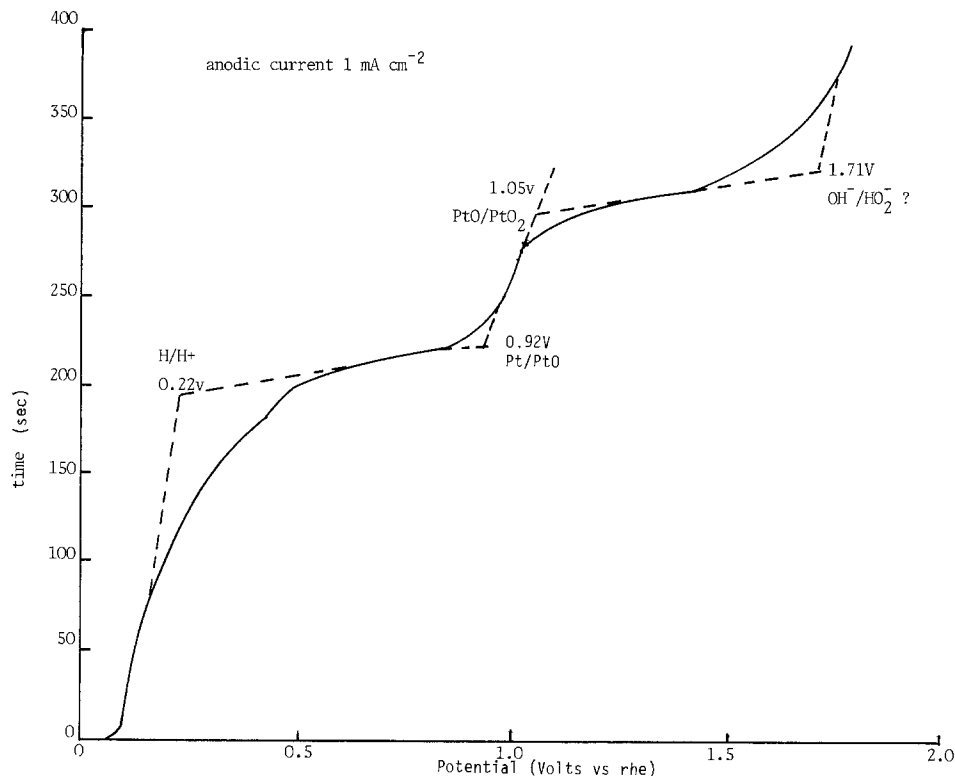
The $(\text{HO}_2^-)_{\text{ps}}$ could evolve oxygen by a further multi-step process.

Figures 5-9 give the V - $\log i$ plots for oxygen evolution on preanodized FEP-bonded RuO_2 , IrO_2 , PtO_2 , Li-doped NiO , Li-doped Co_3O_4 , and PbO_2 electrodes, at 25°C in $5N$ KOH . Table III gives the oxygen evolution potentials for a current density of 1 mA/cm^2 , the couples that are expected to govern oxygen evolution, and the potential values of these couples. The oxygen evolution potential corresponding to a current density of 1 mA/cm^2 was taken to be the minimum potential

for oxygen evolution, since the current potential characteristics at current densities of 1 mA/cm^2 and less deviated from the oxygen evolution Tafel slope for most of the oxides considered. The currents at regions where the oxygen evolution Tafel slope deviates is attributed to the anodic reactions leading to oxidation state changes before the highest oxidation state oxide is formed.

Figure 10 gives the plot of the oxygen evolution potentials for a current density of 1 mA/cm^2 on the six oxides and the respective couples that govern oxygen evolution showing a good correlation. According to this correlation, it could be inferred that the oxides of Ir, Ru, Ni, and Co evolve oxygen only after their surface cations undergo oxidation state transitions and attain the respective potentials of the lower oxide/higher

Fig. 4. Anodic charging curve on reduced PtO_2 at 25°C in 5N KOH.



oxide couple. However, the results suggest that PtO_2 and PbO_2 evolve oxygen at potentials very close to the $\text{OH}^-/\text{HO}_2^-$ couple, without undergoing any formal oxidation state changes.

Table IV gives the lattice type, the cation oxidation number, the cation environment, and the electron dis-

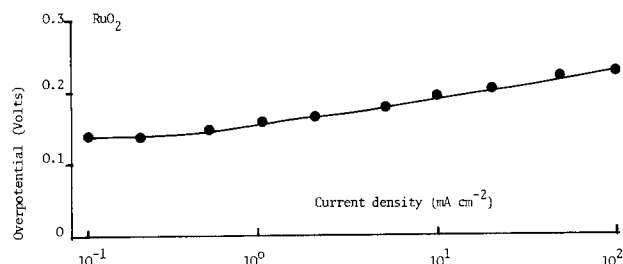


Fig. 5. Tafel plot for oxygen evolution on a preanodized FEP-bonded RuO_2 electrode at 25°C in 5N KOH.

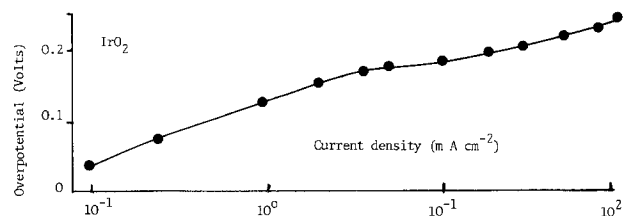


Fig. 6. Tafel plot for oxygen evolution on a preanodized FEP-bonded IrO_2 electrode at 25°C in 5N KOH.

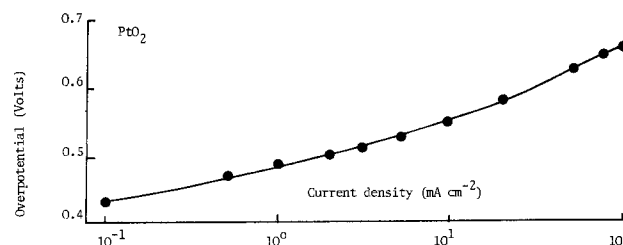


Fig. 7. Tafel plot for oxygen evolution on a preanodized FEP-bonded PtO_2 electrode at 25°C in 5N KOH.

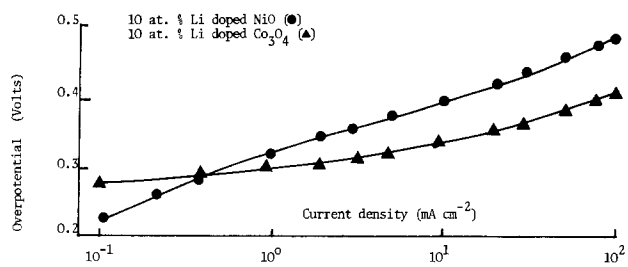


Fig. 8. Tafel plots for oxygen evolution on preanodized FEP-bonded $\text{Li}_{0.3}\text{Co}_{2.7}\text{O}_4$ and $\text{Li}_{0.1}\text{Ni}_{0.9}\text{O}$ electrodes at 25°C in 5N KOH.

tribution in the d orbitals of the cation in the oxides at rest and in the highest oxidation state oxide. Since oxygen evolution is a surface process, it is assumed that the higher oxidation state cation that is formed is in the same environment within the rigid host lattice. All cations except the Co^{2+} cations of the Li-doped Co_3O_4 are in octahedral environment. It is assumed that the cations in the octahedral environment of the lattice have sufficient high field to induce the low spin electronic arrangement. If transitions to higher oxidation states involves removal of electrons from destabilized d orbitals, i.e., from e_g orbitals in octahedral environment (o) and t_{2g} orbitals in tetrahedral environment (t), then the higher oxidation state is stabilized. An example of this is the $\text{Co}^{2+}(\text{t}) \rightarrow \text{Co}^{3+}(\text{t}) \rightarrow \text{Co}^{4+}(\text{t})$ oxidation state transitions in Li-doped

Table III. Oxygen evolution potentials for a current density of 1 A/cm² in 5N KOH at 25°C and the potentials of the couples that govern the minimum potential of oxygen evolution for the six oxides

Oxide	Oxygen evolution potential (V vs. rhe)	Couple governing oxygen evolution	Potential of couple (V)	Ref.
RuO_2	1.394	$\text{RuO}_2/\text{RuO}_4$	1.387	(5)
PtO_2	1.725	$\text{OH}^-/\text{HO}_2^-$	1.760	—
IrO_2	1.360	$\text{IrO}_2/\text{IrO}_3$	1.350	—
PbO_2	1.810	$\text{OH}^-/\text{HO}_2^-$	1.760	—
$\text{Li}_{0.3}\text{Co}_{2.7}\text{O}_4$	1.530	$\text{Co}_2\text{O}_3/\text{CoO}_2$	1.447	(5)
$\text{Li}_{0.1}\text{Ni}_{0.9}\text{O}$	1.550	$\text{Ni}_2\text{O}_3/\text{NiO}_2$	1.434	(5)

Table IV. Electronic properties of oxides

Oxide	Structure	Cation* environment	Cation oxidation number at rest	Number of outer electrons	Oxidation state transition	Electron distribution in degenerate orbital
$\text{Li}_{0.3}\text{Co}_{0.7}\text{O}_4$	normal spinel	t	Co^{2+}	$3d^7$	$\text{Co}^{2+} \rightarrow \text{Co}^{3+}$	$e_g^4 t_{2g}^3 \rightarrow e_g^4 t_{2g}^2$
$\text{Li}_{0.1}\text{Ni}_{0.9}\text{O}$		t	Co^{2+}	$3d^0$	$\text{Co}^{3+} \rightarrow \text{Co}^{4+}$	$e_g^4 t_{2g}^2 \rightarrow e_g^4 t_{2g}^1$
RuO_2	rutile	o	Co^{3+}	$3d^5$	$\text{Co}^{3+} \rightarrow \text{Co}^{4+}$	$t_{2g}^6 e_g^0 \rightarrow t_{2g}^5 e_g^0$
IrO_2		o	Ni^{2+}	$3d^8$	$\text{Ni}^{2+} \rightarrow \text{Ni}^{4+}$	$t_{2g}^4 e_g^2 \rightarrow t_{2g}^0 e_g^0$
PtO_2	rutile	o	Ru^{4+}	$4d^4$	$\text{Ru}^{4+} \rightarrow \text{Ru}^{8+}$	$t_{2g}^4 e_g^0 \rightarrow t_{2g}^0 e_g^0$
PbO_2		o	Ir^{4+}	$5d^5$	$\text{Ir}^{4+} \rightarrow \text{Ir}^{6+}$	$t_{2g}^5 e_g^0 \rightarrow t_{2g}^3 e_g^0$
			Pt^{4+}	$5d^6$		$t_{2g}^6 e_g^0$
			Pb^{4+}	$5d^{10}$		$t_{2g}^6 e_g^4$

* t = tetrahedral. o = octahedral.

Co_3O_4 bringing about $e_g^4 t_{2g}^3 \rightarrow e_g^4 t_{2g}^2 \rightarrow e_g^4 t_{2g}^1$ electron transitions, respectively. The corresponding energy transition could be given as $-12Dq' + 2P \rightarrow -16Dq'' + 2P \rightarrow -20Dq''' + 2P$, where $10Dq$ is the magnitude of the crystal field splitting and P is the pairing energy. However, since an increase in oxidation state of a cation in a fixed environment increases the value of the $10Dq$ (9), assuming the value of P to be constant, it could be stated that $10Dq''' > 10Dq'' > 10Dq'$. Thus, an increase in oxidation state of a cation in a fixed environment brings about a further stability by increasing the magnitude of the crystal field splitting. From the above arguments, $\text{Ni}^{2+}(\text{o}) \rightarrow \text{Ni}^{4+}(\text{o})$ will be energetically feasible, and $\text{Ru}^{4+}(\text{o}) \rightarrow \text{Ru}^{8+}(\text{o})$ forms the stable rare gas configuration of Kr. In the case of IrO_2 , where $\text{Ir}^{4+}(\text{o}) \rightarrow \text{Ir}^{6+}(\text{o})$ transition is postulated, the loss of

crystal field stability by the removal of two electrons from the t_{2g} orbitals in forming Ir^{6+} can be outweighed by the gain in stability due to loss of pairing and an increase in crystal field splitting energy due to the higher oxidation state transition. The stability of Co^{4+} formed by the $\text{Co}^{3+}(\text{o}) \rightarrow \text{Co}^{4+}(\text{o})$ in Li-doped Co_3O_4 could be justified by an argument similar to that put forward for IrO_2 . This discussion shows that the higher oxidation state surface species that are formed on the four oxides under consideration, although chemically unstable and structurally highly strained, are brought about by oxidation state transitions that are energetically feasible.

Pb ion in PbO_2 has an outer electronic arrangement of $5d^{10}$ and therefore oxidation states greater than four are very unlikely for it and have not been reported in general literature. As for PtO_2 , where the Pt^{4+} has an electronic configuration which in the octahedral environment of $t_{2g}^6 e_g^0$ could also be considered to be stable. It could be argued that such a postulation is in contradiction to the previously proposed activity of $\text{Co}^{3+}(\text{o})$, which is of the same electron configuration. However, it must be borne in mind that $\text{Co}^{3+} \rightarrow \text{Co}^{4+}$ transition requires (10) an energy equivalent of only approximately 0.3V, whereas PtO_2 has to be raised from its potential at rest to 2.0V to elevate the oxidation state of Pt from +4 to the next possible state of +6. Therefore, due to the restriction of oxidation state transition in PtO_2 and PbO_2 , oxygen evolution could take place on them by an alternative process.

The exchange current densities for oxygen evolution were evaluated from the polarization data of the six oxides. The exchange current densities are pseudo-values and are based on unit geometric area of the electrode. The pseudoexchange current density of any one oxide will vary, depending on the oxide loading of the electrode. However, since the loading of all six oxide electrodes were normalized, a comparative study of the pseudoexchange current densities is facilitated. Table V gives the pseudoexchange current densities and the Tafel slopes for oxygen evolution on the six oxides. A plot of the negative log of the pseudoex-

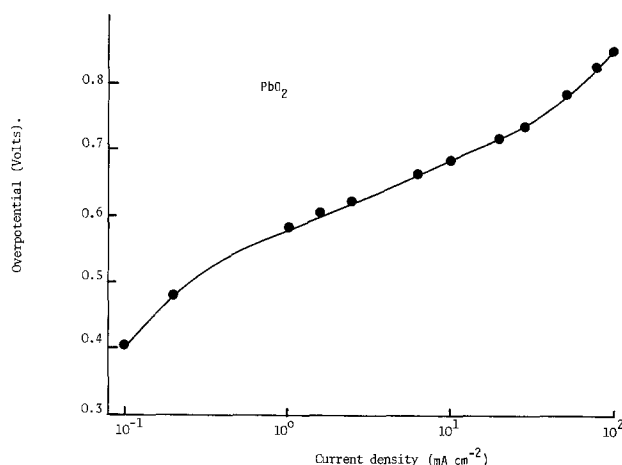


Fig. 9. Tafel plot for oxygen evolution on a preanodized FEP-bonded PbO_2 electrode at 25°C in 5N KOH.

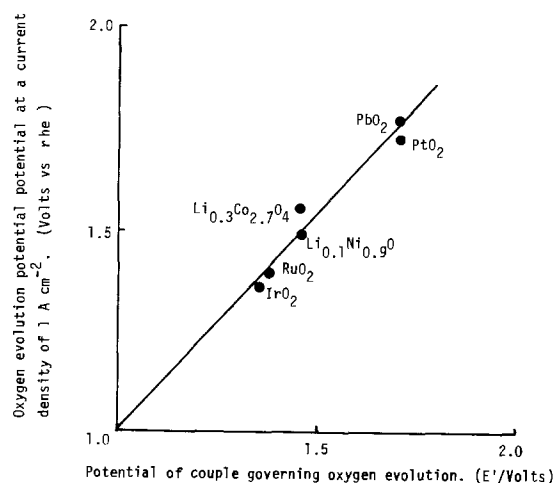


Fig. 10. Correlation of the minimum potential of oxygen evolution at 25°C in 5N KOH of six oxides and the respective potentials that govern oxygen evolution.

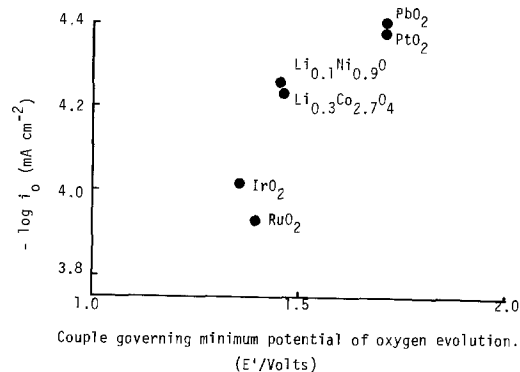


Fig. 11. Relationship of the pseudoexchange current density for oxygen evolution of six oxides at 25°C in 5N KOH and the respective couple that govern oxygen evolution.

Table V. Pseudoexchange current densities and the Tafel slopes for oxygen evolution in 5N KOH at 25°C for preanodized FEP-bonded electrodes of six oxides

Oxide	Pseudoexchange current density $i_0 \times 10^{-5}$ (mA/cm ²)	Tafel slope (V/decade)
RuO ₂	11.7	0.042
PtO ₂	4.2	0.043, 0.113
IrO ₂	9.5	0.033
Li _{0.3} Co _{2.7} O ₄	5.8	0.063
Li _{0.1} Ni _{0.9} O	5.6	0.076
PbO ₂	3.5	0.121

change current densities and the couple governing the minimum potential of oxygen evolution for the six oxides (Fig. 11) does not show any correlation, suggesting that the oxygen evolution rate on the oxides is not totally dependent on the magnitude of the lower oxide/higher oxide couple. Figure 12 gives the plot of the negative log of the pseudoexchange current density vs. the ratio of the lower oxide/higher oxide couple and the Tafel slope for the six oxides and shows good correlation. Therefore, although the minimum potential of oxygen evolution on oxides is determined by the lower oxide/higher oxide couple, the rate of oxygen evolution is also dependent on the Tafel slope. Therefore, the factors that determine the magnitude of the Tafel slope, such as the type and nature of the sites, extent of site coverage, etc., are also important in determining the rate of oxygen evolution.

The trend shown in Fig. 12 can be explained as follows: the Tafel line intercept, which is the overpotential η at unit current density is given $\eta = -b \log i_0$, where b is the Tafel slope and i_0 is the pseudoexchange current density. From Fig. 10, η is proportional to value of the couple governing oxygen evolution, E . Thus E is proportional to $-b \log i_0$, and hence $E/b \propto -\log i_0$.

Conclusions

This study shows that the behavior of oxides towards oxygen evolution can be divided into two groups. In one group, the oxides evolve oxygen by undergoing an increase in the cationic oxidation state before evolving oxygen. The intermediates formed during this process are of the chemisorbed type. Oxygen evolution takes place on these oxides at fairly low overpotentials, very close to the potential of the lower oxide/higher oxide couple. Oxides of Ir, Ru, Ni, and Co belong to this group. The other group of oxides evolve oxygen at fairly high overpotentials close to the potential of the OH⁻/HO₂⁻ couple of 1.77V. This group consists of either oxides that are of stable electronic configuration at rest, e.g., PbO₂ where Pb⁴⁺

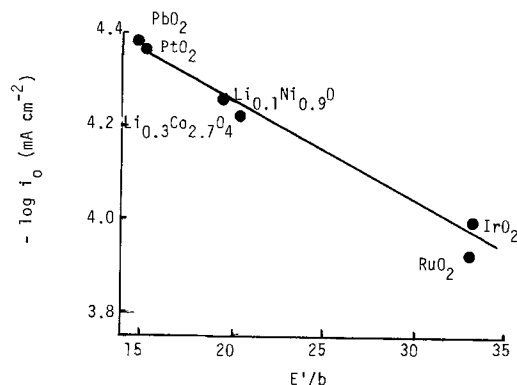


Fig. 12. Relationship of the pseudoexchange current density for oxygen evolution of six oxides at 25°C in 5N KOH and the respective ratio of the couple governing evolution (E') and the Tafel slope (b).

is a d¹⁰ ion and on which further oxidation state transitions are not very possible, or oxides that undergo oxidation state transitions at very high potentials, e.g., PtO₂ having a PtO₂/PtO₃ couple of 2.0V. This study suggests that oxygen evolution on this group of oxides takes place by the formation of physisorbed HO₂⁻ as intermediate.

Acknowledgment

This work was supported by the United Kingdom Science Research Council.

Manuscript submitted June 7, 1982; revised manuscript received Nov. 8, 1983. This was Paper 527 presented at the Minneapolis, Minnesota, Meeting of the Society, May 10-15, 1981.

REFERENCES

1. P. Ruetschi and P. Delahay, *J. Chem. Phys.*, **23**, 560 (1955).
2. A. C. C. Tseung and S. Jasem, *Electrochim. Acta*, **22**, 31 (1977).
3. A. Hickling and S. Hill, *Disc. Faraday Soc.*, **1**, 236 (1947).
4. A. K. Vijh, *Electrochim. Acta*, **17**, 91 (1972).
5. M. Pourbaix, "Atlas d'Equilibres Electrochimiques a 25°C," Gauthiers Villars, Paris (1963).
6. V. S. Bagotzkii, S. S. Sedova, and B. Vasiliev, *Elektrokhimiya*, **4**, 1113 (1968).
7. M. W. Breiter, "Electrochemical Process in Fuel Cells," Springer, New York (1969).
8. R. N. Goldberg and L. G. Hepler, *Chem. Rev.*, **68**, 229 (1968).
9. L. E. Orgel, "Introduction to Transition Metal Chemistry," Methuen (1960).
10. P. Rasiyah, A. C. C. Tseung, and D. B. Hibbert, *This Journal*, **129**, 1724 (1982).

Electrochemical Properties of $\text{WO}_3 \cdot x(\text{H}_2\text{O})$

II. The Influence of Crystallization as Hydration

Nobuyuki Yoshiike and Shigeo Kondo

Matsushita Electric Industrial Company, Limited, Central Research Laboratory, Moriguchi, Osaka, 570 Japan

ABSTRACT

Electrochemical properties of WO_3 films prepared by vacuum evaporation and stored in high humidity atmosphere have been studied in organic electrolytes. Structures of the film have been analyzed by electron diffraction analysis and x-rays. It has been found that the evaporated amorphous WO_3 film is crystallized to form $\text{WO}_3 \cdot \text{H}_2\text{O}$ crystal and furthermore $\text{H}_2\text{WO}_4 \cdot \text{H}_2\text{O}$ from surface layer to bulk layer in high humidity air. Hydrated $\text{WO}_3 \cdot x(\text{H}_2\text{O})$ crystal layer may act as a high resistant layer on the electrochemical reaction, so that the hydrated layer, remarkably, loses the electrochromic activity.

WO_3 is one of the most useful materials for electrochromic displays (ECD) (1-6). At present, a reasonable model for coloration is explained by Faughnan *et al.* (3), whereby the double injection of electrons and protons into the film forms tungsten bronzes. The bronze has a stable memory effect and can be switched back into the original colorless state by reversing the current. Recent studies (7-13) have confirmed that water in the film plays an important role in the coloration and bleaching mechanism. Hurditch (7) has studied the dependence of the coloration phenomenon on the water content in the film. He suggested $\text{WO}_3 \cdot \text{aq}$ as intermediate between a fractionally hydrated form of tungsten oxide and a polytungstic acid. Zeller and Beyeller (8) concluded that the crystal water not only provides a high ionic conductivity which is conditional for a fast electrochromic reaction, but also stabilizes electrocatalytically active surface sites. Reichman and Bard (9) reported that the kinetic behavior of the electrochromic process is attributable to differences in porosity and water content of the film.

The states of water in the WO_3 film may be classified into three groups: physisorbed water, chemisorbed water as hydroxylated, or hydrated water having a crystal structure. The authors (14) have recently confirmed the influence of free water as physisorption and chemisorbed water as hydroxylation and/or hydrolysis on the electrochemical properties of evaporated WO_3 films. In particular, we have suggested that the water adsorbed in the film during the evaporation and from ambient air after the ventilation of the vacuum chamber not only provides a fast electrochromic reaction at first, but reacts gradually with WO_3 by hydroxylation and/or hydrolysis to shift the potential of the cathodic reaction to negative side, and then the hydroxylated film loses the electrochromic coloration density at the same applied potential.

Tungstates (15) may generally be obtained by precipitating tungstate solutions with mineral acids. Paola *et al.* (16) reported the electrochromism in anodically formed tungsten oxide films. They prepared tungstates and measured cyclic voltammetry of the films in H_2SO_4 aqueous electrolytes, and they suggested a new coloration mechanism. Reichman *et al.* (9) also reported the behavior of WO_3 anodic films.

In this paper, we report the formation of tungstate crystals from evaporated amorphous WO_3 films stored in high humidity air and the electrochemical properties of the tungstate films in propylene carbonate electrolytes.

Experimental

Preparation of WO_3 films.— WO_3 films were deposited by an electron beam evaporation method. WO_3 targets (99.99%) were supplied by Furuuchi Kagaku Company, Limited. The deposition rate was 4-5 Å/s, the deposition angle was varied within 40° with a planetary rotation, and the substrate temperature was usu-

Key words: electrochromism, display, hydration, tungsten oxide.

ally maintained at 80°C after keeping at 110°C for 5 min. The total gas pressure in the chamber during the evaporation process was controlled by N_2 gas introduction to be $4-5 \times 10^{-5}$ torr. Deposited WO_3 films were confirmed by electron diffraction analysis to be typically amorphous. Packing density of the film calculated from film thickness, and its weight was 5.38 g/cm³, and the reflection index evacuated from the interference patterns of visible absorption and film thickness was 1.85.

The substrates were In_2O_3 -coated glass (20 Ω/cm²) used for electrochemical measurements and electron diffraction analysis, glass plates for x-ray diffraction analysis, and Al films for electron diffraction analysis.

For the purpose of investigating the influence of humidity on the evaporated films, the films were stored in humidity-controlled air at different conditions with a thermostat (Nagano Kagakukikai, Model NEW LH-20).

Analysis of WO_3 films.—Electron diffraction analyses of the films were carried out with an electron microscope (Nihon Denshi, Model JEM-200CX); the accelerated voltage was 80 kV. The incident beam angle was 5°-6°, and electron diffraction patterns were formed by reflection from surface of WO_3 films.

Direct x-ray diffraction patterns of the films (16,000 Å thick) on glass plates were obtained by using a Philips Model APD-10 goniometer. Cu_α radiation (voltage: 50 kV, current: 40A) was used. The scanning speed was 2° 2θ/min. The d spacings were compared with the ASTM index values and reference papers.

Transmission electron microscope photographs of the film were taken with a positive replica method using the microscope described above.

Electrochemical measurements.—The electrochemical measurements, especially cyclic voltammetry measurements, were performed with a potentiostat (Hokuto Denko, Model HA-301), which was supplied with voltage from a function generator (same company, Model HB-104). The WO_3 film thickness and area were 3000Å and 0.3 cm², respectively. The counter-electrode was a Pt plate, and the reference electrode was a saturated calomel electrode (SCE). The electrolytes were propylene carbonate (PC) solutions containing 0.3M LiClO_4 and 0.03M LiBF_4 . PC (first grade, Wako Junyaku) was freshly distilled under vacuum, LiClO_4 (purity 99%, Mitsuwa Kagaku), and LiBF_4 (purity 93%, Morita Kagaku) were used. Ar gas was bubbled for more than 5 min before measurements. H_2O content in the electrolytes was checked in each case by an Aquacounter (Hiranuma Seisakusho, Model AQ-3B), and these concentrations were typically 0.03-0.05M.

Results and Discussions

Structures of WO_3 films.—Electron diffraction measurements formed by reflection from surface were taken with WO_3 films on Al film substrates stored in

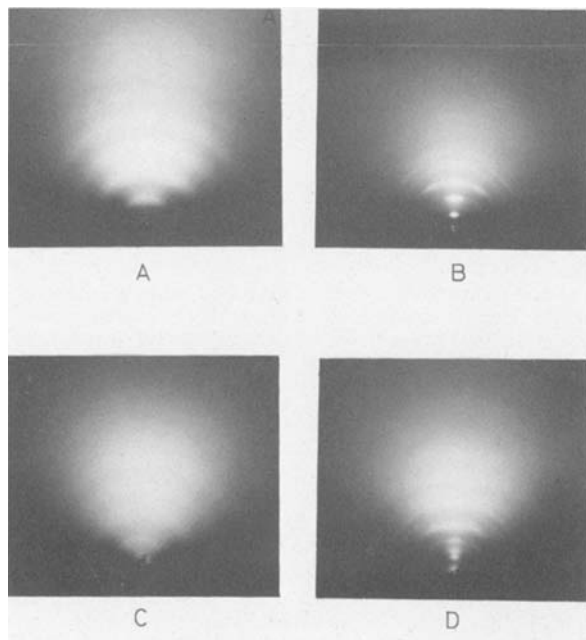


Fig. 1. Electron diffraction patterns of WO_3 films ($16,000\text{\AA}$ thick on Al) stored in different conditions after the storage in air at 25°C and 50% RH for 72h. A: on treatment. B: 40°C and 95% RH for 1h. C: 80°C and 95% RH for 1h. D: 100°C for 1h at 1×10^{-6} torr after treatment B.

different conditions are shown in Fig. 1. The film stored in air at 25°C and 50% RH for 72h was amorphous; the film stored in air at 40°C and 95% RH for 1h had a crystal structure pattern, and the film stored at 80°C and 95% RH for 1h remained amorphous. This will be interpreted as dehydration of the film at high temperatures (i.e., 80°C). An endothermic peak was observed on amorphous WO_3 with differential thermal analysis at around 90°C (19). Once the film was crystallized, no differences in the reflection patterns could be observed even after treatment in a vacuum chamber at 100°C and 1×10^{-6} torr for 1h (Fig. 1d). A surface reflection pattern was also observed with the WO_3 film on In_2O_3 -coated glass stored in air at 40°C and 95% RH for 1h, but it was not as well defined as the film on Al films. The reflection pattern did not appear with the film stored in air at 25°C and 50% RH for long periods (more than 4000h). Hence, the crystallization does not occur under the conditions of <50% RH and < 25°C .

The d spacings with the definite patterns were estimated by using a reference of Au diffraction pattern, and are tabulated in Table I with $\text{WO}_3 \cdot \text{H}_2\text{O}$ values of the ASTM (no. 18-1418) and Glemser (17). Table I shows that the reflection pattern of the film stored in high humidity air can be assigned to $\text{WO}_3 \cdot \text{H}_2\text{O}$ crystal. Needless to say, the d spacings were different from those of the substrate compounds: Al, Al_2O_3 , $\text{Al}(\text{OH})_3$, and/or In_2O_3 . The d spacing of the strongest peak with ASTM values ($d = 3.49\text{\AA}$) was not observed. This may be explained by the crystallization of film with a preferred orientation, because, besides many rings, clear spots were also observed.

X-ray diffraction analyses of the WO_3 films on glass plates which were stored in air at 40°C and 95% RH are shown in Fig. 2. The diffraction pattern was observed with the film after the storage for 24h, but not with the film after 2h. However, a definite electron reflection pattern was observed with the same film stored for 2h. The penetration depth with electron probe is much less than with x-ray, and then surface layer and bulk layer is examined with electron reflection patterns and x-ray diffractions, respectively (20). Therefore, the crystallization may proceed from surface layer to bulk layer.

Table I. Electron diffraction data of WO_3 films stored in air at 40°C and 95% RH for 1h

Experimental Values			WO_3		H_2O	
A	B	C	ASTM Values		Glemser (17)	
d \AA	d \AA	d \AA	d \AA	I/I ₁	d \AA	I/I ₁
5.90	5.32	5.49	5.39	7.5	5.34	7.0
		3.76	3.77	4	3.80	2.0
			3.49	10.0	3.48	10.0
2.86			2.95	6	2.92	3.0
2.67	2.73	2.75	2.687	10	2.70	3.0
			2.626	12	2.62	5.0
2.48			2.570	2.5	2.56	7.0
1.91			1.959	2		
	1.86		1.837	14		
1.76			1.739	10		
	1.58		1.58	2		
1.52			1.52	4		
	1.48		1.47	2		
1.32	1.33		1.34	2		
	1.30		1.30	2		

A: WO_3 ($16,000\text{\AA}$) on Al substrate. B: Another sample same as A. C: WO_3 ($16,000\text{\AA}$) on In_2O_3 -coated glass.

Table II. X-ray diffraction data of WO_3 films ($16,000\text{\AA}$ on glass) stored in air at 40°C and 95% RH for 24h

Experimental values		$\text{H}_2\text{WO}_4 \cdot \text{H}_2\text{O}$ ASTM values		
d \AA	I/I ₁	d \AA	I/I ₁	hkl
6.857	100	6.96	100	010
(5.335)	(3)			
3.437	29	3.47	30	020
2.290	9	2.304	10	030
1.720	2	1.729	6	040

The d spacings of x-ray analyses were compared with $\text{H}_2\text{WO}_4 \cdot \text{H}_2\text{O}$ values of the ASTM (no. 18-1420) and are tabulated in Table II. The peaks at $d = 6.857$,

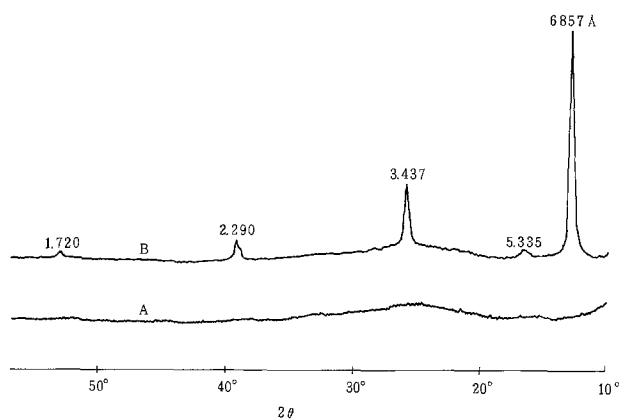
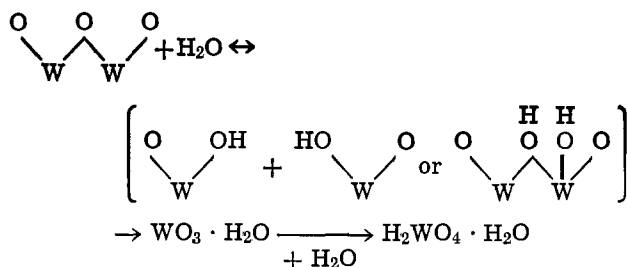


Fig. 2. X-ray diffraction patterns of WO_3 films ($16,000\text{\AA}$ thick on glass plate) stored in air at 40°C and 95% RH for different time. A: 2h. B: 24h.

3.437, 2.290, and 1.720 Å can be assigned closely to the d spacings of the $\{0k0\}$ planes of $\text{H}_2\text{WO}_4 \cdot \text{H}_2\text{O}$, and the intensity ratios agree exactly among themselves. These results may be attributed to the presence of monoclinic $\text{H}_2\text{WO}_4 \cdot \text{H}_2\text{O}$ which crystallized with a preferred orientation of the $\{010\}$ planer parallel to the substrate. The peak at 5.335 Å may be attributed to the presence of a small amount of $\text{WO}_3 \cdot \text{H}_2\text{O}$.

Electron reflection patterns of the film (1.6 μm thick) on In_2O_3 -coated glass stored in air at 40°C and 95% RH for 24h was observed and assigned to $\text{H}_2\text{WO}_4 \cdot \text{H}_2\text{O}$ crystal, but its patterns were not as clear as those on Al. Hence the orientation of crystallization may depend on the surface state of substrates.

Consequently, under the condition of high humidity, it was predicted that a recombination as hydration of the film with dissociation of W-O-W bonding occurs, and the $\text{WO}_3 \cdot \text{H}_2\text{O}$, and furthermore the $\text{H}_2\text{WO}_4 \cdot \text{H}_2\text{O}$, are formed as follows



Transmission electron microscope examinations of WO_3 films by a positive replica method shows that the porous surface layer of amorphous film was changed to a dense and glassy layer by crystallization, as shown in Fig. 3.

Electrochemical properties.—Cyclic voltammograms of the WO_3 films which were stored in different conditions for 1h (after the storage of as-deposited film in air at 25°C and 50% RH for 72h) are shown in Fig. 4. In Fig. 4, the potential cycling started at +1000 mV vs. SCE and returned to -400 mV with a 200 mV/s scan rate. The cathodic current which started at +250 mV

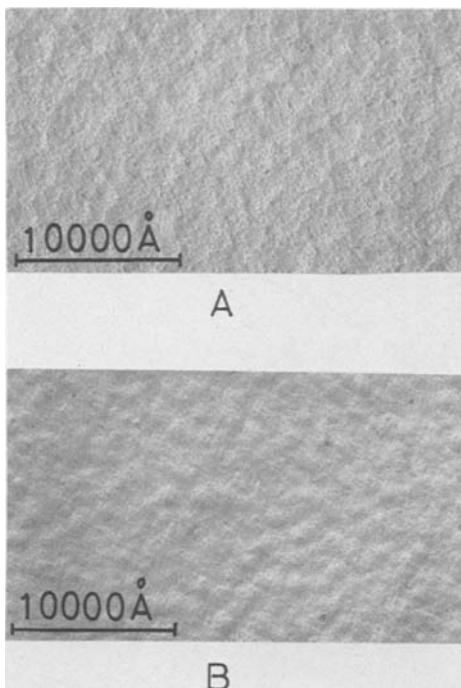


Fig. 3. Transmission electron microscope photographs with a positive replica method of WO_3 films stored in different conditions. A: 25°C and 50% RH for 72h. B: 40°C and 95% RH for 24h after the treatment of A.

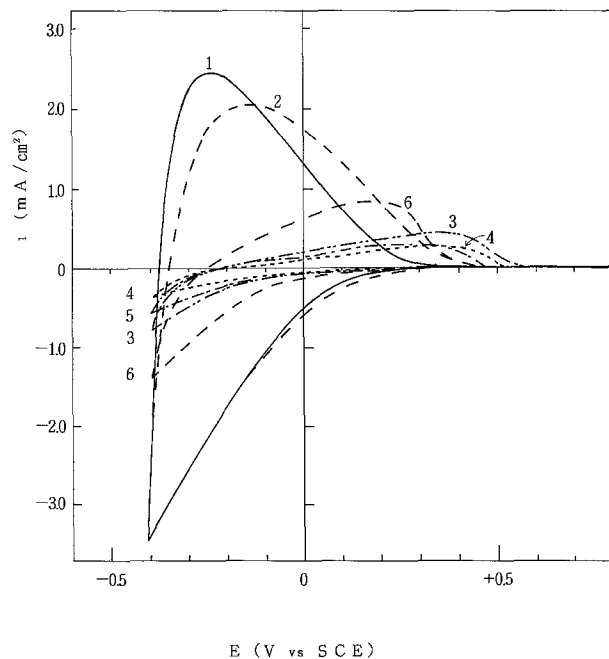


Fig. 4. Cyclic voltammograms at 0.2 V/s scan rate in PC electrolytes of WO_3 films stored in air at different temperatures and 95% RH for 1h after storage in air at 25°C and 50% RH for 72h. Curve 1: no treatment. Curve 2: 25°C. Curve 3: 30°C. Curve 4: 40°C. Curve 5: 60°C. Curve 6: 80°C.

is associated with the coloration reaction of the film, and the anodic current is associated with the bleaching reaction. Figure 4 shows that, in spite of the rarity of change of the starting potential of the cathodic reactions, the cathodic current decreased with the storage in high humidity atmosphere and the peak potential of the anodic current shifted to positive side with the storage. That is, both the cathodic and anodic reactions become slower with the storage, and these changes are assigned to a deterioration of electrochromic activity. The extent of the deterioration was distinguished with the storage at 40°C and 95% RH, and it was smaller with the storage at temperatures higher than 40°C.

Cyclic voltammograms of the films which were stored in air at different relative humidities at 40°C for 1h are shown in Fig. 5. The electrochromic activity of the films decreased with increasing humidity of the atmosphere.

In order to make the detailed behavior of hydrated WO_3 more clear, cyclic voltammograms of freshly prepared films were measured connected in series to various different resistances. These are shown in Fig. 6. Figure 6 shows that the potential of the cathodic reaction does not change, but rather that the cathodic current decreases and the anodic current peak shifts to the positive side with the resistivity of the resistances. This behavior is similar to the cyclic voltammograms of the film having a crystal surface layer (see Fig. 4, curve 4). Therefore, hydrated crystal surface layers may act as a resistant layer against electrochemical reaction. That is, the layer may contribute to the depression of diffusion of proton and/or electron mobility. This effect of crystal surface layer can also be supported with the results of the TEM photograph (Fig. 3) showing the crystal surface to be more dense than the amorphous film.

Consequently, the crystallization will be remarkably different from both the effect of physisorbed water improving the electrochemical reaction and the effect of chemisorbed water shifting the cathodic reaction to negative potentials. In order to prepare ECD's having constant electrochromic properties, the exposure of the WO_3 film to even slightly high humidity atmospheres (i.e., 60% RH) at around room tempera-

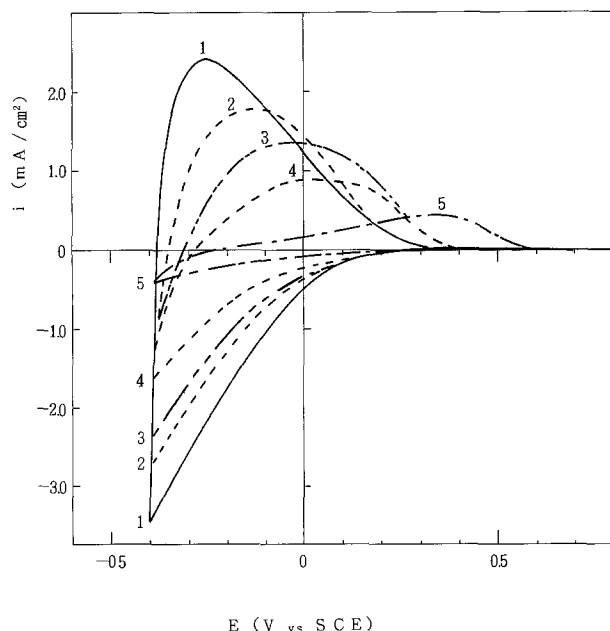


Fig. 5. Cyclic voltammograms at 0.2 V/s scan rate in PC electrolytes of WO_3 films stored in air at 40°C and different humidities for 1h after storage in air at 25°C and 50% RH for 72h. Curve 1: no treatment. Curve 2: 60% RH. Curve 3: 80% RH. Curve 4: 90% RH. Curve 5: 95% RH.

ture to 80°C during storage and assembly must be avoided.

Conclusion

Evaporated amorphous WO_3 can be crystallized to form $\text{WO}_3 \cdot \text{H}_2\text{O}$ crystals and $\text{H}_2\text{WO}_4 \cdot \text{H}_2\text{O}$ crystal from surface layer to bulk layers after storage in high humidity air for relatively short time. The hydrated crystal layer may act as a high resistance layer on the electrochemical reaction so that the electrochromic activity of the film is remarkably deteriorated.

Acknowledgment

We are thankful to T. Kurumizawa, a member of Techno-Research Department, for performing electron and x-ray diffraction analyses and for helpful discussions.

Manuscript submitted April 22, 1983; revised manuscript received Nov. 16, 1983.

Matsushita Electric Industrial Company, Limited, assisted in meeting the publication costs of this article.

REFERENCES

1. S. K. Deb, *Appl. Opt. Suppl.*, **3**, 192 (1969).
2. C. T. Schoot, J. J. Ponjee, H. T. Van dam, R. A. Van doorn, and P. T. Bolwijn, *Appl. Phys. Lett.*, **23**, 64 (1973).
3. B. W. Faughnan, R. S. Crandall, and P. M. Hevman, *RCA Rev.*, **36**, 177 (1975).
4. J. D. E. McIntyre, G. Beni, and J. L. Shay, Abstract

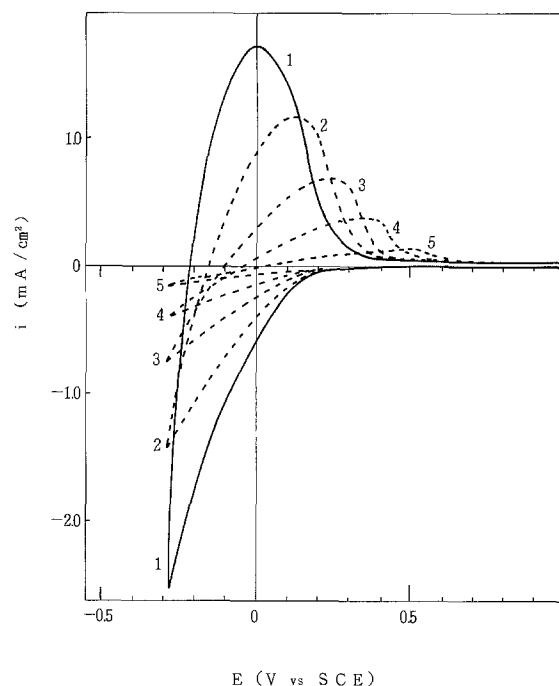


Fig. 6. Cyclic voltammograms at 0.2 V/s scan rate in PC electrolytes of WO_3 films stored in air 25°C and 50% RH for 72h connected in series to different resistances. Curve 1: 0.0Ω. Curve 2: 560Ω. Curve 3: 2 kΩ. Curve 4: 5.6 kΩ. Curve 5: 20 kΩ.

- of the 20th EMC, Santa Barbara (1978).
5. M. M. Nicholson and R. V. Galiardi, *SID Dig.*, **24** (1978).
6. N. Yoshiike, S. Kondo, and M. Fukai, *This Journal*, **127**, 1496 (1980).
7. R. Hurdlich, *Electron. Lett.*, **11**, 142 (1975).
8. H. R. Zeller and H. V. Beyeller, *Appl. Phys.*, **13**, 231 (1977).
9. B. Reichman and A. J. Bard, *This Journal*, **126**, 583 (1979).
10. A. Deneuille, P. Gerard, and P. Billat, *Thin Solid Films*, **70**, 203 (1980).
11. Y. Hajimoto, M. Matsushita, and S. Ogura, *J. Electron. Mater.*, **8**, 301 (1979).
12. L. Pickelman and P. Schlotter, in "Euro Display '81," Proceeding of the First European Display Research Conference, Sept. 16-18, 1980, Munich (1981).
13. T. C. Arnoldussen, *This Journal*, **128**, 117 (1981).
14. N. Yoshiike and S. Kondo, *ibid.*, **130**, 2283 (1983).
15. *J. Chem. Soc.*, 1987 (1930); *Z. Anorg. Chem.*, **265**, 288 (1951).
16. A. Di Paola, F. Di Quarto, and C. Sanseri, *This Journal*, **125**, 1344 (1978).
17. O. Glemser and C. Naumann, *Z. Anorg. Chem.*, **332**, 299 (1964).
18. H. P. Boehm, *Discuss. Faraday Soc.*, **52**, 264 (1971). M. Egashira, M. Nakashima, S. Kawasumi, and J. Seiyama, *J. Phys. Chem.*, **85**, 4125 (1981).
19. J. P. Ramdin, *J. Electron. Mater.*, **7**, 47 (1978).
20. Charless, Barrett, "Structure of Metals," pp. 581-603, McGraw-Hill, New York (1952).

Activation of Glassy Carbon Electrodes by Dispersed Metal Oxide Particles

I. Ascorbic Acid Oxidation

Shaojun Dong and Theodore Kuwana*

Department of Chemistry, The Ohio State University, Columbus, Ohio 43210

ABSTRACT

Various metal oxides (MOx) were dispersed onto a glassy carbon (GC) surface for the purpose of catalyzing the oxidation of ascorbic acid (AH₂). Of the 37 different metal oxides examined, more than 20 showed varying degrees of rate enhancement (henceforth referred to as activation) for AH₂ oxidation. The highest degree of activation was exhibited by those MOx's whose oxidation state of the metal was +3 or higher, such as zirconium oxide, ceric oxide, cobaltic oxide, chromic oxide, stannic oxide, and the previously reported alumina. The double layer capacitance was also observed to increase with MOx/GC's compared to the bare GC electrode. This increase suggested that the surface area of the GC electrodes increased due to the dispersion of MOx. The pH dependence of the AH₂ activation at MOx/GC was considerably different from that at a bare GC electrode and suggested that the enhancement mechanism may involve an acceleration of a proton-transfer step via AH₂ interaction with the MOx/GC surface. A model of the physical structure of the MOx/GC surface is proposed to account for the carbon surface activation.

We recently reported (1, 2) that α -alumina dispersed on glassy carbon surfaces (henceforth referred to as α -Al₂O₃/GC) enhanced the rate of the electrode reaction with ascorbic acid (AH₂), 1,2-dihydroxybenzene (1,2-H₂Q, commonly called catechol), 1,4-dihydroxybenzene (1,4-H₂Q, commonly called hydroquinone), and oxalic acid (H₂Ox). The rate enhancement (henceforth referred to as activation) resulted in the lowering of the overpotential by 200-300 mV with the α -Al₂O₃/GC compared to highly polished, bare GC electrode. Catechol and hydroquinone, the two compounds with product reversibility, exhibited electrochemically reversible cyclic voltammograms at α -Al₂O₃/GC. Adsorption of the electroactive species onto the α -alumina particles also was observed. It was suggested that activation possibly involved an acceleration in the rate of proton transfer by the alumina.

To further assess the nature of the MOx activation, various MOx's, differing in elemental composition and oxidation states, were dispersed onto GC surfaces. The electroactive species used for assessing the extent of activation was ascorbic acid, whose electrochemical behavior is quite sensitive to the surface state of the glassy carbon surface (3, 4). The catalysis of AH₂ through surface modifications, i.e., via immobilization of redox mediators (3, 5, 6), polymeric films (7, 8), spontaneous adsorption (9), and metal adatoms (10, 11) has been reported.

As reported herein, a total of 37 different MOx's were mechanically dispersed onto GC surfaces and examined by cyclic voltammetry (CV). It was surprising to find that more than 20 oxides exhibited some degree of rate enhancement as evidenced by either the anodic peak potential, E_{pa} , shifting to less positive values and/or the peak current, i_{pa} , increasing in comparison to a bare GC electrode. The higher valent, harder refractory oxides, such as ZrO₂, CeO₂, Cr₂O₃, and the previously reported α -Al₂O₃, appeared to give the most pronounced effect to AH₂ oxidation.

In our earlier work with 1 μ m α -Al₂O₃ dispersed on GC, an increase in the double layer capacitance was observed, indicating an increase in the surface area. Also, catechol, hydroquinone, and ascorbic acid were reported to adsorb on this electrode. The extent to which these two factors may be important in the observed activation are discussed. The characteristics of AH₂ oxidation at MOx/GC electrodes are determined using the electrochemical methods of CV, chrono-

amperometry, and chronocoulometry, in addition to experiments performed using electrodes in rotating disk and thin-layer cell configurations.

Experimental

Chemicals.—L-ascorbic acid (Baker Analyzed Reagent Grade) was used as received. All of the metal oxides were from SPEX Industries, Incorporated. Twice distilled water was used for the preparation of solutions. The supporting electrolyte was 0.1M phosphate buffer at pH 2.0 (0.1M ortho-phosphoric acid with 0.1M sodium phosphate added for pH adjustment).

Electrode preparation.—A Kel-F shrouded GC disk (Bioanalytical Systems, Incorporated, West Lafayette, Indiana) with a geometric area of 0.071 cm² and a Tokai glassy carbon, GC-20, (Tokai Carbon, Limited, Tokyo) with a geometric area of 0.43 cm² were used as working electrodes. The surfaces of the GC's were polished successively with emery paper and alumina (Buehler, Limited, Chicago, Illinois, 1.0, 0.3, and 0.05 μ m) on an optical flat (Harrick Scientific Corporation, Ossining, New York) until a mirror-like finish was obtained on the surface. Final polishing was done on a polishing cloth (Buehler). Residual polishing material was removed from surfaces by sonication of the electrodes in a water bath for 30 min during which the water (twice distilled) was changed frequently. An electrode prepared by this procedure will be considered as a "bare" GC (henceforth referred to as GC₀). The metal oxides were dispersed onto the surface by rotating the GC under light hand pressure with a small amount of the desired MOx in slurry form on an optical flat. The MOx/GC surfaces were rinsed with doubly distilled water several times prior to immersion in the test solution. Electrodes were prepared and used immediately for each run.

Equipment and instrumentation.—Cyclic voltammograms were obtained with a BAS (Bioanalytical Systems, Incorporated, West Lafayette, Indiana) cyclic voltammeter Model CV-1B-120 connected to a three-electrode cell. A silver/silver chloride (saturated KCl) electrode served as the reference, and all potentials in the text will be reported with respect to this reference. A Houston (Houston Instrument Company, Austin, Texas) Model 2000 X-Y recorder served to record data. Chronoamperometric and chronocoulometric experiments were conducted with a home-built potentiostat with output capabilities of 150 mA and a rise time of less than 50 μ s. Input pulse signals to the potentiostat were provided by a PAR (Princeton Applied Re-

* Electrochemical Society Active Member.

Key words: metal oxides, particles, ascorbic acid, glassy carbon, electrochemistry.

search Corporation, Princeton, New Jersey) Model 175 waveform generator.

Rotating disk electrochemical experiments were performed with a Pine Instruments (Pine Instruments Company, Greenville, Pennsylvania) Model RDE-3 potentiostat and a Model ASR-165 analytical rotator. The rotating disk electrode (RDE) consisted of a glassy carbon disk shrouded by Teflon with a geometric electrode area of 0.49 cm^2 .

Scanning electron microscopy (SEM) photomicrographs of MO_x/GC surfaces were acquired on a Cambridge Stereoscan Model S4-10 (EG&G Ortec, Oak Ridge, Tennessee) with elemental analysis determined by energy dispersive x-ray (EDX) analysis with an ORTEC 6200 Multichannel Analyzer. Particle size distribution was determined by a computer imaging system (Videoplan by Carl Zeiss, Incorporated, Germany) using enlarged SEM photographs. The distribution function of the particle diameters was determined, as well as the average and the standard deviation of the diameters. The smallest particle diameter that could be imaged with the present system was 5 nm.

Results

Scope of MO_x activation.—Considerable variation of the potential at which AH_2 was oxidized was observed depending on the pretreatment procedure for preparing the GC electrode. With the procedure described in the experimental section, the cyclic voltammograms were found to be quite reproducible from run to run. Typical voltammograms of AH_2 oxidation at a GC_0 in phosphate buffer (pH 2.0) are shown in Fig. 1 (dashed lines). The average E_{pa} value of the broad i-E waves was 0.49V ($\sigma = 0.06\text{V}$ for 60 values), which is close to the previously reported (2) value of $+0.454 \pm 0.05\text{V}$ in $0.05\text{M H}_2\text{SO}_4$. A reverse wave was not observed for AH_2 because of the rapid hydrolysis of the oxidized product to dehydroascorbic acid. Examples of AH_2 oxidation at MO_x/GC are shown in Fig. 1; the solid curves labeled a, b, and c correspond to cyclic voltammograms at CeO_2 , ZrO_2 , and Cr_2O_3 , respectively, dispersed onto GC surfaces in phosphate buffer at pH 2. The effect of these oxides on AH_2 oxidation is considerable, i.e., the CV i-E waves became narrower with the i_{pa} enhanced and the E_{pa} values shifted to less positive potentials by 200–300 mV in comparison to the E_{pa} at GC_0 .

To explore the activation with respect to the elemental and valence composition of MO_x 's, 37 different metal oxides as particles were dispersed onto GC surfaces. The results for AH_2 oxidation (phosphate buffer, pH 2.0) with several of these oxides are tabulated in Table I. More than 20 oxides exhibited some degree of "catalysis," with the more effective activators appearing to be correlated with the higher valent oxides. For example, SnO_2 and PbO_2 exhibited activation, while the lower valent, SnO and PbO , did not. However, care must be exercised in interpreting such results because many oxides may be partially solubilized and/or undergo varying extents of hydration or hydrolysis in the acidic aqueous media. Ascorbic acid is also known to form complexes with certain metal ions (12, 13), although complexation may be minimal in acidic solutions.

Because of the large number of MO_x 's exhibiting activation properties, it was important to disperse particles with known chemical inertness and see whether activation occurred. Zak (2) had previously indicated that garnet/GC and KRS-5/GC did not activate AH_2 oxidation. However, the most inert material for use as a test particle appeared to be synthetic diamond commonly used as metallographic polishing compounds. Such diamond "dust" is often suspended in organic dispersing agent to prevent particle agglomeration. In order to remove the dispersing agent, the diamond particles (Buehler diamond, $1 \mu\text{m}$) were

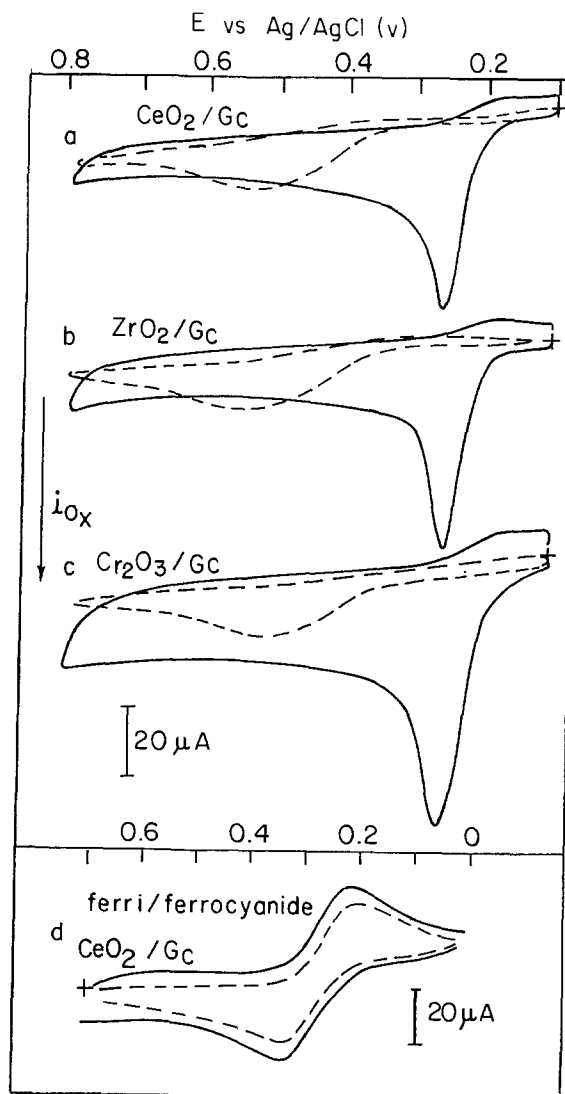


Fig. 1. Cyclic voltammograms of 1 mM ascorbic acid in phosphate buffer at pH 2.0 at GC_0 (dotted line) and at MO_x/GC electrodes (solid line). a: CeO_2/GC . b: ZrO_2/GC . c: $\text{Cr}_2\text{O}_3/\text{GC}$. Cyclic voltammograms for 1 mM ferrocyanide in 1M KCl at GC_0 (dotted line) and CeO_2/GC (solid line) are shown in part d. Scan rate = 100 mV/s.

first washed with acetone in a Soxhlet extractor, filtered and dried, and then washed thoroughly with twice-distilled water. The particles were heated and stored in a vacuum oven at 500°C . They were dispersed onto a GC surface by the usual mechanical abrasion method. The cyclic voltammograms of ascorbic acid, catechol, and hydroquinone at a diamond/GC were essentially unchanged from those at a GC_0 electrode. Thus, this apparent lack of activation by diamond was consistent with its known chemical inertness.

Earlier, it was speculated that the MO_x may accelerate the rate of the proton transfer step since the compounds, such as AH_2 , $1,2\text{-H}_2\text{Q}$, and $1,4\text{-H}_2\text{Q}$, have a common feature of involving protons in the overall reaction. It is therefore interesting to examine the behavior of ferrocyanide/ferricyanide, which undergoes an outersphere, one-electron redox reaction without the participation of any protons. Trace d in Fig. 1 (dotted curve) is a typical i-E wave for ferro-/ferricyanide at a GC_0 electrode. The separation of the cathodic and anodic peak potentials was usually the order of 100–150 mV at glassy carbon and considerably more than the 60 mV characteristics of a reversible electrode reaction. The voltammograms for ferro-/ferricyanide at MO_x/GC 's such as CeO_2 and ZrO_2 remain essentially identical to those at GC_0 , if one corrects for the larger,

Table I. Electrochemical parameters for ascorbic acid^a oxidation at MOx/GC electrode evaluated by cyclic voltammetry

MOx	E_{pa} (V)	$E_{pa/2}$ (V)	$\Delta i_p/i_{p_0}^b$	MOx	E_{pa} (V)	$E_{pa/2}$ (V)	$\Delta i_p/i_{p_0}^b$
MgO	0.285	0.255	0.68	CuO	0.275	0.245	0.80
CaO	0.265	0.230	1.70	ZnO	0.285	0.255	0.60
BaO	0.275	0.245	0.76	CdO	0.285	0.255	0.93
TiO ₂	0.265	0.235	1.72	α -Al ₂ O ₃	0.250	0.220	2.72
ZrO ₂	0.255	0.225	3.00	In ₂ O ₃	0.250	0.225	1.60
CeO ₂	0.255	0.230	2.47	Tl ₂ O	0.285	0.255	1.93
ThO ₂	0.280	0.250	1.75	SiO ₂	0.265	0.230	1.91
V ₂ O ₅	0.280	0.250	1.25	GeO ₂	0.275	0.245	1.96
Nb ₂ O ₅	0.275	0.245	2.33	SnO ₂	0.250	0.220	2.39
Ta ₂ O ₅	0.275	0.245	1.35	SnO	0.43 ^c	—	0.00
Cr ₂ O ₃	0.265	0.230	3.50	PbO ₂	0.265	0.235	2.10
MoO ₃	0.290	0.255	0.62	PbO	0.41 ^c	—	~0.20
H ₂ WO ₄	0.275	0.250	1.91	Sb ₂ O ₃	0.275	0.245	0.70
Fe ₂ O ₃	0.265	0.225	1.95	Bi ₂ O ₃	0.275	0.245	1.57
Co ₂ O ₃	0.250	0.220	2.93	TeO ₂	0.285	0.215	2.13
NiO	0.255	0.225	2.08	(bare GC)	0.49 ^d	—	—

^a 1 mM ascorbic acid in 0.1M phosphate buffer pH 2.0, scan rate = 100 mV/s.

^b i_{p_0} represents peak current at GC. Δi_p represents net increase in the peak current at MOx/GC compared to GC.

^c CV i -E curves are broad and ill-defined.

^d Standard deviation for 60 values.

background charging current. Thus, the ferro-/ferricyanide redox reaction is not markedly affected by the presence of MOx. The scope with respect to compound types is currently being examined to ascertain whether involvement of a proton in the rate-determining step of the redox reaction is a prerequisite to MOx activation.

The presence of MOx on the GC surface was confirmed by elemental analysis using EDX, and the particle dispersion/distribution was determined by SEM. Figure 2 shows SEM photomicrographs of CeO₂, ZrO₂, Co₂O₃ as representative samples of MOx/GC's. The particle size and its distribution were evaluated by particle imaging from enlargements of these SEM photomicrographs. The size distributions for these oxides are given in Fig. 3. The total surface area occupied by MOx ranged from 10% for CeO₂ to 19% for Co₂O₃. In our previous α -Al₂O₃ work, coverages ranged from 20% to 30%. The extent of activation can become coverage dependent if the coverage is too low. However, a detailed study of the coverage dependence has been deferred until a method of fractionating the particles and dispersing them reproducibly is devised. It will then be possible to assess the relationship between the size and coverage to the effectiveness of activation.

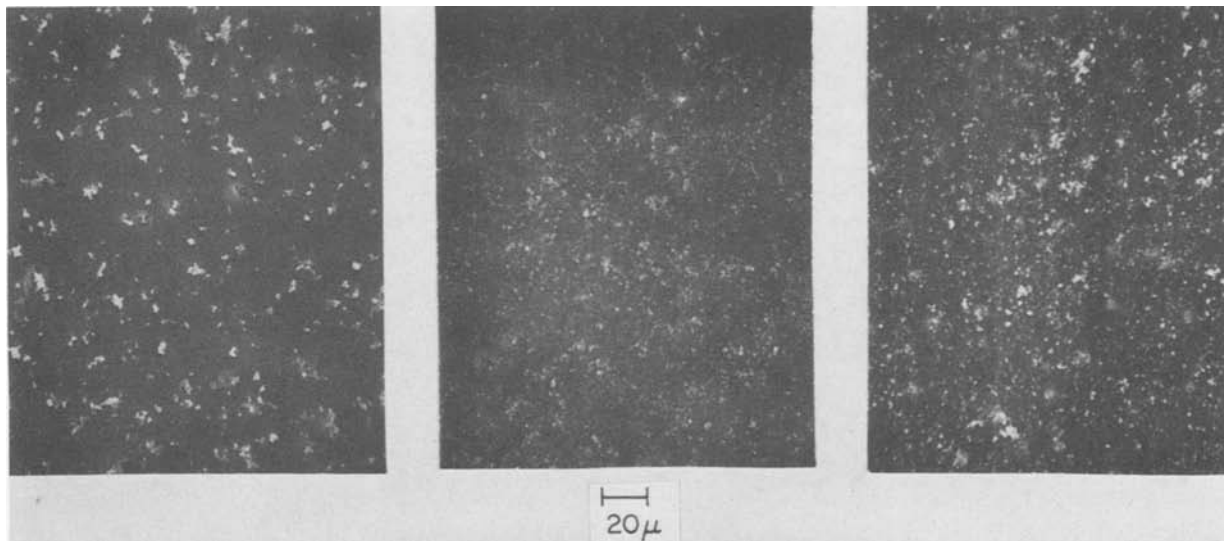


Fig. 2. Scanning electron photomicrographs of MOx/GC electrode surfaces. From left to right: CeO₂, ZrO₂, and Co₂O₃ dispersed on glassy carbon surface. Magnification is 525 \times .

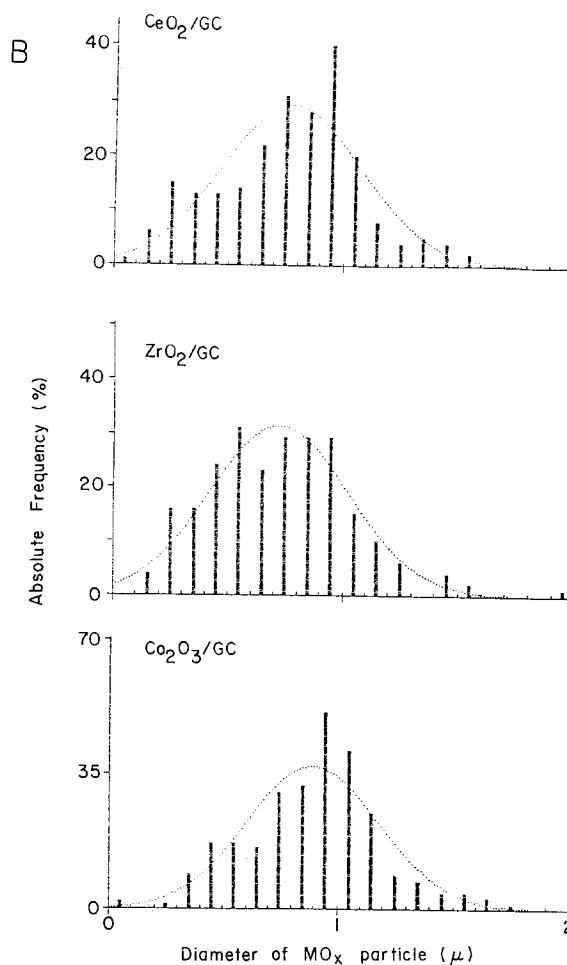


Fig. 3. Size distribution of the MOx particles shown in the scanning electron photomicrographs of Fig. 2. The absolute frequency is plotted vs. the size in micron. From top to bottom; CeO₂, ZrO₂, and Co₂O₃.

Adsorption.—Since the MOx particles are on the average much larger than the width of the diffuse double layer, it is difficult to envision a mechanism of activation. In our earlier work (1, 2) with α -Al₂O₃/GC, surface adsorption by AH₂, catechol, and hydroquinone was evidenced by the shape of the CV i -E

waves, particularly at low concentrations of the electroactive species, where the adsorptive wave predominated. Adsorption was also indicated by the non-zero intercept on the charge axis of the extrapolated plots of Q vs. $t^{1/2}$ from chronocoulometry. Thus, the question arose whether surface adsorption was a prerequisite to activation.

At MOx's such as CeO_2 , ZrO_2 , ThO_2 , and Cr_2O_3 , the plots of the i_p vs. $v^{1/2}$ from CV data for AH_2 were linear and extrapolated to the zero current intercept when corrected for background. Similarly, adsorption of AH_2 on these same electrodes appeared to be absent as evaluated by chronocoulometry. However, varying amounts of adsorption were observed by both CV and chronocoulometry on Co_2O_3 and $\alpha\text{-Al}_2\text{O}_3/\text{GC}$'s. Such variation made it difficult to make quantitative statements with respect to adsorption.

With catechol and hydroquinone, where electrochemical product reversibility is observed, the successive "dump-fill" thin-layer method introduced by Soriaga and Hubbard (14, 15) worked extremely well to examine the question of adsorption. In this method, the electrochemical charge required to exhaustively electrolyze material in a thin-layer cell for the first solution filling, Q_1 , is compared to the second, Q_2 , filling. If a quantity of species in terms of charge, Q_{ads} , is adsorbed and electroactive, then

$$Q_1 = Q_{\text{ads}} + (Q_{\text{soln}})_1 + Q_b$$

where $(Q_{\text{soln}})_1$ is the electroactive species remaining in the solution phase of the thin-layer cell, and Q_b is the background charge. Of course, Q_1 can be calculated and in this case should correspond to Q_T , the total amount of electroactive species introduced into the thin-layer cell by the first filling. If the adsorbed species remains on the electrode surface during the second filling, the charge Q_2 will be

$$Q_2 = Q_1 + Q_{\text{ads}} + Q_b$$

and, hence, the difference between Q_2 and Q_1 provides a means of determining Q_{ads} . This case is illustrated by the plot of Q_1 (triangles) and Q_2 values (open circles) for catechol at ZrO_2/GC as a function of catechol concentration (phosphate buffer, pH 2.0) in Fig. 4. It appears that saturation coverage of the ZrO_2/GC surface is attained at catechol concentrations of 0.1M or higher. Values of Q_1 coincide with those of Q_T (repre-

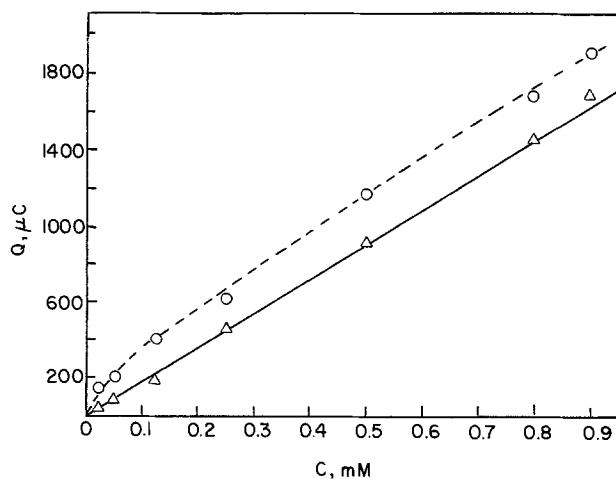


Fig. 4. The charge, Q , in microcoulomb for the first (triangles) and second (open circles) fillings of the thin-layer cell with known concentrations of catechol in phosphate buffer (pH 2.0) at a ZrO_2/GC electrode. The solid line is drawn for the charge calculated from the known concentration of catechol and thin layer volume of $9.35 \mu\text{l}$. The charges, Q_1 and Q_2 , were determined by integrating the area under the voltammetric, current-potential curve obtained at a scan rate of 2 mV/s .

sented by the solid line), which is calculated from the concentration and the thin-layer volume, and assuming a two-electron redox reaction for catechol. The cell volume was determined using known concentrations of ferrocyanide. One can conclude from the coincidence of Q_1 and Q_T that the adsorbed catechol remains electroactive in the potential region of the CV scan. Similar adsorption results have been obtained for catechol and hydroquinone at $\alpha\text{-Al}_2\text{O}_3/\text{GC}$ (1, 2).

For AH_2 , the cyclic voltammograms in the thin-layer cell at CeO_2/GC are illustrated in Fig. 5, traces a (first filling) and b (second filling). Activation at this electrode is clearly seen by comparing the voltammograms of traces a and b with that of trace c, which is at a bare GC electrode. An increase in the background charging current is also evident by comparing traces d(1) and d(2) of Fig. 5. Although the voltammogram for the second filling (trace b) is broader in shape than for the first filling (trace a), the charges, Q_1 and Q_2 , were identical when corrected for Q_b . Similar results were obtained for AH_2 at ZrO_2/GC and the values of Q_1 and Q_2 were identical over a ten-fold concentration range and coincided with Q_T (assuming $n = 2$). Thus, the conclusion can be drawn that, if any AH_2 was adsorbed, it was electroactive in the potential range of the CV scan. However, it is not possible in the case of AH_2 to delineate whether adsorption occurred because the parent AH_2 cannot be electrochemically regenerated.

In the case of AH_2 at $\alpha\text{-Al}_2\text{O}_3/\text{GC}$, considerable variation occurred from experiment to experiment, and Q_1 was often less than Q_T , which initially was taken to mean that the adsorbed AH_2 was not electroactive. However, it was found that if the cell was vacuum degassed prior to filling with deoxygenated solutions of AH_2 , Q_1 was equal to Q_T . Apparently, AH_2 is catalytically oxidized by oxygen in the presence of the

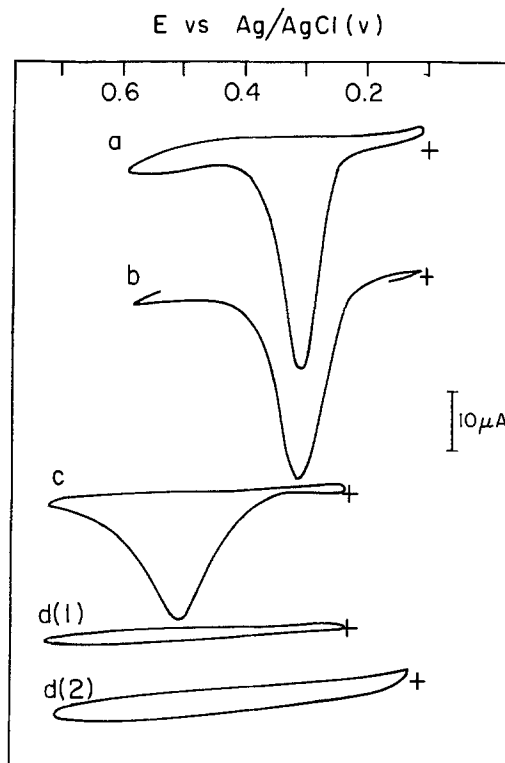


Fig. 5. Current-potential (i - E) curves for the oxidation of 0.75 mM ascorbic acid in phosphate buffer (pH 2.0) at CeO_2/GC for (a) first filling and (b) second filling. Curve (c) is the i - E curve at GC_0 . Curves labeled d(1) and d(2) are background i - E curves at GC_0 and CeO_2/GC , respectively, in phosphate buffer without ascorbic acid. Volume of thin-layer cell was $9.35 \mu\text{l}$, and the scan rate was 2 mV/s .

α -Al₂O₃/GC surface. The rate and stoichiometry of this catalysis has not been quantitated. Further studies on this interesting question of AH₂ adsorption and oxygen catalysis with MOx/GC electrodes will be examined with a newly constructed optical thin-layer cell in which the optical pathlength and the electrode surface area to solution volume are relatively large (16).

Electrode area.—At MOx/GC electrodes, the “double layer” charging current is increased, as is evident from the larger background envelope of the cyclic voltammograms or the background charge during chronocoulometric experiments. This charge is three to four times greater than that at GC₀. Although oxides such as CeO₂, ZrO₂, and α -Al₂O₃ are supposedly insulators, the double-layer charge suggests that there could be a considerable increase in the area of the conductor surface.

The question is whether or not this increase in the area is real. If it is, what is the source? A partial clue to answer this question comes from the observation that the slopes of the i_p vs. $v^{1/2}$ plots for AH₂ oxidation from CV experiments were always slightly larger for the MOx/GC than for the GC₀. Chronoamperometric, chronocoulometric, chronopotentiometric, and rotating disk experiments were conducted to pursue this question of electrode area. If these experiments are conducted under diffusion-controlled conditions, any surface roughness will affect the observed current only at short times; i.e., when the diffusion-layer thickness is comparable to the surface roughness. SEM photomicrographs did not indicate any surface cracks, crevices, or other defects greater in dimension than the maximum 1 μ m particle size (e.g., α -alumina). This meant that the measured geometric area of the electrode should govern the current under diffusional mass-transfer conditions, certainly at times greater than 1s (17, 18). The current functions for these three methods, as normalized to those obtained at GC₀, are tabulated in Table II. In addition to AH₂, data are included for ferricyanide reduction and ferrocyanide oxidation. To check possible differences due to the commercial source of GC and the means by which the electrode is affixed to the cell, Tokai GC-20 and BAS GC electrodes were used. The geometric area of the GC-20 was 0.43

Table II. Normalized current functions of ferricyanide, ferrocyanide, and ascorbic acid at MOx/GC electrode with different methods

Compound (conc)	Normalized current function*		
	CeO ₂ /GC	ZrO ₂ /GC	α -Al ₂ O ₃ /GC
Chronoamperometry: $t\sqrt{i}/(t\sqrt{i})_0$			
Ferricyanide (1 mM)	1.22 ^b (1.11) ^c	1.25 (1.20)	2.27
Ferrocyanide (1 mM)	(1.10)	(1.21)	(1.62)
Ascorbic acid (1 mM, pH 2)	1.15 1.10	1.16 1.04	
(1 mM, pH 8)	1.02 1.14	1.14 1.14	
Chronopotentiometry: $t\sqrt{\tau}/(t\sqrt{\tau})_0$			
Ascorbic acid (10 mM, pH 2)	1.03	1.06	
(10 mM, pH 8)	1.03	1.04	
RDE ^d $(i_1/\omega^{1/2})/(i_1/\omega^{1/2})_0$			
Ascorbic acid (1 mM, pH 2)	[1.13]	[1.16]	
	avg 1.10 $\sigma = 0.06$	1.14 $\sigma = 0.07$	

* Normalized current function at MOx/GC to GC₀ electrode.
^b Data for a BAS GC electrode, geometric area = 0.071 cm².
^c Data enclosed in parentheses for a Tokai glassy carbon (GC-20 grade), geometric area = 0.43 cm².
^d Data enclosed in square brackets for a rotating glassy carbon electrode (Pine Instrument), geometric area 0.49 cm²; rotation rate 100-3600 rpm.

cm² (area defined by the size of the sealing gasket), whereas the BAS electrode had an area of 0.071 cm². Without exception, the normalized current functions for the electroactive species were larger at the MOx/GC than at GC₀. The statistical averages of the normalized current functions, including the RDE results, are 1.10 with a standard deviation of 0.06 at CeO₂/GC, and 1.14 with a standard deviation of 0.07 at ZrO₂. The increase in the current function with MOx/GC electrodes in comparison to GC₀ appears real. Chronoamperometric and chronopotentiometric data were taken over a time period of 1-20s. Any effect of the surface roughness to the *i*-t or *E*-t transients should have been negligible at these times. The situation at the RDE is different, since there is convective-diffusional mass transport. The convective solution flow near the interface of MOx/GC may have been altered with respect to GC₀.

pH studies.—The pH dependence of the E_{pa} and i_{pa} was studied by CV to see the effect of MOx/GC vs. GC₀ to the AH₂ oxidative mechanism. At GC₀, the i_{pa} was independent of pH, whereas at CeO₂/GC, for example, the i_{pa} decreased with increasing pH until ca. pH 6, at which the i_{pa} became independent of pH. i_{pa} and E_{pa} are plotted in Fig. 6 for CeO₂/GC and GC₀. The E_{pa} vs. pH varied with a slope of 52 mV/pH in the acidic region at GC₀ until ca. pH 4, where the E_{pa} became independent of pH. The 52 mV/pH slope is in agreement with a value reported by Sternson (19) at a carbon paste electrode. For CeO₂/GC, the E_{pa} varied with a slope of ca. 42 mV/pH between pH 2 and 5.5 and then continued to decrease in an irregular fashion as pH increased until ca. pH 8. At this pH, the E_{pa} appeared to become independent of pH. The “breaks” in the *E* vs. pH plot in the pH 6-8 region for CeO₂/GC may reflect the pK_a of this surface where the metal oxide is acting as a weak acid. Similar results have been obtained for AH₂ at ZrO₂ at ZrO₂/GC.

The normalized current functions as determined by chronoamperometry, chronocoulometry, and RDE at two different pH values, 2.0 and 8.0, for AH₂ are summarized in Table III. Assuming that these currents are controlled by the mass-transfer rate of AH₂, the difference in the normalized values reflect a difference in the diffusion coefficient(s) of AH₂ at these two pH's. Gerhardt and Adams (20) have reported a *D* value of 0.53₂ (± 0.026) $\times 10^{-5}$ cm²/s at pH 7.4, as determined by the flow injection method. This *D* value is for the ascorbate ion [pK_a is 4.0-4.2 (21-22) for AH₂]. The neutral AH₂ is expected to have a higher *D* value than

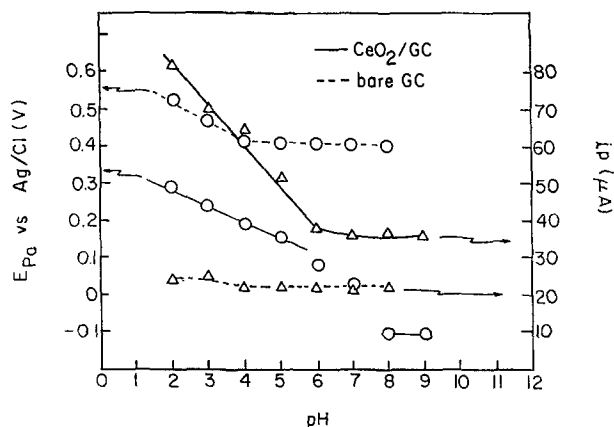


Fig. 6. The anodic peak potentials (circles) and the peak currents (triangles) are plotted for GC₀ (dotted line) and CeO₂/GC (solid line) for 1 mM ascorbic acid oxidation as a function of pH. The peak currents have been background corrected. Buffer was 0.1M phosphate and pH adjusted using 1M NaOH. The data were taken from linear sweep voltammetric *i*-*E* curves. Scan rate was 100 mV/s.

Table III. Current functions of ascorbic acid at MOx/GC and GC₀ taken at pH 2.0 and 8.0

Method (reagent, conc)	Electrode	Current function		
		pH 2	pH 8	ratio (pH 2/pH 8)
Chronoamp. (AH ₂ 1 mM)	bare GC	$i\sqrt{t}$ ($\mu\text{As}^{1/2}$)		
	CeO ₂ /GC	24.1	21.4	1.12
	ZrO ₂ /GC	27.8	21.9	1.27
	CeO ₂ /GC	28.1	24.4	1.15
	ZrO ₂ /GC	26.6	24.3	1.09
Chronopot. (AH ₂ 10 mM)	bare GC	$i\sqrt{\tau}$ ($\mu\text{As}^{1/2}$)		
	CeO ₂ /GC	310.7	299.9	1.04
	CeO ₂ /GC	320.1	309.6	1.03
	ZrO ₂ /GC	326.3	311.0	1.06
RDE (AH ₂ 1 mM)	bare GC	$i\sqrt{\omega}$ ($\mu\text{A}/\text{rpm}^{1/2}$)		
	CeO ₂ /GC	11.3	—	—
	CeO ₂ /GC	12.8	—	—
	ZrO ₂ /GC	13.1	—	—
				avg 1.10 $\sigma = 0.08$

for ascorbate. The average ratio of the normalized current function at pH 2 with respect to pH 8 was 1.10 with a standard deviation of 0.08. Since $(D_{\text{pH}2})^{1/2}/(D_{\text{pH}8})^{1/2}$ is directly proportional to this ratio, a $D_{\text{pH}2}$ value of 0.64×10^{-5} cm²/s is calculated. This $D_{\text{pH}2}$ is an estimated value that needs to be verified by an independent method.

Discussion and Conclusion

Several metal oxides, such as CeO₂, ZrO₂, Co₂O₃, and α -Al₂O₃, dispersed onto a GC surface enhanced the rate of AH₂ oxidation. A tentative model is therefore proposed to explain this enhancement by the MOx particles. In this model, a thin porous layer of carbon and MOx particles, intimately intermixed, adheres to the base GC. The MOx particles protrude from this layer and can be partially covered with carbon. This porous particle mixture with conductive carbon explains why the double layer capacitance increases. The increase in the faradaic current functions, as measured by cyclic voltammetry, chronoamperometry, and chronopotentiometry, can be explained if the assumption is made that there is an additional current component from electroactive material penetrating into the porous layer and MOx particles; the latter depends on the crystallinity and the pore sizes. This model is analogous to a thin polymeric-coated electrode where the polymer is swollen by the solvent, thereby allowing ions and/or electroactive species to penetrate. A major difference of the porous carbon-MOx layer is that electronic conduction via the carbon can occur to the outer periphery of the layer.

In this model, more than one diffusional term controls the mass-transfer, i.e., the usual solution diffusion term, D , and the diffusion inside the porous layer and particle, D_i . Because of the tortuosity of the path inside these latter materials, the magnitude of D_i is much less than that of the solution. Thus, the faradaic current function is enhanced due to the additional current from any electroactive species "adsorbed" in the porous layer and the particles, the time function of this current depending on the value of D_i . The increase in the area, as reflected by the capacitive current, is now rationalized by the presence of this conductive, porous layer.

This proposed model of the MOx/GC surface needs to be further tested by diffusion-kinetic studies at rotating disk electrodes and with ac impedance. Rotating electrodes are ideal probes and have been applied advantageously to similar situations at polymer-coated electrodes (23). However, ac impedance is a powerful method to extract electrical parameters, such as resistive and capacitive terms, and to probe surface

porosity. A long optical-pathlength, thin-layer cell is also under development to help quantitate surface adsorption phenomena (16).

The scope of compound types that can be activated by MOx/GC's is also under study. Preliminary results are consistent with the contention that the involvement of protons in the overall redox process is a prerequisite to the observed-rate enhancement. However, proton involvement alone does not insure activation. For example, the electrochemistry of several aromatic and aliphatic aldehydes were unaffected by α -alumina (24). Thus, the structural features important to activation are currently not understood.

Wightman and co-workers (4) have recently observed an enhanced electrochemical reversibility for ascorbate and ferricyanide at heat-treated (520°-540°C for 2-24h) glassy carbon. Such heat-treatment is undoubtedly removing adsorbed impurities, changing surface topography and functionalities, and increasing the surface area. In this respect, the role of the MOx may be to activate the carbon by creating a fresh carbon surface from the mechanical abrasion process and then maintaining activity by preferentially adsorbing impurities from the solution that would otherwise adsorb on the active sites of the carbon. Quantitating the possible multieffects of dispersed MOx and correlating them to explain the enhancement of charge-transfer rates will be a challenging problem.

Acknowledgments

This work was supported by NSF Grant CHE-8110013 and by the Ohio State University Materials Research Laboratory. We gratefully acknowledge the contributions of J. Zak to the thin-layer experiments, D. Weisshaar to the chronopotentiometric studies, W. H. Kao for assistance with the particle imaging, and M. Porter for helpful discussions. Our appreciations to M. Wightman for an advanced copy of a publication on carbon electrode studies.

Manuscript submitted July 29, 1983; revised manuscript received Nov. 15, 1983.

The Ohio State University assisted in meeting the publication costs of this article.

REFERENCES

- J. Zak and T. Kuwana, *J. Am. Chem. Soc.*, **104**, 5514 (1982).
- J. Zak and T. Kuwana, *J. Electroanal. Chem.*, **150**, 645 (1983).
- J. F. Evans, T. Kuwana, M. H. Henne, and G. P. Royer, *ibid.*, **80**, 409 (1977).
- R. M. Wightman, Personal communication (1983).
- D. C-S. Tse and T. Kuwana, *Anal. Chem.*, **50**, 1315 (1978).
- K. J. Stutts and R. M. Wightman, *Anal. Chem.*, **55**, 1576 (1983).
- M. F. Dautartas and J. F. Evans, *J. Electroanal. Chem.*, **109**, 301 (1980).
- J. Facci and R. W. Murray, *Anal. Chem.*, **54**, 772 (1982).
- H-Y. Cheng, E. Strobe, and R. N. Adams, *ibid.*, **51**, 2243 (1979).
- K. Takamura and M. Sakamoto, *Chem. Pharm. Bull. (Tokyo)*, **27**, 254 (1979).
- K. Takamura and M. Sakamoto, *J. Electroanal. Chem.*, **113**, 273 (1980).
- E. E. Kriss, *Russ. J. Inorg. Chem.*, **23**, 1004 (1978).
- N. P. Evtushenko, K. B. Yatsimirskii, E. E. Kriss, and G. T. Kurbatova, *Zh. Neorg. Khim.*, **22**, 1543 (1977).
- M. P. Soriaga and A. T. Hubbard, *J. Am. Chem. Soc.*, **104**, 2735 (1982); *ibid.*, **104**, 3937 (1982); *ibid.*, **104**, 2742 (1982).
- M. P. Soriaga, P. H. Wilson, and A. T. Hubbard, *J. Electroanal. Chem.*, **142**, 317 (1982).
- J. Zak, M. Porter, and T. Kuwana, *Anal. Chem.*, To be published.
- D. E. Weisshaar and D. E. Tallman, *ibid.*, **55**, 1146 (1983).
- The diffusion layer problem is similar to what is

- encountered at a minigrad electrode; see M. Petek, T. E. Neal, and R. W. Murray, *Anal. Chem.*, **43**, 1069 (1971).
19. M. S. Sternson, M.S. Thesis, University of Kansas, Lawrence, KS (1971).
20. G. Gerhardt and R. N. Adams, *Anal. Chem.*, **54**, 2618 (1982).
21. A. E. Martell and R. M. Smith, "Critical Stability

- Constants," Vol. 3, p. 264, Plenum Press, New York (1979).
22. "The Merck Index," P. G. Stecher, Editor, 8th ed., p. 105 (1968).
23. W. J. Albery and A. R. Hillan, in "Annual Reports C," pp. 424-427, The Royal Society of Chemistry, London (1981).
24. S. Weng and T. Kuwana, Unpublished results.

Stability of Undoped and Oxidized Polyacetylene

R. Huq* and G. C. Farrington*

Department of Materials Science and Engineering, University of Pennsylvania, Philadelphia, Pennsylvania 19104

ABSTRACT

The stability of polyacetylene has been examined by thermogravimetric analysis and measuring the change in its electronic conductivity upon heating in various atmospheres. Samples included unreacted polyacetylene as well as films that had been oxidized chemically, with bromine and iodine, and electrochemically, with AsF_6^- as the anion. Fresh polyacetylene and samples which have been oxidized to the conducting state react rapidly with oxygen in a gaseous atmosphere, especially in the presence of moisture. At room temperature, the reaction with oxygen is largely irreversible, and presumably interrupts the conjugated double bond network of the polymer. The resulting material is not readily oxidized or reduced to an electronically conducting state.

Polyacetylene (Fig. 1) is a simple conjugated organic polymer with quite unusual electrical and electrochemical properties. Films of polycrystalline polyacetylene, which has the general formula, $(\text{CH})_x$, can be easily synthesized by the catalytic polymerization of acetylene. Typical films are composed of fibers of polyacetylene and have extremely high surface areas, generally 40-60 m^2/g .

The extraordinary properties of polyacetylene are observed when it is oxidized or reduced. When polycrystalline polyacetylene films are exposed to various oxidants, such as iodine or bromine, it reacts to form compounds of the type, $(\text{CHX}_y)_x$ (typically, $y < 0.10$). Upon exposure to reducing agents, such as n-butyl lithium, compounds of the type $(\text{Li}_y\text{CH})_x$ result (typically, $y < 0.3$) (1-7). From the viewpoint of electrochemistry, the most intriguing aspect of polyacetylene chemistry is that these reactions can be carried out electrochemically in nonaqueous electrolytes containing appropriate dissolved anions and cations.

If the conditions are gentle, these chemical or electrochemical oxidation/reduction reactions do not attack the conjugated polymer chains, and the reactions are reversible. However, if the reaction conditions are more severe, irreversible attack and interruption of the conjugated polymer network takes place. The reversible reactions are functionally similar to the oxidation reactions of transition metal dichalcogenides, such as TiS_2 . As a result, the oxidized and reduced polyacetylenes have been suggested for use as electrodes in nonaqueous batteries (8).

Extensive studies of the electrical properties of the polyacetylenes have been reported (9-17). However, relatively little work describing the stability of these materials has appeared. Notable exceptions are the contributions of Rolland *et al.* (18) and Yen *et al.* (19). The goals of our research have been to examine those aspects of the stability of fresh and reacted polyacetylene which influence its potential electrochemical applications. We have carried out a systematic study of the stability of fresh and oxidized polyacetylene by monitoring the change in electronic resistivity of samples in contact with argon, oxygen, and air from 20° to 100°C. Thermogravimetric analysis (TGA) and differential scanning calorimetry (DSC) measurements were also carried out.

Experimental Details

The polyacetylene used in this work was supplied by Professor A. MacDiarmid and co-workers in the Department of Chemistry of the University of Pennsylvania. The films were typically about 0.01 cm thick and highly fibrous, with a density of ca. 0.4 g/cm^3 . The films were not subjected to further chemical analysis.

Conductivity was measured in a specially designed glass cell with electrical feed throughs so that experiments could be carried out in various atmospheres. Samples were sandwiched between two Pt mesh electrodes. The electrodes were connected to a computer-controlled Solarton 1170 complex impedance analyzer which was used to measure conductivity. The tempera-

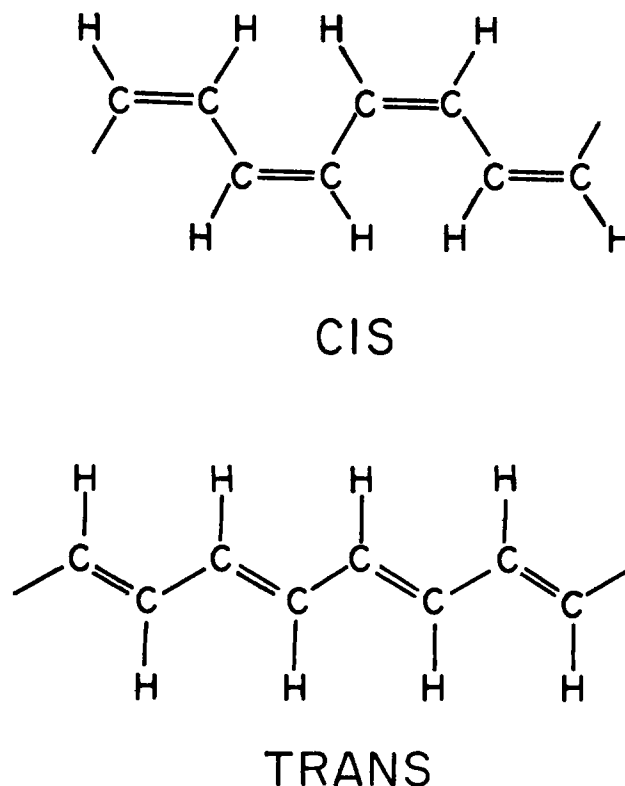


Fig. 1. Cis and trans polyacetylene

* Electrochemical Society Active Member.

ture of the cell was determined and regulated by a thermocouple located about 5 mm from the sample.

All samples were handled and stored under argon or in vacuum. Cell loading was carried out in an argon-atmosphere dry box (Vacuum Atmospheres).

Oxidized samples were prepared either in the conductivity cell, by exposing fresh polyacetylene to small partial pressures of iodine or bromine, or electrochemically. For the *in situ* reactions, a bulb containing the halogen was attached to the cell, and its temperature adjusted to maintain a known vapor pressure of halogen. The onset of oxidation was signalled by a dramatic increase in the electronic conductivity of the sample. Electrochemical oxidation was carried out in a separate electrochemical cell in a propylene carbonate electrolyte containing 1.0M LiAsF₆. The propylene carbonate used to prepare the electrolyte was obtained from Burdick and Jackson; the electrolyte salt from U.S. Steel, Agri-Chemical Division (electrochemical grade). Before use, the electrolyte was percolated through a column of neutral activated alumina (Fisher-Brockman, activity 1). The electrolyte was then pre-electrolyzed between two lithium electrodes. The film was oxidized at a controlled potential of 3.8V vs. Li/Li⁺. The level of oxidation [value of γ in (CHX _{γ})_x] was in the range of 0.02-0.03.

TGA measurements were carried out with a du Pont 951 Thermogravimetric Analyzer and 910 Differential Scanning Calorimeter. Samples weighing 1-2 mg were heated at 5°C/min over the temperature range of 22°-200°C in nitrogen.

Results

Stability of fresh polyacetylene.—The resistivity of samples of unoxidized polyacetylene was about 10¹⁰ Ω-cm, which indicated that the material was quite pure and mainly in the *cis* form (20). The effects of exposing films to argon (99.999%), oxygen (99.996%), and moist air, in that order, for short times (3-5h) are shown in Fig. 2. Between gases, the samples were exposed to a vacuum of about 10⁻⁵ torr for 24h. The vacuum partially reversed the conductivity changes that were observed.

Figure 3 shows the influence of temperature upon the resistivity of films exposed to argon and oxygen. During heating in argon from 25° to 100°C, the conductivity of the material increased with an average activation energy of 0.49 eV (11 kcal/mol) (Fig. 4). Our results agree well with those of Rolland and co-workers (21), who have reported a value of 0.50 eV for fresh, *cis* polyacetylene and 0.30 eV for the *trans* form.

In oxygen, the resistivity initially decreased and then increased dramatically around 65°C, as the material became brittle and was transformed from golden-gray to yellowish-brown. The initial decrease

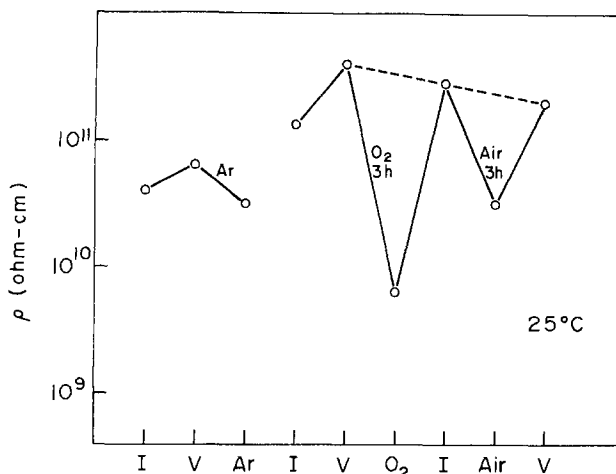


Fig. 2. Room temperature resistivity when (CH)_x film is exposed to Ar, O₂, and air with vacuum after each exposure.

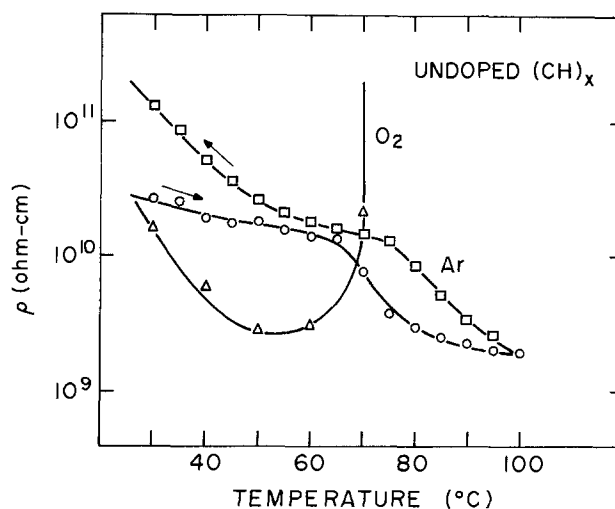


Fig. 3. Influence of temperature on the resistivity of (CH)_x in Ar and O₂.

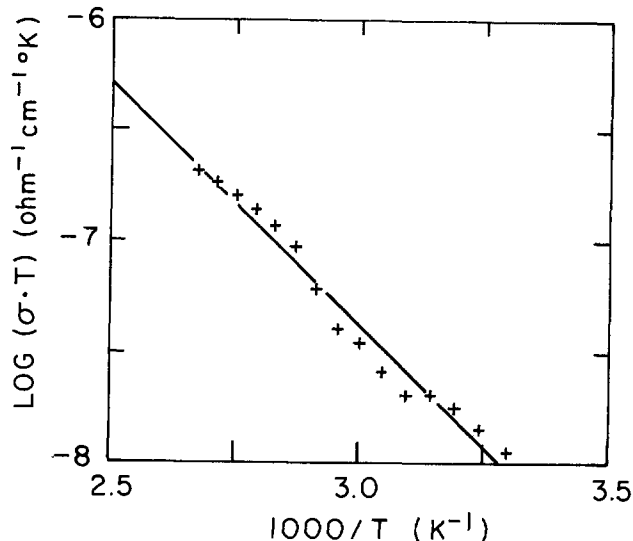


Fig. 4. Arrhenius plot for resistivity of (CH)_x in Ar

in resistivity was small in comparison to the dramatic decrease in resistivity, from 10¹⁰ (Ω-cm) to 10² (Ω-cm), which takes place when a fresh film is exposed to 0.5 torr iodine. We saw no evidence that the overall oxidation reaction was reversible. We found that the oxidation proceeded more rapidly in moist air, and could be observed even at room temperature. Yen *et al.* (19) and Pochan (22) have reported similar results.

These results indicate that, at moderate temperatures, polyacetylene films react readily with oxygen, and more rapidly in the presence of moisture. At lower temperatures the reaction may initially be reversible, but at higher temperatures or longer times it is largely irreversible. The process ultimately destroys the usefulness of polyacetylene as an electrochemical electrode. However, we must note that, under the conditions used in these experiments, oxygen served both as the oxidizing agent and the dopant. Our results do not indicate whether polyacetylene films are stable when exposed to oxygen in an electrolyte which contains another anion which may act as an alternate dopant.

Stability of oxidized films.—The temperature dependence of the resistivity of polyacetylene films which have been oxidized to the conducting state either chemically, by bromine and iodine, or electrochemically, with AsF₆⁻ as the anion, was studied from 25°-100°C (Fig. 5, 6, 7) in argon. The resistivities of films oxidized with bromine or iodine increase at relatively low temperatures. For example, the resistivity of a

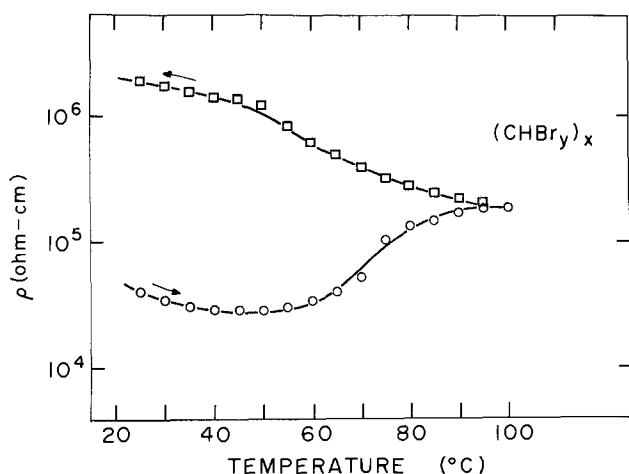


Fig. 5. Influence of temperature on the resistivity of $(\text{CHBr}_y)_x$ in Ar.

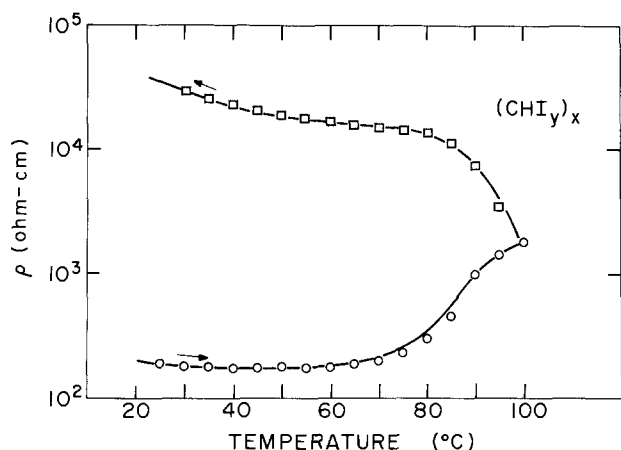


Fig. 6. Influence of temperature on the resistivity of $(\text{CHI}_y)_x$ in Ar.

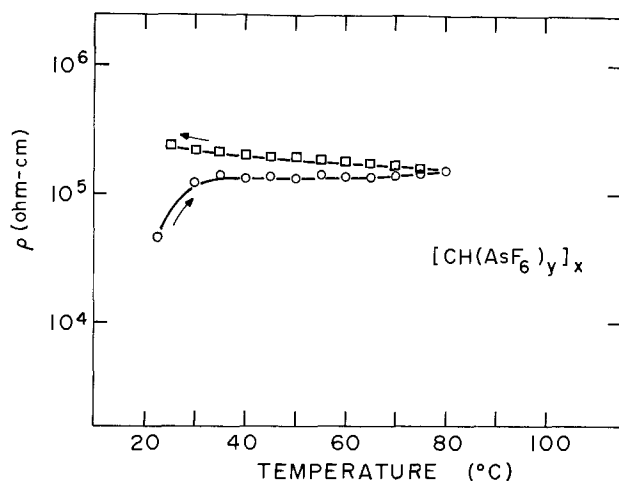


Fig. 7. Influence of temperature on the resistivity of $[\text{CH}(\text{AsF}_6)_y]_x$ in Ar.

film of composition approximately $(\text{CHI}_{0.01})_x$ was reasonably stable from 25° to 55°C. Above 60°C, it slowly rose many orders of magnitude. Figure 8 dramatically illustrates the progressive increase in resistivity observed for an iodine-oxidized film at various temperatures.

In samples oxidized with bromine, the resistivity increase commenced at lower temperatures, around 45°C. Films which had been electrochemically oxidized with AsF_6^- as the anion were stable to considerably higher temperatures, somewhat above 65°C. Rolland

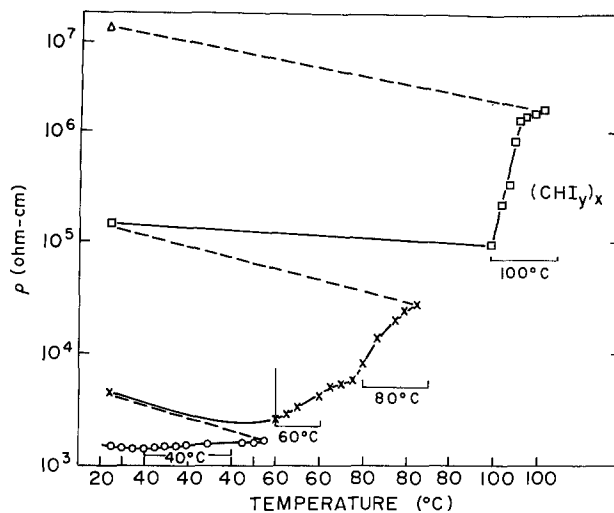


Fig. 8. Influence of heating and cooling cycles on the resistivity of $(\text{CHI}_y)_x$ in Ar.

et al. (18) have found that films oxidized with SbF_5 are stable to about 80°C, whereas films reacted with $\text{CF}_3\text{SO}_3\text{H}$ begin to degrade slightly above 25°C.

It could be argued that the increases in resistivity observed as the temperature was increased were simply the result of the reversible loss of halogen from the films or the homogenization of the oxidant within the bulk fibrils. To test these ideas, we oxidized a sample of polyacetylene in 0.5 torr iodine vapor at 25°C. Its initial resistivity was $2.8 \times 10^2 \Omega\text{-cm}$. After heating to 100°C and cooling to room temperature over 15h in an argon atmosphere (Fig. 6), its resistivity increased to $5.5 \times 10^4 \Omega\text{-cm}$. When the sample was re-exposed to 0.5 torr iodine at room temperature, its resistivity decreased, but only to $1.7 \times 10^3 \Omega\text{-cm}$, a level about eight times its initial value before heating. Subsequent cycles of heating, cooling, and re-exposure to iodine produced a progressive increase in the room temperature resistivity of the sample (Fig. 8). These experiments do not eliminate the possibility that homogenization or halogen loss contribute to the resistivity increases observed. However, our observations indicate that irreversible reaction contributes significantly to the resistivity changes.

In contrast, a sample which had been electrochemically oxidized with AsF_6^- as the guest anion was much more stable (Fig. 7) during heating. With the dopants we investigated, the stability of reversibly oxidized polyacetylene was least with Br^- and greatest with AsF_6^- . Corresponding anion effects were seen in the TGA and DSC results discussed below.

Thermal analysis measurements.—TGA and DSC measurements which complement the conductivity studies were also carried out. Figures 9 and 10 show the resistivity, TGA, and DSC behavior of films oxidized with iodine and bromine, respectively. These experiments were carried out in a nitrogen atmosphere. Ito *et al.* (23) have previously reported that unoxidized polyacetylene does not thermally decompose in nitrogen until above 300°C. They found that unoxidized polyacetylene, whether *cis* or *trans* at the beginning, turned brown without losing weight when heated in vacuum at about 325°C for 5 min. Weight loss was observed to begin around 420°C. They suggested that phenyl groups are first formed at the lower temperature, which then decompose to yield a weight loss at the higher temperature.

With films oxidized with bromine or iodine, we found that weight loss began around 90°C (bromine) and 120°C (iodine). At 160°C, the total weight loss reached 21% for the material oxidized with bromine and 15% for that oxidized with iodine.

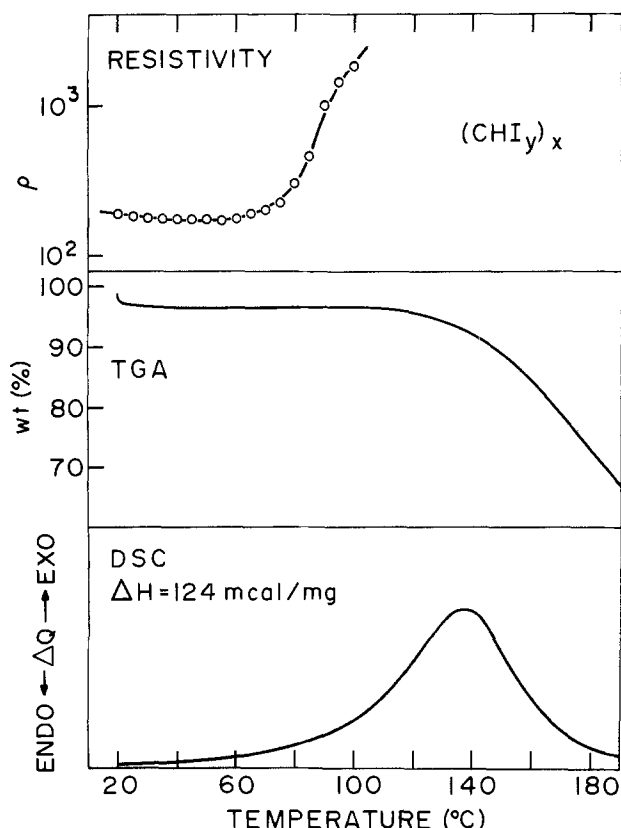


Fig. 9. Resistivity, TGA, and DSC (5°C/min) results for $(\text{CHI}_y)_x$.

DSC analysis over the range of 25°–180°C revealed only one exothermic peak for either the bromine- or iodine-oxidized samples. The peak position varied from 80°C (bromine) to 140°C (iodine) (Fig. 9 and 10). The heat of reaction observed for the decomposition of the iodine-oxidized material was 124 mcal/mg. Pron (24) has also observed the removal of iodine from polyacetylene above 100°C and has concluded that the process is irreversible and occurs by the evolution of HI and a small amount of I_2 .

The TGA and DSC results are completely consistent with the resistivity measurements. However, in all cases we have found that changes in resistivity are the most sensitive and early indications of changes in the sample chemistry.

Conclusions

Oxygen reacts readily with fresh polyacetylene, apparently faster in the presence of moisture. Although the initial stages of oxidation may be reversible, the process is eventually irreversible and presumably involves the interruption of the conjugated double-bond network essential for electronic conductivity in the material. We must point out that, under our experimental conditions, oxygen was both the oxidant and the source of the doping ion. Our results do not demonstrate that oxygen would irreversibly react with polyacetylene if another dopant ion, such as I^- in a solvent, were in contact with the material during exposure to oxygen. In fact, MacDiarmid *et al.* (25) have reported that polyacetylene is stable in an aqueous electrolyte containing either HBF_4 or HF in contact with bubbling oxygen gas. The difference between these conditions and ours is that, in the aqueous electrolyte, oxygen serves only as a source of energy to oxidize the polymer. Further attack of the polymer chain is apparently prevented by the introduction of BF_4^- or F^- , which are stable doping ions.

Polyacetylene films which have been oxidized to the conducting state with bromine or iodine decompose between 45° and 55°C. Films which contain AsF_6^- as

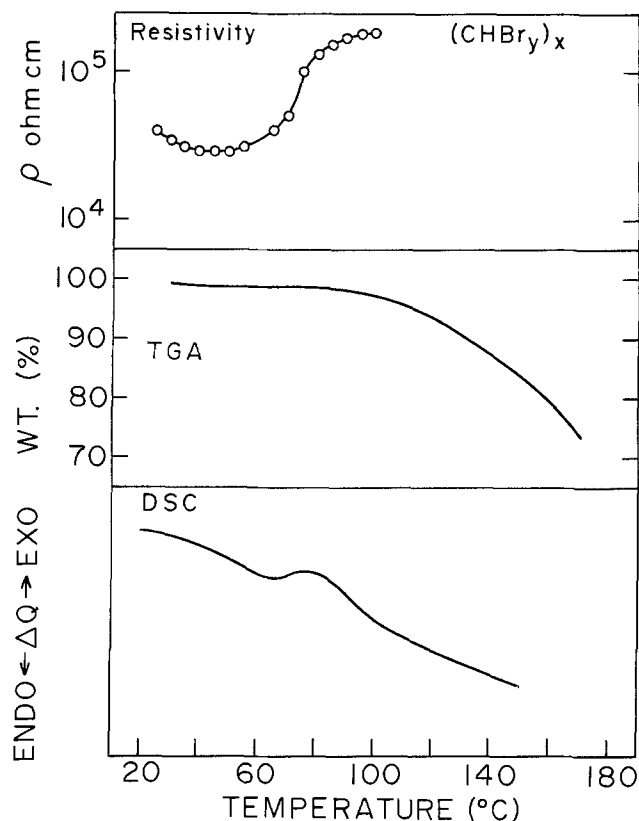


Fig. 10. Resistivity, TGA, and DSC (5°C/min) results for $(\text{CHBr}_y)_x$.

the dopant ion are more stable. The decomposition decreases the electronic conductivity of polyacetylene and ultimately destroys its usefulness as an electrode.

Our results underscore the point that polyacetylene films must be handled in extremely dry and oxygen-free atmospheres, at least when they are not in contact with an electrolyte containing stable dopant anions. Polyacetylene is not a material that forgives casual handling. It is unreasonable to expect reproducible electrochemical results using samples of polyacetylene whose origins are uncertain.

Acknowledgment

This research was supported by the United States Department of Energy.

Manuscript submitted Jan. 17, 1983; revised manuscript received Nov. 21, 1983.

The University of Pennsylvania assisted in meeting the publication costs of this article.

REFERENCES

1. B. R. Weinberger, J. Kauger, A. J. Heeger, A. Pron, and A. G. MacDiarmid, *Phys. Rev. B*, **20**, 223 (1979).
2. N. Suzuki, M. Ozaki, E. Etemad, A. J. Heeger, and A. G. MacDiarmid, *Phys. Rev. Lett.*, **45**, 1209 (1980).
3. K. Seeger and W. D. Gill, *Colloid Polym. Sci.*, **258**, 252 (1980).
4. T. C. Chung, A. Feldblum, A. J. Heeger, and A. G. MacDiarmid, *J. Chem. Phys.*, **74**, 5504 (1981).
5. K. Guekelsberger, P. Rodhammer, E. Gmelin, M. Peo, K. Menke, J. Hocker, S. Roth, and K. Dransfeld, *Z. Phys. B*, **43**, 189 (1981).
6. I. Harada, M. Tasumi, H. Shirakawa, and S. Ikeda, *Chem. Lett.*, 1411 (1978).
7. M. Nechstein, F. Devreun, R. L. Greene, T. C. Clarke, and G. B. Street, *Phys. Rev. Lett.*, **44**, 356 (1980).
8. A. J. Heeger and A. G. MacDiarmid, in "The Physics and Chemistry of Low Dimensional Solids," L. Alcacer, Editor, pp. 353-397, P. Reidel (1980).
9. G. E. Wnek, J. C. W. Chien, F. E. Karasz, M. A.

- Druy, Y. W. Park, A. G. MacDiarmid, and A. J. Heeger, *J. Polym. Sci., Polym. Lett. Ed.*, **17**, 779 (1979).
10. C. K. Chiang, A. J. Heeger, and A. G. MacDiarmid, *Ber. Bunsenges. Phys. Chem.*, **83**, 407 (1979).
 11. R. H. Baughman, S. L. Hsu, G. P. Pez, and A. J. Signorelli, *J. Chem. Phys.*, **68**, 5405 (1978).
 12. D. J. Berets and D. S. Smith, *Trans. Faraday Soc.*, **64**, 823 (1968).
 13. C. K. Chiang, Y. W. Park, A. J. Heeger, H. Shirakawa, E. J. Louis, and A. G. MacDiarmid, *J. Chem. Phys.*, **69**, 5098 (1978).
 14. M. Rolland, P. Bernier, M. Aldissi, C. Linaya, J. Sledz, F. Schue, J. M. Fabre, and L. Giral, *J. Phys. Lett.*, **41**, L165 (1980).
 15. K. Mortensen, M. L. W. Thewalt, Y. Tomkiewica, T. C. Clarke, and G. B. Street, *Phys. Rev. Lett.*, **45**, 1490 (1980).
 16. A. J. Epstein, H. W. Gibson, P. M. Chaikin, W. G. Clark, and G. Gruner, *Phys. Rev. Lett.*, **45**, 1730 (1980).
 17. W. Deits, P. Cukor, M. Rubner, and H. Jopson, *J. Electron. Mater.*, **10**, 683 (1981).
 18. M. Rolland, S. Lefrant, M. Aldissi, P. Bernier, E. Rzepka, and F. Schue, *J. Electron. Mater.*, **10**, 619 (1981).
 19. S. P. S. Yen, R. Somoano, S. K. Khanna, and A. Rembaum, *Solid State Commun.*, **36**, 339 (1980).
 20. H. Shirakawa, T. Ito, and S. Ikeda, *Macromol. Chem.*, **179**, 1565 (1978).
 21. M. Rolland, P. Bernier, and M. Aldissi, *Phys. Status Solidi A*, **62**, K5 (1980).
 22. J. M. Pochan, D. F. Pochan, H. Rommelmann, and H. W. Gibson, *Macromolecules*, **14**, 110 (1981).
 23. T. Ito, H. Shirakawa, and S. Ikeda, *J. Polym. Sci., Polym. Chem. Ed.*, **13**, 1943 (1975).
 24. A. Pron, Ph.D. Thesis, University of Pennsylvania, Philadelphia, PA (1980).
 25. A. G. MacDiarmid, R. J. Mammone, S. J. Porter, and N. L. D. Somasiri, Abstract 92, p. 145, The Electrochemical Society Extended Abstracts, Vol. 83-2, Washington, DC, Oct. 9-14, 1983.

Effects of Phosphoric Acid Concentration on Oxygen Reduction Kinetics at Platinum

K-L. Hsueh,* E. R. Gonzalez,** and S. Srinivasan**¹

Los Alamos National Laboratory, Los Alamos, New Mexico 87545

D-T. Chin**

Department of Chemical Engineering, Clarkson College of Technology, Potsdam, New York 13676

ABSTRACT

The oxygen reduction reaction was investigated at platinum electrodes in phosphoric acid in the concentration range 0.7M (6.6%) to 17.5M (95%) at 25°C using the rotating ring-disk electrode technique. As a complement, cyclic voltammograms on platinum and potentials of zero charge of mercury were obtained as a function of phosphoric acid concentration. The mechanism of the oxygen electrode reaction is discussed in terms of the direct four-electron transfer reduction to water and the formation of hydrogen peroxide as an intermediate in a parallel two-electron transfer reaction. The rate constants of the intermediate reaction steps were calculated from the ring-disk data for various potentials and electrolyte concentrations. The characteristics of the reaction were found to be markedly dependent on the concentration of phosphoric acid. These results are interpreted in terms of changes in oxygen solubility, proton activity, and double layer characteristics when passing over from a water to a phosphoric acid solvent structure.

Concentrated phosphoric acid is presently used as the electrolyte in advanced fuel cells. The factor limiting the efficiency of this fuel cell system is the overpotential for oxygen reduction reaction in the concentrated acid medium. In fact, this reaction is approximately two orders of magnitude slower in concentrated H₃PO₄ than in aqueous solutions of strong acids, such as trifluoromethanesulfonic acid (1, 2).

Previous studies on the reduction of oxygen on platinum in concentrated H₃PO₄ focused on examining the Tafel behavior over a wide temperature range (3-5). The conclusions can be summarized as follows. (i) Three Tafel regions can be observed. Above 0.8V (vs. RHE), a 60 mV Tafel slope is obtained. This slope changes to 120 mV in the region of potentials between 0.8 and 0.6V. Below 0.5V, very high Tafel slopes (over 200 mV) are observed. The mechanism of the reaction in the third region is not completely understood. (ii) Tafel slopes in the intermediate range (120 mV) are independent of temperature, contrary to predictions from electrode kinetic theory. Appleby (5) suggested that this phenomenon could be associated with a change in the double layer structure with tem-

perature. But the question is far from settled. Yeager *et al.* (6) suggested that this phenomenon is due to a compensating effect of the entropic and enthalpic terms in the rate expression. (iii) Rotating ring-disk investigations (7, 8) have shown that the reduction of oxygen in concentrated phosphoric acid follows two parallel paths: a direct four-electron reduction to water and a couple of two-electron transfer reduction reactions to water with hydrogen peroxide as the intermediate. (iv) The rate of the reaction is first order with respect to the oxygen partial pressure (4). (v) The reaction order with respect to proton activity is 3/2 in the low current density region (60 mV Tafel slope) and 1 in the high current density region (120 mV Tafel slope).

The structure and properties of concentrated H₃PO₄ are not well understood, but these certainly are expected to play a role in the slow reduction of oxygen at platinum. Recently, the authors examined the structure of the mercury/concentrated H₃PO₄ interface (9) and concluded that the double layer in concentrated H₃PO₄ is thicker than in aqueous media. Thus, it seems reasonable to assume that a transition with respect to both the interfacial and bulk properties will occur when passing over from a water to a phosphoric acid solvent structure. For this reason, the present study was undertaken to elucidate the effect of the struc-

* Electrochemical Society Student Member.

** Electrochemical Society Active Member.

¹ Leave of absence from LANL; at Institute for Hydrogen Systems, Mississauga, Ontario L5N 1P1, Canada.

Key words: gas, electrode, metals, electrolyte.

ture of H_3PO_4 solutions, ranging in concentration from 7 to 95%, on the kinetics of oxygen reduction at platinum electrodes.

Experimental

The equipment, preparation of the electrode, and the experimental procedure for the rotating ring-disk experiment have already been described (10). The same setup was used for the cyclic voltammetric experiments. Phosphoric acid (85%, electronic grade, J. T. Baker) was treated with 10% hydrogen peroxide (90%, stabilizer free, FMC) and heated to 50°–70°C for 1h. The solution was concentrated to 85% by evaporation at 160°C in Teflon vessels. This solution was diluted with double-distilled water that was previously treated with alkaline permanganate. Further evaporation of the 85% stock solution was done to obtain the 95% concentration. Before use, solutions were pre-electrolyzed for 24h with platinum electrodes to eliminate electroactive impurities.

All potentials were measured against a dynamic hydrogen electrode (DHE). The values were converted to a reversible hydrogen electrode (RHE) scale by measuring, for each solution, the potential difference between the DHE and a floating-type fuel cell hydrogen electrode.

Results and Discussion

Cyclic voltammetry.—Figure 1 shows the cyclic voltammograms on Pt, obtained as a function of H_3PO_4 concentration. No difference was observed for a stationary or a rotating electrode, which is indicative of the absence of impurities in the electrolyte. According to this figure, it is apparent that for concentrations of H_3PO_4 up to about 4M there is no effect on the characteristics of the voltammogram. On the other hand, for higher concentrations, it is observed that the potential of oxide formation commencement progressively shifts to more positive values. Also, the total charges for oxide formation and reduction decrease for these increasing acid concentrations. These findings can be associated with a strong adsorption of phosphate species on the electrode that interferes with the oxide formation. However, the effect may be partly due to a decrease in the activity of water as the concentration of H_3PO_4 increases (11).

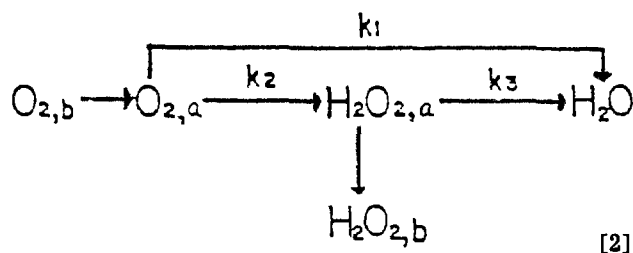
Mass-transfer-corrected Tafel behavior.—The mass-transfer-corrected Tafel behavior for oxygen reduction on platinum for different H_3PO_4 concentrations is shown in Fig. 2. The plots correspond to the equation

$$E = \frac{2.3RT}{\alpha_c F} \log i_0 - \frac{2.3RT}{\alpha_c F} \log \frac{i_{d1} i_d}{i_{d1} - i_d} \quad [1]$$

where α_c is the transfer coefficient, i_0 the exchange current density, i_d the disk current density, and i_{d1} the limiting disk current density. The Tafel plots presented in Fig. 2 are independent of rotation speed. In the region from 0.6 to 0.8V, Tafel slopes are about 120 mV. This result is similar to that obtained by others (3-7, 11) in acid media. Thus, it seems reasonable to conclude that the overall reduction of oxygen is controlled by the first charge transfer step under Langmuir adsorption conditions. Below 0.5V, higher Tafel slopes (> 200 mV/decade) are observed and the current seems to reach a limiting value. Because these limiting currents are not due to mass transfer, a change in the reaction mechanism must be taking place. This change probably involves a chemical rate-determining step, which may be the dissociative adsorption of the oxygen molecule. This point was not investigated further because the potential region lies outside the range of interest for fuel cells.

Mechanistic aspects of electroreduction of oxygen.—Recently, theoretical aspects of the reduction of oxygen on rotating ring-disk platinum electrodes have been considered (10). In this work, it was concluded

that the mechanism proposed by Damjanovic *et al.* (12) is the most appropriate. The reaction scheme is as follows



where a indicates an adsorbed state and b is the bulk of the solution. Two equations for calculating the reaction rate constants k_1 , k_2 , and k_3 are (10)

$$\frac{I_{d1}}{I_{d1} - I_d} = 1 + \frac{k_1 + k_2}{0.62 D_{\text{O}_2}^{2/3} \nu^{-1/6}} \omega^{-1/2} \quad [3]$$

$$\frac{I_d}{I_r} = \frac{1}{N} \left(1 + 2 \frac{k_1}{k_2} + \frac{2(k_1/k_2 + 1)k_3}{0.62 N D_{\text{H}_2\text{O}_2}^{2/3} \nu^{-1/6}} \right) \omega^{-1/2} \quad [4]$$

where I_d and I_r are the disk and ring currents, respectively; I_{d1} is the limiting current on the disk electrode; N is the collection efficiency; ω is the rotational speed; ν is the kinematic viscosity of the electrolyte; and D_{O_2} and $D_{\text{H}_2\text{O}_2}$ are the diffusion coefficients of oxygen and hydrogen peroxide, respectively. Accordingly, plots of $I_{d1}/(I_{d1} - I_d)$ vs. $\omega^{-1/2}$ and I_d/I_r vs. $\omega^{-1/2}$ should yield two straight lines, and the rate constants can be calculated from the intercepts and the slopes of these straight lines. In this way, the values of k_1 , k_2 , and k_3 , as functions of electrode potential for oxygen reduction on Pt, were evaluated from the ring-disk data for various phosphoric acid concentrations (Fig. 3-6).

In all cases, it was found that the ratio k_1/k_2 is greater than 10, which means that most of the oxygen reduces to water directly through the four-electron transfer reaction. Because $k_1 \gg k_2$, the relationship between i and k_1 can be written approximately as

$$i \cong 4FA k_1 c_{\text{O}_2} = 4FA k_1' c_{\text{O}_2} a_{\text{H}^+} \exp \left(- \frac{\alpha_c F}{RT} E \right) \quad [5]$$

Therefore, k_1 should have the same dependence on phosphoric acid concentration as i/c_{O_2} at any potential. This can be seen in Fig. 7 where k_1 , i , and i/c_{O_2} for a potential of 0.7V are plotted as a function of H_3PO_4 concentration. Clearly, k_1 and i/c_{O_2} have the same concentration dependence.

From Fig. 3, 4, and 5, it is apparent that for H_3PO_4 concentrations up to 8M, k_2 has the same potential dependence as k_1 . This means that the rate-determining step is probably the same for both reactions. At higher concentrations, k_2 is surprisingly independent of potential, which means that the rate of the reaction is chemically controlled (chemical step prior to electron transfer step). In this case, the rate of the reaction may be determined by the adsorption of the O_2 molecule, which must be oriented preferentially at the interface in order to lead to H_2O_2 formation. This can be inhibited by a predominance of phosphate species at the interface, which is supported by the fact that the constant value of k_2 shows a marked decrease with the increase in H_3PO_4 concentration.

The behavior of k_3 is similar to that of k_2 (cf. Fig. 5 and 6); k_3 increases with the overpotential in the low overpotential regime and is more or less independent of potential when E becomes more negative than 0.5V vs. RHE. Increased phosphoric acid concentration results in decreased k_3 . It can be shown that the significant decrease in k_2 and k_3 with increasing H_3PO_4 concentration leads to an increase in the faradaic efficiency for the reduction of oxygen to water. This is

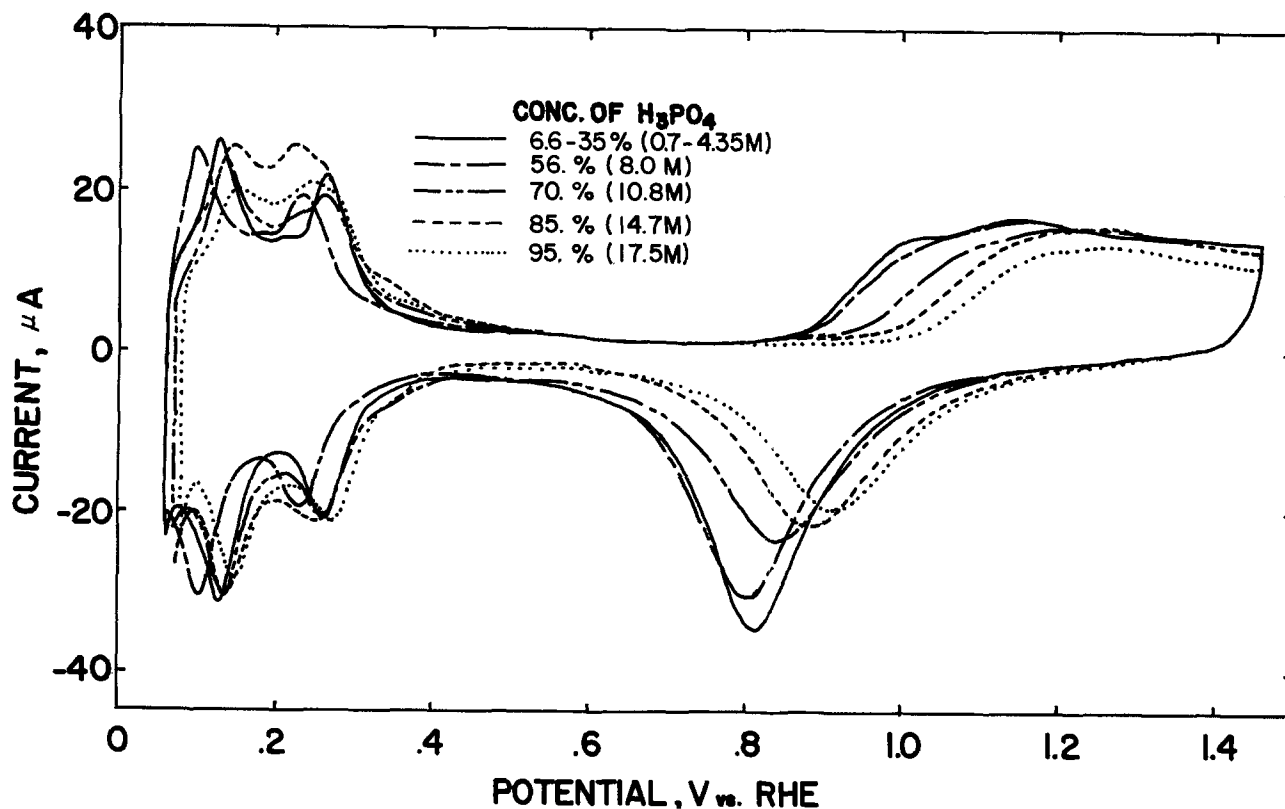


Fig. 1. Cyclic voltammograms on Pt at a scan rate of 50 mV/s in H_3PO_4 over the concentration range 6.6-95 w/o (weight percent) at 25°C.

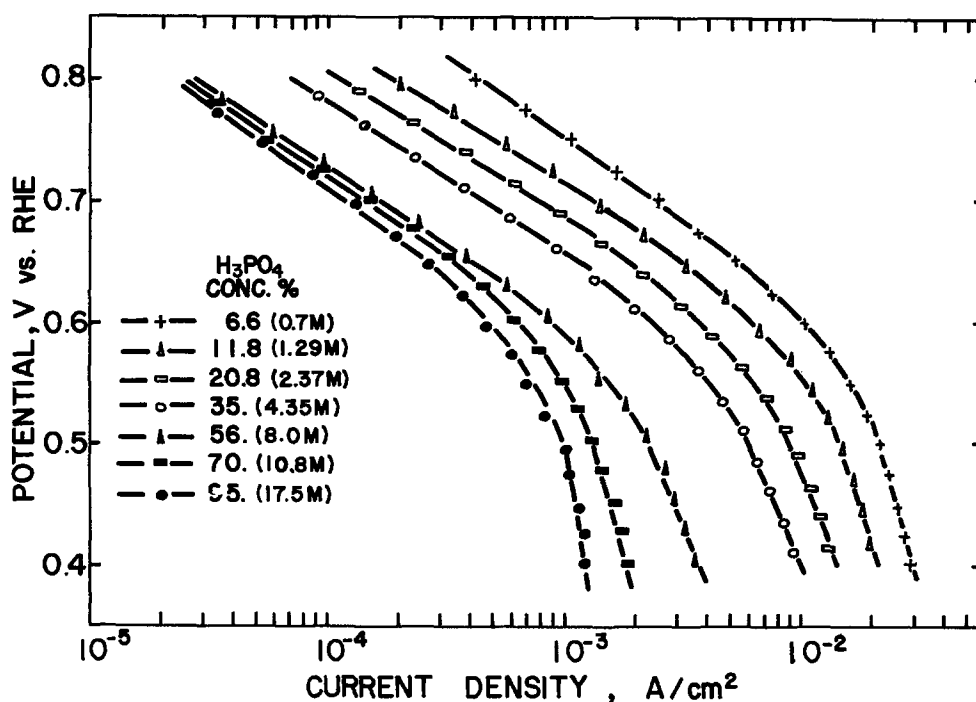


Fig. 2. Mass-transfer-corrected Tafel behavior for oxygen reduction on Pt in H_3PO_4 over the concentration range 6.6-95 w/o at 25°C. Tafel behavior is independent of electrode rotating speed in the 400-3600 rpm region.

important because it means that at the high concentrations used in fuel cells the amount of formation of H_2O_2 is negligible and the faradaic efficiency is close to unity.

Effect of anion adsorption on the rate of oxygen reduction.—The decrease in the oxygen reduction rate with increasing H_3PO_4 concentrations can be attributed to several factors. These include the oxygen solubility, proton activity, and changes in double layer structure. In the region of potential considered, the rate of oxygen reduction in acid media as shown by Eq. [3] is first order with respect to the oxygen concentration and the proton activity (4, 13). Experimental evidence

(14) has indicated that both oxygen solubility and proton activity decrease with increasing H_3PO_4 concentration; one would, therefore, expect a lower oxygen reduction current in concentrated H_3PO_4 solutions.

However, the most significant factor in determining the rate of oxygen reduction may be due to the change in the double layer structure at the electrode/electrolyte interface with H_3PO_4 concentration. A recent study (9) has shown that the double layer thickness is greater at a mercury electrode/concentrated H_3PO_4 interface than at a mercury electrode/aqueous electrolyte interface. Thus, the distance for electron tunneling can be expected to be greater at the electrode/phosphoric

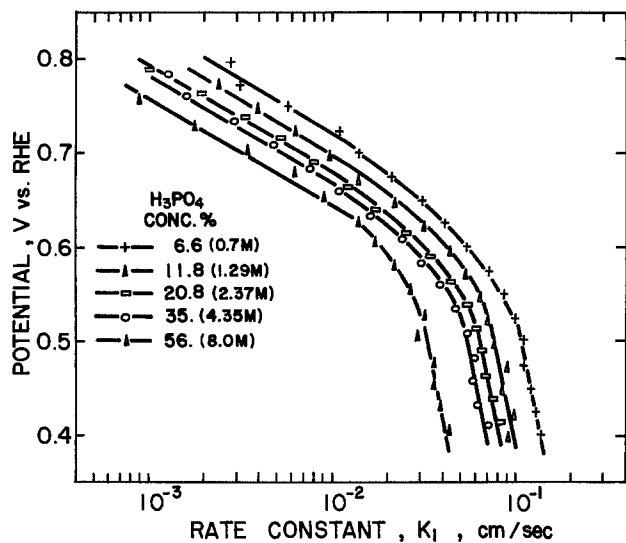


Fig. 3. Potential dependence of rate constant k_1 for oxygen reduction at Pt in H_3PO_4 in the concentration range 6.6-56 w/o at 25°C.

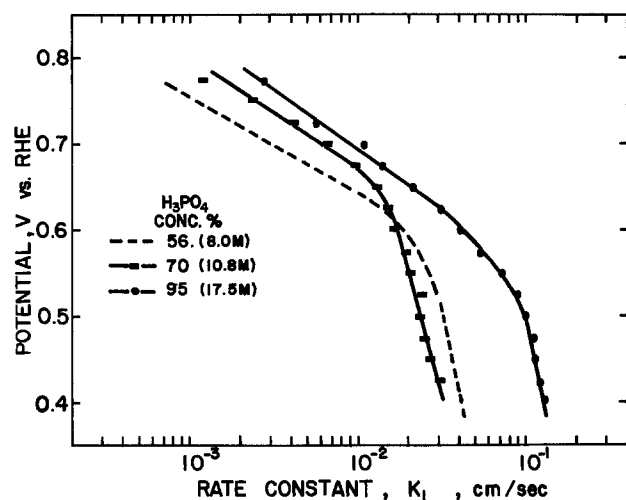


Fig. 4. Potential dependence of rate constant k_1 for oxygen reduction at Pt in H_3PO_4 in the concentration range 56-95 w/o at 25°C.

Fig. 5. Potential dependence of rate constant k_2 for oxygen reduction at Pt in H_3PO_4 in the concentration range 6.6-85 w/o at 25°C.

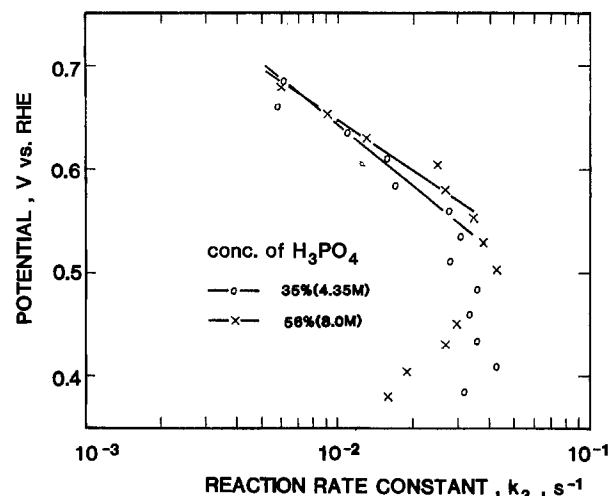
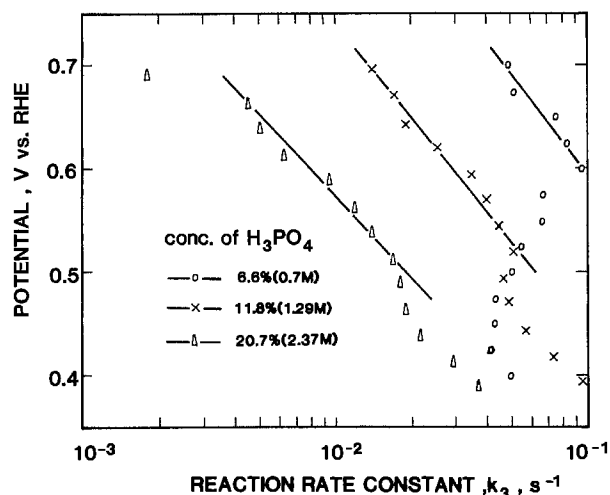
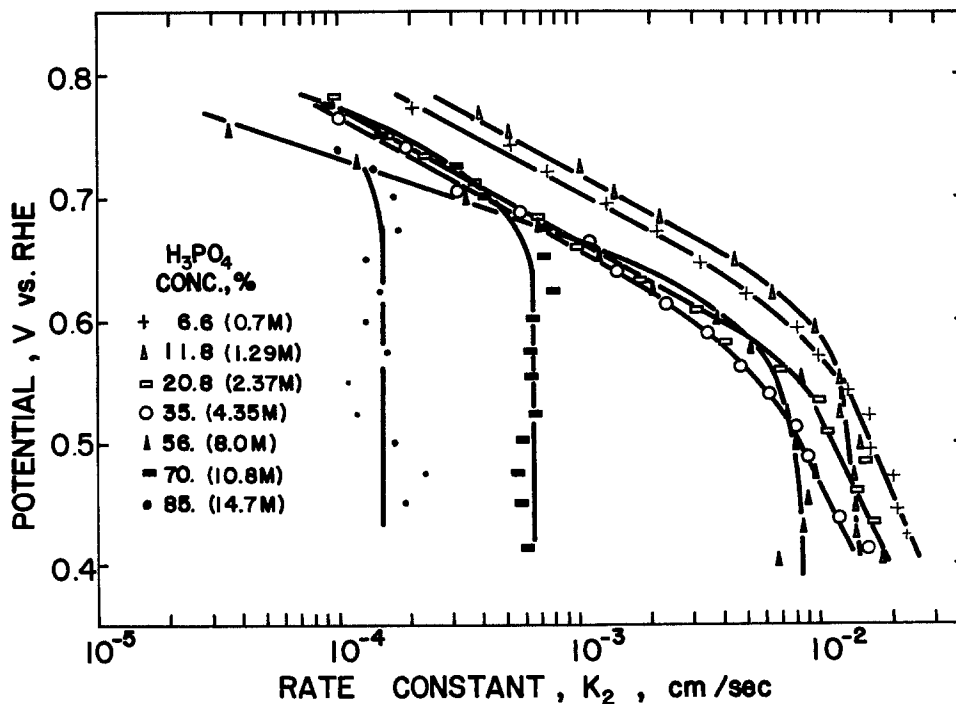


Fig. 6. Potential dependence of rate constant k_3 for oxygen reduction of Pt in H_3PO_4 in the concentration range 6.6-56 w/o at 25°C.

acid interface than at the electrode/aqueous electrolyte interface. At the same time, the presence of phosphate species on the electrode surface could interfere with the adsorption of reactants and/or intermediates. To

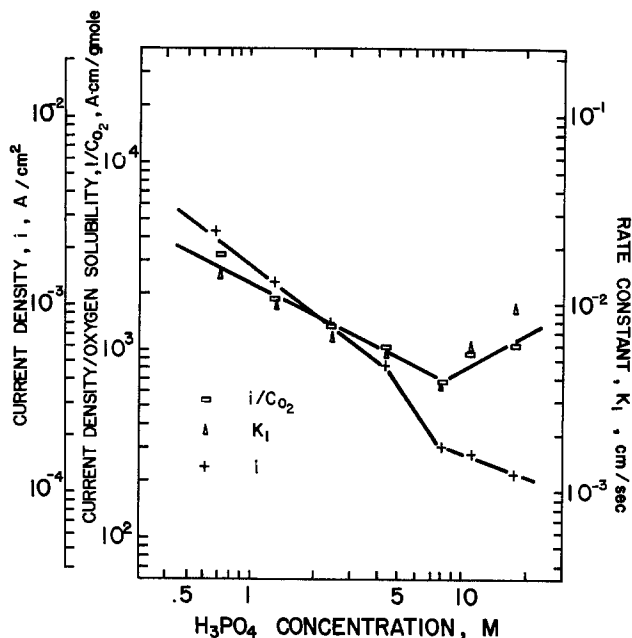


Fig. 7. Dependences of i , i/c_{O_2} , and k_1 for oxygen reduction at Pt on H_3PO_4 concentration at 25°C.

provide further evidence of strong anion adsorption, a separate experiment using a streaming electrode technique (15) was made to determine the effect of phosphoric acid concentration on the potential of zero charge on a mercury electrode. Figure 8 shows the plot of the potential of zero charge (E_z) as a function of H_3PO_4 concentration. A large change of E_z toward more negative values was observed as the concentration of H_3PO_4 increased, which is evidence for increasing adsorption of phosphate species at the interface. The change of E_z with H_3PO_4 concentration is linear, which means that the properties of the double layer undergo a gradual change. It can be expected that the extent of adsorption of the phosphate ion on platinum is at least as much as that on mercury. The presence of phosphate ions on the electrode surface blocks the ac-

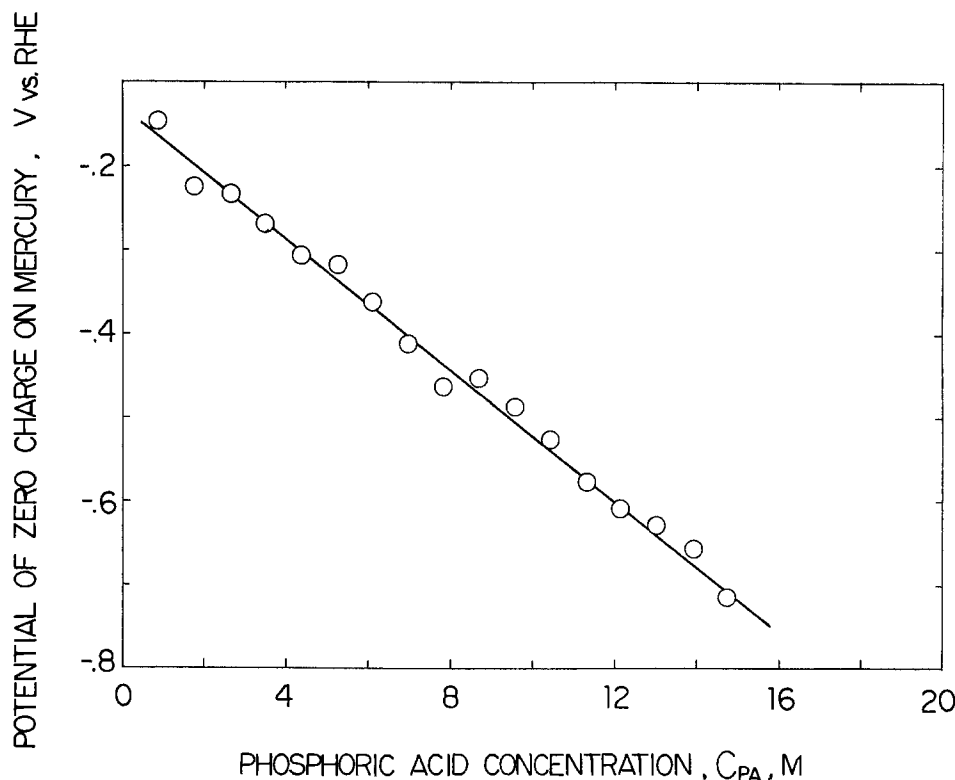


Fig. 8. Dependence of the potential of zero charge on mercury on H_3PO_4 concentration at 25°C.

tive sites for the charge-transfer reaction and causes a decrease in the oxygen reduction current.

The plots of i/c_{O_2} vs. H_3PO_4 concentration (Fig. 7) indicate that the rate of the reaction has a minimum at a certain H_3PO_4 concentration. This behavior has sometimes been observed for electrode reactions in mixed solvents (16). The phenomenon can be attributed to differential solvation between the electrode and the reacting species. Thus, if the latter is preferentially solvated with water molecules while the electrode is covered by phosphate species, a lower rate of reaction should then be expected. On the other hand, if the electrode and the reactant share the same solvating species, as would be the case in dilute or very concentrated phosphoric acid electrolytes, then the activated complex may be nearer the electrode surface and higher rates should be expected.

Conclusions

The results of the cyclic voltammetric and rotating ring-disk electrode experiments make it possible to reach the following conclusions on the effects of phosphoric acid concentration on oxide formation and oxygen reduction kinetics at platinum.

1. At concentrations below 4M, phosphoric acid has hardly any effect on the cyclic voltammograms. Above 4M, there is a progressive shift of the potential for commencement of oxide formation in the positive direction. Strong anion adsorption is indicated.

2. In the potential range 0.8-0.6V, the slope of the mass-transfer-corrected Tafel plots is nearly equal to 120 mV/decade and is practically independent of concentration. Below 0.6V, the slope becomes quite high (≈ 200 mV/decade), and then the current densities tend to a limiting value, which decreases with increasing acid concentration.

3. The mechanism proposed by Damjanovic *et al.*, that is, the four-electron transfer reduction in which the first electron transfer step is rate determining, appears most appropriate at potentials above 0.6V. The limiting current densities are probably due to a rate-determining dissociative adsorption of oxygen.

4. The rate constants for the two (k_2)- and four (k_1)-electron transfer reduction reactions have the same potential dependence. The ratio k_1/k_2 is greater than

10, which again supports the second conclusion. At concentrations above 8M, k_2 is independent of potential, probably because of the need for a preferential orientation of oxygen leading to the formation of H_2O_2 .

5. The decrease in reaction rates at higher concentrations can be attributed to four causes: lower oxygen solubility, lower proton activity, increased specific adsorption of anions, and a thicker double layer. Complementary experiments that yielded the concentration dependence of the potential of zero charge on mercury support the view that specific adsorption of anions is quite strong.

6. Minima in the plots of i/c_{O_2} and of k_1 vs. concentration at a fixed potential illustrate the effects of differential solvation between electrode and reaction species on oxygen reduction kinetics. Similar phenomena have been observed for other reactions in mixed solvents.

Acknowledgments

This work was performed under the auspices of the U.S. Department of Energy. E. R. Gonzalez thanks CNPq, Brazil, for a travel grant to Los Alamos National Laboratory during the summers of 1982 and 1983. The contribution of K-L. Hsueh partially fulfilled requirements toward his Ph.D. degree from the Department of Chemical Engineering, Clarkson College of Technology, Potsdam, New York. The authors wish to thank Dr. E. O'Sullivan of Case Western Reserve University, Dr. S. Gottesfeld of Tel Aviv University, and Dr. S. W. Feldberg of Brookhaven National Laboratory for helpful discussions and suggestions.

Manuscript submitted July 26, 1982; revised manuscript received July 8, 1983. This was Paper 677 pre-

sented at the Montreal, Quebec, Canada, Meeting of the Society, May 9-14, 1982.

Los Alamos National Laboratory assisted in meeting the publication costs of this article.

REFERENCES

1. A. J. Appleby and B. S. Baker, *This Journal*, **125**, 404 (1978).
2. A. A. Adams, R. T. Foley, and H. J. Barger, Jr., *ibid.*, **124**, 1228 (1977).
3. A. J. Appleby, *ibid.*, **117**, 328 (1970).
4. A. J. Appleby, *ibid.*, **117**, 641 (1970).
5. A. J. Appleby, *ibid.*, **117**, 91 (1970).
6. S. J. Clouser, J. C. Huang, and E. Yeager, Abstract 348, p. 572, The Electrochemical Society Extended Abstracts, 82-1, Montreal, Que., Canada, May 9-14, 1982.
7. J. C. Huang, R. K. Sen, and E. Yeager, *This Journal*, **126**, 786 (1979).
8. W. E. O'Grady, E. J. Taylor, and S. Srinivasan, *J. Electroanal. Chem.*, **132**, 137 (1982).
9. E. R. Gonzalez, K-L. Hsueh, and S. Srinivasan, *This Journal*, **130**, 1 (1983).
10. K-L. Hsueh, D-T. Chin, and S. Srinivasan, *J. Electroanal. Chem.*, **153**, 79 (1983).
11. B. E. Conway and D. M. Novak, *This Journal*, **128**, 956 (1981).
12. A. Damjanovic, M. A. Genshaw, and J. O'M. Bockris, *J. Chem. Phys.*, **45**, 4057 (1966).
13. D. B. Sepa, M. V. Vojnovic, and A. Damjanovic, *Electrochim. Acta*, **26**, 781 (1981).
14. K-L. Hsueh, Ph.D. Dissertation, Clarkson College of Technology, Potsdam, New York (1983).
15. D. C. Grahame, R. P. Larsen, and M. A. Poth, *J. Am. Chem. Soc.*, **71**, 298 (1949).
16. T. Biegler, E. R. Gonzalez, and R. Parsons, *Coll. Czech. Chem. Comm.*, **36**, 414 (1971).

Semiconductor Electrodes

LIV. Effect of Redox Couple, Doping Level, and Metal Type on the Electrochemical and Photoelectrochemical Behavior of Silicide-Coated n-Type Silicon Photoelectrodes

Fu-Ren F. Fan, Theresa Varco Shea, and Allen J. Bard*

Department of Chemistry, The University of Texas at Austin, Austin, Texas 78712

ABSTRACT

The surface potentials of silicide-coated n-type silicon photoelectrodes as functions of the potential of solution redox couples and the bias potential show that the Fermi level of these photoelectrodes is strongly pinned at the silicide/Si interface. The built-in potential barrier is consistent with the constancy in the photovoltage observed in solutions containing various reversible couples with redox potentials spanning a range larger than the bandgap of silicon. The performance of these photoelectrodes depends strongly on the metal, the charge transfer kinetics at the silicide/solution interface, and the doping density of silicon substrate.

One approach to stabilizing small bandgap semiconductors against photocorrosion in photoelectrochemical (PEC) cells involves the utilization of a thin noble metal overlayer (1). We have recently demonstrated that noble metal silicide-coated n-Si electrodes and suitably modified forms (e.g., with RuO_2) can photogenerate highly oxidizing species, such as chlorine and oxygen, with durable photoelectrochemical performance in aqueous solutions (2). In the previous work, we proposed that the photovoltage arises at the Si/silicide junction, based on preliminary studies with a few redox species in solution, and suggested several factors which contribute to the high stability and good performance of these photoelectrodes. However, fundamental investigations of the interfacial energetics and the effect of the charge transfer kinetics at the silicide/solution interface on the PEC performance were not

reported. In this paper, we examine the surface potential of these photoelectrodes as functions of the potential of solution redox couples and the bias potential. We also demonstrate that the performance of these silicide-coated n-Si electrodes depends strongly upon the metal, the charge transfer kinetics at the (silicide/solution) interface, and the doping level of silicon substrate. Additionally, we confirm that constant photopotentials are observed on these electrodes for solution couples with redox potentials spanning a range from -0.67 to $+1.1V$ vs. SCE, which is larger than the bandgap of silicon.

Experimental

Silicon substrates for silicide growth were n-Si(100) ($0.02-2.5 \Omega\text{-cm}$) single crystals donated by Texas Instruments and n-Si ($\sim 1 \Omega\text{-cm}$) polycrystals donated by Dr. R. Noufi. Silicides were prepared by procedures reported previously (2). The detailed procedures for

* Electrochemical Society Active Member.

Key words: semiconductor, photoelectrochemistry, silicides.

preparing the ohmic contacts and mounting and sealing the electrodes were also similar to those previously reported (3). The exposed area of the photoelectrodes ranged from 0.1-0.3 cm². The light source, if not otherwise mentioned, was a tungsten-halogen lamp fitted with a 13 cm-thick water filter with an intensity of 65 mW/cm². The voltammetric experiments were performed with the same apparatus and by procedures previously described. Reagent grade chemicals were used without further purification. All solutions were prepared from triply distilled water. All experiments were carried out with the solution under a nitrogen atmosphere. The electrode arrangement used in the measurement of surface potential is illustrated in Fig. 1. For electrodes used in surface potential measurements, a thicker Pt overlayer was deposited on the silicide layer to lower the sheet resistance to <100Ω. A silver contact was made to a portion of silicide overlayer. This Ag layer was sealed, as was the back ohmic contact, with insulating silicone rubber. Strong rectifying behavior in the current-voltage curve was observed between these two contacts indicating the absence of shorts between the two metal layers.

Results and Discussion

Surface potential of Pt-silicide-coated n-Si electrode.—The surface potential (between PtSi and SCE), V_s , of n-Si(Pt) electrode at open circuit was the same as the redox potential of the solution, V° , as measured by an independent Pt electrode (see Fig. 2); this demonstrates that the silicide layer was in equilibrium with the solution redox couples.

In a solution containing supporting electrolyte (0.5M Na₂SO₄, pH 5) only, no appreciable background current was observed at a Pt electrode over the potential range -0.6 to 0.6V vs. SCE and V_s , as shown in curve a of Fig. 3, was essentially equal to the applied potential

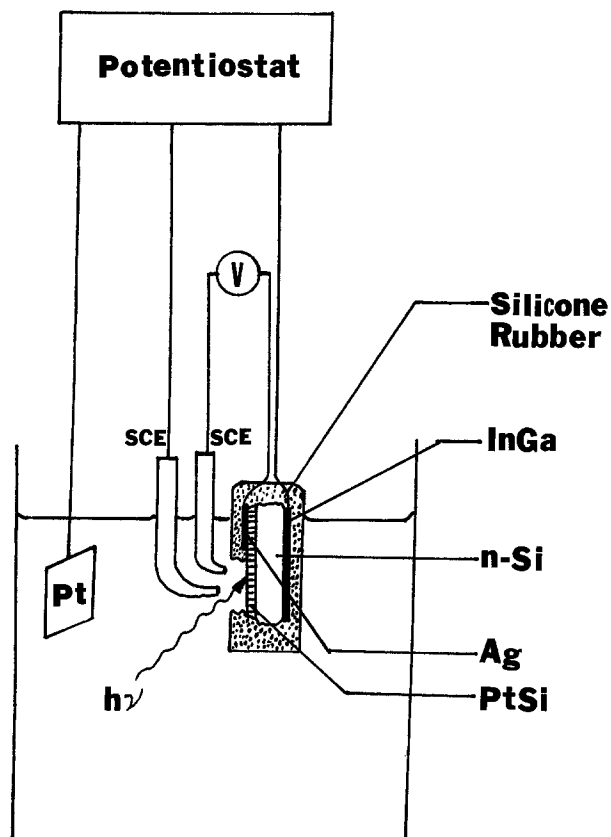


Fig. 1. The setup and the electrode configuration used in the measurement of surface potential of n-Si(Pt) electrode. V is the high impedance voltmeter consisting of a FET operational amplifier (Type NE 536T) in a voltage follower made with an input impedance $> 10^8\Omega$.

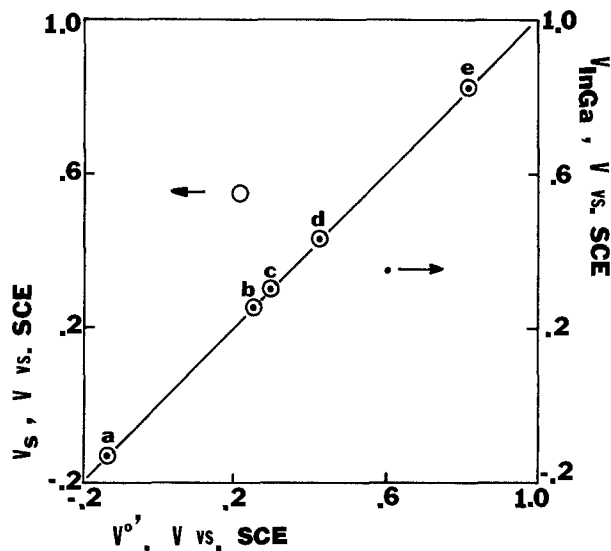


Fig. 2. Surface potential (V_s) and rest potential (V_{InGa}) of n-Si(Pt) electrode vs. potential of redox couples (V°) in 1M KCl. a: Fe-EDTA⁻²⁻. b: Fe(CN)₆^{3-/4-}. c: I⁻/I₃⁻. d: Fe^{2+/3+}. e: Fe(o-phenanthroline)₃^{2+/3+}.

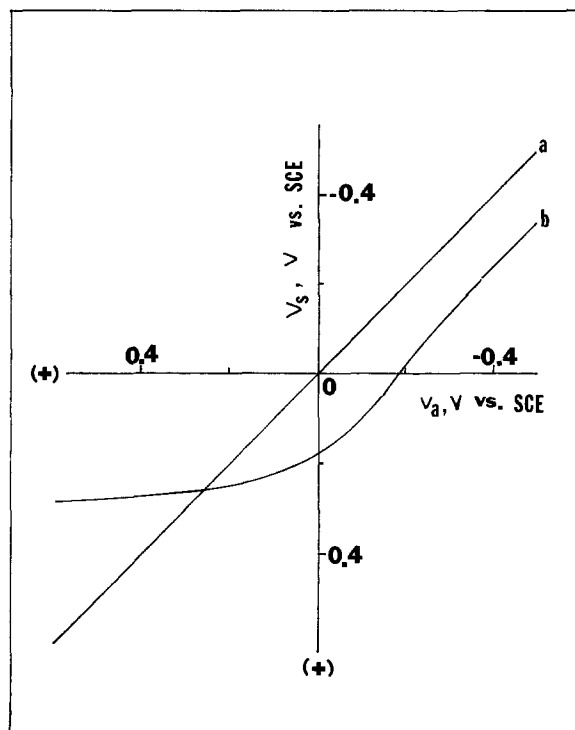
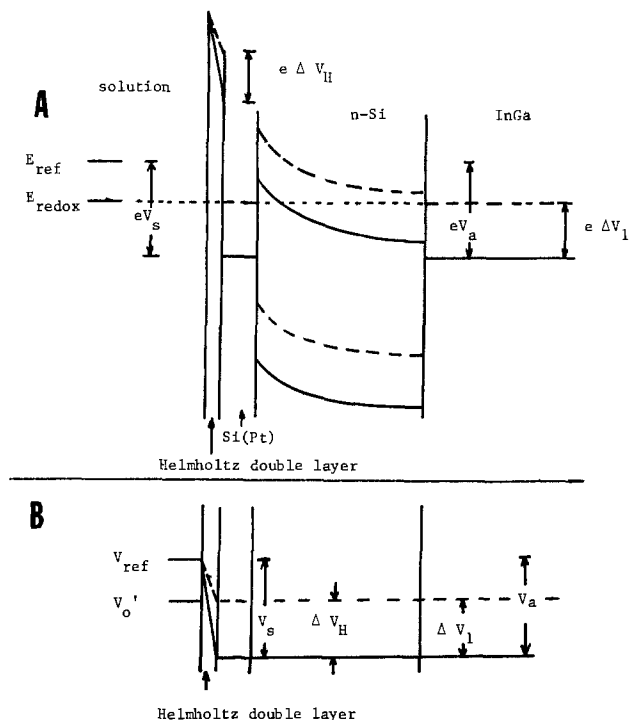


Fig. 3. Surface potential of n-Si(Pt) vs. applied potential in 0.5M Na₂SO₄ (curve a) and in 0.5M Na₂SO₄, 0.5M K₄Fe(CN)₆, and 0.5M K₃Fe(CN)₆ (curve b).

V_a (where V_a is the potential between the ohmic contact to Si and SCE). Since V_s represents the change of the potential drop between PtSi and solution, the results imply that the applied voltage is almost completely absorbed by changes of potential across the Helmholtz double layer (if the potential drop across the diffuse double layer and at the ohmic contact is neglected). (see Scheme I).

When equimolar (0.5M) amounts of Fe(CN)₆³⁻ and Fe(CN)₆⁴⁻ were added to the solution, the rest potential of the n-Si(Pt) electrodes was 0.25V vs. SCE, which is equal to formal potential, V° , of the Fe(CN)₆^{3-/4-} couple. In the dark, a small anodic current was observed when an anodic potential scan (Fig. 4, curve c) was applied to the n-Si(Pt) electrode



Scheme 1. A, top: in terms of interfacial energetics, neglecting the potential drop across the diffuse double layer and at the ohmic contact. $\Delta V_L = \Delta V_H = V_a - \frac{E_{\text{redox}}}{e}$; band-bending unchanged. B, bottom: in terms of distribution of V_a (vs. reference electrode) in the system. Dotted line: no external bias. Solid line: with external bias.

through the InGa ohmic contact. The potential scan generates a peak current at about -0.38V vs. SCE at a scan rate of 100 mV/s due to mass transport limitations (Fig. 4c). The voltammetric curve of PtSi was obtained by applying a potential scan through the front Ag contact to the PtSi. As shown in curve a of Fig. 4, both anodic and cathodic currents were mass-transfer limited.

The current-voltage curve of the n-Si/PtSi diode (current flow and voltage, V_D , between InGa to Si and Ag contact to PtSi) is shown in curve b of Fig. 4. In the reverse bias (anodic bias) direction, the current was essentially the same as that in curve c and was much smaller than the anodic current (shown on curve a of Fig. 4) taking place on PtSi. In the forward bias direction, before mass-transfer limitation took over, the diode current was smaller than the cathodic current (shown on curve a of Fig. 4) on PtSi and was nearly equal to the real current flow through the n-Si(Pt) electrode (shown on curve c of Fig. 4).

The system can thus be modeled as the Si-PtSi diode in series with the PtSi/solution interface. At a given current, V_a is given by the sum of V_D and V_s plus any internal iR drops. As shown in curve b of Fig. 3, in the presence of equimolar $\text{Fe}(\text{CN})_6^{3-}$ and $\text{Fe}(\text{CN})_6^{4-}$, V_s was essentially fixed at V_o' of the $\text{Fe}(\text{CN})_6^{3-/4-}$ couple when V_a was positive of V_o' . When V_a was negative of the potential at which mass-transfer limitation or the electron-transfer kinetics on PtSi becomes important, the change of V_s was equal to the change of V_a . If we assume that the potential drop across the diffuse double layer and at the ohmic contact is negligible, we can calculate the distribution of the applied voltage into the change of band bending, ΔV_b , (which is equivalent to the drop across the diode, V_D), and the change of potential drop across Helmholtz double layer, ΔV_H ; this is plotted in Fig. 5. As shown in this figure, $\Delta V_H \cong 0.0\text{V}$ when V_a is positive of V_o' , indicating that the applied voltage is mainly absorbed inside the semiconductor.

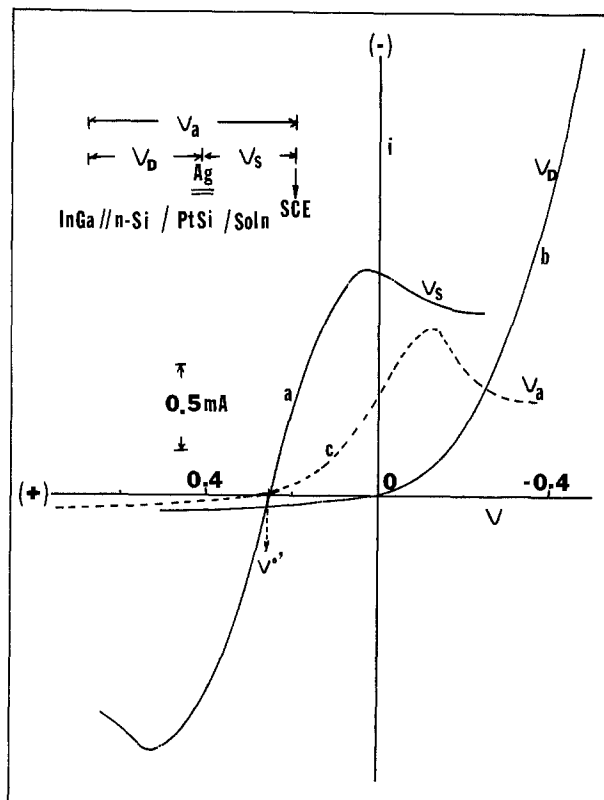


Fig. 4. a: voltammetric curve on PtSi (through Ag contact). b: current-voltage curve of the n-Si/PtSi diode. c: voltammetric curve on n-Si/PtSi (through InGa contact). Scan rate: 100 mV/s and in $0.5\text{M Na}_2\text{SO}_4$, $0.5\text{M K}_3\text{Fe}(\text{CN})_6$, and $0.5\text{M K}_4\text{Fe}(\text{CN})_6$. pH 5. Exposed PtSi electrode area $< 0.1\text{ cm}^2$.

When V_a is negative of V_o' , the applied voltage distributes both in ΔV_H and ΔV_b (Scheme II); ΔV_b approaches a maximum at a potential near the potential at which the peak current through the system was observed. Then ΔV_H increases and ΔV_b decreases steadily because of mass-transfer limitations to the current.

Interfacial energetics.—We have carried out cyclic voltammetry for a variety of redox couples with V_{redox}

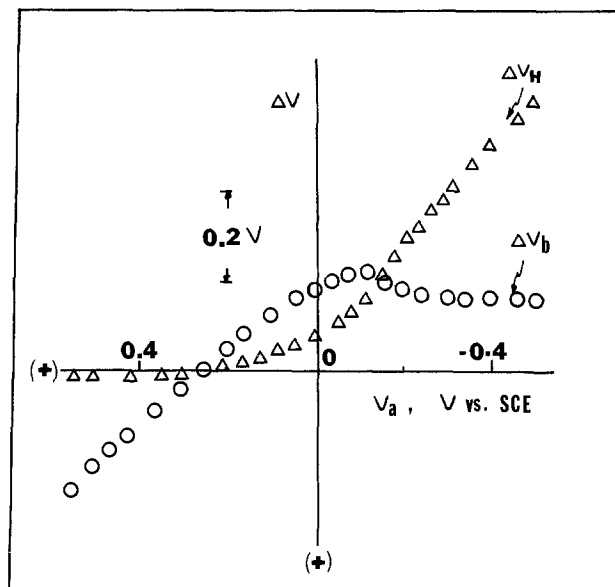
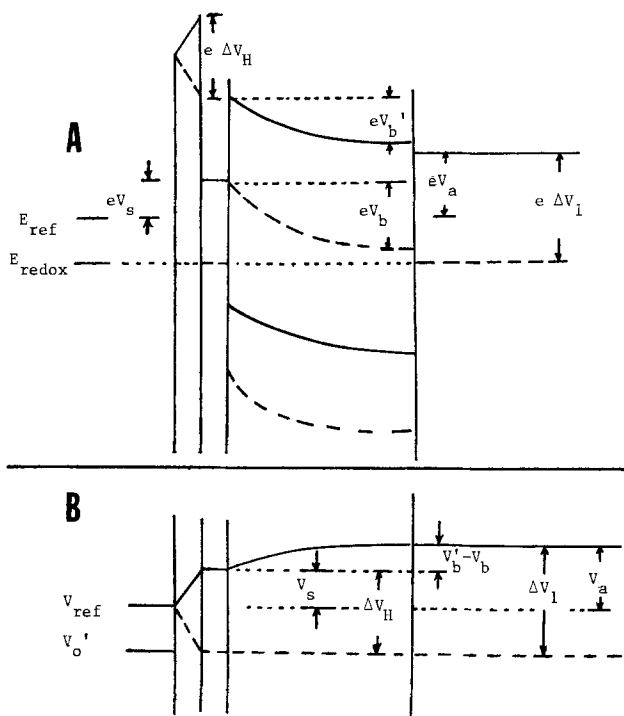
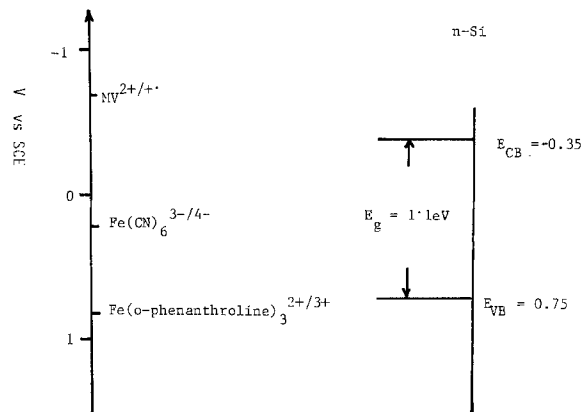


Fig. 5. The change of band-bending, ΔV_b , and the change of potential drop across Helmholtz double layer, ΔV_H , as functions of the applied potential, V_a . Scan rate: 100 mV/s and in $0.5\text{M Na}_2\text{SO}_4$, $0.5\text{M K}_3\text{Fe}(\text{CN})_6$, and $0.5\text{M K}_4\text{Fe}(\text{CN})_6$. pH 5.



Scheme II. A, top: in terms of interfacial energetics. $\Delta V_1 = \Delta V_H + (V_b' - V_b)$ $V_a = V_s + (V_b' - V_b)$; band-bending unchanged. B, bottom: in terms of distribution of V_a (vs. reference electrode) in the system.

values spanning a range that is wider than the bandgap of silicon in aqueous solution (see Scheme III). Those redox couples all show one-electron reversible cyclic voltammograms on a Pt electrode (Fig. 6), so that possible complications caused by different interfacial charge transfer kinetics at the silicide/solution interface are not important. As shown in Fig. 6, in the dark, MV^{2+} is reduced at an n-Si(Ir) electrode with a cathodic peak potential (V_{pc}) of $-0.9V$ vs. SCE. No anodic peak corresponding to the reoxidation of MV^+ was observed in the dark, because of the lack of holes in n-Si and the unfavorable energetics for electron injection from solution species. Under illumination with



Scheme III

65 mW/cm^2 , MV^{2+} is reduced at more negative potential with V_{pc} at $-1.07V$ and reoxidized with V_{pa} at $-1.01V$ vs. SCE due to the photogeneration of holes. With $V_{oc} = |V_{pa}[n\text{-Si(Ir)}] - V_{pa}(\text{Pt})|$ (4, 5), this represents $V_{oc} = 0.4V$ for $MV^{2+/+}$. Similar results were obtained for $\text{Fe}(\text{CN})_6^{3-/4-}$ and $\text{Fe}(\text{o-phenanthroline})_3^{2+/3+}$. This constancy of V_{oc} for various one-electron reversible redox couples with potentials beyond the bandedges of silicon is consistent with our previous results over a more restricted range (2) and suggests that the electrolyte solution species do not interact with silicon substrate. Rather, the interaction is with the silicide overlayer and the interfacial energetics is dominated by this interaction. Apparently, the interfacial energetics depend strongly upon the coverage of silicide on silicon substrate. Electron spectroscopic (AES and XPS) analyses (2, 8) show that most of the silicide layer we prepared were richer in silicon than in metal. Even under those conditions, n-Si(M) electrodes behave as if the surface of Si electrode were wholly covered by a uniform metal layer. The effect of variation of the thickness of the metal overlayer, the annealing conditions, and coverage of silicides or metals on the interfacial energetics is currently under investigation.

Effect of charge transfer kinetics.—The charge transfer kinetics at the electrode/solution interface might

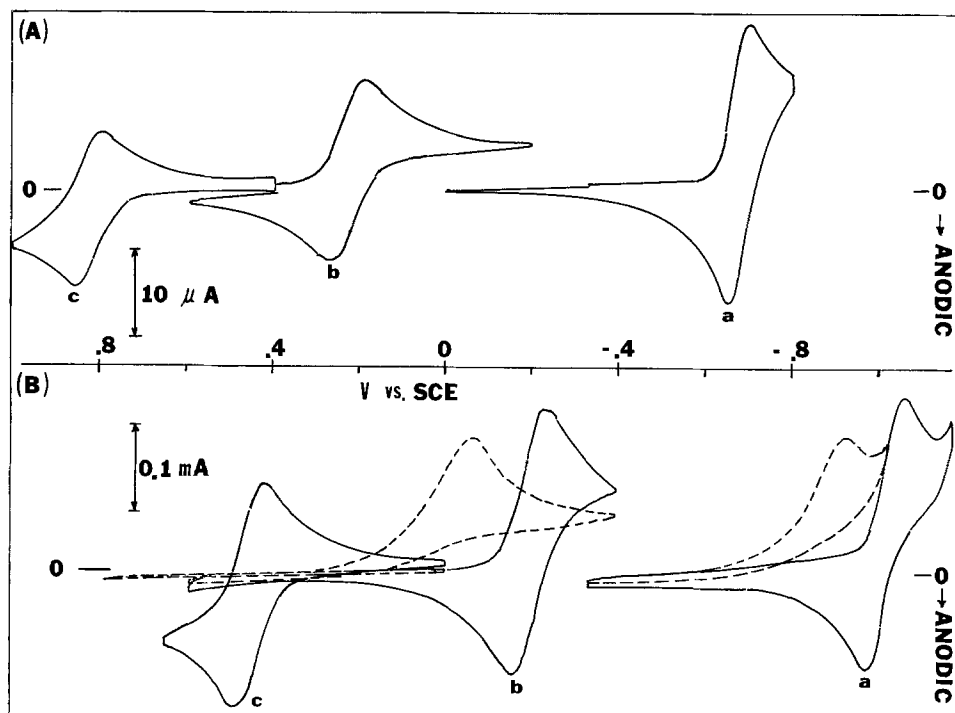


Fig. 6. Cyclic voltammograms of three reversible couples at scan rate of 100 mV/s on Pt (A) and on n-Si(Ir) (B) in the dark (broken lines) and under illumination with 65 mW/cm^2 (solid curves). Curve a: $MV^{2+/+}$. Curve b: $\text{Fe}(\text{CN})_6^{3-/4-}$. Curve c: $\text{Fe}(\text{o-phenanthroline})_3^{2+/3+}$.

affect the potential at which processes occur, as well as the voltammetric behavior of the photoelectrode and the observed photopotentials (6, 7). This was investigated in the following several experiments. The charge transfer kinetics of the Fe(II)/Fe(III) couple was changed by variation of the concentration of chloride ion, $[Cl^-]$. As shown in Fig. 7a, an increase in the concentration of Cl^- increased the rate of Fe(II)/Fe(III) redox reaction at Pt electrode. ΔV_p ($\Delta V_p = V_{pa} - V_{pc}$) decreased from 330 mV at $[Cl^-] = 0.0M$ to 60 mV when $[Cl^-] = 6M$, where the reaction approached reversible behavior, without a significant shift in the midpoint potential. The ratio of the anodic peak current (i_{pa}) vs. the cathodic peak current (i_{pc}) approaches unity when $[Cl^-]$ is increased (9). A similar trend was observed with an n-Si(Ir) electrode under illumination with 80 mW/cm² (see Fig. 7b), although the peak potentials were shifted towards more negative values by about 0.4V, as compared with those on Pt (corresponding to the photovoltage observed on those electrodes). This similarity of behavior suggests that the rate-limiting process under illumination is the kinetics of charge transfer at the Si(M)/solution interface.

Effect of dopant concentration in the silicon substrate and type metal (M) overlayer on the voltammetric behavior of n-Si(M) electrode.—The deposition of a metal onto a semiconductor will usually result in the formation of an ohmic contact or a Schottky barrier, depending on the relative work functions of semiconductor and metal, the surface treatment of semiconductor before deposition, and the interfacial chemistry that occurs upon deposition or during annealing (10). By keeping the conditions for etching, metal deposition, and postannealing constant and varying the doping density of silicon substrate, we found very different voltammetric behavior in the dark and

under illumination (see Fig. 8). The dark oxidation current increased and the reduction current decreased systematically with decreased resistivity of the silicon wafers, suggesting that samples with a higher resistivity form better rectifying junctions with silicide. Corresponding to this behavior, a better photoeffect was observed on samples with higher resistivity. The photoelectron spectroscopic results (8) suggested that metal diffuses a few hundred angstroms into the silicon substrate. The incorporated transition metal could facilitate electron transfer and recombination in the space-charge layer. This effect will be more prominent when the width of the space-charge layer becomes narrower due to higher doping density. The incorporated transition metal in the space-charge layer might also form effective recombination centers that scavenge photo-generated holes and thus degrade the photoeffect. This is consistent with the results shown in Fig. 8.

The effect of the nature of the metal on the voltammetric behavior is summarized in Fig. 9. Several interesting conclusions result from these studies. First, the work function of metals listed in Fig. 9 covers a range of at least 0.8V (11); however, V_{oc} of these silicide-coated n-Si electrodes only covers about 0.25V. This insensitivity of V_{oc} with respect to the work function of metal is basically consistent with the results observed in solid-state devices (12). Secondly, the higher the rectifying ratio (R_r) is (the absolute ratio of the dark reduction current vs. the dark oxidation current at equal potential difference with respect to the rest potential), the better the photoeffect is. Both Pt and Ir show very high R_r values and have high V_{oc} and short-circuit photocurrents (i_{sc}), whereas Ru shows poor R_r , V_{oc} , and i_{sc} . The factors contributing to the poor photoeffect on n-Si(Ru) electrodes are not clear and require further investigation.

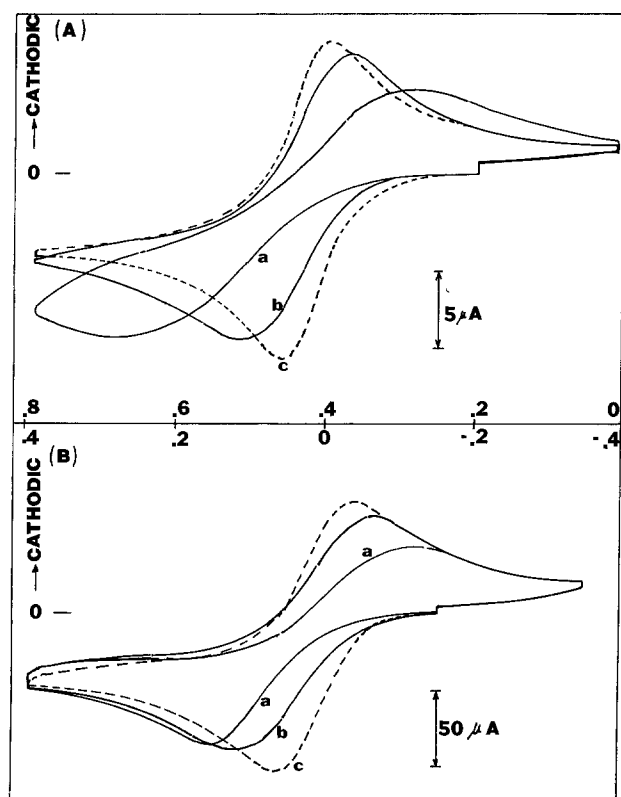


Fig. 7. Cl^- concentration dependence of cyclic voltammograms of Fe^{2+} at scan rate of 100 mV/s on Pt (A) and on n-Si(Ir) (B) under illumination with 80 mW/cm². Curve a: 5 mM $FeSO_4$ in 0.5M H_2SO_4 . Curve b: 5 mM $FeSO_4$ in 0.5M H_2SO_4 and 3M NaCl. Curve c: 5 mM $FeSO_4$ in 1M HCl and 5M LiCl. (Note that potential axis for n-Si(Ir) is shifted by 0.4V w.r.t. that for Pt.)

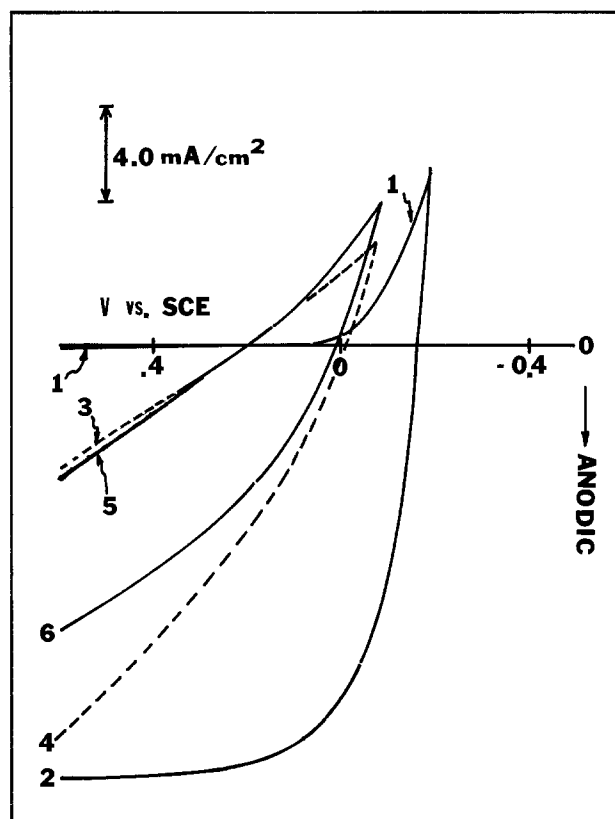


Fig. 8. Effect of doping density on voltammetric behavior of n-Si(Ir) in 0.5M $K_4Fe(CN)_6$, 0.1M $K_3Fe(CN)_6$, and 0.5M Na_2SO_4 . Light intensity at 65 mW/cm². Annealing at 500°C and 10^{-6} torr for 10 min. Curves 1 (in the dark) and 2 (under illumination): 2.5 Ω -cm. Curves 3 (in the dark) and 4 (in the light): 0.2 Ω -cm. Curves 5 (in the dark) and 6 (under illumination): 0.02 Ω -cm.

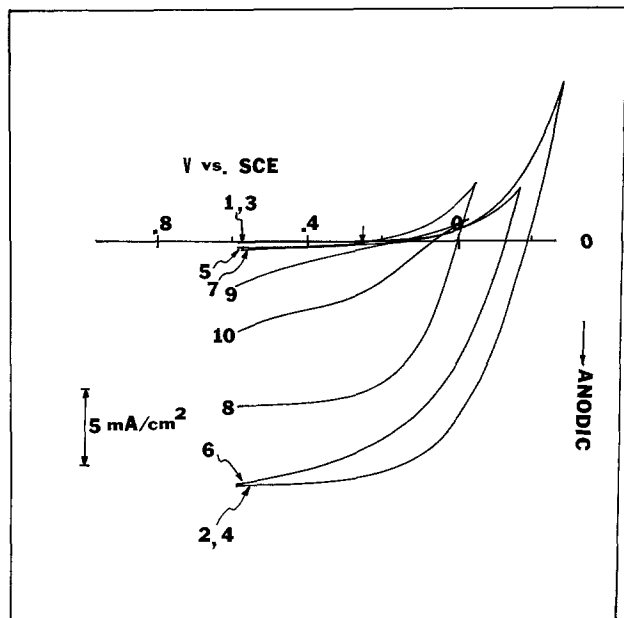


Fig. 9. Voltammetric behavior of n-Si coated with various kinds of metals in 0.5M $K_4Fe(CN)_6$, 0.1M $K_3Fe(CN)_6$, and 0.5M Na_2SO_4 . Light intensity 65 mW/cm^2 . Postannealed at 200°-500°C for 5-10 min. Ir: 1 (dark), 2 (light). Pt: 3 (dark), 4 (light). Rh: 5 (dark), 6 (light). Pd: 7 (dark), 8 (light). Ru: 9 (dark), 10 (light).

In conclusion, the measurement of the surface potential of n-Si electrodes coated with a thin layer of noble metal silicide reveals that changes in the applied potential on these electrodes are mainly absorbed across Helmholtz double layer either in the dark or under illumination. A constancy of open-circuit photovoltage was observed on these electrodes for reversible redox couples which span a potential range larger than the bandgap. These EC and PEC characteristics simulate those found when Fermi-level pinning occurs (13). The interfacial charge transfer kinetics at the silicide/solution interface also plays an important role in the EC and PEC performance, as does the doping density of silicon substrate and the type of metal overlayer.

Acknowledgments

We thank Dr. R. Gerald Keil for his suggestion on the electroplating of ruthenium and Professor Mark S.

Wrighton for his suggestion on the experiment about the constancy of photovoltage with respect to reversible redox couples. The assistance of Professor Gregory A. Hope and Dr. M. Schmerling, as well as the comments and suggestions of Dr. Ronald Wilson, are gratefully acknowledged. The support of this research by the Solar Energy Research Institute and the National Science Foundation (CHE8000682) is gratefully acknowledged.

Manuscript submitted June 27, 1983; revised manuscript received Dec. 5, 1983.

REFERENCES

1. Y. Nakato, T. Obnishi, and H. Tsubomura, *Chem. Lett.*, **19**, 838 (1975); Y. Nakato, K. Abe, and H. Tsubomura, *Ber. Bunsenges. Phys. Chem.*, **80**, 1002 (1976); L. A. Harris, M. E. Gerstner, and R. H. Wilson, *This Journal*, **124**, 1511 (1977); F.-R. F. Fan, G. A. Hope, and A. J. Bard, *ibid.*, **129**, 1647 (1982).
2. F.-R. F. Fan, R. G. Keil, and A. J. Bard, *J. Am. Chem. Soc.*, **105**, 220 (1983).
3. F.-R. F. Fan, B. L. Wheeler, A. J. Bard, and R. N. Noufi, *This Journal*, **128**, 2042 (1981).
4. A. Kohl, Ph.D. Thesis, The University of Texas at Austin, Austin, TX (1978).
5. J. A. Baglio, G. S. Calabrese, E. Kamieniecki, R. Kershaw, C. P. Kubiak, A. J. Ricco, A. Wold, M. S. Wrighton, and G. D. Zoski, *This Journal*, **129**, 1461 (1982).
6. J. Reichmann, *Appl. Phys. Lett.*, **36**, 574 (1980).
7. W. J. Albery, P. N. Bartlett, A. Hammet, and M. P. Dare-Edwards, *This Journal*, **128**, 1492 (1981).
8. G. A. Hope, F.-R. F. Fan, and A. J. Bard, *ibid.*, **130**, 1488 (1983).
9. A. J. Bard and L. R. Faulkner, "Electrochemical Methods: Fundamentals and Applications," Chap. 6, John Wiley and Sons, New York (1980).
10. G. A. Hope and A. J. Bard, *J. Phys. Chem.*, **87**, 1979 (1983); F. T. Wagner and G. A. Somorjai, *J. Am. Chem. Soc.*, **102**, 5494 (1980); M. S. Wrighton, P. T. Wolczanski, and A. B. Ellis, *J. Solid State Chem.*, **22**, 17 (1977).
11. S. M. Sze, "Physics of Semiconductor Devices," 2nd ed., p. 366, Wiley-Interscience, New York (1981).
12. T. C. McGill, *J. Vac. Sci. Technol.*, **11**, 935 (1974); S. Kurtin, T. C. McGill, and C. A. Mead, *Phys. Rev. Lett.*, **22**, 1433 (1969).
13. A. J. Bard, A. B. Bocarsly, F.-R. F. Fan, E. G. Walton, and M. S. Wrighton, *J. Am. Chem. Soc.*, **102**, 3671 (1980).

Redox Conduction: Its Use in Electronic Devices

P. G. Pickup and Royce W. Murray

Kenan Laboratories of Chemistry, University of North Carolina, Chapel Hill, North Carolina 27514

ABSTRACT

A sandwich electrode composed of a film of the electroactive polymer $[Os(bpy)_2(vpy)_2]^{P+}$, sandwiched between a Pt disk electrode and a porous Au film, becomes conductive when the Pt and Au potentials are properly poised in relation to the potential at which the Os(III/II) mixed valent state becomes generated. The potential control is normally judged in relation to a reference electrode. The reference electrode can be shorted to, or made common with, the Au electrode, so that two-terminal potential control circuitry can be employed to cause or not cause redox conduction through the sandwich. Such arrangements are used to illustrate principles for using the sandwich electrode as a two-terminal device that acts in a manner similar to a Zener diode, and as a triode-like three-terminal device in which the current between two terminals is controlled by the potential applied at the third.

That electrochemical charge can be transported through films of redox polymer saturated with electrolyte solution and coated on electrodes has been recognized since 1978 (1). Such films can contain the equiv-

Key words: osmium, polymer modified electrode, electron diffusion, diode, triode.

alent of thousands of monomolecular layers of electroactive sites yet be rapidly oxidized and reduced by the electrode (2). For a pyrazoline polymer, where the electroactive sites were affixed to the polymer lattice, Kaufman *et al.* (3) proposed that charge transport can occur by electron self-exchange reactions between oxi-

dized and reduced pyrazoline sites. When a concentration gradient of oxidized and reduced sites exists, such reactions lead to a net electron current which follows Fick's diffusion law as shown both experimentally (4) for several redox polymers and theoretically (5), and is characterized by a diffusion coefficient (D_{ct}). Diffusion laws also apply when the electroactive site is a counterion of a polyionic film (6), but competitive physical diffusion of the redox site must then be considered (7). In both cases, starting from a fully reduced or oxidized polymer, electron transport (e.g., "redox conduction current") must be accompanied by a net oxidation or reduction of some of the electroactive sites of the polymer, and so is turned on by underlying electrode potentials near the formal potential of the electroactive species in the polymer.

Normally, redox conduction in electroactive polymer films is observed using an electrode contacting the film on one side and an electrolyte solution on the other. To exploit certain of the properties of redox conduction, however, it is of advantage to contact the second side of the polymer film with a structure which can serve as electron donor or acceptor. We have done this with a second electroactive polymer film in the case of bilayer electrodes (8), and most recently in a sandwich electrode (9), with a second electrode (a Au film) which is porous to the contacting electrolyte/solvent bath (Fig. 1). This paper addresses the application of the sandwich electrode to make a simple electronic device which can be used as a two-terminal rectifying device, similar in some respects to a Zener diode, or as a three-terminal device in which the current between two terminals is controlled by the potential applied at the third. The polymer film employed is made by electropolymerization of the vinyl-substituted complex (8, 10) $[\text{Os}(\text{bpy})_2(\text{vpy})_2]^{2+}$ onto a Pt electrode. We should emphasize that the purpose of the study is to demonstrate the concept of making a device based on redox conduction and electrochemical principles.

Figure 1 shows the concentration gradient for Os(III) redox sites in a film of poly- $[\text{Os}(\text{bpy})_2(\text{vpy})_2]^{2+}$ in a sandwich electrode in which the potentials of the two electrodes are controlled so that the left-hand (Pt) electrode acts as electron acceptor and the right-hand electrode (porous Au) acts as electron donor. The

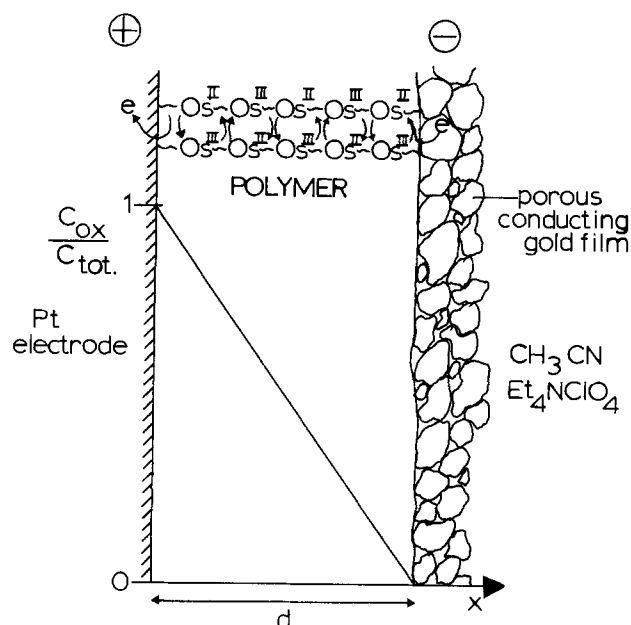


Fig. 1. Sandwich electrode showing schematic representation of the proposed mechanism of redox conduction and a concentration profile for the situation when Au is significantly negative of E° and Pt significantly positive of E° .

current passing through the film shown in Fig. 1 depends upon the concentration gradients of oxidized or reduced Os sites in the film, which are determined by the potentials applied to the two electrodes. In our previous experiments (9), the potentials of the two electrodes were controlled relative to some reference electrode placed in the contacting solution. An analytical expression for the steady-state current as a function of the potentials of the two electrodes (E_{Pt} and E_{Au}) relative to the reference electrode is readily derived, and is formally analogous to the equation for twin-electrode thin layer electrochemistry (10)

$$i = \left[\frac{nFAD_{ct}C_T^2}{\Gamma_T} \right] \left[\frac{1}{1 + \exp[gf(E^\circ - E_{Pt})]} \right] \left[\frac{1}{1 + \exp[gf(E^\circ - E_{Au})]} \right] \quad [1]$$

where C_T and E° are concentration and formal potential of polymer redox sites, Γ_T is surface coverage of redox polymer in mol/cm², f is nF/RT , and g is a constant to correct for the nonideality of the polymer film (9b).

It is useful to consider a three-dimensional plot of Eq. [1] as shown in Fig. 2. Each line on the grid surface in this plot represents current as a function of E_{Pt} at constant E_{Au} or vice versa. Each line then corresponds to a constant oxidized-polymer concentration on one side of the film and thus a concentration gradient and hence current proportioned by the concentration of oxidized polymer on the other side. Take, for example, the trace at $(E_{Au} - E^\circ) = 0$ (whose ends are marked with stars \star), in which there is always a 50% oxidized layer of polymer at the Au electrode. When $E_{Pt} - E^\circ$ is significantly negative (e.g., $-0.2V$), there is no oxidized polymer at the Pt, and so the concentration gradient will be half maximum and a current of $nFAD_{ct}C_T^2/2\Gamma_T$ will flow from Au to Pt. At $(E_{Pt} = E_{Au})$, the concentration gradient and current are zero. At more positive $E_{Pt} - E^\circ$, a limiting current $nFAD_{ct}C_T^2/2\Gamma_T$ flows from Pt to Au as the polymer at the Pt electrode becomes virtually 100% oxidized.

The preceding example presumes control of both Pt and Au electrode potentials relative to a reference electrode potential, which is a three- or four-electrode experiment as used previously (9). Under this circumstance, the current for a given $E_{Pt} - E_{Au}$ potential difference could be found readily from Fig. 2. If now instead one considers not controlling either electrode's

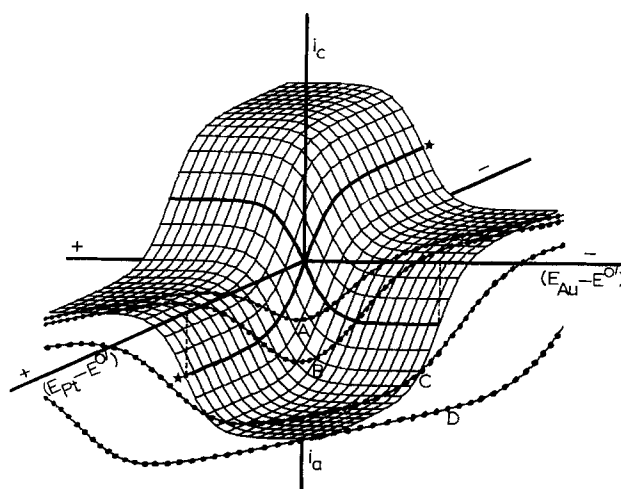


Fig. 2. Three dimensional plot of current at the Pt electrode vs. the Pt electrode potential (E_{Pt}) and the Au electrode potential (E_{Au}) for a Pt/polymer/Au sandwich electrode according to Eq. [1] ($g = 0.8$). The grid extends to $\pm 0.26V$ for the two potential axes, and the current axis is in arbitrary units. Also shown are the loci of the triode-type experiments of Fig. 8 ($-\bullet-\bullet-$).

potential relative to a reference electrode, but just the potential difference $E_{Pt} - E_{Au}$ between them, as would be the case in a two-electrode cell, we see that a given difference between E_{Au} and E_{Pt} no longer defines a unique point on the current-potential surface of Fig. 2. In fact, a range of different currents through the film are possible for any given absolute value of $E_{Pt} - E_{Au}$. Thus, true two-electrode potential control presents a fundamental difficulty. On the other hand, to exploit the sandwich arrangement shown in Fig. 1 in an electronic device, it is desirable to simplify the potential control requirements for the device by using only a two-electrode cell, i.e., controlling only the potential difference between the two electrodes. This paper describes how this can be done while maintaining a usable reference to the current-potential pattern of Fig. 2.

Experimental

The construction of the sandwich electrode has been described elsewhere (9). The electrode assembly consists of six independent Pt disk microelectrodes (tips of wires) sealed in a single Teflon [or glass (9b)] shroud. Five electrodes are coated with 0.1-1.0 μm polymer by reductive electropolymerization of the $[\text{Os}(\text{bpy})_2(\text{vpy})_2]^{2+}$ monomer complex. The whole face of the electrode assembly is then coated with ca. 0.1 μm vapor-deposited gold. The sixth Pt disk serves as a direct electrical contact to the gold film.

The problem of shorts between the gold and the Pt disk described in earlier papers (9a) has now been largely overcome. The multi-electrode assembly allows five sandwich electrodes to be constructed simultaneously, at least one of these is typically not shorted at all, and the others can usually be successfully conditioned (9a) to remove initial shorts.

All experiments were performed in 0.1M $\text{Et}_4\text{NClO}_4/\text{acetonitrile}$. The solutions were normally degassed with N_2 . A conventional, locally built potentiostat and a triangle wave generator were used to apply a variable potential difference across the polymer film and to measure the current through the film. Two-electrode control was effected by connecting both the reference and auxiliary electrode terminals of the potentiostat to the gold film and connecting the working electrode terminal to one of the polymer-coated Pt microelectrodes. The potentiostat is thus used merely as a current follower and can be replaced by an ammeter or some other current measuring device or circuit. A PAR Model 175 Universal Programmer was used when voltage pulses were required, and a second triangle wave generator when two independent potential differences were required. The Ag/AgCl electrode was prepared by (11) depositing AgCl at 0.4 A/cm^2 for 30 min from 0.1M HCl .

Results and Discussion

To determine the current/voltage characteristics of a Pt/poly- $[\text{Os}(\text{bpy})_2(\text{vpy})_2]^{2+}/\text{Au}$ sandwich device in 0.1M $\text{Et}_4\text{NClO}_4/\text{CH}_3\text{CN}$, the potential difference between the Pt and Au electrodes ($\Delta E = E_{Pt} - E_{Au}$) was varied linearly with time, starting from zero with no reference electrode in the cell. A scan speed of 20 mV/s, which would give an almost steady-state response in four-electrode experiments, was used. However, a steady-state (or even near steady-state) response was not obtained at first in this two-electrode experiment. Redox conduction currents were observed, but the potential difference range over which they occurred continually changed with time so that repetitive scans were not reproducible. The direction and rate of the change varied from one experiment to the next. After some time of scanning, the current/voltage pattern did tend to stabilize and become more nearly reproducible, but again the time required for stabilization and the final ΔE potential difference range giving

redox conduction varied from one experiment to the next.

The above behavior can be rationalized with reference to Fig. 2. Since neither the Pt nor Au electrode potentials are independently controlled, but only the potential difference between the two is controlled, a position on the three-dimensional surface of Fig. 2 is not specified. Also, the potentials of the two electrodes (relative to the reference electrode scale), and hence the current, can be influenced by the reactions of impurities such as Au ions from gold oxidation during conditioning, O_2 , or H_2O . One simplifying factor is the very large surface area of the Au electrode relative to that of the Pt, so that a large charge is required to change its potential. [SEM shows the gold film to be made up of small particles. It is porous and exhibits a large charging current (9a).] Thus, as ΔE is varied, so that the polymer film becomes mixed valent and redox conduction occurs, the potential of the Au electrode typically changes by only ca. 50 mV. However, the Au electrode potential does tend to drift with time.

A conceptual solution to this problem would be to charge the polymer to its 50/50 mixed valent state at the start of the experiment. Then both Pt and Au should initially be at E° for the polymer (0.78V vs. Ag/AgCl), and any applied potential difference $E_{Pt} - E_{Au}$ should just cause a redistribution of oxidized and reduced sites. Hence, redox conduction currents should be centered at $\Delta E = 0$. However, even if initially charged, the polymer does not in fact remain for long in the 50/50 mixed valent state, and the potentials of the two electrodes still drift with time. A change to more positive ΔE is probably due to reduction of Au(I) ions from gold dissolution; the more usual change is a lowering of ΔE , presumably due to oxidation of solvent impurities by Os(III) in the film.

Reference electrodes.—The drifting potential problem described above was solved by connecting a reference (or pseudoreference) electrode directly to the Au electrode. In this way, the Au electrode is kept at the reference electrode potential, and its potential does not change as the potential difference between it and the Pt electrode is changed, yet the simplicity of two-electrode potential control is preserved. The reference electrode used has in principle to reversibly pass a charge equal to that required to oxidize half of the redox polymer film (to generate a mixed valent film) without significantly changing its potential. This limits the number of reference electrodes that can be used, but still there are many that are suitable. By using different reference electrodes, it is possible, furthermore, to systematically vary the potential difference at which the sandwich electrode becomes conducting.

Ag/AgCl.— Ag/AgCl proved to be a suitable reference electrode in the experimental arrangement shown in Fig. 3, either with or without chloride added to the reference electrode compartment. Plots of redox conduction current vs. ΔE for this arrangement are shown in Fig. 4a for positive ΔE (where E_{Pt} is more positive than E_{Au}). The potential difference ΔE was scanned continually at 20 mV/s between 0.5 and 1.0V; the first and twentieth cyclical potential scans are shown. The redox conduction wave for the Os(III/II) couple is reasonably reproducible. The only changes over 20 scans are a slight increase in the limiting current (from 7.5 to 8.4 mA/cm^2) and a very slight change in wave-shape. The increase in i_{lim} is of unknown origin, but is also observed in four-electrode redox conduction measurements using this polymer (9b). The slight hysteresis in the forward and reverse waves of Fig. 4a, also observed in four-electrode redox conduction measurements (9b), is of unknown origin, but does diminish at lower scan rates. The current is half of its limiting value at 0.78V ($\Delta E_{1/2}$), which is E° for this polymer vs. Ag/AgCl . The i_{lim} and ($\Delta E_{1/2}$) values obtained

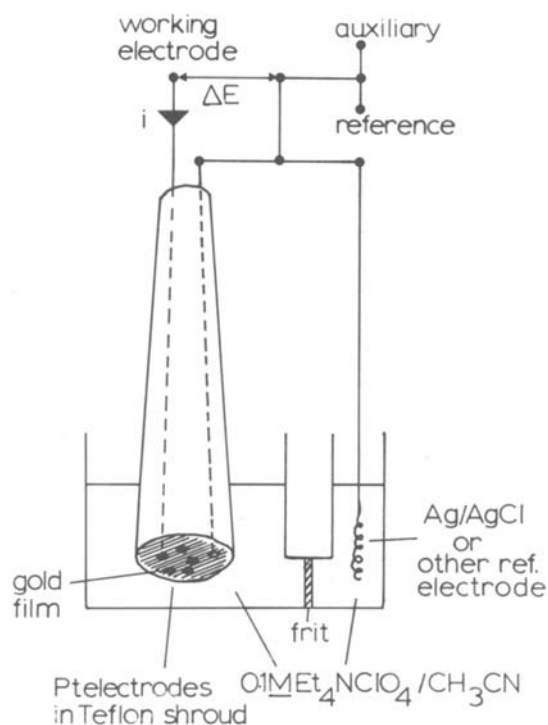


Fig. 3. Schematic representation of the sandwich electrode diode-type device, showing the potentiostat connection for measurement of i vs. ΔE characteristic. Five Pt electrodes are coated with polymer, and one is left bare to serve as a contact to the gold film. Gold is deposited over both electrodes and Teflon shroud in a continuous film. Only one polymer-coated electrode is used at a time; the others do not effect the behavior of the device.

in this experiment are the same as those obtained by using the same electrode in a four-electrode redox conduction experiment.

Figure 4b shows the result for scanning to negative values of ΔE (i.e., E_{Au} more positive than E_{Pt}) for the same electrode used for Fig. 4a. Two waves, with $\Delta E_{1/2} = -1.27$ and -1.48 V, respectively, are observed, which are caused by the Os(II/I) and Os(I/0) mixed valent states ($E^{o'} = -1.27$ and -1.48 V vs. Ag/AgCl). The currents are much higher ($i_{lim} = 0.4$ A/cm²) (9b), but gradually decay during consecutive scans. The decay is probably due to irreversible damage caused to the highly reducing polymer by trace O₂. There is also a hysteresis between the forward and reverse scans which is also observed in four-electrode redox con-

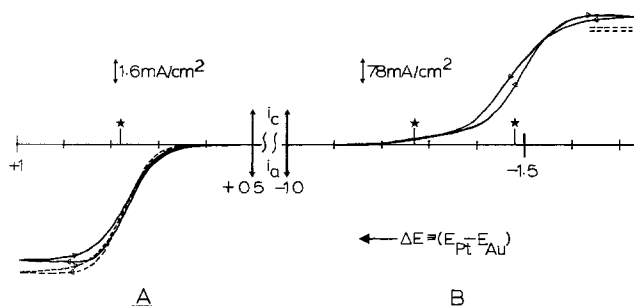


Fig. 4. Current vs. voltage characteristic of the sandwich-electrode device shown in Fig. 3, for a 6.5×10^{-8} mol/cm² poly-[Os(bpy)₂(vpy)₂]²⁺ film with Ag/AgCl reference. Stars mark the formal potentials (vs. Ag/AgCl) of Os(III/II), Os(II/I), and Os(I/0) from left to right, respectively, in the polymer film. Panel A: First (—) and twentieth (---) scans at 20 mV/s. Panel B: First (—) scan and limiting currents (---) of second and third scans at 20 mV/s.

duction experiments, as is the instability. The hysteresis is less at 5 mV/s.

The current/voltage characteristics in Fig. 4a and 4b are typical for the arrangement of Fig. 3. No observable current (at the current sensitivities used) is seen between +0.5 and -1.0V, and so this region is not shown. At potential differences $\Delta E > +1.0$ V, the limiting current remains constant at its limiting value until solvent oxidation commences at between +1.5 and +2.0V (depending upon the solvent dryness and purity). Then the current increases and damage to the sandwich, ultimately shorting, occurs. At potential differences more negative than -2.0V, solvent reduction occurs and destruction of the sandwich is very rapid.

Thus the sandwich shown in Fig. 3 behaves like a Zener diode device with both positive and negative breakdown voltages. These breakdown voltages (ca. +0.7 and -1.2V in this case) are of different magnitude and the conductivity and current vs. ΔE profiles are different. In both cases, an approximately exponential change in current with ΔE is followed by a leveling off to give a limiting current independent of ΔE . As an "electronic conductivity" ($i/\Delta E$) increases to a maximum and then decreases linearly. ("Electronic conductivity" means the effective electronic conductivity if it is imagined that the current is driven by a potential rather than concentration gradient.)

Polyvinyl-ferrocene.—A polyvinyl-ferrocene- (PVF) coated Pt electrode has been shown to be a good reference electrode (12). This polymer reference is attractive for these experiments because it can be deposited in a large amount, relative to the quantity of poly-[Os(bpy)₂(vpy)₂]²⁺, directly upon the Au film, thereby simplifying the device, and when charged to its 1:1 Fe(III/II) state, the PVF^{0/1+} film should poise the gold film at a constant potential. Note that this arrangement (Fig. 5) is a bilayer electrode (8), with a conductor whose potential can be controlled, interposed between two polymer films.

PVF was first tested as a separate reference electrode in the arrangement of Fig. 3. Several drops of a toluene solution of a polyvinyl-ferrocene-siloxane copolymer (PVF-MPS) (Ref. 13, copolymer 4) were sequentially evaporated on a coiled Pt wire, and the polymer film then cross-linked by exposure to moist HCl vapor. Approximately 10⁻⁸ mol of ferrocene sites were present on the electrode. The Os polymer film used contained approximately 10⁻¹¹ mol of redox sites. This Pt/PVF-MPS reference electrode replaced the Ag/AgCl electrode in the arrangement shown in Fig. 3. It was not oxidized before the experiment. Scanning $\Delta E = 0$ to 1V (i.e., E_{Pt} more positive than E_{Au}) at 100 mV/s gave the i vs. ΔE response shown in Fig. 6. The first and tenth scans are shown, in which the positive and negative sweeps for the first scan show significant hysteresis, and the redox conduction wave moves to

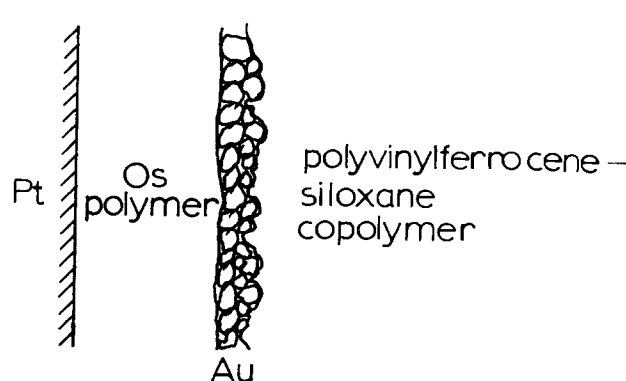


Fig. 5. Schematic representation of a sandwich-electrode diode with a self-contained PVF-MPS polymer reference to keep the gold film at a fixed potential.

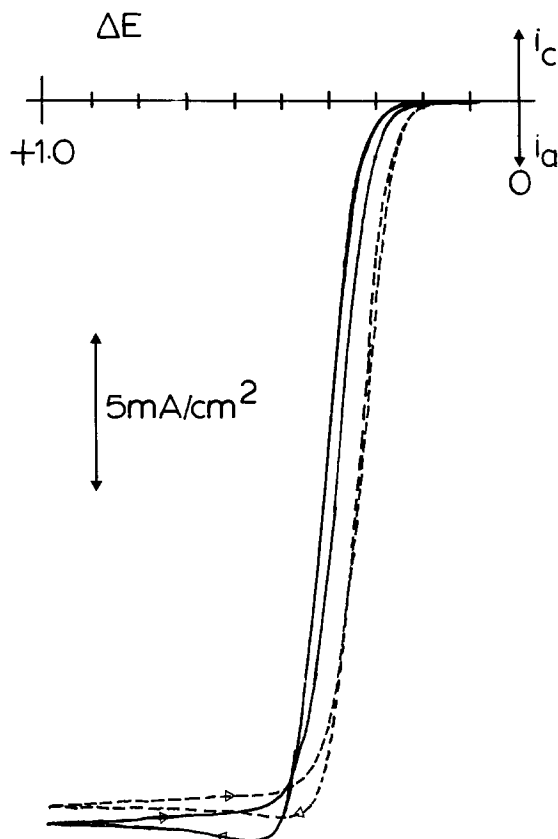


Fig. 6. Current vs. voltage characteristic for the device shown in Fig. 3 with a 2.6×10^{-8} mol/cm² poly-[Os(bpy)₂(vpy)₂]⁺² film and a Pt/PVF-MPS polymer reference electrode. First (—) and tenth (---) scans at 100 mV/s.

somewhat more negative ΔE on subsequent scans. By the tenth scan, the hysteresis is small and there is little change between consecutive scans.

This behavior can be rationalized by considering the oxidation state of the PVF-MPS film. Initially the PVF-MPS film is mainly in the Fe(II) oxidation state, and so its rest potential and that of the Au electrode which it contacts is somewhat more negative, about 0.08V, than E° for PVF-MPS, which is +0.45V vs. Ag/AgCl (13). The E° for the Os(III/II) reaction is +0.78V vs. Ag/AgCl (9), and, accordingly, on the first potential sweep the half-wave potential $\Delta E_{1/2}$ of the Os(III/II) reaction occurring on the Pt electrode is at +0.41V (+0.78 - 0.45 + 0.08). On the subsequent negative scan of the Pt electrode potential vs. that of Au and of the PVF-MPS film, we find that $\Delta E_{1/2}$ occurs at 0.38V vs. SSCE. Thus, in some way the PVF-MPS film has become, on the average, more oxidized during the voltammogram, so that its and the Au electrode potential are more positive. This trend of the PVF-MPS film becoming more oxidized continues, but slows to a very small rate of change as the PVF-MPS gradually becomes more oxidized. Table I contains $\Delta E_{1/2}$ values for the sandwich electrode after a number of different experiments. After long periods of use, the $\Delta E_{1/2}$ sometimes drops below the ideal $\Delta E_{1/2} = +0.33$ V that a 1:1 PVF-MPS mixed valent state should yield, but the difference (90 mV) is not great, and this does not always occur, as illustrated by Table I. When allowed to rest, the $\Delta E_{1/2}$ does become poised at a value near the ideal +0.33V.

Measurements over a ΔE range of +2.0 to -2.0V were also made with the Pt/PVF-MPS reference electrode arrangement of Fig. 3. The results were similar to those obtained with an Ag/AgCl reference electrode (Fig. 4), except that the redox conduction of all three waves occurred at potentials ca. 0.45V more negative,

Table I. $\Delta E_{1/2}$ for both positive and negative scans for the device shown in Fig. 3 with a Pt/PVF-MPS reference electrode.

Scan rate = 100 mV/s.

Operation in chronological order	$\Delta E_{1/2}$ positive, V	$\Delta E_{1/2}$ negative, V
Initial	0.41	0.38
Tenth scan	0.35	0.34
Fifteenth scan	0.34	0.33
After some potential-step experiments	0.30	0.29
After Pt/PVFS had not been used for 30 min	0.36	0.35
After 40 min continual scanning	0.26	0.24
After Pt/PVFS had not been used for 20h	0.36	0.35
After 30 min continual scanning	0.34	0.31

which merely reflects the difference between the potentials of the Ag/AgCl and Pt/PVF-MPS reference electrodes.

An improvement, in terms of practicality, in this device is attained by depositing the PVF-MPS polymer directly onto the gold electrode (Fig. 5). A few drops of the PVF-MPS toluene solution were allowed to evaporate to dryness on the gold-coated sandwich electrode, and the polymer was cross-linked with moist HCl. This electrode assembly gave the same type of current vs. ΔE response, as shown in Fig. 6. Initially, $\Delta E_{1/2}$ was 0.44V, but after a few scans it had dropped to 0.34V, and it soon stabilized at 0.31V. This arrangement is both compact and genuinely "two electrode." The positive and negative "diode" breakdown voltages are clearly determined by the potential of the PVF-MPS, as they were with the Ag/AgCl reference in the previous example.

A triode-type device.—We have shown above that the two-terminal sandwich electrode arrangements of Fig. 3 and of Fig. 5 act in a similar manner to a diode. The diode conductivity (the limiting currents of Fig. 4 and 6) depends on the magnitude and polarity of the applied, two-terminal potential ΔE .

It is possible to apply a second potential difference to produce a device which acts in a similar manner to a triode, as shown in Fig. 7. One potential (ΔE_1) is applied between the Pt and Au electrodes as before, and a second potential difference (ΔE_2), with a common terminal to ΔE_1 , is applied between the Au and Ag/AgCl electrodes. In the circuit in Fig. 7, the current flowing between the Au and Pt electrodes is now also controlled by the potential difference between the Au and Ag/AgCl electrodes, as is demonstrated by the voltammograms shown in Fig. 8. In the traces shown, the potential difference applied across the Os polymer film (ΔE_1), was held constant at 50 mV (curve A), 100 mV (curve B), 300 mV (curve C), or 500 mV

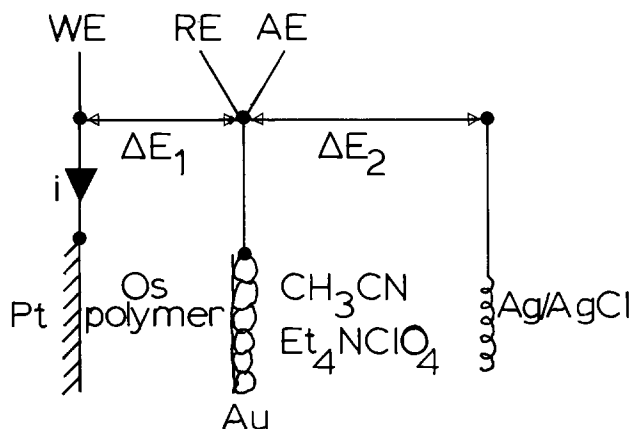


Fig. 7. Circuit for demonstration of the triode-type device. WE, RE, and AE are the three terminals of the potentiostat, which measure current. ΔE_1 and ΔE_2 are supplied by independent triangle wave generators.

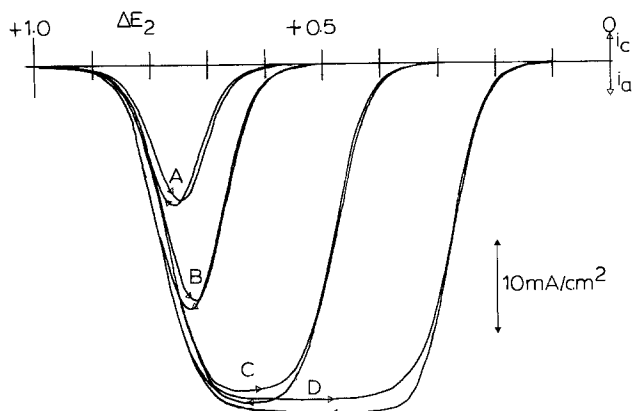


Fig. 8. Current vs. ΔE_2 for the device shown in Fig. 7 at fixed values for ΔE_1 of 50 mV (A), 100 mV (B), 300 mV (C), and 500 mV (D). ΔE_2 was varied linearly at 1 mV/s. 9.1×10^{-8} mol/cm² poly[Os(bpy)₂(vpy)₂]²⁺.

(curve D), while the potential difference between the Au and Ag/AgCl electrodes (ΔE_2) was scanned at 1 mV/s (using a triangle wave generator connected between the Ag/AgCl electrode and the gold electrode contact).

The traces of Fig. 8 can be understood with reference to Fig. 2. The locus of the scans used in Fig. 8 are plotted on Fig. 2 and labeled in the same way (i.e., curve A in Fig. 2 corresponds to $\Delta E_1 = 50$ mV, curve A of Fig. 8). Consider curves A of Fig. 2 and 8. When $\Delta E_2 = 0.0$ V, then $E_{Au} = 0.0$ V (vs. Ag/AgCl), and $E_{Pt} = +0.05$ V (is ΔE_1). Since $E^\circ = 0.78$ V vs. Ag/AgCl for Os(III/II), the polymer is completely reduced, there are no concentration gradients within the film, and no current flows. As ΔE_2 increases and E_{Au} and E_{Pt} both approach E° , both electrodes become capable of driving the Os(II) \rightarrow Os(III) reaction. However, there will always be more oxidized polymer at the Pt electrode than at the Au electrode, because $\Delta E_1 = +0.05$ V, and so electrons will flow from Pt to Au. The difference in [Os(III)] concentration at the two electrodes, and hence the current, will be greatest when $(E_{Pt} - E^\circ) = (E^\circ - E_{Au})$, since at E° the Nernstian plot (Fig. 2) has the largest gradient. As ΔE_2 becomes yet larger, the current decreases to zero as both E_{Pt} and E_{Au} become significantly greater than E° and the polymer film is completely oxidized.

Last, consider curves D of Fig. 2 and 8. When $\Delta E_1 = 500$ mV, following the reasoning for curves A, there exists a range of ΔE_2 values between 0.35 and 0.65 V, for which the film is almost completely oxidized at the Pt electrode and almost completely reduced at the Au electrode. Thus, over this entire region the limiting current of the polymer film continues to flow from Pt to Au.

Response time for the diode-type device.—The rate at which the current passing through the diode-type devices discussed here changes from near-zero to the limiting current, or vice versa, as ΔE passes the breakdown potential, depends on how quickly the osmium polymer can be charged to its mixed valent state. Thus, the diode response time is influenced by the polymer film thickness and the concentration of redox sites, since these determine the total quantity of Os sites in the polymer, and by the rate at which electron diffusion occurs through the polymer as measured by the parameter D_{ct} .

Figure 9 shows the result of repeatedly stepping the potential difference ΔE applied to the sandwich-cell arrangement of Fig. 3, with a Ag/AgCl reference electrode, between 0.0 and +1V at 5s intervals. This stepping program crosses the breakdown potential, as seen with reference to Fig. 6. For each potential step, there is a current spike of ca. ± 0.1 A/cm² (measured by an

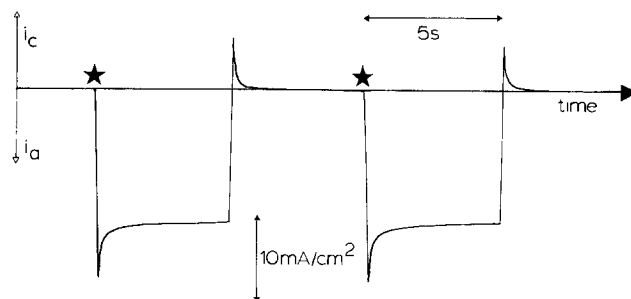


Fig. 9. Current vs. time plot for the device shown in Fig. 3 with a 4.7×10^{-8} mol/cm² poly[Os(bpy)₂(vpy)₂]²⁺ film and an Ag/AgCl reference electrode. The potential difference ΔE across the film was repeatedly stepped from 0.0 to +1V and back (*) at 5s intervals.

oscilloscope) which rapidly decays to either zero or i_{lim} , depending upon the applied potential difference. The rate at which this current decay occurs and the device achieves a stable response should be described by the finite diffusion current-time relation (4d)

$$i = \left[\frac{nFAD_{ct}^{1/2}C_T}{(\pi t)^{1/2}} \right] \left[\sum_{k=0}^{\infty} (-1)^k \left[\exp \left[\frac{-k^2 d^2}{D_{ct} t} \right] - \exp \left[\frac{-(k+1)^2 d^2}{D_{ct} t} \right] \right] \right]$$

This equation allows estimate of the time required to oxidize or reduce, say 99% of the polymer. For the electrode used for Fig. 9, $D_{ct} = 1.6 \times 10^{-9}$ cm²/s as evaluated from the limiting current. Taking $C_T = 1.5 \times 10^{-3}$ mol/cm³ and $d = 3.1 \times 10^{-5}$ cm from Γ_T/C_T , we estimate that the polymer film should be 99% charged in ca. 1s. This is approximately what is experimentally observed (Fig. 9).

(★ D_{ct} was initially 5.0×10^{-9} cm²/s for this electrode, which is in agreement with results reported elsewhere (9). However, prior to the experiment of Fig. 9, this electrode had been used extensively in the somewhat unstable Os(I) and Os(0) states, which caused D_{ct} to gradually decrease to 1.6×10^{-9} cm²/s.)

An undegraded poly-[Os(bpy)₂(vpy)₂]²⁺ film has a D_{ct} of 5×10^{-9} cm²/s. If a sandwich device could be constructed from this polymer with a film thickness as low as 500Å, then by the above analysis, it could be charged to 99% in just 10 ms. This is a reasonable switching time for a diode device in many circumstances, particularly for electrochromic applications which also rely upon electrochemical reactions (14).

Stability.—The stability of the sandwich electrode devices discussed in this paper has been quite variable. Some individual electrodes in the multimicroelectrode assembly are stable for hours of continual use, while others exhibit behavior interpretable as a short between the Pt and Au electrodes after just one scan through the Os(III/II) redox conduction wave. The Os(III/II) redox activity, observed cyclic voltammetrically with a film on a Pt electrode, is also stable for many hours. We believe that the sandwich-electrode assembly is inherently stable and that instability where observed is due to nonoptimum construction methods. In particular, other work in this laboratory (11) has shown that use of glass rather than Teflon for the shroud, and very particular polishing procedures, promotes a much lower incidence of shorting effects. It appears that the shorting often occurs on the edge of the Pt microdisks. Additionally, we have identified a number of conditions which promote instability during use of the electrode: (i) reduction of the polymer to Os(I) or Os(0) causes (eventually) irreversible damage to the polymer and often pro-

duces shorting. (ii) If the potential of the Pt electrode is made too positive (e.g., +2V vs. SSCE), then shorting occurs. (iii) If the electrode assembly is allowed to dry and then is reused, shorting occurs.

We describe our most stable electrode assembly as an illustration of stability that has been achieved. This electrode, which initially demonstrated a limiting current of 38 mA/cm², was used as a diode-type device in the manner of Fig. 3 for ca. 1h scanning ΔE between 0.0 and +1V at 20 or 100 mV/s, then as a triode-type device at scan rates from 1-100 mV/s for ca. 1h, stored under acetonitrile unused for 1h, and then as a triode-type device for a further 2.5h at a scan rate of 1 mV/s. There then followed 23h of nonuse, ca. 1h of use as a diode-type device, 20h of nonuse, and finally measurements of redox conduction of the Os(I) and Os(0) states, during which it shorted. During this sequence of experiments, i_{lim} for Os(III/II) redox conduction increased from 38 to 45 mA/cm² during the first 40 min of use, and then gradually decreased to 35 mA/cm² just before the electrode's fatality.

Since in practical use these devices would be subject to voltage pulses, rather than linear voltage changes, we investigated their stability when subject to 0.0 to +1V voltage pulses with pulse widths between 5s and 0.1 ms. No evidence for decreased stability was observed.

Acknowledgment

This research was supported in part by the Office of Naval Research.

Manuscript submitted Aug. 8, 1983; revised manuscript received ca. Nov. 7, 1983.

REFERENCES

- (a) A. Merz and A. J. Bard, *J. Am. Chem. Soc.*, **100**, 3222 (1978); (b) L. L. Miller and M. R. Van De Mark, *J. Electroanal. Chem.*, **100**, 3223 (1978); (c) R. Nowak, F. A. Schultz, M. Umana, H. Abruna, and R. W. Murray, *ibid.*, **94**, 219 (1978).
- R. W. Murray, in "Electroanalytical Chemistry," A. J. Bard, Editor, Vol. 13, Marcel Dekker, Inc., New York (1984).
- F. B. Kaufman, A. H. Schroeder, E. M. Engler, S. R. Kramer, and J. Q. Chambers, *J. Am. Chem. Soc.*, **102**, 483 (1980).
- (a) N. Oyama and F. C. Anson, *This Journal*, **127**, 640 (1980); (b) P. J. Peerce and A. J. Bard, *J. Electroanal. Chem.*, **114**, 89 (1980); (c) R. J. Nowak, F. A. Schultz, M. Umana, R. Lam, and R. W. Murray, *Anal. Chem.*, **52**, 315 (1980); (d) P. Daum, J. R. Lenhard, D. R. Rolison, and R. W. Murray, *J. Am. Chem. Soc.*, **102**, 4649 (1980).
- (a) E. Laviron, *J. Electroanal. Chem.*, **112**, 1 (1980); (b) C. P. Andrieux and J.-M. Saveant, *ibid.*, **111**, 377 (1980).
- N. Oyama and F. C. Anson, *This Journal*, **127**, 247 (1980).
- (a) D. A. Buttry and F. C. Anson, *J. Am. Chem. Soc.*, **105**, 685 (1983); (b) H. S. White, J. Leddy, and A. J. Bard, *ibid.*, **104**, 4811 (1982); (c) C. R. Martin, I. Rubinstein, and A. J. Bard, *ibid.*, **104**, 4817 (1982); (d) K. N. Kuo and R. W. Murray, *J. Electroanal. Chem.*, **131**, 37 (1982).
- (a) H. D. Abruna, P. Denisevich, M. Umana, T. J. Meyer, and R. W. Murray, *J. Am. Chem. Soc.*, **103**, 1 (1981); (b) P. Denisevich, K. W. Willman, and R. W. Murray, *ibid.*, **103**, 4727 (1981).
- (a) P. G. Pickup and R. W. Murray, *ibid.*, **105**, 4510 (1983); (b) P. G. Pickup, W. Kutner, C. R. Leidner, and R. W. Murray, *ibid.*, To be published.
- L. B. Anderson and C. N. Reilley, *J. Electroanal. Chem.*, **10**, 295 (1965).
- D. T. Sawyer and J. T. Roberts, "Experimental Electrochemistry for Chemists," p. 80, Wiley-Interscience, New York (1974).
- P. J. Peerce and A. J. Bard, *J. Electroanal. Chem.*, **108**, 121 (1980).
- S. Nakahama and R. W. Murray, *ibid.*, To be published.
- M. N. Nicholson and F. A. Pizzarello, *This Journal*, **128**, 1740 (1981).

Electrocatalytic Rate Enhancement of Propylene Epoxidation on Porous Silver Electrodes Using a Zirconia Oxygen Pump

M. Stoukides and C. G. Vayenas*¹

Department of Chemical Engineering, Massachusetts Institute of Technology, Cambridge, Massachusetts 02139

ABSTRACT

Propylene epoxidation and deep oxidation on porous silver electrodes was studied galvanostatically in the solid electrolyte cell C₃H₆, C₃H₆O, CO₂, H₂O, O₂, Ag|ZrO₂(8% Y₂O₃)|Ag, O₂. It was found that when O²⁻ ions are pumped electrochemically to the silver catalyst electrode, the rates of propylene epoxidation and oxidation to CO₂ increase significantly with simultaneous enhancement of the selectivity to propylene oxide. The opposite effect is observed upon reversal of the pumping voltage. The enhancement in the rate of epoxidation and deep oxidation can exceed the rate of O²⁻ pumping by two orders of magnitude. The magnitude of the catalytic rate enhancement depends on the imposed current, anodic gas composition, and catalyst electrode surface area, and is proportional to the pumping voltage. This new phenomenon is similar to that observed with ethylene oxidation and appears to be due to formation of a catalytically active surface silver oxide at the anode.

Stabilized zirconia solid electrolyte cells have been used in recent years as oxygen gauges (1), as fuel cells with H₂, CO, CH₄ (2), and NH₃ (3, 4) as the fuel, as a means of measuring the oxygen activity on working metal catalysts (5, 6), as oxygen pumps to dissociate oxygen containing compounds, such as H₂O (7) and NO (8, 9), and to enhance the rate of certain catalytic reactions such as CO hydrogenation (10).

It was found recently that stabilized zirconia oxygen ion pumps can also be used to influence the product

selectivity of certain catalytic reactions; a porous polycrystalline silver film was used simultaneously as one of the electrodes of a stabilized zirconia oxygen concentration cell and as a catalyst for ethylene oxidation (11, 12). With ethylene and O₂ present at the anode and the cell open-circuited, the silver film acts as a regular catalyst for ethylene epoxidation (i.e., ethylene oxide formation) and deep oxidation (i.e., formation of CO₂). However, it was found that the product selectivity and yield change considerably when external voltages are applied to the cell and O²⁻ ions are pumped to or from the working catalyst. It was found that the selectivity to ethylene oxide (mols ethylene oxide produced/mols ethylene re-

* Electrochemical Society Active Member.

¹ Present address: Department of Chemical Engineering, University of Patras, Patras, Greece.

Key words: solid electrolyte, propylene oxidation, zirconia pump, silver electrode.

acted) can increase or decrease by more than 20% and that the ethylene oxide yield (mols ethylene oxide produced/mols ethylene fed to the reactor) can increase or decrease by more than a factor of two. These phenomena were attributed to the formation of a catalytically active surface silver oxide (11, 12).

In the present communication, we report on similar phenomena observed with propylene oxidation on porous silver electrodes in stabilized zirconia cells. It is shown that the catalytic activity and selectivity of silver for propylene oxidation can be modified considerably by electrochemical oxygen pumping. The results are consistent with the surface silver oxide model proposed for ethylene oxidation (12).

Experimental

A schematic diagram of the apparatus used in the investigation is shown in Fig. 1. It consists of a gas feed system, a stabilized zirconia reactor cell, and a gas analysis system.

The reactor cell shown in Fig. 2 consists of a 1/2 in. id 8 mol percent (m/o) Y_2O_3 stabilized ZrO_2 tube closed flat on the one end, obtained from Zircoa Corning Glass. The reactor volume was 30 cm³. A porous silver catalyst electrode film was deposited on the flat bottom of the zirconia tube by coating with a thin layer of Ag suspension in butyl acetate, followed by drying and calcining at 400°C. Auger electron spec-

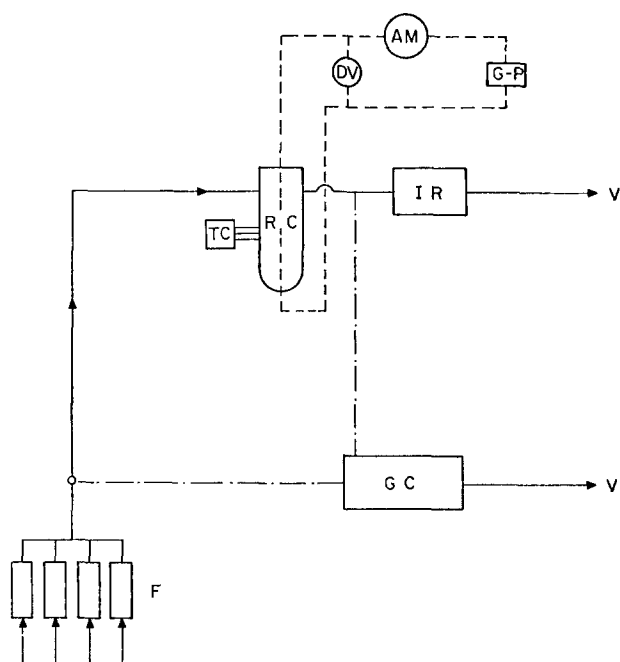


Fig. 1. Schematic diagram of the apparatus: (F) calibrated feed flowmeters, (RC) reactor cell, (TC) temperature controller, (IR) infrared analyzer, (GC) gas chromatograph, (AM) multimeter, (DV) differential voltmeter, (G-P) galvanostat-potentiostat, (V) vent.

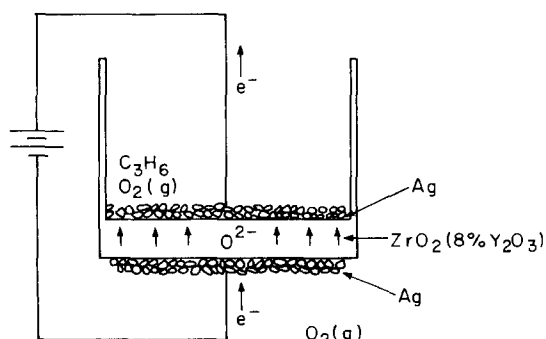


Fig. 2. Schematic diagram of the cell reactor

toscopic analysis showed that the resulting Ag films are fairly clean, with only trace impurities of Na and S (6). A similar Ag film was deposited on the outside bottom wall of the zirconia tube, which was exposed to ambient air.

Several stabilized zirconia reactor cells were used in the course of the present investigation. The electrolyte thickness of each cell was roughly between 150 and 300 μ m. The cells differed in the surface area of the silver catalyst electrode. These areas were determined by measuring the reactive oxygen uptake of the catalyst Q (mols O_2) upon titration with ethylene, as described in detail elsewhere (6). The surface areas of the catalyst electrodes used in the present investigation are given in Table I.

After an induction period which lasted approximately 48h for each new catalyst, the catalyst electrode open-circuit activities and selectivities remained constant ($\pm 2\%$) for several weeks (12). All the data reported here, including surface areas, were obtained after the termination of the induction period.

The reactants were certified standards of propylene diluted in N_2 and Matheson zero-grade air. They could be further diluted in N_2 , in order to maintain the partial pressure of ethylene or oxygen constant during the experiments. Reactants and products were analyzed by on-line gas chromatography. A Porapak Q column was used to separate air, propylene, carbon dioxide, and propylene oxide; a molecular sieve 5A column was used to separate oxygen and nitrogen. The concentration of CO_2 in the reactant effluent stream was also monitored continuously by means of a Beckman 864 Infrared Analyzer.

Constant current or voltage across the cell was applied by means of a AMEL 549 potentiostat-galvanostat. The voltage drop across the cell was monitored with a J. Fluke 891 A differential voltmeter. Current was measured by a J. Fluke 8040 A multimeter. Further experimental details are given in Ref. (11, 12).

Results

Close agreement was observed ($\pm 1\%$) between measured and theoretical EMF values when O_2 , N_2 , or He mixtures of known P_{O_2} were fed through the zirconia cell reactor. This verified the pure ionic conductivity of the solid electrolyte. When propylene-oxygen mixtures are fed through the reactor, the open-circuit EMF E , which reflects the oxygen activity a_{O_2} on the catalyst (5, 6) according to

$$E = (RT/4F) \ln [a_{O_2}/(0.21)] \quad [1]$$

takes values between -10 and -100 mV, indicating that $a_{O_2} < P_{O_2}$, because the intrinsic rate of oxygen adsorption is comparable to the rate of the surface oxidation steps (13).

The effect of oxygen pumping.—The effect of electrochemical oxygen pumping on the rates of propylene epoxidation r_1 and deep oxidation r_2 is shown in Fig. 3. At time $t < 0$ the circuit is open and the silver catalyst electrode acts as a regular catalyst for propylene epoxidation (i.e., conversion to propylene oxide) and deep oxidation (i.e., conversion to CO_2). Since temperature ($395^\circ \pm 1^\circ C$) and gas feed composition ($P_{Pr} \sim 2.8 \cdot 10^{-3}$ bar, $P_{O_2} \sim 0.15$ bar) are maintained constant, the catalyst electrode is at a steady state characterized by $r_{10} = 0.050 \cdot 10^{-7}$ mol/s and $r_{20} = 2.53 \cdot 10^{-7}$ mol/s.

Table I. Catalyst electrode surface areas

Reactor cell	Reactive oxygen uptake Q (mol O_2)
RC1	$4 \cdot 10^{-7}$
RC2	$1.5 \cdot 10^{-7}$
RC3	$7.6 \cdot 10^{-7}$
RC4	$1 \cdot 10^{-7}$
RC5	$10 \cdot 10^{-7}$

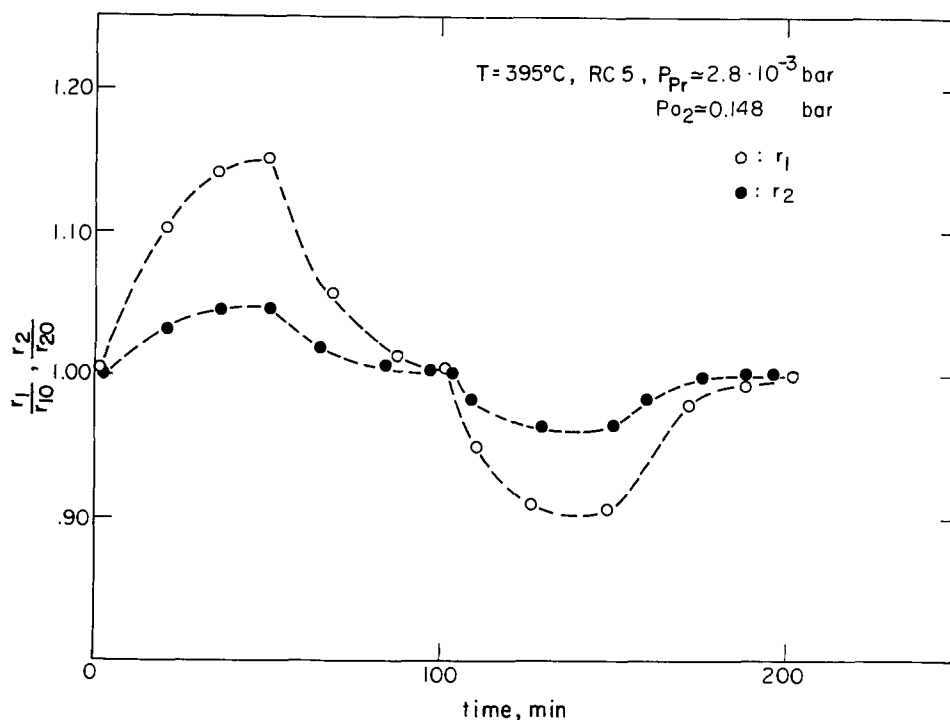


Fig. 3. Transient effect of oxygen pumping during propylene oxidation.

At time $t = 0$, a constant current of $+200 \mu\text{A}$ is applied to the cell. Oxygen ions are pumped to the catalyst. This causes a transient increase in both reaction rates. Figure 3 shows that the relative increase in r_1 is higher than the corresponding relative increase in r_2 ; and thus, the selectivity to propylene oxide increases. The system reaches a new steady state after approximately 30 min. At $t = 50$ min, the circuit is opened and the catalyst returns to its initial steady state, indicating the reversibility of the phenomenon. At $t = 100$ min, a constant current of $-100 \mu\text{A}$ is applied across the cell, so that O^{2-} are pumped from the catalyst. As a result, both rates decrease and so does the selectivity to propylene oxide. Figure 3 shows that when the circuit is opened again, both rates return to their original steady-state values r_{10} and r_{20} .

The rate of oxygen transport through the electrolyte $G_{\text{O}^{2-}}$ can be calculated from the value of the imposed current i ($G_{\text{O}^{2-}} = i/2F$ gramatom oxygen/s). The increase in the rate of oxygen consumption due to the

increase in the rate of epoxidation and deep oxidation during reaction was found to exceed $G_{\text{O}^{2-}}$ by a factor as high as 150. This shows that the catalytic properties of the silver catalyst electrode are changing substantially during oxygen pumping.

Effect of current and pumping voltage.—Figures 4 and 5 show the effect of imposed current on the final steady-state increase in the rates of propylene epoxidation and deep oxidation for two reactor cells which differed in catalyst area. In both cases, temperature and gas phase composition were kept constant throughout the experiments. It can be seen that both rates increase with increasing current up to 250–300 μA , above which they remain practically constant. The effect is qualitatively the same for both rates; however, the relative increase in the rate of epoxidation r_1 is much larger than that in r_2 ; thus, selectivity to propylene oxide increases. It can also be seen from Fig. 4 and 5 that the relative increases in r_1 and r_2 are higher for

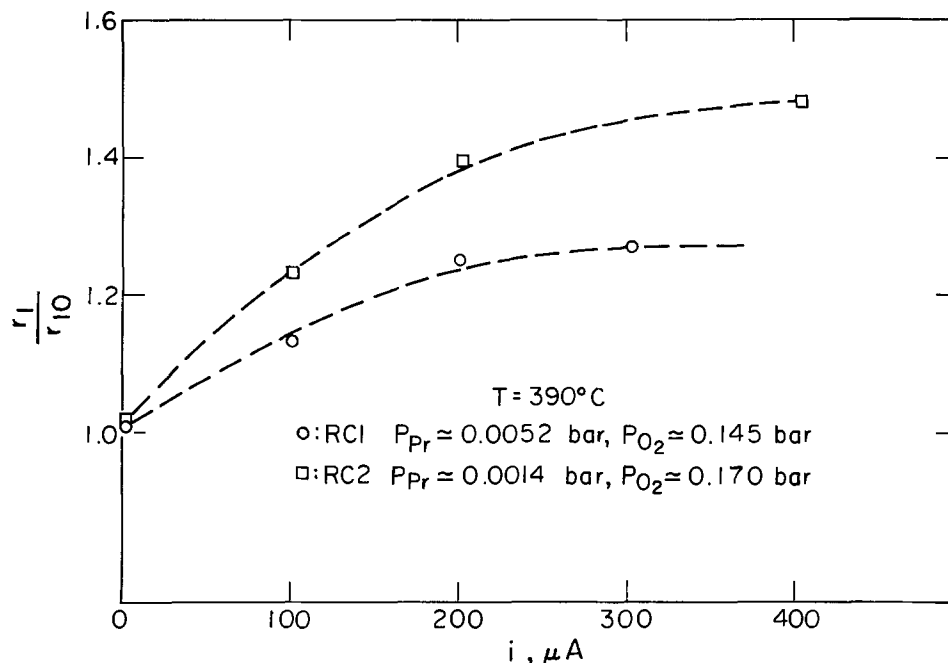
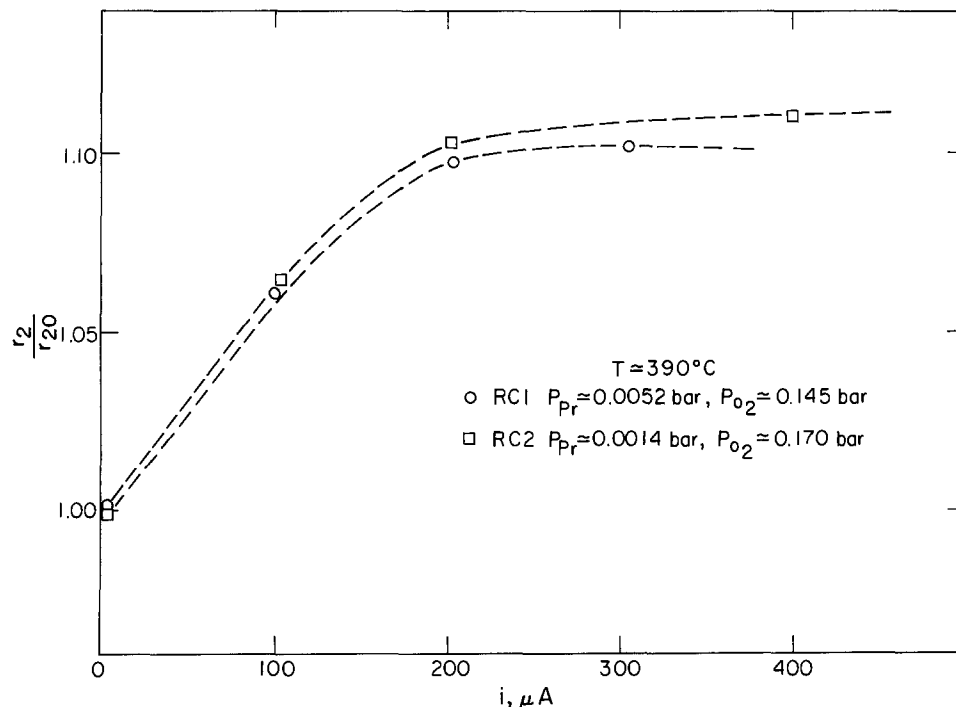


Fig. 4. Steady-state effect of current on the rate of propylene epoxidation.

Fig. 5. Steady-state effect of current on the rate of propylene oxidation to CO_2 .



reactor cell RC2 than for RC1. This is due to the higher catalyst electrode surface area of RC1 as shown in Table I and discussed below.

Figure 6 shows a typical cell voltage response to a galvanostatic step increase in current. At $t < 0$, the circuit is open and the cell voltage equals the open-circuit EMF E given by the Nernst equation [1]. At $t = 0$, a constant current of $200 \mu\text{A}$ is imposed across the reactor cell. The initial sharp rise in V at $t = 0$ corresponds to the ohmic drop iR_c , where R_c is the ohmic resistance of the solid electrolyte and the electrodes. The subsequent gradual increase ΔV to a final asymptotic value corresponds to formation of surface

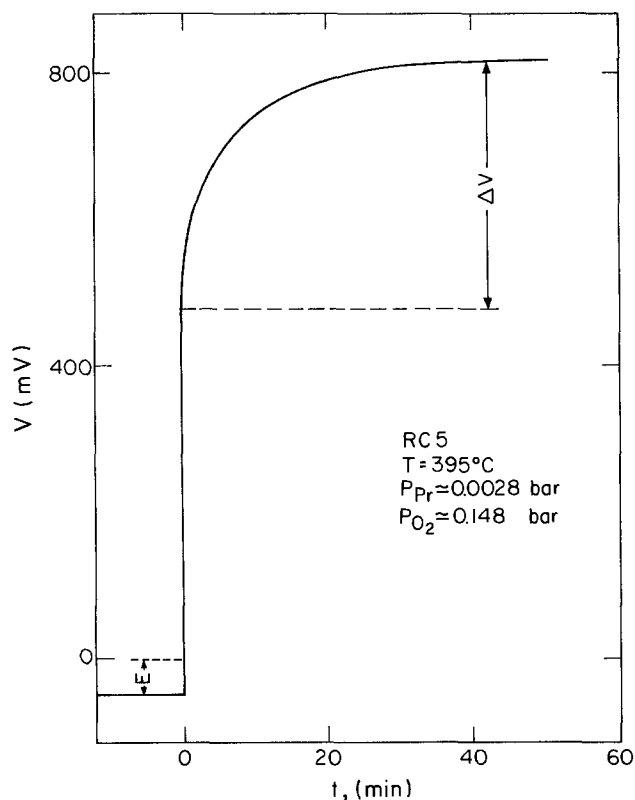


Fig. 6. Galvanostatic transient voltage response

intermediates on the catalyst electrode. A similar voltage behavior was observed during the electrocatalytic oxidation of ethylene (12). One can define the pumping voltage ΔV from

$$\Delta V = V - E - iR_c \quad [2]$$

As shown in Fig. 7, the pumping voltage response during a galvanostatic transient parallels the reaction rate response. Within the accuracy of the measurements, both transients are characterized by the same

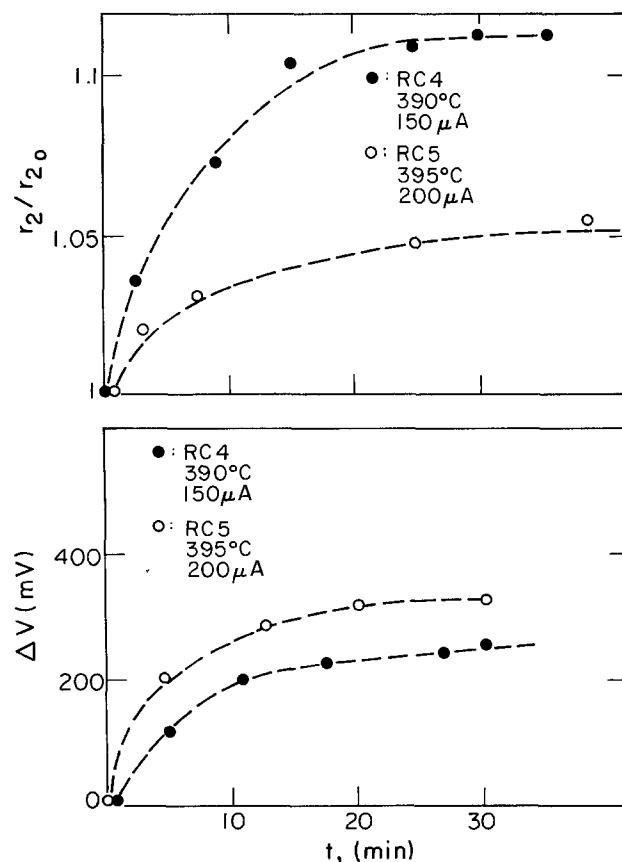


Fig. 7. Galvanostatic transient response of deep oxidation rate and cell overvoltage.

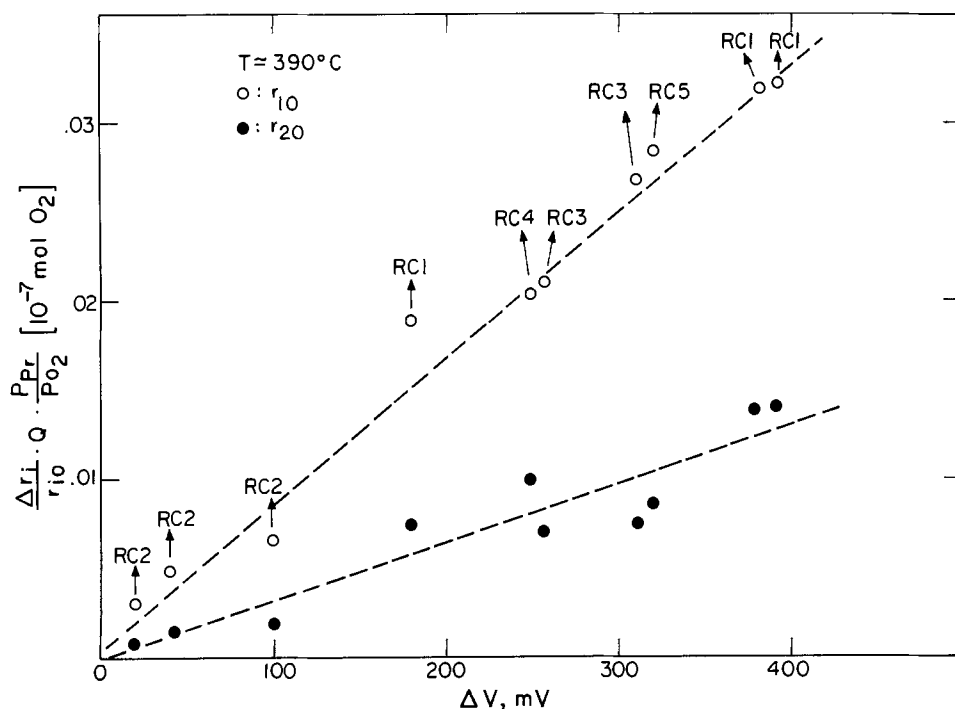


Fig. 8. Effect of pumping voltage, gaseous composition, and catalyst electrode surface area on the rates of propylene epoxidation ($i = 1$, \circ) and deep oxidation ($i = 2$, \bullet).

relaxation time constant τ_0 , defined as the time required for ΔV or Δr_1 and Δr_2 to reach 63% of their final asymptotic values ΔV_{\max} , $\Delta r_{1, \max}$, and $\Delta r_{2, \max}$, respectively. Furthermore, as shown in Fig. 8 and Table II for a given reactor cell and for given temperature and gaseous composition, the steady-state increase in reaction rates $(\Delta r_i)_{\max}$ is roughly proportional to the steady-state pumping voltage $(\Delta V)_{\max}$, i.e.

$$(\Delta r_i)_{\max} = \beta_i (\Delta V)_{\max} \quad [3]$$

The proportionality constants β_i strongly depend on gaseous composition and catalyst electrode surface area, as discussed below.

Effect of surface area and gaseous composition.—Table II contains steady-state data obtained from five different reactors RC1, RC2, RC3, RC4, and RC5. Comparing runs 7 and 9, which were obtained with almost identical pumping voltage, temperature, and gaseous composition, it can be seen that the relative increase in the reaction rates $(\Delta r_i/r_{i0})$ is inversely proportional to the catalyst electrode surface area. Similar conclusions can be reached by comparing runs 2 and 8, which were obtained with almost the same gaseous composition, temperature, and current and comparable pumping voltage. The same behavior has been observed during ethylene oxidation on silver (11, 12).

Similar to ethylene oxidation, the relative increase in the rates of epoxidation and deep oxidation at constant catalyst electrode surface area, temperature, and imposed current is roughly proportional to P_{O_2}/P_{Pr} . This can be seen from runs 7 and 8 of Table II.

Figure 8 contains all the steady-state data of Table II, obtained with five different reactors, and shows that, similarly to ethylene electro-oxidation (12), all the data can be adequately described by one single expression

$$\frac{\Delta r_i}{r_{i0}} \cdot Q \cdot \frac{P_{Pr}}{P_{O_2}} = \alpha_i \Delta V \quad [4]$$

where α_1 , α_2 ($i = 1, 2$) are constants with a ratio $\alpha_1/\alpha_2 = 2.5 \pm 0.5$. Equation [4] contains as a limiting case Eq. [3], which is valid for constant gaseous composition.

In view of the fact that over the range of experimental conditions of the present investigation, r_{i0} are first order in propylene and zero order in oxygen (13), it follows from Eq. [4] that

$$\Delta r_i = K_{i0} \cdot \alpha_i \cdot \Delta V \cdot P_{O_2} \quad [5]$$

where K_{i0} are the intrinsic rate constants for propylene epoxidation ($i = 1$) and deep oxidation ($i = 2$), respectively.

Discussion

The observed phenomena show clearly that the properties of the silver catalyst electrode change significantly during electrochemical oxygen pumping. The increase in the rates of propylene epoxidation and deep oxidation can exceed the rate of oxygen transport through the electrolyte by two orders of magnitude. The selectivity also changes considerably. It can be easily shown that the electrolyte temperature

Table II. Effect of surface area and gas composition on the reaction rates enhancement

Reactor cell	P_{Pr} bar	P_{O_2} bar	Electrode surface area Reactive Q_0 uptake Q_0 (mol O_2)	Current (μA)	Pumping voltage ΔV V	Intrinsic rate		$\frac{\Delta r_1}{r_{10}}$	$\frac{\Delta r_2}{r_{20}}$	Intrinsic selectivity $\frac{r_{10}}{r_{10} + r_{20}} \cdot 10^3$	Selectivity $\frac{r_1}{r_1 + r_2} \cdot 10^2$	Temperature $^{\circ}C$
						r_{10} -mol C_3H_6 /s	r_{20} -mol C_3H_6 /s					
RC1	0.0052	0.145	$4 \cdot 10^{-7}$	100	0.18	$5.8 \cdot 10^{-9}$	$1.8 \cdot 10^{-7}$	0.13	0.06		3.3	390
RC1	0.0052	0.145	$4 \cdot 10^{-7}$	200	0.39	$5.8 \cdot 10^{-9}$	$1.8 \cdot 10^{-7}$	0.22	0.1	3.1	3.45	390
RC1	0.0052	0.145	$4 \cdot 10^{-7}$	300	0.42	$5.8 \cdot 10^{-9}$	$1.8 \cdot 10^{-7}$	0.23	0.1		3.5	390
RC2	0.0014	0.170	$1.5 \cdot 10^{-7}$	100	0.02	$0.6 \cdot 10^{-9}$	$0.19 \cdot 10^{-7}$	0.22	0.06		3.5	400
RC2	0.0014	0.170	$1.5 \cdot 10^{-7}$	200	0.04	$0.6 \cdot 10^{-9}$	$0.19 \cdot 10^{-7}$	0.39	0.1	3.0	3.85	400
RC2	0.0014	0.170	$1.5 \cdot 10^{-7}$	400	0.1	$0.6 \cdot 10^{-9}$	$0.19 \cdot 10^{-7}$	0.45	0.11		4.0	400
RC3	0.0088	0.095	$7.6 \cdot 10^{-7}$	200	0.25	$10 \cdot 10^{-9}$	$5.8 \cdot 10^{-7}$	0.03	0.01	1.7	1.78	395
RC3	0.0046	0.145	$7.6 \cdot 10^{-7}$	200	0.31	$6 \cdot 10^{-9}$	$3.1 \cdot 10^{-7}$	0.11	0.03	1.9	2.1	395
RC4	0.0094	0.09	$1 \cdot 10^{-7}$	150	0.25	$1.7 \cdot 10^{-9}$	$0.8 \cdot 10^{-7}$	0.20	0.11	2.1	2.25	390
RC5	0.0028	0.15	$10 \cdot 10^{-7}$	200	0.32	$5 \cdot 10^{-9}$	$2.5 \cdot 10^{-7}$	0.15	0.045	2.0	2.16	390
RC5	0.0028	0.15	$10 \cdot 10^{-7}$	-100	-0.20	$5 \cdot 10^{-9}$	$2.5 \cdot 10^{-7}$	-0.1	-0.03		1.82	390

cannot rise locally more than 2 K at most, due to i^2R_c heat generated during oxygen pumping. This was also shown by measuring the temperature of the electrolyte at a distance of 1 mm from the two electrodes and observing no measurable temperature rise during pumping. The absence of local catalyst heating due to oxygen pumping is also demonstrated by the fact that upon reversing the direction of pumping, both r_1 and r_2 decrease (Fig. 3).

Internal and external gas phase diffusional limitations at the porous silver catalyst electrode have been shown to be totally negligible under the conditions of these experiments (6, 13). Therefore, it can be safely concluded that it is the intrinsic properties of the silver catalyst which change during electrochemical oxygen pumping.

When oxygen is pumped to the catalyst, the oxygen activity of the catalyst electrode increases dramatically. Thus, it becomes possible to at least partly oxidize the silver catalyst electrode. In previous communications related to ethylene electro-oxidation, it has been shown that the phenomenon involves surface rather than bulk oxidation of the silver crystallites (11, 12). The experimentally observed relaxation time constants of the present investigation show conclusively that this is also the case during propylene oxidation: the polycrystalline Ag films used could typically adsorb $6 \cdot 10^{-7}$ mol O_2 (Table I). Typical currents employed in the present study during the galvanostatic transients were of order 100 μA , corresponding to $2.6 \cdot 10^{-10}$ mol O_2/s transported through the electrolyte. Thus, the time required to fully cover the silver surface with surface oxide is of order 36 min in good agreement with the experimental relaxation times (Fig. 3, 6, 7). Bulk oxidation of the silver catalyst would require approximately $2 \cdot 10^{-4}$ mol O_2 . With $i = 100 \mu A$, this would correspond to relaxation time constants of about 50h. It therefore follows that the observed phenomenon is related to surface oxidation of the silver crystallites.

The observation that the transient rate changes parallel the transient overvoltage behavior (Fig. 7) strongly suggests that the increase or decrease in the rates is caused by a corresponding increase or decrease in the surface concentration of an adsorbed oxygen species or surface silver oxide. This is further corroborated by the striking similarity in the effect of oxygen pumping during ethylene (11, 12) and propylene oxidation on silver catalyst electrodes.

There is previous evidence in the literature for the existence of surface silver oxides, including the work of Seo and Sato (14) who observed a continuous exoelectron emission from silver catalysts during ethylene epoxidation, which was proportional to the rate of epoxidation. They explained their results in terms of formation of surface silver oxide Ag_2O with molecular oxygen ion O_2^- adsorbed on it. This proposed picture seems to be in excellent agreement with the present results, i.e., with

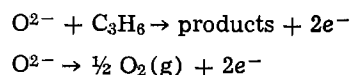
$$\Delta r_1 = K_{i0} \cdot \alpha_1 \cdot (\Delta V) P_{O_2} \quad [5]$$

if the change in the amount of surface silver oxide is proportional to ΔV and the coverage of molecular oxygen adsorbed on the oxide is proportional to P_{O_2} , or at least if the rates of epoxidation and combustion on the silver oxide are first order in oxygen.

Quantitative kinetics.—In previous communications (11, 12), we have denoted the surface oxygen species formed during oxygen pumping by AgO_2^* and its surface concentration by c (mol/cm²). The relationship between Δc and the pumping voltage ΔV can be established by the following analysis. Neglecting the double layer capacitance of the electrode-electrolyte interface, one can split the constant current i imposed during a galvanostatic transient in two parts (15)

$$i = C_{ad} \frac{d(\Delta V)}{dt} + i_{CTR} \quad [6]$$

where i_{CTR} is the current corresponding to the charge transfer reactions, i.e.



and C_{ad} is the adsorption pseudocapacitance of the oxide, which by definition equals (15)

$$C_{ad} = \frac{dq}{dV} = \lambda_0 AF \frac{d(Sc)}{d(\Delta V)} \quad [7]$$

where S is the surface area of the catalyst electrode, q is the charge stored in the oxide, A is the electrolyte surface area, and λ_0 a constant. λ_0 depends on the gas-electrode-electrolyte interline "area" per unit electrolyte area and depends solely on the catalyst porosity. Since all the electrodes used in the present investigation were prepared by the same calcination procedure, it is reasonable to assume they all had similar porosities and thus, similar values of λ_0 .

The experimental observations can be explained quantitatively by making the following assumptions. (i) The oxide pseudocapacitance C_{ad} is constant, in which case, Eq. [7] becomes

$$\Delta(Sc) = \frac{C_{ad}}{\lambda_0 AF} \Delta V \quad [8]$$

(ii) The changes Δr_i in the rates of propylene epoxidation r_1 and deep oxidation r_2 are proportional to the change in the mols of AgO_2^* . Both rates are first order in oxygen.

$$\Delta r_1 = K_1 \cdot P_{O_2} \cdot \Delta(Sc) \quad [9]$$

From Eq. [8] and [9], one obtains

$$\Delta r_1 = K_1 \frac{C_{ad}}{\lambda_0 AF} (\Delta V) P_{O_2} \quad [10]$$

which coincides with the experimental Eq. [5] and with

$$\alpha_1 = \frac{K_1}{K_{i0}} \cdot \frac{C_{ad}}{\lambda_0 AF} \quad [11]$$

It should be noted that according to Eq. [10], Δr_1 and Δr_2 do not depend on the electrode surface area. Finally, to explain the dependence of $\Delta r_1/r_{i0}$ on ΔV and gas phase composition, one can assume that the oxide forms on Ag sites which are inactive for reaction and take into account that at temperatures above 350°C and under open-circuit conditions both r_{i0} and r_{20} are first order in propylene and zero order in oxygen (13)

$$r_{i0} = K_{i0} \cdot Q \cdot P_{Pr} \quad [12]$$

This last equation is not inconsistent with the hypothesis that the rates on AgO_2^* are first order in oxygen, to the extent that the surface concentration of AgO_2^* is small under open-circuit conditions.

Combining Eq. [10]-[12], one obtains the experimental Eq. [4]. Equation [4] shows that for given gaseous composition and pumping voltage, the relative increase in the rates of epoxidation and deep oxidation are inversely proportional to the surface area Q of the catalyst electrode. This is because the intrinsic rates r_{i0} are proportional to Q , while the rate enhancement Δr_1 caused by oxide formation does not depend on Q .

In summary, the effect of oxygen pumping during propylene oxidation on silver is qualitatively identical with the effect during ethylene oxidation (11, 12). This corroborates the proposition that the rate enhancement is caused in both cases by surface oxidation of

the silver catalyst electrode. The use of *in situ* surface science techniques should prove very useful for the elucidation of the exact nature of this surface oxide. Although the exact form of the surface silver oxide is not yet known, the proposed macroscopic model can adequately explain all the experimental observations.

We note that, although zirconia oxygen pumps have been known to dramatically enhance the rate of certain reactions, such as NO decomposition (8) and CO hydrogenation (10), ethylene and propylene oxidation on silver are the first known reactions where oxygen pumping has been shown to cause a change in product selectivity.

Acknowledgments

This research was supported under NSF Grant CPE-8009436 and under a C. and H. Dreyfus Award Grant.

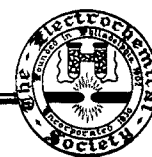
Manuscript submitted May 9, 1983; revised manuscript received ca. Nov. 2, 1983.

REFERENCES

1. C. Wagner, *Adv. Catal.*, **21**, 323 (1970).
2. T. H. Etsell and S. N. Flengas, *This Journal*, **118**,

- 1980 (1971).
3. C. G. Vayenas and R. D. Farr, *Science*, **208**, 593 (1980).
4. R. D. Farr and C. G. Vayenas, *This Journal*, **127**, 1478 (1980).
5. C. G. Vayenas, B. Lee, and J. Michaels, *J. Catal.*, **66**, 34 (1980).
6. M. Stoukides and C. G. Vayenas, *ibid.*, **64**, 18 (1980).
7. J. Weissbart, W. H. Smart, and T. Wydeven, *Aerosp. Med.*, **40**, 136 (1969).
8. S. Pancharatnam, R. A. Huggins, and D. M. Mason, *This Journal*, **122**, 869 (1975).
9. T. M. Gür and R. A. Huggins, *ibid.*, **126**, 1067 (1979).
10. T. M. Gür and R. A. Huggins, *Solid State Ionics*, **5**, 567 (1981).
11. M. Stoukides and C. G. Vayenas, *J. Catal.*, **70**, 137 (1981).
12. M. Stoukides and C. G. Vayenas, in "Catalysis under Transient Conditions," p. 181, ACS Symposium Series **178** (1982).
13. M. Stoukides and C. G. Vayenas, *J. Catal.*, **82**, 45 (1983).
14. M. Sato and J. Seo, *ibid.*, **24**, 224 (1972).
15. J. O'M. Bockris and A. K. N. Reddy, "Modern Electrochemistry," pp. 1020-1035, 1190-1195, Plenum Press, New York (1973).

Technical Notes



Calorimetric Determination of the Heat Generation Rate of Sodium-Sulfur Cells during Discharge and Charge

Reinhard Knoedler*

Brown, Boveri & Cie AG, Central Research Laboratory, Heidelberg, Germany

High temperature sodium-sulfur batteries (beta-batteries) are being developed for electric vehicle propulsion and load leveling applications. As with all battery systems, heat is dissipated during operation due to irreversible polarization losses. It is important to know the rate of this heat generation as precisely as possible, because these data are vital for the design of the cooling equipment. Measurements of this kind were performed already for the high temperature LiAl/FeS system (1, 2). It turned out that, because of the chemistry of this system, there is an almost constant rate of heat dissipation during discharge. In contrast, Na/S-cells are expected to show a more complex behavior because during discharge sodium polysulfides of different composition (Na_2S_x with $x = 3-5$) are generated electrochemically which contribute to the heat generation rate by their entropy change.

In principle, heat rates can be determined either by the adiabatic or the isothermal method. In adiabatic measurements, a cell is operated in a furnace with good heat insulation (vacuum-foil) and low heat capacity. From the temperature gradient and the heat capacity, the heat generation rate can be calculated (3). This method is applicable only for currents of greater than 10-15A, dependent on the cell resistance. Another characteristic of this method is that the cells can be operated only discontinuously. This is because the measuring time is only a few minutes and the states of discharge have therefore to be changed in a

stepwise manner. This is in contrast to the isothermal arrangement (calorimeter), as will be described in the following, where measurements can be carried out only at currents smaller than about 15A and continuous operation is required. Thus, isothermal measurements will complete the data on the thermal properties of Na/S-cells.

Isothermal measurements are generally performed by directly determining the heat flux from the cell at constant temperature (1). The advantage over adiabatic measurements is the considerably higher accuracy. This is due partly to the fact that the value of the heat capacity of the cell, which is not well known, is not needed to obtain the data. In addition, it is experimentally easier to establish good isothermal conditions than good adiabatic conditions (because even a vacuum-multifoil insulation has its losses). As mentioned above, isothermal measurements are useful, especially when relatively long discharge/charge times are to be used and continuous operation is required.

Experimental Arrangement

In contrast to prismatic LiAl/FeS cells (2), where good thermal contact can be obtained rather simply by pressing the cell between flat plates, that process is more difficult with cylindrical Na/S cells. Therefore, each Na/S cell has to be fitted individually into a cylindrical shaped calorimeter in order to provide a good thermal contact. Figure 1 shows the principal features of the calorimeter, which was designed and built for the measurements described below.

* Electrochemical Society Active Member.

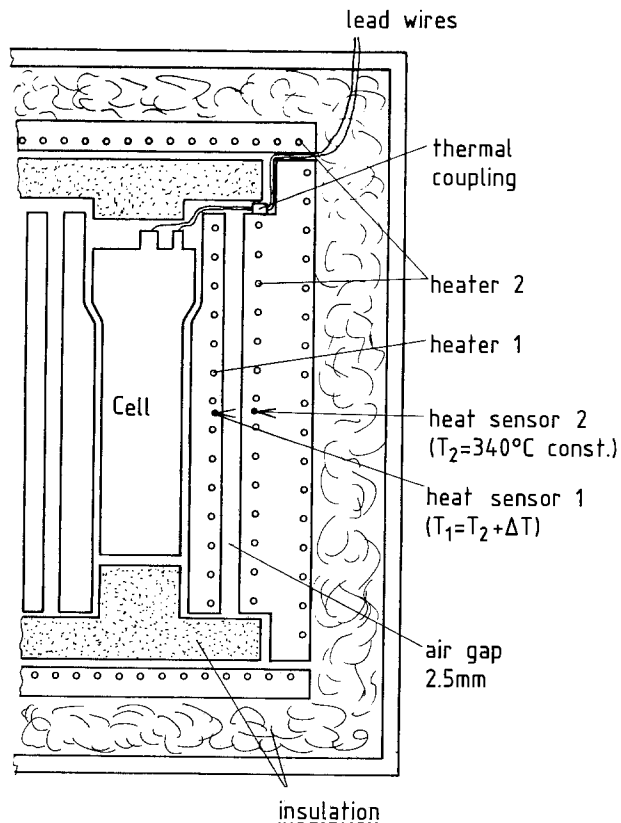


Fig. 1. Schematic for the calorimeter for the determination of heat-generation rates of cylindrical Na/S cells.

The cell is contained inside a furnace consisting of two concentric heaters, H1 and H2. Both are made of two aluminum half-cylinders each. After fixing the heating wire on the outside of one half-cylinder, the other is heat-shrunk unto it, thus giving minimal heat-transfer resistance. Between H1 and H2, a 2.5 mm air gap is provided, which allows the maintenance of a constant temperature gradient. At the top and the bottom of the cell, thermal insulation and additional heaters are placed. This ensures that almost all the heat generated during discharge leaves through the cell wall and thus can be determined. All lead wires

which are coming from the cell (current, voltage, 3 Pt-100 resistance thermometers) are contacted thermally to H2 in order to prevent heat losses. Measurements of vertical temperature distribution showed that ΔT is well below 1°C . This indicates that indeed the heat loss through the wire leads is negligible.

The cells which were tested were taken from a standard series (4). They were about 23 cm long and 3.6 cm in diam. Their capacity was about 44 Ah, and their dc resistance at the beginning of discharge about 15 m Ω . During discharge this value increased a few milliohms. All measurements were carried out at 340°C .

Principle of Operation

With the arrangement described above, the heat flux from the cell during discharge or charge can be measured directly. This is done by maintaining a constant temperature gradient ΔT between H1 and H2, thus fixing the heat flux between H1 and H2 to a constant value, independent of the heat-generation rate \dot{Q}_z of the cell. Therefore, if \dot{Q}_1 is the power output of the heater H1

$$\dot{Q}_1 + \dot{Q}_z = \text{const} = \dot{Q}_{10} \quad [1]$$

\dot{Q}_{10} denotes the power output of H1 when the cell is not being operated. The heat-generation rate of the cell can then be obtained by recording the difference between the power output of H1 with and without cell operation

$$\dot{Q}_z = \dot{Q}_{10} - \dot{Q}_1 \quad [2]$$

At discharge currents of $\approx 15\text{A}$, maximum values of \dot{Q}_z of about 15 W have to be expected. Therefore, \dot{Q}_{10} must be a little higher than this value in order to be able to satisfy Eq. [2]. However, the value should not be too high, because this would decrease the accuracy. For the same reason, the temperature difference ΔT should be as low as possible, say about 10°C . As a consequence, the air gap (2.5 mm) between H1 and H2 was designed to yield a value of the coefficient of the heat transfer of about $1.5\text{ W}/^\circ\text{C}$. Experimentally, a value of $1.1\text{ W}/^\circ\text{C}$, which is near the designed one, was obtained.

Measurements were usually carried out at $\Delta T = 8^\circ\text{C}$ – 15°C , depending on the discharge/charge current. After temperature equilibrium was established, the cell was discharged or charged continuously. Due to the heat generated by the cell, the controller of heater

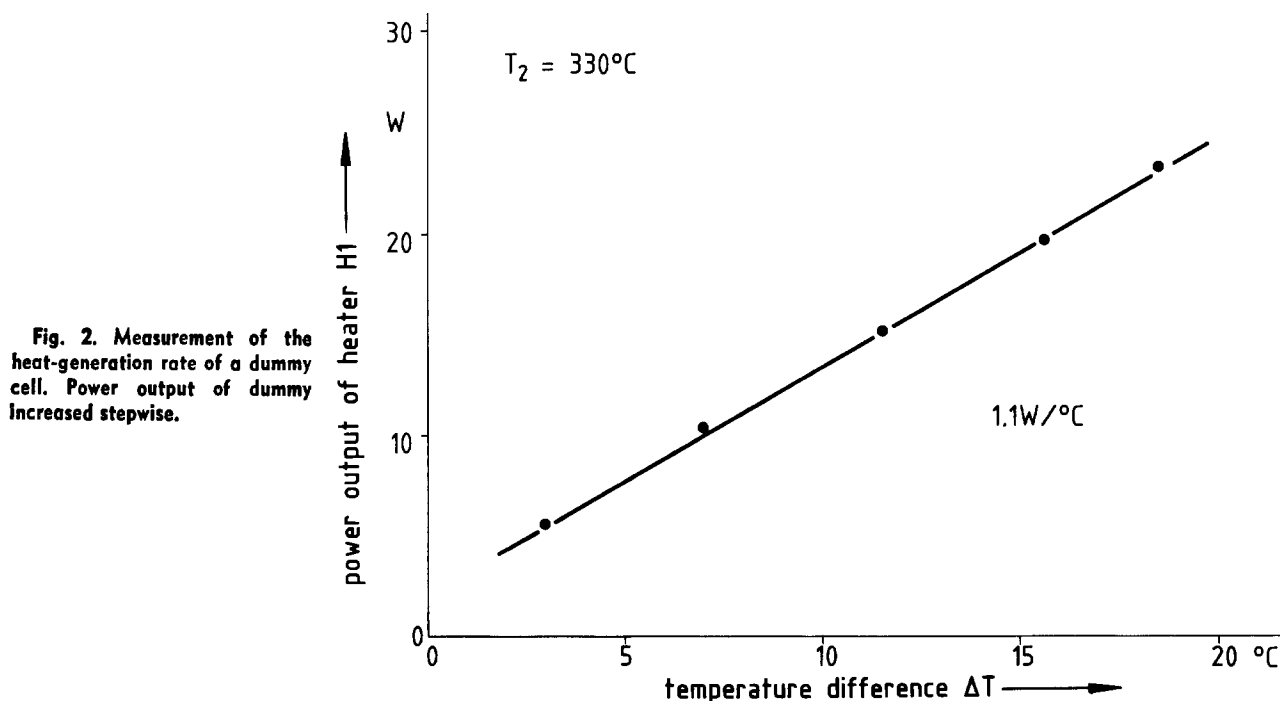


Fig. 2. Measurement of the heat-generation rate of a dummy cell. Power output of dummy increased stepwise.

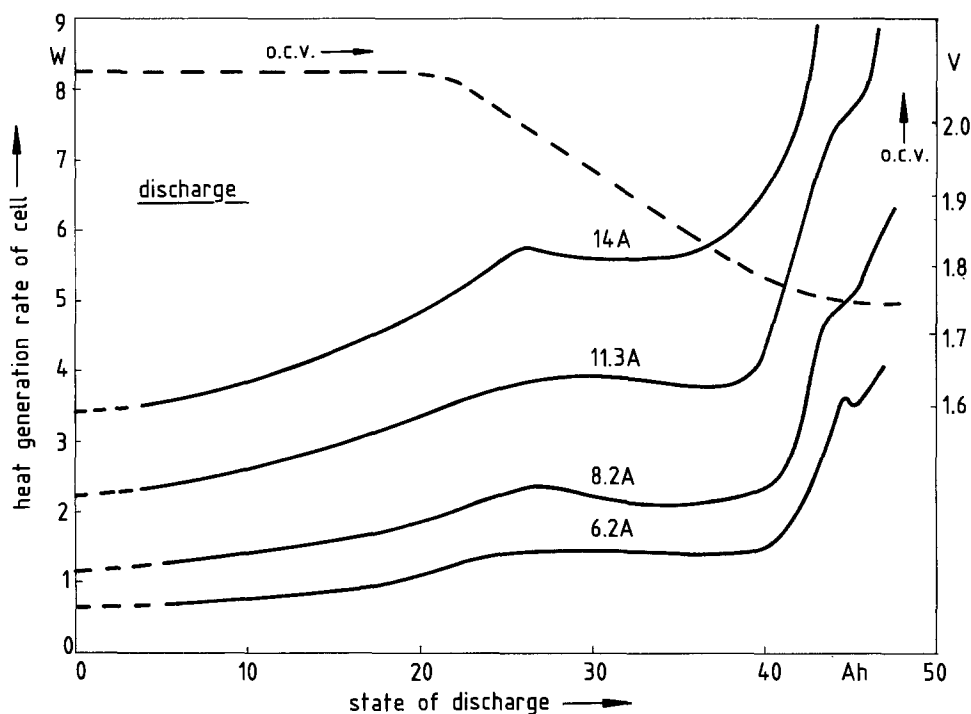


Fig. 3. Heat generation rate of a Na/S cell during discharge with different currents.

H1 adjusts the heating power to a lower value in order to keep ΔT constant. The difference in heating power is, according to Eq. [2], directly the heat-generation rate of the cell. The controller of heater H1 allows the temperature difference to rise several tenths of a degree during the discharge cycle. This small error was corrected by adding 1.1W per $^{\circ}\text{C}$ to the measured \dot{Q}_z value. The accuracy of the measurements was estimated to be $\pm 0.1\text{W}$.

Before testing Na/S cells, a dummy cell with a similar heat capacity and of a similar size was operated in the calorimeter in order to test the general performance. Figure 2 shows the behavior of this dummy cell when its heating power is increased in several steps up to 15.3W. It can be seen that the measured values are in good agreement with those preset at the dummy. The time needed for establishing equilibrium turned out to be about 10 min. This is why it is not possible to discharge the cell in less than about 3-4h, which

means currents of 11-15A. If higher currents are applied, the calorimeter is too slow to follow rapid changes in the heat-generation rate, which indeed are being observed in Na/S cells (see, e.g., Fig. 3).

Results

In Fig. 3, the heat-generation rate of a cell during discharge is shown for different operating currents. The OCV, which is also included in the figure, indicates the transition between the two-phase and the one-phase region as it could be derived from the cell voltage at low discharge currents. The OCV reaches a value of 1.78V at about 40 Ah state of discharge. This voltage corresponds to a composition of Na_2S_3 . According to the phase diagram (5), discharging beyond this value at 340°C is possible until a composition of about $\text{Na}_2\text{S}_{2.7}$ is reached. In the present case, this means a state of discharge of about 45 Ah (i.e., 90% utilization). Beyond this value, the cell is "overdis-

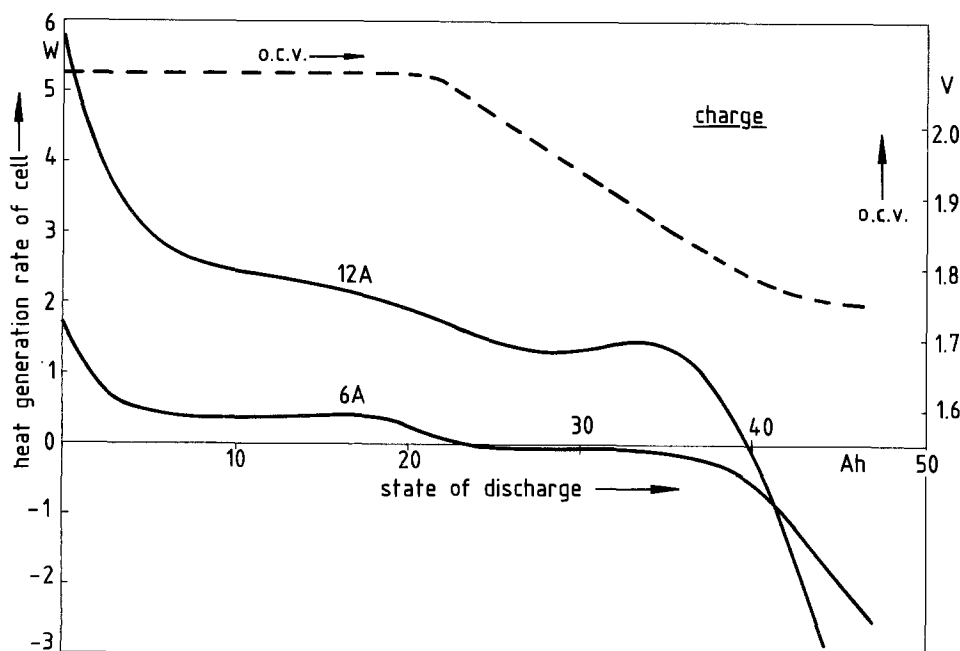
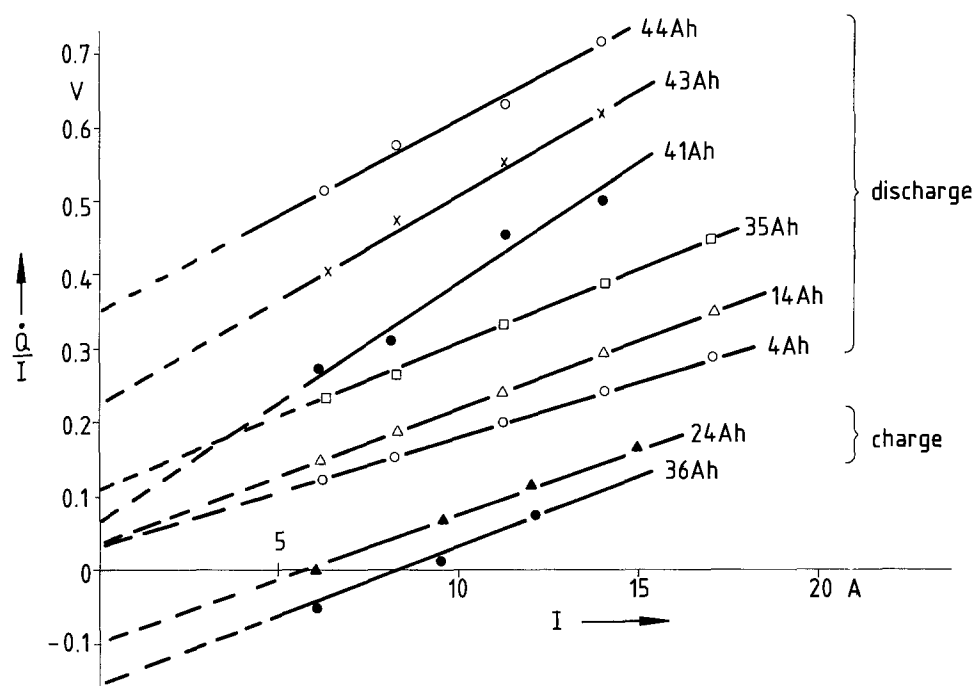


Fig. 4. Heat generation rate of a Na/S cell during charge with different currents.

Fig. 5. Heat generation rate divided by operating current vs. operating current for different states of discharge (0.0 Ah = fully charged, 44 Ah = fully discharged).



charged," which is accompanied by formation of solid Na_2S_2 . Figure 3 shows that in the two-phase region there is a continuous increase in the heat-generation rate. In the middle part of the one-phase region, there is a plateaulike shallow minimum. Near the end of discharge, a sharp rise takes place, and (most pronounced for the smaller currents) a discontinuity is observed at a state of discharge where formation of solid Na_2S_2 can be expected. It should be pointed out that the transition from the two-phase to the one-phase region which can be seen in the OCV does not coincide with the corresponding transition in the heat-generation rate.

Figure 4 shows the heat-generation rate during charging with two different currents. Due to entropy effects, the cell takes up heat from the environment when in the far discharged state. Corresponding to the discharging behavior, a shallow minimum is observed in the one-phase region. Near the fully charged state, the heat-generation rate increases strongly because of the increase in cell resistance. As expected, the values

are considerably smaller than during discharge with the same currents.

Discussion

The heat generation rate \dot{Q} in electrochemical cells can be expressed as (3)

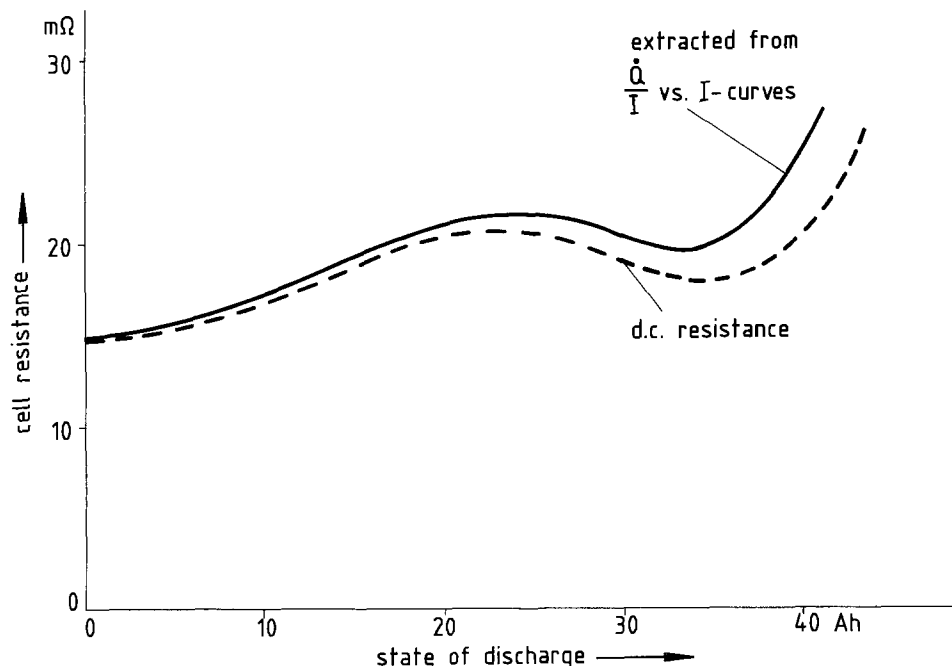
$$\dot{Q} = I \left(\eta \mp T \frac{dE}{dT} \right) \quad [3]$$

where I is the current, η the polarization, and $T \frac{dE}{dT}$ the entropy term. T is the absolute temperature and dE/dT the temperature dependence of the open-circuit voltage. The minus sign is to be applied for discharge, the plus sign for charge. If only resistance polarization is taken into account, then $\eta = IR_z$ where R_z is the dc resistance of the cell. Equation [3] can then be transformed to

$$\frac{\dot{Q}}{I} = IR_z \mp T \frac{dE}{dT} \quad [4]$$

Figure 5 shows a plot of \dot{Q}/I vs. I for different states

Fig. 6. Resistance of a Na/S cell as a function of the state of discharge.



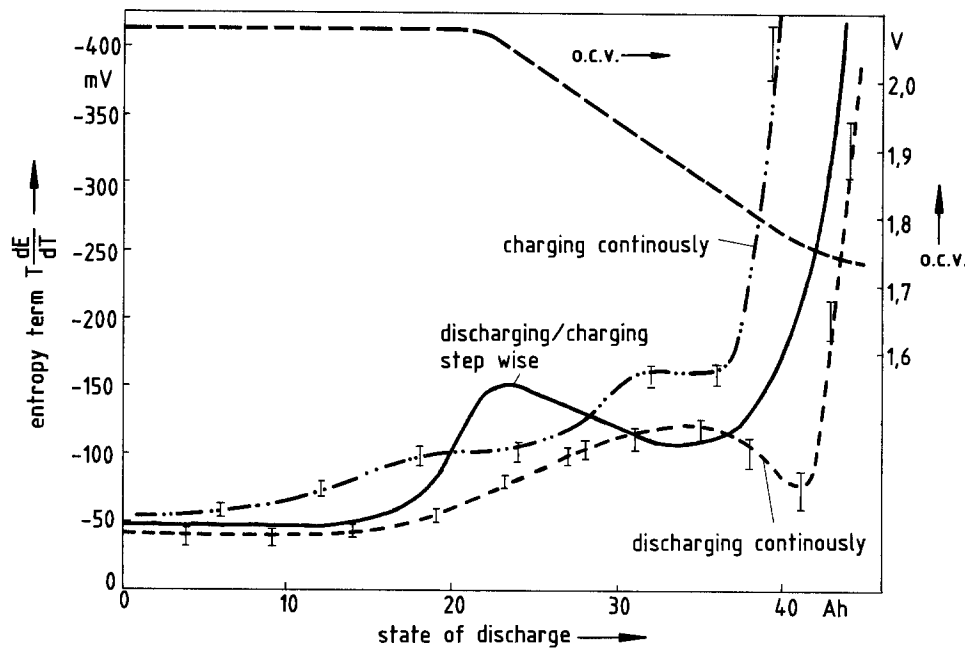


Fig. 7. Entropy term as a function of the state of discharge for different modes of operation.

of discharge and shows that Eq. [4] is indeed valid. From the Y-axis intercept at $I = 0$, the entropy term can be obtained, and from the slope of the straight lines the cell resistance. In Fig. 6 the cell resistance obtained in this manner is plotted together with the dc resistance (at currents beyond 11A) from direct electric measurements. It can be seen that a maximum occurs at the transition between the two-phase and the one-phase region and that at the end of discharge the resistance rises. The two curves are in good agreement within measuring accuracy. A plot of the entropy term, as extracted from Fig. 5, using Eq. [4] is shown in Fig. 7. There is a maximum at the end of discharge, followed by a minimum and a steep increase. The entropy term as obtained from the charge experiments can be seen to be clearly different from that. This suggests that, especially in the one-phase region, equilibrium was not reached.

In contrast to this, the entropy measured during a stepwise (several-hours wait) operation manner (3) showed no difference between charging and discharging. In this case, the maximum occurred in an earlier state of discharge, namely, in the transition region between the one-phase and the two-phase region, and its magnitude is higher than in the continuous mode. All these facts show a considerable dependence on the mode of operation, and this has to be taken into account when thermal management is being considered.

With the data obtained from the measurements described above, it is possible to obtain the overall thermal energy Q_e which is dissipated during a complete cell discharge or charge. Figure 8 shows the result of an integration of the heat-generation rate as it is shown in Fig. 3 and 4 up to 44 Ah. Q_e can also be calculated

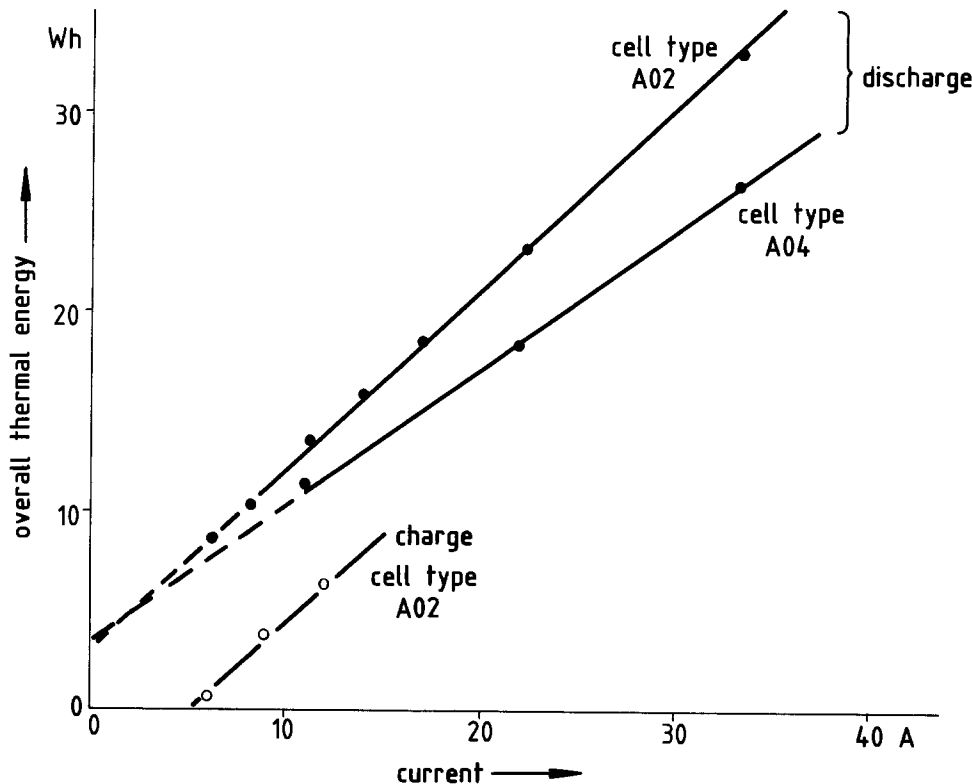


Fig. 8. Overall thermal energy dissipated during a full charge or discharge as function of the current.

culated by

$$Q_e = \int_0^t \dot{Q} dt = C \left(I \int_0^1 R_z dD \mp T \int_0^1 \frac{dE}{dT} dD \right) \quad [5]$$

where D is the state of discharge, going from 0 to 1, and C the capacity of the cell (44 Ah). Therefore, from the slope of the straight lines in Fig. 8, the average resistance can be obtained and from the Y-axis intercept the average entropy term. According to this, even at currents approaching zero, a finite value of the thermal energy of about 4 Wh will be dissipated independent of the cell resistance. In Fig. 8, the data for two cell types with different resistances are plotted. Extrapolation of both lines yield the same Y-axis intercept. In the charging mode there is heat dissipation only with currents greater than 5A; below this value heat is taken up from the environment.

Conclusion

Data have been presented which are necessary for thermal management purposes, especially the design of cooling equipment. It has been shown that the heat-generation rate during discharge depends on the mode of operation. When discharged stepwise, a shallow maximum in the heat-generation rate occurs at the

transition from the one-phase to the two-phase region. In the case of a continuous discharge, this maximum is being shifted to the one-phase region. This behavior shows that the equilibration in Na/S cells takes considerable time, especially in the one-phase region. This must be taken into account in thermal management considerations.

Acknowledgments

This work has been supported by the Bundesministerium fuer Forschung und Technologie (reference ET-4496 A). The author greatly appreciates the assistance of R. Krapf in designing the calorimeter.

Manuscript submitted Sept. 1, 1983; revised manuscript received Dec. 7, 1983.

Brown, Boveri & Cie AG assisted in meeting the publication costs of this article.

REFERENCES

1. H. F. Gibbard, D. M. Chen, and T. W. Olszanski, in "Proceedings of the 16th IECEC Conference," Atlanta, GA (1981).
2. L. D. Hansen, R. H. Hart, D. M. Chen, and H. F. Gibbard, *Rev. Sci. Instrum.*, **53**, 503 (1982).
3. R. Knoedler, *J. Appl. Electrochem.*, **14**, 39 (1984).
4. W. Fischer, *Solid State Ionics*, **3**, 413 (1981).
5. N. K. Gupta and R. P. Tischer, *This Journal*, **119**, 1033 (1972).

Effect of Surface Modification on Subbandgap Response of n-InP Photoelectrodes

D. N. Bose, Y. Ramprakash, and S. Basu

Materials Science Centre, Indian Institute of Technology, Kharagpur, India

Subbandgap response has been shown by Butler to be a sensitive indicator of the nature of the surfaces of GaP and SrTiO₃ photoelectrodes (1, 2). In particular, mechanical damage and cathodic aging were found to enhance the subbandgap response. In this paper, we demonstrate that surface modification of InP by Ru ions diminishes subbandgap response due to removal of surface states from the bandgap, as postulated by Parkinson, Heller, and Miller (3) for the case of n-GaAs. Heat-treatment of InP and anodic dissolution both lead to enhanced subbandgap response. These results are correlated with the increase in flat-band potential due to Ru modification as demonstrated from C-V characteristics, and also with significant changes in the nature of the transient response.

Experimental

n-InP samples were single crystals obtained from Metals Research, England, Sn-doped with $n = 4.7 \times 10^{18} \text{ cm}^{-3}$ and of (111) orientation. Ohmic contacts were made by alloying In-Sn dots at 400°C for 1 min in a hydrogen atmosphere. Surfaces were subsequently etched in concentrated HCl for 15s, whereby a black matte surface was obtained. Specimens were then immersed in the appropriate redox system, i.e., 0.04M Te²⁻/Te₂²⁻ or [Fe(CN)₆]^{4-/3-} for 30 min. After washing, they were immersed in a solution of 0.01M RuCl₃ and 0.1M HNO₃ for 1h to accomplish surface modification. This was followed by gentle washing in triple-distilled water.

The electrochemical cell was a two-electrode system with Pt as a counterelectrode and was illuminated by a 1.5 kW tungsten-halogen lamp adjusted to produce AM1 illumination at the photoelectrode. High purity

argon was bubbled through the redox solutions initially and during experiments in the Te²⁻/Te₂²⁻ redox. Detailed spectral response of the photoelectrodes with and without Ru modification was first studied between 0.4 and 1.2 μm using a Jarrell-Ash monochromator. The steady-state currents were measured using a Keithley 160B multimeter. Subsequently, the subbandgap response was studied using single-crystal InP ($n = 4.7 \times 10^{18} \text{ cm}^{-3}$, 0.055 cm thick) or Si ($n = 9.24 \times 10^{13} \text{ cm}^{-3}$, 0.029 cm thick) as filters with a tungsten-halogen source. The light beam was chopped by a PAR 125A light chopper at 84 Hz and the current output measured across a 10 kΩ load resistance which was fed to a PAR Model 5101 lock-in amplifier. The detection sensitivity was ±0.1 μV. The InP and Si filters acted as optical windows with high energy cutoff at 1.29 and 1.08 eV, respectively, as estimated from their absorption spectra.

Results and Discussion

Figure 1 shows the photocurrent response obtained using a monochromatic beam on n-InP specimens under identical conditions with and without Ru modification in Te²⁻/Te₂²⁻ redox electrolyte. It is evident that the subbandgap response is diminished in both magnitude and spectral extent by the modification. Similar results were also obtained on n-InP crystals grown by gradient-freeze technique in our laboratory.

Subsequent experiments were carried out alternately with white light followed by the use of an InP or Si filter. The ratio of the response provided a method for rapid evaluation of surface properties. Table I indicates that the subbandgap response decreased on Ru modification and that the ratio remained unchanged when this

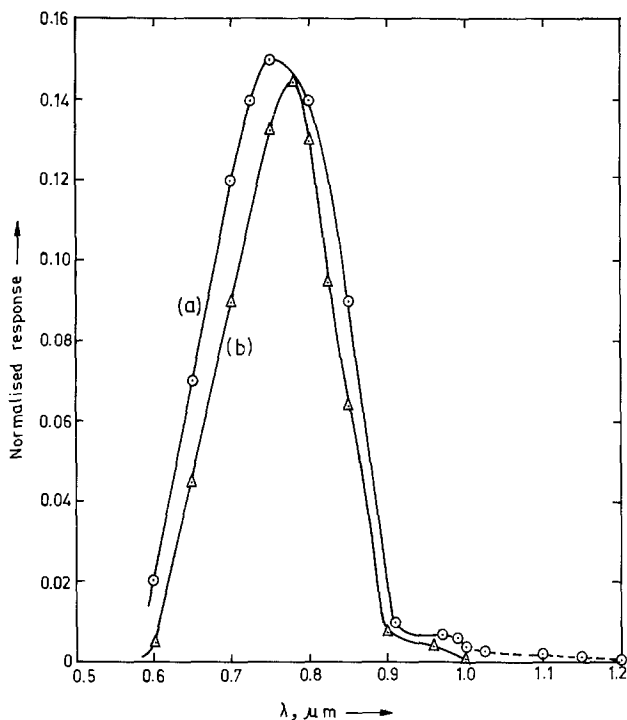


Fig. 1. Spectral response of n-InP in $\text{Te}_2^-/\text{Te}_2^{2-}$ redox, (a) without, and (b) with Ru modification.

electrode was kept in the dark for 24h and thereafter illuminated for 5h. The decrease in response with full AM1 illumination was due to change in color of the redox couple and not to photodissolution. The effect of 0.1M HNO_3 nitric acid without RuCl_3 was negligible, as was confirmed by control experiments.

It was found that Ru modification also increased V_{FB} (from 0.125 to 0.23V), as determined from the C-V characteristics. Similar results were obtained with n-type gradient-freeze-grown InP ($n = 3.2 \times 10^{17} \text{ cm}^{-3}$), in which V_{FB} increased from 0.24 to 0.44V on Ru modification (4).

Experiments with $[\text{Fe}(\text{CN})_6]^{4-/\text{3-}}$ redox showed that the subbandgap response was larger by almost two orders of magnitude, indicating the creation of surface states within the bandgap. The AM1 response was also higher due to more efficient hole transfer. Ru treatment again diminished the subbandgap response. Due to anodic dissolution with this redox after 5h of illumination, the ratio of subbandgap to white-light response increased by a factor of three.

The drastic effect of heat-treatment on InP given in Table II shows that heating for a short time at 500°C in argon atmosphere has a harmful effect on the surface properties due to outdiffusion of phosphorous. Such heat-treatments are commonly encountered in ohmic-contact formation. Our method gives a quick quanti-

Table I. n-InP in 5M NaOH (pH = 10)

		Before modification	Just after modification	24h after modification (dark)	Followed by 5h by AM1 illumination
White light (mV)	A	35.0	35.0	22.0	22.0
	B	60.0	60.0	25.0	20.0
InP filter (μV)	A	4.0	3.0	3.0	3.0
	B	425.0	200.0	240.0	200.0
Si filter (μV)	A	2.3	1.5	1.5	1.5
	B	130.0	100.0	90.0	75.0

A: 0.04M $\text{Te}_2^-/\text{Te}_2^{2-}$ redox.
B: 0.2M $[\text{Fe}(\text{CN})_6]^{4-}$, 0.04M $[\text{Fe}(\text{CN})_6]^{3-}$.

Table II. Effect of heat-treatment on subband response. n-InP in 5M NaOH, 0.04M $\text{Te}_2^-/\text{Te}_2^{2-}$ redox (pH = 10)

Heat-treatment	Response with		
	White light illumination AM1 (mV)	InP filter (μV)	Si filter (μV)
330°C for 5 min	35.0	55.0	22.0
As above, followed by 500°C for 30s	35.0	300.0	100.0

tative estimate of surface deterioration by examining the subbandgap response in $\text{Te}_2^-/\text{Te}_2^{2-}$.

Finally, transient response experiments were carried out (Fig. 2) on unmodified and modified surfaces in $\text{Te}_2^-/\text{Te}_2^{2-}$ redox. These responses were significantly different, the decrease in response after the initial increase on illumination demonstrating the presence of localized states within the bandgap in unmodified surfaces. These centers can be considered to be electron traps, as explained by Dahlberg and Orr (5).

Conclusions

Subbandgap response involves the excitation of carriers from states within the bandgap either in the bulk or at the surface to either band. The variation of photovoltaic response with surface treatment shows the latter is the case. Direct excitation from surface states to either band is known to have a low probability, and hence a two-step process involving excitation in the bulk, followed by charge transfer to surface states within the bandgap, and finally hole transfer to the redox level is envisaged. The subbandgap response demonstrates the decrease in surface-state density due to Ru ion treatment and increases due to dissolution in $[\text{Fe}(\text{CN})_6]^{4-/\text{3-}}$ redox or heat-treatment. The broad similarity of the behavior with InP and Si filters indicates that the surface states extend 0.2-0.3 eV within the bandedges but with decreasing density away from the edges.

The increase in V_{FB} with Ru modification is an indication that Fermi-level pinning due to surface states is removed, while the change in transient response shows

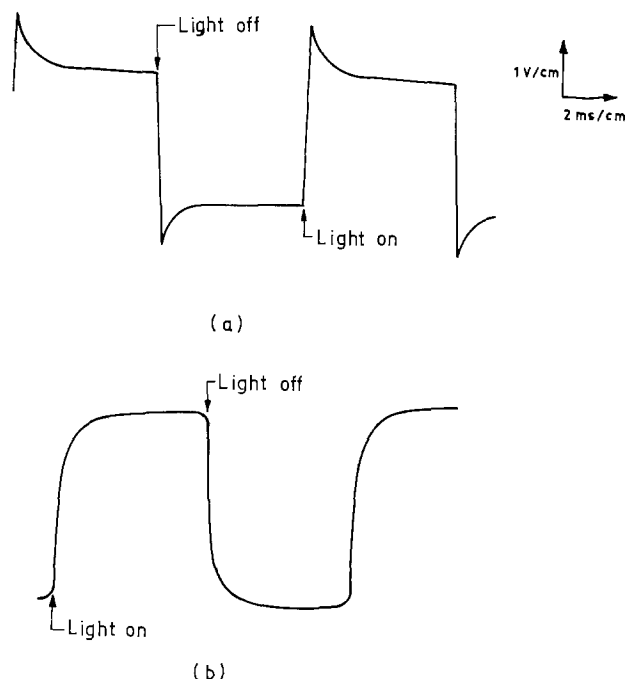


Fig. 2. Transient photovoltaic response (a) without, and (b) with Ru modification.

that Ru modification renders these states inactive in carrier trapping at the surface.

Acknowledgments

The authors are grateful to the C.S.I.R. (India) for the grant of a project in which Y. Ramprakash is a Senior Research Fellow.

Manuscript submitted Feb. 28, 1973; revised manuscript received Oct. 25, 1983.

REFERENCES

1. M. A. Butler and D. S. Ginley, *This Journal*, **128**, 712 (1981).
2. M. A. Butler, M. Abramovich, F. Decker, and J. F. Juliao, *ibid.*, **128**, 200 (1981).
3. B. A. Parkinson, A. Heller, and B. Miller, *ibid.*, **126**, 954 (1979).
4. Y. Ramprakash, S. Basu, and D. N. Bose, in "Proceeding Solar World Congress," Australia, 1983, to be published.
5. S. C. Dahlberg and W. A. Orr, *Surf. Sci.*, **67**, 226 (1977).



The Microstructures and Growth Rates of FeS on Pure and Not-So-Pure Iron

R. A. McKee and R. E. Druschel

Oak Ridge National Laboratory, Oak Ridge, Tennessee 37830

ABSTRACT

The sulfidation rates of iron to $Fe_{1-x}S$ have been measured for three batches of nominally pure iron, and rather significant differences in microstructures and growth rates have been observed. The measurements were made at 700°C over the sulfur pressure range of 1-10³ Pa as part of a study of the general aspects of the microstructures and growth rates of this highly nonstoichiometric sulfide of iron. Apparently due to rather small differences in silicon content, 0-40 ppm, the scale microstructure, scale adhesion, and growth rate vary significantly. Silicon that is dissolved as small Fe_3SiO_4 particles in the iron accumulates at the scale/metal interface during the sulfidation reaction causing a layered growth. The overall reaction rate is reduced at the lowest pressures, but remains unchanged at higher pressures.

In many of the sulfidation studies of iron (1-4), comments about the microstructural development of FeS have included descriptions of a layered growth scale. This layered scale consists of an inner layer of equiaxed grains overgrown by an outer layer of columnar grains. However, in recent work (5) of our own we found that it is possible to form a single layer, columnar growing, sulfide scale on iron. We show, in what follows, that these different characteristics of the scale microstructure are due to specimen purity, and that relatively minor levels of silicon in the iron apparently cause the layer growth that has been the commonly reported microstructure for FeS on iron. Moreover, we can report that, while significant changes do occur in the growth rates, there is no apparent influence on the a- to c-direction growth change with pressure. Of the three batches of nominally pure iron studied, all exhibit the a to c transformation at the same pressure.

Experimental

All measurements were made at 700°C and in pure sulfur vapor. The experimental technique has been documented carefully in a previous publication (5), and no detailed discussion of it will be presented here. However, since we wish to discuss both qualitative and quantitative differences in iron sulfidation rates and microstructures, we ran our experiments in the exact manner that was previously reported (5) except that we used all three batches of material as specimens simultaneously mounted in the apparatus. In this study, as before, we used a multispecimen technique to determine reaction rate constants, *i.e.*, each point on a reaction rate curve was obtained from a separate specimen run for a specific time. This has resulted in an unequaled reproducibility in reaction rate data.

The materials we used were purchased as "Marz grade" iron from Materials Research Corporation (MRC). Three different batches were purchased, and our analyses are reported in Table I. As is clear from a study of Table I, batch A iron is the purest and batch C is the least pure; in fact, batch C could even be called a dilute alloy. Although batch C is much less pure than batch A or B, there is no measurable difference be-

tween the growth rate and microstructure of FeS formed on batches B and C, but a real distinction does exist between batch A and batch B or C.

Results and Discussion

We have investigated the rate of reaction for several batches of "pure" iron, and Fig. 1 and Table II give comparisons between rate data we have obtained as well as data by others. As cited previously (5), the pressure range covered in our data spans the a- to c-direction change that occurs for scale growth in this material. The change in rate that occurs at approximately $p_{s_2} = 10$ Pa is due to an apparently faster rate of diffusion in the c-direction than in the a-direction of FeS. At sulfur pressures below 10 Pa, the

Table I. Composition of iron used in sulfidation studies (ppm by weight)

Impurity	Batch A	Batch B	Batch C
Si	<3.0	40	40
P	0.2	20	10
S	3.0	50	70
Cr	0.6	5	70
Mn	0.3	10	10,000
Co	0.1	20	10
Ni	3.0	6	60
Ga		20	7
As		10	40
Mo		1	4
Sn			10
Sb			1

Table II. Reaction-rate data at 700°C

P_{s_2}, Pa	Batch A		Batch B	
	$k_p^* \times 10^4 \left(\frac{kg^2}{m^4 \times s} \right)$		$k_p^* \times 10^4 \left(\frac{kg^2}{m^4 \times s} \right)$	
1	0.464 (± 0.047)		0.159 (± 0.055)	
10	1.12 (± 0.041)		0.754 (± 0.077)	
100	2.00 (± 0.22)		1.91 (± 0.21)	
1000	2.44 (± 0.32)		2.96 (± 0.28)	

Key words: alloy, corrosion, films, kinetics.

* k_p defined from $(\text{weight of sulfur gain})^2 = k_p t$, t is time.

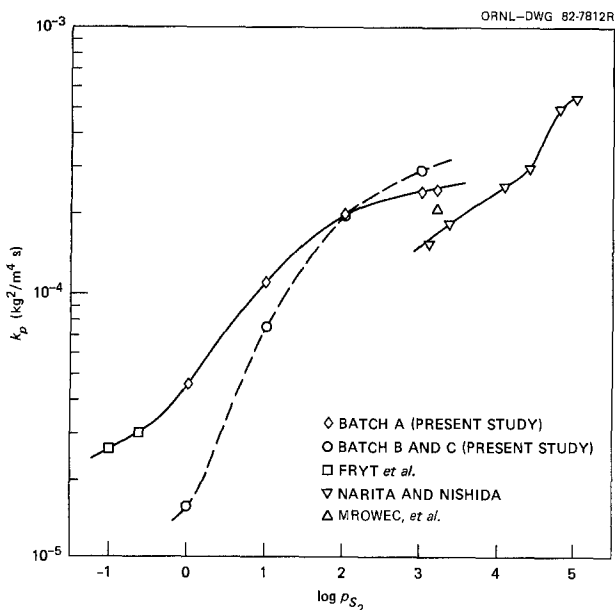


Fig. 1. Reaction rate data for FeS forming on iron at 700°C

major growth direction of the scale is along the a-direction normal to the iron surface, and above 10 Pa a reorientational effect occurs giving only c-direction growth. This happens for all of the materials we used and, therefore, seems to be only dependent on pressure. Similarly, the data obtained illustrate parabolic growth kinetics; Fig. 2 shows data plotted as (thickness of FeS)² vs. time, and for the range of scale thicknesses studied (as great as 240 μm), no departure from parabolic kinetics is observed.

The basic finding that we wish to present and discuss is that sulfide scales formed on nominally pure iron vary significantly in microstructures and growth rates as a result of apparently minor variations in silicon content in the iron. Figures 3 and 4 show examples of the microstructures of FeS formed on iron at 700°C and 1 Pa sulfur pressure (the reaction was

SULFIDATION OF IRON "ALLOY" IN SULFUR VAPOR - 700°C

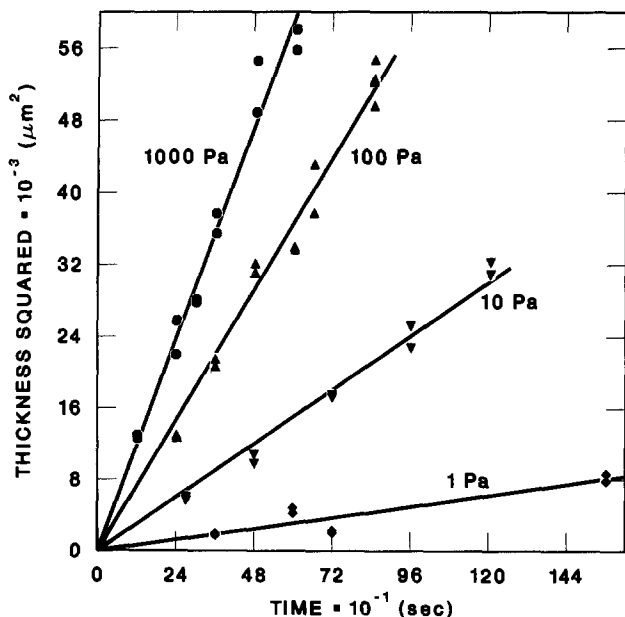


Fig. 2. Scale growth kinetics for FeS forming on batch B or C iron at 700°C. Parabolic kinetics is illustrated; the maximum scale thickness is 240 μm . Each point represents a separate experiment on a different specimen.

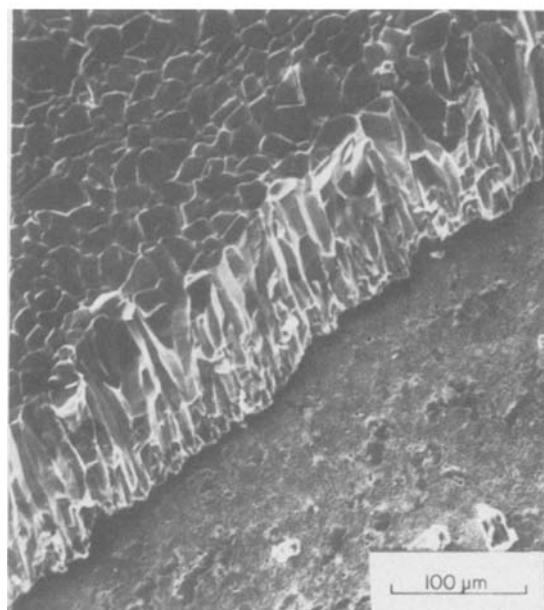
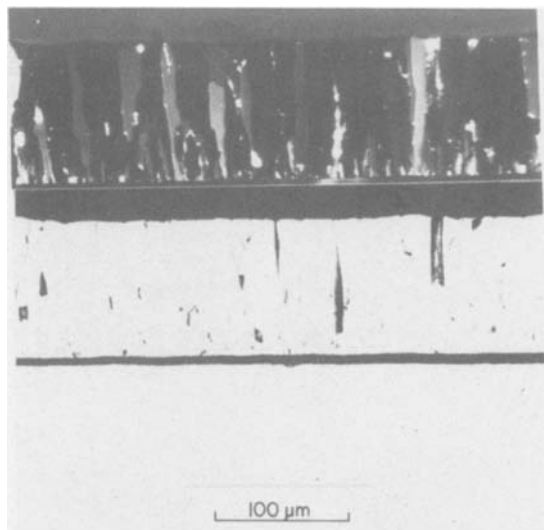


Fig. 3. FeS scale on batch A iron, growth at 700°C, $p_{S_2} = 1$ Pa, reaction time 10 min. The upper portion of the figure shows the scale in cross section in polarized light and bright field illumination, and the lower portion shows an SEM image of the scale at a 45° angle to the surface with a portion of the scale popped off, revealing the metal underlayer.

carried out in pure sulfur vapor). Figure 3 is the result for batch A material, and Fig. 4 is for batches B and C (analyses of these materials are given in Table I).

The lowest silicon content material, batch A, exhibits sulfidation characteristics that have been fully described recently (5), but for comparison here, we see columnar growth with compact single-layer crack-free grains as opposed to the layered structure for the scale formed on batch B, the higher silicon content material. The micrographs in Fig. 3 and 4 are polarized light, bright field, and SEM (scanning electron microscopy) images showing the metal and sulfide phases. The SEM pictures were taken by first popping off a scale segment, then mounting and polishing the specimens for the bright field and polarized light microscopy.

The features to note in Fig. 3 and 4 are the grain sizes of the columnar segments of the scales, the scale/metal interfaces, and the multilayered scale in Fig. 4. In both figures, the outer columnar grains have ap-

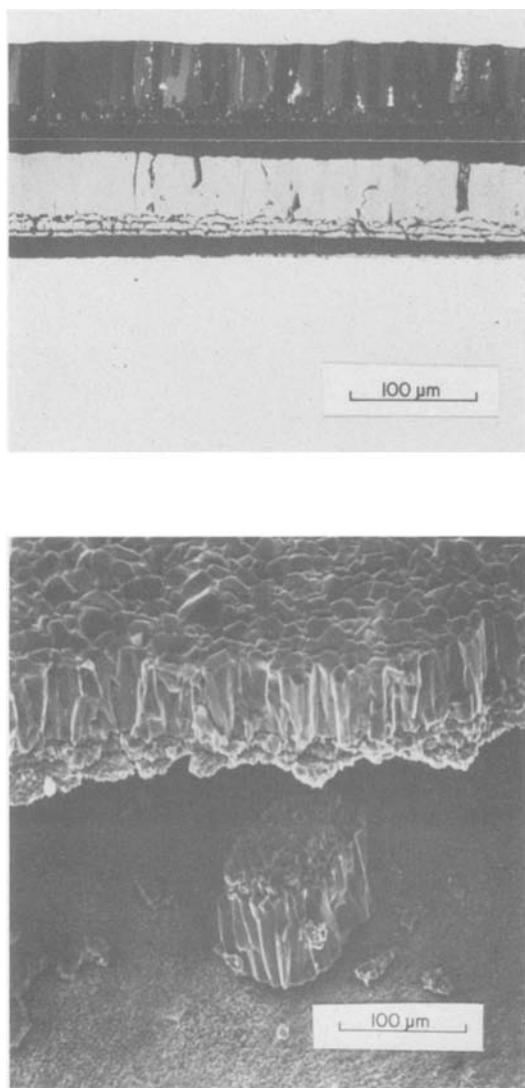


Fig. 4. FeS scale on batch B iron, growth at 700°C, $p_{S_2} = 1$ Pa, reaction time 10 min. The upper portion of the figure shows the scale in cross section in polarized light and bright field illumination, and the lower portion shows an SEM image of the scale at a 45° angle to the surface with a portion of the scale popped off, revealing the metal underlayer.

proximately the same diameter, and the orientational relation for their growth is identical. That is, the grains are highly oriented and grow with their major axis being the a-direction for the hexagonal, pyrrhotite, FeS phase (5). This a-direction is normal to the metal surface, and the individual grains are rotated randomly about this axis. It is at the scale/metal interface that the real distinction in these materials is made. The scale/metal interface is represented as a clean separation of the two phases in Fig. 3 for batch A material; the scale completely detaches on cooling. However, the scale does not separate completely from the metal phase for batch B material, shown in Fig. 4. The innermost layer of the sulfide remains attached, and gross scale separation that does occur on cooling is at a boundary between the layered equiaxed grains of the sulfide itself. Finally, the multilayer aspect of scale growth for batch B or C material is illustrated further in Fig. 5. Figure 5 is a higher magnification of the scale segment that has cracked off, inverted, and is visible in Fig. 4. This scale segment shows that pores have formed between the layers, but it also illustrates that the layers were in intimate contact at temperature, *i.e.*, fractured surfaces are visible at the

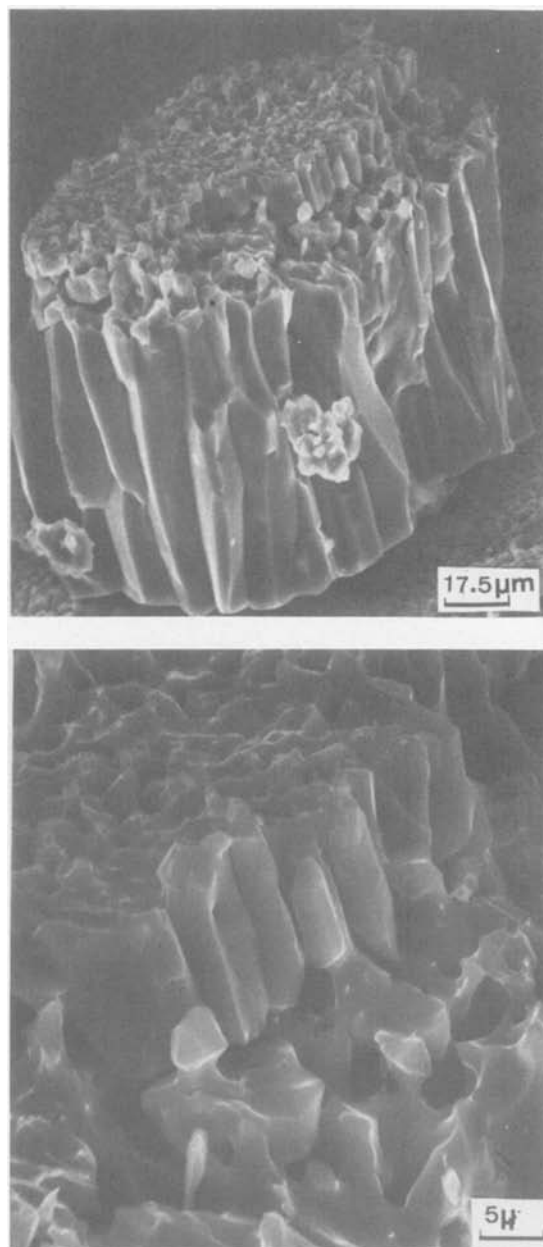


Fig. 5. Scale segment illustrating details of the layered microstructure.

separated layers. We will discuss this feature of the microstructure in more detail later.

In older literature (6), it has been illustrated that commercially pure iron contains fine dispersions (1-2 μm diam), and it was suggested that these particles are oxides and sulfides of Fe or Mn and contain silicon as silicates. If the particles are stable in the iron at a particular reaction temperature, then they could accumulate at the scale/metal interface and potentially influence the microstructure and growth rate of the iron sulfide. We have studied the metal microstructure of the three batches of material that we used in our experiments; they all contain spherical-shaped particles. Bright field photomicrographs show the particles in batch A to be black or opaque while the particles in batches B and C appear to be glassy. Electron microprobe analysis indicates that batch A particles are the monoxide of iron, FeO, but batch B and C particles are the orthosilicate of iron, Fe_2SiO_4 . An examination of what happens when the FeO or Fe_2SiO_4 particles are encountered by the growing sulfide phase is instructive in considering the microstructural development of FeS on iron.

The iron and precipitate particles are primary and secondary contributions to scale growth in our experiments. The primary sulfidation reaction is



and this process occurs by the outward migration of iron ions through the sulfide scale with the sulfide growth actually occurring at the scale/gas interface. The particles, when encountered by the growing Fe-FeS front, are secondary contributions to the scale growth, but the mechanism for their contribution is not so clear. Figure 6 illustrates the metal/scale interface for batch A and B iron; A in the lower and B in the upper micrograph. The spherical-shaped precipitates are shown in the metal phase in both micrographs, but they remain distinguishable and have collected at the Fe/FeS interface in only batch A iron; the black area in both micrographs is mounting material. The silicate particles in batch B iron are not distinguishable in optical light at the interface, but their decomposition at the interface can be detected using x-ray imaging methods. Figure 7 shows back-scattered electron and Si-K α x-ray images of the interface of batch B iron. The silicate particles are visible in the iron, but although a particle can be seen

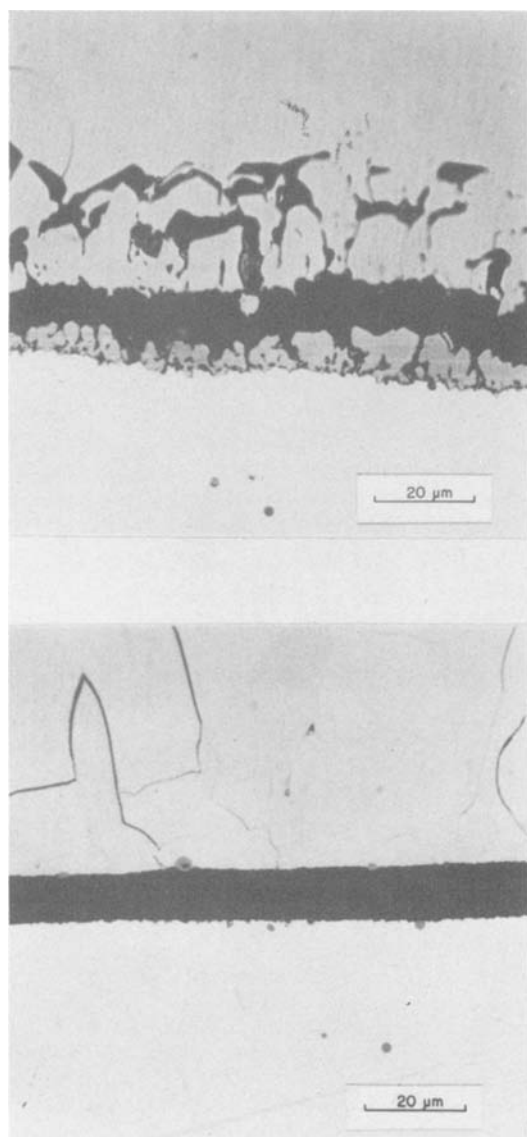


Fig. 6. The metal scale interfaces for batch A and B iron; A in the lower and B in the upper micrograph.

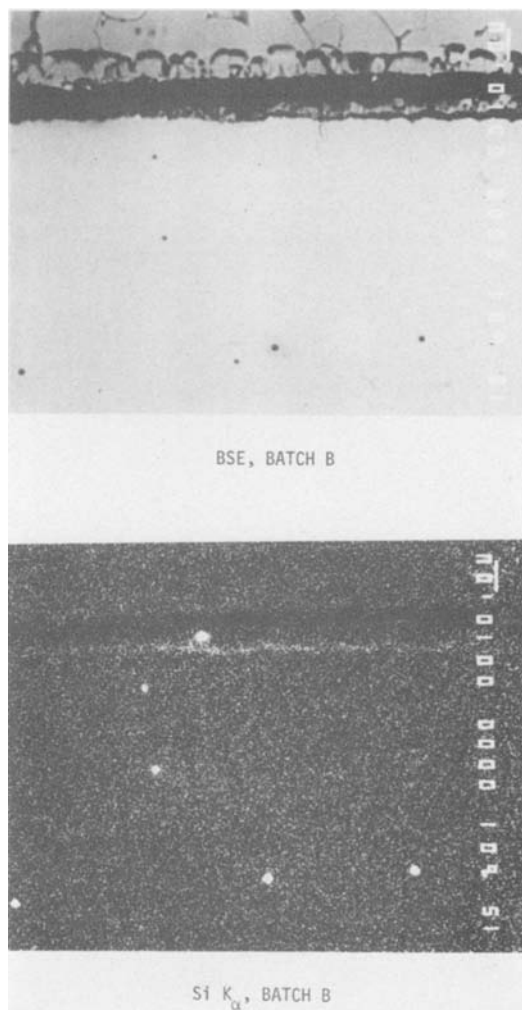
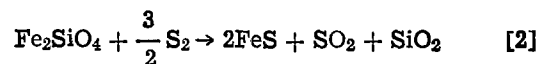


Fig. 7. Back-scattered electron and Si-K α x-ray images of the interface of batch B iron.

at the interface, a decomposition process has occurred leaving the silica to spread along the interface. Moreover, a map of the oxygen K α line shows a similar distribution of oxygen.

The mechanism for decomposition of either an FeO particle or Fe₂SiO₄ particle is essentially the same: sulfur in the environment reacts with the particle to decompose it. However, the decomposition product of the silicate particle is the most interesting. The ortho-silicate will decompose according to



From examinations of the microstructure, the silica spreads along the interface between the Fe and FeS phases (see Fig. 7), and pore formation in the inner equiaxed layers (see Fig. 2 and 3) is likely due to the accumulation of SO₂ in the scale. This SO₂ accumulation and a dissociative migration through the scale could be analogous to the process of carbon in nickel forming CO₂ in the scale during nickel oxidation (7).

With the experiments that we have done thus far, anything past these observations is certainly speculation. However, it seems clear that the silicate particles do decompose leaving silica to spread along the interface. The decomposition is very likely according to Eq. [2]. A final point in this section relating to this secondary contribution to scale growth (decomposition of the silicate particles) is that it is possible that

the layered scale occurs because of a change in mechanism of growth in the vicinity of a particle at the scale/metal interface. The FeS that is formed according to Eq. [1] forms at the scale/gas interface, but the resultant FeS that forms when the particle decomposes, according to Eq. [2] producing SiO₂, SO₂, and FeS, may be at the scale/metal interface giving rise to the equiaxed inner layers. Further experiments have been planned and are in progress to determine the mechanism for particle decomposition and how it relates to the observed scale microstructure.

Conclusion

We have shown that the commonly reported microstructure for FeS formation on iron is a direct result of silicon contamination of the iron. This silicon effect is to reduce the reaction rate and alter the microstructure from ideal columnar crack-free scale growth to a layered microstructure. An additional effect that has been observed, but only qualitatively, is that silicon improves the adherence properties of FeS scale on iron by leaving an inner layer of the scale firmly attached to the metal substrate.

Acknowledgment

Research was sponsored by the Division of Materials Sciences, U.S. Department of Energy under contract W-7405-eng-26 with the Union Carbide Corporation.

Manuscript submitted Sept. 1, 1983; revised manuscript received Nov. 4, 1983.

Oak Ridge National Laboratory assisted in meeting the publication costs of this article.

REFERENCES

1. E. M. Fryt, V. S. Bhide, W. W. Smeltzer, and J. S. Kirkaldy, *This Journal*, **126**, 683 (1979).
2. T. Narita and K. Nishida, *Trans. Jpn. Inst. Met.*, **15**, 314 (1974).
3. R. A. Meussner and C. E. Birchenall, *Corrosion*, **13**, 677 (1957).
4. S. Mrowec, A. Stoklosa, and M. Danielewski, *Oxid. Met.*, **11**, 355 (1977).
5. R. A. McKee and R. E. Druschel, *This Journal*, **130**, 898 (1983).
6. "Metals Handbook," Vol. 7, p. 516, American Society for Metals, Metals Park, OH (1972).
7. D. Caplan, R. J. Hussey, G. I. Sproule, and M. J. Graham, *Oxid. Met.*, **14**, 279 (1980).

Ellipsometry Measurements as Direct Evidence of the Drude Model for Polycrystalline Electrochromic WO₃ Films

David H. Mendelsohn¹ and Ronald B. Goldner*

Department of Electrical Engineering, Tufts University, Medford, Massachusetts 02155

ABSTRACT

The optical constants of polycrystalline electrochromic (EC) tungsten trioxide (WO₃) films, prepared by rf sputtering, were measured by ellipsometry at three wavelengths: 940, 633, and 546 nm. For each wavelength, the optical constants were measured at various states of coloration. It is shown that these measurements provide direct evidence for the validity of the free-electron Drude model (i.e., the reflectivity modulation that is observed in polycrystalline EC films of WO₃ is primarily determined by the density and scattering of the free electrons).

Electrochromic (EC) materials are substances for which the optical properties can be reversibly altered with the passage of an electrical current. It is widely accepted that this involves the injection or extraction of electrons and charge compensating ions (1). Most of the EC research to date has been focused on amorphous materials for display applications. The injected electrons in amorphous EC materials predominantly occupy localized states, and this leads to a modulation of the optical absorptivity.

We have been investigating the possibility of using EC materials for controlling solar and thermal infrared energy transfer through windows as a means of decreasing heating and cooling loads in buildings. Consequently, we are interested in obtaining a modulated reflectivity $R(\lambda)$ (λ = wavelength) characteristic. This translates into the requirement that the injected electrons occupy predominantly delocalized (conduction-band) states; and, therefore, the EC material should exhibit a metallic [Drude (2, 3)] behavior. Such a requirement suggests that a crystalline or polycrystalline state is desirable. Previous work by Schirmer *et al.* (4) supports this view. They performed experiments on recrystallized WO₃ films that had been thermally evaporated. The films were amorphous in the as-deposited state and were recrystallized by a thermal anneal. Their recrystallized films, when deeply colored, exhibited a near-infrared reflectivity close to

35% at 2.5 μm wavelength. They were able to fit their results with a Drude free-electron model using an energy-dependent scattering time, $\tau(E)$.

In another paper (5), we shall report the results of reflectivity measurements on polycrystalline WO₃ films prepared by rf sputtering (for which the 2.5 μm wavelength reflectance of the films in a deeply colored state was found to exceed 60%). We likewise have been able to obtain a Drude fit to the reflectivity data. Ellipsometric studies were made on the same samples to provide a direct test for the validity of the Drude model by measuring the coloration-induced variations in the optical constants, n (refractive index) and k (extinction coefficient) at three wavelengths. In this paper, we wish to report the results of those studies and, in particular, that not only did the results agree with the reflectivity measurements, but, of greater importance, they provided direct proof of the validity of the free-electron Drude model.

Experimental

Polycrystalline samples of WO₃ were prepared by rf sputtering onto a substrate held at $325^\circ \pm 10^\circ\text{C}$ in an atmosphere of 10% oxygen and 90% argon at 40 mtorr² (6). The crystallinity was determined by x-ray diffraction measurements (5). The substrate was tin-doped indium oxide (ITO)-coated glass.³

² The samples were prepared by Dr. Tim Rose, EIC Laboratories, Newton, Massachusetts.

³ The ITO-coated glass (5 Ω/\square Nesatron) was purchased from PPG Industries, Pittsburgh, Pennsylvania.

* Electrochemical Society Active Member.

¹ Present address: Eikonix Corporation, Bedford, Massachusetts 01730.

Measurements were taken to determine the characteristics of the ITO and glass. A prism-coupled optical waveguide (PCOW) apparatus, similar to that used by Tanaka and Ohtuska (8), was used in its "substrate mode" to determine that the glass (n, k) = (1.5225, 0.00) at 633 nm wavelength, estimated to be nondispersive. Note that the notation used here is (n, k) where n is the real part of the complex refractive index \underline{N} and k is the "extinction coefficient," such that $\underline{N} = (n - ik) = n(1 - iK)$; K is the "attenuation index" (7). PCOW measurements were coupled with ellipsometry measurements to determine the parameters of the chemically reduced ITO layer: (n, k, d) = (1.16, 0.10, 0.548 μm) at 940 nm wavelength. At 633 nm wavelength, (n, k, d) = (1.82, 0.01, 0.548 μm). The ITO parameters at 546 nm wavelength were estimated to be the same as those at 633 nm. The ellipsometric measurements were made at 546, 633, and 940 nm. Estimates of uncertainty for the ITO figures are ($\delta n, \delta k, \delta d$) = ($\pm 0.05, \pm 0.02, \pm 0.030 \mu\text{m}$). The step height of monitor sample of WO_3 was $0.560 \pm 0.050 \mu\text{m}$ as measured on a Sloan profilometer. PCOW and ellipsometry measurements agreed with this value, but could not reduce the uncertainty; the film thickness of the WO_3 was a principal source of error in this experiment.

A bath of (approximately) 1N H_2SO_4 with 10% glycerol (by volume) was used as the ion source/electron insulator for coloration and bleaching of the WO_3 layer. A counterelectrode of graphite completed the cell. The *in situ* optical density and reflectivity of the sample were monitored as functions of injected charge, measured by a crude charge integration circuit connected to the cell excitation circuit. Approximately 110 mC/cm² of injected charge were needed to achieve the maximum coloration shown in this data. As the charge was injected in steps and relaxation towards a bleached state occurred between steps, the sum of the injected charges was considerably larger (approximately 270 mC/cm²) than the charge needed to color a sample directly from its bleached state. If

fading (probably oxidation) had not occurred, less injected charge would have been needed to achieve the measured coloration states. After each color or bleach step was completed in the acid bath, the sample was rinsed in deionized water, dried with an argon jet, and measured. The sample was returned to the acid bath at the end of each set of measurements, and the process was continued until the sample had been run through a color/bleach cycle of sequential steps.

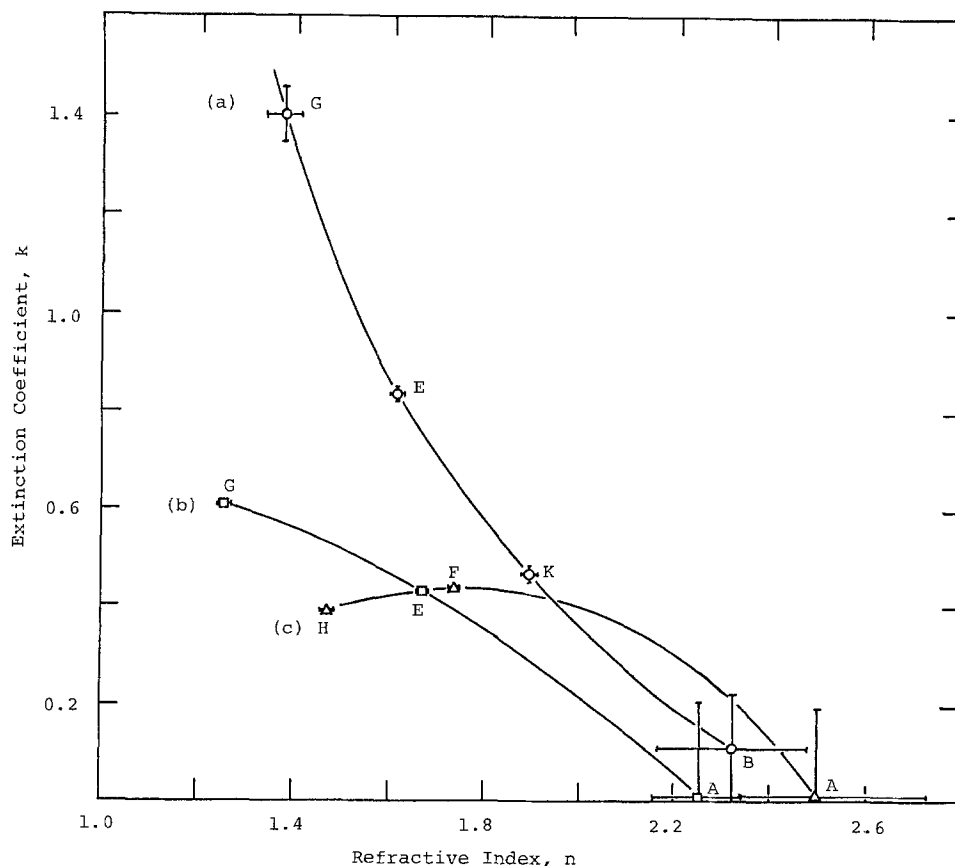
The ellipsometer used was a modified Rudolf Research reflection ellipsometer with a fixed incident angle of 70 degrees. The modifications included the addition of two light sources and a number of apertures, and the application of a silicon detector with a lock-in amplifier for detection of the infrared (940 nm) source. The wavelengths provided were 546 nm (line-filtered Hg lamp source), 633 nm (3.5 mW He-Ne laser), and 940 nm (infrared LED, RCA 1010A). The procedure involved adjusting the polarizer and analyzer for beam extinction with a fixed compensator azimuth of 45 degrees. The compensator, a muscovite mica retarder, was calculated for retardations of 90.0 degrees at 546 nm, 77.7 degrees at 633 nm, and 52.3 degrees at 940 nm. The refractive indexes of the retarder were estimated to be nondispersive and the transmission coefficient of 1.000 was estimated as constant.

The polarizer (P) and analyzer (A) azimuths were recorded for each color/bleach cycle. The P and A values were entered into a modified version of the McCrackin ellipsometry program (available as part of the National Bureau of Standards Technical Note 479) (7). The program was used to obtain delta and psi pairs (the polar coordinates of the complex total reflection of the optical system), from which (n, k) pairs were obtained. In all cases, (n, k) were assumed to be constant throughout the film thickness.

Results and Discussion

The results of this analysis appear in Fig. 1. Three curves are shown to represent the three wavelengths

Fig. 1. Optical constants of rf sputtered electrochromic WO_3 films (polycrystalline, 0.56 μm thick) in various coloration states. a: 940 nm wavelength. b: 633 nm wavelength. c: 546 nm wavelength. A, B = bleached states. E, F, K = intermediate coloration states. G, H = deeply colored states.



used. Each curve begins at its lower-right extreme (k near 0) in its bleached state and moves toward the upper left as the sample is colored. A few data points are shown on each curve to illustrate the effect of experimental uncertainties. Note that the uncertainties of the (n, k) values are greatest in the bleached state. These uncertainties are mainly due to the uncertainty of the WO₃ film thickness. When k is low for a film, there are many possible ellipsometric solutions which may be within the bounds of the top-film thickness uncertainty. As the extinction coefficient k becomes larger, the reflectivity is increasingly characterized by the film properties near the surface. Considerable absorption can cause the ellipsometric solutions to become almost independent of top-film thickness and underlying layer parameters. This explains the reduced uncertainties for the colored film data. Finally, as n becomes very low and k high, the uncertainties in azimuth readings become more significant. This last point explains the increasing uncertainty of the 940 nm data points in the film's most colored states.

One can use the McCrackin ellipsometry software (7) to obtain theoretical reflection intensities for each (n, k) at normal incidence. Such calculations were made so that ellipsometry data could be compared to data obtained from the reflection spectrophotometer. The correlation was good; the data matched to within measurement error in all cases but one point.

The reflection spectrophotometer readings showed that the reflectivity of the WO₃/ITO/glass sandwich was as high as 62% ($\pm 5\%$) at 2.50 μm wavelength (5, 8). Due to the relatively high extinction coefficient in the highly colored state, the reflectivity of the 0.56 μm WO₃ film was virtually independent of the reflectivity of the underlying layers.

The results of the ellipsometry measurements when plotted as k vs. n provide direct qualitative evidence that the reflectivity modulation associated with the charge injection or extraction in polycrystalline WO₃ is caused primarily by a modulation of the free-electron density. Consider the behavior of the optical constants, n and k , in the vicinity of a plasma resonance for a hypothetical free-electron Drude solid with an initial plasma energy, $E_p = 1.0$ eV (Fig. 2). Note that for an observation photon energy above 1.2 eV, n decreases with coloration (with increasing plasma energy or free-electron density), but k increases, i.e., at a fixed photon energy, there is a distinct inverse relationship between n and k which can only be explained by a free-electron model. Furthermore, the amount of decrease in n reaches a maximum and then reduces as the observation energy increases. The amount of increase in k , however, continuously reduces with increasing observation energy. These qualitative Drude model predictions agree with the results of Fig. 1. In Fig. 1, we observe that n decreases and k increases with coloration, and the largest change in

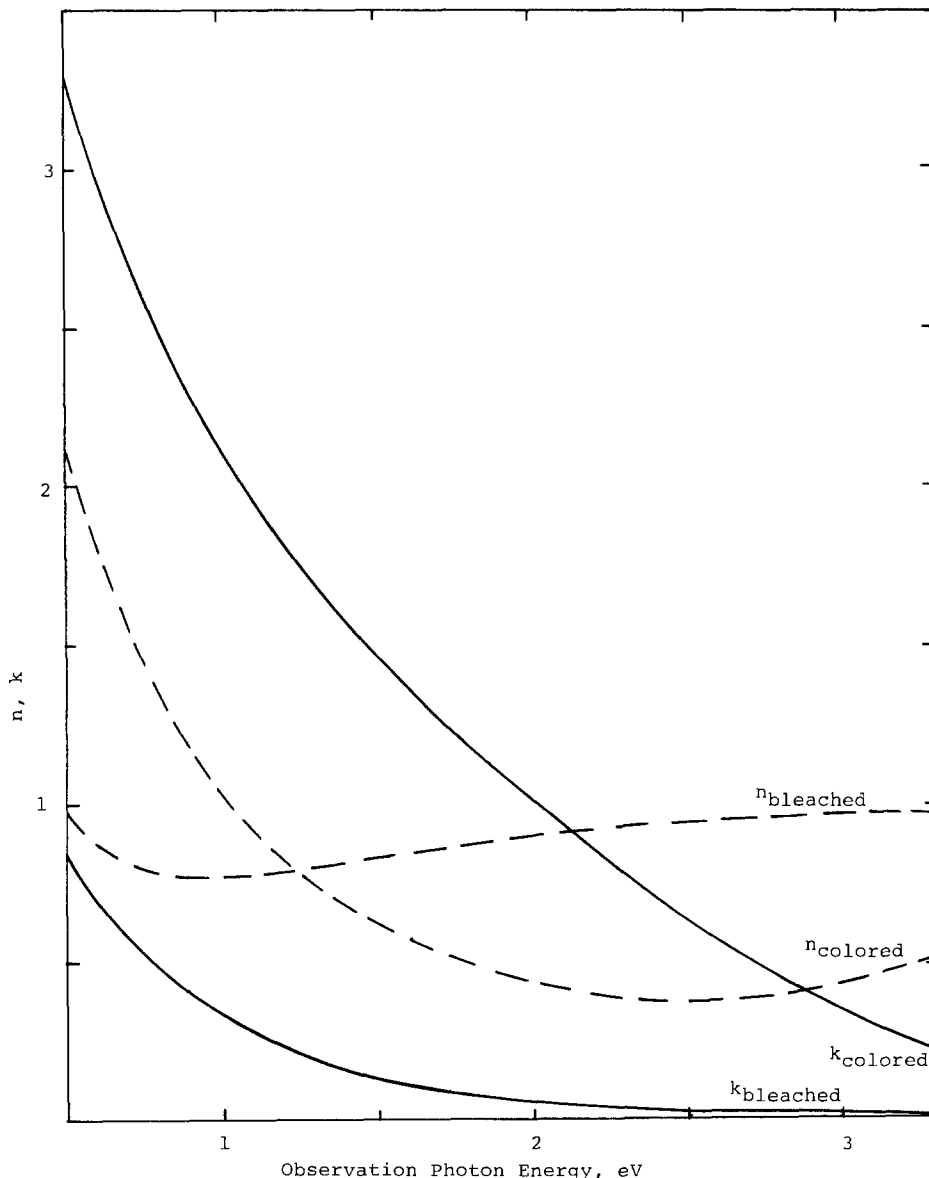


Fig. 2. Illustration of dispersion of optical constants n (refractive index) and k (extinction coefficient) of a hypothetical free-electron Drude solid with two different plasma energies. "Bleached" state plasma energy = 1 eV. "Colored" state plasma energy = 3 eV. Scattering loss energy = 1 eV. The (Drude) equations used were: $\epsilon_1 = 1 - E_p^2/(E^2 + E_\gamma^2)$; $\epsilon_2 = (E_\gamma/E) (E_p^2/[E^2 + E_\gamma^2])$; $n^2 = 1/2 [(\epsilon_1^2 + \epsilon_2^2)^{1/2} + \epsilon_1]$; $k^2 = 1/2 [(\epsilon_1^2 + \epsilon_2^2)^{1/2} - \epsilon_1]$; where E_p = plasma energy, E_γ = scattering loss energy, and E = photon energy.

k occurs at 940 nm with smaller changes at shorter wavelengths. Note that the coloration endpoints show n smallest for the colored sample at 633 nm, with the minimum n values somewhat higher at 940 and 546 nm wavelengths. This observation matches the expected behavior of n in the colored state, based on observations of the "n_{colored}" curve in Fig. 2. (The largest change in n also seems to occur at 633 nm, with smaller changes at 940 and 546 nm. This point is also in agreement with expected results, but is not experimentally well demonstrated because the optical constant uncertainties are very large in the bleached state.)

It should be noted that by using only the free-electron Drude model one cannot account completely for the 546 and 633 nm data of Fig. 1. At 546 nm, the extinction coefficient, k, exhibits a peak at an intermediate coloration state. We tentatively associate this with an absorption arising from increased filling of bound-electron states by some of the injected electrons. This bound carrier absorption saturates at an intermediate coloration state. (The bound states are completely filled.) Subsequently, as more electrons are injected, there is a decrease in bound-state absorption. This arises from an increase in the filling of conduction-band states, i.e., the conduction-band filling leads to fewer initial bound state-to-final conduction band state transitions analogous to the Burstein-Moss effect (9). The slight convexity of the 633 nm data is very likely also caused by bound-electron states. Further research is needed to quantify the relative roles of the bound- and free-electron states; but the data clearly demonstrate the dominating influence of the free electrons on the optical constants of polycrystalline WO₃, especially in the near infrared.

Conclusions

The results of the spectroscopic ellipsometry measurements of the optical constants of polycrystalline WO₃ in various states of coloration are in good agreement with independent reflectivity measurements (which have been found to be well described by a Drude model fit), and provide direct confirmation of the validity of a free-electron Drude model. This clearly demonstrates that the reflectivity modulation observed in polycrystalline WO₃ (and probably in other crystalline electrochromic materials) is associated with a high degree of

modulation of the free-carrier density. It suggests, furthermore, that to develop practical controlled radiant-energy transfer devices using EC materials, the sources of the free-electron carrier scattering in the EC materials must be identified and reduced. We are currently addressing these problems.

Acknowledgments

Some of the polycrystalline WO₃ samples used in this research were kindly provided by Dr. David Rauh and Dr. Tim Rose of EIC Laboratories, Newton, Massachusetts. Tufts University students James Alexander, William Henderson, and David Fitzpatrick aided in the preparation of experimental apparatus and associated software. The authors would also like to gratefully acknowledge the enthusiastic support and encouragement of David Pellish (Department of Energy) and Carl Lampert (University of California, Berkeley, California). This work was supported in part by the U.S. Department of Energy, contract no. DE-AC02-82CE30753.

Manuscript submitted June 21, 1983; revised manuscript received Nov. 10, 1983.

Tufts University assisted in meeting the publication costs of this article.

REFERENCES

1. W. C. Dautremont-Smith, *Displays*, **3**, 3, 67 (1982).
2. J. C. Slater, "Insulators, Semiconductors, and Metals," Vol. 3 of *Quantum Theory of Molecules and Solids*, Chap. 5, McGraw-Hill, New York (1967).
3. F. Wooten, "Optical Properties of Solids," p. 52, Academic Press, New York (1972).
4. O. F. Schirmer, V. Wittwer, G. Baur, and G. Brandt, *This Journal*, **124**, 747 (1977).
5. R. B. Goldner, D. H. Mendelsohn, J. Alexander, W. R. Henderson, D. Fitzpatrick, T. E. Haas, H. H. Sample, R. D. Rauh, M. A. Parker, and T. L. Rose, *Appl. Phys. Lett.*, **43**, 1093 (1983).
6. K. Tanaka and Y. Ohtuska, *J. Appl. Phys.*, **49**, 6132 (1978).
7. F. L. McCrackin, N.B.S. Technical Note 479, U.S. Department of Commerce, National Bureau of Standards (1969).
8. D. H. Mendelsohn, M.S. Thesis, Tufts University, Medford, Massachusetts (1983).
9. T. S. Moss, G. J. Burrell, and B. Ellis, "Semiconductor Opto-Electronics," p. 84, Butterworth Company, Ltd., London (1973).

Analysis of Chemical Vapor Deposition of Boron

Maria Michaelidis*¹ and Richard Pollard**

Department of Chemical Engineering, University of Houston, Houston, Texas 77004

ABSTRACT

A one-dimensional model has been developed which describes the interactions among hydrodynamics, multicomponent heat and mass transfer, and reaction kinetics for chemical vapor deposition of boron from boron trichloride using an impinging jet apparatus. The analysis includes variable physical properties and finite interfacial velocity and has provision for simultaneous homogeneous and heterogeneous reactions. Comparison of theoretical predictions with experimental data suggests that decomposition of BHCl₂ on the surface can control the deposition rate. The model also indicates that homogeneous production of BHCl₂ has a significant effect on the process.

Boron is a hard, light, refractory element that exhibits semiconducting behavior and high corrosion resistance. Consequently, there are many potential applications for boron in electronic components, refrac-

tory coatings, and composite materials. The most common manufacturing technique involves chemical vapor deposition (CVD) from a boron halide in a reducing atmosphere. Typically, a cool reactant stream is passed over a hot, solid surface on which boron is deposited.

Experimental studies of CVD of boron have used either heated filaments (1-4) or the impinging jet apparatus (5-7). In the jet system, the reactant gas mix-

* Electrochemical Society Student Member.

** Electrochemical Society Active Member.

¹ Present address: Department of Chemical Engineering, Washington University, St. Louis, MO 63130.

Key words: boron deposition, impinging jet, modeling.

ture is passed through a nozzle placed at right angles to the heated substrate surface. The gas flows normally to the center of the substrate and then flows away radially in all directions. An analysis (7) of this apparatus identifies regions of importance for mass-transfer and surface kinetics. However, the model assumes equilibrium in the gas phase, and it is not able to account fully for the dependence of the boron deposition rate on process parameters such as substrate temperature and inlet gas composition. Specific kinetic expressions have been proposed for reduction of BCl_3 in hydrogen (2, 3), but transport phenomena were not included in these models and, therefore, their predictive capabilities are questionable.

In this paper, a general approach to the analysis of CVD of boron from BCl_3 is presented. The axisymmetric stagnation point flow configuration is modeled because experimental data are available (5-7) and because the hydrodynamics and mass-transfer characteristics of this system are relatively well understood (8-12). In particular, the region near the stagnation point is uniformly accessible from a mass-transfer standpoint (10) so that a one-dimensional model may be used. The analysis presented here considers multi-component heat and mass transfer, coupled with laminar fluid flow, and simultaneous homogeneous and heterogeneous reactions with finite reaction rates. Variable physical properties are included, as well as a finite interfacial velocity at the reaction surface. With the model, it is possible to explain experimental observations and to identify rate-controlling factors for CVD of boron.

Transport Phenomena

Momentum, heat, and mass transfer for an impinging jet are modeled subject to the following restrictions: (i) steady-state operation, (ii) laminar flow of Newtonian fluid, (iii) no viscous dissipation of energy, (iv) radiation and natural convection neglected, (v) constant total pressure across diffusion layer, (vi) negligible thermal diffusion, and (vii) ideal gas mixture. With these restrictions, the equations of motion and continuity of the fluid become

$$\rho \mathbf{v} \cdot \nabla \mathbf{v} + \nabla \cdot \underline{\underline{\tau}} = 0 \quad [1]$$

$$\nabla \cdot (\rho \mathbf{v}) = 0 \quad [2]$$

where

$$\underline{\underline{\tau}} = -\mu [\nabla \mathbf{v} + (\nabla \mathbf{v})^T] + \frac{2}{3} \mu I \nabla \cdot \mathbf{v} \quad [3]$$

Equations [1]-[3] are simplified further by assuming that the hydrodynamics obtained experimentally can be approximated by the classical axisymmetric stagnation point flow pattern (8). For this ideal case, the velocity component normal to the surface, the gas composition, and the transport properties are independent of radial position. [This is consistent with the observation (7) that the boron deposition rate is uniform close to the stagnation point.]

The transformation of von Kármán (13) suggests that, with cylindrical coordinates, the velocity components can be expressed as

$$v_r = arF(\zeta), \quad v_\theta = 0, \quad v_z = -2\sqrt{av_\infty} H(\zeta) \quad [4]$$

where

$$\zeta = z\sqrt{a/v_\infty} \quad [5]$$

The hydrodynamic parameter a can be correlated with the average nozzle exit velocity and the system geometry (10). For nonuniform, laminar flow at the exit of the circular nozzle used in the experiments (7), a theoretical relationship for a may be used (10, 14)

$$a = \frac{4w}{\pi d^3 \rho} \left(2.464 - 1.0629 \frac{L}{d} + 1.5794 \frac{L^2}{d^2} \right) \quad [6]$$

where $0.05 \leq L/d \leq 0.5$.

Substitution of Eq. [4] into Eq. [1]-[3] gives

$$F - \frac{dH}{d\zeta} = H \frac{d \ln \rho}{d\zeta} \quad [7]$$

$$F^2 - 2H \frac{dF}{d\zeta} = \frac{\rho_\infty}{\rho} \frac{d}{d\zeta} \left(\frac{\mu}{\mu_\infty} \frac{dF}{d\zeta} \right) + 1 \quad [8]$$

It should be noted that a third hydrodynamic equation is not needed because the angular velocity component is zero. The magnitude of the normal velocity component at the surface is related to the mass-transfer rate by the definition for the mass average velocity

$$\underline{v} = \frac{1}{\rho} \sum_i M_i \underline{N}_i \quad [9]$$

where \underline{N}_i is the molar flux of species i . Equation [9] is used in conjunction with the relationship between the fluxes \underline{N}_i and the reaction kinetics (see below) as a boundary condition for Eq. [7]. The boundary conditions for Eq. [8] are

$$F = 0 \quad \text{at} \quad \zeta = 0 \quad [10]$$

$$F = 1 \quad \text{at} \quad \zeta = \infty$$

The fluid density ρ , used in the equations above, is directly related to total gas concentration by

$$\rho = \bar{M}c \quad [11]$$

where $\bar{M} = \sum_i x_i M_i$. The concentration is, in turn, related to pressure with the ideal gas law

$$p = cRT \quad [12]$$

The thermal energy equation can be expressed in dimensionless form as (15)

$$\begin{aligned} -2 \frac{\tilde{C}_p}{\tilde{C}_{p_\infty}} H \frac{dT}{d\zeta} &= \frac{T}{Pr_\infty T_\infty} \left[\frac{k}{k_\infty} \frac{d^2 T}{d\zeta^2} + \frac{dT}{d\zeta} \frac{d(k/k_\infty)}{d\zeta} \right] \\ &+ \frac{sT}{T_\infty} \frac{dT}{d\zeta} + UT \quad [13] \end{aligned}$$

where

$$\left. \begin{aligned} \tilde{C}_p &= \sum_i x_i \tilde{C}_{p_i} \\ Pr_\infty &= \frac{\mu_\infty \tilde{C}_{p_\infty}}{k_\infty \bar{M}_\infty} \\ s &= - \frac{\sum_i J_i \tilde{C}_{p_i}}{\tilde{C}_{p_\infty}} \\ U &= - \frac{\sum_i \tilde{H}_i^* R_i}{T_\infty \tilde{C}_{p_\infty}} \\ J_i &= \underline{J}_i / c_\infty \sqrt{v_\infty a} \\ R_i &= R_i / c_\infty a \end{aligned} \right\} \quad [14]$$

The temperatures of the surface and the bulk fluid are specified as boundary conditions for Eq. [13].

The dimensionless multicomponent diffusion equation is (15, 16)

$$\nabla x_i = \sum_{k \neq i} \frac{x_i J_k - x_k J_i}{D_{ik}} \quad [15]$$

where D_{ik} is a dimensionless transport property for binary interactions, defined as $D_{ik} = c D_{ik}/c_{x\nu_x}$. For a mixture of n species, there are $(n-1)$ independent force balances in the form of Eq. [15], and there are $\frac{1}{2}n(n-1)$ independent transport properties because D_{ii} is not defined and, by Newton's third law of motion, $D_{ik} = D_{ki}$. The mole fractions in Eq. [15] are related by

$$\sum_i x_i = 1 \quad [16]$$

A steady-state material balance in the gas phase is

$$\nabla \cdot \underline{N}_i = R_i \quad [17]$$

where R_i is the net homogeneous rate of production of species i and

$$\underline{N}_i = \underline{J}_i + c_i v \quad [18]$$

In dimensionless form, Eq. [17] becomes

$$\frac{d^2 x_i}{d\zeta^2} = \sum_{k \neq i} \left[\frac{x_i R_k - x_k R_i}{D_{ik}} + \frac{2cH}{c_x D_{ik}} \left(x_i \frac{dx_k}{d\zeta} - x_k \frac{dx_i}{d\zeta} \right) + J_k \frac{d}{d\zeta} \left(\frac{x_i}{D_{ik}} \right) - J_i \frac{d}{d\zeta} \left(\frac{x_k}{D_{ik}} \right) \right] \quad [19]$$

for the one-dimensional problem considered here. There are $n-1$ independent force balances with the form of Eq. [19] which can be used, together with the relationship between the fluxes

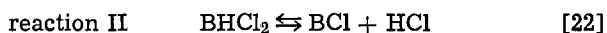
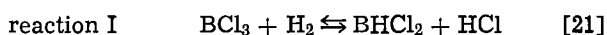
$$\sum_i M_i J_i = 0 \quad [20]$$

to describe mass transfer in a multicomponent system.

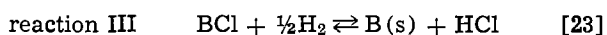
At the surface, $n-1$ Stefan-Maxwell relations, Eq. [15], are combined with Eq. [16] to give the boundary conditions for the composition. Far from the surface, equilibrium compositions at the bulk fluid temperature are specified as boundary conditions.

Chemical Reactions

The equations derived above, which describe the transfer of heat, mass, and momentum for axisymmetric stagnation point flow, can be used to predict the behavior of systems with an arbitrary number of homogeneous and heterogeneous reactions. For CVD of boron from a mixture of boron trichloride and hydrogen, thermodynamic studies (7) indicate that, over the temperature range of interest, five principal species are present in the gas phase: H_2 , HCl , BCl_3 , $BHCl_2$, and BCl . Several mechanisms have been proposed for the formation of boron from BCl_3 (2, 3, 5). Here, it is assumed that BCl_3 can be reduced either homogeneously or heterogeneously by the following reversible reactions



At the surface, the deposition reaction



can also take place.

The net rate of each reaction is regarded as the difference between the rates of forward and backward reactions and can be represented as

$$r_i = [k_{if} \pi x_i^{\nu_{i1}} - k_{ib} \pi x_i^{-\nu_{i1}}] \theta_v^{\nu_i} \quad [24]$$

$$\nu_{i1} > 0 \quad \nu_{i2} < 0$$

The coefficient θ_v represents the interaction between gas phase molecules and the surface; it can be taken as unity for homogeneous reactions. For heterogeneous processes, it is assumed implicitly in Eq. [24] that

dynamic equilibrium is established between the rates of adsorption and desorption. Consequently, θ_v may be regarded as the fraction of active surface sites that is available for adsorption of reactants. It can be related to compositions in the gas phase immediately adjacent to the surface by an expression of the form (17)

$$\theta_v = \frac{1}{1 + \sum_i K_{s,i} x_i^{q_i}} \quad [25]$$

where $K_{s,i}$ is an effective equilibrium constant for adsorption/desorption of species i . The values for exponents n in Eq. [24] and q_i in Eq. [25] are dependent on the specific model chosen for the surface processes.

In Eq. [24], k_{if} and k_{ib} are rate constants for forward and backward reactions, respectively. The exponent ν_{i1} is the stoichiometric coefficient for species i in reaction 1. It is positive for reactants and negative for products, and may be obtained from Eq. [21]-[23], which are assumed to be elementary reaction steps. The temperature dependence of the rate constants in Eq. [24] is assumed to be given by

$$k_{ib} = A_1 e^{-E_1/T} \quad [26]$$

where E_1 can be regarded as an activation energy for reaction 1.

In the model, the kinetic behavior can be described by the following set of independent parameters (15): E_a , $\theta_1 = k_{2b}/k_{1b}$, $\theta_2 = k_{3b}/k_{1b}$, $\theta_3 = k'_{2b}/k'_{1b}$, $\theta_4 = k^2_{1b} e^{E_a/T_s} / c_{x\nu_x} k'_{1b}$, $\theta_5 = e^{-E_a/T_s} c_x a / k'_{2b}$, $K_{s,i}$, q_i , and n . The term E_a represents an activation energy for the deposition process. Different activation energies could be chosen for each reaction, but it is assumed that the temperature dependence of the deposition rate will be dictated by the activation energy for the rate-limiting step. The dimensionless parameters θ_1 and θ_2 describe the relative rates of the heterogeneous reactions, and θ_3 is a ratio of rate constants for the homogeneous reactions. The parameter θ_4 represents the relative rates of the homogeneous and heterogeneous reactions. θ_5 specifies the rate of homogeneous production of BCl , as described by Eq. [22], compared to the mass-transfer rate, as characterized by the hydrodynamic constant a . The quantities $K_{s,i}$, q_i , and n are associated with the details of the adsorption and desorption process at the reaction surface. In some cases (see below), it is possible to incorporate these quantities into the definition for θ_4 .

The forward and backward rate constants are related by an equilibrium constant $K_1 = k_{if}/k_{ib}$, which can be defined in terms of equilibrium reactant and product compositions using Eq. [24]

$$K_1 = \prod_i x_i^{\nu_{i1}} \quad [27]$$

In general, K_1 is related to a pressure-independent equilibrium constant K_{pl} by

$$K_{pl} = p^m K_1 \quad [28]$$

In Eq. [27], the activity of any solid phase is taken to be unity, and, in Eq. [28], m represents the net number of molecules produced by reaction 1. The temperature dependence of K_{pl} is predicted from standard heats of reaction $\Delta H(T)$, with

$$\left[\frac{\partial \ln K_{pl}}{\partial (1/T)} \right]_p = -\Delta H(T)/R \quad [29]$$

and from free energy data at 25°C (18), to give expressions of the form

$$\ln K_{pl} = \alpha_1 + \beta_1/T + \gamma_1 \ln T + \delta_1 T + \epsilon_1 T^2 \quad [30]$$

The coefficients α_1 , β_1 , γ_1 , δ_1 , ϵ_1 used for the reactions are summarized in Table I.

Table I. Equilibrium constants for boron deposition reactions: coefficients for Eq. [30]

Reaction	Eq.	α	$10^4 \beta$	γ	$10^8 \delta$	$10^6 \epsilon$
I	[21]	+17.51	-0.81	-2.08	+0.94	-0.07
II	[22]	-0.11	-3.52	+2.61	-2.69	+0.35
III	[23]	-1.76	+2.78	-1.39	+1.38	-0.13

In the gas phase, the net rate of production of species i is given as

$$R_i = - \sum_j \nu_{ij} r_j \quad [31]$$

At the surface, a similar summation for the heterogeneous reactions represents the molar flux \bar{N}_i from the surface relative to the interface. The variables \bar{N}_i and R_i link the rates of the individual reactions to the equations that describe heat, mass, and momentum transfer for the impinging jet.

Interactions among the governing differential equations are caused directly by the inclusion of a finite interfacial velocity (see Eq. [9]) and variable physical properties in the analysis. Relationships for the temperature and composition dependences of physical parameters needed in the model are summarized in the Appendix.

For CVD of boron, with five species (H_2 , HCl , BCl_3 , $BHCl_2$, and BCl) in the gas phase, the steady-state behavior is described by Eq. [7], [8], [11]-[13], [16], and four Eq. [19] for variables F , H , c , p , T , and x_i . In addition, Eq. [20] and four Eq. [15] are used for the fluxes j_i . These fluxes are eliminated within the computer program by numerical inversion of Eq. [15] and [20]. The governing coupled algebraic equations and nonlinear, ordinary differential equations, subject to the specified boundary conditions, are solved numerically by a finite difference technique accurate to $O(h^2)$ (16, 19, 20). Parameters that must be specified in the model include surface and bulk temperatures, inlet gas composition, hydrodynamic parameter a (related to jet mass flow rate by Eq. [6]), and operating pressure.

Results and Discussion

Initially, simulations were obtained without inclusion of adsorption/desorption effects in the analysis (i.e., $\theta_v = 1$ in Eq. [24]). Figure 1 compares the experimental temperature dependence of dimensionless boron deposition rate with theoretical predictions, for three sets of model parameters (see Table II). The top curve is the locus of maximum deposition rates calculated with the mathematical model. It can be regarded as a combined thermodynamic-mass transfer limit since, for this curve, the reactions are locally at equilibrium but the finite mass-transfer rate through the diffusion layer limits the fraction of the bulk fluid that can reach the surface. The actual deposition rate is smaller than the thermodynamic-mass transfer limit as a result of finite chemical reaction rates, particularly at low substrate temperatures.

The curves in Fig. 1 represent extreme cases, with kinetic parameters chosen to give the "best fit" with different rate-limiting reactions. It can be seen that, with $\theta_v = 1$, the model predictions do not give a satisfactory match with the experimental data. Neverthe-

Table II. Values of kinetic parameters for Fig. 1

Curve Rate-limiting reaction (at surface)	I	II	III
	Eq. [21]	Eq. [22]	Eq. [23]
E_a (K)	9.00×10^8	1.26×10^9	1.20×10^4
θ_1	1.0×10^7	8.0×10^1	1.0×10^4
θ_2	1.0×10^5	8.0×10^1	1.0×10^{-4}
θ_3	1.0×10^9	8.0×10^1	5.0×10^3
θ_4	3.2×10^{11}	7.8×10^3	3.5×10^{13}
θ_5 (at $a = 310 \text{ s}^{-1}$)	6.3×10^{-5}	1.4×10^{-2}	1.3×10^{-4}
θ_v	1.0	1.0	1.0

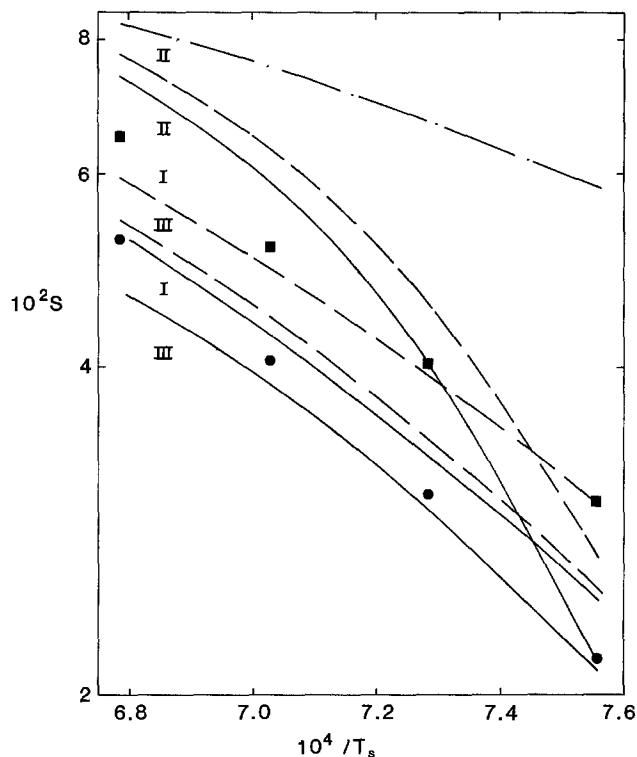


Fig. 1. Dependence of dimensionless boron deposition rate on substrate temperature. $S = \text{actual deposition rate}/c_x \sqrt{v_x a}$. Experimental data (●): $x_{BCl_3} = 0.4$, $L/d = 0.375$; (■) $a = 310 \text{ s}^{-1}$, (●) $a = 626 \text{ s}^{-1}$. Full curves: theoretical predictions for $a = 626 \text{ s}^{-1}$ with different kinetic parameters (see Table II). Dashed curves: theoretical predictions for $a = 310 \text{ s}^{-1}$ with different kinetic parameters. Uppermost curve (— · — ·): thermodynamic-mass transfer limit.

less, they can be used to provide insight into the physical phenomena involved in the process. When heterogeneous decomposition of $BHCl_2$ controls (curves II), the theoretical deposition rate is very sensitive to surface temperature. This is because the equilibrium constant for reaction II is a strong function of temperature (see Table I). For curves I and III, the slopes in Fig. 1 are close to observed results, but, as with curves II, the dependence of S on mass flow rate is unacceptable.

The model has also been used to consider reactions in the gas phase. These homogeneous reactions provide pathways that are in parallel with the surface reactions. If reaction I is rate-limiting, and if it occurs predominantly in the gas phase, the mass-transfer dependence of S in Fig. 1 becomes more acceptable, but the slopes for the curves are too small. Increases in activation energy E_a fail to raise the slopes significantly because their magnitudes are dictated by variations in local compositions with temperature. If reaction II occurs primarily in the gas phase, boron deposition rates are predicted to be at least an order of magnitude smaller than those observed experimentally. The extent of homogeneous reaction II is very small because decomposition can only occur in the narrow high temperature region close to the substrate. Further from the surface (lower gas temperatures), the equilibrium constant is small and this favors the back reaction.

Combinations of kinetic parameters that gave more than one reaction far from equilibrium were also considered, but no significant improvements were obtained. In all cases, it was observed that reaction II tends to dominate the process, especially at low surface temperatures. Furthermore, none of the simulations considered above were able to predict the correct changes in deposition rate with inlet gas composition.

The influence of inlet gas composition on S is presented in Fig. 2, for a specific jet mass flow rate. The

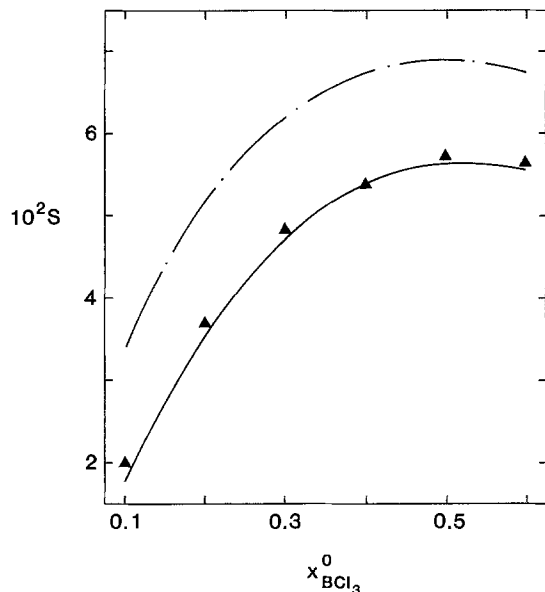


Fig. 2. Dependence of dimensionless boron deposition rate on inlet gas composition. Experimental data (7): $\blacktriangle \sim a = 102 \text{ s}^{-1}$ at $x^0_{\text{BCl}_3} = 0.4$. Full curve: theoretical prediction with kinetic parameters $\theta_1 = 2.3 \times 10^5$, $\theta_2 = 80.0$, $\theta_3 = 8.0 \times 10^4$, $\theta_4 = 4.6 \times 10^{-11}$ at $x^0_{\text{BCl}_3} = 0.4$ (see Eq. [34]), $\theta_5 = 9.0 \times 10^{-8}$ at $x^0_{\text{BCl}_3} = 0.4$, $E'_a = 2.7 \times 10^4 \text{ K}$, $E_a = 3.0 \times 10^3 \text{ K}$. Uppermost curve (— · — · —): thermodynamic-mass transfer limit. $T_s = 1373 \text{ K}$, $T_\infty = 298 \text{ K}$, $p_\infty = 1.013 \times 10^5 \text{ N/m}^2$.

dependence of the thermodynamic-mass transfer limit on $x^0_{\text{BCl}_3}$ results from composition changes near the substrate surface and from changes in the variables ν_∞ and a that are included in the definition of the dimensionless rate of boron production. The deviation of the actual deposition rate from the limiting value is almost independent of composition; both curves show a maximum at $x^0_{\text{BCl}_3} \approx 0.5$.

The close correspondence between theoretical predictions and experimental results is a consequence of the specific values for the kinetic parameters chosen for the model. In particular, the shape of the curve is controlled by the values for n , $K_{s,i}$ and q_i in Eq. [24] and [25]. The results in Fig. 2 are for

$$\theta_v^n = \frac{1}{K_{s,\text{BCl}_3} \sqrt{x_{\text{BCl}_3}}} \quad [32]$$

where

$$K_{s,\text{BCl}_3} = A_s e^{-E_s/T_s} \quad [33]$$

From a physical standpoint, Eq. [32] could imply that BCl_3 is the dominant adsorbed species and that dissociation occurs on adsorption (17).

With this simplified expression for θ_v , it is convenient to redefine the dimensionless kinetic parameter θ_4 to include K_{s,BCl_3}

$$\theta_4 = \frac{k_{21b}^2 e^{-E'_a/T_s}}{c_{\infty} \nu_\infty k'_{1b} K_{s,\text{BCl}_3}^2} \quad [34]$$

where $E'_a = 2E_s - E_a$. In this way, the relevant kinetic parameters for CVD of boron are θ_1 to θ_5 , E_a , and E'_a with $n_{\text{BCl}_3} = \frac{1}{2}$ and $q_i = 0$ otherwise. It should be noted that, by inclusion of θ_v in accordance with Eq. [32], the composition dependence of each heterogeneous reaction rate has been altered and E'_a can now have either a positive or a negative value.

Other relationships for θ_v have been tested. If adsorption of any other species is used in Eq. [32], or if θ_v is taken as unity, the maximum in Fig. 2 is predicted at $x^0_{\text{BCl}_3} > 0.5$. Also, the maximum becomes sharper and moves to smaller compositions as the product n_{BCl_3} is raised. It is conceivable that a satisfactory match could also be obtained with a higher value for

n_{BCl_3} together with additional composition terms in the expression for θ_v (Eq. [25]). However, this would necessitate introduction of extra kinetic parameters, and it is not clear that greater insight into the system behavior would be obtained.

A maximum in deposition rate with inlet gas composition has also been observed in other CVD systems. For silicon deposition from SiCl_4 , an etching reaction between SiCl_4 and silicon has been proposed as an explanation for the effect (21). The analogous reaction for CVD of boron would be



Inclusion of this heterogeneous reaction in the model raises the rate of reaction III (Eq. [23]), but the net deposition rate does not give the maximum observed experimentally.

Figure 3 shows the effect of substrate temperature on boron deposition rate at three mass flow rates. The temperature dependence of the thermodynamic-mass transfer limit corresponds to changes in the binary diffusion coefficients (see Fig. 7). The slope for the actual deposition rates is approximately $1.2 \times 10^4 \text{ K}$. This can be regarded as an apparent activation energy for boron deposition. However, it is emphasized that this value is a combination of E'_a , composition changes, and the temperature dependence of the equilibrium constant for the rate-determining reaction.

With the kinetic parameters that provide a match between experiment and theory, heterogeneous decomposition of BHCl_2 is not in equilibrium, and the rate of this step can control the boron deposition rate, i.e., the ratio of backward to forward reaction rates can be smaller for this step than for the other reactions. However, increases in surface temperature or reductions in mass flow rate tend to reduce the importance of reaction II. Under these circumstances, decomposition of BCl_3 to BHCl_2 (reaction I) becomes more significant. Reaction I occurs both homogeneously

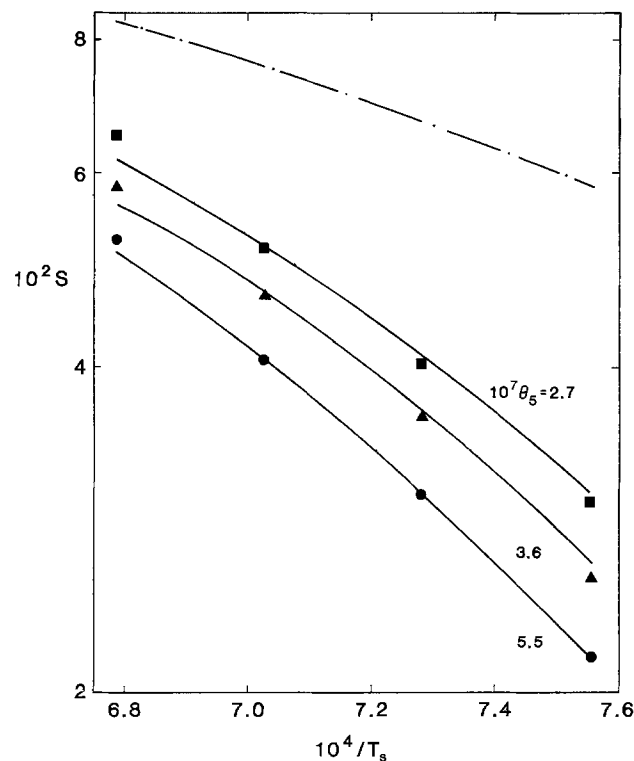


Fig. 3. Dependence of dimensionless boron deposition rate on substrate temperature. Experimental data (7): $\blacktriangle \sim a = 417 \text{ s}^{-1}$, also see Fig. 1. Full curves: theoretical predictions with kinetic parameters as in Fig. 2, unless stated otherwise. Uppermost curve (— · — · —): thermodynamic-mass transfer limit. $x^0_{\text{BCl}_3} = 0.4$, $p_\infty = 1.013 \times 10^5 \text{ N/m}^2$, $T_\infty = 298 \text{ K}$.

and heterogeneously, but most conversion occurs in the gas phase. The extent of the homogeneous pathway determines the dependence of S on mass flow rate, *i.e.*, on θ_5 . (With reaction I in equilibrium, the homogeneous reaction would have a negligible effect on the deposition rate. Consequently, it would be impossible to match theory and experiment at more than one mass flow rate.)

With the value for θ_3 specified in Fig. 2 and 3, homogeneous reaction II is essentially in equilibrium. However, as with the $\theta_v = 1$ results (see above), only a small fraction of the BHC_2 can decompose in the gas phase, and therefore this pathway is unimportant. With $\theta_2 = 80.0$, reaction III is also close to equilibrium. If the kinetic parameters were changed to make reaction III the rate-limiting step, the slopes of the curves in Fig. 3 at low mass flow rates would be too small.

The experimental values of S at 1473 K are slightly higher than the theoretical predictions (see Fig. 3). This might be attributed to natural convection which, for the reactor configuration considered here (7), would tend to raise the actual deposition rates above the results predicted on the basis of forced convection alone. In general, the contribution of natural convection becomes larger as the magnitude of the ratio Gr/Re^2 increases (7, 15). This ratio is largest at high surface temperatures and low jet mass flow rates.

In addition to predicting deposition rates, the model also provides information on changes in compositions, velocities, and physical properties across the diffusion layer. Typical composition profiles are presented in Fig. 4. A maximum in BCl composition is consistent with the fast rate of reaction III. With higher surface temperatures, reaction rates at the surface are increased, and, hence, a small maximum for x_{BHC_2} may be predicted.

An approximate estimate of the diffusion layer thickness can be obtained from the composition profiles, even though some species reach their bulk compositions closer to the surface than others. For the example in Fig. 4, an approximate thickness is 0.2 cm, which is

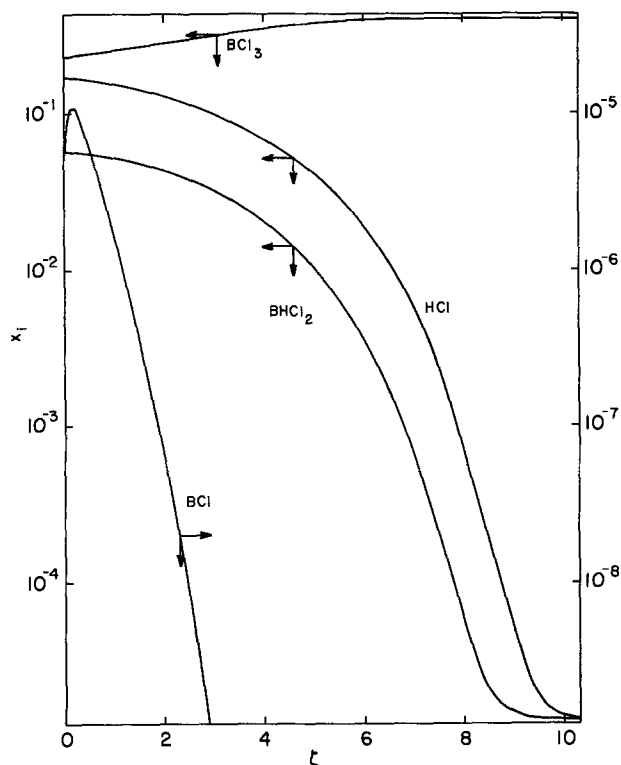


Fig. 4. Composition profiles in diffusion layer adjacent to reaction surface. Parameter values as in Fig. 3, with $\theta_5 = 3.6 \times 10^{-7}$ and $T_s = 1373$ K.

smaller than values for CVD of silicon (15) but larger than values for electrolyte solutions.

For the operating conditions used in Fig. 4, the variations of some physical properties are shown in Fig. 5. The density changes by a factor of 5.5 across the diffusion layer in direct association with changes in T and \bar{M} . Viscosity and thermal conductivity both vary by factors of about 4. These changes distort the velocity profiles from the constant property results (see Fig. 6). With larger values for T_s , variations in μ and ρ are less marked, and the constant physical property solution is approached. Even though the local velocities are influenced by the bulk temperature, the choice for T_s in the model has a negligible effect on the deposition rate. This is primarily because the extent of the gas-phase reactions declines sharply as one moves away from the reaction surface.

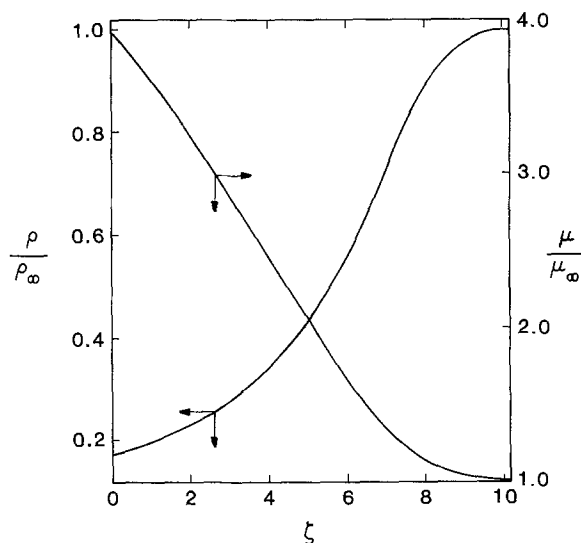


Fig. 5. Dependence of viscosity and density on distance from surface of impinging jet apparatus. Parameter values as in Fig. 4. $\rho_\infty = 1.965$ kg/m³; $\mu_\infty = 1.285 \times 10^{-5}$ kg/m.s; $T_s = 1373$ K.

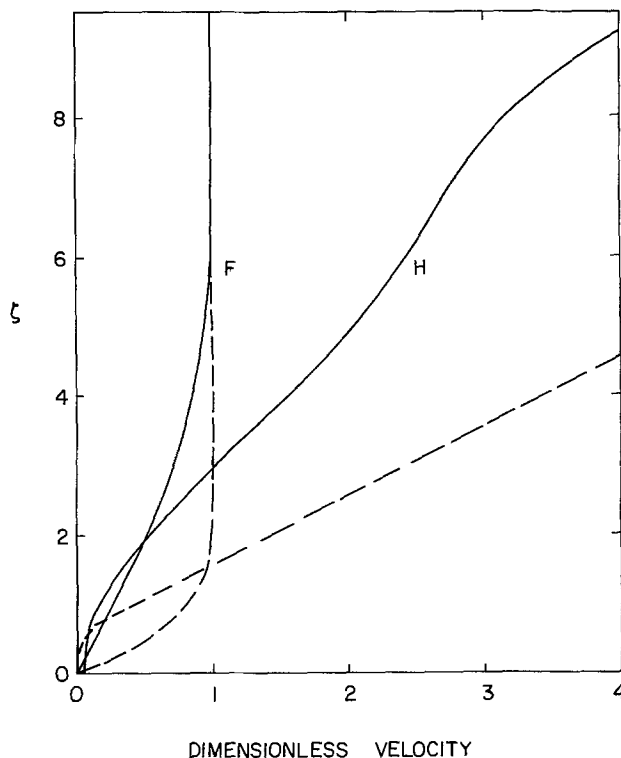


Fig. 6. Velocity profiles for boron deposition at an impinging jet. Parameter values as in Fig. 4. Full curves ~ model predictions. Dashed curves ~ constant property result (8).

Conclusions

A model has been developed which describes the interactions among hydrodynamics, multicomponent heat and mass transport, and reaction kinetics for the impinging jet system. The analysis includes variable physical properties, finite interfacial velocity, and simultaneous homogeneous and heterogeneous reactions.

This model has been used to study CVD of boron from BCl_3 in hydrogen. The effects of inlet gas composition, jet mass flow rate, and surface temperature have been investigated, and several features of the process have been elucidated.

1. With five gas-phase species and a set of seven independent kinetic parameters, the predicted dependence of boron deposition rate on inlet gas composition, jet mass flow rate, and surface temperature matches experimental results.

2. The model indicates that the relative importance of the reactions for CVD of boron is dependent on the operating conditions. Heterogeneous decomposition of BHCl_2 tends to be rate determining, although production of BHCl_2 becomes more important at low mass flow rates and high surface temperatures. The homogeneous pathway for BHCl_2 decomposition is unimportant, whereas the extent of production of BHCl_2 in the gas phase is significant and dictates the effect of mass flow rate on the rate of boron deposition.

3. Inclusion of adsorption/desorption effects, with BCl_3 as the dominant adsorbed species, is able to account for the dependence of deposition rate on inlet gas composition.

4. Physical properties, such as density and viscosity, vary by factors of between 4 and 6, across the diffusion layer and this distorts the fluid flow profiles. The diffusion layer thickness is in the range 1-10 mm.

Acknowledgment

This work was supported by the National Science Foundation (Grant no. CPE-8203554).

Manuscript submitted June 29, 1983; revised manuscript received Dec. 5, 1983.

APPENDIX

Physical Properties

Viscosity.—The temperature dependence of the viscosity of each species in the gas phase is predicted from the Chapman-Enskog kinetic theory (22)

$$\mu_i = \frac{2.6693 \times 10^{-5} \sqrt{M_i T}}{\sigma_i^2 \Omega_{\mu_i}} \quad [\text{A-1}]$$

The parameter σ_i is the collision diameter (18, 23), and Ω_{μ_i} is a dimensionless function which depends on kT/ϵ_i , where ϵ_i is a characteristic energy of interaction between molecules and k is Boltzmann's constant. For each species, Eq. [A-1] is rewritten in the simplified form

$$\mu_i = \delta_{ii} T^{\psi_{ii}} \quad [\text{A-2}]$$

and values for δ_{ii} and ψ_{ii} are given in Table A-I. The viscosity of the gas mixture is calculated with the Wilke correlation (24)

Table A-I. Values for parameters in Eq. [A-2] and [A-7]

Species, i	μ_i ($\text{N} \cdot \text{s}/\text{m}^2$)		k_i ($\text{W}/\text{m} \cdot \text{K}$)	
	$10^7 \delta_{ii}$	ψ_{ii}	δ_{ii}	ψ_{ii}
H_2	2.14	0.66	2.61×10^{-8}	0.74
HCl	1.24	0.85	7.74×10^{-8}	0.95
BCl_3	0.98	0.84	3.51×10^{-5}	0.98
BHCl_2	0.89	0.93	1.12×10^{-5}	0.93
BCl	0.37	0.98	2.27×10^{-5}	1.07

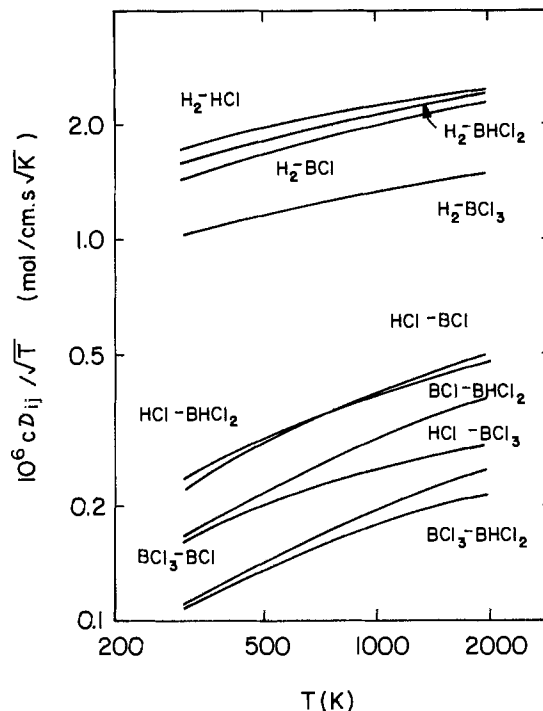


Fig. A-1. Temperature dependence of binary diffusion coefficients

$$\mu_{\text{mix}} = \sum_{i=1}^n \left(x_i \mu_i / \sum_{j=1}^n x_j \phi_{ij} \right) \quad [\text{A-3}]$$

where

$$\phi_{ij} = [1 + (\mu_i/\mu_j)^{1/2} (M_j/M_i)^{1/4}]^2 / [8 + 8M_i/M_j]^{1/2}$$

Diffusivity.—Diffusion coefficients for binary interactions are estimated from (22)

$$\frac{cD_{ij}}{\sqrt{T}} = \frac{2.2646 \times 10^{-5} \left(\frac{1}{M_i} + \frac{1}{M_j} \right)^{1/2}}{\sigma_{ij}^2 \Omega_{D_{ij}}} \quad [\text{A-4}]$$

where σ_{ij} is a mean collision diameter which is taken as $(\sigma_i + \sigma_j)/2$. The dimensionless quantity $\Omega_{D_{ij}}$ is analogous to Ω_{μ_i} used for the viscosity calculations, but the characteristic of the intermolecular potential field should now represent both species i and j , and is assumed to be given by $\epsilon_{ij} = \sqrt{\epsilon_i \epsilon_j}$. Figure A-1 shows the temperature dependence of diffusion coefficients obtained from Eq. [A-4]. In the analysis, a simplified form

$$cD_{ij} = B_{ij} T^{l_{ij}} \quad [\text{A-5}]$$

is chosen with parameters which best fit the curves in Fig. A-1 over the temperature range of interest (see Table A-II).

Specific heat.—The temperature dependence of the heat capacity (18, 25) of each species is obtained from

$$\tilde{C}_{pi} = \alpha_i + \beta_i T + \gamma_i T^2 \quad [\text{A-6}]$$

where the coefficients are summarized in Table A-III.

Table A-II. Values for parameters in Eq. [A-5]

Species		B_{ij}	l_{ij}
i	j		
H_2	HCl	5.73×10^{-7}	0.69
H_2	BCl_3	3.28×10^{-7}	0.70
H_2	BHCl_2	4.35×10^{-7}	0.73
H_2	BCl	3.16×10^{-7}	0.76
HCl	BCl_3	2.18×10^{-8}	0.85
HCl	BHCl_2	2.53×10^{-8}	0.89
HCl	BCl	1.74×10^{-8}	0.95
BCl_3	BHCl_2	1.14×10^{-8}	0.89
BCl_3	BCl	8.60×10^{-9}	0.95
BHCl_2	BCl	1.08×10^{-8}	0.98

Table A-III. Values for parameters in Eq. [A-6]

Species, i	α_i	β_i	γ_i
H ₂	28.95	-4.96×10^{-4}	1.81×10^{-6}
HCl	28.21	2.04×10^{-3}	1.28×10^{-6}
BCl ₃	51.50	4.76×10^{-2}	-1.85×10^{-5}
BHCl ₂	34.94	6.07×10^{-2}	-2.15×10^{-5}
BCl	28.44	1.39×10^{-3}	-5.22×10^{-6}

Thermal conductivity.—An approximate relationship

$$k_i = \delta_{2i} T^{\psi_{2i}} \quad [A-7]$$

is used to describe data (18) for the temperature dependence of k_i (see Table A-I). The thermal conductivity of the mixture is given by an expression analogous to Eq. [A-3]

$$k_{mix} = \sum_{i=1}^n \left(x_i k_i \left/ \sum_{j=1}^n x_j \phi_{ij} \right. \right) \quad [A-8]$$

LIST OF SYMBOLS

a	hydrodynamic constant (s^{-1})
A_1	pre-exponential factor for backward rate constant
A_s	pre-exponential factor for adsorption/desorption equilibrium constant (see Eq. [33])
c	total concentration (mol/cm^3)
c_i	concentration of species i (mol/cm^3)
\tilde{C}_p	molar heat capacity of mixture ($\text{J}/\text{mol} \cdot \text{K}$)
\tilde{C}_{pi}	molar heat capacity of species i ($\text{J}/\text{mol} \cdot \text{K}$)
d	nozzle diam (cm)
D_{ik}	diffusion coefficient for binary interactions (cm^2/s)
D_{ik}	dimensionless diffusion coefficient for binary interactions
E_a	kinetic parameter representing activation energy of rate-limiting step (K)
E'_a	$= 2E_s - E_a$, modified E_a (K)
E_s	activation energy for K_{s,BCl_3} in Eq. [33] (K)
E_1	activation energy for reaction 1 (K)
F	dimensionless radial velocity defined in Eq. [4]
Gr	Grashof number
h	mesh size (m)
H	dimensionless axial velocity defined by Eq. [4]
\tilde{H}_i^*	molar enthalpy of ideal gas (J/mol)
\underline{I}	unit matrix
\underline{J}_i	$= N_i - c_i v$, flux of species i relative to mass average velocity ($\text{mol}/\text{m}^2 \cdot \text{s}$)
J_1	dimensionless J_1
k	Boltzmann constant ($1.3806 \times 10^{-23} \text{ J}/\text{K}$)
k_i	thermal conductivity of species i ($\text{W}/\text{m} \cdot \text{K}$)
k_{if}	forward rate constant for reaction 1
k_{ib}	backward rate constant for reaction 1
k'_{ib}	backward rate constant for homogeneous reaction 1
K_1	equilibrium constant for reaction 1
K_{p1}	equilibrium constant defined by Eq. [28]
$K_{s,1}$	equilibrium constant for adsorption/desorption of species i
L	distance between end of nozzle and substrate surface (cm)
m	exponent in Eq. [28]
M_i	molecular weight of species i
\bar{M}	average molecular weight
n	exponent in Eq. [24]
\underline{N}_i	flux of species i ($\text{mol}/\text{m}^2 \cdot \text{s}$)
p	gas pressure (N/m^2)
Pr	Prandtl number
q_i	exponent in Eq. [25]
r	radial coordinate (m)
r_1	rate of reaction 1
R	universal gas constant ($8.3143 \text{ J}/\text{mol} \cdot \text{K}$)
Re	Reynolds number
R_i	rate of homogeneous production of species i ($\text{mol}/\text{m}^3 \cdot \text{s}$)
\tilde{R}_i	dimensionless R_i
s	dimensionless parameter defined by Eq. [14]
S	dimensionless boron deposition rate
T	temperature (K)

U	dimensionless parameter defined by Eq. [14]
\underline{v}	mass average velocity (m/s)
v_r	radial velocity (m/s)
v_θ	angular velocity (m/s)
v_z	axial velocity (m/s)
w	jet mass flow rate (g/s)
x^{oBCl_3}	inlet mole fraction of BCl ₃
x_i	mole fraction of species i
z	axial distance from disk surface (m)

Greek Symbols

ϵ_{ij}	maximum energy of attraction between molecules i and j (J)
ζ	dimensionless axial distance coordinate defined by Eq. [5]
θ_k	dimensionless kinetic parameter ($k = 1$ to 5)
θ_v	parameter defined by Eq. [24]
μ	fluid viscosity ($\text{kg}/\text{m} \cdot \text{s}$)
ν_{il}	stoichiometric coefficient for species i in reaction l
ν_∞	bulk kinematic viscosity (m^2/s)
ρ	fluid density (kg/m^3)
σ	collision diam for Lennard-Jones potential (m)
$\underline{\tau}$	viscous stress tensor (N/m^2)

Superscripts

*	ideal gas
$\bar{}$	partial molar quantity
\top	transpose

Subscripts

l	reaction l
s	at surface
∞	in bulk

REFERENCES

- D. R. Stern and L. Lynds, *This Journal*, **105**, 676 (1958).
- H. E. Carlton, J. H. Oxley, E. H. Hall, and J. M. Blocher, Jr., in "Chemical Vapor Deposition, Second International Conference," J. M. Blocher, Jr. and J. C. Withers, Editors, p. 209, The Electrochemical Society Softbound Symposium Series, New York (1970).
- P. E. Gruber, *ibid.*, p. 25.
- J.-O. Carlsson, in "Chemical Vapor Deposition, Seventh International Conference," T. O. Sedgwick and H. Lydtin, Editors, p. 332, The Electrochemical Society Softbound Symposium Series, Princeton, NJ (1979).
- G. E. Vuillard, A. Luque, and L. Vandenbulcke, *J. Less-Common Met.*, **47**, 235 (1976).
- L. Vandenbulcke and G. Vuillard, *This Journal*, **123**, 278 (1976).
- L. Vandenbulcke and G. Vuillard, *ibid.*, **124**, 1931 (1977).
- H. Schlichting, "Boundary Layer Theory," McGraw-Hill, New York (1960).
- H. Martin, *Adv. Heat Transf.*, **13**, 1 (1977).
- D.-T. Chin and C.-H. Tsang, *This Journal*, **125**, 1461 (1978).
- G. Wahl and R. Hoffmann, *Rev. Int. Hautes Temp. Refract.*, **17**, 7 (1980).
- J. A. Trainham and R. Pollard, *J. Non-Newtonian Fluid Mech.*, **10**, 281 (1982).
- Th. v. Karman, *Z. Angew. Math. Mech.*, **1**, 233 (1921).
- M. T. Sholtz and O. Trass, *AIChE J.*, **16**, 82 (1970).
- R. Pollard and J. Newman, *This Journal*, **127**, 744 (1980).
- J. S. Newman, "Electrochemical Systems," Prentice-Hall, Inc., Englewood Cliffs, NJ (1973).
- C. G. Hill, Jr., "Chemical Engineering Kinetics and Reactor Design," John Wiley & Sons, Inc., New York (1977).
- JANAF Thermochemical Tables, Published by U.S. National Bureau of Standards, Washington, DC, NSRDS-NBS 37 (1971).
- J. Newman, *Ind. Eng. Chem. Fundam.*, **7**, 514 (1968).
- R. E. White, *ibid.*, **17**, 367 (1978).
- P. van der Putte, L. J. Giling, and J. Bloem, *J. Cryst. Growth*, **31**, 299 (1975).

22. R. B. Bird, W. E. Stewart, and E. N. Lightfoot, "Transport Phenomena," John Wiley & Sons, Inc., New York (1960).
 23. R. A. Svehla, NASA Tech. Report R-132, Lewis Re-

- search Center, Cleveland, Ohio (1962).
 24. C. R. Wilke, *J. Chem. Phys.*, **18**, 517 (1950).
 25. B. Attwood and R. A. J. Shelton, *J. Less-Common Met.*, **20**, 131 (1970).

A Flexible Multilayer Resist System Using Low Temperature Plasma-Deposited Silicon Nitride

B. R. Soller,^{*,1} C. R. Snider,^{*,2} and R. F. Shuman¹

Sperry Research Center, Sudbury, Massachusetts 01776

ABSTRACT

A three-layer resist system which uses positive photoresists for planarizing and imaging and an intermediate layer of plasma-deposited silicon nitride is described. The planarizing layer is 2 μm -thick Shipley AZ[®] 2430. The silicon nitride transfer layer is deposited at low temperature over hard-baked AZ 2430. Photon or electron imaging is done in a thin layer of resist spun on top of the transfer layer. The silicon nitride deposition process is described, and the properties of the resulting film are detailed. The planarizing photoresist is patterned by oxygen reactive ion etching. The vertical etch rate and the degree of isotropy are measured as a function of rf power and oxygen pressure. Controllable and reproducible undercut is achieved with this multilayer resist system. The resist profile is demonstrated to be suitable for lift-off applications or anisotropic etching of the substrate.

Multilayer resists have been employed by many to accomplish high resolution pattern transfer (1-6). The multilayer resists described here consist of three layers (Fig. 1). The bottom layer, the one covering the substrate, is a thick polymer layer which is used to planarize the topography of the substrate. A second layer, the transfer layer, separates the planarization layer from the imaging layer. The transfer layer keeps the imaging resist from mixing with the planarizing material, which may also be a photoresist. A thin imaging resist is then spun on top of the transfer layer. Because the resist is thin and flat, it is possible to achieve high resolution patterns even over complex topography. The imaging resist is exposed and developed and then used as a mask for etching the transfer layer. The etched transfer layer is subsequently used as a mask for reactive ion etching (RIE) of the planarizing layer. The transfer layer is usually an inorganic material which forms a nonerodible mask for oxygen RIE.

One advantage of multilayer resists is their flexibility. Because the planarizing resist is plasma or reactive ion etched, the sidewall profile can be accurately and reproducibly controlled. The thick resist may be vertically etched so the multilayer resist can be used as an etch mask for anisotropic etching of the substrate. The multilayer resist is a better mask for substrate etching than single-layer resist because the transfer layer, rather than an organic resist, is exposed to the plasma. A properly chosen transfer-layer material will stand up to plasma etching better than photoresist. Multilayer resists can also be processed so that the planarizing resist is undercut beneath the transfer layer. This profile is ideal for lift-off applications. The metal thickness is controlled by the thickness of the planarizing resist, making lift-off of thick metals possible. The pattern resolution is controlled independently by imaging in the thin top resist.

Additional flexibility is gained by being able to image in any type of resist. Photo-, E-beam, or x-ray resists can be used as the imaging resist without regard to future harsh processing steps. The resist is used only for lithography and as a mask for etching 1000Å of the transfer material. The imaging resist is usually re-

moved during reactive ion etching of the planarization layer. The multilayer resist system described here is being used in the application of same-level mixed lithography (7). In this application the resist is both optically and E-beam exposed. As a consequence, it is necessary to be able to optically align through the resist. For this reason, a transparent material is necessary for the transfer layer. Silicon nitride was chosen as the transfer material.

Silicon nitride is compatible with both silicon and GaAs technologies. It is currently used in both technologies as a final passivation layer because it serves as an excellent barrier to alkali diffusion. It also has application as an interlevel dielectric in multilayer metallization. Because it has such widespread use in the industry, processing with silicon nitride is routine, and its properties are well characterized. Silicon nitride can be plasma deposited at low temperatures uniformly across a wafer. It is also easily etched in fluorocarbon plasmas. This ease in handling makes silicon nitride a good choice for the transfer-layer material.

This paper will describe a multilayer resist system composed of plasma-deposited silicon nitride and positive photoresists. The processing steps will be described and the applications will be demonstrated.

Experiments

The multilayer resist (Fig. 1) was applied on 3 in. silicon wafers. The planarization layer was typically 1.7-2.0 μm of AZ[®] 2430,³ which was baked at 200°C for 30

³ AZ is a registered trademark of American Hoechst Corporation, Somerville, New Jersey, for their photoresist products.

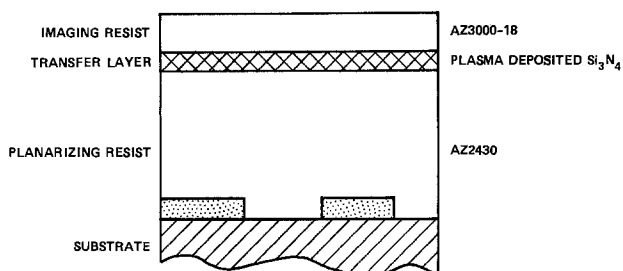


Fig. 1. Multilayer resist structure suitable for E-beam and optical exposure. Reactive ion etching of the planarizing resist leaves either vertical sidewalls or an undercut profile for lift-off applications.

* Electrochemical Society Active Member.

¹ Present address: Digital Equipment Corporation, Hudson, Massachusetts 01749.

² Present address: Alpha Industries, Woburn, Massachusetts 01801.

Key words: plasmas, etching, photoresists, integrated circuits.

min in a convection oven. The silicon nitride transfer layer was applied on top of the hard-baked resist. Thickness of this layer was generally $0.1 \mu\text{m}$.

The silicon nitride was plasma deposited in a modified Technics Planar Etch II reactor, as shown schematically in Fig. 2. The two electrodes, 20.3 cm in diam, were separated by 3.0 cm. Samples were uniformly spaced on the heated platen. The reactant gases entered the chamber through an annular plate, passed a diffusion ring, and flowed radially inward over the samples. The reaction by-products were exhausted through the center hole of the heated deposition plate.

Pressure and gas flow into the reactor were controlled independently. Reactant gases were controlled by a three-gas flow/ratio mass flow controller. This system provided closed-loop flow control and the capability of slaving any two of the gases to a third. Individual gas flows, as well as total-flow rate, were accurately maintained within the chamber. The desired process pressure was controlled independently by using a throttle valve and controller on the exhaust port. Depositions were made at a substrate temperature of 125°C . The platen was heated by a resistance heater sandwiched between the two aluminum plates comprising the platen. Temperature monitoring and control were accomplished by a thermocouple positioned between the plates.

The production of silicon nitride (Si_3N_4) was achieved by coreaction of nitrogen (N_2), ammonia (NH_3), and silane (SiH_4). Silane was introduced in an argon carrier gas, where the SiH_4/Ar ratio was 10/90. Ammonia was added because it is more easily dissociated than nitrogen. The larger concentration of free nitrogen atoms in the plasma resulted in silicon nitride films, which are less silicon rich than the films deposited from N_2/SiH_4 plasmas. The use of ammonia resulted in material having a more uniform index of refraction and thickness.

Under typical deposition conditions, input gas-flow rate ratios were $\text{N}_2/\text{NH}_3/\text{SiH}_4$ equal to 37/4.5/33.5 sccm. A total chamber pressure of 700 mtorr was maintained with the throttle valve. The plasma was sustained with 50W rf power applied to the top electrode from a 30 kHz generator. Under these conditions the deposition rate was $120 \text{ \AA}/\text{min}$.

The properties of the silicon nitride film were characterized using a Rudolph AutoEl ellipsometer. The silicon nitride film was deposited directly on silicon substrates to determine the index of refraction and film thickness. The film thickness uniformity over a 3 in. wafer was determined by using the ellipsometer to

measure thickness at nine points on a wafer. The etch rate in Transene-buffered HF was measured by determining the film thickness before and after a timed etch. Etching in buffered HF was done for several different times, and the etch rates were calculated. The etch rate of the silicon nitride film in a CF_4/O_2 plasma could not be calculated in this way because the plasma changes the reflecting properties of the silicon nitride.

The imaging resist layer was spun on the silicon nitride transfer layer over HMDS adhesion promoter. Generally, $0.5 \mu\text{m}$ -thick AZ 2415 or Microposit 3000-18 was used for pattern definition. These resists could be either optically or E-beam exposed. After the pattern was developed in the imaging resist, it was used as a mask to etch the silicon nitride.

The silicon nitride was etched in a second Technics planar system. The etch gas was 97.5% CF_4 and 2.5% O_2 . The pressure was determined by the gas flow and maintained at 400 mtorr. The wafer was placed on a 20.3 cm grounded electrode, and etching was completed in 48s using 50W applied power. The wafers were given a 9s dip in Transene buffered HF before nitride etching. Following the nitride etch, the wafers were baked at 100°C for 1h.

Reactive ion etching of the planarization layer was done with 13.56 MHz rf power applied to the bottom electrode of a Plasma Therm PK 1241 reactor. The electrode was 25.4 cm in diam, and the chamber volume was 13.5 liters. The applied power was varied between 50 and 450W, while the gas pressure and flow rate were held constant.

The etch gas used was MOS purity oxygen from Matheson. The flow of gas into the chamber was controlled by mass flowmeters. The pressure was held constant by an automatic venetian-blind valve controlled by a capacitance manometer. Pressures between 5 and 100 mtorr were studied. All etching was done with both electrodes maintained at 40°C .

In order to determine the etch rate, the samples were etched for varying time periods such that none of the etches completely removed the resist. Measurements were made from SEM photos of the etch depth and the amount of undercut. Etch rates were calculated from these data. The average etch rate and the standard deviation from the mean are reported. The amount of resist undercut, as measured at the resist-nitride interface, divided by the etch depth for the same time period is defined as the degree of isotropy. The degree of isotropy is a quantitative measure of the resist profile.

Silicon Nitride

The silicon nitride film that was plasma deposited in the system described above had an index of refraction of 1.81 ± 0.02 . This should be compared to the index of refraction of stoichiometric Si_3N_4 , which is 1.98. The lower index of the film deposited in our system suggests that it is nitrogen-rich material. This material can be deposited with a thickness uniformity of better than 5% over the surface of the wafer and less than 3.5% between three 3 in. wafers in the same run. The material which is deposited is more chemically reactive than either thermally deposited silicon nitride or plasma-deposited nitride, which is deposited at a higher temperature. The material being described etches in Transene-buffered HF at $700 \text{ \AA}/\text{min}$. For comparison, plasma nitride deposited at 250°C etches at $500 \text{ \AA}/\text{min}$; the etch rate of material deposited at 325°C is $300 \text{ \AA}/\text{min}$; 750°C thermal nitride etches at $100 \text{ \AA}/\text{min}$ in BHF. In a CF_4/O_2 plasma which is 2.5% O_2 , the etch rate of the 125°C plasma nitride is $1400 \text{ \AA}/\text{min}$. The etch is nearly isotropic, but since only 1000 \AA of nitride is being defined, the pattern dimensions can be preserved by stopping the etch just as the endpoint is reached.

Prior to silicon nitride deposition, the planarizing resist was hard-baked in a convection oven where the

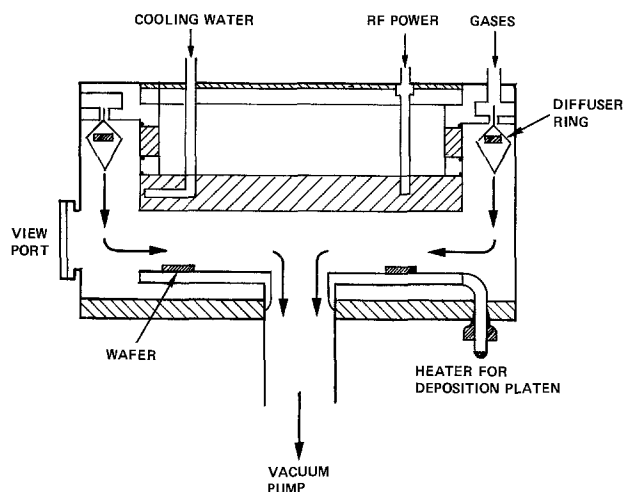


Fig. 2. Schematic drawing of planar reactor for the plasma deposition of silicon nitride. Material is deposited at 125°C by coreaction of N_2 , NH_3 , and SiH_4 with flows 37, 4.5, and 33.4 sccm, respectively, and a total pressure of 400 mtorr. The power is 50W.

minimum bake conditions were 200°C for 30 min. Baking at a temperature lower than 200°C resulted in a wrinkled photoresist layer with a textured silicon nitride layer on top of it. This is illustrated in Fig. 3. During plasma deposition of silicon nitride, the surface of the AZ 2430 planarizing resist was heated to temperatures greater than 125°C. At these temperatures, cellosolve acetate is volatilized from AZ resists and nitrogen gas is also released from decomposition of the photoactive compound (8). If the planarizing resist is not prebaked, these gases will be released during the silicon nitride deposition resulting in a wrinkling of both films. Shaw *et al.* (8) determined that for AZ 1350J photoresist, samples had to be heated to 160°C to remove all volatile components. For AZ 2430, samples must be heated to 200°C to prevent wrinkling.

Under some conditions, the silicon nitride film became completely resistant to a CF_4/O_2 plasma etch. It is believed that the silicon nitride surface becomes oxidized after it is deposited. This oxynitride surface layer can be removed in Transene-buffered HF. It was found that a 9s dip in buffered HF is the minimum time required to completely eliminate this unwanted film. After 9s the "oxide" layer was removed and almost all 1000Å of the silicon nitride film remained. The source of this oxide contamination is still being investigated.

After the CF_4/O_2 plasma etch of the nitride transfer layer, the wafer was baked at 100°C in a convection oven for 1h. The baking step was performed to prevent the nitride erosion seen in Fig. 4, which is a scanning electron micrograph of the multilayer resist after the planarization layer has been etched using the silicon nitride layer as a mask. This nitride erosion results in images substantially smaller than those originally defined in imaging resist, as well as ragged edges on those features. It is believed that the erosion is caused by the presence of fluorine in the plasma at the beginning of the oxygen RIE step. This fluorine may be trapped on the surface of the imaging resist during the CF_4/O_2 plasma etch of the nitride. Microprobe analysis has indicated the presence of fluorine

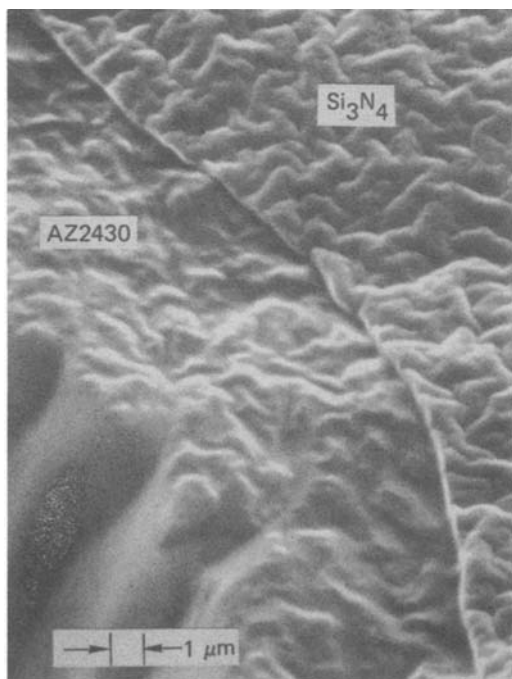


Fig. 3. SEM plots of silicon nitride transfer layer which was deposited on AZ 2430 which was not hard baked. Temperature increase during the deposition process causes both the resist and the nitride film to wrinkle.

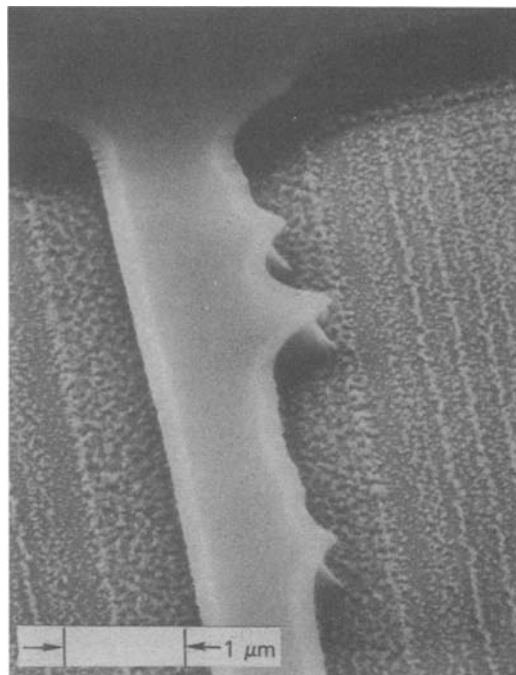


Fig. 4. Multilayer resist after nitride layer and planarization layer are etched. Ragged edges are caused by unwanted fluoride etching of the silicon nitride. The fluorine contamination can be removed by baking the wafer after the nitride etch.

in this layer, while Dobkin and Cantos (9) also found evidence for this in their work. Oxygen RIE removes the top imaging resist as well as the bottom planarizing resist, an interaction which releases the trapped fluorine to react with the silicon nitride transfer layer. The fluorine is only present at the beginning of the O_2 etch, because it is only released from the surface of the imaging resist.

The problem arises when the imaging resist does not have a square profile. Poor resist profiles are dome shaped, being thinner near the edges of the feature than in the middle. If the edges of the imaging resist are removed very early in the oxygen etch, the silicon nitride will be exposed to reactive fluorine. This is probably the cause of the nitride erosion. One solution to the problem would be to have resist profiles which do not have sloping walls, since this would assure that all fluorine is removed from the surface of the photoresist and pumped away before any silicon nitride is uncovered. An empirical solution to the problem has been to bake the sample before the oxygen RIE step is done. It is believed that the baking releases the fluorine from the surface of the photoresist; however, we have been unable to confirm this with a microprobe experiment because the fluorine signals are very small.

Reactive Ion Etching and Profile Control

Once the features were defined in the silicon nitride layer, it was used as a mask for etching the thick planarizing resist. This resist was etched in a low pressure oxygen plasma. The wafers were placed on the powered electrode so that they received high ion bombardment. Figure 5 shows the measured degree of isotropy as a function of chamber pressure and rf power. The degree of isotropy is a quantitative way to describe the profile of the etched resist and silicon nitride mask, and is defined as the lateral etch rate divided by the vertical etch rate. Figure 5 shows that power has very little effect on changing the degree of isotropy. Large variations in the degree of isotropy do occur when the pressure is varied. Completely anisotropic etching occurs only at pressures below 5 mtorr and powers greater than 150W. The dependence

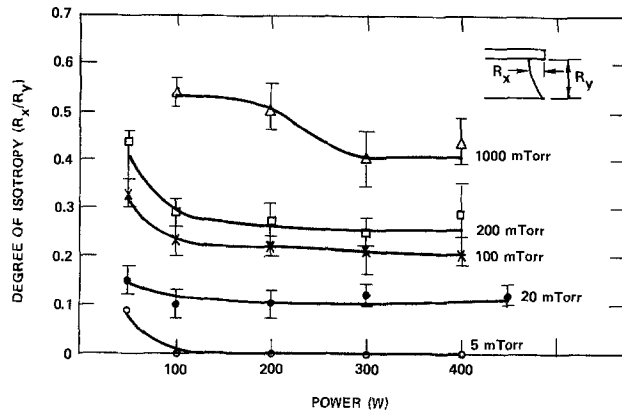


Fig. 5. Degree of isotropy of hard-baked AZ 2430 after oxygen RIE. The ratio of lateral to vertical etch rate is shown as a function of rf power for several system pressures.

of the degree of isotropy on oxygen pressure and rf power will be discussed further in another paper (10).

The vertical etch rate of the planarizing resist is plotted against power for constant pressure values in Fig. 6. Except for the data taken at 100 mtorr, the etch rate increases linearly with power input. At 100 mtorr, the etch rate increases with power, but not linearly. As the rf power input into the system increases over the range studied, the electrons in the plasma acquire a higher average energy. As the electron energy increases, the number of ionizing collisions increases (11). Ionization of the oxygen molecules produces positive ions, which are accelerated vertically toward the wafer by the sheath potential. Increasing the rf power increases both the number of positive ions and the sheath potential so that the vertical etch rate is seen to increase with the power.

The effect of varying the system pressure on the etch rate is more complicated. At low pressures (less than ~ 100 mtorr), the etch rate increases with increasing pressure because the number of reactive species increases with the increasing number of electron-molecule collisions. (There are more O₂ molecules available for collisions at higher pressures.) As the number of molecules increase with increasing pressure, the time between electron-molecule collisions decreases. This shortened time results in lower average electron energy because the electric field has less time to accelerate the electron before it collides (12). The lower average electron energy results in fewer

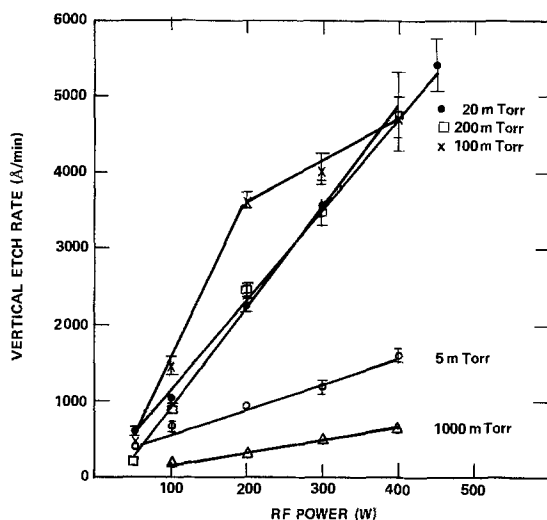


Fig. 6. Etch rates for hard-baked AZ 2430 in an oxygen plasma. The etch rates are given as a function of rf power for several system pressures.

collisions energetic enough to ionize the molecular oxygen. At pressures greater than ~ 100 mtorr, the number of ionizing collisions starts to decrease as the pressure is increased, as seen in Fig. 6.

Reactive ion-etch parameters can be chosen based on the information in Fig. 5 and 6. Gas pressure and rf power determine the degree of isotropy obtained in the planarizing resist profile. The etch rate data are used to determine the etch time to endpoint. Figure 7 shows the multilayer resist which has been defined anisotropically. The imaging resist layer is removed during the oxygen RIE so the SEM photograph only shows the etched transfer and planarization layers. The imaging resist, Microposit 3000-18, was exposed with electrons. By using electron beam lithography, features as small as $0.3 \mu\text{m}$ have been processed with this multilayer scheme. Etching beyond endpoint produces a film on the sidewalls of the planarizing resist on silicon substrates. It is believed that these films are similar to those described by Kinsbron (13). On silicon substrates, the sidewall film is probably some silicon-oxygen compound and is easily removed in buffered HF.

Figure 8 shows the multilayer resist processed with an undercut so it can be used for lift-off definition of metals. The degree of isotropy is 0.25, and $0.4 \mu\text{m}$ of a metal alloy has been deposited over the multilayer resist. The degree of isotropy is reproducible within the error bars shown in Fig. 5. This reproducibility leads to well-controlled lift-off profiles. The thick planarization layer makes it possible to define very tall features. The silicon nitride transfer layer has supported as much as a $1.5 \mu\text{m}$ layer of Ti/Au alloy without any signs of strain. After the metal has been deposited over the multilayer resist, the planarizing resist must be dissolved to carry away the excess metal. Resists baked at 200°C are not soluble in acetone, the usual lift-off solvent. A commercial epoxy remover, Uresolve Plus (Dynaloy, Incorporated), is suitable for removing the hard-baked resist in the final lift-off step. Uresolve Plus is strongly alkaline and is not suitable for lift-off directly on GaAs. Other, less caustic solvents are being sought for this application.

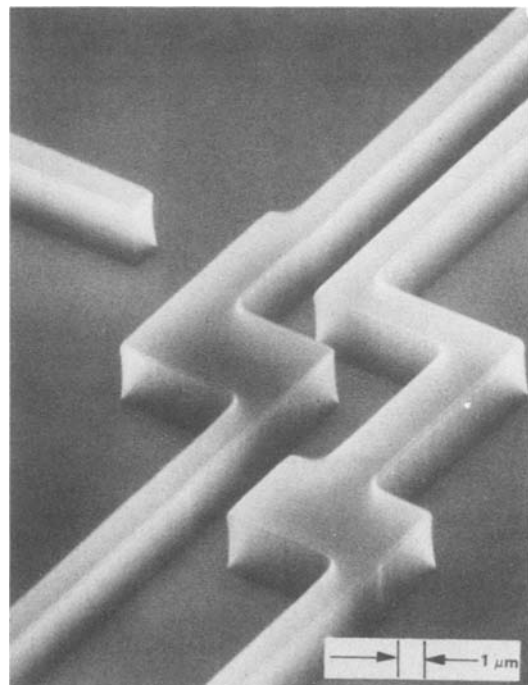


Fig. 7. Anisotropically etched AZ 2430 with a Si₃N₄ mask. The imaging resist which was removed in the oxygen RIE step was patterned using E-beam lithography.

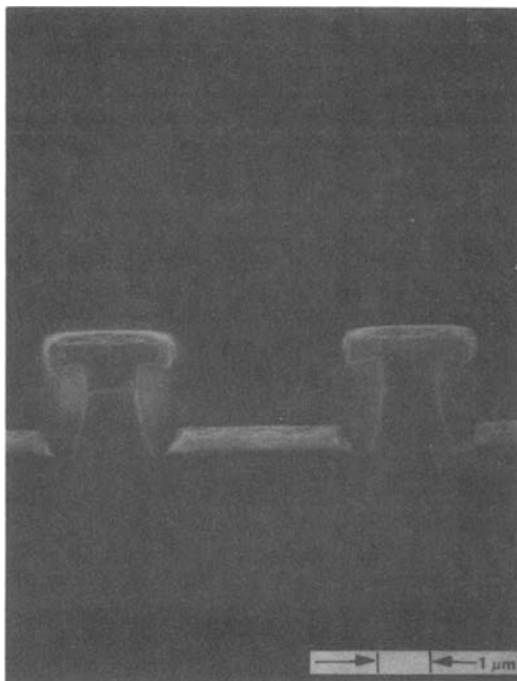


Fig. 8. Multilayer resist processed with an undercut suitable for lift-off metal deposition. $0.4 \mu\text{m}$ of Ti/Au is deposited on the resist structure.

Summary

A very flexible multilayer resist system has been developed using positive resists and plasma-deposited silicon nitride. The low temperature plasma nitride can be uniformly deposited over the surface of the wafer, resulting in a three-layer system which is completely transparent, making optical alignment possible. The imaging resist can be either optically or E-beam exposed, and no charging occurs during the E-beam exposure.

Reactive ion etching of the planarizing resist produces controllable profiles. The profile can be varied from vertical wall to any degree of isotropy desired for a lift-off application. Characterization of the etch rate and degree of isotropy as a function of pressure and power has led to predictable and reproducible resist profiles.

Acknowledgments

The authors wish to thank D. D. Casey and F. H. Spooner for many helpful discussions. The authors are also grateful to L. E. Phaneuf for his technical assistance and to T. D. Berker for the E-beam exposures.

Manuscript submitted July 11, 1983; revised manuscript received Dec. 19, 1983.

Sperry Corporation assisted in meeting the publication costs of this article.

REFERENCES

1. M. Hatzakis, *Solid State Technol.*, **24** (8), 74 (1981).
2. H. Namatsu, Y. Ozaki, and K. Hirata, *J. Vac. Sci. Technol.*, **21**, 672 (1982).
3. E. Bassous, L. M. Ephrath, G. Pepper, and D. J. Mikalsen, *This Journal*, **130**, 478 (1983).
4. J. M. Moran and D. Maydan, *Bell Syst. Tech. J.*, **58**, 1027 (1979).
5. J. Havas and G. Paal, U.S. Pat. 4,202,914 (1978).
6. M. M. O'Toole, E. D. Liu, and M. S. Chang, *Proc. Soc. Photo-Opt. Instrum. Eng.*, **275**, 128 (1981).
7. T. D. Berker, *This Journal*, **130**, 474 (1983).
8. J. M. Shaw, M. A. Frisch, and F. H. Dill, *IBM J. Res. Dev.*, **21**, 219 (1977).
9. D. M. Dobkin and B. D. Cantos, *IEEE Device Lett.*, **en-2**, 222 (1981).
10. B. R. Soller, R. F. Shuman, R. R. Ross, *This Journal*, To be published.
11. A. J. Bell and K. Kwong, *AIChE J.*, **18**, 990 (1972).
12. C. M. Melliar-Smith and C. J. Mogab, "Thin Film Processes," p. 532, Academic Press, New York (1978).
13. E. Kinsbron, W. E. Willenbrock, and H. J. Levinstein, in "VLSI Science and Technology/1982," C. J. Dell'Oca and W. M. Bullis, Editors, p. 116, The Electrochemical Society Softbound Proceedings Series, Pennington, NJ (1982).

Effective Segregation Coefficient of Boron in Silicon Ingots Grown by the Czochralski and Bridgman Techniques

P. S. Ravishankar,* L. P. Hunt,* and R. W. Francis*

Exxon Research and Engineering Company, Solar Electric Conversion Unit, Linden, New Jersey 07036

ABSTRACT

Hall measurements and four-point probe resistivity measurements were used to determine the concentration profile of boron in doped semiconductor silicon ingots grown by Czochralski and Bridgman techniques. The concentration profiles were fitted to the normal segregation equation and the effective segregation coefficient, k_{eff} , was calculated. The average value of k_{eff} for boron was 0.786 ± 0.036 in Czochralski single crystals and 0.803 ± 0.036 in Bridgman polycrystals.

Silicon made by carbothermic reduction of silica in an arc furnace is becoming increasingly important as a source of low cost silicon for solar cells (1-3). The arc furnace-derived silicon normally contains both boron and phosphorus doping impurities which are difficult to assay reliably by chemical analysis. Multiple recrystallization of the arc furnace silicon and Hall measurements on the crystals thus obtained has been suggested as an accurate method of determining boron and phosphorus concentration in arc furnace silicon

(4). The method, however, requires an accurate knowledge of segregation coefficients for these impurities. This information is also necessary to estimate the extent of purification achievable by crystal growth.

An equilibrium distribution coefficient is based strictly on thermodynamic considerations. It is normally calculated from a phase diagram as the ratio of the slope of solidus to liquidus. However, in practice, this value of the distribution coefficient can be approached only at slow growth rates and for solidification from well stirred melts. Therefore, it is customary

* Electrochemical Society Active Member.

Table I. Effective segregation coefficient of boron in single-crystal silicon

Run no.	Crystal diam (cm)	V (cm/h)	R ²	k _{eff} from slope	k _{eff} from intercept	$\left(1 - \frac{k_{\text{eff, intercept}}}{k_{\text{eff, slope}}}\right) \times 100 (\%)$
SPC-89	7.5	5	0.933	0.796	0.755	5.2
SPC-107	5	5	0.959	0.809	0.781	3.5
SPC-91	5	10	0.934	0.780	0.812	-4.1
SPC-106	5	10	0.951	0.757	0.830	-9.6

to define an effective segregation coefficient, k_{eff} , as

$$k_{\text{eff}} = x_s/x_1 \quad [1]$$

where x_s and x_1 are the concentrations (atom fraction) of an impurity in the solid at the solid/liquid interface and the bulk melt, respectively. Unlike the equilibrium coefficient, the value of k_{eff} is dependent on the actual crystal growth conditions such as growth rate, amount of stirring in the melt, etc. Therefore, this value will, in general, be different for different methods of crystal growth.

A survey of the literature for k_{eff} of boron can be somewhat disquieting. For the Czochralski technique, reported values vary from 0.7 to 0.85 (5-7). An even wider range is found for float-zone recrystallized material. Even though 0.8, with only one significant digit, is the traditionally accepted segregation coefficient for boron, it is not certain whether this is an effective or an equilibrium value, k_{eq} .

In this paper, a procedure is reported for the experimental determination of the effective segregation coefficient of boron in specific Czochralski and Bridgman crystal growth systems. The normal segregation equation

$$x_s = x_0 k_{\text{eff}} (1 - g)^{k_{\text{eff}} - 1} \quad [2]$$

is rearranged in logarithmic form as

$$\ln (x_s/x_0) = \ln k_{\text{eff}} + (k_{\text{eff}} - 1) \ln (1 - g) \quad [3]$$

where x_0 is the initial impurity concentration in the melt. A log-log plot of Eq. [3] results in a straight line, and k_{eff} can be calculated from both the slope and the intercept.

Description of Experiments

The Czochralski crystals were grown in a HAMCO CG-2000 Czochralski crystal grower. Crystals of <111> orientation were pulled from a 20 cm diam quartz crucible containing 6 kg of semiconductor grade silicon doped with boron to $\sim 0.3 \Omega\text{-cm}$. The crucible and seed were counter rotated at 15 and 8 rpm, respectively. The operation was carried out in argon at 14 torr. The ingots were grown at constant growth rates of 5 and 10 cm/h. The ingot diameters were not constant, but averaged either 5 or 7.5 cm. Slices were cut at several (about 5) locations along the ingot. Accurate weights for the appropriate crystal sections were measured in order to permit determination of the values of fraction solidified, g , for a given slice. The concentration of boron in the crystal, x_s , was determined by Hall measurements made on the individual slices. Using Eq. [3], a plot of $\ln (x_s/x_0)$ vs. $\ln (1 - g)$ was made. The slope and intercept for the straight line were obtained by a least squares fit.

The Bridgman crystals were grown by a directional solidification of semiconductor silicon doped to $\sim 0.3 \Omega\text{/cm}$. The freezing rates for these crystals ranged from 1 to 2 cm/h. A vertical section of the resulting polycrystalline ingot was etched in NaOH. Several four-point probe measurements were made at various positions (about 10) along the vertical axis. An average resistivity of several (about 4) readings at each location was converted to concentration using the equation suggested by Thurber *et al.* (8). The interface shape for different growth conditions was estimated from experiments where this parameter was

measured independently. From the interface shape, the value of the fraction solidified was calculated geometrically. The g vs. x_s data were treated as described for Czochralski crystals.

Discussion of Results

Single-crystal silicon.—Table I shows k_{eff} calculated from the slope and intercept for Czochralski crystals grown under different conditions. The square of the correlation coefficient R^2 is also shown in the table. Its value close to unity demonstrates a good linear fit to the data. The difference between the value of k_{eff} as estimated from the slope and the intercept is expressed as a percentage error in Table I. Since the intercept value requires a knowledge of x_0 and the slope value is independent of x_0 , the value from the slope should be more reliable. The small variation in k_{eff} from slope can be attributed to errors in the measurement of g . The value from the intercept is within 10% of the slope value. This error probably represents the accuracy with which a few milligrams of boron can be weighed for use as the dopant. In Table II, the mean value of k_{eff} from the slope is given for the crystals grown at the same growth rate and also for all four crystals combined. Within experimental error, the mean k_{eff} seems to be independent of growth rate. Therefore, it can be concluded that k_{eff} is 0.786 ± 0.036 for this particular Czochralski process and equipment.

Though calculation of k_{eq} requires knowledge of the phase diagram, it is possible to estimate this value from k_{eff} . For example, the BPS model (9, 10) relates k_{eff} to k_{eq} , by the equation

$$k_{\text{eff}} = \frac{k_{\text{eq}}}{k_{\text{eq}} + (1 - k_{\text{eq}}) \exp \{-V\delta/D\}} \quad [4]$$

According to Eq. [4], k_{eff} should increase as $(V\delta/D)$ increases. The results given in Table II show that, if anything, the mean k_{eff} decreases slightly as V is increased. This is the basis for the conclusion that the variation of k_{eff} with V is not significant.

Rearranging Eq. [4],

$$\ln [(1 - k_{\text{eff}})/k_{\text{eff}}] = \ln [(1 - k_{\text{eq}})/k_{\text{eq}}] - (V\delta/D) \quad [5]$$

If sufficient data were available at each growth rate, a plot of Eq. [5] should give a straight line of slope (δ/D) and intercept $(\ln [(1 - k_{\text{eq}})/k_{\text{eq}}])$ from which k_{eq} can be calculated. Since sufficient data were not available, this procedure was not carried out. However, it can be concluded that the measured k_{eff} is probably very close to k_{eq} .

Polycrystalline silicon.—The data for polycrystalline silicon is shown in Table III. In some cases, k_{eff} calculated from the intercept deviates by as much as

Table II. Mean k_{eff} as a function of growth rate

Growth rate, (cm/h)	Mean k_{eff} from slope
5	$0.803 \pm 0.083^*$
10	0.796 ± 0.146
Combined data	0.786 ± 0.036

* 95% confidence limits (11, 12).

Table III. Effective segregation coefficient of boron in polycrystalline silicon

Run no.	R ²	k_{eff} from slope	k_{eff} from intercept	$\left(1 - \frac{k_{\text{eff, intercept}}}{k_{\text{eff, slope}}}\right) \times 100(\%)$
EB-38	0.961	0.838	0.928	-10.7
EB-43	0.968	0.767	0.806	- 5.1
EB-98	0.970	0.783	0.568	27.5
EB-99	0.981	0.805	0.698	13.3
EB-104	0.975	0.822	0.683	16.9

Mean k_{eff} from slope = $0.803 \pm 0.036^*$.

* 95% confidence limits.

27.5% from the slope value. As discussed before, this error may be caused by the error in x_0 . It is important to note that the k_{eff} from the slope, which is independent of x_0 , has much less scatter. The mean k_{eff} from the slope for all five of the ingots is 0.803 ± 0.036 . The significance of the difference between this value and the value obtained for Czochralski growth depends on the confidence one wishes to place in the data. However, the higher value of k_{eff} for Bridgman growth is consistent with the fact that there is much less stirring in Bridgman growth than in Czochralski growth.

Conclusions

1. The effective segregation coefficient, k_{eff} , for Czochralski growth is 0.786 ± 0.036 .
2. For the range of growth rates used, k_{eff} is independent of growth rate within experimental error. This suggests that the measured k_{eff} is probably very close to the equilibrium value, k_{eq} .
3. k_{eff} in polycrystalline silicon grown by the Bridgman method is 0.803 ± 0.036 .

Acknowledgments

We wish to acknowledge E. Shipp and L. Younghouse for assistance in the Hall and four-point probe measurements, and R. Sylvain of Solar Power Corporation for growing the crystals.

Manuscript submitted April 11, 1983; revised manuscript received Sept. 21, 1983. This was Paper 215 presented at the San Francisco, CA, meeting of the Society, May 8-13, 1983.

LIST OF SYMBOLS

D	diffusion coefficient (m^2/s)
g	fraction solidified (dimensionless)
k	segregation coefficient (dimensionless)
R	correlation coefficient (dimensionless)
V	growth rate (m/h)
x	concentration (atom fraction)
δ	fictitious stagnant film thickness (m)

Subscripts

eff	effective
eq	equilibrium
s	solid
l	liquid
o	initial

REFERENCES

1. J. A. Amick, J. P. Dismukes, R. W. Francis, L. P. Hunt, P. S. Ravishankar, M. Schneider, R. Sylvain, K. Larsen, and A. Schei, Paper 208 presented at The Electrochemical Society Meeting, San Francisco, CA, May 8-13, 1983.
2. L. P. Hunt and V. D. Dosaj, in "2nd E.C. Photovoltaic Solar Energy Conference," R. Van Overstraeten and W. Palz, Editors, p. 98, D. Riedl Publishing Co., Boston, MA (1977).
3. S. Pizzini, in "Materials and New Processing Technologies for Photovoltaics," J. P. Dismukes, P. Rai-Choudhury, E. Sirtl, and L. P. Hunt, Editors, p. 26, The Electrochemical Society Soft-bound Proceedings Series, Pennington, NJ (1982).
4. L. P. Hunt, J. P. Dismukes, and R. W. Francis, Paper 209 presented at The Electrochemical Society Meeting, San Francisco, CA, May 8-13, 1983.
5. R. N. Hall, *J. Phys. Chem.*, **57**, 836 (1953).
6. H. R. Hub, T. G. Diggs, Jr., and O. B. Cecil, *J. Appl. Phys.*, **42**, 1235 (1971).
7. H. F. Wolf, in "Semiconductors," Wiley-Interscience, New York (1971).
8. W. R. Thurber, R. L. Mattis, Y. M. Liu, and J. J. Filliben *This Journal*, **127**, 2291 (1980).
9. J. A. Burton, R. C. Prim, and W. R. Slichter, *J. Chem. Phys.*, **21**, 1987 (1953).
10. W. R. Wilcox, in "Fractional Solidification," M. Zief and W. R. Wilcox, Editors, Marcel Dekker, New York (1967).
11. C. A. Bennett and N. L. Franklin, "Statistical Analysis in Chemistry and the Chemical Industry," John Wiley and Sons, New York (1954).
12. P. S. Ravishankar, W. R. Wilcox, and D. J. Larson, *Acta Metall.*, **28** (1980).

Study of Electrical Characteristics on Thermally Nitrided SiO₂ (Nitroxide) Films

Chin-Tang Chen, Fang-Churng Tseng, and Chun-Yen Chang

Institute of Electronics and Electrical Engineering, National Cheng Kung University, Tainan, Taiwan, China

Ming-Kwang Lee

Institute of Electronics, National Chiao-Tung University, Hsin-Chu, Taiwan, China

ABSTRACT

A significant influence of thermal nitridation on the electrical characteristics of nitroxide films was found in this study. Nitridation at temperatures lower than 1000°C results in a great negative shift of flatband voltage V_{FB} . However, the value of V_{FB} continuously decreases with the increasing of nitridation time at nitridation above 1000°C. After annealing of nitroxide films in N₂ gas at 1000°C for 30 min, a decrease of V_{FB} , compared with the same nitridation conditions, was observed. From quasi-static C-V measurements, it shows that not only interface fixed charge Q_{ss} but also surface-state density N_{ss} are reduced in the decreasing of V_{FB} after annealing the films in N₂ gas. This effect is more prominent for nitridation at lower temperatures; however, there still exists some degree of reduction in V_{FB} for nitridation at higher temperature and longer time. The negative bias-temperature instability, sometimes called "slow trapping," is revealed by accelerated aging with negative gate bias at elevated temperatures. It is found that the instability problem is more severe for samples which are nitrided at lower temperatures but N₂ annealing can reduce the negative bias-temperature instability. After N₂ annealing, nitroxide films prepared with nitridation above 1150°C provide good properties for MOS devices.

Currently, thermally grown SiO₂ film is used as a gate insulator in MOSLSI's. According to the scaling method (1), a reliable thin insulator is required for VLSI applications. However, due to several serious problems of thin SiO₂ films, including low resistivity to the diffusion of impurities (2, 3), high field instabilities (4-7), and hot electron effects (8-9), we can expect that the quality of SiO₂ films becomes inadequate for VLSI devices when the thickness of the gate oxide is getting thinner.

Thermal nitridation of SiO₂ is considered to be the best candidate to replace SiO₂ as the gate insulator in films less than 300Å thick since this material has demonstrated excellent masking characteristics against diffusion of impurities, remarkable improvement in dielectric breakdown voltages, larger dielectric constant, and good stability of MOS structure (10-12).

In this study, relatively thick nitroxide films (around 650Å), instead of thinner nitroxide films, were chosen because we could eliminate the poor quality factor caused from unreliable thin oxide films. This paper shows that the interfacial characteristics of MOS structure can be improved by applying N₂ annealing on nitrided oxide films.

Experimental

Electrical measurements were made on MOS structures. In this experiment, n-type, (100) oriented silicon wafers, with resistivities ranging from 4 to 7 Ω-cm, were used. These wafers were cleaned in a hot solution of H₂SO₄ + H₂O₂ and rinsed in deionized water. Oxide films with thicknesses of around 650Å were thermally grown on the wafers in the ambient of wet oxygen gas. The oxidized wafers were proceeded to thermal nitridation in ultrapure ammonia gas. The nitridation temperature and time were varied from 900° to 1200°C and from 30 min to 3h, respectively. After this process, the wafers were divided into two groups. There was a group with no additional processing, the others were annealed in nitrogen gas at 1000°C for 30 min. 1 μm in thickness of aluminum was deposited on the wafers, and a metal pad of 100 mil² was then patterned using the conventional lithography and etching techniques. After metallization, the wafers were sintered at 450°C in forming gas for 30 min.

The value of flatband voltage V_{FB} was calculated on C-V curves. Bias-stress tests using an applied volt-

age of -20V were made on MOS capacitors at 300°C for 3 min to reveal the negative bias-temperature instability. A quasi-static C-V technique was used to determine the interface fixed charge Q_{ss} and surface-state density N_{ss} .

Results

For samples without N₂ annealing, the changes of flatband voltages V_{FB} with respect to nitridation temperature and time are shown in Fig. 1. Nitridation at temperatures lower than 1000°C results in a great

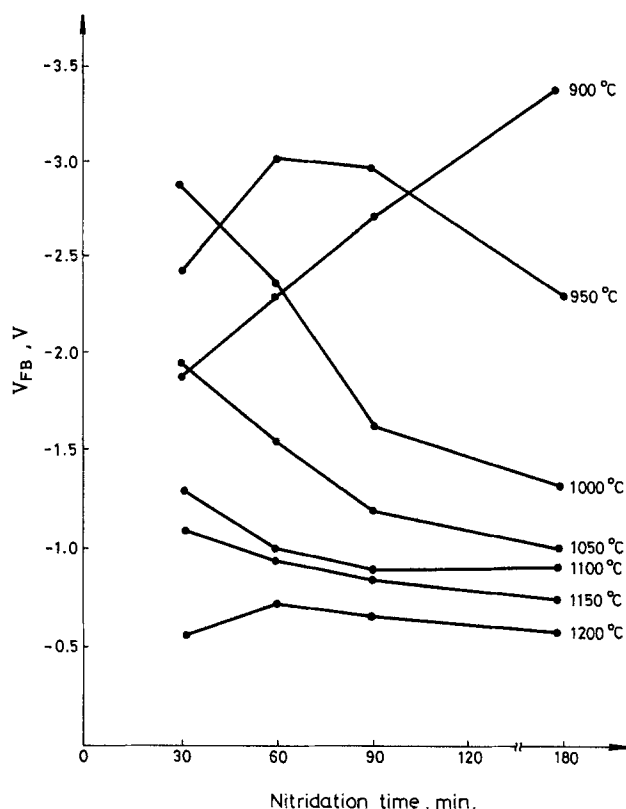


Fig. 1. The changes of flatband voltages V_{FB} with respect to different nitridation temperature and time for samples without N₂ annealing.

Table I. Q_{SS} and midgap N_{SS} vs. nitridation time for samples that were nitrided at 950°C and received N_2 or no N_2 annealing

	NO N_2 annealing				N_2 annealing			
	30 min	60 min	90 min	180 min	30 min	60 min	90 min	180 min
Q_{SS} (cm^{-2})	6.6×10^{11}	5.07×10^{11}	4.92×10^{11}	2.2×10^{11}	5×10^{11}	3.18×10^{11}	2.14×10^{11}	1.04×10^{11}
N_{SS} ($cm^{-2}ev^{-1}$)	7.82×10^{10}	4.68×10^{11}	5.08×10^{11}	5.55×10^{11}	5.78×10^{10}	4.4×10^{11}	4.55×10^{11}	4.96×10^{11}

negative shift of V_{FB} . However, as temperature increases above 1000°C and nitridation time exceeds 90 min, the V_{FB} value rapidly decreases. Figure 2 shows the changes of V_{FB} for samples that were N_2 annealed, the curves have similar tendency of variation to Fig. 1, but V_{FB} is smaller compared with the same nitridation conditions. As temperature increases above 1100°C and reaction for 180 min, the samples have nearly the same value of V_{FB} .

For samples that were N_2 annealed, the decrease of V_{FB} corresponds to the reduction of N_{SS} and Q_{SS} . This can be clearly seen in the representative data shown in Table I. These data are obtained from samples which were nitrided at 950°C by using quasi-static C-V technique.

Table II shows data of midgap N_{SS} and Q_{SS} for samples which were nitrided at 1150°C and had been annealed in N_2 gas. Both Q_{SS} and midgap N_{SS} can be reduced to the order of 10^{10} for a nitridation time longer than 90 min.

Upon negative bias-temperature aging, the slow trapping is revealed in the shift of the high frequency C-V curve to a more negative direction. The magnitude of flatband voltage difference ΔV_{FB} reflects the degree of instability. The dependence of ΔV_{FB} on nitridation temperatures with reaction time varied from 30 to 180 min and is shown in Fig. 3. ΔV_{FB} increases with the

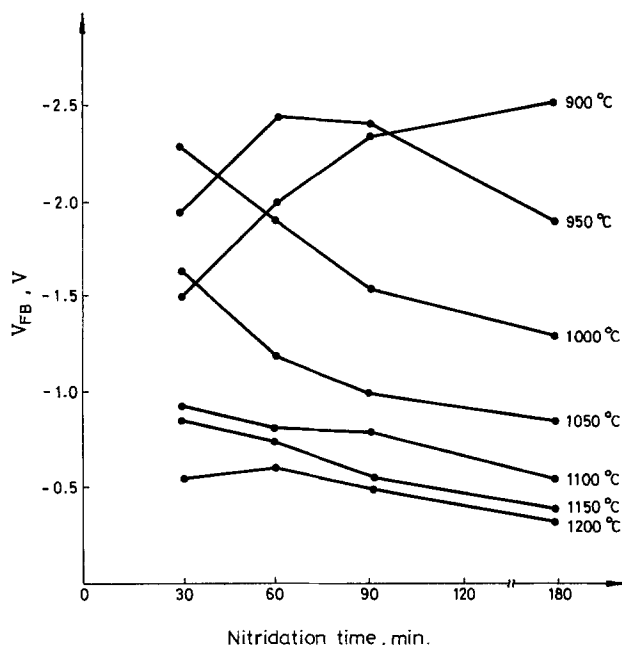


Fig. 2. The changes of flatband voltages V_{FB} vs. various nitridation temperatures and times for samples that were N_2 annealed.

Table II. Data of Q_{SS} and midgap N_{SS} for samples that were nitrided at 1150°C and had been annealed in N_2 gas

	30 min	60 min	90 min	180 min
Q_{SS} (cm^{-2})	1.3×10^{11}	1.1×10^{11}	4.1×10^{10}	3.6×10^{10}
N_{SS} ($cm^{-2}ev^{-1}$)	5.0×10^{10}	4.7×10^{10}	3.5×10^{10}	1.0×10^{10}

increasing of nitridation time for temperatures lower than 1150°C and nearly saturates at higher temperatures of 1150° and 1200°C. However, samples that were N_2 annealed consistently achieve lower ΔV_{FB} values.

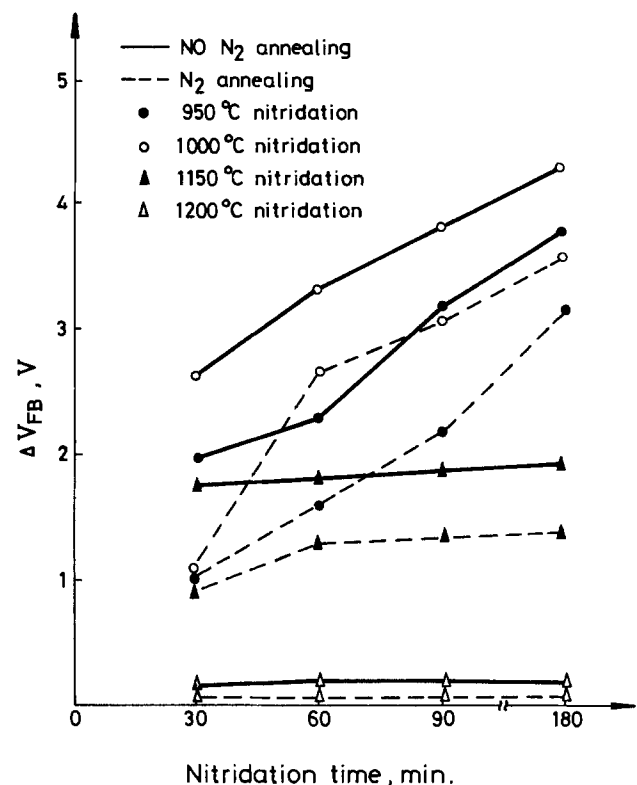


Fig. 3. The dependence of flatband voltage of different ΔV_{FB} on various nitridation temperatures and time for samples with and without N_2 annealing.

Discussion

As seen in Fig. 1, with the increase of nitridation time the negative shift of V_{FB} increases significantly at 900°C and decreases explicitly at elevated temperatures above 1000°C. This phenomenon might be interpreted as the following mechanism. At first, the hydrogen gas produced during ammonia nitridation processing dissolves into the SiO₂ skeleton. Then, the dissolved hydrogen molecules react with the surrounding Si-O bondings, forming the dangling bonds. Both N_{ss} and Q_{ss} , therefore, increase significantly and cause the V_{FB} shift phenomenon (2). The V_{FB} shift consequently is strongly related to the solubility of hydrogen gas in a SiO₂ layer. Since the hydrogen molecule is very small in molecular diameter and has nonpolar characteristics, the solubility of hydrogen in SiO₂ may be assumed to be similar to its solubility in aqueous solution (13). That is, the hydrogen solubility in a SiO₂ layer may decrease with the increase of temperature and be negligibly small at elevated temperatures above 1000°C compared with that at 900°C. Consequently, the dangling bond formation at temperatures above 1000°C is not explicitly seen.

The slow trapping instability can be a major threat to reliability of p-channel MOSFET. The mechanism of slow trapping has not been established. However, the effect is greater when initial Q_{ss} or N_{ss} is large (14, 15). In the case of Table I, N_{ss} exhibits the reverse. Comparing Fig. 3 with Table I, we can conclude that the increase of ΔV_{FB} is due to the increase of N_{ss} .

After N₂ annealing, the atomic bonds at the interface of silicon and nitroxide can be rearranged (16). Both N_{ss} and Q_{ss} are reduced to a certain amount, therefore, V_{FB} and ΔV_{FB} also decrease. This effect is clearly shown in Fig. 2 and Fig. 3.

Conclusion

The electrical characteristics of the nitroxide films were studied. The negative direction shift of V_{FB} due to the deterioration of hydrogen gas can be alleviated by N₂ annealing. Such an anneal also reduces the negative bias-temperature instability.

N₂ anneal is recommended for nitroxide films which are prepared with nitridation above 1150°C to achieve stable device operational characteristics.

Acknowledgments

The authors would like to thank Dr. C. Y. Lu for valuable discussions and Miss S. Y. Wei for typing this manuscript.

Manuscript submitted June 10, 1983; revised manuscript received ca. Nov. 7, 1983.

National Cheng Kung University assisted in meeting the publication costs of this article.

REFERENCES

1. R. H. Dennard, F. H. Gaensslen, H. N. Yu, E. Bassous, and A. Le Blance, *IEEE J. Solid-State Circuits*, **sc-9**, 256 (1974).
2. T. Ito, T. Nakamura, and H. Ishikawa, *This Journal*, **129**, 184 (1982).
3. Y. Hayafuji and K. Kajiwara, *ibid.*, **129**, 2102 (1982).
4. M. Shtatzkes and M. Av-Ron, *J. Appl. Phys.*, **47**, 3192 (1976).
5. C. M. Osburn and S. I. Raider, *This Journal*, **120**, 1369 (1973).
6. ToH. Distefano, *J. Appl. Phys.*, **44**, 527 (1973).
7. E. Harari, *Appl. Phys. Lett.*, **30**, 601 (1977).
8. R. A. Gdula, *This Journal*, **123**, 42 (1976).
9. T. H. Ning, C. M. Osburn, and H. N. Yu, *ibid.*, **123**, 198 (1976).
10. S. P. Muraka, C. C. Chang, and A. C. Adams, *ibid.*, **126**, 996 (1979).
11. T. Ito, H. Arakawa, T. Nozaki, and H. Ishikawa, *ibid.*, **127**, 2248 (1980).
12. T. Ito, T. Nozaki, and H. Ishikawa, *ibid.*, **127**, 2053 (1980).
13. N. A. Lange and G. M. Forker, "Handbook of Chemistry," p. 1092, Handbook Publishers, Inc., Sandusky, OH (1956).
14. S. I. Raider and A. Berman, *This Journal*, **125**, 629 (1978).
15. E. H. Nicollian and J. R. Brews, in "MOS Physics and Technology," pp. 794-798, Wiley, New York (1982).
16. A. K. Sinha and T. E. Smith, *This Journal*, **125**, 743 (1978).

Submicron Epitaxial Films

V. J. Silvestri* and G. R. Srinivasan*

IBM General Technology Division, East Fishkill Facility, Hopewell Junction, New York 12533

B. Ginsberg

IBM T. J. Watson Research Center, Yorktown Heights, New York 10598

ABSTRACT

This work focuses on the quality of epitaxial silicon deposited when the total thickness grown is in the range of 0.5-0.9 μm from the initial physical interface. Shallow junctions were fabricated to evaluate device potential of the thin films. Defect levels were evaluated. The ability to reproduce doping profiles was also evaluated. The studies have shown that the epitaxial silicon deposited to 0.5 μm thickness is suitable for device fabrication.

This study has focused on evaluation of the quality of the epitaxial silicon deposited to thicknesses in the 0.5 μm range. The concerns with regard to the silicon quality this close to a physical interface included: (i) whether doping profiles could be reproduced and thicknesses controlled, (ii) whether defect levels arising from the interface would have an effect on devices, and (iii) whether the silicon obtained would be suitable for device fabrication.

* Electrochemical Society Active Member.

Experimental

The concentration profiles in this study were obtained by spreading resistance measurement technique. Figures containing spreading resistance data show either the raw data of spreading resistance in ohms vs. depth in microns, or data converted to log of the dopant concentration vs. depth from the surface. The spreading resistance data was obtained on samples beveled to angles of 20 min. An Automatic Spreading Resistance Probe (Solid State Measurements, Incorpo-

rated) was employed. Error corrections were made using methods developed by Hu (1). In addition to the spreading resistance data, SIMS data were taken on a number of films for comparison and cross checking (Fig. 5 and 6 show examples of such comparisons). Figure 1 shows a diagrammatic representation of concentration profiles as shown in later figures and discussed below. The physically thin epitaxial films were deposited to a total thickness of 0.5–0.9 μm from the initial growth interface. Sharp transitions (0.06–0.15 μm) from the arsenic n^+ buried layer at a concentration of 1×10^{19} atoms/cm³ in the silicon substrate to a 2×10^{16} atoms/cm³ level were obtainable using the High-Lo Epi process described elsewhere (2–5), which employs a $\text{SiCl}_4\text{-H}_2$ system at atmospheric pressure. Films were deposited at 1050°C in an AMT 1200 epitaxial reactor with different process variations for the epitaxial depositions, as described below. Referring to the schematic concentration profile of Fig. 1, for purposes of discussion, "flat zone" is defined as the distance from the surface to a concentration of 1×10^{17} atoms/cm³ in the epitaxial layer. "Transition region" is the depth required to go from a concentration of 1×10^{17} atoms/cm³ to the subcollector concentration value of 1×10^{19} atoms/cm³.

Occurrence of defects in the films, such as oxidation stacking faults, epitaxial stacking faults, and hillocks, were evaluated using wet chemical decoration techniques similar to those described in previous work (6, 7). Wright etching (8) times were kept to below 1 min because of the thinness of the films. In addition to Wright etch decoration, anodic etch was used to monitor the electrically active defect sites. Etch current characteristics *vs.* time were examined for films in the 0.5–3.0 μm range. For the anodic etching, the epitaxial film surfaces were exposed to a dilute HF solution (used as the electrolyte), while a positive voltage was applied to the substrate wafer. A platinum wire in the solution acted as the cathode. Conditions used for the anodic etching were varied. In general, an HF concentration of 5% was employed. An applied voltage of 2–3V was generally used for the thin films and 10V for the films greater than 1 μm ; 10–60s were typical times employed for the anodic exposure. After Wright etch and anodic etch, microscopic examination of the etched sites was made.

To evaluate the device potential, shallow junctions were formed in the uniformly doped regions. Junctions

were formed in the lightly doped n-type films by diffusion using CVD boron-doped polycrystalline silicon films as a diffusion source. Diffusion was at a temperature of 900°C for 30 min. Breakdown voltages and diode leakage measurements were made on the junctions formed.

Results and Discussion

Concentration profiles.—To develop a sharp concentration profile in the thin films, a preliminary evaluation of autodoping relative to input-dopant concentration was carried out. A series of epitaxial films were deposited wherein all variables were held constant except deposition time (see Table I, runs 1, 2, 3, and 5). These films were deposited on arsenic-doped substrates ($\sim 10^{19}$ atoms/cm³). The process sequence used for these runs included a 17 min prebake and thermal equilibration to 1150°C to produce surface outgassing and to minimize autodoping. This was followed by deposition at 1050°C for the times shown in Table I. A postbake of 1 min followed each deposition time before ramp down. Spreading resistance curves for runs 1, 2, 3, and 5 in this series are plotted in Fig. 2 and show a decreasing sharpness in profile with increasing deposition time at constant doping input. Run 4 in Fig. 2 (curve 4) was grown with no doping introduced to test effectiveness of the dopant input concentration being employed. The fact that this run did not produce a surface concentration or profile significantly different than the other runs indicated that the input concentration of 32 cm³/min of 50 ppm arsine in H_2 was insufficient to affect the film profile and indicated that the profiles obtained were entirely due to autodoping from the substrate. For comparison, curve 6 has been included in Fig. 2. This film was deposited for 22 min with all conditions similar to the 32 cm³ dopant input series except that the dopant was increased to 48 cm³/min. This increased dopant input leads to the sharpness observed in the profile and indicates that intentional doping predominates over autodoping. The importance of determining the proper doping level following prebake to achieve abrupt transitions in thin epitaxial films is thus demonstrated in these experiments.

The effect of varying time at this higher doping input is shown in Fig. 3. The film profiles in this figure were obtained using the same growth conditions as in Table I, except that deposition times of 22, 17, and 14 min were used for curves 7, 8, and 9, respectively. It will be noted that the abrupt profile is retained with the higher doping level with decreasing time even as the films become thinner. The flat zones and transition regions for the curves are given in Table II. Table III summarizes key refinements used to develop the sharp transitions in the films. A High-Lo- (2-5) type process sequence was used. This included a high tem-

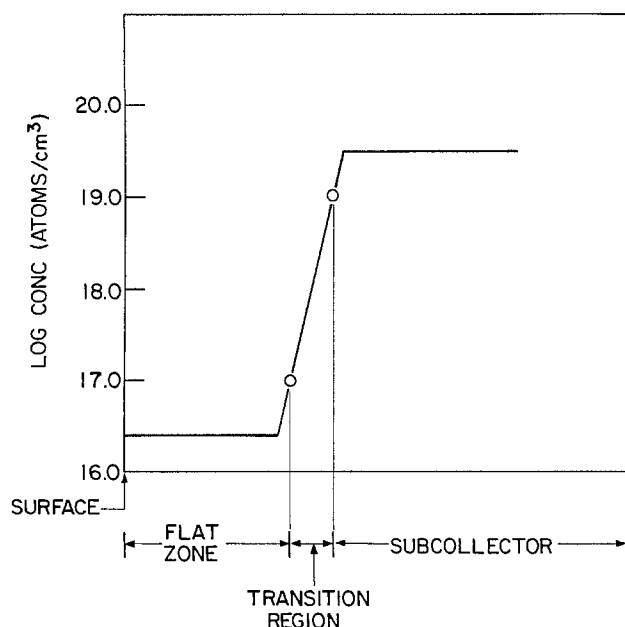


Fig. 1. Diagrammatic representation of concentration profile

Table I. Autodoping evaluation

Run no.	Dep. time (min)	Dep. temp (°C)	H ₂ flow (cm ³ × 10 ⁴ /min)	SiCl ₄ carrier (cm ³ /min)	Dopant source (cm ³ /min)
1	16	1050	9.6	456	32
2	17	1050	9.6	456	32
3	18	1050	9.6	456	32
4	17	1050	9.6	456	0
5	25	1050	9.6	456	32
6	22	1050	9.6	456	48

Table II. Time variation at 48 cm³/min dopant input

Run no.	Flat zone (μm)	Transition region (μm)	Deposition time (min)
7	1.34	0.05	22
8	0.86	0.33	17
9	0.70	0.14	14

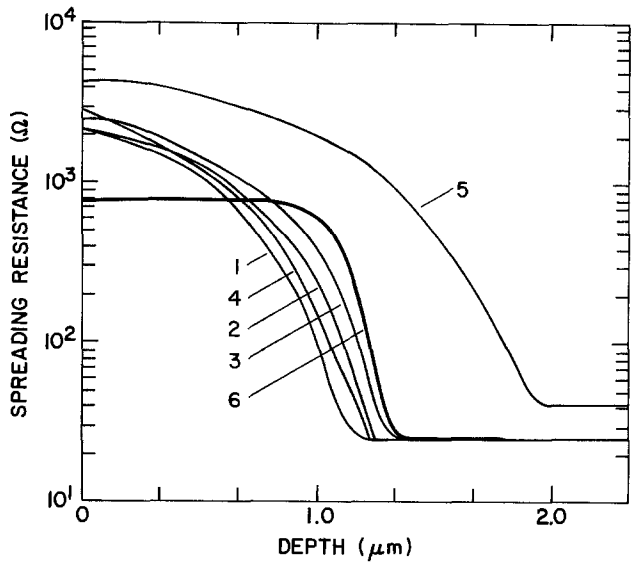


Fig. 2. Doping input and background autodoping

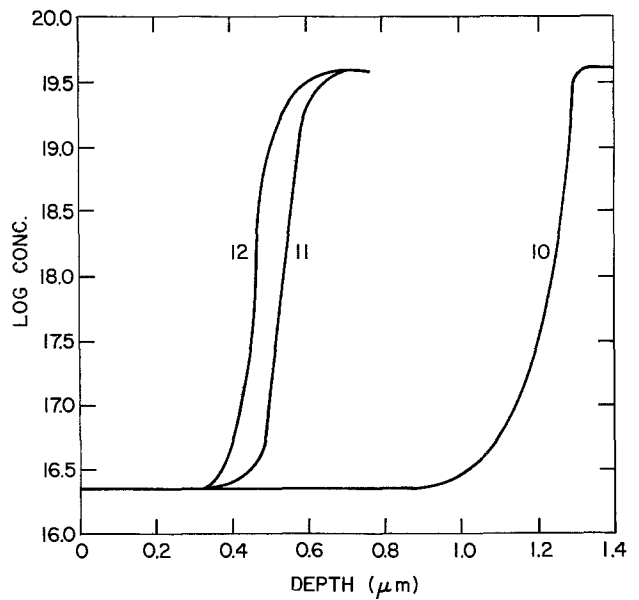


Fig. 4. Comparison of submicron epitaxial film profiles with 1.2 μm film.

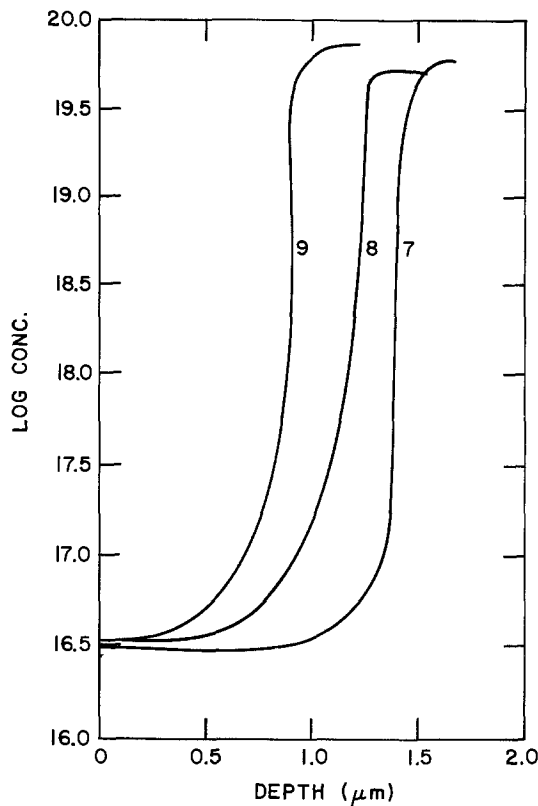


Fig. 3. Doping profile as a function of thickness of epitaxial film

perature prebake at 1150°C, deposition of an undoped layer of epi followed then by deposition of a layer with dopant introduced. Both deposition steps were at 1050°C. Most of these runs had a 2 min deposition of undoped epitaxy. Conditions for these runs are summarized in Table III. Profiles for runs 10, 11, and 12 are shown in Fig. 4. Run 11 achieved many of the epi

Table III. Thin epi (refined process)

Run no.	Flat zone (μm)	Transition region (μm)	Deposition time (min)	
			Undoped	Doped
10	1.09	0.140	2	15
11	0.50	0.087	2	7
12	0.41	0.065	2	6
13	0.53	0.068	3	6
14	0.57	0.079	1	8

characteristics desired, having a flat zone of 0.495 μm and a transition region of 0.087 μm. More detailed features of this particular profile are given in Fig. 5. Figure 6 shows SIMS data for this same film. The concentration of the flat zone, as well as the general overall profile, is slightly higher than the value obtained by spreading resistance; however, the transition region and measured depths are similar. This run had an 1150°C prebake for 15 min. A somewhat thinner film was achieved in run 12 with a doped epi deposition time cut to 6 min. The flat-zone and transition regions are retained, indicating that this process can perhaps be extended to even thinner epi.

Runs 13 and 14 were experiments where total deposition time was held constant while the doped and undoped epi thicknesses were varied. Run 13 had a 3 min undoped region and a 6 min doped region, and

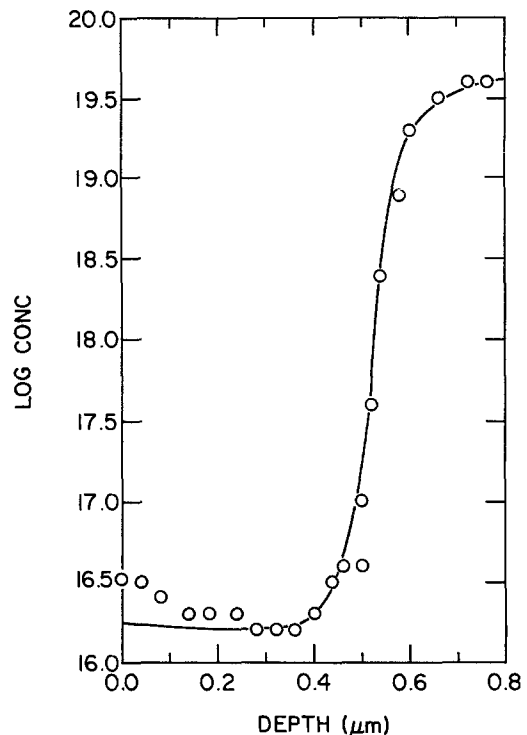


Fig. 5. Spreading resistance As concentration profile in a 0.65 μm thick epitaxial film.

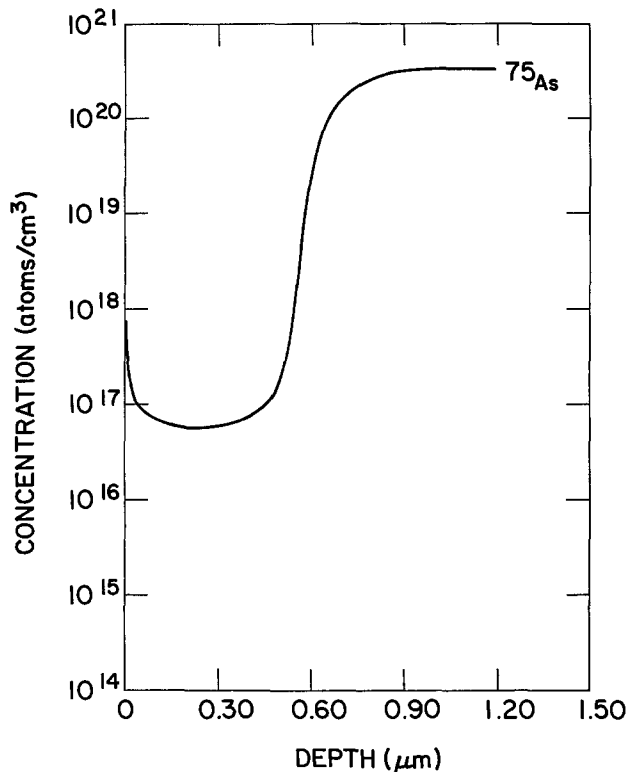


Fig. 6. SIMS As concentration profile in 0.65 μm thick epitaxial film.

14 had a 1 min undoped region and an 8 min doped region. These variations had little effect on the transition region but did change the flat-zone thickness. There seems to be little advantage to making these thickness changes, though further study may be warranted. It would appear more desirable to pursue reducing the temperature of the epi growth in order to improve the sharpness in the transition region.

Reproducibility of the process in duplicating doping profiles was evaluated for a more typically used film deposited on ion-implanted blanket subcollectors doped to $\sim 10^{19}$ atoms/cm³. The results are summarized in Table IV.

Defects.—Defects in the films, such as oxidation stacking faults, epitaxial stacking faults, and hillocks, were examined using wet chemical decoration. Overall defect levels ($\sim 10^2/\text{cm}^2$) were found to be no higher than levels for thicker films (1–2 μm). In addition to Wright etch decoration, anodic etch was used to monitor the electrically active defects in the films. Etch current characteristics *vs.* time were examined for films in the 0.5–3.0 μm range. Current profiles during the anodic etching is a function of epitaxial film doping and thickness as well as defect levels. Films of higher quality (low defect counts) on similarly conductive (n^+) substrates required longer etch times to show a rapid current rise characteristic in the etch curves at punch through to the conductive substrate. The epitaxial stacking faults were more commonly

revealed with the anodic etching treatments. A number of the thin films were oxidized so that the oxide/silicon interface formed was within 0.2, 0.4, and 0.6 μm of the physical epitaxial interface. The oxide was then stripped. Some of the wafers were subjected to Wright etch, and others were to anodic etching. No oxidation stacking faults were observed except in a few instances at the outer edges of wafers. For the anodically treated samples, the etch curve characteristics for the films (representing different distances from the interface) indicate that fewer defects are present as one approaches the epitaxial physical interface. From these observations, it appears that defects arising from the interface are not a limitation in growing thinner films. The anodic etching was done on limited portions of the films. However, extensive sampling of diodes (described below) formed on the thin films was made, and the uniform diode properties overall would indicate electrically active defect levels were sufficiently low such as not to effect the individual devices.

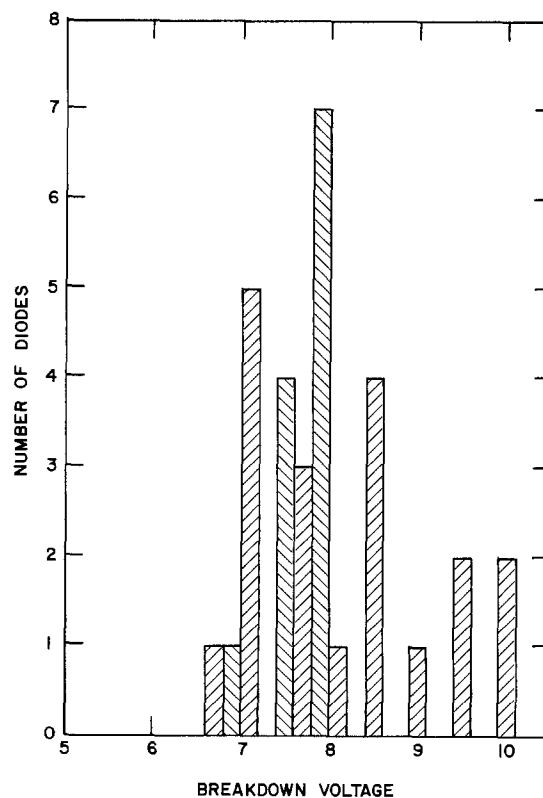


Fig. 7. Typical breakdown voltage distribution for diodes

Table IV. 0.5 μm epi reproducibility

Run no.	Flat zone (μm)	Transition region (μm)	Surface concentration (atoms/cm ³) 10^{19}
Blank Sub 10-1	0.479	0.133	2.08
Blank Sub 10-2	0.573	0.168	3.34
Blank Sub 11-1	0.509	0.142	2.14
Blank Sub 11-2	0.598	0.124	3.03
Blank Sub 12-1	0.566	0.144	2.13
Blank Sub 12.2	0.562	0.157	3.23
		0.143	2.59
		+11.7%	+29%
		-23.3%	-29%

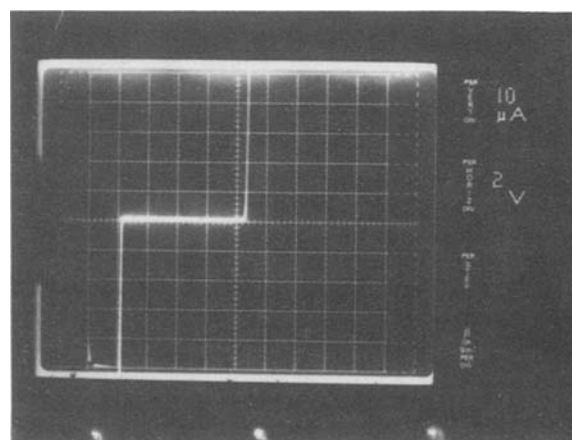


Fig. 8. Forward and reverse diode characteristics

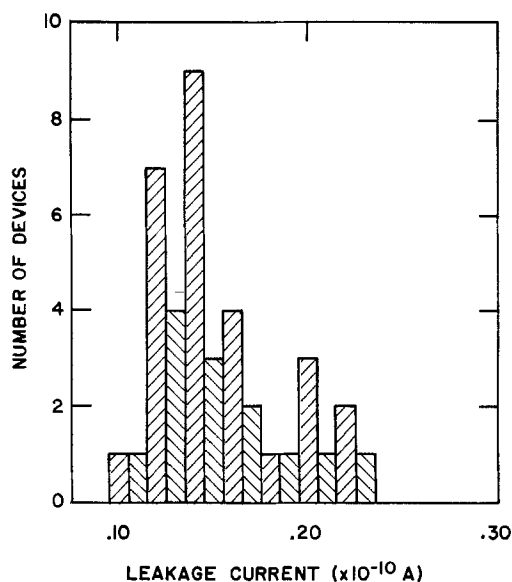


Fig. 9. Typical leakage current distribution for diodes

Diode characterization.—To evaluate the device potential, shallow junctions were formed in the uniformly doped regions, and electrical measurements were made. A histogram of the breakdown voltages is shown in Fig. 7. Forward and reverse diode characteristics are given in Fig. 8. Breakdown voltages of junctions were consistent with film thicknesses and doping concentrations. Leakage measurements on diodes having 40,000 μm^2 areas were in the order of 10^{-11} A. Figure 9 is a histogram of leakage measurements and shows the

epitaxial films to be of excellent quality. Recently, high performance transistor structures have been fabricated and reported for these thin films (0.8-0.9 μm) (9-11).

Acknowledgment

The contributions of members of the IBM Yorktown Bipolar Devices and Circuits Group and Silicon Processing Facility are greatly appreciated.

Manuscript submitted July 14, 1983; revised manuscript received Nov. 4, 1983.

IBM General Technology Division assisted in meeting the publication costs of this article.

REFERENCES

1. S. M. Hu, *Solid-State Electron.*, **15**, 809 (1972).
2. G. R. Srinivasan, U.S. Pat. 4,153,486 (1979).
3. G. R. Srinivasan, *Solid-State Technol.*, **24**, 101 (1981).
4. G. R. Srinivasan, in "Proceedings of the Silicon Processing-Technologies of the '80's Symposium," in press.
5. G. R. Srinivasan, *This Journal*, **127**, 1334 (1980).
6. M. C. Chen and V. J. Silvestri, *ibid.*, **128**, 389 (1981).
7. M. C. Chen and V. J. Silvestri, *ibid.*, **129**, 1294 (1982).
8. M. W. Jenkins, *ibid.*, **124**, 757 (1977).
9. D. D. Tang, P. M. Solomon, T. H. Ning, R. D. Isaac, and R. Burger, *ISSCC* (1982).
10. D. D. Tang, P. Solomon, T. H. Ning, R. D. Isaac, and R. Burger, *IEEE Trans. Electron. Devices*, **ed-29**, Oct. (1982).
11. S. F. Chu, G. R. Srinivasan, H. Bhatia, B. M. Kemple, F. Barson, J. Maur, and J. Riseman, in "VLSI Science and Technology/1982," C. J. Dell'Oca and W. M. Bullis, Editors, p. 306, The Electrochemical Society Softbound Proceedings Series, Pennington, NJ (1982).

Optical Etch-Rate Monitoring: Computer Simulation of Reflectance

P. A. Heimann* and R. J. Schutz*

AT&T Bell Laboratories, Murray Hill, New Jersey 07974

ABSTRACT

We report on a numerical simulation of the signal from a laser etch-rate monitor which utilizes changes in the optical reflectance of a layered structure while the top layer is being etched. The simulation can be applied to structures having several layers. For a strongly absorbing layer such as aluminum ($k = 7.1$), the reflectance is constant until the layer has been etched completely. For a moderately absorbing layer such as a transition-metal silicide (k between 1.5 and 2.5), light can be transmitted through the film and can be reflected from the underlying layers when the silicide has been etched down to a few hundred angstroms thick. The only required parameters are the wavelength of the light, and, for each layer, the indexes of refraction and absorption, the initial thickness, and the etch rate. It can also be applied to cases where portions of the film area are being etched at different rates, such as when part of the film is covered with photoresist. The simulation is applied to several etch processes, including silicide-polysilicon gate and metallization etches. Good agreement is found between experimental and calculated data.

The technique of etch-rate monitoring and endpoint detection by optical reflectance is becoming more widely used (1-3). Advantages of this technique include the simplicity of the apparatus, the insensitivity of the reflectance to changes of the etching gases, process parameters or etch rate, and the fact that it can provide a continuous monitor of the etch rate. In order to make full use of this technique, a detailed simulation of the reflectance vs. etching time is desirable.

When monochromatic radiation is reflected from a layered structure whose transparent (or semi-transparent) top layer is being etched, the intensity of the reflected radiation oscillates. This periodic change in intensity is due to the interference of waves reflected from the outer and interior surfaces of the structure. The signal is relatively easy to explain for a single layer on an opaque substrate. For a multilayered structure, subtle changes in signal,

Electrochemical Society Active Member.

which are meaningful but difficult to interpret intuitively, often occur. Therefore, a computer program has been written to calculate the reflectance of up to four layers plus a substrate and to include the interference from adjacent areas with different structures and etch rates. The program runs on a Honeywell 6000 computer and provides graphic as well as numerical output.

Theory

The theory of multilayer reflectance is described in many books on optics, and will not be repeated here, except for a brief description of the matrix method (4,5) for calculating reflectance. The effect of each layer j (see Fig. 1a) upon the incident light is described by a 2×2 complex matrix C_j

$$C_j = \begin{bmatrix} \exp(i\delta_{j-1}) & \tau_j \exp(i\delta_{j-1}) \\ \tau_j \exp(-i\delta_{j-1}) & \exp(-i\delta_{j-1}) \end{bmatrix} \quad [1]$$

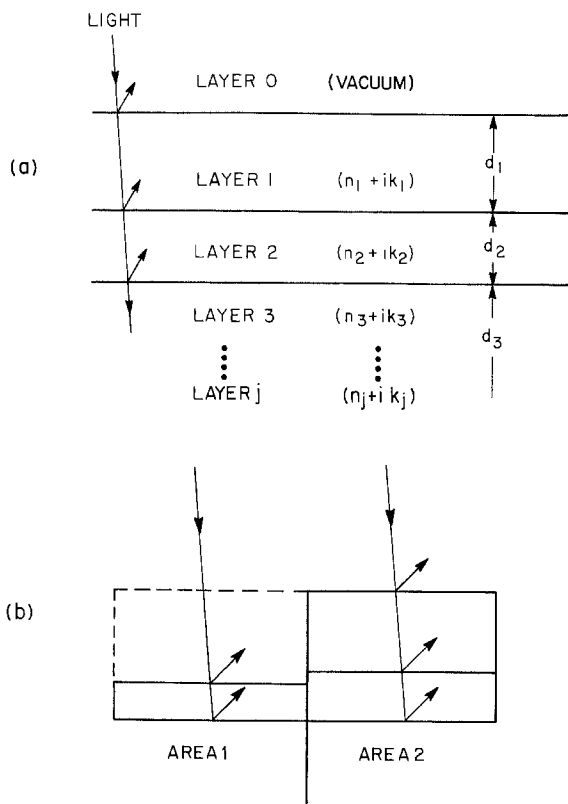


Fig. 1. a: Parameters for calculation of multilayer reflectance. b: Reflectance from more than one type of structure on a wafer. Dashed line shows extra layer of vacuum for multiple-area calculations.

with

$$\bar{r}_j = \frac{\eta_{j-1} - \eta_j}{\eta_{j-1} + \eta_j} \quad [2]$$

$$\eta_j = n_j + ik_j \quad [3]$$

$$\delta_j = 2\pi d_j \eta_j / \lambda \quad [4]$$

Here n_j is the index of refraction of layer j , k_j is its absorption per vacuum wavelength λ , and d_j is the layer thickness. The absorption k_j is related to the attenuation of light through the layer by

$$I/I_0 = \exp(-4\pi k_j d_j / \lambda) \quad [5]$$

where I and I_0 are the transmitted and incident light intensities, respectively.

The matrix C_i is found by setting δ_0 arbitrarily equal to zero, since the phase shift in the external (vacuum) region does not affect the measured reflectance. Matrices for each layer are then multiplied together in the same order as the corresponding layers (top to bottom) yielding a product matrix \bar{C} . The complex reflection coefficient \bar{r} is defined as the ratio of two elements of \bar{C}

$$\bar{r} = \frac{\bar{C}_{21}}{\bar{C}_{11}} \quad [6]$$

and the measured reflectance R is given by

$$R = |\bar{r}|^2 \quad [7]$$

Using this method, some interesting predictions can be made. For example, it is easy to show that the reflectance is a periodic function of the thickness of the top layer (if it is not strongly absorbing), with one period corresponding to a thickness change Δd given by

$$\Delta d = \lambda/2n \quad [8]$$

Therefore, the optical etch-rate monitor signal repeats itself after etching about 2150\AA ($6328\text{\AA} \div 1.47 \div 2$) of silicon dioxide or about 800\AA ($6328\text{\AA} \div 3.90 \div 2$) of polycrystalline silicon (polysilicon), when using a He-Ne laser

source. This is the periodicity which is widely used for optical etch-rate monitoring, since the etch rate is simply the thickness corresponding to one period, divided by the etch time required to make one complete period. It can also be shown that the variation of reflectance with film thickness approximates a sinusoid when the index of refraction is close to 1.0, and becomes less symmetrical as the index gets larger.

Another result is that, when the thickness of any transparent layer ($k_j = 0$) is an integral multiple of the wavelength of the light in the material, i.e.

$$d_j = N(\lambda/n_j), N = 1, 2, 3 \dots \quad [9]$$

then from Eq. [3] and [4] the term $\exp(i\delta_j)$ has the same value as for zero thickness, and it can be shown that the total reflectivity of the structure is the same as it would be if that layer were absent. This is true not only for the top layer, but also for layers deeper in the structure. One can also show that if the thickness is given by

$$d_j = (N + 1/2)\lambda/n_j \quad [10]$$

then the complex reflection coefficient \bar{r} is the negative of the zero-thickness case, but the observed reflectance R is the same. Therefore, a general rule is that a layer which is an integral number of half-wavelengths thick will have the same optical effect as no layer at all. For example, if the oxide in a polysilicon/oxide/silicon structure is one wavelength thick, then the structure looks like polysilicon/silicon. Since heavily doped polysilicon and lightly doped silicon have nearly the same indexes of refraction, the reflectance is practically independent of polysilicon thickness and cannot be used to monitor polysilicon etching. This undesirable effect has been observed experimentally [6].

A third interesting result, from the standpoint of practical application, is the total reflectance when two different areas on the wafer are etching at different rates. This is the case when part of the wafer surface is covered by a low-etch-rate resist and the remaining area is to be etched at a higher rate. For each area, the reflected light has an amplitude and phase which depends upon the film structure of that area, and the light beams reflected from different areas will interfere with each other (see Fig. 1b). The overall effect of these two types of interference (among light reflected from different layers within an area and among light reflected from different areas) can be calculated by adding the complex reflection coefficients \bar{r}_m corresponding to each area, and then taking the squared amplitude of that sum. This model does not include diffraction at the step edges, but the contribution from this effect is expected to be small if the areas are large compared to λ . The interference of the light reflected from different areas will be treated in detail in a subsequent paper (7).

One method of maintaining the proper phase relationship among the various \bar{r}_m 's is to include the space above all the areas (except the highest) as an additional layer, with the index of refraction for vacuum ($n = 1, k = 0$) and with a thickness such that all areas have the same total thickness (see broken line in Fig. 1b). It can be shown that another method, which does not require this additional vacuum layer, is to redefine δ_{m0} for each area m as

$$\delta_{m0} = -\frac{2\pi}{\lambda} \sum_j d_{mj} \quad [11]$$

where the summation is over all layers except the substrate. This latter scheme is easier to incorporate into a computer calculation. If each area m covers a fraction f_m of the total area, then the overall complex reflection coefficient is

$$\bar{r} = \sum_m f_m \bar{r}_m \quad [12]$$

and the reflectance R is found from Eq. [7].

Examples

In this section, we present the results of simulations of optical etch-rate monitor (OERM) signals for various structures, and compare them to experimental results, where available. All of the curves are based upon the 6328\AA red light from a He-Ne laser. Discrepancies be-

tween calculation and experiment can be caused by uncertainty in the values for indexes of refraction and by slowly varying additive signals due to light emitted by the etching gases.

Polysilicon etching.—The standard polysilicon gate technology requires an etch of polysilicon on field oxide. Figure 2 shows the calculated OERM signals for etching 3200Å of polysilicon on top of field oxides of two different thicknesses. Again, the total thickness being etched can be found by counting cycles of the OERM curve. The small signal for the 4305Å oxide is caused by its integral wavelength thickness and demonstrates the effect described earlier (see Eq. [9] and [10]). Figure 3 shows the signal strength (difference between minimum and maximum reflectivity) vs. oxide thickness. One can see that this effect is detrimental only over narrow ranges of oxide thicknesses, and those thickness ranges can be avoided during device fabrication without placing severe constraints upon device design.

In both Fig. 2a and 2b, the endpoint of the polysilicon etch occurs when the reflectance is close to the minimum value observed during the etch. In fact, the reflectance at this endpoint is always less than halfway between the maximum and minimum reflectance values (see Table I). This fact can be incorporated into automated endpoint detection schemes (8).

Silicide-polysilicon etching.—The simulation is also useful for modeling the etching of an optically absorbing

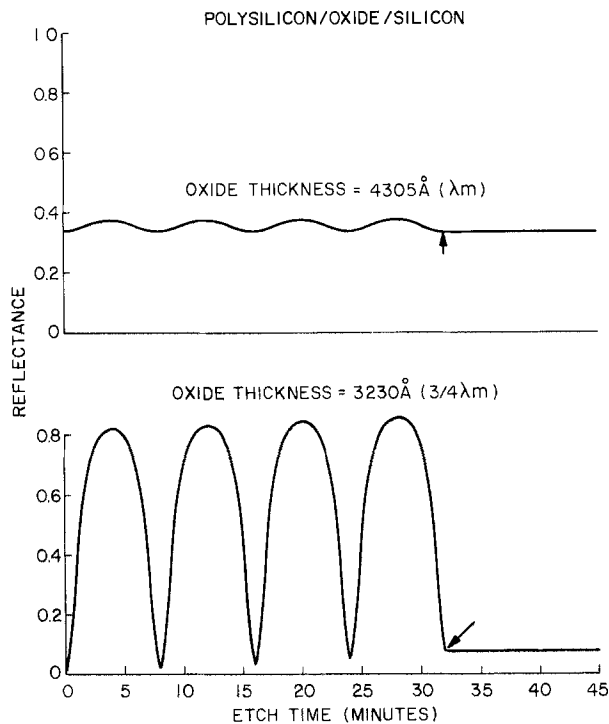


Fig. 2. Calculated OERM signal for etching polysilicon/oxide/silicon structures with two different oxide thicknesses. Polysilicon etch rate is 100 Å/min. Arrow indicates end of polysilicon etching.

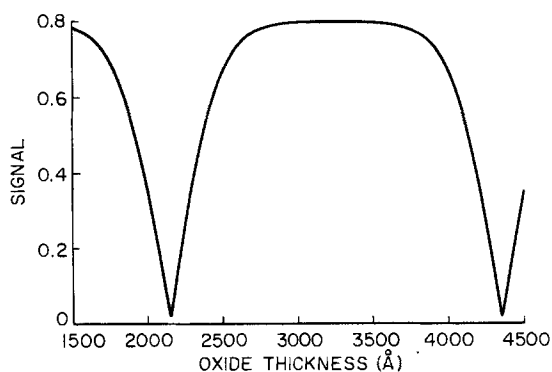


Fig. 3. Variation of signal strength with oxide thickness for polysilicon/oxide/silicon OERM

Table 1. Calculated reflectance during etching of polysilicon/oxide/silicon structure

Oxide thickness (Å)	Reflectance* during polysilicon etch		At endpoint (R _{Final})	$\left[\frac{R_{Final} - R_{Min.}}{R_{Max} - R_{Min.}} \right]$
	Maximum (R _{Max})	Minimum (R _{Min.})		
2050	0.479	0.230	0.335	0.42
2150	0.375	0.335	0.335	0.00
2250	0.477	0.231	0.327	0.39
2350	0.582	0.127	0.311	0.41
2450	0.665	0.055	0.288	0.38
2550	0.728	0.013	0.256	0.34
2650	0.775	0.000	0.222	0.29
3230	0.863	0.073	0.074	0.00

*623.8 nm light, normal incidence.

layer. For a strongly absorbing layer such as aluminum ($k = 7.1$) (9), the reflectance is constant until the layer has been etched completely. For a moderately absorbing layer such as a transition-metal silicide (k between 1.5 and 2.5) (10), light can be transmitted through the film and can be reflected from the underlying layers when the silicide has been etched down to a few hundred angstroms thick. Figure 4 shows calculated OERM signals from etching an aluminum/polysilicon/oxide/silicon structure (a) and a silicide/polysilicon/oxide/silicon structure (b). For the first case, the aluminum is nearly opaque, so the OERM signal is flat during most of the aluminum etch, and it changes only when the metal has been nearly etched away. In this case, the endpoint can be estimated (to within about 100Å) as the point where the signal starts to change. For the second case, the signal starts to change while the silicide is several hundred angstroms thick, and such an estimate would yield a significant error. Figure 5 shows how the structure of the silicide-etch OERM curve

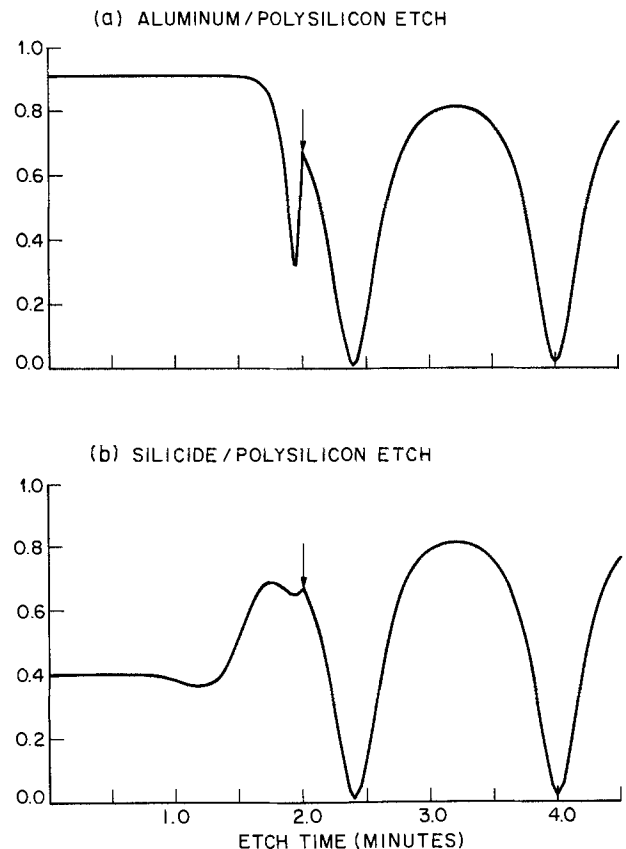


Fig. 4. Calculated OERM signal for structures of aluminum/polysilicon/oxide/silicon (a) and silicide/polysilicon/oxide/silicon (b). In both cases, the top layer is 2000Å thick and etches at 1000 Å/min, the polysilicon is 3404Å thick and etches at 500Å/min, and the oxide is 3229Å thick. Arrows indicate transition from metal or silicide etching to polysilicon etching.

SILICIDE/POLYSILICON ON FIELD OXIDE

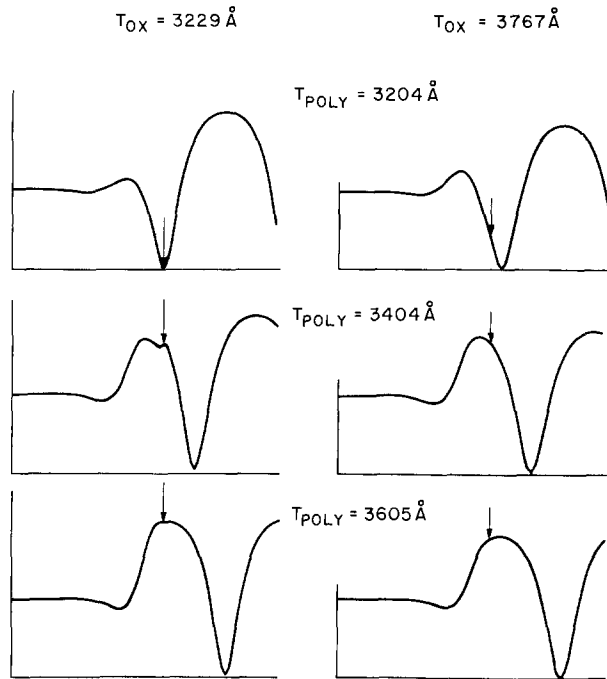


Fig. 5. Calculated OERM signal for a silicide/polysilicon/oxide structure, for various values of polysilicon thickness (T_{POLY}) and oxide thickness (T_{OX}). Arrows indicate transition from silicide etching to polysilicon etching.

is affected by the thickness of the underlying polysilicon and oxide layers. In order to see the OERM curve to determine transition from silicide to polysilicon etching, one needs an accurate knowledge of these thicknesses (note the effects of a change of only 200Å in polysilicon thickness) and one needs to use a model, such as the one described here, to calculate the curve shape expected for those thicknesses. Figure 6 shows an experimentally observed signal from the initial portion of this etch with nominal thicknesses of 3000Å polysilicon and 3500Å oxide. There is fair agreement with the calculated curve in Fig. 5 for 3204Å polysilicon and 3767Å oxide. The slight discrepancy between the calculated and experimental curves is due to uncertainty of the exact thicknesses of the polysilicon and oxide layers, and to a possible change in silicide surface texture during etching. No arrow has been placed in Fig. 6. Had the polysilicon thickness been measured prior to silicide deposition, the OERM curve could have been modeled using this simulation and the location of endpoint on the OERM curve could have been predicted.

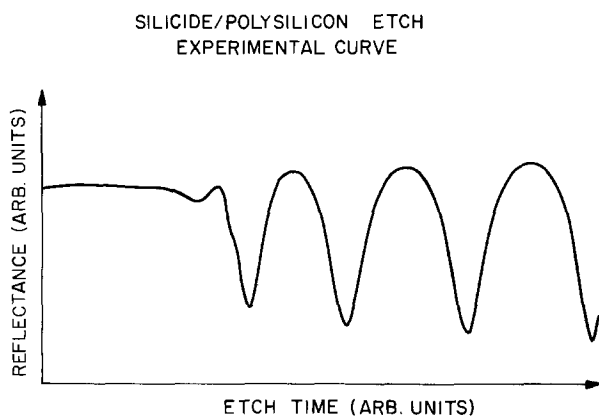


Fig. 6. Experimental OERM signal for silicide/polysilicon/oxide/silicon structure, for the complete silicide etch and the initial portion of the polysilicon etch. Nominal thicknesses are 3000Å polysilicon and 3500 Å oxide.

Multiple areas.—There are cases in which the light beam might be directed onto a region of the wafer containing two different types of layered structures, one of which is covered with photoresist. In some cases, this region could be a structure specialized for optical etch-rate monitoring, such as a diffraction grating (11). In other cases, this region could be the actual device area, which would eliminate the need to devote a large area (about 1-2 mm²) for use as a reflector in etch-rate monitoring. The latter case would be useful if, for instance, such an area would be difficult for an operator to locate, or if it would require an additional mask in a step-and-repeat camera.

As an example of this multiple-area simulation, Fig. 7 shows the calculated OERM signal for 2.0 μm of a metal which has half of its area covered by a resist of index 1.60. The case where there is no resist erosion is shown in Fig. 7a, and the case where the resist etch rate is one-fifth of the metal etch rate is shown in Fig. 7b. One can see that when resist erosion occurs, the OERM signal is quite complicated, since neither the amplitude nor the period remain constant. The average period is shorter here, since a 2 μm etch depth corresponds to 6.3 cycles in the zero-erosion case and to 7.1 cycles in the 1:5 etch-rate-ratio case. If the termination point of the etch process is determined by counting OERM cycles, and if resist erosion is not taken into account, then the etch will be terminated before the desired depth has been reached. This is in agreement with the experimental results of Sternheim *et al.* (3), who found that the optical etch rate monitor yielded a step (in silicon) which, when measured with a stylus instrument, was lower than expected from counting periods of the optical signal. If the resist erosion rate is known, even if only approximately, this simulation can predict the actual number of OERM cycles which will occur during the etch to the desired depth.

Conclusions

The simulation described above is currently in use for calculating multilayer, multiarea reflectance during etching. When combined with analytical calculations and ex-

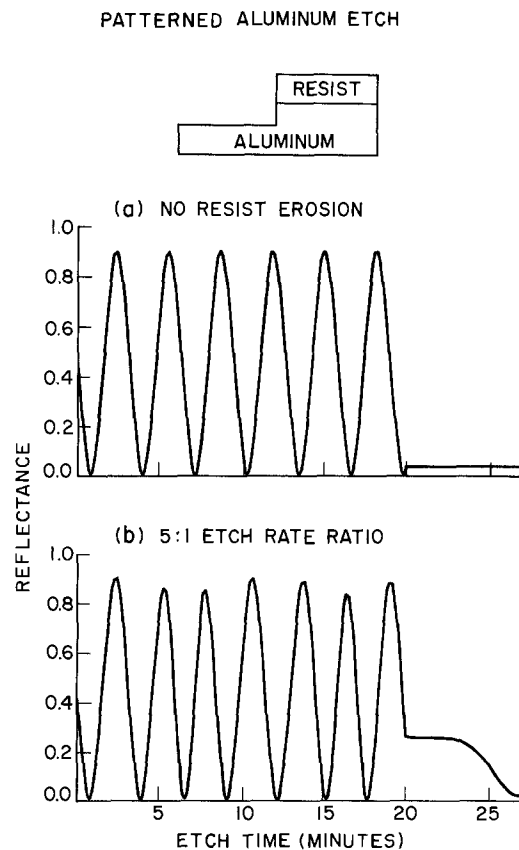


Fig. 7. Calculation of OERM signals obtained from a metal with half of its area covered by resist. Metal etch rate is 1000 Å/min. a: No resist erosion. b: Resist erodes at one-fifth of metal etch rate.

perimental results, it is proving useful for understanding optical etch-rate monitor signals, and for developing new schemes to improve the usefulness of this technique.

Acknowledgments

We give many thanks to H. J. Levinstein, J. M. Moran, A. C. Adams, and P. D. Foo for suggestions and encouragement, to N. Ciampa for silicide etch data, and to D. Alcalay for advice on the use of the Honeywell computer.

Manuscript submitted July 27, 1983; revised manuscript received Dec. 12, 1983. This was paper 160 presented at the San Francisco, California, Meeting of the Society, May 8-13, 1983.

AT&T Bell Laboratories assisted in meeting the publication costs of this article.

REFERENCES

1. H. H. Busta, *Proc. Soc. Photo-Opt. Instrum. Eng.*, **276**, 164 (1981).
2. P. J. Marcoux and P-D. Foo, *ibid.*, **276**, 170 (1981).
3. M. Sternheim, W. Van Gelder, and A. W. Hartman, *This Journal*, **130**, 655 (1983).
4. See, for instance, O. S. Heavens, "Optical Properties of Thin Films," p.48 ff., Academic Press, New York, (1955), but watch out for algebraic errors.
5. P. H. Berning, *Phys. Thin Films*, **1**, 69 (1963).
6. P-D. Foo, Personal communication.
7. P. A. Heimann, to be submitted to *This Journal*.
8. W. S. Lindenberger, Personal communication.
9. American Institute of Physics Handbook, 3rd ed., D. E. Gray, Editor, McGraw-Hill, New York (1972).
10. P. A. Heimann, S. P. Murarka, and J. Rosario, *Mater. Lett.*, **2**, 31 (1983).
11. H.P. Kleinknecht and H. Meier, *This Journal*, **125**, 798 (1978).

Retardation of Boron Diffusion in Silicon

Chol Kim*

Faculty of Science and Technology, Sophia University, Tokyo 102, Japan

ABSTRACT

Boron diffusion profiles incline steeply near diffusion fronts, since the diffusivity decreases from the intrinsic value with decreasing the local boron concentration. The retardation of boron diffusion occurs only when the surface concentration is lower than the intrinsic carrier density at the diffusion temperature.

Various researchers have carried out boron diffusion in silicon, which has surface concentration less than the intrinsic carrier density at the diffusion temperature. The boron diffusion sources employed were B_2O_3 (1), elemental boron (2), and boron-doped oxide (3). In the papers, boron diffusivity was calculated from the boron surface concentration and the diffusion depth, assuming that, in the intrinsic diffusion condition, the boron diffusivity is not dependent on the local concentration and that the boron profile could be described by the complementary error function (erfc). However, the boron diffusivity reported by Ghoshtagore, who employed doped epitaxial silicon layer as the boron source, is much smaller than the intrinsic value (4). In practical boron diffusion, it has often been observed that the actual diffusion depth is much shallower than the value predicted by the erfc or by the Gaussian function with an intrinsic diffusivity.

Recently, it was found that, when boron-excess BN film, deposited on a silicon surface and encapsulated with Si_3N_4 film, was used as a boron diffusion source, the boron surface concentration could be controlled over the range of 2×10^{18} to $2 \times 10^{20} \text{ cm}^{-3}$ according to the deposition temperature of the BN film under proper gaseous flow conditions and held constant during the heat-treatment for boron diffusion (5). This makes it possible to employ the Boltzmann-Matano analysis on the boron diffusion profiles over a wide range of surface concentration, in terms of the diffusivity viewed as a function of the local boron concentration.

Experimental

Mirror finished silicon wafers, having a phosphorus concentration of $2.4 \times 10^{15} \text{ cm}^{-3}$ and (100) orientation, were used as a substrate. On the wafers, the 30 nm layer of boron-excess BN was deposited in the temperature range 440°-830°C under the gaseous flow conditions 50 cm^3/min of 1% B_2H_6 in N_2 , 70 cm^3/min of NH_3 , and 2000 cm^3/min of nitrogen carrier gas. The 30 nm layer of Si_3N_4 was successively formed on the BN surface at 720°C with 20 cm^3/min of 5% SiH_4 in N_2 , 70 cm^3/min of NH_3 , and 2000 cm^3/min of nitrogen carrier gas. The experimental apparatus has been described in a previous paper (6). Boron diffusion into silicon from the BN film was carried out by

heat-treatment in nitrogen atmosphere in the temperature range of 1050°-1200°C for the diffusion time of 15-300 min.

Lee (7) performed a comparison of an incremental sheet resistance profile to analyzed spreading resistance profile of a shallow phosphorus diffusion. Except near the surface, the results were in good agreement. In this study, this spreading resistance technique was employed mainly to obtain the boron diffusion profiles, and the incremental sheet resistance method was also used to determine the surface concentration and the profiles near the surface. The diffusion depth was determined not only by the spreading resistance technique, but also by the spherical drilling and staining technique. The difference between the values of diffusion depth determined by the two methods was within the range of $\pm 5\%$ for all samples tested in this investigation.

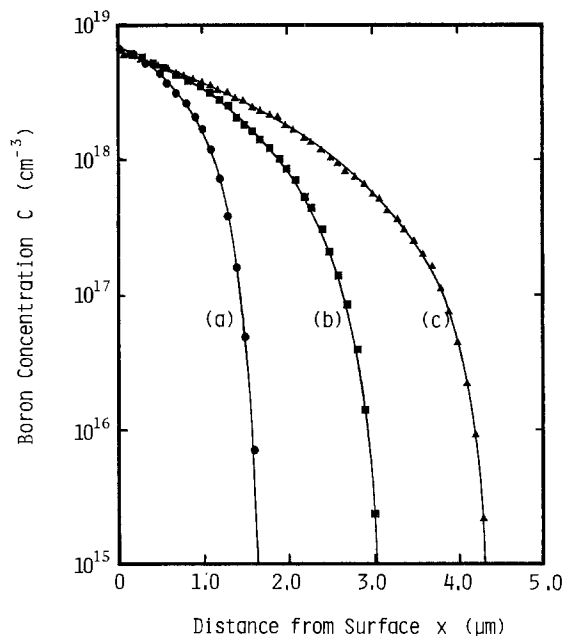


Fig. 1. Boron profiles in silicon. Each curve is for the diffusion time of 50 (a), 130 (b), and 240 (c) min.

* Electrochemical Society Student Member.

Key words: impurity, integrated circuits, CVD.

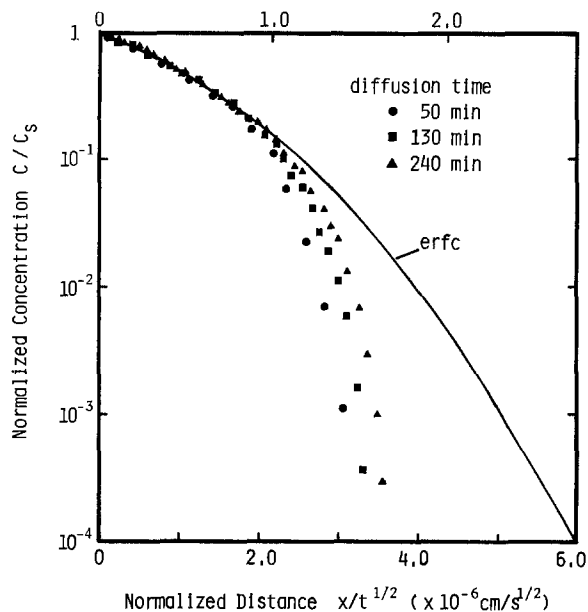


Fig. 2. Normalized profiles. The original data are shown in Fig. 1

Results

The boron diffusion profiles with the surface concentration of $6 \times 10^{18} \text{ cm}^{-3}$, which is lower than the intrinsic carrier density n_i of $2.0 \times 10^{19} \text{ cm}^{-3}$ at the diffusion temperature of 1200°C , are shown in Fig. 1. During the diffusion heat-treatment, the boron surface concentration C_s was constantly kept at $6.5 \times 10^{18} \text{ cm}^{-3}$, and the diffusion depth increased from 1.65 to $4.30 \mu\text{m}$ in proportion to the square root of diffusion time.

Figure 2 is a replot of the profile data shown in Fig. 1, in which the distance from the surface is normalized to the square root of diffusion time, and the boron concentration is also normalized to the surface concentration. The solid line in the figure corresponds to the erfc curve, assuming the intrinsic diffusivity D_i to be $1.4 \times 10^{-12} \text{ cm}^2/\text{s}$. The normalized boron profiles fit the erfc curve only for the normalized concentration more than 0.1, but they differ near the diffusion front, where the profiles inclined steeply above the solid line. The resulting depth of the diffusion front is only 55-60% of the one expected from the erfc curve which assumes the intrinsic diffusivity D_i .

Because the diffusion profiles are coincident when plotted as shown in Fig. 2, the Boltzmann-Matano technique is applicable to calculate the diffusivity D . The boron diffusivity D as a function of the local boron concentration is shown in Fig. 3. For a local concentration higher than $1 \times 10^{18} \text{ cm}^{-3}$, the diffusivity D was constant at the intrinsic value of $1.4 \times 10^{-12} \text{ cm}^2/\text{s}$. However, for any con-

Fig. 3. Boron diffusivity vs. local boron concentration.

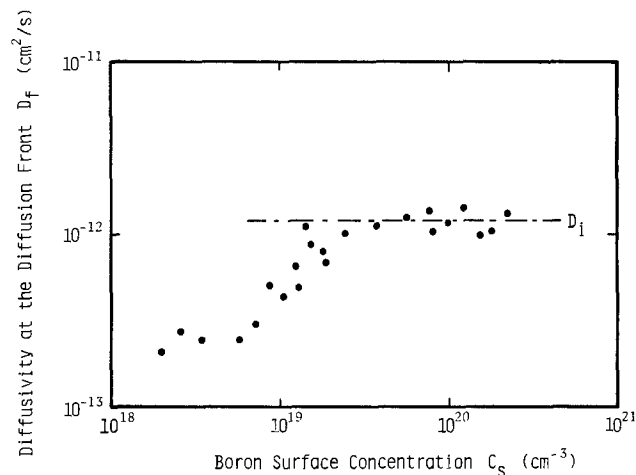
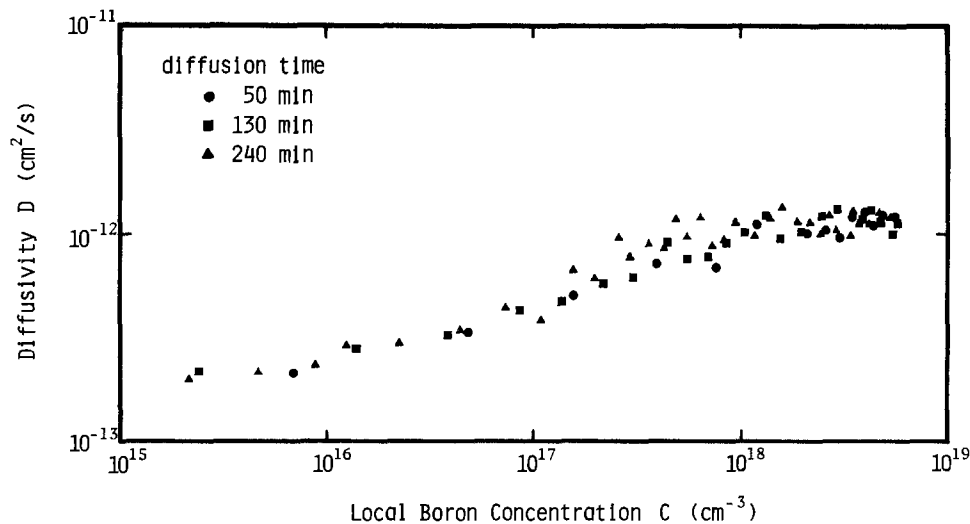


Fig. 4. Boron diffusivity at the diffusion front vs. boron surface concentration.

centration lower than $1 \times 10^{18} \text{ cm}^{-3}$, the diffusivity D decreased with decreasing local boron concentration. For a boron concentration of $1 \times 10^{16} \text{ cm}^{-3}$, the diffusivity is about $2.5 \times 10^{-13} \text{ cm}^2/\text{s}$, that is, $1/4$ of the intrinsic value. As a figure for the retardation of the boron diffusion, we define the diffusivity D_f at the local concentration of $1 \times 10^{16} \text{ cm}^{-3}$.

The boron diffusion with the surface concentration in the range of 2×10^{18} to $2 \times 10^{20} \text{ cm}^{-3}$ was carried out at 1200°C . The diffusion time was chosen so that the resulting diffusion depth would be in the $1.5\text{-}6.0 \mu\text{m}$ range to obtain detailed profile data near the diffusion front where the boron concentration decreased steeply. In all cases, the Boltzmann-Matano analysis was performed, and the diffusivity D was calculated as a function of the local boron concentration. The results are summarized in Fig. 4, in terms of the diffusivity D_f vs. the boron surface concentration C_s . For boron diffusion with the surface concentration higher than the intrinsic carrier density n_i of $2.0 \times 10^{19} \text{ cm}^{-3}$, the diffusivity D_f at the diffusion front agrees with the intrinsic diffusivity D_i shown as a dashed line in the figure. The retardation of boron diffusion at the diffusion front was not observed. For a low surface concentration less than $2 \times 10^{19} \text{ cm}^{-3}$, the diffusivity D_f at the diffusion front was smaller than the intrinsic value.

To confirm the retardation of boron diffusion at lower temperature than 1200°C , boron diffusion was carried out at 1050° , 1100° , and 1150°C . As shown in Fig. 5, the diffusivity D_f at the diffusion front was always smaller than the intrinsic diffusivity D_i for the surface concentration of less than 10^{19} cm^{-3} , even though the diffusivity D_f was coincident with the intrinsic value for the higher surface concentration. The retardation of boron diffusion occurs only when the surface concentration is less than the in-

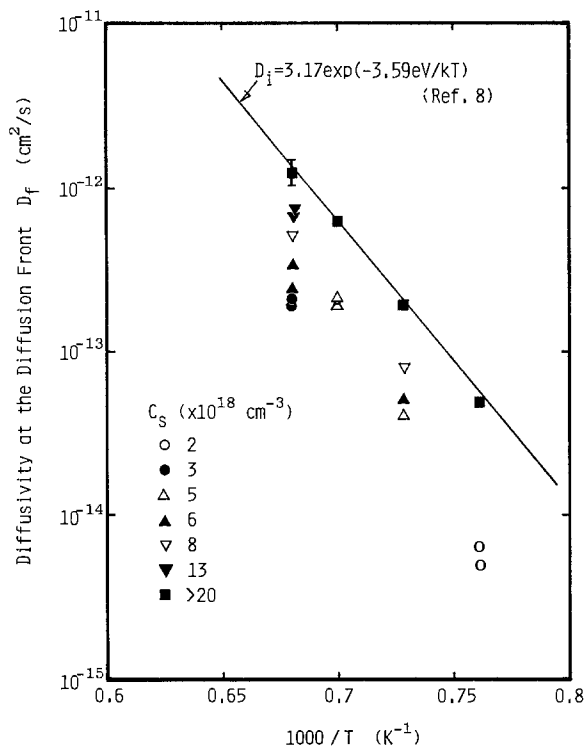


Fig. 5. Boron diffusivity at the diffusion front vs. the reciprocal of diffusion temperature.

intrinsic carrier density n_i at diffusion temperatures in the 1050°-1200°C range. Figure 5 also shows that, under the intrinsic condition, the diffusivity D_f depends not only on the diffusion temperature, but on the surface concentration of diffused layer.

Acknowledgment

The author would like to thank Professor Shono for his helpful discussion and kind suggestions about this work.

Manuscript submitted Aug. 8, 1983; revised manuscript received Dec. 22, 1983.

Sophia University assisted in meeting the publication costs of this article.

REFERENCES

1. A. D. Kurtz and R. Yee, *J. Appl. Phys.*, **31**, 303 (1960).
2. M. Okamura, *Jpn. J. Appl. Phys.*, **8**, 1440 (1969).
3. M. L. Barry and P. Olofsen, *This Journal*, **116**, 854 (1969).
4. R. N. Ghoshtagore, *Phys. Rev. B*, **3**, 389 (1971).
5. C. Kim and K. Shono, Abstract 205, p. 328, The Electrochemical Society Extended Abstracts, Vol. 82-1, Montreal, Quebec, Canada, May 9-14, 1982.
6. K. Shono, T. Kim, and C. Kim, *This Journal*, **127**, 1546 (1980).
7. G. A. Lee, in "Proceedings of Spreading Resistance Symposium," p. 75, Gaithersburg, MD, June 13-14, 1974.
8. R. B. Fair, *This Journal*, **122**, 800 (1975).

Auger Sputter Profiling and Secondary Ion Mass Spectrometry Studies of SiO₂ Grown in O₂/HCl Mixtures

J. W. Rouse and C. R. Helms*

Stanford Electronics Laboratories, Stanford University, Stanford, California 94305

B. E. Deal* and R. R. Razouk*

Fairchild Camera and Instrument Corporation, Palo Alto, California 94304

ABSTRACT

We report on studies of the transport and incorporation of chlorine in SiO₂ during the oxidation of silicon in O₂/HCl mixtures at 1000° and 1100°C using Auger sputter profiling (ASP) and secondary ion mass spectrometry (SIMS). The experimental results obtained were analyzed using general particle-transport considerations including both diffusion and drift components. Data obtained from the SIMS profiles of the chlorine concentration in SiO₂ indicate that chlorine transport is aided by an electrochemical field in the oxide, although this field is undoubtedly not electrical in nature. Data obtained from the ASP profiles show that the Si-SiO₂ interface acts as a sink for chlorine. By fitting the transport relations to the data obtained, an accurate model for chlorine transport is derived.

In recent years, there has been much interest in the effect of chlorine additions to the oxidizing ambient during silicon oxidation (1-42). Chlorine in the grown oxides neutralizes positive alkali ions in the oxide (21), provides better reproducibility in breakdown voltages (11), reduces stacking faults (16), and directly affects the oxidation kinetics (23). In addition, because of the electrochemical similarities between oxygen and chlorine, studies of chlorine incorporation may provide additional insight into the mechanisms of oxide growth.

In this paper, we describe the results of Auger sputter profiling (ASP) and secondary ion mass spectrometry (SIMS) studies of silicon dioxide grown in O₂/HCl ambients. Our ASP and SIMS studies on O₂/HCl-grown oxides may be summarized as follows: (i) high levels of chlorine reside on the oxide side at the SiO₂/Si interface in a region less than 30Å wide. (ii) The total interface chlorine increases

with growth temperature for a fixed oxide thickness. (iii) The total interface chlorine for a fixed temperature increases monotonically with oxide thickness. We believe the evolution of the chlorine distribution can be described in terms of field-driven transport of a chlorine species to the SiO₂/Si interface region where it is incorporated, possibly, in various Si-Cl-O-H complexes. With the arrival of sufficient chlorine a new phase is nucleated, and ultimately SiCl₄ compounds are formed which cause blisters at the interface.

We introduce a simple kinetic model which is consistent with these results to predict the amount of interface chlorine for a given oxidation process, and present data showing the total interface chlorine as a function of oxide-growth temperature and thickness. We will present a brief summary of the conclusions of several studies regarding the distribution of chlorine in HCl-grown oxides and compare these results with our own recent work.

*Electrochemical Society Active Member.

Experimental

To gain an understanding of the effects of various process conditions on chlorine distribution and transport, we examined several sets of sample structures. All oxide thicknesses were determined by ellipsometric measurements. One such set consisted of (100)- and (111)-oriented n-type silicon oxidized in O₂/5% HCl at 1000° and 1100°C. A second sample series consisted of silicon oxidized in dry O₂ at 1100°C to a thickness of 1060Å. This second set was then annealed in Ar/5% HCl at 1100°C for various times. Examination of these sample sets allowed us to evaluate the chlorine transport and incorporation processes with and without the presence of a simultaneous oxidation process. Two additional sample sets consisted of silicon wafers, which underwent complementary sequential growth processes. One sample was oxidized in O₂/5% HCl to 500Å, and this was followed by oxidation in dry O₂ to a total thickness of 1000Å. The other sample was oxidized first in dry O₂ to 500Å and then in O₂/5% HCl to a total thickness of 1000Å. These samples were compared in an effort to determine the stability of chlorine distribution during silicon oxidation in the absence of a chlorine source in the ambient. This also provided an indication of the ability of chlorine to permeate an initial dry O₂ oxide layer. We also examined oxides grown in O₂ with no HCl as controls.

All samples were examined using Auger sputter profiling. To calibrate sensitivity factors, standards of both Si and SiO₂ were investigated using implants of ³⁵Cl⁺ at 50 keV for a total dose of $3.0 \times 10^{15} \text{ cm}^{-2}$. Auger sputter profiling was performed using a Varian high-resolution Auger electron spectrometer. The primary Auger electron beam was operated at 10 μA, 4.5 keV, rastered over an area 600 μm on a side. This gave an electron-beam flux of 3 mA cm⁻² and a power flux of 13.5 W cm⁻². Sputter profiling was performed with Ne⁺ at 1.0 keV with a current density of 36 μA/cm². The sputtering rate was determined to be 27 Å min⁻¹ by comparison with ellipsometric measurements. All experiments were carried out using a liquid nitrogen cryoshroud to minimize background contamination of samples. For these conditions, the Auger depth resolution is better than 30Å (43), and the chlorine detection limit is approximately $1 \times 10^{19} \text{ cm}^{-3}$ in a profiling mode. Secondary ion mass spectrometry (SIMS) analysis was also performed on a representative selection of these samples.¹ The samples were analyzed using O₂⁺ ions at 8 keV.

We have used both Auger sputter profiling and SIMS because the two techniques offer complementary capabilities: Auger provides superior depth resolution (primarily through lower ion energies for sputtering), and SIMS offers superior sensitivity. It is difficult to make statements about absolute concentrations with either technique, however, without resorting to sample standards. The investigation of the implanted standards, however, provided us with a means of determining absolute concentrations in the SIMS experiments to the accuracy afforded by the implant standards. In previous studies of chlorine in SiO₂ using Auger sputter profiling, distortions of the profile due to electron irradiation have been observed. In this study, the conditions described above were chosen so that these effects were not significant. Both ASP and SIMS show some variations in signal sensitivity over a series of experimental runs. In our work, we consistently scaled SIMS data to the Auger data, since our Auger data base for each sample was considerably larger. The resulting concentrations quoted here are good to within 20%, not including errors due to the implant standards. Note that this is a systematic error introduced during the calibration process. Measurements of relative concentration from sample to sample can be expected to yield a precision better than ±20%.

A typical O₂/HCl-grown SiO₂ ASP profile is shown in Fig. 1. The sample is a lightly doped, n-type (100) silicon crystal thermally oxidized at 1100°C to a thickness of 910Å in an ambient containing O₂/5% HCl. In the figure, the peak to peak heights of the differentiated electron energy distribution for several Auger transition energies are shown. The silicon signal shown is due to the 92 eV Si-LVV transition, which is present only in unoxidized elemental silicon; this signal (along with the oxygen) serves as a marker to locate the interface.

¹SIMS analysis performed by C. A. Evans and Associates.

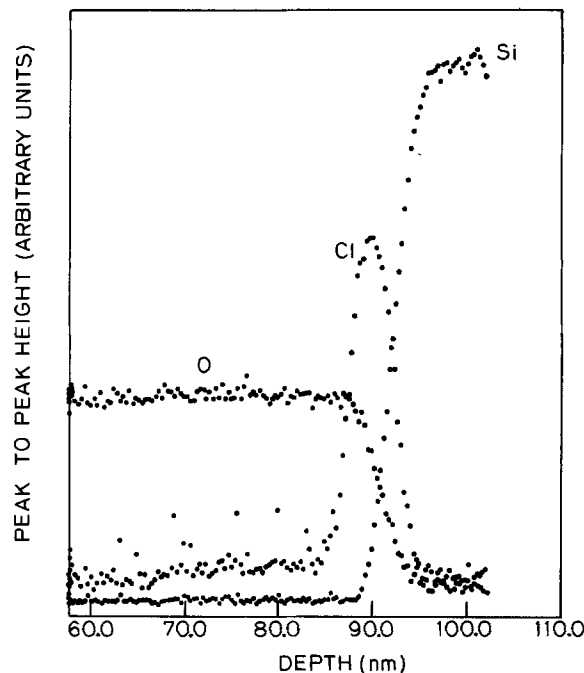


Fig. 1. ASP profile of SiO₂ grown in O₂/5% HCl at 1100°C. This figure records the peak to peak height of the differentiated Auger electron energy distribution curve, for experimental conditions described in the text. The three curves show the depth distribution of oxygen (511 eV), silicon (92 eV), and chlorine 181 eV). The chlorine peak represents a concentration of $1.8 \times 10^{21} \text{ cm}^{-3}$ at a FWHM of 50Å.

The chlorine-interface peak appears in the oxide approximately 10Å from position where the oxygen signal is down by 50% (we define this point as the interface position). The chlorine-peak concentration and FWHM (full width at half maximum) for this sample are $1.8 \times 10^{21} \text{ cm}^{-3}$ and 50Å, respectively. The 50Å FWHM contrasts sharply with the peak widths of from 100-200Å in previous studies (12, 32), and we have, in fact, measured chlorine distributions with FWHM as narrow as 30Å, which is still due in large part to experimental broadening effects. Chlorine levels in the bulk oxide are below our detection limit of $1 \times 10^{19} \text{ cm}^{-3}$ for these operating conditions (chosen to minimize electron-beam effects). We also note a small, gradual rise in chlorine concentration in the SiO₂, which becomes detectable approximately 200Å from the interface. It is also clear that the chlorine levels fall off very quickly in the silicon substrate.

Figure 2 provides an illustration of the complementary features of ASP and SIMS, and shows SIMS and ASP profiles of an n-type, (100) Si sample grown in O₂/5% HCl at 1000°C to 2060Å; the upper panel is on a linear scale, the lower on a semilog scale. The solid curve is the Auger profile showing the very sharply peaked distribution of the interface chlorine. Superimposed on this is the dashed SIMS profile of the same sample. The two curves represent the same total amount of chlorine. Clearly, the ASP technique as used in these experiments has superior depth resolution due to knock-on broadening (43) and ion enhanced diffusion effects for the ion energies employed. SIMS, however, has a superior sensitivity. This is clear from the lower panel, which records on a log scale the bulk oxide chlorine distribution for the same sample. We cannot detect these low chlorine levels with the Auger technique, due to the low electron-beam fluxes necessary to minimize electron-beam effects. The small rise in the chlorine distribution seen with ASP in Fig. 1, however, does seem to be indicative of the clear monotonic increase in chlorine evident in Fig. 2.

At this point, we will address the effects of the electron and ion beams used in these experiments. Previous work by Chou *et al.* (44) shows that the Auger primary electron-beam-activated chlorine in the oxide allowing it to move and caused the chlorine at the surface to desorb. We have profiled SiO₂/Si structures implanted with chlorine and, from these studies, determined to what extent the electron primary beam and ion beam distort the chlorine distribu-

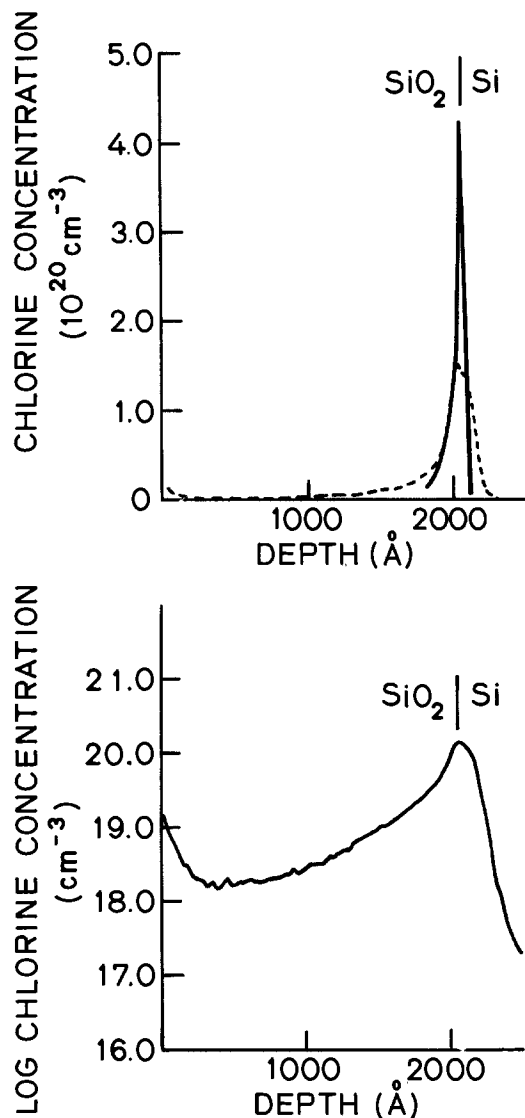


Fig. 2. Chlorine distribution as a function of depth for SiO₂ grown in O₂/5% HCl at 1100°C. Top: linear plot, where solid curve is Auger sputter profile. The profile cuts off at the sensitivity limit for this run. The broken curve is the SIMS profile for the same sample. Note that the total integrated chlorine is approximately the same for the two curves, as expected. Bottom: Log plot of the same SIMS data.

tion (45). The electron beam, consistent with previous work, does enhance chlorine mobility, presumably through the generation of defects in the oxide. The amount of chlorine transport induced by the electron-beam scales with the total charge injected into the sample by the electron beam. One effect is to deplete the chlorine present at the interface. In Fig. 3, we show the total interface chlorine as measured with electron beam fluxes of 3 mA cm⁻² and 100 mA cm⁻², respectively. For our measurements of interface chlorine, we used a flux of 3 mA cm⁻², which was turned on within 100 Å of the SiO₂/Si interface. Thus, we operated within the boxed region in the figure. We conclude that our ASP profiles provide an accurate measure of the interface chlorine distribution.

The ion beam can also be expected to effect the chlorine distribution in our ASP and SIMS profiling experiments. The dominant effect of an ion beam on a particle distribution is to generate a random walk process analogous to a thermal diffusion process (43). Calculations of these effects for the ASP and SIMS profiles described here lead to broadening effects of 20 Å for the ASP results and 150 Å for the SIMS results.

Figure 4 provides further support for the assertion that the ion beam distorts the original distribution only through broadening. We show a SIMS profile of chlorine implanted in SiO₂. Also shown for comparison is the nominal chlorine implant distribution as calculated from implant parameters

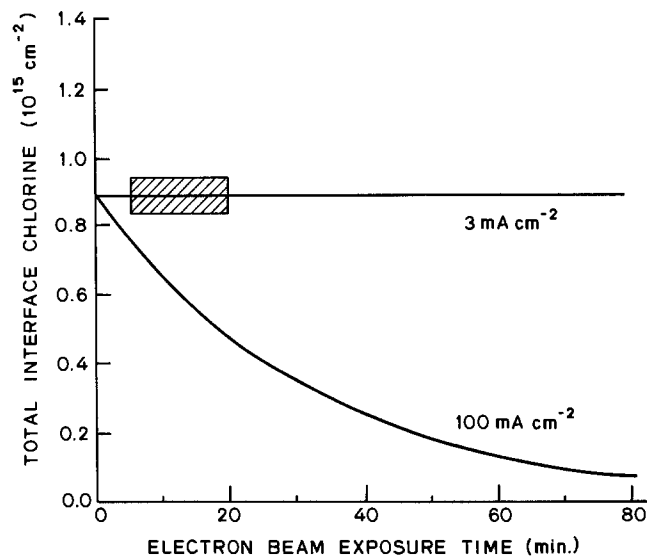


Fig. 3. Total interface chlorine for an oxide grown in O₂/5% HCl at 1100°C as a function of electron-beam-exposure time. Curves are shown for beam fluxes of 3 mA cm⁻² and 100 mA cm⁻². Boxed region denotes flux level and exposure time used in data collection.

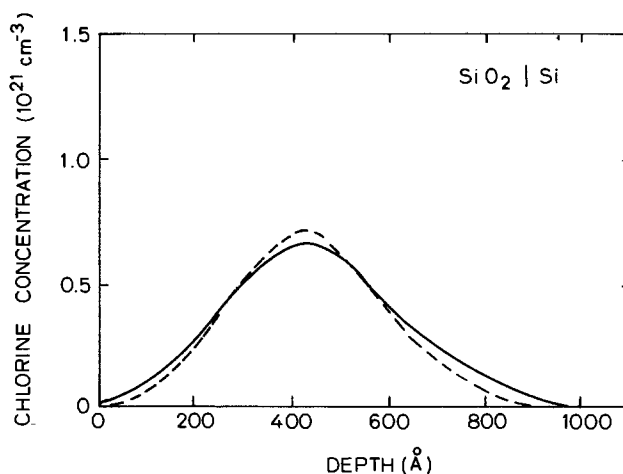


Fig. 4. SIMS profile (solid) of chlorine implanted in SiO₂. ³⁵Cl⁺ was implanted at 50 keV into a 980 Å layer SiO₂ to yield 3.0 × 10¹⁵ cm⁻². The calculated distribution is shown for comparison (dashed).

(46). The SIMS ion beam has broadened the implant distribution in an rms fashion where the broadening is 160 Å.

Theoretical Considerations of Chlorine Transport Through SiO₂

We will briefly present a single-particle transport model for chlorine incorporation in growing SiO₂, and, to establish a working picture, we present a schematic diagram of the SiO₂/Si structure in Fig. 5. The surface and interface denote regions which probably differ significantly in structure and chemistry from the bulk-oxide region, and give rise to the chemical potential sinks there. As used here, we will take the surface to consist of essentially one or two monolayers (ΔX_s), and, as we have seen, the interface region (ΔX_i) is 30 Å or less wide and possibly only a few monolayers thick. We assume that each region is homogeneous with well-defined structural properties. Also shown in Fig. 5 is a schematic diagram of the electrochemical field acting on the chlorine which we have derived from our experimental results. We will say more about the electrochemical field in the discussion section. The key features are chemical potential sinks at the surface and interface which model interfacial-segregation mechanisms, a high chemical potential in the Si, as little Cl dissolves in the Si itself, and a gradient in the electrochemical potential due to a "field" whose origin at this time is uncertain. In discussing the transport properties, we will also assume that the surface

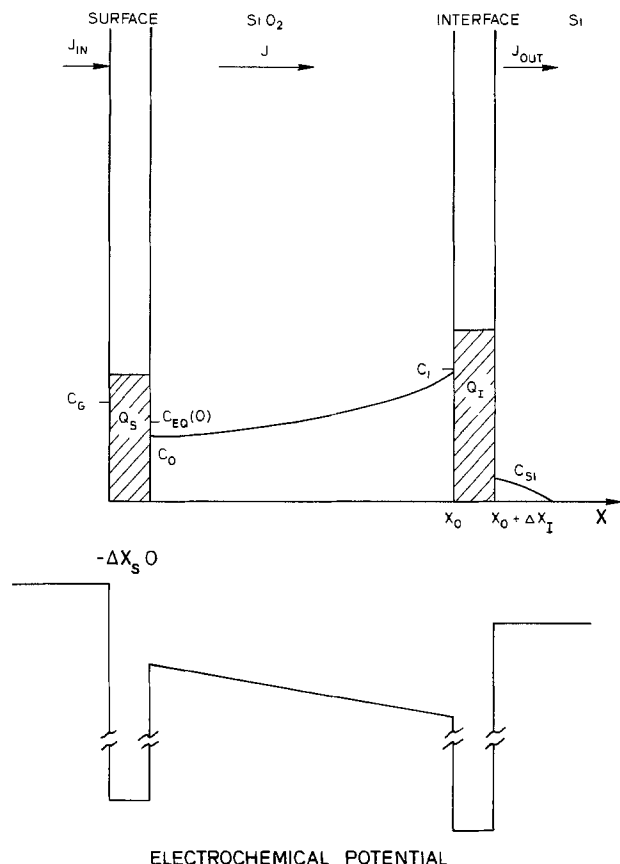


Fig. 5. A, top: Schematic illustration of the SiO_2/Si structure during particle transport. The surface, bulk, and interface regions are each characterized by distinct structural properties. Particle accumulation in the surface and interface is denoted by $Q(\text{cm}^{-2})$. Also shown are the various flux terms. The important concentration levels are C_G (gas phase concentration), $C_{EQ}(0)$ equilibrium concentration in SiO_2 at $x = 0$, C_0 (actual concentration in SiO_2 at $x = 0$), C_1 (concentration in SiO_2 at $x = x_0$), and C_{Si} (concentration in silicon substrate at $x = x_0 + x$). J has been taken as constant through the oxide due to the use of the steady-state approximation. Also, $J_{out} \ll J$ for the conditions of our experiments. B, bottom: Illustration of the potential of the chlorine due to the electrochemical fields acting during oxidation.

and interface regions are so narrow that the concentration is a constant throughout these regions.

Transport in the bulk-oxide region can be described by the equation

$$J(x, t) = -D(x) \frac{\partial C}{\partial x}(x, t) + \mu(x)F(x, t)C(x, t) \quad [3]$$

where D is the diffusion coefficient, μ is the mobility, and F is a general field. The driving force due to F comprises numerous effects, including electric fields, stress fields, chemical bonding, defects, and activity gradients (47-49). As used in this context, it is undoubtedly not due to an electric field, as we will show later.

In addition to Eq. [3], we have the equation of continuity for the case of no recombination or generation giving

$$\begin{aligned} \frac{\partial C}{\partial t} &= -\frac{\partial J}{\partial x} \\ &= -\frac{\partial}{\partial x} \left[-D \frac{\partial C}{\partial x} + \mu FC \right] \end{aligned} \quad [4]$$

To simplify the above equations, we would like to work in the steady-state domain. The necessary condition for steady state is given by Fromhold (47) as

$$t \gg \tau \quad [5]$$

where

$$\frac{1}{\tau} = \frac{D}{4} \left(\frac{F}{k_B T} \right)^2 + \frac{\pi^2 D}{x_0^2} \quad [6]$$

and t is the time required to grow an oxide layer of thickness x_0 . If Eq. [5] is satisfied, all of the time dependent terms in the expansion for $C(x, t)$ are negligible. Physically, steady state implies that the chlorine species is sufficiently dilute and mobile so that it can rapidly respond to any perturbation which causes a deviation from the steady-state condition. Later, we will show that the chlorine transport through the bulk oxide is close to steady state so that this assumption is valid.

In steady state, Eq. [3] becomes

$$J(t) = -D \frac{\partial C}{\partial x} + \mu F(x, t)C(x, t) \quad [7]$$

where J is now constant with position and varying in time, and we have taken D and μ as constant for simplicity. Equation [7] is the general transport equation in steady state. The general solution to Eq. [7] for any time t is then given (using an integrating factor) by

$$C(x, t) = \frac{C(0, t) - J(t) \int_0^x \frac{1}{D} \left[\exp \left(\frac{-1}{k_B T} \int_0^y F(z, t) dz \right) \right] dy}{\exp \left[\frac{-1}{k_B T} \int_0^x F(z, t) dz \right]} \quad [8]$$

where F is the generalized force field of Eq. [3], and $J(t)$ and $C(x, t)$ are related by the boundary conditions [47].

A simple case which appears adequate to describe our results is obtained if F is not a function of x . This gives a linear potential gradient, as shown in Fig. 5. In this case, Eq. [8] can be integrated to give

$$C(x, t) = \frac{C(0, t) - J(t)k_B T / DF(t) \{1 - e^{-F(t)x/k_B T}\}}{e^{-F(t)x/k_B T}} \quad [9]$$

For $F(t) = 0$, this reduces to the familiar diffusion profile in steady state

$$C(x, t) = C(0, t) - \frac{J(t)x}{D} \quad [10]$$

A definite solution for $C(x, t)$ and $J(t)$ from Eq. [9] can be obtained from the boundary condition at the Si-SiO₂ interface. Here again we will apply a simple model that seems adequate to describe our results: namely, that $J(t) = kC(x_0, t)$. This represents a first-order process for chlorine in the SiO₂ to be "trapped" by the Si-SiO₂ interface, since (see Fig. 5) $J_{out} \ll J$. This gives

$$J(x_0) = \frac{C(0, x_0)\mu\phi/(1 - e^{-\phi/k_B T})}{x_0 + \mu\phi e^{-\phi/k_B T}/k(1 - e^{-\phi/k_B T})} = \frac{P}{x_0 + \lambda} \quad [11]$$

and

$$\begin{aligned} C(x, x_0) &= \frac{x_0 J(x_0)}{\mu\phi} \\ &+ e^{\phi x/k_B T x_0} \left\{ C(0, x_0) - \frac{J(x_0)x_0}{\mu\phi} \right\} \end{aligned} \quad [12]$$

where $D/k_B T$ has been replaced by a mobility μ , and F has been replaced by ϕ/x_0 , where ϕ is the electrochemical potential drop across the oxide (as shown in Fig. 5), and the time variable t has been replaced by oxide thickness x_0 . P and λ , as defined in Eq. [11], will be used in subsequent descriptions for simplicity.

The interface chlorine can be calculated by integrating the flux over time. For the case of thermal growth of SiO₂, we can relate oxide thickness and time by (41)

$$x_0 = \sqrt{B} \left(t + \tau + \frac{A^2}{4} \right)^{1/2} - \frac{A}{2} \quad [13]$$

and

$$\frac{dx_0}{dt} = \frac{B}{2x_0 + A} \quad [14]$$

B , A , and τ are constants characteristic of a given oxidation. These equations lead to an expression for interface chlorine Q as a function of x_0

$$Q(x_0) = Q_0 + \frac{P}{B/A} \left[\frac{x_0 - x_1}{A/2} + \left(1 - \frac{\lambda}{A/2} \right) \ln \left(\frac{x_0 + \lambda}{x_1 + \lambda} \right) \right] \quad [15]$$

x_1 is the thickness at which $Q(x_1) = Q_0$. It will be chosen as that value of oxide thickness after an initial period of rapid growth not described by the Deal-Grove growth law [typically $x_1 \approx 200 \text{ \AA}$ (41)]. This expression allows us to calculate the interface chlorine for a given oxide thickness.

Results

In this section, we will present the results of our studies, and we will follow this with a detailed discussion. We begin by looking at samples grown in O₂/HCl. As noted above, Fig. 1 exhibits the features common to all oxides examined in this study. These data were from an oxide grown in O₂/5% HCl at 1100°C. All samples were characterized by bulk oxide chlorine levels below our ASP detection limit of $1 \times 10^{19} \text{ cm}^{-3}$. The position of the peak in chlorine concentration occurs on the oxide side of the interface about 10 Å away from the oxygen signal 50% point. Although this actual value is probably not significant, it does give evidence that the chlorine lies on the "SiO₂ side" of the interface. The chlorine peaks have FWHM of 30-50 Å. Note that these widths are upper limits to the actual distributions. Keeping in mind the effects of electron escape depth and the broadening mechanisms in the ASP process, the actual peak widths would be better described as 30 Å or less, and the interface chlorine could conceivably occupy only a few monolayers in the interface region.

To determine the effects of growth time and temperature on chlorine incorporation, we will use the total chlorine concentration per cm² under the peak as a measure of total interface chlorine. This removes any uncertainty due to profiling broadening factors. Figure 6 shows the total integrated chlorine Q at the interface of the O₂/HCl oxides investigated as a function of growth temperature and oxide thickness for the conditions investigated. Error bars are the standard deviations calculated from several runs for each sample. There is a monotonic increase of interface chlorine with oxide thickness for a fixed-growth temperature. There is also some variation between (100) and (111) sample substrates. From these data, we can see no clear evidence of any saturation in the chlorine concentration over this range of oxide thickness. It appears that the SiO₂/Si interface is a good sink for chlorine up to at least $2 \times 10^{15} \text{ cm}^{-2}$. In fact, from other studies (35), it appears that the chlorine concentration will increase to the point that SiCl_x compounds are formed, resulting in blisters at the interface, although we have no evidence for this effect for these conditions.

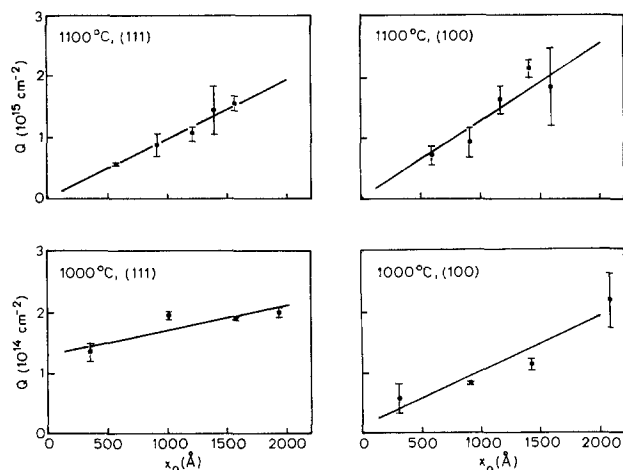


Fig. 6. Total integrated chlorine at the SiO₂/Si interface as a function of oxide growth temperature and thickness for (100) and (111) orientations. Error bars denote standard deviation for several runs. Note the vertical scales of 10^{15} cm^{-2} for 1100°C and 10^{14} cm^{-2} for 1000°C. The straight lines are least square fits to the data points and have been terminated at $x = x_1$ for the samples investigated.

The bulk-oxide chlorine levels were below our ASP detection limit. Because superior signal sensitivity was required and depth resolution is not critical in the bulk oxide, we employed SIMS to examine the chlorine concentration in our O₂/HCl oxides. Figure 7 records on log scales the chlorine distributions of three selected samples as measured by SIMS. The samples were oxidized in O₂/HCl with variations

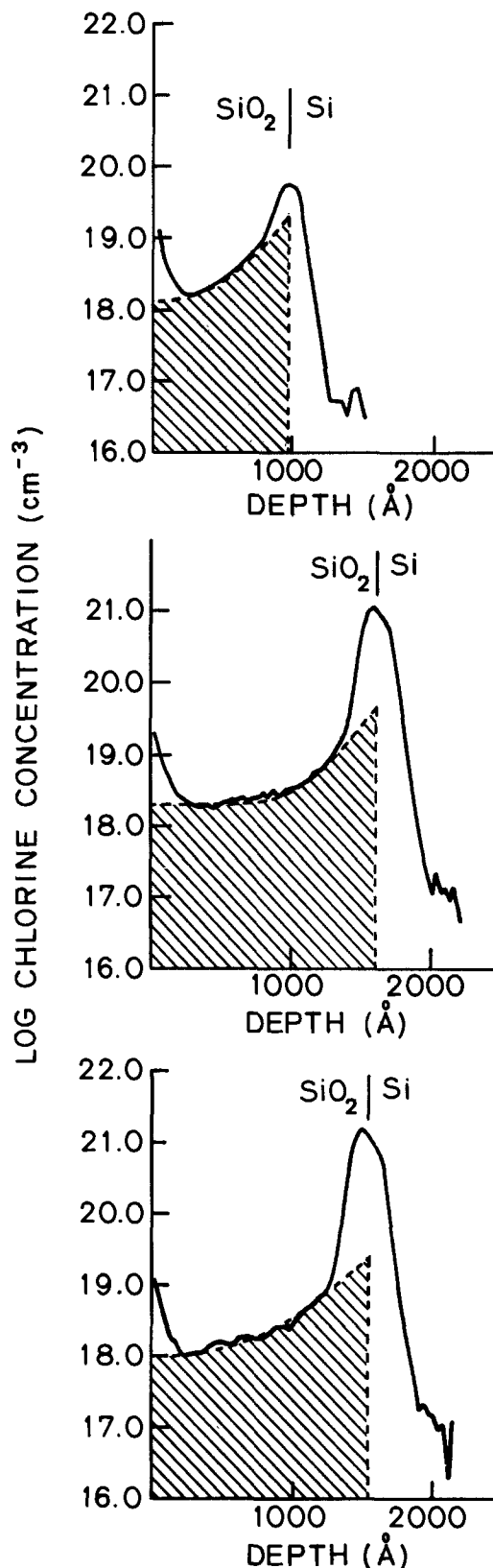


Fig. 7. Log plots of chlorine SIMS profiles. We take the crosshatched areas to be chlorine in the bulk oxide; the remainder is segregated at the surface or interfaces. A, top: SiO₂ grown in O₂/5% HCl at 1000°C. B, middle: SiO₂ grown in O₂/5% HCl at 1100°C. C, bottom: SiO₂ grown in O₂/10% HCl at 1100°C.

in time, temperature, and HCl pressure, as described in the caption.

The results obtained by SIMS for the interfacial-chlorine concentrations were within $\pm 30\%$ of the average values obtained from the Auger studies on the same samples. Part of this error is due to the difference in width of the Auger and SIMS profiles.

In addition, these profiles show a peak in chlorine concentration at the oxide surface as well as the distribution through the bulk SiO_2 . The general features for all the samples investigated were similar. The bulk concentration profile, which we take as the crosshatched area in the figure, is very different from the linearly decreasing profile expected from a simple diffusion process. Instead, the chlorine concentration increases monotonically from its near-surface value to a much higher value near the interface. This profile can, however, be adequately described by the model presented in the previous section, as we will see below.

We have also examined oxides which underwent sequential growth, first in dry O_2 and then in O_2/HCl , and compared these with oxides with the growth sequence reversed. This allowed us to determine the stability of interface chlorine during a dry O_2 oxidation and the ability of chlorine to permeate a dry oxide and accumulate at the SiO_2/Si interface.

The sequential growth samples consisted of p-type (100) Si oxidized at 1100°C in dry O_2 and $\text{O}_2/5\%$ HCl. The dry- O_2 step was the first oxidation step for one set and the second oxidation step for the other set. In each case, the $\text{O}_2/5\%$ HCl and dry- O_2 oxidation steps were performed to yield approximately 500\AA of oxide growth for each step and total oxide thicknesses of approximately 1000\AA . In Fig. 8, we show the incorporation of total interface chlorine as a function of time for the sequentially grown oxides. For comparison, we show the standard O_2/HCl oxide as the solid curve. The broken curve is for an initial O_2 oxidation followed by an O_2/HCl oxidation. For this case, the incorporation proceeds rapidly, the slope of the curve being the same as for the nonsequential O_2/HCl oxidation. Samples grown first in O_2/HCl and then in dry O_2 (dashed dotted curve) show decay of interface chlorine as oxidation proceeds, consistent with diffusion of Cl back through the oxide and into the gas phase.

To determine the stability of interface chlorine when oxidation is not occurring, we have also examined samples grown in $\text{O}_2/5\%$ HCl and then annealed in Ar at 1100°C for

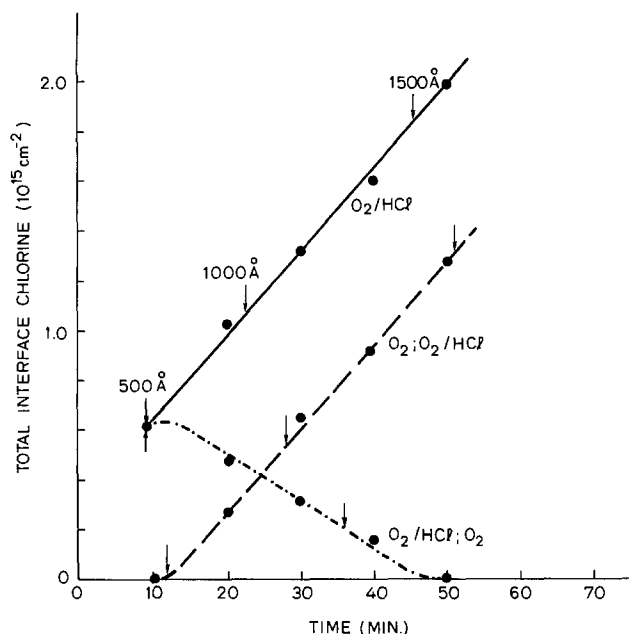


Fig. 8. Total interface chlorine as a function of processing time at 1100°C with 5% HCl. The solid curve is a standard oxidation; the broken curve corresponds to an initial oxidation in dry O_2 to $\sim 500\text{\AA}$ followed by the O_2/HCl oxidation; the dashed-dotted curve corresponds to an O_2/HCl oxidation to $\sim 500\text{\AA}$ thickness followed by an O_2 oxidation. Included are arrows 500\AA oxide thickness increments.

1h. We saw no evidence for depletion of interface chlorine in this case, indicating that oxidation is enhancing reincorporation of Cl from the interface into the SiO_2 or the Cl mobility or both. However, van der Meulen *et al.* (13) have reported depletion of the interface of chlorine by annealing at a higher temperature of 1200°C .

To isolate the importance of the oxidation process on chlorine transport and incorporation, we also examined n-type (100) Si oxidized in dry O_2 at 1100°C to produce oxides 1060\AA thick. These were then annealed for various times in Ar/5% HCl at 1100°C . In Fig. 9, we show the total interface chlorine as a function of time for the samples which were first oxidized in dry O_2 and then annealed in Ar/5% HCl. For comparison, we show the chlorine-incorporation rate for the O_2/HCl and O_2/HCl oxides from the previous figure. We can see that the chlorine-incorporation rate is significantly lower when oxidation is not occurring, even though the interface is stationary, again indicating the effect of the oxidation process on chlorine transport.

Discussion

In this section, we will discuss possible mechanisms occurring during the incorporation of chlorine at the SiO_2/Si interface. Before proceeding, however, it is worthwhile to review briefly some of the earlier studies of chlorine in SiO_2 and to compare and contrast these with our own findings.

Early studies of chlorine distributions in SiO_2 were performed by Kriegler *et al.* (12) and van der Meulen *et al.* (13). Using nuclear backscattering, they found that chlorine present in oxides grown in O_2/HCl mixtures accumulated at high levels in a region roughly $100\text{-}200\text{\AA}$ wide at the SiO_2/Si interface. Total interface chlorine levels ranged from less than $0.06 \times 10^{15} \text{ cm}^{-2}$ for 900°C oxides to $1.7 \times 10^{15} \text{ cm}^{-2}$ for 1150°C oxides. They found the levels of chlorine increased with oxidation temperature and ambient HCl partial pressure. The authors report a depth resolution of 200\AA , which indicates some difficulty in carefully characterizing the chlorine peaks, however.

More recently, Deal *et al.* (33) performed studies similar to those of van der Meulen *et al.* using SIMS, which should be more sensitive than nuclear backscattering to chlorine. They found the same behavior of chlorine segregation to the SiO_2/Si near interface region. They reported that chlorine incorporation increased with oxidation temperature, oxide thickness, and ambient HCl partial pressure. They also noted a somewhat greater level of chlorine for (111) silicon than for (100) silicon at 1100°C . Their SIMS data yielded total chlorine concentrations comparable with the data of van der Meulen *et al.* and a typical FWHM of 150\AA .

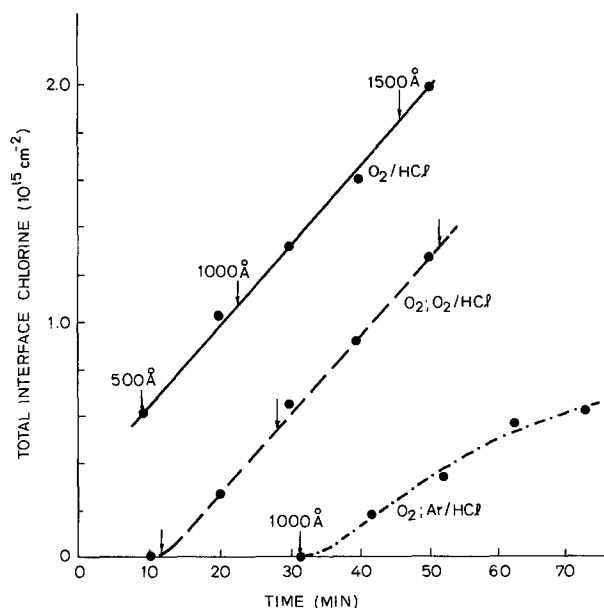


Fig. 9. Total interface chlorine as a function of processing time at 1100°C with 5% HCl. Sequential processes are as indicated. Solid curves begin at the transition points for the sequential processes. Included are arrows 500\AA oxide thickness increments.

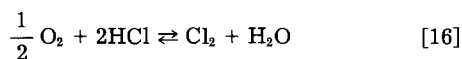
Frenzel and Balk (38) have presented SIMS and Auger data on oxides grown in TCE/O₂ and CCl₄/O₂. They postulated the existence of a laterally inhomogeneous chlorine-rich region at the SiO₂/Si interface which measured 200Å or less in width. They also argue for the presence of an SiO_x transition region at the interface which is roughly 300Å wide. Similar SIMS data by Tsong *et al.* (39) shows chlorine pileup with a 200Å FWHM.

The Frenzel-Balk argument for lateral inhomogeneities in the chlorine distribution relies upon the presence of a chlorine SIMS signal extending into the silicon substrate. They attribute this to nonuniform oxide sputtering rates due to an irregular lateral distribution of chlorine. Chlorine levels in the silicon substrate in our studies, however, prove to be less than our detection limit of $1 \times 10^{19} \text{ cm}^{-3}$, so the argument for lateral inhomogeneities put forth in their paper is not compelling. However, recent work by Monkowski *et al.* (32) shows electron microscopy evidence for an inhomogeneous chlorine phase near the SiO₂/Si interface. Our work suggests that the extent in depth of this new phase is less than 30Å. Finally, the excess silicon observed by Frenzel and Balk in a broad SiO_x phase contains approximately $3 \times 10^{16} \text{ cm}^{-2}$ excess silicon atoms, nearly 20 times the total amount of measured chlorine. It seems probable that the enhancement in the Si Auger signal in the oxide observed in their work is due to an artifact in the ASP experiment.

In our work, we have found levels of interface chlorine in good agreement with results of other groups. In contrast to these earlier studies, however, we have seen that this interface chlorine is distributed over a region less than 30Å wide, and we therefore associate this chlorine directly with the SiO₂/Si interface. The presence of a chemical potential sink for chlorine at the Si-SiO₂ interface, therefore, appears clearly established.

For the chlorine to reach the interface and remain there during oxidation, it must be transported rapidly compared to the interface velocity, and, in addition, the interfacial chlorine must also move with the growing interface. Rapid transport implies that the chlorine distribution quite rapidly reaches steady state. Additional evidence for this comes from our sequential growth studies (Fig. 8). The rate of chlorine incorporation for the O₂/O₂/HCl oxidation (broken curve) rapidly reaches that of the O₂/HCl oxidation, indicating that the velocity of the chlorine is large compared with the Si/SiO₂ interface velocity.

In addition, the rate of chlorine incorporation at the interface is slower for a sequential process with an O₂ oxidation followed by an Ar/HCl anneal. This indicates that the chlorine-transport process is affected by the oxidation process itself. This may come either through a reaction between the HCl and O₂ as



or be due to an effect of the oxidation process on the structure or electrochemical properties of the oxide.

The chlorine profiles obtained through the bulk of the SiO₂ are not linear, indicating that the transport process is not just a simple diffusion mechanism for the chlorine present. A simple model which does describe this profile, as well as the other features of chlorine incorporation, is based on the presence of an electrochemical field driving chlorine transport, as shown in Fig. 5. Within this model, the chlorine distribution in the SiO₂ would be given by Eq. [12], which can be rewritten as

$$C(x, x_0) = C_1(x_0) + e^{\phi x/k_B T} C_2(x_0) \quad [17]$$

The dashed regions of Fig. 7 take this form. The fit of these curves to the profiles with the exception of the surface and interface peaks is excellent, as can be seen from the figures.

The microscopic mechanisms for the effects discussed above is unclear. The interfacial segregation of chlorine is undoubtedly due to lowering of the interfacial free energy due to chemical bonding effects, strain considerations, etc. Work by Monkowski *et al.* indicates that the higher chlorine concentrations SiO_xCl_y compounds form at the interface; the segregated interface chlorine may be a precursor to the formation of these compounds.

The nature of the mechanism responsible for the chlorine distribution in the bulk, which can be described by a constant field acting on the chlorine, is also not clear at all. Possible field sources are stress, activity gradient (due to variations in the number of available chlorine sites in the oxide or interactions with hydrogen present), and electrical fields, among others. The electrical-field mechanism is unlikely, however, since high levels of space charge would be necessary to compensate for the large chlorine concentrations observed; these, in turn, would cause the chlorine-concentration profile to deviate from what is predicted by Eq. [12].

Modeling of Chlorine Transport and Incorporation

In this section, we will use the general transport equations derived above to analytically model chlorine transport through SiO₂. In modeling this process, we will start with Eq. [11], which relates the chlorine flux to oxide thickness. We also have a relationship for the interface-chlorine concentration Q from Eq. [15]. For modeling purposes, it is easier to look at the rate of chlorine incorporation per unit oxide thickness

$$\frac{dQ(x_0)}{dx_0} = \frac{2P}{B} \cdot \frac{x_0 + A/2}{x_0 + \lambda} \quad [18]$$

Looking back at Fig. 6, we see that $Q(x_0)$ is close to a straight line, so that $\lambda \sim A/2$ (unless $A/2, \lambda \gg x_0$ which is not the case for these thicknesses). Values for P for the 100 samples, along with other relevant parameters for the linear fits of Eq. [18] to Fig. 6, are shown in Table I.

For a simple diffusion model, we would expect similar values for P to be obtained for both the 100 and 111 samples, since B does not vary from 100 to 111 orientations. However, P contains the field term which may vary from 100 to 111, and, in addition, A varies from 100 to 111, and we might also expect a variation in λ . In any case, the slopes are within a factor of two of each other (much closer for the 1100°C samples) which is in reasonable agreement if these factors are taken into consideration.

Parameters from the fit of Eq. [17] to the data of Fig. 6 are shown in Table II. Of particular interest is the value of the diffusion coefficient. The values given are considerably smaller than what would be expected from the diffusion of other molecules that diffuse interstitially. This may indicate that the chlorine-transport process involves exchange with the SiO₂ lattice which would lead to the smaller diffusion coefficients. It may also be due to the inclusion in the profiles of chlorine that has exchanged with the lattice and is no longer free to diffuse. Since the product of the diffusion coefficient and the concentration always appears in transport equations, a larger value of the concentration leads to a smaller value of the diffusion coefficient.

Irrespective of the mechanisms involved, we can use the parameters of Tables I and II to calculate the chlorine con-

Table I. Summary of transport parameters for chlorine in SiO₂ samples oxidized in O₂/5% HCl

	O ₂ /5% HCl (100) 1000°C	O ₂ /5% HCl (100) 1100°C
x_1	139Å	171Å
B	$5.8 \times 10^{-14} \text{ cm}^2 \text{ s}^{-1}$	$1.08 \times 10^{-13} \text{ cm}^2 \text{ s}^{-1}$
A	2860Å	749Å
Q_0	$0.25 \times 10^{14} \text{ cm}^{-2}$	$0.22 \times 10^{15} \text{ cm}^{-2}$
P	$3 \times 10^6 \text{ cm}^{-1} \text{ s}^{-1}$	$7 \times 10^6 \text{ cm}^{-1} \text{ s}^{-1}$

Table II. Values for the parameters C_1 , C_2 , ϕ , and D for oxides of thickness x_0

Sample no. Growth Conditions	I	II	III	IV
	5%, 1000°C	5%, 1000°C	5%, 1100°C	10%, 1100°C
x_0 (Å)	980.	2060.	1605.	1525.
C_1 (10 ¹⁶ cm ⁻³)	132.	150.	177.	117.
C_2 (10 ¹⁶ cm ⁻³)	4.29	4.04	1.59	2.16
ϕ (eV)	0.57	0.65	0.74	0.66
D	—	$3 \times 10^{-14} \text{ cm}^2 \text{ s}^{-1}$	$6 \times 10^{-13} \text{ cm}^2 \text{ s}^{-1}$	—

centration at the Si-SiO₂ interface, using either Eq. [15] or [18] (with $\lambda = A/2$) and the chlorine concentration profile through the SiO₂, using Eq. [17].

Acknowledgments

This work was supported by DARPA Contract MDA 903-79-C-0257. In addition, this work has benefited from facilities (equipment) made available to Stanford University by the NSF-MRL Program through the Center for Materials Research at Stanford University.

Manuscript submitted Jan. 8, 1983; revised manuscript received Nov. 11, 1983.

Stanford University assisted in meeting the publication costs of this article.

REFERENCES

1. P. H. Robinson and F. P. Heiman, *This Journal*, **118**, 141 (1971).
2. M. C. Chen and J. W. Hile, *ibid.*, **119**, 223 (1972).
3. R. J. Kriegler, Y. C. Cheng, and D. R. Colton, *ibid.*, **119**, 388 (1972).
4. R. J. Kriegler, *Thin Solid Films*, **13**, 11 (1972).
5. R. J. Kriegler, *Appl. Phys. Lett.*, **20**, 449 (1972).
6. R. S. Ronen and P. H. Robinson, *This Journal*, **119**, 747 (1972).
7. R. J. Kriegler, in "Semiconductor Silicon 1973," H. R. Huff and R. R. Burgess, Editors, p. 363, The Electrochemical Society Softbound Proceedings Series, Princeton, NJ (1973).
8. K. Hirabayashi and J. Iwamura, *This Journal*, **120**, 1595 (1973).
9. G. Baccarani, M. Severi, and G. Soncini, *ibid.*, **120**, 1436 (1973).
10. Y. J. van der Meulen and J. G. Cahill, *J. Electrochem. Mater.*, **3**, 371 (1974).
11. C. M. Osburn, *This Journal*, **121**, 809 (1974).
12. R. J. Kriegler, A. Aitken, and J. D. Morris, *J. Appl. Phys.*, **43**, 341 (1974).
13. Y. J. van der Meulen, C. M. Osburn, and J. F. Ziegler, *This Journal*, **122**, 284 (1975).
14. G. J. Declerck, T. Hattori, G. A. May, J. B. Beaudouin, and J. D. Meindl, *ibid.*, **122**, 436 (1975).
15. H. Shiraki, *J. Appl. Phys.*, **14**, 747 (1975).
16. H. Shiraki, *ibid.*, **15**, 1 (1976).
17. H. Shiraki, *ibid.*, **15**, 83 (1976).
18. Y. Nabeta, T. Uno, S. Kiko, and H. Tsukamoto, *This Journal*, **123**, 1416 (1976).
19. H. Shibayama, H. Masaki, H. Ishikawa, and H. Hasimoto, *Appl. Phys. Lett.*, **29**, 136 (1976).
20. T. Hattori, *This Journal*, **123**, 945 (1976).
21. D. L. Heald, R. M. Das, and R. P. Khosla, *ibid.*, **123**, 302 (1976).
22. A. Rohatgi, S. R. Butler, F. J. Feigl, H. W. Kraner, and K. W. Jones, *Appl. Phys. Lett.*, **30**, 104 (1977).
23. R. E. Tressler, J. Stach, and D. M. Metz, *This Journal*, **124**, 607 (1977).
24. D. W. Hess and B. E. Deal, *ibid.*, **124**, 735 (1977).
25. T. Hattori, *Appl. Phys. Lett.*, **30**, 312 (1977).
26. T. Hattori, *Jpn. J. Appl. Phys.*, **17**, 69 (1978).
27. B. E. Deal, D. W. Hess, J. D. Plummer, and C. P. Ho, *This Journal*, **125**, 339 (1978).
28. B. R. Singh and P. Balk, *ibid.*, **125**, 453 (1978).
29. B. E. Deal, *ibid.*, **125**, 576 (1978).
30. T. Hattori and T. Suzuki, *Appl. Phys. Lett.*, **33**, 347 (1978).
31. E. D. Janssens and G. J. Declerck, *This Journal*, **125**, 1696 (1978).
32. J. Monkowski, R. E. Tressler, and J. Stach, *ibid.*, **125**, 1867 (1978).
33. B. E. Deal, A. Hurrle, and M. J. Schultz, *ibid.*, **125**, 2024 (1978).
34. A. Rohatgi, S. R. Butler, and F. J. Feigl, *ibid.*, **126**, 149 (1979).
35. J. Monkowski, J. Stach, and R. E. Tressler, *ibid.*, **126**, 1129 (1979).
36. H. Frenzel, B. R. Singh, K. Haberle, and P. Balk, *Thin Solid Films*, **58**, 301 (1979).
37. B. R. Singh and P. Balk, *This Journal*, **126**, 1288 (1979).
38. H. Frenzel and P. Balk, *J. Vac. Sci. Technol.*, **16**, 1454 (1979).
39. I. S. T. Tsong, M. D. Monkowski, and J. R. Monkowski, in "Physics of MOS Insulators," S. Pantelides, Editor, (1980).
40. J. W. Rouse, B. E. Deal, C. R. Helms, and R. R. Razouk, in "Proceedings of the AVS Symposium," Detroit, MI (1980).
41. B. E. Deal and A. S. Grove, *J. Appl. Phys.*, **36**, 3770 (1965).
42. J. P. Stagg and M. R. Boudry, *ibid.*, **52**, 885 (1981).
43. S. A. Schwarz and C. R. Helms, *J. Vac. Sci. Technol.*, **16**, 781 (1979).
44. N. J. Chou, C. M. Osburn, Y. J. van der Meulen, and R. Hammer, *Appl. Phys. Lett.*, **22**, 380 (1973).
45. J. W. Rouse and C. R. Helms, To be published.
46. W. S. Johnson and J. F. Gibbons, Thesis, Stanford University, Stanford, CA (1970).
47. A. T. Fromhold, Jr., "Theory of Metal Oxidation," Vol. I, North Holland (1976).
48. R. E. Dickerson, "Molecular Thermodynamics," W. A. Benjamin, Inc. (1969).
49. W. A. Tiller, *This Journal*, **127**, 619 (1980).

Electron-Electron Interactions in Finely Focused Beams of Low Energy Electrons

Y. W. Yau and R. F. W. Pease

Stanford Electronics Laboratory, Stanford University, Stanford, California 94305

T. R. Groves

Hewlett Packard Laboratory, Palo Alto, California 94304

ABSTRACT

Although low current beams of low energy electrons can be finely focused through the use of retarding field focusing optics, it had been suggested that the reduced axial spacing of the low energy electrons could lead to serious defocusing because of electron-electron interactions. However, the Monte Carlo simulation of such electron-electron interactions in the region between final lens and target plane shows that there are no appreciable differences in energy spread and spot diameter with beam currents up to 5 μ A transported through aperture sizes greater than 0.01 mm in radius at energies of 10 keV, 1 keV, and 100 eV. Preliminary experimental results indicate that current density of 250 A/cm² of 1 keV electrons can be obtained by using hairpin tungsten filaments.

Low energy (< 5 keV), low current (<< 1 μ A) electron beams can be finely focused by immersing the target plane in a retarding electrostatic field (Fig. 1) because the spherical and chromatic aberration coefficients C_s and C_c of the total focusing system (i.e., magnetic lens plus retarding field) are greatly reduced (1). At higher currents ($\geq 1 \mu$ A), as

needed in E-beam lithographic systems, the electron-electron interactions can become a limiting factor for the minimum probe diameter obtainable. This is true in conventional higher (≥ 10 keV) energy electron-beam systems (2); in retarding field systems where electrons are slowed down in the region between the final lens and the target

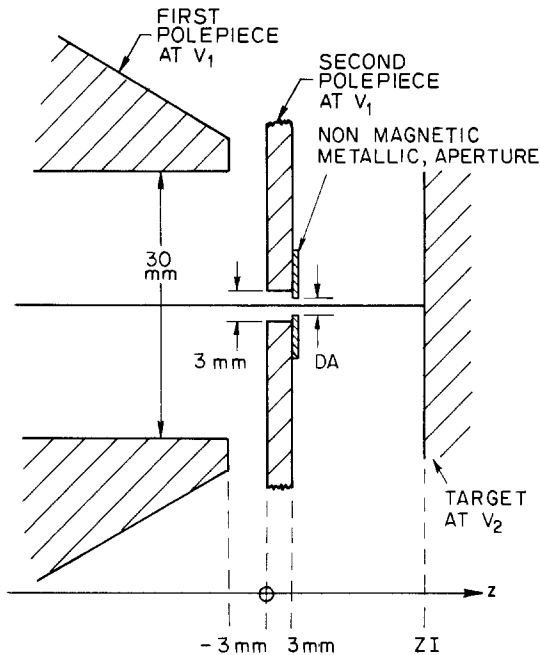


Fig. 1. Final lens region of an electron probe system. In conventional mode, $V_2 = V_1$; in retarding field mode, $V_2 < V_1$.

plane, the electron-electron interactions may set an even lower limit. We report here the results of the Monte Carlo simulation of electron-electron interactions in conventional and retarding field systems. There appears to be little increased effect, and the experimental results are consistent with the conditions specified.

Monte Carlo Simulation

A version of the program described by Groves *et al.* (3) was modified to account for the retarding field and for image charges induced by the target plane.

Initialization.—The simulation starts with a sample of 100 electrons distributed within the aperture area at the exit of the final magnetic lens (Fig. 2). Each electron is assigned a set of randomly generated radial coordinates (x_i, y_i), and zero initial energy spread is assumed. All the electrons are directed toward an ideal geometrical point with an initial energy of 10 keV. In the conventional case, this ideal point is at the focus on the target plane; in the retarding field case, it lies beyond the target plane so that the retarding electrostatic field brings about a focus at the target plane for each beam current, final landing energy, and aperture size. Every electron is also given a time t_i which is determined by the beam current I , i.e., $0 < t_i < 100 \cdot e/I$. The final step of the initialization is to advance all the electrons' positions by

$$\begin{aligned} x_i &= x_i + \dot{x}_i \cdot t_i \\ y_i &= y_i + \dot{y}_i \cdot t_i \\ z_i &= z_i + \dot{z}_i \cdot t_i + at_i^2/2 \end{aligned}$$

Their velocities are modified (if necessary) by

$$z_i = z_i + at_i$$

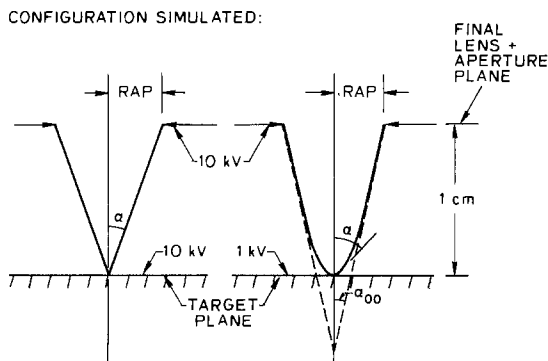


Fig. 2. Conventional and retarding field configurations simulated

where $a = 0$ for conventional case, $a = e(V_2 - V_1)/m_e$ for retarding field case, V_1 is the initial starting voltage, and V_2 is the final target plane voltage.

Stepping.—First, the time of flight between the final lens plane and the target plane is divided into 100 steps of equal time T

$$T = \frac{l/100}{\sqrt{\dot{x}_i^2 + \dot{y}_i^2 + \dot{z}_i^2}}$$

where l is the distance between aperture and target (1 cm in our model). At each step, the Coulomb force and the Lorentz force between all electron pairs are calculated. Then the positions and the velocities of the electrons are updated accordingly. This process goes on until the last electron has reached the target plane. When an electron arrives at the target plane, its position and velocity are recorded. From these recorded data, the spot diameter d , energy spread ΔE , and axial defocusing ΔZ (for conventional cases) are calculated. The spot diameter is determined such that 80% of the total current is included. In conventional cases, the minimum spot may occur at a different axial position from the focus because of electron-electron interactions. The program looks for the minimum spot diameter and its corresponding axial position by extrapolating from the positions and velocities recorded at the target plane. The energy spread is the standard deviation from the mean final energy at the target plane for both configurations.

Results

A fixed-beam current of $5 \mu A$ for different aperture sizes in the conventional arrangement was used to simulate different values of space charge parameter σ (4). As the aperture radius is decreased, the interactions become stronger; this is evident from the increase both in the energy spread and spot diameter of the electron beam. Furthermore, the axial defocusing, zero at negligible interactions, reaches a maximum and then becomes negative as the electron-electron interactions are increased; this is in agreement with the classical space-charge theory (4). Shown in Table I are the two cases of retarding field configurations with final landing energies of 1 keV and 100 eV, respectively. When the aperture radius is 0.1 mm or larger, the energy spread and spot diameter appear to be quite close to their conventional 10 keV counterparts. For very small apertures, however, the electron-electron interactions increase considerably.

Experimental Measurement

A scanning electron microscope (SEM) was modified to investigate the relation between beam diameter and beam current in conventional and in retarding field configurations. The arrangement is shown in Fig. 3. A flat aluminum slab was used as the target plane with a 1000 mesh/in. Ni grid mounted over the 2 mm diam hole. Conventionally, the aluminum target is grounded and the cathode is at -10 kV; in retarding field mode, the target is connected to -9 kV.

Table I. Values of energy spread (ΔE) and minimum beam diameter (d) for the conventional and retarding field configurations for a beam current of $5 \mu A$

RAP (cm)	ΔE (eV)	d (μm)	ΔZ (μm)	
3.0×10^{-2}	0.15	0.06	0	Conventional $V_1 = 10$ kV $V_2 = 10$ kV
1.0×10^{-2}	0.33	0.20	+6	
3.0×10^{-3}	0.88	0.47	+73	
2.0×10^{-3}	1.20	0.69	+156	
1.1×10^{-3}	1.68	1.19	+568	
7.0×10^{-4}	2.04	1.85	+944	
6.0×10^{-4}	2.16	2.04	+1053	
5.0×10^{-4}	2.30	2.34	+866	
4.6×10^{-4}	2.36	2.46	+480	
4.0×10^{-4}	2.45	2.64	-572	
3.7×10^{-4}	2.51	2.76	-1514	Retarding Field $V_1 = 10$ kV $V_2 = 1$ kV $V_1 = 10$ kV $V_2 = 0.1$ kV
3.0×10^{-2}	0.15	0.09	0	
1.0×10^{-2}	0.43	0.21	0	
3.0×10^{-3}	1.04	0.68	0	
3.0×10^{-2}	0.17	0.13	0	
1.0×10^{-2}	0.52	0.29	0	
3.0×10^{-3}	1.18	1.26	0	

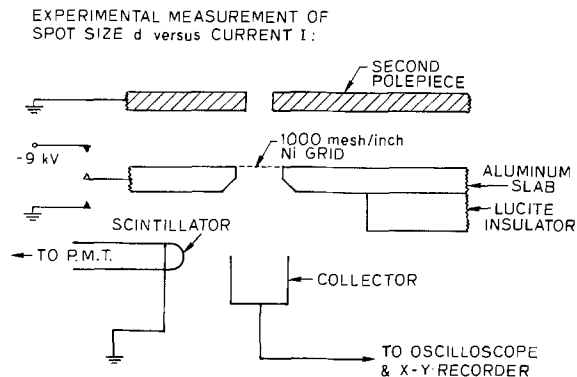


Fig. 3. Experimental arrangement for measuring beam diameter and beam current.

Underneath the mesh grid, a Faraday cup is used to collect the transmitted electrons. As the beam is scanned across the mesh, the signal rise time gives the measurement of the spot diameter and the beam current is measured. Some results are shown in Table II. Because of limitations of the SEM, contributions to the spot diameter arise mainly from the aberrations for large values of RAP, the Gaussian diameter of the source at small values of RAP, and electron-electron interactions in regions other than that between the final lens and target.

Discussion

Dayan *et al.* (5) suggested that a sample size of 100 is inadequate for currents above $10 \mu\text{A}$ at 20 kV because then the sample length becomes as short as the stepping interval. We have restricted the maximum current to $5 \mu\text{A}$ to minimize such an error. As a check on the error, three simulations were carried out with 200 electrons. The discrepancy in values of energy spread and spot diameter between 200- and 100-electrons simulation is about 10%. Furthermore, using a different set of randomly generated numbers, the variation in the results is within 5%. Further credibility to the validity of the Monte Carlo simulation results from the agreement of values of Δz at low values of σ (*i.e.*, serious interactions) with those determined from the classical treatment of the axial defocusing in conventional cases. For example, the maximum axial defocusing occurs at $\text{RAP} = 6 \times 10^{-4} \text{ cm}$ where $\sigma = 2.4$. This is the same value of σ which gives the maximum axial defocus according to Klemperer and Barnett (4).

It is not immediately obvious why the electron-electron interactions are not more serious in the retarding field case. One possible explanation is that the retardation is accompanied by an increase in convergence angle, thus reducing the interactive impulses. The experimental results are consistent with the main conclusion that the extra space-charge effects in the retarding field region has only

Table II

Aperture Radius	Current	Spot Diam	
RAP (cm)	I (μA)	d (μm)	
3×10^{-2}	5.0	2.3	Conventional $V_1 = 10 \text{ kV}$ $V_2 = 10 \text{ kV}$
3×10^{-2}	2.5	1.1	
3×10^{-2}	1.0	1.0	Retarding Field $V_1 = 10 \text{ kV}$ $V_2 = 1 \text{ kV}$
3×10^{-2}	5.0	2.6	
3×10^{-2}	2.5	1.2	
3×10^{-2}	1.0	1.1	

minor overall effect as predicted by Monte Carlo calculation.

Conclusion

1. There is no significant difference in energy spread and spot diameter for the conventional ($V_1 = V_2 = 10 \text{ kV}$) and retarding field ($V_1 = 10 \text{ kV}$, $V_2 = 1 \text{ kV}$ and 100V) configurations for currents up to $5 \mu\text{A}$ for the geometry shown. Hence the advantages of the previously reported low aberrations of the retarding field configuration are not offset by the electron-electron interactions in the final lens and the target plane region.

2. The Monte Carlo space-charge program predicts axial defocusing of high perveance beams in accordance with classical space-charge theory.

3. Experimentally, a current density of 250 A/cm^2 with 1 keV electrons at target plane is obtainable using tungsten hairpin filaments.

Acknowledgment

This work was supported by the Defense Advanced Research Project Agency under Contract No. MDA 903-81-C-0294.

Manuscript submitted Oct. 25, 1982; revised manuscript received Sept. 6, 1983. This was paper 308 presented at the Montreal, Quebec, Canada, Meeting of the Society, May 9-14, 1982.

Stanford University assisted in meeting the publication costs of this article.

REFERENCES

- Y. W. Yau, R. F. W. Pease, A. A. Iranmanesh, and K. J. Polasko, *J. Vac. Sci. Technol.*, **19**, 1048 (1981).
- See, for example, H. C. Pfeiffer, in "Proceedings of the 5th Annual SEM Symposium," p. 113, IIT Research Institute, Chicago, IL (1972).
- T. R. Groves, D. L. Hammond, and H. P. Kuo, *J. Vac. Sci. Technol.*, **16**, 168 (1979).
- O. Klemperer and M. E. Barnett, "Electron Optics," Chap. 8, Cambridge University Press, London (1971).
- P. S. Dayan and G. A. C. Jones, *J. Vac. Sci. Technol.*, **19**, 1094 (1981).

The Effect of Film Thickness on the Electrical Properties of LPCVD Polysilicon Films

N. C. C. Lu

IBM Thomas J. Watson Research Center, Yorktown Heights, New York 10598

C. Y. Lu

The Institute of Electronics, National Chiao-Tung University, Hsin-Chu, Taiwan, China and Department of Electrical and Computer Engineering, North Carolina State University, Raleigh, North Carolina 27650

M. K. Lee, C. C. Shih, and C. S. Wang

The Institute of Electronics, National Chiao-Tung University, Hsin-Chu, Taiwan, China

W. Reuter

IBM Thomas J. Watson Research Center, Yorktown Heights, New York 10598

T. T. Sheng

AT&T Bell Laboratories, Murray Hill, New Jersey 07974

ABSTRACT

The effect of film thickness on the electrical properties of boron-doped LPCVD polysilicon films with doping concentration ranging from 1×10^{17} to 1×10^{19} cm^{-3} has been characterized from 1.2 μm down to 0.1 μm . The resistivity increases exponentially as the film thickness decreases, rather than remaining constant, and the rate of increase is a strong function of doping concentration. After a quantitative study on the physical mechanisms which can affect the resistivity as film thickness decreases, the carrier trapping effect due to grain-size variation at different film thicknesses is shown to be the dominant factor. A trapping model without assuming the depletion approximation can explain well the experimental data and enhances understanding of the resistivity behavior as the polysilicon film thickness decreases.

Polycrystalline-silicon (polysilicon) material is composed of aggregates of single crystal grains with a grain boundary between adjacent grains. The grain boundary is a transitional region between different orientations of neighboring crystallites. Polysilicon films have been widely used in integrated circuits such as silicon gates, interconnections, passivation or isolation layers, diffusion sources, resistors, monolithic distributed RC filters, diodes, active devices, and redundancy programming elements. Its increasing range of applications ensures the importance of this material in the coming era of VLSI.

Since the demand for better performance and higher packing density of VLSI circuits requires the device size to be scaled not only in the horizontal but also in the vertical direction, the thickness of polysilicon films used in most integrated-circuit applications has been scaled from several micrometers (1, 2) down to tenth of a micrometer (3). In addition, the film deposition generally has changed from atmospheric-pressure chemical vapor deposition (APCVD) (1, 2) to low-pressure chemical vapor deposition (LPCVD) (4) for better film quality and higher throughput. As a result, understanding of the thickness scaling effect on the electrical properties of LPCVD polysilicon films in the submicrometer range is important for device design in VLSI circuits.

Kamins (1) studied the thickness dependence of Hall mobility and resistivity in APCVD polysilicon films, which had thickness ranging from 3 to 24 μm and were doped by diffusion with concentrations ranging from 10^{18} to 10^{19} cm^{-3} . Resistivity of these polysilicon films decreases with increasing film thickness. Kamins showed that this decrease in resistivity is due mainly to the increase of mobility. Because an APCVD polysilicon film with thickness larger than several micrometers is composed of a few layers of grains stacked in the thickness direction, the measured mobility is actually an average mobility over the film thickness. The mobility near the top surface is larger in a thicker film because the grain size becomes larger. Mei *et al.* (5) studied the resistivities of APCVD polysilicon films which had thickness down to 0.25 μm and were doped by phosphorus ion implantation with a concentration of 1.2×10^{19} cm^{-3} . The resistivity also decreases with increasing film thickness. It was reasoned that this resistivity increase is due mainly to dopant segregation to the interface between polysilicon film and its underlying oxide layer. Recently, Colinge *et al.* (6) proposed a theoretical equation [Eq. (5) in (6)] for the mobility in polysilicon films, which considers the ef-

fect of film thickness by including the polysilicon/oxide interface scattering mechanism. They used 1.95 μm as the mean free path of electrons in silicon, which implies that if a polysilicon film thickness is reduced to the range of 1.95 μm , the effect due to collisions of electrons to the polysilicon/oxide interface can become a dominant factor to cause the resistivity increase.

The above review shows that the effect of film thickness on the electrical properties of LPCVD polysilicon films at different doping concentrations has not been fully understood and that, in fact, different viewpoints exist on the dominant mechanism for the resistivity changes as the film thickness decreases. In this work, therefore, we first characterized the electrical properties of boron-doped LPCVD polysilicon films which had thickness ranging from 1.2 down to 0.1 μm and doping concentration ranging from 1×10^{17} to 1×10^{19} cm^{-3} . It will be shown that as the film thickness decreases, the resistivity increases exponentially, rather than remaining constant as in conventional resistor materials, and the rate of increase is a strong function of doping concentration. There are several possible physical mechanisms to cause this increase, such as polysilicon/oxide interface scattering, dopant segregation to the grain boundaries, dopant leaching or loss, dopant segregation to the polysilicon/oxide interface, and changes of the number of carriers trapped into grain boundaries because of grain-size variations. A detailed quantitative analysis will show that the dominant mechanism causing the resistivity increase is the carrier trapping effect due to grain-size reduction.

Experimental Results

Sample preparation and measurements.—Undoped polysilicon films 0.1–1.2 μm thick were deposited onto 0.80 μm thick SiO_2 layers thermally grown on silicon wafers. The deposition was done in an LPCVD reactor at 620°C by H_2 ambient pyrolysis of silane with a deposition rate of 80 Å/min. The implanted boron doses were selected to give calculated doping concentrations at three different levels: 1×10^{17} , 2×10^{18} , and 1×10^{19} cm^{-3} . The calculations assumed a uniform dopant profile and no dopant loss. The implantation energies were selected to yield a maximum implantation dose near the center of the polysilicon films. After the devices were patterned by plasma etching, a 0.80 μm -thick CVD oxide layer was deposited at 430°C. Contact windows were opened, and the wafers were divided into two groups. One group had the contact windows implanted heavily with boron to give p^+

contacts; the other group did not have this implantation. All the wafers were then annealed at 900°C for 420 min in N₂ to remove the implantation damage and to ensure uniform dopant distribution. A 1.0 μm-thick aluminum layer was deposited and defined over the contact areas. The contacts were alloyed at 450°C for 20 min in N₂. The devices included different shapes of resistors, van der Pauw structures (8), and cross-bridge structures (8).

The thickness of polysilicon film was measured by an α-step profiler. The grain structure and grain size were studied using transmission electron microscopy (TEM) techniques. Figure 1 shows the typical cross-sectional TEM micrographs. It was found that all the grain structures of undoped and doped samples were conical, and no significant recrystallization was observed, in contrast to the reported grain growth in phosphorus-doped samples in Ref. (9). From thin to thick polysilicon films, the surface roughness becomes worse, and the grain size at the top of the surface, which corresponds approximately to the distance between the hillocks (9), increases. A quantitative measurement of the grain size was performed using top-viewed TEM micrographs shown in Fig. 2. Two methods were used, and the results agreed well. One method was to measure the area of a certain region and to count the number of grains within that area. The average grain size L is calculated from the following equation

$$L = (\text{area}/\text{number of grains})^{0.5}/m \quad [1]$$

where m is the micrograph magnification factor. The other method (10) was to draw a line and to count the number of grains across the line. The average grain size is

$$L = (\text{line length}/\text{number of grains})/m \quad [2]$$

The measured grain size decreases as the film thickness decreases (Fig. 3).

By using the secondary ion mass spectroscopy (SIMS) technique (11), dopant profiles were proven uniform, and no significant dopant loss was observed. The SIMS analysis was done with a 12 keV O₂⁺ beam raster scanned and gated to accept 20% of the central portion. Charging problems were minimized by using the electron flood gun and integration of the secondary ion energy distribution. We used a 50 keV boron implantation with dose of 5×10^{14} cm⁻² as a standard. The measured doping concentrations were within 20% of the projected values. Figure 4 shows typical SIMS profiles of samples which have projected doping levels of 2×10^{18} cm⁻³ and thickness of either 0.2 or 1.0 μm.

Electrical measurements included the I-V characteristics, resistivity, and Hall voltages. Resistivity was always measured over the linear I-V range with small applied bias. Sheet resistances for some high-value resistors were difficult to obtain from the Hall setup and were calculated, therefore, from measured resistance and device geometry.

Results.—The measured sheet resistance vs. film thickness at room temperature is shown in Fig. 5a for a doping

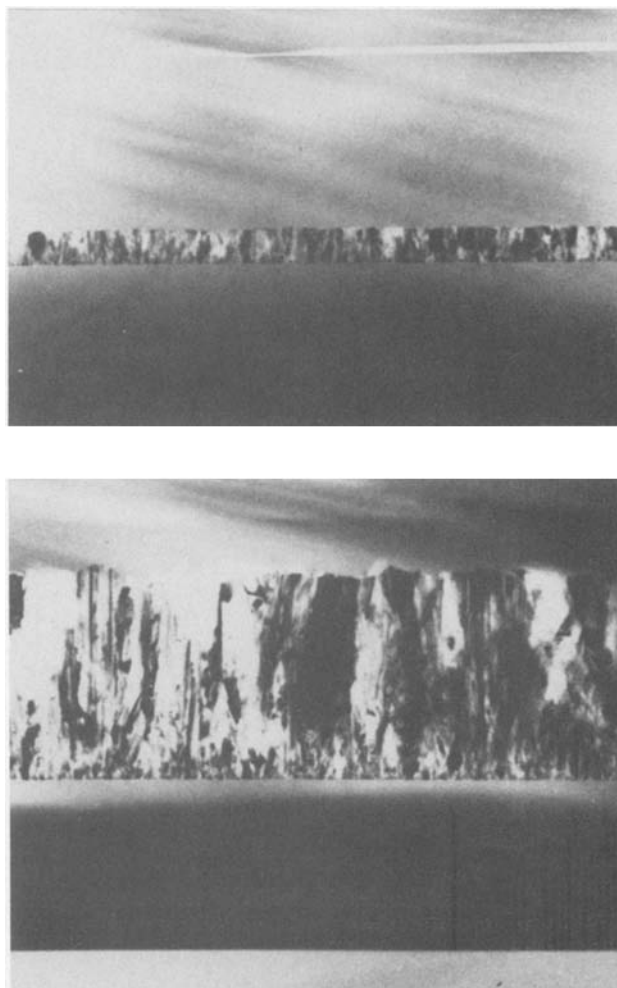


Fig. 1. Cross-sectional TEM micrographs. A, top: $t = 1950 \text{ \AA}$, $N = 1 \times 10^{17} \text{ cm}^{-3}$. B, bottom: $t = 9800 \text{ \AA}$, $N = 2 \times 10^{18} \text{ cm}^{-3}$. t = film thickness, N = doping concentration.

concentration of $1 \times 10^{17} \text{ cm}^{-3}$, and in Fig. 5b for $2 \times 10^{18} \text{ cm}^{-3}$. The contacts between aluminum and polysilicon in samples without p⁺ contact dopants are ohmic at small applied voltage. Inclusion of the p⁺ contact dopants does not significantly affect the sheet resistance. Figure 5a and 5b shows that when the film thickness decreases, the sheet resistance increases exponentially. The thickness dependence of the resistance is considerably larger at a doping concentration of $2 \times 10^{18} \text{ cm}^{-3}$ than at $1 \times 10^{17} \text{ cm}^{-3}$. The resistivity, which can be calculated by multiplying the sheet resistance by the film thickness, is also

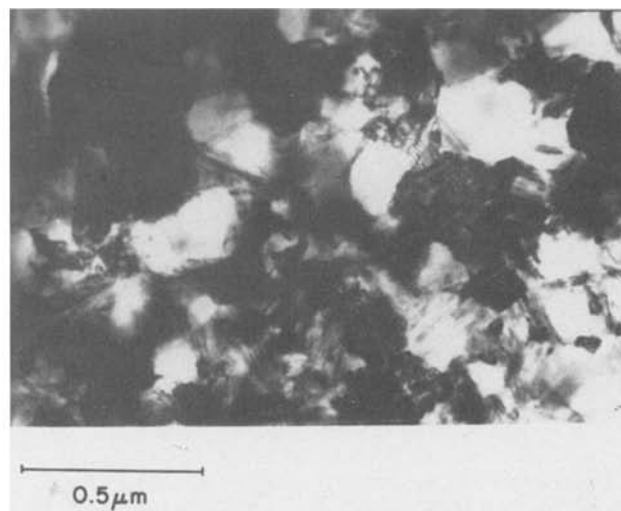
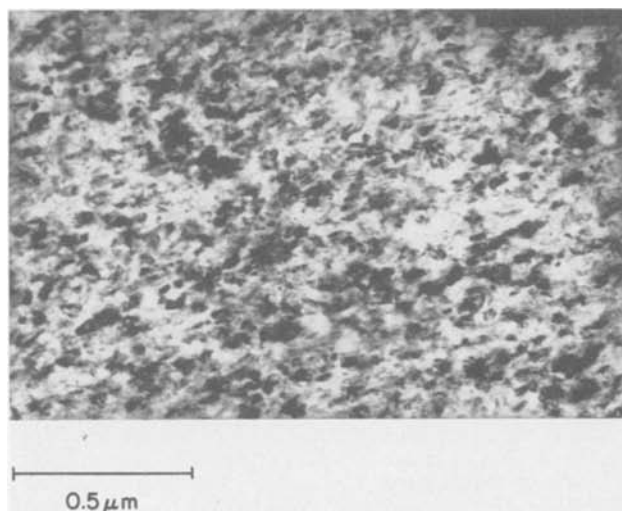


Fig. 2. Top view TEM micrographs of the samples in Fig. 1

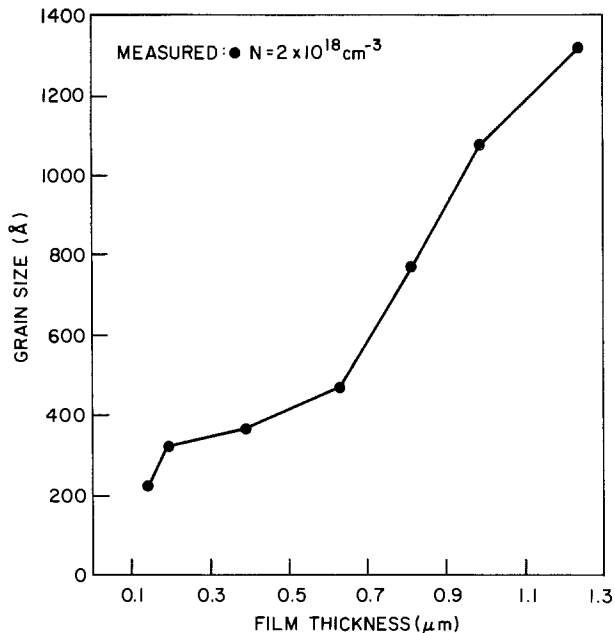


Fig. 3. Measured average grain size vs. film thickness

shown in Fig. 5a and 5b as a function of film thickness. A rapid increase of the resistivity with decreasing film thickness occurs, especially at thickness less than $0.8 \mu\text{m}$. This behavior is different from ohmic resistors of other materials, the resistivity of which is generally independent of thickness.

Theoretical Interpretation

Two theories have been proposed to model the transport properties of doped-polysilicon films. The first is a dopant-segregation model, where the grain boundary serves as a sink to cause preferential segregation of

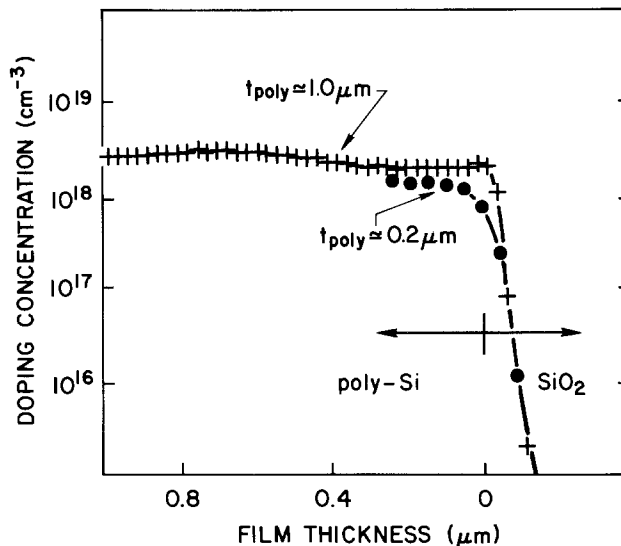


Fig. 4. Measured dopant profiles vs. film thickness

dopant atoms that become inactive at the boundary (12, 13). This model, however, cannot explain the mobility minimum at a critical doping concentration, the temperature dependence of the resistivity, and the hyperbolic-sine I-V behavior of polysilicon resistors at high electric field. The second theory is a carrier trapping model (1, 2, 7, 14-16), where the trapping states inside the grain boundary, due to defects and incomplete atomic bondings, can trap free carriers from the ionized dopants. This process not only reduces the number of free carriers, but also creates a potential barrier surrounding the grain boundary, which impedes the motion of carriers from one crystallite to another. This model better explains the sharp changes of resistivity with doping concentration, the mobility minimum, the temperature dependence of resistivity, and the hyperbolic-sine I-V behavior at high

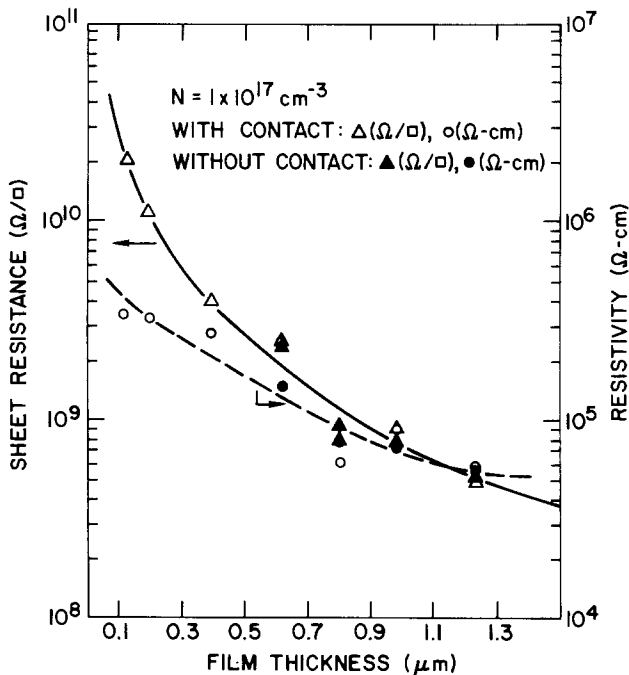
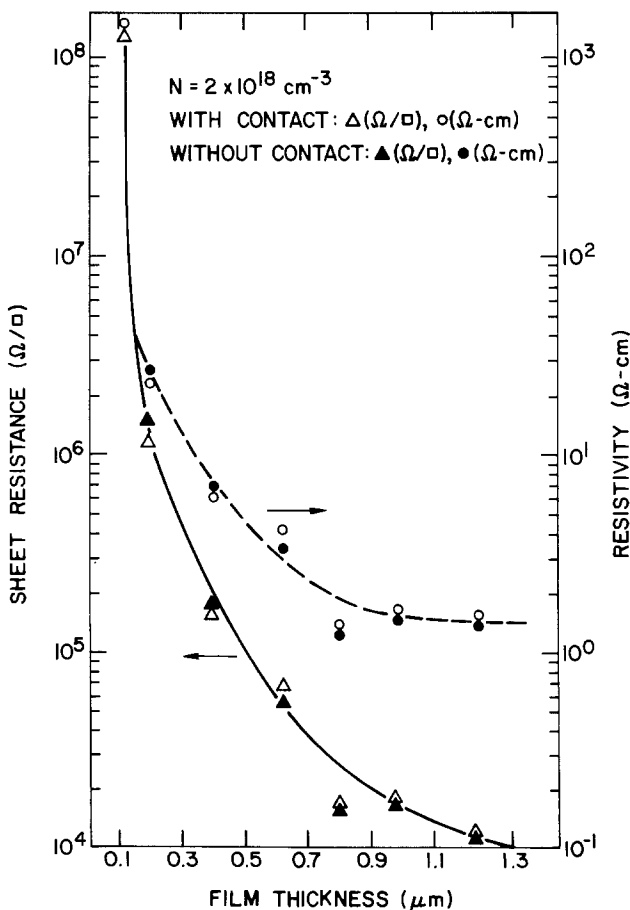


Fig. 5. Measured sheet resistance and resistivity vs. film thickness at room temperature. A, above: $N = 1 \times 10^{17} \text{ cm}^{-3}$. B, right: $N = 2 \times 10^{18} \text{ cm}^{-3}$.



electric field. Even if the dopants do segregate, the trapping model can still be applied, based on an active dopant concentration that can be obtained by subtracting the inactive dopant concentration from the actual doping concentration (15, 17).

For thin-film polysilicon resistors, several physical mechanisms may cause the observed resistivity increase when film thickness decreases. The effect of these mechanisms will be considered individually below.

Scatterings at horizontal grain boundaries and polysilicon/oxide interface.—TEM results on LPCVD films show that the grain structures in all samples having different film thicknesses are conical. In such conical structures, grain boundaries rarely occur in the direction parallel to the polysilicon/oxide interface, in contrast to the randomly stacked grain structures usually observed in APCVD polysilicon films. If the structure had many stacked layers of such horizontal grain boundaries, the resistances of the samples with p⁺ contact dopants could not be the same as those without the contact dopants because the grain boundary is a high resistance region. However, it is found that the resistances of samples with p⁺ contact dopants are approximately equal to those without p⁺ contact dopants. This demonstrates that, even though horizontal grain boundaries may exist occasionally, they do not seriously disturb the current flow, and the possibility of carriers colliding with the horizontal grain boundaries is low. Since the mean free path of carriers in the intrinsic silicon is approximately 200Å,¹ which is much smaller than the thinnest film thickness in our samples, the carriers should have had several collisions before scattering at the polysilicon/oxide interface. As a result, the scattering effects due to both polysilicon/oxide interface and horizontal grain-boundaries should not be the dominant factor responsible for the resistivity increase (18) in LPCVD polysilicon films with thickness down to 0.1 μm. Another piece of indirect evidence to support the conclusion is that when the oxide layer above polysilicon film is removed, the measured resistance does not change too much from the resistance of samples with the top oxide layer present, and the rate of resistivity increase as the films become thinner is almost the same. In addition, that different rates of the resistivity increase at different doping concentrations is difficult to explain based on scattering effect.

Dopant segregation to grain boundaries.—Although the amount of dopant segregation to grain boundaries can be a function of film thickness, Mandurah *et al.* (19) showed that no significant segregation effect occurs in boron-doped polysilicon films. In our boron-doped samples, the grain-boundary segregation should not be the dominant factor for the resistivity increase.

Dopant leaching or loss.—After implantation and before annealing, the samples were coated with a thin layer of low temperature deposited oxide to protect their surfaces from furnace ambient and to prevent loss of dopants during the high temperature process. The SIMS results (Fig. 4) proved that the actual doping concentration in the polysilicon film is close to the projected value within 20% variation, and no significant loss was found even in the thinnest samples.

Segregation to polysilicon/oxide interface.—From the SIMS results as shown in Fig. 4, no significant pileup of the dopants was found at the polysilicon/oxide interface in the samples with doping concentration up to 2×10^{18} cm⁻³. It should be noted that an electron flood gun for charge compensation was employed. While not shown in Fig. 4, the silicon signal remained constant when sputtering through the Si/SiO₂ interface. It has been shown (20) that at normal incidence O₂⁺ bombardment, silicon is completely oxidized to SiO₂. At a doping level of 1×10^{19} cm⁻³, a small pileup of the dopants has been observed; however, its amount is not so significant as to affect the absolute doping level in the film. This effect can become important at higher doping concentration.

¹ The mean free path λ is $v_{th}(m^* \mu / q)$, where v_{th} is thermal velocity of the carriers, $v_{th} = (3kT/m^*)^{0.5}$, and μ is mobility. In intrinsic silicon, $\lambda \approx 237\text{\AA}$ for holes and $\approx 204\text{\AA}$ for electrons at room temperature. In a doped silicon crystallite, λ is even smaller. For example, $\lambda \approx 130\text{\AA}$ at a doping concentration of around 10^{20} cm⁻³.

Carrier trapping.—Before a quantitative calculation of the carrier trapping effect on the resistivity change due to reduction of film thickness, general features of the carrier trapping model are briefly reviewed here. Several assumptions were made in the previous trapping models (2, 15) to simplify the calculation. The polysilicon film is assumed to be composed of identical crystallites having a grain size L , and the grain boundary is assumed to contain Q_T cm⁻² of traps located at an energy level of e_T with respect to the intrinsic Fermi level at the grain boundary (Fig. 6). The traps are assumed to be initially neutral and become charged by trapping carriers. When dopants are added into polysilicon films, some of the mobile carriers around the grain boundary are trapped by the trapping states in the grain boundary, resulting in a depletion region. Using these assumptions, an abrupt depletion approximation was used to calculate the energy band in the crystallites. For a given grain size, since the effective trapping states in the grain boundary are finite, there exist two possible conditions, depending on the doping level. If the doping concentration is high, the crystallite can only be partially depleted and a neutral region remains (Fig. 6b). If the doping level is decreased to a critical doping concentration N^* , the crystallite is totally depleted (Fig. 6c). Because the crystallite becomes totally depleted, the number of free carriers remaining in the crystallite drastically decreases, thus causing a sharp resistivity increase. As the doping level further decreases, the crystallites remain in the condition of total depletion, and resistivity increases at a rather gradual rate. This explains why the resistivity vs. doping concentration curve of polysilicon films has a sharp change in slope near the critical doping level N^* . Similarly, at a given doping concentration, there exists a critical grain size L^* below which the grains are totally depleted. For a grain size around the value of L^* , as the grain goes from partial to total depletion, the resistivity change due to grain size variation is drastic.

As mentioned above, TEM results showed that when polysilicon film thickness is reduced, the grain size decreases. The effect of such grain-size change on the resistivity of polysilicon films will be examined based on the carrier trapping model below.

The previous trapping models (2, 14, 15) using the depletion approximation can clearly describe the transport

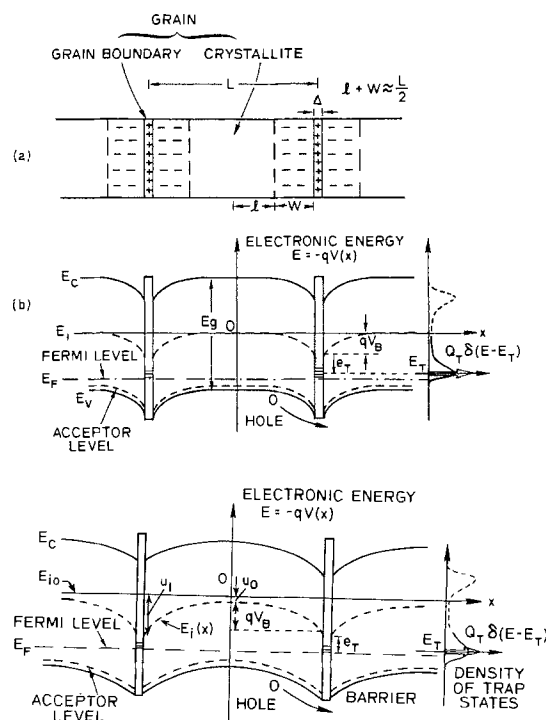


Fig. 6. The polysilicon trapping model. a: One-dimensional grain structure. b: Energy-band diagram of partially depleted grains for p-type dopants. c: Energy-band diagram of totally depleted grains for p-type dopants.

properties of polysilicon films. However, the depletion approximation causes abrupt changes in the resistivity with respect to grain-size variations near the transition between the partial depletion and the total depletion condition (21).² These abrupt changes can be smoothed by using a more accurate solution of Poisson's equation without assuming the depletion approximation (21). Recently, an exact solution for polysilicon resistivity was derived, which can avoid such abrupt changes and is valid over a wide range of doping concentrations, temperatures, and grain sizes (22). In this work, because samples are not very heavily doped and data were measured at room temperature, the exact Fermi-Dirac statistics of free-carrier distribution can be approximated by Boltzmann statistics, thus relaxing our exact analysis (22) to similar equations derived by Board and Darwish (21), except that a more precise formulation of the Fermi level in the bulk silicon E_{i0} as zero energy and assuming the electron (hole) energy positive (negative) for upward and negative (positive) for downward direction (Fig. 6), the Fermi level is

$$E_F = kT \ln \left\{ \frac{1}{4} \exp(E_A/kT) \left[\sqrt{1 + 8(N_A/n_i) \exp(-E_A/kT)} - 1 \right] \right\} \quad [3]$$

where N_A is the doping concentration, n_i is the intrinsic carrier concentration, and impurity level E_A , is (15)

$$E_A = \left(\frac{1}{2} E_g - 0.08 + 4.3 \times 10^{-8} N_A^{1/3} \right) + E_i(0) \quad [4]$$

By solving Poisson's equation and using suitable boundary conditions (21), the relationship of intrinsic Fermi level at grain boundary $E_i(L/2)$ with respect to the intrinsic Fermi level at the center of grain $E_i(0)$ can be calculated from

$$\left(\frac{Q_T^+}{2L_D q N_A} \right)^2 = (u_1 - u_0) + \beta(e^{u_1} - e^{u_0}) + (e^{-u_1} - e^{-u_0}) \quad [5]$$

where $L_D = (2kT\epsilon/q^2 N_A)^{0.5}$, $\beta = kT/q$, u_1 and u_0 are defined as $E_i(L/2)/kT$ and $E_i(0)/kT$, respectively, and the ionized trap density in the grain boundary Q_T^+ is related to the number of metallurgical traps Q_T as follows (2, 15)

$$Q_T^+ = \frac{Q_T}{1 + 2 \exp[u_1 + (e_T - E_F)/kT]} \quad [6]$$

where e_T is the trapping-state energy level with respect to the intrinsic Fermi level at the grain boundary. The corresponding grain size L is given by

$$L = L_D \int_{u_0}^{u_1} [(u - u_0) + \beta(e^u - e^{u_0}) + (e^{-u} - e^{-u_0})]^{-1/2} du \quad [7]$$

By varying u_0 , therefore, the corresponding u_1 and L can be calculated using Eq. [5] and [7].³ The resistivity is then obtained from (15)

$$\rho = \frac{(2\pi m^* kT)^{1/2}}{L q^2 p(0)} \exp(qV_B/kT) \quad [8]$$

where $qV_B = kT(u_1 - u_0)$ and $p(0) = N_A \exp(-u_0)$. For simplicity, crystallite bulk resistivity is not included.

To compare theory to the experimental results, it is necessary to determine m^* , permittivity ϵ , n_i , E_g , L , Q_T , and e_T . The values of single-crystal silicon were used for the first five parameters (15) and L was measured from TEM micrographs (Fig. 3). Q_T and e_T were obtained experimentally from the ρ vs. $1/kT$ curves of polysilicon resistors by using similar procedures described in Ref. (15). The method is valid because the samples used for parameter extraction have doping concentrations away from N^* , and thus the depletion approximation is valid.

² This can be interpreted in terms of film thickness as follows: at a given doping concentration, when film thickness changes such that its grain size is close to L^* , the abrupt depletion approximation becomes invalid.

³ The contents of Eq. [5], [6], and [7] are different from their corresponding expressions in Ref. (21) by including the necessary corrections.

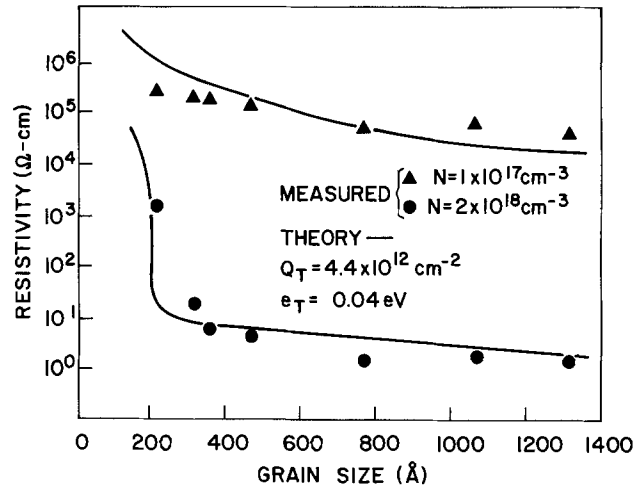


Fig. 7. Measured and theoretical resistivity vs. average grain size of different thickness films.

Also, since Q_T could be precisely determined, the value of e_T was adjusted within a reasonable degree to produce the best results of the ρ vs. L curves. Figure 7 shows the measured resistivities of different thickness films vs. the measured average grain sizes. The theoretical curves agree well with the experimental data and explain the drastic increase of resistivity with decreasing film thickness. Because decrease of film thickness causes reduction of grain size, when the grain size reaches around 210Å at doping concentration of $2 \times 10^{18} \text{ cm}^{-3}$, most of the grains go from partial depletion into total depletion, and the number of free carriers available for conduction drastically decreases, thus causing a sharp increase of resistivity. In contrast, at doping concentration of $2 \times 10^{17} \text{ cm}^{-3}$ for the range of film thickness studied in this work, most of the grains have been totally depleted, and therefore, the changes of resistivity are not so drastic as in those samples with doping concentration of $2 \times 10^{18} \text{ cm}^{-3}$. As a result, the carrier trapping effect due to grain-size variation at different film thicknesses is a dominant factor for the resistivity increase in boron-doped LPCVD polysilicon films as the film thickness decreases ($\geq 1000\text{Å}$).

Conclusions

The effect of film thickness on the electrical properties of boron-doped LPCVD polysilicon films has been studied down to film thickness of $0.1 \mu\text{m}$. It has been found that the resistivity increases exponentially as the film thickness decreases, rather than remaining constant, and the increasing rate is a strong function of doping concentration. After a quantitative study of the physical mechanisms which may affect the resistivity as film thickness decreases, the carrier trapping effect due to grain-size variation at different film thicknesses was shown to be the dominant factor. A trapping model without assuming the depletion approximation can explain the experimental observations well and enhances understanding of the resistivity behavior as polysilicon film thickness decreases. It also shows that when the polysilicon films are employed in VLSI circuits, the sensitivity of the resistivity to the film thickness must be considered in the device design (23).

Acknowledgments

The authors wish to thank the group of Professor L. J. Chen of National Tsing-Hwa University for helping the top-view TEM studies and Dr. L. M. Terman of IBM for helpful comments. This work was partially supported by the National Science Council of the Republic of China.

Manuscript submitted Aug. 26, 1983; revised manuscript received Nov. 28, 1983. This was Paper 234 presented at the Detroit, Michigan, Meeting of the Society, Oct. 17-21, 1982.

IBM T. J. Watson Research Center assisted in meeting the publication costs of this article.

REFERENCES

1. T. I. Kamins, *J. Appl. Phys.*, **42**, 4357 (1971).
2. J. Y. W. Seto, *ibid.*, **46**, 5247 (1975).
3. T. I. Kamins, M. M. Mandurah, and K. C. Saraswat, *This Journal*, **125**, 927 (1978).
4. R. D. Rosler, *Solid State Technol.*, **20**, 63 (1977).
5. L. Mei and R. W. Dutton, *IEEE Trans. Electron. Devices*, **ed-29**, 1726 (1982).
6. J. P. Colinge, E. Demoulin, F. Delannay, M. Lobet, and J. M. Temerson, *This Journal*, **128**, 2009 (1981).
7. N. C. C. Lu, L. Gerzberg, C. Y. Lu, and J. D. Meindl, *IEEE Trans. Electron. Devices*, **ed-30**, 137 (1983).
8. M. G. Buehler, W. R. Thurber, and S. D. Grant, *This Journal*, **125**, 645, 650 (1978).
9. R. Falckenberg, E. Doering, and H. Oppolzer, Abstract 570, p. 1429, The Electrochemical Society Extended Abstracts, Los Angeles, California, Oct. 14-19, 1979.
10. Y. Wada and S. Nishimatsu, *This Journal*, **125**, 1499 (1978).
11. M. A. Frisch, W. Reuter, and K. Wittmaack, *Rev. Sci. Instrum.*, **51**, 695 (1980).
12. M. E. Cowher and T. O. Sedgwick, *This Journal*, **119**, 1565 (1972).
13. A. L. Fripp, *J. Appl. Phys.*, **46**, 1240 (1975).
14. G. Baccarani, B. Ricco, and G. Spadini, *J. Appl. Phys.*, **49**, 5565 (1978).
15. N. C. C. Lu, L. Gerzberg, C. Y. Lu, and J. D. Meindl, *IEEE Trans. Electron. Devices*, **ed-28**, 818 (1981).
16. N. C. C. Lu, L. Gerzberg, C. Y. Lu, and J. D. Meindl, *IEEE Electron. Devices Lett.*, **ed1-2**, 95 (1981).
17. M. M. Mandurah, S. C. Saraswat, and T. I. Kamins, *IEEE Trans. Electron. Devices*, **ed-28**, 1163 (1981).
18. S. Solmi, M. Severi, R. Angelucci, L. Baldi, and R. Bilenchi, *This Journal*, **129**, 1811 (1982).
19. M. M. Mandurah, S. C. Saraswat, C. R. Helms, and T. I. Kamins, *J. Appl. Phys.*, **51**, 5755 (1980).
20. W. Reuter and K. Wittmaack, *Appl. Surf. Sci.*, **5**, 221 (1980).
21. K. Board and M. Darwish, *J. Appl. Phys.*, **51**, 4546 (1980); *ibid.*, **52**, 4351 (1981).
22. C. Y. Lu and N. C. C. Lu, *Solid-State Electron.*, **26**, 549 (1983).
23. N. C. C. Lu, L. Gerzberg, and J. D. Meindl, *IEEE J. Solid-State Circuits*, **sc-17**, 312 (1982).

Polycrystalline Silicon Recrystallization by Combined CW Laser and Furnace Heating

J. Shappir* and R. Adar

School of Applied Science and Technology, The Hebrew University of Jerusalem, Jerusalem, Israel

ABSTRACT

A modified CW argon laser-induced lateral recrystallization of polycrystalline silicon is described. Holding the sample in a furnace at elevated temperature of about 1000°C resulted in significantly reduced thermal gradients and stresses. A wider range of power is allowed for proper recrystallization both on oxide and substrate areas simultaneously. Preferred thermal profiles enabled larger lateral epitaxy of ~50 μm per single scan. The higher substrate temperature resulted also in wider melted areas and high scan rates of 80 cm/s enabling much shorter processing time.

In recent years, intensive effort has been made in different techniques to obtain large area silicon on insulator (SOI) as an alternative substrate for integrated circuits. Besides the obvious advantages of reduced junction capacitance, no device coupling, and no contact spiking, it can eventually lead to three-dimensional integration of electronic devices (1, 2). Gat *et al.* observed (3) that the recrystallization of polysilicon layers on an insulating substrate by a CW laser beam results in grains having dimensions up to $2 \times 25 \mu\text{m}^2$.

In order to fabricate larger-area SOI structures without grain boundaries and with complete control of the crystallographic orientation, seeded lateral epitaxy technique has recently been studied (4, 5). In this technique, a region where the polysilicon is in direct contact with the silicon substrate serves as a seed for lateral crystal growth to the area where the polysilicon is over an insulating layer.

With standard isoplanar technology, lateral epitaxy of 20-30 μm was obtained. Modified coplanar structure with no step between the polysilicon on silicon (PS) and polysilicon on oxide (PO) or the utilization of thin underlying insulators (< 1500Å) resulted in further increase of the lateral epitaxy to 70-80 μm (5, 6).

In the standard laser recrystallization configurations, the silicon wafer is attached to a metal chuck that can be heated up to 700°C (6) and the laser beam raises the layer temperature to above its melting point of 1415°C. Such an arrangement suffers from two major drawbacks: (i) It is difficult to find optimal recrystallization conditions for both the PS and PO areas due to the difference in the vertical heat conduction in the two regions, and (ii) the high lateral thermal gradients are bound to reduce the crystalline quality of the recrystallized layer.

To overcome these two problems, the approach of this work was to raise the substrate temperature to about 1000°C by placing it in a diffusion furnace and use lower laser power to raise locally the polysilicon temperature to its melting point. In this setup, the wafer loses most heat by blackbody radiation rather than by thermal conductance to the metal chuck.

In the following, certain results of this combined laser and furnace recrystallization technique are reported.

Experimental

The experimental setup consisted of the laser, the optics, the scanners, and the furnace, where the wafer was held during the recrystallization process. The laser was a Coherent 18W Ar ion laser, operated in the multiline mode with wavelengths near 0.5 μm. The optical system consisted of two lenses in a beam expanding structure that served both as beam expander and focusing element to obtain an 80 μm diam spot size, at a focal distance of 700 mm. The beam was scanned across the wafer by means of two galvanometer-driven mirrors. The silicon wafer was vacuum held by an adjustable quartz tube which entered the furnace from its back side. The system also included a conventional metal vacuum chuck for comparison purposes. The experimental setup is illustrated schematically in Fig. 1.

The 0.5 μm-thick polycrystalline silicon layer was deposited on a standard isoplanar structure, obtained by local oxidation of the p-type <100> silicon substrate to 0.7 and 1.1 μm oxide thicknesses. As a stabilizing capping layer, use was made of CVD-deposited Si₃N₄ or thermally grown SiO₂ layers of various thicknesses. After the recrystallization step, the capping layers were removed and Secco etch (7) was used to reveal the grain boundaries.

Results

Effects of recrystallization at elevated substrate temperatures.—The main advantage of the recrystalliza-

*Electrochemical Society Active Member.

Key words: laser annealing, recrystallization, silicon on insulator.

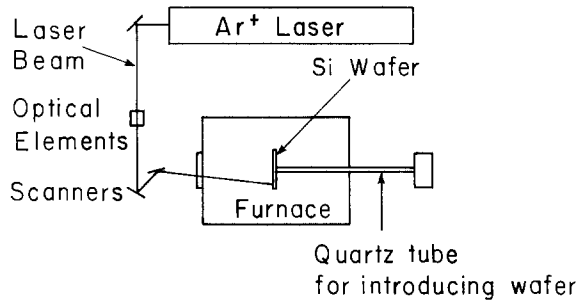


Fig. 1. The experimental setup

tion process at high substrate temperatures is in having a wider window of allowed laser power for good recrystallization both on the PO and PS regions. This can be seen in Fig. 2, where recrystallization was performed with substrate temperatures of 1000°C, 700°C, and 400°C using oxide capping. At low substrate temperature, catastrophic results were observed in the PO regions, while no recrystallization took place in PS regions. As the substrate temperature increased, the difference between the two regions was reduced. At 1000°C, similar results were obtained both in PO and PS regions.

The experimental conditions in Fig. 2d are identical to those of Fig. 2c, with the exception that the wafer was held by the metal chuck at 400°C. It is concluded that the wafer temperature is one of the dominant factors affecting the quality of recrystallization; the way the wafer is held has little influence.

The furnace temperature has also a profound effect on the width of the molten zone of a single laser scan with fixed velocity and power, as shown in Fig. 3.

The thermal gradients and their effect on the lateral epitaxial regrowth.—As was established in previous works (5, 8, 9), the direction of the grains' growth in the recrystallization process is identical to the thermal gradients in the trailing edge of the laser-induced molten zone.

The temperature profile is determined by the laser beam shape, its scan rate, and the thermal conductivity of the sample. Figures 4a and 4b represent typical recrystallization structures in PO regions for low power and scanning velocity and high power and velocity, respectively. The isothermals and the momentary solidification front can be easily traced starting at the top side of the scan and advancing to the bottom side, always at a right angle to the grain boundaries. The resulting profiles are also shown in Fig. 4.

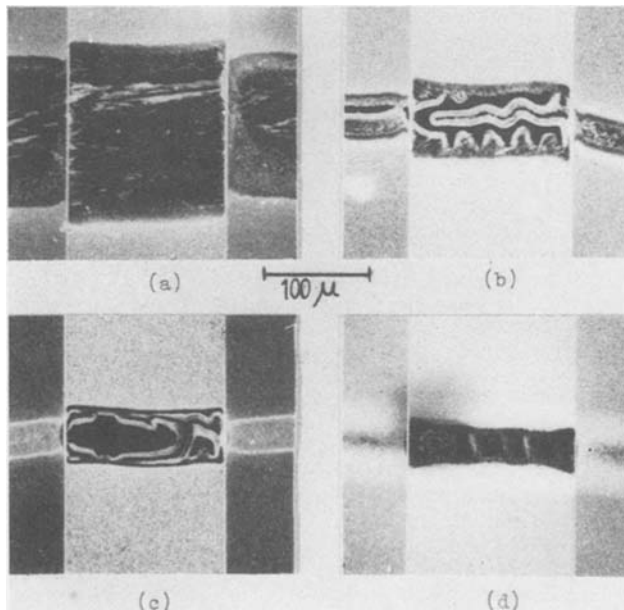


Fig. 2. Recrystallization at furnace temperature of: (a) 1000° (b) 700°, and (c) 400°C. In (d), the wafer is attached to a metal chuck at 400°C. Oxide thickness in PO regions is 1.1 μm. The PO is the center region.

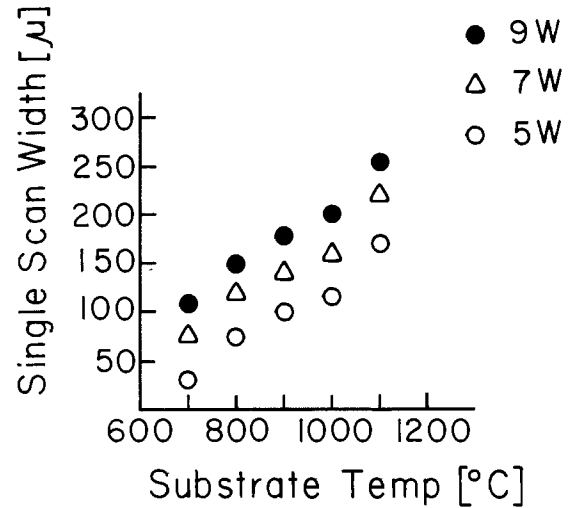


Fig. 3. The dependence of the single-scan molten zone width in the PS regions on the furnace temperature with laser power as a parameter. Scan velocity was 8 cm/s.

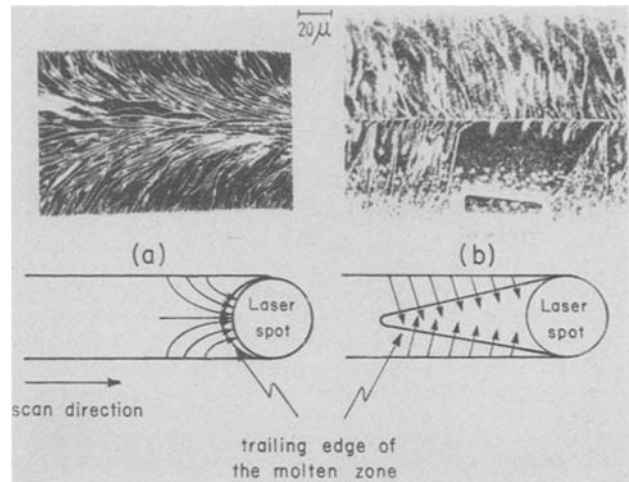


Fig. 4. The structure of the grain boundaries and the momentary solidification front in (a) low power and velocity recrystallization ($P = 4W$, $v = 8$ cm/s) and (b) high power and velocity conditions ($P = 12W$, $v = 80$ cm/s.)

For a given silicon on insulator structure, the substrate temperature and the absorbed heat density determine the cooling time of the layer from its maximal temperature to below the melting point. This cooling time multiplied by the scanning velocity equals the characteristic length of the molten zone behind the moving laser beam.

When this length is smaller than the beam radius, as in Fig. 4a, the profile of the trailing edge of the molten zone is similar to the beam shape, *i.e.*, circular for Gaussian beam. In the case when this length is much larger than the beam dimension, the trailing molten zone no longer follows the beam shape, as seen in Fig. 4b, and the thermal gradients are directed almost perpendicular to the scan direction.

A moving solidification front with a small radius of curvature is known to induce a higher density of defects and dislocations as compared to a flat front (5). This is reflected in the size of the epitaxial lateral distance. The gradient structure in Fig. 4b represents almost flat solidified front, while in Fig. 4a, this front is significantly more curved. The results consistently show more than 50 μm lateral single crystal in the high scan power and rate (Fig. 4b), as compared to less than 25 μm in the slow scanning conditions (Fig. 5). The central horizontal line in Fig. 4b is where the crystals growing from both sides do meet.

In the case of the high scanning velocities of 50-80 cm/s, the molten silicon area is so large that the situation is close, in a sense, to the situation of pulsed-laser recrystal-

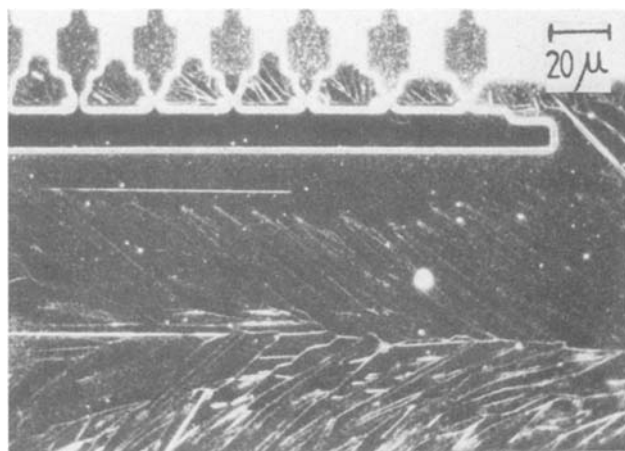


Fig. 5. The lateral epitaxial distance is limited by defect formation to less than $25 \mu\text{m}$ when the gradients are curved, and can be increased to more than $50 \mu\text{m}$ when the solidification front is almost flat (Fig. 4b).

lization. Under such conditions, the thermal gradients are strongly dependent on the layer configuration, *i.e.*, the layout of the PS and PO regions. The vertical thermal conduction is significantly higher in the PS than in PO regions, and thus the PS region is first to solidify, and the recrystallization propagates in all directions away from the PS into the PO region, as shown in Fig. 6.

Thermal effects in the PO-PS border.—Although it is not clear yet what are the exact mechanisms which restrict the lateral epitaxial distance (5, 10), it is agreed upon that moving from the PS into the PO region is a critical step which can introduce high defect density (11, 12). This is demonstrated in Fig. 2a and 7, where a discontinuity in the thermal profile near the interface between the PS and PO region is observed. Figure 8 represents schematically the changes in the maximal temperature along the scan axis shown in Fig. 7. These variations were repeatedly observed in different scanning conditions. In the PS side (regions b and f in Fig. 8), a decrease in the scan width is observed. This implies lower temperatures in these areas, as compared to regions farther away from the PO regions (a and g). This is explained by extra heat flow in the lateral direction to underneath the PO region where the substrate is relatively colder because of the insulating oxide layer. This phenomenon is slightly stronger where the beam passes from the PO to the PS (region f), probably because the lateral conduction of heat opposite the scanning direction is always more efficient. As a consequence of the heat flow from the PS regions, the temperature gradients across the oxide is smaller near the PO edge (regions c and e), and thus a lower cooling efficiency towards the substrate exists there. This, in turn,

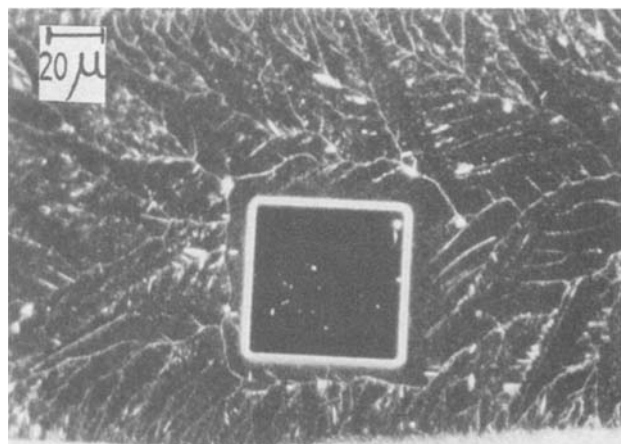


Fig. 6. The lateral epitaxial distance from PS islands in rapid scan and moderate power is less dependent on the scan direction and propagates up to $10 \mu\text{m}$ in the "reversed direction."

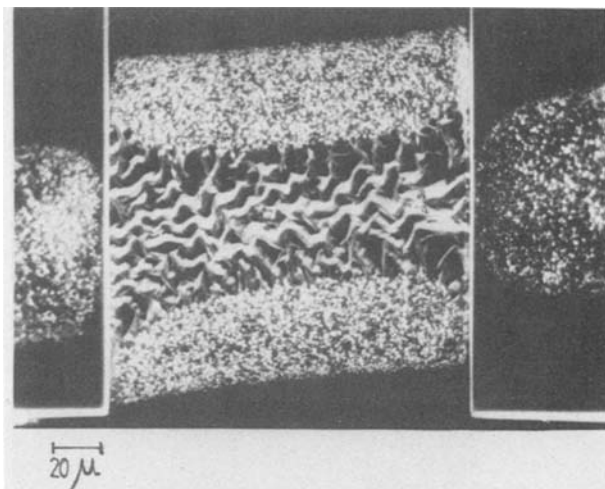


Fig. 7. Variation in the laser effect near the PS-PO interfaces. The PO is the center region.

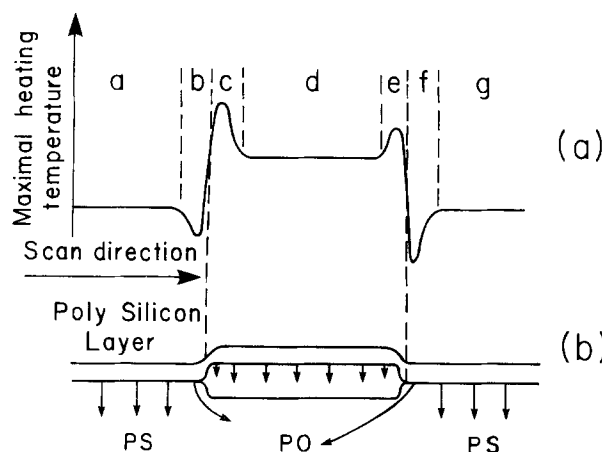


Fig. 8. The variation of the maximal temperature along the scan axis a), can be explained by heat flow to underneath the oxide layer, as shown by the arrows in (b).

leads to higher temperature of the layer which eventually broadens the melted-region width (Fig. 7) and may even cause a local damage in the recrystallized layer just as it starts to propagate into the PO region (Fig. 2a). These findings do not contradict the conclusions of Ohkura *et al.* (13), who claim that in regions b and f the temperature is higher than in regions a and g, since, as shown in Fig. 8, extremely close to the region c the temperature of region b might be still higher than in region a.

Discussion

It was shown that carrying out the lateral, laser-induced, recrystallization at elevated substrate temperatures around 1000°C reduces the thermal stresses significantly, as compared to $400^\circ\text{--}500^\circ\text{C}$ conventional hot-chuck systems. Holding the wafer during this process in a heated furnace implies that the Si wafer loses the absorbed laser power by blackbody radiation.

By means of high velocities and laser power, made possible by the high temperature conditions, certain control over thermal gradients was possible with a fixed-beam shape. An almost flat solidifying front was achieved, resulting in as far as $50 \mu\text{m}$ lateral epitaxy in a single scan. The higher scan rate and the obtained wider molten zone imply also much shorter processing time, as compared to the conventional approach.

Under such recrystallization conditions, lateral seeded epitaxy is observed also when the laser beam moves from the PO to the PS region. The mechanism of the lateral recrystallization in this case is believed to be the same as the "bridging epitaxy" observed in pulsed-laser annealing (14, 15). The lateral bridging obtained is $7\text{--}10 \mu\text{m}$ as compared to only $1.2\text{--}2.5 \mu\text{m}$ previously reported. This im-

proved result is again associated with the high temperature conditions. Another significant advantage of the high substrate temperature is the increase in the laser power window of proper recrystallization both on PS and PO areas.

Finally, it was pointed out that an undesired increase in the thermal discontinuity exists near the oxide edge. This was attributed to lateral heat flow to underneath the oxide. Minimal step in the polysilicon layer structure by silicon etching before the local oxidation step (5) can probably decrease this phenomenon.

In conclusion, it was shown that performing the CW laser-induced lateral recrystallization at elevated substrate temperature can have an important advantage in overcoming some of the technological problems connected with thermal stresses. The high temperature conditions enable also higher area coverage velocities and might lead to larger and better quality epitaxial silicon on insulator structures.

Acknowledgment

The authors would like to thank D. Polotzky, I. Pinsky, and D. Schlossberg, for their valuable help in the construction of the experimental setup and in sample preparation.

Manuscript submitted July 8, 1983; revised manuscript received Oct. 25, 1983.

REFERENCES

1. J. F. Gibbons, K. F. Lee, F. C. Wu, and G. E. J. Eggermont, *IEEE Electron. Devices Lett.*, **ed1-3**, 191 (1982).
2. J. F. Gibbons and K. F. Lee, *ibid.*, **ed1-1**, 117 (1980).
3. A. Gat, L. Gertzberg, J. F. Gibbons, T. J. Magee, J. Peng, and J. D. Hong, *Appl. Phys. Lett.*, **33**, 775 (1978).
4. J. Sakurai, S. Kawamura, H. Mori, and M. Nakano, *Jpn. J. Appl. Phys.*, **20**, L176 (1981).
5. H. W. Lam, R. F. Pinizzotto, and A. F. Tasch, *This Journal*, **128**, 1981 (1981).
6. T. O. Sedgwick, R. H. Geiss, S. W. Depp, V. E. Hanchett, B. G. Huth, and V. Graf, *ibid.*, **129**, 2802, (1982).
7. A. Secco d'Aragona, *ibid.*, **119**, 948 (1972).
8. S. Kawamura, J. Sakurai, M. Nakano, and M. Takagi, *Appl. Phys. Lett.*, **39**, 394 (1982).
9. T. J. Stultz and J. F. Gibbons, *ibid.*, **39**, 498 (1981).
10. G. K. Celler, L. E. Trimble, K. K. Ng, H. J. Leamy, and H. Baumgart, *ibid.*, **40**, 1043 (1982).
11. M. Miyao, M. Ohkura, I. Takemoto, M. Tamura, and T. Tokuyama, *ibid.*, **41**, 59 (1982).
12. T. I. Kamins, T. R. Cass, C. J. Dell'Oca, K. F. Lee, R. F. W. Pease, and J. F. Gibbons, *This Journal*, **128**, 1151 (1981).
13. M. Ohkura, M. Ichikawa, M. Miyao, and T. Tokuyama, *Appl. Phys. Lett.*, **41**, 1089 (1982).
14. M. Tamura, H. Tamura, and T. Tokuyama, *Jpn. J. Appl. Phys.*, **19**, L23 (1980).
15. M. Tamura, M. Ohkura, and T. Tokuyama, *Jpn. J. Appl. Phys., Suppl.*, **21-1**, 193 (1982).

Cleaning of Si and GaAs Crystal Surfaces by Ion Bombardment in the 50-1500 eV Range

Influence of Bombarding Energy and Sample Temperature on Damage and Incorporation

P. Rabinzohn and G. Gautherin

Institut d'Electronique Fondamentale, Université Paris XI, 91405 Orsay-Cédex, France

B. Agius* and C. Cohen

Groupe de Physique des Solides, ENS, Université Paris VII, 75221 Paris-Cédex 05, France

ABSTRACT

Silicon and gallium arsenide single crystals were cleaned in high vacuum by very low energy ion bombardment. High currents (up to 1 mA/cm²) were produced by a triplasmatron source down to energies of 50 eV. *In situ* Auger analyses showed that Si and GaAs clean surfaces are obtained at room temperature for bombarding energies as low as 70 and 50 eV, respectively. The incorporation of bombarding ions and the bombardment-induced disorder were studied *ex situ* by Rutherford backscattering and channeling. For silicon, the incorporation (Ar or Xe) increases linearly with bombarding energy while the Auger signal saturates above 200 eV. This result indicates that at high energies, ions are incorporated at greater depths than the sampling depth of the Auger technique. For GaAs, ion incorporation takes place only above 200 eV. The bombardment-induced disorder increases with the bombarding energy. Above 200 eV, a strong correlation was observed between incorporation and disorder, demonstrating that the latter was stabilized by the incorporated ions. However, at very low energies, a significant disorder remains (10¹⁶ and 5 × 10¹⁵ atom/cm², for Si and GaAs, respectively) for a very small concentration of incorporated ions, indicating the presence of "intrinsic disorder" related to the sputtering mechanism. No influence of the beam current on bombardment-induced incorporation or disorder was detected. For silicon, at very low bombarding energies, the disorder increases with the sample temperature during bombardment, with a noticeable effect already observed at 100°C. This is due to bombardment-enhanced diffusion of the ions and associated damage stabilization. At higher bombarding energies, no temperature dependence was observed because the range of bombarding ions was greater than the diffusion length.

In the preparation of semiconductor devices, the nature of surfaces has been a long standing concern. It is well known today that high quality devices are obtained only from clean and undamaged surfaces. For instance, the production of low resistance ohmic contacts or of high quality and reproducible Schottky diode characteristics (1) is directly related to obtaining such surfaces. But the ease in achieving such a perfect surface depends, of course, on its chemical reactivity, which is very high for

* Electrochemical Society Active Member.

Key words: semiconductor, surfaces, crystallography, sputtering.

most semiconductors. Consequently, the presence of undesirable surface impurities is hard to avoid.

Of all the possible methods of semiconductor surface preparation, chemical etching is most generally used. During or just after this chemical treatment, an inhomogeneous oxide layer is formed. In addition to oxygen, the major impurity was found to be carbon. Other trace elements such as Cl, Br, N, and S may be observed. This latter contamination depends on the etching solution used to remove the native oxide. Many studies have been carried out, on silicon or gallium arsenide, germanium, gallium phosphide, and indium phosphide (2, 3).

An obvious way to be free of the atmospheric native oxide is to proceed under vacuum conditions. One method to achieve a clean well-ordered surface consists of heating the substrate in UHV at a temperature high enough to evaporate the surface oxide, i.e., 1200°C for silicon (4), 550°C for gallium arsenide (5), 800°C for germanium, and 500°C for indium phosphide (3). Thermal desorption can be achieved through the use of a heated filament, by electron beam heating the back side, or by pulsed or continuous laser irradiation (6). Problems such as diffusion of impurities to and from the bulk or departure from stoichiometry in the case of compound semiconductors set limits to this method.

Another approach widely used today is physical sputtering and subsequent annealing. It consists of inert gas ion bombardment followed by heating at a temperature lower than that required for thermal decomposition of the oxide to expel the retained bombarding species and remove the damage induced in the surface region (7). Most studies center around residual ion damage and primary ion retention before and/or after annealing as a function of ion energy, sample temperature during sputtering, and current density. As shown by Sachse *et al.* (8) for Ar bombardment of Si {111}, the behavior of lattice damage and argon trapping as a function of annealing temperature is strongly dependent on the bombarding ion energy. The required annealing temperature was shown to increase with the sputtering ion energy in the range 0.5-2.5 keV. In the same way, Yamada *et al.* (9) pointed out that annealing of Si {100} is achieved at 720°C when the Ar ion energy is less than 1.5 keV. Moreover, Ne and Kr bombardment necessitate lower annealing temperatures than Ar. For 150 eV Ar ion energy from a RF triode arrangement, Koch *et al.* (10) find that an annealing treatment at 600°C for 20 min is sufficient to remove the ion damage for Si. Bean *et al.* (11) have investigated the effect of varying the sample temperature from 25° to 800°C during sputtering of {100} and {111} silicon surfaces with 1 keV Ar⁺ ions. They have studied Ar retention with the help of both AES (Auger electron spectroscopy) and ⁴He⁺ RBS (Rutherford backscattering spectrometry). For as-bombarded samples, the Ar Auger signal decreases when the temperature during sputtering is increased. At the same time RHEED (reflection high energy electron diffraction) patterns show an increasing degree of surface order. However, when AES and RHEED show a fully ordered and Ar-free topmost surface region resulting from 800°C sputtering, ⁴He⁺ RBS and channeling give evidence of disorder and Ar capture. The argon content increases from 1.4×10^{14} to 1.5×10^{15} atoms/cm² when the temperature during sputtering goes from 150° to 800°C. Ar atoms extend approximately 500Å into the bulk for the latter temperature.

Many studies have also been carried out on the effects of ion sputtering on GaAs. The retention of primary ions and near surface stoichiometry have only been probed by AES (12-15). Reference (15) gives an exhaustive compilation of Auger data, in which the Ga over As peak to peak height ratios were used "in order to determine changes in the surface composition more accurately." The results show the formation of an As depleted near surface region for high current density *J* and low temperature *T* and a GaAs stoichiometric surface for low *J* and high *T*. Lower current densities and higher temperatures are required to obtain a stoichiometric surface when the ion energy is increased. Competition between thermal annealing and bombardment damage processes is involved to account for the order-disorder transition of the GaAs surface region (the 20Å probed by AES). These results seem to indicate different trends than those obtained by Bean (11) on the temperature effect of sputtering induced damage for Si. As stated before, the disorder and the implanted primary ions diffuse into the bulk when the temperature is increased and cannot be seen by AES. An important result of the preceding studies (12-15) is that, even at bombarding energies as low as 250 eV, the surface is not Ar-free at room temperature.

From this brief review we can conclude that the preparation of a well-ordered impurity-free surface requires a careful choice of the parameters involved. The aim is to minimize the defects and implanted ions introduced dur-

ing bombardment in order to avoid a too high temperature annealing treatment.

In the present work, we report results on surface cleaning of {100} Si and GaAs crystals by ion bombardment under high vacuum conditions. The near surface composition was checked both by Auger analysis in order to get information on the few topmost surface layers and by nuclear microanalysis to calibrate the Auger results and study deeper layers (on the 100-1000Å range). The surface disorder was studied by channeling. As shown by the literature mentioned above, damage and impurity incorporation usually decrease at low bombarding energy. However, the sputtering efficiency also decreases so that higher current densities are required to achieve proper cleaning in a reasonable time. In this work, we use a triplasmatron source which can produce very high current densities down to energies below 100 eV. We have performed a systematic study of the influence of ion species, ion energy, and ion current density on the damage, and the ion implantation induced by bombardment. Moreover, we determined the lowest energy limit for surface cleaning (for our experimental conditions). We have also studied the effect of substrate heating during bombardment as a function of ion energy. Due to the mobility of point defects and to extended defects nucleation probabilities, the damage induced, even at low ion energy, is expected to vary strongly with the bombardment temperature. The same holds for impurity incorporation which may be related to the mobility of impurity-defect associations. Our results give clear evidence for such dependencies.

Experimental

Apparatus and procedure.—The ultrahigh vacuum stainless steel experimental setup in which the cleaning procedure was carried out is shown in Fig. 1. It is divided into four separable chambers: a sample introduction lock with fast pumping capability, an *in situ* surface analysis chamber with a cylindrical mirror analyzer (CMA) Auger electron spectrometer to monitor the chemical cleanliness of the surface, and an interaction chamber located at the end of the ion gun which consists of a plasma source and a transport chamber. The analysis chamber had a base pressure of $8 \cdot 10^{-10}$ torr obtained with ion pumping. The interaction chamber was pumped to $5 \cdot 10^{-8}$ torr by a turbomolecular pump, then pumped down to less than 10^{-8} torr using a cryopump. A quadrupole mass analyzer was used to monitor residual gas analysis at each stage of the experiments.

The ion source used was of the triplasmatron type which was described elsewhere (16-18). Briefly, it consisted of a miniature duoplasmatron source used as a hot cathode for the auxiliary discharge which took place in the expansion cup located behind the anode of the duoplasmatron. In order to reach a high efficiency, the expansion cup was positively biased with respect to the anode. This source had the advantage that there was no back-diffusion towards the main discharge. Thus, the source parameters and operating conditions were reproducible since the filament was not affected and had a long lifetime. With help of a toroidal magnetic field, the charged and neutral species were separated from the expanding plasma. Neutrals and photons could be used or analyzed in the axis of the plasma source even though this was not undertaken for the present study. Ions and electrons were carried along the strength lines of the magnetic field and separated according to their charge sign when biasing the target. For the cleaning experiments, nonreactive gases were solely employed. The pressure in the interaction chamber was varied from 10^{-5} to 10^{-4} torr depending on the sample current called for: 20-1000 $\mu\text{A}/\text{cm}^2$. This current density can be reached for a bias voltage in the range 50-1500V. The circular section of the ion beam has an intensity distribution peaked at the center with a FWHM (full width at half maximum) of about 20 mm. Mass analysis of the ion beam showed that for Ar bombardment, less than 0.1% of the ionized species were unwanted ions: H₂O⁺, N₂⁺, CO₂⁺, O₂⁺, and the percentage of multi-ionized species did not exceed 0.5%. Energy analysis showed that the energy distribution was centered at

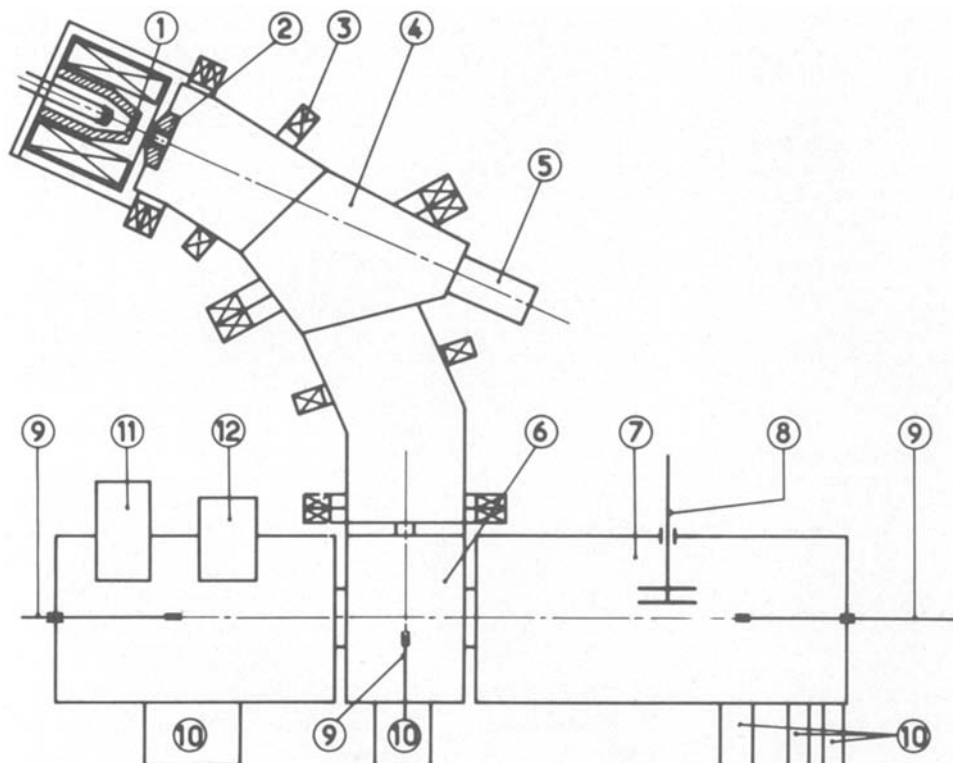


Fig. 1. Schematic representation of the experimental setup showing the triplasmatron source consisting of the duoplasmatron (1) and the expansion cup (2), induction coils (3) giving rise to the toroidal magnetic field in the transport chamber (4). The neutral species path (5) and the charged species-substrate interaction chamber (6) are also shown. The introduction lock chamber (7) with sample holders storage capabilities (8) and the analysis chamber with CMA Auger electrons analyzer (11), and a place reserved for LEED apparatus (12) complete the setup. Also represented are magnetic manipulators (9) and pumping facilities (10).

the bias voltage with a FWHM of 50 eV for Ar^+ and 35 eV for Kr^+ or Xe^+ .

In this study, the samples were {100} oriented p-type Si ($\sim 10^{17}$ - 10^{19} cm^{-3}) doped with B and {100} oriented n-type GaAs ($\sim 10^{18} \text{ cm}^{-3}$) doped with Si. After mechanochemical polishing, they were degreased in trichlorethylene, acetone, and methanol before being etched in HF or HCl solutions for Si or GaAs in order to remove the inhomogeneous oxide layer. Each cleaning stage was conducted in an ultrasonic bath. After being rinsed and dried, the samples were mounted with indium on a molybdenum platform smaller than the sample ($1 \times 1 \text{ cm}^2$) in order to avoid sputter deposition of the substrate holder onto the sample. The holder could be heated with halogen lamps up to 600°C . The temperature was monitored by a Chromel-Alumel thermocouple clamped in the molybdenum. The sample temperature was somewhat underestimated, however, no distinction between the sample and sample-holder temperature will be made in the text.

To check the surface cleanliness, the ion bombardment was stopped and the sample holder transferred into the analysis chamber. The Auger measurements proceeded under normal incidence conditions with an incident electron beam energy of 2 or 3 keV and $2 \mu\text{A}$ beam current provided from a 3 kV electron gun coaxial to the CMA. The beam diameter at the sample surface was about 0.3 mm. The modulation was 3V rms for all the peaks. The sweep rate was 0.1 V/s. The uncertainty in reading the peak position was estimated at $\pm 0.2 \text{ eV}$ for Si, C, and Ar and $\pm 0.3 \text{ eV}$ for O, As, and Ga.

In order to determine the surface disorder and the primary ion implantation, channeling combined with nuclear reaction analysis experiments was performed. For this purpose, the cleaned samples were removed from the "low energy ion" experimental setup and then analyzed with MeV beams obtained from the 2 MeV Van de Graaff accelerator of the Groupe de Physique des Solides de l'ENS. Rutherford backscattering in channeling geometry with $^4\text{He}^+$ ions was used to determine both the extent of lattice disorder and the primary ion concentration. The samples were mounted on a goniometer described previously (19). The energy distribution of the backscattered ions was measured using a 25 mm^2 silicon surface barrier detector with an overall energy resolution of approximately 12 keV FWHM. The detector was mounted on an arm which could be rotated around the chamber central

axis over a range corresponding to scattering angles between 90° and 170° , using an external control. For nuclear reaction analysis, the surface barrier detector was equipped with a Mylar absorber in order to stop the backscattered particles and analyze the nuclear reaction products. The goniometer was equipped with an XY table. Four samples could be placed on the sample holder. This allows one to simultaneously mount crystals and standard references for backscattering and nuclear reaction absolute calibration.

Data analysis.—Auger results.—Auger analyses were performed studying the two Ga and As peaks, and the Ar, Si, O, and C peaks. These peaks were readily identified from the literature. From Auger spectra, quantitative information on the change of the surface stoichiometry can be deduced only if the following conditions were satisfied: (i) the chemical composition of the surface does not change from one sputtering experiment to the other; (ii) the concentration of the elements studied remains constant all over the Auger electron escape depth; (iii) the Auger emission cross sections for all elements and transitions studied are known. Because of these limitations we used AES only as a highly qualitative and sensitive analytical tool to check the surface contamination. In some cases, ratios of peak heights (Ar/Si or As/Ga) were used in order to estimate changes in surface stoichiometry due to bombarding ion incorporation or to preferential sputtering.

Study by channeling of the heavy ion bombardment-induced damage.—The RBS spectra obtained from single crystals when the beam is aligned with a low index crystallographic axis (channeling geometry) exhibit a surface peak and a substrate background which is only a few percent of the one obtained in a "random" geometry. The surface peak, which corresponds to an overall number of atoms/ cm^2 (N_s) is due: (i) to ions backscattered from the very first atomic layers of the crystal (N_0), and (ii) to ions backscattered from atoms displaced from crystallographic sites near the top of the crystal (N_d). The first contribution which can be estimated accurately from Monte Carlo simulations on a perfect crystal (20) is dependent on the incident beam energy. For a given substrate, we have measured the surface peaks at various energies between 500 keV and 1.8 MeV and subtracted the predicted contribution N_0 for each energy. The quantity $N_s - N_0$ was found to be independent of incident beam en-

ergy. This proves that N_c is well estimated and hence that $N_d = N_s - N_c$ does represent the number of atoms displaced from crystallographic sites. In order to obtain the best estimate of N_d we have both to minimize N_c and the substrate background. Since N_c increases with beam energy, most experiments on silicon crystals were performed with low energy beams (500 keV $^4\text{He}^+$). In order to reduce the background/peak ratio, the experiments on silicon were performed by detecting the particles backscattered at grazing angles ($\theta_{\text{lab}} = 110^\circ$ or 120°). This geometry enhances the counting for the surface peak (greater cross section) and lowers the background since the energy loss of the backscattered ions is enhanced. The background was subtracted by drawing a straight line between the minimum background level behind the peak and the top of the surface peak. This procedure was shown to be valid in Ref. (20) by Monte Carlo simulations.

In the case of GaAs, the situation is more complex due to the presence of two elements with a small mass difference. If only the overall amount Ga + As is needed, the experiment can be performed as for Si, at 500 keV and grazing emergence. On the contrary, if the ratio of $[\text{Ga}]/[\text{As}]$ is to be determined, the experiment has to be performed at high energy (≈ 1800 keV) and large θ_{lab} (165°) in order to improve the mass separation.

Typical spectra for Si and GaAs are shown in Fig. 2-4. We also show in the insert the result of the background subtraction performed using an on-line computer.

The absolute amount of Si or GaAs corresponding to the surface peak was obtained by comparison with standards (Ta deposits on light substrates) known with a precision better than 3% (21). The oxygen concentration was obtained by nuclear reaction analysis using the $^{16}\text{O}(d, p)^{17}\text{O}^*$ reaction at 830 keV in a channeling geometry, in order to minimize the counts due to nuclear reactions with the Si background atoms. Using ^{16}O standards (22), we measured a few 10^{15} ^{16}O atom/cm 2 on a Si crystal with a precision better than 3%.

Once the contribution of N_c was subtracted from the surface peak, the number of displaced cations N_d and of oxygen atoms could be compared. It was known in the case of {100} Si (20) that even for chemically polished samples, an excess of displaced Si with respect to the oxide stoichiometry SiO_2 is found. This excess, which can be attributed to reordering of the first atomic planes of the Si crystal, is of about $2-3 \times 10^{15}$ atom/cm 2 . In the case of GaAs, we found that, for a chemically polished sample, the GaAs excess with respect to the oxide stoichiometry $\text{Ga}_2\text{O}_3 + \text{As}_2\text{O}_3$ was less than 1×10^{15} atom/cm 2 . For samples cleaned by low energy ion bombardment, if the Si or GaAs excess with respect to the oxide stoichiometry was not greater than for a chemically polished sample, the total number of displaced atoms measured in a channeling experiment was only indicative of the upper limit of the disorder induced by the bombardment as (i) the latter had removed all the oxides as checked by the *in situ* Auger measurement and (ii) at least the overall disordered layer had been oxidized during the transfer to the channeling chamber. If, on the contrary, the displaced atom excess with respect to the oxide stoichiometry was significantly higher than the excess found for a chemically polished sample, then the number of displaced atoms measured in the channeling experiment represented exactly the total amount of bombardment-induced disorder: all the disordered layer was not oxidized during the transfer.

Results and Interpretation

Room temperature bombardment.—Silicon.—All the results presented here were obtained on {100} silicon. Measurements on {111} Si were in good agreement with the {100} case.

The cleanliness of the samples was checked *in situ* by Auger analysis which also showed us evidence of bombarding Ar implantation. We found that silicon could be cleaned, within AES sensitivity limits, for bombarding energies down to 70 eV. In our experimental conditions, a full cleaning could not be obtained with 50 eV ions after

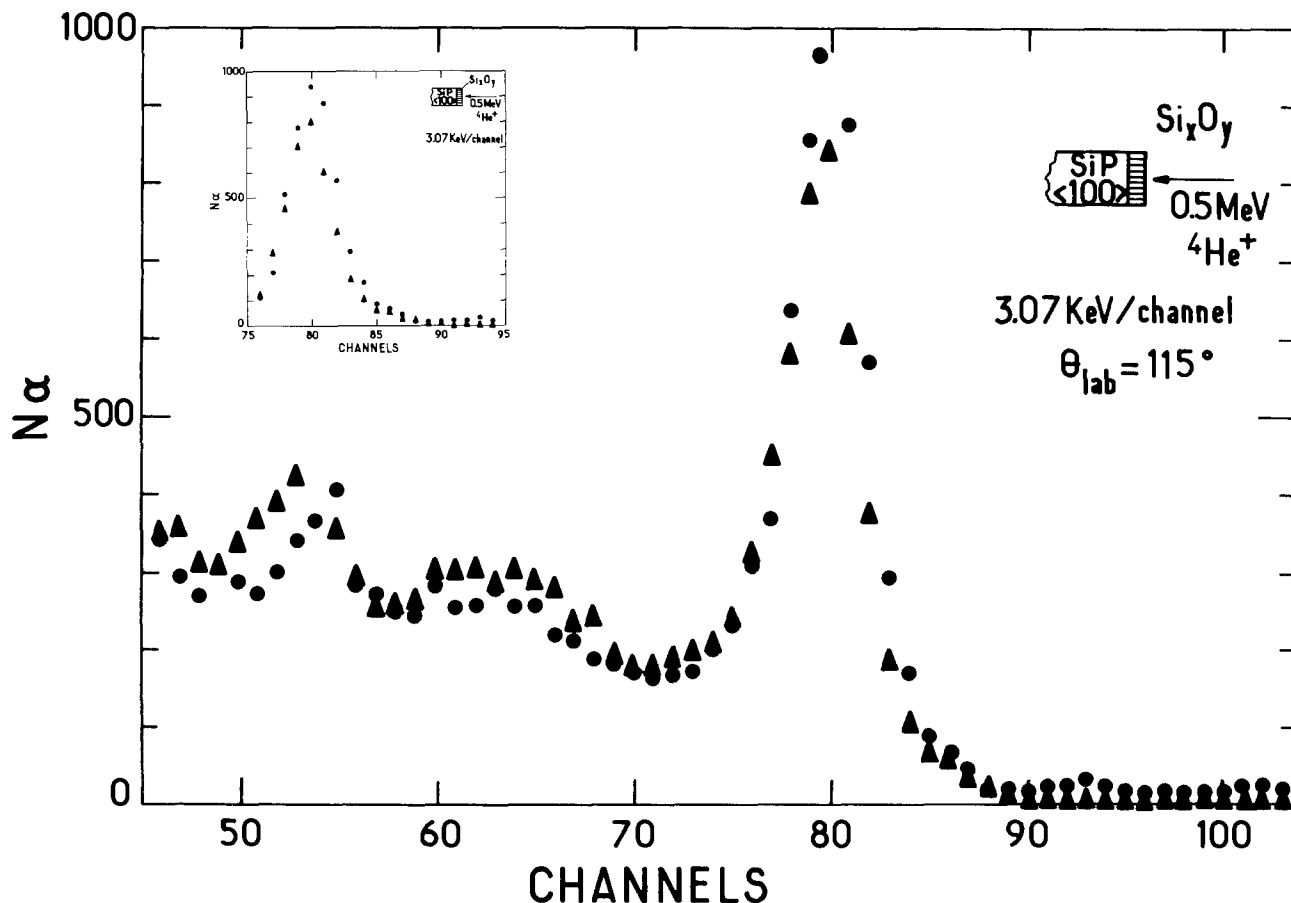


Fig. 2. [100] aligned RBS spectra on chemically polished (▲) and 100 eV Ar^+ -bombarded (●) Si samples. The surface peaks after background subtraction are shown in insert. The chemically polished sample is more oxidized but has less interface disorder than the Ar^+ -bombarded sample, yielding to an overall similar surface peak. The Ar bombardment was performed at room temperature with a 1 mA/cm 2 beam during 30 min.

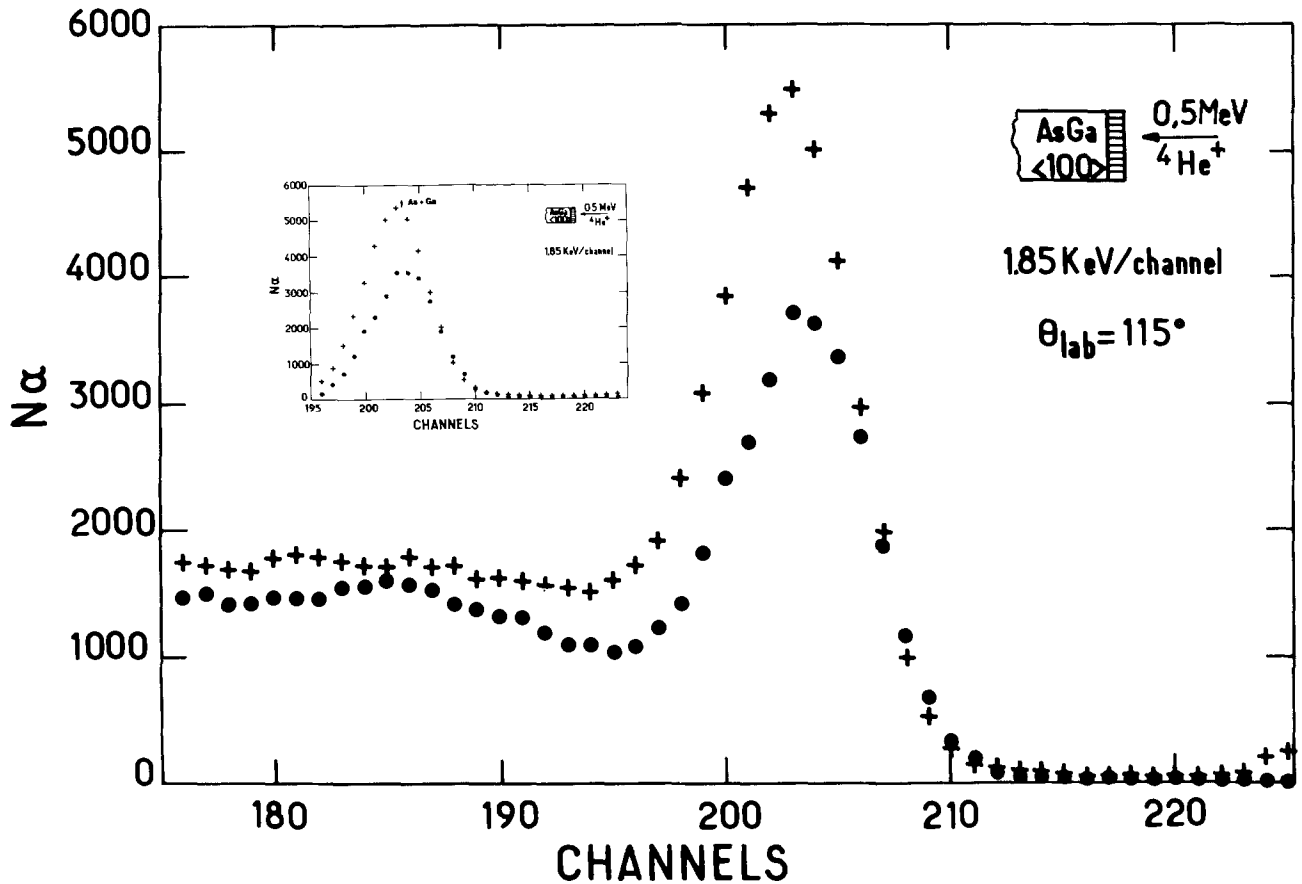


Fig. 3. [100] aligned RBS spectra on chemically polished (\bullet) and 100 eV Ar^+ -bombarded ($+$) GaAs samples. The experimental conditions (E and θ_{lab}) are chosen in order to minimize the background and to obtain the overall contribution of Ga and As atoms in a single surface peak (which is also shown in insert after background subtraction). The Ar^+ bombardment was performed at room temperature with a 1 mA/cm^2 beam during 15 min.

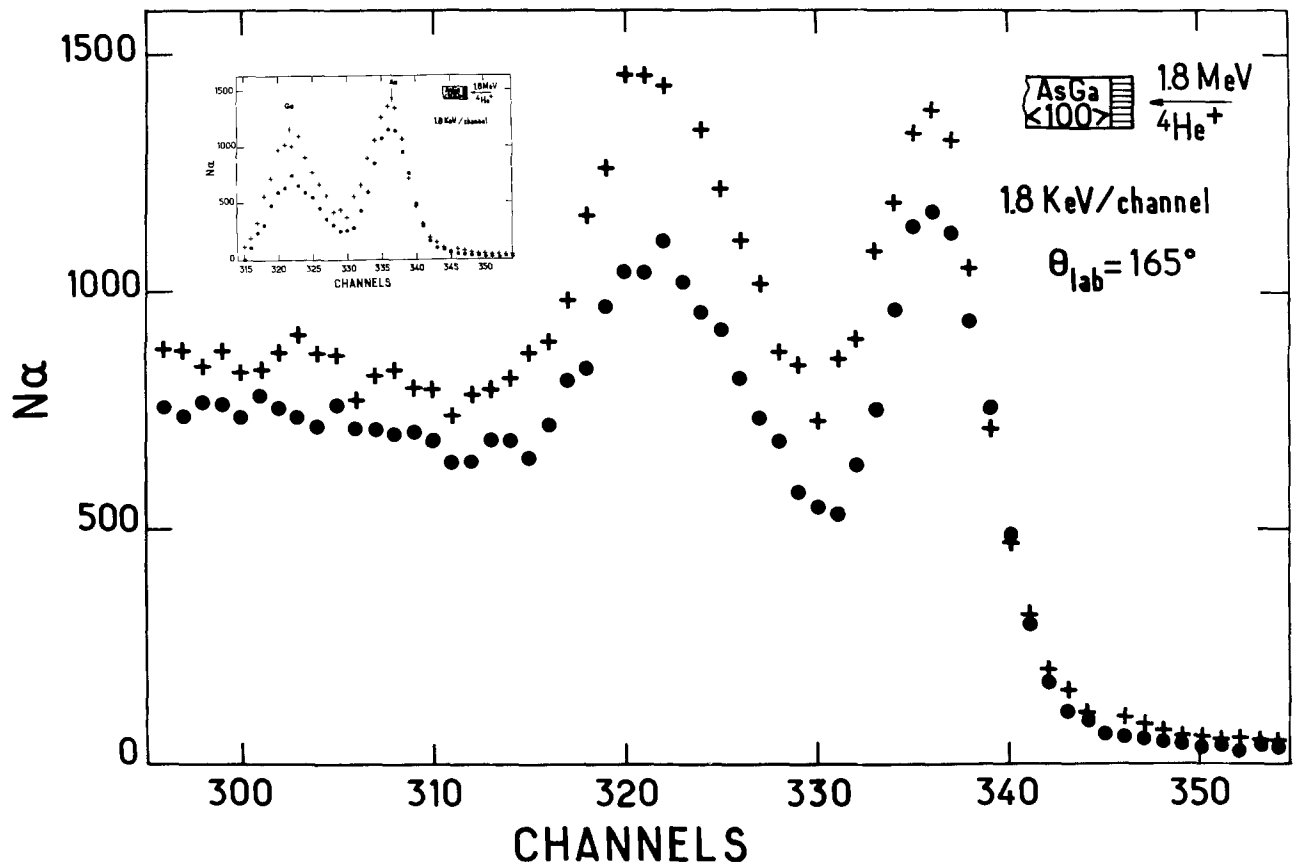


Fig. 4. [100] aligned spectra on the same GaAs samples as in Fig. 3. The experimental conditions (E and θ_{lab}) are chosen to obtain separate surface peaks for As and Ga (these peaks are also shown in insert after background subtraction) and reach the As/Ga ratio for displaced atoms.

hours of bombardment with a beam current density of 1 mA/cm². This could have been due to recontamination from the vacuum.

Influence of Bombardment Energy

Figure 5 compares the variation of the AES Ar signal normalized to the Si signal, and the Ar incorporation measured by RBS as a function of Ar bombarding energy. While the AES signal exhibits a maximum around 200 eV, the Ar incorporation increases linearly with bombarding energy. These results demonstrate that above 200 eV, most of the Ar ions penetrate in the crystal at depths greater than the escape depth of the Auger electrons, *i.e.*, about 10 Å for Ar in Si. The incorporation was measured for the minimum bombarding dose leading to full cleaning; the slope corresponds to $\sim 1.7 \times 10^{14}$ Ar · cm⁻²/100 eV. For instance, at 70 eV, 1.3×10^{14} Ar · cm⁻² were incorporated. For samples bombarded with Xe ions, the RBS analysis also shows a linear increase in the Xe concentration as a function of ion bombarding energy. However, the slope is smaller than for Ar: 0.6×10^{14} Xe · cm⁻²/100 eV (see Fig. 5).

The bombardment-induced disorder was measured by channeling experiments as described previously. The oxygen content due to sample oxidation during transfer to the channeling chamber was always found around $5\text{--}6 \times 10^{15}$ atom · cm⁻². In all cases, the number of displaced Si atoms was significantly greater than the oxidized silicon, assuming the SiO₂ stoichiometry. The Si excess with respect to SiO₂ was always greater than the one observed on a chemically polished sample which was measured to be about 2.5×10^{15} atom · cm⁻² and was in good agreement with Ref. (20). Consequently, we can assume that, in our experiments, the overall displaced Si atoms, oxidized or not, represent precisely the disorder induced by the bombardment. This disorder (N_d) is represented as a function of bombarding energy in Fig. 6. These results correspond of Ne, Ar, and Xe bombardments. In all cases, a strong dependence on bombarding energy was observed. For all the ions, the disorder increased linearly with ion energy

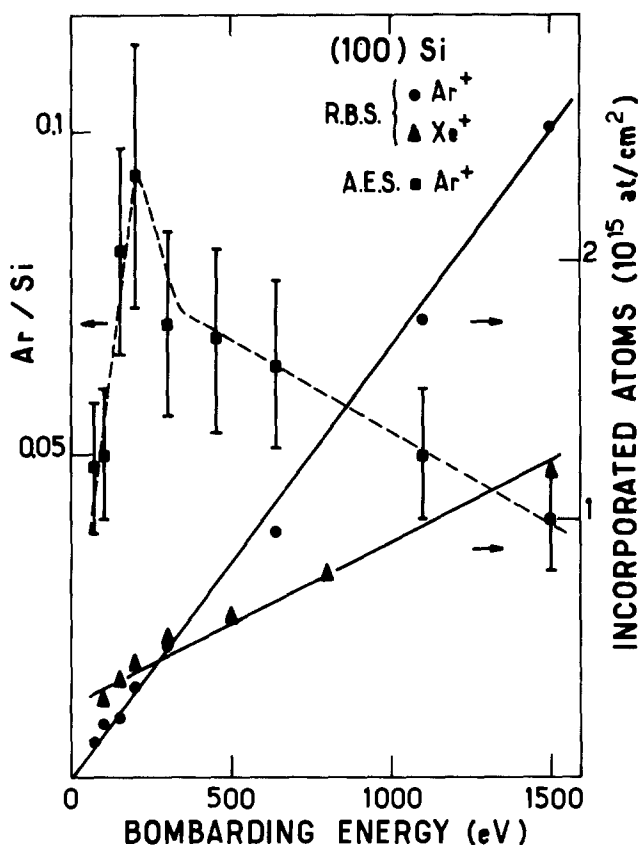


Fig. 5. Comparison of the Ar and Xe incorporation in Si, as a function of bombarding energy, measured in RBS experiments, with the Ar/Si ratio obtained from Auger spectra: room temperature bombardments at 1 mA/cm².

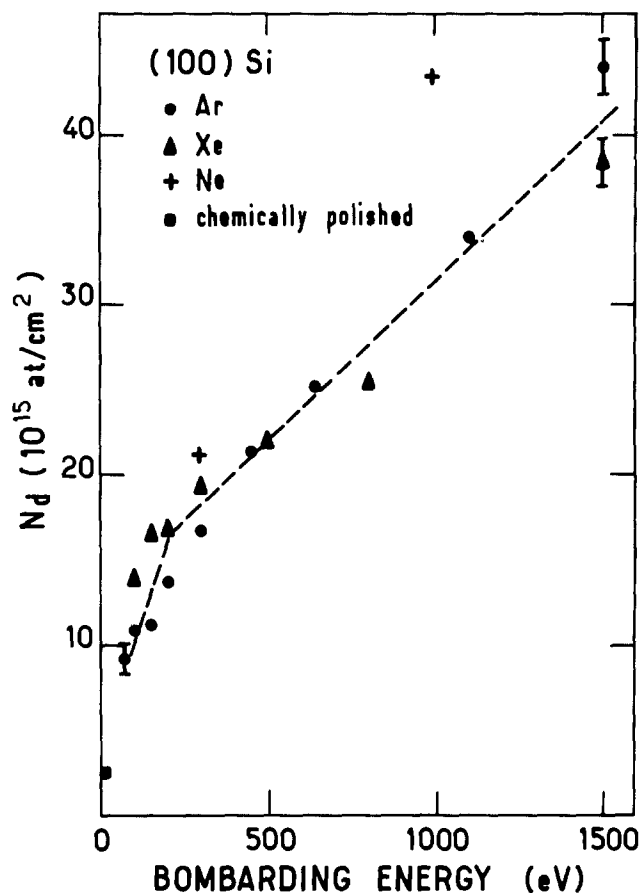


Fig. 6. Overall bombardment-induced disorder in Si with Ne, Ar, and Xe ions, as a function of bombarding energy. Room temperature bombardments at 1 mA/cm². The point corresponding to the chemically polished samples (■) represents the disorder after subtraction of the oxide (SiO₂) contribution.

in the range 200–1500 eV. However, the slope increased significantly for Ne ions. This may well have been due to the fact that, at a given energy, light ions have a greater range and can hence induce disorder over greater depths. Below 200 eV, the damage decreased more rapidly with decreasing energy. It reaches about $8 \cdot 10^{15}$ atom · cm⁻² for Ar at 100 eV. The value corresponding to the disorder at the silicon-silicon dioxide interface for a classically chemically polished sample is also reported in Fig. 6.

From the above results, it appears clear that when the bombarding energy is increased, both the disorder and the ion incorporation increase. Unfortunately, it was not possible to check the Ne incorporation either by Auger or RBS experiments. We have reported in Fig. 7 the ratio of disorder to incorporated atoms as a function of bombarding energy. This ratio is quasi constant above 500 eV, indicating that the disorder may well be stabilized by the incorporated ions. However, at lower energies, the ratio increases markedly indicating the presence of some "intrinsic" disorder not directly connected to bombarding ion incorporation. As a matter of fact, the presence of such a disorder is closely related to the mechanisms of very low energy sputtering. The fact that atoms can be expelled with some efficiency in this energy domain implies some assumptions about the dissipation of the very locally deposited energy. A simple collisional description appears insufficient and "nonlinear" effects must be considered, leading to enhanced sputtering and related disorder formation.

It is of interest to compare our results to those obtained by Yamada *et al.* (9). These authors have also studied in the case of {100} Si the influence of bombarding energy and ion species. The two main differences are: (i) the energy domain explored (1.5 to 4 keV in their case) and (ii) the bombardment dose. Since these authors have carried out an UHV thermal cleaning followed by the adsorption of an oxygen monolayer which had to be sputtered, only 300 μC doses were needed. In our case, we had to remove

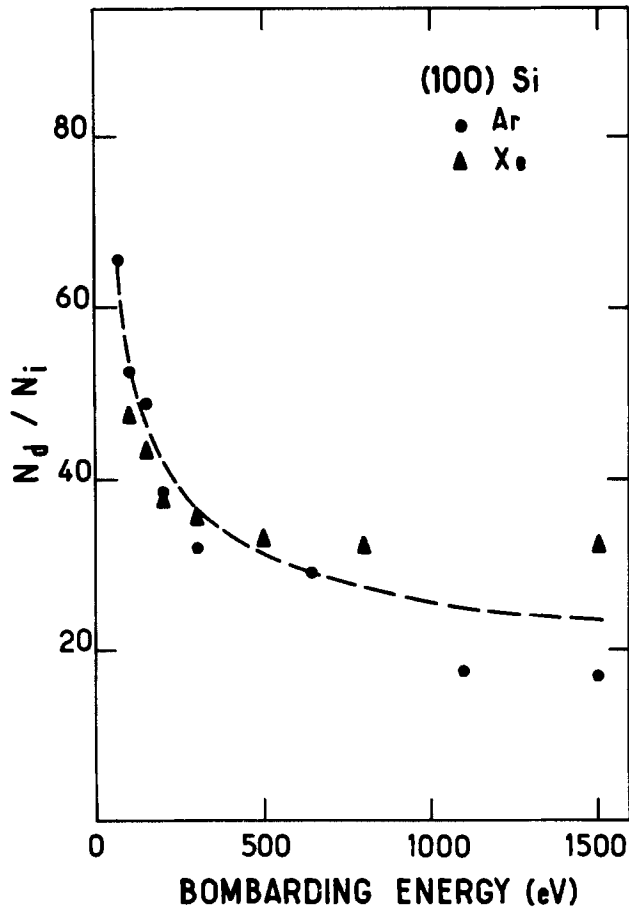


Fig. 7. Ratio of the number of displaced Si atoms to the incorporated bombarding ions (Ar or Xe) as a function of bombarding energy. Room temperature bombardments at 1 mA/cm^2 .

a native oxide with carbon contamination, and so in the same energy range (about 1.5 keV) the doses needed were 50 times higher. Of course, much higher doses were needed for lower bombardment energies. For instance, at 100 eV under 1 mA/cm^2 current density, the dose used in our experiment was about $1.5 \times 10^6 \mu\text{C}$, i.e., nearly four orders of magnitude above the dose used by Yamada *et al.* For bombardment at 4 keV, Yamada *et al.* found a strong increase of the disorder with the ion mass that saturates for masses heavier than 40. This is in contrast with our results below 1 keV, where Ne induces more disorder than heavier ions. For Ar bombardment Yamada *et al.* find, as in our experiment, a linear increase of disorder with bombarding energy. However, the slope of the curve (about 5×10^{15} displaced atoms per keV) is three times smaller than ours. This difference is certainly due to the very low dose used by Yamada *et al.* with respect to this work. It is interesting to notice that, at the same bombarding energy (1.5 keV Ar^+), the disorder induced in our case is about three times greater than in Ref. (9), for a bombarding dose fifty times higher. This result indicates that the damage saturates with bombarding dose. Yamada *et al.* have certainly not reached this steady state while we very likely have. A recent RBS study (24) of 4 keV Ar ion bombardment damage of semiconducting materials supports this statement. This is also confirmed by the fact that we induce, for 100 eV bombardment, a disorder 1.5 smaller than Yamada *et al.* at 1.5 keV, with a bombarding dose about $5 \cdot 10^3$ higher.

Influence of the Beam Current

Ar and Xe bombardments have been undertaken at 100 eV for various current densities between 20 and $1000 \mu\text{A/cm}^2$. At all current densities the bombardments were carried out up to full cleaning. The beam dose required to obtain this result was found to be current density independent, in all cases around 1.5 Cb. Moreover, the disorder induced and the bombarding ion incorporation were also found to be independent of the beam current density.

Gallium arsenide.—The samples were sputtered in the same way as Si.

Auger Results

The minimum energy at which a cleaning can be achieved was found, in our experimental conditions, to be 50 eV with Ar ions, i.e., somewhat smaller than for the silicon case (70 eV). The *in situ* Auger analysis after cleaning reveals that no argon incorporation is detectable below 200 eV bombardment energy (Fig. 8). This is in contrast to the silicon case where argon was detected at all bombardment energies. At energies higher than 200 eV, argon is detected. The Ar/Ga ratio is nearly constant between 300 and 600 eV and decreases for higher bombardment energies. This probably indicates that Ar penetrates to depths greater than the path length of Auger electrons. As Ga and As are heavier than Ar, the Ar incorporation was not measurable by RBS. The Auger spectra also give information about the near surface stoichiometry of the clean samples. This is illustrated in Fig. 9 where the ratio of the Ga and As peaks corresponding to the LMM high energy transitions is reported as a function of bombarding energy. This ratio increases significantly when the bombarding energy increases from 50 to 600 eV and then saturates at a value around 1.85 which is in good agreement with the measured value of Ref. (15).

These results demonstrate that, for low energy bombardment, the very near surface stoichiometry changes with bombarding energy, indicating a preferential sputtering of As. The saturation of the ratio shows that above 600 eV the composition in the depth domain sensed by the Auger technique becomes independent of bombardment energy, which does not exclude stoichiometry modifications at greater depths. It appears from Fig. 9 that low energy Xe bombardments lead to similar results to that of Ar. Moreover, for the two energies for which Xe bombardment were performed (100 and 200 eV), RBS spectra did not show Xe incorporation.

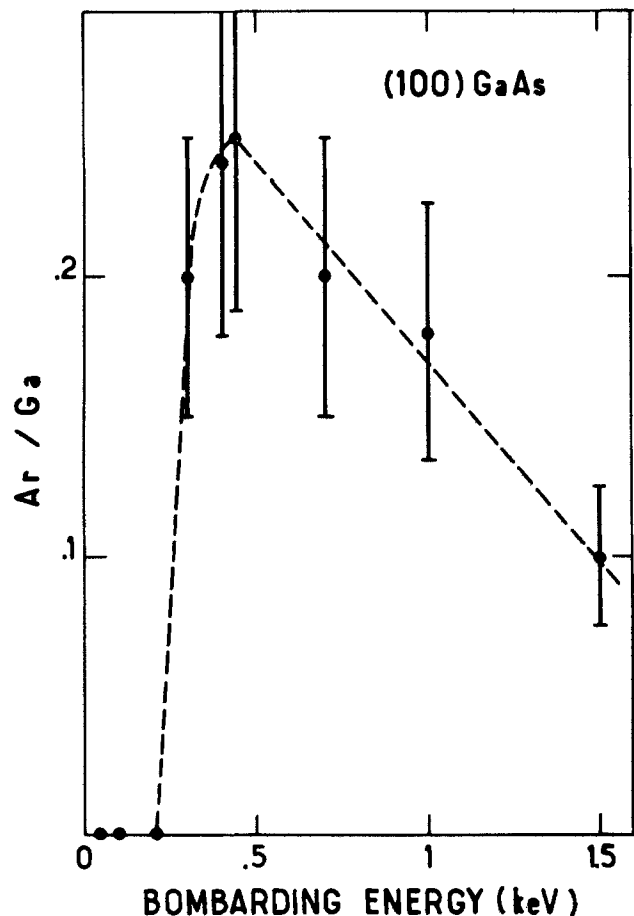


Fig. 8. Ratio of Ar and Ga signals corresponding to Auger spectra recorded on samples bombarded at various energies. Room temperature bombardments at 1 mA/cm^2 .

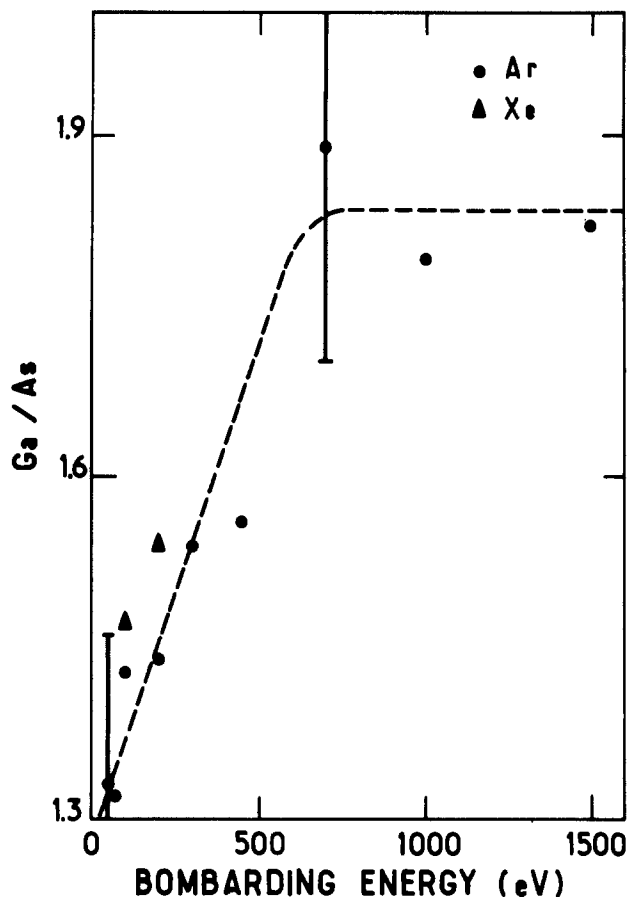


Fig. 9. Ga/As ratio obtained from Auger spectra as a function of bombarding energy (Ar and Xe ions). Room temperature bombardment at 1 mA/cm^2 .

Channeling Results

For all the bombarding energies used, the displaced Ga and As atoms (N_d) measured by surface analysis exceed the number of cations bonded to oxygen atoms, assuming $\text{Ga}_2\text{O}_3\text{-As}_2\text{O}_3$ stoichiometry for the native oxide. The minimum value of this excess, obtained for 50 eV bombardment energy, was about $2.5 \times 10^{15} \text{ atom} \cdot \text{cm}^{-2}$ while for a chemically polished sample, the excess is always smaller than $10^{15} \text{ atom} \cdot \text{cm}^{-2}$. We must hence assume, as for the silicon case, that all the atoms displaced by the bombardment have not been oxidized and that the quantity N_d represents the bombardment-induced disorder. This quantity is reported in Fig. 10 as a function of bombarding energy. Again, a quasi-linear dependence is observed. At 50 eV bombardment, the disorder corresponds to $5 \cdot 10^{15} \text{ atom} \cdot \text{cm}^{-2}$ while it is equal to $22 \times 10^{15} \text{ atom} \cdot \text{cm}^{-2}$ at 1500 eV . The slope is nearly two times smaller than for silicon. This may be due to the fact that the range of bombarding ions being smaller in GaAs than in Si for a given incoming ion, results in ion-induced disorder extending over a smaller range. Disorder is also observed at low energies where no ion incorporation was found.

Channeling experiments were performed with 1.8 MeV $^4\text{He}^+$ beams to distinguish between the displaced gallium and arsenic atoms (Fig. 4). We found in all cases that the ratio $N_{\text{Ga}}/N_{\text{As}}$ has a value between 1 and 1.1. Since the surface peaks represent from 5 to $22 \times 10^{15} \text{ atom} \cdot \text{cm}^{-2}$ depending on the bombarding energy, these results prove that the gallium excess with respect to the GaAs stoichiometry is not greater than about $10^{15} \text{ atom} \cdot \text{cm}^{-2}$. This result, when compared with the very strong departure from stoichiometry seen by Auger analysis, demonstrates that this departure concerns only the very shallow surface region sensed by the Auger technique. As the disorder, in particular at high bombarding energies, extends towards much greater depths, it appears that the correlation between overall disorder and departure from stoichiometry is poor.

Effect of the sample temperature during bombardment.—Silicon samples were heated in the range between

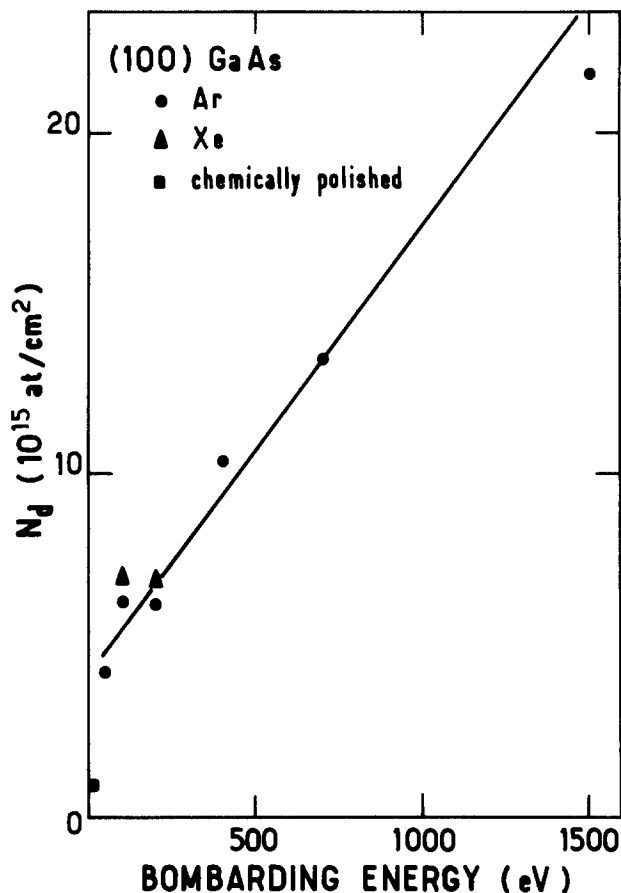


Fig. 10. Overall bombardment-induced disorder in GaAs with Ar and Xe ions as a function of bombarding energy. Room temperature bombardments at 1 mA/cm^2 . The point corresponding to the chemically polished sample (■) represents the disorder after subtraction of the oxide ($\text{Ga}_2\text{O}_3 - \text{As}_2\text{O}_3$).

27° and 550°C during argon bombardment. At 500°C , the effect of bombarding energy between 100 and 1500 eV was also studied. The *in situ* Auger analysis reveals a constantly decreasing normalized Ar signal from 27° to 400°C and no Ar peak above this temperature for a 100 eV bombarding energy (Fig. 11). On the contrary, the RBS analyses of the samples show that, for all bombarding energies, the ion incorporation is independent of the sample temperature during bombardment and is equal to the one found at room temperature. For instance, argon incorporation for 100 eV ion energy is reported in Fig. 11 as a function of the sample temperature. The comparison of Auger and RBS results clearly demonstrates that as soon as the sample is heated above 400°C the incorporated argon ions penetrate to depths greater than the Auger electron path length ($\sim 10 \text{ \AA}$) and do not desorb. These results, obtained for 100 eV bombarding energy are similar to those observed by Bean *et al.* (11) when sputtering with 1 keV ions.

The channeling analysis and oxygen content determination give us the following results: (i) The sample oxidation during the transfer to the channeling chamber is independent of the sample temperature during cleaning (oxygen content is always about $6 \cdot 10^{15} \text{ atom} \cdot \text{cm}^{-2}$). (ii) The number of displaced silicon atoms deduced from the channeling surface peak analysis is much greater than the oxidized silicon atoms and represents, therefore, the bombardment-induced damage. (iii) The temperature dependence of the damage varies with the bombarding energy. At low bombarding energies (100 eV) a very strong increase in the damage is observed when increasing the substrate temperature. As illustrated in Fig. 11, the increase in damage is about $10^{16} \text{ atoms} \cdot \text{cm}^{-2}$ between room temperature and 100°C . A trend towards damage saturation is observed at higher temperatures. Our interpretation of this result is the following. Damage is stabilized by low argon concentration all over the depths where argon diffuses. This diffusion is associated with the mobility of

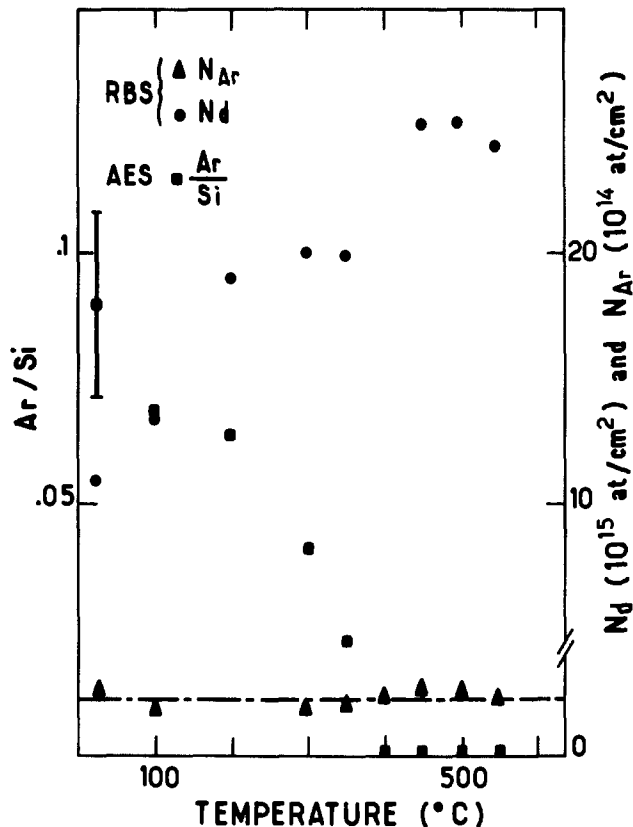


Fig. 11. Temperature dependence for Si samples bombarded with 100 eV Ar^+ and heated during bombardment of: the Ar/Si ratio from Auger spectra (■); the Ar incorporation measured by RBS (▲); and the overall bombardment-induced disorder (●).

the "intrinsic" bombardment-induced damage. It is interesting to note that this process takes place at 100°C. Our interpretation is supported by the study of the damage evolution with bombardment energy, at temperatures higher than room temperature. For instance, in Fig. 12 the variation in the damage, ΔN_{Si} , between 27° and 500°C as a function of bombarding energy is very high at low bombarding energy (19×10^{15} atom \cdot cm⁻² at 100 eV) and decreases rapidly with bombarding energy: at 1500 eV, $\Delta N_{Si} = 0$. This behavior indicates that argon-assisted diffusion takes place over great depths with respect to the perturbed layer corresponding to 100 eV room temperature bombardment, but smaller or of the order of the perturbed layer corresponding to room temperature bombardment at 1500 eV. This is consistent with the value of the damage measured at 100 eV and 500°C. This value (25×10^{15} atom \cdot cm⁻²) is much higher than the one found for 100 eV bombardment at room temperature (7×10^{15} atom \cdot cm⁻²), but significantly smaller than the damage measured for 1500 eV at room temperature (43×10^{15} atom \cdot cm⁻²). Roughly, we can estimate that the argon diffuses during bombardment on heated samples over lengths of the order of 50Å. If this value is great with respect to the implanted argon range (case of 100 eV bombardment), the damage is increased by sample heating. On the contrary, if this value is small with respect to the argon range (case of 1500 eV bombardment) the damage is independent of sample temperature.

We have verified that the effects described above are related to bombardment-enhanced argon diffusion and not to simple thermal diffusion. This is proven by the fact that if room temperature bombarded samples are post annealed up to 500°C, no variation of the bombardment-induced damage or of the argon incorporation is observed.

For higher post annealing temperatures, a full recovery is observed. For instance, when a sample cleaned by 100 eV Ar bombardment at room temperature is post annealed at 550°C, no argon incorporation is found in RBS experiments and the surface peak analysis in channeling shows that the excess between N_d and the oxidized silicon (assuming SiO_2) is equal to the one found for a chem-

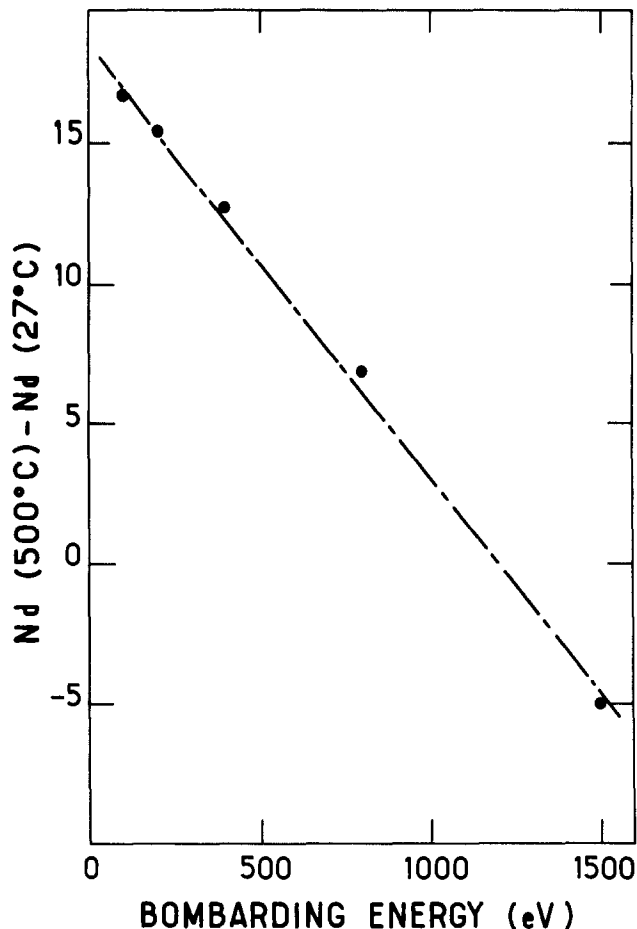


Fig. 12. Difference between the overall bombardment-induced disorders for 500°C and room temperature bombardments with Ar^+ ions (1 mA/cm^2), as a function of bombarding energy.

ically polished sample, i.e., about 2×10^{15} /cm². It must be pointed out that if the bombarding energy is increased, the post annealing temperature required for full recovery is higher [(720°C for bombarding energies around 1 keV as indicated in Ref. (9)]. Since impurity segregation towards the surface may take place above 600°C, it appears that the low temperature needed for recovery when low energy bombardment occurs should be favorable for surface electrical properties in device preparation.

We have also studied the influence of temperature during ion bombardment on GaAs. The experiments were performed at 100° and 200°C for 100 eV argon bombardment energy. No marked temperature dependence was observed for damage. This must be related to the fact that at 100 eV no argon incorporation was detected in GaAs, and, hence, the mechanisms described for the silicon case do not hold.

Summary

We have demonstrated that Si and GaAs crystals can be cleaned at room temperature by very low energy ion bombardment (below 100 eV), using a high intensity source. The bombardment-induced disorder, which does not depend markedly on the beam current, is significantly higher for low ion masses. However, the main effect is the very strong bombarding energy dependence of the disorder and of the bombarding ion incorporation. These two quantities are strongly correlated. When heating the sample during very low energy bombardment, the incorporated ions penetrate deeper into the sample and stabilize more damage. However, even though at very low energies the incorporation is small, some bombardment-induced damage is still present even for room temperature bombardment. This damage is, of course, very low as compared to that observed for standard bombarding conditions around 1 keV. For instance, near 100 eV, the maximum damage corresponds to 10^{16} and 5×10^{15} atom/cm² for Si and GaAs, respectively. Full surface recovery is only achieved by post annealing around 550°C for 20 min

for a Si sample cleaned by 100 eV Ar ions at room temperature. This treatment also removes the incorporated bombarding ions.

Acknowledgments

The authors wish to thank A. Chabrier for his technical assistance, particularly during sample preparation. This work was supported by the Centre National de la Recherche Scientifique (CNRS) under R.C.P. 157 and by the D.A.I.I.

Manuscript submitted July 8, 1983; revised manuscript received Nov. 3, 1983. This was Paper 364 presented at the Denver, Colorado, Meeting of the Society, Oct. 11-18, 1981.

REFERENCES

1. P. M. Lew and C. R. Helms, *J. Vac. Sci. Technol.*, **20**, 691 (1982).
2. T. Oda and T. Sugano, *Jpn. J. Appl. Phys.*, **15**, 1317 (1976).
3. R. H. Williams and I. T. McGovern, *Surf. Sci.*, **51**, 14 (1975).
4. J. M. Charig and D. K. Skinner, *ibid.*, **15**, 277 (1969).
5. G. Laurence, F. Simondet, and P. Saget, *Appl. Phys.*, **19**, 63 (1979).
6. D. M. Zehner, C. W. White, and C. W. Ownby, *Appl. Phys. Lett.*, **36**, 56 (1980); R. C. Rodway, A. G. Cullis, and H. C. Wabber, *Appl. Surf. Sci.*, **6**, 76 (1980).
7. H. E. Farnsworth, R. E. Schlier, T. H. George, and R. M. Burger, *J. Appl. Phys.*, **29**, 1150 (1958).

8. E. W. Sachse, W. E. Miller, and C. Gross, *Solid-State Electron.*, **18**, 431 (1975).
9. I. Yamada, D. Marton, and F. W. Saris, *Appl. Phys. Lett.*, **37**, 563 (1980).
10. F. B. Koch, R. L. Meek, and D. V. McCaughan, *This Journal*, **121**, 558 (1974).
11. J. C. Bean, G. E. Becker, P. M. Petroff, and T. E. Seidel, *J. Appl. Phys.*, **48**, 907 (1977).
12. G. E. McGuire, *Surf. Sci.*, **76**, 130 (1978).
13. A. Van Oostrom, *J. Vac. Sci. Technol.*, **13**, 224 (1976).
14. I. L. Singer, J. S. Murday, and J. Comas, *ibid.*, **18**, 161 (1981).
15. I. L. Singer, J. S. Murday, and L. R. Cooper, *Surf. Sci.*, **108**, 7 (1981).
16. J. Aubert, Ph.D. Thesis, University of Orsay (1972); *C. R. Acad. Sci., Ser. B*, **15**, 537 (1972).
17. J. Aubert, G. Gautherin, and C. Lejeune, in "Proceedings of the 8th International EMIS Conference," G. Anderson and G. Olmen, Editors, Skövde (1973).
18. G. Gautherin and C. Lejeune, *J. Phys. D*, **9**, 1149 (1976).
19. F. Abel, G. Amsel, M. Bruneaux, C. Cohen, and A. L'Hoir, *Phys. Rev. B*, **12**, 467 (1975).
20. L. C. Feldman, P. J. Silverman, and I. Stensgaard, *Nucl. Instrum. Methods*, **168**, 589 (1980).
21. S. Rigo, C. Cohen, A. L'Hoir, and E. Backelant, *ibid.*, **149**, 721 (1978).
22. G. Amsel, J. P. Nadai, C. Ortega, S. Rigo, and J. Siejka, *ibid.*, **149**, 705 (1978).
23. C. C. Chang, in "Characterization of Solid Surfaces," P. F. Kane and G. B. Larabee, Editors, Chap. 20, Plenum Press, New York (1974).
24. R. S. Williams, *Solid State Commun.*, **41**, 153 (1982).

An ^{18}O Study of the Oxidation Mechanism of Silicon in Dry Oxygen

F. Rochet, B. Agius,* and S. Rigo

Groupe de Physique des Solides de l'École Normale Supérieure, Université Paris 7, 75251 Paris Cedex 05, France

ABSTRACT

The mechanism of thermal oxidation of silicon in dry oxygen was studied using ^{18}O as a tracer. SiO_2 layers first grown in natural oxygen were grown further in ^{18}O -enriched oxygen ($^{18}\text{O}_2$) up to thicknesses ranging from 5 to 26 nm at 930°C . ^{18}O profiling was carried out using the nuclear reaction microanalysis. Fixed ^{18}O is found near the Si/ SiO_2 interface (^{18}O FNI) and near the external surface of the oxide (^{18}O FNES). In this work we studied: (i) the possible origins of ^{18}O fixation near the external surface of the oxide (^{18}O FNES) and (ii) the possible growth mechanisms of films of thicknesses ranging from 260 to 5 nm. It was shown that ^{18}O FNES does not seem to be due to some interfering phenomena (network oxygen exchange with water vapor traces or effects connected with the experimental procedure) and is not due to a growth mechanism by Si transport. A step-by-step motion of network oxygen atoms seems to be the more likely to explain ^{18}O FNES. The amount of ^{18}O FNES becomes more important as the original thickness of the film becomes smaller. Even for thicknesses under 20 nm we always found large amounts of ^{18}O fixed near the Si/ SiO_2 interface, which corresponds to growth by oxygen species migrating through the oxide network and without measurable interaction with it (very likely O_2 molecules for thick oxide samples). However for ~ 5 nm thickness films, the amounts of ^{18}O FNES can reach 50% and 80% of the total amount of ^{18}O at O_2 pressures equal to 10 torr and 10^{-1} torr, respectively.

In their well-known model, Deal and Grove (1) put forward two basic assumptions: (i) silica has an open structure allowing interstitial dissolution of atoms or molecules, and (ii) the oxidant is assumed to be molecular. This leads to linear kinetics followed by parabolic growth when diffusion across silica film becomes rate limiting, the corresponding constants being $k_L = kC^*/N_i$ and $k_p = 2D_{\text{eff}}C^*/N_i$, respectively, where C^* is the oxidant solubility, N_i the number of network oxygen atoms per volume unit, k the reaction rate at Si/ SiO_2 interface, and D_{eff} the effective diffusion coefficient. According to Mott (2), one must consider the solubility in "normal" interstitial sites where percolation paths can be opened, so that deep sites do not have any contribution to growth. Revesz and Schaeffer (3) wrote a paper devoted to the same subject using structural considerations. In the case of water vapor oxidation, the kinetics match well with the theory of Deal and Grove, but for dry oxygen oxidation this theory only applies for thicknesses greater than 20-30 nm. Using ^{18}O as a tracer, Rosencher *et al.* (4) have studied the oxygen transport across the film during thermal oxidation. SiO_2

layers first grown in natural oxygen (130-300 nm) were further grown in highly ^{18}O -enriched oxygen for 8.5h at 930°C . The resulting SiO_2 films consisted of two ^{18}O -rich zones, one containing about 7% of the ^{18}O near the SiO_2 surface, and another containing 93% near the Si/ SiO_2 interface, while the bulk ^{18}O concentration was very low (under 0.3%). This shows that for these thicknesses the oxide grows mainly by an interstitial transport of oxygen without reaction with the network, which favors a model based on the transport of molecular oxygen as proposed by Deal and Grove (1). The presence of a small amount of ^{18}O at the external surface, if not due to an interfering phenomenon, might indicate that the existence of another oxygen transport mechanism cannot be entirely rejected.

Kinetics studies for various oxygen pressures p_{O_2} show that: (i) k_p is proportional to p_{O_2} , thus favoring a molecular oxygen transport, and (ii) k_L is found to be proportional to p_{O_2} (1), $p_{\text{O}_2}^{0.6}$ (5, 6), $p_{\text{O}_2}^m$ with m varying from 0.59 to 0.83, as the temperature is varied from 700° to 1000°C for SiO_2 films grown on (111) substrates and with m varying from 0.54 to 0.66 in the temperature range 850° - 1000°C for oxide films grown on (100) substrates (7). The pressure dependence of k_L was interpreted by O_2 reacting with silicon, which leads after calculation to a p_{O_2} law (1), by a

* Electrochemical Society Active Member.

Key words: semiconductors, glass, growth, nuclear reactions.

reaction at the Si/SiO₂ interface involving the presence of both atomic and molecular oxygen, which leads to a $p_{O_2}^m$ law with m lying between 0.5 and 1 (7). Blanc (8, 9) proposed a similar mechanism where the reaction of oxygen atoms predominates. This leads to a $p_{O_2}^{0.5}$ law. Concerning high pressure oxidation (p_{O_2} lying between 1 and 20 atm), Lie *et al.* (10) have recently shown that if k_p is still proportional to p_{O_2} , k_L is proportional to $p_{O_2}^{0.7}$, in the temperature range of 800°-1000°C. Their analysis is based entirely on the Deal-Grove model; they point out that such a pressure dependence of k_L would imply a complex interface reaction mechanism or a contribution due to gas phase transport at the SiO₂/gas interface above 1 atm. Various values can be found for k_p and k_L in the literature. Activation energies are extracted: for k_p and k_L , respectively, Deal and Grove (1) found them equal to 1.2 and 1.8 eV in the temperature range 900°-1200°C, while Irene and Van der Meulen (11) found them equal to 2.2 and 1.5 eV in the temperature range 780°-980°C. More recently, Irene and Dong (12) found in the high temperature range (980°-1150°C) activation energies near to those found in Ref. (1); moreover, they showed that k_p and k_L do not follow an Arrhenius law. Irene (13) has shown that the curvature of the Arrhenius plots of k_L values is consistent with the parallel paths mechanism proposed by Ghez and Van der Meulen (7). One must keep in mind that the typical values of activation energies corresponding to O₂ diffusion, Si-Si, and O-O single bonding are 1.2, 1.8, and 1.5 eV, respectively.

One must also notice that few people (5, 14-16) started oxidation from a well-controlled surface free from native oxide and used during the process an oxygen ambient free from impurities that might have produced water vapor. As a matter of fact, the natural oxide layer remaining at the silicon surface before oxidation may create a source of contamination for the thermal oxide and water traces in the ambient greatly modify the kinetics. A 20% increase in overall rate with only 25 ppm of water vapor in the ambient was reported by Irene *et al.* (17). Hopper *et al.* (5), who worked in clean conditions, try to account for their kinetics assuming that growth is the sum of two mechanisms being both present, corresponding to two linear parabolic reactions, one prevailing at small thicknesses, the other at large ones, with one of the mechanism involving charged species. So they based their assumption on Jorgensen's work (18). Jorgensen succeeded in accelerating or retarding thermal growth because he had an electric current flowed through the oxide; he, therefore, concluded the presence of charged species. This latter work has been criticized by Raleigh (19), who explained Jorgensen's results by stating that an electrolysis due to electrons can induce the transport of charged species different from those involved in "classical" thermal oxidation. Mills and Kroger (20) proposed a transport mechanism involving interstitial O²⁻ as responsible for ionic conduction. This has been discussed by Mott (21), who puts forward the fact that the reaction $O_2 + 4e \rightleftharpoons 2 O^{2-}$ leads to a reaction rate proportional to $p_{O_2}^{0.5}$. Jorgensen considers it proportional to p_{O_2} (22). So, if the transport of oxygen species is generally proposed to explain the oxidation of silicon, Mott (21) examines the existence of silicon vacancies, this being supported by energetic considerations. For film thicknesses above 130 nm, the experiments of Rosencher *et al.* show that it cannot be the major phenomenon responsible for growth (4).

Kinetics for very thin films (thicknesses <20 nm) are generally obtained under low pressure and at low temperature conditions. Thus any comparison with thick oxide kinetics is difficult. Especially one must notice that oxidation rate of (111)-oriented silicon at low pressure is smaller than that of (100)-oriented silicon, contrary to what happens at high pressure ($p_{O_2} > 1$ atm) (23). As well, oxidations are often performed in O₂-inert gas mixtures at atmospheric pressure (6, 24); thus, the amount of water vapor relative to O₂ partial pressure may be not well defined and not so negligible. Considering all the experimental results, it is difficult now to conclude about the type of kinetics laws. Experimental results have been fitted by linear-parabolic (5, 25, 27) or inverse-logarithmic laws (6, 24, 26), although Irene thinks that the linear type is prevailing (27); he explains those rather linear kinetics

by the fact that pores could exist, so that O₂ could run through these pores and have rapid access to Si/SiO₂ interface. Using transmission electron microscopy (TEM), Gibson *et al.* (28) concluded in favor of the existence of micropores. Nevertheless, Revesz (29-30) assumed the existence of channels responsible for an extended transition region of the two regimes of oxidation. As the oxide film thickens, these channels become distorted and the oxidation rate decreases and becomes linear parabolic. Let us emphasize that for Revesz, the channels are intrinsic structural features of noncrystalline SiO₂ and not gross morphological defects. Hopper *et al.* (5) observed that the growth rate varies more rapidly in the thin thickness range (<20 nm) than in the larger one (>30 nm). Fargeix *et al.* (31) interpret the results of Hopper *et al.* considering that "the diffusion through the first hundred angstroms of the oxide layer (near the Si/SiO₂ interface) is slowed down." Previously, the existence of an "interface blocking layer with different transport properties than the bulk oxide" was proposed by Tiller (32).

For very thin films (1.5-6 nm) at 400°C, Fehlner asserts he obtained growth kinetics of inverse-logarithmic type (26) due, as a consequence, to a mechanism involving charged species known as the Cabrera-Mott mechanism (33). In this model, transport is controlled by a high electric field, the potential drop at the film boundaries remaining constant. Kamigaki and Itoh (6) have obtained kinetics which are consistent with such a mechanism in the 950°-1100°C domain and for a partial pressure equal to 10⁻³ atm. Derrien and Commandré (16) worked under ultrahigh vacuum conditions in the range of thicknesses 0-3 nm under low pressure oxygen ambient (from 10⁻⁴ to 10⁻² torr) with temperatures lying between 750° and 1050°C. Evaluating oxide thicknesses by Auger electron spectroscopy, they interpret the kinetics they obtain by a phenomenological model based on charged oxygen diffusion through the oxide layer under the presence of a surface electric field.

The aim of this paper is to present a study of the mechanisms of silicon thermal oxidation in dry oxygen, using ¹⁸O as a tracer.

Experimental Procedures

Thermal Treatments

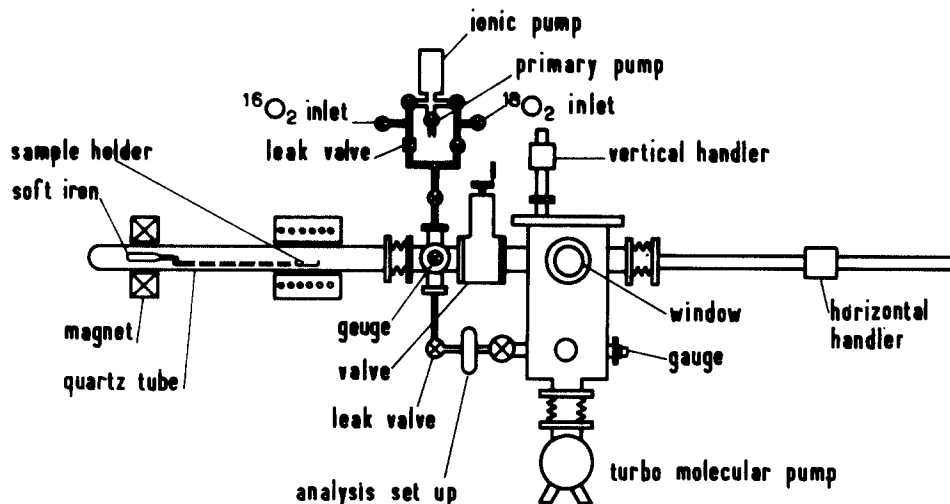
¹⁸O₂ oxidation.—Two kinds of thermal oxidation have been carried out.

Thick (>20 nm) oxide samples.—These samples were supplied by Laboratoire d'Electronique et de Technologie de l'Informatique of Grenoble. (100) oriented silicon wafers of resistivity 4-5 Ω cm were oxidized in a flow of dry natural oxygen to obtain oxide thicknesses between 50 and 260 nm, at atmospheric pressure and at temperatures ranging from 1000° to 1200°C. The 20 nm-thick oxides were grown in a natural O₂/N₂ mixture at 950°C.

Thin (<20 nm) oxide samples.—Oxide films were grown on (100)-oriented silicon wafers (resistivity 4-5 Ω cm), in dry natural oxygen in an ultrahigh vacuum technology (UHVT) furnace (Fig. 1) at 10 torr, 930°C for various durations. After cleaning, the Si substrates were annealed at 150°C under vacuum (10⁻⁹ torr). Then, they were pushed into the hot zone of the quartz tube and treated *in vacuo* (<10⁻⁸ torr) for about 1 min at 930°C. This is sufficient to eliminate the major part of water vapor adsorbed on the sample holders, but no examination of the surface cleanliness was available. This operation was necessary to stay in the realms of 3 ppm for water vapor traces during further oxidation treatments. The procedures for ¹⁸O₂ gas introduction and water vapor control, as well as the measured water traces contents, are identical to those of ¹⁸O₂ gas introduction described below. After growth in ¹⁸O₂, these samples were re-stored in the UHV chamber.

¹⁸O₂ oxidation.—All the ¹⁸O₂ treatments were performed at 930°C in the UHVT furnace (¹⁸O labeling guaranteed above 99%) by expanding ¹⁸O₂ in the 5 liter quartz tube. The ¹⁸O₂ gas previously passed through zeolites (degassed *in vacuo* at 200°C for 48h, which reduced the traces content of water. H₂¹⁸O partial pressure was measured by mass spectrometry using the classical trapping/desorption method in a quartz tube located before the spectrometer head. This was done in order to extract the signal

Fig. 1. Schematic drawing of the UHVT furnace used for thermal treatment in dry $^{18}\text{O}_2$ and $^{16}\text{O}_2$ gas.



corresponding to the water content of the oxidizing ambient from the background due to the continuous formation of water by hydrogenated species reacting with O_2 in the spectrometer head (34). H_2^{18}O partial pressure was never found above 3 ppm of the total pressure. In each experiment, the ^{18}O labeling of the gas was also measured by mass spectrometry.

Samples grown in $^{16}\text{O}_2$ outside the UHVT furnace.—As these samples were grown in $^{16}\text{O}_2$ ambient in a gas flow furnace different from our UHVT furnace, they are exposed to air between two thermal treatments. Thus, before any $^{18}\text{O}_2$ treatment they are introduced in the quartz tube hot zone *in vacuo* (10^{-8} torr) for about 1 min in order to eliminate water vapor adsorbed on the samples holders. One must also add that, if the $^{18}\text{O}_2$ treatments are performed at 930°C , the previous $^{16}\text{O}_2$ growth treatments were carried out at higher temperatures ($1000^\circ\text{--}1200^\circ\text{C}$). One cannot eliminate some "memory effect" on kinetics, as pointed out by Hamasaki (35), who investigated the oxidation kinetics of silicon using two-step oxidation at two different temperatures. He found that "in an initial stage of second oxidation the growth rate of the oxide is different from the oxide's equilibrium growth rate," and that "the difference in these growth rates is due to the difference in the linear growth rate of these two stages." However, we do not think that it might interfere greatly on location of the heavy isotope found near the external surface and near the Si/oxide interface. This is supported by results obtained with *in situ* addition of $^{18}\text{O}_2$ gas in an ambient as described further in the text.

Samples grown or regrown in $^{16}\text{O}_2$ in the UHVT furnace.—These samples (generally thin oxide samples) were introduced again in the hot zone without being exposed to air, which minimized pollutions and/or interfering phenomena due to such an exposure. As a consequence, no ^{16}O content measurement was available before ^{18}O treatments. In some cases, during the thermal treatment we added $^{18}\text{O}_2$ to the $^{16}\text{O}_2$ atmosphere, as the sample was left in the hot zone; this avoided thermal shock but introduced some decrease and evolution of the ^{18}O isotope concentration.

Data Analysis

^{16}O and ^{18}O amounts measurement.—The nuclear reactions $^{16}\text{O}(d,p)^{17}\text{O}^*$ and $^{18}\text{O}(p,\alpha)^{15}\text{N}$ induced by deuteron or proton beams from a 2 MeV Van De Graaff accelerator were used to measure the number of ^{16}O (N_{16}) and ^{18}O (N_{18}) atoms/cm² in the oxide layers (36). Absolute values of N_{16} and N_{18} were determined by comparison to standard references known to within $\pm 3\%$ (37), their relative precision was better than $\pm 1\%$. It is worthy to notice that the sensitivity of the $^{18}\text{O}(p,\alpha)^{15}\text{N}$ reaction is limited to $\sim 8 \cdot 10^{19}$ oxygen atoms/cm³ or $2 \cdot 10^{15}$ oxygen atoms/cm² by the natural abundance of the heavy isotope.

Equivalent ^{16}O and ^{18}O oxide thicknesses were calculated assuming an oxide density equal to that of SiO_2 , i.e., to $2 \cdot 21 (10^{15}$ oxygen atoms/cm²) corresponds to 0.226 nm). For oxide thicknesses lower than 20 nm, such equivalent

thickness was sometimes calculated, but one must keep in mind that departures from SiO_2 stoichiometry might occur (38).

^{18}O concentration-depth profiles.—The ^{18}O concentration depth profiles could be deduced from two different techniques: (i) analysis of the excitation curves of the $^{16}\text{O}(p,\alpha)^{15}\text{N}$ reaction near the 2 keV-wide 629 keV resonance (39), or (ii) step-by-step dissolution combined with nuclear microanalysis.

In the latter procedure, each studied wafer was cut into several pieces, one being kept without being chemically etched, the others being immersed in dilute HF (3% volume in H_2O) for various times. On each piece, the amounts of ^{16}O and ^{18}O were obtained from the nuclear reactions. Such a procedure was necessary when knowing that the particles beam can induce structural modifications (and as a consequence, spatial variations of the dissolution rate) in the impact zone. Thus a thickness nonhomogeneity from one part of sample to the other will be a source of error that must be taken into account. In comparison with the resonant reaction method, the step-by-step dissolution method gives a better depth resolution, and in some cases a better knowledge of local concentration; however, this method is more sensitive to thickness nonhomogeneities.

Results and Interpretation

Study of Oxygen Transport by Chemical Dissolution

The results of ^{16}O and ^{18}O content measurements (N_{16} and N_{18} , respectively) in the oxide *vs.* the different steps of dissolution are shown in Fig. 2 as a function of the total amount of oxygen N_{16} and N_{18} . This oxide was grown up to 47 nm in a dry natural oxygen flow at atmospheric pressure. This was followed by a further growth in $^{18}\text{O}_2$ in the UHVT furnace at 100 torr up to 86.3 nm. We can see after the first step of dissolution a first decrease of the ^{18}O content followed by a plateau. This sheer step is related to the ^{18}O fixed near the external surface of the oxide (^{18}O FNES), whereas the plateau corresponds to a very low ^{18}O -labeled oxide. After this plateau, there appears a linear decrease of the ^{18}O content of the oxide which is related to the dissolution of the layer corresponding to the ^{18}O fixed near the Si/oxide interface (^{18}O). As can be seen, the ^{18}O FNI concentration is nearly constant, and the ^{18}O FNES amount can be estimated to about 7% of the total ^{18}O amount. All these results are in good agreement with a previous work using resonance techniques (4). The ^{16}O results are complementary to ^{18}O observations; the first decrease of N_{16} corresponds to the dissolution of the interfacial layer, while the horizontal line corresponds to the dissolution of ^{18}O FNI. The N_{16} variation in this last case is less than $1 \cdot 10^{15}$ atoms/cm², when the amount of oxygen decreases about $100 \cdot 10^{15}$ atoms/cm². This means that the maximum value of ^{16}O isotopic concentration is equal to 1% at most. Thus, the corresponding ^{18}O labeling must be larger than 99%, i.e., equal to that of the gas (99.5%) within 0.5%; therefore, the heavy isotope found near the Si/SiO₂

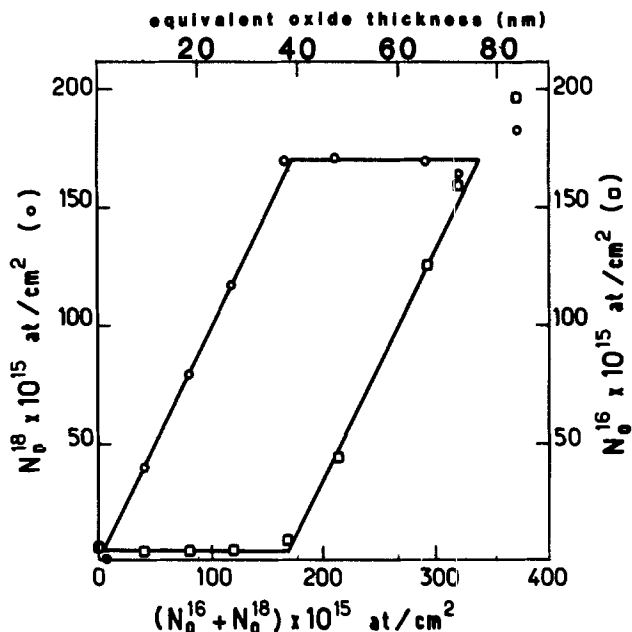


Fig. 2. N_o^{18} (o) and N_o^{16} (□) (in atoms/cm²) obtained after different steps of dissolution as a function of the total amount of oxygen ($N_o^{18} + N_o^{16}$) for an oxide grown to 47 nm in $^{16}\text{O}_2$ and then up to 86.3 nm in $^{18}\text{O}_2$.

interface went through the pre-existing oxide matrix without any measurable interaction with it. Furthermore, the transition between ^{18}O and ^{16}O zone is so abrupt that a possible isotopic mixing due to some network oxygen self-diffusion (see Fig. 5) is not measurable in the range of accuracy of our techniques. Finally, the height of the ^{16}O plateau may correspond to oxygenated species adsorbed on the surface after dissolution and/or to the background of the ^{28}Si (d, p), ^{29}Si reaction. Concerning ^{18}O FNES, this may be due to (i) isotopic exchange between oxygen of the network and water vapor traces, (ii) to some oxide growth by silicon transport, or (iii) to fixation of oxygen due to step-by-step effective motion of network oxygen atoms and an external surface allowing exchange. Let us notice that there is always the possibility of interfering phenomena induced by exposure to air between $^{16}\text{O}_2/^{18}\text{O}_2$ treatments or by the presence of the native oxide at the surface and finally by the treatment under high vacuum at high temperature.

Nature and Origin of ^{18}O Fixed near the External Surface

Effects connected with the experimental procedure.—Between $^{16}\text{O}_2$ growth and $^{18}\text{O}_2$ further growth, the oxide was exposed to the room atmosphere and then treated under vacuum. Could this process be the cause of ^{18}O FNES? To answer this question, we carried out the following experiments.

Sample A (Table I) was oxidized in $^{16}\text{O}_2$ for 18.1 h at 930°C under 8.5 torr up to about 14 nm, and then, instead

of withdrawing it from the furnace, $^{18}\text{O}_2$ gas was introduced up to a total oxygen pressure of 29 torr for 3.5 h at the same temperature. From the ratio of pressures, we deduced the ^{18}O isotopic concentration to be 60%, which was in agreement with mass spectrometer measurements. Results confirm the existence of ^{18}O FNES corresponding to about 16% of the total amount of ^{18}O . Let us notice that for this thinner oxide film the ^{18}O content is larger than those previously obtained: 16% for about 14 nm ^{16}O equivalent thickness instead of 7% for 47 nm. This effect will be studied later. From this experiment we can conclude that the appearance of ^{18}O FNES is not due to an interfering phenomenon related to exposure to air and/or to high temperature vacuum treatments. However, we start from a sample very likely covered with a native oxide, and considering that this oxide might remain at the external surface when growth takes place by a Deal-Grove type mechanism, we can wonder if this native oxide may have the particular property of exchanging its oxygen atoms with those of the $^{18}\text{O}_2$ gas. In order to clarify this situation, a second experiment was carried out.

Sample B (Table I) was grown in an $^{16}\text{O}_2$ flow up to 190 nm and then dissolved down to 140 nm to be sure that the possibly remaining native oxide was removed. Then, this sample was submitted to a further growth in $^{16}\text{O}_2$ for 1.5 h at 930°C under 8 torr, and then $^{18}\text{O}_2$ gas was introduced up to a total pressure of 33 torr for 1.1 h at the same temperature. As can be seen, the presence of the ^{18}O FNES is confirmed: about 30% of the total amount (this result was checked by resonance technique).

Study of the possible mechanisms for the ^{18}O fixation near the external surface.—**Silicon transport.**—We have carried out the following experiments on two films of different original ^{16}O thicknesses (about 50 nm for sample C and 20 nm for sample D). They were subjected to an $^{18}\text{O}_2$ growth under 100 torr for 19 and 1.1 h, respectively. Each sample was cut into two parts. One part was kept as a test sample, the other was treated again in $^{16}\text{O}_2$ (for samples C and D, under 100 torr for 19 and 1.1 h, respectively). The results are summarized in Table II. We can easily see that for sample C the amount of ^{18}O FNES (i.e., N_s^{18}) is reduced by nearly a half, while for the thinner sample (sample D), the decrease is larger (this decrease which is a function of the original thickness will be discussed further). Thus isotopic exchange of oxygen occurs. If the fixation of the heavy isotope near the external surface was due to silicon transport, then the regrowth in an $^{16}\text{O}_2$ ambient would not diminish the surface ^{18}O amount. The Si $^{18}\text{O}_2$ would be unaltered but buried under a layer of Si $^{16}\text{O}_2$. This experiment cannot be used to distinguish between an exchange phenomenon due to water vapor traces and an exchange phenomenon due to a step-by-step effective motion of network oxygen atoms.

Exchange between water vapor traces and network oxygen atoms at the external surface.—In Table III, we calculate the equivalent water vapor pressure which would be necessary to obtain the whole ^{18}O FNES amount if the fixation of oxygen near the surface was entirely due to exchange with vapor traces. This calculation is performed by assuming that: (i) the ^{18}O mobile carrier is the H_2^{18}O

Table I. Measurements of ^{16}O and ^{18}O amounts obtained for two different oxide films (samples A and B) after different steps of dissolution. X_o^{18} is the equivalent ^{18}O oxide thickness. The samples were left in the hot zone when $^{18}\text{O}_2$ gas was added to $^{16}\text{O}_2$ (no thermal shock)

Samples	$^{16}\text{O}_2$ oxidation			$^{16}\text{O}_2 + ^{18}\text{O}_2$ oxidation			Dissolution			
	t (h)	T (°C)	p (torr)	t (h)	T (°C)	p (torr)	t (s)	N_o^{18} (10^{15} at./cm ²)	X_o^{18} (nm)	$N_o^{16} + N_o^{18}$ (10^{15} at./cm ²)
A	18.1	930	8.5	3.50	930	29	0	18.6	4.20	98.5
							4	16.1	3.65	93.0
							8	15.6	3.50	94.5
							13	15.0	3.40	82.5
							20	15.5	3.50	72.0
							0	4.2	0.95	630.0
B*	1.5	930	8.0	1.12	930	33	40	3.0	0.68	586.0
							80	2.9	0.65	530.0
							120	2.9	0.65	495.5
							160	2.7	0.61	444.0
							200	2.6	0.59	411.0
							0	4.2	0.95	630.0

* 190 nm-thick Si^{16}O_2 sample, partially chemically etched to remove the possibly remaining native oxide at the external surface and then regrown in $^{16}\text{O}_2$ (8 torr) for 1.5 h before isotopic treatment.

Table II. Measurements of ^{16}O and ^{18}O total amounts of ^{18}O FNES and ^{18}O FNI amounts (N_s^{18} and N_i^{18} , respectively) obtained for two samples of different original Si^{18}O_2 thicknesses: sample C (~ 50 nm) and sample D (~ 20 nm)

	Samples	N_s^{18} (10^{15} at./cm 2)	X_s^{18} (nm)	N_i^{18} (10^{15} at./cm 2)	X_i^{18} (nm)	$\frac{N_s^{18}}{N_i^{18} + N_s^{18}}$	$N_s^{16} + N_o^{18}$ (10^{15} at./cm 2)	Total oxide thickness (nm)	Technique used
$^{18}\text{O}_2 \rightarrow ^{18}\text{O}$ oxidation sequence	C	9.0	2.030	153.0	34.5	0.055	387.0	87.5	Dissolution Resonance
		8.2	1.850	155.0	35.0	0.050	—	—	
	D	5.7	1.300	14.3	3.2	0.285	109.0	24.6	Dissolution
	$^{16}\text{O}_2 \rightarrow ^{18}\text{O}_2 \rightarrow ^{18}\text{O}$ oxidation sequence	C	3.9	0.880	153.0	34.5	0.025	636.0	144.0
D			1.0	0.226	14.5	3.3	0.064	131.0	29.6

¹ Grown in an $^{18}\text{O}_2$ ambient. Sample C: 930°C, 100 torr, 19h. Sample D: 930°C, 100 torr, 1.1h.

² Regrown in an $^{16}\text{O}_2$ ambient in the same experimental conditions.

molecule, and its equilibrium concentration is proportional to the pressure $P_{\text{H}_2\text{O}}$, ^{18}O , (ii) the ^{18}O labeling of the H_2O traces is equal to 100%, and (iii) the reaction of the water molecules with the SiO_2 network is so fast that the ^{18}O isotopic equilibrium is reached.

Using the mathematical developments presented by Rigo *et al.* (40), we have calculated the equivalent minimum values of water vapor pressure. The corresponding exchanged amount is given by the equation

$$X = \frac{2}{\sqrt{\pi}} Cg^{18} \sqrt{D^*t}$$

where D^* is the effective diffusion coefficient, t the treatment duration, and Cg^{18} the isotopic concentration of water vapor traces. This expression is valid at this temperature for pressures in the 10 torr range. If at very low pressures (in the 10^{-4} torr range) D^* is still proportional to $p_{\text{H}_2\text{O}}$, we can obtain the equivalent water vapor pressure. Let us notice that measurements by mass spectrometer of H_2^{18}O yield values under 3 ppm of the total pressure. If for the thicker oxide samples (thickness ≥ 50 nm) such a hypothesis cannot be rejected, for the thinner oxide films, ^{18}O FNES is not due to an exchange between vapor traces and silicon oxide unless the mechanism assumed above is not valid any longer. As shown below, it would be difficult to explain the observed phenomena by water vapor traces.

Step-by-step effective motion of network oxygen atoms.—If the ^{18}O fixation near the external surface is not due to water vapor traces, we can consider that this exchange phenomenon, as evidenced by the decrease of the ^{18}O FNES amount after treatment in $^{16}\text{O}_2$ (Table II), is related to a step-by-step effective motion of network oxygen atoms. The particular role of the external surface is therefore emphasized: (i) some O_2 molecules are allowed to react at the surface, and then the dissociated species can migrate into the oxide, for example, by a vacancy type or by an interstitial type mechanism, and (ii) this surface allows network oxygen atoms to exchange with those of the O_2 gas. As a matter of fact, the oxygen species migrating through the pre-existing matrix in order to

react at the Si/oxide interface, within our method resolution, apparently do not interact with the network. Consequently, the external surface must exhibit some particular defect configuration that must be seldom encountered in the bulk.

Thickness effect on the respective amounts of ^{16}O fixed either near the surface or near Si/oxide interface.—**Thickness greater than 50 nm.**—Four samples of various original thicknesses X_o^{16} , named E_1 , F_1 , G_1 , and H_1 , were simultaneously treated at 930°C, 100 torr of $^{16}\text{O}_2$ for 8h. Another batch, consisting of samples E'_1 and G'_1 , was subsequently treated under the same conditions in order to control the reproducibility of the experiments. Finally, a third batch, consisting of samples (F_2 and H_2), was treated for 4h. The goal of simultaneous treatments was to avoid irreproducibilities from one treatment to another. The ^{16}O amounts before and after $^{18}\text{O}_2$ treatments and the incorporated ^{18}O amounts are reported in Table IV. Also in Table IV, we represent the equivalent thicknesses X_s^{18} (^{18}O FNES amounts) and X_i^{18} (^{18}O FNI amounts), which were obtained from fits of experimental excitation curves of the nuclear resonant reaction $^{18}\text{O}(p, \alpha)^{15}\text{N}$ with calculated curves assuming an ^{18}O concentration profile. Figures 3 and 4 represent such excitation curves for the samples H_1 and E_1 , respectively. Sample H_1 was tilted at $\theta = 68^\circ$ to separate the surface peak from the interface peak. The corresponding value X_s^{18} is equal to 1.57 nm. This value has been used in a test profile for sample E_1 (Fig. 4, where the dashed line represents the corresponding excitation curve). It appears that this curve cannot fit the experimental one. The surface peak is too great, and thus it is so for X_s^{18} . The profile that allows a good fit of the experimental curve is represented in the inset. It is seen that the corresponding value of X_s^{18} is equal to 0.9 nm, which is a smaller value than for the thinner sample H_1 . This shows that the variations of X_s^{18} observed by this method are relevant. From Table IV, one can notice a significant increase of X_s^{18} when X_o^{16} diminishes. The comparison between samples (E_1 , G_1) and (E'_1 , G'_1) identical treatment duration but nonsimultaneous experiments) shows that X_s^{18} increases with decreasing X_o^{16} in the same way. Samples (F_2 , H_2) treated during 4h show the same behavior and can give some evaluation of the kinetics of X_s^{18} . Between the fourth and eighth treatment hour ($\Delta t = 4\text{h}$), X_s^{18} roughly increases by 35% and by 57% for samples of original thickness $X_o^{16} \approx 178$ nm and $X_o^{16} \approx 47$ nm, respectively. Thus, the surface ^{18}O fixation rate is not linear. Since no appreciable increase of exchanged ^{18}O amounts was observed with decreasing oxide thickness in the case of labeled water vapor treatments (13 torr) (34), the present thickness effect is not indicative of an exchange with water vapor traces unless the phenomenon of exchange between water vapor traces and silica is not the same at very low pressures. The respective parts of ^{18}O FNES and ^{18}O FNI amounts are thus dependent on the original thickness of the oxides in the range 50-260 nm; a similar

Table III. Equivalent water pressure calculated for various oxide thicknesses

Si $^{18}\text{O}_2$ original thickness (nm)	$^{16}\text{O}_2$ oxidation			N_s^{18} (10^{15} at./cm 2)	Equivalent water vapor pressure (ppm)
	t (h)	T (°C)	p (torr)		
~ 50	1.9	930	100	8.4	11
~ 20	1.1	930	100	5.8	85
~ 4	1.0	930	10	3.2	285

This calculation was performed following Ref. (40), where $D^* = 1849$ nm 2 /h at 930°C under 13 torr H_2^{18}O .

Table IV. Results of ^{16}O and ^{18}O measurements (N_o^{16} and N_o^{18}) and of ^{18}O FNES (X_s^{18}) and ^{18}O FNI (X_i^{18}) amounts obtained from fits of experimental excitation curves for thicknesses higher than 50 nm regrown in an $^{18}\text{O}_2$ ambient for two different durations at 930°C under 100 torr

Sample	After $^{16}\text{O}_2$ oxidation		Treatment duration (h)	After $^{18}\text{O}_2$ oxidation						
	N_o^{16} (10^{15} at./cm 2)	X_o^{16} (nm)		N_o^{16} (10^{15} at./cm 2)	X_o^{16} (nm)	N_o^{18} (10^{15} at./cm 2)	X_o^{18} (nm)	X_s^{18} (nm)	X_i^{18} (nm)	$\frac{X_s^{18}}{X_s^{18} + X_i^{18}}$
E ₁	1140	257.6	8	1140	257.6	38.3	8.65	0.90	7.20	0.110
F ₁	790	178.6	8	786	178.0	47.6	10.75	1.15	9.30	0.110
G ₁	374	84.5	8	387	87.5	72.6	16.40	1.30	15.00	0.080
H ₁	209	47.2	8	214	48.3	98.0	22.20	1.57	19.60	0.076
E' ₁	1140	257.6	8	1124	254.0	38.6	8.70	1.15	7.16	0.140
G' ₁	374	84.5	8	403	91.0	74.8	16.90	1.40	15.50	0.080
F ₂	790	178.3	4	765	173.0	26.1	5.90	0.85	4.70	0.150
H ₂	209	47.2	4	204	46.0	58.0	13.10	1.00	12.10	0.076

Table V. Measurement of ^{16}O and ^{18}O total amounts (N_o^{16} and N_o^{18}) and of ^{18}O FNES and ^{18}O FNI amounts (N_s^{18} and N_i^{18}) obtained by step-by-step dissolution combined with nuclear microanalysis for ^{16}O oxide films of original thicknesses ≤ 20 nm

Sample	$^{16}\text{O}_2$ Treatment			$^{18}\text{O}_2$ Treatment							Total equivalent thickness (nm)	
	N_o^{16} (10^{15} at./cm 2)	T (°C)	t (min)	p (torr)	N_o^{18} (10^{15} at./cm 2)	N_i^{18} (10^{15} at./cm 2)	$\frac{N_s^{18}}{N_s^{18} + N_i^{18}}$	$N_o^{16} + N_o^{18}$ (10^{15} at./cm 2)				
J ₁	O ₂ + N ₂ mixture 950°C	84.3	930	67	100.0	3.3	14.70	0.18	101.0	22.8		
J ₂		84.3	930	67	100.0	5.7	14.10	0.28	109.0	24.6		
J ₃		84.3	930	67	100.0	2.9	14.30	0.17	99.0	22.3		
	T (°C)	t (min)	p (torr)									
K	930	30	9	(+)	930	60	9.0	3.2	3.00	0.52	23.0	5.2
L ₁ *	—	60	—	(+)	—	—	9.0	2.1	2.10	0.50	22.4	5.0
L ₂ *	—	60	—	(+)	—	—	1.0	1.4	0.50	0.74	21.0	4.7
L ₃ *	—	60	—	(+)	—	—	0.1	0.5	0.12	0.81	22.1	4.9
M	—	90	—	(+)	—	—	9.0	2.6	3.00	0.46	26.4	5.9
N	—	120	—	(+)	—	—	9.0	2.7	3.20	0.46		

* Samples simultaneously grown in $^{16}\text{O}_2$. No re-exposure to air between two thermal treatments and thus no ^{16}O content measurement available.

study was carried out for thinner samples down to about ~5 nm.

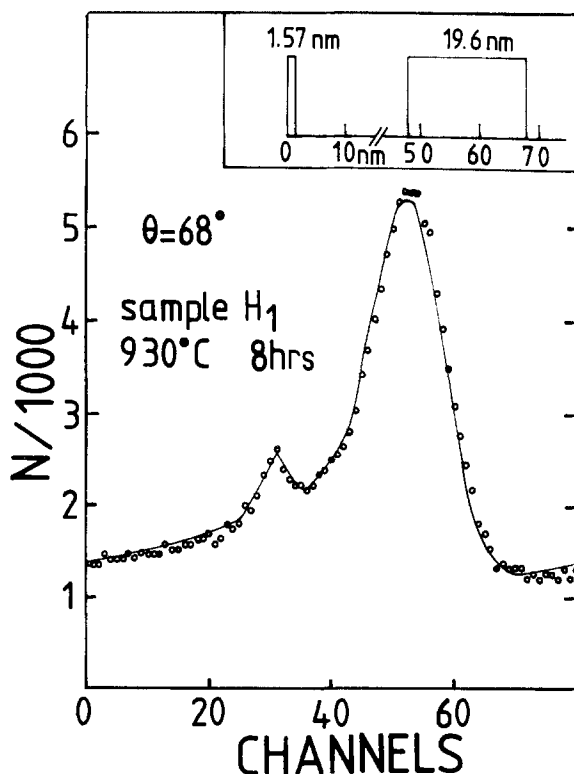


Fig. 3. ^{18}O concentration profile measurement by the nuclear resonance method for sample H₁ of original thickness $X_o^{16} = 47.2$ nm treated in $^{18}\text{O}_2$ at 930°C, 100 torr for 8h. The sample was tilted at $\theta = 68^\circ$. The solid line is the best fit calculated for the profile represented in inset.

Thickness under 50 nm.—The results are reported in Table V. Two groups of samples were treated. First, sample J₁, J₂, and J₃, grown at 950°C in an $^{16}\text{O}_2/\text{N}_2$ mixture up to a thickness of about 19 nm, were subsequently submitted to an $^{18}\text{O}_2$ treatment at 930°C for about 1h, under a pressure of 100 torr. These samples were exposed to air between two thermal treatments. Although we approach the thickness domain where kinetics do not seem to follow the Deal-Grove model (1) any longer, we can notice that ^{18}O is still mainly found near the Si/oxide interface but the ^{18}O FNES amount now is around 20% of the total ^{18}O amount.

Second, samples K, L₁, L₂, L₃, M, and N, grown in the UHVT furnace in dry natural oxygen at 930°C, 9 torr, for various times (30-120 min), were subsequently treated in $^{18}\text{O}_2$, with no re-exposure to air, at 930°C for 1h and various pressures (0.1-9 torr) up to total thicknesses of about 5 nm. In this range of thicknesses, temperature and pressure where Kamigaki and Itoh (6) utilized the Mott-Cabrera model in order to fit the kinetics they found, we always found the heavy isotope located near the Si/oxide interface and near the external surface, but the ^{18}O FNES amounts are around 50% of the whole ^{18}O content when samples are still treated in $^{18}\text{O}_2$ at 9 torr. This ratio increases when the $^{18}\text{O}_2$ treatments are carried out under lower pressures, and can reach 80% of the whole ^{18}O amount at $p_{^{18}\text{O}_2} = 0.1$ torr. It appears that N_i^{18} follows a $p_{^{18}\text{O}_2}^{0.62}$ law, and N_s^{18} seems to follow a log $p_{^{18}\text{O}_2}$ law (N_s^{18} and N_i^{18} corresponding to the ^{18}O FNES and ^{18}O FNI amounts, respectively).

Discussion

As it can be noticed, there is no discontinuity in behavior for oxide films of thicknesses ranging from 260 to ~5 nm, both concerning the location of the heavy isotope and the increase of ^{18}O FNES amounts with decreasing original thickness X_o^{16} .

Fixation near the external surface

This thickness effect on ^{18}O FNES amounts could be interpreted in various ways

Fig. 4. ^{18}O concentration profile measurement by the nuclear resonance method for sample E_1 , of original thickness $X_{0,16} = 257$ nm treated in $^{18}\text{O}_2$ at 930°C for 8h. The solid line is the best fit calculated for the profile represented in inset. The ^{18}O FNES amount determined for sample H_1 was introduced in a trial profile whose theoretical excitation curve is represented by the broken line.

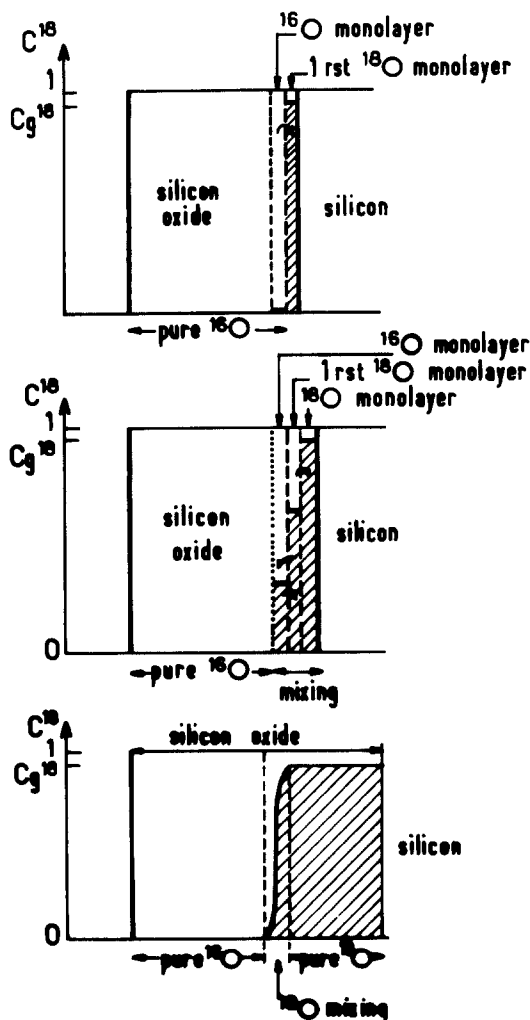
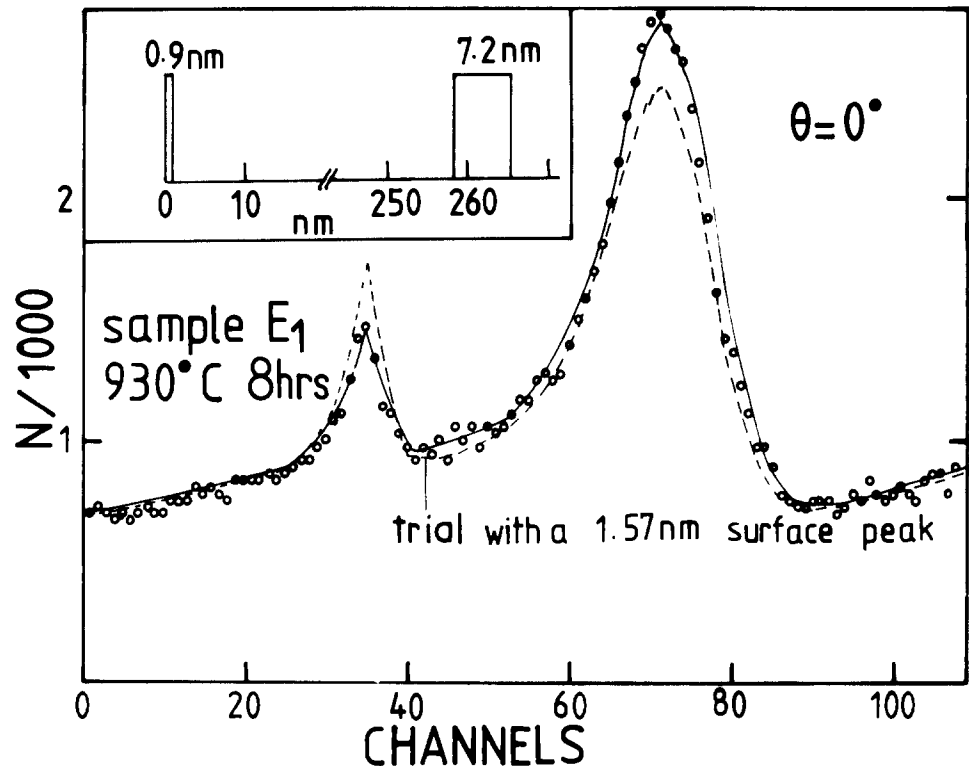


Fig. 5 Mixing effect on the $^{16}\text{O}/^{18}\text{O}$ boundary of a step-by-step effective motion of network oxygen atoms concurrent of an interstitial motion of molecular oxygen for an oxide film grown in $^{18}\text{O}_2$ and then in $^{18}\text{O}_2$.

1. The effect could be a structural change during growth, as observed for very thin films by Agius *et al.* (41). This was previously postulated by Revesz and Schaeffer (3).

2. The effect could be an enhancement of the concentration of oxide defects in connection with the film growth rate. The step-by-step motion of network oxygen atoms could be interpreted by some vacancy or interstitialcy-type mechanism. During oxide growth, defects in excess could be created at the silicon-oxide interface or at the external surface, respectively. Let us emphasize that one observes an injection of interstitial silicon atoms from the SiO_2/Si interface into the silicon substrate (42, 43). This was interpreted by Lin *et al.* (42) as an incomplete oxidation of Si by O_2 creating extra interstitial Si atoms both in the oxide and the Si substrate. The completion of the oxidation is performed through a further oxidation of these interstitial Si in the oxide. As no evidence of a migration of Si atoms was obtained through our labeling experiments, it seems to us that oxygen vacancy type defects generated at the Si/SiO_2 interface could be a reasonable explanation. Moreover, as one observes that the generation of interstitial Si into the Si substrate varies with the oxide growth rate (42, 43), one could imagine that the concentration of network defects in the oxide could be also related to the oxide-growth rate. In the case of network oxygen diffusion by network defects, the effective self-diffusion coefficient of network oxygen atoms is proportional to the concentration of oxide-network defects. Thus, if this defect concentration increases with the oxide-growth rate, the increase of ^{18}O FNES amounts with decreasing thicknesses could be explained.

3. The effect could be the presence of charged defects in the oxide and/or the supply of electronic species whose transport properties and injection at the interfaces are impeded for the thicker films.

Possible microscopic interpretation of the phenomenon of ^{18}O fixation near external surface

We noticed that the oxide surface and oxide bulk have a different behavior with respect to molecular oxygen and that network oxygen atoms can migrate by step-by-step motion; we have tried to explain all these experimental observations by a mechanism involving vacancy type defects, alternative to that proposed by Revesz and Schaeffer (3). The basic defects that we consider here are silicon dangling bonds in excess (one Si dangling bond, charged or not, formally corresponds to half an oxygen

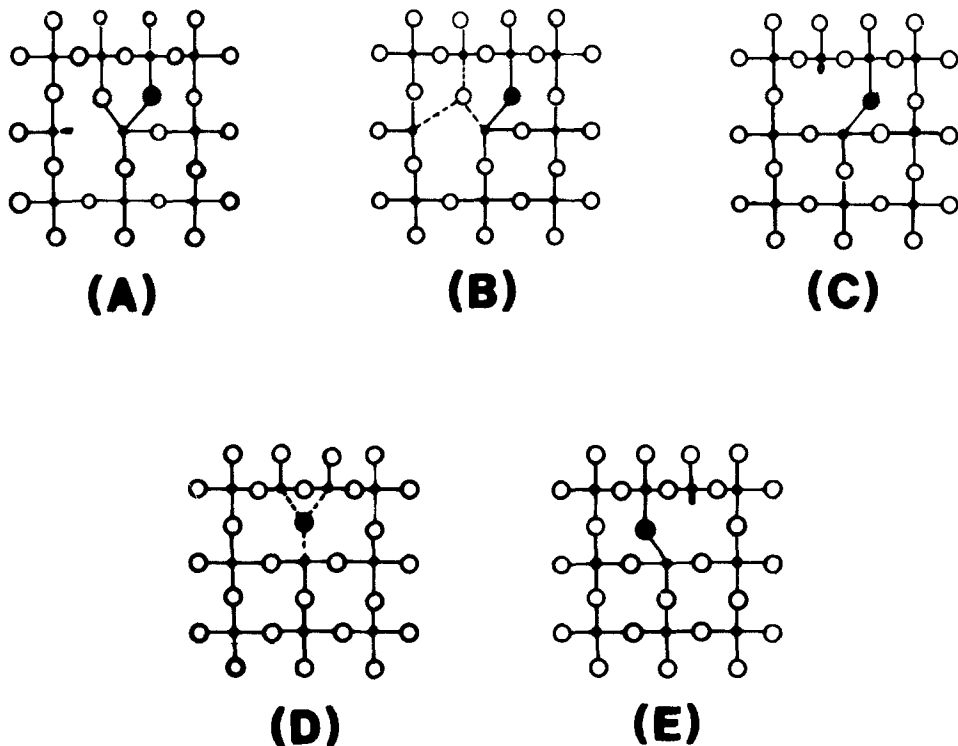
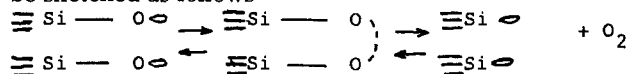


Fig. 6. Schematic drawing of the motion of a labeled oxygen atom of the network when one assumes that the basic oxygen defect is a Si dangling bond. Small circles correspond to Si atoms, and large circles to oxygen atoms (the dark one being a labeled oxygen). Subsequent steps are in alphabetical order. For the sake of simplicity, the charge of the defects (if charged) is not represented.

vacancy). The motion of a labeled oxygen atom is sketched in Fig. 6. In this figure, we describe the motion of the defect considering a threefold-coordinated oxygen as an intermediate step, although the existence of this defect imagined by Lucovsky (44) in bulk silica has been debated (45). As the direct jump of a Si dangling bond would imply the breaking of a Si—O bond in the $\equiv\text{Si}-\text{O}\equiv$ configuration ($d_{\text{SiO}} = 0.6 \text{ nm}$) the breaking of the Si—O bond [$d_{\text{SiO}} = 0.72 \text{ nm}$ (46)] in the threefold-coordinated oxygen configuration would be energetically easier. The particular behavior of the surface compared to that of the bulk is due to the fact that the network is disrupted at the surface. The desorption, adsorption, and breaking of the O_2 molecule at the external surface could be sketched as follows



where two Si dangling bonds (or nonbridging oxygens) are in the vicinity of each other. The symbol — designates a bond between an oxygen atom and a silicon atom; the

symbol \ominus designates a Si or O orbital. For the sake of simplicity, the occupation of these orbitals by electrons (*i.e.*, the charge of the dangling bond) is not represented. The probability of finding such a topological situation is very high at the surface and very small in the bulk. These phenomena are perhaps favored by the supply of electrons at the external surface: an electronic bombardment greatly enhances the oxidation rates even at very low pressure (10^{-3} torr) (47). Figure 7 shows a possible scenario for oxygen exchange between the gas and the network. An interstitialcy mechanism by jumps of $\equiv\text{Si}-\text{O}\cdot$ defects cannot be ruled out. At sufficiently low pressure, where the contribution to growth due to O_2 molecules reacting at the interface Si/SiO₂ might be negligible, the creation of oxygen vacancies in excess might not be necessarily envisaged. As a matter of fact, in low pressure plasma oxidation, no oxidation stacking faults in the Si substrate are observed; apparently, no great amounts of interstitial silicon atoms are generated (48). Consequently, such an interstitialcy mechanism could perhaps exist rather at low pressure.

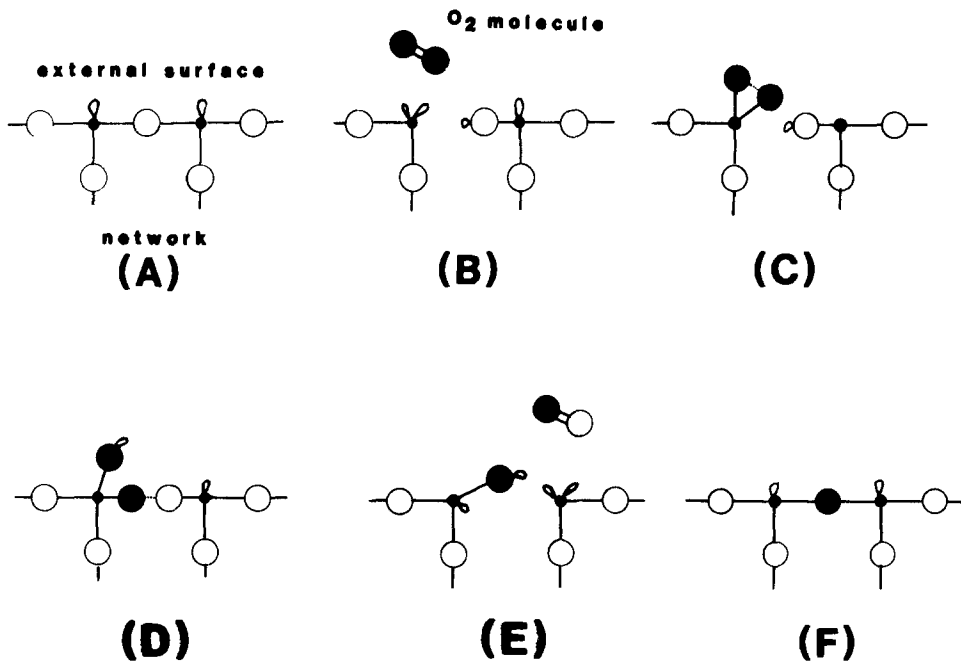


Fig. 7. Schematic drawing of a possible scenario for oxygen exchange between the gas and the network. Small circles correspond to Si atoms. Large circles correspond to oxygen atoms (the dark one being a labeled oxygen). Subsequent steps are in alphabetical order. For the sake of simplicity the charge of the defects (if charged) is not represented.

Fixation near the Si/oxide interface, nature of the migrating oxygen species

As we always find ^{18}O located near the Si/oxide interface, we can wonder about the oxygen species migrating through the film with no interaction with it.

For thick oxide samples (>20 nm), one can think that O_2 molecules are very likely the diffusing species as k_p exhibits a p_{O_2} dependence and an activation energy equal to that found for permeation (1).

For thin oxide samples (<5 nm), for which electrons can tunnel across the film, the dissociation of O_2 molecules into dissociated ions is perhaps enhanced. These hypothetical ions must migrate in the oxide film without interacting with it, as well as O_2 molecules for thicker oxide samples. Mills and Kroger (20) proposed O^{2-} as responsible for ionic conduction. We should notice that this ion is the more energetically difficult to obtain from a free O_2 molecule [462 kcal · mole⁻¹ or 20 eV (49)], but one might wonder why these dissociated species do not apparently interact with the network while migrating. O_2^- species could also be envisaged knowing that at the Si/oxide interface O_2^- can be more easily dissociated as its bond strength is practically that of an O—O single bond [1.5 eV (50)]. As a matter of fact, charged species are involved in a Cabrera-Mott transport mechanism leading to inverse logarithmic laws; such kinetics are observed at pressures under 1 torr (6). Obviously, neutral O_2 molecules are still good candidates for explaining the ^{18}O fixation near the Si/SiO₂ interface even for very thin films. If a Cabrera-Mott mechanism is actually involved for very thin oxide samples and becomes dominant as pressure decreases (6), it may be that the charged species and/or defects accelerated by the electrical field could rather be $\equiv\text{Si}^+$ or $\equiv\text{Si}-\text{O}^-$ defects (or other equivalent defects); in this case the heavy isotope would only be found near the external surface.

Effect of pressure on N_i^{18} and N_s^{18}

Variations of N_i^{18} .—Two cases may be considered. First, that the diffusion of O_2 molecule is the limiting phenomenon. We are only able to conclude that, as the thickness increase is small (<10%), we are not facing a simple bulk-limited diffusion phenomenon where the concentration of diffusing species at the external surface is practically equal to the solubility C^* , this solubility following a Henry's law ($C^* \propto p_{\text{O}_2}$). Second, that a more or less complex reaction of the O_2 molecules at the Si/oxide interface is the limiting phenomenon. Thus, we are not facing a simple first-order reaction, which was already assumed by Ghez and Van der Meulen (7), and later by Blanc (8). A change in O_2 diffusivity connected with a structural change during growth (41) might be also put forward to explain the $p_{\text{O}_2}^{0.62}$ law that we found.

Variations of N_s^{18} .—The variation of N_s^{18} with p_{O_2} for film thicknesses under 5 nm is difficult to interpret at the present time without a better understanding of surface phenomena, bulk diffusion mechanisms, and their relative importance. Nevertheless, noticing that at 10^{-1} torr, N_s^{18} represents more than 80% of the whole heavy isotope amount (see Table V), we could wonder if, in the very small thickness range (<5 nm) and in the range of pressures where our experiments were carried out, we are not facing two concurrent growth mechanisms, one of them related to a vacancy or interstitial type mechanism and much less sensitive pressure decrease.

Conclusion

For oxide thicknesses ranging from 5 to 260 nm, oxygen transport shows two aspects, one being related to oxygen species' migrating through the network with no or little interaction with it (very likely O_2 molecules for thick samples) and reacting with silicon at the Si/oxide interface, and the other being likely related to a step-by-step motion of network oxygen atoms responsible for isotopic exchange near the external surface, this being allowed by some particular nature of the surface. The relative importance of the latter increases as oxide films are thinner and O_2 pressures lower.

Acknowledgments

The authors are very indebted to F. P. Fehlner, E. A. Irene, Sir Nevill Mott, and A. G. Revesz for fruitful dis-

cussions and reading the manuscript. They are very grateful to G. Amsel for his help in the UHVT furnace designing, and to J. Moulin for his technical assistance in the UHTV furnace making. They thank E. d'Artemare and E. Girard for their help in the use of nuclear microanalysis facility of our laboratory. They are indebted to B. Biasse and J. J. Niez from the Laboratoire d'Electronique et de Technologie de l'informatique of Grenoble for their help in ^{18}O oxide preparation. This work was supported by Centre National de la Recherche Scientifique (R. C. P. no. 157) and Centre National d'Etudes des Télécommunications.

Manuscript submitted May 11, 1983; revised manuscript received Dec. 5, 1983.

The Groupe de Physique des Solides de l'Ecole Normale Supérieure assisted in meeting the publication costs of this article.

REFERENCES

- B. E. Deal and A. S. Grove, *J. Appl. Phys.*, **36**, 3770 (1965).
- N. F. Mott, *Proc. R. Soc. London, Ser. A*, **376**, 207 (1981).
- A. G. Revesz and H. A. Schaeffer, *This Journal*, **129**, 357 (1982).
- E. Rosencher, A. Straboni, S. Rigo, and G. Amsel, *Phys. Lett.*, **34**, 254 (1979).
- M. A. Hopper, R. A. Clarke, and L. Young, *This Journal*, **122**, 1216 (1975).
- Y. Kamigaki and Y. Itoh, *J. Appl. Phys.*, **48**, 2891 (1977).
- R. Ghez and Y. J. Van der Meulen, *This Journal*, **119**, 1100 (1972).
- J. Blanc, *Appl. Phys. Lett.*, **33**, 424 (1978).
- J. Blanc, in "Semiconductor Characterization Techniques," P. A. Barnes and G. A. Rozgonyi, Editors, p. 139, The Electrochemical Society Softbound Proceedings Series, Princeton, NJ (1978).
- L. N. Lie, R. R. Razouk, and B. E. Deal, *This Journal*, **129**, 2828 (1982).
- E. A. Irene and Y. J. Van der Meulen, *ibid.*, **128**, 1380 (1976).
- E. A. Irene and D. W. Dong, *ibid.*, **125**, 1146 (1978).
- E. A. Irene, *Appl. Phys. Lett.*, **40**, 74 (1982).
- A. G. Revesz and R. J. Evans, *J. Phys. Chem. Solids*, **30**, 551 (1969).
- J. Derrien and M. Commandre, *Surf. Sci.*, **118**, 32 (1982).
- J. Hollinger, *Appl. Surf. Sci.*, **8**, 318 (1981).
- E. A. Irene and R. Ghez, *This Journal*, **124**, 1757 (1977).
- P. J. Jorgensen, *J. Chem. Phys.*, **37**, 874 (1962).
- D. O. Raleigh, *This Journal*, **113**, 782 (1966).
- T. G. Mills and F. A. Kroger, *ibid.*, **120**, 1582 (1973).
- N. F. Mott, *Philos. Mag. A*, **45**, 323 (1982).
- P. J. Jorgensen, *This Journal*, **114**, 820 (1967).
- S. I. Raider and L. E. Forget, *ibid.*, **127**, 1783 (1980).
- M. Horiuchi, Y. Kamigaki, and T. Hagiwara, *ibid.*, **125**, 768 (1968).
- A. G. Revesz and R. J. Evans, *J. Phys. Chem. Solids*, **30**, 551 (1969).
- F. P. Fehlner, *This Journal*, **119**, 1725 (1972).
- E. A. Irene, *ibid.*, **122**, 1216 (1978).
- J. M. Gibson and D. W. Dong, *ibid.*, **127**, 2722 (1980).
- A. G. Revesz, *Phys. Status Solidi A*, **57**, 235 (1980).
- A. G. Revesz, *ibid.*, **58**, 107 (1980).
- A. Fargeix, G. Ghibaudo, and G. Kamarinos, *J. Appl. Phys.*, **54**, 2878 (1983).
- W. A. Tiller, *This Journal*, **130**, 501 (1983).
- N. Cabrera and N. F. Mott, *Rep. Prog. Phys.*, **12**, 163 (1949).
- F. Rochet, Thèse de Doctorat du 3ème cycle, Université Paris VI, Paris (1981).
- M. Hamasaki, *Solid-State Electron.*, **25**, 479 (1982).
- G. Amsel, J. P. Nadai, E. d'Artemare, D. David, E. Girard, and J. Moulin, *Nucl. Instrum. Methods*, **92**, 481 (1971).
- G. Amsel, J. P. Nadai, C. Ortega, S. Rigo, and J. Siejka, *ibid.*, **149**, 705 (1978); **149**, 713 (1978).
- C. R. Helms, *J. Vac. Sci. Technol.*, **16**, 609 (1979).
- B. Maurel, Thèse de doctorat d'état, Université Paris 7, Paris (1980).
- S. Rigo, F. Rochet, B. Agius, and A. Straboni, *This Journal*, **129**, 867 (1982).
- B. Agius, S. Rigo, F. Rochet, M. Froment, C. Maillot, H. Roulet, and G. Dufour, *Appl. Phys. Lett.*, **44**, 48 (1984).
- M. R. Lin, R. W. Dutton, D. A. Antoniadis, and W. A.

- Tiller, *This Journal*, **127**, 2243 (1980).
43. S. M. Hu, *Appl. Phys. Lett.*, **43**, 449 (1983).
44. G. Lucovsky, *Philos. Mag. B*, **39**, 513 (1979).
45. A. G. Revesz and G. E. Walrafen, *J. Non-Cryst. Solids*, **54**, 323 (1983).
46. A. G. Revesz and G. V. Gibbs, in "Proceedings of the Conference on the Physics of MOS Insulator," G. Lucovsky, S. T. Pantelides, and F. L. Galeener, Editors, p. 92, Pergamon Press, New York (1980).
47. P. Rabinzohn, G. Gautherin, B. Agius, F. Rochet, and S. Rigo, in Extended Abstracts of the 5th International Symposium on Passivity," p. 184, Bordeaux, France, May 30-June 3, 1983, Society de Chemie Physique, Paris (1984).
48. V. Q. Ho and T. Sugano, *IEEE Trans. Electron. Devices*, **ed-27**, 1436 (1980).
49. M. Kh. Karapet'yants, and M. L. Karapet'yants, "Thermodynamic Constants of Organic and Inorganic Compounds," p. 193, Ann Arbor-Humphrey Science Publishers, London (1970).
50. M. Garric, "Cours de Chimie," p. 220, Dunod, Paris (1971).

The Characteristics of Alumina Scales Formed on Fe-Based Yttria-Dispersed Alloys

T. A. Ramanarayanan,* M. Raghavan, and R. Petkovic-Luton

Exxon Research Center, Linden, New Jersey 07036

ABSTRACT

To provide resistance to aggressive environments at elevated temperatures, especially in excess of $\sim 1000^\circ\text{C}$, alloys or coatings which develop $\alpha\text{-Al}_2\text{O}_3$ scales are the best choice. It has been pointed out that the presence of highly stable rare earth oxide dispersoids in high temperature alloys leads to improvements in the corrosion-resistant properties of Al_2O_3 scales formed on such alloys. The present study is directed toward developing an understanding of how the properties of Al_2O_3 scales formed on Fe-based alloys are influenced by yttrium oxide dispersoids in the alloy. The Fe-based alloy system selected for the current study consists of $\sim 20\%$ Cr, $\sim 4.5\%$ Al, $\sim 0.5\%$ Ti, and $\sim 0.5\%$ Y_2O_3 . The oxidation kinetics of the alloy have been established at various oxygen partial pressures in the temperature range 1000°C - 1200°C . The $\alpha\text{-Al}_2\text{O}_3$ scales which result upon oxidation are observed to be columnar, ultrafine grained, and extremely adherent when thermally stressed. Platinum markers initially placed on the alloy surface are found at the oxide/gas interface at the completion of oxidation, suggesting that scale growth occurs by exclusive inward oxygen migration. The ultrafine grain size ($0.5\text{-}1\ \mu\text{m}$) suggests that grain boundaries in the oxide scale are the preferred path for oxygen migration. The fine dispersoid particles in the alloy ($200\text{-}500\text{\AA}$) transform to coarse ($\sim 0.5\ \mu\text{m}$) yttrium aluminum garnet upon incorporation into the Al_2O_3 scale, leading to a garnet-saturated scale. It is suggested that the remarkable adherence of the $\alpha\text{-Al}_2\text{O}_3$ scales is a consequence of a combination of factors. First, yttrium doping promotes the development of a fine-grained $\alpha\text{-Al}_2\text{O}_3$ scale which can effectively relieve oxide growth stresses by diffusional plastic flow. Second, because the alumina scale grows by exclusive inward oxygen transport, growth stresses arising from Al_2O_3 nucleation within an existing scale are avoided.

High temperature alloys or coatings designed to resist aggressive environments at elevated temperatures should be capable of developing a surface oxide layer which is thermodynamically stable, slow growing, and adherent. The three oxides which fit the requirement of slow growth are Cr_2O_3 , SiO_2 , and Al_2O_3 . Of these, chromia is the fastest growing and alumina is the slowest growing. The thermodynamic stability of these oxides is in the order $\text{Al}_2\text{O}_3 > \text{SiO}_2 > \text{Cr}_2\text{O}_3$. At temperatures exceeding $\sim 1000^\circ\text{C}$, chromium oxide scales tend to become unstable; in environments of relatively high oxygen partial pressure, the oxide can vaporize as CrO_3 (1), while under highly reducing conditions the oxide can transform to other more thermodynamically stable phases (2).

For applications in hostile environments at temperatures in excess of $\sim 1000^\circ\text{C}$, Al_2O_3 and SiO_2 scales should be preferred to provide corrosion resistance. While the kinetic stages leading to the development of a continuous-surface oxide layer are certainly of importance, once such an oxide layer is established, the most important consideration is how well the oxide layer adheres to the alloy surface. The factors which influence the adhesion of oxide scales are not well understood. It has been pointed out by several investigators that small amounts of rare earth oxide dispersoids present in the alloy lead to the formation of a more adherent surface-oxide scale (3-17). The literature information in this area was reviewed recently (18-19).

Several mechanisms have been proposed in the literature to explain the dispersoid effect:

1. The oxide scale develops numerous protrusions/pegs which form around rare earth oxide particles in the alloy. These pegs anchor the oxide scale to the alloy.
2. The rare earth oxide particles react with the main oxide scale and form a mixed-oxide layer between the main scale and the alloy. The mixed-oxide layer acts as a "graded seal" improving the stability of the oxide scale under thermal cycling conditions.

3. The rare earth oxide particles in the alloy act as sites on which vacancies generated by the oxidation process condense. The vacancies thus do not coalesce on the scale/metal interface, a process which could lead to oxide spallation.

4. The rare earth element dissolves into the scale and suppresses Al transport in the scale. Thus, growth stresses, otherwise developed by the formation of alumina within an existing scale, are decreased.

Sufficient experimental evidence does not exist to confirm the above mechanisms. Also, most of the published studies point to a combination of mechanisms rather than a single mechanism being operative. Thus, a consistent picture of the dispersoid effect has not emerged.

The purpose of the present investigation is to improve our understanding of the influence of rare earth oxide dispersoids on oxide-scale properties. As the first of a proposed series of investigations, it was decided to examine the properties of alumina scales developed on an Fe-based alloy system containing yttrium oxide as the dispersoid. The results of this study are contained in the present paper.

Materials and Experimental Procedure

The experimental alloy selected for investigation was alloy MA956, made by the International Nickel Company. Two types of samples were used; one had a fine-grained ($\sim 0.2\ \mu\text{m}$) microstructure typical of the as-received condition, while the other had a coarse-grained structure which results upon heat-treating (Fig. 1). The distribution of dispersoid particles is shown in Fig. 2. The particles have been identified by microdiffraction to be YAlO_3 . The specimens were rectangular, $1 \times 1/2 \times 1/16$ in.; the faces were ground to 600 grit SiC and cleaned ultrasonically in acetone.

The kinetics of oxidation was measured by thermogravimetry using a Cahn 1000 electrobalance. The electrobalance was attached to a vertically placed quartz reactor tube; the sample to be oxidized was hung from the balance by

*Electrochemical Society Active Member.
Key words: oxidation, defects, kinetics.

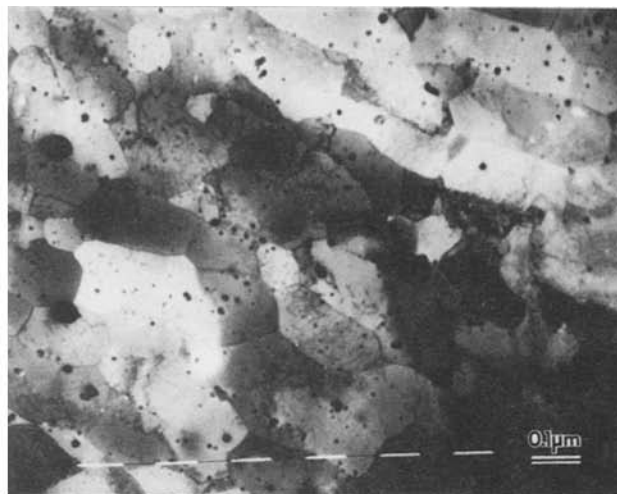
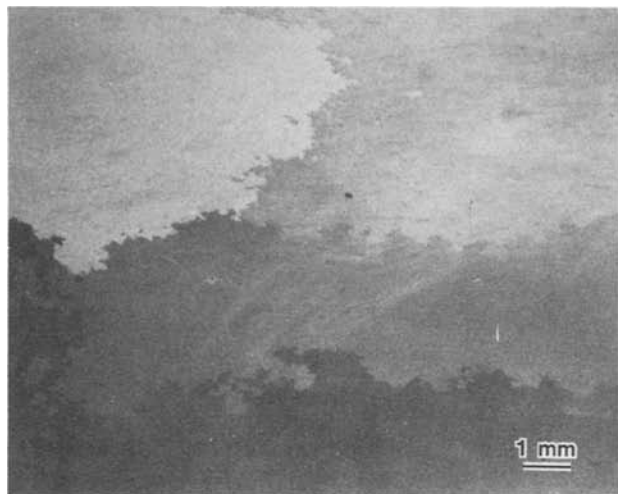


Fig. 1. Fine-grained and coarse-grained MA956 samples used in the study

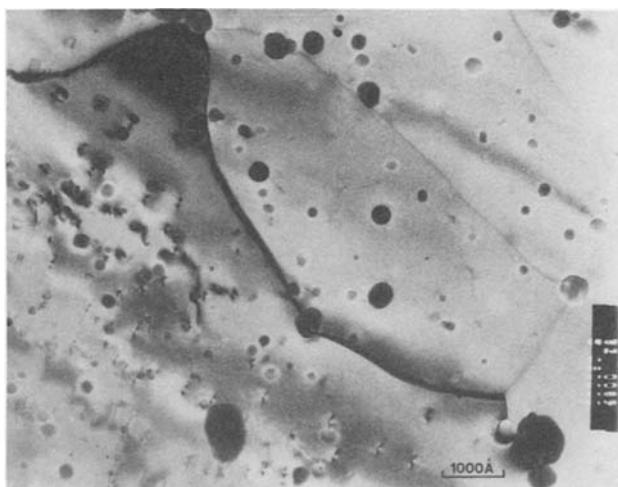


Fig. 2. Dispersoid distribution in alloy MA956

means of a platinum suspension wire. A platinum resistance furnace surrounded the quartz tube; the furnace could be moved up and down hydraulically. The oxidizing gas entered the quartz tube at the bottom and escaped at the top, where it mixed with an argon stream used to provide an inert atmosphere within the electrobalance assembly.

At the start of an experimental run, the sample to be oxidized was hung from the electrobalance and the quartz reactor tube slid into place, the furnace being in the "down" position. The reactor tube was kept under a purging argon stream, and the furnace brought to the oxidation temperature, the sample still being held at room temperature. The argon flow was then replaced by the oxidizing gas or gas mixture, the flow rate being high enough so that mass transport in the gas phase would not be rate controlling. After an interval of ~30 min, the furnace was hydraulically lifted up around the sample so that the sample was positioned within the constant temperature zone ($\pm 1^\circ\text{C}$) of the furnace. It took approximately 10 min for the sample to attain the experimental temperature. An HP 9845T computer was used to collect and analyze weight-gain data.

The oxidation kinetics were investigated in the temperature range $900^\circ\text{--}1200^\circ\text{C}$. The environments used were undried air, dry oxygen, and CO/CO_2 gas mixtures of varying oxygen partial pressures. The adherence of the oxide scales developed on the alloy surface was inferred by weight changes upon rapidly cooling the sample to room temperature by lowering the furnace and/or temperature cycling by raising and lowering the furnace at specific intervals.

Upon completion of the kinetic runs, the morphology and structure of the oxide scales formed on the alloy surface were examined using scanning electron microscopy, trans-

mission electron microscopy, microdiffraction, and secondary ion mass spectrometry.

Results

Most samples were oxidized for periods ranging from 25 to 100h in the thermogravimetric unit. A few samples were oxidized up to 1000h in a separate furnace; kinetic data are not available for these longer-term experiments. The oxide scales were characterized by their excellent adherence; no oxide spallation could be detected upon quenching the sample to room temperature from oxidation temperatures in the range $900^\circ\text{--}1200^\circ\text{C}$ even after oxidation times as long as 100h.

Most of the experimental data were taken in the temperature range $1000^\circ\text{--}1200^\circ\text{C}$. A parabolic rate was obeyed for oxidation times as long as 100h. The slope of a plot of the square of the oxidation weight gain per unit area vs. time is the parabolic rate constant, k_p ($\text{g}^2 \text{cm}^{-4} \text{s}^{-1}$). The rate constant is plotted as a function of temperature in Fig. 3. The data for the fine- and coarse-grained samples fall on the same regression line, the grain size of the alloy having little influence on the oxidation rate. The rate constant can be expressed by the relationship

$$k_p (\text{g}^2 \text{cm}^{-4} \text{s}^{-1}) = 4.2 \times 10^2 \exp(-92,800/RT) \quad [1]$$

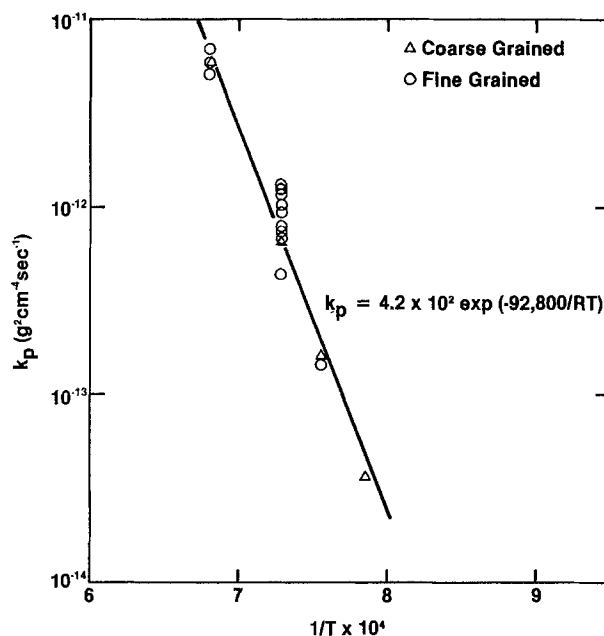


Fig. 3. Parabolic rate constant for $\alpha\text{-Al}_2\text{O}_3$ growth as a function of temperature.

The oxidized samples were fractured under liquid nitrogen and the fracture cross sections examined by SEM. A columnar fine-grained scale morphology was revealed (Fig. 4). The oxide grain sizes were temperature independent when oxidized in the temperature range 1000°-1200°C for times ranging from 25 to 100h, with grains measuring approximately 1-2 μm in length and $\sim 0.5 \mu\text{m}$ across. At 1200°C, upon increasing the oxidation time to 300h, the average grain width increased to 0.75 μm , while after 1000h, the width was approximately 1.25 μm . Thus, the oxide scale remained essentially fine grained even after long oxidation times (Fig. 5). X-ray diffraction analysis showed the scales to be exclusively $\alpha\text{-Al}_2\text{O}_3$.

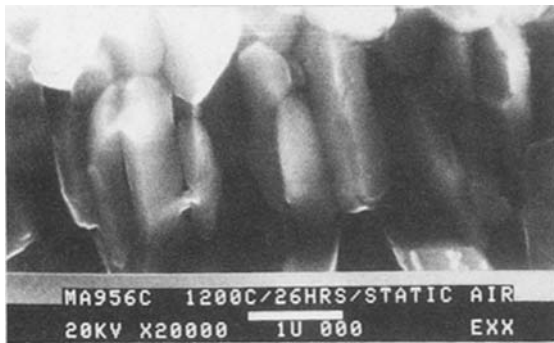


Fig. 4. Columnar fine-grained morphology of $\alpha\text{-Al}_2\text{O}_3$ scales

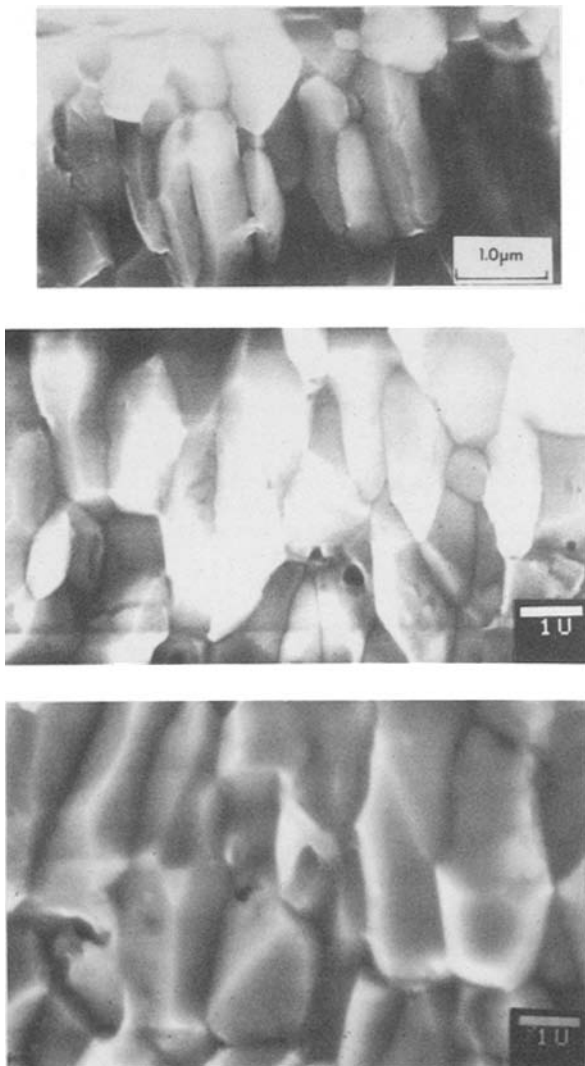


Fig. 5. Dependence of $\alpha\text{-Al}_2\text{O}_3$ grain width on oxidation time. Top: 24h in air, 1200°C. Center: 300h in air, 1200°C. Bottom: 1000h in air, 1200°C.

In order to characterize the oxide films further, thin films were prepared and examined using a Philips EM 400 transmission electron microscope. The films were prepared by first electropolishing the metal away and then ion thinning the oxide scale. In some cases, only ion thinning was used. The TEM investigations again revealed the fine-grained nature of the oxide scale. A thinned section, viewed perpendicular to the oxide/metal interface, reveals the presence of fine microvoids, $\sim 500\text{\AA}$ in size; the voids occur predominantly at oxide grain boundaries (Fig. 6). Microdiffraction analysis in the TEM confirmed the oxide scale to be $\alpha\text{-Al}_2\text{O}_3$.

Further detailed examination of the scale was carried out in order to detect the YAlO_3 particles originally present in the alloy. The only yttrium containing phase found in the oxide scale was yttrium aluminum garnet, $\text{Y}_3\text{Al}_5\text{O}_{12}$. This phase was typically 0.2-0.5 μm in size, as revealed by the TEM micrograph to the left in Fig. 7. The phase was identified by microdiffraction. The [001] diffraction pattern is shown on the right in Fig. 7. The zero layer in this pattern consists of a square grid of {200} reflections, and the third dimension was calculated from the diameter of the ring to be 12.05 \AA , consistent with the lattice parameter of garnet. The garnet phase was located principally in the vicinity of $\alpha\text{-Al}_2\text{O}_3$ grain boundaries. It is interesting to note the coarseness of the garnet phase when compared with the fine YAlO_3 particles present in the alloy (Fig. 2). The size difference is further revealed in the transmission electron micrograph in the vicinity of an oxide/metal interface (Fig. 8).

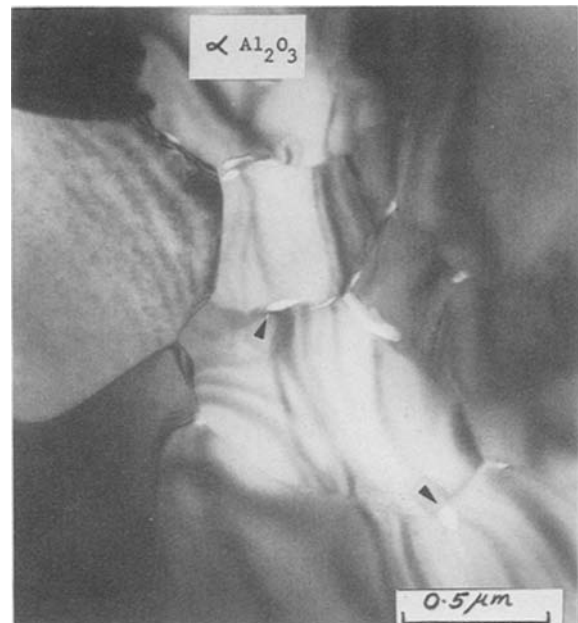


Fig. 6. TEM micrograph of $\alpha\text{-Al}_2\text{O}_3$ revealing grain boundary microvoids.

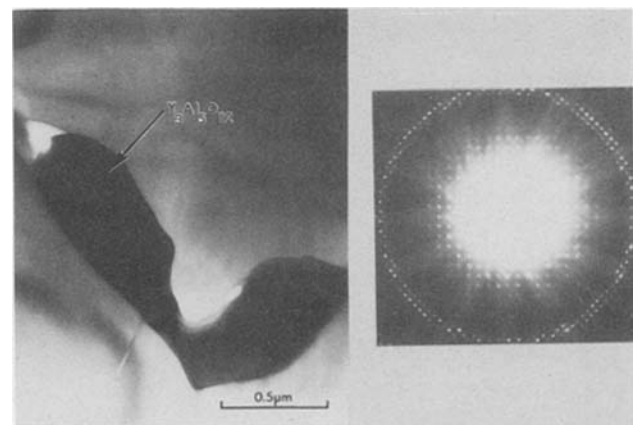


Fig. 7. TEM micrograph and electron diffraction pattern showing the $\text{Y}_3\text{Al}_5\text{O}_{12}$ phase in $\alpha\text{-Al}_2\text{O}_3$.

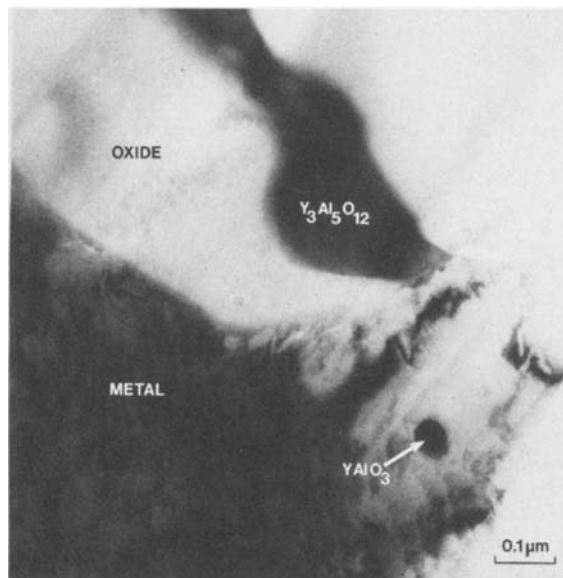


Fig. 8. TEM micrograph in the vicinity of the oxide/metal interface showing coarse $Y_3Al_5O_{12}$ in the oxide and fine $YAlO_3$ in the metal.

In order to determine the distribution of the $Y_3Al_5O_{12}$ phase in a thick $\alpha-Al_2O_3$ scale, a MA 956 alloy specimen was oxidized for 1000h at 1200°C in air and examined in cross section using a Cameca secondary ion mass spectrometer. Ion maps for Al^+ and Y^+ are shown in Fig. 9. The field of view in Fig. 9 is 150 μm ; the positive secondary ions were monitored, sputtered, and excited with a 15 keV beam of O_2^+ . Because the spacial resolution of SIMS is $\sim 0.5 \mu m$, the fine yttrium containing oxides in the metal are not resolved. The $Y_3Al_5O_{12}$ phase in the oxide scale is clearly shown; there is some degree of charging in the Y^+ ion map which has exaggerated the size of the garnet phase. It is clearly seen that the fine $YAlO_3$ particles have dissolved upon entering the oxide scale and reprecipitate as garnet.

A limited number of oxidation experiments were carried out at a lower temperature of 900°C at high oxygen partial pressures. A difference in kinetics was noticed upon oxidizing fine-grained MA 956 samples in undried air and dry oxygen. The kinetics were faster in undried air (Fig. 10). Examination of the oxide scales by TEM revealed that in the air-oxidation case, the alumina scale was made up of a mixture of α - and δ -phases, while in the case of dry oxygen, the scale was exclusively the α -phase. A TEM micrograph of the δ -phase and the corresponding [100] microdiffraction pattern are shown in Fig. 11. The microdiffraction pattern shows a rectangular grid of (010) and (002) reflections. The δ -phase is seen to have a faulted structure and probably al-

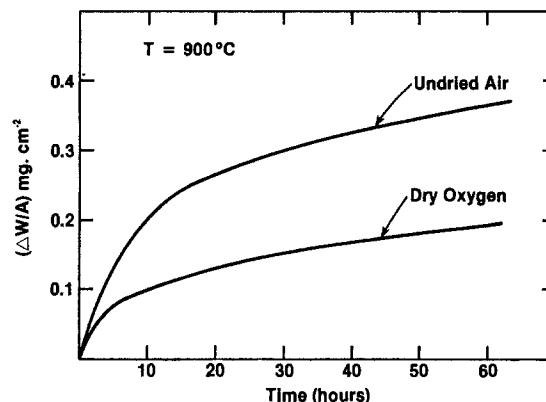


Fig. 10. Oxidation kinetics of MA956 at 900°C

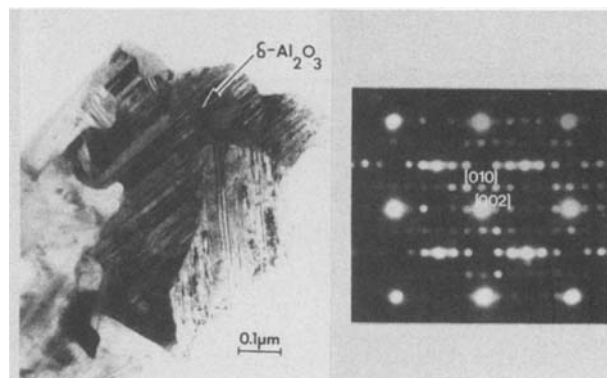


Fig. 11. TEM micrograph and [100] electron diffraction pattern for $\delta-Al_2O_3$ phase.

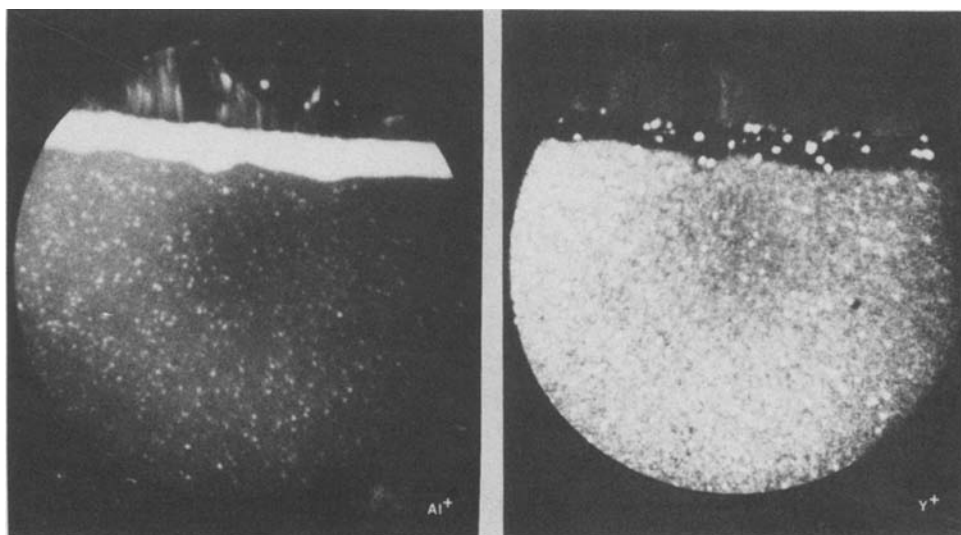
lows more rapid transport of reactant species, as suggested by the kinetic data shown in Fig. 10.

Discussion

Anion migration through Al_2O_3 scale.—Parabolic kinetics of $\alpha-Al_2O_3$ scale growth suggests that the oxide scale growth is limited by diffusional transport through it. To establish whether oxygen or aluminum is the predominant mobile species in the oxide scale, Pt-wire markers were positioned on the alloy surface prior to oxidation. Upon completion of oxidation, the Pt markers remained at the oxide/gas interface, suggesting that scale growth occurred by oxygen transport (Fig. 12).

The diffusivity of oxygen in single-crystalline and polycrystalline (20-30 μm grain size) $\alpha-Al_2O_3$ at 1200°-1800°C has been measured by Oishi and Kingery (20). Between 1400° and 1800°C their data for oxygen diffusivity in single crystalline and polycrystalline $\alpha-Al_2O_3$ are given, respectively, by

Fig. 9. SIMS ion maps for Al^+ and Y^+ in MA956 at 900°C.



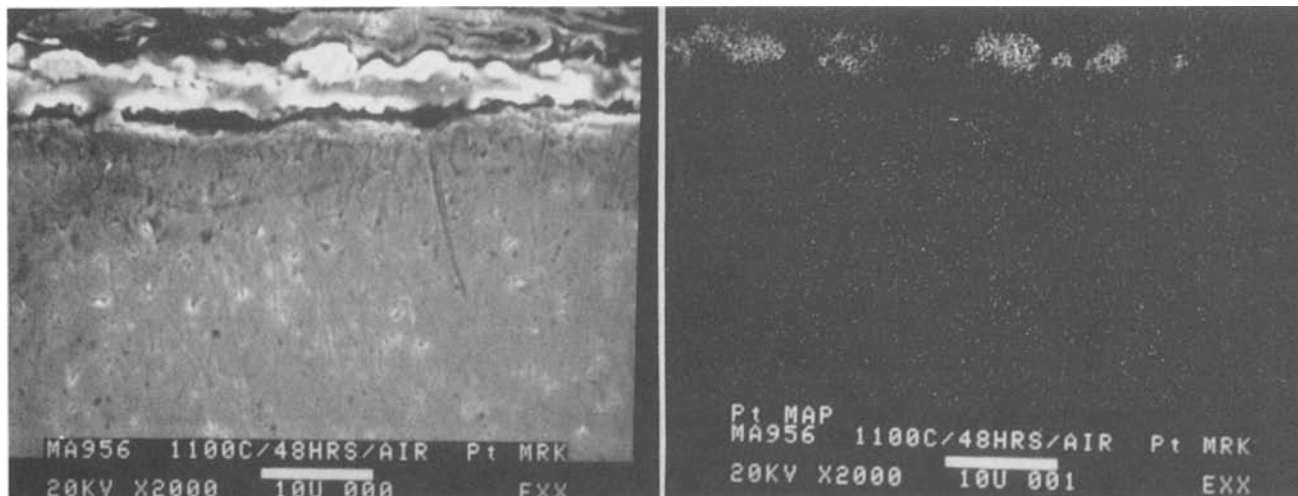


Fig. 12. Platinum marker study showing the inward growth of $\alpha\text{-Al}_2\text{O}_3$ scale by oxygen diffusion

$$D_0^l = 1.9 \times 10^8 \exp(-152,000/RT) \text{ cm}^2/\text{s} \quad [2]$$

$$D_0^{\text{eff}} = 2 \exp(-110,000/RT) \text{ cm}^2/\text{s} \quad [3]$$

where D_0^l denotes the lattice diffusivity of oxygen in the single crystal and D_0^{eff} denotes the effective diffusivity (made up of both lattice and grain-boundary contributions) of oxygen in the polycrystalline sample. Experimental data below 1400°C deviated from the above expressions presumably because of impurities contained in the $\alpha\text{-Al}_2\text{O}_3$ samples.

If the data according to Eq. [2] and [3] are extrapolated to 1200°C , then $D_0^l \sim 5.3 \times 10^{-20} \text{ cm}^2 \text{ s}^{-1}$ and $D_0^{\text{eff}} \sim 9.5 \times 10^{-17} \text{ cm}^2 \text{ s}^{-1}$. The effective diffusivity can be expressed in terms of lattice and grain boundary components as (21)

$$D_0^{\text{eff}} = (1 - f)D_0^l + fD_0^{\text{gb}} \quad [4]$$

where D_0^{gb} represents the grain boundary oxygen diffusivity and f is the fractional volume for grain boundary diffusion. The factor f can be equated to $k\delta/d$ where k is a geometrical constant (k was taken to be 2 in this study), δ is the grain boundary width, and d is the grain width. Thus

$$D_0^{\text{eff}} = D_0^l + \frac{k\delta}{d}(D_0^{\text{gb}} - D_0^l) \cong D_0^l + \frac{k\delta}{d}D_0^{\text{gb}} \quad [5]$$

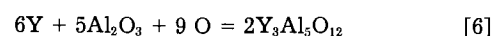
since $D_0^{\text{gb}} \gg D_0^l$

Using the extrapolated values of D_0^{eff} and D_0^l at 1200°C , it is easily seen that for grain sizes in the 20-30 μm range, the effective oxygen diffusivity in $\alpha\text{-Al}_2\text{O}_3$ is predominantly determined by grain boundary diffusion. Also, in view of Eq. [5], the contribution to grain boundary transport would be even higher as the grain width, d , decreases. It can be concluded that in the $\alpha\text{-Al}_2\text{O}_3$ scales formed on Alloy MA 956, in which $d \sim 1 \mu\text{m}$, oxygen transport occurs almost exclusively through the grain boundary.

Incorporation of YAlO_3 particles into inward growing $\alpha\text{-Al}_2\text{O}_3$ scale: yttrium doping.—As discussed earlier, the YAlO_3 particles in the alloy are in the size range 200-500 \AA . Particles in this size range or of this composition have not been detected in the $\alpha\text{-Al}_2\text{O}_3$ scale. Instead, only coarse yttrium aluminum garnet particles in the size range 0.2-0.5 μm have been detected. This phase forms predominantly in the vicinity of $\alpha\text{-Al}_2\text{O}_3$ grain boundaries. Energy dispersive x-ray analysis of the alumina in the grain boundary and bulk regions reveals a strong tendency for yttrium to segregate to the grain boundary (Fig. 13). The analysis in the grain-boundary region is averaged over a width of $\sim 200\text{\AA}$. Grain boundary segregation of yttrium in alumina has also been reported in a previous study (22).

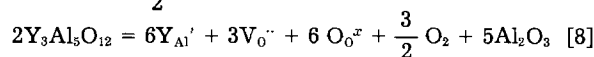
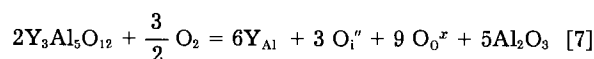
In view of the above findings, it is suggested that the YAlO_3 particles from the alloy dissolve upon incorporation into the oxide/metal interface region. The yttrium rapidly diffuses along the metal/oxide interface and segregates to the Al_2O_3 grain boundary region as the oxide grows into the metal. At some point, the solubility product for $\text{Y}_3\text{Al}_5\text{O}_{12}$ is exceeded in the vicinity of some of the Al_2O_3 grain bounda-

ries, whereupon this phase is precipitated



The oxygen supply for reaction [6] is provided by grain boundary transport. The suggested mechanism is shown schematically in Fig. 14.

The $\alpha\text{-Al}_2\text{O}_3$ scale formed on the alloy may be considered to be saturated with $\text{Y}_3\text{Al}_5\text{O}_{12}$, and the scale will have a certain doped concentration of yttrium, which is predominantly present in the vicinity of grain boundaries. However, the bulk grain is also probably doped with yttrium at lower concentration levels. It has been proposed that doped yttrium tends to reduce Al transport through bulk $\alpha\text{-Al}_2\text{O}_3$ grains (23, 24). Such an effect cannot be expected if yttrium occupies the Al lattice site in $\alpha\text{-Al}_2\text{O}_3$ as a trivalent dopant with zero effective charge. However, El-Aiat and Kröger (25) argue that yttrium might act as a donor Y_{Al} , a yttrium defect with a positive effective charge. In the present discussion, it is considered that yttrium might act as a donor or an acceptor in accordance with the following defect equilibria



The equilibria [7] and [8] imply that defects generally proposed for bulk grains also prevail in the vicinity of grain boundaries. This is appropriate because the high diffu-

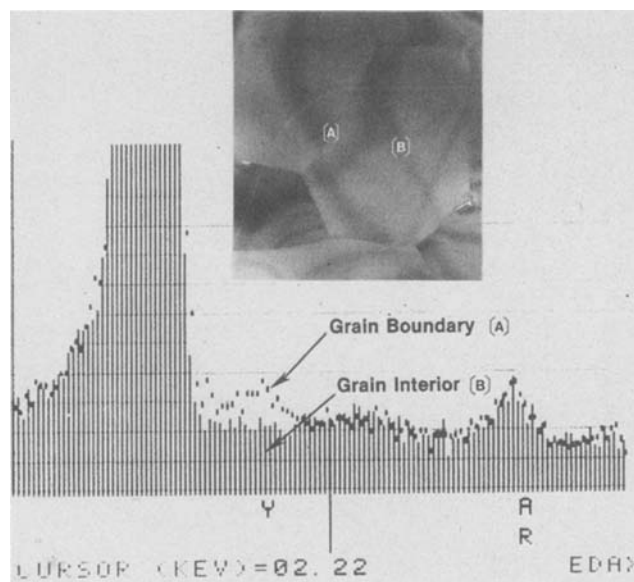
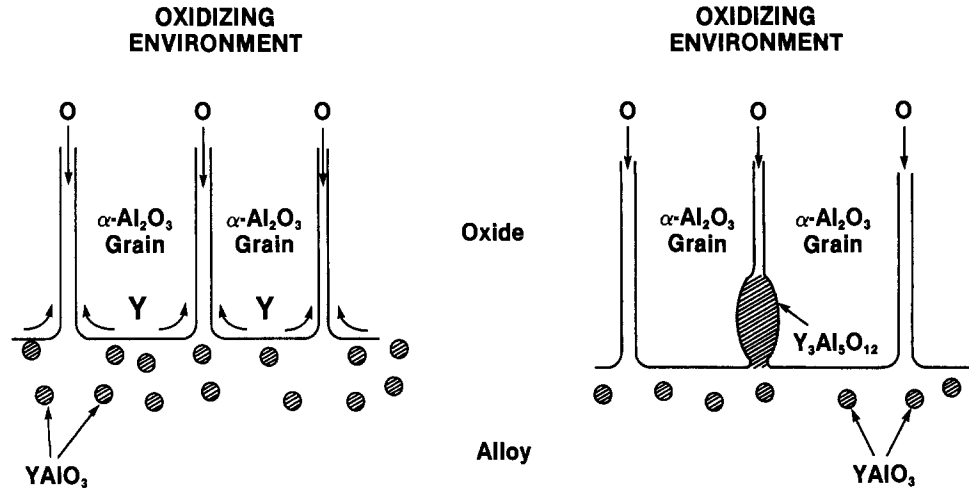


Fig. 13. Grain boundary segregation of yttrium in $\alpha\text{-Al}_2\text{O}_3$

Fig. 14. Mechanism for precipitation of $Y_3Al_5O_{12}$ in $\alpha-Al_2O_3$.



sivity path for rapid transport in the vicinity of an $\alpha-Al_2O_3$ grain boundary is $\sim 100-150\text{\AA}$ wide (26). Wang and Kroger (27) have also used defect descriptions generally used for bulk grains for the grain boundary region.

Alpha Al_2O_3 has a high bandgap of ~ 9.9 eV (28, 29); the concentrations of native defects formed by electronic or ionic disorders is extremely small. Thus, for equilibrium [7], one can use the electroneutrality condition

$$[Y_{Al}'] = 2[O_i''] \quad [9]$$

where [] denotes concentration. Combining the equilibrium constant, K_I , for reaction [7] with Eq. [9],

$$K_I = 64 [O_i'']^3 P_{O_2}^{-3/2} \quad [10]$$

Thus $[O_i''] \propto P_{O_2}^{1/6}$. Since the diffusivity of oxygen will have the same oxygen partial pressure dependence as the major oxygen defect (30)

$$D_0^{gb} = D_0^{*gb} P_{O_2}^{1/6} \quad [11]$$

where D_0^{gb} is the oxygen diffusivity in the vicinity of $\alpha-Al_2O_3$ grain boundary and D_0^{*gb} is the value at 1 atm oxygen partial pressure.

Use of similar arguments to reaction [8] along with the neutrality condition, $[Y_{Al}'] = 2[V_O'']$ leads to

$$K_{II} = 64 [V_O'']^3 P_{O_2}^{3/2} \quad [10.1]$$

$$D_0^{gb} = D_0^{*gb} P_{O_2}^{-1/6} \quad [11.1]$$

Where K_{II} is the equilibrium constant for reaction [8].

Quantitative description of oxidation kinetics.—In the following analysis, the $\alpha-Al_2O_3$ scale is considered to consist of columnar grains having a square cross section of side d . The oxide scale is presumed to grow exclusively by grain-boundary transport of oxygen. The width of the boundary region where rapid transport occurs is designated δ . The oxygen flux during oxide scale growth is considered to occur exclusively in a direction parallel to the grain boundary. The oxygen flux per unit area of the grain boundary is then given by

$$J_0 \text{ (mol cm}^{-2} \text{ s}^{-1}) = -B_0 C_0 \left(\frac{\partial \mu_0}{\partial x} \right) \\ = -\frac{1}{2} B_0 R T C_0 \left(\frac{\partial \ln P_{O_2}}{\partial x} \right) = -\frac{1}{2} D_0^{gb} C_0 \left(\frac{\partial \ln P_{O_2}}{\partial x} \right) \quad [12]$$

where B_0 is the mobility of oxygen (velocity per unit gradient of chemical potential), C_0 is the average oxygen concentration in the oxide in mol cm^{-3} , μ_0 is the chemical potential of oxygen in the oxide, and x the distance coordinate perpendicular to the oxide/metal interface. The oxygen partial pressure at the oxide/gas interface is designated as $P_{O_2}^0$ and at the oxide/metal interface as $P_{O_2}^1$. Per unit area of the oxide scale, the area occupied by grain boundary equals $\sim 2\delta/d$. Thus, the flux, J_0' of oxygen per unit area of the oxide scale is given by

$$J_0' = -D_0^{gb} C_0 \delta d^{-1} \left(\frac{\partial \ln P_{O_2}}{\partial x} \right) \quad [13]$$

Integrating across thickness, Δx , of oxide scale

$$J_0' \Delta x = C_0 \delta d^{-1} \int_{P_{O_2}^1}^{P_{O_2}^0} D_0^{gb} d \ln P_{O_2} \quad [14]$$

Using the relations, $J_0' = 1/16A (d\Delta w/dt)$ and $\Delta x = \Delta w/(\rho_{oxide} f_o A)$, where ρ_{oxide} is the density of $\alpha-Al_2O_3$, Δw is the oxidation weight gain measured thermogravimetrically, A is the cross-sectional contact area between oxide and metal, and f_o is the weight fraction of oxygen, Eq. [14] can be rewritten as

$$\frac{1}{A^2} \int_0^{\Delta w} \Delta w d\Delta w = [16 \rho_{oxide} f_o C_0 \delta d^{-1} \int_{P_{O_2}^1}^{P_{O_2}^0} D_0^{gb} d \ln P_{O_2}] \int_0^t dt \quad [15]$$

Integrating and rearranging

$$\left(\frac{\Delta w}{A} \right)^2 = [59.78 C_0 \delta d^{-1} \int_{P_{O_2}^1}^{P_{O_2}^0} D_0^{gb} d \ln P_{O_2}] t \quad [16]$$

whereby the parabolic rate constant (Fig. 3), k_p , is given by

$$k_p = 59.78 C_0 \delta d^{-1} \int_{P_{O_2}^1}^{P_{O_2}^0} D_0^{gb} d \ln P_{O_2} \quad [17]$$

In integrating Eq. [17], the variation of D_0^{gb} with oxygen partial pressure must be taken into account. If yttrium acts as a donor and leads to the formation of O_i'' defects, then Eq. [11] holds. Combining Eq. [11] and [17]

$$k_p = 358.68 \delta d^{-1} C_0 D_0^{*gb} (P_{O_2}^{0/6} - P_{O_2}^{1/6}) \quad [18]$$

At 1100°C , $p_{O_2}^1 \sim 5 \times 10^{-28}$ atm. The lowest environmental oxygen partial pressure used in the present investigation is $\sim 10^{-14}$ atm. Thus $P_{O_2}^{0/6} \gg P_{O_2}^{1/6}$ so that

$$k_p = 358.68 \delta d^{-1} C_0 D_0^{*gb} P_{O_2}^{0/6} \quad [19]$$

Thus k_p is strongly dependent on the environmental oxygen partial pressure.

If yttrium acts as an acceptor and creates oxygen vacancies as the predominant defects, then, combining Eq. [11.1] and [17]

$$k_p = 358.68 \delta d^{-1} C_0 D_0^{*gb} (P_{O_2}^{-1/6} - P_{O_2}^{0-1/6}) \quad [20]$$

In this case, since $P_{O_2}^{-1/6} \gg P_{O_2}^{0-1/6}$

$$k_p = 358.68 \delta d^{-1} C_0 D_0^{*gb} P_{O_2}^{-1/6} \quad [21]$$

Thus, k_p should be independent of the environmental oxygen partial pressure.

To test whether Eq. [19] or [21] applies, the variation of k_p with oxygen partial pressure has been measured at 1100° and 1200°C . Within limits of experimental error, k_p is found to be independent of the oxygen partial pressure. Typical data at 1100°C are presented in Fig. 15. It is, therefore, suggested that oxygen vacancies rather than interstitials are responsible for grain boundary oxygen transport. Using experimental values for k_p and the average grain width, d , the

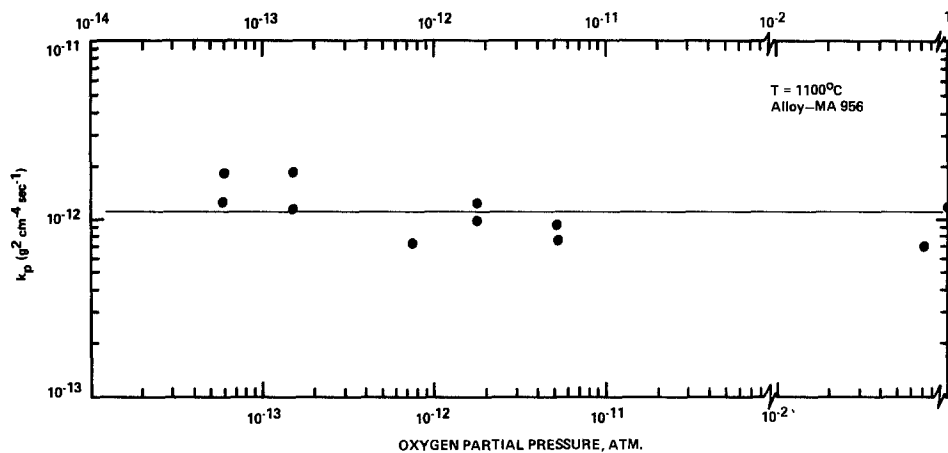


Fig. 15. Variation of k_p with oxygen partial pressure.

following expression has been evaluated for the product δD_0^{*sb}

$$\delta D_0^{*sb} (\text{cm}^3 \text{ s}^{-1}) = 4.92 \times 10^{-2} \exp(-133,940/RT) \quad [22]$$

Equation [22] holds for 1 atm oxygen partial pressure. For other oxygen partial pressures

$$\delta D_0^{*sb} = \delta D_0^{*sb} P_{O_2}^{-1/6} \quad [23]$$

The activation energy term in Eq. [22] is made up of contributions from the temperature dependence of δ and the temperature dependence of D_0^{*sb} .

The present results for δD_0^{*sb} may be compared with values for δD_0^{*sb} calculated from Oishi and Kingery (20)

$$\delta D_0^{*sb} = 1.4 \times 10^{-3} \exp(-110,000/RT) \quad [24]$$

and values measured by Reddy (31)

$$\delta D_0^{*sb} = 8.15 \exp(-142,000/RT) \quad [25]$$

However, no oxygen partial pressure dependencies are available for these values.

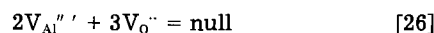
A mechanism for microvoid formation in $\alpha\text{-Al}_2\text{O}_3$ grain boundaries.—The production of voids in oxide scales growing under an oxygen partial pressure gradient is by no means a new phenomenon. Pores have been observed, for example, in oxidized scales of Fe_3O_4 (32), FeO (33), NiO (34), and Al_2O_3 (35, 36). In Fe_3O_4 , FeO , and NiO , the pores were large enough to be detected by optical metallography. Evidence of pore formation in CoO placed under an oxygen partial pressure gradient was obtained by Yurek and Schmalzried (37). A pellet of CoO , initially equilibrated at $P_{O_2} = 0.2$ atm at 1200°C , was placed in a P_{O_2} gradient so that one face was at 0.2 atm and the other face was at 10^{-9} atm. After 1.5h at 1200°C , the crystal developed ~5 volume percent (v/o) porosity. The authors suggested that the pores are formed as a result of cobalt vacancy diffusion from the high P_{O_2} side and subsequent precipitation at the low P_{O_2} side.

The above examples suggest that the formation of pores in oxide scales placed under a P_{O_2} gradient is related to atomic defects in the crystal and occurs by vacancy condensation. In their work on Al_2O_3 scales formed on Ni-Cr-Al alloys, Smialek and Gibala (35) tentatively proposed a model based on oxygen-vacancy supersaturation and condensation to account for void formation. The voids were present both within the grain and in the grain boundary. The model they proposed is schematically indicated in Fig. 16. Assuming oxygen vacancies to be the predominant migrating defect, the solid line in Fig. 16 represents the oxygen vacancy gradient within the scale at a scale thickness, Δx . Local equilibrium is assumed at the metal/oxide and the oxide/gas interfaces. When the oxide has grown to a thickness, $\Delta x'$, the new oxygen vacancy gradient is represented by the dotted line. This implies a supersaturation of oxygen vacancies in the growing scale, which condenses out as voids in establishing the new equilibrium oxygen vacancy gradient.

Elegant though this mechanism is, it suffers from a flaw; if the oxygen vacancy concentration at the oxide/metal interface exceeds the equilibrium value, the interface cannot move, since this would imply an oxygen concentration below that required for oxide/metal equilibrium. To maintain

the oxygen concentration (and, therefore, the oxygen vacancy concentration) at the oxide/metal interface at the equilibrium value, the arriving oxygen flux must overcome any oxygen vacancy supersaturation within the oxide.

The following mechanism is tentatively proposed to account for grain boundary voids in $\alpha\text{-Al}_2\text{O}_3$ scales of the present study. As yttrium dissolves into the $\alpha\text{-Al}_2\text{O}_3$ scale as the scale grows inward, the oxygen vacancy concentration in the vicinity of oxide grain boundaries increases by virtue of reaction [8]. If Schottky defects are assumed in $\alpha\text{-Al}_2\text{O}_3$, the increase in oxygen vacancy concentration must be accompanied by a decrease in the aluminum vacancy concentration in the vicinity of grain boundaries by virtue of the Schottky defect equilibrium



$$K_s = [V_{O}^{\bullet}]^3 [V_{Al}']^2 \quad [27]$$

where K_s is the Schottky defect equilibrium constant. Thus, in attaining the lower aluminum vacancy concentration required by the increase in the oxygen vacancy concentration, the excess aluminum vacancies must condense out in the grain boundary region; this process generates grain boundary microvoids.

Adherence of $\alpha\text{-Al}_2\text{O}_3$ scales.—Of the effects produced by oxide dispersions on the properties of oxide scales on high temperature alloys, the most significant from a technological point of view is the adherence of the oxide scale. In the sense in which the term "adherence" is used in most of oxidation literature, it refers to the resistance of the scale to spallation under the influence of stresses. In isothermal oxidation, one is mainly concerned with growth stresses. In alloy components used in various high temperature processes, additional stresses arise which are thermally in-

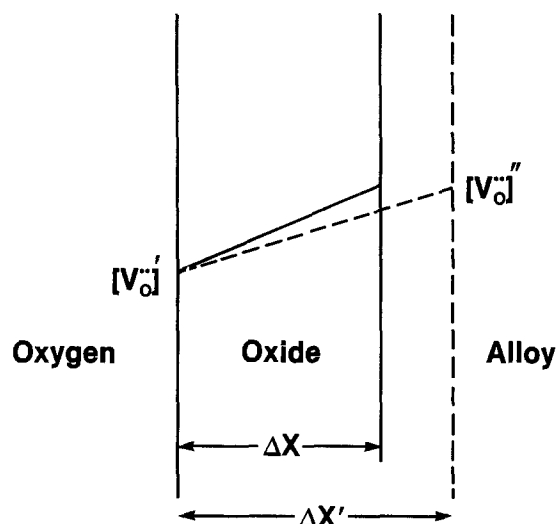


Fig. 16. Schematic oxygen vacancy concentration profile in growing $\alpha\text{-Al}_2\text{O}_3$.

duced (due to temperature oscillations) and/or mechanically induced.

It was pointed out earlier that several mechanisms have been proposed in the literature as contributing to rare earth oxide dispersoid-induced oxide-scale adherence. The most widely accepted mechanism is that the oxide scale develops protrusions (pegs), which form around dispersoid particles in the alloy; these protrusions anchor the scale to the alloy. Giggins and Pettit have suggested the existence of pegs in Co-Cr-Al-Y and Ni-Cr-Al-Y systems (38). Pegs have been observed especially in Hf containing alloys forming alumina, in which internally oxidized HfO_2 particles were present in the alloy subsurface region. Whittle *et al.* (39) have presented evidence for peg formation in Co-Cr-Al-Hf alloys in which the Hf was oxidized to HfO_2 particles. A more dramatic case of pegging has been recently observed by Hindam and Whittle (40) in Fe-10Al-Hf alloys in which subsurface HfO_2 particles were present. They have suggested a mechanism for peg formation according to which HfO_2 particles in the Al_2O_3 scale act as short-circuit paths for oxygen transport. In regions of the scale where HfO_2 particles are present, especially close to the alloy/scale interface, more rapid Al_2O_3 growth occurs, leading to protrusions which envelop HfO_2 .

A detailed examination of the oxide/metal interface was made in the present study to look for any evidence of pegs around dispersoid particles. A TEM micrograph in the vicinity of the oxide/metal interface is shown in Fig. 17. The dispersoid particles are clearly seen in the metal in the vicinity of the oxide/metal interface; there are no pegs around the particles. The absence of pegging is also clearly revealed by the ion maps for Al^+ and Y^+ generated by secondary ion mass spectrometry (Fig. 9). Thus, pegging must be ruled out as a mechanism for adherence in the case of yttria-dispersed alumina forming alloys.

The second mechanism proposed in the literature is that a mixed-oxide phase forms by reaction of the main oxide scale with the rare earth oxide, and this phase is present as a thin layer between the main scale and the alloy. The mixed-oxide phase is supposed to have a thermal expansion coefficient which is intermediate between that for the main scale and the alloy so that a "graded-seal" effect is produced. There is no sound evidence of such a mixed-oxide layer in any reported investigation. In a study of the oxidation of a Cr-5 v/o Y_2O_3 alloy, Seybolt (12) provides tentative evidence for a thin YCrO_3 intervening layer. However, the existence of such a layer has never been confirmed. No mixed-oxide layer could be detected between the $\alpha\text{-Al}_2\text{O}_3$ scale and the alloy in the present investigation.

The third mechanism is based on the argument that vacancies generated in the alloy when an element such as Al is preferentially oxidized can condense at metal/dispersoid interfaces. These vacancies, therefore, are not available to coalesce on the metal/scale interface, a process which can

lead to loss of scale adherence. In their work on the mechanism of oxide-scale adherence on Fe-25Cr-4Al-(Y or Sc) alloys, Tien and Pettit (41) suggested that internally oxidized Sc_2O_3 and Y_2O_3 particles act as sinks for vacancies generated during oxidation. In a comparative study of the oxidation of Ni_3Al and $\text{Ni}_3\text{Al-0.5Y}$ alloys, Kuenzly and Douglass (42) observed condensation of vacancies at the alumina/alloy interface in the case of the yttrium-free alloy. The vacancies were thought to form as the result of a "Kirkendall effect" in the alloy subsurface region upon preferential removal of Al by oxidation. Voids were absent in the yttrium containing alloy and are thought to have condensed around internally oxidized Y_2O_3 particles. However, no microstructural evidence for void condensation around Y_2O_3 particles was presented. Also, the present authors are not aware of published literature data which confirm the presence of voids around dispersoids. Examination of dispersoid particles by TEM in the present study did not show any evidence of void condensation.

In the opinion of the present authors, the improved adherence of $\alpha\text{-Al}_2\text{O}_3$ scales on Y_2O_3 -dispersed alloys is caused by the chemical doping of yttrium into the oxide scale and consequent effects on the relief of growth stresses. It is well documented that during the oxidation process of a metal growth stresses arise. The subject has been reviewed by Stringer (43). It is considered that yttrium doping leads to growth stress relief in two ways: (i) by effecting the formation of a fine-grained oxide scale, and (ii) by retarding Al transport in the scale.

It has been shown that in polycrystalline alumina having grain sizes less than $\sim 15 \mu\text{m}$, diffusional creep is the most important mechanism for plastic deformation (44). The generalized expression for the creep strain rate, $\dot{\epsilon}$, is given by (45, 46)

$$\dot{\epsilon} = \frac{14\Omega}{kTd^2} \left[\frac{(D_{\text{Al}}^{\text{l}} + \pi\delta D_{\text{Al}}^{\text{gb/d}})(D_0^{\text{l}} + \pi\delta D_0^{\text{gb/d}})}{3(D_{\text{Al}}^{\text{l}} + \pi\delta D_{\text{Al}}^{\text{gb/d}}) + 2(D_0^{\text{l}} + \pi\delta D_0^{\text{gb/d}})} \right] \sigma \quad [28]$$

where Ω is the volume of an alumina molecule, the superscripts on D represent the diffusion path (lattice or grain boundary), the subscripts indicate the diffusing species, and σ is the stress under which deformation occurs. It is seen from Eq. [28] that $\dot{\epsilon}$ is extremely sensitive to the grain size. Thus, in the ultrafine-grained $\alpha\text{-Al}_2\text{O}_3$ scale obtained in the present study, plastic deformation can occur with greater ease. The grain size of $\alpha\text{-Al}_2\text{O}_3$ scales grown on dispersoid-free Fe-25Cr-4Al alloys for 1000h at 1200°C is approximately a factor of four larger (47). Thus long-term stability of the oxide scale can be improved by having a fine grain size. Yttrium doping can lead to the retardation of grain growth kinetics in two ways: by forming grain boundary microvoids which, analogous to particles on a grain boundary, can pin the boundary, and by segregating to the grain boundary and decreasing grain-boundary velocity (48).

That relief of growth stresses by plastic flow even when thermally induced stresses are present can improve scale adherence has been shown in an oxidation study of copper carried out some years ago by Sartell *et al.* (49). They showed that when copper is oxidized at a temperature just below 700°C and cooled to room temperature, the oxide scale readily flakes off. However, when the oxidation is carried out at 870°C , the oxide scale remains quite adherent upon cooling to room temperature. The authors argued that in the latter case, growth stresses are relieved by plastic flow at 870°C so that even at a higher level of thermal stresses, the oxide scale formed at the higher temperature is more adherent. Tylecote has shown (50) that above 700°C , copper oxide, Cu_2O , undergoes a transition from elastic to plastic behavior.

The second effect of yttrium doping is to suppress Al transport through $\alpha\text{-Al}_2\text{O}_3$ scales. In their work on Fe-Cr-Al and Fe-Cr-Al-Y alloys, Golightly *et al.* (23, 24) suggested that Y in some unknown fashion decreased the transport of Al in Al_2O_3 . In the yttrium-free alloy, according to these authors, oxygen diffusing inward through $\alpha\text{-Al}_2\text{O}_3$ grain boundaries reacts with Al diffusing outward through $\alpha\text{-Al}_2\text{O}_3$ grains, forming new Al_2O_3 within an existing scale and generating compressive growth stresses. In an effort to relieve these compressive stresses, the oxide tends to grow

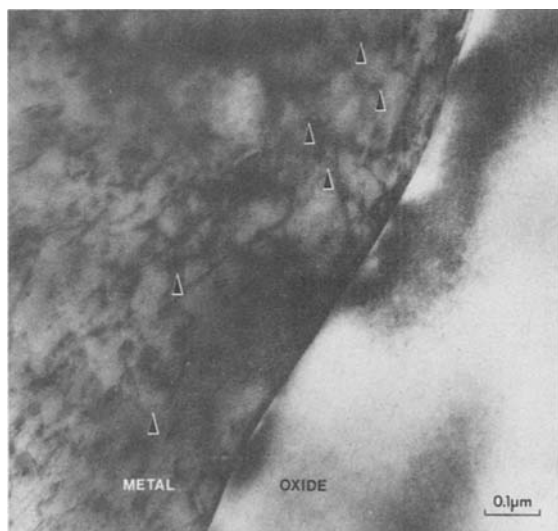


Fig. 17. TEM micrograph in the vicinity of oxide/metal interface revealing absence of micropegging.

laterally, resulting in a convoluted morphology, and becomes detached from the alloy at the convolutions. Such detachment leads to loss of oxide scale adhesion.

Our preliminary work on Fe-25Cr-5Al alloys also shows a convoluted oxide-scale morphology (47). Such convolutions are absent in the oxide scale on MA956. Thus, in agreement with Golightly *et al.* (23, 24), the present authors also feel that yttrium doping in α -Al₂O₃ suppresses Al transport and avoids the build up of compressive stresses otherwise generated by Al₂O₃ formation within existing scale.

If it is assumed that Schottky disorder prevails in α -Al₂O₃, then a mechanism can be proposed for the suppression of Al transport as a result of yttrium doping. As explained previously, in fine-grained α -Al₂O₃ grain-boundary oxygen transport predominates, so that one is dealing with a rather low flux of aluminum. In accordance with our proposed defect reaction [8] for yttrium doping, the concentration [V_O^{••}] is increased by yttrium, especially in the vicinity of Al₂O₃ grain boundaries. In accordance with Eq. [27], the concentration of Al vacancies, [V_{Al}[']] is correspondingly reduced. Since oxygen transport occurs through grain boundary, any reaction between Al and O to form Al₂O₃ within an existing oxide scale must occur in the grain boundary region. Such Al₂O₃ formation is prevented by decreasing [V_{Al}[']] in the grain boundary region, which correspondingly decreases the flux of Al to this region.

Concluding Remarks

In the present study, the influence of yttrium oxide dispersoids in Fe-base alloys on the microstructure and adherence of α -Al₂O₃ scales formed on such alloys has been emphasized. The oxide scale grows by inward oxygen grain boundary transport; the yttrium oxide dispersoid particles dissolve upon incorporation into the scale, and yttrium segregates to the α -Al₂O₃ grain boundary; in consequence, it is suggested that grain growth and Al transport in α -Al₂O₃ are suppressed. These effects in turn can relieve and/or decrease growth stresses in α -Al₂O₃ and improve oxide-scale adherence.

In view of the immense technological importance of α -Al₂O₃ scales, it is suggested that more work should be carried out both on the defect structure and doping characteristics of Al₂O₃. Some papers in the literature suggest that whatever the chemistry of the dispersoid used, there is an improvement in the adherence of the α -Al₂O₃ scale formed on the alloy. While this may indeed be so, the doping effects of elements from different groups of the periodic table are clearly different. Thus, there is a need to understand more clearly the role of dispersoid chemistry in the alloy on oxide-scale properties.

Acknowledgment

The authors gratefully acknowledge the efforts of J. Mumford throughout this experimental study. They wish to thank D. P. Leta for performing the SIMS work and Lydia Massey for her skillful assistance in preparing the manuscript.

Manuscript submitted Jan. 9, 1983; revised manuscript received Nov. 22, 1983.

Exxon Research Center assisted in meeting the publication costs of this article.

REFERENCES

- C. S. Tedmon, *This Journal*, **113**, 766 (1966).
- T. A. Ramanarayanan and R. Petkovic-Luton, *Corrosion*, **37**, 712 (1981).
- C. S. Giggins and F. S. Pettit, *Metall. Trans.*, **2**, 1071 (1971).
- D. P. Whittle, M. E. El-Dashan, and J. Stringer, *Corros. Sci.*, **17**, 879, (1977).
- J. Stringer, B. A. Wilcox, and R. I. Jaffee, *Oxid. Met.*, **5**, 11 (1972).
- G. R. Wallwork and A. Z. Hed, *ibid.*, **3**, 229 (1971).
- J. Stringer and I. G. Wright, *ibid.*, **5**, 59 (1952).
- J. Stringer, A. Z. Hed, G. R. Wallwork, and B. A. Wilcox, *Corros. Sci.*, **12**, 625 (1972).
- H. M. Fowler and B. A. Wilcox, *ibid.*, **17**, 253 (1977).
- H. H. Davis, H. C. Graham, and I. A. Kvernes, *Oxid. Met.*, **3**, 431 (1971).
- I. G. Wright and B. A. Wilcox, *Metall. Trans.*, **5**, 957 (1974).
- A. U. Seybolt, *Corros. Sci.*, **6**, 263 (1966).
- M. S. Seltzer, B. A. Wilcox, and J. Stringer, *Metall. Trans.*, **3**, 2391 (1972).
- I. M. Allam, D. P. Whittle, and J. Stringer, *ibid.*, **13**, 381 (1979).
- H. T. Michels, *ibid.*, **7A**, 379 (1976).
- O. T. Goncel, D. P. Whittle, and J. Stringer, *Corros. Sci.*, **19**, 305 (1979).
- I. G. Wright and J. Stringer, *Metallography*, **6**, 65 (1973).
- D. P. Whittle and J. Stringer, *Philos. Trans. R. Soc. London, Ser. A*, **295**, 309 (1980).
- T. A. Ramanarayanan and R. Petkovic-Luton, To be published.
- Y. Oishi and W. D. Kingery, *J. Chem. Phys.*, **33**, 480 (1960).
- L. G. Harrison, *Trans. Faraday Soc.*, **57**, 1191 (1961).
- B. Bender, D. B. Williams, and M. R. Notis, *J. Am. Ceram. Soc.*, **63**, 542 (1980).
- F. A. Golightly, F. H. Stott, and G. C. Wood, *Oxid. Met.*, **10**, 163 (1976).
- F. A. Golightly, F. H. Stott, and G. C. Wood, *This Journal*, **126**, 1035 (1979).
- M. M. El-Aiat and F. A. Kroger, *J. Am. Ceram. Soc.*, **65**, 280 (1982).
- R. E. Mistler and R. L. Coble, *J. Appl. Phys.*, **45**, 1507 (1974).
- H. A. Wang and F. A. Kroger, *J. Am. Ceram. Soc.*, **63**, 613 (1980).
- W. R. Strehlow and E. L. Cook, *J. Phys. Chem. Ref. Data*, **2**, 163 (1973).
- V. N. Abramov, M. G. Karin, A. I. Kuznetsov, and K. K. Sidorin, *Sov. Phys. Solid State*, **21**, 47 (1979).
- P. Kofstad, "Non-Stoichiometry, Diffusion and Electrical Conductivity in Binary Metal Oxides," p. 104, Wiley-Interscience, New York (1972).
- K. P. R. Reddy, Ph. D. Thesis, Case Western Reserve University, Cleveland, Ohio (1979).
- G. B. Gibbs, *Oxid. Met.*, **7**, 173 (1973).
- S. Taniguchi and D. L. Carpenter, *Corros. Sci.*, **19**, 15 (1979).
- F. N. Rhines and J. S. Wolf, *Metall. Trans.*, **1**, 1701 (1970).
- J. L. Smialek and R. Gibala, NASA Technical Memorandum 79259 (1979).
- J. L. Smialek, NASA Technical Memorandum 81676 (1981).
- G. J. Yurek and H. Schmalzried, *Ber. Bunsenges. Phys. Chem.*, **79**, 225 (1975).
- C. S. Giggins and F. S. Pettit, Report no. ARL75-0234, Pratt and Whitney Aircraft Division, United Technologies Corporation, Middletown, CT (1975).
- D. P. Whittle, I. M. Allam, and J. Stringer, in "Materials and Coatings to Resist High Temperature Corrosion," D. Holmes and A. Rahmel, Editors, p. 55, Applied Science Publishers, London (1978).
- H. Hindam and D. P. Whittle, *This Journal*, **129**, 1147 (1982).
- J. K. Tien and F. S. Pettit, *Metall. Trans.*, **3**, 1587 (1972).
- J. D. Kuenzly and D. L. Douglass, *Oxid. Met.*, **8**, 139 (1974).
- J. Stringer, *Corros. Sci.*, **10**, 513 (1970).
- R. M. Cannon, W. H. Rhodes, and A. H. Heuer, *J. Am. Ceram. Soc.*, **63**, 46 (1980).
- R. S. Gordon, *ibid.*, **56**, 147 (1973).
- R. M. Cannon and R. L. Coble, in "Deformation of Ceramic Materials," R. C. Bradt and R. E. Tressler, Editors, p. 61, Plenum Press, New York (1975).
- T. A. Ramanarayanan and M. Raghavan, Research in progress.
- J. W. Cahn, *Acta Metall.*, **10**, 789 (1962).
- J. A. Sartell, R. J. Stokes, S. H. Bendel, T. L. Johnston, and C. H. Li, *Trans. Metall. Soc. AIME*, **215**, 420 (1959).
- R. F. Tylecote, *J. Inst. Metals*, **78**, 301 (1950).

Capacitance-Voltage Technique for the Determination of Carrier Concentrations in Thin Film Photoanodes

C. S. Blair* and D. W. Hess**

Materials and Molecular Research Division, Lawrence Berkeley Laboratory, and Department of Chemical Engineering, University of California, Berkeley, California 94720

Carrier concentrations in thin film iron oxide and titanium oxide photoanodes are determined using a metal/insulator/semiconductor structure. Capacitance-voltage measurements of this structure are distinct from the usual liquid junction impedance measurements, because results of the present study are not dependent upon electrolyte/semiconductor interface properties. Further, determination of the conductivity of the photoanode films permits the calculation of carrier mobilities.

The electrical properties of materials used as liquid junction solar cells ultimately determine their energy conversion efficiency. Two of the most important electrical properties are the flatband potential and the carrier concentration. The carrier concentration is particularly significant since it determines the space charge region thickness and the depth available for light absorption in the semiconductor surface. These properties are usually determined from impedance measurements of the photoelectrochemical cell by plotting $1/C^2$ vs. voltage, thereby generating a Mott-Schottky plot (1).

Experimental difficulties in performing capacitance measurements of solid/liquid interfaces have been previously discussed (2-6). Most of these difficulties involve complex interactions between the semiconductor and the electrolyte. For instance, specific ion adsorption on the semiconductor surface and variation of the Helmholtz layer capacitance with voltage have been suggested as causes of nonlinear Mott-Schottky plots and non-Nernstian electrode behavior (2). The presence of surface states and electrode surface treatments also have been a strong influence on Mott-Schottky plot linearity (3, 4). Further, the difficulty of interpreting nonlinear Mott-Schottky plots has been addressed (2, 5, 6). In this paper, a technique capable of measuring semiconductor electrode carrier concentration without the use of an electrolyte is described.

Capacitance-Voltage Technique

Impedance measurements in photoelectrochemical cells are used to ascertain the thickness of the semiconductor space charge or depletion region. In n-type semiconductors, this region is initially formed by the net flow of electrons from the semiconductor into the electrolyte. However, a depletion region can also be formed merely by applying an electric field across a semiconductor. If a dielectric layer is present on the semiconductor surface, high electric fields can be applied without initiating current flow. This latter structure is called a metal/insulator/semiconductor (MIS) capacitor, and is the basis of many solid-state devices.

Capacitance-voltage measurements of the MIS structure represent a well-established diagnostic technique utilized in the fabrication of integrated circuits. The usual goal of MIS measurements is the determination of dielectric properties such as dielectric constant and electronic charge levels in the insulating film. In these investigations, the electrical properties of the semiconductor (usually silicon) are well known. However, as will be indicated below, electrical properties of the semiconductor can also be obtained. A number of reviews discuss the high frequency capacitance-voltage technique in detail (7, 8), so only a brief description will be given here.

The total capacitance of the MIS structure is given by the series capacitance of the insulator and the semiconductor

$$1/C = 1/C_I + 1/C_{sc} \quad [1]$$

Here, C is the total capacitance, C_I the insulator capacitance, and C_{sc} the semiconductor space charge capacitance, all per unit area.

If a positive potential is applied to a dielectric layer above an n-type semiconductor, majority carriers (electrons) accumulate at or near the semiconductor/insulator interface, giving essentially zero depletion width. In this case, $1/C_{sc}$ is negligible compared to $1/C_I$, and the total capacitance is the insulator capacitance. As the voltage becomes negative, electrons are driven away from the dielectric/semiconductor interface, and a depletion region is formed. This depletion or space charge region presents an additional capacitance in series with the dielectric capacitance (Fig. 1). As the negative potential is increased, more electrons are repelled from the semiconductor surface, and the depletion region widens, thereby increasing the space charge capacitance, and reducing the overall capacitance due to the series combination given in Eq. [1]. When sufficiently negative voltages are applied so that minority carriers (holes for an n-type semiconductor) are attracted to the surface, the space charge region has reached its maximum value, and the capacitance remains nearly constant with further increases in potential. Of course, the maximum width of the depletion region is dependent upon the doping level and the dielectric constant of the semiconductor.

The maximum and minimum capacitance values can be used to calculate the charge concentration, N , in the semiconductor (8, 9).

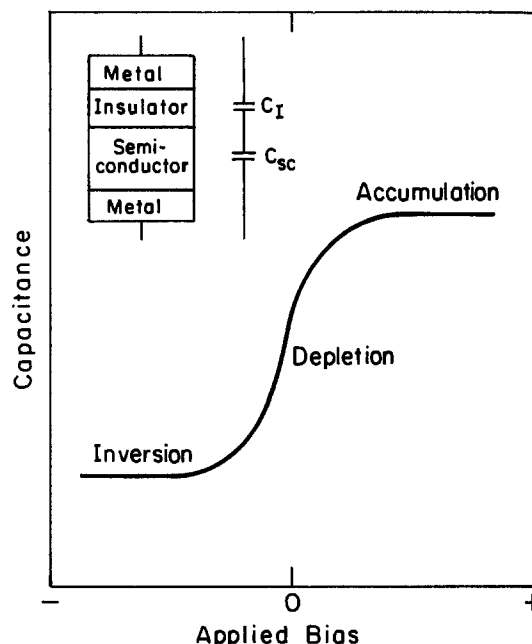


Fig. 1. Theoretical high frequency capacitance-voltage plot of an MIS structure. Inset at the upper left indicates the origin of the two series capacitances for this structure.

*Electrochemical Society Student Member.

**Electrochemical Society Active Member.

Key words: capacitance-voltage, photoanodes, carrier concentration, plasma-enhanced deposition.

$$N = \frac{2C_1^2 \psi_s(\text{inv})}{e\epsilon_s\epsilon_0 \left(\frac{C_{\text{max}}}{C_{\text{min}}} - 1 \right)^2} \quad [2]$$

where

$$\psi_s(\text{inv}) = (\sqrt{\alpha^2 + V'} - \alpha)^2$$

$$\alpha = \frac{1}{C_1} \left(\frac{eN\epsilon_s\epsilon_0}{2} \right)^{1/2}$$

$$V' = V - V_{\text{FB}}$$

In these equations, ϵ_s is the dielectric constant of the semiconductor, e is the electronic charge, ϵ_0 the permittivity of free space, and $\psi_s(\text{inv})$ is the semiconductor surface potential at inversion. The surface potential was estimated by the method of Goetzberger and Nicollian (9). V_{FB} , the flatband potential, was estimated by Heiman's method (10).

The slope of the central portion (depletion region) of the curve is also related to the carrier density by the expression (7)

$$\frac{dC}{dV} = C^3 \frac{1}{\epsilon_0\epsilon_s eN} \quad [3]$$

which upon integration becomes

$$\frac{1}{C^2} = \frac{2}{\epsilon_0\epsilon_s eN} (V - V_0) + \frac{1}{C_1^2} \quad [4]$$

It is important to note that Eq. [3] was obtained in a depletion approximation. However, as long as the space charge layer thickness is greater than twice the extrinsic Debye length, λ , where

$$\lambda = \left(\frac{2kT\epsilon_s\epsilon_0}{e^2N} \right)^{1/2} \quad [5]$$

Equations [3] and [4] represent good approximations (11). In the present case, 2λ is $\sim 20\%$ of the depletion layer thickness at inversion. In Eq. [4], V_0 is a constant which accounts for interface and/or insulator charges. Naturally, this expression is similar to the usual Mott-Schottky relation, but V_0 is not related to the electrolyte dependent flatband potential.

Experimental

All photoelectrodes analyzed in this study were deposited thin films. Iron oxide films were deposited onto iron substrates (Puratronic Foil, Alfa Products) by the RF glow discharge reaction of iron pentacarbonyl and oxygen (12). Substrate temperatures ranged from 350°-500°C, and plasma power densities were 0.079-0.4 W/cm². Under these conditions, α -Fe₂O₃ was the only phase detected by x-ray diffraction in the polycrystalline films. Further, in

all cases, film densities were approximately 90% of the theoretical density. Titanium dioxide films were deposited on titanium substrates by a similar glow discharge process using titanium tetrachloride and oxygen as gas phase reactants (13).

MIS structures were produced by electron beam evaporation (the Temescal electron gun was operated at 7 kV and 400 mA) of a layer (500-3000Å) of quartz on top of the metal oxide films. Electrical contact was made by evaporating aluminum dots (0.46 mm²) onto the quartz film through a shadow mask.

Capacitance was measured with a Boonton Capacitance meter (Model 71A) operating at 1 MHz. A voltage ramp was used to apply dc bias across the film (-10 to +10V) at a scan speed of 0.04 V/s. Small signal capacitance vs. applied voltage at 1 MHz was recorded on a Hewlett-Packard 7045A X-Y recorder. A Keithley Model 179 digital multimeter measured current for resistivity determination. A General Radio Model 1650-A impedance bridge was used for capacitance measurements for Mott-Schottky plots at 1 kHz, and resistance measurements at 1 kHz. Semiconductor resistance and dielectric constant measurements were carried out by evaporating aluminum contacts directly onto the semiconductor films.

Results and Discussion

The results of C-V and other electrical measurements for selected Fe₂O₃ and TiO₂ samples are summarized in Table I. The dielectric constant of the iron oxide films varied from 60 to 113, with high values corresponding to higher RF power levels and substrate temperatures. These values are in reasonable agreement with those reported in the literature for bulk iron oxide [80-120 for the α -crystal form (2, 14), and approximately 10 for the γ -form (15)]. The dielectric constant measured for the titanium dioxide film is consistent with that found for single-crystal rutile (*i.e.*, 180) along the C-axis (16). Iron oxide film resistivity varies over two orders of magnitude, depending upon deposition conditions. Similarly, the resistivity of bulk iron oxide varies from 10 to 10¹⁰ Ω -cm depending on processing conditions (2, 17).

Relative capacitance (C/C_1) data from two Fe₂O₃ films of thickness 1.7 μm (sample 1) and 1.9 μm (sample 2) are shown in Fig. 2. Note that positive bias voltage in this plot refers to that voltage applied to the dielectric of the MIS structure. It is clear that sample 1 shows a nearly theoretical shape (7, 8). Using Eq. [2], the carrier concentration for sample 1 is $5.3 \times 10^{15} \text{ cm}^{-3}$. On the other hand, sample 2 shows somewhat unusual behavior, in that a very large potential (10V) is required to bias the sample into inversion. Such behavior is probably due to the rather thick insulator deposited on this film, and the high dielectric constant iron oxide film. The carrier concentration for the second sample is $1.3 \times 10^{16} \text{ cm}^{-3}$.

According to Eq. [4], a plot of $1/C^2$ vs. bias voltage should yield a straight line. Note, however, in this case voltage is referenced to that applied to the film substrate, rather than to the aluminum contact atop the dielectric. Indeed, in agreement with Eq. [4], both samples 1 and 2 yield a straight line on such a plot (Fig. 3), with carrier

Table I. Deposition conditions and electrical properties of thin film photoanodes

Power (W)	Temperature (°C)	Thickness (μm)	Electron concentration* (cm^{-3})	Dielectric constant (at 1 MHz)	Resistivity (Ω -cm)	Electron mobility ($\frac{\text{cm}^2}{\text{V}\cdot\text{s}}$)
50	500	2.1	4.6×10^{15}	113	2.0×10^4	0.068
	450	2.4	2.3×10^{15}	104	4.6×10^4	0.059
	400	1.9	1.7×10^{16}	94	6.5×10^3	0.055
	350	1.7	6.5×10^{15}	63	1.9×10^4	0.050
25	500	0.51	1.7×10^{16}	60	5.7×10^3	0.063
TiO ₂ films						
10	430	1.2	9.4×10^{14}	160	1.1×10^6	0.0060
	600	4.4	1.0×10^{15}	160	1.0×10^6	0.0063

* Electron concentrations were determined from application of Eq. [4].

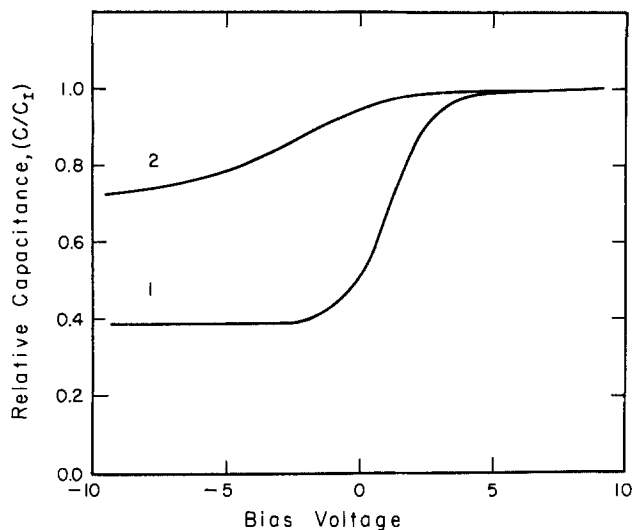


Fig. 2. Variation of relative capacitance with dc voltage for the Al/SiO₂/Fe₂O₃ MIS structure. The SiO₂ thicknesses are 0.064 μm for sample 1 (1.7 μm Fe₂O₃) and 0.125 μm for sample 2 (1.9 μm Fe₂O₃). See Table I for additional information on these samples.

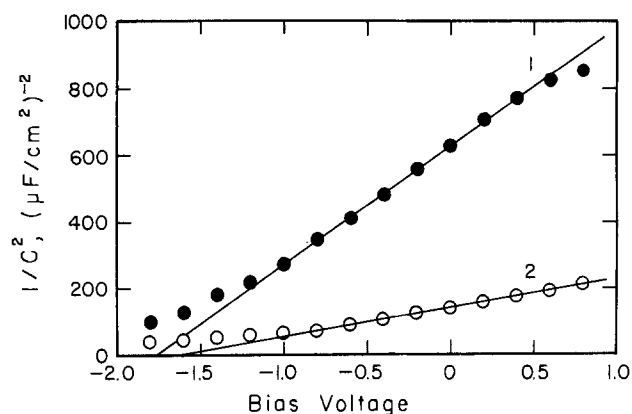


Fig. 3. Analysis of capacitance-voltage data according to Eq. [4], for the samples of Fig. 2. The slopes of the lines are related to the carrier concentrations. Resulting values of the carrier concentration are given in Table I.

concentrations of 6.5×10^{15} and $1.7 \times 10^{16} \text{ cm}^{-3}$, respectively. These values are in reasonable agreement with results given above from application of Eq. [2].

For comparison purposes, a number of the iron oxide samples described in Table I were studied using the Mott-Schottky technique. In nearly all cases, the resulting plots were nonlinear, and the results were difficult to reproduce. For the sample deposited at 500°C and 50W, a linear Mott-Schottky plot was obtained, but the carrier concentration from this plot was $7 \times 10^{18} \text{ cm}^{-3}$, an unexpectedly high value.

The reasons for this discrepancy are not clear. The Mott-Schottky plot measurements were all made using the impedance bridge at 1 kHz, while the C-V plots were performed at 1 MHz. However, variations in the dielectric constant of the various Fe₂O₃ films investigated were insignificant for these two frequencies. Further, the discrepancy does not appear to be due to Helmholtz layer capacitance; such a series capacitance would result in a decrease in the total capacitance. On the other hand, surface states are known to act as an impedance in parallel to the depletion layer capacitance (3, 18). This may lead to the higher capacitance values observed here. Indeed, semiconductor-solution interactions are known to lead to the formation of surface states for Fe₂O₃, TiO₂, and other materials (19-21).

As observed in Table I, carrier concentrations for the plasma-deposited iron oxide films vary over two orders of magnitude, yet no consistent trends relating the effects of film deposition conditions to carrier concentrations are evident. Other workers have also noted the

difficulties of controlling the conductivity of undoped bulk polycrystalline α-iron oxide materials (2).

Electron mobilities of the plasma-deposited films were calculated from the equation

$$\mu = 1/N\rho p \quad [6]$$

where μ is the electron mobility, and ρ is the resistivity of the film. These values are also given in Table I. The present results are within reported values (10^{-1} to $10^{-5} \text{ cm}^2/\text{V}\cdot\text{s}$) for bulk iron oxide (22). Titanium dioxide film mobilities are somewhat low compared to the literature value of $0.1 \text{ cm}^2/\text{V}\cdot\text{s}$ for bulk polycrystalline material (23). However, the literature values are from samples reduced at 1450°C for 2h, thereby resulting in higher electrical conductivities than the samples in this study.

Conclusions

The metal/insulator/semiconductor capacitance-voltage technique appears to be a useful technique for obtaining semiconductor carrier concentrations for thin film photoanodes. This technique allows the measurement of semiconductor properties independent of electrolyte. The properties of thin film SiO₂ insulators are well-known, and interactions between the semiconductor and the insulator are less complex and better understood than those of a liquid junction. The C-V method also displays self-consistency. For example, at positive bias, the capacitance appropriate to the insulator film thickness is obtained. Moreover, the capacitance-voltage data can be analyzed according to Eq. [2] and [4] in order to calculate two independent values of carrier concentration, which serve as an internal check on the experimental technique.

Acknowledgements

The authors would like to thank L. M. Williams for supplying the TiO₂ samples used in this study. This work was supported by the Division of Materials Sciences, Office of Basic Energy Sciences, U.S. Department of Energy under Contract No. DE-AC03-76SF00098.

Manuscript submitted July 18, 1983, revised manuscript received Oct. 31, 1983.

REFERENCES

- H. Gerischer, in "Physical Chemistry: An Advanced Treatise," Vol. IXA, Chap. 5, Academic Press, New York (1970).
- J. H. Kennedy and K. W. Freese, *This Journal*, **125**, 723 (1978).
- F. Cardon and W. P. Gomes, *J. Phys. D.*, **19**, L63 (1978).
- M. A. Butler, R. D. Nasby, and R. K. Quinn, *Solid State Commun.*, **19**, 1011 (1976).
- K. S. Yun, S. M. Wilhelm, S. Kapusta, and N. Hackerman, *This Journal*, **121**, 85 (1980).
- F. Mollers, H. J. Tolle, and R. Memming, *ibid.*, **121**, 1160 (1974).
- K. H. Zaininger and F. P. Heiman, *Solid State Technol.*, **13**, 49 (May, 1970); *ibid.*, 46 (June, 1970).
- S. M. Sze, "Physics of Semiconductor Devices," Wiley-Interscience, New York (1969).
- A. Goetzberger and E. H. Nicollian, *Appl. Phys. Lett.*, **9**, 444 (1966).
- F. B. Heiman, *IEEE Trans. Electron Devices*, **ed-13**, 885 (1966).
- K. Ziegler, E. Klausmann, and S. Kar, *Solid State Electron.*, **18**, 189 (1975).
- D. M. Wroge and D. W. Hess, in "Plasma Processing," R. G. Frieser and C. J. Mogab, Editors, p. 30, The Electrochemical Society Softbound Proceedings Series, Princeton, NJ (1981).
- L. M. Williams and D. W. Hess, *J. Vac. Sci. Technol.*, **A1**, 1810 (1983).
- R. K. Quinn, R. D. Nasby, and R. J. Baughman, *Mater. Res. Bull.*, **11**, 1011 (1976).
- O. Jantzen, *Z. Angewand. Phys.*, **18**, 560 (1965).
- R. J. H. Clark, "The Chemistry of Titanium and Vanadium," Elsevier Publishing Co., New York (1978).
- F. J. Morin, *Phys. Rev.*, **83**, 1005 (1951).
- P. J. Boddy, *J. Electroanal. Chem.*, **10**, 199 (1965).
- R. J. Atkinson, A. M. Posner, and J. P. Quirk, *J. Phys. Chem.*, **71**, 550 (1967).
- R. H. Wilson, *This Journal*, **127**, 228 (1980).
- A. Heller, K. C. Chang, and B. Miller, *ibid.*, **124**, 697 (1977).
- F. J. Morin, *Phys. Rev.*, **93**, 1195 (1954).
- R. G. Breckenridge and W. R. Hosler, *ibid.*, **91**, 793 (1953).



Optimized Collection of AC Impedance Data

M. W. Kendig,* A. T. Allen,* and F. Mansfeld*

Rockwell International Science Center, Thousand Oaks, California 91360

INTRODUCTION

The low corrosion rate of well inhibited systems and high capacitance values make it necessary to extend the collection of electrochemical impedance data to very low frequencies. In addition, several orders of magnitude of the impedance have to be measured accurately between the value for the solution resistance at high frequencies, and the polarization resistance at low frequencies. An additional problem arises from the changes of the corrosion kinetics with time, which occur for the majority of corrosion systems. These factors place severe limitations on the validity of data (and their analysis) obtained in the traditional manner with a transfer function analyzer where the impedance for each frequency is measured individually over several cycles. We have developed a new approach in which the current measuring resistor of an autoranging PAR model 276 interface is adjusted continuously to match the impedance to be measured. The use of a filter allows accurate measurements with only one cycle per frequency at frequencies below 1 Hz. Experimental data have been obtained for iron in tapwater with various inhibitors and in deionized water with low frequency limits between 0.4 and 10 mHz.

EXPERIMENTAL APPROACH

A Solartron 1174 transfer function analyzer (TFA) and a PAR 173 potentiostat containing a model 276 current amplifier interface communicate via an IEEE-488 bus with a HP9825 desktop computer (1). The communication between the 276 interface and the computer allows optimization of the gain of the current amplifier during the collection of the impedance spectrum. For frequencies below 1 kHz, the computer selects the current measuring resistor R_m of the 276 interface so that R_m relates to the impedance modulus $|Z|$ by

$$\log R_m = \text{int} (\log(3|Z|)) \quad [1]$$

*Electrochemical Society Active Member.

The integer function, int , determines the largest integer less than or equal to the argument. This procedure limits the output signal of the interface so as to avoid phase shift errors, but maintains a high enough signal level for accurate measurement of the current. Since no switching occurs during the actual data collection by the TFA, switching transients pose no problems for the measurement. Above 1 kHz, a preselected R_m is used in order to minimize the phase shift of the current amplifier. At each frequency down to 1 Hz, ten cycles are sampled. Below 1 Hz, in addition to optimizing the gain of the interface, the computer signals the interface to introduce a 1 μF capacitor in parallel with R_m thereby giving the interface a low-pass filtering capability. In addition, the computer signals the TFA to reduce the data sampling rate to one cycle of current and voltage signals at each frequency below 1 Hz. Thus, below 1 Hz the speed of the measurement is increased by a factor of ten over the previous method of integration over ten cycles while good signal-to-noise resolution is maintained due to filtering.

EXPERIMENTAL RESULTS

The following experimental results serve as illustration of the type of impedance spectra which have been obtained with the approach discussed above. The electrode was a rotating 4340 steel cylinder (RCE) at 144 rad/s.

Figure 1 shows the results for exposure to 0.5 N NaCl open to air. A simple spectrum is obtained, which is characterized by one time constant in a frequency range between 10^5 Hz and $5 \cdot 10^{-3}$ Hz. Excellent agreement is observed between the experimental results and a fit to a theoretical model of the impedance as:

$$Z = R_\Omega + \frac{R_p}{1 + (j\omega CR_p)^\alpha} \quad [2]$$

where R_Ω is the electrolyte resistance, C the capacitance calculated from the frequency ω_m of

the maximum of the imaginary component Z'' ($C = (\omega_m R_p)^{-1}$), R_p is the polarization resistance and α is the (negative) slope of the capacitive part of the Bode-plot. The parameters used for the curve fitting in Fig. 1 have been obtained with the CIRFIT - computer program (2). The data in Fig. 1 cast some doubt on the results and the model proposed by Bonnel et al. (3) and Duprat et al. (4), who reported the occurrence of a second time constant at low frequencies (<0.1 Hz) for a carbon steel rotating disk electrode in 3% NaCl.

Figure 2 shows Bode-plots in tapwater containing NaNO_2 as inhibitor. Measurements were extended to $0.4 \cdot 10^{-3}$ Hz. Using the integration method (5) R_p was calculated to be $4.15 \cdot 10^6$ ohm ($2.85 \cdot 10^6$ ohm \cdot cm 2) for $t = 2.9$ h. Curve fitting according to Eq. 1 gave good agreement for this R_p -value and $R_Q = 39$ ohm, $C = 29.4$ μF and $\alpha = 0.88$ in the capacitive range. Deviations occur below 10 mHz. The measurement with a lower limit of $5 \cdot 10^{-3}$ Hz was performed in 76 min.

Data obtained in deionized water are shown in Fig. 3 for two exposure times. Despite the low conductivity of this test medium accurate data can be obtained for frequencies below 200 Hz. The fit between the experimental data for an exposure of 2.5 h and the model of Eq. 1 is very good. The solution conductivity increased continuously during the first day of testing due to build-up of corrosion products.

REFERENCES

1. F. Mansfeld, M. W. Kendig and S. Tsai, *Corrosion* **38**, 570 (1982).
2. M. W. Kendig, E. M. Meyer, G. Lindberg and F. Mansfeld, *Corr. Sci.* **23**, 1007 (1983).
3. A. Bonnel, F. Dabosi, C. Deslouis, M. Duprat, M. Keddam and B. Tribollet, *J. Electrochem. Soc.* **130**, 753 (1983).
4. M. Duprat, F. Moran and F. Dabosi, *Corr. Sci.* **23**, 1047 (1983).
5. M. W. Kendig and F. Mansfeld, *Corrosion* **39**, 466 (1983).
6. F. Mansfeld and M. W. Kendig, *Werkstoffe und Korrosion* **34**, 397 (1983).

Manuscript submitted Dec. 14, 1983;
revised manuscript received Jan. 30,
1984.

Rockwell International Science
Center assisted in meeting the publi-
cation costs of this article.

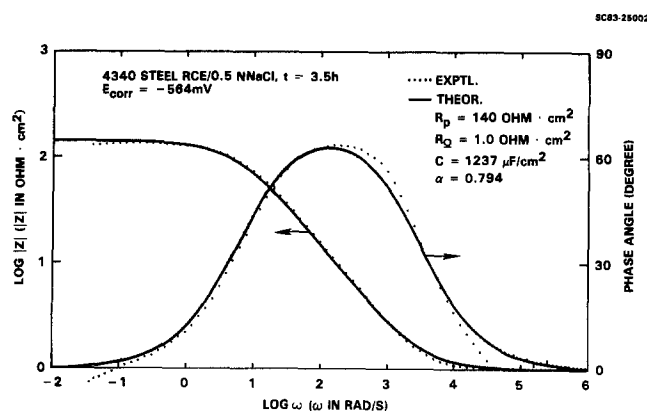


Fig. 1. Bode plots for 4340 steel RCE in 0.5 N NaCl.

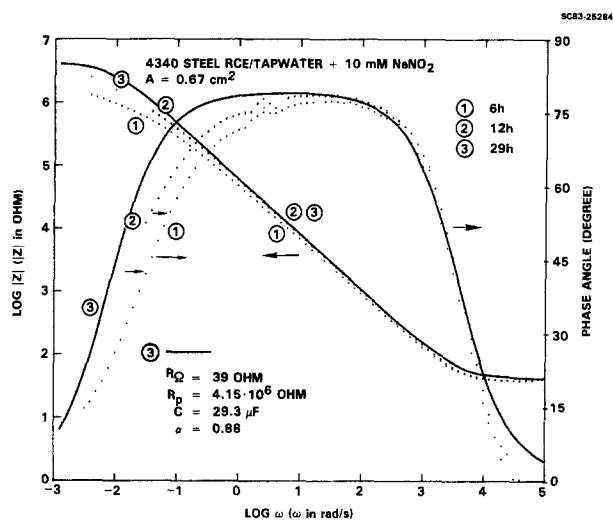


Fig. 2. Bode-plots for 4340 steel RCE in tapwater containing NaNO_2 .

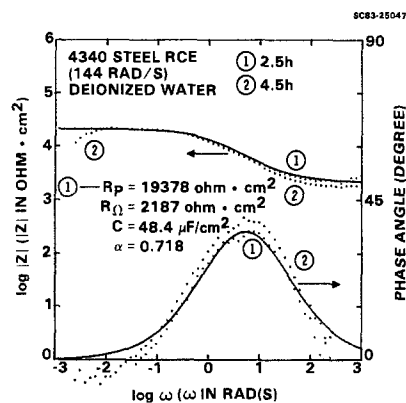


Fig. 3. Bode-plots for 4340 steel RCE in deionized water.

Method for Increasing the Conductivity of Silver-Doped Polyimides

A. Auerbach

General Electric Company, Corporate Research and Development, Schenectady, New York 12301

Recently there have been a number of communications describing the doping of polyamic acids with electropositive metal salts.^{1,2}

The metal cation is reduced to the metal during a cure cycle to obtain metal doped polyimide films. The authors found substantial increases in conductivity as compared to undoped polyimide films. In some cases palladium mirrors formed on the polymer surface. Although most of their work involved palladium salts, they pointed out that other metal salts could be used.

We report an improved processing method which has allowed us to form both silver mirrors and/or thin film silver conductors using silver nitrate dissolved in commercial polyamic acids. Using our technique we have achieved conductivities orders of magnitude above those previously reported, and comparable to vapor deposited silver films.

The method involves spin coating a substrate material (e.g. alumina, glass, polymer coated metal or glass, etc.) with one of the mixtures listed in Table 1. Spin rates between 2000 to 4000 rpm are used, depending on the viscosity of the mixture chosen. The samples are then dried in a cross flow oven to form a dry skin. After drying, the samples can be handled or stored for future use. The last step involves a high temperature bake. The specimens are baked for a period at 360°C under a blanket of carbon powder. The carbon blanket accelerates the reduction of the silver cation to metallic silver; while allowing the polyamic acid to imidize. Lower bake temperatures can be used, but then a longer bake period is required.

Figure 1 shows the silver mirror formed on two substrate materials -- glass and alumina -- using the above processing and mix 1 of Table 1. The mirror formed on the alumina substrate is conductive (100Ω/sq.). More highly conductive films are generated using either mix 8 or 9 in Table 1. A S.E.M. of one such surface is shown in Figure 2.

At 30,000 magnification the small silver ellipsoids are readily apparent and measure from 1000Å to 3000Å across. X-ray analysis of one ellipsoid shows a prominent silver peak. A S.I.M.S. analysis relative to an evaporated silver standard further verified the presence of elemental silver since the two spectra virtually overlapped.

During our investigation of the above reduction reaction to determine the optimum N-methyl pyrrolidone (NMP)/AgNO₃/polyamic acid ratio to use, we observed the following trends. When too much of the solvent NMP is added (i.e. NMP rich ratio), then the evaporation of the NMP during the bake step prevents oxygen from reaching the polymer surface and little reduction occurs during the imidization. When, on the other hand, too much AgNO₃ is added then the reduction interferes with the imidization of the polyamic acid and the film quality is degraded. Also the silver nitrate can be added in one of two ways; either directly to the polyamic acid or via NMP. If added directly, then the weight ratio of AgNO₃ to polyamic acid should be less than or equal to one, so no reaction product forms and thus eliminating the need to filter the solution. If added via NMP, then the excess solvent must be removed prior to the bake or it interferes with both the silver reduction and the imidization. The best results have been achieved using the mixtures and cure schedules listed in Table 1.

In closing, we point out that the present technique is general, and could be used with any electropositive metal salt and polyamic acid. It is a useful method for making metal laced polyimide films. The films are durable and can be patterned and etched, thereby making this a useful alternative to vacuum deposited thin films.

ACKNOWLEDGMENTS

The pictures provided by the scanning electron microscopy group are appreciated. Support of this work by the General Electric Company is also appreciated.

Manuscript submitted Jan. 4, 1984; revised manuscript received ca. Feb. 2, 1984.

General Electric Company assisted in meeting the publication costs of this article.

REFERENCES

1. A. K. St. Clair, et al., J. Am. Chem. Soc., 102, 876 (1980).
2. L. T. Taylor et al., Org. Coat. Plast. Chem., 43, 635 (1980).

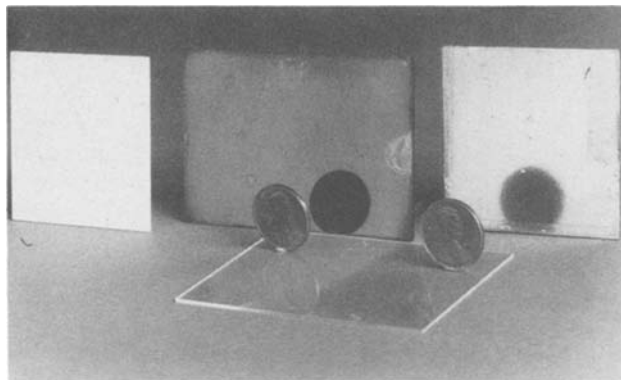


Fig. 1. Left to right: alumina substrate (2.54 x 2.54 cm), polyimide-AgNO₃ mirror formed on glass slide, and mirror formed on alumina substrate. Shadow of penny is visible only on the mirrored surface, not on the alumina substrate.

TABLE 1

MIX	POLYAMIC ACID	AgNO ₃	AgNO ₃ /NMP (33%/67%)	AgNO ₃ /NMP (25%/75%)	DRYING TIME	FIRING TIME 370°C	SURFACE RESISTANCE
1)	5 grams	.5 grams			10 min 180°C	25 min	>100/Ω/sq.
2)	5 grams		3 grams		1 hr 200°C	10 min	~10 ⁸ Ω/sq.
3)	5 grams		8 grams		1 hr 200°C	10 min	~1000 Ω/sq.
4)	10 grams	1.5 grams			10 min 180°C	8 min	1-1000 Ω/sq.
5)	3 grams		3 grams		10 min 180°C	7 min	~1-100 Ω/sq.
6)	3 grams		6 grams	6 grams	10 min 180°C	8 min	~1-100 Ω/sq.

PyraML-5057^aPyraLN-2530^a

a - Dupont registered trademark

b - Measured with a Hewlett-Packard meter model number 4275A; using the four probe technique.

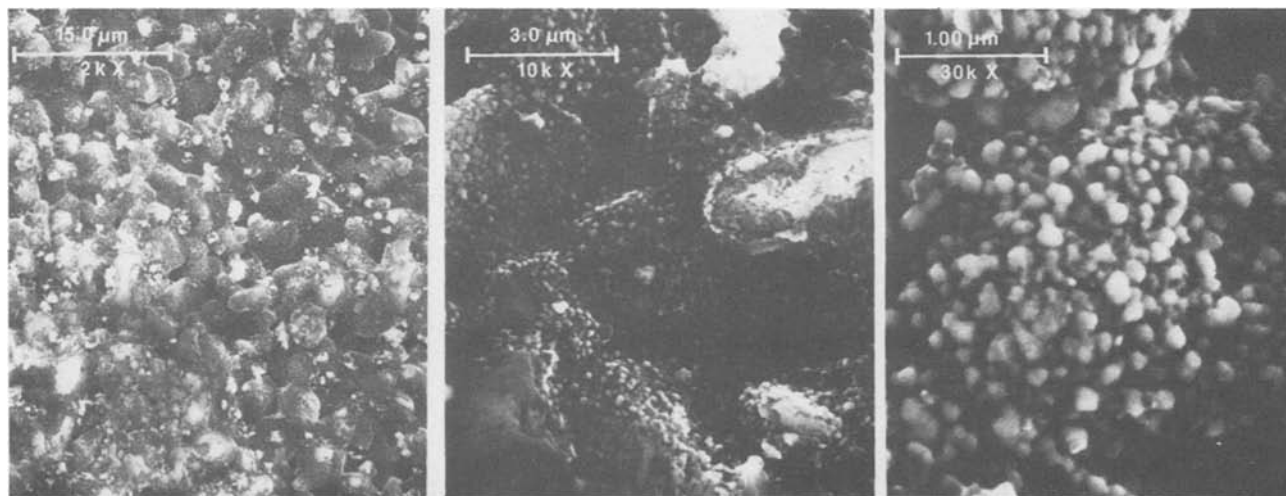


Fig. 2. SEM photographs of conductive polyimide-silver-coated alumina substrate at 2000, 10,000, and 30,000 X magnification, as indicated.

Electroless Deposition of CdTe Thin Films

R. N. Bhattacharya and K. Rajeshwar*

Department of Chemistry, The University of Texas at Arlington, Arlington, Texas 76019-0065

R. N. Noufi*

Solar Energy Research Institute, Golden, Colorado 80401

INTRODUCTION

Of the emerging materials for solar cell applications, CdTe is one candidate which has received much attention in recent years (1). Two features in the optical characteristics of this material are particularly attractive for photovoltaic conversion of sunlight: (a) its energy bandgap of 1.5 eV, which provides an optimal match with the solar spectrum and thus facilitates its efficient utilization; and (b) the direct mode of the main optical transition, which results in a large absorption coefficient and in turn permits the use of thin layers (1-2 μm) of active material.

Electrodeposition methods have been successfully employed for the fabrication of cadmium chalcogenide thin films in general (2) and CdTe in particular (3). In principle, both anodic as well as cathodic deposition is possible, although more precise control of film stoichiometry is obtained with the latter approach. Difficulties have been reported in the introduction of p-type dopants in electrodeposited CdTe layers (3b); however, efficient CdS/CdTe heterojunction devices have been fabricated from either n-CdTe layers (3d) or p-type films obtained by suitable treatment of the electrodeposited n-type material (3e).

In this paper, we describe a new electroless method for the fabrication of CdTe thin films for photovoltaic applications. This method, unlike its closely-related electrochemical counterpart, has the advantage of simplicity in that it does not require instrumentation for potentiostatic or galvanostatic control and is therefore particularly promising for routine fabrication of a large number of thin

films. The electroless method is based on short-circuiting the thin film substrate to an easily oxidizable redox component (e.g. Al, Cd) in the electrolytic bath. This component can be even recycled if necessary in a practical system.

EXPERIMENTAL

Substrates for film growth were either Ti or Nesatron^R glass (PPG Industries, Pittsburgh, Pennsylvania). They were degreased and cleaned prior to use. In the case of Ti, the substrate treatment sequence additionally included an abrading step, a subsequent etch in 10% HF and a final annealing procedure in Ar stream (containing $\approx 0.5\%$ O₂) at 650°C for 5 min. All chemicals were of Analar^R or Pura-tronic^R grade purity. Deionized water was used in all cases.

The electrolytic bath nominally contained 1.0×10^{-2} M CdOAc and 1.0×10^{-2} M TeO₂. The latter was brought into solution in NaOH; the pH being subsequently adjusted to ≈ 2 by addition of 10% H₂SO₄. In a typical electroless deposition run, the bath was first thermostatted at the required temperature. The substrates were then suspended in solution with a Cu alligator clip suitably clamped such that intimate contact of the latter with the solution was facilitated. Film formation was facile and visible to the naked eye. The aluminum contained in the clip screw sets up the short-circuited local cell via the dissolution reaction: $\text{Al} \rightleftharpoons \text{Al}_{(\text{aq})}^{3+} + 3 \text{e}^-$ ($E^0 = 1.66 \text{ V}$). This was confirmed by connecting an Al wire instead to the substrate; film formation was immediately evident. Another variant of this method would be to substitute the CdOAc in the bath with a Cd foil short-circuited to the substrate. This foil

*Electrochemical Society Active Member.

would then act both as a source of Cd species as well as of electrons for the cathodic deposition reaction. (Note that the free-energy gain from the formation of CdTe shifts the Cd deposition potential less negative from the standard value of -0.40 V; cf. Ref. 4).

Deposition was invariably carried out at temperatures above ambient (40 - 60°C). Films thus obtained had better physical characteristics (grain size and morphology) than those deposited at room temperature as shown by scanning electron microscopy (SEM).

X-ray diffraction analyses were obtained on a Rigaku Rotaflex Model RU 200 instrument using $\text{CuK}\alpha$ radiation. EDAX/SEM measurements were done on a Philips Model P 505 unit. Photoelectrochemical (PEC) characterization of majority carrier type in the semi-conducting films was carried out in a conventional three-electrode electrochemical cell using a Princeton Applied Research (PAR) Model 173 potentiostat/galvanostat in conjunction with a Model 175 Universal Programmer and a Model 179 digital coulometer. An alkaline solution of polysulfide (prepared from Na_2S , S and NaOH) was used as the electrolyte in these experiments. To protect the CdTe film from corrosion, a thin (≈ 0.1 μm) layer of α - PbO_2 was deposited on the CdTe surface by electroless deposition from a bath containing 1.0×10^{-2} M PbOAc , 1.2 M NH_4OAc and 6×10^{-2} M $\text{K}_2\text{S}_2\text{O}_8$ (5). The light source for the PEC measurements was an ELH tungsten-halogen lamp whose output intensity was measured on a radiometer/photometer (EG&G Model 450-1). No corrections were made for the attenuation of light by reflection and solution absorption in the PEC cell. Optical measurements on the CdTe thin films were performed on a Cary Model 219 spectrophotometer. Film thicknesses were measured on a Sloan Dektak instrument (Sloan Technology Corp., Santa Barbara, California).

RESULTS AND DISCUSSION

Films of varying thickness in the range 0.15 - 2 μm were routinely grown on both Ti and Nesatron^R substrates. Data from optical measurements on films in the latter case were processed via

the relationship: $\alpha = (d_2 - d_1)^{-1} \ln T_1 T_2$ where d_1 and d_2 are two different film thicknesses and T_1 and T_2 are the corresponding transmittances (6). A typical plot of α^2 vs. energy using these data, is shown in Figure 1. The energy band-gap, obtained from extrapolation of the linear portion of the plot, is 1.4 eV. The difference between this value and that reported for single-crystal CdTe (1.5 eV, cf. Refs. 1, 7) is easily accommodated within the propagated error limits associated with the measurement of d and T .

Although not obvious from these optical data, some free Te was also often incorporated in the fabricated CdTe layers. This is illustrated by the EDAX spectrum (Figure 2a) for a typical CdTe film grown on Ti substrate. The Cd:Te ratio increases from $\approx 25:60$ for the as-deposited film to $\approx 55:45$ for films annealed at 590°C for 30 min (cf. Figure 2b). Further evidence for the compositional changes on annealing is provided by X-ray diffraction data (Table 1). The as-deposited films in this case contained CdTe in both hexagonal and cubic modifications and Te in the hexagonal form. The thermal treatment obviously resulted in the loss of free Te and in complete conversion of CdTe to the hexagonal form.

Figure 3 contains typical results from the PEC experiments. These data are for a CdTe film grown on Ti in the as-deposited condition. The dark current is largely due to the presence of conducting α - PbO_2 on the film surface (see above). On illumination, the film potential shifts in the positive direction at open circuit. The enhancement of cathodic current flow is consistent with the creation of minority carriers (electrons in this case) in the underlying CdTe layer (some contribution to the cathodic photocurrent also comes from the free Te present in this layer). The situation here is akin to the Si/ITO/electrolyte interface studied previously by us (8). That the Te layer is only partially responsible for the p-type conductivity behavior observed here was shown by additional experiments involving electroless CdTe films wherein lower amounts of TeO_2 were incorporated in the initial

deposition bath. Cathodic current flow enhancement on illumination was still observed although X-ray diffractograms showed no evidence for free Te.

After thermal treatment of the CdTe thin films and subsequent growth of a α -PbO₂ layer, the PEC data were consistent with n-type behavior (i.e. enhancement of anodic current flow on band-gap illumination). Apart from the loss of any free Te by the thermal treatment, the Cd:Te ratio in the CdTe phase is also increased by this treatment, finally leading to excess Cd in the film as shown by EDAX. Such changes in the defect chemistry and consequent effects on conductivity on thermal treatment are well-known for CdTe (7).

In summary, a simple electroless method has proved useful for the fabrication of CdTe thin films. The film composition (Cd:Te ratio) can be varied by suitable thermal treatment of these films. A PEC method for ascertaining majority carrier type in semiconductor thin films has been demonstrated. This method is especially suited to cases where more conventional Hall or hot-probe measurements would be precluded by the high conductivity of the substrate.

Further optimization of the electroless method, introduction of various dopants in the film and fabrication of heterojunction devices based on these films are in progress.

ACKNOWLEDGEMENTS

This research was made possible by a sub-contract (No. XL-3-03048-01) from the U.S. Department of Energy and the Solar Energy Research Institute.

REFERENCES

- (a) Proc. of the 2nd Symposium on Cadmium Telluride, Strasbourg, France, 1976, edited in Rev. Appl. Phys., 12 (1977); (b) K. Zanio, "Cadmium Telluride," Vol. 13 of "Semiconductors and Semimetals," a series edited by R.K. Willardson and A.C. Beer, Academic Press, New York (1978).
- (a) J.F. McCann and M. Skylas Kazacos, J. Electroanal. Chem., 119, 409 (1981); see also references therein; (b) L.S.R. Yeh, P.G. Hudson, and A. Damjanovic, J. Appl. Electrochem., 12, 153, 343 (1982); (c) D.J. Miller and D. Haneman, Solar Energy Mat., 4, 223 (1981); (d) R.A. Boudreau and R.D. Rauh, Solar Energy Mat., 7, 385 (1982); (e) M. Tomkiewicz, T. Ling, and W.S. Parsons, J. Electrochem. Soc., 129, 2016 (1982); (f) G.J. Houston, J.F. McCann, and D. Haneman, J. Electroanal. Chem., 134, 37 (1982); (g) A.S. Baranski, W.R. Fawcett, K. Garner, A.C. McDonald, J.R. MacDonald, and M. Selen, J. Electrochem. Soc., 130, 579 (1983); (h) R.N. Bhattacharya, Solar Energy Mat., in press.
- (a) M.P.R. Panicker, M. Knaster, and F.A. Kroger, J. Electrochem. Soc., 125, 566 (1978); (b) R.L. Rod, R. Banshah, O. Stafudd, B.M. Basol, and P. Nath, USDOE Final Report DOE/ET/23008-T1, submitted by Monosolar Inc., Santa Monica, CA (1980); (c) Z. Shkedi and R.L. Rod, Proc. 14th IEEE Photovoltaic Specialists' Conference, p. 472 (1980); (d) G. Fulap, M. Doty, P. Meyers, J. Betz, and C.H. Liu, Appl. Phys. Lett., 40, 327 (1982); (e) B.M. Basol, E.S. Tseng, and R.L. Rod, paper presented at the 16th IEEE Photovoltaic Specialists Conference, San Diego, CA (1982).
- F.A. Kroger, J. Electrochem. Soc., 125, 2028 (1978).
- R.N. Bhattacharya and P. Pramanik, Bull. Mater. Sci., 2, 287 (1980).
- J.N. Gan, J. Tauc, V.G. Lambrecht, Jr., and M. Robbins, Phys. Rev., B12, 5797 (1975).
- D. deNobel, Philips Res. Rep., 14, 361 (1959).
- G. Hodes, L. Thompson, J. DuBow, and K. Rajeshwar, J. Am. Chem. Soc., 105, 324 (1983).

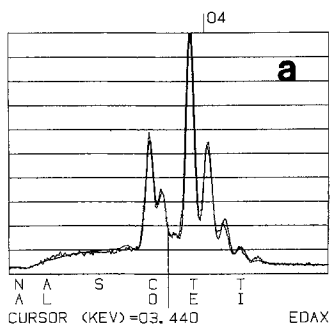
Manuscript submitted Dec. 8, 1983.
The University of Texas assisted in meeting the publication costs of this article.

Table 1
PARTIAL X-RAY DIFFRACTOGRAM DATA AND PEAK ASSIGNMENTS
FOR CdTe THIN FILMS PREPARED BY ELECTROLESS METHOD

Observed	Hexagonal CdTe				Reported ^{a)}				Hexagonal Te			
	2 θ	d, Å	hkl	hkl	2 θ	d, Å	hkl	hkl	2 θ	d, Å	hkl	hkl
Before thermal treatment												
23.80	3.735	100	002	23.70	3.740	100	111		27.58	3.230	100	102
27.70	3.218	100		25.27	3.520	80	101	39.28	2.290	50	220	
38.45	2.330	44		39.25	2.295	100	110	46.42	1.954	30	311	
46.20	1.963	22		45.42	1.965	75	112					
After thermal treatment (500°C for 30 min, see text)												
23.90	3.720	100										
39.45	2.280	91										
45.58	1.990	49										

^{a)} Source: ASTM X-ray Powder Diffraction File (Nos. 18-193, 4-0554 and 15-770).

13-JUL-83 01:00:05
RATE: CPS TIME 90LSEC
00-40KEV; 20EV/CH PRST: 90LSEC
A: ELEEELECTROLESSB;
FS= 2610 MEM: A/B FS= 2610



22-JUL-83 06:05:26
RATE: CPS TIME 90LSEC
00-40KEV; 20EV/CH PRST: 90LSEC
A: EEO1 COTE EL B;
FS= 2504 MEM: A/B FS= 2504

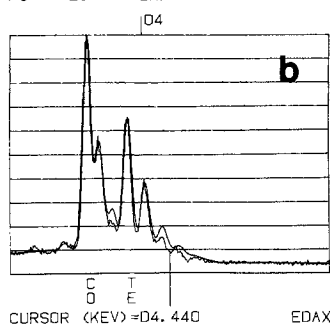


Fig. 2. EDAX spectra for a CdTe thin film prepared by electroless method on Ti substrate before (a) and after (b) thermal treatment (see Text). The electron beam energy was 20 keV. Both the actual spectra and the computer fit to these spectra generated from the peak assignments are shown.

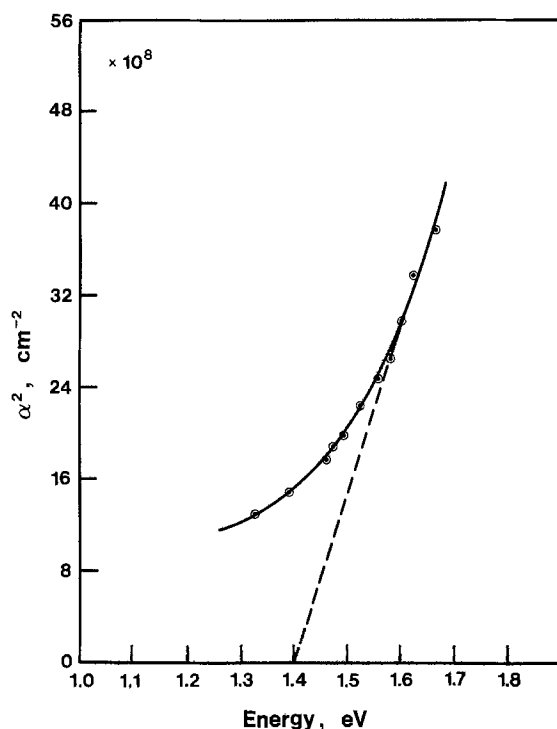


Fig. 1. Typical plot of α^2 vs. light energy (α = adsorption coefficient) for CdTe thin films fabricated by the electroless method.

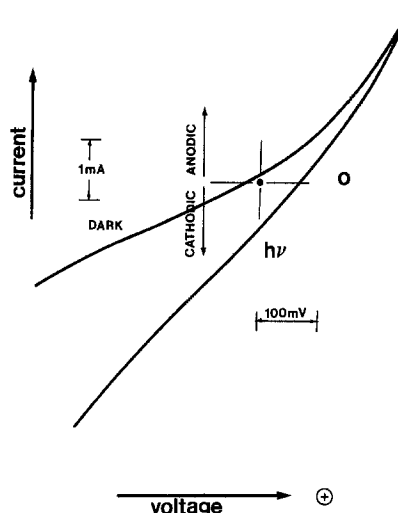


Fig. 3. Comparison of steady-state current voltage behavior in the dark and under illumination for a CdTe thin film fabricated by the electroless method on Ti substrate. The electrolyte contained 3M each of Na₂S, NaOH, and S and was quiescent. The electrode had a protective coating of α -PbO₂ (see text). The potential scan rate was 100 mV/s and the uncorrected light intensity was ~ 60 mW/cm².

Germanium Implantation into Silicon

An Alternate Pre-Amorphization/Rapid Thermal Annealing Procedure for Shallow Junction Formation

D. K. Sadana

Microelectronics Center of North Carolina, Research Triangle Park, North Carolina 27709

W. Maszara, J. J. Wortmann, and G. A. Rozgonyi*

North Carolina State University, Raleigh, North Carolina 27650

W. K. Chu

University of North Carolina, Chapel Hill, North Carolina 27514

INTRODUCTION

Control of electric charge in the surface region of modern miniature Si devices is achieved by shallow ($0.5\mu\text{m}$) dopant implantation followed by a furnace or rapid thermal annealing (RTA) treatment.⁽¹⁾ However, for light impurities, such as B, complete amorphization of the surface layer by ion implantation does not occur even at high doses (10^{15} cm^{-2}) and an extended tail in the B distribution is usually observed due to channeling during implantation.^(2,3) Removal of partially amorphous implantation damage is difficult to achieve on subsequent annealing. Furthermore, high doses of smaller covalent radii dopants create a dislocation network in the implanted region in addition to several other kinds of extended defects. Therefore, recent shallow implants of light impurities are conducted into pre-amorphized Si substrates and then furnace⁽⁴⁾ or rapid thermally annealed⁽⁵⁾ to circumvent the problems addressed above. The pre-amorphization is usually achieved by multiple energy self-implantation of Si to very high doses (10^{-16} cm^{-2}). Since Ge has infinite solid solubility in Si, and it does not appear to alter the electrical properties of Si significantly, we have amorphized Si prior to dopant implant with Ge rather than a typical multi energy Si implant. A similar approach is being investigated by others.^(6,7) The presence of large covalent radius Ge on substitutional site in Si is expected to compensate the lattice strain that arises after subsequent high dose shallow implant/annealing of impurities like B or P. This should prevent the formation of a dislocation network which would otherwise be present without Ge. In this communication, RTA behavior of pre-amorphized surface layers in Si produced by Ge implantation with or without subsequent BF_2 implant is presented. A comparison between RTA results from Si and Ge induced amorphous surface layers is also discussed.

EXPERIMENTAL

Silicon wafers of (100) orientation were implanted with Ge^+ to a dose of 10^{16} cm^{-2} . The implantation was conducted at 300keV at either liquid nitrogen (LN) or room temperature (RT). Some of the wafers were subsequently implanted with 42 keV BF_2^+ at RT to a dose of $2 \times 10^{15}\text{ cm}^{-2}$. Both types of wafers then underwent RTA at 1100°C for 10 seconds in an intense incoherent light system. The structural characterization on all cross-section samples was performed by bright-field transmission electron microscopy (TEM) whereas both bright-field and weak-beam TEM were performed on plan view samples. The atomic profiles of B, F and Ge before and after the RTA were obtained by secondary ion mass spectrometry (SIMS).

RESULTS AND DISCUSSION

Figures 1a and b show typical XTEM micrographs from a Ge implanted (at LN or RT) sample before and after RTA at 1100°C for 10 seconds. From these micrographs and their corresponding diffraction patterns (not shown) it was found that the unannealed sample contained a 4000Å wide amorphous layer extending from the surface (Fig. 1a). Upon annealing at 1100°C for 10 seconds, defect-free regrowth occurred in the amorphous region (Fig. 1b). However, the amorphous/crystalline interfacial region in the annealed sample contained a discrete layer of small dislocation loops typical of the coalescence of straggling ion damage.⁽⁸⁾ The RBS/MeV He^+ channeling from the samples of Figure 1a and b indicated that 92% of Ge occupied substitutional lattice sites after the RTA.⁽⁹⁾ Comparison of the Ge profiles from the unannealed and annealed samples show that very little redistribution of Ge occurs on RTA.⁽⁹⁾

The XTEM micrograph from the subsequently shallow (42 keV) BF_2 implanted but unannealed sample showed that there was no change in the width of the original amorphous layer. The RTA of this sample showed that essentially

*Electrochemical Society member.

key words: rapid thermal annealing, Ge, implantation, TEM, SIMS, damage

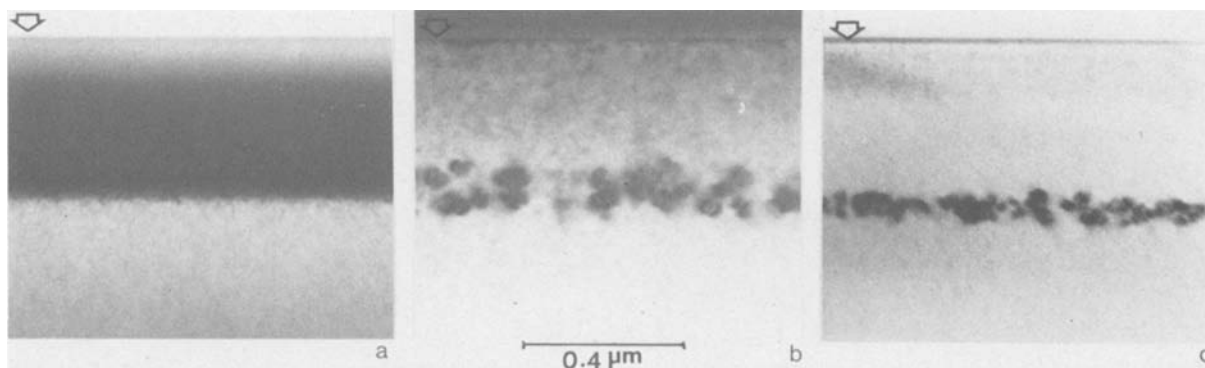


Figure 1. $\text{Ge}^+ \longrightarrow$ (100) Si, 300 keV, 10^{16} cm^{-2} , XTEM micrographs showing (a) a continuous amorphous layer (dark band) in the unannealed sample (b) dislocation loops due to straggling ion damage at the amorphous/crystalline interface in the RTA (1100°C/10 sec) sample (c) same as (b) but with shallow BF_2 implant (42 keV, $2 \times 10^{15} \text{ cm}^{-2}$).

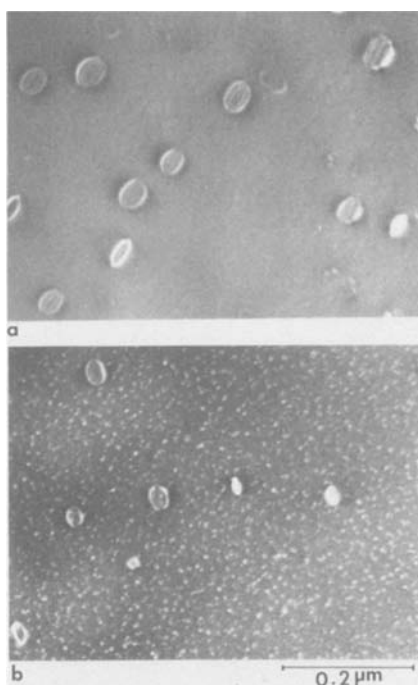


Figure 2. Weak-beam TEM plan view micrographs, (a) corresponding to Fig. 1b and (b) corresponding to Fig. 1c. Note a high density of fine clusters ($\approx 50\text{\AA}$) in Fig. 2b.

defect-free regrowth again occurred in the originally amorphous region (Fig. 1c). Hair-pin shaped dislocations (not shown) were occasionally observed in this region (type II defects in ref. 5). Small dislocation loops due to straggling ion damage were also present in the interfacial region. Although the bright field XTEM micrograph did not show any surface damage (type III in ref. 5), the

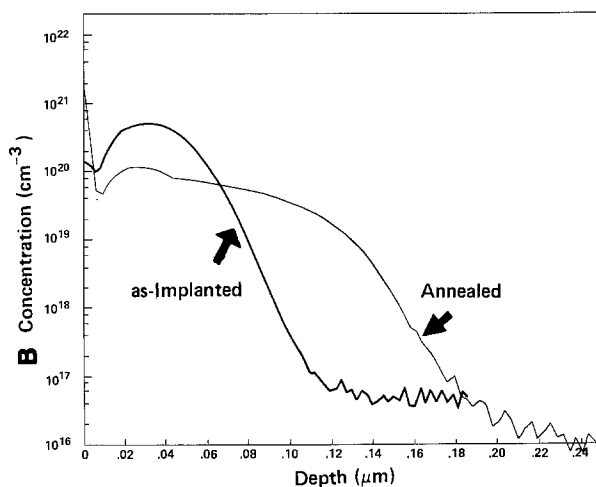


Figure 3. SIMS profiles of boron before and after RTA at 1100°C/10 sec.

weak-beam TEM micrograph (Fig. 2b) from a plan view sample corresponding to the surface region of Figure 1c revealed a high density of uniformly distributed fine defect clusters ($\approx 50\text{\AA}$). Such clusters were absent in a similar TEM micrograph (Fig. 2a) from the sample without the BF_2 . A similar phenomenon has been observed on RTA of self-implanted samples with a shallow BF_2 layer. (5)

The B and F profiles from the samples of Fig. 1c before and after the RTA are shown in Figures 3 and 4. The as-implanted profiles of both B and F showed Gaussian distributions with peaks occurring at 300Å (Fig. 3) and 250Å (Fig. 4). The peak concentrations of B and F were found to be $5 \times 10^{20} \text{ cm}^{-3}$ and $8 \times 10^{20} \text{ cm}^{-3}$ respectively. During

RTA,²¹ however, a high concentration ($\approx 10^{21} \text{ cm}^{-3}$) of B was found to segregate toward the surface which created a pile-up there. Pronounced diffusion into the deeper regions (up to $0.2 \mu\text{m}$) also occurred (Fig. 3). The F profile from the RTA sample did not show high surface concentrations. The F peak remained at R_p although it became narrower as compared to that in the unannealed sample indicating its precipitation at this depth. Diffusion of F toward the peak was observed from either side of the peak. Comparison of the weak-beam TEM results with the SIMS data in Figs. 3 and 4 confirms that the fine clusters are related to the presence of B and/or F.

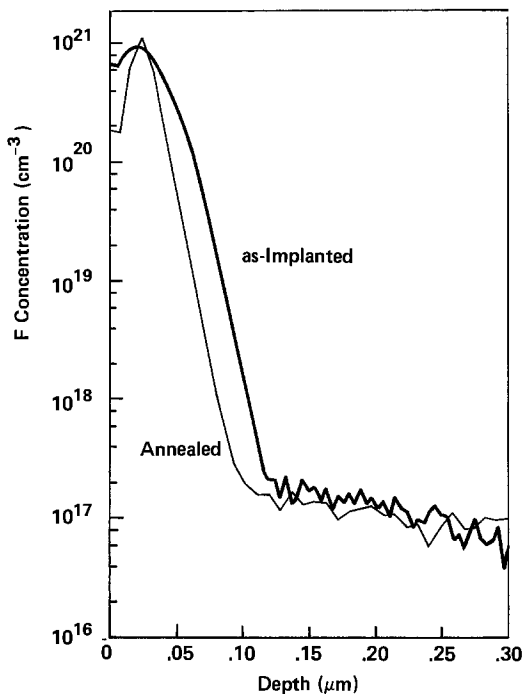


Figure 4. SIMS profiles of fluorine before and after RTA at $1100^\circ\text{C}/10 \text{ sec.}$

From the results presented above, it appears that Ge can be a suitable alternative for pre-amorphization of Si. The structural quality obtained after RTA of the pre-amorphized layer with or without BF_2 is comparable to or better than that achieved in the Si-implanted case.^(5,6) For example, in both procedures three types of major secondary defects are found to be present with BF_2 : (I) surface damage (II) 'hair-pin' shaped dislocations within the implanted region and (III) dislocation loops due to straggling ion damage at the amorphous crystalline interface. However, in the Ge implanted samples the density of type II defects is an order of magnitude less than that in the Si implanted samples. The nature of the surface damage in

Manuscript submitted Dec. 28, 1983;
revised manuscript received Jan. 24,
1984.

the two cases is also found to be different. For example, in the Ge case only uniformly distributed fine defect clusters are observed in the surface region (Fig. 2b). In the Si case microtwins and other irregular structures are observed in addition to the clusters. Comparison of atomic profiles of F show that the redistribution of F in both the unannealed and annealed samples can be significantly reduced in the Ge case. However, the B profiles following BF_2^+ implantation show qualitatively similar results in the two cases although B segregation at the surface is more pronounced in the Ge case than the Si case. Experiments on RTA behavior of shallow B^+ and As^+ into Ge implanted Si are now underway. The electrical results from these samples will be published elsewhere.

ACKNOWLEDGEMENTS

The authors would like to thank Ed Myers, Calvin Carter and Jian Liu of NC State University, Terje Finstead of UNC-CH and Tim Sands of UC Berkeley for stimulating discussions and help provided during the course of this work. Thanks are also due to Dieter Griffis of NC State University for the SIMS measurements and Pam Johnson for typing the manuscript skillfully. This work was partially supported by the ONR.

REFERENCES

1. T.O. Sedgwick, *VLSI Science & Tech.* Eds: C.J. Dell'Oca and W.M. Bullis, The Electrochemical Society, Princeton, NJ (1982) pp.130.
2. W.K. Hofker, Philips Res. Dept. Suppl. 8 (1975) PhD Thesis.
3. D.K. Sadana, S. Shatas and A. Gat, *Proc. Inst. Phys.* (London) 1983 (in Press).
4. M.Y. Tsai and B.G. Streetman, *J. App. Phys.* 50 183 (1979).
5. W. Maszara, C. Carter, D.K. Sadana, G.A. Rozgonyi, J. Liu and J.J. Wortman, *Beam-Solid Interactions and Transient Thermal Annealing of Materials*, J.C.C. Fan and N.M. Johnson (Eds.) North Holland (1984).
6. T.E. Seidel, R. Knoell, F.A. Stevie, G. Poli and B. Schwartz, to be published in *VLSI 1984*, K. Beam and G.A. Rozgonyi (Eds.)
7. P.V. Pavlov, V.I. Pashkov and E.V. Dobrokhotov, *Sov. Phys. Solid State* 15 2257 (1974).
8. D.K. Sadana, J. Fletcher and G.R. Booker, *Electronics Lett.* (Britain) 15 615 (1977).
9. D.K. Sadana, E. Myers, J. Liu, T. Finstead and G.A. Rozgonyi, in ref. 5.

Microelectronics Center of North Carolina assisted in meeting the publication costs of this article.

Simulation of Anomalous Be Diffusion in Semi-Insulating InP

C. W. Farley and B. G. Streetman*

Department of Electrical Engineering, The University of Texas at Austin, Austin, Texas 78712

BACKGROUND

This study considers the anomalous diffusion of implanted Be during thermal annealing reported in this journal by Oberstar et al. (1). Secondary ion mass spectroscopy (SIMS) studies of annealed Be implants into semi-insulating (SI) InP revealed Be profiles with relatively flat tails and abrupt leading edges. Furthermore, the diffusion front penetrated less as the anneal temperature increased (Ref. 1, Figs. 3 and 4), contrary to the expectations of conventional diffusion theory. Concentration dependent diffusion has been reported for both shallow (2-5) and deep (6,7) acceptor impurities in compound semiconductors. In order to understand the anomalous migration of Be we have attempted to simulate the effects of impurity concentration and implantation-related damage on redistribution during annealing.

SIMULATION METHOD AND RESULTS

The unannealed impurity profile is calculated for an implant dose of 10^{15} cm^{-2} , a projected range of 4000 Å and a straggle of 800 Å.

Diffusion simulation is accomplished with a discrete transformation of the continuity equation for the position-dependent diffusion coefficient, reported previously in this journal (Ref. 8, Eq.[16]). In our model we assume that the diffusion coefficient is reduced in regions where the impurity concentration is larger than a specified value C_{max}

$$D_0(T), \quad C < C_{\text{max}}$$

$$D_0(T) \times D_r(T), \quad C > C_{\text{max}}$$

where

$$D_0(T) = D_0 \times \exp[-U_a/kT]$$

$$D_r(T) = D_{r0} \times \exp[U_v/kT]$$

and D_0 and D_{r0} are constants.

The shape of simulated profiles was found to be largely dependent on the degree to which the diffusion coefficient was reduced at high concentrations. For slight redu-

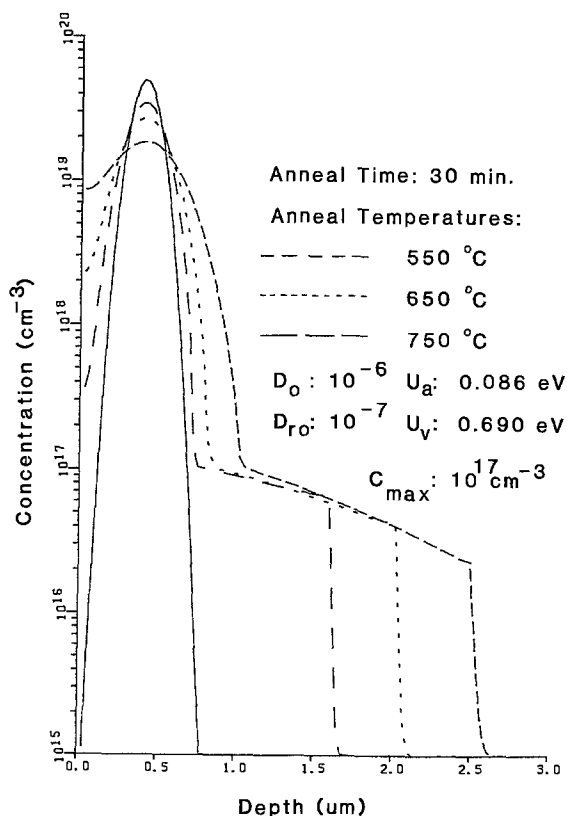


Fig. 1. Isochronal anneals showing retrograde penetration of the diffusion front.

Manuscript submitted Jan. 27, 1984; revised manuscript received Feb. 3, 1984.

The University of Texas at Austin assisted in meeting the publication costs of this article.

* Electrochemical Society Active Member

Key Words: anneal, migration, implantation, semiconductor.

ctions ($D_r > 10^{-2}$) the profiles resemble "ideal" diffusion curves. However, when D_r is less than 10^{-2} the profiles become markedly "non-ideal" and resemble the profiles seen by Oberstar for high dose implants (1). Simulations using this model show retrograde behavior similar to that reported by Oberstar only when $U_a \ll U_v$. However, as the anneal temperature increases simulated profiles become more peaked (Fig. 1) whereas the experimental profiles diffuse and flatten out. Since Oberstar suggested the possible role of defect structures, we modified the reduction factor to include the influence of damage (largely vacancies at the anneal temperatures) so that

$$D_o(C_d) = D_{ro} \quad , \quad C_d < C_{max}$$

$$D_{ro} \times \sqrt{C_{max}/C_d} \quad , \quad C_d > C_{max}$$

where C_d is the defect concentration. These defects are assumed to anneal and diffuse more rapidly at high temperatures. Simulations using various defect diffusion coefficients and annealing rates yield similar results and suggest that initially rapid redistribution at high concentrations is slowed by structures whose gettering ability does not initially decrease upon annealing.

DISCUSSION

Release of Be atoms from regions of high concentration appears to be the rate-limiting factor in the diffusion process. However, the rate of release cannot be described simply by thermally enhanced vacancy generation or by the release of atoms gettered to point defects at or near the peak of the profile since these mechanisms would allow deeper penetration at higher anneal temperatures. It is probable that relatively immobile damage clusters created by the high implant dose do not anneal at lower temperatures but do so at higher temperatures by dissociating into a larger number of rapidly diffusing point defects. Therefore, the gettering ability of the implantation-induced damage should remain constant or possibly increase before declining as the point defects begin to anneal. This model explains the variation with implant dose and annealing time observed by Oberstar (1).

Anomalous Be diffusion was reported only in (SI) and not vapor phase epitaxy (VPE)

material (Ref. 1, Fig. 6). A possible explanation is that the competition of two impurity species (e.g. Be and Fe) for the same lattice sites modifies the diffusion kinetics. If we assume that Be diffuses as a fast interstitial and as a slow substitutional, we would expect to see rapid diffusion in regions where $C_{Be} < C_{Fe}$ since the interstitial fraction of Be should be increased by the presence of Fe. As expected, deep penetration of Be was observed experimentally to occur at levels up to the original concentration of the compensating dopant.

CONCLUSION

In summary, we have developed a model for the diffusion coefficient which gives results similar to those observed by Oberstar for Be-implanted InP. Simulation profiles suggest that Be probably diffuses by an interstitial mechanism and indicate that release of Be from the peak of the profile is a critical determinant of the final distribution. The presence of Fe and Cr on the In sublattice reduces the availability of substitutional sites for Be, which explains why the effect occurs in SI and not VPE material. It is apparent from this and other work that rapid diffusion of acceptors is inherent in SI GaAs and InP and that accurate descriptions of diffusion behavior cannot be simply formulated.

ACKNOWLEDGEMENT

This work was supported in part by the DoD Joint Services Electronics Program through Air Force Office of Scientific Research (AFSC) contract F49620-82-C-0033.

REFERENCES

1. J.D. Oberstar, B.G. Streetman, J.E. Baker, and Peter Williams, This Journal, 129, 1312 (1982).
2. H.C. Casey, M.B. Panish, and L.L. Chang, Phys. Rev., 162, 162 (1967).
3. L.L. Chang and H.C. Casey, Solid-State Electron., 7, 481 (1964).
4. T. Itoh and Y. Kushiro, J. Appl. Phys., 42, 5120 (1971).
5. P.K. Tien and B.I. Miller, Appl. Phys. Lett., 34, 701 (1979).
6. M.R. Brozel, E.J. Fonlkes, Brian Tuck, N.K. Coosivami, and J.E. Whitehouse, J. Phys. D: Appl. Phys., 16, 1085 (1983).
7. B. Tuck and G.A. Adegboyega, J. Phys. D: Appl. Phys., 12, 189 (1979).
8. R. Kwor and C. Paz de Arrujo, This Journal, 130, 1586 (1983).

CdGeP₂ Photoelectrochemical Cells

B. Scrosati* and L. Fornarini

Dipartimento di Chimica, University of Rome, Rome, Italy

Substantial interest has been lately devoted to ternary chalcopyrite semiconductors as photoanodes in liquid junction solar cells. So far the attention has been focussed on ternary chalcogenides in the I-III-VI₂ family, such as CuInS₂ (1,2) and CuInSe₂ (3) and in the II-III₂-VI₄ family, such as CdIn₂S₄ (4) and CdIn₂Se₄ (5,6).

These compounds show very promising photoelectrochemical properties (1-6) and this has prompted us to extend the investigation to other ternary semiconductors having chalcopyrite-type structures. In this respect, we have considered the II-IV-V₂ compounds and here we report preliminary results on the photoelectrochemical behavior of n-CdGeP₂ in liquid electrolyte cells.

Samples of CdGeP₂ single crystals have been kindly provided by Bell Laboratories. The experimental techniques for assembling the photoelectrochemical cells and for the measurements of the current-voltage curves, have been described previously (7).

In figure 1, curve *a*, is shown the normalized spectral response of the CdGeP₂ electrode in a Na₂SO₄ aqueous solution. The response at 770 nm indicates an energy gap of 1.6 eV, in good agreement with the literature data (8).

Current-voltage curves of the

* Electrochemical Society Active Member.

Key words: photoelectrochemistry,
ternary semiconductors.

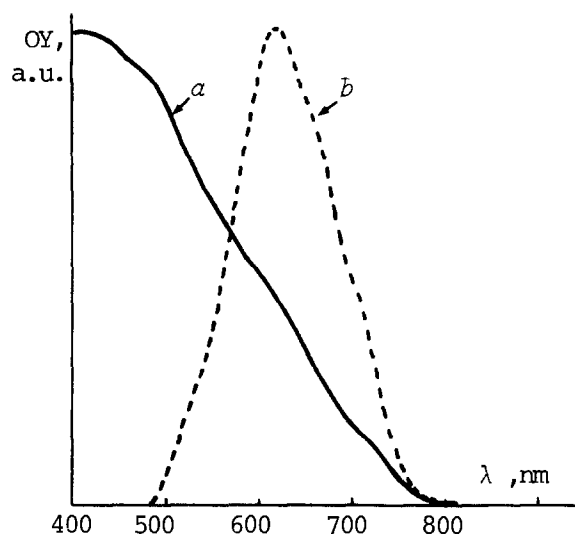


Figure 1-Normalized spectral response of the n-CdGeP₂ electrode in the Na₂SO₄ solution (curve *a*) and in the I₂/I⁻ solution (curve *b*).

the CdGeP₂ semiconductor electrode in the dark and under illumination, reveal a consistent photoeffect (figure 2). Therefore, the behavior of this electrode was evaluated in a regenerative photoelectrochemical cell, using a Pt counter electrode and a I₂/I⁻ redox couple in aqueous solution. The output power characteristic, illustrated in figure 3, shows a good fill-factor (FF=0.37) and a high open circuit voltage (V_{oc}=0.64 V). The photocurrent density and thus the power conversion efficiency are still confined to relatively modest values. This is due to the absorption of the dark iodine solution at short wavelengths (see

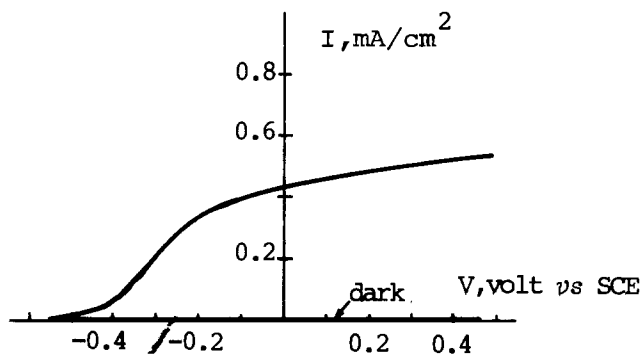


Figure 2-Dark and photocurrent-voltage curves for the n-CdGeP₂ electrode in a 0.5M Na₂SO₄ solution. Illumination: 80 mW/cm².

curve *b* of figure 1) and probably to high surface state recombination, since untreated CdGeP₂ crystals have been used in this preliminary test.

Preliminary results indicate a good stability of the CdGeP₂ photoanode against photocorrosion. Therefore, work is in progress in our laboratory to evaluate the most appropriate electrolyte and the most suitable surface treatments, to finally increase the conversion efficiency of these promising CdGeP₂ photoelectrochemical solar cells.

ACKNOWLEDGEMENTS

The authors wish to thank Dr. J. L. Shay of Bell Laboratories for having graciously provided the CdGeP₂ single crystals and the University of Rome (Progetto di Ateneo) for the financial support.

Manuscript submitted Nov. 28, 1983; revised manuscript received Jan. 30, 1984.

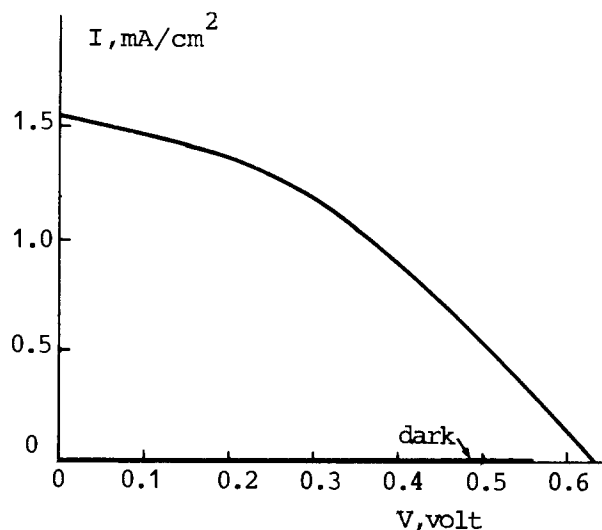


Figure 3-Output characteristic of a n-CdGeP₂/I₂, I₂ (0.2 M, 0.02M)/Pt photoelectrochemical cell, under a 80 mW/cm² illumination. Conversion efficiency: 0.6%

REFERENCES

- 1)-M. Robbins, K. J. Bachmann, V. G. Lambrecht, F. A. Thiel, J. Thomson Jr., R. G. Vadimsky, S. Menzes, A. Haller, B. Miller, This Journal, 125, 831 (1978).
- 2)-H. J. Lewerenz, H. Goslowsky, 4th International Conference on Photochemical Conversion and Storage of Solar Energy, Jerusalem, Israel, 1982.
- 3)-Y. Mirovsky, D. Cahen, Appl. Phys. Lett., 40(8), 727 (1982).
- 4)-G. F. Epps, R. S. Becker, This Journal, 129, 2628 (1982).
- 5)-R. Tenne, Y. Mirovsky, Y. Greenstein, D. Cahen, This Journal, 129, 1506 (1982).
- 6)-L. Fornarini, F. Stirpe, E. Cardarelli, B. Scrosati, Solar Cells, in press.
- 7)-G. Razzini, M. Lazzari, L. Peraldo Bicelli, F. Lévy, L. De Angelis, F. Galluzzi, E. Scafe, L. Fornarini, B. Scrosati, J. Power Sources, 6, 371 (1981).
- 8)-J. L. Shay, J. H. Wernick, 'Ternary Chalcopyrite Semiconductors Growth, Electronic Properties and Applications', Pergamon Press, 1975.

A Pronounced Cation Effect on Performance and Stability of Cd-Chalcogenide/Polysulfide Photoelectrochemical Cells

S. Licht, R. Tenne, H. Flaisher, and J. Manassen

Department of Plastics Research, The Weizmann Institute of Science, Rehovot 76100, Israel

Variation of the alkali cation in aqueous polysulfide solutions is found to have a dramatic effect on Cd-chalcogenide photoelectrochemical cell (PEC) stability and conversion characteristics. The cation species, although not directly involved in the electrochemical reactions, is important since it is the predominant ionic species in solutions.

Crystals of CdSe (0.25 cm², 5 ohms cm from Cleveland Crystals) were polished with 5 micron alumina powder, etched for twenty seconds in 1:4 (HNO₃/HCl)_{conc} and then submerged in polysulfide solution to dissolve possibly elemental selenium formed. Ohmic contacts were made with In-Ga alloy. Etching procedures were found to be not critical for the effects found. Alkali hydrosulfide solutions were prepared by saturation of the relevant aqueous alkali hydroxide solution with H₂S. Saturation with H₂S was monitored by volume, mass, pH and temperature changes. Polysulfide solutions were obtained by addition of sulfur and alkali hydroxide. Solutions were prepared, stored and utilized under strict exclusion of air. The light source was a stabilized tungsten/halogen lamp. Standard electrochemical equipment was used for measuring the IV and rest potentials.

Solution conductivity was measured with a Radiometer CDM 2d conductivity meter ($\pm 0.5\%$) using a calibrated CDC 104 cell of cell constant one. Cation activity was measured with a calibrated Beckman 39137 cation selective electrode versus standard calomel electrode. The electrode was calibrated against alkali hydroxide and alkali chloride solutions of known activity (1).

Figure 1 presents the output of an etched CdSe electrode as a function of time in four polysulfide solutions containing equal concentrations of, respectively, Li, Na, K and Cs and the striking differences in stability are obvious. The same cationic dependence is found when measuring the current/voltage behavior as shown in Table I, where the short circuit current as well as fill factors are seen to increase appreciably from Li to Cs.

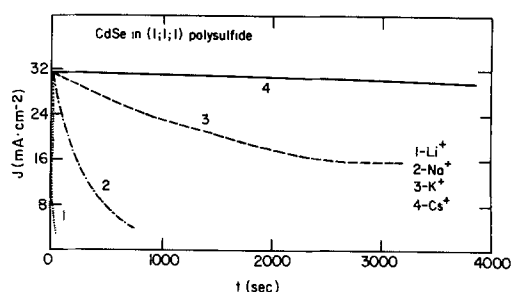


Fig. 1. Output stability of CdSe in polysulfide solutions with different cationic species (2 AM1).

Table I. Experimentally measured rest potentials and calculated photoelectrochemical data for solutions which are 1M in OH⁻, S⁼ and S as a function of cationic species at room temperature.

Cation	Polysulfide rest potential (volts vs. SCE)	Open circuit voltage (volts)	Short circuit current (mA/cm ²)	Relative efficiency
Li ⁺	-0.740	0.650	9.2	1
Na ⁺	-0.748	0.742	17.3	4.06
K ⁺	-0.768	0.747	18.7	5.09
Cs ⁺	-0.775	0.757	20.0	5.67

In order to check whether a similar effect is also found in ordinary electrochemical systems, polarization effects were measured on Cu₂S electrodes under dark conditions. Cu₂S is known to be kinetically fast in the polysulfide system (2). A one cm² Cu₂S electrode, prepared from brass gauze as described in ref. 2 was tested in the one molar, polysulfide solutions. Polarization losses decreased in the order Li > Na > K > Cs, with losses in the Li solution being approximately four times greater than those for the cesium polysulfide electrolyte.

The measured specific solution conductivity and cation activity for the various polysulfide solutions are presented in Table II.

Manuscript received Jan 16, 1984.

Table II. Measured cation activities and specific conductivities for aqueous polysulfide solutions one molar in hydroxide, sulfide and sulfur and containing exclusively lithium, sodium, potassium or cesium cations.

Cation	Li ⁺	Na ⁺	K ⁺	Cs ⁺
Activity	.57	.69	.86	
Conductivity (mho/cm)	.230	.265	.365	.372

The Beckman cation selective electrode was not sufficiently responsive in cesium polysulfide and cesium hydroxide solutions to estimate the cesium ion activity.

The variation of conductivity (Table II) is consistent with the known variation of alkali salt and alkali cation mobilities. However, the variation of activity contradicts the known behavior of the alkali halides. Evidently it is this enhancement of both activity and conductivity which favors the large cation effect observed.

The known decrease in alkali halide activity from lithium to cesium salts is generally understood to reflect the increased hydration of the cations with low atomic number. This results in a decrease in free water and therefore to an increase in effective concentration of the ion. The opposite trend is observed here for the polysulfide solutions and is similar to the observed trend for alkali hydroxides.

The experimental effects are consistent with the model of localized hydrolysis introduced by Robinson and Harned (3), as will be elaborated in a future publication.

The Weizmann Institute of Science assisted in meeting the publication costs of this article.

- References
1. B.E. Conway, "Electrochemical Data," Elsevier Publ. Co., London (1952).
 2. G. Hodes, J. Manassen and D. Cahen, J. Electrochem. Soc., 127, 544 (1980).
 3. R.A. Robinson and H.S. Harned, Chem. Rev., 28, 419 (1941).

New Binder System for Low Temperature Alkaline Electrodes

L. B. Berk and C. T. Liu

Westinghouse Electric Corporation, Research and Development Center, Pittsburgh, Pennsylvania 15235

INTRODUCTION

A binder for a hydrophobized, porous, gas-fed electrode must perform two fundamental tasks, it must blend the support and catalyst into a conductive, gas-and-electrolyte-permeable structure and it must impart hydrophobicity to the electrode without substantially decreasing the activity of the electrode. Presently, polytetrafluoroethylene (PTFE) and fluorinated polyethylene (FEP) are the binders of choice for gas-fed electrodes. Prior to this wide-spread acceptance of PTFE, polypropylene and polyethylene whiskers and powders were used as binders. The PTFE electrodes quickly supplanted these electrodes due to better performance and life characteristics. However, the extreme hydrophobicity of PTFE (which necessitates a compromise between long life and good performance), its difficult processing characteristics (high temperatures and toxic fumes) and its high cost have limited the optimization of PTFE-bound electrodes. This has led to a search for a replacement for PTFE as a binder for low-temperature, gas-fed electrodes.

NOVEL BINDER

Two alternative binders have been found to replace PTFE and FEP. These binders are fibrillated polyethylene and fibrillated polypropylene marketed by Hercules/Solvay under the tradenames Pulpex E (polyethylene) and Pulpex P (polypropylene). Table I, taken from Pulpex product literature, lists the characteristics of the Pulpex materials. Their most important features, as will be described in a more complete paper to be published later, are their high surface area ($10 \text{ m}^2/\text{gm}$), large diameter (20μ), and length (1mm). The high surface area gives the fiber strong binding ability and decreases the amount of Pulpex necessary. The large diameter compensates for lower chemical stability in the presence of superoxides and peroxides. Further, polyethylene and polypropylene are sufficiently hydrophobic to be used as hydrophobizing agents in the absence of PTFE or FEP.

EXPERIMENTS AND RESULTS

The Pulpex was obtained in both P (polypropylene) and E (polyethylene) forms. The fibers turned from white to gray when trace amounts of carbon were introduced, which showed a high degree of interaction between the fibers and carbon. Initial tests on 40 cm^2 , 0.03 cm thick electrodes in 25% KOH showed no electrolyte leakage at room temperature for over 1500 hours in the absence of potential. Thus encouraged, 40 cm^2 , two-layer electrodes were fabricated and tested in 25% KOH. The electrodes were cycled against a nickel counter on a 4 hour $12.5 \text{ mA}/\text{cm}^2$ charge and a 4 hour $25 \text{ mA}/\text{cm}^2$ discharge.¹ Two effects were noted. When electrodes made with Pulpex E were hot-pressed at 125°C the electrodes performed well but leaked quickly. When electrodes made with Pulpex E were hot pressed at 135°C they performed poorer than the 125°C electrodes but had a much longer leak-free life. Therefore electrodes were made using the additive package shown in Table II using Pulpex P (melting point 165°C) in the active, hydrophilic layer and Pulpex E (melting point 132°C) in the hydrophobic layer. The electrodes were pressed at 135°C . The small amount of PTFE was added as a dusting agent.

The performances of two such electrodes are shown in Figure 1. The electrodes were cycled in the bifunctional mode (25 mA discharge for four hours, 12.5 mA charge for four hours). Performance is better than similar, Teflon-based electrodes of the same structure. Figure 2 shows a similar Pulpex electrode run in discharge only.

One interesting feature of the Pulpex-bound electrode is that the hydrophobicity is controlled more by the processing temperature than the amount of the binder and even the presence or absence of small amounts of PTFE. Processing the electrode above the melting point of the polymer makes leak-resistant electrodes without comprising gas-permeability. This ability to use two distinct by interchangeable polymers is an advantage not

available with PTFE.

SUMMARY

Suitable alternatives to PTFE and FEP have been found in fibrillated polyethylene and fibrillated polypropylene. The materials can be used with or without the fluorocarbons. The new binders have processing advantages over PTFE (two distinct forms, lower pressing temperatures). Further the cost (approximately \$1.50/lb) is significantly lower than PTFE. Preliminary tests on the binders have shown them to be competitive with PTFE in terms of performance and cycle life.

ACKNOWLEDGMENT

We would like to thank DOE and Lawrence Livermore Laboratories for supporting this work under Contract 7335709. We would also like to thank Hercules/Solvay for supplying samples of Pulpex.

REFERENCES

1. A complete description of the experiment will be published at a later date.

Table I

Polymer	Pulpex E polyethylene	Pulpex P polypropylene
Specific gravity	.96	.90
Melting point, °C	132	165
Fiber length, mm average	0.6 - 1.2	0.8 - 1.5
Fiber diameter, μ	10 - 40	20 - 40
Surface area (BET, N ₂) m ² /gm	6 - 15	5 - 10

Table II

Hydrophilic Layer
10 gms 3.5 wt% silverized Shawinigan
Black with 0.3 gms PTFE

3 gms WC 12 w/o Co
2 gms FeWO₄
2 gms NiS
2 gms Pulpex P

Hydrophobic Layer
10 gms 3.5 wt% silverized Shawinigan
Black (without PTFE)

2 gms Pulpex E

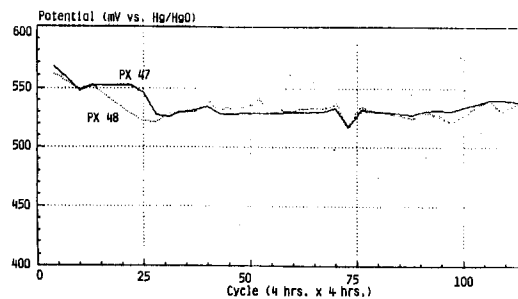


Figure 1a. Charge at 12.5 mA/cm²

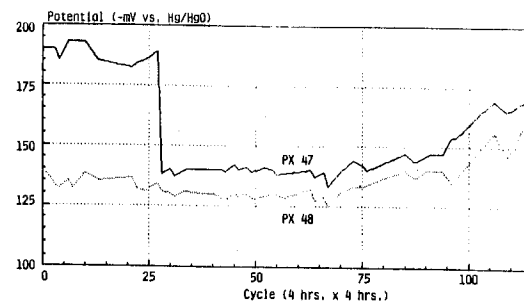


Figure 1b. Discharge at 25 mA/cm². The high initial potentials of PX47 were due to an experimental error.

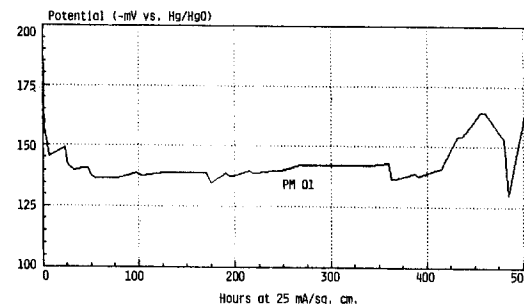


Figure 2. Constant discharge at 25 mA/cm².

Manuscript received Jan. 17, 1984.

Westinghouse Electric Corporation assisted in meeting the publication costs of this article.

Time-Resolved Microwave Conductivity (TRMC): Photoeffects at Semiconductor/Electrolyte Interfaces

M. Kunst, G. Beck, and H. Tributsch

Hahn-Meitner-Institut für Kernforschung Berlin, Bereich Strahlenchemie, D-1000 Berlin 39, Germany

We report a method to study charge generation and transport at interfaces by following the change of the conductivity induced by a light pulse, via detecting the corresponding change of microwave absorption. The possibilities of the methods are demonstrated in an investigation of charge carrier generation and transport at the semiconductor/aqueous electrolyte interface. The method presented here has been originally applied to the study of charge carriers in homogeneous non- and low-conductivity compounds (1,2) and is here firstly applied to interfacial systems.

The method uses the proportionality between the relative change of reflected microwave power $\frac{\Delta p}{p}$ and the conductivity $\Delta\sigma$ induced by a light pulse in a solid embedded in a waveguide system (2,4):

$$\frac{\Delta p}{p} = A \Delta\sigma$$

$\Delta\sigma$ is composed of two parts (3,4), i.e. $\Delta\sigma_i$ the induced conductivity of free ionic and electronic charge carriers and $\Delta\sigma_p$ the conductivity due to electric energy absorption of induced dipoles. Although TRMC can also be used to investigate light-induced changes of dipole moments, $\Delta\sigma_i$ dominates in semiconductors with high quantum yields and mobilities in the initial charge separation processes (2,3).

key words: photoelectrochemistry, microwave absorption, interfaces, charge separation, electrode reactions

Hence:

$$\frac{\Delta p}{p} = A \Delta\sigma_i = A \sum_i N_i \mu_i e$$

N_i : concentration of induced charge carriers of the i th kind,
 μ_i : respective mobility; and
 e : elementary charge

The electrochemical cell consists of a plastic tube screwed into the center of a short-circuited waveguide section (Fig. 1). The tube is closed at one end by the semiconductor working electrode, which in our experiment is a thin platelet of n-WSe₂. The tube is filled with supporting electrolyte (K₂SO₄). A Pt-wire is used as counter- and reference-electrode during the measurement.

Microwaves (30 GHz) are directed in a waveguide system (Fig. 2) to the semiconductor electrode positioned perpendicular to the direction of microwave propagation. The reflected microwaves from the semiconductor/electrolyte interface are directed via a circulator to the detector. The detector output signal, which is proportional to the change of microwave power for small signals as in our experiment, is recorded on a storage oscilloscope as a function of time after excitation. Excitation is provided by a frequency-doubled Nd:YAG laser ($\lambda = 530$ nm, pulse width 20 ns FWHM).

The Current Voltage curves (Fig. 3) show increases in photocurrent with electrode potential up to 6 V without saturation. The induced conductivity (inserts Fig. 3) shows a fast decaying part (decay time mainly determined by

the laser pulse) giving way to a much slower decay. Two observations are made: a) The signal maximum and the height of the slower decaying part increase with electrode potential. b) The increase of the slower part is relatively larger (Fig. 4).

Both the peak amplitude of the TRMC signal and the electrode photocurrent vary at fixed potential approximately in a linear way with the light intensity (illumination with laser light - producing up to 10^{14} photons per pulse - and with a Xe-lamp - up to 500 mWcm^{-2} - respectively). The geometry of the front contact has within the accuracy of the measurements no influence on the time constants observed. Experiments with ring contacts yielded analogous results.

The results can be interpreted in terms of recombination in the space charge region (fast decay) and the consumption of the separated charge carriers (slower decay). The fact that under illumination with a Xe-lamp saturation of photocurrent is not observed indicates that substantial polarization losses occur at the n-WSe₂/electrolyte interface. The increase of the maximum signal height under anodic polarization thus represents an enhancement of the initial yield by an increase of the electric field in the space charge region (reduced geminate recombination). The larger electric field leads also to a higher concentration of separated charge carriers due to diminished recombination. This results in the more pronounced increase of the slower decaying part.

Charge transfer reactions in the surface can be identified by several decay constants in the slowly decaying part which can be distinguished at longer timescales not displayed here. The qualitative conductivity data can be expressed in absolute conductivity units by a calibration procedure (4). However, the most difficult problem confronting quantitative evaluation in terms of mobilities, cross sections and concentration of reaction partners of the induced charge carriers appears to be the inhomogeneous absorption of the exciting light and consequently

the inhomogeneity of the kinetics of the produced charge carriers still enhanced by the space charge field.

From the above it is evident that TRMC can be used to monitor charge separation and transport at the semiconductor/electrolyte interface to obtain information not easily accessible otherwise. Quantitative evaluation should permit determination of cross sections of the various charge carrier reactions. An intriguing possibility is also acquisition of data concerning the intensity and depth of the space charge field from the influence of the electrode potential on the cross sections and on the initial yield where measurements at several wavelengths of the exciting light can be used. As TRMC permits measurements without supporting electrolyte, the influence of the double layer can be investigated.

The use of TRMC is not limited to the study of transient conductivity changes at semiconductor/electrolyte interfaces. Other interfacial systems (e.g. semiconductor/metal) can be studied with the set-up shown here and a small adaptation permits also to investigate the steady-state case.

ACKNOWLEDGEMENT

It is a pleasure to thank Drs. M.P. Haas, J. M. Warman and H.J. Lewerenz for stimulating discussion and helpful suggestions.

REFERENCES

1. J.M. Warman, P.P. Infelta, M.P. de Haas and A. Hummel, *Can.J.Chem.*, **55**, 2249 (1977).
2. J.M. Warman, Interuniversity Reactor Institute Report No. 134-81-22.
3. M.P. de Haas and J.M. Warman, *Chem. Phys.* **73**, 35 (1982).
4. M. Kunst, G. Beck and H. Tributsch, publication in preparation.

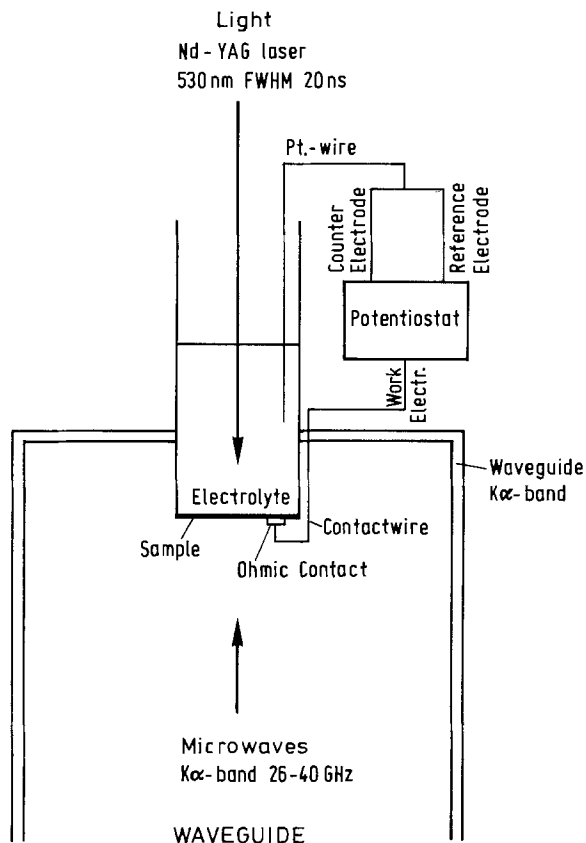


Fig. 1 Electrochemical set-up to measure the reflected microwave power level of a $n\text{-WSe}_2$ working electrode.

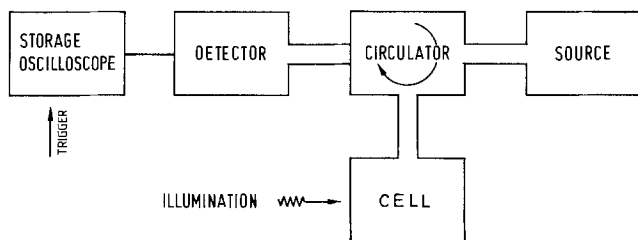


Fig. 2 Microwave Equipment

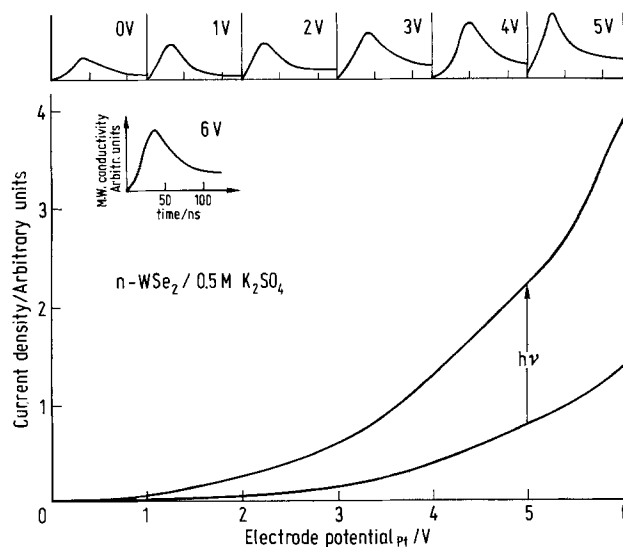


Fig. 3 Photocurrent (excitation source Xe-lamp) and dark current in an electrochemical cell with $n\text{-WSe}_2$ working electrode and a Pt-wire as counter- and reference-electrode as a function of the electrode potential.

Inserts show the induced microwave conductivity at the electrode potentials given as a function time in a $n\text{-WSe}_2$ working electrode.

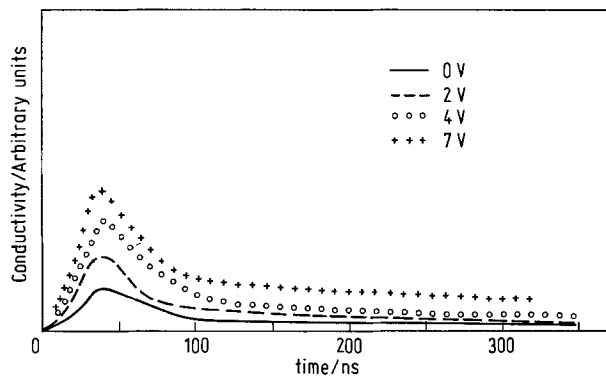


Fig. 4 Induced microwave conductivity as a function of time at electrode potentials indicated.

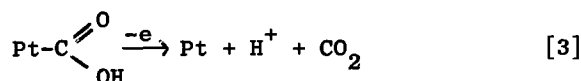
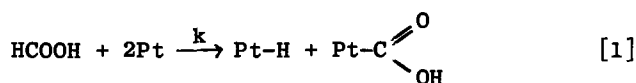
Manuscript submitted Nov. 5, 1983;
revised manuscript received Jan. 15,
1984.

The Rates of Oxidation of HCOOH and DCOOH at Lead Adatom-Covered Pt Anodes

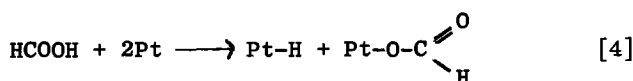
Anjam Razaq and Derek Pletcher*

Department of Chemistry, The University, Southampton SO9 5NH, England

During the last six months, there have been two international symposia on electrocatalysis (1,2). At both, there have been extensive discussions on the mechanism of formic acid oxidation and these have served to highlight the fundamental difference between the accepted mechanisms at Pt electrodes and at Pt surfaces in the gas phase. Electrochemists have generally accepted the mechanism proposed by Capon and Parsons (3), i.e.



where the initial step is cleavage of a C-H bond in a dissociative adsorption process. In contrast, the data from the study of the decomposition of formic acid at a gas-Pt interface has generally been interpreted in terms of initial cleavage of the O-H bond, i.e.



The main evidence for step [1] as the rate determining process in anodic oxidation is the absence of a strong pH effect. In this note we wish to report further evidence based on the measurement of the rate of oxidation of HCOOH and DCOOH, using the now, well-known Pb adatom effect to overcome the poisoning of the Pt surface (4). In earlier papers (5,6) we have shown that the rate of oxidation of formic acid is determined either by diffusion in solution or a chemical reaction sensitive to surface conditions and taken to be reaction [1] above. In addition, we described an analysis of the chronoamperometric data leading to a rate constant for the chemical step. We believed that the observation of a strong kinetic isotope effect between the acids DCOOH and HCOOH would support the conclusion of the

*Electrochemical Society Active Member.

cleavage of the C-H, but not the O-H bond, in the determining step.

Experimental.--All the procedures have been described in detail elsewhere (5,6). The DCOOH was formed by dissolving Merck DCOOD in the HClO₄ electrolyte.

Results and Discussion.--Cyclic voltammograms were run for a Pt electrode in solutions of (a) 0.1M HCOOH and (b) 0.1M DCOOH both in 1M HClO₄ containing 1 mM Pb²⁺. Figure I shows the forward sweeps for experiments at 0.1V s⁻¹. It can be seen that the I-E curves are very similar in shape and the main

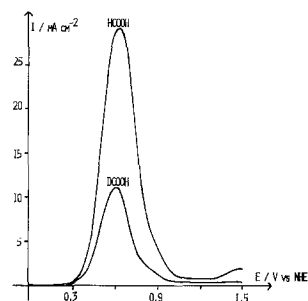


Figure I I-E curves for (a) 0.1M HCOOH and (b) 0.1M DCOOH in 1M HClO₄ + 1mM Pb²⁺

features are the high current density peaks, E_p close to +0.60V vs NHE although it is also clear that the peak current densities are quite different, that for DCOOH being lower by a factor of 2.7. The curve for HCOOH is identical to that reported earlier (5,7) and the peak has been interpreted in terms of the coverage by Pb adatoms. The peak potential corresponds to θ_{Pb} = 0.5, the most active surface, where the adatoms are arranged over the surface so as to give a maximum number of two Pt surface atoms adjacent to each other for reaction [1] to occur but few sites where there are sufficient Pt sites for poison to form. At lower potentials some of the surface is completely covered by Pb and at higher potentials θ_{Pb} < 0.5 and some of the surface becomes poisoned.

While the difference in peak current

densities for HCOOH and DCOOH clearly implies cleavage of the C-H bond in the rate determining step, it is difficult to estimate a ratio of rate constants from the linear sweep curves. Hence the chronoamperometric technique was used. For each acid in 1M HClO₄ + 1 mM Pb²⁺, the potential was stepped from +0.2V (where the surface is fully covered by Pb) to +0.6V (where $\theta_{Pb} = 0.5$ and oxidation of formic acid occurs at a maximum rate) and the I-t responses were recorded over the time range 0.1 to 100 s. In both cases, falling I-t transients were observed and these were analysed by plotting It^2 vs t^2 , see figure II.

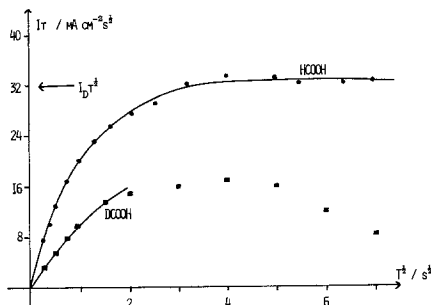


Figure II Chronoamperometric data for 0.1M HCOOH & DCOOH in 1M HClO₄ + 1mM Pb²⁺.

The curve for HCOOH is very similar to that expected for an electrode reaction under mixed diffusion-kinetic control. Initially It^2 increases but beyond 10 s it reaches a plateau value from which the diffusion coefficient may be evaluated as $0.83 \times 10^{-5} \text{ cm}^2 \text{ s}^{-1}$. With DCOOH the response is not so ideal. It will be shown below that the curve again fits well to mixed control but only up to 4 s; at longer times the value of It^2 falls below the expected value, never reaching the diffusion limit (the same plateau as for HCOOH) and indeed It^2 passes through a peak and then falls. This is the behaviour expected if the electrode surface poisons slowly; certainly it would not be surprising if the DCOOH were to contain a higher level of impurity than the Analar HCOOH.

The I-t data was further analysed using a modification of the procedure of Delahay and Oka (8) developed earlier (5) for the case where the kinetic limitation arises from reaction [1]. In this method the ratio I/I_D at each t on the rising part of the It^2 vs t^2 plot is used to calculate a value of $k \theta_{Pb}(1-\theta_{Pb})t^{3/2}/D$ which can then be replotted versus $t^{3/2}$. Such plots should be linear and k may be estimated from the slope since D is known and $\theta_{Pb} = 0.5$ at 0.6V. Figure III shows such plots for HCOOH and DCOOH where the data for the latter acid was evaluated assuming the true diffusion limited current is the same as

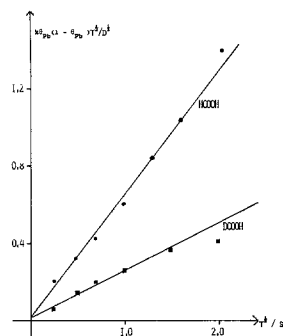


Figure III Analysis of chronoamperometric data.

for HCOOH. Good linear plots are obtained and the values of k for HCOOH and DCOOH were 7.6×10^{-3} and $2.9 \times 10^{-3} \text{ cm s}^{-1}$ respectively.

The ratio of the rate constants, $k_{\text{HCOOH}}/k_{\text{DCOOH}}$, of 2.6 clearly supports the hypothesis that it is the C-H bond which is cleaved in the chemical process leading to the kinetic limitation of the current. Hence it remains our conclusion that at Pt/Pb surfaces, the oxidation of formic acid is under mixed control by diffusion and a chemical process leading to cleavage of the C-H bond and whose rate reflects the surface, both coverage (4,5,7) and choice of adatom (6). The mechanism [1] - [3] meets all the requirements.

REFERENCES

1. "The Chemistry and Physics of Electrocatalysis", The Electrochemical Society Meeting, San Francisco, May 1983.
2. "Electrocatalysis: Theory, Practice and Further Developments", Neunkirchen, W. Germany, September 1983.
3. A. Capon and R. Parsons, *J. Electroanal. Chem.*, **45**, 205 (1973).
4. R.R. Adzic, *Israel J. Chem.*, **18**, 166 (1979) and references therein.
5. D. Pletcher and V. Solis, *J. Electroanal. Chem.*, **131**, 309 (1981).
6. I. Fonseca, J. Lin-Cai and D. Pletcher, *J. Electrochem. Soc.*, **130**, (1983), 2187.
7. R.R. Adzic, D.N. Simic, D.M. Drazic and A.R. Despic, *J. Electroanal. Chem.*, **61**, 117 (1975) and **65**, 587 (1975).
8. P. Delahay and S. Oka, *J. Am. Chem. Soc.*, **82**, 329 (1960).

Manuscript submitted Nov. 4, 1983.

Electrochemical Intercalation of Lithium into an Active Carbon

Yoshio Takasu*, Masao Shiinoki, and Yoshiharu Matsuda*

Faculty of Engineering, Yamaguchi University, 2557 Tokiwadai, Ube 755, Japan

INTRODUCTION

Besides metal oxides, sulfides and fluorocarbons, materials such as polyacetylene and carbon fiber have recently been proposed for cathode of lithium cells.¹⁻⁶ Many investigators insisted that some cathode reactions in lithium cells involve the intercalation of lithium into the cathode. Active carbon can also be expected to offer incorporation sites for lithium because it is composed of many fine graphite-like crystallites (i.e. turbostratic structure).⁷⁾ Lithium might intercalate into the inter-layer of the crystallites.

In this research, the authors have examined whether lithium ions intercalate into an active carbon cathode in an organic solvent containing a lithium salt.

EXPERIMENTAL

Active carbon made from coal (Futamura Chemicals Co. Ltd., Taiko-GL-30) and graphite powder (Nakarai Chemicals Co. Ltd., C-325) were used as active materials. X-ray diffraction spectra of these active materials are shown in Fig.1. In this region graphite has a strong diffraction peak from the plane at 26.5° which is characteristic of the graphite structure. On the other hand, active carbon has only a weak peak at this angle, but has three broad peaks around 21.2° , 23.5° , and 43° . These peaks originate from graphite-like crystallites having turbostratic structure. Active carbon (or graphite powder) [150 mg] was dried at 60°C , mixed with polyethylene powder [25 mg], and then press-molded [4500 kg cm^{-2}] to a tablet cathode [13 mm in diam, ca.1 mm in thickness]. The tablet was mounted on a frame made of poly-tetrafluoroethylene, and the electrical contact was made with a platinum plate [13 mm in diam] connected to a spring wire. This platinum plate was brought into contact with the tablet cathode. Since the geometric area of the cathode faced to the electrolyte solution was 0.95 cm^2 (corresponding to 72% of the cross section of the tablet cathode), about 108 mg of carbon material would be effective as the active material. The electrolytic cell was a glass beaker filled with 100 ml of an electrolyte solution composed of a mixture of propylene carbonate and 1,2-

dimethoxyethane in volume ratio of 1 : 1 containing 1.0 mol dm^{-3} of LiClO_4 . The counter electrode and the reference were a platinum plate [2 x 3 cm^2] and SCE, respectively. Prior to electrical measurements, the electrolyte solution was deoxygenated by blowing high purity nitrogen. The electrolytic cell was thermostated at 25°C . The amount of lithium intercalated (or partly adsorbed) into active carbon was determined by an atomic absorption spectrometry, after the cathode material was ignited and dissolved in nitric acid.

RESULTS AND DISCUSSION

Figure 2 shows the discharge curves of the carbon cathodes at 0.21 mA cm^{-2} current density. The electrode potential of active carbon cathode gradually dropped with an increase of discharge time, reached a minimum value, ca. -1.4 V vs. SCE , at 0.3 A h g^{-1} discharge, and then rose slowly. On the other hand, that of the graphite cathode rapidly dropped with the discharge. Figure 3 shows the relation between the amount of lithium detected in the cathode and the charge passed. The straight line in the figure shows a theoretical value assuming that all the charge passed is utilized for the discharge of lithium ions. After about 0.3 A h g^{-1} discharge, the derivation of experimental value from the theoretical line was observed. This discharge capacity corresponds to that during a period from the start of discharge to the time at which the cathode potential gave the minimum value. The X-ray diffraction spectrum (c) in Fig.1 is of the cathode after 0.6 A h g^{-1} discharge. The appearance of some new diffraction peaks around 32° , 37° , and 40° suggests that the discharged lithium intercalates into active carbon. Adsorption of lithium over the active carbon might partly occur, however, it would occur no change in the X-ray diffraction spectra. Beyond ca. 0.3 A h g^{-1} discharge, other cathodic reaction without the adsorption and/or intercalation of lithium into active carbon would dominantly occur, because the electrode potential rose again and the amount of lithium taken into active carbon showed a deviation from the value theoretically presumed. One of the probable reaction beyond ca. 0.3 A h g^{-1} discharge is the cathodic reduction of some organic ions which were formed on the platinum anode as a result of anodic solvent decomposition. To prove this possibility, analyses of the electrolytes are now being made.

* Electrochemical Society Active Member

If we assume that the active carbon was composed only of carbon before the discharge, and lithium homogeneously intercalated into the active carbon, the composition of sample (e) (e.g., in Fig.3) should be LiC_5 .

REFERENCES

1. K.M.Abraham, J.L.Goldman, and M.D.Dempsey, *This Journal*, **128**, 2493 (1981).
2. M.S.Whittingham, *ibid.*, **123**, 315 (1976).
3. P.J.Nigrey, D.MacInnes, Jr., D.P.Nairns, and A.G.MacDiarmid, *ibid.*, **128**, 1651 (1981).
4. L.W.Shacklette, R.L.Elsembaumer, R.R.Change, J.M.Sowa, D.M.Ivory, G.G.Miller, and R.H.Baughman, *J.C.S.Chem.Comm.*, 361 (1982).
5. M.Nawa, T.Nogami, and H.Mikawa, *Proc.*, 23rd. Battery Symposium in Japan, 65p, (1982).
6. Y.Matsuda, M.Morita, and H.Katsuma, *DENKI KAGAKU*, **51**, 744 (1983).
7. R.E.Flanklin, *Proc.Roy.Soc.*, **A209**, 196 (1951).

Manuscript submitted Nov. 31, 1983;
revised manuscript received Jan. 17, 1984.

Yamaguchi University assisted in meeting the publication costs of this article.

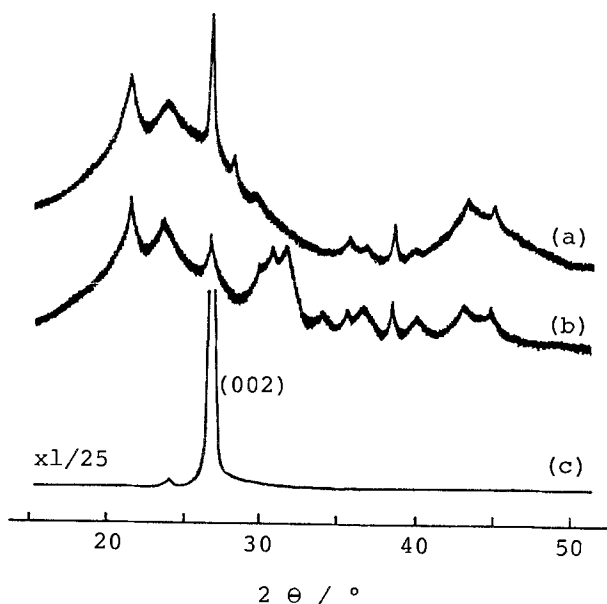


Fig.1. X-ray diffraction spectra of a graphite and active carbon electrode before and after discharge in PC-DME(1 : 1)- LiClO_4 (1 mol dm^{-3}) at 25°C .

- (a) : before discharge,
(b) : after discharge (0.6 A h g^{-1}),
(c) : graphite,
X-ray source : $\text{CuK}\alpha$.

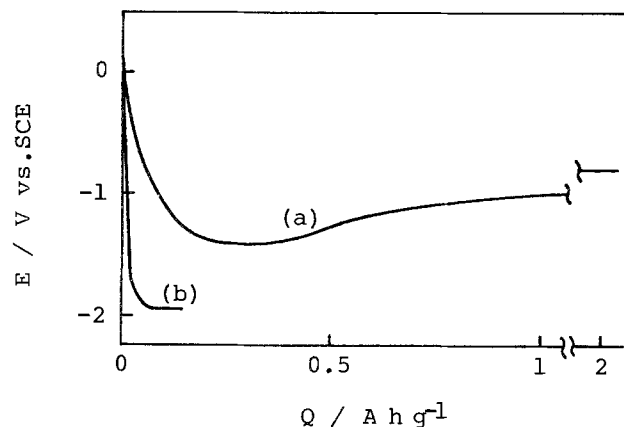


Fig.2. Discharge curves of an active carbon and a graphite electrode in PC-DME(1 : 1)- LiClO_4 (1 mol dm^{-3}) at 25°C .

- (a) : active carbon,
(b) : graphite,
Current density : $0.20 \text{ mA}/0.95 \text{ cm}^2$.

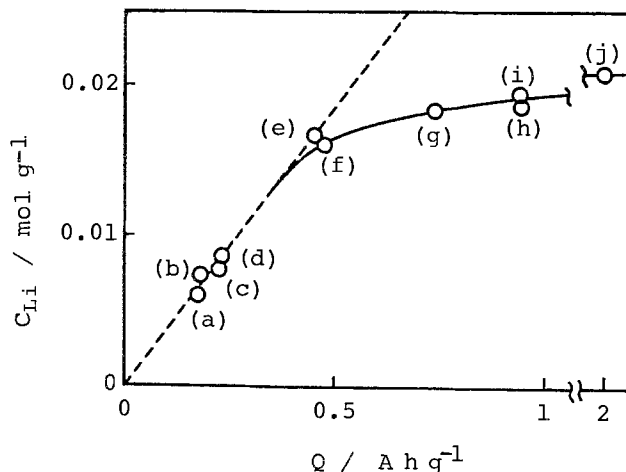


Fig.3. The relation between the amount of lithium detected in cathodes and the charge passed.

The broken line shows the theoretical value in which all the charge passed is used for the discharge of lithium ions to adsorb and/or intercalate into the cathode through an one-electron reaction.



Transport Properties of Aluminum Chloride-Thionyl Chloride-Based Electrolytes

S. Szpak*

Naval Ocean Systems Center, San Diego, California 92152

H. V. Venkatesetty*

Honeywell Corporate Technology Center, Bloomington, Minnesota 55420

ABSTRACT

Conductance, viscosity, and density of $\text{AlCl}_3\text{-SOCl}_2$ -based electrolyte solutions with and without sulfur dioxide and sulfur and varying concentration of lithium chloride have been determined as a function of temperature. While the data on $\text{AlCl}_3\text{-SOCl}_2$ system can be interpreted in terms of solute-solvent interaction forming adducts, those in the presence of sulfur dioxide and lithium chloride have been interpreted in terms of ion-ion and ion-solvent interactions and equilibria involving ion pairs and triple ions with complex anions such as Al_2Cl_7^- and $\text{Al}_3\text{Cl}_{10}^-$. Data on energy of activation for conductance and for viscous flow along with Walden product are in agreement with this interpretation. The unusually high electrolytic conductance observed for these concentrated electrolyte solutions and the energy of activation data are interpreted in terms of the hopping mechanism for conductance. The implication of increased complexity of solution structure on mass transport during Li/SOCl_2 battery discharge is discussed.

The development of a Li/SOCl_2 battery capable of high discharge rates has only recently been undertaken. To achieve this goal, two design approaches are being explored: the thin cell technology and the use of flowing electrolyte (1). In both approaches, the battery performance is believed to be limited by the positive electrode.

The relationship between the electrode structure and performance at low discharge rates was examined by, among others, Dey (2) and Christopulos and Gilman (3). The effect of electrocatalysts was explored by Venkatesetty (4). At high discharge rates, structural characteristics of the electrode, its catalytic surfaces, as well as the physico-chemical properties of the electrolyte, are expected to play a dominant role. This was confirmed, in part, by results of Klinedinst and Domeniconi (5), Dey and Bro (6), and, most recently, Szpak and Driscoll (7).

The least explored aspect of Li/SOCl_2 technology is the transport properties of the $\text{AlCl}_3\text{-SOCl}_2\text{-LiCl}$ electrolyte. As Li/SOCl_2 cells are discharged, composition of the electrolyte changes and becomes complex due to the formation of LiCl , sulfur dioxide, and sulfur. In particular, as the concentration of these products builds up, the structure and, therefore, transport properties of the electrolyte solution change, and this change will affect the battery performance.

The purpose of this communication is to extract structural information and transport modes from the data on conductance, viscosity, and density of AlCl_3 in SOCl_2 containing known concentrations of sulfur and sulfur dioxide and varying concentrations of LiCl as a function of temperature.

Experimental

Thionyl chloride was mixed with triphenylphosphite [16 volume percent (v/o)] while cooling and then distilled under positive pressure of dry nitrogen. The distillate was redistilled with a cutoff point at 80°C ; the middle fraction of the second distillation was used in this study. An anhydrous AlCl_3 (Fluka, AG) and an anhydrous, AR grade LiCl (Malinkrodt) were used as received. Sulfur, U.S.P. powder, sublimed, and anhydrous SO_2 were used without additional purification. All chemicals were weighed inside a dry box and maintained under dry argon. Solutions were prepared in another dry box. A known volume of the electrolyte solution was placed in an Erlenmeyer flask fitted with a sidearm bubbler, through which SO_2 was passed from a lecture bottle. Precautions were taken to minimize any loss of SOCl_2 . After admitting SO_2 , the flask was stoppered, volume change and weight were noted, and the concentration of dissolved SO_2 was calculated.

Conductivity measurements were carried out in specially designed cells, as shown in Fig. 1. The electrode assembly (A) consisting of platinum rods sealed into glass tubes and attached to a glass joint, was placed into a graduated cylinder (B). As illustrated, this cylinder is connected through a side arm and a two-way stopper to another graduated cylinder (C), in which the concentrated solution is stored. The desired composition of solution was obtained upon mixing of electrolyte in B with a calculated quantity admitted from C. Because of the electrode assembly design, mixing was continued until a constant conductivity was measured. The conductance cell was thermostated in an oil bath and/or water-methanol bath, and the deviations in temperature were 0.1° , 0.05° , and 0.5°C in the ranges of -20° to 0°C , 0° to 50°C , and 50° to 70°C , respectively. Low temperature was maintained in water-methanol bath with a Brinkmann Lauda IC-6 cooler.

* Electrochemical Society Active Member.
 Key words: $\text{SOCl}_2\text{-AlCl}_3\text{-LiCl}$ electrolyte, conductance, viscosity, Li/SOCl_2 battery.

EST

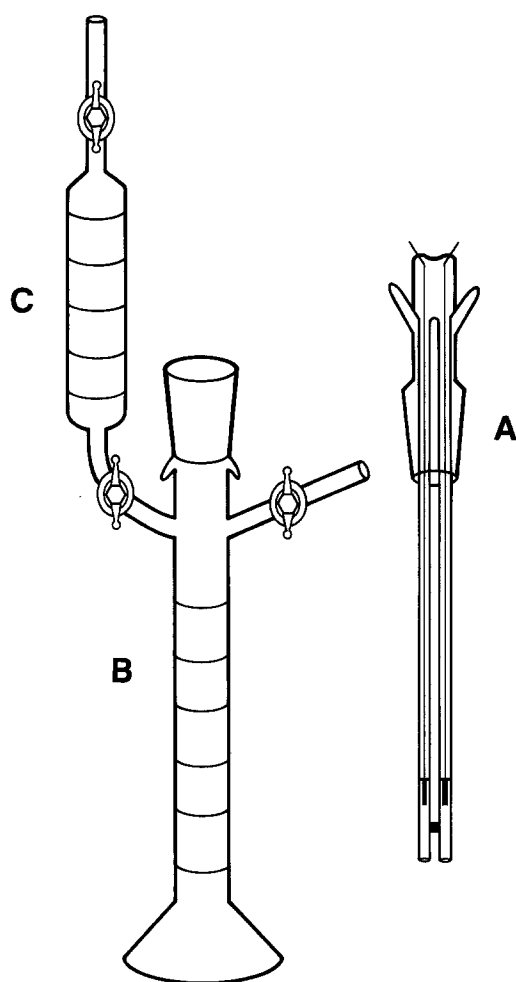


Fig. 1. Conductance dilution cell. A: electrode assembly. B: dilution cell. C: graduated cylinder for storage of concentrated solutions.

Density data were used to make corrections for concentrations at different temperatures.

Conductance cell calibration and solution conductance measurements were made using a Jones bridge and accessories previously described (8). The solution resistances were measured at frequencies of 1, 3, 5, and 10 kHz and extrapolated to an infinite frequency.

Viscosities of the solutions were measured using the Cannon-Ubbelohde dilution viscometer immersed in a suitable bath with a guard-tube attachment to exclude moisture from the solution. The bath temperatures were controlled to within 0.1°C and the time to within 0.1s. The viscometer constant was determined using viscosity standards provided by the Cannon Instrument Company (9).

The densities of the electrolyte solutions were determined using Pyrex dilatometers sealed at the top and calibrated with methanol and distilled water.

Results

Extensive experimental data on transport properties of the $\text{AlCl}_3\text{-SOCl}_2\text{-LiCl}$ system have been presented elsewhere (10). Here, only a limited set of data, needed to illustrate specific points, will be used.

Conductance.—The conductance data are given in the following order: specific conductance, equivalent conductance, and energy of activation.

Specific conductance, σ .—Results, shown in Fig. 2, indicate no substantial change in specific conductance with a three-fold increase in the AlCl_3 concentration. In contrast, upon addition of even small amounts of LiCl , a significant increase in conductance is observed, as seen in Fig. 3. This observation suggests that the

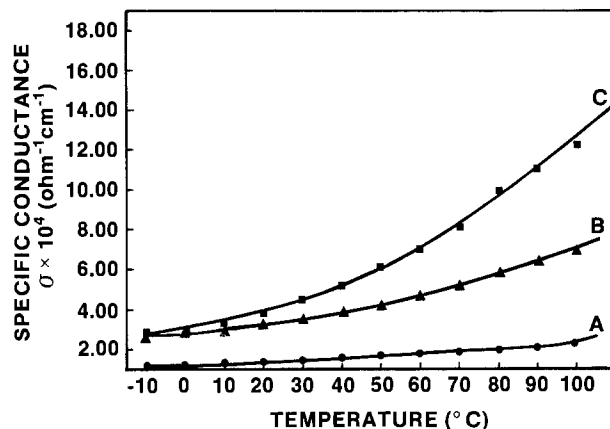


Fig. 2. Specific conductance of $\text{AlCl}_3\text{-SOCl}_2$ electrolyte as function of temperature. Curve A: 1.5M AlCl_3 . Curve B: 3.0M AlCl_3 . Curve C: 4.5M AlCl_3 .

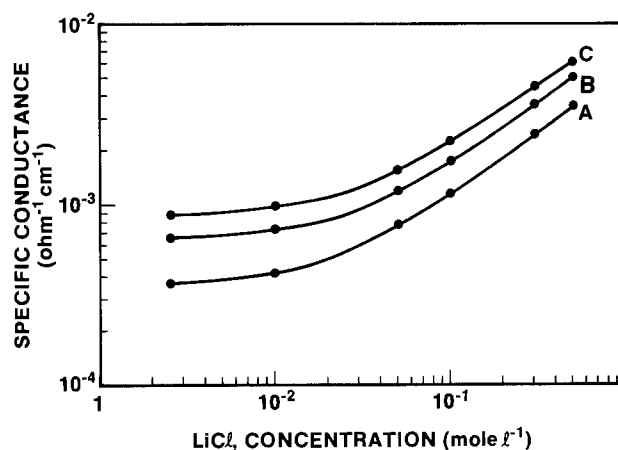


Fig. 3. Specific conductance of 4.5M $\text{AlCl}_3\text{-SOCl}_2$ electrolyte as function of LiCl concentration. Curve A: 15°C . Curve B: 40°C . Curve C: 60°C .

($\text{SOCl}_2 \cdot \text{AlCl}_3$) adduct does not increase the self-ionization of the SOCl_2 except at higher concentrations.

Addition of SO_2 renders the $\text{AlCl}_3\text{-SOCl}_2\text{-LiCl}$ system more conductive. As illustrated in Fig. 4 and 5, this increase depends on temperature and, for a selected

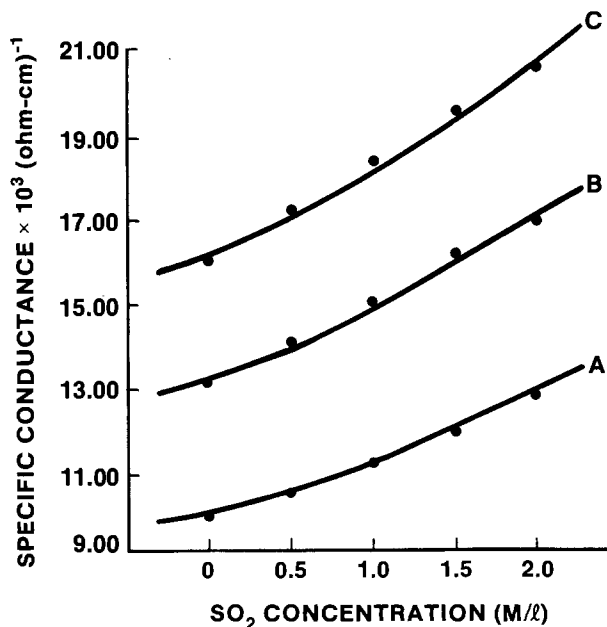


Fig. 4. Specific conductance as a function of SO_2 concentration. Electrolyte: 3.0M $\text{AlCl}_3\text{-SOCl}_2\text{-1.5M LiCl}$. Curve A: 10°C . Curve B: 30°C . Curve C: 50°C .

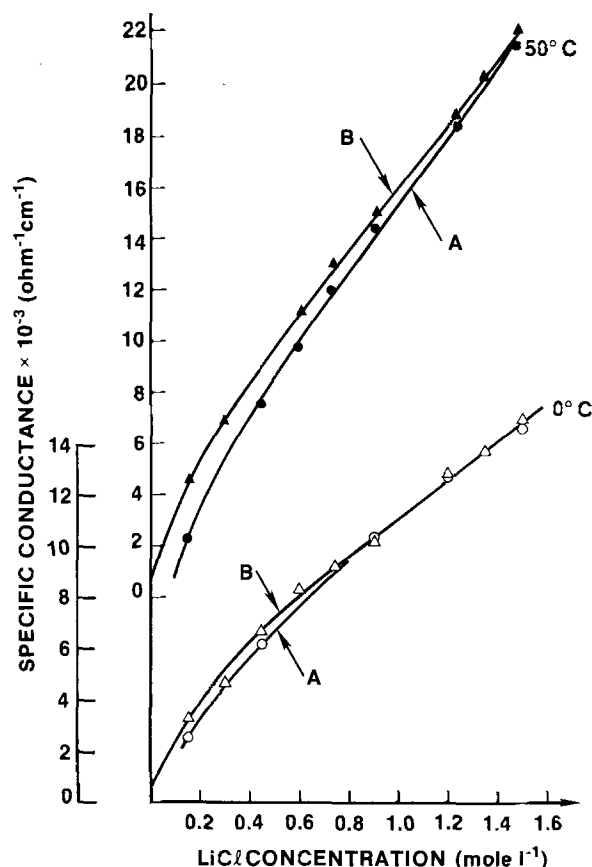


Fig. 5. Effect of dissolved SO₂ on specific conductance at 0° and 50°C. Electrolyte: 1.5M AlCl₃-SOCl₂-xLiCl. Curve A: without SO₂. Curve B: containing 0.5M SO₂.

AlCl₃ concentration, the amount of dissolved SO₂ (Fig. 4) and dissolved LiCl (Fig. 5).

Equivalent conductance, Λ .—As shown in Fig. 3, the specific conductance of the (SOCl₂ · AlCl₃ + SOCl₂) electrolyte increases by an order of magnitude upon the addition of LiCl. This behavior suggests that the dissolved LiCl provides the conducting species and that the equivalent conductivities can be calculated accordingly.

Plots of equivalent conductivities vs. the square root of LiCl concentration, shown in Fig. 6, indicate that these solutions are weak electrolytes. This behavior is expected if we consider that the (SOCl₂ · AlCl₃ + SOCl₂) is a low dielectric solvent (11). Evidently, as the concentration of LiCl increases, the equivalent conductance at first decreases rapidly, and then changes moderately; it tends to exhibit a minimum particularly at higher AlCl₃ concentrations.

Energy of activation.—The energy of activation for conductance in the AlCl₃-SOCl₂-LiCl system is tabulated in Table I. Evidently, in the absence of LiCl, the energy of activation increases with the AlCl₃ concentration. Such a trend indicates the formation of large aggregates involving AlCl₃ and SOCl₂ components.

It is noteworthy that energies of activation for this system are considerably larger than those measured for the solutions of LiAlCl₄ in SOCl₂ (8).

Viscosity, η .—Additional structural information can be obtained from the analysis of viscosity data. To facilitate this analysis, the viscosity data are assembled in the form of Batschinski-Hildebrand plots (12, 13) and a Jones-Dole relation (14). The tabulation of energies of activation for the viscous flow completes the presentation of experimental data results (Table I).

Batschinski-Hildebrand equation.—The Batschinski-Hildebrand equation, Eq. [1], relates the fluidity, ϕ ,

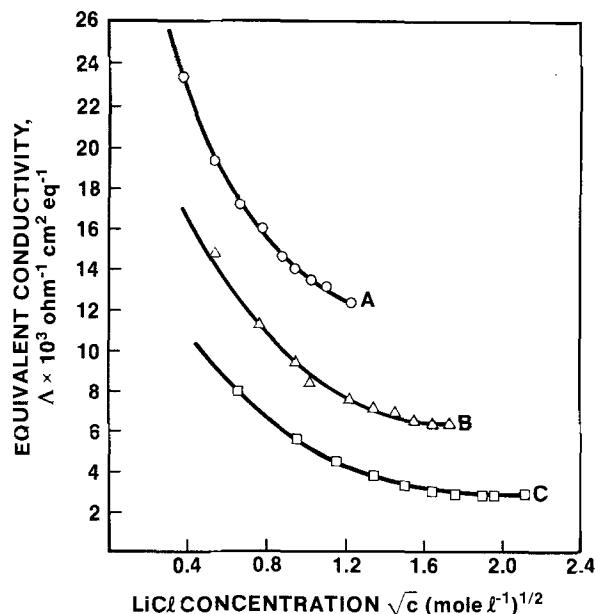


Fig. 6. Equivalent conductance as a function of LiCl concentration. Electrolyte: AlCl₃-SOCl₂-xLiCl; temperature = 20°C. Curve A: 1.5M AlCl₃. Curve B: 3.0M AlCl₃. Curve C: 4.5M AlCl₃.

to the specific excess volume, $(v - v_0)$, alternatively, to the ratio of occupied to unoccupied volume, $(v - v_0/v_0)$

$$\phi = B(v - v_0)/v_0 \quad [1]$$

The B constant is not an adjustable parameter, but a property of a liquid measuring its ability to absorb momentum generating the newtonian flow (13). Thus, its value depends on the molecular size and shape, and, in a qualitative way, may yield information on the molecular structure. The intrinsic volume, v_0 , is defined by Eq. [2]

$$v_0 = \lim_{\phi \rightarrow 0} v \quad [2]$$

i.e., it is obtained by an extrapolation of the $\phi(v)$ curve to zero. Physically, v_0 is the specific volume of a substance in the solid state provided that on solidification molecules preserve all of their degrees of freedom (13).

A typical plot of the $\phi(v)$ curves for the AlCl₃-SOCl₂-LiCl system, and specifically for the 1.5M AlCl₃, is shown in Fig. 7. Plots for other concentrations are

Table I. Energies of activation for conductance and viscous flow

Electrolyte composition (SOCl ₂ + 0.5M S + 0.5M SO ₂)		E (conduct.) kcal/mol	E (viscous) kcal/mol
AlCl ₃ /M	LiCl/M		
—	—	—	1.61
1.5	—	—	2.11
1.5	0.15	1.3	2.16
1.5	0.30	1.3	—
1.5	0.45	—	2.14
1.5	0.60	1.3	2.14
1.5	0.90	1.5	2.16
1.5	1.2	1.5	2.09
1.5	1.5	1.5	2.06
3.0	—	—	2.34
3.0	0.3	2.4	—
3.0	0.6	—	2.65
3.0	0.9	2.3	—
3.0	1.2	—	2.84
3.0	1.5	2.3	—
3.0	1.8	—	3.23
3.0	2.1	2.4	—
3.0	2.4	—	3.30
3.0	2.7	2.3	—
3.0	3.0	2.4	3.37
4.5	—	—	3.27
4.5	0.45	3.1	3.86
4.5	0.9	3.3	3.92
4.5	1.8	3.1	4.24
4.5	2.7	3.8	4.41
4.5	3.6	4.1	4.25
4.5	4.5	3.9	4.51

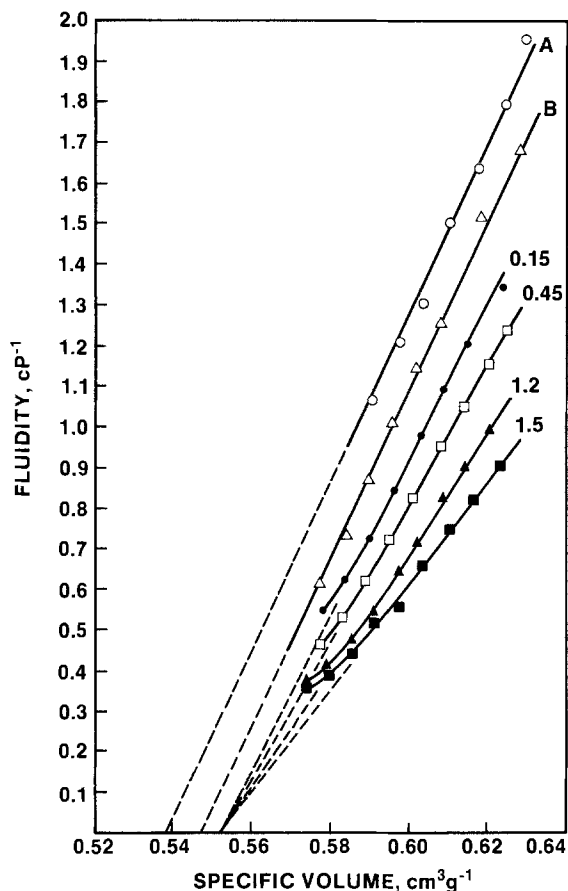


Fig. 7. Electrolyte fluidity vs. volume. Electrolyte: 1.5M AlCl_3 - SOCl_2 - $x\text{LiCl}$ containing 0.5M SO_2 . Curve A: SOCl_2 only. Curve B: $\text{SOCl}_2 + 1.5\text{M AlCl}_3$ only. Other curves: electrolyte containing LiCl in the indicated concentrations.

similar; the corresponding B and v_0 values are tabulated in Table II. It is noteworthy that, in the absence of dissolved SO_2 , the curvature of $\phi(v)$ is substantially reduced.

Jones-Dole equation.—Because the AlCl_3 - SOCl_2 -LiCl system contains charged species, it is expedient to examine the viscosity data in terms of the Jones-Dole equation, which is only valid for moderate concentrations, Eq. [3]

$$\eta = \eta_s(1 + A\sqrt{c} + Bc) \quad [3]$$

Here η is the shear viscosity of the electrolyte, η_s is that of the solvent, and c is the concentration of the ion producing salt. A is a positive constant which can be calculated theoretically and which accounts for the contribution due to the ion-ion interaction. The B coefficient, on the other hand, is an empirical constant and can be either positive or negative (14).

Table II. Values of B and v_0 in Eq. [4] for the AlCl_3 - SOCl_2 -LiCl system

Composition AlCl_3/M	LiCl/M	B/cP^{-1}	$v_0/\text{cm}^3\text{g}^{-1}$
—	—	11.24	0.5385
1.5	—	11.16	0.5471
	0.15	10.41	0.5510
	0.6	9.03	0.5523
	1.2	8.19	0.5523
3.0	—	8.95	0.5523
	0.6	7.49	0.5540
	1.2	6.91	0.5561
	1.8	5.92	0.5561
4.5	3.0	4.84	0.5561
	—	8.44	0.5572
	0.45	6.88	0.5572
	1.8	4.93	0.5673
	2.7	3.28	0.5673
	4.5	3.15	0.5673

The B coefficient is obtained from the plot of $(\eta_r - 1)/\sqrt{c}$ vs. \sqrt{c} , where $\eta_r = \eta/\eta_s$. Examples of the Jones-Dole plots are shown in Fig. 8 for the SOCl_2 -1.5M AlCl_3 and for the 1.5M AlCl_3 - SOCl_2 - $x\text{LiCl}$ systems. In the AlCl_3 - SOCl_2 system, the B coefficient is small and positive (curves a and b at 0° and 50°C, respectively). Upon addition of LiCl, the B coefficient becomes negative (curves a' and b' at 0° and 50°C, respectively). Evidently, in the first case, SOCl_2 is the solvent and AlCl_3 is the salt, whereas in the second case 1.5M $\text{AlCl}_3 + \text{SOCl}_2$ is the solvent and LiCl is the salt.

Energy of activation, E_η .—At high concentrations, structural information is usually sought through the determination of the energy of activation. Temperature effects, expressed in terms of energy of activation, are summarized in Table I and in Fig. 9 and 10. In particular, Fig. 9 shows the energy of activation for SOCl_2 (curve A) and SOCl_2 containing dissolved AlCl_3 (curves B, C, and D for 1.5, 3, and 4.5M solutions of AlCl_3 , respectively). Evidently, the addition of AlCl_3 increases the energy of activation for the viscous flow, with the increase being quite noticeable at higher AlCl_3 concentrations. The effect of the addition of LiCl is illustrated in Fig. 10. It is seen that the $\log \eta$ vs. $1/T$ lines are parallel and displaced upwards with the increase in the LiCl concentration.

Discussion

Measurements of transport properties, e.g., viscosity, diffusivity, and conductivity, are often the source of information concerning molecular aspects of liquids (15-17). These are phenomenological coefficients describing the response of a structureless liquid to the

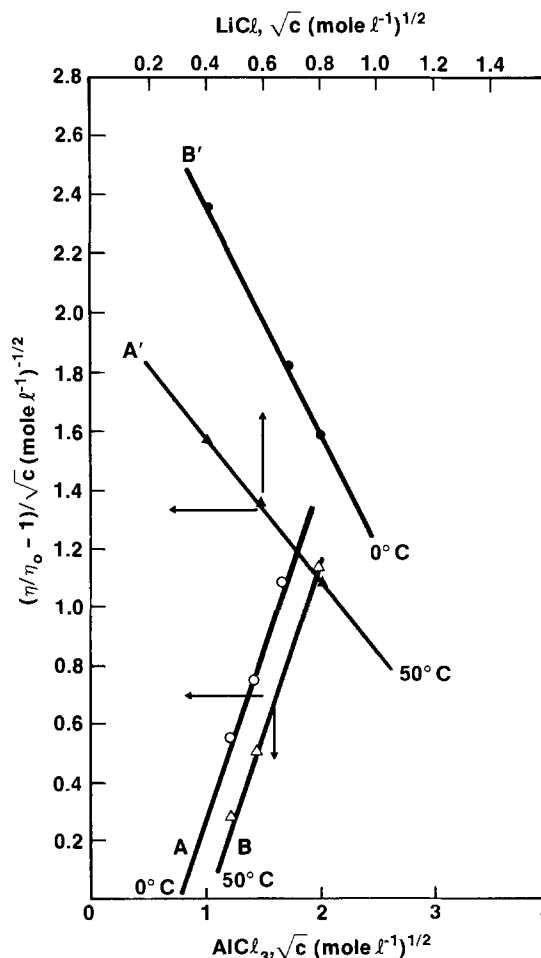


Fig. 8. Effect of LiCl concentration on B coefficient in the Jones-Dole equation. Curves a and b for the SOCl_2 - AlCl_3 system at 0° and 50°C, respectively. Curves a' and b' for 1.5M AlCl_3 - SOCl_2 - $x\text{LiCl}$ at 0° and 50°C, respectively.

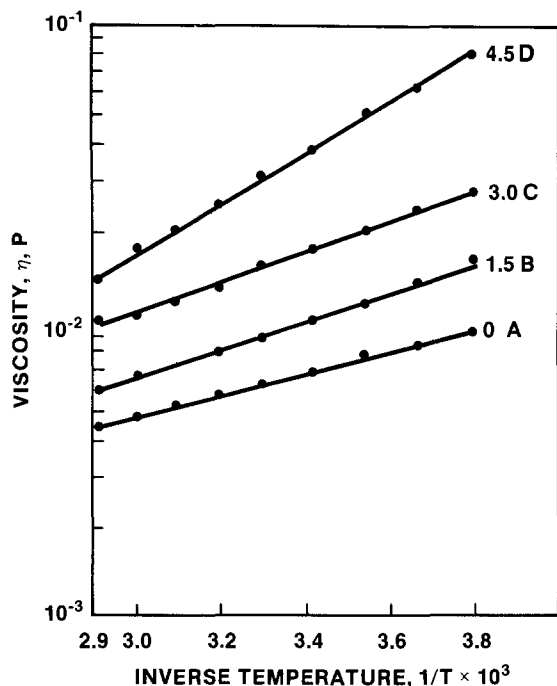


Fig. 9. Plot of viscosity vs. $1/T$. Curve A: SOCl₂ alone. Curves B, C, and D: for 1.5M AlCl₃-SOCl₂, 3.0M AlCl₃-SOCl₂, and 4.5M AlCl₃-SOCl₂, respectively.

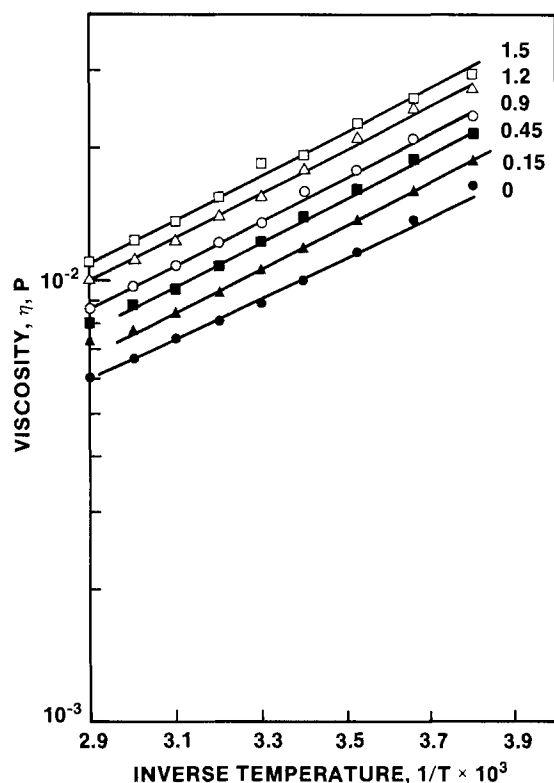


Fig. 10. Plot of viscosity vs. $1/T$. Electrolyte: 1.5M AlCl₃-SOCl₂-LiCl. Molarity of LiCl indicated alongside.

action of forces generated by the velocity, chemical, and electrical potential gradients, respectively. On the microscopic level, however, liquids are not homogeneous entities, *i.e.*, the condition of continuum cannot be satisfied. In concentrated solutions, especially in solvents of low dielectric constant, new ionic and molecular species appear. Moreover, ion pairs, triple ions, etc., may interact with solvent dipoles, forming complex structures, thus making interpretation of conductance and viscosity data difficult and, at times, ambiguous.

To obtain progressively better insight into the molecular structure of this system, we start with the discus-

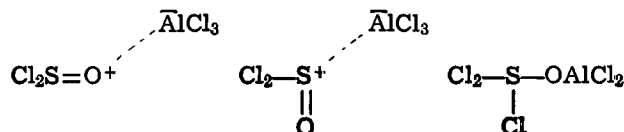
sion of relevant elements of coordination chemistry and examine the conductance and viscosity data against this background.

The SOCl₂-AlCl₃-LiCl system.—Thionyl chloride is a nonaqueous, aprotic solvent that undergoes a process of self-ionization to yield SOCl⁺ and Cl⁻ ions with $K = 10^{-4}$ (18). It has a tetrahedral arrangement of electron pairs with three σ bonds and a lone pair of electrons. Its molecular shape is that of a triangular pyramid. It is an exceedingly weak donor, with a donor number of 0.4 on the Gutmann scale (19). Because it possesses a strong affinity to Cl⁻ ions, it is useful in the synthesis of chloro-complexes.

The covalent AlCl₃ is a strong acceptor, and its dissolution in SOCl₂ can be viewed as the donor-acceptor reaction

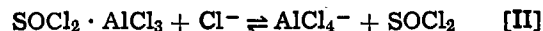


Both 1:1 and 1:2 adducts have been isolated (20, 21). In the solution, particularly when an excess of SOCl₂ is present, the 1:1 adduct, an undissociated compound, is dominant. As the AlCl₃ concentration is increased, the formation of a quasi 1:2 adduct is favored. However, spectroscopic evidence suggests that the 1:2 adduct is, in fact, the 1:1 adduct with a loosely attached second AlCl₃ molecule (20). Three structures are possible for the SOCl₂ · AlCl₃ complex



Of these, the Raman spectra are consistent with the first structure, *i.e.*, where the oxygen atom is the donor.

In the presence of Cl⁻ ions, generated by either self-ionization of SOCl₂ or by the addition of LiCl, the SOCl₂ · AlCl₃ adduct forms anionic complexes with a simultaneous release of SOCl₂



If the source of Cl⁻ ions is the self-ionization of SOCl₂, then, with an increase in the AlCl₃ concentration, the acidity of solution increases and shifts the equilibrium in the direction to promote the formation of higher complexes, *e.g.*, Al₂Cl₇⁻, Al₃Cl₁₀⁻, particularly at higher temperatures.

Sulfur dioxide, which has been added to simulate actual conditions in a discharging cell, is a nonlinear molecule with a triangular planar arrangement of electron pairs with two σ bonds and a lone pair of electrons. It can act both as Lewis acid or base, depending upon environment, and, when dissolved in another solvent, such as SOCl₂, it can also act as a cosolvent (22), but it does not interact chemically (19). It can function as an acceptor toward Cl⁻ ions, forming SO₂ · Cl⁻ complex (19, 23); it can also enter preferentially into Li⁺ ion solvation sheet (24).

The dissolved sulfur exists as a S₈ molecule, which, at low concentrations, exhibits weak electrolytic dissociation: S₈ \rightleftharpoons S₂²⁺ + S₆₋₂²⁻ (18).

Conductance.—The conductance in molecular liquids is, as a rule, a specific function of the solvent-solute system (17). This assertion is particularly true if the solute is potential electrolyte, *i.e.*, a covalent salt, and if its dissolution occurs only on account of reaction between the solute and the solvent: here, between AlCl₃ and SOCl₂ (Eq. [I]). In this system, therefore, electrostatic considerations are likely to play a lesser role than the molecular forces, and the dependence on square root of concentration should be limited. However, it would appear that electrostatic considerations should dominate the dissolution of an ionic salt such as LiCl. However, the dissolution of LiCl in the (SOCl₂ · AlCl₃ + SOCl₂) solvent does not occur via

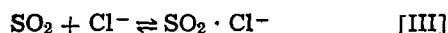
the weakening of electrostatic forces, but rather through a chemical reaction of an anionic complex formation (Eq. [I]). Consequently, when we increase the concentration of LiCl, it may not necessarily be the number of Li⁺ ions but their interaction with a solvent that determines the conductance.

Because the 1:1 SOCl₂ · AlCl₃ adduct remains undissociated, the addition of AlCl₃ to SOCl₂ should not substantially change the solution conductivity. However, at high concentrations of AlCl₃ the 1:2 adduct dominates, new equilibria are established, and the number of charged species increases, principally due to a higher affinity for complex formation. The temperature effects (Fig. 2) substantiate this conclusion.

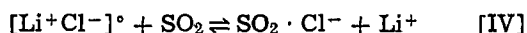
Upon addition of even small amounts of LiCl, the solution conductivity increases many fold, as shown in Fig. 3. This marked increase in conductivity, their linear dependence on concentration of LiCl, and temperature effects, suggest that both the number of charged species and their mobility are affected, in accordance with Eq. [II].

The equivalent conductance data (Fig. 6) indicate that the AlCl₃-SOCl₂-LiCl solutions behave as weak electrolytes. Equivalent conductances decrease with increasing LiCl concentration, reaching what appears to be a minimum, especially at higher AlCl₃ concentrations. This behavior is in agreement with theoretical predictions that the decrease in conductance with an increasing concentration of the electrolyte is due to the formation of ion pairs, triple ions, and more complex aggregates (25).

Plots of log Λ vs. log c are linear with an approximate slope of $-\frac{1}{2}$, thus confirming the formation of ion pairs (11). Further support for the formation of ion pairs and other complex aggregates is to be found in the observed effect of the dissolved SO₂ on the electrolyte conductivity, illustrated in Fig. 4 and 5, which is due, probably, to an increase in the number of charged species by a mechanism identical to that suggested by Moshtev and Zlatilova (23)



The dissolved SO₂ molecules form adducts with Cl⁻, alternatively, with AlCl₃ and thus reduce the ion pair formation



The effect of SO₂ is more pronounced in the case of 1.5M AlCl₃-SOCl₂-LiCl solutions than in the case of 3M AlCl₃. At the present time, it is not possible to provide adequate interpretation because of enormous complexity of this system.

Viscosity.—The $\phi(v)$ relationship for the SOCl₂, with the B value of 11.2 cP⁻¹, is typical for many molecular liquids, e.g., CCl₄. Evidently, the addition of small amounts of AlCl₃ does not substantially change the capacity of SOCl₂ to absorb the momentum generating the newtonian flow, since curve b is nearly parallel to curve a in Fig. 7. The addition of larger amounts of AlCl₃ decreased the numerical value of the B constant somewhat, thus indicating moderate changes in molecular structure. This moderate change in structure is consistent with the formation of the 1:2 adduct (20).

The addition of LiCl, however, clearly affects the numerical value of the B constant, indicating substantial structural changes. Of special interest is the development of a curvature at low $(v - v_0)/v_0$ ratios (i.e., at low temperatures). The development of such curvatures indicates that molecular crowding has occurred (12). Another feature of the $\phi(v)$ plots is the independence of the intrinsic specific volume with LiCl concentration, i.e., the linear portion of the $\phi(v)$ curve intersects the V -axis at the same point. The intrinsic volume is thus affected by the addition of AlCl₃, but not by the addition of LiCl. Such a behavior is consistent

with an increase in the number of molecules and is in accordance with the hole theory of liquids (11). It can be interpreted as indicating that the addition of LiCl breaks up the adduct molecules, in agreement with Eq. [II].

Stokes and Mills (21) express the left-hand side of Eq. [3] as a sum of contributions due to ion-ion interaction (η_{10}) and ion-solvent interaction (η_{20}). The latter can be further split to account for the size and shape of an ion, inclusive of solvation sheet (η_{21}), alignment of polar molecules by local electric field, a kind of molecular stiffening (η_{22}), and finally to the destruction of solvent structure (η_{23}). Of these, all are positive contributors, except for the last, which is negative.

The small and positive B coefficient indicates a low concentration of charged species when AlCl₃ is the only component dissolved in SOCl₂. This observation is in agreement with the conductance measurements (Fig. 2) and with the Batschinski-Hildebrand plots (Fig. 7); both suggest negligible change in SOCl₂ structure, except at much higher AlCl₃ concentrations. Upon addition of LiCl to the (1.5M)AlCl₃-SOCl₂ solution, the B coefficient becomes negative. Since η_{21} and η_{22} are positive contributors, it follows that $\eta_{21} + \eta_{22} < \eta_{23}$, i.e., it is consistent with the conductance data.

The Jones-Dole equation is valid for moderate concentrations. At higher concentrations, the structural information is usually sought through the energy of activation measurements. To bring into focus the relationship between the energy of activation and the fluid structure, we apply the Eyring equation in the form of

$$\eta = (Nh/V_m) \exp(\Delta G^*/RT) \quad \text{[4]}$$

where N is the Avogadro number, V_m is the molar volume, h is the Planck constant, and ΔG^* is the minimum value of additional free energy needed, or the smallest amount of work that must be done, to bring the system into the intermediate position. Upon substitution $\Delta G^* = \Delta H^* - T\Delta S^*$, Eq. [4] has the same form as the empirical equation

$$\eta = A \exp(E_a/RT) \text{ with } \Delta H^* = E_a \quad \text{[5]}$$

where $A = f(\Delta S)$ has a physical meaning indicating an ordering process when the molecules pass from the initial to the transition state. Temperature effects, expressed in terms of energy of activation, are summarized in Table I and in Fig. 9 and 10. In particular, Fig. 9 shows the energy of activation of SOCl₂ (curve a) and for SOCl₂ containing dissolved AlCl₃.

Walden product.—The Walden rule states that, if the moving charged particle is the same, then the product remains constant in solvents of different viscosities. This rule follows from the applicability of the Stokes law, and, in general, is a good approximation in aprotic solvents. The constancy of the product is assured when the energy of activation for the viscous flow and the migration in an electric field are the same, which, in turn, implies that the same or similar configurational changes occur when the system responds to either driving force.

A plot of the product, constructed for the 1.5M AlCl₃-SOCl₂-LiCl, as a function of temperature and LiCl concentration is shown in Fig. 11. Evidently, the product is not constant, i.e., in agreement with the energy of activation data tabulated in Table I. The variation of the product in the same solvent arises from a number of reasons: (i) the Stokes law is not applicable, i.e., on the microscopic scale the solvent is not continuous, or the transport in an electric field occurs via the jumping of charged species between neighboring aggregates, Eq. [IV]; (ii) size of the charged particle varies with temperature and/or concentration, i.e., the degree of dissociation may change; and (iii) in a complex system, new equilibria may be

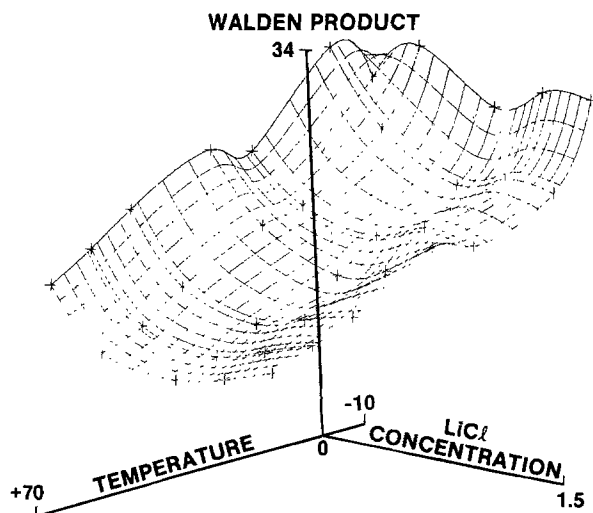


Fig. 11. Plot of Walden product as function of composition and temperature. Electrolyte: 1.5M AlCl₃-SOCl₂-xLiCl.

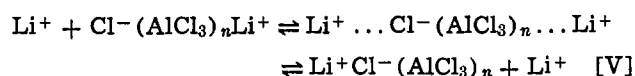
established with a change in composition and temperature.

In a system where $E_{\eta} > E_{\Lambda}$, in particular when $E_{\eta} = nE_{\Lambda}$ ($n > 1$) there exists a relationship

$$\Delta^n \eta = \text{const.} \quad [6]$$

Consequently, plots of $\log \eta$ vs. $\log \Lambda$ should be linear with the slope giving the value of n . Such a relationship was found with n values from 1.33 for 1.5M AlCl₃ to 4.5 for 4.5M AlCl₃ electrolytes. These values indicate that larger configurational changes take place at high AlCl₃ concentrations and suggest that conductance is controlled by small, positive ions (most likely solvated Li⁺ ions), whereas the viscous flow is governed by large negative aggregates.

Mechanism of conductance.—One of the characteristics of the AlCl₃-SOCl₂-LiCl system, with or without dissolved sulfur and sulfur dioxide, is its fairly high conductance in a solution of high viscosity. The high viscosity is attributed to the formation of large ionic aggregates, thus suggesting that small positive ions have high transference number. The failure of the applicability of Stokes law is consistent with the hopping mechanism of the type proposed by Reger *et al.* (25)



In this mechanism, the Li⁺ ion jumps between successive molecules (aggregates). Evidently, the larger the aggregates, the larger the distance between the incoming and leaving Li⁺ ion and, therefore, the higher the conductivity. Because of the existence of a number of aggregates of various sizes in equilibrium with each other, further analysis would be hopeless.

Relevance to battery technology.—The operational characteristics of batteries, especially those employing porous electrodes, depend on the kinetics of charge transfer reaction, the transport in the electrolyte phase, and the resistivity of the electrode matrix. In Li/SOCl₂ batteries, the first two factors play a major role because they change with the change in electrolyte composition, *i.e.*, with the degree of battery discharge.

Regarding the electrolyte as a ternary system, *i.e.*, omitting dissolved SO₂ and elemental sulfur, we can follow the change in the composition on the Gibbs' triangle, shown in Fig. 12. Hence, the pure components, *i.e.*, SOCl₂, LiCl, and AlCl₃, are represented at respective apexes, the binaries of the system are read along the sides of a triangle, and the ternary points are found within the domain of a triangle. The change in

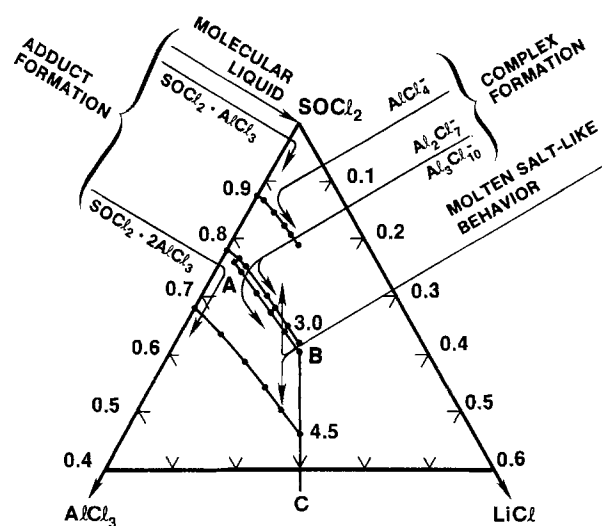


Fig. 12. Representation of structural changes on the Gibbs' triangle.

the composition for the initial 3.0M AlCl₃ in SOCl₂ is shown in Fig. 12 by the heavy line. In practice, initial conditions are chosen to assure maximum conductivity and maximum amount of SOCl₂.

Structural changes and, therefore, transport properties change with composition. Thus, pure SOCl₂ is a molecular liquid. Upon addition of AlCl₃, the viscosity and conductivity data indicate a weak interaction along the binary AlCl₃-SOCl₂, except when $x > 0.3$, *i.e.*, where some structural changes occur. These changes are associated with the formation of new aggregates. Because of limited conductivity, those compositions are not suitable electrolytes for high discharge-rate applications.

Substantial structural changes occur with the addition of LiCl. Formation of ionic complexes (Eq. [I]) results in an increased conductivity. The low ratio of E_{η}/E_{Λ} suggests that transport properties are controlled by hole formation, and a correlation between the diffusion coefficient and viscosity can be used in examining the mass transport. Such a correlation becomes less valid as the battery is being discharged, *i.e.*, along the heavy line in Fig. 12. As we approach curve c, and especially close to the line indicating precipitation of LiCl, the formation of triple ions and other aggregates dominates the electrolyte structure. Within this region, the electrolyte is better represented by molten salt. Here, the conductance most likely occurs through a hopping mechanism, and transport is by migration rather than diffusion. It is also likely that the mechanism of SOCl₂ reduction changes when less SOCl₂ is available.

Conclusions

1. In AlCl₃-SOCl₂ solutions containing low AlCl₃ concentrations, the same structural changes affect conductance and viscosity governed by hole formation. As the AlCl₃ concentration increases approaching 4.5M, structural changes and adduct formation take place.

2. Addition of LiCl at all levels of AlCl₃ concentration increases electrolytic conductance. Formation of ion pairs, triple ions, and large aggregates becomes dominant. The analysis of viscosity data suggests the destruction of solvent structure.

3. Sulfur dioxide in the AlCl₃-SOCl₂ system acts as a cosolvent with increased conductance, particularly at low AlCl₃ concentration and low temperatures. This is attributed partly to SO₂ · Cl⁻ interaction minimizing ion pair formation and partly to preferential solvation of lithium ion by SO₂.

4. The Walden product and then energy of activation for conductance and viscous flow indicates that the

conductivity at high AlCl_3 concentration and in the neighborhood of neutral solutions is governed by positively charged small ions, whereas the viscous flow is controlled by the negatively charged large aggregates.

5. A hopping mechanism for conductance seems to be operative in concentrated solution of $\text{AlCl}_3\text{-SOCl}_2$ containing lithium chloride.

Acknowledgments

This work was funded by Naval Sea Systems Command (NAVSEA 63R-32) and constitutes a fraction of a program to establish a technology base for high discharge-rate Li/SOCl_2 batteries. We thank Mr. F. Romano (NAVSEA 63R-32) for his interest and support.

Manuscript submitted June 15, 1983; revised manuscript received Dec. 15, 1983. This was Paper 440 presented at the Montreal, Quebec, Canada, Meeting of the Society, May 9-14, 1982.

Honeywell, Incorporated assisted in meeting the publication costs of this article.

REFERENCES

1. S. Szpak and H. V. Venkatesetty, Paper 29 presented at the 13th International Power Sources Symposium, Brighton, England, 1982.
2. A. N. Dey, *This Journal*, **126**, 783 (1980).
3. J. A. Christopolos and S. Gilman, in "Proceedings of the 10th Intersociety Energy Conversion Engineering Conference," IEEE, Newark, DE (1975).
4. H. V. Venkatesetty, U.S. Pat. 4,252,875 (1981).
5. K. A. Klinedinst and M. J. Domeniconi, *This Journal*, **127**, 539 (1980).
6. A. N. Dey and P. Bro, *ibid.*, **125**, 1574 (1978).
7. S. Szpak and J. R. Driscoll, *J. Power Sources*, To be published.
8. H. V. Venkatesetty and D. J. Saathoff, *This Journal*, **128**, 773 (1981).
9. Bulletin no. 90, Cannon Instrument Co., State College, PA.
10. H. V. Venkatesetty and S. Szpak, *J. Chem. Eng. Data*, **28**, 47 (1983).
11. R. M. Fuoss and F. Accascina, "Electrolytic Conductance," Interscience Publishers, Inc., New York (1959).
12. J. A. Batschinski, *Z. Phys. Chem.*, **84**, 643 (1913).
13. J. H. Hildebrand, *Science*, **174**, 490 (1971); *Faraday Discuss. Chem. Soc.*, **66**, 151 (1978).
14. R. H. Stokes and R. Milles, "Viscosity of Electrolytes and Related Topics," Pergamon Press, New York (1965).
15. J. Frenkel, "Kinetic Theory of Liquids," Dover Publications, Inc., New York (1946).
16. H. Eyring and M. S. Jhon, "Significant Liquid Structures," John Wiley and Sons, New York (1969).
17. J. O'M. Bockris and A. K. N. Reddy, "Modern Electrochemistry," Plenum Press, New York (1972).
18. H. Spandau and E. Brunneck, *Z. Anorg. Chem.*, **270**, 201 (1952); *ibid.*, **278**, 197 (1955).
19. V. Gutmann, "Coordination Chemistry in Non-Aqueous Solutions," Springer-Verlag, Wien (1968).
20. D. A. Long and R. T. Bailey, *Trans. Faraday Soc.*, **59**, 594 (1963).
21. H. Hecht, *Z. Anorg. Chem.*, **254**, 37 (1947).
22. H. V. Venkatesetty, in "Proceedings of the 16th Intersociety Energy Conversion Engineering Conference," p. 788, IEEE, Newark, DE (1981).
23. R. V. Moshtev and P. Zlatilova, *Electrochim. Acta*, **27**, 1107 (1982).
24. C. R. Kraus, *J. Phys. Chem.*, **60**, 129 (1956); *ibid.*, **58**, 673 (1954).
25. A. Reger, E. Peled, and E. Gileadi, *J. Phys. Chem.*, **83**, 873 (1979).

A Spectroscopic Investigation of Lithium Dithionite and the Discharge Products of a Li/SO_2 Cell

Robert L. Ake

Department of Chemical Sciences, Old Dominion University, Norfolk, Virginia 23508

Donald M. Oglesby*

Virginia Chemicals Incorporated, 3340 West Norfolk Road, Portsmouth, Virginia 23703

William P. Kilroy*

Naval Surface Weapons Center, White Oak, Silver Spring, Maryland 20910

ABSTRACT

Infrared, x-ray, and electron spin resonance spectroscopic studies of laboratory-synthesized $\text{Li}_2\text{S}_2\text{O}_4$ are reported. Spectra of cathode samples from Li/SO_2 cells discharged at -30° , 25° , and 70°C are compared with the spectra of the laboratory-prepared $\text{Li}_2\text{S}_2\text{O}_4$. The principal discharge material is confirmed to be $\text{Li}_2\text{S}_2\text{O}_4$. The 70°C discharge is shown to produce a different set of products from the discharges at the lower temperatures.

Although lithium dithionite, $\text{Li}_2\text{S}_2\text{O}_4$, has been assumed to be the sole discharge product of Li/SO_2 batteries, the evidence has been based on qualitative information (1) and various voltammetric investigations often performed under conditions dissimilar to commercial cells. Quantitative analysis of commercial Li/SO_2 cells discharged at 25°C at low current densities has recently been performed (2, 3). Under these conditions, $\text{Li}_2\text{S}_2\text{O}_4$ is the discharge product. However, preliminary chemical analysis performed at NSWC on Li/SO_2 cells discharged under more abusive conditions

such as high temperature discharge, revealed the presence of other sulfur products.

The principal discharge product, $\text{Li}_2\text{S}_2\text{O}_4$, has recently been synthesized and its thermal decomposition studied (4). Differential thermal analysis of the synthetic material reveals that it decomposes exothermally releasing approximately $3.4 \text{ kcal mol}^{-1}$. The products formed in the decomposition are Li_2SO_3 , SO_2 , and S.

Previous spectroscopic studies of dithionites have centered on the sodium salt (5). The current study examines the laboratory-prepared $\text{Li}_2\text{S}_2\text{O}_4$ by x-ray, infrared, and electron spin resonance spectroscopies and compares the spectroscopic characteristics with

* Electrochemical Society Active Member.
Key words: $\text{Li}_2\text{S}_2\text{O}_4$, Li/SO_2 cells.

those of the discharge products of the Li/SO₂ cell formed under various discharge temperatures.

Experimental

The Li₂S₂O₄ was synthesized in the manner previously described (4). It was determined to be 92% pure by the method of Kilroy (6). The lithium salts used for comparison were obtained commercially and used without further purification. The Li/SO₂ cell cathode discharge products were obtained by discharging a series of ½ A-size commercial Li/LiBr/SO₂ cells at a constant 40 mA at various temperatures (−30°, 25°, 70°C) to a 2.0V cutoff. The cells were equilibrated 1h at the discharge temperature prior to discharge. After discharge, the cells were opened under helium, whereupon the cathodes were powdered in an agate mortar and divided. Half of the cathode was washed several times with doubly distilled and oxygen-free acetonitrile. Duplicate discharges were run at each temperature.

X-ray diffraction patterns were recorded using a GE XRD-5 diffractometer with a copper target operated at 50 kV and 20 mA. The scan rate was 2° min^{−1} with a chart speed of 1 in. min^{−1}. The signal levels ranged between 500 and 5000 cps for the maxima and were recorded with a time constant of 0.5 or 1.0s.

The samples were prepared by grinding the solid material with an agate mortar and pestle in a dry box continually flushed with dry nitrogen. The ground material was uniformly applied to a microscope slide coated with silicone vacuum grease. The slides were transported to the diffractometer in a desiccator, which was placed inside a nitrogen-filled glove bag specially mounted over the goniometer. The slides with samples were mounted on the goniometer, and the diffraction patterns were recorded. All powder patterns were recorded at room temperature.

The infrared spectra were recorded using a Nicolet 7199 FT-IR spectrometer employing a bandpass between 4000 and 400 cm^{−1} with 4 cm^{−1} resolution. The samples used to obtain the infrared spectra were prepared by grinding approximately 1–2 mg of sample with 100 mg of dry infrared-grade KBr in an agate mortar and pestle for 4 min. The grinding was done in a dry box. The mixture was pressed into a pellet 1 cm in diam and 0.5 mm thick. The sample compartment was swept with dry nitrogen during the recording of the spectrum.

A Varian 4502 spectrometer operating at 9.1 Gc with the Varian temperature accessory was used to obtain the ESR spectra at various temperatures. The temperature was monitored with a Chromel-constantan thermocouple inserted into a sample tube filled with DC200 silicone fluid. The sample temperature was determined in the cavity both before and after each spectrum was taken. The G values were obtained by comparison with a standard sample of known G value, diphenylpicrylhydrazyl.

The Li₂S₂O₄ samples for ESR were contained in Varian cylindrical, 5 mm id, thin-wall quartz cells open at the top to permit the escape of any SO₂ produced. Samples sealed under vacuum or under dry nitrogen gave the same results. ESR spectra could not be obtained for cathode samples contained in a 5 mm tube, so the samples were contained in a capillary positioned in the center of a 5 mm sample tube.

Results and Discussion

X-ray spectroscopy.—An analyzed sample of Li₂S₂O₄ was prepared electrochemically by one of us (2); the x-ray pattern of this same sample has been previously reported (7). This study compares the x-ray diffraction patterns of duplicate cathode samples from commercial cells discharged at several temperatures with that of a synthetic Li₂S₂O₄ sample. The results are shown in Table I. In each cathode sample, the peaks

observed in the synthetic sample of Li₂S₂O₄ are present, although not always with exactly the same intensity ratios. This result indicates that Li₂S₂O₄ is the major crystalline cathode product resulting from the discharge of a commercial Li/SO₂ cell. Small crystals of a nearly colorless material which could be seen in the cathode material prior to sample preparation are quite likely crystals of Li₂S₂O₄, which is insoluble in the electrolyte, acetonitrile.

However, some additional peaks were noted in the x-ray diffraction patterns. In the pattern from the unwashed cathode material discharged at −30°C two peaks (*d* = 3.98 and 2.84Å) attributable to LiBr, the battery electrolyte, were recorded. These two peaks disappeared upon washing the cathode material with dry doubly distilled acetonitrile. The resulting pattern after washing contained only those peaks recorded in the synthetic Li₂S₂O₄ pattern. The intensity distribution from the washed cathode sample was not the same as the pattern from the highest purity Li₂S₂O₄, but did resemble that of a synthetic Li₂S₂O₄ of lower purity. The diffraction pattern from a cathode sample washed with CS₂ still showed the peaks attributed to LiBr. The presence of LiBr was not clearly detected in the diffraction patterns from other unwashed cathode samples.

Other additional peaks were noted in the diffraction pattern of an unwashed cathode sample discharged at 70°C according to the procedure followed for the other discharges. A minor peak (*d* = 2.88Å) can be attributed to LiBr. The major additional peaks match up with two major peaks of a Li₂SO₃ · H₂O sample recorded for comparison (*d* = 3.14 and 4.15Å). Li₂SO₃ is a decomposition product of Li₂S₂O₄. Exposure of the unwashed cathode to air increased the background intensity at *d* = 3.93Å, indicative of Li₂SO₄ · H₂O resulting from air oxidation of an oxy-sulfur compound. None of the cathode samples gave diffraction patterns that would indicate the presence of Li₂S, which has its most intense peak at *d* = 3.29Å. However, analyses on cathodes from cells discharged at 70°C reveal that sulfide is present (8, 9). The sulfide is present in less than 10% of the overall sulfur species and appears bound in the carbon infrastructure. This may account for its absence in the x-ray spectra.

Infrared spectroscopy.—Infrared analyses studies of sodium salts and available lithium salts were compared with the infrared bands obtained from several SO₂ cells discharged at various temperatures. Table II summarizes the composite frequencies of the vibration bands and relative intensities of the sodium and lithium dithionites and cathode samples. Three factors combine to hinder interpretation of portions of the spectra: (i) with the exception of a few, lithium oxy-sulfur compounds are not available; (ii) the lab-synthesized Li₂S₂O₃ is 90% pure, containing primarily sulfite and some other impurities, such as thio-sulfate, which may introduce weak bands or shoulders; (iii) the carbon-Teflon cathode introduces a matrix which introduces heterogeneity into the sample or dilutes the spectra. This latter factor may explain some subtle differences in the spectra of Fig. 1. This is most apparent with the O-S-O symmetric bending vibration occurring at 647 cm^{−1}.

Dithionite spectra.—The dithionite ion should show four fundamental S-O stretching frequencies, two symmetric modes, and two asymmetric modes. The two asymmetric S-O stretching modes which occur at higher frequency than the symmetric modes are split more in Li₂S₂O₄ than in Na₂S₂O₄. The symmetric stretching modes are not perceptibly split in Na₂S₂O₄, whereas in Li₂S₂O₄ the fundamental is shifted to lower frequency and shows a pronounced intense shoulder on the high energy side. Such differences may be attributed to the differences on the force field exerted by the sodium and lithium ions in the crystal. The

Table I. X-ray diffraction patterns of $\text{Li}_2\text{S}_2\text{O}_4$ and cathode samples from Li/SO_2 cells discharged at various temperatures

Diffraction angle 2θ	Interplane spacing, d (Å)	Relative intensities, 10.0 = max								$\text{Li}_2\text{S}_2\text{O}_4$	Comment
		Cathodes									
		Discharge temperatures and treatment after discharge									
		-30°C		25°C		70°C		70°C*			
		Unwash	Wash	Unwash	Wash	Unwash	Wash	Unwash	Wash		
20.4	4.35	2.9	3.5	4.4	4.4	6.1	6.2	5.5	4.9	6.4	
21.45	4.14							2.2			Li_2SO_4
22.3	3.98	0.7									LiBr
23.9	3.72	5.3	6.4	7.1	7.8	7.2	7.8	7.0	6.9	10.0	
27.5	3.24	3.4	4.3	5.6	5.9	6.5	6.4	6.8	6.7	9.4	
28.4	3.14							4.2			Li_2SO_4
30.2	2.96	2.1	2.1	2.9	2.7	3.4	3.2	3.1	3.8	6.4	
31.0	2.88							1.2			LiBr
31.5	2.84	0.9									LiBr
33.6	2.67	10.0	10.0	10.0	10.0	10.0	10.0	10.0	10.0	9.7	
35.3	2.54	6.0	6.7	5.4	5.5	5.6	5.3	5.5	5.6	5.4	
40.1	2.25	0.9	1.3	1.1	0.9	0.9	0.9	1.0	1.0	1.4	

* 70°C represents a cathode from a second cell discharged at 70°C.

Table II. Infrared frequencies and relative intensities for $\text{Na}_2\text{S}_2\text{O}_4$, $\text{Li}_2\text{S}_2\text{O}_4$, and cathode samples from Li/SO_2 cell discharged at various temperatures

$\text{Na}_2\text{S}_2\text{O}_4$	$\text{Li}_2\text{S}_2\text{O}_4$	Cathodes								Unwashed	Washed
		Discharge temperatures and treatment after discharge									
		-30°C		-30°C a		25°C		70°C			
		Unwashed	Washed	Washed	Unwashed	Washed	Unwashed	Washed	Unwashed	Washed	
1235 (w)	(1244) (sh)	1239 (w)	1244 (w)	1244 (w)	1244 (w)	1244 (w)	1241 (m)	1242 (m)	1238 (w)	1244 (m)	
1147 (mw)	(1182) (sh)	1193 (w)	1183 (w)	1180 (sh)	1182 (w)	1182 (w)	1165 (m)	1234 (m) 1160 (m)	1155 (m)	1165 (m)	
1054 (str)	1085 (str)	(1105) (sh)	(1110) (sh)	1113 (str)	1088 (str)	1087 (str)	1088 (str)	1086 (str)	1122 (sh)	1091 (str)	
1031 (str)	1034 (str)	1080 (str)	1078 (str)	1082 (m)	1031 (str)	1029 (str)	1028 (str)	1020 (str)	1110 (sh)	1091 (str)	
974 (sh)	978 (sh)	1032 (str)	1030 (str)	1031 (m)	978 (sh)	(978) (sh)	969 (m)	968 (m)	1094 (m)	1021 (str)	
921 (str)	(912) (sh)	(940) (sh)	(940) (sh)	944 (sh) 975 (w)	906 (str)	907 (str)	905 (str)	904 (str)	1019 (str)	970 (m)	
899 (str)	899 (str)	906 (str)	904 (str)	946 (w) 917 (sh)	(662) (sh)	(661) (vw)	664 (m)	661 (m)	967 (str)	970 (m)	
620 (w)	647 (w)	645 (w)	646 (w)	906 (m)	(643) (w)	(641) (vw)	645 (w)	645 (w)	949 (sh)	970 (m)	
542 (w)	542 (m)	542 (m)	542 (m)	542 (w)	543 (w)	541 (m)	544 (mw)	543 (mw)	949 (sh)	970 (m)	
512 (m)	507 (m)	504 (m)	503 (m)	511 (w) 504 (w)	502 (m)	503 (m)	501 (mw)	502 (mw)	630-640 (mw) 640 (mw) 560 (w)	545 (mw)	

* 70°C represents a cathode from a second cell discharged at 70°C.

-30°C a is a sample from a cathode discharged at -30°C but exposed to the atmosphere.

(str) strong, (m) moderate, (mw) moderate to weak, (w) weak, (vw) very weak, (sh) shoulder.

All frequencies are in cm^{-1} . Frequencies in parentheses have been estimated.

possibility also exists that the two salts have different crystal structures. However, the IR spectrum of the lithium salt sufficiently resembles that of the sodium salt to suggest that the $\text{S}_2\text{O}_4^{2-}$ ion geometry in crystalline $\text{Li}_2\text{S}_2\text{O}_4$ is C_{2v} , as it is in the sodium salt.

The IR spectra of 92% pure $\text{Li}_2\text{S}_2\text{O}_4$ has been previously reported by the authors (10); the IR bands are tabulated in Table II. The top of Fig. 1 shows the IR spectra of 85% pure $\text{Li}_2\text{S}_2\text{O}_4$. The three principal bands at 1082, 1034, and 899 cm^{-1} , and two moderate bands at 540 and 506 cm^{-1} , are essentially the same as that reported for the purer sample. Some weak bands and shoulders may be caused by impurities, i.e., the 647 cm^{-1} band in the 92% sample is attributed to the principal impurity, Li_2SO_3 . Additional weak bands or shoulders occur in the 85% sample (Fig. 1) at 1182, 963, and 639 cm^{-1} , which are in excellent agreement with the 1180, 965, and 642 cm^{-1} bands of hydrated Li_2SO_3 . The band near 1130 cm^{-1} may be due to sulfate.

IR spectra of cells discharged at -30° and 25°C.—The infrared spectra of cathode samples discharged at -30° and 25°C are compared with $\text{Li}_2\text{S}_2\text{O}_4$ in Fig. 1. The spectra of these cathodes strongly resemble the spectrum of $\text{Li}_2\text{S}_2\text{O}_4$. Washing the cathode material with acetonitrile has a negligible effect on the infrared spectra of these samples. The major discharge product

at these two temperatures is $\text{Li}_2\text{S}_2\text{O}_4$, a result in accord with the x-ray results. The weak bands reported in Table II appear to be due to trace amounts of decomposition or oxidation products.

IR spectra of cells discharged at 70°C.—Major bands.—The infrared spectra of cathodes from cells discharged at the higher temperature (70°C) are shown in Fig. 2. Obvious differences from those discharged at the two lower temperatures are observed. The spectra resemble those of $\text{Li}_2\text{S}_2\text{O}_4$, but the intensity pattern of the bands is altered. The strong peaks at 1091, 1021, and 910 cm^{-1} correspond to the strong peaks in the $\text{Li}_2\text{S}_2\text{O}_4$ spectrum. The moderately weak bands at 545 and 503 cm^{-1} match well with the moderate asymmetric bending vibrations occurring at 542 and 507 cm^{-1} for $\text{Li}_2\text{S}_2\text{O}_4$. However, the infrared spectral evidence strongly shows that the higher temperature discharge produces a different distribution of products than the discharges at lower temperature. Four new moderately intense bands appear at \sim 1244, 1165, 970, and 663 cm^{-1} . In addition, discharge of other cathodes reveal the appearance of bands at \sim 1110, 1130, 944, and 630-640 cm^{-1} .

The high frequency IR band observed at 1240 cm^{-1} (1242 and 1238 cm^{-1} in Fig. 2) can be generated by S-O stretching vibrations of several oxy-sulfur anions,

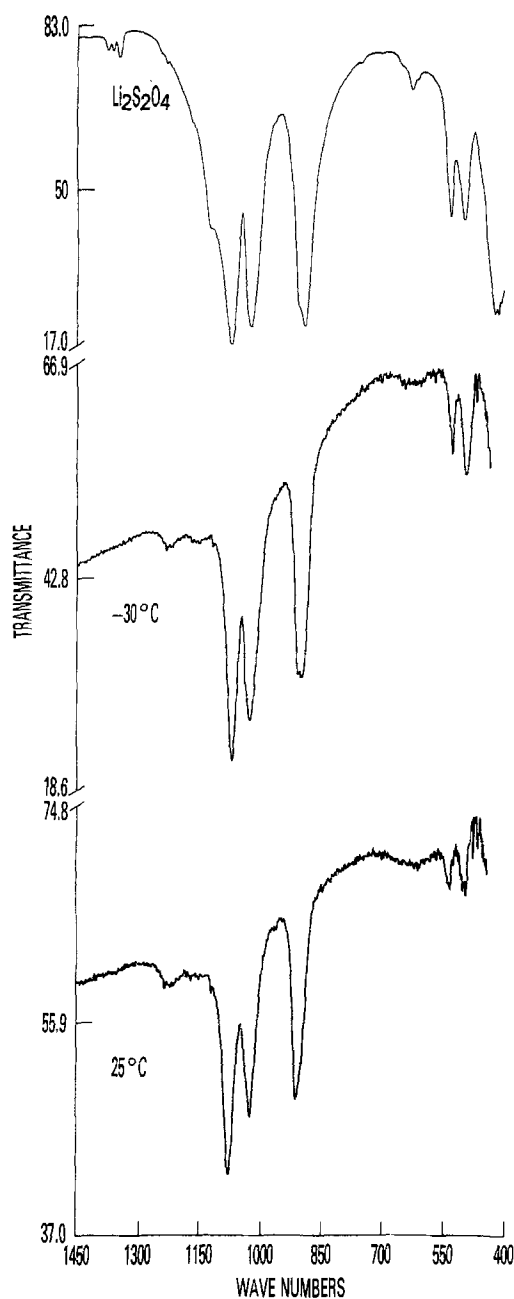


Fig. 1. Infrared spectra of $\text{Li}_2\text{S}_2\text{O}_4$ and the cathode product from a Li/SO_2 cell discharged at -30° and 25°C .

including pyrosulfate $\text{S}_2\text{O}_7^{2-}$, dithionate $\text{S}_2\text{O}_6^{2-}$, and polythionates $\text{S}_x\text{O}_6^{2-}$ ($x = 3 \rightarrow 6$). The presence of pyrosulfate can be ruled out due to the absence of bands in the 700 and 800 cm^{-1} region of the infrared spectrum (11). The di- or poly-thionates have their most intense bands at $\sim 1240 \text{ cm}^{-1}$ (12-14). Polythionates differ by exhibiting a strong IR band near 1035 cm^{-1} (12, 15). This was confirmed by comparing the IR spectra of the sodium di- and tetra-thionates. The tetrathionate had characteristic bands at 1238, 1030, and 635 cm^{-1} . The anhydrous dithionate exhibited strong bands at 1244 and 998 cm^{-1} , a moderate triplet at $\sim 590, 580$, and 560 cm^{-1} , and had a weak band at $\sim 528 \text{ cm}^{-1}$. The critical distinction between the dithionate (995-1000 cm^{-1} band) and the polythionate (1035-1045 cm^{-1} band) is masked in the mixture containing $\text{Li}_2\text{S}_2\text{O}_4$, which absorbs at 1034 cm^{-1} . Additional precaution is warranted on evaluating the 1240 cm^{-1} region. Very pure $\text{Na}_2\text{S}_2\text{O}_6$ exhibits a relatively simple IR pattern at 1244 cm^{-1} , whereas spectral data reported for $\text{K}_2\text{S}_2\text{O}_6$ reveal a complex IR spectra in this region (16). In the absence of the lithium polythionates, dis-

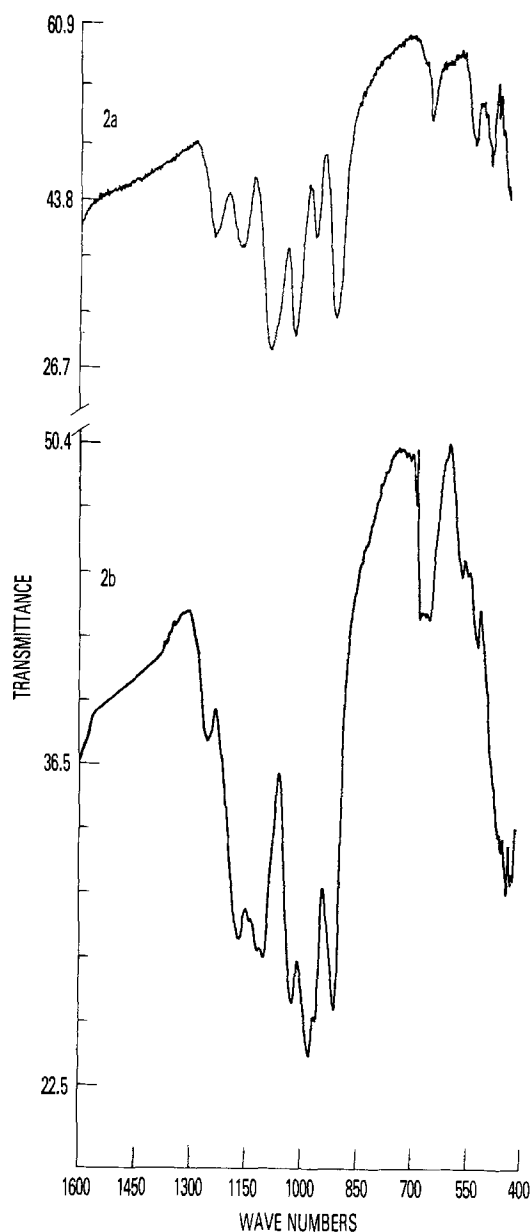
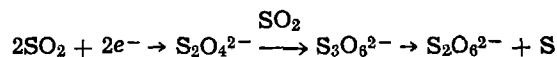


Fig. 2. Infrared spectra of cathodes taken from two different Li/SO_2 cells discharged at 70°C . Curve a: washed cathode no. 1. Curve b: unwashed cathode no. 2.

tinction between the di- and poly-thionates cannot be unambiguously determined by IR in the presence of $\text{Li}_2\text{S}_2\text{O}_4$. Analysis employing the method of Murthy (17), currently in progress at NSWC (8), indicates dithionate formation. A hint of the 998 cm^{-1} band appears near the 1021 cm^{-1} peak, but is not obvious in the spectra. A band at 560 cm^{-1} is observed, which may or may not be associated with a lithium thionate. The thionate concentration may be insufficient in the presence of the predominant dithionite ($\text{S}_2\text{O}_4^{2-}$) for this band to be observed. The presence of a di- or tri-thionate can be explained by the redox scheme



The presence of sulfur was confirmed in the 70°C discharged cathode. The cathodes were washed with carbon disulfide. The carbon disulfide was evaporated, and the residue was confirmed to be sulfur by spot tests and differential scanning calorimetry. The sulfur could be produced through the above mechanism or as a result of the thermal decomposition of the lithium dithionite.

An unidentified band appears at $\sim 1160\text{ cm}^{-1}$ (1165 and 1155 cm^{-1} in Fig. 2) in the 70°C discharge which is not present in the low temperature discharges. Although S_2O has been observed as a minor constituent by mass spectroscopy and has IR bands at 1165 and 679 cm^{-1} (a shoulder at 679 cm^{-1} is seen in Fig. 2), this possibility appears remote, since S_2O is unstable at ambient temperature. A solution of SO_2 in CH_3CN exhibits a predominant peak at 1160 cm^{-1} . However, the possibility of the carbon cathode retaining the $\text{CH}_3\text{CN-SO}_2$ only at the 70°C and not at the -30° and 25°C discharges rules out $\text{CH}_3\text{CN-SO}_2$. Anhydrous Li_2SO_4 has a strong broad-band centered near 1140 cm^{-1} , whereas the hydrate displays split peaks at 1170 and 1110 cm^{-1} (18). Moisture content of the carbon may influence the position of the sulfate band. Although the presence of sulfate is strongly suggested by other bands, e.g., 661 cm^{-1} , an unequivocal assignment cannot be determined, since the unavailable lithium polythionates are likely to also absorb in this region.

A strong IR band is observed at 968 cm^{-1} . Recently, a similar band at 970 cm^{-1} was reported by Bowden *et al.*, which they attributed to be dithionate based on a comparison with IR spectra of $\text{Na}_2\text{S}_2\text{O}_6$ (19). However, a sample of $\text{Na}_2\text{S}_2\text{O}_6$, analyzed at $>99\%$ purity by standard methods, exhibited a band at 998 cm^{-1} . We attributed the band at 968 cm^{-1} to the presence of Li_2SO_3 . This was confirmed by comparing the spectra with that of Li_2SO_3 , which displayed a strong band at 967 cm^{-1} . The symmetric and asymmetric O-S stretching modes of the sodium salt give rise to a strong absorption around 970 cm^{-1} , and often the two fundamentals are seen separately at 970 and $930\text{--}940\text{ cm}^{-1}$ (12, 20). Such a splitting as observed in Fig. 2b explains the peak at 908 cm^{-1} and the shoulders observed from 940 to 949 cm^{-1} . Similarly, the symmetric S-O bend observed at $630\text{--}640\text{ cm}^{-1}$, which appears in the spectra of the unwashed cathode of Fig. 2b, is also attributed to Li_2SO_3 . The presence of Li_2SO_3 was observed in the x-ray pattern of this same cathode.

The washed cathode has a moderate band at $\sim 661\text{ cm}^{-1}$ and the hint of a weak peak near 612 cm^{-1} . The location of these bands are in excellent agreement with the IR spectra of anhydrous Li_2SO_4 , which exhibit strong and moderate bands at 660 and 612 cm^{-1} , respectively. The intensity and frequency of these bands may be influenced by the moisture content of the carbon cathode. Instead of two sharp bands, hydration produces a single broad-band near 634 cm^{-1} (18).

The spectra of the unwashed cathode (Fig. 2b) reveals a more complex IR pattern. In addition to the band near 657 cm^{-1} , there is another band in the $630\text{--}640\text{ cm}^{-1}$ region with a shoulder at $\sim 613\text{ cm}^{-1}$. The band at 657 cm^{-1} (664 and 657 cm^{-1} in Table II) and shoulder at 613 cm^{-1} appear consistent with the spectra of anhydrous Li_2SO_4 . The peak in the $630\text{--}640\text{ cm}^{-1}$ region is attributed to sulfite.

The bands $540\text{--}545\text{ cm}^{-1}$ and $504\text{--}500\text{ cm}^{-1}$ are in excellent agreement with similar bands observed for $\text{Li}_2\text{S}_2\text{O}_4$.

Minor IR bands.—The IR spectra of one of the unwashed cathodes from the 70°C discharged cells displayed several minor peaks and shoulders.

The shoulder at 1122 cm^{-1} could be due to the S-O stretching high frequency bands of sulfate, sulfite, or SOBr_2 ; the latter displays a single high frequency band at 1121 cm^{-1} (12).

The small shoulder at 1110 cm^{-1} is consistent with the presence of sulfate or sulfite. The hydrated lithium salts showed bands at 1113 cm^{-1} [1110 cm^{-1} , Ref. (18)] and $\sim 1108\text{ cm}^{-1}$, respectively. An infrared spectrum of a cathode sample from a -30°C discharged cell that had been exposed to air for 4 days developed an intense band at 1113 cm^{-1} . X-ray analysis confirmed this to be lithium sulfate. Similarly, the IR spectrum of a

washed cathode from a 70°C discharged cell that had been stored 4 months in a vacuum desiccator showed the development of a shoulder near 948 cm^{-1} as well as a peak at 1108 cm^{-1} . On opening the desiccator, a strong odor of SO_2 was noticed. These peaks may be due to sulfite, resulting from limited oxidation in an SO_2 atmosphere or slow decomposition of $\text{Li}_2\text{S}_2\text{O}_4$. Unlike the sodium salt, $\text{Li}_2\text{S}_2\text{O}_4$ is unstable. When 92% pure $\text{Li}_2\text{S}_2\text{O}_4$ was stored in a closed vial at ambient temperature, iodometric analysis nearly 1 yr later revealed only $\sim 8\%$ dithionite remaining.

The peaks at $630\text{--}646\text{ cm}^{-1}$ (Table II) and shoulder at $\sim 513\text{ cm}^{-1}$ are attributed to lithium sulfite. The IR pattern of $\text{Li}_2\text{SO}_3 \cdot 3\text{H}_2\text{O}$ has bands at 643 and 511 cm^{-1} . The nonappearance (Fig. 2a) and appearance (Fig. 2b) of the ($940\text{--}949\text{ cm}^{-1}$) band is consistent with the behavior previously reported for sulfite (12).

The incongruous bands at 1009 and 560 cm^{-1} in one of the 70°C cathodes could be an artifact, but might be a part of the spectrum of an unavailable lithium salt, such as a di- or poly-thionate.

The possibility of thiosulfate ($\text{S}_2\text{O}_3^{2-}$) and/or metabisulfite ($\text{S}_2\text{O}_5^{2-}$) cannot be ruled out under some discharge conditions. The spectra of $\text{Li}_2\text{S}_2\text{O}_3$ and $\text{Na}_2\text{S}_2\text{O}_5$ were recorded and have several bands in common with the observed cathode spectra. Thiosulfate has been reported in D-size Li/SO_2 cells (21), and iodometric studies on these same $\frac{1}{2}$ A-size cells indicate thiosulfate (2, 8). Additionally, hydrolysis of dithionite in an aqueous acid medium is well known to produce thiosulfate. Mass spectroscopy studies on carbon cathodes from commercial SO_2 cells were found to contain as much as 18% water upon heating to 275°C (8). Moist carbon cathodes may be a suitable acidic medium to promote hydrolysis. Similarly, water has been reported to promote the decomposition of dithionite to both thiosulfate and metabisulfite (22).

The spectra of $\text{Li}_2\text{S}_2\text{O}_3$ has major broad bands at ~ 1112 and 1000 cm^{-1} , a moderate band near 680 cm^{-1} , and a weak band at 550 cm^{-1} . The 1000 and 550 cm^{-1} bands are not far removed from the observed incongruous peaks, and a hint of a 679 cm^{-1} shoulder is present in Fig. 2.

Sodium metabisulfite—displayed bands at ~ 1180 , a $1056\text{--}1068$ doublet, 978 , 653 , 568 , and 415 cm^{-1} resemble the pattern, if not the intensity, of several weak to moderate bands in Table II. However, the absence of the strong bands in the $\sim 1060\text{ cm}^{-1}$ region is an argument against the presence of metabisulfite. Since acceptance of this manuscript, a recent paper has reported that metabisulfite is present in cells discharged at 72°C (24).

ESR spectroscopy.—Electron spin resonance (ESR) studies were carried out on the cathodes from the discharged cells and compared with laboratory-synthesized $\text{Li}_2\text{S}_2\text{O}_4$. The solid $\text{Li}_2\text{S}_2\text{O}_4$ synthesized in the laboratory displays a strong ESR signal with G values of 2.0076 , 2.0053 , and 2.0036 . The signal has been attributed to the presence of the SO_2^- radical anion in the sample (5), and arises from the homolytic cleavage of the disulfide bond in dithionite.

The effects of temperature on the ESR spectra of $\text{Li}_2\text{S}_2\text{O}_4$ can be seen in Fig. 3. At low temperature the signal is broad. It sharpens and splits as the temperature is raised. The intensity of the signal increases dramatically with temperature reaching a maximum at 220°C , corresponding to the approximate exothermic decomposition temperature of the dithionite, whereupon the ESR signal decays quickly and irreversibly. This behavior implicates SO_2^- in the thermal decomposition of $\text{Li}_2\text{S}_2\text{O}_4$.

The half-field signal ($\Delta m = 2$) at low temperatures for crystalline $\text{Li}_2\text{S}_2\text{O}_4$ has been reported (4). The presence of the half-field signal is evidence for the interaction of trapped pairs of radicals in well-defined

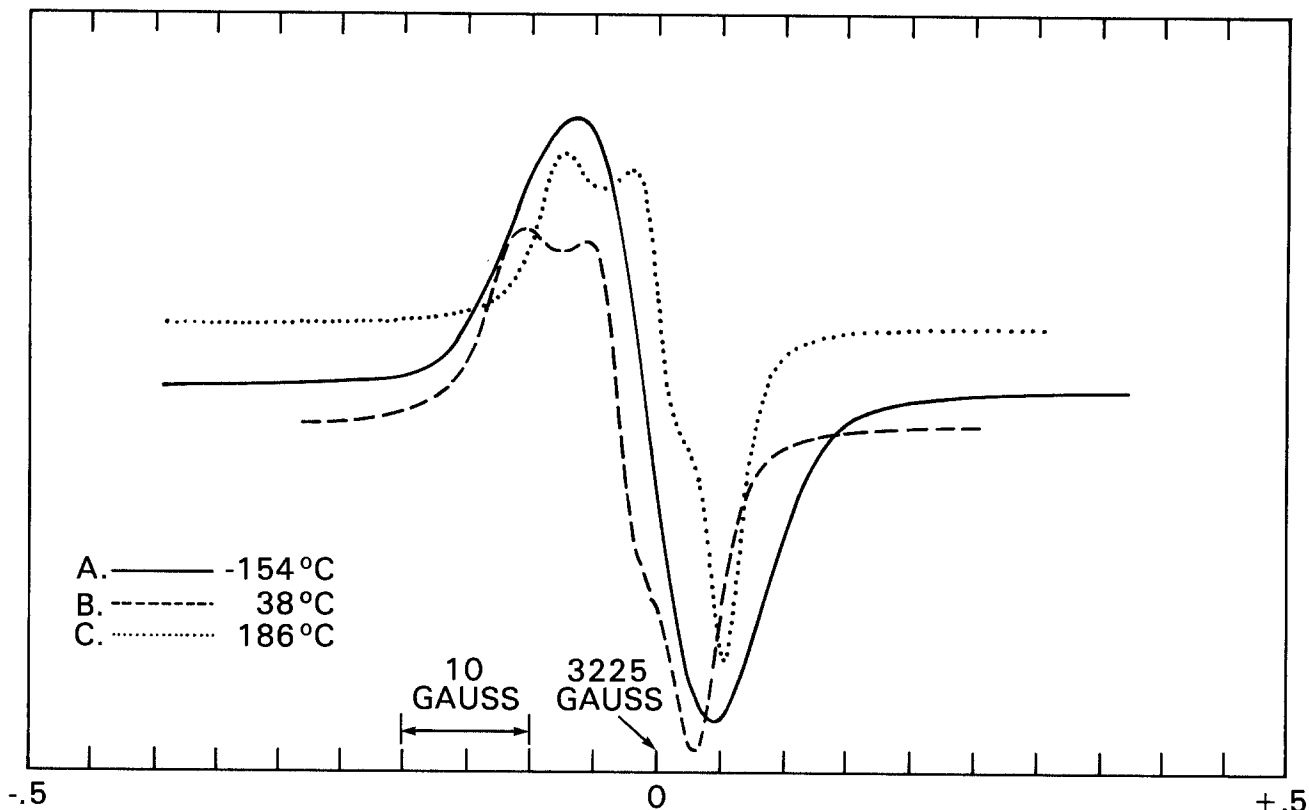


Fig. 3. The effects of temperature on the ESR spectra of Li₂S₂O₄

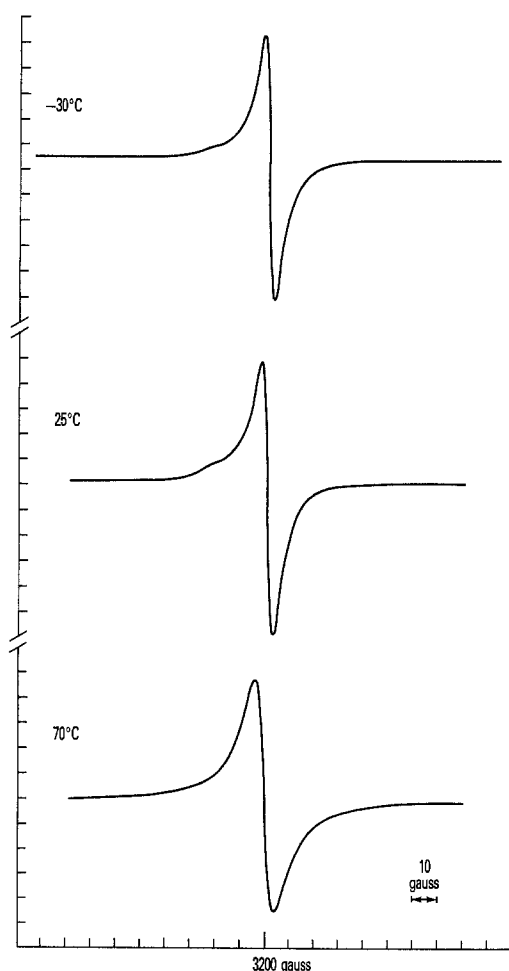


Fig. 4. ESR spectra of unwashed cathodes from discharged Li/SO₂ cells (a, top curve) -30°C, (b, middle curve) 25°C, (c, bottom curve) 70°C. All spectra taken at room temperature.

locations within the lattice. Intensity considerations indicate that the splitting of the $\Delta m = 1$ transition should be considerable. However, paired $\Delta m = 1$ transitions attributable to interacting radicals could not be identified, most probably because of dipolar broadening from a large anisotropic zero field splitting. In addition, no ³³S hyperfine splittings were observed in the Li₂S₂O₄ samples.

ESR spectra of unwashed cathode samples are shown in Fig. 4. Washing the cathode samples with acetonitrile did not significantly affect the spectra. The cathodes discharged at -30° and 25°C differ little from each other, with the exception that the 25°C cell has more of a lower field signal, which is attributed to the dithionite. The obvious reason for this is that the 25°C cell has more capacity than the -30°C cell, and consequently more dithionite. The spectra of the cathode material discharged at 70°C are similar to those of the lower temperature discharges, but they are broader and less structured, indicating a greater amount of radical interaction or the presence of new radical species.

As shown in Fig. 5, the cathode spectra from the 25° and -30°C discharges have been interpreted as a sum of the spectra of two species: one due to the Li₂S₂O₄, and the other due to a radical species associated with the cathode carbon material, Shawinigan black. The spectra could be reproduced reasonably well by a mixture of ~5% Li₂S₂O₄ in carbon. It is not clear what role, if any, the carbon-based radical plays in the decomposition or discharge chemistry.

Conclusion

Laboratory synthesized Li₂S₂O₄ has been characterized by x-ray, infrared, and electron spin resonance spectroscopy.

The spectroscopic characteristics of the Li₂S₂O₄, together with the IR spectra of Li₂SO₃, Li₂S₂O₃, Li₂SO₄, and several sodium salts, were used to study the cathode products from Li/SO₂ cells discharged at -30°, 25°, and 70°C. Li₂S₂O₄ was confirmed to be essentially the major product formed at -30° and 25°C using x-ray and IR spectroscopy. The 70°C discharged cathode revealed a different set of products. The principal prod-

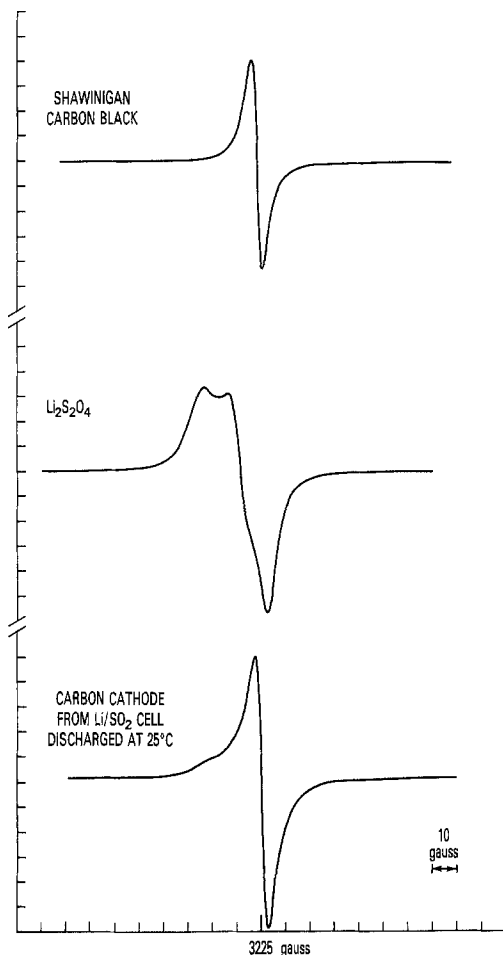
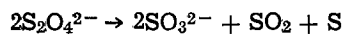
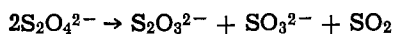


Fig. 5. ESR spectra for shawinigan black, solid $\text{Li}_2\text{S}_2\text{O}_4$, and carbon cathode from a Li/SO_2 cell discharged at 25°C .

uct was dithionite. The presence of sulfite, sulfur, and $\text{Li}_2\text{S}_2\text{O}_6$ or $\text{Li}_2\text{S}_n\text{O}_6$ was confirmed. Sulfate also appears to be present. Some thiosulfate or metabisulfate may be present.

Thermal decomposition of dithionite (4, 23), as indicated below



may account for some of these products. Thermal stability studies of dithionite are in progress.

Results of ESR studies on $\text{Li}_2\text{S}_2\text{O}_4$ at different tem-

peratures implicate the SO_2^- radical in the thermal decomposition mechanism of $\text{Li}_2\text{S}_2\text{O}_4$. A radical species associated with the cathode carbon material is also present.

Acknowledgment

This work was supported by the Naval Surface Weapons Center "High Energy Batteries for Weapons" Block Program. The assistance of Dennis Mitchell, Thomas N. Robeson, and Charles E. Fisher is greatly appreciated for the preparation of lithium dithionite.

Manuscript submitted Sept. 16, 1983; revised manuscript received Jan. 4, 1984.

The Naval Surface Weapons Center assisted in meeting the publication costs of this article.

REFERENCES

1. P. Bro, H. Y. Kang, C. Schlaikjer, and H. Taylor, *IECEC*, 432 (1975).
2. W. P. Kilroy and C. R. Anderson, *J. Power Sources*, 9, 397 (1983).
3. M. W. Rupich, L. Pitts, and K. M. Abraham, *This Journal*, 129, 1857 (1982).
4. D. M. Oglesby, R. L. Ake, and W. P. Kilroy, in "Proceedings of the 30th Power Sources Symposium," Atlantic City, NJ, June 7-12, 1982, The Electrochemical Society, Inc., p. 127 (1983).
5. E. G. Janzen, *J. Phys. Chem.*, 76, 157 (1972).
6. W. P. Kilroy, *Talanta*, 27, 343 (1980).
7. D. W. Ernst, *This Journal*, 129, 565 (1982).
8. W. P. Kilroy, Unpublished data.
9. W. P. Kilroy, *Talanta*, 30, 419 (1983).
10. R. L. Ake, D. M. Oglesby, and W. P. Kilroy, Abstract 298, p. 483, The Electrochemical Society Extended Abstracts, Vol. 82-2, Detroit, Michigan, Oct. 17-21, 1982.
11. V. A. Simon and H. Wagner, *Z. Anorg. Allg. Chem.*, 311, 102 (1961).
12. "Inorganic Sulfur Chemistry," G. Nickless, Editor, pp. 162-170, Elsevier, New York (1968).
13. W. G. Palmer, *J. Chem. Soc.*, 1552 (1961).
14. M. Schmidt and T. Sand, *J. Inorg. Nucl. Chem.*, 26, 1179 (1964).
15. R. M. Golding, *J. Chem. Phys.*, 33, 1666 (1960).
16. K. Buijs, *J. Inorg. Nucl. Chem.*, 24, 229 (1962).
17. A. R. Murthy, *Curr. Sci. (India)*, 22, 371 (1953).
18. F. A. Miller and C. H. Wilkens, *Anal. Chem.*, 24, 1253 (1952).
19. W. L. Bowden, L. Chow, D. DeMuth, and R. Holmes, Abstract 11, p. 17, The Electrochemical Society Extended Abstracts, Vol. 83-1, San Francisco, California, May 8-13, 1983.
20. W. E. Dasant and D. Morrison, *J. Inorg. Nucl. Chem.*, 26, 1122 (1964).
21. J. Godin, M. Farrington, and C. Gardener, Abstract 53, p. 89, The Electrochemical Society Extended Abstracts, Vol. 83-2, Washington, DC, Oct. 9-14, 1983.
22. Y. Yoshikawa, H. Okazaki, and T. Yamaguchi, U.S. Pat. 3,411,875 (1968).
23. "Specialty Inorganic Chemicals," A. Thompson, Editor, p. 59, Burlington House, London (1980).
24. W. L. Bowden, L. Chow, D. L. DeMuth, and R. W. Holmes, *This Journal*, 131, 229 (1984).

Mathematical Modeling of the Lithium, Thionyl Chloride Static Cell

I. Neutral Electrolyte

Keh-Chang Tsauro* and Richard Pollard**

Department of Chemical Engineering, University of Houston, Houston, Texas 77004

ABSTRACT

A mathematical model of the Li-LiAlCl₄, SOCl₂-C static cell with neutral electrolyte is presented. The model considers a whole prismatic cell consisting of negative electrode, separator, electrolyte reservoir, and positive electrode. Physical phenomena described are ohmic potential drop and diffusion potential in the electrolyte, changes in porosity and electrolyte composition due to electrochemical reactions, local reaction rates, and diffusion, convection, and migration of electrolyte. The theoretical results show the trends in behavior observed experimentally. The effects of state of charge, initial electrolyte composition, electrode thickness and porosity, and current density are presented, and factors that can limit cell performance are identified.

The Li-LiAlCl₄/SOCl₂-C primary cell has received considerable attention as a high energy density power source (1-4). A mathematical model is needed to predict the operational characteristics of the system and to assess the influence of changes in design parameters on the cell performance.

Models have been proposed to describe the behavior of flooded porous electrodes (5). Specific systems that have been investigated include electrodes with sparingly soluble reactants such as the Ag-AgCl and Cd-Cd(OH)₂ couples (6), and electrodes of zinc (7) and of lead dioxide (8, 9).

Far less effort has been directed toward modeling complete cells and, up until now, only the lead acid battery (10, 11) and the LiAl/FeS molten salt battery (12, 13) have been analyzed in detail. In this paper, a one-dimensional model is presented for the lithium, thionyl chloride system with a neutral electrolyte. A whole prismatic cell is considered, consisting of negative electrode, separator, electrolyte reservoir, and positive electrode (see Fig. 1). The model can be used to identify system limitations and to help guide experimental research.

Model Development

The analysis is based on the macroscopic theory of porous electrodes in which the solution and matrix phases are treated as superposed continua without regard for the geometric details of the pores (14). With this approach, one can obtain a consistent framework for the description of isothermal transport processes in the electrolyte (5).

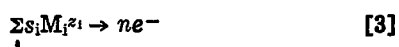
A material balance for species *i* is given by

$$\frac{\partial(\epsilon c_i)}{\partial t} = a_{j_{in}} - \nabla \cdot \underline{N}_i \quad [1]$$

where \underline{N}_i is the flux of species *i* in the pore solution averaged over the cross-sectional area of the electrode and where $a_{j_{in}}$ represents the transfer rate of species *i* from the solid phases to the pore solution per unit electrode volume. The superficial current density in the pore solution is due to the movement of charged species

$$\underline{i}_2 = F \sum_i z_i \underline{N}_i \quad [2]$$

and, as a consequence of electroneutrality, the divergence of the total current density is zero. For a single electrode reaction of the form



Faraday's law can be expressed as

$$a_{j_{in}} = - \frac{s_{ij}}{nF} = - \frac{s_i}{nF} \nabla \cdot \underline{i}_2 \quad [4]$$

provided that double-layer charging is ignored.

A material balance on the solid phases indicates how the electrode porosity changes with the extent of reaction at each location within the electrode (5)

$$\frac{\partial \epsilon}{\partial t} = \sum_{\text{solid phases}} \frac{\tilde{V}_i}{nF} \nabla \cdot \underline{i}_2 \quad [5]$$

The flux of mobile species in the electrolyte can be attributed to the combined effects of diffusion, migration, and convection. For the neutral Li/SOCl₂ cell, the electrolyte is regarded as a concentrated mixture of lithium cations and chloroaluminate anions in thionyl chloride. Inversion of the multicomponent diffusion equations yields explicit relationships for the fluxes (5, 15)

$$\underline{N}_+ = -\epsilon D \nabla c_e + \frac{t_+ \underline{i}_2}{z_+ F} + c_+ \underline{v} \quad [6]$$

$$\underline{N}_- = -\epsilon D \nabla c_e + \frac{t_- \underline{i}_2}{z_- F} + c_- \underline{v} \quad [7]$$

$$\underline{N}_o = -\epsilon D \nabla c_o + c_o \underline{v} \quad [8]$$

where the subscripts +, -, e, and o refer to Li⁺, AlCl₄⁻, LiAlCl₄, and SOCl₂, respectively, and where *D* is the effective diffusion coefficient of the electrolyte. The volume average velocity, $\underline{v} = \sum_i \tilde{V}_i \underline{N}_i$, has been

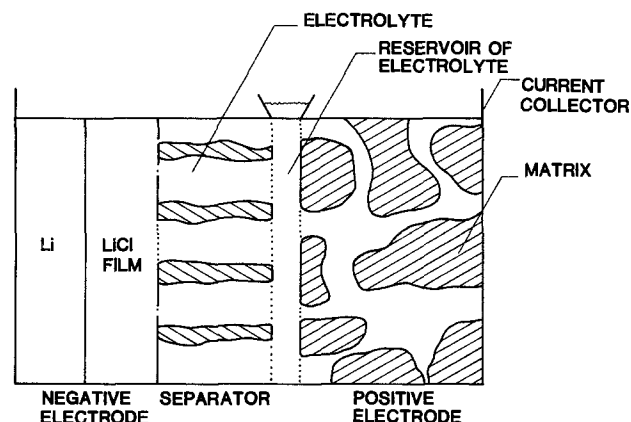


Fig. 1. Schematic diagram of Li-LiAlCl₄/SOCl₂-C static cell

* Electrochemical Society Student Member.

** Electrochemical Society Active Member.

Key words: porous electrodes, cell performance, galvanostatic discharge.

chosen as the reference frame because physical data for LiAlCl_4 , SOCl_2 electrolytes are often correlated with the concentration (see Appendix). Substitution of Eq. [6]-[8] into the material balance Eq. [1] and rearrangement gives an overall conservation equation

$$\frac{\partial e}{\partial t} + \nabla \cdot \underline{v} = a \left[\nabla_{\text{O}^{\ominus}} j_{\text{O}^{\ominus}} + \frac{\nabla_{\text{e}^{\ominus}} t_{+}^{\ominus}}{\nu_{+}} j_{+n} + \frac{\nabla_{\text{e}^{\ominus}} t_{-}^{\ominus}}{\nu_{-}} j_{-n} \right] - \nabla_{\text{e}^{\ominus}} \frac{i_2 \cdot \nabla t_{+}^{\ominus}}{z_{+} + \nu_{+} F} - \epsilon \frac{D}{c_0 \bar{V}_0} (\nabla c_e) \cdot \nabla \bar{V}_e \quad [9]$$

The movement of electrons in the matrix phase is governed by Ohm's law

$$\underline{i}_1 = -\sigma \nabla \Phi_1 \quad [10]$$

where σ is the effective matrix conductivity. In the electrolyte, the variation in solution potential is given by (5)

$$\frac{i_2}{\kappa} = -\nabla \Phi_2 - \frac{1}{F} \left(\frac{s_{+}}{\nu_{+}} + \frac{t_{+}^{\ominus}}{z_{+} + \nu_{+}} - \frac{s_0 c_e}{n c_0} \right) \nabla \mu_e \quad [11]$$

where Φ_2 is measured with a reference electrode that has stoichiometric coefficients s_i and number n of electrons transferred, and μ_e is the chemical potential of the electrolyte (16)

$$\mu_e = \nu RT \ln (c_e f_{+} - a^{\theta} -) \quad [12]$$

Equation [10] may be subtracted from Eq. [11] to obtain variations in the overpotential $\eta = \Phi_1 - \Phi_2$ directly (17).

Polarization equations are needed to express the dependence of the local rate of each reaction on the various concentrations and on the potential difference driving force at the reaction interface. Electrode kinetics do not follow fundamental laws that can be expressed as reliably as Ohm's law or the law of conservation of matter. Therefore, the polarization relationships will be subject to further refinement as one tries to account not only for the charge transfer mechanism but also for electrode morphology, formation of covering layers, and mass transport to and from reaction sites. It is common to begin with a polarization equation of the form

$$j = a i_0 [e^{\alpha_s F \eta_s / RT} - e^{-\alpha_c F \eta_s / RT}] \quad [13]$$

where η_s is the local value of the surface overpotential, $\eta_s = \eta - U_w$, and where the exchange current density i_0 can be written as

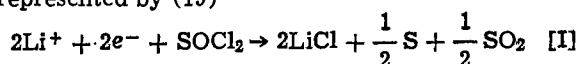
$$i_0 = i_{0,\text{ref}} \pi \left(\frac{c_{i,w}}{c_{i,\text{ref}}} \right)^{\gamma_i} \frac{\pi a_k \gamma_k}{k} \quad [14]$$

The activity a_k for a pure solid reactant or product may be taken as unity. The theoretical open-circuit potential for a reaction is given by (18)

$$U_w = U^{\theta} - U_{\text{re}}^{\theta} + \frac{RT}{n_{\text{re}} F} \sum_i s_{i,\text{re}} \ln \left(\frac{c_{i,\text{re}}}{\rho_0} \right) - \frac{RT}{nF} \sum_i s_i \ln \left(\frac{c_{i,w}}{\rho_0} \right) \quad [15]$$

provided that activity coefficient corrections can be neglected. The potential U_w is equal to zero if the reference electrode has a reaction of the same kind as the working electrode, measured at the composition prevailing locally at the surface of the working electrode.

The complicated processes in the positive electrode are represented by (19)



It is assumed that the S and SO_2 produced by reaction [I] dissolve in the electrolyte (20). Furthermore, the

model supposes that, as a result of low solubility in the neutral electrolyte (20, 21), pure LiCl precipitates instantaneously and passivates a fraction of the active surface area of the carbon matrix in accordance with

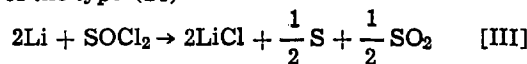
$$a = a^{\circ} [1 - (\epsilon_{\text{LiCl}} / \epsilon_p)^p] \quad [16]$$

The magnitude of the exponent p reflects the morphology of the LiCl precipitate: large values represent long, needle-like crystals, whereas small values imply that flat, passivating films are produced (6, 22). Inclusion of the initial porosity in Eq. [16] corresponds, indirectly, to a dependence of crystallite shape on mechanical constraints (23). Any effects of factors such as temperature, current density, or impurities on the morphology are not considered in the initial analysis.

The overall discharge reaction at the negative electrode is



A LiCl film forms over the surface of the lithium by a reaction of the type (24)



It is assumed that reaction [II] occurs at the lithium surface, and that lithium ions are transported through the LiCl film and transferred to the electrolyte. The LiCl film can be described as a solid electrolyte interphase (SEI) with an outer porous layer (25, 26). However, neither detailed transport properties for the SEI nor local porosities for the porous layer are available. Consequently, the present analysis makes several simplifying assumptions. The film is regarded as a homogeneous region that can be characterized by a single bulk conductivity. This conductivity is used in Eq. [10] to calculate the potential drop across the film. The potential difference η_s at the Li/LiCl film interface is determined from Eq. [13] with j/a replaced by I and with i_0 independent of concentration. As a discharge proceeds and lithium is consumed, it is assumed that growth of the LiCl film and forces from outside the cell or from LiCl precipitation in the cathode maintain contact between Li, LiCl film, and separator. If a gap does develop in the anode, the potential drop across this region would need to be included in the calculation of electrode resistance.

With the simplified model for the anode, it is not necessary to determine the concentration profile for lithium ions in the film. However, the SOCl_2 flux N_0 across the film must be calculated to assess the changes in film thickness. If convection terms are omitted from Eq. [6]-[8] and physical properties are taken as constant, the SOCl_2 concentration profile within the film is linear. Under these circumstances, the SOCl_2 flux is given by

$$N_0 = \frac{D_f}{\delta_f} [(c_0)_b - (c_0)_a] \quad [17]$$

where D_f is an effective diffusivity for SOCl_2 in the film, δ_f is the film thickness, and $(c_0)_b$ and $(c_0)_a$ are reactant concentrations at the separator and lithium interfaces, respectively. Reaction [III] is expected to be very fast, and, therefore, $(c_0)_a$ is taken to be zero. The flux in Eq. [17] is equal to the reaction rate r_{III} per unit separator area.

The production of LiCl by reaction [III] can alter either the porosity or the thickness of the protective film (25, 26). If only thickness changes are significant, a mass balance gives

$$\frac{d\delta_f}{dt} = s_{\text{LiCl,III}} \tilde{V}_{\text{LiCl}} r_{\text{III}} \quad [18]$$

As a discharge proceeds, increases in δ_f tend to lower the conversion rate, as predicted by Eq. [17]. A reduction in film porosity would also show this trend,

but indirectly, through changes in the effective diffusivity D_f .

The temperature is assumed to be uniform throughout the cell sandwich, but it can change with time in response to reversible heat effects, Joule heating, overpotentials associated with electrode reactions, and corrosion at the negative electrode. The first law of thermodynamics gives

$$C \frac{dT}{dt} = \left(U_o - V - T_o \frac{\partial U_o}{\partial T} \right) I - h_o(T - T_A) + (\Delta H_R)r_{III} \quad [19]$$

where C is the cell heat capacity per unit separator area, and h_o is the heat transfer coefficient between the cell and the surroundings. The total cell voltage V is obtained by integration of local matrix and electrolyte potential gradients in the electrodes and separator, in accordance with Eq. [10] and [11]. Kirchhoff's voltage law requires inclusion of the surface overpotentials (with appropriate signs) at the front of each electrode, as well as the difference in potential between the two types of reference electrode at one location. Resistances of the electrolyte reservoir and current collector can also be included.

The Li-LiAlCl₄/SOCl₂-C system can be described by local variables c_e , \underline{v} , ϵ , j , i_2 , and η and by the governing Eq. [1] (for the electrolyte), [4], [5], [9], [11] (in conjunction with Eq. [10]), and [13], subject to the following boundary conditions: (i) at the LiCl film/separator interface

$$\begin{aligned} \text{(a) } i_2 &= I \\ \text{(b) } c_i, \underline{N}_i &\text{ continuous} \end{aligned} \quad [20]$$

(ii) at the positive electrode/reservoir interface

$$\begin{aligned} \text{(a) } i_2 &= I \\ \text{(b) } c_1 &\text{ continuous} \\ \text{(c) } \frac{\partial}{\partial t} \left(\frac{V_R}{A} c_1 \right) &= \underline{N}_I - \underline{N}'_I \end{aligned} \quad [21]$$

(iii) at the positive electrode/current collector interface

$$\begin{aligned} \text{(a) } i_2 &= 0 \\ \text{(b) } \underline{v} &= 0 \\ \text{(c) } \underline{N}_I &= 0 \end{aligned} \quad [22]$$

where \underline{N}_i and \underline{N}'_i in Eq. [21] are the species fluxes that enter and leave the reservoir, respectively. (It should be noted that the subscript i in Eq. [20]-[22] refers to any species in the electrolyte. Also, the term "continuous" means that a variable is assigned only one value at the location in question, but that this value can change with time during cell discharge.) The electrolyte composition is assumed to be uniform across the reservoir. In the separator, the governing equations can be simplified with

$$\begin{aligned} \text{(a) } i_2 &= I \\ \text{(b) } j &= 0 \\ \text{(c) } \epsilon &= \epsilon_s \end{aligned} \quad [23]$$

The initial conditions are taken as

$$\begin{aligned} \text{(a) } c_i &= c_i^o \\ \text{(b) } \epsilon &= \epsilon^o \end{aligned} \quad [24]$$

The governing equations constitute a set of coupled, ordinary, nonlinear differential equations at each time step which are cast into finite difference form accurate to $O(h^2)$, and solved simultaneously by a numerical technique (16). Each nonlinear equation is linearized properly to assure convergence, and each time-dependent equation is programmed symmetrically between the old time-step and the present one, in order to attain stability.

Results and Discussion

Figure 2 shows composition profiles across a typical cell sandwich at several times during a constant current discharge of 80 mA/cm². When the discharge is started, lithium ions are introduced into the electrolyte by passage through the LiCl film at the negative electrode. They are then transported across the porous separator to the positive electrode, where they can react cathodically to form LiCl, in accordance with Eq. [1]. A concentration profile develops because the transference number of Li⁺ is not unity and because a chemical reaction can occur at the surface of the negative electrode. Consequently, diffusion aids migration in the transport of lithium ions across the cell.

The details of the composition variations can be attributed to the combined effects of diffusion, migration, convection, and electrochemical reaction. An

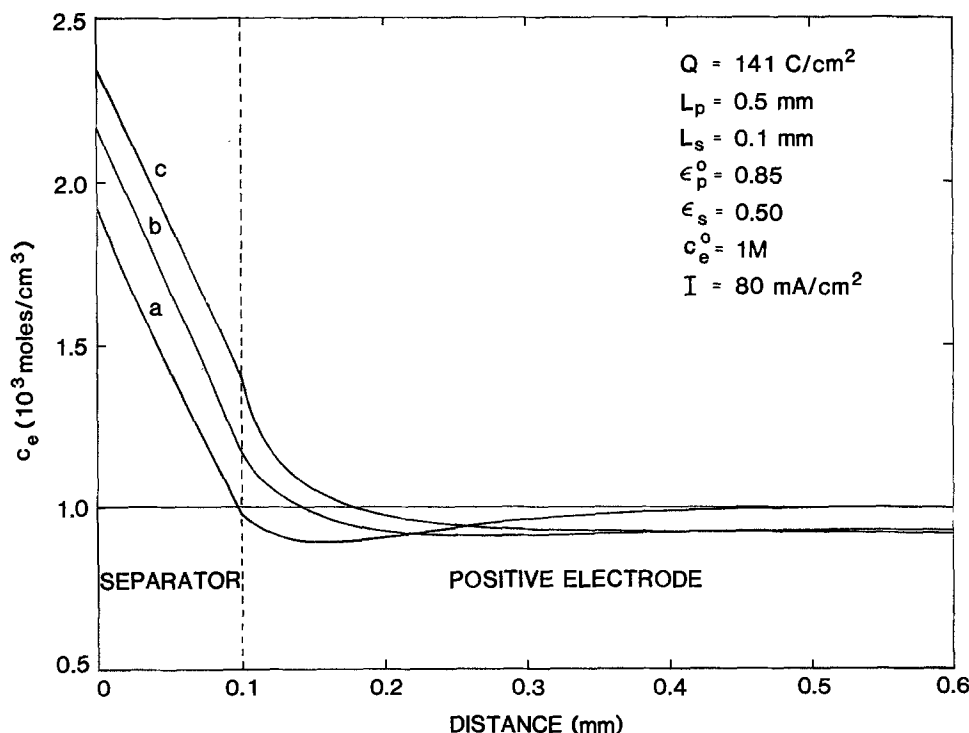


Fig. 2. Position dependence of electrolyte composition at different utilizations. Utilization is calculated on the basis of moles of SOCl₂ available: (a) 0.58%; (b) 3.70%; (c) 9.10%. Simulation parameters are presented in Tables I and II and in the Appendix.

almost constant composition gradient is established across the separator that corresponds to the flux of lithium ions needed for the specified current density. Porosity changes in the positive electrode accentuate local composition changes, and this, in turn, tends to raise the overall concentration level in the separator as discharge proceeds. The contribution of convection, which arises primarily from the influx or squeezing out of electrolyte as the porosity alters, is expected to be small for this system, ($v \sim O(10^{-5})$ cm/s). However, it is included in the analysis to ensure that the accuracy of the electrolyte material balances is retained (12).

The transfer current in the positive electrode is shown in Fig. 3, for several utilizations. The large electrode surface area of a typical carbon matrix material such as Shawinigan black (27) helps to create fast reaction kinetics. As a result, a highly nonuniform reaction distribution, dominated by ohmic effects, is obtained. Throughout the discharge, most of the reaction occurs near the electrode/reservoir interface and, because $\sigma/\kappa \gg 1$ (14), only a small amount of current is transferred near the back of the electrode. Precipitation of LiCl at the reaction zone close to the front of the electrode reduces the surface area available for reaction. This tends to increase the penetration depth (5) for the reaction and make the reaction distribution more uniform. Precipitation also reduces the porosity and, hence, the local effective conductivity of the electrolyte. For this reason, the transfer current in the region of lowest porosity (at the front face of the electrode) is larger at higher utilizations (see Fig. 3, curves b and c). The transfer current near the back of the electrode decreases in response to the concentration dependent term in the Ohm law relationship for the electrolyte.

Figure 4 shows microstructures in the positive electrode at a given depth of discharge for three discharge rates. The volume fraction of LiCl ($\epsilon_{\text{LiCl}} = \epsilon_p^0 - \epsilon_p$) corresponds directly to the cumulative reaction distribution, as dictated by integration of Eq. [5]. Most of the precipitation occurs near the electrode/reservoir interface, in keeping with the transfer current profiles

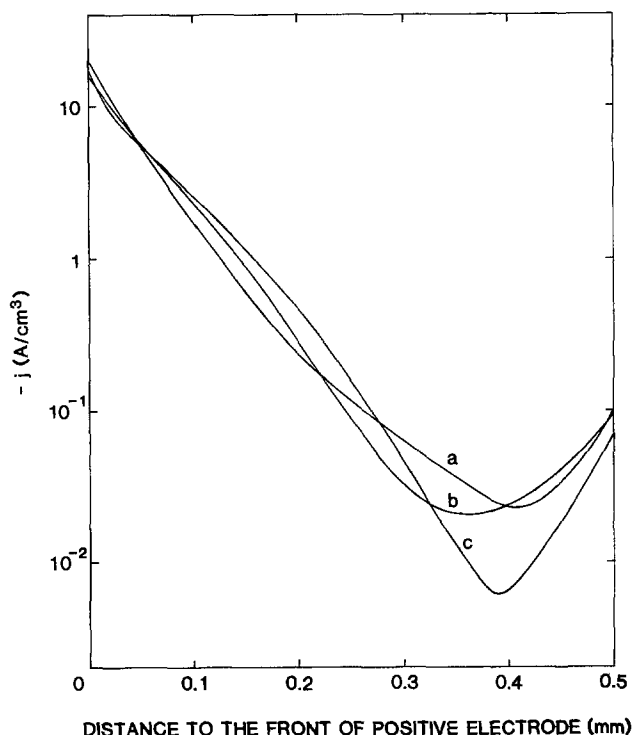


Fig. 3. Reaction distribution in the positive electrode at different utilizations. (a) 0.58%; (b) 3.70%; (c) 9.10%. Simulation parameters as in Fig. 2.

presented in Fig. 3. At higher current densities, the distribution is less uniform, particularly at the front of the electrode. The effect of current density on the porosity at this location is more noticeable at greater depths of discharge.

Figure 5 shows the predicted dependence of total cell voltage on utilization for three discharge rates. The increase in electrolyte conductivity in the separator, which results from a local change in solution concentration (see Fig. 2), overcomes the increase in potential drop associated with growth of the LiCl film and gives a small voltage rise shortly after the beginning of discharge. At higher current densities, the electrolyte concentration in the separator increases more rapidly, and this makes the initial voltage rise more distinct. However, an initial voltage rise is not predicted for cells with $c_e^0 \gtrsim 1.5M$ because changes in electrolyte conductivity are less significant at high concentrations (see Eq. [A-1]). For all three curves, the sharp reduction in cell voltage at the end of discharge is caused by the localized porosity reduction at the front face of the positive electrode. The plugging of porous electrodes has been cited as a possible cause of failure in other cells (7, 12, 28). Before the onset of failure, the cell voltage remains relatively constant. The shape of the voltage curve is steeper and the cell lifetime is shorter at higher current densities because the reaction distribution in the positive electrode is less uniform and, to a lesser extent, because there is less time for diffusional processes to take place. The triangle on the 40 mA/cm² curve indicates the onset of precipitation of sulfur in the cell. This is calculated on the basis of a saturation concentration of 1M, a uniform sulfur distribution, and the stoichiometry of Eq. [I]. In principle, sulfur deposition could reduce the porosity close to the reaction front in the cathode and hence control the cell lifetime. However, experimental evidence (23) indicates that sulfur precipitates in voids away from the LiCl, and does not interfere with discharge significantly. Therefore, formation of solid sulfur has not been included in the present model.

The dependence of cell lifetime on initial porosity in the positive electrode and on galvanostatic discharge rate is summarized in Fig. 6. With a smaller ϵ_p^0 , less space is available to accommodate LiCl crystals and the pores at the cathode face are blocked more readily. In the absence of reaction distribution effects, the lifetime-porosity relationship would be linear (29). The predicted nonlinearity results from the dependence of deposit morphology on ϵ_p^0 (see Eq. [16]).

Figure 7 shows that cell lifetime is expected to increase with electrode thickness, but that the effect is relatively small above a certain value of L_p . Overall, variations are caused by changes in local reaction rates within the electrode. If an electrode is thinner than the penetration depth of approximately 0.3 mm (see Fig. 4), the magnitude of the transfer current is higher locally in order to satisfy the total current density

$$I = \int_0^{L_p} j dy \quad [25]$$

The increase in j is most significant at the front face of the electrode, and the cell fails rapidly by plugging of pores with LiCl at this location. For electrodes thicker than the penetration depth, small but finite transfer currents are predicted behind the reaction front (see Fig. 3). This gradually accounts for a larger proportion of the total current density as thickness is increased and, as the distribution of reaction and LiCl precipitation become more uniform, cell lifetime is extended.

The influence of initial electrolyte concentration on cell lifetime is presented in Fig. 8. As c_e^0 is increased from zero, the electrolyte conductivity becomes larger, the reaction distribution becomes more uniform and,

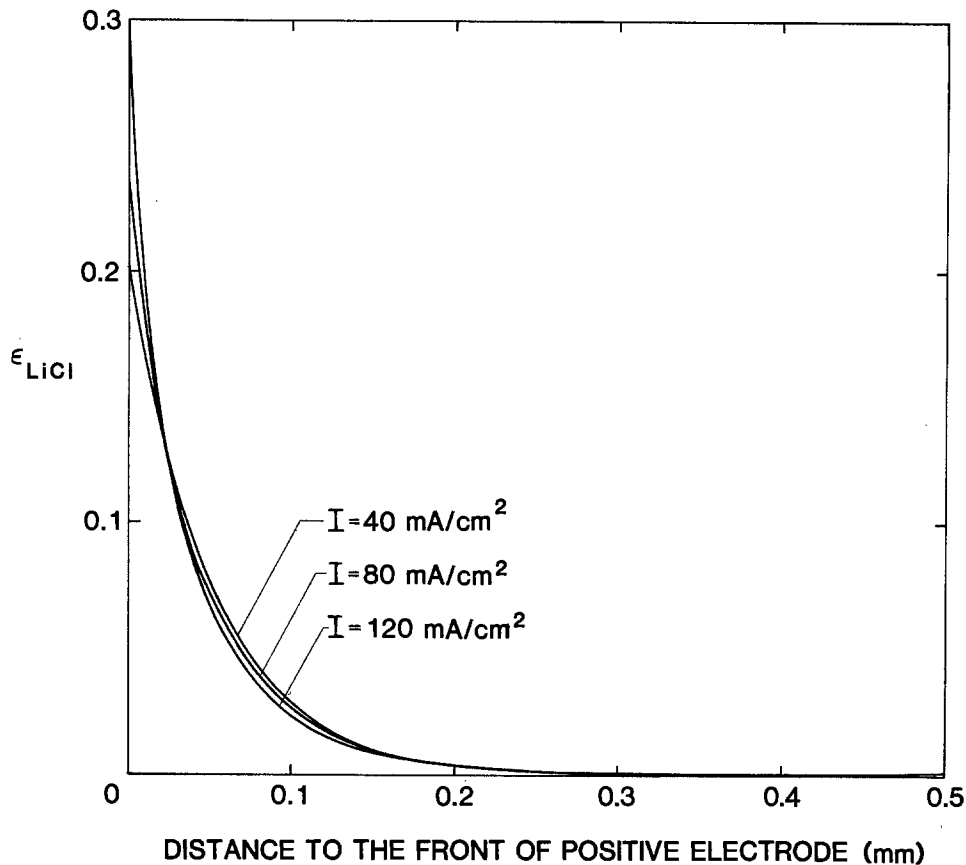


Fig. 4. Distributions of ϵ_{LiCl} in the positive electrode at different discharge rates for a utilization of 3.4%. Parameters as in Fig. 2, except as indicated.

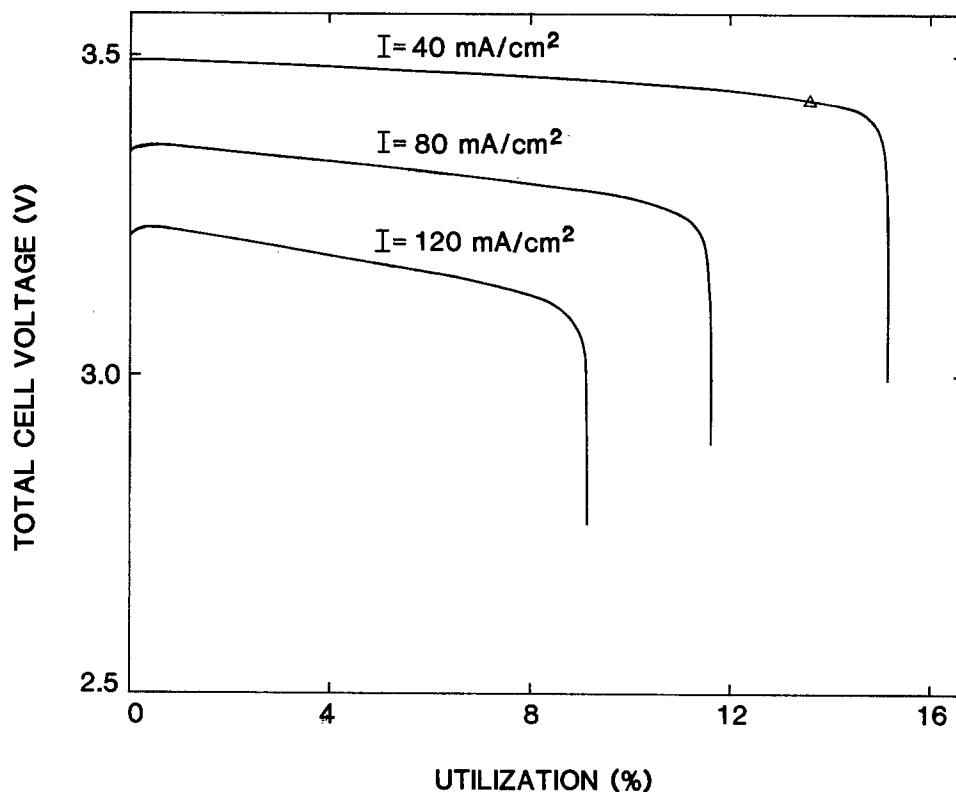


Fig. 5. Theoretical discharge curves at different constant current densities. Parameters as in Fig. 2, except as indicated.

hence, the discharge lasts longer. At higher concentrations, the conductivity approaches a constant value (see Eq. [A-1]), and the concentration dependence of the exchange current density dominates the cell behavior. A higher value of i_0 reduces the penetration depth in the cathode, forces the reaction closer to the front of the electrode, and, in turn, reduces the cell lifetime.

Many of the theoretical results described above are in close agreement with experimental observations. It is difficult to make detailed quantitative comparisons

because published experimental results do not include all the input data required for the model. However, the maximum in cell lifetime at $c_e^0 = 1.5M$ compares favorably with the optimum of $1.6M$ obtained in the laboratory (21). Also, the trends in behavior shown in Fig. 6 and 7 are supported by experimental results (22, 30-32), as are details such as the initial voltage rises in Fig. 5 (21, 30) and the LiCl distributions in Fig. 4 (31). Nevertheless, it is necessary to compare additional factors and to access critically the sensitivity of model predictions to the input data.

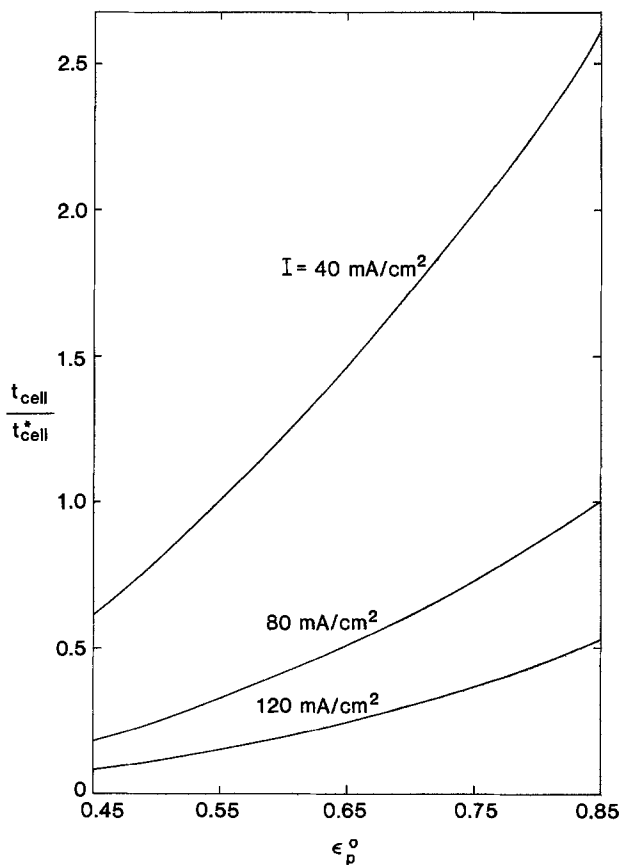


Fig. 6. Dependence of cell lifetime on discharge current density and initial electrode porosity. Simulation parameters as in Fig. 2, except I and ϵ_p^0 . The lifetime of the cell described in Fig. 2 is denoted by t_{cell}^* .

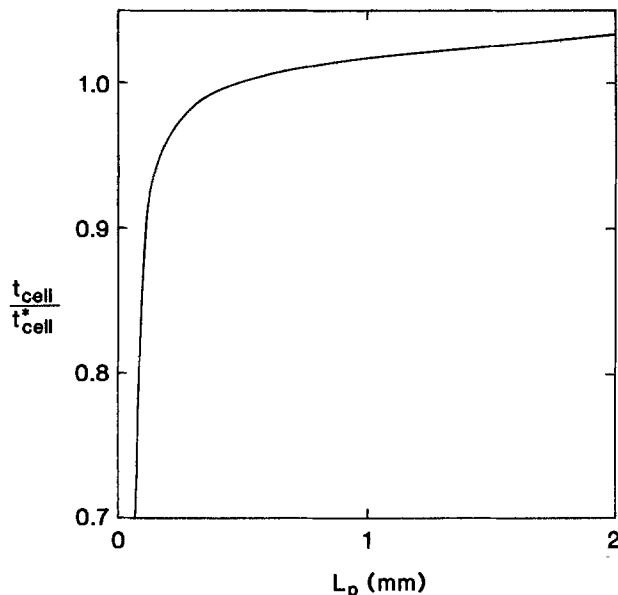


Fig. 7. Dependence of cell lifetime on positive electrode thickness. Simulation parameters as in Fig. 2, except L_p ; t_{cell}^* as defined for Fig. 6.

One difference between theoretical and experimental results is that predicted cell voltages are approximately 500 mV higher than those obtained in actual cells (30). The sensitivity of model predictions to several parameters that could affect cell voltage is discussed below.

1. *Positive electrode matrix conductivity.*—If σ_p is reduced by a factor of 200, the predicted voltage only falls by 170 mV. Also, significant LiCl deposition is

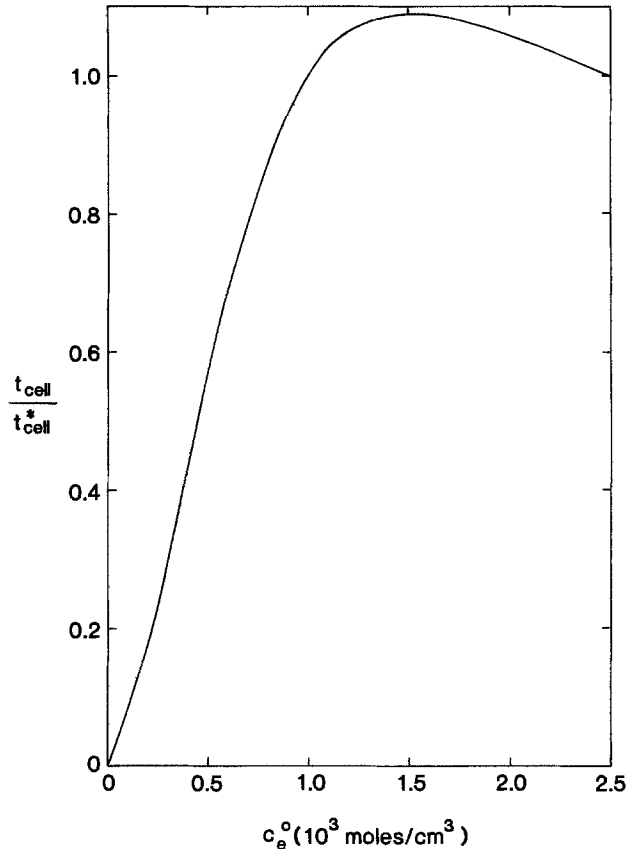


Fig. 8. Dependence of cell lifetime on initial electrolyte concentration. Simulation parameters as in Fig. 2, except c_e^0 ; t_{cell}^* as defined for Fig. 6.

predicted near the current collector, which is contrary to experimental observations (23, 31).

2. *Exchange current density for positive electrode reaction.*—Figure 9 indicates that reducing $a^0 i_{o,ref}$ by two orders of magnitude has a relatively small effect on the total cell voltage but extends the cell lifetime significantly. To reduce the cell voltage to the experimentally observed value of approximately 3V, it would be necessary to use $a^0 i_{o,ref} = O(10^{-6})$ A/cm². With this value, the reaction distribution in the cathode is relatively uniform, and predicted utilizations are considerably greater than those attainable in practice.

3. *Exchange current density for negative electrode reaction.*—With a smaller value of i_o , the potential drop across the Li/LiCl interface is increased and, hence, the cell voltage is lowered. If, for example, i_o is reduced by a factor of 100 to 1.0×10^{-8} A/cm², the cell voltage becomes approximately 3.1V for $I = 80$ mA/cm². In contrast to 1 and 2 above, this change does not introduce other discrepancies with experimental observations.

4. *Conductivity of LiCl film at negative electrode.*—A straightforward reduction of σ_f reduces the cell voltage V , but gives a much larger dependence of V on discharge rate than is actually obtained (30, 31).

Table I. Kinetic parameters used in model

Parameter	Negative electrode		Positive electrode	
	Value	Value	Value	Parameter
$\alpha_a = \alpha_c$	0.5	1.0	1.0	$\alpha_a = \alpha_c$
η	1.0	2.0	2.0	η
s_+	-1.0	-2.0	-2.0	s_+
s_o	0.0	-1.0	-1.0	s_o
γ_{Li^+}	0.0	1.0	1.0	γ_{Li^+}
i_o^0 (A/cm ²)	1.0×10^{-6}	20.0	20.0	$a^0 i_{o,ref}$ (27, 37) (A/cm ²)
$\sigma_{LiCl, III}$	2.0	1.0×10^{-8}	1.0×10^{-8}	$c_{o,ref}$ (mol/cm ³)

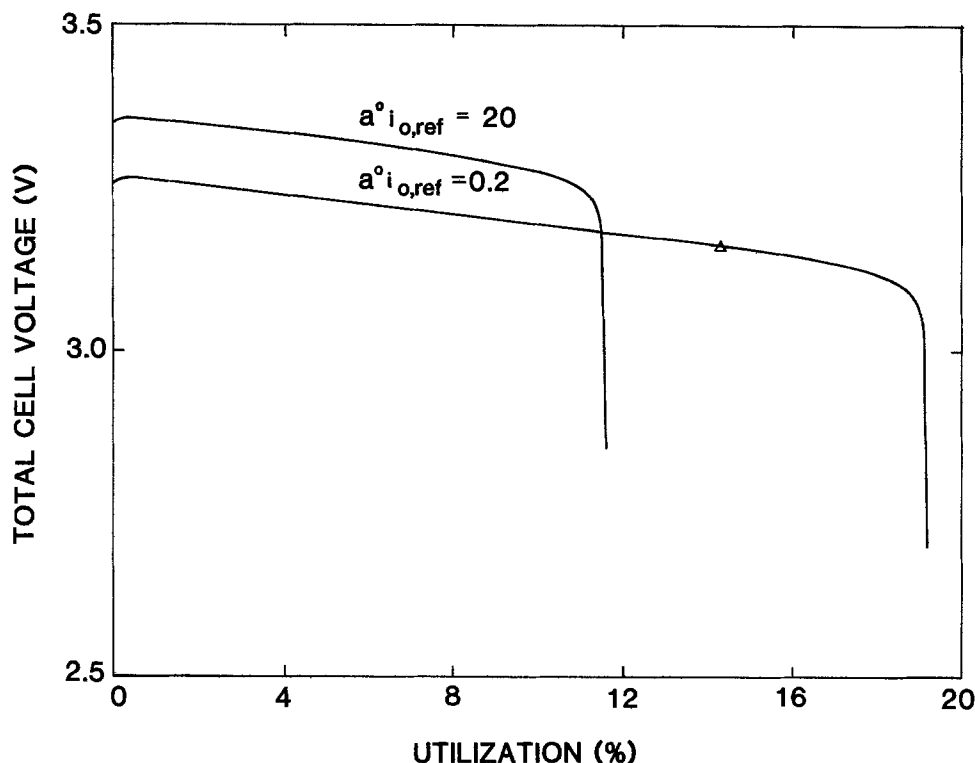


Fig. 9. Dependence of galvanostatic discharge curve on $a^{\circ}i_{o,ref}$. Simulation parameters as in Fig. 2, except $a^{\circ}i_{o,ref}$.

However, this does not exclude LiCl film resistance as an explanation for the voltage discrepancy, because the nature of the film, and hence σ_f , might change with current density (25, 26). This possibility is supported by the dependence of cell coulombic efficiency λ on discharge rate. If a constant value of D_f is used in the simulations, λ is almost independent of current density. It is necessary to assume that D_f depends on I (see Table II) to give coulombic efficiencies that are close to experimental values (21). Theoretical predictions for λ are given in Table III. A large value of σ_f also imparts too great a slope to the discharge curves because the film thickness increases during discharge (see Eq. [18]). However, in practice, disruption of the film could give an effective film resistance that is less dependent on utilization.

These results suggest that factors 3 and 4 are more likely to be responsible for the voltage discrepancy than factors 1 and 2.

With values for the total cell voltage that are too high, the magnitude of the heat-generation rate will be underestimated (see Eq. [19]). Consequently, predicted cell temperatures are expected to be lower than those obtained experimentally. However, it should be noted that overall cell temperature changes depend markedly on experimental conditions: test cells might be operated isothermally, adiabatically, or with well-

defined heat-transfer conditions, and battery modules might include facilities for thermal management.

Temperature changes during discharge can have a significant impact on cell behavior. As the temperature rises, increases in the conductivity and diffusivity of the electrolyte, and a reduction in the driving force term $F\eta/RT$ for the electrochemical reaction, make the reaction distribution more uniform and prolong the cell lifetime. However, an increase in positive electrode exchange current density would tend to offset this change. With the assumption of constant i_o , isothermal and adiabatic runs give the shortest and longest cell lifetimes, respectively. For the 80 mA/cm² discharge in Fig. 5, the model predicts a 14% difference in t_{cell} for these two extreme cases. This is in qualitative agreement with experimental data (30). In both cases, the rate of heat generation by chemical reaction declines during discharge, primarily because the film thickness increases and the SOCl₂ flux through the film is reduced (see Eq. [18]). The magnitude of this effect is illustrated by the changes in coulombic efficiency with depth of discharge, as shown in Table III.

In addition to the cell temperature and the positive electrode exchange current density, several other factors can influence cell lifetime:

1. *Electrode expansion.*—In practice, the plugging of pores at the end of discharge may be delayed by swelling of the positive electrode as a result of LiCl precipitation. If expansion occurs to accommodate the volume made available by consumption of lithium, it is possible that additional LiCl will precipitate before cell failure. For the operating conditions specified in Fig. 2, a 75% increase in LiCl deposition is feasible, provided that it can occupy all the free space generated. The maximum usable cell capacity can be sensitive to the

Table II. Physical parameters used in analysis

Parameter	Value
U_o (1, 30, 38) (V)	3.64
$\partial U_o / \partial T$ (38) (V/K)	1.026×10^{-3}
U_w (V)	0.0
C (J/cm ² · K)	0.2
h_o (39) (W/cm ² · K)	6.0×10^{-4}
p	0.1
$\Delta H_{R, III}$ (40) (J/mol of SOCl ₂ consumed)	-7.2×10^6
$T_A = T_o$ (K)	293.15
\bar{V} (cm ³ /mol)	77.97
\bar{V}_{LiCl} (39) (cm ³ /mol)	20.50
\bar{V}_{SOCl_2} (2) (cm ³ /mol)	72.63
δt° (cm)	4.0×10^{-4}
σ_f (mho/cm)	5.0×10^{-4}
V_R/A (cm)	0.01
f_{-}	0.5
D_f (cm ² /s)	$2.0 \times 10^{-7} \times I^{-1.7}$
f_{+}	1.0

Table III. Dependence of coulombic efficiency (%) on discharge rate and utilization. Simulation parameters as in Fig. 2.

Utilization (%)	I (mA/cm ²)		
	40	80	120
1	89.4	84.3	80.6
5	90.6	86.9	84.4
9	91.5	88.5	86.2

details of the expansion process because (i) increases in free volume for LiCl and in utilization are, in principle, synergistic, and (ii) the matrix conductivity can change locally and alter the cell behavior (see above).

2. *Transfer coefficients for positive electrode reaction.*—If the values of α_a and α_c are changed from 1.0 to 0.5, the reaction distribution becomes more uniform and, to a first approximation, the cell lifetime is doubled.

3. *Polarization equation for positive electrode.*—If the anodic term in Eq. [13] is neglected (on the basis of the irreversibility of reaction [I] (33)), the relationship between j and η_s is modified at small values of η_s . With the relation

$$j = -ai_0 e^{-\alpha_c F \eta_s / RT} \quad [26]$$

the reaction distribution is less uniform and, hence, the maximum cell lifetime is reduced. For the cell in Fig. 5 with $I = 80 \text{ mA/cm}^2$, t_{cell} is reduced by 25%. However, the use of Eq. [26] rather than Eq. [13] does not alter the overall trends in cell behavior significantly.

4. *Cation transference number.*—If a larger value of t_+ is used in the analysis, the concentration and reaction distributions become more uniform, and the cell lifetime increases (see Table IV). Changes in t_{cell} are dictated by a reduction in the magnitude of the concentration dependent term in the Ohm law relationship for the electrolyte rather than by variations in local solution conductivity or exchange current density. Table IV also indicates that composition variations do not control the dependence of usable cell capacity on discharge rate.

5. *Electrolyte diffusion coefficient.*—By analogy with changes in t_+ , an increase in D reduces concentration gradients and increases cell lifetime. With twice the value of D given in the Appendix, the model predicts an 8% increase in maximum utilization at 80 mA/cm^2 .

6. *Temperature dependence of cell potential.*—Recent experimental results (34) indicate that a negative value for $\partial U_o / \partial T$ (cf. Table II) may be more appropriate. In this case, the rate of heat generation within the cell will be higher. For nonisothermal systems, this will lead to an increase in t_{cell} (see above).

7. *Reservoir volume.*—An increase in V_R^0/A attenuates the composition changes at the front of the positive electrode. With $c_e^0 \approx 1.5M$, this reduces the electrolyte conductivity and, in turn, the cell lifetime. The effect is relatively small: a tenfold increase in V_R^0/A is needed to reduce the lifetime by 9% at 80 mA/cm^2 .

8. *Morphology parameter, p .*—The extent to which LiCl crystals reduce the surface area available for further reaction can have a profound effect on the discharge characteristics. If the value of p is increased from 0.1 to 0.3 and 0.5, the cell lifetime declines by 28% and 38%, respectively. This is a direct result of an increase in local values for ai_0 during discharge and, correspondingly, a less uniform cumulative reaction distribution.

Equation [16] assumes implicitly that some surface area remains active until the local porosity reaches zero. If the deposit morphology causes passivation before plugging occurs, the reaction would be able to

Table IV. Dependence of dimensionless cell lifetime ($t_{\text{cell}}/t_{\text{cell}}^*$) on discharge current density and cation transference number. Simulation parameters as in Fig. 2.

I (mA/cm ²)	t_+		
	0.5	0.75	1.0
80	1.00	1.12	1.21
120	0.53	0.61	0.66

penetrate further into the cathode and the discharge time would be extended. As with electrode swelling, this change would make the decline in cell voltage near t_{max} less sharp. Longer cell lifetimes may also be predicted if a significant quantity of LiCl can dissolve into the electrolyte and diffuse away from the reaction zone to favorable sites for precipitation.

The sensitivity of t_{cell} to the parameter p suggests that the effectiveness of additives (35, 36) on increasing cell lifetime could be associated with changes in the deposit morphology. However, it is necessary to isolate the influence of additives on each of the possible effects described above to help clarify their impact on the cell performance.

Conclusions

A mathematical model has been developed that can describe the time-dependent and position-dependent behavior of a complete Li-LiAlCl₄/SOCl₂-C static cell with neutral electrolyte. Composition and reaction distributions can be predicted, as well as variations in volume fractions of individual phases and electric potential across the cell. The results of the theoretical analysis show the general trends in discharge behavior that are observed experimentally. The model predicts that high internal resistance can develop in the positive electrode as a result of low local porosities which are, in turn, caused by large-volume, solid reaction products. Consequently, the maximum usable cell capacity can be dictated by the nonuniformity of the reaction distribution at the front of the positive electrode. Variations in cell design or operation that alleviate local plugging of pores should be able to prolong cell lifetime. The model also indicates an optimum initial electrolyte concentration of approximately 1.5M and a range of acceptable positive-electrode thicknesses.

Acknowledgments

This work was funded by the Naval Sea Systems Command (NAVSEA code 63R32) and constitutes a fraction of a major program to establish a technology base for high rate lithium, thionyl chloride batteries. We wish to thank Mr. Frank Romano for his continued interest.

Manuscript submitted April 22, 1983; revised manuscript received ca. Sept. 16, 1983.

APPENDIX

Physical properties of the Li-LiAlCl₄/SOCl₂-C system

Electrolyte conductivity.—The dependence of bulk electrolyte conductivity on composition and temperature is described by

$$\kappa_e = \begin{cases} ac_e e^{-E/T} & c_e \leq 1M \\ b(1 - e^{-dc_e + f}) e^{-E/T} & 1M < c_e < 1.73M \\ be^{-E/T} & c_e \geq 1.73M \end{cases} \quad [A-1]$$

where $a = 48.97$, $b = 6.843 \times 10^{-2}$, $d = 4032.0$, $f = 2.9$, and $E = 361.0 \text{ K}$ (1, 41). The effective conductivity in the porous media is estimated from

$$\kappa = \epsilon \kappa_e / \zeta^2 \quad [A-2]$$

where the tortuosity factor ζ^2 is directly related to porosity by

$$\zeta = e^{(1-q)/2} \quad [A-3]$$

and the constant q is taken as 1.5 (42).

Diffusion coefficient.—The diffusion coefficient is assumed to be independent of electrolyte concentration, and to have the same dependence on temperature as electrolyte conductivity

$$D_e = 3.35 \times 10^{-5} e^{-361/T} \quad [A-4]$$

The molecular diffusion coefficient in the porous media can be characterized by

$$D = D_0/\zeta^2 \quad [\text{A-5}]$$

together with Eq. [A-3].

Matrix conductivity.—In general, the matrix conductivity can be influenced by the volume fraction of the conducting phases, the inherent conductivity of each solid phase, and the manner in which the particles of conducting phases are interconnected. However, in the present model, the matrix conductivity is assumed to be unaffected by precipitation of LiCl, and is expressed as

$$\sigma_p = \sigma_{p,0}(1 - \epsilon_p^0)^q \quad [\text{A-6}]$$

where (27) $\sigma_{p,0} = 45.5$ mho/cm and $q = 1.5$.

LIST OF SYMBOLS

a	interfacial area per unit electrode volume (cm^{-1})
a_k	relative activity of solid species k
$a^{\theta+}$	property expressing secondary reference state (cm^3/mol)
A	cross-sectional area of electrode (cm^2)
c_e	$= c_+/\nu_+ = c_-/\nu_-$ molar concentration of electrolyte (mol/cm^3)
c_i	concentration of species i (mol/cm^3)
C	cell heat capacity ($\text{J}/\text{cm}^2 \cdot \text{K}$)
D	diffusion coefficient (cm^2/s)
D_f	effective diffusivity of SOCl_2 in LiCl film (cm^2/s)
f_{+-}	mean molar activity coefficient of electrolyte
F	Faraday's constant (96,487 C/eq)
h	mesh size (cm)
h_0	heat transfer coefficient ($\text{W}/\text{cm}^2 \cdot \text{K}$)
ΔH_R	heat of reaction for the reaction defined by Eq. [III] (J/mol of SOCl_2 consumed)
i_0	exchange current density for positive electrode reaction (A/cm^2)
i_0'	exchange current density for negative electrode reaction (A/cm^2)
i_1	superficial current density in matrix phase (A/cm^2)
i_2	superficial current density in pore phase (A/cm^2)
I	superficial current density to an electrode (A/cm^2)
j	$= \nabla \cdot i_2$, transfer current per unit electrode volume (A/cm^3)
j_{in}	pore wall flux of species i ($\text{mol}/\text{cm}^2 \cdot \text{s}$)
L	electrode thickness (cm)
M_i	symbol for the chemical formula of species i
n	number of electrons transferred in electrode reaction
N_i	superficial flux of species i ($\text{mol}/\text{cm}^2 \cdot \text{s}$)
p	morphology parameter defined by Eq. [16]
Q	cell capacity (based on moles of SOCl_2) (C/cm^2)
r_{III}	reaction rate of chemical reaction (mol of SOCl_2 consumed/ $\text{cm}^2 \cdot \text{s}$)
R	universal gas constant ($8.3143 \text{ J}/\text{mol} \cdot \text{K}$)
s_i	stoichiometric coefficient of species i in electrode reaction
t	time (s)
t_{cell}	cell lifetime (s)
t_{cell}^*	lifetime of the cell described in Fig. 2 (s)
t_i^{\square}	transference number of species i with respect to the volume average velocity
T	absolute temperature (K)
T_A	temperature of surroundings (K)
T_0	initial temperature (K)
U_w	theoretical open-circuit potential for the reaction at the composition prevailing locally at the electrode surface, relative to a reference electrode of a given kind (V)
U^{θ}	standard electrode potential for reaction (V)
U_0	open-circuit cell potential (V)
\bar{v}^{\square}	volume average velocity (cm/s)
\bar{V}	total cell voltage (V)
\tilde{V}	molar volume (cm^3/mol)
\tilde{V}_i	partial molar volume of species i (cm^3/mol)
V_R	reservoir volume (cm^3)
z_i	valence or charge number of species i

Greek Letters

α_a	transfer coefficient in anodic direction
α_c	transfer coefficient in cathodic direction
γ_i, γ_k	exponents in Eq. [14]

δ_f	LiCl film thickness (cm)
ϵ	porosity or void volume fraction
ϵ_{LiCl}	volume fraction of LiCl
ζ	tortuosity defined by Eq. [A-3]
η	$\Phi_1 - \Phi_2$
κ	effective solution conductivity (mho/cm)
λ	coulombic efficiency
μ_e	chemical potential of electrolyte (J/mol)
ν	$= \nu_+ + \nu_-$, number of mols of ions into which a mol of electrolyte dissociates
ν_+, ν_-	number of cations and anions into which a molecule of electrolyte dissociates
ρ_0	density of pure solvent (g/cm^3)
σ	effective matrix conductivity (mho/cm)
Φ_1	electric potential in the matrix (V)
Φ_2	electric potential in the solution (V)

Subscripts

a	Li electrode/LiCl film interface
b	LiCl film/separator interface
e	electrolyte
f	LiCl film
o	solvent
p	positive electrode
re	reference electrode
ref	reference condition
s	separator
w	at the electrode surface
$+$	cation
$-$	anion
III	reaction (III)
∞	bulk property

Superscript

o	initial value
-----	---------------

REFERENCES

- J. J. Auborn, K. W. French, S. I. Lieberman, V. K. Shah, and A. Heller, *This Journal*, **120**, 1613 (1973).
- W. K. Behl, J. A. Christopoulos, M. Ramirez, and S. Gilman, *ibid.*, **120**, 1619 (1973).
- K. A. Klinedinst, *ibid.*, **128**, 2507 (1981).
- A. N. Dey and N. Hamilton, *J. Appl. Electrochem.*, **12**, 33 (1982).
- J. Newman and W. Tiedemann, *AICHE J.*, **21**, 25 (1975).
- J. S. Dunning, Dissertation, University of California, Los Angeles, CA (1971).
- W. G. Sunu, Dissertation, University of California, Los Angeles, CA (1978).
- K. Micka and I. Rousar, *Electrochim. Acta*, **18**, 629 (1973); *ibid.*, **19**, 499 (1974).
- D. Simonsson, *J. Appl. Electrochem.*, **3**, 261 (1973).
- W. Tiedemann and J. Newman, in "Battery Design and Optimization," S. Gross, Editor, p. 23, The Electrochemical Society Softbound Proceedings Series, Princeton, NJ (1979).
- W. Tiedemann and J. Newman, *ibid.*, p. 39.
- R. Pollard and J. Newman, *This Journal*, **128**, 491 (1981).
- R. Pollard and J. Newman, *ibid.*, **128**, 503 (1981).
- J. Newman and C. W. Tobias, *ibid.*, **109**, 1183 (1962).
- J. Newman and T. W. Chapman, *ibid.*, **19**, 343 (1973).
- J. Newman, "Electrochemical Systems," Prentice-Hall, Englewood Cliffs, NJ (1973).
- R. Pollard, Dissertation, University of California, Berkeley, CA (1979).
- R. White, Dissertation, University of California, Berkeley, CA (1977).
- J. C. Bailey and J. P. Kohut, in "Power Sources 8," J. Thompson, Editor, p. 17, 12th International Power Sources Symposium, Brighton, England (1980).
- J. R. Driscoll, G. L. Holleck, and D. E. Toland, in "Proceedings of the 27th Power Sources Symposium," Atlantic City, NJ, June 21-24, 1976, p. 28.
- J. R. Driscoll, Personal communication.
- J. S. Dunning, D. N. Bennion, and J. Newman, *This Journal*, **120**, 906 (1973).
- S. Szpak and J. R. Driscoll, *J. Power Sources*, To be published.
- A. N. Dey, *Electrochim. Acta*, **21**, 377 (1976).

25. E. Peled, *J. Power Sources*, **9**, 253 (1983).
26. R. V. Moshtev, Y. Geronov, and B. Puresheva, *This Journal*, **128**, 1851 (1981).
27. A. N. Dey, *ibid.*, **126**, 2052 (1979).
28. D. Gidaspow and B. S. Baker, *ibid.*, **120**, 1005 (1973).
29. N. Marincic, *J. Appl. Electrochem.*, **5**, 313 (1975).
30. K. A. Klinedinst and M. J. Domeniconi, *This Journal*, **127**, 539 (1980).
31. A. N. Dey, *Thin Solid Films*, **43**, 131 (1977).
32. A. N. Dey, *This Journal*, **123**, 1262 (1976).
33. W. K. Behl, in "Proceedings of the 27th Power Sources Symposium," Atlantic City, NJ, June 21-24, 1976, p. 30.
34. N. A. Godshall and J. R. Driscoll, Paper 40 presented at The Electrochemical Society Meeting, Washington, DC, Oct. 9-14, 1983.
35. H. V. Venkatesetty, U.S. Pat. 4,279,973 (1981).
36. L. R. Giattino, U.S. Pat. 4,167,608 (1979).
37. M. J. Madou and S. Szpak, Submitted to *This Journal*.
38. C. R. Schlaikjer, F. Goebel, and N. Marincic, *This Journal*, **126**, 513 (1979).
39. R. H. Perry and C. H. Chilton, "Chemical Engineers' Handbook," 5th ed., McGraw-Hill, New York (1973).
40. R. C. Weast, "CRC Handbook of Chemistry and Physics," 58th ed., CRC Press, Cleveland, Ohio (1978).
41. NOSC Tech. Note 1083, S. J. Szpak, Ed., (Nov. 1981).
42. R. E. Meredith and C. W. Tobias, *Adv. Electrochem. Electrochem. Eng.*, **2**, 15 (1962).

Mathematical Modeling of the Lithium, Thionyl Chloride Static Cell

II. Acid Electrolyte

Keh-Chang Tsaur* and Richard Pollard**

Department of Chemical Engineering, University of Houston, Houston, Texas 77004

ABSTRACT

A mathematical model for a complete Li/SOCl₂ static cell with acid electrolyte is presented. Concentrated solution theory is extended to account for the presence of two neutral species in the electrolyte. The effects of initial acid concentration, positive electrode thickness, and galvanostatic discharge rate on cell performance are elucidated. Results are compared with equivalent cells that use a neutral electrolyte.

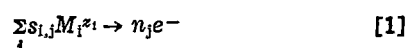
The discharge capacity of a Li/SOCl₂ reserve cell can be increased by addition of excess AlCl₃ to the electrolyte (1). A mathematical model is needed to explain the effects of the acid on cell behavior and to assess the influence of changes in design parameters on the system performance. For this analysis, it is necessary to extend concentrated solution theory to account for the presence of AlCl₃ in the electrolyte.

The multicomponent diffusion equation has been used to describe the effects of convection, diffusion, and migration in concentrated solutions with two or more electroactive constituents (2-4), and in mixtures of two binary molten salts with a common ion (5). In this paper, a consistent set of transport equations is presented for a binary electrolyte in two neutral solvents. The equations are used in conjunction with the macroscopic theory of porous electrodes (6) to describe the behavior of the Li-LiAlCl₄, AlCl₃/SOCl₂-C primary cell. System limitations are identified and results are compared with cells that use a neutral electrolyte (7). The cell configuration that is analyzed is shown in Fig. 1 of Ref. (7).

Model Development

The material balance equation, the relationship for the superficial current density in the pore solution, and Ohm's law for the solid phases are the same as in the neutral electrolyte model (7). However, many of the other governing equations need to be modified to include simultaneous electrochemical and chemical reactions and the details of the transport phenomena in the acid electrolyte.

For simultaneous reactions of the form



Faraday's law can be expressed as

$$a_{j,in} = - \sum_j \frac{s_{i,j}}{n_j F} a_{i,nj} + s_{i,0} R_0 \quad [2]$$

provided that double-layer charging can be ignored. The last term on the right side of Eq. [2] represents the production of species *i* by a chemical reaction with stoichiometric coefficient *s*_{*i,0*} and reaction rate *R*₀. The transfer current per unit electrode volume $\nabla \cdot i_2$ is related to the average transfer current density for each reaction by

$$\nabla \cdot i_2 = \sum_j (a_{i,n})_j \quad [3]$$

A material balance on the solid phases indicates how electrode porosity changes as a result of chemical and electrochemical reactions at each location within the electrode

$$\frac{\partial \epsilon}{\partial t} = \sum_{\text{solid phases}} \left(\sum_j \frac{s_{i,j} \tilde{V}_1}{n_j F} (a_{i,n})_j - s_{i,0} \tilde{V}_1 R_0 \right) \quad [4]$$

The complicated acid electrolyte (1) is regarded as a concentrated mixture of Li⁺ ions and AlCl₄⁻ ions in AlCl₃ and SOCl₂ (species 1, 2, 3, and 4, respectively). Inversion of the multicomponent diffusion equations yields explicit relationships for the fluxes

$$\begin{aligned} N_1 &= -\epsilon v_1 D_1 \nabla c_e - \epsilon v_1 D_3 \nabla c_3 + \frac{t_1 \square i_2}{z_1 F} + c_1 \underline{v} \square \\ N_2 &= -\epsilon v_2 D_1 \nabla c_e - \epsilon v_2 D_3 \nabla c_3 + \frac{t_2 \square i_2}{z_2 F} + c_2 \underline{v} \square \\ N_3 &= -\epsilon D_2 \nabla c_e - \epsilon D_4 \nabla c_3 + \frac{t_3 \square i_2}{F} + c_3 \underline{v} \square \\ N_4 &= -\epsilon D_5 \nabla c_e - \epsilon D_6 \nabla c_3 + \frac{t_4 \square i_2}{F} + c_4 \underline{v} \square \end{aligned} \quad [5]$$

* Electrochemical Society Student Member.

** Electrochemical Society Active Member.

Key words: porous electrodes, cell performance, galvanostatic discharge.

where the diffusion coefficients and the transference numbers are related to binary interaction parameters, as shown in the Appendix. The six independent transport properties for this system are chosen to be D_1 , D_2 , D_3 , t_1^\square , t_3^\square , and the electrolyte conductivity κ . If D_2 and D_3 are taken to be zero (see Appendix), substitution of the fluxes in Eq. [5] into the material balance relation (Eq. [1] of Ref. (7)) yields

$$\frac{\partial e}{\partial t} + \nabla \cdot \mathbf{y}^\square = a \left[\frac{t_2^\square \bar{V}_e}{\nu_1} j_{1n} + \frac{t_1^\square \bar{V}_e}{\nu_2} j_{2n} + \bar{V}_3 j_{3n} + \bar{V}_4 j_{4n} \right] - \bar{V}_e \frac{i_2 \cdot \nabla t_1^\square}{\nu_1 z_1 F} - \epsilon D_1 \nabla c_e \cdot \nabla \bar{V}_e - \epsilon D_5 \nabla c_e \cdot \nabla \bar{V}_4 - \epsilon D_4 \nabla c_3 \cdot \nabla \bar{V}_3 - \epsilon D_6 \nabla c_3 \cdot \nabla \bar{V}_4 \quad [6]$$

The dependence of solution potential on the current density i_2 can be derived by inversion of the multi-component diffusion equations (5). For the LiAlCl_4 , AlCl_3 electrolyte, one obtains

$$\frac{i_2}{\kappa} = -\nabla \Phi_2 - \frac{1}{F} \left(\frac{t_1^\square}{z_1 \nu_1} + \frac{s_1}{n \nu_1} - \frac{s_4 c_e}{n c_4} \right) \nabla \mu_e - \frac{1}{F} \left(t_3^\square + \frac{s_3}{n} - \frac{s_4 c_3}{n c_4} \right) \nabla \mu_3 \quad [7]$$

where Φ_2 is measured with a reference electrode that has stoichiometric coefficients s_1 and number n of electrons transferred. The composition dependent terms on the right side of Eq. [7] include the diffusion potentials of the electrolyte and the acid. The chemical potentials μ_e and μ_3 are defined in Eq. [A-5] and [A-6], respectively.

The Butler-Volmer equation is used to represent the dependence of the local current density due to reaction j on the surface overpotential $\eta_{sj} = \eta - U_{j,w}$

$$a i_{nj} = a i_{oj} [e^{\alpha_{sj} F \eta_{sj} / RT} - e^{-\alpha_{sj} F \eta_{sj} / RT}] \quad [8]$$

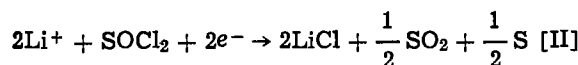
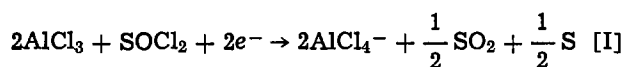
where the exchange current density i_{oj} can be written as

$$i_{oj} = i_{oj,ref} \pi \left(\frac{c_{i,w}}{c_{i,ref}} \right)^{\gamma_i} \quad [9]$$

and the theoretical open-circuit cell potential for reaction j is given by (8)

$$U_{j,w} = U_j^\theta - U_{re}^\theta + \frac{RT}{n_{re} F} \sum_i s_{i,re} \ln \left(\frac{c_{i,re}}{\rho_o} \right) - \frac{RT}{n_j F} \sum_i s_{i,j} \ln \left(\frac{c_{i,w}}{\rho_o} \right) \quad [10]$$

The discharge processes in the positive electrode are represented by two simultaneous reactions (1)



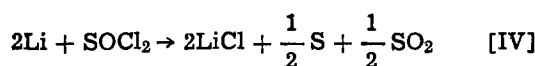
Equation [8] is used to describe the rate of each reaction, and changes in the active surface area of the carbon matrix are predicted with (7)

$$a = a^0 [1 - (\epsilon_{\text{LiCl}}/\epsilon_p^0)^p] \quad [11]$$

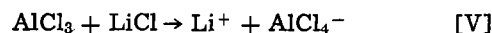
At the negative electrode, the overall discharge reaction is



and the LiCl film formation reaction is (9)



The SOCl_2 flux through the LiCl film to the Li surface is related to the rate of chemical reaction [IV] by Eq. [17] of Ref. (7). In addition, the LiCl at both electrodes can be dissolved chemically by the acid in accordance with



The dissolution rate at the negative electrode is assumed to be proportional to the acid concentration at the LiCl/separator interface

$$r_v = k_1 (c_a)_b \quad [12]$$

It is assumed that dissolution depends on the local acid concentration, the volume fraction of LiCl crystals, and the morphology parameter p

$$R_o = k_2 c_a (\epsilon_{\text{LiCl}})^p \quad [13]$$

The thickness of the protective film on the lithium surface can be altered by reactions [IV] and [V]. If the film porosity is constant, a mass balance gives

$$\frac{d\delta_f}{dt} = (s_{\text{LiCl,IV}} r_{\text{IV}} + s_{\text{LiCl,O}} r_v) \bar{V}_{\text{LiCl}} \quad [14]$$

The heat-balance equation is modified to account for simultaneous chemical and electrochemical reactions

$$C \frac{dT}{dt} = \sum_j \left[\left(U_{oj} - T_o \frac{\partial U_{oj}}{\partial T} \right) \int_0^{L_p} \frac{(-a i_{nj})}{I} dy - V \right] I - h_o (T - T_A) + (\Delta H_{R,\text{IV}}) r_{\text{IV}} + (\Delta H_{R,\text{V}}) \left(r_v + \int_0^{L_p} R_o dy \right) \quad [15]$$

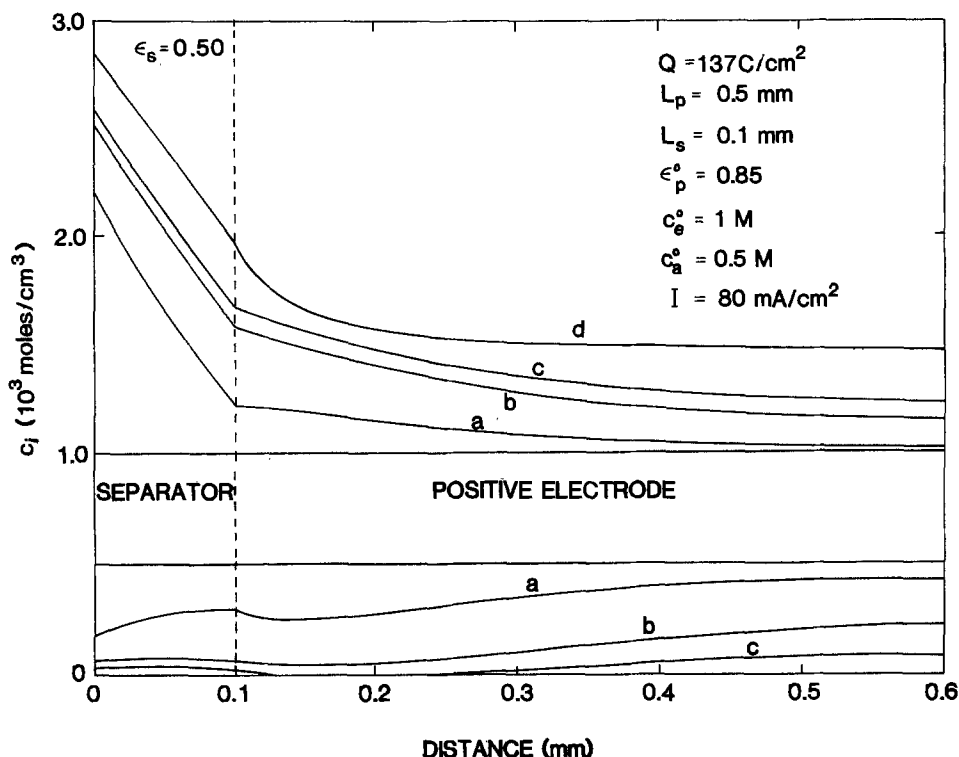
The Li-LiAlCl₄, AlCl₃/SOCl₂-C system can be described by the local variables c_e , c_a , \mathbf{v}^\square , ϵ , $a i_{n\text{I}}$, $a i_{n\text{II}}$, i_2 , and η , and by the governing Eq. [3], [4], [6], [7], and [8], together with material balances for acid and electrolyte. The initial conditions and the boundary conditions for these equations have been presented previously (7). These relationships constitute a set of coupled, ordinary, nonlinear differential equations at each time step which are cast into finite difference form accurate to $O(h^2)$, and solved simultaneously by a numerical technique (10).

Results and Discussion

Composition profiles for acid and electrolyte and the corresponding reaction distributions in the positive electrode are shown in Fig. 1 and 2, respectively, at several times during galvanostatic discharge of a typical cell sandwich. The open-circuit potential for reaction [I] is significantly larger than the one for reaction [II] (see Table I), and, therefore, reaction [I] prevails early in the discharge. This lowers the overall level of acid in the cell and raises the electrolyte concentration above its original value. The positive slopes for the acid concentration curves at the negative electrode/separator interface result from chemical dissolution of the LiCl film at the anode. The discontinuities in concentration gradients at the front of the positive electrode reflect the presence of the reservoir at this location and the porosity difference between the separator and the cathode. The production of electrolyte by reaction [I] makes this effect more noticeable than in cells with neutral electrolyte.

The initial current density distribution for electrochemical reduction of acid (see curve a, Fig. 2) represents a balance between the low κ/σ ratio, which makes the reaction rate highest at the cathode face, and $a^0 i_{o,ref}$, which is low enough to allow the reaction to penetrate into the electrode. As discharge proceeds, the current density at the front of the positive electrode is maintained by diffusion of acid from the reservoir and sepa-

Fig. 1. Position dependence of composition at different utilizations. Utilization is calculated on the basis of moles of SOCl_2 available: (a) 0.60%; (b) 1.49%; (c) 1.79%; (d) 11.36%. The lower curves represent acid concentration profiles, the upper curves electrolyte concentration profiles. Simulation parameters are presented in Table I, and in Fig. 2 of Ref. (7).



rator and by an increase in the driving force for electrochemical reaction. However, the electrolyte becomes depleted in acid directly behind this region, and the transfer current tends to zero locally (see curves c).

After approximately 31s, the potential difference, $\Phi_1 - \Phi_2$, becomes large enough to initiate the neutral reaction as a sharp front at the electrode/reservoir interface. Once the neutral reaction has begun, it dominates the cell behavior. Reaction [I] continues at the back of the electrode, but the acid concentration

is very low and only a small fraction of the current is transferred in this way. Also, acid that remains in the separator continues to diffuse into the cathode and react, but the effect is negligible for the discharge conditions specified in Fig. 1 and 2. The neutral reaction distributions are not influenced significantly by the cell history or the acid reaction, and they correspond closely to those predicted for cells with neutral electrolyte (7).

The independent nature of the two electrochemical reactions in the cathode is also illustrated by the total cell-voltage characteristics shown in Fig. 3. For each discharge curve, the higher voltage region is associated with the acid reaction, and the lower voltage plateau is representative of the neutral reaction. The cell behavior on the lower plateau is very similar to that for the neutral electrolyte system (7), and the cell fails by plugging of pores with LiCl at the front face of the cathode. The major contribution of the acid reaction is to delay the onset of LiCl formation in the positive electrode and, therefore, to extend the cell lifetime. The shape of the theoretical discharge curves agrees closely with experimental results for comparable cells (1, 11). Reasons for discrepancies in the exact values of the voltages have been discussed in detail previ-

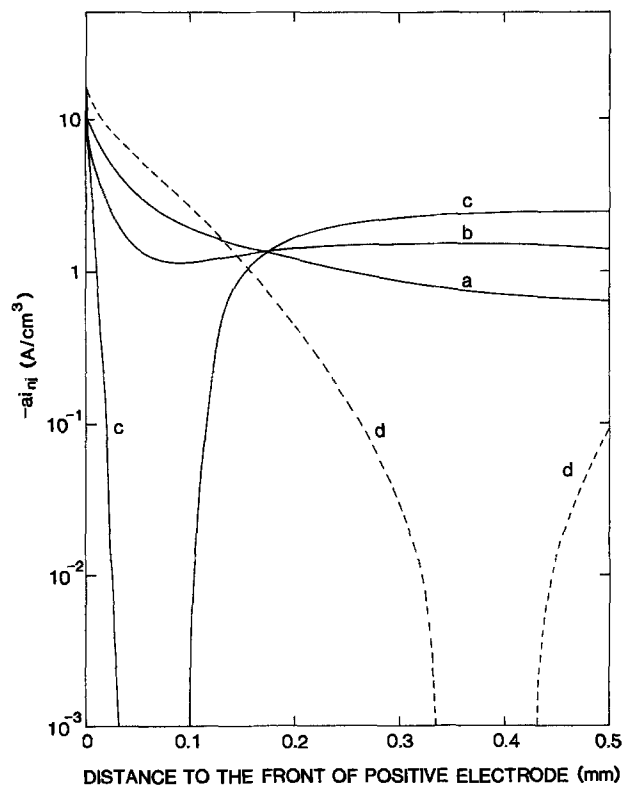


Fig. 2. Reaction distributions in the positive electrode at different utilizations: (a) 0.60%; (b) 1.49%; (c) 1.79%; (d) 11.36%. Simulation parameters as in Fig. 1. —: acid reaction (a_{iII}). - - -: neutral reaction (a_{iIII}).

Table I. Simulation parameters used in analysis

Parameter	Value
$U_{r1}^0 - U_{r2}^0$ (1, 13) [V]	0.31
$U_{r1}^0 - U_{r2}^0$ (1, 13, 14) [V]	0.0
U_{0I} (1, 13) [V]	3.95
$\partial U_{0I} / \partial T$ (V/K)	1.026×10^{-8}
\tilde{V}_{AlO_2} [15] (cm^3/mol)	54.65
k_1 (cm/s)	4.0×10^{-4}
k_2 (s^{-1})	1.0×10^{-2}
$c_{a, \text{ref}}$ (mol/cm^3)	1.0×10^{-8}
$\alpha_{aI} = \alpha_{eI}$	1.0
η_{I1}	2.0
S_{B1I}	2.0
S_{B2I}	-2.0
S_{A1I}	-1.0
$S_{L1O1,IV}$	2.0
$S_{L1O1,0}$	-1.0
$\alpha_{0I, \text{ref}}$	0.2
f_s	1.0
k_{∞} (1, 13, 16) (mho/cm)	$9.1 \text{ CAICl}_3 e^{-301/T}$
$\Delta H_{n,v}$ (J/mol of LiCl dissolved)	-6.0×10^4
$D_2 = D_a$	0.0
t_{2III}	0.0

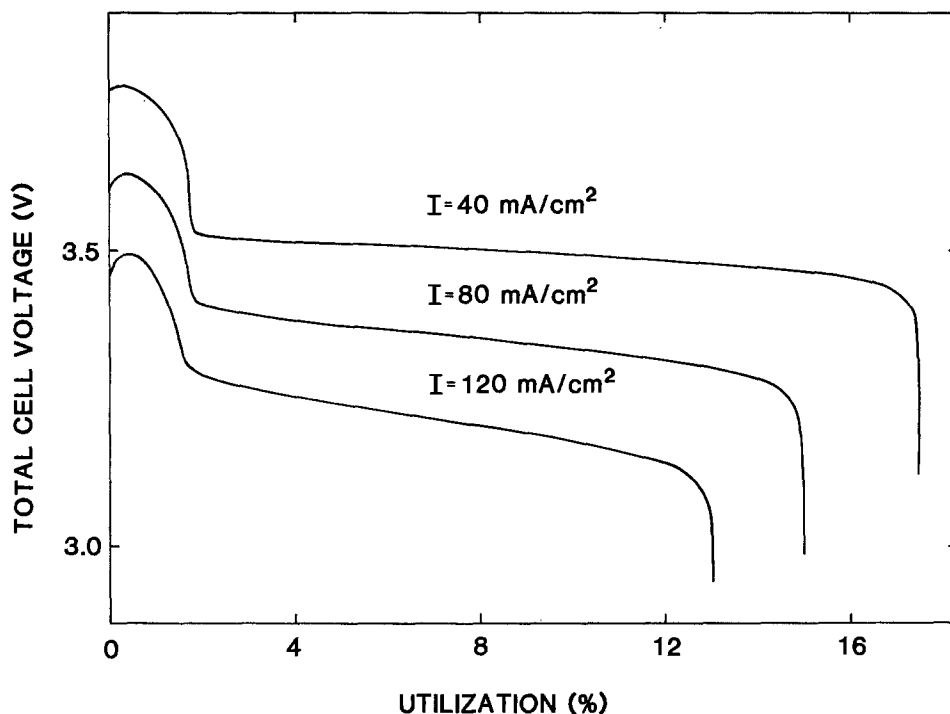


Fig. 3. Theoretical discharge curves at different constant current densities. Simulation parameters as in Fig. 1, except as indicated.

ously (7). These differences do not alter the physical interpretation of the cell behavior described below.

The small voltage rise shortly after the beginning of discharge is caused by an increase in electrolyte conductivity in the separator as the local electrolyte concentration changes. The rises are slightly more pronounced than those predicted for comparable neutral cells because, initially, chemical dissolution of LiCl at the negative electrode is faster than the film formation reaction [IV], so that the thickness and the resistance of the LiCl film decreases.

The acid portion of each curve declines from a maximum voltage as acid is consumed at the front of the positive electrode and the surface overpotential becomes more negative (see Eq. [8]). The width of the acid region of the voltage-utilization curve depends primarily on the quantity of acid available for reaction near the cathode/reservoir interface, but it is also affected by the discharge rate. At higher current densities, there is less time for the chemical reaction to take place at the anode, and, consequently, a greater proportion of the original acid can react electrochemically in the positive electrode. However, higher values of I also necessitate higher surface overpotentials, and the cell voltage is lower. This can allow the neutral reaction, and hence the lower plateau, to begin at a smaller utilization (see Fig. 3). Subsequently, the acid and neutral reactions can occur simultaneously in the positive electrode for a longer period of time, but this does not alter the voltage of the lower plateau significantly.

Other factors also influence the shape of the acid region of a discharge curve. Reductions in the values of the kinetic parameters (α_{ol}^0 , α_{al} , α_{cl}) are analogous to an increase in I : the driving force needed to transfer current is larger, and this leads to a smaller voltage maximum and to earlier initiation of reaction [II]. An increase in the initial acid concentration gives a higher electrolyte resistance at $t = 0$, but the voltage rises quickly due to rapid dissolution of LiCl at the anode (see Eq. [12]). This reduces the resistance across the negative electrode and, through changes in κ , across the separator. Also, the surface overpotential for the cathode reaction is smaller, in accordance with Eq. [8]. For these reasons, the predicted voltage maximum is higher for cells with large values of c_a^0 . In addition, more acid is available for reaction in the cathode, and

the width of the acid region, and hence the cell lifetime, is increased.

Figure 4 shows the dependence of the increase in lifetime on c_a^0 with $c_{e,a}^0 = 1M$. If the acid cell is compared with an identical cell that uses neutral electrolyte with initial concentration

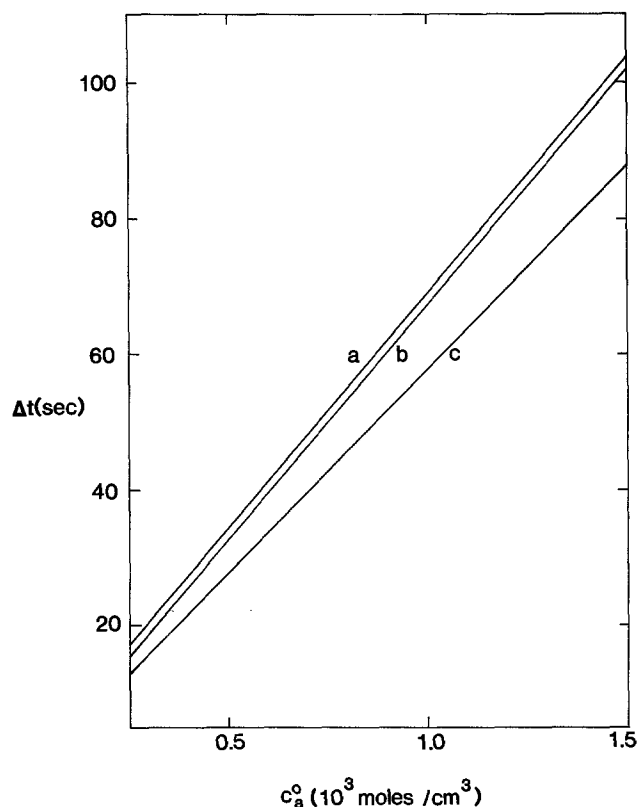


Fig. 4. Dependence of increase in cell lifetime on initial acid concentration. Δt = lifetime of acid cell - lifetime of comparable neutral cell that has initial electrolyte concentration $c_{e,n}^0$, as defined by Eq. [16]. Curve a represents values calculated from the stoichiometry of reaction [1]. Curve b represents values predicted with the heat capacity data given in Table II of Ref. (7). Curve c represents values predicted under isothermal conditions. Simulation parameters as in Fig. 1, except as indicated.

$$c_{e,n}^0 = c_{e,a}^0 + c_a^0 \quad [16]$$

the increase in lifetime is almost identical to the value calculated from the stoichiometry of reaction [I]. Very similar behavior is predicted with different values of $c_{e,a}^0$ and I . This result indicates that, over a wide range of operating conditions, cells with acid electrolyte can be regarded as a combination of (i) a neutral electrolyte cell with $c_{e,n}^0$ given by Eq. [16], and (ii) an acid reservoir that delays formation of LiCl crystals in the positive electrode. However, it should be noted that the closeness of curves a and b in Fig. 4 is rather fortuitous. As c_a^0 is increased, the rate of the chemical-dissolution reaction at the anode becomes faster, and a smaller proportion of the acid is available for electrochemical reaction (see above). This is compensated for by the heat of the reaction $\Delta H_{R,V}$, which raises the average cell temperature and hence increases the usable cell capacity on the lower voltage plateau (7). The magnitude of these effects is indicated by curve c, which shows the predicted effect of c_a^0 for an identical cell that is operated isothermally. In practice, the proximity of the actual time increase and the one based on stoichiometry will depend on factors such as the thermal characteristics of the system, the details of the dissolution reaction at the anode, the presence of impurities, and the mechanism for the chemical and electrochemical reactions of $AlCl_3$ in the cathode.

At present, there is considerable uncertainty concerning the complex physical processes that take place at the negative electrode under acid and neutral conditions. The model for the LiCl film described in Ref. (7) is an oversimplification, and it cannot be expected to explain observed behavior completely. In particular, theoretical values for the coulombic efficiency λ (see Table II) are close to the results for neutral cells (7), whereas experimental values are typically 10-20% lower (11). The predicted dependence of λ on I and utilization is a direct consequence of the reduction in film thickness by dissolution with acid and the corresponding increase in the flux of $SOCl_2$ to the lithium surface. With larger values for the rate constant k_1 , only small increases in dissolution rate can be obtained because a mass transfer limitation is reached [$(c_a)_b = 0$]. Even if all the acid available in the separator and reservoir (26% of the total) could react chemically at the anode, λ could only be close to the experimental result at low utilizations. At higher depths of discharge, when no acid remains, the LiCl film grows and the efficiency increases (7). Alteration of the film structure by the acid, e.g., higher porosity, or disruption of the film during discharge may be able to explain experimental observations. Also, formation of adducts (12) or complexes (1) may reduce the rate of $AlCl_3$ consumption in the cathode. This could allow more $AlCl_3$ to be transported to the anode and hence could lead to greater film dissolution by reaction [V].

In the simulations presented above, all the $AlCl_3$ is used up before cell failure. With thicker electrodes, a proportion of the acid remains at the back of the electrode at the end of discharge. Figure 5 shows that, under these circumstances, the increase in lifetime will be smaller than that calculated on the basis of the total amount of original acid and the stoichiometry of reaction [I]. This implies that, if it is considered desirable to use large quantities of acid in the cell, it may be

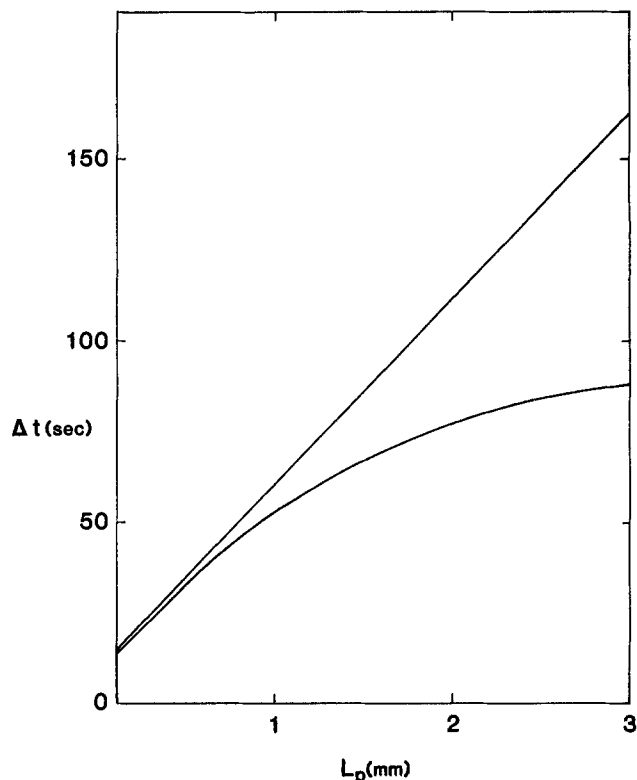


Fig. 5. Dependence of increase in cell lifetime on positive electrode thickness. The basis of comparison is described in Fig. 4. The straight line represents values predicted from the stoichiometry of reaction [I]. Simulation parameters as in Fig. 1, except as indicated.

preferable to add a large reservoir at the front of the cathode rather than increase the electrode thickness. However, at lower discharge rates or with higher diffusion coefficients, the amount of unused acid is reduced. This is because more acid is able to reach the front of the electrode and delay the onset of reaction [II]. In all cases, acid from the separator, the reservoir, and the front region of the cathode is expected to react completely before the cell fails. The overall effect of this acid is independent of whether it reacts chemically or electrochemically because the net effect is always a delay in plugging of the electrode pores. With the particular rate constants used in the simulations, the electrochemical reaction dominates.

Conclusions

A mathematical model has been developed that can describe the time-dependent and position-dependent behavior of a complete Li/ $SOCl_2$ static cell with acid electrolyte. In many respects, a cell with acid electrolyte can be regarded as a combination of an equivalent neutral electrolyte system and an acid reservoir. At the cathode, the $AlCl_3$ reacts preferentially at small depths of discharge. This delays the precipitation of LiCl crystals at the front of the electrode and, therefore, extends the cell lifetime. The theoretical predictions suggest that the increase in cell lifetime depends primarily on the quantity of acid added to the electrolyte. However, if the cathode is too thick, a proportion of the acid will be isolated at the back of the electrode and will be unable to react before the end of discharge. It should also be noted that the results depend on the model chosen to represent dissolution and formation of LiCl at the anode and on the thermal characteristics of the cell.

Acknowledgment

This work was funded by the Naval Sea Systems Command (NAVSEA code 63R-32) and constitutes a fraction of a major program to establish a technology

Table II. Dependence of coulombic efficiency (%) on discharge rate and utilization. Simulation parameters as in Fig. 1.

Utilization (%)	I (mA/cm ²)		
	40	80	120
1.0	89.0	84.3	80.7
5.0	89.9	86.7	84.4
9.0	90.9	88.3	86.2

base for high rate lithium, thionyl chloride batteries. We wish to thank Mr. Frank Romano for his continued interest.

Manuscript submitted April 22, 1983; revised manuscript received ca. Sept. 16, 1983.

APPENDIX

Derivation of Transport Equations

The multicomponent diffusion equation for an isothermal, isobaric system is expressed as (10)

$$c_i \nabla \mu_i = \sum_j K_{ij} (\underline{v}_j - \underline{v}_i) = RT \sum_j \frac{c_i c_j}{c_T \mathcal{D}_{ij}} (\underline{v}_j - \underline{v}_i) \quad [\text{A-1}]$$

For a mixture of n species, a set of $(n-1)$ independent force balances defines the binary interaction parameters \mathcal{D}_{ij} , which are functions of temperature, pressure, and composition. In porous media, each \mathcal{D}_{ij} is related to the transport coefficient \mathcal{D}_{ij}^0 for the bulk electrolyte by $\mathcal{D}_{ij} = \mathcal{D}_{ij}^0/\xi^2$, where ξ is a tortuosity factor. The parameter ξ is a characteristic of the microscopic electrode structure and can be associated with the porosity by a relation of the form (6), $\xi^2 = 1/\sqrt{\epsilon}$. The number of independent transport properties in Eq. [A-1] is $n(n-1)/2$ because \mathcal{D}_{ii} is not defined and, by Newton's third law of motion, $\mathcal{D}_{ij} = \mathcal{D}_{ji}$. Specific combinations of these properties correspond to transport parameters that can be measured directly.

For the Li^+ , AlCl_4^- , AlCl_3 , and SOCl_2 system, the three independent diffusion equations may be rearranged, with the introduction of the superficial current density, to give expressions for fluxes based on a reference velocity representative of the bulk motion of the electrolyte. For example, with the solvent reference velocity \underline{v}_4 , one obtains

$$\begin{aligned} \underline{N}_1 &= c_1 \underline{v}_1 = -\frac{\epsilon v_1 c_e^2}{\alpha} \nabla \mu_e \\ &\quad - \epsilon v_1 c_e c_3 \left(\frac{K_{13} + K_{23}}{\alpha \psi} \right) \nabla \mu_3 + \frac{t_1^4 t_2}{z_1 \mathbf{F}} + c_1 \underline{v}_4 \\ \underline{N}_2 &= c_2 \underline{v}_2 = -\frac{\epsilon v_2 c_e^2}{\alpha} \nabla \mu_e \\ &\quad - \epsilon v_2 c_e c_3 \left(\frac{K_{13} + K_{23}}{\alpha \psi} \right) \nabla \mu_3 + \frac{t_2^4 t_2}{z_2 \mathbf{F}} + c_2 \underline{v}_4 \\ \underline{N}_3 &= c_3 \underline{v}_3 = -\frac{\epsilon c_3^2}{\psi} \left[1 + \frac{(K_{13} + K_{23})^2}{\alpha \psi} \right] \nabla \mu_3 \\ &\quad - c_3 c_3 \frac{(K_{13} + K_{23})}{\alpha \psi} \nabla \mu_e + \frac{t_3^4 t_2}{\mathbf{F}} + c_3 \underline{v}_4 \\ \underline{N}_4 &= c_4 \underline{v}_4 \end{aligned} \quad [\text{A-2}]$$

where

$$\begin{aligned} \mu_e &= v_1 \mu_1 + v_2 \mu_2 \\ \psi &= K_{13} + K_{23} + K_{34} \\ \alpha \psi &= K_{34} (K_{13} + K_{23}) + (K_{14} + K_{24}) \\ &\quad (K_{13} + K_{23} + K_{34}) \\ t_1^4 &= \frac{1}{\alpha \psi} (K_{23} + K_{24}) (K_{13} + K_{23} + K_{34}) \\ &\quad - (K_{13} + K_{23}) K_{23} \\ t_2^4 &= 1 - t_1^4 \\ t_3^4 &= \frac{c_3}{\psi} \left(\frac{K_{13} t_1^4}{z_1 c_1} + \frac{K_{23} t_2^4}{z_2 c_2} \right) \end{aligned} \quad [\text{A-3}]$$

and the subscripts 1, 2, 3, and 4 represent Li^+ , AlCl_4^- , AlCl_3 , and SOCl_2 , respectively.

In the computer simulation, the volume average velocity, defined by

$$\underline{v}^\square = \sum_i \bar{V}_i \underline{N}_i \quad [\text{A-4}]$$

is used as the reference frame for the diffusion flux because physical data for the LiAlCl_4 , AlCl_3 , SOCl_2 electrolyte are correlated with concentration. Substitution of the thermodynamic relations

$$\mu_e = \nu RT \ln (c_e f_{12} a_{12}^0) \quad [\text{A-5}]$$

$$\mu_3 = RT \ln (c_3 f_3 a_3^0) \quad [\text{A-6}]$$

and Eq. [A-4] into Eq. [A-2] gives Eq. [5] in the main text. The transport properties in Eq. [5] are related to the friction coefficients K_{ij} by the following equations

$$\begin{aligned} D_1 &= \frac{c_e}{\alpha \psi} \nu RT \left(1 + \frac{d \ln f_{12}}{d \ln c_e} \right) [c_4 \bar{V}_4 \psi + c_3 \bar{V}_3 K_{34}] \\ D_2 &= \frac{c_3}{\alpha \psi} \nu RT \left(1 + \frac{d \ln f_{12}}{d \ln c_e} \right) [K_{13} + K_{23} \\ &\quad + c_3 \bar{V}_3 K_{34} + \psi (c_4 \bar{V}_4 - 1)] \\ D_3 &= \frac{c_e}{\alpha \psi} RT \left(1 + \frac{d \ln f_3}{d \ln c_3} \right) [c_4 \bar{V}_4 (K_{13} + K_{23}) \\ &\quad - c_3 \bar{V}_3 (K_{14} + K_{24})] \\ D_4 &= \frac{c_3}{\alpha \psi} RT \left(1 + \frac{d \ln f_3}{d \ln c_3} \right) [(1 - c_3 \bar{V}_3) \\ &\quad (K_{14} + K_{24}) + c_4 \bar{V}_4 (K_{13} + K_{23})] \\ D_5 &= \frac{c_4}{\alpha \psi} \nu RT \left(1 + \frac{d \ln f_{12}}{d \ln c_e} \right) [c_3 \bar{V}_3 K_{34} \\ &\quad - (1 - c_4 \bar{V}_4) \psi] \\ D_6 &= \frac{c_4}{\alpha \psi} RT \left(1 + \frac{d \ln f_3}{d \ln c_3} \right) [(c_4 \bar{V}_4 - 1) \\ &\quad (K_{13} + K_{23}) - c_3 \bar{V}_3 (K_{14} + K_{24})] \end{aligned} \quad [\text{A-7}]$$

$$t_1^\square = t_1^4 - c_1 z_1 Q' - c_1 z_1 \bar{V}_3 t_3^4$$

$$t_2^\square = t_2^4 - c_2 z_2 Q' - c_2 z_2 \bar{V}_3 t_3^4$$

$$t_3^\square = -c_3 Q' + (1 - c_3 \bar{V}_3) t_3^4$$

$$t_4^\square = -c_4 Q' - c_4 \bar{V}_3 t_3^4 \quad [\text{A-8}]$$

where

$$Q' = \frac{t_1^4 \bar{V}_1}{z_1} + \frac{t_2^4 \bar{V}_2}{z_2} \quad [\text{A-9}]$$

In addition, the effective conductivity within the pores (5) may be written in terms of K_{ij} as

$$\frac{1}{\kappa} = \frac{1}{\epsilon z_1 c_1 \mathbf{F}^2} \left[\frac{t_3^4 K_{23}}{c_3} - \frac{t_2^4}{z_2 c_2} (K_{23} + K_{24}) + \frac{K_{12}}{z_1 c_1} \right] \quad [\text{A-10}]$$

Only six of the transport properties defined in Eq. [A-7], [A-8], and [A-10] are independent. The quantity Q' cannot be measured, but it can arbitrarily be taken to be zero (6). In the analysis of the Li/SOCl_2 acid electrolyte cell, it is assumed that the contribution of diffusion to the flux of a species arises solely from the concentration gradient of that species. In this way, the parameters D_2 and D_3 are taken to be zero. Furthermore, the effect of migration on the flux of AlCl_3 is neglected, so that the transference number t_3^\square also becomes zero. The three independent transport properties that can still be chosen are taken to be D_1 , t_1^\square , and κ . The other properties (D_4 , D_5 , and D_6) are expressed in terms of these variables, for example

$$D_4 = \frac{\left(1 + \frac{d \ln f_3}{d \ln c_3} \right) \bar{V}_e}{\left(1 + \frac{d \ln f_{12}}{d \ln c_e} \right) \nu \bar{V}_3} \cdot D_1 \quad [\text{A-11}]$$

LIST OF SYMBOLS

a	interfacial area per unit electrode volume (cm^{-1})
$a^{\theta_{12}}, a^{\theta_3}$	property expressing secondary reference state (cm^3/mol)
c_a	molar concentration of AlCl_3 (mol/cm^3)
c_e	$= c_1/\nu_1 = c_2/\nu_2$ molar concentration of electrolyte (mol/cm^3)
$c_{e,a}^{\circ}$	initial electrolyte concentration of a cell that uses an acid electrolyte (mol/cm^3)
$c_{e,n}^{\circ}$	initial electrolyte concentration of a cell that uses a neutral electrolyte (mol/cm^3)
c_i	molar concentration of species i (mol/cm^3)
C	cell heat capacity ($\text{J}/\text{cm}^2 \cdot \text{K}$)
\mathcal{D}_{ij}	diffusion coefficient for interaction of species i and j (cm^2/s)
D_i	($I = 1 - 6$), diffusion coefficient defined by Eq. [A-7] (cm^2/s)
f_{12}	mean molar activity coefficient of electrolyte
f_3	molar activity coefficient of AlCl_3
F	Faraday's constant (96,487 C/eq)
h	mesh size (cm)
h_0	heat transfer coefficient ($\text{W}/\text{cm}^2 \cdot \text{K}$)
$\Delta H_{R,IV}$	heat of chemical reaction (J/mol of SOCl_2 consumed)
$\Delta H_{R,V}$	heat of chemical reaction (J/mol of LiCl dissolved)
i_0	exchange current density (A/cm^2)
\underline{i}_2	superficial current density in pore phase (A/cm^2)
i_{nj}	local current density due to reaction j (A/cm^2)
I	superficial current density to an electrode (A/cm^2)
j_{in}	pore wall flux of species i ($\text{mol}/\text{cm}^2 \cdot \text{s}$)
k_1	rate constant of reaction [V] at anode (cm/s)
k_2	rate constant of reaction [V] at cathode ($1/\text{s}$)
K_{ij}	friction coefficient for interaction of species i and j ($\text{J} \cdot \text{s}/\text{cm}^5$)
L	electrode thickness (cm)
M_i	symbol for the chemical formula of species i
n_i	number of electrons transferred in electrode reaction j
\underline{N}_i	superficial flux of species i ($\text{mol}/\text{cm}^2 \cdot \text{s}$)
\underline{p}	morphology parameter defined by Eq. [11]
Q	cell capacity (based on moles of SOCl_2) (C/cm^2)
Q'	parameter defined by Eq. [A-9]
r_{IV}	reaction rate of chemical reaction [IV] (mole of SOCl_2 consumed/ $\text{cm}^2 \cdot \text{s}$)
r_V	reaction rate of chemical reaction [V] at anode (mol of LiCl dissolved/ $\text{cm}^2 \cdot \text{s}$)
R	universal gas constant (8.3143 J/mol \cdot K)
R_0	reaction rate of chemical reaction [V] at cathode ($\text{mol}/\text{cm}^3 \cdot \text{s}$)
$s_{i,i}$	stoichiometric coefficient of species i in electrode reaction j
$s_{i,0}$	stoichiometric coefficient of species i in chemical reaction [V]
$s_{i,IV}$	stoichiometric coefficient of species i in chemical reaction [IV]
t	time (s)
t_i^{\blacksquare}	transference number of species i with respect to the volume average velocity
t_i^{Δ}	transference number of species i with respect to the velocity of SOCl_2
Δt	lifetime of acid cell — lifetime of comparable neutral cell that has an initial electrolyte concentration $= c_{e,n}^{\circ}$ (s)
T	absolute temperature (K)
T_A	temperature of surroundings (K)
T_0	initial temperature (K)
$U_{j,w}$	theoretical open-circuit potential for reaction j at the composition prevailing locally at the electrode surface, relative to a reference electrode of a given kind (V)
U_j^{θ}	standard electrode potential for reaction j (V)
U_0	open-circuit cell potential (V)
$\underline{v}^{\blacksquare}$	volume average velocity (cm/s)
\underline{v}_i	velocity of species i (cm/s)
\bar{V}	total cell voltage (V)
\tilde{V}	molar volume (cm^3/mol)
\bar{V}_i	partial molar volume of species i (cm^3/mol)
z_i	valence or charge number of species i

Greek Letters

α	a combination of friction coefficients defined by Eq. [A-3] ($\text{J} \cdot \text{s}/\text{cm}^5$)
α_a	transfer coefficient in anodic direction
α_c	transfer coefficient in cathodic direction
γ_i	exponent in Eq. [9]
δ_f	LiCl film thickness (cm)
ϵ	porosity or void volume fraction
ϵ_{LiCl}	volume fraction of LiCl
ζ	tortuosity factor
η	$\Phi_1 - \Phi_2$
κ	effective solution conductivity (mho/cm)
λ	coulombic efficiency
μ_i	chemical potential of species i (J/mol)
ν	$= \nu_1 + \nu_2$, number of mols of ions into which a mol of electrolyte dissociates
ν_1, ν_2	number of cations and anions into which a molecule of electrolyte dissociates
ρ_0	density of pure solvent (g/cm^3)
σ	effective matrix conductivity (mho/cm)
Φ_2	electric potential in the solution (V)
ψ	a combination of friction coefficients defined by Eq. [A-3] ($\text{J} \cdot \text{s}/\text{cm}^5$)

Subscripts

a	AlCl_3
b	LiCl film/separator interface
e	electrolyte
f	LiCl film
i	anion, cation, or solvent
j	reaction j
p	positive electrode
re	reference electrode
ref	reference condition
s	separator
w	at the electrode surface
1	Li^+
2	AlCl_4^-
3	AlCl_3
4	SOCl_2
I	reaction [I]
II	reaction [II]
IV	reaction [IV]
V	reaction [V]
∞	bulk property

Superscript

0	initial value
---	---------------

REFERENCES

1. K. A. Klinedinst and M. J. Domeniconi, *This Journal*, **127**, 539 (1980).
2. J. Newman, D. Bennion, and C. W. Tobias, *Ber. Bunsenges. Phys. Chem.*, **69**, 608 (1965).
3. J. Newman, *Adv. Electrochem. Electrochem. Eng.*, **5**, 87 (1967).
4. W. G. Sunu and D. N. Bennion, *This Journal*, **127**, 2007 (1980).
5. R. Pollard and J. Newman, *ibid.*, **126**, 1713 (1979).
6. J. Newman and W. Tiedemann, *AIChE J.*, **21**, 25 (1975).
7. K. C. Tsaur and R. Pollard, *This Journal*, **131**, 975 (1984).
8. R. White, Dissertation, University of California, Berkeley, CA (1977).
9. A. N. Dey, *Electrochim. Acta*, **21**, 377 (1976).
10. J. Newman, "Electrochemical Systems," Prentice-Hall, Englewood Cliffs, NJ (1973).
11. J. R. Driscoll, Personal communication.
12. D. A. Long and R. T. Bailey, *Trans. Faraday Soc.*, **59**, 594 (1963).
13. J. J. Auburn, K. W. French, S. I. Lieberman, V. K. Shah, and A. Heller, *This Journal*, **120**, 1613 (1973).
14. C. R. Schlaikjer, F. Goebel, and N. Marincic, *ibid.*, **126**, 513 (1979).
15. R. H. Perry and C. H. Chilton, "Chemical Engineers' Handbook," 5th ed., McGraw-Hill, New York (1973).
16. NOSC Tech. Note 1083, S. J. Szpak, Editor, (November 1981).

Accelerated Evolution of Hydrogen on Freshly Generated Metal Surfaces in Aqueous Solution

G. T. Burstein and M. A. Kearns

Department of Metallurgy and Materials Science, University of Cambridge, Cambridge, CB2 3QZ, England

ABSTRACT

Data have been obtained which describe quantitatively the rate of evolution of hydrogen on freshly generated surfaces of Fe, Cr, and their binary alloys. At low electrode potentials, creation of the new metal surface causes large acceleration of the rate of hydrogen evolution. The succeeding decay of cathodic current with time is relatively small; long after its creation, the new surface remains catalytically active towards hydrogen evolution provided the potential remains low. The kinetics of each stage of the process are defined and presented as a function of the metal composition.

The scratched rotating disk electrode has proved a valuable probe for the investigation of the rapid initial reactions which occur when metal surfaces are generated in aqueous electrolytes under potential control (1-7). Efforts have so far been focused on the elucidation of anodic processes occurring in a range of metal/electrolyte systems. These have included measurements of the rapid initial rates of anodic reactions (1-9), kinetics of oxide film growth (8, 9), and the effects of anions on these (1, 2). Although cathodic current transients have been documented at sufficiently low potentials (2-9), these have not been analyzed in detail.

Preliminary work on the scratched chromium electrode at low electrode potential in alkaline solution has shown that the hydrogen evolution reaction can be accelerated on scratching, and that the accelerated rate of reaction can continue for periods long after the scratching process is complete (10). The present work sets out the results of similar studies of iron, chromium, and a range of their binary alloys in a potential range where scratching gives rise to a net cathodic current due to the hydrogen evolution reaction occurring upon the scratch surface.

The phenomenon of enhanced or retarded diffusivity of hydrogen atoms through metals accompanying plastic deformation has been studied for some time (11). Despite the recent debate (12-14) concerning the measurements and mechanism of this process, enhanced diffusion of hydrogen in metals undergoing plastic deformation may well be involved in the mechanisms of some localized environment-dependent failure modes, such as corrosion fatigue and hydrogen embrittlement (15-17). For the scratched electrode, enhanced rates of hydrogen evolution are possible (10), and there thus exists the likelihood of a combination of enhanced hydrogen discharge and subsequent rapid transport through the metal substrate. Such processes may be envisaged as having repercussions for environment-sensitive failure of metals.

Experimental

Full details of the potentiostatically controlled scratched electrode technique have been presented previously (1-7). The technique is designed for measurement of both the instantaneous and subsequent events that occur when a fresh metal surface is created in solutions under electrochemical control. The disk electrodes used in this work were made from Cr, Fe, and a range of iron/chromium binary alloys of compositions 5%, 20%, and 50% Cr. These are designated as Fe-5Cr, Fe-20Cr, and Fe-50Cr, respectively. The metals were pure (Fe, BISRA, impurities in weight percent [w/o]: C 0.006, Si 0.006, S 0.0066, Al 0.004, O 0.001, N 0.016, Mn <0.005, and Cr Ex-iodide, 99.995%); the alloys were synthesized by arc melting in a copper hearth. The melts were inverted several times, cooled to room temperature, homogenized at ~1473 K and annealed at ~873 K. They were ground to a 1200 grit finish before

use. Some work was also carried out on pure nickel (Johnson Matthey, Specpure). Scratches generated on rotating disks of these materials were of different widths and depths according to the hardness of the metal. Thus for Fe, Fe-5Cr, and Fe-20Cr the scratches measured ~2 mm × 40 μm × 4 μm, for Fe-50Cr, ~2 mm × 35 μm × 3 μm, and for pure Cr, ~2 mm × 26 μm × 2 μm. The stylus contact time for an electrode rotation rate, ω , of 100 Hz was ~1 ms.

The electrolyte used throughout this work was 1.0M KOH prepared from AR reagent and doubly distilled water. It was deoxygenated by thorough purging with purified nitrogen before and during use. Experiments were performed at ambient temperature of 292 ± 2 K.

Electrodes were controlled to constant potential for a period of time sufficient to produce a steady-state current on the whole electrode before a scratch was initiated. In some cases, the surface consisted of the initial air-formed film before cathodization. In other cases, a preprogrammed anodic treatment in the working electrolyte was provided before cathodic treatment. This is described below.

Cathodic current transients due to scratching were recorded on a range of transient recorders set to different sensitivities and time scales so that the entire event could be recorded for as long as necessary. Some transients were prepared with the transient recorders set to the pretrigger mode so that any possible pre-trigger events could also be recorded.

Results

In this work, only scratches which gave rise to a net cathodic current transient are discussed. Anodic current transients will be presented elsewhere.

Figure 1a shows a current transient generated by scratching Cr in 1.0M KOH at a potential of -1405 mV (NHE). The base current, which represents the steady-state current flowing from the entire electrode surface before scratching is negative and is due to steady-state evolution of hydrogen. The potential is more negative than the thermodynamic equilibrium potential for the hydrogen electrode reaction of -827 mV (NHE) at pH 14, 1 atm of H₂. The scratch is initiated at the point identified by A in Fig. 1a and lasts for ~1 ms. This period is the stylus contact time, t_c , after which the scratching process is complete.

From this region of machining by the diamond stylus, it is possible to define the maximum observed current density flowing on the scratch surface by measuring the maximum rate of current generation as the scratch is being formed. It is given by (2)

$$i_s = \frac{1}{2\pi r \omega y} \frac{dI}{dt} \quad [1]$$

where dI is the increase in total current in time dt , y the scratch width, and r is its distance from the center of rotation.

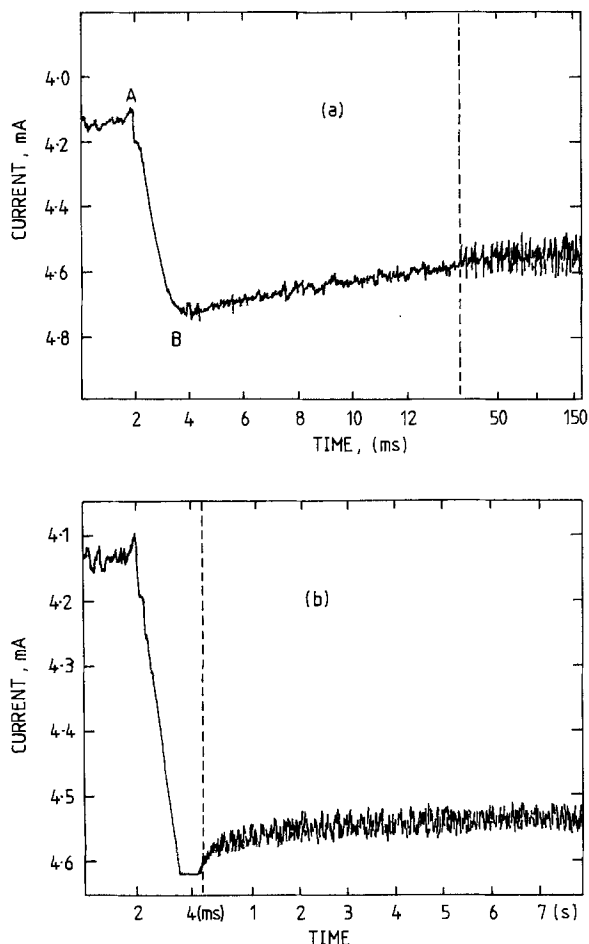


Fig. 1. Cathodic current transient recorded on scratched Cr in 1.0M KOH at a potential of -1405 mV(NHE). The diagram shows the use of different current sensitivities and time scales (a and b) to detect the current decay. The time interval A to B is equal to the stylus contact time, t_c .

For Fig. 1a the current increases in the cathodic direction during scratching. After completion of the scratch, the current decays with time; at any instant t , the current density on the scratch is given by

$$i_s(t) = \frac{[I(t) - I_b]}{2\pi r \omega y t_c} \quad [2]$$

where $I(t)$ is the total current flowing from the whole electrode at time t and I_b is the base current flowing from the whole electrode before scratching. The quantity $2\pi r \omega y t_c$ is the surface area of the scratch. It is not corrected for the depth of the scratch (which is small, see above); neither is it corrected for the microscopic surface roughness. This form of Eq. [2] is only valid if the creation of the scratch makes a negligible difference to the base current density, i_b . For most practical purposes this is true; however, as $i_s(t)$ decays towards i_b , the formula must be modified to incorporate the change in I_b which occurs on scratching. The modification in essence allows for the fact that $i_s(t)$ decays towards i_b , and not towards zero. In such a case

$$i_s(t) = \frac{[I(t) - I_b]}{2\pi r \omega y t_c} + i_b \quad [3]$$

and in practice this occurs for $i_s(t) < \sim 10i_b$.

Figure 1b shows the same current transient as Fig. 1a recorded on a more sensitive current scale for a far greater period of time; it is immediately clear that the scratch current does not decay back to the base level I_b , even after 5s. The final steady-state scratch current density is denoted by $i_s(\infty)$ (calculated from Eq. [2])

and provides the new steady state of the scratch surface. This new steady-state cathodic reaction is accelerated when compared with the original steady state, i_b .

The base current I_b , displayed in Fig. 1a, shows a small decrease immediately prior to stylus contact. This feature is common to all such cathodic transients and is caused by interference with the original steady-state evolution of hydrogen by the approaching diamond stylus. It is thus necessary to examine the pre-trigger base current in detail to provide an accurate measure of I_b . Figure 2 shows another transient, this time with the transient recorder set in the pretrigger mode. The current before scratching is now displayed for a period of 1s, and the current after scratching for 1s. Since in the experiments the stylus requires some 30–40 ms to reach the surface, Fig. 2 gives an accurate measure of the variation in I_b both before and during the trigger period. It demonstrates that the approach of the stylus provides only a very small change in I_b , and the difference $I(t) - I_b$ used to evaluate $i_s(\infty)$ (see Eq. [2]) is not significantly affected.

Current transients of the type shown in Fig. 1 and 2 were recorded for Fe, Fe-5Cr, Fe-20Cr, Fe-50Cr, and Cr, over a range of potentials in 1.0M KOH. The values of i_s for pure Cr are shown in Fig. 3 as a function of potential together with measured values of i_b (the steady-state current density flowing from unscratched rotating electrodes [also 100 Hz]). The values of i_s lie almost 2 orders of magnitude higher than i_b . Also shown plotted in Fig. 3 are the values of the new steady-state cathodic current density $i_s(\infty)$. These also lie at considerably higher values than i_b . The potential marked with an arrow in Fig. 3 gives the bare surface mixed potential, E_{ms} ; at more positive potentials, the scratch current transients give net anodic currents.

Figure 3 shows that Tafel's law is obeyed for each of i_b , i_s , and $i_s(\infty)$. The measured range of these graphs for i_s and $i_s(\infty)$ is necessarily somewhat limited because of both the proximity of E_{ms} and the very high current densities involved. Nevertheless, Tafel's law is obeyed over some 1.5 orders of magnitude in $i_s(\infty)$ and ~ 1 order in i_s . The Tafel slopes are listed in Table I. At high current densities, the graphs deviate from linear Tafel behavior, a consequence of the ohmic resistance of the electrolyte. This resistance and consequent ohmic potential drop is smaller for the scratch (7) than it is for the disk (18) at similar current den-

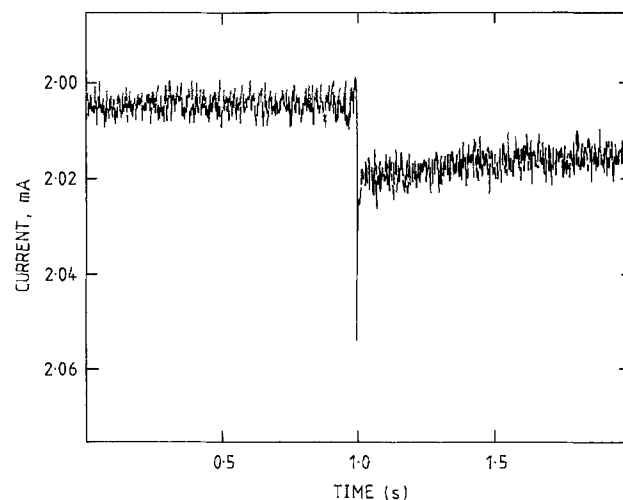


Fig. 2. Cathodic current transient recorded on pure Cr in 1.0M KOH at a potential of -1305 mV (NHE), in the pretrigger mode. It shows the steady-state base current for 1s prior to the scratch event and clearly illustrates the difference in steady-state current density on the electrode before and after scratching.

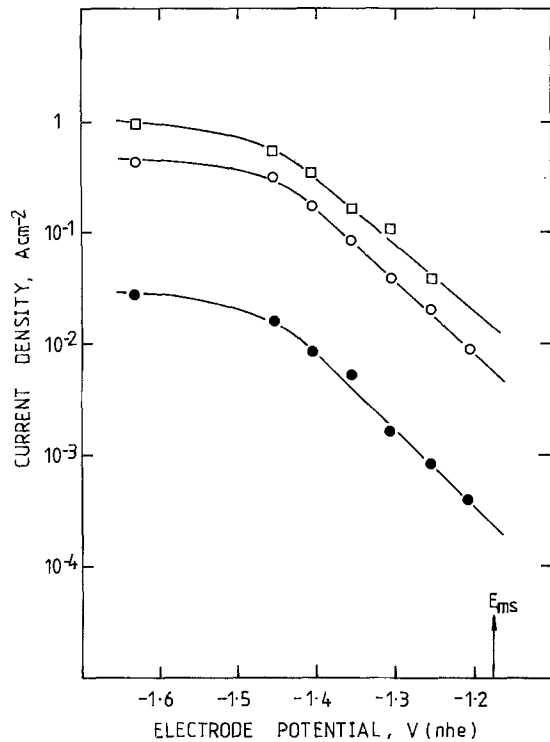


Fig. 3. Cathodic current density on pure Cr as a function of potential. Instantaneous scratch current density, i_s (\square). Steady-state scratch current density, $i_s(\infty)$ (\circ). Steady-state current density on unscratched Cr, i_b (\bullet).

sities. Thus i_b deviates from Tafel's law at lower values than i_s and $i_s(\infty)$.

Similar data were obtained for pure Fe and for the three Fe-Cr alloys (Fe-50Cr, Fe-20Cr, and Fe-5Cr). These are present in Fig. 4-7, respectively. Each of the five metals displays linear cathodic Tafel behavior for i_s , $i_s(\infty)$, and i_b and the Tafel slopes are listed in Table I. For constant potential the i_s values show an increase with increase in the Fe content. The same trend is found for i_b value for the five metals.

To estimate the effects of anodic pretreatment of the electrodes before cathodic scratch transients were prepared, an experiment was performed in which pure chromium was subject to different anodic potentials, each for a period of 30s. Each electrode was then potentiostatically pulsed to the cathodic region (-1345 mV [NHE]), allowed to achieve a steady state, and scratched. Graphs of i_b , i_s , and $i_s(\infty)$ are shown as a function of the potential of anodic pretreatment of Cr in Fig. 8. Also shown are the corresponding parameters for Cr which carried simply the original air-formed film; these are plotted at $E = -355$ mV (NHE) since this was the steady-state open-circuit potential. Each of the three values of current density is independent of electrode pretreatment.

Discussion

Since in this electrolyte, only H_2O is capable of electrochemical reduction, the current transients described above are due to accelerated evolution of hydrogen on the scratch. It is quite remarkable that a high rate of hydrogen evolution continues long after the scratch has

Table I. Cathodic Tafel slopes for hydrogen evolution in 1.0M KOH

Metal	$-\partial E/\partial \log i_b$ (mV)	$-\partial E/\partial \log i_s$ (mV)	$-\partial E/\partial \log i_s(\infty)$ (mV)
Fe	150	134	147
Fe-5Cr	128	144	138
Fe-20Cr	130	128	123
Fe-50Cr	132	144	149
Cr	135	144	158

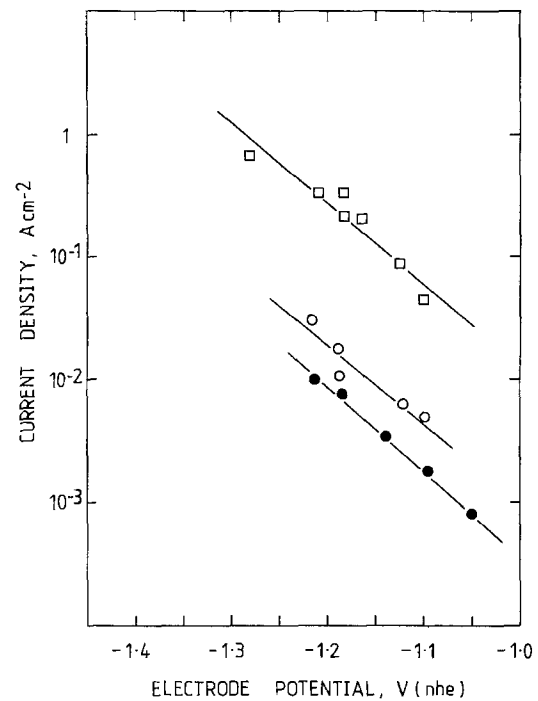


Fig. 4. Cathodic current density vs. potential for pure Fe. Instantaneous scratch current density, i_s (\square). Steady-state scratch current density, $i_s(\infty)$ (\circ). Steady-state current density on unscratched Fe, i_b (\bullet).

been formed. The effect of $i_s(\infty)$, which represents a new steady-state rate of hydrogen evolution long after the scratch has been formed, can be observed visually by applying a scratch to a stationary specimen held at constant potential within the required range (see Fig. 3-7). Under these circumstances, the effect is seen as a string of hydrogen bubbles decorating the scratch surface. Photomicrographs of this phenomenon are shown in Fig. 9. The photograph 9a was taken ca. 10s after completion of the scratch; 9b was taken ca. 600s

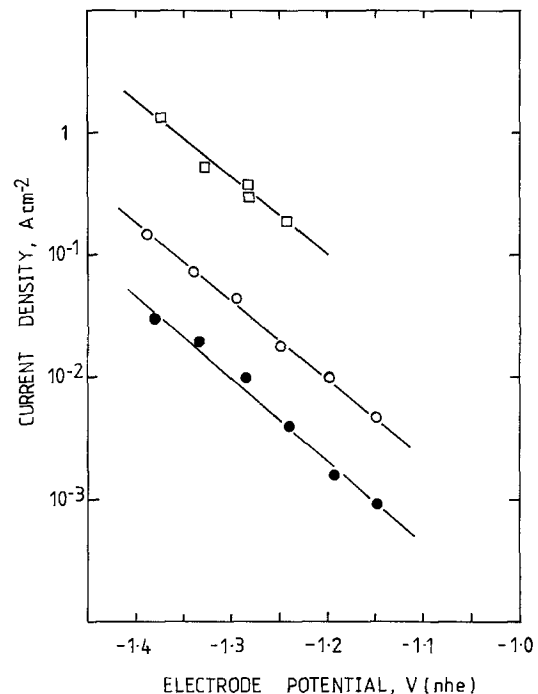


Fig. 5. Cathodic current density vs. potential for Fe-50Cr. Instantaneous scratch current density, i_s (\square). Steady-state scratch current density, $i_s(\infty)$ (\circ). Steady-state current density on unscratched Fe-50Cr, i_b (\bullet).

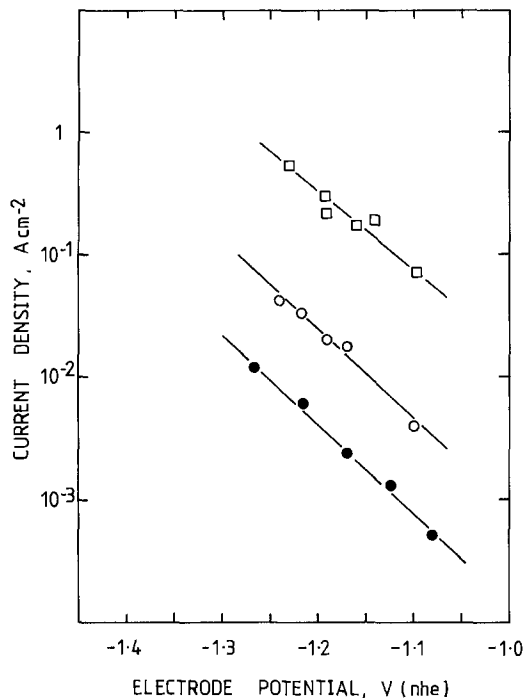


Fig. 6. Cathodic current density vs. potential for Fe-20Cr. Instantaneous scratch current density, i_s (\square). Steady-state scratch current density, $i_s(\infty)$ (\circ). Steady-state current density on unscratched Fe-20Cr, i_b (\bullet).

after scratching. Both depict a scratch on pure chromium in 1.0M KOH at $E = -1255$ mV (NHE). The figures show a high density of hydrogen bubbles along the length of the scratch, and this has been observed to persist for >1.2 ks. It is clearly a permanent feature of the newly created surface. The effect of the scratch is therefore irreversible.

The cathodic Tafel slopes described in Table I are all of similar magnitude and represent a single-electron transfer reaction as the rate-determining step. This is

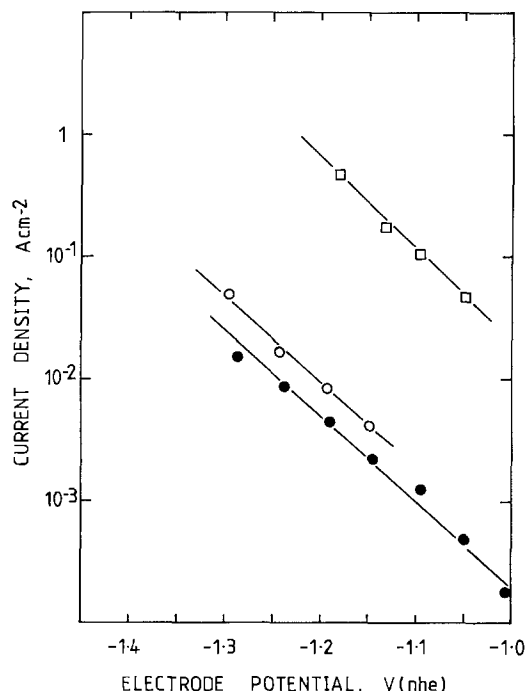


Fig. 7. Cathodic current density vs. potential for Fe-5Cr. Instantaneous scratch current density, i_s (\square). Steady-state scratch current density, $i_s(\infty)$ (\circ). Steady-state current density on unscratched Fe-5Cr, i_b (\bullet).

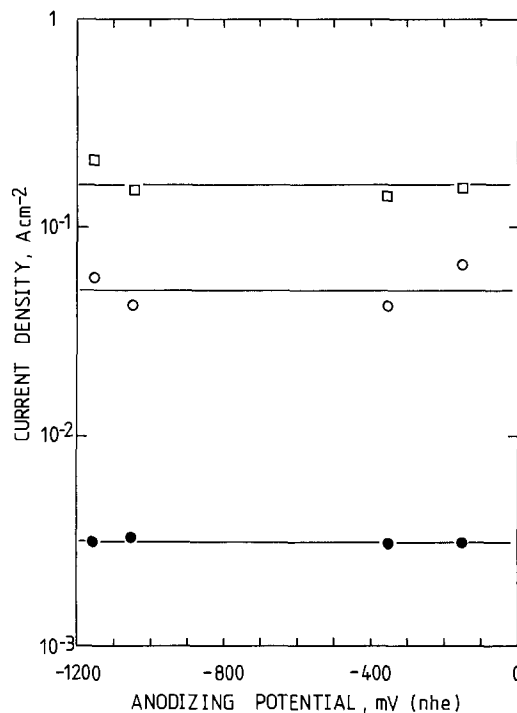
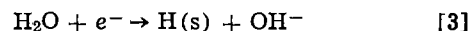


Fig. 8. Dependence of cathodic current density i_s (\square), $i_s(\infty)$ (\circ), and i_b (\bullet) at $E = -1345$ mV (NHE) on the anodizing potential for Cr in 1.0M KOH.

consistent with Tafel slopes found in the steady state for hydrogen evolution in alkaline solutions on a range of metals (19, 20). The reaction may be written as



where H(s) is a hydrogen atom adsorbed to the surface. The kinetics of the reaction follow

$$i = i_0 \exp \left[\frac{\beta F \eta}{RT} \right] \quad [4]$$

and this equation is obeyed for each of i_b , i_s , and $i_s(\infty)$. Recombination of the adsorbed hydrogen atoms must be fast.

Values of the exchange current densities are clearly different for each of these current density parameters. They are evaluated by extrapolation of each of the Tafel lines to $E = -827$ mV (NHE), which is the equilibrium potential for the hydrogen evolution reaction at pH 14 and 1 atm of H_2 . The exchange current densities are designated as i_{b0} , i_{s0} , and $i_{s0}(\infty)$, and are listed in Table II.

The values of i_{b0} which represent the unscratched steady-state surface show an increase with decrease in Cr content of the alloy. The value found for pure Fe (2×10^{-5} A cm^{-2}) is about an order higher than that recorded earlier ($\sim 10^{-6}$ A cm^{-2}) (19, 20). Variation of i_{b0} with the mol fraction of Cr, X_{Cr} in the alloy is shown in Fig. 10.

A similar trend with mol fraction of Cr is found for i_{s0} , and this too is shown in Fig. 10. The variation of both $\log i_{b0}$ and $\log i_{s0}$ is linear in X_{Cr} and gives $\partial \log i_{b0} / \partial X_{\text{Cr}} = -1.14$ and $\partial \log i_{s0} / \partial X_{\text{Cr}} = -1.03$. The two values are very similar.

Table II. Exchange current densities for the hydrogen electrode reaction in 1.0M KOH

Metal	i_{b0} (A cm^{-2})	$i_{s0}(\infty)$ (A cm^{-2})	i_{s0} (A cm^{-2})
Fe	1.9×10^{-5}	3.2×10^{-5}	1.05×10^{-3}
Fe-5Cr	8.3×10^{-6}	3.0×10^{-5}	1.0×10^{-3}
Fe-20Cr	6.2×10^{-6}	3.0×10^{-5}	5.4×10^{-4}
Fe-50Cr	2.9×10^{-6}	2.9×10^{-5}	3.2×10^{-4}
Cr	6.7×10^{-7}	3.0×10^{-5}	8.5×10^{-5}

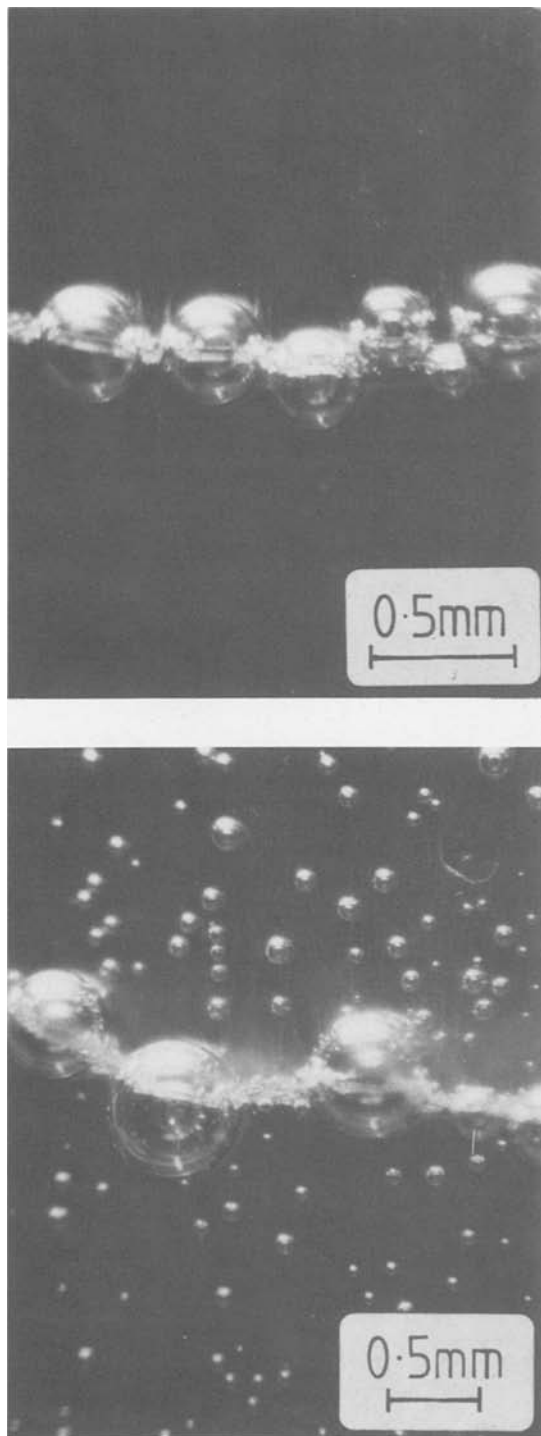


Fig. 9. Photomicrographs of H_2 bubbles evolved from the scratched area of a pure Cr electrode under potentiostatic control at -1255 mV (NHE) in $1.0M$ KOH. A, top: picture taken ca. 10s after scratching. B, bottom: picture taken ca. 600s after scratching.

The new steady-state current density on the scratch, $i_{s0}(\infty)$, is, however, invariant with X_{Cr} (see Fig. 10). It is striking that all these scratch surfaces, after re-establishment of a steady state, exhibit such similar activity towards hydrogen evolution.

It should be noted that the experimental data obtained for both Cr and Fe (Fig. 3 and 4) extend to potentials below those for which the metals can equilibrate with their bulk oxides at pH 14 (21). This implies that the original oxide films are not totally reduced electrochemically since the post-scratch steady-state current density [$i_s(\infty)$] is greater than the pre-scratch steady state (i_b) even at potentials where electrochemical reduction is possible. Only mechanical

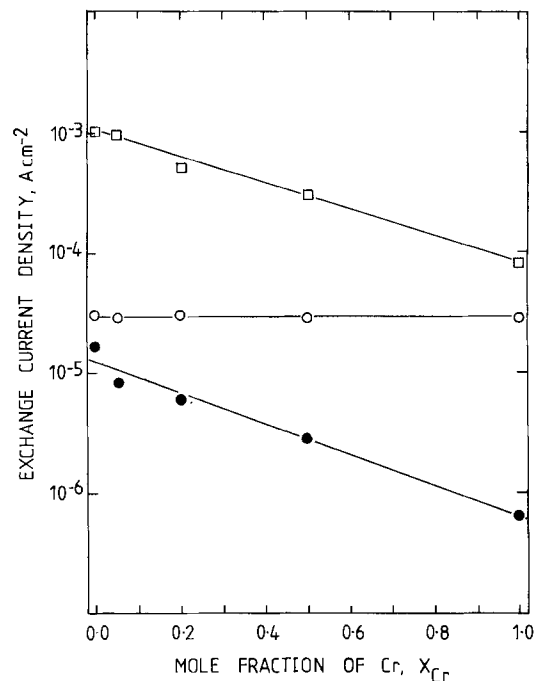


Fig. 10. Variation of exchange current densities i_{s0} (\square), $i_{s0}(\infty)$ (\circ), and i_{b0} (\bullet) with alloy composition for the Fe-Cr binary alloy system in $1.0M$ KOH.

methods can remove these oxide films entirely, and, provided the electrode potential remains low, such oxides cannot reform.

The decay in cathodic current density from its maximum value of i_s to the new steady-state $i_s(\infty)$ is explicable in a number of ways. For iron, all the cathodic scratch data lie below the thermodynamic equilibrium potential for bulk oxide formation, as shown in Fig. 4 (20). Nevertheless, some evidence exists for the presence of a monolayer of adsorbed FeOH on Fe at very low potentials (3, 4), and it seems likely that this monolayer could form over the surfaces generated as described above. Such a monolayer of film would retard evolution of H_2 and thereby reduce i_s to $i_s(\infty)$. Similar behavior is expected to occur for Cr at very low potentials: much of the data shown in Fig. 3 occurs, however, at potentials where bulk oxides can form, and the presence of such oxides would retard hydrogen evolution further. For the alloys one therefore expects the newly created oxide to contain more Cr than Fe (Fig. 5-7), and it is expected that an increase in Cr content would give a decrease in i_{b0} , since reduction of H_2O would occur on surfaces carrying increased amounts of bulk chromium oxides. The difference in the oxide composition before and after scraping gives rise to the difference between i_b and $i_s(\infty)$.

Alternatively, hydrogen bubbles may be generated beneath the film at the metal film interface and cause continuous disruption of the film. If this occurred only on the newly created film, then $i_s(\infty)$ would again be different from i_b . The third possibility is the saturation of the surface with H atoms from the reduction process. Such adsorbed H atoms can follow either of two possible paths after discharge: they can form H_2 bubbles which leave the surface, or they may be absorbed into the metal matrix. These H atoms can also give rise to reduction of any oxide film being formed over the scratch surface. The relative rates of each of these processes must be that which controls the new steady-state $i_s(\infty)$. It is clearly not possible to achieve this steady state electrochemically in the absence of fresh surface generation. This mechanism is still under investigation.

The catalytic effect can be described by a catalytic acceleration factor, defined by the ratio $i_{so}(\infty)/i_{bo}$. This ratio is independent of electrode potential for each metal. The quantity is shown in Fig. 11 as a function of the mol fraction of Cr (X_{Cr}) in the alloy. It is greatest for pure Cr. For comparison the instantaneous catalytic acceleration factor (i_{so}/i_{bo}) is also shown: this value is approximately independent of X_{Cr} .

It is noteworthy that not all metals which display underpotential behavior of the type thought to give rise to FeOH [e.g., CuOH on Cu (6)] display the behavior described above. Attempts to establish the behavior for Cu and Ni in 1.0M KOH gave no evidence of the existence of a new steady state after scratching at very negative potentials. A cathodic scratch transient for Ni is shown in Fig. 12. Decay of this cathodic current transient is complete in ~ 20 ms to within the lower limits of current detection in these experiments. The acceleration, if it exists, is therefore small.

The effect may have important repercussions with respect to the hydrogen embrittlement and stress-corrosion cracking of steels. Several articles have already been published concerning the effects of plastic strain applied to metals on the hydrogen diffusivity through the metals (11-14). For nickel, the presence of plastic strain appears to enhance the diffusivity of hydrogen in thin membranes; for $2\frac{1}{4}$ Cr-1 Mo steel, diffusion is retarded. The diffusion rate must, at least initially, depend on the surface activity of adsorbed hydrogen atoms, which in turn depends on the rate of discharge. It may also be important in stress-corrosion and corrosion fatigue crack propagation where the bare metal surface created by plastic strain (15) may cause enhanced discharge of hydrogen as the cathodic process to reoxidation of the bare metal at the crack tip. If the electrochemical potential at the crack tip remains low, hydrogen discharge will occur rapidly and permanently. The consequent increased diffusion rate of H atoms into the metal ahead of the crack tip may accelerate the onset of embrittlement. This situation will arise where the propagating crack is a region of restricted access to oxygen and the environment of poor conductivity.

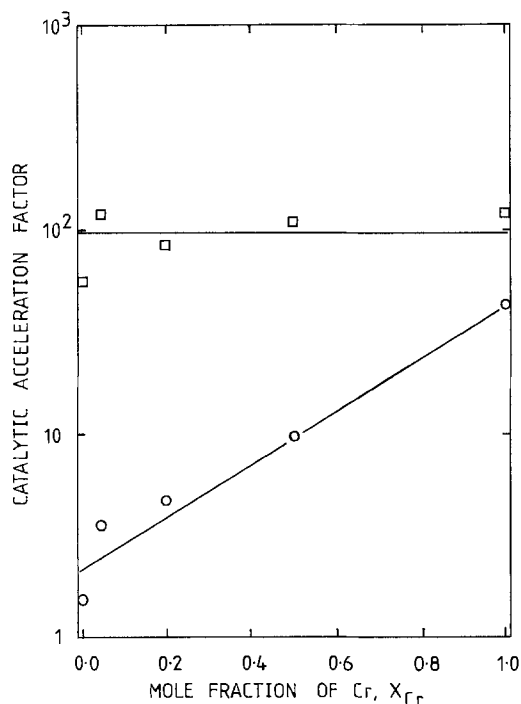


Fig. 11. Graphic representation of catalytic acceleration factor for evolution of hydrogen in 1.0M KOH: $\frac{i_{so}}{i_{bo}}$ (□) and $\frac{i_{so}(\infty)}{i_{bo}}$ (○) for Fe-Cr binary alloys.

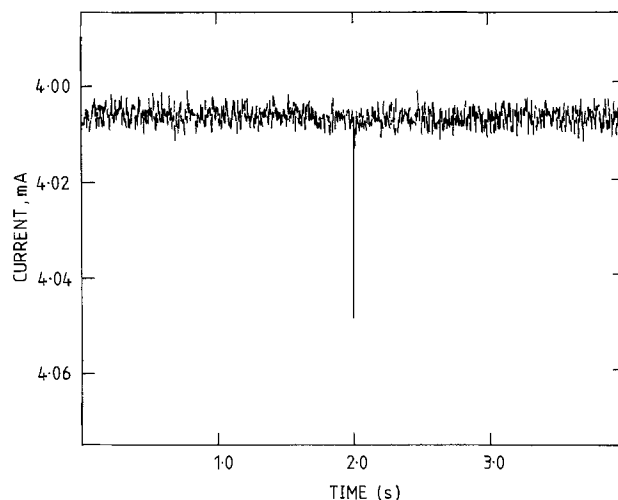


Fig. 12. Cathodic scratch current transient for Ni in 1.0M KOH at a potential of -1155 mV (NHE) recorded in the pretrigger mode. Within the resolution of the transient, the decay in current is complete.

Conclusions

1. Generation of a bare metal surface on Fe, Cr, and Fe-Cr alloys at low potential in aqueous solution causes accelerated evolution of hydrogen.
2. This accelerated reaction is a permanent feature of the newly created metal surface. Such surfaces cannot repair themselves without alteration of the electrode potential.
3. The behavior occurs both above and below the thermodynamic reversible potential for equilibrium between Cr and its oxides.
4. The steady-state rate of hydrogen evolution after generation of the new metal surface is similar for Fe, Cr, and their binary alloys.

Manuscript received March 31, 1983.

REFERENCES

1. F. P. Ford, G. T. Burstein, and T. P. Hoar, *This Journal*, **127**, 1325 (1980).
2. G. T. Burstein and D. H. Davies, *Corros. Sci.*, **20**, 1143 (1980).
3. G. T. Burstein and D. H. Davies, *This Journal*, **128**, 33 (1981).
4. G. T. Burstein and G. W. Ashley, *Corrosion*, **39**, 241 (1983).
5. G. T. Burstein and R. C. Newman, *Electrochim. Acta*, **25**, 1009 (1980).
6. G. T. Burstein and R. C. Newman, *This Journal*, **128**, 2270 (1981).
7. H. J. Pearson, G. T. Burstein, and R. C. Newman, *ibid.*, **128**, 2297 (1981).
8. G. T. Burstein and P. I. Marshall, *Corros. Sci.*, **23**, 125 (1983).
9. G. T. Burstein and R. D. K. Misra, *Electrochim. Acta*, **28**, 825 (1983).
10. G. T. Burstein, M. A. Kearns, and J. Woodward, *Nature*, **301**, 692 (1983).
11. R. M. Latanision and H. Opperhauser, Jr., in "Proceedings of the 3rd International Conference on Strength of Metals and Alloys," p. 472, Institute of Metals and Iron and Steel Institute (1973).
12. M. Kurkela and R. M. Latanision, *Scr. Metall.*, **13**, 927 (1979).
13. R. Otsuka and M. Isaji, *ibid.*, **15**, 1153 (1981).
14. M. Kurkela and R. M. Latanision, *ibid.*, **15**, 1157 (1981).
15. R. N. Parkins, in "Corrosion," 2nd ed., L. L. Shriener, Editor, Chap. 8.1, Butterworths, London (1976).
16. A. T. Stewart, in "Mechanisms of Environment Sensitive Cracking of Materials," P. R. Swann, F. P. Ford, and A. R. C. Westwood, Editors, p. 400, Metals Society, London (1977).
17. A. R. Troiano, *Trans. ASME*, **52**, 54 (1960).

18. J. Newman, *This Journal*, **113**, 501 (1966).
 19. N. Pentland, J. O'M. Bockris, and E. Sheldon, *ibid.*, **104**, 182 (1957).
 20. R. Parsons, "Handbook of Electrochemical Con-

- stants," p. 97, Butterworths, London (1959).
 21. M. Pourbaix, "Atlas of Electrochemical Equilibria in Aqueous Solutions," pp. 256, 307, Pergamon Press, Oxford (1966).

The Electrochemistry of Glassy 60Ni-40Nb in Aqueous Media

N. C. Grant and M. D. Archer*

Department of Physical Chemistry, University of Cambridge, Cambridge CB2 1EP, England

ABSTRACT

The electrochemistry of glassy melt-spun 60 atom percent (a/o) Ni-40 a/o Nb was investigated at moderate temperatures in various aqueous media. The alloy was very corrosion resistant to most acids and alkalis, but it was attacked by aqueous HF. Cyclic voltammograms of the glassy alloy in 15M NaOH indicated the existence of a thin nickel oxide corrosion layer from which niobium was absent. Linear sweep voltammetry in the oxygen evolution region, constant current chronopotentiometry, and rest potential decay measurements confirmed that the alloy surface in alkali consisted of nickel oxides. Chronopotentiometry in 0.5M H₂SO₄ at 30°C indicated the formation of a thin niobium oxide corrosion film which did not prevent oxygen evolution. Anodization in concentrated neutral KCl caused severe corrosion. On cathodization in acid, the glassy alloy absorbed ca. 14 a/o hydrogen and was severely embrittled. Attempted hydrogen permeation experiments caused ribbon fracture; as-quenched and low temperature-annealed glasses behaved differently in this respect.

The vitrification of metallic alloys affects all their properties, including their electrochemistry. The novel and useful combination of toughness, strength, and corrosion resistance which can be produced (1, 2) has stimulated much research into the electrochemistry of glassy metals. To date, most work has been on Fe- and Ni-based glasses containing ca. 20 atom percent (a/o) metalloid (3), some of which have remarkable magnetic properties (4). This paper is a contribution to the work on metal-metal glasses and examines the electrochemical properties of melt-spun glassy 60Ni-40Nb in a range of aqueous media at or near room temperature. The behavior of this alloy in more aggressive high-temperature aqueous media is reported in the following paper (5). The alloy 60Ni-40Nb was chosen as a typical representative of the T₁T₂ type of metallic glass, in which T₁ is an early transition metal and T₂ a late one.

Relatively little electrochemical work has been carried out on metal-metal glasses. Glassy Cu-Zr (6), Ti-Ni (7), and Al-Fe (8) have been investigated, and there is only one brief report on glassy (100-x) Ni-xNb (9). Polyphasic crystalline Ni-Nb alloys have been examined by Trusov *et al.* (10) in 3M HCl and 1M H₂SO₄ and by Sugimoto *et al.* (11, 12) in 25 weight percent (w/o) KOH.

The composition 60Ni-40Nb is very close to one of the eutectic compositions in the Ni-Nb phase diagram (13), so glasses of this composition are readily formed, though a wider compositional range is possible; Giesen *et al.* (14) have reported the melt spinning of Ni-Nb glasses containing 25-60 a/o Ni. Glassy Ni-Nb alloys were first prepared in 1967 (15), and since then they have been well characterized. Data are available on their structure (16-18), electronic structure (19), electrical resistivity (20), mechanical properties (14, 21), and some thermal properties (14). Information on the production of amorphous 60Ni-40Nb (22) and 50Ni-50Nb (23) by laser glazing, and on ion implantation damage in amorphous and crystalline 60Ni-40Nb (24), is available.

Experimental

Three electrode voltammetry was performed with a Hi-Tek DT 11001 potentiostat and PPR1 function generator. Galvanostatic experiments were made using a Time Electronics constant current source. Solutions

were prepared from AR-grade chemicals and triply distilled water, and were sparged with nitrogen.

Ni and Nb electrodes were made from Specpure materials (Johnson Matthey, Royston, Herts). Cylinders of metal were embedded in thermosetting plastic to give circular electrodes of diameter 0.7 cm (Nb) and 0.5 cm (Ni). Crystalline ingots of 60Ni-40Nb were produced by melting appropriate masses of Ni (99.99%) and Nb (99.9%) (Goodfellow Metals, Limited, Cambridge) under argon in an arc furnace. Glassy 60 a/o Ni-40 a/o Nb ribbons, typically 2 mm wide and 20 μm thick, were formed by the melt spinning technique (25). The ribbons were spun in air and hence possessed a thin, air-formed film. No crystallinity was discernible by x-ray diffractometry. Glassy 60Ni-40Nb electrodes of known area were made by affixing lengths of ribbon to glass supports and masking the edges with epoxy cement. All electrodes were polished before use with Hyprez 1 μm diamond paste, washed with ethanol, and dried. Ag/AgCl (3M or saturated KCl) reference electrodes were used in acid solutions, and Hg/HgO (1M NaOH) reference electrodes were used in alkaline solutions. The reference electrodes were housed in Luggin capillaries positioned within 0.5 mm of the working electrode surface. IR compensation was not applied, because IR drop was negligible except at the highest current densities used in Fig. 3.

The transport of hydrogen through the glassy alloy was studied using the dual electrochemical permeation cell of Devanathan and Stachurski (26). The ribbons under study, which were all ca. 30 μm thick, were mounted between two Teflon flanges in which slits had been machined to expose 0.288 cm² of ribbon on either side. The two flanges were then sandwiched between the two glass vessels which formed the two compartments of the cell. The inner faces of the two Teflon flanges were coated with epoxy cement prior to assembly to ensure a watertight seal. In one compartment of the assembled cell, hydrogen was generated at constant current on the ribbon surface, which acted as a cathode. The galvanostatic circuit comprised a dc power supply, a large resistor, and a platinum anode isolated behind a frit. In the other cell compartment, the other surface of the ribbon was the anode of a three-electrode potentiostatic experiment, in which the reference electrode was Hg/Hg₂SO₄ (saturated K₂SO₄). The potential of this face of the ribbon was maintained at 0.256V NHE, which is sufficiently positive to oxidize all hydrogen permeating

* Electrochemical Society Active Member.
 Key words: glassy metal, Ni-Nb alloy.

the ribbon. Thus, the permeation current is a measure of the instantaneous flow of hydrogen out of the ribbon.

In both compartments of the permeation cell, the electrolyte was 0.56M H₂SO₄. Initially, both compartments were sparged with nitrogen, but it was subsequently found that background currents were negligible in aerated solution, so the practice was discontinued. All permeation experiments were performed at room temperature.

Results and Discussion

Glassy 60Ni-40Nb proved to be generally very resistant to electrochemical corrosion. In 30 day immersion tests in aerated, unstirred 1M HCl, 30% NaOH, 10% FeCl₃, and aqueous polythionic acid (27), the weight loss of freely corroding specimens was undetectable (<0.3 mg dm⁻² day⁻¹); the samples appeared unchanged at the end of the tests. Sugimoto *et al.* (12) have reported that crystalline Ni-Nb alloys containing >47% Ni also showed negligible weight loss in 20 day immersion tests in aerated 25% KOH at 25°C. The only aqueous medium that caused evident attack on freely corroding glassy 60Ni-40Nb was hydrofluoric acid; in aerated, unstirred 5% HF at room temperature, the weight loss in an 80h test corresponded to a corrosion rate of 142 mg dm⁻² day⁻¹, and the samples were blackened and embrittled. Under the same conditions the corrosion rate of crystalline Ta is >593 mg dm⁻² day⁻¹ (28). Figure 1 shows the free corrosion potentials E_{corr} of Ni, Nb, and glassy 60Ni-40Nb in 5% HF and three other media. In HF, Nb adopts a free corrosion potential close to that of the Nb/NbF₇²⁻ couple [$E^\circ = -0.355\text{V NHE}$ (29)] and dissolves as fluoride complexes. Ni is extremely resistant to HF, being protected by a layer of insoluble fluorides, and the glassy alloy adopts an intermediate corrosion potential. Nb also dissolves slowly in 1M NaOH, forming niobates. Ni is resistant to alkalis, being protected by a film of hydrated oxides, and as the corrosion potentials (Fig. 1) show, the glassy alloy again adopts a potential intermediate be-

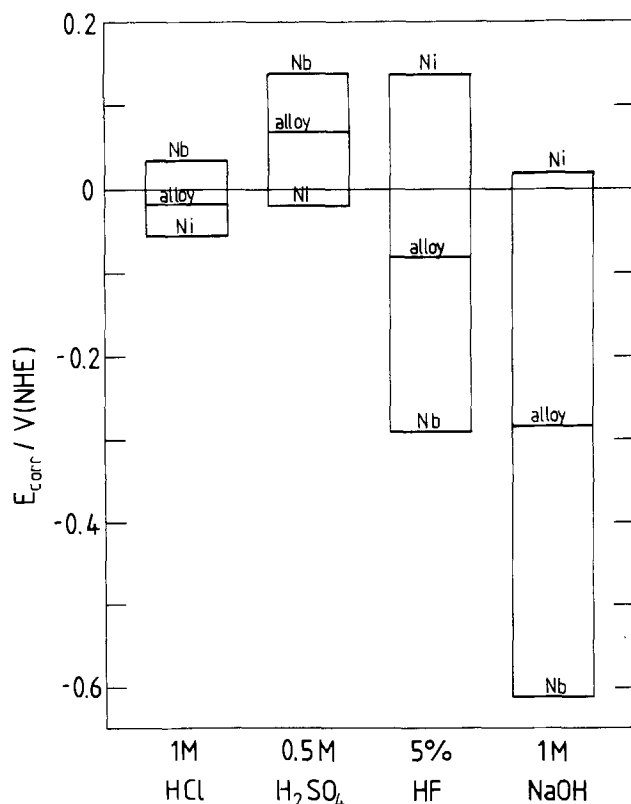


Fig. 1. The free corrosion potential E_{corr} adopted by Ni, Nb, and glassy 60Ni-40Nb in aqueous media at 19°C. Glassy 60Ni-40Nb is indicated by the word "alloy."

tween those of its two components. In 1M HCl and 0.5M H₂SO₄, Ni dissolves and Nb is passivated by a layer of Nb₂O₅, so that Nb adopts a more noble corrosion potential than Ni, and the glassy alloy again exhibits an intermediate corrosion potential.

We established from high temperature electrochemical work (5) that, in alkaline media at 150° and 300°C, Nb is leached from the alloy surface, leaving a nickel oxide corrosion layer, whereas in acidic media Ni is leached from the alloy surface, leaving a niobium oxide scale. At these high temperatures, the corrosion layers reach a thickness of the order of microns, and the dissolved component is chemically detectable in solution. At room temperature, similar chemical behavior is likely, although the corrosion films are evidently much thinner and the quantities of Ni dissolving in acid, and Nb in alkali, will be correspondingly much smaller. Results to be described (Fig. 3 and 6) provide confirmatory evidence that the corrosion films formed on the glassy alloy at room temperature are indeed chemically similar to those formed at higher temperatures. However, in room temperature tests on the glassy metal, we could not detect any dissolution of Ni in acid or of Nb in alkali. In the first test, 1 cm⁻² of abraded ribbon surface was polarized at 100 $\mu\text{A cm}^{-2}$ for 17.5h in 1 cm³ of 0.5M H₂SO₄. No nickel was detected in the resulting solution by the dimethyl glyoxime test, implying a Ni dissolution rate of <0.08 mg dm⁻² day⁻¹. [We note that Trusov *et al.* (10) have reported an apparently abrupt cessation of the ability of Nb to passivate Ni-Nb crystalline alloys in 1.5M H₂SO₄ and 3M HCl between the compositions 75Ni-25Nb and 85Ni-15Nb.] In the second test, 1 cm² of abraded ribbon surface was polarized at 10 mA cm⁻² for 17.5h in 1 cm³ of 30% KOH. No precipitate of Nb₂O₅ appeared on neutralization and dilution of the resulting solution.

The cyclic voltammograms (CV's) of the glassy alloy were recorded in a range of aqueous media corrosive either to nickel or to niobium. No features other than oxygen and hydrogen evolution were observed (at a sensitivity of 1 $\mu\text{A cm}^{-2}$) in the case of the following room temperature solutions: acidic NaClO, 10M NH₄F, 10% FeCl₃, 1M Na₂S₂O₃, 0.6M Na₂S₂O₃ + 0.9M KCl, 1M H₃PO₄, 0.5M H₃PO₄ + 0.5M HCl, 1M HCl + 0.5M H₂SO₄. The CV's in the region of hydrogen evolution, particularly in 1M H₃PO₄, resembled those of palladium in acid. This suggested that the glassy alloy absorbed some of the evolved hydrogen.

The only procedure we discovered which caused thick corrosion layers to be produced on glassy 60Ni-40Nb at room temperature was anodization in strong neutral chloride solutions. Chlorine evolution from concentrated KCl produced Ni(II) in solution and a cloudy precipitate of Nb₂O₅. A thick (~10 μm) striated corrosion layer, shown in section in Fig. 2a, was formed on the glassy metal. The face of the scale was cracked into blocks, as shown in Fig. 2b. It seems probable that the presence of chloride or chlorine causes the growing corrosion layer to crack and hence be unprotective. The films formed by oxygen evolution do not crack, being totally featureless at magnifications up to 5000 \times ; hence, they are protective and much thinner.

It is of interest to note that Trusov *et al.* (10) observed a current efficiency of only $2 \times 10^{-3}\%$ for anodic dissolution from a crystalline 75Ni-25Nb alloy polarized at 50 mA cm⁻² in 3M HCl for 24h. We also found no evidence of corrosion when the glassy alloy was anodized in 1M HCl. The much greater corrosive power of neutral KCl must be attributed to the higher pH.

Figure 3 shows the CV's of the glassy alloy and crystalline Ni and Nb in 15M NaOH at room temperature. Nb (Fig. 3b) gives a large anodic peak at low potential due to dissolution as a niobate, and partial passivation occurs at higher potentials. Sugimoto *et al.*

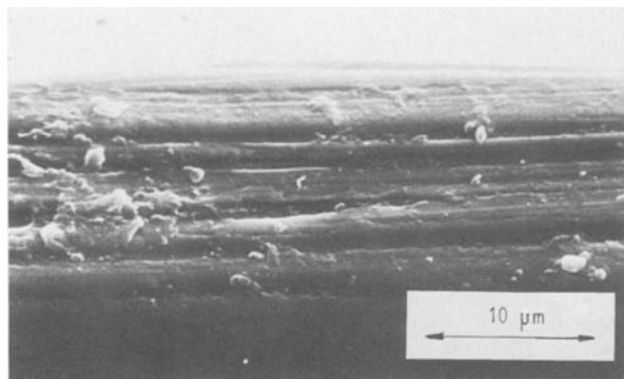
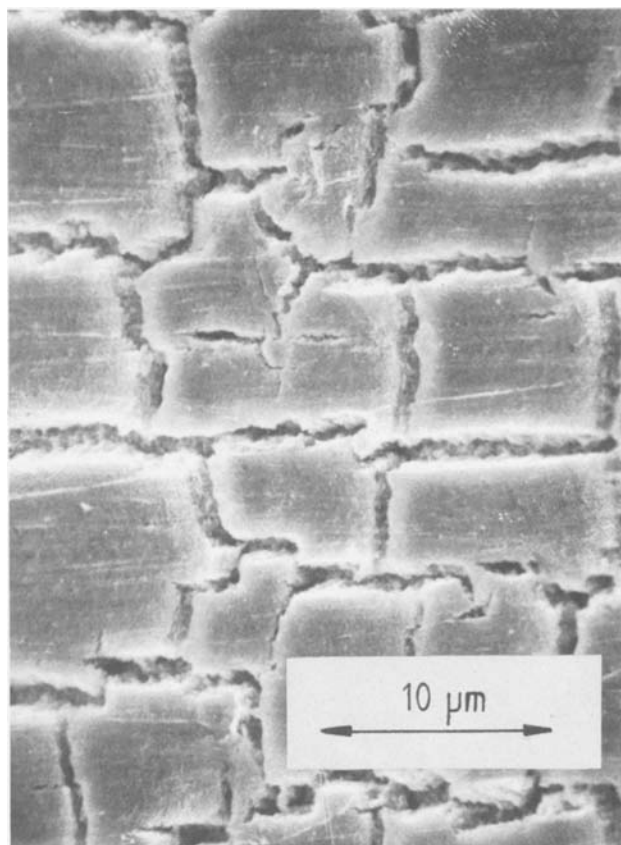


Fig. 2. Scanning electron micrographs of the corrosion layer formed on glassy 60Ni-40Nb by chlorine evolution at room temperature. A, above: sectional view. B, right: face-on view. The sample was anodized for 10 min at 100 mA cm^{-2} in 1 M KCl .



(12) have reported similar behavior for Nb in 25% KOH at 25°C . Ni (Fig. 3c) shows no active dissolution region, but rather a conjugate pair of peaks, I and II. The glassy alloy (Fig. 3a) shows a very similar pair of peaks, I at 0.43V and II at 0.29V NHE. We ascribe these features to a composite $\text{Ni}_3\text{O}_4/\text{Ni}_2\text{O}_3/\text{NiO}_2$ surface transformation, for reasons discussed below in connection with Fig. 5. The CV of the glassy alloy (Fig. 3a) does not show the Nb dissolution region of Fig. 3b, indicating that the nickel oxide surface film formed in NaOH contains very little elemental Nb. Any Nb originally present in the glassy alloy surface (probably as an oxide) must have dissolved chemically before the first electrochemical experiment. At lower concentrations of NaOH, the nickel oxide transformation peaks in the CV of the glassy alloy are much less pronounced; in 1 M NaOH , they were not observable.

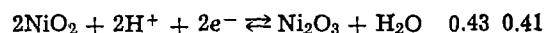
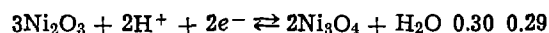
The linear sweep voltammograms (LSV's) of glassy 60Ni-40Nb and crystalline Ni in the oxygen evolution region are shown in Fig. 4. The medium chosen (30% KOH at 70°C) is typical of those used in alkaline water electrolyzers. Freshly polished electrodes were used for comparability, because the behavior of these anodes is fairly time dependent, although not very sweep-rate-dependent, as a comparison of Fig. 4b and 4c shows. The oxygen evolution characteristics of the glassy alloy (Fig. 4a) closely resemble those of Ni, which is consistent with the view that the alloy surface is composed of nickel oxides.

The redox transformations of the corrosion films formed on the glassy alloy in 30% KOH at 70°C were further investigated by constant-current chronopotentiometry and by measurement of the decay of the rest potential after anodic potentiostasis. Curve 1 of Fig. 5a shows the first galvanostatic experiment on a freshly polished electrode. At $t = 0$, prior to the passage of current, the rest potential of the glassy alloy was -0.75V NHE, and when the anodic current of 10 mA cm^{-2} was applied, the potential rose rapidly to a plateau at 0.47V , maintained for 0.29s , before it rose further to a second plateau at 0.67V , at which point

oxygen evolution occurred. When the current was reversed, the potential fell to a plateau at 0.365V , maintained for 0.21s , and then fell rapidly again to a second plateau at -1.27V , at which point hydrogen evolution occurred. A train of successive anodic and cathodic half-cycles of 2.8s duration was applied. The second, seventh, and tenth cycles are also shown in Fig. 5a. The cathodic plateau at 0.365V lengthened slightly with sweep number, but the general features of the chronopotentiogram were reproducible. Figure 5b shows the decay in rest potential of a glassy alloy electrode after it had been held at a potential of 2.1V for 5s . This decay curve is qualitatively very similar to the cathodic chronopotentiograms, showing a potential arrest at 0.365V , although the decay takes much longer at open circuit than when a cathodic current is passed. Similar work on Ni in alkali produces charging curves very similar to those of Fig. 5. For example, the anodic and cathodic plateaus observed by Briggs *et al.* (30) in 1 M KOH at 25°C and a charging current of 2 mA cm^{-2} were 0.53 and 0.47V NHE, respectively.

Equilibrium thermodynamics must be cautiously applied in considering these results, since the temperatures are moderate and the rates of change of current and potential are high. However, the two processes most probably responsible for these features, and their redox potentials, E_1 and E_2 , interpolated or calculated from the literature (31, 32) for (i) 15 M NaOH at room temperature (calculated pH 17) and (ii) 30% KOH at 70°C (calculated pH 14.9), respectively, are

$$E_1 \quad E_2$$



The literature on the electrochemical formation of these nickel oxides on nickel is conflicting. Macdonald and Owen (33), from a consideration of the thermodynamics, assign the potential arrests in the chronopotentiogram to the conversion of Ni_2O_3 to NiO_2 , but the observation, by x-ray diffractometry of *in situ* elec-

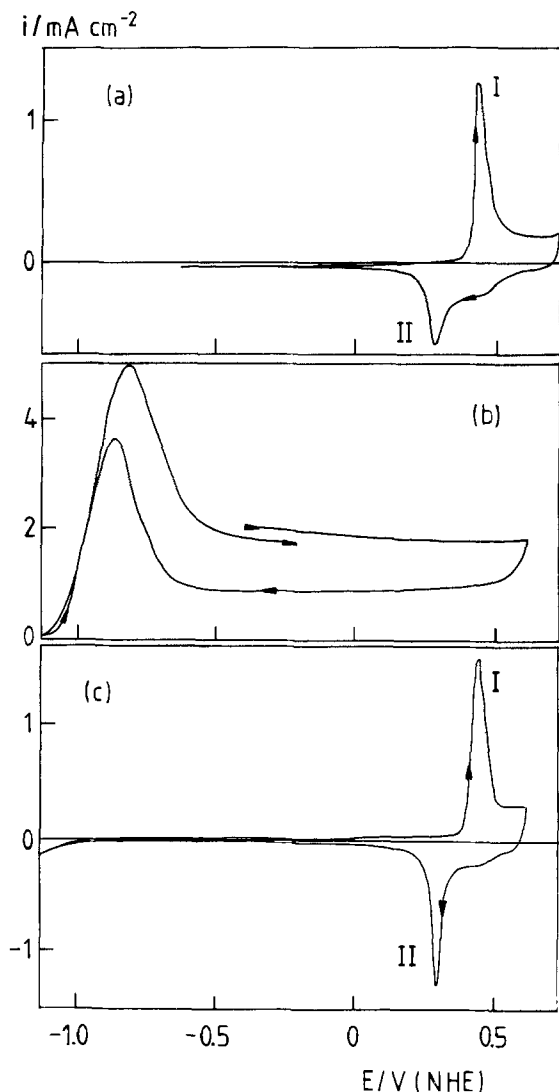


Fig. 3. Cyclic voltammograms of (a, top) glassy 60Ni-40Nb, (b, center) Nb, and (c, bottom) Ni in 15M NaOH at room temperature. Sweep rate: 100 mV s⁻¹.

trodes (34, 35), of the conversion of Ni(OH)₂ to β -NiOOH at this potential cannot be lightly dismissed. However, NiO₂ is reported to be amorphous to x-rays (32, 33), and there is magnetic evidence for the production of Ni(IV) in the electrochemical oxidation of Ni(OH)₂ (38, 39).

At 150° and 300°C in alkali, two closely spaced but distinct peaks are observed in the CV's of both Ni and glassy 60Ni-40Nb (5). We have ascribed these to the Ni₃O₄/Ni₂O₃ and Ni₂O₃/NiO₂ transformations. At lower temperatures, these transformations will be slower. As we have already noted, the potential arrests observed in the galvanostatic experiment of Fig. 5 (0.47 and 0.365V) are comparable with the anodic and cathodic peak potentials (0.43 and 0.29V, respectively) in the CV of the glassy alloy (Fig. 3c). From a comparison of these potentials with E_1 and E_2 above, we conclude that the peaks of Fig. 3 and the potential arrests of Fig. 5 are probably composites of the Ni₃O₄/Ni₂O₃ and Ni₂O₃/NiO₂ redox processes.

The constant-current chronopotentiograms of glassy 60Ni-40Nb and crystalline Nb in 0.5M H₂SO₄ at 30°C are shown in Fig. 6a. On passage of the anodic current, the potential of the glassy alloy rises smoothly and then levels off as oxygen evolution occurs. When the current is reversed, the potential falls rapidly to the hydrogen evolution plateau at -0.38V NHE, although there is a brief arrest at -0.10V. The decay of the rest potential of a glassy alloy electrode after anodic

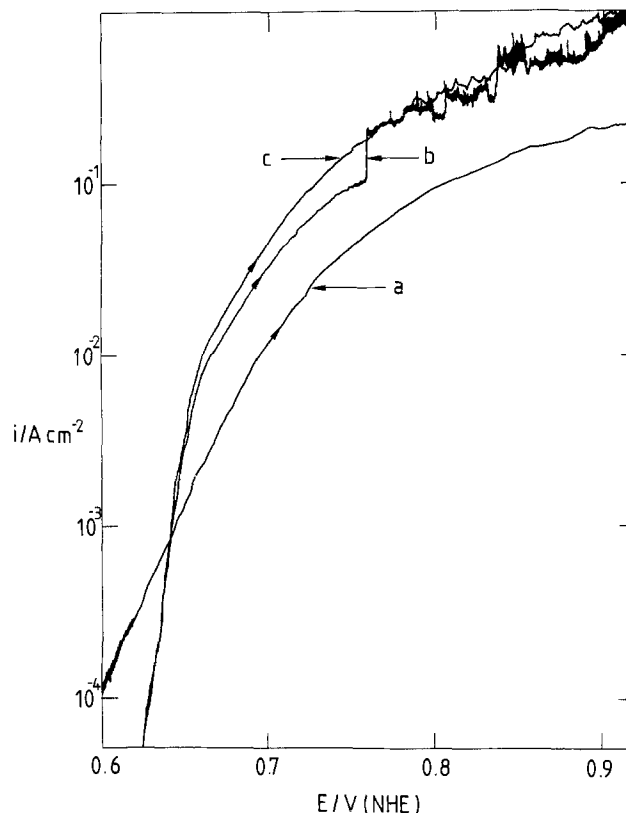


Fig. 4. Linear sweep voltammograms of freshly polished electrodes in 30% KOH at 70°C. Curve a: glassy 60Ni-40Nb; sweep rate 1 mV s⁻¹. Curve b: Ni, sweep rate 1 mV s⁻¹. Curve c: Ni, sweep rate 10 mV s⁻¹.

potentiostasis (Fig. 6c) is qualitatively similar, though again much slower. The glassy alloy is exhibiting a niobium oxide-like surface in this acidic medium, although niobium itself behaves rather differently on anodic charging. The Nb potential continues to rise without oxygen being evolved, as a resistant layer of Nb₂O₅ thickens on the surface. As the potential passes through the range 10-150V, the film exhibits the expected range of interference colors. Film breakdown occurs at about 160V.

The smooth rise in potential of the glassy alloy on passage of the anodic current can be ascribed to thickening of the film, which is evidently less resistive when formed on the glassy alloy substrate than on pure Nb. It is never possible to grow thick Nb₂O₅ films on the glassy alloy surface in acidic conditions because oxygen evolution occurs at quite modest overpotentials. The features in the glassy alloy discharge curve cannot be assigned with certainty. However, the rapidity of the potential decay in Fig. 6b compared with the potential rise is worthy of note: in the film growth region ($t = 0$ to $t = 104$ s in the anodic half-cycle) the charge passed was 10.4 mC cm⁻², whereas in the cathodic half-cycle ($t = 0$ to $t = 10$ s after current reversal) the charge passed before the onset of hydrogen evolution was only 1 mC cm⁻². The potentials of all the Nb/Nb oxide couples are so low that it is quite possible that a niobium oxide film persists on the electrode during hydrogen evolution.

The kinetics of hydrogen evolution on glassy 60Ni-40Nb in acidic solutions are complicated by absorption of hydrogen into the alloy, which readily occurs on cathodization. This uptake of hydrogen manifests itself both physically and electrochemically. Physically, the absorption of hydrogen results in the expansion of the metal (as shown by the curling of an initially straight piece of ribbon when hydrogen is evolved on one side only) and its embrittlement. Prolonged hy-

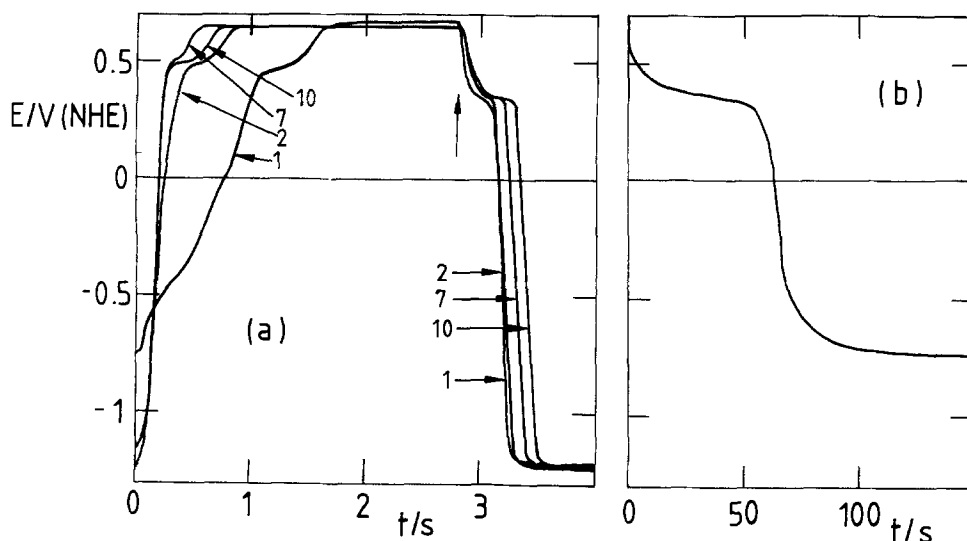


Fig. 5. A, left: galvanostatic charging curves of glassy 60Ni-40Nb in 30% KOH at 70°C. Between $t = 0$ and $t = 2.8$ s, the anodic current density was 10 mA cm^{-2} . At $t = 2.8$ s (marked with a vertical arrow) the current was reversed. The electrode was polished before the first cycle only. B, right: decay of open-circuit potential of glassy 60Ni-40Nb in 30% KOH at 70°C after potentiostasis at 2.1V NHE for 5s.

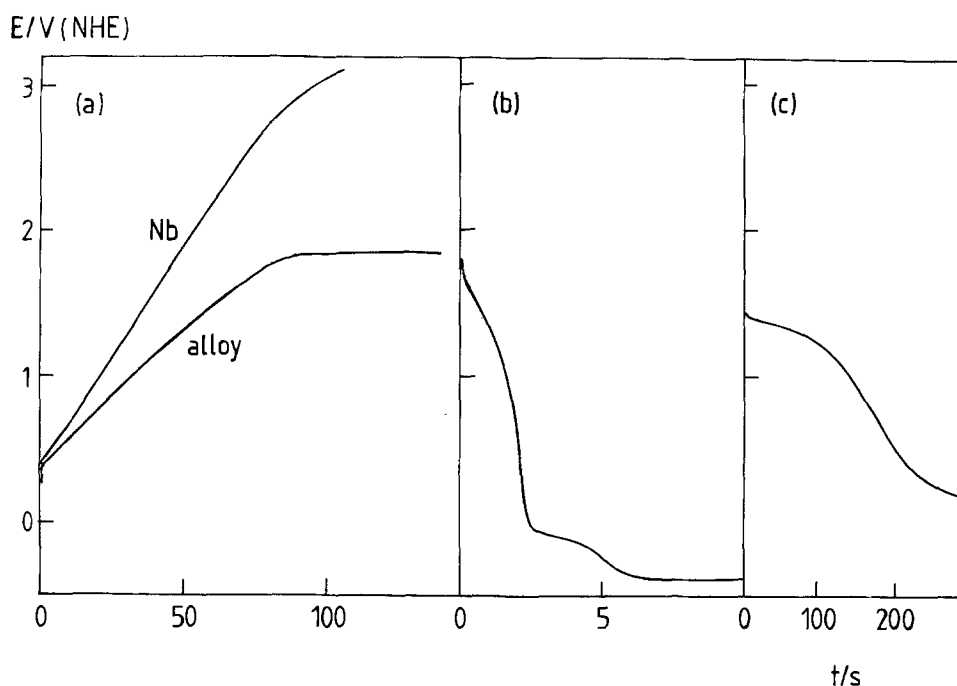


Fig. 6. A, left: galvanostatic charging curve of glassy 60Ni-40Nb (indicated by the word "alloy") in 0.5M H₂SO₄ at 30°C. Anodic current density $100 \mu\text{A cm}^{-2}$. The anodic charging curve for Nb under the same conditions is shown for comparison. B, center: discharge curve for glassy 60Ni-40Nb after current reversal (at $t = 300$ s in Fig. 6a). C, right: decay of open-circuit potential of glassy 60Ni-40Nb in 0.5M H₂SO₄ at 30°C after potentiostasis at 2.2V NHE for 300s.

drogen evolution causes the alloy to become friable and to disintegrate. Electrochemically, the absorption of hydrogen results in non-Tafel behavior and time dependence in the hydrogen evolution region, the overpotential increasing with time and the Tafel slope decreasing from its initial value of $115 \text{ mV decade}^{-1}$. This time dependence was not noted by Naka *et al.* (9), but they showed that the hydrogen evolution overpotential increases with increasing x in the alloys $(100 - x)\text{Ni}-x\text{Nb}$.

Considerable quantities of hydrogen are dissolved by glassy 60Ni-40Nb on cathodization. For example, after 70h potentiostasis at -0.3V NHE in $1\text{M H}_2\text{SO}_4$ at room temperature, the hydrogen content (measured with a Strohlein H-mat) corresponded to the atomic composition 86.5(60Ni-40Nb)-13.5H. Even after this time, the hydrogen content was still rising slowly, so this is not a limiting composition. The composition 78(60Ni-40Nb)-22H was reached by three days cathodization at 1A in $0.56\text{M H}_2\text{SO}_4$. The high solubility of hydrogen in the glassy alloy is not surprising since both its components form hydrides: up to $\text{NbH}_{2.97}$ (40) and a distinct $\text{NiH}_{0.7}$ phase (41) can be formed electrochemically. Crystalline 10Ni-90Nb and 31Ni-69Nb are also hydrogen embrittled by cathodic polarization in 25% KOH (11); the spalled surface layers produced

by 20 days' immersion at the free corrosion potential had the composition $\text{NbH}_{0.89}$ (12).

These indications of the absorption of hydrogen by the glassy alloy led us to the permeation experiments illustrated in Fig. 7-9, initially undertaken with the aim of measuring the diffusion coefficient of hydrogen in the material. Figure 7 shows typical transients for as-quenched, polished ribbons and two different generating currents i_{gen} . Experiments on different ribbon samples yielded qualitatively similar results. The permeation current did not increase smoothly with time to a constant limiting current, as it does for simple diffusion, but rather exhibited pronounced variations about a roughly linearly increasing mean. The breakthrough time (*i.e.*, the time at which the permeation current is first observed) was long and irreproducible, varying by an order of magnitude. This is probably due to varying amounts of residual or reformed oxide film on the ribbon surfaces. When the generating currents were switched off the permeation currents fell rapidly to zero, as illustrated in Fig. 7a. This indicates that mechanical failure of the alloy had occurred, shorting the ribbon bielelectrode.

Figure 8 illustrates the rather different transients obtained on ribbons annealed *in vacuo* for 30 min at 642°C : this anneal produced no crystallinity detectable

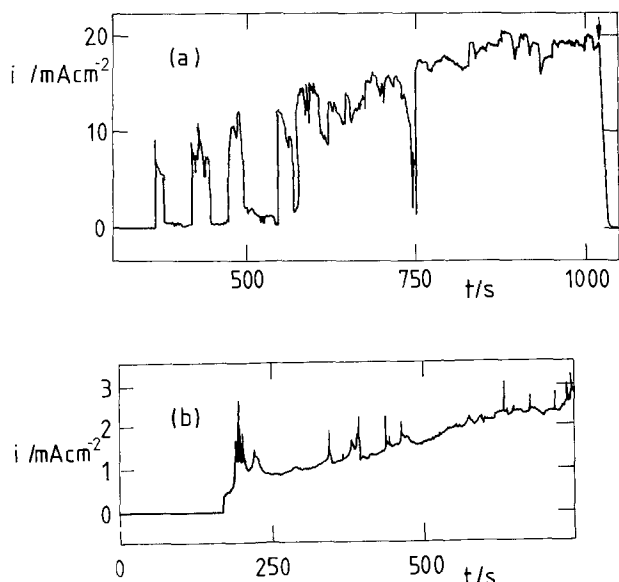


Fig. 7. Electrolytic hydrogen permeation currents for unannealed, polished glassy 60Ni-40Nb foils for generating currents i_{gen} of (a, top) 20.8 mA cm^{-2} and (b, bottom) 3.8 mA cm^{-2} . The vertical arrow indicates the time at which the generating current was switched off.

by x-ray diffractometry. The rising transient for the annealed glassy alloy is much smoother, though the shape is still not that predicted theoretically for simple diffusion under well-defined boundary conditions. The breakthrough times are still very irreproducible. The decay on switching off i_{gen} remains very abrupt, whereas for simple diffusion it should be gradual. Figure 8b shows a transient obtained with an annealed ribbon, cold-rolled to 95% of its original thickness, and subsequently polished. Evidently cold-rolling has little effect on the permeation characteristics: even severe cold-rolling to 75% of the original thickness did not modify the general form of the transients observed on annealed ribbons.

These results differ greatly from those obtained from permeation experiments on crystalline metals such as Pd and Ni (42) or Fe (43). Hydrogen atoms diffuse through these metals in an essentially non-cooperative manner, so that permeation currents rise and fall smoothly. The cause of the behavior observed with glassy 60Ni-40Nb is not the glassy structure per se, for Latanision *et al.* (6) and Lin and Johnson (44) have observed normal permeation transients for Fe-Ni-P-B glasses; rather, we attribute the observed behavior to the mechanical damage inflicted on the Ni-Nb alloy by hydrogen uptake. Ribbon fracture occurs as the permeation experiment progresses. This is made evident in two ways. First, leakage between the two cell compartments can be observed, and the ribbon dis-

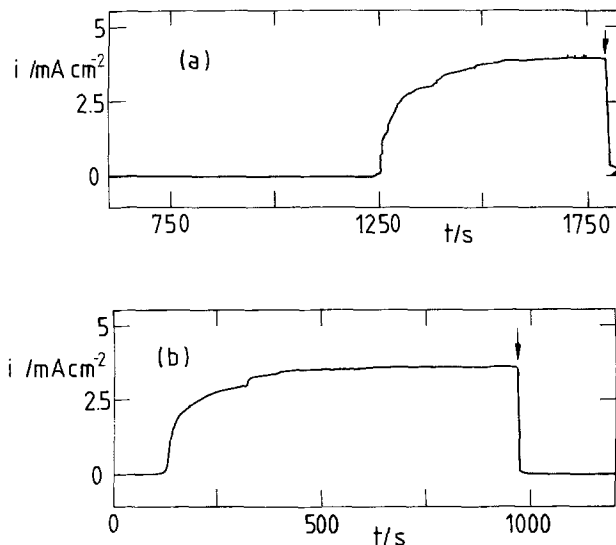


Fig. 8. Electrolytic hydrogen permeation currents for glassy 60Ni-40Nb foils. A, top: ribbon annealed and polished. B, bottom: ribbon annealed, cold-rolled, and polished. The generating current was 3.8 mA cm^{-2} for both a and b, and the ribbons were annealed *in vacuo* for 30 min at 642°C . The vertical arrows indicate the times at which the generating currents were switched off.

integrates on handling. Second, the permeation current becomes equal to the generating current: this occurs when a sufficiently large channel of electrolyte is formed by cracking the ribbon to short the bielectrode completely out of the circuit. This condition is attained in Fig. 9a and 9b, which were obtained using lower generating currents on annealed ribbons. Little or no hydrogen permeates the ribbons before the abrupt increase in permeation current that indicates mechanical failure. Fragments of fractured ribbon examined microscopically at magnifications up to $1500\times$ showed brittle fracture surfaces which were often decorated with microcracks.

The very irregular form of the permeation transients obtained for the as-quenched ribbons as compared with the much smoother transients for the annealed ribbons is of interest. In as-quenched melt-spun ribbons, a high concentration of diffuse defects exists. In particular, excess free volume may be distributed over a number of atomic sites (45). Annealing relaxes the glassy structure and reduces the excess free volume. Low temperature annealing often causes some loss in ductility (46), and does so in 60Ni-40Nb. Cold-rolling introduces shear bands. The similarity of Fig. 8a and 8b shows that the introduction of shear bands does not significantly alter the permeation of the annealed alloy by hydrogen. Since it is unlikely that the surface films (which are no doubt present on both ribbon faces) are significantly different for annealed as com-

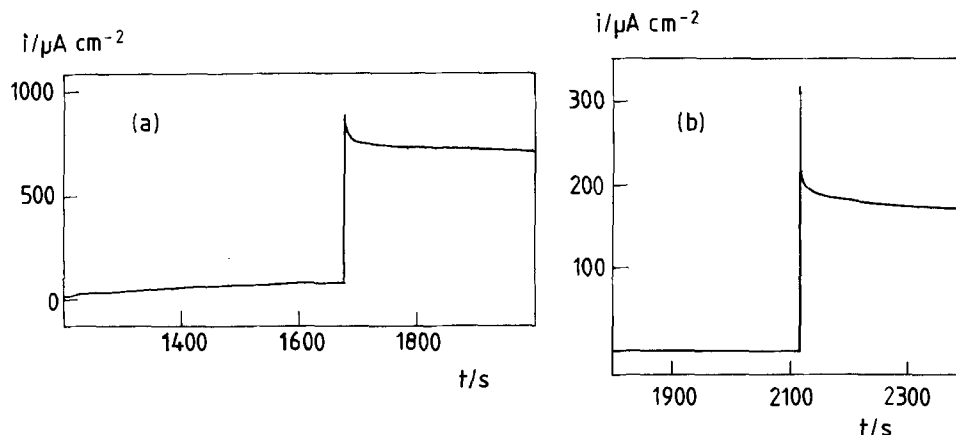


Fig. 9. Electrolytic hydrogen permeation currents for annealed, polished glassy 60Ni-40Nb foils for generating currents of (a, left) $695 \mu\text{A cm}^{-2}$ and (b, right) $174 \mu\text{A cm}^{-2}$.

pared with as-quenched ribbons, it follows that the difference in bulk structure must be responsible for the difference in permeation behavior. Hydrogen embrittlement is thought to occur by concentration of the hydrogen in regions in which its Gibbs energy is lowest. This causes local expansion of the solid; cracking then occurs in response to the stress created by nonuniform expansion. In the as-quenched glass, hydrogen could accumulate in the quenched-in diffuse defects, resulting in a nonuniform distribution of hydride phase and severe embrittlement: this occurs when crystalline Nb is cathodically charged (40, 47). In the annealed material, the structure is much more homogeneous, and thus the absorbed hydrogen is likely to be less localized. Consequently, the annealed glassy alloy fails in a less dramatic manner than the as-quenched material.

Acknowledgments

We thank R. J. McKim for weight loss measurements on glassy 60Ni-40Nb and B. H. Harji for checking the cyclic voltammograms.

Manuscript submitted June 21, 1983; revised manuscript received Dec. 30, 1983.

The University of Cambridge assisted in meeting the publication costs of this article.

REFERENCES

- P. Chaudhari, B. C. Giessen, and D. Turnbull, *Sci. Am.*, **242**, 98 (1980).
- C. Grant and R. McKim, *New Sci.*, **94**, 637 (1982).
- Y. Waseda and K. T. Aust, *J. Mater. Sci.*, **16**, 2337 (1981).
- Passim, "Glassy Metals I," Topics in Applied Physics, Vol. 46, H. J. Guntherodt and H. Beck, Editors, Springer-Verlag, Berlin (1981).
- N. C. Grant and M. D. Archer, *This Journal*, **131**, 1004 (1984).
- R. M. Latanision, J. C. Turn, Jr., and C. R. Compeau, in "Proceedings of the 3rd International Conference on Mechanical Behaviour of Materials," Vol. 2, K. J. Miller and R. F. Smith, Editors, p. 475, Cambridge, England, 1979, Pergamon, Oxford (1980).
- M. Naka, K. Asami, K. Hashimoto, and T. Masumoto, in "Proceedings of the 4th International Conference on Titanium," H. Kimura and O. Izumi, Editors, p. 2677, AIME, New York (1980).
- G. Faninger, D. Merz, and H. Winter, in "Proceedings of the 2nd International Conference on Rapidly Quenched Metals," N. J. Grant and B. C. Giessen, Editors, Massachusetts Institute of Technology, Cambridge, MA (1976).
- M. Naka, K. Hashimoto, T. Masumoto, and I. Okamoto, in "Proceedings of the 4th International Conference on Rapidly Quenched Metals," T. Masumoto and K. Suzuki, Editors, Japan Institute of Metals, Sendai, Japan (1982).
- G. N. Trusov, E. P. Gochalieva, B. A. Goncharenko, and V. S. Mikheev, *Sov. Electrochem.*, **13**, 895 (1977).
- K. Sugimoto, G. Belanger, and D. L. Piron, *Surf. Technol.*, **9**, 83 (1979).
- K. Sugimoto, G. Belanger, and D. L. Piron, *Corrosion*, **36**, 437 (1980).
- M. Hansen, "Constitution of Binary Alloys," 2nd ed., p. 1010, McGraw-Hill Inc., New York (1958).
- B. C. Giessen, M. Madhava, D. E. Polk, and J. Vander Sande, *Mater. Sci. Eng.*, **23**, 145 (1976).
- R. C. Ruhl, B. C. Giessen, M. Cohen, and N. J. Grant, *Acta Metall.*, **15**, 1963 (1967).
- H. S. Chen and Y. Waseda, *Phys. Status Solidi A*, **51**, 593 (1979).
- E. Svab, E. Forgacs, F. Hajdu, N. Kroo, and J. Takas, *J. Non-Cryst. Solids*, **46**, 125 (1981).
- S. Basak, R. Clarke, and S. R. Nagel, *Phys. Rev. B*, **20**, 3388 (1979).
- S. R. Nagel, J. Tauc, and B. C. Giessen, *Solid State Commun.*, **22**, 471 (1977).
- S. R. Nagel, J. Vassiliou, P. H. Horn, and B. C. Giessen, *Phys. Rev. B*, **17**, 462 (1978).
- S. H. Whang, D. E. Polk, and B. C. Giessen, in "Proceedings of the 4th International Conference on Rapidly Quenched Metals," T. Masumoto and K. Suzuki, Editors, p. 1365, Japan Institute of Metals, Sendai, Japan (1982).
- H. W. Bergmann and B. L. Mordike, in "Proceedings of the Conference on Metallic Glasses: Science and Technology, Budapest, 1980," Vol. 1, C. Hargitai, I. Bakonyi, and T. Kemeny, Editors, p. 173, Central Research Institute for Physics, Budapest, Hungary (1981).
- V. M. Kyashkin, G. S. Zhdanov, and L. I. Mirkin, *Dokl. Akad. Nauk. SSSR*, **249**, 1118 (1979).
- M. D. Reichtin, J. Vander Sande, and P. M. Baldo, *Scr. Metall.*, **12**, 639 (1979).
- D. Pavuna, *J. Non-Cryst. Solids*, **37**, 133 (1980).
- M. A. V. Devanathan and Z. Stachurski, *Proc. R. Soc. London, Ser. A*, **270**, 90 (1962).
- ASTM Standard Recommended Practice, Designation: G35-73 (1973).
- J. Bentley, in "Corrosion," 2nd ed., L. L. Shreir, Editor, Ch. 5, p. 64, Newnes-Butterworth, London (1976).
- M. Cottin and M. Haissinsky, *J. Chim. Phys.*, **47**, 731 (1950).
- G. W. D. Briggs, E. Jones, and W. F. K. Wynne-Jones, *Trans. Faraday Soc.*, **51**, 1433 (1955).
- R. Parsons, "Handbook of Electrochemical Constants," p. 58, Butterworths, London (1959).
- R. L. Cowan and R. W. Staehle, *This Journal*, **118**, 557 (1971).
- D. D. MacDonald and D. Owen, in "High Temperature High Pressure Electrochemistry of Aqueous Solutions," D. deG. Jones, J. Slater, and R. W. Staehle, Editors, pp. 513-523, International Corrosion Conference Series, NACE, Houston, TX (1976).
- S. U. Falk, *This Journal*, **107**, 661 (1960).
- A. J. Salkind and P. F. Bruins, *ibid.*, **109**, 356 (1962).
- M. LeBlanc and E. Mobius, *Z. Elektrochem.*, **39**, 753 (1933).
- M. LeBlanc and R. Muller, *ibid.*, **39**, 264 (1933).
- J. Labat, *Ann. Chem.*, **9**, 399 (1964).
- P. Pacault and J. Labat, *Compt. Rend.*, **258**, 5421 (1964).
- G. Brauer and H. Muller, *J. Inorg. Nucl. Chem.*, **17**, 102 (1961).
- T. Bonizewski and G. C. Smith, *Phys. Chem. Solids*, **21**, 115 (1961).
- M. D. Archer and N. C. Grant, Unpublished results.
- P. K. Subramanyan, in "Comprehensive Treatise of Electrochemistry," Vol. 4, J. O'M. Bockris, B. E. Conway, E. Yeager, and R. E. White, Editors, Ch. 8, Plenum Press, New York (1981).
- R.-W. Lin and H. H. Johnson, *J. Non-Cryst. Solids*, **51**, 45 (1982).
- F. Spaepen, *ibid.*, **31**, 207 (1978).
- J. Latuskiewicz, P. G. Zielinski, and H. Matyka, in "Proceedings of the 4th International Conference on Rapidly Quenched Metals," T. Masumoto and K. Suzuki, Editors, p. 1381, Japan Institute of Metals, Sendai, Japan (1982).
- T. Schober and H. Wenzl, in "Hydrogen in Metals II," Vol. 29 of Topics in Applied Physics, G. Alefeld and J. Völkl, Editors, p. 11, Springer-Verlag, Berlin (1978).

The Electrochemistry of Glassy 60Ni-40Nb in Some High Temperature Aqueous Media

N. C. Grant and M. D. Archer*

Department of Physical Chemistry, University of Cambridge, Cambridge CB2 1EP, England

ABSTRACT

The high temperature aqueous electrochemistry of glassy melt-spun 60Ni-40Nb was investigated. Glassy 60Ni-40Nb subjected to cyclic voltammetry (CV) in 1*m* NaOH at 150°C undergoes corrosion, which produces niobates in solution and a thick scale of nickel oxide on the alloy. The latter yields CV peaks due to the Ni₃O₄/Ni₂O₃ and Ni₂O₃/NiO₂ transformations. In 1*m* NaHSO₄ at 300°C, the glassy alloy corrodes to yield Ni(II) in solution, and an adherent layer of Nb₂O₅ is formed on the electrode surface. The glassy alloy takes up substantial quantities of hydrogen at its rest potential in this medium. In 1*m* Na₂CO₃ at 150°C, behavior similar to that in 1*m* NaOH is observed, except that the glassy alloy takes up some hydrogen at its rest potential. In 1*m* Na₂CO₃ at 300°C, some hydrogen uptake again occurs at the rest potential, and a scale of nickel oxide is formed on the glassy alloy, but no oxide transformation peaks are observed in the CV because they are obscured by facile oxygen evolution at this high temperature. The assignment of features in the CV of glassy 60Ni-40Nb was made by comparison with similar experiments on crystalline Ni and Nb, and with thermodynamic data at the same temperature, and by *ex situ* microscopical examination of ZnSe-coated cross sections of the corroded electrodes.

In the preceding paper (1), we showed that glassy 60Ni-40Nb is extremely resistant to most forms of electrochemical attack at room temperature except hydrogen embrittlement. Alloys generally exhibit electrochemical properties characteristic of all their principal ingredients. Binary Ni-Nb alloys should possess the resistance to acidic media characteristic of Nb and the resistance to alkaline media characteristic of Ni. However, crystalline Ni-Nb alloys are brittle, whereas the glassy alloy is tough and flexible. This useful combination of good mechanical properties and high resistance to room-temperature corrosion stimulated the present study of the behavior of glassy 60Ni-40Nb under more extreme conditions, in four acidic and alkaline media at 150° or 300°C. As far as we know, no previous studies on high temperature aqueous electrochemistry of glassy alloys have been reported. Glassy 60Ni-40Nb is well suited to such a study, since its crystallization temperature is 650°C (2), so there is no risk of crystallization occurring during work at 300°C.

Experimental

Glassy 60Ni-40Nb ribbons, typically 2 mm wide and 20 μm thick, were formed by the melt-spinning technique (3) as previously described (1).

Conventional three-electrode experiments were carried out using a Chemical Electronics linear sweep generator and TR40/3A potentiostat, and a Bryans XY 26000 A4 chart recorder. The electrochemical experiments were performed in a PTFE beaker housed in a mild steel autoclave. Standpipes in the autoclave lid carried the electrode and thermocouple leads and access to an argon line. The temperature of the autoclave was controlled by a Perkin-Elmer precision oven.

Working electrodes of glassy 60Ni-40Nb were produced by spot-welding 5 cm lengths of ribbon to a platinum wire which passed through the appropriate standpipe. 1 mm diam wires of Ni (99.999%) and Nb (99.95%), obtained from Johnson Matthey Limited, Royston, Herts., England, were also used as working electrodes. The welded joint between the platinum and the electrode material was positioned well above the solution meniscus. Nevertheless, it is likely that the platinum was in exiguous contact with the solution. Prior experiments on the electrochemistry of platinum in aqueous solutions at high temperatures showed that any current derived from the platinum was negligible compared with those derived from the working electrode proper.

* Electrochemical Society Active Member.

Key words: glassy metal, nickel-niobium alloy, high temperature electrochemistry.

The counterelectrode was a concentric cylinder of platinum gauze. A dynamic hydrogen electrode (DHE) polarized at 1 mA cm⁻² (4) was used as the reference electrode. The potential of this electrode lies 50 ± 20 mV below the reversible hydrogen evolution potential at each temperature and pH (5). The potential of the DHE with respect to the normal hydrogen electrode (NHE) is given, therefore, by

$$E(\text{NHE}) = (RT/F) \ln [H^+] - 0.05V$$

Since the pH dependence of the thermodynamic potentials for oxygen evolution, hydrogen evolution, and oxidation state transformations of metal oxides (e.g., Ni₃O₄/Ni₂O₃) is the same as that of the DHE, the potentials observed for such processes *vs.* the DHE at various pH's can be compared with the corresponding standard potential on the NHE scale simply by addition of 50 mV to the potential observed *vs.* DHE

$$E(\text{DHE}, \text{pH} \neq 0) = E(\text{NHE}, \text{pH} = 0) - 0.05V$$

The DHE was used in this work because it is one of the few reference electrodes robust enough to withstand temperatures of 300°C. The hydrogen generated during its use is sufficient to saturate the solutions at both 150° and 300°C, but hydrogen is very sparingly soluble at these temperatures.

Aqueous solutions of NaOH, NaHSO₄, and Na₂CO₃, of concentration 1*m* at room temperature, were prepared from AR chemicals and doubly distilled water. 80 cm³ of solution were used in each experiment. The working electrodes were cleaned before each run by washing, first in acetone and then in distilled water. The autoclave was assembled and flushed three times with high purity argon at 1000 psi. It was then sealed under 400 psi argon, placed in the oven, and heated. Heating to 150°C took about 1h, and heating to 300°C about 1.5h; during this period the working electrodes were at open circuit. It was not possible to apply cathodic protection against corrosion during the warm-up period because glassy 60Ni-40Nb is subject to severe hydrogen embrittlement (1).

Heating the solutions changes their densities and causes appreciable loss of water by evaporation. The calculated molality and pH of each high temperature solution used are given in Table I. The vapor pressure and density of pure water were used in calculation of these figures, which are therefore approximate. The equilibrium constants needed for the pH calculations were taken from the literature (6, 7). In calculating the current density, the immersed area of each

Table I. Calculated molality and pH of nominally 1m solutions

Medium	Molality	pH (molal units)
NaOH 150°C	0.99	11.2
NaHSO ₄ 300°C	0.94	3.2
Na ₂ CO ₃ 150°C	0.99	11.0
Na ₂ CO ₃ 300°C	0.94	11.3

working electrode was corrected for the effects of evaporation and the change in solution density.

Used working electrodes and free corrosion specimens were mounted in a thermosetting plastic and ground and polished to expose a cross section. This procedure fractured the mechanically weaker specimens. The samples were examined with an optical microscope and with a Cambridge Instruments S410 scanning electron microscope equipped with an EDAX facility. The samples for optical examination were coated with a thin (<100 nm) film of vapor-deposited ZnSe (8, 9). The purpose of this coating is illustrated in Fig. 1. The color produced by destructive interference between light reflected from the air-film and the film-substrate interfaces depends on the optical properties, and hence on the chemical identity, of the substrate. Thus chemically different areas in the substrate appear differently colored. ZnSe is used because its high refractive index produces good color contrast. By examination of one specimen both by EDAX and by ZnSe interferometry, the interference colors can be chemically assigned. Many specimens can then be quickly identified by the ZnSe technique. Uniformity of thickness in the ZnSe coating is required for this technique to be reliable. This was assessed by reference to a steel washer placed next to the specimen. ZnSe deposition was continued until the color of the coated washer was the same in all samples. Unfortunately, the black-and-white reproductions of Fig. 4, 7, and 10 do not convey all the detail of the colored originals.

Pourbaix Diagrams

Thermodynamic data on the Ni-H₂O and Nb-H₂O systems assist the assignment of features in the cyclic voltammograms. Figure 2a, taken from Cowan and Staehle (10), shows the Pourbaix diagram for Ni at 300°C, which is broadly similar to the room temperature diagram. Some extrapolations and approximations were used in the compilation of the high temperature diagram, which must therefore be used with caution. Table II summarizes the relevant data for the anhydrous oxides. Hydration of the oxides shifts these standard potentials only slightly. For example, at room

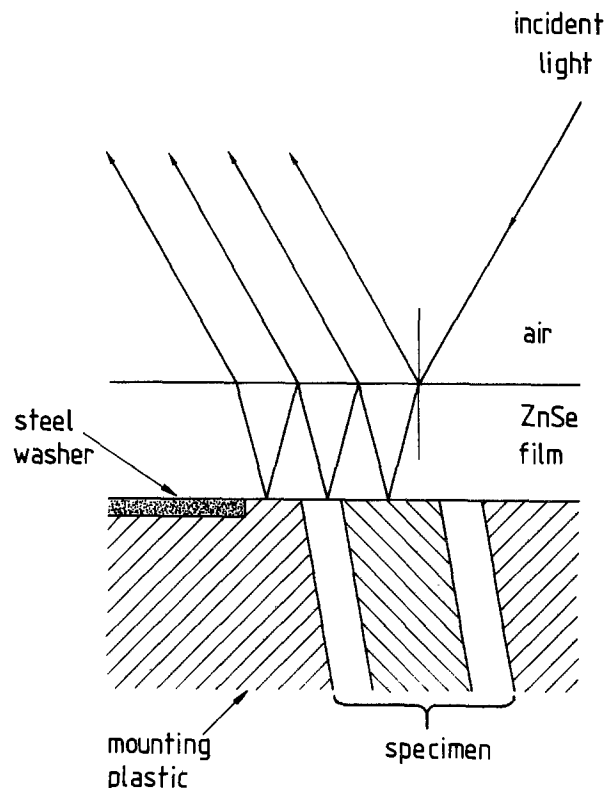


Fig. 1. Metallographic examination of corrosion films by ZnSe coating technique.

temperature the Ni/Ni(OH)₂ potential is only 6 mV below the Ni/NiO potential (11).

Figure 2b shows our calculated Pourbaix diagram for Nb at 300°C. The diagram shows data for the phases Nb, NbO, NbO₂, and Nb₂O₅ only, because of the lack of thermodynamic data on niobium hydrides and niobates. However, Nb₂O₅ does dissolve in strong alkali to form niobates. Figure 2b was calculated from enthalpy and heat capacity data on niobium and its oxides (12) and on water (13). The equilibrium potentials of the niobium/niobium oxide couples are all well below the hydrogen evolution potential. The effect of temperature is again slight, as shown in Table III.

It is worth noting that at 150°C, and more particularly at 300°C, oxide-transformation CV peaks usually appear much nearer their thermodynamic potentials

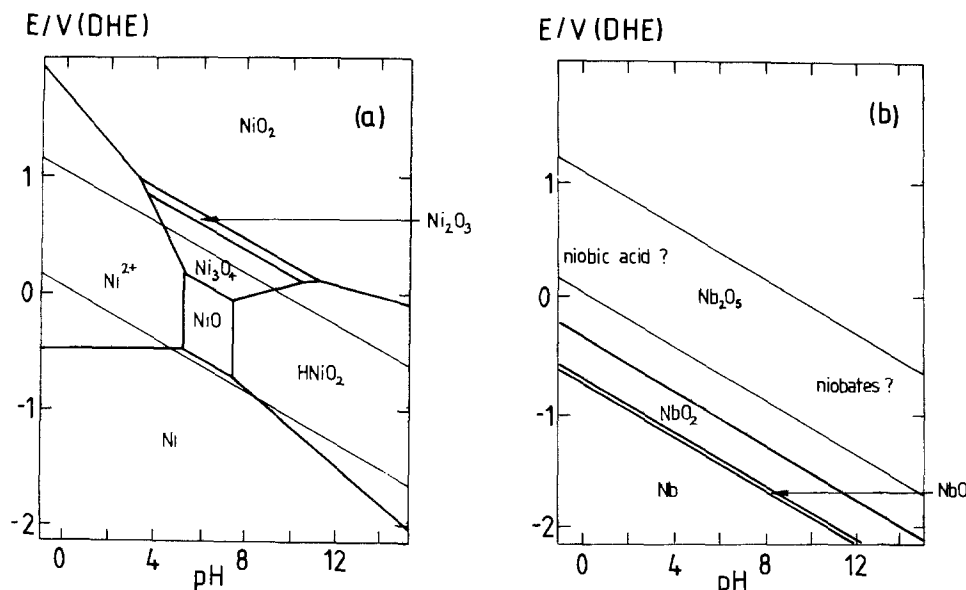


Fig. 2. Pourbaix diagrams for (a, left) Ni and (b, right) Nb at 300°C. The concentration of dissolved ions in the Pourbaix diagram of Ni is 10⁻⁶M. The upper faint line represents oxygen evolution, and the lower, hydrogen evolution.

Table II. Standard potentials at 150° and 300°C for nickel oxide transformations and hydrogen and oxygen evolution*

	Eq. no.	$E(150^\circ\text{C})$	$E(300^\circ\text{C})$
$\text{H}_2 \rightleftharpoons 2\text{H}^+ + 2e^-$	[1]	0.05	0.05
$4\text{OH}^- \rightleftharpoons 2\text{H}_2\text{O} + \text{O}_2 + 4e^-$	[2]	1.18	1.07
$\text{Ni} + \text{H}_2\text{O} \rightleftharpoons \text{NiO} + 2\text{H}^+ + 2e^-$	[3]	0.13	0.08
$3\text{NiO} + \text{H}_2\text{O} \rightleftharpoons \text{Ni}_3\text{O}_4 + 2\text{H}^+ + 2e^-$	[4]	0.87	0.83
$2\text{Ni}_3\text{O}_4 + \text{H}_2\text{O} \rightleftharpoons 3\text{Ni}_2\text{O}_3 + 2\text{H}^+ + 2e^-$	[5]	1.33	1.29
$\text{Ni}_2\text{O}_3 + \text{H}_2\text{O} \rightleftharpoons 2\text{NiO} + 2\text{H}^+ + 2e^-$	[6]	1.44	1.40

* Expressed in V vs. DHE and taken from Cowan and Staehle (10) with the addition of 0.05V to convert to the DHE scale.

Table III. Standard potentials at 150° and 300°C for niobium oxide transformations*

	Eq. no.	$E(150^\circ\text{C})$	$E(300^\circ\text{C})$
$\text{Nb} + \text{H}_2\text{O} \rightleftharpoons \text{NbO} + 2\text{H}^+ + 2e^-$	[1]	-0.71	-0.75
$\text{NbO} + \text{H}_2\text{O} \rightleftharpoons \text{NbO}_2 + 2\text{H}^+ + 2e^-$	[2]	-0.66	-0.71
$2\text{NbO}_2 + \text{H}_2\text{O} \rightleftharpoons \text{Nb}_2\text{O}_5 + 2\text{H}^+ + 2e^-$	[3]	-0.29	-0.34

* Expressed in V vs. DHE and calculated from the data of Gerasimov (12).

than at room temperature, because they are usually kinetically controlled and hence occur faster at higher temperatures. Thus Pourbaix diagrams are a more reliable guide to peak assignment at high temperatures than they are at room temperature.

Results and Discussion

0.99M NaOH at 150°C.—Figure 3 shows steady-state cyclic voltammograms (CV's) for glassy 60Ni-40Nb and crystalline Nb and Ni. Niobium (Fig. 3b) dissolves freely as niobates in this strongly alkaline medium at low potentials, and shows some tendency to passivate at higher potentials. The rest potential E_r (see Table IV) was very low (-0.315V DHE): niobate and hydrogen formation are presumably the balancing processes at E_r . Nb behaves similarly at room temperature in 15M NaOH although the active dissolution peak is then smaller (1). Macleary (14) records the corrosion rate of Nb in 5% NaOH at 98°C as 9390-18,780 mg dm⁻² day⁻¹, which is equivalent to a corrosion current density of 1.15-2.3 mA cm⁻².

Nickel did not dissolve on repeated cycling between 0.02 and 1.55V DHE, i.e., within the effective hydrogen and oxygen evolution potentials in this medium. Its CV (Fig. 3c) showed two reproducible peaks, I and II, which can be assigned by comparison with the thermodynamic data of Table II. Peak I in Fig. 3c is at 1.39V DHE, and peak II is at 1.22V. The mean value, 1.30V, agrees well with Eq. [5] of Table II for the Ni₃O₄/Ni₂O₃ couple. Over the sweep rate range 0.5-2.5 mV s⁻¹, the charge under peak II was constant at 118 ± 10 mC cm⁻², confirming that reaction of a surface, rather than a dissolved, species is occurring.

Glassy 60Ni-40Nb has a CV (Fig. 3a) that indicates Ni-like behavior of the surface. Nb was detected in solution after this experiment by the precipitation of Nb₂O₅ on neutralization, and the ZnSe technique (Fig. 4) showed that only nickel oxide was present in the corrosion layer. Nb also dissolved from specimens freely corroding in this medium. We conclude that,

Table IV. Rest potentials E_r in V vs. DHE

Medium		60Ni-40Nb	Ni	Nb
1M NaOH	150°C	0.625-0.725	0.775	-0.315
1M NaHSO ₄	300°C	0.015-0.060	0.052	-0.030-+0.030
1M Na ₂ CO ₃	150°C	0.020	0.455	-0.27
1M Na ₂ CO ₃	300°C	0.01-0.07	—	—

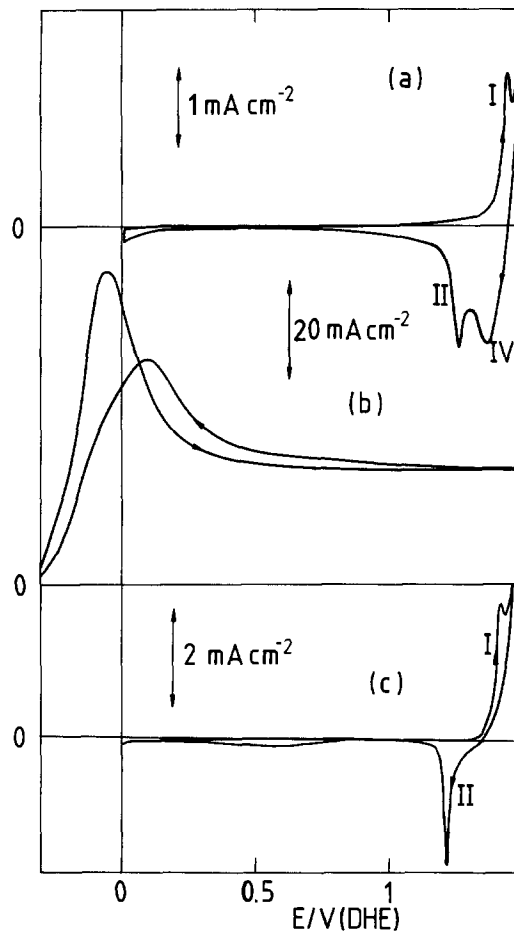


Fig. 3. CV's of (a, top) glassy 60Ni-40Nb, (b, center) Nb, and (c, bottom) Ni in nominally 1M NaOH at 150°C. Sweep rates: (a) 25.5, (b) 30, and (c) 25.8 mV s⁻¹.

during the warm-up period for the experiment of Fig. 3a, Nb has dissolved and the CV consequently shows the transformations of the nickel oxide corrosion layer remaining. In addition to peaks I and II, which were also obtained on crystalline Ni, an additional cathodic peak IV was observed at 1.39V DHE. This peak did not appear unless the anodic sweep limit was above 1.49V. We infer that there is an anodic peak (peak III) concealed under the current due to oxygen evolution, and

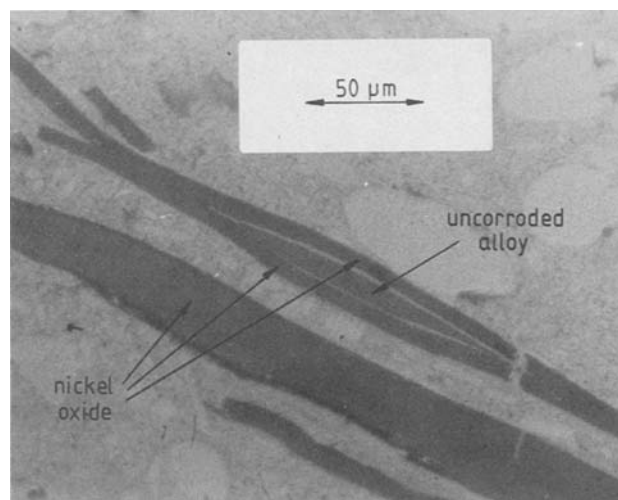


Fig. 4. Optical micrograph of ZnSe-coated cross section of glassy 60Ni-40Nb after the experiment of Fig. 3a.

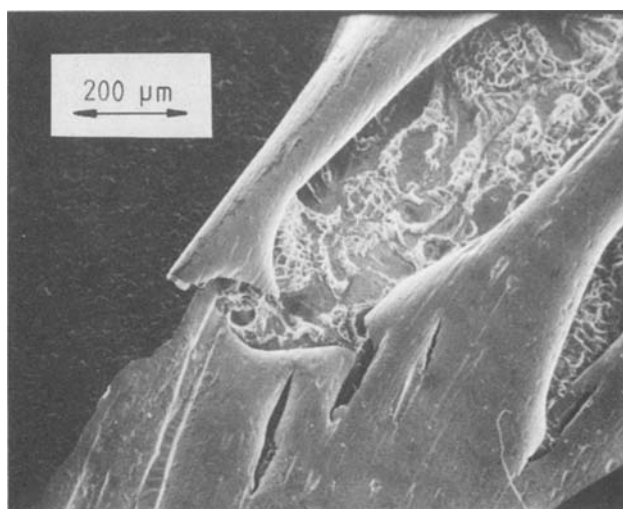


Fig. 5. Scanning electron micrograph of the surface of glassy 60Ni-40Nb after the experiment of Fig. 3a.

that peak IV is its conjugate reduction peak. [Peak III can be seen in the CV of Ni in $1\text{m Na}_2\text{CO}_3$ at 150°C (Fig. 8a)]. The potentials of peaks I and II in Fig. 3a are 1.44 and 1.30V DHE, respectively, and, as for Ni itself, we ascribe these to the $\text{Ni}_3\text{O}_4/\text{Ni}_2\text{O}_3$ transformation. Assuming that the concealed peak III is at 1.49V, the average of the peak potentials of peaks III and IV is 1.44V DHE, in agreement with Eq. [6], and we therefore ascribe these two peaks to the $\text{Ni}_2\text{O}_3/\text{NiO}_2$ transformation.

At 150°C in 1m NaOH , the rest potentials (Table IV) of Ni and the glassy alloy are high and approach the $\text{NiO}/\text{Ni}_3\text{O}_4$ potential. It is noteworthy that at 150°C , the CV's show distinct $\text{Ni}_3\text{O}_4/\text{Ni}_2\text{O}_3$ and $\text{Ni}_2\text{O}_3/\text{NiO}_2$ transformations at roughly the thermodynamically predicted potentials. At room temperature in 15M NaOH (1), these two peaks were not resolvable.

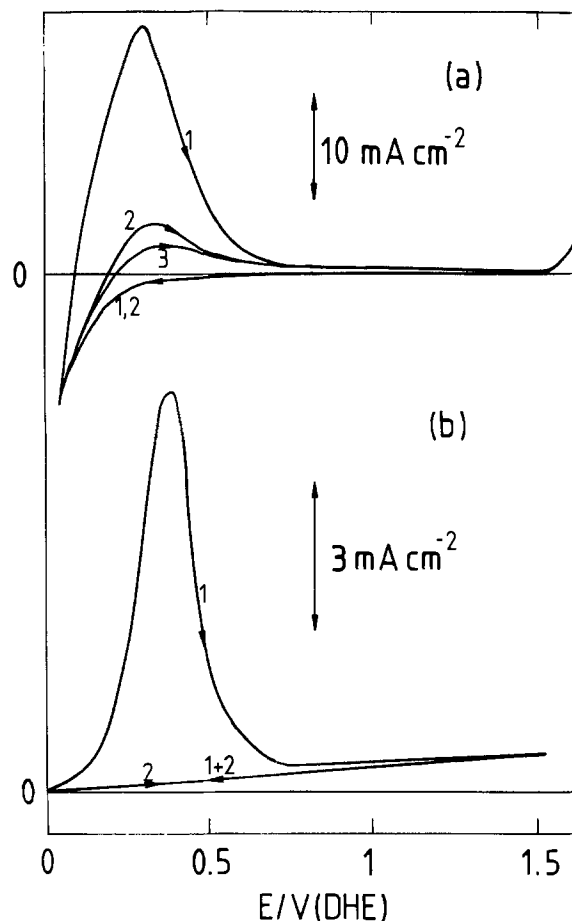


Fig. 6. CV's of (a, top) glassy 60Ni-40Nb and (b, bottom) Nb in nominally 1m NaHSO_4 at 300°C . Sweep rates: (a) 26.2 mV s^{-1} , (b) 25 mV s^{-1} .

We can estimate the thickness of the oxide film involved in these redox processes from the charge under

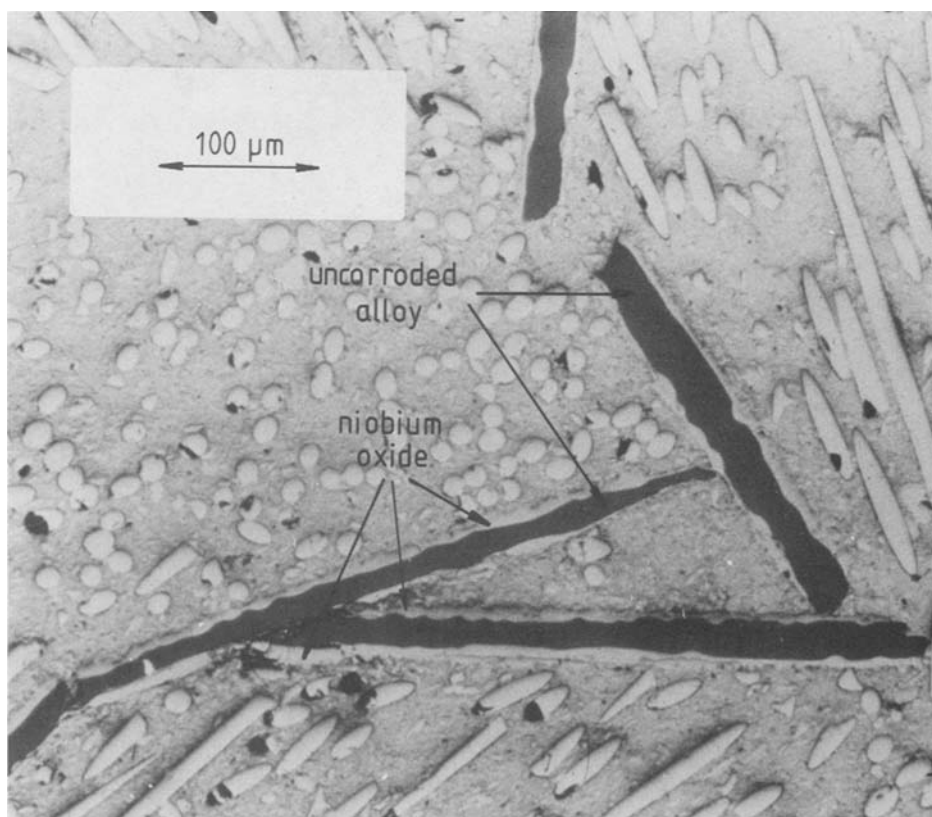


Fig. 7. Optical micrograph of ZnSe-coated cross section of a free corrosion specimen of glassy 60Ni-40Nb after immersion in nominally 1m NaHSO_4 at 300°C for 70h.

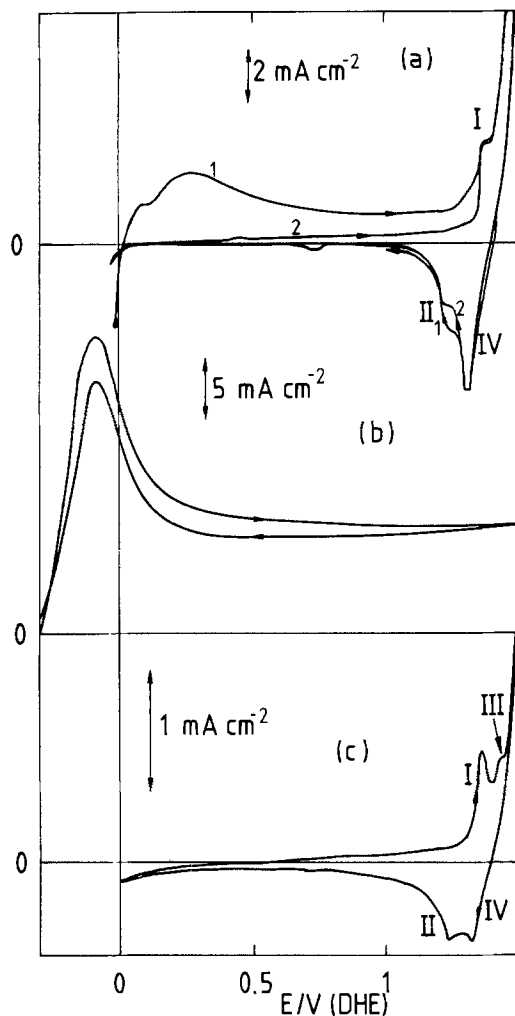


Fig. 8. CV's of (a, top) glassy 60 Ni-40Nb, (b, middle) Nb, and (c, bottom) Ni in nominally 1M Na_2CO_3 at 150°C. Sweep rates: (a) 26.5, (b) 30, and (c) 25.5 mV s^{-1} .

the peaks. The charge under either peak I or peak II in Fig. 3a is 13.8 mC cm^{-2} . Assuming that the surface density of Ni atoms is the mean of that for $\text{Ni}_3\text{O}_4 \cdot 2\text{H}_2\text{O}$ ($7.93 \times 10^{14} \text{ cm}^{-2}$) and Ni_2O_3 ($1.073 \times 10^{15} \text{ cm}^{-2}$), this charge is equivalent to the transformation of about 40 monolayers. The corrosion scale formed by CV is much thicker than this, as is evident from Fig. 4. Only the superficial region of the corrosion layer is redox-active in cyclic voltammetry.

Figure 4 shows a ZnSe photograph of the cross-sectioned glassy electrode of Fig. 3a. The corrosion layer was not strongly adherent, and, on drying the electrode, part of it spalled off, as shown in the scanning electron micrograph of Fig. 5. The scale was lifted entirely off the substrate by the mounting and cross sectioning procedure, as can be seen in the upper fragment of Fig. 4. This has a central portion of uncorroded alloy, which appears orange in color under the ZnSe coating, encased in a corrosion layer ca. $6 \mu\text{m}$ thick, which, from its purple color, can be identified by comparison with the corrosion scale formed on nickel itself as nickel oxide. The lower fragment shown in Fig. 4 contains no uncorroded alloy and consists entirely of nickel oxide. We could not reliably distinguish between the possible oxidation states of this scale by the ZnSe interference colors, but it appeared to be duplex in nature.

0.94M NaHSO_4 at 300°C.—Crystalline Ni dissolves so rapidly in this acidic medium that no cyclic voltammogram could be obtained for it. The behavior of Nb and glassy 60Ni-40Nb is shown in Fig. 6, from which it is apparent that in this medium the alloy exhibits a Nb-

like surface. This is confirmed by the ZnSe photograph of a free corrosion specimen (Fig. 7). This shows a central orange portion of uncorroded alloy covered by an adherent, featureless film ca. $8 \mu\text{m}$ thick that appears colorless under the ZnSe coating. This was shown by EDAX to be a niobium oxide, presumably Nb_2O_5 . Analysis of the solution after the experiment of Fig. 6a showed no dissolved Nb, but rather a high concentration of dissolved Ni. Of the nickel initially present in the glassy alloy sample, about one-third was present as Ni(II) in solution at the end of the experiment.

As Fig. 6 indicates, neither Nb nor glassy 60Ni-40Nb initially yielded a steady-state CV in 1M NaHSO_4 . During the warm-up period, both specimens assumed rather low rest potentials (Table IV). A large anodic peak at 0.30V was seen on the first positive-going sweep (numbered 1 in Fig. 6), but this decreased in magnitude with each succeeding sweep until after about five it was completely absent. In the case of the alloy, it would be possible to attribute this peak to Ni(II) formation. However, this cannot be the case for Nb, and the similarity in the CV's of the two materials suggests that they have the same cause. We tentatively ascribe this transient peak to the oxidation of hydrogen generated

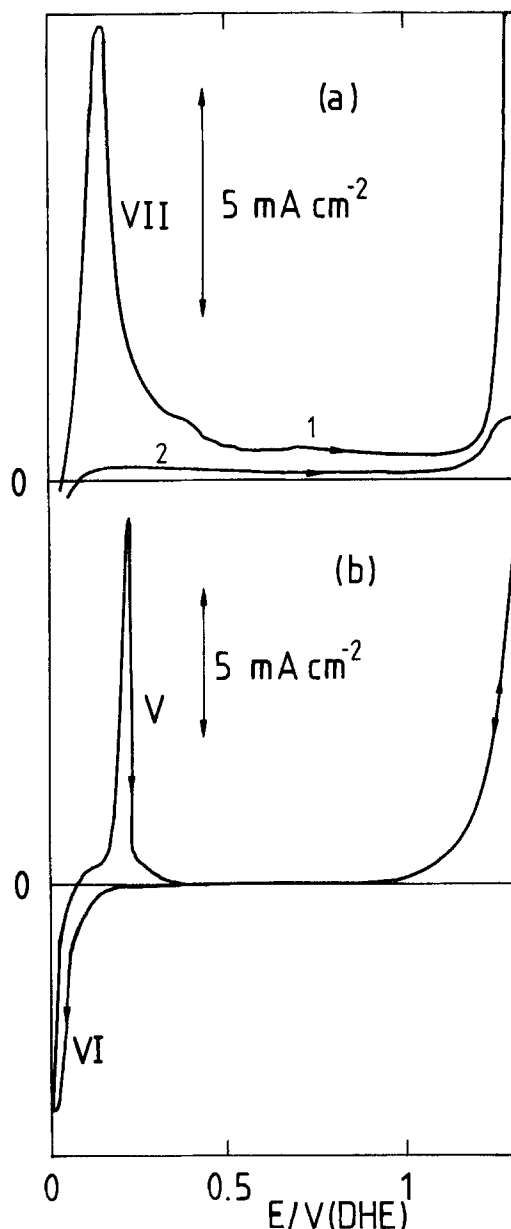


Fig. 9. CV's of (a, top) glassy 60Ni-40Nb, and (b, bottom) Ni in nominally 1M Na_2CO_3 at 300°C. Sweep rates: (a) 0.4 and (b) 22.2 mV s^{-1} .

at E_r and absorbed by the niobium or the Nb-like surface of the glassy alloy during the warm-up period. The rest potentials are sufficiently negative to indicate hydrogen generation and Nb_2O_5 film growth (and, in the case of the alloy, Ni(II) formation) as probable balancing processes at E_r . Moreover, other evidence supports the hypothesis that these two materials are likely to take up hydrogen at their rest potentials in acidic solution: the glassy alloy dissolves substantial quantities of hydrogen on cathodization (1). Niobium is also known to form hydrides on cathodization (15, 16).

The charges under the first sweep peaks were 0.29 and 0.07 C cm^{-2} for the glassy alloy (Fig. 6a) and Nb (Fig. 6b), respectively. Oxidation of a monolayer of hydrogen atoms requires only *ca.* 1.5 mC cm^{-2} , so if the peaks are due to the oxidation of absorbed hydrogen, substantial amounts of hydrogen have been generated on, and absorbed by, both Nb and 60Ni-40Nb at E_r in the warm-up period. Possibly some of the hydrogen generated by the reference electrode is also absorbed during warm-up. The decline of the peak with sweep number would be expected, because once the potential cycling has started, the amount of hydrogen generated by the relatively brief excursions to negative potentials would be negligible on this current scale. The large concentration of Ni(II) found in solution after the experiment of Fig. 6a must have dissolved during the warm-up period, since no peak due to Ni(II) formation appears in the steady-state CV of the glassy alloy.

0.99m Na₂CO₃ at 150°C.—Figure 8 shows CV's of 60Ni-40Nb, Nb, and Ni in nominally *1m Na₂CO₃* at 150°C. Behavior broadly similar to that in *1m NaOH* at 150°C is observed. Nb (Fig. 8b) has a very low rest potential in this medium (Table IV). A substantial peak at -0.091V , due to dissolution of Nb as niobates, and a tendency to passivate at higher potentials are again observed in its CV: however, the critical current density and passivation potential are both lower than in the more alkaline *1m NaOH* (Fig. 3b). Ni does not dissolve in *1m Na₂CO₃*, and its CV (Fig. 8c) again indicates the surface transformations $\text{Ni}_3\text{O}_4/\text{Ni}_2\text{O}_3$ (peaks

I and II, centered at 1.28V DHE) and $\text{Ni}_2\text{O}_3/\text{NiO}_2$ (peaks III and IV, centered at 1.35V DHE). These potentials are slightly low compared with the thermodynamic values of Eq. [5] and [6] of Table II, but this is partly because the peak maxima are shifted by the steep backgrounds against which they appear. It is interesting that peak III, ascribed to the superficial oxidation of Ni_2O_3 to NiO_2 , is observed in *1m Na₂CO₃*, but not in *1m NaOH*, at 150°C. Glassy 60Ni-40Nb (Fig. 8a) also shows the Ni oxide transformation peaks I, II, and IV, less well defined than in *1m NaOH*, but peak III is here obscured. The midpoint potentials for the $\text{Ni}_3\text{O}_4/\text{Ni}_2\text{O}_3$ and $\text{Ni}_2\text{O}_3/\text{NiO}_2$ peaks in Fig. 8a are 1.36 and 1.43V DHE, respectively. The ZnSe technique confirmed that the corrosion scale formed on the glassy alloy was nickel oxide.

The first sweep conducted on the glassy alloy (numbered 1 in Fig. 8a) differed from that observed in *1m NaOH* at 150°C in that a substantial peak at 0.27V was observed on the first sweep, but not on subsequent ones. This could be due either to the oxidation of hydrogen absorbed during the warm-up period, as proposed for the transient 0.30V peak observed in the CV in *1m NaHSO₄* (Fig. 6a), or to niobate formation: the position of this peak, 0.36V positive of the niobate formation peak of Fig. 8b, and the rest potential (0.02V DHE) suggest that the oxidation of absorbed hydrogen is probably predominant, but the shoulder at 0.077V might be niobate formation. The rest potential of the glassy alloy is much higher in *1m NaOH* at 150°C than it is in *Na₂CO₃*, and it is therefore to be expected that no transient hydrogen oxidation peak should appear in the first sweep in NaOH. No niobate was found in the cooled solution after the experiment of Fig. 8a, although the above evidence shows that it must have dissolved from the alloy during warm-up. However, the corroded electrode was covered with a crystalline niobate that presumably precipitated from the carbonate solution on cooling.

0.94m Na₂CO₃ at 300°C.—At positive potentials, Nb dissolved in this medium so rapidly that no CV was obtainable. The behavior of glassy 60Ni-40Nb and Ni

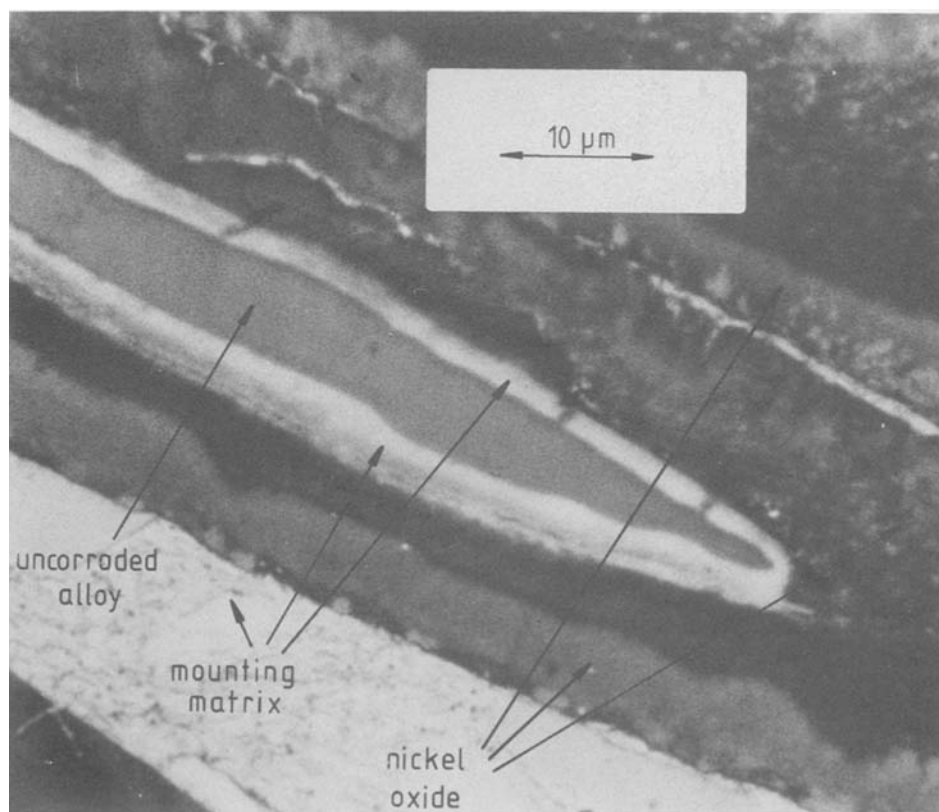


Fig. 10. Optical micrograph of ZnSe-coated cross section of a free corrosion specimen of 60Ni-40Nb after immersion in nominally *1m Na₂CO₃* at 300°C for 24h.

is shown in Fig. 9a and 9b, respectively. The ZnSe photographs showed that both electrodes had developed thick (ca. 10 μm) nickel oxide corrosion scales during an experiment of 20h duration. The previously observed $\text{Ni}_3\text{O}_4/\text{Ni}_2\text{O}_3$ and $\text{Ni}_2\text{O}_3/\text{NiO}_2$ transformations are, however, now not seen in either CV, presumably because they are hidden under the current due to oxygen evolution. Instead of being subject to a substantial overpotential as it is at lower temperatures, this now appears in the region of the standard $\text{O}_2/\text{H}_2\text{O}$ potential, which at 300°C is 1.07V DHE, below the higher oxide conversion potentials (Eq. [5] and [6], Table II). On both glassy 60Ni-40Nb and Ni, oxygen evolution reaches a current density of 1 mA cm^{-2} at ca. 1.2V DHE. The nickel oxide corrosion layer is evidently able to sustain oxygen evolution at a negligible overpotential at this temperature. Miles *et al.* (17) have reported that the exchange current for oxygen evolution on Ni in 50 weight percent KOH increases sharply between 150° and 264°C. By contrast, on the Nb_2O_5 layer formed on the glassy alloy in 1M NaHSO_4 (Fig. 6a), oxygen evolution commenced only above 1.5V DHE even at 300°C, and this layer is presumably rather resistive.

The CV of nickel showed two sharp peaks at low potentials, V and VI in Fig. 9b, which were not observed at 150°C. These occur at 0.26 and 0.06V DHE, respectively. Peak V is probably due to a surface reaction, rather than to the oxidation of a solution species. This was shown by stopping the CV at the cathodic limit or just negative of peak V for various lengths of time. The height of peak V was unaffected in both cases, so the hypothesis that peak VI is caused by generation of hydrogen in solution, and peak V by its oxidation, is probably wrong. Reference to Table II shows that peaks V and VI could be due to the Ni/NiO transformation, although the absence of any peaks due to the NiO/Ni₃O₄ transformation is then anomalous.

Peak VII (Fig. 9a) at 0.15V DHE, observed only during the first positive going sweep on the glassy alloy, is also difficult to assign. It is possible that the cathodic peak VI would have appeared in this CV had the potential been taken lower, but lower potentials were avoided because they caused hydrogen embrittlement. It is not possible to decide whether peak VII is due to oxidation of absorbed hydrogen or to niobate formation: both of these were also thought possible in the CV obtained at 150°C (Fig. 8a).

Figure 10 and 11 show ZnSe photographs and Ni and Nb EDAX maps of the same portion of a specimen of glassy 60Ni-40Nb freely corroded in 1M Na_2CO_3 at 300°C for 20h. (Corroded working electrodes gave very similar results.) All three pictures show a central portion, appearing orange under the ZnSe coating, which from its Ni:Nb ratio can be positively identified as the uncorroded alloy. The duplex corrosion film contains Ni, but not Nb. Some Nb containing crystals can be seen in Fig. 11c to have formed on top of this corrosion film. These are the niobates which dissolved from the alloy at 300°C, but which precipitated on cooling because they are insoluble at room temperature. As for 1M Na_2CO_3 at 150°C, no Nb was detected in the cooled solution after CV of the glassy alloy.

Conclusions

In the high temperature acidic medium (1M NaHSO_4 at 300°C), some Ni dissolves from glassy 60Ni-40Nb at its free corrosion potential, and the alloy surface becomes covered by a strongly adherent layer of Nb_2O_5 . In the three high temperature alkaline media (1M Na_2CO_3 at 150° and 300°C, and 1M NaOH at 150°C), niobium dissolves as niobates and the alloy becomes covered by a scale of nickel oxide, which is less adherent than the acid-formed Nb_2O_5 layer. Thus, as at room temperature (1), the glassy alloy possesses a combination of the corrosion-resistant properties of

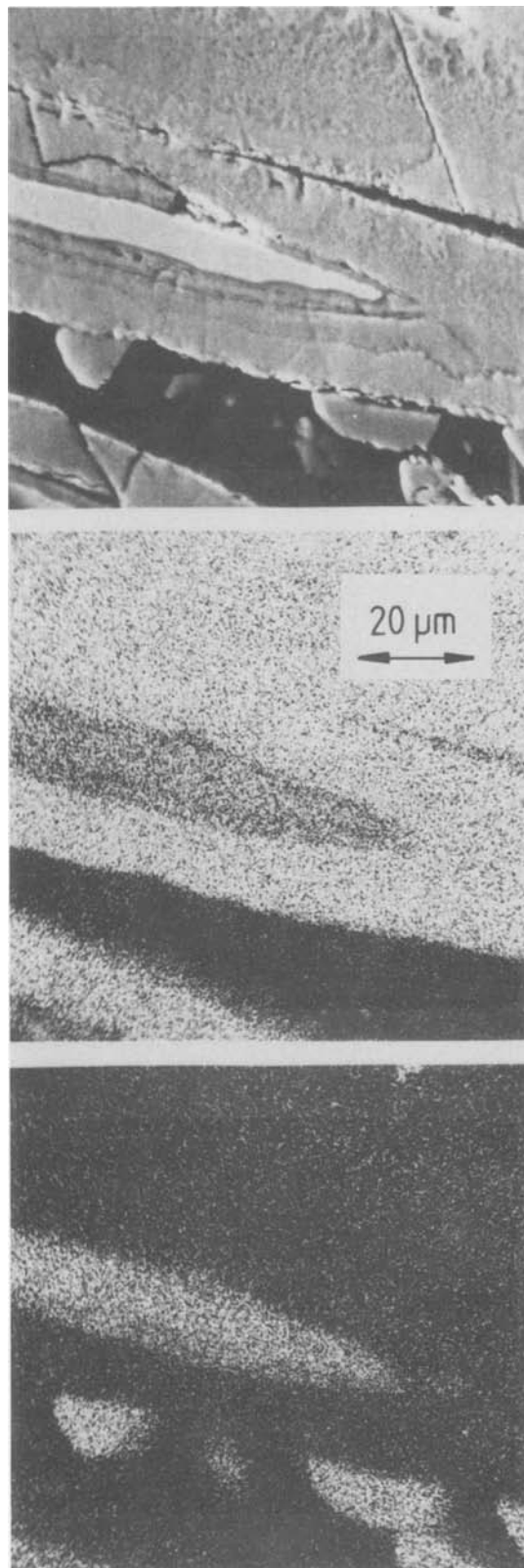


Fig. 11. a, top: scanning electron micrograph of the area shown in Fig. 9, b, center: Ni EDAX map of the same area, c, bottom: Nb EDAX map of the same area.

Ni and Nb, though the corrosion scale formed at 150° and 300°C is too thick with respect to the ribbon thickness to regard the material as usefully resistant to corrosion at high temperatures in these aggressive media.

Acknowledgment

N.C.G. gratefully acknowledges sponsorship of a SERC/CASE award and provision of laboratory facili-

ties by the Central Electricity Research Laboratories, Leatherhead, England.

Manuscript submitted June 21, 1983; revised manuscript received Sept. 23, 1983.

The University of Cambridge assisted in meeting the publication costs of this article.

REFERENCES

1. N. C. Grant and M. D. Archer, *This Journal*, **131**, 997 (1984).
2. B. C. Giessen, M. Madhava, D. E. Polk, and J. Vander Sande, *Mater. Sci. Eng.*, **23**, 145 (1976).
3. D. Pavuna, *J. Non-Cryst. Solids*, **37**, 133 (1980).
4. J. Giner, *This Journal*, **111**, 376 (1964).
5. G. J. Bignold and D. de G. Jones, in "Proceedings of the British Nuclear Energy Society Conference of 1974," S. F. Pugh, Editor, p. 120, British Nuclear Energy Society, London (1975).
6. R. C. Murray, Jr. and J. W. Cobble, in "Proceedings of the 41st International Water Conference, 1980," p. 295, Engineering Society of Western Pennsylvania, Pittsburgh, PA (1980).
7. W. L. Marshall and E. U. Franck, in "Proceedings of the 9th International Conference on Properties of Steam, 1979," J. Straub and K. Scheffler, Editors, p. 506, Pergamon Press, Oxford, England (1980).
8. W. Pepperhoff, *Arch. Eisenhüttenwes.*, **32**, 269 (1961).
9. R. Castle, D. F. Liebert, and I. S. Woolsey, CERL Internal Report RD/L/N 20/78 (1978).
10. R. L. Cowan and R. W. Staehle, *This Journal*, **118**, 557 (1971).
11. M. Pourbaix, "Atlas of Electrochemical Equilibria in Aqueous Solutions," p. 330, Pergamon Press, Oxford, England (1966).
12. Ya. I. Gerasimov, A. N. Krestovnikov, and A. S. Shakhov, "Chemical Thermodynamics in Non-Ferrous Metallurgy," Vol. 3, p. 163 ff, Springfield, VA (1965).
13. "CRC Handbook of Chemistry and Physics," CRC Press, Inc., Boca Raton, Florida, 61st ed., 1980.
14. D. L. Macleary, *Corrosion*, **18**, 67t (1962).
15. C. K. Dyer and J. S. L. Leach, *Electrochim. Acta*, **20**, 151 (1975).
16. G. Brauer and H. Muller, *J. Inorg. Nucl. Chem.*, **17**, 102 (1961).
17. M. H. Miles, G. Kissel, P. W. T. Lu, and S. Srinivasan, *This Journal*, **123**, 332 (1976).

An Examination of Current Fluctuations during Pit Initiation in Fe-Cr Alloys

Ugo Bertocci* and Ye Yang-Xiang†

National Bureau of Standards, Center for Materials Science, Washington, DC 20234

ABSTRACT

Random fluctuations of the passive current for Fe-Cr alloys of various Cr content were examined, in borate buffer and in the same solution with 0.1M NaCl added. Frequency spectra of these fluctuations were recorded before and during pit initiation. No detectable fluctuations were observed in the absence of chlorides, where pitting does not occur. Comparison with the current noise measured before pit initiation indicates that the most important role of the aggressive ions is that of increasing the chance of local breakdown of the passive film. Frequency spectra give information concerning the time constants of the various processes, including repassivation. No correlation was found between the rate of attack during pitting and noise amplitude.

During the induction period leading to pitting, a number of workers have observed, under potentiostatic conditions, sudden current bursts (1), but little is known about their shape and frequency content. Some authors (2) have proposed that a dynamic equilibrium exists between random events of breakdown of the passive film and its repair by repassivation, and that pitting would occur when the repassivation rate is too slow compared to the rate of local attack. Such a description of the processes leading to the breakdown of a passive film suggests that random fluctuations (that is, current noise) should be observed.

The availability of sensitive methods for detecting and analyzing current fluctuations under potentiostatic conditions (3) and previous experimental results showing a large increase in the amplitude of the noise spectra after the onset of pitting (4) suggest that it would be useful to examine in detail the current noise during the induction period before pitting starts, as well as during the pitting transients. Also of special importance is the examination of the role of alloy composition on the current fluctuations under pitting and nonpitting conditions.

The purpose of this work was to collect data concerning the amplitude and frequency of the current noise

before and after the onset of pitting and to examine the influence of metal composition and, to a limited extent, of the electrode potential on the noise spectra. As materials to be studied, three Fe-Cr alloys were chosen, with increasing Cr concentrations ranging from 5 to 12 to 20 atom percent (a/o) in Cr, so as to increase their resistance to corrosion and pitting.

Experimental Procedures

Materials, chemicals, and cells.—The electrodes were small rods prepared by vacuum melting, followed by swaging and annealing. The rods were sheathed in polytetrafluoroethylene and their cross sections, with a surface of 0.1 cm², were mechanically polished down to 600 grit paper. The solution employed for most of the experiments was a 1:1 mixture of saturated boric acid and saturated sodium tetraborate (B:B), to which 0.1M NaCl was added. The pH of the solution was about 8. Some measurements were made in B:B without addition of chloride. All chemicals were of analytical grade and the water was doubly distilled.

The cell employed for the measurements had a Pt counterelectrode, separated from the working electrode compartment by a coarse glass frit, and two reference electrodes, one made of a large Pt sheet, which was used as the sensor for the potentiostat, and a saturated calomel electrode (SCE), which was used to monitor the electrode potential. The Pt electrode, in spite of its lack of a well-defined potential, was fairly stable, drifting a few mV in the course of several

* Electrochemical Society Active Member.

† Visiting Guest Scientist from China.

Key words: chlorides, chromium alloys, corrosion, electrochemical noise, passivity breakdown, pitting.

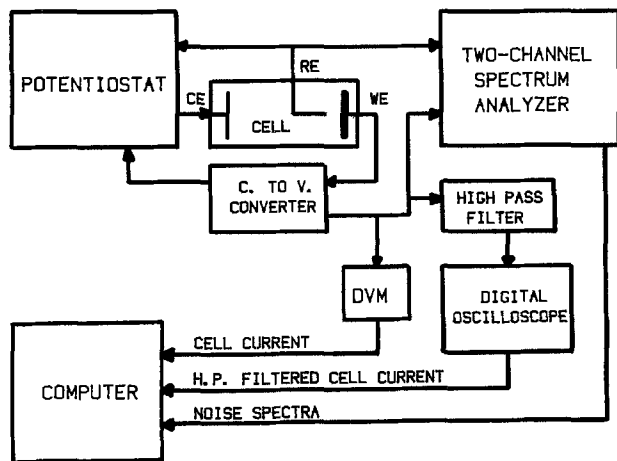


Fig. 1. Block diagram of the measuring system

hours. The atmosphere above the solution was air, and the cell was shielded mechanically with foam rubber and electrically by a double enclosure of mu-metal sheet.

Instrumentation.—The instrumentation employed was very similar to that described previously (3), with modifications in the layout as shown in Fig. 1. The three measuring instruments, that is, spectrum analyzer, DVM reading the dc current, and digital oscilloscope recording the high-pass filtered current, were connected to a computer, which was capable of triggering and controlling them and monitoring the spectrum analyzer for overloads.

For the study of the pitting transients the digital oscilloscope, connected in parallel to the current channel of the spectrum analyzer, started storing the trace when the fluctuations exceeded a set value. The onset of pitting was monitored by the dc current read by the DVM: when the current density exceeded a few microamperes per square centimeter, the computer triggered the spectrum analyzer while taking a current reading every second for 200s. For every pitting transient so examined, therefore, the data obtained were: (i) an unfiltered current density vs. time curve, sampled at 1s intervals, showing the increase in current due to pit formation; (ii) an oscillographic record of the current, sampled at 20–50 ms intervals, high-pass filtered at 30 mHz, which lasted from 50 to 100s and included a portion of the time immediately pre-

ceding the start of pitting, showing any fluctuations before pit initiation; and (iii) noise spectra of the voltage and the current, as well as the cross-power spectrum, taken from the moment the pit started and averaged over a time of a few minutes.

Data processing.—The processing of the spectra taken followed the method described in a previous paper (4), but was executed under computer control (5), so that the separation between the stochastic and deterministic part of the signal, after subtraction of the average instrumental noise, was accomplished for all 128 frequency values of a spectrum in less than 1 min after completion of the acquisition, and plots and printouts were immediately produced.

Optical examination.—The presence of pits on the surface after the pitting transients was confirmed by optical microscopy. The correlation with the current data was 100%.

Selection of the conditions for observing pitting.—Because of the large gain of the amplifiers and the low cutoff frequency of the high-pass filters, it was necessary to have a sufficiently long period, of the order of several minutes, from the establishment of the potential chosen for the pitting experiment to the actual pit initiation, in order for the instrumentation to recover from the overload caused by the manual adjustment of the potentiostat control voltage. However, it was highly desirable to cut the induction period relatively short. With these limits in mind, a number of preliminary tests, either slow potentiodynamic scans or long duration potentiostatic runs, was carried out, observing the effect of pH, chloride concentration, and potential-time schedules on the onset of pitting.

The procedure adopted after these tests was to employ a neutral borate buffer containing 0.1M of NaCl as the solution, to carry out the experiments at 300 mV vs. SCE for the 20% Cr alloy, at 100 mV for the 12% Cr alloy, and at -50 mV for the 5% Cr alloy. The other important point was that the surface had to be immersed into the solution less than 20 min after polishing. As for the manner of setting the desired potential, an operation which was found to be one of the most critical points, the procedure consisted in turning the potentiostat on at the open-circuit potential and then raising to the desired value manually by 50 mV steps and waiting 3–4 min at each potential.

The potentials chosen for the study are obviously higher than the "pitting potential." For instance, if the potential was raised quickly, pitting occurred with

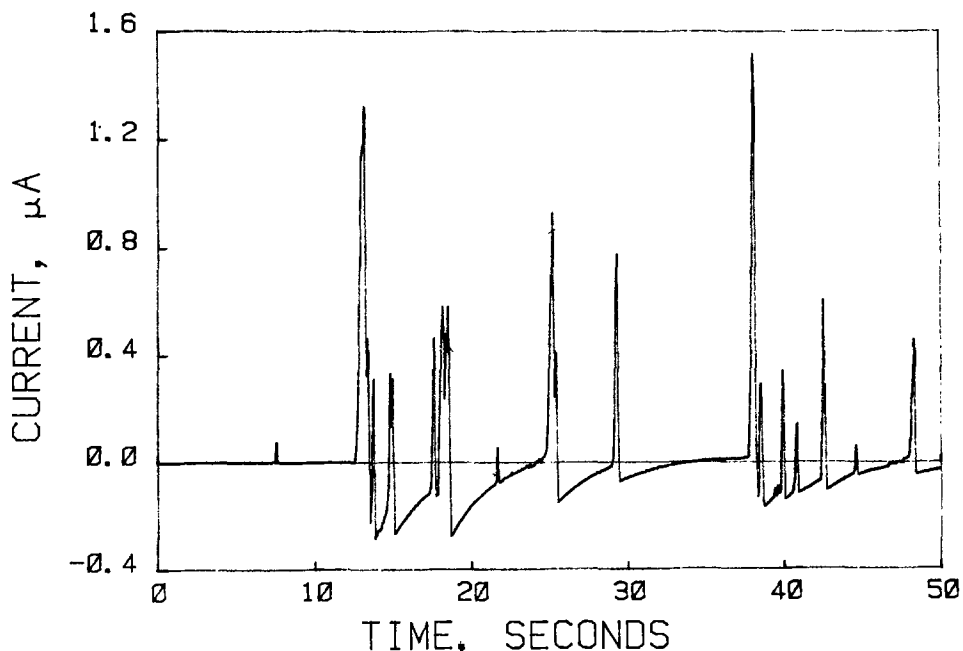


Fig. 2. High-pass filtered time record of the current fluctuations of a Fe-12% Cr electrode in borate buffer plus 0.1M NaCl, before pit initiation. $E = 50$ mV vs. SCE. H. P. filter: 3 dB down at 30 mHz. Sampling rate: 50 ms.

high probability 50-100 mV below the value selected. If the potential was raised very slowly, with long pauses to let the passive film grow, it could be raised even a few hundreds of mV higher without observing any pit information, at least for a few hours.

Noise Spectra in the Absence of Pitting

Spectra of the current fluctuations were taken in boric acid/borate buffer without chlorides, where pitting does not occur. All three alloys were tested, and measurements taken at the same potentials at which pitting was studied in the NaCl-containing solutions. After subtraction of the instrumental noise, no electrode-generated random noise could be detected. In these conditions, therefore, taking the surface area into account, a maximum limit for the electrochemical noise can be established; this limit is of the order of $0.1 \text{ nA/cm}^2 \sqrt{\text{Hz}}$ between 1 Hz and 1 kHz, increasing to about $10 \text{ nA/cm}^2 \sqrt{\text{Hz}}$ at 50 mHz, because of the increasing instrumental noise at lower frequencies.

Noise data could also be collected in boric acid/borate buffer plus 0.1M NaCl before pitting started. During this induction period, isolated current transients were observed, as shown, for instance, in Fig. 2. Because of the low number of such current spikes, the averaging procedure of the spectrum analyzer tends to distort the results so that spectra taken in different frequency ranges (and therefore with different acquisition times) are not consistent in amplitude with one another. However, comparison between spectra of different alloys acquired under the same conditions are valid. Figure 3 shows that the noise increases with decreasing Cr content, and that the amplitude of each spectrum is essentially independent of frequency. This suggests that the current transients before pitting occur at random intervals and are spikes with rise and decay times shorter than 10 ms. This is in agreement with the oscillographic records such as Fig. 2, where only sudden transients can be seen. The spikes also disappear suddenly (at the sampling rate of 50 ms). The subsequent undershoots are an artifact of the 30 mHz high-pass filter.

Low frequency fluctuations, however, were detected on a 5% Cr alloy which had a freshly prepared surface and was brought rapidly at the measurement potential, another indication that film thickness and stability are critically dependent on the previous history of the electrode, particularly the duration of the various potentials. The record of the fluctuations before and at the moment of the start of the first pit is shown in

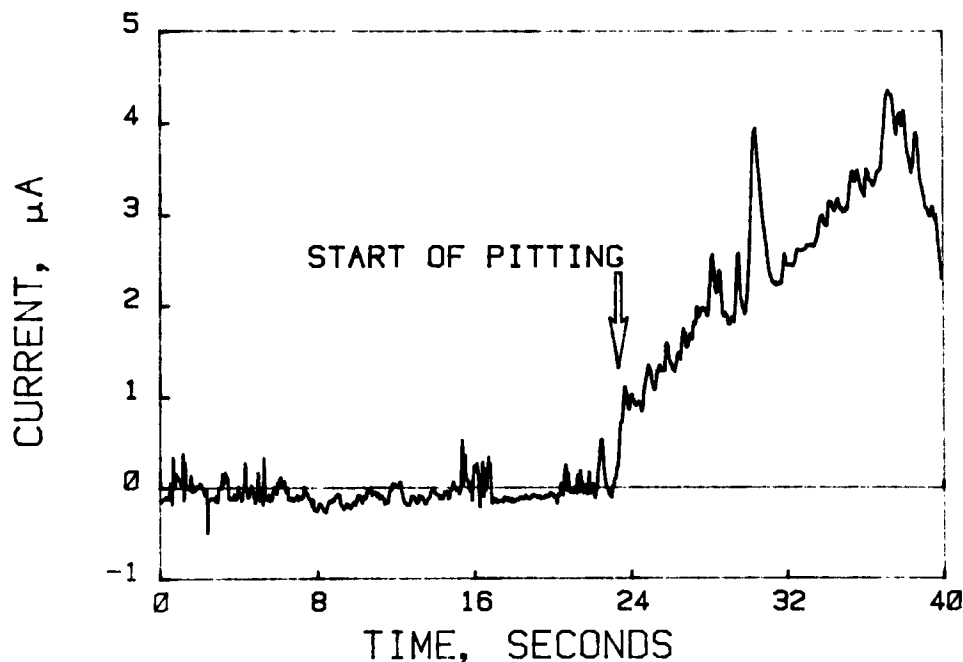


Fig. 4. High-pass filtered time record of the current fluctuations of a Fe-5% Cr electrode in borate buffer plus 0.1M NaCl, during pit initiation. $E = -50 \text{ mV}$ vs. SCE. H. P. filter: 3 dB down at 30 mHz. Sampling rate: 50 ms.

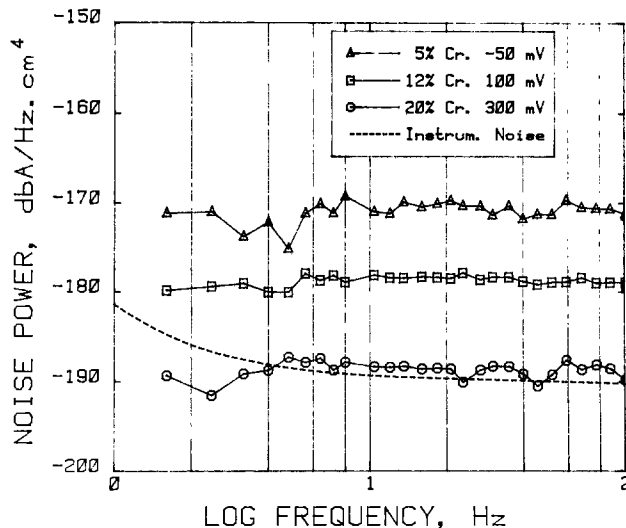


Fig. 3. Spectra of the random current fluctuations in borate buffer plus 0.1M NaCl before the onset of pitting.

Fig. 4, while spectra are shown in Fig. 5 for two potentials, both lower than the one employed for the pitting experiments. At -100 mV the amplitude plateau and the slope, close to -20 dB/decade , indicate fluctuations with a frequency of about 0.2 Hz and an amplitude of $1 \mu\text{A/cm}^2$. At even lower potential, the frequency of the large fluctuations is less than 0.1 Hz. For the higher Cr alloys, no such low frequency noise was observed before the start of pitting.

Pitting Transients

Once a pit starts growing, the current density increases in a roughly linear fashion, at least for 300-400s. It is impossible, therefore, to have strictly stationary conditions. However, if a high-pass filter eliminates the very low frequency components of the current density, remarkably consistent and reproducible spectra can be obtained, averaging over the period of linear increase of the current. The linearity can be taken as an indication that the growth of only one pit is being observed.

Examples of the current density vs. time plots recorded from the beginning of the pit growth are shown in Fig. 6. Average slopes and their standard deviations are given in Table I. A more detailed view of the

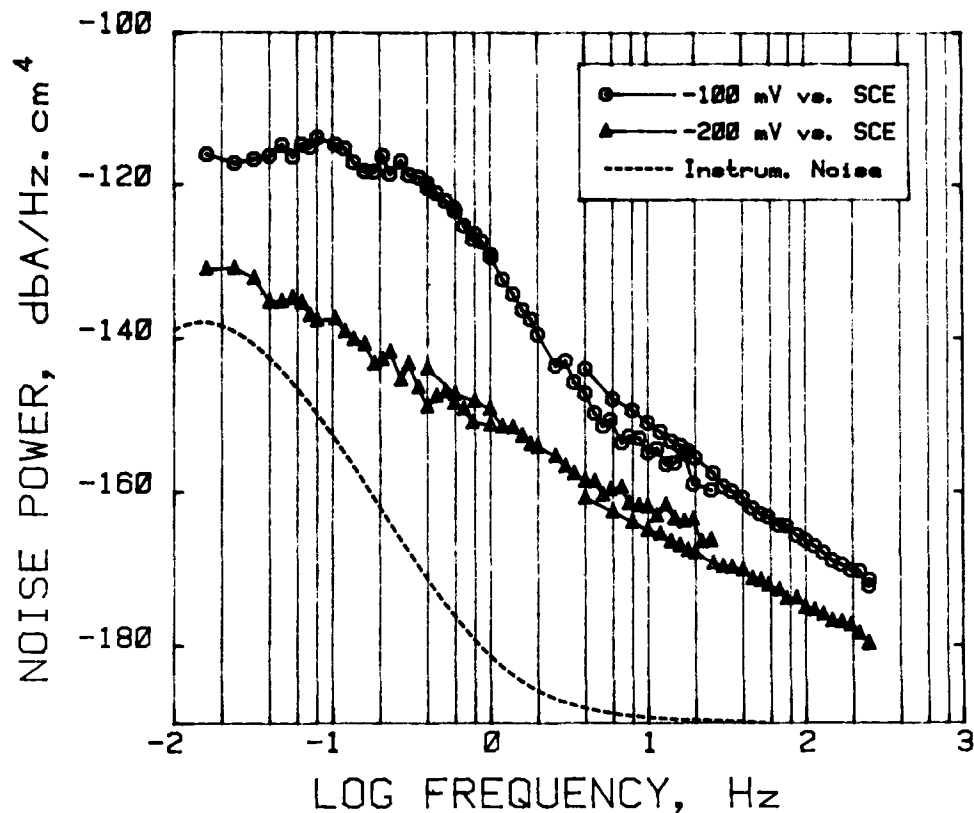


Fig. 5. Spectra of the random current fluctuations of freshly prepared Fe-5% Cr electrode in borate buffer plus 0.1M NaCl, before the onset of pitting.

fluctuations during pit initiation is given by the high-pass filtered record shown in Fig. 7.

No significant difference could be found between the slopes of the 12% and the 20% alloys, while the pits on the 5% Cr alloy grew almost twice as fast. If one considers the potential applied, it is evident that even after the protective film has been broken (pitting initiated), the higher Cr content slows down the attack.

The spectra of the random fluctuations of the current during the pitting transients are shown in Fig. 8, 9, and 10. The scatter from test to test was found to be in general less than 10 dB at the same frequency. It appears, therefore, that the difference in the results at 200 and 300 mV for the 20% Cr alloy (Fig. 8) is significant.

The tendency to larger amplitudes with higher potentials regardless of Cr concentration is detectable, although the difference between the spectrum of the 5% Cr alloy at -50 mV and the 12% Cr alloy at 100 mV is very small. It should be pointed out, however, that the amplitude of the current fluctuations does not

seem to be closely correlated with the magnitude of the corrosion current, which, on the average, increased twice as fast on 5% Cr than on the other two alloys.

The spectra, except possibly for the 20% Cr alloy, decrease monotonically with increasing frequency. A tendency to a low frequency plateau in Fig. 8 would indicate fluctuations of a period of about 10s and an amplitude of $100 \mu\text{A}/\text{cm}^2$. The spectra of the 5% and 12% Cr alloys break clearly into two segments, with a low frequency slope of about 30 dB/decade and a high frequency slope of about 15 dB/decade, beginning at 20 Hz. They cannot, therefore, be interpreted in terms of an exponential decay of the fluctuations, which would give a 20 dB/decade slope, but point to a more complex kinetics. The two slopes are less clearly evident for the 20% Cr alloy. The high frequency slope is close to 20 dB/decade and begins approximately at 10 Hz for the 200 mV data and 20 Hz at 300 mV.

Discussion

The results presented here show that in the absence of an aggressive ion such as Cl^- there are no detectable random fluctuations in the current density. Therefore, the description of a passive film as being in a continuous state of local breakdown, followed by rapid repassivation of the exposed surface, is not supported by the experimental evidence, unless the occurrence of these breakdown events is well below one every 10 min and/or it does not involve more than 10^5 atoms. Such a number is obtained by considering that a current burst of $3 \cdot 10^{-10}\text{A}$ for $3 \cdot 10^{-3}\text{s}$ would clearly contribute to the noise spectrum. The charge involved would correspond to the oxidation of some $3 \cdot 10^5$ atoms, a surface area of $0.03 \mu\text{m}^2$, or less, if the oxide is more than 1 atom layer thick.

Table I. Average slopes and standard deviations

%Cr	Slope, $\mu\text{A}/\text{s}$	Std dev, $\mu\text{A}/\text{s}$	E , mV vs. SCE	No. of tests
5	3.2	1	-50	9
12	1.7	0.4	100	5
20	1.6	0.4	300	7

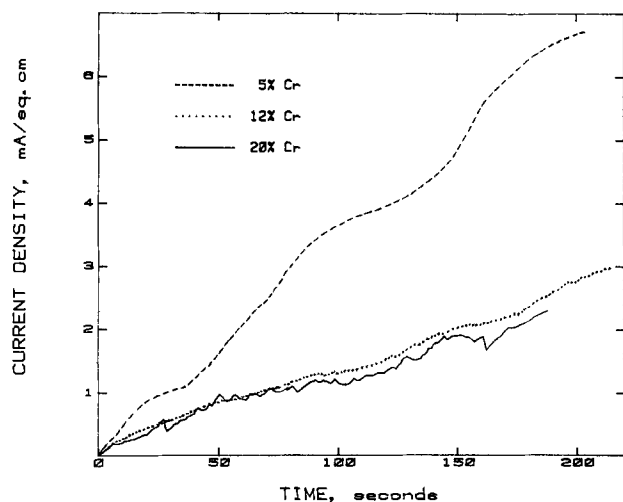


Fig. 6. Unfiltered time records of the current density after the start of the first pit.

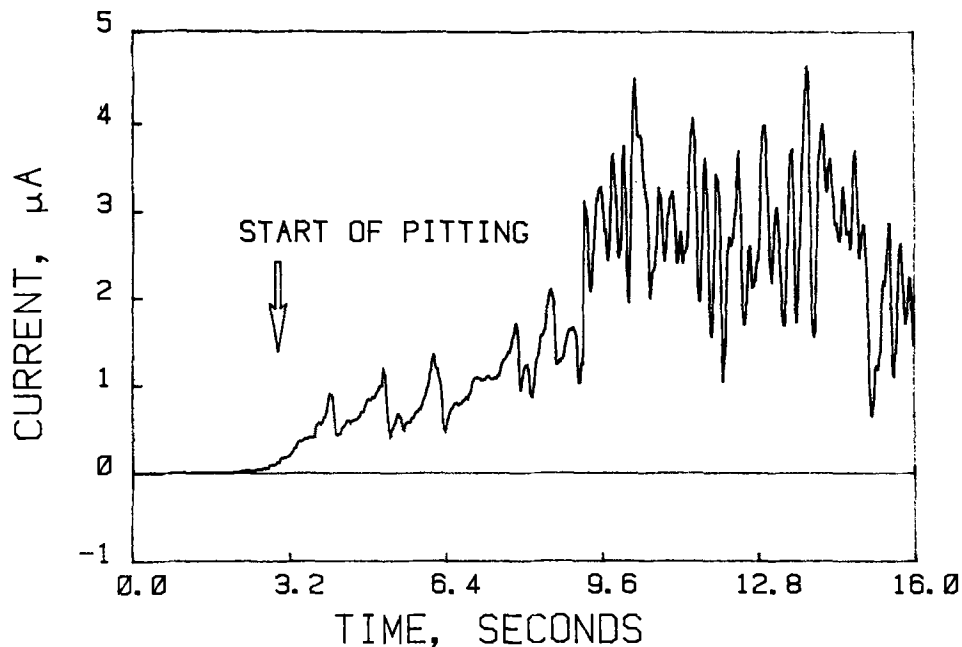


Fig. 7. High-pass filtered time record of the current fluctuations of a Fe-20% Cr electrode in borate buffer plus 0.1M NaCl during pit initiation. $E = 400$ mV vs. SCE. H. P. filter: 3 dB down at 30 mHz. Sampling rate 20 ms.

In the presence of chlorides, current transients can be detected during the induction period, the spikes being of the order of $1 \mu\text{A}$ (see Fig. 2 and 3). Smaller, frequent fluctuations have been observed only for the 5% Cr alloy, for which the low chromium content confers little corrosion resistance. For the 12% and 20% Cr alloys, these current spikes are rather rare: Fig. 2 was chosen because there was a somewhat larger number of them in a limited time (about one every 3s), but it was more common to see a spike every 0.5 min. On the 20% Cr alloy, the transients not immediately followed by the start of the pitting were even rarer, and between them no fluctuations could be observed at a detection limit of the order of 30 pA. The conclusion one draws is that for the corrosion resistant alloys during the induction period very few points on the surface undergo a burst of dissolution, and therefore each point where passivity fails momentarily has a

relatively large probability (for the 20% Cr at 300 mV, of the order of 0.5) to develop into a pit. Considering that no such transients are observed in the absence of chlorides, the conclusion is that the most important effect of the Cl^- lies in increasing the chance of local breakdown rather than in affecting the repassivation rate.

The flat spectra of Fig. 3, as well as the corresponding time records as in Fig. 2, indicate that the corrosion resistant alloys repassivate rapidly, in times less than 10 ms, even in the presence of chlorides. These values are shorter than the repassivation time constants of about 15 ms reported by Kruger and Ambrose (6) for steels with similar Cr content, but in more concentrated chloride solutions.

Once the pits have started, the spectra of the fluctuations represent the complex interplay of the progressive spreading of the pit-area, local repassivation at

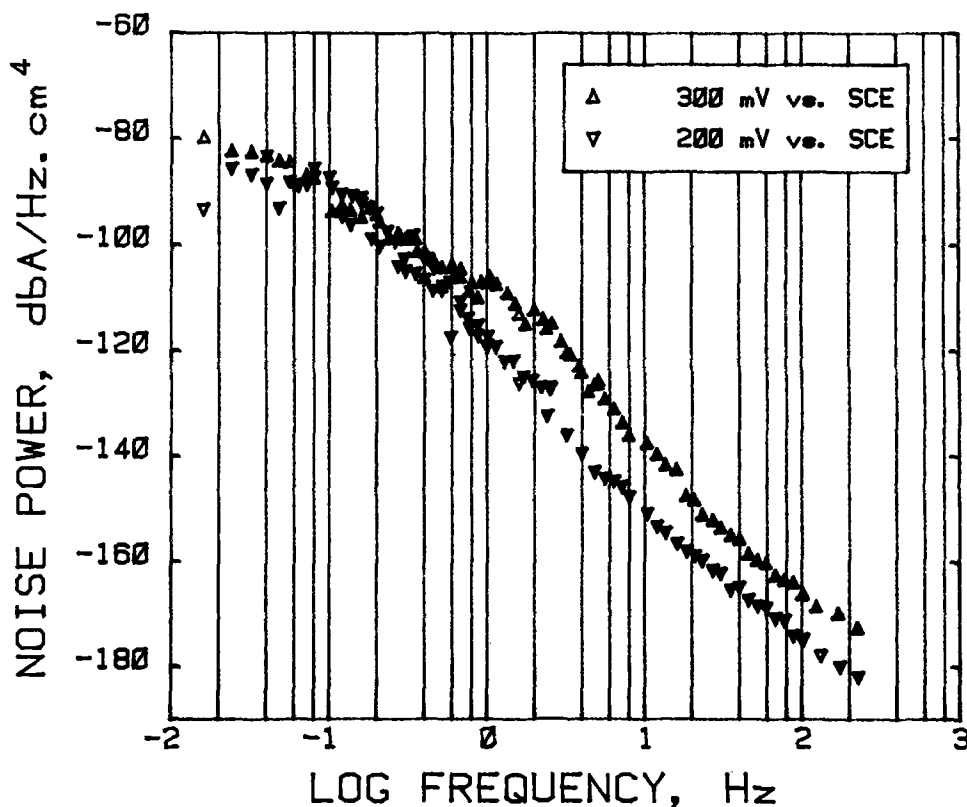


Fig. 8. Spectra of the random current fluctuations of Fe-20% Cr electrode in borate buffer plus 0.1M NaCl during pitting.

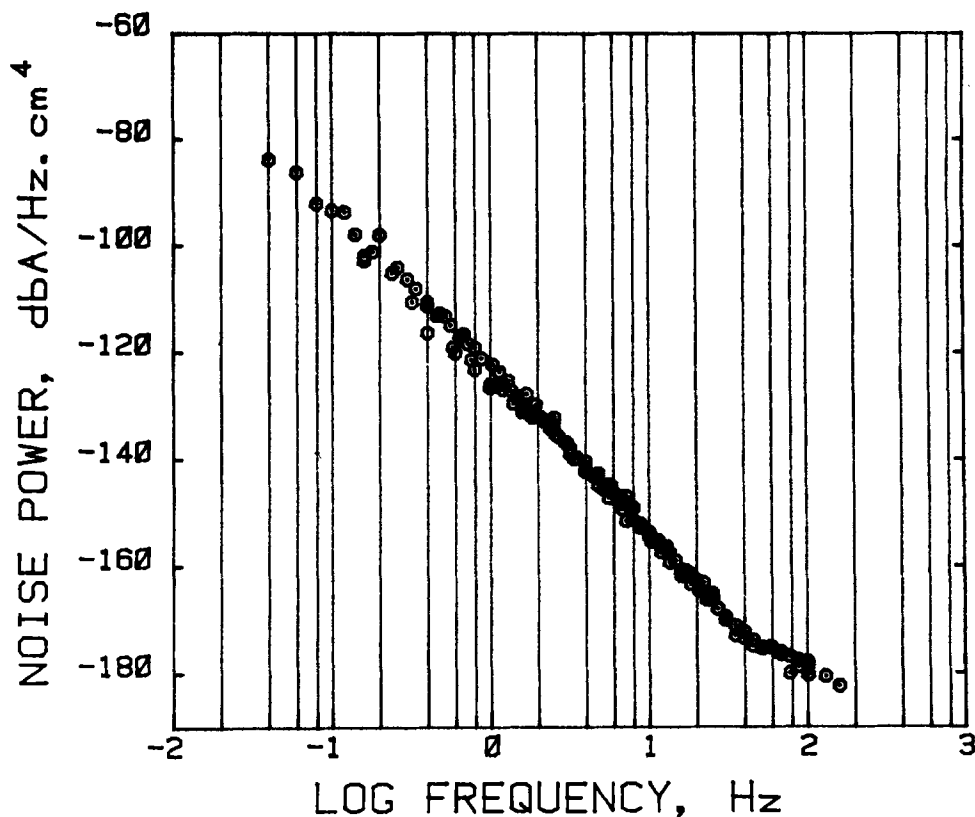


Fig. 9. Spectra of the random current fluctuations of Fe-12% Cr electrode in borate buffer plus 0.1M NaCl during pitting.

the edges and of fluctuations of the composition of the solution inside the pit, which probably account for the large amplitudes, close to $10 \mu\text{A}$, with periods of tens of seconds. The fact that amplitude plateaus are not observed once pitting starts is not due to the limited frequency range investigated, but is probably because the condition is nonstationary, with pits growing and current steadily increasing. Nonstationarity has been invoked as an explanation for low frequency noise (7).

It is likely that the fastest process observed is still repassivation, which determines the high frequency

end of the spectra. For the 20% Cr alloy where the high frequency slope is close to 20 dB/decade, such an interpretation seems reasonable: the time record of Fig. 7, for instance, shows that often the decreases in current are faster than the increases. A comparison of the spectrum of Fig. 8 with that obtained before pitting initiation (Fig. 3) shows that for the same amplitude of about -170 dB the induction period spectrum is flat up to 100 Hz, while after pit initiation the amplitude decreases. The time constant for repassivation has be-

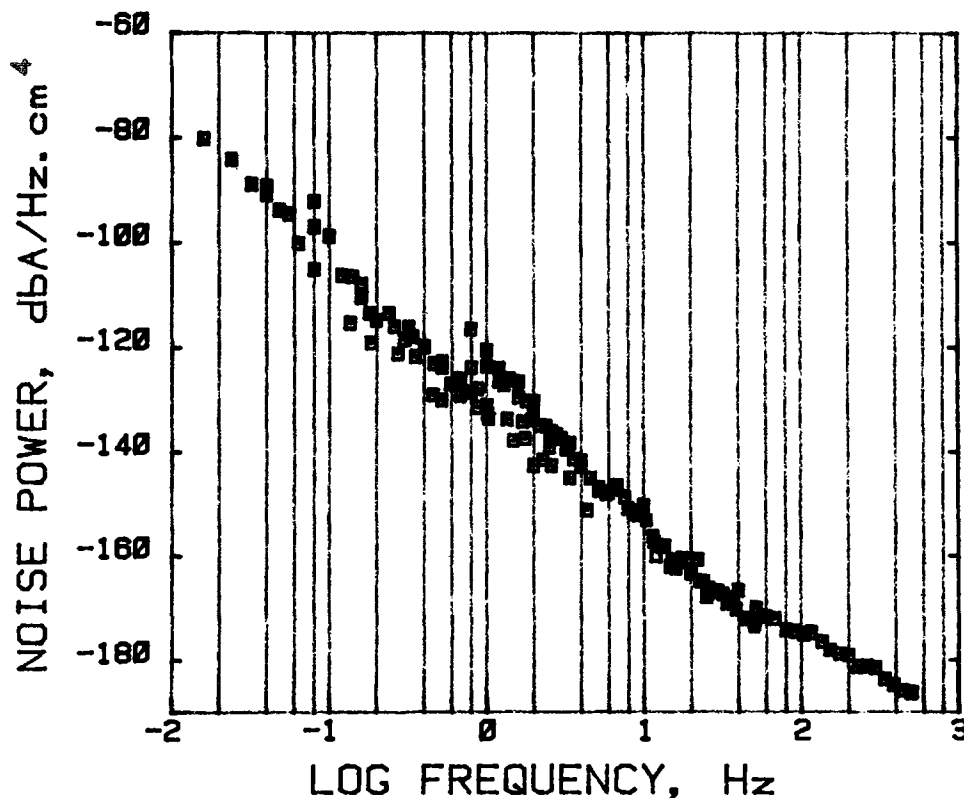


Fig. 10. Spectra of the random current fluctuations of Fe-5% Cr electrode in borate buffer plus 0.1M NaCl during pitting.

come longer than 10 ms, reflecting the more aggressive local environment in the pit.

Finally, fluctuation amplitudes do not seem to be related to the magnitude of the average current density; rather, they increase with the degree of resistance to corrosion of the alloy. For the 20% and 12% Cr alloys, the fluctuations represent a larger fraction of the average current than for the 5% Cr alloy. For instance, at 0.1 Hz, the amplitude of the fluctuations is of the order of $3 \cdot 10^{-5}$ A/cm² for the high Cr alloys and about $7 \cdot 10^{-6}$ A/cm² for the 5% Cr alloy, while the rate of attack, as shown in Fig. 6, is about twice on the latter. Therefore, in this case, where localized corrosion is the source of the current, no correlation between total current density and noise amplitude has been found, as reported for generalized corrosion (8).

Manuscript received June 7, 1983.

The National Bureau of Standards assisted in meeting the publication costs of this article.

REFERENCES

1. G. C. Wood, W. H. Sutton, J. A. Richardson, T. N. K. Riley, and A. G. Malherbe, "Localized Corrosion," NACE-3, Houston, TX (1974); G. Okamoto, T. Sugita, S. Nishiyama, and K. Tachibana, *Boshoku Gijutsu*, **23**, 439, 445 (1974); G. Okamoto and T. Shibata, in "Passivity of Metals," R. P. Frankenthal and J. Kruger, Editors, p. 646, The Electrochemical Society Monograph Series, Princeton, NJ (1978); B. P. Löchel and H-H. Strehblow, *Werkst. Korros.*, **31**, 353 (1980).
2. K. Videm, Kjeller Report DR-149, Institutt for Atomenergi, Kjeller, Norway (1974). See also: J. Kruger, "Passivity and its Breakdown on Iron and Iron Base Alloys," R. W. Staehle and H. Okada, Editors, p. 91, NACE, Houston, TX (1976); M. Janik-Czachor, G. C. Wood, and G. E. Thompson, *Brit. Corros. J.*, **15**, 154 (1980).
3. R. W. Shideler and U. Bertocci, *NBS J. Res.*, **85**, 211 (1980); U. Bertocci, *This Journal*, **127**, 1931 (1980).
4. U. Bertocci, *ibid.*, **128**, 520 (1981).
5. U. Bertocci, *Mater. Prot. (China)*, **3**, 11 (1982).
6. J. R. Ambrose, NBS Internal Report 78-1429, p. 40 (1977).
7. M. S. Keshner, *Proc. IEEE*, **70**, 212 (1982).
8. K. Hladky and J. L. Dawson, *Corros. Sci.*, **22**, 231 (1982).

Development of a High Temperature pH Electrode for Geothermal Fluids

Leonard W. Niedrach* and William H. Stoddard

General Electric Company, Corporate Research and Development Center, Schenectady, New York 12301

ABSTRACT

This work demonstrates the applicability of a stabilized zirconia pH sensor to high temperature measurements on brines containing as much as 20 weight percent NaCl and 100 ppm hydrogen sulfide. Throughout the program, stable operation was achieved, and measured pH values from 3 to 9 were in good agreement with calculated values. Differences were generally less than 0.5 pH unit at 285°C, and it is not yet certain whether the discrepancies are associated with the measured or calculated values of the pH. Two sensors were operated at 285°C for periods of 11 days, and one was employed in successive tests for a total of 37 days. At the end of this period, the sensor was still satisfactory, and it was forwarded to the sponsoring laboratory, PNL, for further tests. Although most of the work was performed at 285°C, a limited amount of testing was done at lower temperatures: 95°, 150°, and 225°C. Sensors prepared from in-house tubes and from tubes obtained from an outside supplier performed well at 95°C for extended periods, in spite of earlier difficulties with the standard ceramic at this temperature. There is still, however, some uncertainty concerning the adequacy of our seals, particularly in cycling between 285°C and lower temperatures. In a brief experiment, one sensor was operated satisfactorily at 285°C and 5000 psi pressure. (Normal operation was at 1200 psi.)

In previous papers (1, 2), a new approach to high temperature pH measurements was described, in which an oxygen ion conducting ceramic membrane—stabilized zirconia—is employed in a sensor somewhat analogous to the glass electrode. The new sensor retains the specificity of the glass electrode, is equally insensitive to interference from redox active species, and possesses markedly superior resistance to attack by aqueous media at high temperatures.

Although the earlier work has established the feasibility of the concept, the performance of the new sensor has not been demonstrated under a wide variety of conditions. Its applicability to measurements on geothermal brines has been the focus of the present work.

A major aim has been to demonstrate that the performance of the sensor does not suffer in the presence of hydrogen sulfide and high concentrations of saline. The test system, protocols, and experimental results with simulated brines are discussed in the present paper.

Experimental

Sensor design.—Figure 1 shows the structural details of the sensor used in most of the work. The ceramic was a ¼ in. od tube of yttria-(8.0 weight percent [w/o]) stabilized zirconia (obtained from Corning Glass Works, Ceramics Products Division, Solon, Ohio, their composition 1372). It was retained in a Conax Type EG-125 Gland (Conax Corporation, Buffalo, New York) with a seal consisting of Teflon,¹ Vespel,¹ silver, and alumina elements as shown. On the basis of previous work (1, 2), we selected a dry copper/cuprous oxide mixture as our preferred internal junction. This was done for several reasons: (i) we had found it to be readily prepared by simple mixing of the powders and packing into the tube, (ii) when prepared in this fashion, it had been found to be extremely stable and reproducible, (iii) unlike aqueous internals, it permits ready designation of the active region of the sensor because it does not wet the wall with a conducting film, and (iv) in the absence of an internal aqueous phase, seal fabrication is simplified.

¹ Teflon and Vespel are registered trademarks of E. I. du Pont de Nemours and Company.

* Electrochemical Society Active Member.

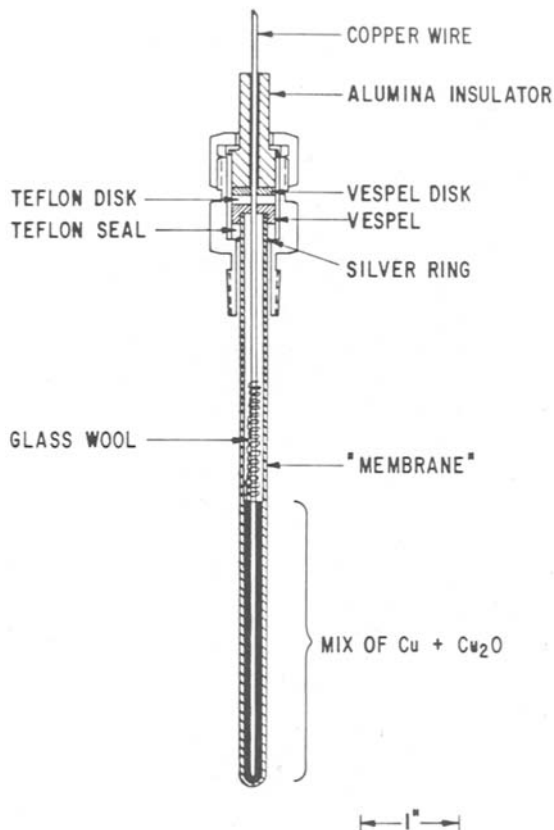


Fig. 1. Schematic diagram of preferred sensor for use with geothermal brines.

For the junction we employed a 1:1 (by weight) mixture of finely divided copper and cuprous oxide (Fisher Copper Metal-Electrolytic Dust, purified; Baker Cuprous Oxide Powder, Analyzed Reagent) to a depth of 2 in. A 30 mil copper wire served as the contact and lead from the sensor.

Test equipment.—A diagram of the test system is shown in Fig. 2. Fabricated of titanium and glass, it paralleled a stainless steel system used earlier (1, 2).

Provision was made for pumping water, acid, base, and simulated brines containing carbonate buffers and sulfides into the heated and pressurized titanium autoclave which had a capacity of 1 liter. It was also possible to introduce aliquots of more concentrated acid or base to bring about more rapid changes in pH. The main pump was a Pulsfeeder Model LS-20 with a titanium head manufactured by the Interpace Corporation, Rochester, New York. All fittings and other parts of the pressurized section were also made of titanium.

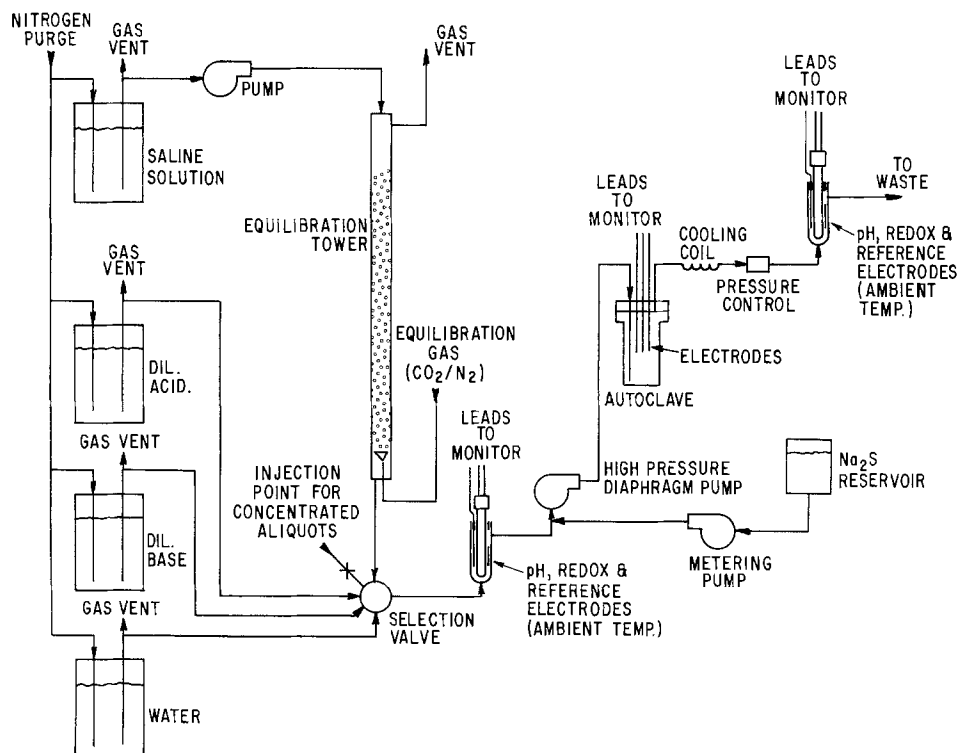
Inserted into the head of the autoclave were the sensor, a platinized platinum electrode (for monitoring the redox potential of the solution), and two reference electrodes. The latter were essentially like those described by Danielson (3), but we eliminated his zirconia thread. As a result, bubbles that formed upon depressurization of the system during cooling resulted in open circuits. Generally one reference electrode was freshly charged with 0.1M KCl in each run.

All streams that entered the autoclave were purged with nitrogen to reduce the oxygen concentration to low levels. To control the pH of the brine solutions before they entered the autoclave, they were contacted with carbon dioxide-nitrogen mixtures in a packed column following a procedure described by Syrett, *et al.* (4). The pH and redox potential of the solutions entering the autoclave were monitored at ambient conditions with a commercial glass combination electrode (Ingold)² and a platinum flag, respectively, both referred to a common reference electrode. Similar measurements were made at ambient conditions on the stream emerging from the autoclave. In this way, irreversible chemical changes occurring during passage through the autoclave could be detected. Provision was also made for sampling the streams and for checking the flow rate.

Rather than incorporate low concentrations of sulfide in the master feed solutions, from which it might be lost through volatilization or oxidation, we elected to inject a more concentrated solution of sodium sulfide into the brine stream just before it entered the high pressure diaphragm pump. The injection point is indicated in Fig. 2. A Harvard Syringe Pump Model 1100 with a 20 ml syringe was used for the injection.

² Registered trademark of Ingold Electrodes, Incorporated, Andover, Massachusetts.

Fig. 2. System for evaluating sensors with simulated geothermal brines.



Temperature of the autoclave was controlled with a Leeds and Northrup Electromax III proportional controller. High temperature pH and potential measurements were made with a Keithly Type 616 electrometer multiplexed with an Orion 855 Electronic Switch. The potentials of the pH sensor, the platinized-platinum redox probe, the autoclave, and the second reference electrode were all measured against the same primary reference electrode. The lower temperature measurements (pH and redox potential of the inlet and outlet streams to the autoclave) were made with an Orion Model 801 Digital pH meter, again multiplexed with an Orion Model 855 Electronic Switch. All potentials and the temperature were recorded on a Linear Instruments Corporation three-channel recorder.

Test protocols.—The initial series of tests were designed to determine the stability of the sensors under a variety of conditions. A key element was an exposure for several days to simulated brines covering a range of pH values. In each case, a calibration curve was obtained during the first two days by determining the response to a change from 1 mm HCl to 1 mm NaOH. Then the sensor was aged for about a week in a selected saline solution covering a range of conditions. During this period, potentials were monitored to check for drift or degradation. The carbon dioxide level of the brine solution was then changed to induce a pH change, and the response of the sensor was monitored and compared with the best estimate that could be made theoretically for the high ionic strength solutions involved. Finally, after an overnight flush of the system with water, the calibration curve was rechecked by determining the response of the sensor to a transition from 1 mm acid to 1 mm base. In a few runs, additional steps were introduced into the test protocols.

Sulfide analysis.—In order to control the sulfide concentration in the entering solution and to ascertain that it was maintained during passage through the autoclave, sulfide analyses were required on an occasional basis. For this purpose, a colorimetric method involving the reduction of methylene blue was found satisfactory. The procedure is provided in the "Methods Manual" (5) for a Hach Direct Reading Engineer's Laboratory, Model DR-EL/4, which was used for the analyses. With proper care to protect samples, reagents and diluting water from air, quite satisfactory results were obtained.

pH calculations.—In order to estimate the pH values of the brine solutions, we adapted a computer program developed by Syrett *et al.* (4) which was directed towards saline solutions containing varying amounts of carbonic acid and hydrogen sulfide, but which made no provision for the presence of salts of the above acids. As described elsewhere (6), we broadened the program to allow for the presence of such salts by including a term in the overall equation for mass and charge balance for the equivalent base required to form such salts from the acids; *i.e.*, the last term in the following equation

$$a_{H^+} + a_{H_2S} - a_{H^+} (K_3[H_2S] \gamma_0 + K_1[H_2CO_3] \gamma_0 + K_W) - 2(\gamma_1/\gamma_2)(K_1K_2[H_2CO_3]\gamma_0 + K_3K_4[H_2S]\gamma_1) + a_{H^+} + 2\gamma_1 \sum_0^m m [M^{m+}] = 0 \quad [1]$$

We have also added terms for the activity coefficients of the undissociated acids, since these deviate significantly from 1.0 in concentrated brines, as evidenced by solubility data in the presence of salts (7, 8).

In order to relate directly to our experimental protocols, an additional variation was introduced into the program to permit the derivation of the ambient temperature 25°C composition on the basis of the NaCl

content, the equivalent base concentration (from the amounts of sodium bicarbonate, sodium carbonate, and sodium sulfide added) of the starting solution, and the percent carbon dioxide in the equilibrating gas. Following this the composition at a second temperature of interest (285°C in most of our experiments) is made from the 25°C values.

The dissociation constants and most of the additional thermodynamic data required for the calculations were those used by Syrett *et al.* which they, in turn, had adopted from Naumov *et al.* (9). In addition, we employed data from Seidell (7) to derive the solubility coefficient for carbon dioxide at 25°C in terms of the partial pressure as well as γ_0 at 25°C. In turn, γ_0 at 285°C was estimated from the data of Ellis and Golding (8) for the solubility of carbon dioxide in water and sodium chloride solutions above 100°C. For extrapolation to 4.278m, their data, which extended only to 2.0m NaCl, was fitted by least squares to the Setchenow equation

$$\log \gamma_0 = \log (K/K^\circ) = BC \quad [2]$$

where K° is the solubility coefficient in water, K is the coefficient in brine at concentration C , and B is a constant. For the more dilute brines having an ionic strength of about 0.1m or less, γ_0 was assumed to be equal to 1.0.

To obtain the pH for any given set of conditions, Eq. [1] in combination with the various dissociation equilibria for the two acids is solved using the Newton-Raphson iterative technique. This, in turn, permits the calculation of the concentrations of all other relevant species. Using this program, the ambient temperature and 285°C pH values and concentration profiles for all of the carbonate solutions used in this work were calculated. Details of the program and a full tabulation of the calculated results will be found elsewhere (6).

Results and Discussion

Operation on brines at 285°C (runs GB-1 through GB-6).—This series of experiments was performed with a group of brines covering a variety of conditions, including high and low salinity (20% and 0.2% NaCl), a range of pH (3.2-9.1 at 285°C), and a range of hydrogen sulfide concentrations (0.0-100 ppm). All of the conditions, including calculated pH values, are listed in Table I. For each run, the solution employed during the extended aging period is marked with an asterisk in Table I. The other solutions were employed more briefly, in order to obtain response data over a wide range of conditions. In general, the sensors were exposed to the aging solution for periods of from 4 to 10 days, but, as will be noted, one sensor was used for three successive runs and accumulated over 37 days exposure to a variety of conditions at 285°C. In one run, GB-2, the sensor cracked and no useful data were obtained.

Run GB-1.—Virgin sensor Y-45 was employed along with two identical, newly fabricated reference electrodes, RD-9 and RD-10, both filled with 0.1m KCl. Both reference electrodes had potentials of 97 mV against a commercial silver-silver chloride electrode containing 3.0m KCl (Ingold) when immersed in 0.1m KCl at 25°C. Their resistances measured under the same conditions were 3.0×10^5 and $2.2 \times 10^5 \Omega$, respectively.

The run extended over a period of 11 days; operating conditions and potentials of the glass electrodes in the ambient temperature streams as well as those of the zirconia electrode as measured against their respective references are summarized in Fig. 3. Only data obtained with the acidic, alkaline, and saline solutions are shown because considerable scatter was present with the unbuffered water.

In greater detail, the system was brought to temperature with aerated water flowing through the auto-

Table I. Compositions of feed solutions used in runs GB-1 through GB-6

Run no.	Brine no.	[NaCl], <i>m</i>	Equivalent base** <i>m</i>	[H ₂ S] ppm	Percent CO ₂ in equilibrating gas	Calculated pH	
						25°C	285°C
GB-1	1A*	4.278 (20%)	0.109	—	1.0	8.6	8.6
	1B	4.278	0.109	—	100.0	6.6	7.8
GB-2	2A*	4.278	0.00109	—	100.0	4.6	5.8
GB-3	3A	4.278	(containing 0.001 <i>m</i> HCl)	—	N ₂	3.3	3.5
	3B	4.278	(containing 0.001 <i>m</i> NaOH)	—	N ₂	10.7	7.8
	3C (= 1A)	4.278	0.109	—	1.0	8.6	8.6
GB-4	3Cs*	4.278	0.110	10	1.0	8.6	8.6
	3Ds	4.278	0.110	10	100.0	6.6	7.8
	4A (= 2A)	4.278	0.00109	—	100.0	4.6	5.8
	4As*	4.278	0.00168	10	100.0	4.8	6.0
	4Bs	4.278	0.00168	10	1.0	6.8	7.3
GB-5	5As*	0.0342 (0.2%)	0.100	10	1.0	8.7	9.0
	5Bs	0.0342	0.100	10	100.0	6.7	8.2
GB-6	6A	0.0342	0.00100	—	100.0	4.8	6.4
	6As*	0.0342	0.00159	10	100.0	5.0	6.5
	6Bs*	0.0342	0.00159	10	1.0	6.9	7.9
	6Ca	0.0342	0.00688	100	100.0	5.6	7.1
	6Ds	0.0342	0.00688	100	1.0	7.4	8.2
	6E	0.0342	(containing 10 ⁻⁴ <i>m</i> HCl)	—	N ₂	5.1	5.2
	6F	0.0342	(containing 10 ⁻⁴ <i>m</i> HCl)	—	N ₂	4.1	4.2
	6G	0.0342	(containing 10 ⁻³ <i>m</i> HCl)	—	N ₂	3.1	3.2
	6H	0.0342	(containing 10 ⁻³ <i>m</i> NaOH)	—	N ₂	9.9	7.2
	6I	0.0342	(containing 10 ⁻³ <i>m</i> NaOH)	—	N ₂	10.9	8.2

* Solution used for aging tests.

** From added sodium bicarbonate and carbonate and the injected Na₂S.

clave. Initial calibration was accomplished with aerated sulfuric acid and sodium hydroxide, the standard procedure used in earlier work (2). The system was then flushed with water and was subsequently deaerated. Additional calibrations were then undertaken with deaerated hydrochloric acid and sodium hydroxide. Upon observation that the potentials from the latter solutions were in satisfactory agreement with those from the former aerated solutions, operation was shifted to the brine equilibrated with 1% carbon dioxide in nitrogen. Operation on this solution was continued for 4 days.

Prior to termination, the brine was equilibrated with 100% carbon dioxide in order to introduce a pH change. About 4h were required before the potentials from the various monitoring points were on plateaus. The system was then flushed with water, and the following day transitions to 0.001*m* hydrochloric acid and then to 0.001*m* sodium hydroxide were undertaken in order to obtain new calibration points that could be compared with the starting values. Finally, the system was flushed with water and cooled.

Upon opening the autoclave and examining the sensor, it was found to be sound and showed no visual signs of degradation. The two reference electrodes,

Table II. Comparison of measured and calculated values of pH: run GB-1. Sensor Y-45. *T* = 285°C.

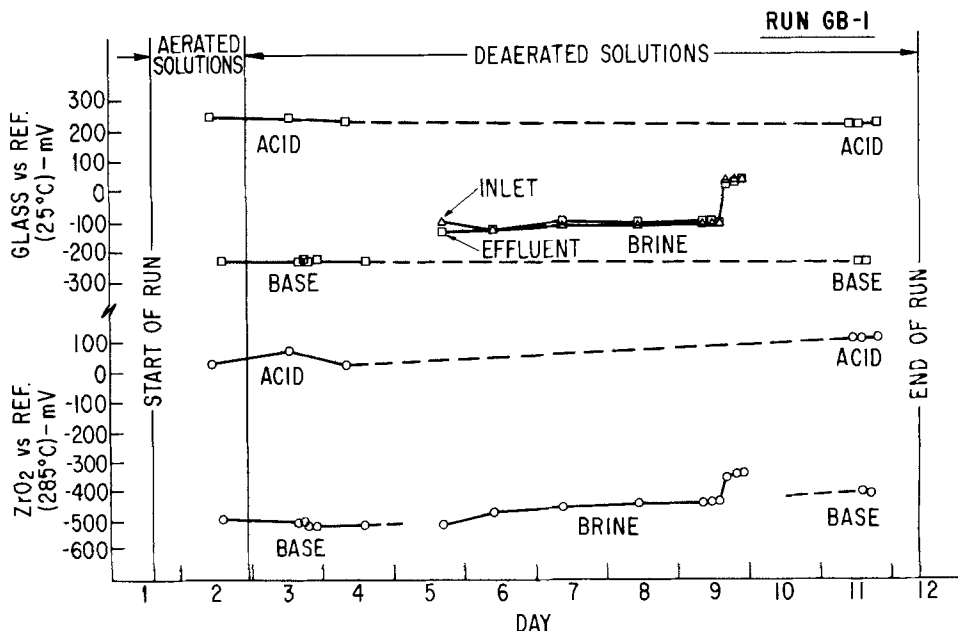
Solution	pH		
	Calc.	Meas.	Δ
A	8.9	8.6	-0.3
B	8.3	7.6	-0.7

however, did contain gas bubbles, and their rest potentials could not be compared with their initial values against a commercial reference electrode.

Although very little drift occurred with the ambient temperature sensors throughout the run, some did occur at 285°C. This point is brought out more clearly by the data in Fig. 4, which shows calibration curves at the start and finish of the run. Similar drift was observed at 285°C with the platinum electrode.

The pH values for the brine solutions derived from the calibration curves in Fig. 4 are summarized in Table II. Because of the drift and the fact that the data points were obtained closer to the final than the initial calibration, the high temperature pH values were determined on the basis of the final calibration curve for the zirconia sensor.

Fig. 3. Potentials of zirconia sensor at 285°C and glass electrodes at 25°C vs. their respective reference electrodes during run GB-1.



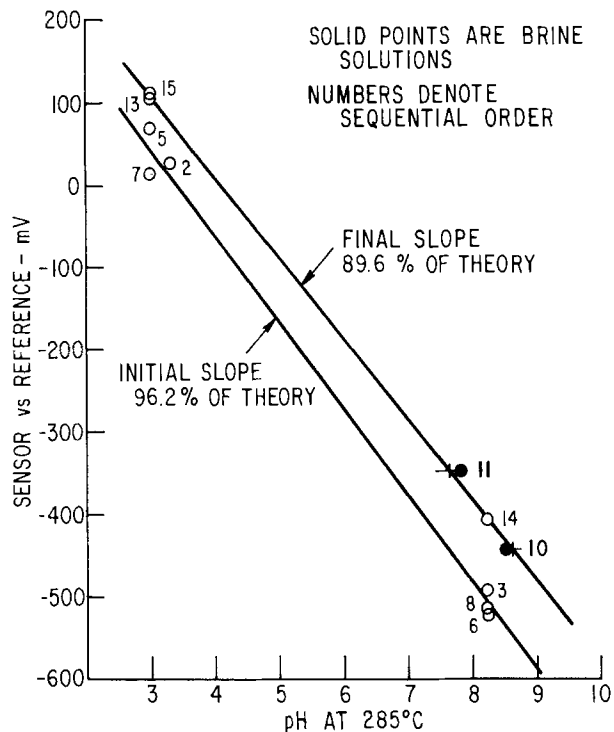


Fig. 4. Calibration curves for zirconia sensor at 285°C (run GB-1)

The drift in the calibration curve with time is a phenomenon that we have encountered previously (2). It appears to be associated with changes in the internal chloride concentration in the reference electrode. Because such drift was not reported in the original description of the electrode (3), it may reflect our omission of the internal zirconia thread from the structure. Such a thread might reduce convection in the internal electrolyte and thereby improve stability. Alternatively, our zirconia junction might have been more porous than that used previously.

Run-GB-3.—This was essentially a repeat of run GB-1, with the exception that sulfide was introduced into the brine. A new sensor Y-47 was employed. The two reference electrodes were also new; RD-13 was filled with 0.1*m* KCl and RD-14 with a 20 w/o NaCl solution.

Following the initial calibration steps, two additional steps were introduced when the system was operated briefly with brines 3A and B containing 0.00109*m* HCl and NaOH, respectively, both in 20% NaCl. This was followed by the transition to the carbonate buffered brine solution equilibrated with 1% CO₂ in N₂. After

Table III. Sulfide analyses of stock solution and effluent

Day of run	Brine	Stock solution* (ppm)	Effluent (ppm)
5	Cs	1162	9.3
9	Cs	1040	7.3
11	Cs		8.3
11	Ds		7.7

* Nominally 1200 ppm. At the flow ratios employed, 1200 ppm in the stock solution would give 11 ppm in the feed to autoclave.

a day's operation on the simple brine, sulfide injection was started to maintain the level at about 10 ppm for a period of 7 days. No detectable change occurred in the output of the pH sensor upon the addition of the sulfide. At the conclusion of this aging period, a pH change was induced by equilibrating the brine with carbon dioxide while retaining the sulfide concentration at 10 ppm. Finally, the sensor was recalibrated with acid and base after flushing the brine from the system with water.

The complete run lasted 11 days. Conditions and potentials of the ambient and high temperature pH sensors vs. their respective reference electrodes are summarized in Fig. 5. During operation on the sulfide, analyses of the stock solution and the effluent were performed with the results in Table III. Since input conditions were adjusted for 11 ppm in the feed to the autoclave, a small loss on passage through the system seems to have occurred. This is undoubtedly real and probably reflects reaction with metal and corrosion products in the system.

The potentials of the two nonidentical reference electrodes were found to converge during the run. Initially, the electrode containing 20% NaCl was 40-50 mV negative to that containing the 0.1*m* KCl. At the end of the run this difference had fallen through zero and was slightly positive. Upon draining the filling solutions from the two, they were both found to contain ~ 1.5*m* NaCl. Clearly the concentrations had converged during exposure to the brine. It is probable, however, that considerable dilution may have occurred during the last day or so of operation on the calibrating solutions and the water and during cool down.

At the conclusion of the run, pH values of the various solutions were read from the calibration curves. Those for the brines containing HCl and NaOH were read from the initial curve, and those containing the carbonate from the final. The measured and calculated values are listed in Table IV. Moderate deviations of the same order of magnitude are seen in all cases. In

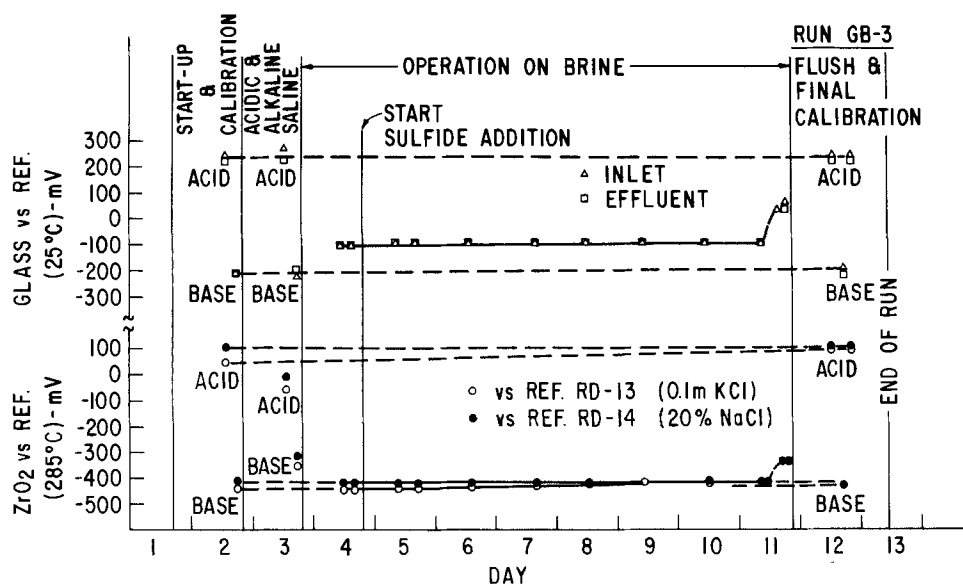


Fig. 5. Potentials of zirconia sensor at 285°C and glass electrodes at 25°C vs. their respective reference electrodes during run GB-3.

Table IV. Comparison of measured and calculated values of pH at 285°C

Solution	Calculated	Measured	Δ	$\gamma_{H^+}(\gamma_{OH^-}) \cdot \text{Calc. from measured pH}$
A	3.5	4.1	+0.6	0.079
B	7.8	7.1	-0.7	0.057
Cs	8.6	8.2	-0.4	—
Ds	7.8	7.4	-0.4	—

$$\gamma_{H^+} = a_{H^+}/C_{H^+} = 10^{-pH}/C_{H^+}$$

$$\gamma_{OH^-} = K_w/(a_{H^+} \cdot C_{OH^-}) = K_w/(10^{-pH} \cdot C_{OH^-}).$$

an effort to assess the cause of the discrepancies, it is of interest to calculate activity coefficients for the hydrogen and hydroxide ions from the experimental data obtained with the simpler solutions, A and B. These values, listed in Table IV, are considerably lower than a value of 0.288 derived from the computer program.

It is suggested that the observed deviations in pH result more from a failure of the computer program to properly estimate activity coefficients of the "trace" constituents (*i.e.*, the hydrogen and hydroxide ions) of the brine solutions than from shortcomings in the measurements with the sensor-reference electrode combination. This suggestion is supported by experience with mixed electrolytes at lower temperatures (10, 11). Much available data indicates that the activity coefficients of trace constituents differ markedly from those of macro constituents in mixed electrolytes. The model of Syrett *et al.*, from which the present computer program was derived, assumes that all are the same.

Run GB-4.—This run was similar to GB-3 except that the brine used for aging was more acidic. A new sensor Y-48 was employed along with two new reference electrodes, one containing 0.1M KCl, the other 3.0M KCl. About 10 ppm of hydrogen sulfide was added to the brines from the start. Aging on the more acidic brine extended over a period of 7 days. Summary data are recorded in Fig. 6. Again some drift was evident, but, as expected, this was greater with the 0.1M KCl reference electrode than with the more concentrated. A comparison of measured and calculated pH values for this and the next two runs will be included in a more general discussion that follows.

Run GB-5.—This run differed from the previous four in that the brine concentration was at the 0.2% level.

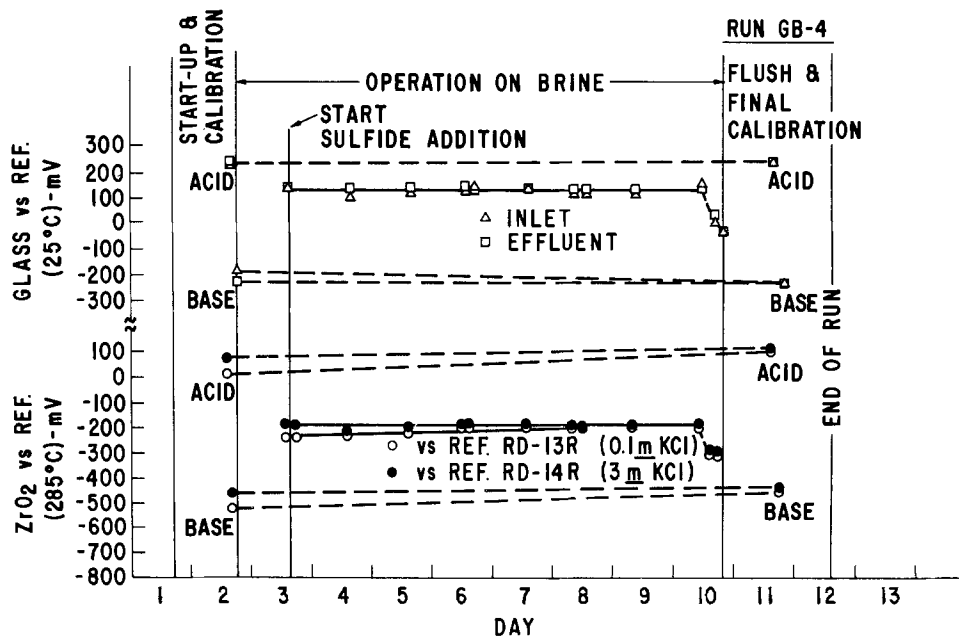
The hydrogen sulfide concentration was maintained at the 10 ppm level. Sensor Y-48 was continued in use from the previous run, but new reference electrodes containing 0.1M KCl and 0.2% NaCl solutions were employed. Aging was performed in the more alkaline brine for a period of about 10 days.

In contrast to the earlier runs, the drift in potentials with time was towards lower values rather than higher. This is to be expected for the 0.1M KCl reference because chloride should be lost to the more dilute brine solution being monitored. It would be expected that the output of the sensor *vs.* the 0.2% NaCl reference would have remained constant, but some drift did occur in this case as well. The summary data are recorded in Fig. 7.

Run GB-6.—This run was carried out as a continuation of the previous one without changing the sensor or the reference electrodes. Only the brine was changed to one of more acidic character by lowering the equivalent base concentration from 0.1 to 0.001M. Conditions and data are summarized in Fig. 8. After about 7 days' operation on the brines containing 10 ppm hydrogen sulfide, the level was raised to 100 ppm for 2 days. This had no apparent effect apart from that associated with the pH change resulting from the introduction of an increased amount of equivalent base in the form of the sodium sulfide. Later in the run, the sensor was exposed successively to 0.2% brine solutions 6E through 6I containing different levels of free hydrochloric acid and sodium hydroxide. Operation was straightforward throughout, and the sensor remained in excellent condition after 37 days of almost continuous operation through three consecutive runs.

General.—It has been evident above that quite satisfactory agreement has been seen between measured and calculated pH values in the individual runs. The accumulated data from the several individual experiments are combined and interrelated in Fig. 9 and 10. The former includes all of the data from runs GB-1 through GB-4 with the 20% brines, and the latter the data from runs GB-5 and GB-6 for the 0.2% brines. It is again clear that the data correlate extremely well and cluster about the line representative of perfect agreement over the full pH range from 3 to 9. As discussed in connection with run GB-3, the deviations between the measured and calculated values may well reflect shortcomings in the calculations rather than the sensors.

Fig. 6. Potentials of zirconia sensor at 285°C and glass electrodes at 25°C vs. their respective reference electrodes during run GB-4.



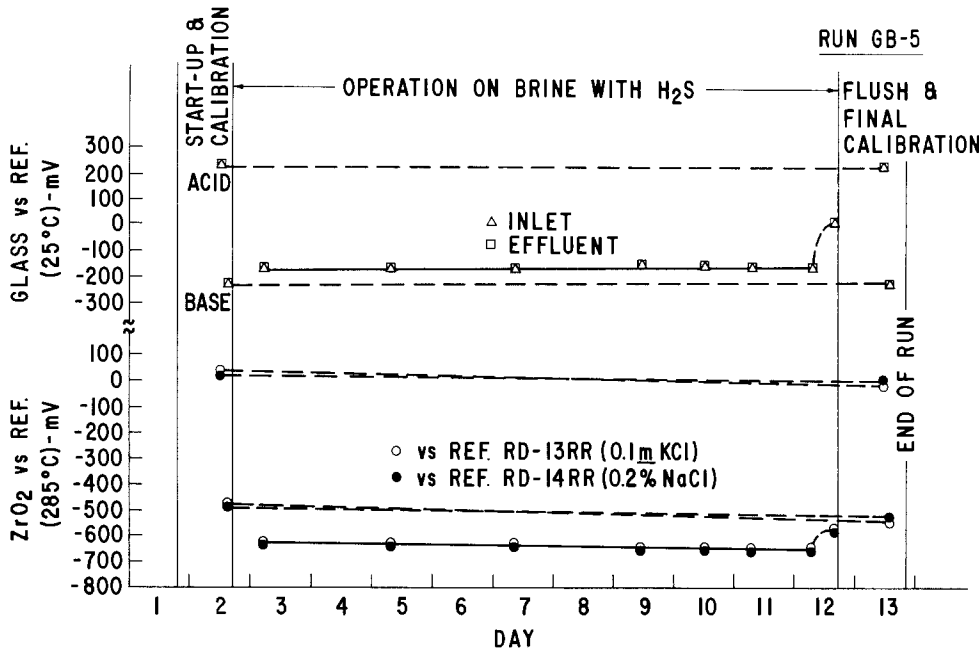


Fig. 7. Potentials of zirconia sensor at 285°C and glass electrodes at 25°C vs. their respective reference electrodes during run GB-5.

Reproducibility of performance.—An indication of the reproducibility of the sensor-reference electrode combination is given in Fig. 11, in which calibration curves from five different runs are shown. In each case, the initial calibration curve was obtained with a fresh reference electrode containing 0.1m KCl. Three different sensors were involved in these measurements: Y-45 in runs GB-1 and GB-2, Y-47 in GB-3, and Y-48 in GB-4 and GB-5. A spread of about 0.5 pH unit is evident for a given output voltage among the initial calibration curves.

If such reproducibility could be maintained, it would probably be acceptable for many applications without the need for later recalibration. Unfortunately, significant shifts in the calibration curves occur after prolonged operation because of the exchange of chloride between the reference electrode and the solution being monitored. In monitoring a brine, the extent of the shift is limited because of the finite concentration of chloride in the solution. In monitoring a 20% brine (4.278m NaCl) using a reference containing 0.1m KCl, the theoretical limit on the drift is $\log(4.278/0.1)$ or 1.6 pH units. The maximum drift observed during the present tests fell short of this limit by a factor of about two. In monitoring solutions containing no chloride,

larger drifts are possible through continuous loss of chloride to very low concentrations.

While considerable displacement of the calibration curves is encountered, the slope remains quite stable. This suggests that in operation single-point calibrations might prove highly satisfactory. In view of the relative stability of the calibration curve obtained against the reference containing 20% sodium chloride in run GB-3, there would seem the real possibility that a reference electrode might be devised to match a given brine field and thereby give very stable performance in that field. This would be somewhat dependent upon the actual stability of brine levels in the field. Even in such a case occasional recalibration would seem in order.

Performance of sensors at lower temperatures (runs GB-7 and GB-11/13).—As noted in an earlier report (12), the standard ceramic has a history of becoming sluggish in response during continuous operation at 95°C. The performance at 95°C has also been poor after brief operation at 285°C, even though the same sensor might again perform excellently for weeks at the higher temperature. This behavior has been attributed, at least in part, to structural shortcomings in the

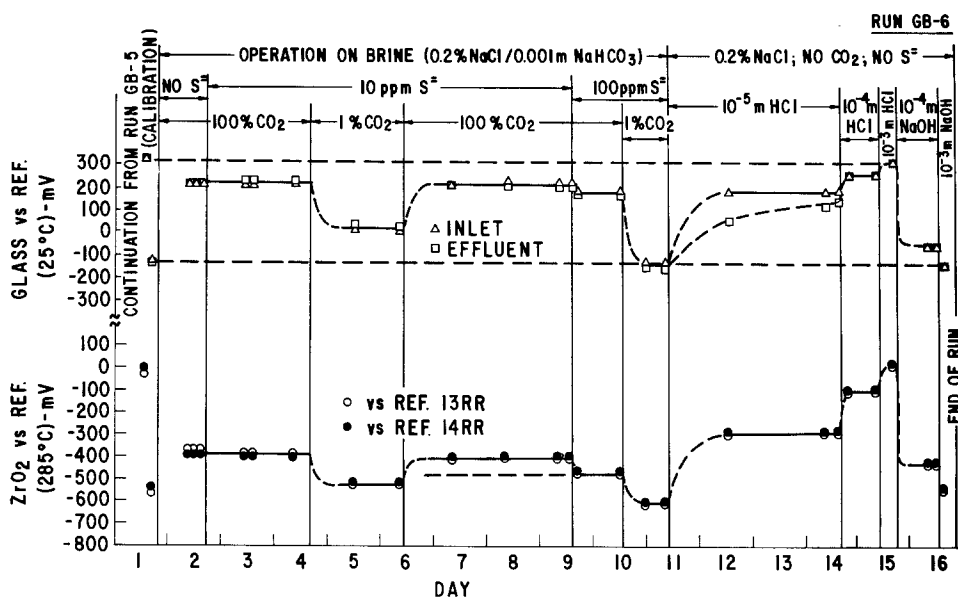


Fig. 8. Potentials of zirconia sensor at 285°C and glass electrodes at 25°C vs. their respective reference electrodes during run GB-6.

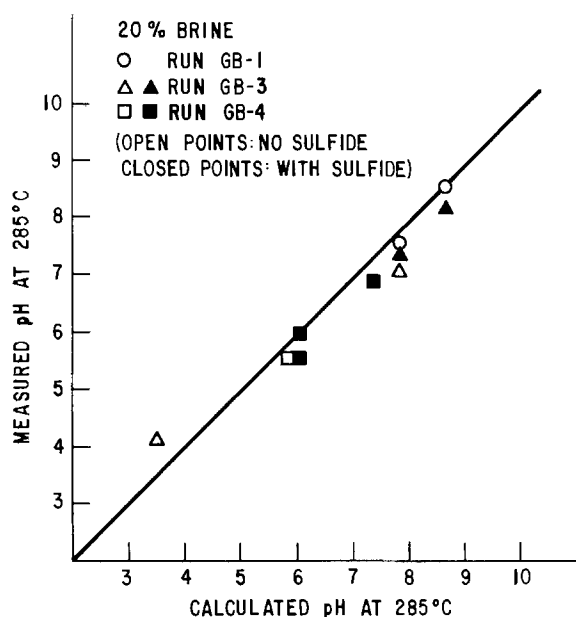


Fig. 9. Correlation between measured and calculated pH at 285°C for all 20% brines.

ceramic (12). For this reason, low temperature testing was delayed until the end of the present program in order to take advantage of the possible availability of improved materials at that time. This was indeed the case, and four new experimental tubes—all yttria-stabilized zirconia—were used in tests at lower temperatures. One of these was a dense ceramic made in house. Used for the fabrication of sensor SP-8 it was similar to the material used for sensor SP-4 in Ref. (6), which performed well at 95°C for over a month of continuous operation. The other three tubes were obtained from NGK-Locke Insulators, Limited, of Japan. Used in sensors NGK-A2, NGK-B, and NGK-C1, they were prepared with different process modifications, all of which gave dense ceramic. The tube in NGK-C1 differed from normal in that it incorporated a larger diameter collar on the open end of the tube. This permitted a seal modification that more closely resembled that of a conventional Conax fitting, which, it was hoped, would solve some of our seal problems. Unfortunately, this hope was not realized: stress con-

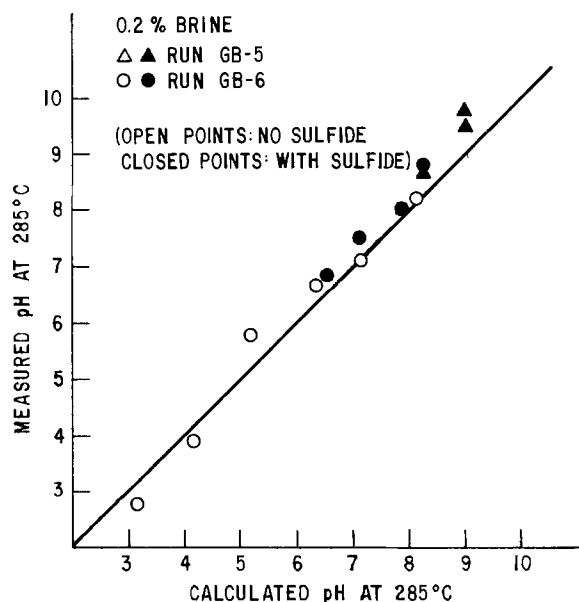


Fig. 10. Correlation between measured and calculated pH at 285°C for all 0.2% brines.

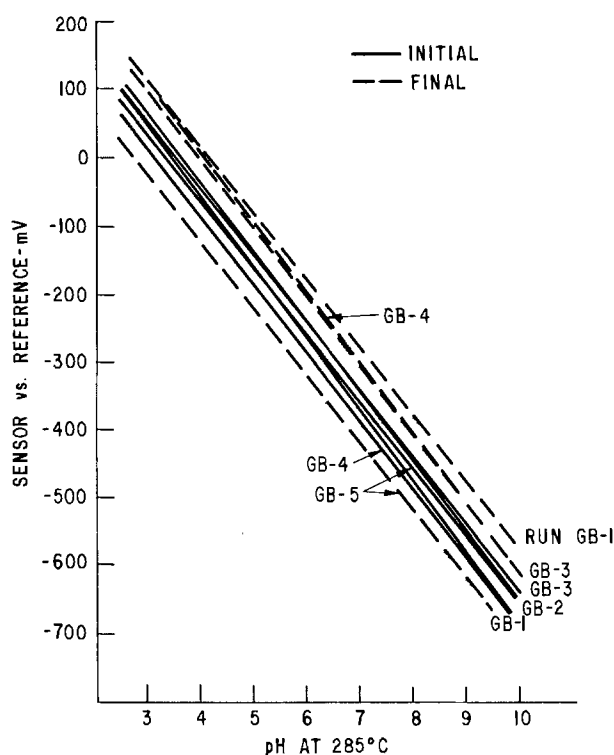


Fig. 11. Data showing reproducibility of calibration curves from run to run. All reference electrodes initially contained 0.1M KCl.

centration at the junction of the larger diameter collar with the smaller diameter tube resulted in circumferential cracking at that location. Although a disappointment, these initial failures would not seem to be intrinsic to the structure.

None of the new tubes were of the same diameter as those normally employed, and slight modifications to the Conax fittings were required. To expedite the tests, it was necessary to employ stainless steel fittings for the purpose, and for this reason all of the tests were performed with simple aqueous solutions rather than brines, i.e., in water, dilute sulfuric acid, and dilute base. This was not felt to be a serious shortcoming because excellent correlation between the performance of the zirconia sensor on such simple solutions and on brines had by this time been demonstrated in the tests at 285°C.

In run GB-7, three sensors SP-8, NGK-A2, and NGK-B were tested in parallel at temperatures of 95°, 150°, 225°, and 285°C. Both the pH response and the resistance of each sensor were determined at each temperature. In order to ascertain whether deleterious changes occurred at the elevated temperatures, a retest at 95°C was performed after each step to a higher temperature. The test results are summarized in Fig. 12.

It is evident that sensor NGK-A2 was erratic from the start, and distinct evidence of failure was obtained from the resistance measurement during the second test at 95°C. Quite clearly, a crack had developed to allow shunting across the ceramic.

The other two sensors performed excellently up through the operation at 285°C, although one set of response data for NGK-B at 95°C was lost through an instrument malfunction. Following the exposure at 285°C, the subsequent response at 95°C was poorer for both. In the case of NGK-B the low resistance at this point again indicated a shunt across the ceramic, most likely because of a crack. The resistance of SP-8 remained high, however. It is therefore difficult to reach a firm conclusion concerning its decline in performance at 95°C. It could result from degradation of the ceramic, but it could also result from leakage of electrolyte

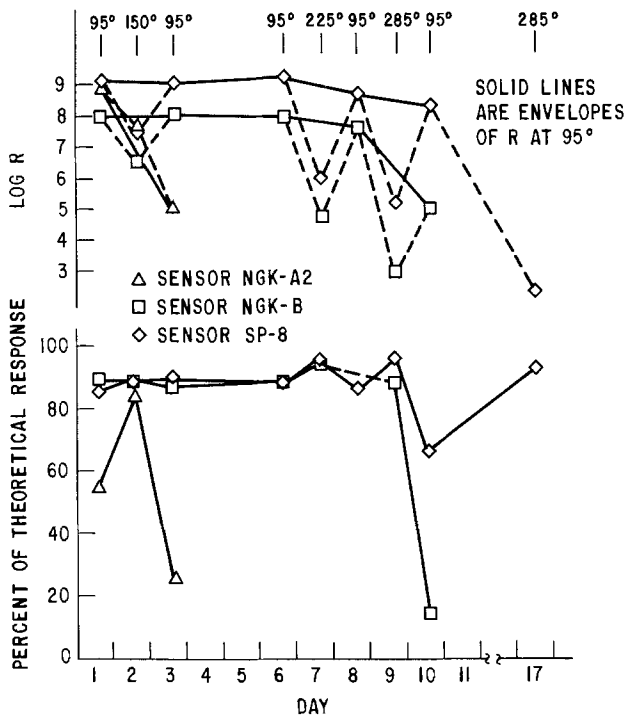


Fig. 12. Response and resistance data for several sensors tested alternately at 95°C and higher temperatures.

around the seal to form an electrolytic shunt sufficient to degrade performance. We have long suspected such a possibility in connection with our present seals, but further work will be required to confirm it.

In view of the declining performance at 95°C, a final test was performed on SP-8 at 285°C. As anticipated from past experience, the response remained excellent at the higher temperature. At this point, the run was terminated and the system cooled to ambient for removal of the sensors. Both NGK-A2 and NGK-B were found to be cracked. Sensor SP-8 remained solid. However, because a curvature had developed during firing it had been necessary to assemble this sensor *in situ* while the Conax fitting was mounted in the lid of the autoclave. We were unsuccessful in removing the sensor from the lid without cracking the ceramic tube.

Sensor NGK-C1 was evaluated in a separate test, run GB-11/13. It was first assembled with a new seal adapted to the collar on the as-received tube. Circumferential cracking occurred during initial operation at 95°C, and again later in the tests. As a result, inconclusive data were obtained with this sensor.

Although the present series of tests were not completely satisfying, they do indicate that ceramics can

be made that are more stable in low temperature service than the standard Corning ceramic used in the bulk of the tests and most of the earlier work. It is, however, not yet clear whether the degradation in performance of the new ceramics at low temperatures is a reflection of changes in the ceramic or of defects in the seals. While we strongly suspect the latter, this point requires resolution. In the interim, it appears likely that it will be possible to operate sensors employing one of the new ceramics for extended times at low temperature (i.e., 95°-150°C) if excursions to higher temperatures are avoided.

Operation at 5000 psi.—The ability of the new pH sensor to operate at 5000 psi and 285°C was demonstrated in a single experiment in which only water, dilute sulfuric acid, and dilute sodium hydroxide were employed as test fluids. Data obtained from the short run are summarized in Table V. They demonstrate the ability of the sensor to withstand the 5000 psi pressure at 285°C and to respond to a pH transient under these conditions. Upon completion of the test, the pH sensor remained intact.

Conclusions

It is concluded from this work that the present sensors should perform well in geothermal brines over a range of temperatures if given sufficient attention to calibration and seal maintenance. Clearly, however, care must be exercised to obtain high quality ceramics, particularly with regard to surface integrity and freedom from surface pores. Improved seals between the ceramic tubes and the metal fittings are also required for long-term, routine use in the field.

Acknowledgments

The investigation described in this report was authorized under prime contract DE-AC-06-76-RLO-1830 for the United States Department of Energy, Division of Geothermal Energy. It was performed by General Electric Company, Corporate Research and Development, for the Pacific Northwest Laboratory, operated by Battelle Memorial Institute for the U.S. Department of Energy. The constructive guidance provided by George A. Jensen, Project Officer for the Pacific Northwest Laboratory, is gratefully acknowledged. We are also grateful to M. J. Danielson of the Pacific Northwest Laboratory for helpful suggestions regarding seals and reference electrodes. S. Prochazka of General Electric Corporate Research and Development was extremely helpful by fabricating several high density zirconia tubes from highly purified, yttria-stabilized zirconia kindly prepared by C. Scott of the General Electric Lighting Research Laboratory, Cleveland, Ohio. P. Buckley facilitated the work at the elevated pres-

Table V. Summary of operating conditions and data from high pressure run GB-10. $P = 5000$ psi. $T = 285^\circ\text{C}$.

Lapsed time (hr)	Temp ($^\circ\text{C}$)	Pressure (psi)	Solution in autoclave	Measured potentials (mV)			Notes
				Glass electrode at 25 $^\circ\text{C}$	Sensor at 285 $^\circ\text{C}$	Pt Electrode at 285 $^\circ\text{C}$	
0.0	25	Ambient	Water				Start pressurization Start heating Increase pressure
0.1	25	1250	Water				
1.8	288	1250	Water	-10	-475	-75	
2.0	285	5000	Water				Inject 4.0 cm ³ 0.1m H ₂ SO ₄
2.1	285	4900	Water	50	-492	-8	
2.2							
2.6	285	5150	~0.0005m H ₂ SO ₄	216	-68	394	
3.4	285	5150	~0.0005m H ₂ SO ₄	202	-81	400	
3.7	285	5150	~0.0005m H ₂ SO ₄	199	-86	400	
			~0.0005m H ₂ SO ₄ mean	206	-78	398	
3.7							Inject 8.0 cm ³ 0.2m NaOH
4.0	285	5150	~0.001m NaOH	-225	-508	-78	
4.1	285	5150	~0.001m NaOH	-225	-511	-82	
4.4	284	5100	~0.001m NaOH	-220	-510	-74	
4.8	285	5100	~0.001m NaOH	-217	-506	-66	
7.0	285	5100	~0.001m NaOH	-216	-480	-22	
			~0.001m NaOH mean	-221	-503	-64	
			Δ mV (acid to base)	427	425	462	
			Theoretical	473	543	543	
			Percent of Theory	90	78	85	

sure by providing one of the protective cells in his high pressure laboratory. W. T. Grubb and L. King assisted with the sulfide analyses and made their Hach Model DR-EL/4 colorimeter available for this purpose.

Manuscript submitted July 18, 1983; revised manuscript received Jan. 19, 1984.

General Electric Company assisted in meeting the publication costs of this article.

REFERENCES

1. L. W. Niedrach, *Science*, **207**, 1200 (1980).
2. L. W. Niedrach, *This Journal*, **127**, 2122 (1980).
3. M. J. Danielson, *Corrosion*, **35**, 201 (1979).
4. B. C. Syrett, D. D. Macdonald, H. Shih, and S. S. Wing, "Corrosion Chemistry of Geothermal Brines. Part 2: High Salinity Brine," Final Report to NSF (RANN) and DOE, Washington, DC (1977).
5. "Methods Manual for Hach Direct-Reading Engineer's Laboratory Model DR-EL/4," Hach Chemical Company (1980).
6. L. W. Niedrach and W. H. Stoddard, "The Development of a High Temperature pH Electrode for Geothermal Fluids. Final Report-Task III and Year-End Summary," Report PNL 4651, Pacific Northwest Laboratory, Battelle Memorial Institute, United States Department of Energy, Division of Geothermal Energy, Washington, DC (1981).
7. A. Seidell and W. F. Linke, "Solubilities of Inorganic and Metal-Organic Compounds," Vol. I, pp. 467 ff, D. Van Nostrand Co., Inc., London (1958).
8. A. J. Ellis and R. M. Golding, *Am. J. Sci.*, **261**, 47 (1963).
9. G. B. Naumov, B. N. Ryzhenko, and I. L. Khodakovskiy, "Handbook of Thermodynamic Data," p. 243, transl. U.S. Geological Survey, Washington, DC (1974).
10. R. A. Robinson and R. H. Stokes, "Electrolyte Solutions," Second Edition (Revised), p. 432, Butterworths, London (1970).
11. H. S. Harned and R. A. Robinson, "Multicomponent Electrolyte Solutions," p. 13, Pergamon Press, London (1968).
12. L. W. Niedrach and W. H. Stoddard, "The Development of a High Temperature pH Electrode for Geothermal Fluids. Final Report-Task I," Report PNL 3857 UC-66, Pacific Northwest Laboratory, Battelle Memorial Institute, United States Department of Energy, Division of Geothermal Energy, Washington, DC (1981).

Considerations of the Stability of Pit Repassivation during Pitting Corrosion of Passive Metals

T. Okada

Industrial Products Research Institute, M.I.T.I., Yatabe, Tsukuba, Ibaraki 305, Japan

ABSTRACT

The repassivation of pits, by which pitting corrosion initiated in an aggressive environment ceases, is studied from the kinetic point of view. Consideration of irreversible thermodynamic stability suggests that the repassivation process starts as soon as the monolayer formation of the metal oxide becomes stable at the bottom of the pit. The critical pitting potential is defined so that the rate of the monolayer formation of the metal oxide overcomes the rate where the monolayer oxide changes to the halide. It is shown that the repassivation potential is very close to the critical pitting potential, whereas the pit initiation potential is intrinsically different and coincides only when the passive film is very thin. The present study presents the theoretical significance of the repassivation potential as a characteristic value of pitting.

The pitting potential, an important characteristic of the pitting of passive metals, is of practical significance because this value gives some indication of the relative pitting resistance of the metal in a corrosive environment. However, different workers have obtained different values, even for the same metal in the same environment (1-3). For example, there are two kinds of potentials observed experimentally: the potential at which the first pit appears when a specimen is positively polarized in a solution containing aggressive ions,¹ and the potential below which pits, once initiated, can be stopped.² These two potentials are experimentally distinguished from each other. However, they occasionally appear to be coincident, if determined in a way that eliminates time lag (9, 10).

Pitting is a complex series of processes consisting of corrosion, material transport, induced local polarization, and the subsequent local concentration of ionic species. Theoretical attempts have been made considering the thermodynamic stability of newly formed phases (11), ionic exchange (12), passive film flaws and crystallographic factors (3, 13, 14), mechanical factors (6, 15), and transport of ionic species (16, 17), but these attempts have not been successful in explaining the kinetic features of pitting.

Key words: pitting corrosion, irreversible thermodynamics, repassivation, oxide film.

¹This potential is called the pitting potential (4) or the breakdown potential (5, 6).

²The protection potential (7) or the repassivation potential (8).

An irreversible thermodynamic consideration has been applied successfully to pitting (18). The complicated phenomena of pitting can be treated by considering the stability of the whole system undergoing pitting corrosion. It has further been shown that pit initiation in an aggressive environment can be thought of as a probability event (19).

It should be recognized that very few theoretical attempts have been successful in predicting the occurrence of the two kinds of characteristic potentials stated above. They are assumed to coincide if the time required for their occurrence is eliminated (9), but they are considered experimentally to be intrinsically different from each other (20, 21).

In this study, the repassivation process of hemispherical pits is discussed in relation to the irreversible thermodynamic stability theory, to see if there is any relationship between pit initiation and the repassivation processes.

Theory

It is sometimes observed in hemispherical pits that dissolution at the pit bottom resembles anodic brightening. Hoar *et al.* (6, 13) reported that the "contaminated oxide" film forms on metal surfaces during anodic brightening, and that the metal dissolves rapidly through this film. Although it is not clear whether this kind of film also forms at the pit bottom during pitting corrosion, it is plausible that a nonprotective salt film composed of dissolved metal cations and concentrated

aggressive anions occurs at the pit bottom, and dissolution of the metal is greatly enhanced.

In order for the repassivation of pits to occur, oxygen atoms need to be supplied to the corroding metal surface in sufficient quantity. According to Hoar (22) H₂O plays an important role in the initial passivation processes of metals. Therefore, H₂O should occur in the nonprotective film which is formed at the pit bottom, and take part in the repassivation process by concentration at the metal surface.

Assume that the nonprotective film is a "hydrous metal halide" with a large ionic conductivity.³ According to the linear phenomenological equations of irreversible thermodynamics, fluxes participating in the entropy production are expressed as linear formulas of all conjugated forces (23). A concentration gradient of H₂O would arise so as to counteract the H₂O flux accompanying the ionic fluxes (24). The flux of the dissolving metal cation would be the largest, and the concentration of H₂O would be lower in the inner part of the hydrous halide layer, if the pitting reaction proceeds quickly. However, as the potential of the metal decreases, it will bring about a decrease in the rate of the metal dissolution reaction and also an increase in H₂O concentration at the metal surface, so that the repassivation process can be initiated. The potential at this point is referred to as the repassivation potential.

Repassivation process.—Oxide film thickening.—Suppose that at the pit bottom where metal is dissolving beneath the nonprotective film of thickness, l , a metal oxide with an area s_0 and a thickness d is formed on the metal surface. Figure 1 shows this system schematically. l is assumed to be much smaller than the size of the pit, so that material transport in this system can be expressed by one-dimensional formulas with the axis normal to the metal surface. The model of the system is depicted in Fig. 2, in which each portion of the phase is denoted by numerals.

Consider the change in entropy production $\delta^d P$ caused by the increase in oxide film thickness from d to $d + \delta d$, with its area s_0 remaining constant. $\delta^d P$ can be divided into two parts, $\delta_J^d P$ due to the change in fluxes and $\delta_X^d P$ due to the change in forces

$$\delta^d P = \delta_J^d P + \delta_X^d P \quad [1]$$

According to the general evolution criterion of irreversible thermodynamics, a system in a fixed boundary condition moves toward the direction where $\delta_X^d P$ decreases until it reaches a steady state (25)

$$\delta_X^d P \leq 0 \quad [2]$$

Changes in the system resulting from the oxide film thickening from d to $d + \delta d$ are: a change in material transport in the oxide film, a change in the reaction at the interface between the oxide and the hydrous halide, a change in material transport in the hydrous halide, a change in the reaction at the interface between the hydrous halide and the electrolyte solution, and a change in material transport in the solution. Other changes are considered to be trivial. The contributions of these changes to $\delta_X^d P$ will be denoted as $\delta_X^d P_{MO}$, $\delta_X^d P_{MO/MX}$, $\delta_X^d P_{MX}$, $\delta_X^d P_{MX/S}$, and $\delta_X^d P_S$, respectively. Here it is assumed that all these changes occur in the area shadowed by s_0 , and changes in the other portions are ignored,⁴ since the ionic conductance of the hydrous halide is very large. It is also assumed that heat flux is neglected because the temperature is kept constant throughout the system.

³ Perhaps this is not the same in composition as the "halide nuclei" which have been assumed to form in a passive film (19). The halide nuclei break through the passive film, whereas the nonprotective film forms on the bare surface of the metal, and the rate of metal dissolution is much larger. Here the differences between them are disregarded as far as notations are concerned.

⁴ Actually, the change in the reaction which occurs on the passive film surface would contribute to $\delta_X^d P$, but the result remains unchanged even if this contribution is taken into account.

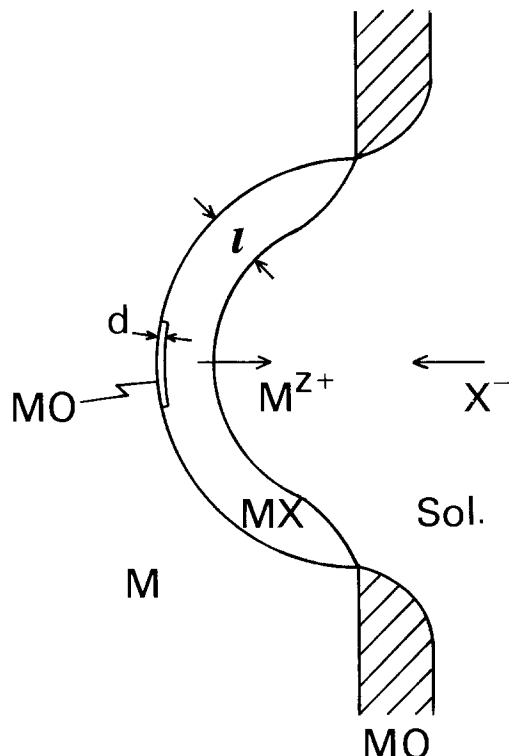


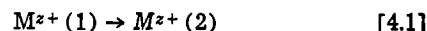
Fig. 1. Illustration of a pit which is repassivating. M: metal. MO: oxide film. MX: nonprotective metal halide. Sol.: solution.

In the oxide film, ionic conduction J_M and J_O of M^{z+} and O^{2-} ions is caused by the potential drop $\Delta\Phi_0$ across the film. The changes in the affinity in this phase are mainly due to the change in $\Delta\Phi_0$, so that

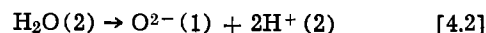
$$T\delta_X^d P_{MO} = (zFJ_M - 2FJ_O) \left(\delta\Delta\Phi_0 - \frac{\Delta\Phi_0}{d} \delta d \right) s_0 \quad [3]$$

with the flux J_i ($i = M, O$) expressed by the exponential formula (19, 26).

At the oxide-hydrous halide interface, metal dissolution



and oxide formation



take place simultaneously. The current density for each reaction is

$$i_M = k_M \exp\left(\frac{\mu_M(1)}{RT}\right) \exp\left(\frac{\nu_X \mu_X(2)}{RT}\right) \exp\left(\frac{\alpha_M z F \Delta\Phi_{MO/MX}}{RT}\right) \quad [5.1]$$

$$i_O = k_O \exp\left(\frac{\mu_W(2)}{RT}\right) \exp\left(\frac{2\alpha_O F \Delta\Phi_{MO/MX}}{RT}\right) \quad [5.2]$$

in which k_M and k_O are rate constants, $\mu_i(p)$ ($i = M, X, W; p = 1, 2$) is the chemical potential of M^{z+} , X^- , and H_2O in each phase, ν_X is the stoichiometric coefficient of X^- participating in the metal dissolution reaction, α_M and α_O are "transfer coefficients," and $\Delta\Phi_{MO/MX}$ is the Galvani potential difference at the interface between the oxide and the hydrous halide. Then

$$T\delta_X^d P_{MO/MX} = \frac{i_M s_0}{zF} [\delta\mu_M(1) - \delta\mu_M(2) + zF\delta\Delta\Phi_{MO/MX}] + \frac{i_O s_0}{2F} [\delta\mu_W(2) - 2\delta\mu_H(2) - \delta\mu_O(1) + 2F\delta\Delta\Phi_{MO/MX}] \quad [6]$$

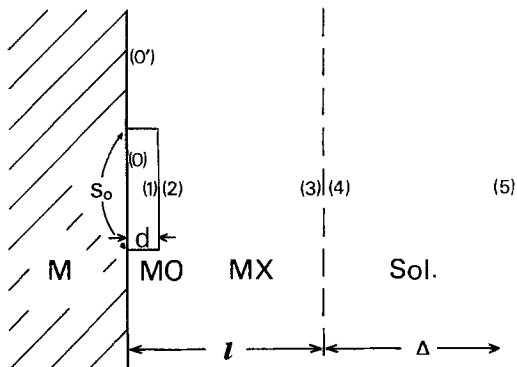


Fig. 2. Schematic representation of phases at the pit bottom. M: metal. MO: oxide film. MX: nonprotective metal halide. Sol.: solution. Numerals indicate portions in each phase.

Linear phenomenological equations (23, 24) can be applied to the material transport in the hydrous halide, because the ionic conductance in this phase is very large. Fluxes J'_w , J'_M , J'_X , and J'_H of H_2O , M^{z+} , X^- , and H^+ are expressed by

$$J'_w = L'_{ww}\Delta\mu'_w + L'_{wi}\Delta\tilde{\mu}'_i \quad [7.1]$$

$$J'_i = L'_{iw}\Delta\mu'_w + L'_{ik}\Delta\tilde{\mu}'_{k \neq i} + L'_{ii}\Delta\tilde{\mu}'_i, \quad i = M, X, H \quad [7.2]$$

where L' are phenomenological coefficients and $\Delta\mu'$ or $\Delta\tilde{\mu}'$ are gradients of chemical or electrochemical potentials in the halide

$$\Delta\mu'_w = \frac{\mu_w(2) - \mu_w(3)}{l - d} \quad [8.1]$$

$$\Delta\tilde{\mu}'_i = \frac{\tilde{\mu}_i(2) - \tilde{\mu}_i(3)}{l - d} = \frac{\mu_i(2) - \mu_i(3)}{l - d} + \frac{z_i F \Delta\Phi_X(2, 3)}{l - d} \quad [8.2]$$

and $\Delta\Phi_X(2, 3)$ is the potential drop across the hydrous halide at the shadowed area by s_0 . Rewriting Eq. [7.2]

$$J'_i = \bar{n}'_i v'_i \Delta\tilde{\mu}'_i \quad [7.3]$$

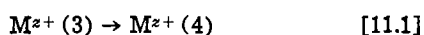
and regarding for simplicity the component given by the following equation as constant

$$L'_{iw} \frac{\Delta\mu'_w}{\Delta\tilde{\mu}'_i} + L'_{ik} \frac{\Delta\tilde{\mu}'_{k \neq i}}{\Delta\tilde{\mu}'_i} + L'_{ii} = \bar{n}'_i v'_i \quad [9]$$

here \bar{n}'_i and v'_i are the mean concentration and the mobility per unit force of i , respectively, in the hydrous halide. The following is then obtained

$$T\delta_X^d P_{MX} = \sum_{i=W, M, X, H} J'_i \left\{ \delta\mu_i(2) - \delta\mu_i(3) + z_i F \delta\Delta\Phi_X(2, 3) - [\mu_i(2) - \mu_i(3) + z_i F \Delta\Phi_X(2, 3)] \frac{\delta(l - d)}{l - d} \right\} s_0 \quad [10]$$

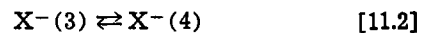
Metal ions dissolves at the interface between the hydrous halide and the electrolyte solution



The current density of this reaction is

$$i'_M = k'_M \exp\left(\frac{\mu_M(3)}{RT}\right) \exp\left(\frac{\nu_H \mu_H(4)}{RT}\right) \exp\left(\frac{\alpha'_M z F \Delta\Phi_{MX/S}}{RT}\right) \quad [12.1]$$

where ν_H is the stoichiometric coefficient of H^+ participating in the metal dissolution reaction and $\Delta\Phi_{MX/S}$ is the Galvani potential difference at the interface between the hydrous halide and the solution. It is assumed that the hydrous halide is in equilibrium between formation and decomposition



so that the following equilibrium condition holds

$$F\Delta\Phi_{MX/S} = \mu_X(3) - \mu_X(4) \quad [12.2]$$

Then it is obtained

$$T\delta_X^d P_{MX/S} = \frac{i'_M s_0}{zF} \{ \delta\mu_M(3) - \delta\mu_M(4) + zF\delta\Delta\Phi_{MX/S} \} \quad [13]$$

Assuming linear phenomenological equations for material transport in the electrolyte solution

$$J''_w = L_{ww}\Delta\mu''_w + L_{wi}\tilde{\Delta\mu}''_i \quad [14.1]$$

$$J''_i = L_{iw}\Delta\mu''_w + L_{ik}\tilde{\Delta\mu}''_{k \neq i} + L_{ii}\tilde{\Delta\mu}''_i, \quad i = M, X, H \quad [14.2]$$

in which L are phenomenological coefficients and

$$\Delta\mu''_w = \frac{\mu_w(4) - \mu_w(5)}{\Delta} \quad [15.1]$$

$$\Delta\mu''_i = \frac{\tilde{\mu}_i(4) - \tilde{\mu}_i(5)}{\Delta} = \frac{\mu_i(4) - \mu_i(5)}{\Delta} + \frac{z_i F \Delta\Phi_S(4, 5)}{\Delta} \quad [15.2]$$

where Δ is the thickness of the diffusion layer which extends from the interface to the bulk of the solution and $\Delta\Phi_S(4, 5)$ is the potential drop across this layer. Taking as previously

$$L_{iw} \frac{\Delta\mu''_w}{\Delta\tilde{\mu}''_i} + L_{ik} \frac{\tilde{\Delta\mu}''_{k \neq i}}{\Delta\tilde{\mu}''_i} + L'' = \bar{C}_i v_i \quad [16]$$

to be constant, where \bar{C}_i and v_i are the mean concentration and the mobility per unit force of i , respectively, in the solution. Assuming Δ to be unchanged

$$T\delta_X^d P_S = \sum_{i=W, M, X, H} J''_i \{ \delta\mu_i(4) - \delta\mu_i(5) + z_i F \delta\Delta\Phi_S(4, 5) \} s_0 \quad [17]$$

The current density passing through the oxide film changes from i to $i + \delta i$ when the oxide film thickness changes from d to $d + \delta d$. Suppose that the change occurs so slowly that no charges or materials are accumulated locally in the area shadowed by s_0 , similar to a steady-state condition. In this case, equations of continuity hold with respect to the current (19).

Chemical potentials of M^{z+} and O^{2-} ions in the oxide film are described by the equilibrium condition (27)

$$2\delta\mu_M(1) + z\delta\mu_O(1) = 0 \quad [18]$$

Also, equilibrium conditions are assumed for chemical potentials of M^{z+} and O^{2-} or H^+ and X^- , in the hydrous halide

$$\delta\mu_M(p) + z\delta\mu_X(p) = 0, \quad p = 2, 3 \quad [19.1]$$

$$\delta\mu_H(p) + \delta\mu_X(p) = 0, \quad p = 2, 3 \quad [19.2]$$

The chemical potential of H_2O at the hydrous halide-solution interface is assumed to remain constant

$$\delta\mu_w(3) = 0 \quad [19.3]$$

Equation [8.2] combined with the continuity equation gives

$$\Delta\mu'w = c'i + c'_M\Delta\mu'_M + c'_X\Delta\mu'_X + c'_H\Delta\mu'_H \quad [20.1]$$

with

$$c'_1 = \frac{1}{zFL'_{MW} - FL'_{XW} + FL'_{HW}} \quad [20.2]$$

$$c'_i = \frac{zFL'_{Mi} - FL'_{Xi} + FL'_{Hi}}{zFL'_{MW} - FL'_{XW} + FL'_{HW}}, \quad i = M, X, H \quad [20.3]$$

An equilibrium condition is assumed for the chemical potentials of H^+ and X^- , in the solution

$$\delta\mu_H(4) + \delta\mu_X(4) = 0 \quad [21]$$

Concentrations of species are fixed in the bulk of the solution

$$\mu_i(5) = \mu_i^S, \quad i = M, X, H \quad [22]$$

It is obtained from Eq. [14.2] and the continuity equation that

$$\Delta\mu''w = c_1i + c_M\Delta\mu''_M + c_X\Delta\mu''_X + c_H\Delta\mu''_H \quad [23.1]$$

with

$$c_1 = \frac{1}{zFL_{MW} - FL_{XW} + FL_{HW}} \quad [23.2]$$

$$c_i = \frac{zFL_{Mi} - FL_{Xi} + FL_{Hi}}{zFL_{MW} - FL_{XW} + FL_{HW}} \quad [23.3]$$

Fluxes of X^- and H^+ in the diffusion layer of the solution are very small compared with that of M^{z+} in the area shadowed by s_0 , because of their small consumption rate in that area

$$J''_i \ll J''_M, \quad i = X, H \quad [24]$$

It is seen from Eq. [11.2] that $\delta i'_M \doteq \delta i$. For simplicity, put $\nu_X \doteq z$.

Following the similar treatments as in literature (19), the force component of the entropy change $\delta_X^d P$ can be expressed as follows

$$\begin{aligned} T\delta_X^d P &= T\delta_X^d P_{MO} + T\delta_X^d P_{MO/MX} + T\delta_X^d P_{MX} \\ &\quad + T\delta_X^d P_{MX/S} + T\delta_X^d P_S \\ &= (A - B)s_0\delta i + (C - D)s_0\delta(l - d) \\ &\quad + E\delta\Delta\Phi_{MO/MX} + F\delta\Delta\Phi_{MX/S} + G\delta\Delta\Phi_S(4, 5) \end{aligned} \quad [25.1]$$

Here A, B, C, D, E, F , and G are positive variables, and

$$\begin{aligned} A &\equiv \frac{RT}{zF} \left(1 + \frac{i_0}{i_M} \right) + \frac{RT}{(z + \nu_H)F} \\ &\quad + \frac{RTid}{\alpha^{\circ}_M z F a_i^{\circ} + 2\alpha^{\circ}_O F a_i^{\circ}} + \frac{i(l - d)}{\Delta_X} \\ &\quad + \frac{i_{0W}}{F} c'_w(l - d) \\ &\quad + \left\{ c_1 J''_w + (J''_M + c_M J''_w) \frac{1}{zF\bar{C}_M\nu_M} \right\} \Delta \end{aligned} \quad [25.2]$$

$$B \equiv \frac{i'_M \Delta}{z^2 F^2 \bar{C}_M \nu_M} \quad [25.3]$$

$$C \equiv \frac{i_{0W}}{F} c'_w i - J'_w c'_w i \quad [25.4]^5$$

$$D \equiv \frac{i^2 \lambda_X}{\Delta_X} \quad [25.5]$$

$$E \equiv \left\{ i - \frac{1}{zF} \left(1 + \frac{i_0}{i_M} \right) (i_M \alpha_M z F + 2i_0 \alpha_O F) \right\} s_0 \quad [25.6]$$

$$F \equiv i'_M \frac{z(1 - \alpha'_M)}{z + \nu_H} s_0 \quad [25.7]$$

⁵ See Appendix A.

$$G \equiv i'_M s_0 \quad [25.8]$$

$$\text{with } i^{\circ}_M = zFJ_M \quad [25.9]$$

$$i^{\circ}_O = -2FJ_O \quad [25.10]$$

$$\Delta_X \equiv z^2 F^2 \bar{n}'_M \nu'_M + F^2 \bar{n}'_X \nu'_X + F^2 \bar{n}'_H \nu'_H \quad [25.11]$$

$$\frac{i_{0W}}{F} \equiv \left\{ \frac{1}{zF'} - \frac{1}{zF} \left(1 + \frac{i_0}{i_M} \right) \right\} i_0 + J'_w \quad [25.12]$$

$$c'_w \equiv c'_1 + \frac{c'_M z F - c'_X F + c'_H F}{\Delta_X} \quad [25.13]$$

$$c'_w i \equiv c'_1 i + \frac{c'_M J'_M}{\bar{n}'_M \nu'_M} + \frac{c'_X J'_X}{\bar{n}'_X \nu'_X} + \frac{c'_H J'_H}{\bar{n}'_H \nu'_H} \quad [25.14]$$

and λ_X is a positive constant of the order of magnitude of 1 (19), which satisfies

$$\frac{\lambda_X}{\Delta_X} i^2 = -\frac{1}{\Delta_X} i^2 + \frac{J'_M{}^2}{\bar{n}'_M \nu'_M} + \frac{J'_X{}^2}{\bar{n}'_X \nu'_X} + \frac{J'_H{}^2}{\bar{n}'_H \nu'_H} \quad [25.15]$$

The current density i passing through the oxide film is controlled mainly by the resistance of the film, and it can be expressed by an exponential formula with respect to the electric field in the oxide, then

$$\delta i = -\frac{zF}{RT} \frac{\alpha^{\circ} a}{d} \Delta\Phi_0 i \frac{\delta d}{d} \quad [26]$$

It is easily seen that B in Eq. [25.3] cancels the sixth member of A in Eq. [25.2] so that $A - B > 0$, and also clearly $C - D < 0$, then using Eq. [26]

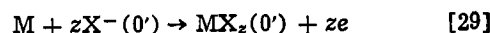
$$(A - B)s_0\delta i + (C - D)s_0\delta(l - d) < 0 \quad [27]^6$$

Ignoring the terms $\delta\Delta\Phi_{MO/MX}$, $\delta\Delta\Phi_{MX/S}$, and $\delta\Delta\Phi_S$ (4, 5), because the change in $\Delta\Phi_0$ due to the oxide film growth is the major contribution

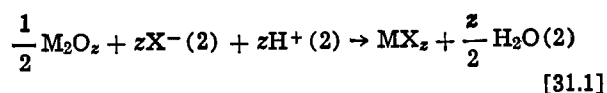
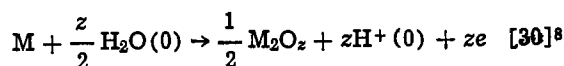
$$T\delta_X^d P < 0 \quad [28]$$

is obtained. This shows that the oxide film formed on the metal surface at the pit bottom continues to grow until it reaches a steady state and stops growing, provided that the film is not very thin.⁷

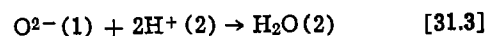
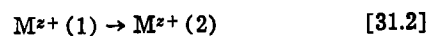
Repassivation process.—Oxide film extension.—Suppose that the oxide film extends its area from s_0 to $s_0 + \delta s_0$ with thickness d remaining constant. At the portion δs_0 the reaction



ceases and a series of reactions appear



Here the reaction [31.1] consists of two steps



The current density and the affinity of reactions [30], [31], and [29] are denoted as i_1, i_2 , and i_3 , and A_1, A_2 , and A_3 , respectively

⁶ See Appendix B.

⁷ I was shown in a previous paper on pit initiation (19) that hemispherical halide nuclei produced on the surface of the passive film can grow inwards when the radius surpasses the critical value r^* . A concentration of the current to local points on the surface is needed for this. Actually, if the halide layer was in contact with the passive film and consumed it from the outside, it would not have resulted in the breakdown of passivity but only a thinning of the passive film, which would stop as the steady state is reached. This is shown by the similar consideration stated in this section.

⁸ The conclusion remains unchanged if the reaction [30] is replaced by $M + zH_2O \rightarrow M(OH)_z + zH^+ + ze$.

$$i_1 = k_{MO} \exp\left(\frac{\nu_W \mu_W(0')}{RT}\right) \exp\left(\frac{\alpha_{MO} z F \Delta \Phi_{M/MO}}{RT}\right) \quad [32.1]$$

$$i_2 = k_{OX} \exp\left(\frac{\mu_M(1)}{RT}\right) \exp\left(\frac{\nu_X \mu_X(2)}{RT}\right) \exp\left(\frac{\alpha_{OX} z F \Delta \Phi_{M/MOX}}{RT}\right) \quad [32.2]$$

$$i_3 = k_{MX} \exp\left(\frac{\nu'_X \mu'_X(0')}{RT}\right) \exp\left(\frac{\alpha_{MX} z F \Delta \Phi_{M/MOX}}{RT}\right) \quad [32.3]$$

and

$$A_1 = \mu_M + \frac{z}{2} \mu_W(0') - \frac{1}{2} \mu_{M_2O_z} - z \mu_H(0') + z F \Delta \Phi_{M/MO} \quad [33.1]$$

$$A_2 = \mu_M(1) - \mu_M(2) - z F \Delta \Phi_{M/MOX} \quad [33.2]$$

$$A_3 = \mu_M + z \mu_X(0') - \mu_{MX_z} + z F \Delta \Phi_{M/MOX} \quad [33.3]$$

The thickness of the oxide film d remains unchanged, so that

$$\mu_O(1) + 2\mu_H(2) - \mu_W(2) - 2F \Delta \Phi_{M/MOX} = 0 \quad [33.4]$$

If at least one atomic layer of the oxide is involved, $i_1 \stackrel{*}{=} i_2$, then the force component of the entropy production caused by the above reaction is

$$T \delta_X^s P_{MXO} = \frac{i_1 + i_2}{2zF} (A_1 + A_2 - A_3) \delta s_O$$

$$= \frac{i}{F} \left\{ \frac{1}{2} [\mu_W(0') - \mu_W(2)] - [\mu_H(0') - \mu_H(2)] + F (\Delta \Phi_{M/MO} - \Delta \Phi_{M/MOX}) \right\} \delta s_O \quad [34]$$

The following equations are used in the above formula

$$\frac{i_1 + i_3}{2} = i \quad [35]$$

$$\mu_M(1) + \frac{z}{2} \mu_O(1) = \frac{1}{2} \mu_{M_2O_z} \quad [36.1]$$

$$\mu_M(2) + z \mu_X(0') = \mu_{MX_z} \quad [36.2]$$

The increase in the area of the oxide film by δs_O , with thickness d constant, causes further changes: a change in material transport in the hydrous halide, a change in the reaction at the interface between the hydrous halide and the solution, and a change in material transport in the solution. The force components of the entropy production changes due to these processes are designated as $\delta_X^s P_{MX}$, $\delta_X^s P_{MX/S}$, and $\delta_X^s P_S$, respectively.

The total change in the entropy production $\delta_X^s P$ due to the change in forces is, neglecting for simplicity, the flux of X^- in the solution which accompanies the reaction [29]

$$T \delta_X^s P = T \delta_X^s P_{MXO} + T \delta_X^s P_{MX} + T \delta_X^s P_{MX/S} + T \delta_X^s P_S$$

$$= (A' - B') (1 - \epsilon) (i_1 - i_3) \delta s_O - (C' - D') i \delta s_O \quad [37.1]$$

where ϵ is a correction due to the secondary current in the area shadowed by δs_O , and A' , B' , C' , and D' are positive variables defined by

$$A' \equiv \left(J'_W - \frac{i}{2F} \right) c'_W (l - d) + \frac{i}{\Lambda_X} + \frac{RT}{(z + \nu_H) F}$$

$$+ \left\{ c_I J''_W + (J''_M + c_M J''_W) \frac{1}{z F \bar{C}_M \nu_M} \right\} \Delta \quad [37.2]$$

$$B' \equiv \frac{i'_M \Delta}{z^2 F^2 \bar{C}_M \nu_M} \quad [37.3]$$

$$C' \equiv \frac{1}{F} \delta \mu_H(2) - \frac{z(1 - \alpha'_M)}{z + \nu_H} (1 - \epsilon) \delta \Delta \Phi_{MX/S}$$

$$- (1 - \epsilon) \delta \Delta \Phi_S(4, 5) \quad [37.4]$$

$$D' \equiv \Delta \Phi_{M/MO} - \Delta \Phi_{M/MOX} \quad [37.5]$$

The following relationships are used in the above equation

$$\delta i = (i_1 - i_3) \frac{\delta s_O}{|\delta s_O|} \quad [37.6]$$

$$\mu_W(0') - \mu_W(2) \stackrel{*}{=} -\delta \mu_W(2) = c'_W \delta i \quad [37.7]$$

where Eq. [37.7] is obtained from Eq. [7.3], [9], [19.2], [19.3], and [20.1] with $\delta(l - d) = 0$.

Taking into account that the fourth member of A' cancels B' , it is seen that $A' - B' > 0$. For a very thin oxide film $\Delta \Phi_{M/MOX} \stackrel{*}{=} \Delta \Phi_{M/MO}$, so that $D' = 0$. It is apparent also that $i_1 - i_3 < 0$. Then Eq. [37.1] becomes

$$T \delta_X^s P < 0 \quad [38]$$

It is shown therefore that the oxide film formed on the pit bottom by reaction [30] leads to the repassivation of pits, if the rate of the oxide formation surpasses the rate at which it dissolves by [31.1], so that at least a monolayer oxide film can exist

$$i_1 > i_2, \text{ at } d = a \quad [39]$$

If the film thus extending is too thick, D' should rise in Eq. [37.1], and the above conclusion cannot necessarily hold. This suggests the repassivation mechanism, whereby a very thin (but more than monolayer) oxide film first appears and extends over the whole active surface on the pit bottom, then increases its thickness, resulting in complete repassivation.

The repassivation potential.—It has been shown by the above considerations that the oxide film formed on the pit bottom which satisfies Eq. [39] can grow continuously and lead to repassivation. A critical condition exists, at which $i_1 = i_2$ for a monolayer oxide film. The potential at this condition shall be called the critical pitting potential E_{cp} . Substituting Eq. [33.4] into Eq. [32.2] for i_2 and equating it with Eq. [32.1] for i_1

$$\Delta_c \Phi_{M/MO} = \frac{RT}{\alpha_{MO} z F} \ln \left(\frac{k_{OX}}{k_{MO}} \right) + \frac{1}{\alpha_{MO} z F} \left\{ \mu_M(1) - \nu_X \mu_X(2) + \frac{z}{2} \alpha_O [\mu_O(1) + 2\mu_H(2) - \mu_W(2)] - \nu_W \mu_W(0') \right\} \quad [40]$$

The chemical potential of H_2O in the hydrous halide should attain a critical value at this condition at the interface with the metal

$$\mu_W(0') = \mu_W(2) = \mu^*_{W} \quad [41.1]$$

During pitting corrosion, a concentration of X^- and H^+ in the solution in contact with the hydrous halide should be kept above critical values (28, 29), so that

$$\mu_X(4) = \mu^*_{X} \quad [41.2]$$

$$\mu_H(4) = \mu^*_{H} \quad [41.3]$$

From Eq. [7.3], [9], [12.2], [14.2], [15.2], [16], [22], [33.4], [40], [41.2], and [41.3], the potential of the metal E_{cp} at this critical condition is

$$E_{cp} = \Delta_c \Phi_{M/MO} + \Delta_c \Phi_{M/MOX} + \Delta_c \Phi_{MX}(2, 3)$$

$$+ \Delta_c \Phi_{MX/S} + \Delta_c \Phi_S(4, 5) = E^*_{cp} + \frac{\nu_X - z \alpha_{OX}}{\alpha_{MO} z} [\Delta_c \Phi_{MX}(2, 3)$$

$$+ \Delta_c \Phi_{MX/S}] + \frac{1}{\alpha_{MO} z F} \left\{ \frac{\nu_X J'_X}{\bar{n}'_X \nu'_X} + \frac{z(\alpha_{MO} + \alpha_{OX}) J'_H}{\bar{n}'_H \nu'_H} \right\} l$$

$$+ \frac{RT}{F} \ln \left(\frac{\gamma_X(4) C^*_{X}}{\gamma_X S C_{X^s}} \right) - \frac{\Delta}{F} \frac{J''_X}{\bar{C}_X \nu_X} \quad [42.1]$$

with

$$E^*_{cp} \equiv \frac{RT}{\alpha_{MO}zF} \ln \left(\frac{k_{OX}}{k_{MO}} \right) + \frac{1}{\alpha_{MO}zF} \left[\mu^*_{MO} - \left\{ \frac{z(\alpha_{MO} + \alpha_{OX})}{2} + \nu_W \right\} \mu^*_W + \nu_X \mu^*_X + z(\alpha_{MO} + \alpha_{OX}) \mu^*_H \right] \quad [42.2]$$

where μ^*_{MO} is the chemical potential of the metal oxide of stoichiometric composition $M_2O_{z(\alpha_{MO} + \alpha_{OX})}$

$$\mu^*_{MO} \equiv \mu_M(1) + \frac{(\alpha_{MO} + \alpha_{OX})}{2} \mu_O(1) \quad [42.3]$$

and $\gamma_X(4)$ and γ_X^S are the activity coefficients, C^*_X is the critical X^- concentration, and C_X^S is the concentration of X^- in the bulk of the solution

$$\mu_X(4) = \mu^*_X = \mu^\circ_X + RT \ln [\gamma_X(4) C^*_X] \quad [42.4]$$

$$\mu_X^S = \mu^\circ_X + RT \ln (\gamma_X^S C_X^S) \quad [42.5]$$

Fluxes of species other than M^{z+} should be very small at the stage where the oxide film is formed, so that $J'_X \approx 0$, $J'_H \approx 0$, and $J''_X \approx 0$. Because of the large electrical conductance of the hydrous halide and the small current density during repassivation, it is seen that

$$\Delta c_{\Phi_X}(2,3) + \Delta c_{\Phi_{MX/S}} = \Delta \Phi^*_{MX/S} = \text{const.} \quad [42.6]^9$$

From the above equations it follows that

$$E_{cp} = E^*_{cp} + \frac{RT}{F} \ln \left(\frac{\gamma_X(4) C^*_X}{\gamma_X^S C_X^S} \right) \quad [43]$$

A critical potential at which the monolayer of oxide can appear is thus determined.¹⁰

In order for the repassivation to proceed, i_1 should be larger than i_2 at the appearance of the monolayer of the oxide so that it can grow. The rates i_1 , i_2 , and i_3 of the reactions [30], [31.1], and [29] at the pit bottom are illustrated schematically in Fig. 3. In the figure, the repassivation starts as the potential of the metal becomes $E < E_{cp}$. It should be noted, however, that the oxide film needs to grow, and this growth results in the decrease in the current, and hence the decrease in concentration of X^- and H^+ below the critical values given by Eq. [41.2] and [41.3] so that protection of metal surface is completely accomplished against corrosion. Then pitting stops absolutely. From this it follows that the repassivation potential is not strictly consistent with the critical pitting potential defined by Eq. [43], but the two potentials may be considered to be quite closely related to each other.

Discussion

If the potential of a metal is decreased from the state where pitting is in progress, it eventually brings about repassivation and stops the pitting. The steps in repassivation are as follows: a thin oxide film forms on the metal surface which, in contact with the nonprotective film, is strongly corroding at the pit bottom, then the oxide film extends over the active area of the pit, and finally becomes a passive film which prevents dissolution of the metal (see Fig. 4).

The pit repassivation potential referring to this stage sometimes shows discrepancies with the pit initiation potential by several tenths of a volt (1, 7, 21). Theories of pitting corrosion with considerations of local destruction-repair processes of a passive film (30), local dissolution through passive film flaws (14), or

⁹ If the rate of formation of the hydrous halide is considered to be so small that $l \rightarrow 0$, then $\Delta \Phi^*_{MX/S} \approx 0$.

¹⁰ It was not explicitly taken into account in Eq. [43] that the oxide film formed on the metal surface becomes stable through the amount of surface free energy. Actually this contribution should be included in μ^*_{MO} in Eq. [42.3].

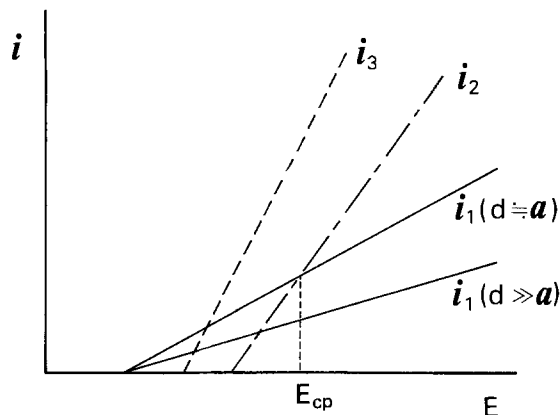


Fig. 3. Variations of i_1 , i_2 , and i_3 as a function of the potential of the metal E . Units of axes are arbitrary. i_1 : rate of the oxide formation. i_2 : rate of the oxide dissolution. i_3 : rate of the metal dissolution. E_{cp} : critical pitting potential.

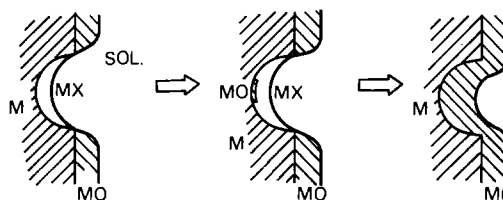


Fig. 4. Illustration of a process leading to pit repassivation. M: metal. MO: oxide film. MX: nonprotective metal halide. Sol.: solution.

thermodynamic stability of forming phases (11, 12) cannot successfully explain the existence of the above two potential values. The transport-based acidification theory (31, 32) explained the phenomena, but it could not always be the case for hemispherical brightening pits.

The present theory suggests that the repassivation potential is very close to the critical pitting potential defined by Eq. [43]. However, the pit initiation potential includes probability factors due to fluctuations, as reported previously (19), and thus depends on the history of the specimen, such as the passive film thickness or other experimental conditions. The case can exist where a high anodic polarization is required for pit initiation or, in an extreme case pits cannot be initiated at all. This is in contrast to the case of repassivation, and this discrepancy comes from the difference in the electrical conductance of the passive film and the nonprotective halide film.

The pit initiation potential coincides with the critical pitting potential E_{cp} only when the passive film becomes very thin (Appendix C). This is in accordance with the experimental results using the "scratch method" (9). Among various methods of measuring pitting potentials, the potentiokinetic method seems advantageous because of its ease, but application merits caution because of the time lag for the occurrence of pitting (1). If the critical pitting potential defined by Eq. [43] is recognized as a characteristic value of pitting, then the repassivation potential determined experimentally acquires practical importance, because it can be repeatedly measured by a potentiokinetic method as compared to the pit initiation potential (21). Thus, the significance of the pit repassivation potential should be stressed, both theoretically and experimentally (7, 20, 21).

Manuscript submitted May 4, 1983; revised manuscript received Dec. 10, 1983.

The Industrial Products Research Institute assisted in meeting the publication costs of this article.

APPENDIX A

It is obtained from Eq. [7.2], [7.3], [20.2], and [20.3]

$$-J'_{\text{w}} \left(c'_{\text{i}} + \frac{c'_{\text{M}}J'_{\text{M}}}{\bar{n}'_{\text{M}}v'_{\text{M}}} + \frac{c'_{\text{X}}J'_{\text{X}}}{\bar{n}'_{\text{X}}v'_{\text{X}}} + \frac{c'_{\text{H}}J'_{\text{H}}}{\bar{n}'_{\text{H}}v'_{\text{H}}} \right) s_0 =$$

$$-J'_{\text{w}}c'_{\text{I}}(zFL'_{\text{MW}} - FL'_{\text{XW}} + FL'_{\text{HW}})\Delta\mu'_{\text{w}}s_0 \quad [\text{A-1}]$$

as $c'_{\text{I}} < 0$ and $\Delta\mu'_{\text{w}} < 0$, the right-hand side becomes positive.

APPENDIX B

It is seen from Eq. [25.4] and [25.5] that $C \ll D$. Using Eq. [25.2], [25.3], and [26], and assuming a constant thickness of the hydrous halide l

$$(A - B)s_0\delta i + (C - D)is_0\delta(l - d) =$$

$$- \left\{ O \left(\frac{\Delta\Phi_0}{d} \right) - O \left(\frac{i\lambda_{\text{X}}}{\Delta x} \right) \right\} is_0\delta d \quad [\text{B-1}]$$

The electric field in the oxide film is much stronger than that in the hydrous halide, so that above equation becomes negative with the increase in d .

APPENDIX C

In order for pitting to occur on the passive metal, hemispherical halide nuclei whose radius is larger than the critical value r^* should be generated in the passive film (19). In Eq. [51] of Okada (19), a small thickness of the passive film, and hence a large current density passing through the halide nuclei, results in a small r^* , and pitting is more easily initiated. In the extreme case when the thickness of the passive film is as small as the order of a , $i = i_1 = i_2$ at the critical pitting potential E_{cp} and becomes even greater as the potential is raised. A critical condition is realized in this case for pit initiation, in which the halide nuclei with the smallest size of a can grow and lead to pitting. Moreover, the potential drop across the halide nuclei takes a minimum value of about RT/F , so that the potential at this condition is very close to E_{cp} . If the potential is lower than this value, an oxide film of any thickness can grow, and is not broken by the halide nuclei.

REFERENCES

1. W. Schwenk, *Corros. Sci.*, **5**, 245 (1965).
2. Z. Szkarska-Smialowska and M. Janik-Czachor, *Br. Corros. J.*, **4**, 138 (1969).

3. M. Janik-Czachor, G. C. Wood, and G. Thompson, *ibid.*, **15**, 154 (1980).
4. W. Schwenk, *Corrosion*, **20**, 129t (1964).
5. T. P. Hoar and D. C. Mears, *Proc. R. Soc. London, Ser. A*, **294**, 486 (1966).
6. T. P. Hoar, *Corros. Sci.*, **7**, 341 (1967).
7. M. Pourbaix, L. Klimzack-Mathieu, Ch. Mertens, J. Pourbaix, Cl. Vanleugenhaghe, L. de Munck, J. Laureys, L. Neelemans, and M. Warzee, *Corros. Sci.*, **3**, 239 (1963).
8. L. I. Freiman and Lap Le Min, *Z. Phys. Chem.*, **252**, 65 (1973).
9. N. Pessall and C. Liu, *Electrochim. Acta*, **16**, 1987 (1971).
10. K. J. Vetter and H.-H. Strehblow, "Localized Corrosion," p. 240, NACE, Houston (1974).
11. K. J. Vetter, *Ber. Bunsenges. Phys. Chem.*, **69**, 683 (1965).
12. Ja. M. Kolotykin, *Corrosion*, **19**, 261t (1963).
13. T. P. Hoar, D. C. Mears, and G. P. Pothwell, *Corros. Sci.*, **5**, 279 (1965).
14. J. A. Richardson and G. C. Wood, *ibid.*, **10**, 313 (1970).
15. N. Sato, *Electrochim. Acta*, **19**, 1683 (1971).
16. H. Kaeshe, *Z. Phys. Chem. N.F.*, **34**, 87 (1962).
17. W. Schwenk, *Corros. Sci.*, **3**, 107 (1963).
18. T. Okada and T. Hashino, *ibid.*, **17**, 671 (1977).
19. T. Okada, *This Journal*, **131**, 241 (1984).
20. M. Pourbaix, *Corrosion*, **26**, 431 (1970).
21. T. Okada, *Denki Kagaku*, **49**, 584 (1981).
22. T. P. Hoar, *This Journal*, **117**, 17C (1970).
23. D. D. Fitts, "Nonequilibrium Thermodynamics," Chap. 4, McGraw-Hill, New York (1962).
24. S. G. Schultz, "Basic Principles of Membrane Transport," Chap. 4, Cambridge University Press, Cambridge, England (1980).
25. P. Glansdorff and I. Prigogine, "Thermodynamic Theory of Structure, Stability and Fluctuations," Chap. 9, Wiley-Interscience, London (1974).
26. K. J. Vetter, "Electrochemical Kinetics," Chap. 6, Academic Press, New York (1967).
27. H. J. Engell, *Z. Phys. Chem. N.F.*, **7**, 158 (1956).
28. K. E. Heusler and L. Fischer, *Werkst. Korros.*, **27**, 551 (1976).
29. N. Sato, *This Journal*, **129**, 260 (1982).
30. K. Videm, Kjeller Report KR-149, Institute for Atomenergi, Kjeller, Norway (1974).
31. J. R. Galvele, *This Journal*, **123**, 464 (1976).
32. J. R. Galvele, *Corros. Sci.*, **21**, 551 (1981).

Dye Loaded Polymer Electrodes

III. Generation of Photogalvanic Effects at n-SnO₂ Electrodes Coated with Poly(4-Vinyl Pyridine) Films Containing Rose Bengal

Prashant V. Kamat and Marye Anne Fox*

Department of Chemistry, University of Texas, Austin, Texas 78712

ABSTRACT

Conducting SnO₂ electrodes precoated with poly(4-vinyl pyridine) can electrostatically bind an anionic dye, rose bengal, within the protonated polymer matrix. When this modified electrode was dipped into an aqueous solution containing a suitable redox couple and illuminated in the dye absorption band, anodic photogalvanic effects were seen. The improved photogalvanic performance of the dye-loaded polymer electrodes has been attributed to high dye concentrations near the electrode surface, longer lived excited states, and stabilization of the photogenerated electroactive species.

One area of recent interest relevant to the direct conversion of light energy to electrical energy is the study of dye-redox systems capable of generating photogalvanic effects (1, 2). Despite continuing efforts to improve the performance of photogalvanic cells, the sunlight engineering efficiency has remained low.

* Electrochemical Society Active Member.

Key words: photogalvanic effects, polymer-coated electrodes, rose bengal, modified electrodes, semiconductor electrodes.

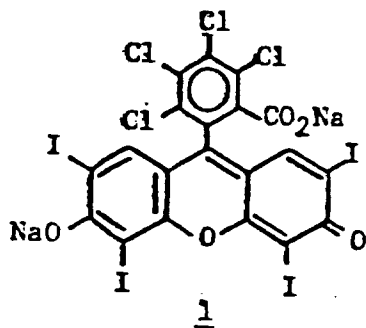
Thionine-Fe(II) system, a widely studied photogalvanic system, has yielded important information on the photochemical and electrochemical determinants of power conversion efficiency in photogalvanic cells (4-6). High concentrations (0.01-0.1M) of the light absorbing dye are thought to be necessary to optimize the efficiency of these photogalvanic cells (7), but recent work suggests that use of such high dye concentrations in homogeneous solution may lead to wastage

of absorbed quantum energy via self-quenching and competitive absorption (8).

Other attempts to improve the performance of photogalvanic cells have involved either improved cell design [e.g., thin layer cells with transparent electrodes (3)] or the use of nonhomogeneous media [e.g., microemulsions (9a), gels (9b), membranes (10), or chemical bonding of the dye to a polymer chain (11)]. So far, however, no major breakthroughs in improving the efficiency of light-to-electrical energy conversion have been achieved.

In our earlier studies, we showed that anionic dyes can be successfully incorporated into protonated poly(4-vinyl pyridine) (PVP) films (12). The electroactivity of these dyes could still be retained in the films, and these dye-loaded polymer electrodes exhibited several interesting electrocatalytic properties (12, 13). Furthermore, the excited states of several xanthene dyes could be stabilized by dispersing them in a polymer film (14). Up to an order of magnitude enhancement in fluorescence yield was seen on microencaging the dye within a polymer (15).

In our continuing investigation of dye-loaded polymer electrodes, we have sought to generate and study photoelectrochemical effects at these modified electrodes. We now present our results on the photogalvanic effects induced by sensitization by rose bengal 1



electrostatically held within a PVP film coated on conducting SnO₂ electrodes and immersed in an aqueous solution containing a suitable galvanic redox couple.

Experimental

Materials.—Rose bengal, 1 (Fisher Scientific), was chromatographically purified (16) over 200-300 mesh silica (E. Merck) using a 35:65 mixture of acetone:ethanol as the eluent. Poly(4-vinyl pyridine), PVP, was used as supplied by Polysciences. All other chemicals were analytical reagents and were used without further purification. All aqueous solutions were made with Millipore-filtered water.

Preparation of dye-loaded polymer electrodes.—Highly conducting SnO₂ electrodes, cut from NESA glass (PPG Industries), were cleaned and dried (13). The conductive surface of the glass plate was then coated with a PVP film by applying a solution of 1% PVP in ethanol and allowing the solvent to evaporate. The PVP-coated electrode (SnO₂/PVP) was then soaked for 10 min in an aqueous solution of 1 (ca. 1 mM) buffered to pH 3 with 0.1M CF₃COONa and CF₃COOH. The electrode was then washed thoroughly with water. Coloration of the PVP film confirmed the incorporation of the dye into the polymer film. Such electrodes will be referred to as SnO₂/PVP/1. Typically, the polymer films were 0.1 μm thick (as determined with a Sloan Dektak surface profilometer) and had a surface coverage of 2-10 × 10⁻⁹ mol/cm² of the dye. (In other words, one could achieve a dye concentration up to 1M in the polymer film.) Dye deposited within the polymer was tightly bound and did not leak into solution during the time scale of the experiment.

Photoelectrochemical measurements.—The photoelectrochemical cell was a standard three-compartment cell equipped with Pt foil (2 cm²) as counterelectrode and a saturated calomel electrode (SCE) as reference. The SnO₂/PVP/1 electrode (2 cm²) was illuminated with a collimated beam from a 250W halogen lamp, filtered with a 460 nm cutoff filter (Corning). The illuminated semiconductor was placed within 1 cm of the dark metallic counterelectrode. The equilibrated solution resistance was ~1 kΩ. Light intensity at the illuminated electrode was 120 mW/cm². For excitation with selected wavelengths, a Bausch and Lomb high intensity grating monochromator was inserted in the path of illumination beam. Absorption spectra were recorded with a Hewlett Packard 8450 spectrophotometer. Photovoltages and photocurrents were measured with a Keithley (Model 177) microvoltmeter. Flash photolysis and pulse radiolysis experiments were carried out with standard equipment available at the Center for Fast Kinetic Research, University of Texas at Austin. Details of analogous pulse experiments have been reported elsewhere (14).

Results and Discussion

Excited state characteristics.—A typical absorption spectrum of SnO₂/PVP/1 is shown in Fig. 1. 1 incorporated within the polymer film retains its absorption characteristics, but exhibits a red shift in its absorption maximum (λ_{max} = 572 nm in the PVP film, 558 nm in ethanol). Such a red shift in the absorption maximum has been attributed to microencagement of the dye by the polymer, consequences of which have been discussed in detail elsewhere (14). A high monomer-to-dimer ratio, determined by the relative intensity of the absorbance at the peak maximum (monomer) and at the (dimeric) shoulder, indicated little aggregation of the dye in the polymer film. Thus, despite achieving high dye concentrations (around 1M) in the 0.1 μm thick PVP film, most of the dye is held in monomeric form.

With SnO₂ electrodes coated by direct electron deposition of thionine (12), the dye absorption spectrum exhibited a broadened absorption band, suggesting substantial aggregation form. Since aggregated dye does not significantly contribute to the generation of photogalvanic effects (18), observation of only small currents with such modified electrodes is understandable. With our present dye-loaded polymer electrodes, in contrast, it is possible to achieve relatively high concentrations of photoactive monomeric dye near the electrode surface. Dye loaded films of optical densities near 1.0, which allowed efficient absorption of the incident photons, could be prepared easily.

Other excited state properties of 1 in homogeneous and polymer containing solutions are given in Table I. An interesting feature of polymer microencagement is seen in the stabilization of the triplet state of the dye. A similar increase in the excited-state lifetimes of xanthenes was also seen upon incorporating them into the polymer films cast on SnO₂ electrodes (14). An increased dye excited-state lifetime is expected to increase the efficiency of generation of electroactive

Table I. Excited state characteristics of rose bengal in ethanol

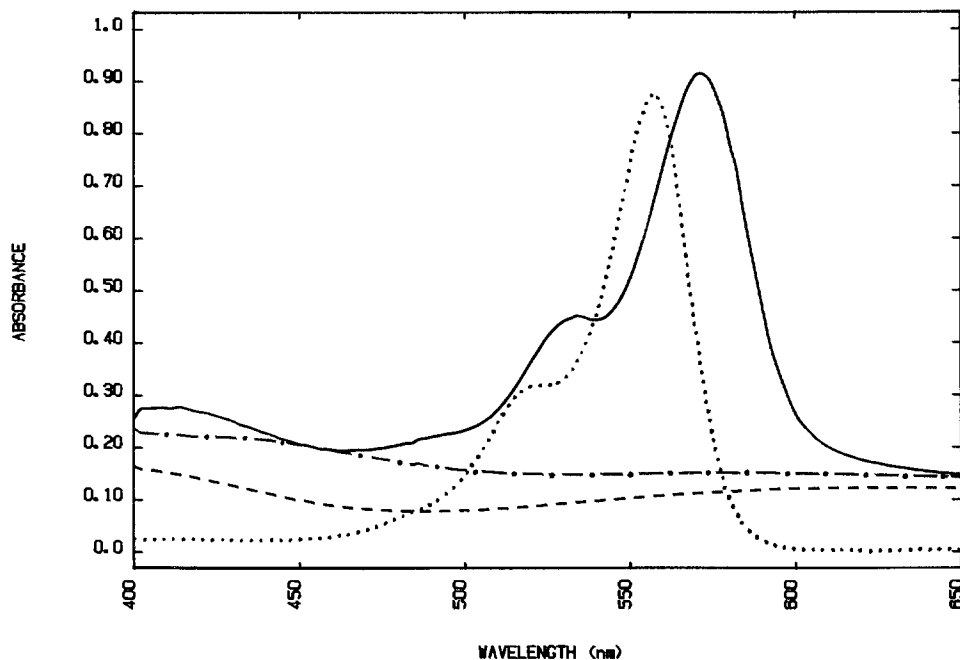
	No PVP	0.01M PVP
Abs. Max, S ₀ - S ₁ (nm)	558.00	565.00
Em. Max, S ₁ - S ₀ (nm)	580.00	586.00
τ _r ^b S ₁ - S ₀ (ns)	0.66	1.10
Abs. Max, T ₁ - T _n (nm)	600.00	610.00
τ ₃ ^c T ₁ - S ₀ (μs)	90.00	205.00
k _q ^a (10 ⁸ m ⁻¹ s ⁻¹)	2.90	0.30

^a Specific rate for the ground state quenching of triplet dye in ethanol at room temperature.

^b Radiative lifetimes.

^c Measured from the decay of τ-τ absorption.

Fig. 1. Absorption spectra of transparent n-SnO₂ at various stages of modification: (---) native SnO₂; (-·-·-) SnO₂/PVP; (—) SnO₂/PVP/1 and (····) 10⁻⁵M 1 in ethanol.



reduced forms of the dye by enhancing the effective Fe(II) electron transfer quenching sphere.

Photogalvanic effects in homogeneous solution.—Photogalvanic effects produced by 1 and several redox systems in homogeneous solution have been described before. With a solution containing 1 and EDTA, a photovoltage and a photocurrent of 19 mV and 0.025 $\mu\text{A}/\text{cm}^2$, respectively, are observed (19) with light intensities such as we used here. This photocurrent is two orders of magnitude lower than that attained with our polymer-modified electrode (see below).

The results of photogalvanic experiments obtained by backface illumination of SnO₂ in contact with a homogeneous solution containing the Fe(II)/(III) couple are listed in Table II. Upon excitation in the absorption band of the dye, Fe(II) ions quench the excited dye, producing an electroactive reduced form of 1. The specific rate of quenching of triplet 1 ($2.0 \times 10^{-5}\text{M}$) by Fe(II), monitored with nanosecond laser flash kinetics, was $4.5 \times 10^8 \text{M}^{-1} \text{s}^{-1}$ in 0.1M CF₃COONa (pH 3.5). A longer lived transient of $\sim 800 \mu\text{s}$ lifetime, observed by recovery from bleaching of 1 at 540 nm, was also detected. We believe this long-lived transient, which was identical with one produced by pulse radiolysis of an aqueous solution of 1 (probably a reduced form of 1), is produced as a result of electron transfer between triplet 1 and Fe(II) and that it is responsible for the observed photogalvanic effect.

The maximum photovoltage and photocurrents obtained at unmodified SnO₂ electrodes were -30 mV and $0.35 \mu\text{A}/\text{cm}^2$. The poor performance of this photo-

galvanic cell could be attributed to the low concentration of the electroactive reduced dye at the electrode surface and to the competition between dye and Fe^{III} in quenching the anodic current by back electron transfer at the working electrode.

Photogalvanic effects at SnO₂/PVP/1.—When the unmodified SnO₂ electrode was replaced by SnO₂/PVP/1 in the same solution, the magnitude of the photogalvanic effect was greatly enhanced. Since the major contribution to the observed effect came from the dye present in the film rather than from dye in solution (Table II), optimal photoeffects were obtained with the SnO₂/PVP/1 in the absence of dye in the electrolyte. The optimum electrolyte Fe(II) concentration was found to be $\sim 0.01\text{M}$. This same concentration of Fe(II) was then employed in the experiments to be discussed below.

A typical photogalvanic response at SnO₂/PVP/1 to illumination is shown in Fig. 2. The response was instant and reproducible in the presence of Fe(III)/Fe(II). Even after extended irradiation periods (several hours), more than 75% of the original photovoltage is retained. Upon increasing the dye content in the polymer film (Table III), increased photocurrents were observed with dye surface coverage up to $4.5 \times 10^{-9} \text{ mols}/\text{cm}^2$. Further increase in the dye coverage, i.e., to concentrations giving optical densities >0.5 , did not increase the photocurrents.

Our dye-loaded polymer electrodes could be illuminated from either the back face or through solution (Scheme 1). With front-face illumination, only a small fraction of the light reaches the electrode surface

Table II. Photogalvanic effect in rose bengal-Fe(II) system^a

[1] (10 ⁻⁵ M)	[Fe(II)] ^b (10 ⁻² M)	SnO ₂		SnO ₂ /PVP/1	
		Photovoltage ^c (mV \pm 5 mV)	Anodic photocurrent ^c ($\mu\text{A} \pm 0.01 \mu\text{A}$)	Photovoltage ^c (mV \pm 5 mV)	Anodic photocurrent ^c ($\mu\text{A} \pm 0.1 \mu\text{A}$)
0.0	0.5	0	0.0	-100	1.5
0.0	1.0	0	0.0	-135	2.5
0.0	2.5	0	0.0	-90	2.5
2.0	0.5	-15	0.1	-95	1.5
2.0	1.0	-33	0.6	-110	2.5
2.0	2.5	-20	0.3	-75	2.4
4.0	1.0	-30	0.7	-105	2.4

^a Electrode area = 2 cm², electrolyte: 0.1M CF₃COONa (pH 3).

^b At open circuit with no applied potential, we assume the Fe(II)/Fe(III) to be significantly dominated by Fe(II).

^c Photovoltage and photocurrent refer to open-circuit and short-circuit conditions, respectively.

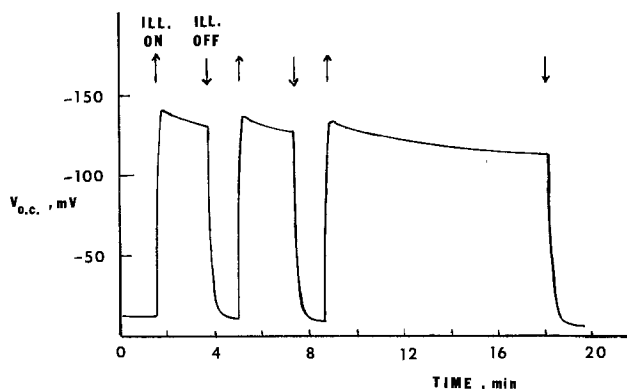
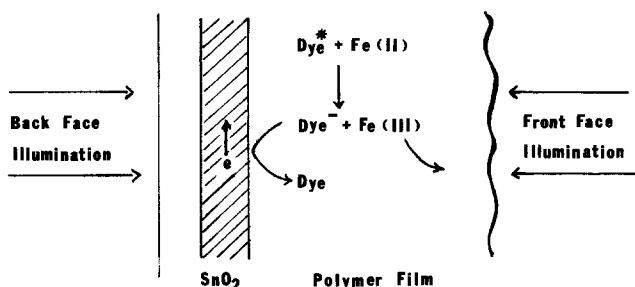


Fig. 2. Response of photogalvanic effect at (A) $\text{SnO}_2/\text{PVP}/\underline{I}$ and its stability over extended period of illumination. Film thickness = $0.1 \mu\text{m}$. Surface coverage of $\underline{I} = 4 \times 10^{-9} \text{ mol/cm}^2$. Electrode area = 2 cm^2 . Electrolyte = 0.01M FeSO_4 , $0.1\text{M CF}_3\text{COONa}$ (pH 3).

and, in fact, front-face illumination of $\text{SnO}_2/\text{PVP}/\underline{I}$ led to a drastic decrease in the short-circuit current at high dye surface coverages. Since nearly the same photocurrents were observed when the illumination was done from the front or back face of dye containing polymer-coated electrodes of lower optical density, these observations suggest that the dye molecules dispersed close to the electrode surface, i.e., the first few monolayers, are responsible for generating the photogalvanic effect. Thicker films led to decreased photocurrents in both front- and back-face illumination, presumably because of reduced mass transport through the thick layer. A similar dependence of the magnitude of the photocurrent on the polymer film thickness was observed with Nafion-coated SnO_2 electrodes loaded with $\text{Ru}(\text{bpy})_3^{2+}$, where slow charge transport in the thick films limited the generation of photocurrent (20).

Figure 3 shows the photoaction spectrum observed at $\text{SnO}_2/\text{PVP}/\underline{I}$. The maximum observed around 565 nm coincides with the (S_0 - S_1) absorption band of the dye. This confirmed our suspicion that the observed effect was initiated upon dye excitation. The observed photocurrent spectrum is rather broad due to the wide-band excitation source, but the correspondence of the single peak in the photoaction spectrum with the monomer absorption band confirms the previously reported observation (18) that only monomeric dye is active in producing photogalvanic effects.

The dependence of photocurrent and photovoltages on light intensity are shown in Fig. 4. The photocurrent varied linearly, while the photovoltage increased logarithmically with the incident light intensity. Similar dependence on the light intensity has been observed also in homogeneous thionine-ferrous systems (4, 9, 18).



Scheme I. Schematic diagram representing possible modes for the generation of photogalvanic effects at a dye-loaded polymer electrode.

Table III. Influence of varying dye concentration in $\text{SnO}_2/\text{PVP}/\underline{I}$ on the generation of photogalvanic effect^a

Total surface coverage of \underline{I} 10^{-9} mol/cm^2	Anodic photocurrent ($\mu\text{A} \pm 0.1 \mu\text{A}$)	
	Front face	Back face
0.0 ^b	0.0	0.0
2.0 ^b	2.5	3.3
4.5 ^b	3.2	3.6
6.0 ^b	1.5	3.1
15.0 ^b	0.8	3.0
5.0 ^c	0.8	1.0

^a In deaerated 0.01M FeSO_4 , $0.1\text{M CF}_3\text{COONa}$ (pH 3); electrode area = 2 cm^2 .

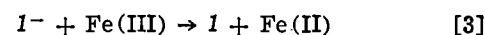
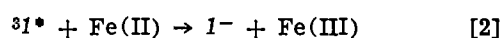
^b $0.1 \mu\text{m}$ thick film.

^c $0.5 \mu\text{m}$ thick film.

The influence of a sacrificial redox system on the magnitude of the observed photogalvanic effect at $\text{SnO}_2/\text{PVP}/\underline{I}$ was also determined. When an aqueous solution of 0.02M EDTA was employed as the redox electrolyte, up to 250 mV of photovoltage and $2 \mu\text{A/cm}^2$ of photocurrents were observed. However, the photocurrents observed with EDTA were neither as reproducible nor as stable as with the Fe(II)/Fe(III) redox system. Decreased photovoltages and photocurrents were seen in successive illumination periods. After $\sim 10 \text{ min}$ illumination, the initial photocurrent had diminished to less than half of its original value. Presumably, the dye in the polymer film undergoes some irreversible photochemical reaction with EDTA and hence loses its photoelectrochemical activity.

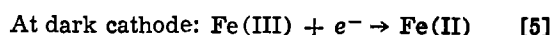
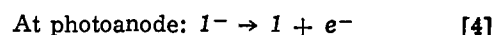
Mechanism.—Our earlier electrochemical studies have indicated that the electroactivity of anionic dyes incorporated in the protonated PVP film could be retained almost completely when in contact with a reversible aqueous redox system (12-14). The polymer film can be regarded as the statistical equivalent of several monolayers (21), where charge propagation occurs through electron hopping between adjacent reduced and oxidized states.

We therefore propose the following mechanism to account for photocurrent production. Upon illumination of $\text{SnO}_2/\text{PVP}/\underline{I}$, dye \underline{I} in the PVP film is excited. Fe(II) , also present in the PVP film (22), quenches the long-lived triplet state of the dye, producing an electroactive reduced form of \underline{I} (Eq. [1] and [2])



If the back electron transfer (Eq. [3]) is retarded, \underline{I}^- undergoes heterogeneous electron transfer to the SnO_2 electrode, leading to an anodic current flow. While \underline{I}^- generated close to the surface can quickly transfer charge to the electrode, a species further from the electrode surface must propagate its charge via either diffusion or an electron hopping mechanism. The results of front- and back-face illumination (Table III) experiments suggest that this propagation is not efficient and that only the dye molecules in the first few monolayers (close to the electrode surface) contribute to the generation of photogalvanic effects.

Photochemically generated Fe(III) , Eq. [2], because of additional electrostatic repulsion between cationic PVP and the more positively charged Fe(III) , is repelled from the film into solution. Fe(III) then will ultimately be reduced at the counterelectrode, thereby completing the redox cycle. The net electrochemical reactions can therefore be represented as



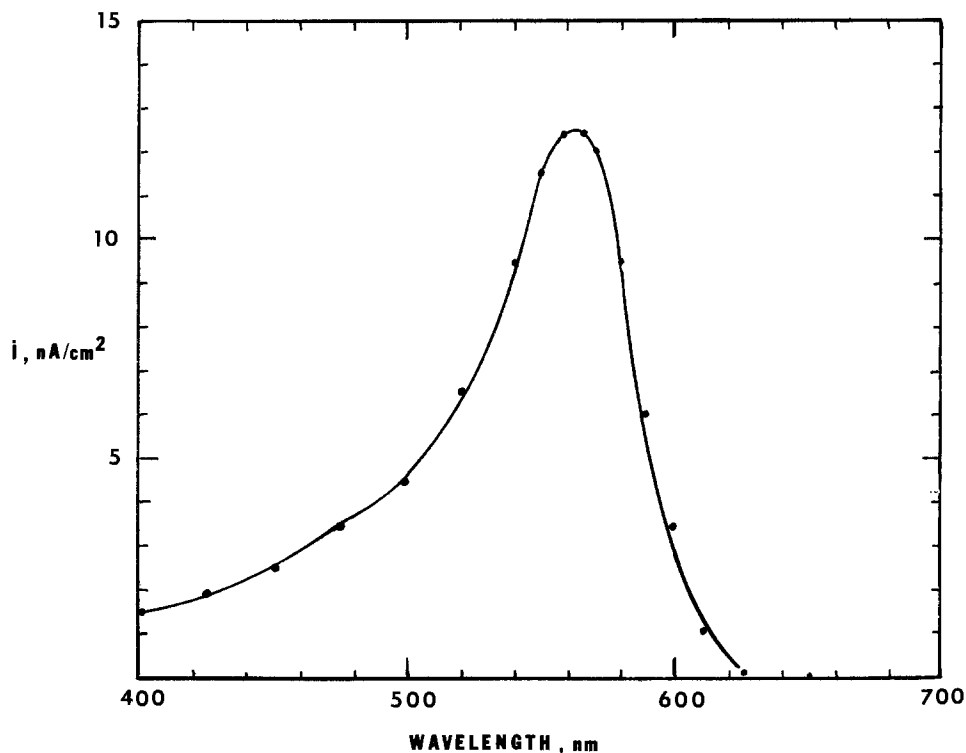


Fig. 3. Photocurrent action spectrum of $n\text{-SnO}_2/\text{PVP}/\underline{I}$ in $0.01M \text{FeSO}_4$, $0.01M \text{CF}_3\text{COONa}$ ($\text{pH } 3$). Film thickness $0.1 \mu\text{m}$. Surface coverage of $\underline{I} = 4 \times 10^{-9} \text{ mol/cm}^2$.

Thus, reactions [1]-[5] constitute a photogalvanic conversion of light energy into electricity without an accompanying net chemical change in the electrolyte.

Power characteristics and sunlight engineering efficiency.—The current-voltage power characteristics of a photogalvanic cell consisting of $\text{SnO}_2/\text{PVP}/\underline{I}$ as the photoanode, Fe(II)/Fe(III) as the mobile redox carrier, and Pt foil as the dark cathode are given in Fig. 5. The load resistance was varied with a $100 \text{ k}\Omega$ variable resistor. The maximum power output (P_{max}) obtained was $0.1 \mu\text{W/cm}^2$ at an incident white light intensity of 100 mW/cm^2 . The fill factor for the photogalvanic cell employing $\text{SnO}_2/\text{PVP}/\underline{I}$ was 0.31, comparable to the values reported for photogalvanic cells employing the thionine-ferrous system (3).

The overall engineering efficiency of this solar energy conversion as determined from the ratio of

power output of the photogalvanic cell to the incident power was found to be $\sim 10^{-2}\%$. Because of the limited absorption of the visible light by the dye \underline{I} ($\lambda_{\text{max}} = 570 \text{ nm}$), more than 80% of the incident light is not utilized. Nonetheless, this efficiency is an order of magnitude higher than that obtained in an analogous photogalvanic cell in which this same dye is dissolved in or adsorbed from homogeneous solution.

The important feature of such dye-loaded polymer electrodes in improving the performance of photogalvanic cells are that very high dye concentrations (up to $1M$) can be achieved near the electrode surface, that dye aggregation is minimal, and that retardation of self-quenching leads to longer lived excited states, which in turn increases the efficiency of generation of the electroactive reduced species. Furthermore, specific electroselectivity of the modified electrodes is an important criterion in achieving better efficiency in pho-

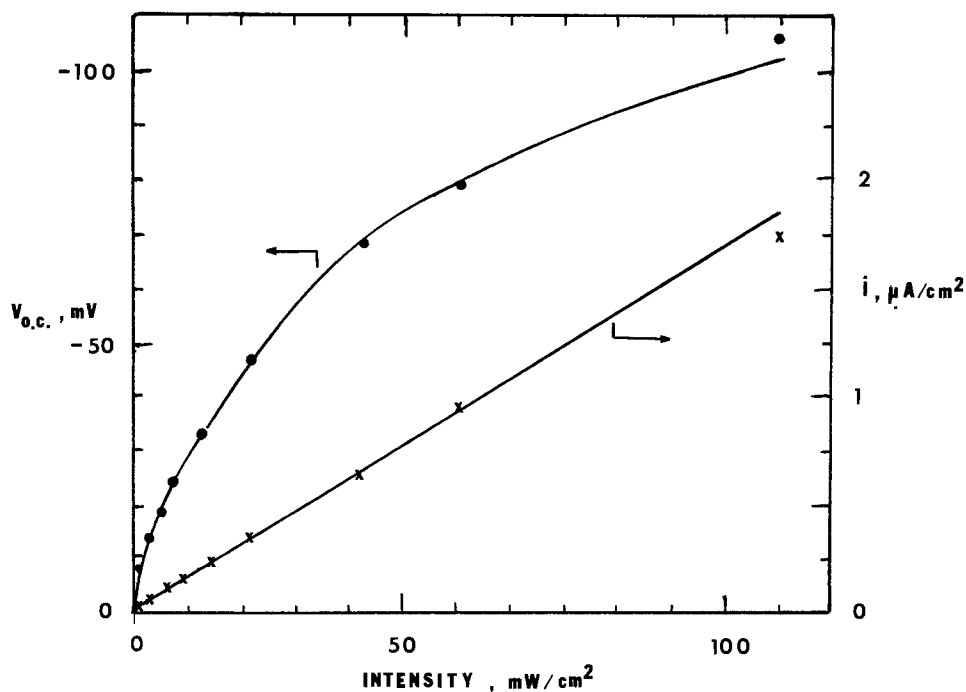


Fig. 4. Light intensity dependence of anodic photocurrent (i) open-circuit photovoltage (OCP) of a photogalvanic cell employing $n\text{-SnO}_2/\text{PVP}/\underline{I}$ in $0.01M \text{FeSO}_4$, $0.1M \text{CF}_3\text{COONa}$ ($\text{pH } 3$). Film thickness = $0.1 \mu\text{m}$. Surface coverage of $\underline{I} = 4 \times 10^{-9} \text{ mol/cm}^2$.

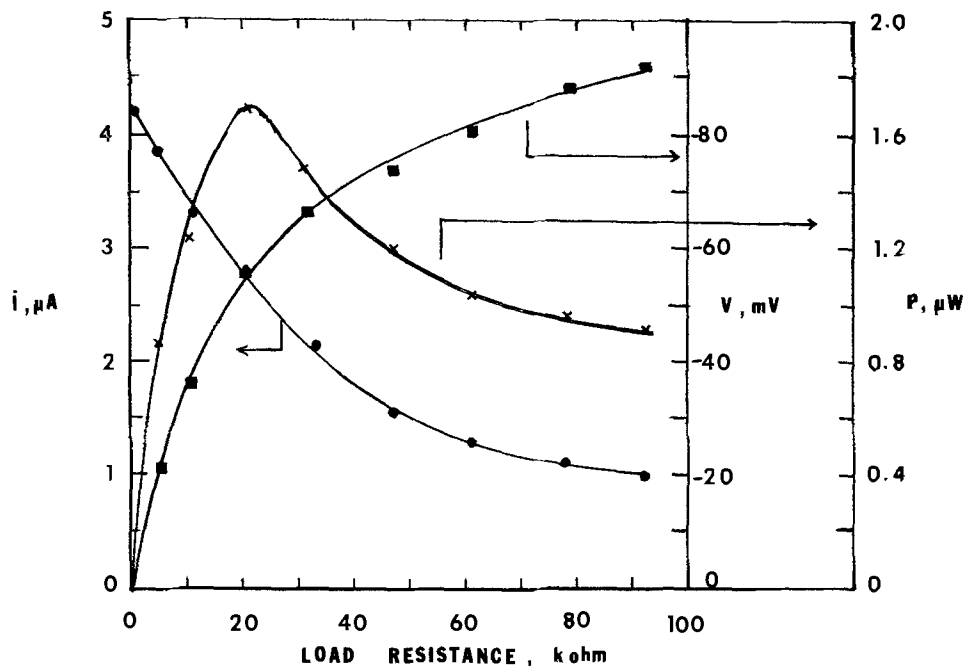


Fig. 5. Characteristics of photogalvanic cell with $n\text{-SnO}_2/\text{PVP}/\text{I}$ photoanode and Pt "dark" cathode in 0.01M FeSO_4 , 0.1M CF_3COONa (pH 3). Photovoltage V (\blacksquare), anodic photocurrent i (\bullet), power output, P (\times) at varying load resistance. Film thickness = 0.1 μm . Surface coverage of I^- = 4×10^{-9} mol/cm². Electrode area = 2 cm².

photogalvanic cells (6, 17). The electroselectivity of the polymer-coated photoanode towards the I^-/I couple is increased because alternate quenching redox couples, e.g., species of increased positive charge like Fe(III) , are electrostatically repelled from the cationic film. The expulsion of Fe(III) from the PVP film also serves to retard the back electron transfer between reduced form of I^- and Fe(III) . This, in turn, stabilizes the electroactive reduced species in the polymer film. Similar arguments have been put forth for a thionine-ferrous system in membrane-mediated reactions (10).

Conclusions

A simple technique has been developed to incorporate an anionic dye into a cationic polymer film coated on a conductive SnO_2 electrode. Excitation of the dye-loaded polymer films adhering to optically transparent electrodes immersed in a solution containing a suitable redox couple led to photogalvanic effects. The enhanced photogalvanic performance of this system has been attributed to the presence of a high dye concentration at the electrode surface, to longer lived excited states of the dye in the polymer film, and to the electrostatic characteristics of the polymer in controlling access of charged redox couples to the illuminated electrode. These dye-loaded polymer electrodes should improve the fabrication of thin layer photogalvanic cells.

Acknowledgments

This research was supported by the U.S. Department of Energy, Division of Chemical Sciences, Fundamental Interactions Branch. M.A.F. is grateful for support as an Alfred P. Sloan Research Fellow and as a Camille and Henry Dreyfus Teacher-Scholar.

Manuscript submitted Aug. 15, 1983; revised manuscript received Dec. 7, 1983.

REFERENCES

- M. D. Archer and M. I. C. Ferreira, in "Photochemical Conversion and Storage of Solar Energy," J. S. Connolly, Editor, p. 201, Academic Press, New York (1982).
- N. N. Lichtin, in "Solar Power and Fuels," J. R. Bolton, Editor, p. 119, Academic Press, New York (1977).
- D. E. Hall, J. A. Eckert, N. N. Lichtin, and P. D. Wilder, *This Journal*, **123**, 1705 (1976).
- P. V. Kamat, M. D. Karkhanavala, and P. N. Moorthy, *Ind. J. Chem.*, **18A**, 206 (1979).
- M. Z. Hoffman and N. N. Lichtin, in "Solar Energy: Chemical Conversion and Storage," R. R. Hautala, R. B. King, and C. Kubal, Editors, p. 153, The Humana Press, Clifton, NJ (1979).
- (a) R. Gomer, *Electrochim. Acta*, **20**, 13 (1975); (b) W. J. Albery and M. D. Archer, *J. Electroanal. Chem.*, **86**, 1 (1978).
- W. J. Albery and A. W. Foulds, *J. Photochem.*, **10**, 41 (1979).
- P. V. Kamat and N. N. Lichtin, *ibid.*, **18**, 197 (1982).
- (a) N. S. Dixit and R. A. Mackay, *J. Phys. Chem.*, **86**, 4593 (1982); (b) K. Shigehara, M. Nishimura, and E. Tsuchida, *Electrochim. Acta*, **23**, 855 (1978).
- M. Gokalp and E. L. Cussler, *J. Membr. Sci.*, **11**, 53 (1982).
- (a) R. Tamilarasan and P. Natrajan, *Ind. J. Chem.*, **20A**, 213 (1981); (b) K. Shigehara, H. Sano, and E. Tsuchida, *Makromol. Chem.*, **179**, 1531 (1978).
- P. V. Kamat and M. A. Fox, *J. Electroanal. Chem.*, To be published.
- P. V. Kamat and M. A. Fox, submitted to *J. Am. Chem. Soc.*
- P. V. Kamat and M. A. Fox, *J. Phys. Chem.*, To be published.
- P. V. Kamat and M. A. Fox, *Chem. Phys. Lett.*, **92**, 595 (1982).
- L. E. Cramer and K. G. Spears, *J. Am. Chem. Soc.*, **100**, 224 (1978).
- W. J. Albery, A. W. Foulds, K. J. Hall, and A. R. Hillman, *This Journal*, **127**, 654 (1980).
- D. E. Hall, W. D. K. Clark, J. A. Eckert, N. N. Lichtin, and P. D. Wilder, *Am. Ceram. Soc. Bull.*, **56**, 408 (1977).
- H. Tsubomura, Y. Shimoura, and S. Fujiwara, *J. Phys. Chem.*, **83**, 2103 (1979).
- M. Krishnan and A. J. Bard, *J. Am. Chem. Soc.*, To be published.
- C. P. Andrieux, J. M. Dumas-Bouchiat, and J. M. Saveant, *J. Electroanal. Chem.*, **116**, 159 (1980).
- (a) N. Dyama and F. C. Anson, *Anal. Chem.*, **52**, 1192 (1980); (b) K. Shigehara, N. Oyama, and F. C. Anson, *J. Am. Chem. Soc.*, **103**, 2552 (1981).

Semiconductor Electrodes

LV. Differential Photocurrent Determination of Absorption Coefficient and Diffusion Length in p-GaP Photoelectrochemical Cells

Bob L. Wheeler, G. Nagasubramanian, and Allen J. Bard

Department of Chemistry, The University of Texas at Austin, Austin, Texas 78712

ABSTRACT

The differential photocurrent (DPC) method, which involves simultaneous modulation of the incident radiation (at f_1) and the applied potential (at f_2) with detection of the intermodulation photocurrent (at $|f_2 - f_1|$), was employed in the determination of α and L for p-GaP in contact with aqueous solutions of Eu^{3+} . Typical values of α determined by this technique were (450 nm) $6.9 \times 10^4 \text{ cm}^{-1}$ and (400 nm) $8.1 \times 10^4 \text{ cm}^{-1}$. The value of L obtained was $0.10 \pm 0.01 \mu\text{m}$, which is smaller than that found for high purity p-GaP in solid-state devices and is attributed to traps or recombination centers in the p-GaP electrode material.

Radiant-to-electrical energy conversion at a semiconductor electrode in contact with an electrolyte in a liquid junction photoelectrochemical (PEC) cell is often controlled by the optical absorption coefficient, α , and the minority carrier diffusion length, L , of the semiconductor. In principle, by measuring the photocurrent under monochromatic illumination as a function of potential, one can obtain the necessary information for the computation of α and L . The Gärtner model and its variations (1-5) are the simplest models for the photocurrent density, j , at the semiconductor/liquid interface. This model assumes that minority carriers generated within the electric field of the space-charge layer (scl) are swept to the interface where they react; recombination within the scl is neglected. Carriers generated outside the scl must diffuse to it. Only those carriers within a distance L of the edge of the scl [where $L = (D\tau)^{1/2}$; D is the diffusion coefficient and τ is the lifetime of the minority carriers] are swept to the interface. More rigorous and complex models for the photocurrent have been proposed (4, 5); these include the effects of surface recombination, bulk and scl recombinations, slow charge-transfer kinetics at the interface, etc. These models are much more difficult to apply to actual experimental studies, however, because they involve many adjustable parameters and numerical solutions or digital simulations rather than analytical solutions. Hence, the Gärtner-like model is frequently used, and we apply this model here in a first attempt at determining α and L by the differential photocurrent (DPC) method—a method first proposed for solid-state devices by Sukegawa *et al.* (6).

The Gärtner equation can be written (1-3)

$$j = KqI\{1 - [e^{-\alpha w}/(1 + \alpha L)]\} \quad [1]$$

where w is the thickness of the scl and is a function of the potential, V , with respect to the flatband potential V_{FB} , and is given by

$$w = [(2\epsilon\epsilon_0/qN)(|V - V_{\text{FB}}|)]^{1/2} \quad [2]$$

ϵ is the dielectric constant of the semiconductor and ϵ_0 is the permittivity of free space, N is the donor or acceptor density, and V is the applied potential with respect to the flatband, V_{FB} . When an ac voltage of amplitude V_0 is superimposed on the dc potential, the variation in space-charge layer thickness, Δw , is given by

$$\Delta w = \epsilon\epsilon_0 V_0 / qNw \quad [3]$$

These equations were used by Sukegawa *et al.* (6). In Eq. [1], K includes terms that are independent of V and the intensity, I , such as the reflectivity of the electrode, etc. The photocurrent density can thus be represented as a function of $|V - V_{\text{FB}}|$ or w (Fig. 1). As

$w \rightarrow \infty$; $j \rightarrow j_{\text{sat'd}} = KqI$. At $V = V_{\text{FB}}$ or $w = 0$, j is given by

$$[j]_{w=0} = KqI[\alpha L/(1 + \alpha L)] \quad [4]$$

The slope of the j vs. w curve at any point is given by

$$(dj/dw) = KqI\alpha e^{-\alpha w}/(1 + \alpha L) \quad [5]$$

In particular, at $w = 0$

$$(dj/dw)_{w=0} = KqI\alpha/(1 + \alpha L) \quad [6]$$

Within the framework of the model, α and L can be obtained from Eq. [4]-[6], since

$$j_{w=0}/(dj/dw)_{w=0} = L \quad [7]$$

$$\ln(dj/dw) = \ln[KqI\alpha/(1 + \alpha L)] - \alpha w \quad [8]$$

with α obtained from the slope of the plot of $\ln(dj/dw)$ vs. w . Note that transformation of the experimentally accessible j vs. V to j vs. w plot requires knowledge of V_{FB} and N ; these can be obtained from a Mott-Schottky plot ($1/C^2$ vs. V) (7). In principle, the actual photocurrent-potential plots could be used in Eq. [7] and [8]. However, since the value of j at $w = 0$ can be very small, the values of L computed from directly measured j vs. V plots are inaccurate. Sukegawa *et al.* (6) developed the differential photocurrent (DPC) technique for obtaining the equivalent data for the determination of α and L .

Basis of DPC method.—The DPC method involves the modulation of the applied potential with a small amplitude (*e.g.*, 12 mVpp) sine wave at a frequency f_2 and the simultaneous modulation of the light intensity at a frequency f_1 with detection of the intermodulated photocurrent at $|f_2 - f_1|$. The intensity of the modulated light is maintained at a low level to prevent changes in dopant density and space-charge layer width from photoeffects alone (8). Figure 2 illustrates these principles. The small signal ac voltage brings about a change (Δw) in the space-charge layer width (w). This change in w produces a change in j , and this change in photocurrent, Δj , is represented by Eq. [5] (*i.e.*, $\Delta j/\Delta w$ approaches dj/dw for small depths of modulation). When the applied potential $V + V_0 \sin \omega_2 t$, where V_0 is the peak amplitude of the small superimposed ac voltage and $\omega_2 = 2\pi f_2$ is the ac angular frequency

$$\Delta w = \epsilon\epsilon_0 V_0 \sin(\omega_2 t) / qNw \quad [9]$$

In the course of one ac cycle, the maximum change in the scl width would be proportional to $2V_0$. However, a more meaningful value for use as the voltage change during a cycle would be the effective voltage or root-mean-square (rms) voltage. The peak-to-peak ac voltage ($2V_0$) is related to the rms voltage (V_{rms}) by

$$V_{\text{rms}} = 0.707 V_0 \quad [10]$$

* Electrochemical Society Active Member.

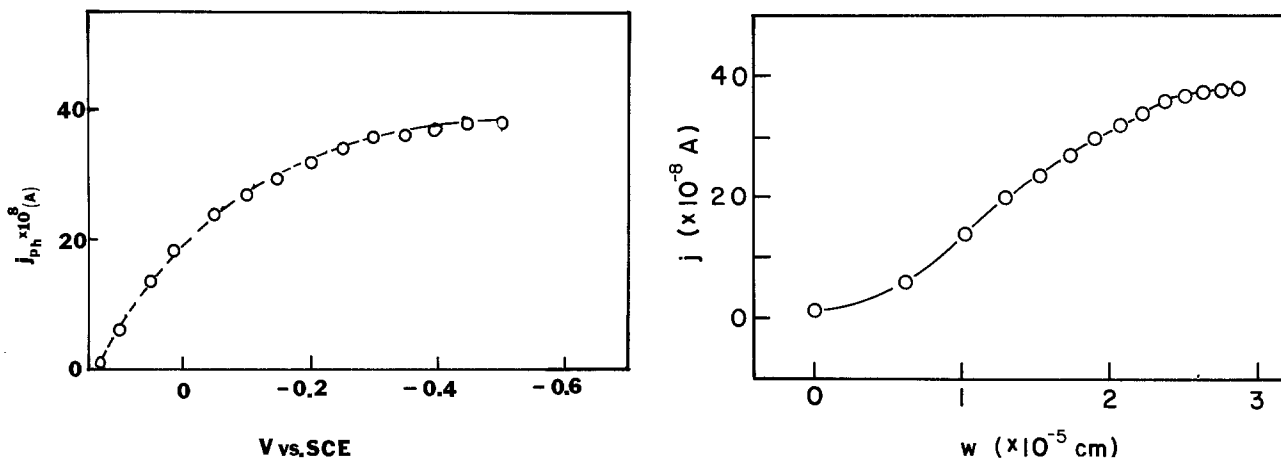


Fig. 1. A, left: plot of photocurrent (j) vs. applied dc bias (V) for a hypothetical case. B, right: plot of j vs. w , the space-charge layer width for the same case.

Hence, $2V_{rms}$ was employed in the computation of Δw from Eq. [3]. When the incident photon flux is modulated with angular frequency of $\omega_1 = 2\pi f_1$, the intensity of illumination varies as

$$I(t) = I_0(1 + m \sin \omega_1 t) \quad [11]$$

where m is the depth of modulation and $2I_0$ is the maximum incident photon flux. In our experiments, the depth of modulation can be set approximately equal to 100%, and, hence, Eq. [11] reduces to

$$I(t) = I_0(1 + \sin \omega_1 t) \quad [12]$$

It is evident from Eq. [1] that upon changing the space charge layer width w by Δw there is a corresponding change in j by Δj . This is expressed by the following relationship

$$\begin{aligned} J &= j + \Delta j = KqI \{1 - [e^{-\alpha(w+\Delta w)/(1+\alpha L)}]\} \\ &= KqI \{1 - [e^{-\alpha w/(1+\alpha L)}](e^{-\alpha \Delta w})\} \\ &= KqI \{1 - [e^{-\alpha w/(1+\alpha L)}](1 - \alpha \Delta w)\} \\ j + \Delta j &= KqI \{1 - [e^{-\alpha w/(1+\alpha L)}]\} \\ &\quad + KqI \alpha \Delta w e^{-\alpha w/(1+\alpha L)} \quad [13] \end{aligned}$$

Substitution of the time varying quantities $I(t)$ and

Δw from Eq. [12] and [9] into Eq. [13] gives the amplitude of the photocurrent, j , at ω_1

$$j(\omega_1) = KqI_0 [1 - e^{-\alpha w/(1+\alpha L)}] \quad [14]$$

and the differential photocurrent, Δj at Δw

$$\Delta j(\Delta w) = (KqI_0/2) [\alpha/(1+\alpha L)] (e^{-\alpha w}) (\epsilon \epsilon_0 V_0/qNw) \quad [15]$$

The derivations of Eq. [14] and [15] are given in the Appendix.

The values of Δw can be computed from Eq. [3] and [10] as a function of w .

Two lock-in amplifiers, one set at ω_1 and the other at $|\omega_1 - \omega_2|$, were used to detect the photocurrent; thus, both j (at ω_1) and Δj (at $|\omega_1 - \omega_2|$) can be recorded simultaneously. From the computed values of Δw and measured Δj , one can make a plot of $\ln(\Delta j/\Delta w)$ vs. w (Eq. [8]). The slope of the plot yields α at the wavelength of measurement. The Y-intercept of the plot, corresponding to $w = 0$, yields $[\Delta j/\Delta w]_{w=0}$. The value of α obtained previously, can be inserted in Eq. [1], and a plot of j vs. $e^{-\alpha w}$ extrapolated to $e^{-\alpha w} = 1$ (corresponding to $w = 0$) yields $[j]_{w=0}$. From these values, L can be computed from Eq. [7]. In addition to the DPC technique, a wealth of information pertaining to the experimental determination of L is available in the literature. These include the surface photovoltage technique (9-11), the electron bombardment of Schottky barriers (12), the photoluminescent-saturation measurement (13), and various other techniques (14-18). In most of these studies, one needs to know α to evaluate L . Since in many cases α is not known, it has to be determined separately, usually from absorbance measurements (19-24).

We report here DPC studies of single-crystal p-GaP and n-MoSe₂ semiconductors contacting liquid electrolytes containing Eu^{3+/2+} and K₄Fe(CN)₆, respectively, as redox couples. The adaptation of this method reported here has the advantage that the measurements are conducted with the semiconductor in the same configuration normally used in PEC cells, unlike the other techniques mentioned. One drawback, however, is that any deleterious effects the electrolyte has on the semiconductor, such as surface recombination or formation of surface states, could affect the measurement. An example of this is the absorption of light by redox couples. In solid-state measurements, no new chemical species are formed, and the light incident on the semiconductor is constant with respect to time. This is not necessarily the case with semiconductors in PEC cells. Species are generated at the photoelectrode with different absorption characteristics than the original form. If these generated species absorb at the wavelength of interest, errors will be caused by the time-

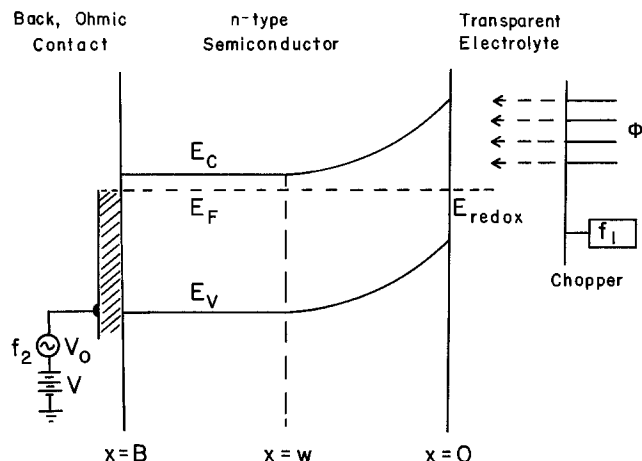


Fig. 2. Schematic of energy-band diagram illustrating the principle of measurement. Φ is the incident photon flux density chopped at an angular frequency of $\omega_1 = 2\pi f_1$; $2V_0$ is the peak-to-peak amplitude of the small signal ac voltage at an angular frequency of $\omega_2 = 2\pi f_2$; V is the applied dc reverse bias; $x = 0$, w , and B represent, respectively, the interface, space-charge layer width, and the back of the crystal where the ohmic contact is made; E_c = conduction bandedge; E_F = Fermi level; E_V = valence bandedge; E_{redox} = redox potential.

dependent filter effect. For this reason, as well as the good kinetics, $\text{Eu}^{3+/2+}$ and $\text{Fe}(\text{CN})_6^{3-/4-}$ were chosen as redox couples.

Experimental

The single-crystal semiconductors employed in this study were p-GaP and n-MoSe₂. The procedures for mounting and etching the electrodes are given elsewhere (25). The solution used with p-GaP was 0.1M EuCl_3 in 1M HClO_4 , and that used with n-MoSe₂ was 0.2M $\text{K}_4\text{Fe}(\text{CN})_6$ adjusted to pH 8 with KOH. Solutions were bubbled with prepurified N_2 prior to use, and N_2 was passed over the solutions during the experiment. A single-compartment electrochemical cell of 40 ml capacity with an optically flat window was used for all experiments. The counterelectrode was a large-area (40 cm²) Pt gauze, and the reference electrode was a saturated calomel electrode (SCE) with a KCl-saturated agar plug immersed directly into the cell. All potentials are expressed relative to the SCE unless otherwise specified.

A PAR Model 173 Potentiostat and a PAR Model 175 Universal Programmer (Princeton Applied Research Corporation, Princeton, New Jersey) were used to obtain the cyclic voltammograms, which were recorded on a Model 2000 X-Y recorder (Houston Instruments, Austin, Texas).

The ac impedance studies (26) utilized the lock-in amplifier technique, which yields the in-phase and the out-of-phase components of an ac signal superimposed on a dc voltage ramp. The ac signal (12 mV peak to peak) at different frequencies was obtained for input into the potentiostat from a Model 200 CD wide-range oscillator (Hewlett-Packard, Palo Alto, California). The output from the potentiostat, which was a voltage proportional to the current flowing between the working electrode (semiconductor) and the counterelectrode, was separated into its components at 0° and 90° with respect to the sine wave input by using a PAR Model 5204 lock-in amplifier and recorded with a Model 6432 (Soltec, Sun Valley, California) X-Y₁Y₂ recorder.

The experimental apparatus used for obtaining the differential photocurrent is shown in Fig. 3. A 2.5 kW Xe lamp (Schoeffel Instrument Company, Westwood, New Jersey) and monochromator (Jarrell-Ash Model 82560, Waltham, Massachusetts), with appropriate slits to achieve a bandpass of ~10 nm, were used as the

monochromatic light source. The light was modulated at 1111 Hz with a PAR Model 192 variable-frequency chopper. The ac frequency from the wide-band oscillator was adjusted to 1511 Hz with an amplitude of 12 mV peak to peak at the input of the potentiostat. A PAR Model 5204 lock-in amplifier was used to measure the photocurrent, j , which is the magnitude of the current present at the input of the lock-in with a frequency equal to the light chopping frequency, 1111 Hz. The much weaker (~1000×) differential photocurrent signal, Δj , was measured with a Model 5206 lock-in amplifier (EG&G, Princeton, New Jersey) equipped with an EG&G Model 5010 plug-in filter operated in the bandpass mode. The differential photocurrent is the magnitude of the current at the input of the lock-in with a frequency equal to the difference in the light chopping frequency and the ac modulation frequency, here arbitrarily kept at 400 Hz (1511 Hz - 1111 Hz). This signal was more conveniently recorded as $\log \Delta j$ by using the log of the magnitude output of the Model 5206. A reference signal for the lock-in at this beat frequency was obtained by passing f_1 from the chopper and f_2 from the oscillator, both adjusted to 0.8V peak to peak with voltage dividers, into the multiplier-filter circuit. The multiplier was constructed with an MC 1494L chip (Motorola, Incorporated) with the attendant circuitry as described in the product application information (27). The output, which consisted of a signal with frequency components at $f_1 + f_2$ and $f_2 - f_1$, was filtered to obtain only $f_2 - f_1$. This filter consisted of the bandpass output of a variable gain, state variable filter (28) constructed from an ECG 997 quad operational amplifier chip (Sylvania, Waltham, Massachusetts). Further filtering or amplification was found to be unnecessary for the reference channel of the EG&G 5206. Power for the circuit was supplied by a Harrison 6205B dual dc power supply (Hewlett-Packard). The potentiostat, programmer for dc ramp (2 mV/s), and X-Y₁Y₂ recorder were the same as mentioned previously.

As an independent check, L was determined by the surface photovoltage technique. The procedure used was that reported previously by Kamieniecki (29) and others (30). A tungsten-halogen lamp with power input controlled with an autotransformer was used as a light source. Monochromatic light was obtained with a grating monochromator (Model 7240, Oriel Corporation, Stamford, Connecticut). The lock-in amplifiers and

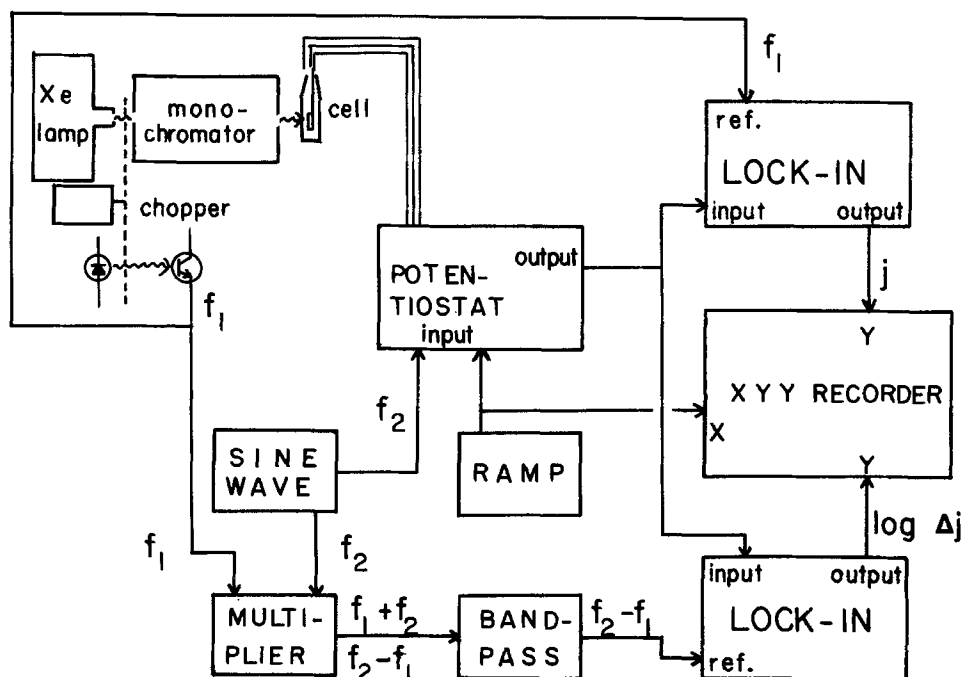


Fig. 3. Apparatus used for recording both the photocurrent (j) and the differential photocurrent (Δj). For details, see the Experimental section.

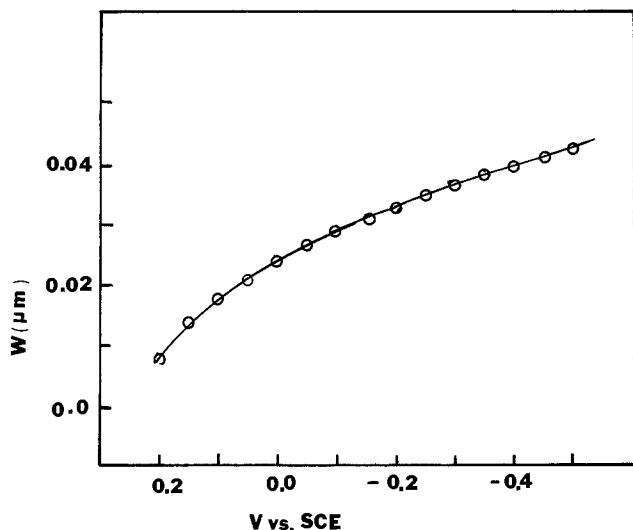


Fig. 4. Plot of the space-charge layer width as a function of applied bias for p-GaP in aqueous solutions containing Eu^{3+} as redox couple.

chopper are the same as previously described. The light intensity was monitored with a pyroelectric detector with a quartz window (Model P1-45Q, Molectron Corporation, Sunnyvale, California). In the surface photovoltage measurements, the solvent was acetonitrile (Spectrum Chemical Manufacturing Corporation, Gardena, California, spectrophotometric grade) and the electrolyte 0.01M tetra-n-butylammonium tetrafluoroborate (Southwestern Analytical Chemicals, Austin, Texas) which had been dried under vacuum at 100°C for 24h after recrystallization from acetone-ether. The solvent-electrolyte solution was stirred with activated alumina (Woelm Alumina N-Super I, Woelm Pharma GmbH and Company, Eschwege, Germany) decanted into the cell and deaerated and kept under a He atmosphere. The reference and counterelectrodes were the same as those used in the DPC measurement.

Results and Discussion

Computation of w and Δw .—For the determination of both w and Δw , one needs to know the value of N , the net doping density, and V_{FB} ; these can be obtained from the Mott-Schottky plot (7). The values of N and V_{FB} obtained from such a plot for p-GaP are $3.7 \times 10^{17} \text{ cm}^{-3}$ and $+0.22\text{V vs. SCE}$, respectively, in $\text{Eu}^{3+/2+}$ aqueous solution. The space-charge layer width, w , is related to N and V (where V is the applied potential) by Eq. [2]. Upon inserting the values of N and V into Eq. [2], the resulting plot of w vs. V for p-GaP in aqueous $\text{Eu}^{3+/2+}$ solution is obtained (Fig. 4). The values of Δw at different potentials were computed by Eq. [3]; the corresponding values of w were taken from Fig. 4. For computation of Δw , a value of $2V_{\text{rms}}$ instead of $2V_0$ was used. The reasons for this are discussed in detail above. The values of w and Δw from Eq. [2] and [3], respectively, are given in Table I as a function of V . Note, in Table I, that as the space-

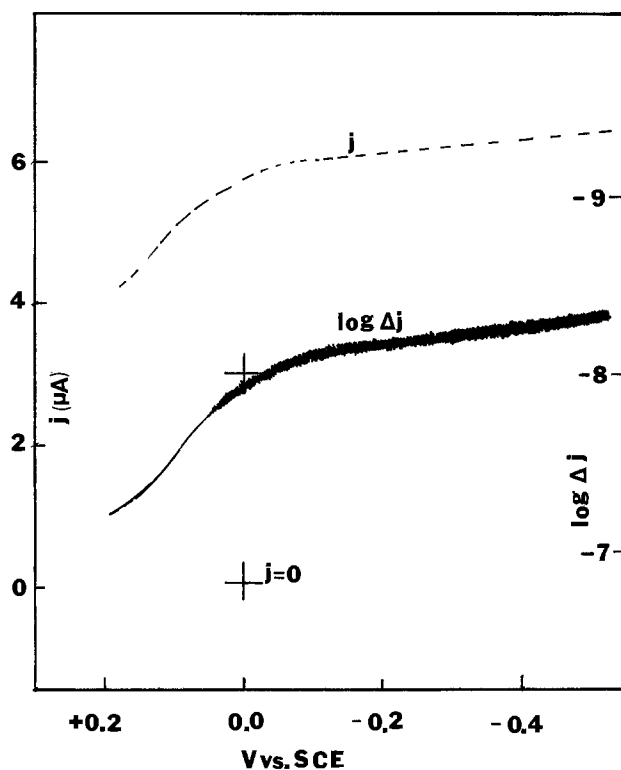


Fig. 5. j and Δj vs. V for p-GaP in aqueous solution containing Eu^{3+} as redox couple. The wavelength of irradiation is 400 nm. $f_1 = 1.111 \text{ kHz}$ and $f_2 = 1.511 \text{ kHz}$.

charge layer width increases, Δw decreases at a given ac modulation.

Plots of Δj and j vs. V .—Under reverse bias conditions, the dark current densities for the semiconductors used in this work were less than $1 \mu\text{A}$. Typical plots of Δj at $\Delta f = 400 \text{ Hz}$ (1511 Hz) and j at 1111 Hz vs. applied bias, V , are given in Fig. 5 for p-GaP in aqueous solution containing $\text{Eu}^{3+/2+}$ as the redox couple. Frequencies 1111 and 1511 Hz correspond, respectively, to the chopping frequency f_1 , of the incident photon flux and the small signal ac frequency, f_2 , superimposed on the dc ramp, V . The plots in Fig. 5 are given for an incident photon energy of 3.1 eV (corresponding to 400 nm). The ordinate for the Δj (400 Hz) vs. V plot is given on a logarithmic scale. Similar results were obtained when the two modulating frequencies f_1 and f_2 were varied by $\pm 20\%$ while maintaining the Δf constant at 400 Hz for ease of filtering. Similar plots of Δj (400 Hz) and j were obtained for irradiation energies in the range 2.7–3.54 eV. Consider Fig. 5, where the photocurrent rises steadily reaching saturation around -0.1V . As j rises, Δj decreases monotonically tending to 0 at -0.1V where j reaches saturation.

Determination of α and L .—From the values of Δw in Table I and the Δj values at corresponding poten-

Table I. Typical values of w , Δw , Δj , and $\ln \Delta j/\Delta w$ for p-GaP in aqueous solution containing $\text{Eu}^{3+/2+}$ at two wavelengths

V (V vs. SCE)	$w \times 10^6$ (cm)	$\Delta w \times 10^{20}$ (m)	$\lambda = 400$ (nm)		$\lambda = 450$ (nm)	
			$\Delta j \times 10^9$ (A)	$\ln (\Delta j/\Delta w)$	$\Delta j \times 10^9$ (A)	$\ln (\Delta j/\Delta w)$
-0.5	4.253	2.504	4.786	2.950	1.000	1.384
-0.45	4.103	2.596	5.011	2.960	1.047	1.394
-0.4	3.947	2.699	5.248	2.967	1.097	1.402
-0.35	3.784	2.815	5.623	2.994	1.159	1.415
-0.3	3.614	2.947	5.888	2.994	1.245	1.440
-0.25	3.436	3.100	6.456	3.036	1.318	1.447
-0.2	3.248	3.279	6.606	3.002	1.413	1.460
-0.15	3.049	3.494	7.244	3.031	1.514	1.466
-0.1	2.835	3.757	7.943	3.051	1.660	1.485
-0.05	2.604	4.090	9.120	3.104	1.820	1.493

tials, from Fig. 5, plots of $\ln \Delta j/\Delta w$ vs. w were obtained (Fig. 6). The Δj and $\ln \Delta j/\Delta w$ values from these plots for p-GaP are given in Table I. A least squares fit was made for the computation of the slope and the Y-intercept. In this fit, a few points very close to V_{FB} were not included, since these points do not fall on the same line as data obtained at larger bias further into the depletion region. The reasons for the deviation are discussed below. The Y-intercept and the slope give, respectively, $(\Delta j/\Delta w)_{w=0}$ and the absorption coefficient, α . The α and $(\Delta j/\Delta w)_{w=0}$ at different wavelengths are given in Table II. This value of α is in good agreement with literature values (31), and is in the range 10^4 - 10^5 cm^{-1} at the wavelengths studied. The value of α at a particular wavelength was inserted into Eq. [1] and a plot of j vs. $e^{-\alpha w}$ obtained (Fig. 7). The j values corresponding to various selected potentials were obtained from Fig. 5. The $[j]_{w=0}$ obtained by extrapolating the plot in Fig. 7 to $e^{-\alpha w} = 1$ correspond-

ing to $w = 0$ at different wavelengths is given in Table II. The extrapolation was made by least squares analysis. Once again, for the least squares fit, values of j close to V_{FB} were neglected. The probable reasons for this positive deviation at small values of V can be attributed to a nonuniform doping density and near-surface recombination. If the impurity concentration is not uniform, w will be different in different regions of the semiconductor, since w varies as $N^{-1/2}$. For example, very close to the surface, if N is larger than the bulk doping density ($3.7 \times 10^{17} \text{ cm}^{-3}$), the actual value of w will be smaller than the computed one, giving a larger Δw . Moreover, if j rises sluggishly to saturation, the Δj will be larger than if j rises precipitously to saturation. The sluggish rise to saturation may be due to the recombination of photogenerated carriers. Thus, the larger Δj and smaller Δw can give rise to a positive deviation. No attempt was made, however, to account for this positive deviation, since one

Fig. 6. Plot of w (μm) vs. $\ln(\Delta j/\Delta w)$ for p-GaP in aqueous solution containing Eu^{3+} as redox couple; conditions are the same as in Fig. 5. Open circles represent data not used in the least squares fit.

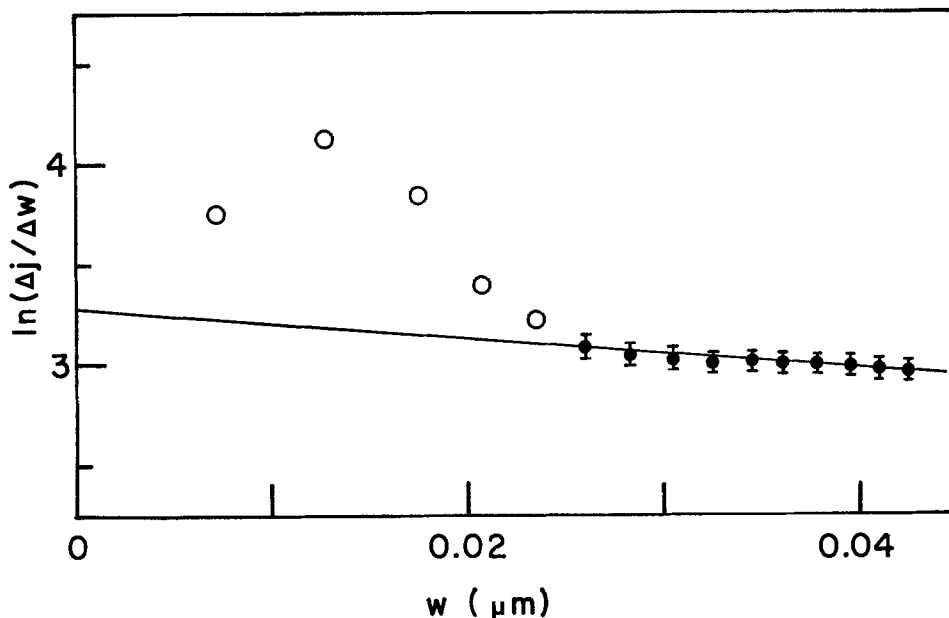


Fig. 7. Plot of $e^{-\alpha w}$ vs. j for p-GaP in aqueous solution containing Eu^{3+} as redox couple; conditions are the same as in Fig. 5.

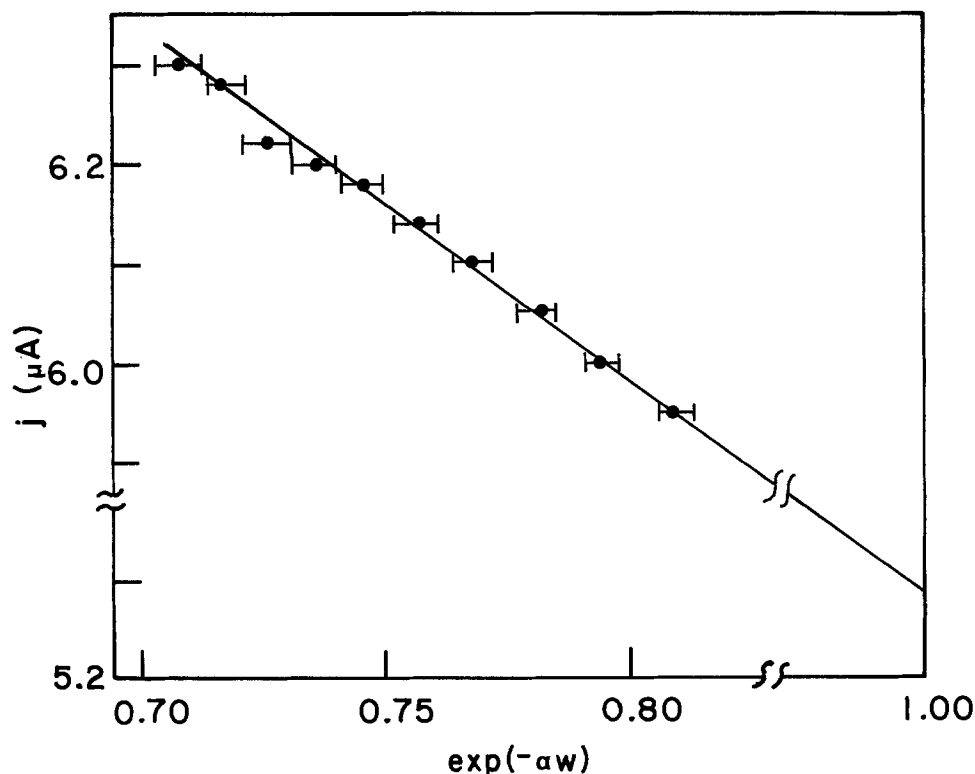


Table II. Values of α , L , and the parameters used to compute them; p-GaP; $\text{Eu}^{3+/2+}$

λ (nm)	α (cm^{-1})	$[\Delta j/\Delta \omega]_{\omega=0}$ (A/m)	$[j]_{\omega=0}$ (A)	L (μm)
450	6.9×10^4	5.35	1.09×10^{-6}	0.11
400	8.1×10^4	26.90	5.28×10^{-6}	0.10
350	3.6×10^5	142.33	10^{-7}	(~ 0.001)

needs to know the values of different parameters, such as surface recombination rate, bulk recombination rate, etc., under actual use conditions. Since these parameters are not easily determined, the values of j and $(\Delta j/\Delta \omega)$ close to V_{FB} were neglected.

The minority carrier diffusion length, L , was obtained from Eq. [7] from the values of $[j]_{\omega=0}$ and $(\Delta j/\Delta \omega)_{\omega=0}$. The values of L at different wavelengths are given in Table II. The literature values of L for p-GaP span a range 0.1-3 μm (15, 31). The minority carrier diffusion length, L , is related to the minority carrier lifetime, τ , and diffusion coefficient, D , by $L = (D\tau)^{1/2}$. The defects and the steps existing in the crystal can act as killer traps or recombination centers for minority carriers resulting in a drastic reduction in the minority carrier lifetime (32). Further, ions adventitiously incorporated into the lattice can also reduce the lifetime, τ . For example, Partin *et al.* (33) have shown that diffusion of cobalt into VPE n-GaAs_{0.6}P_{0.4} produced a considerable reduction of the diffusion length. Although L has been shown to be a function of doping density (15), the values of L obtained here ($\sim 0.1 \mu\text{m}$) are at the lower end of the range of values reported for similar doping densities. This suggests that the sample studied has a rather high number of recombination centers. Note that the value of L at 350 nm appears to be practically zero because the condition $\alpha\omega < 1$ is not satisfied. If $\alpha\omega > 1$, all the light will be absorbed within the space-charge layer with the result that there is no photocurrent attributable to diffusion of carriers from the semiconductor bulk.

Surface photovoltage measurement.—The value of L determined by the DPC technique was independently

checked by the surface photovoltage (SPV) technique (9-11, 29, 30). In this technique, the semiconductor electrode at open circuit is illuminated with chopped monochromatic radiation of energy slightly greater than the bandgap (E_g) of the semiconductor. The accumulation of minority carriers at the surface of the semiconductor produces a SPV. The SPV signal is capacitively coupled into the 10 Mohm impedance of a lock-in amplifier for amplification and measurement. The light intensity is adjusted to produce the same value of SPV at different wavelengths of excitation. The monochromatic light intensity required to produce this constant SPV signal is plotted against the reciprocal absorption coefficient for each wavelength. The α values for the wavelength range (500 nm – 440 nm) studied were those reported by Beckmann and Memming (34). The resultant linear plot is extrapolated to zero intensity, and the negative intercept value is the effective diffusion length. The results obtained by this technique are given in Fig. 8 for the same p-GaP sample studied by the DPC technique. The value of L obtained by least squares analysis of the data was $0.2 \pm 0.1 \mu\text{m}$. The uncertainty was the standard deviation of the values of L obtained from four different surface photovoltage values. The value of L agrees, within experimental uncertainty, with the value obtained by the DPC technique.

Effects of surface states on Δj - V behavior.—The claim by Sukegawa *et al.* (6) that this DPC technique is free from the effects of surface states does not appear to be valid. Surface states are known to affect the I-V behavior and may cause Fermi level pinning. These can be identified in different ways, including ac impedance measurements (26) and low frequency capacitance methods (35). We have studied the surface states on n-MoSe₂ in aqueous $\text{K}_4\text{Fe}(\text{CN})_6$ solutions by the ac conductance method (36). A typical plot of G_p (0° component) *vs.* V at 100 Hz is given in Fig. 9. The large hump in the range 0.1-0.45V can be attributed to the presence of surface states. DPC measurements were made with this electrode and plots of j and Δj *vs.* V are shown in Fig. 10. The dip in the Δj *vs.* V plot occurs in the same potential range in which G_p *vs.* V exhibits

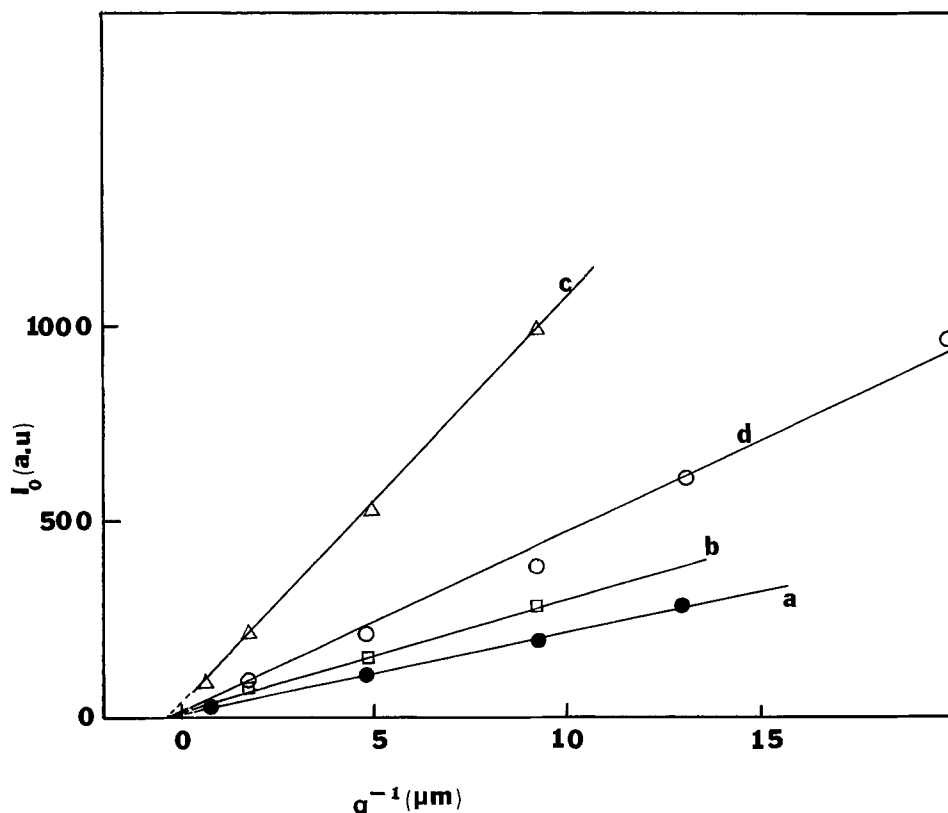
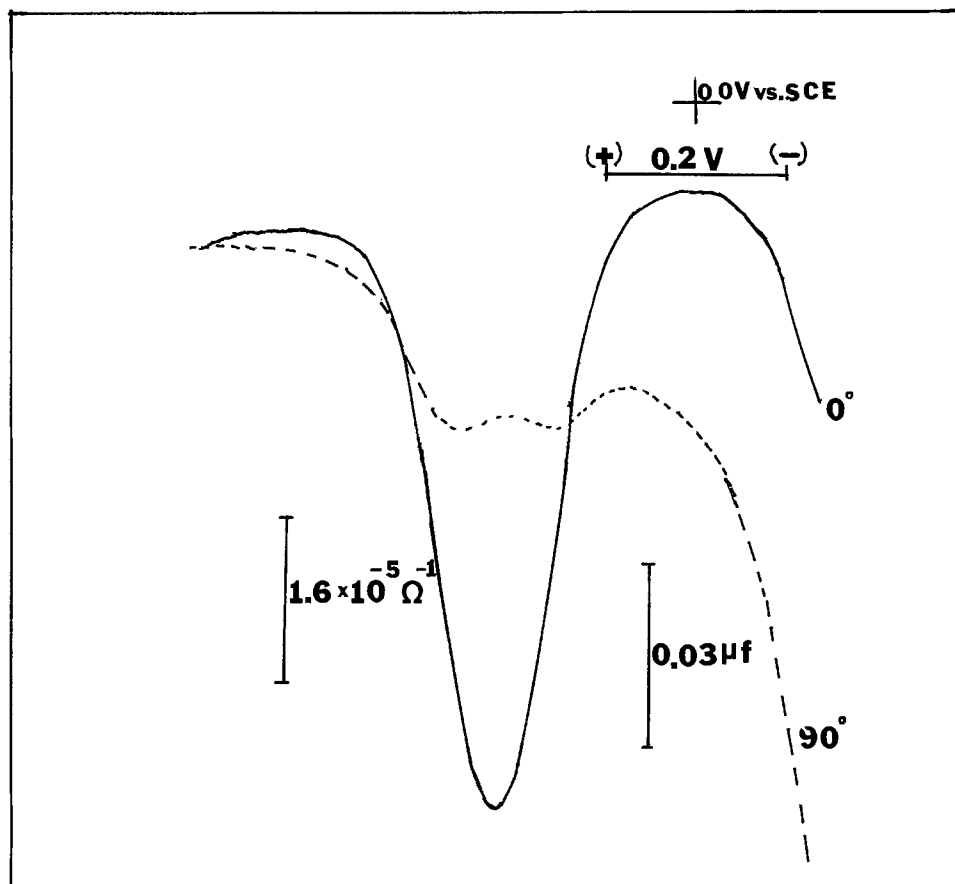


Fig. 8. Relative photon intensity (I_0 in arbitrary units) *vs.* inverse absorption coefficient (α^{-1}) for p-GaP in acetonitrile, 0.01M tetra-n-butylammonium tetrafluoroborate. Chopped at 87 Hz. Surface photovoltage was kept at: (a) 0.075 mV, (b) 0.1 mV, (c) 0.25 mV, and (d) 0.5 mV. The sensitivity of I_0 for SPV = 0.5 mV was $0.5 \times$ all others.

Fig. 9. G_p (in-phase component) vs. V for n-MoSe₂ in aqueous solution containing K₄Fe(CN)₆ as redox couple. $f = 100$ Hz.



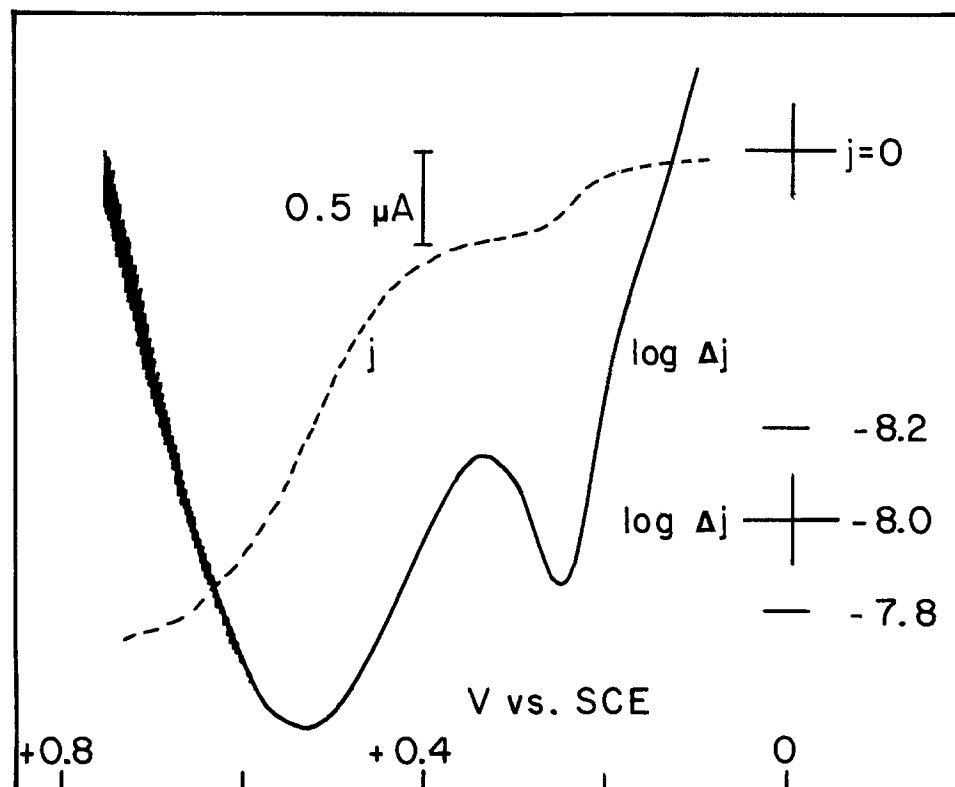
a hump; this dip is also ascribed to surface states. Consider the functional relationship between j and Δj . While j increases steadily, Δj decreases monotonically, and when $j \rightarrow j_{\text{sat}}$, $\Delta j \rightarrow 0$. However, when there is an inflection in the steady increase in j , there is a dip in the Δj vs. V plot. This inflection in the increase in j can be attributed to surface states acting as recombination centers. While the functional relationship between

j and Δj explains qualitatively the dip in Δj vs. V , a quantitative estimate of the density of surface states and the time constant of the surface states still needs to be addressed.

Conclusions

To our knowledge, this is the first time that the DPC method has been employed in liquid junction PEC cells. The absorption coefficient, α , for p-GaP is in the

Fig. 10. j and Δj vs. V for n-MoSe₂ in aqueous solution containing K₄Fe(CN)₆ as redox couple. The wavelength of irradiation is 500 nm. Modulation frequencies: $f_1 = 1.111$ kHz and $f_2 = 1.511$ kHz.



range 10^4 - 10^5 cm^{-1} in the wavelength range studied. This is in good agreement with that reported in the literature. However, L for our p-GaP is much smaller than the literature value for good-quality GaP crystals. This may be due to the existence of steps, defects, or incorporated metal ions. Finally, the results on n-MoSe₂ suggests that this method can be used to locate and identify surface states. The DPC method cannot be used in liquid junction PEC cells to determine α and L when surface states are present, the semiconductor decomposes under optical illumination, or the diffusion length is larger than the width of the crystal. These three factors precluded the measurement of α and L for Si, GaAs, and InP by this method in PEC cells.

Acknowledgments

The support of this work by the Solar Energy Research Institute and the National Science Foundation (CHE8304666) is gratefully acknowledged. B. L. W. wishes to acknowledge the generous support of The Electrochemical Society in the form of the Colin Garfield Fink Summer Fellowship.

Manuscript submitted July 22, 1983; revised manuscript received Dec. 28, 1983.

The University of Texas assisted in meeting the publication costs of this article.

APPENDIX

Introduction of the expression for the two modulated quantities, illumination ($I(t)$, Eq. [12]) and Δw (expressed as applied voltage, Eq. [9b]) into Eq. [13] leads to the total time dependent photocurrent.

$$J(t) = KqI_0(1 + \sin \omega_1 t) [1 - e^{-\alpha w} / (1 + \alpha L)] \\ + KqI_0(1 + \sin \omega_1 t) [e^{-\alpha w} \alpha / (1 + \alpha L)] \\ [(\epsilon_0 / qNw) V_0 \sin \omega_2 t] \quad [\text{A-1}]$$

or collecting terms

$$J(t) = KqI_0(1 + \sin \omega_1 t) [1 - e^{-\alpha w} / (1 + \alpha L)] \\ + KqI_0 [\alpha / (1 + \alpha L)] (e^{-\alpha w} \epsilon_0 V_0 / qNw) \\ \times [\sin \omega_2 t + (\sin \omega_1 t) \sin \omega_2 t] \quad [\text{A-2}]$$

From trigonometric identity

$$\sin A (\sin B) = 1/2 [\cos (A - B) - \cos (A + B)]$$

Equation [A-2] can be rewritten as

$$J(t) = KqI_0(1 + \sin \omega_1 t) [1 - e^{-\alpha w} / (1 + \alpha L)] \\ + KqI_0 [\alpha / (1 + \alpha L)] (e^{-\alpha w} \epsilon_0 V_0 / qNw) \times [\sin \omega_2 t \\ + 1/2 [\cos (\omega_1 - \omega_2) t - \cos (\omega_1 + \omega_2) t]] \quad [\text{A-3}]$$

Of the various signals present in the second term in Eq. [A-3], the major difference frequency component ($|\omega_2 - \omega_1|$) can be separated using a lock-in amplifier. The first term on the right-hand side in Eq. [A-3] is proportional to the photocurrent j , and the amplitude is given by

$$j(\omega_1) = KqI_0 [1 - e^{-\alpha w} / (1 + \alpha L)] \quad [\text{A-4}]$$

The amplitude of the major difference frequency ($|\omega_2 - \omega_1| = \Delta\omega$) component, the second term on the right-hand side in Eq [A-3] is expressed as

$$\Delta j(\Delta\omega) = (KqI_0/2) [\alpha / (1 + \alpha L)] e^{-\alpha w} \epsilon_0 V_0 / qNw \quad [\text{A-5}]$$

Dividing Eq. [A-4] by Eq. [A-5] gives

$$j_{w=0} / [\Delta j / \Delta w]_{w=0} = KqI_0 L [\alpha / (1 + \alpha L)] \\ / [(1/2) KqI_0 \alpha / (1 + \alpha L)] = 2L$$

Therefore

$$L = j_{w=0} / 2 [\Delta j / \Delta w]_{w=0}$$

REFERENCES

- W. W. Gärtner, *Phys Rev.*, **116**, 84 (1959).
- M. A. Butler, *J. Appl. Phys.*, **48**, 1914 (1977).
- J. Reichman, *Appl. Phys. Lett.*, **36**, 574 (1980).
- H. Reiss, *This Journal*, **125**, 937 (1978).
- (a) R. H. Wilson, *J. Appl. Phys.*, **48**, 4292 (1977); (b) D. Laser and A. J. Bard, *This Journal*, **123**, 1833 (1976).
- T. Sukegawa, T. Watanabe, T. Mizuki, and A. Tanaka, *IEEE Trans. Electron Devices*, **ed-27**, 1251 (1980).
- G. Nagasubramanian, B. L. Wheeler, F-R. F. Fan, and A. J. Bard, *This Journal*, **129**, 1742 (1982).
- J. A. Turner and A. J. Nozik, *Appl. Phys. Lett.*, **41**, 101 (1982).
- E. Y. Wang, C. R. Baraona, and H. W. Brandhorst, Jr., *This Journal*, **121**, 973 (1974).
- S. S. Li, *Appl. Phys. Lett.*, **29**, 126 (1976).
- W. E. Phillips, *Solid-State Electron.*, **15**, 1097 (1972).
- C. J. Wu and D. B. Wittry, *J. Appl. Phys.*, **49**, 2827 (1978).
- C. J. Hwang, *J. Appl. Phys.*, **40**, 3731 (1969).
- B. L. Smith and M. Abbott, *Solid-State Electron.*, **15**, 361 (1972).
- P. D. Dapkus, W. H. Hackett, Jr., O. G. Lorimor, G. W. Kammlott, and S. E. Haszko, *Appl. Phys. Lett.*, **22**, 227 (1973).
- M. L. Young and D. R. Wight, *J. Phys. D*, **7**, 1824 (1974).
- E. H. Stupp and A. Milch, *J. Appl. Phys.*, **48**, 282 (1977).
- R. J. Lender, S. Tiwari, J. M. Borrego, and S. K. Ghandhi, *Solid-State Electron.*, **22**, 213 (1979).
- F. Bassani, in "Optical Properties of Solids," E. D. Haidemenakis, Editor, pp. 4-6, Gordon and Breach, Science Publishers, New York (1970).
- F. Bassani and G. Pastori Parravicini, "Electronic States and Optical Transitions in Solids," p. 153, Pergamon Press, New York (1975).
- A. V. Nurmikko, D. J. Epstein, and A. Linz, in "Optical Properties of Highly Transparent Solids," S. S. Mitra and B. Bendow, Editors, pp. 443-449, Plenum Press, New York (1975).
- J. Tauc, in "Proceedings of the International School of Physics 'Enrico Fermi.' Course 34. The Optical Properties of Solids," J. Tauc, Editor, pp. 63-89, Academic Press, New York (1966).
- A. J. Bard and L. R. Faulkner, "Electrochemical Methods. Fundamentals and Applications," p. 586, John Wiley and Sons, New York (1980).
- W. C. Dash and R. Newman, *Phys. Rev.*, **99**, 1151 (1955).
- (a) P. A. Kohl, S. N. Frank, and A. J. Bard, *This Journal*, **124**, 225 (1977); (b) F-R. F. Fan and A. J. Bard, *ibid.*, **128**, 945 (1981).
- G. Nagasubramanian, B. L. Wheeler, G. A. Hope, and A. J. Bard, *ibid.*, **130**, 385 (1983).
- "Motorola Linear Integrated Circuits, Series C," pp. 6-60-6-73, Motorola Inc. (1979).
- D. Lancaster, "Active Filter Cookbook," pp. 156-162, Howard W. Sams and Co., Inc., Indianapolis, IN (1975).
- E. Kamieniecki, *J. Vac. Sci. Technol.*, **20**, 811 (1982).
- "Annual Book of ASTM Standards," pp. F391-73T, ASTM, Philadelphia, PA (1975).
- (a) M. L. Young and D. R. Wight, *J. Phys. D*, **7**, 1824 (1974); (b) B. L. Smith and M. Abbott, *Solid-State Electron.*, **15**, 361 (1972); (c) S. A. Abagyan and V. K. Subashiev, *Sov. Phys. Solid State*, **6**, 2529 (1965); (d) V. K. Subashiev and G. A. Chalikian, *Phys. Status Solidi*, **13**, K91 (1966).
- H. J. Lewerenz, A. Heller, and F. J. Disalvo, *J. Am. Chem. Soc.*, **102**, 1877 (1980).
- D. L. Partin, A. G. Milnes, and L. F. Vassamillet, *This Journal*, **126**, 1584 (1979).
- K. H. Beckmann and R. Memming, *ibid.*, **116**, 368 (1969).
- K. Kobayashi, Y. Aikawa, and M. Sukigara, *Chem. Lett.*, 679 (1981).
- G. Nagasubramanian, B. L. Wheeler, and A. J. Bard, *This Journal*, **130**, 1680 (1983).

Effect of Contact Between a Current Collector and a Polyacetylene Electrode on Electrochemical Behavior in Polyacetylene/Lithium Batteries

Show-An Chen and Yeong-Cherng Chiou

Chemical Engineering Department, National Tsing Hua University, Hsinchu, Taiwan 300, China

ABSTRACT

Organic batteries with a polyacetylene film (PA) as the anode, a lithium strip as the cathode, and lithium perchlorate dissolved in propylene carbonate as the electrolyte are constructed. Charging and discharging characteristics of three batteries with different types of PA electrode are investigated. Type a PA electrode involves mechanical pressed contact of nickel gauze with the upper portion of the PA electrode; charging and discharging of the battery are difficult due to the semiconducting characteristic of the PA. Type b involves a PA film which has one side coated with a sputtered palladium (Pd) film; good contact of the Pd current collector with the PA electrode makes charging and discharging easily manageable. Type c involves an iodine-doped PA film; the battery is easily charged and discharged, but cleaning the surface of the lithium electrode is necessary after a few cycles.

Organic batteries, in which one or two electrodes are composed of organic polymer, have drawn great attention because of its lightweight and high energy density since MacDiarmid's team discovered a battery with polyacetylene (PA) electrodes (1-4). Immediately after this discovery, other conducting polymers, such as poly(p-phenylene) (PPP), were also found to be potential material for the electrodes (5-7). In these two polymers, PA was investigated more for its use as an electrode than PPP in the open literature (1-4) for its higher durability and ease in being prepared. In the battery, a salt, lithium perchlorate, dissolved in an organic solvent, propylene carbonate, was usually used as an electrolyte. During charging, the PA, connected to a positive terminal of dc power source, was partly oxidized to polycarbonium ions $[(CH)^{y+}]_x$ with a corresponding number of counter A^- ions adsorbed and changed to $[(CH)^{y+}A_y^-]_x$. The PA connected to the negative terminal was partly reduced to polycarbanion $[(CH)^{y-}]_x$ with a corresponding number of counter M^+ ion adsorbed and changed to $[(CH)^{y-}M_y^+]_x$. During discharge, the former electrode was reduced and the latter oxidized, with both tending to recover their original states although it was claimed that PA could be used for both electrodes. However, the battery was not investigated in detail for its charging and discharging characteristics. Among the reports on organic batteries involving PA, lithium is usually used as a counterelectrode (2-4).

Since the pristine PA is a semiconductor, good contact between the current collector and PA is essential for efficient charging and discharging. Two types of current collectors were reported in the literature on the PA electrode: (i) a metal wire such as platinum (Pt) which was attached to the PA by mechanical-pressed contact (3, 4); and (ii) a piece of 52 mesh platinum gauze, similar in area to the PA film, was connected to the lead, a platinum wire, by spot welding (8). Differences between these two types in charging and discharging were not reported.

In this work, we investigate the charging and discharging characteristic of the first type current collector mentioned above and two other types: (i) a thin film of palladium (Pd) which was formed on one side of a PA electrode by using sputtering technique; and (ii) iodine-doped PA (this electrode itself also served as a current collector).

Experimental

Materials.—The PA film was synthesized using Shirakawa's method (9). Identification of the film, produced

through the use of IR, density measurement, DSC, and porous surface area measurement, was made in the previous paper (10). The lithium strip was obtained by cutting a lithium rod of synthetic grade (Merck). Lithium perchlorate used as an electrolyte was of analytical grade from Fluka. Propylene carbonate of synthetic grade and toluene and tetrahydrofuran (THF) of LC grade from Merck were purified by adding molecular sieves and then storing for three days to remove a minor amount of moisture. The iodine was reagent grade from Wako.

The PA electrode, which had one side coated with a Pd film, was obtained by sputtering Pd on one side of the PA film in argon gas at a pressure between 10^{-7} and 10^{-2} torr for 8 min at room temperature, using a sputter SPF-210B from Aneva Company. The amount of Pd deposition was about 1.36 mg/cm^2 . The resulting Pd-coated PA film was tested to see whether the Pd was uniformly and continuously distributed on the PA surface by measuring the resistivity on the Pd-coated side. The resistivity was about $10\text{-}40\Omega$ everywhere as measured by making contact between two probes (0.5 cm apart) and the Pd surface. This indicates that the Pd coating was a continuous film.

The iodine-doped PA electrode was obtained by immersing the pristine PA film in iodine/toluene (163 mg/20g) solution for 30 min and then washed successively with toluene for at least three times until no appreciable color appeared in the toluene. The resulting PA film was stored in toluene for one day. The toluene appeared to be clear during the storage. The film was then dried in a dynamic vacuum for at least 30 min. This doped PA film $[(CH)I_{0.028}]_x$ had a conductivity of $0.093 (\Omega\text{-cm})^{-1}$ as measured by the two-probe method.

Construction of organic batteries.—The dimensions of the PA films used as electrodes were about 4 cm in length, 1 cm in width, and 0.1-0.4 mm thick, unless specified otherwise. For all cases, the upper 0.5 cm portion was clipped with a folded nickel gauze, which had the same width as the film, by a pressure of about 7000 lb/cm^2 . After pressing, a conductivity measurement was made by connecting one probe to the nickel gauze and the other probe to the other end of the PA film, in order to assure that the film was not damaged by the pressing. The PA electrode and the counterelectrode (a lithium strip of about 3.5 cm in length, 1 cm in width, and 0.3 cm thick), separated by a glass filter paper, were then installed in a vacuum-tight glass vessel. These two electrodes were about 1 cm apart. The lower part of the vessel was for storing the electrolyte solution (0.3M lithium perchlorate in

Key words: conduction, diffusion, polymer.

propylene carbonate) of about 20 ml. The upper part was equipped with a Teflon valve and two tungsten wires, with their middle parts sealed in the glass wall. The outer ends of the wires were connected to the power source, while the two inner ends were each welded with a small steel clamp for connecting to the electrode. In the cell, about 3 cm of the PA electrode was immersed in the electrolyte solution.

After the whole assembly was set up, the electrolyte solution was injected. The apparatus was connected to a vacuum line, pumped for 5 min, and then introduced with argon gas. During dynamic vacuum pumping, small bubbles arising from the film were observed, indicating that the gas inside the porous area of the PA was pumped out. Since propylene carbonate has a high boiling point and a very low vapor pressure at room temperature, this pumping did not affect the concentration of the electrolyte solution. This cycle of pumping and adding argon gas was repeated three times. The cell was then ready for the charging experiment.

During charging, a constant voltage of 4-6V was applied for a certain period of time. The current passing through was recorded.

During discharge, the two electrodes were brought into contact with or without a standard resistor. The current discharged and voltage across the electrodes were recorded using a digital multimeter and recorder.

Results and Discussion

Results of the charging and discharging of the three types of batteries having various current collectors for the PA electrodes are given below. In each case, the counterelectrode was a lithium strip, and the electrolyte solution used was the same.

Type a.—PA film having the upper portion clipped with a folded nickel gauze.—Charging this battery was accomplished by first applying 1V to the whole PA electrode (45 mg) immersed in the electrolyte solution, supplying a current of 2.5 μ A to begin and rising to 4 μ A. This was to increase the conductivity of the portion of the PA in contact with the nickel gauze and also that above the liquid level. After 2 min, the PA electrode was raised so that its top edge was 1 cm above the liquid level. The applied voltage was then increased to 4V, and the current was increased to 10 μ A and after 2 min, to 13 μ A. The applied voltage was further increased to 5V, which gave a current of 27 μ A. Keeping the applied voltage at 5V for 26h, it finally gave a steady current of about 285 μ A. The resulting open-circuit voltage (OCV) was 3.85V, and the initial short-circuit current (SCC) was 3.21 mA. As described above, the rate of charging was slow.

In order to understand the distribution of perchlorate ions in the PA electrode after charging and discharging, the PA electrode, after charging, was washed with THF, dried in a dynamic vacuum for three cycles, and then subjected to resistivity measurement in an argon atmosphere using a pair of probes which were bound together and had a fixed distance of 0.12 cm. Note that the measured values were dependent on the pressure applied to the two probes. The data shown in Fig. 1(a) are the minimum resistivity at each location. The resistivity of the portion immersed in the electrolyte solution during charging had a resistivity lower than that above the solution.

After the resistivity measurement, the PA electrode was again placed with the battery which gave an OCV of 3.85V and an initial SCC of 102 μ A. After a short-circuit current for 120 min, the SCC was reduced to 15 μ A, and the total charges released were $Q_{out} = 0.16C$. The PA electrode was then washed with THF and dried in a dynamic vacuum for three cycles. Its resistivity was then measured in various locations. The differences in resistivity between the portion in contact with nickel gauze and that immersed in solution

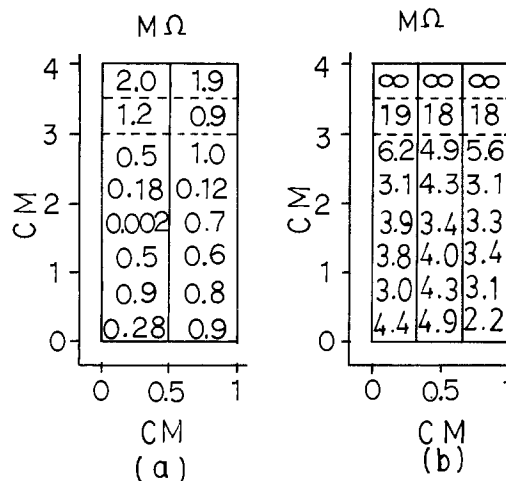


Fig. 1. (a) Resistivity of type a polyacetylene electrode after charging by applying a constant voltage of 5V for 26h; (b) resistivity of type a polyacetylene electrode after discharging without an external resistor for 120 min.

are shown in Fig. 1(b). The former had extremely high resistance while the latter had considerably lower resistance. The residual anions adsorbed in the PA fibrils diffused to the solution during discharging at an extremely slow rate, since electrons were difficult to transfer to the nickel gauze due to the decreased conductivity of the PA. A similar experiment was performed by MacDiarmid (2, 3), in which platinum wire 0.1 cm diam instead of nickel gauze was wound on the same portion of the PA electrode. The same difficulty in charging and discharging was found. Thus, the current collector in contact with the upper part of the PA film is not suitable for the organic battery.

Type b.—PA film having one side coated with palladium.—PA, 2.9 cm long, 1 cm wide, and 0.12 mm thick (14 mg), and coated with Pd on one side by the sputtering method, was used as an anode. Charging of the battery was performed by applying a constant voltage of 4.3V for 35 min; the current *vs.* time is shown in Fig. 2 where Q_{in} was 2.2C. This battery had an OCV of 3.87V and initial SCC of 17.4 mA. In comparison to type a, the rate of charging was much faster. SCC *vs.* time is also shown in Fig. 2 where $Q_{out} = 1.575C$ and the coulombic efficiency $\eta (= Q_{out}/Q_{in})$ was 0.72. It was then recharged under the same constant voltage of 4.3V for 102 min, giving an OCV of 3.8V. The SCC *vs.* time curve is shown in Fig. 3 where $Q_{in} = 6.3C$. It was then discharged by connecting it to an external resistor of 33.6 k Ω and stopped at the voltage, 1.2V. The curves of current and voltage *vs.* time are shown in Fig. 3 where $Q_{out} = 5.33C$ and η was 0.84. The actual coulombic efficiency would have been higher than 0.84 if discharging was stopped at zero voltage. It seems that lower rate of withdrawn current would lead to a higher coulombic efficiency. This, together with the electrochemical behavior of the PA electrode are demonstrated below.

For the first cycle of charging in Fig. 2, the current was high at first and then decreased to a nearly constant level. This indicates that PA fibrils [the PA used had fibrillar morphology (11)] having direct contact with the Pd would first lose electrons easily, allowing a high rate of perchlorate ion diffusion to the surface and interior of the PA fibrils accompanying a charge transfer. This made the initial current high. After these fibrils were oxidized by the perchlorate ions (the first in 5 min), they then became more conductive, causing the other fibrils next to them to lose electrons easily to the Pd current collector. These pristine fibrils started being oxidized by perchlorate ions. This electron transfer process was slower than that for the fibrils in direct contact with the Pd, making the cur-

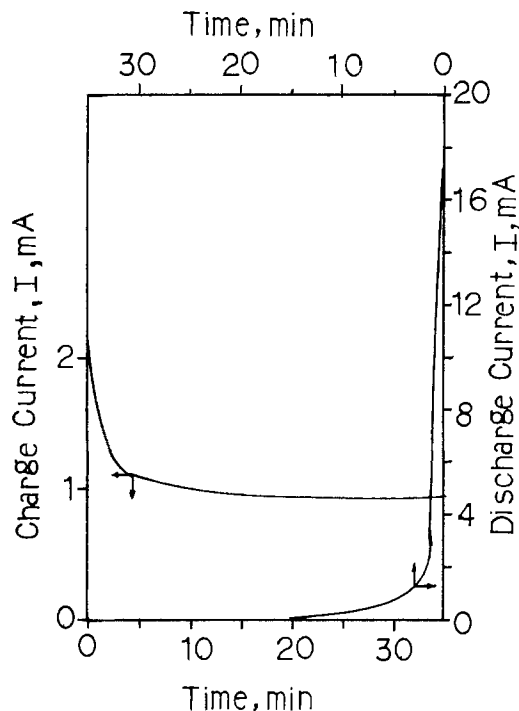


Fig. 2. Current variations with time of the battery with type b polyacetylene electrode during the first cycle charging by applying a constant voltage of 4.3V for 35 min and first cycle discharging without an external resistor.

rent drop to a lower level. This process continued until all the fibrils were oxidized sufficiently by perchlorate ions at the applied voltage. During discharge without external resistance, the rate of current withdrawn was so fast that most charges were withdrawn within 5 min. This rapid diffusion of perchlorate ions from the surface and interior of the fibrils in direct contact with the Pd coating would cause these fibrils to become less conductive. This caused the perchlorate ions bonded on the surface of the fibrils, located far from the Pd coating and parts of those located inside the interior of the fibrils, difficult to diffuse out. After 15 min discharging, the current dropped to zero, but perchlorate ions that originally oxidized the PA were still retained in the fibrils.

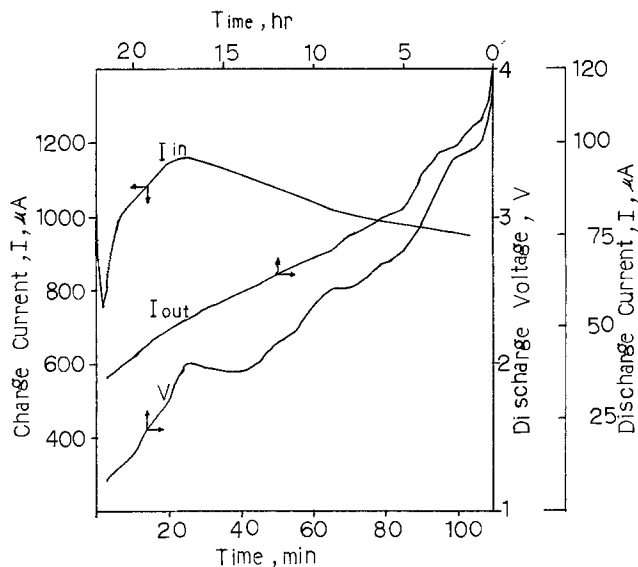


Fig. 3. Current and voltage variations with time of the battery with type b polyacetylene electrode during the second cycle charging by applying a constant voltage of 4.3V for 102 min and second cycle discharging with an external resistor of 33.6 k Ω .

For the second cycle of charging in Fig. 3, the current was high at the first instant, dropped quickly within 2 min, increased to its maximum at 25 min, and then dropped slowly. This can be attributed to the fact that the PA fibrils in direct contact with the Pd were reduced to a nearly neutral state from the discharging of the first cycle and electrons would be lost easily at first, making the initial current high. The rest of the PA fibrils (without direct contact with Pd) would still retain a certain amount of perchlorate ions after discharging in the first cycle and would provide reasonable conductivity for the transfer of electrons to the Pd coating. They were all able to release electrons and to be oxidized by the diffused-in perchlorate ions. The more they were oxidized by the perchlorate ions the more conductive they were, leading to an increase in current until saturation was reached at the fibril surface where the current was at a maximum. After this stage, the perchlorate ions started to diffuse into the interior of the fibrils. Since the diffusion is more difficult inside the solid, the rate of diffusion was slower than that of the surface oxidation stage. Thus, the current started to fall. This charging characteristic of the battery after the first cycle remained the same for another five cycles. The discharging curve (for the case with an external resistor of 33.6 k Ω) in Fig. 3 shows that the lower rate of current withdraw for the second cycle provided higher coulombic efficiency than the higher rate of current withdraw for the first cycle. This is due to the fact that slow release of current would allow more perchlorate ions located inside the fibrils and on the surface of the fibrils far from the Pd coating to diffuse out.

Note that this battery with Pd-coated PA as an anode has a coulombic efficiency similar to that proposed by Kaneto *et al.* (8) in which Pt gauze, having the same area as a PA electrode, was used as a current collector. However, the present method provides a lighter current collector.

For practical uses, good reversibility and stability of the cell are of importance. The PA/Li cells were found to be reversible if the extent of oxidation of PA was low, about 2.2%, under an applied voltage below about 3.75V (8). Above this voltage, degradation of PA due to reaction with the propylene carbonate and lithium perchlorate might occur. In our case, the applied voltage (4.3V) was higher and the degradation of PA could occur. But within 20 cycles of charge-discharge, no appreciable degradation was observed. As to cell stability, contamination of the electrolyte and electrodes by oxygen and moisture is highly probable during installation of the cell or due to insufficient purification and should be reduced to a minimum. Any trace of air can cause the cell voltage to fall sharply on standing. The stability can be increased after several charge-discharge cycles, possibly because the $(\text{CH}^{\nu+})_x$ species acted as a scavenger for impurities initially, as observed by Kaneto *et al.* (8). The same result was also obtained in our case.

Type c.—Iodine-doped PA film.—For the iodine-doped PA electrode, 18.4 mg of pristine PA was doped with 5.03 mg of iodine to give $[(\text{CH})\text{I}_{0.028x}]$. A battery with it as an anode was charged by applying a constant voltage of 6V for 0.5h to give an OCV of 4.2V and a SCC of 22.4 mA. The current input increased slightly with time with $Q_{1,\text{in}} = 14\text{C}$, as shown in Fig. 4. The discharging curve (without an external resistor) in Fig. 4 gave $Q_{1,\text{out}} = 5.28\text{C}$ and $\eta = 0.38$. In the second cycle, charging for 0.5h under 6V gave an OCV of 4.08V, a SCC of 14 mA, and $Q_{2,\text{in}} = 8.64\text{C}$, while discharging gave $Q_{2,\text{out}} = 3.6\text{C}$ and $\eta = 0.42$. The increase in η in the second cycle is due to the part of the perchlorate ions in and on the fibrils during the first cycle that was not completely released. In the charging of the second cycle, small streams with brown color were bleeding from the PA electrode during the first 5-10 min, within which the rate of increasing current

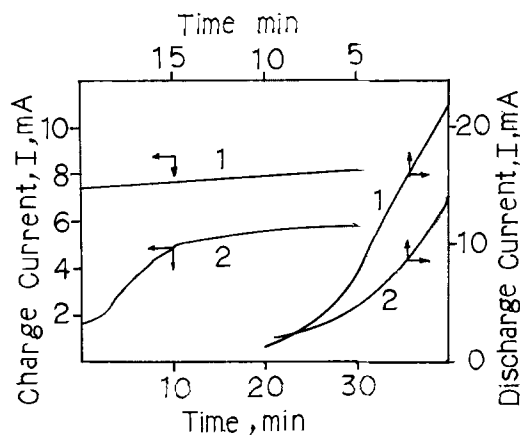


Fig. 4. Current variations with time of the battery with type c polyacetylene electrode during the first and second cycle chargings by applying a constant voltage of 6V for 30 min and, during this two cycle discharging, without external resistor.

was high. This indicates that molecular iodine was released to the solution.

Note that during charging, current variations with time for the first and second cycles are different. For the first cycle, it increased linearly with time. This indicates that the PA electrode was quite conductive everywhere. As the degree of oxidation by perchlorate ions increased, it became more conductive. However, even at the end of charging, the PA was not oxidized to an equilibrium state at the applied voltage. For the second cycle, the current was low first then increased rapidly in 8 min to a higher level. This can be attributed to the fact that the applied voltage not only oxidized the PA, but also the ions, I^- , I_3^- , and I_5^- . After discharging, most perchlorate ions were driven off to the solution, making the PA electrode less conductive. However, as more perchlorate ions doped on the PA electrode, it became more conductive, leading to an increase in the charging current. This charging characteristic remained the same after the first cycle for another four cycles. After the fifth cycle, the surface of the lithium electrode became darker, due to the reaction with iodine from the solution. The charging became more difficult, and the SCC was lower. However, if the surface of the lithium electrode was scratched to remove the reaction product, lithium iodide, the battery was recovered to its original capacity for energy storage.

Conclusion

1. Pristine polyacetylene, without good contact and a large contacting area with a current collector, is not

suitable for use as an electrode due to its semiconducting characteristic when dopant ions are lost.

2. Good contact of a current collector with a polyacetylene electrode is essential for efficient charging and discharging. Thin coating of an inert metal on one side of the polyacetylene film obtained by sputtering method is a promising current collector. This allows the polyacetylene film to become a workable electrode.

3. Directly increasing the conductivity of a polyacetylene film by adding dopant is also a possible way to promote the polyacetylene film for use as an electrode, provided that the dopant concentration in the electrolyte solution is not harmful for the lithium electrode.

Acknowledgment

The authors wish to thank Dr. Choh H. Li for introducing them into the interesting field of organic batteries and for valuable suggestions and discussion. We would also like to thank the National Science Council for financial aid.

Manuscript submitted July 14, 1983; revised manuscript received Dec. 20, 1983.

REFERENCES

1. *Chem. Engr. News*, Jan. 26, p. 39 (1981).
2. D. MacInnes, Jr., M. A. Drug, P. J. Nigrey, D. P. Nairns, A. G. MacDiarmid, and A. J. Heeger, *J. Chem. Soc., Chem. Commun.*, 317 (1981).
3. P. J. Nigrey, D. MacInnes, Jr., D. P. Nairns, A. G. MacDiarmid, and A. J. Heeger, in "Conductive Polymers," R. B. Seymour, Editor, p. 227, Plenum Press, New York (1981).
4. P. J. Nigrey, D. MacInnes, Jr., D. P. Nairns, A. G. MacDiarmid, and A. J. Heeger, *This Journal*, **128**, 1651 (1981).
5. *Chem. Engr. News*, Oct. 12, p. 34 (1981).
6. R. L. Elsenbaumer, L. W. Shacklette, J. M. Sowa, R. R. Chance, D. M. Ivory, G. G. Miller, and R. H. Baughman, *Polymer Preprints*, Vol. 1, p. 132, American Chemical Society Meeting (1982).
7. L. W. Shacklette, R. L. Elsenbaumer, R. R. Chance, J. M. Sowa, D. M. Ivory, G. G. Miller, and R. H. Baughman, *J. Chem. Soc., Chem. Commun.*, 361 (1982).
8. K. Kaneto, M. Maxfield, D. P. Nairns, A. G. MacDiarmid, and A. J. Heeger, *J. Chem. Soc., Faraday Trans. 1*, **78**, 3417 (1982).
9. H. Shirakawa and S. Ikeda, *Polym. J. (Jpn.)*, **2**, 231 (1971).
10. S.-A. Chen and L.-S. Li, *Makromol. Chem.*, **4**, 503 (1983).
11. A. J. Epstein, H. Rommelmann, R. Fernquist, H. W. Gibson, M. A. Druy, and T. Woerner, *Polymer*, **23**, 1211 (1982).

Piezo-Electrocapillary Effect: A New Effect Observed in Porous Anodic Oxide Films

J. J. Bernstein*¹ and R. M. White*

Department of Electrical Engineering and Computer Sciences, University of California, Berkeley, California 94720

ABSTRACT

A new effect, the Piezo-Electrocapillary (PEC) effect, has been observed in wet, porous anodic Al_2O_3 films subject to ultrasonic bulk compressional waves. When wetted with a high resistivity polar liquid, these films behave as if they were piezoelectric in that they act as transducers for ultrasonic waves. This is due to the motion (in response to an acoustic wave) of charged liquid located within a Debye length of the inner pore walls which creates an electrical current and externally measurable alternating voltage. As derived in this paper and confirmed by experiments, the voltage output depends on the resistivity, compressibility, and viscosity of the liquid. Transducer sensitivity equal to that of sputtered ZnO $10\ \mu\text{m}$ thick has so far been obtained.

The PEC effect is explained here in detail for the first time, although it has been reported previously (1). Because of this effect, wet porous anodic-oxide films act much like piezoelectric films in response to bulk compressional ultrasonic waves. The porous anodic-oxide films studied here are known to have an array of very fine pores aligned with their axes parallel to the film normal (2). Anodic Al_2O_3 films are also known to have residual electric space charge frozen in the oxide, resulting from the ionic currents which form the oxide during anodization (3-7). This results in a considerable effective surface charge on the Al_2O_3 surface. The liquid in the pores contains a compensating charge equal and opposite to the charge in the porous oxide; the liquid moves relative to the porous oxide in response to an acoustic wave (Fig. 1), creating an alternating electrical current and voltage.

The PEC effect is an extension to ultrasonic frequencies of the electroosmotic effect (8), which describes the steady-state coupling between mass flow and electrical current in a charged capillary. Although we have assumed an array of circular cross section pores in our analysis, any two-phase medium with a charged interface oriented parallel to the direction of acoustic wave propagation should exhibit the PEC effect. In the anodic films studied here, the large specific interfacial area, the large difference in the acoustic phase velocities of the oxide and the liquid, and the large interfacial charge density make the effect very strong, resulting in transducer sensitivity comparable to piezoelectric films such as sputtered ZnO that is $10\ \mu\text{m}$ thick.

In our theoretical treatment of the PEC effect, we first derive the fluid flow in a narrow capillary with a compressional wave propagating along the capillary axis. We then combine this flow with the charge distribution in the capillary to derive the voltage (potential difference from one end of the capillary to the other) across the porous film. In the Experimental Results section, we demonstrate the agreement of this theory with the measured dependence of the PEC voltage on liquid parameters such as resistivity, compressibility, and viscosity.

Experimental Procedures

Porous anodic films were produced by anodizing aluminum at a constant current density of $160\ \text{A}/\text{m}^2$ for 0.5 and 2.5h at 20°C in 10 weight percent (w/o) H_2SO_4 . Before anodization, the aluminum sheet substrates (alloy 5052-H32) were mechanically polished to a $0.25\ \mu\text{m}$ surface finish with diamond polishing compound. This alloy contains 2.5% Mg, 0.1% Cu, Mn, and Zn, 0.25% Cr, and a sum of Si + Fe = 0.45%. Before testing, and between tests with different liquids, the porous anodic films were cleaned ultrasonically in methanol and dried.

Film thickness was measured by abrading a cylindrical groove in the film (Philtec 2015 sectioner) and then profiling the groove with a Tencor Alpha-Step. We consider this to be more reliable than ellipsometry on porous films. The 0.5h anodized film was $8\ \mu\text{m}$ thick, and the 2.5h anodized film was $32\ \mu\text{m}$ thick.

The arrangement used to measure the PEC voltage is shown in Fig. 2. A piezoelectric transducer (Panametrics V311,10) was electrically pulsed by a Panametrics 5052PR pulser to provide a short duration acoustic signal centered at 10 MHz. The maximum particle displacement of the acoustic pulse was 1.6 nm. The acoustic waves were delayed by an aluminum buffer rod (to prevent electromagnetic interference between the pulser's electric signal and the PEC signal), passed through the liquid-filled gap, and into the porous film (Fig. 2). The PEC voltage signal was taken between the body of the anodized aluminum sample and the buffer rod. Some experiments were also performed with the sample inverted, in which case a voltage sensing electrode was placed on top of the anodic film. The PEC voltage was the same whether the acoustic waves were incident from the front of the sample (the anodic film side) or the back (the aluminum substrate).

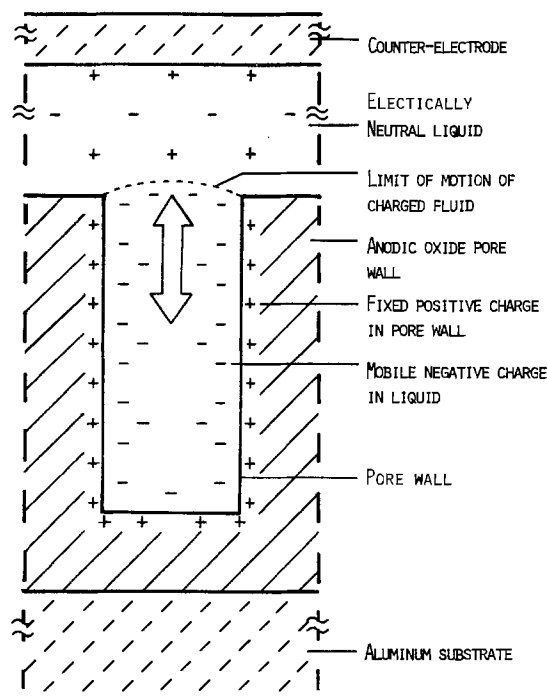


Fig. 1. Motion of charged fluid in a pore, shown here in cross section, produces a current in response to an oscillating acoustic wave (elements not drawn to scale). The boundary between charged and neutral fluid regions is shown as a curved, dotted line at the pore mouth, although the boundary is actually about 1 Debye length thick.

*Electrochemical Society Active Member.

¹Present address: Solavolt International, P.O. Box 2934, Phoenix, Arizona 85062.

Key words: ultrasonic transducer, piezoelectric, space charge.

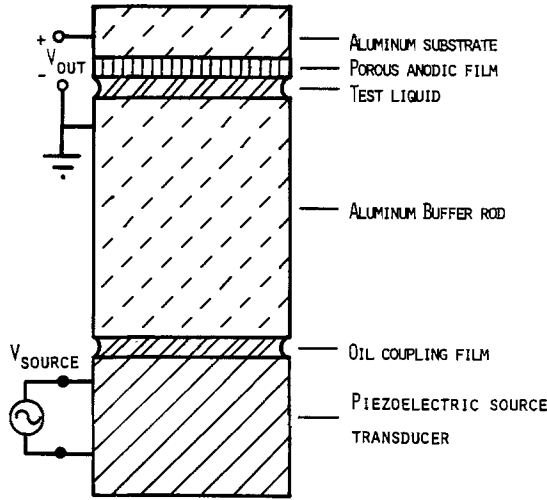


Fig. 2. Experimental setup used to measure PEC voltage. The output voltage is taken from the substrate to the buffer rod (elements not drawn to scale).

Acoustic Wave Motion in a Capillary

Biot's theory (9) of acoustic waves in two-phase media shows that there exist two bulk compressional modes in a fluid-filled porous medium: a fast mode, in which the fluid and solid move in phase, and a slow mode, in which they move out of phase. In addition, recent experimental work (10) has shown that efficient mode conversion from an incident compressional wave to the slow-wave mode can occur at the boundary of the porous layer.

The velocity distribution for a compressional acoustic wave at frequency ω propagating along a fluid-filled pipe in the z direction is (11)

$$v_z(r,z) = v_z(z) \left(\frac{2}{kR} \right)^2 \left(\frac{J_0(kr)}{J_0(kR)} - 1 \right) \quad [1]$$

where J_0 is the Bessel function of the first kind of order 0, r is the radial distance from the center of the pipe, R is the pipe inner diam, and k is a complex constant given by

$$k = (1 - j) \sqrt{\frac{\omega}{2\nu}} \quad [2]$$

where ω is the angular frequency of the acoustic excitation and ν is the kinematic shear viscosity of the fluid in the pipe (Fig. 3). For $kR \ll 1$ (the case of interest for a capillary), Eq [1] reduces to

$$v_z(r,z) = v_z(z) \left(1 - \frac{r^2}{R^2} \right) \quad [3]$$

which is the familiar case of Poiseuille flow. Note that $v_z(r,z)$ has been separated into a product of $v_z(r) \times v_z(z)$ so that each one can be dealt with separately.

In the absence of an acoustic wave, the net charge of liquid plus oxide in a thin layer between z and $z + dz$ is zero. We are interested in the flow of liquid relative to the pore wall, since only relative flow can produce a net charge in a pore cross section and hence a local change in the net charge. One boundary condition on $v_z(z)$ is

$$v_z(r,L) = 0 \quad [4]$$

at the closed end of the capillary. We assume that the acoustic wave creates a known oscillating z -directed particle velocity v_0 at the pore mouth ($z = 0$) and this is the other boundary condition

$$v_z(0,0) = v_0 \quad [5]$$

The equation of motion of a compressible viscous fluid in a capillary of radius R is (12)

$$\frac{\partial^2 v_z(z)}{\partial z^2} = -\alpha \rho_m \omega^2 v_z(z) + \frac{8j\omega\alpha\mu}{R^2} v_z(z) \quad [6]$$

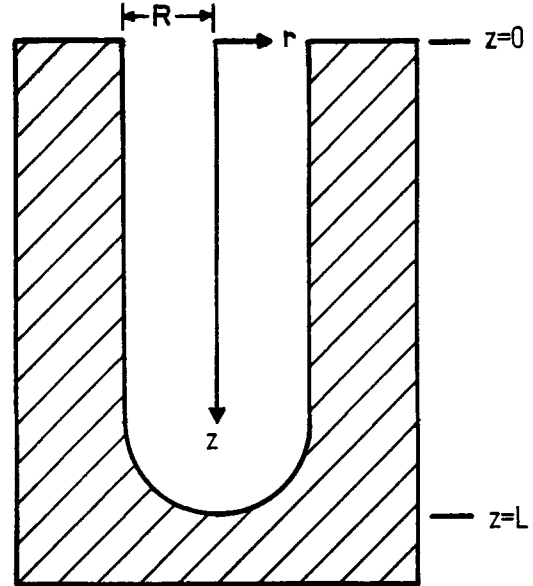


Fig. 3. Diagram of pore, showing coordinates used in the derivation of the PEC effect.

where $v_z(z)$ is the particle velocity in the z direction at $r = 0$, α is the isothermal compressibility of the fluid ($\alpha = -1/V \partial V / \partial P$), ρ_m is the mass density of the fluid, V is volume, P is pressure, and μ is the viscosity of the fluid. The first term on the right represents the inertial reaction of the fluid, and the second term represents the viscous damping. For the films we studied and for frequencies below the GHz range, the inertial term is negligible, yielding

$$\frac{\partial^2 v_z(z)}{\partial z^2} = \frac{8j\omega\alpha\mu v_z(z)}{R^2} = 2j\beta^2 v_z(z) \quad [7]$$

where $\beta = [4\omega\alpha\mu/R^2]^{1/2}$. The solution to this equation is simply

$$v_z(z) = A_1 e^{\beta z(1+j)} + A_2 e^{-\beta z(1+j)} = v_0 e^{-\beta z} \cos(\beta z) \quad [8]$$

The velocity wave oscillates and decays with a characteristic length of $1/\beta$, which implies that increasing the film thickness beyond $2/\beta$ should have little effect on the voltage output. Unfortunately, we cannot compare film thickness to $1/\beta$ because R and hence β are unknown for our experimental films.

The strain in the fluid in the z direction is the derivative with respect to z of the z -directed particle displacement

$$S_z(z) = \frac{\partial u_z}{\partial z} = \frac{1}{j\omega} \frac{\partial v_z(z)}{\partial z} = \frac{-\sqrt{2}\beta v_0}{j\omega} e^{-\beta z} \cos\left(\beta z - \frac{\pi}{4}\right) \quad [9]$$

The strain as a function of z and r is

$$S_z(r,z) = S_z(z) \left(1 - \frac{r^2}{R^2} \right) = \frac{-\sqrt{2}v_0}{j\omega} e^{-\beta z} \cos\left(\beta z - \frac{\pi}{4}\right) \left(1 - \frac{r^2}{R^2} \right) \quad [10]$$

This strain will be used to compute the net charge density when an acoustic wave perturbs the charge in a fluid-filled capillary.

Perturbation of Charge in a Capillary by an Acoustic Wave

In this section we calculate how the acoustic wave perturbs the fluid charge and gives rise to the PEC effect.

In cylindrical coordinates, the solution of Poisson's equation for the charge density ρ_{e0} in a capillary unperturbed by any acoustic wave is (13)

$$\rho_{e0}(x) = \frac{\sigma I_0(x)}{\lambda I_1(x_0)} \quad [11]$$

where λ is the Debye length in the fluid, σ is the surface

charge density on the capillary wall, $x = r/\lambda$, $x_0 = R/\lambda$, and $I_0(I_1)$ is the modified Bessel function of the first kind, of order zero (one). For $\lambda \gg R$ ($x_0 \ll 1$), the radial charge distribution is approximately constant and equal to $\rho_{e0} = 2\sigma/R$. For $\lambda \ll R$ ($x_0 \gg 1$), $I_0(x)$ is approximately exponential, and the charge density becomes negligible at distances greater than several Debye lengths from the pore wall

$$\rho_{e0} \approx \frac{\sigma}{\lambda} e^{x-x_0} \left(\frac{x_0}{x}\right)^{1/2}, \quad x_0 \gg 1 \quad [12]$$

The net charge in a pore cross section between z and $z + dz$ is zero in the absence of an acoustic wave, since the charge on the pore wall and the charge in the fluid cancel each other. A positive strain S (a dilation) in the negatively charged fluid reduces the local charge density and creates a net positive charge $\rho_e(z)$ which is equal to the integral of the strain S times the unperturbed charge distribution ρ_{e0} over the cross section. The net charge is

$$\begin{aligned} \rho_e(z) &= -\int_0^R \rho_{e0} S_z(r, z) 2\pi r dr \\ &= -\frac{\sigma S_z(z)}{\lambda I_1(x_0)} \int_0^R I_0(x) \left(1 - \frac{r^2}{R^2}\right) 2\pi r dr \\ &= S_z(z) (2\pi R \sigma) \gamma(x_0) \end{aligned} \quad [13]$$

where we have defined a function $\gamma(x_0)$ to take into account the overlap of the charge distribution $I_0(r/\lambda)$ and the r dependence of the z velocity, $(1 - r^2/R^2)$

$$\begin{aligned} \gamma(x_0) &= \frac{\int_0^R \rho_{e0}(r) \left(1 - \frac{r^2}{R^2}\right) 2\pi r dr}{\int_0^R \rho_{e0}(r) 2\pi r dr} \\ &= \frac{1}{x_0 I_1(x_0)} \int_0^{x_0} I_0(x) \left(1 - \frac{x^2}{x_0^2}\right) x dx \end{aligned} \quad [14]$$

Notice that since the velocity peaks at the pore axis and the charge density peaks at the pore wall, significant overlap of charge and velocity occurs only if $\lambda \geq R$. In the limiting case $\lambda \gg R$ (very dilute solution) $I_0(x) \approx 1$, $I_1(x) \approx x/2$, and $\gamma(x_0) \approx 1/2$. In the other limiting case of concentrated solutions, we can use the asymptotic forms of the Bessel functions and integrate (14), obtaining $\gamma(x_0) \approx 2/x_0 = 2\lambda/R$.

Having integrated out the r dependence of the charge distribution and condensed it into the variable γ , we now examine the z dependence as given in the strain wave [9]. Substituting the strain [9] into Eq. [13] gives the charge distribution as a function of z (Eq. [15]), but we have left out an important part of the charge. The narrow region near the pore mouth (Fig. 1) contains charged fluid which, on alternate half cycles, is uncompensated by pore wall charge. We approximate this uncompensated fluid charge as a delta function at the pore mouth ($z = 0$) of sufficient magnitude to satisfy electrical neutrality over the entire pore. Since the liquid only moves about 1 nm, the delta function approximation is a good one. Without this approximation, the problem is very difficult because both the charge distribution and the fluid flow are no longer confined to the pore and are therefore three dimensional. For an oxide with n pores/m²

$$\begin{aligned} \rho_e(z) &= \frac{2\pi n R \sigma \gamma}{j\omega} \left(\frac{\partial v_z(z)}{\partial z} + \delta(z) v_z(z) \right) \\ &= \psi \left(\frac{\partial v_z(z)}{\partial z} + \delta(z) v_z(z) \right) \end{aligned} \quad [15]$$

where we have temporarily combined all the constants in the term ψ .

The voltage across the film, V_{out} can be written as a function of the charge density using the fundamental laws of electrostatics

$$\begin{aligned} V_{out} &= \frac{-1}{\epsilon_{pore}} \int_0^L \rho_e(z) (L - z) dz \\ &= \frac{-\psi}{\epsilon_{pore}} \int_0^L (L - z) \left(\frac{\partial v_z(z)}{\partial z} + \delta(z) v_z(z) \right) dz \end{aligned} \quad [16]$$

where ϵ_{pore} is an area weighted average of the dielectric constants of the oxide and the liquid. Integration of Eq. [16] by parts yields

$$V_{out} = \frac{\psi}{\epsilon_{pore}} \int_0^L v_z(z) dz \quad [17]$$

Substituting for $v_z(z)$ from Eq. [8] and integrating gives

$$\begin{aligned} V_{out} &= -\frac{\psi v_0}{\epsilon_{pore} 2\beta} = -\frac{2\pi n R \sigma \gamma v_0}{j\omega \epsilon_{pore} 2\beta} \\ &= \frac{\pi n R^2 \sigma \gamma v_0}{j\omega^{3/2} \epsilon_{pore} 2(\alpha\mu)^{1/2}} \end{aligned} \quad [18]$$

The sensitivity of the film as a transducer can be expressed as the output voltage per unit particle displacement

$$\frac{V_{out}}{u_z(0)} = \frac{j\omega V_{out}}{v_0} = \frac{(\pi n R^2) \sigma \gamma}{2\omega^{1/2} \epsilon_{pore} (\alpha\mu)^{1/2}} \quad [19]$$

in units of V/m. This is the main theoretical result of the paper, and will now be discussed in order to find the conditions of greatest transducer output.

The term $(\pi n R^2)$ is the pore area fraction. It is typically about 0.5 and can never be greater than one. The term σ , the surface charge density on the inner pore wall, depends on the conditions of the anodization in a poorly understood fashion. Thus far, an empirical approach has been taken to optimize σ . The term γ can be assumed to be 0.5 for liquids of sufficiently high resistivity such as deionized water and reagent-grade solvents. For a given anodic film, the main parameters affecting the magnitude of the PEC effect are the resistivity, compressibility α , and viscosity μ ; therefore these were chosen for experimental study.

Experimental Results

Using the arrangement shown in Fig. 2, various liquids were tested in two different porous anodic films using the same acoustic excitation. The measured PEC voltages are plotted in Fig. 4 as a function of $(\alpha\mu)^{-1/2}$. Although there is some experimental scatter, the data from each film appear to lie on a straight line, as predicted by [19].

It was experimentally observed that nonpolar liquids such as benzene, CCl₄, and cyclohexane resulted in the same PEC voltage as a dry film, about 30 times smaller than and opposite in polarity from the PEC voltage obtained with a liquid such as methanol. The nonpolar liquids apparently do not solvate the ions remaining after anodization on the inner pore wall and therefore result in an effectively zero Debye length.

The resistivity of the liquid can affect the PEC voltage in two ways: first, by its effect on the Debye length and therefore γ , as outlined previously, and second, by its effect on dielectric relaxation for frequencies $f \leq (2\pi\rho\epsilon)^{-1}$ (where ρ is the resistivity and ϵ is the dielectric constant of the liquid). Figure 5 shows PEC voltages for a given film wetted with a series of aqueous K₂SO₄ solutions prepared by successive dilutions. The large change in PEC voltage occurs at the resistivity predicted by dielectric relaxation, 2300 Ω -cm.

If we assume the dropoff in PEC voltage with increasing salt concentration is due to the decrease in Debye length and therefore γ , we can calculate the pore diameter from the condition $\gamma = 1/4 \approx 2\lambda/R$, or $R \approx 8\lambda$. Using the measured concentration at which the PEC voltage falls to half its maximum value (1.4×10^{-3} M), the pore radius is

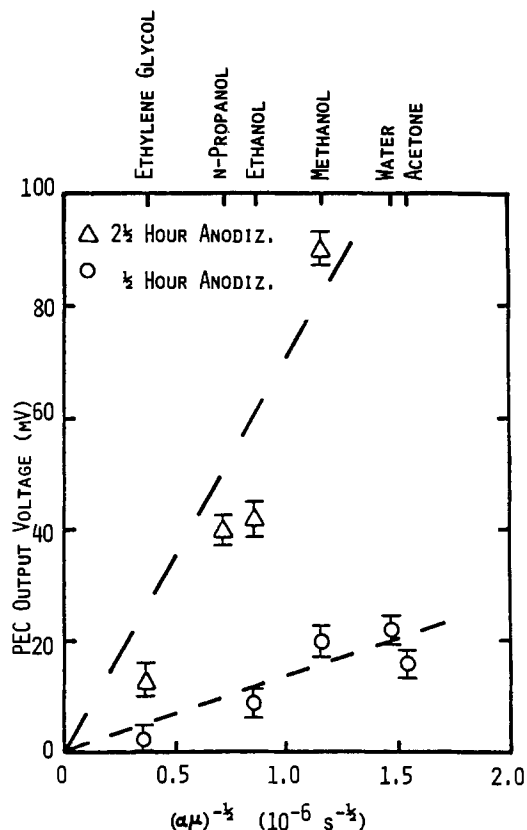


Fig. 4. Measured PEC voltages in two porous anodic films (anodized for 0.5 and 2.5h, respectively) as a function of the compressibility-viscosity ($\alpha\mu$) product of the test liquid for a variety of liquids.

calculated to be 4.7 nm, which is comparable to the results of published TEM studies on similar porous anodic-oxide films (2).

Summary and Conclusions

A new effect has been observed, in which porous, wet anodic-oxide films act as transducers for ultrasonic waves. A theory was derived to explain this effect using the known equations for the fluid flow and charge distribution in a capillary. The derived equations have been confirmed by experiments showing the dependence of PEC output voltage on the resistivity, compressibility, and viscosity of the liquid saturating the film. Based on Eq. [19], the optimal fluid for a PEC transducer is polar, has a small viscosity times compressibility product, and has a high resistivity. When used with methanol, these anodic Al_2O_3 films have shown themselves to be as sensitive to 10 MHz ultrasonic waves as sputtered ZnO films that are 10 μm thick.

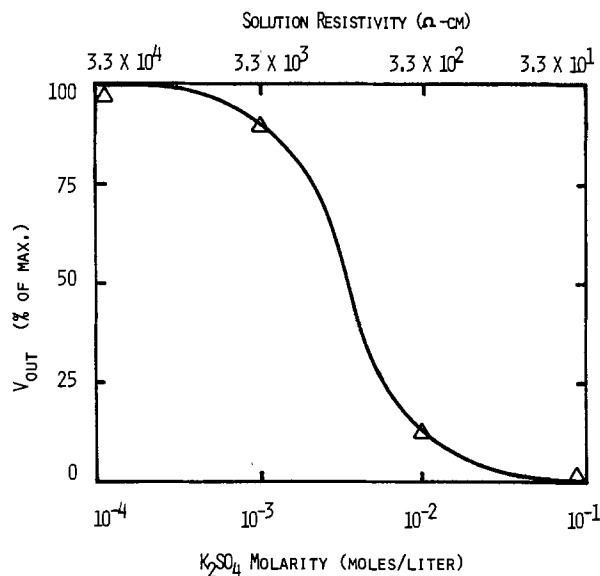


Fig. 5. Measured PEC voltages as a function of resistivity and concentration of an aqueous K_2SO_4 solution.

Acknowledgments

This research was supported by NSF grant ENG78-22193. In addition, one of the authors (J.B.) gratefully acknowledges the support of a Hertz foundation graduate fellowship.

Manuscript submitted May 19, 1983; revised manuscript received Nov. 15, 1983.

REFERENCES

1. J. J. Bernstein and R. M. White, Paper presented at IEEE Ultrasonics Symposium, Boston, Nov. 1980.
2. L. Young, "Anodic Oxide Films," Chap. 16, Academic Press, New York (1961).
3. J. J. Bernstein and R. M. White, Paper presented at IEEE Ultrasonics Symposium, San Diego, 1982.
4. Imoto Tatsuyo, Kanematsu Futoshi, Saito Joichi, and Murakawa Takao, *Keikinzoku*, **25**, 237 (1975).
5. J. Siejka, A. Morawski, J. Lagowski, and H. C. Gatos, *Appl. Phys. Lett.* **38**, 552 (1981).
6. A. W. Davies and R. E. Collins, *Electron. Lett.*, **5**, 462 (1969).
7. A. R. Champion, *J. Appl. Phys.*, **40**, 3766 (1969).
8. J. S. Newman, "Electrochemical Systems," pp. 193-201, Prentice Hall, Englewood Cliffs, NJ (1973).
9. M. A. Biot, *J. Acoust. Soc. Am.*, **28**, 168 (1956).
10. T. J. Plona and D. L. Johnson, Paper presented at IEEE Ultrasonics Symposium, Boston, (Nov. 1980).
11. L. E. Kinsler and A. R. Frey, "Fundamentals of Acoustics," 2nd ed., p. 239, John Wiley and Sons, New York (1962).
12. I. B. Crandall, "Theory of Vibrating Systems and Sound," pp. 96-97 and Appendix A, D. Van Nostrand Co., New York (1926).
13. J. S. Newman, *ibid.*, p.193.

Manuscript submitted Sept. 21, 1982; revised manuscript received Dec. 29, 1983.

REFERENCES

1. W. M. Vogel and J. T. Lundquist, *This Journal*, **117**, 1512 (1970).
2. H. R. Kunz and G. A. Gruver, *ibid.*, **122**, 1279 (1975).
3. A. J. Appleby, *ibid.*, **117**, 328, 641 (1970); A. J. Appleby and A. Borucka, *ibid.*, **116**, 1212 (1969).
4. R. N. Hazeldine and J. M. Kidd, *J. Chem. Soc.*, 4228 (1954).
5. R. Battino and H. L. Clever, *Chem. Rev.*, **66**, 395 (1966).
6. J. G. Riess, *Ann. Anesthesiol. Fr.*, 391 (1974).
7. E. P. Wessler, R. Iltis, and L. C. Clark, *J. Fluorine Chem.*, **9**, 137 (1977).
8. T. M. Reed, III, in "Fluorine Chemistry," Vol. 5, J. H. Simmons, Editor, p. 211, Academic, New York (1964).
9. E. Yeager, P. Bindra *et al.*, EPRI EM-505, June (1977).
10. T. J. Balicheva, V. I. Ligus, and Yu. Yu. Fialkov, *Russ. J. Inorg. Chem.*, **18**, 917 (1973).
11. L. I. Komarow and I. Z. Fisher, *Sov. Phys. JEPT*, **16**, 1358 (1963).
12. J. E. Walrafen, *J. Chem. Phys.*, **42**, 485 (1965).

Stability Analysis of Electrochemical Reactors via Liapunov Theory

I. The CSTER System

Thomas Z. Fahidy

Department of Chemical Engineering, University of Waterloo, Waterloo, Ontario, N2L 3G1 Canada

ABSTRACT

The effect of perturbations in the concentration and temperature of the inflow electrolyte and electrolytic current on the steady-state concentration and temperature of the electrolyte in the reactor are studied by an algebraic theory, in terms of appropriate Liapunov functions. The analysis is illustrated by the stability behavior of an electrolytic copper recovery process.

The purpose of studying the stability of an electrolytic reactor is to find out what the effect of perturbations in process variables is on overall reactor performance. One may specifically ask whether a reactor perturbed via changes in electrolyte flow rate, inlet concentration and/or temperature, electric current, etc. will eventually regain its prior steady state, or reach a new steady state. Such information is of obvious importance for the design and control of electrolytic reactors. There are, in principle, two ways of obtaining information on stability on the basis of a mathematical model. First, one may solve the governing set of differential equations for every kind of perturbation as an input function. This is a time consuming and wasteful exercise, since a stable solution to a nonlinear differential equation upon one particular forcing function does not guarantee stability under different forcing. A second and much more powerful approach is via Liapunov functions which allow an essentially algebraic analysis of the stability problem, thus offering a significant shortcut. The purpose of this paper is to present a stability analysis of a certain class of electrolytic reactors which can be modeled as a continuous-flow stirred-tank system (CSTER), in terms of a suitable set of Liapunov functions. The analysis is illustrated numerically by a copper-ion recovery process where the results of the Liapunov approach and simulated transient responses are compared. The analysis of electrolytic reactors modeled in terms of distributed parameters will be the subject of further communications.

Theory

Fundamental notions of Liapunov analysis.—A non-autonomous dynamic system represented by its governing set of differential equations

$$\dot{x} = f(x, t) \quad [1]$$

is asymptotically stable within a region R if there exists at least one scalar function $V(x, t)$ which satisfies the following conditions

$$V(x, t) > 0 \text{ for } x \neq 0, t \geq 0 \quad [2]$$

$$V(0, t) = 0; t \geq 0 \quad [3]$$

$$\dot{V}(x, t) = \frac{\partial V}{\partial t} + x \cdot \text{grad } V(x, t) < 0; x \neq 0, \text{ in R} \quad [4]$$

Then, $V(x, t)$ is a Liapunov function of this system in R. The elements of vector x are the state variables of the system whose steady state is 0. If R is the entire vector space, the system is asymptotically stable in the large (ASL). Rigorous definitions (not needed for the purpose of this paper) and detailed proofs of associated theorems are available in the literature (e.g. Ref. 1-6).

Among the large variety of Liapunov functions proposed by numerous researchers, certain quadratic forms have been found to be particularly powerful. For autonomous systems with governing equation $\dot{x} = f(x)$, the ma-

trix Q and its Liapunov function $V(x) = x'Qx$ has to be positive definite in such a manner that the time derivative $\dot{V}(x) = \dot{x}'Qx + x'Q\dot{x}$ is negative definite. The extension of this principle to arbitrary nonautonomous systems is by no means straightforward, as shown by Petrovski (7); an elegant method based on the convex/concave properties of functions by Mangasarian (8) and the averaging of radius curvature method by Luus (9) require a good deal of mathematical sophistication. When the nonautonomous system is represented by the governing set of equations

$$\dot{x} = f(x) + \xi(t) \quad [5]$$

one appropriate Liapunov function may be defined, following Berger (10, 11), as

$$V(x, t) = x'Qx + \int_t^\infty \xi'(\theta)M\xi(\theta) d\theta \quad [6]$$

where Q and M are appropriately chosen positive definite matrices. This approach may lead to rather cumbersome algebraic manipulations and a better alternative may be to choose

$$V(x, t) = y'Qy + \int_t^\infty \xi'(\theta)M\xi(\theta) d\theta \quad [7]$$

where $y = x - \phi$; $\phi = \int_0^t \xi(\theta) d\theta$. In the sequel, this alternative will be further explored.

It is instructive to note at this point that failure of finding a suitable Liapunov function does not prove system instability, although there exist specific Liapunov-based methods, such as Chetaev's instability theorem (2), for proving instability. The strength of the approach lies in its converse: even if only one single Liapunov function can be found (which satisfies Eq. [2]-[4]), stability within a certain region R is guaranteed. The size of the stability region depends, however, on the Liapunov function chosen, and a systematic search for the true stability domain may not be a trivial exercise.

State variable representation of an electrolytic reactor represented by a CSTER model.—Consider an electrolytic reactor consisting of a rectangular tank with a single pair of parallel-plate electrodes. The electrolyte is well mixed, and during (potentiostatic or galvanostatic) electrolysis there is one dominant reaction occurring at each electrode. Then the governing set of equations is the mass balance and the heat balance (12)

$$V_t \dot{c} = qc_0 - qc - I/zF \quad [8]$$

$$m_e C_p \dot{T} = GC_p T_0 - GC_p T - Q_L + I^2 R_e - I \Delta H_H / zF \quad [9]$$

The heat loss term may be written as

$$Q_L = \frac{k_1}{d_1} A_1 (T - T_f) + \sum_{i=2}^6 U_i A_i (T - T_a) + h_6 A_6 (T - T_a) \quad [10]$$

In steady state, there is no variation with time, hence $\dot{c} = \dot{T} = 0$ and Eq. [8]-[10] may be solved for steady-state

*Electrochemical Society Active Member

Keywords: stability, electrolysis, Liapunov functions, CSTER, copper recovery.

values c_0^* , c^* , T_0^* , T^* , and I^* , assuming that T_r and T_a remain constant and that the various physical parameters are constant (or may be approximated by appropriately computed average values). Dimensionless state variables can then be defined as $x_1 \equiv (T - T^*)/T_0^*$ and $x_2 \equiv (c - c^*)/c_0^*$, while the dimensionless forcing functions are taken as $\xi_1 \equiv (T_0 - T_0^*)/T_0^*$ and $\xi_2 \equiv (c_0 - c_0^*)/c_0^*$. Further, the following dimensionless quantities may be assigned

$$R \equiv \frac{kV_t}{m_e q C_p T_0^*} \left(\frac{I^2}{\sigma} - \frac{I^{*2}}{\sigma^*} \right) \quad [11]$$

$$S \equiv \frac{V_t \Delta H_R}{m_e q C_p T_0^* z F} (I - I^*) \quad [12]$$

$$Q \equiv \frac{1}{q z F c_0^*} (I - I^*) \quad [13]$$

$$\psi \equiv 1 + \frac{V_t k_1 A_1}{q m_e c_p d_1} + \frac{V_t}{q m_e C_p} \left[\sum_{i=2}^5 U_i A_i + h_6 A_6 \right] \quad [14]$$

$$\theta \equiv \frac{q}{V_t} t \quad (\text{dimensionless time})$$

Then, the dimensionless state equations equivalent to Eq. [8] and [9] are

$$\frac{dx_1}{d\theta} = -\psi x_1 + R - S + \xi_1 \quad [15]$$

$$\frac{dx_2}{d\theta} = -x_2 - Q + \xi_2 \quad [16]$$

where ξ_1 and ξ_2 represent time varying perturbations in the electrolyte inlet temperature and concentration. Note that R is nonzero, since $\sigma \neq \sigma^*$ due to variations in T and c .

Liapunov analysis of perturbations decaying in time.—If sporadic (random) disturbances are disregarded, perturbations in an electrolytic reactor may be broadly classified as either time decaying or persistent. In the former case, the decaying perturbation $\xi(t)$ would be bounded by a properly chosen exponential envelope

$$\left| \xi_i(t) \right| \leq A_i e^{-\lambda_i t} \quad i = 1, 2 \quad [17]$$

where A_i and λ_i are constant parameters. In galvanostatic electrolysis, Eq. [15] and [16] are simplified to

$$\frac{dx_1}{d\theta} = \psi x_1 + R + \xi_1 \quad [18]$$

$$\frac{dx_2}{d\theta} = -x_2 + \xi_2 \quad [19]$$

In potentiostatic electrolysis, this simplification is not possible, but the principle of the approach presented below is similar. Considering Eq. [5] and [7] and given the decaying nature of $\xi(t)$, the Liapunov derivative may be written as

$$\dot{V}(x, \theta) = y' Q y + y' Q \dot{y} - \xi'(t) M \xi(t) \quad [20]$$

where the overdot denotes differentiation with respect to dimensionless time θ . The matrix Q will be constructed as

$$\begin{pmatrix} 1 & \beta \\ \beta & \alpha^2 \end{pmatrix}; \alpha^2 - \beta^2 > 0 \text{ and matrix } M \text{ will be constructed as}$$

$$\begin{pmatrix} 2\mu_1 & 0 \\ 0 & 2\mu_2 \end{pmatrix}; \mu_1 > 0; \mu_2 > 0; \text{ thus, both } Q \text{ and } M \text{ are posi-}$$

tive definite. A convenient choice is $\beta = 0$; consequently, if the inequality

$$\begin{aligned} \dot{V}/2 = & -\psi x_1^2 - \alpha^2 x_2^2 - \mu_1 \xi_1^2 - \mu_2 \xi_2^2 + \\ & \psi x_1 \xi_1 + R x_1 - R \xi_1 + \alpha^2 \xi_2 < 0 \end{aligned} \quad [21]$$

$$x_1 \neq 0; x_2 \neq 0$$

is satisfied within a certain region R of electrolyte temperature and concentration, then any perturbation originating within this region will allow the system to regain asymptotically its 0 steady state. At small times past the onset of a perturbation, x_1 , x_2 , their time derivatives and R are reasonably close to zero, thus if μ_1 and μ_2 are sufficiently large positive scalars, Eq. [21] will be satisfied. At large times, ξ_1 and ξ_2 will be reasonably close to zero, hence

$$\lim_{t \rightarrow \infty} \dot{V}/2 = -\psi x_1^2 + R x_1 - \alpha^2 x_2^2 \quad [22]$$

which represents the autonomous case, *i.e.*, when $\xi = 0$. It follows that the stability of CSTER exposed to decaying perturbations of the form given by Eq. [17] is essentially determined by its stability conditions related to sudden changes in its state variables (*i.e.*, electrolyte temperature and concentration). The analysis is therefore, reduced to the one previously discussed (12). In the case of potentiostatic electrolysis, the foregoing analysis has a straightforward extension, provided that variations in the electric current are not strong enough to generate secondary (parasitic) reactions. If, for instance, current is the only forcing function, Eq. [15] and [16] may be modified to

$$\frac{dx_1}{d\theta} = -\psi x_1 + \Gamma_1(\theta); \Gamma_1(\theta) \equiv R(\theta) - S(\theta) \quad [23]$$

$$\frac{dx_2}{d\theta} = -x_2 + \Gamma_2(\theta); \Gamma_2(\theta) \equiv -Q(\theta) \quad [24]$$

and if an exponential decay-envelope condition

$$\left| \Gamma_i(\theta) \right| \leq \beta_i e^{-\gamma_i \theta}; i = 1, 2 \quad [25]$$

may again be assigned in the manner of Eq. [17], similar results are obtained. Note that the minimum numerical value of α is determined by the autonomous subsystem, and so long as $\alpha \geq \alpha_{\min}$, its magnitude is immaterial.

Liapunov analysis of persistent perturbations.—In this section, the theorem of Malkin (2), described in the Appendix, is employed to study CSTER stability in the case of persistent perturbations in electric current. The state variable equations are rewritten as

$$\frac{dx_1}{d\theta} = -\psi x_1 + R(\theta) - S(\theta) + \xi_1(\theta) \quad [26]$$

$$\frac{dx_2}{d\theta} = -x_2 - Q(\theta) + \xi_2(\theta) \quad [27]$$

The Malkin formalism requires rearrangement in the vector form

$$\begin{pmatrix} \frac{dx_1}{d\theta} \\ \frac{dx_2}{d\theta} \end{pmatrix} = \begin{pmatrix} -\psi x_1 \\ -x_2 \end{pmatrix} + \begin{pmatrix} R(\theta) - S(\theta) + \xi_1(\theta) \\ -Q(\theta) + \xi_2(\theta) \end{pmatrix}$$

or its equivalent

$$\frac{dx}{d\theta} = X(x, \theta) + Y(x, \theta) \quad [28]$$

In fact, X is not dependent implicitly on time and

$$V(x) = x' Q x \quad [29]$$

$$= x_1^2 + \alpha^2 x_2^2 \quad (\beta = 0) \quad [30]$$

is one of its Liapunov functions. Proceeding now to the perturbed system, if m_1 and m_2 are the largest magnitudes of x_1 and x_2 , respectively, due to a persistent perturbation, then by inspection.

$$W(x) = 0 \quad [31]$$

$$W_1(x) = m_1^2 + \alpha^2 m_2^2 \quad [32]$$

and since, $\dot{V}(x) = -2\psi x_1^2 - 2\alpha^2 x_2^2$, an obvious choice is

$$W_2(x) = \psi x_1^2 + \alpha^2 x_2^2 \quad [33]$$

To find the bound M on the partial spatial derivatives of $V(x)$, we obtain from Eq. [30] $\partial V/\partial x_1 = 2x_1$ and $\partial V/\partial x_2 = 2\alpha^2 x_2$; hence an obvious bound is

$$M = \sqrt{2(m_1^2 + \alpha^2 m_2^2)} \quad [34]$$

Let $\Omega(A)$ denote the region of stability of subsystem $X(x)$, defined by the $\|x\| < A$ inequality; a suitable numerical value of A is obtained from the $\dot{V}(x) < 0$ condition, differentiating Eq. [30]. If the magnitude of the persistent perturbation is bounded, so will be R , S , Q , and ξ , hence there exists a non-negative scalar μ_2 such that

$$\|Y(x, \theta)\| = \sqrt{(R - \xi + \xi_1)^2 + (-Q + \xi_2)^2} \leq \eta_2 \quad [35]$$

If, for instance, the persistent perturbation is a sinusoidal current wave, and ξ has the form of Eq. [17], η_2 may be chosen as the magnitude of Y at zero time and $\epsilon = \sqrt{m_1^2 + m_2^2}$. Since at large times the response x will be confined in a stricter sense, i.e., $\lim_{t \rightarrow \infty} |x_1| \leq a_1$ and $\lim_{t \rightarrow \infty} |x_2| \leq a_2$ such that $a_1 < m_1$ and $a_2 < m_2$, that stability region

$$\lim_{t \rightarrow \infty} \epsilon = \sqrt{a_1^2 + a_2^2}$$

may replace for practical purposes the rigorous but cautious result of Malkin's theorem, when the transient effects have vanished. Finally, the $\|x(0)\| < \eta_1$ condition is clearly satisfied for any $\eta_1 > 0$ if the system is initially at rest. Hence a CSTER obeying the conditions stated in this section is stable in the Malkin sense; its electrolyte temperature and concentration will fluctuate within finite limits so long as persistent perturbations in the CSTER are bounded. It follows immediately that if the perturbations are oscillatory, then so will be the electrolyte temperature and concentrations, with magnitudes eventually bounded by bounds related to the numerical values of a_1 and a_2 .

Application: Stability Analysis of a Metal Recovery Process

For the sake of numerical illustration and comparison with simulated transient response a CSTER, where copper is deposited from an aqueous cupric sulfate solution on a metal cathode and oxygen is generated at an inert anode, is considered. The following data apply: $d_1 = 7$ mm; $V_t = 0.3881$ m³; $k_1 = 0.313$ W/m²·K; $h_1 = 4.61$ W/m²·K, $i = 2, \dots, 5$; $h_6 = 18$ W/m²·K; $k = 1.47$ m⁻¹; $s = 0.68$ m; $A_E = 0.4624$ m²; $d_E = 0.002$ m; $m_e = 425.5$ kg; $C_p = 4186$ J/kg·K; $\Delta H_r = 221.6$ kJ/mol Cu; $C_o^* = 850$ mol/m³; $G = 0.3$ g/s; $I^* = 41.6$ A (18% of the limiting current); $T_o^* = 25^\circ\text{C}$; $T_A = 20^\circ\text{C}$; and $T_F = 20^\circ\text{C}$. The dependence of electrolyte density and conductivity on concentration and temperature is represented by statistical regressions based on literature data (13)

$$\rho = 1014.3 + 0.1484c - 0.5T \text{ kg/m}^3 \quad [36]$$

$$\sigma = 6.5676 \times 10^{-3} C^{0.706} T^{0.55} \text{ S/m} \quad [37]$$

$$c: \text{ mol/m}^3; T: ^\circ\text{C}$$

valid for the $98.9 < c < 1322$ and $20 < T < 70$ range. Under these circumstances, $c^* = 62.06$ and $T^* = 69$ represent the steady state. It is assumed that Eq. [36] and [37] hold for temperatures and concentrations encountered under the stated conditions, although they may be somewhat outside the validity range of the regression.

Case I: galvanostatic electrolysis, perturbation occurring in the electrolyte inlet concentration and temperature.—Assuming that the effect of temperature and

concentration on m_e , C_p , and ΔH_r is negligible, Eq. [11]–[14] yield $S = 0$, $Q = 0$, $\psi = 32.657$, and

$$R(\theta) = \frac{81.0292}{\sigma} - 65.1842 \quad [38]$$

As shown previously (12), the expression in Eq. [22] is less than zero for $\alpha > 3.4$, and if the magnitude of perturbations $\|\xi\|$ does not exceed the region R defined by the validity domain of Eq. [36] and [37], asymptotic stability is

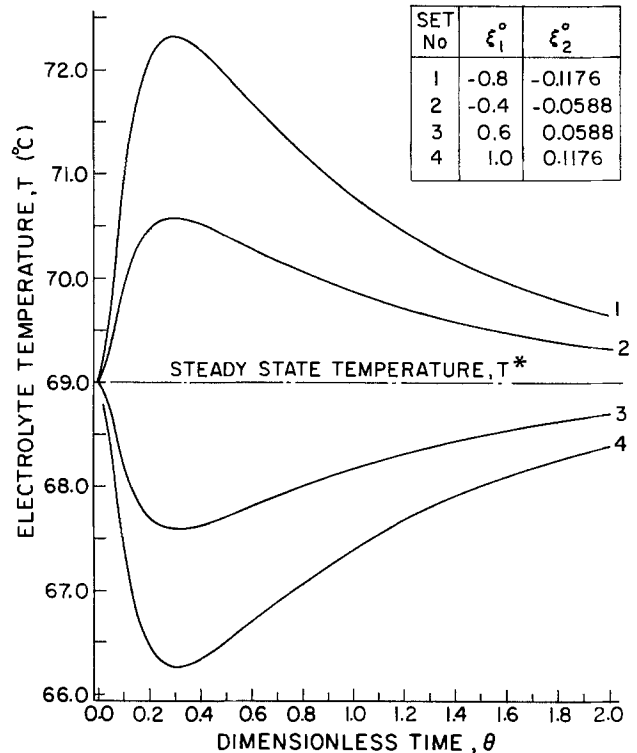


Fig. 1. Simulated variation of the transient electrolyte temperature with time in the copper-recovery process.

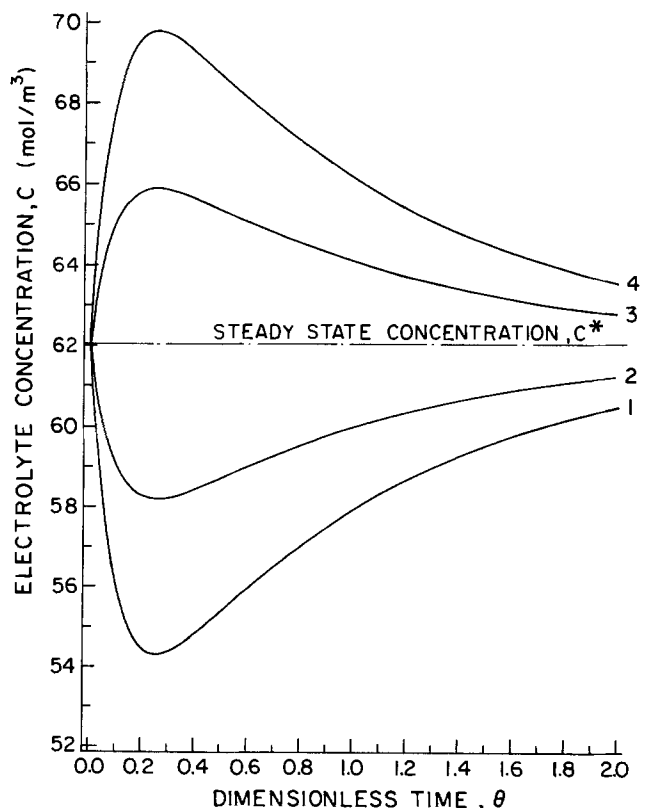


Fig. 2. Simulated variation of the transient electrolyte concentration with time in the copper-recovery process (as in Fig. 1).

guaranteed by the choice of sufficiently large values of μ_1 and μ_2 in Eq. [21]. Typical transients for this case are shown in Fig. 1 and 2 where the numerical form of Eq. [18] and [19]

$$\frac{dx_1}{d\theta} = -32.657x_1 + R(\theta) + \xi_1^0 \epsilon^{-5\theta} \quad [39]$$

$$\frac{dx_2}{d\theta} = -x_2 + \xi_2^0 \epsilon^{-10\theta} \quad [40]$$

was solved via digital computer; the numerical values $\lambda_1 = 5$ and $\lambda_2 = 10$ were arbitrarily chosen. Note that Eq. [40] has the analytical solution

$$x_2 = \frac{\xi_2^0}{\lambda_2 - 1} \left[\epsilon^{-\theta} - \epsilon^{-\lambda_2 \theta} \right] \quad [41]$$

but Eq. [39], being a nonlinear equation coupled with Eq. [38], has to be solved by a numerical technique. The course of curves can be explained by qualitative reasoning: consider, *e.g.*, the instance where ξ_1^0 and ξ_2^0 are both positive, meaning a positive perturbation in T_0 and C_0 , resulting in an increase in σ , and a decrease in R . Since electrolysis is galvanostatic, the increase in σ means a decrease in the rate of Joule heat generation, which leads to a drop in the electrolyte temperature. As time progresses, the decrease in T leads to a decrease in σ , and hence R and the rate of Joule heat generation begins to increase. The net result is that $dx_1/d\theta$ will be less and less negative and $dx_2/d\theta$ less and less positive. They both become zero at a crossover point ($\theta \approx 0.3$ in the simulated example). Past the crossover point, continuing increases in the rate of Joule heat generation and electrolyte conductivity result in a monotonic increase in T and a monotonic de-

crease in c until they reach the previous steady state, at sufficiently large times. A similar (although inverse) argument applies to the $\xi_1^0 < 0$, $\xi_2^0 < 0$ set.

Case II. electrolysis with a sinusoidal perturbation in electric current and decaying perturbation in electrolyte inlet concentration and temperature.—As before, $\psi = 32.657$ but Eq. [11]–[14] yield

$$R(\theta) = 0.046829 \frac{I^2}{\sigma} - 65.1974 \quad [42]$$

$$S(\theta) = 0.03658 I - 1.5216 \quad [43]$$

$$Q(\theta) = 0.009029 I - 0.3756 \quad [44]$$

The electric current is assumed to have the functional form

$$I = 41.6 + 3.4 \sin 51.06\theta \text{ amp} \quad [45]$$

with an oscillation angular frequency of $\omega = 1 \text{ h}^{-1}$. The numerical form of Eq. [18] and [19]

$$\frac{dx_1}{d\theta} = -32.657 x_1 + R(\theta) - S(\theta) + \xi_1^0 \epsilon^{-5\theta} \quad [46]$$

$$\frac{dx_2}{d\theta} = -x_2 - Q(\theta) + \xi_2^0 \epsilon^{-10\theta} \quad [47]$$

can be solved via a digital computer if ξ_1^0 and ξ_2^0 are specified; a typical solution is shown in Fig. 3, illustrating bounded oscillations predicted by Liapunov analysis via Malkin's theorem. In this instance ($\xi_1^0 = 1.0$; $\xi_2^0 = 0.1176$), the variation domains are $0.2 \leq x_1 \leq 0.24$ and $-0.0036 \leq x_2 \leq 0.0023$, corresponding to variation domains $64 \leq T \leq 75$ and $59 \leq C \leq 64$. Since the variation of R between -13.8 and $+17.26$ is much larger than the varia-

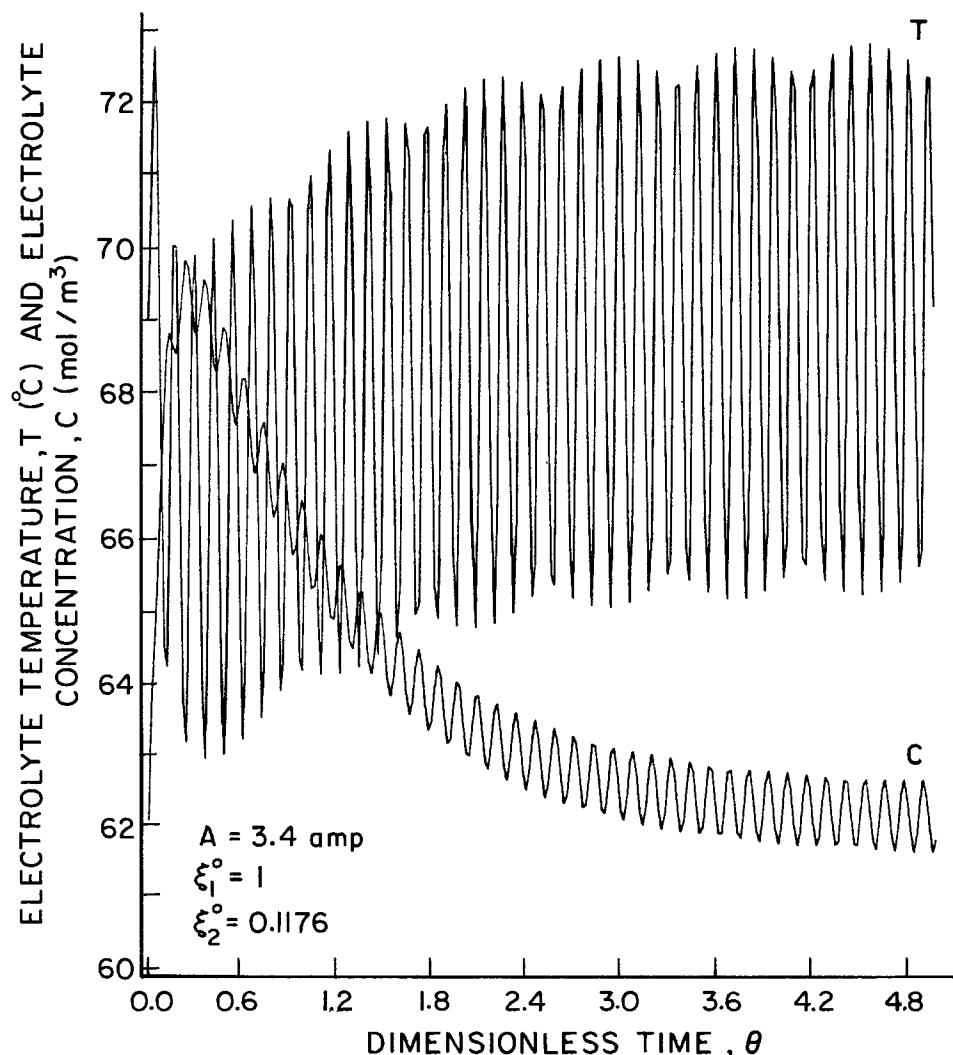


Fig. 3. The response of electrolyte temperature and concentration to a sinusoidal perturbation in the current.

Table I. Parameters of the Malkin stability theorem in a persistently perturbed CSTER

Initial Conditions								
$\xi_1(0)$	$\xi_2(0)$	η_2	α_1	α_2	m_1	m_2	M_{\min} (Eq. [34] $\alpha = 3.4$)	ϵ
-0.8	-0.1176	16.34	0.30	0.0036	0.720	0.0100	1.02	0.72
-0.4	-0.0588	16.74	0.30	0.0024	0.320	0.0055	0.45	0.32
0.6	0.0588	17.74	0.30	0.0017	0.300	0.0046	0.42	0.30
1.0	0.1176	18.14	0.30	0.0012	0.400	0.0092	0.56	0.40

$$R(\theta) = 0.046829 \left(\frac{I^2}{\sigma}\right) - 65.1974. S(\theta) = 0.03658I - 1.5216. Q(\theta) = 0.009029I - 0.3756. I = 41.6 + 3.4 \sin 51.06 \theta, \text{ amp.}$$

Table II. The effect of the current perturbation amplitude on the stability parameters

A (amp)	η_2	α_1	α_2	m_1	m_2	M_{\min}	ϵ
1.8	12.13	0.160	0.00065	0.254	0.00911	0.36	0.254
2.5	14.34	0.225	0.00918	0.318	0.00916	0.45	0.318
3.4	18.14	0.300	0.00120	0.400	0.00920	0.57	0.400

$\xi_1^\circ = 1.0. \xi_2^\circ = 0.1176. R(\theta), S(\theta),$ and $Q(\theta)$: as in Table I. $I = 41.6 + A \sin 51.06 \theta, \text{ amp.}$

tion of Q (-0.03; -0.104) or S (-0.14; 0.124), Eq. [35] may be simplified to $\|Y(x, \theta)\| \approx \sqrt{(R + \xi_1)^2 + \xi_2^2} \leq \eta_2$. Similar arguments may be made for all initial perturbation conditions $\xi(0)$; pertinent Malkin parameters for selected cases (including the computer-simulated case) are shown in Table I. The effect of the current perturbation amplitude on the stability parameters is indicated in Table II; it is interesting to note that the $\eta_2(\epsilon)$ relationship is essentially linear in this particular case

$$\eta_2 = 1.83 + 40.68 \epsilon \quad [48]$$

Thus, if the amplitude of the current oscillation is known, the norm of the oscillatory temperature/concentration response can be quickly estimated without an experimental determination or a computer simulation of their variation with time. This is an important property of the Liapunov-function-based approach to stability.

The foregoing analysis, although powerful within its scope, suffers from one restriction: the dependence of pertinent physical parameters on electrolyte concentration and temperature has to be known in the form a quantitative relationship (e. g., Eq. [36] and [37]). This restriction applies equally to the simulation of the CSTER model, and, for that matter, to any attempt of quantitative performance analysis. In the absence of reliable physical and chemical data for a given electrolyte, the power of the stability study described in this paper is limited. When such data are available, its usefulness for electrolytic process control is rather obvious; much more work will, however, be required to explore its full potential.

Manuscript submitted July 25, 1983, revised manuscript received ca. Nov. 30, 1983.

The University of Waterloo assisted in meeting the publication costs of this article.

APPENDIX

Malkin's Stability Theorem for Systems Under Persistent Perturbations

In this section, Malkin's theorem for the stability of a system described by its governing equation (Eq. [28]) is summarized; for a proof, consult Ref. (2). Here, $Y(x, \theta)$ represents persistent perturbations and $X(x, \theta)$ the dynamic system subjected to such perturbations. It is assumed that if there are no perturbations, the nonautonomous system

$$\frac{dx}{d\theta} = X(x, \theta); X(0, t) = 0 \quad [A-1]$$

(all $t \geq 0$)

has a Liapunov function $V(x, t)$ in a region $\Omega(A)$ where A is a suitably chosen bound on $\|x\|$; i.e., $\|x\| < A$. For t

≥ 0 , the subsystem [A-1] is asymptotically stable within this region. Let there exist three positive definite functions such that for $t \geq 0$

$$W(x) \leq V(x, t) \leq W_1(x) \quad [A-2]$$

$$\dot{V}(x, t) \leq -W_2(x) \quad [A-3]$$

within Ω . Furthermore, let all partial spatial derivatives of $V(x, t)$ be bounded, i.e., there exists a positive scalar M such that for $t \geq 0$, the condition

$$\left| \frac{\partial V}{\partial x_i} \right| \leq M; i = 1, 2, \dots, n \quad [A-4]$$

is satisfied within Ω . Then, given a positive scalar ϵ such that $0 < \epsilon < A$, the system given by Eq. [28] is stable in the following sense

$$\|x(0)\| < \eta_1(\epsilon); \eta_1 > 0 \quad [A-5]$$

$$\|x(t)\| < \epsilon; t > 0 \quad [A-6]$$

provided that $\|Y(x, t)\| < \eta_2(\epsilon), \eta_2 > 0$; for all $\|x\| < \epsilon$ and $t \geq 0$, i.e., the perturbations are bounded. Thus, the system will not leave a certain domain of its state variables, although it may never reach a constant steady state. Equations [A-5] and [A-6] are the mathematical expression of Malkin stability.

LIST OF SYMBOLS

A_1	area of the electrolytic tank bottom
A_i	$i = 2, \dots, 5$ the four sidewall areas of the electrolytic tank
A_6	area of the electrolyte surface
c	electrolyte concentration. c^* : its steady-state value.
c_0	inlet electrolyte concentration. c_0^* : its steady-state value.
C_p	specific heat capacity of the electrolyte
d_b	thickness of the electrolytic tank bottom
F	Faraday's constant
G	inlet mass flow rate of electrolyte
h_6	heat transfer coefficient related to the electrolyte surface (including evaporation)
I	electric current
k	geometric shape factor (for resistance calculations)
k_t	thermal conductivity of the electrolytic tank
m_e	mass of electrolytic in electrolytic tank
q	inlet volumetric flow rate of electrolyte
R_e	electric resistance of electrolyte in the electrolytic tank
T	electrolyte temperature. T^* : its steady-state value.
T_0	inlet electrolyte temperature. T_0^* : its steady-state value.
T_a	ambient temperature
T_f	temperature of the electrolyte tank floor
t	time
U_i	$i = 2, \dots, 5$ overall surface-to-ambient heat-transfer coefficient related to the four sidewalls of the electrolytic tank
V_r	effective volume of the electrolytic reactor
z	number of electrons participating in the electrode reaction of interest
ΔH_R	heat of reaction of electrode reaction of interest
ρ	density of electrolyte
σ	electric conductivity of electrolyte

REFERENCES

1. R. E. Kalman and J. E. Bertram, *J. Basic Eng.*, **82**, 371 (1960).
2. J. F. LaSalle and S. Lefschetz, "Stability by Liapunov"

- ov's Direct Method with Applications," Academic Press, New York (1961).
3. T. L. Saaty and J. Bram, "Nonlinear Mathematics," pp. 235-254, McGraw-Hill, New York (1964).
 4. H. Hochstadt, "Differential Equations," pp. 234-243, Holt, Reinhart and Winston, New York (1965).
 5. D. D. Perlmutter, "Stability of Chemical Reactors," Prentice Hall, Englewood Cliffs, NJ (1972).
 6. R. C. Dorf, "Time Domain Analysis and Design of Control Systems," Addison-Wesley, Palo Alto, CA (1965).
 7. I. G. Petrovski, "Ordinary Differential Equations," Sec. 49, 150-158, Dover, New York (1966).
 8. O. L. Mangasarian, *J. SIAM Control, Ser. A.*, **1**, 311 (1963).
 9. L. Lapidus and R. Luus, "Optimal Control of Engineering Processes," Sec. 6.6, 396-409, Blaisdell Publishing Co., Waltham, MA (1967).
 10. J. S. Berger, *Diss. Abst.*, **26**, 244 (1965).
 11. J. S. Berger and D. D. Perlmutter, *Chem. Eng. Sci.* **20**, 147 (1965).
 12. T. Z. Fahidy, *J. Appl. Electrochem.*, To be published.
 13. D. C. Price, H. Larsson, and W. G. Davenport, *Nouv. J. Chim.*, **4**, 78 (1980).

Mass Transfer in Parallel Plate Electrolyzers with Two-Phase Liquid-Liquid Flow

Po-Yen Lu^{*,1} and Richard C. Alkire*

Department of Chemical Engineering, University of Illinois, Urbana, Illinois 61801

ABSTRACT

The enhancement of mass transfer to a solid surface by addition of a dispersed immiscible second liquid phase was investigated with use of the electrochemical limiting current method. The electrolyzer consisted of a divided parallel plate cell in which electrolyte flowed upward past vertical electrodes. Three electrolytes were used: aqueous ferricyanide, aqueous ferricyanide containing inert dispersed droplets of toluene, and aqueous iodide containing dispersed toluene droplets in which was dissolved the reactant, iodine. Experiments were carried out under controlled variation of flow rate, droplet size, organic volume fraction, and electrode material. Experiments were performed both with and without use of a turbulence promoter. It was found that the overall mass-transfer rate could be separated into three elements: (i) the single-phase mass-transfer rate, (ii) the enhancement of mass transfer owing to the physical action of dispersed liquid droplets, and (iii) the still further enhancement of mass transfer owing to the presence of reactants dissolved in the dispersed droplets. For sparingly soluble reactants, it was found that the mass-transfer enhancement achieved by extraction of reactants from a dispersed second liquid phase could be orders of magnitude larger than the other two mass-transfer mechanisms.

The attainment of high mass-transfer rates is important for many electrochemical processes, but is difficult to achieve when the reacting species are sparingly soluble. Under such conditions, two approaches are generally used. The first approach emphasizes increasing the solubility of reactant species, for example, by adjustment of pH, by using a cosolvent, by using a solvent other than water, or by using surfactant salts which solubilize micelles of reactant molecules. The second approach emphasizes increasing the mass-transfer coefficient by using high flow rates, turbulence promoters, or porous electrodes. While each of these procedures exhibit certain advantages, the search for still superior methods continues.

In this investigation, the enhancement of mass transfer to an electrode surface by addition of a dispersed second liquid phase was studied. The use of two liquid phases in an electrolytic operating scheme has the attractive feature that mass-transfer rates can be significantly improved while also maintaining high ionic conductivity and low pressure drop across the cell.

The advantages associated with using an emulsion as an electrochemical feedstock were recognized in the 1903 patent of Kempf (1) who oxidized benzene in sulfuric acid to produce quinone and hydroquinone. More recent electroorganic synthesis examples include those reported by Dey (2), Udupa (3), Fremery (4), Millington (5), and Seco (6), among others. Additional applications may be found in the field of flow batteries and hydrometallurgy. While these processes depend critically upon two-phase operation for their success, there are relatively few papers which investigate the fundamental principles which are involved.

The events which occur in such systems are complex and include, for example, modification of the flow field

near the electrode surface by the dispersed droplets, and perhaps also wetting the electrode surface by the dispersed phase. Such events exert a profound influence on mass-transfer processes near the electrode surface, particularly when reactants are sparingly soluble in the continuous phase but highly soluble in the dispersed phase.

While the mass-transfer literature in the field of liquid-liquid systems is voluminous (7), most of these nonelectrochemical studies do not include all of the salient features needed for application of the results to electrochemical applications. In particular, electrochemical processes require that reactants be supplied from the two-phase mixture to an adjacent solid surface where electrochemical reaction occurs and, in addition, that electrical current be able to flow through the solution by an ionic path to the reactive region on the electrode surface. The following paragraphs summarize recent studies on several aspects of the overall electrochemical problem.

The effect of inert dispersed particles on mass transfer to a solid electrode has been investigated recently for several systems. These systems include mass transfer of dissolved oxygen to the wall of a corroding pipeline through which a slurry of sand flows (8), and mass-transfer enhancement at a rotating disk electrode by action of impinging solid particles dispersed in the solution (9). These studies illustrate that significant mass-transfer enhancement occurs owing to the presence of a second (solid) phase dispersed in the electrolyte.

The effect of dispersed liquid droplets upon mass transfer at a solid electrode surface was studied by Dworak *et al.* (14-16). The studies were conducted on a horizontal electrode facing upward, operated under turbulent flow conditions. It was found that the addition of hexane (density: 0.6 g/cm³) had no effect on the rate of mass transfer of ferricyanide to the electrode, but that the addition of carbon tetrachloride (density: 1.6 g/cm³) enhanced mass-transfer rates by up to 30%. These studies differ from the present investigation in which laminar flow conditions were studied at vertical electrodes past which fluid flowed in an upward direction.

*Electrochemical Society Active Member.

¹Present address: AT&T Bell Laboratories, Murray Hill, New Jersey 07974.

Key words: mass transport, laminar, two-phase flow, parallel plates, electrolyzer.

Dworek *et al.* also reported that the use of highly turbulent emulsion flow prevented contact between the emulsified phase and the electrode. In related studies, Kinoshita *et al.* (17) indicated that the interfacial contact area between electrode and droplets of the dispersed phase is an important parameter which influences the magnitude of mass-transfer enhancement which is observed. These observations indicate that partial wetting of the surface by the dispersed phase may be critically important for enhancing mass-transfer rates.

While the effect of turbulence promoters on mass transfer has been studied in one-phase electrolytic systems (18-20), no previous mass-transfer measurements are known to exist for the use of turbulence promoters in two-phase systems.

The influence of rising gas bubbles at vertical electrodes has been widely studied (10), as has been the influence of electrolytic gas evolution, which creates intense local stirring (11). The combined effect on mass transfer of rising bubbles plus bubble evolution, as observed in chlorate electrolysis, was found to be a linear addition of two mass-transfer coefficients (12, 13). This concept will be used in the present study, and appears in the form of Eq. [1] below.

The foregoing survey indicated that there have been relatively few measurements of mass-transfer rates in electrochemical systems having liquid-liquid electrolyte. The purpose of this investigation was to characterize experimentally the different phenomena which control the overall mass-transfer process, and to establish the dependence of the different phenomena upon operating conditions (21).

The hypothesis for the present study, which was verified by the results presented below, was that the overall mass-transfer limiting current is a linear sum of three effects: (i) the mass transfer caused by the flow of the continuous phase, (ii) the mass-transfer enhancement caused by physical disruption of the mass-transfer boundary layer near the electrode surface owing to the presence of dispersed droplets, and (iii) the still further mass-transfer enhancement which arises from extraction of reactive species from the dispersed droplets, which may be in intimate contact with the electrode and thus serve as a source of reactant deep within the mass-transfer boundary layer. The three elements of the overall process are characterized below by three coefficients (k_i) according to the equation

$$i_L = nFk_1c_1 + nFk_2c_1 + nFk_3c_2 \quad [1]$$

The first term (nFk_1c_1) is the one-phase convective flow term where the mass-transfer coefficient k_1 is that which is commonly reported for single-phase flow, and the concentration c_1 is the concentration of reactant in the continuous phase. The second term (nFk_2c_1) represents the mass-transfer enhancement by the disturbance mechanism. The third term (nFk_3c_2) represents the mass-transfer enhancement which is brought about by the extraction mechanism, where the concentration c_2 is the concentration of reactant in the discontinuous phase from which extraction occurs. Measurements of k_1 , k_2 , and k_3 are reported in this paper for a parallel plate electrochemical cell through which flows electrolyte containing two solvent phases.

Apparatus

Electrochemical cell.—Figure 1 shows a diagram of the cell assembly in which the path of electrolyte flow in both electrode compartments is indicated. The cell was positioned vertically so that fluid entered at the bottom, flowed upward past the electrodes, and exited at the top. The cell was machined from two blocks of polypropylene which were clamped together with a silicon O-ring seal. Electrical contact to electrodes was made with titanium screws pressed into the back side of the electrodes. The cross section of the flow channel in the working electrode compartment was 0.2×3.0 cm.

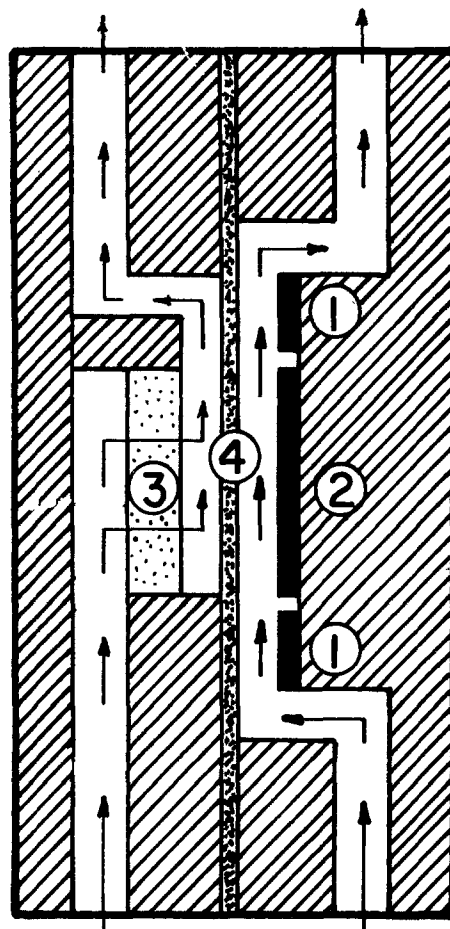


Fig. 1. Cross-sectional view of electrochemical cell, not drawn to proportion. Arrows indicate fluid flow path in the two-compartment cell. Components include: (1) reference electrodes; (2) planor working electrode; (3) porous counterelectrode, and (4) separator.

Two types of working electrode materials were investigated: graphite (Poco) and ruthenized titanium (DSA, Diamond Shamrock). The area of the working electrode which was exposed to the electrolyte was 3×27 cm. The surface roughness of the graphite electrode was $< 1 \mu\text{m}$, and of the DSA was $< 4 \mu\text{m}$. The surface roughness was less than 10% of the thickness of the mass-transfer boundary layer, and may, therefore, be regarded as "smooth." Two reference electrodes were positioned in the cell, at the entrance and exit region as illustrated in Fig. 1. The reference electrodes were of the same composition as the working electrode and had an exposed area of 3×10 cm in contact with the electrolyte. The counterelectrode was made of porous ruthenized titanium (Gould Incorporated, and Diamond Shamrock), through which electrolyte flowed as indicated in Fig. 1. The counterelectrode had the same exposed area as the working electrode.

A separator of microporous polypropylene (Daramic, W. R. Grace & Company) was used for most of the experiments reported below for which turbulence promoters were not placed in the working electrode compartment. The separator had support ribs in the direction of flow so that the working electrode compartment was thereby segmented into four channels, each of which measured 0.2×0.75 cm. For a small number of experiments, a turbulence promoter (Vexar 549V300BD, E.I. du Pont de Nemours and Company) was used in which case a membrane (Nafion, N-415, E.I. du Pont de Nemours and Company) was used to prevent cross-flow between the two compartments.

Flow system.—A diagram of the flow system is shown in Fig. 2 and includes five flowmeters denoted FA through FE (Gilmont 4, Ti float), five valves denoted VA through VE (glass/Teflon stopcocks), a glass reservoir (4 liters), and two pumps (March, TE-MDX-MT3). In the res-

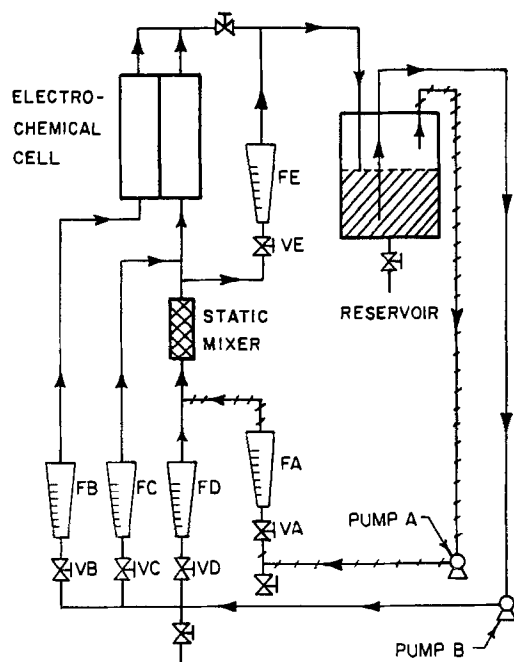


Fig. 2. Flow system used for preparation and recirculation of two-phase liquid-liquid mixtures.

ervoir, the two-phase mixture separated cleanly into aqueous and nonaqueous layers. All tubing was 3/8 in. id polypropylene except for the section between the static mixer and the cell inlet, which was 1/4 in. id; the same id as the static mixer.

An in-line static mixer was used to generate droplets of the organic phase dispersed in the continuous aqueous phase (Kenics, 1/4"-40-174-0), with 20 Ti elements in 1/4 in. glass housing). The correlation between mean droplet size and the Weber number was available from the manufacturer (22).

Valves VA and VD were used to control the two-phase volume fraction and droplet size produced in the static mixer. Valve VE was used to bypass some of the fluid around the cell so that the combination of small droplets and slow flow past the electrode could be investigated. Similarly, valve VC was used to add aqueous phase to the flow exiting from the static mixer so that the combination of large droplets and fast flow past the electrode could be studied. Valve VB was used to control the flow through the counterelectrode compartment.

Electrical system.—The measurement of electrical current at various applied potentials between working and reference electrode was made with a potentiostatic power supply (built in-house) driven by a function generator (PAR 175) and displayed on an X-Y recorder (Houston, 2000).

Procedures

Solutions were prepared by mixing analytical grade reagents, and deionized distilled water. The solution for measurement of the single-phase mass-transfer coefficient k_1 was 0.01M potassium ferricyanide, 0.01M potassium ferrocyanide, and 0.2M sodium sulfate in water. The solution for measurement of the disturbance mechanism coefficient, k_2 , was the same ferric/ferrous cyanide solution except that toluene was added. The solution for measurement of the extraction mechanism coefficient, k_3 , was 0.01M potassium iodide and 0.2M sodium sulfate in water equilibrated with a toluene solution containing 0.165N iodine. The concentrations of ferricyanide and of iodine were determined by titration (23).

The interfacial tension between aqueous and organic phases was measured with the duNouy method which used a tensiometer (Fisher, Model 20). The density was measured by weighing a known volume of solution, and the viscosity was determined with an Ostwald viscome-

ter. The diffusion coefficients of electroactive species were measured by using a rotating disk electrode.

Current-voltage traces were obtained under steady flow conditions with use of a scan rate of 5 mV/s. Additional details may be found in the original thesis (21).

Results and Discussion

The experimental strategy for obtaining mass-transfer coefficients k_1 , k_2 , and k_3 (see Eq. [1]) was as follows: (i) The one-phase convection mass-transfer coefficient, k_1 , was found from measurement of the mass-transfer limiting current in a one-phase aqueous solution containing ferricyanide. (ii) The effect of an inert second phase (disturbance mechanism) was found by dispersing toluene in the solution of ferricyanide. The inert toluene droplets served to disturb flow near the electrode surface and, thus, to enhance the mass transfer of ferricyanide to the electrode surface. The limiting current was thus attributed to the one-phase rate (nFk_1c_1) plus the physical disturbance owing to the inert dispersed droplets (nFk_2c_1). By subtracting nFk_1c_1 found previously from the measured limiting current, the enhancement owing to disturbance alone was thus obtained. (iii) The effect of a reactive second phase (extraction mechanism) was investigated with use of water/toluene dispersions containing the iodine/iodide redox couple. The iodine reactant is highly soluble in the dispersed organic phase. The reactive droplets serve both to disturb and also to replenish the mass-transfer boundary layer near the electrode surface. The limiting current was thus attributed to the one-phase rate (nFk_1c_1) plus the disturbance attributed to the dispersed droplets (nFk_2c_1) and the replenishment of iodine reactant by extraction from the droplets (nFk_3c_2). By subtracting nFk_1c_1 and nFk_2c_1 (found previously) from the measured limiting current, the enhancement owing to the extraction mechanism was obtained. Since the partition constant of iodine between the toluene and the aqueous phases was approximately 100 to 1, the mass-transfer resistance of iodine in the organic phase could be ignored (24, 25).

The physical properties of the solutions used in this study are summarized in Table I. The Reynolds numbers reported below were calculated on the basis of the hydraulic diameter of the working electrode compartment which, for the channels measuring 0.2×0.75 cm, was 0.315 cm.

It was found that repeated experiments were reproducible to within 1% for one-phase flow, and to within 10% for two-phase flow. The interested reader may refer to the original thesis for additional details (21).

One-phase results.—For fully developed laminar flow between two parallel plates, the average limiting current density over an electrode may be found by integration of Eq. [105-9] in Ref. (26).

$$i_L = 1.4675 \frac{nFDc_1}{s} \left(\frac{\nu}{hDL} \right)^{1/3} \quad [2]$$

Table I. Physical properties

Aqueous ferricyanide solution:			
Density		1.06 g/cm ³	
Viscosity		0.94 cP	
Diffusion coefficient of ferricyanide ion		6.5 × 10 ⁻⁶ cm ² /s	
Aqueous iodide solution:			
Density		1.06 g/cm ³	
Viscosity		0.94 cP	
Diffusion coefficient of iodine (or triiodide)		8.0 × 10 ⁻⁶ cm ² /s	
Iodine-toluene solution equilibrated with aqueous iodide solution:			
Iodine conc in toluene phase	Interfacial tension (dyn/cm)	Density (g/cm ³)	Viscosity (cP)
0.1N	30.67 ± 0.42	0.868	0.546
0.2N	30.73 ± 0.46	0.877	0.550
0.4N	29.37 ± 0.32	0.897	0.554
0.6N	29.00 ± 0.50	0.918	0.571

In this study, the Reynolds number based on hydraulic diameter was used to compare mass-transfer results. Over the range $130 < Re < 1000$, experimental data agreed with Eq. [2] to within 3%. Above $Re = 1000$, experimental data lie slightly above Eq. [2], probably owing to hydrodynamic entrance effects. For example, at $Re = 1250$ (the maximum value used in this study), the limiting current was observed to be 20% greater than expected by Eq. [2]. Limiting current data were obtained with both graphite and DSA, and showed no dependence upon electrode material.

Two-phase results.—In this section, results are given for the disturbance mechanism (k_2), the extraction mechanism (k_3), and for the effect of turbulence promoters.

Because toluene is lighter than water, droplets tend to rise as they are carried upward by flow through the cell. In this study, the maximum slip velocity of droplets, computed from Stokes' law, was 1 cm/s; most experiments were carried out under conditions where the slip velocity was significantly less than 1 cm/s. In addition, the average flow rate (for both phases combined) varied from about 30 cm/s down to about 1 cm/s. Thus, the effect of gravitational forces on the data reported below should be negligible. The conditions where gravitational forces are most likely to influence data are for slow flow of solutions containing large droplets and large volume fractions of the organic phase; such operating conditions, however, lead to poor mass-transfer enhancement and would not, therefore, be likely to be of practical interest.

Disturbance mechanism.—Based on Eq. [1] in the absence of the extraction mechanism ($k_3 = 0$), simple rearrangement gives

$$i_L - nFk_1c_1 = nFk_2c_1 \quad [3]$$

The data shown in Fig. 3(a) represent the quantity nFk_2c_1 (that is, measured limiting current density minus nFk_1c_1) for various conditions of reactant concentration, flow rate, droplet size, volume fraction, and electrode material. All data illustrate a linear relationship between nFk_2c_1 and reactant concentration; therefore, it was concluded that the disturbance mechanism is an additive effect as expressed in Eq. [1]. In the act of "subtracting nFk_1c_1 ," the experimental data reported above were used rather than the theoretical results expressed by Eq. [2]. The following paragraphs summarize the effect of important variables on the disturbance coefficient k_2 .

Volume fraction influences mass transfer as indicated in Fig. 4(a) for graphite electrodes and Fig. 4(b) for DSA electrodes. For both types of materials, the enhancement of mass transfer was greatest at a volume fraction of about 40% organic. Above about 80% organic, the mass-transfer is less than would be found in the absence of the organic phase. The loss of reactivity at high volume fraction may either be owing to coverage of the electrode by the nonconducting organic phase, or to coalescence by large droplets which are less effective in enhancing mass transfer.

Droplet size influences the mass-transfer rate as illustrated in Fig. 5(a) for graphite and Fig. 5(b) for DSA electrodes. For the size range studied, it was found that smaller droplets and higher organic volume fractions gave slightly better mass-transfer enhancement. The difference between behavior of graphite and of DSA was found to be small. Because the mass-transfer enhancement by smaller droplets was not dramatic, and because the energy required to generate droplets increases as the 3.5 power of the diameter, it may not be worthwhile to employ extremely small droplets. This study did not, however, include consideration of surfactants which would stabilize suspensions of very small droplets.

Velocity increases the mass-transfer rate. Figure 6(a) illustrates the velocity dependence of that portion of the overall rate attributable to the disturbance mechanism. That is, the ordinate of every point was obtained by subtracting the corresponding value of nFk_1c_1 from the measured value. The slopes of the lines shown in Fig. 6(a) vary between 0.7 and 1.0, and are thus appreciably greater than the velocity dependence of k_1 , the one-phase coefficient (0.33) indicated by Eq. [2]. That is, the relative significance of the disturbance mechanism increases with flow velocity.

Electrode material has a generally small influence on the disturbance mechanism as may be seen by comparing Fig. 4(a) with Fig. 4(b), and Fig. 5(a) with Fig. 5(b). These results suggest that there was no significant difference between electrodes in coverage of electrode surface by the organic phase, and that the enhancement owing to the disturbance mechanism was controlled primarily by flow conditions.

Extraction mechanism.—Rearrangement of Eq. [1] gives

$$i_L - nFk_1c_1 - nFk_2c_1 = nFk_3c_2 \quad [4]$$

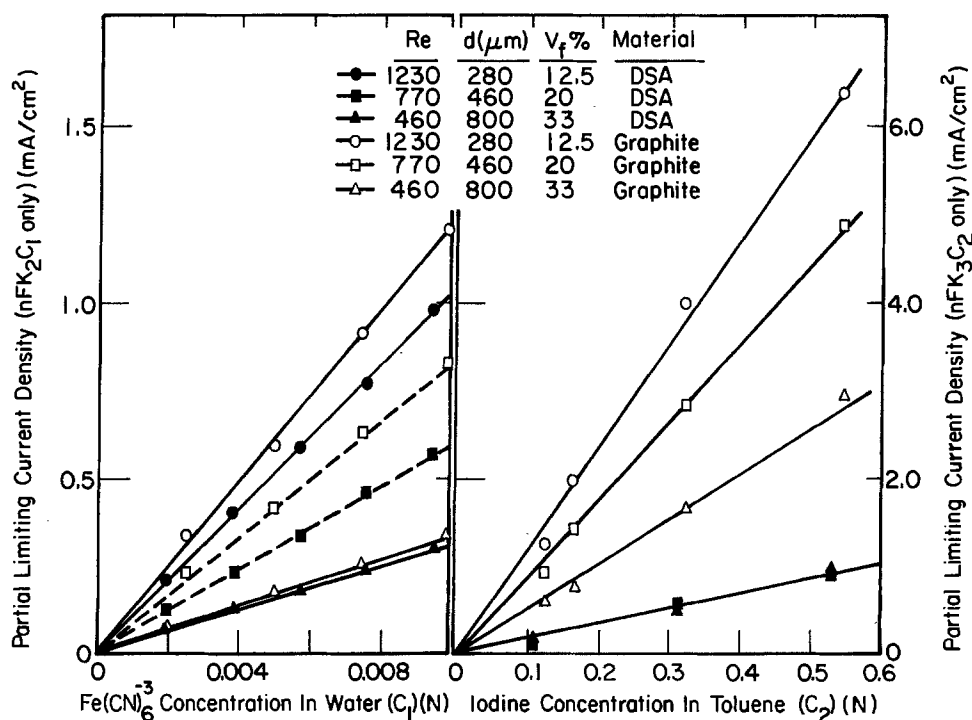


Fig. 3. Demonstration of the validity of the linear additive model, Eq. [1]. (a, left) data are for disturbance mechanism, (b, right) data are for extraction mechanism.

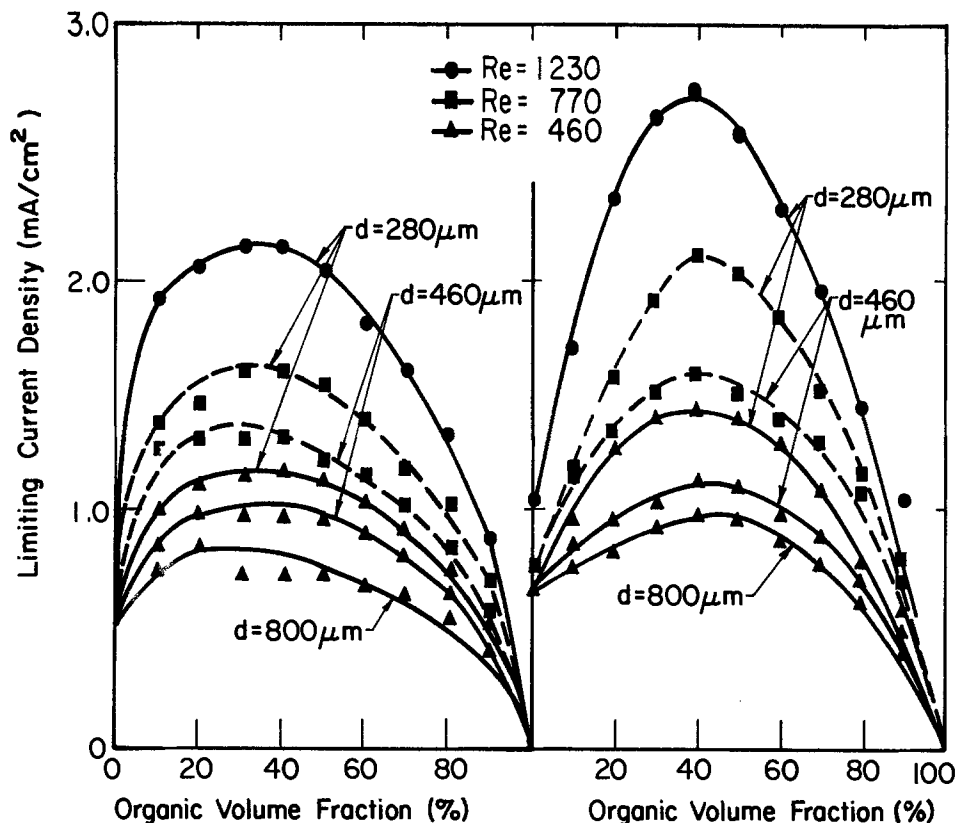


Fig. 4. Effect of electrode material and volume fraction on mass-transfer rate in two-phase flow. (a, left) data are for graphite electrodes, $c_1 = 0.0076N$ (b, right) data are for DSA electrodes, $c_1 = 0.0095N$.

The data shown in Fig. 3(b) represent the quantity nFk_3c_2 (that is, measured limiting current density minus nFk_1c_1 and minus nFk_3c_1) for various conditions of reactant concentration, flow rate, droplet size, volume fraction, and electrode material. It should be noted that the quantity nFk_3c_2 is as large as, or larger than, the limiting current for the one-phase base case. All data illustrate a linear relationship between nFk_3c_2 and reactant concentration in the dispersed phase. Therefore, it was concluded that the extraction mechanism is an additive effect as expressed in Eq. [1]. The following paragraphs summarize the effect of important variables on the extraction coefficient k_3 .

Volume fraction influences the extraction mechanism as indicated in Fig. 7(a) and Fig. 7(b) for graphite and DSA electrodes, respectively. The data in Fig. 7 illustrate only the effect of the extraction mechanism (nFk_3c_2) in that the effects of one-phase transfer and of the disturbance mechanism have been subtracted off as indicated by Eq. [4]. A significant difference is seen between the behavior of the two electrode materials. Also, in contrast to data shown in Fig. 4, the extraction mechanism does not exhibit a volume fraction at which the effect passes through a maximum. It is therefore suggested that, for high volume fractions, the surface becomes wetted with

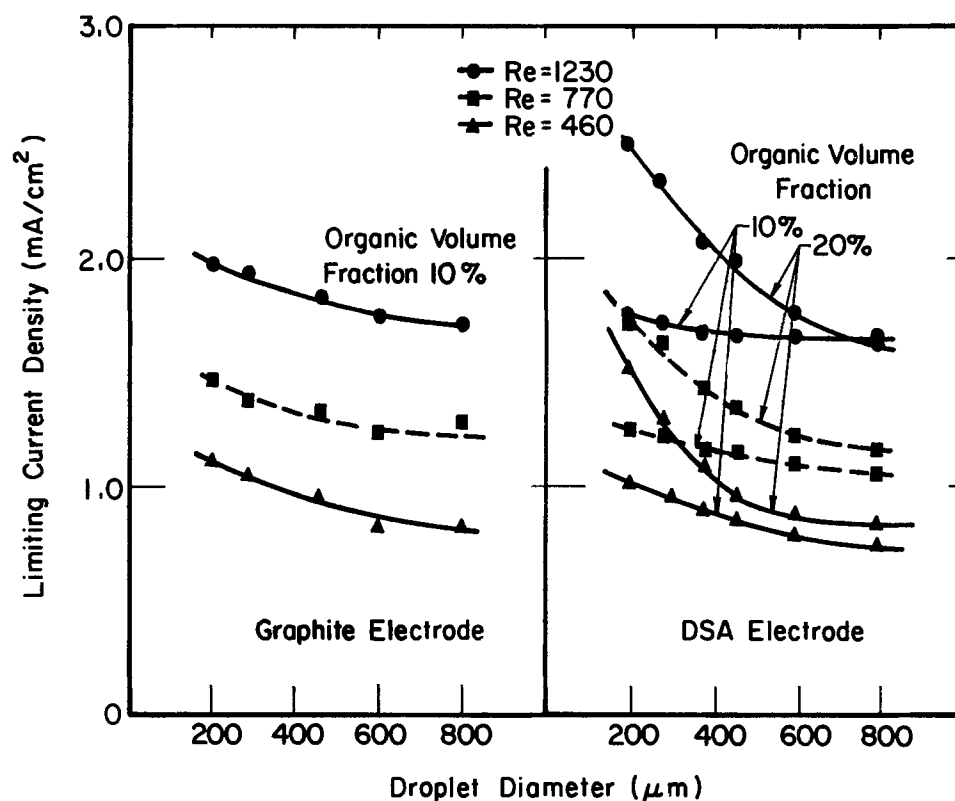


Fig. 5. Effect of dispersed droplet size on mass-transfer rate in two-phase flow. (a, left) data are for graphite electrodes, $c_1 = 0.0076N$; (b, right) data are for DSA electrodes, $c_1 = 0.0095N$.

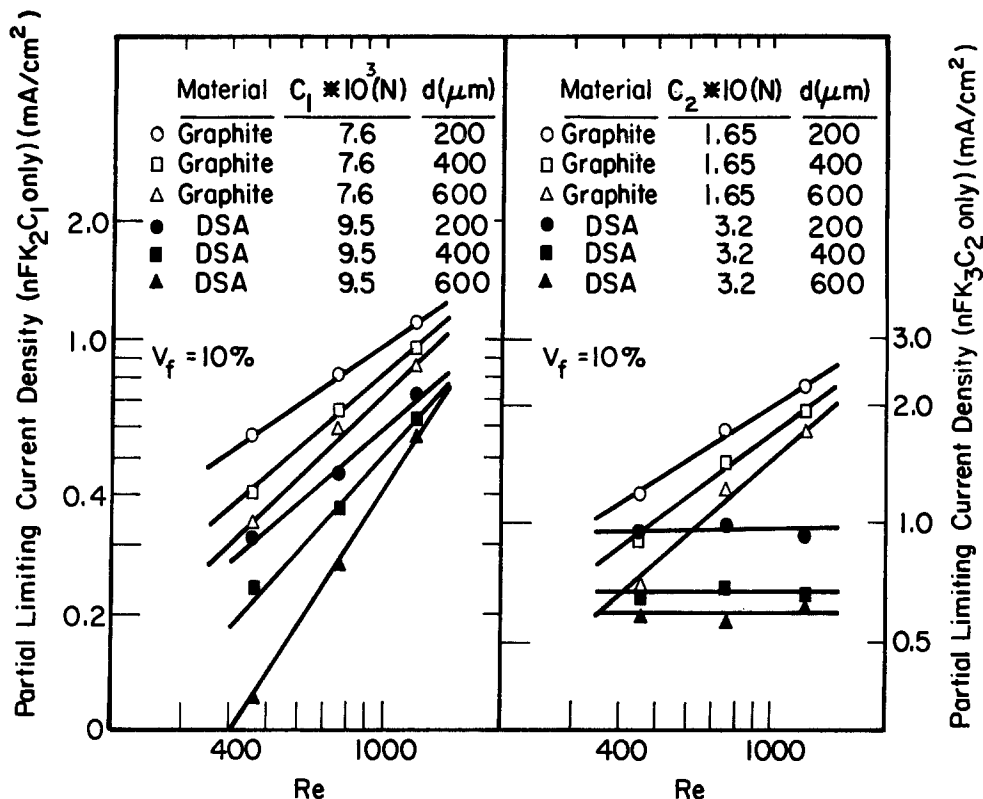


Fig. 6. Effect of velocity on mass-transfer enhancement in two-phase flow. (a, left) data are for disturbance mechanism, (b, right) data are for extraction mechanism.

the organic phase and that, although a portion of the surface may thus be shielded by nonconducting liquid, the shielding is more than compensated by the highly concentrated reactants which are thereby brought into intimate contact with the remaining reactive portion of the electrode surface.

Droplet size influences mass transfer by the extraction mechanism as shown in Fig. 8(a) and Fig. 8(b) for graphite and DSA electrodes, respectively. It may be seen that the enhancement was much more pronounced on the graphite electrode than on the DSA electrode even though the reactant concentration used for the DSA electrodes was about twice that used for the graphite electrodes. On

graphite, the enhancement was larger for the smaller droplets.

Based on Fig. 8, it is suggested that the graphite electrode is partially wetted by the dispersed phase. Small droplets probably hit the electrode and adhere as small puddles, while larger droplets adhere as larger puddles. For the same coverage of electrode by the organic phase, small puddles provide a larger total perimeter for supplying the reactant to the electrode surface, and thus serve to enhance the mass-transfer rate by the greater amount.

By comparison of Fig. 8(a) with Fig. 8(b), it is seen that the DSA electrode exhibited negligible mass-transfer en-

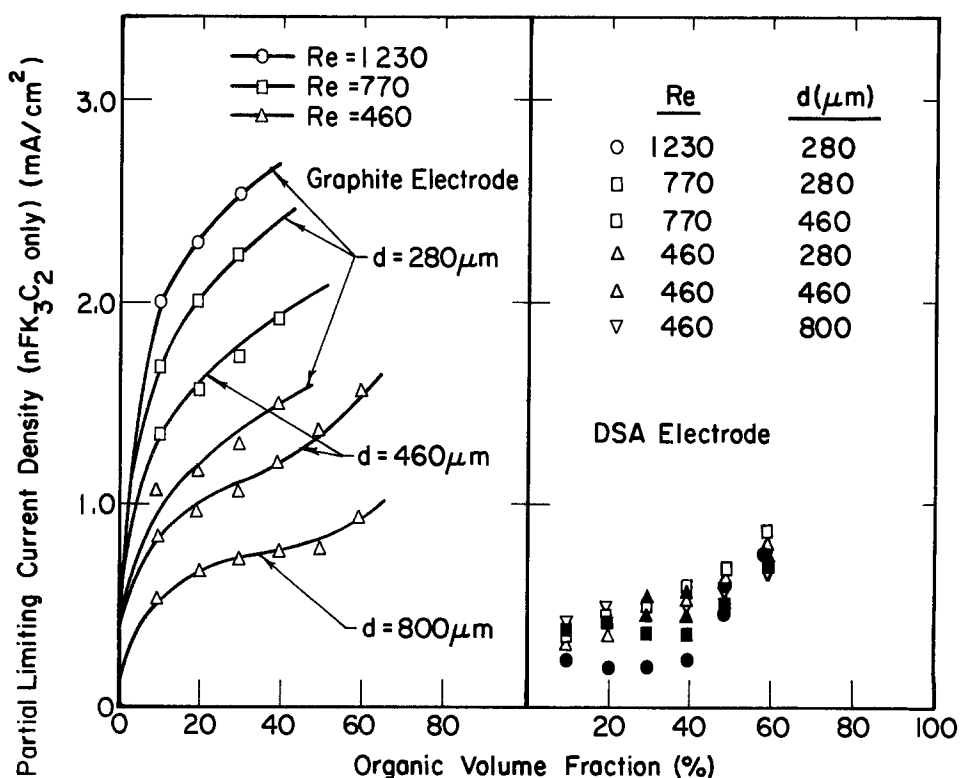


Fig. 7. Effect of electrode material and volume fraction on mass-transfer enhancement by the extraction mechanism. (a, left) data are for graphite electrodes, $c_2 = 0.165N$; (b, right) data are for DSA electrodes, $c_2 = 0.32N$.

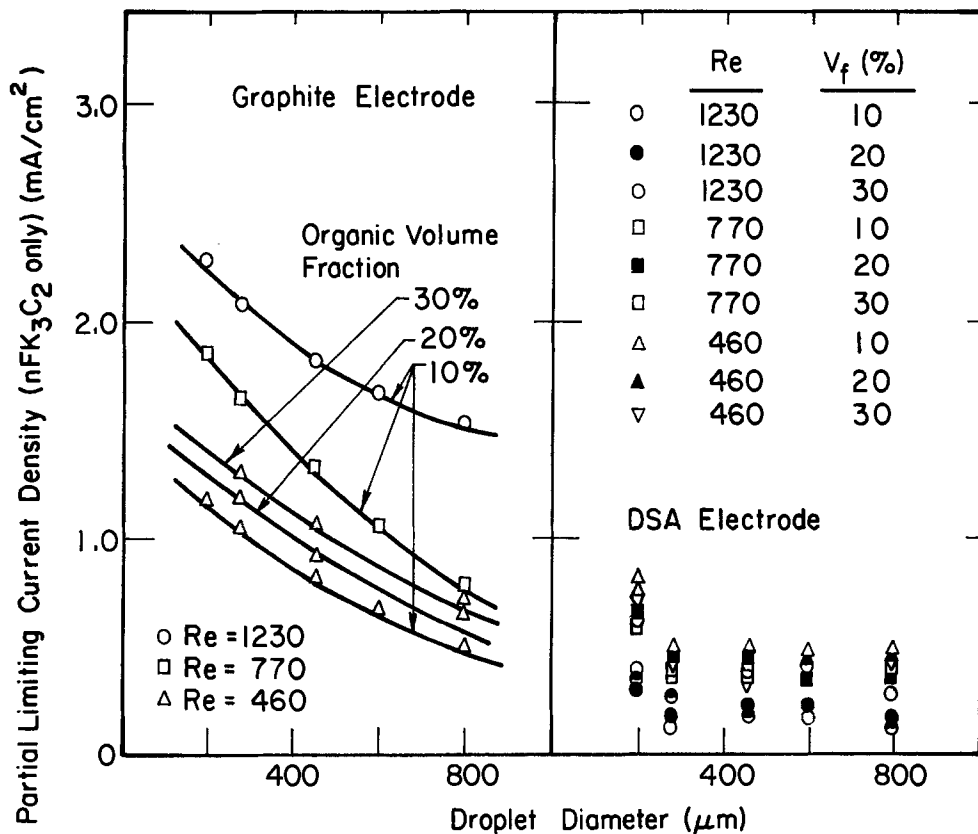


Fig. 8. Effect of electrode material and droplet size on mass-transfer enhancement by the extraction mechanism. (a, left) data are for graphite electrodes, $c_2 = 0.165N$; (b, right) data are for DSA electrodes, $c_2 = 0.32N$.

enhancement by the extraction mechanism. It is therefore suggested that the DSA material is not wet by the reactive dispersed droplets.

Velocity effect for the extraction mechanism alone is shown in Fig. 6(b) for both graphite and DSA electrodes. For the graphite electrode, the enhancement by extraction depends upon flow rate to the power of between 0.6 and 1.0, while, for DSA electrodes, the enhancement is independent of flow rate. The difference lies in the ability of the two electrode materials to utilize the reactive droplets which are brought to the surface region by the fluid flow conditions.

Electrode materials clearly exhibit a profound influence upon the extraction mechanism, in contrast to a minor influence upon the disturbance mechanism. It is suggested that the affinity between the surface and the dispersed phase controls the extraction mechanism. The DSA electrode is an oxide surface which is quite polar in comparison with graphite; by the same token, water is a strong polar molecule in comparison with toluene. Therefore, the nonpolar organic droplets are more likely to wet the nonpolar graphite electrode surface than the polar DSA surface. The absence of significant mass-transfer enhancement observed by Dworak *et al.* (14-16) may be in part owing to their use of Ni electrodes.

Turbulence promoter.—When a turbulence promoting grid is placed into a flow channel, then the definition of Reynolds number becomes ambiguous since it is no longer clear which characteristic dimension should be used to correlate results. Therefore, for evaluation of turbulence promoters, mass-transfer rates were compared on the basis of the volumetric flow rate through the cell instead of the Reynolds number. For one-phase flow, Fig. 9 provides experimental mass-transfer data and, for comparison, also shows the prediction of Eq. [2] for the expected mass-transfer rate without the turbulence promoter. It may be seen that an enhancement of up to sevenfold in mass-transfer rate was achieved by use of the turbulence promoter. Such enhancement, however, was achieved at the expense of substantially increased pumping power.

For two-phase flow containing an inert dispersed phase and a turbulence promoter, the mass-transfer rates

shown by the dashed lines in Fig. 10 were found. By comparison of these data with Fig. 9, it was found that the addition of the inert second phase degraded mass-transfer performance in cells containing turbulence promoters. It is suggested that the plastic turbulence promoter was easily wet by the dispersed phase, and thus facilitated coverage of the electrode surface by the nonconducting inert organic phase. In addition, the mass-transfer rate in the presence of the turbulence promoter was not influenced by the droplet size of the inlet fluid; evidently, the turbulence promoter acted as a static mixer and produced its own two-phase flow conditions regardless of variation in droplet size in the feed stream.

For two-phase flow containing a reactive dispersed phase, the data connected by solid lines in Fig. 10 illustrate results on graphite electrodes for several conditions of flow rate, droplet size, and volume fraction. It may be seen that the enhancement by presence of the second

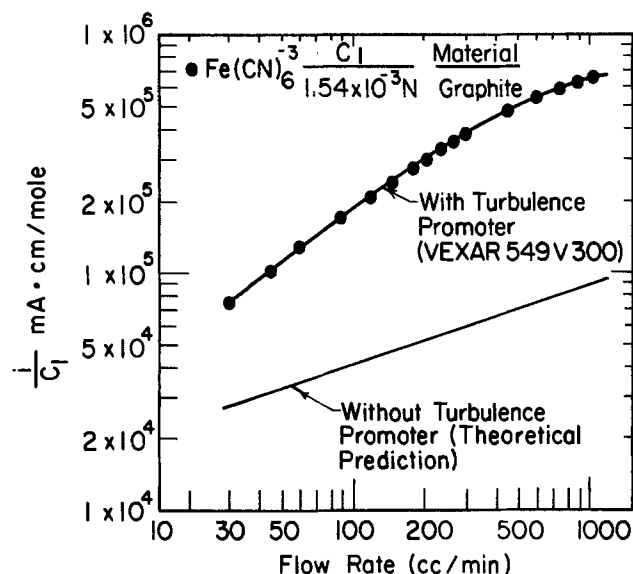


Fig. 9. Effect of turbulence promoter on mass-transfer rate in one-phase system, graphite electrodes, $c_1 = 0.00154N$ ferricyanide.

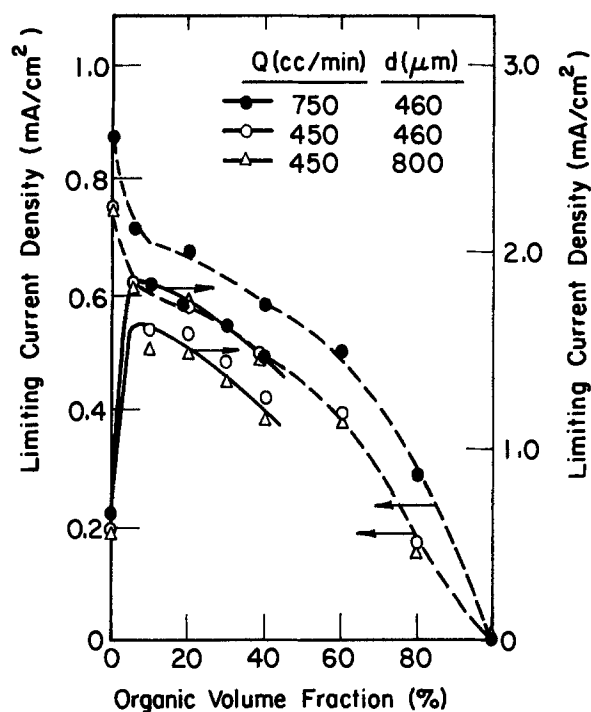


Fig. 10. Effect of turbulence on mass-transfer rate in two-phase system, with variation of volume fraction, flow rate, and droplet size. Graphite electrodes with Vexar 549V300 turbulence promoter. (Dashed line) data are for an inert dispersed phase, $c_1 = 0.00154N$ (solid line) data are for a reactive dispersed phase, $c_1 = 0.00102N$ and $c_2 = 0.08N$.

phase occurs but achieves a maximum at 10% volume fraction or less. The enhancement improves with flow rate but is insensitive to droplet size in the feed stream. Above a volume fraction of 10%, there is a decay in mass-transfer performance, owing probably to electrode coverage by organic phase.

Examples.—It should be emphasized that the concentration of reactive species used in the solutions investigated in this study was kept low in order to simplify measurement of mass-transfer limited behavior. As a consequence, the current densities reported in the figures are much lower than would be required of industrial processes. However, the use of higher reactant concentrations, particularly in the dispersed organic phase, would increase current density significantly. For example, consider Fig. 7(a) in which a current density of 2.5 mA/cm² is obtained from dispersed droplets containing reactant at 0.165*N*. If, instead, an organic reactant dissolved at 10*M* would be used in the dispersed phase, then mass-transfer limiting current density would increase to on the order of 150 mA/cm².

For typical operating conditions ($Re = 1000$, $V_t = 10\%$, $d = 500 \mu m$, graphite electrode), if the value of k_1 is unity (a reference value), then Fig. 4(a) suggests that k_2 is also about unity, and Fig. 8(a) indicates that k_3 is about 0.1. Thus, the relative importance of the individual mechanisms can be ascertained if these mass-transfer coefficients are multiplied by the corresponding concentrations as shown for several cases in Table II. It may be seen that the extraction mechanism dominates the other two mechanisms when the solubility of the reactant in the continuous phase is less than 10% of the solubility in the dispersed phase. For low solubility of reactant in the continuous phase (Case 1), the extraction mechanism serves to increase the mass-transfer rate by a factor of 1000 over that obtained with one-phase flow. If the solubility of the reactant in the aqueous solution is greater than that in the dispersed phase (Case 5), then the presence of the second phase serves to approximately double the mass-transfer rate, but at the expense of increased process complexity.

The relative importance of the individual mass-transfer mechanisms can be used in the design of two-phase sys-

Table II. The relative importance of the mass-transfer enhancement mechanisms with respect to the reactant concentrations in both the continuous and the dispersed phase solutions ($k_1 = 1$, $k_2 = 1$, $k_3 = 0.1$)

Case	c_1 (mol/ liter)	c_2 (mol/ liter)	$k_1 c_1$ One-phase convective flow mechanism	$k_2 c_1$ Disturbance mechanism	$k_3 c_2$ Extraction mechanism
1	0.001	10	0.001	0.001	1
2	0.01	10	0.01	0.01	1
3	0.1	10	0.1	0.1	1
4	1.0	10	1.0	1.0	1
5	10.0	10	10.0	10.0	1

tems. For example, if the largest term in Eq. [1] is $nFk_1 c_1$, then there is no advantage in introducing the dispersed phase into the cell; increasing the reactant solubility in the aqueous solution, or mass-transfer coefficient k_1 , would be the best procedure. If the largest term in Eq. [1] is $nFk_2 c_1$, then any inexpensive and stable inert dispersed phase could be introduced into the cell in order to enhance mass transfer. But if the largest term in Eq. [1] is $nFk_3 c_2$, then the reactant should be introduced in the dispersed phase.

Conclusions

Mass transfer in parallel plate electrolyzers with two-phase liquid-liquid flow was investigated by the electrochemical limiting current method. The overall mass-transfer rate was found to follow a linear additive model, expressed in Eq. [1], for which contributions to the overall rate included the one-phase convective flow (k_1), the disturbance by presence of the second phase (k_2), and the replenishment of reactant by extraction from the second phase (k_3). The experimental approach enabled the overall mass-transfer rate to be separated into the individual mechanisms. The important variables for coefficients k_2 and k_3 included dispersed phase volume fraction, droplet size, flow velocity, electrode material, and the presence of a turbulence promoter.

The significant results of this investigation are summarized as follows: (i) mass-transfer enhancement by the disturbance mechanism k_2 is insensitive to electrode material, while enhancement by the extraction mechanism k_3 is higher on nonpolar (graphite) than on polar (DSA) electrode surfaces. (ii) An increase in organic phase volume fraction leads to mass-transfer enhancement by both disturbance and extraction mechanisms, over a volume fraction range of about 0-80%. (iii) The effect of flow rate is to increase all mass-transfer coefficients; the velocity dependence of the coefficients is 0.33 for k_1 , 0.7-1.0 for k_2 for both types of electrode materials, and 0.6-1.0 for k_3 on graphite. With DSA electrodes, there was no discernible improvement in k_3 upon increasing flow velocity. (iv) Over the range of droplet sizes studied, the coefficients k_2 and k_3 varied by less than a factor of two, and were greatest for high volume fractions, for small droplets, and on graphite. (v) Mass-transfer enhancement by the disturbance mechanism k_2 was small in comparison with that achieved by a turbulence promoter in one-phase flow. Mass-transfer enhancement by the extraction mechanism k_3 can be significantly greater than that achieved with a turbulence promoter in one-phase flow.

In this study, emphasis has centered on mass-transfer enhancement. Other reasons for introducing a dispersed immiscible second phase may also exist for electrochemical applications. For example, extraction of a desired reaction product into a second phase may help protect it from undergoing further degradation reactions to unwanted by-products. Also, a second phase may be useful for continuous extraction of unwanted reaction products from a cell during operation, for example, polymeric surface tars. For these reasons, the continued investigation of electrolysis in the presence of two-phase liquid systems appears to be warranted.

A macroscopic approach was used in the present study in order to separate the overall mass-transfer sequence

into several component steps. Further study will require improved understanding of microscopic features such as interaction of dispersed droplets with the mass-transfer boundary layer, as well as mass transfer during droplet impingement and wetting of the electrode surface. The consideration of surfactants would add a major new variable to those included in this study. Surfactants would be expected to play an influential role both in two-phase flow and wetting phenomena, and also in the electrochemistry of the surface reactions.

The experimental results reported in this study represent only a small number of possible combinations of important variables. In particular, only one mixture of solvents was studied, and only one reactor configuration was used. Additional experimental studies in different systems would contribute toward better understanding of enhancement coefficients k_2 and k_3 in order that they may be related to system parameters with use of generalized dimensionless correlations.

Acknowledgments

This work was carried out under partial sponsorship of Gould Incorporated (Subcontract 20474G of DOE-EPRI Contract DE-AC02-78ET29345, EPRI Project RP635-2) and by the National Science Foundation (Grant CPE-80-08947). Some electrode materials were supplied by Ronald A. Putt of Gould Incorporated, Rolling Meadows, Illinois.

Manuscript submitted Aug. 1, 1983; revised manuscript received Nov. 22, 1983.

LIST OF SYMBOLS

c_1	reactant concentration in the aqueous phase solution, mol/cm ³
c_2	reactant concentration in the organic phase solution, mol/cm ³
d	dispersed droplet size, μm
D	diffusion coefficient, cm ² /s
F	Faraday's constant, 97,487 C/equiv
h	gap of the flow channel, cm
i_L	average limiting current density over the electrode length L , A/cm ²
k_1	mass-transfer coefficient due to the one-phase convective flow, cm/s
k_2	mass-transfer coefficient due to the disturbance mechanism, cm/s
k_3	mass-transfer coefficient due to the extraction mechanism, cm/s

L	length of electrode, cm
n	Faraday's per mol of substance electrolyzed
Re	Reynolds number based on hydraulic diameter
S	electrode material
s	stoichiometric coefficient of species in electrode reaction
v	fluid velocity, cm/s
v_1	organic dispersed phase volume fraction

REFERENCES

1. T. Kempf, German Pat. 117,251 (1903).
2. B. B. Dey, T. R. Govindachari, and S. C. Rajagopalan, *J. Sci. Ind. Res.*, **4**, 559 (1946).
3. K. S. Udupa, G. S. Subramanian, and H. V. K. Udupa, *Bull. Acad. Pol. Sci.*, **9**, 45 (1961).
4. M. Fremery, H. Hover, and G. Schwarzlose, *Chem.-Ing.-Tech.*, **46**, 635 (1974).
5. J. P. Millington, *Chem. Ind. (London)*, **18**, 780 (1975).
6. M. Seko, *Chem. Econ. Eng. Re.*, **7**, 20 (1975).
7. G. S. Laddha and T. E. Degaleesan, "Transport Phenomena in Liquid Extraction," McGraw-Hill Book Co., New York (1978).
8. J. Postlethwaite and D. N. Holdner, *Can. J. Chem. Eng.*, **54**, 255 (1976).
9. G. C. Pini and P. L. DeAnna, *Electrochim. Acta*, **22**, 1423 (1977).
10. N. Ibl, *Chem.-Ing.-Tech.*, **35**, 353 (1963).
11. L. J. J. Janssen, *Electrochim. Acta*, **23**, 81 (1978).
12. T. R. Beck, *This Journal*, **116**, 1038 (1969).
13. R. C. Alkire and P.-Y. Lu, *ibid.*, **126**, 2118 (1979).
14. R. Dworak, H. Feess, and H. Wendt, *AIChE Symp. Ser.* **185**, **75**, 38 (1979).
15. R. Dworak and H. Wendt, *Ber. Bunsenges. Phys. Chem.*, **81**, **8**, 728 (1977).
16. R. Dworak and H. Wendt, *ibid.*, **81**, **8**, 864 (1977).
17. K. Kinoshita, S. C. Leach, and C. M. Ablow, Final Report for EPRI Contract RP 370-2 (Jan. 1982).
18. A. Storck and F. Coeuret, *Electrochim. Acta*, **22**, 1155 (1977).
19. F. Schwager, P. M. Robertson, and N. Ibl, *ibid.*, **25**, 1655 (1980).
20. A. Storck and D. Hutin, *ibid.*, **26**, 127 (1981).
21. P.-Y. Lu, Ph.D. Thesis, University of Illinois, Urbana, IL (1982).
22. S. J. Chen, KTEK-5, Kenics Corp. (July 1972).
23. M. Louis, "Handbook of Analytical Chemistry," ed.-1 McGraw-Hill, New York (1963).
24. M. Yamaguchi, T. Fujimoto, and T. Katayama, *J. Chem. Eng. Jpn.*, **8**, 361 (1975).
25. M. Yamaguchi and T. Katayama, *ibid.*, **10**, 280 (1977).
26. J. Newman, "Electrochemical Systems," p. 318, Prentice Hall, Inc., Englewood Cliffs, NJ (1973).

Zinc Selenide Photoelectrodes

Efficient Radiative Recombination in a Stable Photoelectrochemical Cell

Patricia M. Smiley, Richard N. Biagioni, and Arthur B. Ellis*

Department of Chemistry, University of Wisconsin-Madison, Madison, Wisconsin 53706

ABSTRACT

Photoluminescence (PL) and electroluminescence (EL) from single-crystal, n-type, Al-doped ZnSe (ZnSe:Al) electrodes have been studied. These samples exhibit both edge emission ($\lambda_{\text{max}} \sim 460$ nm) and subbandgap emission when excited at several ultrabandgap wavelengths. The latter PL band is particularly intense, with a measured radiative quantum yield of $\sim 10^{-1}$ to 10^{-2} ; the transition appears to be at least partially self-activated (SA) in origin, based on previously reported PL data. Excited-state communication involving the two emissive states is inferred from time-resolved PL measurements. Stable photoelectrochemical cells (PEC's) can be constructed from n-ZnSe:Al electrodes and aqueous diselenide or ditelluride electrolytes. Applied potential quenches both of the photoanodes' PL bands roughly in parallel. The extent of PL quenching is consistent with a dead-layer model previously used to describe quenching in Au-ZnSe Schottky diodes. When used as a dark cathode in aqueous, alkaline peroxydisulfate electrolyte, EL from ZnSe:Al electrodes is observed. PL and EL spectral distributions are similar and indicate that the same emissive excited states are populated in the two experiments. Measured EL efficiencies, $\sim 10^{-4}$ to 10^{-6} at -2.2 and -1.8 V vs. SCE, respectively, are much smaller than PL efficiencies. Possible sources of the discrepancies are discussed.

Keen interest in photoelectrochemical cells (PEC's) has focused attention on the excited-state properties of the semiconductor electrodes which serve as the key element of these devices (1). We and others have studied photoluminescence (PL) and electroluminescence (EL) from a variety of II-VI and III-V semiconductor electrodes in an effort to determine the effect of PEC parameters on the solids' excited-state deactivation routes (2). In general, measured radiative quantum yields, ϕ_r , of these materials have been small, $\sim 10^{-3}$ - 10^{-5} . We describe in this paper an electrode, n-ZnSe:Al, whose emission competes favorably ($\phi_r \sim 10^{-1}$ - 10^{-2}) with other deactivation paths in stable, efficient PEC's. As observed with other semiconductor electrodes (3), the PL of n-ZnSe:Al electrodes can be perturbed and EL initiated by interfacial charge-transfer processes. We show that PL quenching by applied potential is compatible with a dead-layer model used to describe such quenching in other PEC's (4, 5) and in Au-ZnSe Schottky diodes (6).

Experimental

Materials.—Single crystal (111) plates of n-type ZnSe:Al (~ 2 ppm Al based on arc emission spectroscopy) were generously provided by North American Philips Corporation, Briarcliff Manor, New York; the samples ($\sim 5 \times 5 \times 0.25$ mm) had been cut from boules which were obtained from Eagle-Picher Industries, Miami, Oklahoma, and had been subsequently heat-treated in molten Zn at 950°C for 24h to lower their resistivity to ~ 1 - 10 Ω -cm. Twinned areas may be present below the surface in some of the samples employed. Sample carrier concentrations of $\sim 10^{17}$ - 10^{18} cm^{-3} were estimated from both dc Hall measurements (7) and Mott-Schottky data. In the former measurement, a Varian Associates Model V-2301-A dc electromagnet producing a field of ~ 0.5 kG was employed. Capacitance measurements of the ZnSe:Al electrodes were made at 1.0 and 0.8 kHz in 1M OH^- and diselenide electrolytes, respectively, using an Ithaco Dynatrac 391 lock-in voltmeter, EG&G PAR Models 173 potentiostat and 175 programmer, and a Wavetek Model 182A 4MHz function generator. Electrodes were prepared by etching the solids for 20s with 1:40 Br_2/MeOH (v/v), making ohmic contact to the Se-rich crystal face by soldering with In, and then mounting the solid as an electrode as described previously (8). Resistivity in some samples was deliberately enhanced by heat-treatment with Se (Alfa; m3N purity). For these experiments, an ~ 10 mg sample of ZnSe:Al was placed in a quartz tube with ~ 0.2 mg of Se. The quartz ampul was evacuated (~ 0.1 torr), sealed to a volume of ~ 3 cm^3 , and heated at 700°C in a Lindberg furnace for ~ 30 s.

After its removal from the ampul, the solid was etched until bright PL was observed; then it was mounted as an electrode. Sulfide, diselenide, and ditelluride electrolytes were prepared as described previously (9, 10), except that after the solid Na_2Se was washed with NaOH, it was dissolved in conc KOH to yield solutions whose compositions were ~ 10 M KOH/0.25M Se^{2-} . During PEC experiments, the electrolytes were vigorously stirred and blanketed with N_2 . Preparation of peroxydisulfate electrolyte has been described (11). MgO powder was obtained from Baker Chemical Company.

PL properties.—Front-surface PL spectra at ambient temperature and at 77 K were obtained with the Aminco-Bowman spectrophotofluorometer described previously (3). The high pressure Xe lamp of the instrument was used in conjunction with an interference filter (Edmund Scientific) for 405 nm excitation; a Corning 3-72 filter was used to prevent this light from reaching the detection optics. All PL and EL spectra were corrected for detector sensitivity from 350 nm to 800 nm using a procedure previously described (3). The correction factors were incorporated into a computer program for use with an Apple II Plus Computer. Spectra were digitized, corrected by the program, and plotted on an Epson printer.

Measurements of ϕ_r were made by placing the ZnSe:Al samples and MgO powder (reference) in turn in a quartz cuvette positioned in the Aminco-Bowman spectrometer's sample compartment as previously described (3, 12). The sample was irradiated "head on" with the spectrometer's high pressure Xe lamp; interference filters (FWHM is ~ 10 nm, except for 366 nm, where it is ~ 30 nm) were used to isolate the desired excitation wavelengths. Both the reflected and emitted intensities were corrected for relative detector response.

The dependence of ϕ_r on incident intensity was probed using the near-UV lines of a Coherent Radiation CR-12 Ar⁺ laser (351 and 364 nm doublet). Samples were mounted with epoxy on a glass rod and positioned at $\sim 45^\circ$ to both the laser beam and the emission detection optics. PL spectra were run as a function of incident intensity which was varied with Melles Griot neutral density filters; the EG&G radiometer was used to measure incident intensity in conjunction with a glass slide serving as a beam splitter.

Time-resolved PL data were obtained in air with a pulsed N_2 laser (337 nm) and N_2 -pumped dye laser (460 nm) using instrumentation and techniques previously reported (13). Peak intensities of ~ 3 and 30 kW/cm^2 were used in these experiments with essentially no difference in the resulting decay curves.

PEC experiments.—A flat-faced quartz cell equipped with a side arm was employed for most PEC measure-

* Electrochemical Society Active Member
Key words: zinc selenide, luminescence, photoelectrochemistry

ments. Long-term stability experiments in diselenide and ditelluride electrolytes were conducted as described previously with an n-ZnSe:Al working electrode and a Pt foil counterelectrode (8). A polyethylene bag was attached to the top of the cell and purged with N₂ during the experiments.

Photoaction spectra were obtained as previously described (14) using transparent selenide electrolyte. The output of a 150W Xe lamp (Oriel) was monochromatized for excitation; lamp intensity was measured with the EG&G radiometer whose response from 350-800 nm was corrected with the manufacturer's calibration factors. Photocurrents were measured at -1.0V vs. SCE.

A standard three-electrode potentiostatic setup was used for obtaining *i*LV data. Excitation at 366, 405, and 436 nm (200W, high pressure Osram Hg lamp with interference filters) was used; lenses and masks were used to fill the exposed electrode area with light. Electrochemical measurements were made with an EG&G PAR Model 174 potentiostat; *i*-V curves were recorded on a Houston Model 2000 X-Y recorder. Steady-state PL intensity in operating PEC's was influenced by production of colored Se₂²⁻ and Te₂²⁻ species. A pulse technique was employed to minimize this problem during the generation of *i*LV curves. The technique consisted of pulsing the electrode between open circuit and increasingly positive potentials. Typically, the electrode sat at open circuit for 500 ms, then was pulsed for 57 ms to a potential which increased by 5 mV with each cycle. The *i*-V curves obtained in this manner were identical to steady-state *i*-V curves. PL was detected with the EG&G radiometer covered by a 600 nm interference filter. Output signals were displayed on a Tektronix Model RM503 oscilloscope equipped with a camera; sweep rates which resulted in potential steps of ~10 mV/s permitted an entire PL intensity-V curve to be photographed with one exposure of ~2 min. Incident light intensity was measured by inserting a mirror (~80% reflectivity) and reflecting the light into the EG&G radiometer. The weakness of the edge PL required use of the near-UV lines of the Ar⁺ laser and the Aminco-Bowman spectrometer for generation of *i*LV curves in which both PL bands could be monitored.

EL properties.—EL spectra were obtained in 5M NaOH/0.1M K₂S₂O₈ electrolyte by pulsing the electrode between 0.0V (8s) and a potential cathodic of ~ -1.7V vs. SCE (1s), while slowly scanning the monochromator of the emission spectrometer (12 nm/min), as described previously (11). At potentials where they could be obtained, steady-state EL spectra were essentially identical to those generated by the pulse technique.

Instantaneous EL efficiencies were determined as described previously (3). The total emitted energy per pulse measured with an EG&G Model 550-3 pulse integration module was converted to 600 nm photons using the manufacturer's correction factor at that wavelength.

Results and Discussion

Single crystal samples of cubic n-ZnSe doped with Al (~2 ppm) and having carrier concentrations of ~10¹⁷–10¹⁸ cm⁻³ were employed in these studies. Sections below describe the PL properties of these solids, their perturbation by PEC parameters, and EL from the solids.

PL spectra.—Near-UV excitation of n-ZnSe:Al crystals produces effulgent, orange emission. The 295 K PL spectrum of the material (Fig. 1) is dominated by a broad band (FWHM ~115 nm) with λ_{max} ~ 600 nm; a weaker, sharper band (FWHM ~10 nm) peaking at ~460 nm is also present. The latter transition, whose intensity is reported to be very sensitive to preparative conditions (15), occurs near the bandgap energy [E_g ~ 2.7 eV (16)]. Although the band's origin in our samples is unknown, its designation as edge emission appears apt based on its energetic proximity to E_g and its temperature dependence: Fig. 1 indicates that the band blue shifts by ~0.09 eV to 445 nm upon cooling to 77 K, consistent with the temperature co-

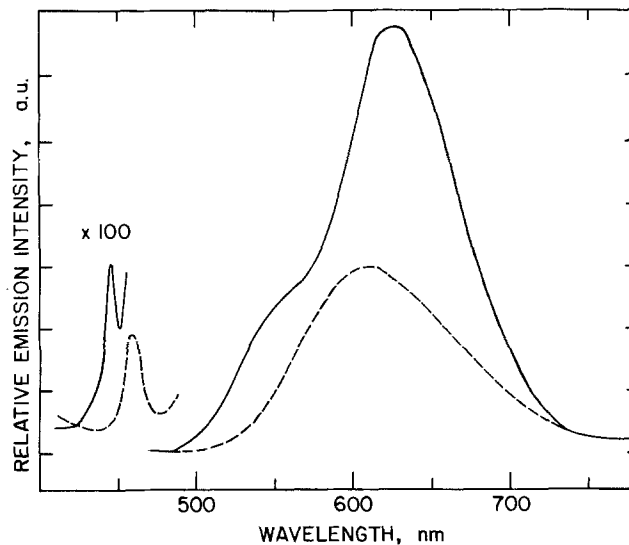


Fig. 1. Corrected, front-surface PL spectra of n-ZnSe:Al at 295 K (dashed line) and 77 K (solid line). Both spectra were taken at the same sensitivity (a 100-fold increase in sensitivity was used in scanning the 410-480 nm region). The sample was excited with identical intensities of 405-nm light without disturbing the experimental geometry.

efficient of -4.1×10^{-4} eV/K reported for exciton emission from cathodoluminescence studies (16b).

An intense orange band at ~630 nm has been reported for many ZnSe samples and assigned as self-activated (SA) PL; the transition is believed to involve a deep trapping level arising from a complex based on a Zn vacancy, V_{Zn}, and a next-neighbor donor impurity such as Al_{Zn} (Al on a Zn site) (17). Our spectra are somewhat more complex, but accord well with spectra reported by Bouley *et al.* (15). Figure 1 reveals that the band at 600 nm seen at 295 K splits into two bands with λ_{max} ~ 630 and 550 nm at 77 K. The former, likely the SA band, has been assigned to complexes involving a neutral (V_{Zn}Al_{Zn}) or ionized defect [(V_{Zn}Al_{Zn})⁻], while the latter was ascribed to a defect involving Al and an alkali metal impurity (15). For convenience, we will refer to the 600 nm transition as a SA band, although we emphasize that its origin is not fully established in our samples.

PL efficiency.—As previously noted, samples of n-ZnSe:Al are highly emissive. We have employed a technique to obtain φ_r values which, using a common geometry, compares light reflected from a nonabsorbing material with light reflected and emitted from a sample (12). Table I presents a compilation of measured φ_r values obtained in air for the SA emission using several different excitation wavelengths. The tabulated values, uncorrected for self-absorption and internal reflectivity, are substantial, ranging from ~2-5%. Large radiative efficiencies are also supported by the modest doubling of φ_r observed when samples are cooled to 77 K. Similar efficiencies and thermal behavior were reported for the ZnSe:Al samples studied by Bouley *et al.* (15). The decline in φ_r with excitation wavelength (Table I) suggests the presence of a nonemissive near-surface region: reported absorptivities increase substantially below 460 nm (18), so that a nonemissive layer is expected to reduce φ_r as it absorbs larger fractions of incident light.

PL decay times.—Time-resolved PL properties were studied in air using the 337 and 460 nm outputs of a N₂ laser and N₂-pumped dye laser, respectively. Measurements of the edge PL band were limited by the duration of the laser pulse, indicating a decay time of ≤7 ns. A similar limitation was observed for the risetime of the SA band and its initial decay. After the peak intensity of the band had dropped ~30%, however, a much longer nonexponential decay was observed with typical τ_{1/e} values being ~1 μs. These properties were independent of the excitation wavelengths employed and of the PL wavelength monitored.

Table I. PL properties and measurements of efficiency in n-ZnSe:Al-based PEC's^a

Electrode ^b	λ_{ex}, nm^c	ϕ_r^d	ϕ_x^e	$(1 - \frac{\phi_r}{\phi_{TFB}})^f$	ϕ_x at η_{max}^g	E_v at η_{max}, V^h	$\eta_{max} (%)^i$
As received	366	0.02	0.37	0.16	0.25	0.90	6.6
	405	0.03	0.25	0.11	0.18	0.85	4.9
	436	0.04	0.18	0.09	0.14	0.85	4.2
	460	0.05					
Treated	366		0.60	0.38	0.42	0.85	10.4
	405		0.31	0.17	0.23	0.72	5.3
	436		0.22	0.13	0.13	0.73	3.3

^a PL properties related to use of n-ZnSe:Al electrodes in PEC's. Most of the properties are derived from iLV curves generated with a three-electrode potentiostatic setup (n-ZnSe:Al working electrode, Pt foil counterelectrode, and SCE reference electrode). To optimize transparency, experiments with 366 nm light were conducted in 10M KOH/0.25M Se²⁻/0.001M Se₂²⁻ electrolyte; for 405 and 436 nm light, an electrolyte of 8M KOH/0.2M Te²⁻/0.002M Te₂²⁻ was employed. The electrode, having an exposed surface area of ~0.25 cm², was excited with ~0.5-2.0 mW of power.

^b The n-ZnSe:Al sample was used either "as received" or treated with Se as described in the Experimental section and text.

^c Excitation wavelength. A 150W high pressure Xe lamp or 200W high pressure Hg lamp equipped with interference filters was employed for ϕ_r data and iLV curves, respectively.

^d Radiative quantum efficiencies obtained in air for the SA band. Values are uncorrected for self-absorption and internal reflectivity.

^e Measured photocurrent quantum efficiency at -1.0V vs. SCE. Values are uncorrected for solution absorption and reflective losses.

^f Fractional PL quenching between -1.0V vs. SCE and the flatband potential, approximated here as the open-circuit potential. PL intensity was monitored at 600 nm.

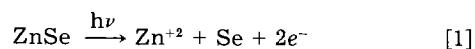
^g Measured photocurrent quantum efficiency at the potential corresponding to maximum optical-to-electrical energy conversion efficiency.

^h Output voltage at the maximum energy conversion point. The diselenide and ditelluride redox potentials were -0.95 and -1.10V vs. SCE, respectively.

ⁱ (Maximum electrical power out divided by input optical power) \times 100.

Mechanistically, the different temporal behavior of the edge and SA bands is an important result in that it indicates that the corresponding excited states are not thermally equilibrated (19). Initiation of the SA emission is also addressed by the data. Although the rapid risetime for the SA band could reflect population via the excited state responsible for edge emission, our data are also consistent with population from a yet higher energy state when ultrabandgap wavelengths are employed; in the latter case, the strong lattice coupling characteristic of deep traps provides a relaxation mechanism for rapid population of the SA state in parallel with population of the state leading to edge emission. Excited-state communication by either of the schemes outlined is also supported by steady-state measurements using the near-UV lines of an Ar⁺ laser; over an incident intensity range of $\sim 10^{-2}$ - 10^1 mW/cm², the intensities of the edge and SA PL bands maintain a constant ratio.

PEC properties.—Although n-ZnSe has been used as an electrode in PEC's (18, 20), the material has not, to our knowledge, been stabilized to the extent that it can be used for efficient conversion of optical energy to electricity; decomposition according to Eq. [1] has previously been observed in several electrolytes (20a, 20b, 20f). The ability to stabilize n-CdX (X = S, Se, Te) electrodes with polychalcogenide



electrolytes suggested their use with n-ZnSe electrodes (9). In an initial experiment with sulfide electrolyte (1M OH⁻/1M S²⁻), decomposition still obtained: photocurrent

fell rapidly, and pitting of the surface occurred. However, PEC's constructed from n-ZnSe:Al, a Pt counterelectrode, and (di)selenide or (di)telluride electrolyte were stable. Table II demonstrates that little electrode weight loss accompanies long-term experiments in these electrolytes. Other evidence of stability includes relatively constant photocurrents and lack of surface damage in the prolonged experiments, as well as observation of competitive electrolyte oxidation (9).

We obtained photoaction spectra of our samples near short circuit in a transparent selenide electrolyte. Figure 2 reveals that, as expected, photocurrent rises sharply at ~460 nm, roughly the bandgap energy. The enhanced efficiency of e⁻-h⁺ pair separation with decreasing wavelength is consistent with the reported trend in absorptivities (18) and with the decline in electric field strength with distance from the interface (21).

Current-voltage curves, shown in Fig. 3, reveal that photocurrent in diselenide electrolyte onsets at ~-2.0V vs. SCE at moderate light intensities of ~10 mW/cm², yielding an open-circuit voltage of ~1.0V. The photocurrent quantum efficiency, ϕ_x , is relatively low for these PEC's. Table I shows that even the least deeply penetrating wavelength, 366 nm, yields a short-circuit ϕ_x value of only ~0.4. We attribute the low ϕ_x values to narrow depletion widths, W , and short hole diffusion lengths, L_p , in these materials: W is calculated to be ~300-1000Å at short circuit in our materials,¹ and L_p has been reported to be only ~10²Å for comparably doped ZnSe materials (20e). We estimate from PL data (*vide in-*

¹ A static dielectric constant of 8.7 was used in calculating W (20d).

Table II. Stabilization of n-ZnSe:Al photoelectrodes^a

Expt.	Electrolyte ^b	Electrode (mol \times 10 ⁴) ^c		Electrons ^d (mol \times 10 ³)	Avg i_c ^e mA	t, h	Output voltage, V	λ_{ex}, nm^f
		Before	After					
1	Se _n ²⁻	0.81	0.80	2.06	0.063	87.5	0.36	366
2	Se _n ²⁻	1.80	1.68	3.72	0.075	133	0.75	366
3	Te _n ²⁻	0.88	0.84	3.19	0.100	85.5	0.63	436
4	Te _n ²⁻	1.25	1.23	2.46	0.055	120	0.55	436

^a All experiments were run under N₂ in stirred solutions in a two-electrode PEC (working electrode and Pt foil counterelectrode) in diselenide or ditelluride electrolyte.

^b Electrolyte compositions are given in Table I. The initially colorless solutions became dark brown and deep purple as Se_n²⁻ and Te_n²⁻ were formed, respectively, during the course of the experiments. Final Se_n²⁻ and Te_n²⁻ concentrations were ~0.002 and 0.004M, respectively.

^c Mols of crystal determined by weight before and after photoelectrochemistry. Crystals used in experiments 1, 2, and 3 chipped while being demounted and were not fully recovered. Surface areas were 0.08, 0.18, 0.09, and 0.12 cm² for the solids of expt. 1-4, respectively.

^d Mols of electrons in the external circuit determined by integrating photocurrent-time plots.

^e Average photocurrent passed during experiment; for current densities, divide by the electrode areas given in c above.

^f Excitation wavelength provided by a 200W high pressure Hg lamp equipped with interference filters.

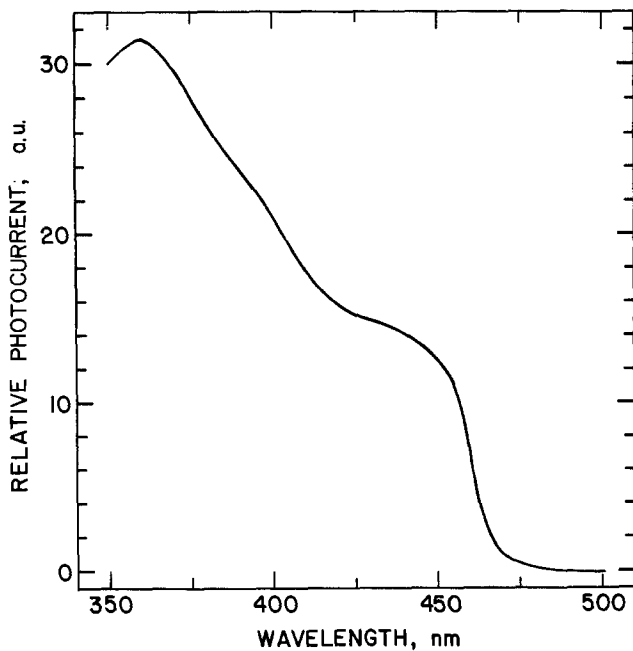


Fig. 2. Photoaction spectrum for a n-ZnSe:Al-based PEC in optically transparent selenide electrolyte; the electrode was held at $-1.0V$ vs. SCE. The plotted values of relative photocurrent have been corrected for variation in light intensity as a function of wavelength. Although the optical pathlength was minimized, the spectrum is not corrected for electrolyte absorption.

fra) that the 366 nm absorptivity of ZnSe is $\sim 6.8 \times 10^4 \text{ cm}^{-1}$, so that a significant fraction of e^-h^+ pairs would be created beyond the depth where holes can be collected by diffusion into the drift region. Despite the modest ϕ_x values, Table I demonstrates that n-ZnSe:Al-based PEC's can still yield substantial efficiencies for the conversion of monochromatic light to electricity, values of $\sim 5\text{-}7\%$ for 366 nm excitation being typical. In the protracted experiments of Table II, energy conver-

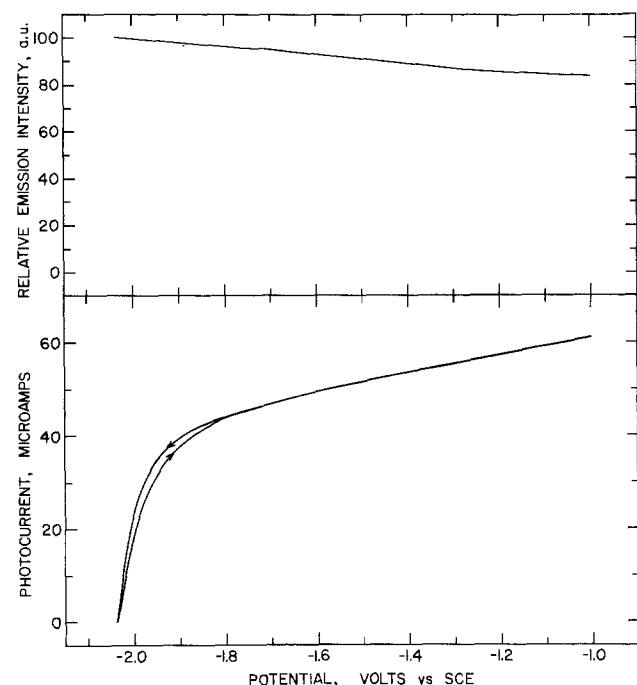


Fig. 3. Photocurrent (bottom frame) and PL intensity (top frame) monitored at $\lambda_{\text{max}} \sim 600 \text{ nm}$ vs. potential for a n-ZnSe:Al electrode excited at 366 nm in $10M \text{ KOH}/0.25M \text{ Se}_2^-/0.001M \text{ Se}_2^{2-}$ electrolyte. The incident light irradiated the $\sim 0.2 \text{ cm}^2$ exposed area of the electrode with $\sim 0.60 \text{ mW}$ of power. The iLV curves were generated using a pulse technique described in the Experimental section. The electrolyte redox potential was $-0.95V$ vs. SCE.

sion efficiencies of up to $\sim 3\text{-}4\%$ (366 nm experiments) were sustained for several days.

Of particular interest to us are changes in PL properties which accompany the use of the semiconductor as an electrode. Figure 4 demonstrates that in passing from open circuit to short circuit, the two PL bands are quenched roughly in parallel by the applied electric field. The spectral distribution is invariant over the potential range of Fig. 3, permitting changes in PL intensity to be monitored at a single wavelength. Simultaneous measurements of current, PL intensity, and potential (iLV) data are illustrated in Fig. 3 and summarized in Table I. The table reveals that PL quenching obtains with all of the excitation wavelengths employed.

Quenching of semiconductor PL by applied potential is a well-documented phenomenon in both semiconductor/metal- (6, 22) and PEC-based (2, 3) Schottky-barrier systems. A dead-layer model which quantifies PL quenching in the solid-state systems has recently been found applicable to PEC's based on n-CdSe and n-GaAs (4, 5). In its simplest form, the model states that e^-h^+ pairs formed within some fraction of the depletion width are swept apart by the field and do not contribute to PL. The mathematical form of the model is given by Eq. [2]

$$\frac{\phi_r}{\phi_{\text{rFB}}} = \exp(-\alpha'D) \quad [2]$$

where D is the dead-layer thickness; ϕ_r and ϕ_{rFB} are the radiative quantum efficiencies at an in-circuit potential and at flatband potential (approximated here as the open-circuit potential); and $\alpha' = \alpha + \beta$ with α and β the solid's absorptivities for the exciting and emitted light, respectively.

The dead-layer model was recently shown to be applicable to PL from a Au-ZnSe Schottky diode; PL intensity-voltage curves obtained with 442 nm light could roughly be fit by assuming that D has a functional dependence like that of W [D proportional to $(V - V_{\text{rFB}})^{1/2}$] (6). For the n-ZnSe:Al-based PEC's, PL quenching curves like that shown in Fig. 3 can be similarly fit, although discrepancies occur near open circuit. Such discrepancies, also noted for n-GaAs-based PEC's, may indicate that potential applied in this regime is partitioned between the semiconductor and the Helmholtz layer (4).

Another quantitative test of the dead-layer model, independence of D on optical penetration depth, is presently precluded by a lack of reliable absorptivities for n-ZnSe:Al. However, qualitative accord is indicated by the enhanced PL quenching at short circuit with de-

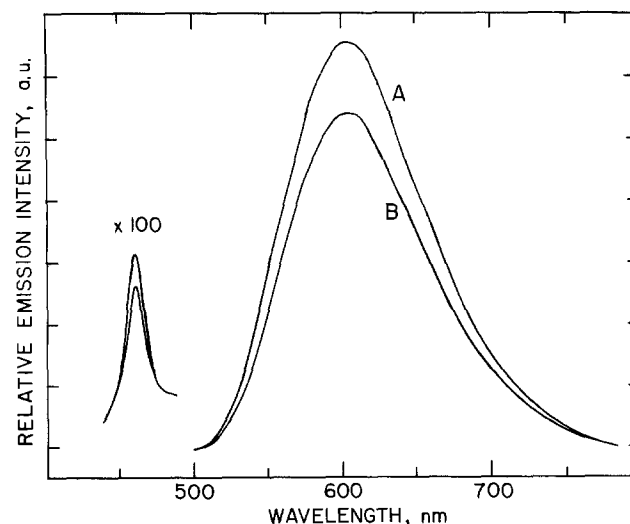


Fig. 4. Corrected PL spectra of a n-ZnSe:Al electrode excited with the near-UV lines (351, 364 nm) of an Ar^+ laser in the diselenide electrolyte of Fig. 3. Curves A and B were taken at -2.0 (open circuit) and $-1.0V$ vs. SCE, respectively. Both spectra were taken in an identical sample geometry.

creasing wavelength and penetration depth, Table I. If the dead-layer model is assumed applicable to these PEC's, it yields, using $\alpha \sim 3 \times 10^4 \text{ cm}^{-1}$ for 436 nm light (6), absorptivities of $\sim 4 \times 10^4$ and $6 \times 10^4 \text{ cm}^{-1}$ at 405 and 366 nm, respectively.

The effect of carrier concentration on PL quenching was also qualitatively consistent with the dead-layer model. As was found in the solid-state study (6), more resistive samples, prepared by heating ZnSe:Al in an evacuated ampul with Se, exhibited greater PL quenching, as shown in Table I. The wider electric fields of these samples were also manifest in larger ϕ_r values. Taken as a unit, we believe our data provide good evidence for describing PL quenching in n-ZnSe:Al-based PEC's in terms of a dead-layer model.

A final point of interest concerns the parallel quenching of the two PL bands illustrated in Fig. 4. Although we are unable to definitively establish the mechanism for populating the SA state (*vide supra*), the parallel quenching is consistent with separation of e^-h^+ pairs prior to population of this state.

EL properties.—We have found that n-ZnSe:Al electrodes mimic other II-VI electrodes (3) in exhibiting EL when used as a cathode in aqueous, alkaline, peroxydisulfate electrolyte. EL from n-ZnSe under anodic polarization has also been reported (23). The key step involved in populating the emissive excited state has been proposed to be hole injection by $\text{SO}_4^{\cdot -}$ radical anions formed by reduction of $\text{S}_2\text{O}_8^{2-}$ (24). As in previous studies, we have obtained EL spectra using a pulse technique: while the emission monochromator is swept, the electrode is pulsed repetitively between a potential where no current is observed (0.0V for 8s) and a potential sufficiently cathodic to initiate EL (1s pulse). We find that EL is initiated to the dark-adapted eye at $\sim -1.7\text{V vs. SCE}$, roughly the onset of dark cathodic current in the electrolyte of $5\text{M OH}^-/0.1\text{M S}_2\text{O}_8^{2-}$.

Figure 5 presents the EL spectrum of an n-ZnSe:Al electrode. Both the edge and SA emission bands are evident, and a comparison with Fig. 1 indicates that the relative intensities of the bands are similar in the two spectra. The overall spectral similarity indicates that the same two emissive excited states are populated in both experiments.

Besides spectral distributions, we have also measured lower limit integrated EL efficiencies, $\bar{\phi}_{\text{EL}}$, using techniques and approximations previously described (3). For n-ZnSe:Al electrodes, we obtain $\bar{\phi}_{\text{EL}}$ values of $\sim 10^{-6}$ and 10^{-4} at -1.8 and -2.2V vs. SCE , respectively. These num-

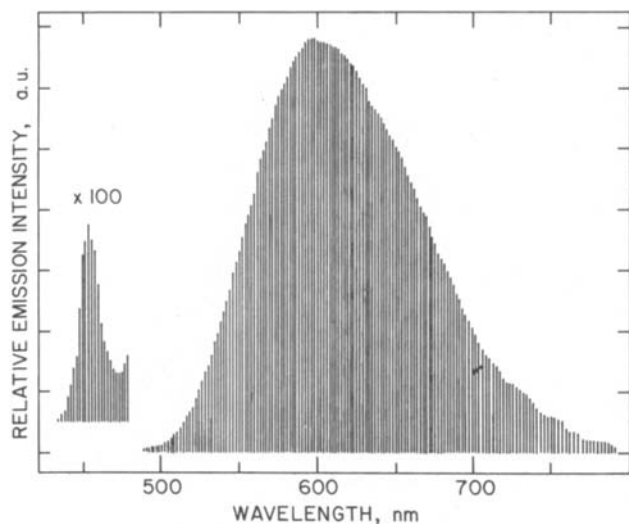


Fig. 5. Corrected EL spectrum of a n-ZnSe:Al electrode obtained in $5\text{M OH}^-/0.1\text{M S}_2\text{O}_8^{2-}$ electrolyte. The electrode was continuously pulsed between 0.0 (8s) and -2.0V vs. SCE (1s), while the emission spectrometer was swept at 12 nm/min . A 100-fold increase in sensitivity was used in scanning the 400-480 nm spectral region.

bers are of interest because $\bar{\phi}_{\text{EL}}$ (photons emitted per holes injected) can be factored into an efficiency for excited-state population, ϕ_{ES} (excited states populated per holes injected) and the PL radiative efficiency, ϕ_r (photons emitted per excited states populated). Samples of n-CdS_xSe_{1-x} ($0 \leq X \leq 1$) exhibit $\bar{\phi}_{\text{EL}}$ and ϕ_r values which are nearly equal, suggesting ϕ_{ES} is near unity for these samples. In contrast, our $\bar{\phi}_{\text{EL}}$ values for n-ZnSe:Al are lower than the measured ϕ_r of $\sim 10^{-1}\text{--}10^{-2}$ by a factor of $10^{-2}\text{--}10^{-4}$. The discrepancy in the two efficiencies may be due to a low value of ϕ_{ES} but more likely reflects the different spatial regions involved in the two modes of excited-state population. In particular, EL is expected to originate, on average, from nearer the semiconductor surface than PL, owing to its initiation by interfacial charge transfer. A lower ϕ_r value for the (near-)surface region due to nonradiative surface recombination could then account for the observed low EL efficiencies. Such a nonemissive near-surface region has already been suggested to account for the variation of PL efficiency with excitation wavelength. Reduction of the electrode surface during the EL experiment (3) may also contribute to the discrepancy.

Acknowledgments

This work was generously supported by the Office of Naval Research. A.B.E. gratefully acknowledges support as an Alfred P. Sloan Fellow (1981-1983). Dr. Brian Fitzpatrick of North American Philips is thanked for generously providing the samples used in this study as well as for helpful discussions. Alan Huelsman and William Hobson are thanked for experimental assistance and helpful discussions.

Manuscript submitted Sept. 15, 1983; revised manuscript received Dec. 1, 1983. This was Paper 348 presented at the Washington, DC, Meeting of the Society, Oct. 9-14, 1983.

REFERENCES

- (a) A. Heller, *Acc. Chem. Res.*, **14**, 154 (1981); (b) A. J. Bard, *Science*, **207**, 139 (1980); (c) M. S. Wrighton, *Acc. Chem. Res.*, **12**, 303 (1979); (d) A. J. Nozik, *Ann. Rev. Phys. Chem.*, **29**, 189 (1978).
- A. B. Ellis, *J. Chem. Ed.*, **60**, 332 (1983), and references therein.
- H. H. Streckert, J. Tong, M. K. Carpenter, and A. B. Ellis, *This Journal*, **129**, 772 (1982), and references therein.
- W. S. Hobson and A. B. Ellis, *J. Appl. Phys.*, **54**, 5956 (1983).
- R. Garuthara, M. Tomkiewicz, and R. P. Silberstein, *ibid.*, **54**, 6787 (1983).
- K. Ando, A. Yamamoto, and M. Yamaguchi, *Jpn. J. Appl. Phys.*, **20**, 679 (1981).
- O. Lindberg, *Proc. IRE*, **40**, 1414 (1952).
- B. R. Karas and A. B. Ellis, *J. Am. Chem. Soc.*, **102**, 968 (1980).
- A. B. Ellis, S. W. Kaiser, J. M. Bolts, and M. S. Wrighton, *ibid.*, **99**, 2839 (1977).
- W. S. Hobson and A. B. Ellis, *Appl. Phys. Lett.*, **41**, 891 (1982).
- H. H. Streckert, B. R. Karas, D. J. Morano, and A. B. Ellis, *J. Phys. Chem.*, **84**, 3232 (1980).
- M. S. Wrighton, D. S. Ginley, and D. L. Morse, *ibid.*, **78**, 2229 (1974). See Ref. (3) for previous applications of the technique to semiconductor electrodes.
- M. M. Olken, R. N. Biagioni, and A. B. Ellis, *Inorg. Chem.*, **22**, 4128 (1983).
- M. K. Carpenter, H. H. Streckert, and A. B. Ellis, *J. Solid State Chem.*, **45**, 51 (1982).
- J. C. Bouley, P. Blanconnier, A. Herman, Ph. Ged, P. Henoc, and J. P. Noblanc, *J. Appl. Phys.*, **46**, 3549 (1975).
- (a) M. Cardona, *J. Appl. Phys.*, **32S**, 2151 (1961); (b) B. Sermage, *Solid-State Electron.*, **21**, 1361 (1978).
- (a) D. Curie and J. S. Prener, in "Physics and Chemistry of II-VI Compounds," M. Aven and J. S. Prener, Editors, Chap. 9.4, North-Holland Publishing Co., Amsterdam (1967), and references therein; (b) S. Iida, *J. Phys. Soc. Jpn.*, **25**, 177 (1968); (c) G. Jones and J. Woods, *J. Lumin.*, **9**, 389 (1974); (d) S. Satoh and K. Igaki, *Jpn. J. Appl. Phys.*, **22**, 68 (1983).
- P. Lemasson, A. Etcheberry, and J. Gautron, *Electrochim. Acta*, **27**, 607 (1982).
- (a) B. DiBartolo, "Optical Interactions in Solids," Ch.

- 18.3, John Wiley and Sons, New York (1968); (b) P. J. Wagner, in "Creation and Detection of the Excited State," Part A, Vol. I, A. A. Lamola, Editor, Ch. 4, Marcel Dekker, New York (1971).
20. (a) R. Williams, *This Journal*, **114**, 1173 (1967); (b) J. Gautron, P. Lemasson, F. Rabago, and R. Triboulet, *ibid.*, **126**, 1868 (1979); (c) P. Lemasson, J. Gautron, and J.-P. Dalbéra, *Ber. Bunsenges. Phys. Chem.*, **84**, 796 (1980); (d) P. Lemasson, J.-P. Dalbéra, and J. Gautron, *J. Appl. Phys.*, **52**, 6296 (1981); (e) J. Gautron and P. Lemasson, *J. Cryst. Growth*, **59**, 332 (1982); (f) B. S. H. Royce, F. Sánchez-Sinencio, R. Goldstein, R. Muratore, R. Williams, and W. M. Yim, *This Journal*, **129**, 2393 (1982).
21. H. Gerischer, *J. Electroanal. Chem. Interfacial Electrochem.*, **58**, 263 (1975), and references therein.
22. R. E. Hollingsworth and J. R. Sites, *J. Appl. Phys.*, **53**, 5357 (1982) and references therein.
23. J. Gautron, J.-P. Dalbéra, and P. Lemasson, *Surf. Sci.*, **99**, 300 (1980).
24. (a) K. H. Beckmann and R. Memming, *This Journal*, **116**, 368 (1969); (b) R. Memming, *ibid.*, **116**, 785 (1969); (c) B. Pettinger, H. R. Schöppel, and H. Gerischer, *Ber. Bunsenges. Phys. Chem.*, **80**, 849 (1976).

Interdiffusion in Cryolite Melts

I. LiF-AlF₃

E. W. Dewing*

Alcan International, Limited, Kingston Laboratories, Kingston, Ontario, K7L 4Z4, Canada

ABSTRACT

The modifications to equations based on Fick's laws necessary when density changes are caused by electrolysis are considered. The quantity found experimentally is D/α , where D is the diffusion coefficient and α is $\partial \ln c / \partial \ln N$, N being the equivalent fraction, and c the concentration. For melts with $N_{\text{AlF}_3} = 0.136$, chronopotentiometric experiments gave $D/(\text{m}^2 \text{s}^{-1}) = \exp\{[-3980 \pm 221]/T - [15.904 \pm 0.184]\}$, with a standard deviation of $\pm 3.9\%$ in the range $1128 < T < 1273$ K. For melts with $N_{\text{AlF}_3} = 0.25$, $D/(\text{m}^2 \text{s}^{-1}) = \exp\{[-5532 \pm 266]/T - [14.609 \pm 0.225]\}$ with a standard deviation of $\pm 3.3\%$. For melts with higher AlF_3 contents, where chronopotentiometry was not applicable, the relaxation of EMF-time transients after electrolysis on copper cathodes was determined. With a melt with $N_{\text{AlF}_3} = 0.25$, for which D is given above, the contribution to the EMF of changing electrolyte composition at the interface could be calculated and subtracted to yield the transient due to the Al-Cu alloy formed on the surface of the wire. For other electrolyte compositions, this contribution of the alloy could then be subtracted. The Fick's law values of D were extraordinarily high, rising to $10^{-7} \text{ m}^2 \text{ s}^{-1}$ at $N_{\text{AlF}_3} = 0.685$ and $T \sim 1270$ K. This seems to be due to the strong thermodynamic driving force in the system since multiplying D by $\partial \ln c / \partial \ln N$ gives thermodynamic diffusivities in the normal range of $0.5\text{--}5 \times 10^{-9} \text{ m}^2 \text{ s}^{-1}$.

To understand mass-transfer phenomena in aluminum electrolysis cells, a knowledge of interdiffusion coefficients in cryolite systems is needed. Although the NaF-AlF₃ system is obviously of chief interest, the LiF-AlF₃ system is much easier to work with and has been used to develop methods.

There are two barriers to be surmounted before any results can be achieved. On the theoretical side, cryolite melts show quite nonideal density behavior, so that the usual assumption of no volume change during diffusion is not valid. At the same time, the melts show strong negative deviations from thermodynamic ideality. On the experimental side, there is no satisfactory way of making a small electrode of known surface area from liquid aluminum, and chronopotentiometry, which is the best method available for dilute solutions, is not suitable for the concentrated mixtures which are the subject of interest.

To look first at the experimental problems, all electrochemical methods for studying diffusion rely on measuring a perturbation of potential caused by a transient current (or vice versa); they differ only in the form of the transient. Chronopotentiometry is unique in that the excursion in concentration of the species of interest is great enough that it drops to zero. The resulting change of potential is large and easily detected, and any distortion of the shape of the potential-time curve by overpotentials or other factors is of no importance. Likewise, it matters little in what form the electrolysis product is left; provided the reactant is removed from solution, a transition in potential will be observed. Thus the method is very simple, provided that the solution is sufficiently dilute that the diffusion coefficient can be regarded as constant between the starting concentration and zero; if not, as in all other transient techniques, analysis of precise measurements of electrode potentials must be made.

To interpret a potential-time transient, it is not necessary that the solutions be ideal, but it is necessary that the

thermodynamics be known so that potential changes can be interpreted as concentration changes. Fortunately, for LiF-AlF₃ melts, this is the case (1, 2). However, even then there are two problems: (i) if current is passing at the time of the measurement there will be a resistive drop and there may be an activation (or other) overpotential, and (ii) if, in the present case, Al is being deposited as an alloy rather than as pure metal, there will be an $(RT/3F) \ln \alpha_{\text{Al}}$ term of unknown magnitude and varying with time. The solution to the first of these problems is to use a relaxation method where a current is passed and then switched off, the decay of the potential towards its initial value being observed. [Wen, *et al.* (3) have used such a method in studying diffusion in solid "LiAl."] The second problem is more difficult. It cannot be obviated by using a pure Al electrode, since there seems to be no way of defining a known (small) area and making electrical connection without contamination from insulator and conductor materials. The solution has been to deposit Al on a solid metal (Cu) substrate and accept the fact that the surface will be an alloy of varying composition. The contribution of this alloy to the electrode potential will not be a function of the melt composition, so that if it can be determined in any one melt where the diffusion coefficient can be found by other methods, its value can be applied to all other compositions.

The course of action has thus been (i) determine the diffusion coefficient by chronopotentiometry in a fairly dilute [10 mol percent (m/o)] solution of AlF₃, (ii) make relaxation measurements at the same composition to determine the contribution of the Al-Cu alloy to the total potential, and (iii) subtract that contribution from measurements with other melts.

Theory

The theory of the effect of volume changes during diffusion has been considered by Vallet *et al.* (4) in connection with the analogous LiF-BeF₂ system. They employed the methods of irreversible thermodynamics. An alternative treatment solely in terms of Fick's laws is given here.

*Electrochemical Society Active Member.

Key words: fused salts, chronopotentiometry, EMF, relaxation.

The problem is that volume changes during electrolysis can of themselves modify concentration gradients.

We start with Fick's first law

$$J = -D \frac{\partial c}{\partial x} \quad [1]$$

in the one-dimensional case as the definition of D , the chemical diffusion coefficient. (Common symbols not defined in the text are listed at the end.) In the steady-state, neither concentrations nor volumes are changing with time and no problem exists.

Let us now consider the unsteady state, and derive a modified form of Fick's second law. Any change of composition is sufficiently small that D can be taken as constant. Two parallel planes, normal to the X-axis and a distance δx apart, cut off a volume v , in a channel of unit cross section. Because it has unit cross section, δx and v are numerically equal. If the number of equivalents of the substance in question in the given volume is n , then

$$c = n/v \quad [2]$$

and its differential, in the case where v is not constant, is

$$\begin{aligned} dc &= (1/v)dn - (n/v^2)dv \\ &= (1/v)dn - c(d \ln v) \end{aligned} \quad [3]$$

The volume v is now defined as holding a constant number of fluoride ions, *i.e.*, only Li^+ and Al^{3+} ions are allowed to cross the bounding planes, and the resulting composition and density changes may cause a change in volume. Electrical neutrality requires that the fluxes of Li^+ and Al^{3+} be chemically equivalent so that c can represent the concentration of either AlF_3 (most convenient) or LiF .

In a time interval dt the change in n is given by the difference of the fluxes in and out of the volume, or

$$dn = (J_x - J_{x+\delta x}) dt = -(\partial J/\partial x) \cdot v \cdot dt \quad [4]$$

since $v = \delta x$. From Eq. [3] and [4]

$$\begin{aligned} \partial c/\partial t &= (1/v)(\partial n/\partial t) - c(\partial \ln v/\partial t) \\ &= -(\partial J/\partial x) - c(\partial \ln v/\partial t)(\partial c/\partial t) \end{aligned} \quad [5]$$

and hence, by differentiation of Eq. [1]

$$\partial c/\partial t = D(\partial^2 c/\partial x^2) - c(\partial \ln v/\partial t)(\partial c/\partial t) \quad [6]$$

Rearrangement gives

$$[1 + c(\partial \ln v/\partial t)](\partial c/\partial t) = D(\partial^2 c/\partial x^2) \quad [7]$$

In the case that v is constant, this reduces to the usual form of Fick's second law. The term in brackets can be written

$$\begin{aligned} 1 + c(\partial \ln v/\partial t) &= 1 + (c/v)(\partial v/\partial t) \\ &= (v \partial c + c \partial v)/(v \partial c) \\ &= (1/v)(\partial cv/\partial c) \\ &= (1/v)(\partial n/\partial c) \end{aligned} \quad [8]$$

At this point we must note that, if V is the volume containing 1 mol of F^- ions and N is the equivalent fraction of the species in question, then

$$n/v = N/V = c \quad [9]$$

so that

$$(1/v)dn = (1/V)dN \quad [10]$$

and

$$\begin{aligned} 1 + c(\partial \ln v/\partial t) &= (1/V)(\partial N/\partial c) \\ &= \partial \ln N/\partial \ln c \end{aligned} \quad [11]$$

Thus Eq. [7] can be written

$$\partial c/\partial t = D(\partial \ln c/\partial \ln N)(\partial^2 c/\partial x^2) \quad [12]$$

$$= \alpha D (\partial^2 c/\partial x^2) \quad [13]$$

where $\alpha = \partial \ln c/\partial \ln N$. Equation [13] is exactly like Fick's second law except that αD has replaced D , and if a similar substitution is made in the first law (which is used in re-

lating flux J to current density i in setting boundary conditions), then all the usual solutions to the equation are valid. Thus, in the case of constant i , and with a transport number of Li^+ ions of t_{Li^+} (with respect to F^-)

$$\alpha i t_{\text{Li}^+}/\mathbf{F} = \alpha J = -\alpha D(\partial c/\partial x) \quad [14]$$

and the Sand equation for the reduction of concentration in time t becomes

$$\begin{aligned} c^0 - c &= (2\alpha i t_{\text{Li}^+}/\mathbf{F})(t/\alpha\pi D)^{1/2} \\ &= (2i t_{\text{Li}^+}/\mathbf{F})(\alpha t/\pi D)^{1/2} \end{aligned} \quad [15]$$

c goes to zero at the transition time $t = \tau$. Thus, what one measures is not αD but D/α .

Just as it is assumed that the changes in concentration are sufficiently small for D to be considered constant, so α also is assumed constant.

Vallet *et al.* (4) found that in the $\text{LiF}-\text{BeF}_2$ system the partial equivalent volumes were not only effectively constant across the system but also almost equal to one another so that, in fact, there was no volume change during diffusion. That is not the case in the present system. Figure 1 shows the value at 1200 K of the term α (with c being taken as the concentration of AlF_3) based on the density measurements of Matiašovský and Malinovský (5). It is within 10% of unity in the range from pure LiF up to $N_{\text{AlF}_3} = 0.5$ (*i.e.*, the Li_2AlF_6 composition, since N_{AlF_3} is the equivalent fraction), and then drops to less than 0.1 as $N_{\text{AlF}_3} = 0.75$ (*i.e.*, LiAlF_4) is approached.

In a system with significant deviations from thermodynamic ideality it is of interest to calculate a diffusivity (D_{th}) based on the thermodynamic driving force, which is the gradient of the chemical potential. Thus Fick's first law (Eq. [1]) is written

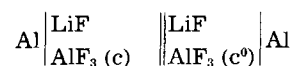
$$J = -cD_{\text{th}}(\partial \ln a/\partial x) = -(cD_{\text{th}}/RT)(\partial \mu/\partial x) \quad [16]$$

so that $D_{\text{th}} = D$ if $a \propto c$. In general (6, 7)

$$D_{\text{th}} = D(\partial \ln c/\partial \ln a) \quad [17]$$

In the $\text{LiF}-\text{AlF}_3$ system, the transport number of Li^+ ions is essentially equal to unity, and has been taken as such. [The experimental value (2) is $t_{\text{Li}^+} = 0.957$ at 1073 K and $N_{\text{AlF}_3} = 0.5$.]

For the relaxation measurements, it is necessary to know the relationship between EMF and composition for the cell



and it is (2)

$$E = (RT/3\mathbf{F})(\ln[a_{\text{AlF}_3}/a^0_{\text{AlF}_3}] - 3 \ln[a_{\text{LiF}}/a^0_{\text{LiF}}]) \quad [18]$$

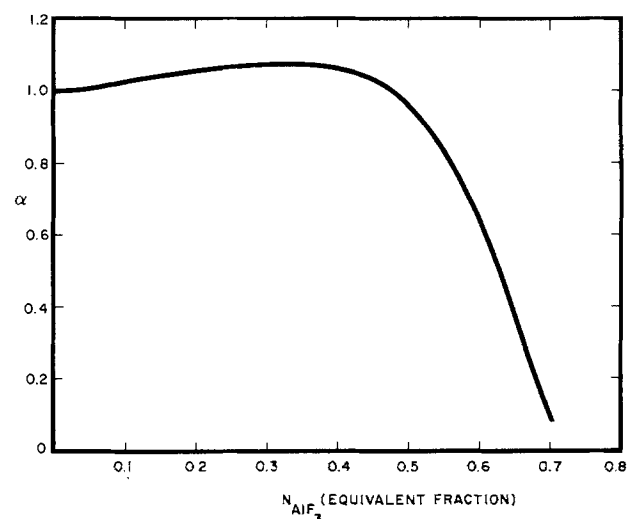


Fig. 1. Variation with composition of the term α for AlF_3 in the system $\text{LiF}-\text{AlF}_3$.

where a and a^0 represent activities on the two sides. It has been found that the activities can be represented adequately by an association model (1, 2)



for which the equilibrium constant in terms of mol fractions is given by

$$\ln K = 6104/T - 2.987 \quad [20]$$

and this expression has been used.

Experimental

The heart of the data gathering system was a Hewlett-Packard 3437A voltmeter connected to an HP85 computer. Resolution was 0.1 mV up to ± 199.9 mV and 1 mV up to ± 1.999 V, with a maximum sampling rate of 4000 readings/s. Each time a reading was taken, an output pulse was available from the voltmeter, and a simple counting circuit with a transistor switch turned the current on and off at the times required. In this way, the experiment was synchronized with the voltmeter operation, rather than vice versa.

Melts were made up by weight from reagent-grade LiF and sublimed AlF_3 , and were contained in copper crucibles made from 13 mm pipe. A 25 mm length was cut off, and its end was squeezed closed in a vise and welded with a gas-oxygen torch; the metal was then cleaned with nitric acid. The crucible was suspended in a vertical tube furnace by Chromel and Alumel wires attached to two holes drilled near its top. The temperature could be determined by measuring the EMF between them, and they also served as current and potential leads for the electrolysis (see Fig. 2).

About 200 mg of Al was added to the crucible so that when it served as anode Al would dissolve and not Cu.

The furnace tube was stainless steel of 35 mm id. Argon was passed in at the bottom, and the top was covered with a sheet of FIBERFRAX.

The cathode and the reference electrode were made from 0.5 mm copper wire, and were held in place by a twin-bore alumina insulator. This was mounted at the top in the stage of an old microscope, so that the wires could be positioned horizontally and moved vertically through a precise distance. After the wires had been in the furnace for at least 10 min and thermal expansion had ceased, the tip of the cathode was positioned at the surface of the melt by observing the sudden change of amplitude of an applied ac signal when the wire made contact. The wire was then lowered by a measured distance (usually 7 mm). The reference wire, immersed approximately the same distance, was plated with Al. Its absolute potential was

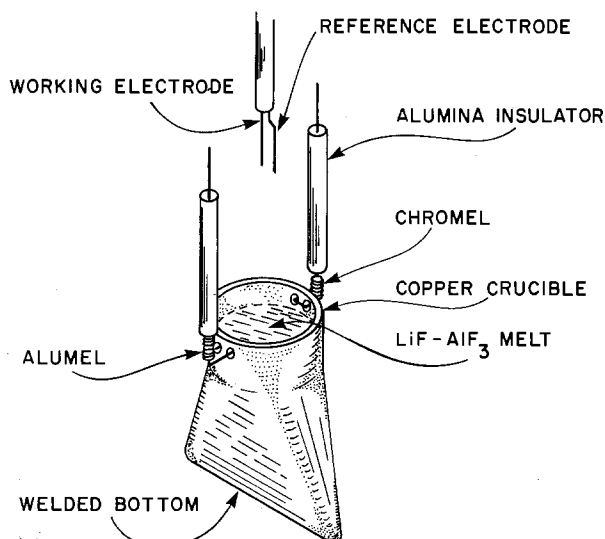


Fig. 2. Schematic diagram of electrochemical cell

not known, but all that was required was that its potential stay constant for the 1s needed to make a measurement.

The dc current supply was a Hewlett-Packard 6224B which delivered up to 3A in the constant-current mode. The starting transient was reduced by disconnecting the output capacitor and by setting the voltage limit only about 1V above the value needed to pass the desired current. Current densities were 7-22 A cm^{-2} . A Tektronix 7623A storage oscilloscope was useful in setting up experiments, but it proved inadvisable to connect it and the HP-3437A voltmeter at the same time as some electrical interference occurred.

When the voltmeter was used on its most sensitive range for the relaxation measurements an arbitrary bias was inserted into the reference circuit to ensure that the voltmeter remained on scale.

A typical chronopotentiometric plot is shown in Fig. 3. The point of inflection was found by numerical differentiation of the readings in the computer.

Diameters of the wires used ranged from 0.5-0.65 mm and were measured with a micrometer. In calculating the surface area, allowance was made for the expansion of the diameter between room temperature and the temperature of the experiment. (Since the immersion was set after the wire was hot, no correction for length was necessary.)

Results

Chronopotentiometry.—The correction for curvature of the wire is given by MacDonald (8) as

$$c^0 - c = 2i\sqrt{t}/(nF\sqrt{\pi D}) - it/(2nF\tau) + \dots \quad [21]$$

where τ is the radius of the electrode. The first term is the Sand equation, while the second is the correction. For chronopotentiometric experiments, it is easiest to make the correction by defining an effective concentration c' as

$$c' = c^0 + it/(2nF\tau) \quad [22]$$

and then using the Sand equation as usual.

Provided transition times were not longer than 0.75s, the values of D calculated were independent of current density. For longer times the apparent values of D increased, and beyond about 1s disturbances appeared in voltage-time curves, so there is little doubt that convec-

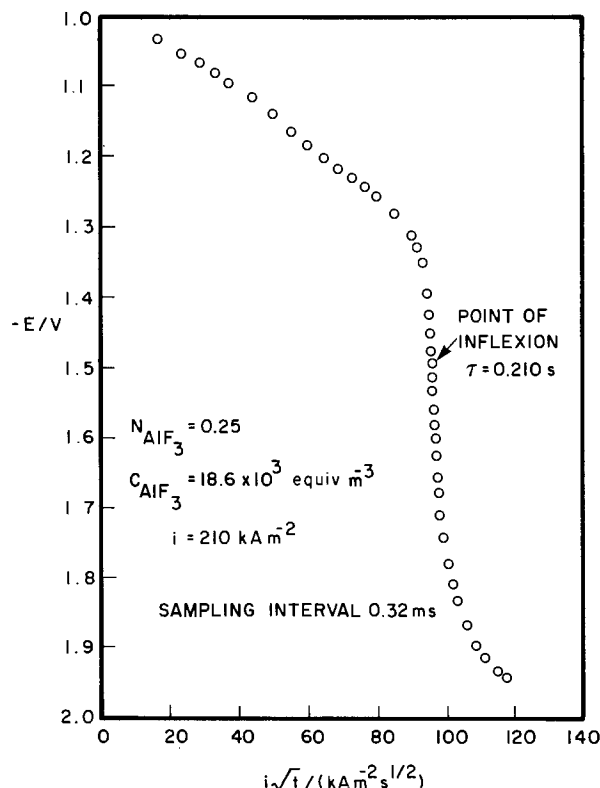


Fig. 3. Typical chronopotentiometric plot

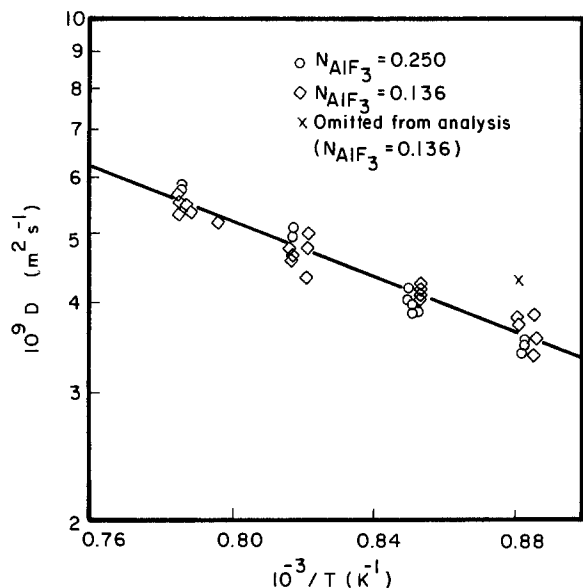


Fig. 4. Chronopotentiometric diffusion coefficients for AlF_3 in LiF-AlF_3 melts

tion was starting. Only measurements with transition times $\leq 0.75\text{s}$ were accepted.

Figure 4 shows the results obtained for melts with $N_{\text{AlF}_3} = 0.136$ and 0.25 (5 and 10 m/o). Although at any one temperature the values of D do not differ significantly with composition, thereby satisfying one of the essential conditions for use of the Sand equation, the Arrhenius slopes are significantly different. With one result out of 36 rejected, the rest may be expressed by

$$N_{\text{AlF}_3} = 0.136$$

$$D/(\text{m}^2 \text{s}^{-1}) = \exp[-3980 \pm 221/T - [15.904 \pm 0.184]] \quad [23]$$

$$N_{\text{AlF}_3} = 0.250$$

$$D/(\text{m}^2 \text{s}^{-1}) = \exp[-5532 \pm 266/T - [14.609 \pm 0.225]] \quad [24]$$

where the uncertainties are statistical standard errors, and the standard deviations are, respectively, $\pm 3.9\%$ and $\pm 3.3\%$.

The relaxation method.—The relaxation method is handled formally by starting a current i at time zero, and superimposing on it a current $-i$ at time t_1 , at which time the current is turned off. Thus the characteristic quantity $i\sqrt{t}$ in the Sand equation is replaced by $(i\sqrt{t} - i\sqrt{t-t_1})$, a quantity which is conveniently represented by m' . [This symbol is adopted since, apart from the factor $2/\sqrt{\pi}$, it is the same as the semi-integral of the current used by Grenness and Oldham (9) and given the symbol m . m' has been used previously by Dewing *et al.* (10).] The melt composition at the interface should depend only on the value of m' , regardless of the combination of i , t , and t_1 used to obtain it.

When electrolysis occurs at a copper wire and Al-Cu alloy forms, the composition of the alloy on the surface varies with time. If the penetration of Al into Cu is also a diffusion-limited process the same parameter m' should serve to characterize the extent to which such diffusion has occurred, even though several phases of alloy, with differing diffusion coefficients, participate. For a given value of m' there should then be the same composition of alloy on the surface and the same contribution to the potential of the electrode. As an example, Fig. 5 shows some results at 950°C . Three curves for different current densities have been superimposed as well as can be by adding constants to the EMF's. (This is permissible and necessary because the absolute potential of the reference electrode is not known and varies from run to run. It is thus only differences of potential which mean anything.)

The discrepancies at high values of m' (*i.e.*, for 10-20 ms after turning off the current) show that some stage of the

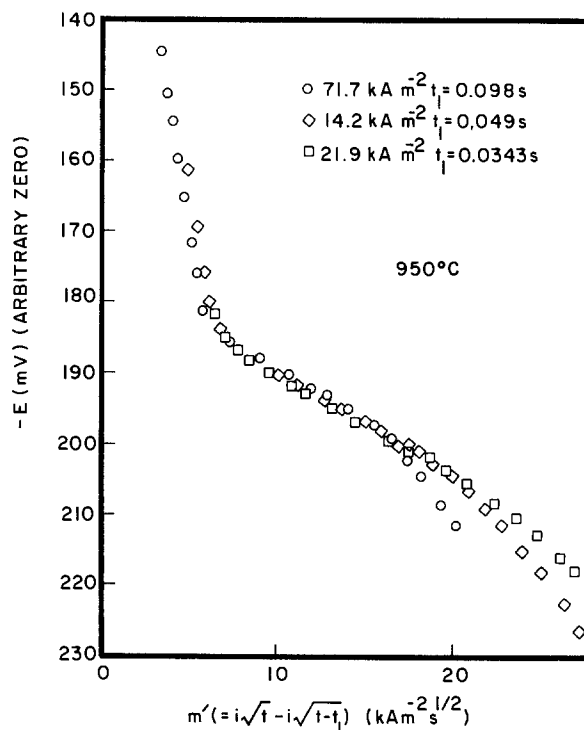


Fig. 5. Variation of potential after turning off current at time t_1

overall process is not entirely diffusion limited, implying a departure from local equilibrium. In principle, it could be in the alloy or it could be in the melt. If the latter, it would presumably be due to unequal rates of discharge of AlF_4^- and AlF_6^{3-} ions. If the former, it would probably be due to slow crystallization of a solid phase from the liquid alloy initially formed. In the calculations which follow, it will be assumed for the moment that the melt is at equilibrium and the departure lies with the alloy; if the ultimate results are not satisfactory, it could suggest that the converse is true.

Experimentally, the contribution of the Al-Cu alloy to the total EMF was determined with the $N_{\text{AlF}_3} = 0.25$ mixture, for which the diffusion coefficient is now known from Eq. [24]. For any given value of m' , the composition of the melt in contact with the electrode can be calculated, and hence $\partial c/\partial m'$, and from the activity model values of $\partial E/\partial c$ are found (Table I). Multiplication gives $\partial E/\partial m'$ for the electrolyte, and subtraction from the experimental value gives the contribution of the Al-Cu alloy. This is shown in Fig. 6 (which represents the same runs as Fig. 5). The steep rise in EMF at the left-hand side almost certainly represents a surface which is no longer liquid; the almost-flat plateau probably represents a two-phase solid-liquid region (in which, of course, at equilibrium the potential should be completely constant).

From the point of view of measuring diffusion coefficients, the higher current densities appear to be preferable. The region of steeply rising potential below $m' = 7$ is best avoided, since a small error in m' will cause a large error in the potential. On the other hand, values of m' high enough to be in the region where the curves di-

Table I. Contribution of Cu-Al alloy to total EMF. Measured on melt with $N_{\text{AlF}_3} = 0.25$ eq fraction

Temp $^\circ\text{C}$	Region of m'	$\partial E/\partial m'$ (total)	$\partial c/\partial E$ (melt)	$\partial c/\partial m'$ (melt)	$\partial E/\partial m'$ (melt)	$\partial E/\partial m'$ (Cu-Al)	Mean
860	7-16	-1.36	192	-207	-1.08	-0.28	-0.30
860	7-16	-1.40	192	-207	-1.08	-0.32	
900	8-19	-1.47	185	-190	-1.03	-0.44	-0.40
900	8-19	-1.40	185	-190	-1.03	-0.37	
950	8-18	-1.38	177	-172	-0.97	-0.41	-0.41
950	8-18	-1.39	177	-172	-0.97	-0.42	
1000	10-20	-1.45	169	-157	-0.93	-0.52	-0.52
1020	12-22	-1.28	169	-151	-0.90	-0.38	

Units of m' are $\text{kA m}^{-2} \text{s}^{1/2}$, of E mV, and of c eq of $\text{AlF}_3 \text{ m}^{-3}$.

Table II. Results for LiF-AlF₃ melts

$N_{\text{AlF}_3}^*$	Temp °C	$\partial E/\partial m'$ (total)	$\partial E/\partial m'$ (melt)	$\partial c/\partial E$ (melt)	α	$10^9 D$ m^2s^{-1}	$\frac{\partial \ln c}{\partial \ln \alpha}$	$10^9 D_{\text{th}}$ m^2s^{-1}
0.500	860	-2.26	-1.96	68.7	0.99	7.5	0.115	0.86
	860	-2.30	-2.00	68.7	0.99	7.2	0.115	0.82
	900	-2.17	-1.77	69.0	0.97	8.9	0.122	1.1
	900	-2.11	-1.71	69.0	0.97	9.5	0.122	1.2
	950	-1.83	-1.42	65.7	0.95	14.9	0.128	1.9
	950	-2.07	-1.66	65.7	0.95	10.9	0.128	1.4
	1000	-1.85	-1.33	67.2	0.93	15.9	0.137	2.2
	1000	-1.86	-1.34	67.2	0.93	15.7	0.137	2.1
	1020	-2.10	-1.72	66.9	0.92	9.5	0.137	1.3
	1020	-1.83	-1.45	66.9	0.92	13.4	0.137	1.8
	0.562	860	-2.34	-2.04	59.4	0.83	7.7	0.103
860		-2.58	-2.28	59.4	0.83	6.2	0.103	0.64
900		-2.07	-1.67	57.0	0.81	12.2	0.104	1.3
900		-2.15	-1.75	57.0	0.81	11.1	0.104	1.2
950		-1.90	-1.49	54.0	0.78	16.5	0.105	1.7
950		-1.92	-1.51	54.0	0.78	16.0	0.105	1.7
1000		-1.41	-0.89	50.7	0.75	50	0.105	5.3
1000		-1.70	-1.18	50.7	0.75	29	0.105	3.0
1020		-1.70	-1.32	49.5	0.74	24	0.105	2.5
1020		-1.61	-1.23	49.5	0.74	27	0.105	2.9
0.618		860	-2.96	-2.66	40.5	0.58	6.8	0.0748
	900	-2.26	-1.86	37.8	0.56	15.5	0.0735	1.1
	900	-2.16	-1.76	37.8	0.56	17.3	0.0735	1.3
	950	-3.36	-2.95	34.5	0.54	7.1	0.0718	0.51
0.685	860	-2.77	-2.47	6.27	0.14	80	0.0135	1.1
	860	-2.91	-2.61	6.27	0.14	71	0.0135	0.97
	950	-2.94	-2.53	6.15	0.15	85	0.0150	1.3
	950	-2.88	-2.47	6.15	0.15	89	0.0150	1.3
	1000	-2.47	-1.95	6.09	0.17	165	0.0158	2.6
	1000	-2.50	-1.98	6.09	0.17	160	0.0158	2.5
	1020	-2.42	-2.04	6.27	0.18	150	0.0167	2.5
	1020	-2.60	-2.22	6.27	0.18	127	0.0167	2.1

* Equivalent fraction. Units of m' are $\text{kA cm}^{-2} \text{s}^{1/2}$, of E mV, and of c eq of $\text{AlF}_3 \text{ m}^{-3}$.

verge mean that any results are suspect. At current densities of $140\text{--}220 \text{ kA m}^{-2}$, therefore, results are only accepted for $8 < m' < 18$ (at 950°C). In this region, moreover, the curves are substantially straight, and that greatly facilitates the calculations since the slope can be determined by least squares. Table I shows the region of m' accepted at each temperature and the calculation of the contributions due to the $N_{\text{AlF}_3} = 0.25$ melt and to the Cu-Al alloy. No curvature corrections were made since all the times involved were short.

Table II shows results for $N_{\text{AlF}_3} > 0.5$. Runs where the standard deviation of the points from the least squares straight line was greater than ± 1 mV were rejected.

Figure 7 shows the values of $-\partial E/\partial m'$ at 950°C as a function of composition; the upward trend is obvious. The contribution of the composition of the Al-Cu alloy is seen to be a relatively small part of the total.

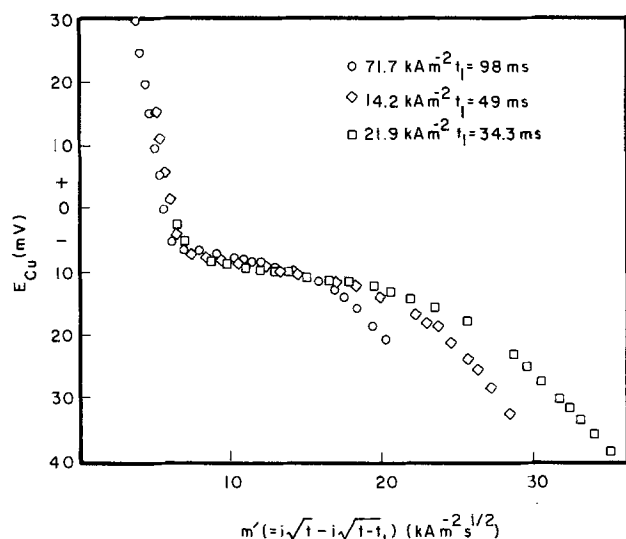


Fig. 6. Variation of potential of Al-Cu alloy after turning off current at time t_1 .

The calculation of the diffusion coefficient is straightforward. $\partial c/\partial E$ is calculated from the thermodynamic model and the densities, and the quantity α is also found from the densities. It will be seen that for the $N_{\text{AlF}_3} = 0.685$ melt, α is very small and, since it varies very rapidly with composition, correspondingly uncertain.

Discussion

There have been no previous diffusion measurements in LiF-AlF₃ melts with which the present results can be compared.

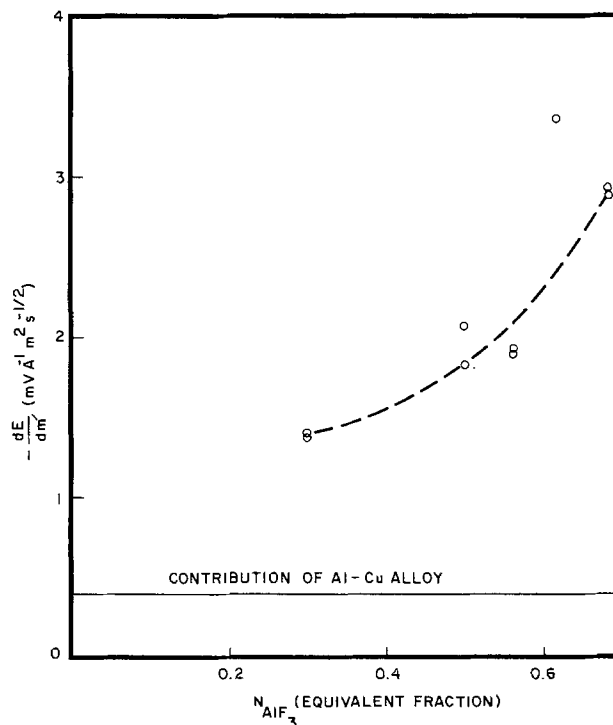


Fig. 7. Slope of the plateau on the plot of potential against m' at 950°C

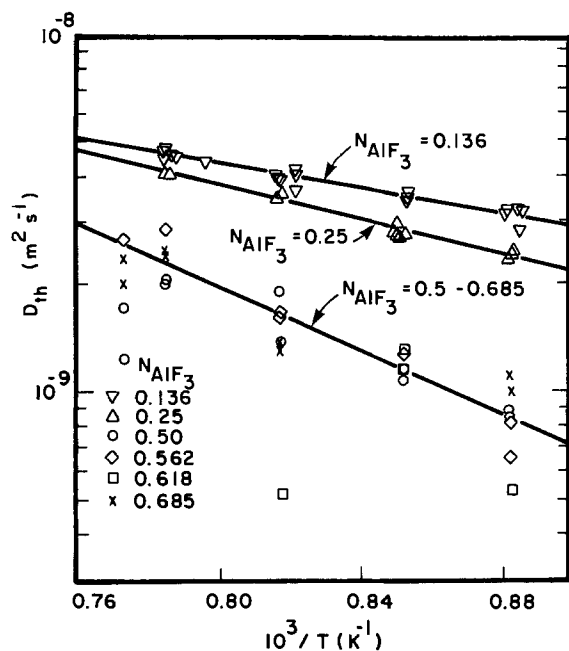


Fig. 8. Thermodynamic diffusivity

Despite the introduction of the density-correction term α , the most conspicuous feature of Table II is that some of the values of D , especially at the $N_{\text{AlF}_3} = 0.685$ composition, are extraordinarily high. Values above $10^{-8} \text{ m}^2 \text{ s}^{-1}$ are unusual, and above $10^{-7} \text{ m}^2 \text{ s}^{-1}$ are, as far as the author is aware, unprecedented. And yet the values of $\partial E/\partial m'$ measured in the experiments vary (with composition) by less than a factor of 3 (see Fig. 7) and the upward trend in $-\partial E/\partial m'$ with composition would in itself correspond to a downward trend in D .

Values of D_{th} calculated from Eq. [17] are shown in Fig. 8. Whereas the Fick's law diffusion coefficients vary (at a given temperature) over a range of a factor of 20, the thermodynamic values cover only a factor of 3.5. Furthermore, the values are nearly all in the range $0.5\text{--}5 \times 10^{-9} \text{ m}^2 \text{ s}^{-1}$, which is quite normal. It is thus clear that the very high Fick's law values originate from the high thermodynamic driving force in these nonideal melts. Since NaF-AlF₃ melts show even greater deviations from ideality, one may anticipate that high diffusion coefficients will again be observed.

The thermodynamic diffusivity decreases substantially between $N_{\text{AlF}_3} = 0.136$ and 0.5, but thereafter remains constant. The drop is presumably associated with the appearance of the bulky AlF_6^{3-} and AlF_4^- groups.

Acknowledgments

The experimental measurements were made with the cooperation of Mr. G. Stratford, and the pulse counting circuit and switch were designed and made by Mr. W. J. A. Green. I am indebted to Dr. J. Braunstein of the Oak Ridge National Laboratory, Oak Ridge, Tennessee, for discussion of the problems associated with density changes, and to the referees for valuable suggestions.

Manuscript submitted Aug. 26, 1982; revised manuscript received Aug. 17, 1983. This was Paper 252 presented at the Montreal, Quebec, Canada, Meeting of the Society, May 9-14, 1982.

The Aluminum Company of Canada, Limited, assisted in meeting the publication costs of this article.

LIST OF SYMBOLS

a, a^0	Activity
c	Concentration (eq m^{-3})
c'	Effective conc, incorporating curvature correction
c^0	Conc at time zero (eq m^{-3})
c_1, c_2	Conc of components 1 and 2
E	Electrode potential (V)
F	96,487 C/eq
i	Current density (A m^{-2})
J	Flux ($\text{eq m}^{-2} \text{ s}^{-1}$)
K	Equilibrium constant
m'	$\sqrt{\pi/2} \times$ semi-integral of i ($\text{A m}^{-2} \text{ s}^{1/2}$)
N	Eq fraction
n	Number of equivalents
R	Gas constant = $8.3143 \text{ J K}^{-1} \text{ mol}^{-1}$
r	Radius of electrode (m)
t	Time (s)
t_{Li^+}	Transport number of Li^+ ions
V	Volume containing 1 mol of F^- (m^3)
v	Volume (m^3)
x	Distance (m)
α	Density correction factor = $V(\partial c/\partial N)$
μ	Chemical potential
τ	Chronopotentiometric transition time (s)

REFERENCES

1. E. W. Dewing, *Metall. Trans. B*, **11**, 245 (1980).
2. E. W. Dewing, *This Journal*, **123**, 1289 (1976).
3. C. J. Wen, B. A. Boukamp, R. A. Huggins, and W. Weppner, *ibid.*, **126**, 2258 (1979).
4. C. E. Vallet, H. R. Bronstein, and J. Braunstein, *ibid.*, **121**, 1429 (1974).
5. K. Matiašovský and M. Malinovský, *Collect. Czech. Chem. Commun.*, **56**, 3746 (1971).
6. L. S. Darken, *Trans. AIME*, **175**, 184 (1948).
7. W. Weppner and R. A. Huggins, *This Journal*, **124**, 1569 (1977).
8. D. D. MacDonald, "Transient techniques in electrochemistry," p. 178, Plenum Press, New York (1977).
9. M. Grenness and K. B. Oldham, *Anal. Chem.*, **44**, 1121 (1972).
10. E. W. Dewing, R. Dorin, and H. J. Gardner, Unpublished results.

Reactions of Coal and Model Coal Compounds in Room Temperature Molten Salt Mixtures

David S. Newman,^{*,1} Randall E. Winans, and Robert L. McBeth

Argonne National Laboratory, Chemistry Division, Argonne, Illinois 60439

ABSTRACT

A 2:1 AlCl_3 -pyridinium chloride molten salt solution was used as the reaction medium for the alkylation of diphenylethane and a bituminous coal by 2-propanol. Probably accompanying the room temperature Friedel-Crafts alkylation is a reduction of $\text{C}=\text{O}$ to $\text{C}-\text{OH}$. Completely deuterated 2-propanol did not react at all with the pyridinium ring. The pyridinium chloride serves to lower the temperature at which the AlCl_3 is able to catalyze the reactions. The pyridinium chloride also catalyzes the Friedel-Crafts alkylation.

In recent years, many authors have focused their attention on organic reactions in molten salt mixtures containing aluminum chloride (1-4) and on organic reactions in molten antimony trichloride (5, 6). Both AlCl_3 and SbCl_3 are strong Lewis acids and are good catalysts for Friedel-Crafts alkylations.

Schlossberg and co-workers have shown that alkylation is a beneficial treatment for coal prior to liquefaction by alkylating several different coals under Friedel-Crafts conditions in an autoclave at 373-423 K (7). Larsen and Kuemmerle discussed the F-C alkylation and depolymerization of coal in a review article (8) and suggested that an understanding of the mechanism of these reactions would considerably increase our understanding of the solubilization of coal and, by implication, our ability to liquefy coal.

Based on these studies, we undertook an investigation of systems in which F-C alkylations would proceed with ease and with minimal damage to the molecular subunits making up the coal macromolecule. The reaction medium we selected was a 2:1 mixture of AlCl_3 and pyridinium chloride, $\text{C}_5\text{H}_6\text{NCl}$. This mixture is liquid at or near room temperature, relatively easy to prepare, and inexpensive—a very important consideration for coal chemistry. Moreover, the melt and the pyridinium salt have both been fairly well characterized (9-11). All of our alkylation reactions were done under nitrogen at or near room temperature. Diphenylethane (bibenzyl) was used as our model coal compound because it has both aryl and alkyl bonds typical of those in coals, and it has been extensively studied under a variety of conditions. The coal chosen for our initial investigation was a high sulfur, high volatile C bituminous coal, and 2-propanol was used as the alkylating agent.

Experimental Details

Preparation of the coal.—A 10g sample of PSOC-244 high sulfur coal [C 55.8%, H 7.5%, N 0.95%, S 7.5% (total), ash 19.5%, and O 12% (by difference)] was ground with water in a shatter box for 15 min and then, after drying, was demineralized using an aqueous HF/HCl solution. The demineralization was carried out by adding 100 ml concentrated HCl to the coal slurry which had been placed in a Teflon beaker. To this mixture, we added 100 ml of 48% HF and allowed the system to react for 48h. The resulting demineralized coal was filtered, vacuum dried, and analyzed. [C 64%, H 5%, N 1.1%, S 6.23% (total), ash 3.9%, and O 19.8% (by difference).] The HCl/HF treatment removed most of the silicate and other inorganic material from the coal.

Preparation of reaction media.—Reagent grade anhydrous aluminum chloride (Cerac 99.9%) and $\text{C}_5\text{H}_6\text{NCl}$ (Eastman Kodak), which had been distilled at 219°C and thoroughly dried, were used without further purification because the impurities in these compounds are far fewer than impurities originating from random fluctuations in composition in any given coal sample.

*Electrochemical Society Active Member.

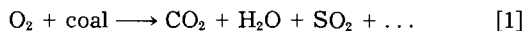
¹Permanent address: Department of Chemistry, Bowling Green State University, Bowling Green, Ohio 43403.

In a dry box, a 2:1 mixture of the AlCl_3 and $\text{C}_5\text{H}_6\text{NCl}$ was prepared by weighing the requisite amount of AlCl_3 into a 100 ml three-neck flask. To the AlCl_3 was added the appropriate amount of $\text{C}_5\text{H}_6\text{NCl}$. The mixture would spontaneously melt, forming a clear to grayish viscous liquid. The liquid was decanted and maintained indefinitely in a dry box. We then added weighed amounts of coal or model compounds, alkylating agents, etc., to portions of this melt. The reaction vessel was removed from the dry box, placed in a constant temperature bath, and the reaction mixture stirred with a magnetic stirrer. A nitrogen atmosphere was maintained in the three-neck flask throughout the course of the reaction.

Treatment and characterization of reaction products.

—After the predetermined requisite amount of time had elapsed, the reaction was carefully quenched by first cooling the closed reaction vessel in ice water and then dropping small pieces of ice, one at a time, into the reaction vessel so as not to raise the melt temperature substantially. After all of the AlCl_3 had reacted with the water, the aqueous slurry was extracted with various organic solvents and the extracted material analyzed by high performance liquid chromatography (HPLC), gas chromatography-mass spectrometry (GC/MS) (12, 13), and a gas chromatograph-microwave plasma detector-computer system (GC/MPD) (14).

The main feature of the GC/MPD-computer system is an Applied Chromatography System MPD-850 which is an emission spectrometer with a helium plasma source. The spectrometer is connected to a GC and is able to simultaneously detect the elements C, H, D, S, F, Cl, O, or N. The output from the spectrometer is amplified digitally and transferred to a VAX 11/780. By using suitable standards, we can obtain empirical formulas or detect the presence of deuterium in labeling experiments with these instruments with an accuracy of $\pm 5\%$. An inlet system allowing direct entry of solid coal into the MPD was designed to facilitate the analysis of nonvolatile coal or coal products. This inlet system or "solid probe" consists of a platinum tube which serves as a furnace and is heated directly by two leads connected to the output of a dc power supply (HP 6259 B). Both the rate and the amount of heating can be controlled by the power supply. The temperature inside the inlet tube is easily monitored by means of a thermocouple. A Teflon T tube connector, attached to the inlet tube by one of its arms and to a gas source by its central channel, conducted the necessary carrier gas or gases into the system. The sample itself was held in a hollow cylinder of platinum gauze welded to a platinum rod and inserted directly into the furnace through the unattached arm of the T tube (along the principal axis of the platinum furnace). With the sample in place and the carrier gas flowing, the sample was heated to the desired temperature, usually 1100°C, to ensure complete combustion. The combustion products were fed directly into the MPD. The combustion of coal can be described by the equation



The products of this reaction are atomized by the plasma and the emission spectra of the atoms analyzed by the MPD. The GC/MPD was also used to quantitatively analyze the coal for the presence of deuterium. In our original study (15), we were unable to obtain quantitative information and were able to detect the presence of deuterium only qualitatively. A weighed deuterated coal sample was pyrolyzed at 800°C under high vacuum and the pyrolysis products collected in three different fractions each of known weight. The first fraction was volatile material trapped at liquid nitrogen temperatures. The second fraction was CH_2Cl_2 soluble material and the third fraction was residual char. The trapped volatiles were taken up in CH_2Cl_2 , injected into the GC/MPD, and the elements C, H, and ^2H were analyzed. The second CH_2Cl_2 fraction was analyzed the same way. Using suitable deuterium labeled standards, the areas under the chromatogram peaks were calibrated and the percentage of each element in the two fractions was calculated. The char was assumed to contain no deuterium.

Measurement of the coal solubility in molten salt.—The solubilities of the starting coal and the alkylated coal were measured by filtering at temperature a slurry of coal in the melt using a medium porosity glass frit in the cell, shown schematically in Fig. 1. The cell itself was maintained in a constant temperature glass-enclosed oven. The molten salt-coal solution passed through the frit when a positive nitrogen pressure was maintained in the top portion of the cell and a partial vacuum was maintained in the bottom portion. The solubility was simply the percentage weight difference between the original coal and the coal residue that did not pass through the frit.

Results and Discussion

Model compounds and solvent system.—In order to characterize the role of the solvent and assess the extent of

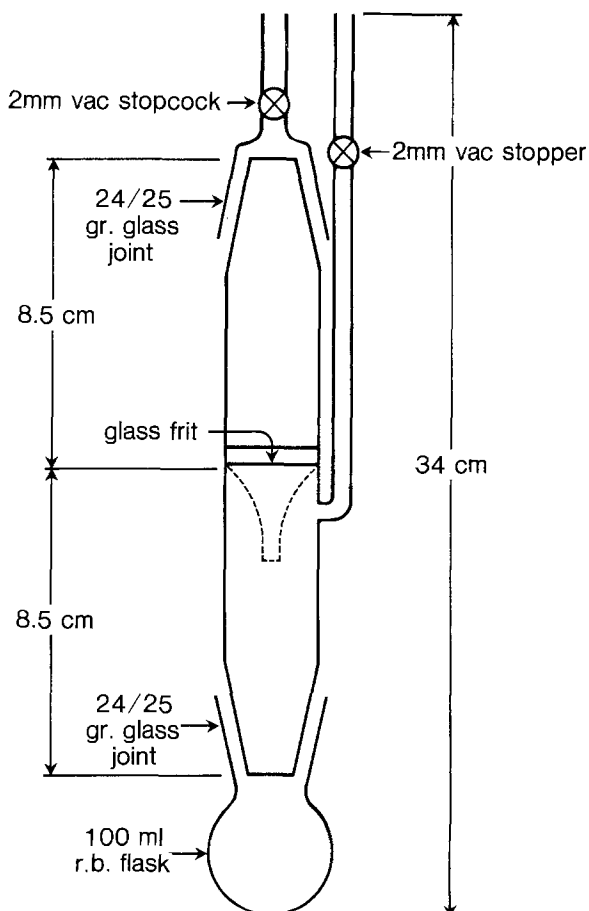


Fig. 1. Glass frit filter cell

autoalkylation of the 2-propanol or the bibenzyl, a series of experiments was performed in which either the 2-propanol or the bibenzyl or a mixture of the two was allowed to react in the melt.

Autoalkylation of 2-propanol formed an orange red material which contained a series of high molecular weight polymers, most of which were nonvolatile. No alkylated pyridines were identified.

Autoalkylation of bibenzyl gave a series of polymers as well as a low yield of monomeric material. The compounds, produced by the bibenzyl reaction and identified by gel permeation chromatography and GC/MS, are listed in Fig. 2. Our results are consistent with those of Heredy and Neuworth (16) who used model compounds in phenol to show that, under Friedel-Crafts conditions, methylene chains can be broken and the resulting species can alkylate other aromatic compounds. In our system, which lacked phenol or another hydrogen source, alkylation proceeded faster than bond cleavage although aryl and methylene bonds were indeed broken at the low reaction temperatures. The molecular weights of the alkylation products were determined by gel permeation chromatography and ranged from 78 (benzene) to approximately 10,000. One aspect of this reaction which deserves comment is the formation of compound 5 which was identified by its mass spectrum. For this compound to form, the aryl carbon bond of bibenzyl had to cleave even though the temperature was less than 40°C. The bond energy for this bond is 414 kJ/mol which means that either the AlCl_3 or the $\text{C}_5\text{H}_6\text{NCl}$ or both are catalyzing the reaction.

To discover if the pyridinium ion would react with alkylating agent under reaction conditions, 1.6g of 2-propanol- d_8 and 1.8g bibenzyl were allowed to react in the 2:1 $\text{AlCl}_3/\text{C}_5\text{H}_6\text{NCl}$ solution at 30°C for 4h. The reaction was quenched with water, as described previously, and extracted with hexane. The aqueous layer was neutralized with NaOH and an aliquot passed through the MPD. No deuterium was detected in the instruments' deuterium channel, indicating that no ring proton exchange or alkylation of the pyridine ring occurred despite the favorable environment for alkylation reactions (17). This means the principal role of the pyridinium chloride in the

Chromatogram Peak Number	Compound	% of Total
1.	Isopropylbenzene	1.2
2.	Disopropylbenzene	2.6
3.	Triisopropylbenzene	6.1
4.	Bibenzyl	9.2
5.	Isopropylbibenzyl	7.3
6.	Diisopropylbibenzyl	18.0
7.	Unidentified	4.2
8.	Triisopropylbibenzyl	21.0
9.	Tetraisopropylbibenzyl	25.5
10.	Pentaisopropylbibenzyl	4.8
(toluene identified in HPLC)		99.9

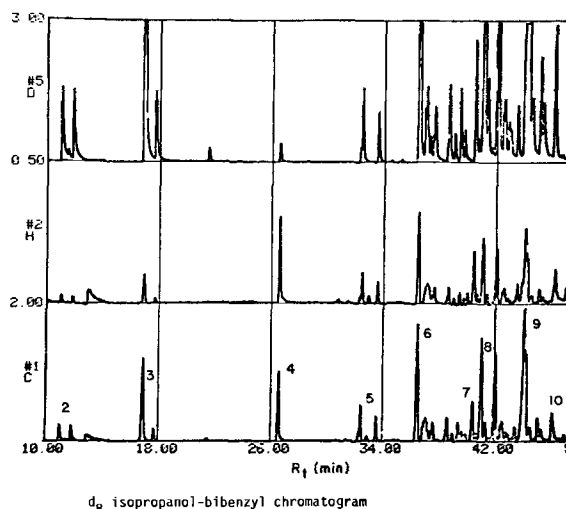


Fig. 2. Chromatogram of compounds formed from the alkylation of bibenzyl by 2-propanol- d_8 .

melt is to lower the temperature at which the AlCl_3 catalyzes the various reactions. The 2-propanol- d_6 reacted with the bibenzyl to form a series of alkylated phenyl derivatives (Fig. 2) as expected. Approximately 85% of the initial bibenzyl reacted within the 4h and about 40% of its aliphatic carbon bonds were cleaved. The alkylation products were identified by GC/MPD and GC/MS. From these results, we conclude that the alkylating agent preferentially alkylates bibenzyl rather than itself. The earlier experimental results, in which no deuterium was found on the pyridine ring, still did not indicate if the nitrogenic proton of the pyridinium ion, N-H^+ , had exchanged with any of the 2-propanols' deuterium atoms. To ascertain whether or not exchange had occurred, the $^1\text{H-NMR}$ spectrum of a 2:1 $\text{AlCl}_3/\text{C}_5\text{H}_5\text{NCl}$ melt was obtained on a CFT-80 with variable temperature capability. The spectrum showed a striking nitrogen broadened triplet at 70°C (Fig. 3) indicating that, in the pure melt, exchange was not occurring because if it was, the proton could not reside on the nitrogen long enough to couple with it, but would give a sharp singlet (10, 11). Our spectrum is similar to that reported by Angell and Shuppert (9) for a similar melt at 148°C , but our ring proton resolution is not as good because of our lower temperature. This spectrum, incidentally, is excellent evidence for the fact that there are few, if any, free Cl^- ions in the melt. If a substantial concentration of free Cl^- ions were present, the N-H^+ would appear as a sharp singlet in the $^1\text{H-NMR}$ spectrum (11). The dominant anionic species is probably Al_2Cl_7^- as suggested by Gale and Osteryoung (18, 19). The cation is, of course, the pyridinium ion, and the environment is distinctly unfavorable for exchange.

When a quantity of 2-propanol- d_6 , equivalent to the $\text{C}_5\text{H}_5\text{NCl}$, is added to the melt, the brownish-orange polymeric material formed again and remained suspended. The $^1\text{H-NMR}$ spectrum changed markedly with respect to the nitrogen-broadened triplet, so prominent in the pure melt, and formed a very broad singlet peak. The integrated area under the N-H^+ peak was reduced from approximately one-sixth that of the ring proton area to approximately one-twelfth, indicating that exchange was complete and the system had equilibrated. It is assumed that it was the hydroxyl deuterium that exchanged with the N-H^+ . This implies that the N-H^+ is available to catalyze various proton catalyzed reactions and broadens the scope of the $\text{AlCl}_3/\text{C}_5\text{H}_5\text{NCl}$ melt as a reaction medium.

Reactions with coal.—A sample of the HF/HCl demineralized HVC coal was added to the $\text{AlCl}_3/\text{C}_5\text{H}_5\text{NCl}$ melt and allowed to mix with it for 20h at 30°C . The black slurry was then quenched and the coal separated from the melt and analyzed to assure us that no substantial elemental changes had occurred. No distinction was made between the melt soluble and melt insoluble coal fractions; both were combined. The elemental analysis was substantially the same as before [C 66%, H 4.8%, N 1.25%, S 6.46% (total)]. To detect changes in average molecular

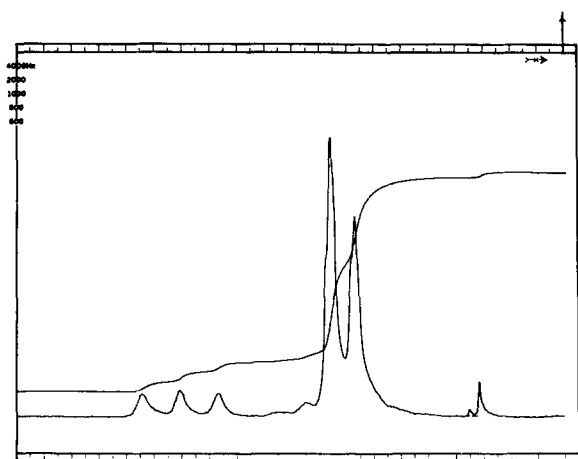


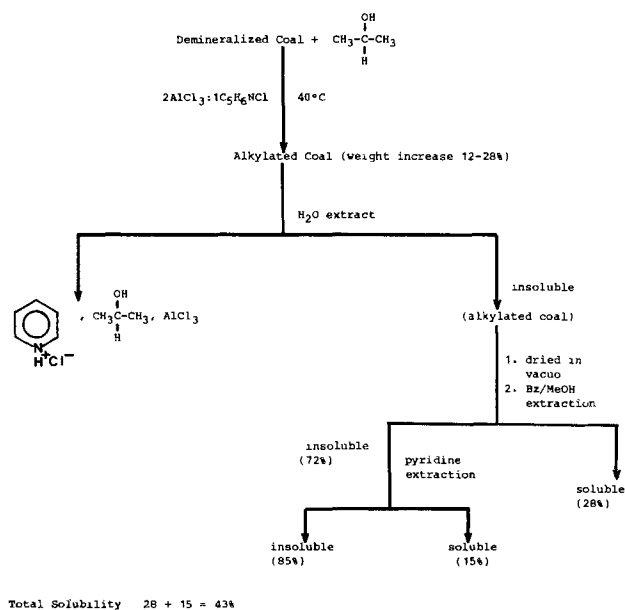
Fig. 3. $^1\text{H-NMR}$ spectrum of $2\text{AlCl}_3/\text{C}_5\text{H}_5\text{NCl}$ at 70°C

weight of the coal that may have occurred through bond cleavage, autoalkylation, etc., the solubility of the reacted coal in a 3:1 benzene-methanol solution was compared with that of the unreacted coal in the same solvent. The solubility of the reacted coal was 6.3% by weight and the solubility of the unreacted coal was 9.8% by weight. Considering the errors involved in recovery and the relatively low solubilities of the two coals, there is not very much difference. Nevertheless, it is possible that some internal change such as autoalkylation did occur while the coal was in the melt.

The reaction between the demineralized coal and the 2-propanol is shown schematically in Fig. 4. We initially used long reaction times ($> 15\text{h}$) and low temperatures (30°C), but subsequently found that shorter reaction times and higher temperatures (40°C - 45°C) gave smaller weight increases, lower ash content, and higher solubilities in organic solvents. From our model compound reactions and chemical analyses, we can say with some assurance that the increase in weight is due to isopropyl groups bonding to the coal.

The larger weight increases that we were able to achieve with this reaction represent the addition to the coal of approximately 15 alkyl groups per 100 carbons, which is more than the number reported by Kroger for the alkylation of high vitrinite coals using isopropyl chloride and AlCl_3 in CS_2 at 45°C (20, 21). This strongly suggests that the 2:1 $\text{AlCl}_3/\text{pyrCl}$ melt is the best medium yet found for Friedel-Crafts alkylation of coal and may, in fact, have general synthetic importance (22).

The molecular weight distribution of the benzene/methanol soluble fraction of the alkylated coal was obtained by gel permeation chromatography with a UV detector set at 254 nm. Four μ -styrogel columns were used in series for the separation. Three had 100\AA nominal pore diameters and one had 500\AA nominal pore diameters. The chromatogram is shown in Fig. 5. The molecular weights ranged from 4400 to less than 100 with the largest fraction being in the neighborhood of 560. Since 254 nm is the region of the spectrum in which aromatic molecules strongly absorb light, a conclusion that can be drawn from this chromatogram is that there are either polymers containing aromatic units or double and triple bonds (which also absorb at 254 nm) dissolved in the benzene/methanol solution. These entities could not have easily originated from the alkylating agent and, therefore, had to come from the coal. The average molecular weight distribution of the soluble fraction of alkylated coal is quite low and is preliminary evidence for concluding that depolymerization is accompanying alkylation (23, 24).



Total Solubility $28 + 15 = 43\%$

Fig. 4. Schematic diagram of the reaction between 2-propanol and demineralized P50C-244 coal.

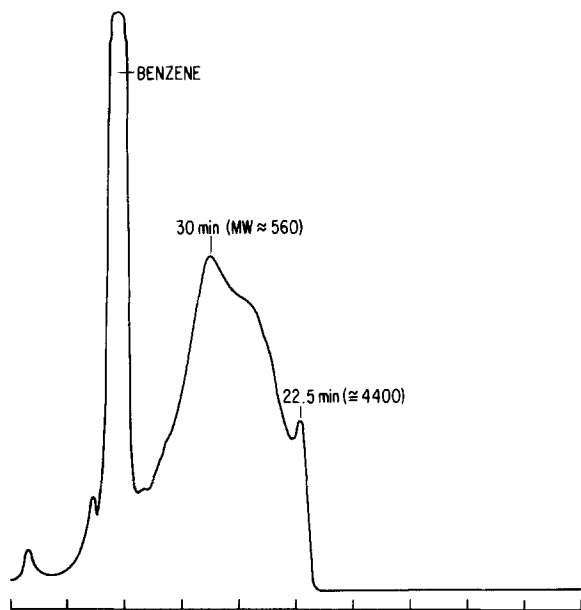


Fig. 5. Gel permeation chromatogram of the benzene/methanol soluble portion of alkylated coal.

A portion of the benzene/methanol soluble fraction of the alkylated coal was analyzed via the solid probe of the GC/MPD and was found to contain sulfur in about the same proportion as in the original coal. This was considered proof that at least some of the original coal was dissolving. It is impossible for the sulfur to have originated from the alkylating agent. The sulfur compounds probably were liberated by breaking a methylene-sulfur bond (25).

To further characterize the alkylation reaction and understand its effect on the coal's solubility, as well as to prove beyond a reasonable doubt that the 2-propanol alkylated the coal rather than polymerized and then attached itself loosely to the coal's surface, we decided to measure the net solubility of the coal rather than the solubility of coal plus added alkyl groups, which is the quantity usually reported in the literature. To do this, we alkylated a 0.722g sample of coal with 2-propanol- d_8 . The coal increased its weight 0.084g or about 12%. We then extracted 0.6482g of this deuterated coal with benzene/MeOH (3:1) and pyrolyzed the residue, which weighed 0.481g. The three fractions were analyzed for C, ^1H , and ^2H , using the technique described earlier. The residue contained 0.0146g of ^2H . The ^2H initially present in the starting sample weighed 0.018g. This means that the insoluble coal remaining after benzene/MeOH extraction contained 81.11% of its original ^2H and 18.9% of the deuterated alkylating agent dissolved along with the coal. The net coal solubility is therefore

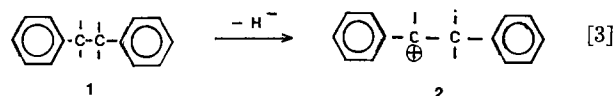
$$100 \times \left[\frac{0.167 \times (0.189 \times 0.0675)}{0.684 - \left[\frac{(0.648 \times 0.084)}{0.806} \right]} \right] = 28\%$$

This should be compared with the 6.3-9% solubility of the nonalkylated coal and represents a significant increase in solubility with relatively little alteration of the structural units that comprise the coal. An interesting result of this experiment, besides proving that the 2-propanol alkylated the coal and not itself, is that at least 10% more coal dissolved than alkylating agent. In all likelihood, the principal reason for the increase in the alkylated coal's solubility is a decrease in the cross-linking between the coal macromolecules, which causes the coal to swell. In several of our alkylation reactions, the coal and 2-propanol, which were in the form of a slurry in the media, turned to a "pudding-like" material. We interpreted this to be partially caused by a swelling of the coal. In our system, the decrease in the extent of cross-linking is due to the scission of methylene and aryl-methylene bonds which is a

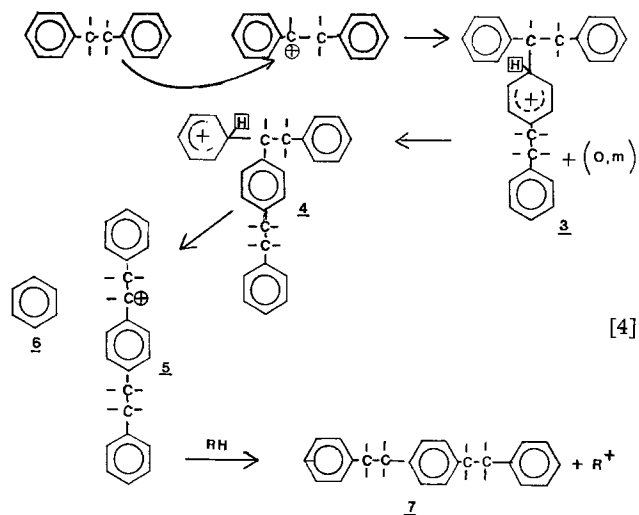
secondary, but important, by-product of the Friedel-Crafts alkylation, as shown in our model compound studies. The decrease in cross-linking permits the solvent to solvate previously inaccessible interior units of the coal macromolecule, which may not have been as completely alkylated as exterior portions, and increase the coal's solubility above what it would have been in the absence of alkylation. Stating this conclusion slightly differently, swelling of the coal, which is a result of a by-product of the Friedel-Crafts reaction, is the important process for increasing the coal's solubility and causing the substantial solubility differential between alkylating agent and coal. To sharpen this argument, we measured the alkylated coals' solubility in the molten salt because coals are notoriously insoluble in highly polar or ionic solvents. The original demineralized coal had a molten salt solubility of 6.5% while the alkylated coals' solubility was 15.9%. The most plausible explanation for this substantial increase in solubility is the Al_2Cl_7^- and $\text{C}_5\text{H}_8\text{H}^+$ ions were able to penetrate the interstices of the coal macromolecule and solvate severed sections of the coal.

Comparing the solubilities of the alkylated and nonalkylated coals in various solvents shows that the alkylated coal is in all cases considerably more soluble. Since increased cross-linking, Scholl reactions and autoalkylation are also possible (17) in the melt; an obvious conclusion that can be drawn from our results is that at low temperatures (40°C), alkylation, depolymerization, and reduction of intermolecular cross-linking are proceeding at a faster rate than Scholl reactions, autoalkylation, and internal cross-linking. This means that alkylation by 2-propanol in $2\text{AlCl}_3 \cdot 1\text{C}_5\text{H}_8\text{NCl}$ is a useful technique for coal solubilization. It also means that coal solubility is not a linear function of weight increase, but depends in a complex manner on all of the external conditions.

Reaction mechanisms.—The reaction mechanisms that can be given in detail and with some degree of confidence are those involved with autoalkylation of bibenzyl and the alkylation of bibenzyl with 2-propanol. The first step in the autoalkylation of bibenzyl is the removal of a hydride ion from the bibenzyl to generate the carbonium ion



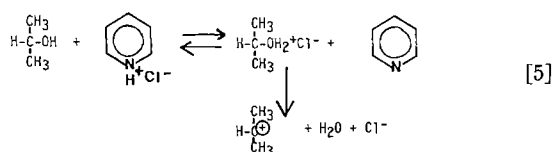
Another bibenzyl molecule then attacks the carbonium ion and the reaction proceeds via the scheme shown below



Both compounds **6** and **7** were identified by GC/MS and HPLC, and R^+ continues the chain reaction. This scheme is quite similar to the Friedel-Crafts transalkylation mech-

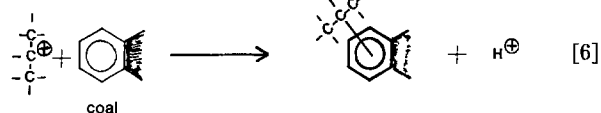
anism suggested by Roberts and Roengsumran for isotopically labeled *n*-propylbenzene (26).

The alkylation of the bibenzyl by the 2-propanol has for its initial step

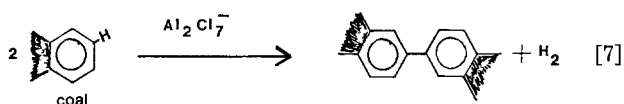


The propyl carbonium ion is then attacked by the bibenzyl forming the various products we have isolated. It should be kept in mind that we did not observe extensive autoalkylation of bibenzyl in the presence of 2-propanol.

In all likelihood, the principal reaction mechanism for the coal alkylation by 2-propanol is similar to Eq. [5] with the carbonium ion then reacting with aryl sites in the coal



Competing with this reaction are Scholl type reactions of the form (27)



Surprisingly, Scholl reactions did not occur to any great extent in the bibenzyl-2-propanol experiments, but there was evidence for this type of reaction in the bibenzyl autoalkylation.

As a result of the formation of compounds 5 and 6 (Eq. [4] as well as the slight decrease in the solubility of the demineralized coal in benzene/methanol, one cannot rule out the possibility that Eq. [7] is competing with Eq. [6]. The substantial increase in the alkylated coal's benzene/methanol solubility relative to the nonalkylated coal, even taking into account that some of the soluble material was the alkylating agent, together with the production of toluene, benzene, ethyl benzene, and other reduced species in the model compound reaction, suggests that a reduction reaction of some sort is also occurring in addition to the other processes already mentioned. Moreover, a similar study of I11 no. 6 coal has given us spectroscopic evidence for the reduction of a carbonyl group to a hydroxyl group (28). This reduction probably results from the protonation of a carbonyl oxygen and the subsequent hydride extraction from either the isopropyl alcohol or hydride donors in the coal itself. Isopropyl alcohol is known to be a good hydride donor, and acetone was observed as a reaction product.

Conclusion

A 2:1 $\text{AlCl}_3/\text{C}_5\text{H}_5\text{NCl}$ solution is an excellent reaction medium for both Friedel-Crafts alkylation and depolymerization of coal. The low temperatures at which the reactions occur in this melt further enhance the ease of handling of the reaction products and prevent the decomposition of the molecular subunits comprising this coal. However, a large variety of coals and model coal compounds remain to be studied before a firm conclusion as to the detailed mechanisms and scope for these intriguing reactions can be determined. It is also our opinion, in agreement with other authors, that alkylation is a beneficial treatment of coal prior to liquefaction, and if combined with an oxyalkylation like that described by

Liotta, may become an extremely important method of liquefying coal (29, 30).

Acknowledgments

This work was supported by the Office of Basic Energy Sciences, Division of Chemical Sciences, U.S.D.O.E. D. S. Newman wishes to thank the Argonne Division of Educational Programs for awarding him a Fossil Energy Faculty Research Residency during the summer of 1980. This program is funded by the U.S. Department of Energy-Fossil Energy.

Manuscript submitted Jan. 14, 1983; revised manuscript received Jan. 19, 1984. This was Paper 660 presented at the Hollywood, FL, Meeting of the Society, Oct. 5-10, 1980.

Argonne National Laboratory assisted in meeting the publication costs of this article.

REFERENCES

1. A. C. Buchanan, III, A. S. Dworkin, and G. P. Smith, *J. Am. Chem. Soc.*, **102**, 5262 (1980).
2. V. R. Koch, L. L. Miller, and R. A. Osteryoung, *ibid.*, **98**, 5277 (1976).
3. J. Robinson and R. A. Osteryoung, *ibid.*, **102**, 4415 (1980).
4. J. Robinson and R. A. Osteryoung, *ibid.*, **101**, 323 (1979).
5. A. S. Dworkin, M. I. Potsma, J. Brynestad, L. L. Brown, L. O. Gilpatric, and G. P. Smith, *ibid.*, **101**, 5299 (1979).
6. G. P. Smith, A. C. Buchanan, III, A. S. Dworkin, M. Sorlie, and M. V. Buchanan, in "Third International Symposium on Molten Salts," G. Mamantov, M. Blander, and G. P. Smith, Editors, p. 393, The Electrochemical Society Softbound Proceedings Series, Pennington, NJ (1981).
7. R. H. Schlosberg, R. C. Neavel, P. S. Maa, and M. L. Gorbaty, *Fuel*, **59**, 45 (1980).
8. J. W. Larsen and E. W. Kuemmerle, *ibid.*, **55**, 162 (1979).
9. C. A. Angell and J. W. Shuppert, *J. Phys. Chem.*, **84**, 538 (1980).
10. V. C. Reinsborough, *Aust. J. Chem.*, **23**, 1473 (1970).
11. D. S. Newman, W. Rohr, and D. Kirklin, *This Journal*, **119**, 798 (1972).
12. M. H. Studier, R. Hayatsu, and R. E. Winans, in "Analytical Methods for Coal and Coal Products," Vol. II, C. Carr, Jr., Editor, p. 43, Academic Press, New York (1978).
13. R. Hayatsu, M. H. Studier, L. P. Moore, and E. Anders, *Geochim. Cosmochim. Acta*, **39**, 471 (1975).
14. R. E. Winans, R. G. Scott, R. L. McBeth, and R. Hayatsu, *J. Am. Chem. Soc.*, To be published.
15. D. S. Newman, R. E. Winans, and R. L. McBeth, in "Third International Symposium on Molten Salts," G. Mamantov, M. Blander, and G. P. Smith, Editors, p. 425, The Electrochemical Society Softbound Proceedings Series, Pennington, NJ (1981).
16. L. A. Heredy and M. B. Neuworth, *Fuel*, **41**, 221 (1962).
17. H. L. Jones and R. A. Osteryoung, *Adv. Molten Salt Chem.*, **3**, 121 (1975).
18. R. J. Gale and R. A. Osteryoung, *Inorg. Chem.*, **17**, 2728 (1978).
19. R. J. Gale and R. A. Osteryoung, *ibid.*, **18**, 1603 (1979).
20. C. Kroger, H. DeVries, *Liebigs Ann.*, **35**, 652 (1962).
21. C. Kroger, H. B. Rabe, B. Rabe, *Petrochemia*, **16**, 21 (1963).
22. P. Treichel, University of Wisconsin, Private communication.
23. L. A. Heredy, L. A. Kostyo, and M. B. Neuworth, *Fuel*, **43**, 414 (1964).
24. L. A. Heredy, L. A. Kostyo, and M. B. Neuworth, *ibid.*, **44**, 125 (1965).
25. D. P. Mobley and A. T. Bell, *ibid.*, **59**, 507 (1980).
26. R. M. Roberts and S. Roengsumran, *J. Org. Chem.*, **46**, 3689 (1981).
27. A. T. Balaban and C. D. Nenitzescu, in "Friedel-Crafts and Related Reactions," Vol. II, Interscience, New York (1963-1965).
28. D. S. Newman, R. E. Winans, and L. Basile, *Appl. Spectrosc.*, In press.
29. R. Liotta, *Fuel*, **58**, 724 (1979).
30. R. Liotta, K. Rose, and E. Hippo, *J. Org. Chem.*, **46**, 277 (1981).

Equilibrium Concentrations of FeS₂ and FeS in LiCl-KCl Eutectic Melts

Ram A. Sharma and Randall N. Seefurth*

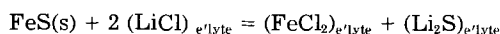
General Motors Research Laboratories, Warren, Michigan 48090-9055

ABSTRACT

Solubilities of FeS₂ in LiCl-KCl eutectic melts between 720 and 900 K are represented by the equation

$$\log(\text{mol fraction, } X_{\text{FeS}_2}) = -\frac{5157.33}{T} + 0.666 \pm 0.125$$

They were measured by a new optical technique. This was necessitated by an excessive scatter in the solubility data determined by chemical analysis of the melts after establishing equilibria between the melts and FeS₂ by diffusion and counterdiffusion. The solubility of FeS in these melts determined chemically also had an excessive scatter. In addition, the optical technique was inadequate, as no solid FeS sample could be satisfactorily used. Therefore, the solubilities were calculated from the equilibrium constant of the reaction



using relevant thermodynamic data.

Rechargeable cells are being developed using Li-Al or Li-Si negative electrodes, iron sulfide or iron disulfide positive electrodes, and LiCl-KCl melts contained in boron nitride cloth separators as electrolytes (1-3). These cells have performed for over 10,000h (2), but the specific energy starts declining after about 3000h. Post-test examination of some of the compact cells which had Li-Al electrodes indicated very fine iron particles associated with lithium sulfide particles within the boron nitride separators (4). The degradation in performance of these cells may be caused by the loss of positive electrode active materials through their solubilities in the electrolyte. The iron sulfides in the positive electrodes themselves might have dissolved slightly in the electrolyte and reacted with dissolved lithium yielding iron and lithium sulfide particles. Boron nitride fibers could provide nucleating sites for their deposition. Therefore, it is necessary to have solubility data for the iron sulfides to evaluate this hypothesis. The following investigation was a part of this effort and was conducted to measure the solubilities of FeS and FeS₂ in LiCl-KCl eutectic electrolyte at different temperatures.

As a first attempt, the solubilities were measured by equilibrating the LiCl-KCl melts with the respective solutes inside specially designed sealed silica capsules at different temperatures and determining the solute contents by chemical analysis. A large scatter was observed in these measurements. This scatter was caused by the difficulty in chemically determining the very low contents of the solutes in the equilibrated melts. Therefore, a new optical technique was developed. In general, this technique consists of sealing weighed amounts of solute and solvent inside a transparent silica capsule under vacuum. The capsule is slowly heated inside a furnace equipped with viewing ports. After the electrolyte has melted, the solid solute particle is observed occasionally with a microscope. At a certain temperature, the solute dissolves completely in the melt, and the solubility is determined from the weighed amounts of solute and solvent and the observed temperature of dissolution. The technique was tested by determining the solubilities of Li₂S in LiCl-KCl eutectic melts. These solubility data were in agreement with data in the literature (5).

Experimental

Materials.—Electrolytes obtained from two sources were used in these studies. First, LiCl of 99.6% purity and KCl of 99.9% purity were combined to form the eutectic mixture [58 mol percent (m/o) LiCl-42 m/o KCl; mp = 625 K (6)]. This mixture was purified by bubbling chlorine through the melt at 775 K for 4h, and subsequently

*Electrochemical Society Active Member.

removing the chlorine by bubbling with helium for 1h. Second, a high purity eutectic was obtained from Anderson Physics Laboratory and used for the majority of the tests.

A section of a large naturally occurring crystal of pyrite (FeS₂) was cleaved off and broken into sample-size pieces. These pieces were analyzed under a microscope capable of 30X magnification, and only pieces having smooth and shiny surfaces [indicating no entrapped silica (SiO₂) impurities] were selected for testing. Chemical analyses of such specimens revealed an iron content of 46.3 weight percent (w/o) compared to the theoretical value of 46.55 w/o.

Inside a helium-atmosphere dry box, a quantity of high purity FeS (63.1 w/o Fe by chemical analysis against 63.53 w/o theoretical Fe) was placed in a graphite container with a tightly fitting cover which was cleaned by firing at about ~1300 K in a helium atmosphere. The container was placed in a flat-bottom silica tube which was closed with a rubber stopper having helium inlet and outlet ports. The silica tube was taken out of the dry box and positioned in a high frequency furnace heating coil. The graphite container was heated to ~1550 K, kept at this temperature for about 30 min, and then cooled in flowing helium. The silica tube with its content was transferred into a dry box. The FeS lump was taken out of the graphite container and crushed into small pieces for use in the solubility measurements using the chemical technique.

Apparatus and procedure.—*Chemical analysis technique.*—Sealed silica (Vycor) capsules of different designs, as shown in Fig. 1, were used to hold the melts. These different designs were tested in an attempt to minimize the convective transport of fine undissolved solute particles during equilibration (*i.e.*, to attain equilibrium by diffusion and counterdiffusion only) and to minimize compositional changes due to transport of the melt from the different compartments of the capsule during quenching. To further reduce the chances of convective transport of the solute particles, silica shot was placed on the inner small solute tube. Any errors due to segregation were avoided by using the whole amount of melt from the lower limb. The results from these different designs were similar, therefore, the capsule of the design shown in Fig. 1a was arbitrarily used.

Before use, the silica capsules were cleaned a few times with soap and water, then with alcohol, and dried at 475 K. They were fired in hydrogen at 1100 K for 1h.

Inside a helium-atmosphere dry box, enough LiCl-KCl eutectic mixture was melted in the silica capsules (Fig. 1A, 1B, 1C) to fill only the bottom extensions. After removing gas bubbles from the melt, the second smaller

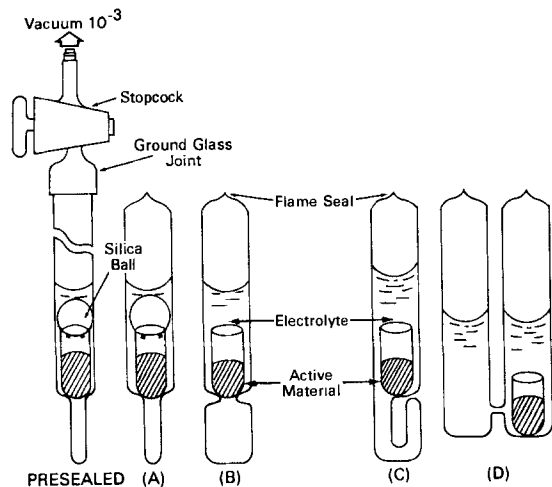


Fig. 1. Schematic representation of the silica containers used for solubility measurements (chemical technique).

tube with the solute reactant pieces (FeS or FeS₂) was placed inside the silica capsule. An additional amount of LiCl-KCl mixture was slowly added, taking care to keep the mixture molten and to submerge the smaller tube completely. The melt was slowly solidified, avoiding gas bubble entrapment. The silica capsules were then taken out of the dry box and sealed under a vacuum of $\sim 10^{-3}$ torr.

A layer of thermal insulation was placed in the bottom of a stainless steel container, 200 mm long and 57 mm id. Eight stainless steel tubes, 150 mm long and 14 mm id, were positioned in the container, and the annular space was filled with sand. The sealed silica capsules were placed inside the smaller stainless steel tubes which were then covered by another layer of thermal insulation.

A vertical tubular furnace (450 mm long, 75 mm diam) with a uniform temperature zone about 150 mm long was used to heat the melts. The other instruments used in conjunction with the furnace included a proportional band temperature controller, a potentiometer, and calibrated Chromel-Alumel thermocouples.

The stainless steel container was placed in the predetermined uniform temperature zone of the vertical tubular furnace, and the empty space in the furnace was packed with thermal insulation. The furnace was heated to a desired temperature and kept at this temperature for the equilibration period. From the results of experiments carried out for different lengths of time, the equilibration period was determined to be about 15 days. However, the test samples were generally allowed to equilibrate about 30 days, and in some cases even 55 days. At the end of the equilibration period, the samples were quenched in oil, the limb containing the equilibrated solidified melt was broken off, and the solubility was determined by chemical analysis of the total contents in the limb for iron.

In the case of silica capsule D (Fig. 1), the same preparatory procedure was followed except the smaller silica tube with the solute was positioned at the very beginning, the LiCl-KCl mixture was added in stages and melted until the level of the melt was above the capillary. During the equilibration period, the silica capsule was not placed in the smaller stainless tube; rather, it was submerged into the sand inside the bigger stainless steel container.

Optical technique.—The transparent test capsules were made by closing one end of a 10 cm-long piece of 25 mm od silica tube and adding a neck (20 cm long by 15 mm od) to the open end. A ground glass joint was attached to the neck, while the base of the capsule was provided with a small protrusion (3 mm deep by 5 mm id) for facilitating sample location. The capsules were washed with soap and water, acetone, and finally distilled water using an ultrasonic cleaner. They were oven dried at 375 K and cooled to room temperature. A preweighed solute sample was inserted into each capsule which was then transferred into a helium-atmosphere (typically less than 1

ppm O₂, N₂, or H₂O) dry box. Predetermined amounts of LiCl-KCl eutectic were weighed inside the dry box and placed inside the respective capsules. Each capsule was closed inside the dry box, using a ground glass joint and stopcock assembly. The loaded capsule was then removed from the dry box and sealed at the base of the neck under a vacuum of $\sim 10^{-3}$ torr using common glass-blowing techniques. A liquid nitrogen cold trap was used between the mechanical pump and the capsule to prevent back diffusion of vapors from the pump into the sample zone.

A description of the apparatus used in this optical technique is shown in Fig. 2. Briefly, the sealed capsule, together with three calibrated thermocouples and two optical prisms, was mounted in a stainless steel test fixture to insure system rigidity. Two of the thermocouples were positioned near the bottom of the melt area, the other near the top. This fixture was inserted into a two-zone, vertical tubular clamshell heating element furnace (3.8 cm id by 40 cm long). One of the lower thermocouples was used in conjunction with a proportional-band temperature controller to control the temperature of the lower furnace zone. The other two thermocouples were used in conjunction with a digital temperature-readout system and a data-acquisition system to monitor the melt temperature. The top furnace zone (above the sample zone) was heated only to maintain a constant temperature throughout the test zone. It was regulated manually by means of an autotransformer.

Initially, the furnace was equipped with two viewing ports, which with the aid of the prisms, allowed transmission of light from the source through the test capsule to the microscope. Later, a third port, opposite the lower port, was introduced for versatility in lighting and observing the sample. The ports were covered with transparent silica plates to eliminate air circulation, while the top and bottom of the furnace were closed with thermal insulation. A 300W xenon lamp was used to illuminate the sample capsule, and a stereomicroscope capable of 70X magnification was used to view the sample.

After the electrolyte was melted, the solid solute particle was observed occasionally with the microscope. The temperature was slowly raised in steps. Near the dissolution temperature, it was increased in approximately 5° increments and kept at each temperature at least 6h. At a certain temperature, the solute would dissolve completely in the melt, and the solubility was determined from the weighed amounts of solute and solvent and the observed temperature of dissolution.

Results and Discussion

FeS₂ solubility.—The solubilities of FeS₂ in LiCl-KCl eutectic melts at different temperatures determined by the

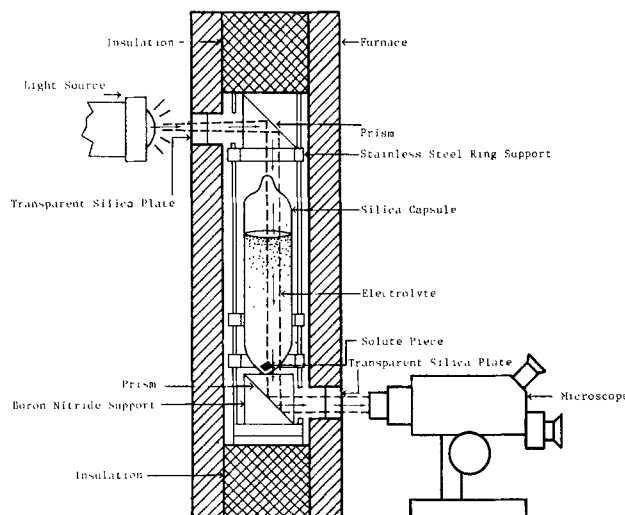


Fig. 2. Schematic diagram of the solubility apparatus (optical technique)

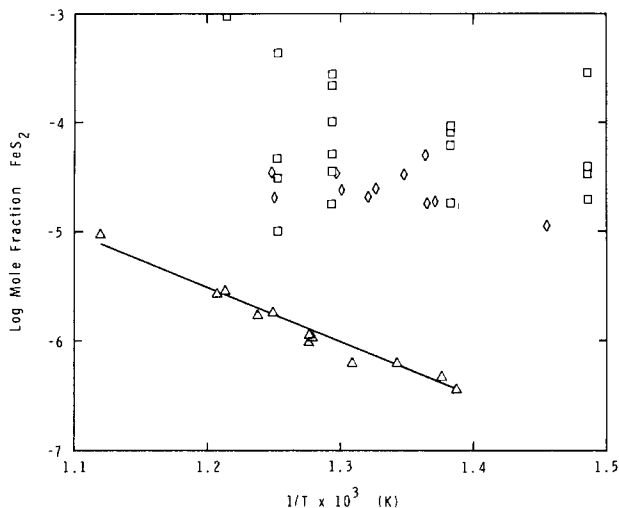


Fig. 3. Solubility of FeS₂ (pyrite) in LiCl-KCl eutectic electrolyte melts. Δ : optical technique. \square : chemical technique. \diamond : Hall (7).

chemical analysis technique are presented in Fig. 3. An excessive scatter in the data is observed. This scatter may be due to the difficulty in determining the very low solute content of the solidified melt by chemical analysis. However, the lower limits of the solubility are in agreement with those determined by a filtration technique (Fig. 3) reported by Hall (7).

The solubility of 12 FeS₂ samples in LiCl-KCl eutectic electrolyte at different temperatures determined using the optical technique are given in Table I. They are also represented graphically in Fig. 3, where the solid line represents a least squares fit to the data. The FeS₂ solubility data between 720 and 900 K can be further represented by the equation

$$\log X_{\text{FeS}_2} = -\frac{5157.33}{T} + 0.666 \pm 0.125 \quad [1]$$

where X_{FeS_2} = mol fraction of FeS₂ in eutectic salt and T = temperature in degrees K. The error caused by the uncertainties in the weights and temperature measurements fall within the scatter of the data. These results indicate FeS₂ is markedly less soluble in eutectic than that determined by the above equilibrium techniques. At comparable temperatures, the solubility appears to be two to three orders of magnitude less than in the above studies.

The slope from Fig. 3 can be used to calculate the relative partial molar enthalpy of solution of FeS₂ in the LiCl-KCl melt. At equilibrium between the pure solid FeS₂ and the melt

$$\mu_{(s)} = \mu_{(l)} \quad [2]$$

where $\mu_{(s)}$ and $\mu_{(l)}$ are the chemical potentials of FeS₂ in the solid and liquid phases, respectively. If pure solid FeS₂ is defined as the standard state, then

$$\mu_{(s)} - \mu_{(s)}^0 = \mu_{(l)} - \mu_{(s)}^0 = \overline{\Delta H} - T \overline{\Delta S} = 0 \quad [3]$$

Table I. Solubility of FeS₂ (pyrite) in LiCl-KCl eutectic melts

Sample	FeS ₂ wt (μg)	Eutectic wt (g)	Mol Fraction FeS ₂	Dissolution Temp (K)
1	26	11.15	1.09×10^{-6}	782
2	45	12.51	1.68×10^{-6}	808
3	14	10.57	6.17×10^{-7}	764
4	9	11.70	3.58×10^{-7}	721
5	800	40.00	9.32×10^{-6}	893
6	245	40.00	2.85×10^{-6}	824
7	62	30.00	9.63×10^{-7}	783
8	171	30.00	2.66×10^{-6}	828
9	73	30.00	1.13×10^{-6}	783
10	117	30.00	1.82×10^{-6}	800
11	40	30.00	6.21×10^{-7}	745
12	10	10.00	4.66×10^{-7}	727

where $\overline{\Delta H}$ is the relative partial molar enthalpy of solution and $\overline{\Delta S}$ is the relative partial molar entropy of solution. In addition

$$\mu_{(l)} - \mu_{(s)}^0 = RT \ln a_{\text{FeS}_2} = RT \ln \frac{X'_{\text{FeS}_2}}{X_{\text{FeS}_2}} \quad [4]$$

where R is the gas constant, a_{FeS_2} is the activity of FeS₂ with respect to pure solid FeS₂, X'_{FeS_2} is any mole fraction of FeS₂ below the solubility limit, and $1/X_{\text{FeS}_2}$ is the activity coefficient of FeS₂ on the assumption that it remains constant below its solubility limit. Also

$$\overline{\Delta S} = \overline{\Delta S}^{\text{ex}} + \overline{\Delta S}^{\text{id}} = \overline{\Delta S}^{\text{ex}} - R \ln X'_{\text{FeS}_2} \quad [5]$$

where $\overline{\Delta S}^{\text{ex}}$ is the excess partial molar entropy of solution and $\overline{\Delta S}^{\text{id}}$ is the ideal partial molar entropy of solution.

By substituting the value of $\mu_{(l)} - \mu_{(s)}^0$ from Eq. [4] and that of $\overline{\Delta S}$ from Eq. [5] into Eq. [3], and rearranging the terms, the following equation can be obtained

$$\ln X_{\text{FeS}_2} = -\frac{\overline{\Delta H}}{RT} + \frac{1}{R} \overline{\Delta S}^{\text{ex}} \quad [6]$$

Therefore, the slope of a plot between $\ln X_{\text{FeS}_2}$ and $1/T$ will be equal to $-\overline{\Delta H}/R$.

Proceeding in this manner, the partial molar enthalpy of solution of FeS₂ was calculated from the data presented in Fig. 3. It was calculated to be 23.5 kcal/mol, which is about twice that of Li₂S [13 kcal/mol (5)]. This higher enthalpy indicates a greater degree of difficulty for FeS₂ to be accommodated into the melt.

FeS solubility.—The solubilities of FeS determined by the chemical analysis technique (Fig. 4) had an excessive scatter similar to that observed in the case of FeS₂ solubilities. In addition, an attempt at measuring the solubility of FeS by the optical technique was unsuccessful. The FeS samples (Appendix A) appeared to absorb electrolyte, increase in size, and develop tree-like structures on their upper surfaces. They dissolved in the electrolyte only after the temperature surpassed ~ 900 K. The tree-like structure and slow dissolution prior to 900 K may be due to the formation of "J-phase" (8). Therefore, the solubilities were calculated as follows.

Calculation of the Solubility of FeS

The dissolution of FeS in LiCl-KCl melts may be represented by the reaction



This reaction has been used in the reverse direction by Saboungi *et al.* (8), to determine the solubility of FeS in the electrolyte by an electrochemical technique. The equilibrium constant (K) for the reaction in terms of the activities (a_i) of the reactants and products is given by

$$K = \frac{a_{\text{FeCl}_2}^* a_{\text{Li}_2\text{S}}}{a_{\text{LiCl}}^2 a_{\text{FeS}}} \quad [8]$$

where $a_{\text{FeCl}_2}^*$ is the activity of FeCl₂ with respect to an infinitely dilute solution as the standard state, such that $a_{\text{FeCl}_2}/X_{\text{FeCl}_2} = 1$ when X , the mole fraction of FeCl₂ $\rightarrow 0$. The activities of the other compounds are with respect to pure solids as their standard states. Therefore $a_{\text{FeS}} = 1$ and

$$K = \frac{X_{\text{FeCl}_2} X_{\text{Li}_2\text{S}} \gamma_{\text{Li}_2\text{S}}}{a_{\text{LiCl}}^2} \quad [9]$$

where $\gamma_{\text{Li}_2\text{S}}$ is equal to the reciprocal of the saturation mole fraction of Li₂S, $X_{\text{Li}_2\text{S}}^{\text{sat}}$. This is true on the assumption that the activity coefficient of Li₂S is constant below the saturation mole fraction. This assumption is reasonable when the values of the saturation mole fractions are very small (Table II). As per the dissolution reaction, $X_{\text{Li}_2\text{S}}$ is equal to X_{FeCl_2} , then

$$K = \frac{X_{\text{FeCl}_2}^2 \gamma_{\text{Li}_2\text{S}}}{a_{\text{LiCl}}^2} \quad [10]$$

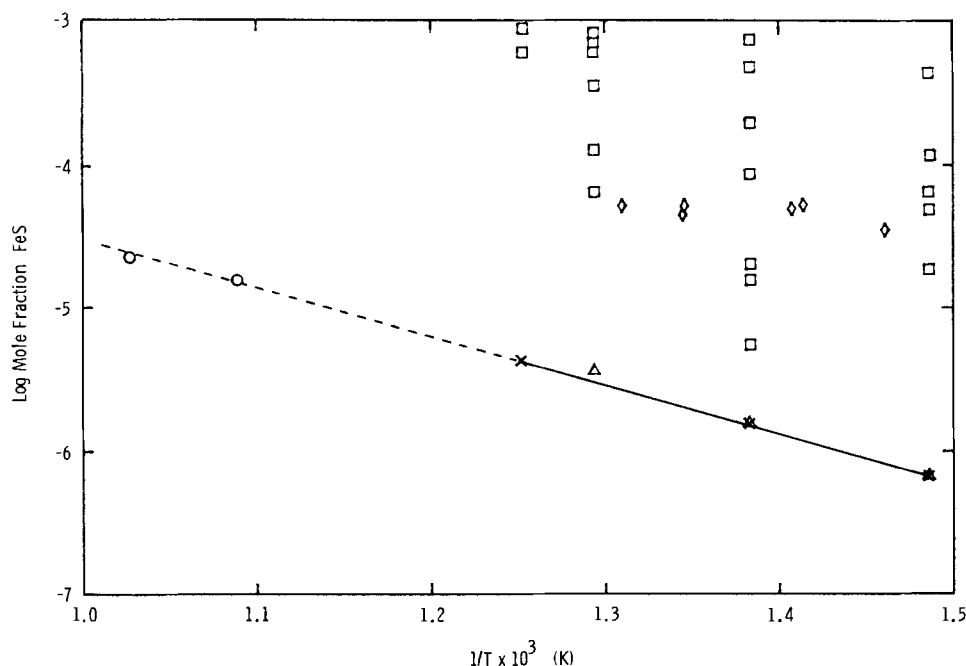


Fig. 4. Solubility of FeS in LiCl-KCl eutectic electrolyte melts. □: chemical technique. ○: optical technique. △: Saboungi *et al.* (8). ◇: Hall (7). X: present calculated values.

The standard free energy change (ΔG^0_R) of reaction [7] is given as

$$\Delta G^0_R = \Delta G^0_{Li_2S} + \Delta G^*_{FeCl_2} - \Delta G^0_{FeS} - 2\Delta G^0_{LiCl} \quad [11]$$

The standard state of $\Delta G^*_{FeCl_2}$ is again an infinitely dilute solution such that $a_{FeCl_2}/X_{FeCl_2} = 1$ when $X_{FeCl_2} \rightarrow 0$, while the standard states for the other compounds are pure solids. Using Eq. [11] and the data given in Table II, ΔG^0_R is calculated to be 27,909, 28,232, and 28,793 cal at 673, 723, and 800 K, respectively. Since

$$\Delta G^0_R = -RT \ln K \quad [12]$$

by substituting Eq. [10] into Eq. [12] we get

$$\Delta G^0_R = -RT \ln \frac{X^2_{FeCl_2} \gamma_{Li_2S}}{\alpha^2_{LiCl}} \quad [13]$$

The α_{LiCl} in the LiCl-KCl eutectic melts at different temperatures has been reported elsewhere (9) and is given in Table II. It is assumed that the α_{LiCl} remains constant on the dissolution of FeS in the LiCl-KCl melt.

Taking the values of ΔG^0_R calculated above and the data in Table II the mol fractions of FeCl₂ were calculated using Eq. [13]. They were found to be 6.5×10^{-7} , 1.5×10^{-6} , and 4.16×10^{-6} at 673, 723, and 800 K, respectively (Fig. 4). As per reaction [7], these equilibrium concentrations of FeCl₂ are also the solubilities of FeS in LiCl-KCl eutectic melts at the respective temperatures.

The standard free energy change of reaction [7] can also be calculated by considering the following individual reactions

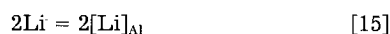
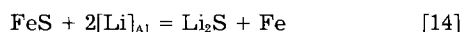


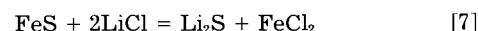
Table II. Pertinent thermodynamic data used for calculating the equilibrium constant for reaction [7] and the FeS concentration in LiCl-KCl melts

Temp (K)	α_{LiCl}	$X^{sat}_{Li_2S}$	ΔG^0 , cal per mol, for			
			LiCl	FeS	Li ₂ S	FeCl ₂ *
673	0.865	0.000655	-84,409	-24,143	-99,650	-65,402
723	0.753	0.001320	-83,425	-24,317	-98,950	-63,985
773	0.668	0.002040	-82,450			-62,568
800	0.635	0.003090	-81,923	-24,600	-97,850	-61,803

α_{LiCl} from Ref. (9). $X^{sat}_{Li_2S}$ from Ref. (5). ΔG^0 for LiCl from Ref. (12). ΔG^* for FeCl₂ from Appendix B. ΔG^0 for FeS from Appendix C. ΔG^0 for Li₂S from Appendix D.



which add up to



Tomczuk *et al.* (10) report the potential of reaction [14] to be 1.343, 1.338, and 1.333V at 673, 723, and 773 K, respectively. Sharma and Seefurth (11) report the potentials for reaction [15]. Calculating the free energy changes of reactions [14] and [15] and combining them with the free energy changes of reaction [16] (12) and reaction [17] (Appendix B), the free energy change (ΔG^0_R) for reaction [7] was calculated to be 27,760, 28,284, and 28,013 cal at 673, 723, and 773 K, respectively. Proceeding as before, the solubility of FeS in LiCl-KCl eutectic melts was calculated from the values of ΔG^0_R for reaction [7]. The solubility was found to be 6.9×10^{-7} , 1.6×10^{-6} , and 3.2×10^{-6} at 673, 723, and 773 K. These values are in good agreement with the values calculated above and with those reported by Saboungi *et al.* (8) from their measurements and from similar calculations using the solubility product concept, etc. (Fig. 4). In addition, two FeS samples having dissolution temperatures above 900 K were run using the optical technique. The solid line in Fig. 4, representing a least squares fit to the calculated solubility data, extrapolates well through these high temperature points. Also, the calculated FeS solubility values are comparable with the solubilities of FeS₂ in the LiCl-KCl eutectic melt at corresponding temperatures.

Proceeding as in the case of FeS₂, the partial molar enthalpy of solution for FeS was calculated from the slope of Fig. 4. It was found to be 15.6 kcal/mol.

Calculation of the solubility of FeS in Li₂S-saturated electrolyte.—Since the cell electrolyte is saturated with Li₂S during discharge, it is of significant importance to determine the solubility of FeS in the saturated melt. This can be determined from relation [13], where α_{Li_2S} becomes unity upon saturation. Using the values of ΔG^0_R calculated above and the data in Table II, the mol fraction of FeCl₂ in Li₂S-saturated LiCl-KCl eutectic melts were calculated to be 7×10^{-10} , 2×10^{-9} , and 4.5×10^{-9} at 673, 723, and 773 K, respectively. These mol fractions which are equivalent to the solubilities of FeS at the respective temperatures are about three orders of magnitude smaller than those in the unsaturated melt.

Solubilities of Other Iron Sulfide Containing Compounds

The determination of the solubilities of the compounds, Li₂S · FeS (13), Li₂Fe₂S₄ (13), and Li_{2+x}Fe_{1-x}S₂ (13) in the

eutectic electrolyte is not possible, because at equilibrium, most of the Li_2S is leached out of these compounds by the electrolyte, leaving behind iron compounds in the solid state. In this situation, final iron sulfide concentration in the electrolyte will be that of the electrolyte saturated with Li_2S . Under the assumption that there is an equilibrium between the compound and the electrolyte, then the concentrations of iron sulfide and Li_2S in the electrolyte will correspond to their activities in the compound. These concentrations should be smaller than those in the electrolyte in equilibrium with the pure phases of unit activities. The compound $\text{Li}_3\text{Fe}_2\text{S}_4$ coexists with FeS_2 , so the iron concentration and sulfur concentration of species in the electrolyte should be the same whether the compound is equilibrated with FeS_2 or $\text{Li}_3\text{Fe}_2\text{S}_4$. That means if there is no polysulfide in the electrolyte in equilibrium with FeS_2 or Li_2S , then there should not be any polysulfide in the electrolyte in equilibrium with $\text{Li}_3\text{Fe}_2\text{S}_4$. The same reasoning can be extended to discount the presence of polysulfide in the electrolyte in equilibrium with $\text{Li}_{2+r}\text{Fe}_{1-r}\text{S}_2$, etc.

Manuscript submitted June 23, 1983; revised manuscript received Nov. 14, 1983. This was Paper 784 presented at the San Francisco, California, Meeting of the Society, May 8-13, 1983.

General Motors Research Laboratories assisted in meeting the publication costs of this article.

APPENDIX A

Preparation of FeS Samples for the Optical Technique

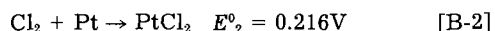
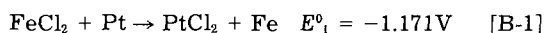
Two batches of FeS were prepared for use as solubility samples for the optical technique. The first batch was made by fusing 99% pure FeS, as described earlier. Chemical analyses of postfusion samples indicated an overall purity of >99.6% and an iron content of 63.77 w/o Fe compared to 63.53 w/o theoretical Fe. When tested, these samples did not dissolve uniformly in the electrolyte. Evidently a phase change occurred which slowed down the dissolution process.

The second batch of FeS was prepared from FeS_2 . Twenty-five mg of FeS_2 particles were placed in a small pyrolytic graphite crucible, and together with another crucible of Fe particles (105 mg) were sealed under vacuum in a quartz vessel. This vessel was heated to ~915 K and allowed to equilibrate for 6 days. The resultant particles were porous appearing under a microscope, indicating loss of sulfur, but there was not enough sample for chemical analysis. When tested, these samples were not wetted and floated on top of the electrolyte.

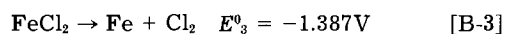
APPENDIX B

Calculation of ΔG^* for FeCl_2

The standard potential (E^0) of a Fe/FeCl₂ electrode vs. a Pt(II)-Pt(O) reference electrode in a LiCl-KCl eutectic melt at 723 K has been reported to be 1.171V by Laitinen and Liu (14). This is for an infinitely dilute solution as the standard state such that $a_{\text{FeCl}_2}/X_{\text{FeCl}_2} = 1$ when $X_{\text{FeCl}_2} \rightarrow 0$. They have also reported E^0 for a Cl_2/Cl^- electrode vs. the reference in the eutectic at 723 K to be 0.216V (14). Therefore, the standard formation potential of FeCl_2 with infinite dilution as the standard state can be calculated by combining the following reactions



and obtaining

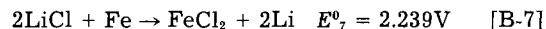
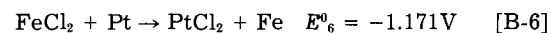


Since

$$\Delta G^*_{\text{FeCl}_2} = -n\mathbf{F}E^0_3 \quad [\text{B-4}]$$

where n is the number of equivalents and \mathbf{F} is the Faraday constant, then $\Delta G^*_{\text{FeCl}_2}$ is calculated to be -63,985 cal/mol at 723 K.

A check of this $\Delta G^*_{\text{FeCl}_2}$ calculation was made by using the standard potential of Li(O)-Li(I), which was computed to be -3.410V for a 17.39 molar Li(I) concentration in LiCl-KCl eutectic solvent (14), and considering the following reactions



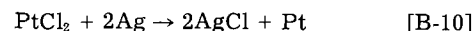
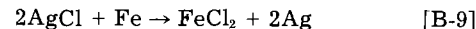
Proceeding as above, ΔG^0 for reaction [B-7] was calculated to be 103,290 cal at 723 K. The $\Delta G^*_{\text{FeCl}_2}$ can then be calculated from the relation

$$\Delta G^*_{\text{FeCl}_2} = 2\Delta G^*_{\text{LiCl}} + \Delta G^0 \quad [\text{B-8}]$$

In this case, ΔG^*_{LiCl} is assumed to be ΔG^0_{LiCl} , the standard free energy of formation of pure LiCl. This assumption indicates that the activity of LiCl in the eutectic is not much different from its mole fraction. Using $\Delta G^*_{\text{LiCl}} = -83,425$ cal/mol (12), the $\Delta G^*_{\text{FeCl}_2}$ was calculated by relation [B-8] to be -63,560 cal/mol at 723 K. This value is in excellent agreement with the -63,985 cal/mol calculated above.

The value of $\Delta G^*_{\text{FeCl}_2}$ at other temperatures (673 and 800 K) was calculated using the temperature coefficient of the standard free energy of formation of pure solid FeCl_2 . This temperature coefficient was calculated to be 28.335 cal/K from the data reported in the JANAF tables (12). The values of $\Delta G^*_{\text{FeCl}_2}$ at 673 and 800 K were calculated to be -65,402 and -61,803 cal/mol, respectively.

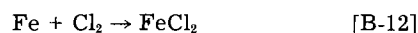
A second check of the $\Delta G^*_{\text{FeCl}_2}$ calculations can be made using the work of Saboungi *et al.* (8). They report the potential (E) of a Fe/FeCl₂ electrode vs. a AgCl/Ag electrode (8.4×10^{-3} mol fraction AgCl) in a LiCl-KCl eutectic melt to be 256.66, 231.58, and 209.09 mV at 673, 723, and 773 K, respectively. The potential of the Fe/FeCl₂ electrode vs. a standard AgCl/Ag electrode (standard state such that $a_{\text{Ag}}/X_{\text{Ag}} = 1$ when $X_{\text{Ag}} \rightarrow 0$) was calculated to be 0.5339, 0.5294, and 0.5275V at the respective temperatures, and the corresponding standard free energies were found to be -24,630, -24,422, and -24,335 cal/mol at the same temperatures. The standard formation potential of a Fe/FeCl₂ electrode vs. a Cl^-/Cl_2 electrode was then calculated by combining the reactions



and



to obtain



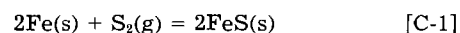
Using the potentials 0.637 and 0.216V for reactions [B-10] and [B-11] reported by Laitinen and Liu (14), and 0.5294V for reaction [B-9] (derived above), the potential of reaction [B-12] was calculated to be 1.382V at 723 K. Proceeding as above, $\Delta G^*_{\text{FeCl}_2}$ was then calculated to be -63,754 cal/mol at 723 K, once again in good agreement with the value derived above.

A second method was used to check the values of $\Delta G^*_{\text{FeCl}_2}$ at other temperatures. The standard free energy of formation of AgCl, ΔG^*_{AgCl} , was calculated using the $\Delta G^*_{\text{FeCl}_2}$ value and the standard free energy change of reaction [B-9] (-24,422 cal/mol, reported above). It was found to be -19,666 cal/mol at 723 K. The values of ΔG^*_{AgCl} at 673 and 773 K were then calculated using the temperature coefficient of the standard free energy of formation of pure solid AgCl (15). The temperature coefficient was found to be 11 cal/K between 600 and 700 K, and 8 cal/K between 700 and 800 K (15). The ΔG^*_{AgCl} was calculated to be -20,216 and -19,266 cal/mol at 673 and 773 K, respectively. Using these values and the standard free energy changes for reaction [B-9] (-24,630 and -24,335 cal/mol, reported above), the values of $\Delta G^*_{\text{FeCl}_2}$ were calculated to be -65,062 and -62,867 cal/mol at 673 and 773 K, respectively. These values are once again in very good agreement with the values of $\Delta G^*_{\text{FeCl}_2}$ calculated above.

APPENDIX C

Calculation of ΔG^0 for FeS

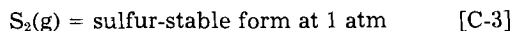
Rosenqvist (16) represents the standard free energy change for the reaction



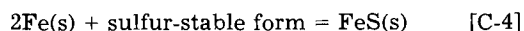
by the equation

$$\Delta G^{\circ} = 71,500 + 25.25 T \quad [\text{C-2}]$$

Richardson and Jeffes (17) give the value of ΔG° at different temperatures for the reaction



Combining reactions [C-1] and [C-3] gives the following reaction



The standard free energies of formation of FeS were calculated from reaction [C-4] using Eq. [C-2], and the corresponding values for reaction [C-3] from Ref. (17). The ΔG° for FeS was calculated to be -24,143, -24,317, and -24,600 cal/mol at 673, 723, and 800 K, respectively.

APPENDIX D

Calculation of ΔG° for Li₂S

The heat of formation, ΔH_{298} , for Li₂S was obtained from the literature. It is reported to be -107, 400 ± 200 cal by Juza and Uphoff (18).

Assuming

$$\frac{S_{298} \text{ of Cu}_2\text{S}}{S_{298} \text{ of Cu}_2\text{O}} = \frac{S_{298} \text{ of Li}_2\text{S}}{S_{298} \text{ of Li}_2\text{O}} \quad [\text{D-1}]$$

the entropy, S_{298} , for Li₂S was calculated from literature data (19). It was determined to be 11.605 cal/deg/mol. The relevant data for lithium ($S_{298} = 6.95 \pm 0.1$ cal/deg/mol, $\Delta H_m = 700$ cal, and mp = 454 K) and for sulfur ($S_{298} = 7.78$ cal/deg/mol, $\Delta H_m = 400$ cal, and mp = 392 K) were also taken from Ref. (19). Combining these data, the entropy of formation, ΔS_{298} , for Li₂S was calculated to be -10.075 cal/deg/mol.

Using the equation

$$\Delta G^{\circ} = \Delta H^{\circ} - T\Delta S^{\circ} \quad [\text{D-2}]$$

and taking into consideration the free energy of fusion of the components (see above), the standard free energy of formation, ΔG° , for Li₂S was calculated at various temperatures. These values are reported in Table II. Re-

cently, ΔG° for Li₂S was measured using an EMF method (10). The reported value of -100,220 cal at 700 K is in good agreement with the values calculated above.

REFERENCES

1. Chemical Engineering Division, Argonne National Laboratory, Argonne, Illinois, Report no. ANL-76-81, July 1976.
2. J. S. Dunning, T. G. Bradley, and E. J. Zeitner, *Proc. IECEC*, **11**, 491 (1976).
3. L. R. McCoy and L. A. Heredy, *ibid.*, **11**, 485 (1976).
4. R. A. Murie, *ibid.*, **12**, 349 (1977).
5. R. A. Sharma and R. N. Seefurth, Abstract 342, p. 550, The Electrochemical Society Extended Abstracts, Vol. 82-2, Detroit, MI, Oct. 17-21, 1982.
6. S. I. Berezina, A. G. Bergman, and E. L. Bakumskoya, *Russ. J. Inorg. Chem. Eng. Transl.*, 1120 (1963).
7. J. E. Hall, Personal communication.
8. M. L. Saboungi, J. J. Marr, and M. Blander, *This Journal*, **125**, 1567 (1978).
9. R. N. Seefurth and R. A. Sharma, *ibid.*, **112**, 1049 (1975).
10. Z. Tomczuk, M. F. Roche, and D. R. Vissers, *ibid.*, **128**, 2255 (1981).
11. R. A. Sharma and R. N. Seefurth, *ibid.*, **123**, 1763 (1976).
12. JANAF Thermochemical Tables, published by U.S. Department of Commerce (1971).
13. R. A. Sharma, *This Journal*, **123**, 448 (1976).
14. H. A. Laitinen and C. H. Liu *J. Am. Chem. Soc.*, **80**, 1015 (1958).
15. C. E. Wicks and F. E. Block, "Thermodynamic Properties of 65 Elements—Their Oxides, Halides, Carbides and Nitrides," Bureau of Mines Bulletin 605, U.S. Government Printing Office, Washington, DC (1963).
16. T. Rosenqvist, *J. Iron Steel Inst. London*, **179**, 37 (1954).
17. F. D. Richardson and J. H. E. Jeffes, *ibid.*, **171**, 165 (1952).
18. R. Juza and W. Uphoff, *Z. Anorg. Chem.*, **287**, 113 (1956).
19. O. Kubaschewski and C. B. Alcock, "Metallurgical Thermo-Chemistry," 5th Ed., Pergamon Press, New York (1979).

Electrochemical Measurements on Pt, Ir, and Ti Oxides as pH Probes

K. Kinoshita*¹ and M. J. Madou*

SRI International, Menlo Park, California 94025

ABSTRACT

Open-circuit potential and impedance measurements were performed on Ti, Pt, and Ir oxides. It was found that the pH dependence of the open-circuit potential of the various oxide electrodes shows a Nernstian behavior and that the response time of the potential to a change in pH for the more conductive oxides on Pt and Ir is comparable to that of the commercial glass pH electrode. Impedance measurements allowed flatband potential determinations on polycrystalline TiO₂ only in highly conductive solutions. In these solutions, the pH dependence of the flatband potential is Nernstian. For less conductive solutions, it was impossible to deduce the exact flatband potential from the intercept of $1/C_s^2$ vs. V on the V -axis.

The results of an electrochemical study on Zr-ZrO₂ electrodes for possible use to monitor pH of aqueous solutions from measurements of open-circuit potential (OCP) and flatband potential (V_{FB}) were presented elsewhere (1). In general the OCP on conductive metal oxides gives a fast Nernstian response to pH; the problem is that the OCP also is influenced by other redox couples (e. g., O₂), since the Helmholtz potential drop in such cases is dominated by electron exchange reactions. Measurements of V_{FB} on appropriately doped oxides, on the other hand, are usually independent of the redox potential of the solution

since the potential drop in the Helmholtz layer is dominated here by adsorption/desorption of specific ions (e. g., H⁺). Because a too insulating oxide film is formed on Zr, the Zr-ZrO₂ electrode in its present state of development does not appear to offer much promise for measuring pH via OCP. The V_{FB} method for pH probing failed also in this case because we were unable to dope the ZrO₂ appropriately (1). In the present paper, data are presented on the continuation of electrochemical studies on metal oxide electrodes, which are intended for monitoring pH at high temperature (up to 300°C), where glass pH electrodes, e. g., would be unstable. Measurements of OCP and V_{FB} at room temperature of Ti, Pt, and Ir oxides prepared by anodic and thermal oxidation are discussed in this paper. Platinum and titanium oxides were selected because of their anticipated stability in water at tempera-

*Electrochemical Society Active Member.

¹Present address: Lawrence Berkeley Laboratory, Berkeley, California.

Key words: flatband potential, Mott-Schottky curves, anodic oxide, space charge capacitance.

tures from 25° to 300°C (2). Iridium oxide is also supposedly stable between 25° and 250°C (3, 4). In a future publication, we will report on pH measurements with these oxides at higher temperatures and pressures.

Experimental Details

Preparation of oxide electrodes.—The TiO₂ electrodes were prepared from coupons of Ti foil (0.2 mm thick, 99.9+%, Astro Metallurgical Corporation, Wooster, Ohio), etched in HF/HNO₃ solution, and then electrochemically or thermally oxidized. The anodic oxide films were produced by using a constant voltage of 40 (T-79A) or 80V (T-79B) applied between the Ti coupon and a Pt counter-electrode in 1N H₂SO₄. An anodic oxidation time of 15 min was used. The oxide film obtained at 40V was light green and that at 80V was purple.

If we use the potential dependence of 14 Å/V reported by Schultze *et al.* (5), the oxide thicknesses at 40 and 80V are 560 and 1120Å, respectively. Note that higher values of the potential dependence have also been used to calculate the thickness of the TiO₂ layer. For example, Archibald (6) used 20 Å/V in his calculations.

Thermally grown TiO₂ films (T-87) were produced by heating Ti coupons at 550°C for 1h in flowing O₂ that was saturated with water vapor at 23°C. A gray oxide film was obtained that was identified by x-ray diffraction to be rutile. The oxide film thickness of 650Å was calculated using the rate constant for parabolic oxidation reported by Kubaschewski and Hopkins (7).

The procedure used to prepare the Ir oxide electrodes was similar to that described by Ardizzone *et al.* (8). A small Ti coupon (0.2 mm thick, 1 cm²) was dipped into an aqueous solution containing dissolved IrCl₃. The coupon was removed and gently heated with an air gun to crystallize the IrCl₃ (dissolved in water) on the titanium surface. After each deposition, the coupon was heated in an air oven for about 10 min to decompose the chloride salt. This procedure was repeated three times, and then a final heat-treatment was conducted at the same temperature for 4h. Two temperatures were used to form IrO₂: 400°C (I-47) and 500°C (I-54).

X-ray diffraction analysis indicated that IrO₂ was obtained by this procedure. The oxide surfaces were not examined in detail by electron microscopy, and no estimate of the oxide thickness is available. Ardizzone *et al.* found by scanning electron microscopy of IrO₂, which was produced by a method similar to the one used in our study, that a cracked, dry mudlike layer was obtained.

Several methods were used to obtain Pt oxide layers on Pt electrodes. Initially, the oxide was produced by oxidation of a Pt bead electrode that was immersed in molten NaNO₃ at 420°C; this procedure was used by Dobson *et al.* (4) in their studies of metal-metal oxide electrodes. A variation of this method was also used to produce a Pt oxide film. In this method, NaNO₃ and Na₂PtCl₆ were dissolved in water. The tip of a Pt bead electrode was dipped into the solution and then gently heated after removal from solution to coat the electrode surface with a mixture of the two salts. The electrode was next heated at 500°-550°C for 2h in air to form the oxide layer. This procedure was repeated three times to form an orange-brown oxide layer.

Another method to produce an oxide layer on Pt involved coating the bead electrode with Pt(NH₃)₂(NO₂)₂ dissolved in nitric acid and then heating to 400°C in air for 10 min. This procedure was repeated three times, and then a final heat-treatment at the same temperature for 3.5h was used (electrode P-57). X-ray diffraction analysis of the oxides obtained by the methods described here indicate the presence of PtO, but not PtO₂. The study by Dobson *et al.* (4) showed that only PtO₂ was obtained by oxidation in molten NaNO₃. However, Every and Grimsley (9) reported that a mixture of PtO and PtO₂ was obtained by oxidation of Pt in KNO₃ at 400°C. Furthermore, the predominant oxide was PtO and not PtO₂; the mol ratio of PtO to PtO₂ was approximately 7.

Electrochemical measurements.—The methods and procedures that were used to measure the OCP and impedance of the metal oxide electrodes are described elsewhere (1). Because TiO₂ showed a photoresponse to the fluorescent lights in the laboratory, the electrochemical studies were conducted with the oxide electrode in the dark.

The response time of Pt and Ir oxide electrodes to changes in pH was compared with that of a commercial glass pH electrode. This comparison was made by using the metal oxide electrode and a glass pH electrode for indicator electrodes in a potentiometric titration of H₃PO₄ with NaOH. About 100 ml of H₃PO₄ solution containing the glass pH electrode and either the Pt or Ir oxide electrode was deaerated by nitrogen. Then controlled amounts of 5N NaOH were added as the titrant, and the potential of the two electrodes was recorded on a strip chart recorder.

Discussion of Results

Open-circuit potential measurements.—The OCP of TiO₂ electrodes, which were prepared by thermal and anodic oxidation, are plotted as a function of pH in Fig. 1. In general, the OCP measurements were conducted for about 24h in each buffer solution, although the steady-state potential (± 4 mV) was reached in about 6h. The data in Fig. 1 show that the TiO₂ prepared by thermal oxidation (T-87) has an OCP-pH response with a slope of -59 mV/pH, which is indicative of a Nernstian behavior for this electrode. But the TiO₂ prepared by anodic oxidation at 40V (T-79A) and 80V (T-79B) does not show a Nernstian response to pH. At pH 2-6, these oxide electrodes showed only a weak response of OCP to pH (-0.031 mV/pH), while at higher pH, OCP was essentially unchanged.

The IrO₂ obtained by thermal decomposition of IrCl₃ on a Ti substrate yielded the OCP-pH curves shown in Fig. 2. The OCP measurements that were made on the electrodes soon after the thermal treatment ("fresh" electrode) are represented in Fig. 2 by the solid symbols. The OCP responds to pH of the buffer solution in a manner predicted by the Nernst equation. Furthermore, the relationship of OCP to pH closely agrees with the data reported by Ardizzone *et al.* (8), which is represented by the dashed line in Fig. 2.

Immediately after testing, the fresh oxide electrodes were stored in distilled water for 2 weeks. The OCP measurements were repeated with the electrodes ("aged" electrode), and the data are represented in Fig. 2 by the open symbols. It is apparent that the aged electrodes still exhibit the Nernstian behavior in the buffer solutions, but

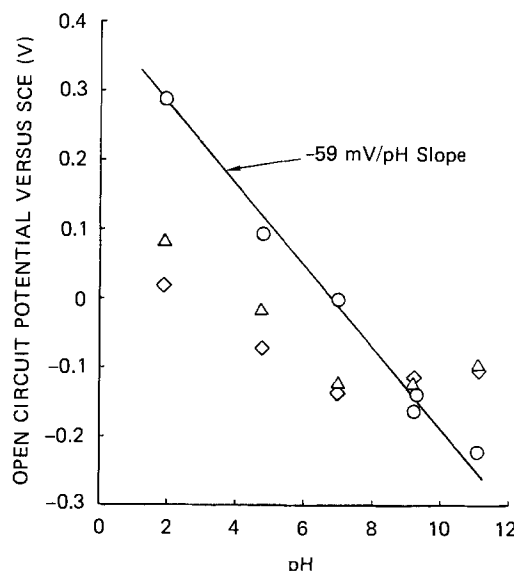


Fig. 1. Open-circuit potential of TiO₂ electrodes in different pH buffers: (◇) T-79A, (△) T-79B, and (○) T-87.

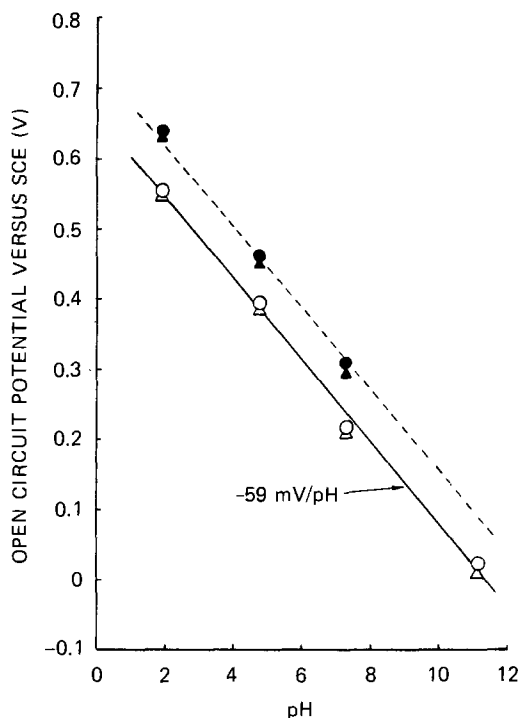
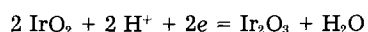


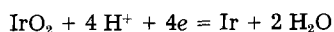
Fig. 2. Open-circuit potential of fresh (solid symbols) and "aged" (open symbols) iridium oxide electrodes (\blacktriangle , \triangle) I-47, (\bullet , \circ) I-54. Dashed line is the OCP-pH dependence for Ir_2O_3 electrode reported by Ardizzone *et al.* (8).

OCP has shifted in the negative direction by about 0.080V. The OCP measurements on the oxide obtained by thermal decomposition of IrCl_3 at 400° (I-47) and 500°C (I-54) showed similar response of the fresh and aged electrodes. Apparently, the oxides formed by decomposition of IrCl_3 at 400° and 500°C are not significantly different to affect the OCP response; and the OCP of both electrodes became more negative by the same amount upon aging in distilled water.

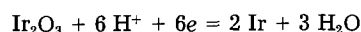
Extrapolating the OCP in Fig. 2 to pH = 0 gives a value of 0.902V (SHE) for the aged oxide electrode. The value for OCP of the fresh electrode at pH = 0 is 0.982V (SHE), which Ardizzone *et al.* (8) reported is close to the equilibrium potential for the reaction



Pourbaix (10) listed two other reactions that have the same equilibrium potential (*i.e.*, 0.926V)



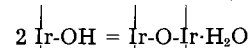
and



Insufficient information is available from the present study to unequivocally determine which reaction represents the OCP-pH dependence shown in Fig. 2. As the IrO_2 was deposited on a Ti substrate, possibly no metallic iridium is present, and the reaction proposed by Ardizzone *et al.* (8) seems more likely. The shift of OCP in the negative direction that is observed with the aged electrode suggests that a change in the properties of the oxide film occurs during storage in distilled water. Pourbaix (10) summarized some of the observations that have been reported on the stability of IrO_2 . Apparently, $\text{IrO}_2 \cdot \text{H}_2\text{O}$ prepared by treating a boiling solution of alkali metal iridochloride with KOH or NaOH in air is soluble in HCl, HNO_3 , and H_2SO_4 . However, on aging the oxide becomes practically insoluble in all acids.

This observation suggests that the IrO_2 undergoes a physical/chemical change to produce a more corrosion-resistant oxide. The shift in OCP with aging of the iridium oxide electrodes in Fig. 2 may possibly be due to a change in the oxide with time. For example, Buckley *et al.* (11)

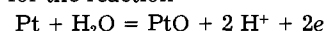
suggest that the oxide film on Ir, which consists of oxygen-bridged hydrated oxy-hydroxide species, can undergo a structural change with the formation or destruction of an iridium/oxygen bridge by a process such as



The water remains in the oxide. Accompanying the structural change in the oxide is a change in the equilibrium potential of the oxide.

We want to caution here that extrapolation and comparison to Pourbaix data for the present oxide might be somewhat dangerous; our oxides here are highly defective and partially hydrated compared to the well-defined oxide phases used to construct the Pourbaix diagrams. These comparisons and extrapolations for IrO_2 and the other oxides described here should only be used as a guide for trends.

The Nernstian behavior of a Pt oxide electrode (P-57) is illustrated in Fig. 3, along with data for the OCP-pH response of oxide electrodes of Ir, Ti, and Zr (1). The OCP at pH = 0 for the Pt oxide electrode is 0.982V (*vs.* SHE). This potential is in good agreement with the equilibrium potential (11) for the reaction



which has E° (25°C) = 0.980V at pH = 0. The corresponding electrochemical reactions for PtO/PtO_2 and $\text{PtO}_2/\text{PtO}_3$ have equilibrium potentials of 1.045 and 2.000V, respectively (12). On the basis of the close agreement between the equilibrium potential and OCP, the reaction given above can adequately describe the pH response of the Pt electrode, P-57. Furthermore, support for the above reaction is provided by the results of the x-ray diffraction analysis, which detected the presence of PtO on the Pt electrode. This implies a solid-state-type reaction where a water-related species diffuses in and out of the PtO film during oxidation/reduction cycles.

The pH dependence of OCP for the various oxide electrodes that appear to show a Nernstian behavior (except Zr oxide electrode at alkaline pH) are plotted in Fig. 3. The OCP for the four metal oxide electrodes at a given pH decreases in the following order: Pt, Ir, Ti, and Zr oxides. Several interesting parallels between this order and chemical/electrochemical properties of these metal oxides can be drawn (see data in Table I). The general trend in the order of OCP follows that of E° and the free energy for the selected couples listed in Table I. However, the difference in OCP between the oxides of Ir and Ti and between the oxides of Ti and Zr is less than the corresponding differences in E° .

The oxides of Pt and Ir are good electronic conductors (15) that exhibit a Nernstian response to pH. Moreover, the OCP values extrapolated to pH = 0 are close to the E° for some possible redox reactions involving the oxidation-reduction of the metal itself. A Mott-Schottky type of measurement on such oxides to obtain the V_{FB} as a means of pH measurement is impossible (see impedance results). Thus with these oxides, OCP is the parameter that can be used to monitor pH.

The oxide on Zr is very insulating, and a Nernstian behavior in response to pH is only approached (very slowly)

Table I. Comparison of OCP, E° , and V_{FB} for various metal oxide electrodes at pH = 0 and free energy of formation of metal oxides

Oxide	OCP <i>vs.</i> SHE (V)	E° <i>vs.</i> SHE (V) ^a	V_{FB} <i>vs.</i> SHE (V)	Free energy (cal/mol) ^a
Pt	0.982	0.982 (Pt/PtO)	NA	-11,510 (PtO)
Ir	0.902	0.926 (Ir/IrO ₂)	NA	-28,000 (IrO ₂)
Ti	0.642	-0.910 (Ti ₂ O ₃ /TiO ₂) ^c	0.150 ^e	-196,300 (TiO ₂) ^b
Zr	0.382	-1.553 (Zr/ZrO ₂) ^b	-0.830 ^d	-256,620 (ZrO ₂) ^b

^a Values obtained from Pourbaix (12).

^b Hydrated oxide.

^c Value obtained by extrapolation of data by Vandermolen *et al.* (14) to pH = 0.

^d Value obtained by extrapolation of data by Clechet *et al.* (13) to pH = 0.

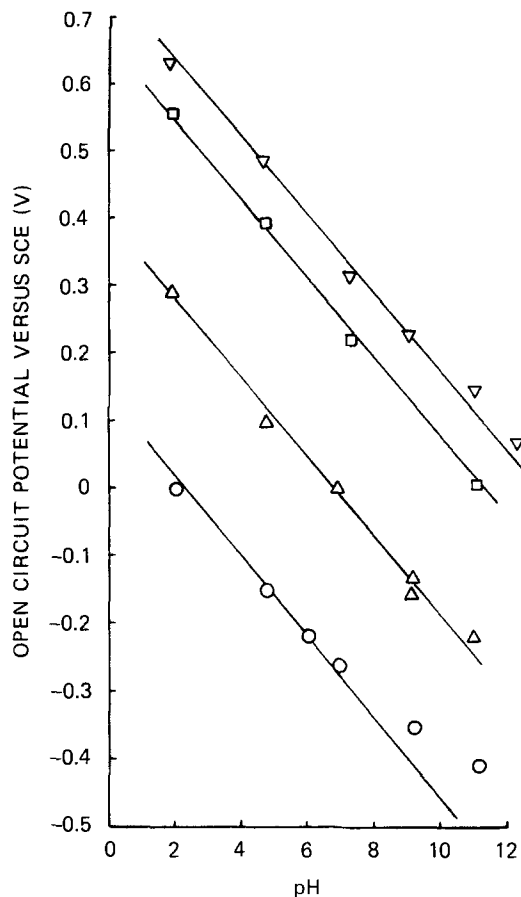


Fig. 3. Open-circuit potential of metal oxide electrodes in different pH buffers. Metal oxides of (∇) Pt, (\square) Ir, (Δ) Ti, and (\circ) Zr. Solid line has slope of -59 mV/pH.

by either the "bare" Zr surface or by certain ZrO_2 films, presumably containing pinholes (1). Extrapolating OCP to $pH = 0$ yields OCP approximately equal to 0.39 V (vs. SHE), which cannot be readily associated with any of the equilibrium reactions presented by Pourbaix (12) for the Zr- H_2O system (see also Table I). It is most likely that we are dealing with a mixed potential in this case. If ZrO_2 could be appropriately doped, V_{FB} determination for pH measurements should be possible (1).

Anodically and thermally grown TiO_2 films on Ti form an intermediate case, since they behave as highly doped semiconductors (see impedance results). It was shown that the OCP response was better for thermally grown TiO_2 (T-87) than for anodically grown TiO_2 (T-79A and T-79B). We believe that this is because the thermally grown film has more pinholes than an anodically grown one. Equilibrium might be reached faster at these sites where the thin oxide is present. The OCP response to pH for thermally grown TiO_2 is better than for ZrO_2 , and V_{FB} determination with Mott-Schottky-type measurements is possible. Our impedance results will show, though, that V_{FB} determination on polycrystalline TiO_2 poses some problems, especially in low conductivity media. Extrapolating OCP to $pH = 0$ yields an OCP that cannot be readily associated with any E° for the Ti- H_2O system (see also Table I) and presumably indicates that the measured OCP here is a mixed potential.

As a general rule, the more insulating a material, the less likely a pH probe can be developed on the basis of an OCP measurement. But, the more insulating the oxide, the better the possibility for a pH probe based on V_{FB} determination on the appropriately doped material.

The transient potential response of the metal oxide electrodes and the glass electrode during the potentiometric titration of H_3PO_4 by $5N$ NaOH is represented by the results in Fig. 4. In this figure, the potential transients for the glass electrode and the Pt oxide electrode (P-57) in the same solution are recorded during the addi-

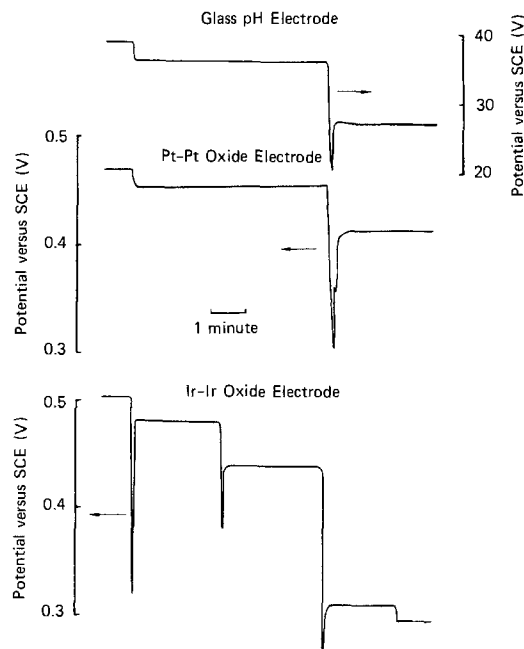


Fig. 4. Transient response of potential of metal oxide electrodes and glass pH electrode during addition of various amounts of $5N$ NaOH titrant.

tion of two aliquots of titrant. The potential transients for the Ir oxide electrode (I-47) were recorded during the potentiometric titration of another H_3PO_4 solution. The potential transients for the Ir oxide electrode show the response after the addition of four aliquots of $5N$ NaOH of different volumes. In these experiments, small amounts of $5N$ NaOH were added from a burette to the deaerated acid solution after a steady-state potential was established.

The data in Fig. 4 are representative of the type of transient potential response that was observed during the titration experiments. As expected, when NaOH is added to the acid solution the steady-state potentials that are recorded change in the direction indicative of higher pH. The apparent overshoot in the potential transient that is evident after addition of the titrant, which then returns to a steady-state potential, is believed to be an artifact (insufficient stirring, for example) related to the experimental arrangement and procedure. The results in Fig. 4 show that the response of the potential of the metal oxide electrodes to changes in pH is comparable to that of the commercial glass pH electrode. At least under the conditions of these titration experiments, the two metal oxide electrodes show a satisfactory response to rapid changes in solution pH.

Impedance measurements.—Impedance measurements on Pt oxide electrodes were performed with a frequency response analyzer (Solartron Model 1172) controlled by a microcomputer. A plot of the imaginary component of the impedance at 1000 Hz of a Pt oxide electrode in an aqueous solution of $1M$ KCl + HCl ($pH = 1.4$) vs. the applied voltage showed several humps (see also Ref. (16), Fig. 3b) and did not lead to a linear $1/C_s^2$ vs. V plot (with C_s the apparent series capacitance).

If C_s could be identified with C_{sc} , the space charge capacitance inside the oxide, C_s would be expected to follow a Mott-Schottky relationship

$$\frac{1}{C_s^2} = \frac{2}{qN_D\epsilon\epsilon_0} (V - V_{FB} - \frac{kt}{q}) \quad [1]$$

for an n-type oxide semiconductor. In this equation, N_D is the donor density, ϵ is the dielectric constant of the semiconductor, ϵ_0 is the dielectric constant in vacuum, and q is the charge of the electron.

The slope of the Mott-Schottky plot is proportional to the concentration of dopant in the semiconductor, and

the intercept with the V-axis at $1/C_s^2 = 0$ yields V_{FB} (if the term kT/q is neglected). The value of $1/\omega C_s$ at 1000 Hz and +2V SCE was only a few ohms per cm^2 of electrode area. Most of the change in the potential drop at this conductive metal oxide electrode interface occurs in the Helmholtz layer, and C_s does not correspond to the capacitance of the space charge layer (C_{sc}) inside the oxide. Impedance measurements on Ir oxide were not attempted, since the conductivity of this oxide is high (15). It is also expected that here V_{FB} determination with the Mott-Schottky plots will be impossible.

Impedance measurements on polycrystalline TiO_2 on Ti that is anodically or thermally grown lead to Mott-Schottky plots exhibiting a break. This is illustrated in Fig. 5 for an oxide that is anodically grown at a constant voltage of 40V in 1N H_2SO_4 (T-79A) and measured in a solution of 1M KCl + HCl (pH \approx 1.4 specific resistivity = 9.6 Ω cm). The value of $1/\omega C_s$ for T-79A at 1000 Hz and +2V vs. SCE in this solution was around 200 Ω/cm^2 of electrode area, about a factor of 100 higher than for the platinum oxide electrode. In this case, a major fraction of the change in potential drop occurs in the space charge layer of the semiconductor, and Mott-Schottky type measurements are possible. Sample T-79B (anodically grown at 80V in 1N H_2SO_4) and T-87 (thermally grown oxide) also showed a break in the Mott-Schottky plots and had similar values for $1/\omega C_s$ at the same potential and frequency.

A break in the Mott-Schottky plots and the frequency dispersion observed in Fig. 5 were not expected. The type of frequency dispersion, where the different Mott-Schottky curves measured at different frequencies converge to one point on the V-axis, as observed in the lower part of the Mott-Schottky curves in Fig. 5, is described in more detail in Ref. (17) and (18). In Ref. (17) it is shown that this type of frequency dispersion (B-type behavior) does not prohibit true V_{FB} determination. A break in the Mott-Schottky plots, as illustrated in Fig. 6, was also shown [e.g., Kennedy *et al.* (19)] for sintered titanium dioxide and sintered iron dioxide, and by P. Richardson *et al.* (20) for flamed iron and titanium foils. Schultze *et al.* (5) showed a Mott-Schottky plot for thin anodically formed films on Ti foil that had three regions with different slopes. These authors discussed different possible explanations for the change in the slope of Mott-Schottky plots: different kinds of donors contributing to the measured capacitance, inhomogeneous doping, layers of different properties, and, at higher potential, the whole film being totally depleted of charge carriers (exhaustion).

At high anodic potentials (> 2V vs. SCE in solution of pH \approx 1.4) specimen T-79A (40V sample) and T-79B (80V sample, double the thickness of T-79A) have almost the same value of $1/\omega C_s$ for the same frequency. Therefore we can exclude the possibility of exhaustion, since, in that case, $1/\omega C_s$ would have been proportional to the thickness of the whole film. It is not easy to distinguish between the other possibilities. Assuming that two different kinds of donors contribute to the measured capacitance, we can calculate approximately the concentration of each donor.

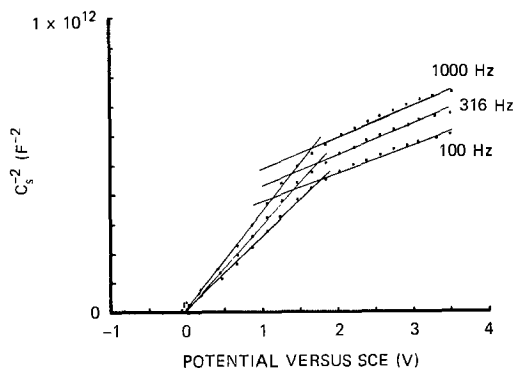


Fig. 5. Plot of $1/C_s^2$ vs. potential of TiO_2 electrode (T-79A) in a solution of 1M KCl + HCl (pH \approx 1.4). Specific resistivity \approx 9.6 Ω cm.

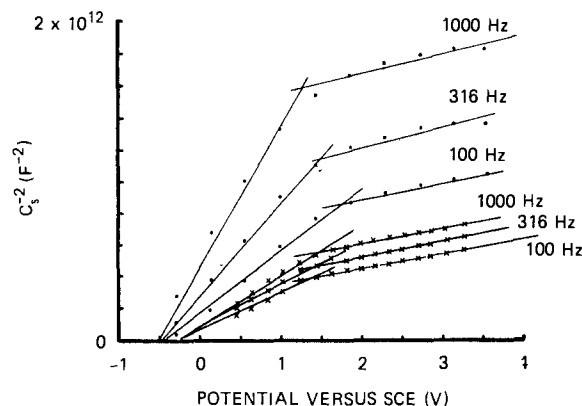


Fig. 6. Plot of $1/C_s^2$ vs. potential of TiO_2 electrode (T-79A) in a commercial buffer solution (pH = 7) (○) and in a 1M KCl solution (pH \approx 6.8) (×). Electrode surface area, 0.455 cm^2 . Frequencies used: from highest curves in each set towards lowest curve, 1000, 316, and 100 Hz.

From the highest slope of the Mott-Schottky curve at 1000 Hz in Fig. 5, a donor concentration of $1.6 \times 10^{19} \text{ cm}^{-3}$ is estimated, and from the lowest slope, $3.9 \times 10^{19} \text{ cm}^{-3}$. These calculations assume a semiconductor dielectric constant ϵ of 173 (see Eq. [1]).

The photocurrent on anodically grown TiO_2 (T-79A) under intense UV illumination in the same solution as for the measurements represented in Fig. 5 exhibited an onset occurring at about the same voltage as the intercept on the V-axis of the lower part of the $1/C_s^2$ vs. V plots (\approx 0.0V vs. SCE) shown in Fig. 5, indicating that this intercept corresponds indeed to the true V_{FB} of this material.

The intercept with the V-axis of the part of the Mott-Schottky plot with the highest slope is pH dependent, and changes in high conductivity solutions (1M KCl + HCl or KOH; specific resistivity \approx 10 Ω cm) by roughly -60 mV per pH unit. The -60 mV/pH unit slope was observed by other authors on single-crystalline TiO_2 in highly conductive media (21-23). Significantly, it was also shown by Dutoit *et al.* (23) that for TiO_2 the V_{FB} was independent of the redox couple present in solution. The independency of the V_{FB} on redox potential in solution for most wide bandgap semiconductors is discussed in detail in reference (24). The V_{FB} of polycrystalline TiO_2 electrodes that were anodically grown could thus be used to monitor pH; unfortunately, the accuracy of the determination is poor (\pm 50 mV). The reproducibility is poor also because of changes in the slope of the Mott-Schottky curves and the consequent changes in the extrapolated V_{FB} as a function of time of exposure to the electrolyte. For practical use of the V_{FB} for monitoring pH, the measurements must also be possible in electrolyte solutions at low concentration.

In Fig. 6, we show Mott-Schottky curves at three different frequencies on sample T-79A in a commercial buffer solution of pH = 7 (specific resistivity = 176 Ω cm) and in a 1M KCl solution at a pH of \approx 6.8 (specific resistivity = 8.9 Ω cm). Mott-Schottky curves obtained in the low conductivity solution have an intercept with the V-axis that is shifted towards cathodic potentials with respect to the intercept of the curves measured in the high conductivity solution of the same pH. The values for $1/C_s^2$ at the same potential are larger and show more frequency dispersion in the case of the low conductivity solution. This is because the Helmholtz layer capacitance in the low conductivity solution is comparable in magnitude to the space charge capacitance. The total measured capacitance is then given by

$$\frac{1}{C_s} = \frac{1}{C_{sc}} + \frac{1}{C_H} \quad [2]$$

with C_{sc} being the semiconductor space charge capacitance, and C_H the Helmholtz capacitance.

De Gryse *et al.* (25) have shown that under those circumstances Eq. [1] should be replaced by

$$\frac{1}{C_s^2} = \frac{1}{C_H^2} + \frac{2}{qN_D\epsilon\epsilon_0} (V - V_{FB} - kT/q) \quad [3]$$

In this case, the Mott-Schottky plot will be parallel to the one measured in the high conductivity solution, and the intercept with the V-axis is

$$V_o = V_{FB} + kT/q - \frac{qN_D\epsilon\epsilon_0}{2C_H^2} \quad [4]$$

From Fig. 6 it is clear that the predicted parallel shift is only observed at high anodic potential. At potentials closer to the V_{FB} , the two sets of Mott-Schottky curves are not parallel, and Eq. [3] does not apply. Thus the V_{FB} on anodically grown polycrystalline TiO_2 cannot be obtained in low conductivity solutions from Eq. [4], as we are unable in this case to relate V_{FB} directly to V_o . In another publication (18), we show that V_{FB} measurements in high resistivity solutions (between 10^4 and $10^5 \Omega \text{ cm}$) are possible by a careful choice of electrode material (low N_D , low ϵ) and cell arrangement. Flatband potential measurements are thus an important alternative to OCP measurement, but the selected oxide semiconductor should not only have a wide bandgap but also a low dielectric constant and a low doping level. The anodically grown TiO_2 formed here clearly does not provide such a film.

Conclusion

This study shows that the pH response of the OCP of the highly doped conductive oxides on Pt and Ir provides a sensitive and fast means of pH measurements in aqueous solutions at room temperature; unfortunately, the OCP is also dependent on the oxidation/reduction potential of the solution. The OCP response to pH for the less conductive TiO_2 films is in general less reliable than for Pt and Ir oxides. The determination of V_{FB} as a means of measuring pH turned out to be possible only for the polycrystalline TiO_2 films in highly conductive solutions. The V_{FB} is less influenced than the OCP by the oxidation/reduction potential of a certain solution because the Helmholtz potential drop is dominated by adsorption/desorption phenomena of protons rather than electron exchange. If semiconductor electrodes could be used that have a higher impedance in depletion than the TiO_2 films used here, then V_{FB} determination could be done also in solutions of lower conductivity.

Acknowledgments

The authors wish to acknowledge the Electric Power Research Institute, and Dr. T. O. Passell, Project Manager, for the support of this work under Contract No. RP1168-1.

Manuscript submitted Aug. 8, 1983; revised manuscript received Nov. 27, 1983. This was Paper 830 presented at

the San Francisco, California, Meeting of the Society, May 8-13, 1983.

SRI International assisted in meeting the publication costs of this article.

REFERENCES

1. M. Madou and K. Kinoshita, *Electrochim. Acta.*, To be published.
2. J. B. Lee, *Corrosion*, **37**, 467 (1981).
3. J. V. Dobson, T. Dickinson, and P. R. Snodin, *J. Electroanal. Chem.*, **69**, 215 (1976).
4. J. V. Dobson, P. R. Snodin, and H. R. Thirsk, *Electrochim. Acta*, **21**, 287 (1981).
5. J. W. Schultze, U. Stimming, and J. Weise, *Ber. Bunsenges. Phys. Chem.*, **86**, 276 (1982).
6. L. C. Archibald, *Electrochim. Acta*, **22**, 657 (1977).
7. O. Kubaschewski and B. E. Hopkins, "Oxidation of Metals and Alloys," Second Ed., p. 214, Butterworths, London (1962).
8. S. Ardizzone, A. Carugate, and S. Trasatti, *J. Electroanal. Chem.*, **126**, 287 (1981).
9. R. L. Every and R. L. Brimsley, *ibid.*, **9**, 165 (1965).
10. M. Pourbaix, "Atlas of Electrochemical Equilibria in Aqueous Solutions," p. 347 "National Association of Corrosion Engineers, Houston, Texas, (1974).
11. D. N. Buckley, L. D. Burke, and J. K. Mulcahy, *J. Chem. Soc. Faraday Trans. 1*, **72**, 1896 (1976).
12. M. Pourbaix, "Atlas of Electrochemical Equilibria in Aqueous Solutions," p. 397 National Association of Corrosion Engineers, Houston, Texas, (1974).
13. P. Clechet, J. M. Martin, R. Olier, and C. Vollouy, *C. R. Acad. Sci. Paris*, **181C**, 887 (1976).
14. J. Vandermolen, W. P. Gomes, and F. Cardon, *This Journal*, **127**, 324 (1980).
15. A. K. Vijh, "Electrochemistry of Metals and Semiconductors," p. 129, Marcel Dekker, Inc., New York (1973).
16. M. W. Breiter, *J. Electroanal. Chem.*, **7**, 38 (1964).
17. E. C. Dutoit, R. L. Van Meirhaeghe, F. Cardon, and W. P. Gomes, *Ber. Bunsenges. Phys. Chem.*, **80**, 1206 (1975).
18. M. Madou, K. Kinoshita, and M. C. H. McKubre, *Electrochim. Acta.*, To be published.
19. J. H. Kennedy and K. W. Frese, *This Journal*, **5**, 723 (1978).
20. P. Richardson, P. Ang, and A. Sammells, "Proceedings of the 4th World Hydrogen Energy Conference," T. N. Veziroglu, Editor, p. 805, Pergamon Press, New York (1982).
21. G. Cooper, J. A. Turner, and A. J. Nozik, in "Photoelectrochemistry: Fundamental Processes and Measurement Techniques," W. L. Wallace, A. J. Nozik, S. K. Deb, and R. H. Wilson, Editors, p. 456, The Electrochemical Society Softbound Proceedings Series, Pennington, NJ (1982).
22. J. M. Bolts and M. S. Wrighton, *J. Phys. Chem.*, **80**, 2641 (1976).
23. E. C. Dutoit, F. Cardon, and W. P. Gomes, *Ber. Bunsenges. Phys. Chem.*, **80**, 475 (1976).
24. S. R. Morrison, "Electrochemistry at Semiconductors and Oxidized Metal Electrodes," p. 60-78, Plenum Press, New York (1980).
25. R. De Gryse, W. P. Gomes, F. Cardon, and J. Vennik, *This Journal*, **122**, 711 (1975).

Effect of PTFE Coverage on the Performance of Gas Evolving Electrodes

O. Teschke*

Grupo de Hidrogenio, Instituto de Fisica, UNICAMP, Campinas, Sao Paulo, Brasil

F. Galembek

Instituto de Quimica, UNICAMP, Campinas, Sao Paulo, Brasil

ABSTRACT

The effect of nickel electrode partial coverage with polytetrafluoroethylene (PTFE) on the electrode performance for the hydrogen evolution reaction (HER) was investigated. We show that for low current densities the only effect of the electrode coverage is to decrease the effective area. For medium current densities ($>10 \text{ mA/cm}^2$), coverage with PTFE has an overall beneficial effect in the electrode performance even with the resulting decrease in electrode surface area. Finally, for high current densities, in a regime of violent bubble release (1 A/cm^2), coverage effect is decreased but still significant.

In a gas evolving electrode, due to the magnitude of the diffusion coefficients, only a fraction of the electrode surface will interchange electrons at any given moment. This is due to partial surface coverage by bubble formation, which blocks part of the electrode surface. As a result, localized high current densities are observed on certain parts of the electrode surface. Recently, metal perforated diaphragms were partially coated with PTFE and were tested as water electrolyzer separators (1). It was shown that the PTFE coated metal is a bubble scavenger, having an overall beneficial effect on electrolyzer performance. Teflon bonded electrodes have also been used in water electrolyzers. However, it is still not clear how much, if at all, the performance of Teflon bonded porous electrodes is better than platinized or plain electrodes for gas evolution reaction and what the overall effect of PTFE on the performance of gas evolving electrodes is (2, 3).

In this work, we investigated the effect of partial electrode surface coverage with PTFE on the electrode performance for the hydrogen evolution reaction (HER).

Experimental

Circular stainless steel plates with an area of 10 cm^2 and 1 mm thick were initially plated in a Watts solution at 80°C . The plated sample was rotated about its axis at a constant speed in order to smooth out local electric field differences. All samples were prepared from the same stainless steel plate. The plate was initially washed in a detergent solution, mechanically scrubbed, and then cleaned in the following sequence (4): (i) degreasing in methanol for 15 min; (ii) washing in an alkaline bath (KOH 10%) for 5s; (iii) rinsing in distilled water; (iv) washing in an acid bath (H_2SO_4 5%) for 5s; and (v) washing in distilled water.

The nickel-plating solution consisted of the following compounds dissolved in distilled water: $\text{NiSO}_4 \cdot 6\text{H}_2\text{O}$, 300 g l^{-1} , $\text{NiCl}_2 \cdot 6\text{H}_2\text{O}$, 45 g l^{-1} , and H_3BO_3 , 30 g l^{-1} . The resulting solution was stirred at 80°C in a Pyrex beaker. The counterelectrode was a nickel sheet. The solution was heated to 80°C prior to each experiment. The total nickel plating time was 12 min. The current density was approximately 10 mA/cm^2 . After plating, the plates were washed with distilled water and dried.

PTFE T30 Teflon dispersion was dialyzed against water to remove the stabilizing surfactant and diluted to ca. 1% in distilled water. The dispersion was then allowed to settle within long (ca. 60 cm) glass cylinders for 15 min, after which time the lower 10% of the cylinder contents were discarded. The dispersion was allowed to settle again, and after 1h the upper half of the cylinder contents were also discarded. To prevent excessive coagulation, 1% sodium laurylsulfate was added to the remaining dis-

persion, for storage. Prior to use, it was drained from a stored, settled dispersion and replaced by distilled water.

PTFE T30 Teflon¹ dispersion was sprayed onto the electrode surface, allowed to dry, and heated in an oven preheated to 370°C . It was left at this temperature for 15 min and cooled by direct exposure to room air. The electrode surface was then washed in an acidic solution to remove the oxides formed, and another layer of nickel was electrolytically deposited on the electrodes. The purpose of this second deposition is to give mechanical stability to the Teflon layer. A photograph of the resulting surface is shown in Fig. 1. If a second nickel layer is not deposited, due to bubble formation, most of the Teflon will be removed from the surface by adsorbing to the gas-liquid interface. Deposition of a second nickel layer prevents the release of the Teflon layer even for high current densities (1 A/cm^2). During the second deposition, the current density was the same as in the first one.

The electrolytic cell employed for current density vs. potential drop measurements was a straight-walled cylindrical Pyrex beaker with a PTFE cover machined to fit (5). The cell containing 30 weight percent (w/o) KOH electrolyte was immersed in a water bath at 80°C . The test electrode and a larger planar platinum electrode were positioned facing each other at a distance of about 4 cm. The electrodes were soldered to a copper wire, and this connection was insulated with silicone rubber. The anode was not submitted to any special treatment. A membrane was inserted between them and kept fixed by a supporting frame. Mercury-mercury oxide electrodes were used as reference electrodes. ($E_{\text{Hg}/\text{HgO}} = 43 \text{ mV/NHE}$ in 5N

¹ Obtained from E. I. du Pont de Nemours and Company.

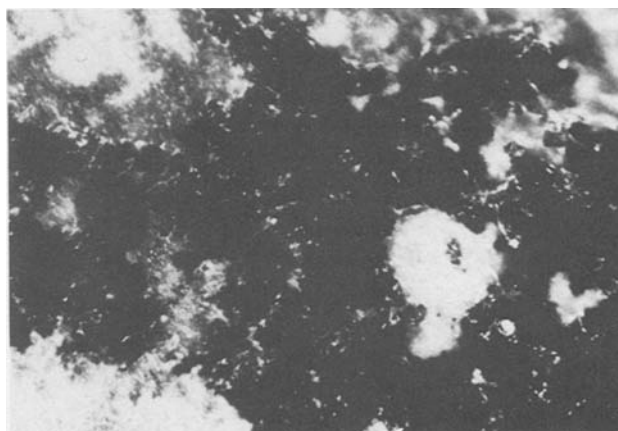


Fig. 1. Optical micrograph of a PTFE partially covered nickel surface (400 \times).

* Electrochemical Society Active Member.

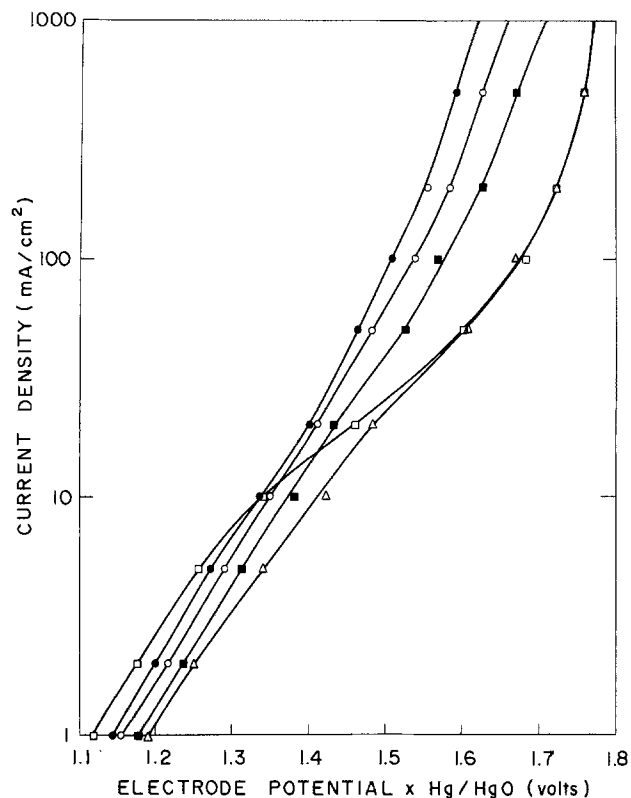
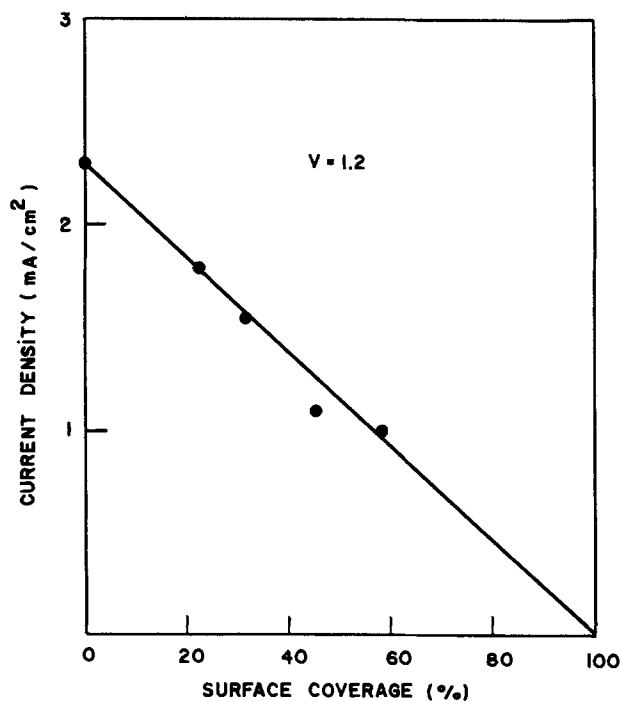


Fig. 2. Tafel plot for the H_2 evolution reaction using partial covered surface electrodes. \square : uncovered. \bullet : 20% coverage. \circ : 40% coverage. \blacksquare : 60% coverage.

KOH solution). The Hg/HgO electrode was inserted into a Luggin probe. The Luggin tip was positioned at the center of the working electrode. The characterization of the electrode was done by measuring cell voltage drop during electrolysis at different conditions, using a current interrupter technique (6) in order to obtain the IR-free electrode voltage.

Results

A number of electrodes was prepared, within surface coverage ranging from zero (uncovered) to 60%. Surfaces of the electrode samples were examined by optical mi-



croscopy. A typical micrograph is shown in Fig. 1. The irregular light (white) pattern observed corresponds to the PTFE deposit, and the dark areas are those of uncovered nickel. The picture was taken after the electrode was operated in HER regime for more than 2h at 1 A/cm². The light and dark tones indicate an irregular topography of the deposit surface. One may clearly observe that the PTFE particles are partially covered by nickel to aid their retention, mechanically. Nickel overlayers give mechanical strength to the Teflon deposits. The edge of the nickel deposit should operate very efficiently since the edges of electrodes are known to operate as efficient bubble generators. Since the metal is better wetted than PTFE, these bubbles should move from the nickel edges to the PTFE surface spontaneously.

Results of current vs. voltage measurements for the electrodes tested are shown in Fig. 2. The current densities shown in Fig. 2 are obtained by dividing the total current I by the geometric area of the circular electrodes (10 cm²). It may be seen that Teflon coverage has a significant effect on the electrode performance. Teflon coated electrodes operated at 500 mA/cm² have lower overvoltage than plain electrodes and are thus more efficient than these.

Discussion

The electrode area covered by PTFE does not participate in electron-transfer reactions, but it draws gas bubbles from the metallic sites, thus leaving more free to adsorb ions from the electrolytic solution and to reduce them. The electrode surface may be seen, then, as a mosaic of regions with different degrees of hydrophobicity, some more hydrophobic (PTFE coated) which can thus draw gas bubbles from the more hydrophilic ones (non-PTFE coated). Current density electrode potential curves obtained by the galvanostatic pulse method show three distinct regions. First, at low current densities (<10 mA/cm²), hydrogen is obtained at sufficiently low rates to diffuse away into the solution without bubble formation. In this region, PTFE coverage is not effective, and uncovered electrodes perform better than the coated ones. Above 10 mA/cm², the uncovered electrodes' overvoltage increases sharply due to bubble formation and concurrent loss of electroactive area. This is not observed in the

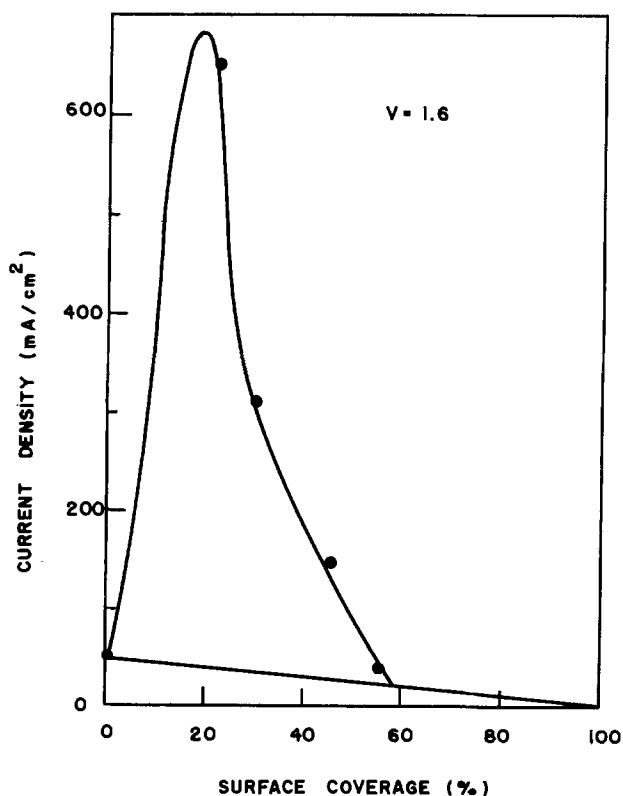


Fig. 3. Current densities versus surface coverage for a voltage of (A, left) $V = 1.2V \times Hg/HgO$ and (B, right) $V = 1.6V \times Hg/HgO$

coated electrodes, which perform better in this region because of the bubble scavenging action of the Teflon coated sites, as predicted by the Marangoni effect.

The size of the bubbles in the electrolyte increase when we have PTFE partial covered electrodes due to hydrophobicity of PTFE coating. The effect of the PTFE coverage on the cell ohmic resistance is discussed in Ref. (1).

Once formed in an electroactive (metallic) surface site, a gas bubble may stay there for a relatively long time until removed by convection, stirring, or flotation. A neighboring PTFE surface will cause bubble displacement, leading to lower total interfacial free energy and leaving metallic surface free for further action. Of course, this will not be observed when metal-electrolyte and PTFE-electrolyte contact angle are close.

At very high current densities ($>1 \text{ A/cm}^2$), violent bubble release and thermal convection should be the major factors leading to surface uncoverage. However, at the highest current density used in our experiments, most coated electrodes were more efficient than the uncoated ones.

Figures 3a and 3b showing current densities as a function of electrode surface coverage at given voltages (V) x Hg/HgO can further elucidate the points under discussions. At $V = 1.2$, current densities decrease linearly with coverage, due to surface loss. The straight line between 0% and 100% coverage represents the expected behavior based on surface availability. At $V = 1.6$, current densities are up to 12 times larger than in uncovered electrodes, but they decrease at higher degrees of surface coverage.

Of course, at very high coverages, current densities should approach zero.

In this work, we chose to cover nickel electrodes with Teflon particles in the 10-100 μm size range, following a simple argument: gas bubbles in the 10 μm (and up) radius range should float rapidly in aqueous media. Bubbles much smaller than this would tend to remain dispersed in water, increasing electrolyte resistance and should thus be avoided. Further theoretical and experimental work is required to define the optimum Teflon-particle size and surface coverage to achieve lower electrode overvoltages.

Acknowledgment

This work was supported by CESP-Companhia Energética de São Paulo.

Manuscript submitted Dec. 12, 1982, revised manuscript received ca. May 4, 1983.

UNICAMP assisted in meeting the publication costs of this article.

REFERENCES

1. O. Teschke and F. Galembeck, *This Journal*, **130**, 33 (1983).
2. L. W. Niedrach and H. R. Alford, *ibid.*, **112**, 117 (1965).
3. A. C. C. Tseung and P. R. Vossie, *Electrochim. Acta*, **21**, 315 (1976).
4. O. Teschke and D. M. Soares, *This Journal*, **130**, 306 (1983).
5. O. Teschke, D. M. Soares, and C. A. P. Évora, *J. Appl. Electrochem.*, **13**, 371 (1983).
6. "Handbook of Fuel Cell Technology," C. Berger, Editor, Prentice Hall, Englewood Cliffs, NJ (1968).

Technical Note



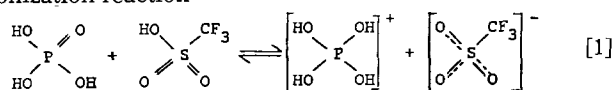
Ionization of Trifluoromethane Sulfonic Acid in Phosphoric Acid Raman Studies

R. Kötz,¹ S. Clouser,^{*2} S. Sarangapani,^{*3} and E. Yeager^{*}

Case Center for Electrochemical Sciences and the Chemistry Department, Case Western Reserve University, Cleveland, Ohio 44106

Much effort has been directed by various investigators (1-3) to optimize platinum catalysts for O_2 reduction in concentrated phosphoric acid. Relatively little attention, however, has been given so far to the acid-base properties of this electrolyte, and the possibility of modifying these properties so as to improve the current-voltage characteristics of platinum catalyzed O_2 cathodes. Through modifications of the acid-base properties, it may also be possible to increase the stability of dispersed Pt and slow down the oxidation of the carbon support.

The proton activity of concentrated H_3PO_4 can be controlled by treating the acid as a parent solvent system and changing its acid-base properties by the addition of strong acids and strong bases. Trifluoromethane sulfonic acid (TFMSA) is one of the strongest protonic acids (4) and, when added to concentrated H_3PO_4 , is expected to increase the proton activity according to the following ionization reaction



^{*} Electrochemical Society Active Member.

¹ Permanent address: Brown Boveri & Company, Research Center, CH-5405 Baden, Switzerland.

² Permanent address: Gould, Incorporated, Foil Division, Eastlake, Ohio 44094.

³ Permanent address: Giner, Incorporated, Waltham, Massachusetts 02154.

In addition to providing a source of protons, this fluorinated acid may also increase the solubility and perhaps also the diffusion coefficient of O_2 . The solubility of O_2 in fluorinated solvents is known to be relatively high (5-8).

In the present work, the acid-base properties of the $\text{H}_3\text{PO}_4\text{-CF}_3\text{SO}_3\text{H}$ have been studied using Raman spectroscopy (for the first time).

Experimental

85% orthophosphoric acid was obtained from Mallinckrodt and purified by treating it first with hydrogen peroxide, then with hydrogen over Pt black, and finally by conventional pre-electrolysis. The details of this purification method have been described elsewhere (9). Higher concentrations of the acid were obtained by distilling water out of the 85% acid. TFMSA was purchased from Alfa-Ventron and distilled twice in an all-glass vessel in an N_2 environment before use. The first 10% of the distillate and last 10% of the residue were discarded. As obtained, the TFMSA was pale straw colored but the doubly distilled acid was colorless.

The Raman spectra were recorded with a Spex Ramanlog spectrometer and Coherent Radiation Model CR-8 argon ion laser. The power output of the laser was 150 mW at the sample at 514.5 nm. The $\text{C}13$ NMR spectra of the doubly distilled $\text{CF}_3\text{SO}_3\text{H}$ and also a 10% $\text{CF}_3\text{SO}_3\text{H}$ solu-

tion in 85% H_3PO_4 were checked with a Varian XL-100 Fourier transform NMR spectrometer and found to contain only the four peaks expected for the CF_3 group. This provides evidence for only one type of carbon in a CF_3 environment to within $\sim 0.1\%$ purity.

The boiling point of the purified $\text{CF}_3\text{SO}_3\text{H}$ was 162°C as compared with a literature value of 162°C (4) at 1 atm. It is unlikely that the purified acid contained significant water since the temperature was constant to within at least 0.5°C during the second distillation. The boiling point of the monohydrate was 210°C .

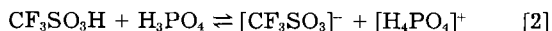
Results and Discussion

The Raman studies⁴ have been carried out in the $\text{CF}_3\text{SO}_3\text{H}\text{-H}_3\text{PO}_4$ mixtures principally to establish whether the $\text{CF}_3\text{SO}_3\text{H}$ is completely ionized in the mixture, and to see if there are any unusual species present in the mixtures.

In Fig. 1 are compared the Raman spectra obtained in doubly distilled pure TFMSA (spectrum A), purified 85% H_3PO_4 corresponding to a mol fraction $X_{\text{H}_3\text{PO}_4} = 0.5$ (spectrum B), and a 10% by volume solution of TFMSA in 85% H_3PO_4 corresponding to $X_{\text{TFMSA}} = 0.0426$, $X_{\text{H}_3\text{PO}_4} = 0.479$, and $X_{\text{H}_2\text{O}} = 0.479$ (spectrum C).

The insert in this figure indicates the Raman spectrum for 10% by volume TFMSA in 100% H_3PO_4 corresponding to $X_{\text{TFMSA}} = 0.062$. The spectrum for the TFMSA- H_3PO_4 solution is the sum of spectra A and B with the exception of an additional vibrational band at 1033 cm^{-1} , which is due to the S—O stretching vibration of the $[\text{CF}_3\text{SO}_3]^-$ anion. This frequency assignment has been made in accord with the published infrared spectra of aqueous solutions of TFMSA and mixtures of TFMSA with other acids (10). Since the TFMSA molecule has no center of symmetry, most of the observed Raman lines are also present in the infrared absorption spectrum.

It is not clear whether the $[\text{CF}_3\text{SO}_3]^-$ ion indicated by the Raman band at 1033 cm^{-1} is formed as a result of the formation of a $[\text{H}_4\text{PO}_4]^+$ cation or H_3O^+ from H_2O in the concentrated H_3PO_4 , according to the reactions



⁴ Some consideration is also being given to carrying out infrared measurements which should be more directly sensitive to the H_3O^+ vs. H_4PO_4^+ species, but cell windows present a problem.

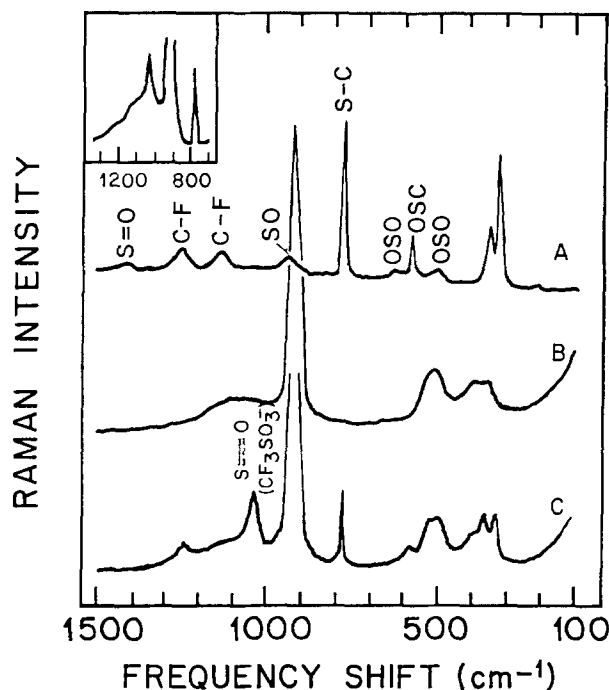
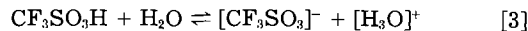


Fig. 1. Raman spectra of (A) pure TFMSA, (B) 100% H_3PO_4 , (C) 10% (volume) TFMSA in 85% H_3PO_4 . Insert: 10% TFMSA in 100% H_3PO_4 . Excitation: 514.5 nm argon ion laser line; slit width: $400\ \mu\text{m}$; resolution: 5 cm^{-1} . Relative sensitivity: (A) 500 k, (B) 50 k, and (C) 100 k.



If reaction [3] is predominant, the H_3O^+ species would differ from that encountered in ordinary acid solutions because there would be insufficient water to solvate it to the usual hydronium ion $[\text{H}_3\text{O} \cdot 3\text{H}_2\text{O}]^+$ or $[\text{H}_9\text{O}_4]^+$. Rather, the $[\text{H}_3\text{O}]^+$ could probably be solvated predominantly by H_3PO_4 to form $[\text{H}_3\text{O} \cdot 3\text{H}_3\text{PO}_4]^+$ with the protons of the $[\text{H}_3\text{O}]^+$ interacting with the O of the O = P of the H_3PO_4 .

To check into this further, the dependence of the intensity of the 1033 cm^{-1} peak on TFMSA concentration has been examined in the H_3PO_4 . The integrated peak intensity of the vibrational band at 1033 cm^{-1} (corresponding to the S—O stretch in the CF_3SO_3^- anion) has been measured relative to that of the 772 cm^{-1} peak as a function of the concentration of the TFMSA added in pure water and 85% H_3PO_4 (see Fig. 2). The band at 772 cm^{-1} is attributed to the C-S vibration of both the TFMSA molecule and its anion and hence depends only on the total amount of TFMSA added. Consequently, the I_{1033}/I_{772} ratio is related to the fraction of the TFMSA which is ionized. This intensity ratio is related to the concentrations of the ionized (C_1) and unionized (C_2) $\text{CF}_3\text{SO}_3\text{H}$ by an equation of the form

$$I = \frac{I_{1033}}{I_{772}} = \frac{(k_1)_{1033}C_1}{(k_1)_{772}C_1 + (k_2)_{772}C_2} = \frac{(k_1)_{1033}X_1}{(k_1)_{772}X_1 + (k_2)_{772}X_2} \quad [4]$$

where X_i is the mol fraction of the subscripted species and $(k_1)_{1033}$, $(k_1)_{772}$, and $(k_2)_{772}$ are the molar Raman scattering coefficients and will be assumed to be constant [see, e.g., Ref. (12)]. Note that the total number of mols is not changed by reactions [2] and [3]. If the equilibrium constants for the reactions are larger compared to unity, then for $X_1 < 0.5$

$$X_1 = X_{\text{H}_3\text{PO}_4}^0 + X_{\text{H}_2\text{O}}^0 \quad [5]$$

and

$$X_2 = X_{\text{CF}_3\text{SO}_3\text{H}}^0 - X_1 \quad [6]$$

where the superscripted symbols correspond to the mol fractions on the basis of the initially added components. Equation [4] can then be rearranged to the form

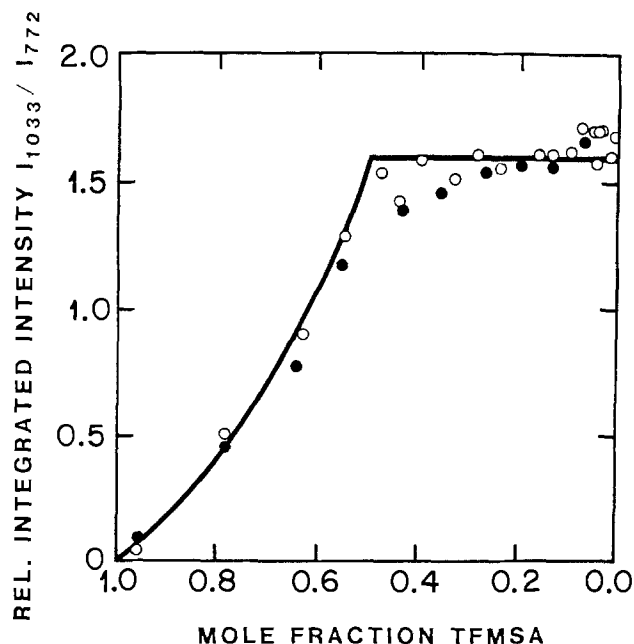


Fig. 2. Ratio of integrated peak intensity of the 1033 cm^{-1} Raman peak (corresponding to S—O in CF_3SO_3^-) to that of the 772 cm^{-1} peak (corresponding to C-S) as a function of the TFMSA concentration. Laser excitation: 514.5 nm (argon). Open points: TFMSA in H_2O ; solid points: TFMSA in 85% H_3PO_4 ; full line: calculation for TFMSA in H_2O assuming that one H_2O is needed to ionize one TFMSA and $(k_1)_{772} = (k_2)_{772}$.

$$\frac{y}{I} = \frac{(k_2)_{772}}{(k_1)_{1033}} - \left[\frac{2(k_2)_{772} - (k_1)_{772}}{(k_1)_{1033}} \right] \cdot y \quad [7]$$

where

$$y = 1 - X_{\text{CF}_3\text{SO}_3\text{H}} = X_{\text{H}_3\text{PO}_4} + X_{\text{H}_2\text{O}}$$

An identical equation is obtained for the $\text{CF}_3\text{SO}_3\text{H}-\text{H}_2\text{O}$ mixture except that $y = X_{\text{H}_2\text{O}}$. If only the water in the $\text{H}_3\text{PO}_4/\text{H}_2\text{O}$ system is capable of solvating the proton, then Eq. [7] is replaced by

$$\frac{y}{I} = \frac{2(k_2)_{772}}{(k_1)_{1033}} - \left[\frac{3(k_2)_{772} - (k_1)_{772}}{(k_1)_{1033}} \right] \cdot y \quad [8]$$

Thus, a comparison of the plots of y/I vs. y for the $\text{CF}_3\text{SO}_3\text{H}-\text{H}_2\text{O}$ and the $\text{CF}_3\text{SO}_3\text{H}-\text{H}_3\text{PO}_4-\text{H}_2\text{O}$ can indicate whether the H^+ of the $\text{CF}_3\text{SO}_3\text{H}$ is solvated by H_3PO_4 , as well as H_2O in the 85% H_3PO_4 or just by the H_2O . Plots of y/I vs. y are given in Fig. 3.

The agreement of the data for the binary and ternary systems with the general form of Eq. [7] is satisfactory considering the difficulty of obtaining accurate values for the ratio y/I as y and I both approach zero. Furthermore, the data for the binary and ternary system coincide reasonably well, indicating that the H_3PO_4 , as well as H_2O solvate the proton. If only the H_2O participated in the proton solvation, then the intercept for the ternary system would be twice as great as for the binary system and the intercept of the linear region at low values of y with the limiting y/I value would be at 0.66 rather than 0.5 (see dashed line in Fig. 3).

At lower concentrations in the H_3PO_4 solutions, however, it is not possible with these data to say what fraction of the protons are in the form of H_3O^+ and H_4PO_4^+ . In principle, it should be possible to establish the ionization constants for the TFMSA in the water and H_3PO_4 -water solutions from the curvature in the region between the two linear portions of each curve, but the accuracy does not appear sufficient with the present measurements even if more points were available. Infrared absorption measurements of the OH stretch in the H_3O^+ and H_4PO_4^+ species or proton NMR appear more promising approaches to establishing the predominant species in these solutions.

The half-width of the 1033 cm^{-1} peak has also been examined as a function of TFMSA in both pure water and 85% H_3PO_4 (see Fig. 4). The half-width decreases substantially with dilution in the TFMSA-water solutions approaching the instrumental line width at low concentrations under the particular operating conditions used in these experiments. In contrast, the half-width is essen-

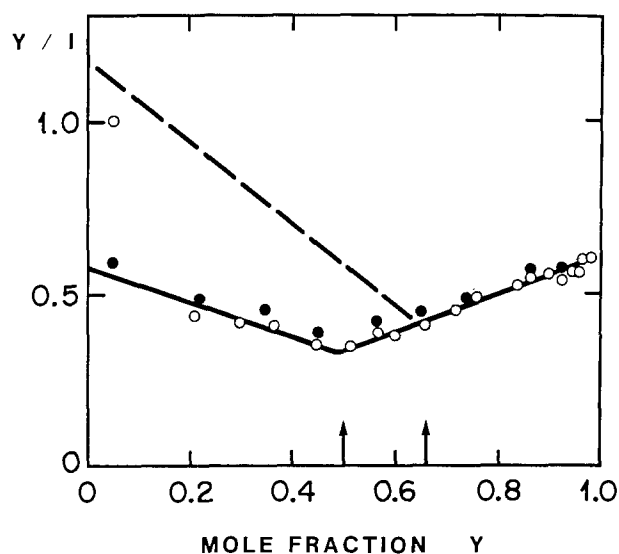


Fig. 3. Ratio y/I as a function of y where y is the mole fraction of H_2O (○) or 85% H_3PO_4 (●). The relative intensity I is taken from Fig. 2. The calculated results for Eq. [7] (—) and [8] (---) are also given.

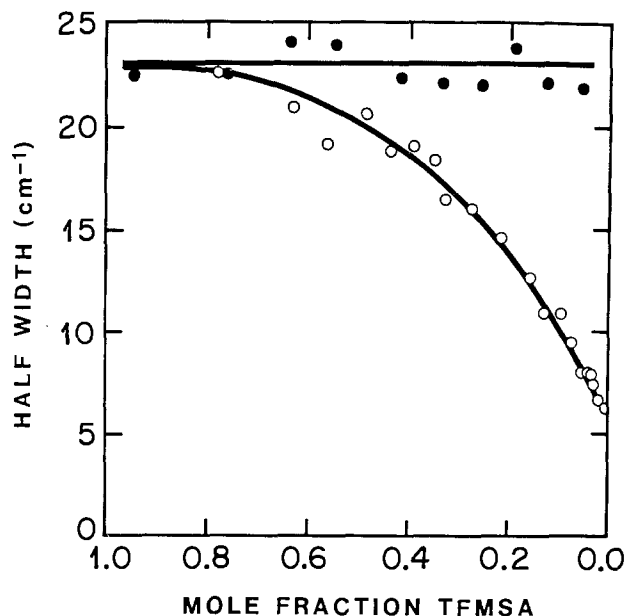


Fig. 4. Half-width of the 1033 cm^{-1} Raman line vs. concentration of trifluoromethane sulfonic acid in water (open points) and 85% H_3PO_4 (solid points).

tially independent of TFMSA concentration in the 85% H_3PO_4 .

The sources of line width broadening in liquids are severalfold and are the subject of considerable discussion (11). For an anisotropic polarizable rotor such as CF_3SO_3^- , they include rotational diffusion in addition to collision processes, hydrogen bond formation kinetics, and ion pair and ionization kinetics at the very high concentrations involved in concentrated acids, such as involved in the present study. Further, the CF_3 internal rotor, partially restricted by hydrogen bonding to H_2O and H_3PO_4 molecules, can also contribute to line broadening. No one of these factors, however, appears capable of explaining the wide line widths and the concentration dependence in water and lack of such in 85% H_3PO_4 in Fig. 4. Depolarization Raman measurements and NMR measurements would prove helpful in interpreting this behavior.

A few NMR measurements have been performed by the authors on the $\text{CF}_3\text{SO}_3\text{H}-\text{H}_3\text{PO}_4-\text{H}_2\text{O}$ solutions. The proton-spin resonance measurements using a 60 MHz Varian EM 360 permanent magnet NMR spectrometer indicate only a single proton peak at room temperature at concentrations varying from 0 to 100% $\text{CF}_3\text{SO}_3\text{H}$ in 85% H_3PO_4 . If any of the equilibria such as those represented by Eq. [2] and [3] were relatively slow, then more than one type of proton signal would be expected; thus, implying that all the equilibria are fast on the NMR time scale. The line width of the proton peak decreases with increasing $\text{CF}_3\text{SO}_3\text{H}$ concentration. The C-13 spectra of the pure $\text{CF}_3\text{SO}_3\text{H}$ and 10% by volume solutions of this acid in 100% H_3PO_4 showed the expected four peaks with no anomalies or impurity peaks evident.

Conclusion

The Raman spectroscopy studies indicate that the TFMSA is essentially completely ionized in H_3PO_4 and $\text{H}_3\text{PO}_4-\text{H}_2\text{O}$ solutions for a mole fraction X_{TFMSA} below 0.4. NMR measurements on the mixed acid solutions indicate only one proton spin resonance line and the expected C-13 spectrum for the CF_3SO_3^- . Therefore, the acid ionization processes are quite fast. The protons in the mixed acid solutions are most likely in the forms $(\text{H}_4\text{PO}_4)^+$ and $(\text{H}_3\text{O})^+$.

Acknowledgment

The authors are pleased to acknowledge the support of this research by the Electric Power Research Institute and the U.S. Department of Energy.

Manuscript submitted Sept. 21, 1982; revised manuscript received Dec. 29, 1983.

REFERENCES

1. W. M. Vogel and J. T. Lundquist, *This Journal*, **117**, 1512 (1970).
2. H. R. Kunz and G. A. Gruver, *ibid.*, **122**, 1279 (1975).
3. A. J. Appleby, *ibid.*, **117**, 328, 641 (1970); A. J. Appleby and A. Borucka, *ibid.*, **116**, 1212 (1969).
4. R. N. Hazeldine and J. M. Kidd, *J. Chem. Soc.*, 4228 (1954).
5. R. Battino and H. L. Clever, *Chem. Rev.*, **66**, 395 (1966).
6. J. G. Riess, *Ann. Anesthesiol. Fr.*, 391 (1974).
7. E. P. Wessler, R. Iltis, and L. C. Clark, *J. Fluorine Chem.*, **9**, 137 (1977).
8. T. M. Reed, III, in "Fluorine Chemistry," Vol. 5, J. H. Simmons, Editor, p. 211, Academic, New York (1964).
9. E. Yeager, P. Bindra *et al.*, EPRI EM-505, June (1977).
10. T. J. Balicheva, V. I. Ligus, and Yu. Yu. Fialkov, *Russ. J. Inorg. Chem.*, **18**, 917 (1973).
11. L. I. Komarow and I. Z. Fisher, *Sov. Phys. JEPT*, **16**, 1358 (1963).
12. J. E. Walrafen, *J. Chem. Phys.*, **42**, 485 (1965).



Electron Injection and Avalanche during the Anodic Oxidation of Tantalum

J. M. Albella,* I. Montero, and J. M. Martínez-Duart

Instituto de Física del Estado Sólido (CSIC) and Departamento de Física Aplicada, C-12, Universidad Autónoma, Cantoblanco, Madrid-34, Spain

ABSTRACT

The consequences of the avalanche-breakdown model during the growth of anodic tantalum oxide in H_3PO_4 electrolytes are discussed. Typical values of the injected current density at the electrolyte-oxide interface, the impact ionization coefficient, and the electric field during anodization have been determined from the anodization characteristics at a constant current. The results are interpreted assuming that the injected current has its origin in the electrolyte anions incorporated into the oxide during the anodization process.

The anodic oxidation of valve metals is a process of high technical and scientific interest because of its implications in the manufacturing of electrolytic capacitors, in the preparation of passivating layers in thin film technology, and in the growth of protective and decorative films (1). The practical limit to the maximum thickness of the oxide reached in the anodization process is given by the breakdown voltage across the film. There is a great amount of literature concerning the nature of the breakdown process, and some empirical relations between the breakdown voltage and anodization parameters have been established (2). Kadari and Klein have studied the electrical breakdown during the anodic growth of Ta_2O_5 and Al_2O_3 and explained it by the theory of stochastic succession of avalanches (3). Recently, Ikonopisov has put forward a model of breakdown caused by the avalanche of electrons injected at the electrolyte/oxide interface during anodization (4). This model is able to explain the well-known linear dependence of the breakdown voltage on the logarithm of the electrolyte resistivity. Lately, the model has been extended by Albella *et al.* to explain the curvature of the voltage curve as a function of time in anodization experiments of tantalum at a constant current density (5). In the present paper, we further examine the implications of this model. In particular, by a careful determination of the slope of the voltage curve, dV/dt , the injected current density, j_0 , and the ionization coefficient of the avalanche have been calculated from the anodization curves of tantalum at a constant current. The results are interpreted on the basis of an alternative model for the injected electronic current at the electrolyte/oxide interface.

Theory

Figure 1 shows the mechanism of avalanche breakdown proposed by Ikonopisov. In this model, an electronic current j_0 is supposed to be injected from the electrolyte to the oxide conduction band by a Schottky mechanism. Other injection mechanisms, such as the Fowler-Nordheim tunneling, have been suggested, for example, by Kadary and Klein (3). The injected electrons are accelerated towards the anode by the strong

field of anodization, causing an avalanche breakdown when a certain critical electron current is reached.

In a simple avalanche model of breakdown during anodic oxidation, one can assume that the electronic current density, j_0 , injected to the conduction band of the oxide from the electrolyte/oxide interface, increases exponentially according to an avalanche process (4). Therefore, the electronic current density at the anode, j_e , should be given by: $j_e = j_0 e^{\alpha d}$, where α is the impact ionization coefficient and d is the distance traveled by the primary electrons on their way to the anode. As a first approximation, one can assume d equal to the total oxide thickness.

In anodization experiments at constant current density, j_t , the oxide thickness increases linearly with the voltage ($d = aV$). As a consequence, the differential equation regulating the growth of potential with time is given by

$$\frac{dV}{dt} = Kj_t \quad [1]$$

where j_t is the ionic current density of anodization, and K is the unitary anodization rate, given by

$$K = \frac{ME}{10F\rho} \quad [2]$$

In this formula, M is the molecular weight of the resulting oxide, F the Faraday constant, ρ the oxide density, and E the electric field during anodization (1). Taking into account the presence of the avalanche electronic current j_e during the anodization, the ionic current will be: $j_i = j_t - j_e$, so that

$$\frac{dV}{dt} = K(j_t - j_e) = K(j_t - j_0 e^{\alpha d}) = K(j_t - j_0 e^{\alpha' V}) \quad [3]$$

with α' equal to $\alpha \cdot a$.

The three parameters K , j_0 and α' of Eq. [3] can be obtained through an accurate determination of the variation of the dV/dt values with the voltage in the range of voltages where no scintillation sparks appear. By operating in Eq. [3], one obtains

$$\ln \left(1 - \frac{1}{Kj_t} \frac{dV}{dt} \right) = \ln \frac{j_0}{j_t} + \alpha' V = \ln \left(\frac{j_e}{j_t} \right) \quad [4]$$

* Electrochemical Society Active Member.

Key words: dielectrics, current efficiency, transport.

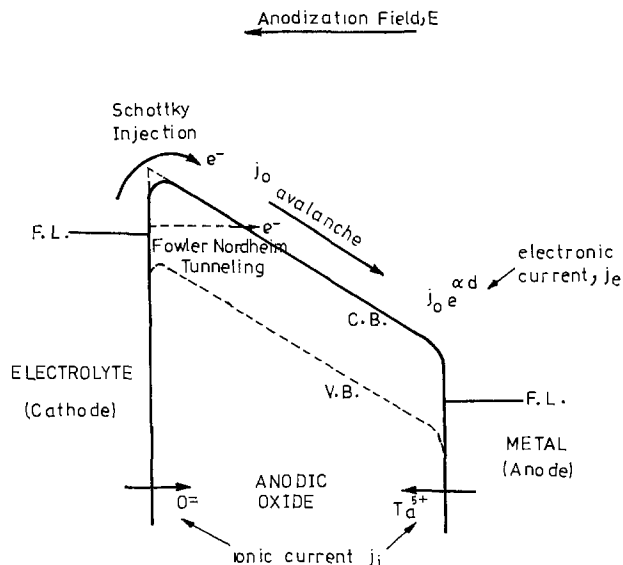


Fig. 1. Schematic representation of the band structure and the avalanche breakdown mechanism during anodization.

Therefore, a graphic representation of the values of $\ln \left(1 - \frac{1}{Kj_t} \frac{dV}{dt} \right)$ as a function of the anodization voltage, V , must fit a straight line whose slope is α' , and the intersection with the ordinate axis is given by $\ln(j_0/j_t)$. The first step in this calculation is to find the value of the constant K . An approximate value of K can be obtained from the extrapolated value of dV/dt at $V = 0$, which from Eq. [3], and with the additional condition $j_0 \ll j_t$, is given by

$$K = \frac{(dV/dt)_{V=0}}{j_t} \quad [5]$$

However, in order to find a more accurate value of K , α' , and j_0 , we have followed an iterative method of least squares fitting of the experimental values of dV/dt to the theoretical Eq. [3].

Experimental

In our experiments, tantalum foil from Reframet Hoboken, of 99.96% purity, was anodized at a constant current density. Previously, the samples were cleaned and chemically polished following standard treatments (5). In order to avoid the creeping of the electrolyte and the spurious effects at the edges of the foil during anodization, a sample holder was used (see Fig. 2), which only exposed to the electrolyte a circular area of $1.18 \pm 0.04 \text{ cm}^2$ of the foil. Optical microscope observations of the anodized area showed that the penetration of the electrolyte under the holder was always less than $10 \mu\text{m}$ wide, resulting in a variation of the surface area during the anodization less than 0.4%. During the experiments, the total current supplied by the source was kept constant within $\pm 0.1\%$. All anodization experiments were performed in an electrolyte of phosphoric acid dissolved in water (0.01%) giving a resistivity of $2280 \Omega \cdot \text{cm}$. By using a stirred thermostat bath, the temperature of the electrolyte close to the sample was always maintained at $20^\circ \pm 0.2^\circ\text{C}$.

Figure 2 shows the experimental setup used in our experiments. The data acquisition system, composed of the HP 3497A digital voltmeter (input impedance $> 10^7 \Omega$) and the HP85 microcomputer, allowed us to obtain directly the variation of the anodization voltage with time, its derivative, and the parameters j_0 , K , and α' which best fit the dV/dt curves. In the measurement of the $\Delta V/\Delta t$ values, the voltage increments were always kept below a few volts. Therefore, fixed time intervals of measurement were adjusted according to

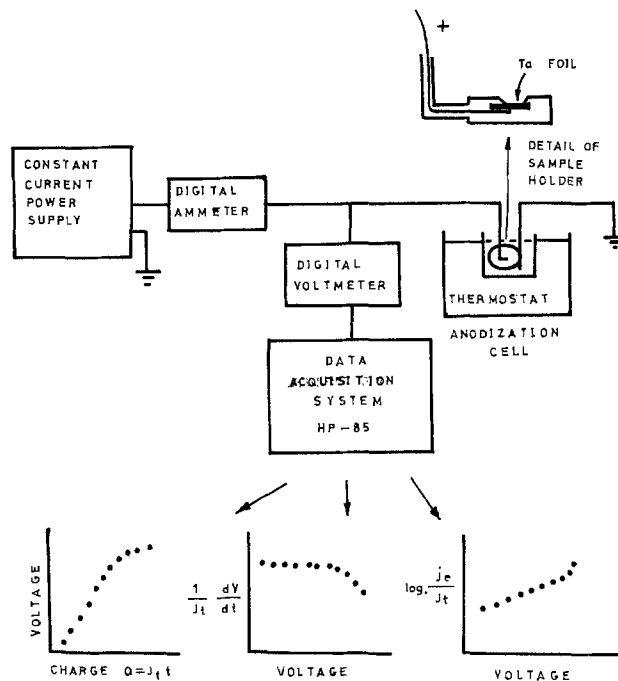


Fig. 2. Experimental setup

the magnitude of the anodization current. Taking into account the resolution in the measurement of voltage (1 mV) and time ($10 \mu\text{s}$) the overall error in the derivative was always below 0.1%. It is important to emphasize that the voltage-time curves are generally reported in the literature as being linear, even at high anodization voltages. However, the nonlinearity effects, which become more apparent in the derivative curve, are very important, since they can be related to the avalanche and breakdown mechanisms.

Results and Discussion

Figure 3 (curves a-e) gives some examples of the variation of the unitary anodization rate ($1/j_t$) (dV/dt) vs. V in typical experiments at different current densities. As can be observed, there is a slight diminution of the $(1/j_t)$ (dV/dt) values with the anodization voltage, until the scintillation voltage, V_s , is reached. For voltages higher than V_s , the experimental values of dV/dt are erratically scattered, due to the onset of the breakdown process. According to the method previously described, we have computed from the data shown in Fig. 3, the values of K , j_0 , and α' in Eq. [4]; this should fit the computed values of $\ln(j_0/j_t)$ to a straight line.

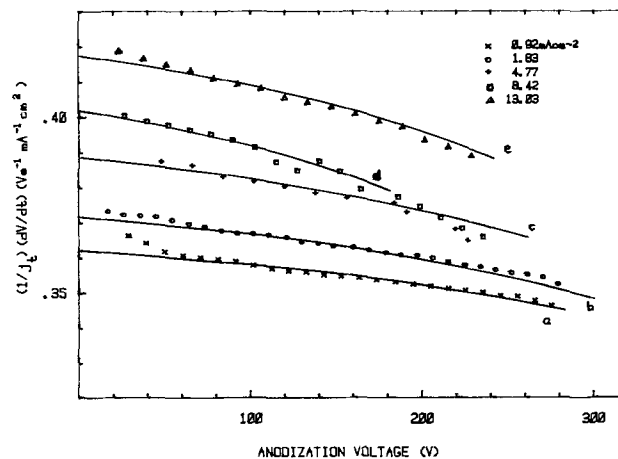


Fig. 3. Unitary anodization rate as a function of the anodization voltage for different current densities (lines indicate the theoretical values calculated according to the model by a least squares fitting).

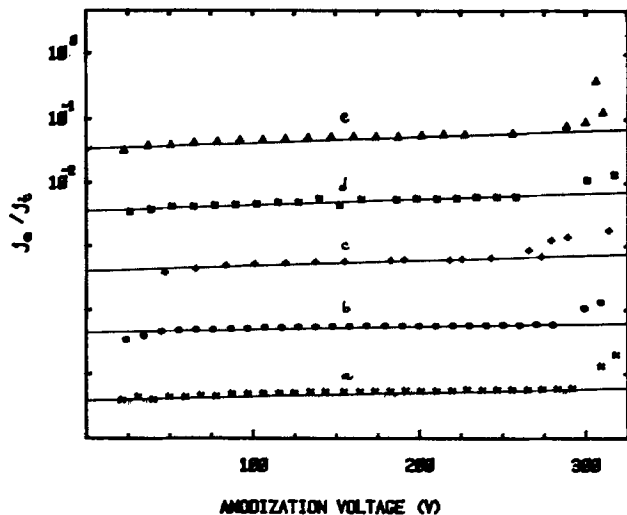


Fig. 4. Fitting of the experimental values of $\ln(j_e/j_i)$ to a linear variation with the anodization voltage, according to Eq. [4] (symbols as in Fig. 3). There has been a vertical displacement of the curves so that each straight line is bounded between the 10^{-1} and 10^{-2} values of j_e/j_i , as for the top line.

The adjustment is shown in Fig. 4. As it can be appreciated, a good linearity in the calculated values of $\ln(j_e/j_i)$ is obtained within a wide range of the anodization voltage.

The electric field E present during anodization can be directly evaluated from Eq. [2], once the value of K has been determined. Using the value of $\rho = 8.03 \text{ g} \cdot \text{cm}^{-3}$ for the density of the oxide (6), Fig. 5 gives a plot of the calculated values of the electric field as a function of the ionic current density $j_i = j_t - j_e$. As can be observed, there exists an approximate exponential dependence of the ionic current on the electric field, in agreement with the experimental results obtained by Dell'Oca and Young (dashed curve in Fig. 5) based on the direct measurement of the oxide thickness corresponding to a definite anodization voltage (7). According to Dignam's analysis (8) of the high field ionic conduction in solids, the field E , and therefore dV/dt , decreases as the film grows. Specifically, the exponential dependence of E on the thickness d for a fixed current density j should be the same as the dependence of E on j for fixed d . This fact implies that the predicted diminution of E during the film growth should be the same as the increase of the field with the ionic current density (see Fig. 5). It might appear at first that the variation of dV/dt measured in our work could be caused by this effect. However, a straightforward

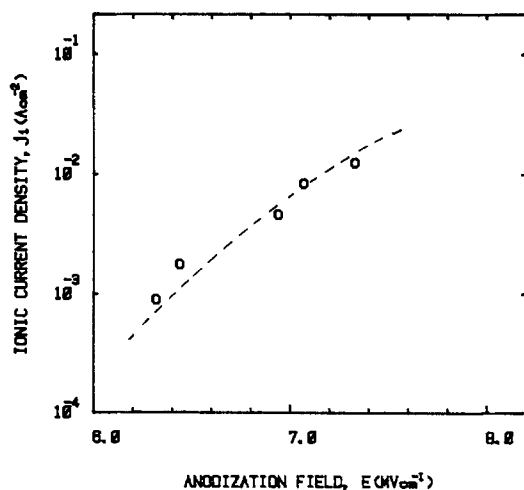


Fig. 5. Ionic current density as a function of the anodization field [the broken line corresponds to the results of Ref. (7)].

calculation shows that the variations in our values of dV/dt and the decrease in E predicted by Dignam's model differ by a factor of about four. For example, from Fig. 3, the decrease in E [calculated from the variation of $(1/j_i)$ (dV/dt) for a tenfold increase of voltage (20 to 200V)] is on the average 3% for a given current density. However, the increase shown by E for a 1 decade change in current density in Fig. 5 is nearly 12%.

It is interesting to compare the calculated values of the injected electronic current, j_e , and the ionic current of anodization. The log-log plot of Fig. 6 gives a straight line whose slope is nearly 45° , thus indicating that the electronic current varies linearly with the ionic current, independently of the value of the total anodization current. The quotient j_e/j_i is about $4 \cdot 10^{-2}$ which means that for the particular anodization electrolyte used in this work, the electronic current amounts to 4% of the ionic current. This value of the electronic current might seem too high when compared with the reported values of the current efficiency during anodization. As it is known, in the case of tantalum, the current efficiency is close to 100% in experimental conditions similar to ours (9). Furthermore, if the electronic current calculated in this work were injected from the electrolyte into the oxide, it would give rise to a visible evolution of oxygen at the oxide surface. However, no bubbles were observed at anodization voltages below the sparking voltage. Although one may speculate that the reduction of the slope dV/dt may be produced by a decrease of the electric field caused by local heating in the film, this does not seem likely in view of the facts that this effect is exhibited at voltages well below the sparking voltage and that some of the experiments were performed at very low current densities.

Within the analysis of the possible causes of the electronic current present during the anodization, one finds the remarkable fact that the above ratio of the injected electronic current to the ionic current coincides with the reported ratio of the mol concentration of anions incorporated into the outer part of the oxide per mol of Ta^{5+} , which is in the range of 3-5% for the electrolyte used in this work (10, 11). Therefore, one tentatively could associate this "electronic" current with the movement of charged anions across the electrolyte/oxide interface. In fact, according to Amsel *et al.* (9), the way by which the electrolyte species are incorporated into the oxide seems to be in the form of PO_4^{3-} anions. As a consequence, there must be an ionic current through the electrolyte/oxide interface associated with

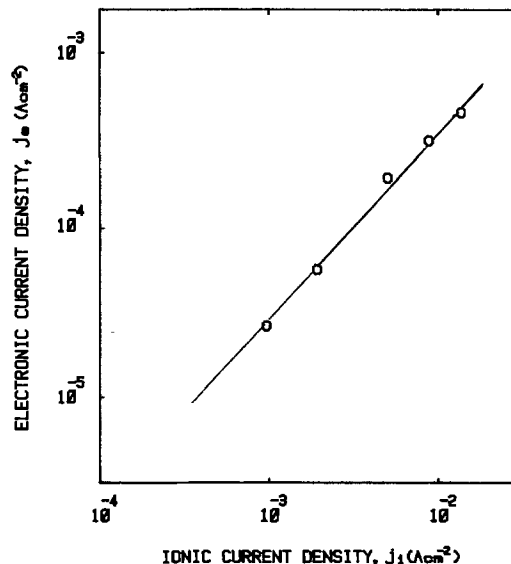


Fig. 6. Electronic vs. ionic current densities during anodization

the charge transported by these anions. This view is further supported by recent experiments (12) performed with H_3PO_4 electrolytes in different concentrations, which show a strong correlation between the quotient j_0/j_i and the corresponding anion concentration incorporated into the oxide.

Given the absence in the literature of a detailed mechanism of the incorporation of the electrolyte ions into the oxide lattice, it is difficult to put forward a model that can explain the onset of the avalanche process proposed in this work. However, some speculations can be made. One of the possible reactions for the incorporation of the PO_4^{3-} anions suggested by Amsel *et al.* (9) is $\text{PO}_4^{3-} \rightarrow \text{PO}_3^- + \text{O}^-$. Under these circumstances, the PO_3^- ions could act as a source of electrons acting like donor levels. The resulting electrons, probably liberated by a Poole-Frenkel mechanism, can then be accelerated by the strong anodization field, bringing about the avalanche multiplication.

On the basis of the above model, the primary electrons are expected to travel a distance to the anode less than the oxide thickness because the electrons are liberated from sites within the outer layer of the oxide. Some observations about this distance can be made from the calculated values of the ionization coefficient, $\alpha = \alpha'/a$. Table I shows the calculated values of α , using for a the value given by $a = 1/E$. As it can be observed, α increases with the anodization field, in agreement with the avalanche theories (13), although the absolute values of α are somewhat lower than the ones reported in the literature. Kadary and Klein, for example, obtain a value of $\alpha = 1.1\text{--}1.4 \times 10^5 \text{ cm}^{-1}$ from electroluminescence and pulse breakdown measurements in Ta_2O_5 films (3, 14), which is more than twice the value obtained in this work. Since the values of α of Table I are obtained through the product αd , a better agreement of α with the published values results if one considers that the distance traveled by the primary electrons is smaller than d . In relation to this, the ionization coefficient for aluminum oxide calculated by Shimizu (15), on the basis of the results of Ikonopisov *et al.* (16), is $\alpha = 2 \cdot 10^4 \text{ cm}^{-1}$. Shimizu objected that this value is too low for the Ikonopisov's model to be accepted. However, this objection can be partially disregarded in the light of our model for the origin of the primary electron current.

Another important question which often arises is whether the electronic current reaching the anode ($j_0 e^{\alpha d}$, according to this work) is high enough to cause the breaking down of the tantalum oxide. At present, there is not a definite answer to this matter. As it can be appreciated from Fig. 4, the avalanche electronic current departs from the exponential dependence, increasing at a faster rate, when the anodization voltage

approaches the sparking voltage. One can assume that, under these circumstances, a new avalanche process starts, which is triggered by the field originated by the spatial charge left by the ionized atoms. The role of the spatial charge has been studied in detail by Kadary and Klein (3) in their theory of stochastic succession of avalanches, and it might be the direct cause of the abnormal rise of the electronic current at high voltages.

Conclusions

The experimental results on the anodization rate of tantalum in an H_3PO_4 electrolyte with different current densities in a wide range of voltages show a good fit to the theoretical curves obtained under the hypothesis of an exponential increase of electronic current present during anodization. This fact provides strong evidence of the avalanche breakdown model in anodic oxides proposed by Ikonopisov (4), and lately extended by Albella *et al.* (5), in order to explain the scintillation process. On the origin of the primary electrons causing the avalanche breakdown, we propose that these electrons, instead of being injected through the electrolyte/oxide interface, are originated within the oxide itself by the ionization of the electrolyte impurities incorporated into the oxide film during the anodization.

Acknowledgments

We would like to thank Professor S. Ikonopisov and Ms. M. Machkova (Higher Institute of Chemical Technology, Sofia, Bulgaria) for helpful discussions regarding the avalanche mechanisms. We are also indebted to the Comisión Asesora de Investigación Científica y Técnica, Spain, for partial support of this work.

Manuscript submitted April 4, 1983; revised manuscript received Jan. 15, 1984.

Universidad Autonoma assisted in meeting the publication costs of this article.

REFERENCES

1. L. Young, "Anodic Oxide Films," p. 4, Academic Press, London (1961).
2. F. J. Burger and J. C. Wu, *This Journal*, **118**, 2039 (1971).
3. V. Kadary and N. Klein, *ibid.*, **127**, 139 (1980).
4. S. Ikonopisov, *Electrochim. Acta*, **22**, 1077 (1977).
5. J. M. Albella, I. Montero, and J. M. Martinez Duart, *Thin Solid Films*, **58**, 307 (1979).
6. A. J. Schrijner and A. Middelhoek, *This Journal*, **111**, 1167 (1964).
7. C. J. Dell'Oca and L. Young, *ibid.*, **117**, 1548 (1970).
8. M. J. Dignam, *ibid.*, **126**, 2188 (1979).
9. G. Amsel, C. Cherki, G. Feuillade, and J. P. Nadai, *J. Phys. Chem. Solids*, **30**, 2117 (1969).
10. J. J. Randall, W. J. Bernard, and R. R. Wilkinson, *Electrochim. Acta*, **10**, 183 (1965).
11. J. J. Randall, *ibid.*, **20**, 663 (1975).
12. I. Montero and J. M. Albella, in "Proceedings of the IX International Vacuum Congress, p. 121, Asocacion Española del Vacio, Madrid (1983).
13. J. J. O'Dwyer, "The Theory of Electrical Conduction and Breakdown in Solid Dielectrics," p. 219, Oxford University Press, London (1973).
14. V. Kadary and N. Klein, *This Journal*, **128**, 749 (1981).
15. K. Shimizu, *Electrochim. Acta*, **26**, 1691 (1981).
16. S. Ikonopisov, A. Girginov, and M. Machkova, *ibid.*, **24**, 451 (1979).

Table I. Impact ionization coefficient α for different anodization fields

E (MV cm^{-1})	α (cm^{-1})
6.30	2.1×10^4
6.42	2.4×10^4
6.92	2.7×10^4
7.05	3.7×10^4
7.31	3.8×10^4

Sputtering Yield of Carbon Atoms in Organic Materials for Oxygen Bombardment

H. Gokan and S. Esho

NEC Corporation, Microelectronics Research Laboratories, Miyamaeku, Kawasaki 213, Japan

ABSTRACT

Etching mechanisms for organic materials in oxygen ion-beam etching has been discussed in terms of sputtering yield of carbon atoms. The sputtering yield, which is defined by the number of sputtered carbon atoms per O_2 ion, exceeds the value of 2 under high oxygen pressure conditions. Mass analysis indicates that the final product during etching is CO. The main reaction for carbon consumption is assumed as being $2C + O_2^+ + nO_2 \rightarrow 2(n+1)CO$, where the nO_2 term expresses the reaction with neutral oxygen molecules. Net sputtering yield is expressed by three factors; physical sputtering, chemical reaction with accelerated oxygen ions, and the ion-assisted reaction with neutral oxygen molecules. The etching model, considering the ion-assisted reaction, qualitatively explains the increase in sputtering yield with decreasing acceleration energy (decreasing current density) and with increasing oxygen pressure.

Reactive ion etching in oxygen plasma has become highly attractive, since it was applied to the etching of thick organic layers in multilevel resist systems (1). The etching provides organic patterns in submicron dimensions with high aspect ratio. However, the etching mechanism for organic materials has not yet been fully understood. In reactive ion etching (RIE), generally, it is difficult to control ion energy and ion current density as well as to separate the radical-species contribution to the etching. However, in oxygen ion-beam etching (IBE), the effect of fundamental parameters, such as acceleration energy and current density on the etch rates, can be investigated qualitatively (2-4), since etching characteristics are investigated in a more controlled environment. In the present paper, etching characteristics and etching mechanism for organic materials are discussed in terms of sputtering yield of carbon atoms for oxygen bombardment.

Etch Rate Measurement

An ion-beam etching system with Kanfan ion source was used in the experiments. Oxygen pressure was monitored at the top of the diffusion pump. Etch-

Key words: oxygen ion-beam etching, resists, sputtering yield.

ing samples were mounted on a water-cooled rotary stage using a heat-sink material, Electron grease (5).

Figure 1 shows etch rates of PMMA and/or Au as a function of oxygen pressure for acceleration energies ranging from 200 to 750 eV. The exposed area of PMMA to the ion beam was about 1 cm^2 . The etch rate for PMMA increases with increasing oxygen pressure and tends to level off at high acceleration energies. Figure 2 shows the loading effect on the etch rate for PMMA. The abscissa shows the exposed area of the PMMA to the ion beams. The data were taken under the condition of 2×10^{-4} torr (2.6×10^{-2} Pa) oxygen pressure, 0.82 mA/cm^2 current density, and 500 eV acceleration energy. It is found that the etch rate slightly decreases when increasing the exposed area of the PMMA. The resist-etch rate was measured for argon bombardment. Figure 3 shows energy dependence for AZ1350J etch rate normalized at 1 mA/cm^2 current density. The reason why AZ1350J is used instead of PMMA is that AZ1350J is more stable than PMMA under high energy argon ion-beam etching conditions (6). The scattering of data observed at energies lower than 200 eV may be due to the effect of the residual background oxygen

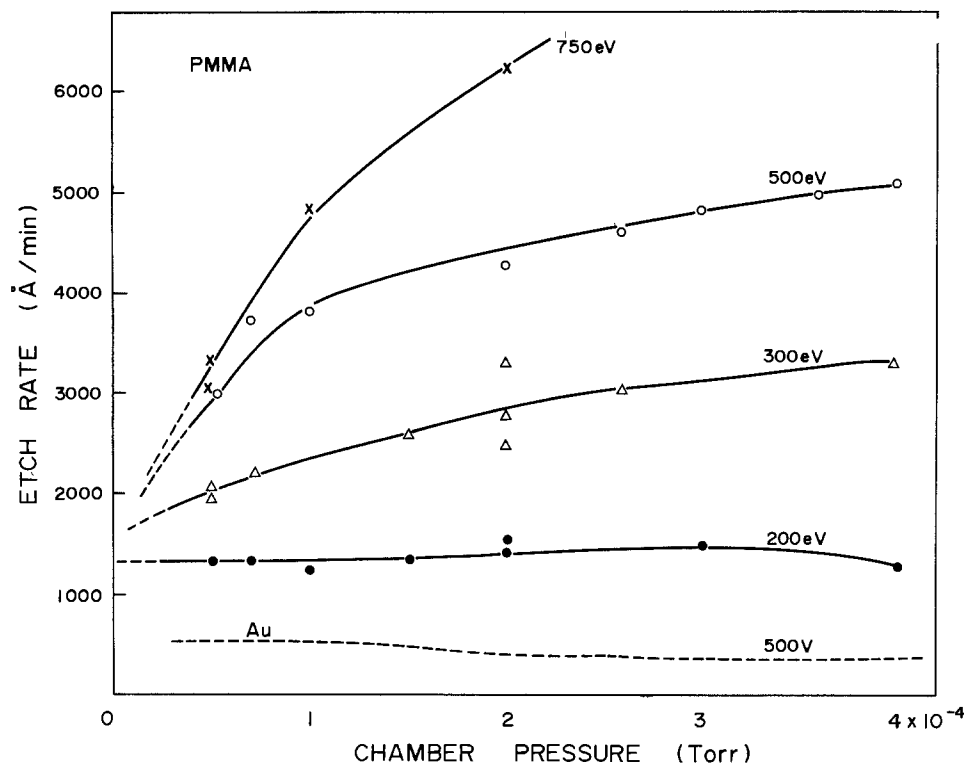


Fig. 1. Etch rates for PMMA and Au as a function of oxygen pressure.

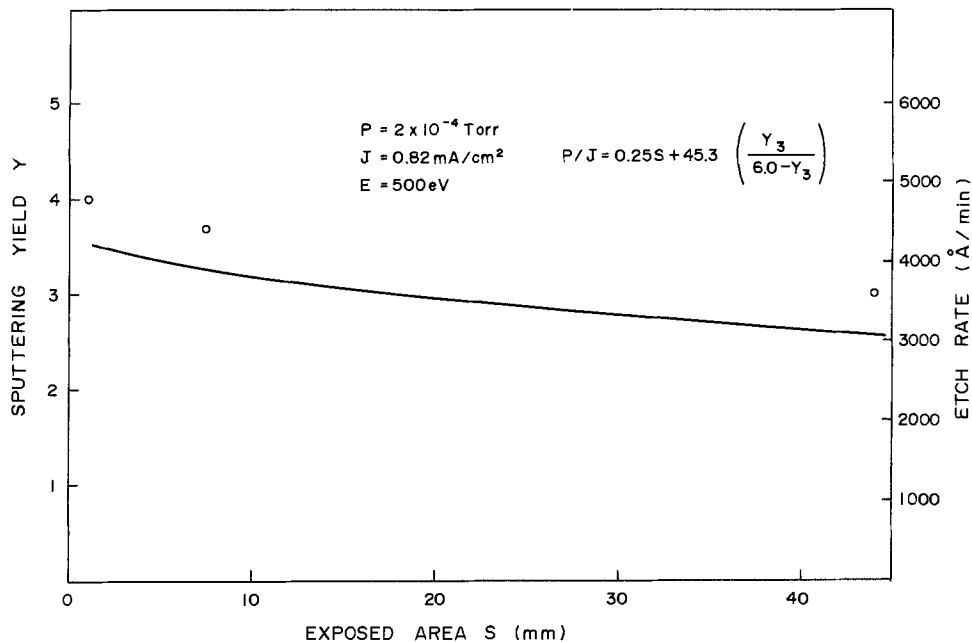


Fig. 2. Etch rate and effective carbon sputtering yield vs. sample area exposed to ion beams.

pressure. Sputtering yields of Au for argon and oxygen bombardments are shown for comparison.

Mass Spectrometric Measurement

For oxygen ion-beam etching, final etch products of PMMA were analyzed by means of a quadrupole mass spectrometer. Oxygen pressure during etching was 5×10^{-5} torr (6.7×10^{-3} Pa). Mass spectra before and during etching are shown in Fig. 4a and 4b. A marked difference in the mass spectra is noticed at CO and H₂ peaks. However, only a small change is observed at CO₂ and H₂O peaks. These results contradict the report that the etch products of stripped photoresist in an oxygen plasma are mainly H₂O, CO₂, and CO (8). This is because, in the present etching system, radical species contribution to the etching is negligibly small (5). Figure 5 shows intensity changes in each species as a function of the acceleration energy. The etch rate for PMMA is also shown for comparison. It was found that, with the increase in etch rate, CO intensity increases, while O₂ intensity decreases.

Definition for Sputtering Yield

Sputtering yield Y_c of carbon atoms in metal-free organic polymers is given by

$$Y_c = \rho V N_c / 60 M J$$

$$= \rho V N_c / 60 N M J \quad [1]$$

where ρ denotes the polymer density (g/cm^3), V the etch rate ($\text{\AA}/\text{min}$), N_c the number of carbon atoms in a monomer unit, N the total number of atoms in a monomer unit, \bar{M} the average atomic weight in a monomer unit (g), M the atomic weight in a monomer unit (g), and J the ion current density (mA/cm^2). Since ρ/\bar{M} is empirically almost constant in metal-free organic polymers, Y_c is expressed by $Y_c \propto V/J \cdot N/N_c$. However, in ion-beam etching, etch rates for organic materials are found to linearly depend on $N/(N_c - N_o)$ factor, not on N/N_c , as reported in the previous paper (5), where N_o denotes the number of oxygen atoms in a monomer unit. This result suggests that the sputtering yield of metal-free organic materials for oxygen bombardment should be considered due to the sputtering yield of "effective" carbon atoms. The term "effective" means subtracting the number of oxygen atoms from that of carbon atoms in polymers. The yield is defined by

$$Y = \rho V (N_c - N_o) / 60 M J \quad [2]$$

Using Eq. [2], effective carbon sputtering yields were calculated from the etch rate data for PMMA, as shown in Fig. 6, where the values of 1.36 and 100 were

used for ρ and M , respectively. Since the current density varies depending on oxygen pressure and acceleration energy, the values are shown in parentheses. The yield increases with increasing oxygen pressure and tends to level off. On the contrary, the yield decreases with increasing acceleration energy under high oxygen-pressure conditions.

Etching Model

Mass spectroscopic analysis suggests that the main reaction for carbon consumption in polymers is expressed by



As shown in Fig. 6, the sputtering yield under high oxygen pressure condition was much higher than 2. However, the maximum sputtering yield of carbon atoms derived from Eq. [3] is 2, provided that the physical sputtering yield is negligibly small. Therefore, Eq. [3] should be modified to closely describe the high sputtering yield. By assuming the contribution of neutral oxygen molecules, a sputtering yield larger than 2 is explained by

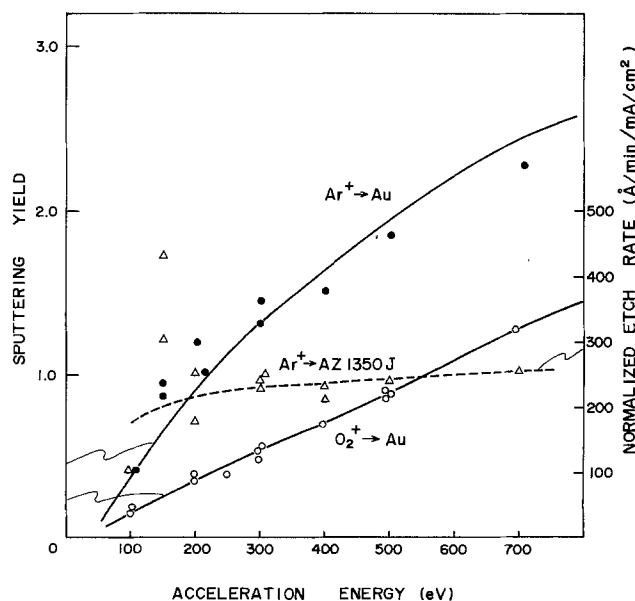
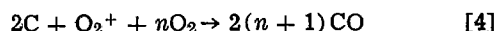


Fig. 3. Acceleration energy dependence of AZ1350J etch rate for argon bombardment.

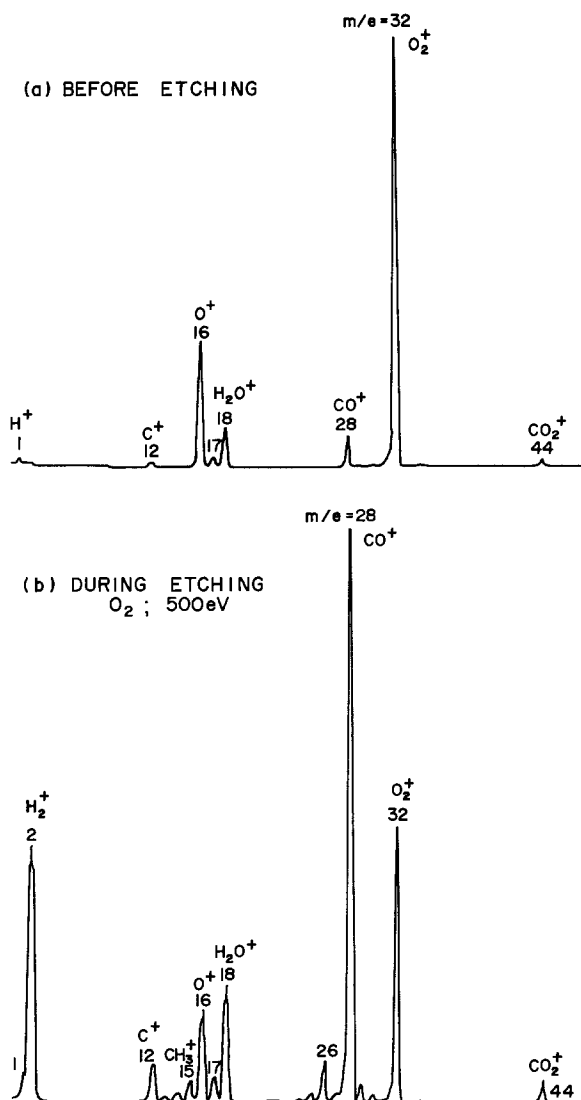


Fig. 4. Mass spectra before and during oxygen ion-beam etching of PMMA.

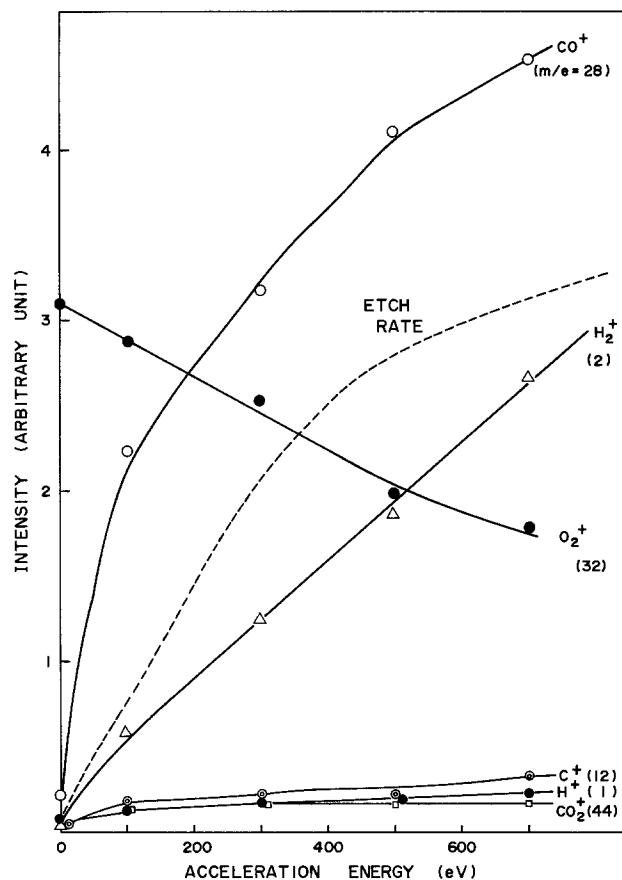


Fig. 5. Mass spectra for CO, H₂, and CO₂ as a function of acceleration energy. Etch rate for PMMA is shown for comparison.

The other possible factor, which explains the increase in sputtering yield under a high oxygen-pressure condition, is the charge transfer: conversion of a fraction of the ion beam into energetic neutrals. This leads to underestimating the current density under high oxygen-pressure conditions. Since the charge transfer increases with increasing oxygen pressure, the sputtering yield apparently increases with increasing oxygen

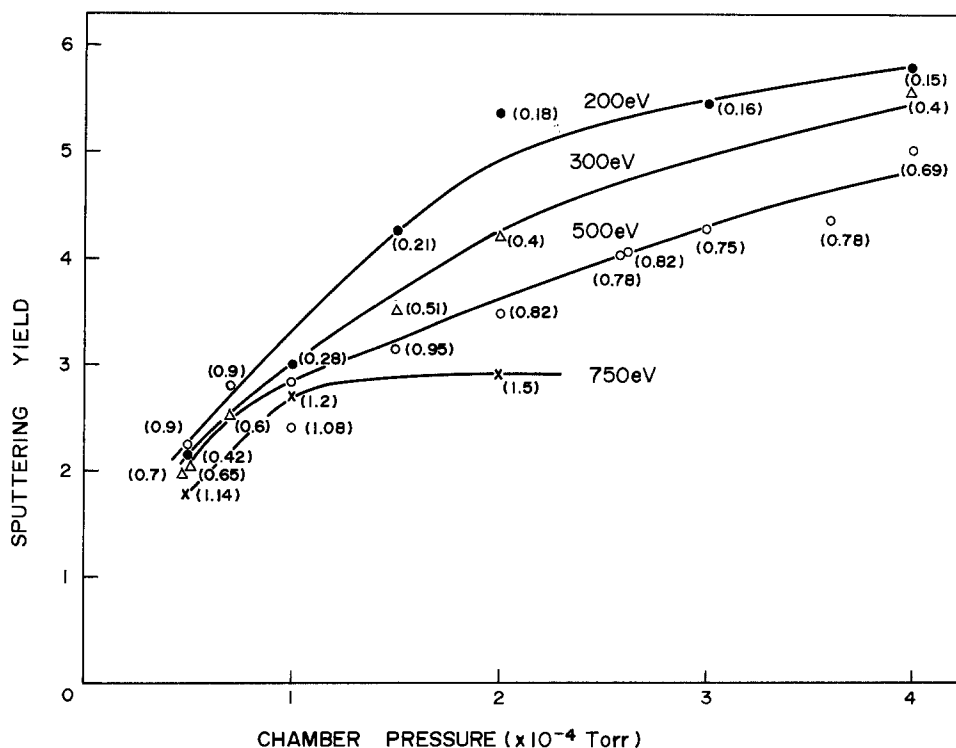


Fig. 6. Effective carbon sputtering yield vs. oxygen pressure at 200, 300, 500, and 750 eV acceleration energies.

pressure. The experimental results ruled out the contribution of charge transfer to the yields. That is, as shown in Fig. 1, the sputtering yield for Au does not increase with oxygen pressure in the range presently examined. According to Mayer *et al.* (4), the net sputtering yield of effective carbon atoms in polymer is expressed by three components.

$$Y = Y_1 + Y_2 + Y_3 \quad [5]$$

The first term, Y_1 , is due to physical sputtering yield. The second term, Y_2 , represents chemical sputtering yield due to the accelerated O_2^+ beams itself. Provided that all the incident O_2 reacts with carbon atoms to form the final product of CO, Y_2 equals 2. The last term, Y_3 , represents the sputtering yield due to the ion-assisted chemical reaction (3, 4, 9) with neutral oxygen molecules. Observation of H_2 as etch products suggests that the O_2 bombardment generates a high density of radical sites in the polymers. Neutral oxygen molecules can adsorb on these sites and react with the carbon atoms to form the volatile product CO. The ion-assisted etch rate is represented by the product of the number of oxygen molecules incident on the polymers and the probability of hitting the activated sites left in the polymers. For an equilibrium state, etch rate V is given by

$$V \propto JY_3 = (P - \beta JSY_3)(1 - KJY_3/DJ) \quad [6]$$

where Y_3 denotes the sputtering yield due to ion-assisted reaction, J the ion current density, S the sample area exposed to oxygen ion beam, and D the number of activated sites generated by the accelerated ion-beam incidence per unit current density, respectively. Constants are α , β , and K . The term βJSY_3 represents the loading effect; dilution of the number of oxygen molecules due to the product formation. Equation [6] is written by

$$P/J = \beta SJY_3 + D/\alpha K \cdot (Y_3/(D - KY_3)) \quad [7]$$

Net sputtering yield Y is given by

$$Y = Y_1 + Y_2 + Y_3(P/J, S) \quad [8]$$

Equation [8] suggests that net sputtering yield should be expressed as a function of P/J ratio. Figure 7 shows the net sputtering yield Y as a function of P/J ratio for acceleration energies, where P and J are expressed in the unit of 10^{-5} torr and mA/cm², respectively. At $P = 0$, sputtering yield $Y_1 + Y_2$ represents the reaction of the beam itself. This inherent sputtering yield is given by the ordinate intercept shown in Fig. 7. The term $Y_1 + Y_2$ equals 1.4, which is mostly independent of the acceleration energy. Using Eq. [8], constants are determined so as to fit the data shown in Fig. 2 and 7. Constants α and β are determined to be 0.13 and 0.25, respectively. The values of D/K are also determined to be 6.0 for 500 eV and 4.9 for 200 eV acceleration energies. Although the number of activated sites D generated by the accelerated ion beam per unit current density, generally, strongly depends on acceleration energy, the result indicates that the energy dependence of D is small.

The value of D is considered to be proportional to the physical sputtering yield Y_1 at a fixed ion-beam incidence. The physical sputtering yield is estimated from the data shown in Fig. 3. The sputtering yield of Au for oxygen bombardment is about half as large as that for argon bombardment. This represents the difference in physical sputtering yield, since Au does not chemically react with oxygen. Therefore, the physical sputtering yield for carbon atoms during oxygen bombardment is estimated to also be half as large as that for argon. From the result, Y_1 is estimated to be about 0.16 at 500 eV acceleration energy, using Eq. [2]. This physical sputtering yield shows little dependence on acceleration energies, at least at values higher than 200 eV. This coincides with the estimate that D differs by only 20% between 200 and 500 eV acceleration energies. The fact that the physical sputtering yield for carbon atoms in polymers has little acceleration energy dependence may be explained as follows. For a target having atomic arrays, the general overall collision process is similar to a diffusion process of mobile atoms, where some of the atoms reach the surface with sufficient energy to collide with and liber-

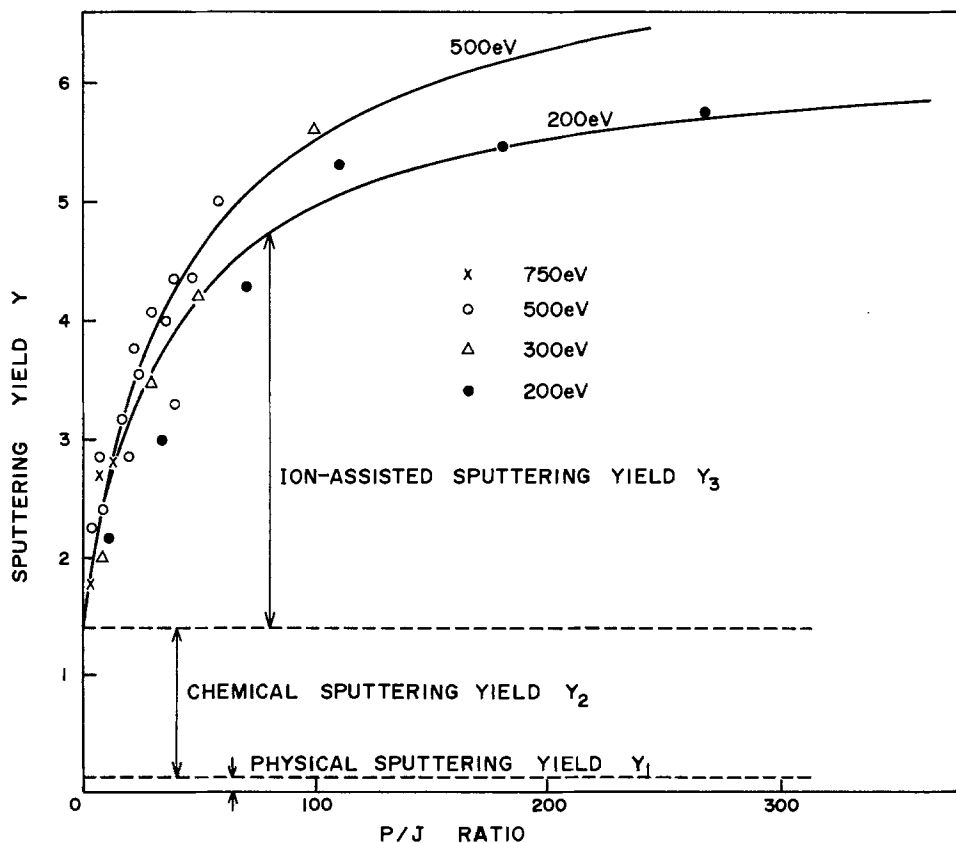


Fig. 7. Calculated sputtering yield vs. oxygen pressure. Sputtering yield is made up of three components; physical sputtering yield Y_1 , chemical sputtering yield Y_2 , and ion-assisted chemical sputtering yield Y_3 .

ate surface atoms. However, since the polymer network is basically two dimensional, momentum transfer process between target atoms and accelerated ions may be terminated only in neighboring polymer chains. Ions with high acceleration energies penetrate the polymers, and surface atoms cannot effectively be liberated by incoming ions at high acceleration energy.

The theoretically fitted curves are described for 500 and/or 200 eV acceleration energies in Fig. 2 and 7. Chemical sputtering yield Y_2 is estimated to be about 1.24. This means that about 38% of the incoming O_2 does not react with and is recoiled from the surface. The increase in sputtering yield with decreasing acceleration energy is attributed to the decrease in current density. This analysis would be useful to describe the observed phenomena and predict the etching characteristics in ion etching with reactive beams.

Conclusion

Oxygen ion-beam etching of organic polymers has been discussed from the view point of "effective" carbon sputtering yield. Mass spectrometric analysis indicates that the final products during etching are mainly H_2 and CO. By assuming the ion-assisted chemical reaction of carbon atoms with neutral oxygen molecules, oxygen pressure, and acceleration energy dependences of sputtering yield are analytically explained. Increase in sputtering yield with decreasing acceleration energy is attributed to the relative increase in an oxygen pressure to current density ratio.

Acknowledgments

The authors would like to thank Mr. K. Matsumi and Dr. K. Yoshimi for encouragement. The authors also would like to thank H. Tsuge and Y. Kato for fruitful discussions.

Manuscript submitted Sept. 12, 1983; revised manuscript received Jan. 28, 1984.

NEC Corporation assisted in meeting the publication costs of this article.

REFERENCES

1. J. M. Moran and D. Maydan, *Bell System Tech. J.*, **58**, 1027 (1979).
2. T. M. Mayer, R. A. Barker, and L. J. Whitman, *J. Vac. Sci. Technol.*, **18**, 349 (1981).
3. T. M. Mayer and R. A. Barker, *This Journal*, **129**, 585 (1982).
4. T. M. Mayer and R. A. Barker, *J. Vac. Sci. Technol.*, **21**, 757 (1982).
5. H. Gokan, M. Itoh, and S. Esho, *ibid.*, **B2**, 34 (1984).
6. H. Gokan, S. Esho, and Y. Ohnishi, *This Journal*, **130**, 143 (1983).
7. J. M. E. Harper, J. J. Cuomo, P. A. Leary, G. M. Summa, H. R. Kaufman, and F. J. Bresnock, *ibid.*, **128**, 1077 (1981).
8. R. F. Reichelderfer, J. M. Welty, and J. F. Battey, *ibid.*, **124**, 1927 (1977).
9. J. W. Coburn and Harold F. Winters, *J. Vac. Sci. Technol.*, **16**, 391 (1979).

Interaction Between Water and Scaled CMOS FET's with Phosphosilicate Glass Passivation Films

M. Noyori and Y. Nakata

Matsushita Electric Industrial Company, Limited, Central Research Laboratory, Moriguchi, Osaka 570, Japan

ABSTRACT

A phosphosilicate glass (PSG) passivation film (4 weight percent phosphorus) was deposited onto complementary MOS (CMOS) FET's by chemical vapor deposition. After exposure to water vapor (85°C/85% RH), the CMOS FET's were tested at a high temperature bias of 150°C. It was found that a threshold voltage shift or transconductance (GM) degradation occurs pronouncedly in p-channel FET's under gate negative-bias stress, compared with in n-channel FET's under gate positive stress. Furthermore, it was found that there is a critical exposure time at 85°C/85% RH to enhance the shift and degradation. Finally, it was confirmed that the shift and degradation characteristics observed in this study are similar to instabilities due to gate negative bias in hydrogen ambient atmosphere.

Chemically deposited phosphosilicate glass (PSG) is widely used as a top passivation film in MOS LSI's. The PSG film reacts easily with water. Interaction mechanisms between water and the PSG film have been studied by a number of researchers (1, 2). However, as far as we know, interactions between water and MOS FET's with the PSG film have not been studied sufficiently, especially in regard to scaled MOS FET's (3), although the effects of water involved in the gate oxide of n-channel MOS FET's on electrical instabilities have been studied by some researchers (4).

However, scaled CMOS LSI's with the PSG passivation film have been developed and are widely used. The question of reliability problems due to moisture on scaled CMOS LSI's has become extremely important. This is because a small amount of water can induce more severe degradation in scaled devices than in conventionally designed devices.

This paper describes electrical instabilities in scaled CMOS FET's with the PSG passivation film, which was exposed to water vapor, under high temperature bias stress.

Experimental

Device preparation.—p- and n-channel polysilicon gate FET's were tested in this study. In this CMOS device, an n-type (100), 2-3 Ω cm substrate was used, and an n-channel FET was formed in a p-well. The gate length was typically 3 μ m, and additional FET's with a gate length of between 2 and 20 μ m, and a gate oxide thickness of 65 nm, were fabricated in order to investigate the gate-length dependence of electrical instabilities. Phosphorus was doped into the polysilicon gate by $POCl_3$ diffusion in both p- and n-channel FET's. The source and drain were formed by implantation of arsenic or boron ion followed by heat-treatment. After the source and drain implantation, CVD SiO_2 film (300 nm thickness) was deposited onto the substrate at 430°C using a mixed gas composed of SiH_4 and O_2 . The CVD SiO_2 film was densified during heat-treatment at 900°C for 40 min in nitrogen gas. Following the aluminum metallization, the PSG passivation film was chemically deposited onto the substrate using a mixed gas composed of SiH_4 , PH_3 , and O_2 with the substrate at 430°C. The deposition rate was about

100 nm/min. The thickness was 0.8 μm . The phosphorus concentration in the PSG film was typically 4 weight percent (w/o).

Test procedure.—First, devices with the PSG film mounted in nonsealed ceramic packages were exposed to water vapor (85°C/85% RH) for 0–336h. After that, the devices were sealed with metal lids in nitrogen gas at a maximum temperature of 350°C for 10 min. Subsequently, the devices were tested at 150°C under the bias conditions ('1' in Fig. 1). The gate negative and positive bias stresses were applied to p- and n-channel FET's, respectively. These gate bias stresses are also applied to the devices under practical operating conditions.

Measured parameters.—The threshold voltage (V_t) and transconductance (GM) in the nonsaturated region were measured, as shown in Fig. 2, with respect to the p-channel FET. V_t and GM were calculated from I-V characteristics. V_t was defined as the gate voltage (V_g), at the drain current (I_d) of zero, extrapolated from two points ($I_d = 3$ and 6 μA); GM was defined as the value of the slope obtained from the two points. Devices were measured at room temperature.

Experimental Results

p-Channel vs. n-channel instabilities.— V_t shift (ΔV_t) and GM degradation (GM/GM_0) in p- and n-channel FET's are shown in Fig. 1. The devices were exposed

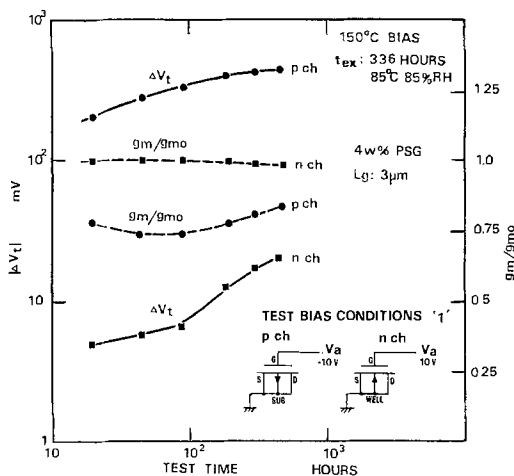


Fig. 1. Time dependence of V_t shift and GM degradation under bias condition '1' at 150°C on p- and n-channel FET's exposed to 85°C/85% RH for 336h. GM_0 means the initial value of GM (after the exposure).

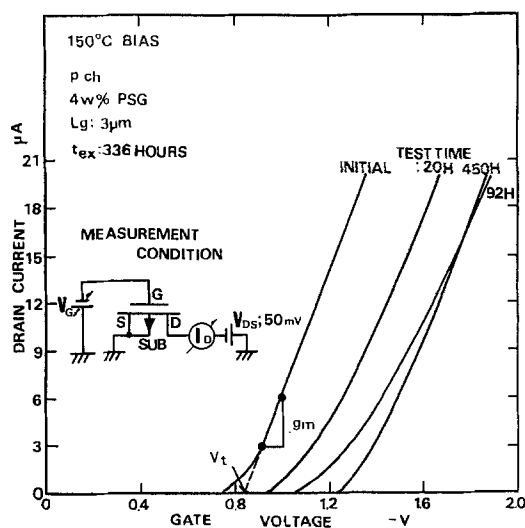


Fig. 2. Typical I-V characteristics of the p-channel FET exposed to 85°C/85% RH for 336h under bias stress '1' at 150°C.

to 85°C/85% RH for an exposure time (t_{ex}) of 336h before the test. It was found that V_t shift and GM degradation in p-channel FET's are much more pronounced than those in n-channel FET's. The V_t shift was towards negative and positive directions in the p- and n-channel FET's, respectively. On p-channel FET's, while $|\Delta V_t|$ increases and saturates with test time, GM degrades relatively early, after which it shows some recovery. Typical I-V characteristics under bias stress are shown in Fig. 2.

Gate length dependence of the instabilities.— V_t shift and GM degradation strongly depend on the gate length or channel length of the FET's. The gate-length dependences of V_t shift are shown in Fig. 3. It was found that $|\Delta V_t|$ increases with the decrease of the gate length in both p- and n-channel FET's. The curves of devices with a silicon nitride passivation film (SIN) shown in Fig. 3 will be discussed below. These results indicate that water-induced instabilities will become more severe with the downscaling of devices, especially in p-channel devices.

Exposure time dependence of the instabilities.—p-Channel FET's were exposed to 85°C/85% RH for several different lengths of exposure time (t_{ex}) for 0 to 336h. Neither ΔV_t nor GM degradation was observed under exposure to water vapor without bias stress. V_t shifts under bias stress are shown in Fig. 4. $|\Delta V_t|$ strongly depends on t_{ex} , that is, $|\Delta V_t|$ increases with the increase of t_{ex} . The relation between $|\Delta V_t|$ at a test time of 500h is shown in Fig. 5. It was found that there is a critical exposure time ($t_{\text{ex,cr1}}$) to enhance additional V_t shift. The time was found to be about 11h. The characteristics of 8 w/o PSG will be discussed later.

Analysis and Discussions

Mechanism.—In order to make clear that the V_t shift and GM degradation shown in Fig. 1 or the gate-length dependence shown in Fig. 3 were caused by water diffusion through the PSG film, the p-channel FET's using a plasma-enhanced silicon nitride (SIN) passivation film (0.8 μm thick) instead of the PSG film were tested after exposure to 85°C/85% RH for 336h. The

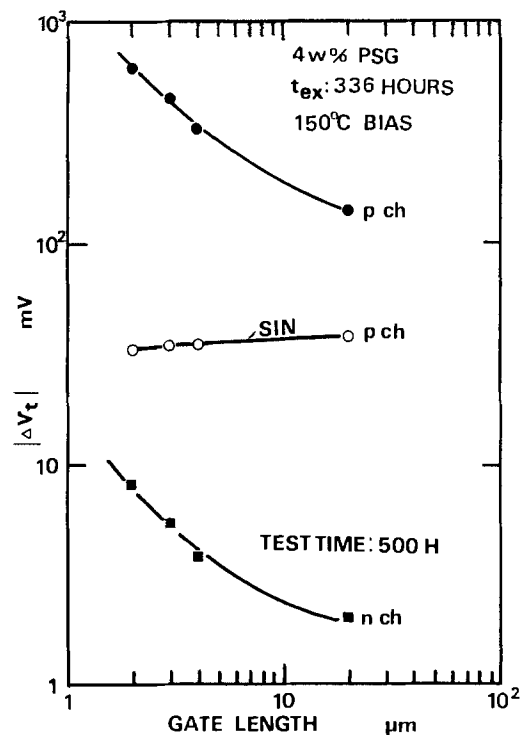


Fig. 3. The gate-length dependences of ΔV_t at 500h under bias stress '1' on p- and n-channel FET's with the PSG film or silicon nitride (SIN) film exposed to 85°C/85% RH for 336h.

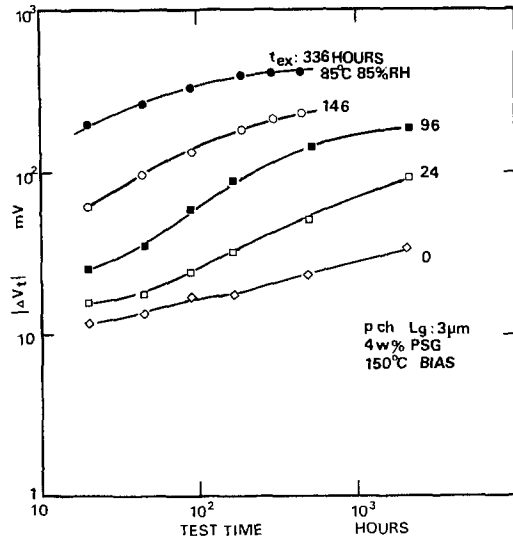


Fig. 4. Time dependences of V_t shift under bias stress 'I' at 150°C on p-channel FET's exposed to $85^\circ\text{C}/85\% \text{RH}$ for t_{ex} between 0 and 336h.

values of $|\Delta V_t|$ of the p-channel FET's with the silicon nitride film were much less than those of the PSG film, and the devices did not show the gate-length dependence. The test result on V_t shift is shown in Fig. 3. These discrepancies probably result from the difference between the silicon nitride and the PSG films in their protective ability against water attack. In our previous study (5), it was found that the impurity involved in plastic encapsulation, which probably contains moisture, can diffuse into the gate oxide or Si/SiO₂ interface not through the polysilicon gate but through the periphery of the polysilicon gate under high temperature bias stress. Furthermore, it was found that the gate length dependence of the V_t shift results from the impurity diffusion. Therefore, the gate-length dependence found in this study can also probably be explained by the diffusion-path model that water absorbed in the PSG film, resulting from exposure to water vapor, should diffuse to the interface through the periphery of the gate.

Judging from I-V characteristics shown in Fig. 2, not only fixed positive charges but also surface states were generated in the p-channel FET's under the bias stress because I-V characteristics were found to shift along the voltage axis not in a parallel mode; that is, the slope of I-V characteristic (GM) was found to

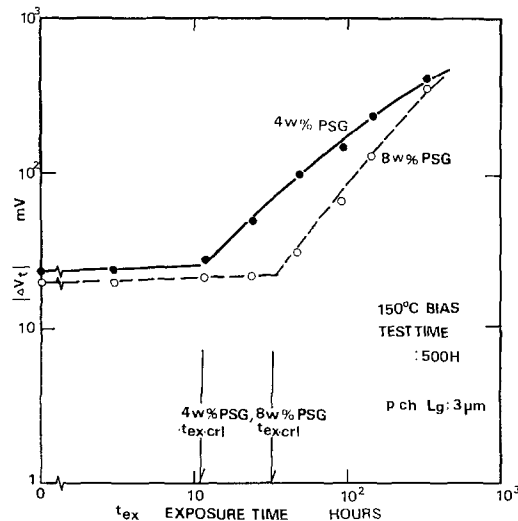
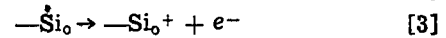
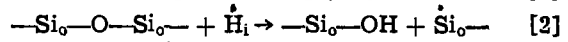
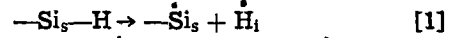


Fig. 5. Exposure time (t_{ex}) dependences of V_t shift at 500h under bias stress 'I' at 150°C , on p-channel FET's with 4 w/o PSG and 8 w/o PSG films.

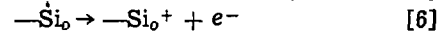
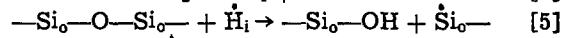
change. Two kinds of instabilities induced by the gate negative bias stress have been reported. One is the "slow trapping" (6, 7), and the other is the "secondary slow trapping" (3, 8). In these instability mechanisms, positive fixed charges and surface states are generated at the Si/SiO₂ interface, as observed in this study. Therefore, the instability mechanism observed here is suspected to be similar to these mechanisms.

The instability induced by the slow trapping can be observed not only in MOS FET's with the PSG film, but also in FET's with the silicon-nitride film. The V_t shift of FET's with the silicon nitride film shown in Fig. 3 is considered to be caused by this mechanism. This shift does not depend on the gate length because the origin of this instability is considered to be the defect of the interface related to a hydrogen-silicon bond. Jeppson *et al.* (6) proposed the following reactions

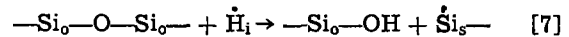
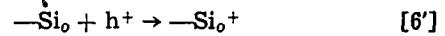


where Si_s means a silicon atom at the surface bonded to other silicon atoms, while Si_o means a silicon atom in the oxide. "." means a dangling bond, and $\dot{\text{Si}}_s$ is assumed to form a surface state. H_i is an interstitial hydrogen.

The instability induced by the secondary slow trapping can be observed in the device with the PSG film, and this instability showed a slight gate-length dependence (5). The origin of this instability is considered to be moisture (or hydrogen). We proposed the following reactions [4]-[7], in the previous study (8)



or



Concerning the instability mechanism observed in this study, it is conceivable that reactions similar to the secondary slow trapping occur at the interface. The major difference of the situation between this mechanism and the secondary slow trapping is probably the amount of water reacted with the interface. That is, the amount of the water in this instability, especially on the device exposed to water vapor for long periods, is much more than the amount of water in the secondary slow trapping. As a result of this difference, the V_t shift or GM degradation in this study is much more pronounced than that in the secondary slow trapping.

ΔV_t and GM degradation increase with the increase of t_{ex} . $|\Delta V_t|$ vs. GM/GM₀ characteristics are shown in Fig. 6, setting t_{ex} as a parameter. The characteristics of the device marked with "H₂" in Fig. 6 will be discussed below. It was found that the characteristics are independent of the value of t_{ex} before GM recoveries, and that the recovery characteristics strongly depend on t_{ex} . These results indicate that the ratio of fixed charge/surface-state formation before the GM recovery does not depend on the amount of water initially absorbed in the PSG film.

Critical exposure time.—In order to analyze the origin of the critical exposure time ($t_{\text{ex,cr1}}$), the reaction between the PSG film and water was investigated. It should be noted that a little ΔV_t occurs in the device exposed for the exposure time below $t_{\text{ex,cr1}}$, as shown in Fig. 5. However, the value of $|\Delta V_t|$ is much less than that of the device exposed for a longer time than $t_{\text{ex,cr1}}$.

PSG film (4 w/o phosphorus, 0.8 μm thick) deposited on a silicon substrate was exposed to $85^\circ\text{C}/85\% \text{RH}$ for 240h. After the exposure, an infrared spectrum was measured by a double-beam infrared spectrometer,

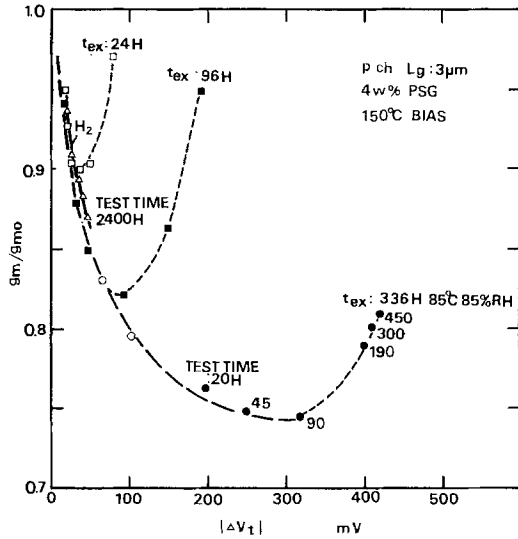
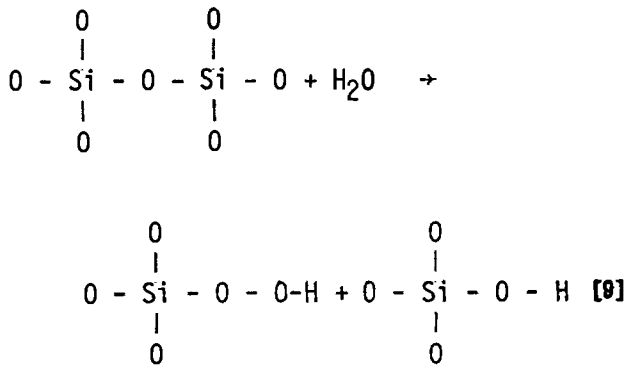
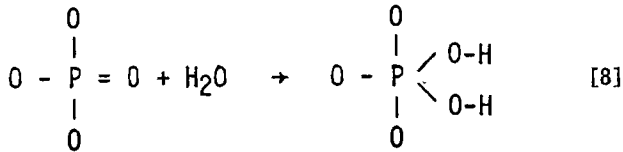


Fig. 6. ΔV_t vs. G_m/G_{m0} characteristics of p-channel FET's exposed to 85°C/85% RH for t_{ex} between 24 and 336h, under bias stress '1' at 150°C. In respect to the characteristic curve on t_{ex} of 336h, 20, 45, and 90h, etc., mean test time under bias stress '1' at 150°C. The curve marked with "H₂" shows the characteristic curve on the p-channel FET with the PSG film, which was mounted in a ceramic package filled with 10 v/o hydrogen gas and was not exposed to water vapor, under bias stress '1' at 150°C for 2400h.

and compared with the spectrum of the film as grown. A typical infrared spectrum is shown in Fig. 7. In the spectrum of the exposed PSG film, the intensity of the peak at 1330 cm^{-1} corresponding to P = O bond decreases. Two new absorption peaks emerge at 930 and 3650 cm^{-1} , which correspond to Si—O—H and H—O—H groups, respectively. From these results, which agree well with the spectrum observed by Levin (1), the interaction between water and the PSG film can be described by the following reactions [8] and [9], in addition, to being physically absorbed in the PSG film.



Furthermore, triple layers composed of undoped silicate glass (USG) (20 nm thick), PSG (30 nm), and USG (20 nm) were formed on a silicon substrate with thermally grown SiO₂. The USG films were formed by the chemical vapor deposition method. The PSG film was formed by the same conditions mentioned previously, except for the thickness and deposition rate. The silicate glass layer was exposed to 85°C/85% RH for either 1 or 17h. After storage in a desiccator at room temperature for 10 days, the profiles of

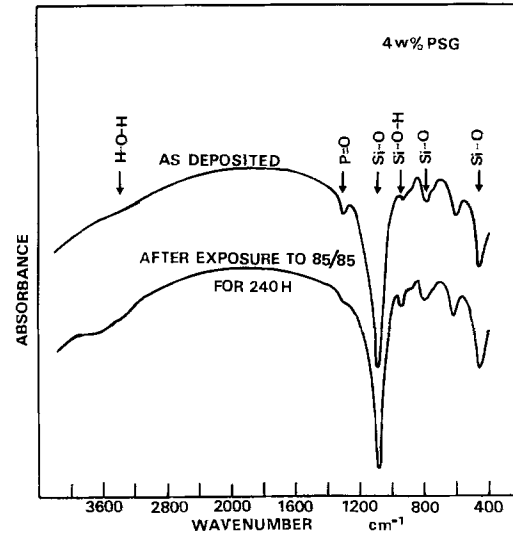


Fig. 7. The infrared spectrum of the PSG film exposed to 85°C/85% RH for 240h, compared with one of the PSG film as grown.

hydroxyl, hydrogen, and phosphorus concentrations were measured by secondary ion mass spectrometry (SIMS). The PSG film in this experiment is much thinner than that of the film in other experiments. This results from the prevention of charging up in the film under the SIMS measurement. The measurement results are shown in Fig. 8. It was found that hydroxyl and hydrogen concentrations in the PSG film are greater than those in the USG films. These profiles indicate that water diffused into the PSG film can move less easily than water diffused into the USG film.

From these two experiments using the infrared spectrometer and SIMS, it is speculated that diffused water bonded to phosphorus is fixed more firmly than diffused water bonded to Si or absorbed physically on an SiO₂ surface. In the case of a relatively small amount of water vapor diffusing into the PSG film, the former type of water is probably dominant. In the case of a large amount of water vapor, however, the latter type of water cannot be neglected. The critical exposure time is considered to result from the types of water diffused into the PSG film. If this assumption

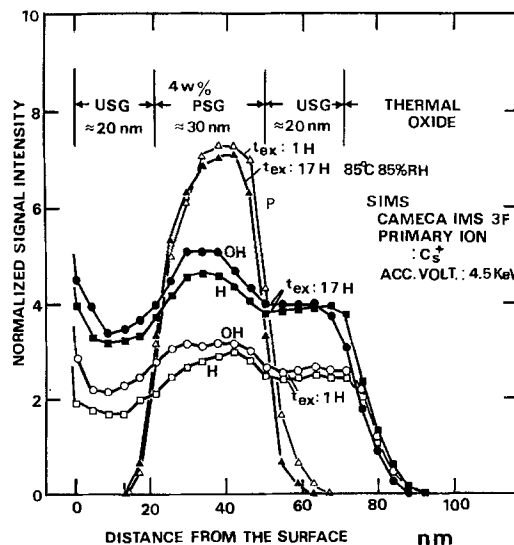


Fig. 8. Phosphorus, hydrogen, and hydroxyl concentrations in the triple layers composed of USG/PSG/USG exposed to 85°C/85% RH for either 1 or 17h, measured by SIMS. Signal intensities of phosphorus, hydrogen, and hydroxyl were normalized by signal intensity of silicon ions.

is right, the critical exposure time should depend on the phosphorus concentration in the PSG film. In order to confirm the assumption, the p-channel FET's with 8 w/o phosphorus PSG film were tested under bias stress, after exposure to 85°C/85% RH for several kinds of t_{ex} . The test results are shown in Fig. 5. It was found that $t_{ex,cr1}$ of the 8 w/o PSG film is much longer than that of the 4 w/o PSG film.

Instabilities under bias stress in hydrogen ambient.— In the instability due to the exposure to water vapor, hydrogen probably plays an important role, as expected from reactions [4]-[17]. In order to confirm the reactions, p- and n-channel FET's with the PSG film were mounted in ceramic packages filled with a mixed gas composed of 10 volume percent (v/o) hydrogen and 90 v/o nitrogen. The FET's were tested at 150°C under the bias stress ('1' and '2' shown in Fig. 9). Test devices and test conditions are shown in Table I. Test results are shown in Fig. 9. It was found that ΔV_t in p-channel FET's (1p and 3p) with the shorter channel filled with 10 v/o H_2 occur more pronouncedly than in the p-channel FET's (2p and 4p) filled with 100% N_2 , under both bias stresses. However, a significant difference of ΔV_t was not observed in n-channel FET's (1n to 4n).

Furthermore, ΔV_t in a p-channel FET is more pronounced under bias '2' (3p) where a channel current flows than under bias '1' (1p), where no channel current flows. This result suggests that holes play important roles in the reaction at the interface in the p-channel FET's, as well as in the n-channel FET's where Fair *et al.* reported that V_t shifts were induced by the reaction between hydrogen and hole under a certain bias stress (9). At bias '1,' effective holes contributing to the reaction will be furnished only by thermal excitation; however, in bias '2,' holes will be prepared by electrical excitation in addition to the thermal one, especially in the short-channel FET's. This bias-stress dependence of ΔV_t was also found in the p-channel FET's (5p and 6p) exposed to water vapor, as shown in Fig. 9.

V_t shift vs. GM/GM₀ characteristics on the p-channel FET filled with 10% H_2 are shown in Fig. 6. It was found that this characteristic is similar to characteristics on the p-channel FET exposed to water vapor. However, significant recovery characteristics of GM was not observed in the device filled with 10 v/o H_2 , in spite of the bias stress for relatively long hours of testing (2000h). The reason for this is still unclear. There are two kinds of possibilities. One is that the test time is not long enough for the GM recovery to occur. The other is that GM recovery is induced by interaction between hydroxyl and the defects related to induced surface states, as described in the previous study (8). As there is no source of hydroxyl ions in the device filled with 10 v/o H_2 , GM recovery should not occur.

Summary and Conclusions

The instabilities under high temperature bias stress for scaled p- and n-channel FET's with the PSG passivation film exposed to water vapor have been in-

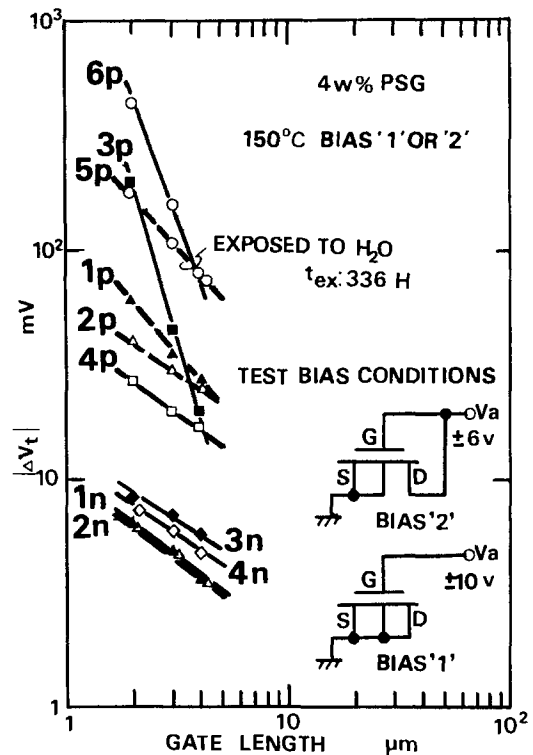


Fig. 9. The gate-length dependence of ΔV_t on p- and n-channel FET's filled with 10 v/o hydrogen or with 100 v/o nitrogen at bias conditions '1' and '2' compared with p-channel FET's exposed to 85°C/85% RH at the two bias conditions. Meanings of labels are shown in Table I.

vestigated, and, as a result, it can be concluded that:

1. The V_t shift and GM degradation occur much more pronouncedly in p-channel FET's under gate negative bias than in n-channel FET's under gate positive bias.
2. The V_t shift in the p-channel FET's strongly depends on the gate length.
3. The V_t shift in the p-channel FET's under high temperature bias stress strongly depends on the exposure time to water vapor. Furthermore, there is a critical exposure time to water vapor to enhance additional V_t shift.
4. The critical exposure time, which depends on phosphorus concentration in the PSG film, probably results from interaction between phosphorus and water in the PSG film.
5. Instabilities under high temperature bias stress after the exposure to water vapor are similar to those under high temperature bias stress in hydrogen ambient, for example, on the gate length dependence of V_t shift, characteristics of ΔV_t vs. GM/GM₀, the differences of ΔV_t and GM degradation between p- and n-channel FET's, and applied bias-stress dependence of V_t shift.

Acknowledgments

The authors are grateful to S. Horiuchi and T. Ishihara for their helpful comments and discussion of this

Table I. Test devices and test conditions on the experimental results shown in Fig. 9

Label	p/n Channel	Gas	Exposure to 85/85 before sealing	Bias condition	Test hours
1p	p	10% H_2 + 90% N_2	no	'1'	500
2p	p	100% N_2	no	'1'	500
3p	p	10% H_2 + 90% N_2	no	'2'	500
4p	p	100% N_2	no	'2'	500
5p	p	100% N_2	yes	'1'	18
6p	p	100% N_2	yes	'2'	18
1n	n	10% H_2 + 90% N_2	no	'1'	500
2n	n	100% N_2	no	'1'	500
3n	n	10% H_2 + 90% N_2	no	'2'	500
4n	n	100% N_2	no	'2'	500

work, and to K. Kirihara for her testing and measurement of the devices, and to T. Tsukamoto and K. Kamikawaji for the SIMS and infrared spectrometer measurements, respectively.

Manuscript submitted Oct. 11, 1983; revised manuscript received Jan. 24, 1984.

Matsushita Electric Industrial Company, Limited assisted in meeting the publication costs of this article.

REFERENCES

1. R. M. Levin, *This Journal*, **129**, 1765 (1982).
2. N. Nagashima, H. Suzuki, K. Tanaka, and S. Nishida, *ibid.*, **121**, 434 (1974).
3. M. Noyori, H. Higuchi, and T. Ishihara, in "Proceedings of 20th Annual Reliability Physics Symposium," p. 113, San Diego, CA (1982).
4. F. J. Feigl, D. R. Young, D. J. DiMaria, S. Lai, and J. Calise, *J. Appl. Phys.*, **52**, 5665 (1981).
5. M. Noyori and Y. Nakata, in "Proceedings of the 21st Annual Reliability Physics Symposium," p. 60, Phoenix, AZ (1983).
6. K. O. Jeppson and C. M. Svensson, *J. Appl. Phys.*, **48**, 2004 (1977).
7. A. K. Sinha and T. E. Smith, *This Journal*, **125**, 743 (1978).
8. M. Noyori, *IEEE Trans. Reliab.*, **r-32**, 323 (1983).
9. R. B. Fair and R. C. Sun, *IEEE Trans. Electron. Devices*, **ed-28**, 83 (1981).

Preparation and Characterization of Plasma-Deposited Silicon Nitride

C. Blaauw

Bell-Northern Research, Ottawa, Ontario, Canada K1Y 4H7

ABSTRACT

This paper reports on the preparation and characterization of films of plasma silicon nitride, deposited on Si substrates from SiH_4 , NH_3 , and Ar. It is shown that the deposition rate and uniformity of the films are strongly affected by the cleaning and loading of the reactor. Pinhole densities are reduced by increase of both the film thickness and the deposition temperature. Several parameters were systematically varied, including the deposition temperature (20°-500°C), RF power (10-300W), chamber pressure (0.5-1.4 torr), and gas flow rates. At 500°C specular films are grown with the following characteristics: refractive index 1.9-2.1, pinhole density 5 cm^{-2} at $1.0 \mu\text{m}$ thickness, 100 Å/min etch rate in buffered HF, and good stability to annealing. Relationships between deposition parameters and film characteristics, including deposition rate, etch rate, and index of refraction, are discussed in terms of current understanding of the deposition process. An explanation is offered for differences in the effect of RF power level on deposition rates observed by other investigators.

Silicon nitride is a hard, chemically inert, dielectric material which forms an excellent diffusion barrier with respect to H_2O , Na, and many other ionic species. It is used extensively in semiconductor technology for the fabrication of thin films for interlayer insulation, device passivation, and mechanical protection. The use of plasma-enhanced chemical vapor deposition (as compared to conventional CVD) has the advantage that the substrate can be held at a relatively low temperature (200°-400°C) during film deposition. It can therefore be used in applications where previous device fabrication steps do not allow higher processing temperatures. It has been shown that silicon nitride films deposited by this technique can provide good adhesion, have good crack resistance, and provide good step coverage. In this paper, results are reported on the preparation and characterization of films of plasma silicon nitride deposited on Si substrates from mixtures of SiH_4 , NH_3 , and Ar.

Experimental

A small, research-oriented plasma reactor, the Tegal P1 100, was used for this work. A schematic diagram of the reaction chamber is shown in Fig. 1. Chamber and electrode assembly are made of aluminum. The gas mixture enters the chamber through a matrix of small holes in the (hollow) upper electrode. The lower electrode contains the substrate and is electrically floating. The electrode area and the distance between the electrodes are $15 \times 15 \text{ cm}$ and 2.5 cm, respectively. The chamber and electrode assembly were cleaned in an RF plasma, using a CF_4 -5% O_2 gas mixture.

The substrates used were polished, single-crystal silicon wafers. For most experiments wafers of 10 cm diam were used, located in a depression on a thin Al

sample holder placed on the electrode. For some runs, wafers of 5 cm diam were used, placed off-center against a ridge at the back of the electrode. The wafers were cleaned prior to deposition using the RCA procedure (1).

Pinhole detection was done electrochemically, using a Gasonics pinhole detector. The wafers are placed in a metal disk (cathode) immersed in methanol. A ring anode, also immersed in the methanol, is held above the wafer, at an applied potential of 40V. At pinhole locations, the substrate is exposed to the methanol, hydrogen evolution takes place, and a stream of bubbles is observed. A Rudolph automatic ellipsometer using a He-Ne laser ($\lambda = 6328\text{\AA}$) was used to measure film thickness and index of refraction. Etch rate measurements were done using buffered HF (NH_4F : HF = 13:2) at 25°C.

Results and Discussions

Film integrity.—The topography of the films was investigated by scanning electron microscopy. Specular films were obtained up to $1 \mu\text{m}$ thickness. At larger thicknesses, a light surface roughness was sometimes observed. The effect of gas composition, RF power, film thickness, and substrate temperature on the pinhole density was investigated. Results are shown in Fig. 2 and 3. The pinhole density was not affected by film composition or RF power density. However, a decrease of the pinhole density with increasing film thickness and deposition temperature was observed.

Nonuniformity of the deposition.—The effect of deposition parameters on the uniformity of the deposition was investigated. It was found that for depositions using SiH_4 -rich gas mixtures the deposition rate decreased with increasing radial distance, whereas for SiH_4 -poor gas compositions the opposite occurred. Re-

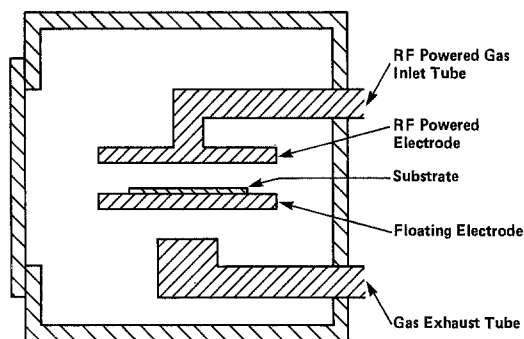


Fig. 1. Diagram of the electrode and gas inlet and exhaust assembly of the Tegal PI 100 plasma reactor.

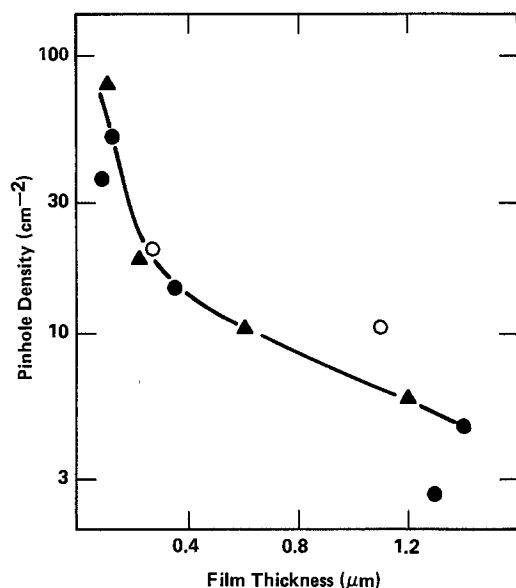


Fig. 2. Effect of film thickness and gas composition on the pinhole density of films of plasma-SiN_x on Si. Deposition conditions: ● Ar = 200 sccm, SiH₄ = 5 sccm, NH₃ = 44 sccm; ○ Ar = 200 sccm, SiH₄ = 10 sccm, NH₃ = 40 sccm; ▲ Ar = 200 sccm, SiH₄ = 17 sccm, NH₃ = 33 sccm.

sults for two depositions are shown in Fig. 4. Several factors are thought to affect the deposition uniformity. Two of these are the radial variation in gas composition due to the differing depletion rates of SiH₄ and NH₃ during the deposition, and the uniform gas flow through the upper electrode, which would give a radial velocity proportional to the radial distance. However, it is not clear how these factors would lead to a radial nonuniformity profile depending on the SiH₄/NH₃ ratio.

A third factor affecting deposition rates is the accumulative amount of deposition following a plasma cleaning of the chamber. Figure 5 shows deposition rate profiles, obtained for a series of consecutive 4 min depositions on 5 cm diam wafers located off-center on the electrode following a plasma cleaning. The deposition-rate profile varied considerably during the first several minutes of deposition; this was followed by a gradual decrease of the deposition rate, eventually reaching a plateau after about 20 min of deposition. When a 10 cm diam wafer was substituted near the end of this series, a deposition profile similar to that obtained during the first deposition was obtained, but at a lower average rate. These results indicate a general decrease in deposition rate as the electrodes are covered with a layer of silicon nitride and that local loading effects are also important. It is thought that the plasma may be affected by the changing surface properties of the electrodes and substrates, as

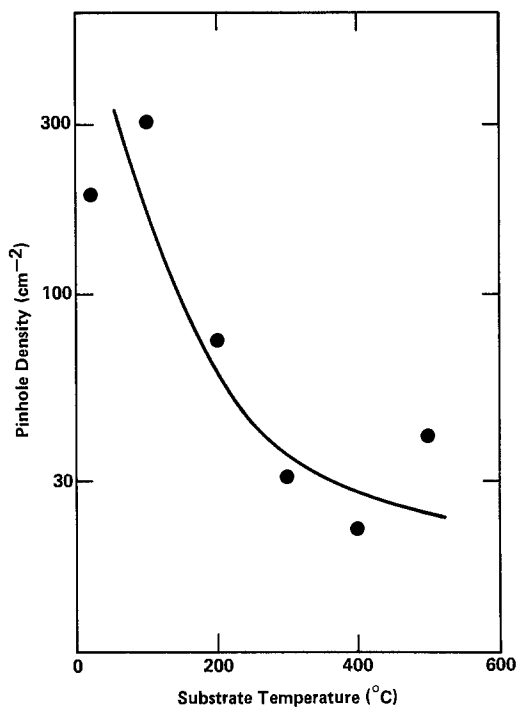


Fig. 3. Effect of substrate temperature on the pinhole density of 1000 Å thick films of plasma-SiN_x on Si. Deposition conditions: RF power 150W, chamber pressure 0.9 torr. Gas flow rates: Ar = 200 sccm, SiH₄ = 6 sccm, NH₃ = 44 sccm.

they are covered by an insulating layer of dielectric film.

The effect of substrate temperature.—In Fig. 6 the effect of substrate temperature on the index of refraction, the deposition rate, and the etch rate is shown. The significant decrease in etch rate with increasing substrate temperature has been observed by other investigators (2, 3), and is thought to be due to a decrease in hydrogen content of films deposited at higher temperatures. Work done by Chow *et al.* (4) for films of plasma silicon nitride deposited in a number of reactors has shown the etch rate in buffered HF to be very sensitive to hydrogen content and that hydrogen content decreases with increasing deposition temperature. This was also observed in other work (5). From the report of Chow *et al.* (4), we deduce that the hydrogen content in our films decreased from ≈40% at 20°–200°C to ≈20% at 500°C. Additional evidence

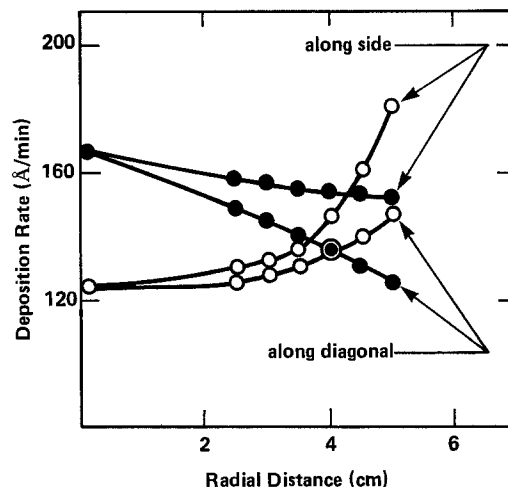


Fig. 4. Nonuniformity of the deposition rate for films of SiN_x on Si. Deposition conditions: T = 300°C, chamber pressure 0.7 torr, RF power 150W, gas flow rates: Ar = 160 sccm. ● SiH₄ = 8 sccm, NH₃ = 42 sccm; ○ SiH₄ = 4 sccm, NH₃ = 46 sccm.

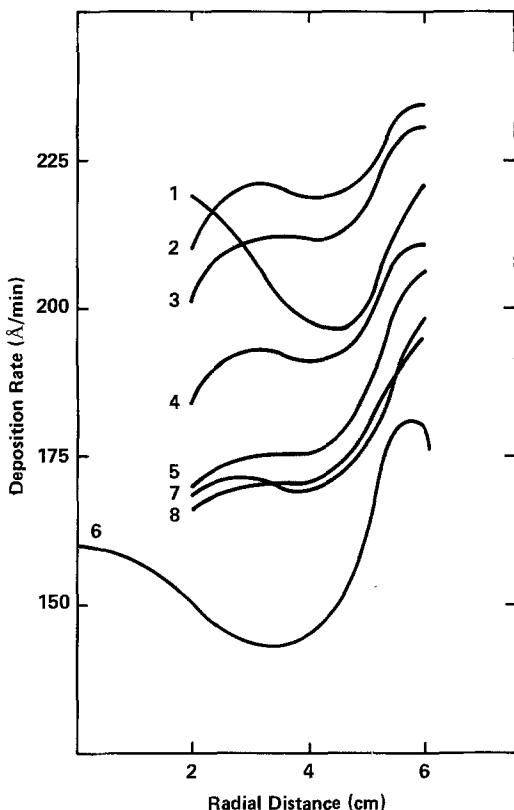


Fig. 5. Radial deposition rate distributions for consecutive 4 min depositions on 5 cm diam Si wafers, placed off-center on the electrode, following a plasma cleaning of the reactor chamber. The sixth deposition was done on a 10 cm diam wafer.

for a decreased hydrogen content at higher deposition temperatures is the effect of annealing on the films. It was found that films deposited at 300°C formed blisters which lifted from the substrate, after annealing in a nitrogen ambient at 600°C. This effect has been reported previously (6) and attributed to hydrogen diffusion and accumulation at the film-substrate interface. Films deposited at 500°C remained stable following annealing up to 700°C.

The increase in n with temperature was also observed by other investigators (3, 7, 8), and related to the increase in density of the films (9). The deposition rate vs. temperature curves suggest that at least two mechanisms are involved. A decrease in deposition rate with increasing temperature has been observed more often, in the range of 20°-300°C (7, 8), and may be related to the increase in film density with temperature. At higher temperatures, we observed a reversal of this trend to an increasing deposition rate. It is thought that this is the result of an increase in the rate of diffusion of reactive species to the substrate, due to the higher gas temperature.

The effect of RF power.—In Fig. 7 the effect of RF power on the index of refraction, the deposition rate, and the etch rate is shown. Experiments by Reinberg (8) have shown that the dissociation of SiH_4 and NH_3 increases with RF power and that dissociation of all SiH_4 and NH_3 molecules takes place at a power density (per unit of substrate electrode area) of $\approx 70 \text{ mW/cm}^2$. It is therefore to be expected that deposition rates will increase with RF power density to this value, and then remain constant. This is in agreement with results obtained by other workers, where values of power density can be extracted from the reported results. For power densities $< 60 \text{ mW/cm}^2$, a linear increase of the deposition rate with RF power has been observed (8, 10), whereas for power densities $> 100 \text{ mW/cm}^2$, a constant value was found (9, 11). In other work (3), the RF power range spans the transition region, as a

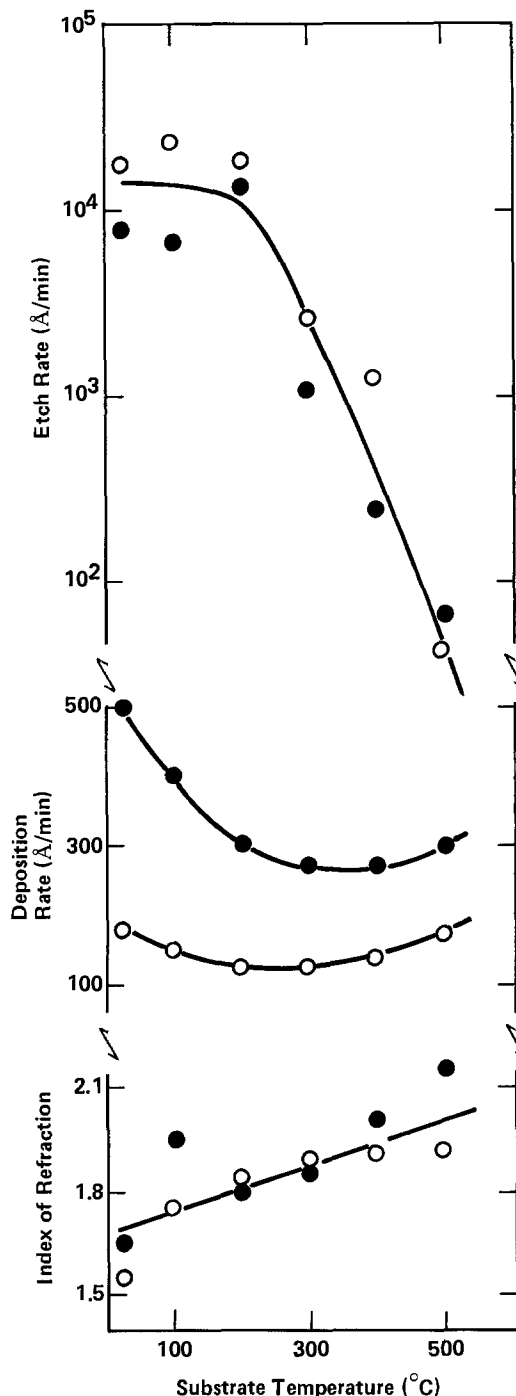


Fig. 6. Effect of substrate temperature on index of refraction, deposition rate, and etch rate in buffered HF for films of SiN_x on Si. Deposition conditions: RF power 150W, gas flow rates: $\text{SiH}_4 = 6 \text{ sccm}$, $\text{NH}_3 = 44 \text{ sccm}$. ● Ar = 200 sccm, chamber pressure = 0.9 torr; ○ Ar = 160 sccm, chamber pressure = 0.7 torr.

change from a linear increase to a more constant value is observed. Our experiments were done at power densities in the range 50-1000 mW/cm^2 . Therefore, little dependence of the deposition rate on RF power is to be expected. However, increase in power level in this region may increase the degree of dissociation of the reacting species and also the temperature of the gas. Both effects would result in a decrease of hydrogen content of the films and therefore a decrease in etch rate, as was observed. Thus it appears that RF power affects the growth rate of silicon nitride primarily through the degree of dissociation of the reactants and increase of power beyond the level at which all re-

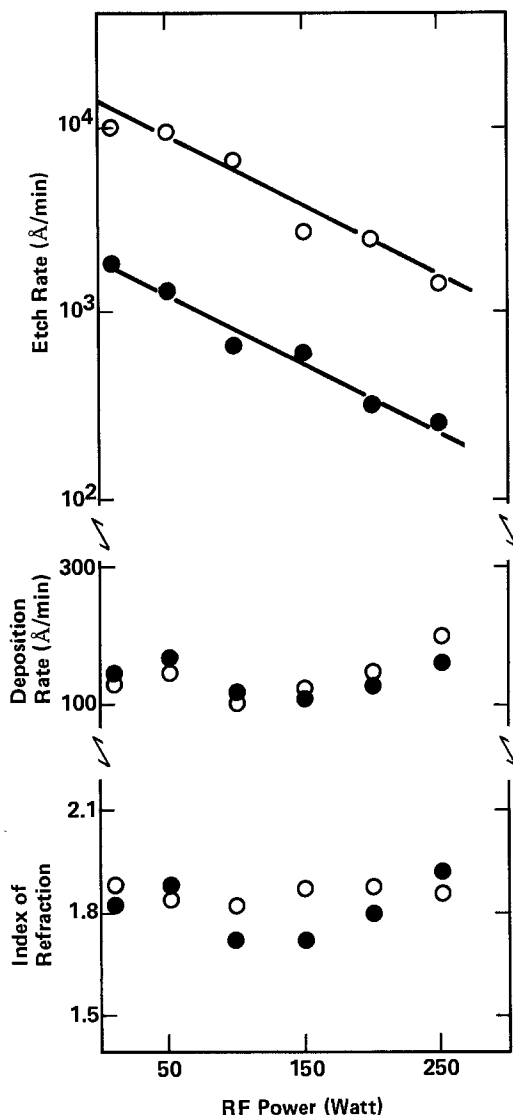


Fig. 7. Effect of RF power on index of refraction, deposition rate, and etch rate in buffered HF for films of SiN_x on Si. Deposition conditions: $T = 300^\circ\text{C}$, chamber pressure = 0.7 torr. Gas flow rates: ● $\text{SiH}_4 = 8$ sccm, $\text{NH}_3 = 42$ sccm, Ar = 200 sccm; ○ $\text{SiH}_4 = 6$ sccm, $\text{NH}_3 = 44$ sccm, Ar = 160 sccm.

actants are partially dissociated does not significantly effect the deposition process.

The effect of gas composition.—For several values of chamber pressure and total gas flow rate, the effect of varying the SiH_4/NH_3 ratio in the gas composition was investigated. Increasing the SiH_4/NH_3 ratio in the gas mixture increases the Si/N ratio in the deposited films. This trend has been well established in previous work (7, 12-14). Because an increase in Si/N corresponds to an increase in n (8), we expect n to increase with increasing SiH_4/NH_3 ratio. Figure 8 confirms this trend, which is generally observed (3, 7, 8, 10-13) and is also seen when N_2 instead of NH_3 is used as the nitriding agent (15, 16). For two films, the Si/N ratio was determined by Auger electron spectroscopy, using a sample of CVD- Si_3N_4 as a reference. Values found for the Si/N ratio were 1.17 and 1.43. The indexes of refraction of these films were 1.95 and 2.17, respectively. From the correlation between Si/N ratio and n , an estimate of the density, σ , of the films can be obtained (8). For both samples a value of $\sigma \approx 2.2$ g/cm² is found, which is a typical value for plasma silicon nitride (7, 8, 17). Using this value of σ , we find that the range of $1.8 < n < 2.1$ corresponds to a range in composition of $1.0 < \text{Si}/\text{N} < 1.3$, within the range of $\approx 0.7 < \text{Si}/\text{N} < 1.5$ reported by most workers (7, 13, 16-18).

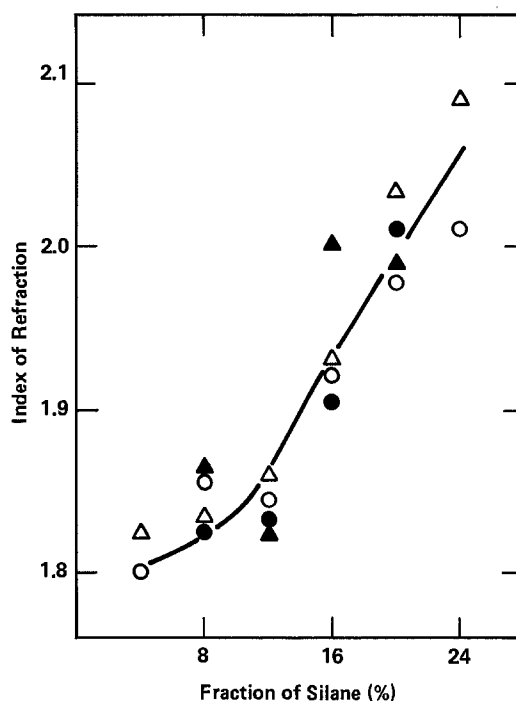


Fig. 8. Effect of gas composition on the index of refraction for films of SiN_x on Si. The fraction of silane is defined as $\text{SiH}_4/(\text{SiH}_4 + \text{NH}_3)$. Deposition conditions: $T = 300^\circ\text{C}$, RF power = 150W, gas flow rates; Ar/($\text{SiH}_4 + \text{NH}_3$) = 3.2. ● $\text{SiH}_4 + \text{NH}_3 = 35$ sccm, chamber pressure = 0.5 torr; ○ $\text{SiH}_4 + \text{NH}_3 = 50$ sccm, chamber pressure = 0.7 torr; ▲ $\text{SiH}_4 + \text{NH}_3 = 35$ sccm, chamber pressure = 0.7 torr; △ $\text{SiH}_4 + \text{NH}_3 = 50$ sccm, chamber pressure = 1.0 torr.

The etch rate was found to be strongly correlated with the index of refraction, as is shown in Fig. 9, where data for films deposited under various conditions of chamber pressure and gas flow are shown. Similar results were reported by other workers (3, 10). The significant increase in the etch rate for $n < 1.9$ indicates that films in that region are more susceptible to corrosion and that the refractive index may be a sensitive test of etch rate in applications where a direct measurement is impractical.

Chamber pressure and total gas flow rate did not affect n or the etch rate, i.e., the film composition. The deposition rate increased with pressure and with SiH_4/NH_3 ratio and was on the order of $5[\text{SiH}_4]$, where $[\text{SiH}_4]$ is the silane partial pressure in millitorr and the deposition rate is in angstroms per minute.

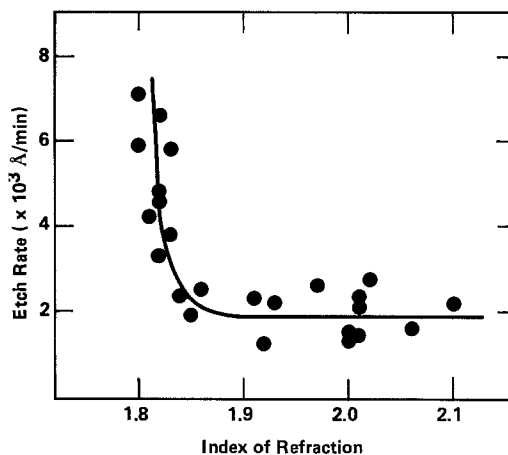


Fig. 9. Etch rate in buffered HF vs. index of refraction for films of SiN_x on Si, deposited at various gas flow rates and chamber pressures at $T = 300^\circ\text{C}$ and 150W RF power.

Conclusions

The effect of process parameters on film characteristics was determined for plasma-deposition of films of silicon nitride, deposited on Si substrates from mixtures of SiH₄, NH₃, and Ar. The effects of variations in the substrate temperature, RF power, and gas composition on the deposition rate, the etch rate, and the index of refraction are consistent with present understanding of the deposition process. Furthermore, the following results were obtained:

1. Pinhole densities can be reduced by increasing film thickness or the substrate temperature.
2. Uniformity of the deposition is affected by the composition of the reactant gas mixture and by the thickness of the layer of silicon nitride already present on the electrodes following previous depositions. Plasma cleaning of the reactor chamber prior to each deposition is required to obtain repeatability of the deposition rates.
3. An explanation is given for differences between the effects of RF power on deposition rate reported by different workers.
4. The relationship between index of refraction and etch rate in buffered HF suggests that the former may be a good indicator for the quality of the films, although the relationship may be reactor dependent.

Acknowledgments

We wish to thank M. Johnson of Bell-Northern Research for Auger electron spectroscopy. This work was partially supported by the Canadian Government as part of the Industrial Research Assistance Program.

Manuscript submitted May 12, 1983; revised manuscript received ca. Nov. 18, 1983.

Bell-Northern Research assisted in meeting the publication costs of this article.

REFERENCES

1. W. Kern and D. A. Puotinen, *RCA Rev.*, **31**, 187 (1970).
2. E. A. Taft, *This Journal*, **118**, 1341 (1971).
3. R. S. Rosler, W. C. Benzing, and J. Baldo, *Solid State Technol.*, **19**, 45 (June 1976).
4. R. Chow, W. A. Lanford, W. Ke-Ming, and R. S. Rosler, *J. Appl. Phys.*, **53**, 5630 (1982).
5. T. Yoshimi, H. Sakai, and K. Ianaka, *This Journal*, **127**, 1853 (1980).
6. W. Kern and R. S. Rosler, *J. Vac. Sci. Technol.*, **14**, 1082 (1977).
7. A. K. Sinha, H. J. Levinstein, T. E. Smith, G. Quintana, and S. E. Haszko, *This Journal*, **125**, 601 (1978).
8. A. R. Reinberg, *J. Electron. Mater.*, **8**, 345 (1979).
9. A. K. Sinha and E. Lugujo, *Appl. Phys. Lett.*, **32**, 245 (1978).
10. R. S. Rosler and G. M. Engle, *Solid State Technol.*, **22**, 88 (1979).
11. K. I. Kirov, S. S. Georgiev, B. G. Pantchev, and J. B. Koprinarova, *Thin Solid Films*, **72**, L9 (1980).
12. F. Sequeda and R. E. Richardson, *J. Vac. Sci. Technol.*, **18**, 362 (1981).
13. H. J. Stein, V. A. Wells, and R. E. Hampy, *This Journal*, **126**, 1750 (1979).
14. S. Yokoyama, M. Hirose, and Y. Osaka, *Jpn. J. Appl. Phys.*, **20**, L117 (1981).
15. J. R. Hollahan and R. S. Rosler, in "Thin Film Processes," J. L. Vossen and W. Kern, Editors, Academic Press, New York (1978).
16. M. J. Helix, K. V. Vaidyanathan, B. G. Streetman, H. B. Dietrich, and P. K. Chatterjee, *Thin Solid Films*, **55**, 143 (1978).
17. W. A. Lanford and M. J. Rand, *J. Appl. Phys.*, **49**, 2473 (1978).
18. A. K. Sinha and T. E. Smith, *ibid.*, **49**, 2756 (1978).

Chromium as a Diffusion Barrier Between NiSi, Pd₂Si, or PtSi and Al

M. Bartur* and M-A. Nicolet*

California Institute of Technology, Pasadena, California 91125

ABSTRACT

We show that the thermal instability that is observed in Schottky diodes with an Al film on NiSi, Pd₂Si, or PtSi contact to <Si> can be removed by proper deposition of a Cr layer, 1000-2000Å thick, between the Al and the underlying silicide layer. The structure can be formed by sequential evaporation of Ni, Pd, or Pt, Cr, and Al, and subsequent thermal annealing to form the contact silicide and sinter the Al contact. Isochronal annealing for 30 min over the temperature range of 350°-500°C shows that the barrier holds electrically at 450°C and fails at 500°C. Forward I-V measurements are used to determine the barrier height, and elemental profiles are investigated using backscattering spectrometry. The successful utilization of the Cr barrier depends on the deposition conditions. Bilayers of Cr and Al deposited at high rates in another vacuum evaporator consistently reacted more rapidly than those usually observed by us and also reported in the literature. We believe that under usual deposition conditions the impurities incorporated in the films are essential for the successful operation of Cr as a sacrificial barrier.

Silicide contacts to Si have received much attention recently and are widely used as material to form ohmic contacts, Schottky rectifiers, IR detectors, and interconnects for integrated circuits. The compatibility of thick Al films with silicide layers is a problem of practical interest, since Al remains a preferred metal for the final contact to other devices or to bonding pads. The direct contact between Al and near-noble metal silicides is unstable: metallurgically, Al forms metal compounds (PtAl₂, NiAl₃, or PdAl₃), and elec-

trically, the Schottky barrier height (SBH) changes when all the silicide layer is consumed.

In a previous paper (1), we suggested that the Al-silicide contact system can be stabilized with a sacrificial barrier between the Al layer and the silicide. A sacrificial barrier exploits the fact that thin adjacent films that react and form a compound often do so in a laterally very uniform fashion. A barrier layer that reacts uniformly with Al and silicide on either side of it effectively maintains a separation of the Al from the silicide as long as the barrier layer is not fully consumed by these reactions. This point in time is predictable when the two reaction rates are known as

* Electrochemical Society Active Member.

Key words: diffusion barriers, chromium barrier, contact metallurgy, solid-solid interfaces.

a function of temperature, provided that precautions are taken to avoid impurities in the films that might alter the reaction kinetics. We have suggested the use of Ti, V, or Cr for such barrier material.

In this paper, we evaluate Cr as a diffusion barrier between Al and NiSi, Pd₂Si, or PtSi. We chose Ni, Pd, and Pt silicides because they can be formed uniformly and reproducibly at relatively low temperatures on a Si substrate. Platinum and palladium silicides are widely utilized in Si contact structures. They also span a wide range of usable SBH (0.66, 0.74, and 0.85 eV for NiSi, Pd₂Si, and PtSi, respectively). We characterize the electrical stability of the contact structure using barrier height measurements as an indicator for the integrity of the Si-silicide interface.

The main results of this study are twofold. We first establish that with films deposited in a conventional fashion Cr does indeed act as the sacrificial barrier model predicts. These results also agree with most observations reported in the literature. We additionally show, however, that Cr fails as a diffusion barrier when the films are deposited in a separate evaporation system and at high rates. Evidence suggests that impurities are critically associated with these different behaviors. In what follows, we therefore distinguish between results obtained with the "slow" or the "fast" evaporation systems.

Experimental Procedures

The Schottky diodes for our study were prepared on 0.003 Ωcm $n^+ \langle 111 \rangle$ silicon substrates covered with a 10 μm thick 10 Ωcm n -type epi-layer. The contact areas (1.16×10^{-2} cm^2) were photolithographically defined and opened using a buffered HF in a SiO₂ layer which was deposited on the wafers by low temperature chemical vapor deposition (CVD). Prior to the loading for metal deposition, the wafers were etched for 10s in 1:10 HF. The metals (Ni, Pd, or Pt), Cr, and Al were sequentially evaporated without breaking the vacuum at pressures less than 5×10^{-7} torr. The depositions were conducted in two systems which are constructed similarly: both use ion pumps and E-guns. The only difference was the deposition rate of the metal layers. In the first ("slow") system, the deposition rate was 10-30 $\text{\AA}/\text{s}$ with intermittent holds due to the manual control, while in the other ("fast") system, the depo-

sition was maintained automatically at a fixed rate of 50 $\text{\AA}/\text{s}$. We also prepared samples only with silicide (no Cr or Al) and without the Cr barrier. For comparison, the silicides of some samples were prepared *in situ* (at 400°C) before the Cr and Al were deposited. Large area samples were prepared simultaneously for backscattering spectrometry (BS) analysis. Subsequent heat-treatments were performed in a vacuum furnace at pressures less than 8×10^{-7} torr, or in N₂ flow in an open-tube furnace.

The SBH was determined from fits of the forward I-V data to the ideal thermionic emission model. The reverse saturation current and Norde plots were also employed, where feasible, to confirm the results. Elemental profiles were detected using BS with a 2 MeV ⁴He⁺ beam.

Results and Discussion

Thin film interactions.—To perform as a sacrificial barrier, Cr must react uniformly with the top Al film and with the bottom silicide layer. It is known that Cr reacts uniformly with Al, forming CrAl₇(2). The Cr consumption rate is $4.5 \times 10^{-14} \times \exp(-1.91 \text{ eV}/kT)$ $\text{\AA}^2 \text{ s}^{-1}$ (2) for annealing in dry nitrogen atmosphere at 300°-450°C temperature range. The reaction of Cr with Pd₂Si has been investigated by Olowolafe *et al.* (3), who demonstrated the uniform layer-by-layer growth of CrSi₂ on Pd₂Si. Also, Zingu *et al.* (4) have clearly shown that the growth rate of CrSi₂ with an interposed Pd₂Si layer is equal to or slower than that on Si, depending on the Pd₂Si thickness. Previous studies of CrSi₂ growth on PtSi(5, 6) or NiSi(6) have demonstrated a uniform layer-by-layer growth of CrSi₂.

Utilizing our slow system, we have investigated the reaction of Cr films with PtSi and NiSi films on Si. For these studies, we have used an initial configuration of Si/metal/Cr or Si/metal silicide/Cr; upon annealing, the former will transform into the latter at temperatures much below those at which Cr begins to react. The uniform formation of CrSi₂ on PtSi is shown in Fig. 1. Similar results are observed for $\langle \text{Si} \rangle/\text{NiSi}$ substrates. There is no detectable (using BS) mixing between the growing CrSi₂ layer and the underlying silicide. We have shown (7) that the growth rate of CrSi₂ on $\langle \text{Si} \rangle/\text{PtSi}$ is slower than on $\langle \text{Si} \rangle$ substrate at the same temperatures. Also, there is a delay time

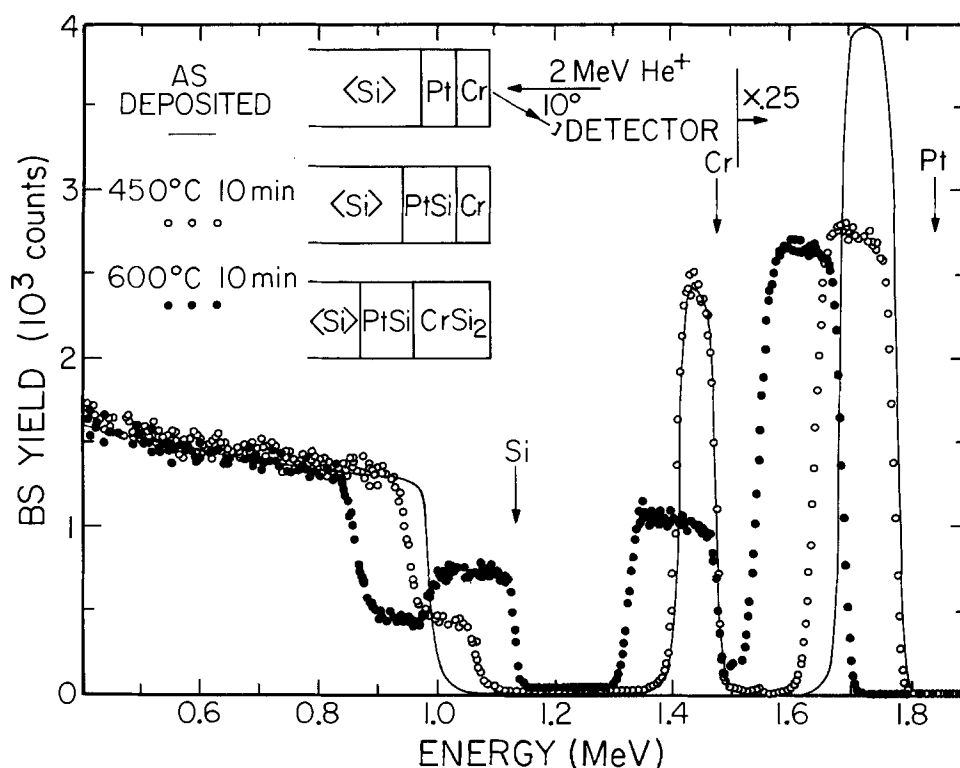


Fig. 1. Silicide formation of Pt/Cr bilayer. First platinum silicide is formed and then at higher temperatures chromium disilicide is formed.

before the CrSi_2 formation starts. This delay time is longer for Si/metal/Cr structures than for Si/silicide/Cr structures that were formed using *in situ* heater.

Chromium was evaluated metallurgically as a diffusion barrier between Pd_2Si and Al (8) and electrically between PtSi and Al (9). It was shown (8) that Cr acts as sacrificial barrier and inhibits the interaction of Al and Pd_2Si for up to 90 min at 500°C . No electrical evaluations of this contact structure were reported. But, it has been reported that for PtSi there is a sharp drop in the SBH after the Cr layer is completely consumed by CrAl_7 formation (9). We conclude that, metallurgically, Cr is adequate for a sacrificial barrier on top of NiSi and PtSi from our studies ("slow" system), and for Pd_2Si from the results of Ref. (3), (4), and (8).

Electrical stability.—Technologically, the process of sequential deposition without silicide formation (metal/Cr/Al) is preferable, since it eliminates the need for *in situ* heating and allows for a single sintering step outside of the evaporator. In our electrical measurements, we found no basic difference between the behavior of the Si/silicide/Cr/Al and the Si/metal/Cr/Al structures. The reason is that the metal silicide forms much before any other reaction takes place in the above structures. Our shortest annealing time will transform all the metal under the Cr barrier to the silicide layer. We thus consider only the Si/metal/Cr/Al structures and compare them with the Si/metal/Al and the Si/silicide structures. The samples discussed in the following sections were produced in the "slow" Cr evaporation system and annealed in vacuum.

NiSi.—Failure of the Si/NiSi/Al contact structure has been reported (10-12) to occur at 400°C after a very short annealing. The compound NiAl_3 forms, and the SBH rises above 760 mV. For such samples, we observed SBH as high as 800 mV following 350°C , 20 min vacuum annealing. However, isochronal annealing of $\langle\text{Si}\rangle/600\text{\AA}$ Ni/ 700\AA Cr/ 6000\AA Al structures for 20 min at 350° , 400° , and 450°C produced no change in the SBH (Fig. 2). Based on Ref. (1), a failure is predicted

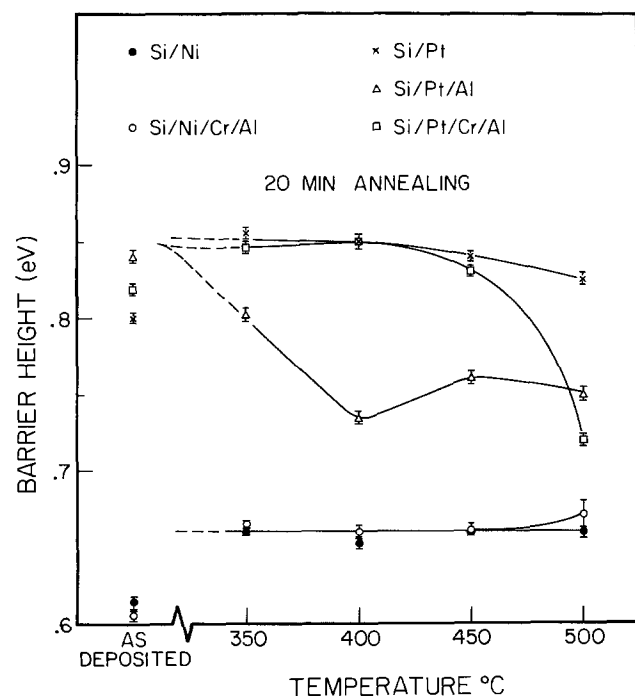


Fig. 2. Schottky barrier height (SBH) of isochronal anneal of: ● $\langle\text{Si}\rangle/590\text{\AA}$ Ni, ○ $\langle\text{Si}\rangle/600\text{\AA}$ Ni/ 700\AA Cr/ 6000\AA Al, × $\langle\text{Si}\rangle/700\text{\AA}$ Pt, △ $\langle\text{Si}\rangle/500\text{\AA}$ Pt/ 5700\AA Al, and □ $\langle\text{Si}\rangle/630\text{\AA}$ Pt/ 1350\AA Cr/ 9440\AA Al. (Formed in "slow" deposition system.)

after 20 min at 465°C . At 500°C for 20 min, the barrier indeed fails. The SBH rises from 667 (which is the barrier height of NiSi) to 680 mV with an increase in the ideality factor. We presume that this is due to localized failures, similar to the failure mode that was suggested for tungsten barrier (12).

Pd_2Si .—The instability of the Si/ Pd_2Si /Al structure has been thoroughly investigated (13-15). A complex ternary phase is observed upon annealing at temperatures as low as 200°C (16). The SBH first decreases after 10 min at 300°C and then rises above its initial value (13). We show that the electrical stability of a $\langle\text{Si}\rangle/650\text{\AA}$ Pd/ 1700\AA Cr/ 7000\AA Al structure at 450°C is maintained for about 120 min (Fig. 3). The barrier height of Pd_2Si , 0.74 eV, is maintained and the ideality factor is constant before the contact fails. Calculation based on our model (1) predicts about 100 min before the barrier is fully consumed; this agrees well with the facts.

PtSi.—The high value of the SBH of PtSi (850 mV) makes this contact very sensitive to any change at the Si/PtSi interface. It has been reported (17) that the Si/PtSi/Al structure shows a reduction in the SBH when all the Pt in the silicide is transformed to PtAl_2 . We find, for Si/Pt/Al sample, an immediate decrease of SBH after 350°C , 20 min annealing of samples without a Cr barrier ($\langle\text{Si}\rangle/500\text{\AA}$ Pt/ 5700\AA Al, see Fig. 2). Also, BS spectra indicate that the atomic composition of the reacted layer is quite Al rich (about 1:6 Pt-to-Al atomic ratio) and that about 0.25 atomic percent (a/o) Pt is contained in the remaining Al layer. The effect of thermal annealing on a $\langle\text{Si}\rangle/700\text{\AA}$ Pt sample is described in Fig. 2 also, because for this silicide, the SBH is altered by annealing (18) even without Al. Figure 2 shows that, after 20 min of annealing, the contact structure $\langle\text{Si}\rangle/630\text{\AA}$ Pt/ 1350\AA Cr/ 9500\AA Al starts to fail above 450°C , where there is a slight decrease in the SBH of PtSi from 0.85 to 0.83 eV. The sacrificial barrier model predicts (1) failure after 20 min at 485°C , which we consider to be excellent agreement. After this 450°C annealing, BS analysis reveals that indeed there is a reaction between the Al and

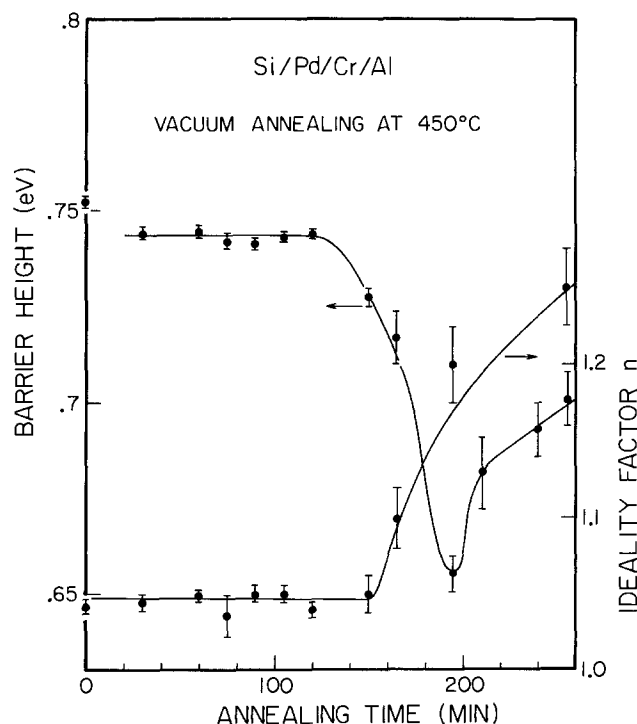


Fig. 3. Schottky barrier height (SBH) of $\langle\text{Si}\rangle/650\text{\AA}$ Pd/ 1700\AA Cr/ 7000\AA Al as function of isothermal vacuum annealing at 450°C . The ideality factor is also depicted. (Formed in "slow" deposition system.)

PtSi, but presumably not all the PtSi is consumed. Following a 500°C, 20 min annealing, Pt (at low concentration) was detected in the CrAl₇ layer and, as seen from the electrical measurements, the contact has failed.

Impurities effect.—To check our results, we also prepared samples in the “fast” vacuum evaporator. In this case, reduced contamination levels (particularly of O₂) are expected. In a previous study (19) done with the “slow” system, about 7 a/o was detected (using SIMS) in the as-deposited Cr layer. For Cr films deposited in the “fast” system, we found by BS that the Cr reaction rate with Al was about ten times faster than predicted in Ref. (1) at 460°C or than observed with the “slow” system. This annealing was conducted in an open-tube furnace with N₂ flow. When the annealing was conducted in vacuum, the CrAl₇ formation rate was at least 100 times faster than the “slow” case. These samples had a very thick (2 μm) Al layer, but, apparently, the impurities from the annealing environment diffuse quite easily through the Al layer at 460°C. It is important to note that even for such high reaction rates the CrAl₇ forms quite uniformly.

To check the effect of impurities in the Al layer, we prepared a sample in the “fast” system, but stopped the Al deposition after about 2000 Å. The system was opened to air briefly (thin Al oxide formation), and then pumped down again and the deposition was finished (in similar vacuum conditions) until about 2 μm Al was deposited. In these samples, no reaction was observed after 3h at 460°C, and, electrically, the barrier height of the underlying NiSi was maintained. These results directly demonstrate that impurities do indeed affect this contact structure.

Sacrificial barrier holding time.—The holding time of the Cr barrier prepared in the “slow” system reported above and in Ref. (9) agrees quite well with our prediction based on individual reaction rates (1).

However, the results obtained with the fast system indicate that these rates are system dependent. The rates of reaction between Cr and Al reported in Ref. (2) and those extracted from holding times of Pd₂Si/Cr/Al (8), PtSi/Cr/Al (9), and our studies are all consistent with each other, although different systems are involved. One is thus forced to conclude that at least the Cr/Al reaction must be relatively insensitive to impurities above some threshold, but very sensitive below that. The identification of the impurities that affect the Cr/Al reaction, and its quantitative characterization therefore emerges as one of the important issues raised by the present study. A corollary of these observations is that the notion of a sacrificial barrier may have to be reconsidered, because it is conceivable that in reality impurities must always be present to realize that concept.

Titanium films have also been investigated for sacrificial barrier application. One would expect, in light of the preceding comments, that inconsistencies should appear in the holding times reported for barrier structure prepared in different systems. Indeed, conflicting results exist as to the usefulness of Ti as a barrier. Solomonson *et al.* (20) show that Ti really works as a sacrificial barrier and reacts uniformly with the silicide and the Al layer. Merchant *et al.* (9) also tested Ti as a barrier between PtSi and Al; they found that the SBH is constant as long as some unreacted Ti is left. However, the same system was reported by Ting and Crowder (21) to fail much faster than predicted by our original model (1). From their data, we deduce a Ti consumption rate of about 140 Å² s⁻¹ at 400°C, while we predict only 20 Å² s⁻¹ based on Bower (22).

Conclusions

The concept of a sacrificial barrier depends on two assumptions: (i) that the reactions at both interfaces of the barrier layer be laterally uniform, and (ii) that

the reaction rates be known and reproducible. The fulfillment of these assumptions will allow the design of a sacrificial barrier as outlined in Ref. (1). In the cases of Cr and Ti, we find vast variations in the reaction rates with Al, depending on the deposition conditions. The second requirement of known and reproducible reaction rates then is not fulfilled. That fairly consistent values for the Cr-Al reaction have nevertheless been reported by independent investigators strongly suggests that impurities may actually help in equalizing reaction rates. By the same token, impurities may also improve the lateral uniformity of a reaction by reducing grain boundary diffusion. The successful implementation of a sacrificial barrier may thus ultimately depend on the presence of impurities, in which case the concept of a sacrificial barrier emerges as a mere special case of a stuffed barrier. The sacrificial barrier may then be implemented for specific cases and in specific systems where impurities are incorporated consistently from run to run.

Practically, the control of impurities in film deposition or during annealing is difficult. A deliberate incorporation of impurities in the barrier (making it a stuffed barrier) in an amount which exceeds that needed to slow the reaction is a preferable procedure. The utilization of Cr (23) or Al (24) doped with oxygen has been suggested by others. It was shown (19) that oxygen in the Si is more effective in slowing down CrSi₂ formation than oxygen in the Cr, probably because of the fact that Si is the moving species. Since in CrAl₇ formation Al is expected to be the moving species (2), it may very well be that impurities in the Al layer have a dominant role in slowing the reaction rate. Indeed, we observed no degradation of the SBH even after 500°C when the Al was “stuffed” with impurities: most probably oxygen.

Chromium can be utilized as a barrier between Al and NiSi, Pd₂Si, and PtSi at 450°C, if the appropriate amount of impurities is incorporated in the film. Our study does not quantify this amount, but from our experience we can say that the evaporation performed at pressure higher than 1 × 10⁻⁶ torr at a rate lower than 10 Å/s will result in films with a sufficient amount of impurities to make the barrier effective.

Acknowledgments

The authors wish to thank M. Parks for careful typing of the manuscript, and Solid-State Devices, Incorporated (A. Applebaum, President) for partial financial and technical support.

Manuscript submitted Sept. 15, 1983; revised manuscript received Dec. 27, 1983. This was Paper 295 presented at the Washington, DC, Meeting of the Society, Oct. 9-14, 1983.

The California Institute of Technology assisted in meeting the publication costs of this article.

REFERENCES

1. M-A. Nicolet and M. Bartur, *J. Vac. Sci. Technol.*, **19**, 786 (1981).
2. J. K. Howard, R. F. Lever, P. J. Smith, and P. S. Ho, *ibid.*, **13**, 68 (1976).
3. J. O. Olowolafe, M-A. Nicolet, and J. W. Mayer, *J. Appl. Phys.*, **47**, 5182 (1976).
4. E. C. Zingu, C. Comrie, and R. Pretorius, *ibid.*, **54**, 2392 (1983).
5. R. Pretorius, J. O. Olowolafe, and J. W. Mayer, *Philos. Mag.*, **37**, 327 (1978).
6. M. O. Naudé, R. Pretorius, and D. J. Maris, *Thin Solid Films*, **89**, 339 (1982).
7. A. Barcz and M. Bartur, Paper presented at Materials Research Society Meeting, Boston, November 1983, and published in “Thin Films and Interfaces II” J. E. E. Baglin, D. R. Campbell, and W. K. Chu, Editors, Elsevier, North Holland, New York, In press.
8. J. O. Olowolafe, M-A. Nicolet, and J. W. Mayer, *Solid-State Electron.*, **20**, 413 (1977).

9. P. Merchant and J. Amano, *J. Vac. Sci. Technol.*, **21**, 459 (1983).
10. E. Hökelek and G. Y. Robinson, *Thin Solid Films*, **53**, 135 (1978).
11. M. Bartur and M-A. Nicolet, *ibid.*, **91**, 89 (1982).
12. M. Bartur and M-A. Nicolet, *Appl. Phys. Lett.*, **39**, 822 (1981).
13. H. Grinolds and G. Y. Robinson, *J. Vac. Sci. Technol.*, **14**, 75 (1977).
14. U. Köster, P. S. Ho, and J. E. Lewis, *J. Appl. Phys.*, **53**, 7436 (1982).
15. C. J. Kircher, *ibid.*, **47**, 5394 (1976).
16. P. S. Ho, J. E. Lewis, and U. Köster, *ibid.*, **53**, 7445 (1982).
17. H. H. Hosack, *ibid.*, **44**, 3476 (1973).
18. E. Calleja, J. Garrido, J. Piqueras, and A. Martinez, *Solid-State Electron.*, **23**, 591 (1980).
19. C.-D. Lien, L. S. Wieluński, M-A. Nicolet, and K. M. Stika, *Thin Solid Films*, **104**, 235 (1983).
20. G. Solomonson, K. E. Holm, and T. G. Finstad, *Phys. Scr.*, **24**, 401 (1981).
21. C. Y. Ting and B. L. Crowder, *This Journal*, **129**, 2590 (1982).
22. R. W. Bower, *Appl. Phys. Lett.*, **23**, 99 (1973).
23. H. M. Dalal, M. Ghafghaichi, L. A. Kasprzak, and H. Wimpfheimer, U.S. Pat. 4,214,256 (1980).
24. W. K. Chu, J. K. Howard, and J. F. White, U.S. Pat. 4,204,472 (1980).

Crosslinking Reactions in Negative Electron Resists Composed of Halogenated Aromatic Polymers

Saburo Imamura, Toshiaki Tamamura, Ken Sukegawa, Osamu Kogure, and Shungo Sugawara

Nippon Telegraph and Telephone Public Corporation, Ibaraki Electrical Communication Laboratory, Polymer Section, Tokai, Ibaraki 319-11, Japan

ABSTRACT

Crosslinking reactions in halogenated aromatic polymers which provide useful negative electron resists with high dry etching durability and high contrast were studied. Halogenated aromatic polymers show characteristic features, such as the saturation of crosslinking reactivity with an increase of halogen content and little postirradiation polymerization effect. The reactivity saturation is dependent not on the ring size or main chain structure of the aromatic polymer, but on the kind of halogen atom. The larger halogen atoms tend to exhibit more rapid saturation with halogen content, suggesting a steric effect. The strong participation of radical species formed by the dissociation of the carbon-halogen bond in the crosslinking reaction was verified from studies of radical scavenger effect and electron spin resonance spectroscopy. Considerable amounts of radical species remain after the crosslinking reaction has finished in vacuum, but remain in polymer films without crosslinking because of the high glass-transition temperatures of aromatic polymers and decreasing chain reactivity by halogen atoms, resulting in negligible postirradiation polymerization.

Almost all negative electron resists recently developed for microfabrication involving dry etching technology are derived from aromatic polymers (1-7). This is, in principle, due to the fact that aromatic polymers have relatively high stability against various dry-etching processes and high glass-transition temperatures (T_g), which may help to depress the swelling of crosslinked polymer chains. Polystyrene- (PSt) based polymers have been extensively studied as negative electron resists, because of the availability of PSt, even in a mono-disperse form (8, 9). As the crosslinking reactivity of PSt is very low, various reactive groups such as halogens or epoxy groups were introduced into PSt structure to enhance sensitivity. The use of halogenated groups as a crosslinking unit is preferable to get high resolution, as well as high sensitivity, because these groups can be used to crosslink polymer chains via step-wise reaction (10). However, polymers containing bonds such as epoxy or vinyl groups often crosslink via chain reaction, resulting in very high sensitivity but relatively low resolution (11).

We have synthesized a high performance negative electron resist, chloromethylated polystyrene (CMS), by the chloromethylation of nearly mono-disperse polystyrene (1). The chloromethyl group has proved to give PSt the highest crosslinking reactivity among various halogen groups (2). CMS has a contrast (γ) of 1.4-2.2, depending on the molecular weight and dispersity of the resist used, and shows excellent dry etching durability. For further improvement of the resolution of CMS, we have changed the starting polymer from PSt to nearly mono-disperse poly- α -methylstyrene, which has a much higher T_g (165°C) than PSt (95°C) (6). A new negative electron resist, chloromethylated poly- α -methylstyrene (α M-CMS) exhibits a contrast of 2.2-3.0, which is as high as that of nearly

mono-disperse PSt, and has excellent dry-etch durability and thermal stability. The sensitivity of α M-CMS is about half that of CMS, but still is 30 times higher than PSt when the same molecular weight polymers are used.

As reported previously, an interesting feature is observed in the resist performance of CMS and iodinated PSt (IPS) (5). This is the saturation of crosslinking reactivity with increasing reactive group content. Though the introduction of a small amount of halogen groups drastically increases the sensitivity of PSt, halogen groups introduced beyond a certain level do not contribute further to sensitivity of PSt. Another interesting observation in halogenated PSt resists is a freedom from postirradiation polymerization, which is defined as a phenomenon in which the crosslinking reaction lasts in the very high vacuum of the electron exposure machine. Postirradiation polymerization causes a lithographic nonuniformity in the developed resist thickness and variation of pattern sizes on a wafer according to the exposure order of patterns (12). In this paper, the crosslinking reactivity of various halogenated aromatic polymers was investigated by varying the polymer structure and measuring the ESR spectra as a function of temperature for these polymers, in order to elucidate the reaction mechanism of halogenated aromatic polymers as negative electron resists.

Experimental

Polymer preparation.—Figure 1 shows the structures of the halogenated aromatic polymers used in this study. Polymers with various ring structures were selected. CMS was obtained from Toyo Soda Manufacturing, and α M-CMS was synthesized as described in the previous paper (6). Chloromethylated poly (β -naphthyl methacrylate) (CMN) was prepared by the chloromethylation of poly(β -naphthyl methacrylate).

Key words: resists, electron beam lithography, polymer resists.

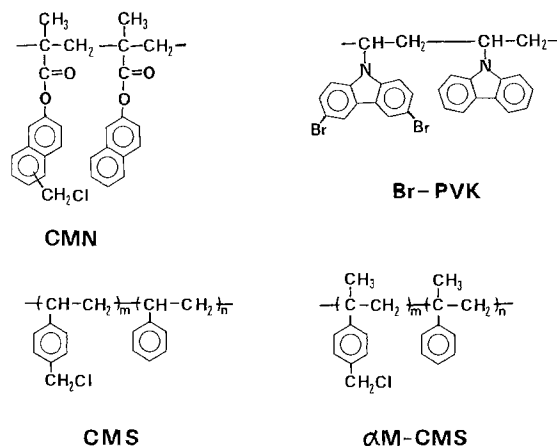


Fig. 1. Chemical structures of halogenated aromatic polymers

β -naphthyl methacrylate monomer was synthesized from methacrylic acid and β -naphthol using dicyclohexylcarbodiimide as a dehydration agent. The monomer was purified by repeated recrystallizations. Poly(β -naphthyl methacrylate) was prepared by azo-bis-isobutyronitrile (AIBN) initiated radical polymerization in toluene at 60°C in a sealed tube for 12h. The polymers were isolated by pouring the solution into methanol, washing with methanol repeatedly, and purifying by reprecipitation from tetrahydrofuran (THF) into methanol. Chloromethylation was carried out in chloromethyl methyl ether with SnCl_4 as a catalyst. Copolymers of β -naphthyl methacrylate and glycidyl methacrylate (NGC) with various monomer feed ratios were prepared and purified using the same procedure as described for poly(β -naphthyl methacrylate). Brominated polyvinylcarbazole (Br-PVK) was synthesized from polyvinylcarbazole, obtained from Anan Koryo Company, Limited, and N-bromosuccinimide using benzoyl-peroxide initiator. Poly-1,2-butadiene was obtained from Japan Synthetic Rubber Company, Limited.

Characterization.—Molecular weight parameters (\bar{M}_w and \bar{M}_n) were determined using gel permeation chromatography with a Hitachi Model 675 GPC and a Toyo Soda Model HLC-802UR GPC. Molecular weight measurements were calibrated with the standard polystyrene. The eluting solvents were methylethyl ketone (MEK) for CMS and α M-CMS and THF for other polymers. The chloromethylation ratio of CMS, α M-CMS, and CMN were calculated on the basis of chlorine content from the elemental analysis of polymers. Bromine content in Br-PVK was also determined by the elemental analysis. A maximum of two bromine atoms can be introduced into a carbazole ring. The glycidyl methacrylate (GMA) content of NGC was determined by measurement of the absorption at 310 nm due to the naphthalene ring in the polymer.

The glass-transition temperatures (T_g) of the polymers were determined with a Rigaku Differential Thermal Analysis Unit. Electron spin resonance (ESR) spectra of irradiated polymers were measured with a JEOL JES-PE-3X spectrometer equipped with a temperature-control unit. Powder samples for ESR measurement were evacuated at 10^{-6} torr for 24h and then sealed in a quartz tube before high energy beam exposure. Two kinds of irradiation, ^{60}Co γ -ray source and 150W high pressure mercury lamp with a collimated exposure system, were used to generate radical species in the resist. The sealed samples were irradiated for a specified period before ESR measurement.

Resist working.—Polymers were dissolved in xylene for CMS and M-CMS or in monochlorobenzene for other polymers and then spin-coated onto a silicon wafer having a 1 μm SiO_2 film 0.5–0.8 μm thick. Pre-

baking was carried out under a nitrogen atmosphere at 70°C for NGC, 95°C for CMS and CMN, and 135°C for Br-PVK and α M-CMS for 20 min. The sensitivity of resists to electron beam exposure was examined by exposure with a computer-controlled electron beam exposure machine ESM-301 or ELS-5000 (ELIONIX Company). The accelerating voltage used was 20 kV. The exposed films were developed by dipping in a suitable developer. MEK was used for CMS and α M-CMS, and THF or monochlorobenzene was used as the developer for other polymers. After development, the resist film was rinsed by dipping the sample in isopropanol. The resist thicknesses before and after development were measured with a Talystep (Taylor-Hobson). The electron beam sensitivity was expressed as D_0 , defined as the minimum dose required to form an insoluble gel on the substrate. Since the sensitivity of crosslinking negative resists is proportional to the initial molecular weight, we use the product of D_0 and \bar{M}_w as the measure of polymer reactivity to eliminate the effect of molecular weight. The temperature dependence of resist sensitivity was measured with a temperature-controlled sample stage, details of which are described by Harada (13).

Results and Discussion

Relation between reactivity and reactive group content.—Normally, for polymers in which the chemical composition is constant since

$$D_0 = K/\bar{M}_w G_c$$

where K is constant and G_c is G value of crosslinking. This is obeyed by many crosslinking polymers at low dose (moderate to high molecular weight). The relationship between resist sensitivity and halogen content has been reported in detail for CMS (2) and IPS (5). The sensitivity of IPS shows a saturation beyond about 20 mol percent (m/o) of iodination, whereas the reactivity saturation is observed beyond 40 m/o in CMS. We have measured this relation for various polymers shown in Fig. 1, to clarify the origin of this saturation. Table I summarizes molecular weight parameters, reactive group contents, and $D_0 \times \bar{M}_w$ for the polymers examined.

Figure 2 shows the reactivity of α M-CMS and CMS as a function of chloromethylation ratio (CR). α M-CMS gives the almost same CR dependence as that of CMS. It is very interesting that a quite similar relation

Table I. Molecular weight parameters, reactive group content, and $D_0 \times \bar{M}_w$ of the polymers examined

Polymer	$\bar{M}_w (\times 10^4)$	\bar{M}_w/\bar{M}_n	RG content*	Reactivity $D_0 \times \bar{M}_w$
PNM	8.3	3.4	0	positive
CMN-1	6.1	3.8	0.86	0.26
CMN-2	9.5	3.8	0.18	0.45
CMN-3	8.1	4.5	0.62	0.32
CMN-4	10.0	5.1	0.34	0.30
CMN-5	10.9	4.4	0.17	0.39
CMN-6	14.4	5.5	0.25	0.40
CMN-7	9.0	3.6	0.05	0.72
CMN-8	9.0	3.4	0.42	0.27
PVK	90	4.9	0	2.9
Br-PVK-1	104	4.8	1.04	0.34
Br-PVK-2	79	3.6	1.50	0.38
Br-PVK-3	9.8	3.7	1.89	0.23
Br-PVK-4	92	4.1	0.51	0.31
Br-PVK-5	96	5.3	0.26	0.33
Br-PVK-6	91	5.2	0.14	0.38
NGC-1	5.4	3.6	0.05	8.0
NGC-2	6.1	3.9	0.18	4.5
NGC-3	3.0	2.7	0.36	1.3
NGC-4	5.7	3.2	0.55	0.88
NGC-5	5.3	3.5	0.76	0.32

* RG content; reactive group content.

PNM: poly(β -naphthyl methacrylate); CMN: chloromethylated poly(β -naphthyl methacrylate); PVK: polyvinylcarbazole. Br-PVK: brominated polyvinylcarbazole. NGC: copolymer of β -naphthylmethacrylate and glycidyl methacrylate.

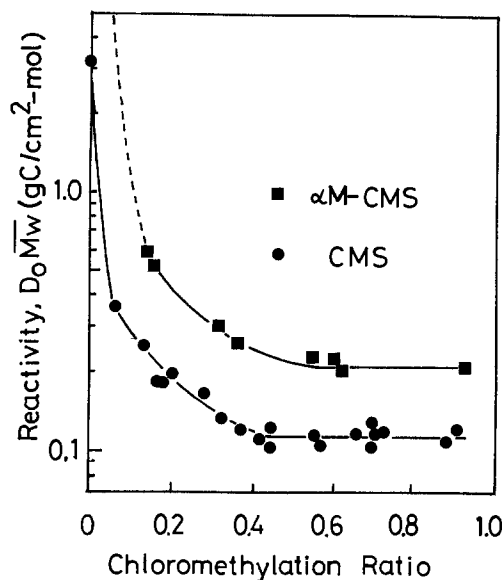


Fig. 2. Reactivity of CMS and α M-CMS as a function of molar chloromethylation ratio.

is also observed for CMN, as shown in Fig. 3. All of these polymers have the chloromethyl group as a crosslinkable unit, but their main chain structures are different. CMS and α M-CMS contain benzene ring, while CMN is a methacrylic polymer containing naphthalene ring. PSt, the parent polymer of CMS, is a negative resist, while α M-CMS and CMN have a parent polymer which acts as a positive resist. A small degree of chloromethylation changes α M-CMS and CMN from positive to negative tone. These results suggest that the reactivity saturation observed at about 0.4 of CR is a common feature of the chloromethyl group.

However, the reactivity of Br-PVK, which has a carbon-bromine bond as a reactive group and the carbazole group as an aromatic ring, saturates above about 30 m/o with bromination ratio, as shown in Fig. 4. By taking into account that IPS which has a carbon-iodine bond which shows a reactivity saturation at about 0.2, it can be concluded that the saturation in halogenated aromatic polymers is almost independent of aromatic-ring size and main chain polymer

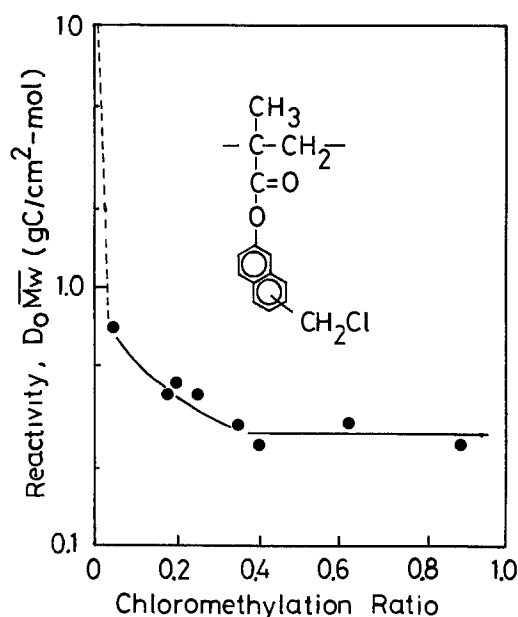


Fig. 3. Reactivity of CMN as a function of molar chloromethylation ratio.

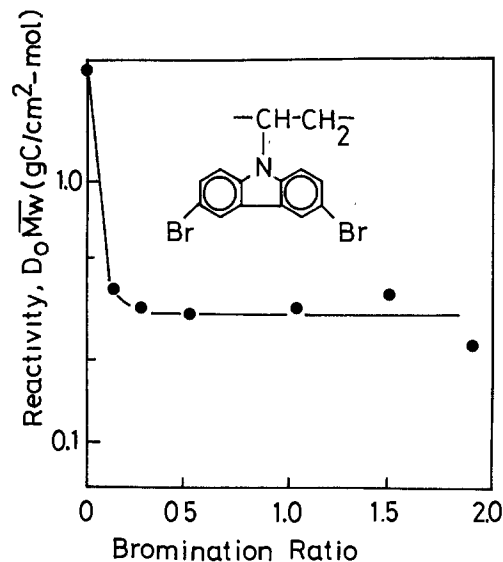


Fig. 4. Reactivity of Br-PVK as a function of molar bromination ratio.

structure, but is closely related to the kind of halogen atom.

To confirm that the reactivity saturation phenomenon is only observed in halogenated aromatic polymers, the sensitivity of NGC copolymerized with amounts of glycidyl methacrylate unit was investigated. Figure 5 shows the sensitivity curves for NGC and Br-PVK. NGC has low contrast in comparison with Br-PVK. This suggests that NGC crosslinks via chain reactions. Figure 6 indicates no saturation, but rather linear increase of reactivity with GMA content. The same results were obtained for epoxydized polybutadiene (PB) (14) and copolymers of styrene and glycidyl methacrylate (4).

Postirradiation polymerization effect.—Many negative electron resists, such as COP and SEL-N, suffered from postirradiation polymerization (15), which causes nonuniformities in pattern width and thickness on a wafer after development according to the order of exposure. CMS is known to show little postirradiation polymerization effect.

To elucidate the relation between this effect and polymer structure, various polymers were tested. For the evaluation of postpolymerization, the thickness of developed patterns after leaving the sample in an exposure machine for a given period was compared with resist thickness developed immediately after exposure. The results are shown in Table II and Fig. 7. Clearly, the postirradiation polymerization effect in halogenated aromatic polymers is negligible. PB which is a rubber material shows enormous postirradiation polymerization. COP and NGC, which both have the

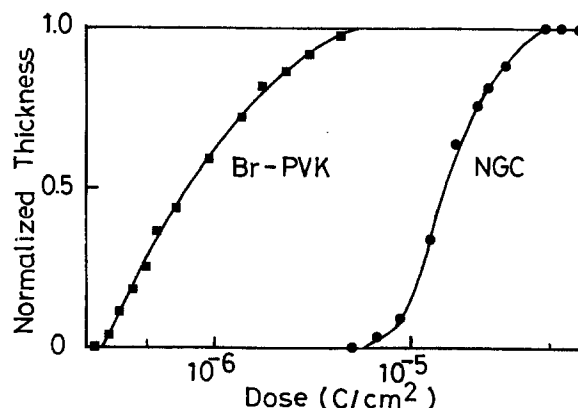


Fig. 5. Sensitivity curves for Br-PVK-1 and NGC-2

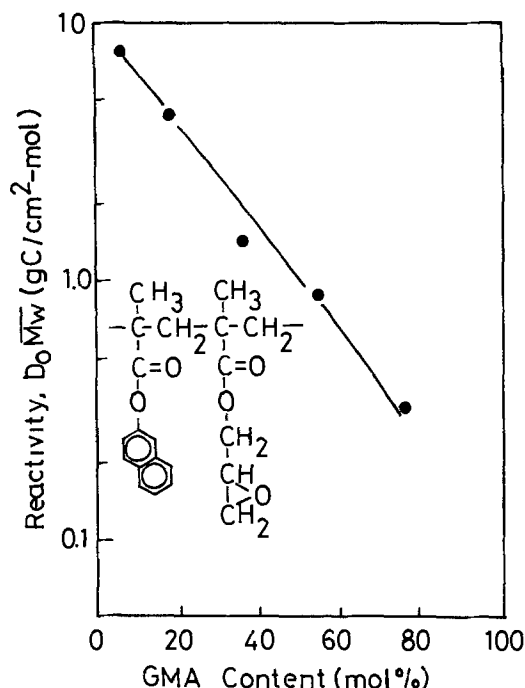


Fig. 6. Reactivity of NGC as a function of GMA content

epoxy group, show a moderate degree of postirradiation polymerization, but the effect is more obvious in COP than in NGC. This could be due to the difference in the T_g of these polymers.

Thus, it can be concluded that polymers with the reactive groups such as vinyl and epoxy group and moreover low T_g tend to result in more postirradiation polymerization. Chain reaction by reactive groups such as vinyl and epoxy group could be a major factor for postirradiation polymerization, but the degree strongly depends on the mobility of polymer chains, that is, T_g .

Effect of radical scavenger.—In order to determine whether neutral radical species are involved in the crosslinking reaction of halogenated polymers, the effect of radical scavenger on the resist sensitivity was measured. As a radical scavenger, diphenylpicrylhydrazyl (DPPH) was added to CMS and α M-CMS resist films. When the crosslinking reaction occurs via radical intermediates, the electron beam sensitivity should be decreased with the addition of radical scavenger (12). Figure 8a shows the variations of the sensitivity curve for CMS with the addition of DPPH. In Fig. 8b, S/S_0 , where S and S_0 are defined as electron beam sensitivity with and without the addition of DPPH, is plotted

Table II. Postirradiation polymerization of electron negative resists

Polymer	Reactive group	T_g ($^{\circ}$ C)	Reactivity $D_0 \times M_w$ (gC/cm ² -mol)	Postirradiation polymerization	Ref.
COP		10	0.023	obvious	(22)
PGMA		78	0.028	moderate	(23)
PB		-25	0.05	obvious	This paper
CMS		110	0.12	little	(2)
α M-CMS		170	0.23	little	This paper
IPS		156	0.42	little	(5)
CMN		113	0.28	little	This paper

T_g : glass transition temperature. COP: copolymer of glycidyl methacrylate and ethyl acrylate. PGMA: poly(glycidyl methacrylate). PB: poly(1,2-butadiene). CMS: chloromethylated polystyrene. α M-CMS: chloromethylated poly(α -methylstyrene). IPS: iodinated polystyrene. CMN: chloromethylated poly(β -naphthyl methacrylate). Ar: phenyl group.

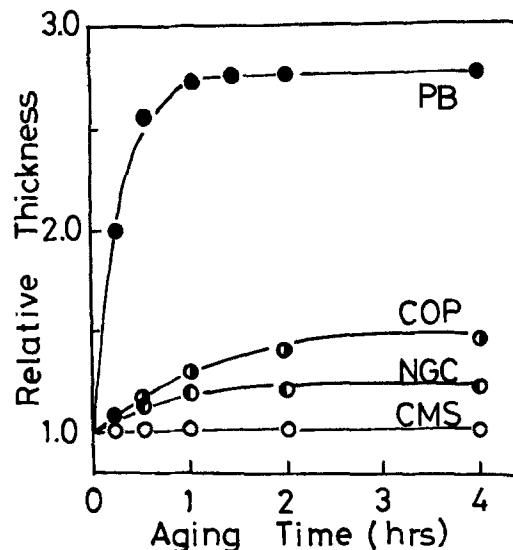


Fig. 7. Postirradiation polymerization effect in negative electron resists. Relative thickness is defined as T/T_0 , where T and T_0 are the resist thickness after development with and without retaining in the exposure machine.

against the concentration of DPPH for both CMS and α M-CMS. The sensitivity decreases are observed as the increase of DPPH concentration, which strongly suggests the participation of radical species.

Electron spin resonance (ESR) spectroscopy.—To detect radical species, ESR spectroscopy was studied for various polymers. Figure 9 shows typical ESR signals from CMS and PSt irradiated with 1 Mrad ^{60}Co γ -rays at room temperature. The CR of CMS was 0.71. The signal intensity from CMS is much larger than that of PSt at room temperature, indicating that large amounts of radicals are formed in CMS by high energy exposure and that they still remain alive. Deep UV exposure gave the same results. The ESR signal height of various CMS's are plotted against CR at the same dose in Fig. 10. The quantity of radical species increased almost proportionally with the increase in chloromethylation ratio. These results seem inconsistent with the results of reactivity saturation, but can be explained in terms of the high stability of these radicals. The variation of ESR signal height at room temperature with the aging time in a vacuum is shown in Fig. 11, where only a small decrease in signal intensity was observed, indicating a high stability of the radicals in the solid state. Since it is known that benzyl chloride is easily decomposed by γ -ray irradiation forming relatively stable benzyl radicals [G value for this scission is 4.3 (15)], radical species detected by ESR can be assigned to the benzyl-type radicals in CMS. Figure 12 shows ESR signals from CMS, benzyl chloride, and p-chloromethyltoluene irradiated with high pressure mercury lamp at -120°C . Though hyperfine structure was not finely detected because of spectrum broadening, the ESR signals from low molecular weight materials, especially in the case of p-chloromethyltoluene, were in close agreement with that of CMS. A portion of total radicals formed by the C-Cl bond dissociation in the chloromethyl group would disappear by a radical coupling reaction to produce a crosslink bond, but most remain in a stable form. In CMS, since it has more chloromethyl groups, more radical species form, but the number of stable radicals which are not involved in crosslinking may also increase, causing reactivity saturation. The details of the reaction mechanism will be discussed later.

The high stability of radical species could be attributed to the high T_g of the aromatic polymers, which may restrict the molecular motion of radicals to produce crosslinking bond. To test this speculation, film

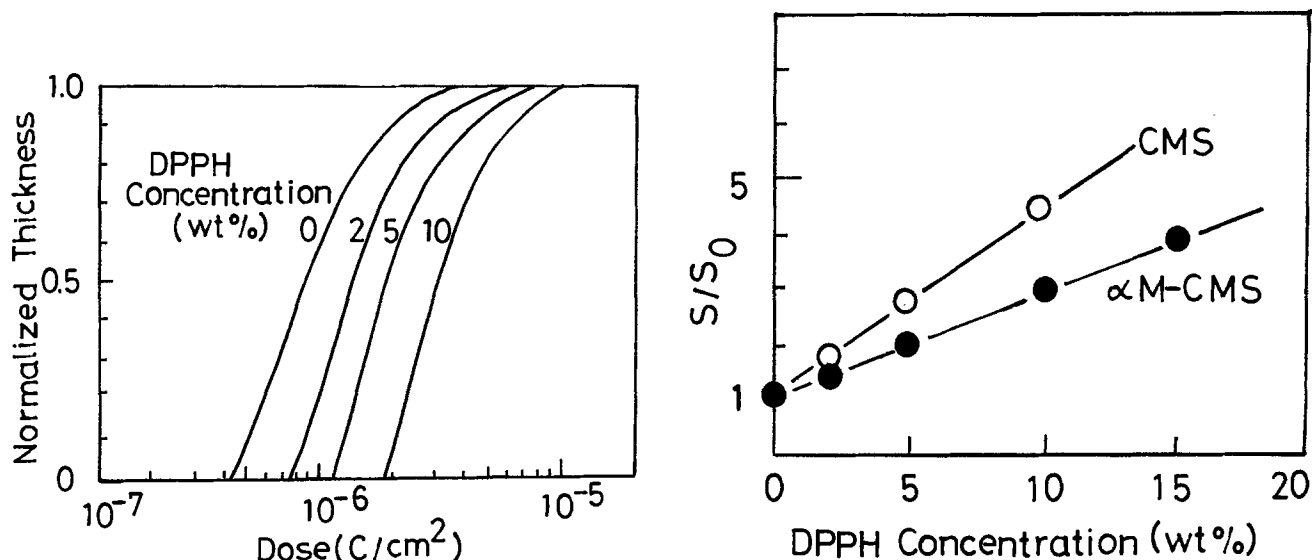


Fig. 8. Sensitivity curves for CMS (a, left) and sensitivity variations for CMS and α M-CMS (b, right) as a function of radical scavenger concentration. S and S_0 are defined as electron beam sensitivity with and without the addition of diphenylpicrylhydrazyl, DPPH.

temperature dependences of the ESR signal and electron beam sensitivity were measured. Figure 13 shows these results for CMS and α M-CMS. When the film temperature of CMS was raised to 60°C, the ESR signal intensity started to decrease and was small when the temperature was higher than T_g . The sensitivity of CMS increased with an increase in film temperature, and this dependence closely corresponded to that of the ESR intensity. In the case of α M-CMS, which has a T_g of 170°C much higher than that of CMS, raising the temperature at first showed little effect on both ESR signal intensity and the sensitivity. From 80°-90°C, the signal intensity gradually decreased, while the sensitivity increased with increasing temperature. However, even at 140°C, the ESR signal intensity of α M-CMS was still strong and the sensitivity enhancement due to temperature was not so large. These very close correlations between the temperature dependences of ESR spectral intensity and sensitivity strongly suggest that radical species detected by ESR spectroscopy have

the potential to crosslink polymer, but are firmly fixed in the film without crosslinking in a temperature region well below T_g . With increasing temperature, the restriction in the movement of these trapped radical species becomes less, and crosslinking bonds are formed from these radicals, leading the decrease of ESR signal height. The reason for the onset of motion in these radicals below T_g in both polymers may be related to the local relaxations of polymer chains around this temperature region.

Further evidence indicating the close relation between film temperature and the lifetime of radical species was demonstrated by an ESR study of PB film. A relatively strong and stable ESR signal was observed when a PB film was irradiated with a high pressure Hg lamp at -70°C, as shown in Fig. 14. This signal could not be detected at room temperature. Figure 15 shows the decrease in the ESR signal of PB irradiated at -70°C with aging time at various temperatures. Radicals disappeared rapidly upon raising the temperature. It is known that in the radiation-

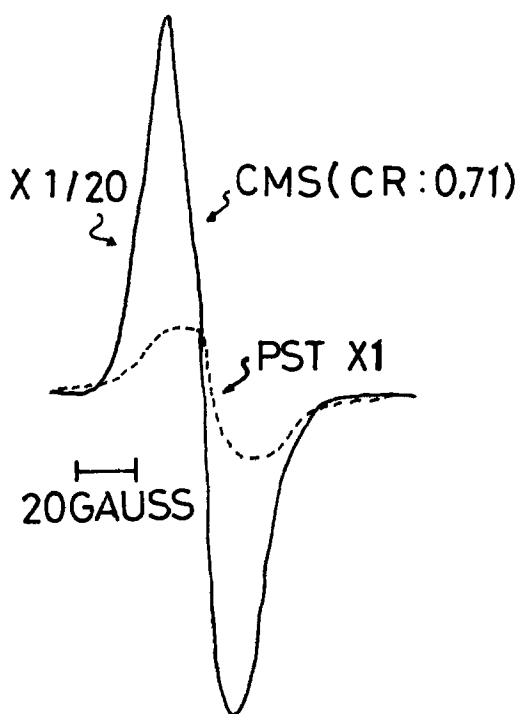


Fig. 9. ESR signals of CMS and PSt irradiated with 1 Mrad ⁶⁰Co γ -rays. CMS signal is drawn on a scale of one-twentieth.

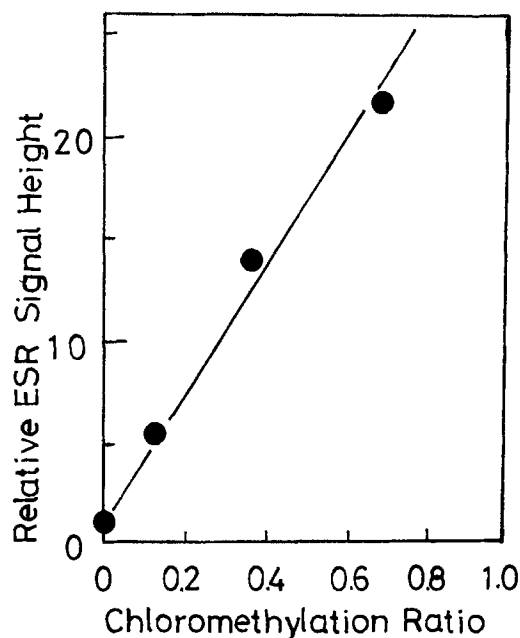


Fig. 10. Variation of ESR signal height as a function of molar chloromethylation for CMS after irradiation with 1 Mrad ⁶⁰Co γ -rays.

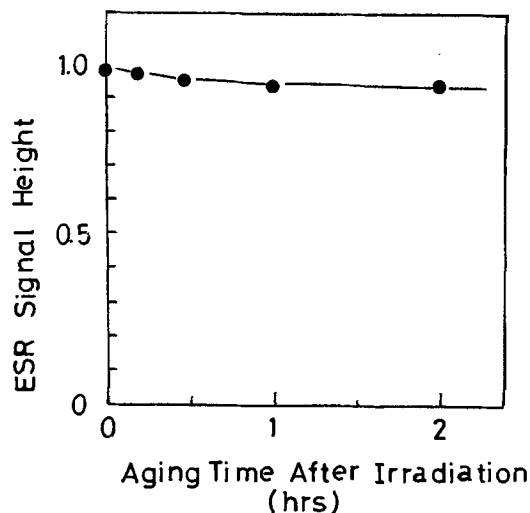


Fig. 11. Variation of the ESR signal height at room temperature with aging time.

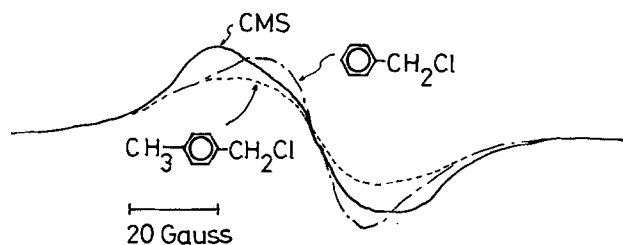


Fig. 12. ESR signals from CMS, benzylchloride and *p*-chloromethyltoluene after irradiation with high pressure mercury lamp at -120°C .

induced radical polymerization of a solid vinyl monomer such as acrylonitrile, propagating radicals can be detected by ESR at low temperature, and the post-irradiation polymerization carried out by heating (16). This suggests that PB vinyl-type radicals remain unreactive below T_g but easily crosslink via chain reactions above T_g .

Crosslinking mechanism of halogenated aromatic polymers.—Reactivity saturation.—In a previous paper (2), we proposed a crosslinking reaction mechanism for CMS resist, which is summarized in Fig. 16. The results obtained in this study support this mechanism. In halogenated polymers, major crosslinking reactions start from the dissociation of carbon-halogen bonds as shown in reaction [1]. The formation of radical species by this dissociation was confirmed by the ESR spectroscopy in this study. Reaction [2] is the crosslinking between two benzylic radicals. Reaction [3] is hydro-

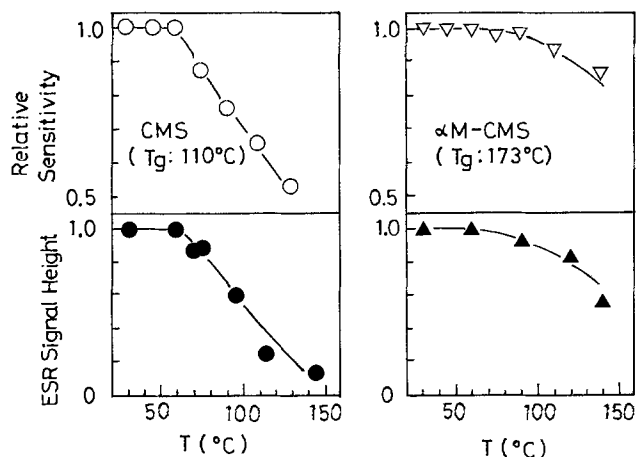


Fig. 13. Temperature dependences of the ESR signal intensity and electron beam sensitivity of CMS and $\alpha\text{M-CMS}$.



Fig. 14. ESR signal of polybutadiene irradiated with a high pressure Hg lamp at -70°C .

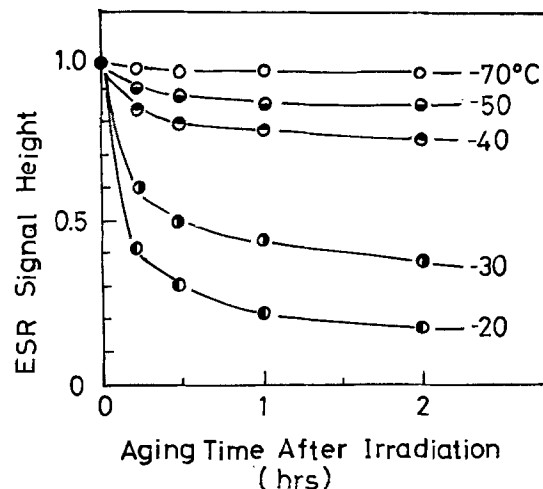


Fig. 15. Aging of the ESR signal intensity in PB at various temperatures. The films were irradiated with the Hg lamp at -70°C and left at a constant temperature during the ESR measurements.

gen subtraction by halogen atoms. When radicals formed by this reaction have a potential to crosslink polymer chains, reactions [4] and [5] can occur. In PSt-type resists, methine hydrogen atoms are readily abstracted by halogen atoms, forming benzylic-type radicals. This type of radical could crosslink polymer chains, because its structure is quite the same as that of radicals derived from the reaction [1] in CMS resist. In this case, a cleavage of the carbon-halogen bond makes two reactive radicals.

Some portion of the radicals in reaction [1] disappear via a recombination reaction, which was suggested as the reason for the reactivity saturation in IPS from kinetic analysis by Shiraishi *et al.* (5). However, we cannot agree with this idea, because no reasonable explanation for the relation between halogen content and recombination reaction rate was provided. Our results in Fig. 10 indicate that more radical species survive in more halogenated polymers, strongly suggesting that the total number of radicals formed by electron beam exposure is also increased.

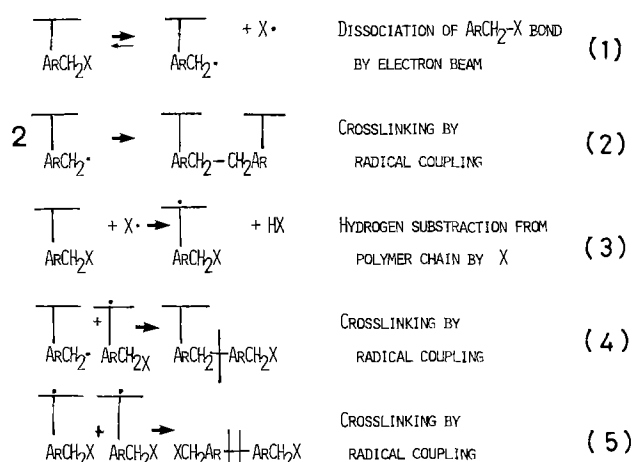


Fig. 16. Proposed crosslinking reaction mechanism for CMS resist

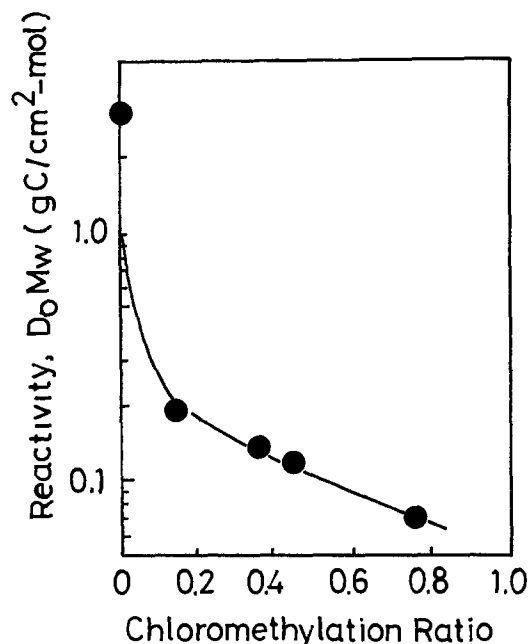


Fig. 17. Reactivity of CMS at 100°C as a function of molar chloromethylation ratio.

The fact that the chloromethyl group gives almost identical dependence between the reactivity and CR, despite a large difference in polymer chain structure, and that larger halogen atoms cause a more rapid saturation, allows us to propose a steric effect on the reactivity saturation. By assuming that two radicals must be located within a certain distance for the coupling reaction, we can explain all of the results with respect to the reactivity saturation. That is, more halogenation could make the average distance between two polymer chains longer, and large halogen atoms further increase this distance. The van der Waals radii of halogen atoms, 1.8Å for Cl, 1.95Å for Br, and 2.15Å for I, seem to correlate with the results of reactivity saturation. The high T_g 's of aromatic polymers may prevent the coupling reaction of two radicals which are separated slightly too far from each other. Since these trapped radicals can be released by heating the resist films, the reactivity of CMS samples with various CR was compared at 100°C, nearly equal to T_g , in order to confirm our model. As shown in Fig. 17, the reactivity saturation is not observed, although the dramatic increase at low CR is still present.

An alternative interpretation for the reactivity saturation may be the energy migration. The fact that CMS shows a high sensitivity to deep-UV light and CMN exhibits a response to mid-UV light indicates that the reaction proceeds via photoexcited states, mainly the triplet state of the halogenated aromatic ring (17). In the case of UV exposure, the same dependence between reactivity and CR was observed, indicating that the same reaction mechanism is operative as in electron beam exposure. It is known that halogenated aromatic rings can act as very effective trapping sites for triplet energy migration in aromatic polymer films (18). When UV light is absorbed in unsubstituted aromatic polymers, the excited states formed can be trapped by various sites, such as excimer sites or structural defects during migration among aromatic rings (19). Since in a slightly halogenated aromatic polymer excited energy is mainly "trapped" by the halogenated aromatic ring, very efficient dissociation of the carbon-halogen bonds are realized. This speculation can readily explain the abrupt sensitivity increase with very low halogen content. Thus, when the halogen content is high enough to form efficient traps, the dominant factor determining the sensitivity of halogenated aromatic polymers

will be not the content of reactive group, but the yield of photoexcited states, thus making reactivity independent of the halogen content. In order to verify this assumption, the primary processes of photophysics in resist films must be investigated.

Postirradiation polymerization.—Experiments with respect to the temperature dependence of ESR and electron beam sensitivity in CMS resists have clearly revealed the reason why little postirradiation polymerization occurs with halogenated aromatic polymers. The high T_g of the aromatic polymer prevents the reactive radical species surviving after the exposure at room temperature from crosslinking, and the low degree of chain reaction with the halogen group in the crosslinking reaction limits the reactions preceding postirradiation polymerization.

By contrast, the situation seems to be complex simple in epoxy-type resists. Recently, Tada studied the postirradiation polymerization effect of poly(glycidyl methacrylate) (PGMA) and PSt by using ESR spectroscopy (20). PSt showed a very weak ESR signal, which is consistent with our result. However, in PGMA, which is a highly sensitive negative resist containing epoxy groups, two kinds of radicals were detected. Short-lived radicals, observed only at low temperature, were assigned to those formed by the cleavage of epoxy rings. The relatively stable and stronger signal was assigned to radicals formed by the scission of the methacrylic main chain. He concluded that postirradiation polymerization in PGMA occurs via the coupling reaction between the latter radicals which survive at room temperature and decrease with time. This does not seem plausible, because main chain scission in methacrylic polymers is a positive-resist reaction. Actually, PGMA changes resist mode from negative to positive when exposed to deep-UV light which is absorbed not by the epoxy group but by the methacrylic unit, suggesting that the crosslinking reactivity of radicals formed by the main-chain scission is not significant.

However, Ohnishi *et al.* also demonstrated that stable radical species are associated with the postirradiation polymerization of COP containing the glycidyl methacrylate unit and the vinyl-type negative resist SEL-N (12). That is, the addition of DPPH considerably decreased the postirradiation polymerization and the kinetic, assuming that the radical coupling reaction occurs during postirradiation polymerization can explain the experimental results. The chain reaction in epoxy group is believed to proceed via ionic polymerization (21). The initiating species is generated by radiation and may be an anion radical, a cation, or a cation radical. The exposure-generated initiator attacks an epoxy moiety and cleaves it to generate a reactive oxygen species which can open a second epoxy group and generate a crosslinking. It is interesting that the addition of DPPH also decreased the sensitivity of these resists. These results indicate that radical species play an important role not only in the postirradiation polymerization but also in the chain-type crosslinking by the epoxy group. However, the origin and the structure of radical species in COP resist are not known, and the crosslinking reaction scheme in epoxy-type resists has not been well understood.

Conclusion

Various aromatic polymers were synthesized to elucidate the crosslinking mechanism of negative electron resists composed of halogenated aromatic polymers. The reactivity saturation with halogen content observed in CMS or IPS is a common behavior in halogenated aromatic polymers, but is not observed in aromatic polymers containing double-bond or epoxy groups. The saturation occurs more rapidly in polymers having larger halogen atoms. More halogenation and larger halogen atoms could make the separation

between reactive sites longer, causing the saturation of crosslinking reactivity. However, a sudden increase in the reactivity of lightly halogenated polymer may be attributed to the effective collection of excited-state energy migrating in the film due to trapping at the halogenated aromatic ring.

The significant participation of radical species in the crosslinking reaction has been demonstrated by ESR spectroscopy of irradiated polymers. The strong ESR signal observed in CMS or α M-CMS can be assigned to a benzyl-type radical formed by the dissociation of the chloromethyl group. This radical species gradually disappears with increasing temperature, and a quite similar variation is observed in the increase of resist sensitivity with temperature. This result strongly suggests that the observed radical species are associated with the crosslinking reaction. Taking into account that little postirradiation polymerization is observed in halogenated aromatic polymers, we propose that these radical species are tightly fixed in rigid polymer chains because of the high T_g of aromatic polymers. Both the high T_g and the step-wise reaction by the halogen group are responsible for the negligible postirradiation polymerization effect.

Acknowledgments

The authors are greatly indebted to Dr. S. Tagawa of Tokyo University and Mr. K. Murase for valuable discussion. They also thank Miss K. Iimura for her assistance in exposing resists.

Manuscript submitted June 12, 1983; revised manuscript received Jan. 20, 1984.

Nippon Telegraph and Telephone Public Corporation assisted in meeting the publication costs of this article.

REFERENCES

1. S. Imamura, *This Journal*, **126**, 1628 (1979).
2. S. Imamura, T. Tamamura, K. Harada, and S.

- Sugawara, *J. Appl. Polym. Sci.*, **27**, 937 (1982).
3. E. D. Feit and L. E. Stillwagon, *Polym. Eng. Sci.*, **17**, 1058 (1980).
4. L. F. Thompson, L. E. Stillwagon, and E. M. Doerries, *J. Vac. Sci. Technol.*, **15**, 938 (1978).
5. H. Shiraishi, Y. Taniguchi, S. Horigome, and S. Nonogaki, *Polym. Eng. Sci.*, **20**, 1054 (1980).
6. K. Sukegawa and S. Sugawara, *Jpn. J. Appl. Phys.*, **20**, 1583 (1981).
7. H. S. Choong and F. J. Kahn, *J. Vac. Sci. Technol.*, **19**, 1121 (1981).
8. J. H. Lai and L. T. Shepherd, *This Journal*, **126**, 696 (1979).
9. E. D. Feit and L. E. Stillwagon, *Polym. Eng. Sci.*, **17**, 1058 (1980).
10. T. Kobayashi and E. Arai, *J. Appl. Phys.*, **52**, 4785 (1981).
11. N. Atoda and H. Kawakatsu, *This Journal*, **123**, 1519 (1976).
12. Y. Ohnishi, M. Itoh, K. Mizuno, H. Gokan, and S. Fujiwara, *J. Vac. Sci. Technol.*, **19**, 1141 (1981).
13. K. Harada, *J. Appl. Polym. Sci.*, **27**, 1441 (1982).
14. S. Nonogaki, H. Morishita, and N. Saitou, *Appl. Polym. Symp.*, **23**, 117 (1974).
15. G. R. A. Johnson, M. C. Sauer, Jr., and J. M. Warman, *J. Chem. Phys.*, **50**, 4933 (1969).
16. R. Penssason and A. Dorkin, *J. Polym. Sci.*, **C4**, 881 (1963).
17. S. Imamura and S. Sugawara, *Jpn. J. Appl. Phys.*, **21**, 776 (1982).
18. B. Ranky and J. F. Rabek, "Photodegradation, Photooxidation and Photostabilization of Polymers," John Wiley & Sons, London (1975).
19. D. A. Holden and J. E. Guillet, *Macromolecules*, **13**, 289 (1980).
20. T. Tada, *This Journal*, **129**, 1070 (1982).
21. L. F. Thompson, C. G. Willson, and M. J. Bowden, "Introduction to Microlithography," American Chemical Society, Washington, D.C. (1983).
22. L. F. Thompson, J. P. Ballantyne, and E. D. Feit, *J. Vac. Sci. Technol.*, **12**, 1280 (1975).
23. Y. Taniguchi, Y. Hatano, H. Shiraishi, S. Horigome, S. Nonogaki, and K. Naraoka, *Jpn. J. Appl. Phys.*, **18**, 1143 (1979).

A Photoelectrochromic Memory and Display Device Based on Conducting Polymers

Olle Inganäs and Ingemar Lundström

Laboratory of Applied Physics, Department of Physics and Measurement Technology, University of Linköping, S-581 83 Linköping, Sweden

ABSTRACT

We report a new photoelectrochromic system for information storage and display applications. This system is based on the electrochromic properties of thin films of electrochemically generated conducting polymers. These materials can be switched between two states of optical absorption: a highly absorbing, almost-black film in the oxidized state, and an almost-transparent film in the reduced state. On an n-type semiconductor surface, oxidation of the conducting polymer requires illumination of the semiconductor surface. A thin film of conducting polymer photoelectrochemically generated onto a semiconductor surface can thus be reversibly bleached by a cathodic potential and blackened by anodic potential simultaneous with a light pulse. Such a device works as an optical memory which can be erased electrically and written optically with a scanning modulated light beam. We report on initial studies of the n-Si/poly(N-methylpyrrole) system in acetonitrile electrolyte.

The photoelectrochemical generation of thin films of conducting polymers (1) on semiconductor surfaces can be employed for pattern generation and optical information storage, but has so far only been used for corrosion protection of the surface (1, 2). The growth of a conducting polymer on a surface, metallic or semiconducting, leads to stronger light absorption—the polymer is generally brown/black—and decreased optical reflectance. A development of this read-only mem-

ory (ROM) is based on the electrochromic effects reported for polypyrrole and polypyrrole derivatives (3, 4). After electrochemical polymerization at a metal electrode, reversal of the potential applied to the polymer film leads to the reduction of the conducting polymer to an insulating and almost-transparent state. This process can be reversed by applying anodic bias. The electrochromic properties of conducting polymers are presently investigated for display purposes (5). Repeated switching of films up to 10^6 cycles has been obtained (6).

Key words: optical memories, photoelectrochemistry, electrochromics, poly(N-methylpyrrole).

In an electrochemical polymerization, oxidation of the monomer to be electropolymerized is suppressed at an n-type semiconductor in the absence of minority charge carriers. These can be generated by light. This is equally true for the oxidation of the reduced polymer film on a semiconductor surface. Thus the oxidized state is reached by applying anodic bias and illuminating the surface. This photoelectrochromic effect can be used for optical storage of information or for display purposes. Similar systems have been reported using metal deposition at semiconductor surfaces (7), photoelectroreduction of heptylviologen at p-GaAs (8) and reversible reduction and photoelectrooxidation of Prussian blue on TiO_2 surfaces (9). All of these systems are based on semiconducting photoelectrodes which generate photocurrents, giving reduction of metal ions or organic molecules or oxidation of a thin film deposited on a semiconductor substrate. The generation of patterns is due to a scanning or modulated light source. Similar electrochemical reactions have also been used on metal electrodes for display purposes (10).

We report studies of a system based on a conducting polymer on n-Si surfaces in an organic electrolyte. This system differs with respect to the first two reported systems in that the electrochromic effect occurs within a thin solid film anchored onto the surface, and that the semiconductor surface is protected by this film (11). It also differs with respect to the third system in that only a fraction of the thin film is actually reduced/oxidized with the polymer (3a), whereas the Prussian blue is fully reduced/oxidized (9). The poly(N-methylpyrrole) polymer was chosen because it is more stable than the pyrrole polymer in electrochromic applications (4).

Experiments

Single crystal n-type silicon ($0.02\text{--}0.03\ \Omega\text{cm}$) (111) were mounted on glass slides using epoxy. An In/Ga eutectic was used for the back contact. After cleaning and etching the front surface (10% HF, 10s), it was transferred to an 0.1M/0.1M N-methylpyrrole/tetraethylammonium perchlorate electrolyte in acetonitrile.

The photoelectrochemical formation of the polymer was performed at 1.0V vs. a saturated calomel electrode (SCE), potentiostated in a three-electrode, two-compartment system. Nitrogen was bubbled through the solution before polymerization in order to exclude oxygen. A tungsten/halogen lamp provided homogeneous illumination at $175\ \text{mW}/\text{cm}^2$ on the $2\ \text{cm}^2$ silicon surface. Different thicknesses of polymer films were used, as calculated from the number of coulombs transferred. The samples corresponded to $80\text{--}100\ \text{mC}/\text{cm}^2$, and the films were smooth and blue/violet. The thickness can be estimated to $0.1\text{--}0.2\ \mu\text{m}$.

The photoelectrochromic studies were performed in a 0.1M $\text{Et}_4\text{NClO}_4/\text{CH}_3\text{CN}$ electrolyte, with oxygen present. No iR compensation was used. The reflectance of the silicon electrode was measured with a very simple setup, consisting of a red LED fed with a sinewave (274 Hz) illuminating the surface at approximately 45° angle of incidence. The primary reflected beam entered a light detector, giving a signal proportional to the reflected-light intensity. This was fed to a lock-in amplifier. The light used for photooxidation (write light) was entered via an optic fiber. No correction was made for light reflected from the windows of the optical cuvette enclosing the electrolyte or from other reflecting surfaces.

Results

The reflectance from a surface coated with the polymer decreases for the samples studied to approximately 25% of that of a bare-silicon surface. When switching the polymer by applying cathodic bias, the reflectance increases. A potentiostatic cycle (Fig. 1) applied to a sample from cathodic potentials towards anodic po-

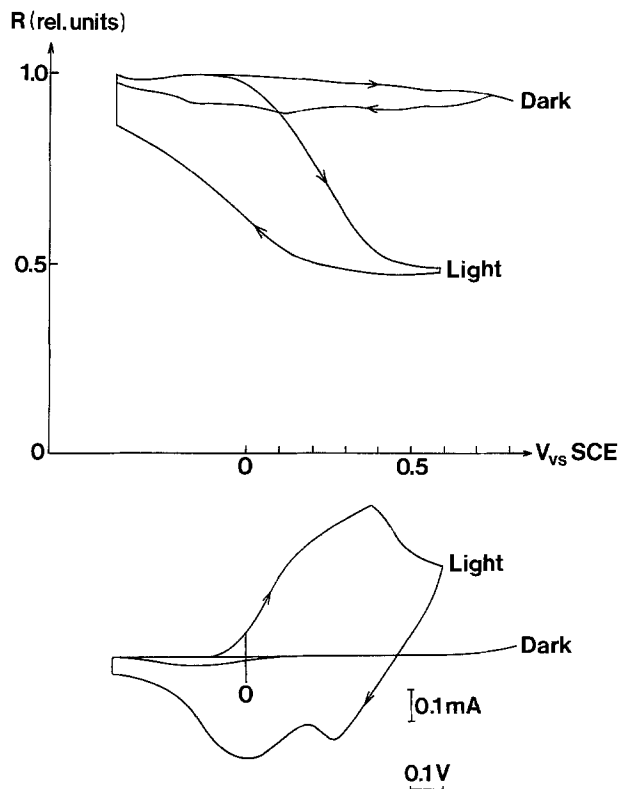


Fig. 1. Upper curve: the optical reflectance from the surface is recorded as a function of potential. The strong decrease of reflectance occurs during the flow of photogenerated-hole currents. With no write-light impinging on the surface, a small change of reflectance still occurs. This is due to the red LED light and light from the surroundings. Lower curve: potentiostatic sweep at $10\ \text{mV}/\text{s}$ from $-0.4\ \text{V}$ vs. SCE to 0.6 and $0.7\ \text{V}$ vs. SCE of an n-Si/poly(N-methylpyrrole) structure ($80\ \text{mC}/\text{cm}^2$) in the presence and absence of light (approximately $25\ \text{mW}/\text{cm}^2$). The electrolyte was $0.1\ \text{M}\ \text{Et}_4\text{NClO}_4$ in CH_3CN . Only a very small leakage current flows during the sweep in dark. With light on, oxidation of the film starts at $0.0\ \text{V}$ vs. SCE, and the oxidation current reaches a maximum at $0.4\ \text{V}$ vs. SCE.

tential, with and without the write-light ($25\ \text{mW}/\text{cm}^2$), shows the gradual decrease of optical reflectance as light-induced currents flow. In the absence of the write-light, only small changes of the reflectance occur, which probably are due to the LED-light induced photocurrent. After the oxidation of the polymer to the absorbing state, reduction in a two-peaked wave occurs in the range of 0.3 to $-0.2\ \text{V}$ vs. SCE. The optical contrast, in this case approximately 50%, has not been optimized, and can probably be increased by judicious choice of film thickness, angle of incidence, and geometry.

From Fig. 1 it is concluded that writing using a light pulse can be done at potentials more positive than $0.0\ \text{V}$ vs. SCE, and that the erasing process requires at least the potential $0.0\ \text{V}$ vs. SCE. However, it must be noted that the rate of change of the reflectance is highly dependent on the choice of writing and erasing potentials. In Fig. 2 a plot is shown of the reflectance as a function of charge transferred on light-induced oxidation of the film at $0.7\ \text{V}$ vs. SCE at three different light intensities, obtained by the use of gray density filters. Even though the starting points are somewhat different, the R vs. Q graph is identical in shape with light intensities varying over one order of magnitude. The reduction process of the film is also identical for these states, as shown by the cathodic side of the graph. The coulometric efficiency of the process (i.e., the fraction of the anodic charge that is removed during the cathodic polarization) is between 75% and 95%. This points to the possibility of side reactions occurring. It can

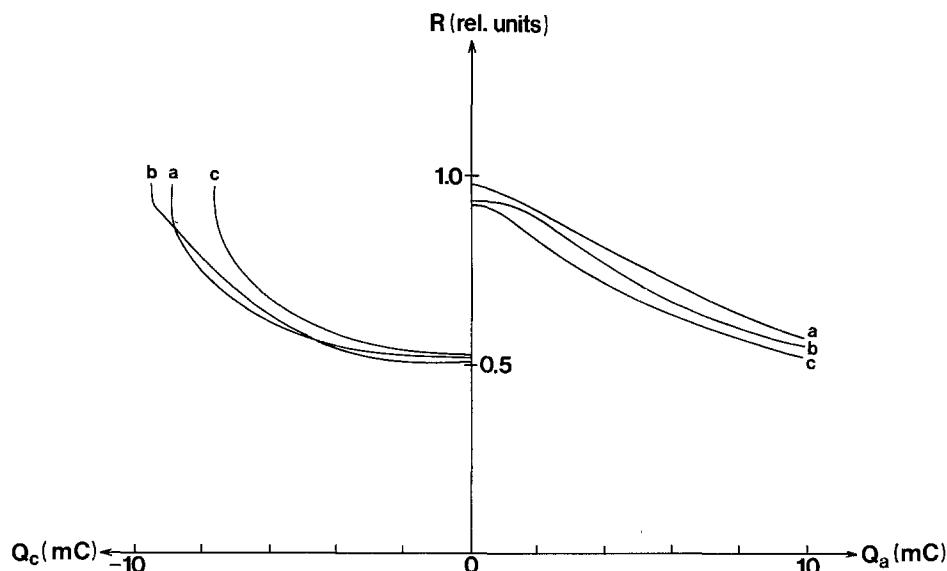


Fig. 2. Reflectance vs. charge transferred during three cycles. The right-hand side of the diagram shows the anodic process (write phase) at a potential of 0.7V vs. SCE and at three different light intensities, (a) 100%, (b) 49%, and (c) 9.8% of 25 mW/cm², obtained using gray filters. The left-hand side shows the subsequent cathodic erase phases at -0.7V vs. SCE.

also be concluded from the graph that a minor increase of the reflectance occurs without a perceptible amount of charge being transferred. It should be observed that the graphs are nonlinear in Q .

The oxidation of the polymer to the fully oxidized state occurs with only a fraction of the sites in the polymer being affected (3). Continued oxidation beyond this point leads to only small changes of the optical absorption. Furthermore, the coulometric efficiency tends to decrease with increasing anodic charge.

Discussion

Three parameters are of essential importance for optimizing the switching time of the memory: writing potential, light intensity, and erase potential. The writing gets faster with more anodic potential, as this will bring about a more efficient collection of minority charge carriers. The intensity of light determines the number of charge carriers available for collection. A more cathodic erasing potential should be chosen for rapid switching. However, these potentials should also be chosen so as to give lasting operation, that is, within the stability range of the electrolyte and of the polymer material. Side reactions on the semiconductor surface must also be avoided, as the adhesion of the polymer film is of essential importance with respect to the lifetime of a device.

N-methylpyrrole polymers show much wider stability ranges than do pyrrole polymers (12), and very anodic (>1.0V vs. SCE) write potentials can be chosen without deterioration. However, a strong, focused light beam at 0.1-1 W/cm² will give a very rapid write process, and it may be preferable to use this parameter for optimization of the write process. The reduction of the polymer is probably the process determining the duration of the write/erase cycle, and this can only be enhanced by applying strong cathodic bias. The stability results on poly(N-methylpyrrole) indicate that it should be possible to go to at least -1.0V vs. SCE. The minimal time of switching reported on metals is 0.1s (3, 5).

The nonlinear relationship of reflectance vs. charge transferred may be a difficulty if the structure should be used as an exposure meter, but need not be a problem when used for digital storage in memory and display devices. Optimization of the device also requires choice of the thickness of the polymer with respect to the contrast required, as well as the time required for write/erase cycles. These considerations may be conflicting, as a thick film will be intrinsically slower in cathodic switching, and also slower in anodic writing: less light will be transmitted through the film, generating photocurrent required for oxidation of the

film. However, a thin film may not give the contrast required. Further development of the device would have to address this question.

As to the stability of the electrochromic material, it is reported (13) that oxygen does not affect the redox process of poly(N-methylpyrrole), neither after exposure to atmosphere nor with oxygen present in the electrolyte. With polypyrrole, oxygen attacks both the reduced and oxidized form of the polymer. This is related to the redox potential of the polymer, which is more anodic with the methyl-substituted polymer. With polypyrrole, the presence of water in the organic electrolyte strongly affects the cyclic voltammograms of the redox process (14). It has also been shown that stable electrochromic switching is obtained with aqueous electrolytes (6, 15), at least with some of the electrochemically prepared conducting polymers. No systematic study of the electrochromic characteristics of different electrolytes has been reported.

A major drawback of the system studied is the instability of the oxidized polymer in contact with electrolyte: it will spontaneously revert to the reduced state at open-circuit conditions. The transparent reduced state, on the other hand, appears to be stable.

Conclusion

We have demonstrated the possibility of constructing a photoelectrochromic device based on a semiconductor surface modified with a photoelectrochemically generated conducting polymer. This device could be used as an optical storage memory that can be erased and rewritten. It can also be used as a display device where light is used to alter the optical state of the display, lowering the power-supply requirements. It could also be used as both an optically and electrically readable exposure meter.

The electrochemical growth of conducting polymers on p-type semiconductors is also possible. On a p-type surface, reduction of the polymer to the transparent state is not possible without light, as no electrons are available for reduction (7). This opens up the possibility of a complementary optical device.

The propagation of light in thin films, one of the basic components of optronics, can also be controlled through the use of semiconductor/polymer devices. For instance, optical coupling of two light beams through a thin film of conducting polymer could be used for light amplification.

The use of a liquid electrolyte is one of the major drawbacks of photoelectrochromic systems, and substitution with a solid-state electrolyte would be very attractive. Earlier work in our laboratory (16) has shown the feasibility of using thin films of a polymer

electrolyte, polyethylene oxide, as a contact to semiconductors coated with thin films of conducting polymers. Preliminary experiments show that photoinduced oxidation of the polymer also occurs in these systems, and this indicates the possibility of extending the photoelectrochromic effects to a polymer electrolyte.

Acknowledgments

Advice from Dr. Robert Bjorklund is much appreciated. This work was supported by the National Swedish Board for Technical Development.

Manuscript submitted Sept. 26, 1983; revised manuscript received Jan. 3, 1984.

The Linköping Institute of Technology assisted in meeting the publication costs of this article.

REFERENCES

1. R. Noufi, D. Tench, and L. F. Warren, *This Journal*, **127**, 2310 (1980).
2. T. Skotheim, I. Lundström, and J. Prejza, *ibid.*, **128**, 1625 (1981).
3. (a) A. F. Diaz and J. I. Castillo, *J. Chem. Soc., Chem. Commun.*, **397** (1980); (b) A. F. Diaz, U.S. Pat. 4,304,465 (1981).
4. K. K. Kanazawa, A. F. Diaz, M. T. Krounbi, and G. B. Street, *Synth. Metall.*, **4**, 119 (1981).
5. M. Gazard, J. C. Dubois, M. Champagne, F. Garnier, and G. Tourillon, *J. Phys. (Paris)*, **44**, 537 (1983).
6. R. Bjorklund and I. Lundström, Personal communication.
7. T. Inoue, A. Fujishima, and K. Honda, *This Journal*, **127**, 1582 (1980).
8. B. Reichman, F.-R. F. Fan, and A. J. Bard, *ibid.*, **127**, 333 (1980).
9. D. DeBerry and A. Viehbeck, *ibid.*, **130**, 249 (1983).
10. I. F. Chang, in "Nonemissive Electrooptic Displays," A. R. Kmetz and F. K. von Willisen, Editors, Plenum Press, New York (1976).
11. T. Skotheim, L. G. Petersson, O. Inganäs, and I. Lundström, *This Journal*, **129**, 1737 (1982).
12. A. Mohammadi and O. Inganäs, Unpublished results.
13. A. F. Diaz, J. I. Castillo, J. A. Logan, and W. Y. Lee, *J. Electroanal. Chem.*, **129**, 115 (1981).
14. E. M. Genies, G. Bidan, and A. F. Diaz, *ibid.*, **149**, 101 (1983).
15. F. Garnier, G. Tourillon, M. Gazard, and J. C. Dubois, *ibid.*, **148**, 299 (1983).
16. T. Skotheim and I. Lundström, *This Journal*, **129**, 894 (1982).

A Study of Contamination during Reactive Ion Etching of SiO₂

M. Valente¹ and G. Queirolo*

SGS-Ates Componenti Elettronici SpA, Agrate Brianza, Milano, Italy

ABSTRACT

Plasma-wall interaction during the reactive ion etching of silicon dioxide was studied with Auger electron spectroscopy. An Al containing film was observed to deposit on the substrate to be etched, slowing down or even stopping the etching process; a fluorocarbon film due to CHF₃ plasma polymerization was also found to grow on the contaminating film. The coverage of the cathode surface by a thick continuous fluorocarbon film effectively avoids this plasma-wall interaction, and allows the etching process to continue to the SiO₂/Si interface.

Reactive ion etching (RIE) of SiO₂ in a fluorine deficient discharge (e.g., CHF₃ plus O₂, or CF₄ plus H₂, in suitable ratios) is an anisotropic and selective dry etching technique widely employed to delineate contact holes in VLSI devices. The etching mechanism is not yet sufficiently understood, though it is evident that a polymer formation process is in competition with the etching of SiO₂. The predominance of either polymerization or etching depends on the energy of the impinging ions, the nature of the material, and the ratio of the two gases.

The presence of a significant voltage between the RF electrode and the discharge is of importance because the substrates undergo bombardment by energetic ions (100–500 eV being typical energies). Since the energy threshold for sputtering of metals is exceeded, it is not surprising that purely physical sputtering effects take place, when the cathode is partially or totally covered by certain metals (1) or when a nonerodable metal mask is used in place of a standard photoresist one (2). This consideration is not applied to all metals, but only to those whose fluorides are not volatile.

The aim of this paper is to demonstrate the nature of contaminants during RIE of SiO₂ with Auger electron spectroscopy (AES); we also illustrate the role played by such contaminants and suggest a remedy to completely eliminate the source of contamination in our particular system.

Experimental

Etching system.—All the experiments were performed within a commercial etching system,² with both RIE and plasma etching (PE) capabilities. The etching gas was a mixture of CHF₃ and O₂; the operating pressure was kept constant at 10.7 Pa (80 mtorr); flow rates were held at 60.0 sccm for CHF₃ and 4.0 sccm for O₂. The gas pressure was monitored with an ion gauge and a capacitive manometer;³ RF power density (at 13.56 MHz) was kept at 0.3 W cm⁻². Substrate temperature was monitored and maintained constant at 22°C.

The system is pumped by a two-stage Roots pump backed by a two-vane rotary pump, and has a base pressure of 0.013 Pa (1.10⁻⁴ torr). The system described here was originally designed for use with chlorine containing gas; hence, aluminum and aluminum oxide were chosen as electrode materials.

AES system.—All the measurements given here were performed within a Varian scanning Auger microprobe, equipped with a variable aperture CMA and LaB₆ cathode. The base pressure of the system is 3 · 10⁻⁸ Pa (2 · 10⁻¹⁰ torr). The primary energy and current were adjusted to minimize sample charging problems and to prevent electron beam-induced reduction or desorption effects. Ar⁺ or Xe⁺ ion etching was performed in order to obtain some in-depth information.

*Electrochemical Society Active Member.

¹ Present address: Montefiuos, Via Bonfadini 148, I-20138 Milano, Italy.

Key words: reactive ion etching, Auger analysis, contamination.

² PK 2440, made by Plasma-Therm Incorporated, Kresson, New Jersey 08053.

³ Baratron Type 220, AHS, made by MKS Instruments, Burlington, Massachusetts 01803.

Sample preparation.—RIE experiments were performed using as a test vehicle a MOS device with contact hole dimensions of approximately 3 μm . Auger measurements were performed on much larger areas. A preliminary scanning electron analysis showed, in fact, that the residues found in the contact holes, and described below, were also present in these areas. The layer to be etched was composed of densified phosphorus silica glass (PSG), about 0.9 μm thick and with a phosphorus content of about 10 w/o; the PSG was deposited over a 0.1 μm thick film of thermal silicon dioxide. HPR 204⁴ resist 1.3 μm thick was used; it was hard-baked (140°C, 30 min) before the etching, in order to enhance its stability during the process.

Results with the RIE system in its original configuration.—Samples processed in the RIE system in its original configuration, as described above, showed the presence of a contaminating residue. In some cases, due to this residue, the etching process failed to reach the silicon dioxide/silicon interface and stopped somewhere in between. In other cases, roughening of the surface was evident, with different morphology, depending on the amount of contamination (see SEM photographs in Fig. 1). This film is of an insulating nature, and its uppermost layer originates a quite singular charging phenomenon, described by the $E \cdot N(E)$ vs. E spectrum of Fig. 2.

The spectrum is severely distorted at energies lower than about 250 eV; in particular, no emission was found at energies lower than 140 eV. On the other hand, no

⁴ Hunt Chemical Corporation.

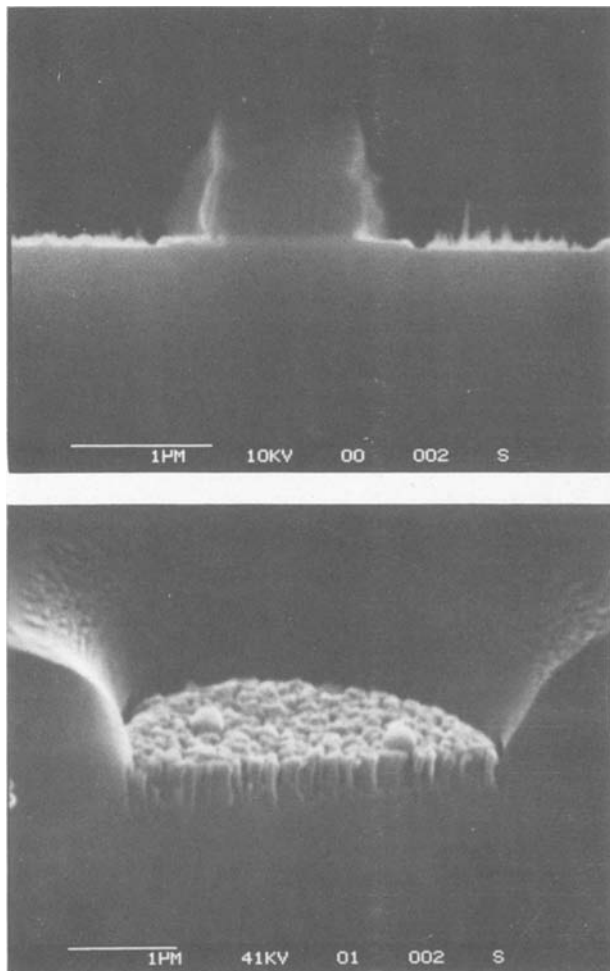


Fig. 1. SEM photographs, showing surface texturing: (a, top) in presence of slight amounts of contaminant (b, bottom) in presence of a heavy contamination.

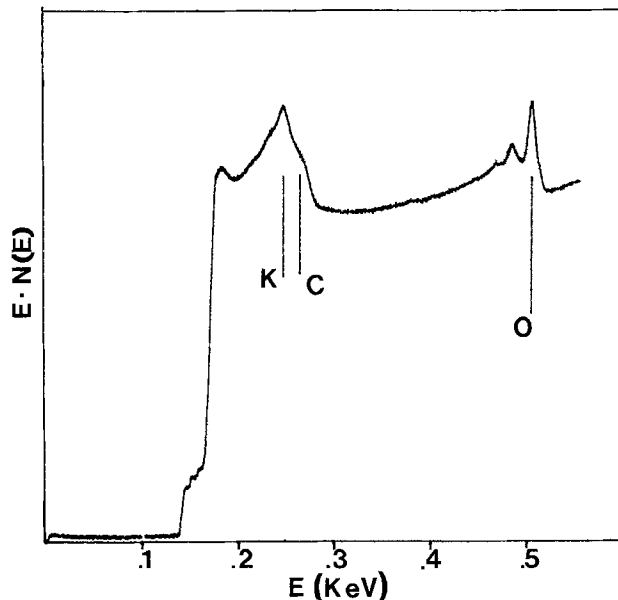


Fig. 2. Auger spectrum recorded during analysis of the insulating film (surface); K is an accidental contamination in this particular sample.

effect at all was noticed on higher energy peaks (like O_{KII}) which were found to be at their correct energy. This fact means that the higher energy Auger electrons see the sample as neutral, and only the low energy secondary and Auger electrons are affected by the phenomenon. At present, the origin of this behavior is not clear, but it is conceivable that a double layer of negative and positive charges is created in the surface layer; in this case, only electrons generated within this double layer will be affected.

The spectrum distortion decreases as soon as the sample is etched with Ar or Xe ions, and nearly disappears after etching for a few seconds, or after the removal of only a few angstroms. At this point, the AES analysis shows the presence of Al, Si, C, O, and F (Fig. 3). Both the energy and shape of Al and Si peaks are typical of some bonded states (for instance Al₂O₃ or SiO₂). Observation of the peak-to-peak height of the peaks during the ion etching shows that F and C are contained in a film grown over the Al contaminating film.

In general, F adsorbed on Si or Al is very easily desorbed by the electron beam used for the AES analysis, even at current density as low as 10⁻² A/cm², at 2 keV beam energy. On the contrary, the F contained in the fluorocarbon layer exhibits a noticeably strong stability and is only partially desorbed after an electron dose which is several orders of magnitude greater than the above figure. This stability suggests a very strong bond between C and F, similar, for instance, to that found in PTFE [poly(tetrafluoroethylene)]. This statement is in agreement with the data contained in the literature (3), reporting that a Teflon-like polymeric film is one of the main products in a CHF₃ discharge.

For the above considerations, the active role played by the materials exposed to the plasma is evident. Al and Al₂O₃ at the cathode surface are converted, in a CHF₃ discharge, to aluminum fluoride; due to its very low vapor pressure at room temperature, this compound cannot be removed. A similar behavior is described in Ref. (2) for Al and Cu in CF₄ discharge. Such a compound is sputtered from the surface of the cathode by the high energy (500 eV) ions impinging on it; after multiple collisions with the gas molecules, it is eventually scattered back onto samples mounted on the cathode, where it can act as a nonuniform mask and texture the surface. Although the proposed mechanism is still rather speculative, it is a good work-

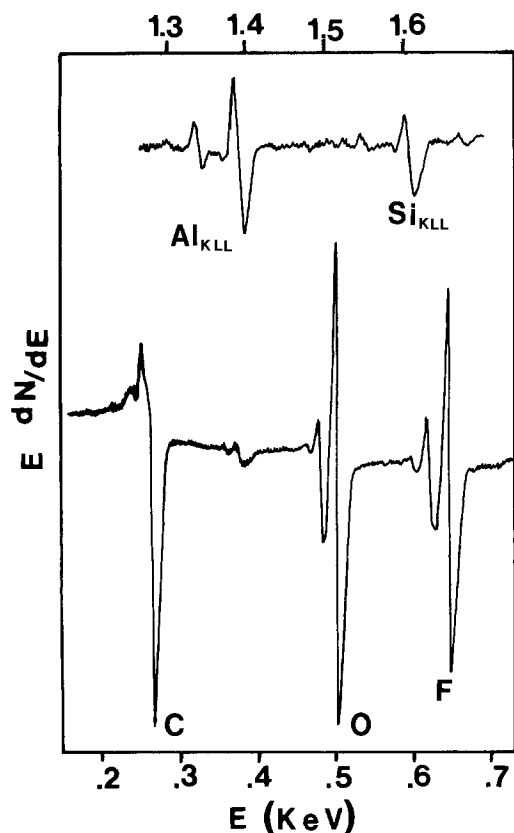


Fig. 3. Auger spectrum of the sample of Fig. 2 after a short ion-etch.

ing hypothesis and explains all our experimental observations.

Reactor chamber passivation.—In order to fully demonstrate the above statement, we envisaged a procedure that would allow us to passivate the cathode surface and avoid contamination. The configuration of the reactor was reverted to the PE mode, and RF power was fed to the upper electrode, the lower electrode being grounded. A pure CHF_3 (60 sccm) discharge was ignited at the same power density and pressure used for previous RIE experiments in order to deposit a polymer film of thickness higher than $0.5 \mu\text{m}$ over the exposed surfaces of the reaction chamber. In order to further study the nature of the fluorocarbon film without interference from the Al contamination, some (100) polished silicon test wafers were introduced into the chamber during a deposition run. Ellipsometric measurements performed on these samples yielded a refractive index value of 1.39, in agreement with the figure reported for PTFE films (1.30-1.40). Auger analysis showed only C and F; the film appeared to be richer in F than PTFE (see Fig. 4 and 5). A mass spectrometric analysis performed during He reactive ion etching of the former sample showed a high concentration of HF being released by the film under He^+ bombardment. Therefore, we supposed that the fluorocarbon film is a PTFE film, encapsulating large amounts of HF. After the passivation treatment, we restored the initial configuration and processed a few runs with the parameters used previously.

Results after chamber passivation.—No roughening effect was found on samples processed on the passivated RIE system. When the etching process was stopped before reaching the SiO_2/Si interface, an optically clean SiO_2 surface was obtained; interferometric measurements of the remaining SiO_2 thickness were now possible, whereas in the previous experiments ambiguous results were usually obtained. In samples

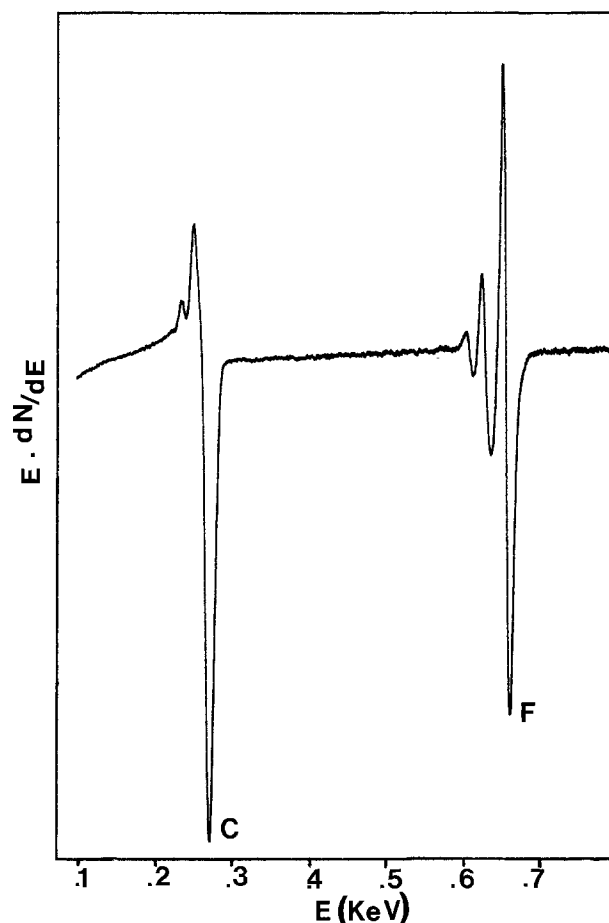


Fig. 4. Auger spectrum of the fluorocarbon film, deposited on the lower electrode, in the PE configuration.

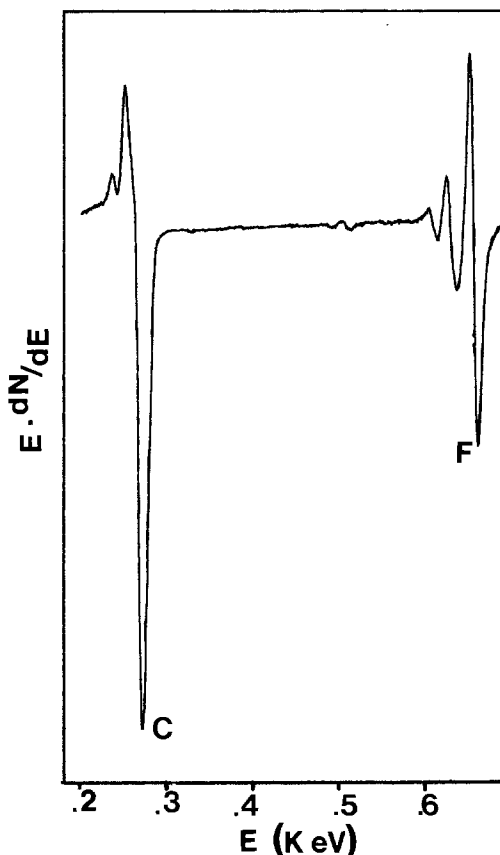


Fig. 5. Auger spectrum of a PTFE film on silicon.

where the etching had been completed, the silicon surface exhibited very high reflectance without any residue. This was in contrast with the samples processed in the unpassivated chamber. In both cases, no contaminant was detected by AES analysis.

Summary and Discussion

To summarize, any metal on the cathode that is not reactive ion etched by the plasma (*i.e.*, whose halide is not sufficiently volatile) will contaminate the SiO₂ samples, leading to anomalously low etch rates, polymer deposition, roughening of the surface, degradation of the electrical device parameters [as found in Ref. (1, 4)]. We have demonstrated that if a deposition cycle in the PE configuration was performed previously under suitable conditions (without any load), a polymer film can be grown on the cathode that will prevent any contamination in the following etching cycle. This solution can be considered preferable to the use of a perforated catcher plate, described in Ref. (1), because it does not simply minimize this effect but completely eliminates it. On the other hand, this procedure has the disadvantage of requiring periodical regrowth of the polymer film which is consumed dur-

ing the etching cycle. 0.5 μm thick film can last for only one etching cycle, but a thicker polymer film can be grown for more etching cycles.

Acknowledgments

We wish to thank Dr. M. Bergoglio of the Istituto Metrologico Colonnetti, Torino, for calibrating the MKS 220 AHS capacitive manometer, against an interferometric manobarometer.

Manuscript submitted June 3, 1983; revised manuscript received Dec. 19, 1983.

SGS-Ates Componenti Elettronici SpA assisted in meeting the publication costs of this article.

REFERENCES

1. L. M. Ephrath and R. S. Bennett, *This Journal*, **129**, 1822 (1982).
2. G. C. Schwartz, L. B. Rothman, and T. J. Schopen, *ibid.*, **126**, 464 (1979).
3. L. M. Ephrath and E. J. Petrillo, *ibid.*, **129**, 2282 (1982).
4. L. M. Ephrath and D. J. Di Maria, *Solid State Technol.*, **182** (April 1981).

Molybdenum Taper Dry Etching

Tetsuo Hosoya, Shin-ichi Ohfuji, and Toshitaka Shibata

Nippon Telegraph and Telephone Public Corporation, Atsugi Electrical Communication Laboratory, 1839, Ono, Atsugi-shi, Kanagawa Prefecture, 243-01 Japan

ABSTRACT

A taper dry etching technique for molybdenum films is proposed. The dry etching characteristics of oxygen-doped Mo films in a CCl₄-O₂ discharge are studied. It is found that oxygen-doped Mo films are etched at a higher rate than oxygen-undoped Mo film and that, in oxygen-doped Mo films, undercutting occurs differently from oxygen-undoped Mo film. Making use of the Mo etching characteristics, tapered Mo patterns with little linewidth loss to resist patterns are obtained by plasma etching of the Mo double layer, namely an oxygen-doped Mo film over an oxygen-undoped Mo film. The taper angle is varied from 40° to 60° by varying the thickness ratio of the oxygen-doped Mo film to the total Mo double layer. This technique promises to improve an interconnection yield in LSI's through reduction of wiring disconnection or shorts over the tapered-Mo steps.

In order to increase LSI packing density, pattern dimensions must be fine. For highly accurate transfer of a resist pattern to the lower material, dry etching techniques, especially anisotropic etching techniques such as reactive ion etching, are effective. This is because directional etching prevents the occurrence of undercutting and produces etched patterns whose dimensions differ little from those of the resist patterns.

However, patterns etched by this kind of etching method have a vertical edge profile, that is, the etched pattern sidewalls are perpendicular to the substrate. Etched patterns having the vertical profile are undesirable for the following interconnection metallization process, since metallization becomes thin or discontinuous where it passes over the etched pattern edges, and, as a result, the metal interconnection yield deteriorates.

One method for improving the metal-interconnection yield without making great changes in LSI-fabrication processes is to produce an etched pattern with tapered sidewalls. Several papers have been published which have reported on taper dry etching techniques, such as tapered via etching using an erodible masking material (1) and tapered silicon etching in which a positive bias is applied to the cathode of a parallel-plate reactor with the wafers placed on the anode (2).

This paper proposes a taper dry etching technique for molybdenum films. Mo films have been used as self-

aligned gates and interconnections for MOS LSI's (3, 4). It is known that vacuum-deposited Mo films on SiO₂ are polycrystalline and have a fiber structure, and that the Mo film resistivity increases as the oxygen content in the grain boundary increases (5). Therefore, in order to obtain Mo films with low resistivity, it is essential to eliminate oxygen from the Mo-deposition atmosphere. However, it has been found that the Mo-film etching rate depends on the oxygen content in the etching atmosphere (6, 7).

The dry etching characteristics for oxygen-doped Mo films were studied. It became clear that oxygen-doped Mo films were etched at a higher rate than Mo films containing no oxygen, and that oxygen-containing Mo films were undercut during etching, while undoped films were not. A Mo double layer was formed by depositing the oxygen-doped Mo film on the undoped Mo film. Tapered Mo patterns were obtained in the lower Mo film after dry etching with AZ resist pattern masks.

The experimental procedure is first described. Next, dry etching characteristics for oxygen-doped Mo films and oxygen-undoped Mo film are discussed. Finally, Mo taper dry etching is realized and discussed in application to LSI fabrication processes.

Experimental Procedure

Mo films were deposited by the reactive-sputter method on SiO₂ which was formed on a 3 in. Si wafer by thermal oxidation. The apparatus for Mo sputter depo-

sition was of a RF planar-magnetron type. An 8 in. Mo disk was used as the target. The purity of the Mo disk was more than 99.95%. The distance between the target and the wafer holder was 80 mm. The holder was turned at 7 rpm. The vacuum chamber was evacuated by a turbo-molecular pump to 3×10^{-7} torr. Ar gas was introduced and kept at a constant pressure of 7.5×10^{-3} torr during Mo sputter deposition by adjusting the Ar-gas flow rate. For oxygen-doped Mo films deposition, O₂ gas was introduced simultaneously with Ar gas. The Ar-gas pressure was maintained at 7.5×10^{-3} torr. The O₂-gas pressure, which was measured in the absence of Ar gas, was varied to 2.5×10^{-4} torr of the maximum pressure. Each gas pressure was controlled by adjusting each gas flow rate. The oxygen concentration in Mo films was varied by controlling the O₂-gas pressure. The wafer holder was at room temperature. RF power density was 4.8 W/cm², and the Mo deposition rate was 120 Å/min.

The apparatus used for Mo dry etching was a parallel-plate reactor (IPC Model 5200), as shown in Fig. 1. The RF power (13.56 MHz) was capacitively coupled to the top electrode. The bottom electrode and the chamber walls were grounded. The wafers were placed on the bottom electrode. The surfaces of the top and bottom electrodes were covered with quartz plates in order to avoid heavy metal contamination to the wafers. The distance between the top and bottom electrodes was 25 mm in the wafer area. A CCl₄-O₂ mixed gas was used as the etching gas in order to obtain a high Mo etching rate and a large etching rate ratio of Mo to SiO₂ (7). The total etching gas pressure and RF-power density were studied to determine suitable conditions for Mo etching. The etching rate for Mo films increased with the total etching gas pressure and with RF-power density. The etching rate ratio of Mo to SiO₂ and photoresist increased with the total pressure and with decreasing the RF-power density. The results of these studies were used to pick a suitable process condition for further studies. Namely, the total pressure and the RF power density were fixed to be 0.2 torr and 0.1 W/cm².

Results and Discussion

Oxygen-doped Mo film structure.—The relation between oxygen concentration in Mo films and the Mo-film structure was studied. The oxygen concentration in Mo films was estimated by Auger electron spectroscopy (AES) analysis. The film structure was investigated by x-ray diffraction. The average grain size was determined from the diffraction peak linewidth. It became clear from AES analysis that Mo films which were not intentionally doped contained about 3 atom percent (a/o) oxygen. The relation between oxygen concentration in films and the x-ray diffraction peak height for as-deposited Mo films is shown in Fig. 2 (8). The Mo films exhibit a strong <110> orientation in the

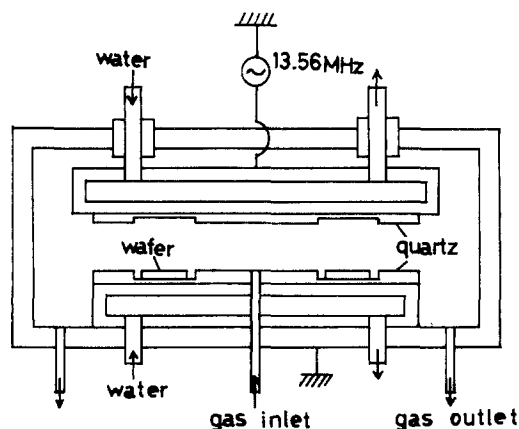


Fig. 1. Etching chamber diagram

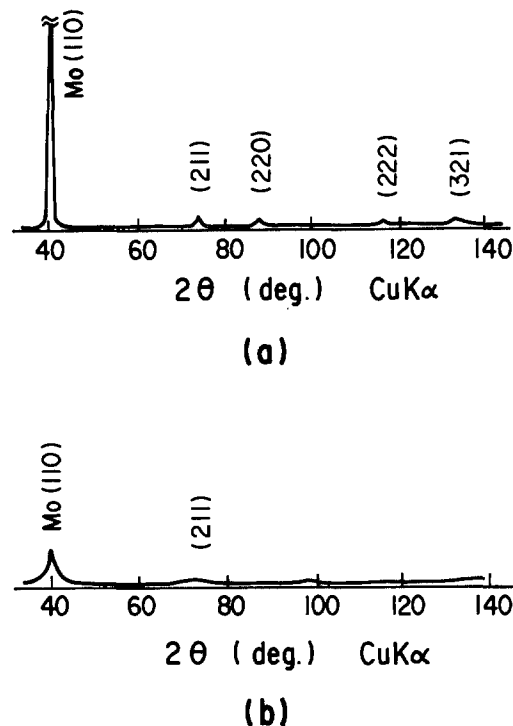


Fig. 2. X-ray diffractometer traces from as-deposited Mo films. (a) oxygen undoped. (b) 20 a/o oxygen doped (8).

growth direction at low oxygen doping, and lose the <110> preferred orientation with increasing oxygen doping. The Mo grain size decreases while increasing the oxygen doping. Mo films were amorphous in structure at oxygen doping levels greater than 30 a/o. Thus, at the Mo-deposition stage, oxygen in Mo films is considered to weaken the preferred orientation and to decrease the Mo grain size in Mo films. It was observed that molybdenum oxide was not formed in oxygen-doped Mo films during the deposition stage. However, MoO₂ was formed in oxygen-doped Mo films which were annealed in an N₂ atmosphere at a temperature above 800°C.

Etching characteristics of oxygen-doped Mo films.—**Etching rate.**—The Mo films and SiO₂ etching depths were measured by Talystep, and the etching rate was estimated by dividing the etching depths by the etching time. The photoresist etching rate was obtained by measuring the difference in the thickness before and after etching. The etching rates for Mo films, photoresist, and SiO₂ are shown in Fig. 3 as a function of the fractional O₂ content of the feed gas (O₂/CCl₄ + O₂). SiO₂ is hardly etched in these etching conditions. Etch rates of AZ resist are small. Thus, etching rate ratios of Mo films to SiO₂ and AZ resist are sufficiently large. In Mo film etching at over 80% and at 0% for the fractional O₂ content, a film was deposited on the Mo films during etching and etching did not advance smoothly. It is thought that inferior oxygen compounds of Mo were produced for O₂ concentrations above 80% in a CCl₄-O₂ discharge and polymer was deposited for an O₂ concentration at 0%. In Fig. 3, two remarkable characteristics are found in Mo film etching rates; the etching rate increased with the fractional O₂ content of the feed gas (7), and the etching rate increased with the oxygen concentration in Mo films. These two characteristics suggest that oxygen is needed to enhance the Mo etching in a CCl₄-O₂ discharge. Oxygen contained in Mo films, as well as oxygen in etching gas (7), is considered to contribute to the formation of molybdenum oxychloride compounds, which are volatile at low temperature.

In Fig. 4, the etching rates for Mo films are shown as a function of (110) Mo grain size. The oxygen con-

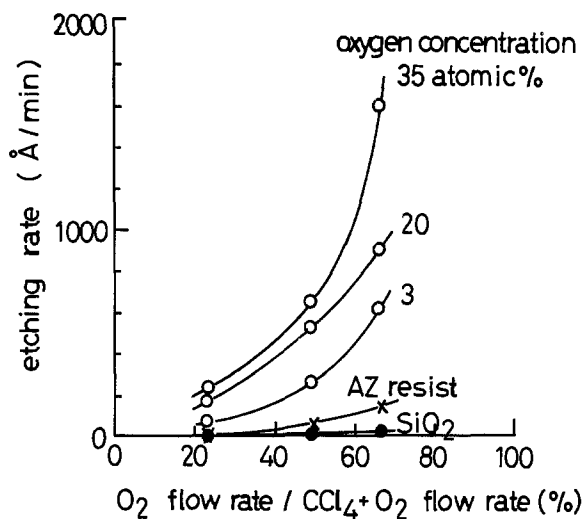


Fig. 3. Etch rates for Mo films, AZ photoresist, and SiO₂ as a function of O₂ percentage in the feed gas.

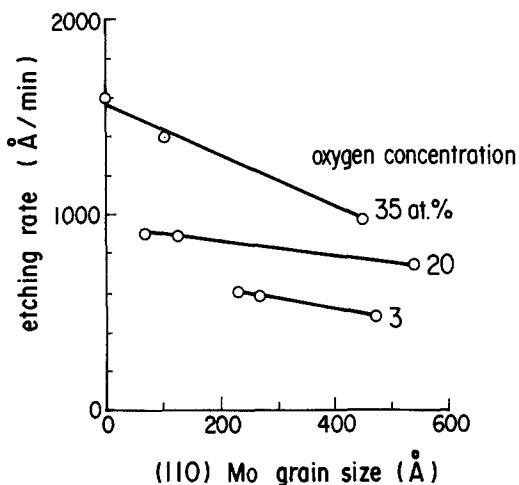
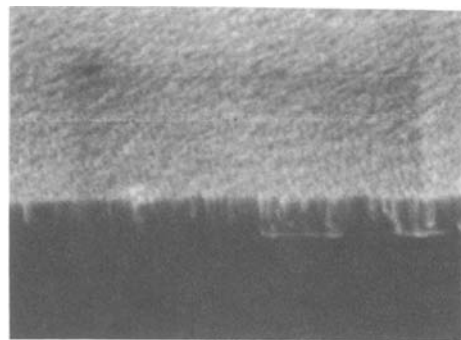


Fig. 4. Etch rates for Mo films as a function of (110) Mo grain size.

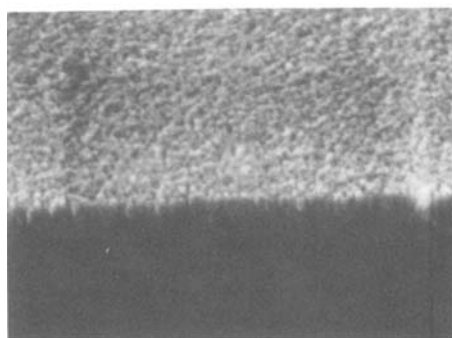
centrations in Mo films were set at 20 and 35 a/o. The Mo grain size was increased by annealing in an N₂ atmosphere at temperatures of 600° and 800°C after Mo film deposition on an SiO₂ substrate. It is found that the etching rate for Mo films increases with the oxygen concentration in Mo films and with decreasing the Mo grain size in Mo films. Figure 5 shows SEM photographs of etched Mo films. It is suggested that Mo films are etched by Mo grain unit similar to Mo films etching using CF₄ + O₂ plasma (9). This tendency is noticeable for oxygen-doped Mo films (Fig. 5b).

Thus, it is believed that the increase in the etching rate for oxygen-doped Mo films is due to the effects of the existence of oxygen in Mo films and of the decrease in Mo grain size in Mo films.

Etched profile.—Figure 6 shows SEM photographs of etched cross sections of oxygen-undoped Mo film (Fig. 6a) and oxygen-doped Mo film (Fig. 6b). Undercutting similar to wet chemical etching is observed for the oxygen-doped Mo films, whereas oxygen-undoped Mo films show no such undercutting. A dependency of single-crystalline Mo etching rate on orientation was investigated. Results are shown in Table I. A Mo (111) plane and a Mo (100) plane were etched at a slightly higher rate than a Mo (110) plane. The Mo film etching characteristics by CF₄ + O₂ plasma have been reported elsewhere (9). In that study, it was indicated that the etching rate at grain boundaries is extremely large and the etching rate for a (111) plane is three times as large as that for a (110) plane. The under-



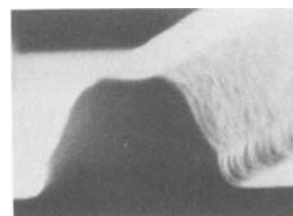
(a)



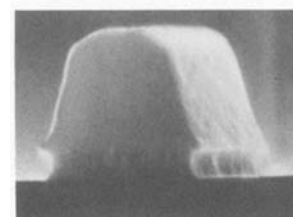
(b)

0.5 μm

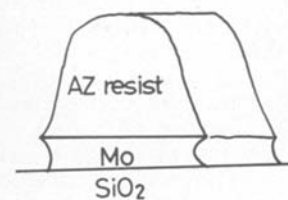
Fig. 5. SEM photographs of Mo films etched. (a) oxygen undoped. (b) 20 a/o oxygen doped.



(a)



(b)



1 μm

Fig. 6. SEM photographs of etched cross sections of Mo films. (a) oxygen undoped. (b) 20 a/o oxygen doped.

cutting process has been interpreted as follows; (i) radicals hardly reach a pattern sidewall before just

Table I. Single Mo etching quantity dependency on orientation

Mo etching quantity ($\mu\text{g}/\text{cm}^2 \cdot \text{min}$)	Single Mo orientation		
	(110)	(111)	(100)
	36	44	45

etching because Mo grains around the pattern prevent the lateral motion of radicals; (ii) undercutting occurs after radicals arrive at the sidewall in the over-etching stage. The etched profile of the undoped Mo film (Fig. 6a) can be interpreted in general on the analogy of Mo films etching by $\text{CF}_4 + \text{O}_2$ plasma. However, the oxygen containing Mo films (Fig. 6b) consist of small-size Mo grains with random orientation. Then, it is believed that the etching advanced isotropically, and that consequently undercutting occurred in the oxygen containing Mo films.

Mo taper dry etching using a Mo double layer.—The etching characteristics for oxygen-doped Mo films are such that the oxygen-doped Mo films were etched at a higher rate than oxygen-undoped Mo film, and, in the oxygen-doped Mo films, undercutting occurred in a manner differing from that in the oxygen-undoped Mo film. Making use of these dry etching characteristics, a tapered Mo pattern was obtained. The experimental procedures are as follows. A Mo double layer was formed on SiO_2 . This structure consisted of an oxygen-doped Mo film for the upper layer and an undoped Mo film for the lower layer. The Mo double layer total thickness was fixed to be 3300Å. The thicknesses for the oxygen-doped Mo film/the oxygen-undoped Mo film were varied from 700Å/2600Å to 1650Å/1650Å. The oxygen concentrations in the upper layer were set to be 20 and 35 a/o, respectively. AZ resist patterns were formed on the Mo double layer film. These samples were etched under etching conditions such that the O_2 flow rate was 67% of the $\text{CCl}_4 + \text{O}_2$ gas mixture.

SEM photographs of cross sections of the etched Mo double layer are shown in Fig. 7. A 700Å/2600Å thick and 20 a/o oxygen-doped Mo film structure are shown in Fig. 7a. A tapered etching pattern was obtained in the lower, undoped layer. The tapered pattern has the features that the deviation in width for the bottom of the lower Mo layer is small in regard to the resist pattern and that the tapered shape is convex, differing from the case in which undercutting occurred. The taper angle obtained in the lower layer, measured as an angle made to the substrate surface, was 60° in the structure, as shown in Fig. 7. The angle varied from 40° for a 1650Å/1650Å structure to 60° for a 700Å/2600Å structure at an oxygen concentration of 20 a/o in the oxygen-doped Mo film. The taper angle was controlled by varying the thickness ratio of oxygen-doped Mo film to the total Mo double layer.

The reason for the tapered profile in the lower layer is considered to be as follows. The upper layer, oxygen-doped Mo film, was etched with an undercut, which resulted in the formation of a space between the resist and the lower layer of the Mo film. The etchant entered into the space and side etching of the upper layer advanced. At the same time, the lower layer was etched at the surface under the space. Thus, the taper was produced in the lower layer of the Mo film. The reason for the tapered shape being convex is considered to be the presence of a high etch rate region in the top of the lower layer. This region, which is illustrated in Fig. 7a, was produced probably due to stress rather than O_2 diffusion. This is because the high etch rate (1200Å/min) cannot be explained only by the diffused O_2 concentration shown in Fig. 8.

The other feature of the etched pattern of the Mo double layer is the generation of a reversed taper in

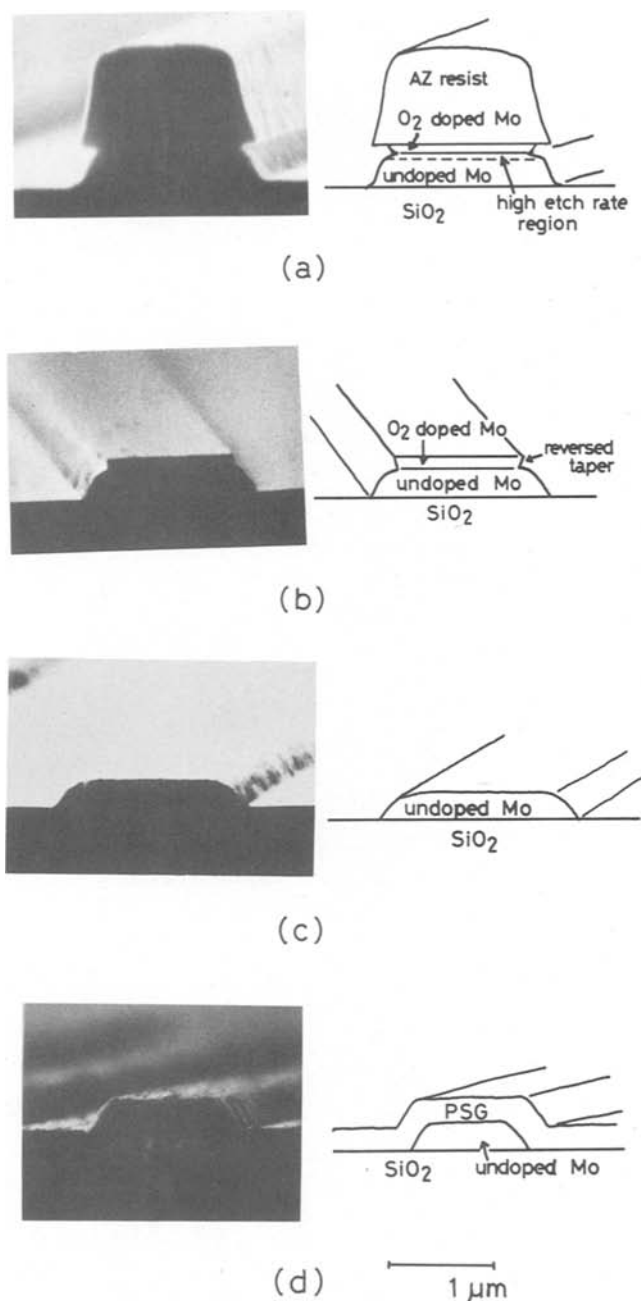


Fig. 7. SEM photographs of etched cross sections of the Mo double layer whose structure is 700Å/2600Å thick and 20 a/o oxygen-doped Mo film for the upper layer. (a) just after etching. (b) after ashing the resist. (c) after etching the upper layer selectively. (d) after PSG deposition over the Mo patterns without glass-reflow treatment.

the upper layer, as shown in Fig. 7a and 7b. The depth profile of oxygen in the Mo double layer investigated by AES analysis is shown in Fig. 8. The piling up of oxygen at the boundary was not found. Therefore, it is thought that the reversed taper in the upper layer was not produced by the piling up of oxygen at the boundary but by stress or disorder in the grain size at the boundary.

Application of Mo taper dry etching.—In order to apply the Mo taper etching technique to LSI fabrication processes, it was necessary to remove the upper O_2 containing layer selectively, after the etching of the Mo double layer pattern. The etching rate ratio for the oxygen-doped Mo films to the oxygen-undoped Mo film is shown in Fig. 9 as a function of flow rate ratio of $\text{O}_2/\text{CCl}_4 + \text{O}_2$. It is observed that the etching

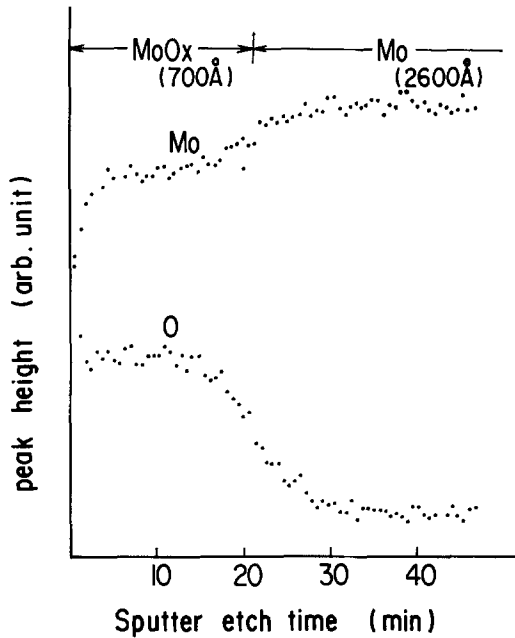


Fig. 8. Depth profile of oxygen in Mo double layer investigated by AES analysis.

rate ratio for the oxygen-doped Mo films to the oxygen-undoped Mo film increases, while decreasing the O₂ flow rate ratio. The 33% O₂ flow rate ratio condition was applied to selective etching of oxygen-doped Mo film. An SEM photograph of the tapered Mo pattern after removing the oxygen-doped Mo film is shown in Fig. 7c. It is obvious that, after selectively etching the upper layer, the reversed taper was cut away and a Mo pattern which had a gentle taper was obtained without serious changes in the pattern dimensions. Figure 7d shows a cross section of the structure in which PSG was deposited over the Mo pattern tapered at 60° without glass-reflow treatment. PSG was deposited with a uniform thickness along the taper, and the good covering of PSG over the tapered Mo pattern was obtained.

Next, the possibility of applying the Mo taper dry etching technique to LSI fabrication processes is discussed with respect to electrical characteristics.

The relation between the PSG coverage angle and the Al electrode resistance was investigated. PSG was deposited on Mo patterns without performing glass-reflow treatment. Al films were deposited on the PSG by the sputter-deposition method using an Al target

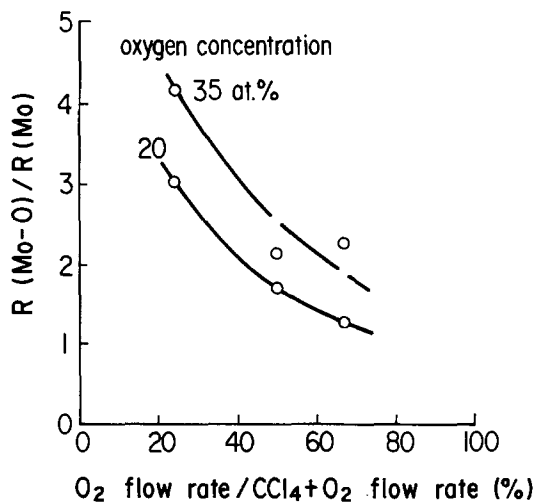


Fig. 9. Etch rate ratio for oxygen-doped Mo films to oxygen-undoped Mo film [$R(\text{Mo-O})/R(\text{Mo})$] as a function of O₂ percentage in the feed gas.

containing 2 a/o Si. AZ resist stripe patterns, as shown in Fig. 10, were formed on the Al films. The Al films were etched by a dry etching method. The AZ resist was removed, and the Al electrode resistances were measured after annealing them at 450°C for 30 min in a H₂ atmosphere diluted with N₂. The results are shown in Fig. 11. The mean value for the Al electrode resistance and the standard deviation of the resistance for a 60° taper angle in the Mo pattern decreased by one-half, when compared to values for a 90° taper angle of the Mo pattern. It is noticeable that Al disconnection or shorts, which are caused by thinning of Al lines or Al remaining at the bottom of steps, rarely occurred for the Mo pattern taper angles under 60°.

The Mo-film resistivity and the Mo-film contact resistance to Al were investigated in relation to the oxygen concentration in Mo film. The results are shown in Table II. The resistivity for Mo films containing 35 a/o oxygen was at most twice that for undoped Mo film after annealing at 1000°C for 20 min in an N₂ atmosphere. The contact resistance of Mo films to Al was almost constant, regardless of the oxygen concentration in Mo films. These results reduce the concern for leaving oxygen-doped Mo films on the tapered Mo

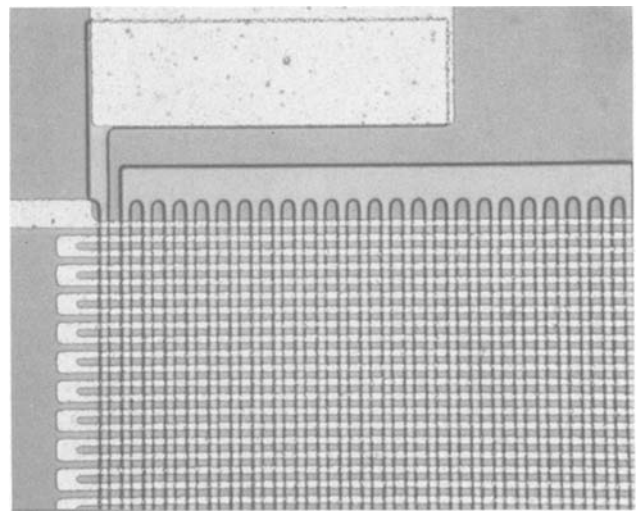


Fig. 10. Al stripe patterns over the Mo steps covered with PSG

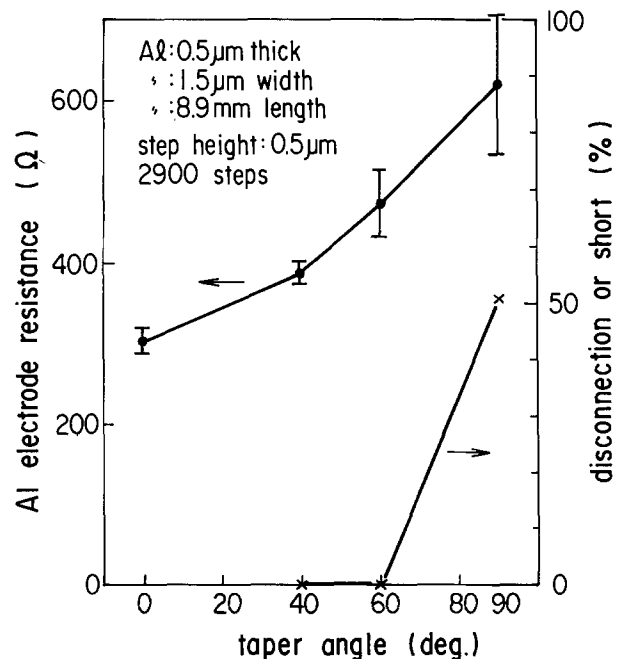


Fig. 11. Al electrode resistance and disconnection or shorts vs. Mo pattern taper angles.

Table II. Mo film resistivity and contact resistance for Mo films to Al

Oxygen concentration in Mo films (a/o)	Mo film resistivity ($\Omega\text{-cm}$)	Contact resistance for Mo film to Al (Ω/cm^2)
3	9.6×10^{-6}	5.3×10^{-8}
20	1.6×10^{-5}	5.5×10^{-8}
35	2.3×10^{-5}	4.1×10^{-8}

patterns and ease the process for etching oxygen-doped Mo films from the tapered Mo patterns. Thus, the possibility of applying the Mo taper dry etching technique to LSI fabrication processes has been demonstrated.

Conclusion

In plasma etching of Mo films using a $\text{CCl}_4 + \text{O}_2$ mixed gas, it was found that oxygen-doped Mo films were etched at a higher rate than oxygen-undoped Mo film and that, in oxygen-doped Mo films, undercutting occurred in a manner different from that observed for oxygen-undoped Mo film.

Using the characteristics of dry etching for oxygen-doped and undoped Mo films, tapered Mo patterns were obtained by plasma etching of the Mo double layer. The tapered Mo patterns have desirable features; for example, the deviation in pattern width for the etched Mo pattern to the resist pattern is small, and the tapered shape is convex. The taper angle is varied from 40° to 60° by varying the thickness ratio of oxygen-doped Mo film to the total Mo double layer. Good coverage of PSG over the tapered Mo pattern is obtained.

It was found that disconnection or shorts of Al electrodes over the tapered Mo steps covered with PSG layer rarely occurred for taper angles of under 60° .

It was observed that oxygen in Mo films did little to worsen the resistivity characteristics for Mo films and contact resistance for Mo films to Al.

The Mo taper dry etching technique promises to improve an interconnection yield in LSI's through reduction of wiring disconnection or shorts over the tapered Mo steps.

Acknowledgments

The authors wish to thank T. Kitayama and T. Matsumoto for supporting this work, and H. Oikawa, C. Hashimoto, and M. Oda for their technical advice.

Manuscript submitted June 18, 1983; revised manuscript received Jan. 3, 1984.

Nippon Telegraph and Telephone Public Corporation assisted in meeting the publication costs of this article.

REFERENCES

1. J. A. Bondur and R. G. Frieser, Abstract 109, p. 288, The Electrochemical Society Extended Abstracts, Vol. 80-1, St. Louis, Missouri, May 11-16, 1980.
2. R. H. Bruce and A. R. Reinberg, *This Journal*, **129**, 393 (1982).
3. F. Yanagawa, K. Kiuchi, T. Hosoya, T. Tsuchiya, T. Amazawa, and T. Mano, *IEEE Trans. Electron. Devices*, **ed-27**, 1602 (1980).
4. E. Arai and N. Ieda, *IEEE J. Solid-State Circuits*, **sc-13**, 333 (1978).
5. H. Oikawa, *J. Vac. Sci. Technol.*, **15**, 1117 (1978).
6. K. Hirata, Y. Ozaki, M. Oda, and M. Kimizuka, *IEEE Trans. Electron. Devices*, **ed-28**, 1323 (1981).
7. Y. Kurogi and K. Kamimura, *Jpn. J. Appl. Phys.*, **21**, 168 (1982).
8. S. Ohfuji, C. Hashimoto, T. Amazawa, and J. Murota, *This Journal*, To be published.
9. M. Oda and K. Hirata, in "Proceedings of the Second Symposium on Dry Processes," p. 87, Institute for Electrical Engineering, Tokyo, Oct. 29-30, 1980.

An Etch for Delineation of Defects in Silicon

K. H. Yang*

IBM Corporation, East Fishkill Laboratory, Hopewell Junction, New York 12533

ABSTRACT

An investigation of the $\text{CrO}_3\text{-H}_2\text{O-HF}$ system shows that preferential etching of crystal defects on silicon surfaces is very sensitive to the concentration ratio of CrO_3 to HF. This leads to development of a new etch consisting of one part by volume of 1.5 molal (M) CrO_3 (150 g/l H_2O) and one part of 49% HF. This etch can delineate a wide variety of crystal defects with sharp definition. The shape of dislocation etch pits is uniquely determined by the orientation of wafer surfaces and dislocation lines.

Preferential etch is a simple and fast technique to evaluate the structural perfection of a single crystal. For silicon crystals, such a technique is widely used to crop dislocation-free crystal sections and also to delineate process-induced defects in silicon wafers. A reliable preferential etch is, therefore, extremely valuable in crystal-growth technology and device-failure analysis.

There are several preferential etches currently available for silicon crystals (1-5). Dash etch (1) requires an etch time of several hours and is unsuitable for fast evaluation of crystal perfection. Sirtl etch (2) favors (111) surfaces but fails to reveal dislocation etch pits on (100) surfaces. Due to the increased demand of (100) wafers, three etches have been developed for (100) surfaces (3-5). Secco etch (3) and Schimmel etch (4) yield relatively poorly defined

circular dislocation etch pits. Wright etch (5), in general, gives sharp definition for crystal defects induced by hot processing. However, it is relatively insensitive to dislocations generated during crystal growth. As a result, development of an improved etch for (100) crystals is highly desirable. Furthermore, the influence of chemical composition that leads to the difference in etching characteristics between these etches has not been discussed and is still poorly understood.

This study investigated the capability of the $\text{CrO}_3\text{-H}_2\text{O-HF}$ system for preferential etching. The results lead to the development of an improved etch. This etch is capable of delineating a wide variety of defects on crystal surfaces of different orientations and electrical resistivities. In most cases, manual agitation or ultrasonic vibration is not necessary during the application of this etch.

Experimental

The materials used for this study were mainly 125 mm slugs and 100 mm wafers of p-type, (100) silicon

* Electrochemical Society Active Member.
Key words: silicon, preferential etch, crystal defects, defect delineation.

crystals (1-20 Ω -cm). A group of p-type (110) wafers and n-type (111) wafers (0.5-2 Ω -cm) was also selected for defect delineation. The surface of the slugs was chemically polished, and that of the wafers was chemically-mechanically polished. During etching, one slug or one wafer was placed horizontally and etched in a plastic beaker without the application of manual or ultrasonic agitation. For as-grown slugs and wafers, a volume of 500 ml etch and a relatively long etching time of 10-15 min were used in order to enhance defect delineation for visual inspection. For hot-processed wafers, a volume of 200 ml etch and an etching time of 2-3 min were used. The volume was decreased proportionally for smaller wafers. After etching, the wafers were rinsed, dried, and examined with the optical microscope using Nomarski interference contrast. The validity of etch figures was compared with x-ray topographs. Some of these etch figures were further investigated in a transmission electron microscope (TEM).

Artifacts in the size of several microns were occasionally observed on the wafer surfaces etched longer than 5 min. The artifacts could be easily eliminated by placing the wafer vertically during etching, or by step etching at an interval of 3 min, or by etching in a 30°-tilt cup rotating at 6-8 rpm. All three methods yielded etch figures with sharp definition, smooth background, and freedom from artifacts.

Etching characteristics.—CrO₃-H₂O-HF system.—An investigation of the CrO₃-H₂O-HF system was carried out using different concentrations of CrO₃ and HF. In the first group of these solutions, the volume ratio of CrO₃ solution and HF (49%) remained one to one. The concentration of CrO₃ molal (*M*) in the stock solution and the concentration ratio, *m*, of CrO₃ and HF expressed in *M*/%, in the etch are given in Table I. The value of *m* is an indicator of oxidizing power in the etch. By gradually increasing the concentration of CrO₃, we observed a substantial change in the definition of dislocation etch pits. At a CrO₃ concentration of 0.5*M* (*m* = 0.01, Y1 etch (see Table Ia) gives relatively ill-defined round etch pits (Fig. 1a). The etch rate of the Y1 etch is relatively low. It requires about 30 min to develop a reasonable size of etch pits. As the CrO₃ concentration increases to 1.0*M* (*m* = 0.02), the shape

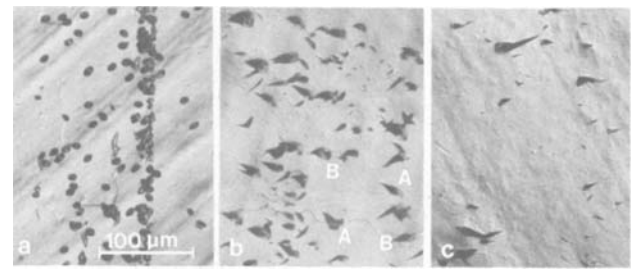


Fig. 1. Influence of CrO₃ conc. on the definition of etch pits on a (100) slug. A, left: 30 min Y1 etch (0.5*M*). B, center: 15 min Y3 etch (1.5*M*). C, right: 15 min Y5 etch (2.5*M*).

of etch pits delineated by Y2 etch becomes better defined. In the range of 1.5-2.0*M* CrO₃ concentration (*m* = 0.03-0.04), Y3 and Y4 etches yield well-defined etch pits (Fig. 1b). As the CrO₃ concentration increases to 2.5*M* (*m* = 0.05), Y5 etch reveals only a low density of dislocation etch pits (Fig. 1c). This indicates a decreasing capability of preferential etching. At a 3.0*M* CrO₃ concentration (*m* = 0.06), Y6 etch has an absence of preferential etching, and the etched surface is featureless, similar to that revealed by the Sirtl etch (5.0*M* CrO₃).

In the second group investigated, the volume of CrO₃ solution and HF was kept at a two-to-one ratio. By increasing the CrO₃ concentration from 1.0 to 2.0*M*, a substantial change in the capability of preferential etching was again observed. At 1.0*M* CrO₃ concentration (*m* = 0.041), Y7 etch reveals well-defined etch pits similar to those obtained by Y3 etch. However, Y7 etch has a slow etch rate and requires about 60 min to develop a reasonable size of etch pits. Because of the slow etch rate, the investigation of CrO₃ concentrations below 1.0*M* was stopped. As the CrO₃ concentration increases to 1.5*M* (*m* = 0.061), Y8 etch reveals only a very low density of dislocation etch pits, indicating a decreasing capability of preferential etching. At 2.0*M* CrO₃ concentration (*m* = 0.082), Y9 etch lacks the capability of preferential etching.

In the third group investigated, the volume ratio of CrO₃ solution and HF is kept at two to three. At 2.0*M* CrO₃ concentration (*m* = 0.027), Y10 etch gives well-defined etch pits. But it also gives artifacts due to vigorous bubble formation. As the CrO₃ concentration increases to 3.0*M* (*m* = 0.041), preferential etching in Y11 is absent.

The dependency of preferential etching on the concentration ratio *m* was also observed on (111) surfaces. The etch composition and the etching characteristics are given in Table Ib. Figure 2a shows that at *m* = 0.01, Y1 etch again gives round dislocation etch pits. As *m* increases to 0.03, Y3 etch yields well-defined triangular pits, Fig. 2b. The definition of the triangular pits shows no significant changes even as *m* increases to 0.204 (Y16) (Fig. 2c). The capability of preferential etching decreases at *m* = 0.408 (Y17 etch), and finally ceases at *m* = 0.612 (Y18 etch).

The results of this study indicated that preferential etching of dislocations takes place only at a proper concentration ratio *m* of CrO₃ and HF in the etch. The influence of *m* is much more critical on (100) surfaces than on (111) surfaces. The optimum composition of the etch applicable to both (100) and (111) surfaces is that of Y3 and Y4 etches. The etching rate of these two etches is about 1.5 μ m/min. The Y3 etch is chosen for further defect delineation.

K₂Cr₂O₇-H₂O-HF system.—The K₂Cr₂O₇-H₂O-HF system was also investigated for preferential etching. Because of the low solubility of K₂Cr₂O₇ in water, the concentration of K₂Cr₂O₇ cannot be changed significantly. The results of our investigation show that the optimum composition is nearly the same as Secco's (3).

Table I. Etching characteristics of CrO₃-HF-H₂O system. One part by volume of CrO₃ solution and one part of HF (49%)

a. (100) Silicon surfaces			
Etch	CrO ₃ , <i>M</i> Stock soln	<i>m</i> , <i>M</i> /% in etch	Remarks
Y1	0.5	0.010	Round etch pits develop after 30 min
Y2	1.0	0.020	Poorly defined etch pits
Y3	1.5	0.031	Well-defined etch pits
Y4	2.0	0.041	Well-defined etch pits
Y5	2.5	0.051	Capability of preferential etching decreases. Reveals low density of etch pits
Y6	3.0	0.062	Reveals very low density of etch pits
b. (111) Silicon surfaces			
Etch	CrO ₃ , <i>M</i> Stock soln	<i>m</i> , <i>M</i> /% in etch	Remarks
Y1	0.5	0.010	Round etch pits
Y3	1.5	0.030	Well-defined etch pits
Y15*	5.0	0.102	Well-defined etch pits
Y16	10.0	0.204	Well-defined etch pits
Y17†	10.0	0.408	Capability of preferential etching decreases. Reveals low density of etch pits
Y18**	10.0	0.612	Reveals very low density of etch pits

* Sirtl etch.

† 2 parts 10*M* CrO₃ and 1 part HF.

** 3 parts 10*M* CrO₃ and 1 part HF.

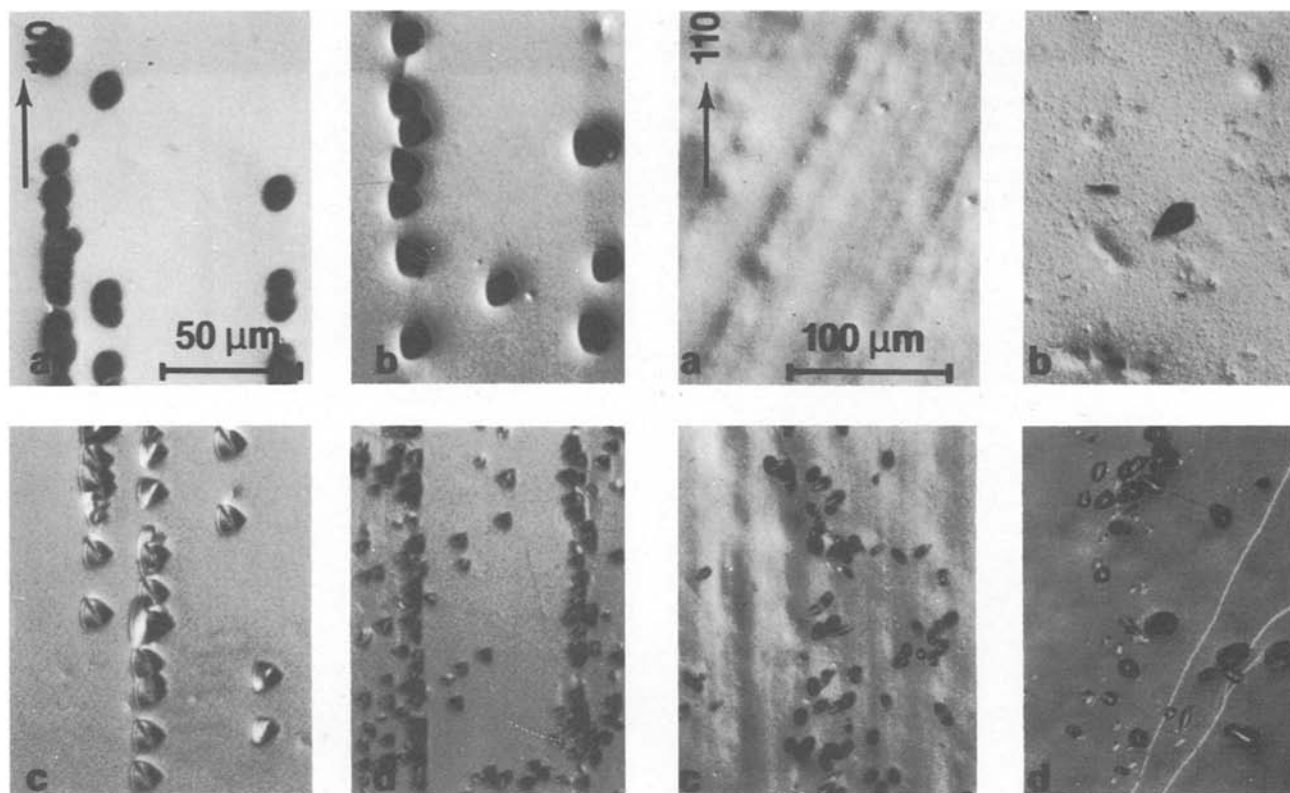


Fig. 2. Influence of CrO_3 conc. on the definition of etch pits on a (111) wafer. A, top left: 15 min Y1 etch (0.5M). B, top right: 5 min Y3 etch (1.5M). C, bottom left: 3 min Y16 etch (10M). D, bottom right: 4 min Y17 etch.

Defect delineation.—Dislocation etch figures.—Dislocation etch figures delineated by the Y3 etch have an excellent correlation with dislocations revealed by the x-ray topography. Figure 3a is the x-ray topograph of a 125 mm (100) slug showing slip dislocations generated during crystal growth. Figure 3b is the etched surface of the same slug. An excellent correlation is clearly established between Fig. 3a and 3b. When the etched surface is examined at high magnification, well-defined etch pits along slip directions are observed (see Fig. 3c). In most cases, the etch pits assume the shapes of A and B, and, in some cases, the square shape C. The pits result from dislocations lying at a steep inclination to the wafer surface.

A comparison of existing etches with Y3 etch is given in Fig. 4. Figure 4a shows that Sirtl etch (2) yields a featureless surface and fails to reveal etch pits as reported previously (3, 5). After 30 min of etching, Wright etch (5) generates a very low density of well-defined etch pits, Fig. 4b. Both Secco etch (3) and Schimmel etch (4) develop ill-defined round etch pits, as shown in Fig. 4c and 4d. A comparison of Fig. 4 with Fig. 1b and 3c clearly indicates that Y3 etch

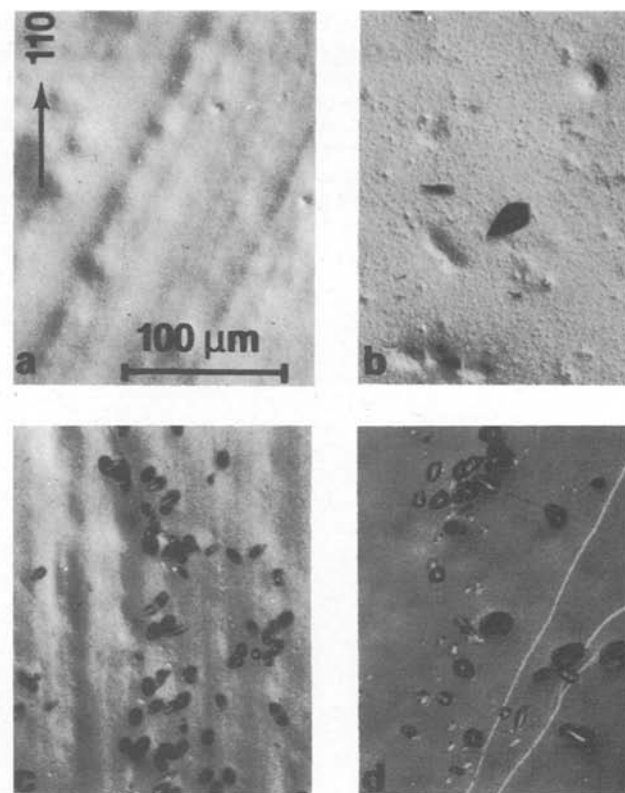


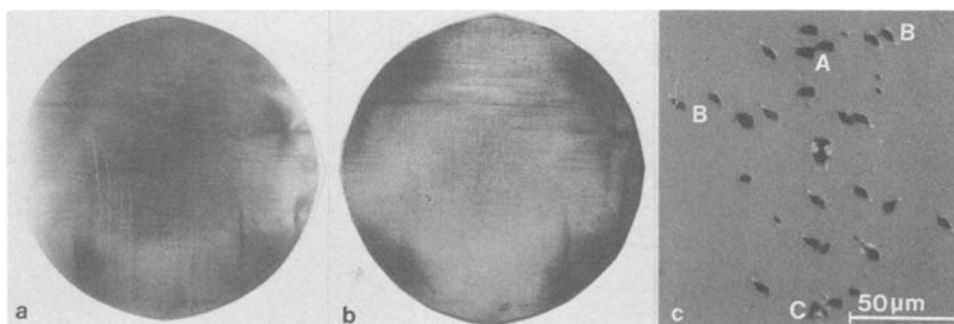
Fig. 4. Four quarters of a highly dislocated 125 mm (100) slug. A, top left: after 5 min Sirtl etch. B, top right: after 30 min Wright etch. C, bottom left: after 10 min Secco etch. D, bottom right: after 10 min Schimmel etch.

gives a better definition of dislocation etch pits on (100) surfaces.

The Y3 etch is also capable of delineating dislocations lying nearly parallel to the surface. This type of dislocation is frequently observed as dislocation networks in as-grown crystals (Fig. 5a) and as misfit dislocations in phosphorus-diffused layers (Fig. 5b). Application of the Wright etch (5), however, fails to delineate those dislocation networks in Fig. 5a and reveals the misfit dislocations in a lower density and a weaker contrast as shown in Fig. 5c. This clearly indicates that the Y3 etch is more sensitive for delineating this type of dislocations.

The Y3 etch is also capable of revealing dislocations on (111) and (110) silicon surfaces. For (111) surfaces, the triangular etch pits revealed by Y3 etch were already shown in Fig. 2b. Figure 6 shows that both Sirtl and Wright etches produce similar triangular pits, while Secco and Schimmel etches yield round pits. Figure 7 shows two types of dislocation etch figures delineated by Y3 etch on a longitudinal (110) slice cut from a 125 mm (100) crystal. One type is etch pits of slip dislocations, which assume three com-

Fig. 3. Slip dislocation in a 125 mm (100) slug. A, left: x-ray topograph. B, center: 15 min Y3 etched surface. C, right: a portion of B at high magnification showing dislocation etch pits.



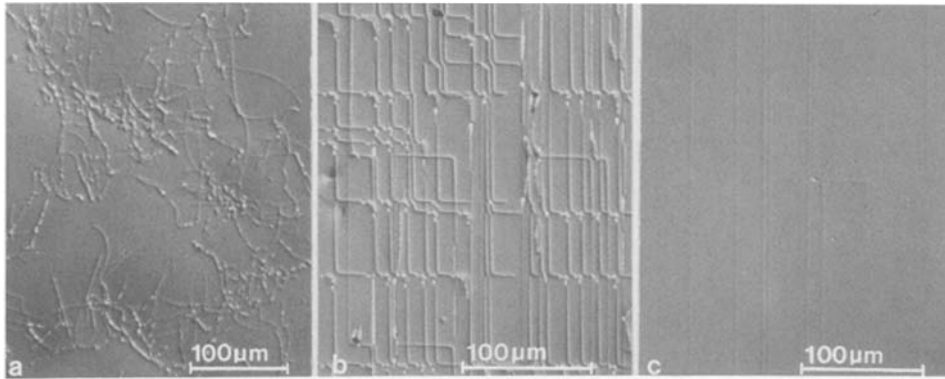


Fig. 5. A, left: dislocation networks on a 125 mm (100) slug delineated by 10 min Y3 etch. B, center: misfit dislocations in a phosphorus-diffused layer delineated by 2 min Y3 etch. C, right: same as B, with 5 min Wright etch.

mon shapes of A, B, and C (Fig. 7a). The shape C is an inversion of the shape B. It is interesting to note the unique shape of etch pits on the (100), (111), and (110) surfaces revealed by this etch. The other type is a group of dislocations lying nearly in the (110) surface (Fig. 7b). Once these dislocations intersect the edge surface, they form etch pits (indicated by arrows).

Swirl patterns.—Swirl patterns are usually observed in a silicon wafer containing substantial oxygen precipitation after hot processings. Figure 8a is an x-ray topograph of such a pattern. Figure 8b is the same wafer after etching. A comparison between Fig. 8a and 8b clearly indicates that the etched surface gives a much more pronounced resolution of the patterns. Examination of Fig. 8b at high magnification shows that some of the etch figures can be clearly identified as oxide precipitates with punch-out dislocation loops (indicated by arrows in Fig. 8c). The formation of dislocation loops due to punch-out from oxide precipitates has been reported previously (6, 7).

However, the majority of the etch figures is beyond the resolution at this magnification. TEM investigation shows that the defects are oxide precipitates with punch-out dislocation loops in a complex form (Fig. 8d).

Oxidation-induced stacking faults.—Stacking faults of both surface and bulk types are often observed in sili-

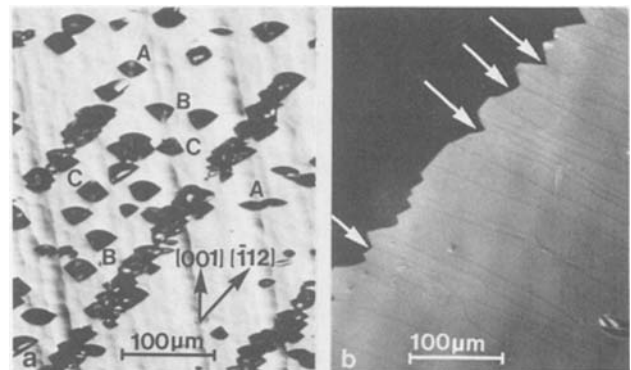


Fig. 7. Etch figures in a (110) slice delineated by 10 min Y3 etch. A, left: dislocation etch pits. B, right: a group of dislocations lying on the (110) surface.

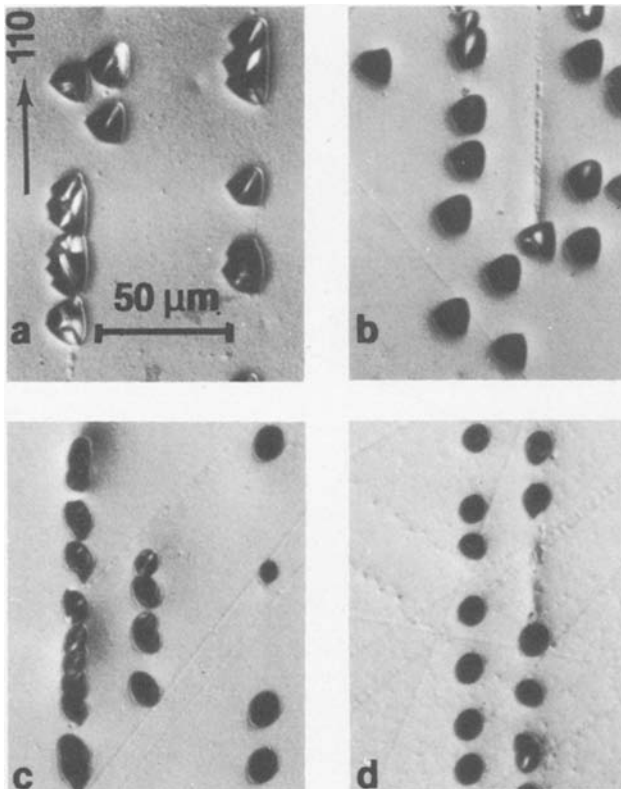


Fig. 6. Etch figures on a (111), phosphorus-doped wafer after oxidation. A, top left: 3 min Sirtl etch. B, top right: 15 min Wright etch. C, bottom left: 5 min Secco etch. D, bottom right: 5 min Schimmel etch.

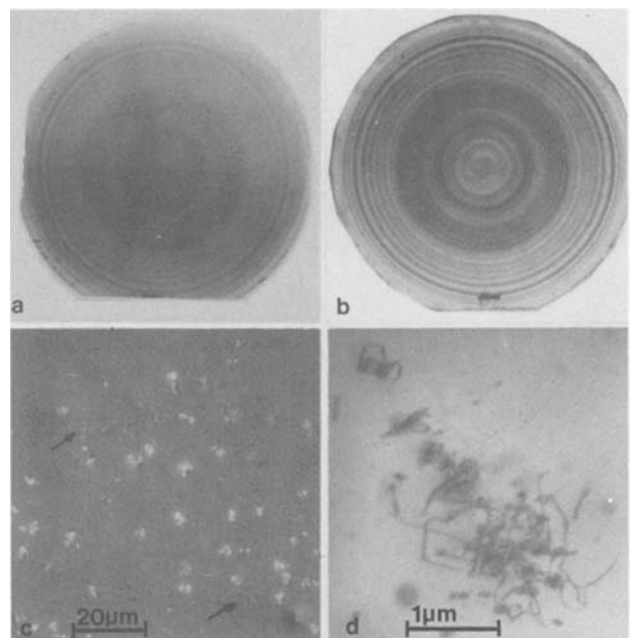


Fig. 8. Swirl patterns in a 100 mm (100) wafer. A, top left: x-ray topograph. B, top right: 5 min Y3 etched surface. C, bottom left: a portion of B at high magnification. D, bottom right: TEM micrograph showing the majority of the etch figures that are precipitate-dislocation complexes.

con wafers after thermal oxidation. Figure 9a shows that the Y3 etch can simultaneously delineate surface faults and unfaulted loops with sharp definition on a (100) surface. These faults are first delineated by 10s of etching. This results in a straight line at the fault location. After subsequent N_2 anneal, most of the faults become unfaulted loops.

Stacking faults of bulk type are shown in Fig. 9b. Most of the faults contain a pit at the fault center. TEM investigation shows that the pit arises from oxide precipitates which act as nucleation centers for fault formation, Fig. 9c.

The resolution of swirl patterns and stacking faults as shown is at least comparable with that revealed by Wright etch (5). However, Y3 etch requires a shorter etching time and no manual agitation. Application of Y3 etch to reveal dislocations on polycrystalline surfaces, resistivity striations in highly doped crystals, and p-n junctions also yields satisfactory results.

Discussion

Mechanism of preferential etching.—The results of this study show that the definition of dislocation etch pits is mainly controlled by the concentration ratio m of CrO_3 and HF. Table I shows that for (100) surfaces, preferential etching takes place only for m below $0.04M CrO_3/\%HF$. The shape of dislocation etch pits is well defined in the range of 0.03 and $0.04M CrO_3/\%HF$. Below $0.03M CrO_3/\%HF$, the shape becomes relatively ill-defined. For (111) surfaces, well-defined etch pits are observed in a wide range of m from 0.03–0.20. Below 0.03, the shape of etch pits becomes ill-defined and above 0.20, the capability of preferential etching decreases.

These results are further supported by our evaluation of existing etches (2–5). For example, Secco, Schimmel, and Y1 etches generate similar round pits on both (100) and (111) surfaces because their oxidizing power is too weak (low m). The value of m is 0.01 for Schimmel and Y1 etches, and 0.003 for Secco etch. The oxidizing power of Sirtl etch ($m = 0.10$) is optimum for (111) surfaces, but is too strong for (100) surfaces. As a result, it favors (111) surfaces but fails to delineate etch pits on (100) surfaces. The m value of Wright etch is difficult to estimate because it contains a combination of conc. HNO_3 and CrO_3 . The etching characteristics of Wright etch, however, are very similar to those of Y6 etch ($m = 0.062$). This suggests that the oxidizing power of Wright etch is slightly too high for (100) surfaces.

The dependence of preferential etching on the concentration ratio m of CrO_3 and HF can be understood

from the following reasoning. The formation of a dislocation pit arises mainly from the strain field associated with a dislocation (8) and/or impurities segregated at a dislocation (9). The strain field and/or the impurity segregation produce a surface potential between the site of a dislocation and the surrounding perfect crystal. The surface potential causes a difference in the etching rate. During the course of etching, HF dissolves silicon when the silicon surface is oxidized by CrO_3 . If the CrO_3 concentration is too high, the strong oxidizing power of CrO_3 tends to minimize the surface potential to a negligible extent. As a result, preferential etching is absent. If the CrO_3 concentration is too low, etching due to HF dissolution is predominant, and the shape of etch pits becomes ill defined. Therefore, the concentration ratio m is very critical to the definition of etch pits.

Influence of surface orientation.—This reasoning can also be extended to explain the influence of surface orientation on preferential etching. As shown before, preferential etching occurs more easily on (111) surfaces than on (100) surfaces. For the low-index surfaces, the surface energy of silicon (10) increases according to the order of $(111) < (110) < (100)$. The surface potential between a dislocation and its surrounding crystal is therefore greater on the (111) surfaces than on the (100) surfaces. The greater surface potential makes preferential etching of (111) surfaces possible with an etch of higher oxidizing power, such as Sirtl etch (2). The (111) etch, however, may not be applicable to the (100) surface. On the contrary, a (100) etch should also be applicable to the (111) surface.

Significance of etch figures.—The etch figures of dislocations are mainly determined by the inclination of dislocations to the surface. For dislocations lying nearly parallel to the surface, dislocation lines are observed. For dislocations lying at a steep inclination to the surface, etch pits result. The basic unit of an etch pit is bounded by the direction of (111) planes intersecting to the surface. The shape of an etch pit can be considered as a superimposition of different sizes of basic units etched at different time intervals along a dislocation. This is shown schematically in Fig. 10.

For the (111) surface, the basic unit is a triangle with three sides in $<110>$ directions. A superimposition of these units along a dislocation in the $[110]$ direction results in an etch pit in the shape of Fig. 10a, in agreement with the shape observed in Fig. 2b and 2c.

For the (100) surface, the basic unit is a square. A superimposition of these squares along two dislocation directions, $[1\bar{1}0]$ and $[2\bar{1}\bar{1}]$, results in two shapes of etch pits as shown in Fig. 10b. These two shapes are frequently observed, as shown in Fig. 3c.

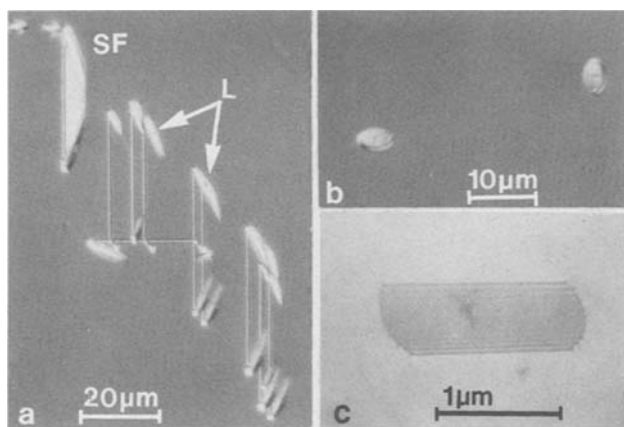
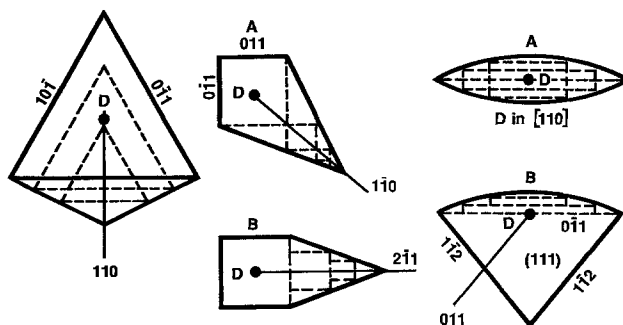


Fig. 9. A, left: oxidation-induced stacking faults (SF) of surface type and unfaulted loops (L) in a (100) wafer delineated by 2 min Y3 etch. B, top right: bulk-type stacking faults delineated by 2 min Y3 etch. Note that the faults contain a pit at the fault center. C, bottom right: TEM micrograph showing that the pit arises from an oxide precipitate.



A. (111) Surface

B. (100) Surface

C. (110) Surface

Fig. 10. Schematic drawing of dislocation etch pits on (A, left) (111) surfaces, (B, center) (100) surfaces, and (C, right) (110) surfaces. D refers to the emergence of a dislocation to the surface. Solid line refers to the shape of an etch pit. Dashed line refers to the basic unit of an etch pit.

For the (110) surface, there are four (111) planes intersecting the surface. Two, the $(\bar{1}\bar{1}\bar{1})$ and the $(\bar{1}\bar{1}\bar{1})$ planes, are perpendicular to the surface, and the other two, the (111) and the $(\bar{1}\bar{1}\bar{1})$ planes, make an angle of 35.3° to the surface. During the course of etching, preferential etch attacks the (111) and the $(\bar{1}\bar{1}\bar{1})$ planes first before reaching the $(\bar{1}\bar{1}\bar{1})$ and the $(\bar{1}\bar{1}\bar{1})$ planes. Therefore, the basic unit is a line in the $[1\bar{1}0]$ direction resulting from the intersection of the (111) and the $(\bar{1}\bar{1}\bar{1})$ planes on the (110) surface. However, etching also takes place at a slower rate in the $[001]$ direction perpendicular to the line. As a result, the basic unit becomes a rectangle. In Fig. 7a, the dislocations lie approximately in three $\langle 110 \rangle$ directions on the $(\bar{1}\bar{1}\bar{1})$ slip plane and slip along the $[\bar{1}\bar{1}2]$ direction on the (110) surface. For those dislocations in the $[110]$ direction perpendicular to the surface, the shape of etch pits can be considered as a superimposition of different sizes of rectangles, and results in shape A in Fig. 10c and 7a. For those dislocations in the $[011]$ direction, preferential etching initiates on both the (111) and $(\bar{1}\bar{1}\bar{1})$ planes, and then proceeds along the $[011]$ dislocation direction. This results in an etch pit consisting of two parts. One part due to preferential etching of the $(\bar{1}\bar{1}\bar{1})$ plane is the upper half of shape A. The other part due to preferential etching of the $[011]$ dislocation emerging to the (111) plane is bounded by the intersections of the (111), $(\bar{1}\bar{1}\bar{1})$, and $(\bar{1}\bar{1}\bar{1})$ planes on the (110) surface. This part is a triangle with three sides in the $[\bar{1}\bar{1}2]$, $[112]$, and $[110]$ directions. These two parts join together at the common line in the $[110]$ direction, and result in an etch pit of shape B, as shown in Fig. 10c and 7a. For the same reason, the dislocations in the $[10\bar{1}]$ direction produce a pit of shape C, an inversion of shape B.

Formation of artifacts.—Artifacts in the size of several microns are occasionally observed in some areas of the etched surface. The formation of the artifacts arises mainly from the fact that Cr^{+6} , once reduced to Cr^{+3} , reacts with F^- to form a green powder of CrF_3 . The CrF_3 powder tends to precipitate on the etched surface and form artifacts in the form of mounds. The rate of CrF_3 formation is much slower in the Y3 etch than in Schimmel and Wright etches. This allows one to use the Y3 etch without manual agitation or ultra-

sonic vibration. Elimination of the artifacts can be easily achieved through the use of three methods described in the Experimental section.

Conclusions

The results of this study lead to the following conclusions:

1. An investigation of the $\text{CrO}_3\text{-H}_2\text{O-HF}$ system shows that preferential etching of dislocations is mainly controlled by the concentration ratio m of CrO_3 and HF.
2. The optimum composition of the newly developed etch consists of one part by volume of 1.5M CrO_3 and one part of 49% HF.
3. This etch is capable of delineating various crystal defects on the (100) surface, as well as on the (111) and the (110) surfaces. The shape of dislocation etch figures is uniquely determined by the orientation of wafer surfaces and the orientation of dislocation lines.

Acknowledgments

The author is indebted to Dr. G. H. Schwuttke, Dr. W. A. Westdorp, and Dr. T. Tan for their helpful discussions. Technical support from Mr. C. Hoogenboom and Mr. W. James is gratefully acknowledged.

Manuscript submitted May 4, 1983; revised manuscript received Jan. 18, 1984.

IBM Corporation assisted in meeting the publication costs of this article.

REFERENCES

1. W. C. Dash, *J. Appl. Phys.*, **27**, 1193 (1956).
2. E. Sirtl and A. Adler, *Z. Metallkd.*, **52**, 529 (1961).
3. F. Secco d'Aragona, *This Journal*, **119**, 948 (1972).
4. D. G. Schimmel, *ibid.*, **126**, 479 (1979); S. M. Hu, *J. Vac. Sci. Technol.*, **14**, 17 (1977).
5. M. W. Jenkins, *This Journal*, **124**, 757 (1977).
6. T. Y. Tan and W. K. Tice, *Philos. Mag.*, **30**, 615 (1976).
7. K. H. Yang, H. F. Kappert, and G. H. Schwuttke, *Phys. Status Solidi A*, **50**, 221 (1978).
8. N. Carbrero, in "The Surface Chemistry of Metals and Semiconductors," H. C. Gatos, Editor, p. 71, John Wiley and Sons, Inc., New York (1960).
9. H. C. Gatos and M. C. Levine, "Chemical Behavior of Semiconductors: Etching Characteristics," Technical Report 293, AFESD-TDR-63-33, Massachusetts Institute of Technology, Cambridge, MA (1963).
10. R. J. Jaccodine, *This Journal*, **110**, 524 (1963).

Rapid Annealing Using Halogen Lamps

Juri Kato and Seiichi Iwamatsu

Suwa Seikosha Company, Limited, Fujimi Plant, Fujimi-machi, Suwa-gun, Nagano, Japan

ABSTRACT

A few seconds halogen lamp annealing (HLA) technology is evaluated from the viewpoint of practical application to complementary metal oxide semiconductor (CMOS) very large scale integration (VLSI) processing. $^{49}\text{BF}_2$, ^{11}B , and ^{31}P ion-implanted silicon layers have been investigated on their isothermal short-time annealing behavior of junction leakage current, recrystallization, activation, and junction depth. We have found that a few seconds annealing of 800°C is enough to crystalline regrow the $^{49}\text{BF}_2$ or ^{31}P ion-implanted amorphous layer, to activate $^{49}\text{BF}_2$ or ^{31}P ion-implanted dopants, to form titanium silicide, and to reduce the area leakage current of both n^+p^- and p^-n^- junctions without dopant diffusion. But activation of $^{11}\text{B}^+$ ion-implanted dopants, reduction of perimeter leakage current, molybdenum silicide formation, and phosphosilicate glass (PSG) reflow require a little higher temperature heat-treatment.

Application of short-time annealing (1) technologies to VLSI fabrication processing have become of great interest from the scaling down of electronic device dimensions, which requires shallower junctions. Re-

Key words: ion implantation, annealing behavior, silicon, p-n junction, silicide formation, PSG reflow.

cently, various short-time annealing technologies have been intensively investigated in activation of ion-implanted layers, using pulsed laser (2), electron beam (3), graphite heater (4), flash lamp (5), high intensity arc lamp (6), and halogen lamp (7-9). From the viewpoint of practical application to VLSI fabri-

cation, halogen lamp annealing (HLA) has many advantages. Halogen lamps irradiate a large area at one time in nitrogen gas at atmospheric pressure, cassette-to-cassette, single-wafer processing realizes excellent repeatability, and cold-wall process reduces risk of contamination. The drain gaussian impurity profile fabricated with HLA reduces short-channel effects and hot-carrier effects (10) compared to the drain abrupt impurity fabricated by melting annealing with pulsed laser. A few-second HLA was already applied (8, 9) to 256 kbit CMOS ROM fabrication and realized a good yield over a 4 in. diam wafer.

This paper describes the basic characteristics of ion-implanted silicon with a few second HLA such as, crystalline regrowth, activation of dopant, diffusion, and junction-leakage current. The application of HLA for CMOS VLSI processing is also discussed.

Heating with Halogen Lamps

The halogen lamp system is a radiant furnace with quartz tungsten halogen lamps. The heating chamber is composed of 24 halogen lamps; 12 lamps at top and bottom, respectively, facing each other. The wavelength of the incoherent light ranges from 0.3 to 3.0 μm . The effective volume of the heating chamber is 200(W) \times 264(D) \times 80(H) mm^3 . A silicon wafer is supported on four pointed quartz pins between the top and bottom lamps, keeping a distance of 40 mm from each lamp unit. Radiation from both lamp units is absorbed in the top and bottom surfaces of the wafer. After these lamps are put out, the wafer is cooled only by its radiation to the surroundings. Figure 1 shows one of the temperature-time profiles of the wafer. We have used a 5s rising time throughout this study. We define the annealing conditions by the maximum temperature and its soak time (1). According to this definition, Fig. 1 is the profile of 1100°C and 5s annealing. The temperature is measured by a Chromel-Alumel thermocouple attached to the bottom surface of the wafer.

Regrowth

Czochralski-grown silicon crystal of (100) orientation of 8-12 $\Omega\text{-cm}$ n-type resistivity and 6-9 $\Omega\text{-cm}$ p-type resistivity were used for the experiments. The wafers were chemically and mechanically polished on one side, and the peripheral edges of the wafers were rounded. Wafers were implanted with ^{11}B , $^{49}\text{BF}_2$, ^{31}P , or ^{40}Ar ions, and were annealed with halogen lamps in nitrogen gas at atmospheric pressure for a few seconds.

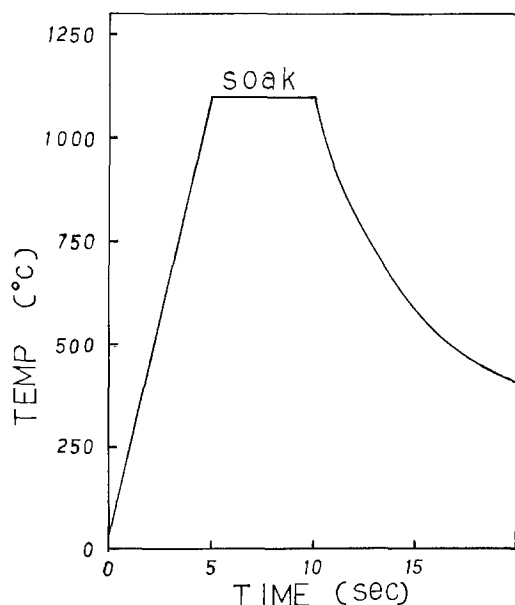


Fig. 1. Temperature-time profile of 5s rising time, 5s soak time, and 1100°C max temp HLA.

The surface regrowth of ion-implanted layers were measured by low energy electron diffraction (LEED) (11). Figure 2 shows the LEED patterns for ^{31}P , 60 keV, $1 \times 10^{15} \text{ cm}^{-2}$ ion-implanted silicon and for $^{49}\text{BF}_2$, 60 keV, $4 \times 10^{15} \text{ cm}^{-2}$ ion-implanted silicon. Both ion-implanted layers with a 600°C and 10s HLA show no Kikuchi line, and the surfaces are still amorphous. Both LEED patterns with an 800°C and 10s HLA show Kikuchi lines (11), and the surfaces are crystalline. Figure 3 shows the combinations of HLA times and

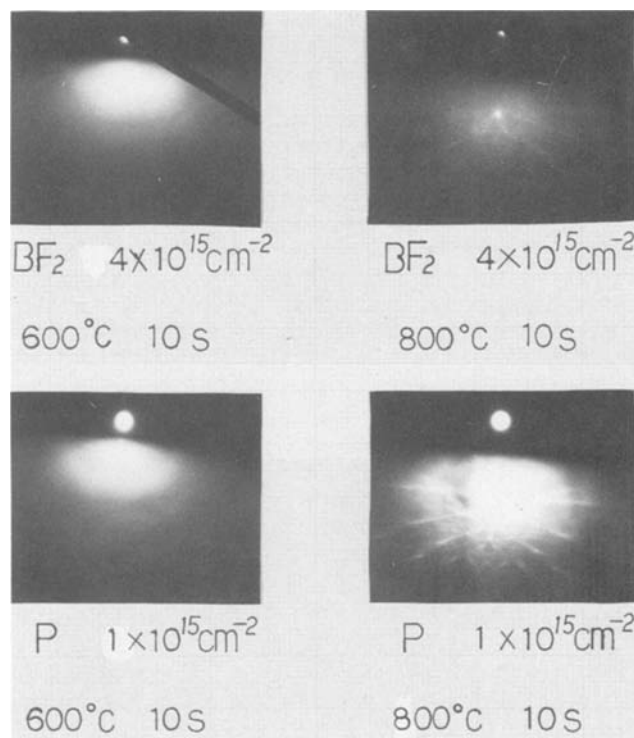


Fig. 2. LEED patterns of ^{31}P , 60 keV, $1 \times 10^{15} \text{ cm}^{-2}$ ion-implanted silicon and of $^{49}\text{BF}_2$, 60 keV, $4 \times 10^{15} \text{ cm}^{-2}$ ion-implanted silicon with HLA.

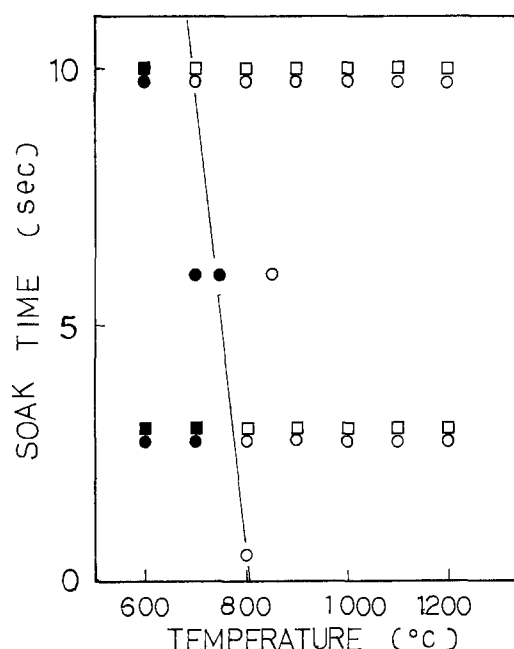


Fig. 3. Regrowth as a function of HLA time and temperature. \square , \blacksquare : $^{49}\text{BF}_2$, 60 keV, $4 \times 10^{15} \text{ cm}^{-2}$ ion-implanted silicon. \circ , \bullet : ^{31}P , 40 keV, $4 \times 10^{15} \text{ cm}^{-2}$ ion-implanted silicon. \bullet , \blacksquare : amorphous layer. \circ , \square : crystalline layer.

temperatures which are sufficient for crystalline regrowth of samples implanted with ^{31}P , 40 keV, $4 \times 10^{15} \text{ cm}^{-2}$ (open circle) or $^{49}\text{BF}_2$, 60 keV, $4 \times 10^{15} \text{ cm}^{-2}$ (open square).

It is shown that a minimum of about 700°C and 10s HLA or 800°C and 1s HLA is required for the crystalline regrowth of ^{31}P or $^{49}\text{BF}_2$ ion-implanted layer. The wafers that were implanted with ^{11}B ions have Kikuchi lines irrespective of HLA time and temperature. The ^{11}B , 40 keV, $4 \times 10^{15} \text{ cm}^{-2}$ ion-implanted layers without HLA were still crystalline. The wafers that were implanted with ^{31}P , 60 keV, $1 \times 10^{15} \text{ cm}^{-2}$ and ^{40}Ar , 60 keV, $1 \times 10^{14} \text{ cm}^{-2}$ and were annealed at 1000°C for 10s have Kikuchi lines. But the wafers that were implanted with ^{31}P , 60 keV, $1 \times 10^{15} \text{ cm}^{-2}$ and more than $1 \times 10^{15} \text{ cm}^{-2}$ ^{40}Ar , 60 keV and were annealed at 1000°C for 10s have no Kikuchi line. ^{40}Ar inhibits the regrowth of ^{31}P ion-implanted layer. The samples which were implanted with ^{40}Ar as well as ^{31}P or $^{49}\text{BF}_2$ recrystallized slower than those which were not implanted with argon (12). According to the LEED patterns, ^{11}B ion-implanted layers require no HLA, $^{49}\text{BF}_2$ or ^{31}P ion-implanted layers require a 700°C and 10s HLA, and high dose ^{40}Ar ion-implanted layers require more than a 1000°C and 10s HLA in order to crystallize the surface of silicon.

Diffusion

The scaling down of CMOS VLSI device dimensions requires shallower junctions of both p-type and n-type source-drain regions. High temperature and long time heat-treatment causes diffusion of dopant in both the vertical and lateral directions, which, if excessive, can constrain the density of LSI designs. HLA could control both vertical and lateral redistribution of source-drain region to the minimum, thus easing the short channel effect (9). This section determines the maximum HLA cycle which causes little diffusion of the dopant. The junction depths were measured by spreading resistance method. Figure 4 shows the junction depths as a function of HLA temperature. Soak time is 3s throughout Fig. 4. One (closed circle) was implanted with ^{11}B , 40 keV, $4 \times 10^{15} \text{ cm}^{-2}$ through 400\AA SiO_2 . The other (closed square) was implanted with $^{49}\text{BF}_2$, 60 keV, $4 \times 10^{15} \text{ cm}^{-2}$ through 400\AA SiO_2 . The junction depth of ^{11}B ion-implanted layer becomes deeper as the HLA temperature goes above 800°C .

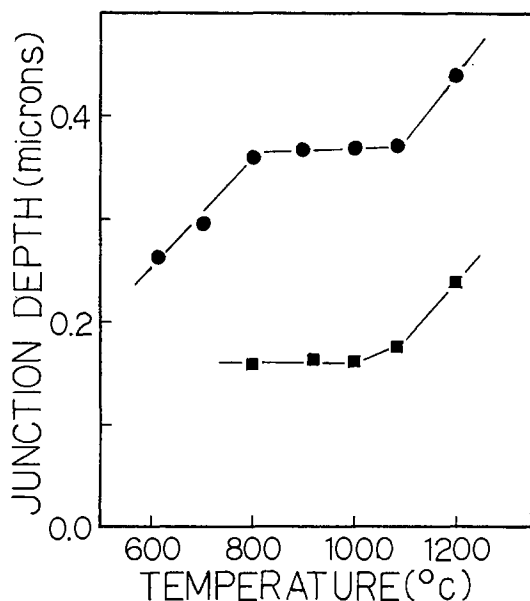


Fig. 4. Junction depth of ^{11}B , 40 keV, $4 \times 10^{15} \text{ cm}^{-2}$ through 400\AA SiO_2 ion-implanted layer (●) and of $^{49}\text{BF}_2$, 60 keV, $4 \times 10^{15} \text{ cm}^{-2}$ through 400\AA SiO_2 ion-implanted layer (■) as a function of HLA temperature. Soak time is 3s.

While HLA temperatures change from 800° to 1100°C , junction depths of both ^{11}B and $^{49}\text{BF}_2$ ion-implanted layers, respectively, do not change. A 1200°C and 3s HLA causes diffusion of the dopant about 1000\AA . It is shown that the maximum of HLA time and temperature which causes little diffusion is 1100°C and 3s for both ^{11}B and $^{49}\text{BF}_2$ ion-implanted layers. Figure 5 shows the junction depths of ^{31}P , 40 keV, $4 \times 10^{15} \text{ cm}^{-2}$ through 400\AA SiO_2 ion-implanted layer as a function of HLA temperature. The one-soak time (open-triangle) is 3s. The other soak time (closed triangle) is 10s. A 1200°C and 10s HLA causes diffusion of the ^{31}P dopant about 2000\AA . It is shown that the maximum of HLA temperature and time which causes little diffusion is 1100°C and 10s for ^{31}P ion-implanted layer. This result almost coincides with ^{11}B and $^{49}\text{BF}_2$ ion-implanted layers. From the viewpoint of LSI miniaturization, HLA should be carried out within the B region in HLA time-temperature space (see Fig. 15).

Sheet Resistivity

Sheet resistivities were measured by means of the four-probe method. Figure 6 compares the ^{11}B , 40 keV, $4 \times 10^{15} \text{ cm}^{-2}$ ion-implanted layer with the $^{49}\text{BF}_2$, 60 keV, $4 \times 10^{15} \text{ cm}^{-2}$ ion-implanted layer as a function of HLA temperature. Soak time is 3s throughout Fig. 6. As HLA temperature goes up, the sheet resistivity of ^{11}B ion-implanted layer becomes lower slowly. There is no rapid drop for ^{11}B . It is shown that more than a 1000°C and 3s HLA is required for the activation of ^{11}B ion-implanted layer. In addition to the data shown in Fig. 6, carrier concentrations were measured by spreading resistance method. As the HLA temperature goes up from 600° to 1200°C , the maximum carrier concentration increases for ^{11}B . However, the sheet resistivity of $^{49}\text{BF}_2$ ion-implanted layer drops rapidly at 800°C and 3s HLA. The rapid drop in sheet resistivity at 800°C corresponds to the crystalline regrowth of the amorphous layer at the surface (Fig. 3). While HLA temperature changes from 800° to 1100°C , the maximum carrier concentration does not increase for $^{49}\text{BF}_2$ and the sheet resistivity does not change so much. The further reduction in sheet resistivity above 1100°C is due to the increment of the maximum carrier concentration and of the junction depth (Fig. 4). The difference of sheet resistivity between ^{11}B and $^{49}\text{BF}_2$ ion-implanted layers above 1100°C HLA is mainly due to the difference of junction depth between ^{11}B and $^{49}\text{BF}_2$ (Fig. 4). The

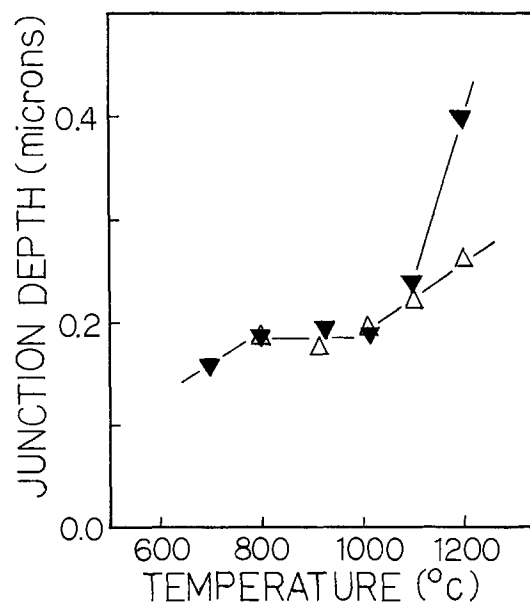


Fig. 5. Junction depth of ^{31}P , 40 keV, $4 \times 10^{15} \text{ cm}^{-2}$ through 400\AA SiO_2 ion-implanted layer as a function of HLA temperature. Soak times are 3s (△) and 10s (▼).

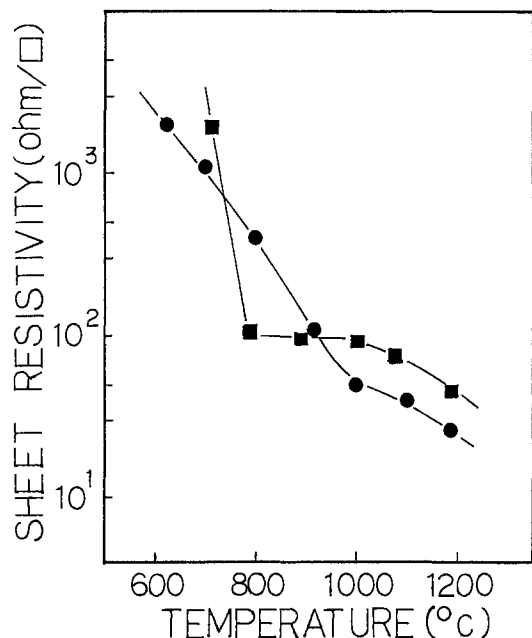


Fig. 6. Sheet resistivity of ^{11}B , 40 keV, $4 \times 10^{15} \text{ cm}^{-2}$ ion-implanted (\bullet) and of $^{49}\text{BF}_2$, 60 keV, $4 \times 10^{15} \text{ cm}^{-2}$ ion-implanted layer (\blacksquare) as a function of HLA temperature. Soak time is 3s.

sheet resistivity difference between ^{11}B and $^{49}\text{BF}_2$ from 800° to 900°C HLA is due to the recrystallization effect of $^{49}\text{BF}_2$ amorphous layer at the surface. And the sheet resistivity difference below 700°C is explained because $^{49}\text{BF}_2$ ion-implanted layer is still amorphous and ^{11}B ion-implanted layer is crystalline. Figure 6 indicates that $^{49}\text{BF}_2$ ion-implanted layer is more suitable than ^{11}B ion-implanted layer for CMOS VLSI fabrication with low temperature and few second HLA. Figure 7 shows the sheet resistivity of ^{31}P , 40 keV, $4 \times 10^{15} \text{ cm}^{-2}$ ion-implanted layer as a function of HLA temperature. One soak time (open triangle) is 3s. The other (closed triangle) is 10s. The abrupt drop in the sheet resistivity at 700°C and 10s HLA or 800°C and 3s HLA is due to the regrowth of the amorphous layer (Fig. 3). After recrystallization, the sheet resistivity be-

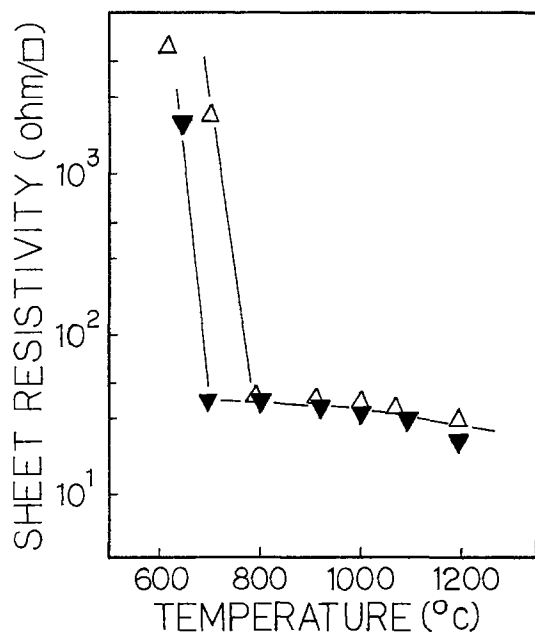


Fig. 7. Sheet resistivity of ^{31}P , 40 keV, $4 \times 10^{15} \text{ cm}^{-2}$ ion-implanted layer as a function of HLA temperature. Soak times are 3s (\triangle) and 10s (\blacktriangledown).

comes lower very slowly as the HLA temperature goes up. Activation of dopant and crystalline regrowth of amorphous layer occur at the same time for both $^{49}\text{BF}_2$ and ^{31}P ion-implanted layers.

A 700°C and 10s or an 800°C and 3s HLA is enough to activate and to crystalline regrow both the $^{49}\text{BF}_2$ and ^{31}P ion-implanted layers. But, ^{40}Ar ion-implanted amorphous layers do not reduce HLA time and temperature of regrowth or of activation. Figure 8 shows the sheet resistivity of ^{31}P ion-implanted layer and of ^{11}B ion-implanted layer as a function of ^{40}Ar dose. More than $1 \times 10^{15} \text{ cm}^{-2}$ ^{40}Ar ion-implanted silicon is amorphous. But ^{40}Ar ion-implanted amorphous layers require more than a 1000°C and 10s HLA in order to regrow and activate dopant. As ^{40}Ar dose goes up, the sheet resistivities of both ^{11}B and ^{31}P ion-implanted layers become higher. The results lead to the conclusion that ^{40}Ar inhibits the activation of ^{11}B and ^{31}P . This ^{40}Ar effect with HLA is the same as that with laser annealing and furnace annealing (13). In Fig. 8, the sheet resistivity of ^{31}P ion-implanted layer is more affected by ^{40}Ar dose compared to that of ^{11}B ion-implanted layer, because the depth of ^{11}B dopant is much deeper than the depth of ^{40}Ar dopant and the depth of ^{31}P dopant is nearly the same as that of ^{40}Ar dopant. The growth rate of $^{49}\text{BF}_2$ or ^{31}P ion-implanted amorphous layer is significantly higher than that of ^{40}Ar as well as $^{49}\text{BF}_2$ or ^{31}P ion-implanted layer. And a 700°C and 10s HLA or an 800°C and 3s HLA activates and regrows $^{49}\text{BF}_2$ and ^{31}P ion-implanted amorphous layers.

Junction Leakage Current

This section describes the electrical characteristics of junction diodes fabricated by the silicon gate CMOS FET process using a few second HLA, and especially puts emphasis on the reverse-bias leakage current as a function of HLA time and temperature. A few second HLA was applied to the silicon gate CMOS FET process. Table I shows the fabrication processing steps that we have used in this experiment. 4 in. diam silicon wafers of n-type 8-12 $\Omega\text{-cm}$ resistivity and (100) orientation were used for the substrate.

This process adopted the halogen lamp system for annealing high dose implanted source-drain layers in place of conventional furnace. At process step 10, the

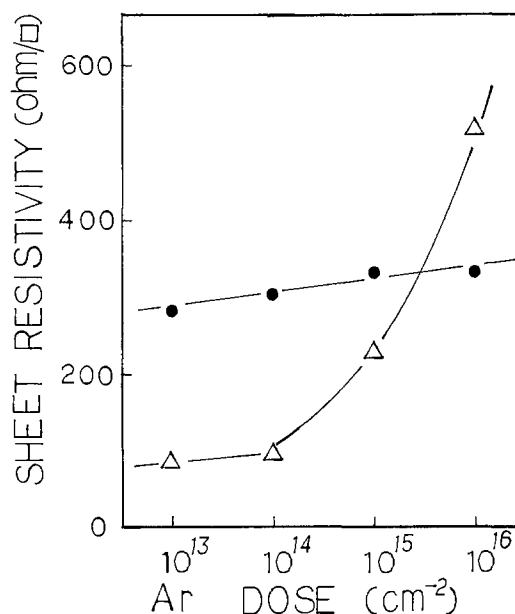


Fig. 8. Sheet resistivity of ^{31}P , 60 keV, $1 \times 10^{15} \text{ cm}^{-2}$ ion-implanted layer (\triangle) and of ^{11}B , 60 keV, $1 \times 10^{15} \text{ cm}^{-2}$ ion-implanted layer (\bullet) as a function of ^{40}Ar , 60 keV dose. The HLA's are 1000°C and 10s for ^{31}P ion-implanted layers and 900°C and 10s for ^{11}B ion-implanted layers.

Table I. Process steps

Process steps	Contents
1. n-well implant	^{31}P
2. p-well implant	^{11}B
3. Well drive-in	Furnace anneal
4. Field oxide	LOCOS (14) technology
5. Gate oxide	SiO_2
6. Gate electrode	n ⁺ -polysilicon
7. p-type diffusion	^{11}B or $^{49}\text{BF}_2$ ion-implant
8. n-type diffusion	^{31}P ion-implant
9. CVD	PSG or silicate glass
10. HLA (halogen lamp annealing)	A few seconds annealing
11. Contact window	
12. Metallization	Al-Si

wafers were annealed by the halogen lamp system in nitrogen gas at atmospheric pressure for a few seconds. This heating treatment must realize the activation and crystalline regrowth of ion-implanted source-drain region, lessen the junction leakage current, lessen the sheet resistivity of polysilicon (9) or silicide, and densify or flow the phosphosilicate glass (PSG). Three diodes were used in this study. The first has $1000 \times 1000 \mu\text{m}^2$ junction area and $4000 \mu\text{m}$ perimeter. This was used for measuring the leakage current per unit area. The other two diodes have same junction area ($100 \times 100 \mu\text{m}^2$ and $4 \times 2500 \mu\text{m}^2$) but different perimeters (400 and $5008 \mu\text{m}$). They were used for measuring the leakage current per unit length of perimeter. The leakage currents were measured at 5V reverse bias in darkness. Figure 9 shows the 5V reverse-bias area leakage current density as a function of HLA time and temperature. The filled circles stand for ^{11}B , 40 keV, $4 \times 10^{15} \text{cm}^{-2}$ through 400\AA SiO_2 ion-implanted junctions. The open triangles represent ^{31}P , 60 keV, $4 \times 10^{15} \text{cm}^{-2}$ through 400\AA SiO_2 ion-implanted junctions. HLA soak time was 6s throughout this figure. The leakage currents were measured at 24°C . These leakage currents are mainly due to damages in the bulk depletion region.

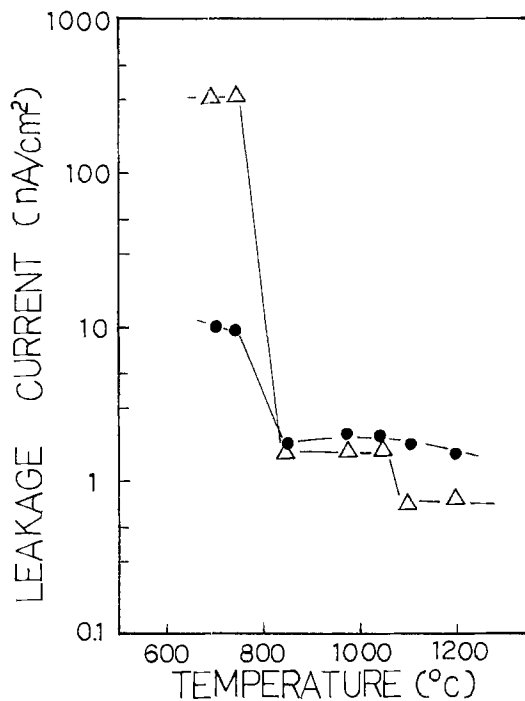


Fig. 9. 5V reverse-bias area junction leakage current density as a function of HLA temperature for ^{11}B , 40 keV, $4 \times 10^{15} \text{cm}^{-2}$ through 400\AA SiO_2 ion-implanted junctions (●) and for ^{31}P , 60 keV, $4 \times 10^{15} \text{cm}^{-2}$ through 400\AA SiO_2 ion-implanted junctions (Δ). Soak time is 6s. The leakage current was measured at 24°C in darkness.

The shape of ^{31}P ion-implanted junction area leakage current density is similar to the behavior of the sheet resistivity, which is shown in Fig. 7. The rapid drops in both leakage current and sheet resistivity at 800°C HLA correspond to the crystalline regrowth of the amorphous region. The small drop at 1100°C HLA is related to motion of the junction depth, which is shown in Fig. 5. It is shown that crystalline regrowth of the amorphous region reduces the area leakage current density. An 800°C and 6s HLA realizes the area leakage current of $\leq 1.5 \text{ nA/cm}^2$. But, a little motion of junction depth, 1100°C and 6s HLA, is necessary to reduce the area leakage current of ^{31}P ion-implanted junctions to the levels of the junctions with 950°C and 30 min furnace annealing ($\leq 0.8 \text{ nA/cm}^2$). The area junction leakage of the sample implanted with ^{11}B has a small drop at 800°C . This is the same as that of ^{31}P . This is consistent with LEED patterns on ^{11}B ion-implanted silicon having Kikuchi lines, but ^{11}B ion-implanted layers have damage in the bulk depletion region. An 800°C and 6s HLA is necessary to get out the damage and to reduce the area leakage current to the level of $\leq 2 \text{ nA/cm}^2$. The reduction of area leakage current density due to motion of junction depth is not significant in the case of ^{11}B ion-implanted junctions. This may be due to the lightness of ^{11}B ion or to the depth ($\approx 0.4 \mu\text{m}$) of the junctions. In the case of $^{49}\text{BF}_2$ ion-implanted junctions, an 800°C and 6s HLA reduces the area leakage current to the level of $\leq 2 \text{ nA/cm}^2$, too. From the viewpoint of CMOS VLSI fabrication, an 800°C and 6s HLA is good enough for both P channel and N channel source-drain region to reduce the area leakage current uniformly over a 4 in. diam wafer. But the perimeter leakage current becomes dominant (15) in VLSI, because the scaling down of electric devices in VLSI causes the area-to-perimeter ratio of the junction to decrease. When the value of the perimeter length (cm) is about 1000 times as large as the value of the area (cm^2), the perimeter leakage current is not negligible. An 800°C and 6s HLA reduces the perimeter leakage current, too. But the uniformity of the perimeter leakage current with an 800°C and 6s HLA is not good. Figure 10 shows the 5V reverse-bias perimeter leakage current at 80°C as a function of HLA temperature. Soak time was 6s throughout this figure. The leakage current was measured at 80°C in darkness. The filled circles stand for ^{11}B , 40 keV, $4 \times 10^{15} \text{cm}^{-2}$ through 400\AA SiO_2 ion-implanted junctions. Open triangles stand for ^{31}P , 60 keV, $4 \times 10^{15} \text{cm}^{-2}$ through 400\AA SiO_2 ion-implanted junctions. The shapes of both ^{31}P and ^{11}B ion-implanted junction perimeter leakage current are similar to the behavior of the area leakage current density, for temperatures below 1000°C (see Fig. 9). Above 1000°C , higher temperature HLA gets lower and more uniform perimeter leakage current for both ^{31}P and ^{11}B ion-implanted junctions. This means that the deeper junctions have lower and more uniform perimeter leakage current density. Figure 11 shows 5V reverse-bias perimeter leakage current at 80°C as a function of HLA temperature. Soak time is 6s throughout this figure. The leakage current is measured at 80°C in darkness. Closed squares represent $^{49}\text{BF}_2$, 60 keV, $4 \times 10^{15} \text{cm}^{-2}$ through 400\AA SiO_2 ion-implanted junctions. Open triangles are for ^{31}P , 40 keV, $4 \times 10^{15} \text{cm}^{-2}$ through 400\AA SiO_2 ion-implanted junctions. An 800°C and 10 min furnace annealing was carried out before HLA throughout this figure. Figure 11 indicates that higher temperature HLA reduces perimeter leakage current for both $^{49}\text{BF}_2$ and ^{31}P ion-implanted junctions. In addition to the data shown in Fig. 10, the perimeter leakage was measured with the sample at room temperature and found to be less than $10^{-15} \text{ A}/\mu\text{m}$ for 1100°C and 6s HLA samples. Perimeter leakage currents may depend much on the perimeter struc-

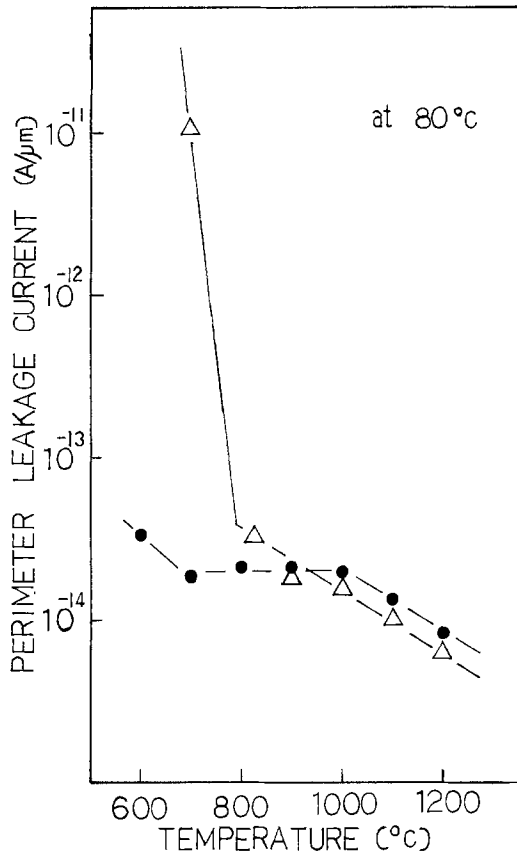


Fig. 10. 5V reverse-bias perimeter junction leakage current as a function of HLA temperature for ¹¹B, 40 keV, $4 \times 10^{15} \text{ cm}^{-2}$ through 400Å SiO₂ ion-implanted junctions (●) and for ³¹P, 60 keV, $4 \times 10^{15} \text{ cm}^{-2}$ through 400Å SiO₂ ion-implanted junctions (Δ). Soak time is 6s. The leakage current was measured at 80°C in darkness.

tures of junctions. More work is needed to determine the dependence of perimeter leakage current on the perimeter structure.

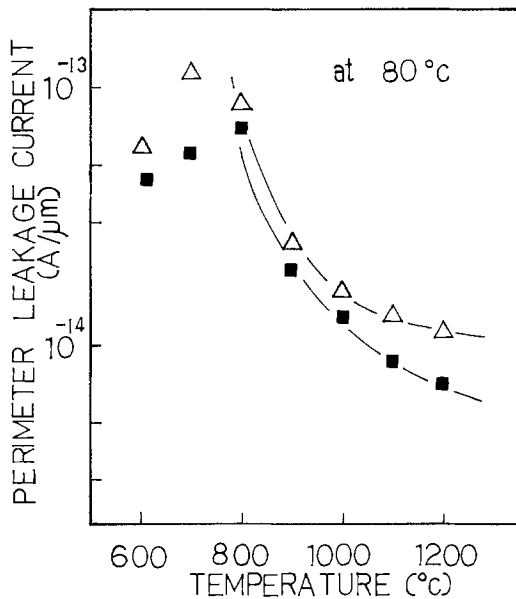


Fig. 11. 5V reverse-bias perimeter junction leakage current as a function of HLA temperature for ⁴⁹BF₂, 60 keV, $4 \times 10^{15} \text{ cm}^{-2}$ through 400Å SiO₂ ion-implanted junctions (■) and for ³¹P, 40 keV, $4 \times 10^{15} \text{ cm}^{-2}$ through 400Å SiO₂ ion-implanted junctions (Δ). Two annealings, an 800°C and 10 min furnace annealing and a 6s HLA, for each data point. The leakage current was measured at 80°C in darkness.

Other Applications of HLA

In current CMOS VLSI fabrication processing, refractory-metal silicide gates and interconnects are used to reduce gate resistivity and contact resistivity. From the practical viewpoint of fabrication CMOS VLSI, it is preferable to keep the silicide formation temperature as low as possible in order to avoid the dopant redistribution in source and drain regions. Figure 12 shows sheet resistivities of titanium (Ti) silicide and molybdenum (Mo) silicide (16) as a function of HLA temperature. Soak time is 10s throughout this figure. Sheet resistivities were measured by a four-point probe. Filled circles stand for Mo silicide which was formed on 4 in. diam wafer, 1000Å elemental Mo was sputtered on (100)-oriented silicon substrates and was annealed with halogen lamps to form silicide. Open circles represent Ti silicide which was formed on 4 in. diam wafer, 1000Å elemental Ti was sputtered on (100)-oriented silicon substrates and was annealed with halogen lamps to form silicide. All results in Fig. 12 are for unpatterned deposited layers. Both metal films did not peel or crack during a few second HLA. It is shown that a 900°C and 10s HLA reduces the sheet resistivity of Mo silicide to 5 Ω/□ and a 700°C and 10s HLA reduces the sheet resistivity of Ti silicide to 2 Ω/□. The surface silicide formation was assured by ion microprobe analysis and by LEED. A 1000°C and 10s HLA is enough to form silicide and reduce sheet resistivity for both Mo and Ti without dopant redistribution. At process step 10 in Table I or after the contact window is open, the HLA heating treatment densifies or flows the phosphosilicate glass (PSG). Figure 13 shows SEM cross-sectional view of plasma etched contact opening in 10 m/o, 10,000Å thick PSG for before flow, after a 1100°C and 3s HLA, and after a 1200°C and 3s HLA. A 1200°C and 3s HLA is enough to planarize the surface of contact holes. A 1100°C and 3s HLA slightly smooths the edge of contact holes. It is shown that 10 m/o PSG flow needs more than a 1100°C and 3s HLA. This means that it is difficult to flow 10 m/o PSG without dopant redistribution. When HLA is applied to CMOS VLSI mass production, we must consider the flatness of wafer, slip-line free, and uniformity of electrical characteristics. In annealing rapidly, it occurred as a problem that the wafer was bent and slip lines were produced. The whole wafer annealed with halogen lamps is heated up and cooled down isothermally,

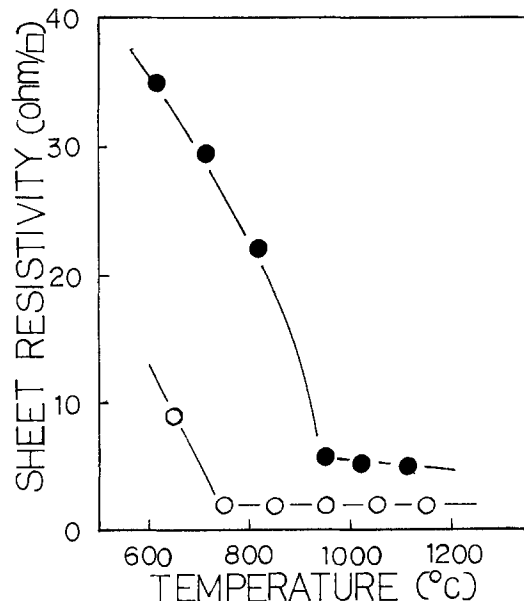


Fig. 12. Sheet resistivity of 1000Å Ti (○) on silicon and of 1000Å Mo (●) on silicon as a function of HLA temperature. Soak time is 10s.

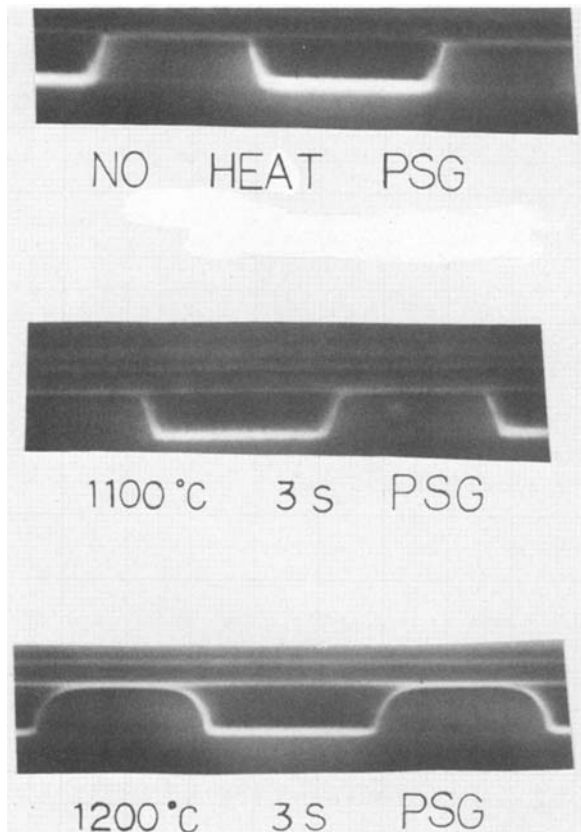


Fig. 13. SEM cross section of contact openings in 10 m/o, 10,000 Å PSG before and after a 1100°C and 3s HLA and after a 1200°C and 3s HLA.

but the thermal losses around the peripheral edge of the wafer generated the drop in temperature (17), which caused the stress. The wafer-edge rounding made the wafer less susceptible to slip. When the temperature of HLA was below 1000°C and the time of HLA was <10s, slip was not induced and the wafers were flat enough to align the photopatterning in CMOS VLSI fabrication. Above 1100°C HLA, leveling the peripheral temperatures of the wafer was required. As a measure of leveling, the peripheral edge of the wafer was heated by peripheral and circular sublamp in addition to the main irradiation, with the result that the whole wafer had the same temperature. By this measure, slip lines disappeared and the peak to valley flatness of the wafer after 1200°C and 10s HLA became as small as (9) that of the conventional furnace-annealed wafer. Figure 14 shows the standard deviation of sheet resistivity within a 4 in. diam wafer as a function of peripheral and circular sublamp power which levels the temperature of the peripheral edge of the wafer. The wafers were implanted with ^{11}B , 40 keV, $4 \times 10^{15} \text{ cm}^{-2}$ and were annealed at 1100°C for 6s. The average sheet resistivity is 28.44 Ω/\square . The optimum 10% sublamp power realized 1.05% standard deviation over a 4 in. diam wafer. The rounded peripheral edge of the wafer and the optimum peripheral and circular sublamp power realize slip-line free, flatness of wafer, and uniformity of electrical characteristics below 1200°C and within 10s HLA.

Summary

Figure 15 shows HLA time-temperature space for CMOS VLSI fabrication. HLA time-temperature region A is insufficient to regrow the ion-implanted amorphous layer. HLA time-temperature region B is enough to crystalline regrow the $^{49}\text{BF}_2$ and ^{31}P ion-implanted amorphous layers, to activate $^{49}\text{BF}_2$ and ^{31}P dopant, to form Ti silicide, and to reduce the area

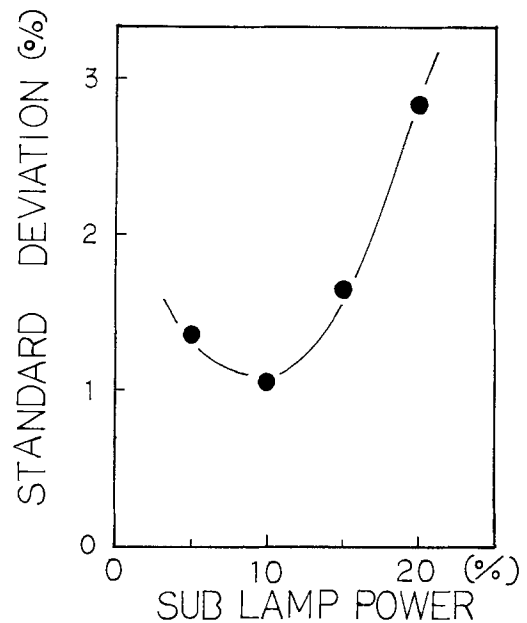


Fig. 14. Standard deviation of sheet resistivity within 4 in diam wafer as a function of peripheral and circular sublamp power. The wafers were implanted with ^{11}B , 40 keV, $4 \times 10^{15} \text{ cm}^{-2}$ and were annealed with a 1100°C and 6s HLA. Average sheet resistivity is 28.44 Ω/\square .

junction leakage current without dopant redistribution. HLA time-temperature region C is enough to crystalline regrow the $^{49}\text{BF}_2$ and ^{31}P ion-implanted amorphous layers, to activate ^{11}B , $^{49}\text{BF}_2$, and ^{31}P dopant, to form Ti silicide and Mo silicide, to flow 10 m/o PSG, and to reduce both area and perimeter leakage current with a little (about 1000 Å) dopant redistribution. More than 1000 Å dopant diffusion occurs with HLA time-temperature region D. From the viewpoint of practical application to VLSI fabrication, a few second HLA is substituted for the furnace annealing without changing conventional processing steps, and it is an effective tool, especially for CMOS VLSI mass production.

Acknowledgments

The authors obtained cooperation from Dr. Hiramoto, Managing Director, Dr. Arai, Laboratory Chief, and Mr. Shimizu of Ushio Denki Company, Limited, and Mr. Mizukami of Tokyo Electron Company Limited, in per-

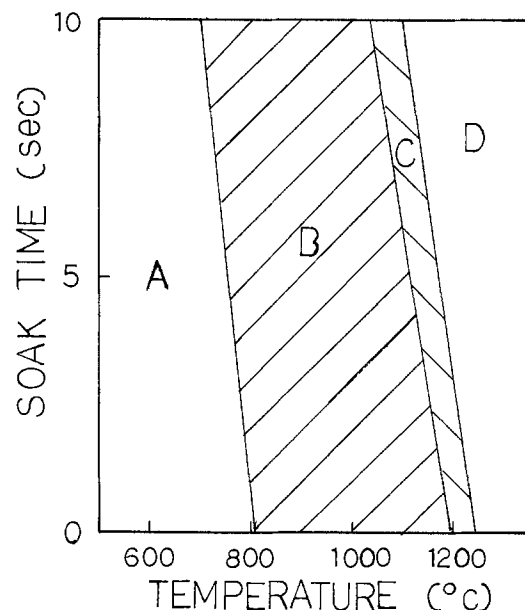


Fig. 15. HLA time-temperature space for CMOS VLSI fabrication

forming experiments for this study. The authors tender the sincerest thanks to them. Also, particular thanks are due to Mr. Mizuno, General Manager, Mr. Ogata, Chief Engineer, and Mr. Takenaka of Suwa Seikosha Company, Limited, Fujimi Plant, for helpful discussion and cooperation in manufacturing CMOS FET's.

Manuscript submitted Nov. 11, 1983; revised manuscript received Jan. 5, 1984. This was Paper 216 presented at the Detroit, Michigan, Meeting of the Society, Oct. 17-21, 1982.

Suwa Seikosha Company, Limited, assisted in meeting the publication costs of this article.

REFERENCES

1. T. O. Sedgwick, *This Journal*, **130**, 484 (1983).
2. L. C. Kimerling and J. L. Benton, in "Laser and Electron Beam Annealing of Materials," C. W. White and P. S. Peercy, Editors, p. 385, Proceedings of the 1979 Materials Research Society Conference in Boston, Academic Press, New York (1980).
3. H. J. Stein, J. A. Knapp, and P. S. Peercy, in "Laser and Electron Beam Interaction with Solids," Vol. 4, B. R. Appleton and G. K. Celler, Editors, p. 319, Proceedings of the 1981 Materials Research Society Conference in Boston, Elsevier, North-Holland (1982).
4. R. T. Fulks, C. J. Russo, P. R. Hanley, and T. I. Kamins, *Appl. Phys. Lett.*, **39**, 604 (1981).
5. J. T. Lue, *ibid.*, **36**, 73 (1980).
6. R. A. Powell, T. O. Yep, and R. T. Fulks, *ibid.*, **39**, 150 (1981).
7. K. Nishiyama, M. Arai, and N. Watanabe, *Jpn. J. Appl. Phys.*, **19**, L563 (1980).
8. S. Iwamatsu, J. Kato, Y. Nakazaki, T. Hiramoto, T. Arai, and R. Igarashi, Abstract 216, p. 348, The Electrochemical Society Extended Abstracts, Vol. 82-2, Detroit, MI, Oct. 17-21, 1982.
9. S. Iwamatsu and J. Kato, *J. Vac. Soc. Jpn.*, **25**, 735 (1982).
10. E. Takeda, T. Makino, and T. Hagiwara, Extended Abstracts of the 15th Conference on Solid State Devices and Materials, p. 261, Japanese Journal of Applied Physics, Tokyo, Aug. 30-Sept. 1, 1983.
11. W. R. Runyan, "Semiconductor Measurements and Instrumentation," p. 252, Texas Instruments Electronics Series, Dallas, TX (1975).
12. L. Csepregi, E. F. Kennedy, T. J. Gallagher, J. W. Mayer, and T. W. Sigmon, *J. Appl. Phys.*, **48**, 4234 (1977).
13. A. Milgram and M. Delfino, Abstract 229, p. 368, The Electrochemical Society Extended Abstracts, Vol. 82-2, Detroit, MI, Oct. 17-21, 1982.
14. J. A. Appels, E. Kooi, M. M. Paffen, J. J. H. Shatorgé, and W. H. C. G. Verkuylen, *Philips Res. Rep.*, **25**, 118 (1970).
15. A. E. Michel, F. F. Fang, and E. S. Pan, *J. Appl. Phys.*, **45**, 2991 (1974).
16. R. T. Fulks, R. A. Powell, and W. T. Stacy, *IEEE Electron Devices Lett.*, **ed-3**, 179 (1982).
17. T. R. Anthony and H. E. Cline, *J. Appl. Phys.*, **49**, 5774 (1978).

Some Properties of Semi-Insulating and Si-Implanted GaAs

P. K. Bhattacharya¹ and J. K. Rhee²

Department of Electrical and Computer Engineering, Oregon State University, Corvallis, Oregon 97331

ABSTRACT

Various measurement techniques have been used to characterize semi-insulating and Si-implanted and annealed GaAs. Hall, photoconductivity, and photoinduced current transient measurements yield almost identical energy values for the compensating deep centers in the semi-insulating materials. In undoped GaAs, the dominant donor level, EL2, is at 0.73 ± 0.02 eV below the conduction band, and in Cr-doped GaAs the dominant Cr acceptor level is at 0.82 ± 0.01 eV below the conduction band. In Si-implanted GaAs where implantation has been made directly into the wafer, there are two dominant trapping centers: a 0.52 eV electron trap and a 0.15 eV hole trap. In materials implanted through a silox encapsulant, these centers are absent. Instead, a slow transient, with its time constant almost independent of sample temperature, is observed. It is believed that the transient arises from interface states. Several other electron and hole traps have been observed in semi-insulating and implanted GaAs.

The fabrication of GaAs field effect transistors (FET's) and other microwave devices requires the availability of reliable semi-insulating (SI) substrate materials. The quality of these materials has changed significantly in the last few years. Most of the recent investigations (1-6) on Cr-doped and undoped SI GaAs have been directly related to the electrical and optical properties of the deep compensating levels in these materials. The techniques which have been predominantly used are photoluminescence, dc and ac photoconductivity, and electron paramagnetic resonance (EPR) spectroscopy. Some transport properties in SI GaAs have been determined by Look (7) and Martin *et al.* (8). In addition to the known properties of the compensating deep levels in SI materials, it is important to determine the thermal emission properties of these levels, *viz.*, their activation energies and capture cross sections for electrons and holes. There is also little report on the thermal-emission properties of other defect or impurity levels which might be present. Such information would aid in a better under-

standing of the electrical properties and compensation mechanisms in semi-insulating materials and the active layers subsequently grown on them.

Deep level defects in Cr-doped and undoped SI GaAs, including the compensating levels, were detected and characterized in this study by the photoinduced current transient (PICT) measurement technique, first reported by Hurtes *et al.* (9). This technique must be employed since it is not possible to perform conventional capacitance transient or deep-level transient spectroscopy (DLTS) measurements with Schottky barriers fabricated on materials exhibiting high resistivity. The nature of the traps were inferred by performing the PICT experiments with intrinsic and extrinsic optical excitation. The energy position of some of the more dominant defect levels were also obtained from the variation of the photoconductivity with incident photoexcitation energy and from analyses of these spectra. Transport parameters in the semi-insulating materials were measured at high temperatures using the van der Pauw technique. The variation of resistivity, Hall mobility, and Hall coefficient with temperature, for $T > 350$ K, were determined. The compensation in the materials and other important transport parameters were determined from a solution of appropriate charge neutrality equations.

¹ Present address: Department of Electrical and Computer Engineering, University of Michigan, Ann Arbor, Michigan 48105.

² Present address: Cray Research Incorporated, Chippewa Falls, Wisconsin.

Key words: ion implantation, deep levels, transport properties, high resistivity gallium arsenide.

Recent progress in ion implantation as a means of controlled doping of elemental and compound semiconductors has led to significant advances in the technology and fabrication of integrated circuits (IC). Implantation of high energy donor ions into SI GaAs and subsequent thermal or laser annealing produce n-type active layers whose thickness and carrier concentration can be controlled by the implant dose and energy. Deep level defects induced by the implant-and-anneal procedure can produce deleterious effects in the performance of FET's and similar devices. Some results on deep levels in Si-implanted and annealed GaAs:Cr (5, 10, 11) have recently been reported, but no detailed studies have yet been made.

Transient capacitance and DLTS measurements were performed on implanted and annealed SI GaAs:Cr and undoped GaAs. Transient current measurements were also made directly on GaAs FET's fabricated by ion-implantation technology. In addition to thermal emission from the deep compensating centers, outdiffusing from the substrate, emission from dominant electron and hole traps and several other traps with thermal activation energies ranging from 0.15 ± 0.01 to 0.90 ± 0.01 eV has been detected and characterized.

Materials Description and Device Fabrication

The semi-insulating (SI) GaAs samples used for this study were grown either by the liquid encapsulation Czochralski (LEC) or by the horizontal Bridgeman (HB) technique and were nominally oriented in the (100) direction. Wafers for the study were generally taken from the midsection of the boules. The undoped LEC material was near stoichiometric. The Cr-doped HB material was usually As rich. The resistivity in the samples is $\sim 10^7 \Omega\text{-cm}$ at room temperature. The same samples were either implanted directly with $^{28}\text{Si}^+$ at an energy of 100 keV, or through a 1000Å silox mask at an energy of 130 keV. Annealing was done at 800° or 850°C for 20 min in an ambient of flowing forming gas ($\text{H}_2:\text{N}_2 = 10:90$) with the implanted layer protected by a 2000Å silox encapsulating layer.

Devices for photoinduced current transient measurements were made from samples of SI GaAs $5 \times 5 \text{ mm}^2$ in area and 200-300 μm thick. A semitransparent circular Au film (diam = 1.5 mm, thickness $\approx 100\text{-}200\text{\AA}$) was deposited on the polished top surface, and a thicker Au layer ($\sim 1000\text{\AA}$) was deposited on the entire opposite face by evaporation under a vacuum of $\sim 10^{-6}$ torr. Similar devices were made by evaporating Cr or eutectic Au-Ge contacts, but they gave rise to low S/N ratio during the measurements.

Circular Au dots with $(1\text{-}2) \times 10^{-3} \text{ cm}^2$ area and 300-500Å thick were evaporated on the implanted and annealed layers to form Schottky diodes for transient capacitance and DLTS measurements. Evaporated and alloyed Au-Ge/Ni ohmic contacts for the diodes were formed on the implanted layers.

Field effect transistors for the transient measurements were fabricated by conventional photolithography and lift-off techniques. The FET's have both gate length and width of 100 μm and source-gate and gate-drain spacings of 5 μm each. Symmetrical samples for Hall measurements were made from the semi-insulating and ion-implanted layers by evaporating small-area ohmic contacts at the four corners and subsequent alloying.

Results and Analysis

Semi-insulating GaAs.—Transport measurements.—Variations of the Hall coefficient, R_H , and dark conductivity, σ , with inverse temperature are shown in Fig. 1 and 2 for SI GaAs:Cr and undoped GaAs. The variations are almost linear in the temperature range of interest. The measured transport parameters at 400 K in SI GaAs:Cr and undoped GaAs are listed in Tables I and II, respectively.

In semi-insulating materials, where two-carrier transport can be assumed to be operative, the appropriate charge-neutrality equations can be solved to obtain expressions for the temperature-dependent conductivity and Hall factor. The position of the Fermi level can also be determined accurately from such an analysis, where full ionization for the shallow levels is assumed. Two distinct cases arise. If the compensat-

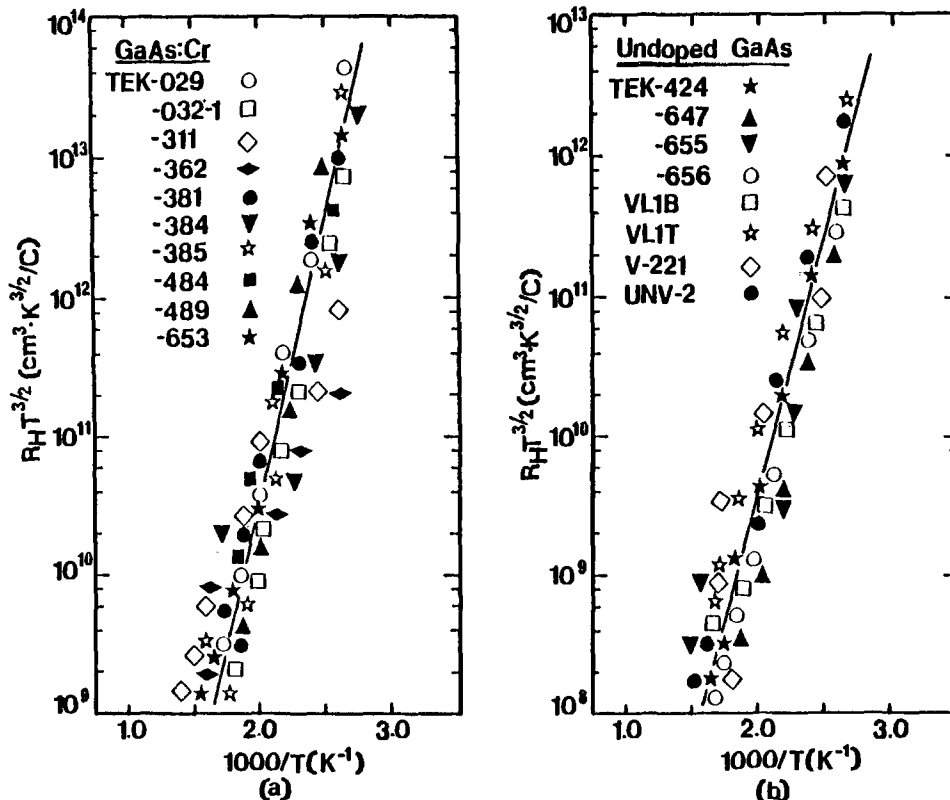


Fig. 1. Measured and calculated variation of $R_H T^{3/2}$ with inverse temperature in (a, left) SI GaAs:Cr and (b, right) SI undoped GaAs.

ing deep level is an acceptor then it can be shown that (12)

$$\sigma(T) = \frac{q\mu_n N_v}{g_{AA} b} [CR - 1] \left\{ \exp\left(-\frac{E_{AA}}{kT}\right) + \frac{g_{AA}^2 b N_c}{N_v (CR - 1)^2} \exp\left(-\frac{E_G - E_{AA}}{kT}\right) \right\} \quad [1]$$

and

$$R_H(T) = r \frac{g_{AA}}{qN_v (CR - 1)} \frac{\exp\left(\frac{E_{AA}}{kT}\right) - g_{AA}^2 b^2 N_c \exp[(3E_{AA} - E_G)/kT]/N_v (CR - 1)^2}{\{1 + g_{AA}^2 b N_c \exp[(2E_{AA} - E_G)/kT]/N_v (CR - 1)^2\}} \quad [2]$$

where $CR = N_{AA}/(N_D - N_A)$. However, if the compensating deep level is a donor, then it can be shown that (12)

$$\sigma(T) = q\mu_n [CRU - 1] g_{DD} N_c \left\{ \exp[-(E_G - E_{DD})/kT] + \frac{N_v \exp\left(-\frac{E_{DD}}{kT}\right)}{g_{DD}^2 [CRU - 1]^2 N_c} \right\} \quad [3]$$

and

$$R_H(T) = r [CRU - 1] \frac{g_{DD}}{qN_v} \frac{\{\exp(E_{DD}/kT) - b^2 [CRU - 1]^2 g_{DD}^2 N_c \exp[(-E_G + 3E_{DD})/kT]/N_v\}}{\{1 + b [CRU - 1]^2 g_{DD}^2 N_c \exp[(-E_G + 2E_{DD})/kT]/N_v\}} \quad [4]$$

where $CRU = N_{DD}/(N_A - N_D)$. In these equations $b = \mu_n/\mu_p$, r is scattering factor which can be taken as unity unless it is strongly temperature dependent, g_{AA} and g_{DD} are the degeneracy factors of the deep compensating acceptor and donor levels, respectively, and N_c and N_v are the density of states in the conduction and valence bands, respectively. The ionization energies E_{AA} and E_{DD} for the acceptors and donors, respectively, are measured from the top of the valence band.

In the samples studied by us, Cr impurities create a deep acceptor in Cr-doped SI GaAs. In the undoped samples, however, compensation is known to occur because of the presence of a deep donor acting as an

electron trap, commonly known as EL2 (13). Therefore, both sets of equations given above are applicable to the materials under study. The solid lines in Fig. 1a and 1b, and 2a and 2b are the theoretically calculated temperature-dependent Hall constant and conductivity in Cr-doped and undoped high resistivity GaAs. The good agreements in each case indicate that the electrical properties of present-day GaAs substrates can be predicted by the models described above. Values for

the deep acceptor and donor concentrations, N_{AA} and N_{DD} , and their energy depth measured from the conduction bandedge, were estimated by fitting the experimental values of $R_H T^{3/2}$ and σ . The estimated values of $(E_G - E_{AA})$ and $(E_G - E_{DD})$ are listed in Tables I and II, and of N_{AA} and N_{DD} are listed in Tables III and IV.

Photoinduced current transient measurements.—Intrinsic photoexcitation generates electron-hole pairs just underneath the circular Au film of the device used. The excess carriers are captured by electron or hole

traps in the sample, if they exist. After removal of the photoexcitation, detrapping due to the thermal reemission gives rise to a transient current between the two contacts. Typical values of the bias applied between the Au contacts varied from 8 to 10V. Arrhenius plots for the emissions detected in SI GaAs:Cr and undoped GaAs are shown in Fig. 3 and 4, respectively. For experiments with intrinsic photoexcitation, the distinction between electron and hole emissions can be made by observing the direction of the transient-current variation. It should be noted that the activation energies, ΔE_T , listed in Fig. 3 and 4 were obtained from

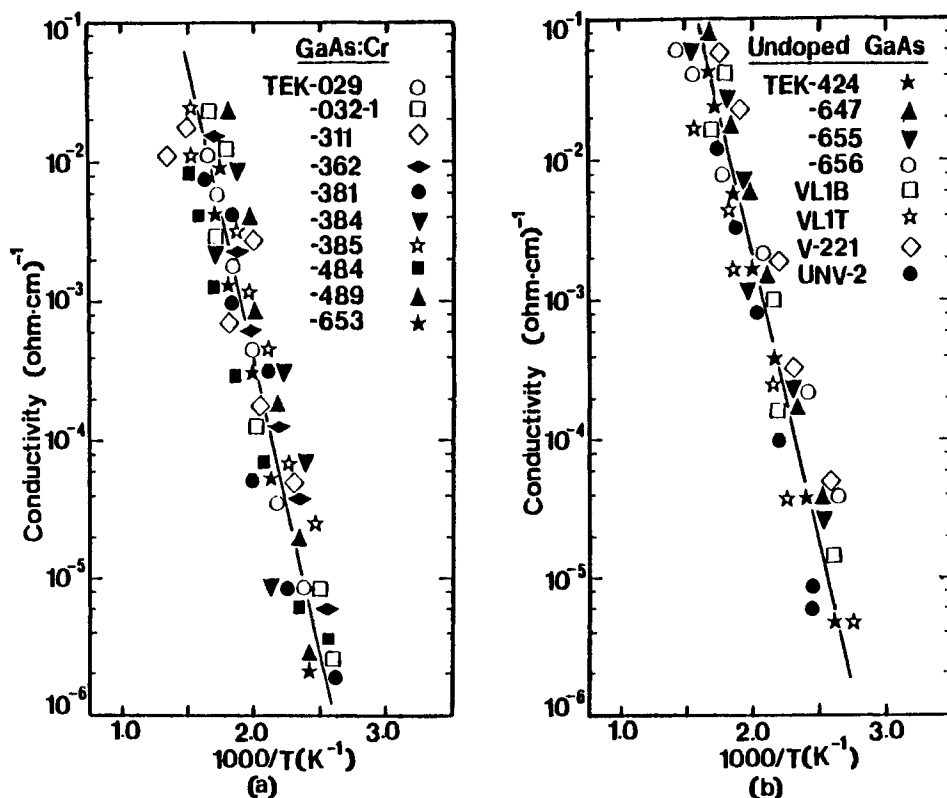


Fig. 2. Measured and calculated variation of dark conductivity, σ , with inverse temperature in (a, left) SI GaAs:Cr and (b, right) SI undoped GaAs.

Table I. Transport data on SI GaAs:Cr obtained (HB) from Hall measurements, Fermi energy values at 400 K, and energy positions of deep acceptor levels

Sample*	$(qR_H)^{-1}$ at 400 K (cm^{-3})	μ_H at 400 K ($\text{cm}^2/\text{V} \cdot \text{s}$)	Slope of $\ln(R_H T^{3/2})^{-1}$ (eV)	$(E_G - E_{AA})$ From analysis (eV)	$(E_G - E_F)$ at 400 K From analysis (eV)
TEK 029	5.8×10^9	2020	0.82	0.81	0.64
TEK 0321	1.7×10^{10}	2100	0.84	0.83	0.60
TEK 311	2.0×10^{11}	275	0.65	0.83	0.52
TEK 362	4.0×10^{10}	790	0.66	0.83	0.57
TEK 381	7.2×10^9	2450	0.80	0.81	0.63
TEK 384	1.0×10^{10}	1880	0.80	0.82	0.62
TEK 385	6.0×10^{11}	560	0.85	0.84	0.48
TEK 484	1.7×10^{10}	1770	0.81	0.82	0.60
TEK 489	2.8×10^{10}	1950	0.86	0.83	0.58
TEK 653	1.1×10^{10}	1250	0.87	0.83	0.62

* Samples are from wafers obtained from the midsection of a single boule.

Table II. Transport data in SI undoped GaAs (LEC) obtained from Hall measurements, Fermi energy values at 400 K, and energy positions of deep donor levels

Sample*	$(qR_H)^{-1}$ at 400 K (cm^{-3})	μ_H at 400 K ($\text{cm}^2/\text{V} \cdot \text{s}$)	Slope of $\ln(R_H T^{3/2})^{-1}$ (eV)	$(E_G - E_{DD})$ From analysis (eV)	$(E_G - E_F)$ at 400 K From analysis (eV)
TEK 424	1.25×10^{11}	890	0.76	0.74	0.53
TEK 647	7.8×10^{11}	780	0.67	0.72	0.47
TEK 655	2.3×10^{11}	2950	0.71	0.72	0.51
TEK 656	4.2×10^{11}	1350	0.68	0.73	0.49
UNV2	3.2×10^{10}	600	0.77	0.75	0.58
VL1B	1.9×10^{11}	1425	0.65	0.71	0.52
VL1T	7.5×10^{10}	1475	0.74	0.74	0.55
V221	1.85×10^{11}	2075	0.71	0.72	0.52

* Samples represent two boules.

the slopes of $\ln(T^2\tau)$ vs. $1/T$ plots and include the barrier energy ΔE_B . Similarly, the capture cross sections, σ_c , were obtained from the emission rate prefactor of the detailed balance equation. The true capture cross section of the centers can be obtained from a measurement of the thermal-capture rates (14). In some cases, hole emission was confirmed by repeating the measurements with suitable extrinsic photoexcitation. In this case, the trap population in a large region between the contacts is directly altered.

Photoconductivity spectra in semi-insulating GaAs.—These measurements were performed to confirm some of the results obtained from PICT and high temperature Hall measurements and to detect deep levels which may not have been revealed by the previous measurements. The spectra were recorded in the spectral range 0.4–1.5 eV with a Jarrel-Ash monochromator with an appropriate combination of filters. The device configuration was the same as that for the PICT measurements. The constant electric field across the samples varied in the range $(1.0\text{--}3.5) \times 10^2$ V/cm.

Typical spectra in SI GaAs:Cr at 100 and 203 K are shown in Fig. 5a. Chromium in GaAs is usually located in a Ga site giving rise to a deep lying acceptor impurity. Four charge states of the Cr-related centers

have been reported (15), giving rise to multiple activation energies between 0.56 to 0.9 eV (16). The onset at 0.65 eV has been observed by several investigators and is probably related to oxygen (16, 17). The rise in photosensitivity at 0.81 eV is probably due to Cr (3, 16). The peak at 0.95 eV has been attributed to the intratransition from the 5T_2 ground state to the 5E excited state of Cr^{2+} (18), which is usually observed closer to 0.9 eV. With reference to Fig. 5b, which depicts the typical photoconductivity spectra for SI undoped GaAs, the onset at 0.73 eV has been observed by several investigators and is attributed to the deep donor (19, 20). The transition at 1.2 eV has been observed by Williams (21) and Farbe (22), but its origin is as yet unknown. The peak at 0.9 eV is probably due to an intrastate transition of the donor level. The sharp onsets in both spectra ~ 1.4 eV indicate the bandedge in GaAs.

Si-implanted and annealed SI GaAs.—Electrical properties.—In wafers implanted through silox, the activation of Si was $\sim 40\%$. Variations of activation with implant dose and mobility with sheet electron concentration in undoped GaAs implanted through silox are depicted in Fig. 6a and 6b. The room-temperature Hall mobilities measured in implanted samples in the course of this study are among the highest values attained in device-quality implanted GaAs.

Table III. Shallow and deep donor and acceptor level concentrations and compensation ratios in SI GaAs:Cr (HB) determined from analysis of Hall-effect data

Sample	N_{AA} (cm^{-3})	N_D (cm^{-3})	N_A (cm^{-3})	$\frac{N_{AA}}{N_D - N_A}$
TEK 029	4.2×10^{10}	3.0×10^{16}	2.1×10^{16}	4.6
TEK 0321	2.3×10^{10}	2.8×10^{16}	2.0×10^{16}	2.8
TEK 311	1.19×10^{17}	2.0×10^{17}	1.0×10^{17}	1.19
TEK 362	1.9×10^{16}	7.5×10^{16}	6.5×10^{16}	1.9
TEK 381	2.5×10^{16}	2.9×10^{16}	2.1×10^{16}	3.1
TEK 384	3.5×10^{16}	3.3×10^{16}	2.3×10^{16}	3.5
TEK 385	1.08×10^{16}	9.4×10^{16}	8.4×10^{16}	1.08
TEK 484	2.5×10^{16}	3.6×10^{16}	2.6×10^{16}	2.5
TEK 489	1.8×10^{16}	3.1×10^{16}	2.2×10^{16}	2.0
TEK 653	3.0×10^{16}	3.5×10^{16}	2.5×10^{16}	3.0

Table IV. Shallow and deep donor and acceptor level concentrations and compensation ratios in SI undoped GaAs (LEC) determined from analysis of Hall-effect data

Sample	N_{DD} (cm^{-3})	N_D (cm^{-3})	N_A (cm^{-3})	$\frac{N_{DD}}{N_A - N_D}$
TEK 424	2.1×10^{17}	9.0×10^{16}	9.8×10^{16}	26.25
TEK 647	1.4×10^{16}	1.0×10^{17}	1.1×10^{17}	140.0
TEK 655	4.3×10^{16}	9.0×10^{16}	1.0×10^{16}	43.0
TEK 656	3.2×10^{17}	2.3×10^{16}	2.7×10^{16}	80.0
UNV2	2.2×10^{17}	1.8×10^{17}	2.1×10^{17}	7.3
VL1B	7.2×10^{16}	2.2×10^{16}	2.4×10^{16}	36.0
VL1T	3.0×10^{16}	2.1×10^{16}	2.3×10^{16}	15.0
V221	3.5×10^{16}	1.7×10^{16}	1.8×10^{16}	35.0

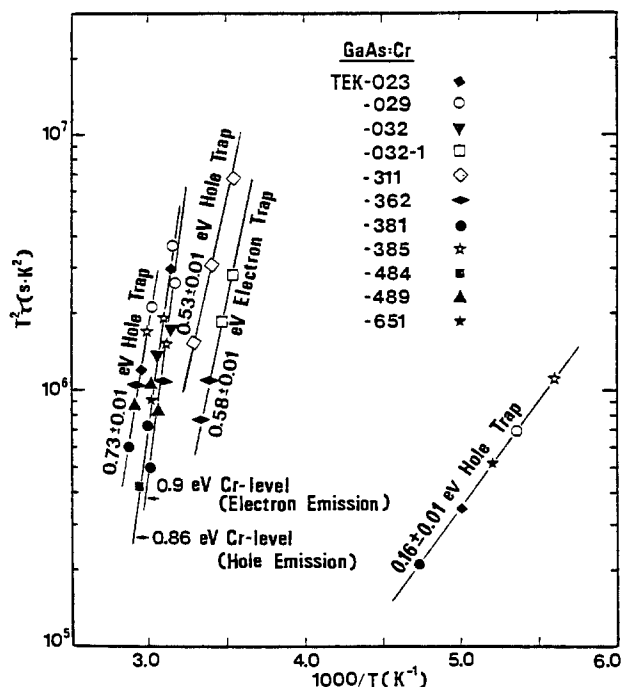


Fig. 3. Arrhenius plots for electron- and hole-trap levels in SI GaAs:Cr detected by PICT measurements. The symbols located arbitrarily represent the different samples and are not data points.

Variation of the Hall mobility with temperature in two Si-implanted GaAs:Cr samples with high electron mobilities is shown in Fig. 7. The solid lines indicate the theoretically calculated mobilities taking into account the relevant scattering mechanisms. Average values of N_A and N_D obtained for the two samples are 0.9×10^{16} and $2.0 \times 10^{16} \text{ cm}^{-3}$, respectively.

Transient capacitance measurements.—Transient capacitance and photocapacitance measurement techniques were used to detect and characterize deep levels in implanted and annealed SI GaAs:Cr and undoped GaAs. Majority and minority carrier trap levels in the depletion region of Schottky barriers made from n-type samples can be filled by a bias or an optical pulse, respectively. The capacitance change of the diode due to thermal emissions from deep levels is monitored by a 1 MHz capacitance bridge and recorded. The activa-

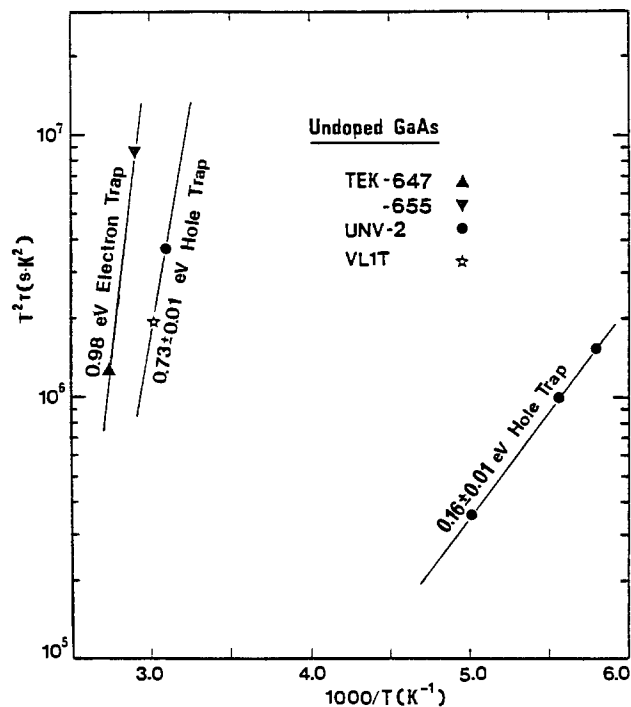


Fig. 4. Arrhenius plots for electron- and hole-trap levels in SI undoped GaAs detected by PICT measurements. The symbols located arbitrarily represent the different samples and are not data points.

tion energy and the thermal capture cross section of the various traps are determined from the measured thermal-carrier emission rates at several fixed temperatures. The trap concentration, N_T , is estimated from the free-carrier concentration and the capacitance change at the termination of the filling pulse. It may be noted that the sensitivity of the measurements, which is primarily determined by the noise added to the transient signal, set the detection limit for traps. It was estimated that traps with concentration 10^{-4} times lower than the free-carrier concentration in the sample would not be detected.

The characteristics of electron and hole-trap levels detected in the implanted and annealed SI GaAs:Cr samples directly implanted with different doses of Si are listed in Table V. The samples implanted were

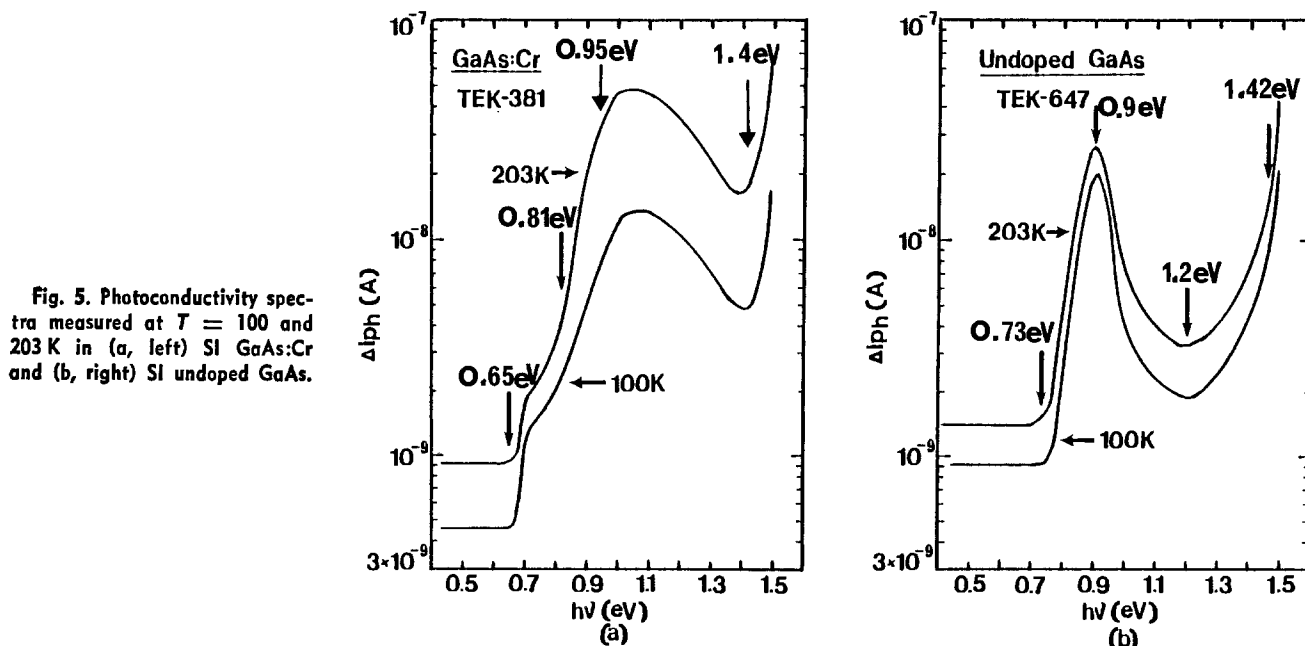
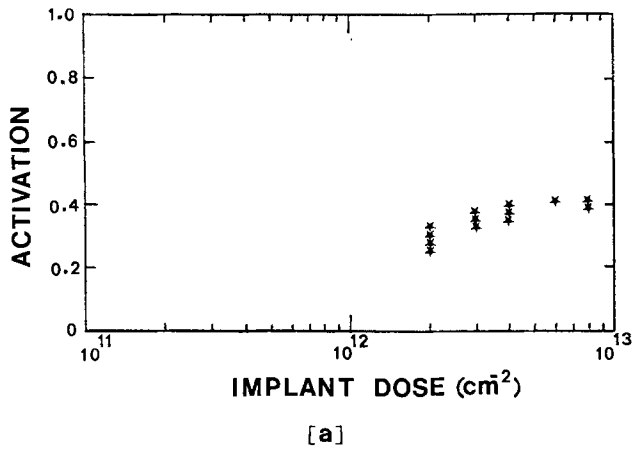
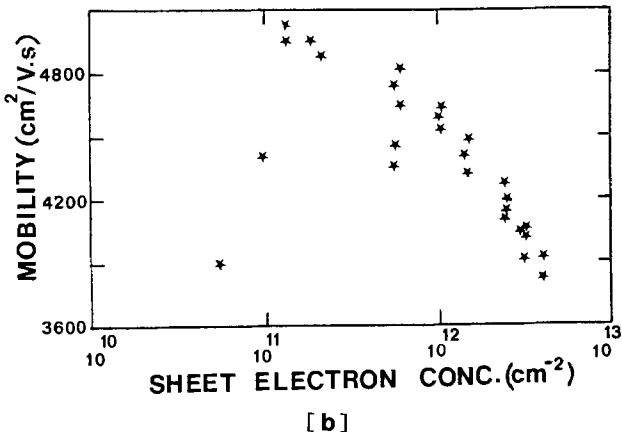


Fig. 5. Photoconductivity spectra measured at $T = 100$ and 203 K in (a, left) SI GaAs:Cr and (b, right) SI undoped GaAs.



[a]



[b]

Fig. 6. Variation of (a, top) Si activation with implant dose and (b, bottom) sheet electron concentration with electron mobility at room temperature.

those listed in Tables I and III and similar wafers. These results are representative of over 30 samples characterized in this study. The electron-trap levels with $\Delta E_T = 0.17 \pm 0.01$ and 0.21 ± 0.01 eV do not appear consistently and are ascribed to unknown impurities and/or defects. Chromium is observed to be present, as evidenced by the 0.85 ± 0.01 eV hole emis-

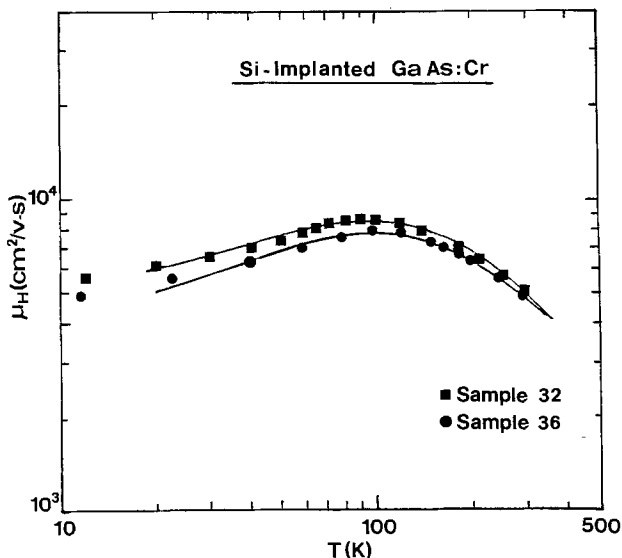


Fig. 7. Variation of Hall mobility with temperature in two Si-implanted and annealed GaAs:Cr samples. Sample 32 was implanted with $8 \times 10^{11} \text{ cm}^{-2}$ and sample 36 with $2 \times 10^{12} \text{ cm}^{-2}$ Si⁺, respectively. The solid lines indicate the calculated mobilities.

Table V. Characteristics of deep levels in Si-implanted and annealed Si GaAs:Cr determined by DLTS measurements

Sample*	Implant dose (10^{12} cm^{-2})	Electron trap		Hole trap	
		ΔE_T (eV)	σ_a (cm^2)	ΔE_T (eV)	σ_a (cm^2)
41	1.0	0.53	1.3×10^{-18}	0.84	1.4×10^{-18}
		0.21	3.1×10^{-21}	0.16	5.8×10^{-23}
36	2.0	0.51	1.5×10^{-18}	0.85	1.3×10^{-18}
		0.17	5.3×10^{-23}	0.15	5.9×10^{-23}
31	2.0	0.51	1.6×10^{-18}	0.84	1.4×10^{-18}
		0.17	5.3×10^{-23}	0.14	6.0×10^{-23}
26	4.0	0.52	1.4×10^{-18}	0.86	1.2×10^{-18}
		0.16	5.5×10^{-23}	0.14	6.0×10^{-23}
21	4.0	0.52	1.4×10^{-18}	0.86	1.2×10^{-18}
		0.18	5.2×10^{-23}	0.14	6.0×10^{-23}
14	8.0	—	—	0.86	1.2×10^{-18}
45	10.0	0.53	1.3×10^{-18}	0.85	1.3×10^{-18}
		—	—	0.15	6.0×10^{-23}

* Thermal annealing of all samples was done at 800°C for 20 min in flowing forming gas.

sion. The electron-trap level with $\Delta E_T = 0.52 \pm 0.01$ eV and the hole-trap level with $\Delta E_T = 0.15 \pm 0.01$ eV were consistently detected in the implanted and annealed Si GaAs:Cr samples. These two trap levels are also the dominant centers in Si-implanted VPE GaAs (26). Arrhenius plots for the two traps are shown in Fig. 8.

Results from the transient-capacitance measurements described above were corroborated by transient measurements on GaAs FET's fabricated on the same GaAs:Cr wafers by ion-implantation technology. A suitable quiescent reverse bias is applied to the Schottky gate of the FET so that near-pinch-off condition exists in the channel. An injection pulse is applied to the gate for the detection of majority-carrier traps. With this pulse, trap levels formerly within the depletion region are filled with electrons. As the trapped electron population returns to equilibrium by thermal emission, the drain-source current, I_{DS} , also returns to its quiescent value. Photoexcitation was used to alter the population of minority-carrier traps. Values of ΔE_T and σ_a for various electron and hole emissions observed in the channel region of GaAs FET's are listed in Table VI. The 0.52 ± 0.01 and 0.15 ± 0.01 eV electron and hole-trap levels, respectively, are again observed consistently.

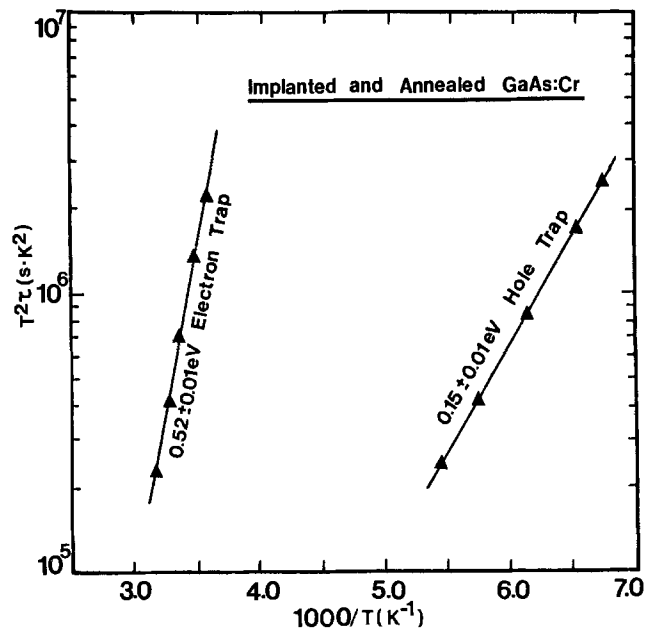


Fig. 8. Dominant electron and hole traps in Si-implanted and annealed GaAs:Cr with the ions being implanted directly.

Table VI. Characteristics of deep levels in GaAs FET's in Si GaAs:Cr fabricated by ion-implantation technology. The data used were obtained from measurement of transient I_{DS} at several fixed temperatures.

Sample	Implant dose (10^{12} cm $^{-2}$)	Electron trap		Hole trap	
		ΔE_T (eV)	σ_n (cm 2)	ΔE_T (eV)	σ_p (cm 2)
FET 8	2.0	0.52	1.4×10^{-18}	0.94 0.15	1.4×10^{-18} 5.9×10^{-20}
FET 15	3.0	0.51	1.5×10^{-18}	0.86 0.14	1.2×10^{-18} 6.0×10^{-20}
FET 16	3.0	0.52	1.4×10^{-18}	0.85 0.16	1.3×10^{-18} 5.8×10^{-20}
FET 18	4.0	0.53	1.4×10^{-18}	0.85	1.3×10^{-18}
FET 20	4.0	0.53	1.2×10^{-18}	0.86 0.15	1.2×10^{-18} 5.9×10^{-20}

Similar measurements were repeated on Cr-doped and undoped SI GaAs implanted with various doses of Si through a silox protective layer. The results are very different. Minority carrier trapping has not yet been studied by us in detail in these materials, and the following discussion is related only to electron traps in the n-type implanted layers. On application of a majority-carrier pulse at any fixed temperature during transient capacitance measurements, a decreasing capacitance transient was observed. The time constant of this transient is of the order of several seconds and is almost independent of temperature. No other transient was observed in these materials. When deep-level transient spectroscopy (DLTS) measurements were performed on the same samples with a majority-carrier pulse sequence, no peaks due to electron trapping were observed. Any feature due to the slow transients described above would be absent, since the rate windows and delays in this measurement are of the order of milliseconds.

Discussion

The values of N_{DD} , N_{AA} , N_D , and N_A derived from analysis of our data reflect the concentration of background impurities and of the deep levels in present-day semi-insulating GaAs. With the exception of sample TEK 311 (Table III), N_D , N_A , and N_{AA} in Cr-doped samples are $\sim 10^{16}$ cm $^{-3}$. Similarly, in undoped samples, N_D , N_A , and $N_{DD} \sim 10^{16}$ - 10^{17} cm $^{-3}$. An exception is sample TEK 647 (Table IV), which can be considered as an anomaly.

The hole trap with $\Delta E_T = 0.86 \pm 0.01$ eV detected in almost all the SI GaAs:Cr samples, is attributed to Cr (23). The 0.90 ± 0.01 eV electron trap level detected in the same samples is attributed to electron emission from the Cr centers (14). The 0.58 ± 0.01 and 0.53 ± 0.01 eV electron and hole-trap levels, respectively, are ascribed to unknown impurities. The electron trap may be identical to the 0.60 eV electron trap reported by Fairman and Oliver (24) in SI GaAs and center EL3 (0.575 eV) reported by Martin *et al.* (13) in VPE GaAs. The hole trap has thermal activation energy and capture cross section very similar to trap HS1 (0.58 eV) reported by Mitonneau *et al.* (25) in LPE GaAs. The 0.73 ± 0.01 eV hole-trap level, also detected in SI undoped GaAs, has a thermal-activation energy very similar to trap B (0.71 eV) detected by Lang and Logan (14) in LPE GaAs which is related to a native defect. However, the thermal hole-capture cross sections of the latter center are at least 2 or 3 orders higher than for the 0.73 eV centers detected in this study. The 0.16 eV hole-trap level, detected for the first time in this study, can probably be ascribed to native defects since it was detected in both SI GaAs:Cr and undoped GaAs. Fewer deep levels were detected in SI undoped GaAs. The 0.98 ± 0.01 eV electron-trap level, detected for the first time in this study, can be ascribed to unknown impurities. Further studies are necessary to elucidate its origin. The dominant

electron trap EL2 is present in all samples, but is not clearly observed in the transient measurements due to the presence of other electron and hole traps in the same temperature range.

The presence of Cr was confirmed by high temperature Hall and photoconductivity measurements. Similarly, the presence of the deep-donor level at $E_c - 0.73$ eV detected by high temperature Hall measurement on SI undoped GaAs was confirmed by the photoconductivity measurements. Both these deep levels have thermally activated capture cross sections, expressed by $\sigma_n = \sigma_\infty \exp(-\Delta E_B/kT)$, and $\Delta E_B = 80$ and 250 meV have been measured for the EL2 and Cr level, respectively (26). These values indicate the capture process at these centers by multiphonon emission due to lattice relaxation. The relaxation is much larger for the Cr center than for the EL2 center.

It emerges from our studies that there are two dominant centers in directly implanted and annealed SI GaAs, the 0.53 eV electron trap and the 0.15 eV hole trap. The traps are absent when implantation is done through a silox encapsulant. It is therefore thought that the more severe damage in the directly implanted samples is in some way responsible for the creation of these centers, which may be related to native defects. The 0.53 eV electron trap was annealed after a half-hour heat-treatment at 700°C under H $_2$ flow without any encapsulation. The observation of the same centers in Si-implanted VPE GaAs (27) also favors their relation to native defects.

Implantation through an encapsulant will reduce the thickness of the damaged layer, and, therefore, for the same carrier concentration, the depletion layer of a Schottky diode made on such a layer will reach closer to the active-layer substrate interface. However, in material implanted directly, the depletion-layer edge is further removed from the interface. We therefore believe that the slow transients observed in samples implanted through an encapsulant arises from non-discrete levels at the active-layer substrate interface. These emissions may also be partly responsible for backgating effects observed in FET's made from such materials.

Acknowledgments

The authors are grateful to Dr. R. Y. Koyama, and Dr. V. B. Rao for their help and to Professor J. S. Blakemore for useful discussions. The work has been supported by the National Science Foundation under grant ECS-8011917.

Manuscript submitted July 22, 1983; revised manuscript received Dec. 20, 1983. This was Paper 360 presented at the San Francisco, California, Meeting of the Society, May 8-13, 1983.

REFERENCES

1. P. F. Lindquist, *J. Appl. Phys.*, **48**, 1262 (1977).
2. M. Castagne, J. Bonnafé, J. C. Manificier, and J. P. Fillard, *ibid.*, **51**, 4894 (1980).
3. K. Kitahara, K. Nakai, A. Shibatomi, and S. Ohkawa, *ibid.*, **50**, 5339 (1979).
4. T. Mizutani, T. Honda, S. Ishida, and Y. Kamusaki, *Solid-State Electron.*, **25**, 885 (1982).
5. R. D. Fairman, R. T. Chen, J. R. Oliver, and D. R. Chen, *IEEE Trans. Electron. Devices*, **ed-28**, 135 (1981).
6. See, for example, the relevant publications in "Semi-Insulating III-V Materials," J. D. Rees, Editor, Shiva Publications Ltd., England (1980).
7. D. C. Look, *J. Appl. Phys.*, **48**, 5141 (1977).
8. G. M. Martin, J. P. Farges, G. Jacob, J. P. Hallais, and G. Poibland, *ibid.*, **51**, 2840 (1980).
9. Ch. Hurtes, M. Boulou, A. Mitonneau, and D. Bois, *Appl. Phys. Lett.*, **32**, 821 (1978).
10. H. Kanber, M. Feng, D. B. Ruby, and G. E. Stillman, Paper presented at the 23rd Electronic Materials Conference, Santa Barbara, CA (1981).
11. K. L. Wang and G. P. Li, Paper presented at the 23rd Electronics Materials Conference, Santa

- Barbara, CA (1981).
12. J. K. Rhee and P. K. Bhattacharya, *J. Electron. Mater.*, **11**, 979 (1982).
 13. G. M. Martin, A. Mitonneau, and A. Mircea, *Electron. Lett.*, **13**, 192 (1977).
 14. D. V. Lang and R. A. Logan, *J. Electron. Mater.*, **4**, 1053 (1975).
 15. J. S. Blakemore, in "Semi-Insulating III-V Materials," J. D. Rees, Editor, p. 29, Shiva Publications, Ltd., England (1980).
 16. P. K. Vasudev and R. H. Bube, *Solid-State Electron.*, **21**, 1095 (1978).
 17. A. L. Lin and R. H. Bube, *J. Appl. Phys.*, **47**, 1859 (1976).
 18. G. K. Ippolitova, E. M. Omel'yanovskii, and L. Ya. Pervova, *Sov. Phys. Semicond.*, **9**, 864 (1976).
 19. A. L. Lin, E. Omelianovski, and R. H. Bube, *J. Appl. Phys.*, **47**, 1852 (1976).
 20. Y. Tokumaru, *Jpn. J. Appl. Phys.*, **9**, 95 (1970).
 21. E. W. Williams, *Br. J. Appl. Phys.*, **18**, 253 (1967).
 22. E. Farbe, *C.R. Acad. Sci. (France)*, **B270**, 848 (1970).
 23. G. M. Martin, in "Semi-Insulating III-V Materials," J. D. Rees, Editor, p. 13, Shiva Publications, Ltd., England (1980).
 24. R. D. Fairman and J. R. Oliver, *ibid.*, p. 83.
 25. A. Mitonneau, G. M. Martin, and A. Mircea, *Electron. Lett.*, **13**, 667 (1977).
 26. D. V. Lang and R. A. Logan, *J. Electron. Mater.*, **4**, 1053 (1975).
 27. P. K. Bhattacharya, J. K. Rhee, S. J. T. Owen, J. G. Yu, K. K. Smith, and R. Y. Koyama, *J. Appl. Phys.*, **52**, 7224 (1981).

Mercury-Pressure-Induced Epitaxy of HgCdTe

H. Ruda, L. Jedral, J. Lagowski,* and H. C. Gatos**

Massachusetts Institute of Technology, Cambridge, Massachusetts 02139

ABSTRACT

A new method for the epitaxial growth of HgCdTe from solution is presented, in which growth is induced under isothermal conditions by an increase in the mercury pressure (pressure-induced epitaxy). A growth kinetics model is developed from mass-transport considerations and is successfully used to explain the experimental dependence of the growth velocity, the layer thickness, and the layer composition on the growth time, the solution height, and the applied pressure differential. Spontaneous nucleation was considered, and it was not found to be limiting.

Increased efforts have been recently devoted to epitaxial growth of HgCdTe layers for IR applications. It has been established that the major difficulty in the growth from solution in open systems is associated with the losses of mercury due to the high mercury pressure (1). In a modified-LPE configuration (1) this difficulty is essentially overcome by the control of the Hg pressure over the whole thermal program, thus preventing Hg loss, which is critical for controlling the solid composition. We have recently shown that in HgCdTe, control of the Hg pressure can be used not only to stabilize the properties of thermally grown layers, but also to induce epitaxial growth with an overpressure of Hg while the temperature of the system is kept constant (2).

Pressure-induced epitaxy (PIE) of HgCdTe is the subject of the present theoretical and experimental study designed to establish quantitatively the characteristics of the new growth process. The theoretical model considers pressure-induced Hg transport in the Te-rich solution as the driving force for the growth. The theoretical relationships are compared with experimental results on HgCdTe layers obtained in an open-system slider boat from tellurium-rich solution.

Process and phenomena.—HgCdTe is a three-component system, which during liquid-phase epitaxial growth exists in three phases. According to the Gibbs' phase rule, there are only two degrees of freedom for such a system, e.g., temperature and pressure. In standard LPE, the pressure is maintained constant, and a temperature decrease is used as a driving force for epitaxial growth. In PIE the situation is reversed, i.e., the temperature is maintained constant, while Hg-pressure increase stimulates growth. In the HgCdTe system, the mercury partial pressure far exceeds either cadmium or tellurium pressures, and thus at a constant temperature the composition of all phases, to good approximation, is controlled by the mercury pressure.

In PIE, a Te-rich solution is maintained at a constant temperature, and the required supersaturation is induced as follows: the temperature of a mercury reser-

voir, in equilibrium with the Te solution, is raised, thereby generating a mercury flux from the reservoir to the growth solution. Mercury is taken up by the solution, resulting in a supersaturation of the solute in solution. The solute gradient across the solution acts as the driving force for solute transport towards the substrate/solution interface, and results in epitaxial growth of HgCdTe on the substrate.

A theoretical model of the PIE growth must consider three processes: (i) transport of Hg, in the vapor phase, to the surface of the solution; (ii) transport of excess Hg (solute) in the solution; and (iii) epitaxial growth on the substrate and associated segregation of the solute (solution) species.

In the following treatment, we will make simplifying approximations in order to reduce the three-phase transport problem to a manageable dimension. The first approximation concerns the surface condition of the solution. We assume that at the initial equilibrium with the vapor, the whole solution is at a constant composition, C_{i0} . Upon raising the Hg reservoir temperature $T_1 \rightarrow T_1 + \Delta T$, the surface of the solution will change its composition to $C_1^i = C_{i0} + \Delta C_1$, where ΔC_1 is a function of ΔT . The capacity of the Hg reservoir and the Hg-vapor transport should be sufficient to maintain a constant value of C_1^i during the growth after an initial transient, which has not been considered here.

The solute transport in the solution and growth on the substrate will be treated in a standard way commonly used in describing the LPE growth. Accordingly, we will assume diffusion-controlled solute transport toward the growth interface, which advances with a (growth) velocity sufficiently small to be ignored in the diffusion equation. The (growth) velocity is, of course, included in the flux-conservation condition. Diffusion in the solid state will be neglected. This assumption, which is commonly made for III-V compounds, is less justified for HgCdTe, and its validity may impose a lower limit on the growth velocity and upper limits on the overall time the layer is kept at elevated temperatures.

The pertinent set of equations used to describe the PIE involves the diffusion equation (contained between

* Electrochemical Society Active Member.

** Electrochemical Society Honorary Member.

Key words: CdHgTe, epitaxial growth, pressure-induced epitaxy.

$x = 0$ and $x = l$)

$$D_1 \frac{\partial^2 C_1}{\partial x^2} = \frac{\partial C_1}{\partial t} \quad [1]$$

the flux-conservation equation at the advancing growth interface

$$D_1 \frac{\partial C_1}{\partial x} \Big|_{x=0} = v \cdot [C_1^s - C_{10}] \quad [2]$$

where C refers to the solute concentration in solution, C^s to its value in the solid, and D is the solute diffusivity. x is a position coordinate. The solution height is l , at coordinate $x = l$ from the solid/liquid interface; v refers to the growth velocity and t to the growth time, while other parameters are defined as before.

The boundary conditions on the solution concentration are

$$\begin{aligned} C_1 &= C_{10} \quad \text{at } t = 0 \quad \text{for all } x \\ C_1 &= C_{10} \quad \text{for } x = 0 \quad \text{at any time} \\ C_1 &= C_1^s \quad \text{at } x = l \quad \text{for } t > 0 \end{aligned} \quad [3]$$

Growth kinetics.—For the HgCdTe system, Eq. [1]-[3] should be solved for two components, i.e., Hg and Cd. However, in the simplified growth-kinetics model presented here we will neglect the effect of Cd on the Hg transport. According to Barnes (3), the solution of Eq. [1] and [3] gives the Hg concentration $C(x, t)$ as

$$\begin{aligned} [C(x, t) - C_{10}] &= (C_1^s - C_{10}) \cdot \left(\frac{x}{l}\right) \\ &+ \frac{2}{\pi} \sum_{n=1}^{\infty} \left\{ \frac{(-1)^n \cdot C_1^s - C_{10}}{n} \right\} \sin\left(\frac{n\pi x}{l}\right) \\ &\exp\left(\frac{-Dn^2\pi^2 t}{l^2}\right) + \frac{4C_{10}}{\pi} \sum_{n=1}^{\infty} \left(\frac{1}{2m+1}\right) \\ &\sin\left(\frac{(2m+1) \cdot \pi x}{l}\right) \exp\left[\frac{-D(2m+1)^2\pi^2 t}{l^2}\right] \end{aligned} \quad [4]$$

From [4] and [2], one gets the expression for the growth velocity

$$\begin{aligned} v &= \frac{D}{l(C^s - C_{10})} \left[\Delta C + \left\{ 2 \sum_{n=1}^{\infty} [(-1)^n \right. \right. \\ &\quad \left. \left. \cdot C_1^s - C_{10}] \exp\left(\frac{-Dn^2\pi^2 t}{l^2}\right) \right\} \right. \\ &\quad \left. + \left\{ 4C_{10} \sum_{n=1}^{\infty} \exp\left(\frac{-D(2m+1)^2\pi^2 t}{l^2}\right) \right\} \right] \end{aligned} \quad [5]$$

where $\Delta C \equiv (C_1^s - C_{10})$ the layer thickness, d , as a function of time, is given by

$$\begin{aligned} d &= \frac{\Delta C}{(C^s - C_{10})} \left(\frac{D}{l}\right) \left[t - \frac{l^2}{6D} \right] \\ &- \frac{2l}{\pi^2 (C^s - C_{10})} \cdot \left[\sum_{n=1}^{\infty} \left[\frac{(-1)^n \cdot C_1^s - C_{10}}{n^2} \right] \right. \\ &\quad \left. \exp\left(\frac{-Dn^2\pi^2 t}{l^2}\right) + 2C_{10} \sum_{n=1}^{\infty} \frac{1}{(2m+1)^2} \right. \\ &\quad \left. \exp\left(\frac{-D(2m+1)^2\pi^2 t}{l^2}\right) \right] \end{aligned} \quad [6]$$

In Fig. 1, the layer thickness, d , is calculated according to Eq. [6] and is plotted vs. time. It is seen that after a certain transient period $t \gtrsim t_c$, t_c can be approximated as $\approx (0.35l^2/D)$, and the layer thickness

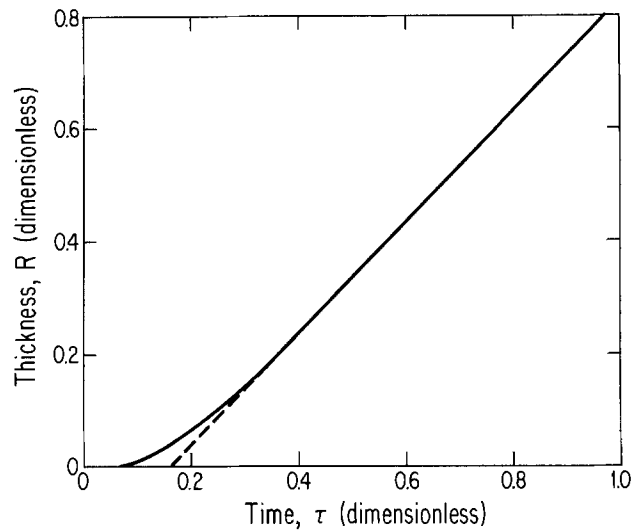


Fig. 1. Dimensionless plot of layer thickness vs. growth time. Curve a represents exact solution, and curve b the steady-state approximation.

becomes a linear function of time which corresponds to steady-state growth with a constant velocity. The value of this steady-state growth velocity is

$$v \approx \frac{\Delta C}{C^s - C_{10}} \cdot \frac{D}{l} \quad [7]$$

and the layer thickness becomes

$$d \approx \left(\frac{\Delta C}{C^s - C_{10}}\right) \cdot \frac{D}{l} \left(t - \frac{l^2}{6D}\right) \quad [8]$$

Equations [7] and [8] predict an inverse dependence of the growth velocity and of the layer thickness on solution height, and a linear dependence on ΔC , which itself is dependent on the thermal step across the reservoir ΔT_{Hg} . The quantitative relationship between ΔC and ΔT is not the same for PIE in an open and in a closed system. In a closed system, one can expect direct proportionality between ΔC and small changes of the reservoir temperature ΔT_{Hg} , i.e., $\Delta C = \zeta \Delta T_{\text{Hg}}$ where ζ is a constant.¹ In an open system, however, the mercury pressure over the solution is not uniquely defined by the reservoir temperature. In such a system, a higher reservoir temperature is required to generate a mercury pressure equivalent to that in the closed system. Thus, a specific dependence $\Delta C(\Delta T_{\text{Hg}})$ cannot be readily predicted for an open system, although for small values of ΔT_{Hg} one can still expect a linear dependence of ΔC on ΔT_{Hg} .

The maximum layer thickness.—As in thermal step cooling LPE, the maximum layer thickness for a given change in Hg concentration, ΔC_{Hg} at the surface, will be limited by depletion of cadmium from solution. Hg is not a limiting factor, since it is continuously supplied for vapor transport from the Hg reservoir. A mass balance for cadmium gives

$$\int_0^l C_{\text{Cd}}(x) dx = lC_{\text{Cd}}^0 - d_{\text{max}}C_{\text{Cd}}^s \quad [9]$$

Clearly, in practice, growth will cease before d reaches d_{max} (for a given ΔC_{Hg} at the surface). But for prolonged growth time

$$C_{\text{Cd}}(x) = \begin{cases} C_{\text{Cd}}^0 & : x = 0 \\ C_{\text{Cd}}^s & : x = l \end{cases} \quad [10]$$

Therefore, substitution of Eq. [10] in [9] gives

¹ See Appendix for more detailed treatment.

$$d_{\max} = -\frac{l}{2} \cdot \frac{\Delta C_{\text{Cd}}}{C_{\text{Cd}}^s} : \Delta C_{\text{Cd}} \equiv C'_{\text{Cd}} - C^o_{\text{Cd}} \quad [11]$$

Following Ref. (4), in which mass transfer is determined by a temperature drop at constant pressure, the same approach is applied here to a case of constant temperature but variable pressure. This gives

$$\frac{\Delta C_{\text{Cd}}}{\Delta C_{\text{Hg}}} \equiv \Lambda = \left\{ \frac{z(k-1) + z(2y-1)}{(1-z)(2y-1) - z(k-1)} \right\} \quad [12]$$

and to rewrite Eq. [11] in the form

$$d_{\max} = \frac{l}{2C_{\text{Cd}}^s} \cdot \left\{ \frac{z(k-1) + z(2y-1)}{(1-z)(2y-1) - z(k-1)} \right\} \cdot \Delta C_{\text{Hg}} \quad [13]$$

where z and y refer to composition of the Te-rich solution $(\text{Hg}_{1-z}\text{Cd}_z)_{1-y}\text{Te}_y$ and $k \equiv (x/z)$.

The growth efficiency, E , can be defined as a ratio of the actual layer thickness, d , over the maximum layer thickness, d_{\max} . From [8] and [13], one gets

$$E = \frac{2C_{\text{Cd}}^s D}{(C_{\text{Hg}}^s - C_{\text{io}}) \Lambda} \cdot \frac{1}{l^2} \left[t - \frac{l^2}{6D} \right] \quad [14]$$

Thus, the growth efficiency increases strongly as the solution thickness decreases.

Growth stability.—In PIE, supersaturation is created in the solution region away from the growth interface. This growth configuration can lead to a spontaneous nucleation in the solution rather than on the substrate. We will analyze the possibility of spontaneous nucleation (SN) in terms of the value of the maximum effective supersaturation that may exist in solution, ΔT_{eff} . This supersaturation corresponds to the maximum constitutional gradient that can exist across the solution.

That is

$$\Delta T_{\text{eff}} = m_{\text{Hg}} [C(l, t) - C(0, t)] :$$

$$m_{\text{Hg}} = \frac{\Delta T}{\Delta C} \Big|_l ; \Delta T_{\text{eff}} = m_{\text{Hg}} \Delta C_{\text{Hg}} \quad [15]$$

Using Eq. [15] and $m_{\text{Hg}} = 993.5^\circ\text{C}/\text{fraction}$ (5) we can evaluate $\Delta T_{\text{eff}} \simeq 1.5^\circ\text{C}$ as the maximum effective supercooling to cause spontaneous nucleation. This value is of the same order as typical supercooling in thermal-LPE growth, and hence we do not expect spontaneous nucleation to occur.

Comparison with Experiment

PIE growth procedure.—Experiments were performed using tellurium-rich solutions of $(\text{Hg}_{1-z}\text{Cd}_z)_{1-y}\text{Te}_y$ of initial composition $z = 0.06$ and $y = 0.80$, in an open-tube slider boat system (6). A two-zone gold reflection coated furnace, with the capability to independently control a growth and a mercury zone, was employed. Growth experiments were performed on polished and etched (111)A CdTe surfaces, $10 \times 10 \text{ mm}^2$ in area. The experimentally determined liquidus temperature for this solution was $501^\circ \pm 0.5^\circ\text{C}$, with a mercury reservoir temperature of $294^\circ \pm 0.5^\circ\text{C}$, under a flowing hydrogen ambient. Direct observation of the surface of the solution through the semitransparent gold reflection-coated furnace enabled a visual determination of the liquidus at work.

The experimental procedure was as follows: complete melting of the solution was achieved at a constant solution temperature T , and reservoir temperature, ($T_o < T_1$). The reservoir was then raised to a temperature, T_1 , to establish the equilibrium mercury pressure above the solution at its liquidus. The system

Table I. Typical growth parameters

Run no.	T (°C)	T ₁ (°C)	T ₂ (°C)	t (min)	l (mm)	d (μm)	z Composition
133	501	294	297	45	2.0	31	0.20
148	501	294	297	15	2.0	13	0.23
140	501	294	300	22.5	2.0	29	0.18
141	501	294	295	22.5	2.0	22	0.22
145	501	293	297	22.5	1.6	38	0.17
149	501	293	297	22.5	3.1	15	0.20

was then allowed to equilibrate for 30-60 min, after which period the substrate was brought into contact with the solution and allowed to thermally equilibrate (5-10 min). The temperature of the reservoir was then increased. Growth experiments were performed for durations ranging from 5 to 45 min, using solution thicknesses of 1.5-3.5 mm and ΔT of 0° - 7°C . Experiments were terminated by sliding the solution off the substrate and cooling the system down. Table I summarizes the growth data for typical PIE layers. Generally, the layers appeared smooth and mirrorlike to the naked eye. Cross sections of PIE layers indicated that excellent thickness uniformity was attained, and quite sharp infrared optical transmission spectra (see Fig. 2) indicate good compositional homogeneity.

Layer thickness vs. growth time.—Experimental results on the dependence of the layer thickness on growth time are given in Fig. 3. The experiments were carried out at a constant growth temperature, using the same solution composition and height and the same magnitude of temperature increase of the Hg reservoir.

As can be seen in Fig. 3, the experimental results can be approximated very well by a straight line consistent with Eq. [8] describing steady-state PIE growth. The calculated value of the Hg diffusivity in solution is $D = 4.44 \times 10^{-5} \text{ cm}^2/\text{s}$ and the value of $\Delta C/(C^s - C_o) \simeq 7.45 \times 10^{-3}$. The diffusivity value is close to the values of around $3 \cdot 10^{-5} \text{ cm}^2/\text{s}$ reported by Ambrozimov *et al.* (7).

Layer thickness vs. solution height.—Experimental data on the layer thickness vs. solution height are given in Fig. 4. All other growth parameters were kept constant. The temperature increase of the Hg reservoir was $\Delta T = 4^\circ\text{C}$ and the growth time $t = 22.5 \text{ min}$. The experimental data are consistent with the inverse proportionality $d \sim 1/l$ predicted by the present theo-

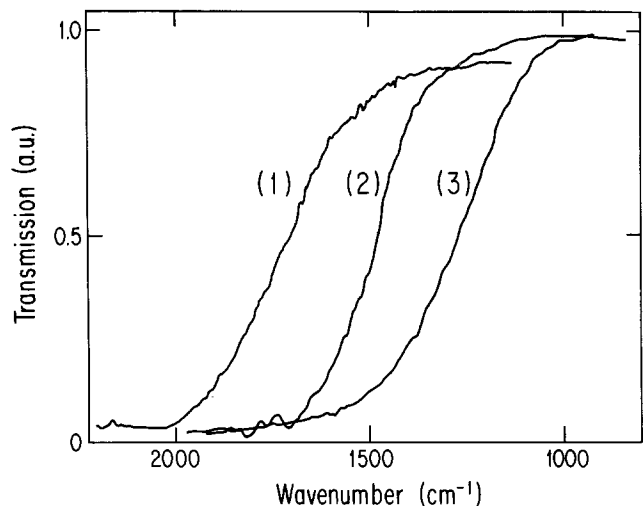


Fig. 2. Room temperature optical transmission spectra of typical layers. Curves (1)-(3) correspond to layer runs numbered 129, 116, and 240, respectively. The relationship used to determine alloy composition was $\lambda_{\text{co}}(\mu\text{m}) = [1.28x - 0.2 + 0.264x^3 + 4.22 \times 10^{-4}T(\text{K}) [1 - 2.08x]]^{-1}$ from Ref. (10). The roots of this equation were found numerically with a Newton-Raphson procedure.

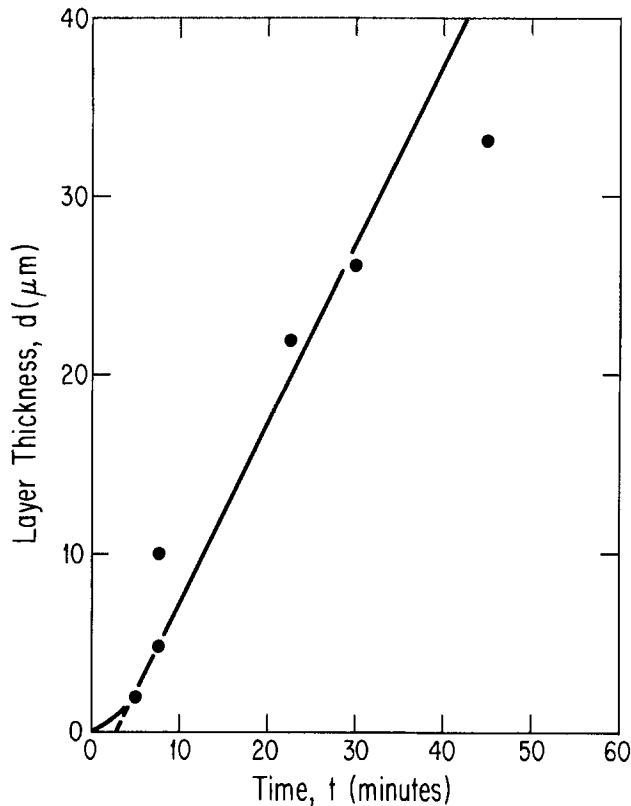


Fig. 3. Layer thickness vs. growth time. $\Delta T = 3^\circ\text{C}$, $l = 2$ mm. Points are experimental, line is derived from theory (see text). t_c is calculated at 5.23 min, and $d_{\text{max}} \sim 50$ μm .

retical model. The line in Fig. 4 is calculated from Eq. [8] using $D = 4.4 \times 10^{-5}$ cm^2/s and $\Delta C/(C^s - C_0) = 5.6 \times 10^{-3}$, i.e., exactly the same parameters used to account for the results in Fig. 3.

Layer thickness vs. temperature step, ΔT_{Hg} .—As pointed out in previous sections, the supersaturation ΔC required for the growth is caused by the increase in Hg reservoir temperature. In an open system, $\Delta C(\Delta T_{\text{Hg}})$ is an important empirical relationship essential for control of the growth process. This relationship can be derived from the experimental dependence of the layer thickness on ΔT_{Hg} . Such experimental data are given in Fig. 5 for the layers grown under identical values of other growth parameters ($l = 0.2$ cm and $t = 22.5$ min). Using Eq. [8] and the diffusivity value $D = 4.4 \times 10^{-5}$ cm^2/s , we have determined $\Delta C(\Delta T_{\text{Hg}})$ for our growth system. As shown in Fig. 5, ΔC increases approximately linearly with ΔT_{Hg} . However, it tends to saturate at higher ΔT_{Hg} values. This saturation is most likely an apparent one, and it probably reflects the depletion of solute (Cd) from the solution; this becomes a growth limiting factor at higher growth rate.

It is of interest to compare $\Delta C(\Delta T_{\text{Hg}})$ with a similar relationship for a closed system. Such dependence calculated according to data of Ruda *et al.* (2) is given by the dashed line in Fig. 5. As can be expected, the closed-system relationship is much steeper. For example, $\Delta T_{\text{Hg}} = 3^\circ\text{C}$ in an open system is equivalent to an effective $\Delta T \approx 2^\circ\text{C}$ in the closed system (8).

Electrical and optical characteristics of the layers.—Layer composition was measured using electron microprobe analysis and infrared optical transmission spectra. Typical spectra for three layers are shown in Fig. 2.

Electrical properties of the layers were measured using a standard Hall apparatus in the van der Pauw configuration at 300 and 77 K, on as-grown and annealed layers. All layers were annealed under saturated mercury atmosphere for 6h at $280 \pm 5^\circ\text{C}$. Table II presents the electrical properties of a selection of

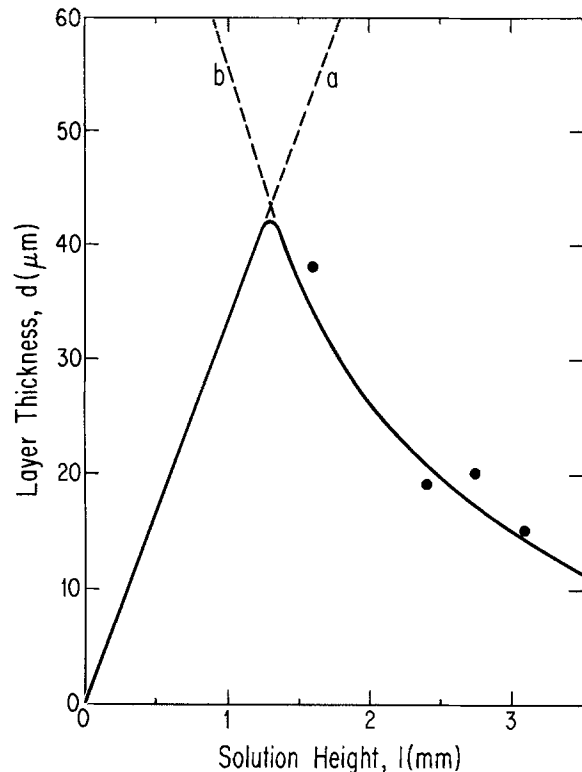


Fig. 4. Layer thickness vs. solution height. $\Delta T = 4^\circ\text{C}$, $t = 22.5$ min. Points are experimental. Line a is calculated for $d = d_{\text{max}}$, and line b from the theory (see text for fit parameters).

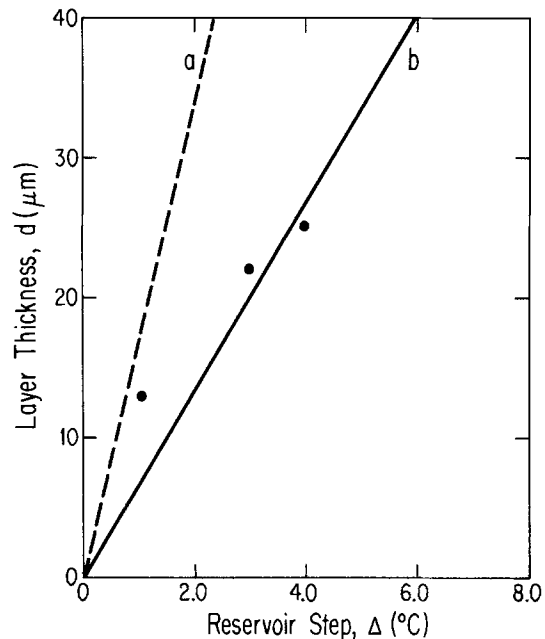


Fig. 5. Layer thickness vs. Hg-reservoir temperature increase. $l = 2$ mm, $t = 22.5$ min. Points are experimental, and solid lines are calculated (see text).

PIE layers. Electron mobilities in excess of 10^5 cm^2/Vs at 77 K with carrier concentrations in the low 10^{15} cm^{-3} were obtained. These compare favorably with present LPE layers (9).

Summary and Conclusions

We have developed a simplified theoretical model of pressure-induced epitaxial growth which quantitatively accounts for the growth-kinetics data obtained with HgCdTe layers grown from Te-rich solution.

PIE growth proceeds under isothermal conditions and is stimulated by Hg adsorption on the surface of

Table II. Electrical properties of PIE layers (after annealing)

Run no.	l (mm)	ΔT ($^{\circ}\text{C}$)	t min	α	d (μm)	$\rho \cdot 10^2$ (Ωcm)	$\mu \cdot 10^{-3}$ ($\text{cm}^2/\text{V}\cdot\text{s}$)	$n \cdot 10^{-16}$ (cm^{-3})	$\rho \cdot 10^2$ (Ωcm)	$\mu \cdot 10^{-4}$ ($\text{cm}^2/\text{V}\cdot\text{s}$)	$n \cdot 10^{-16}$ (cm^{-3})
111	1.6	4	50	0.17	64	0.41	13.0	12.0	0.82	10.2	0.96
116	1.4	3	35	0.20	50	2.70	2.0	12.0	4.40	3.1	0.45
129	2.0	3	30	0.22	26	3.00	2.5	8.3	0.80	1.7	4.60
134	2.0	3	25	0.20	20	2.00	4.4	7.1	1.70	2.1	1.70
135	2.0	3	30	0.22	20	2.40	7.3	3.5	1.30	4.2	1.10
144	2.0	4	22.5	0.17	20	0.50	11.3	10.9	0.45	32.2	0.42

the solution. The growth kinetics can be controlled by a temperature increase of an Hg reservoir and by the thickness of the solution.

Using PIE, we have grown $\text{Hg}_{0.8}\text{Cd}_{0.2}\text{Te}$ layers with typical growth velocities between 0.5 and 1.5 $\mu\text{m}/\text{min}$. Layers up to about 40 μm thick were grown of quality comparable to thermal-LPE layers.

Acknowledgment

The authors are grateful to the Advanced Research Projects Agency for financial support.

Manuscript submitted Aug. 8, 1983; revised manuscript received Jan. 5, 1984.

The Massachusetts Institute of Technology assisted in meeting the publication costs of this article.

APPENDIX

Relationship Between ΔC and ΔT_{Hg}

At its initial equilibrium condition (i) at the liquidus, the state of system may be defined in terms of two temperatures (T, T_1), where T refers to the isothermal solution temperature and T_1 to the initial reservoir temperature. Final equilibrium (f) may similarly be specified by the couple (T, T_2), where $T_2 = (T_1 + \Delta T_{\text{Hg}})$ and is the final reservoir temperature.

In the closed-system context, these two equilibrium states may be expressed as

$$a^i(T) = \frac{P^i(T)}{P^o(T)} = \frac{P^o(T_1)}{P^o(T)} = C_{10}\gamma^i(T) \quad [\text{A-1}]$$

$$a^f(T) = \frac{P^f(T)}{P^o(T)} = \frac{P^o(T_2)}{P^o(T)} = C_{10}\gamma^f(T)$$

where $a(T)$, $\gamma(T)$, $P^o(T)$, and $P^i(T)$ refer to mercury activities, mercury activity coefficients, pure mercury pressures, and mercury pressures over the solution, respectively.

In the open-system context, the mercury pressure over the solution is not uniquely defined by the reservoir: generally, a high reservoir temperature is required compared with the closed system to generate the equivalent mercury pressure. In the open system, $P^o(T_1)$ and $P^o(T_2)$ should be replaced by $P^o(T_1)$ and

$P^o(T_2)$ where $T_1 \neq T_1'$ and $T_2 \neq T_2'$, and generally $T' > T_1'$ and $T_2' > T_2$. From Eq. [A-1] and the above considerations

$$C_{10}^i = C_{10} \frac{\gamma^i(T)}{\gamma^f(T)} \cdot R$$

$$R \equiv \begin{cases} P^o(T_2)/P^o(T_1) : & \text{Closed system} \\ P^o(T_2)/P^o(T_1') : & \text{Open system} \end{cases} \quad [\text{A-2}]$$

Therefore

$$\Delta C = C_{10} \left[\frac{\gamma^i(T)}{\gamma^f(T)} \cdot R - 1 \right] \quad [\text{A-3}]$$

In the closed-system context for small ΔT_{Hg} (8)²

$$R \approx \left\{ \left(\frac{7136 \Delta T_{\text{Hg}}}{T_1 \cdot T_2} \right) + 1 \right\} \quad [\text{A-4}]$$

Therefore, from Eq. [A-3] and [A-4] the closed-system case may be generalized to

$$\Delta C = \xi \Delta T_{\text{Hg}}, \quad \text{where } \xi \text{ is constant} \quad [\text{A-5}]$$

²Phase data used to obtain mercury pressure above solution at 501 $^{\circ}\text{C}$: mercury reservoir temperature of 260 $^{\circ}\text{C}$ implied.

REFERENCES

1. T. C. Harman, *J. Electron. Mater.*, **9**, 945 (1980).
2. H. Ruda, P. Becla, J. Lagowski, and H. C. Gatos, *This Journal*, **130**, 228 (1983).
3. C. Barnes, *Physics*, **5**, 4 (1934).
4. J. Mroczkowski and H. R. Vydyanath, *This Journal*, **128**, 655 (1981).
5. P. Becla, Personal communication.
6. L. Jedral, H. Ruda, P. Becla, J. Lagowski, and H. C. Gatos, *This Journal*, **130**, 1615 (1983).
7. V. N. Ambrozimov, A. V. Vanyukov, T. N. Saburova, and A. S. Tomson, *Izv. Akad. Nauk SSSR Neorg. Mater.*, **12**, 1676 (1976).
8. T. Tung, L. Golonka, and R. F. Brebrick, *This Journal*, **128**, 451 (1981).
9. See, for example, (a) Y. Nemirowski, *J. Electron. Mater.*, **11**, 133 (1982); (b) J. L. Schmit, R. J. Hager, and R. A. Wood, *J. Cryst. Growth*, **56**, 485 (1982).
10. J. L. Schmit and E. L. Stelzer, *J. Appl. Phys.*, **40**, 4865 (1969).

Oxidative Removal of Photoresist by Oxygen/Freon® 116 Discharge Products

J. J. Hannon and J. M. Cook

AT&T Bell Laboratories, Allentown, Pennsylvania 18103

ABSTRACT

Microwave discharge products of a few percent of C_2F_6 in O_2 have been used for the study of the removal of Shipley AZ 1350J photoresist as a function of time and temperature. The removal rate was found to increase with increasing C_2F_6 concentration. The activation energy of removal has been determined for C_2F_6 concentrations ranging from 0.048 to 0.81 volume percent. Initially, the activation energy decreases rapidly to 0.34 eV for C_2F_6 concentrations ranging from 0.048% to 0.10% and continues to decrease with increasing C_2F_6 concentrations to approximately 0.16 eV at 0.81% C_2F_6 . The results reported apply to the removal of Shipley AZ 1350J photoresist, but are likely to indicate the oxidative-removal trends of other organic residues.

The gas-phase, oxidative removal of organic materials from semiconductor surfaces during various processing steps has become rather common in the microelectronics industry. These organic materials are generally present either in bulk amounts as photoresists and encapsulants, or as residual, trace contaminants. The former, which must be removed to allow further processing, failure analysis, etc., generally are fairly thick, on the order of several microns. The latter, whose removal can be categorized more as cleaning, are usually only a few thousand angstroms or so thick and are more readily completely removed.

Although we are more concerned with the cleaning category of the removal processes, it is often easier to monitor removal rates as functions of various process parameters by using bulk amounts of organic materials such as photoresist. Since oxidative degradation of organics is primarily a process occurring at the surface of the material being oxidized (1), the results for bulk amounts should be valid for trace amounts as well.

In the work reported here, we have examined the enhancement of the oxidative removal rate of Shipley AZ 1350J photoresist (Shipley Company, Newton, Massachusetts 02162) by the addition of small amounts of Freon® 116 (C_2F_6) to the oxygen before discharging. This removal of photoresist by plasma discharge methods was first suggested by Irving in 1968 (2) and has been the subject of many papers (3-10) since then. Most of the removal studies described utilized apparatus wherein the photoresist-coated samples were contained in the discharge itself, or else immediately adjacent to it. In either case, the photoresist was likely to be subjected to the particles and radiation present in the discharge, both of which can assist in the oxidation of the material since it has an activation energy in the neighborhood of 0.5 eV (3, 11). However, in our case, as in others (9, 10, 12), the circuits to be cleaned are separated from the environment of the discharge. This not only removes the materials from the possibly harmful effects of the discharge, but also allows better control of the process parameters owing to a better understanding of the various phenomena involved in the downstream reactions.

One factor that must be considered when separating the circuits from the discharge is the essentially complete cessation of photoresist removal (when using O_2 , O_2/N_2 , O_2/H_2 or O_2/H_2O) unless supplemental energy (usually heat) is supplied to the material. However, when fluorocarbons are present, either as additives to the O_2 before discharge or in the materials being oxidized, the removal continues readily (9, 12, 13). We have observed an increase in the oxygen atom concentration downstream of the discharge when a few percent of either CF_4 or C_2F_6 was mixed with the O_2 (14), by using an electron paramagnetic resonance (EPR)

spectrometer. Moreover, we have detected fluorine atoms as well, even for very low concentrations of C_2F_6 , which supports the assertion of the F atoms' participation in the reactions (12, 13, 15).

Finally, while only photoresist removal rates are presented here, it is believed that these results are representative of the oxidative removal behavior of other organic residues.

Experimental Apparatus

The experimental apparatus used for this investigation has been described previously (11) and is shown in Fig. 1. Essentially, it consists of an evacuated quartz tube (22.5 mm id) with a Microtron 200 microwave generator operating at 75W that is used to generate the discharge using an Evenson-type (16) microwave cavity. The gas flow through the tube was measured with a Matheson mass flowmeter Model 8160. Adjustment of a throttling valve at the vacuum pump controlled the pressure in the tube, which was measured by an MKS Instruments, Incorporated capacitance manometer. A Research, Incorporated, Variac-controlled, mini-spot IR heater with an Omega proportional controller and a thermocouple at the sample surface was used to control the temperature of the substrate, which was supported in a Teflon carrier.

Test Vehicle

The test vehicles consisted of square ceramic substrates, 14 mm on a side (area ≈ 2 cm²) coated on one surface with approximately 10 μ m of Shipley AZ 1350J photoresist. After fabrication, the substrates were baked at 140°C for 50 min in a nitrogen atmosphere to drive off any volatile components associated with the photoresist processing, leaving a surface coating density of approximately 1 mg/cm².

Experimental Procedure and Results

Each test specimen was individually weighed several times on a microbalance, and the average weight of each sample determined before and after exposing the substrate to the microwave discharge effluent. The maximum variation from measurement to measurement was less than $\pm 0.005\%$. The distance of the substrate from the microwave cavity was 33 cm unless otherwise specified. The flow rate and chamber pressure were $118 \pm$ sccm and 1.0 torr, respectively, in all cases. These values were chosen because of earlier work (11) with pure O_2 that showed that this resulted in reasonable photoresist removal rates.

Figure 2 shows the effects of time and temperature on the photoresist removal rate for two concentrations (0.103 and 0.81%) of C_2F_6 . In one instance, the substrate temperature was maintained at approximately 150°C, while it was uncontrolled in the second. For the case where the temperature was controlled, the substrates were allowed to stabilize for about 1 min prior

Key words: integrated circuits, etching, discharge, oxidation.

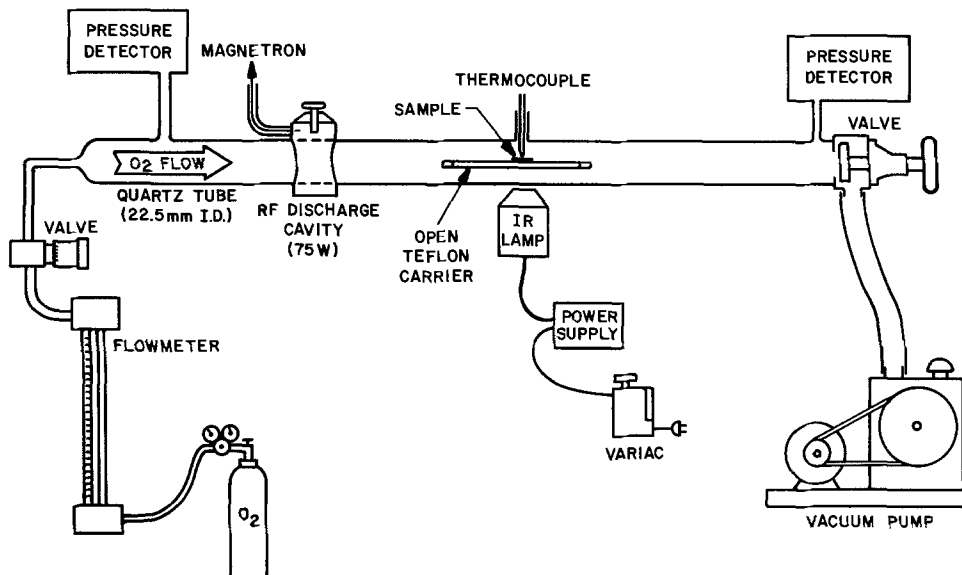


Fig. 1. Schematic of discharge and reaction apparatus.

to initiation of the discharge. The substrates shown were individually processed to simplify photographing, and are therefore not intended to be quantitative, but rather serve only to indicate the qualitative aspects of the removal process. The thickness of the photoresist was essentially the same for all substrates. It is evident from the photographs that the reaction is greater on the edge of the substrate closest to the discharge, as

would be expected. Also, increasing either the C_2F_6 concentration or the substrate temperature resulted in an increase in the reaction rate. In addition, higher operating temperatures resulted in a more uniform removal over the entire substrate surface, although the more rapid removal upstream is still evident. This increased uniformity is likely due to greater temperature homogeneity across the surface as compared to the case with no external heating.

Figure 3 shows plots of substrate surface temperature as a function of discharge time, for substrates with and without photoresist, in a 0.497% C_2F_6/O_2 atmosphere. The data shown are for substrates located 33, 22, and 11 cm from the microwave cavity. The increase in temperature on the surface of the substrates without photoresist results from heating by gas from the discharge. Initially, the temperature increases rapidly, essentially stabilizing after approximately 50s. The temperature of the surface of substrates with photoresist results from heating by the discharge gas as well as from heat generated in the combustion of the photoresist surface. The peak temperature seems to occur when the surface area of the photoresist is approximately 1/4 of its original surface area.

The increase in surface temperature on a single photoresist substrate as a function of discharge time for C_2F_6 concentrations ranging from 0.048 to 4.61% is shown in Fig. 4. The temperature generated with a particular concentration is reproducible to within $\pm 5^\circ C$ on any given day under similar test conditions: i.e., chamber wall conditions, distance of substrate from microwave cavity, etc. This is within the accuracy of the temperature measuring system used. Larger

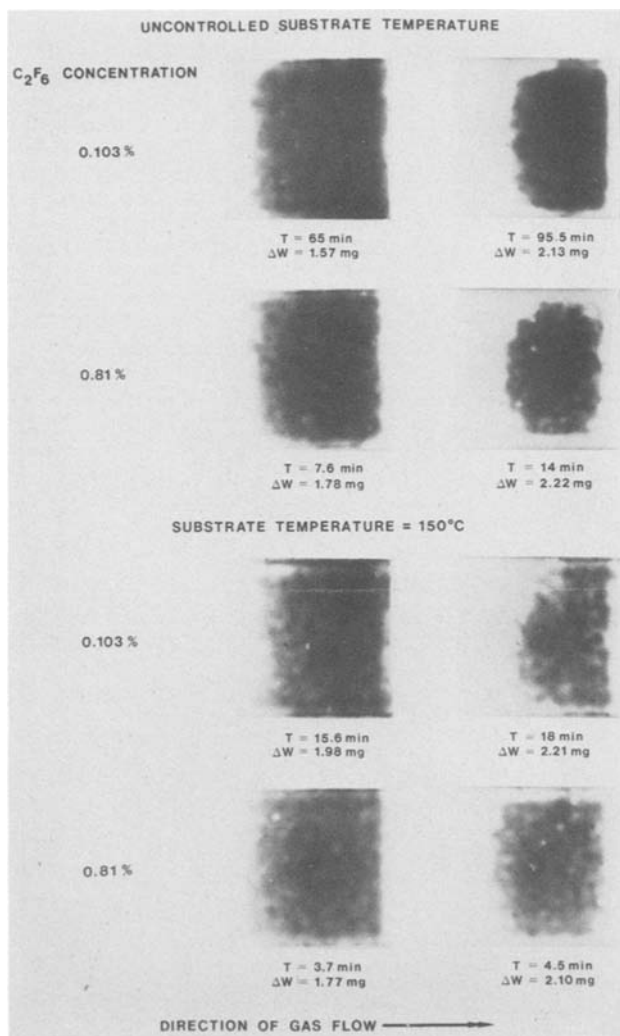


Fig. 2. Photographs of the effects of time and temperature on photoresist removal for two concentrations of C_2F_6 .

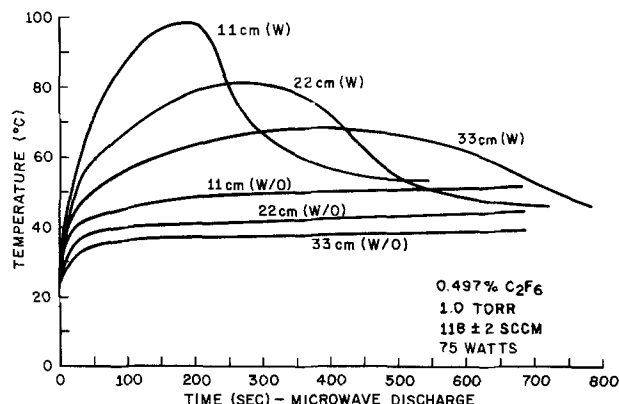


Fig. 3. Substrate surface temperature as a function of discharge time in 0.497% C_2F_6 mixture for coated and uncoated substrates.

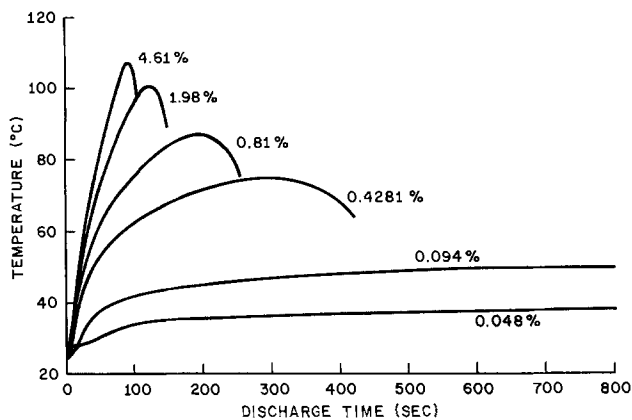


Fig. 4. Substrate surface temperature as a function of discharge time and C_2F_6 concentration.

temperature variations were observed in the case of a newly reconditioned quartz chamber.¹ The temperature generated at the surface of the photoresist substrate, during the initial run after reconditioning, was approximately 20°C higher than that measured prior to reconditioning. This effect was temporary and lasted only until the walls of the chamber had reached a steady-state condition with the discharge effluent flowing through the tube. The variation of temperature with resist removal suggests that the temperature might be useful as an endpoint detector. However, since there is a considerable delay between complete removal of resist and the attainment of a steady-state temperature, and this varies depending upon conditions, it would be a difficult method to implement for endpoint detection.

Photoresist weight loss, as a function of discharge time for uncontrolled temperature and C_2F_6 concentration is shown in Fig. 5 and 6. Pressure and flow rate are the same as mentioned previously, i.e., 1.0 torr and 118 ± 2 sccm. After the initial heating period of <1 min, the mass removed is approximately linear with time of exposure. The data have been fitted to a straight line by the least squares method. The removal

¹Reconditioning consisted of etching with 48% HF for 25 min followed by a DI water rinse. The chamber was then pumped overnight before introducing 0.103% C_2F_6 .

Fig. 5. Photoresist weight loss as a function of time and C_2F_6 concentration and no temperature control.

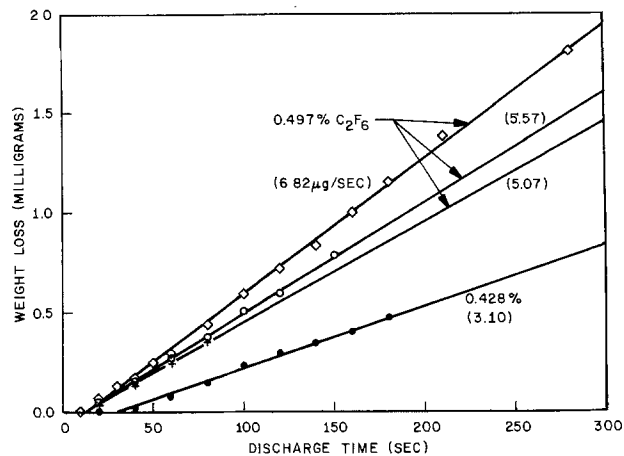
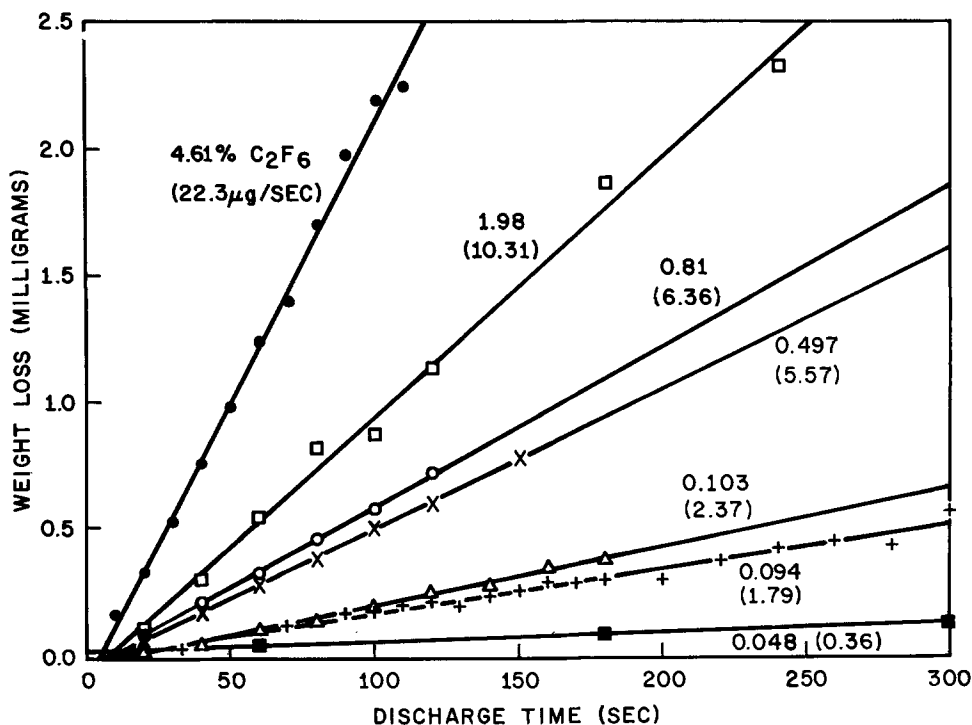


Fig. 6. Comparison of weight loss for two similar mixtures

rates shown in parentheses are in micrograms per second.

In Fig. 5, uncontrolled-temperature weight loss data are plotted for C_2F_6 concentrations ranging from 0.048% to 4.61%. The removal rate increased from 0.36 to 22.3 $\mu\text{g/s}$ with increasing C_2F_6 concentrations.

During the initial investigation with 0.497% C_2F_6 , problems with the balance were detected. Subsequently, two additional experiments were performed. These data are plotted in Fig. 6. Initially, a removal rate of 6.82 $\mu\text{g/s}$ was obtained. The later experiments resulted in values of 5.07 and 5.57 $\mu\text{g/s}$, which agree reasonably well. The small differences observed were attributed to a lack of cooling of the microwave cavity during one experiment, which resulted in a slightly higher substrate temperature and thus the slightly higher removal rate. Also included in Fig. 6 are data for 0.428% C_2F_6 concentration, which resulted in a removal rate of 3.1 $\mu\text{g/s}$. While this value is considerably lower than that of the 0.497% mixture, it does seem the more reasonable of the two when compared to other mixtures. (Unfortunately, this mixture was exhausted, necessitating the use of the 0.497% mixture.)

Two separate experiments were run where the substrate surface temperature was controlled. Weight loss as a function of both time and temperature, for C_2F_6

concentrations of 0.048%, 0.103%, 0.497%, and 0.81% was determined. Temperatures ranged from 120° to 200°C in 20° increments. The substrates were stabilized at temperature for approximately 2 min prior to the discharge's being initiated. The photoresist removal rates given below represent the time period that the ceramic surface area was still completely covered by the resist.

Initially, removal rates were determined for temperatures of 140°, 160°, and 180°C and produced unexpected results in some of the cases having the higher C₂F₆ concentrations. In the second investigation, the range of temperatures was expanded to more accurately determine the activation energy of removal. Before the second investigation, the quartz tube was reconditioned by etching in HF, as discussed earlier. In Table I removal rates as a function of temperature and C₂F₆ concentration are listed for both investigations.

With 0.103% C₂F₆ at 200°C, a residue was observed to deposit on the substrate carrier and the chamber wall approximately 5-6 cm downstream from the test substrate. The carrier and chamber walls were subsequently cleaned by allowing the microwave discharge to operate at uncontrolled temperature for several minutes.

Photoresist weight loss as a function of time for a C₂F₆ concentration of 0.81% at 140° and 180°C with no discharge is shown in Fig. 7. The substrates were allowed to stabilize at temperature approximately 1 min prior to starting the test. Although there is considerable scatter in the data, especially at the higher temperature, there is some indication that reaction of the gas with the photoresist may occur at higher temperatures without the discharge products, although at a much slower rate. However, at the higher temperature the photoresist may well be decomposing. Removal rates determined are 0.07 and 0.73 μg/s at 140° and 180°C, respectively. This effect was not taken into consideration when determining activation energies, since its exclusion does not affect the trends.

Arrhenius plots of the log of $\frac{R}{P} T^{1/2}$ vs. $\frac{1}{T}$ for the various C₂F₆ concentrations are plotted in Fig. 8 for

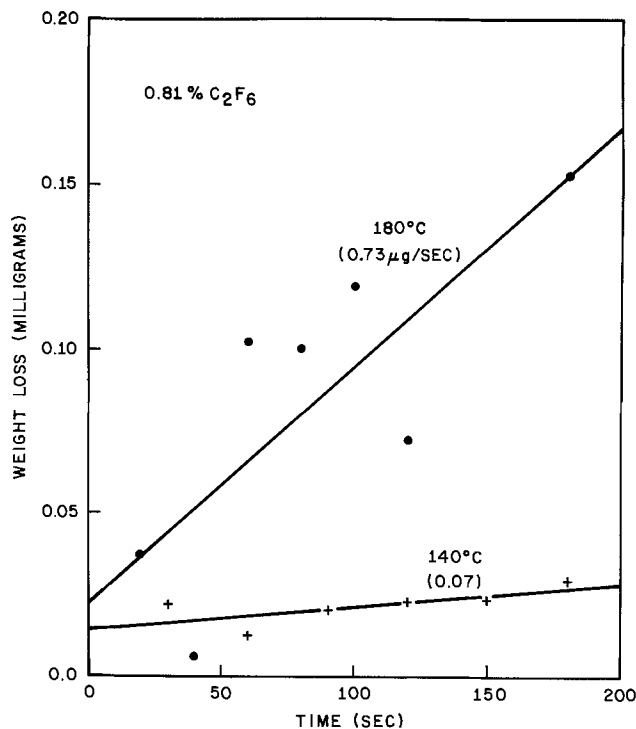


Fig. 7. Weight loss as a function of time and temperature with no discharge.

data from the second investigation. The data are fitted by the least squares method (in exponential form) with the E_{act} for each concentration given in parenthesis. The activation energy of removal as a function of C₂F₆ concentration is plotted in Fig. 9. In general, the activation energy increases with decreasing C₂F₆ concentration ranging from approximately 0.16 eV at 0.81% to 0.34 eV at 0.048% C₂F₆. Activation energies determined from the initial investigation agree rea-

TABLE I					
Removal Rates of Shipley AZ 1350J Photoresist (μg/sec)					
		Percent C ₂ F ₆ Concentration			
Temp (°C)	Investigation	0.048	0.103	0.497	0.81
120	I				
	II	1.20	1.95		9.15
140	I	1.58	4.51	12.55	13.37
	II	1.71	2.41	11.35	10.27
160	I	1.81	5.93	14.40	13.45
	II	2.38	3.79	14.29	13.48
180	I	3.28	8.60	14.19	17.16
	II	3.88	5.50	18.42	15.27
200	I				
	II		7.98		
Activation Energy of Removal (eV)					
	I	0.37	0.35	0.07	0.13
	II	0.34	0.34	0.22	0.16

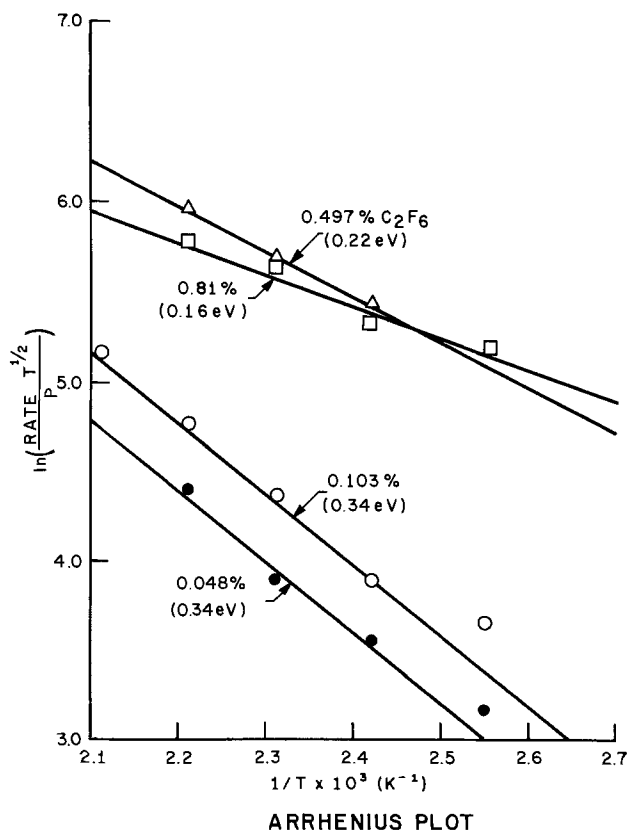


Fig. 8. Activation energy plots for several concentrations

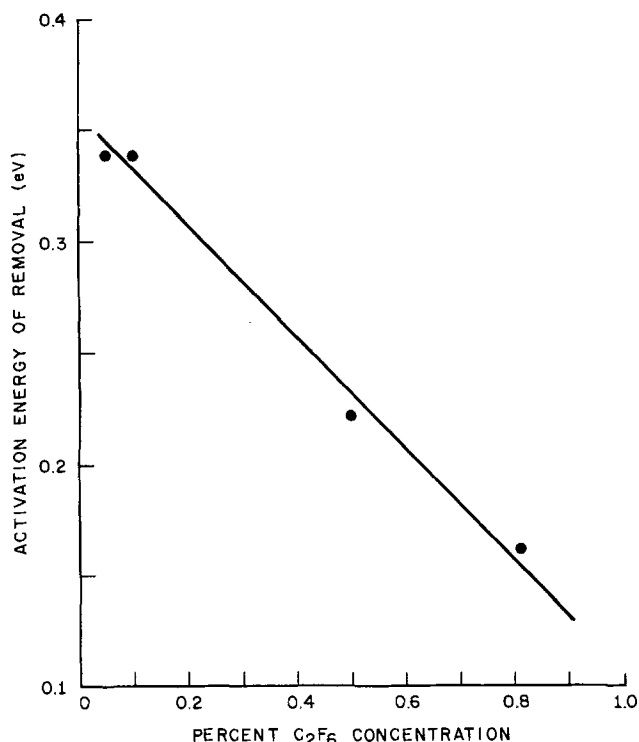


Fig. 9. Activation energy variation with C₂F₆ concentration

sonably well and are listed in Table I. These results agree with the suggestions of Mogab (15) with respect to variation of activation energy with changing C₂F₆ concentration.

In Fig. 10 are plotted the relative oxygen and fluorine atom concentrations as functions of the percentage of C₂F₆ in oxygen. (The term "relative" applies only to each species individually; the absolute relationship between the concentrations of the two species is not known, excepting that [F] < [O].) These concentrations were measured at the same distance from the discharge as the substrates had been placed. It can be seen that while the oxygen atom concentration rises rather rapidly and then reaches essentially a plateau, the fluorine atom concentration continues to increase. The observation that the rate increases (and the E_{act} decreases) with increasing C₂F₆ content can be explained by the fluorine atoms' concomitant increase. Very likely the fluorine atoms abstract hydrogen atoms or add to double bonds to form excited complexes that then dissociate. In either case, the fluorine atoms react far more rapidly than do oxygen atoms (17, 18) and by so doing, render numerous sites quite reactive to the excess oxygen atoms and molecules.

Conclusions

The removal rate of Shipley AZ 1350J photoresist, when subjected to microwave discharge products of a C₂F₆/O₂ mixture, increases with increasing C₂F₆ concentrations. Activation energies determined agree reasonably well for both investigations reported here as well as with results determined from EPR spectroscopy studies conducted previously (11). Initially, the activation energy decreases rapidly to about 0.3 eV for C₂F₆ concentrations ranging from 0.048% to 0.10% and continues to decrease with increasing C₂F₆ concentrations to approximately 0.16 eV at 0.81% C₂F₆.

The results reported here may be used to help select appropriate C₂F₆ concentrations and temperatures for application to device processing. The uncontrolled-temperature results would be valid for process application only if very large amounts of photoresist are to be removed from a single sample such that the heat of combustion significantly increases the sample tempera-

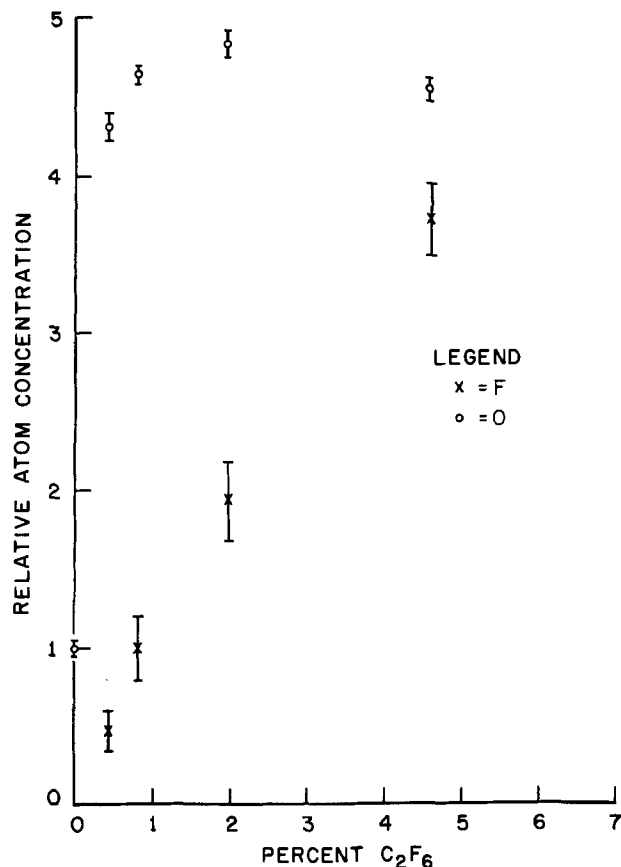


Fig. 10. Relative oxygen and fluorine atom concentrations downstream as functions of C₂F₆ concentration.

ture. The data show that the temperature drops substantially once the bulk of the organic material has been removed from the sample.

Care should be taken to maintain the condition of the chamber, since the surface of the chamber can have a great affect on the concentration of the active species. This is especially evident for a newly reconditioned quartz chamber. Once the system is operated for a specified time prior to device processing, the chamber walls reach a point of passivation such that the results are reproducible.

Redeposition of removed material can be a problem, but can be avoided by operating at lower temperatures ($\approx 160^\circ\text{C}$) with no more than 2% C₂F₆ by volume.

Finally, in all our work, as noted, no removal of photoresist was observed in the absence of fluorocarbon doping or supplemental heating. This is in contrast to the observations of Dzioba *et al.* (10), who observed rather rapid removal in a system analogous to ours while using pure oxygen. Our results agree with those reported both by Wang and Galernt (9) and Horiike and Shibagaki (12). This suggests that in the work of Dzioba *et al.* (10) energy was being supplied to the photoresist in some fashion, perhaps via UV radiation from the plasma.

Acknowledgments

We would like to thank Dr. B. W. Benson for enlightening discussions, technical assistance, and his helpful critical review of this paper. In addition, the help of J. S. Solga for test-specimen weight measurements is gratefully acknowledged.

Manuscript submitted Aug. 22, 1983; revised manuscript received Feb. 3, 1984.

AT&T Bell Laboratories assisted in meeting the publication costs of this article.

REFERENCES

1. R. H. Hansen, J. V. Pascale, T. De Benedictis, and P. M. Rentzepis, *J. Polymer Sci. A*, **3**, 2205 (1965).
2. S. M. Irving, in "Kodak Photoresist Seminar Proceedings," Vol. 2, p. 26, Eastman Kodak Co., Rochester, NY (1968).
3. R. L. Bersin, *Solid State Technol.*, **13**, 39 (1970).
4. H. G. Hughes, W. L. Hunter, and K. Ritchie, *This Journal*, **120**, 99 (1973).
5. E. P. G. T. van de Ven and H. Kalter, Abstract 124, p. 332, The Electrochemical Society Extended Abstracts, Vol. 76-1, Washington, DC, May 2-7, 1976.
6. E. O. Degenkolb, C. J. Mogab, M. R. Goldrick, and J. E. Griffiths, *Appl. Spectrosc.*, **30**, 520 (1976).
7. J. F. Battey, *This Journal*, **124**, 147 (1977).
8. B. B. Stafford and G. J. Gorin, *Solid State Technol.*, **20**, 51 (1977).
9. C. W. Wang and B. Galernt, *ibid.*, **24**, 121 (1981).
10. S. Dzioba, G. Este, and H. M. Naguib, *This Journal*, **129**, 2537 (1982).
11. J. M. Cook and B. W. Benson, *ibid.*, **130**, 2459 (1983).
12. Y. Horiike and M. Shibagaki, in "Semiconductor Silicon 1977," H. R. Huff and E. Sirtl, Editors, p. 1071, The Electrochemical Society Softbound Proceedings Series, Princeton, NJ (1977).
13. G. N. Taylor and T. M. Wolf, *Tech. Paper Reg. Tech. Conf. Soc. Plast. Eng.*, 174 (1979).
14. J. M. Cook, J. J. Hannon, and B. W. Benson, in "Proceedings of the Sixth International Symposium on Plasma Chemistry," M. I. Baulos and R. J. Munz, Editors, p. 616, IUPAC, Montreal, Que., Canada, July 24-28, 1983.
15. C. J. Mogab, Unpublished results.
16. F. C. Fehsenfeld, K. M. Evenson, and H. P. Broida, *Rev. Sci. Instrum.*, **36**, 294 (1965).
17. R. E. Huie and J. T. Herron, in "Progress in Reaction Kinetics," K. R. Jennings and R. B. Cundall, Editors, p. 1, Pergamon Press, New York (1975).
18. R. Foon and M. Kaufman, *ibid.*, p. 81.

Cleaning of a Rough Rigid Surface: Removal of a Dissolved Contaminant by Convection-Enhanced Diffusion and Chemical Reaction

Radhakrishna Chilukuri¹ and Stanley Middleman

Department of Applied Mechanics and Engineering Sciences, University of California, San Diego, La Jolla, California 92093

ABSTRACT

A model is formulated with which one may calculate the rate of disappearance of a species dissolved in fluid trapped in a microscopic cavity of a surface. The model accounts for diffusion, convection, and chemical reaction. Solutions are carried out, and a numerical example is worked out in order to show the representative time scales of these interacting processes.

When a solid surface is contaminated by a liquid spill, or processed through a series of liquid chemical baths, removal of the liquid is usually effected by a cleaning procedure that involves soaking, flushing, or wiping of the surface. In most situations, the bulk of the contaminating liquid is removed by such action. Several examples may be cited that suggest the need to examine the details of removal of contaminants that may be trapped within the microscopic architecture of the surface:

1. A rough metal may be cleaned to the point that only a miniscule fraction of contaminant remains in the microscopic "valleys" of the surface. If the contaminant is reactive, however, continued exposure of the surface to the contaminant may lead to a deleterious change in the surface properties of the metal.

2. If the contaminant has very high toxicity (possible examples would be radiation or biological hazards) then continued exposure of personnel to the surface would be intolerable, even though "nearly all" of the contaminant had been removed by mechanical means.

3. In the semiconductor industry, one purposefully creates a surface architecture with length scales of the order of 0.1-1 μm on silicon wafers. These wafers must then be washed prior to subsequent chemical steps (such as chemical vapor deposition), and ultimately cleaned of submicron particulates. Traditional gross methods of flushing and wiping may be insufficient to clean such a surface adequately.

If we confine our attention to microscopically rough (or patterned) surfaces, say with length scales of order $\leq 100 \mu\text{m}$, then it is clear that mechanical flushing and wiping may not be an effective means of decontamination. It is necessary, in order to evaluate a proposed or existing mechanical decontamination procedure, to deter-

mine the hydrodynamics induced within a microscopic "pore" or "cavity" in a surface by the external macroscopic flow field. Studies which are in progress have, in general, distinguished between two kinds of hydrodynamic phenomena that occur in cavities in a surface, within which a contaminated liquid resides.

1. In one, the liquid is effectively trapped, but the external cleaning flow can induce circulation within the cavity. If the contaminant is diffusible, then the removal of contaminant is controlled by convective diffusion, and the efficiency of removal depends upon the hydrodynamics within the cavity. The problem of convective diffusion from a circulating flow within a two-dimensional rectangular cavity has been treated recently by Chilukuri and Middleman (1).

2. In the second type of cavity flow, the external flow may penetrate the cavity and remove some of the entrapped liquid. Our studies of this problem are in an early stage, but it appears that on the scale of interest, there would always be a sizable region of trapped liquid which can be set in circulation, but not displaced, from the cavity (2).

Figure 1 illustrates some of these ideas.

Model Formulation

It should be apparent that under conditions such that displacement of a contaminant does not occur (at all, or at a sufficiently high rate), it will be necessary to assist the decontamination process in some way. One possibility is chemical detoxification or decontamination. The study presented herein investigates detoxification of a trapped contaminant. We consider a toxic species T which may react with a neutralizing or detoxifying agent D to produce a harmless neutral product N. The reaction scheme is taken to be according to

¹ Present address: JAYCOR, San Diego, California 92138

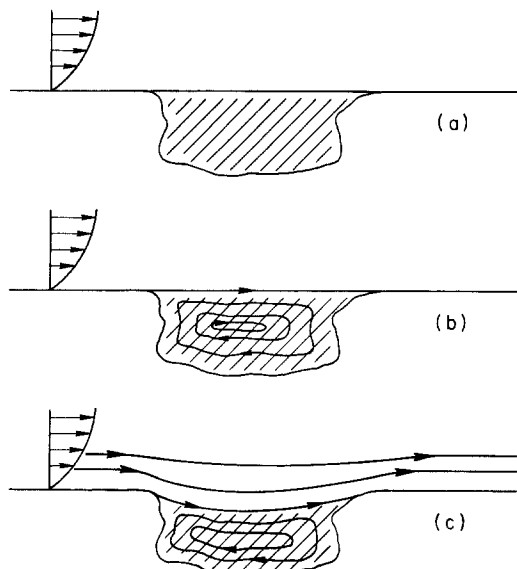


Fig. 1. A, top: a microscopic pore contains contaminated liquid, and a flushing flow is imposed in the space above the pore. B, middle: under some conditions, the pore fluid is induced to circulate, but is not displaced from the pore. C, bottom: under other conditions, some of the original fluid displaced from the pore, but, ultimately, a limit to displacement occurs, and there is a streamline which divides the external flow from the internal circulating flow.



where k is the specific reaction rate, defined so that

$$r = k C_T C_D \quad [2]$$

where C_T (C_D) is the molar concentration of the toxic (detoxifying) species, and r is the number of mols of T converted by reaction [1], per unit of volume and time.

The species conservation laws for T and D are, including convection and diffusion

$$\frac{\partial C_T}{\partial t} + u \cdot \nabla C_T = \mathfrak{D}_T \nabla^2 C_T - k C_T C_D \quad [3]$$

$$\frac{\partial C_D}{\partial t} + u \cdot \nabla C_D = \mathfrak{D}_D \nabla^2 C_D - k C_T C_D \quad [4]$$

Here u is the velocity vector within the cavity, and species T and D may have different diffusion coefficients \mathfrak{D}_T and \mathfrak{D}_D .

We will illustrate the analysis by studying a two-dimensional rectangular cavity, as shown in Fig. 2, and assume that the cavity flow is closed, i.e., no streamlines cross the plane $y = H$. In an earlier study (1), we have calculated the velocity field in a closed cavity, assuming either constant velocity or constant shear stress, along $y = H$. In this

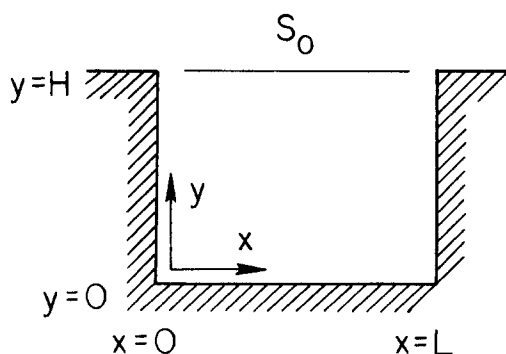


Fig. 2. Definition sketch of the cavity geometry. Over the region $(0 \leq x \leq L)$, the plane $y = H$ is a streamline across which there is diffusion, but no flow. A constant shear stress S_0 is assumed along that line in the example problem presented here.

paper, for the sake of illustration, we take the constant shear boundary condition.

Boundary conditions on concentration take the form

$$n \cdot \nabla C_T = n \cdot \nabla C_D = 0 \quad [5]$$

on the walls of the cavity, where n is the normal to the surface. This expresses impermeability of the walls. Along the boundary $y = H$ we assume

$$C_T = 0 \quad [6]$$

$$C_D = C_{D_0}$$

Initial conditions are

$$C_T = C_{T_0}$$

$$C_D = 0 \quad [7]$$

within the cavity. Equations [3] and [4] are nonlinear, because of the assumption of nonlinear reaction rate in Eq. [2]. Note that the equations are coupled through the reaction terms. It is necessary to solve the equations numerically. A finite difference method is used, and details are described by Chilukuri (2). The velocity field u must be obtained separately, also by numerical methods, and a general discussion of the method and results may be found in our earlier works on this topic (1, 2).

Results

The set of equations presented above was solved for the concentrations C_T and C_D within the cavity, as a function of time. Results are illustrated here for $\mathfrak{D}_T = \mathfrak{D}_D = \mathfrak{D}$, and $H = L$.

It is useful to present results in terms of the following dimensionless groups

$$\text{Stoichiometric ratio } R = C_{D_0}/C_{T_0} \quad [8]$$

$$\text{Peclet number } Pe = S_0 L^2 / \mu \mathfrak{D} \quad [9]$$

where S_0 is the shear stress along $y = H$.

$$\text{Kinetic number } K = k L^2 C_{T_0} / \mathfrak{D} \quad [10]$$

We will be interested in the half-time $t_{1/2}$ required for the concentration within the cavity to be reduced to one-half its initial value of C_{T_0} . If there is no chemical reaction, removal of contaminant is by the mechanism of convection-aided diffusion.

The degree to which reaction aids removal of the contaminant may be measured by a factor we call the Enhancement Ratio

$$E1 = t_{1/2}^0 / t_{1/2} \quad [11]$$

where $t_{1/2}^0$ is the half-time in the absence of reaction.

Figure 3 shows some typical results for the Enhancement Ratio, $E1$, as a function of K and R , for $Pe = 100$. As is to be expected, $E1$ approaches unity as K vanishes. For large K (i.e., fast reactions) the enhancement is controlled by the Peclet number and the stoichiometric ratio, R . Figure 4 shows the asymptotic value of $E1$ for large K as a function of R , for two Peclet numbers. Figure 5 shows the effect of Peclet number on $E1$ vs. K , at a value of $R = 10$.

While nondimensionalization is an aid to compact presentation of these results, there is an accompanying obscuring of the meaning and import of the results. It is useful, then, to consider some direct numerical interpretations of the results through the presentation of a case study.

Let us begin with a review of possible mechanisms of decontamination. Figure 6 shows a cavity in a surface, with four possible modes of removal of a contaminant from the cavity. In Fig. 6a we suggest that the external hydrodynamics (agitation, sonication, spray flushing, wiping, or brushing) is capable of physically and instantaneously removing fluid with contaminant from the cavity. This is not a realistic prospect for small cavities, as our studies of the hydrodynamics are suggesting. Nevertheless, the case forms a lower bound on the time re-

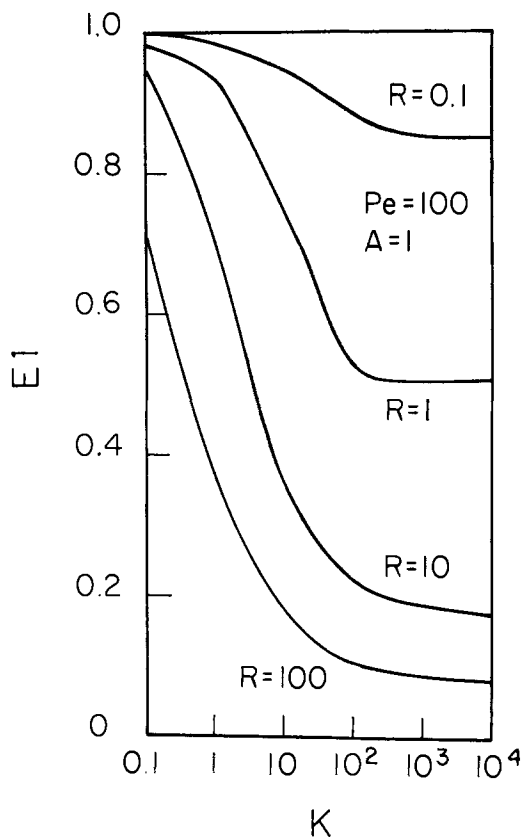


Fig. 3. Enhancement ratio in the presence of chemical reaction

quired to clean the cavity. The time is instantaneous, as assumed above. However, we have not detoxified the contaminant.

In some practical cases, it may be sufficient to remove the contaminant from a small cavity, and then dilute it within the large body of cleaning fluid. In other cases, however, it may be necessary to neutralize the contaminant chemically. This is the case of interest here.

If the fluid in the cavity is instantaneously removed and mixed into the external cleaning fluid, and if D is the

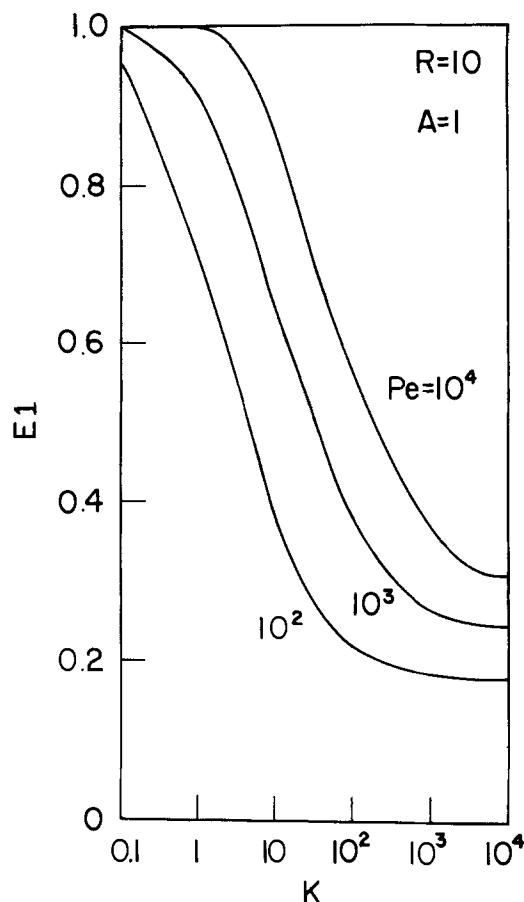


Fig. 5. Effect of reaction rate and Pe on $E1$.

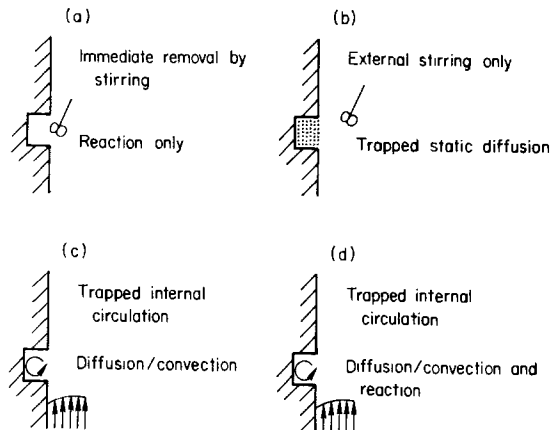


Fig. 6. Modes of removal of a contaminant from a cavity. A, top left: immediate removal from the cavity: reaction only. B, top right: static diffusion from the cavity to a well-stirred exterior. C, bottom left: trapped but circulating fluid in the cavity. Circulation aids diffusion. D, bottom right: as in C, but with chemical reaction as well.

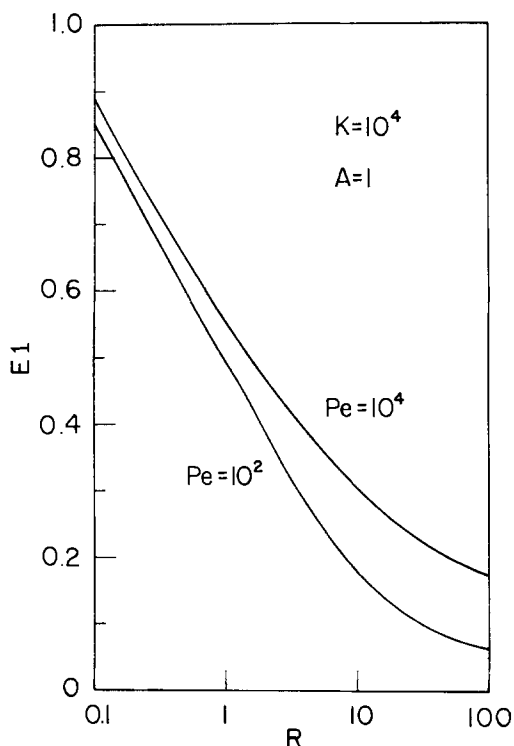


Fig. 4. Asymptotic value of $E1$ for large K

dilution ratio (cavity volume/cleaning fluid volume), then chemical neutralization occurs according to Eq. [2], and we write

$$-\frac{dC_T}{dt} = kC_T C_D \quad [12]$$

$$\left. \begin{aligned} C_D &= C_{D\infty} \\ C_T &= DC_{T_0} \end{aligned} \right\} \text{at } t = 0$$

We assume that the external concentration of neutralizing chemical C_D is related to the initial concentration of contaminant in the cavity, so that (as in Eq. [8])

$$C_{D\infty} = RC_{T_0} \quad [13]$$

If we let ξ be the fraction of contaminant neutralized, then

$$C_T = DC_{T_0}(1 - \xi) \quad [14]$$

and

$$\begin{aligned} C_D &= C_{D_0} - DC_{T_0} \xi \\ &= RC_{T_0} - DC_{T_0} \xi \end{aligned} \quad [15]$$

Then Eq. [12] becomes

$$\frac{d\xi}{dt} = kC_{T_0}R(1 - \xi) \left(1 - \frac{D}{R}\xi\right) \quad [16]$$

The solution for $\xi(t)$ is easily found to be

$$\frac{1}{1 - \frac{D}{R}} \ln \left(\frac{1 - \frac{D\xi}{R}}{1 - \xi} \right) = kC_{T_0}Rt \quad [17]$$

The half-time for neutralization then follows upon setting $\xi = 1/2$ in Eq. [17]. Results are shown in Fig. 7. We are now prepared to make numerical comparisons of the modes of removal illustrated in Fig. 6.

We choose the following parameters:

$$\begin{aligned} L &= 10^{-2} \text{ cm (100 } \mu\text{m)} \quad \text{square cavity (} A = 1) \\ \mathcal{D} &= 10^{-6} \text{ cm}^2/\text{s} \\ \mu &= 0.1 \text{ poise} \\ S_0 &= 10 \text{ dyn/cm}^2 \\ C_{T_0} &= 10^{-4} \text{ mol/cm}^3 \\ k &= 10^6 \text{ cm}^3/\text{mol}\cdot\text{s} \\ R &= 10 \\ D &= 10^{-4} \end{aligned}$$

With these parameters we find

$$\begin{aligned} \text{Pe} &= 10^4 \\ K &= 10^4 \end{aligned}$$

Neutralization via instantaneous removal, dilution, and reaction.—We find

$$(kC_{T_0}D)t_{1/2} = 0.693 \times 10^{-5} \quad [18]$$

or the expected half-time is

$$t_{1/2} = 0.693 \cdot 10^{-3} \text{ s} \quad [19]$$

For all practical purposes, the neutralization is instantaneous.

Our hydrodynamic studies suggest that it is not realistic to anticipate that Fig. 6a offers a realistic picture of the physics of this situation. For small cavities, it is much more likely that fluid in a cavity is effectively trapped, and that diffusion plays an important role in removal of the contaminant and its neutralization.

Again with reference to Fig. 6, we examine these other modes of decontamination.

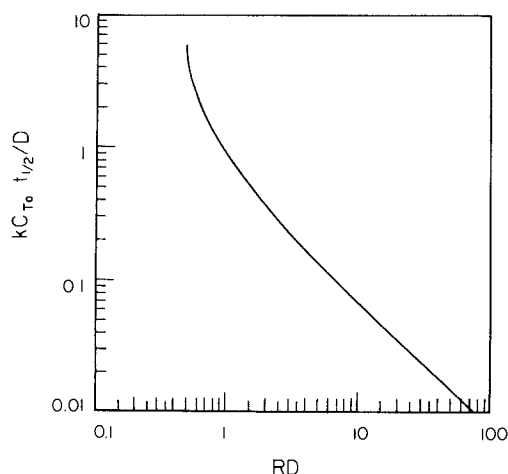


Fig. 7. Half-time for neutralization of contaminant

Diffusion from a trapped and static liquid in a cavity; no reaction.—We have a classical diffusion problem defined by Eq. [3] with $u = 0$ (static liquid) and $k = 0$ (no reaction). Equations [5]–[7] for C_T provide the boundary conditions. The solution of this problem is available in such standard references as Bird *et al.* (3), and from it we find that the half-time for removal is

$$\frac{\mathcal{D}t_{1/2}}{L^2} = 0.194A^2 \quad [20]$$

For the parameters chosen, this gives

$$t_{1/2} = 19.4 \text{ s} \quad [21]$$

Note how much slower the diffusion process is in comparison to the reaction process.

However, diffusion can be accelerated by circulation induced by an external flow. This is the topic of our earlier study (1), and Fig. 6c shows the physics envisioned.

Diffusion from a trapped but circulating liquid in a cavity; no reaction.—We must find an enhancement factor E by which the static diffusion half-time is reduced. For $\text{Pe} = 10^4$ and a square cavity, we find (1; Fig. 3) $E = 5 \times 10^{-2}$. Hence, circulation induced by the external flow speeds up the diffusion process by a factor of 20, and we find

$$t_{1/2} = 0.97 \text{ s} \quad [22]$$

Before proceeding, let us remark on the kind of flushing or wiping flow that would give a shear stress of 10 dyn/cm^2 across the top of the cavity, as assumed here. Suppose we have a surface being cleaned by a rotating cylindrical brush, as suggested in Fig. 8. We imagine the case where, to protect the surface, the brush does not actually contact the surface, but instead comes within a small distance b of the surface. For a linear velocity U the shear stress would be given by

$$S_0 = \mu_t U/b \quad [23]$$

where μ_t is the viscosity of the flushing fluid. For water at 20°C ($\mu_t = 10^{-2}$ poise), using a 2.5 cm radius brush with a clearance b above the surface of $100 \mu\text{m}$ ($b = 10^{-2}$ cm), at a rotational speed of 40 rpm, we find $S_0 = 10 \text{ dyn/cm}^2$. Thus the numbers used here, while arbitrary, are within the range of reasonable operation of equipment.

Reaction and convection-aided diffusion within the cavity.—The half-time for case c, approximately 1s, while quite a bit longer than that of case a, seems short enough to be suitable for a cleaning operation. It is interesting to inquire into the possibility of still faster removal of the contaminant from the cavity through the aid of a chemical neutralizing agent. Instead of assuming, as in case a, that the contaminant is removed bodily from the cavity and then neutralized via reaction, we examine the rate of neutralization due to diffusion of the species D into the cavity, within which it reacts. Of course, this is the mathematical model posed in Eq. [1]–[7]. Figure 5 (for $K = 10^4$, $\text{Pe} = 10^4$, and $R = 10$) gives an enhancement factor $E1 = 0.31$. Thus, for reaction and convection-aided diffusion within the cavity we find (using Eq. [11] and [22])

$$t_{1/2} = 0.3 \text{ s} \quad [24]$$

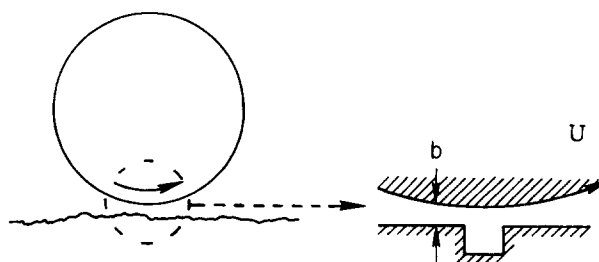


Fig. 8. Simple model of a rotating-brush cleaner

This is still quite a bit larger than the value to be expected if the cavity fluid could be removed (case a).

From a practical point of view, one would control the rate of cleaning by exercising some control over the characteristics of the brush or jet-spray apparatus that is typically used in surface cleaning. As our model demonstrates, it is the shear stress exerted by the brush- or jet-driven flow across the cavity surface that affects the rate of removal of a contaminant. This shear stress appears in the model only in the Peclet number (Eq. [9]).

Our earlier work (1) predicts that in the range of Peclet numbers of likely occurrence (say $\geq 10^3$ - 10^6), convection aids removal by a factor E which is linearly and inversely proportional to Peclet number, *i.e.*

$$E \sim Pe^{-1} \quad [25]$$

Thus, all other physical and geometrical parameters remaining the same, the removal time is reduced by a factor that is linear in shear stress S_0 . In a brush cleaner, the shear stress may be controlled through the rotational speed of the brush as well as the proximity of the brush to the surface to be cleaned. In a jet-spray apparatus, the dynamics are more complex, and depend upon the jet velocity and the proximity and orientation of the jet with respect to the target surface. The mathematical model illustrated here should be useful to those concerned with the design, improvement, and utilization of cleaning systems, when used in conjunction with appropriate laboratory studies of the cleaning of real surfaces.

Conclusions

A mathematical model has been formulated with which one can assess the time scales associated with removal (by convection-aided diffusion and/or by a neutralization reaction) of a chemical contaminant from a small cavity in a surface. Idealizations of the geometry make solutions possible via relatively simple numerical methods. In principle, more complex geometries and external flows could be considered, but at considerable increase to the cost of computation.

For a fluid hydrodynamically trapped within a cavity, but capable of circulation induced by the external

flushing flow, the time for removal of a diffusible contaminant is strongly dependent on circulation within the cavity. The degree of effectiveness of circulation, and the effectiveness of a neutralization reaction, can be assessed using the models presented here.

Acknowledgment

Numerical computations were supported by the Army Research Office under its contract DAAG29-80-K-0058. We gratefully acknowledge this support.

Manuscript submitted Sept. 7, 1983; revised manuscript received Dec. 19, 1983.

LIST OF SYMBOLS

A	aspect ratio (H/L)
$C_T(C_D)$	concentration of toxic (detoxifying) species (mol/cm ³)
\mathcal{D}	diffusivity in the cavity liquid (cm ² /s)
D	dilution ratio (cavity volume/cleaning fluid volume)
E	enhancement ratio
E_1	enhancement factor for chemical reaction
H	depth of cavity (cm)
k	specific reaction rate (cm ³ /mol-s)
K	dimensionless reaction rate constant ($kC_{T_0}L^2/\mathcal{D}$)
L	length of cavity (cm)
Pe	Peclet number, ($S_0L^2/\mu\mathcal{D}$)
R	concentration ratio (C_{D_0}/C_{T_0})
Re	Reynolds number ($\rho u_c L/\mu$)
Sc	Schmidt number (ν/D_T)
S_0	shear stress at $y = A$ (dyn/cm ²)
t	time (s)
u	velocity vector (cm/s)

Greek Letters

μ	viscosity of cavity liquid (poise)
ξ	fractional conversion

REFERENCES

1. R. Chilukuri and S. Middleman, *Chem. Eng. Commun.*, **22**, 127 (1983).
2. R. Chilukuri, Ph. D. Thesis, University of California, San Diego, La Jolla, CA (1982).
3. R. B. Bird, W. E. Stewart, and E. N. Lightfoot, "Transport Phenomena," John Wiley and Sons, Inc., New York (1960).

Electroluminescence and Photoluminescence of GaAs in Aqueous Redox Electrolytes

Franco Decker,* Milton Abramovich, and Paulo Motisuke

Instituto de Física, UNICAMP, Campinas, Sao Paulo, Brazil

ABSTRACT

Spectral resolved electroluminescence has been observed for n-GaAs in the presence of different hole injecting redox electrolytes from 0.8 to 1.25 μm . Photoluminescence spectra were obtained for n-GaAs in the same electrolytes. Luminescence was observed both in bandgap and subbandgap energy ranges. The presence of a deep acceptor level, attributed to Ga vacancies, is inferred. Efficient charge transfer to this level and/or to the valence band can be observed with a suitable choice of the redox electrolyte.

The occurrence of hole injection from a redox electrolyte into the valence band and/or into an intermediate level (deep level and/or surface state), of a semiconducting electrode can be detected via electroluminescence (EL). This phenomenon has been observed with the one-electron redox injecting electrolyte $\text{Fe}(\text{CN})_6^{3-/4-}$ for GaP (1, 2), and more recently for GaAs by Decker *et al.* with the couples $\text{Fe}^{2+/3+}$, $\text{Ce}^{3+/4+}$, $\text{Fe}(\text{CN})_6^{3-/4-}$ (3). In that work, the mechanism of hole injection was elucidated by the use of the rotating ring-disk technique as well as by elec-

troluminescence. Ring-disk results that are in excellent agreement with the ones in Ref. (3) were also published by Menezes and Miller (4). The electroluminescence measurements reported in Ref. (3) were not spectrally resolved because of instrumental limitations. The present publication is, therefore, mostly devoted to the investigation of the EL spectra up to 1.25 μm , of the relationship between the spectra and the redox electrolyte used, and to the comparison with photoluminescence (PL) spectra of GaAs. Interesting comparisons can be made with previous works on EL from GaAs (5) and from II-VI binary and ternary compounds (6-9). In those papers, the injecting species was a highly active intermediate, like $\text{OH} \cdot$

*Electrochemical Society Active Member.

Key words: semiconductor/electrolyte junctions, luminescence.

or SO_4^{2-} , resulting from the reduction of peroxide or persulfate. The energy-level distribution of such an injecting species is poorly defined, and therefore little information on the energy level at which the hole-injection process takes place can be extracted from the spectra. Using one-electron redox couples like $\text{Fe}^{2+/3+}$, $\text{Ce}^{3+/4+}$, $\text{Fe}(\text{CN})_6^{3-/4-}$, on the contrary, the energetic conditions for hole injection into the valence band or into some intermediate level of GaAs can be analyzed more carefully. Moreover, the use of a redox ion as a hole injecting species allows a steady-state measurement of an EL spectrum, once the mass transport of the electrolyte to the electrode surface is well defined. In practice, this procedure can be employed only if the surface conditions of the electrode do not change too much during the measurement. If drastic changes occur (like from an oxide-coated to a hydride-coated surface) quenching of radiative recombination can take place and a distorted and weaker spectrum results. It is therefore very important to control the electrode potential during EL measurements, since adequate electron concentration at the semiconducting electrode surface has to be maintained. At the same time, side reactions giving H_2 evolution have to be avoided.

Very large cathodic potentials can induce either hole injection due to high concentration of intermediates (10, 11) or ion injection and migration (12, 13) into the semiconducting electrode. Both phenomena can cause luminescence; high cathodic polarization has therefore been avoided in our work in order to confine our study to EL resulting from hole injection by the redox electrolytes.

Experimental Techniques

Electroluminescence.—The use of redox ions in low (10^{-3} – $10^{-2}M$) concentration as the hole injecting species requires an efficient stirring of the electrolyte, in order to guarantee diffusion-controlled hole injection and current high enough to yield detectable EL signals. In Ref. (3) the rotating disk technique was used in order to guarantee efficient mass transport and constant current. Here, this technique is impractical because the image of the rotating electrode onto the spectrometer slit is unstable, causing fluctuations of the detected EL signal. Stirring by means of magnetic stir-bars or other mechanical devices produces enormous oscillations in the hole-injection current and therefore in the EL intensity as well. The best configuration has been found to be an electrolyte jet impinging onto a stationary electrode, the electrolyte flux being sustained by an all-Teflon rotary pump that fills an intermediate reservoir (Fig. 1). The electrolyte level in

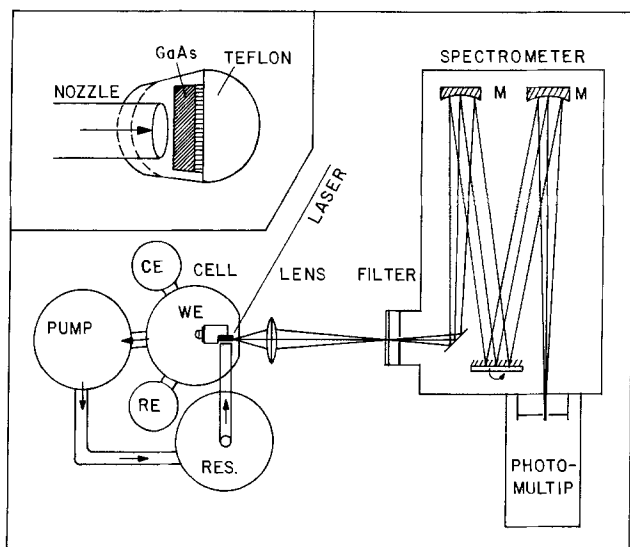


Fig. 1 Top view of the experimental setup for photoluminescence and electroluminescence. The inset shows the electrode mounting in detail (side view).

this reservoir is constantly kept ~ 10 cm higher than that in the main cell, to which the electrolyte flows simply by gravity. EL intensity fluctuations of a few percent and even smaller current oscillations have been achieved in this way. The GaAs electrode is set in front of the nozzle (with 1–2 mm separation) and sideways to the cell flat Pyrex window, so that the image of its front edge can be focused onto the spectrometer slit. The EL originating from the flat-crystal surface exposed in front of the nozzle can also contribute to the signal as long as defocusing is not too severe. The optical setup consists of a collecting lens, a long pass filter with cutoff at $0.7 \mu\text{m}$, a Spex spectrometer, and a S-1 EMI photomultiplier. The spectral sensitivity of the photomultiplier decays very steeply for λ greater than $1.1 \mu\text{m}$. Consequently, the photomultiplier relative spectral response was compared to that of a flat photoacoustic photodetector, and correction factors were derived for wavelengths in the range 0.7 – $1.25 \mu\text{m}$. The photomultiplier was cooled with liquid air in order to achieve maximum signal-to-noise ratio. The slit widths of the spectrometer were kept at 1.0 mm in most experiments, which brings a spectral resolution of 16\AA at $\lambda = 1.0 \mu\text{m}$. Measurements of EL for λ greater than $1.3 \mu\text{m}$ were not possible with the present experimental setup both because of photomultiplier insensitivity and because of strong IR absorption in the aqueous electrolyte. A different setup will be assembled for EL measurements in this IR region.

The electronic apparatus consisted of conventional potentiostat and programmer, voltmeter, electrometer, and a double-pen strip-chart recorder. The EL and PL spectra were obtained by driving the spectrometer at the constant speed of $5 \text{\AA} \text{ s}^{-1}$. The electrochemical cell and the reservoir were made of Pyrex and connected to each other and to the pump by Tygon tubes. The three-electrode configuration was always used, and all potentials will be referred to the saturated calomel reference electrode (RE). The electrolytes were prepared with triply distilled H_2O and with high purity reagents. The presence of oxygen did not affect our measurements; therefore, it was unnecessary to deaerate the electrolytes. Graphite was used as the counterelectrode (CE). An n-GaAs sample from Laser Diode Company, doped with a Si concentration at $5 \times 10^{17} \text{ cm}^{-3}$, was used as the working electrode (WE). The ohmic contact was obtained by the evaporation of Sn followed by annealing under N_2 atmosphere during 2 min at 400°C . The sample was mounted on a Teflon rod (as shown in Fig. 1) with the crystallographic (100) face exposed to the solution. The semiconductor surface was etched in $\text{H}_2\text{SO}_4:\text{H}_2\text{O}_2$ (1:1 by volume) prior to use.

Photoluminescence.—The same setup described for EL was used for the PL measurements. The photoexcitation was made by means of a 3 mW He-Ne laser from Spectra Physics focused on GaAs front crystal edge. In this way, the same alignment for PL and EL could be used.

Experimental Results

Photoluminescence of GaAs.—PL of GaAs in air or vacuum has been widely studied for several years, as a function of temperature, doping, and various other parameters (14). It is well known that heat-treatments and surface contamination may affect PL. First, we ran the photoluminescence spectrum at room temperature and in air of GaAs sample as received from the factory, with mirror-like surface finishing. The spectrum (not corrected for photomultiplier sensitivity) is labeled as PL⁰ in Fig. 2: a very strong band-to-band transition is observed in $0.87 \mu\text{m}$, and a weaker and much broader band shows up around $1.1 \mu\text{m}$ (note the 30-fold increase in sensitivity in the IR region).

PL and EL in $\text{Fe}(\text{CN})_6^{3-}$ pH 13.—The GaAs electrode was assembled as previously shown, etched, and introduced into the electrochemical cell filled with a 30 mM $\text{K}_3\text{Fe}(\text{CN})_6 + 0.1M$ KOH electrolyte. This electrolyte composition was chosen because it is well known that

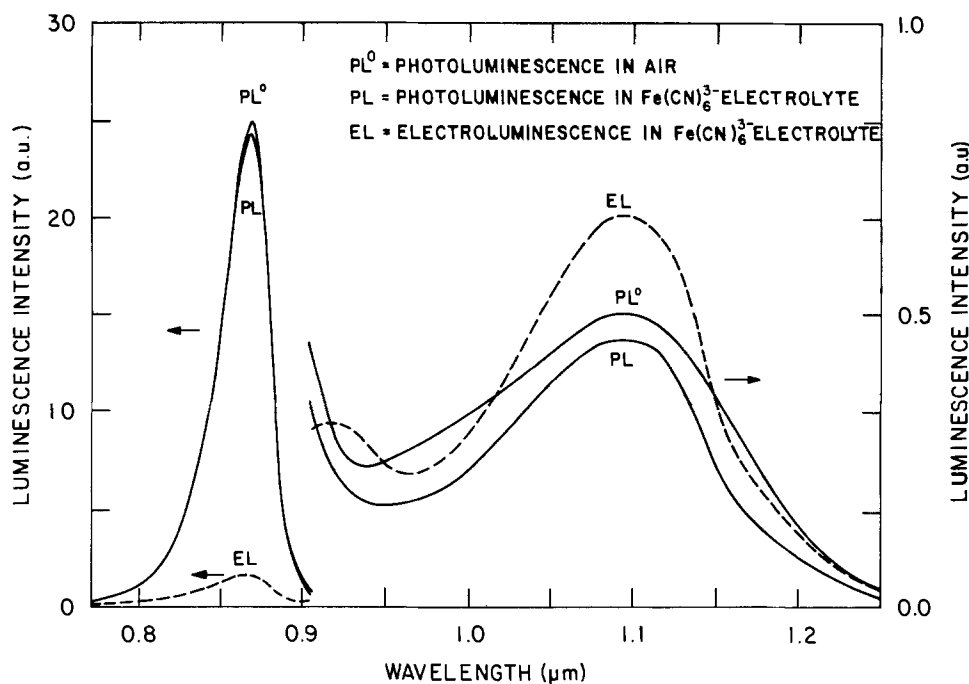


Fig. 2. Uncorrected photoluminescence (solid lines) and electro-luminescence (dashed lines) spectra of n-GaAs in air (PL°) and in aqueous $0.03M K_3Fe(CN)_6 + 0.1M KOH$ electrolyte (PL and EL). During PL, the GaAs electrode was held at open circuit; during EL, at $-1.75V$.

$Fe(CN)_6^{3-}$ injects holes into GaAs in alkaline solutions (3, 4, 15). The PL spectrum (Fig. 2) was obtained with no potential applied to the GaAs electrode. This spectrum is virtually identical to the one obtained in air in the band-to-band region, and shows only minor changes in the IR. It is therefore clear that none of the features observed in the photoluminescence spectra depends on contact with the electrolyte, *i.e.*, the electrolyte ions have no specific effect on PL. When potential is applied to the electrode, and the laser switched off, luminescence from the electrode appears as soon as a cathodic current flows in the cell (Fig. 3). At $-1.75V$, the EL intensity is maximum and very stable in time at all wavelengths (see Fig. 4). Therefore, a steady-state EL spectrum (shown in Fig. 2) was ob-

tained at a constant $-1.75V$ potential. In the EL spectrum both bands at 0.87 and 1.1 μm are observed; however, the intensity of the 0.87 μm band is now much weaker than that observed in PL. A better analysis of the PL and EL spectra can be made after multiplying the measured intensities by the correction factors and after normalization to the same peak height at 0.87 μm . This is shown in Fig. 5. The band-to-band recombination spectrum in the EL is broader than in the PL (see Table I), which is mainly due to the enhancement of the short wavelength side of the peak. In the IR region, the emitted intensities level off in both spectra; however, the ratio of this intensity to that in 0.87 μm is much larger in the EL spectrum than that in PL. It is unfortunate that the photomultiplier is so insensitive for wavelengths greater than 1.25 μm and therefore that the long wavelength tail of the IR peak cannot be seen with this experimental setup. A structure is seen at 0.93 μm in EL, but since it did not appear in all EL measurements, we shall not discuss it.

The complete dependence of EL with electrode potential at constant wavelength is shown in Fig. 3. EL appears

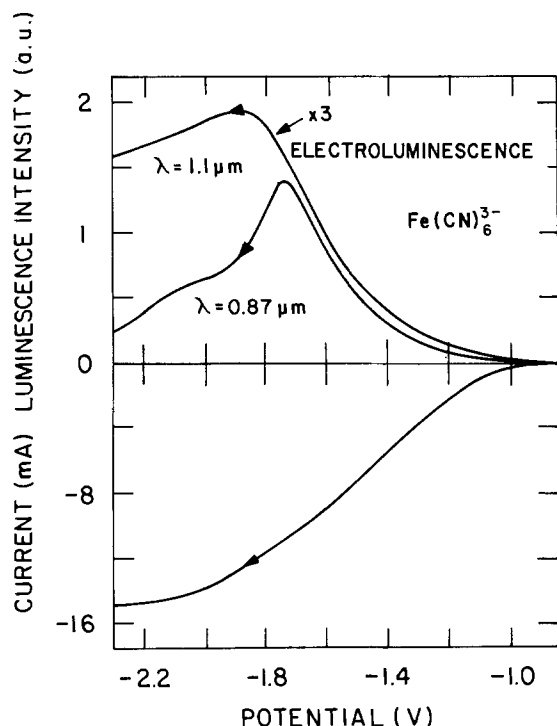


Fig. 3. Current-potential curve for n-GaAs in aqueous $0.03M K_3Fe(CN)_6 + 0.1M KOH$ in the dark (lower part). The corresponding EL intensities recorded as a function of applied potential for two different wavelengths are shown in the upper part. Note the three-fold increase in sensitivity for EL in $\lambda = 1.1$ μm . The potential was swept at a constant rate of -20 $mV s^{-1}$.

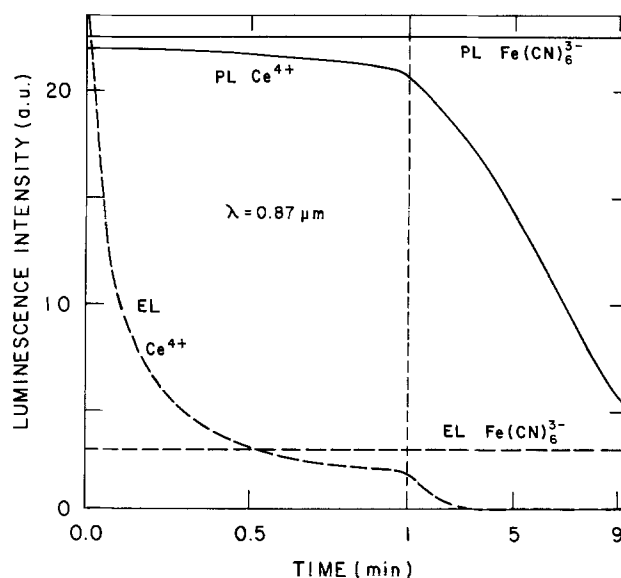


Fig. 4. Time dependence of PL (solid lines) and EL (dashed lines) of n-GaAs in $0.03M K_3Fe(CN)_6 + 0.1M KOH$ and in $0.03M Ce(SO_4)_2 + 1.0M H_2SO_4$. At $t = 0$, either the laser was switched on (PL), or the electrode potential was stepped from 0 to $-1.75V$ (EL).

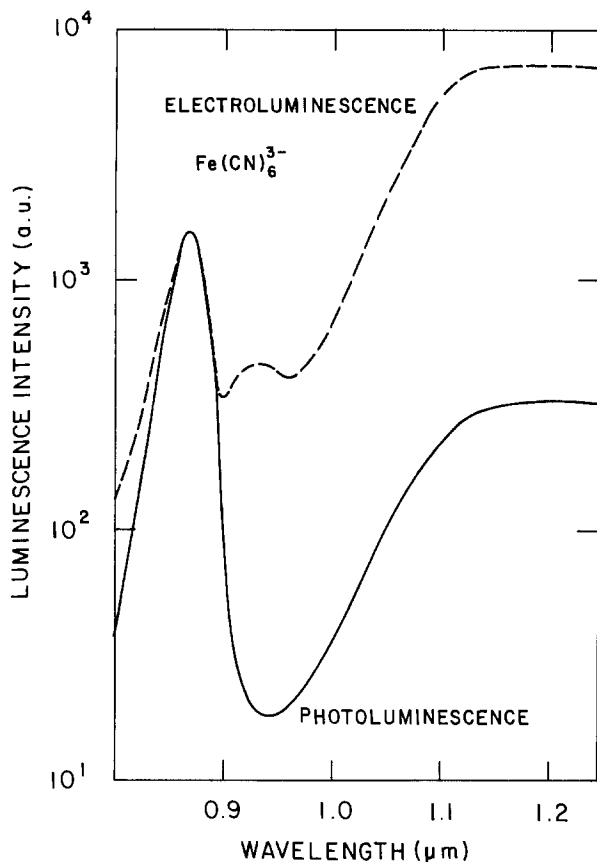


Fig. 5. PL (solid line) and EL (dashed line) spectra of n-GaAs after correction for photomultiplier efficiency and normalization to the same peak height in 0.87 μm . Electrolyte and polarization conditions are the same as in Fig. 2.

only with cathodic currents, starting for $V < -1.0\text{V}$. This is in agreement with previous observations (3), which were confined, however, to $\lambda < 0.9\ \mu\text{m}$. For potentials more cathodic than -1.8V , EL at $\lambda = 0.87\ \mu\text{m}$ is quenched abruptly while EL at $\lambda = 1.1\ \mu\text{m}$ decays slowly and eventually becomes constant.

PL and EL in Fe^{3+} and Ce^{4+} , pH 0.—Electrolytes with 0.03M Fe^{3+} or 0.03M Ce^{4+} in 1.0M H_2SO_4 were used because the equilibrium potentials of these couples are located either in the GaAs bandgap ($\text{Fe}^{2+/3+}$) or overlap with the GaAs valence band ($\text{Ce}^{3+/4+}$).

A number of experimental difficulties arise, however, in acid electrolytes. Although the potential dependence of PL and EL was observed to be similar to that observed at pH 13 (with the exception of a 0.6V shift in the onset of EL), no electrode potential could be found at which EL would be stable during the time required to measure a complete spectrum. PL intensities at fixed wavelength and potential decrease with time, contrary to what occurs in 0.1M KOH. The variation of PL and EL intensities with time are shown in Fig. 4 for Ce^{4+} and $\text{Fe}(\text{CN})_6^{3-}$. An exchange of Ce^{4+} by Fe^{3+} showed a similar decrease in PL and EL intensities with time.

It became clear to us that photocorrosion takes place at the laser spot on the GaAs electrode and the corrosion products are not dissolved quickly enough at pH 0. Corrosion products like gallium oxides are probably left on the surface [see also Ref. (16)], resulting in PL quenching. In fact, moving the laser spot to another region of the electrode restores the initial intensity of PL.

In order to measure EL, we had to apply the same technique previously employed by Ellis *et al.* (6, 7) which consists in short (2s) forward-bias pulses alternated by longer (20s) time intervals in which the GaAs-electrolyte junction is reverse biased. At the same time, the spectrometer was driven at constant speed. The two EL spectra, relative to Fe^{3+} or Ce^{4+} ions in the same 1M H_2SO_4 support

Table I. Characteristics of the luminescence spectra of n-GaAs grown from the melt in the bandgap region (first two columns) and ratios between the luminescence intensities, corrected by photomultiplier efficiency, at 0.87 and 1.1 μm (third column)

	Peak position (Å)	Bandwidth FWHM (Å)	$\frac{I_{0.87}}{I_{1.1}}$
PL ^o in air	8700	343	6.24
PL in $\text{K}_3\text{Fe}(\text{CN})_6 + \text{KOH}$	8700	345	6.71
EL in $\text{K}_3\text{Fe}(\text{CN})_6 + \text{KOH}$	8680	392	0.30
EL in $\text{Ce}(\text{SO}_4)_2 + \text{H}_2\text{SO}_4$	8680	390	0.35
EL in $\text{Fe}_2(\text{SO}_4)_3 + \text{H}_2\text{SO}_4$	8660	408	0.08

electrolyte, are shown in Fig. 6. It is important to notice that the spectra were obtained one after the other without removing either the cell or the electrode. The redox electrolyte was substituted, and otherwise the same experimental conditions were maintained, so that the EL intensities of both spectra can be directly compared. The following remarks are important: (i) the EL with Ce^{4+} is more intense than that with Fe^{3+} , by a factor of 10 in 0.87 μm and by a factor of only 2.2 in 1.1 μm (note the different scales in which EL intensities for Fe^{3+} and for Ce^{4+} are shown in Fig. 6) and (ii) in the Fe^{3+} EL spectrum, the IR peak is more intense than the peak in 0.87 μm .

The more relevant data from PL and EL spectra in the three electrolyte are summarized in Table I.

Discussion and Conclusions

The PL and EL spectra give a valuable insight into processes related to radiative recombination and charge transfer across the semiconductor-electrolyte interface. The band-to-band recombination emission spectrum of the n-GaAs with maximum at $\sim 0.87\ \mu\text{m}$ is observed in PL as well as in EL, but in the latter the spectrum appears slightly broader and its peak is shifted to shorter wavelength, as shown in Fig. 5 and Table I. Since this broadening occurs almost exclusively in the high energy tail we attribute the difference to self-absorption effects, *i.e.*, on average, EL is produced nearer to the GaAs-electrolyte interface than PL. Similar conclusions about EL spectra broadening were drawn by Ellis *et al.* (6); they compared EL and PL spectra of cadmium-sulfo-selenide electrodes. This conclusion is valid for any material where the penetration depth α^{-1} of the exciting photons is of the same order, or greater than the diffusion length L of the injected minority carriers. In particular, for n-GaAs α^{-1} is $\sim 0.3\ \mu\text{m}$ (at $\lambda = 0.63\ \mu\text{m}$) and L_p is of the same order of magnitude, as long as the hole lifetime is in the order of 10^{-9}s . The last hypothesis was not experimentally confirmed here but can be taken as reasonable, since at the semiconductor-electrolyte interface the surface recombination velocity is high (17).

The subbandgap emission bands with its maximum at $\sim 1.1\ \mu\text{m}$, uncorrected to photomultiplier spectral response, are also observed in PL and EL on samples grown from the melt. However, samples grown by us by liquid phase epitaxial (LPE) technique showed no measurable PL signal in this subbandgap spectral region, although a similar laser beam was used to induce bandgap emission of the same intensity as above. Both LPE and melt-grown samples are doped only with Si. However, the LPE samples have a lower density of defects, in particular Ga vacancies, than the crystals grown from the melt. Since there is a good agreement between the energetic position of the subbandgap peak observed by us with that cited in the literature on photoluminescence of GaAs (18), we attribute the 1.1 μm emission band to radiative transition from shallow donor states to deep acceptor states created by gallium vacancies. In the following, only n-GaAs grown from the melt will be considered. As shown in Fig. 2, the spectra of PL with the sample immersed in electrolyte or in air are almost identical, *i.e.*, the electrolyte ions have no specific effect on PL. However, the overall intensities in EL as well as in PL may decrease

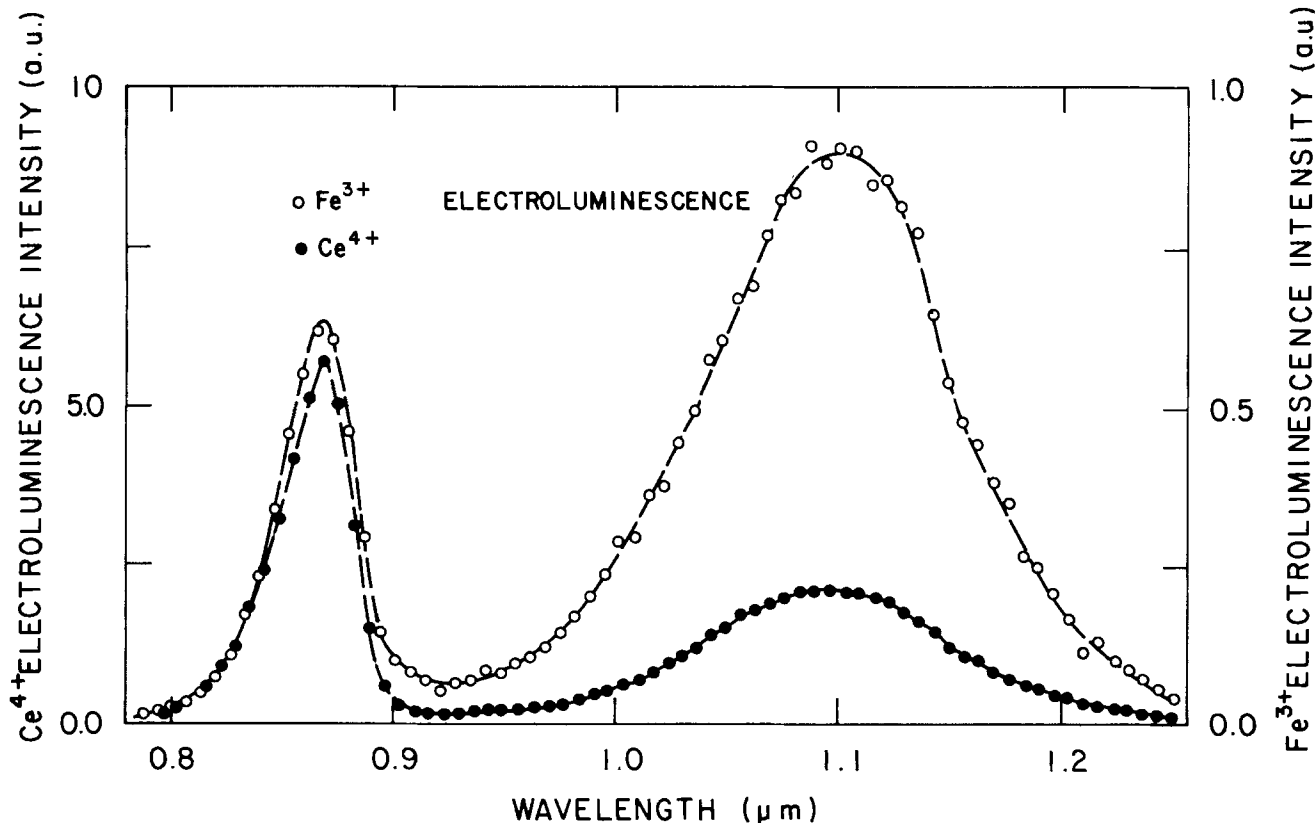


Fig. 6. Uncorrected EL spectra of n-GaAs in $0.01M \text{Fe}_2(\text{SO}_4)_3 + 1.0M \text{H}_2\text{SO}_4$ and in $0.03M \text{Ce}(\text{SO}_4)_2 + 1.0M \text{H}_2\text{SO}_4$. The electrode potential was continuously pulsed between 0 (20s) and $-1.75V$ (2s), while the emission spectrum was scanned at 5 \AA s^{-1} . Note the tenfold increase in sensitivity in order to record the spectrum in the $\text{Fe}_2(\text{SO}_4)_3$ electrolyte.

in time, with a time constant depending on the electrolyte composition (see Fig. 4). The photoluminescence quenching in the presence of the electrolyte was attributed to electrode-surface degradation due to photocorrosion effects, which, in fact, can be observed with the naked eye.

The most remarkable difference between PL and EL spectra is the variation of the ratio between the near-bandgap emission peak intensity to the subbandgap emission intensity ($I_{0.87}/I_{1.1}$). As shown in Fig. 5 and Table I, this ratio is smaller by a factor of 22 in EL than PL when the electrolyte is a solution of $\text{K}_3 \text{Fe}(\text{CN})_6 + \text{KOH}$, and by a factor of 78 when the electrolyte is changed to $\text{Fe}_2(\text{SO}_4)_3 + \text{H}_2\text{SO}_4$. This variation can be due to one or more of the following:

1. The density of the acceptor centers is higher in the region near to the GaAs-electrolyte interface. Gallium vacancies, in particular, may have higher density closer to the surface as a consequence of corrosive reactions taking place at the interface.

2. The band-to-band radiative transition is quenched by a more competitive nonradiative recombination at the GaAs electrolyte surface.

3. The electron-transfer rate is larger at the intra-bandgap state energy (gallium vacancy state) than at the valence bandedge energy. We shall discuss this point in the following.

An energy-band diagram is sketched in Fig. 7 for the semiconductor-electrolyte interface, taking as 0.3 eV the distance of the acceptor level (E_{INT}) from the valence bandedge (E_{VB}) of GaAs. This value is in agreement both with the known energy position of gallium vacancies and with our corrected PL and EL spectra, which show a maximum around $1.2 \mu\text{m}$ (Fig. 5). In the electrolyte side, the unoccupied energy levels of Fe^{3+} and Ce^{4+} are depicted as gaussian distributions that have their maximum at an energy E_{R} above the Fermi level of the couple (taken as the redox potential). The rearrangement energy E_{R} is ~ 1.2 and ~ 1.5 eV for the Fe^{3+} and for Ce^{4+} , respectively, (19). The proper matching between electrodes and elec-

trolyte energy levels is obtained knowing the flatband potential of GaAs, which nearly coincides with the conduction bandedge E_{CB} in our n-type samples. The value of -0.5 eV vs. NHE (pH = 0) was chosen for E_{CB} , in agreement with data from the literature (3, 4, 20). The unoccupied energy levels of $\text{Fe}(\text{CN})_6^{3-}$ could also be included in the diagram, provided the shift with pH of the GaAs energy levels is taken into account. For the sake of simplicity, however, we shall consider in Fig. 7 only the energy level distributions corresponding to the Fe^{3+} and Ce^{4+} ions. Due to the redox potentials of the two couples, Ce^{4+} should easily inject holes into the valence band of GaAs, but Fe^{3+} should not. This was indeed confirmed by previous work (3, 4). Here, we did observe bandgap luminescence with Fe^{3+} , although ten times weaker than with Ce^{4+} (Fig. 6). Bandgap luminescence indicates unequivocally hole injection into the valence band. This can be attributed either to an underpotential reduction of Fe^{3+} by valence-band electrons and/or to an upper shift of the GaAs bandedges during the $-1.75V$ potential pulse used in the present EL measurements. This pulse technique differs from the potential sweep technique used previously by Decker *et al.* (3), allowing higher EL intensities. From the EL measurements, and from Fig. 7, we conclude:

1. $\text{Fe}(\text{CN})_6^{3-}$, Ce^{4+} , and Fe^{3+} inject holes both into the valence band and into the intra-bandgap state.

2. The ratio $I_{0.87}/I_{1.1}$ falls from 0.3 [Ce^{4+} , $\text{Fe}(\text{CN})_6^{3-}$] to 0.08 (Fe^{3+}), indicating that the Fe^{3+} injects holes less efficiently into the valence band than the other electroactive species do.

3. The rate of hole injection for Ce^{4+} and $\text{Fe}(\text{CN})_6^{3-}$ is comparable; for Fe^{3+} this rate is lower, both at E_{INT} and at E_{VB} .

Since the energy-level distribution in the electrolyte is very broad, a good overlap of both the deep level and the valence band with empty levels in the electrolyte occurs. Consequently, the electron transfer from the semiconductor to the redox ion can occur isoenergetically, the initial state being either at the valence bandedge or in the

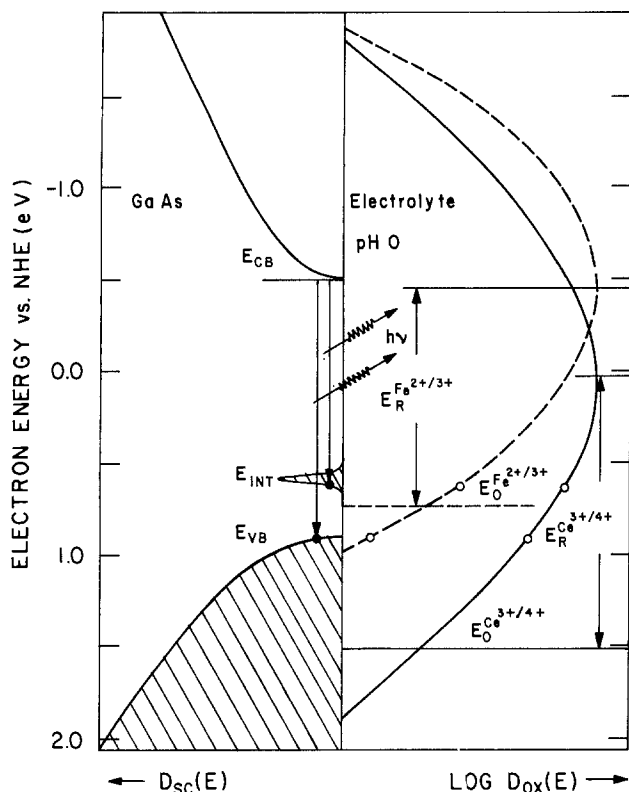


Fig. 7. Energy band diagram for the n-GaAs/redox electrolyte interface. In the semiconductor, the dashed areas represent filled states. E_{CB} and E_{VB} indicate the conduction and the valence band edges; E_{INT} is the energy of the deep level attributed to Ga vacancies. In the electrolyte, the solid and dashed parabolas represent the energy-level distribution of the empty Ce^{4+} and Fe^{3+} states, respectively. E_O^F represents the standard redox potentials, and E_R represents the so-called arrangement energy for the redox couples. The following symbols are used to illustrate the electron transfer across the semiconductor/electrolyte interface. Filled dots: initial states. Open dots: final states. The vertical arrows in the GaAs indicate the radiative transitions taking place in the semiconductor after the electron transfer has occurred.

deep intra-bandgap level. In fact, the energy level model for the semiconductor-electrolyte interface (21) assumes isoenergetic charge transfer, since negligible phonon emission during electron transfer is expected (22). For a single level E , the charge transfer rate is proportional to the density of occupied states in the solid and of unoccupied states in the electrolyte. One can see from Fig. 7 that the density of empty states in the electrolyte is larger at E_{INT} than at E_{VB} . The electron transfer at E_{INT} is then kinetically favored, unless the density of states at the valence band edge overwhelms the density of states at the intra-bandgap level. The small ratios $I_{0.87}/I_{1.1}$ we observed in electroluminescence indicate, indeed, high charge transfer rate at E_{INT} . Our experiments with Fe^{3+} and Ce^{4+} in H_2SO_4 indicate also that the competition between charge transfer to the intra-bandgap state and charge transfer to the valence band is regulated by the redox potential of the couple. As a general conclusion, electroluminescence in aqueous redox electrolytes is a technique sensitive per se to the presence of intra-bandgap states. This conclusion agrees well with previous results of EL measurements on GaP (1).

Finally, the charge transfer from the conduction band of GaAs cannot be excluded. In fact, Fig. 7 shows that the capture of conduction-band electrons can also occur at a high rate without violation of the principle of isoenergetic charge transfer. Indeed, simultaneous charge transfer to distinct energy levels is unavoidable with small bandgap semiconducting electrodes in the presence of aqueous redox electrolytes.

Acknowledgments

The financial support from FINEP and CNPq is gratefully acknowledged.

Manuscript submitted Sept. 29, 1983; revised manuscript received Jan. 4, 1984.

REFERENCES

1. K. H. Beckmann and R. Memming, *This Journal*, **116**, 368 (1969).
2. Y. Nakato, A. Tsumura, and H. Tsubomura, in "Photoeffects at Semiconductor-Electrolyte Interfaces," A. J. Nozik, Editor, p. 145, ACS Symposium Series, American Chemical Society, Washington, DC (1981).
3. F. Decker, B. Pettinger, and H. Gerischer, *This Journal*, **130**, 1335 (1983).
4. S. Menezes and B. Miller, *ibid.*, **130**, 517 (1983).
5. B. Pettinger, H. R. Schöppel, and H. Gerischer, *Ber. Bunsenges. Phys. Chem.*, **80**, 849 (1976).
6. H. H. Streckert, J. Tong, M. K. Carpenter, and A. B. Ellis, *This Journal*, **129**, 772 (1982).
7. H. H. Streckert, J. Tong, and A. B. Ellis, *J. Am. Chem. Soc.*, **104**, 581 (1982).
8. H. H. Streckert, B. R. Karas, D. J. Morano, and A. B. Ellis, *J. Phys. Chem.*, **84**, 3232 (1980).
9. H. H. Streckert, J. Tong, M. K. Carpenter, and A. B. Ellis, *Proc. Electrochem. Soc.* **82-3**, 633 (1982).
10. D. J. Bernard and P. Handler, *Surf. Sci.*, **40**, 141 (1973).
11. H. Gerischer, N. Müller, and O. Haas, *J. Electroanal. Chem.*, **119**, 41 (1981).
12. M. A. Butler and D. S. Ginley, *The Electrochem. Soc. Meeting*, **79-2**, 1577 (1979).
13. M. A. Butler and D. S. Ginley, *Appl. Phys. Lett.*, **36**, 845 (1980).
14. "Proceedings of the Tenth International Symposium on Gallium Arsenide and Related Compounds," Albuquerque, New Mexico, Sept. 19-22, 1982, G. E. Stillman, Editor, Institute of Physics Conference Series no. 65 Bristol, England (1983); E. W. Williams and H. B. Bebb, in "Semiconductors and Semimetals," Vol. 8, R. K. Willardson, Editor, p. 321, Academic Press, New York (1972); V. Swaminathan, N. E. Schumaker, and J. L. Zilko, *J. Lumin.*, **22**, 153 (1981); A. Mircea-Roussel and S. Makran-Ebeid, *Appl. Phys. Lett.*, **38**, 1007 (1981).
15. H. Gerischer, *Ber. Bunsenges. Phys. Chem.*, **69**, 578 (1965).
16. V. A. Myamlin and Y. V. Pleskov, "Electrochemistry of Semiconductors," p. 99, Plenum Press, New York (1967).
17. A. Heller, in "Photoeffects at Semiconductor-Electrolyte Interfaces," A. J. Nozik, Editor, p. 57, ACS Symposium Series, American Chemical Society, Washington, DC (1981).
18. "Semiconductors and Semimetals," Vol. 8, R. K. Willardson, Editor, pp. 324, 359-373, Academic Press, New York (1972); V. Swaminathan, N. E. Schumaker, and J. L. Zilko, *J. Lumin.*, **22**, 153 (1981).
19. F. Willig and K. P. Charlé, *Faraday. Discuss.*, **74**, 9 (1982).
20. R. Memming, *Ber. Bunsenges. Phys. Chem.*, **81**, 732 (1977).
21. H. Gerischer, *Z. Phys. Chem. N. F.*, **27**, 48 (1961).
22. R. R. Dogonadze, A. M. Kuznetsov, and A. A. Cherenko, *Russ. Chem. Rev.*, **34**, 759 (1965).

Thermodynamic Stability of Manganese Phosphides from High Temperature Solid-State Galvanic Cells

Clifford E. Myers and Diana J. Simpson

Department of Chemistry, State University of New York at Binghamton, Binghamton, New York 13901

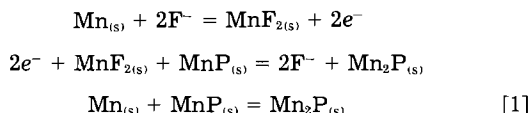
ABSTRACT

The solid-state cells, $\text{Mn, MnF}_2/\text{CaF}_2/\text{MnF}_2, \text{MnP, Mn}_2\text{P}$ and $\text{Mn, MnF}_2/\text{CaF}_2/\text{MnF}_2, \text{Mn}_2\text{P, Mn}_3\text{P}$ have been studied in the temperature range 867-1067 K. The EMF's, together with data from the literature, were used to calculate enthalpies of formation (from red P), $\Delta H_{f, 298.15}^0/R$: MnP , -13.9 ± 1.0 kK; Mn_2P , -20.6 ± 1.0 kK; Mn_3P , -21.8 ± 1.0 kK. The results are in excellent agreement with data reported earlier from this laboratory.

Although the thermodynamic stabilities of the manganese phosphides have been studied in several laboratories (1-4), there are no data in the literature on the stability of Mn_3P other than what may be inferred from the published phase diagram (5). Mn_3P melts incongruently to give liquid and $\text{Mn}_2\text{P}_{(s)}$, which may be taken as evidence that its stability is marginal relative to $\text{Mn} + \text{Mn}_2\text{P}$. Baratashvili *et al.* (2) have reported measurements in the temperature range 851-1067 K on the solid-state cell



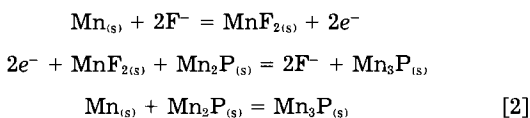
for which the cell reactions are



The results of their study were shown to be consistent, within experimental uncertainty, with a combination of results from combustion calorimetry (1) and vaporization studies (3) on $\text{MnP}_{(s)}$. They are also consistent with a combination of results from vaporization studies (3, 4) on $\text{MnP}_{(s)}$ and $\text{Mn}_2\text{P}_{(s)}$. Hence the use of solid-state galvanic cells appears to give reliable results in the Mn-P system, and it was decided to set up cell I as a check on technique and then to study the cell



for which reactions are



The enthalpy of formation of $\text{Mn}_3\text{P}_{(s)}$ is given by

$$\Delta H_{f, 298.15}^0(\text{Mn}_3\text{P})/R = \Delta H_{298.15}^0[2]/R - \Delta H_{f, 298.15}^0(\text{Mn}_2\text{P})/R$$

where $\Delta H_{298.15}^0[2]$ is the enthalpy change for reaction [2].

Experimental

The cell assembly shown in Fig. 1 was constructed following a design (6) generously provided by Dr. Reginald Faircloth. The electrolyte was a 25.3 mm diam \times 2.1 mm thick polished calcium fluoride optical window which was supported by a mullite porcelain tube held in place by a steel compression spring located below the hot zone. The lower electrode pellet (Mn, MnF_2) was supported by a molybdenum or graphite pellet holder set within a molybdenum support block mounted on a smaller mullite porcelain tube placed inside the first and supported rigidly by a brass tube located below the hot zone. The upper electrode pellet (MnF_2, Mn phosphides) was positioned by a second pellet holder which was held in place by a stainless steel plate attached to two stainless steel rods pulled down by tension springs located below the hot zone. Electrical leads of molybdenum wire were connected to the

Key words: Enthalpy of formation, enthalpy of atomization, Mn_3P , Mn_2P , MnP .

respective pellet holders, and a Chromel-Alumel thermocouple was mounted in the support block. The thermocouple was calibrated *in situ* against a U.S. National Bureau of Standards copper freezing-point standard. The entire assembly was enclosed in a mullite porcelain tube which was connected to a vacuum/argon gas system. The argon entered the assembly from the bottom of the apparatus and exited through a slot in the inner ceramic tube and through a stainless steel tube outside the electrolyte-

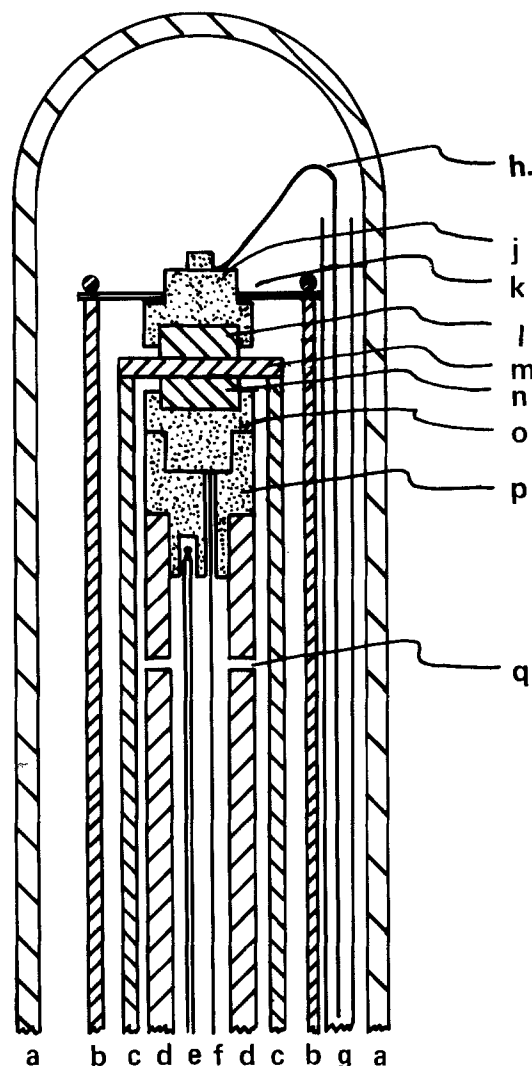


Fig. 1. Solid-state galvanic cell assembly. A: outer ceramic tube. B: stainless steel rods. C: ceramic tube electrolyte support. D: inner ceramic tube. E: thermocouple. F: lower molybdenum lead. G: stainless steel tube. H: upper molybdenum lead. J: upper electrode-pellet holder. K: stainless steel plate. L: upper electrolyte pellet. M: CaF_2 electrolyte. N: lower electrode pellet. O: lower electrode-pellet holder. P: molybdenum support. Q: slot.

support tube. The arrangement was such that argon which had come in contact with one electrode pellet did not subsequently come in contact with the other. The argon, stated by the supplier to be 99.998% pure, was passed over activated alumina at room temperature and titanium metal at 600°C before entering the apparatus. In addition, a strip of tantalum foil was placed around each pellet holder to act as a getter for oxygen. In each run, the assembly was first heated under a vacuum of about 10^{-5} torr for several hours to remove adsorbed gases. After being cooled to room temperature, the assembly was brought to atmospheric pressure with argon, and the argon continued to flow slowly through the assembly as it was brought up to temperature, as measurements were made, and as the assembly was cooled again to ambient temperature. The EMF of the cell was measured with a Keithley Model 660A guarded dc differential voltmeter.

The manganese used in the lower electrode pellet and for synthesis of the samples was "flake" obtained from SPEX, Incorporated, and had a stated purity of 99.89%. The red phosphorus used for preparing the samples was obtained from CERAC/Pure, Incorporated, and had a stated purity of 99.9%. The manganese difluoride used in the electrode pellets was obtained from Atomergic Chemical Corporation and had a stated purity of 99.9%. The calcium fluoride disks were purchased from Harshaw Chemical Company, Incorporated. The mullite porcelain tubes were obtained from McDanel Refractory Porcelain Company. The phosphide samples were prepared and characterized in the manner described earlier (7).

The electrode pellets were prepared by pressing an intimate mixture (1:1 by weight) of the powdered components under a load of 10 tons. The pellet materials were examined by x-ray powder diffraction after each run to ensure that the desired component materials were indeed present.

Results

Data collected for the two cells are given in Fig. 2 and Tables I and II.¹ The line in Fig. 2 is calculated from the equation given by Baratashvili *et al.* (2) for the EMF of cell [I]. Despite the efforts described above to exclude oxygen, there was evidence in some runs of formation of green MnO on the surface of the electrode pellets; however, the results did not appear to be affected by the oxide. In a number of runs on cell [I], the EMF, although otherwise in agreement, increased slightly with increasing temperature rather than decreasing as required by the

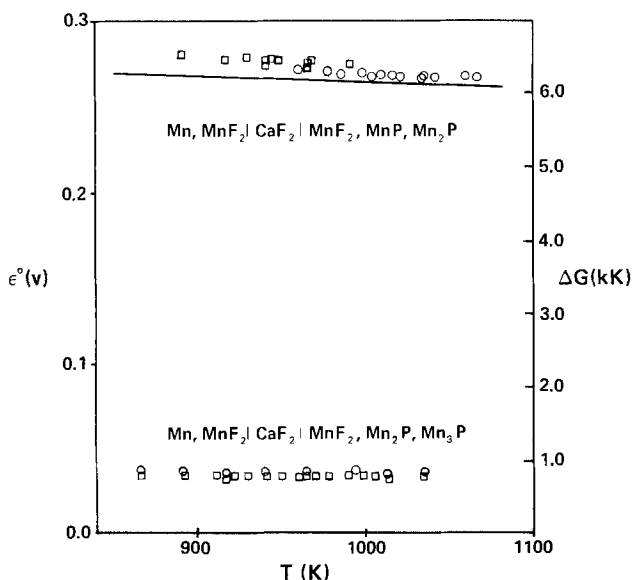


Fig. 2. EMF data, cells [I] and [II]. Line from equation in Ref. (2)

Table I. Cell [I]

T(K)	EMF (mV)	log K	$\Delta\phi^1/R$	$\Delta H_{298.15}^0/R$ (kJ)
Run A				
966	273	2.848	-0.565	-6.88
941	275	2.945	-0.563	-6.91
917	278	3.056	-0.560	-6.99
891	281	3.179	-0.557	-7.02
917	278	3.055	-0.560	-6.97
941	277	2.967	-0.563	-6.96
991	275	2.797	-0.568	-6.95
968	277	2.884	-0.565	-6.98
948	278	2.956	-0.563	-6.99
930	279	3.024	-0.562	-7.00
945	278	2.965	-0.563	-6.98
966	276	2.880	-0.565	-6.95
Run B				
1034	266	2.593	-0.579	-6.77
1060	268	2.548	-0.587	-6.84
1040	268	2.597	-0.590	-6.83
1016	268	2.659	-0.574	-6.80
999	269	2.714	-0.569	-6.81
979	270	2.780	-0.567	-6.82
1005	268	2.688	-0.570	-6.79
1020	267	2.638	-0.575	-6.78
1041	267	2.585	-0.581	-6.80
1067	267	2.522	-0.589	-6.82
1060	267	2.539	-0.587	-6.82
1035	268	2.610	-0.579	-6.82
1009	268	2.677	-0.571	-6.80
986	269	2.750	-0.567	-6.80
961	272	2.853	-0.565	-6.86

thermodynamics of the cell reaction. Numerous unsuccessful attempts were made to eliminate this anomaly; these included ensuring that the cell was not subject to temperature gradients, as well as changing electrode contact materials and lead wires. None of these was effective in eliminating the anomalous behavior in an unambiguous manner. In any case, the only data shown in Fig. 2 and Tables I and II are those which did not exhibit this anomalous variation of the EMF with temperature. Thermal functions for MnP and Mn₂P were those used earlier (3); those for Mn were taken from the compilation of Hultgren *et al.* (8). There are no heat capacity nor entropy data for Mn₃P in the literature, and these were estimated. The entropy of Mn₃P was taken to be $S_{298.15}^0/R = 12.44$, which is the value (9) for Mn₃Si, and the heat capacity at high temperatures, $C_p/R = 11.42 + 5.083 \times 10^{-3}T - 1.409 \times 10^{-5}T^2$ was based on the heat capacities (10) of MnP and Mn₂P.

Table II. Cell [II]

T(K)	EMF (mV)	log K	$\Delta\phi^1/R$	$\Delta H_{298.15}^0/R$ (kJ)
Run A				
917	35.4	0.389	-0.168	-0.98
965	34.5	0.360	-0.173	-0.97
1013	35.0	0.348	-0.181	-1.00
1035	35.6	0.347	-0.189	-1.02
867	37.3	0.434	-0.161	-1.01
892	36.5	0.412	-0.165	-0.99
917	36.2	0.398	-0.168	-0.99
941	36.0	0.386	-0.170	-1.00
965	36.0	0.376	-0.173	-1.00
990	36.1	0.368	-0.175	-1.01
1035	34.1	0.332	-0.189	-0.99
1035	35.2	0.343	-0.189	-1.01
Run B				
1013	32.4	0.322	-0.181	-0.93
917	31.6	0.347	-0.168	-0.89
867	35.0	0.407	-0.161	-0.95
867	34.3	0.399	-0.161	-0.95
867	34.3	0.399	-0.161	-0.94
892	34.2	0.386	-0.165	-0.94
917	33.9	0.372	-0.168	-0.94
965	33.5	0.350	-0.173	-0.94
990	33.5	0.341	-0.175	-0.95
1013	33.6	0.334	-0.181	-0.96
1035	33.9	0.330	-0.181	-0.98
1006	33.8	0.339	-0.178	-0.96
998	33.9	0.342	-0.176	-0.96
990	33.9	0.345	-0.175	-0.96
978	34.0	0.350	-0.174	-0.96
970	34.1	0.354	-0.173	-0.96
960	34.1	0.357	-0.172	-0.95
950	34.1	0.362	-0.171	-0.95
941	34.0	0.364	-0.170	-0.95
930	34.0	0.368	-0.169	-0.95
922	34.0	0.372	-0.168	-0.94
911	34.0	0.376	-0.167	-0.94

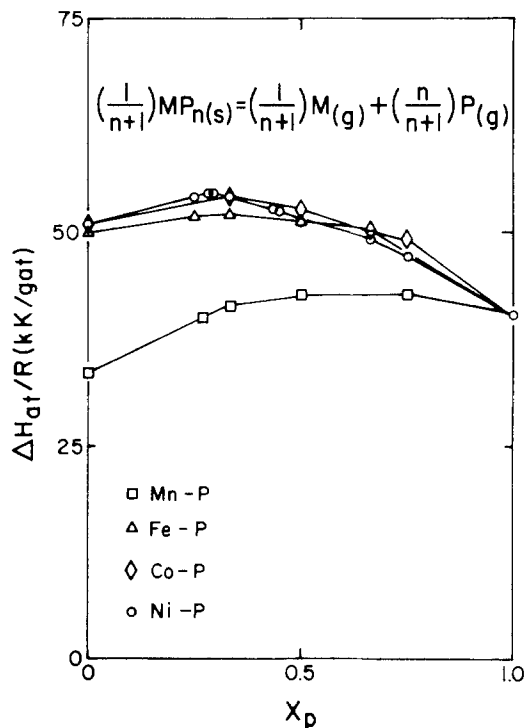


Fig. 3. Atomization enthalpies of transition metal phosphides

Primary thermodynamic data for the two cell reactions are given in Table III. The second law datum is, for each cell, a weighted average (by the number of points) of the second-law enthalpies from the two runs with each cell. For comparison, data are included which were calculated from the equation given by Baratashvili *et al.* (2) for the temperature variation of the EMF of cell [I]. Uncertainty limits are based on differences in second-law enthalpies for replicate runs, uncertainties in published and estimated heat capacities and in estimated entropies, and on scatter in experimental data. Derived stability data for the manganese phosphides from this and previous studies using third-law values are given in Table IV. Data from this laboratory using different techniques show good internal consistency within experimental uncertainty; the enthalpy of formation of MnP obtained by combustion calorimetry (1) appears to be too low. As shown in Fig. 3, the atomization enthalpy of Mn₃P (per gram atom) is such that it is barely stable with respect to Mn₂P and Mn, as had been suggested above.

Acknowledgment

The authors wish to thank Dr. Reginald Faircloth for the description of the cell assembly used as a model for the one described above. Also, thanks are due McDanel Refractory Porcelain Company for a donation of some of

Table III. Primary thermodynamic data

Cell	Reaction	$\Delta H_{298.15/R}^{\circ}$ (second law) (kK)	$\Delta H_{298.15/R}^{\circ}$ (third law) (kK)
[I]	$\text{Mn}_{(s)} + \text{MnP}_{(s)} = \text{Mn}_2\text{P}_{(s)}$	-7.2 ± 1.0	-6.9 ± 0.5^a
[II]	$\text{Mn}_{(s)} + \text{Mn}_2\text{P}_{(s)} = \text{Mn}_3\text{P}_{(s)}$	-0.91 ± 1.0	-0.97 ± 0.5^a

^aThis work.

^bBaratashvili *et al.* (2).

Table IV. Derived stability data (from third-law values)

Compound	$\Delta H_{298.15/R}^{\circ}$ (from red P) (kK)	$\Delta H_{298.15/R}^{\circ}$ (kK)	Source
MnP	-11.6		a
	-13.8 ± 1.0	87.5 ± 1.0	b, c
	-13.7 ± 1.5	87.4 ± 1.5	b, d
	-13.9 ± 1.0	87.6 ± 1.0	c, d
Mn ₂ P	-20.8 ± 1.0	128.1 ± 1.0	c
	-20.6 ± 1.5	127.9 ± 1.5	b, d
Mn ₃ P	-21.8 ± 1.0	162.7 ± 1.0	c, e

^aCombustion calorimetry (1).

^bDissociation pressures above MnP-Mn₂P (3).

^cCongruent vaporization of Mn₃P (4).

^dCell [I] (this work).

^eCell [II] (this work).

the mullite tubing. Some of the measurements were made by Scott M. Gross. This work was supported by the U.S. Department of Energy.

Manuscript submitted *ca.* Oct. 18, 1983; revised manuscript received Jan. 5, 1984.

The Foundation of the State University of New York at Binghamton assisted in meeting the publication costs of this article.

REFERENCES

- S. A. Shchukarev, M. P. Morozova, and T. A. Stol'yarova, *J. Gen. Chem. USSR (Engl. Transl.)*, **31**, 1657 (1961).
- I. B. Baratashvili, A. A. Nadiradze, I. A. Makharadze, and L. S. Shvartsman, *Dokl. Phys. Chem. (Engl. Transl.)*, **224**, 1008 (1975).
- C. E. Myers, E. D. Jung, and E. L. Patterson, *Inorg. Chem.*, **19**, 532 (1980).
- C. E. Myers, G. A. Kisacky, E. L. Patterson, and R. A. Mevorach, *This Journal*, **129**, 2343 (1982).
- S. Rundqvist, *Acta Chem. Scand.*, **16**, 287, 992 (1962).
- R. Faircloth, U.K. Atomic Energy Establishment, Harwell, Personal communication (1970).
- C. E. Myers, *High Temp. Sci.*, **6**, 309 (1974).
- R. Hultgren, P. D. Desai, D. T. Hawkins, M. Gleiser, K. K. Kelley, and D. D. Wagman, "Selected Values of the Thermodynamic Properties of the Elements," pp. 301-308, American Society for Metals, Metals Park, OH (1973).
- S. M. Letun, P. V. Gel'd, and N. N. Serebrennikov, *Russ. J. Inorg. Chem. (Engl. Transl.)*, **10**, 683 (1965).
- I. A. Makharadze, I. B. Baratashvili, D. Sh. Tsagarishvili, and G. G. Gvelesiani, *Inorg. Mater. (Engl. Transl.)*, **11**, 515 (1975).

Reaction of Cobalt in SO₂ Atmospheres at Elevated Temperatures

Nathan S. Jacobson

National Aeronautics and Space Administration, Lewis Research Center, Cleveland, Ohio 44135

Wayne L. Worrell*

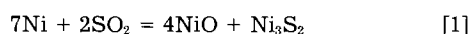
University of Pennsylvania, Department of Materials Science and Engineering, Philadelphia, Pennsylvania 19104

ABSTRACT

The reaction rate of cobalt in SO₂-argon environments has been measured at 650°, 700°, 750°, and 800°C. Product scales consist primarily of an interconnected sulfide phase in an oxide matrix. At all temperatures, the rapid diffusion of cobalt outward through the interconnected sulfide appears to be important. At 650°C, the reaction rate slows dramatically after 5 min due to a change in the distribution of these sulfides. At 700° and 750°C, the reaction is primarily diffusion controlled; values of $D_{Co}(CoS)$ calculated from this work show favorable agreement with values of $D_{Co}(CoS)$ calculated from previous sulfidation work. At 800°C, a surface step becomes rate limiting.

Metals and alloys may be exposed to complex gas environments at elevated temperatures in a variety of industrial applications. Often, combustion of fossil fuels will lead to sulfur oxides which may have deleterious effects on the metal or alloy in question. Nickel and cobalt are important base metals used in turbine components. However, both these metals corrode dramatically faster in SO₂ than in O₂. For nickel at 600°C, the ratio of rates is about 10⁶; for cobalt at 750°C this ratio is about 10⁸. In this laboratory, extensive work has been done on the reaction of nickel with SO₂ and equilibrated SO₂-O₂ mixtures (1, 2). In order to determine if some of the same principles hold for the reaction of cobalt with SO₂, similar experiments were conducted for this metal.

The results for nickel corrosion in SO₂-argon mixtures can be summarized as follows. A porous oxide layer forms during the initial stages of reaction and SO₂ diffuses down the pores to the oxide/metal interface, where the oxygen activity is low enough so that nickel sulfide is thermodynamically stable. Nickel sulfide then forms as a thin layer between the metal and oxide and also grows into the pores of the oxide. A network of interconnected sulfides forms in the oxide matrix and acts as rapid diffusion paths for nickel to the scale/gas interface. These rapid diffusion paths account for the faster reaction rates in SO₂ than in O₂. At the scale/gas interface, the following reaction occurs



Scale growth is initially linear, indicating that a surface step is rate controlling. However, during the later stages of reaction, scale growth obeys an apparent parabolic rate law, since diffusion of nickel outward is primarily rate controlling.

Other investigators have reported that cobalt reacts with SO₂ similarly to nickel (3-10). However, there are still many questions about the details of the reaction mechanism. Among the earliest investigations is that of Konev *et al.* (4), who exposed nickel and cobalt to CO₂ and SO₂ mixtures. For nickel, an outer layer of NiO and an inner layer of Ni₃S₂ were detected. However, for cobalt only CoO was detected. Alcock *et al.* (5) exposed cobalt at 688°C to 2SO₂:1 O₂ streams for 2h. They observed the metal with a thin layer of CoS, followed by a thick layer of CoO, followed by a thin layer of CoSO₄. More recently, Singh and Birks (6) have studied cobalt corrosion in SO₂-argon mixtures from 500° to 900°C. They observed a thin sulfide layer (Co₉S₈) adjacent to the metal followed by a mixed oxide-sulfide layer (CoO-Co₉S₈), and they proposed that the inner sulfide layer forms by penetration of SO₂ into a porous oxide layer, a mechanism similar to that observed for nickel. Holthe and Kofstad (7) have also studied cobalt corrosion in SO₂ from 800° to 1000°C at 10, 100, and 760 torr. They also see duplex scales of oxides

and sulfides. Although tests for sulfate are inconclusive, they suggest that a very thin layer of sulfate may form on the oxide surface. Gesmundo and DeAsmundis (8) have studied cobalt corrosion in 1 atm SO₂ from 450° to 1200°C. At 600° and 700°C, they report approximate parabolic kinetics with increasing deviations at higher temperatures. Finally, Gillot and Garnier (9) have examined cobalt corrosion in SO₂ from 450° to 1200°C at various SO₂ pressures. Generally, at low temperatures they see parabolic kinetics and at higher temperatures linear kinetics. In summary, previous investigators agree that the reaction of cobalt and SO₂ leads primarily to cobalt sulfide and cobalt oxide. However, the kinetics of the reaction are still not clear.

In this work, measurements were taken from 650° to 800°C, below the cobalt-sulfur eutectic. Particular attention was paid to the time dependence of scale growth in order to determine which step is rate limiting and to understand the mechanism of this reaction.

Experimental

High purity (99.999% pure) cobalt sheet was obtained from Johnson Matthey Chemicals, Limited. Metallic impurities detected were Si at 3 ppm and Al, Ca, Cu, Fe, Mg, and Ag (each) < 1 ppm. This sheet was cut into rectangular specimens roughly 15 × 10 × 1 mm. All samples were ground to 600 grit on SiC papers. Most of the samples were further polished to 0.05 μm on alumina wheels. This final polishing step had no major effect on the kinetics of the reaction or morphology of the product layer. However, 0.05 μm polishing did give better reproducibility between runs, particularly at the lower temperatures. After polishing, sample dimensions were measured, and the sample was cleaned in xylenes and acetone.

A diagram of the experimental apparatus is shown in Fig. 1. Weight gains were measured with a Sartorius Model 4104 balance, which had an accuracy of ±0.06 mg/cm² in this system. The output of the balance was connected to a microprocessor with a crystal controlled clock which was set to transmit weight gains to a printer at 1 min intervals. The sample was heated by a Hoskins alloy wound furnace, controlled to ±1°C by an ECS Model 6823 controller. This furnace was mounted on tracks for ease in loading and removing the sample. Sulfur dioxide-argon gas mixtures enter from the bottom of the quartz reaction tube. Note the presence of a porous alumina ceramic directly below the sample to bring the temperature of the reaction gas up to that of the sample. In order to prevent the hot sulfur dioxide from entering the balance mechanism, a counterstream of argon was passed through the top of the balance. All gases were dried over Drierite; argon was also deoxygenated over BASF copper catalyst (150°-200°C) or titanium sponge (700°C). Flow rates were controlled and monitored with Tylan Model FC-260 mass flow controllers.

*Electrochemical Society Active Member.
Key words: cobalt, corrosion, sulfur dioxide.

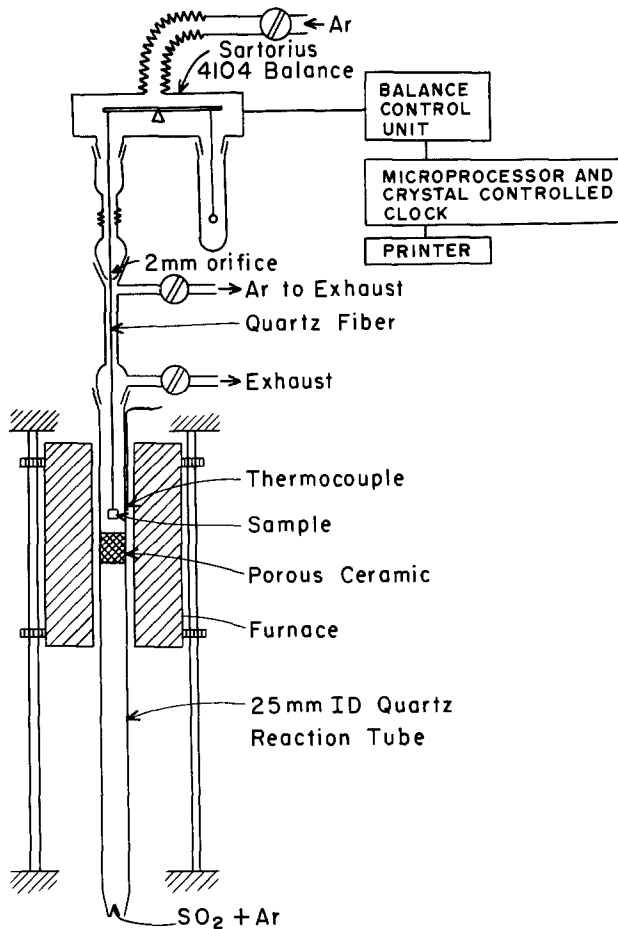


Fig. 1. Schematic of experimental apparatus

One concern with this type of apparatus is the possibility of forming a thin oxide layer during specimen loading and thermal equilibration. In order to avoid this, the following procedure was employed. With the furnace at room temperature, the sample was loaded into the reaction tube. Next, the system was evacuated to better than 0.02 torr and backfilled with a 5% H₂/Ar mixture. This mixture was passed over the sample during furnace

heat-up. After about 1/2h, the furnace was slid over the sample and allowed to come to thermal equilibrium for about 2h. Then the flow of H₂/Ar was stopped and the system flushed with gettered argon for several minutes. After this, the flow of argon was stopped and the SO₂-argon mixture admitted to begin a run.

After a run, the furnace was lowered and the specimen rapidly cooled. The reaction gases were stopped and replaced with a stream of gettered argon. When the furnace had cooled to room temperature, the sample was removed from the reaction tube. Phases present were determined with x-ray diffraction and scale morphology examined with a scanning electron microscope. In order to examine scale cross sections, a ~1 mm thick layer of copper was electroplated on the sample from a copper sulfate solution. The plated sample was mounted and polished to 1 μm with diamond paste. Samples had to be very gently polished to avoid separation at the scale/metal interface.

Results

Figures 2 through 5 show kinetic results for 650°, 700°, 750°, and 800°C. Six to eight runs were performed at each temperature; the rate constants and final weight gains agreed to ±10%. Flow rates were chosen so that gas-phase diffusion was not rate limiting (11). For each temperature, experiments were done at linear flow rates of 40.7 and 61.1 cm/min at STP. These had little influence on the reaction rates.

The three lower temperature reactions exhibit parabolic regions of different duration. At 650°C, the sample reacts rapidly for the first 5 min and then reacts according to a slow parabolic rate for the next 2h. At 700° and 750°C, the sample follows a parabolic rate from the beginning of the reaction, with rate constants of 2.91 ± 0.31 and 7.18 ± 0.44 mg²/cm⁴-min, respectively. This is shown in Fig. 4. Note that after 30 min at 700°C and 60 min at 750°C, the parabolic rates tend to decrease. At 800°C, the sample reacts rapidly according to a linear rate law (K_L = 1.2 ± 0.1 mg/cm²-min) for about 30 min. After this, the sample reacts quite slowly.

All four temperatures produced the same product phases: CoO-Co₉S₈-CoS. Some investigators have reported only CoO and Co₉S₈ (6, 8, 9). It is possible that in their cases CoS decomposed on cooling, since it is unstable below 460°C. Samples run at each temperature were checked for sulfate with x-ray diffraction and a method based on the higher solubility of CoSO₄ in water than cobalt sulfides and oxides (12). The samples were placed in

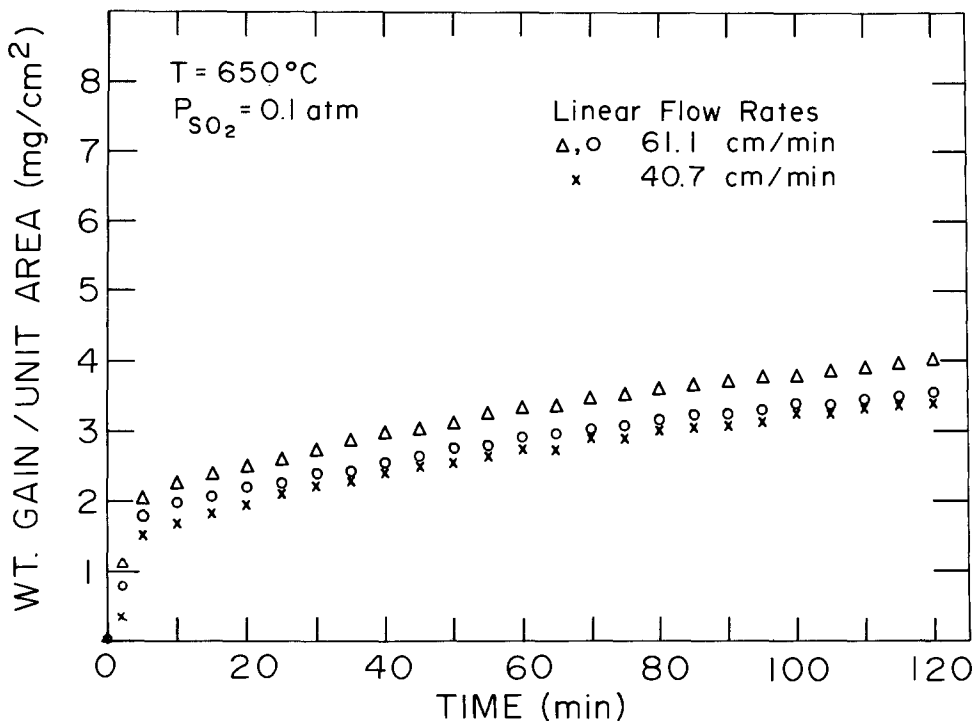


Fig. 2. Reaction of cobalt with SO₂ at 650°C.

Fig. 3. Reaction of cobalt with SO_2 at 700° and 750°C.

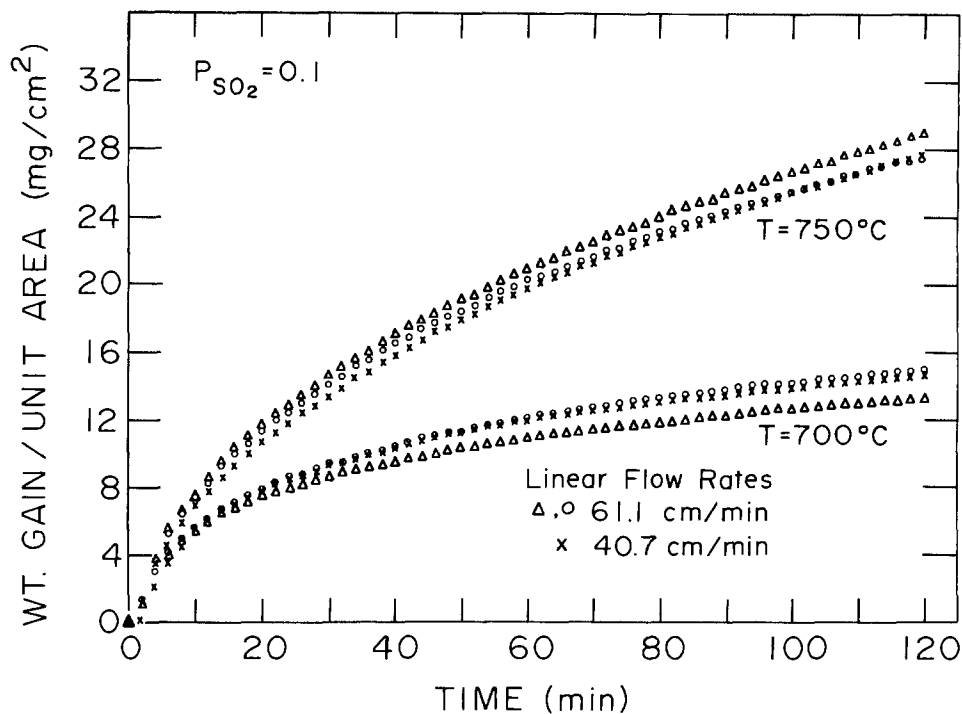
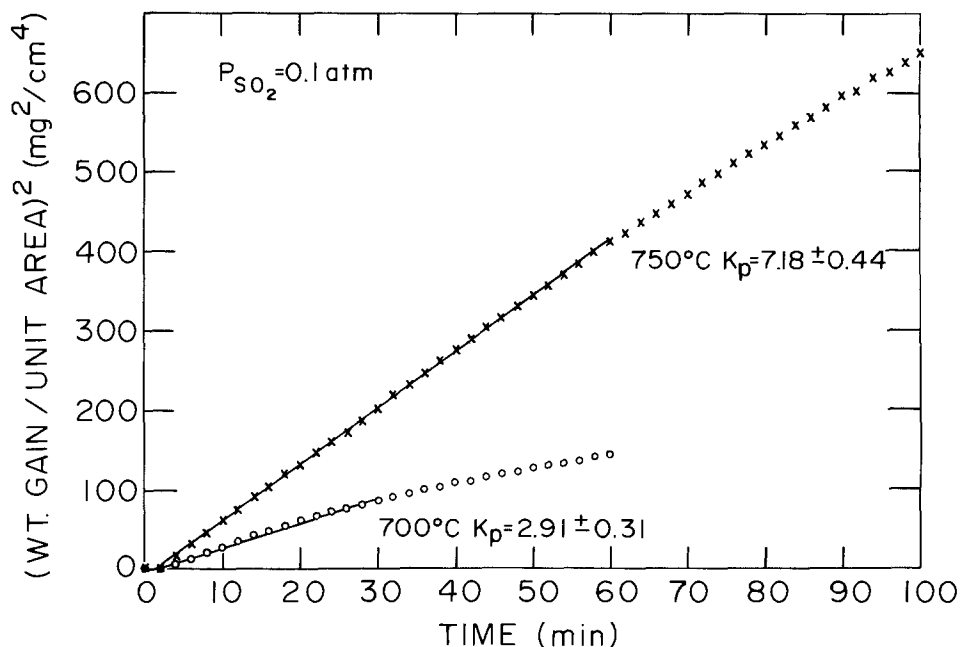


Fig. 4. Parabolic plot of Fig. 3



5 ml distilled water for several minutes and the water was checked for cobalt cations with an atomic absorption spectrometer. The concentration of cobalt cations for all samples was less than 1 ppm, which is the limit of resolution of the instrument. This indicates that if a sulfide layer is present, it is less than 100Å thick.

The morphology of the reaction product varied with temperature. The morphology of the reaction product formed at 650°C is shown in Fig. 6-10. The inner scale consisted of a fine distribution of sulfide in oxide matrix (Fig. 6 and 8). This inner scale grew during the first few minutes of reaction. The outer scale consisted of larger sulfide regions in the oxide matrix, which is also shown in Fig. 8. There is no clear evidence of an inner pure sulfide layer adjacent to the metal. However, the sulfide layer may be very thin or lost due to problems with scale/metal separation at this temperature.

At 700°, 750°, and 800°C, a morphology similar to that for nickel at 600°C is observed. There is a thin sulfide band adjacent to the metal, followed by a duplex sulfide-oxide layer. This morphology develops with the first few min-

utes of reaction. Figure 11 shows a cross section of a sample run at 750°C for 2h. The darker areas are the sulfide and the gray area is the oxide matrix. The sample consists of a ~1 μm thick sulfide layer adjacent to the metal followed by an oxide matrix with a fairly even distribution of sulfide. This sulfide band and sulfide distribution were evident in samples run at the three higher temperatures. Four point resistivity measurements gave very low values (~0.5 Ω-cm), indicating that the sulfides are interconnected. Sulfides have a higher electrical conductivity than oxides and therefore an interconnected sulfide structure should give these low resistivity values.

Discussion

Figure 12 shows the cobalt stability diagram as a function of oxygen and sulfur potentials at 650°C (13, 14). Also shown is a line indicating the sulfur and oxygen potentials due to SO_2 dissociation. It is likely that the oxygen content of the system is 1 ppm or higher, due to the manufacturer's reported oxygen impurities in the reaction gas. Figure 12 shows that under 0.1 atm SO_2 and 1

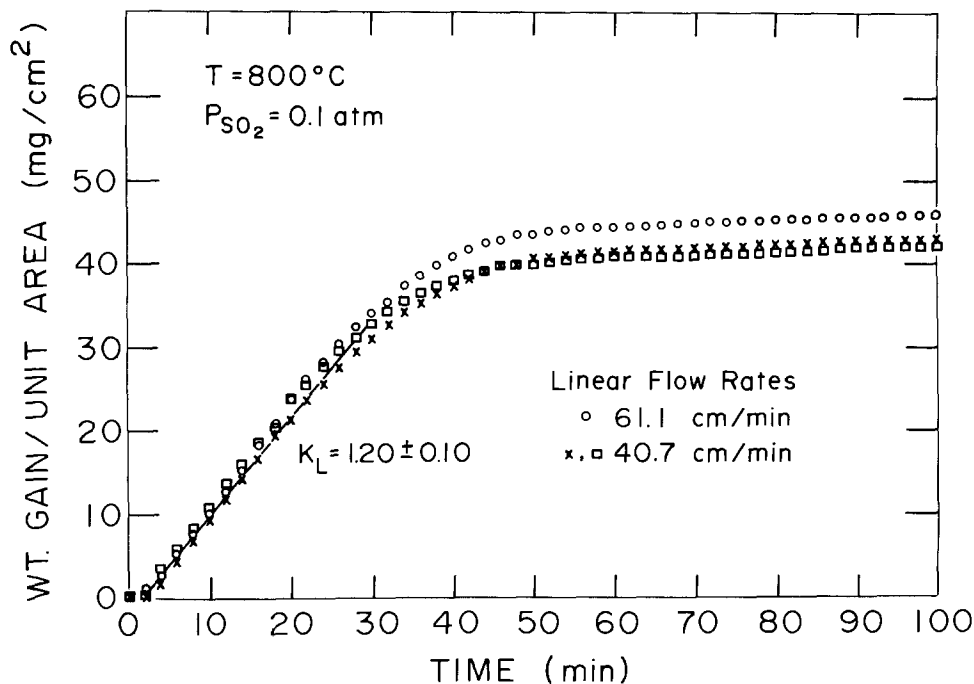


Fig. 5. Reaction of cobalt with SO₂ at 800°C.

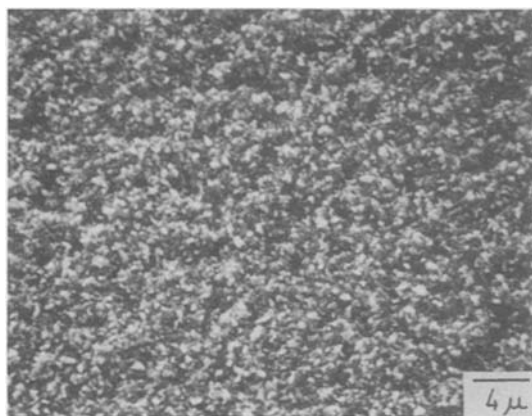


Fig. 6. Surface of a sample reacted for 3 min in 10% SO₂-argon at 650°C. The light areas are the sulfide, the dark areas are the oxide.

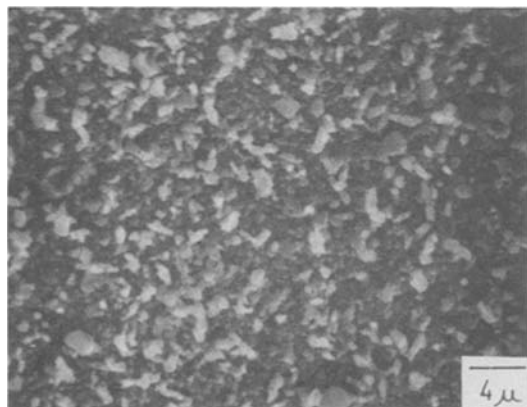


Fig. 7. Surface of a sample reacted for 5 min in 10% SO₂-argon at 650°C. There are less sulfides and those that remain have become larger.

ppm O₂, cobalt sulfate is the stable phase. This is also true at 700°C. A similar situation exists for nickel at 600°C (1, 2). At 750° and 800°C, cobalt oxide is stable under 0.1 atm SO₂ and 1 ppm O₂. As indicated in Fig. 12, cobalt sulfide is thermodynamically stable at the oxygen potential that must exist near the scale/metal interface.

The accepted theory of formation of an inner sulfide layer (1, 2, 6) is based on the initial formation of a porous

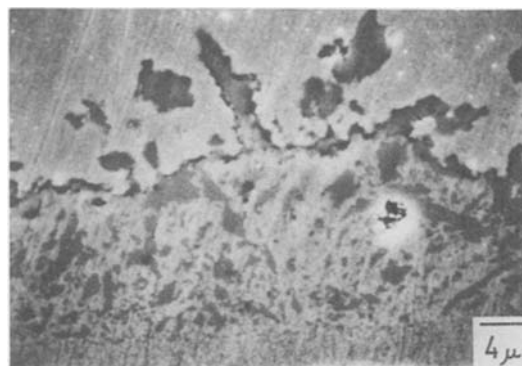


Fig. 8. Cross section of a sample reacted for 2h at 650°C for 2h. Note the fine distribution of sulfide in the oxide matrix at the bottom. This was closest to the metal.

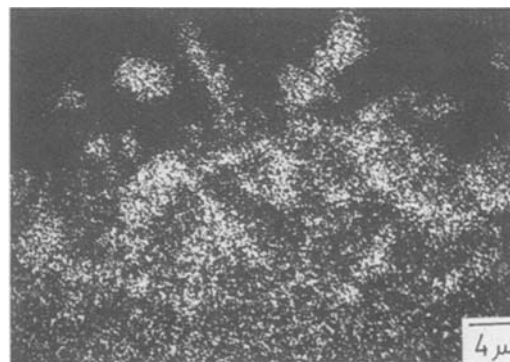


Fig. 9. Sulfur map of Fig. 8. Note the sulfide flames projecting into the gas phase.

metal oxide. SO₂ penetrates this oxide through the micropores and reacts to form sulfide at the oxide/metal interface where the oxygen potential is low. This process very likely occurs in the reaction of cobalt and SO₂, since the inner sulfide layer forms in the first few minutes of reaction. However, it is still not clear how sulfide forms at or near the scale/gas interface. Some investigators have proposed that sulfide forms via a sulfate intermediate, which exists at the scale/gas interface (15). However, sulfate is stable only at the lower temperatures (650° and 700°C) and a sulfate layer has not been detected. Figures 8

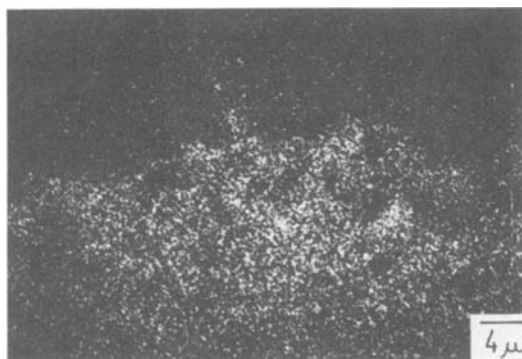


Fig. 10. Oxygen map of Fig. 8

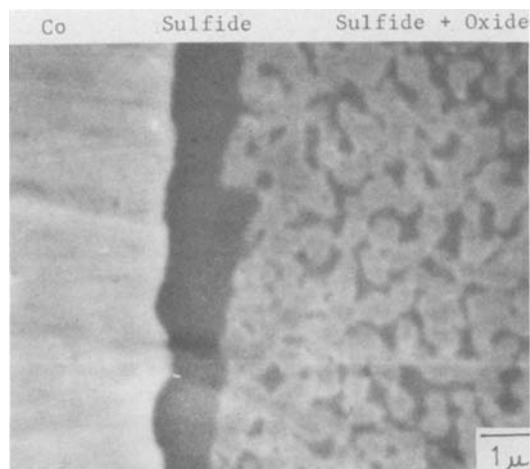


Fig. 11. Cross section of a sample reacted for 2h at 750°C. The sulfide is the darker area.

to 10 show a cross section of a sample reacted at 650°C and the large sulfide flames that project into the gas phase. Thus, one must conclude that the scale does not equilibrate with the gas.

Before discussing the kinetics of the reaction of cobalt and SO_2 , it is necessary to examine previous work on cobalt sulfidation (16-18). When cobalt reacts with 1 atm sulfur vapor, an inner Co_9S_8 layer forms and an outer CoS layer forms. Inert markers are observed between the two

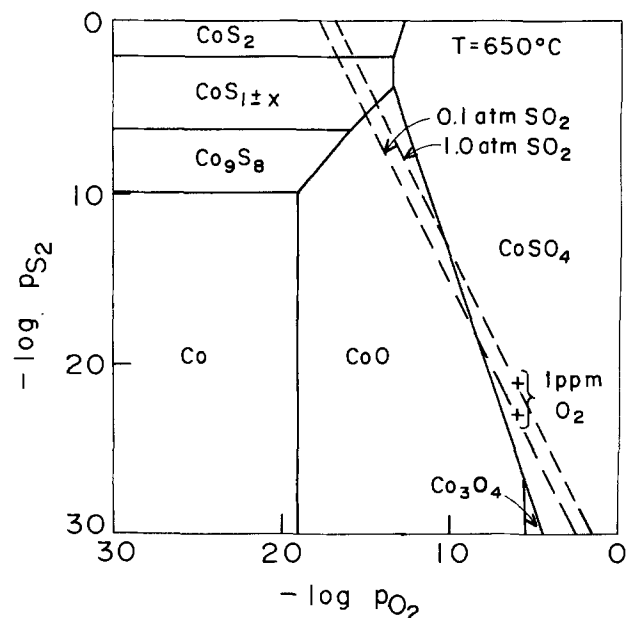


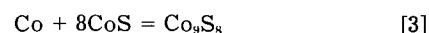
Fig. 12. Stability diagram of cobalt in a sulfur-oxygen atmosphere at 650°C.

layers, suggesting that sulfur moves inward to form Co_9S_8 and cobalt moves outward to form CoS (16). From 500° to 750°C, cobalt reacts with sulfur vapor according to a parabolic rate law (17). It has been suggested that the diffusion of cobalt outward is rate limiting (18). Based on this, the diffusivity of cobalt in CoS can be calculated.

In a previous paper (1), it was shown that the parabolic rate constant is related to the metal ion diffusivity by the following expression

$$k_p = -2 D_{\text{Co}} c_{\text{Co}} \frac{\alpha f}{\beta \gamma} \Delta \ln a_{\text{Co}} \quad [2]$$

Here k_p is the parabolic rate constant ($\text{g}\cdot\text{cm}^{-2}\cdot\text{s}^{-1}$), D_{Co} is the diffusion coefficient of cobalt in CoS ($\text{cm}^2\cdot\text{s}^{-1}$), c_{Co} is the concentration of cobalt in CoS ($\text{g}\cdot\text{cm}^{-3}$), f is the volume fraction of CoS ($f = 1$ for a single phase), and β and γ are conversion factors which relate the emerging flux of cobalt to weight gain. α is a factor based on the distribution of sulfide. For a single phase or an evenly distributed phase in an oxide matrix, $\alpha = 1$; for isolated islands of sulfide in an oxide matrix, $\alpha = 0$; and for an uneven distribution of sulfide in an oxide matrix, $1 > \alpha > 0$. Expression [2] can be applied to the data of Mrowec and Werber (17) in order to calculate $D_{\text{Co}}(\text{CoS})$. Using the density of CoS (19): $\beta = 1.84$, $\gamma = 0.52 \text{ cm}^3\cdot\text{g}^{-1}$, and $c_{\text{Co}} = 3.53 \text{ g}\cdot\text{cm}^{-3}$. The cobalt activity difference can be calculated from the activity at the $\text{Co}_9\text{S}_8/\text{CoS}$ interface, which is determined by

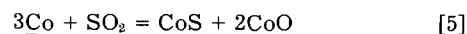


and the activity at the scale/gas interface, which is determined by



Table I lists the values of $D_{\text{Co}}(\text{CoS})$ at each of the temperatures used in this study. Also shown are $D_{\text{Co}}(\text{CoO})$ in 1 atm oxygen (20) which are several orders of magnitude lower than $D_{\text{Co}}(\text{CoS})$. The values of $D_{\text{Co}}(\text{CoO})$ are for diffusion in a single crystal; however, they are within 10% of those calculated from oxidation of polycrystalline specimens (21). Given this kinetic background, the experimental results for the reaction of cobalt in sulfidizing-oxidizing environments can be discussed.

Consider first the reaction of cobalt with SO_2 at 700° and 750°C. As mentioned, conductivity measurements indicate the sulfides are interconnected and fairly evenly distributed (Fig. 11 and 13) in the oxide matrix. Thus, Eq. [2] can be applied and the diffusivity of cobalt in CoS can be calculated from the measured parabolic rate constants. These diffusivities can then be compared to those calculated from the data of Mrowec and Werber (17). To apply Eq. [2] to the data presented here: $\alpha = 1$, $\beta = 2.76$, and $\gamma = 0.62 \text{ cm}^3\cdot\text{g}^{-1}$. The volume fraction of sulfide was estimated by placing a grid over Fig. 13 and determining what fraction of the area was occupied by sulfide. This gave a value of 0.40, which was in agreement with the value of 0.42 obtained from the stoichiometry of the reaction



The change in cobalt activity can be estimated by the difference between the cobalt activity at the $\text{Co}_9\text{S}_8/\text{CoS}$ interface and the cobalt activity at the gas/scale interface,

Table I. Diffusivities of cobalt in CoO and CoS

Temperature °C	$D_{\text{Co}}(\text{CoO})$ Ref. (20)	$D_{\text{Co}}(\text{CoS})$	
		Calculated from Ref. (17)	This work
650	1.45×10^{-11}	3.9×10^{-9}	-----
700	3.82×10^{-11}	9.8×10^{-9}	2.2×10^{-8}
750	9.15×10^{-11}	2.7×10^{-8}	4.2×10^{-8}
800	2.02×10^{-10}	4.6×10^{-8}	-----

which is set by Eq. [5]. The values of $D_{Co}(CoS)$ calculated from the reaction of cobalt and SO_2 are listed in Table I. The agreement with the values calculated from Mrowec and Werber's sulfidation data is reasonable, indicating that under these conditions the diffusion of cobalt outward through the interconnected sulfides is primarily rate limiting.

It is important to recognize that the reaction cannot be entirely diffusion controlled. This is because the scale does not equilibrate with the gas, *i.e.*, sulfide is observed at the scale surface and this means a substantial change in sulfur activity at the gas/scale interface. The reaction probably undergoes mixed control, with diffusion being the major contributor to the rate and a surface step being the minor contributor. This explanation also accounts for some of the differences in the diffusivities calculated from sulfidation and those calculated from sulfidation-oxidation.

As mentioned previously, both the 700° and 750°C parabolic plots (Fig. 4) show slower parabolic rates after 30 and 60 min, respectively. This is very likely due to a changing sulfide distribution in the oxide matrix as shown in Fig. 13 and 14. Figure 13 shows a portion of the scale which grew during the first hour at 750°C. Note the fairly even distribution of sulfide, indicating $\alpha = 1$. Figure 14 shows a portion of the scale which grew after 1h; the sulfide is now unevenly distributed, containing sulfide regions connected by constricted sulfide channels. Now $\alpha < 1$ which results in a slower parabolic rate.

This change in reaction rates due to a change in sulfide distribution is also evident at 650°C. Figure 2 show the reaction is quite rapid for the first 5 min and then slows down for the next 2h. During the first 3 min of reaction, a microstructure develops with many sulfides poking out of the oxide matrix into the gas phase (Fig. 6). These many available transport paths account for the rapid rate observed at the start of the reaction. After 5 min of reaction, the scale surface contains less sulfides and those

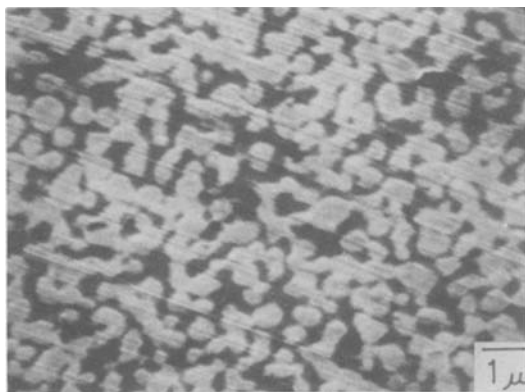


Fig. 13. Inner portion of duplex region of a sample reacted at 750°C for 2h. Note the even sulfide distribution (darker region).

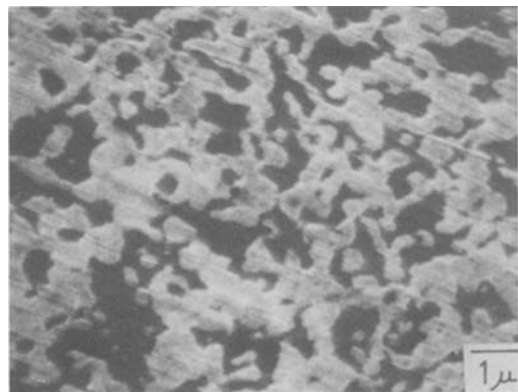


Fig. 14. Outer portion of duplex region of a sample reacted at 750°C for 2h. Note the uneven sulfide distribution.

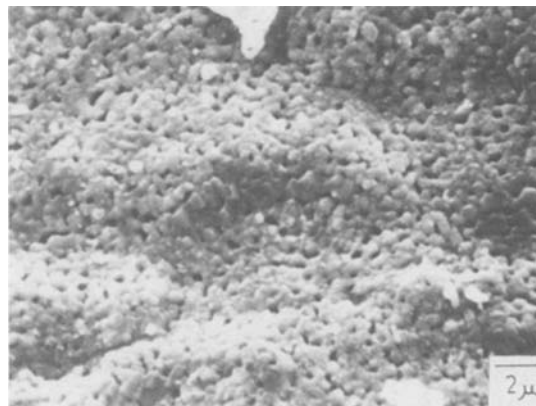


Fig. 15. Underside of a scale formed in 2h at 800°C. This is an oxide matrix and the voids are areas where there was once sulfide.

that remain grow larger (Fig. 7). A cross section (Fig. 8) suggests that the larger regions of sulfide are connected by constricted areas of sulfide. These two factors, the smaller amount of sulfide and the constrictions in the interconnected network, may limit cobalt ion diffusion outward and result in a slower rate.

At 800°C, the reaction initially shows a rapid linear rate and then slows dramatically after about 40 min. The linear rates suggest that cobalt diffusion outward is so rapid that an interfacial reaction, presumably SO_2 dissociation, becomes rate limiting. The latter reaction stage is more difficult to interpret. When a sample which had reacted for 2h at 800°C was cooled, the scale separated at the sulfide layer-duplex layer interface. Figure 15 shows the portion of the duplex layer which was adjacent to the sulfide layer. Note there are voids where there were once sulfides, only the oxide matrix is visible. It is possible that void formation causes a decrease in scale/metal contact area, which slows the reaction.

Conclusions

In the reaction of cobalt with SO_2 at 650°-800°C, the rapid diffusion of cobalt outward through an interconnected sulfide phase is important. The different kinetic behavior observed in this temperature range is due both to the increasing diffusivity of cobalt and differing morphologies of the product phase. At 650°C, the rates are initially rapid due to many available sulfide channels. After about 5 min, the rates decrease due to a decreased number of sulfide channels. At 700° and 750°C, diffusion of cobalt through these sulfides is primarily rate limiting and the calculated $D_{Co}(CoS)$ calculated compare favorably with those calculated from a previous sulfidation study. At 800°C, diffusion through the sulfides is so fast that an interfacial step becomes rate limiting.

Acknowledgment

This work was partially supported by the NSF Materials Research Program under Grant No. DMR-9923647 at the University of Pennsylvania.

Manuscript submitted Aug. 4, 1983; revised manuscript received Jan. 9, 1984. This was Paper 427 presented at the Washington, DC, Meeting of the Society, Oct. 9-14, 1983.

National Aeronautics and Space Administration—Lewis Research Center assisted in meeting the publication costs of this article.

REFERENCES

1. K. L. Luthra and W. L. Worrell, *Metall. Trans.*, **9A**, 1055 (1978).
2. K. L. Luthra and W. L. Worrell, *ibid.*, **10A**, 621 (1979).
3. G. Pannetier and L. Davignon, *Bull. Soc. Chim., France*, **7**, 1509 (1964).
4. V. N. Konev, A. M. Borgantsoev, and N. V. Suntsoev, *Prot. Met. (Engl. Transl.)*, **5**, 590 (1969).
5. C. B. Alcock, M. G. Hocking, and S. Zador, *Corros. Sci.*, **9**, 111 (1969).
6. P. Singh and N. Birks, *Oxid. Met.*, **12**, 23 (1978).
7. K. Holthe and P. Kofstad, *Corros. Sci.*, **20**, 919 (1980).

8. F. Gesmundo and C. DeAsmundis, in "Behavior of High Temperature Alloys in Aggressive Environments," pp. 435-447, Metals Society, London (1980).
9. B. Gillot and D. Garnier, *Ann. Chim. Paris*, **5**, 483 (1980).
10. H. Nakai, E. Ataka, and T. Saegusa, *J. Jpn. Inst. Met.*, **44**, 207 (1980).
11. G. H. Geiger and D. R. Poirier, "Transport Phenomena in Metallurgy," p. 532, Addison-Wesley Publishing Co., Reading, MA (1973).
12. A. M. Comey and D. A. Hahn, "A Dictionary of Chemical Solubilities," MacMillan Co., New York (1921).
13. C. B. Alcock, *Int. J. Appl. Radiat. Isot.*, **3**, 139 (1958).
14. "JANAF Thermochemical Tables," 2nd ed., D. R. Stull and H. Prophet, Editors, National Bureau of Standards, Washington, DC (1971).
15. P. J. Ficalora, *Oxid. Met.*, **18**, 19 (1982).
16. V. I. Arkharov and E. B. Blankova, *Phys. Met. Metallogr. (Engl. Transl.)*, **8**, 452 (1959).
17. S. Mrowec and T. Werber, *ibid.*, **14**, 114 (1962).
18. A. Davin, *Cobalt*, **30**, 19 (1966).
19. C. D. Hodgman, "Handbook of Chemistry and Physics," 39th ed., Chemical Rubber Publishing Co., Cleveland, OH (1957).
20. R. E. Carter and F. D. Richardson, *Trans. AIME*, **200**, 1244 (1954); **203**, 336 (1955).
21. P. Kofstad, "Nonstoichiometry, Diffusion, and Electrical Conductivity in Oxides," p. 244, Wiley, New York (1972).

RF Recrystallization of Polycrystalline Silicon on Fused Silica for MOSFET Devices

Y. Kobayashi, A. Fukami, and T. Suzuki

Hitachi, Limited, Hitachi Research Laboratory, Hitachi, Ibaraki 319-12, Japan

ABSTRACT

A new zone melting recrystallization method that uses an RF-heated carbon susceptor in fabrication of silicon on insulator (SOI) structures has been developed. A fused silica substrate, on which a 0.5-1.0 μm thick polycrystalline silicon film had been deposited, was encapsulated with a 1.2 μm thick CVD- SiO_2 layer. This was moved across the carbon susceptor, which had a narrow high temperature zone. The continuous silicon films that were recrystallized had grains several tenths to a few millimeters wide, a few centimeters long, and a film orientation of (100). The electron mobility of MOSFET's fabricated on the films was about 700-1000 cm^2/Vs , which was higher than that of (100) orientated bulk single-crystal silicon. However, as some cracks occurred in the film, it was formed as islands and then the islands were recrystallized. This recrystallized silicon was a single crystal with an orientation of (111) and showed no cracks. The electron field effect mobility of the islands was about 300-600 cm^2/Vs , which was smaller than that of the recrystallized continuous film because of the (111) orientation. In order to obtain silicon without cracks and with an orientation of (100), a method that connected the polycrystalline silicon islands with narrow strips was proposed based on a thermal connection of silicon.

Silicon on insulator (SOI) structures offer many advantages for display devices such as active liquid crystal displays, for high speed integrated circuits and for three-dimensional circuits. The structures are produced by melt regrowth methods using laser beams (1, 2), electron beams (3-5), and incoherent energy sources such as strip carbon heaters (6-8) and arc lamps (9, 10). The laser and electron beam recrystallization methods have the potential to produce three-dimensional circuits, but have a small throughput. On the other hand, zone melting recrystallization using incoherent energy sources is not suitable for three-dimensional circuits because the entire wafer must be heated. However, a high quality silicon layer can be obtained, without seeding, as can high throughput (6-11). Therefore, this method is suitable for manufacturing very high speed circuits and display devices.

In the zone melting recrystallization method, temperature control in the melted silicon region and its proper distribution are necessary to prevent agglomeration of the melted silicon and to obtain a good surface uniformity.

The authors have developed a novel zone melting regrowth method using an RF-heated carbon susceptor, in which temperature and shape of the melted zone can be easily observed and controlled (11). This article describes the method and the results obtained while investigating the quality of the recrystallized silicon films produced.

RF-Heated Zone Melting Regrowth Method (RF-ZMR Method)

Figure 1 shows the recrystallization method. The upper figure (a) is a cross-sectional view of the apparatus, and the lower figure (b) is a schematic blowup of the wafer and carbon susceptor area. A 0.5-1.0 μm thick poly-

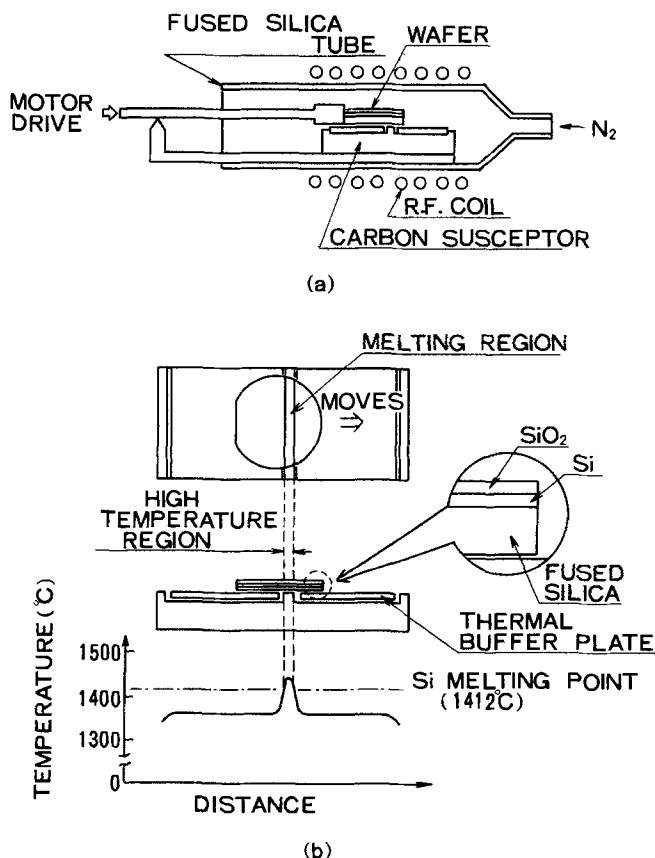


Fig. 1. (a, top) Schematic diagram and (b, bottom) illustration of the zone melting recrystallization method.

crystalline silicon film was deposited by decomposition of monosilane (SiH_4) on an optically polished, fused silica substrate. The silicon surface was then covered with a 1.2 μm thick layer of silicon dioxide by decomposition of tetraethoxysilane ($\text{Si}(\text{OC}_2\text{H}_5)_4$) at 760°C. This wafer was moved across the carbon susceptor surface (speed: 0.1-2 mm/s), which was RF-heated, and had the temperature distribution reproduced in Fig. 1b. In the high temperature region (1 or 2 mm wide), where the polycrystalline silicon was melted, a higher heat flow from the RF-heated carbon susceptor came into contact with samples. In the low temperature regions, the heat flow was partially shielded by fused silica or carbon thermal buffer plates. The temperature of the high temperature region, measured using an optical pyrometer, was about 1450°C; 100°C higher than that of other regions. Melting and regrowth took place in a nitrogen atmosphere which was evaporated from liquid nitrogen and was not passed through a purifier. The silicon layer was melted in the high temperature region and then, after moving on, was solidified to form a regrown layer.

Figure 2 is a photograph, taken during recrystallization, of the melted silicon. The vertical dark bands were shadows produced by the work coil, while the large circular region was the wafer (diam = 50 mm). The central light-colored strip was the high temperature region, while the slightly darker narrow ellipse inside it was the melted silicon region. The area of the melted silicon was probably darker than that of the surrounding unmelted silicon due to the lower emissivity of melted silicon as compared to unmelted silicon. The photograph demonstrated that the melted silicon could be easily observed and that recrystallization conditions could be easily controlled.

Characteristics of the Recrystallized Silicon

Figure 3 shows (a) an optical micrograph of an etched silicon surface after recrystallization and (b) its schematic. The etchant composition was $\text{HF}:\text{HNO}_3:\text{CH}_3\text{COOH} = 1:50:50$ (6). There were many elongated subgrains and cracks. The sizes of the subgrains were several tens of micrometers wide and several hundreds of micrometers long. All cracks were parallel or perpendicular. These crack patterns implied two things: (i) that the orientation of the recrystallized silicon was (100), because the direction of the cracks was $\langle 110 \rangle$ for single-crystal silicon; and (ii) that the subgrain boundaries were small angle grain boundaries, because the cracks were straight even when they crossed the subgrain boundaries. These points were studied in detail using transmission electron microscopy (TEM).

Figure 4 is a TEM of the recrystallized silicon. Three diffraction patterns which correspond to the indicated region are also shown. Dislocations and subgrain boundaries could be observed. The diffraction patterns showed that orientations of the three regions were (100). All the

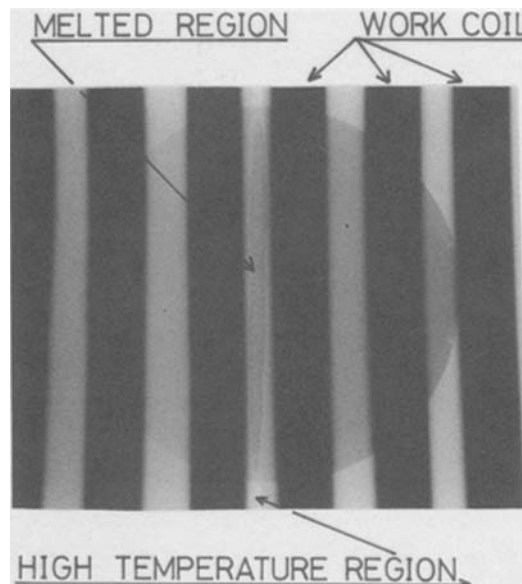


Fig. 2. Photograph of the melted silicon region during recrystallization obtained by using an infrared transmitting glass filter.

patterns had the same rotation angle within one degree or less, verifying the conclusion that the subgrain boundaries were small angle grain boundaries.

Figure 5 is a magnified photograph of one diffraction pattern. The Kikuchi lines and bands could be clearly observed, indicating that the crystalline quality of the recrystallized silicon was high. Results of the TEM observations corresponded to those observed for the etched silicon surface.

Next, the subgrain boundary was studied using TEM. A subgrain boundary has been assumed to consist of an array of dislocations (8). Figure 6 is a 1000 keV TEM photograph of a subgrain boundary. Individual dislocations could be seen on the subgrain boundary; that is, the boundaries consisted of discrete dislocations. When the deviation of the orientation was estimated from the distance between these dislocations, a value of about 0.6 deg was obtained.

As shown in Fig. 7, an Al-gate n-channel MOSFET was fabricated on the recrystallized silicon, in order to investigate its electrical properties. The gate length and width were 20 and 723 μm , respectively. The thickness of the gate oxide film was 1000Å.

Figure 8 shows electrical characteristics of (a) a MOSFET fabricated on recrystallized silicon and (b) a MOSFET fabricated on bulk single-crystal silicon using the same process as the SOI/MOSFET fabrication. Electron mobility could be obtained from these characteris-

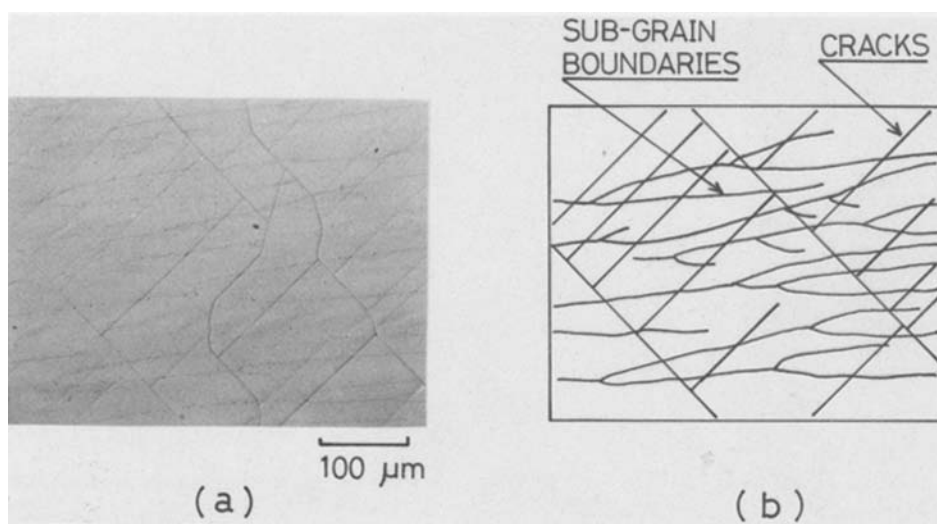


Fig. 3. (a, left) Optical micrograph of an etched silicon surface after recrystallization. (b, right) Schematic of the same optical micrograph.

Fig. 4. Transmission electron micrograph of a recrystallized silicon layer, and diffraction patterns from each subgrain area.

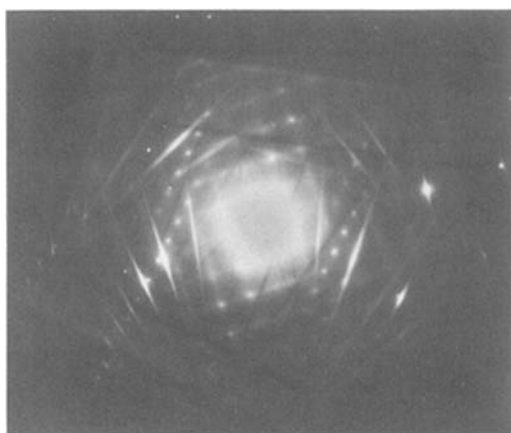
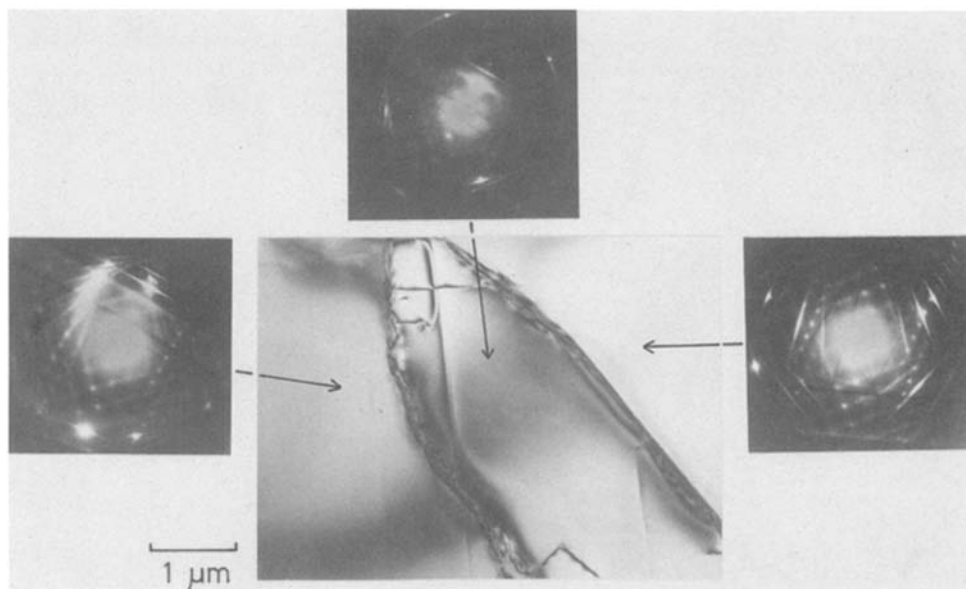


Fig. 5. Magnified photograph of a diffraction pattern

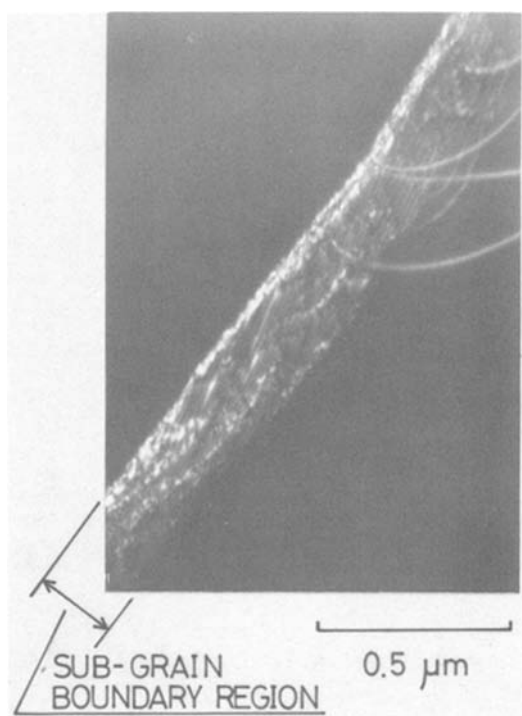


Fig. 6. 1000 kV transmission electron micrograph of a subgrain boundary.

tics. The maximum electron mobility in the saturated region of the recrystallized silicon was about $1020 \text{ cm}^2/\text{Vs}$, while the average value was about $860 \text{ cm}^2/\text{Vs}$. On the other hand, the electron mobility of bulk silicon was about $600 \text{ cm}^2/\text{Vs}$. That is, the mobility of the recrystallized silicon was about 1.4 times that of the bulk silicon. The reason for the higher electron mobility observed in the recrystallized silicon was tensile stress in the silicon due to a difference in the thermal expansion coefficients of fused silica substrate and silicon. The tensile stress in a (100) silicon plane reduced the effective mass of an electron, which increased electron mobility (7, 11-13).

These experimental results described above verified that this RF-ZMR method produced a high quality recrystallized silicon on a fused silica substrate.

Recrystallization of Polycrystalline Silicon Islands

In structures such as silicon on fused silica, cracking caused by the stress in the recrystallized silicon is a serious problem, as previously shown in Fig. 3. Figure 9a is a photograph of the surface of a MOSFET fabricated on recrystallized silicon having some cracks, while Fig. 9b

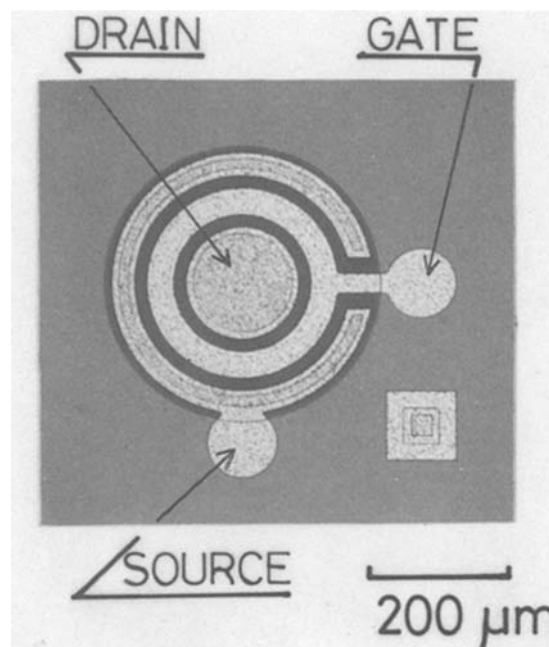


Fig. 7. Photograph of a MOSFET fabricated from recrystallized silicon.

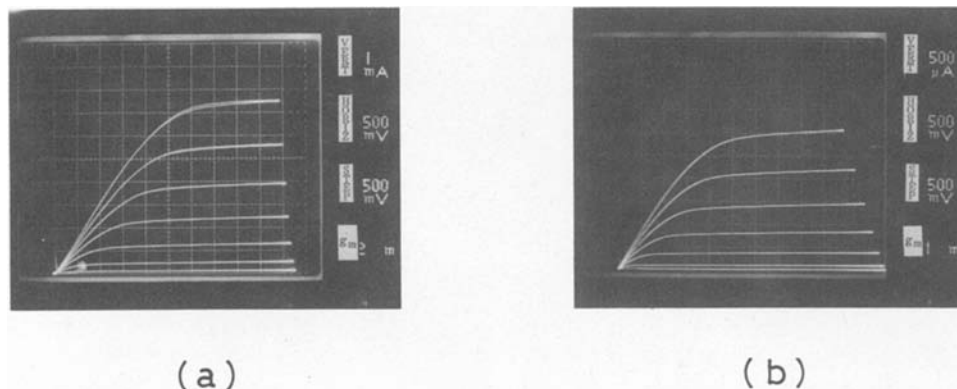


Fig. 8. Electrical characteristics of MOSFET fabricated from (a, left) recrystallized silicon and (b, right) single-crystal bulk silicon.

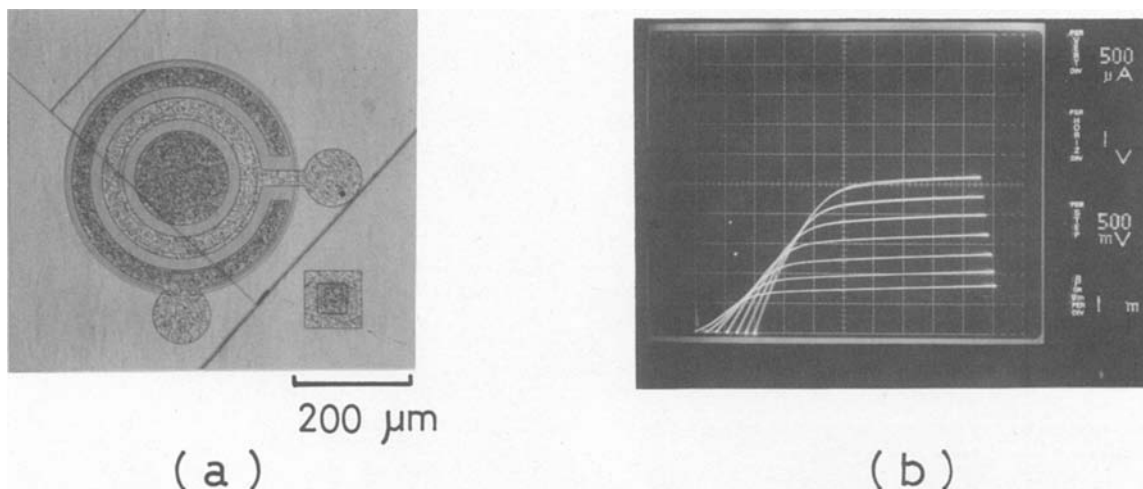


Fig. 9. (a, left) Photograph of a recrystallized silicon surface. (b, right) Electrical characteristics of a MOSFET having cracks.

shows its electrical characteristics. The characteristics of the devices were abnormal, indicating the necessity of eliminating cracks in the recrystallized silicon. Therefore, reduction of stress by forming silicon islands (14, 15) was tried.

The polycrystalline silicon film was etched with a dry etching technique to form islands with areas from 5×5

μm^2 to $4 \times 4 \text{ mm}^2$. Subsequent processes were the same as for the continuous silicon described above. The crack density of the recrystallized silicon was measured after the encapsulating SiO_2 layer was etched off.

As shown in Fig. 10, cracks disappeared when recrystallized islands of polycrystalline silicon were less than $250 \times 500 \mu\text{m}^2$ in size when silicon thickness was $0.5 \mu\text{m}$, and

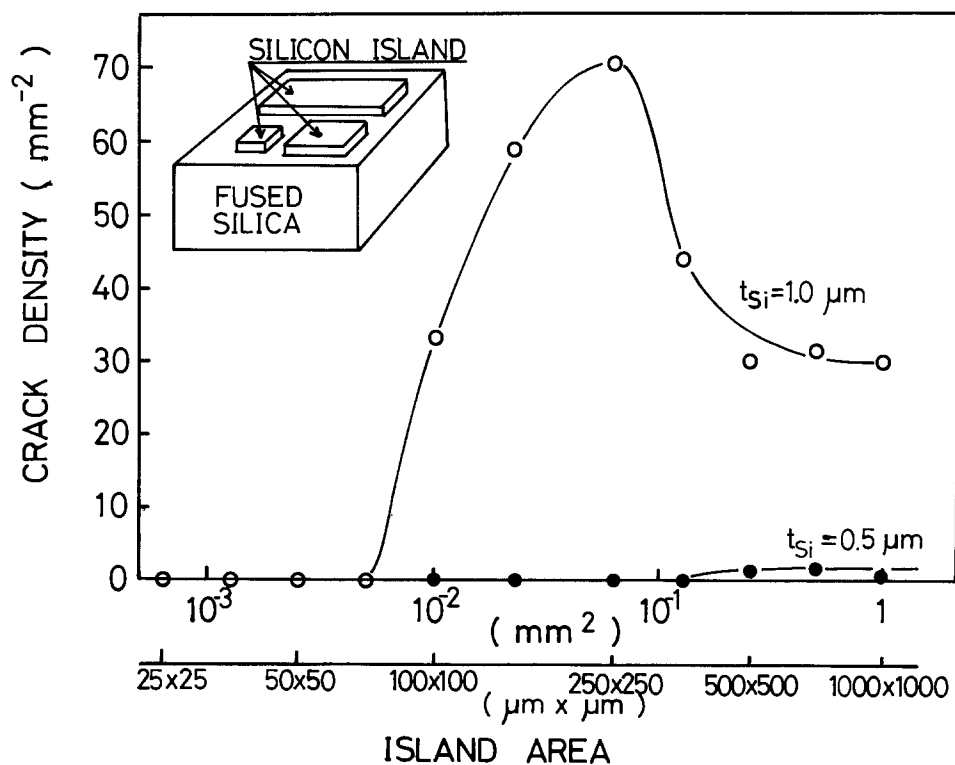
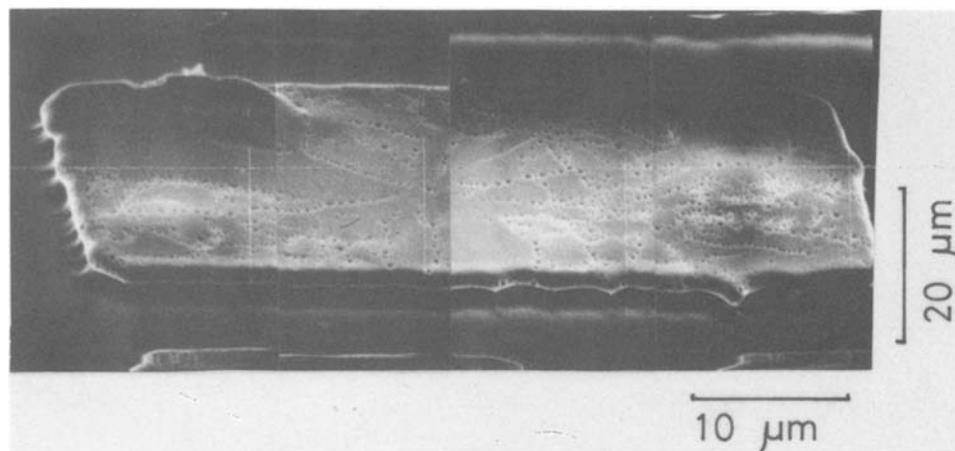


Fig. 10. Relationship between crack density and island area.

Fig. 11. SEM photograph of Sirtl-etched surface of recrystallized silicon island.



when the islands were less than $50 \times 100 \mu\text{m}^2$ in size when the silicon thickness was $1 \mu\text{m}$.

Figure 11 shows a SEM photograph of the Sirtl-etched (16) silicon surface. The lines of dark dots were etch pits, corresponding to dislocations. These indicated that recrystallized silicon islands had some subgrain boundaries consisting of arrays of discrete dislocations, but no grain boundaries. Their absence indicated that the recrystallized silicon in an island was a single crystal. The orientation of the recrystallized silicon islands was observed with a TEM technique. Figure 12 shows a typical diffraction pattern for one island, and indicates its orientation was (111). Figure 13 shows an optical micrograph of the silicon island surface which was wider than the one in



Fig. 12. A typical diffraction pattern of the recrystallized silicon.

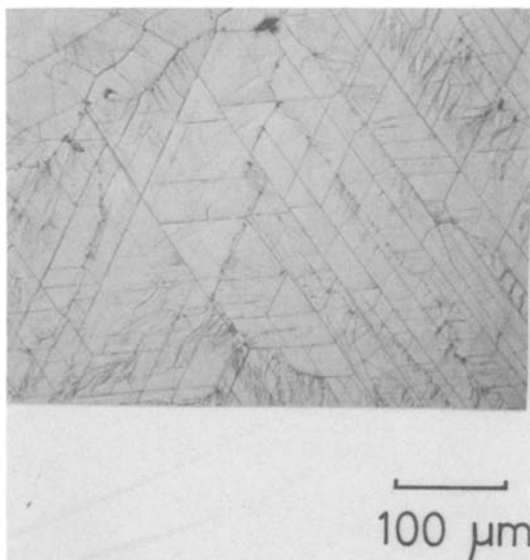


Fig. 13. Crack shapes in a silicon island which is wider than that for which no cracks occurred.

which no cracks occurred. As shown in this figure, there were many cracks and their arrangements were those of equilateral triangles. This meant that the orientation of the island was (111), because a crack line was $\langle 110 \rangle$. Orientations of all another islands were justified by the arrangements of the cracks, and were (111).

In order to study the electrical properties of the recrystallized silicon islands, ring type, Al-gate, and n-channel, MOSFET's were fabricated on them. The thickness of the gate oxide film was 1200\AA . Gate length and width were 20 and $680 \mu\text{m}$, respectively. Figure 14 shows the field effect mobilities of devices with a drain voltage of 0.1V. These mobilities depended on the threshold voltages of the devices. The reference MOSFET's were also fabricated in bulk silicon with an orientation of (111) using the same fabrication process. The field effect mobility of a device on the recrystallized silicon island was the same as that of a device on bulk silicon with an orientation of (111) for the same device threshold voltages. Leakage current was also measured at a drain voltage of 5V and found to be $1.5 \times 10^{-11} \text{ A}/\mu\text{m}$.

As described above, cracks were eliminated by recrystallization of the island polycrystalline silicon on fused silica substrate. The recrystallized silicon island was a single crystal having an orientation of (111), ensuring good electrical properties. However, tensile stress could not increase the electron mobility, such as in recrystallization of a continuous polycrystalline silicon film, because of the island orientation. Consequently, it was necessary to obtain (100) oriented silicon by recrystallizing in order to produce a high speed switching MOSFET. The difference in orientation of continuous and island silicon is discussed next.

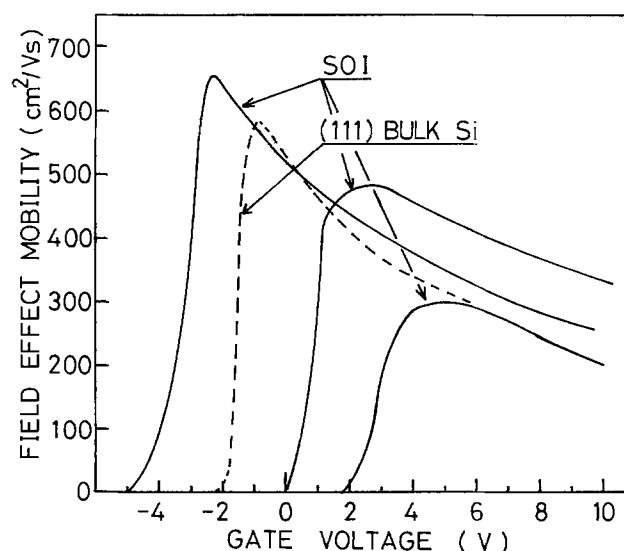
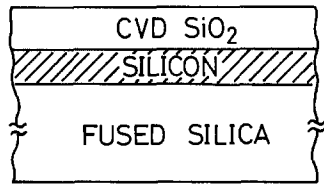
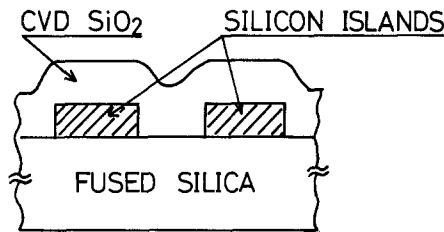


Fig. 14. Field effect mobility of MOSFET's fabricated on recrystallized silicon.

THERMAL CONDUCTIVITY(W /mK)	
FUSED SILICA, CVD-SiO ₂	1.9
SILICON	84



A) IN CASE OF CONTINUOUS SILICON



B) IN CASE OF SILICON ISLANDS

Fig. 15. Schematics of the orientation difference between (a, top) recrystallization of a continuous silicon layer and (b, bottom) of silicon islands.

Figure 15 illustrates the orientation difference of continuous and island silicon. In the continuous silicon, heat flowed smoothly in a direction parallel to the surface of the silicon because the silicon was sandwiched between the SiO₂ film and the fused silica substrate, both of which had thermal conductivity coefficients two orders lower than that of silicon. On the other hand, in the island silicon, heat was held in the melted silicon region because the silicon was completely enclosed by the SiO₂ layer and the fused silica. So, the difference in orientation might be caused by a difference in heat flow during silicon recrystallization. In this recrystallization method, the melted region could be directly observed during the recrystallization, as shown in Fig. 2. A microscope was used to observe whether the islands were melted or solidified. Supercooling of the melted silicon island occurred at a temperature of more than 200°C below the melting point of silicon, supporting the above explanation.

Based on this explanation, a method for obtaining crackless and (100) oriented silicon on fused silica was proposed. As shown in Fig. 16, silicon was formed as an island in order to eliminate cracking. The islands were then connected to each other with fine polycrystalline

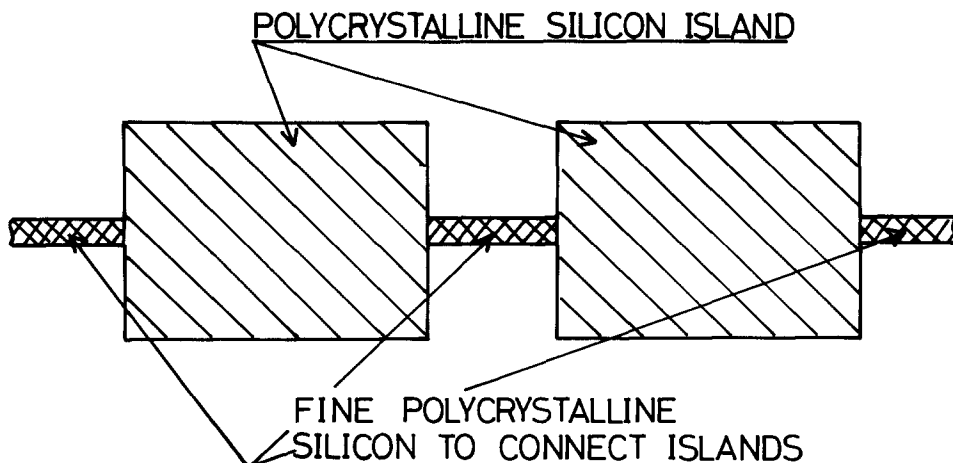


Fig. 16. Schematics of a connected silicon island pattern.

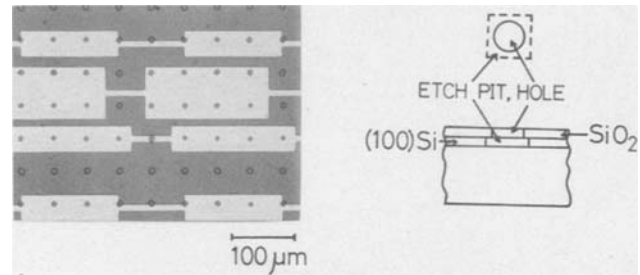


Fig. 17. Orientation of the recrystallized silicon islands which are connected with fine silicon regions.

silicon in order to achieve a smooth heat flow, and the polycrystalline silicon was recrystallized.

Figure 17 shows the orientation of silicon recrystallized by this method. The orientation was studied with the etch pit method (17) (figure schematic). The shape of the etch pits was square, indicating the orientation of the recrystallized silicon was (100) and the rotation angles of the squares were all the same within an island. Hence, the island silicon was a single crystal.

Conclusion

A new zone melting recrystallization method using an RF-heated carbon susceptor has been developed. This method allowed easy control of the temperature on the melted silicon region, an important factor in zone melting recrystallization. In continuous silicon film, the orientation of the film was (100) and the electron mobility was 700-1000 cm²/Vs. However, there were some cracks in the film. In the island silicon, recrystallized islands were single crystal with an orientation of (111) and without cracks. The electron field effect mobility was 300-600 cm²/Vs. These experimental results verified that (100) orientation was important for high speed devices which need high electron mobility in case of silicon on fused silica substrate. In order to obtain high quality crystalline silicon without cracks and with an orientation of (100), a recrystallization of connected polycrystalline silicon islands was also developed.

Acknowledgments

The authors would like to express their sincere thanks to Professor T. Imura and Dr. H. Saka for taking the 1000 kV transmission electron micrographs and their useful discussions regarding crystalline quality. They would also like to thank Dr. T. Takasuna and Dr. M. Okamura for their guidance and encouragement.

Manuscript submitted Oct. 12, 1983; revised manuscript received Jan. 19, 1984.

Hitachi, Limited assisted in meeting the publication costs of this article.

REFERENCES

1. M. Tamura, M. Ohkura, and T. Tokuyama, *Jpn. J. Appl. Phys.*, Suppl. 1, **21**, 193 (1981).
2. H. W. Lam, Z. P. Sobczak, R. F. Pinizzotto, and A. F. Tasch, Jr., *IEDM Tech. Dig.*, 559 (1980).
3. K. Shibata, T. Inoue, and T. Takigawa, *Appl. Phys. Lett.*, **39**, 645 (1981).
4. T. I. Kamins and B. P. Von Herzen, *Electron. Dev. Lett.*, **2**, 313 (1981).
5. H. Ishiwara, M. Nakano, H. Yamamoto, and S. Furukawa, *Jpn. J. Appl. Phys.*, Suppl. 1, **22**, 607 (1983).
6. E. W. Maby, M. W. Geis, Y. L. LeCoz, D. J. Silver-smith, R. W. Mountain, and D. A. Antoniadis, *Electron. Dev. Lett.*, **2**, 241 (1981).
7. B.-Y. Tsaur, J. C. C. Fan, and M. W. Geis, *Appl. Phys. Lett.*, **40**, 322 (1982).
8. R. F. Pinizzotto, H. W. Lam, and B. L. Vaandrager, *ibid.*, **40**, 388 (1982).
9. T. J. Stultz and J. F. Gibbons, *ibid.*, **41**, 824 (1982).
10. A. Kamgar and E. Labate, *Mat. Lett.*, **1**, 91 (1982).
11. Y. Kobayashi, A. Fukami, and T. Suzuki, *Electron. Dev. Lett.*, **4**, 132 (1983).
12. Y. Kobayashi, M. Nakamura, and T. Suzuki, *Appl. Phys. Lett.*, **40**, 1040 (1982).
13. C. Herring, *Bell Syst. Tech. J.*, **34**, 237 (1955).
14. T. I. Kamins and P. A. Pianetta, *Electron. Dev. Lett.*, **1**, 214 (1980).
15. W. G. Hawkins, J. G. Black, and C. H. Griffith, *Appl. Phys. Lett.*, **40**, 319 (1982).
16. E. Siltl and A. Adler, *Z. Metallkd.*, **52**, 529 (1961).
17. M. W. Geis, H. I. Smith, B.-Y. Tsaur, J. C. C. Fan, E. E. May, and D. A. Antoniadis, *Appl. Phys. Lett.*, **40**, 158 (1982).

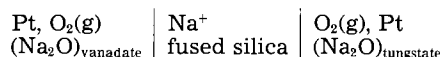
Thermodynamic Properties of Na₂O-V₂O₅ Melts, 1030-1210 K

S. K. Mittal* and J. F. Elliott

Department of Materials Science and Engineering, Massachusetts Institute of Technology, Cambridge, Massachusetts 02139

ABSTRACT

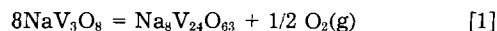
The following electrochemical cell was employed for this study



The activity of Na₂O on Na₂O-V₂O₅ melts was measured in the temperature range of 1030-1210 K for melt compositions of $x_{\text{V}_2\text{O}_5} \geq 0.50$. The measured activities of Na₂O show large negative deviations from ideality. The activity of V₂O₅ was obtained by integrating the Gibbs-Duhem equation. The values of the partial molar and molar-free energies and enthalpies of mixing for the Na₂O-V₂O₅ system were calculated from the results. The free energies of formation of the compounds Na₂O · 6V₂O₅, Na₂O · 3V₂O₅, and Na₂O · V₂O₅ were estimated in the temperature range of 500°-600°C.

Vanadium and sodium are impurities in fuel oils and coals. In combustion, these elements are oxidized to vanadium oxide (V₂O₅) and sodium oxide (Na₂O), and in combination these oxides may form liquids whose melting temperatures may be as low as 600°C (Fig. 1). The liquid phase in the Na₂O-V₂O₅ system is extremely corrosive to the metal and ceramic parts of combustion systems, and corrosion of these parts degrades the performance of energy conversion systems and may cause economic loss. To improve our understanding of the corrosive action of liquids containing Na₂O and V₂O₅, a study of the thermodynamic properties of the Na₂O-V₂O₅ was undertaken. The results are reported here.

The Na₂O-V₂O₅ binary system has been studied by several investigators (1-3). Kolta *et al.* (1) have determined the Na₂CO₃-V₂O₅ phase diagram, as shown in Fig. 1, using DTA and x-ray diffraction methods. Kolta *et al.* (1) employed platinum crucibles to contain their samples. In the composition range of pure V₂O₅ to 75 mol percent (m/o) Na₂CO₃, they found that the Na₂CO₃-V₂O₅ system is essentially a Na₂O-V₂O₅ system because of complete evolution of CO₂ from the Na₂CO₃-V₂O₅ mixtures. Kolta *et al.* detected five compounds in this binary system at the following mol ratios of V₂O₅/Na₂O: 6/1, 3/1, 1/1, 1/2, and 1/3. During solidification of Na₂O-V₂O₅ melts at high V₂O₅ concentrations (m/o V₂O₅ ≈ 75%), oxygen is evolved from the sample by the following reaction



However, in the liquid phase the vanadium exists in the pentavalent state (V⁵⁺) only, and the weight of the Na₂O-V₂O₅ melt is equal to the sum of the weights of Na₂O and V₂O₅ only.

Lin (4) attempted to measure the activity of sodium oxide in the Na₂O-V₂O₅ binary system at 1179 K by an electrochemical cell employing sodium-β-alumina as the solid

electrolyte. However, he encountered serious difficulties because the Na₂O-V₂O₅ melt crept up the sodium-β-alumina electrolyte and penetrated a high temperature cement seal in his cell. In addition, the melts attacked the electrolyte and dissolved some alumina. This attack increased with higher activities of sodium oxide in the working melt.

Koehler (5) has measured the heats of formation of NaVO₃(c), Na₂V₂O₇(c), and Na₃VO₄(c) at 298.15 K by applying sodium hydroxide solution colorimetry. King and Weller (6) have determined the heat capacities and entropies at 298.15 K for the same compounds. These data were extrapolated to higher temperatures to evaluate enthalpies, entropies, and free energies of formation for the corresponding compounds by Mah (7) and Kubaschewski (8).

Experimental

A concentration emf cell was employed to measure the activity of sodium oxide in Na₂O-V₂O₅ melts. Because of the instability of sodium-β-alumina in Na₂O-V₂O₅ melts, fused silica was used as the solid electrolyte. Doremus (9) has shown that the transference number of Na⁺ ions in fused silica is essential unity. Mittal and Elliott (10) demonstrated that fused silica performs satisfactorily as a sodium-ion solid electrolyte for open-circuit emf measurements when the activity of sodium oxide in the melts is less than 10⁻¹³ and in the temperature range of 1050-1200 K. The work of Doremus (9) and Veltri (11) on the specific conductivity, σ, of fused silica has been extrapolated to the temperature range of interest (1050-1200 K). This extrapolation yields values of approximately 10⁻⁶ Ω⁻¹cm⁻¹ between 1050 and 1200 K, and these values of σ are considered large enough to establish a stable chemical-potential gradient of sodium across the fused-silica solid electrolyte.

Theoretical considerations.—The following electrochemical cell was employed to obtain the activities of so-

* Electrochemical Society Student Member.
Key words: glass, cell, free energy.

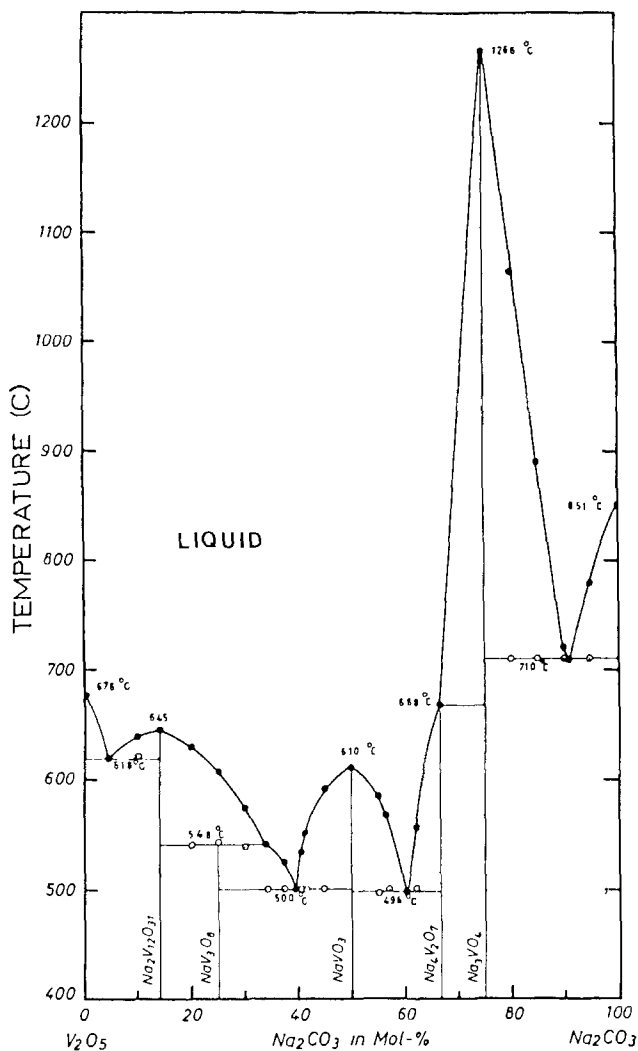
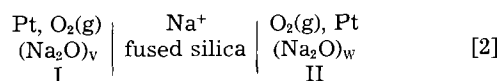
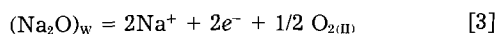


Fig. 1. The phase diagram V₂O₅-Na₂CO₃ (1)

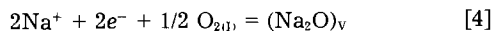
dium oxide in Na₂O-V₂O₅ melts



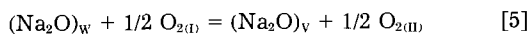
where the subscripts V and W designate sodium oxide in the Na₂O-V₂O₅ melt and the Na₂O-WO₃ reference melt, respectively. The anodic and cathodic half-cell reactions are



and



respectively. Here O_{2(I)} and O_{2(II)} are the oxygen pressures at the cathode and the anode, respectively. The overall reaction can be written as



The Nernst equation for reaction [5] is

$$\log \mathcal{A}_{(\text{Na}_2\text{O})_V} = \log \mathcal{A}_{(\text{Na}_2\text{O})_W} + 1/2 \log [(p_{\text{O}_2})_{\text{I}} / (p_{\text{O}_2})_{\text{II}}] - 2F\epsilon / (2.303RT) \quad [6]$$

Thus the activity of sodium oxide in the cathode melt is obtained directly from the cell potential if the two pressures of oxygen and the activity of sodium oxide in the anode melt are known. In Eq. [6], ϵ is the reversible emf of the cell, R is the universal gas constant, F is the Faraday constant, and p_{O_2} is the partial pressure of oxygen. The partial pressure of oxygen over each melt was 1 atm during the measurements.

The activity of sodium oxide in Na₂O-WO₃ binary melts has been measured by Lin and Elliott (12). Their results expressed in terms of the partial molar free energy of mixing of Na₂O, G_N^M , in the Na₂O-WO₃ system at 1200 K are as follows

$$G_N^M = -95.10 - 347.2 x_w \quad (\text{kJ/mol}) \quad [7]$$

for $0.53 \leq x_w \leq 0.80$. The term x_w is the mol fraction of WO₃ in the Na₂O-WO₃ binary melt. The partial molar enthalpy of mixing of Na₂O (H_N^M) in the same system is given by

$$H_N^M = -709.80 + 262.57/x_w \quad (\text{kJ/mol}) \quad [8]$$

This equation applies in the composition range $0.53 \leq x_w \leq 0.80$ and the temperature range $1113 \text{ K} \leq T \leq 1230 \text{ K}$. The standard state for Na₂O is pure liquid Na₂O at 1 atm pressure.

The temperature range for the experiments was $1030 \text{ K} \leq T \leq 1210 \text{ K}$, so the experimental results of Lin and Elliott (12) for the Na₂O-WO₃ system were extrapolated to the lower temperature using the Gibbs-Helmholtz equation

$$\left| \frac{\partial(G_N^M/T)}{\partial(1/T)} = H_N^M \right|_{p, x_N} \quad [9]$$

and Eq. [7] and [8].

Materials preparation.—The Na₂O-V₂O₅ melts were prepared from mixtures of reagent-grade sodium carbonate (Mallinckrodt 7527) and reagent-grade vanadium pentoxide (Fisher V-7). The required amount of sodium carbonate was weighed into a platinum crucible and dried at 700 K (427°C) for 8h. The vanadium pentoxide was dried in a separate platinum crucible at 523 K (250°C) for 6h, and then the vanadium pentoxide was added to the crucible containing the sodium carbonate. The sample was mixed with a spatula, and the mixture was fused in a flowing stream of pure dry argon. All of the Na₂CO₃ reacted with the V₂O₅ above 1000 K to yield a Na₂O-V₂O₅ melt. The final weight of the melt was checked to ensure that all the CO₂ had been expelled. The agreement between the calculated theoretical weight of the Na₂O-V₂O₅ mixture and that measured after fusion was within 1% of the weight of Na₂O in the sample. The total weight of the Na₂O-V₂O₅ melt was approximately 2.5g.

The Na₂O-WO₃ reference melt was prepared by a procedure similar to that employed by DeYoung and Elliott (13). The compositions of the Na₂-WO₃ melt used were $x_w = 0.564$ and 0.5499 .

Measurements.—The general arrangement of the electrochemical cell used is shown in Fig. 2, and is similar to that employed earlier by DeYoung and Elliott (13). There are two principal differences in the current work. First, the solid electrolyte in these experiments was a tube of clear fused silica (General Electric 214, clear fused quartz, 6.2 mm od) which was closed at one end with a gas torch. Second, to ensure a good contact, the platinum lead wire to the cathode was twisted several times around another piece of platinum wire that was spot-welded to the crucible. Thus the platinum crucible became an electrode (cathode).

The temperature of the cell was measured by a Pt/Pt-10% Rh thermocouple calibrated against the melting point of gold (1337 K). A high impedance ($\sim 10^9 \Omega$) Beckman pH meter (Model no. 101900) was employed to measure the emf of the cell.

An atmosphere of pure oxygen was maintained over both the Na₂O-V₂O₅ melt and the Na₂O-WO₃ reference melt. The flow rate of oxygen gas was 75 ml/min over the Na₂O-V₂O₅ melt and 5 ml/min over the reference melt. Before passing into the cell, the streams of oxygen were dried.

The cell potential was periodically measured until it became steady; this required approximately 2h. Each cell

¹ Subsequently, the subscripts W, N, and V will denote WO₃, Na₂O, and V₂O₅, respectively.

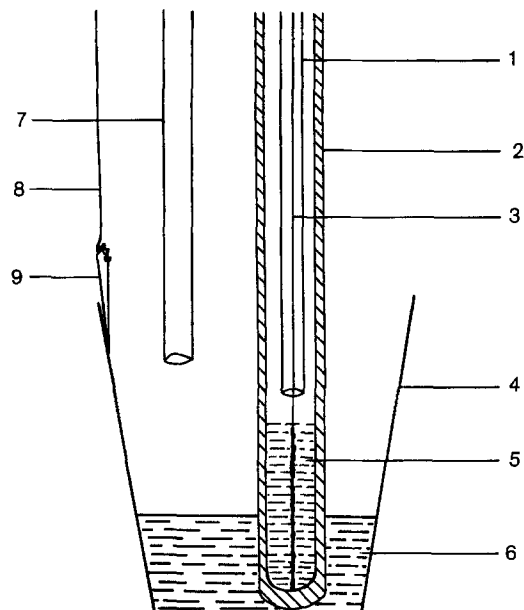


Fig. 2. The electrochemical cell. 1: alumina tube. 2: fused-silica electrolyte. 3: Pt lead wire. 4: Pt crucible. 5: $\text{Na}_2\text{O}\text{-WO}_3$ reference melt. 6: working melt. 7: inlet gas tube. 8: Pt lead wire. 9: Pt wire hook.

was operated for about 10h. Reversibility of the cell was checked by cycling the cell temperature and, for a few cells, by polarizing the cell with an external current source. After polarization with 0.6 mA of current for approximately 10s, the potential of a cell returned to within 2 mV of the initial value within 20s and to within ± 0.05 mV in approximately 5 min.

After the experiment, the end of the fused-silica tube in contact with the $\text{Na}_2\text{O}\text{-V}_2\text{O}_5$ melt was sectioned and inspected. There was no attack on the tube by the $\text{Na}_2\text{O}\text{-WO}_3$ reference melt. The wall of the fused silica in contact with the $\text{Na}_2\text{O}\text{-V}_2\text{O}_5$ working melt, however, was dissolved to an extent that depended on the melt composition and temperature. No penetration by the melt through the wall of the fused silica electrolyte was observed. The dissolution of fused silica was greatest at higher temperatures and at higher sodium oxide contents in the melt ($x_N > 0.40$).

At high activities of sodium oxide (i.e., $\mathcal{A}_N > 10^{-6}$), the platinum crucible was attacked. Thus satisfactory measurements could be made only for compositions below $x_N \approx 0.5$.

Results

The activity of sodium oxide was calculated from the potential of the cell, the activity of sodium oxide in the cathode melt (Eq. [7] and [8]), and the pressures of oxygen at each electrode with the use of Eq. [6]. The results are shown in Fig. 3. The line through each set of data is a least squares line, the equation of which is

$$\log \mathcal{A}_N = A/T + B \quad [10]$$

where A and B are coefficients obtained in the correlation and T is the absolute temperature. The partial molar enthalpy and entropy of mixing, H_N^M and S_N^M , for sodium oxide for each composition of the anode melt are then obtained by the equations

$$H_N^M = 2.303 R \times A \quad [11]$$

and

$$S_N^M = 2.303 R \times B \quad [12]$$

The values of A and B and of the enthalpies and entropies of mixing of sodium oxide that were obtained from the data and Eq. [11] and [12] are listed in Table I.

The standard state for Na_2O in the analysis is the pure liquid at 1 atm pressure. The results obtained may be converted to the standard state of pure solid Na_2O by the

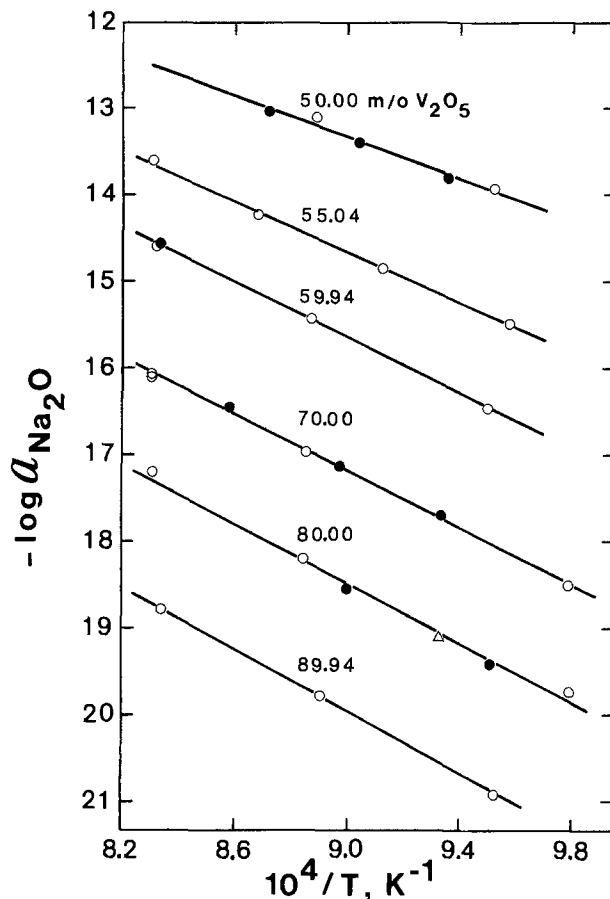


Fig. 3. Temperature dependence of $\log \mathcal{A}_{\text{Na}_2\text{O}(l)}$ in the $\text{Na}_2\text{O}\text{-V}_2\text{O}_5$ binary system.

equation

$$\log \mathcal{A}_N(\text{solid ss}) = \log \mathcal{A}_N(\text{liquid ss}) + 3020.9/T - 2.20 \quad [13]$$

which was obtained from data in the JANAF tables (14).

Thermodynamic Calculations

Thermodynamic properties of V_2O_5 .—The activity coefficient and excess partial molar free energy of V_2O_5 were calculated from the data for the activity of sodium oxide by the Gibbs-Duhem equation in the form

$$\log \gamma_V(x_V) = \log \gamma_V(x_V = 1) - \int_{x_V=1}^{x_V} (x_N/x_V) d \log \gamma_N \quad [14]$$

and then

$$G_N^{\text{EX}} = 2.303 RT \log \gamma_V \quad [15]$$

The range of temperature of this study was 1030–1210 K, and the melting point of pure V_2O_5 is 943 K (14), so that the value of $\log \gamma_V$ ($x_V = 1$) in the calculations is zero, i.e., the pure liquid is the standard state. The integral in Eq. [14] was evaluated graphically. However, it was found that $\log \gamma_N$ was linear with respect to x_V in the range of $0.7 < x_V < 0.9$, and extrapolation of the line to $x_V = 1$ gave a value of -19.91 for the property at 1125 K. The values obtained for the excess partial molar free energies for Na_2O and V_2O_5 are shown in Table II. The molar properties shown in the table were obtained by the relationship

$$G^{\text{EX}} = G_N^{\text{EX}} \cdot x_N + G_V^{\text{EX}} \cdot x_V \quad [16]$$

Figure 4 shows the activities of Na_2O and V_2O_5 in the $\text{Na}_2\text{O}\text{-V}_2\text{O}_5$ binary system at 1125 K.

The partial molar enthalpies of V_2O_5 , H_V^M , were obtained by integration of the Gibbs-Duhem equation as follows

$$H_V^M(x_V) = H_V^M(x_V = 1) - \int_{x_V=1}^{x_V} (x_N/x_V) d H_V^M \quad [17]$$

Table I. Thermodynamic properties of Na₂O* in Na₂O-V₂O₅ melts, 1030-1200 K

m/o V ₂ O ₅ **	Eq. [10] and Fig. 3			H _N ^M kJ/mol	S _N ^M J/mol · K
	-A × 10 ⁻³	-B	s (log a _N)†		
89.94	17.85 ± 0.15	3.89 ± 0.14	0.018	-342 ± 3	74.5 ± 3
80.00	17.16 ± 0.42	3.04 ± 0.39	0.070	-329 ± 8	58.2 ± 7
70.00	16.41 ± 0.22	2.42 ± 0.19	0.039	-314 ± 4	46.3 ± 4
59.94	16.02 ± 0.08	1.24 ± 0.07	0.013	-307 ± 2	23.8 ± 1
55.04	14.48 ± 0.14	1.64 ± 0.13	0.020	-277 ± 3	49.1 ± 10
50.00	11.98 ± 0.55	2.56 ± 0.50	0.056	-229 ± 11	49.1 ± 10

*Pure liquid Na₂O at 1 atm pressure is the standard state.

**Composition as made up.

†Standard deviation.

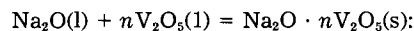
Table II. Values of excess free energies and of enthalpies of mixing in the Na₂O-V₂O₅ system

x _v	T = 1125 K, kJ/mol*			1055 K - 1200 K, kJ/mol		
	-G _N ^{EX}	-G _V ^{EX}	-G ^{EX}	-H _N ^M	-H _V ^M	-H ^M
1.00	424.1	0	0	353 ± 3	0	0
0.899	404.1	1.4	41.9	341 ± 3	0.7	35
0.800	378.9	5.8	80.5	329 ± 3	3	68
0.700	355.0	13.9	116.3	317 ± 3	7	100
0.600	324.8	30.5	148.4	305 ± 3	13	130
0.550	305.0	45.2	162.0	279 ± 4	33	143
0.500	278.0	69.8	173.9	229 ± 11	78	153

*Uncertainty in excess free energy quantities is as follows: s (G_N^{EX}) = ± 1.5 kJ/mol; s (G_V^{EX}) = ± 1.6 kJ/mol; s (G^{EX}) = ± 1.1 kJ/mol.

As shown in Table I, H_N^M is a linear function of x_v from 0.7 to 0.9 H_v. Extrapolating the line gives a value of -352.6 kJ/mol for H_N^M at N_v = 1. At this composition, H_v^M is 0. The results of the graphical integration of Eq. [17] are shown in Table II. Also shown there are values of H^M obtained by use of the equation for enthalpies that is equivalent to Eq. [16].

Standard free energy of compounds.—The standard free energy of formation of a compound from its constituent oxides at a given temperature was obtained by the relationship



$$\Delta G^\circ = 2.303RT(\log a_N + n \log a_V) \quad [18]$$

The values of log a_N and log a_V were extrapolated from 1125 K to 773 and 873 K by use of the Gibbs-Helmholtz equation (Eq. [9]). It was necessary to assume that H_N^M

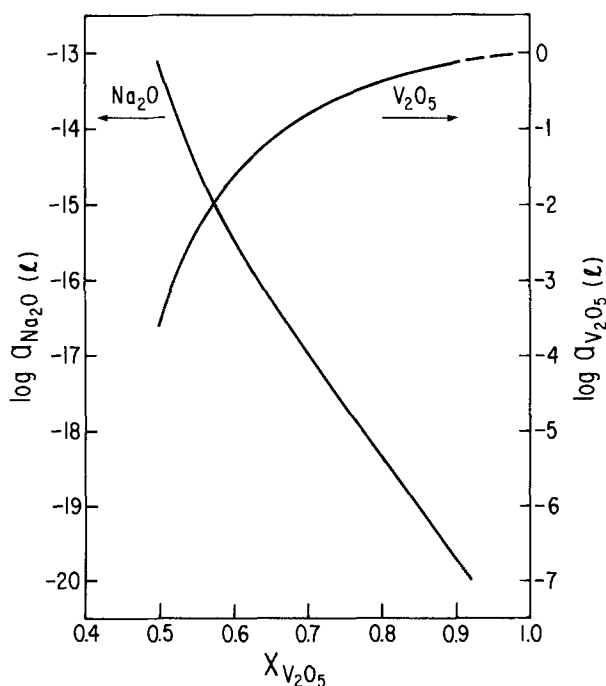


Fig. 4. Log a_{Na₂O} and log a_{V₂O₅} in the Na₂O-V₂O₅ binary system at 1125 K.

and H_v^M are constant over this temperature range. The value of the log of the activity for each of the components in Eq. [18] was obtained at the composition on the liquidus envelope of a compound at the two temperatures noted above. Once the standard free energy of formation of the compound was found, the integral molar free energy of mixing for the composition of the compound G^M was then obtained by dividing the standard free energy by n + 1. The enthalpy change for reaction [18] was obtained by applying once again the Gibbs-Helmholtz equation (Eq. [9]) to the standard free energies of formation of the compound that had been obtained at 773 and 873 K. The three compounds of interest in the system are Na₂O · 6V₂O₅, Na₂O · 3V₂O₅, and Na₂O · V₂O₅. The results of the calculations are shown in Table III.

The standard free energy of formation of each of the compounds from the elements, ΔG_f^o, is obtained by adding the standard free energies of formation of the constituent oxides to Eq. [18]. The resulting equation is

$$\Delta G_f^\circ(\text{Na}_2\text{O} \cdot n\text{V}_2\text{O}_5) = \Delta G_{18}^\circ + \Delta G_f^\circ[\text{Na}_2\text{O}(l)] + \Delta G_f^\circ[\text{V}_2\text{O}_5(l)] \quad [19]$$

The results of these calculations for the three compounds are also shown in Table III. Values for the standard free energies of formation of the simple oxides were obtained from the JANAF tables (14).

Discussion

The integral molar free energy of mixing, G^M, was calculated over the composition range studied at the temperatures 773 and 873 K, and the results are shown in Fig. 5 and 6, respectively. According to the Na₂O-V₂O₅ binary phase diagram shown in Fig. 1, at 773 K (500°C), the compounds Na₂O · 6V₂O₅, Na₂O · 3V₂O₅, and Na₂O · V₂O₅ are stable. The stability of the compounds and the liquid phase (at the eutectic) predicted in Fig. 5 are in good agreement with the published phase diagram. Similar agreement is observed between the phase stability predicted in Fig. 6 at 873 K (600°C) and the Na₂O-V₂O₅ phase diagram.

The calculated value of ΔG_f^o(Na₂O · V₂O₅) from the current work is approximately 30 kJ/mol (or 1.7%) less negative than the value calculated by Mah (7) in the temperature range 773-873 K. This difference could arise from the assumption of constant values of H_N^M and H_v^M from 1200 to 773 K for the calculation of ΔG_f^o(Na₂O · V₂O₅) at 773 and 873 K. Mah estimated the values of ΔG_f^o(Na₂O · V₂O₅) up to 1000 K using the solid standard state for Na₂O · V₂O₅. Her values of ΔG_f^o(Na₂O · V₂O₅) have been extrapolated to 1200 K using the heat capacity of the liquid compound as 261.2 J/mol K, and have been corrected to the liquid standard state for Na₂O · V₂O₅ by employing a standard entropy of melting, ΔS_m^o, of 24.7 J/mol K. This value of ΔS_m^o is similar to those for the compounds Na₂WO₄ (14) and Na₂MoO₄ (15) (i.e., ~24.5 J/mol K). The resulting value of the heat of melting, ΔH_m^o, for Na₂O · V₂O₅ is 21.8 kJ/mol. In Fig. 7, the calculated values of ΔG_f^o[Na₂O · V₂O₅(l)] from the current work are compared to those values extrapolated from Mah's data. The difference in the two sets of values for ΔG_f^o[Na₂O · V₂O₅(l)] is less than 10 kJ/mol (0.6%) for the temperature range shown. No data exist in the literature for a comparison of the results for Na₂O · 3V₂O₅ and Na₂O · 6V₂O₅.

Table III. Thermodynamic properties of $\text{Na}_2\text{O} \cdot 6\text{V}_2\text{O}_5$, $\text{Na}_2\text{O} \cdot 3\text{V}_2\text{O}_5$, and $\text{Na}_2\text{O} \cdot \text{V}_2\text{O}_5$

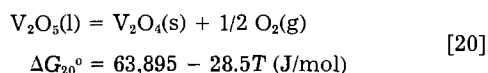
Compound	Temp (K)	ΔG_f° (kJ/mol)	ΔH_f° (kJ/mol)	ΔS_f° (J/mol K)	Ref.
$\text{Na}_2\text{O} \cdot 6\text{V}_2\text{O}_5(\text{s})$	773	$-7,990 \pm 40$	-9,980	-2,570	Present study
	873	$-7,740 \pm 40$	-9,980	-2,570	
$\text{Na}_2\text{O} \cdot 3\text{V}_2\text{O}_5(\text{s})$	773	$-4,310 \pm 21$	-5,290	-1,270	Present study
	873	$-4,250 \pm 21$	-5,290	-1,270	
$\text{Na}_2\text{O} \cdot \text{V}_2\text{O}_5(\text{s})$	773	$-1,850 \pm 9$	-2,230	-500	Present study
	873	$-1,800 \pm 9$	-2,230	-500	
$\text{Na}_2\text{O} \cdot \text{V}_2\text{O}_5(\text{s})$	773	-1,880	-2,290	-530	(7)
	873	-1,830	-2,290	-530	

*Uncertainties are (14): $s[\Delta G_f^{\circ}(\text{Na}_2\text{O})] = \pm 4.2$ kJ/mol; $s[\Delta G_f^{\circ}(\text{V}_2\text{O}_5)] = \pm 6.5$ kJ/mol.

The $\text{Na}_2\text{O}\text{-V}_2\text{O}_5$ melts show extremely large negative deviations from ideality, as seen from the values of G^{EX} and H^{M} in Table II. These values are more than 50% more negative than the values of G^{EX} and H^{M} at $x_N = 0.3$ and 0.4 in the $\text{Na}_2\text{O}\text{-SiO}_2$ system from measurements by Neudorf and Elliott (16) in the temperature range 1055-1200 K. The data of Neudorf and Elliott (1273-1373 K) were extrapolated to the current temperature range (1055-1200 K) by employing the Gibbs-Helmholtz equation. This indicates that V_2O_5 is a more acidic oxide than is SiO_2 , and it would appear that at high concentrations of V_2O_5 nearly all the oxygen anions from the Na_2O react with the :V-O-V: network for form :V-O groups, which would result in a very low activity of Na_2O .

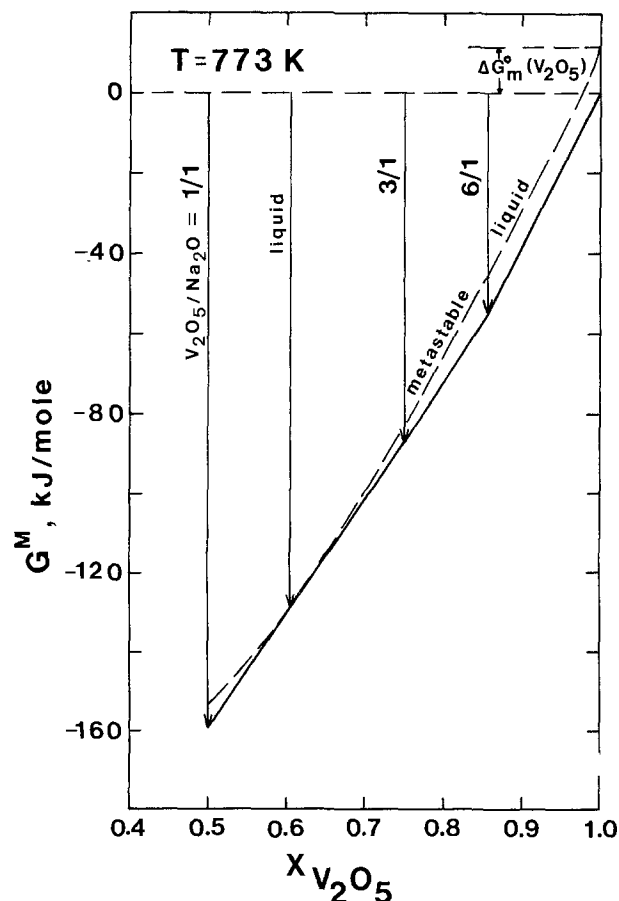
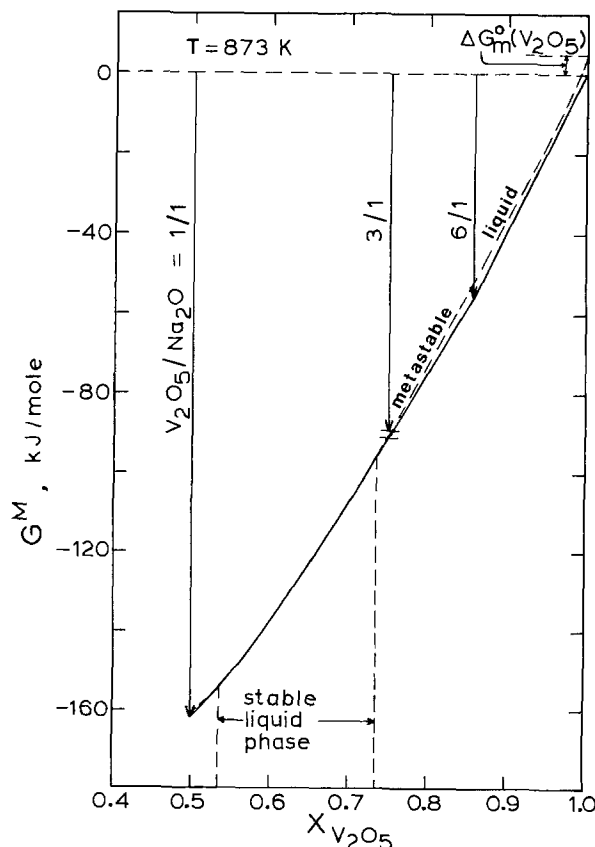
Errors.—There are three principal sources of error in the experiments: (i) error due to reduction of V_2O_5 to V_2O_4 , (ii) uncertainty in the experimental measurements, and (iii) error due to dissolution of the fused-silica electrolyte in the $\text{Na}_2\text{O} \cdot \text{V}_2\text{O}_5$ melt.

Liquid V_2O_5 may be reduced to V_2O_4 by the following reaction



where the values of ΔG_f° for $\text{V}_2\text{O}_4(\text{s})$ and $\text{V}_2\text{O}_5(\text{l})$ are from the JANAF tables (14). The equilibrium partial pressure of O_2 for reaction [20] is 2.6×10^{-3} atm at 1200 K and 4.5×10^{-3} atm at 1055 K. In these experiments, the partial pressure of O_2 in the gas was always greater than 0.40 atm, so no solid V_2O_4 formed from the molten V_2O_5 . Also, according to Block-Bolten and Sadoway (17), there is no nonstoichiometry in liquid V_2O_5 , arising from the presence of V_2O_4 in solution for $p_{\text{O}_2} > 0.06$ atm at 1200 K. Therefore, the error due to nonstoichiometry of the V_2O_5 in the $\text{Na}_2\text{O}\text{-V}_2\text{O}_5$ binary melts is considered to be unimportant.

A detailed analysis of the uncertainties in the measured and calculated thermodynamic quantities was carried out (18). The estimated random uncertainty in the measurement of the cell temperature was ± 1.0 K and in the measurement of the cell emf was ± 1.0 mV. Combining these errors (18) leads to an uncertainty in $\log \mathcal{A}_N$ of ± 0.014 . In the $\text{Na}_2\text{O}\text{-V}_2\text{O}_5$ melts, an estimated uncertainty in weighing of $\pm 0.006\text{g}$ (± 1 weight percent [w/o] Na_2O) during melt preparation yields an uncertainty in the concentration of Na_2O of ± 0.25 m/o and an uncertainty in the concentration of V_2O_5 of ± 0.08 m/o for a total sample weight ($\text{Na}_2\text{O} + \text{V}_2\text{O}_5$) of 2.5g. Using the maximum slope of the curve of $\log \mathcal{A}_N$ vs. x_N , an uncertainty in m/o Na_2O of ± 0.25 produces an uncertainty in $\log \mathcal{A}_N$ of ± 0.07 . The uncertainty in the composition of the $\text{Na}_2\text{O}\text{-WO}_3$ reference melt (m/o

Fig. 5. G^{M} in the $\text{Na}_2\text{O}\text{-V}_2\text{O}_5$ binary system at 773 KFig. 6. G^{M} in the $\text{Na}_2\text{O}\text{-V}_2\text{O}_5$ binary system at 873 K

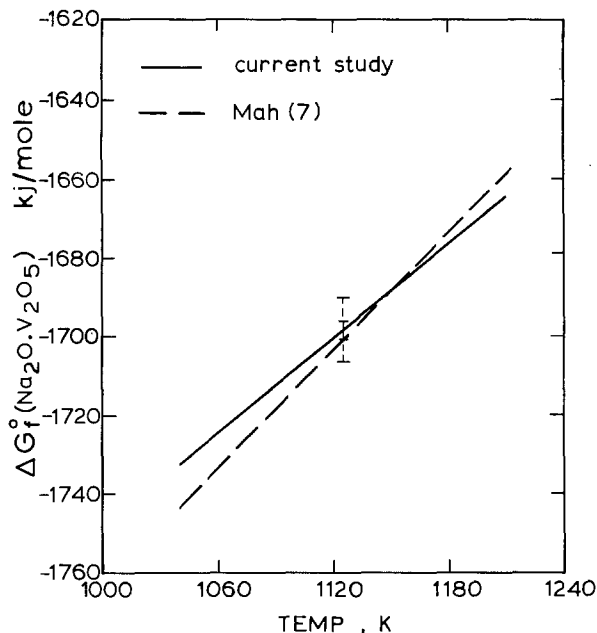


Fig. 7. The standard free energy of formation of Na₂O · V₂O₅(1) from the elements. Horizontal bars indicate estimated uncertainties in lines.

WO₃ of ± 0.01) causes an error in $\log \mathcal{A}_N$ of ± 0.0013 . Combining all the random errors (19) due to measurement of temperature and emf, and due to uncertainties in melt compositions, results in a total estimated random error in $\log \mathcal{A}_N$ of ± 0.071 . From the least squares line fits to the experimental data, the maximum standard deviation in $\log \mathcal{A}_N$ is ± 0.07 , as shown in Table I. This value (± 0.07) is in good agreement with the total estimated random error in $\log \mathcal{A}_N$ of ± 0.071 . A random error in $\log \mathcal{A}_N$ of ± 0.071 corresponds to a maximum random uncertainty in G_N^{EX} of ± 1.5 kJ/mol at 1125 K. The random errors in H_N^{M} and S_N^{M} are estimated to be ± 9 and ± 2.7 J/mol K, respectively.

A further error in the electrochemical cell experiments arises from the dissolution of the fused-silica electrolyte into the V₂O₅ containing melts. There is a maximum solubility of 2.5 w/o SiO₂ in liquid V₂O₅ at 1200 K according to the V₂O₅-SiO₂ phase diagram (20). However, a fused-silica rod continued to be attacked by a pure V₂O₅ melt even though the saturation concentration of silica of 2.5 w/o was reached (20, 21). This apparently anomalous behavior resulted from silica reprecipitating as quartz or crystalite because the chemical potentials of these crystalline forms are slightly less than that of the silica in the vitreous state. It would appear that the same effect was present with the cell measurements of this study. The apparent solubility of silica in the melt as estimated from the volume of silica removed from the exterior of the electrolyte tube varied with the V₂O₅ content of the melt and the time of operation of the cell. For example, the weight of silica removed ranged from 0.9% to 1.9% of the weight of the melt for times of 6-9.5h exposure and melt compositions of 90, 80, and 70 m/o V₂O₅. For melts containing 50 m/o, the equivalent figure was 5 w/o or less. With a melt of pure sodium sulfate in which the activity of sodium oxide was controlled in the range of 10^{-14} to 10^{-16} , there was no attack of the silica electrolyte for exposures of 15-30h at 1170-1256 K. There was also no attack of these electrolytes by Na₂O-WO₃ melts in which the activity of Na₂O was near 10^{-14} .

The available information on the nature of the Na₂O-V₂O₅-SiO₂ system is much too limited to make a quantitative evaluation of the effect of SiO₂ on the measured values of $\log \mathcal{A}_{\text{Na}_2\text{O}}$. An estimate of the effect can be made, however, on the basis that silica and vanadium oxide, as VO_{2.5} are acids and behave similarly in the Na₂O-VO_{2.5}-SiO₂ system. The actual melt on which the measurements were made is in the ternary system, whereas the results of the study are applied to the Na₂O-VO_{2.5} binary system. In making the correction, the composition of the ternary sys-

tem is calculated on the basis that 2.5 w/o silica was added to the initial binary melt. This addition is 0.033-0.037 mole fraction of silica for the melt compositions studied. It is then assumed that the value of $\log \mathcal{A}_{\text{Na}_2\text{O}}$ is constant along lines of constant concentration of sodium oxide in the ternary system, i.e., for lines of constant SiO₂ + VO_{2.5}. Thus the values of $\log \mathcal{A}_{\text{Na}_2\text{O}}$ are obtained for the binary Na₂O-VO_{2.5} system. Conversion of the compositions in the ternary system back to compositions in the Na₂O-V₂O₅ system provides the estimate of the correction that is to be applied to the lines plotted in Fig. 5. The corrections in $\log \mathcal{A}_{\text{Na}_2\text{O}}$ range from -0.002 to -0.011 in the composition range from 90-50 m/o V₂O₅, respectively. When compared to other sources of uncertainty in the study, this correction is insignificant.

Summary

The activity of Na₂O in the liquid phase of the Na₂O-V₂O₅ system has been measured between 1055 and 1200 K by employing an electrochemical cell. The partial molar thermodynamic quantities for Na₂O and V₂O₅ and the integral molar quantities for the liquid have been evaluated.

The values of ΔG_f° , ΔH_f° , and ΔS_f° for the compounds Na₂O · V₂O₅, Na₂O · 3V₂O₅, and Na₂O · 6V₂O₅ have been calculated in the temperature range 873-773 K. The calculated data on Na₂O · V₂O₅ from the current work is within 1.7% (± 30 kJ/mol) of the data calculated by Mah (7).

The Na₂O-V₂O₅ melts show large negative deviations from ideality which is indicative of the strong chemical interaction between the two components (Na₂O and V₂O₅) in the melt.

Acknowledgment

The authors express their appreciation to the National Science Foundation for financial support of this work (contract no. 7923671-CPE and contract no. DMR-7923671).

Manuscript submitted May 19, 1983; revised manuscript received Dec. 30, 1983.

Massachusetts Institute of Technology assisted in meeting the publication costs of this article.

REFERENCES

- G. A. Kolta, I. F. Hewaidy, and N. S. Felix, *Z. Erzbergbau Metallhuettenwes.*, **25**, 327 (1972).
- H. Flood and H. Sorum, *Tidsskr. Kjem. Bergves. Meten.*, **3**, 55 (1943).
- V. V. Illarionov, R. P. Ozerov, and E. V. Kil'disheva, *Zh. Neorg. Khim.*, **22**, 883 (1957).
- R. Lin, Sc. D. Thesis, Massachusetts Institute of Technology, Cambridge, MA (1980).
- M. F. Koehler, *U. S. Bur. Mines Rep. Invest.*, 5700 (1960).
- E. G. King and W. W. Weller, *ibid.*, 5715 (1961).
- A. D. Mah, *ibid.*, 6727 (1966).
- O. Kubaschewski, *Nat. Phys. Lab. U.K. Rep.*, DCS-7 (1970).
- R. H. Doremus, *Phys. Chem. Glasses*, **10**, 28 (1969).
- S. K. Mittal and J. F. Elliott, *Metall. Trans.*, to be published.
- R. D. Veltri, *Phys. Chem. Glasses*, **4**, 221 (1963).
- R. Lin and J. F. Elliott, *Metall. Trans. A*, **14**, 1713 (1983).
- D. H. DeYoung and J. F. Elliott, in "Proceedings of the Carl Wagner Symposium," 110th AIME Meeting, The Metallurgical Society of AIME, Warrenton, PA (1981).
- JANAF Thermochemical Tables, published by U.S. National Bureau of Standards (1982).
- O. Kubaschewski and C. B. Alcock, "Metallurgical Thermochemistry," 5th ed., Pergamon Press, New York (1979).
- D. Neudorf and J. F. Elliott, *Metall. Trans. B*, **11**, 607 (1980).
- A. Block-Bolton and D. R. Sadoway, *ibid.*, **14**, 231 (1983).
- S. K. Mittal, Sc. D. Thesis, Massachusetts Institute of Technology, Cambridge, MA (1983).
- Y. Beers, "Introduction to the Theory of Error," pp. 26-36, Addison-Wesley, Reading, MA (1957).
- N. C. Gravette, D. Barham, and L. R. Barrett, *Trans. J. Br. Ceram. Soc.*, **65**, 199 (1966).
- M. R. Goldman, Ph. D. Thesis, University of London, London (1963).

The Composite Insertion Electrode

Theoretical Part. Equilibrium in the Insertion Compound and Linear Potential Dependence

S. Atlung,* B. Zachau-Christiansen, K. West, and T. Jacobsen*

Fysisk-Kemisk Institut, The Technical University of Denmark, DK 2800 Lyngby, Denmark

ABSTRACT

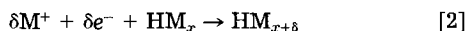
The specific energy obtainable by discharge of porous insertion electrodes is limited by electrolyte depletion in the pores. This can be overcome using a solid ion conductor as electrolyte. The term "composite" is used to distinguish these electrodes from porous electrodes with liquid electrolyte. The theoretical basis for such electrodes is discussed and, using a simplified model, equations are derived to describe the distribution of potential and current during discharge/charge operation. Under the assumption that the insertion compound particles are small enough to ensure equilibrium, and that the local electrode potential depends linearly on the degree of insertion, these equations are solved to obtain analytical expressions for the discharge curve. It is shown that the parameters which determine the discharge behavior for a given discharge current are simply related to the effective ionic and electronic conductivities, the thickness of the electrode, the volume fractions, and the slope of the potential curve.

From a specific energy point of view, batteries with insertion electrodes have the advantage that the overall cell process



only includes a minimum of components, and no changes in overall electrolytic composition.

The reaction at the positive electrode



is a topochemical reaction where the monovalent cation M^+ is inserted in the "host compound," H . δ is an infinitesimal increment in the degree of insertion x and the compound HM_x , for $x \leq n$, forms a single phase.

Hence Eq. [2] can take place in both directions with a minimum of structural changes. This should make it possible to design secondary batteries with long cycle life. Li is the metal most used for this type of batteries, but Eq. [2] is known to occur with Na^+ (1), K^+ (2), and Ag^+ (3) as well.

Many insertion compounds are known primarily from the groups of dichalcogenides (4), but lately also oxides, in particular, vanadium oxides, have been studied (5).

Based on the Li/TiS_2 couple, practical battery investigations have shown (6-8) that a specific energy in the range of 100-150 Wh/kg is a realistic goal for moderate temperature batteries. This can be compared with the 50-60 Wh/kg goal for advanced lead acid systems.

The limitations met with in the design of insertion compound batteries originate primarily from the low mobility of the M^+ cation in the electrolytes used (9). Alkali metal anodes dictate the use of nonaqueous electrolytes, either organic solvents with a M salt (10), or solid ionic conductors (7).

The dynamics of insertion cathodes.—Equation [2] is basically a solid-state reaction, whose rate is controlled by diffusion of M^+ into the insertion compound particle. This type of electrode kinetics has been discussed in relation to battery performance in earlier papers (11, 12). It was concluded that insertion cathodes should be made with small particles arranged in a porous structure in order to obtain acceptable specific energies at heavy loads. In a porous electrode, the utilization of the active materials depends on the transport in the active particles, electrode porosity and thickness, and electrolyte properties. By choosing small enough cathode particles, the influence of transport in these can be eliminated without impairing the packing density (11). For example, in the case of the Li/TiS_2 system, a particle size smaller than 1-2 μm ensures that even for 2-4h loads, the Li concentration in the particles is practically uniform.

The impedance for the interfacial charge transfer reaction can be assumed negligible for insertion reactions (13)

*Electrochemical Society Active Member.

Key words: electrode, insertion, solid state, discharge.

and, accordingly, reaction [2], under these circumstances, proceeds close to equilibrium. Hence, the obtainable material utilization in the porous cathode is limited by transport phenomena in the electrolyte in the pores.

These problems were discussed in a previous publication (14), where it was concluded that the utilization of a porous cathode, designed for maximum energy density, was limited by local depletion of electrolyte salt in the cathode. This depletion occurs when the local transfer current consumes more M^+ ions than the amount supplied by diffusion and migration. In Ref. (12) it was indicated that the electrolyte depletion was a consequence of the transport of the anion and could be delayed or suppressed if the anion mobility was low enough. Thus, a low anion and a high cation mobility should be beneficial for material utilization. However, one might fear that the corresponding decrease in conductivity and the appearance of "diffusion potentials" would offset the gain.

A quantitative study was undertaken in Ref. (14) from which Fig. 1 is reproduced. It is obvious from this figure that the electrode performance is dramatically improved by decreasing anion mobility to a low value, regardless of the increase in electrolyte resistance. This points to the use of solid ion conductors with only one ionic species mobile as electrolytes in "porous" electrodes. To indicate the difference between electrodes with liquid electrolytes and solid electrolytes, the term "composite electrodes" is coined to describe these "all solid-state" electrodes.

Composite Electrodes

In experiments with solid ionic conductors it has been the practice to mix the electrode substance with electrolyte powder (15). So far no discussion of this procedure and the expected advantages is found in the literature.

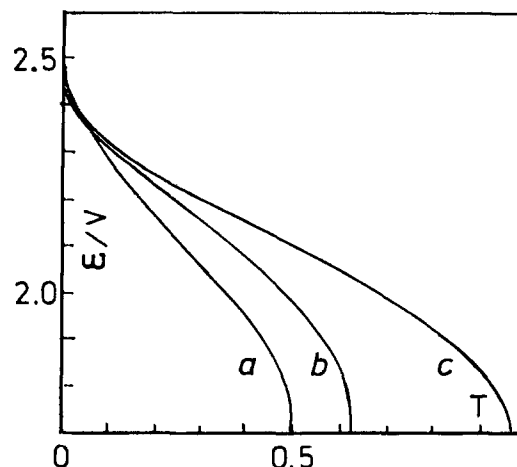


Fig. 1. Calculated discharge curves for porous electrode with liquid electrolyte. Cationic mobility kept constant, different values of t (a, b, c). $a = 0.8$, $b = 0.1$, and $c = 0.01$. For further details see Ref. (14).

For reversible batteries, a composite electrode can hardly be imagined with other electrode systems than insertion compounds because participation of electrolyte compounds in the cell reaction would destroy the structure. Even with insertion compounds the volume changes associated with charge and discharge might cause difficulties. The composite electrode must be made by mixing powders of the insertion compound and the solid electrolyte and consolidating this mixture on a metal grid serving as current collector.

The structure of a composite electrode is shown in Fig. 2. It is essential that the insertion material and the electrolyte form two interwoven contiguous networks with maximum contact area, and that the number of voids or isolated particles is at a minimum. The realization of such a structure is difficult; it can, however, be facilitated using a "soft" electrolyte like $\text{LiI-Al}_2\text{O}_3$ (16) or a small amount of polymeric electrolyte (17) to improve the contact between electrolyte and electrode particles (18).

The composite electrode concept is an imperative prerequisite for the construction of an all solid-state battery system exploiting the advantages associated with electrolytes conducting only the inserted ion.

Such a system can be operated at a moderately increased temperature, 100°-150°C. In the first place, this improves the rather low conductivity of solid electrolytes at room temperature. Assuming an activation energy for ionic transport of 0.3 eV, raising the temperature from 25° to 150°C will improve the battery rate capability by a factor of five. Also, the rate of the insertion process will be improved permitting use of less "active" insertion compounds or larger particles.

Operation of organic electrolyte batteries at increased temperature has until now not been successfully demonstrated, partly from safety considerations, and partly due to the tendency for solvent intercalation in layered materials. It is obvious that the composite electrode should be combined with a layer of solid electrolyte as a separator. The most promising electrolyte materials, Li_3N and $\text{LiI-Al}_2\text{O}_3$, are thermodynamically stable against Li, and this, possibly in connection with the increased temperature, improves the cyclability of the Li electrode considerably (18).

From a construction point of view, the possibility of stacking a number of cells to a high voltage unit without serious containment problems should improve overall specific energy. Hence, the expected advantages associated with the composite electrode concept warrants a closer study of its theoretical and practical aspects.

Theoretical Treatment

Model description.—It is assumed that the electrode is a flat pellet of thickness, l , (Fig. 3). The length coordinate is z , with $z = 0$ at the current collector. The electrode potential, ϵ_c is measured at the current collector with reference to an electrode reversible to M^+ placed at $z = l$. π is the Fermi potential in the electronically conducting insertion compound and ϕ the Galvani potential in the electrolyte. Hence

$$\epsilon_c = \pi_0 - \phi_1 \quad [3]$$

where $\pi_0 = \pi(z = 0)$ and $\phi_1 = \phi(z = l)$.

Due to the equivalence between the electrolyte and insertion compound, it is natural to use the macrohomogeneous model as introduced by Newman and Tobias (19). According to this model, each point is associated with local values of π , ϕ , ionic current density, i_i , and electronic current density, i_e . The electrochemical reaction causes a transfer current, i_t , measured per unit volume electrode. These variables are all functions of position, z , and time, t .

We further ascribe an effective electronic conductivity, κ_e , and a corresponding ionic conductivity, κ_i , to the electrode structure as such. These quantities then include the effect of tortuosity and volume fraction of the insertion and the electrolyte components, respectively. Neglecting volume changes due to charge/discharge, κ_i can be considered constant in time and space, when a true solid

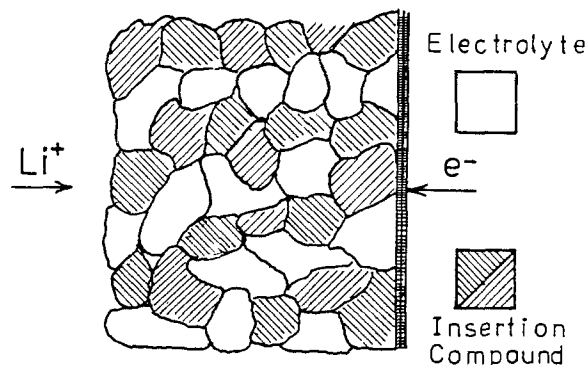


Fig. 2. Composite electrode concept (two dimensional)

ionic conductor is used. This makes all the difference between the treatment of the composite and the porous electrode with liquid electrolyte, where composition and conductance of the electrolyte changes with time and position.

For some insertion compounds, the electronic conductivity of the pure substance, κ_e^0 , can change considerably with the amount of inserted ion. However, the effective value of κ_e in the electrode can be controlled by conducting additives like graphite, etc.

In the following, κ_e is considered constant, the interfacial charge transfer is assumed to be in equilibrium, and the local concentration of inserted ion in each insertion compound particle is uniform. Also, electrical gradients perpendicular to the Z -axis are assumed negligible. Under these assumptions, the transport equations are

$$i_i = -\kappa_i \frac{d\phi}{dz} \quad \text{and} \quad i_e = -\kappa_e \frac{d\pi}{dz} \quad [4]$$

and the conservation of mass and charge requires

$$i_t = \frac{\partial i_i}{\partial z} \quad \text{and} \quad i_i + i_e = i^* \quad [5]$$

i^* is the discharge/charge current density (counted negative for cathodic, i.e., discharge currents). The local single electrode potential is given as

$$\epsilon = \pi - \phi \quad [6]$$

and Eq. [4]-[6] give the porous electrode relation (20)

$$\frac{\partial^2 \epsilon}{\partial z^2} = i_t \left(\frac{1}{\kappa_i} + \frac{1}{\kappa_e} \right) \quad [7]$$

with the boundary conditions for constant current discharge

$$z = 0, i_e = i^*; \quad z = l, i_i = i^* \quad [8]$$

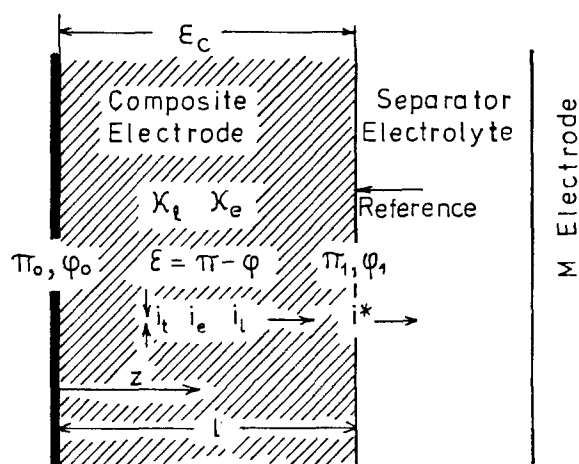


Fig. 3. Specification of composite electrode model

which on the strength of Eq. [4] and [5] can be written as

$$\begin{aligned} z = 0, \partial\epsilon/\partial z &= -i^*/\kappa_e \\ z = l, \partial\epsilon/\partial z &= i^*/\kappa_l \end{aligned} \quad [9]$$

The insertion electrode potential.—In porous and composite insertion electrodes, the reaction is distributed through the electrode, mainly as a result of the change in potential associated with the change in the local degree of insertion caused by the discharge/charge process. A characteristic for insertion compounds is that their equilibrium potential depends strongly on the degree of insertion. One example of this dependence is the relation proposed by Armand (21) for TiS_2/Li

$$\epsilon = \pi - \phi = \epsilon^\theta + RT/F[\ln[(1-X)/X] - f[X - 0.5]] \quad [10]$$

where $X = x/n$ is the degree of insertion, f an "interaction parameter," and ϵ^θ a standard potential for the insertion compound/electrolyte in question.

The interaction parameter, f , expresses approximately the effect of the electrostatic interactions associated with the insertion process (23) and dominates the dependence of the potential on X . The typical range for the linear term is $10 < f < 20$, e.g., 16 for TiS_2 .

A relation of the form Eq. [10] presumes that the insertion takes place in a monophasic region. If, for example, new phases are formed during insertion, the EMF composition relation will exhibit plateaus, and relations like Eq. [10] are only valid within limited regions.

In Fig. 4, we have depicted the TiS_2/Li potential as measured (29) and calculated from Eq. [10]. In this case, it is obvious that a simple linear dependence

$$\epsilon = \epsilon^* - kX \quad [11]$$

is a good approximation. Although other insertion compounds may show this behavior only in a limited range, it is believed that Eq. [11] brings out the characteristic features of insertion electrodes compared with other battery electrodes like HgO , AgCl , and PbO_2 .

The working potential.—The working potential is given by Eq. [3]. In case of a significant contribution from the electronic resistance in the insertion compound network, ϵ_c cannot be identified with the local electrode potential

ϵ_1 at $z = l$. Many insertion compounds have a high electronic conductance as, e.g., TiS_2 , while other compounds interesting from a battery point of view show a rather low electronic conductivity, e.g., some of the vanadium oxides.

Until now there still remains some uncertainty as to the influence of electronic resistivity on battery performance, although it was a main topic in some of the first works on porous electrodes (24).

The following treatment is quite general and based on the local potentials: $\epsilon_1 = \epsilon(z = l) = \pi_1 - \phi_1$ and $\epsilon_0 = \epsilon(z = 0) = \pi_0 - \phi_0$. From Eq. [3], we have

$$\epsilon_c = \pi_0 - \phi_1 = \pi_1 - \phi_1 - (\pi_1 - \pi_0) \quad [12]$$

and from Ohms law (κ_e constant)

$$\pi_1 - \pi_0 = -\frac{1}{\kappa_e} \int_0^l i_c dz \quad [13]$$

and using Eq. [4] and [7]

$$i_c = \int_z^l i_t dz = \frac{\kappa_e \kappa_l}{\kappa_e + \kappa_l} \int_z^l \frac{\partial^2 \epsilon}{\partial z^2} dz \quad [14]$$

Performing the integration and using the boundary conditions in Eq. [9] we obtain

$$\epsilon_c = \frac{1}{\kappa_e \kappa_l} (\kappa_e \epsilon_1 + \kappa_l \epsilon_0 + li^*) \quad [15]$$

At this stage, it is convenient to introduce the parameters ϵ_1^0 and ϵ_0^0 to express the potential difference which would develop across the electrode, if all the current passed through the ionically conducting network or the electronically conducting network, respectively

$$\epsilon_1^0 = -i^*l/\kappa_l; \quad \epsilon_0^0 = -i^*l/\kappa_e \quad [16]$$

As it will appear later, these two parameters and k determine the behavior of the electrode over the entire discharge range. With these ϵ_c can be written as

$$\epsilon_c = \frac{\epsilon_1^0 \cdot \epsilon_1}{\epsilon_1^0 + \epsilon_0^0} + \frac{\epsilon_0^0 \cdot \epsilon_0}{\epsilon_1^0 + \epsilon_0^0} - \frac{\epsilon_1^0 \cdot \epsilon_0^0}{\epsilon_1^0 + \epsilon_0^0} \quad [17]$$

The ratio $\beta = \epsilon_0^0/\epsilon_1^0 = \kappa_l/\kappa_e$ expresses the influence of increasing the electronic resistance for a fixed value of the ionic resistance. Using β , we get

$$\epsilon_c = \frac{1}{1 + \beta} \epsilon_1 + \frac{\beta}{1 + \beta} \epsilon_0 - \frac{\beta}{1 + \beta} \epsilon_1^0 \quad [18]$$

Mathematical treatment.—It is characteristic for porous and composite electrodes that the transport in the two phases is coupled through the local electrode potential $\epsilon = \pi - \phi$. As ϵ is given by the local value of X , which depends on the local degree of discharge, the time dependence of the electrode behavior is introduced. If, as assumed, the insertion compound particles are in equilibrium, then

$$\frac{\partial X}{\partial t} = -\frac{i_t}{Fvc^0} \quad [19]$$

where c^0 is the saturation concentration ($x = n$) and v is the volume fraction of insertion compound. Combining this with Eq. [7] and [16], we get

$$\frac{\partial X}{\partial t} = \frac{i^*l}{Fvc^0(\epsilon_0^0 + \epsilon_1^0)} \frac{\partial^2 \epsilon}{\partial z^2} \quad [20]$$

For convenience, dimensionless variables and groups are introduced. For a battery discharge at constant current, the obvious time unit is the time needed to discharge the battery completely. At equilibrium conditions this is

$$\tau_D = -F l v c^0 / i^* \quad [21]$$

keeping in mind that cathodic currents are negative. τ_D is the "stoichiometric" discharge time and can be consid-

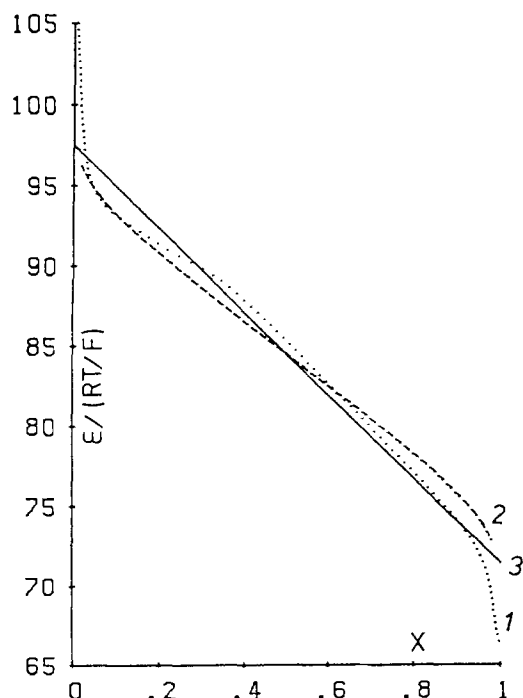


Fig. 4. Insertion electrode potential. (1) measured Ref. (29), (2) approximation according to Eq. [10], and (3) linear approximation ($\epsilon^* = 2.49\text{V}$, $k = 0.67\text{V}$).

ered a measure of the intensity of the discharge. Equivalent terminology is used in the battery industry, e.g., a "5h load." The dimensionless time

$$T = t/\tau_D = -ti^*/F\ell v c^0 \quad [22]$$

is then identical to the degree of discharge.

Introducing dimensionless length, Z , and potential, E

$$Z = z/l; E_j^m = F\epsilon_j^m/RT; \text{ and } K = Fk/RT \quad [23]$$

transforms Eq. [20] and [9] into

$$\frac{\partial X}{\partial T} = -\frac{1}{E_1^0 + E_e^0} \frac{\partial^2 E}{\partial Z^2} \quad [24]$$

$$Z = 0, \partial E/\partial Z = E_e^0; Z = 1, \partial E/\partial Z = -E_1^0$$

where

$$E_j^0 = \frac{F^2 \ell^2 v c^0}{RT\tau_D \kappa_j} \quad (j = e, l) \quad [25]$$

and the potential relation in Eq. [10] into

$$E = E^0 + \ln[(1 - X)/X - f(X - 0.5)] \quad [26]$$

and Eq. [11]

$$E = E^* - KX \quad [27]$$

Equations [24] and [26] or a corresponding potential relation form two simple nonlinear simultaneous second-order differential equations from which E or X can be found as functions of T and Z by well-known numerical methods. Here we will use the linear relation in Eq. [27] to obtain an analytical solution. Equations [24] and [27] give

$$\frac{\partial X}{\partial T} = \frac{K}{E_1^0 + E_e^0} \frac{\partial X^2}{\partial Z^2} \quad [28]$$

Together with the boundary conditions in Eq. [24], this relation shows that the discharge in a composite electrode proceeds in the same way as diffusion (according to Ficks second law) in a bounded domain $0 \leq Z \leq 1$ with constant flux at the two boundaries.

In the dimensionless units used above, the quantity $K/(E_1^0 + E_e^0)$ is equivalent to a diffusion coefficient which in dimensioned units is

$$D_c = \frac{k}{\mathbf{F} \cdot \mathbf{v} \cdot c^0 \left(\frac{1}{\kappa_l} + \frac{1}{\kappa_e} \right)} \quad [29]$$

To describe the discharge characteristics of the electrode at the given load a "load factor," L_c , is introduced

$$L_c = \frac{\tau_c}{\tau_D} = \frac{E_1^0 + E_e^0}{K} = (1 + \beta)E_1^0/K \quad [30]$$

$$= \frac{|i^*| \cdot l}{k} \left(\frac{1}{\kappa_e} + \frac{1}{\kappa_l} \right)$$

where τ_c is the time constant for the electrode: ℓ^2/D_c .¹ The solution of Eq. [28] can be obtained by combining solutions for the equivalent heat conduction phenomena (25) as discussed in the Appendix.

The two solutions below are written using L_c and $E_e^0 = \beta \cdot E_1^0$ to demonstrate the influence of additional electronic resistance

$$X = T + \frac{E_1^0}{K} \left\{ \frac{1 + \beta}{2} Z^2 - \beta Z + \frac{\beta}{3} - \frac{1}{6} + \frac{2}{\pi^2} \sum_{n=1}^{\infty} \frac{(-1)^n}{n^2} \exp[-n^2 \pi^2 T/L_c] [\beta \cos n\pi Z - \cos n\pi(1 - Z)] \right\} \quad [31]$$

and²

¹In Ref. (11), the reciprocal of L_c was used, called Q .

²ierfc is the first integral of the erfc function. See Ref. (25).

$$X = 2 \frac{E_1^0}{K} \frac{\sqrt{T}}{L_c} \sum_0^{\infty} \left[\text{ierfc} \frac{2n + 1 + Z}{2\sqrt{T}/L_c} + \text{ierfc} \frac{2n + 1 - Z}{2\sqrt{T}/L_c} + \beta (\text{ierfc} \frac{2n + Z}{2\sqrt{T}/L_c} + \text{ierfc} \frac{2n + 2 - Z}{2\sqrt{T}/L_c}) \right] \quad [32]$$

These relations are most conveniently treated by considering "long time" and "short time" behavior separately. To obtain an acceptable battery capacity, L_c should be less than one. For $T > L_c/3$, the sum of exponentials in Eq. [31] vanishes, giving the long time approximation

$$X = T + \frac{E_1^0}{K} \left(\frac{1 + \beta}{2} Z^2 + \beta Z + \frac{\beta}{3} - \frac{1}{6} \right) \quad [33]$$

This concentration profile is a parabola with minimum value at $Z = \beta/(1 + \beta)$. The values of X at the back and front are

$$Z = 0, X_0 = T + (2\beta - 1)E_1^0/6K \quad [34]$$

$$Z = 1, X_1 = T + (2 - \beta)E_1^0/6K$$

Using Eq. [18] and [11], the dimensionless working potential is found as

$$E_c = E^* - KT - (E_1^0 + E_e^0)/3 \quad [35]$$

$$= E^* - KT - (1 + \beta)E_1^0/3$$

For "short time," an approximation can be obtained from Eq. [32] observing that, for small values of T/L_c , all terms except those with $n = 0$ in the summations vanish, (ierfc $1.5 < 0.01$). Also, for Z near zero, only the term with ierfc $(Z/2\sqrt{T}/L_c)$, and for Z near one, only ierfc $((1 - Z)/2\sqrt{T}/L_c)$ remains. Hence, the short time approximation is

$$X = 2 \frac{E_1^0}{K} \sqrt{\frac{T}{L_c}} \left(\text{ierfc} \frac{1 - Z}{2\sqrt{T}/L_c} + \beta \text{ierfc} \frac{Z}{2\sqrt{T}/L_c} \right) \quad [36]$$

showing that the profile is composed of two semi-infinite diffusion profiles starting from $Z = 1$ and $Z = 0$, respectively. They both travel inward and at $Z = \beta/(1 + \beta)$ they meet, building up the parabola given by Eq. [33]. The values of X at the back and front of the electrode are [ierfc(0) = $1/\sqrt{\pi}$]

$$Z = 0, X_0 = 2 \frac{\beta E_1^0}{K} \sqrt{\frac{T}{\pi L_c}} \quad [37]$$

$$Z = 1, X_1 = 2 \frac{E_1^0}{K} \sqrt{\frac{T}{\pi L_c}}$$

Then using Eq. [11] and [18], the dimensionless working potential is

$$E_c = E^* - \frac{2}{\sqrt{\pi}} \frac{1 + \beta^2}{(1 + \beta)^{3/2}} \sqrt{KE_1^0 \cdot T} - \frac{\beta}{1 + \beta} E_1^0 \quad [38]$$

This relation demonstrates the \sqrt{t} dependence, typically for semi-infinite diffusion, but it also contains a constant term for $t = 0$ which is largest for $E_1^0 = E_e^0$, ($\beta = 1$).

Equations [35] and [38] are asymptotic solutions for $T \rightarrow \infty$ and $T \rightarrow 0$, but they are both very good approximations over a large range. Equating dE_c/dT from these two expressions, a transition point is found for

$$T_t = \left[\frac{1 + \beta^2}{(1 + \beta)^2} \right]^2 \frac{L_c}{\pi} = \frac{(1 + \beta^2)^2}{(1 + \beta)^3} \frac{E_1^0}{\pi K} \quad [39]$$

and, at this point, the true value for E_c deviates less than 0.01($E_e^0 + E_1^0$) from the values calculated from Eq. [35] and [38]. Thus, these two relations cover the range $0 < T < 1 - L_c/3$ with a sufficient precision for all practical purposes.

The low potential region.—Physically, X can never exceed 1, and, thus, Eq. [35] or [38] are only valid for $T < T_{sat}$,

where T_{sat} is found by equating X to 1 in Eq. [34] or [37]. For practical batteries, a utilization of more than 50% is usually required and hence, only the use of Eq. [34] is relevant. From this, T_{sat} is

$$\beta \leq 1, T_{\text{sat}} = 1 - (2 - \beta) \frac{E_1^0}{6K} = 1 - \frac{2 - \beta}{6(1 + \beta)} L_c \quad [40]$$

$$\beta \geq 1, T_{\text{sat}} = 1 - (2\beta - 1) \frac{E_1^0}{6K} = 1 - \frac{2\beta - 1}{6(1 + \beta)} L_c$$

For $\beta = 0$ and $\beta \rightarrow \infty$, T_{sat} is $1 - L_c/3$, and for $\beta = 1$, T_{sat} is $1 - L_c/12$. At T_{sat} the insertion compound becomes saturated either at the surface (for $\beta < 1$) or at the current collector ($\beta > 1$). For $\beta = 1$, the saturation occurs simultaneously at the surface and at the current collector.

However, the discharge of the inner parts of the electrode can continue for $T > T_{\text{sat}}$. For $\beta < 1$, due to the transport of M^+ in the ionic conducting network to the non-saturated inner parts, and for $\beta > 1$, correspondingly through transport of electrons in the electronic conducting network of (saturated) insertion compound. In this way the electrode can, in principle, be discharged to 100% utilization.

This part of the discharge is characterized by a boundary between the saturated and still active part of the electrode; the boundary moving inwards for $\beta < 1$. From this boundary on, the electrode reaction proceeds as usual and Eq. [24] will apply. However, the boundary condition $dE/dZ = -E_1^0$ should now be applied to the moving boundary between the saturated and the active part of the electrode. For $\beta > 1$, saturation starts at the current collector. The total current is now carried by the electronic conducting network to the boundary, which is now moving forward but still subjected to the boundary condition $dE/dZ = E_e^0$. For $\beta = 1$, two boundaries starting at each end move against each other. In Fig. 5, we have depicted the development of concentration profiles in the electrode with T for different characteristic values of β .

A simple analytical solution of Eq. [24] with moving boundary conditions has not been found. However, an approximate solution for the position of the boundary can be found if one assumes that the shape of the concentration profile remains parabolic as for $T < T_{\text{sat}}$. This appears reasonable when $1 - T_{\text{sat}}$ is small.

The analytical solutions are only simple for E_e^0 or $E_1^0 = 0$ or in the symmetrical case $E_e^0 = E_1^0$. For $\beta = 0$ let the boundary between the outer saturated and the inner ac-

tive region be at $Z = Z^*$. Then, using the boundary conditions at $Z = 0$ and $Z = Z^*$ and the assumption about a parabolic shape, the concentration profile ($0 \leq Z \leq Z^*$) is found to be

$$X = \frac{E_1^0 Z^2}{2KZ^*} - \frac{E_1^0}{2K} Z^* + 1 \quad [41]$$

As the total inserted amount is T , Z^* can be found from

$$T = \int_0^{Z^*} X dZ + 1 - Z^* \quad [42]$$

resulting in

$$Z^* = \sqrt{3K(1 - T)/E_1^0} \quad [43]$$

For $\beta = 1$ ($E_e^0 = E_1^0$), we have two boundaries, Z_1^* and Z_2^* , symmetrical about $Z = 1/2$. With the same procedure as above, we get

$$Z_1^* = 1/2 + \sqrt{3K(1 - T)/2E_1^0} \quad [44]$$

$$Z_2^* = 1/2 - \sqrt{3K(1 - T)/2E_1^0}$$

At the boundaries, the local electrode potential according to Eq. [11] is $E^* - K$. If $E_e^0 = 0$, we get the working potential directly as

$$E_c = E^* - K - E_1^0(1 - Z^*) \quad [45]$$

And for $E_e^0 = E_1^0$ ($\beta = 1$)

$$E_c = E^* - K - E_1^0(1 - Z^*) - \frac{F}{RT} \int_{Z_1^*}^{Z_2^*} \pi dZ \quad [46]$$

Inserting Eq. [43] in [45] and Eq. [44] in [46] and evaluating the integral as for Eq. [18], we get as a common result

$$E_c = E^* - K - E_1^0(1 - \sqrt{3K(1 - T)/(\beta + 1)E_1^0}) \quad [47]$$

valid for $\beta = 0$ and 1.

The final working potential at $T = 1$ is thus estimated as

$$E_c(T = 1) = E^* - K - E^0 \quad [48]$$

where E^0 is E_1^0 for $\beta \leq 1$ or E_e^0 for $\beta \geq 1$.

Discussion

The basic Eq. [28] demonstrates that in the region where $X < 1$ the composite electrode behaves like a non-porous insertion electrode. The apparent diffusion coefficient depends, according to Eq. [29], on the slope of the EMF curve, on the conductivities, and on the specific capacity ($c^0 \cdot v$) of the electrode.

Using available data for the $\text{TiS}_2/\text{Li}_3\text{N}$ combination,³ a value of $D_c \approx 10^{-5} \text{ cm}^2 \text{ s}^{-1}$ is obtained at 170°C . This relatively high value allows construction of batteries with a high materials utilization and a good packing density even at heavy loads.⁴

To illustrate this further, the discharge curve, i.e., the working voltage, ϵ_c , as a function of degree of discharge, T , can be calculated for an electrode with known values of k , ϵ_1^0 , ϵ_e^0 , and ϵ^* . This can be done using Eq. [38], [35], and [47], successively, observing that the discharge curve can be divided in three regions: the \sqrt{T} region, the linear part, and the low potential region characterized by a $\sqrt{1 - T}$ dependence. The transition points between these regions as given by Eq. [39] and [40] are determined by the load factor L_c defined in Eq. [30]. The case $\epsilon_1^0 \gg \epsilon_e^0$ ($\beta = 0$) is of considerable practical interest and may serve as an illustration of the characteristic course of the discharge curve. Using dimensioned units ($k = RTK/F$, $L_c = \epsilon_1^0/k$), the three regions can be described thus

³ $C^0 = 0.026 \text{ mol cm}^{-3}$, $K = 22$, $\kappa_e \gg \kappa_1 \approx 2.5 \cdot 10^{-3} \Omega^{-1} \text{ cm}^{-1}$ at 170°C , $v = 0.5$.

⁴ It has been experimentally shown that although the $\text{TiS}_2/\text{Li}_3\text{N}$ combination is thermodynamically unstable, it is kinetically stable. Batteries with $\text{TiS}_2/\text{Li}_3\text{N}$ composite electrodes have been cycled more than 500 times (30).

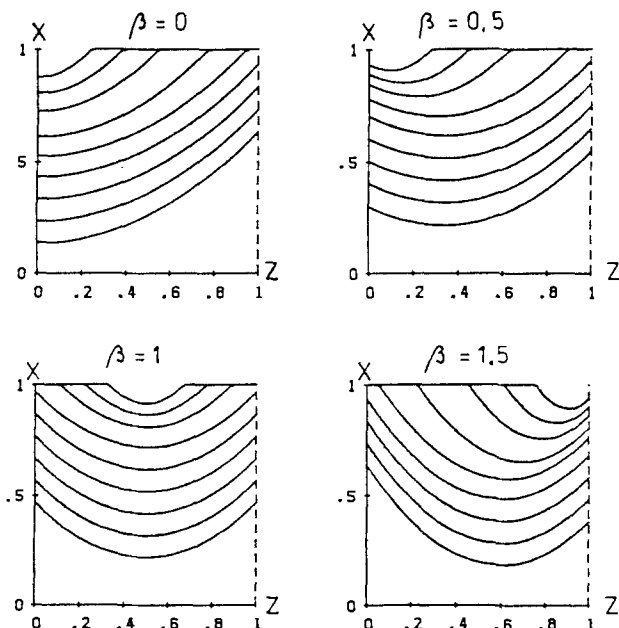


Fig. 5. Calculated concentration profiles in composite electrode. Different values of $\beta = \kappa_1/\kappa_e$ as indicated. E_1^0/K kept constant. Counted from lowest value of X , $T = 0.3, 0.4, 0.5, 0.6, 0.7, 0.8, 0.9, 0.95$, and 0.98 .

$$T < L_c/\pi;$$

$$\epsilon_c = \epsilon^* - \frac{2}{\sqrt{\pi}} \sqrt{\epsilon_1^0 k \cdot T}$$

$$L_c/\pi < T < 1 - L_c/3; \quad [49]$$

$$\epsilon_c = \epsilon^* - \epsilon_1^0/3 - k \cdot T$$

$$1 - L_c/3 < T < 1;$$

$$\epsilon_c = \epsilon^* - k - \epsilon_1^0 (1 - \sqrt{3k(1-T)/\epsilon_1^0})$$

In Fig. 6, discharge curves for $L_c = 1$ and different combinations of k and ϵ_1^0 are depicted. The effect of an additional electronic resistance ($\beta > 0$) is illustrated in Fig. 7. Contrary to the case for $\beta = 0$, there is according to Eq. [38] an initial ohmic voltage drop: $\epsilon_e^0/(1 + \beta)$. In a complete battery, this will be observed in addition to the voltage drop across the separator electrolyte. The \sqrt{T} part of the curve is flattened due to the factor $(1 + \beta^2)/(1 + \beta)^{3/2}$ in Eq. [38] ($= 0.7$ for $\beta = 1$). The linear part is further depressed by $\epsilon_e^0/3$, but the linear range is extended at the expense of the \sqrt{T} and the $\sqrt{1-T}$ regions, delaying the appearance of the more sloping last part of the discharge. The end-point voltage ($T = 1$) is, however, the same as for $\beta = 0$ cf. in Eq. [48].

In general, the course and position of the discharge curve are determined by k and ϵ^* , characteristic for the insertion compound, and by the quantities ϵ_1^0 and ϵ_e^0 , which besides the electronic and ionic conductivities κ_e and κ_i , combine the influence of the discharge current, the thickness of the electrode, and the volume fraction and saturation concentration of the insertion compound.

ϵ^* and k are thermodynamic quantities given by the affinity of the cathode reaction in Eq. [2]. k in particular depends on the interactions associated with the insertion reaction. The ϵ_e^0 's as given by Eq. [16] contain the effective conductivities κ_e and κ_i . The magnitudes of these are critical for the battery performance. It should be realized that these conductivities are effective values, including the effects of volume fraction, tortuosity, contact resistance between particles, and voids in the electrode. All this adds up to a considerable reduction in the effective

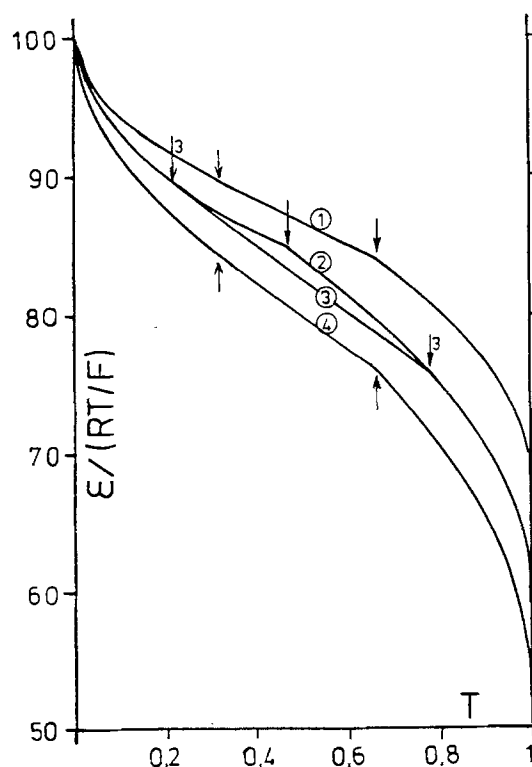


Fig. 6. Calculated discharge curves. $\kappa_e \gg \kappa_i$. (1) $E_1^0 = 16, K = 16$; (2) $E_1^0 = 24, K = 6$; (3) $E_1^0 = 16, K = 24$; and (4) $E_1^0 = 24, K = 24$. Transition points indicated by arrows.

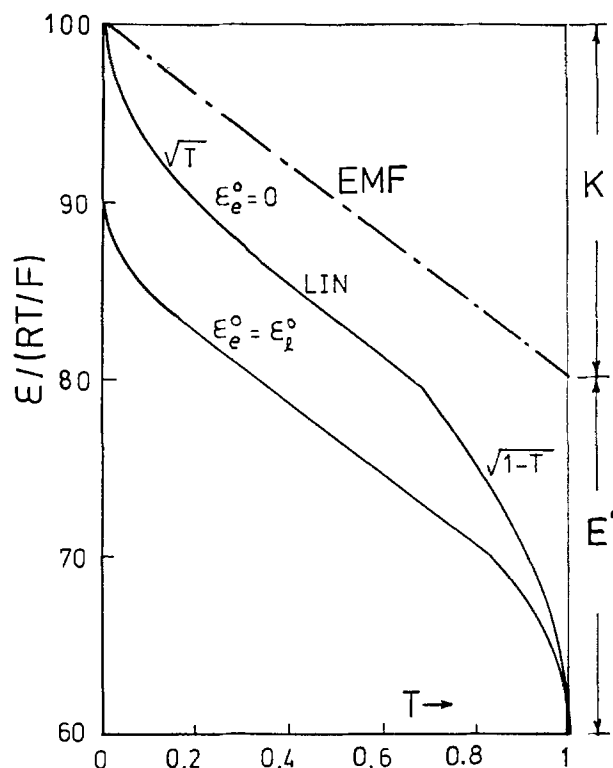


Fig. 7. Calculated discharge curves demonstrating the effect of electronic resistance. Parameters as indicated.

conductivities compared with those of the pure substances.

As the electrolyte and insertion compound particles act as nonconducting diluents for each other, some guidance as to the magnitudes of the effective values can be obtained from the study of conductivities of heterogeneous systems as carried out by Meredith and Tobias (26) and later discussed by Newman and Tiedemann (27). According to these authors, κ_i and κ_e can be estimated from the volume fractions and the conductivities of the pure substances κ_i^0 and κ_e^0 by the relations

$$\kappa_i/\kappa_i^0 = (1 - v)^\alpha; \quad \kappa_e/\kappa_e^0 = v^\alpha \quad [50]$$

where the exponent α has a value in the range $1.5 < \alpha < 2.5$. Using Eq. [50], ϵ_e^0 and ϵ_1^0 can be written as

$$\epsilon_1^0 = F \frac{l^2 c_0 v}{\tau_D \kappa_i^0 (1 - v)^\alpha} = - \frac{l}{\kappa_i^0 (1 - v)^\alpha} \cdot i^*$$

and [51]

$$\epsilon_e^0 = F \frac{l^2 c^0}{\tau_D \kappa_e^0 v^{\alpha-1}} = - \frac{l}{\kappa_e^0 v^\alpha} \cdot i^*$$

From these relations, it can be estimated how the different design parameters and the discharge regime influence the course of the discharge curve and thus, the obtainable materials utilization. For example, for different loads it is obvious that the ratio l^2/τ_D should remain constant for a given electrode composition in order not to change the discharge behavior.

Due to the uncertainty present in estimates of the effective conductivities, it is certainly a safer approach to consider the effective κ 's as phenomenological parameters characteristic for a given electrode composition, grain size, and fabrication technique, and to measure them directly on a sample electrode.

This can be done using blocking electrodes for M^+ ions and electrons, respectively, considering the composite as a mixed conductor, and using the methods discussed, e.g., by Rickert (28). It is important in these measurements to observe the requirement of electrochemical equilibrium between the insertion compound and the electrolyte.

Alternatively, estimates of $\epsilon_e^0 + \epsilon_i^0$ and k can be found from the discharge curves when the current is chosen low enough to allow development of the linear region. In these cases, k is the slope of the linear part, while the position of the discharge curve (corrected for the potential difference across the separator) according to Eq. [35] or [49] allows determination of $\epsilon_e^0 + \epsilon_i^0$ for a given current. In cases $\kappa_e \gg \kappa_i$ ($\beta = 0$), the potential difference across the separator can be found from the instantaneous voltage transient when switching the current on or off.

As mentioned above, a consequence of the immobility of the compensating charges in the electrolyte is the possibility to discharge the composite electrode until $T = 1$, as discussed in the derivation of Eq. [47]. However, the predictions which can be made for this part of the discharge are less precise than the predictions for the square root and linear regions. First it must be realized that the assumption about a linear potential/composition relation has limited validity. For $X > 0.95$, a relation like Eq. [10] is a better approximation to the potential dependence, thus causing a steeper slope of the discharge curve and a lower end-point voltage. Also for that part of the discharge, where only a small part of the electrode is active, the assumptions about equilibrium in the insertion compound particles and on the surface of these cannot be maintained because of the high final local current transfer. For $T > 0.95$ the influence of these limitations must be studied using a numerical technique as discussed in our previous paper (14).

Conclusion

The discharge behavior of a composite electrode containing a finely divided insertion electrode material can be adequately described by the ionic and electronic conductivities of the composite and the slope of the EMF/composition curve for the insertion compound.

Using reasonable approximations, the course of the discharge curve for a given electrode can be calculated analytically for a specified constant current load. Due to the immobility of the compensating charges in the solid electrolyte, theory predicts that a materials utilization near 100% can be obtained to an acceptable discharge end point.

The possibility of realizing these advantages depends on the availability of a good solid ion conductor for the inserted ion. The fulfillment of this requirement is facilitated by the possibility of operating this type of electrode at a moderately increased temperature.

Technologically, the realization of the composite electrode concept requires the development of a fabrication technique which results in a structure consisting of two contiguous networks of electrolyte and insertion compounds in intimate contact.

Manuscript submitted Feb. 24, 1983; revised manuscript received Aug. 26, 1983.

APPENDIX

The heat conduction problem (25)

$$0 \leq x \leq l, V = 0 \text{ for } t = 0$$

$$\frac{\partial V}{\partial x} = 0 \text{ for } X = 0; \frac{dV}{dx} = \frac{F^0}{K} \equiv A \text{ for } x = l \quad [\text{A-1}]$$

$$\frac{\partial V}{\partial t} = \kappa \frac{\partial^2 V}{\partial x^2}; \kappa = \frac{K}{\rho c} \equiv \gamma$$

has (loc.cit.) the solutions

$$V = A\gamma \cdot t/l + A(x^2/2l - l/6) - \frac{2}{\pi^2} \sum_1^{\infty} \frac{(-1)^n}{n^2} \exp[-n^2\pi^2\gamma t/l^2] \cos n\pi x/l$$

and

$$V = 2A\sqrt{\gamma t} \sum_0^{\infty} \left(\operatorname{ierfc} \frac{(2n+1)l+x}{2\sqrt{\gamma t}} + \operatorname{ierfc} \frac{(2n+1)l-x}{2\sqrt{\gamma t}} \right) \quad [\text{A-2}]$$

Equations [24] and [28] can be written

$$U = U(Z, T) \quad 0 \leq Z \leq 1; U(Z, 0) = 0$$

$$\partial U/\partial Z = \alpha_1, Z = 0; \partial U/\partial Z = \alpha_2, Z = 1$$

$$\frac{\partial U}{\partial T} = \gamma \frac{\partial^2 U}{\partial Z^2} \quad [\text{A-3}]$$

Let $R = R(\tau, T)$ and $S = S(s, T)$ be defined by

$$\frac{\partial R}{\partial T} = \gamma \frac{\partial^2 R}{\partial \tau^2}; \quad \frac{\partial S}{\partial T} = \gamma \frac{\partial^2 S}{\partial s^2}$$

$$S = R = 0, T = 0; \quad s = 1 - \tau$$

$$\partial R/\partial \tau = 0, \tau = 0; \quad \partial R/\partial \tau = -\alpha_1, \tau = 1 \quad [\text{A-4}]$$

$$\partial S/\partial s = 0, s = 0; \quad \partial S/\partial s = \alpha_2, s = 1$$

Then, $U = R + S$ is a solution to [A-3]. From Eq. [A-1], for $l = 1$, $x = \tau = 1 - Z$, and $A = -\alpha_1$

$$R = -\alpha_1\gamma T - \alpha_1(1/3 - Z + \frac{Z^2}{2} - \frac{2}{\pi^2} \sum_1^{\infty} \left[\frac{(-1)^n}{n^2} \exp[-n^2\pi^2\gamma T] \cos n\pi(1 - Z) \right])$$

And for $x = s = Z$, $A = \alpha_2$

$$S = \alpha_2\gamma T + \alpha_2 \left(Z^2/2 - 1/6 - \frac{2}{\pi^2} \sum_1^{\infty} \left[\frac{(-1)^n}{n^2} \exp[-n^2\pi^2\gamma T] \cos n\pi Z \right] \right)$$

leading to

$$U = (\alpha_2 - \alpha_1)\gamma T + (\alpha_2 - \alpha_1)Z^2/2 + \alpha_1 Z - \alpha_1/3 - \alpha_2/6 \quad [\text{A-5}]$$

$$- \frac{2}{\pi^2} \sum_1^{\infty} \frac{(-1)^n}{n^2} \exp[-n^2\pi^2\gamma T] [\alpha_2 \cos n\pi Z - \alpha_1 \cos n\pi(1 - Z)]$$

or using Eq. [A-2]

$$U = 2\sqrt{\gamma T} \left[\alpha_2 \sum_0^{\infty} \left(\operatorname{ierfc} \frac{2n+1+Z}{2\sqrt{\gamma T}} + \operatorname{ierfc} \frac{2n+1-Z}{2\sqrt{\gamma T}} \right) - \alpha_1 \sum_0^{\infty} \left(\operatorname{ierfc} \frac{2n+Z}{2\sqrt{\gamma T}} + \operatorname{ierfc} \frac{2n+2-Z}{2\sqrt{\gamma T}} \right) \right] \quad [\text{A-6}]$$

Inserting $\gamma = K/(E_e^0 + E_i^0) = 1/L_c$ and $\alpha_1 = -E_e^0/K = -\beta E_i^0/K$, $\alpha_2 = E_i^0/K$ in Eq. [A-5] and [A-6] gives Eq. [31] and [32].

LIST OF SYMBOLS

c^0	saturation concentration of inserted ion in insertion compound
f	interaction parameter in Eq. [10]
i^*	overall discharge/charge current density
i_e	local electronic current density
i_i	local ionic current density
i_t	transfer current per unit electrode volume
k	slope of linearized Eq. [11]
l	thickness of composite electrode
n	amount of M^+ in HM_x at saturation and also variable in Eq. [31] and [32]
t	discharge/charge time, time coordinate
x	amount of M in HM_x
v	volume fraction of insertion compound
z	length coordinate $0 \leq z \leq l$
D_c	apparent chemical diffusion coefficient for M^+ in composite
H	insertion compound
M^+	inserted ion

T in RT/F , Kelvin temperature

Dimensionless Variables and Groups

E dimensionless potential, $E_i^m = \epsilon_i^m F/RT$ (for significance of superscripts and subscripts see ϵ)
 K $k \cdot F/RT$
 L_c load factor, τ_c/τ_D
 X degree of insertion, $X = x/n$
 T degree of discharge, $T = t/\tau_D$
 Z length coordinate, $Z = z/l$
 Z* boundary between saturated and active part of electrode

Greek Letters

α exponent in Eq. [50]
 β ratio of ionic to electronic conductance and also $\beta = \epsilon_e^0/\epsilon_i^0$
 ϵ insertion compound electrode potential, $\epsilon = \pi - \phi$
 ϵ_θ standard potential in Eq. [10].
 ϵ_0, ϵ_1 ϵ at back and front of electrode, respectively
 ϵ_c working potential of electrode
 ϵ^* electrode potential before discharge
 ϵ_e^0 $-i^* \cdot l/\kappa_e$
 ϵ_i^0 $-i^* \cdot l/\kappa_i$
 ϕ Galvani potential in electrolyte
 κ_e, κ_i effective electronic, ionic conductivities in composite (bulk values)
 κ_e^0, κ_i^0 electronic, ionic conductivities of insertion compound and solid electrolyte
 π Fermi potential in insertion compound ($\pi = -\bar{\mu}_e/F$)
 τ_c time constant for composite electrode = l^2/D_c
 τ_D stoichiometric discharge time = $-F \cdot v \cdot c^0 \cdot l/i^*$

REFERENCES

- G. H. Newman and J. P. Klemm, *This Journal*, **127**, 2097 (1980).
- G. H. Newman and J. P. Klemm, *ibid.*, **129**, 230 (1982).
- A. Bottini, M. Lazzari, G. Razzini, B. Rivolta, G. De Felici, M. A. Voso, and B. Scrosati, *J. Electroanal. Chem.*, **98**, 165 (1979).
- M. S. Whittingham, *Prog. Solid State Chem.*, **12**, 41 (1978).
- D. W. Murphy, P. A. Christian, F. D. DiSalvo, and J. V. Waszczak, *Inorg. Chem.*, **18**, 2800 (1979).
- L. H. Gaines, R. W. Francis, G. H. Newman, and B. M. L. Rao, 11th Intersociety Energy Conversion Engineering Conference, Stateline, NV (1976).
- C. C. Liang, A. V. Joshi, and N. E. Hamilton, *J. Appl. Electrochem.*, **8**, 445 (1978).
- J. R. Rea, G. S. Kelsey, H. C. Kuo, and M. Kallianidis, *Solid State Ionics*, **3/4**, 267 (1981).
- S. Atlung, *Prog. Batt. Solar Cells*, **2**, 96 (1979).
- R. Jasinski, in "Advances in Electrochemistry and Electrochemical Engineering," Vol. 8, P. Delahay and C. W. Tobias, Editors, p. 291 (1972).
- S. Atlung, K. West, and T. Jacobsen, *This Journal*, **126**, 1311 (1979).
- S. Atlung, K. West, and T. Jacobsen, in "Materials for Advanced Batteries," D. W. Murphy, J. Broadhead, and B. C. H. Steele, Editors, p. 275, Plenum Press, New York (1980).
- K. West, T. Jacobsen, B. Zachau-Christiansen, and S. Atlung, Extended Abstract A 11, 32nd ISE Meeting, Dubrovnik (1981).
- K. West, T. Jacobsen, and S. Atlung, *This Journal*, **129**, 1480 (1982).
- J. E. Oxley and B. B. Owens, in "Power Sources 3. Proceedings of the 7th International Power Sources Symposium," D. H. Collins, Editor, p. 537, Oriel Press, Newcastle (1971).
- C. C. Liang and L. H. Barnette, *This Journal*, **123**, 453 (1976).
- M. B. Armand, J. M. Chabagno, and M. J. Duclot, in "Fast Ion Transport in Solids," Vashista *et al.*, Editors, p. 131, Elsevier, Amsterdam (1979).
- S. Atlung, S. Skaarup, B. Zachau-Christiansen, and K. West, Progress Report No. 2, Advanced Battery Design, EEC Contract EE/E2/429/80/DK/H (1982).
- J. S. Newman and C. Tobias, *This Journal*, **109**, 1183 (1962).
- J. de Levie, in "Advances in Electrochemistry and Electrochemical Engineering," Vol. 6, P. Delahay and C. W. Tobias, Editors, p. 329 (1967).
- M. Armand, Thesis, Grenoble (1978).
- A. J. Berlinsky, W. G. Unruh, W. R. McKinnon, and R. R. Haering, *Solid State Commun.*, **31**, 135 (1979).
- T. Jacobsen, K. West, and S. Atlung, *Electrochim. Acta*, **27**, 1007 (1982).
- J. J. Coleman, *Trans. Electrochem. Soc.*, **90**, 545 (1946).
- H. S. Carslaw and J. C. Jaeger, "Heat Conduction in Solids," 2nd ed., p. 112, 310, Oxford, London (1959).
- R. E. Meredith and C. W. Tobias, in "Advances in Electrochemistry and Electrochemical Engineering," Vol. 2, P. Delahay and C. W. Tobias, Editors, p. 15 (1965).
- J. Newman and W. Tiedeman, *AICHE J.*, **21**, 25 (1975).
- H. Rickert, "Einführung in die Elektrochemie fester Stoffe," p. 107, Springer, Berlin (1973).
- K. West, T. Jacobsen, B. Zachau-Christiansen, and S. Atlung, *Electrochim. Acta*, **28**, 97 (1983).
- B. Knutz and S. Skaarup, 4th Internat. Conf. Solid State Ionics, Grenoble (1983).

Technical Notes



Rare Earth-Activated Niobates

W. A. McAllister

North American Philips Lighting Corporation, Bloomfield, New Jersey 07003

Alkaline earth niobate phosphors were described some time ago (1, 2), the best materials being calcium and cadmium niobates ($\text{Ca}(\text{Cd})\text{Nb}_2\text{O}_6$) emitting in the blue and having the columbite structure. Other niobates with intrinsic blue emission are based on the fergusonite structure (3), e.g., yttrium niobate (YNbO_6), and have been shown to be good hosts for activation by other rare earths. Energy is transferred from host to activator giving, in the case of Eu^{+3} , emission largely that of the latter species. Since there were no reports of a similar role for the calcium or cadmium niobates, we have investigated the luminescence characteristics of these materials, their

solid solutions, and rare earth activated materials derived therefrom.

Experimental

Phosphors were prepared by reacting SL grade calcium carbonate (GTE) and cadmium oxide (99.99% American Metals and Chemicals) with optical grade Kawecki-Berylco niobium pentoxide; rare earths, when present, were 99.99% Molycorp oxides. Firing was in air or nitrogen (Tb-activated materials only) for 2h at $1100^\circ\text{--}1400^\circ\text{C}$, the higher temperature being required for high calcium [>50 m/o (mol percent)] members of the series. A slight excess of Nb_2O_5 was also required in these latter formulations to suppress formation of the $\text{Ca}_2\text{Nb}_2\text{O}_7$ structure (4).

*Electrochemical Society Active Member.

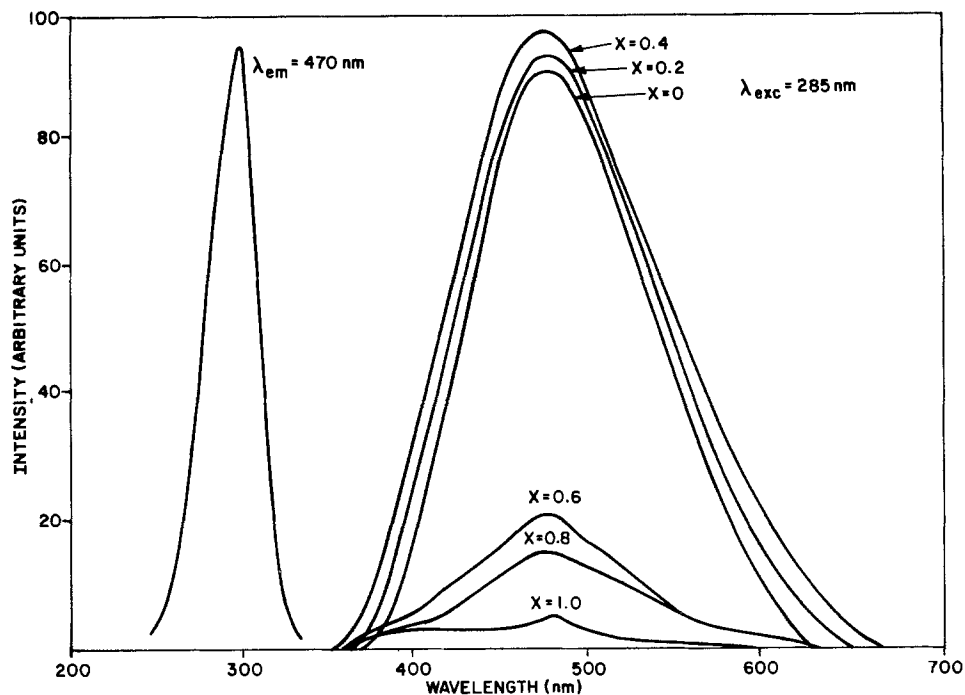


Fig. 1. Spectral characteristics of $\text{Ca}_{1-x}\text{Cd}_x\text{Nb}_2\text{O}_6$ phosphors.

Product purity was ascertained by x-ray diffraction using a Philips Model APD instrument. Brightness comparisons were made using filtered radiation from a low pressure mercury discharge as the source, a Spectra Brightness Spot meter as the detector. Other spectral characteristics were measured using a Perkin-Elmer MPF44-B instrument with a microprocessor unit for correcting spectra.

Results

Although all phosphors in the solid solution series $\text{Ca}_{1-x}\text{Cd}_x\text{Nb}_2\text{O}_6$ have a broad emission band peaked at 470 nm for excitation peaked sharply at 285 nm, the cadmium-rich members are superior (Fig. 1). The best such material has an emission spectrum similar to "Blue Halo" and with a peak intensity about 75% of that of the latter under 254 nm excitation.

The rare earths were introduced, with sodium as a charge compensating species for substitution on the divalent Ca^{2+} cation site, as activators in the $\text{Ca}_{1-x}\text{Cd}_x\text{Nb}_2\text{O}_6$ series. Only those discussed below gave characteristic

Ln^{3+} emission, excitation being via a charge transfer band of the host at 285 nm and in the 350-500 nm range where the host emits and rare earth f-f transitions occur. The rare earth concentration for best Ln^{3+} emission ranged from 5 to 12%; the brightest generally being noted for the cadmium end member of the series (Table I). The exceptions were in the terbium activated group, the fired group products having tan body colors indicating some (unknown) amounts of Tb^{4+} species and precluding meaningful comparisons.

The emission spectra of the $\text{Ca}_{0.4-2x}\text{Cd}_{0.6}\text{Nb}_2\text{O}_6:\text{Ln}_x\text{Na}_x$ group are depicted in Fig. 2-6. All have considerable host emission except europium which has only the characteristic 612 nm emission.

Discussion

In niobates, excitation is due to transfer of an electron from one of the highest filled molecular orbitals on an adjacent oxygen (O^{2-}) to one of the lowest unfilled orbitals located on the Nb^{5+} ion (5). The columbite structure of these materials is characterized by edge sharing of nio-

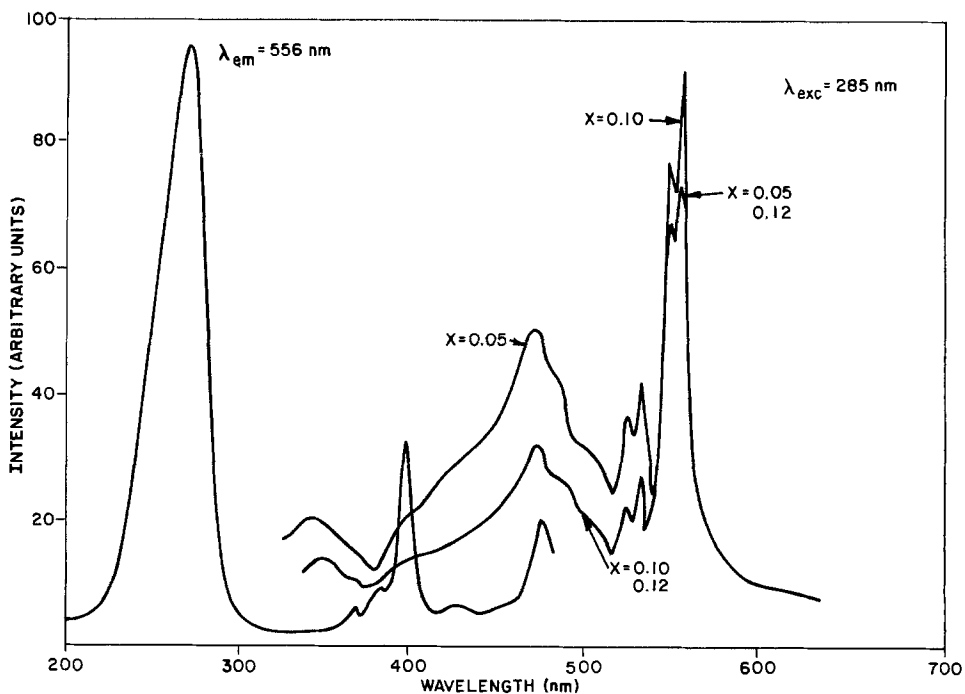


Fig. 2. Spectral characteristics of $\text{Ca}_{0.4-2x}\text{Er}_x\text{Na}_x\text{Cd}_{0.6}\text{Nb}_2\text{O}_6$ phosphors.

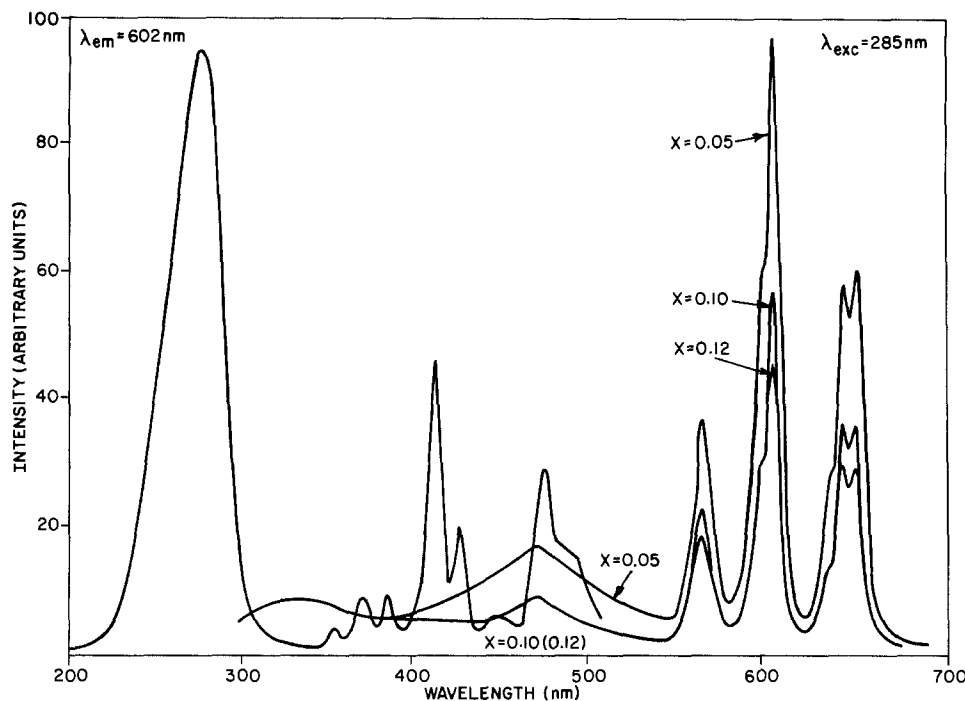


Fig. 3. Spectral characteristics of $Ca_{0.4-2x}Sm_xNa_xCd_{0.6}Nb_2O_6$ phosphors.

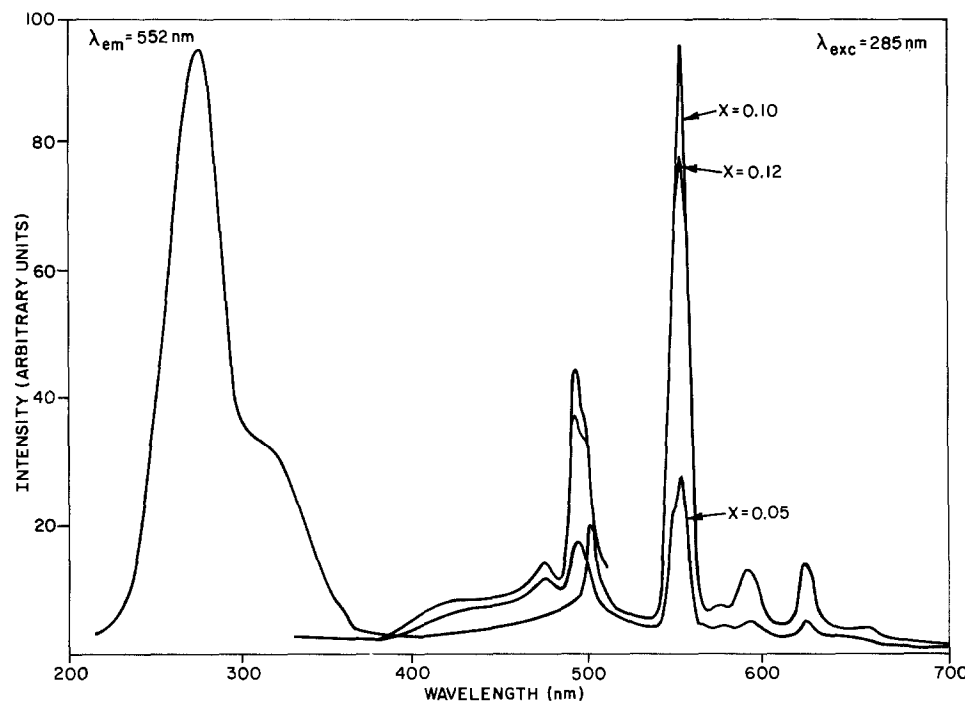


Fig. 4. Spectral characteristics of $Ca_{0.4-2x}Tb_xNa_xCd_{0.6}Nb_2O_6$ phosphors.

bate (NbO_6) octahedra, which are further joined at corners to form chains oriented along the C axis; the divalent spe-

cies bridging these chains are in a distorted cubic array of oxygen ions (6). Since all of the $Ca_{1-x}Cd_xNb_2O_6$ phosphors

Table I. Effect of cadmium concentration on $Ca_{1-x}Cd_xNb_2O_6:Ln^{+3}/Na^{+1}$ emission ($\lambda_{ex} = 285$ nm)

Activator	Concentration (mol)		Relative peak intensity	
	Cadmium		470 nm	Ln^{+3}
0.10 Er	0.9		80	100
	0.6		30	90
	0.2		10	10
0.05 Sm	0.9		10	100
	0.6		10	90
	0.2		20	20
0.10 Tb	0.8		15	30
	0.6		10	90
	0.2		20	20
0.12 Eu	0.76		1	90
	0.66		1	87
	0.20		1	10
0.10 Dy	0.8		30	95
	0.6		30	90
	0.2		10	15

Table II. Depreciation of $Ca_{1-x}Cd_xNb_2O_6:Ln^{+3}Na_y^{+1}$ phosphors

Activator	x	y	Depreciation (%)*		
			ft-L	Red ($\lambda_{ex} = 254$ nm)	Blue
Erbium	1.0	0.1	22	31	23
	0	0.1	0	4	1
Samarium	1.0	0.05	17	18	43
	0	0.05	9	10	2
Terbium	1.0	0.1	27	40	60
	0	0.1	14	23	80
Dysprosium	1.0	0.1	33	31	32
	0	0.1	5	4	3
Europium	1.0	0.12	17	17	90
	0	0.12	1	1	10
None	1.0	0	36	38	44
	0	0	18	16	14

*After 100h exposure under a quartz Sterilamp *in vacuo*.

Fig. 5. Spectral characteristics of $\text{Ca}_{0.4-2x}\text{Eu}_x\text{Na}_x\text{Cd}_{0.6}\text{Nb}_2\text{O}_6$ phosphors.

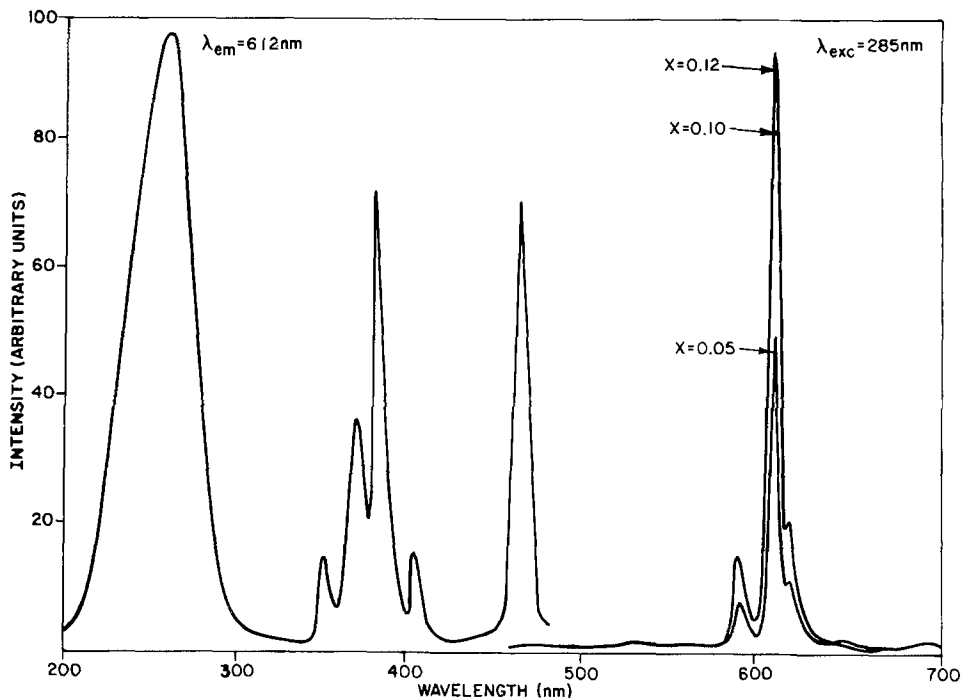
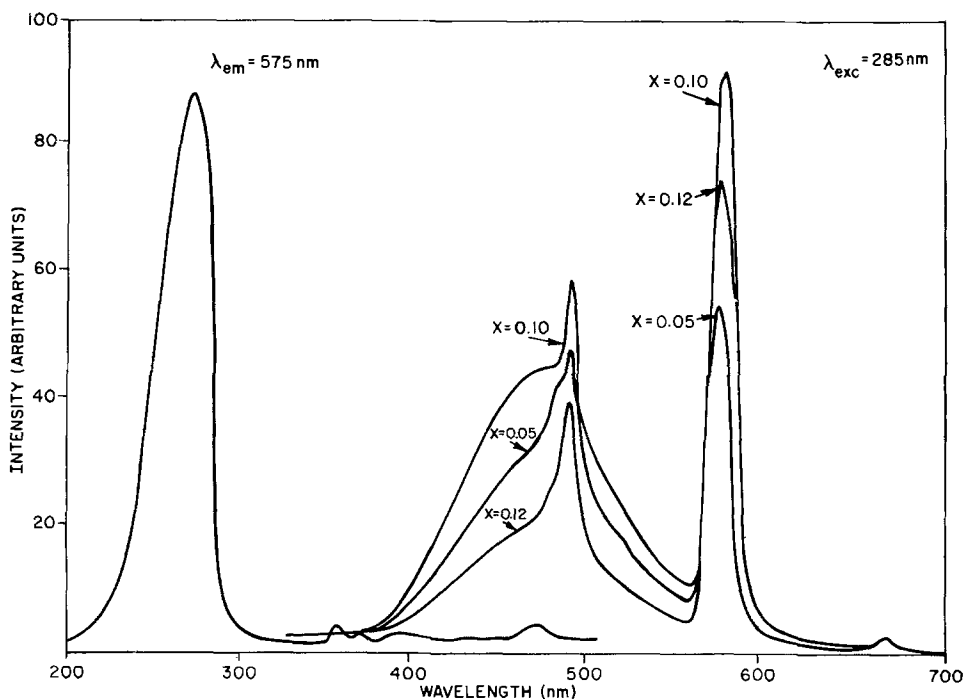


Fig. 6. Spectral characteristics of $\text{Ca}_{0.4-2x}\text{Dy}_x\text{Na}_x\text{Cd}_{0.6}\text{Nb}_2\text{O}_6$.



have the columbite structure, the superiority of cadmium-rich materials must be associated with differences in the divalent ions. Although their orbital radii are similar (7), the three calcium 3p orbitals and five cadmium 4d orbitals differ in directional characteristics. In the poorly defined site symmetry, the latter may overlap with the adjacent oxygen ions, the result being delocalization of the metal d electrons to the oxygens which, in turn, are coupled to the niobium metal ions. The presence of these electrons enables their participation in the $\text{O}^{2-} \rightarrow \text{Nb}^{5+}$ charge transfer and enhancement of the luminescence intensity; the calcium 3p orbitals apparently do not participate to as great an extent in this electron sharing.

This superiority of cadmium-based host materials extends to those in which the divalent metal ions were replaced by $\text{Ln}^{+3}\text{-Na}^{+1}$ combinations. Although the ratio of rare earth/host emission intensities varied with the

lanthanide, phosphors without calcium had the greatest overall intensity for all rare earths. In all cases, the rare earth must compete with niobate for energy to generate the Ln^{+3} emission and only europium is very successful. However, the plaque brightness of the europium-activated niobate is only 35% that of $\text{Y}_2\text{O}_3\text{:Eu}$, indicating considerable energy dissipation in an otherwise efficient host material. This may be due to the electron delocalization implied by orbital overlap. The attendant electron mobility could lead to color center formation by trapping at defects, *e.g.*, sodium vacancies, always present in solids. Evidence for such was noted by exposing plaques of host and rare earth-activated niobates of both calcium and cadmium to the radiation (254 + 185 nm) from a quartz Sterilamp, in an evacuated glass apparatus for 100h. The resulting depreciation was considerably greater for cadmium niobate materials (Table II), and the body

color darkening, which accompanies color center formation, was very apparent.

Acknowledgment

The writer is indebted to J. Livingston for x-ray diffraction analyses and E. Chen for technical assistance.

Manuscript submitted Aug. 2, 1983; revised manuscript received ca. Jan. 20, 1984.

North American Philips Lighting Corporation assisted in meeting the publication costs of this article.

REFERENCES

1. A. Wachtel, *This Journal*, **111**, 534 (1964).
2. G. Blasse and A. Brill, *Z. Phys. Chem. (Wiesbaden)*, **57**, 187 (1968).
3. G. Blasse, *J. Lumin.*, **14**, 231 (1976).
4. E. M. Levin and H. F. McMurdie, *Phase Diagrams for Ceramists*, 106 (1975 Supplement).
5. G. Blasse, *J. Inorg. Nucl. Chem.*, **26**, 1191 (1964).
6. J. P. Cummings and S. H. Simonsen, *Am. Mineral.*, **55**, 90 (1970).
7. J. T. Waber and D. T. Cromer, *J. Chem. Phys.*, **42**, 4116 (1965).

Use of Plasma-Deposited Si₃N₄ as an Oxidation Mask in the Fabrication of GaAs Shallow-Homojunction Solar Cells

G. W. Turner and M. K. Connors

Lincoln Laboratory, Massachusetts Institute of Technology, Lexington, Massachusetts 02173-0073

The optimum junction depth in shallow-homojunction n⁺/p/p⁺ GaAs solar cells is approximately 500Å (1). In the fabrication of these cells, the technique of anodic oxidation and stripping is utilized for thinning the n⁺ layer from its as-grown thickness, which is generally 1000-1500Å, and the final oxidation step is employed to form an antireflection (AR) coating. High efficiency cells have been fabricated with either a tin front contact grid applied before anodic oxidation (1) or a gold front contact grid applied after the final oxidation (2). However, neither metallization scheme is ideal.

Since a passivating oxide layer is formed on Sn during anodic oxidation, Sn contacts can be electroplated on the n⁺ GaAs surface prior to the oxidation process. This procedure is advantageous because it permits the solar cell current and voltage to be monitored after successive oxidation steps, making it convenient to optimize the thickness of the n⁺ layer. However, the bulk electrical conductivity of Sn is only about one-fifth that of Au. Therefore, to obtain comparable series resistance requires the use of thicker Sn layers, which can lead to additional shadowing losses because of the expansion of the contact grid line-width during electroplating. In addition, there is evidence from scanning electron microscopy that an interfacial oxide layer can be formed between the Sn and GaAs during anodic oxidation. Such a layer can increase the contact resistance and therefore decrease the cell fill factor and conversion efficiency.

Unlike Sn, Au does not become passivated during anodic oxidation. Previously, therefore, it has been necessary to deposit Au contact grids after the completion of the thinning process, making it impossible to monitor the cell characteristics after successive oxidations. Furthermore, the reduction in the thickness of the n⁺ layer separating the contacts from the junction increases the risk that extended high temperature operation will lead to junction degradation due to the diffusion of Au into the GaAs.

Plasma-deposited Si₃N₄ has been used in MOS technology as a final passivation layer (3), since it provides an inert barrier to Na and H₂O contamination and can be deposited at a relatively low temperature. In this study, we have found that Au contacts can be protected from dissolution during anodic oxidation by coating them with a film of plasma-deposited Si₃N₄. The use of this technique makes it possible to take advantage of the higher conductivity of Au while retaining the ability to monitor cell performance after the successive oxidation steps. Plasma-deposited Si₃N₄ has been used previously for antireflection coatings on InP solar cells (4), Si solar cells (5), and

InP/InGaAsP light-emitting diodes (6), but not in the fabrication of GaAs solar cells.

Experimental Procedure and Film Properties

The basic solar cell structure was prepared by using vapor-phase epitaxy to grow successive p⁺, p, and n⁺ GaAs layers on p⁺ GaAs substrates, as described previously (2). The Au contacts were formed by either electroplating or evaporation of Au layers 0.3-1.0 μm thick. The protective Si₃N₄ films were deposited at rates of ~160 Å/min in a Plasma-Therm PK1250 multiversion system. The substrate temperatures were in the range of 100°-200°C. The relative flow rates of N₂, SiH₄, and NH₃ were about 30:1.6:1, and the deposition pressure was 0.55 torr. The RF power density was 0.07 W/cm² at 13.56 MHz.

The Si₃N₄ films were characterized by several techniques. Index of refraction and thickness measurements were made at a number of points on each film with a Rudolph Research Auto EL-III automatic ellipsometer. The index of refraction was generally found to be 2.00 ± 0.04, and the thickness uniformity was approximately 5% over 2 in. diam test wafers. The reproducibility of the films was confirmed by wet etch tests in a solution of 20:1 H₂O:HF, which consistently gave etch rates of 1000-2000 Å/min.

Because the n⁺ layer is so thin in shallow homojunction GaAs solar cells, the quality of the n⁺/p junction is very sensitive to damage to the GaAs surface. Any such damage caused by the plasma deposition process or by stress incorporated in the Si₃N₄ film could significantly increase the leakage current, thus degrading the open-circuit voltage and fill factor of the cells. To test the effect of the deposition process, we etched off the anodic oxide layer from a high efficiency solar cell that had been fabricated by our conventional technique (2) and measured the cell I-V characteristics. A film of Si₃N₄ about 2000Å thick was deposited on the n⁺ GaAs surface and then removed, after which the I-V characteristics were re-measured. The open-circuit voltage and fill factor of the cell were found to be unchanged. In contrast, deposition and removal of pyrolytic SiO₂ and PSG generally resulted in degradation of these parameters.

We have demonstrated the low intrinsic stress of the plasma-deposited Si₃N₄ films by using a Tropel 9000 interferometer to examine GaAs and Si wafers before and after deposition of films about 2000Å thick. There was no detectable change in the free-standing radius of curvature of the wafers. To evaluate the intrinsic tensile stress, a membrane deflection technique (7) was used for measurements on films deposited on several Si wafers. The average stress was 9×10⁸ dyn/cm², well below the values of ~4×10⁹ dyn/cm² that were measured by the same tech-

nique for Si_3N_4 films deposited by low pressure chemical vapor deposition.

Solar Cell Results

The optimum thickness of Si_3N_4 to be used for protection masks was determined by experiments on shallow homojunction solar cells fabricated by the procedure shown in Fig. 1. An $n^+/p/p^+$ structure was grown by vapor-phase epitaxy, a 3000Å Au layer was deposited by evaporation on the as-grown GaAs surface and patterned to form a front contact grid, and the entire surface was covered with a layer of Si_3N_4 . Next, a photoresist etch mask was defined over the contact fingers, making certain that there was sufficient overlap for sidewall coverage, and the Si_3N_4 between the fingers was removed with a dilute HF etch. The remaining photoresist was removed, an electrical contact was made to the back of the sample, the sample was mounted face up on a glass slide with a low-melting point wax, and anodic oxidation was performed in the manner described previously (2). Measurements on solar cells fabricated by this procedure showed that a layer of Si_3N_4 2000-3000Å thick is sufficient to protect the Au fingers during anodic oxidation without producing any detectable degradation in the cell parameters.

The Si_3N_4 masking process was then used in fabricating a number of shallow-homojunction solar cells with anodic oxide AR coatings. The I-V characteristic of the best 0.51 cm^2 cell is shown in Fig. 2. The open-circuit voltage V_{oc} is 0.97V, the short-circuit current density J_{sc} is 24.7 mA/cm^2 , and the fill factor is 0.84, giving an AM1 conversion efficiency of 20.1%. This fill factor is higher than the best values that have been obtained for shallow homojunction GaAs cells fabricated using earlier metallization procedures (6). For a 0.0925 cm^2 , 20% AM1 cell fabricated on the same wafer, the diode factor A is 1.1 and the reverse saturation current density J_0 is 1×10^{-17} A/cm^2 . These values were determined from the $\log J_{sc}$ vs. V_{oc} data plotted in Fig. 3 by fitting the straight line shown with the diode equation $J_{sc} = J_0 [\exp(qV_{oc}/kT) - 1]$, where q is the electronic charge, k is Boltzmann's constant, and T is the absolute temperature. These values of A and J_0 are the same as the best values previously obtained (8), confirming the fact that the plasma deposition process does not cause junction degradation.

Conclusion

We have demonstrated a new process that utilizes plasma-deposited Si_3N_4 films for protective masks in the fabrication of high-efficiency GaAs solar cells. The use of gold front contact metallization during anodic oxidation has made it possible to prepare cells with fill factors higher than those previously obtained. Plasma deposition

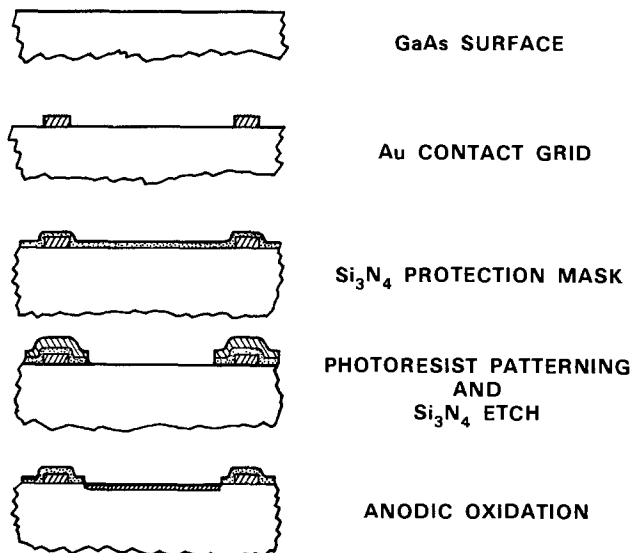


Fig. 1. Solar cell fabrication procedure using Si_3N_4 protection mask

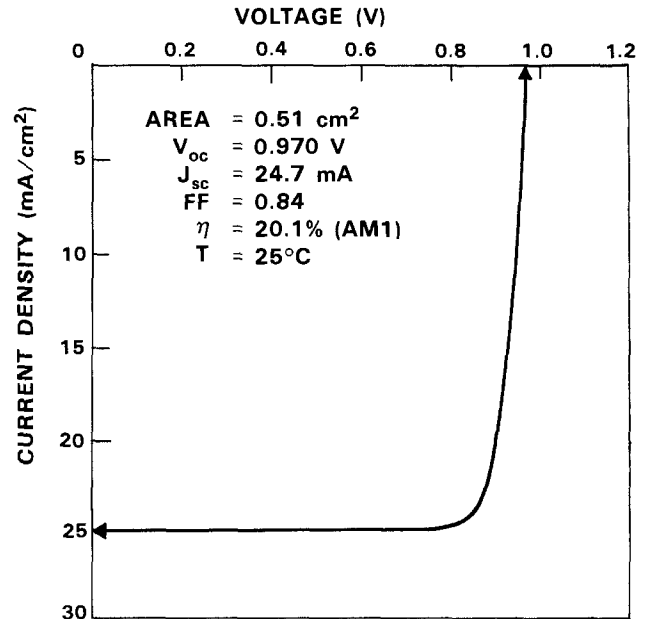


Fig. 2. Photocurrent density as a function of voltage for GaAs cell with 20% conversion efficiency at AM1.

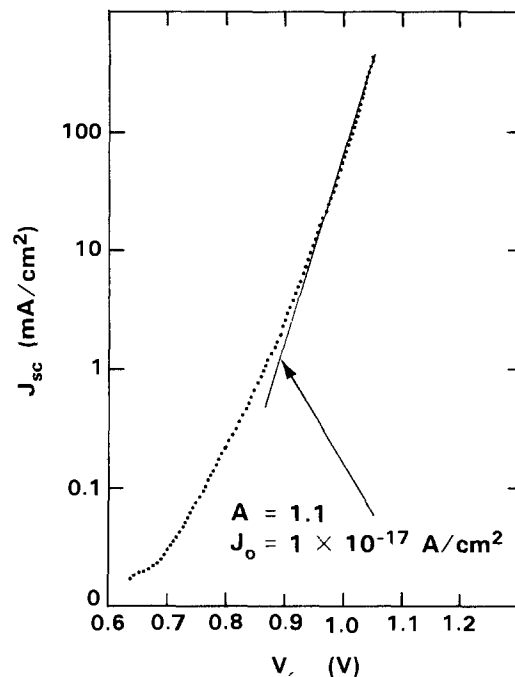


Fig. 3. Short-circuit current density J_{sc} as a function of open-circuit voltage for a 0.0925 cm^2 cell fabricated on the same wafer as the cell of Fig. 2.

of Si_3N_4 can be used on these shallow-junction GaAs devices with no degradation of junction properties. This process may be useful for other devices that employ anodic oxidation or require deposition of Si_3N_4 in their fabrication.

Acknowledgments

The authors are grateful to R. L. Chapman, B. D. King, R. W. McClelland, W. L. McGilvary, P. M. Nitishin, and B-Y. Tsaur for technical assistance, to E. I. Bromley for performing the stress measurements, and to J. C. C. Fan and A. J. Strauss for helpful discussions. This work was sponsored by the Solar Energy Research Institute, the National Aeronautics and Space Administration, and the Department of the Air Force.

Manuscript submitted July 25, 1983; revised manuscript received Jan. 4, 1984.

Massachusetts Institute of Technology assisted in meeting the publication costs of this article.

REFERENCES

1. C. O. Bozler, J. C. C. Fan, and R. W. McClelland, in "7th International Symposium on GaAs and Related Compounds, p. 429, Institute of Physics and Physical Society, London (1979).
2. J. C. C. Fan, C. O. Bozler, and R. L. Chapman, *Appl. Phys. Lett.*, **32**, 390 (1978).
3. A. K. Sinha, H. J. Levinstein, T. E. Smith, G. Quintana, and S. E. Haszko, *This Journal*, **125**, 601 (1978).
4. G. W. Turner, J. C. C. Fan, and J. J. Hsieh, *Appl. Phys. Lett.*, **37**, 400 (1980).
5. F. W. Sexton, *Sol. Energy Mat.*, **7**, 1 (1982).
6. R. H. Burton, Unpublished result.
7. E. I. Bromley, J. N. Randall, D. C. Flanders, and R. W. Mountain, *J. Vac. Sci. Technol., J. Vac. Sci. Technol.*, **4**, 1364 (1983).
8. J. C. C. Fan, G. W. Turner, R. P. Gale, and C. O. Bozler, in "Conference Record 14th IEEE Photovoltaic Specialists Conference," p. 1102, IEEE, New York (1980).

The Effect of Particle Size on the Electrical Conductivity of CuCl (Al₂O₃) Composites

M. R-W. Chang,¹ K. Shahi,² and J. B. Wagner, Jr.*

Center for Solid State Science and Departments of Chemistry, Mechanical, and Aerospace Engineering and Physics, Arizona State University, Tempe, Arizona 85287

The purpose of this note is to report the effect of dispersoid size on the electrical conductivity, σ , of CuCl containing insoluble Al₂O₃ particles. Enhanced conductivity of electrolytes containing Al₂O₃ was first reported by Liang (1). Subsequently, Jow and Wagner (2) studied the CuCl (Al₂O₃) system but utilized only two particle sizes (0.06 and 0.3 μm Al₂O₃). Shahi and Wagner (3) studied AgI (Al₂O₃) using Al₂O₃ of 0.06, 0.3, 1, 3, 8, and 15 μm size, but only at 24°C. For AgI containing 30 mol percent (m/o) Al₂O₃ they reported an enhancement for all particle sizes; although for samples containing 1, 3, 8, and 15 μm , there was very little change in conductivity (see Fig. 1). In the present work, a similar study was carried out for CuCl (Al₂O₃) between 25° and 390°C.

CuCl, 99.999% pure from Apache Chemicals, Incorporated, was dried at 100°C under vacuum for at least 10h. The particle size of this CuCl was about 3 μm . Alumina, 99.98% pure from Adolf Meller, was dried under vacuum at about 700°C for at least 12h. Weighed amounts of the two powders were mixed, sealed in a quartz tube, and heated at 580°C (mp of CuCl = 493°C) for 8h. The product was quenched to 25°C, pulverized, and pressed at 85 kpsi into pellets, 9.5 mm diam \times 2-3 mm thick. The densities were 90% theoretical. The pellets were sandwiched between 99.999% copper electrodes. Purified argon flowed over the sample, which was annealed at 380°C for 5h prior to onset of measurement using 1 kHz ac.

After measurements, selected samples were thermally etched under vacuum at 350°C for about 7 min and then examined by a SEM which was fitted with an EDAX analyzer. The grain size of the CuCl matrix was 5-15 μm , with \sim 10 μm being the most usual. Agglomeration was not observed for Al₂O₃ of sizes $>$ 1 μm , but did occur for the smaller sizes. Figure 2 shows a plot of $\log \sigma$ vs. $1/T$ for undoped CuCl containing 0.06 and 0.3 μm Al₂O₃. The maximum enhancement occurred at 10 m/o of 0.06 μm Al₂O₃. This is in reasonable agreement with data of Jow and Wagner (2), who found the maximum enhancement at 20 m/o for 0.06 μm Al₂O₃ in CuCl. Jow and Wagner (2) have previously shown that the electronic conductivity of CuCl (Al₂O₃) was negligible compared to the ionic conductivity. In addition to uncertain degrees of agglomeration, the grain size of the matrix plays an important role, as has been shown quantitatively for AgCl (Al₂O₃) by Khandkar (4). Figure 3 shows an Arrhenius plot of $\log \sigma$ vs. $1/T$ for CuCl containing 10 m/o Al₂O₃ of 1, 3, 8, and 15 μm particle size.

We attempted to fit the data for the larger particle sizes to the classical model for a two-phase mixture of an insu-

lator embedded in a conductor (5-7)

$$\sigma(\text{composite}) = \left[\frac{1-f}{1+0.5f} \right] \sigma_0 \quad [1]$$

where $\sigma(\text{composite})$ is the total conductivity of the composite, σ_0 is the conductivity of the matrix CuCl without the Al₂O₃, and f is the volume fraction of the insulator, Al₂O₃. This equation did not adequately represent the data at 100°C. According to the space charge model of Jow and Wagner (2), the enhancement, $\Delta\sigma$, is

$$\Delta\sigma \approx 3 \sum_i e u_i < \Delta n_i > \lambda \left(\frac{1}{r_i} \right) \left(\frac{f}{1-f} \right) \quad [2]$$

where e = electronic charge, u_i = mobility of i th species, Δn_i = change in concentration of i th species, λ = space-charge layer thickness, f = volume fraction, and r_i = radius of insulator particle (assumed spherical). In the present studies for 10 m/o Al₂O₃, the conductivities for all samples (except 15 μm), even those with decreased ionic conductivities, were proportional to the reciprocal of r_i , as shown in Fig. 1. Likewise for AgI for the smaller particle sizes, the plot of $\log \sigma$ vs. \log particle size yields a slope of minus one. These data are consistent with Eq. [2].

At 100°C, the data on CuCl (Al₂O₃) are in good agreement with the report of Shahi and Wagner (3) who showed that Al₂O₃ of 1 μm diam resulted in a very small enhancement of σ for AgI (Al₂O₃) at 24°C. However, Shahi

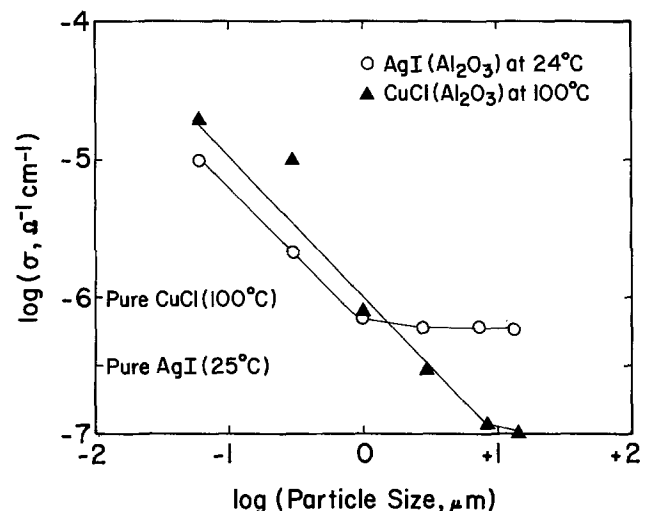


Fig. 1. Logarithm of conductivity vs. logarithm of particle size for CuCl containing 10 m/o of dried Al₂O₃ at 100°C and for AgI containing 30 m/o of dried Al₂O₃ at 24°C. The slope of the straight lines is -1, in accord with Eq [2].

*Electrochemical Society Active Member.

¹Present address: Applied Beam Technology, Freemont, CA 94538.

²Present address: Department of Physics and Advanced Materials Science Centre, Indian Institute of Technology, Kanpur, India.

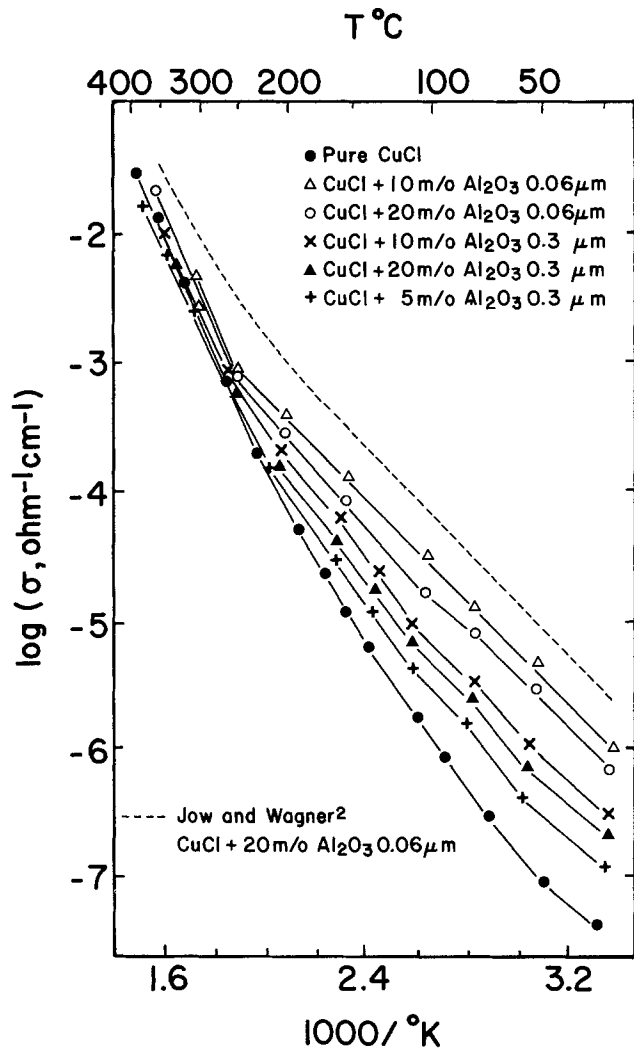


Fig. 2. Arrhenius plot for CuCl (Al_2O_3) for Al_2O_3 particle sizes of 0.06 and 0.3 μm .

and Wagner found that the larger diameter particles yielded almost no change in σ .

While the smaller particle sizes which result in an enhancement exhibit an Arrhenius behavior such that the conductivity approaches that of CuCl without Al_2O_3 at elevated temperatures ($\sim 250^\circ\text{C}$), the samples with the larger particle sizes (1, 3, 8, 15 μm) do not show such behavior. In these cases, the slopes of the $\log \sigma$ vs. $1/T$ plots are approximately parallel to the CuCl without Al_2O_3 additions. In the case of CuBr (Al_2O_3), the conductivity of a composite containing 10 m/o of 8 μm Al_2O_3 initially was lower than that of CuBr without Al_2O_3 , but for $200 \leq T \leq 300^\circ\text{C}$, σ exhibited a very small enhanced conductivity (8). In the present studies, the experimental error was about one-half logarithm unit for the larger particle sizes (Fig. 3). We attribute the scatter in the data in part to the difference between CuBr (Al_2O_3) and CuCl (Al_2O_3).

In summary, the conductivity of CuCl containing Al_2O_3 of 0.06, 0.3, 1, 3, 8, and 15 μm particle size has been measured between 25° and 390°C . The conductivity is enhanced for the 0.06 and 0.3 size Al_2O_3 for temperatures lower than $\sim 250^\circ\text{C}$, the maximum enhancement being over an order of magnitude for 10 m/o 0.06 Al_2O_3 at 25°C .

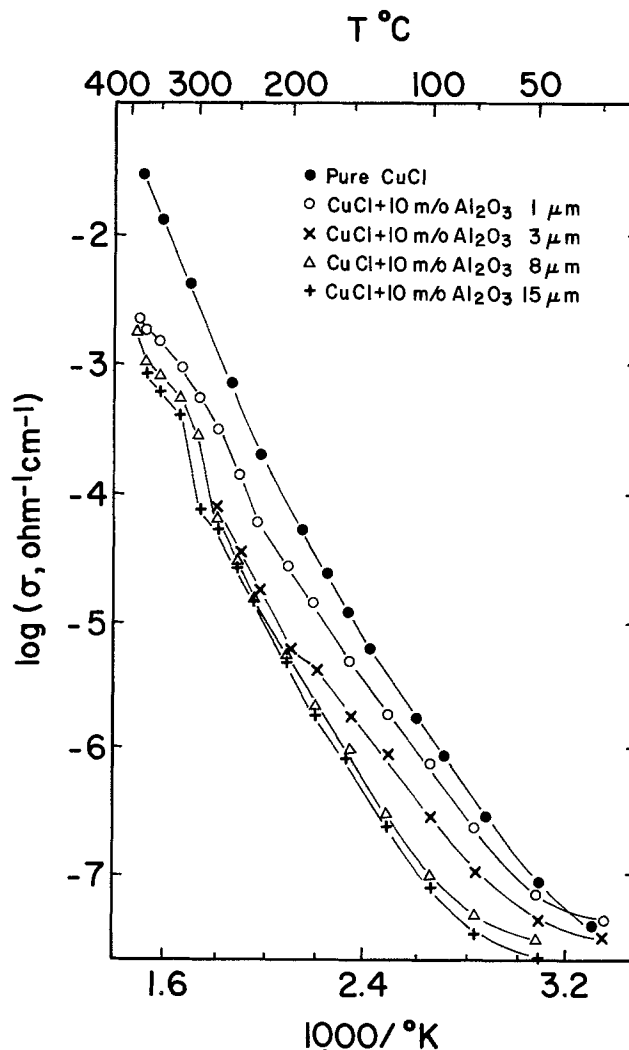


Fig. 3. Arrhenius plot for CuCl (Al_2O_3) for Al_2O_3 particle sizes of 1, 3, 8, and 15 μm .

Acknowledgment

This research was supported under NASA contract NAS 8-32937.

Manuscript submitted Aug. 25, 1983; revised manuscript received Jan. 18, 1984. This was Paper 367 presented at the Boston, Massachusetts, Meeting of the Society, May 6-11, 1979.

Arizona State University assisted in meeting the publication costs of this article.

REFERENCES

1. C. C. Liang, *This Journal*, **120**, 1289 (1973).
2. T. Jow and J. B. Wagner, Jr., *ibid.*, **126**, 1963 (1979).
3. K. Shahi and J. B. Wagner, Jr., *ibid.*, **128**, 6 (1981).
4. A. Khandkar, MS. Thesis, Arizona State University, Tempe, AZ (1982).
5. R. E. Meredith and C. W. Tobias, *Adv. Electrochem. Engr.*, **2**, 15 (1962).
6. J. C. Maxwell, "Treatise on Electricity and Magnetism," 2nd ed., Vol. 1, p. 435, Clarendon Press, Oxford (1881).
7. Lord Raleigh, *Philos. Mag.*, **24**, 481 (1892).
8. R. M. Dubec and J. B. Wagner, Jr., Abstract 135, p. 346, The Electrochemical Society Extended Abstracts, Vol. 79-2, Los Angeles, CA., Oct. 14-19, 1979.



A Rotating Disk Electrode Apparatus for the Study of Fuel Cell Reactions at Elevated Temperatures and Pressures

J. McBreen,* W. E. O'Grady,* and R. Richter

Brookhaven National Laboratory, Department of Applied Science, Upton, New York 11973

INTRODUCTION

Much of the recent improvement in performance of phosphoric acid fuel cells has been due to fuel cell operation at elevated temperatures ($\sim 205^\circ\text{C}$) and pressures (8A) (1). Further increases in temperature and pressure are contemplated (1). Apart from increased performance, pressurization minimizes electrolyte loss via vaporization and it significantly increases the volumetric power density as a result of decreases in conduit sizes etc. Performance improvements accrue from an increase in the Nernst potential, and decreases in the activation over-voltages at both electrodes.

All previous studies of oxygen reduction in phosphoric acid have been carried out at atmospheric pressure (2-10). Recent work has confirmed that results on smooth platinum are applicable to carbon supported platinum electrocatalysts in fuel cell electrodes (9,10). This communication describes a rotating disc electrode apparatus for the study of fuel cell reactions at elevated temperatures and pressures. Preliminary data for oxygen reduction in 89.5% H_3PO_4 at temperatures up to 205°C and pressures up to 7.6A are presented.

EXPERIMENTAL

System Design.--The key to a hermetic rotating seal was the use of a ferrofluidic seal (Ferrofluidics Corp.). For this application a water cooled seal with fluorocarbon base magnetic fluid was used. Once the hermetic rotating seal had been achieved the remainder of the design involved provisions for the electrode drive, gas feed, sealed electrical feed-throughs and temperature control of the H_3PO_4 electrolyte. A schematic of the overall system is shown in Fig. 1.

The electrode drive consisted of a DC motor (Indiana General Motor Products) with a motor controller (B&B Motor and Control Corp.). The drive was coupled to the rotating seal via a flexible coupling. The

electrical leads were stainless steel wires that were fed through Conax compression fittings.

Temperature control was achieved through the use of a temperature controller and two cartridge heaters which fitted snugly inside quartz tubes. Uniform heating could be achieved by simply rotating the electrode at 400 rpm during the heating operation. This also resulted in rapid equilibrium between the overhead gas and dissolved gases.

The Cell.--The cell and cover were machined from PTFE. The cell dimensions were 8.5 cm ID x 8 cm H. The cell had a platinum counter electrode and a dynamic hydrogen reference electrode in a quartz Luggin capillary tube.

Experimental Procedure.--The methods for cell cleaning, phosphoric acid purification and platinum disc electrode preparation have been described previously (10). The cell was filled with 300 ml of electrolyte and placed in the vessel. The vessel was evacuated and backfilled with oxygen (5 psi) three times. The electrolyte was heated and runs were started at 150°C . The electrochemical measurements were done in a manner described previously (10). The cell was filled with 300 ml of electrolyte and placed in the vessel. Temperatures were increased in $\sim 25^\circ\text{C}$ intervals and pressures in 1A intervals. Thermal equilibrium could be achieved in 40 min and gas-solution equilibrium (i.e., a stable limiting current) in ~ 15 min. To avoid electrolyte composition changes, no runs were done at less than 3A above 175°C .

RESULTS AND DISCUSSION

Figure 2 shows Tafel plots for oxygen reduction in 89.5% H_3PO_4 . Up to 175°C and at pressures close to atmospheric the Tafel slope was ~ 120 mV/decade and was invariant with temperature. This anomalous behavior has been reported before (5,8,9). However,

on increasing the pressure to 3A at 175°C, the Tafel slope decreased to a value of $\sim RT/F$. At pressures above 3A the current was proportional to the oxygen pressure, indicating a first order dependence with respect to oxygen pressure. The change in Tafel slope indicates a mechanism change with increasing oxygen coverage of the platinum. The reason for this is not understood at this time. However, these results indicate that in addition to the Nernst effect and the oxygen reaction order effect there is a concomitant decrease in the Tafel slope. Thus, the electrochemical reasons for pressurization of phosphoric acid fuel cells are very cogent indeed.

ACKNOWLEDGEMENTS

The authors acknowledge the help of S. J. Majeski and W. J. Johnson of BNL in designing the pressure vessel and the help of G. A. Schoener of BNL in the design of the drive system.

REFERENCES

1. A. J. Appleby, "Acid Fuel Cell Technology: An Overview", Abstracts of The National Fuel Cell Seminar, Orlando, Florida, November 13-16, Courtesy Associates, Inc., Washington, DC (1983), pp. 1-5.
2. A. J. Appleby, *This Journal*, **117**, (1970).
3. P. N. Ross, *ibid.*, **126**, 78 (1979).
4. J. C. Huang, R. K. Sen and E. Yeager, *ibid.*, **126**, 786 (1979).
5. W. M. Vogel and J. T. Lundquist, *ibid.*, **117**, 1512 (1970).
6. H. R. Kunz and G. A. Gruver, *ibid.*, **122**, 1279 (1975).
7. L. J. Bergoli, *Electrochim. Acta* **23**, 489 (1978).
8. W. E. O'Grady, E. J. Taylor and S. Srinivasan, *J. Electroanal. Chem.* **132**, 137 (1982).
9. J. McBreen, H. Olender and S. Srinivasan, *Proceedings of Symposium on Electrocatalysis*, W. O'Grady, P. N. Ross Jr. and F. G. Will, Editors, The Electrochemical Society, Inc., Pennington, NJ (1982), pp. 120-130.
10. P. N. Ross, *ibid.*, pp. 24-38.

Manuscript received Feb. 3, 1984.
Brookhaven National Laboratory assisted in meeting the publication costs of this article.
*Electrochemical Society Active Member.

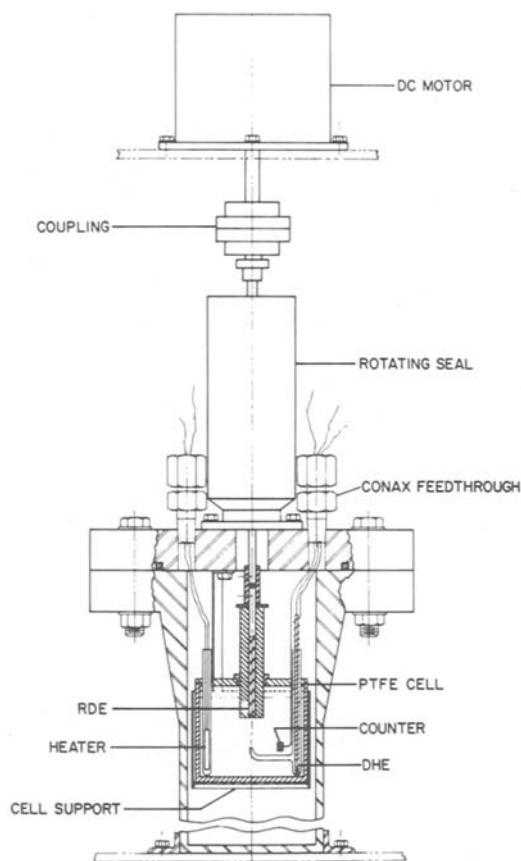


Figure 1. High Pressure rotating disc assembly.

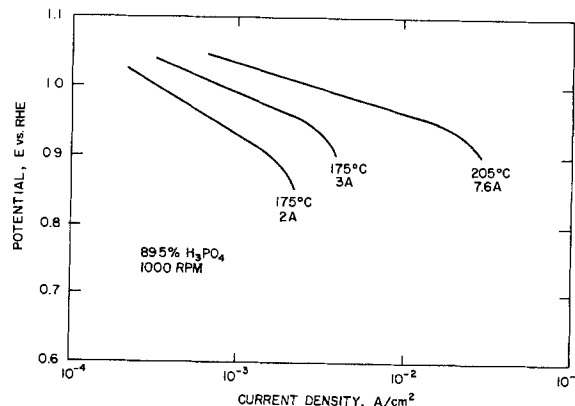


Figure 2. Tafel plots for oxygen reduction in 89.5% H_3PO_4 ; pressures and temperatures are given on the figure.

This research was performed under the auspices of the U.S. Department of Energy under Contract No. DC-AC02-76CH00016.

TiSi₂/n⁺Poly-Si Gate Electrode Patterning by Plasma Etching Using CF₂Cl₂O₂

Toshiaki Yachi

Nippon Telegraph and Telephone Public Corporation, Musashino Electrical Communication Laboratory, Musashino-shi, Tokyo, 180 Japan

The most generally used gate electrode material in MOS-integrated circuits technology is doped polycrystalline silicon. Recently, with continuously decreasing device dimensions, the relatively high sheet resistance of poly-Si becomes a limiting factor for device performance. This has led to work currently going on to incorporate refractory metal silicides into the device fabrication process (1). In order to keep the well-established quality of the poly-Si gate technology, a double layer of refractory metal silicide on top of doped poly-Si is commonly used (2).

One of the key problems in introducing refractory metal silicide/poly-Si double layers into the fabrication process is an appropriate patterning technique full-filling the demands of LSI circuits. Some reactive ion etching of refractory metal silicide/poly-Si double layers has been reported using CF₂/O₂ for MoSi₂- and WSi₂- based double layers (2, 3), and using SF₆/Cl₂ and CF₄/Cl₂ for Ta-silicide- and TiSi₂- based double layers (4, 5). These techniques, however, require stringent control for obtaining proper etching profile without a poly-Si undercut (3, 4).

The author has carried out an investigation on the plasma etching of TiSi₂/n⁺poly-Si double layers using CF₂Cl₂/O₂. A TiSi₂/n⁺poly-Si pattern with proper etching profile without a poly-Si undercut has easily been produced without pattern width reduction.

Experimental

The etching experiments were performed in a batch-type commercially available planar plasma etching system, as shown in Fig. 1. The rf power (13.56 MHz) was applied to the upper electrode (cathode) via a tuning network. The forward power was held at 400W. The cathode and the anode were also covered by quartz glass. The pumping system consists of a rotary pump and a roots blower. During the etch cycle, the pressure was maintained at 17Pa with a 50 sccm flow of CF₂Cl₂/O₂ gas. The substrate table temperature was also kept 22°C by water-cooling.

The 4 inch Si wafers used for the experiments were prepared in the following way: After growing a thin (50 nm) thermal SiO₂, 0.3 μm phosphorus-doped poly-Si was deposited using chemical vapor deposition. Ti and Si were deposited simultaneously by rf planar magnetron-

sputtering from two independent sources, one a titanium (99.94-percent pure) target and the other a poly-Si (99.999-percent pure) target. Prior to Ti and Si mixed film deposition, a dip in buffered HF removed the native oxide on top of the poly-Si. This Ti and Si mixed film is 0.2 μm in thickness. The Ti concentration is about 50 at. %.

Subsequently, the wafers were annealed at 800°C for 20 minutes in argon using a furnace. X-ray diffraction studies detect only TiSi₂ and Si crystalline phases in the annealed double layers. The sheet resistance of the annealed TiSi₂/n⁺poly-Si double layers is 1 Ω/□. The interface between TiSi₂ and n⁺poly-Si is still clear.

Lithography was accomplished by conventional photolithography in 1.2 μm positive resist AZ1370. Post-baking was performed at 180°C for 10 minutes.

Etch rates were determined by the film thickness decrease in CF₂Cl₂/O₂ plasma, which was measured by creating a step and then using the Taley Step Height Reader. For evaluating the various etch profiles for the TiSi₂/n⁺poly-Si double layers, scanning electron microscope (SEM) analysis has been carried out.

Results

Figure 2 presents the TiSi₂, n⁺poly-Si and resist AZ1370 etch rates as a function of CF₂Cl₂/O₂ gas composition. It was found that the etch rate for the as-deposited Ti and Si mixed film was not reproducible. A TiSi₂ formation anneal for 20 minutes in argon at 800°C was carried out to stabilize the silicide film etch rate. At low O₂ concentrations, the TiSi₂ etches faster than n poly-Si and AZ1370. In the 10-20-percent O₂ concentration range, the TiSi₂ to resist etch rate ratio is 7:1. At low O₂ concentrations, a relatively large etch selectivity of poly-Si over SiO₂, which is necessary for gate electrode patterning, has also been observed (etch rate ratio = 5:1).

Figure 3 shows an SEM micrograph after CF₂Cl₂ (50): O₂(0) etching. It can be seen that the TiSi₂ is etched strictly anisotropically, whereas the n⁺poly-Si shows no undercut and a proper positive slope. At 20-percent and below O₂ concentrations, similar etching profiles were obtained. Moreover, the O₂ addition decreases the residue near pattern edges which is shown in Fig. 3. No undercut of the n⁺poly-Si is consistent with the

Key Words: Films, Integrated Circuits, SEM, Etching

fact that the n^+ poly-Si is also etched perfectly anisotropically in CF_2Cl_2/O_2 at low O_2 concentrations. The proper positive slope of the n^+ poly-Si is consistent with the facts that the n^+ poly-Si to resist AZ1370 etch rate ratio is relatively small, as shown in Fig. 2, and that the resist pattern is semicircular, owing to $180^\circ C$ postbaking. These facts also indicate that the n^+ poly-Si pattern is produced in a pattern width equal to the resist pattern width before etching.

In conclusion, $TiSi_2/n^+$ poly-Si pattern with proper etching profile has easily been produced without pattern width reduction by the plasma etching using CF_2Cl_2/O_2 . This method is very useful for $TiSi_2/n^+$ poly-Si gate electrode patterning in LSI fabrication.

Acknowledgements

The author would like to thank A. Ishimoto and T. Serikawa for helpful technical discussions.

References

- (1) S.P. Murarka, *J. Vac. Sci. Technol.*, **17**, 775 (1980).
- (2) B.L. Crowder and S. Zirinsky, *IEEE Trans. Electron Devices*, **ed-26**, 369 (1979).
- (3) F.R. White, C. W. Koburger, D. L. Harmon and H. J. Geipel, *This Journal*, **129**, 1330 (1982).
- (4) H. J. Mattausch, B. Hasler and W. Beinvogl, *J. Vac. Sci. Technol. B*, **1**, 15 (1983).
- (5) K. L. Wang, T. C. Holloway, R. F. Pinizzotto, Z. P. Sobczak, W. R. Hunter and A. F. Tasch, Jr., *IEEE Trans. Electron Devices*, **ed-29**, 547 (1982).

Manuscript submitted Oct. 31, 1983; revised manuscript received Feb. 22, 1984.

Nippon Telegraph and Telephone Public Corporation assisted in meeting the publication costs of this article.

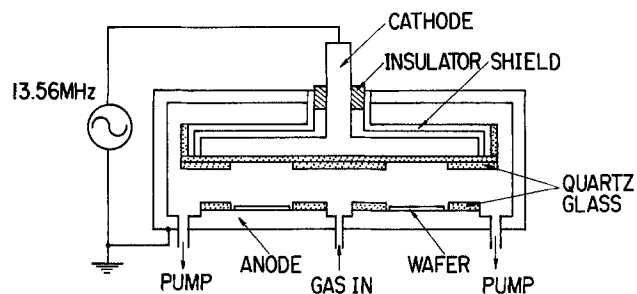


Fig. 1 Planar plasma etching apparatus diagram

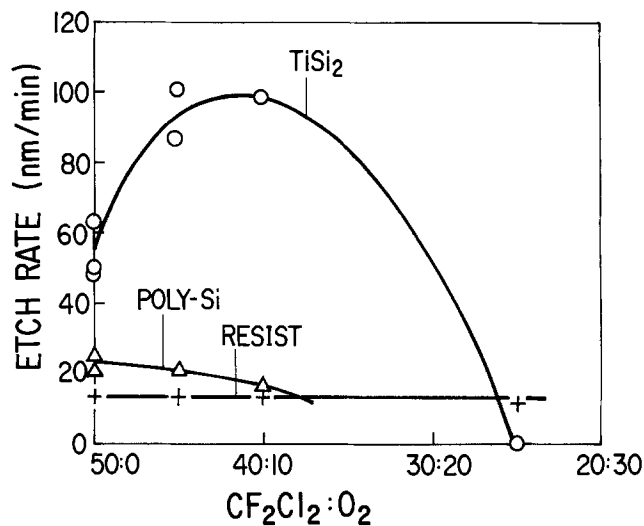


Fig. 2 Etch rates for $TiSi_2$, n^+ poly-Si and resist as a function of gas composition $CF_2Cl_2:O_2$.

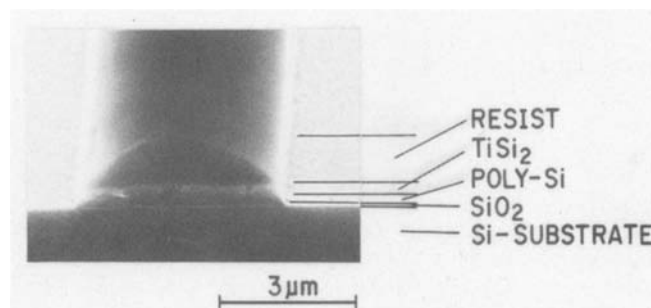


Fig. 3 SEM micrograph of profile after etching through $TiSi_2/n^+$ poly-Si in $CF_2Cl_2(50):O_2(0)$.



International Trade in Semiconductors: Challenges and Opportunities

William K. Krist

Assistant U.S. Trade Representative for Industrial Trade Policy, Executive Office of the President, Washington, DC 20506

I am pleased to meet with The Electrochemical Society to discuss some of the challenging trade issues that confront the semiconductor industry. Your industry has long been considered the symbol of American inventiveness and ingenuity. Because the products of your industry form the basic building blocks for many high technology industries, increasing numbers of nations are coming to view production of semiconductors as vital to their future. As a result, today you are facing a serious international challenge—a challenge that has led some to question your industry's, and indeed our nation's basic approach to free trade and to our industrial competitiveness.

In many ways, the challenges faced by your industry form the backdrop for the broader trade policy debate now raging in our country. Because your industry's problems are part and parcel of this broader issue of our approach to trade policy, let me talk briefly about our basic trade posture, before describing specific semiconductor issues in more detail.

U.S. Trade Policy Objectives

As you know, since the end of World War II, the United States has led the Western nations in developing a system of international rules to govern world trade, and has fostered a system based on open markets, economic freedom, and interdependence. This fundamental United States objective has been based on recognition that protectionist actions greatly facilitated the descent into the Great Depression and World War II.

This system of open trade has greatly contributed to world growth, and indeed to our substantial economic achievements. World trade grew substantially faster (7.1%) than world commodity production (4.9%) during the last two decades.

For the United States, in just the last 10 years trade has doubled as a percentage of GNP, reaching 13%. Twenty percent of what we manufacture, and 40% of our agricultural output is exported. Most of the new manufacturing jobs created in the United States in recent years have been in industries involved in international trade. Moreover, the economic interdependence that has fomented the spectacular economic growth of the postwar era has also ensured that withdrawal from this process is all but impossible. Even a country with a large and expanding internal market like the United States is increasingly dependent on the international economy for its economic well-being. Never again will the United States be able to confine its economic concerns to its domestic market. We are in international trade to stay, and we believe we have a pressing national interest in seeing this system function and flourish.

The May 30 Summit of Industrialized Nations recognized this stake in the national commitment to "halt protectionism and, as recovery proceeds, to reverse it by dismantling trade barriers." The Summit leaders also

took the courageous step of calling for a new round of trade liberalizing international negotiations in GATT.

Keeping Trade Fair

Although our position is firmly against protectionism, it cannot be over emphasized that, under United States and international rules, countries have agreed to a framework for the conduct of international trade. The purpose of this framework is to ensure that countries benefit from trade equally, and that trade flows are determined by comparative advantage to the greatest extent possible.

If a country deviates from these agreed rules, actions to restore equal competition are not only acceptable but ethically and legally right. These actions, taken in accordance with domestic and international law, must not be confused with protectionism. Through vigorous enforcement of our unfair trade statutes, we must ensure that Americans are not unfairly deprived of their jobs by other governments' trade or market distortions.

However, our target must be unfair competition, not imports in general. Imports provide needed competition for our domestic producers and more choice and lower prices for consumers. They also symbolize an important fact—that we are living in an interdependent world.

In our negotiations for fair and open trade, it is important to produce tangible results. Unless we do, the perception will grow that our trading partners refuse to play by the same rules as we do. Fair and open trade in the Japanese and European markets is important to United States industry because of the current size of these markets and their long-term growth potential.

Market Access for Semiconductors

The semiconductor industry is an area of dynamic growth with a history of intense competition and rapid technological change. The current world market for semiconductors of \$15 billion is projected to grow to \$60 billion by 1990.

Our industry's share of this global market is currently some 55%. However, our share has been declining, and, in fact, is down from 64% in 1975. The Japanese have become our principal competitors, as their share rose from 19.3% to 33%.

The United States Semiconductor Industry Association argues eloquently that this past competition has not been on an even footing. For example, the SIA points out that the Japanese have protected their home market over several decades, relative to our market. The Japanese Government gave substantial aid in the form of financial assistance, research and development, and exemptions from the general antitrust provisions of Japanese law. This assistance enabled Japanese firms to launch an export drive with high products at very low prices.

A historical analysis of Japanese legislation and government policies shows government support commencing as early as 1957, when MITI was authorized to exempt

Z
R

computers and semiconductors from antitrust prosecution and to provide financial assistance. From 1971 to 1978, MITI was authorized not only to instruct firms to take concerted action exempted from antitrust prosecution and to provide financial assistance, but to adopt "rationalization plans" for the industry. This latter step was taken to avoid "excessive" competition among competing Japanese firms.

Although the Japanese protest that these were actions taken in the past, which have since ceased, they are instructive in explaining the concentration of production in six semiconductor manufacturers, each of whom is part of a Japanese industrial conglomerate. This ensures large financial resources are available for necessary capital investment to maintain an increased market share. The Japanese producers also tend to specialize in particular product lines which further tends to reduce head-on competition.

Access to Technology

Another important area of comparison is that of access to technology. Although the United States does control export of some technologies through export administration regulations, export of semiconductors to free-world destinations is essentially free of restriction, and foreign-owned firms are allowed access to patents and technology resulting from United States Government-sponsored research and development. In most cases, United States companies are vested with patent rights and can license the technology flowing from work done under government contract. In contrast, in Japan, there are a number of barriers to technology flow including approval by MITI as to whether Japanese national interests would be served by licensing of technology. Thus, to date, technology flow has been a one-way street in the direction of Japan.

Japanese Success

The success of the Japanese semiconductor effort can be best demonstrated by examining the specific case of the 64K RAM (random access memory). Market protection, government financial assistance, and identification of this product as a priority reduced the costs and risks for Japanese firms of rapid and large-scale investment in 64K RAM production capacity. This capacity buildup resulted in aggressive pricing, and today the Japanese have captured a substantial majority of the world market for the 64K RAM.

Japanese semiconductor successes are not confined only to the 64K RAM. By 1975, Japanese global trade in semiconductors had shifted from a deficit to a surplus. Furthermore, the perennial United States semiconductor trade surplus with Japan had turned into a deficit of close to \$200 million by 1982.

We are understandably concerned with this situation and are working closely with the United States industry to address their primary goal—opening up the Japanese market. In this context, a series of discussions, which we have held with the Japanese Government, resulted in the establishment of a bilateral working group on high technology trade issues. This working group reached an agreement to establish a data base of current information on trade in semiconductors. Monthly data on bookings and billings in the United States and Japanese markets of a selected list of semiconductors is now being collected from nearly all United States and Japanese producers. The participating firms on both sides will be provided with the aggregate figures showing the trends and trade flows. Once aggregated, the data will be reviewed by the working group, which will enable both United States government and industry to monitor trends and respond quickly to problems on the basis of a set of agreed facts.

In response to United States industry's desire to remove barriers to the United States semiconductor sales in Japan, and to establish a trade regime as free as possible from government interference, we have presented the Japanese with a series of proposals for promoting semi-

conductor imports to Japan. The Japanese have agreed to consider these and possibly generate ideas of their own for improving access to sales in the Japanese market. Our objective is to implement an agreed import program by November of this year.

European Community Targeting

In evaluating future international competition in the semiconductor industry, one should also take note of the recent "technological push" implemented by the European Community in order to achieve parity with, if not superiority over, American and Japanese competitors. The program, entitled ESPRIT (European Strategic Program for Research and Development in Information Technology), allots \$1.5 billion (financed on a 50-50 basis by the Community and European Industry) to a five-year research program commencing in 1984. The program aims at establishing a new technological base for the next generation of products in the information technology sector in five key areas: advanced microelectronics, information processing, software technology, office automation, and computer-integrated manufacturing. This EC program is designed to counter a trend in which the Community went from a trade surplus in 1975 to a 1981 trade deficit of \$5 billion, which doubled to \$10 billion in 1982.

Tariffs

As of April 1, 1983, Japan and the United States had cut import duties on semiconductor products from 10.1 and 5.6%, respectively, to 4.2%. This action was five years ahead of the schedule set for the Tokyo Round Tariff Negotiations. In contrast to this, the EC is holding their tariffs at 17%, but are temporarily suspending duties for some products in order to enable downstream users to obtain supplies. The high tariffs have not proved successful to date, since the EC industry capacity is inadequate to fill any gap which might be created by a reduction of imports. In short, in our view, EC input protectionism is hurting, not helping, their own industry.

Government Initiatives

In addition to ensuring fair and open trade in semiconductors with our trading partners, there are other steps that can and should be taken to improve the competitiveness of the United States semiconductor industry.

Antitrust.—We are encouraging more joint research and development within the industry. One leading example is the formation of the Microelectronics and Computer Technology Corporation (MCC), an umbrella organization composed of major United States semiconductor computer firms which will sponsor research and development projects in the field of microelectronics and computer science.

The Administration is proposing amendments to existing antitrust legislation to encourage more joint research and development. We believe this will help the United States' competitive position by promoting efficient use of scarce technical personnel and achieving desirable economies of scale. It will give United States industry the ability to match the collaborative efforts on research and development in high technology areas undertaken by Japanese and European competitors.

The Export Trading Company Act of 1982 is also designed to encourage joint actions to increase competitiveness in world trade.

To further research, the Department of Defense is investing \$300 to \$400 million in a multiyear project related to semiconductors scheduled for completion in 1984.

Need for new relationships.—As we move forward in an increasingly interdependent world economy we simply can no longer afford the types of antagonistic relationships that have all too often existed between management and labor, industry and government. These sectors have historically considered themselves far apart with no common objectives. We simply must move toward a new spirit of cooperation. This can be accomplished if we all

pay more attention to our long-term goals which contain far more similarities than dissimilarities. For example, business labor, as much as needs a motivated and a profitable company that can fulfill its pension obligations. Recognition of this interdependence is critical for all industries in meeting the Japanese challenge.

Education.—The responsibility for ensuring a leadership position in the world economy rests not only with the Federal Government, but with a commitment to excellence on the part of each individual. The general decline of primary and secondary education poses a significant long-term threat to our economic vitality. Evidence of this decline is documented all too clearly by the recent findings of the President's National Commission on Educational Excellence. The Commission reported widespread deficiencies in the fundamentals of English, mathematics, and science.

Proper education is a *sine qua non* in high technology industries. We must consistently reexamine our educational system to ensure that it is doing the job. The Japanese population today is almost completely literate against an estimated 20% rate of illiteracy in the United States. Japanese students score high in mathematics, physical sciences, and other related areas which are important building blocks in later degrees in engineering, chemistry, and other sciences.

America has long been distinguished for the best products of her education system—the scientists, doctors, writers, engineers, and teachers who make possible sustained progress in discovery and invention and who fueled America's technological primacy in the world. Yet even the contribution of these intellectual and scientific leaders is undermined by the lack of financial incentives and social prestige accorded to them. During the seventies, the number of engineers graduating from American universities decreased sharply.

The President is interested in counteracting this trend and has proposed programs to award substantial grants to those undertaking doctoral research. Further, he has proposed measures to increase the number of math and science teachers for elementary and secondary education.

Training

Another implication of the world's rapidly changing economy is that education and professional training must become an on-going process for the many Americans whose jobs will be increasingly affected by evolving technology. The private sector now funds roughly \$30 to \$40 billion each year to update the needed skills of its employees. Such programs are of critical importance, and the President's proposal for a job voucher tax credit should encourage employers to do more on the job training for new employees.

We need to retrain displaced workers as well. The President has proposed a tenfold increase in funds to train displaced workers under the Job Training Partnership Act for which we fought last year. The program should be very promising because of greater private sector participation.

Funding

The long-term view must similarly be incorporated in new and innovative approaches to increasing the availability of low cost capital to fuel the tremendous innovativeness that characterizes yours and other industries. One example is the venture capital area which was extremely healthy through most of the sixties but which evaporated in 1969 following an increase in the capital gains tax from 25 to 49%. When the capital gains tax was reduced to 28% in 1978, venture capital investment doubled in one year and further increased in 1981 when the tax was reduced from 28 to 20%.

With this favorable United States tax policy, we anticipate that the pool of venture capital will continue to grow and will provide favorable conditions for entrepreneurs to increase the cutting edge of technological innovation. Many venture capitalists not only put up the initial funding but help in the development of markets, provide legal and financial services, and then help the company go public at an appropriate stage of development.

Cost of Capital

While today's climate for equity financing is excellent, certain penalties have been attached to this form of funding in the past. Not the least of these is the pressure for short-term profits brought by shareholders. Emphasis on such accounting criteria as earnings per share, which have little relationship to the long-term economic growth and viability of the corporation, have tended to place undue pressures on management for the "quick fix." This same approach has often been used in determining bonuses for managers.

Japanese firms, on the other hand, with their reliance on debt rather than equity financing and with the large financial reserves available to the conglomerates to which they belong, would appear to be better situated to make decisions which will benefit the long-term interests of their companies. Their situation is helped by the government funded research and development for such designated fields as the fifth generation computer, the super computer, new electronic devices, and by Japan Development Bank loans at special interest rates for specific areas of the semiconductor industry.

In addition to increased access to capital in the United States, our cost of capital must be reduced. A major aspect of the reduction of the cost of capital is to bring inflation under control, and this Administration has accomplished that. However, interest rates must be further reduced.

Conclusion

Our free trade position continues to be heavily challenged. Our growing trade deficit (\$76 billion headed toward \$100 billion) will lead to further attacks on the open trade system. On the positive side, the strong economic recovery continues in the United States on a broad basis. Second quarter real GNP growth has now been revised upward from 9.2 to 9.7%. The inflation rate for the 12 months ending in July is 2.4%—the smallest since January 1966.

As the economy continues to recover and industries feel more secure, pressures against an open trade policy should diminish, provided we deal with the deficit.

The immediate future of your industry is an enviable one of having to scramble to meet demand. Clearly, had protectionist measures been taken last year they would seem inappropriate today. We believe as you continue to emphasize the competitiveness of your industry in a better overall economic climate that you will meet the Japanese challenge which is now moving from one of improving technologies imported from the United States to "forward engineering" and the development of original technologies.

To do this, however, you will need to continue your history of innovativeness. No one should underestimate the proven ability of the Japanese to move very quickly into product development in selected areas. United States industry will need to speed up its own reaction time. In this effort, we are prepared to work closely with you to ensure that world competition is fair competition and that the United States regulatory and investment climate is inductive to growth.

Manuscript submitted Nov. 31, 1983. This was Paper 266 presented at the Washington, DC, Meeting of the Society, Oct. 9-14, 1983.



A Rotating Disk Study of the Corrosion Behavior of Cu-9.4Ni-1.7Fe Alloy in Air-Saturated Aqueous NaCl Solution

C. Kato¹ and H. W. Pickering*

Department of Materials Science and Engineering, The Pennsylvania State University,
University Park, Pennsylvania 16802

ABSTRACT

Results using a rotating disk electrode (RDE) clarify the mechanism of corrosion of commercial Cu-9.4Ni-1.7Fe alloy in aerated 3.4 weight percent NaCl solution at room temperature. The loosely adherent corrosion product (mainly $\text{Cu}_2(\text{OH})_3\text{Cl}$) formed under rotating conditions consists of two layers. Additional support is obtained for the existence of a third inner layer which is very thin and adherent to the metal surface. The anodic Tafel slope on this corrosion-product-covered sample is $60 \text{ mV decade}^{-1}$ and is independent of rotation speed, consistent with a slow step for the anodic reaction being ionic transport in electrolyte within the porous corrosion-product layer. Results using Pd deposits on the corrosion-product surface show that the rate of the cathodic reaction (oxygen reduction) may be under reaction (charge transfer) control rather than transport control through a corrosion-product inner layer. It follows that the good corrosion resistance of the cupronickels in seawater may be due to a poor catalytic nature of the corrosion-product surfaces for the oxygen-reduction reaction.

Commercial Cu-9.4Ni-1.7Fe alloy (Cu10 Ni) has been used successfully as condenser tubes in saline environments (1-4). Although it is generally believed that the source of corrosion resistance of this alloy is a protective inner layer of the otherwise porous corrosion products which develop on its surface in seawater, results presented herein support an alternative protection mechanism.

In laboratory experiments in aerated 3.4 weight percent (w/o) NaCl solution at room temperature, these corrosion-product layers thickened during the first 10³h (5, 6). Anodic and cathodic polarization curves produced on the corrosion-product-covered alloy surface showed that both the anodic (metal dissolution) and cathodic (oxygen reduction) reaction rates and thus the corrosion rate of the alloy decrease as the corrosion products form. However, the amount of reduction in the cathodic rate is much larger than that of the anodic rate. In a similar experiment conducted in natural seawater, Ijesseling and Kroughman (7) also found rate reductions for both the anodic and cathodic reactions up to a certain stage of the corrosion-product formation. Thereafter, only the cathodic rate decreased, while the anodic-reaction rate held constant. Both of these results suggest that the cathodic reaction is most affected by the formation of the corrosion-product layers in aerated seawater and in 3.4 w/o NaCl solution. North and Pryor (8) also observed reduced anodic- and cathodic-reaction rates and suggested that the reductions are due to the increased anodic (ionic) and cathodic (electronic) resistances during formation of the layer. They and other investigators over the years (9, 10) have suggested that the decreased corrosion rate is correlated with the defect structure of the corrosion product layers: specifically, of a thin inner layer next to the alloy surface. Recently, however, another mechanism

based on reaction control of the oxygen reduction reaction has been suggested by Kato *et al.* (5, 6).

Compositional and structural investigations showed that the corrosion product consists of at least two adherent layers: a relatively thick porous outer layer composed of mainly $\text{Cu}_2(\text{OH})_3\text{Cl}$, and a thin inner layer composed of Cu_2O (6, 7). The alloying elements Ni and Fe were concentrated in the middle portion of the corrosion products where the exact structure is not known (6, 7). In this investigation, as a continuation of our previous work (5, 6), the kinetics of the anodic and cathodic reactions were studied using a rotating Cu-9.4Ni-1.7Fe disk electrode in aerated 3.4 w/o NaCl solution.

Experimental

Materials and specimen preparation.—The composition and mechanical properties of the Cu-9.4Ni-1.7Fe alloy (Cu10 Ni) sheet material (0.17 cm thick) in the solutionized condition (850°C for 30 min, water quench) are given elsewhere (5). Disk specimens were cut from the alloy master sheet, polished successively down to 600 grit, immersed in deaerated 10 volume percent H_2SO_4 for 10 min to remove the air-formed oxide, degreased in acetone with ultrasonic surface cleaner for 10 min, rinsed in methanol and stored (\lesssim 20h) in a desiccator. Then, the alloy disk was soldered to a copper wire and mounted in a plexiglass sample holder which exposed 0.70 cm² of sample surface, and inserted into the solution.

For the open-circuit immersion treatments, the alloy disk was rotated at 800 rpm in 300 ml of an aerated 3.4 w/o NaCl solution. Water-saturated compressed air was bubbled through the solution during immersion. The immersion treatments were conducted for various lengths of time up to 10 days. For the 10 day immersion, the solution was changed at 7 days in order to duplicate a procedure used previously for longer term tests which was designed to avoid an accumulation of Cu and Ni ions (5, 6). The initial pH was ad-

* Electrochemical Society Active Member.

¹ Present address: Kawasaki Steel Company, Research Laboratories, Chiba, Japan.

Key words: cupronickels, catalyzed O_2 reduction, condenser tubes, marine corrosion.

justed to 7.5 using NaOH. It tended to slowly drift upward (few tenths of a pH unit after 7 days).

For the polarization measurement, the Cu10Ni disk electrode was transferred from the open-circuit immersion cell to a conventional three-electrode cell equipped for rotation of the sample. For comparison, polarization measurements were also made on fresh alloy disk electrodes after the above-described sample preparation. Electrical contact was made between the specimen and a stainless steel shaft by a Cu wire. The shaft was supported by two frictionless carbon bearings, mounted in plexiglass, which completed the circuit. Either water-saturated compressed air or purified nitrogen gas was bubbled through the 3.4 w/o NaCl solution during the polarization measurements. A saturated calomel electrode was used as the reference electrode. The potential is reported on the standard hydrogen electrode scale.

Transfer of the sample from the immersion cell to the electrochemical cell was quick enough so that the surface of the specimen remained wet, thereby avoiding crack formation in the corrosion products (5). The potential was preset at -100 mV, so that on contact with the solution the sample was at this value while also rotating at 500 rpm. After about 15 min, by which time a quasi-steady current was reached, a potential scan rate of 0.03 mV s^{-1} was applied in the more noble direction. The anodic polarization curve was found to be the same as for a "steady-state" method.¹ In some measurements, rotations up to 2000 rpm were used to investigate the rotation-speed dependence of the polarization curve.²

Another set of experiments was conducted to study the roles of the outer and inner parts of the adherent corrosion product in the corrosion process. Following immersion and overnight drying in a desiccator, the outer part of the corrosion products was removed with poly-tape. Then, polarization curve measurements in both aerated and deaerated 3.4 w/o NaCl electrolyte solution were conducted on the adherent inner layer. Furthermore, on some specimens, palladium was deposited on the inner-layer surface from an aqueous solution, in order to study the effect of a more catalytic surface on the oxygen-reduction reaction.

Conventional x-ray diffraction SEM methods were utilized to characterize the corrosion products formed during the immersion treatments. The test specimens were always duplicated, so that the freshly made corrosion product was used for each characterization analysis.

Results

Polarization curves on fresh surfaces.—Polarization curves measured on fresh rotating disk electrode (RDE) surfaces are shown in Fig. 1. The intersection of curves B' (anodic metal dissolution) and C (true oxygen reduction) is the corrosion current ($20 \mu A cm^{-2}$) and the corrosion potential ($+5$ mV). The rotation-speed dependence of the anodic (metal dissolution) polarization curves on fresh surfaces are shown in Fig. 2. Above -30 mV, a distinct Tafel line is observed. The anodic polarization curves are less polarized at higher rpm, while the Tafel slope is constant (60 – 62 mV decade⁻¹). At potentials higher than those in Fig. 2 ($+70$ to $+170$ mV), the Tafel slope was higher at ~ 80 mV decade⁻¹. A plot of current density vs. square root of the rotation speed at constant potential (Fig. 3) shows a linear relation with an extrapolation which goes through the origin. The cathodic oxygen-reduction polarization curves are dependent on the rotation speed (Fig. 2); however, the rate decreases rather than increases with increasing rpm.

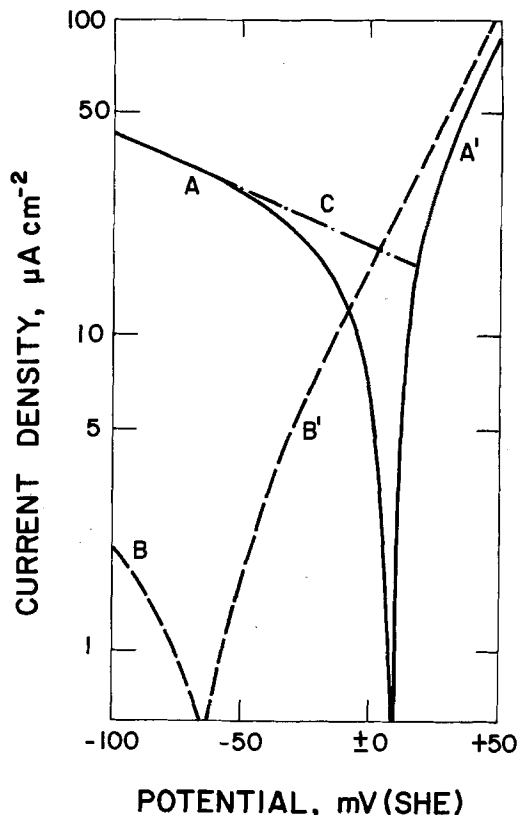


Fig. 1. Polarization curves on the fresh Cu10Ni surfaces. Curves A and A': measured in air-saturated solution. Curves B and B': measured in deaerated solution. Curve C: calculated true oxygen reduction. Rotation speed is 500 rpm.

Open-circuit corrosion.—SEM examination of corroded Cu10Ni RDE samples following immersion, showed two well-defined corrosion product layers (Fig. 4). Their thicknesses were 2.5 – $5 \mu m$ and approximately $5 \mu m$ for the outer porous and relatively dense (middle) layers, respectively. Otherwise, the corrosion products are as reported for immersion in relatively quiescent solution (6). The total (scraped) corrosion product contained both Cu_2O (in small amount) and $Cu_2(OH)_3Cl$, whereas corrosion product which could be stripped with tape showed only $Cu_2(OH)_3Cl$.

Polarization curves on corroded samples.—For the corroded RDE samples, the rate of reduction of the corrosion products was measured (deaerated solution) at -100 mV and 500 rpm (Fig. 5). The quasi-steady-state value on the 5 day corroded sample was $0.9 \mu A cm^{-2}$ cathodic, which was essentially the same, considering a rather poor reproducibility, as the current on the fresh surface ($1.5 \mu A cm^{-2}$ cathodic), indicating no substantial reduction of the corrosion products. Similar results were obtained at 1200 and 1900 rpm. These experiments also clearly showed that the current is always higher in aerated than in deaerated solution. At -100 mV, there was no visible change in the surfaces of either the 0 or 5 day samples.

Both the anodic and cathodic reaction rates are reduced by formation of the corrosion products, and, hence, the corrosion rate decreases with time (Fig. 6), in agreement with previously reported corrosion rates for this alloy-solution system (5). Both the anodic and cathodic currents for the corroded samples are also independent of the rotation speed. Near the corrosion potential, the anodic curves exhibit Tafel behavior with a slope of about 60 mV decade⁻¹ (Fig. 6 and 7). After stripping the (detachable) corrosion products, a higher anodic rate occurs on the inner layer (curve B in Fig. 7) which approximately equals that on a fresh surface (C), and the anodic reaction main-

¹ Potential was shifted manually every 10 mV, and at each potential a quasi-steady-state current was observed before changing the potential.

² Rotation speeds up to 6000 rpm are expected to produce laminar, rather than turbulent, flow for the size of the disk electrode, $r = 0.5$ cm (11).

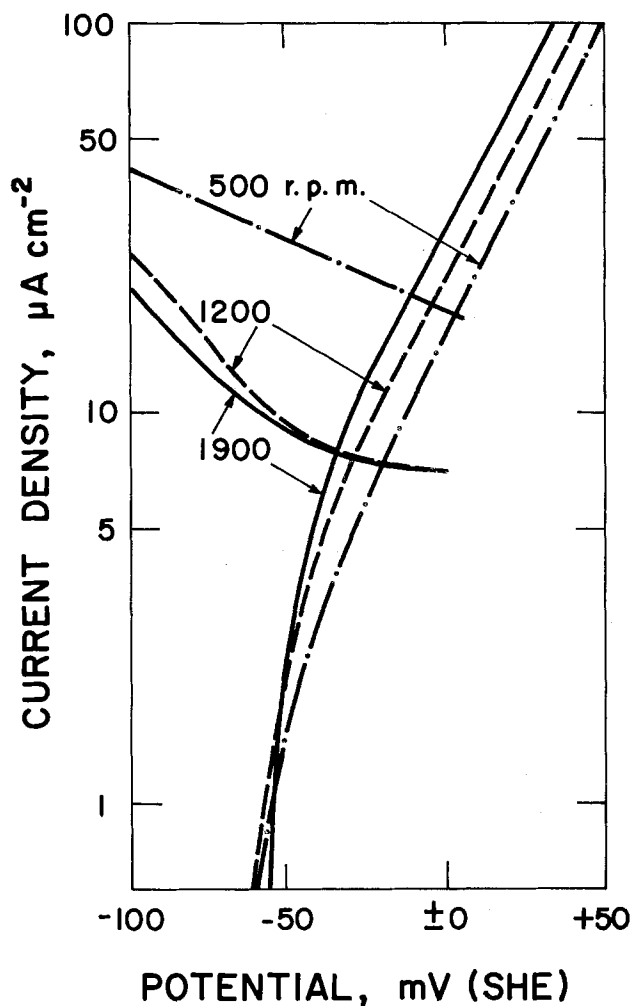


Fig. 2. Rotation speed dependence of the polarization curves on the fresh surface. Cathodic curves measured in air-saturated solution, anodic curves in deaerated solution.

tains a Tafel slope of 60 mV decade⁻¹. In addition, an even higher cathodic current can be produced by the application of a Pd coating on the inner layer (curve D in Fig. 7). The anodic curve B (inner layer) in Fig. 7 and the cathodic curve D (Pd-coated inner layer) are rotation-speed dependent, e.g., at -30 mV, the current increases for both reactions by about 20% for an increase from 500 to 1200 rpm. This is virtually the same dependence for the anodic reaction as in Fig. 2 for a fresh surface.

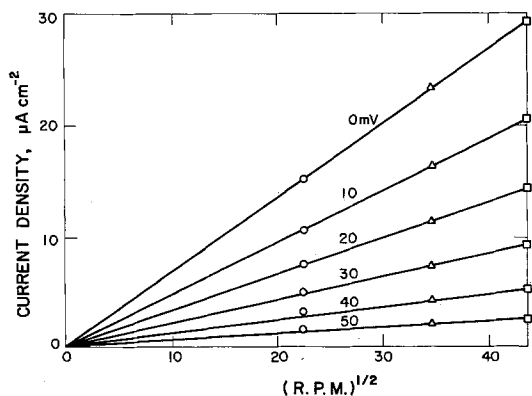


Fig. 3. Anodic current density vs. square root of the rotation speeds on the fresh surface at various potentials vs. SHE in de-aerated solution.

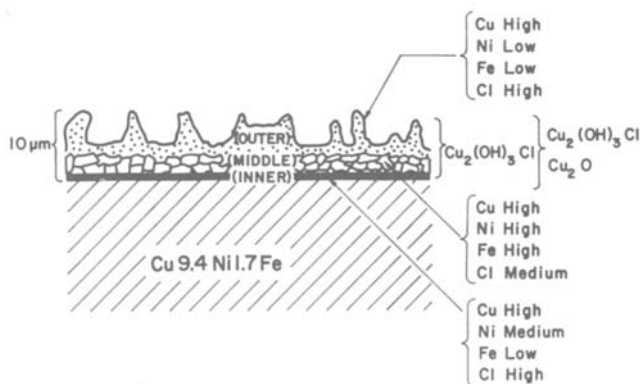
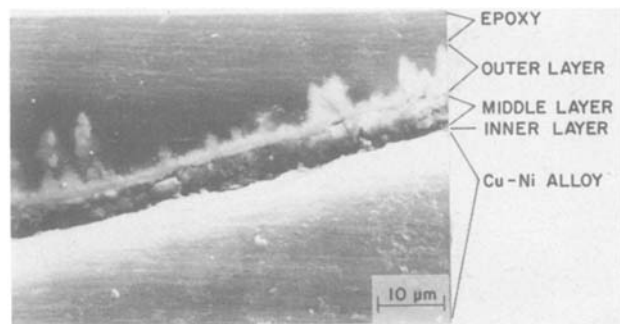


Fig. 4. SEM micrograph (a, top) and schematic (b, bottom) of the cross section of a RDE sample after a 5 day immersion in aerated 3.4 w/o NaCl solution (800 rpm) showing corrosion product layers. Relative amounts of elements based on ESCA and EDX analyses at different locations within the corrosion product (6, 20).

Discussion

Early stage of Cu10 Ni alloy corrosion in 3.4 w/o NaCl solution.—When Cu10 Ni alloy is immersed in 3.4 w/o NaCl solution, visible corrosion products start developing on the alloy surface within 8 min (6). This early stage of the corrosion process was studied by making anodic and cathodic polarization curves on fresh RDE surfaces of the alloy.

The anodic metal dissolution curves on freshly prepared Cu10 Ni surfaces showed a Tafel slope of 60 mV per current decade and a rotation speed dependence which, in a plot of current vs. $\omega^{1/2}$, gives a straight line

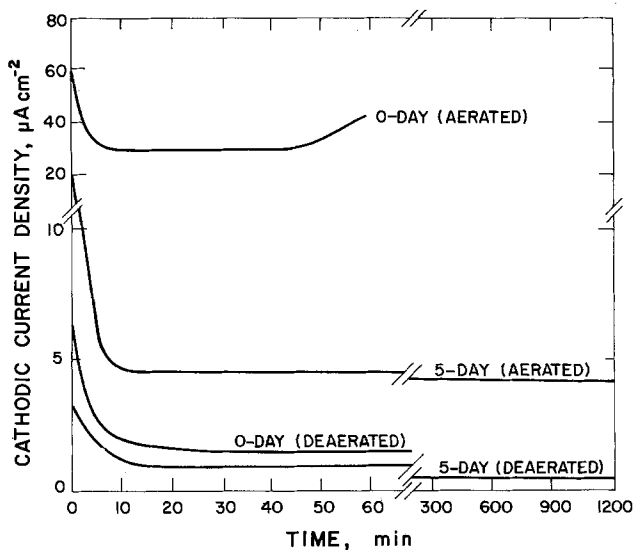


Fig. 5. Cathodic current-density transient at -100 mV (SHE) and 500 rpm on freshly polished and 5 day corroded Cu10 Ni in aerated and deaerated 3.4 w/o NaCl solution.

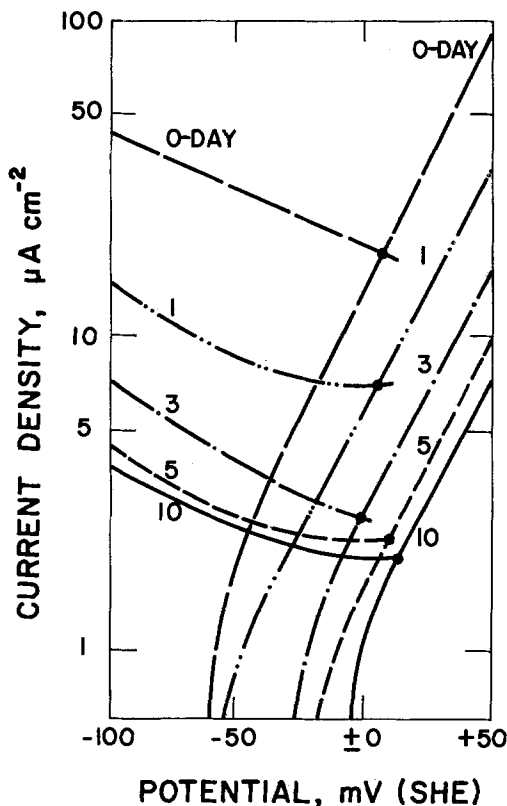


Fig. 6. Polarization curves measured after various periods of corrosion.

through the origin (Fig. 2 and 3). These features are also seen in the dissolution of pure Cu in HCl (12, 13) and in NaCl (14), although the half-power dependency is not always seen (15). Higher Tafel slopes have been reported for the fresh Cu10Ni alloy in HCl solution, viz., 130 mV decade⁻¹ (13) and 70-80 mV decade⁻¹ (16), as well as at overpotentials higher than those used in the present study (3.4 w/o NaCl solution), where 80 mV decade⁻¹ was obtained instead of the 60 mV decade⁻¹ shown in Fig. 2.

The 60 mV decade⁻¹ Tafel slope for the freshly polished Cu-Ni alloy and the half-power dependency of the anodic dissolution current on the rotation speed (Fig. 3) are indicative of a mass-transfer-controlled anodic dissolution step, which is the same as that already established for copper (12-15). Thus, transport of either Cl⁻ ion to the surface or a copper chloride complex ion away from the surface could be the rate-determining step. If the anodic process at open circuit is controlled by diffusion of CuCl₂⁻ away from the surface, as is most often suggested (12-14), then the concentration of CuCl₂⁻ at the alloy/solution interface can be approximately obtained from

$$[\text{CuCl}_2^-]_s = \frac{i}{D_{\text{CuCl}_2^-} F} \cdot \delta \quad [1]$$

where $[\text{CuCl}_2^-]_s$ is the concentration of CuCl₂⁻ at the alloy/solution interface, i is the current and will be taken as the corrosion current in the following calculation, $D_{\text{CuCl}_2^-}$ is the diffusion coefficient of CuCl₂⁻, F is the Faraday constant, and δ is the diffusion layer thickness, which can be calculated by utilizing the Levich equation

$$\delta = 0.643 \omega^{-1/2} \nu^{1/6} D^{1/3} \text{CuCl}_2^- \quad [2]$$

where ω is the rotation speed and ν is the kinematic viscosity. Using typical values of ω , ν , and $D_{\text{CuCl}_2^-}$ (8.33 Hz, 0.01 cm² s⁻¹, and 0.6×10^{-5} cm² s⁻¹)³, one

³ Taken to be the same as the room temperature diffusion coefficients of CuCl⁺ and CuCl₂⁻ (17).

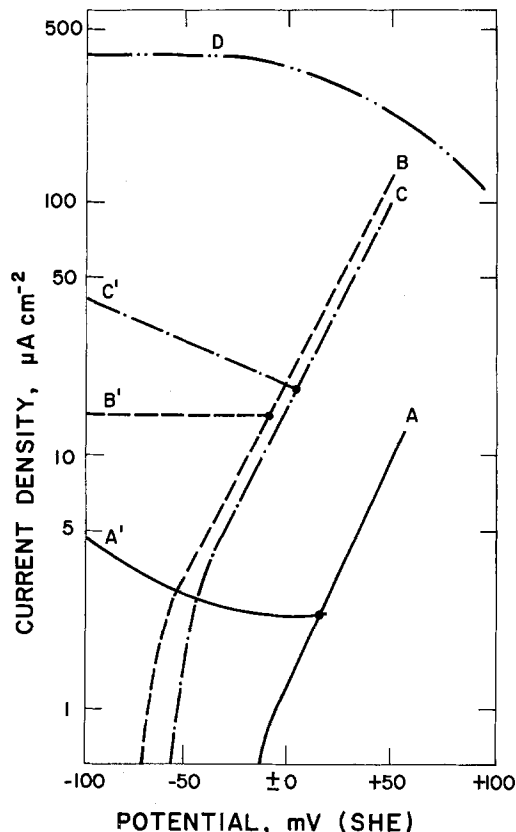
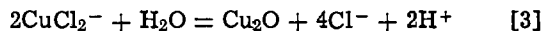


Fig. 7. Effect of the adherent (inner) and the detachable (outer) corrosion-product layers on the polarization curves: Curves A and A' are 5 day; B and B' are 5 day stripped; C and C' are fresh surface; D is 5 day, stripped, Pd-coated.

obtains the diffusion layer thickness of 18 μm. The corrosion current obtained on a rotating (500 rpm), freshly polished sample is determined by the intersection of the anodic and cathodic polarization curves and is about 20 μA cm⁻² (Fig. 6). Using these values of i and δ , the concentration of CuCl₂⁻ from Eq. [1] is $6.2 \times 10^{-5} M$.

Bacarella and Griess (14) and other investigators (18) suggested that the relatively high concentration of CuCl₂⁻ at the metal surface causes hydrolysis of CuCl₂⁻ and produces Cu₂O by the reaction



It follows from their results that the minimum concentration of CuCl₂⁻ to form Cu₂O for our experimental conditions is $5.5 \times 10^{-6} M$. Thus, the concentration ($6.2 \times 10^{-5} M$) obtained in this study is favorable for the formation of Cu₂O. This is still true, although more marginally so, if a more precise calculation is made in which the Ni and Fe contributions to the corrosion current are taken into account. The x-ray powder diffraction analysis of the corrosion products clearly shows the presence of Cu₂O after the 5 day corrosion. Lesser amounts of Cu₂O, below the detection capability of the technique, were presumably present at earlier stages.

The cathodic current transients in Fig. 5 show an initial drop followed by a quasi-steady state. The initial drop on the 0 day samples may be due to reduction of air-formed oxide, reaction with impurities, and/or formation of Cu₂O or other oxides which have a poorer catalytic nature (as compared to the fresh alloy surface) for the reduction of oxygen or impurities. Resolving these possibilities is difficult because of the typically rather slow rate of reaction (low exchange current density) of oxygen reduction on metal surfaces and the effects of impurities. These factors were less of an issue once the surface was covered with

corrosion products, as indicated by a better reproducibility of the transients on 5 day than on 0 day samples.

The mechanism of oxygen reduction on a Pt electrode has been well documented (19), and its Tafel slope is 110 mV decade⁻¹. However, on the freshly polished Cu10 Ni alloy, the Tafel slope is not well defined and varies between 200-260 mV decade⁻¹. The oxygen reduction rate shows an unusual rotation-speed dependency, decreasing with increase in the rotation speed. Only the last-listed of the above explanations of the initial drop of the current is also consistent with this result, i.e., regarding corrosion-product formation at the immersion potential of -100 mV. As the rotation speed increases, increasing amounts of the corrosion products may form, in accord with the effect of rotation speed on the anodic-reaction rate (Fig. 2). If so, as the rpm increases, the cathodic polarization curves are increasingly measured on the adherent solid corrosion products with their poorer catalytic nature, rather than on the alloy surface. In the same way, the observed decrease in corrosion rate with time (Fig. 6) could occur because of the decreasing catalytic activity of the surface for the oxygen-reduction reaction as the corrosion products form. The possibility of a reaction-controlled corrosion process is further indicated by the results with Pd and also by other results in sulfide-contaminated solutions (see below).

Corrosion mechanism of Cu10 Ni alloy after the 5 day immersion.—After a 5 day immersion of the RDE in the NaCl solution, the corrosion product layers are well developed on the alloy surface. Based on SEM, ESCA, and x-ray diffraction investigations, they consist of three layers (6, 20): a very porous outer layer with high concentrations of Cu and Cl; a relatively porous middle layer which contains a particularly high concentration of Ni; and a very thin inner layer which contains Cu and considerable amounts of Cl and Ni, though it is lower in Cl and higher in Ni than found for a stationary electrode (Fig. 4b). The inner layer is invisible in Fig. 4a; the presence of Cl after 60s of ion sputtering on the inner-layer surface (6, 20) shows that the layer under examination is still within the corrosion products. The detachable outer and middle layers were identified as Cu₂(OH)₃Cl. The thin inner layer was not identified directly, but is probably Cu₂O, since the x-ray diffraction analysis on the total scraped corrosion product showed Cu₂O, whereas the stripped corrosion product layers did not. The approximate thickness of the inner layer is estimated to be between 5 and 500 nm. The lower limit is obtained from the ion sputtering rate of 5 nm min⁻¹. The upper limit is based on the resolution in the micrograph. These results for the rotating alloy samples are similar to those reported for the stationary sample (5, 6), except for the finding of the middle layer which is clearly identified in Fig. 4a.

A well-developed corrosion product produces the following changes in the anodic polarization curves compared to those for a fresh Cu10 Ni surface: (i) they shift to more noble potentials while keeping a Tafel slope of 60 mV per decade current (Fig. 6) and (ii) they become independent of rotation speed. Another set of anodic polarization measurements conducted on the inner layer of the corrosion products (after stripping the loosely adherent corrosion products) showed that the curve on the inner layer (curve B, Fig. 7) is nearly identical to the curve on the fresh surface (curve C) and is rotation-speed dependent. This indicates that the outer loosely adherent layer rather than the inner layer is responsible for the changes found in the anodic polarization curves. The Tafel slope of 60 mV per decade current indicates a mass-transfer-limited anodic-reaction rate (12, 13). Since the anodic polarization curves of corroded samples are independent of the rotation speed, transport

of ions through the solution boundary layer next to the electrode surface cannot be the rate-determining step (rds) of the anodic reaction, in contrast to the situation for the fresh Cu10 Ni surface. Rather, diffusion of these ions in the electrolyte within the porous corrosion-product layer is the likely rds of the anodic reaction for corroded samples.

The important effect of establishing well-defined hydrodynamic conditions at the electrode surface is dramatically illustrated by comparison of the above anodic polarization behavior with prior work which did not employ the RDE (5). For the less well-defined hydrodynamic conditions, the Tafel slope varied from 70 to 110 mV decade⁻¹ with increasing length of the corrosion period. Actually, the 60 mV decade⁻¹ value in the present work is for a lower overpotential region; this region could be examined in the present work because of less current oscillation with the RDE. The 60 mV decade⁻¹ value is taken as a more correct Tafel slope, and is consistent with a particular rds, as discussed above. Another difference is the larger shift with the RDE of the anodic polarization curves (to more noble potentials) in going from a fresh surface to a corroded one. Thus, the anodic reaction plays a somewhat larger role in reducing the corrosion rate in the case of flowing systems than was found for quiescent solution (5), but still is only of secondary importance compared to the cathodic reaction.

Like the anodic curves, the cathodic oxygen-reduction curves were more polarized after the formation of the corrosion-product layer. The polarization measurements conducted on the outer-layer surface (curve A in Fig. 7) and on the inner-layer surface (curve B) showed no dependence on rotation speed. In contrast, with Pd⁴ on the inner layer the oxygen reduction rate was much higher and was rotation-speed dependent (curve D). Thus, neither diffusion of the reactants nor the products in the solution boundary layer is the rate-determining step, except in the presence of Pd. The fact that Pd, a well-known catalyst for oxygen reduction, greatly increases the oxygen-reduction rate supports the theory that the good corrosion resistance of Cu10 Ni alloys in seawater is due to the poor catalytic nature of the corrosion products for the oxygen-reduction reaction. It, nevertheless, is not a decisive result because one cannot rule out the possibility that Pd penetrated to the metal surface, in which case it could have short circuited electron flow through a protective inner layer. Some recent work in this laboratory in a H₂S containing aqueous solution (20), summarized next, yielded data which are, however, consistent only with a reaction, rather than transport-controlled, process.

Corrosion mechanism of Cu 10 Ni alloy in sulfide solution.—The corrosion product formed on the Cu10 Ni alloy during immersion in sulfide-contaminated (~5 ppm) 3.4 w/o NaCl solution was found to be multi-layered. The inner layer has a very small thickness, approximately the same atomic ratio of Cu to Ni to Cl but also containing a small amount of sulfide (2 a/o), and identical anodic polarization curves to that obtained on the inner layer in the sulfide-free solution (curve B, Fig. 7). The cathodic polarization curves obtained on the samples corroded in the sulfide-contaminated solution, however, show a diffusion limiting high rate of reaction similar to that obtained on the Pd-coated inner layer in Fig. 7 (curve D). However, the reaction was found to be very slow on the stripped sample, whereas it should have been unchanged after stripping if the role of the sulfide had been to increase the conductivity of a poorly conducting inner layer. Thus, sulfide increases the cathodic reaction kinetics, presumably by increasing the catalytic nature of the

⁴The exchange current density of oxygen reduction is very high on Pd, about one order of magnitude greater than on Pt (21).

surface of the corrosion products for the oxygen-reduction reaction. The low rate of reaction on the inner-layer surface after stripping could then be attributed to an insufficient level of sulfide on its (fracture) surface to significantly increase the catalytic nature of this surface for the oxygen-reduction reaction.

Conclusions

The loosely adherent corrosion products developed on rotating Cu-9.4Ni-1.7Fe alloy samples immersed in aerated 3.4 w/o NaCl solution have been found to be composed of two layers: a relatively dense middle layer and a porous outer layer. Data obtained on the composition of these loosely adherent corrosion products are largely supportive of earlier data reported for stationary electrodes (6). The presence of an inner corrosion-product layer which is very thin, adherent to the metal, and contains Cu_2O is indicated by the data.

The formation of these layers under rotating conditions produced a greater reduction in the corrosion rate than in the case of their formation under the relatively quiescent conditions of a stationary electrode. Most of the decrease in corrosion rate for either condition is due to a decrease in the rate of oxygen reduction.

For the fresh surface, the Tafel slope is 60 mV decade⁻¹ and is rotation-speed dependent. This indicates that a transport step in the aqueous boundary layer is the anodic rds. In the presence of the corrosion product, the Tafel slope is also 60 mV decade⁻¹ [in contrast to the variable 70-110 mV decade⁻¹ found for stationary electrodes (5)] but is rotation-speed independent. In this case, diffusion of ions in electrolyte within the porous corrosion products is the likely rds of the anodic reaction. Results for the cathodic reaction, though not decisive, support a reaction-control mechanism for the corrosion process. This is a (new) understanding of the good corrosion-resistant character of the CuNi alloys in seawater based on a low exchange current density for the oxygen-reduction reaction, consistent with other results (20) for sulfide-contaminated solutions. The results in sulfide, additionally, appear decisively to rule out transport mechanisms based on a protective inner corrosion-product layer.

Acknowledgments

The authors gratefully acknowledge the financial support of the National Science Foundation, Metallurgy Program, Division of Materials Research under Con-

tract no. DMR80-10828, and of the Applied Research Laboratory of The Pennsylvania State University.

Manuscript submitted Sept. 7, 1982; revised manuscript received Jan. 20, 1984.

The Pennsylvania State University assisted in meeting the publication costs of this article.

REFERENCES

1. G. L. Bailey, *J. Inst. Metals*, **79**, 243 (1951).
2. W. C. Stewart and F. L. LaQue, *Corrosion*, **8**, 259 (1952).
3. S. D. Reynolds, Jr. and F. W. Perment, *Mater. Perform.*, **13**, September (1974).
4. H. Leidheiser, Jr., "The Corrosion of Copper, Tin, and Their Alloys," p. 85, John Wiley and Sons, Inc., New York (1971).
5. C. Kato, B. G. Ateya, J. E. Castle, and H. W. Pickering, *This Journal*, **27**, 1890 (1980).
6. C. Kato, J. E. Castle, B. G. Ateya, and H. W. Pickering, *ibid.*, **127**, 1897 (1980).
7. F. P. Ijesseling and J. M. Kroughman, in "Proceedings of 6th European Congress of Metallic Corrosion," p. 181, Society of Chemical Industry, London, Sept. 19-23 (1977).
8. R. F. North and M. J. Pryor, *Corros. Sci.*, **10**, 297 (1970).
9. R. G. Blundy and M. J. Pryor, *ibid.*, **12**, 65 (1972).
10. J. M. Popplewell, R. J. Hart, and J. A. Ford, *ibid.*, **13**, 295 (1973).
11. Yu. V. Pleshov and V. Yu. Filinovskii, "The Rotating Disk Electrode," p. 360, Translated from Russian by H. S. Wroblowa, Translation edited by H. S. Wroblowa and B. E. Conway, Consultants Bureau, New York and London (1976).
12. C. H. Boniglio, H. C. Albaya, and O. A. Cobo, *Corros. Sci.*, **13**, 295 (1973).
13. J. O'M. Bockris, B. T. Rubin, A. Despic, and B. Lorvecek, *Electrochim. Acta*, **17**, 973 (1972).
14. A. L. Bacarella and J. C. Griess, Jr., *This Journal*, **120**, 461 (1973).
15. M. Braun and K. Nobe, *ibid.*, **126**, 1666 (1979).
16. M. C. Walton and P. A. Brook, *Corros. Sci.*, **17**, 317 (1977).
17. R. White, J. A. Trainham, and J. Newman, *This Journal*, **124**, 669 (1977).
18. K. D. Efrid, *Corrosion*, **31**, 77 (1975).
19. A. Damjanovic, in "Modern Aspects of Electrochemistry," Vol. 5, p. 369, J. O'M. Bockris and B. E. Conway, Editors, Plenum Press, New York (1959).
20. C. Kato, H. W. Pickering, and J. E. Castle, *This Journal*, **131**, 1225 (1984).
21. J. Hoare, in "Encyclopedia of Electrochemistry of the Elements," Vol. 2, p. 209, A. J. Bard, Editor, Marcel Dekker, New York (1974).

Effect of Sulfide on the Corrosion of Cu-9.4Ni-1.7Fe Alloy in Aqueous NaCl Solution

C. Kato¹ and H. W. Pickering*

Department of Materials Science and Engineering, The Pennsylvania State University, University Park, Pennsylvania 16802

J. E. Castle

Department of Metallurgy and Materials Technology, University of Surrey, Guildford, GU2 5XH, England

ABSTRACT

The effects of sulfide contamination (5 ppm) on the corrosion mechanism of Cu-9.4Ni-1.7Fe alloy were studied in 3.4 weight percent (w/o) NaCl solution at room temperature. Compared to the sulfide-free solutions (i), the thickness of the corrosion products formed in the sulfide solution is much greater, and (ii) the anodic polarization curves measured in clean 3.4 w/o NaCl solution after immersion in the solution containing sulfide are somewhat less polarized but are otherwise similar, whereas (iii) the cathodic polarization curves are very much less polarized (100 times). This much increased cathodic rate is mainly responsible for the increased corrosion rate caused by prior exposure to a solution containing sulfide. After stripping the loosely adherent corrosion products containing sulfide, the corrosion rate fell to a negligible level comparable to that obtained for sulfide-free corroded samples. These results show that sulfide increases the corrosion rate through its effect on the outer corrosion products, rather than on the thin inner layer next to the metal. Since the outer corrosion products are porous, it follows that sulfide's dominant role is that of a catalyst for the oxygen reduction reaction. This explanation is consistent with other results for sulfide-free corroded samples.

Serious corrosive attack of the commercially available Cu-9.4Ni-1.7Fe alloy (Cu10 Ni) has been a problem in naval ships in polluted seawater. Such attack has been attributed to contamination of the seawater environment by sulfide (1-6). Dissolved oxygen is the normal oxidant in unpolluted seawater. In polluted seawater or subsequently in unpolluted (clean) seawater, higher rates of corrosive attack are expected in its presence (1, 5-8).

The usually good corrosion resistance of the Cu10 Ni alloy in seawater is generally attributed to the nature of its corrosion products. These corrosion products have been identified as Cu_2O and $\text{Cu}_2(\text{OH})_3\text{Cl}$ (9-14). They consist of an outer porous layer, a relatively dense middle layer and a very thin inner layer (10-12). The outer and middle layers are loosely adherent and can be removed with adhesive tape. Based on polarization measurements (9, 11), it was concluded that (i) the anodic (metal dissolution) reaction is controlled by diffusion of ions in electrolyte within the porous, loosely adherent corrosion products, (ii) the cathodic reaction (oxygen reduction) may be under reaction control, and (iii) the low corrosion rates of the Cu-Ni alloys in neutral chloride solutions may be due to the mechanism in (ii). Other explanations of the corrosion-resistant character of the cupronickels in seawater which rely on other rate-determining steps and/or are based on the inner layer have been suggested, but these have been questioned based on recent polarization data (9, 11) and are shown to be inconsistent with data in this paper. More generally, our results support the concept of reaction-control as the basis for a corrosion-resistant alloy rather than the classical protective layer concept, *i.e.*, one based on a poisoned surface for charge transfer of the cathodic reaction(s).

In sulfide-contaminated natural or simulated seawater, the corrosion products are modified and the corrosion rate sharply increases. Bates and Popplewell (1) measured the corrosion rate of the Cu10 Ni alloy in sulfide-contaminated (10 ppm) simulated seawater. They used alternating sulfidation and aeration periods in an effort to simulate service conditions involving polluted seawater, and avoided simultaneous sulfidation/aeration since sulfide levels could not be main-

tained due to reaction with the oxygen. They suggested that the higher corrosion rates are due to a highly defective Cu_2O layer containing Cu_2S which permits rapid ionic and electronic transport through it. More recently, Hack and Gudas (5, 6) and Eiselstein *et al.* (8) have shown that very high rates of corrosion, matching those of service failures, occur during simultaneous exposure to sulfide and oxygen. MacDonald *et al.* (2), using deaerated solutions, attributed the effect of sulfide to an increase in kinetics of the anodic reaction, since it changed from cuprous oxide formation in the sulfide-free solution to cuprous sulfide formation in the sulfide-polluted solution. As such, oxygen reduction was not the cathodic reaction, and the corrosion potential shifted in the less noble direction with sulfide addition.

Our previous work (9-11) has focused on the corrosion mechanism of Cu-Ni alloy in simulated unpolluted seawater (NaCl solution). This paper describes the effects of sulfide addition to a 3.4 weight percent (w/o) NaCl solution on the corrosion mechanism of Cu-9.4Ni-1.7Fe alloy.

Experimental

The composition and mechanical properties of the commercial Cu-9.4Ni-1.7Fe alloy, sample preparation, immersion, and polarization procedures are the same as described in previous papers of this series (9-11).

The sulfide-contamination solution was prepared by bubbling a $\text{H}_2\text{S}/\text{H}_2$ gas mixture through a 3.4 w/o NaCl solution which had been first deaerated with purified [anhydrous calcium sulfate (Drierite) and copper at 400°C] nitrogen. The 99.6% H_2S was dried using phosphorous pentoxide, the 99.99% H_2 was dried using drierite and magnesium perchlorate, and oxygen was removed by passing over magnesium at 400°C. The gases were then mixed using conventional flowmeters containing silicon oil (for H_2S) or dibutyl phthalate (for H_2).

For an immersion experiment, a disk sample of Cu10 Ni was rotated at 800 rpm first in the aerated sulfide-free (clean) solution for 23h, and then for 1h in a deaerated solution containing 5-8 ppm sulfide² and a pH between 7.0 and 7.5 at room temperature ($23 \pm 2^\circ\text{C}$).

* Electrochemical Society Active Member.

¹ Current address: Kawasaki Steel Company, Research Laboratories, Chiba, Japan.

² Total sulfide, including H_2S , HS^- , and S^{2-} [in the approximate ratio of 1:1:10⁻⁵ (15)], measured using a sulfide ion electrode; oxygen and sulfide were not mixed due to their tendency to react.

For the flow rate used, these values were obtained in about 30 min, see Table I. This cycle was repeated for up to 10 days total time.

Immediately after the immersion tests, some of the samples were rinsed with distilled water and transferred to a conventional three electrode electrochemical cell for polarization curve measurements in sulfide-free 3.4 w/o NaCl solution at 500 rpm, unless otherwise indicated. The 3.4 w/o NaCl solution was either deaerated (with purified N_2 gas) or aerated for some of the cathodic curves using compressed air. The polarization curves were measured from -100^3 to $+150$ mV at a potential scanning rate of 0.03 mV s^{-1} . This immersion/polarization procedure most closely follows that of experiments on sulfide-free corroded samples (9-11) which are used as a basis of comparison, and also may be an encountered corrosion situation in seawater. Corrosion currents were obtained in polarization plots by extrapolation of the cathodic curve (oxygen reduction) in order to obtain the intersection with the anodic curve measured in deaerated solution.

Following established procedures (9, 10), the corrosion products which formed during open-circuit corrosion were analyzed with x-ray diffraction, SEM, and ESCA. Moreover, EDX analyses could be conducted on the cross section of the corrosion products, since they were much thicker than those obtained in the sulfide-free solution.

Results

Compositional and structural analyses.—The corrosion products formed during immersion were separated into an outer loosely adherent and an inner adherent layer, as reported for sulfide-free solution (11). The loosely adherent corrosion products were black and the adherent inner layer was a dull reddish brown. X-ray diffraction analyses of the loosely adherent black corrosion product and of the total corrosion products scraped off the sample both show Cu_2S and $Cu_2(OH)_3Cl$. However, identification is not possible for Cu_2O , whose peaks overlap the Cu_2S and $Cu_2(OH)_3Cl$ peaks. These layers are seen in Fig. 1.

ESCA results are compared in Table II for the sulfide-free (clean) solution and the solution containing sulfide for the surfaces shown in Fig. 2. In all three locations, the Cu to Ni ratio is similar for the solution containing sulfide and the sulfide-free solution: Cu strongly predominates in locations A and C, whereas, Ni is in (slight) majority in location B. The sulfur peak was identified as sulfide (S^{--}). The concentration of S^{--} decreases from position A to C, whereas the concentration of chloride is highest at C and lowest at B for layers formed in the solution containing sulfide, see Table II.

In cross section, the adherent inner layer is too thin to be seen, however, the outer porous layer and multiple lamellae of a middle layer can be seen by SEM, Fig. 3. These loosely adherent outer and middle layers are thicker than those developed after clean corrosion (11); as such they are suitable for EDX analysis. The elemental spectrums obtained at positions D, E, and F (Fig. 3) are shown in Fig. 4 and indicate a unique

^a Electrode potential is reported on the standard hydrogen electrode scale.

Table I. Typical time variations of pH and sulfide concentration in the 3.4 w/o NaCl solution from the start of bubbling with the H_2S/H_2 gas mixture

Time (min)	pH	Sulfide concentration mol/liter	ppm
0	7.50	0	0
15	7.10	4.3×10^{-5}	1.4
30	7.05	2.2×10^{-4}	7.0
60	7.05	1.9×10^{-4}	6.0
90	7.00	2.3×10^{-4}	7.0

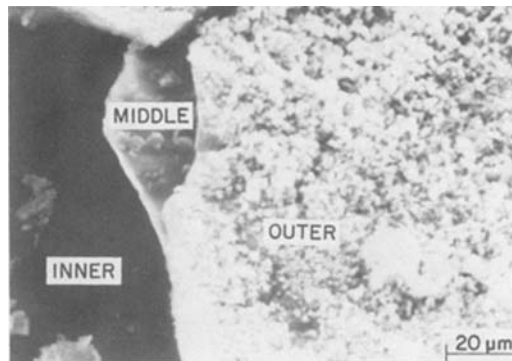


Fig. 1. SEM micrograph of the surface of a Cu10 Ni sample after a 10 day immersion in the 3.4 w/o NaCl solution containing sulfide and partial (tape) stripping of the corrosion products. Left: only adherent inner layer remains. Right: highly porous middle and outer layers still adherent after stripping.

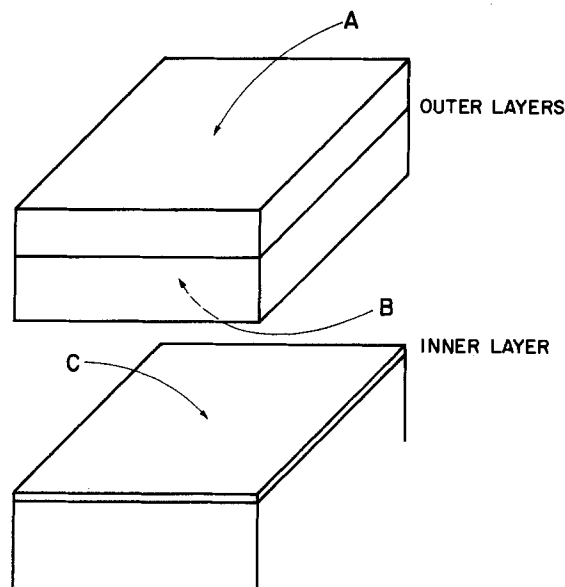


Fig. 2. Schematic showing stripped corrosion product and an adherent (very thin) corrosion product layer on the sample surface.

composition for each location. Based on the data obtained by x-ray diffraction, ESCA, and SEM with EDX, the corrosion products formed in the sulfide solution are shown in Fig. 5.

Polarization curve measurements.—Cathodic polarization of the Cu10 Ni sample following the corrosion

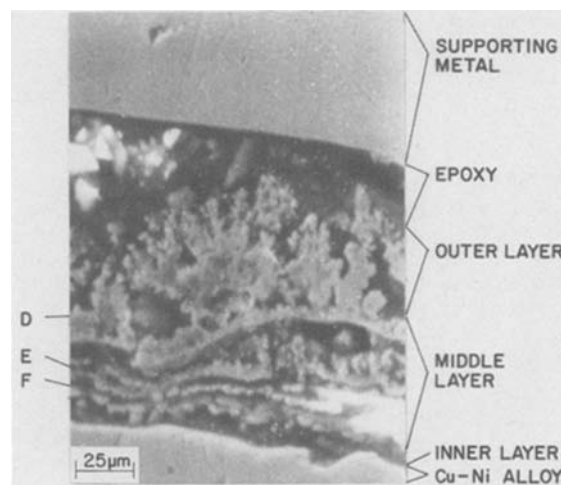


Fig. 3. SEM micrograph of the cross section of a Cu10 Ni sample after a 5 day sulfide corrosion experiment.

Table II. ESCA semiquantitative analysis (relative a/o) of corrosion products developed during the corrosion tests in sulfide-free solution or solution containing sulfide for locations A, B, and C (Fig. 2)

Sample	Location Etching time (s)*	Element	A			B			C		
			0	15	60	0	15	60	0	15	60
3 day clean	Cu	14	19	32	14***	7	17***	20	21	27	
	Ni	ND**	ND**	ND**	17***	19	13***	10	13	13	
	O	62	49	50	—	50	—	62	56	49	
	Cl	24	33	19	—	21	—	8	10	11	
5 day clean† (stationary)	Cu	20	—	—	15	15	18	12	33	26	
	Ni	1	—	—	17	12	18	4	4	4	
	O	62	—	—	45	62	55	64	41	44	
	Cl	16	—	—	21	11	8	21	22	26	
3 day sulfide	Cu	—	27	34	18	16	11	23	26	29	
	Ni	—	5	3	24	22	11	4	5	5	
	S	—	6	10	7	6	2	<2	<2	<2	
	O	—	52	41	42	49	67	56	51	46	
5 day sulfide	Cl	—	10	12	8	7	7	18	19	20	
	Cu	14	16	25	14	13	6	16	18	20	
	Ni	12	6	7	26	21	13	8	9	11	
	S	6	6	8	4	3	4	2	2	2	
	O	56	55	43	46	51	64	53	45	41	
	Cl	13	17	17	10	12	13	22	26	26	

* Approximate sputtering rate of 5 nm min⁻¹ (Ar ion, 10 μA, 5 keV).
 ** None detectable.
 *** O and Cl levels are assumed to be 50 and 20 a/o, respectively.
 † Data are for a stationary, rather than rotating, electrode (10).

experiment may cause reduction of the corrosion products in addition to oxygen reduction. The rate of reduction of the corrosion products was measured by holding a sulfide-corroded sample at a constant potential of -100 mV in the deaerated sulfide-free 3.4 w/o NaCl solution, and the current transient was compared with similar data obtained on a freshly prepared noncorroded (0 day) Cu10 Ni surface, Fig. 6. Initially, a relatively high current (80 μA cm⁻²) is measured on the 5 day sulfide-corroded Cu10 Ni sample in the deaerated (sulfide-free) solution, and this current decreases with time. The charge passed is mainly due to the reduction of the corrosion products, since no other species can be reduced in this inert gas-purged solution at -100 mV, as shown for the fresh sample (bottom curve in Fig. 6). However, the rate of reduction of the corrosion products is between one and two orders of magnitude lower than the rate of oxygen

reduction (top curve in Fig. 6), and was, therefore, ignored in subsequent polarization measurements.

Post-test anodic and cathodic polarization curves (sulfide-free solution) produced on the samples after 3, 5, and 10 day sulfide corrosion tests are compared with those produced after a 5 day sulfide-free corrosion test (11) in Fig. 7. Sulfide corrosion causes about a 100-fold increase in the cathodic current and a slight increase in the anodic current of the respective polarization curves. The corrosion rate increases from ~2 μA cm⁻² for the 5 day sulfide-free (clean) corrosion test to 400 μA cm⁻² for the 5 day sulfide corrosion test, and the corrosion potential shifts from +10 to +160 mV, Table III. The corrosion currents obtained on samples corroded for more than 5 days are not reproducible, varying between 100-500 μA cm⁻², and random detachment of portions of the corrosion-product layer occurs.

A sulfide-corroded sample which has been stripped with tape shows a much reduced cathodic rate and increased anodic rate compared to an unstripped sample (Fig. 8). Both reaction rates on the inner layer are

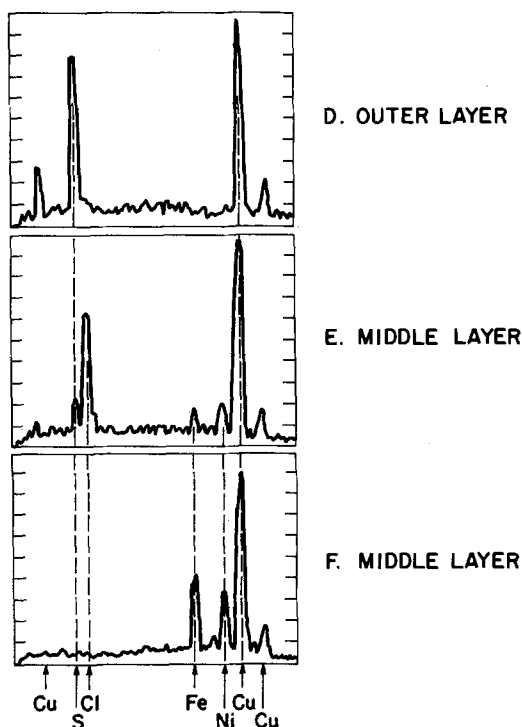


Fig. 4. EDX analyses of locations D, E, and F in Fig. 3 of the corrosion products after a 5 day sulfide corrosion experiment.

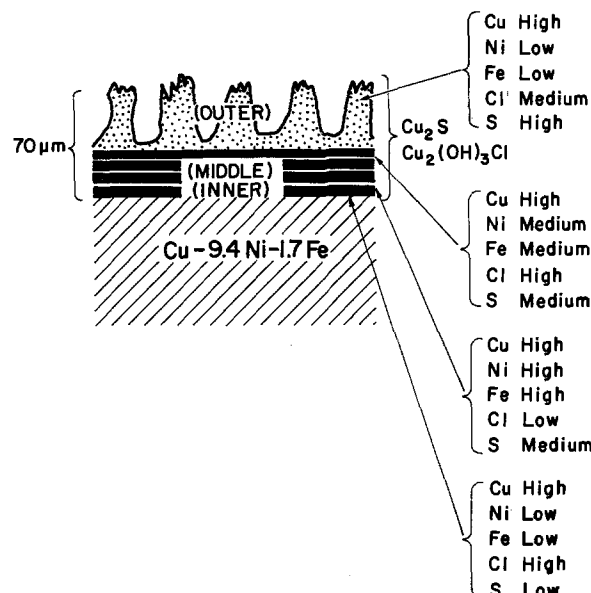


Fig. 5. A schematic of the cross section of the corrosion products on the Cu10 Ni surface after a 5 day sulfide corrosion experiment.

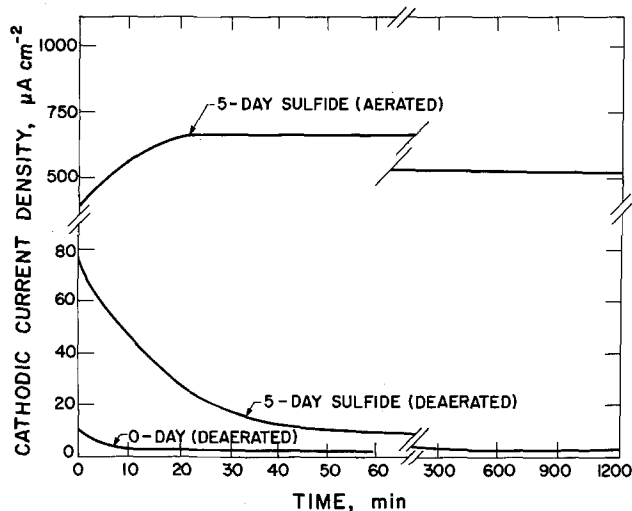


Fig. 6. Post-test cathodic current-density transient at -100 mV (SHE) in sulfide-free aerated and deaerated 3.4 w/o NaCl solution on 5 day sulfide-corroded samples. Transient for a fresh (0 day) sample also presented.

similar to those on the inner layer of samples corroded in sulfide-free (clean) solution (11).

Discussion

Comparison of the corrosion products formed in the sulfide corrosion test with those formed in the sulfide-free (clean) test (11) show the following. Those developed in the sulfide-contaminated solution are much thicker ($\sim 70 \mu\text{m}$ vs. $10 \mu\text{m}$ for a 5 day immersion). Both exhibit highly porous and easily detachable outer layers and an adherent very thin inner layer. The thicker sulfide corrosion products are black in color and contain Cu_2S and $\text{Cu}_2(\text{OH})_3\text{Cl}$, whereas those formed in the sulfide-free solution are dull tan and contain Cu_2O and

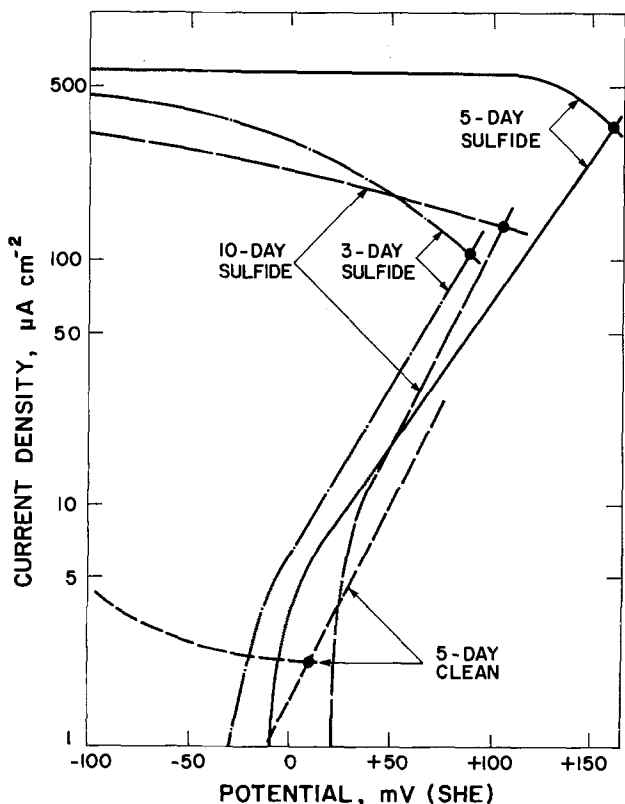


Fig. 7. Post-test polarization curves measured on the Cu10 Ni sample following the sulfide corrosion tests and following a 5 day sulfide-free (clean) corrosion test (11).

Table III. Corrosion currents and potentials of sulfide-degraded Cu10 Ni samples measured in sulfide-free 3.4 w/o NaCl solution. Same for Cu10 Ni samples which had been corroded instead in sulfide-free (clean) 3.4 w/o NaCl solution (11).

Time	Sulfide Potential vs. SHE (mV)	Sulfide Current ($\mu\text{A cm}^{-2}$)	Clean Potential vs. SHE (mV)	Clean Current ($\mu\text{A cm}^{-2}$)
1h	—	—	+5	18.0
1 day	—	—	+5	7.0
3 day	+80	100	+5	2.5
5 day	+160	400	+10	2.2
10 day	+100	150	+10	2.0

$\text{Cu}_2(\text{OH})_3\text{Cl}$ (11). The adherent inner layers developed in both solutions are very similar and have the following properties: (i) they are brown in color, adherent to the alloy, and thinner than could be resolved in SEM cross-sectional study, i.e., $\ll 500$ nm. (ii) They contain relatively high concentrations of Cl^- anions [~ 25 atomic percent (a/o)] and Cu and Ni cations [~ 30 a/o] with Cu predominating (ratio of 2-5 to 1).

The corrosion potentials for the sulfide-degraded alloy are more noble (80-160 mV SHE) than in the case of corrosion product formed in sulfide-free solution (5-10 mV SHE), Table III. The reason for the more noble corrosion potential is the greatly improved catalytic nature of the outer corrosion products containing sulfide for the oxygen reduction reaction, as discussed next. A shift of the corrosion potential in the noble direction for aerated solution is in contrast to a shift in the negative direction for deaerated solution (2, 3).

The polarization curves produced on the inner layer after stripping the loosely adherent outer corrosion products actually show a much reduced oxygen reduction rate compared to that on the outer corrosion

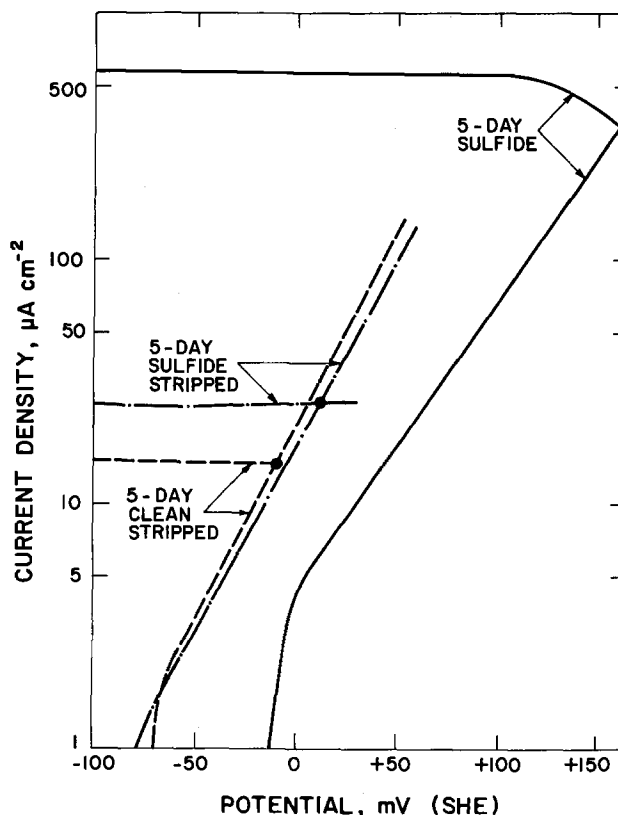


Fig. 8. Effect of the adherent (inner) layer and of the detachable (outer) layer of the corrosion products produced in the sulfide-contaminated solution and in the clean solution (11) on the polarization curves.

products containing sulfide (Fig. 8). This reduced rate is about the same (slightly higher) as that obtained on inner layers which had been produced in clean (sulfide-free) solution (Fig. 8). Thus, it is the effect of sulfide on the detachable porous outer layer which totally degrades the normally good corrosion resistant character of the Cu10 Ni alloy in neutral chloride solution. A similar increased rate of oxygen reduction was observed when Pd, a well-known catalyst for oxygen reduction, was applied as a deposit on the inner layer (11). Thus, it is concluded that the porous corrosion-product surface containing sulfide is a good catalyst for the oxygen reduction reaction, whereas normally (in the absence of sulfide incorporation during its formation) it is a poor catalyst for this reaction. This high rate of oxygen reduction ($\sim 500 \mu\text{A cm}^{-2}$) is of the same magnitude as the localized (e.g., pitting) corrosion rate in service failures [$700 \mu\text{A cm}^{-2}$ (16)], and is much larger than service failures when compared on a uniform corrosion or charge-passed, rather than localized corrosion, basis. To maintain this high rate, electron migration must be adequate through the corrosion product to the sites of the pore surfaces where oxygen reduction occurs. Electron migration is, therefore, concluded to be a relatively easy (fast) process. Similarly, the much lower anodic current on the inner layer ($2\text{--}30 \mu\text{A cm}^{-2}$) implies that its surface is a poor catalyst for the oxygen reduction reaction. The polarization data also show that ionic transport in the solid corrosion products is either adequate or not involved to an appreciable extent in the corrosion process; the latter could be the case if the inner, as well as outer, layer is porous so that an aqueous path for ionic transport penetrates to the metal surface.

High oxygen reduction rates on sulfide compounds, such as Co_3S_4 , FeS_2 , and PbS , have been reported by several investigators (17-19). The rate appears to increase with the number of unpaired d electrons per atom. Another interesting phenomenon is an affect of sulfide composition. It was shown that a sulfide of composition $\text{Fe}_{0.5}\text{Ni}_{0.5}\text{S}_2$ is 40 times more active than FeS_2 for oxygen reduction (20). Other catalyzed cathodic processes have also been reported for iron sulfides formed in steel (21). In the present work, the transition metals of Ni and Fe are alloyed with Cu. The ESCA examination revealed that these alloying elements coexist with sulfide in the loosely adherent layers with a relatively high concentration. Therefore, the very high oxygen reduction rate can be expected to be due to a much increased catalytic nature of the corrosion products containing sulfide coupled with normally adequate electronic and ionic conductances.

Conclusions

Corrosion products of Cu_2S and $\text{Cu}_2(\text{OH})_3\text{Cl}$ are developed on Cu-9.4Ni-1.7Fe alloy in sulfide-contaminated 3.4 w/o NaCl solution. Similar to the products developed in sulfide-free solution, the sulfide corrosion products consist of outer porous layers and a thin inner adherent layer. These corrosion products are much thicker (7 times) than those developed in sulfide-free solution (11) and yield a corrosion current in sulfide-free 3.4 w/o NaCl solution, which is much higher ($400 \mu\text{A cm}^{-2}$) than when the corrosion products are formed in the sulfide-free solution ($\sim 2 \mu\text{A cm}^{-2}$). This high corrosion rate, which matches or exceeds that of service failures, is attributed to the much

increased catalytic nature of the porous corrosion products for the oxygen reduction reaction when they contain sulfide.

An explanation of the corrosion-resistant character of the cupronickels in neutral chloride solutions given previously (9-11), i.e., reaction control of the oxygen reduction reaction, was confirmed by a systematic study of the anodic and cathodic polarization behavior of the sulfide-degraded Cu-Ni alloy. A definitive result was the finding that whereas sulfide-degraded Cu10 Ni has a very high corrosion rate, the rate falls to negligible levels when the porous corrosion-product layers are stripped from the sample leaving only the thin inner layer attached to the sample. The salient point is that sulfide causes degradation of the corrosion resistance through its effect on the porous layers, rather than on the adherent inner layer. This result also rules out other mechanisms of protection which involve a slow transport step and/or which postulate that the inner layer is protective in the sense of severely restricting electronic or ionic transport.

Acknowledgments

Mr. R. H. West of the University of Surrey performed the ESCA analysis. The authors gratefully acknowledge the financial support of the National Science Foundation, Metallurgy Program, Division of Materials Research under Contract DMR 80-10828, and of the Applied Research Laboratory of The Pennsylvania State University.

Manuscript submitted Sept. 7, 1982; revised manuscript received Jan. 30, 1984.

REFERENCES

1. J. F. Bates and J. M. Popplewell, *Corrosion*, **31**, 269 (1975).
2. D. D. MacDonald, B. C. Syrett, and S. S. Wing, *ibid.*, **35**, 367 (1979).
3. B. C. Syrett, D. D. MacDonald, and S. S. Wing, *ibid.*, **35**, 409 (1979).
4. B. C. Syrett and S. S. Wing, *ibid.*, **36**, 73 (1980).
5. H. P. Hack and J. P. Gudas, *Mater. Perform.*, **18**, 25 (March 1979).
6. J. P. Gudas and H. P. Hack, *Corrosion*, **35**, 67 (1979).
7. B. C. Syrett, *Corros. Sci.*, **21**, 187 (1981).
8. L. E. Eiselstein, B. C. Syrett, S. S. Wing, and R. D. Caligiuri, *NACE Corrosion*, Reprint 59 (1982).
9. C. Kato, B. G. Ateya, J. E. Castle, and H. W. Pickering, *This Journal*, **127**, 1890 (1980).
10. C. Kato, J. E. Castle, B. G. Ateya, and H. W. Pickering, *ibid.*, **127**, 1897 (1980).
11. C. Kato and H. W. Pickering, *ibid.*, **131**, 1219 (1984).
12. F. P. Ijesseling and J. M. Kroughman, in "Proceedings of 6th European Congress on Metallic Corrosion," p. 181, Society of the Chemical Industry, London (1977).
13. J. M. Popplewell, R. J. Hart, and J. A. Ford, *Corros. Sci.*, **13**, 295 (1973).
14. R. G. Blundy and M. J. Pryor, *ibid.*, **12**, 65 (1972).
15. W. Stumm and J. J. Morgan, "Aquatic Chemistry," p. 97, Wiley-Interscience, New York (1970).
16. H. Hack, Private communication.
17. S. M. Ahmed, *Int. J. Min. Process.*, **5**, 163 (1978).
18. S. M. Ahmed, *ibid.*, **5**, 175 (1978).
19. T. Biegler, *J. Electroanal. Chem. Interfacial Electrochem.*, **70**, 265 (1976).
20. H. Behret, H. Binder, and G. Sandstede, *Electrochim. Acta*, **20**, 111 (1975).
21. D. D. MacDonald, B. Roberts, and J. B. Hyne, *Corros. Sci.*, **18**, 411 (1978), and references therein.

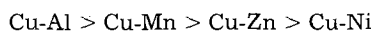
The Mechanism of Dealloying of Copper Solid Solutions and Intermetallic Phases

M. J. Pryor* and J. C. Fister

Olin Corporation, Metals Research Laboratories, New Haven, Connecticut 06511

ABSTRACT

Potentiostatic experiments in 0.5N NaCl at $-0.25 V_{SHE}$ show that the kinetics of dealloying of copper base binary alloys fall in the order



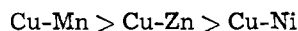
For the solutes Al and Zn, the kinetics of dealloying may be expressed by the relationship

$$\text{Log } S_e = K C_s$$

where S_e is the excess solute dissolved and C_s is the atom percent solute. K is related qualitatively to the reversible potential of the solute element. It is shown that dealloying cannot propagate into the alloys by diffusion of solute from the bulk to the surface. Instead, dealloying is maintained by solution intrusion under conditions where continuous solute paths exist in the alloy and where solute removal results in atomic rearrangement of the depleted alloy.

Extensive studies have been conducted on the dealloying of copper base alloys and particularly Cu-Zn alloys. An earlier significant issue was whether dealloying involved selective removal of Zn atoms from the lattice (1-5) or whether zinc and copper dissolved proportionately from the alloy with the copper subsequently being redeposited on the alloy surface (6-10). Except for a few special cases, this does not now appear to be a major issue. Stillwell and Turnipseed (1) succeeded in dealloying ϵ brass in dilute HCl first to γ , then to β , and finally to α brass. Pickering (5) also succeeded in dealloying ϵ and γ brass to more copper-rich intermetallic compounds in deaerated sodium sulfate solution. In these cases, there was no significant doubt that the mechanism of dealloying involved selective removal of Zn atoms from the lattices of the intermetallic phases. More recently, one of the authors (11) has shown that Cu-Mn alloys can be dealloyed in sodium chloride solution without a change in grain size or shape, thereby extending proof of selective removal of solute atoms to the solid solution region.

A second and more fundamental mechanistic issue involves the means by which dealloying is maintained over more than a few atom layers. Pickering and Wagner (12), in a study of the selective dissolution of copper from Au-Cu alloys and zinc from Cu-Zn alloys, proposed that dealloying was supported by solid-state diffusion. Because the diffusion rate of solute at room temperature is much too low to maintain the dealloying kinetics, they suggested that the selective electrochemical dissolution of more electronegative solute atoms from the alloy surface resulted in vacancy injection into the alloy. Diffusion of solute atoms to the surface was believed to be greatly accelerated by rapid divacancy diffusion, thereby permitting propagation of the dealloying process. This concept has been embraced by other investigators (13). In contrast, one of the authors (11) pointed out that the kinetics of dealloying of three copper solid solutions followed the order of



but that the diffusion coefficients did not fall in the same qualitative order. A mechanism involving electrochemical removal of more electronegative solute atoms from the surface, followed by rapid collapse of residual Cu atoms into equilibrium lattice positions, was considered to open up the surface to solution ingress and to maintain dealloying in depth by this

means. A later paper by the same author (14) suggested that diffusion through a segregated surface zone enriched in zinc could also account for the kinetics of dealloying of α brass in sodium chloride solution.

A study of the dealloying characteristics of a Cu-18.7 atom percent (a/o) Al alloy in sodium chloride solution (15) was intended to throw light on whether dealloying kinetics were controlled primarily by electrochemical factors or by diffusion. The study was somewhat inconclusive because of a large difference in a/o solute in the Cu-Al alloy (18.7 a/o) compared with the previously studied Cu-Mn, Cu-Zn, and Cu-Ni alloys (27.8-31.5 a/o solute).

The present study was conducted with the view of being able to compare the dealloying kinetics of Cu-Mn, Cu-Zn, Cu-Al, and Cu-Ni alloys over a broad composition range. In the case of Cu-Zn and Cu-Al alloys, the composition range was extended to encompass most of the intermetallic phases in these systems. Experimental study was largely conducted by a series of mass-balance experiments conducted at a potential of $-0.25 V_{SHE}$. This potential was selected on the basis of previous work on Cu solid solutions (11, 14, 15) conducted over a potential range of -0.5 to $+0.5 V_{SHE}$. At $-0.25V$, the anodic corrosion of Cu in sodium chloride containing dissolved oxygen is not completely suppressed, thereby permitting the selectivity of dealloying to be determined. In addition, the effects of grain size and cold work were investigated on α brass. Extensive diffusion calculations were conducted in an attempt to determine whether enhanced room temperature diffusion could account for dealloying kinetics.

Experimental and Results

Materials.—Three Cu-Zn intermetallic phases and five Cu-Al intermetallic phases were prepared from OFHC copper and high purity Zn or Al additions. The alloys were melted in air in a graphite crucible and poured into a preheated steel mold measuring $1.5 \times 2.5 \times 10$ cm. The phases investigated, together with their chemical compositions, are listed in Table I. The castings were homogenized for 16-18h in dry argon at the temperatures shown in Table I. Selected alloys were water quenched (Table I) to retain the desired phase.

Cu-Zn, Cu-Ni, and Cu-Mn solid solutions were prepared in the form of annealed sheet 0.075 mm thick in the same fashion as was described in earlier publications (11, 14, 16). A Cu-77.6 a/o Mn alloy was solution annealed at 800°C and water quenched (Table I).

* Electrochemical Society Honorary Member.

Key words: aqueous corrosion, dealloying, copper, aluminum, manganese, nickel, zinc.

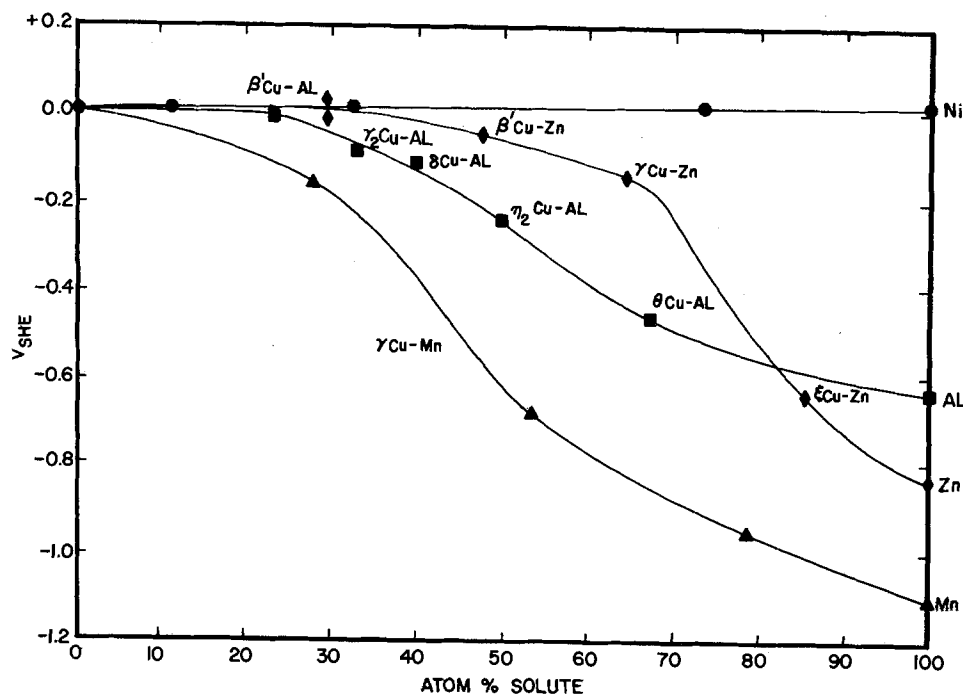


Fig. 1. Relationship between corrosion potential and solute content for Cu-Al, Cu-Mn, Cu-Ni, and Cu-Zn alloys in 0.5N NaCl at 25°C.

Cu-29.4 a/o Zn alloy sheet 0.075 cm thick was fabricated with grain sizes of 8.5 μm by annealing for 1h at 420°C, 50 μm by annealing for 1h at 550°C, and 119 μm by annealing for 1h at 650°C.

Cold-rolled Cu-29.4 a/o Zn alloy sheet 0.075 mm thick was fabricated by annealing for 1h at 550°C at a thickness of 0.10 mm and cold-rolling 25% to 0.075 mm and by annealing for 1h at a thickness of 0.150 mm and cold-rolling 50% to 0.075 mm.

Experimental method.—Surface preparation of the cast and rolled specimens was mechanical and involved light unlubricated end milling followed by careful degreasing in benzene. Cast specimens were coated with Microstop to above the water line except for an exposed area of around 3 cm². Sheet specimens were masked with 3M pressure-sensitive tape no. 470. The exposed area was 1 cm² for Cu-53 a/o Mn and 10 cm² for all other alloys.

All corrosion experiments were carried out in 0.5N NaCl prepared from reagent-grade sodium chloride and deionized-distilled water. The solutions contained dissolved air, and experiments were carried out with the solutions freely exposed to the atmosphere. Experiments were conducted for 20h at 25° ± 0.05°C, using 200 ml of solution per specimen. Mass balance experiments were conducted potentiostatically at -0.25 V_{SHE}, where selective removal of electronegative solutes predominates (11, 14, 15). The mass balance experiments together with studies of surface morphology were carried out as described in previous publications (11, 14, 15), except that the microanalyses were performed using an Instrumentation Laboratory Plasma 10D Spectrometer.

Results.—Figure 1 shows the relationship between corrosion potential in 0.5N NaCl and composition for

Table I. Alloy compositions and heat-treatments

Alloy	Phase	Homogenizing temp (°C)	Water quench
Cu-47.3 a/o Zn	β'	600	Yes
Cu-63.3 a/o Zn	γ	600	No
Cu-83.6 a/o Zn	ϵ	500	No
Cu-22.7 a/o Al	δ	800	Yes
Cu-34.1 a/o Al	γ_2	800	No
Cu-39.2 a/o Al	δ	600	No
Cu-48.9 a/o Al	η_2	500	No
Cu-67.7 a/o Al	θ	500	No
Cu-77.6 a/o Mn	γ solid solution	800	Yes

Cu-Al, Cu-Mn, Cu-Ni, and Cu-Zn alloys. Only alloying with Mn results in a substantial depression of corrosion potential at atom percentages of solute less than 50 a/o.

Figure 2 shows the relationship between excess solute dissolved from the alloys¹ and atom percentage of

¹ Obtained by taking the weight of copper removed from the alloy, calculating the associated weight of solute from the alloy composition, and subtracting from the measured weight of solute dissolved from the alloy.

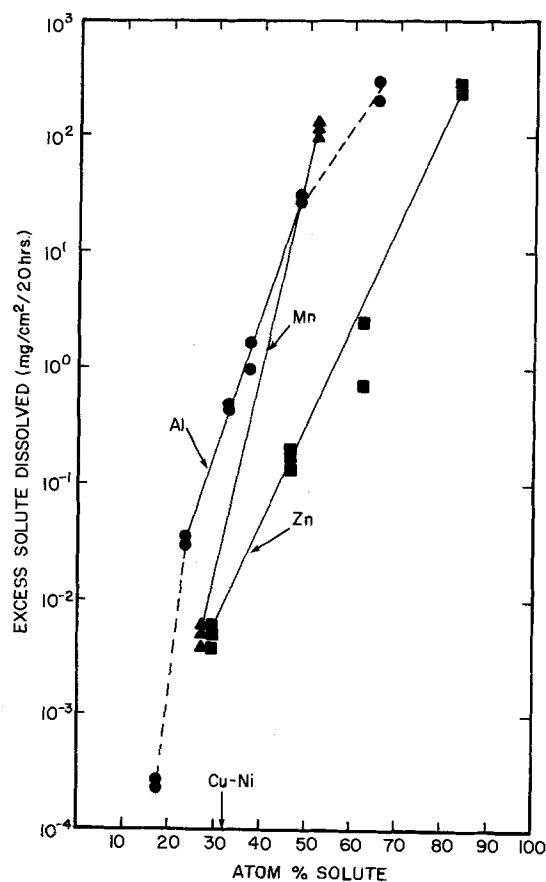


Fig. 2. Relationship between excess solute removed and solute content for Cu-Al, Cu-Mn, and Cu-Zn alloys held at -0.25 V_{SHE} in 0.5N NaCl at 25°C.

solute at a potential of $-0.25 V_{SHE}$. Only the Cu-31.5 a/o Ni alloy was resistant to dealloying. With the exception of the two terminal points on the Cu-Al curves, the results for Cu-Al and Cu-Zn alloys may be expressed by a general relationship

$$\log S_e = KC_s \quad [1]$$

where S_e is the excess solute concentration ($\text{mg}/\text{cm}^2/20\text{h}$) dissolved from the alloy and C_s is the atom percent of solute in the alloy. It is evident from Fig. 2 that, with the exception of the Cu-53 a/o Mn alloy, dealloying kinetics at constant atom percent solute fall in the order

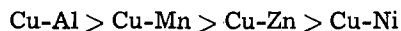
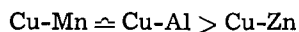


Figure 3 shows that the selectivity of solute removal at $-0.25 V_{SHE}$ as a function of atom percent solute of Al, Mn, and Zn. It is clear that selectivity of preferential dissolution of solute atoms at constant atom percent solute is in the order



Of the various alloys studied from the mass balance standpoint, only θ Cu-Al, ϵ Cu-Zn, and Cu-53 a/o Mn exhibit corrosion potentials more active than $-0.25 V_{SHE}$. Figure 4 shows the current vs. time plot for the Cu-53 a/o Mn alloy over the 20h experiment. Calculation shows that the net anodic current flow only accounts for a Mn weight loss of around $1 \text{ mg}/\text{cm}^2/20\text{h}$, i.e., less than 1% of the total Mn dissolved from the specimen; the preponderance of the weight loss is likely galvanic in nature due to the presence of α Mn in the grain boundaries. The cathodic reaction is the reduction of oxygen dissolved in the electrolyte.

Figures 5-7 shows scanning electron micrographs of dealloyed surfaces of two Cu-Al alloys and one Cu-Mn alloy. Figure 5 is the dealloyed residue of δ Cu-Al. The surface composition² approximates that of β' Cu-Al.

²Surface compositions were determined by SEM microprobe measurements. The values reported are the average solute contents of localized elements of the dealloyed surface and subsurface to a depth of around $1 \mu\text{m}$.

Table II. Effect of grain size and cold work on the dealloying kinetics of Cu-29.4 a/o Zn at $-0.25 V_{SHE}$

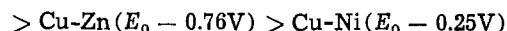
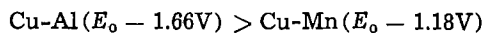
Grain size (μm)	Cold reduction (%)	Excess Zn dissolved $\mu\text{g}/\text{cm}^2/20\text{h}$
8.5	0	7.8, 8.6, 5.8
50	0	5.0, 6.9, 3.8
119	0	6.8, 3.6, 4.2
52	25	5.0, 6.5, 3.3
57	50	3.8, 4.6, 6.2

Figure 6 is the dealloyed surface of γ_2 Cu-Al with the residual surface composition being α Cu-Al containing approximately 14 a/o Al. Figure 7 is the dealloyed surface of Cu-53 a/o Mn. The dealloyed residue is γ Cu-Mn containing around 4 a/o Mn. Substantial grain boundary corrosion is evident.

Table II shows the effect of grain size and cold work on the dealloying kinetics of Cu-29.4 a/o Zn in 0.5N NaCl at $-0.25 V_{SHE}$. There appears to be no significant effect of either grain size or cold work on the dealloying kinetics of this alloy.

Discussion

Figure 2 shows that, at constant atomic concentrations of electronegative solutes, dealloying kinetics fall in the qualitative order



i.e., the more active is the standard potential of the solute element, the faster will be the dealloying rate. This conclusion is similar to one made earlier by one of the authors (11), except that the critical data for the Cu-Al system was not known at that time. Figure 1 shows that neither the corrosion potentials of the solute elements nor the corrosion potentials of the alloys themselves relate to dealloying kinetics. Instead, these kinetics are related to the standard potentials of the solute elements with the copper acting as a solvent

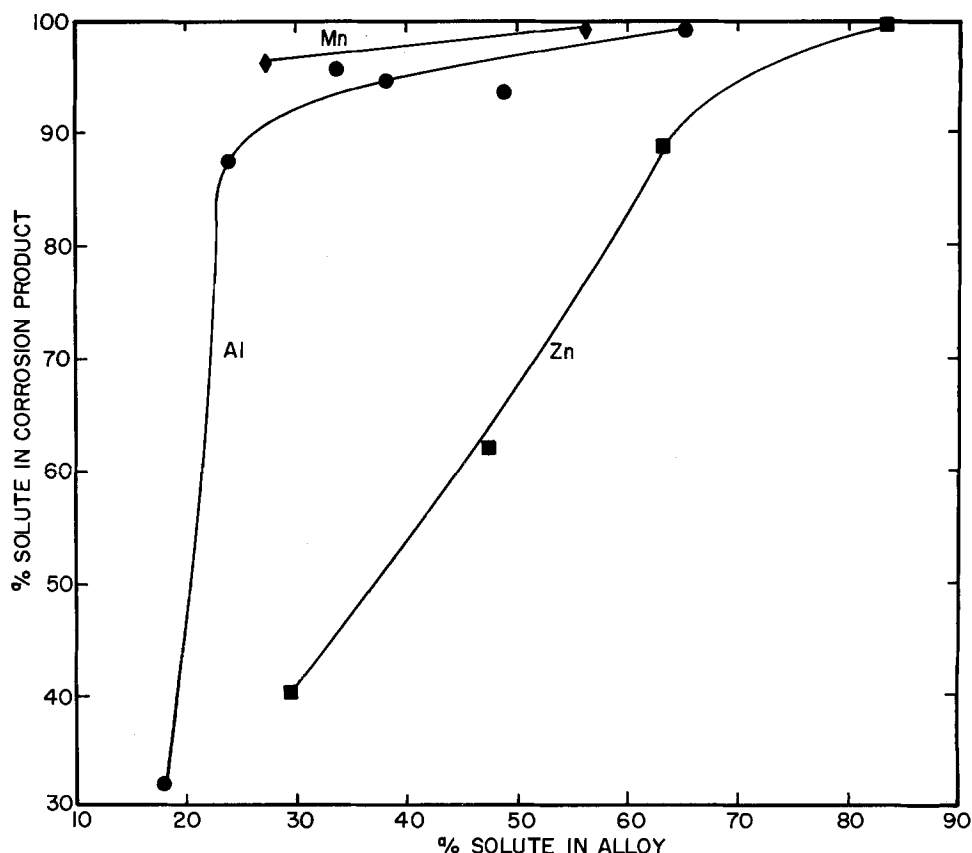


Fig. 3. Relationship between percentage of solute dissolved and solute content for Cu-Al, Cu-Mn, and Cu-Zn alloys held at $-0.25 V_{SHE}$ in 0.5N NaCl at 25°C.

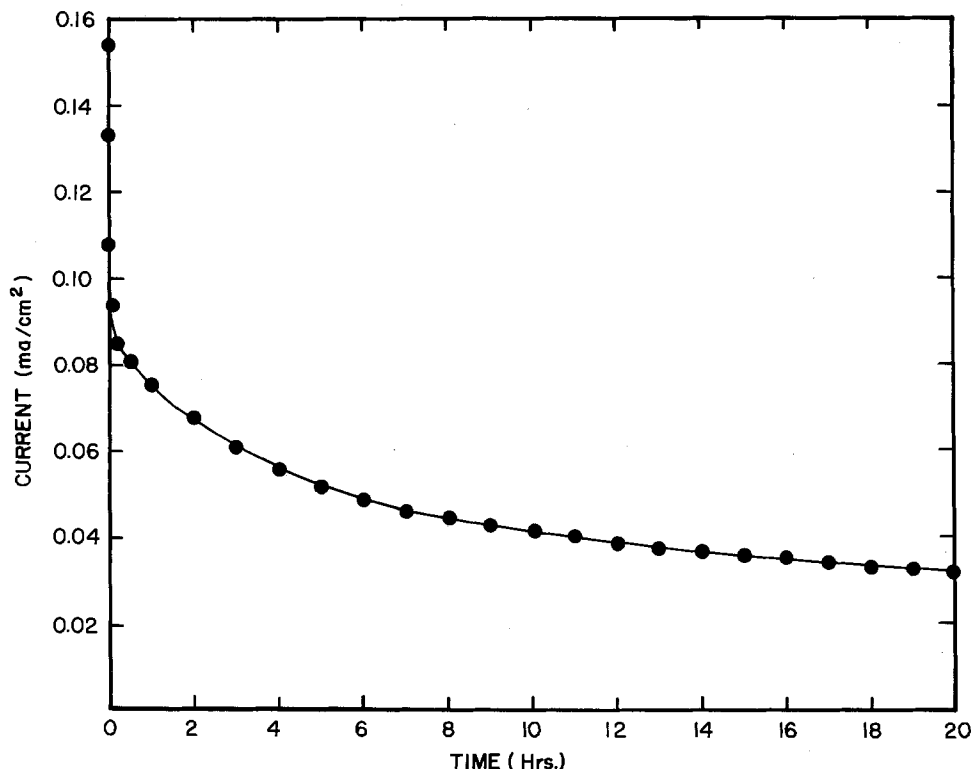


Fig. 4. Relationship between time and the anodic current drawn from a Cu-53 a/o Mn alloy held at $-0.25 V_{SHE}$ in 0.5N NaCl at 25°C.

(15). The only deviation from the foregoing relationship is provided by the dealloying behavior of the Cu-53 a/o Mn alloy, which exhibits a very high dealloying rate. At equilibrium, this alloy consists of a γ solid solution in equilibrium with α Mn (17). The present alloy was prepared using a final solution anneal (750°C for 2h) in the γ solid-solution phase field followed by water quenching in the hope of yielding a metastable single-phase alloy (11). There is no doubt from Fig. 7 and also from previous work (11) that, despite the water quenching to room temperature, there was precipitation of α Mn at the grain boundaries, as evidenced by the severe intergranular corrosion. The galvanic corrosion of this more anodic grain boundary phase is believed to account in the main for the unusually high dealloying rate of this alloy. In addition, the γ solid solution in this alloy loses the vast bulk of its Mn content, without the necessity of passing through intermediate phases having progressively slower dealloying kinetics. Indeed, the Mn content of the residual solid solution at $-0.25 V_{SHE}$ is

quite similar to that reported earlier (11) for dealloying at a potential of $0.00 V_{SHE}$.

At around 30 a/o solute, where the complication of decomposition of γ Cu-Mn solid solutions is avoided, calculations from the results in Fig. 2 show that the relationship

$$S_e = Ae \frac{-B}{\eta} \quad [2]$$

is reasonably well obeyed where S_e is the excess solute removed. A and B are constants and η , the approximate overpotential, is the difference between the set potential of the alloys ($-0.25 V_{SHE}$) and the standard potential of the solute atoms.

Figure 3 shows that the selectivity of solute removal is poor in the range of around 20-30 a/o solute for Cu-Al and Cu-Zn alloys. At higher solute contents, the selectivity falls in the order

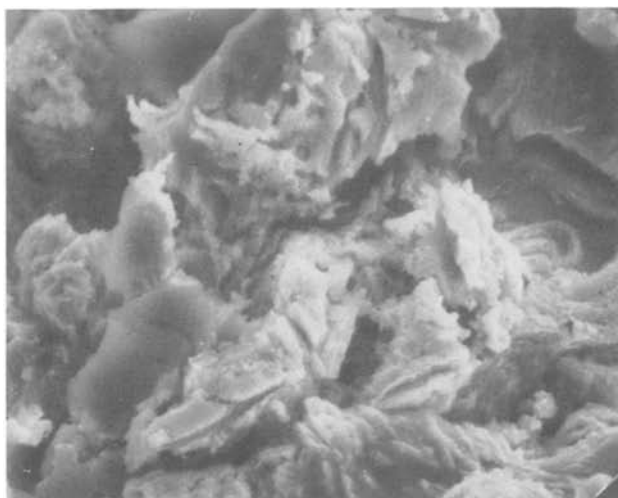
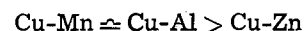


Fig. 5. Surface of δ phase Cu-Al dealloyed for 20h at $-0.25 V_{SHE}$ in 0.5N NaCl at 25°C ($\times 2000$).

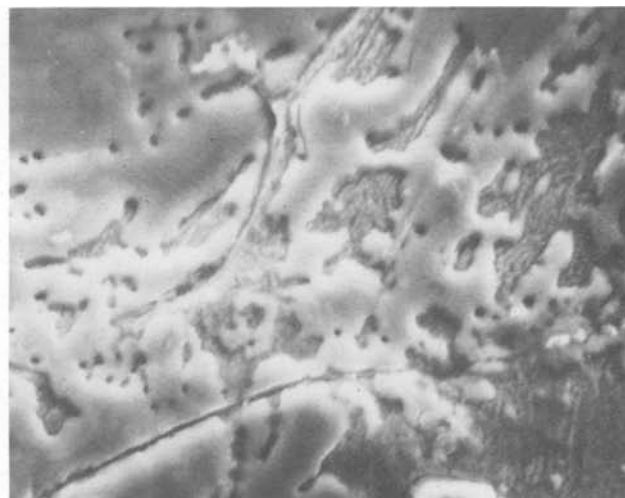


Fig. 6. Surface of γ phase Cu-Al dealloyed for 20h at $-0.2 V_{SHE}$ in 0.5N NaCl at 25°C ($\times 2000$).

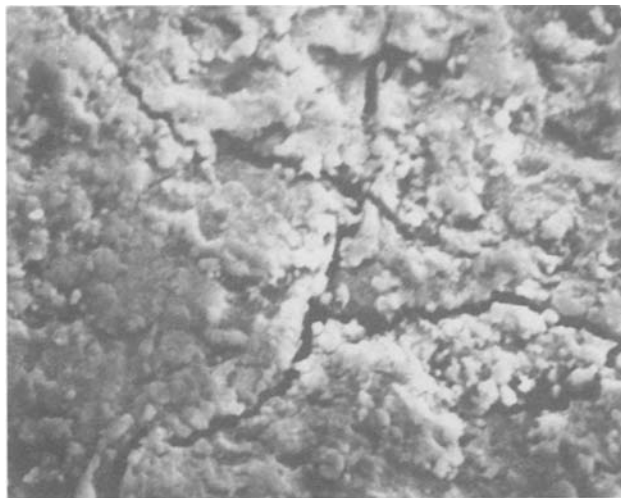


Fig. 7. Surface of Cu-53 a/o Mn dealloyed for 20h at $-0.25 V_{SHE}$ in 0.5N NaCl at 25°C ($\times 2000$).

This may be attributed to the higher fields operating on Mn and Al atoms in the lattice than Zn.

Having established that electrochemical factors primarily control the kinetics of dealloying, it remains to determine whether solid-state diffusion plays any role in the propagation of the dealloying process. The fact that dealloying kinetics can be expressed by a general equation

$$\log S_e = KC_s \quad [1]$$

where K is related to E_0 for the various solutes, makes control by solid-state diffusion an unlikely eventuality. Other considerations may be brought to bear to confirm this view. For instance, the presence of vacancies or divacancies as proposed by Pickering and Wagner (12) only serve to increase the chemical diffusion rate in an alloy. Assuming that vacancies or divacancies are present in comparable concentrations in a range of alloys, then, in order for vacancy aided diffusion to be rate determining, the calculated room temperature chemical diffusion coefficients should fall in at least the same qualitative order as the dealloying kinetics. Table III contains calculated chemical room temperature diffusion coefficients for a variety of copper alloys of interest. The high temperature source data from which the results in Table III were calculated were taken from Ref. (18) (Cu-Zn), (19) (Cu-Mn), and (20) (Cu-Al). Of the values calculated, the lowest diffusion coefficient is for Cu-53 a/o Mn, which has one of the highest dealloying rates. A Cu-27.8 a/o Mn alloy dealloys at a substantially faster rate than Cu-18.7 a/o Al alloy, yet the room temperature diffusion coefficients are almost identical. The same Cu-Mn alloy dealloys faster than Cu-29.4 a/o Zn, but has a diffusion coefficient four orders of magnitude lower. Clearly, bulk diffusion coefficients at room temperature in no way correlate with dealloying kinetics.

Pickering and Wagner (12) suggested that divacancies had a sufficient diffusion rate to support the dealloying process in Au-Cu. They suggested an approximate relationship

$$D = D_{\square\square} N_s \square\square \quad [3]$$

where D is the diffusivity in the vicinity of the surface, $D_{\square\square}$ is the diffusivity of a divacancy and $N_s \square\square$ is the mol fraction of divacancies in the vicinity of the alloy surface. If one is to double the solute concentration of a copper alloy susceptible to dealloying, and one removes all the solute atoms from a constant volume in the surface and subsurface region, then the maximum increase in vacancy concentration is a factor of 2 and that of divacancies³ is a factor of 4. This would result at most in a quadrupling of the divacancy-enhanced diffusion rate. Reference to Fig. 2 shows that as the atom percent solute is increased from 30% to 60%, the dealloying rate increases by 2½-3 orders of magnitude, i.e., quite inconsistent with a vacancy-enhanced diffusion model.

The Cu-Al system provides a further check of the lack of influence of diffusion kinetics on dealloying kinetics. Table IV shows the calculated room temperature diffusion coefficients for terminal α phase and for Cu-Al intermetallic phases. There is a sharp 13 orders of magnitude increase in diffusion coefficient on passing from the α to the β' phase field. Thereafter, as aluminum content is increased, there is no large systematic change in diffusion coefficient. Despite this, as one increases the aluminum content from that in the β' phase to that in the θ phase, dealloying kinetics increase by some 4 orders of magnitude without an increase (actually, a modest decrease) in diffusion coefficient. A change of this magnitude is irreconcilable with the modest accelerating effect of vacancies or divacancies described above.

The foregoing considerations argue strongly that there is no relationship between dealloying kinetics and diffusion kinetics, irrespective of whether the solid-state diffusion is vacancy (or divacancy) enhanced, deformation enhanced, or not. The only logical conclusion that can be reached is that solid-state diffusion does not control the propagation of dealloying in copper alloys.

One of the authors had suggested (14) that the kinetics of room temperature diffusion could be rationalized with measured dealloying rates of a Cu-29.4 a/o Zn alloy if it was assumed that surface segregation of solute atoms occurred. Calculations from a treatment of surface segregation by Stüwe and Jager (21) indicated that the surface composition might approach that of disordered β brass. Using the much higher diffusion coefficient of disordered β brass, it was possible in this one case to rationalize diffusion kinetics with dealloying kinetics. A similar treatment is also contained in Table III for some of the alloys in this investigation. Column 2 contains segregated surface compositions in alloys of interest calculated from Stüwe and Jager's treatment (21). Column 4, headed "Surface," shows the room temperature diffusion coefficients in the segregated surfaces. Here, the disagreement between calculated diffusion coefficients and dealloying kinetics is even more pronounced than in the case of the bulk values. The diffusion coefficient for the segregated Cu-29.5 a/o Zn alloy is 10 orders of mag-

³ At very low divacancy concentrations only.

Table III. Calculated chemical room temperature diffusion coefficients

Alloy	Calculated (21) surface composition (300 K)	Diffusion coefficient (\tilde{D}) at 300 K (cm^2/s)	
		Bulk	Surface
Cu-18.7 a/o Al	Cu-15.5 a/o Al	2.58×10^{-34}	3.3×10^{-34}
Cu-27.4 a/o Zn	Cu 35.3 a/o Zn	1.64×10^{-30}	8.5×10^{-34}
Cu-27.8 a/o Mn	Cu-33.1 a/o Mn	1.15×10^{-34}	2.6×10^{-34}
Cu-53 a/o Mn	Cu-43.5 a/o Mn	3.19×10^{-40}	5.14×10^{-38}
Cu-31.5 a/o Ni	Cu-14.3 a/o Ni	2.39×10^{-38}	1.74×10^{-38}

Table IV. Calculated room temperature diffusion coefficients for terminal α phases and Cu-Al intermetallic phases

Aluminum a/o	Phase	\tilde{D} at 300 K (cm^2/s)
18.7	α	2.58×10^{-34}
22.7	β'	1.74×10^{-31}
34.1	γ_2	1.77×10^{-34}
39.2	δ	1.89×10^{-34}
48.9	η_2	2.95×10^{-28}
67.7	θ	3.34×10^{-28}

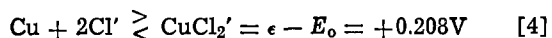
nitude higher than the other diffusion coefficients, but, with the exception of the Cu-18.7 a/o Al alloy, has the lowest dealloying rate found in this investigation. In summary, neither diffusion coefficients calculated on the basis of bulk composition or on the basis of surface segregation have any qualitative relationship with dealloying kinetics in Fig. 2.

An alternate propagation mechanism based on solution intrusion was suggested earlier by one of the authors (11). At around 50 a/o solute, there are clearly many continuous paths of electronegative solute element throughout a copper alloy susceptible to dealloying. These electronegative atoms in the surface and subsurface region may be easily removed by electrochemical means. Once they are removed electrochemically, the remaining copper atoms find themselves in highly unstable lattice positions. They must collapse rapidly under the influence of electrostatic forces to equilibrium lattice positions, and in so doing will create small copper-rich nuclei and new surfaces.

Forty and co-workers (22-24) in electrooptical studies of the dealloying of Au-Ag alloys containing 50 a/o Au or less in HNO₃ have proposed a mechanism involving growth of Au islands by surface diffusion succeeded by slower tunneling into the alloy. They observed dealloyed residues similar to those observed on Cu-53 a/o Mn [Fig. 9 and 10 from Ref. (11)] and somewhat less similar to the dealloyed residue from δ Cu-Al (Fig. 5). If the Forty *et al.* mechanism is applied to the Cu alloys of this study, it is clear that the surface diffusion of Cu must be rapid enough so as not to be rate limiting for the overall dealloying process. Further, the application of this model to Cu-Zn and Cu-Al alloys containing 50 a/o Cu or less is more problematical, because, under our experimental conditions, dealloying yields more copper-rich intermetallic compounds rather than essentially pure copper. Notwithstanding the difficulties outlined above, surface diffusion represents the most viable explanation for the growth of Cu from the initial nuclei or indeed, from that of the more Cu-rich intermetallic compounds.

As the solute contents of the alloys are reduced to values significantly below 50 a/o, continuous paths of solute atoms tend to be found in increasingly linear arrays, *i.e.*, at grain boundaries, edge and misfit dislocations, etc. This is likely due to these arrays containing an enhanced solute content. As shown in Fig. 6, the morphology of the dealloyed residue changes to one containing discrete channels of fairly large diameter. Similar morphologies have been reported on α Cu-Zn (14) and α Cu-Al (15) dealloyed at more noble potentials.

The nature of the electrolyte is important in the dealloying process particularly at relatively lower solute contents. Pickering and Byrne's work on brass (4) was conducted in deaerated sodium sulfate solution. In this electrolyte, the copper current ceases sharply at around 0.0 V_{SHE}. At more active potentials, only solute atoms were removed. In the sodium chloride electrolyte, a copper current can be maintained at potentials more active than 0.0 V_{SHE} by virtue of the reaction (22)



Under no conditions studies in this work was the re-

moval of solute 100% selective (Fig. 3), and some copper atoms were always removed electrochemically at -0.25 V_{SHE}. The ability to remove some copper atoms electrochemically at -0.25 V puts less of a premium on complete continuity of electrochemically active solute atoms in the alloy lattice, thereby permitting easier propagation of the dealloying process. Indeed, Fig. 3 shows that the dealloying of Cu-Zn and Cu-Al α solid solutions is comparatively nonselective in the range of 20-30% solute.

Acknowledgments

The authors thank the Brass Group of the Olin Corporation for its support of this work. They also wish to thank Dr. L. Lin for conducting the diffusion calculations, together with Mr. A. F. Beck, Mr. J. Conrod, and Mr. E. Olander for assistance with the experimental work.

Manuscript submitted May 26, 1983; revised manuscript received Jan. 10, 1984.

The Olin Corporation assisted in meeting the publication costs of this article.

REFERENCES

1. C. W. Stillwell and E. S. Turnipseed, *Ind. Eng. Chem.*, **26**, 740 (1934).
2. C. P. Polushkin and H. L. Shuldener, *Trans. AIME*, **161**, 214 (1945).
3. E. E. Langenegger and F. P. A. Robinson, *Corrosion*, **25**, 137 (1969).
4. H. W. Pickering and P. J. Byrne, *This Journal*, **116**, 1492 (1969).
5. H. W. Pickering, *ibid.*, **117**, 8 (1970).
6. G. D. Bengough and R. May, *J. Inst. Metals*, **32**, 81 (1924).
7. L. Kenworthy and W. G. O. Driscoll, *Corros. Technol.*, **2**, 247 (1955).
8. M. Pruna, B. LeBoucher, and P. LaCombe, *Rev. Inst. Fr. Pet.*, **6**, 145 (1951).
9. K. Hashimoto and S. Ogiva, *Trans. Jpn. Inst. Met.*, **4**, 42 (1963).
10. V. F. Lucey, *Br. Corros. J.*, **1**, 9 (1965).
11. D. S. Keir and M. J. Pryor, *This Journal*, **127**, 2138 (1980).
12. H. W. Pickering and C. Wagner, *ibid.*, **114**, 698 (1967).
13. A. P. Pchelvikov, A. D. Sitnikov, I. K. Marshakov, and V. V. Losev, *Electrochim. Acta*, **26**, 600 (1981).
14. M. J. Pryor and K. K. Giam, *This Journal*, **129**, 2157 (1982).
15. M. J. Pryor, *ibid.*, **130**, 1625 (1983).
16. R. G. Blundy and M. J. Pryor, *Corros. Sci.*, **12**, 65 (1972).
17. M. Hansen, "Constitution of Binary Alloys," p. 597, McGraw Hill Book Co., Inc., New York (1958).
18. C. J. Smithells, "Metals Reference Book," 5th Ed., pp. 895, 911, 922, Butterworths, London (1976).
19. Y. Iijima, K. Hirano, and K. Sato, *Trans. Jpn. Inst. Met.*, **18**, 835 (1977).
20. H. Oikawa, T. Obara, and B. Karashima, *Metall. Trans.*, **1**, 2969 (1970).
21. H. P. Stüwe and I. Jager, *Acta Metall.*, **24**, 605 (1976).
22. A. J. Forty and P. Durkin, *Philos. Mag.*, **42**, 295 (1980).
23. A. J. Forty and G. Rowlands, *ibid.*, **43**, 171 (1981).
24. A. J. Forty, *Gold Bull.*, **14**, 1 (1981).
25. A. Moreau, *Electrochim. Acta*, **26**, 497 (1981).

Rotating Ring-Disk Electrode Studies of Cu-Ni Alloy Electrodissolution in Acidic Chloride Solutions

I. A Commercial Cu-Ni (90/10) Alloy

H. P. Lee* and Ken Nobe**

Department of Chemical Engineering, University of California, Los Angeles, California 90024

ABSTRACT

The electrodissoolution behavior of a commercial Cu-Ni (90/10) alloy with 1.7% Fe in deoxygenated acidic chloride solutions has been studied with rotating ring-disk electrodes. Alloy electrodissoolution was examined at various rotation rates, potentials, and Cl^- and H^+ concentrations. Potentiostatic experiments indicate selective electrodissoolution of Ni in the apparent Tafel region; high rates of Fe electrodissoolution are measured near the rest potential. Formation of a film consisting of mainly CuCl was discerned to begin at about the peak potential. At higher potentials where a current minimum and a current plateau are observed, electrodissoolution is nonselective and under mass-transfer control. In this region, cuprous chloride complexes are the only electro-oxidation product of the Cu component. However, at potentials above the current-plateau region, the Cu component also electro-oxidizes to cupric ions. Above the current-plateau region, electrodissoolution continues to be nonselective but under mixed activation and mass-transfer control.

An understanding of the mechanism of Cu-Ni alloy dissolution requires knowledge of the dissolution kinetics of both pure Cu and Ni. It is known that copper in chloride solutions electro-oxidizes to cuprous chloride complexes. In general, the anodic dissolution of copper in chloride solutions is under diffusion control (1-4) and is independent of pH (1-3). The reaction order with respect to Cl^- is two for low chloride solutions ($< 1M$) and is greater than two for higher chloride concentrations (1-3). Bengali and Nobe (5) have found that the electrodissoolution of Ni in chloride solutions in the active region is under charge-transfer control. The reaction orders are 0.5 for Cl^- and -0.5 for H^+ in solutions in which both H^+ and Cl^- concentrations are less than $1M$, but first order for both Cl^- and H^+ for $1 \leq [\text{H}^+] \leq 5M$ and $1 \leq [\text{Cl}^-] \leq 5M$.

Although the electrodissoolution of copper in chloride solutions has been extensively studied (1-4), the anodic dissolution of copper-based nickel alloys in acidic chloride media has not received much attention. Walton and Brook (6) investigated the electrochemical behavior of (90/10) and (60/40) Cu-Ni alloys in 1/3 to 3M hydrochloric acid at a sweep rate of 5 mV/s. Two current plateaus and a current minimum were observed for the (90/10) Cu-Ni alloy. In the active region, cuprous species were detected as the dissolution product, and at much higher potentials, cupric species were found by means of a rotating ring-disk electrode. Bockris *et al.* (7) studied the electrodissoolution of Cu-Ni alloys in 1N HCl with the electrolyte flowing at a velocity of 0.5 cm³/s. They obtained an anodic Tafel slope of 130 mV/decade for (90/10) Cu-Ni alloy and concluded that the overall dissolution reaction in this region is charge-transfer controlled. Cahan and Hayes (8) reported that Tafel slopes for (30-90% Cu) Cu-Ni alloys 1N HCl are about 80 mV/decade. They concluded from partial current data of a (50/50) Cu/Ni alloy that the overall reaction is controlled by the dissolution of Ni. Kato *et al.* (9) found the anodic Tafel slope to be 70 mV/decade for the dissolution of Cu-9.4Ni-1.7Fe in air-saturated NaCl solution. Current minimum, current plateaus, and film formation were observed.

In this work, electrodissoolution kinetics of Cu-Ni (90/10) alloy (with 1.7% Fe) are studied with a rotating disk and ring-disk electrodes in various pH and chloride concentrations. The selectivity of alloy component dissolution is also investigated using the rotat-

ing ring-disk electrode and atomic absorption spectrophotometry during potentiostatic polarization.

A rotating ring-disk electrode has been specially designed for these studies to permit the disk to be easily changed. Since the electrode design enables rapid disk replacement, acquisition of electrode kinetic data is greatly facilitated.

Experimental

Details of the rotating disk assembly have been described elsewhere (10). The rotating ring-disk electrode design is shown in Fig. 1. Parts A and B of the rotating ring-disk electrode are machined from 3/4 in. diam stainless steel rod (Type 304) into the shape shown in Fig. 1. The lower part of the outer surface of A and the upper part of the inner surface of B are threaded. As Fig. 1 shows, B can be unscrewed from A so that a tight-fitted disk can be easily inserted in or out of B. A 1/16 in. thick pure gold sheet was silver soldered to the bottom steel surface of B and then machined to the ring shape. The disk radius is 0.240 in. (0.610 cm) and the inner and outer radii of the ring are 0.267 in. (0.678 cm) and 0.478 in. (1.214 cm), respectively. This design is convenient for experiments in which the disk electrodes have to be replaced often. A PAR 173 potentiostat was used to control the disk

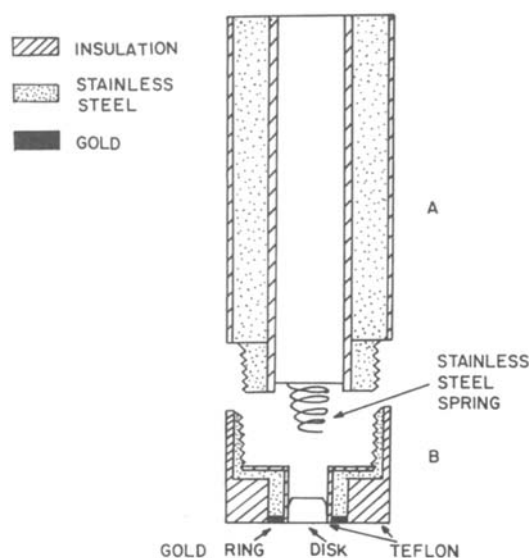


Fig. 1. The rotating ring-disk electrode assembly

* Electrochemical Society Student Member.

** Electrochemical Society Active Member.

Key words: electrodissoolution kinetics, mass transfer, Cu-Ni alloy.

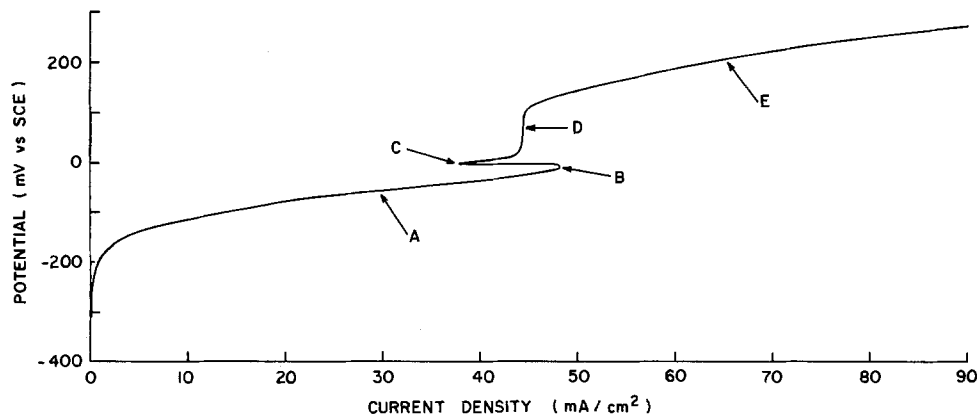


Fig. 2. Anodic polarization of Cu in 0.5M HCl + 0.5M NaCl, 1000 rpm.

potential, and a Tacussel potentiostat Type PRT 10-0.5L was used for the ring. In these experiments, the ring potentials were set at +600 mV vs. SCE (saturated calomel electrode) to register the cuprous species current and at -100 mV to detect cupric species. Collection efficiencies, N , for each ring-disk electrode were calculated with the equation developed by Alberly and Bruckenstein (11). Experimental and theoretical values were compared using pure copper disk electrodes and agreed to within 1%.

The disk electrodes were made from a commercial Cu-Ni (90/10) alloy with a nominal composition of 88.8 weight percent (w/o) Cu, 9.4% Ni, 1.7% Fe, and 0.1% others. Electrodes were polished with alumina paper of various grit (no. 240, no. 400, and no. 600) and were rinsed in double-distilled water. The electrodes were then degreased with hot benzene in a soxhlet column and annealed under vacuum (5×10^{-5} torr) at 760°C for 4h. Two types of constant ionic strength electrolytes were used:

1. Constant acid concentrations
 - a. 1M (HClO₄ + HCl) [Cl⁻] = 0.1, 0.2, 0.4, 0.7, 1M
 - b. 4M (HClO₄ + HCl) [Cl⁻] = 1, 2, 3, 4M
2. Constant chloride concentrations
 - a. 1M (NaCl + HCl) [H⁺] = 0.01, 0.05, 0.1, 0.5, 1M
 - b. 5M (NaCl + HCl) [H⁺] = 1, 2, 3, 4M

The hydrochloric acid, sodium chloride, and perchloric acid were Baker-analyzed reagent grade. Water was first deionized and then double distilled from permanganate solutions. All electrolytes were deoxygenated with prepurified nitrogen gas for at least 12h prior to an experiment. The experiments were carried out at about 23°C. Sweep rates were maintained at 0.5 mV/s at the disk for both rotating disk and ring-disk electrodes, while the ring was set at a constant potential. Lower sweep rates indicated the same polarization behavior in the apparent Tafel region and above the current-plateau region. Copper, iron, and nickel solution concentrations in 1N HCl solutions during anodic potentiostatic polarization were analyzed with a Perkin-Elmer atomic absorption spectrophotometer. All potentials were measured relative to a saturated calomel electrode (SCE). Potentials have been corrected for IR drop (unless otherwise noted) and liquid-junction potentials.

Results

Anodic polarization behavior.—Typical anodic polarization of copper in chloride solutions is shown in Fig. 2. The first feature observed as the potential increases above the rest potential is the apparent Tafel region A (this "apparent" Tafel behavior does not represent a charge transfer-controlled process), and it is followed by a current peak B. From that point on, the current decreases as the potential increases

until the current reaches a minimum at C. A current plateau region occurs at D, and then the current increases with potential E.

The rate of cuprous species formation during the anodic dissolution was monitored by the ring electrode. This experiment was first performed using pure Cu as the disk. Figure 3 shows that the Cu disk and the ring current coincide in the Tafel region. This means that cuprous species are the only electro-oxidation products of the Cu disk in this region. Above the peak potential, the ring current stays constant as the potential increases. Cupric ions were detected by the ring electrode above the current-plateau region. However, the cupric-ring current did not correspond quantitatively to the increase in the disk current in the region E. Therefore, separate potentiostatic polarization experiments with the ring-disk electrode and atomic absorption spectrophotometer were performed to determine the rate of cupric ion formation in the higher potential region. This result is also shown in Fig. 3.

For the 90/10 Cu-Ni alloy, the disk and the cuprous-ring currents are shown in Fig. 4. The disk and the ring current do not coincide in the apparent Tafel region as observed for pure Cu due to the dissolution of the Ni component in the alloy (and a small amount of Fe). Above the peak potential, the cuprous current remains constant with increase in potential. Cupric

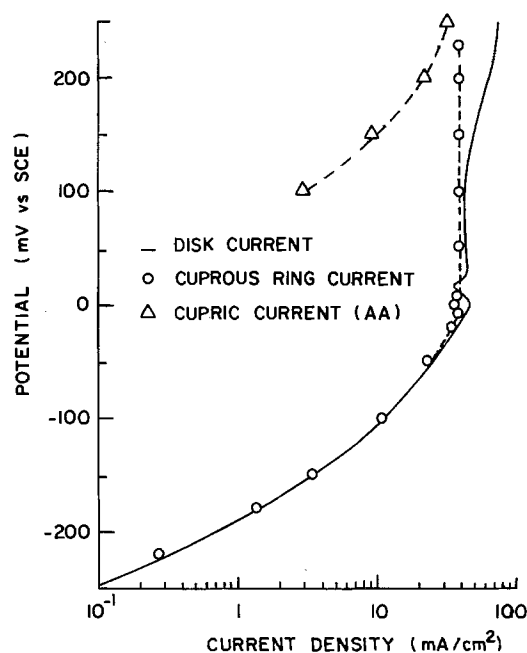
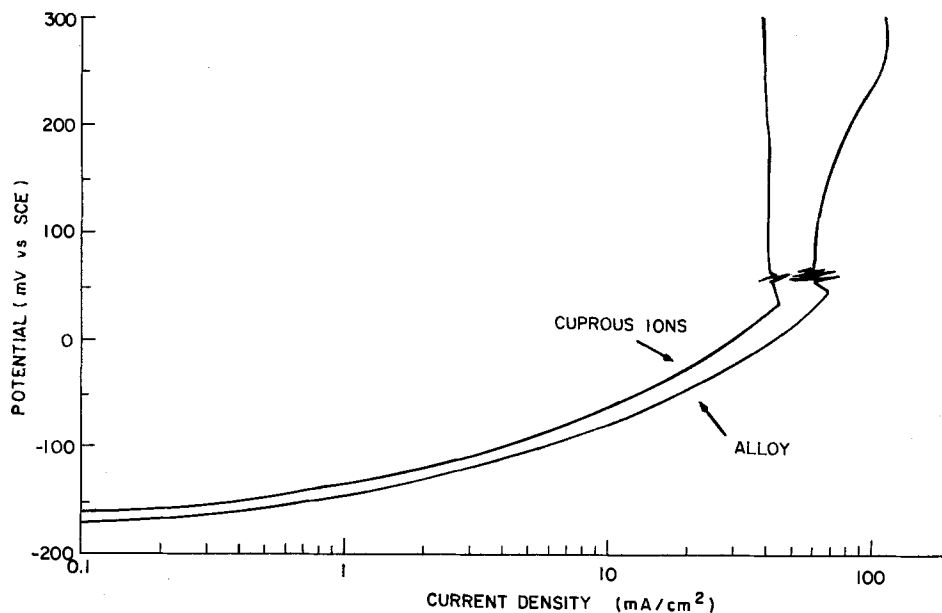


Fig. 3. Comparison of the Cu disk and the ring (cuprous) currents during Cu electrodisolution in 1M HCl, 1000 rpm. Not corrected for IR drop.

Fig. 4. Comparison of the Cu-Ni (90/10) alloy disk and ring (cuprous) current in 1M HCl, 1000 rpm. Not corrected for IR drop.



species are also detected at potentials above the current-plateau region.

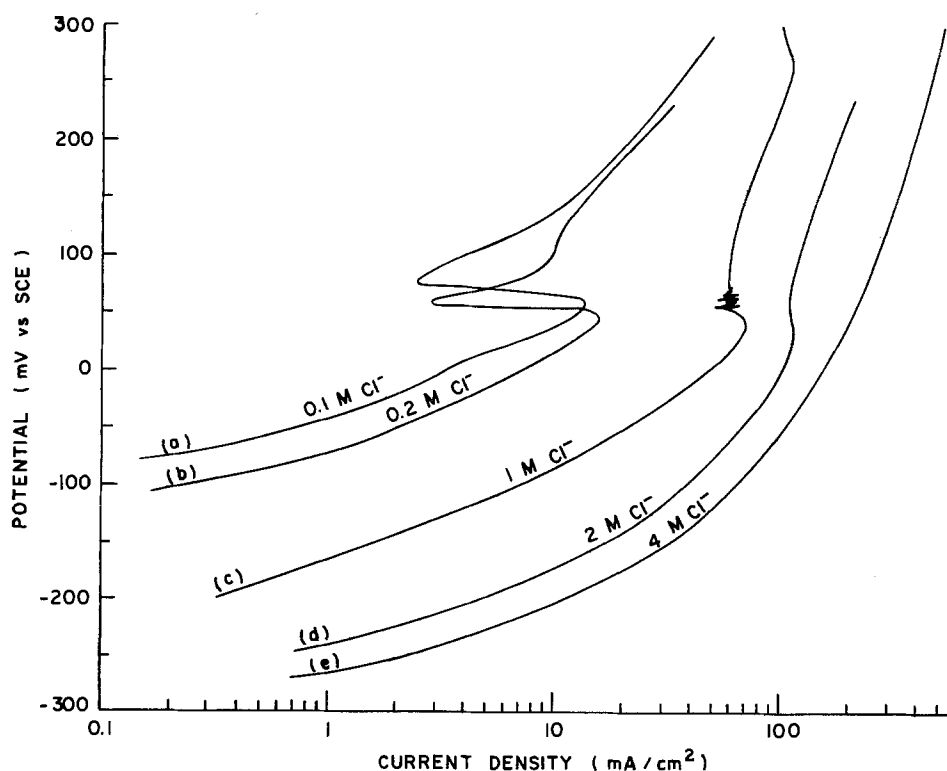
Effect of chloride and hydrogen ion concentrations on alloy electrodisolution.—The effect of chloride ions on anodic polarization of the Cu-Ni alloy is shown in Fig. 5. Anodic currents increase, but the depth of the current minimum decreases with increase in chloride concentration. At low Cl^- concentrations ($\leq 0.1M$), the current-plateau region was not observed. Above $[\text{Cl}^-] = 2M$, the current minimum virtually disappears. As chloride concentrations were increased further, peak and minimum currents, as well as the current-plateau region, could no longer be discerned.

As shown in Fig. 5, there is a strong chloride effect on the alloy-dissolution rate. Figure 6 shows that at a constant rotation rate of 700 rpm, the current density in the apparent Tafel region increases tenfold with increase in chloride concentration from 0.1 to 0.7M. The Tafel slope for Cu-Ni alloy dissolution is 70 mV/

decade. At -80 mV, the reaction orders for Cl^- are 1.3 for $[\text{Cl}^-] < 1M$ and 1.6 for $[\text{Cl}^-] > 1M$. Figure 7 shows the dissolution rate of the Cu component (cuprous-ring current) during the alloy dissolution shown in Fig. 6. The Tafel slope for Cu component dissolution is approximately 60 mV/decade. The reaction orders with respect to Cl^- for Cu component dissolution are 1.9 and 2 at low and high chloride concentrations, respectively. The dissolution rate of the Ni component (with a small amount of Fe) has been obtained (Fig. 8) by subtracting the cuprous current (Fig. 7) from the disk current (Fig. 6). The Tafel slope for Ni component dissolution is 100 mV/decade, and the reaction order with respect to Cl^- at both high and low chloride concentrations is approximately one.

The effect of hydrogen ions on alloy and Cu component dissolution is shown in Fig. 9 and 10. At $[\text{H}^+] < 1M$, both the disk and cuprous-ring currents are

Fig. 5. The effect of chloride ions on the anodic polarization of the alloy in (curves a-c) 1M ($\text{HClO}_4 + \text{HCl}$), and (curves d and e) 4M ($\text{HClO}_4 + \text{HCl}$), 700 rpm. Not corrected for IR drop.



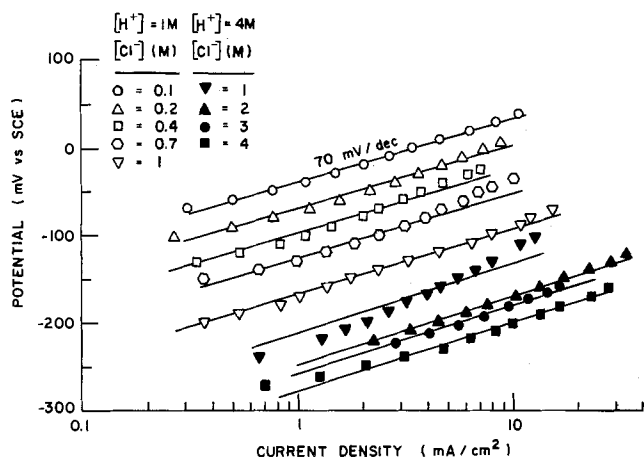


Fig. 6. The effect of chloride ions on alloy electrodisolution in the apparent Tafel region, 700 rpm.

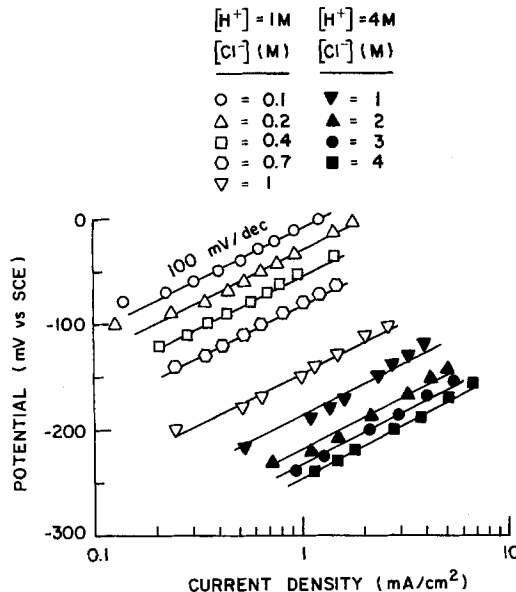


Fig. 8. The effect of chloride ions on the electrodisolution of the Ni component of the alloy in the apparent Tafel region, 700 rpm.

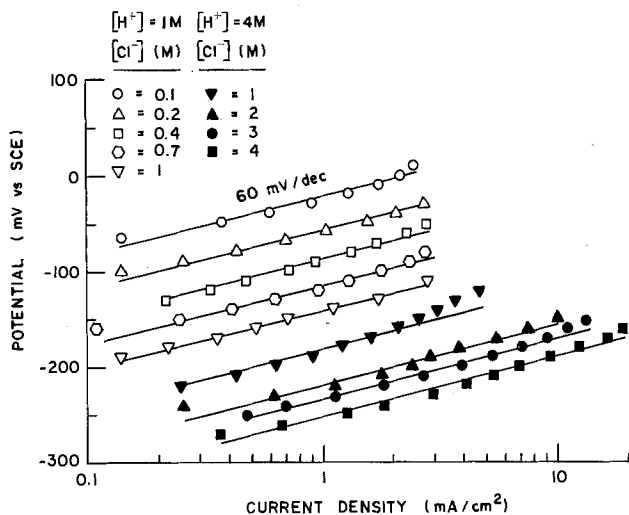


Fig. 7. The effect of chloride ions on the electrodisolution of the Cu component (ring current) of the alloy in the apparent Tafel region, 700 rpm.

independent of H^+ concentrations. At $[H^+] > 1M$, an increase in $[H^+]$ increases the anodic currents. However, the magnitude of the increase is not as large as that observed for chloride ions. At $[H^+] > 1M$, the H^+ reaction orders are 0.6 for the alloy-disk dissolution and 0.5 for Cu-component (ring current) dissolution. The Ni-component dissolution was also studied. At low

$[H^+]$, a significant effect of H^+ was not observed. However, at high $[H^+]$, the rate of Ni-component dissolution increases with increase in $[H^+]$ (Fig. 11), and the reaction order with respect to H^+ is 0.6.

Mass-transfer effects on alloy electrodisolution.— Alloy electrodisolution increases with increase in rotation rate. Figure 12 shows that the dependence on rotation rate varies with potential. At potentials slightly above the rest potential, the slope of the log-log plot of the current vs. rotation rate is 0.36. At -100 mV, dependence on rotation rate is greater at rotation rates below 2000 rpm than above 2000 rpm. As shown in Fig. 12, the slope below 2000 rpm is 0.36, but decreases to 0.2 at higher rotation rates. At the current minimum and the current-plateau region, the anodic current varies as the square root of the rotation rate following the Levich relation. However, at potentials above the current-plateau region, where cupric ions are also detected as a reaction product, the slope decreases to 0.4.

Selective alloy electrodisolution.— Selective alloy electrodisolution depends strongly on the applied potential. Selective dissolution of the most active (but minor) component, Fe, is observed at and in the neighborhood of the rest potential (data not shown). However, at higher potentials ($\cong -200$ mV), the rate of

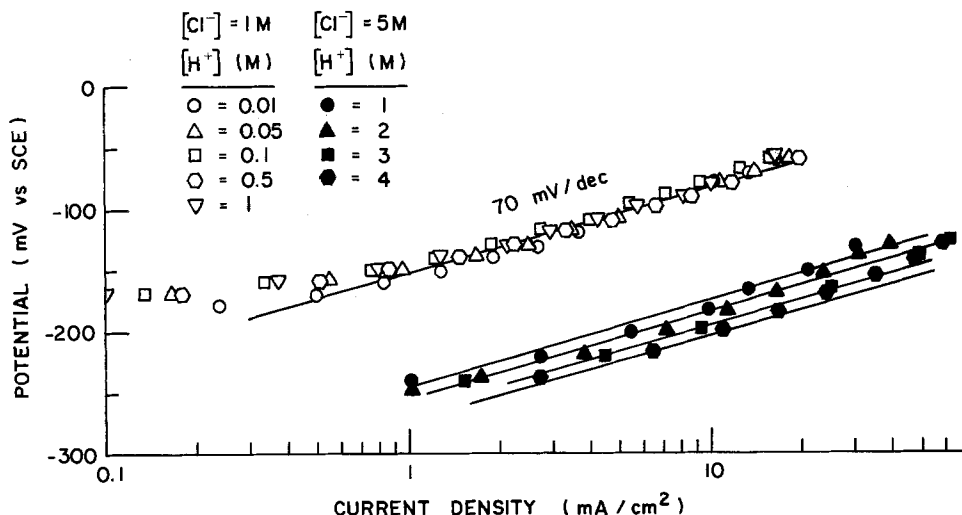


Fig. 9. The effect of hydrogen ions on alloy electrodisolution in the apparent Tafel region, 1000 rpm.

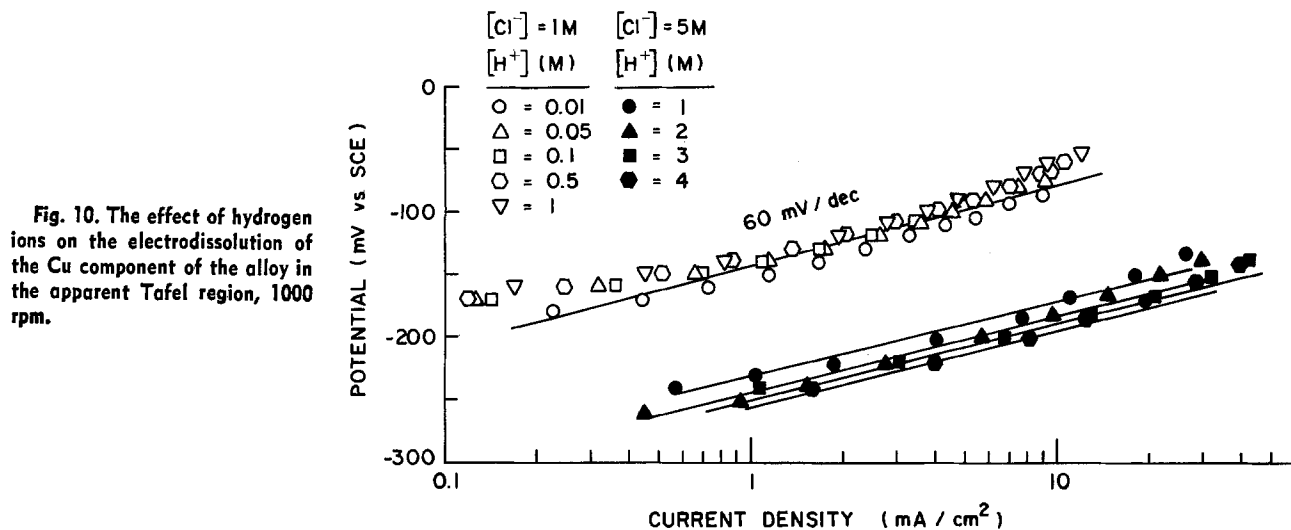


Fig. 10. The effect of hydrogen ions on the electro-dissolution of the Cu component of the alloy in the apparent Tafel region, 1000 rpm.

Fe dissolution is too low to be measured with sufficient accuracy.

Figure 13 shows Cu component electro-dissolution of the alloy at different potentials using data obtained by both the rotating ring-disk electrode and atomic absorption spectrophotometry (the results are obtained by setting the alloy at each potential for about 1h). At -170 mV, only 50 w/o of the alloy dissolved is Cu. As the potential increases Cu electro-dissolution increases. Nonselective dissolution is attained at about the current minimum (≈ 0 mV) when the relative composition of the dissolved species is the same as that of the bulk alloy. In the selective dissolution region (≤ -50 mV); the Cu component electro-oxidizes only to cuprous species. In the nonselective dissolution region above the current plateau (≥ 50 mV), electro-oxidation of Cu to both cuprous and cupric species is obtained. It should be noted that the difference between 100 w/o and the amount of Cu species dissolved (in w/o) is the solution composition of Ni(Fe).

The effect of Fe (1.7%) on alloy electro-dissolution.—Iron has a significant effect on alloy electro-dissolution at low potentials. Figure 14 compares the dissolution rates of 90/10 Cu-Ni alloys with and without Fe at low potentials. At -180 mV, both the disk and cuprous-ring currents for the alloy with Fe are significantly less than that without Fe. Thus, the presence of Fe substantially decreases alloy dissolution and strongly diminishes the propensity of the Cu component for electro-dissolution near the rest potential. As the potential increases, the difference between the alloy and the Cu-component electro-dissolution rates for both alloys is virtually the same.

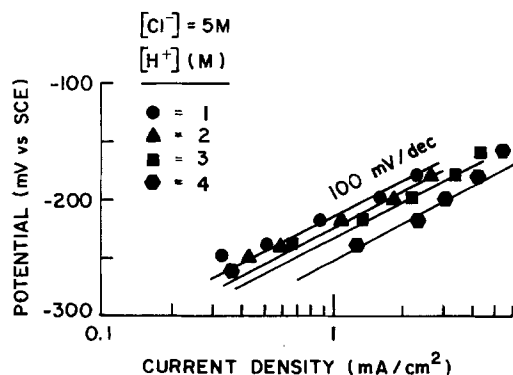


Fig. 11. The effect of hydrogen ions on the electro-dissolution of the Ni component of the alloy in the apparent Tafel region, 1000 rpm.

Discussion

Figure 3 shows that for pure copper electro-dissolution in chloride solutions, cuprous species are the only reaction products from the rest potentials to potentials

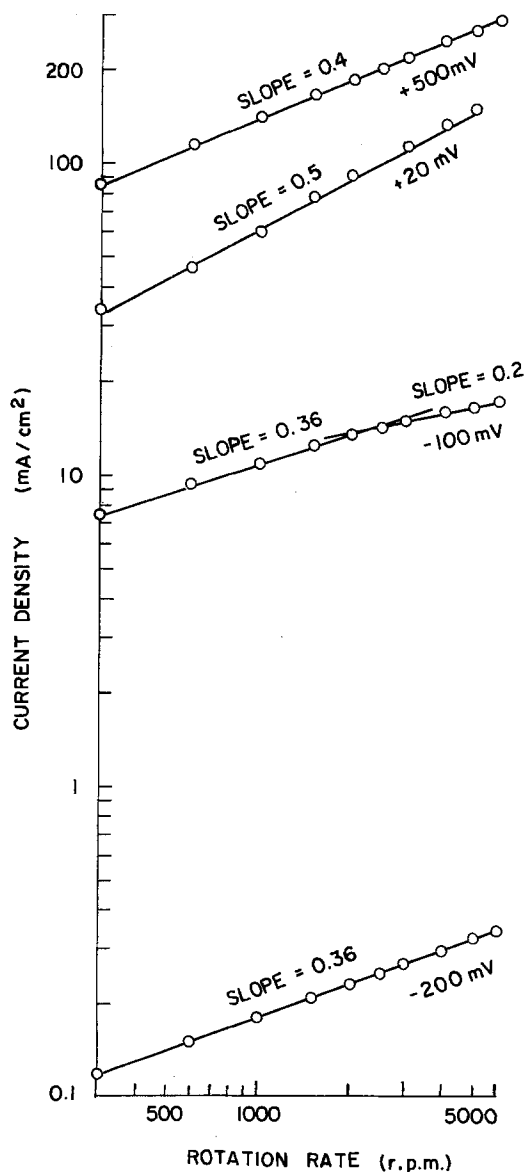


Fig. 12. The effect of rotation rate on the electro-dissolution of the alloy in 1M HCl.

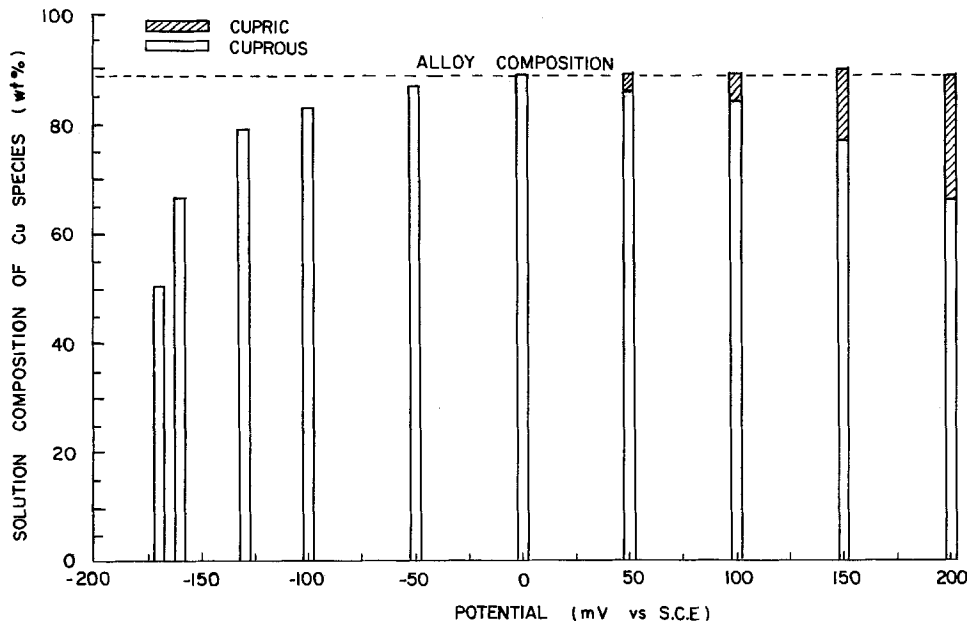
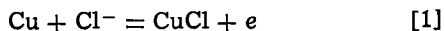


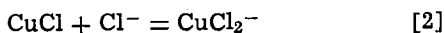
Fig. 13. Electrodisso- lution of copper species from the alloy in 1M HCl as a function of poten- tial (≈ 1 h potentiostatic polar- ization at each potential), 700 rpm.

slightly below the potential of the current peak. The reactions are as follows



where

$$E^e = -0.105 - (RT/F) \ln [\text{Cl}^-], \quad \text{V vs. SCE} \quad [1']$$

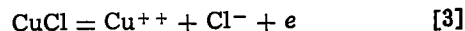


where

$$K_2 = 6.61 \times 10^{-2} \quad [2']$$

In this region, the CuCl film formation step (Eq. [1]) is slow relative to the film dissolution step (Eq. [2]), precluding buildup of film. Film formation is not discerned until about the peak potential. Moreau *et al.* (12) concluded from their results that the CuCl film begins to form at potentials just below the peak potential. At this point when the film starts to build up, the first step (Eq. [1]) is fast compared to the second step (Eq. [2]).

At the current minimum and in the current-plateau region (Fig. 2 and 3), the cuprous ring current remains constant. In this region, the rate of Cu electrodisso- lution to cuprous-chloride complexes is propor- tional to the square root of the rotation rate following the Levich relation, as shown by Braun (4) and in this study (results not shown). At higher potentials (region E in Fig. 2), cupric ions are detected, as shown in Fig. 3. These results have also been reported by Walton and Brook (6), who suggest that Cu^{++} is formed by electro-oxidation of the CuCl film

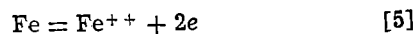
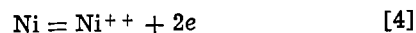


where

$$E^e = 0.295 + \frac{RT}{F} \ln [\text{Cu}^{++}][\text{Cl}^-], \quad \text{V vs. SCE} \quad [3']$$

In the apparent Tafel region for pure Cu in chloride solutions, the anodic Tafel slopes of 60 mV/decade are obtained in accord with the results of others (1-4). The chloride reaction order is 2 (data not shown), which is also in agreement with others (1-4). How- ever, at higher chloride concentrations, cuprous tri- chloride and tetrachloride complexes may form in significant amounts, so that chloride reaction orders greater than 2 may be obtained.

For 90/10 Cu-Ni alloy (with 1.7% Fe), the cuprous- ring current and the alloy disk are not equivalent below the peak potential (Fig. 4) as observed for pure Cu (Fig. 3). The reason for this difference between the alloy and pure Cu is that, in addition to the Cu electro- disso- lution reactions (Eq [1] and [2]) for pure Cu, the alloy disk current represents Ni and Fe electrodisso- lution rates



The Fe reaction is especially significant near the rest potential, as shown in Fig. 13. At higher potentials, cupric ions are produced, as observed for pure Cu, probably via Eq. [3].

If the electrodisso- lution of the alloying elements is similar to the pure metals, it is expected that the elec-

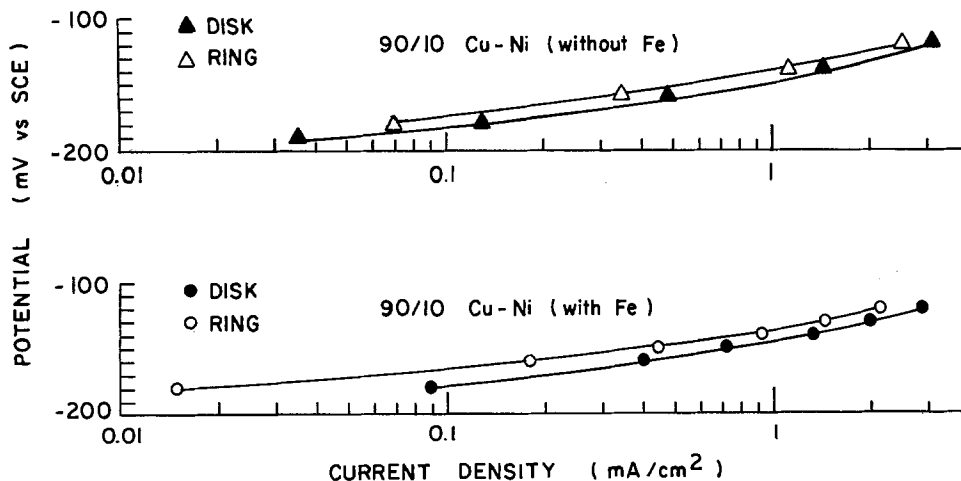


Fig. 14. Effect of Fe on Cu-Ni (90/10) alloy and the Cu component electrodisso- lution in 0.5M HCl + 0.5M NaCl, 700 rpm.

trodissolution of both Ni and Fe components is activation controlled (5, 14) and the Cu component is mass-transfer controlled (1-4). The anodic Tafel slopes for the alloy are approximately 70 mV/decade for chloride concentrations of 0.1-4M (Fig. 6), as reported by other investigators (6, 9, 15). The Cl^- reaction orders for alloy electrodisso- lution obtained from the results in Fig. 6 are 1.3 for low Cl^- concentrations and 1.6 for high Cl^- concentrations. These parameters for alloy electrodisso- lution compare with anodic Tafel slopes of 60 mV/decade (Fig. 7) and 100 mV/decade (Fig. 8) for Cu component and Ni component (with Fe) electro- disso- lution, respectively. The Cl^- reaction orders for Cu-component electrodisso- lution are 1.9 and 2.0 for low Cl^- and high Cl^- concentrations (Fig. 7), respec- tively. The Cl^- reaction order for the Ni-component electrodisso- lution is approximately 1 (Fig. 8). The param- eters for the Cu component are essentially the same as those obtained for pure copper (as discussed above). The anodic Tafel slopes for pure Ni in chloride solu- tions have been reported to range from 75 to 120 mV/ decade (5, 16, 17). The Cl^- reaction orders have been reported to be 0.5 (low Cl^- concentrations) and 1 (high Cl^- concentrations) for pure Ni (5). Thus, the param- eters for the Ni component roughly approximate the values obtained for pure Ni.

Mass-transfer dependence of alloy electrodisso- lution is shown in Fig. 12. Complete mass-transfer control of alloy electrodisso- lution is not observed between the rest potential and just below the peak potential where the CuCl film begins to form. This is shown by the slope less than 0.5 for the $\log i$ vs. \log rotation rate plots at potentials of -200 and -100 mV. The slope of 0.36 suggests mixed-activation and mass-transfer control with both Ni and Fe components under activation control and the Cu component under mass-transfer control. At potentials of the current-minimum and current- plateau region ($+20$ mV), alloy electrodisso- lution clearly follows the Levich relation and indicates that the dissolution of the CuCl film (Eq. [21]) is the domi- nant process in this potential region and is under mass- transfer control. Above the current-plateau region, mixed control is again indicated, as shown in Fig. 12 ($+500$ mV), with Eq. [2] the mass-transfer control process and Eq. [3] under activation control. Walton and Brook reported similar mixed mass-transfer and activation-control behavior (6).

Selective electrodisso- lution of Ni is observed at potentials below the peak potentials, as shown in Fig. 13. At potentials near the rest potential, Fe electrodisso- lution, the minor alloying element, is dominant (data not shown). As the potential is increased (Fig. 13), selective electrodisso- lution of Ni is progressively dimi- nished (above -200 mV, the electrodisso- lution rate of Fe is too small to be measured) up to -50 mV. The current-plateau region occurs above 0 mV where electrodisso- lution is nonselective and the cuprous chlo- ride complex is the only electro-oxidation product of the Cu component. As Fig. 13 shows, at potentials

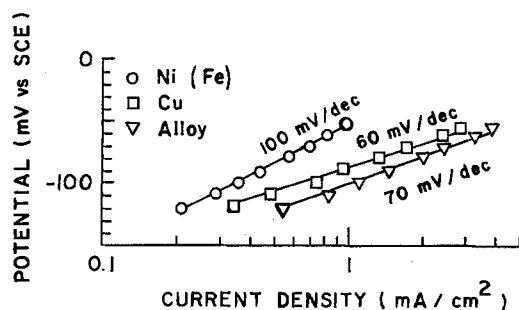


Fig. 15. Electrodisso- lution of the alloy and the Cu and Ni components in 0.6M HClO_4 + 0.4M HCl in the apparent Tafel region, 700 rpm.

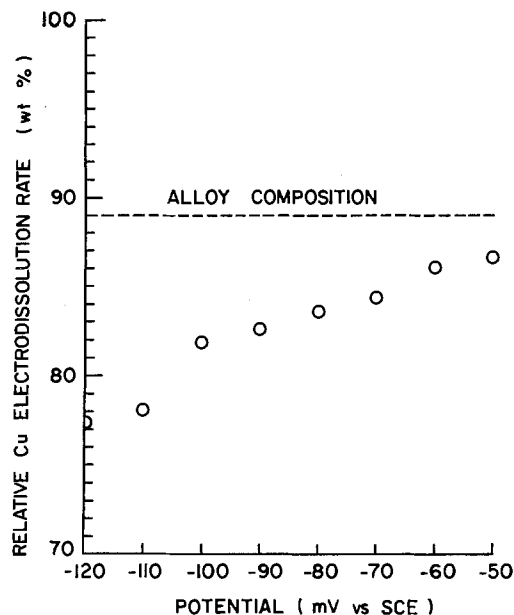


Fig. 16. Selective alloy electrodisso- lution at potentials ≤ -50 mV. Data from Fig. 15.

above this region alloy electrodisso- lution continues to be nonselective, but an increasing fraction of the Cu component electro-oxidizes to the cupric state.

Figure 15 provides the basis for a quantitative mea- sure of selective alloy electrodisso- lution at potentials ≤ -50 mV. As the potential is increased, the differ- ence between the currents of the Cu component and the Ni component increases and reaches at -50 mV a Cu:Ni(Fe) weight ratio of 6.46. This ratio compares with the value of 8 for the bulk alloy. The results of Fig. 15 are expressed, in Fig. 16, as the electrodisso- lution rate of the Cu component relative to that of the alloy between -120 and -50 mV. At -120 mV, the relative rate in terms of w/o Cu is 77.5%. There is a steady increase in the relative rate as the potential is increased, and the value of 86.5% is attained at -50 mV. The latter approaches the bulk-alloy composition of 88.8% Cu, which indicates nonselective electrodisso- lution. This point is reached at approximately the potential of the current minimum (> 0 mV), where complete mass-transfer control of the electrodisso- lution process is observed.

Acknowledgment

This work is part of the University of California Sea Water Desalination Program.

Manuscript submitted ca. March 20, 1983; revised manuscript received Jan. 18, 1984.

The University of California assisted in meeting the publication costs of this article.

REFERENCES

1. T. Hurlen, *Acta Chem. Scand.*, **15**, 1231 (1961).
2. C. H. Bonfiglio, A. C. Albaya, and O. A. Cobo, *Corros. Sci.*, **13**, 717 (1973).
3. A. L. Bacarella and J. C. Griess, *This Journal*, **120**, 459 (1973).
4. M. Braun and K. Nobe, *ibid.*, **126**, 1666 (1979).
5. A. Bengali and K. Nobe, *ibid.*, **126**, 1118 (1979).
6. M. E. Walton and P. A. Brook, *Corros. Sci.*, **17**, 317 (1977).
7. J. O'M. Bockris, B. T. Rubin, A. Despic, and B. Lovrecek, *Electrochim. Acta*, **17**, 973 (1972).
8. B. Cahan and R. Haynes, *J. Electroanal. Chem.*, **22**, 339 (1969).
9. C. Kato, J. E. Castle, B. G. Ateya, and H. W. Pickering, *This Journal*, **127**, 1890 (1980).
10. H. P. Lee, M.S. Thesis, University of California, Los

- Angeles, CA (1980).
11. W. J. Albery and S. Bruckenstein, *Trans. Faraday Soc.*, **62**, 1920 (1966).
 12. A. Moreau, J. P. Frayret, J. Del Rey, and R. Pointeau, *Electrochim. Acta*, **27**, 1281 (1982).
 13. R. S. Cooper and J. H. Bartlett, *This Journal*, **105**, 109 (1958).
 14. H. C. Kuo, Ph.D. Dissertation, University of California, Los Angeles, CA (1975).
 15. G. L. Bauerle and K. Nobe, *Corrosion*, **37**, 426 (1981).
 16. A. Moon and K. Nobe, *ibid.*, **33**, 300 (1977).
 17. M. L. Kronenberg, J. C. Banter, E. Yeager, and F. Hovorka, *This Journal*, **110**, 1007 (1963).

Passive Films on Iron: The Mechanism of Breakdown in Chloride Containing Solutions

Tong E. Pou, Oliver J. Murphy,* Vaneica Young, and John O'M. Bockris*

Department of Chemistry, Texas A&M University, College Station, Texas 77843

Luis L. Tongson

Physics Department, Pennsylvania State University, Worthington Scranton Campus, Dunmore, Pennsylvania 18512

ABSTRACT

An examination has been made of the mechanism of breakdown of passive films on iron in borate buffer solution (pH = 8.4) caused by chloride ions. Various electrochemical kinetic criteria were measured. XPS, SIMS, and ISS studies were made of the systems used in the electrochemical work. The rate of breakdown was found to be proportional to c_{Cl^-} and c_{H^+} and exponentially dependent on the electrode breakdown potential and field drop in the oxide film. XPS data showed that when chloride ions caused breakdown, the O_{total}/Fe and H_2O/Fe ratios changed from 2 to 1.5 and 0.5 to 0.1, respectively. SIMS data revealed that heating passive films up to 200°C drove out water from the films and that chloride ions penetrated the whole film thickness on breakdown. ISS data indicated that on changing from a passive to a depassivated film, the O/Fe ratio changed from 2.07 to 1.5. Discussion of the electrochemical kinetic data shows that it is inconsistent with adsorption-displacement models, pore models, and chemico-mechanical models, but is not inconsistent with ion-exchange processes, point-defect models, and hydrated polymeric oxide models. Confrontation of the spectroscopic data with the expectations of the latter three models shows some points of agreement with all these models, but the data taken together is most consistent with the hydrated polymeric oxide model.

Study of the mechanism of breakdown of passive films by anions, and, in particular, chloride ions, presumes a knowledge of the passivation process. Although theories in relation to the chloride effects on passive films abound (1, 2), models with respect to the nature of the latter can, at present, be summarized into two types (3-5).

The crystalline oxide model.—In this model (6-11), the protective nature of the layer which forms upon the surface of a metal under a particular form of oxidation is supposed to be connected with the crystal structure of the film. In the case of iron, the film is considered to be a duplex layer consisting either of an inner layer of Fe_3O_4 and an outer layer of $\gamma-Fe_2O_3$ (6, 10) or of $\gamma-Fe_2O_3$ alone (7, 11). The undeniable presence of water in connection with passive films formed in aqueous environments is interpreted to be due either to hydrogen stabilization of $\gamma-Fe_2O_3$ in the outer regions (12, 13) or to adsorbed water on the surface of the film (14).

The hydrated polymeric oxide model.—Inherent in this model (15-17) is the essential role played by water in transforming the properties of "iron oxide" to those of the protective passive layer. How the water does this varies with the author (15-20).

The essential concept is that the water is supposed to maintain the thin film amorphous, and the word "polymer" is used with the meaning that the bound water (21) "pulls together" the iron oxide in such a fashion that it is difficult for the Fe^{2+} ions from the metal base beneath the film to diffuse to the hydration sites at the oxide/solution interface.

The various theories of passive film breakdown (1, 2, 22) provoke numerous dilemmas, among which the two most in need of resolving are the following: (i) the distribution of hydrogen, or water, within passive

films (13, 15-20, 23), or (ii) the distribution of chloride ions in the bulk of passive films after exposure to chloride containing solutions (2, 24).

The present paper reports the application of both electrochemical and spectroscopic techniques to these problems.

Experimental

Electrodes.—Working electrodes were iron disks approximately 1 mm thick and 6 × 6 mm square (99.99% purity, Alfa Ventron Corporation, Danvers, Massachusetts). They were mechanically polished with 320-, 400-, 500-, and 600-grade silicon carbide paper and then finished with diamond paste of 6-0.25 μ m grain sizes to give a bright mirror surface. After polishing, electrodes were washed with methanol and several times with triply distilled water, dried, and stored *in vacuo*. Each electrode was prepared fresh with a fine-grade diamond paste and washed before use. Electrodes were mounted in a Teflon holder, as described previously (25).

The counterelectrode was a platinum gauze arranged in a half-cylindrical shape opposite the working electrode and had a surface area at least 100 times larger than the iron disk electrode. Its arrangement opposite the iron anode allowed the latter electrode to function unimpeded by depolarization reactions arising from the hydrogen gas evolved during polarization of the large cathode.

The reference electrode was a Hg/HgO, 1N KOH electrode. The calomel electrode was avoided because of the possibility of solution contamination with chloride ions. Potentials in this paper are referred to the normal hydrogen electrode.

Solution preparation.—Solutions were prepared from triply distilled water of conductivity, κ , less than $10^{-6}\Omega$ cm⁻¹ and were made up as buffer solutions consisting of 0.275M analytical-grade sodium tetraborate, mixed

* Electrochemical Society Active Member.

with 0.15M analytical-grade boric acid. The solution pH was 8.4. All solutions were pre-electrolyzed in a separate cell attached to the working cell at a constant current density of about $20 \mu\text{A cm}^{-2}$ using two large platinum gauze electrodes, each about 100 cm^2 in area. The pre-electrolysis time was of the order of 15h.

Removal of air-formed oxide films.—The working electrode was pretreated by cathodic polarization at -0.74V (NHE) (26) for 30 min to remove air-formed oxides. The solution used for this reduction of the electrode, and which contained evolved hydrogen gas, was removed from the main cell by a purified nitrogen gas pressure, and a new pre-electrolyzed solution introduced into the cell in contact with the electrode.

The rest potential of the working electrode prepared under these conditions was -0.5V (NHE).¹ Electrodes prepared in this manner were used as base electrodes in all subsequent experiments, i.e., when an experimental potential pertinent to the passivation experiments was applied, the electrode was prepared as described above, and this new potential was impressed by means of a potentiostatic step onto the resting potential of pure iron.

Formation of the passive layer.—The typical passive film which was used in all experiments was formed at 0.3V (NHE) for a time interval of 50 min, unless otherwise stated. The current decreased continuously during the time of passivation, finally reaching a value of the order of $1 \mu\text{A cm}^{-2}$. Integration of the current/time curve showed that the total charge passed was around 6 mC cm^{-2} . Assuming that the oxide present was Fe_2O_3 , the film thickness would be in the region of 26Å.

Having formed the passive film, the solution present was displaced by purified nitrogen gas, and a solution containing chloride ions was introduced. The solutions which were introduced at this point were either variable in chloride-ion concentration at fixed pH (8.4) or variable in pH at fixed chloride concentration (0.1 or 0.5M) and were of constant ionic strength. Passivated specimens were exposed to these solutions at the potential of film growth (unless otherwise stated) for various times prior to, at, and after breakdown. Induction times (τ)² for breakdown were established under the various conditions used, chloride-ion concentration, pH, passive-film thickness, and the potential at which the electrode was held at in the chloride solutions.

Spectroscopic analyses of passive films.—**Transfer of samples to XPS spectrometer.**—Solutions which had been used in the formation of passive films, or in the depassivation of such films, were pressed out of the cell by means of purified nitrogen gas pressure, the electrode being left in contact with the latter. The cell was then quickly filled with triply distilled water from an attached reservoir and released by nitrogen gas pressure. This was repeated a second time. The cell with the electrode still in place and under a nitrogen gas atmosphere was then removed to a dry box filled with nitrogen gas and opened therein, the electrode being removed, washed again thoroughly with triply distilled water, and transferred to a glass vial filled with nitrogen gas. The vial was sealed, placed in a Dewar containing liquid nitrogen, and then removed from the glove box. The Dewar was transferred to another laboratory in the chemistry building and placed in another nitrogen containing glove box, which was attached to the XPS sample chamber. The electrode

¹The relaxation of the film-free potential to one of -0.5V (NHE) was caused by the needed change of solution. Reference to Wroblowa, *et al.* (27), who studied film formation on iron at the same pH and potential regions as used here, shows that at -0.5V (NHE) a prepassive film of submonolayer thickness is formed.

²The induction time will vary with the age of the film. However, significant effects have been measured only over times in the 100-1000 min range (28).

was once more removed from the original vial and on warming up was placed in the XPS analysis chamber.

The XPS spectra were recorded by use of an HP 5950A ESCA spectrometer, equipped with monochromatized Al $K\alpha$ radiation. The sample probe was encased in a dry box, employing a nitrogen atmosphere filtered with oxisorb cartridge ($\text{O}_2 < 5 \text{ ppm}$). A Surface Science Laboratories Model 259 angular distribution probe was used. The photoelectron detection angle relative to the sample surface, θ , was varied from 8° – 58° (~ 5 – 30Å). A Hewlett Packard 9825A computer was interfaced to the system. A Surface Science Laboratories software package (9825 Data System Rev E) made possible background subtraction and peak deconvolution.

The atomic ratio of O to Fe was calculated according to the relation (29)

$$\frac{N_{\text{O}}}{N_{\text{Fe}}} = \frac{I_{\text{O}} \sigma_{\text{Fe}}}{I_{\text{Fe}} \sigma_{\text{O}}}$$

where N_{O} and N_{Fe} equal the number of atoms of oxygen and iron, I_{O} and I_{Fe} are the corresponding intensities, and σ_{O} and σ_{Fe} are the corresponding cross sections. The relative cross sections, $\sigma_{\text{Fe}}/\sigma_{\text{O}}$, was taken (30) as 1.45.

Transfer of samples to SIMS and ISS spectrometers.—In these cases, analyses were performed in laboratories far from that in which the original experiments had been carried out. Electrodes were treated as described above and were placed in glass vials, the tops of which were carefully sealed using Teflon tape and screw caps. They were opened under inert gas conditions and placed in the respective spectrometer chambers.

The SIMS measurements were performed on a Gatan Model 591C SIMS-SIPS ion microprobe at the Materials Research Laboratory, Pennsylvania State University, Dunmore, Pennsylvania. The ion beam consists of a Colutron ion source, Wein mass filter, and two electrostatic lenses. The ion gun chamber is pumped with a turbomolecular pump. The target chamber can be evacuated to 10^{-10} torr with a second turbomolecular pump and titanium sublimation pump. The secondary ions are detected with an Extranuclear quadrupole mass spectrometer with a Spheric-El energy filter.

The operating parameters were: probe ion beam $^{40}\text{Ar}^+$, beam voltage of 7 keV, beam current of 90 nA, and a sample chamber pressure during analysis of 5×10^{-9} torr. The ion beam of $\sim 70 \mu\text{m}$ diam was rastered over an area of $1.2 \times 1.2 \text{ mm}$. The signal was gated so that the data were collected over a central area of $0.36 \times 0.36 \text{ mm}$. The sputtering rate was determined as 0.3Å s^{-1} , using a $102\text{Å SiO}_2/\text{Si}$ standard.

The ISS analyses were carried out with a Leybold-Heraeus LHS 10 surface analysis system at the Solar Energy Research Institute, Golden, Colorado.

The operating parameters were: probe ion beam $^3\text{He}^+$, primary beam energy 1 kV, beam current of 94 nA, and a sample chamber pressure during analysis of 1.4×10^{-7} torr. The ion beam $\sim 200 \mu\text{m}$ was rastered over an area of $2 \times 2 \text{ mm}$. The signal was gated so that the data were collected over a central area of $1 \times 1 \text{ mm}$. The sputtering rate was determined as 1.3 Å min^{-1} , using as a standard the etch rate for the iron substrate in conjunction with a mechanical profiler.

The atomic ratio of O to Fe was calculated using the equation (31)

$$\frac{N_{\text{O}}}{N_{\text{Fe}}} = \frac{I_{\text{O}} \sigma_{\text{Fe}}}{I_{\text{Fe}} \sigma_{\text{O}}}$$

where N_{O} and N_{Fe} equal the number of atoms of oxygen and iron, I_{O} and I_{Fe} are the corresponding ISS peak intensities, and σ_{O} and σ_{Fe} are the corresponding cross

sections. The relative cross section, σ_{Fe}/σ_0 , taken was the mean of those found in the literature, 6.6 (31) and 8.8 (32), yielding a value of 7.7.

Results

The results of the investigations can be divided into four parts, corresponding to the techniques used.

Electrochemical techniques.—The normal passivation curve for iron is shown in Fig. 1 and corresponds to a sweep rate of 0.2 mV s^{-1} .

In Fig. 2, the log of the breakdown rate (v) is plotted as a function of chloride-ion concentration in the buffered borate solutions to which passivated electrodes were exposed.

It can be seen that

$$\delta \log v / \delta \log c_{Cl^-} = 1$$

where $v (= 1/\tau)$ is the rate of the reaction leading to the breakdown of the passive layer. The process has a reaction order of unity at constant potential [0.3V (NHE)].

The corresponding variation of the log of the breakdown rate with hydrogen ion concentration is shown in Fig. 3. It transpires upon examining this plot that

$$\delta \log v / \delta \log c_{H^+} = 0.66$$

In Fig. 4, the log of the breakdown rate as a function of the electric field across the passive film, for films grown at a constant potential of 0.3V (NHE) for vari-

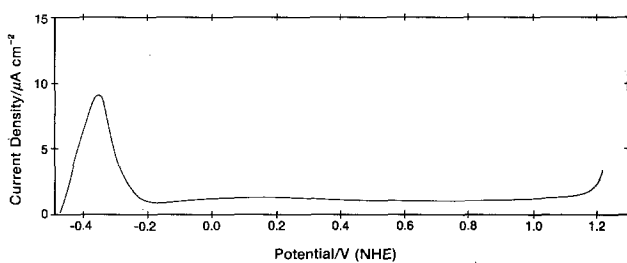


Fig. 1. Current/potential curve for a clean iron electrode in borate buffer solution, $\text{pH} = 8.4$. Scan rate: 0.2 mV s^{-1} .

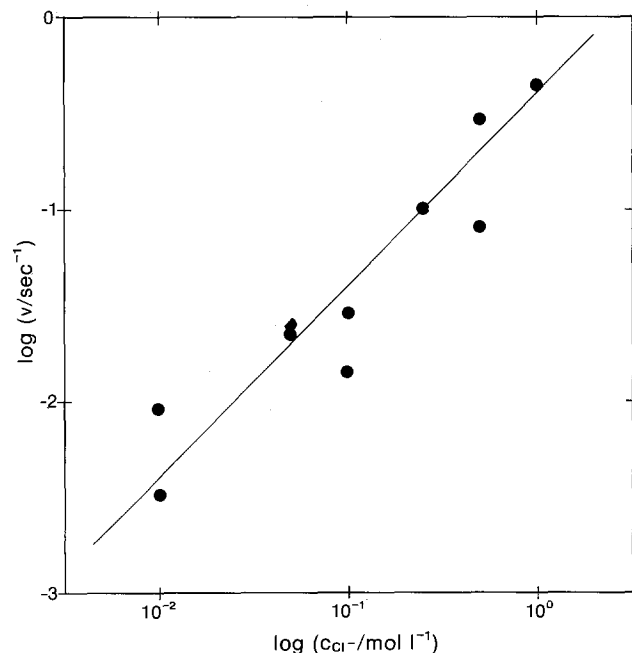


Fig. 2. Variation of the log of the breakdown rate, v , as a function of chloride-ion concentration. Film growth conditions: 0.3V (NHE) in borate-buffer solution. Breakdown conditions: 0.3V (NHE) in chloride containing borate-buffer solution.

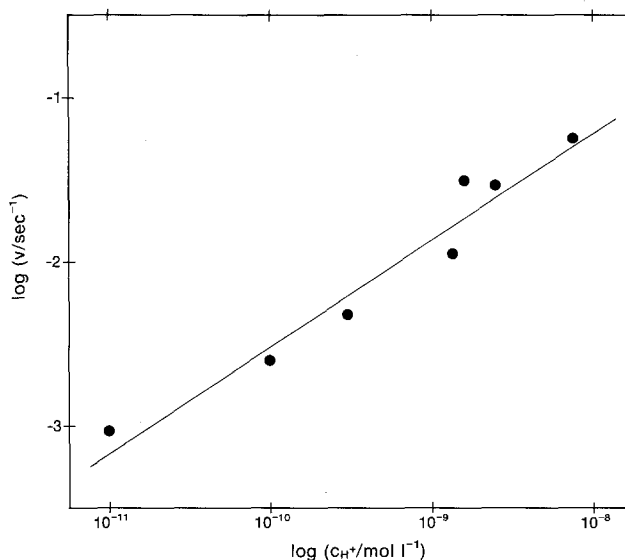


Fig. 3. Dependence of the log of the breakdown rate, v , on hydrogen-ion concentration. Film growth conditions: 0.3V (NHE) in borate-buffer solution. Breakdown conditions: 0.3V (NHE) in solutions of variable pH containing 0.1M NaCl.

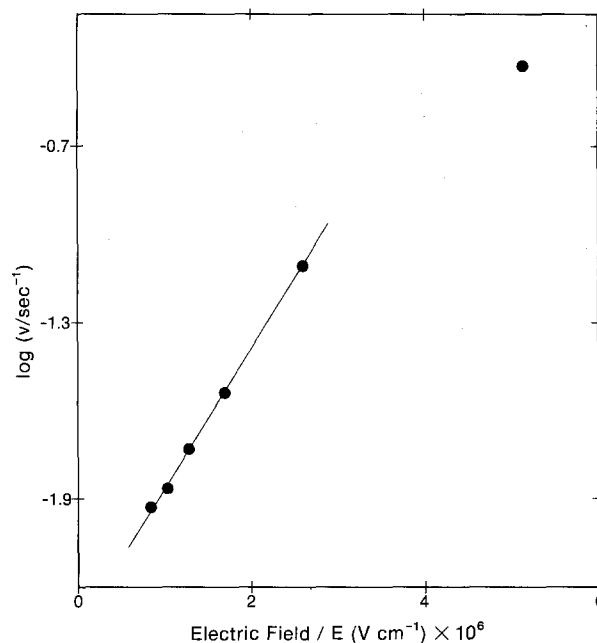


Fig. 4. Variation of the log of the breakdown rate, v , as a function of the electric field, E , across the film. Film growth conditions: 0.3V (NHE) in borate-buffer solution for various times and, hence, various film thicknesses. Breakdown conditions: 0.3V (NHE) in borate-buffer solution containing 0.1M NaCl.

ous times is presented. Film thicknesses were estimated by utilizing the charge passed in forming the films and by assuming that the passive layer consists of Fe_2O_3 . The slope of the graph

$$\delta \log v / \delta E = 0.48 \times 10^{-6} \text{ V}^{-1} \text{ cm}$$

The dependence of the log of the breakdown rate on the breakdown potential, V , is given in Fig. 5. It can be ascertained from the figure that³

$$\delta \log v / \delta V = 4.1 \text{ V}^{-1}$$

XPS spectra.—Several analyses were made with XPS. In Fig. 6 is shown the binding energy curve cor-

³The value given here is, of course, not to be taken simplistically, because the V is referenced to other potentials and is only a measure of the potential difference across the film.

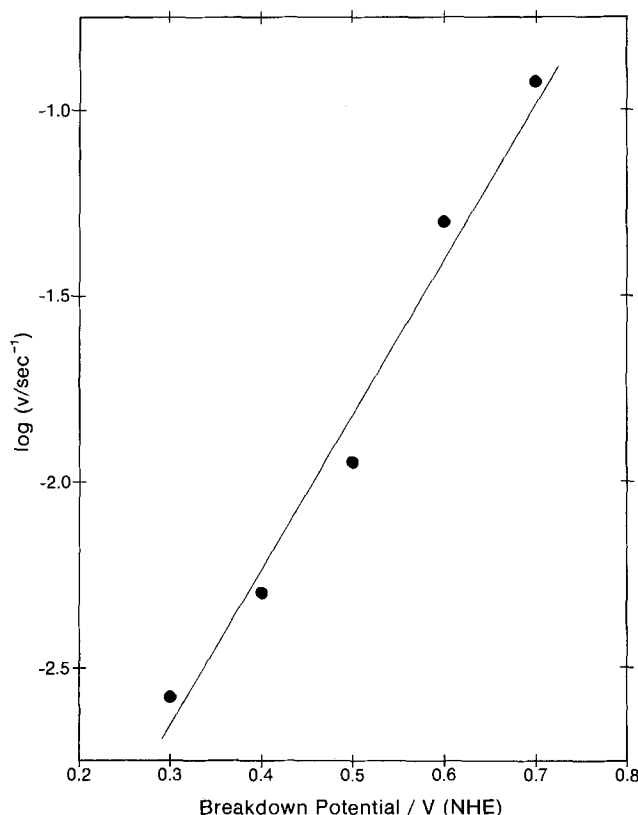


Fig. 5. Dependence of the log of the breakdown rate, v , on the breakdown potential, V . Film growth conditions: 1.0V (NHE) in borate-buffer solution. Breakdown conditions: borate-buffer solution containing 0.1M NaCl.

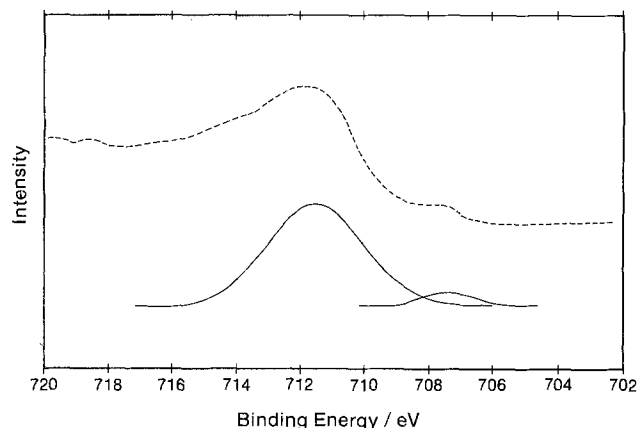


Fig. 6. XPS spectrum for Fe $2p_{3/2}$ for the passive film formed on iron in borate-buffer solution at 0.3V (NHE).

responding to iron (Fe $2p_{3/2}$). It can be seen that after deconvolution metallic iron shows up at a binding energy of 707.4 eV (33), while iron in the oxidized state, Fe^{3+} , is seen at a binding energy of 711.5 eV (34). The passive film prepared at 0.3V (NHE) contains exclusively ferric iron with no ferrous iron content (Fe $^{2+}$ binding energy 708.5-709.5 eV) (34, 35).

In Fig. 7 is shown the O 1s spectra. On deconvoluting the spectra, three peaks were obtained. The peak with binding energy of 530.3 eV is attributed to O $^{=}$ (25, 34, 36), while the peak at 531.8 eV is assigned to OH $^{-}$ (14, 34, 36) and the peak at 533 eV to H $_2$ O (25, 35).

In Table I, XPS results are given for an electron escape angle, θ of 38 $^{\circ}$ ($\sim 22\text{\AA}$), corresponding to passive films prepared at three different potentials. The ratio O_{total}/Fe is about 2 for all potentials, and the H $_2$ O/Fe ratio averages 0.5. The ratios, O/Fe and OH/

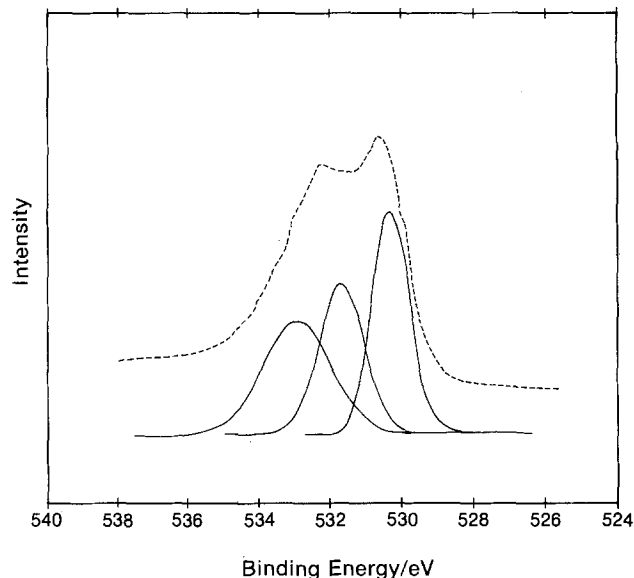


Fig. 7. XPS spectrum for O 1s for the passive film formed on iron in borate-buffer solution at 0.3V (NHE).

Fe, are less clear, but if each pair is added together and averaged, a value of approximately 1.5 is obtained.

In Table II, similar results are shown as a function of escape angle, θ , for a passive film prepared at 0.3V (NHE). The ratio of O_{total}/Fe corresponding to an escape angle of 8 $^{\circ}$ ($\sim 5\text{\AA}$) is 2.61, higher than the expected 2.0. The average value of the ratio H $_2$ O/Fe is 0.77. The average of the sum of the ratios, O/Fe and OH/Fe, is 1.46.

The effects of the exposure of passive films to chloride ions for times after breakdown for three escape angles, θ , 18 $^{\circ}$ ($\sim 11\text{\AA}$), 38 $^{\circ}$ ($\sim 22\text{\AA}$), and 58 $^{\circ}$ ($\sim 30\text{\AA}$) are presented in Table III. The ratio O_{total}/Fe has decreased to ca. 1.5. However, more strikingly, the ratio H $_2$ O/Fe is lowered considerably to about 0.1. The average of the sum of the O/Fe and OH/Fe ratios yields 1.53.

ISS spectra.—A typical ISS spectrum of a passive film prepared at 0.3V (NHE) in borate solution (pH = 8.4) is shown in Fig. 8. Two peaks can be seen, the first one at an energy ratio $E/E_0 = 0.53$ corresponds to oxygen and the second one with an energy ratio $E/E_0 = 0.83$ is for iron.⁴

⁴Leybold-Heraeus ISS energy ratio (E/E_0) data for the elements for various bombarding ions applicable to the scattering geometry used.

Table I. O_{total}/Fe , H $_2$ O/Fe, OH/Fe, O/Fe, and (OH + O)/Fe ratios at an electron escape angle $\theta = 38^{\circ}$ ($\sim 22\text{\AA}$) from XPS of passive films on iron formed at various potentials in borate solution (pH = 8.4) for 50 min

Potential V (NHE)	O_{total}/Fe	H $_2$ O/Fe	OH/Fe	O/Fe	(OH + O)/Fe
+0.30	2.1	0.7	0.6	0.82	1.42
+0.065	1.88	0.2	0.77	1.11	1.88
-0.20	1.97	0.5	0.74	0.74	1.58

Table II. O_{total}/Fe , H $_2$ O/Fe, OH/Fe, O/Fe, and (OH + O)/Fe ratios at various electron escape angles, θ , from XPS of passive films formed on iron at +0.30V (NHE) in borate solution (pH = 8.4) for 50 min

Angle, θ	O_{total}/Fe	H $_2$ O/Fe	OH/Fe	O/Fe	(OH + O)/Fe
8 $^{\circ}$ ($\sim 5\text{\AA}$)	2.61	0.91	0.83	0.99	1.82
18 $^{\circ}$ ($\sim 11\text{\AA}$)	2.03	0.84	0.58	0.77	1.35
38 $^{\circ}$ ($\sim 22\text{\AA}$)	2.09	0.69	0.58	0.83	1.41
58 $^{\circ}$ ($\sim 30\text{\AA}$)	1.96	0.65	0.52	0.76	1.28

Table III. O_{total}/Fe , H_2O/Fe , OH/Fe , O/Fe , and $(OH + O)/Fe$ ratios at various electron escape angles, θ , from XPS of passive films after breakdown in an 0.1M chloride containing borate-buffered solution (pH = 8.4) at 0.3V (NHE)

Angle, θ	O_{total}/Fe	H_2O/Fe	OH/Fe	O/Fe	$(OH + O)/Fe$
18° (~11Å)	1.51	0.10	0.6	0.88	1.48
38° (~22Å)	1.52	0.09	0.69	0.91	1.60
58° (~30Å)	1.51	0.12	0.55	0.96	1.51

Plots of the atomic ratio O/Fe , derived from the ISS spectra, as a function of depth, are presented in Fig. 9 for a passive film formed in borate solution at 0.3V (NHE) and for a similar film broken down in a borate-buffered chloride solution at the latter potential. In the case of the film which has not been exposed to chloride solution, the ratio is close to 2, while for the film after breakdown in buffered chloride solution, it is 1.5.

SIMS spectra.—The SIMS data are presented in three aspects.

In Fig. 10, the OH^-/O^- ratios are given as a function of depth for passive films formed in borate solution at 0.3V (NHE) and subsequently thermally treated under a flowing argon gas atmosphere at various temperatures for 15 min. As the temperature increases, the OH^-/O^-

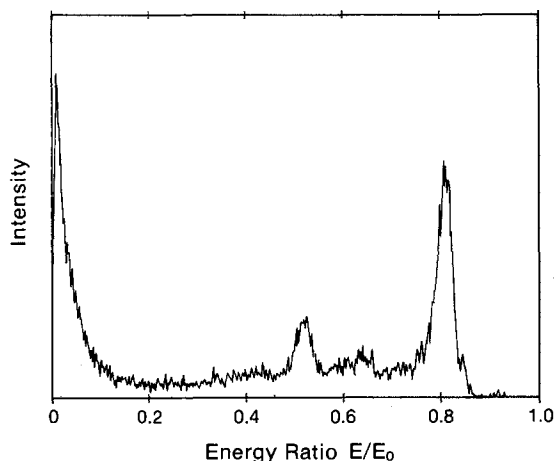


Fig. 8. ISS spectrum of passive film on iron formed in borate-buffer solution at 0.3V (NHE).

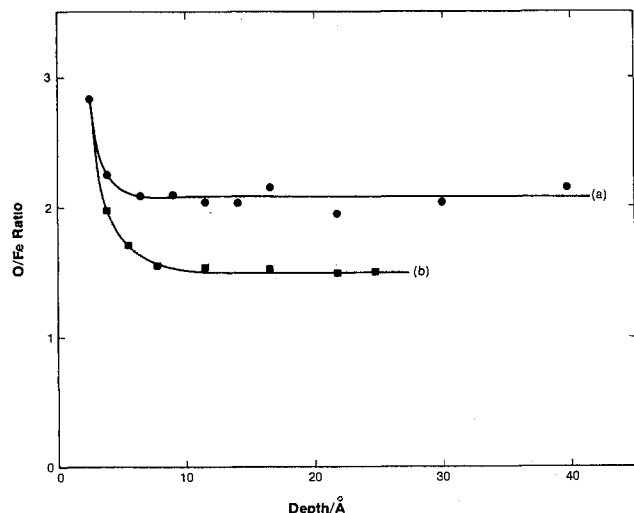


Fig. 9. O/Fe ratio as a function of depth, Å, into the passive film on iron from ISS depth profiling: (a) film formed in borate buffer solution at 0.3V (NHE); (b) passive film after breakdown [0.3V (NHE) in borate-buffer solution containing 0.5M NaCl].

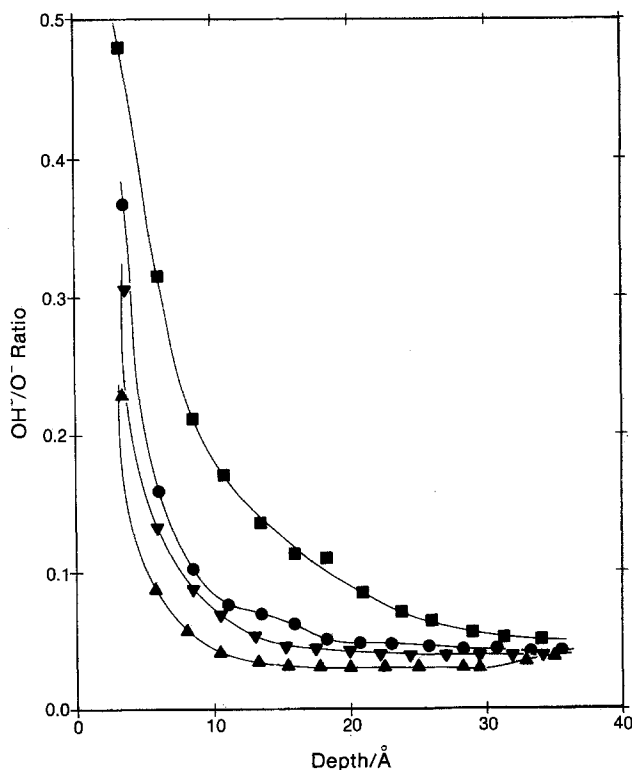


Fig. 10. Variation of OH^-/O^- ratio with depth into passive films formed in borate buffer solution at 0.3V (NHE). Annealing temperatures under an argon gas flow were: (■) 25°C; (●) 70°C; (▼) 160°C; (▲) 200°C.

O^- ratio decreases. The ratios of OH^-/O^- for temperatures above room temperature are reduced.

The Cl^- peak height intensities, as a function of depth, presented in Fig. 11 for passive films formed at 0.3V (NHE) in borate solution and subsequently exposed to a borate-buffered chloride containing solution for times of 40, 80, 163, 205, and 420s, i.e., for times before and after breakdown (~160s), show some

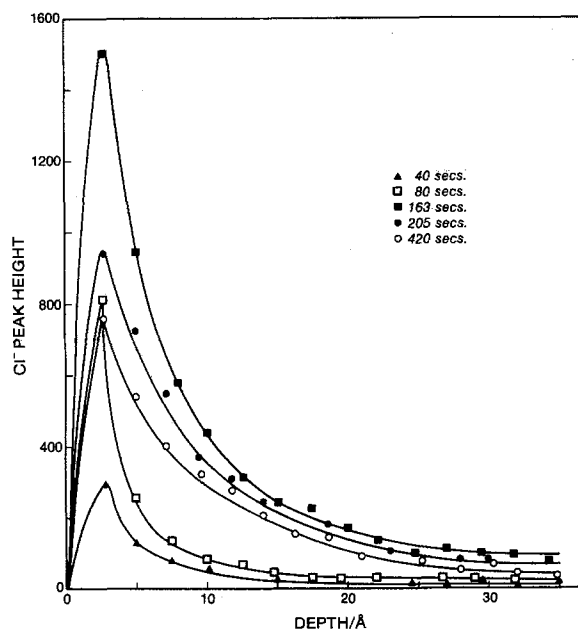


Fig. 11. Variation of Cl^- peak height intensities as a function of depth into passive films formed in borate-buffer solution at 0.3V (NHE) and subsequently exposed to a borate-buffer solution containing 0.5M NaCl at this potential for various times.

interesting features: (i) for increasing exposure times (40, 80, and 163s) up to breakdown time, increasing amounts of chloride ions penetrate the passive films, reaching a maximum around breakdown, (ii) for exposure times longer than breakdown, however, namely, 205 and 420s, a decrease in the chloride content of the passive films becomes apparent, the Cl^- concentration within the film being now anomalously lower for the larger exposure time (420s). Chloride ions penetrate passive films right up to the metal/film interface.

The positive SIMS O^+ peak height signals as a function of depth into the same passive films as used in obtaining the data shown in Fig. 11 are given in Fig. 12. The O^+ signals are seen to increase as the depth into the films increases, undergo a constant value for the bulk of the films, and decay as the passive film/metal interfaces are reached.

Discussion

Electrochemically derived kinetic data.—Criteria derived from the data presented in Fig. 2-5, and which are conveniently summarized in Table IV, may now be compared for consistency with leading models for passive film breakdown.

Adsorption-displacement models.—In one approach (37, 38), the events leading to breakdown involve the adsorption of Cl^- and simultaneous displacement of oxygen from the monolayer said to constitute the passive layer in this model. As soon as the chloride ion is adsorbed, dissolution is facilitated (39, 40).

It has been shown that the film breakdown kinetics depend upon the electric field across the film at constant potential (various thicknesses) (41) (Fig. 4) and at constant thickness (with various applied breakdown potentials) (Fig. 5), so that concepts inherent in the Uhlig theory are negated.

In another view (42), adsorption of a small number of chloride ions around an iron cation on the surface of a passive film gives rise to the formation of a complex, which is supposed to dissolve more readily than the corresponding aquo complex.⁵ The local thinning, which would be caused, and the associated stronger local anodic field at the site of removal, will cause further cations to diffuse to the surface, where they will complex with halide ions and dissolve.

A reaction order of unity with respect to chloride ion, found here for the depassivation reaction, appears contradictory; the view demands an order equal to the number of Cl^- ions in the complex.

Ion exchange processes.—Penetration of aggressive ions through passive films by ion exchange processes, e.g., Cl^- for lattice O^{2-} (1), or via cation vacancies (44, 45), has also been considered. A reaction order of unity with regard to chloride ion is consistent with this view. The dependence of lattice-breakdown velocity upon electric-field strength (Table IV) is consistent with the fact that diffusion of chloride ions in the lattice will be exponentially aided by a field. The pH dependence seems anomalous to this view.

⁵ The implied greater stability of the chloride over the aquo complex seems dubious (43).

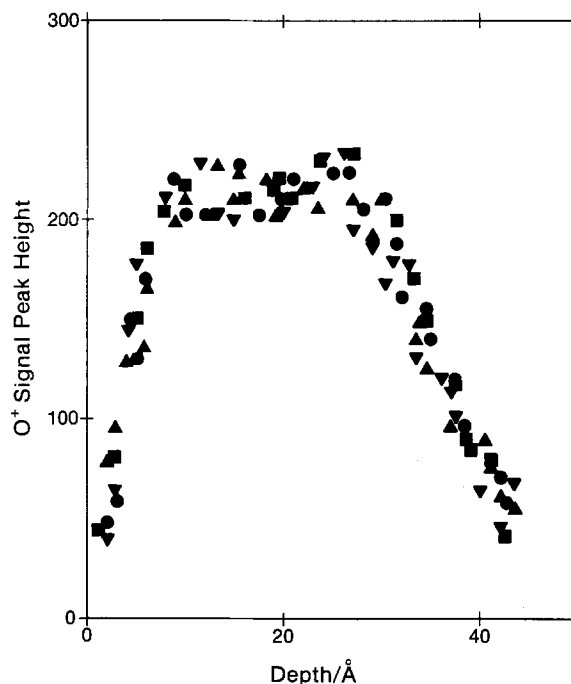


Fig. 12. Variation of O^+ peak height as a function of depth into passive films utilized in obtaining the data presented in Fig. 11.

Pore models.—The basic supposition is that all passive layers contain flaws or are porous in nature (46, 47). Chloride ions pass through the pores and make contact with the iron lattice. Complexes are formed which diffuse upward to the outer film/solution interface. Pits are formed at the bottom of each pore. Continuation of this process would give rise to greatly increased anodic current densities tantamount to film breakdown.

It is to be expected that this model would be dependent directly on the chloride-ion concentration but that it would not be dependent on the concentration of hydrogen ions.

The point-defect model.—Cation diffusion from the metal/film to the film/solution interface results only in dissolution, a consequence of which is the formation of metal holes at the metal/film interface, which normally tend to disappear into the bulk of the metal (22). However, when the cation diffusion rate is greater than the rate of disappearance of holes into the metal bulk, voids form at the metal/film interface. When a void of sufficient size is formed, local collapse of the passive film occurs, which subsequently dissolves faster than at any other region of the film, leading to pit growth.

The effect of chloride ions on this process would be to increase the potential difference across the film and, therefore, enhance Fe^{2+} diffusion to the surface (22). A consequence of this is seen as increased void formation and breakdown.

Table IV. Summary of data from electrochemical kinetic study of passive-film breakdown

Parameter investigated	Kinetic law followed	Rate dependence
Rate of breakdown dependence on chloride ion concentration at constant potential, thickness, and pH	$v = k c_{\text{Cl}^-}$	$\delta \log v / \delta \log c_{\text{Cl}^-} = 1$
Rate of breakdown dependence upon hydrogen-ion concentration at constant potential, thickness, and Cl^- concentration	$v = k c_{\text{H}^+}$	$\delta \log v / \delta \log c_{\text{H}^+} = 0.66$
Rate of breakdown dependence on electric field, E , across the film at constant potential, pH, and Cl^- concentration	$v = k e^{BE}$	$\delta \log v / \delta E = 0.48 \times 10^{-6} \text{ V}^{-1} \text{ cm}$
Rate of breakdown dependence on breakdown potential at constant thickness, pH, and Cl^- concentration	$v = k e^{BV}$	$\delta \log v / \delta \log V = 4.1 \text{ V}^{-1}$

A model of this kind fits the criteria of Table IV rather well except for the pH dependence, which should be zero on this model.

The chemico-mechanical models.—Adsorption of ions, e.g., Cl^- , on passive film surfaces lowers the interfacial tension at the film/solution interfaces, which results in the formation of cracks or flaws when the repulsive forces between the adsorbed ions are sufficiently large (48). Rupture of passive films can also arise from electrostriction pressure effects (49, 50). The effect of film thickness and reduced interfacial tension, as a result of Cl^- adsorption on the surface of a passive film, on increasing the electrostriction pressure above a critical value to bring about breakdown was considered.

This view does not seem consistent with the linearity of the breakdown rate with chloride concentration. Thus, chloride occupancy of the surface and the corresponding reduction of interfacial tension would depend upon an isotherm. At the higher chloride-ion concentration in solution, a nonlinear region of the isotherm would be reached, and, hence, surface tension would no longer be linear with concentration. A linearity of breakdown rate with chloride-ion concentration (as is observed) would not be expected.

The hydrated polymeric oxide models.—After the Cl^- ion adsorbs on the outside of the passive layer and begins to diffuse inward toward the iron base, it meets with the bound water molecules (17, 51), which, in this model, are the essential cementing elements of the stable passive layer (15-18, 20). The chloride ions displace water molecules (or hydroxyl ions), since chloride ion is a stronger Lewis base than the latter (52), and form chloride containing iron complexes, which then diffuse upward and outward to the solution (53).

As chloride ions displace water molecules, the breakdown rate would be proportional to the chloride-ion concentration. The presence of increasing amounts of protons in solution, which are known (54) to adsorb on oxide surfaces, would give rise to a weakening of $\text{M}-\text{O}-\text{M}$ and $\text{M}-\text{O}-\text{H} \cdots \text{O}-\text{M}$ bonds as a result of conversion to $-\text{OH}$ and $-\text{OH}_2$ groups, respectively. With increasing hydrogen-ion concentration, such processes would lead to a weakened passive-film structure. Thus, the observed rate of breakdown dependence on hydrogen-ion concentration is interpretable qualitatively in terms of interaction of protons with surface hydroxyl groups, surface water molecules, and surface lattice oxygen. The exponential dependence of breakdown rate upon field strength (Table IV) would be consistent with the dependence of the chloride-ion diffusion rate upon field.

Thus, the kinetic data presented in this paper is sharply inconsistent with the adsorption-displacement models proposed by Kolotyrkin (37), Uhlig (38), and Hoar (42), flaw or pore models (46, 47), and chemico-mechanical models (48-50), but is not inconsistent with ion-exchange processes (1, 45, 46), point-defect models (22), or the hydrated polymeric oxide model (15-17, 20).

XPS data.—The spectroscopic data (Fig. 6-12) will be utilized in leading to a distinction between the alternative models mentioned above.

The lack of a ferrous-ion signal on deconvoluting the $\text{Fe } 2p_{3/2}$ spectra (cf. Fig. 6) is not surprising, in view of the potential at which the film was grown, namely, 0.3V (NHE). This is 0.2V more positive than the Flade potential for the solution pH used. This view contrasts with the work of Sato *et al.* (55), who found Fe^{2+} ions at less positive potentials (and at transpassive potentials).

For passive films grown at various potentials, the observed $\text{O}_{\text{total}}/\text{Fe}$ ratio of about 2 and $\text{H}_2\text{O}/\text{Fe}$ ratio of ca. 0.5 at a constant depth for each film (cf. Table I)

are consistent with the model in which the passive film is constituted essentially of $\text{Fe}_2\text{O}_3 \cdot \text{H}_2\text{O}$. In respect to the O/Fe ratio, the value is not consistent with the model, which requires 1.5, whereas the value observed is around 0.9. However, if one takes the average of the sum of the O/Fe and OH/Fe ratios, a value of approximately 1.5 is obtained. To rationalize this result, it may be taken that the lattice water is bound by means of hydrogen bonding to the lattice O^{2-} ions, so that the XPS sees a pseudohydroxylated structure. The schematic shown in Fig. 13 shows a type of structure which might be consistent with a value of 1.5.

Table II shows the effect of XPS analyzing depth on various relevant ratios. The $\text{O}_{\text{total}}/\text{Fe}$ and the $\text{H}_2\text{O}/\text{Fe}$ ratios are higher than that required by the polymer model near the surface, but they correspond to that required as one goes into the depth of the film. The extra water near the surface may seem reasonable in terms of water adsorbed in the double layer.

In Table III, the effect of chloride ions on the relevant ratios is tabulated. The $\text{O}_{\text{total}}/\text{Fe}$ ratio is down to 1.5 from 2.0. This corresponds to what would be expected if Cl^- ions removed water in the process of depassivation (13, 23). More strikingly still, the ratio of $\text{H}_2\text{O}/\text{Fe}$ goes down to 0.1 after exposure to Cl^- ions, in marked consistence with the model. The average of the sum of $(\text{OH} + \text{O})/\text{Fe}$ is 1.5, after Cl^- addition, in accordance with a dehydrated structure after depassivation. The fact that the OH/Fe ratios of a film after breakdown (Table III) are similar to those of the nonexposed passive films (Tables I and II) is possibly due to residual hydrogen, in the form of hydroxyl groups, remaining in the passive film, or, more probably, due to corrosion product buildup, e.g., $\text{Fe}(\text{OH})_3$, throughout the layer after breakdown.

Ion scattering spectroscopy data.—This is shown in terms of O/Fe ratios (cf. Fig. 9). After the first 5Å, the ratio for a passive film attains a value of about 2, just what is required of the polymer model without chloride exposure. The O/Fe ratio after chloride addition has the constant value of 1.5, as is needed by the polymer model. The constant values obtained also indicate a single oxide phase throughout the thickness of the passive films.

SIMS data.—With respect to depth, it is seen that the OH^-/O^- ratios (Fig. 10) reach a high of 0.5 near

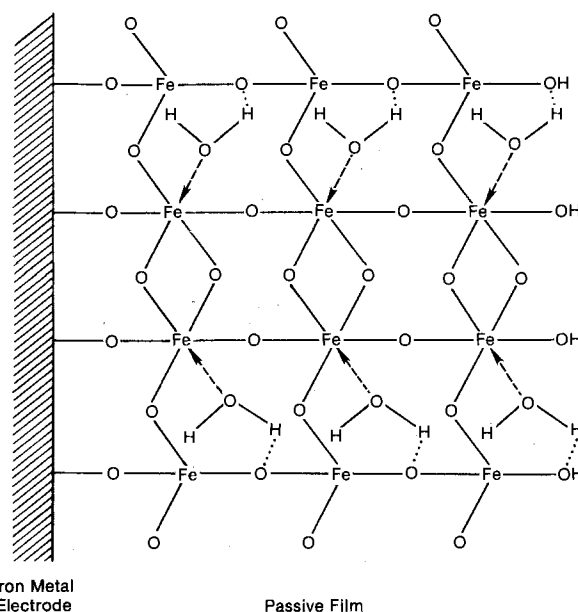


Fig. 13. Schematic representation of the hydrated passive film on iron.

the surface and level off in the bulk of the films at less than 0.1. The modelistic ratio for the polymer structure, e.g., $\text{Fe}_2\text{O}_3 \cdot \text{H}_2\text{O}$, is about 0.3, but SIMS is qualitative, and, therefore, the numerical discrepancy does not seem significant. However, what is significant is the temperature effect. It is seen that, qualitatively, the fall of the OH^-/O^- ratios with increase of temperature is consistent with the removal of water as the key aspect of the effect of temperature on passive films.

The data presented in Fig. 11 establishes chloride penetration into passive films on iron on being exposed to chloride-ion solutions as a result of events leading to breakdown. The requirement of water within passive films to facilitate chloride-ion penetration of the latter has been stressed in the case of the breakdown of passivated titanium alloys (52). With respect to the surprising decrease of chloride ions with time in passive films (cf. Fig. 11), some dissolution of the passive film itself takes place, as is evidenced by the rotating ring-disk work of Heusler and Fischer (53), which showed Fe^{3+} species arising after exposure of passivated iron disks to chloride solution.

From the data presented in Fig. 12, the interfacial passive film region is about 5Å thick, and the region between 10 and 27Å corresponds to films with constant properties. After 27Å, the fall off in the O^+ signal indicates that the interface with the iron substrate is reached. A film thickness of ca. 27-30Å for a growth potential of + 0.3V (NHE) is in excellent agreement with the ellipsometric data of Sato *et al.* (55). It is also possible to conclude from this data (Fig. 12) with regard to the effect of chloride ions that the thickness of passive films clearly remains unchanged for various times of exposure to chloride ions before and after breakdown (41).

It must be pointed out, however, that the data derived from SIMS analyses is qualitative in nature (56, 57). In the SIMS process, complications associated with matrix effects (58, 59), preferential sputtering (60, 61), and knock-on effects (62) in sputtering can arise. Only a general picture, at best, can be deduced from such data.

Conclusion

The electrochemical kinetic evidence excludes adsorption-displacement models (37, 38, 42), pore models (46, 47), and chemico-mechanical models (48-50), but leaves open a choice among ion-exchange processes (1), point-defect models (22), or the hydrated polymeric oxide model (15-17, 20) in the case of the breakdown of passive films on iron in chloride solutions. With respect to the spectroscopic evidence, though none of the data is by itself conclusive, yet, taken together, they point in favor of the polymeric oxide model.

Acknowledgments

Support of this work by the Department of the Interior (DOI) under grant no. 14-34-0001-9446 and to Dr. W. McCoy for discussion is gratefully acknowledged. We greatly appreciate the performance of ISS analyses at Solar Energy Research Institute, Golden, Colorado, and, in particular, acknowledge Dr. A. W. Czanderna, Dr. R. Pitts, and Dr. T. Thomas for this service. We would like to thank Dr. R. P. Frankenthal, AT&T Bell Laboratories, Murray Hill, New Jersey, for pointing out to us the ISS cross-sectional ratio, $\sigma_{\text{Fe}}/\sigma_{\text{O}} = 8.8$. The authors are also grateful to Mrs. Lynn McCartney-Murphy for her editing and typing of this manuscript.

Manuscript submitted July 21, 1983; revised manuscript received Jan. 13, 1984.

Texas A&M University assisted in meeting the publication costs of this article.

REFERENCES

1. J. Kruger, in "Passivity and Its Breakdown on Iron and Iron-Base Alloys," R. W. Staehle and H. Okada, Editors, p. 91, NACE, Houston, Texas (1976).
2. M. Janik-Czachor, *This Journal*, **129**, 513C (1981).
3. N. D. Tomashov and G. P. Chernova, "Passivity and Protection of Metals Against Corrosion," Plenum Press, New York (1967).
4. R. P. Frankenthal and J. Kruger, Editors, "Passivity of Metals," The Electrochemical Society Monograph Series, Princeton, NJ (1978).
5. N. Sato and G. Okamoto, in "Comprehensive Treatise of Electrochemistry," Vol. 4, J. O'M. Bockris, B. E. Conway, E. Yeager, and R. E. White, Editors, pp. 193-245, Plenum Press, New York (1981).
6. M. Nagayama and M. Cohen, *This Journal*, **109**, 781 (1962).
7. G. L. Foley, J. Kruger, and C. J. Bechtold, *ibid.*, **114**, 936 (1967).
8. C. Wagner, *Ber. Bunsenges. Phys. Chem.*, **77**, 1090 (1973).
9. J. W. Schultze, in "Passivity of Metals," R. P. Frankenthal and J. Kruger, Editors, p. 82, The Electrochemical Society Monograph Series, Princeton, NJ (1978).
10. M. Cohen, D. Mitchell, and K. Hashimoto, *This Journal*, **126**, 442 (1979).
11. K. Kuroda, B. D. Cahan, Gh. Nazri, E. Yeager, and T. E. Mitchell, *ibid.*, **129**, 2163 (1982).
12. M. C. Bloom and L. Goldenberg, *Corros. Sci.*, **5**, 623 (1965).
13. H. T. Yolken, J. Kruger, and J. P. Calvert, *ibid.*, **8**, 103 (1968).
14. S. C. Tjong and E. Yeager, *This Journal*, **128**, 2251 (1981).
15. G. Okamoto and T. Shibata, *Corros. Sci.*, **10**, 371 (1970).
16. W. E. O'Grady and J. O'M. Bockris, *Surf. Sci.*, **10**, 249 (1973).
17. G. Okamoto, *Corros. Sci.*, **13**, 471 (1973).
18. R. W. Revie, B. G. Baker, and J. O'M. Bockris, *This Journal*, **122**, 1460 (1975).
19. H. Saito, T. Shibata, and G. Okamoto, *Corros. Sci.*, **19**, 693 (1979).
20. W. E. O'Grady, *This Journal*, **127**, 555 (1980).
21. V. P. Tayal, B. K. Srivastava, and D. P. Khandelwal, *Appl. Spectros. Rev.*, **16**, 43 (1980).
22. C. Y. Chao, L. F. Lin, and D. D. Macdonald, *This Journal*, **128**, 1187, 1194 (1981).
23. O. J. Murphy, J. O'M. Bockris, T. E. Pou, D. L. Cocke, and G. Sparrow, *ibid.*, **129**, 2149 (1982).
24. M. Janik-Czachor, G. C. Wood, and G. E. Thompson, *Br. Corros. J.*, **15**, 154 (1980).
25. D. L. Cocke, P. Nilsson, O. J. Murphy, and J. O'M. Bockris, *Surf. Interface Anal.*, **4**, 94 (1982).
26. J. O'M. Bockris, G. Genshaw, and V. Brusich, *Symp. Faraday Soc.*, **4**, 177 (1970).
27. H. Wroblowa, V. Brusich, and J. O'M. Bockris, *J. Phys. Chem.*, **75**, 2823 (1971).
28. J. R. Ambrose and J. Kruger, in "Proceedings of the Fourth International Congress on Metallic Corrosion," N. E. Hamner, Editor, p. 698, NACE, Houston, Texas (1972).
29. S. N. K. Chaudhari, F. C. Chang, K. L. Chang, and V. Y. Young, *Anal. Chem.*, **53**, 2048 (1981).
30. K. Asami, K. Hashimoto, and S. Shimodaira, *Corros. Sci.*, **17**, 713 (1977).
31. M. A. Wheeler, *Anal. Chem.*, **41**, 146 (1975).
32. R. P. Frankenthal and D. L. Malm, *This Journal*, **123**, 186 (1976).
33. K. Asami, K. Hashimoto, and S. Shimodaira, *Corros. Sci.*, **16**, 387 (1976).
34. K. Asami and K. Hashimoto, *ibid.*, **17**, 559 (1977).
35. K. Asami, K. Hashimoto, and S. Shimodaira, *ibid.*, **16**, 35 (1976).
36. N. S. McIntyre and D. G. Zetaruk, *Anal. Chem.*, **49**, 1521 (1977).
37. Y. M. Kolotyrkin, *This Journal*, **108**, 209 (1961).
38. H. P. Leckie and H. H. Uhlig, *ibid.*, **113**, 1262 (1966); *ibid.*, **116**, 906 (1969).
39. J. O'M. Bockris, D. Drazic, and A. Despic, *Electrochim. Acta*, **4**, 325 (1961).
40. S. Asakura and K. Nobe, *This Journal*, **118**, 13 (1971); **118**, 19 (1971).

41. C. L. McBee and J. Kruger, in "Localized Corrosion," R. W. Staehle, B. F. Brown, and J. Kruger, Editors, p. 252, NACE, Houston, Texas (1974).
42. T. P. Hoar and W. R. Jacob, *Nature*, **216**, 1299 (1967).
43. J. E. Huheey, "Inorganic Chemistry Principles of Structure and Reactivity," p. 363, Harper & Row, New York (1978).
44. M. A. Heine, D. S. Keir, and M. S. Pryor, *This Journal*, **112**, 29 (1965).
45. M. J. Pryor, in "Localized Corrosion," R. W. Staehle, B. F. Brown, and J. Kruger, Editors, p. 2, NACE, Houston, Texas (1974).
46. J. A. Richardson and G. C. Wood, *Corros. Sci.*, **10**, 313 (1970); *This Journal*, **120**, 193 (1973).
47. K. Hashimoto and K. Asami, *Corros. Sci.*, **19**, 251 (1979).
48. T. P. Hoar, *ibid.*, **7**, 355 (1967).
49. N. Sato, *Electrochim. Acta*, **16**, 1683 (1971).
50. N. Sato, *This Journal*, **129**, 255 (1982).
51. O. J. Murphy, J. O'M. Bockris, T. E. Pou, L. L. Tongson, and M. D. Monkowski, *ibid.*, **130**, 1792 (1983).
52. P. Fugassi and E. H. Haney, in "Titanium Science and Technology," R. I. Jaffee and H. M. Burte, Editors, p. 2611, Plenum Press, New York (1973).
53. K. E. Heusler and L. Fischer, *Werkst. Korros.*, **27**, 551, 788 (1976).
54. S. M. Ahmed, in "Oxides and Oxide Films," Vol. 1, A. K. Vijh, Editor, p. 319, Marcel Dekker, New York (1972).
55. N. Sato, K. Kudo, and R. Nishimura, *This Journal*, **123**, 1419 (1976).
56. K. Wittmaack, *Surf. Sci.*, **89**, 668 (1979).
57. H. W. Werner, in "Applied Surface Analysis," T. L. Barr and L. E. Davis, Editors, p. 81, ASTM, Philadelphia, PA (1980).
58. G. R. Sparrow and S. R. Smith, in "Surface Contamination," Vol. 2, K. L. Mittal, Editor, p. 635, Plenum Press, New York (1979).
59. B. C. Lamartine, J. V. Czarnecki, and T. W. Haas, *Appl. Surf. Sci.*, **16**, 207 (1983).
60. D. K. Murti, R. Kelly, Z. L. Liau, and J. M. Poate, *Surf. Sci.*, **81**, 571 (1979).
61. E. Taglauer, *Appl. Surf. Sci.*, **13**, 80 (1982).
62. S. A. Schwarz and C. R. Helms, in "Springer Series in Chemical Physics," Vol. 9, H. A. Storms *et al.*, Editors, p. 15, Springer-Verlag, Berlin (1979).

Mass Transfer Analysis of Electrodeposition Through Polymeric Masks

Edward C. Hume, III*

IBM General Technology Division, Hopewell Junction, New York 12533

William M. Deen and Robert A. Brown

Department of Chemical Engineering, Massachusetts Institute of Technology, Cambridge, Massachusetts 02139

ABSTRACT

A tertiary current-distribution model is developed for predicting two-dimensional shape change during electrodeposition through polymeric masks. The cathode geometry studied consists initially of a parallel array of microscopic, rectangular trenches, the trench bottoms being conductive metal, and the trench walls being formed from insulating mask material. Concentration polarization, activation polarization, and a stagnant diffusion-layer treatment of convective mass transport are incorporated into the model equations. Boundary integral equation methods and Euler-predictor, trapezoid-corrector time integration are used to calculate the deposit-shape history as it depends on geometrical parameters, the level of convection, and the degree of polarization.

Using photolithography techniques and materials developed for the manufacture of integrated circuits, it has become possible to create electroforming molds on a micron- or even submicron-size scale. In the semiconductor industry, these microscopic electroforming molds are termed mask structures, so that the process of electroforming with them is called electroplating through polymeric masks. The individual steps in this process are described elsewhere (1). When metal is electrodeposited through a mask under the proper conditions, the deposit conforms faithfully to the dimensions of the mask pattern. Hence this process can be used to fabricate metal structures that preserve the pattern resolution obtainable with current lithography technology (2).

Romankiw *et al.* (3) have compared this technique to other procedures used to obtain patterned microscopic metal structures. The techniques of wet chemical etching, reactive ion etching, sputter etching, and ion milling cannot etch wholly in one direction. To varying extents they degrade the resolution of the mask pattern by lateral spread of the etching species. Lift-off techniques involving the evaporative deposi-

tion of a metal are more faithful to the mask pattern, but it is only with difficulty that features much taller than they are wide can be obtained. Electroplating through masks does not have this aspect-ratio limitation. In view of its advantages, electroplating through masks is beginning to see use in the fabrication of magnetic bubble memories (2), thin film recording heads (4), masks for x-ray lithography (5), fresnel-zone plates and submicron gratings for x-ray diffraction (6), and interconnection networks for microelectronic circuitry (7).

This work is a theoretical investigation into the mass-transfer aspects of the electrodeposition step of this metallization process. The masked electrode is distinguished by feature sizes that are small relative to the concentration boundary-layer thickness, and by the separated, recessed cathodic areas. We derive a model which emphasizes the importance of diffusional limitations in influencing the evolving shape of the electrodeposit. Other theoretical studies of electrode shape evolution either have not considered tertiary current-distribution effects (8-11), have considered tertiary effects but do not apply to microprofiles (12), or have only considered the limiting current case (13). Among the studies just cited, only Alkire *et al.* (8) have considered a discontinuous electrode geometry.

* Electrochemical Society Active Member.

Key words: current density, moving boundary, boundary element method, electrodeposition.

Theoretical Formulation of the Model Problem

A microprofile is defined as a feature of electrode topography whose size rivals or is smaller than the thickness of the concentration boundary layer adjacent to the electrode surface (14). Microprofiles of an electrode present an uneven surface to mass transfer by diffusion and convection because raised parts of the profile are more accessible to mass transport of the reacting species from the bulk electrolyte. In the process of electrodeposition through masks, the cathode layout is determined photolithographically, so that typical feature sizes are 1-100 μm . The thickness of the concentration boundary layer can be approximated from measurements or calculations of the mass-transfer coefficient. Under conditions of gentle stirring, an effective film thickness of 50-100 μm is typical. Hence deposited features will be within the size domain of the microprofile.

Kardos and Foulke (14) have presented an extensive review of electrodeposition on microprofiles. They present theoretical estimations and experimental results to support the relatively large importance of diffusional and convective effects in determining the distribution of current density on a microprofile. For a microprofile, ohmic influences are negligible as compared to concentration and activation overpotentials in determining the local pattern of current distribution. Neglecting the role of plating bath additives, variation in the current density on a microprofile is primarily due to the variation in mass transfer by diffusion or convection of the depositing species.

We consider the case of a single depositing species in a supporting electrolyte bath. The reduced importance of the potential field in the vicinity of a microprofile electrode feature leads to a simplification of the current-distribution analysis. The portion of the electrode overpotential that is not attributed to changes in the concentration field of the depositing species is assumed constant. The contribution of migration to transport of the minority depositing species is negligible, and solution of the potential field is unnecessary.

The cell geometry considered is illustrated in Fig. 1. At the cathode, where the deposition occurs, a prototypic pattern of evenly spaced, identical rectangular trenches is considered. This might represent a mask for a grating or a group of circuit lines. Since the potential field only influences the deposit growth through its constant contribution to the cathodic overpotential, details of the anode geometry are not considered. Conceptually, the anode is parallel to and located far above the masked-electrode plane.

Convective effects are included in the analysis in an approximate manner by modeling the concentration boundary layer as an equivalent stagnant film adjacent to the electrode surface. The thickness of this film is inversely proportional to the mass-transfer coefficient.

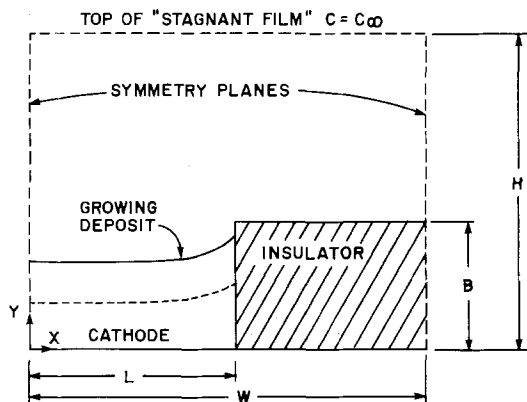


Fig. 1. Two-dimensional model geometry

A thinner film corresponds to greater agitation and a faster rate of deposition. Outside of the stagnant film, all species are assumed to be at their bulk concentrations.

This approximation neglects the effects of the local flow pattern on mass transfer in the trench, a simplification which is valid for small features and moderate rates of agitation. In reality, flow over the top of the trench will induce recirculating motion within the trench. If $\dot{\gamma}$ is the characteristic velocity gradient on the surface of the mask and L is the half-width of the trench, then the characteristic velocity of the recirculating motion is $\sim 0.01\dot{\gamma}L$ (15). Accordingly, the Peclet number that characterizes the importance of this recirculating motion relative to diffusion is $Pe \sim 0.01\dot{\gamma}L^2/D$, where D is the diffusion coefficient of the depositing species. For example, with $L = 10 \mu\text{m}$, $D = 10^{-5} \text{ cm}^2/\text{s}$, and $\dot{\gamma} = 100 \text{ s}^{-1}$ (characteristic of a vigorous, but laminar shear flow), $Pe \sim 0.1$, and diffusion will be dominant.

It is assumed that a single cathodic-deposition reaction occurs and that the current density normal to the cathode surface is described by a concentration-dependent Tafel equation (16)

$$i_{\text{cath}} = -i_0 (C_s/C_\infty)^\beta \exp(-\alpha_c \eta_s F/RT) \quad [1]$$

The surface overpotential, η_s , is found as the sum of the concentration overpotential, η_c , and a constant

$$\eta_s = -\eta_c + \text{const.} \quad [2]$$

$$\eta_c = -(RT/zF) \ln(C_\infty/C_s) \quad [3]$$

As discussed above, the constant corresponds to the level of applied potential, which influences the current level but is much less important than the concentration field in affecting current density uniformity. The expression [3] for the concentration overpotential is valid for a minority reacting species in a supported electrolyte, as shown by Newman (16).

We assume that the bulk concentration and the diffusivity of the reacting species are constant during the deposition and that the rate of shape change of the deposit is slow compared to the establishment of the concentration field. The last assumption is based on an estimated Peclet number for the advance of the cathode of 10^{-5} , using 10^{-6} cm/s as a typical velocity for the cathode surface (7).

With these assumptions the deposit growth is modeled by solving Laplace's equation for the concentration field

$$\nabla^2 C = 0 \quad [4]$$

subject to the following boundary conditions. First, the cathode current density is proportional to the diffusive flux of the reacting species normal to the cathode

$$i_{\text{cath}} = \underline{n} \cdot zFD \nabla C, \text{ cathode surface} \quad [5]$$

Here \underline{n} is the surface normal vector which points into the deposit surface from the electrolyte. Usually the current density is described by Eq. [1]. We are also interested in solving for the limiting current distribution for comparison. For this special case, the concentration of the limiting reactant at the cathode is set to zero

$$C = 0, \text{ cathode surface (limiting current)} \quad [6]$$

The cathode current density also determines the rate of cathode movement. Assuming a current efficiency of unity, and denoting the surface velocity as V_s , the cathode velocity in the direction of the surface normal is given as

$$\underline{n} \cdot V_s = \frac{M}{z\rho F} i_{\text{cath}} \quad [7]$$

The cathode current density is negative, indicating that growth is into the electrolyte. At the bulk solution-

diffusion layer interface, the reacting species is at its bulk concentration

$$C = C_\infty, \quad Y = H \quad [8]$$

Finally, there is no flux across planes of symmetry or insulating surfaces

$$\underline{n} \cdot \nabla C = 0, \quad \text{insulator, symmetry planes} \quad [9]$$

The equation set is recast in nondimensional variables by using the trench half-width as the characteristic length and defining

$$\begin{aligned} x &\equiv X/L & c &\equiv C/C_\infty \\ y &\equiv Y/L & v_s &\equiv V_s t_0/L \\ h &\equiv H/L & \tau &\equiv \frac{DC_\infty Mt}{\rho L^2} \equiv \frac{t}{t_0} \\ \nabla &\equiv L \tilde{\nabla} \end{aligned} \quad [10]$$

Upon substitution, Eq. [1]-[9] become

$$\frac{\partial^2 c}{\partial x^2} + \frac{\partial^2 c}{\partial y^2} = 0 \quad [11]$$

$$c = 1, \quad y = h \quad [12]$$

$$\underline{n} \cdot \nabla c = -\xi c^{\beta + (\alpha_c/z)}, \quad \text{cathode surface} \quad [13]$$

$$c = 0, \quad \text{cathode surface (limiting current)} \quad [14]$$

$$\underline{n} \cdot \nabla c = 0, \quad \text{insulator, symmetry planes} \quad [15]$$

$$\underline{n} \cdot v_s = \underline{n} \cdot \nabla c, \quad \tau > 0 \quad [16]$$

where the polarization parameter, ξ , is defined as

$$\xi \equiv \frac{Li_\infty}{zFDC_\infty} \exp[-\alpha_c F(\eta_s + \eta_c)/RT] \quad [17]$$

This use of the term polarization parameter differs from its use in describing secondary-current distributions. Here it is a measure of diffusional mass-transfer limitations compared to electrode-kinetic limitations.

At any time, Eq. [11]-[15] are used to determine the concentration field along the cathode, which is then used to advance the cathode according to Eq. [16]. Repetition of this process results in a history of the deposit shape and its local growth rate starting from the initial condition of a flat profile.

The model equations are sufficiently complex so that numerical solution is required. Prentice and Tobias (17) have recently surveyed numerical methods for solutions to current-distribution problems. Of the methods used to date for moving boundary electrochemical problems, the finite-element method (FEM) (8, 10, 13) and the finite-difference method (FDM) (9, 11, 12) are the most general. In the present study, we have found it advantageous to use an integral-equation technique appropriate for Laplace's equation, referred to as the boundary element method (BEM). The BEM is the method of choice for this investigation primarily for two reasons. First, it incorporates the isoparametric mapping advantage of the FEM. That is, the basis functions that are used to interpolate the concentration field are also used to interpolate the system boundaries. The ability to conveniently represent curved or deforming boundaries is therefore built into the method. Second, by using an integral-equation form of Laplace's equation, it is possible to reduce a problem from a form involving an entire region to a form involving data only along the region's boundary. This reduction in dimensionality of the problem can result in computational savings, especially if only surface values of dependent variables are sought. Unlike the FDM or the FEM, which generate banded, symmetric matrix problems, the BEM results in a matrix problem that is full and asymmetric. The economy of the technique hinges on the reduction of the problem to only the sys-

tem boundaries and the concomitant savings in the number of node points. Its use has been demonstrated by several authors (18-23).

The mathematical formulation of the BEM is derived from the requirement that weighted residual integrals of Laplace's equation vanish over the domain, Ω

$$\int_{\Omega} w_i \nabla^2 c d\Omega = 0 \quad [18]$$

Here $w_i = w_i(x, y; x_i, y_i)$ is a weighting function that is defined with reference to a node point (x_i, y_i) and an observation point (x, y) . By integrating by parts twice and using the divergence theorem, Eq. [18] is reduced to

$$\begin{aligned} - \int_{\Omega} c \nabla^2 w_i d\Omega + \int_{\Gamma} c (\underline{n} \cdot \nabla w_i) d\Gamma \\ - \int_{\Gamma} w_i (\underline{n} \cdot \nabla c) d\Gamma = 0 \end{aligned} \quad [19]$$

where $d\Gamma$ is used to signify integration over the system boundaries, Γ . The first integral taken over the domain is eliminated by choosing w_i to be a Green's function (fundamental solution) for Laplace's equation. The general, two-dimensional BEM formulation is based on using the free space Green's function

$$w_i(x, y; x_i, y_i) \equiv -\frac{1}{4\pi} \ln[(x - x_i)^2 + (y - y_i)^2] \quad [20]$$

which satisfies $\nabla^2 w_i(x, y; x_i, y_i) + \delta(x - x_i) \delta(y - y_i) = 0$. Here δ is the Dirac delta function. Substituting Eq. [20] into Eq. [19] results in the integral form of Laplace's equation

$$\begin{aligned} \theta_1 c_i - \frac{1}{2\pi} \int_{\Gamma} c (\underline{n} \cdot \nabla \ln(r)) d\Gamma \\ + \frac{1}{2\pi} \int_{\Gamma} \ln(r) (\underline{n} \cdot \nabla c) d\Gamma = 0 \end{aligned} \quad [21]$$

where $r \equiv \sqrt{(x - x_i)^2 + (y - y_i)^2}$, and θ_1 depends on the point, (x_i, y_i) , at which the equation is applied. When (x_i, y_i) is outside the domain, $\theta_1 = 0$; when (x_i, y_i) is inside the domain, $\theta_1 = 1$; and when (x_i, y_i) is on the domain boundary, as is the usual case, θ_1 equals the interior angle of the domain divided by 2π . For the usual smooth surface point, $\theta_1 = 1/2$.

A matrix formulation of the BEM is constructed by choosing a set of nodal points along the boundary. The values of the concentration and its normal derivative, $dc/dn \equiv \underline{n} \cdot \nabla c$, on the boundary are interpolated by a set of one-dimensional finite element basis functions $\{\Phi_i(s)\}$. Each function is written in a local coordinate s that accounts for the orientation of the particular segment of the boundary. The concentration and its derivative on the boundary are expressed as

$$c[x(s), y(s)] = \sum_{i=1}^N \Phi_i(s) c_i \quad [22]$$

$$\frac{dc}{dn}[x(s), y(s)] = \sum_{i=1}^N \Phi_i(s) d_i$$

where the coefficients $\{c_i\}$ and $\{d_i\}$ are determined from the solution of the weighted residual equations. The shape of each segment of the boundary is also interpolated by this finite element basis according to the isoparametric mappings

$$x = \sum_{i=1}^N \Phi_i(s) x_i, \quad y = \sum_{i=1}^N \Phi_i(s) y_i \quad [23]$$

The summations in Eq. [22] and [23] are formally over

all nodes on the boundary; however, for the quadratic basis functions used here, only three terms are nonzero at any location.

Substituting the basis functions and boundary conditions of Eq. [12]-[15] into Eq. [21] results in an algebraic equation for each node point (x_i, y_i)

$$\begin{aligned} \theta_i c_i - \frac{1}{2\pi} \int_{\Gamma_d} \underline{n} \cdot \nabla \ln(r) d\Gamma \\ - \frac{1}{2\pi} \int_{\Gamma_i, \Gamma_c} (\Sigma \Phi_j c_j) [\underline{n} \cdot \nabla \ln(r)] d\Gamma \\ + \frac{1}{2\pi L} \int_{\Gamma_d} [\ln(r)] [\Sigma \Phi_j (dc/dn)_j] d\Gamma \\ - \frac{\xi}{2\pi L} \int_{\Gamma_c} [\ln(r)] (\Sigma \Phi_j c_j)^{\beta + (\alpha_c/z)} d\Gamma = 0 \quad [24] \end{aligned}$$

where r measures the distance from the point (x_i, y_i) . The integrals in Eq. [24] are nonzero only along specified boundary segments, as indicated by the notation. The segment types are Γ_c (cathode), Γ_i (insulator or symmetry plane), and Γ_d (top of diffusion layer).

The boundary conditions for a well-posed problem specify either c , dc/dn , or a relationship between them, at every point along the surface. Therefore, application of Eq. [24] using each node as a base point results in a set of simultaneous equations for the unknown nodal values of $\{c_i\}$ and $\{d_i\}$. The matrix formulation for this problem

$$\underline{A} \underline{X} + \underline{F} + \underline{Q} = 0 \quad [25]$$

is obtained by defining

$$A_{ij} \equiv \begin{cases} \int_{\Gamma_i, \Gamma_c} \Phi_j [\underline{n} \cdot \nabla \ln(r)] d\Gamma - 2\pi \theta_i \delta_{ij}, & \text{for } X_i = c_i \\ -\frac{1}{L} \int_{\Gamma_d} \ln(r) \Phi_j d\Gamma, & \text{for } X_i = d_i \end{cases} \quad [26]$$

$$X_i \equiv \begin{cases} c_i & \text{for } \Gamma_i, \Gamma_c \\ d_i & \text{for } \Gamma_d \end{cases} \quad [27]$$

$$F_i \equiv \int_{\Gamma_d} \underline{n} \cdot \nabla \ln(r) d\Gamma \quad [28]$$

$$Q_i \equiv \frac{\xi}{L} \int_{\Gamma_c} [\ln(r)] (\Sigma \Phi_j c_j)^{\beta + (\alpha_c/z)} d\Gamma \quad [29]$$

In Eq. [25], the vector \underline{Q} has a nonlinear dependence on the unknown cathode-surface concentrations. Solution to the matrix equations is accelerated using Newton-Raphson iteration, where the components of the Jacobian are found from the A matrix and from explicit differentiation of Q_i with respect to c_j .

The integrals needed in the above terms are done numerically using a ten-point Gauss-Legendre quadrature rule, except when the base point coincides with the portion of the boundary being integrated. In this case, integrals with $\ln(r)$ singularities result, and a four-point quadrature formula that accounts for the singularity is applied (24). We have found that better numerical accuracy is obtained if θ_i is calculated by difference, as described by Brebbia (22), rather than directly from the interior angle of the domain at (x_i, y_i) . The derivation summarized here for the Tafel polarization expressed in Eq. [1] also applies to the limiting current case, *mutatis mutandis*.

A Euler-predictor, trapezoid-corrector scheme is used to determine the time evolution of the cathode surface, according to Eq. [16]. The method has second-order accuracy in time, with local error being $O(\Delta t)^3$, and therefore offers a similar level of approximation in time to what quadratic basis functions offer in the

spatial representation. Irrespective of the integration scheme used, the error in the calculated position of the deposit surface must increase with time. This is because the problem is physically and mathematically unstable, as will be discussed in the next section.

The calculation procedure is presented in detail elsewhere (25).

Results and Discussion

A definitive analysis of error in the numerical solutions is not possible since analytical solutions are not available. However, an estimate of the solution error was obtained by analyzing the convergence of the solution as the number of nodal points was increased. Figure 2 shows the root-mean-square (rms) differences in the concentration values at the cathode nodes for solutions obtained with varying total nodes, relative to the solution obtained with 240 total nodes. The observed solution convergence rate was slightly less than quadratic for the calculation with the nonlinear Tafel kinetics and somewhat faster than quadratic for the linear limiting current calculation. There was close agreement between the solutions obtained with a small number of nodes and the solutions obtained using 240 nodes.

A strong indication that the solutions obtained were converging to the correct result was the rapid convergence of the overall mass balance, also shown in Fig. 2. The mass balance was obtained by integrating the net current over the surfaces of the domain. This imbalance was expressed as a fraction of the total current at the cathode boundary. The slopes of the mass-balance curves in Fig. 2 indicate that the mass-balance error was proportional to the node spacing raised to the third power, and was comparable to solution error convergence rates for the Galerkin finite-element method applied to Laplace's equation using biquadratic elements (26).

Figure 3 may be used as a guide to estimate computation expense. In Fig. 3, the CPU time needed on a Honeywell 6180 mainframe computer to obtain a concentration field solution at a single time step is plotted as a function of the number of nodes in the solution. The rate of growth of execution time with the number of nodes suggests that formulation of the integral terms dominated the computation expense,

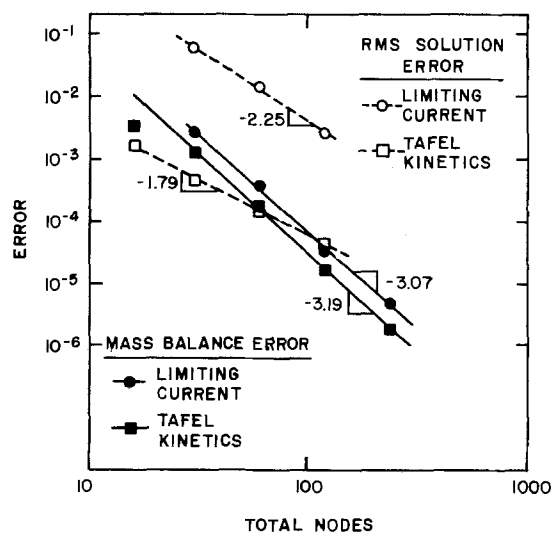


Fig. 2. Convergence of the overall mass balance and of the concentration solution at the cathode surface. Imbalance of the mass flow over the boundaries is expressed as a fraction of the average cathode current. The concentration-field error is the root-mean-square error at the cathode relative to the solution obtained using 240 total nodes. Slopes for the linear regression lines are as indicated.

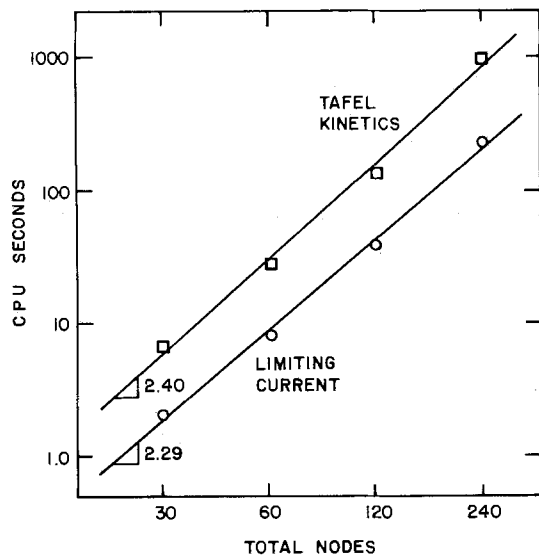


Fig. 3. Computation time as a function of the number of nodes, for solution of the initial concentration field on a Honeywell 6180 mainframe computer.

since this grows with the square of the number of nodes and the expense of solving the simultaneous equation set scales as the third power of the same number. Given a sufficient number of nodes, the cost of solving the simultaneous equation set will eventually dominate the computation time.

For each time step, the concentration field had to be solved for twice, and for the deposition history of a profile, a sequence of time steps was needed. The results were insensitive to the size of the time step that was used. For most problems a simulation composed of five time steps agreed to within a few percent with simulations that used many smaller time steps. When the current distribution was nearly uniform, even fewer time steps were needed. Simulations that involved filling a deeper trench area, or that involved a less uniform current distribution were more sensitive to the time step and were handled accordingly.

Reaction kinetics, trench geometry, and deposition time are each important in determining the deposit-shape history. The kinetic factors include β , α_c , z and ξ . The values of β , α_c , and z were fixed throughout this study at 0.58, 0.36, and 2, respectively. These values are appropriate for a copper acid-sulfate bath and are based on the statistical study of Caban and Chapman (27). The most important kinetic factor is the polarization parameter (Eq. [17]), ξ . It is a measure of mass-transfer limitations compared to electrode-kinetic limitations. Increasing the Tafel exchange current density corresponds to a more active electrode surface and a higher value of ξ . However, larger diffusivity and bulk concentration of the depositing species decrease mass-transfer limitations and thus decrease ξ . ξ also incorporates the effect of applied cell potential on the electrode reaction; for a higher applied cell potential, ξ will grow exponentially. As ξ becomes infinite, the interfacial concentration becomes zero, and limiting current behavior results.

In Fig. 4, the effect of ξ on the average current density across the initial, flat cathode surface is portrayed. The three curves represent different levels of convection, or thicknesses of the diffusion film, h . Two regimes of electrochemical cell behavior are identified. When $\xi < 0.01$, the kinetic resistance of the electrode reaction controls the rate of reaction, and the current is independent of h . The solution of the concentration field in this low current regime was nearly constant at the bulk value, and the current density was nearly uniform over the cathode surface. At high levels of ξ , mass transfer controlled the electrodeposition. The total current was insensitive to the precise level of ξ ;

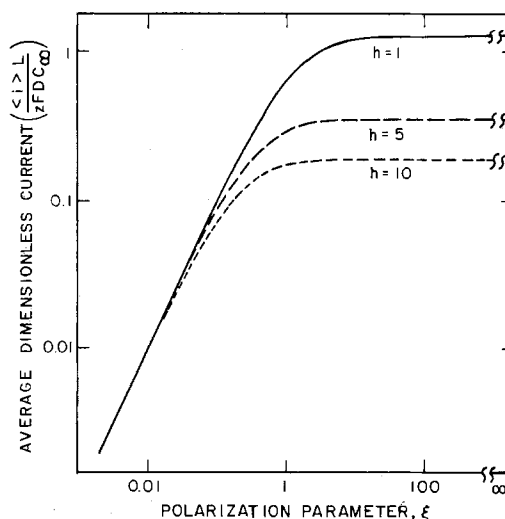


Fig. 4. Average initial current density as a function of the polarization parameter and diffusion film thickness, for $b = 0.2$ and $w = 2$.

the cell geometry and the thickness of the diffusion film determined the deposition pattern. Only at intermediate values of ξ were both mass transfer and kinetics important in setting the deposition history.

In Fig. 4, the polarization scale is broken so that the current values from the limiting current calculations are shown on the extreme right. There was a smooth approach of the nonlinear (finite ξ) solutions to the separately calculated limiting current (infinite ξ) solutions. This confirmed the consistency of the underlying calculations.

The value of ξ had a strong influence also on the thickness variations of the deposit shape. In Fig. 5, deposit profiles are drawn to show the influence of ξ after sufficient current has passed to fill either 35% or 70% of the trench area, denoted by $\Lambda = 0.35$ and $\Lambda = 0.70$. Figure 5 shows only the right half of a symmetrical trench deposit, being consistent with the model cell geometry of Fig. 1. For the cases depicted in Fig. 5, the initial trench depth was 20% of the trench half-width. The pattern of nonuniformity depicted in Fig. 5 is in accord with expectation. The right-hand side of the cathode received additional current from the area above the insulating resist material. The deposit on the left-hand side of the diagram corresponds to

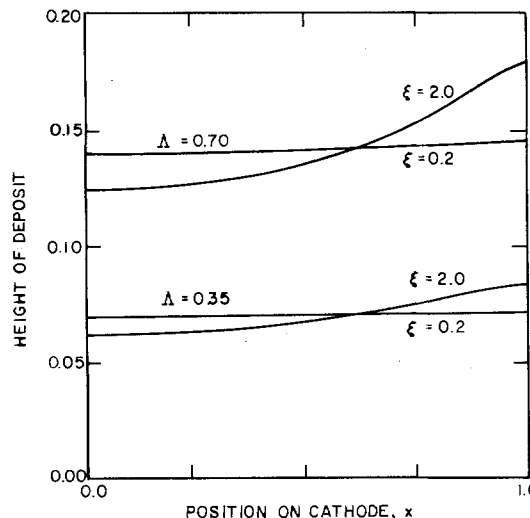


Fig. 5. Deposit profiles for two values of the polarization parameter, when the trench area is 35% or 70% full, and $h = 5$, $b = 0.2$, and $w = 2$.

the center of the trench and only received current from the cell area above it. Therefore, as ξ was increased and mass-transfer effects became more important, the deposit grew fastest next to the trench wall. The profile was flat as it approached the left side of the diagram. This was predictable from the symmetry condition that was imposed for the center of the trench.

Except near the limiting current, the deposit profiles calculated for other conditions were similar to those depicted in Fig. 5. The maximum deposit was at the trench wall, and the minimum was at the trench centerline. A smooth curve connected the two extrema, and the curve became flat as it neared the centerline minimum. As the limiting current was approached and the current distribution became less uniform, it was possible to develop rippled deposit shapes. In this case, the predicted node locations along the cathode surface were alternately above or below some average curve.

This rippling is due to an underlying physical instability of the deposition process. A point on the cathode surface that rises above the neighboring surface receives more current because it is more accessible. The enhanced deposition caused by the increased current accelerates the growth of the nonuniformity. The perturbation analysis of Fedkiw (28), for a primary current distribution, indicates that shorter wavelength, sinusoidal electrode profiles will grow faster than longer wavelength ones. Our numerical simulations are consistent with this result in two ways. First, when rippling occurred, it had the periodicity of the node spacing, which is the lowest ripple wavelength that can be accommodated in the boundary-element approximation. Second, refining the approximation by introducing more nodes caused rippled deposits to appear at lower currents, indicating that the shorter wavelength ripples had a faster rate of growth.

In addition to the node spacing, the formation of ripples was influenced to an unknown extent by the accumulation of calculation error. Fortunately, rippled surfaces were found only near the limiting current, and after a substantial degree of deposit growth. Prentice and Tobias (17) report similar instability phenomena which they suppressed, arbitrarily, by numerically smoothing their node locations. No smoothing procedure was employed in the present study.

An effective means of parameterizing the usual deposit shapes as they evolve in time is to express the difference in deposit thickness as a fraction of the maximum thickness. That is, the index of nonuniformity is defined as

$$\Delta Y \equiv (Y_{\max} - Y_{\min})/Y_{\max} \quad [30]$$

The extent of the deposit is described by Δ (deposit area/trench area). Plots of ΔY vs. Δ are used to illustrate the effects of the various geometric parameters on the nonuniformity of the deposit. With reference to Fig. 1, recall that the following geometric factors are defined as dimensionless ratios to the trench half-width, L ; h , the upper limit of the diffusion film; b , the depth of the trenches before deposition; and w , the overall symmetry width. To elicit the effect of these parameters on the deposit formation, it is convenient to define a standard set of parameter values as a reference case. For this purpose we choose $h = 5$, $b = 0.2$, and $w = 2$.

Figure 6 displays the effect of varying the level of convection, as expressed by h , at three values of the polarization parameter, ξ . The other geometric parameters, b and w , are held at their reference values. For a given value of ξ , increased convection (lower h) resulted in a more uniform deposit. With higher levels of convection, the diffusion film was thinner, mass-transfer limitations were lessened, and current from above the insulating resist mask that caused uneven deposition made a smaller contribution to the total current. It is convenient to regard the area above the

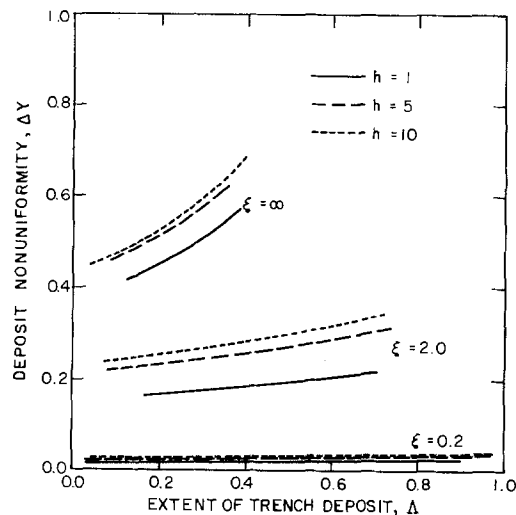


Fig. 6. Effect of diffusion film thickness on the development of deposit nonuniformity, for $b = 0.2$ and $w = 2$.

insulating resist mask as a reservoir of the depositing reactant. As mass-transfer limitations become more pronounced, the additional mass flow from this reservoir promotes uneven deposition.

The curves in Fig. 6 fall into groups showing the importance of ξ in setting the nonuniformity of the deposit. At the low value, $\xi = 0.2$, the influence of the trench geometry was only weakly felt and the profiles varied by only a few percent in thickness. One might suppose that the level of current at $\xi = 0.2$ is only a small fraction of the limiting current, in view of the predicted uniformity of profile shapes. It is surprising to note that for the $h = 5$ intermediate case, the current was at 39% of the limiting current level for the unfilled trench. The corresponding figures for $h = 1$ and 10 are approximately 15% and 57% of the limiting current, respectively. When ξ was 2.0, the current level for the $h = 5$ case was at 91% of the limiting current.

In Fig. 7, the effect of varying the overall symmetry width (w) is shown, with h and b held constant. As already noted, the dimensionless cathode half-width is always defined as 1.0. The results were again consistent with the idea of the insulator area functioning as a reservoir of the depositing reactant. When the overall symmetry width approached the cathode width ($w = 1.1$), there was little mass flow available from the vanishing insulator area. If the insulator area were

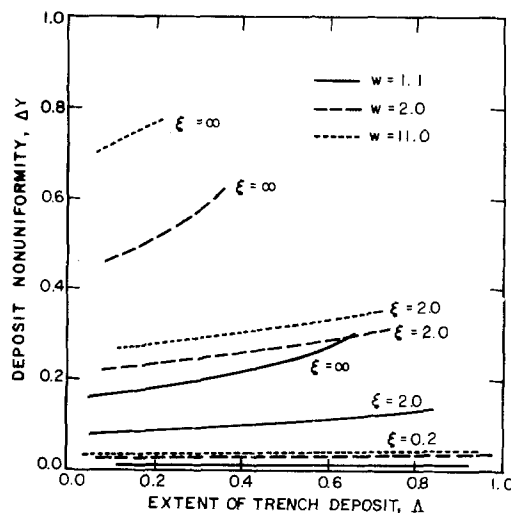


Fig. 7. Effect of the trench spacing on the development of deposit nonuniformity for $h = 5$ and $b = 0.2$.

eliminated, a uniform one-dimensional current distribution would result. With a larger insulating area, mass flow to the cathode edge was augmented.

The effect of varying trench depth (b) is shown in Fig. 8. As the initial trench was made deeper, the current density became more uniform, since the mass flow from above the insulator was able to diffuse laterally to a greater extent before reaching the cathode surface. With progressively greater amounts of deposition, the deeper trenches became shallower and developed current distributions that were similar to those of trenches that were initially shallow. As any given deposit approached the top of the trench area, it encountered the least uniform current distribution of its history. For a deeper trench, this late growth had a smaller effect on the overall uniformity index (ΔY), because ΔY was normalized by the maximum thickness of the deposit.

A word of explanation concerning the end points of the curves in Fig. 6-8 is in order. The calculations assumed that the deposit height along the insulator wall was always below the top of the insulator. Since the profiles can become sharply curved, the deposit can reach the top of the insulator when there is still a large portion of the trench area unfilled. The different curve lengths in Fig. 6-8 were caused by varied times for termination of the calculations, because of this trench-overrun phenomenon.

Summary and Conclusion

Theoretical predictions have been made for deposit shapes resulting from the use of photolithographically prepared mask structures. The analysis emphasizes the effect of concentration variations in determining the pattern of current nonuniformity on the exposed cathode, represented as a set of parallel, microscopic trenches. We have treated the applied cell potential as a constant contribution to the cathodic overpotential. This analysis is appropriate when ohmic influences on the local variation of current density are negligible compared to concentration and activation overpotentials.

The results show a strong dependence of deposit shape on the polarization parameter, ξ , which expresses the importance of mass-transfer limitations relative to electrode-kinetic limitations. For large values of ξ , where mass-transfer limitations predominate, additional mass flow from the area above the inactive masking material to the cathodic surface causes enhanced deposition rates at the electrode edges adjacent to the mask. This edge effect can be diminished by reducing

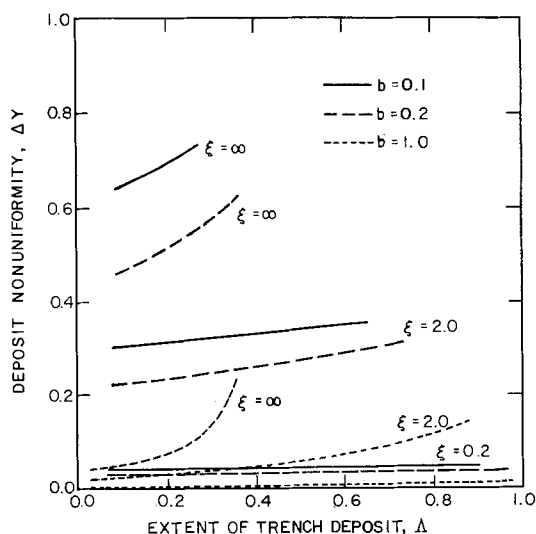


Fig. 8. Effect of the trench depth on the development of deposit nonuniformity, for $h = 5$ and $w = 2$.

the fractional area of the substrate that is masked, by increasing the agitation of the bath, or by increasing the thickness of the mask pattern. Reducing the applied cell potential corresponds to reducing ξ . This diminishes mass-transfer limitations and smooths the current distribution but slows the deposition rate. The tradeoff is such that deposit profiles formed at 40% of the limiting current show only a small degree of height variation, for the geometry considered.

The boundary element method was found to be effective for solving this electrochemical current distribution problem, which involves Laplace's equation. The method is especially useful for irregular and deforming domains because it accommodates them in a regular way using isoparametric mapping. Comparatively few nodal points are needed to obtain an accurate current-distribution solution since the problem is only discretized over the boundary surface of the domain. The present analysis can be readily extended to other mask geometries, including nonperiodic and three-dimensional patterns. For the latter case, the relative compactness of the boundary-element method is particularly advantageous. The boundary-element method is also applicable to the unsteady diffusion equation (19), which would allow our analysis to be extended to pulsed cell potentials. However, the boundary-element method only applies to field equations where a Green's function is available, and does not apply directly to current-distribution problems where diffusion and migration are both important.

Acknowledgments

This work was supported by the Department of Chemical Engineering, Massachusetts Institute of Technology, and by the IBM Corporation through a fellowship awarded to E.C.H.

Manuscript submitted Aug. 5, 1983; revised manuscript received ca. Jan. 31, 1984.

The IBM Corporation assisted in meeting the publication costs of this article.

LIST OF SYMBOLS

A	formulation matrix
b	dimensionless depth of trench before deposition
B	dimensional depth of trench before deposition (m)
c	dimensionless concentration of the depositing species
c_i	dimensionless concentration at the nodal point i
C	concentration of the depositing species (g mol/m^3)
C_s	concentration of the depositing species at the cathode surface (g mol/m^3)
C_∞	bulk concentration of the depositing species (g mol/m^3)
d_i	dimensionless normal concentration gradient, $\underline{n} \cdot \nabla c$, at the nodal point i
D	diffusivity of the depositing species (m^2/s)
F	Faraday's constant (96,500 C/g equiv.)
\underline{F}	vector resulting from matrix formulation
h	dimensionless thickness of the diffusion film
H	dimensional thickness of the diffusion film (m)
i_{cath}	current density normal to the cathode surface (A/m^2)
i_∞	exchange current density corresponding to the bulk concentration of the depositing species (A/m^2)
L	half-width of the cathode trench (m)
M	molecular weight of the depositing species (g/mol)
\underline{n}	normal vector pointing from the electrolyte into the deposit
\underline{Q}	vector of nonlinear contributions
r	radial distance from the point i
R	gas constant (8.32 J/g mol K)
t	time (s)
t_0	characteristic dimensionless time, $\rho L^2 / DC_\infty M$
T	absolute temperature (K)

v_s	dimensionless velocity of the cathode surface
\vec{V}_s	dimensional velocity vector of the cathode surface (m/s)
w	dimensionless symmetry width
w_i	weighting function based at the i th node point
X	dimensional symmetry width (m)
x	horizontal coordinate, dimensionless
x_i	horizontal coordinate of node i
X	dimensional horizontal coordinate (m)
\underline{X}	vector of unknown concentrations and fluxes
y	vertical coordinate, dimensionless
y_i	vertical coordinate of node i
Y	dimensional vertical coordinate (m)
ΔY	deposit nonuniformity index, Eq. [30]
z	valency of the depositing species and the number of electrons in the deposition reaction (g equiv./g mol)

Greek Characters

α_c	cathodic transfer coefficient
β	concentration dependence exponent of the exchange current density
$\dot{\gamma}$	velocity gradient (s^{-1})
Γ	the boundary surface of the model domain
Γ_c	cathode surface contour
Γ_d	diffusion film surface contour
Γ_i	insulator or symmetry plane surface contour
δ	Dirac delta function
δ_{ij}	Kronecker delta function, $\delta_{ij} = 1$ if $i = j$, otherwise $\delta_{ij} = 0$
η_s	surface overpotential
η_c	concentration overpotential
Θ_i	constant related to position of the point i
Λ	trench deposit area/total trench area
ξ	polarization parameter
ρ	density of the cathodic deposit (g/m^3)
τ	dimensionless time
Φ_i	quadratic polynomial basis function centered at nodal point i
Ω	two-dimensional region where Laplace's equation applies
∇	dimensional gradient operator
∇	dimensionless gradient operator

REFERENCES

- L. T. Romankiw, Abstract 462, p. 1165, The Electrochemical Society Extended Abstracts, Vol. 79-2, Los Angeles, CA, Oct. 14-19, 1979.
- E. Spiller, R. Feder, J. Topalian, E. Castellani, L. Romankiw, and M. Heritage, *Solid State Technol.*, **19**, 62 (1976).
- L. T. Romankiw, S. Krongelb, M. C. Blakeslee, A. T. Pfeiffer, and B. J. Stoeber, Abstract 474, p. 1190, The Electrochemical Society Extended Abstracts, Vol. 79-2, Los Angeles, CA, Oct. 14-19, 1979.
- L. T. Romankiw, S. Krongelb, D. A. Thompson, R. Anderson, E. E. Castellani, P. M. McCaffrey, A. T. Pfeiffer, and B. J. Stoeber, Abstract 465, p. 1170, The Electrochemical Society Extended Abstracts, Vol. 79-2, Los Angeles, CA, Oct. 14-19, 1979.
- W. D. Buckley, J. F. Nester, and H. Windischmann, *This Journal*, **128**, 1116 (1981).
- D. C. Shaver, D. C. Flanders, N. M. Ceglie, and H. I. Smith, *J. Vac. Sci. Technol.*, **16**, 1626 (1979).
- A. M. Tuxford and L. T. Romankiw, Abstract 223, p. 551, The Electrochemical Society Extended Abstracts, Vol. 74-2, New York, Oct. 13-17, 1974.
- R. Alkire, T. Bergh, and R. L. Sani, *This Journal*, **125**, 1981 (1978).
- J. Riggs, Ph.D. Thesis, University of California, Berkeley, CA (1977).
- R. Sautebin, H. Froidevaux, and D. Landolt, *This Journal*, **127**, 1096 (1980).
- G. Prentice and C. Tobias, *ibid.*, **129**, 78 (1982).
- G. Prentice and C. Tobias, *ibid.*, **129**, 316 (1982).
- R. Sautebin and D. Landolt, *ibid.*, **129**, 946 (1982).
- O. Kardos and D. G. Foulke, in "Advances in Electrochemistry and Electrochemical Engineering," Vol. 2, P. Delahay and C. Tobias, Editors, Wiley-Interscience, New York (1962).
- N. R. Jackson and B. A. Finlayson, *J. Non-Newtonian Fluid Mech.*, **10**, 55 (1982).
- J. Newman, "Electrochemical Systems," Chap. 20, Prentice Hall, Englewood Cliffs, NJ (1973).
- G. Prentice and C. Tobias, *This Journal*, **129**, 72 (1982).
- J. A. Liggett, *J. Hydraulics Div., ASCE*, **103**, 353 (1977).
- J. A. Liggett and J. R. Salmon, *Int. J. Num. Meth. Eng.*, **17**, 543 (1981).
- R. P. Shaw, *Int. J. Heat Mass Transfer*, **17**, 693 (1974).
- J. C. Lachat and J. O. Watson, *Int. J. Num. Meth. Eng.*, **10**, 991 (1976).
- C. A. Brebbia, "The Boundary Element Method for Engineers," John Wiley, New York (1978).
- C. A. Brebbia and S. Walker, "Boundary Element Techniques in Engineering," Newnes-Butterworths, Boston (1980).
- A. H. Stroud and D. Secrest, "Gaussian Quadrature Formulas," Prentice Hall, New York (1966).
- E. C. Hume III, Ph.D. Thesis, Massachusetts Institute of Technology, Cambridge, MA (1983).
- G. Strang and G. J. Fix, "An Analysis of the Finite Element Method," Prentice Hall, Englewood Cliffs, NJ (1973).
- R. Caban and T. W. Chapman, *This Journal*, **124**, 1371 (1977).
- P. Fedkiw, *ibid.*, **127**, 1304 (1980).

Efficiency of Splitting Water with Semiconducting Photoelectrodes

Michael F. Weber* and Michael J. Dignam*

Department of Chemistry, University of Toronto, Toronto, Ontario, Canada M5S 1A1

ABSTRACT

Solar conversion efficiencies for splitting water with semiconducting photoelectrodes are calculated from basic thermodynamic principles combined with transport properties matching those of the best materials presently available. Assuming no further constraints, we derive in this way "upper limit" estimates of efficiencies achievable via semiconductor photoelectrochemical cells (PEC's), operating with no external electrical bias. Both one- and two-photon configurations are considered. A one-photon PEC is found to have an "upper limit" efficiency of ~7% (AM 1.2 solar energy to chemical potential energy stored as H_2). For two-photon configurations, the "upper limit" for a p-n PEC is ~10%, while for a tandem PEC it is ~18%. The tandem cell configuration is the least sensitive to the choice of materials parameters and transport losses and yields the highest efficiencies. Significant increases in conversion efficiencies result from assuming lower oxygen overpotentials and higher photoelectrode fill factors than have been achieved so far, with the latter being the more important, however.

The free energy required to split water reversibly into H_2 and O_2 gases at room temperature is about

* Electrochemical Society Active Member.

Key words: solar, semiconductor, EMF, energy conversion.

1.23 eV per electron transferred. As a large fraction of solar radiant energy is represented by photons of energy greater than 1.23 eV, one can be misled into believing that reasonable solar energy conversion effi-

ciencies are achievable by splitting water with an electrically unbiased, low bandgap semiconductor. Certain thermodynamic losses, however, are associated with this process. On conversion of photon energy to free energy, there is an entropy price to be paid which is entirely analogous to that associated with heat energy conversion in a Carnot engine (1). In addition to this inevitable loss, there are energy losses associated with bulk and interfacial transport, *i.e.*, with nonradiative recombination, interfacial kinetics (overpotentials), and band bending in the semiconducting element(s) making up the electrode(s). In the following, we show that on choosing transport properties matching those of the best materials presently available, these losses require that a semiconductor of bandgap ~ 2.4 eV be used to achieve the "upper limit" efficiency for conversion of solar energy to chemical free energy as H_2 via an unbiased single-photon photoelectrode. The use of such a large bandgap material for photoconversion excludes most of the solar radiant energy, resulting in a fairly low "upper limit" efficiency. However, much higher efficiencies are possible using multiple photon devices that combine the energies of two or more photons to effect the transfer of a single electron (2).

The aim of this paper is to calculate the "upper limit" efficiencies for splitting water with semiconductor devices. We define the "upper limit" efficiency as that calculated including all essential thermodynamic losses, and transport losses, assuming transport properties matching those of the best materials presently available, but, otherwise, the efficiencies are optimized with no further constraints. Three specific photoelectrochemical cell (PEC) configurations are considered: single bandgap photoelectrode with dark auxiliary electrode, separately illuminated single bandgap photoanode and photocathode, and two-bandgap photoelectrode with dark auxiliary electrode. The first has been widely studied, following Fujishima and Honda's paper on TiO_2 photoanodes (3). In the paper, Fujishima and Honda proposed using a p-type photocathode to replace the Pt auxiliary electrode. This second configuration has since been explored by several workers (4-7). This configuration is commonly called a p-n PEC. Various ways of making devices in the third configuration have been proposed and tested by Wagner and Shay (8), Nozik (9, 10), and Morisaki *et al.* (11). Fan (12) has called this optical series, electrical series arrangement a tandem cell, but has performed calculations for photovoltaic (dry) devices only.

Calculating the thermodynamic maximum open-circuit voltage of a quantum absorbing system is relatively straightforward. Such calculations have been carried out by Ross (13), Ross and Hsiao (14), and Ross and Collins (15). They derived expressions for the maximum power obtainable from such systems as well. Bolton (16) and Bolton and Hall (17) have extended these results to two-photon processes and applied them to several fuel generation reactions and to photobiological systems. The resulting voltage and power maxima are almost twice as high as the efficiencies usually achieved with single-crystal devices. The difference is of course due to the transport losses mentioned above. In photoelectrochemical junctions, a further parameter is involved, namely the flatband potential, V_{FB} , of the semiconductor, as this determines the relative alignment of the semiconductor bands and the redox energy levels of the electrolyte.

We do not make estimates for any particular choice of materials, but have chosen transport properties that are upper limits for any material to date. Bandgap energies, E_g , and V_{FB} , on the other hand, are chosen freely to optimize the conversion efficiencies in the hope that materials can be found with the desired E_g and V_{FB} .

Open-Circuit Potentials

The free energy, $\Delta\mu$, or voltage, $\Delta\mu/e$, available from the electrodes of a PEC cannot be easily measured because ohmic contacts are not made at one or both of the appropriate interfaces. However, the concept is just as useful, and its existence real, as for solid-state devices. The voltage output of a solid-solid junction is derived from the difference between the quasi-Fermi levels for electrons and holes in the space charge region. Similarly, the free energy driving force for an electrochemical junction is determined by the difference between the two quasi-Fermi levels. Gerischer (18-20) has stressed this repeatedly, pointing out that the EMF derived from a doped n-type semiconductor is given by

$$\Delta\mu = kT \ln [(p + \Delta p^*)/p] \quad [1]$$

i.e., by the increase in the hole quasi-Fermi level upon illumination, where p is the hole concentration in the dark, and Δp^* is the change in the hole concentration upon illumination. In the dark, there is only one common Fermi level.

Thus, for a single-photon photoelectrochemical junction to function, bias-free, for the photoelectrolysis of water, it is not a sufficient condition that the energy bandedges of the semiconductor straddle the electrochemical redox energy levels for H^+/H_2 and O_2/OH^- . Rather, the electron and hole quasi-Fermi levels must straddle these electrochemical potential levels, with sufficient extra separation to allow for band bending, overpotentials, and interfacial recombination.¹ In other words, the open-circuit potential, $\Delta\mu_{max}/e$, of a PEC must be considerably larger than 1.23V. The open-circuit potential of either a good single-crystal silicon p-n junction or Schottky barrier is usually ~ 0.6 V, which is considerably less than the bandgap of 1.14 eV. One can then see qualitatively that for a single bandgap device, a bandgap almost twice 1.23 eV will be required for splitting water.

If two semiconductor devices are connected in electrical series, the total $\Delta\mu$ is the sum of the $\Delta\mu$'s for each device. An example of a tandem cell is shown in Fig. 1. In this case, the hole quasi-Fermi level in semiconductor I must lie sufficiently below the O_2/OH^- redox level, and the electron quasi-Fermi level in semiconductor II must lie sufficiently above the H^+/H_2 level, in order to take care of the various free energy losses. It is

¹Redox levels and quasi-Fermi levels are electrochemical potentials for electrons. Net electron flow is forbidden except from higher to lower electrochemical potentials. A common misconception is that net electron flow is determined by the relative alignment of bandedges and redox levels.

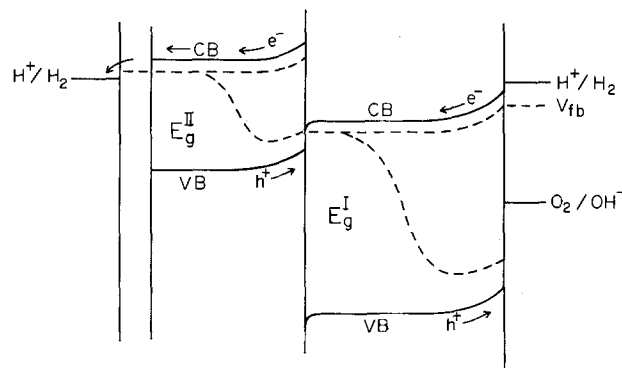


Fig. 1. Example of a tandem PEC which divides the solar spectrum into high and low energy photons by sequential irradiance of materials with different bandgaps. An n-n isotype junction is shown here for simplicity, along with the photoelectrochemical junction, but other configurations are possible. Electrons from the high bandgap material enter the valence band of the low bandgap material where low energy photons boost them to the conduction band.

evident that smaller bandgap materials may be successfully used in this device compared to a single bandgap device.

Calculations and Results

We begin by calculating the open-circuit potential, $\Delta\mu_{\max}/e$, obtainable in a semiconductor of bandgap, E_g , in the presence of both radiative and nonradiative recombination. Using a more general formulation than Gerischer, Ross (13) has developed equations for the electrochemical potential difference, $\Delta\mu$, between the lower and upper electronic states of a two-state system. He assumes that all substrates within each band are in thermal equilibrium, *i.e.*, he assumes the validity of the quasi-Fermi level description. Thus, a common chemical potential characterizes all electrons within a single band (13). A more recent formulation of the problem has been given by Ross and Collins (15), upon which we base our present analysis. Ross has shown (13-15) that the gross rate of radiative recombination per unit area is given by

$$[\exp(\Delta\mu/kT)] \int I_{BB}(\nu) \alpha(\nu) W d\nu \quad [2]$$

where $\alpha(\nu)$ is the absorption coefficient and W is the thickness. The net rate is less because of reabsorption of that radiation in other parts of the absorber, and is given by

$$[\exp(\Delta\mu/kT)] \int I_{BB}(\nu) \epsilon(\nu) d\nu \quad [3]$$

where $\epsilon(\nu)$ is the spectral emissivity and I_{BB} is the photon flux of thermal blackbody radiation over all directions

$$I_{BB} = 8\pi n^2 (\nu/c)^2 [\exp(-h\nu/kT)], \quad h\nu \gg kT \quad [4]$$

where n is the refractive index, and all other symbols are conventional. The rate of nonradiative recombination, treated as simply a constant K times the gross rate of radiative recombination given by [2], is given by

$$K[\exp(\Delta\mu/kT)] \int I_{BB}(\nu) \alpha(\nu) W d\nu \quad [5]$$

At open circuit, all carriers recombine, *i.e.*, the rate of photon absorption, I_g , for $h\nu > E_g$, equals the total rate of carrier recombination. Using this condition, we obtain

$$\Delta\mu_{\max} = kT \ln I_g - kT \ln [\int I_{BB}(\nu) \epsilon(\nu) d\nu + KW \int I_{BB}(\nu) \alpha(\nu) d\nu] \quad [6]$$

Equations [2] and [3] were derived for a simple two-state system. Nonradiative recombination requires mid-gap states however, so Eq. [6] is not generally valid. For example, $\Delta\mu_{\max}$ must vanish in the dark, which is predicted by Eq. [6] only if $K = 0$. The error is small at normal illumination intensities, however, as we demonstrate below. For semiconductors, $KW\alpha(\nu) \gg \epsilon(\nu)$ for all ν so the first integral in Eq. [6] can be neglected.

To evaluate the second integral in Eq. [6], we must assume some general functional form for the absorption coefficient $\alpha(\nu)$. The simplest form, a step-function, was found to give considerable error in predicting open-circuit potentials. The integral is heavily weighted for values of $h\nu$ near the bandgap, so a realistic form for $\alpha(\nu)$ must increase more slowly as a function of ν than does a step function. For simplicity, we assume a simple linear dependence on ν

$$\alpha(E) = a(E/E_g - 1), \quad E = h\nu \geq E_g \quad [7]$$

Neglecting higher order terms in kT/E_g , we obtain

$$\Delta\mu_{\max} = E_g - kT \ln [8\pi(kT)^2 n^2 E_g K a L / c^2 h^3 I_g] \quad [8]$$

in which we have replaced the sample thickness W by L where $L = L_m$, the minority carrier diffusion length, if $L_m \leq W$, while $L = W$ if $L_m \geq W$. This last condition was chosen for the following reason. Ross' derivation of $\Delta\mu$ is based on the assumption that the quasi-Fermi levels for both electrons and holes are constant through-

out the semiconductor. This is essentially an assumption of high carrier mobility or long diffusion length. In considering this approximation, he argues (21) that this case produces the highest efficiency, so its use is consistent with our aim of calculating "upper limit" efficiencies. However, the assumption becomes unphysical in the case of thick solids for which $W \gg L_m$. Parts of the solid that cannot communicate via diffusing carriers, cannot affect the separation of quasi-Fermi levels in the illuminated space charge region. Thus, we have limited the region of importance to the smaller of L_m and W .

Other than the bandgap energy, E_g , all material parameters are contained in the product $n^2 K a L$. To test Eq. [8] for silicon, we use the following values for the parameters: $n = 4$, $L = W = 10^{-1}$ cm, $a = 10^3$ cm $^{-1}$ (obtained from the absorption spectrum), $E_g = 1.14$ eV, and $I_g = 2.5 \times 10^{17}$ cm $^{-2}$ s $^{-1}$ for AM 1.2. For good single-crystal silicon, $K \sim 600$ (15). With these values, Eq. [8] predicts an open-circuit potential for silicon of $\Delta\mu_{\max}/e = 0.60$ V. Good single-crystal silicon junctions give $V_{oc} = 0.57$ V (22). The highest reported value for silicon under AM 1.2 illumination is 0.614 V, obtained with $W = 0.03$ cm (23). For $L = 0.03$ cm, Eq. [8] yields $V_{oc} = 0.63$ V. Upper limit values were expected, as we have not considered other minor losses.

Values of n , K , $\alpha(\nu)$, and L are, of course, not available for as yet undiscovered materials with bandgaps chosen to optimize conversion efficiency. Therefore, in all cases, we assume a value of $n^2 K a L = 3.3 \times 10^6$, which gives a value of 0.57 V for $\Delta\mu_{\max}/e$ in silicon. Direct bandgap materials have higher values of a , but lower values of L_m than silicon, leaving $n^2 K a L$ relatively unchanged. Using this value for $n^2 K a L$, we obtain for CuInSe $_2$, with $E_g = 1.0$ eV, a $\Delta\mu_{\max}/e$ of 0.44 V. This agrees quite well with the best observed value of 0.437 V (24). For amorphous silicon, with $E_g = 1.7$ eV, we obtain 1.1 V, which is higher than the best values of 0.9 V. Amorphous silicon undoubtedly has a much higher recombination rate than the value of K used here. Therefore, the values of $\Delta\mu_{\max}$ which we calculate with Eq. [8] can be considered as "upper limit" estimates.

Extracting carriers, *i.e.*, drawing a current to produce power, always reduces $\Delta\mu$. The reduction of $\Delta\mu$ from $\Delta\mu_{\max}$ is due to band bending and interfacial recombination losses. "Lower limits" for these losses are introduced here by taking experimental I-V curves from the best single-crystal devices. For different bandgaps, these response curves are scaled to the appropriate open-circuit voltage and saturation current densities, as described below. The value of $\Delta\mu$ at any operating current can be obtained from these response curves.

For the two-photon tandem cell, we assume that a large bandgap material can be joined physically to a smaller bandgap photovoltaic device such that the latter can provide an electrical bias for the former, for example, by a transparent ohmic contact. The photovoltaic could be a p-n junction, Schottky barrier, etc. We further assume that all radiation not absorbed in the larger bandgap semiconductor can reach the lower bandgap material.

The remaining parameters and transport characteristics necessary to calculate "upper limit" efficiencies are introduced as follows: (i) All photovoltaic I-V curves for different bandgap materials are modeled after that for a silicon single-crystal p-n junction with $V_{oc} = 0.57$ V, $I_{sc} = 37$ mA/cm 2 , $ff = 0.82$ (22). The open-circuit potential for a given bandgap is the $\Delta\mu_{\max}/e$ calculated from Eq. [8], I_s is determined from the AM 1.2 spectrum and the absorption spectrum given below in (iii). (ii) All photoelectrode curves are modeled after that for O $_2$ evolution on one of our thin films of TiO $_2$ at 300 nm. The curve shape is essentially the same as that for single-crystal TiO $_2$ at

330 nm (25) and very close to that for H₂ evolution on Pt-overcoated InP as reported by Heller *et al.* (26). Photocurrent onset is assumed to occur at V_{FB}. An optimum value of V_{FB} is chosen, as described in (iv). (iii) To calculate the saturation current density I_s, the quantum efficiency of all materials was assumed to increase linearly from zero at hν = E_g to unity at hν > E_g + 0.2 eV. This approximation is similar to the one made for α(ν) in calculating Δμ_{max}, but is more convenient for this application. (iv) Various values of flatband are found for different materials, so we have assumed no restrictions here. For an n-type photoanode of bandgap E_g, we choose V_{FB} so that, with AM 1.2 illumination driving a potential of Δμ_{max}/e, the quasi-Fermi level for holes is just far enough below the O₂/OH⁻ level to include the overpotential for oxygen evolution, η_{O₂}. This is illustrated in Fig. 2. For the case shown there, the bandgap is not wide enough for splitting water unless an additional electrical bias is supplied.

Although the overpotential changes with current density, it does so roughly logarithmically, and so is essentially constant over the limited range of current density of interest for these calculations.

Thus, the optimum value for V_{FB} is one that causes the hole quasi-Fermi level to be η_{O₂} below the O₂/OH⁻ level during AM 1.2 illumination. For more cathodic values of V_{FB}, hole transfer is impeded kinetically. However, sufficient band bending will increase the hole concentration at the interface, thus lowering the hole quasi-Fermi level and allowing the reaction to proceed. This could change the I-V response curve and, depending on the kinetics, conceivably either raise, or lower, the efficiency for different cases. For values of V_{FB} more anodic than optimum, a higher bias voltage is required. This latter case is always deleterious and leads to lower efficiencies. (v) For the initial set of calculations, the overpotentials were set at 400 mV for O₂ evolution and 50 mV for H₂ evolution. On most semiconductors and metals, the value of η_{O₂} is much higher than 400 mV at 10 mA/cm². This choice of overpotential, and the possibility of catalytic overcoatings, is discussed later in detail. (vi) All calculations use the AM 1.2, 100 mW/cm² summer total solar spectrum impinging on a flat plate collector as measured by Boer (27). The radiation incident on the photovoltaic ele-

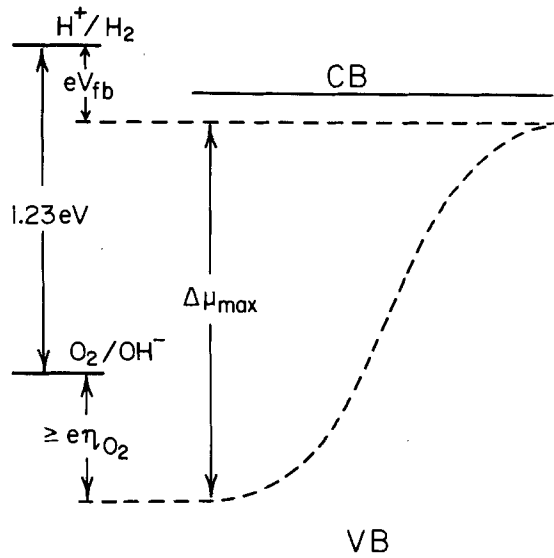


Fig. 2. Energy diagram for the photoanode-electrolyte interface. The hole quasi-Fermi level must lie at least η_{O₂} below the O₂/OH⁻ level to overcome the kinetic hindrance of charge transfer (overpotential).

ment is corrected for the light absorbed in the wide bandgap photoanode. No corrections are made for reflection losses. (vii) All efficiencies are determined by a graphical method for each type of PEC configuration.

Tandem PEC

Efficiencies are determined by combining the I-V photoresponse curves of the photovoltaic and the photoanodic junctions. The photovoltaic junction acts to bias the photoanodic junction to the required potential anodic of V_{FB}. The operating current, i_{op}, is given uniquely by the intersection of the photovoltaic I-V curve with that of the photoanode, as this quantity must be equal at both interfaces. Examples are given in Fig. 3 and 4 for different photoanode and photovoltaic bandgaps. Any excess carriers recombine as they normally would for individual operation of either device at the operating current density. The efficiency of

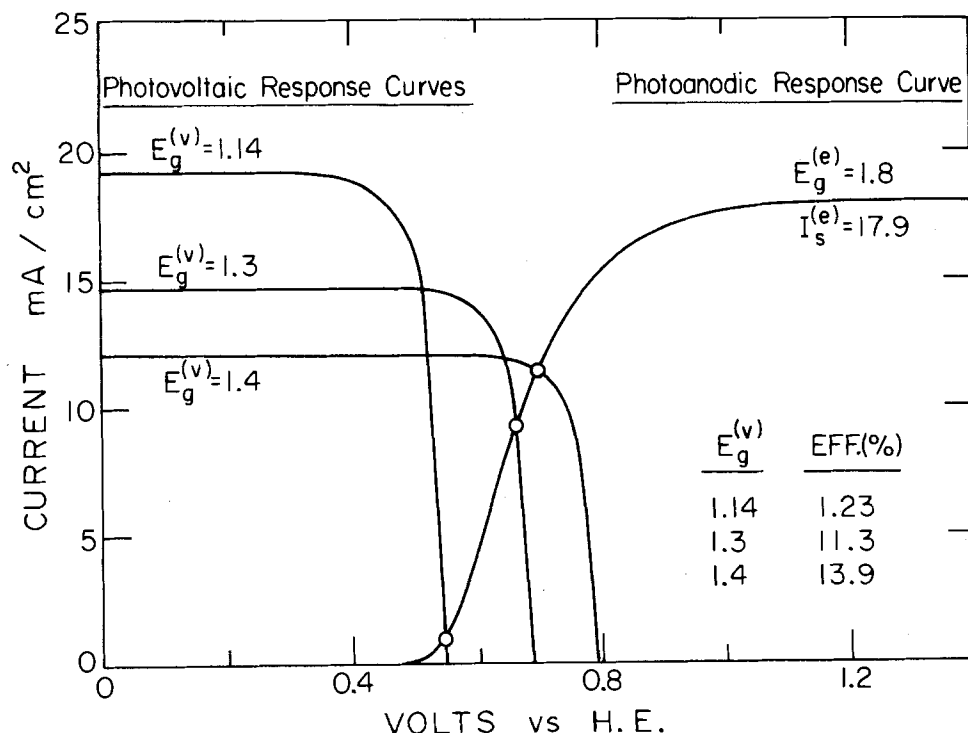


Fig. 3. Current-voltage curves for three cases of a 1.8 eV bandgap photoanode on top of a low bandgap photovoltaic. In each case, the operating current is given by the intersection of the two curves (circled position).

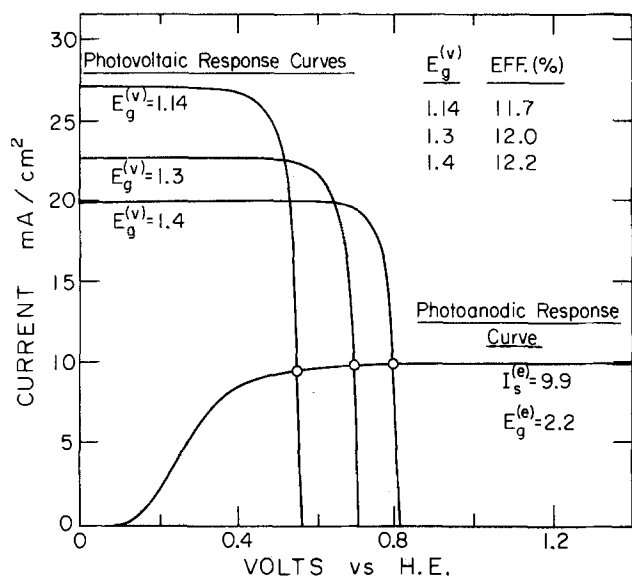


Fig. 4. Current-voltage curves for three cases of a 2.2 eV bandgap photoanode on top of a low bandgap photovoltaic. In each case, the different combinations of bandgaps result in nearly equal efficiencies.

conversion of incident solar radiant energy to stored chemical potential energy (as H_2) is given by i_{op} (mA/cm^2) $\times 1.23V/100$ (mW/cm^2). Obviously, lower bandgap materials give higher photocurrent densities, but the tradeoff is the larger bias voltage needed. In Fig. 3, we see that a bandgap combination of 1.14 (silicon) and 1.8 eV gives nearly equal saturation currents in each, but that the silicon cannot provide the high bias needed to operate a 1.8 eV bandgap photoanode. Recall that the minimum photocurrent onset potential is determined by the requirement that the quasi-Fermi level for holes lie 0.4 eV below the O_2/OH^- level. In addition, we have allowed for the 50 mV of overpotential for H_2 evolution at the metal cathode by shifting the photoanode I-V curves by that amount. The efficiency is markedly improved if a 2.0 eV bandgap photoanode is employed. With still higher bandgaps, such as 2.2 eV, shown in Fig. 4, the efficiency begins to drop because of the smaller saturation photocurrent. The two photojunctions are in electrical as well as optical series, so the efficiency can become limited by the saturation current of either one of them.

Curves of efficiency vs. photoanode bandgap are displayed in Fig. 5 for three photovoltaic bandgaps. The efficiency curve for a photovoltaic bandgap of 1.5 eV is not shown here, but is comparable to that for 1.3 eV. Efficiency contours as a function of both bandgaps are displayed in Fig. 6. The overall maximum efficiency occurs for a photovoltaic bandgap ~ 1.4 eV and a photoanode bandgap ~ 1.95 eV, and is 16.7%. This efficiency is for solar to chemical potential energy as H_2 gas. Photovoltaic solar cells driving an electrolysis cell at 1.68V ($\sim 75\%$ efficiency) must operate at 22.3% to match this performance.

Although the above results were obtained for photoanodes, the same results apply to photocathodes on photovoltaics. With the latter, however, the overpotential for O_2 evolution is easier to reduce, since it involves the dark electrode, and hence could be substantially less than 400 mV. This is discussed in detail later.

p-n PEC

The assumptions and I-V curve shapes used for the tandem PEC are applied here as well. The optimum flatband potential for the photoanode is chosen in the same way. For the photocathode, the flatband is chosen so that the quasi-Fermi level for electrons lies 50 mV

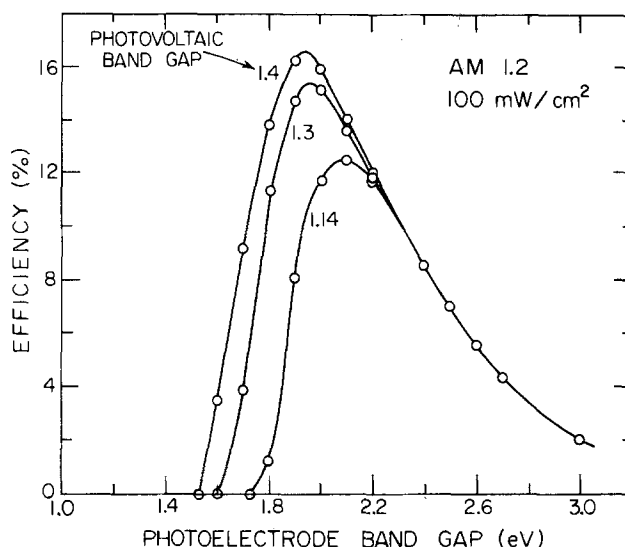


Fig. 5. Conversion efficiency of a tandem PEC as a function of both first (photoanode) and second (photovoltaic) absorber bandgap energies. Smooth curves were drawn through the circled points, which were obtained from Fig. 3 and 4 and others (not shown).

above the H^+/H_2 level during AM 1.2 illumination. Photocurrent onset is assumed to occur at flatband in each case. The operating current of the cell is determined graphically by plotting the absolute values of anodic and cathodic I-V curves and noting the intersecting point. In calculating the efficiency, the operating current must be halved to obtain the current per cm^2 under illumination. Again the trade-off of saturation currents and onset potentials produces a maximum in the efficiency. Examples are shown in Fig. 7 and 8. Efficiency vs. bandgap is plotted in Fig. 9, with a peak efficiency of 9.8% occurring for a bandgap of 1.75 eV. The analysis is for both equal bandgaps and areas for the photoanode and photocathode, but the maximum efficiency does not increase for unequal bandgaps on keeping the I-V curves of the same form.

Single-Photon PEC

Finally, the single-photon photoelectrolysis cell is considered. We graphically analyze the case of a photoanode and dark cathode. The analysis is the same for

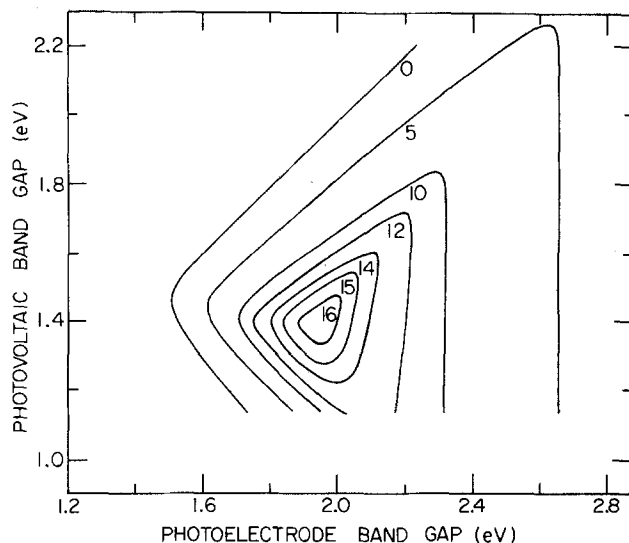


Fig. 6. Conversion efficiency contours (in %) for a tandem PEC as a function of first and second absorber bandgaps. These contours were generated directly from the information in Fig. 5 and similar graphs (not shown).

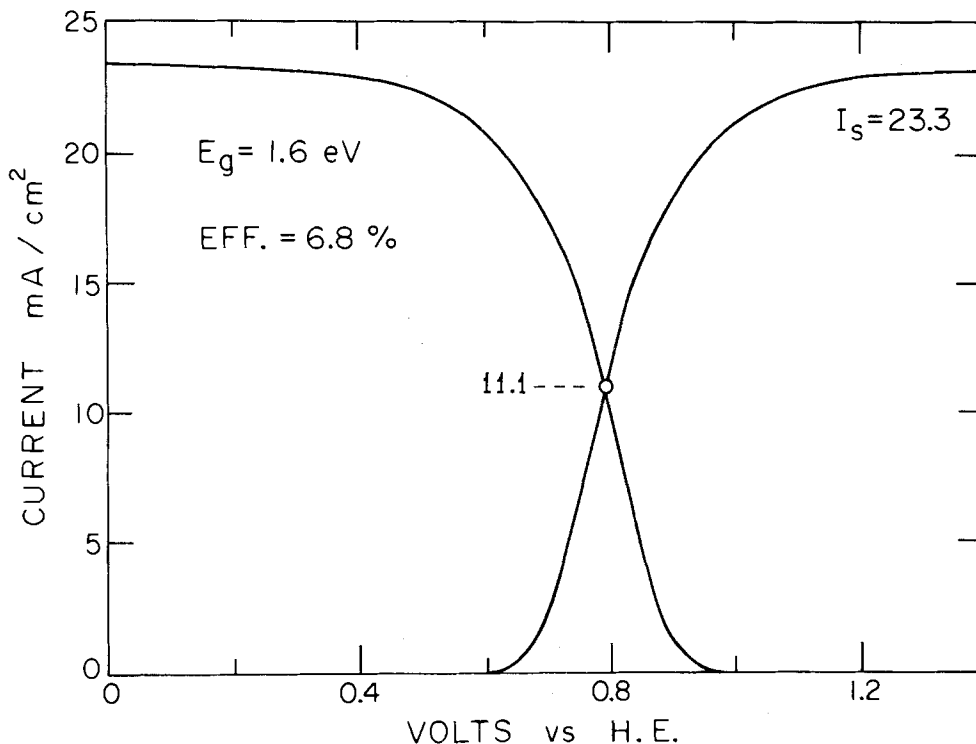


Fig. 7. Current-voltage curves for a p-n PEC with photoanode and photocathode having the same area, and each with a bandgap of 1.6 eV. As for the tandem PEC, the operating current is given by the intersection point.

a photocathode and dark anode if the same overpotentials are assumed. In either case, the operating current density for bias-free operation corresponds to setting $V = 0$ (Fig. 10). As for the tandem PEC, we have included the 50 mV for H_2 evolution by shifting the I-V response curve 50 mV in the anodic direction. The maximum efficiency obtained is seen to be $\sim 4.5\%$ at $E_g \cong 2.6$ eV. For AM 2, or AM 1.2 under hazy atmospheric conditions, the scattering of higher energy photons causes this to drop to about 3%.

Discussion

Considerable attention was given to the choice of oxygen overpotential used in these calculations. Different materials exhibit a wide range of overpotentials, with temperature and electrolyte composition being

important factors. Increasing the temperature lowers the overpotential, but doing so also lowers the voltage obtainable from any semiconductor. The latter is a well-known result, and is born out by Eq. [8]. Running a cell at $100^\circ C$ vs. $25^\circ C$ increases the recombination voltage losses by some 150 mV. This is roughly equal to the resulting decrease in overpotential. Thus, for photoanodes we considered only room temperature values for η_{O_2} , and only for smooth electrodes. Some roughening of photoelectrodes may be possible, but is limited because of the need to maintain a proper internal space charge field for efficient electron-hole separation.

Apart from the simple factor of real surface area, many O_2 evolution catalysts exhibit an abrupt increase in Tafel slope at higher current densities. For example,

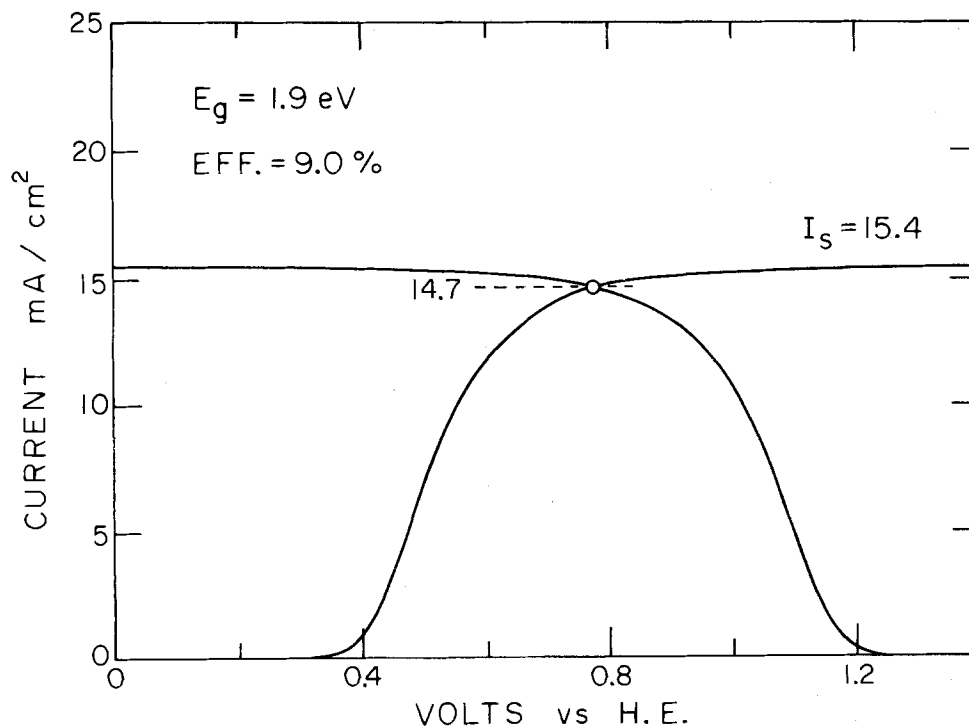
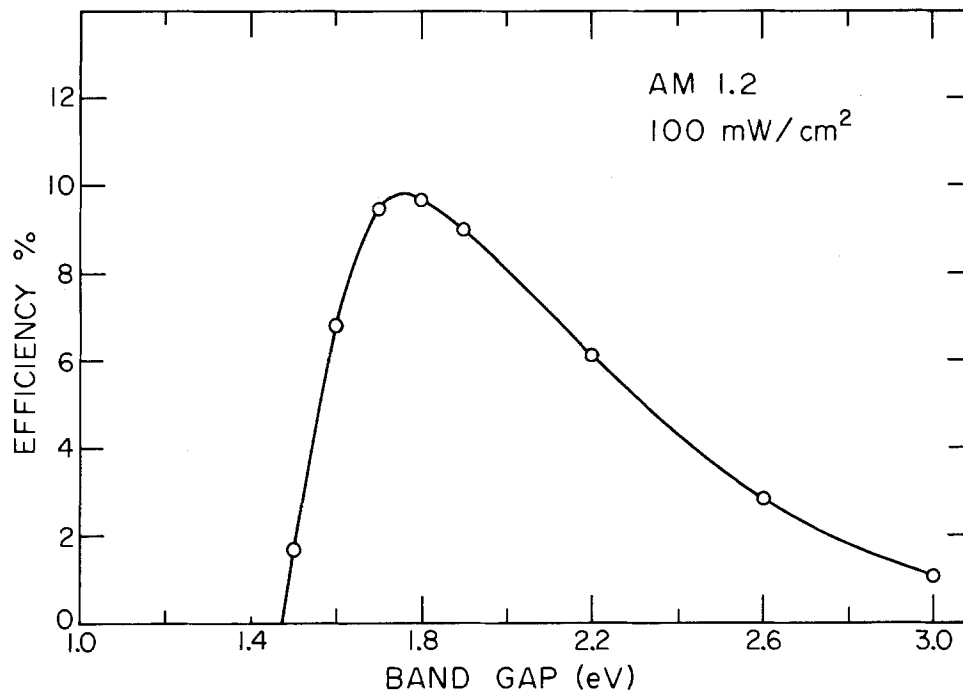


Fig. 8. As for Fig. 7, but for a bandgap of 1.9 eV.

Fig. 9. Conversion efficiency of a p-n PEC as a function of the common bandgap energy.



a Pt-black electrode can evolve oxygen at 10 mA/cm², 75°C, 3M KOH, with $\eta_{O_2} = 180$ mV (28); but the overpotential increases to 700 mV at 25°C in 1M KOH on smooth Pt at the same current density (29). For high surface area NiCo₂O₄, η_{O_2} equals 200 mV at 75°C, 10 mA/cm², in 3M KOH (27), but the overpotential increases to 440 mV at 25°C in 1.2M KOH (30).

A new catalyst of lanthanum nickelate (31) exhibits an η_{O_2} of only 270 mV at 25°C, 10 mA/cm², for a sintered powder electrode (surface area not reported). Very low overpotentials of ~ 100 mV at 12.5 mA/cm² have recently been reported, after long term tests, for lead ruthenate catalysts (28). These results were obtained at 75°C, in 3M KOH with heavy catalyst loading of high surface areas. Adding ~ 100 mV for room temperature operation, assuming no change in Tafel slope, and another 100 mV for low surface area electrodes, η_{O_2} is about 300 mV at 10 mA/cm².

Unless the photoanode material itself is highly catalytic, some catalyst such as one of the above must be

deposited on the electrode in a thin film or island configuration without blocking either the incident radiation or interfacial hole transfer, and without increasing surface recombination or delaying the photocurrent onset. As this would be difficult to achieve, we have chosen the value of 400 mV as the lower limit for the oxygen evolution overpotential on a photoanode. For PEC's with a dark anode at 25°C, a value of 200 mV seems entirely possible and will be selected for this case. Repeating the analysis for $\eta_{O_2} = 200$ mV, a maximum efficiency of 18.2% occurs for a photovoltaic bandgap of 1.3 eV and photoelectrode bandgap of 1.87 eV. This is only an increase of 1.5% in efficiency over that for the case of $\eta_{O_2} = 400$ mV.

A p-n PEC of course uses no dark electrode, but repeating the analysis anyway for $\eta_{O_2} = 200$ mV gives a maximum efficiency of 11.5%, with a common bandgap of 1.67 eV. The gain of 1.7% is about the same as for the tandem cell. With a single-photon PEC, the efficiency increases from 4.5 to 7.1% at a bandgap of 2.4 eV, a gain of 2.6%. Since the voltage at which the cells store energy is fixed at 1.23V, the increase in efficiency is due only to the increased rate of photon collection made possible by using materials with smaller bandgaps.

A major source of efficiency loss lies in the slow rate of rise of photocurrent with voltage for photoelectrodes. In the terminology of photovoltaics, photoelectrodes have low fill factors. This high transport loss enters twice for the p-n PEC. If we again use $\eta_{O_2} = 400$ mV, but instead replace the normal photoelectrode I-V curve with one modeled after the photovoltaic curves used above, considerable gains in the maximum efficiency result. The p-n PEC maximum efficiency changes the most; from 9.8 to 14.7% at $E_g = 1.55$ eV. The maximum single-photon cell efficiency increases from 4.5 to 8.4% at $E_g = 2.4$ eV, and the tandem PEC from 16.7 to 20.3% with $E_g^I = 1.85$ eV and $E_g^{II} = 1.25$ eV. These gains are considerably larger than those attained by a 200 mV reduction in overpotential.

For the case of high fill factor and 200 mV oxygen evolution overpotential, the maximum efficiency of 22% occurs for a tandem cell with $E_g^I = 1.8$ eV and $E_g^{II} = 1.15$ eV. A p-n PEC peaks at 16.6% for $E_g = 1.4$ eV, and the single-photon cell peaks at 11.6%, at $E_g = 2.2$ eV. In all cases, we have used the optimum value of the flatband potential, as described above. From Fig. 2, one can see that an anodic shift in the

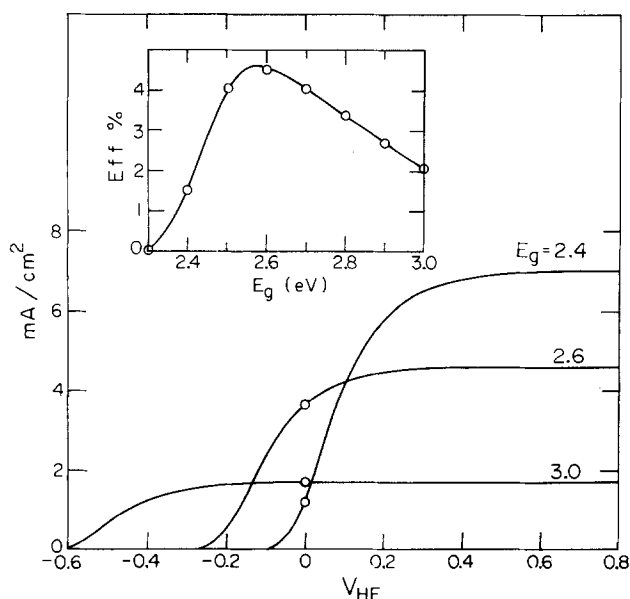


Fig. 10. Current-voltage curves for a single-photon photoanode for various bandgaps, with inset figure for conversion efficiency vs. bandgap.

Table I. Conversion efficiencies (solar to stored H₂) in percentages as a function of the oxygen overpotential and fill factor* for the solid-electrolyte junction

System	Low fill factor		High fill factor	
	$\eta_{O_2}/400$ mV	200 mV	400 mV	200 mV
Single-photon cell	4.5	<u>7.1</u>	8.4	11.6
p-n PEC	<u>9.8</u>	11.5	14.7	16.6
Tandem PEC	16.7	<u>18.2</u>	20.3	22

* By fill factor we mean the rate of increase of photocurrent from flatband. "Low" refers to values observed for TiO₂ (25) and InP (26). "High" refers to values observed for silicon p-n photocells (22).

flatband can be treated as equivalent to a higher oxygen overpotential. All the cases just described will be treated in more detail in a forthcoming publication (32), where the analysis is extended to include three- and four-photon devices.

Summary and Conclusions

The various cases and resulting efficiencies are summarized in Table I. The underlined values are the "upper limit" efficiencies based on transport properties matching those of the best materials presently available, and hence, represent current realistic goals for these systems. If one includes reflection losses, the efficiency values must be reduced by up to 10% of their value, as the AM 1.2 total, not direct, solar spectrum was used for the calculations. We have not included resistance losses in the electrolyte and separator membrane, but these would be important in an engineering analysis.

We draw three conclusions that are probably of greater significance than the actual calculated efficiencies. First, improving the fill factor would be potentially more rewarding than reducing the oxygen overpotential. Secondly, the single-photon cell efficiency is most sensitive to changes in transport loss factors such as fill factor and overpotential. The p-n PEC efficiencies are less sensitive to these loss factors, followed by the tandem cell efficiencies which are the least sensitive. Thirdly, for equal loss factors, the tandem cell would yield the highest efficiency, followed by the p-n PEC, then by the single-photon device.

Acknowledgment

The authors wish to acknowledge the financial support of the Natural Sciences and Engineering Research Council of Canada.

Manuscript submitted Dec. 29, 1982; revised manuscript received Dec. 12, 1984.

REFERENCES

1. R. T. Ross, *J. Chem. Phys.*, **45**, 1 (1966).
2. J. R. Bolton, A. F. Haught, and R. T. Ross, in "Photochemical Conversion and Storage of Solar Energy," J. S. Connolly, Editor, Chap. 11, Academic Press, New York (1981).
3. A. Fujishima and K. Honda, *Nature*, **238**, 37 (1972).
4. H. Yoneyama, H. Sakamoto, and H. Tamura, *Electrochim. Acta*, **20**, 341 (1975).
5. A. J. Nozik, *Appl. Phys. Lett.*, **29**, 152 (1976).
6. J. McCann and J. O'M. Bockris, *Nature*, **266**, 610 (1977).
7. C. Levy-Clement, A. Heller, W. A. Bonner, and B. A. Parkinson, *This Journal*, **129**, 1701 (1982).
8. S. Wagner and J. L. Shay, in "Semiconductor Liquid-Junction Solar Cells," A. Heller, Editor, p. 231, The Electrochemical Society Softbound Proceedings Series, Princeton, NJ (1977).
9. A. J. Nozik, Second International Conference on the Photochemical Conversion and Storage of Solar Energy, Cambridge, England (1978).
10. A. J. Nozik, *Faraday Discuss. Chem. Soc.*, **70**, 7 (1980).
11. H. Morisaki, T. Watanabe, M. Iwase, and K. Yazawa, *Appl. Phys. Lett.*, **29**, 338 (1976).
12. J. C. C. Fan, B.-Y. Tsaur, and B. J. Palm, 16th IEEE Photovoltaics Special Conference, p. 692, San Diego, CA (1982).
13. R. T. Ross, *J. Chem. Phys.*, **46**, 4590 (1967).
14. R. T. Ross and T.-L. Hsiao, *J. Appl. Phys.*, **48**, 4783 (1977).
15. R. T. Ross and J. M. Collins, *J. Appl. Phys.*, **51**, 4504 (1980).
16. J. R. Bolton, *Science*, **202**, 705 (Nov. 17, 1978).
17. J. R. Bolton and D. O. Hall, *Ann. Rev. Energy*, **4**, 353 (1979).
18. H. Gerischer, *This Journal*, **113**, 1174 (1966).
19. H. Gerischer, in "Solar Power and Fuels," J. R. Bolton, Editor, Chap. 4, p. 77, Academic Press, New York (1977).
20. H. Gerischer, in "Semiconductor Liquid-Junction Solar Cells," A. Heller, Editor, p. 1, The Electrochemical Society Softbound Proceedings Series, Princeton, NJ (1977).
21. R. T. Ross, *Appl. Phys. Lett.*, **35**, 707 (1979).
22. R. J. Stirn, in "Low Cost Polycrystalline Silicon Solar Cells," p. 333, NSF, Dallas (1976).
23. R. T. Young, G. A. van der Leeden, R. L. Sandstrom, R. F. Wood, and R. D. Westbrook, *Appl. Phys. Lett.*, **43**, 666 (1983).
24. R. Hsiao, W. S. Chen, and R. A. Mickelsen, "Polycrystalline Thin Film Review," p. 55, SERI, Golden, CO (1983).
25. R. Potter, *Faraday Discuss. Chem. Soc.*, **70**, 126 (1980).
26. A. Heller, *Acc. Chem. Res.*, **14**, 154 (1981).
27. K. W. Boer, *Sol. Energy*, **19**, 525 (1977).
28. H. S. Horowitz, J. M. Longo, and H. H. Horowitz, *This Journal*, **130**, 1851 (1983).
29. A. Damjanovic, A. Dey, and J. O'M. Bockris, *Electrochim. Acta*, **11**, 791 (1966).
30. P. Rasiyah and A. C. C. Tseung, Abstract 530, p. 1305, The Electrochemical Society Extended Abstracts, Vol. 81-1, Minneapolis, MN, May 10-15, 1981.
31. T. Otagawa and J. O'M. Bockris, *This Journal*, **129**, 2391 (1982).
32. M. F. Weber and M. J. Dignam, in "Proceedings of the 5th World Hydrogen Energy Conference," Toronto, Ont., Canada, July (1984).

Thin Film Photoelectrochemistry: Iron Oxide

K. Itoh[†] and J. O'M. Bockris*

Department of Chemistry, Texas A&M University, College Station, Texas 77843

ABSTRACT

Fe₂O₃ photoelectrodes offer advantages in respect to simplicity. However, at normal thickness, the efficiency is low. In this paper, the consequences of reducing the thickness of the oxide below that of the space-charge region is investigated. Allowing the light transmitted through the first electrode to be incident on further semitransparent electrodes should give a gain over a normal (ca. 1 μm thick) electrode of ca. three times for ten successive electrodes. The theory is experimentally tested. It is quantitatively in agreement with experiment for values of the hole-solution transfer-rate constant (for water oxidation) of $6 \times 10^{-2} \text{ cm s}^{-1} \text{ M}^{-1}$ and a model in which 1/4 of any change in applied p.d. occurs across the Helmholtz layer.

It is well known that Fe₂O₃ has interesting properties as a photoanode (1-8). However, the efficiency is poor [corresponding to a maximum photocurrent of a few hundred μA · cm⁻² at one sun (6-8)], because of a low absorption coefficient (α) as well as low carrier mobilities (μ) (2, 4). Thus, much light is absorbed outside the space-charge region, and, consequently, many of the corresponding holes are not subject to an effective internal field in transport to the surface. However, if an Fe₂O₃ layer were made with a thickness comparable to or less than that of the space-charge region in a thick electrode, and if the substrate on which Fe₂O₃ is deposited were transparent, light transmitted through the electrode could be utilized by a second electrode. Repetition of this principle should allow most of the incident light to be absorbed within the space-charge regions. Thus, the effect of the disadvantages of Fe₂O₃ could be reduced.

A simple model is used to quantify this concept. It is shown that ten layers of films each with thickness 600Å deposited on SnO₂- and/or In₂O₃-coated glass substrates increase the photocurrent compared with that of a thick electrode by a factor of up to 4.

Photocurrent Electrode-Thickness Dependence for a Thin Film

The photocurrent-potential (*i_p*-*V*) characteristics of thin films is different from that of thick electrodes in a potential range where the space-charge region of thickness $W = (2\epsilon\epsilon_0 V_s / eN_d)^{1/2}$, exceeds the film thickness *d*, where ε represents the dielectric constant of Fe₂O₃, ε₀ is that of vacuum, *V_s* is the Schottky barrier height, *e* is electronic charge, and *N_d* is the donor density (9).

In the potential region in question, the electric field in the Fe₂O₃, $\vec{E} (= -dV/dx)$, is approximately $-V_s/d \equiv -E$, since the SnO₂ substrate employed here is highly conductive (cf. Fig. 1). Then the diffusion equation for holes in the thin layer of Fe₂O₃ can be expressed as follows

$$D \frac{d^2 p}{dx^2} + \mu E \frac{dp}{dx} - p/\tau + I_0 e^{-\alpha x} = 0 \quad [1]$$

Here, *D* represents the diffusion coefficient of holes, *p* is the hole density, μ is the hole mobility, τ the hole lifetime, α the absorption coefficient, *I₀* the light intensity, and *x* the distance from the electrode-solution interface. The lifetime of holes in the film was assumed to be independent of position, i.e., recombination centers (rather than electron-hole collisions) in the film bulk are regarded as the predominant source of loss, since the electron density in a positively biased film is several orders of magnitude smaller than that in the bulk.

These assumptions are reasonable for the situation in which α and μ are small and the film is thin. Otherwise, surface recombination may be the dominating mode of loss.

One boundary condition can be taken for the Fe₂O₃-SnO₂ interface, where a particularly high concentration of surface traps can be taken to imply (cf. Fig. 1)

$$p(d) = 0 \quad [2]$$

Also, at the boundary of Fe₂O₃ with the solution

$$D \left(\frac{dp}{dx} \right)_{x=0} + E p(0) = k_{vH} p(0) = \frac{i_p}{e} \quad [3]$$

Here, *k_{vH}* represents the rate constant of the interfacial reaction between holes in Fe₂O₃ and reactants in solution; the p.d. in the Helmholtz layer is *V_H*.

The solution of Eq. [1], [2], and [3] is given by Eq. [4].

$$p(x) = A \exp(-ax) + B \exp(bx) + C \exp(-\alpha x) \quad [4]$$

Here

$$A = \frac{C[(k_{vH} - aD)e^{-\alpha d} - (k_{vH} + aD - v)e^{bd}]}{(k_{vH} + bD)e^{bd} - (k_{vH} - aD)e^{-\alpha d}} \quad [5]$$

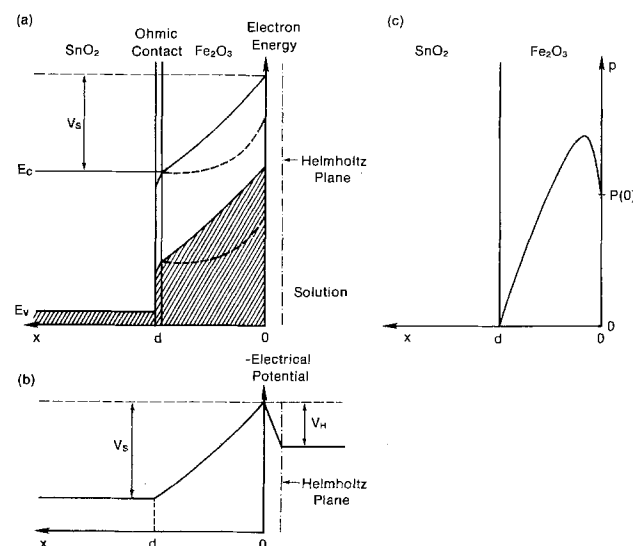


Fig. 1. a: Schematic energy-level diagram for an Fe₂O₃ film-SnO₂ junction. The thickness of the ohmic contact region is regarded as negligible in the text. The dotted line represents a Schottky barrier with a width smaller than *d*. *V_s* is the potential difference (p.d.) across an Fe₂O₃ film. b: Schematic diagram of electrical potential in the electrode and in solution. *V_H* is the Helmholtz layer p.d. c: Schematic diagram of the distribution of hole concentration in the film; *p(d) = 0* was chosen as one boundary condition.

* Electrochemical Society Active Member.

[†] On leave from Department of Chemistry, Faculty of Engineering, University of Tokyo, Tokyo, Japan.

$$B = \frac{C[(k_{vH} + \alpha D - v)e^{-\alpha d} - (k_{vH} + bD)e^{-\alpha d}]}{(k_{vH} + bD)e^{bd} - (k_{vH} - \alpha D)e^{-\alpha d}} \quad [6]$$

$$C = \frac{\alpha I_0}{1/\tau + \alpha v - D\alpha^2} \quad [7]$$

$$a = (\sqrt{v^2 + 4D/\tau} + v)/2D \quad [8]$$

$$b = (\sqrt{v^2 + 4D/\tau} - v)/2D \quad [9]$$

$$v = \mu E(V_s/d) \quad [10]$$

The photocurrent i_p is given by Eq. [3] as $i_p = ek_{vH}p(0)$.

$$i_p = \frac{ek_{vH}CD[a(e^{bd} - e^{-\alpha d}) - b(e^{-\alpha d} - e^{-\alpha d}) - \alpha(e^{bd} - e^{-\alpha d})]}{(k_{vH} + bD)e^{bd} - (k_{vH} - \alpha D)e^{-\alpha d}} \quad [11]$$

It is noteworthy that there are two distinct potential differences at the interface: one, V_s , is the Schottky barrier height; the other, V_H , is the Helmholtz potential difference (p.d.) in solution. In the absence of a high concentration of surface states, the value of V_H is constant with change of external potential. However, with a high concentration of ionized surface states (e.g., 10^{15} cm^{-2} , 1/10 ionized), V_H varies with total applied p.d. (10). The value of V_H at the flatband condition (i.e., $V_s = 0$), V_H^0 , is not necessarily 0 (10). Therefore, the total p.d. V measured from the flatband potential (V_{FB}) can be represented as $V = V_s + (V_H - V_H^0) = V_s + \Delta V_H$. The ratio $V_s/V = \gamma$ is regarded in this paper as a parameter.

Equation [11] is plotted in Fig. 2. It shows i_p as a function of the total potential, V at a thickness of 800Å, with varying γ .

k_{vH} can be represented phenomenologically as (11)

$$k_{vH} = ck_0 \exp[\beta \Delta V_H / (k_B T / e)] \quad [12]$$

where k_B represents Boltzmann's constant, T is the temperature, c is the concentration of reducing species in solution, and k_0 and β ($\beta \sim 0.5$) are parameters.

Deduction of Photocurrent of a Stack of Thin Film Electrodes

The advantage of thin film for electrode materials having properties similar to those of Fe_2O_3 is an enhanced internal field, but the disadvantage is reduced absorption of light, compared with a thick film, respectively. Consequently, increased current density can only be obtained by stacking several electrodes together.

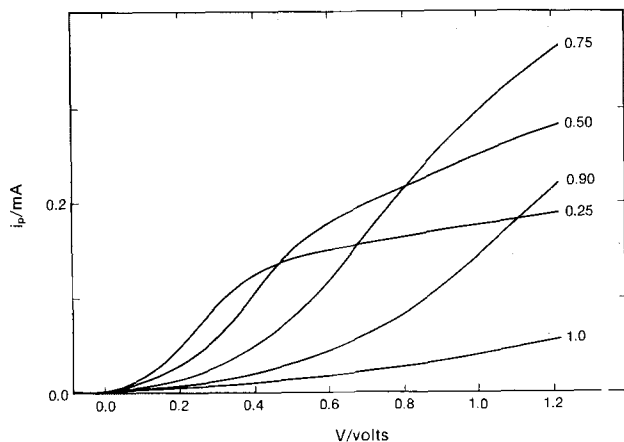


Fig. 2. Calculated i_p - V curves based on Eq. [11] for different values of γ . Parameters used were $d = 800\text{Å}$, $\mu = 0.01 \text{ cm}^2 \text{ V}^{-1} \text{ s}^{-1}$, $\alpha = 10^4 \text{ cm}^{-1}$, $ck_0 = 10 \text{ cm s}^{-1}$, $\beta = 0.5$, $\tau = 2 \times 10^{-9} \text{ s}$, and $I_0 = 10^{17} \text{ s}^{-1} \text{ cm}^{-2}$.

Here we consider a stack of film electrodes: each electrode is in contact with solution; light from the same source passes through each electrode (cf. Fig. 3). Let the transmittance of an Fe_2O_3 film and that of the conducting substrate be f and g , respectively. Then the light intensity after the m th electrode, I_m , can be represented as follows

$$I_m = fgI_{m-1} = \dots = (fg)^m I_0 \quad [13]$$

The amount of light absorbed by the m th layer equals $(1-f)I_{m-1}$. Hence, the light absorbed by n Fe_2O_3 layers, A_n , is

$$\begin{aligned} A_n &= \sum_{m=1}^n (1-f) I_{m-1} \\ &= I_0(1-f) \sum_{m=1}^n (fg)^{m-1} \\ &= I_0(1-f)(1-f^n g^n)/(1-fg) \end{aligned} \quad [14]$$

Therefore, light absorbed by Fe_2O_3 , increases by a factor of $A_n/A_1 = (1-f^n g^n)/(1-fg) \equiv L_n$. The total photocurrent i_T is obtained as¹

$$i_T = L_n i_p \quad [15]$$

where i_p is given by Eq. [11].

Figure 4 shows the i_T - d relations for a stacked system with varying values of the number of electrodes, n , namely $n = 1, 4, 10, 20$, and ∞ . Here, b was taken as 0.90, a typical value for SnO_2 - and/or In_2O_3 -coated glass (13). The values of μ , τ , α , and V were taken as $0.01 \text{ cm}^2 \text{ V}^{-1} \text{ s}^{-1}$, $2 \times 10^{-9} \text{ s}$, 10^4 cm^{-1} (2), and 1V, respectively; μ was assumed to be the same as the electron mobility (4), considering that both the conduction band and valence band of Fe_2O_3 are d bands (12). The value of τ is known from the literature (9) on other materials to have the order of magnitude 10^{-9} - 10^{-10} s; it was varied here between 0.1 and 100×10^{-9} s.

It is clear from Fig. 4 and 5 that i_p can be increased by stacking electrodes having an optimal value of thickness. For the conditions chosen for the plots of Fig. 4 and 5, the optimum thickness is 500Å, which value is smaller than the space-charge region width W , which is about 1500Å in a thick electrode at $V_s = 1\text{V}$.

¹ Thus, the value of i_p refers to a fixed potential controlled by an external potentiostat. It represents the current density for the first electrode. The current across the second electrode will be this same i_p (as the potential is held the same at each electrode), multiplied by a fraction representing the light incident upon it, compared with that incident upon the first. The currents for each electrode add. The expression [15] represents this reasoning for n electrodes.

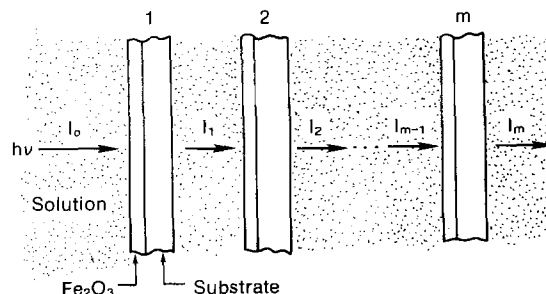


Fig. 3. Schematic diagram of stacked film electrodes, Light intensity after the m th electrode is I_m .

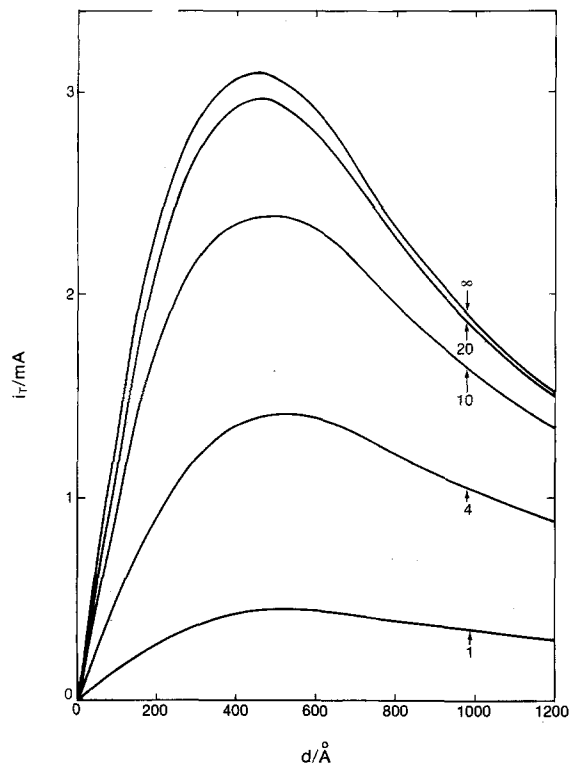


Fig. 4. Dependence of i_T on d for a stack of film electrodes. The numbers of electrodes are shown in the figure, namely, 1, 4, 10, 20, and ∞ . Parameters were taken, $b = 0.90$, $V = 1V$, $\tau = 2.7 \times 10^{-9}s$, $\gamma = 0.75$, $ck_0 = 30 \text{ cm s}^{-1}$, $\beta = 0.5$, and $I_0 = 10^{17} \text{ s}^{-1} \text{ cm}^{-2}$.

Experimental

Fe_2O_3 thin films were deposited onto conducting glass made by coating the glass with SnO_2 and/or In_2O_3 by the use of a spray pyrolysis technique (13). A 0.1M FeCl_3 ethanolic or iso-propyl alcoholic solution containing 0.1M HCl was sprayed onto heated conducting glass substrates (350°C) in air by the use of an all-

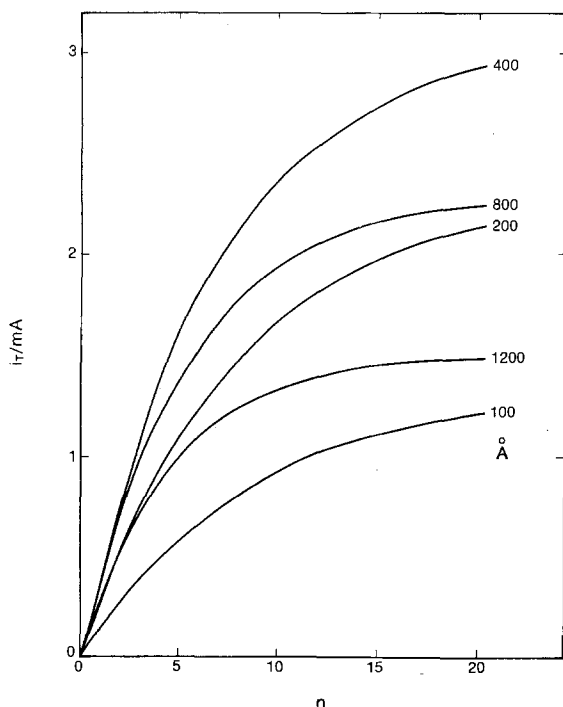


Fig. 5. Dependence of i_T on the number of stacked electrodes for different film thickness, d . Parameters chosen are the same as those in Fig. 4.

glass atomizer and N_2 as carrier gas. The substrate temperature was monitored by the use of a thermocouple. The thickness of the films were followed by observing interference colors. Approximately 40\AA of Fe_2O_3 film was deposited by one spraying (i.e., 0.5 cm^3 of the FeCl_3 solution); 1-2 min intervals were taken between each spraying to avoid excess cooling of the substrate.

Figure 6 shows the construction of the thin film Fe_2O_3 electrode. The electrode area exposed to the solution was 1.0 cm^2 ; the other part of the Fe_2O_3 film was covered with silicone sealant, and an ohmic contact was taken at the SnO_2 or In_2O_3 surface.

The electrochemical measurements were performed in a glass cell with a quartz window, and the usual equipment: a potentiostat and a programmer. A 200W Hg-Xe lamp and a solar simulator were used as light sources.

Results

Films deposited on glass as well as onto conducting glass were uniform and hard, having a mirror-like surface. They were transparent and brown in color up to 40 sprayings ($\sim 1600\text{\AA}$). Sheet resistances of Fe_2O_3 films formed on glass substrates were high ($> 20 \text{ M}\Omega$).

Figure 7 shows typical experimental i_p - V curves obtained on 10 and 15 times sprayed films in alkaline solution. No difference in behavior was observed upon change from SnO_2 to In_2O_3 as substrate. Fe_2O_3 deposited onto TiO_2 made from heated Ti foil was also tested, but it gave less photoactivity than did Fe_2O_3 on conducting glass. The 15 times-sprayed film exhibited good photoactivity (curve a in Fig. 7). The photocurrent was stable, and no corrosion was observed. Illumination from the back side of the electrode gave consistent photocurrents with front illumination, except in the wavelength region less than 350 nm where light absorption due to In_2O_3 and SnO_2 occurs. Photocurrents from In_2O_3 and SnO_2 themselves were negligible.

The 10 times-sprayed film showed less photoactivity (curve b Fig. 7) for water oxidation than the 15 times-sprayed film. However, after the addition of 0.5% of H_2O_2 to the electrolyte (5), the 10 times-sprayed films showed a photoactivity as high as for the 15 times-sprayed one [curves c and d in Fig. 7].

The dependence of the photocurrent on the film thickness (i_p - d curve) was examined in the presence and absence of H_2O_2 in the electrolyte. The i_p - d curve for H_2O_2 oxidation (curve b in Fig. 8) was similar to the theoretical curve (Fig. 4), while that for water oxidation showed some quantitative discrepancy (curve a in Fig. 8) in that no current was observed for the first five sprayings, and the i_p number of sprayings, relation tended to an asymptote.

By stacking electrodes, one behind the other, each electrode being in contact with solution, the photocurrent increased, as expected. Figure 9 shows the photocurrent dependence on the number of 15 times-sprayed electrodes for water oxidation (a similar result was

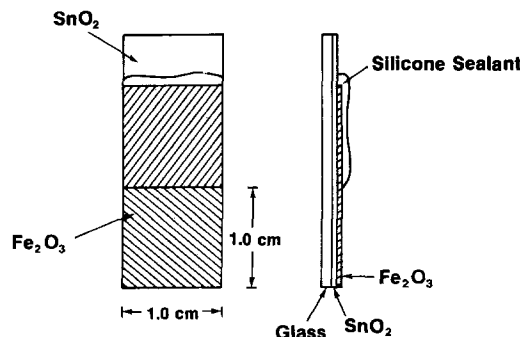


Fig. 6. Construction of a thin film Fe_2O_3 electrode

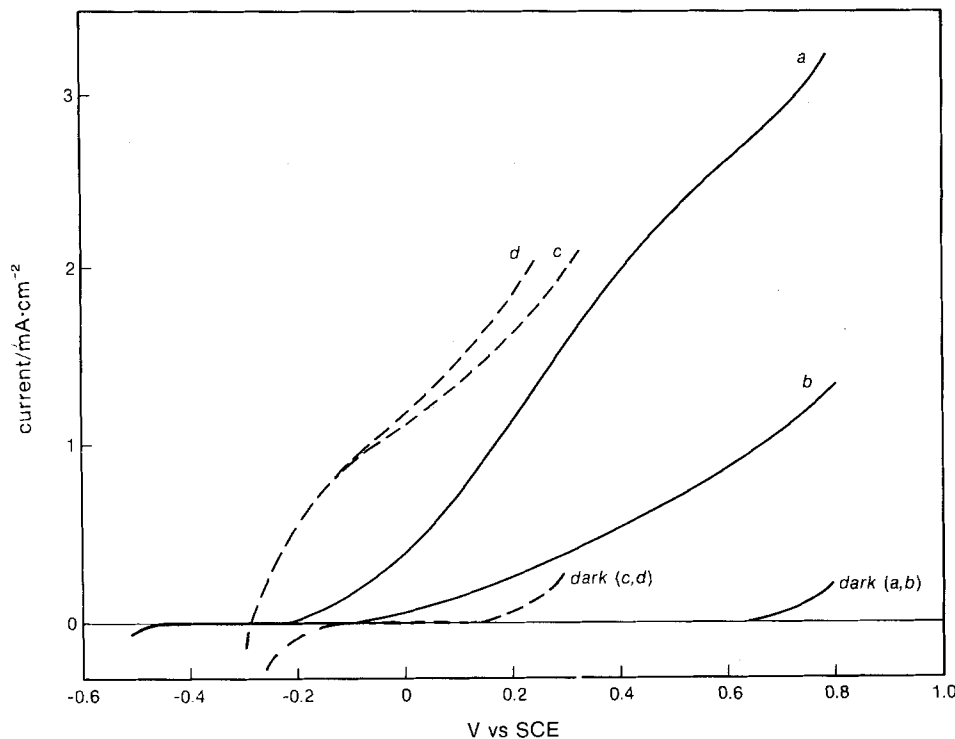


Fig. 7. Photoactivities of a thin film Fe_2O_3 electrode on conducting electrode. a, c: 15 times-sprayed film. b, d: 10 times-sprayed film. Light intensity was 325 mW cm^{-2} , Hg-Xe 200W lamp without filters. Solution was $0.5M \text{ Na}_2\text{SO}_4 + \text{NaOH}$ (pH 13) for a, b, and $0.5M \text{ H}_2\text{O}_2$ was added for c, d. Corrections for iR drops due to the resistance of SnO_2 and of In_2O_3 films ($0.5V$ at most) were made.

obtained for H_2O_2 oxidation). Simulated solar light was used as a light source.

In Fig. 8, theory and experiment are compared. The circles are the experimental points. The agreement is good ($\tau = 2.7 \times 10^{-9}\text{s}$, $\gamma = 0.75$, $d = 600\text{\AA}$). If the theoretical curve in Fig. 9 (see also Fig. 5) was extrapolated, it reached an asymptotic value of 1.6, 1.9, and $2.0 \text{ mA} \cdot \text{cm}^{-2}$ for a number of electrodes in the stack, $n = 10, 20$, and ∞ , respectively (see Discussion).

Discussion

Films made by the pyrolysis technique, with thickness of less than 1000\AA , give good photoactivities when they are deposited onto suitable substrates. The highly conducting SnO_2 and In_2O_3 act as materials with lower work functions than the n-type Fe_2O_3 film, so that there is an ohmic junction at the Fe_2O_3 -substrate interfaces. Conversely, for Fe_2O_3 - TiO_2 junctions (which give smaller currents), the smaller flatband potential

of TiO_2 compared with Fe_2O_3 implies a nonohmic contact for electrons at the solid-solid boundary.

The difference in i_p - V characteristics between those measured in H_2O_2 and H_2O oxidation can be interpreted by the use of Eq. [11] with appropriate values of k_0 and γ . Figures 10 and 11 show i_p - V curves calculated for typical cases. Figure 10 shows the calculated curves for water oxidation for some values of k_0 ; curves are normalized to unity at $V = 1.2V$. Experimental values fit with the calculated curve quite well at $ck_0 = 3.5 \text{ cm} \cdot \text{s}^{-1}$ ($k_0 = 6.4 \times 10^{-2} \text{ cm} \cdot \text{s}^{-1} M^{-1}$; $c = 55M$) and $\gamma = 0.75$. Figures 11a and 11b show similar curve fittings for H_2O_2 oxidation for different film thickness. The consistency of calculation with experiment is good again. For both the 6 times-sprayed film and the 15 times-sprayed film, the best value of ck_0 was $30 \text{ cm} \cdot \text{s}^{-1}$ ($k_0 = 2.0 \times 10^2 \text{ cm} \cdot \text{s}^{-1} M^{-1}$; $c = 0.15M$). The value of γ was 0.75, the same as for water. These results support the specific model assumptions

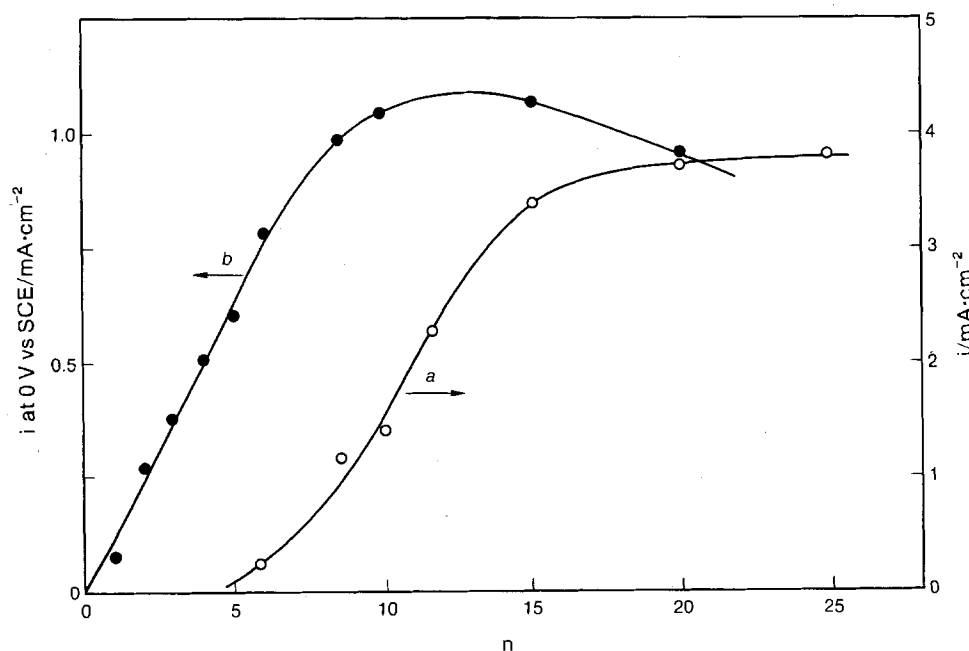


Fig. 8. Experimental photocurrent-film thickness dependence for water (a) and H_2O_2 (b) oxidation.

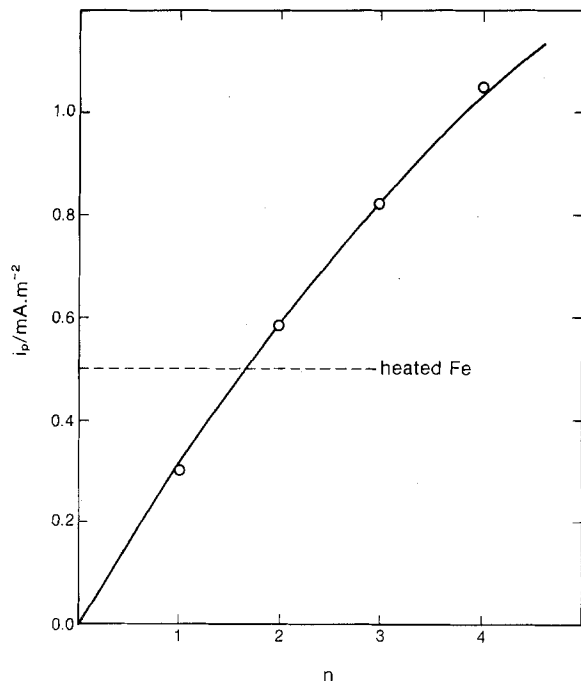


Fig. 9. Photocurrent dependence on the number of 15 times-sprayed electrodes stacked. The solid line is the calculated curve from Eq. [15] $d = 600\text{\AA}$ ($\alpha = 0.95$) and $b = 0.90$. Open circles are experimental values. Experimental condition is pH 13, 0.6V vs. SCE, and light intensity 1 sun from a solar simulator.

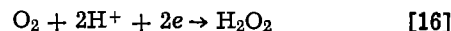
upon which the present calculation is based; the electric field in the film can be taken as uniform, and V may be divided into two parts, i.e., V_s and ΔV_H .

The values of γ and k_o can be tested by virtue of those in the literature although only a few experimental values have so far been reported. Theoretically, γ can vary from 1 to 0 (10). A pure Schottky barrier model requires $\gamma = 1$, and complete Fermi-level pinning corresponds to $\gamma = 0$. Vanden Berghe *et al.* observed that a fraction of 0.9 of the applied voltage changes occur over the depletion region of n-type single-crystalline ZnO electrodes ($N_d \approx 10^{18} \text{ cm}^{-3}$) in contact with aqueous solution (14). Considering

that the electrodes we employed are polycrystalline, the value $\gamma = 0.75$ seems acceptable.

Morrison estimated the reactivity (electron-capture rate) of oxidizing agents at n-type ZnO surface (15). Typical results from his work recalculated in terms of k_o , are $1 \times 10^2 - 8 \times 10^3 \text{ cm s}^{-1} M^{-1}$ for $\text{Fe}(\text{CN})_6^{3-}$ for different pH values, $6 \text{ cm s}^{-1} M^{-1}$ for Ce^{4+} , $< 10^{-3} \text{ cm s}^{-1} M^{-1}$ for Cu^{2+} and V^{3+} . In his experiment, the energy differences between the conduction bandedge and E_{redox} 's are 0.7-1.6 eV, which values are of the same order as those between the valence bandedge and E_{redox} in our experiment; $\sim 1.4 \text{ eV}$ for water and $\sim 1.8 \text{ eV}$ for H_2O_2 oxidation. The value of k_o or cK_o which we found consistent with our experiments, $k_o = 6.4 \times 10^{-2} \text{ cm s}^{-1} M^{-1}$ for water and $2.0 \times 10^2 \text{ cm s}^{-1} M^{-1}$ for H_2O_2 oxidation, are reasonably consistent with these.

Charge accumulation may occur in the film when hole consumption is slow, giving rise to an accelerated electron-hole recombination rate. This may be the case with water oxidation in the relatively low bias region. H_2O_2 acts as a strong reducing agent, i.e., a hole scavenger, at the illuminated photoanode due to the less positive potential (0.86V vs. NHE) needed for the reaction



than that of water oxidation (1.23V vs. NHE) (16). Consequently, hole consumption by H_2O_2 occurs faster than by water, and hence electron-hole recombination is suppressed; the charge transfer rate ck_o for H_2O_2 is ca. 10 times that for water in Fig. 10 and 11. The i_p - d relation for H_2O_2 oxidation (curve b in Fig. 8) is consistent with the theoretical one in Fig. 4. However, the experimental results for water oxidation did not show significant currents until 5 sprayings (curve a in Fig. 8). This may arise from the fact that if the film is sufficiently thin, the diffusion length for electrons from the SnO_2 layer extends over a greater portion of the film than when it is thicker, hence causing enhanced recombination. To deal with this, the distance dependence of τ should be taken into account in Eq. [1].

It has been shown above that the experimental results of Fig. 9 showing experiments on stacks of two, three, and four electrodes are consistent with Eq. [15]. This shows that, if some ten electrodes were brought together in the manner suggested, the multiplying

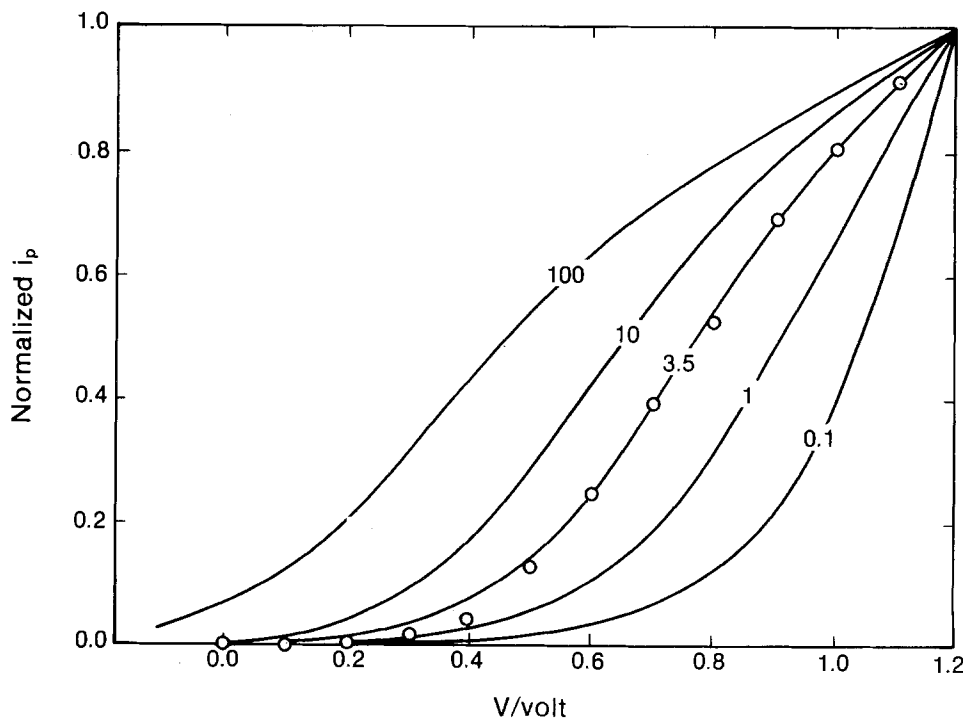


Fig. 10. Theoretical calculation of i_p - V curves for water oxidation based on Eq. [11] for different values of ck_o (cm s^{-1}). Circles are experimental values for a 15 times-sprayed film. The values of parameters, d , τ , β , and γ are the same as those in Fig. 4; note that $d = 600\text{\AA} = 15 \times 40\text{\AA}$. V_{FB} was taken as -0.5V vs. SCE.

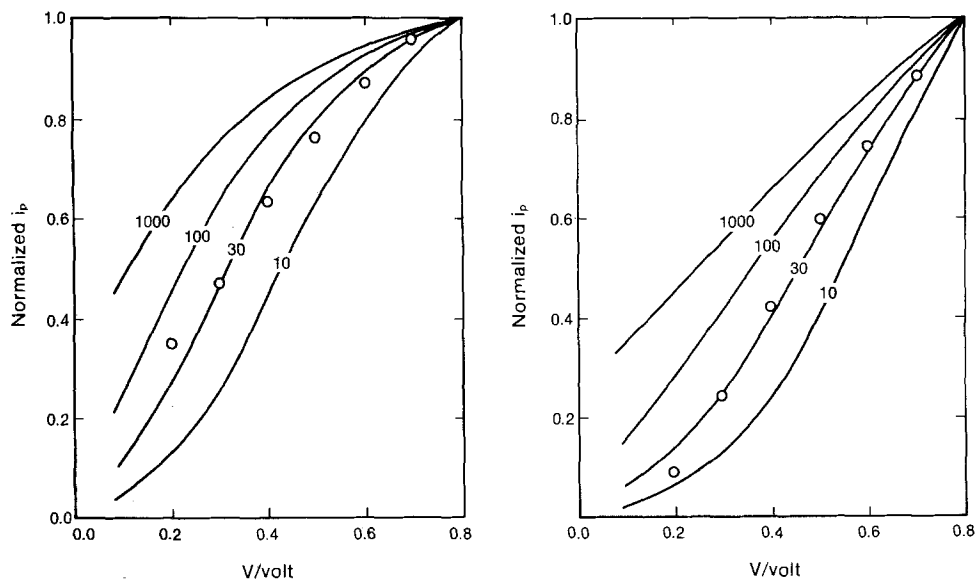


Fig. 11. Calculated curves for H_2O_2 oxidation for different values of ck_0 and d . $d = 240\text{\AA}$ ($6 \times 40\text{\AA}$) in a, and $d = 600\text{\AA}$ ($15 \times 40\text{\AA}$) in b. Circles are experimental values for a 6 times-sprayed film in a and for a 15 times-sprayed film in b. Other parameters are the same as those in Fig. 10.

factor over the result for a thin film electrode would be about $5.3\times$. Thin electrodes of the type used here give around 0.3 mA cm^{-2} (0.6V/SCE , $\text{pH} \approx 13$, 1 sun, solar simulator), so that a ten-stack cell should give around 1.6 mA cm^{-2} . A "thick" electrode ($1\text{ }\mu\text{m}$) under similar conditions but prepared by holding an iron foil in a natural gas flame gives about 0.5 mA cm^{-2} . An increase of more than three times may therefore be expected from stacking.

Further increase in i_p could be obtained by improvement of the film. An increase of τ is important. This might be accomplished by changing the spraying condition, including substrate temperature, dopant, and carrier gas, and thus changing the crystallite size. Furthermore, a catalyst introduced on the surface of the films might cause an increase in the k_0 in Eq. [12], and hence make the onset of i_p shift in the negative direction.

The thin films were observed stable for 12h. No stability tests were made for further hours.

Conclusion

If a photoanode has a low value of the carrier mobility and/or the absorption coefficient, an increase in current up to four times can be obtained in a device in which about ten thin (e.g., 600\AA) semiconductor layer electrodes are placed one behind the other.

Manuscript submitted Aug. 15, 1983; revised manuscript received Dec. 18, 1983.

Texas A&M University assisted in meeting the publication costs of this article.

REFERENCES

1. K. L. Hardee and A. J. Bard, *This Journal*, **123**, 1024 (1976).
2. R. K. Quinn, R. D. Nasby, and R. J. Baughman, *Mater. Res. Bull.*, **11**, 1011 (1976).
3. L. S. R. Yeh and N. Hackerman, *This Journal*, **124**, 833 (1977).
4. J. H. Kennedy and K. W. Freese, *ibid.*, **124**, 723 (1978).
5. A. F. Sammells and P. G. P. Ang, *ibid.*, **126**, 1831 (1979).
6. H. L. Sanchez, H. Steinfink, and H. S. White, *J. Solid State Chem.*, **41**, 90 (1982).
7. F-T. Lion and C. Y. Yang, *This Journal*, **129**, 342 (1982).
8. R. Shinar and J. H. Kennedy, *ibid.*, **130**, 848 (1983).
9. J. Reichman, *Appl. Phys. Lett.*, **36**, 574 (1980).
10. M. Green, *J. Chem. Phys.*, **31**, 200 (1959).
11. J. O'M. Bockris and A. K. N. Reddy, "Modern Electrochemistry," p. 845, Plenum Press, New York (1970).
12. W. A. Harrison, "Electronic Structure and the Properties of Solids," p. 430, W. H. Freeman and Company, San Francisco (1980).
13. K. L. Chopra, R. C. Kainthla, D. K. Pandya, and A. P. Thakoor, in "Physics of Thin Films," Vol. 12, G. Hass, M. H. Francombe, and J. L. Vossen, Editors, p. 167, Academic Press, New York (1982).
14. R. A. L. Vanden Berghe, F. Cardon, and W. P. Gomes, *Surf. Sci.*, **39**, 368 (1973).
15. S. R. Morrison, *ibid.*, **15**, 363 (1969).
16. M. Pourbaix, "Atlas of Electrochemical Equilibria in Aqueous Solutions," p. 112, Translated by J. A. Franklin, Pergamon Press, New York (1966).

A New Electrochemical Determination of Potassium Ion Concentration with Immobilized Valinomycin Disk

Minoru Kumakura and Isao Kaetsu

Japan Atomic Energy Research Institute, Takasaki Radiation Chemistry Research Establishment, Takasaki, Gunma, Japan

Shoichi Adachi

Japan Immunoresearch Laboratories Company, Limited, Takasaki, Gunma, Japan

ABSTRACT

A new electrochemical determination of potassium ion concentration in serum with immobilized valinomycin disk was studied, in which the disk having porous structure was prepared by radiation polymerization of hydrophilic monomer at low temperature. The method was based upon the measurement of the current resulting from liberated potassium ion in the disk. The sensitivity varied with the pore size in the porous polymer matrix of the disk, which depends on monomer concentration. Potassium ion concentration ranging from 0.4 to 10 mM/l can be easily assayed with precision of 2% by using 20 μ l of sample. The correlation between potassium ion concentrations in sera measured by flame photometry and by the present method was good ($r = 0.91$).

Determination of sodium and potassium ion concentration in blood serum is important in diagnostic assay, so that various methods have been developed (1-3). The average concentration ranges of sodium and potassium ion in serum of normal humans are 134-143 and 3.5-5.4 mM/l, respectively. Thus, the concentration range is very narrow, so that an analysis method with a high precision is needed. Furthermore, for the diagnostic assay of these ions, a speedy operation is usually necessary. From these points, a flame photoscopic method and electrochemical method with ion-selective electrodes, which have a relatively high sensitivity, have been used (1). However, these methods consist of complicated large apparatus and their response times are relatively long.

In this paper, a new electrochemical determination method with immobilized valinomycin disk, obtained by radiation polymerization, is described. Valinomycin is dissolved in an appropriate organic solvent placed in a convenient liquid-membrane electrode assembly giving rise to an electrode with selectivity ratios of the order of 5000:1 for potassium over sodium; such a selectivity ratio is considerably higher than those of about 8:1 for cation-sensitive glass electrodes (4, 5). The high selectivity of the electrode makes it a very useful sensor for analytical and biomedical measurements in which potassium ion determinations are usually required in the presence of comparable or larger concentrations of sodium ion. Thus, valinomycin has been utilized as the membrane component of ion-selective electrodes capable of *in vitro* or extracorporeal potassium analysis (5-9), in which valinomycin-impregnated membranes using usually polyvinyl chloride (PVC) have been used for the construction of solid-state electrodes. The methods using these sensors based on the diffusion and trapping of potassium ion in the valinomycin-impregnated PVC membranes, in which electrode potentials are measured. We have developed an electrochemical method with immobilized valinomycin disk having a porous structure in which the currents resulting from potassium ions in the disk are measured.

Experimental

Instrumentation.—A regulated dc power supply having current measurement equipment, PAB 350-0.2 (Kikusui Electronics Corporation, Tokyo) was used to supply a constant potential at 20.0V and to measure the current. An Atomic Absorption and Flame Emission

Key words: potassium ion, electrochemical determination, immobilized valinomycin disk.

Spectrophotometer, AA-8200 (Nippon Jarrell Ash Company, Limited, Kyoto) was used for comparison of the assay.

Reagents.—Valinomycin and potassium chloride were obtained from Sigma Chemical Company, St. Louis, Missouri, and Wako Pure Chemical Industries, Limited, Osaka, respectively.

2-Hydroxyethyl methacrylate (HEMA) was obtained from Mitsubishi Gas Chemical Company, Limited, Tokyo.

Preparation of reagents.—Standard potassium solutions were prepared using potassium chloride and doubly distilled water. Freshly centrifuged serum was used throughout. HEMA was purified by base extraction and distillation to remove an inhibitor and impurity prior to use.

Immobilization of valinomycin by radiation polymerization.—Monomer (HEMA), valinomycin (5% w/v), and water were mixed, poured into a 20 \times 0.8 cm (diam) glass tube, and used quickly shaken. Without delay, the tube was frozen at -78°C and irradiated (1 Mrad) by γ -ray from a ^{60}Co source. After irradiation, valinomycin immobilized in the polymer matrix formed was removed from the tube and sliced into thin disks (20 μm thick, 0.8 cm diam) at low temperature with cryostat Model EF-FCS (Bright Institute Company, Limited, England), and then dried with a lyophilizer (Kyowa Vacuum Engineering Company, Limited, Tokyo).

Measurement of potassium ion concentration with immobilized valinomycin disk.—An immobilized valinomycin disk was immersed in the standard potassium solution or serum sample (20 μl) for 10-30 min, and washed with doubly distilled water. The washed disk was placed on a glass plate (18 \times 18 \times 0.15 mm) and heated at 120°C with a heater. After heating, potassium ion with the disk was measured by the instrument as shown in Fig. 1. The disk placed on the plate was put into a sample cell constructed with two platinum electrodes, containing doubly distilled water (2.0 ml). A constant potential of 10V was applied to the electrode with the size of 20 \times 20 \times 0.5 mm. After 1.0 min, the currents based on the liberation of potassium ion from the polymer matrix of the disk were measured at 25°C .

Results and Discussion

Characterization of immobilized valinomycin disk.—The relationship between potassium-ion concentration and current is shown in Fig. 2. The current increased

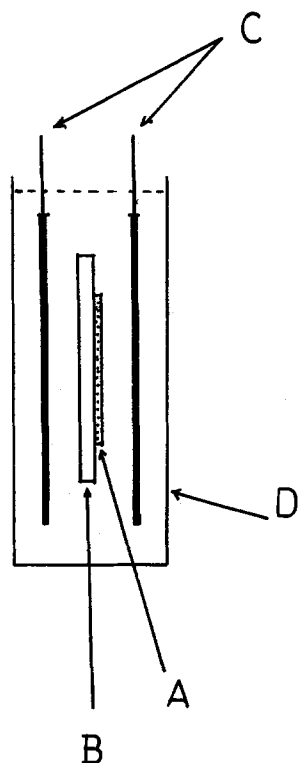


Fig. 1. Construction of the sample cell for the measurement of potassium ion. A: immobilized valinomycin disk. B: glass plate. C: electrode. D: sample cell.

linearly with increasing potassium-ion concentration, and this indicated that immobilized valinomycin disk reacts efficiently with potassium ion to form a complex, and its disk-potassium complex liberates available potassium ion by heat-treatment. According to the typical current-potassium-ion concentration curve in Fig. 1, it was found that a linear relationship between current and potassium-ion concentration holds up to a potassium-ion concentration of 0 mM/l and the slope of the curve was obtained to be $4.50 \mu\text{A} (\text{mM/l of potassium ion})^{-1}$ with a standard error of $0.20 \mu\text{A} (\text{mM/l of potassium ion})^{-1}$. The detection limit for potassium ion in the present method was found to be 0.4 mM/l. The bond of potassium ion and valinomycin in the polymer matrix of the disk is weak, so that its bond is

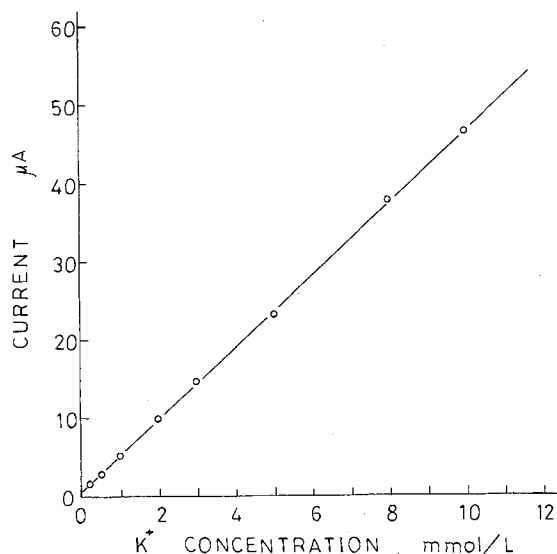


Fig. 2. Relationship between potassium ion concentration and current. HEMA monomer concentration: 50% v/v.

broken by heat-treatment and then potassium ion is liberated from the disk-to-water system. The liberated potassium ions act as the carrier of the current. Thus, the heating of the disk on the plate was necessary for the dissociation of the bond in the potassium-valinomycin complex. After heat-treatment, the present method attributed simply to the measurement of conductivity of potassium-ion aqueous solution.

It is known that potassium ion-valinomycin complex is retained with hydrogen bond-stabilized framework, in which all the ester carbonyl groups become involved in ion-dipole interaction with potassium ion (10). Complexation is accompanied by conformational reforming of the molecule in which the three ester carbonyl groups are oriented within the ring to form a hexadentate system of oxygen atoms about the cation. From the situation of such a complex formation, it is proposed that valinomycin immobilized in the polymer matrix of the disk should have a large mobility to react with potassium ion. The polymer matrix of the disk obtained by radiation polymerization of hydrophilic HEMA at low temperature had a soft sponge-like porous structure, as shown in Fig. 3, in which valinomycin is trapped on the surface of the porous polymer matrix. The soft porous polymer matrix having large surface area gives a very convenient situation for the formation of potassium ion-valinomycin complex. The formation of the porous structure was one of the most characteristic features of the polymer matrix obtained by the present method, and its mechanism was due to small ice particles formed at low temperature (-78°C), at which the radiation polymerization was carried out, melting as the temperature rose to room temperature after irradiation. The soft porous polymer matrix of the disk obtained by the present method was different from the rigid, blocky polymer which was developed for ion-selective electrodes resulting from PVC, poly(siloxane), etc. (5-9, 11). Since the porosity of the porous polymer matrix was large (50%-80%) and the pore diameter was 1-10 μm , the diffusion of potassium ion would not be affected by the polymer matrix.

Effect of monomer concentration on the current.—The effect of monomer concentration on the current was studied by varying HEMA concentration in the

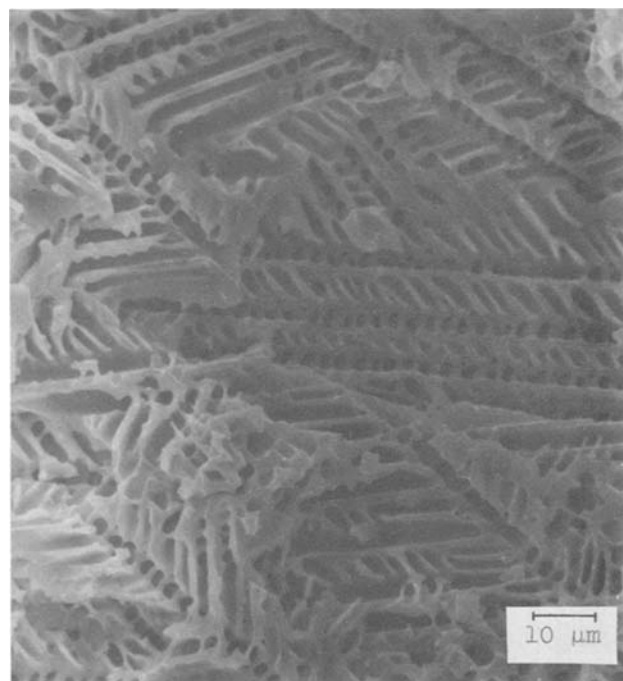


Fig. 3. Scanning electron microphotograph of the surface of immobilized valinomycin disk. HEMA monomer concentration: 50% v/v.

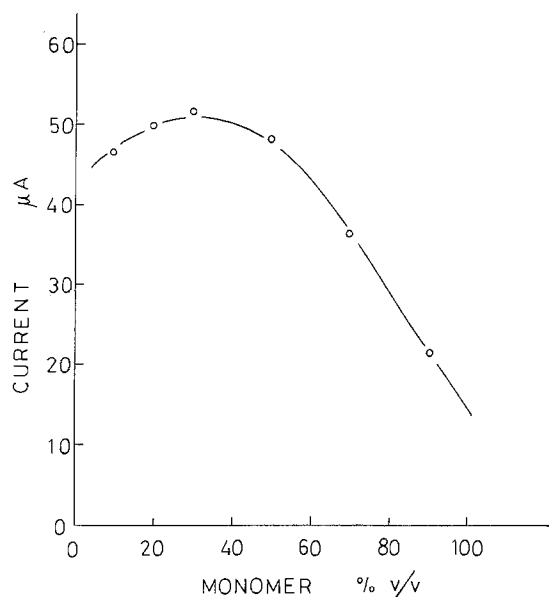


Fig. 4. Effect of HEMA monomer concentration on the current. Potassium ion concentration: 10 mM/l.

immobilization of valinomycin. The relationship between the current and HEMA concentration is shown in Fig. 4. The current increased and had a maximum and then decreased with increasing HEMA concentration. From this result, it was found that optimum monomer concentration exists for the sensitivity. The decreases of the current at lower and higher monomer concentrations were probably due to the leakage and the entrapping of valinomycin, respectively, because the nature, such as porosity and flexibility of the disk, depended on monomer concentration. That is, the disks from lower monomer concentrations below 10% gave a very soft polymer matrix having large pore sizes above 10 μm in diameter, while those from high monomer concentrations above 70% a very rigid polymer matrix having small pore sizes below 0.5 μm . The trapping yield of valinomycin in the immobilization at lower monomer concentrations would be low, and then the apparent content of valinomycin in the disk is low, so that the apparent sensitivity of the disk became low. However, valinomycin in the disks from high monomer concentrations was trapped rigidly in the polymer matrix, in which the mobility of valinomycin suffered, and it did not appear to react with potassium ion. Thus, the optimum monomer concentration range giving high sensitivity appeared to be 20%-50%, in which the disk was flexible and gave suitable state for the complex formation of valinomycin with potassium ion.

The porous structure in the disk obtained from such an optimum monomer concentration lead to the increase of the diffusion rate of potassium ion into the disk. After heat-treatment of the disk, potassium ion can be easily released throughout the pore of the porous polymer matrix. In fact, the response time in which the current became constant was very short (<1.0 min).

Reproducibility and precision.—A standard potassium ion solution of 5.00 mM/l was measured ten times using the disks. A coefficient of valinomycin of 2% was obtained.

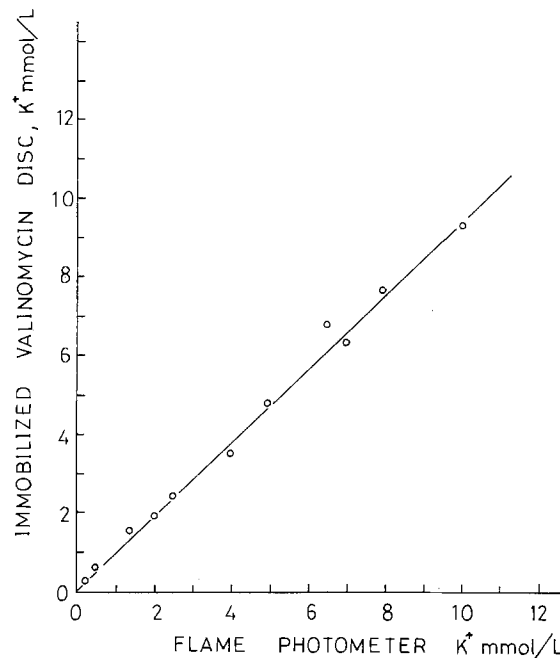


Fig. 5. Comparison of determinations of the concentration of potassium ion in serum by flame photometry and immobilized valinomycin disk method.

Comparison study with flame photometry.—Figure 5 shows the good agreement between flame photometry and the present method, which is based on different calibration procedures in the two techniques applied. The linear regression analysis of potassium ion gave a correlation coefficient of 0.91.

We conclude from these results that the immobilized valinomycin disks having porous polymer matrix obtained by radiation polymerization at low temperature provides a new simple electroanalytical procedure for the determination of potassium ion in serum samples.

REFERENCES

1. K. Takahara, *Rinshyo Kensa*, **22**, 821 (1978).
2. L. A. R. Pioda, W. Simon, H.-R. Bosshard, and H. Curtius, *Clin. Chim. Acta*, **29**, 289 (1970).
3. D. Ammann, R. Bissig, Z. Cimerman, U. Fiedler, M. Guggi, W. E. Morf, M. Oehme, H. Osswald, E. Pretsch, and W. Simon, in "Ion and Enzyme Electrodes in Biology and Medicine," p. 22, Urban and Schwarzenberg, Munich (1976).
4. M. S. Frant and J. W. Ross, Jr., *Science*, **167**, 978 (1970).
5. E. Eyal and G. A. Rechnitz, *Anal. Chem.*, **43**, 1090 (1971).
6. O. H. LeBlance, Jr. and W. T. Grubb, *ibid.*, **48**, 1658 (1976).
7. L. A. R. Pioda, V. Stankova, and W. Simon, *Anal. Lett.*, **2**, 665 (1969).
8. J. L. Walker, Jr., *Anal. Chem.*, **43**, 89A (1971).
9. J. L. Hill, L. S. Gettes, M. R. Lynch, and N. C. Herbert, *Am. J. Physiol.*, **235**, H455 (1978).
10. M. M. Shemyakin, Yu. A. Ovchinnikov, V. T. Ivanova, V. K. Antonov, E. I. Vinogradova, A. M. Shkrob, G. G. Malenkov, A. V. Evstratov, I. A. Laine, E. I. Melnik, and I. D. Ryabova, *J. Membr. Biol.*, **1**, 402 (1969).
11. T. Akiyama, K. Kinoshita, Y. Horita, and E. Niki, *Nihon Kagakkai Shi*, **10**, 1431 (1980).

Correlations Between Transport Properties, ¹HNMR Spectra, and Structure of Molten Methylpyridinium Iodides

David S. Newman* and Rex M. Stevens*

Department of Chemistry, Bowling Green State University, Bowling Green, Ohio 43403

ABSTRACT

The equivalent conductance, viscosity, and ¹HNMR spectra of the four molten methylpyridinium iodides were measured as a function of temperature, and correlations between structure, spectra, and transport properties were made. In addition, an interesting new compound was found in the 2-methylpyridinium iodide melt.

In earlier studies of molten pyridinium salts, we found that a melt's transport properties, thermodynamic properties, and ¹HNMR spectrum were affected by the presence or absence of a methyl substituent and by the position of this methyl group on the pyridine ring (1-3). From these observations, we concluded, among other things, that hydrogen bonding between the nitrogenic proton and the halide ion strongly influenced the melt's structure, as well as its transport properties. In the methylpyridinium iodides, hydrogen bonding does not occur (4), so by comparing their transport properties and ¹HNMR spectra with those of the chlorides and bromides, a more accurate assessment of the influence of hydrogen bonding on the chloride and bromide melts can be made.

The suggestion that molten organic salts have relatively weaker repulsive forces between ions than inorganic salts, and also possess the general property that the ratio of the energy of activation for viscosity, E_η , to the energy of activation for equivalent conductance, E_Λ , is about equal to 1.1, is explored further, and the consequences and causes of this ratio are discussed. The existence of an interesting new species present in the 2-methylpyridinium iodide melt is postulated, and the role of complex species in determining the melt's properties is discussed.

Experimental

The methylpyridinium iodide salts were synthesized by methods already described in the literature (3, 5), with the exception that the appropriate methylpyridine was mixed with an equal quantity of petroleum ether rather than benzene. Anhydrous HI gas was bubbled through the solution following a 10 min nitrogen purge that removed air from the system. White crystals of the methylpyridinium salt began to precipitate after about 1 min. All four iodides turned bright yellow upon melting; the yellow color disappearing upon freezing.

Density measurements were made using the modified Lipkin bicapillary arm pycnometer (6), together with a fiber-optic light pipe that greatly facilitated seeing the graduation markings on the pycnometer, which was immersed in a constant-temperature oil bath.

Conductivity measurements were made with a Jones bridge at a frequency of 1000 Hz using a capillary cell with cylindrical platinum electrodes.

Chemical analysis of the salts was done by determining the iodide concentration using a standard KIO₃ solution to titrate the iodide (7).

Viscosities were measured with a Cannon-Fenske viscometer. The ¹HNMR spectra were obtained using the variable temperature probe of a Varian CF¹T 20 NMR machine and external reference standards. Since the salts are hygroscopic, all transfer operations were done in a dry box.

* Electrochemical Society Active Member.

Key words: fused salts, conductance, viscosity, tunneling.

Results

The densities of the four methylpyridinium iodide isomers are listed as a function of temperature in Table I together with each salt's melting point. It should be noted that the 2-methyl iodide is considerably less dense than the other isomers and lies in the density range of the molten bromides (1, 6).

The logs of the equivalent conductances plotted as a function of T^{-1} are shown in Fig. 1, and it is evident that the conductance of 2-mepyr/HI does not fall on the same curve as the conductances of the other three isomers. The logs of the absolute viscosities vs. T^{-1} are shown in Fig. 2. The viscosity values for N-mepyr I differ somewhat from those reported earlier by us (2) and are more accurate.

Table II lists the equivalent conductances and viscosities of the twelve methylpyridinium halides at a common temperature of 425 K. The chloride and bromide data are from earlier studies (1, 2).

This temperature has been selected as the reference temperature because it lies within the accessible liquid range of most of the salts. For the salts whose liquid range does not include 425 K, extrapolated values are used. In the absence of ideal glass-transition temperatures or normal boiling points, which are natural reference states (8), a common temperature is the most valid reference state from which to compare transport properties.

Table I. The densities of the four methylpyridinium iodide salts as a function of temperature

$$\rho = A - B/T \text{ (K)}$$

Salt	A	B ($\times 10^4$)	T _m (°C)	Temp. range °C
4-mepyr/HI	1.995	8.377	171	171-200
3-mepyr/HI	1.968	7.779	92	93-143
2-mepyr/HI	1.591	7.057	94	94-130
N-mepyr/I*	1.943	6.880	117	117-187

* See Ref. (4).

Table II. Equivalent conductances and viscosities of the twelve methylpyridinium halides at 425 K

Isomer	$\Lambda \text{ cm}^2 \text{ (eq)}^{-1}$	$\eta \text{ (cp)}$
2-mepyr/HCl	6.68	3.90
3-mepyr/HCl	8.58	3.87
4-mepyr/HCl	6.61	3.06
N-mepyrCl	10.50	6.24
2-mepyr/HBr	7.76	4.78
3-mepyr/HBr	8.41	6.65
4-mepyr/HBr	6.55	5.41
N-mepyrBr	9.00	7.27
2-mepyr/HI	16.44*	1.32*
3-mepyr/HI	7.76*	3.93*
4-mepyr/HI	7.97*	3.97*
N-mepyrI	8.16	5.26

* Extrapolated value.

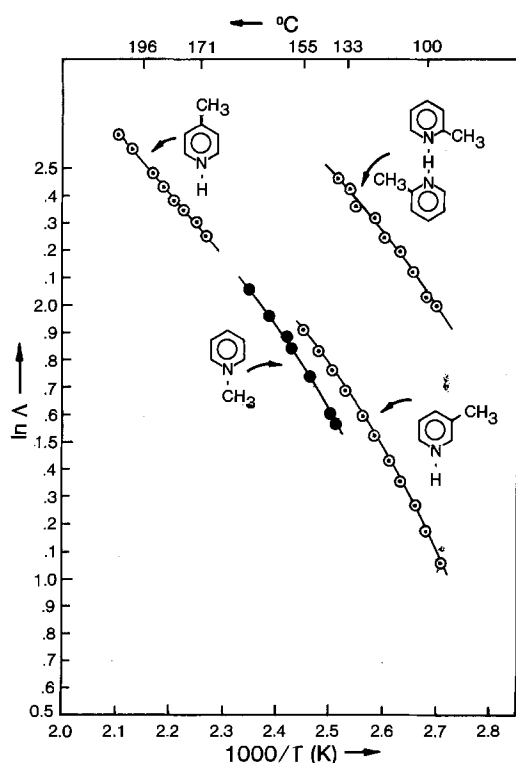


Fig. 1. $\ln \Delta$ vs. T^{-1} for each of the four methylpyridinium iodides.

The ^1H NMR spectrum of molten 4-mepyr/HI at 174 K is shown in Fig. 3. The reference here is $(\text{CH}_3)_2\text{SO}_2$ and appears in the spectrum. No temperature dependence was observed for any peak over the temperature range studied. Figure 4 shows the ^1H NMR spectrum of 3-mepyr/HI, and Fig. 5 shows the spectrum of 2-mepyr/HI. DMSO is the reference in both of these melts, but is not shown. Table III lists the chemical shifts, δ , for the three isomers, all corrected to a DMSO reference. DMSO is approximately 2.60

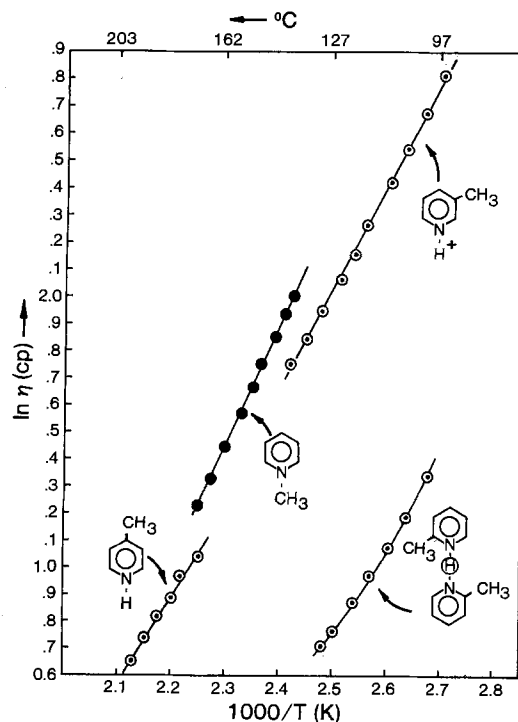


Fig. 2. $\ln \eta$ vs. T^{-1} for each of the four methylpyridinium iodides.

Table III. Proton chemical shifts for 4, 3, and 2-methylpyridinium iodide vs. DMSO (ppm)

Salt	N-H	α	β	γ	CH ₃	Temp. range (K)
4-mepyr/HI	12.1	7.03	6.08	—	0.64	447
3-mepyr/HI	12.32-12.23	6.93	6.10	6.58	0.50	369-418
2-mepyr/HI	12.84-13.10	6.30	5.22	5.75	0.27	369-400

ppm downfield from TMS. The N—H⁺ proton in the 3-methyl melt showed a small upfield shift of the N—H⁺ peak position with increasing temperature, whereas the ring proton chemical shifts were temperature independent. In the 2-methyl salts, the N—H⁺ proton chemical shift showed a rather striking temperature dependence, moving upfield 0.0083 ppm/K. This temperature dependence is larger than any we have yet measured and is in an unexpected direction. Moreover, the integrated area under the N—H⁺ peak was approximately 0.5, rather than 1, as it was in each of the other two spectra.

Chemical analysis of six different 2-mepyr/HI salt samples (each analysis in triplicate) indicated a methylpyridine to iodine ratio of 1.99 to 1.

Discussion

μ-hydrogenbis (2-methylpyridinium) iodide [$(\text{C}_6\text{H}_7\text{N})_2\text{H}^+\text{I}^-$].—These data are compelling evidence for the existence of a dimeric species in the 2-methyl-

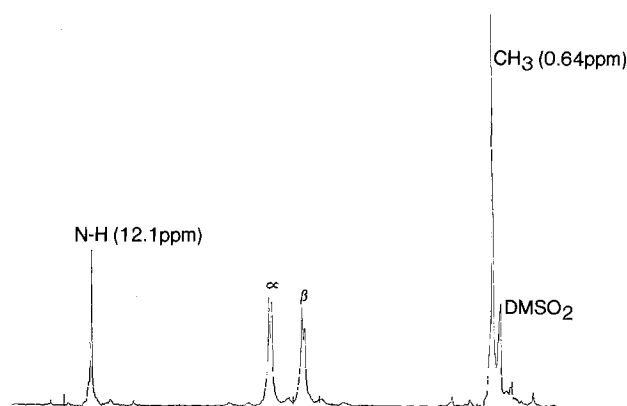


Fig. 3. ^1H NMR spectrum of 4-methylpyridinium iodide at 172°C

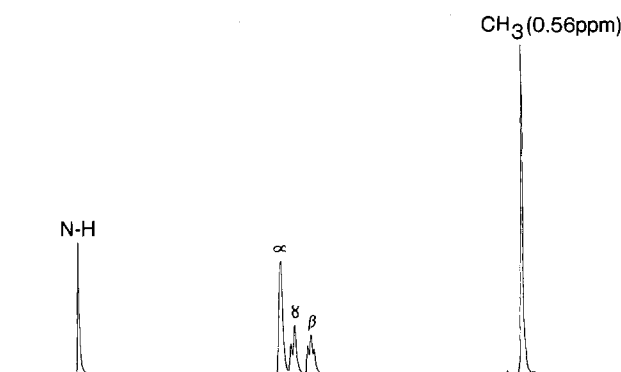


Fig. 4. ^1H NMR spectrum of 3-methylpyridinium iodide at 134°C

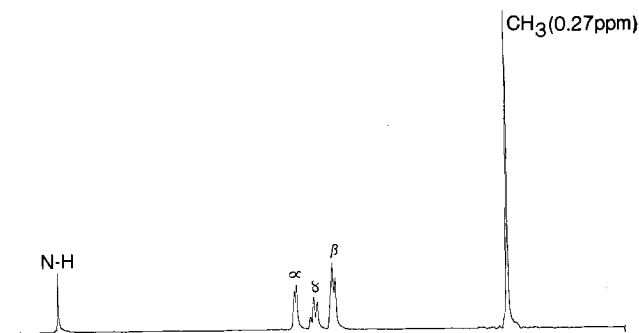


Fig. 5. ^1H NMR spectrum of μ -hydrogenbis(2-methylpyridinium) iodide.

pyridinium iodide melt. In the liquid state, this μ -hydrogenbis(2-methylpyridinium) iodide consists of a dimeric cation, the structure of which is shown in Fig. 6, and an I^- anion. There are two principal reasons why the 2-methyl iodide is different from the

other pyridinium salts studied to date. The $\text{N}-\text{H}^+$

does not hydrogen bond with the I^- , as it does with the Cl^- and Br^- ions, so it is able to form a bond with the partially negative nitrogen (9) on the "second" methyl pyridine ring, and the CH_3 groups on the "2" positions sterically prevent the large I^- from disrupting the

$\text{N}-\text{H}-\text{N}$ bond once it forms. Precedents

for this pyridinium-pyridine type of structure do exist in the literature. X-ray and neutron diffraction studies show $[(\text{C}_5\text{H}_5\text{N})_2\text{H}]^+ [\text{ZnBr}_{3/2}\text{Cl}_{3/2}(\text{C}_5\text{H}_5\text{N})]^-$ to possess a

$\text{N}-\text{H}-\text{N}$ bond (10), and IR together with

neutron diffraction indicate "4-aminopyridine hemiperchlorate ($\text{C}_5\text{H}_5\text{N} \cdot \frac{1}{2} \text{HClO}_4$)" also has a strong

$\text{N}-\text{H}-\text{N}$ bond (11). More importantly, however,

this structure correlates very well with transport properties, ^1H NMR spectra, and density.

The average shielding at a nucleus cannot be measured directly by NMR, so there will be some ambiguity in accounting for the upfield chemical shift of the bridging proton. Nevertheless, it can be said with some certainty that the upfield shift with increasing temperature is caused by the bridging proton becoming more shielded by the bonding electrons, rather than less deshielded by the aromatic ring currents. The average chemical shift difference, $\Delta\sigma_{\text{av}}$, is given by the equation

$$\Delta\sigma_{\text{av}} = \sigma_{\text{av}}(\text{A}) - \sigma_{\text{av}}(\text{B}) \\ = \sigma_{\text{av}}^{\text{p}}(\text{A}) + \sigma_{\text{av}}^{\text{d}}(\text{A}) - \sigma_{\text{av}}^{\text{p}}(\text{B}) - \sigma_{\text{av}}^{\text{d}}(\text{B})$$

where A and B are different magnetic environments and $\sigma_{\text{av}}^{\text{p}}$ and $\sigma_{\text{av}}^{\text{d}}$ are the paramagnetic and diamagnetic contributions, respectively. Employing literature values for the relevant molecular parameters and several plausible assumptions, σ_{av} for the bridging proton can be calculated to a fairly accurate first approximation using a modification of the technique developed by

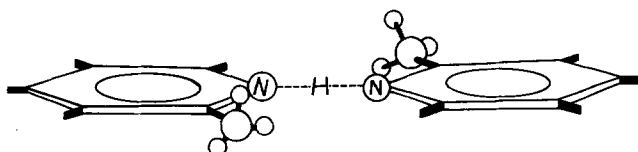


Fig. 6. Structure of μ -hydrogenbis(2-methylpyridinium) cation

Shuppert and Angell (12). $\Delta\sigma_{\text{av}}$ can then be estimated by comparing this calculation with σ_{av} (TMS) at 10 ppm. The bare proton has a σ_{av} of -20.9 ppm relative to TMS (13). A single electron in a 1s orbital shields this bare proton $+17.7$ ppm (13), but a better shielding value is $+21.4$ ppm because the electrons surrounding a bonded hydrogen are less diffuse than in a hydrogen atom (14). Emsley has calculated a net positive charge of 0.21 units on the nitrogenic proton in an isolated pyridinium ion (9). However, the more recent computation of Goldstein and Ragle placed a net positive charge of 0.32 units on this proton or a net 1s orbital population of 0.68 electrons (4). Using the newer value and assuming, first, that a 2-methylpyridinium "monomer" and a pyridinium ion are not significantly different with respect to the nitrogenic proton's 1s orbital population and, second, that both methylpyridine rings make identical contributions to the bond in the dimeric cation, the 1s orbital population will be $0.68 + (0.32/2) = 0.84$ electrons.

The chemical shift at the bridging proton also depends on the electric field arising from charges on other atoms in the molecule. This dependence is described by the equation (9, 15)

$$\sigma^{\text{E}} = -6.58 \times 10^{-22} \sum_i q_i \cos \theta_i r_i^{-2} \\ - 3.34 \times 10^{-23} \sum_i q_i^2 r_i^{-4}$$

where the coefficients are in coulombs, the q_i are the formal charges, θ_i the angle between the bond, and the vector is r_i . It is obvious that these electric field effects will cancel by virtue of symmetry. For example, the electric field due to the partial negative charge on one nitrogen will exactly cancel the field due to the other nitrogen. This leaves only shielding caused by ring currents to be estimated, and this cannot differ significantly from that in benzene, the extra charge on the nitrogen nucleus being almost exactly canceled by the redistribution of electronic charge (4, 16). We use, therefore, Johnson and Bovey's predicted values of shielding contributions from ring currents in aromatic hydrocarbons (17, 18) to calculate the ring-current contribution to the chemical shift in the cation.

We assume that the $\text{N}-\text{H}-\text{N}$ bond length is 0.27

nm, as measured by Roziere *et al.* for 4-aminopyridine hemiperchlorate (11), that both methylpyridine rings are in the same plane, and that at any intermediate distance between the two nitrogens the ring current contributions are additive. The calculated values are listed in Table IV. These data show that the region, or "box" where the bridging proton has a high probability of being found has a relatively invariant ring current shielding contribution. At a distance of about ± 0.07 nm from the plane of the rings, the negative shielding begins to decrease, but the positive 1s shielding also decreases. Since the electronic shielding is about an order of magnitude larger than the ring current deshielding and since it decreases at least as sharply with distance, it will almost certainly dominate. Consequently, it is highly unlikely that the upfield shift with increasing temperature is caused by decreased

Table IV. Ring current shielding

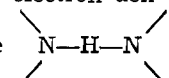
Distance from reference nitrogen (nm)	Shielding in plane of ring (ppm)	Shielding ± 0.05 nm from plane of ring
0.097	-2.47	-2.94
0.111	-2.42	-2.34
0.135	-2.50	-2.46
0.159	-2.42	-2.34
0.173	-2.47	-2.49

deshielding. The only other plausible explanation is the one we offer. Calculating the chemical shift, we obtain (relative to TMS)

$$\Delta\sigma_{av} = [(0.84 \times 2.14) - (2.50) - (20.9)] = -15.42 \text{ ppm}$$

$$\Delta\sigma_{meas} = (-15.44 \text{ to } -15.70) \text{ ppm}$$

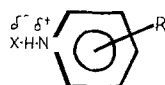
The excellent agreement between theory and experiment is no doubt partly fortuitous because of the many assumptions made and because both the CH_3 group and the I^- have unknown, but opposite, contributions to the chemical shift which probably cancel. Nevertheless, the agreement offers strong support for our conclusions. Because the peak moves upfield, the shielding of the proton must increase. Since the bond itself weakens slightly as temperature increases, the only plausible explanation for the increased electron den-

sity about the bridging atom is that the 

bond is asymmetric to begin with, the proton is lying, on the average, closer to one nitrogen than the other, and electron density is being localized around it for longer periods of time. It should be kept in mind that the nonbonding electrons of nitrogen are less delocalized in the pyridinium ion than in the pyridine (9, 16). This means that the bridging proton lies in a double minimum-potential well between the two halves of the pyridinium-pyridine cation and tunnels back and forth between the two minima. The tunneling frequency will be strongly dependent on the relative orientation of one nitrogen to the other. As temperature rises, the nitrogens move away from the appropriate position for maximum tunneling to occur, so that the tunneling frequency diminishes much faster than the frequency of hopping over the barrier increases (19, 20). The proton thus resides in its well for longer time intervals and becomes more and more shielded with increasing temperature. If the proton resided in a deep single-minimum well for a long period of time on the NMR time scale, its resonance peak would be a nitrogen-broadened triplet, as it is in the molten $\text{C}_5\text{H}_5\text{NH}^+\text{Al}_2\text{Cl}_7^-$ spectrum (21, 22), and the proton would become more acidic and less shielded as temperature increased.

Equivalent conductance.—The data in Table II show that at 425 K the conductances of the three N-methyl salts increase in the order $\text{I}^- < \text{Br}^- < \text{Cl}^-$, and that the increase is substantial. This further strengthens our contention that these salts are principally anionic conductors in the molten state. If one assumes that the mobility of the cation is roughly constant in all three melts, the only plausible explanation for the observed increase in Λ between the three salts is that the halide ion's mobility increases from I^- to Cl^- . Consequently, the fraction of the current carried by the anion also increases. In all likelihood, the iodide ion's mobility and the methylpyridinium ion's mobility are somewhat similar, the difference in ionic radius compensating for the difference in ionic mass.

Comparing the Λ 's of the 4-methyl halides with those of the N-methyl salts shows that the percentage differences in conductance, $[(\Lambda_N - \Lambda_4)/\Lambda_N] \times 100$, are 37% for the chlorides, 27.2% for the bromides, and only 2.3% for the iodides. This large difference is almost certainly due to the formation of complexes of the sort



which form in the Cl^- and Br^- melts because of hydrogen bonding. Complex formation reduces the effective number of charge carriers per unit volume at any instant and thus reduces the conductivity. The

larger percentage difference between chloride conductivities than between bromide conductivities is exactly what is expected if the Cl^- ion is both more mobile than the Br^- ion and forms a stronger bond with a $\text{C}_5\text{H}_7\text{NH}^+$ ion. In effect, the hydrogen bonding immobilizes a greater number of faster moving species in the chloride melt and fewer slower species in the bromide melt, thus giving the observed result. This conjecture is confirmed by the fact that at 425 K $\Lambda_{4, \text{meCl}} \approx \Lambda_{4, \text{meBr}}$, but Λ_{NmeCl} is about 14% larger than Λ_{NmeBr} .

The 2.3% difference in conductance between the two symmetrical iodide melts is further confirmation that in iodides hydrogen bonding is not a factor. This is the sort of difference expected from steric considerations only. This small difference in Λ confirms our earlier hypothesis (1) that the 4-methyl pyridinium chloride and bromide conductivities would be about the same as the respective N-methyl conductivities if not for hydrogen bonding. This means our calculated values for the association constants (0.11 for the chloride melt and 0.062 for the bromide melt) based on this assumption are probably fairly accurate.¹

Viscosity.—The iodide viscosities are difficult to explain, especially in context with our other observations. It is evident from the data in Table II that at 425 K each iodide is less viscous than the corresponding bromide and, with the exception of 3-mepyrHI, less viscous than the corresponding chloride. However, each bromide melt is more viscous than its corresponding chloride melt, which implies that something unique is occurring in the iodides to reverse the expected trend. Part of the explanation is the absence of hydrogen bonds, but, obviously, something else must be occurring. The yellow color of the melt and the relatively low electron affinity of iodine are indicative of the presence of complex species, and we suggest these may be charge-transfer complexes having long enough lifetimes to lower each iodide melt's viscosity relative to what it would be if no neutral species were present (23). Since the forces of attraction between neutral molecules and between ions and neutral molecules are much weaker and fall off much more rapidly as a function of internuclear distance than the forces of attraction between ions, the higher the concentration of CT or other neutral complexes, the lower the viscosity, other things being equal.

The apparently "normal" conductivities of the N-methyl melts, i.e., $\text{Cl}^- > \text{Br}^- > \text{I}^-$, in the presence of abnormal iodide viscosities ($\text{I}^- < \text{Cl}^- < \text{Br}^-$) again imply a different iodide melt structure. The formation of relatively stable iodide complexes causes local liquid relaxation (24), which reduces viscosity. These complexes do not contribute to the conductivity, so that charge is being carried at any instant by fewer ions per unit volume than in the other two N-methyl melts, but these ions are fairly mobile.

The explanation for the μ -iodide melt's high conductivity and low viscosity is not at all clear, but it would seem to be directly related to the melt's low density. Because the density is much lower than that of the other iodides, there is a greater probability for "holes" to form, due to local density fluctuations, which an I^- ion can move into. Moreover, the dimer itself contributes to liquid relaxation by shielding the proton's charge, which further reduces viscosity.

Energies of activation.—Table V lists energies of activation for viscosity, E_η , and for equivalent conductance, E_Λ , assuming Arrhenius behavior for all of the iodide melts. Several melts, most notably 2-mepyr-I, deviated slightly from strict Arrhenius behavior, but the limited temperature range and precision of the data did not warrant the use of the three-

¹Table V in Ref. (1) contains several incorrect entries. The correct K_A 's are the ones listed here. The G 's for the Cl^- and Br^- melts are 7.8 and 9.8 kJ/m, respectively.

Table V. Energies of activation for viscosity and conductance

Salt	E_{η} (J/mol)	E_{Λ} (J/mol)	E_{η}/E_{Λ}
N-mepyrI	27.6	26.2	1.05
4-mepyrI	27.6	19.2	1.43
3-mepyrI	30.9	26.7	1.15
2-mepyrI	26.4	18.5	1.42

parameter VTF equation. In any case, the E_{η}/E_{Λ} ratios did not change significantly as a function of temperature. As is true for all other organic salts studied, the ratios are between 1 and 1.5 and considerably less than the ratios for typical inorganic salts, which range between 2 and 5 (25). We consider this difference to be quite significant and indicative of a fundamentally different transport mechanism occurring in organic molten salts. In inorganic melts, repulsive forces dominate, there is a 10%-20% expansion on melting (26), and, as a result, large density fluctuations occur. Therefore, a small positive ion requires considerably less energy to move than an entire molecule or ion pair. In organic melts, repulsive forces are mitigated by attractive forces, there is little, if any, expansion upon melting, and density fluctuations are quite small. Therefore, it takes nearly as much energy for a halide ion to "waffle" by a pyridinium ion as it does for a pyridinium halide ion pair to waffle by another halide or ion pair. Since a given density fluctuation will be still slightly less likely to accommodate the motion of a larger cation than a smaller anion, the E_{η} is always a bit larger than E_{Λ} . The relatively high E_{η}/E_{Λ} ratio of 1.4 for the μ -iodide melt is consistent with our explanation for its unusual transport properties. The reason why the 4-methyl melt's ratio is also 1.4 is not yet clear.

Based on the energies of activation obtained here as well as those measured elsewhere, we suggest classifying those salts whose E_{η}/E_{Λ} ratio is between 1.0 and 1.5 as "soft" salts, and those salts whose E_{η}/E_{Λ} ratio is between 2 and 5 as "hard" salts. This terminology may even be more apt in molten salt systems than in acid-base theory because those salts whose E_{η}/E_{Λ} ratios are 1:1, and therefore considered soft, are easily polarizable and have relatively weak repulsive forces. However, the inorganic salts, particularly at melt temperatures, do behave to a good first approximation as charged hard spheres.

Errors.—We estimate the errors involved in the iodide measurements to be slightly greater than in the chloride and bromide measurements, probably because there are two decomposition pathways, one being photochemical, the other being thermal. This led to a slightly lower precision in our measurements, since it was impossible to exactly duplicate both the thermal and photochemical history of a given melt. With this in mind, we estimate the error in density to be $\pm 1\%$ (the precision was $\pm 0.3\%$ overall, and in the case of 4-mepyrI $\pm 0.1\%$). The error in equivalent conductance $\pm 2\%$ and the error in viscosity $\pm 3\%$.

Conclusion

By obtaining correlations between structure, transport properties, and ^1H NMR spectra of a series of isomeric melts in which no hydrogen bonding occurs, we are better able to assess the contribution of hydrogen bonding to structure and transport properties of those melts in which hydrogen bonding plays an important role. In addition, we have found that by studying a series of compounds in a systematic way, we were able to detect the presence of an interesting new compound that otherwise might have gone unnoticed.

Acknowledgments

We would like to thank Julie Nemeth for performing the iodide analyses. We would also like to thank Dow Corning for contributing the 710 silicon oil for our constant temperature bath.

Manuscript submitted July 8, 1983; revised manuscript received Jan. 26, 1984. This was Paper 647 presented at the Hollywood, Florida, Meeting of the Society, Oct. 5-10, 1980.

The Teletype Corporation assisted in meeting the publication costs of this article.

REFERENCES

- D. S. Newman, R. R. Rhinebarger, D. Siconolfi, and O. A. Banjoko, *This Journal*, **128**, 2331 (1981).
- D. S. Newman, R. T. Tillack, D. P. Morgan, and W. C. Wan, *ibid.*, **124**, 856 (1977).
- D. S. Newman, W. Rhor, D. Kirklin, and H. D. Frame, *ibid.*, **119**, 797 (1972).
- N. Goldstein and J. L. Ragel, *J. Chem. Phys.*, **70**, 5072 (1979).
- M. S. Rozhdestvenskii and L. M. Brode, *Zh. Prikl. Khim. (Leningrad)*, **10**, 722 (1937).
- D. S. Newman, D. P. Morgan, and R. T. Tillack, *J. Chem. Eng. Data*, **21**, 279 (1976).
- A. I. Vogel, "A Text Book of Quantitative Inorganic Analysis," pp. 360-361, Longman's Green and Company, London (1951).
- J. Wong and C. A. Angell, "Glass Structure by Spectroscopy," Chap. 1, Marcel Dekker, Inc., New York (1976).
- J. W. Emsley, *J. Chem. Soc. A*, 1387 (1968).
- B. E. Villarreal-Salinas and E. O. Schlemper, *J. Cryst. Mol. Struct.*, **8**, 217 (1978).
- J. Roziere, J. M. Williams, E. Grech, Z. Malarski, and L. Sobczyk, *J. Chem. Phys.*, **72**, 6117 (1980).
- J. W. Shuppert and C. A. Angell, *ibid.*, **67**, 3050 (1977).
- W. H. Flygare, "Molecular Structure and Dynamics," Chap. 6, Prentice Hall, Inc., Englewood Cliffs, NJ (1978).
- J. A. Pople, W. G. Schneider, and H. J. Bernstein, "High Resolution Nuclear Magnetic Resonance," p. 175, McGraw-Hill, New York (1959).
- A. D. Buckingham, *Can. J. Chem.*, **38**, 300 (1960).
- H. Seel and H. Gunter, *J. Am. Chem. Soc.*, **102**, 7051 (1980).
- C. E. Johnson and F. A. Bovey, *J. Chem. Phys.*, **29**, 1012 (1958).
- J. W. Emsley, J. Feeney, and L. H. Sutcliffe, "High Resolution Nuclear Magnetic Resonance Spectroscopy," Vol. 1, Appendix B, Pergamon Press, London (1965).
- J. O'M. Bockris and S. U. M. Kahn, "Quantum Electrochemistry," Chap. 9, Plenum Press, New York (1979).
- J. R. DeLaVega, *Acc. Chem. Res.*, **15**, 185 (1982).
- C. A. Angell and J. W. Shuppert, *J. Phys. Chem.*, **84**, 538 (1980).
- D. S. Newman, R. E. Winans, and R. L. McBeth, in "Third International Symposium on Molten Salts," G. Mamantov, M. Blander, and G. P. Smith, Editors, pp. 425-438, The Electrochemical Society Softbound Proceedings Series, Pennington, NJ (1981).
- E. M. Kosower, J. A. Skorcz, W. M. Schwarz, and J. W. Patton, *J. Am. Chem. Soc.*, **82**, 2188 (1960).
- D. S. Newman and P. B. Bikkani, in "Fourth International Symposium on Molten Salts," M. Blander, K. E. Johnson, M-L. Sabungi, and D. S. Newman, Editors, pp. 206-216, The Electrochemical Society Softbound Proceedings Series, Pennington, NJ (1984).
- H. Bloom and E. Heymann, *Proc. R. Soc. London, Ser. A*, **188**, 392 (1947).
- J. O'M. Bockris and A. K. N. Reddy, "Modern Electrochemistry," Vol. 1, p. 525, Plenum/Roseta Editions, New York (1973).

Determination of Internal Cation Mobilities in the Molten System (Li-K)Cl at 723 K

R. Takagi,¹ H. Shimotake,* and K. J. Jensen

Argonne National Laboratory, Chemical Engineering Division, Argonne, Illinois 60439

ABSTRACT

Internal cation mobilities of Li^+ and K^+ in the system (Li-K)Cl were determined experimentally using the counter current electromigration method over the temperature range 700-778 K, with initial equivalent fractions of KCl of 0.356, 0.416, and 0.451. The relative difference in internal cation mobilities of Li^+ and K^+ was found to reach as much as 7% in this range.

Lithium-aluminum/iron sulfide cells that contain multicomponent molten salt electrolytes such as (Li-K)Cl mixture are currently under development for energy-storage applications (1). During charge or discharge of such cells, composition gradients of ions, Li^+ and K^+ are induced within the molten salt by the electrode reactions. As a result, the salt compositions are shifted locally from the liquidus range, and precipitation of a solid phase may occur. In lithium/sulfide cells, which are operated at a temperature range of 400°-430°C in (Li-K)Cl eutectic, Askew and Holland (2) noted that the lithium electrode was severely polarized when discharged at high current densities. They conjectured that the polarization was caused by precipitation of LiCl at the lithium electrode. Willars *et al.* (3) found that the cell capacity was inversely proportional to discharge rate, and the result was interpreted in terms of electrolyte phase separation at the iron sulfide electrode. Braunstein and Vallet (4) and Pollard and Newman (5) calculated current-induced composition profiles of LiCl and KCl in lithium/sulfide cells containing (Li-K)Cl electrolyte. Furthermore, Vallet *et al.* (6) predicted a composition profile that indicates an increased KCl concentration near the cathode. More recently, they presented direct evidence of KCl precipitation (7). Furthermore, they have shown that the composition profile depends not only on the initial composition of the electrolyte, but also on the current density and distance between electrodes. The high KCl concentration also favors the formation of J-phase ($\text{LiK}_6\text{Fe}_{24}\text{S}_{26}\text{Cl}$) in the iron sulfide electrode (8). Transition time required for the separation of the components, which was estimated by Braunstein and Vallet (5), is correlated with the transference number and diffusion coefficient. However, transference number is directly related to the emf because the concentration polarization is involved. Thus it is necessary to know the mobilities of the ions at the operating temperature for accurate determination of the transference numbers. At present, the experimental data reported on the mobilities of Li^+ and K^+ in the system (Li-K)Cl are limited to the temperatures at 913 (9) and 1100 K (10), which are much higher than the normal operating temperature of lithium/iron sulfide cells, *i.e.*, 723 K.

In this study, the internal cation mobilities, *i.e.*, the cation mobilities relative to the common anion, were measured in the system (Li-K)Cl at the cell operating temperature range by the counter current electromigration method developed by Klemm (11) and Okada (12).

Experimental

Figure 1 is a schematic diagram of the electromigration cell. The system consists of a sample melt reservoir made of an alumina tube (a), that has a 2.54 cm id and a length of 35 cm, containing a sample

salt mixture (b), a quartz electromigration tube (d) with a main tube that is 0.4 cm id and 20 cm long, which has been packed with quartz powder (80-100 mesh) (g) and sealed with quartz wool (f), an aluminum electrode (j) that is 0.8 cm id and 7 cm long, encased in a boron nitride tube (i) attached to a nickel lead wire (h), and a thermocouple covered with an alumina sheath (e). The electromigration tube, the aluminum electrode, and thermocouple are immersed in an electrolysis vessel (1) that has a 3.8 cm id and is 43 cm long, made of alumina containing (Li-K)Cl eutectic melt (k). The entire system is assembled inside a glove box containing a high purity helium atmosphere. The (Li-K)Cl mixtures were prepared from LiCl and KCl (polarographic grade) supplied by Anderson Physics Laboratory.

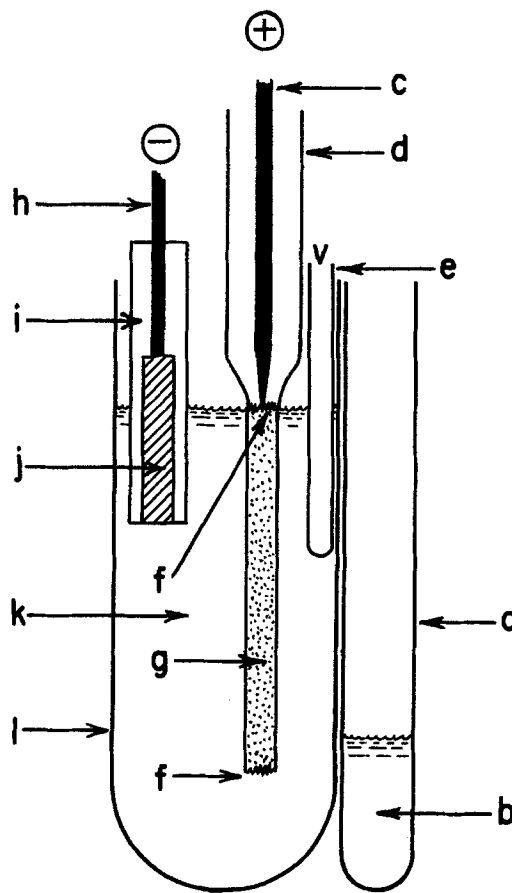


Fig. 1. Electromigration cell. a: alumina vessel. b: mixture under investigation. c: graphite electrode. d: electromigration tube. e: thermocouple. f: quartz wool. g: quartz powder (80-100 mesh). h: Ni lead wire. i: BN sleeve. j: Al mesh metal electrode. k: salt bath [(Li-K)Cl eutectic composition]. l: alumina vessel.

* Electrochemical Society Active Member.

¹ Present address: Tokyo Institute of Technology, Tokyo, Japan.

The experimental procedure was as follows: the electromigration tube packed with dry quartz powder was first immersed in the molten salt mixture to be tested in the sample melt reservoir. The tube filled with the sample melt was then transferred into the molten salt bath held in the electrolysis vessel. The electromigration was carried out by passing a current, 100 mA at about 100V for 4-7h supplied by a dc power supply. The transported charge, Q , was determined by a copper coulometer. After electromigration had occurred, the electromigration tube was removed from the salt bath and immediately quenched to room temperature. The upper part of the tube was then cut into eight pieces, each ~ 1.5 cm long. The salt in each piece was dissolved in distilled water and the quantity of Li^+ and K^+ was determined by emission or atomic absorption spectrophotometry. The variation of the composition of Li^+ and K^+ along the electromigration tube allowed the construction of composition profile.

Results and Discussion

The initial equivalent fraction of KCl, p_K , in the (Li-K)Cl mixtures was varied from 0.356 to 0.451, and the temperature was selected in the liquidus region according to the phase diagram (13). The relative difference in the internal cation mobilities, ϵ_{12} , is defined by

$$\epsilon_{12} = (b_{\text{Li}} - b_{\text{K}}) / \bar{b} \quad [1]$$

where \bar{b} is the average value of b 's, and related to the equivalent conductivity, Λ , by

$$\bar{b} = \Lambda / F = p_{\text{Li}} b_{\text{Li}} + p_{\text{K}} b_{\text{K}} \quad [2]$$

where F is the Faraday constant. From Eq. [1] and [2], one can obtain

$$b_{\text{Li}} = (\Lambda / F) (1 + \epsilon_{12} p_{\text{K}}) \quad [3]$$

$$b_{\text{K}} = (\Lambda / F) (1 - \epsilon_{12} p_{\text{Li}}) \quad [4]$$

The values of ϵ_{12} for the different equivalent fractions of K^+ at the different temperatures are calculated from the chemical analysis and the transported charge balances (11, 12) based on the concentration profile along the electromigration tube, an example of which is shown in Fig. 2. The experimental conditions and results are also listed in Table I. The value of ϵ_{12} obtained in this study at $p_K = 0.416$ and $T = 711$ K is estimated to be -0.06 , which reasonably agrees with $\epsilon_{12} = -0.10$ at $p_K = 0.41$ determined by Moynihan and

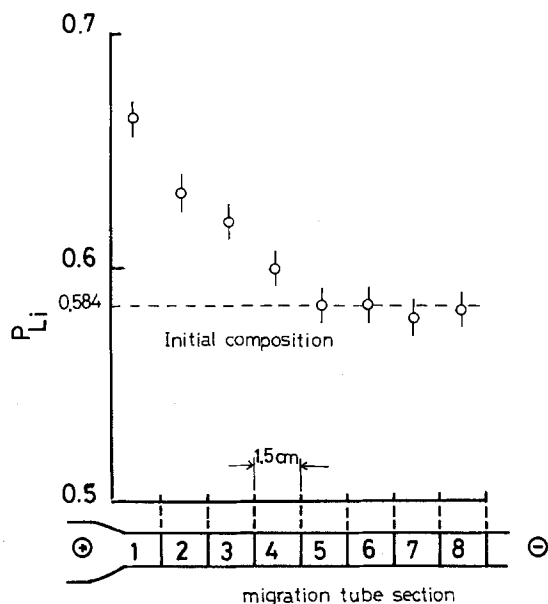


Fig. 2. Typical profile of concentration in the migration tube (run 5).

Table I. Experimental conditions and results

Run	T/K	p_{Li}	Q/C	ϵ_{12}
1	712	0.644 ± 0.008	1219	$-0.014 \ 0.015$
2	760		2156	$-0.035 \ 0.004$
3	777		2503	$-0.048 \ 0.008$
4	700	0.584 ± 0.008	1740	$-0.049 \ 0.007$
5	721		1699	$-0.071 \ 0.015$
6	778		2127	$-0.092 \ 0.007$
7	737	0.549 ± 0.008	1613	$-0.070 \ 0.008$
8	775		2030	$-0.072 \ 0.007$

Laity (9) at the same temperature using the Hittorf method. The point at which the difference in the internal mobilities of Li^+ and K^+ reached zero was designated as the Chemla crossing point (14), which is a function of temperature. The Chemla crossing point at $p_K = 0.356$ was estimated to be at 700 K, extrapolated from experimental values. This extrapolated point is plotted in Fig. 3 together with values for the Chemla crossing point estimated with the reported results (9, 10). In the region represented by the area below the curve obtained by connecting these points, the mobility of Li^+ is greater than that of K^+ .

The internal mobilities, b_{Li} and b_{K} , were calculated from Eq. [3] and [4] using the equivalent conductivity data available in the literature (15). The isotherms of the results at 723 and 772 K are shown in Fig. 4, which indicates that the mobility of Li^+ becomes less than that of K^+ at these temperatures over the concentration range of this study. This interacting phenomenon in which a large cation, K^+ , migrates faster than a small cation, Li^+ , has been known in other systems and was designated as the Chemla effect (12). The other system in which this phenomenon was first observed was (Li-K)Br (16), and later simulated by a model based on the molecular dynamics (17, 18).

It has been experimentally shown that the internal mobility of Li^+ , b_{Li} , is expressed by

$$b_{\text{Li}} = A \exp(-E/RT) / (V - V_0) \quad [5]$$

where E and V_0 are constants, R is the gas constant, and V is the molar volume of the system. The reciprocal value of b_{Li} obtained in this study is plotted in Fig. 5 against the molar volume of the system together with that obtained by Moynihan and Laity (9). This figure shows that within the experimental range the relationship expressed by Eq. [5] holds in the present system. The constants for the solid lines in Fig. 5 are $A = 1.16 \text{ cm}^5 \text{ V}^{-1} \text{ s}^{-1}$, $V_0 = (43.7 - 0.0259T) \text{ cm}^3 \text{ mol}^{-1}$, and $E = 33.1 \text{ kJ mol}^{-1}$. As for the mobility of K^+ , its reciprocal shows similar linear relationships with

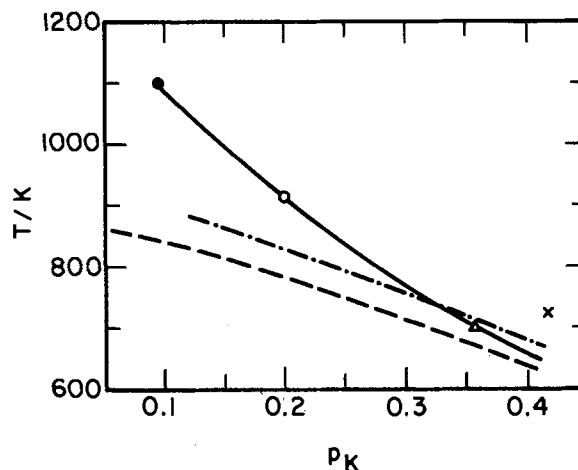


Fig. 3. Temperature of crossover composition and of liquidus composition. ●: (10). ○: from Ref. (9). Δ: this work. ----: liquidus temperature (13). - · - ·: 50 K above liquidus temperature. ×: the eutectic composition of 723 K.

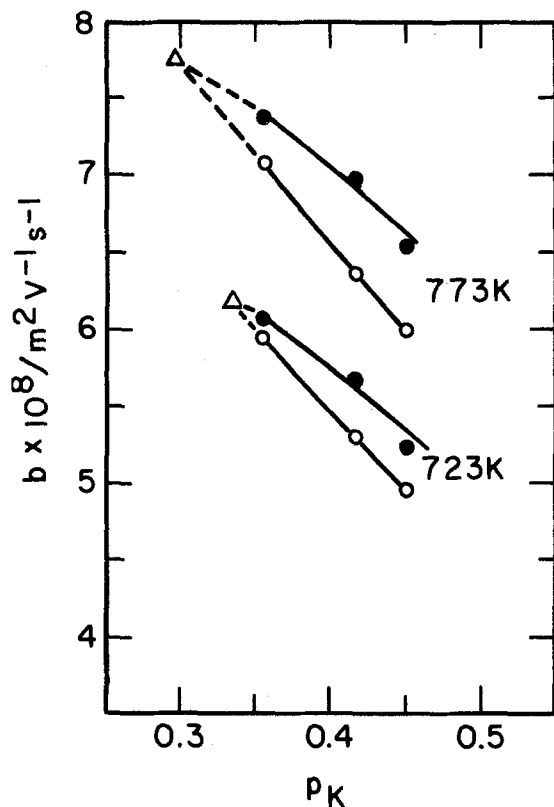


Fig. 4. Isotherms of internal cation mobilities against equivalent fractions of KCl at 723 and 773 K. \circ : b_{Li} . \bullet : b_K . Δ : the Chemla crossing points estimated from Fig. 3.

molar volume of the system at temperatures 773 and 913 K, as shown in Fig. 6. The parameters for K^+ are $A = 6.18 \text{ cm}^5 \text{ V}^{-1} \text{ s}^{-1}$, $V_o = (75.8 - 0.0743T) \text{ cm}^3 \text{ mol}^{-1}$, and $E = 40.7 \text{ kJ mol}^{-1}$. The curve at 723 K deviates considerably from linearity. Similar non-linearity was observed with large cations such as Rb^+ in the molten nitrates at lower temperatures (14).

The transference number of species i , t_i is related to the mobility of species i , b_i , by the following equation in a binary system

$$t_i = p_i b_i / (p_1 b_1 + p_2 b_2) \quad [6]$$

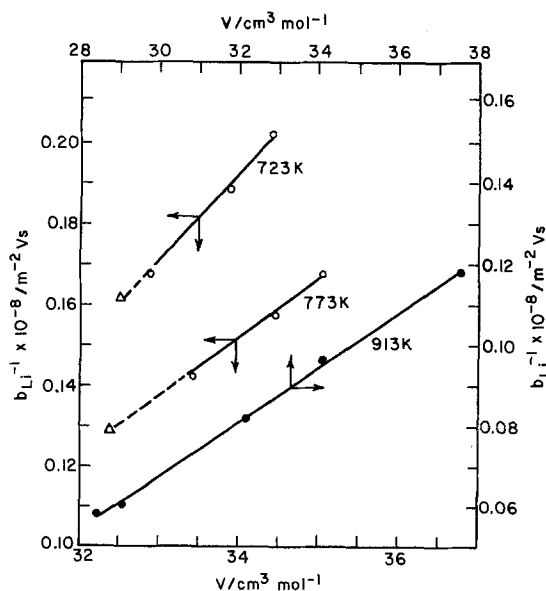


Fig. 5. The reciprocal of internal mobilities of Li^+ plotted vs. molar volume. \circ : this work. \bullet : from Ref. (9). Δ : the Chemla crossing points.

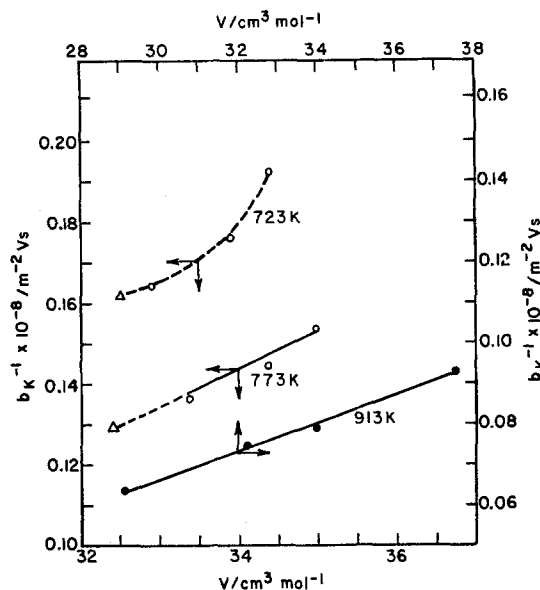


Fig. 6. The reciprocal of internal mobilities of K^+ plotted vs. molar volume using the same symbols as in Fig. 5.

Therefore

$$t_i/p_i = b_i / (p_1 b_1 + p_2 b_2) \quad [7]$$

When $b_1 = b_2$, one can obtain $t_i/p_i = 1$, which is frequently used as an approximation for the transference number. However, the present study shows the values of t_{Li}/p_{Li} and t_K/p_K to be 0.97 and 1.04 at $T = 723 \text{ K}$ and near the eutectic composition, i.e., $p_K = 0.416$, respectively. The relative difference in internal cation mobilities, which is equal to $(t_{Li}/p_{Li} - t_K/p_K)$, reaches as much as -7% in this system. Since the eutectic composition (x in Fig. 3) is located above the solid line in Fig. 3, where t_K base line is larger than p_K , transition time for phase separation becomes shorter than that estimated from the assumption $t_K = p_K$. For example, the value of $t_K/p_K = 1.04$ determined by this study at $p_K = 0.416$ and $T = 723 \text{ K}$ gives about 8% less transition time than that estimated using the assumption $t_K = p_K$. The discrepancy becomes more pronounced at higher concentration of KCl. However, increased concentration of LiCl lowers t_K and brings t_K to below the value of p_K , resulting in the favorable condition for the cell operation. However, the addition of LiCl to the eutectic salt mixture also results in a higher liquidus temperature, causing the precipitation of the salt component. In such case, the operating temperature of the cell must be kept sufficiently high to maintain the stable cell operation. Usually the cell operating temperature is kept at least 50 K above the liquidus temperature of the salt. For example, changing the electrolyte composition from $p_K = 0.415$ to $p_K = 0.36$ raises the liquidus temperature of salt to 673 K. A cell containing this salt requires an operating temperature of 723 K for the stable operation.

EMF, ϕ , due to the concentration polarization can be calculated by

$$\phi = \frac{1}{F} \int_0^{\Xi} \frac{1 - t_{Li}}{1 - p_{Li}} \frac{d\mu_{LiCl}}{dx} dx \quad [8]$$

where μ is chemical potential and Ξ is the separation distance between electrodes (4). With the boundary conditions $p_{Li} = 0.52$ at $x = 0$ and $p_{Li} = 0.72$ at $x = \Xi$ and assuming $t_{Li} = p_{Li}$ and an ideal solution, one can obtain $D = 20.4 \text{ mV}$. A similar calculation can be carried out, using t_{Li} , estimated from Eq. [6], and $\phi = 20.7 \text{ mV}$ is obtained. Therefore, as far as EMF of this system is concerned, the assumption of $t_i/p_i = 1$ seems to be satisfactory.

Conclusion

The internal cation mobilities of Li^+ and K^+ in the system (Li-K) Cl were determined experimentally over

the temperature range 700–778 K, with initial equivalent fractions of KCl of 0.356, 0.416, and 0.451. The Chemla effect was observed in this system.

The transference numbers calculated from the internal mobilities showed a discrepancy from the relationship $t_i/p_i = 1$, which is frequently used as an approximation for transference number.

Manuscript submitted Aug. 2, 1982; revised manuscript received Dec. 9, 1983.

Argonne National Laboratory assisted in meeting the publication costs of this article.

LIST OF SYMBOLS

A	constant in Eq. [6] ($\text{cm}^5 \text{V}^{-1} \text{s}^{-1}$)
b_i	internal mobility of cation i ($\text{cm}^2 \text{V}^{-1} \text{s}^{-1}$)
\bar{b}	average value of mobilities defined by Eq. [2] ($\text{cm}^2 \text{V}^{-1} \text{s}^{-1}$)
p_i	equivalent fraction of cation i
t_i	internal transport number of cation i
E	constant in Eq. [5] (kJ mol^{-1})
Q	transported charge (C)
T	temperature (K)
V	molar volume of the system ($\text{cm}^3 \text{mol}^{-1}$)
V_0	constant in Eq. [5] ($\text{cm}^3 \text{mol}^{-1}$)

Greek Letters

ϵ_{12}	relative difference in internal mobilities defined by Eq. [1]
Λ	equivalent conductivity ($\text{S cm}^2 \text{mol}^{-1}$)
μ	chemical potential (kJ mol^{-1})
Ξ	separation distance between electrodes (cm)
Φ	EMF due to the concentration polarization (V)

REFERENCES

1. P. A. Nelson *et al.*, "Progress Report for the Period 11/78-3/79," ANL-79-39, Argonne National Laboratory, Argonne, IL (1979).
2. B. A. Askew and R. Holland, Abstract 56, p. 138, The Electrochemical Society Extended Abstracts, Vol. 73-2, Boston, Oct. 7-11, 1973.
3. M. J. Willars, J. G. Smith, and R. W. Glazebrook, *J. Appl. Electrochem.*, **11**, 355 (1981).
4. J. Braunstein and C. E. Vallet, *This Journal*, **126**, 960 (1979).
5. R. Pollard and J. Newman, *ibid.*, **128**, 491 (1981).
6. C. E. Vallet, D. E. Heatherly, R. L. Sherman, and J. Braunstein, *ibid.*, **129**, 49 (1982).
7. C. E. Vallet, D. E. Heatherly, and J. Braunstein, in "Transport Processes in Electrochemical Systems," R. S. Yeo, T. Katan, and D-T. Chin, Editors, p. 122, The Electrochemical Society Soft-bound Proceedings Series, Pennington, NJ (1982).
8. C. A. Melendres, C. C. Sy, and B. Tani, *This Journal*, **124**, 1060 (1977).
9. C. Moynihan and R. Laity, *J. Phys. Chem.*, **68**, 3312 (1964).
10. M. Smirnov, K. Aleksandrov, and K. Khokhlov, *Electrochim. Acta*, **22**, 543 (1977).
11. A. Klemm, *Z. Naturforsch.*, **1**, 252 (1946).
12. K. Kawamura, I. Okada, and Odawara, *ibid.*, **30a**, 69 (1975).
13. M. Hansen, "Constitution of Binary Alloys," Metallurgy and Metallurgical Engineering Series, 2nd ed., McGraw Hill (1958).
14. I. Okada, R. Takagi, and K. Kawamura, *Z. Naturforsch.*, **36a**, 381 (1981).
15. E. R. Van Artsdalen and I. S. Yaffe, *J. Phys. Chem.*, **59**, 118 (1955).
16. J. Perie, M. Chemla, and M. Gignoux, *Bull. Soc. Chim. Fr.*, 1249 (1961).
17. I. Okada, R. Takagi, and K. Kawamura, *Z. Naturforsch.*, **35a**, 493 (1980).
18. F. Lantelme and P. Turq, *J. Chem. Phys.*, **77**, 3177 (1982).

Porous Electrodes

I. Numerical Simulation Using Random Network and Single-Pore Models

Michael Kramer and Micha Tomkiewicz*

Department of Physics, Brooklyn College of the City University of New York, Brooklyn, New York 11210

ABSTRACT

A random network model is introduced to simulate the porous metal-electrolyte interface. This is the first time that an attempt has been made at defining a model for this system that maintains the random nature of the rough topology. A previously utilized model for this system, the single-pore model, is explored and extended. The models are compared, and the results of the random network model are found to be in qualitative agreement with the single-pore models.

The porous metal electrode is a subject of intense theoretical and applied interest. Although widely utilized in electrochemical systems, especially in battery technology, very little is known in detail about the porous interface from first principles, aside from a general knowledge of how the porous electrode's behavior deviates from flat-electrode behavior. Specifically, it would be useful to know how the complicated topology of the porous metal electrode contributes to the electrical properties of the interface. Previous attempts at modeling the porous electrode are presented in the review article by DeLevie (1). The macroscopic model (2) treats the electrode-electrolyte system as a superposition of two continua, one of the electrode matrix and one of the solution matrix that fills all the unoccupied space. The solution is assigned an effective conductivity, and the interface is considered to have an effective capacitance per unit area. The single-pore model is based on a one-dimensional representation of

a pore as a transmission line (see Fig. 5) which represents a pore of "average pore length." These models, however, do not account for the random distribution of pores in a true porous solid, nor for a complicated surface topology. We have chosen to introduce a three-dimensional model of the rough interface based on the random-network lattice that has proven to be so useful in representing conduction in inhomogeneous materials and related percolation problems (3-5). AC impedance measurements are widely used experimentally for the *in situ* characterization of electrochemical systems under equilibrium conditions. In conducting these measurements on porous electrodes, the complex topology of the electrode in various states of charge yields ambiguous data, not subject to a unique interpretation. The computer simulation allows us to examine the impedance of the system as a function of given charge accumulation modes at the electrode-electrolyte interface. The model is not intended to portray the dc operation of the electrode, but rather to provide a means for understanding the interface. Using an IBM/

* Electrochemical Society Active Member.

Key words: electrode, impedance, battery, topography.

370 computer, we construct our model and calculate its complex impedance, $Z(\omega)$, in the frequency range of 1 Hz to 1 MHz. Based on this impedance spectrum, we model the system in terms of passive elements (6).

In this paper, we will present our model in detail, discuss preliminary results, and compare these results with the "DeLevie model." We will also discuss further work being done to utilize this model for a more detailed characterization of the interface.

The "Random" Network Model

We consider a simple system, in which a 1 cm³ porous metal electrode is immersed in electrolyte, along with a counterelectrode. Only the bottom (1 cm²) surface of the electrode is exposed to the electrolyte. The electrode is allowed to discharge, allowing for a buildup of a semiconductor on the metal surfaces exposed to the electrolyte. To explore the electrical behavior of this system, we note that we may define a local conductivity, $\sigma(\vec{r})$, the bulk conductivity at point \vec{r} in our system. Rather than attempt to solve for the current distribution using the electrostatic equations for the continuous case, we transform the problem into one requiring the solution of a discrete set of Kirchoff's law equations (a finite difference approximation to the continuum problem (3)). We subdivide our bulk system into a regular cubic mesh of points $\{r_i\}$ ($i = 1, S$) and assign to each branch of the mesh a conductivity that represents the conductivity of the surrounding bulk in that region of space. Let the conductance of the circuit branch that connects node i and j be denoted as g_{ij} , the voltage at node i be V_i , and the net current into node i be I_i . We then have $(S-1)$ equations of the form

$$\sum_j g_{ij}(V_i - V_j) = I_i \quad [1]$$

or in matrix notation

$$G \cdot V = I$$

where G is the conductance matrix ($G_{ii} = \sum_j g_{ij}$ and $G_{ij} = -g_{ij}$), V is a vector containing the voltages on each node with respect to ground, and I is a vector containing the net current inputs to each node. We may solve these simultaneous equations for the V 's on all the nodes, and for the total impedance of the system. A detailed presentation of the algorithm that we have employed follows.

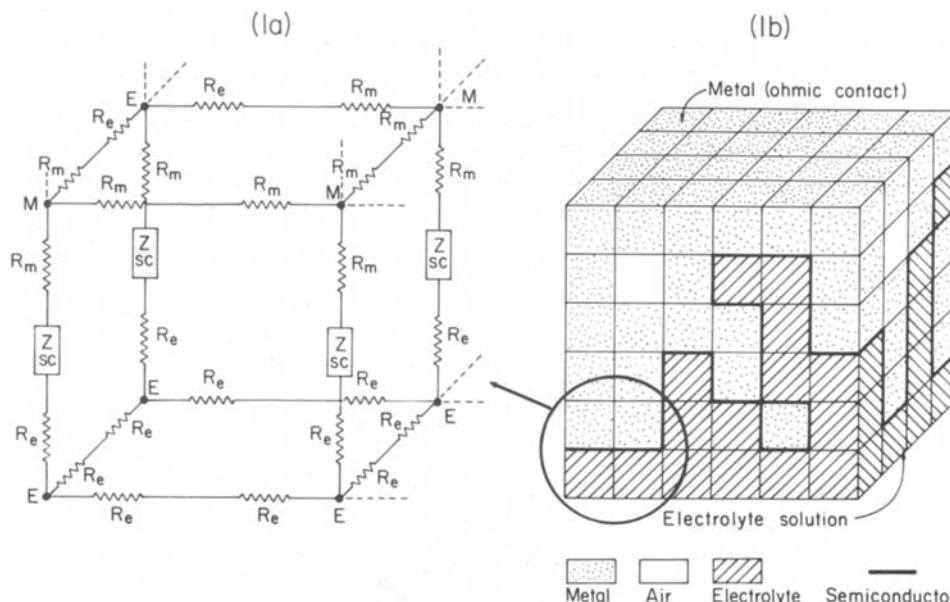
We define a three-dimensional cubic lattice, $A(i, j, k)$, where i, j , and k range from 1 to N , and $N^3 = S$, the total number of nodes. N is chosen so that it is sufficiently large to approximate an infinite system. Construction of the electrode is simulated using a random

number generator to place "metal" at various points in the lattice, until the desired porosity is reached. A check is made of the resulting electrode to insure that it is continuous and that no pieces of metal are "hanging" in midair. Any disjointed pieces of metal are removed, and are randomly replaced on the remaining available lattice points. This process is repeated until a continuous electrode of the desired porosity is obtained. Lattice plane $k = 1$ is defined as electrolyte, to represent the solution; the electrode itself begins at lattice plane $k = 2$. The electrolyte is allowed to "seep" into the pores in the electrode until all accessible pores are filled, by searching for continuous electrolyte paths from the $k = 1$ plane throughout the electrode. Any point on the lattice which has been left empty (i.e., no metal was placed there, and electrolyte was precluded from penetrating to that site) is considered to be "air."

Each lattice point represents a node in a three-dimensional circuit network, (see Fig. 1), and each pair of nodes defines a circuit branch in the network. The impedance of each branch is determined by the characteristics of the two surrounding nodes. Thus, for example, if $A(1, 1, 1)$ is electrolyte and $A(1, 2, 1)$ is also electrolyte, the circuit branch defined by those nodes will consist of two series resistors of resistance R_e (the resistance of a microscopic section of the electrolyte). If $A(1, 1, 2)$ is metal and $A(1, 2, 2)$ is metal, then the circuit branch defined by those two nodes will be two series resistors of value R_m (the resistance of a microscopic section of the metal). Finally, the branch defined by $A(1, 1, 1)$ -electrolyte, and $A(1, 1, 2)$ -metal, is represented by an R_m and an R_e resistor in series, with the addition of a parallel R-C element in series with them to represent the semiconductor-electrolyte interface that results (see Fig. 2). Any circuit branches leading into nodes that are defined as "air" are taken to be of infinite resistance.

The values that we have chosen to use as our unit impedances for the individual components of metal, electrolyte, and semiconductor are presented in Fig. 2. These values were obtained by taking the values of bulk impedance for a 1 cm³-sized sample (we chose numbers characteristic of Zn and ZnO) and scaling them down to the magnitude of a unit pore size: approximately 10 μ diam. We define a characteristic time constant of the interface, $\tau = R_p C$. These components are assembled into a system, as described above (see Fig. 3), and the total impedance of the system is calculated. The total impedance is then rescaled by an appropriate factor that normalizes the whole system to a 1 cm³ size. Thus, an attempt is made to obtain im-

Fig. 1. Representation of the three-dimensional lattice in terms of circuit elements. Figure 1b shows our model in terms of a checkerboard pattern of bulk components of metal, electrolyte, semiconductor, and air. Figure 1a depicts our representation of a corner of Figure 1b in terms of a network of circuit elements. Z_{sc} is the impedance of the semiconductor layer on the interface (see Fig. 2).



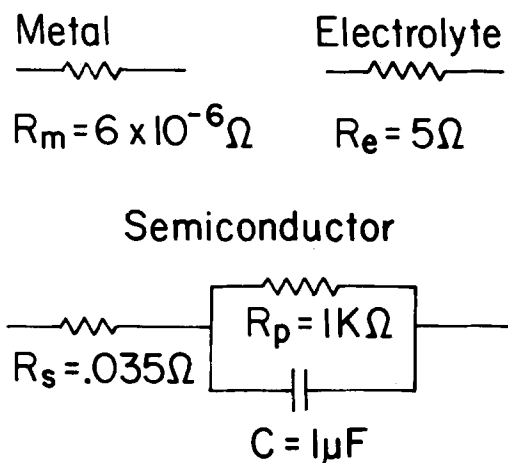


Fig. 2. Equivalent circuits used to represent the microscopic components of the system (metal, electrolyte, semiconductor, etc.).

pedance data with numbers representative of that which might be encountered in a real system.

Once the electrical network has been defined, the computer sets up the Kirchoff's law equations. Due to the fact that our model includes reactive circuit elements, the quantities G , V , and I in Eq. [1] are complex, and may be represented as 2S-1 equations of the form

$$\begin{pmatrix} G_r & -G_i \\ G_i & G_r \end{pmatrix} \begin{pmatrix} V_r \\ V_i \end{pmatrix} = \begin{pmatrix} I_r \\ I_i \end{pmatrix} \quad [2]$$

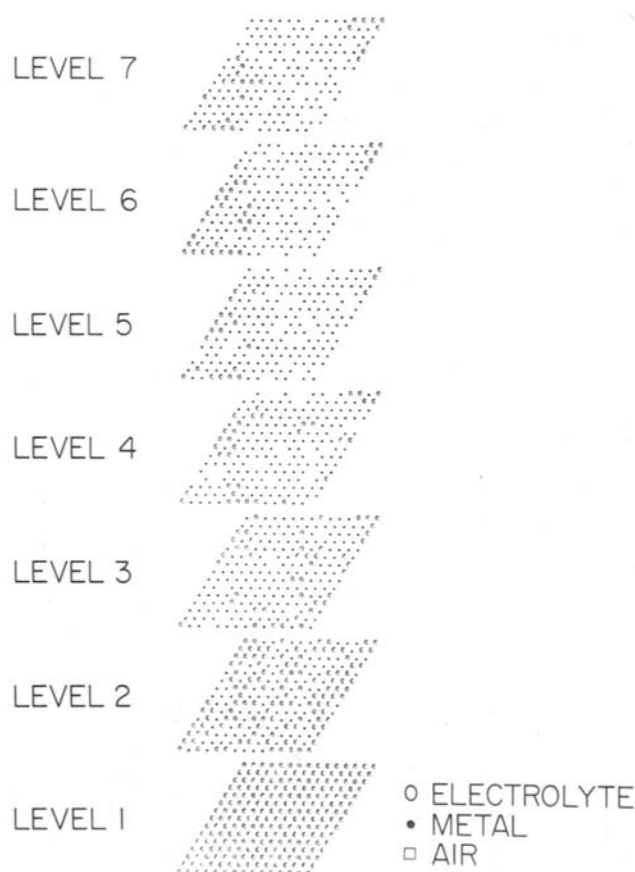


Fig. 3. The random network lattice used to generate the data for Fig. 4. At this porosity of 0.3, the electrolyte does not fully penetrate the lattice. (Actually, the penetration of the electrolyte into the pores seems to conform to classical percolation theory. At porosities above 0.35, the liquid starts to penetrate through the electrode).

where the subscripts r and i stand for the real and imaginary components, respectively.

A known current is sent uniformly into all the bottom nodes (so as to eliminate the "edge effects" that would result if the current were sent only into one node), and the impedance of the system is calculated between one node on the electrolyte plane (1, 1, 1) and one node of the top electrode plane (N, N, N) by solving for the V 's on all the nodes.

For a system of $N = 15$ (a lattice of size $15 \times 15 \times 15$ with 3375 nodes) there are up to 6748 equations to be solved. This is a formidable computer problem. Indeed, the task would be prohibitive without taking advantage of the fact that the conductance matrix, G , is a sparse-symmetric coefficient matrix.

A number of techniques exist for the solution of this class of problems. A widely used method for solving the simultaneous equations in the random resistor lattice is the Gauss-Seidel iteration procedure with over-relaxation (5). This is a very economical method, in both execution time and storage space. A serious drawback of this technique is the relatively strict requirements that it places on the coefficient matrix in order for convergence to be achieved, namely, that the matrix be either diagonally dominant, or at least positive definite (7). For Kirchoff's law problems with purely resistive components, diagonal dominance is assured, since the diagonal elements of the conductance matrix are simply the sum of the off diagonal elements. In our problem, with complex impedances, we find that at frequencies for which the real conductance approaches the same order of magnitude as the imaginary conductance, the Gauss-Seidel procedure does not converge. This is due to the form of the equation in Ref. (2) where there are many more off diagonal elements due to the G_i values. When these imaginary components are large, the matrix is no longer diagonally dominant nor positive definite.

For most of our computations, we have resorted to the use of a Gaussian elimination routine which takes advantage of both the sparseness and the symmetry of the G coefficient matrix (8). Only the nonzero elements in the upper half-triangle of the matrix are stored, and an efficient pivoting strategy is chosen to minimize nonzero matrix fill during the pivoting and to minimize the number of multiplications required in the solution. In practice, the technique is approximately an order of magnitude more expensive to use than Gauss-Seidel in both speed and storage requirements. The advantage of using the Gaussian elimination technique is that a solution is guaranteed for almost any problem. The solutions obtained from the Gauss-Seidel procedure (in the range in which convergence is reached) are in complete agreement with the results obtained using the modified Gaussian elimination technique.

Figure 3 presents a system constructed with a porosity of 0.30, and the resulting impedance of the system as a function of frequency is plotted in Fig. 4. We have identified three basic regions of interest in the frequency range spanned by our results. Region I is the low frequency range, in which our system seems to behave as a parallel RC combination (see Fig. 4). Region II is in the mid-frequency range, with an impedance spectrum that cannot be represented using passive elements, and Region III is representative of a series RC combination. The variation of the impedance data as a function of system size is presented in Fig. 5 from size $N = 5$ to $N = 15$. For the results presented here, $N = 15$ was used to ensure proper statistical representation of an infinite system.

The Single-Pore Model

It is interesting to compare, at least qualitatively, the results from our three dimensional model with the results obtainable from the single pore model previously mentioned (1).

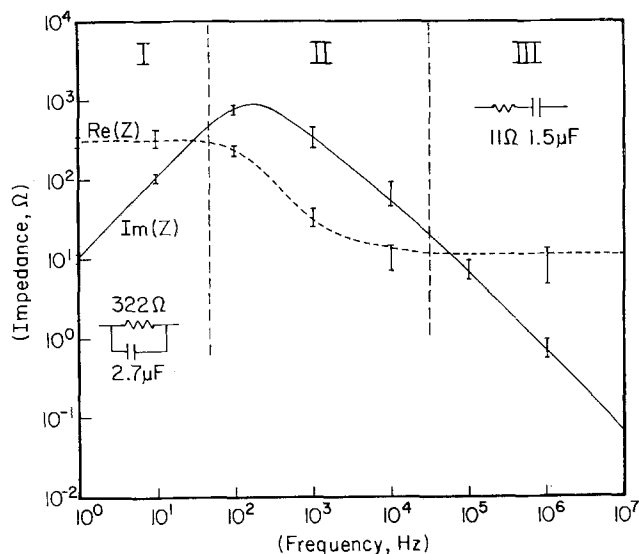


Fig. 4 Impedance spectrum from the random network model at a single porosity (0.3), and a single random number. Three frequency regimes are identified, and we have modeled two regimes with a simple passive-element model. The bars on each curve represent the variations in the data when various random-number seeds are used to construct the lattice. For each random-number seed, the shape of the impedance spectrum is almost identical.

DeLevie, following on the heels of other researchers [Daniel-Bek (9) and others], suggested that each pore in a porous electrode may be thought of as having a uniformly distributed electrode and electrolyte resistance throughout its length. As such, the single pore may be modeled as in Fig. 6a, where R is the resistance per unit length of the electrolyte solution in-

side the pore and Z is the impedance of the electrode-electrolyte interface. The current voltage relationships of this circuit may be expressed as a differential equation, and a solution may be obtained for the total impedance of the circuit as (1)

$$Z_o = (RZ)^{1/2} \coth(\rho L) \quad [3]$$

where R and Z are defined above, $\rho = (R/Z)^{1/2}$, and L is the length of the pore. This is the main, and currently utilized (10), result from this model. The main characteristics of the calculation are: (i) although flat electrode impedances vary as a function of Z , porous surface impedances will be dependent on $(RZ)^{1/2}$, and (ii) the contribution of the electrode surface deep inside the pore is negligible, $1/\rho$ becoming the characteristic "penetration depth." If $\rho L \gg 1$, the pore behaves like a semi-infinite one.

In order to utilize these results for comparison with the random network model, we must introduce a value for Z , and we must also combine the single-pore transmission-line impedances to form a complete rough electrode. The former is accomplished by defining the electrode-electrolyte interface as a standard parallel RC model, as depicted in Fig. 6b. We have used the same numerical values for the individual components as those in the random network model (here they are shown already normalized to the $10 \mu\text{m}$ single-pore size). As a result

$$Z = r_s + \frac{R_p}{1 + \omega^2 \tau^2} - j \frac{\omega \tau R_p}{1 + \omega^2 \tau^2} \quad [4]$$

where $\tau = R_p C$. Substituting Eq. [4] into Eq. [3] and simplifying, we get

$$Z_o = \sqrt{\frac{RP}{2}} \frac{e^{2x} - e^{-2x}}{e^{2x} + e^{-2x}} \times \left\{ \left[(\beta + \alpha)^{1/2} + \frac{2 \sin 2\theta}{e^{2x} - e^{-2x}} (\beta - \alpha)^{1/2} \right] + j \left[(\beta - \alpha)^{1/2} - \frac{2 \sin 2\theta}{e^{2x} + e^{-2x}} (\beta + \alpha)^{1/2} \right] \right\} \quad [5]$$

where we have defined the following quantities

$$P = \frac{R_p}{1 + \omega^2 \tau^2}$$

$$\alpha = 1 + \frac{r_s}{P}$$

$$\beta = (\alpha^2 + \omega^2 \tau^2)^{1/2}$$

$$x = L \left(\frac{R}{P} \right)^{1/2} \frac{1}{\sqrt{2}\beta} (\beta + \alpha)^{1/2}$$

$$\theta = L \left(\frac{R}{P} \right)^{1/2} \frac{1}{\sqrt{2}\beta} (\beta - \alpha)^{1/2} \quad [6]$$

A log-log plot of the relationship between Z and f (for a single pore) is presented in Fig. 7. It is interesting to note the similarity in shape between the impedance spectrum of the single-pore model (even though we are only considering a single pore) and that of our random network model (Fig. 4). The advantage of considering a single pore at the present stage is that it is the only system for which we have an analytic result (Eq. [5]), which may be used to derive expressions for the impedance in different frequency ranges.

We define three frequency regimes:

1. The low frequency range ($\omega \tau \ll 1$)

$$\text{Re}(Z_o) \simeq K$$

$$\text{Im}(Z_o) \simeq K\omega\tau$$

[7a]

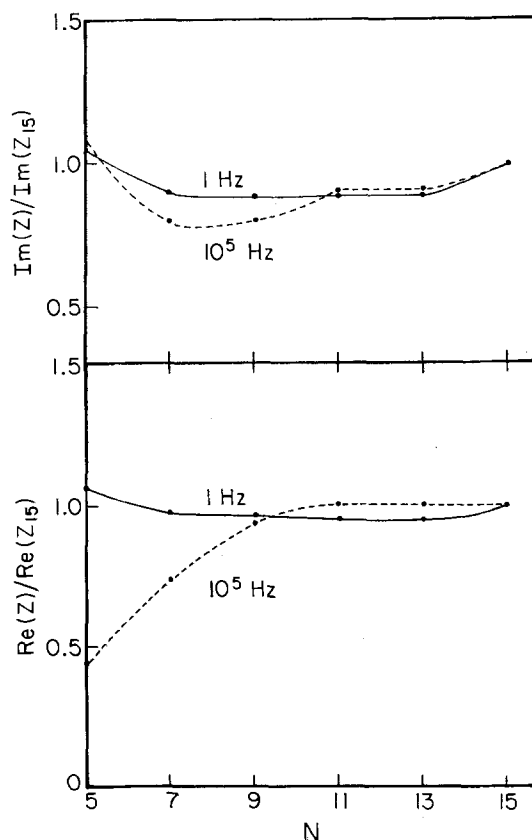


Fig. 5. The impedance in the random network model as a function of system size. All values are normalized to the impedance of lattice size $15 \times 15 \times 15$ ($N = 15$).

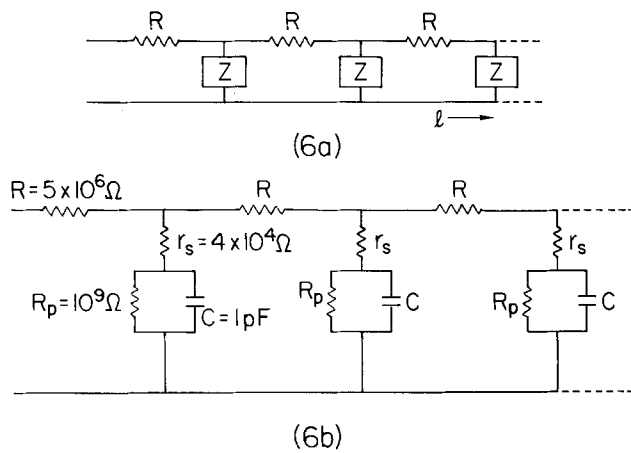


Fig. 6. The DeLevie model of a single pore. Figure (6a) presents the general transmission-line model. (6b) presents the value we have chosen for R , the electrolyte impedance, and our specific model for Z , the electrode-electrolyte interface inside the pore.

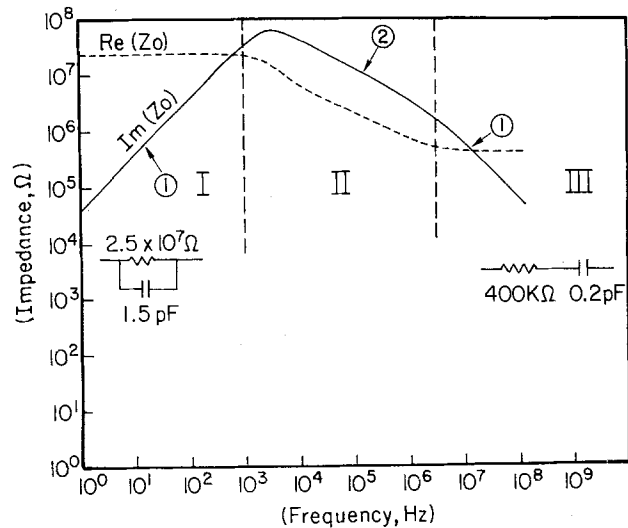


Fig. 7. Impedance spectrum from the DeLevie model, single pore. The sections of the curve labeled 1 are areas in which the imaginary impedance plot is of slope = 1 on the log-log plot, and the impedance in these ranges may be modeled by the two passive elements models shown. The section of the curve labeled 2 has a slope of 1/2 (see Eq. [7a]-[7c]).

where K (independent of frequency) is given as

$$K = \sqrt{RR_p} \frac{e^{2x} - e^{-2x}}{e^{2x} + e^{-2x} + 2}$$

and x is

$$x \approx L(R/R_p)^{1/2}$$

The notable features of Eq. [7a] are the frequency independence of the real part and the slope 1 dependence (on the log-log plot) in the imaginary part of the impedance (see Region I on Fig. 7).

2. The intermediate frequency range ($\omega\tau \gg 1$, but $r_s\omega\tau/R \ll 1$)

$$Re(Z_o) = Im(Z_o) = \sqrt{\frac{RR_p}{2}} \frac{1}{\sqrt{\omega\tau}} \quad [7b]$$

This results in the slope $-1/2$ line in Region II of Fig. 7.

3. The high frequency range ($\omega\tau \gg 1$ and $r_s\omega\tau/R_p \gg 1$)

$$Re(Z_o) = \sqrt{Rr_s}$$

$$Im(Z_o) = \frac{1}{2} \sqrt{\frac{R}{r_s}} \frac{R_p}{\omega\tau} \quad [7c]$$

which results in a frequency independent real impedance, and the slope -1 line in the imaginary impedance, as can be seen in Region III of Fig. 7.

In addition to the frequency limits, it was also assumed that $R_s/R_p \ll 1$, and that $R > r_s$ by at least an order of magnitude (which is usually the case).

To combine the single pores into a unified metal-electrolyte system, we extend DeLevie's model slightly. We define an X-Y plane and divide it into N^2 squares, and randomly place a rectangular-width pore on the X-Y plane with its length extending in the Z direction. The length of the pore, L , is also randomly chosen to be from 1 to N , and the pore width, W , is selected so that there is a Gaussian distribution about $W = 2$ (to prevent a few very wide pores from "taking over" the whole electrode). More random-sized pores are randomly placed on the X-Y plane until the desired porosity is reached. We may then solve for the total impedance of the system by adding up all the parallel impedances due to the individual pores, using Eq. [5] to represent the impedance of each pore. The impedances of the nonporous sections of the electrode are also added on to the total impedance.

The results, for a porosity of 0.3 and $N = 40$, are presented in Fig. 8. The criteria for choosing N was based on considerations similar to those used to choose N in the random network model, namely, that the results be independent of N and statistically independent of the random number. This phase of the calculation was performed on an IBM PC.

Discussion of Results

There is a qualitative agreement between the random network model and the single-pore model. A comparison of the passive elements representation of the two systems (Fig. 4 and Fig. 8) also yields order-of-magnitude quantitative agreement. One discrepancy between the two models is the definite shift in the location of the "mid-frequency peak" in Fig. 8 as compared to the random network and single-pore results. A major difference between the two models in construction, is the fact that in the random network the pores interact with each other as in a true porous electrode, while in the DeLevie model each pore is kept separate from the others, and is a separate channel. The favorable comparison of the two models would seem to bear out DeLevie's assertion that "the disregard of crosslinks [between the pores] presumably does not introduce a significant error" (1). Nevertheless, this

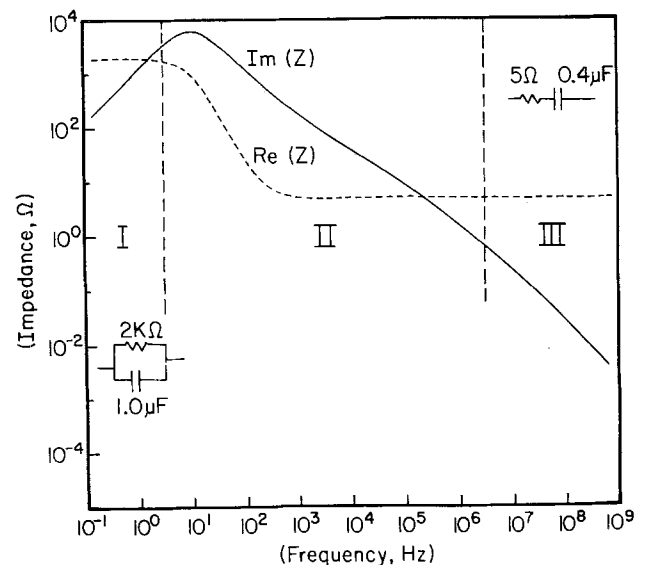


Fig. 8. Impedance data from DeLevie model, randomly distributed pores. Porosity = 0.3, $N = 40$.

can be a useful starting place for an explanation of a discrepancy between the two.

The behavior of the system impedance in the random network model may be somewhat inferred from the values of the constituent components that make up the system. The low frequency (real and imaginary) impedance in Fig. 4 reflects the values of R_p and C of the unit (semiconductor) interface, although the 300Ω value of $Re(Z)$ is noticeably lower than the $1\text{ k}\Omega$ R_p . In the high frequency regime, C dominates, totally shunting out R_p , the only contribution to the real impedance being R_e . This provides us with an indication that the total behavior of the porous-metal system may be inferred from the values of the components that make up the complicated surface topography. Our ultimate goal is to generate a detailed picture of the macroscopic interface from the impedance data of the microscopic components that make up the system. This will be considered further in a subsequent paper, along with an exploration of the physical significance of the passive elements model of the entire system.

We will also examine the correlation between the single-pore analytic results (in the various frequency limits) and the random network model. Only a single porosity has been considered thus far, but an exploration of the random network model at different porosities is in order. Although some rough surfaces may exhibit a conduction percolation threshold (11, 12), we do not expect to see any classical percolation in our system. This is due to the fact that we have constrained the system to be above the percolation threshold by the requirement that the metal electrode be continuous. We would, however, expect to see some less dramatic system dependence on porosity.

Acknowledgments

We would like to express our special gratitude to Dr. Philip E. Seiden from IBM, Thomas J. Watson Re-

search Center, for helping us to formulate the Random-Network problem. We would also like to thank Dr. Itzhak Webman from Exxon, for helpful discussions during the initial phases of the project. This work was supported by the Office of Naval Research under Contract N00014-81-K-0339.

Manuscript submitted July 14, 1983; revised manuscript received Feb. 14, 1984.

Brooklyn College assisted in meeting the publication costs of this article.

REFERENCES

1. R. DeLevie, in "Advances in Electrochemistry and Electrochemical Engineering," Vol. 6, P. Delahay and C. W. Tobias, Editors, p. 329, John Wiley and Sons/Interscience, New York (1967).
2. J. S. Newman and C. W. Tobias, *This Journal*, **109**, 1183 (1962).
3. S. Kirkpatrick, *Rev. Mod. Phys.*, **45**, 574 (1973).
4. I. Webman, J. Jortner, and M. H. Cohen, *Phys. Rev. B*, **14**, 4737 (1976).
5. I. Webman, J. Jortner, and M. H. Cohen, *ibid.*, **11**, 2885 (1975).
6. M. Tomkiewicz, *This Journal*, **126**, 2221 (1978).
7. Carnahan, Luther, and Wilkes, "Applied Numerical Methods," p. 300, John Wiley and Sons, New York (1969).
8. G. E. Forsythe, M. A. Malcom, and C. B. Moler, "Computer Methods for Mathematical Computations," Prentice Hall, Inc., Englewood Cliffs, NJ (1977).
9. V. S. Daniel'-Bek, *Zh. Fiz. Khim.*, **22**, 697 (1948).
10. S. A. G. R. Karunathilaka and N. A. Hampson, *J. Appl. Electrochem.*, **10**, 357, 603 (1980).
11. M. H. Cohen and M. Tomkiewicz, *Phys. Rev. B*, **26**, 7097 (1982).
12. M. H. Cohen, J. K. Lyden, and M. Tomkiewicz, *Phys. Rev. Lett.*, **47**, 13 (1981).

Study of the Initial Stages of Anodic Oxidation of Polycrystalline Silver in KOH Solutions

Maria Hepel* and Micha Tomkiewicz*

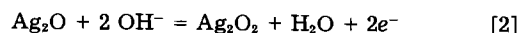
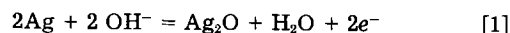
Department of Physics, Brooklyn College of the City University of New York, Brooklyn, New York 11210

ABSTRACT

Growth of the anodic Ag_2O film on a polycrystalline silver disk electrode in 1 mol dm^{-3} KOH solution at ambient temperature has been examined using a variety of electrochemical techniques. On the basis of the experimental results, a solid-state model of silver electrode covered by a thin semiconductor film with a finite ionic conductivity has been proposed. It has been found that under potentiostatic control, thickness of the oxide film adjusts very quickly to the hydrodynamic conditions by a deposition/dissolution process, and the steady-state oxidation currents fulfill the Levich equation for RDE, despite the fact that the electrode is covered by a thin Ag_2O film. In the case of thicker films, after completion of nucleation and growth, changes in the hydrodynamic conditions do not influence the oxidation current, and adjustment of the thickness of the oxide film to new hydrodynamic conditions proceeds at slower rate because of the slowness of the solid-state diffusion step. The Ag_2O nucleation and growth peak has been observed in chronoamperometric transients above potential of $+240\text{ mV}$ (vs. Ag/AgCl). It has been observed that the nucleation and growth peak decreases as the convective diffusion is accelerated by the rotation speed of the RDE. The dependence of the oxidation current upon the rotation speed vanishes gradually during the Ag_2O nucleation and growth process.

Porous silver oxide electrodes in conjunction with zinc, cadmium, iron, or hydrogen electrode serve as cathodes in various batteries (1). The silver electrodes offer excellent cycle life when used in rechargeable cells (1-4). In spite of development of commercial rechargeable silver-zinc batteries and the numerous investigations on the electro-oxidation of silver in alkaline solutions, the basic electrochemical processes involved are still not well understood. Apparently simple, consecutive oxidation

scheme



is complicated by adsorption processes, nucleation overvoltages, solid-state diffusion, and dissolution of Ag(I) in form of hydroxy complexes. The resulting cyclic voltammogram for polycrystalline smooth electrode consists of five anodic peaks (see Fig. 1), of which only two are associated with the formation of bulk Ag_2O and Ag_2O_2 .

*Electrochemical Society Active Member.

Key words: anode, films, nucleation, transients, battery.

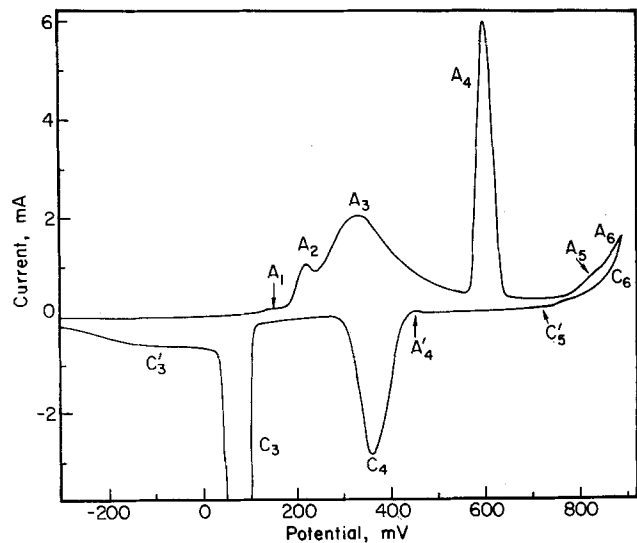


Fig. 1. The CV characteristic for the polycrystalline silver electrode (geometric area $A = 0.385 \text{ cm}^2$) in 1 mol dm^{-3} KOH solution at 22°C . Potential cycles 6-8 between -650 and $+900 \text{ mV}$ vs. Ag/AgCl, $\nu = 10 \text{ mV/s}$, quiet solution, $E_{\text{cond}} = -1240 \text{ mV}$.

Our present objective is to study the initial stages of the oxidation of smooth polycrystalline silver electrode.

Commencement of silver oxidation has been ascribed by Giles *et al.* (5, 6) on the basis of impedance measurements, to its dissolution in form of $\text{Ag}(\text{OH})_2^-$ complexes. According to Brezina *et al.* (7), the multilayer surface oxides are formed in the region of peak A_1 (see Fig. 1), while Giles *et al.* (5, 6) proposed a mechanism in which a monolayer of Ag_2O is completed in the region of the first oxidation peak. Droog *et al.* (8) and Ambrose *et al.* (15) treated their peak as A_1 on the basis of the recalculation of the electrode-potential scale, but, previously (5, 9, 10), this peak was compared to the peak A_2 of other authors (11-14). Ambrose and Barradas (15) conclude on the basis of ring-disk study that in the A_1 region the dissolution of silver(I) as $\text{Ag}(\text{OH})_2^-$ occurs, giving linear Koutecky-Levich plots, $i^{-1} = f(\omega^{-1/2})$. However, no further conclusions could have been drawn from the potential dependence of the determined values of the anodic current at $\omega \rightarrow \infty$. Earlier, the ring-disk technique has been applied by Miller (16). In this study, the supersaturation in the vicinity of the electrode surface has been observed at the foot of the A_3 peak; the peaks A_1 and A_2 have not been observed on his freshly polished electrodes. Tilak *et al.* (9), Perkins *et al.* (10), and Stonehart (11) have treated the peak A_1 as an artifact (carbonate impurities, electrode etching, etc.). Droog *et al.* (8) attribute it to a complex situation in which at least two reactions are involved. They have proven that the change in carbonate concentration does not influence the A_1 peak potential. On the basis of the combined electrochemical and ellipsometric studies, the same authors (8) conclude that the A_1 peak is due to the silver dissolution and the formation of a surface monolayer. The peak A_2 has been identified by Dirkse and de Vries (12) as AgOH . To similar conclusions came Stonehart (11), neglecting dissolution of adsorbed and volume films of AgOH . Other hypotheses have also been proposed: oxidation of adsorbed hydrogen (13), preferential oxidation of surface silver atoms of low coordination number (16, 17), and electrodisolution of silver with eventual formation of a surface of Ag_2O monolayer (9, 10). The latter point of view has been associated (10) with the fact that no photoeffects were observed in the A_2 region. It has been found that the onset of the photocurrent on voltammetric characteristics for semiconducting $n\text{-Ag}_2\text{O}$ film electrode takes place after the peak A_2 is completed (10, 18).

The aging effects in the initially formed oxide film have been considered by Arvia and co-workers (19). The electrochemistry of silver in KOH solutions at elevated

temperatures has been studied by Macdonald and co-workers (25-28).

In this study, we examine the initial stages of the electro-oxidation of silver and growth of the semiconducting oxide films on polycrystalline silver electrodes in alkaline environment. The aim of this work is to describe the solid-state transport processes across the thin Ag_2O anodic film starting from first monolayers. The influence of different parameters on the total oxidation current is discussed. On the basis of the performed experiments, we propose a steady-state model of the Ag/ Ag_2O electrode in the region of the space-charge buildup in the growing film. The linear scan voltammetry (LSV), linear potential scan coulometry (LPSC), cyclic voltammetry (CV), and rotating disk electrode (RDE) techniques have been used in measurements.

Experimental

A standard plexiglass electrolytic cell of about 100 cm^3 capacity was used in this study. A fritted glass tube was used to separate the Pt-foil counterelectrode from the main cell compartment. A silver rod (Johnson-Matthey) pressed into a Teflon holder was used as a working electrode; its active surface area was 0.385 cm^2 . A Model EC-219 rotating disk electrode (IBM Instruments, Incorporated) was also used in experiments with controlled hydrodynamics. The potentials were measured against the double-junction silver/silver chloride electrode (Sargent-Welch Scientific Company) with internal saturated KCl solution and external 1 mol dm^{-3} KNO_3 solution. The latter one was exchanged each day to avoid contamination of the main solution (KOH) by chloride ions.

An EG&G Model 173 potentiostat, equipped with a Model 179 digital coulometer and Model 175 universal programmer, was used for voltammetric and chronocoulometric measurements. The experimental plots were recorded on a Hewlett-Packard Model 7044 A XY-plotter.

All the chemicals used were of analytical-grade purity. The solutions were prepared with deionized water ($18 \text{ M}\Omega$) obtained using a Milli-Q purification system. Before the measurements, silver electrode was polished with $0.05 \mu\text{m}$ alumina (Fisher Scientific Company), washed with deionized water, and dried in a vacuum. The solutions were deoxygenated by nitrogen bubbling.

Results

A well-developed full CV characteristic for polycrystalline silver electrode in 1 mol dm^{-3} KOH solution can be obtained after approximately six cycles between -650 and $+900 \text{ mV}$ vs. Ag/AgCl reference electrode. Such a voltammogram is presented in Fig. 1 for the potential scan rate of 10 mV/s . All the faradaic activity start at potentials positive to -300 mV vs. Ag/AgCl. In consecutive cycles, only small changes (increase) in the peak heights are observed, and they are due to increasing real surface area of the electrode. It is seen, that in the anodic scan, five current peaks are observed and they are designated A_1 through A_5 . The current increase at the positive limit of the voltammogram is associated with the oxygen-evolution reaction.

The formation of bulk Ag_2O and Ag_2O_2 can be ascribed (5, 6, 8-10, 12-21) to peaks A_3 and A_4 , respectively. In the potential region of the peak A_3 , at the foot of the oxygen-evolution wave, the highest silver oxide, Ag_2O_3 , is formed, as has also been reported in Ref. (22, 23, 25, 29-32). The peaks A_1 and A_2 correspond to the initial stages of the silver oxidation.

When the electrode is conditioned in solution at open circuit for a long time (*e.g.*, 24h) significant changes are seen in the LSV peak structure (Fig. 2). The peak A_2 is not observed, and the peak A_3 is much sharper than normally obtained on freshly polished electrode and also is higher than the peak A_4 corresponding to the nucleation and growth of the argentic oxide. Furthermore, upon successive cycles, large changes are observed in the relative amplitude and the position of the various peaks. After about

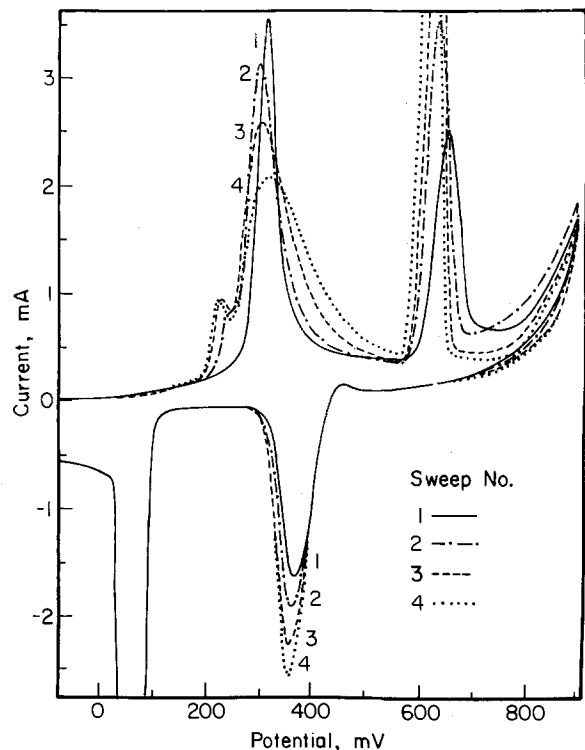


Fig. 2. Consecutive runs (1-4) of the cyclic voltammogram for a stationary silver electrode conditioned for 24h in 1 mol dm⁻³ KOH solution. Scan rate: 10 mV/s. Potential limits: -650 and +900 mV. $A = 0.385$ cm².

four cycles, a stable voltammogram emerges. This evolution is shown in Fig. 2.

Potential region of the peak A₁.—The current prewave A₁, hardly seen in Fig. 1, is presented in enlarged scale in Fig. 3 for a set of potential scan rates ranging from 10 to 200 mV/s. When the anodic inversion potential E_i is equal +180 mV (as in Fig. 3), a full anodic wave is developed only at $v \leq 10$ mV/s. In the reverse scan, the peak C₁ is observed for all values of v . The half-peak width increases with v and approaches approximately 60 mV at $v = 200$ mV/s. The dependence of the peak height upon the potential scan rate is presented in Fig. 4.

The amount of charge consumed during LSV experiment can be calculated by integrating the voltammetric

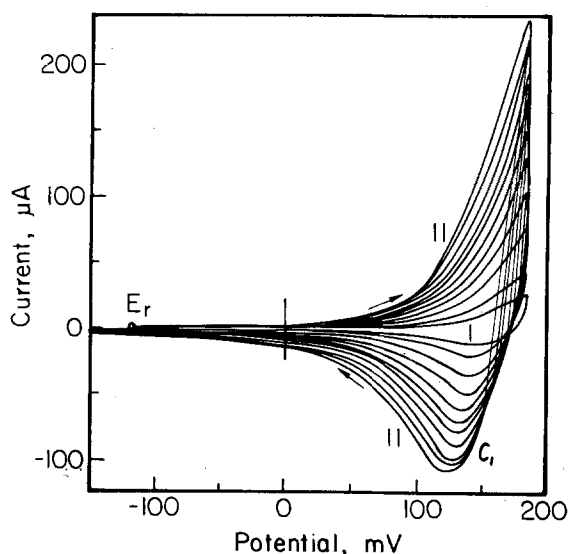


Fig. 3. The LSV characteristics for the Ag electrode in 1 mol dm⁻³ KOH solution in the region of peaks A₁ and C₁, for the potential scan rate v [mV/s]: (1)10, (2)20, (3)40, (4)60, (5)80, (6)100, (7)120, (8)140, (9)160, (10)180, (11)200, $A = 0.385$ cm².

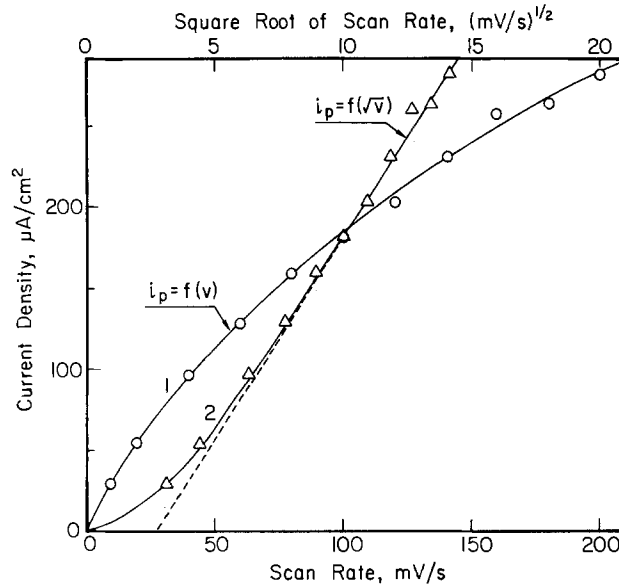


Fig. 4. The dependence of the cathodic peak current (C_1) upon the potential scan rate (curve 1) and the square root of the scan rate (curve 2). Solution: 1 mol dm⁻³ KOH.

characteristic. The charge Q plotted vs. the electrode potential gives then the LPSC characteristic. The same result can be obtained by the use of an electronic digital coulometer with analog output. Typical LPSC characteristics obtained in this way for the initial stage of silver oxidation are presented in Fig. 5. The experimental conditions are similar to the LSV curves shown in Fig. 3, except that E_i is now equal to +200 mV, and the scan rates down to 1 mV/s are applied. Despite a fall of the LSV currents, the total anodic charge increases significantly as v decreases. The total cathodic charge Q_c does not compensate the anodic one Q_A and is always lower by about 1.2-1.5 times. The slower the potential scan, the larger the unrecovered charge.

Note, that all the charge peaks on the LPSC curves in Fig. 5, appear exactly at the same potential. It corresponds to the isopotential point E_x in the family of the respective LSV characteristics. In this case, $E_x = 175$ mV.

As shown by Droog *et al.* (8), the cathodic peak C_1 increases as the anodic potential limit E_i is shifted toward more positive values. We have observed the same effect

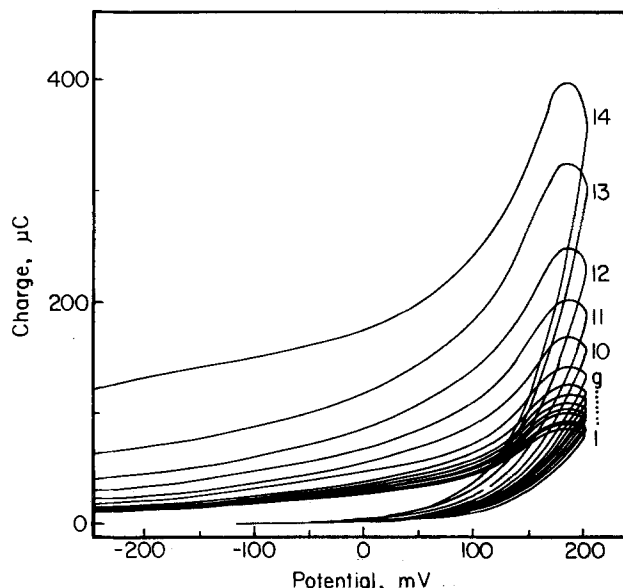


Fig. 5. The LPSC curves for the initial stage of silver oxidation and reduction in 1 mol dm⁻³ KOH solution. Potential scan rates v [mV/s]: (1)200, (2)180, (3)160, (4)140, (5)120, (6)100, (7)80, (8)60, (9)40, (10)20, (11)10, (12)5, (13)2, (14)1, $A = 0.385$ cm².

on a stationary polycrystalline silver electrode. It is interesting now to compare this effect with the LSV curves obtained under different hydrodynamic conditions. A set of LSV characteristics with changing E_i obtained on the rotating silver disk electrode (RDE) is presented in Fig. 6. No effect of E_i is observed up to $E_i = 220$ mV, unless fast potential scans are applied. The significance of this observation is discussed in the Discussion section.

Dissolution effects in the formation of a thin Ag_2O film.—The steady-state anodic oxidation currents measured on silver RDE at different angular velocities, in the potential range 180–250 mV, fulfill the Levich equation

$$i = 0.62nFAD^{2/3}\nu^{-1/6}\omega^{1/2}(C_s - C^*) \quad [3]$$

where D is the diffusion coefficient of the diffusing species, ν is the kinematic viscosity of the solution, C_s and C^* are the concentrations of the diffusing species at the electrode surface and in the solution bulk, respectively, ω is the angular velocity of the rotating disk, and the other symbols have their usual meaning.

The plot of the linear relations $i = f(\sqrt{\omega})$ for different electrode potentials under steady-state conditions is presented in Fig. 7. (The rotation speed $\bar{\omega}$ is expressed in rpm; $\bar{\omega} = [60/2\pi]\omega$). It is evident from Fig. 7 that the surface concentration C_s increases with increasing potential up to approximately +250 mV. Above +250 mV, the situation is much more complex because of commencement of the growth of the bulk Ag_2O film. This process proceeds via the nucleation and growth mechanism (21) with the control by a solid-state transport through the underlying basal layer.

The chronoamperometric curves presented in Fig. 8 illustrate the nucleation and growth of Ag_2O film at $E = +260$ mV on RDE at 5990 rpm and on a stationary electrode. Note that the charge under the nucleation and growth peak is much greater for the stationary electrode than for the RDE. It is not unreasonable to assume that a thicker film is formed in the former case. The problem then arises what is the dependence of the oxidation current upon the hydrodynamic conditions in different stages of the Ag_2O film growth and what is the role of the oxide dissolution processes. From many experiments per-

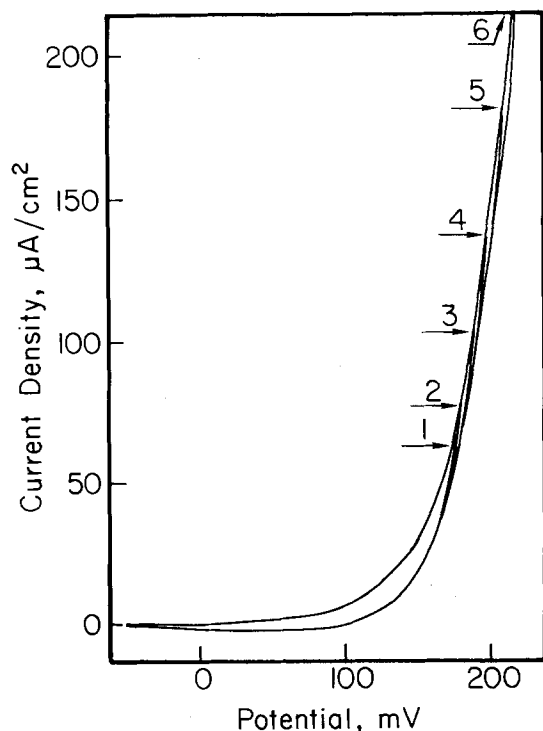


Fig. 6. The slow-scan, LSV characteristics for a rotating polycrystalline silver disk electrode in 1 mol dm^{-3} KOH solution for different values of the anodic inversion potential E_i [mV]: (1)185, (2)182, (3)190, (4)200, (5)210, (6)220. Conditions: $\nu = 1$ mV/s, $\omega = 5990$ rpm.

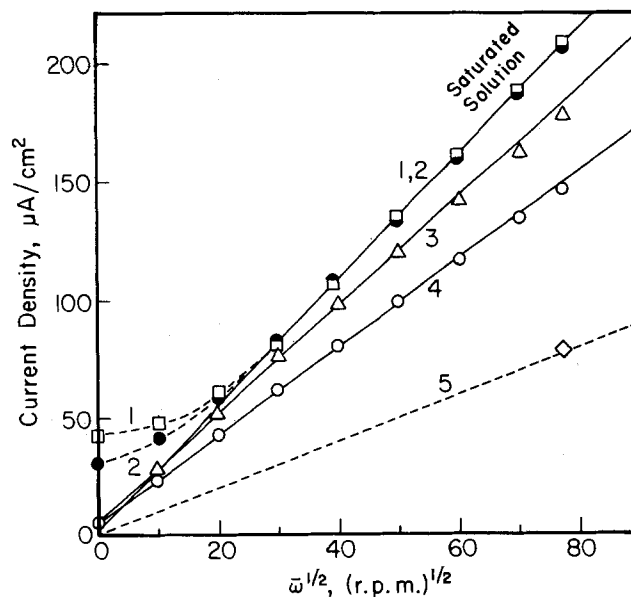


Fig. 7. Dependence of the steady-state oxidation current i_a upon the square root of the rotation speed $\sqrt{\omega}$ [in: (rpm) $^{1/2}$] of the silver RDE for different electrode potentials E [mV vs. Ag/AgCl]: (1)260, (2)250, (3)230, (4)200, (5)180. Solution; 1 mol dm^{-3} KOH.

formed to answer these questions, we present below three typical examples which explain the results in terms of the relaxation of the oxidation current after the perturbation of the transport rate in solution.

The current-time curve shown in Fig. 9 was obtained after anodization of the silver disk electrode at constant potential $E = +260$ mV and $\omega = 0$ for 10 min until the nucleation and growth peak had been completed. This curve is a continuation of the curve 1 from Fig. 8. A very small response to the change of the hydrodynamic conditions is then observed (compare branch A obtained at $\omega = 0$ with branch B at $\omega = 5990$ rpm in Fig. 9), and the current returns to the previous value after stopping the disk rotation (branch C, $\bar{\omega} = 0$). However, a longer rotation at $\bar{\omega} = 5990$ rpm (branches D and E) causes a gradual increase in the oxidation current which finally approaches a steady-state level. If now the disk is stopped again, the current falls down, but the nucleation and growth process start again, leading to the transient similar to that presented in

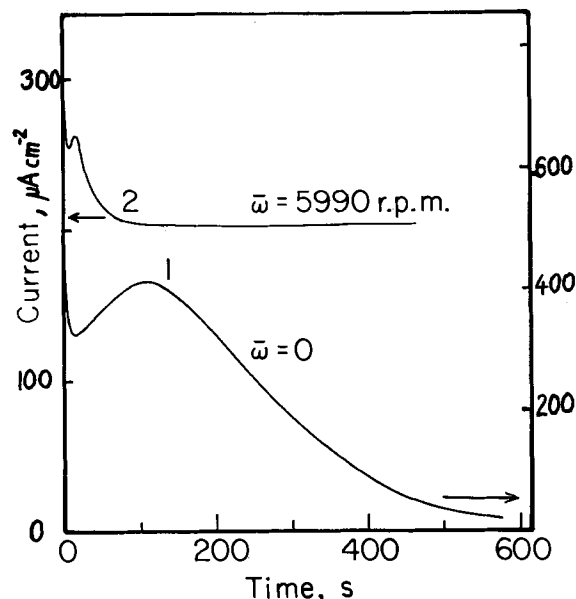


Fig. 8. Typical chronoamperometric transients obtained on a stationary (1) and rotating (2) silver disk electrodes at $E = +260$ mV (vs. Ag/AgCl) in 1 mol dm^{-3} KOH solution. Curve 2: $\omega = 5990$ rpm. Current scale: right for curve 1, left for curve 2.

Fig. 9. The current-time transient obtained on a silver disk electrode after depositing of the Ag_2O film for $\tau_d = 600\text{s}$. The branches A-E of the transient correspond to the rotation speed of the disk ω : (A,C)0 and (B,D,E)5990 rpm. Solution: $1\text{ mol dm}^{-3}\text{ KOH}$; $E = +260\text{ mV}$ (vs. Ag/AgCl), $A = 0.192\text{ cm}^2$.

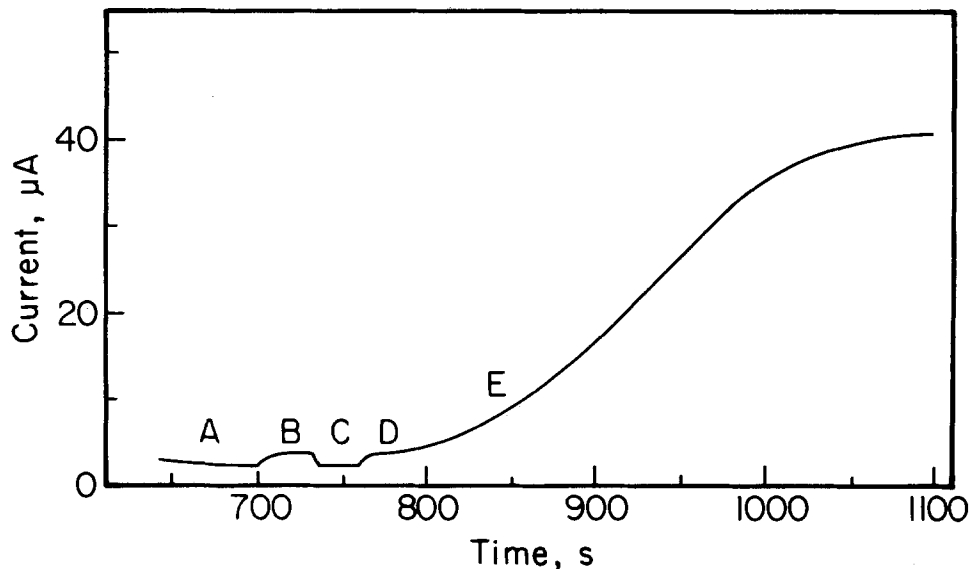


Fig. 10. The transients shown in Fig. 10 illustrate the short-term rotation-speed dependence of the oxidation current in different stages of the Ag_2O film growth. Approximately steady-state anodic current at $\omega = 5990\text{ rpm}$ is observed after about 2 min ($E = +260\text{ mV}$). At the point A, disk rotation was stopped. The $i - \omega$ relations at different times (points B through G) are represented by the arrow whose length is equal to the difference Δi between the current at $\omega = 5990\text{ rpm}$ (measured after 25s) and the current at $\omega = 0$. Each arrow represents a separate experiment because the disk rotation for 25s influences the nucleation and growth peak at $\omega = 0$, which becomes more expanded in time. As seen in Fig. 10, the dependence of the oxidation current upon ω vanishes gradually during the Ag_2O nucleation and growth process.

At the potential $E = +230\text{ mV}$, the nucleation and growth of the Ag_2O film is not observed, and adjustment of the anodic current after changing rotation speed of the disk electrode proceeds faster. This situation is illustrated in Fig. 11 and can be compared to those described above.

Discussion

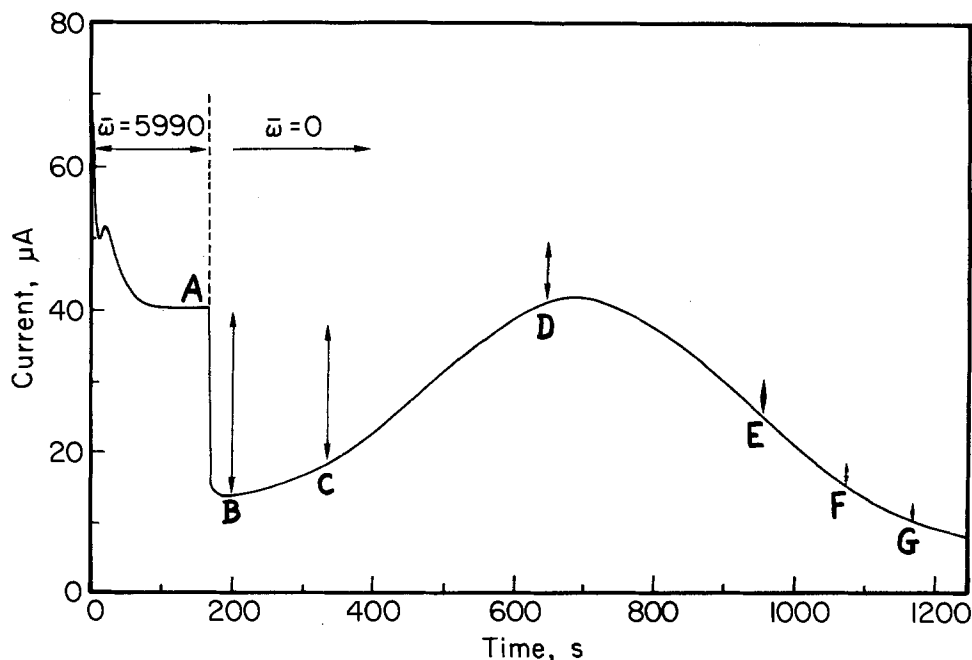
The voltammetric characteristics of silver electrodes in alkaline solutions are influenced by many factors, of which the following seem to be the most important: (i) pretreatment of the electrode surface, (ii) roughness fac-

tor and surface structure, (iii) hydrodynamic conditions, (iv) solution impurities, (v) illumination, and (vi) electrode history (i.e., conditioning potentials, cycling, potential programs of previous experiments, etc.). Most of the present literature contradictions concerning silver oxidation can be explained when specific experimental conditions and procedures are taken into account.

The general oxidation path at the silver electrode in the potential range -300 through $+900\text{ mV}$ is shown in Fig. 1 (cycling between -650 and $+900\text{ mV}$). There are five anodic peaks, A_1 through A_5 . On the basis of our experiments, we list the conditions under which A_1 and A_2 peaks can be observed: unstirred solution, electrode roughened by strong oxidation and oxide stripping, solution not saturated with Ag(I) -hydroxy complexes. Similar peak structure has recently been reported by Droog *et al.* (8) and Teijelo *et al.* (except the feature A_5).

It is clear from our measurements (Fig. 2, 6) that the first two peaks A_1 and A_2 do not appear on the voltammogram for polycrystalline silver electrode conditioned for a long time or when the solution is stirred and is not saturated with Ag(I) . The surface restructuring processes are evidently involved in the conditioning step. The reconstruction of the surface monolayers and formation of the thermodynamically more stable atomic configurations with some preferential crystallographic orien-

Fig. 10. The short-term effect (marked by the length of arrows) of changing the rotation speed of the filmed silver disk electrode from 0 to 5990 rpm in different stages of the Ag_2O film growth. The current-time transients were obtained at $\omega = 5990\text{ rpm}$ (branch A) and 0 rpm (branch B). Each arrow represents a separate experiment in which the transient was interrupted at the time (marked by arrow) by turning the rotation on ($\omega = 5990\text{ rpm}$) and reading the value of current after 25s. $E = 260\text{ mV}$ (vs. Ag/AgCl), $A = 0.192\text{ cm}^2$.



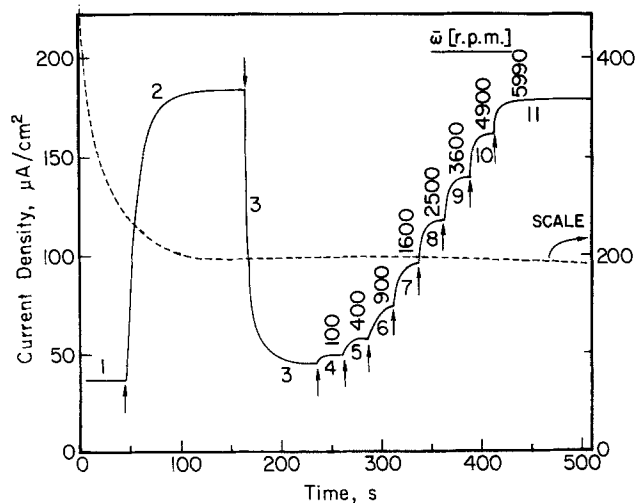
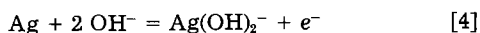


Fig. 11. The current response on the change in the rotation speed of the filmed polycrystalline silver disk electrode at $E = 230$ mV (vs. Ag/AgCl) in 1 mol dm^{-3} KOH solution; ω [rpm]: (1) 10, (2) 5990, (3) 0, (4) 100, (5) 400, (6) 900, (7) 1600, (8) 2500, (9) 3600, (10) 4900, (11) 5990. Dashed curve: initial current-time transient at 5990 rpm (current scale $\times 2$).

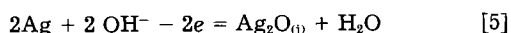
tations on a polycrystalline material can be considered. Eventually, it may concern even a few monolayers. Note, that some authors (14, 17) identify the peak A_2 with the preferential oxidation of surface atoms of low coordination number. Also, in this case (Fig. 2, curve 1) the peak A_3 has a different shape than that seen in Fig. 1; it is sharp and much higher than the peak A_4 for the Ag_2O_2 nucleation and growth.

This indicates that Ag_2O nucleation process (A_3) is highly retarded on reconstructed surfaces and starts spontaneously when the solution becomes supersaturated at the electrode surface and the potential reaches sufficiently positive value. Before the first monolayer of Ag_2O film starts to grow, the reaction of silver dissolution according to Giles and Harrison (5) can be represented by the equation

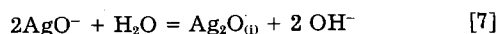
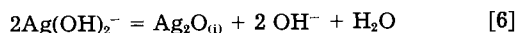


assumed also by other authors (15).

The initial stage of Ag_2O formation proceeds via the net electrochemical reaction [5] which in our opinion is presumably composed from a few elementary steps



or by the precipitation mechanism which is generally accepted for thicker Ag_2O films (9, 15, 16, 21, 22). In the latter case the reactions that might be involved are the following



The subscript (i) was used at Ag_2O in the reaction Eq. [5]-[18] to denote differences between consecutive monolayers (at least between the first, adsorbed layer and the bulk Ag_2O layers). The complexes $\text{Ag}(\text{OH})_2^-$ and AgO^- are prevailing Ag(I) species in the solution (16, 32). The reaction Eq. [5] has been proposed for the formation of the adsorption Ag_2O film (5). For the next monolayers, the same equation can be used as a total reaction for the film growth, but it has been found on the basis of the RRDE experiments (15, 16), that the important step in the mechanism is precipitation of Ag_2O from the supersaturated solution via the nucleation and growth process. Dignam *et al.* (33) and other authors (9, 21, 34) pointed out the significance of the solid-state transport in the Ag_2O film formation.

Initial stages of silver oxidation.—Determination of the contributions of the initial silver-dissolution process and the Ag_2O adsorption reaction to the total current is difficult because no mechanistic studies have been performed which could give a better insight into the reactions involved.

Comparison of our LSV characteristics for the region of peak A_1 (Fig. 3 and 6) shows a significant influence of the dissolution processes at the RDE, where the effect of the increasing inversion potential E_i on the cathodic currents is not observed. The results of the LPSC measurements (Fig. 5) at a stationary electrode can be explained by loss of charge due to the dissolution at $E_i < 200$ mV.

On the basis of the RDE experiments (Fig. 7 and other data), we can calculate the surface concentration C_s of the Ag(I) species at different potentials using Levich Eq. [3]. For a reversible electroreduction of metallic silver, one can expect a linear relation $\log C_s$ vs. potential E with a slope $(\delta E / \delta \log C_s) = 59.16$ mV. However, in our case (Fig. 12), the slope is 73 mV at higher potentials and about 90 mV at lower potentials. The potential region where the slope 73 mV is observed corresponds to the region of the change in optical parameters ($\delta\Delta$) in the ellipsometric studies of Droog *et al.* (8) and can be associated with the influence of the adsorption process.

Effect of the solid-state transport and nucleation and growth phenomena on the potentiostatic transients under different hydrodynamic conditions.—At potentials $E > 250$ mV, the bulk Ag_2O is formed, however, the Ag(I) surface concentration C_s maintains the saturation value. The dependence of the steady-state oxidation currents vs. $\sqrt{\omega}$ is still similar to that represented by the curve for $E = 250$ mV, although adjustment of the film thickness during the change in the rotation speed takes place (Fig. 9-11). This fact seems to be a natural consequence of the interrelations between the varying rate of convective diffusion in the solution and the mass transport within the solid film. The electrical conductivity of Ag_2O is very low [$\sigma = 10^{-8}$ S/cm (33)], and, basically, one might assume a constant field approximation

$$E = -\frac{d\phi}{dx} = \text{const.} \quad [9]$$

for the potential distribution across the Ag_2O film, similarly to that, for example, for niobium oxide (35) or iron oxides (36). In consequence, adjustment of the film thickness to the changed hydrodynamic conditions would require in this case a change in the potential drop across the film. But, because of the observed constancy of $C_s = C_s^{\text{sat}}$

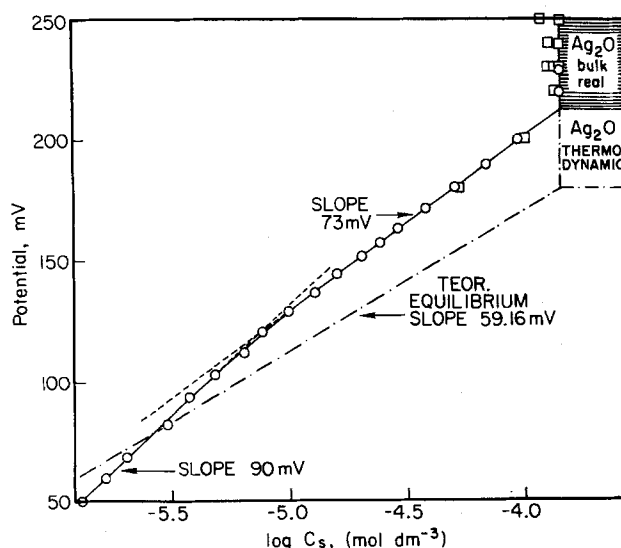


Fig. 12. Plot of the electrode potential vs. the logarithm of the surface Ag(I) concentration calculated from experimental steady-state oxidation currents using Levich Eq. [3]. Solution: 1 mol dm^{-3} KOH.

at varying ω (i.e., linearity of the Levich plot) under steady-state conditions, it seems that constant potential drop rather than constant field is maintained in the oxide film. Work is underway in our laboratory to address this question, using impedance measurements, and the results will be reported in the forthcoming publications.

Finally, we would like to emphasize one characteristic feature of the system behavior: the invariance of the LSV peak currents A_2 and A_3 with respect to the rotation speed ω as was reported by Tilak *et al.* (8) and Hampson *et al.* (17), as compared to the rotation speed dependence of the oxidation currents at constant potentials in the potential region of the LSV peak A_2 that is reported here (Fig. 8-11). A possible explanation of this fact is that in the LSV experiments ($v = \text{const.}$), the film thickness increases following the continuous changes in the electrode potential. In the case of the nucleation and growth, the current peak is determined by the increasing real surface area. An acceleration of the rotation speed causes a longer delay before the commencement of the nucleation and growth process, and this is manifested by a shift of the peak potential. The peak currents, however, remain undisturbed by the dissolution processes. The nucleation and growth peaks seen in Fig. 8 and 10 correspond probably to the same processes as those at the LSV peak A_3 because a further potential scan applied in the direction of positive potentials shows only peak A_4 (Ag_2O formation).

Conclusion

The steady-state oxidation currents measured on the polycrystalline silver RDE fulfill the limiting Levich equation, despite the fact that the electrode is covered by a thin Ag_2O film. When the hydrodynamic conditions are changed by the change of the rotation speed of the disk, the anodic current adjusts to the new value. The rate of this adjustment indicates that the solid-state transport processes and changes in the film thickness are involved. However, the final value of the current indicates that the saturation of the solution with respect to Ag(I) is maintained. A steady-state model of the metal/semiconductor electrode undergoing dissolution is thus proposed. In the case of thick Ag_2O films, the solid-state diffusion control of the anodic processes can occur. At the same constant electrode potential, thicker films are obtained under conditions of slower mass transport in the solution. This conclusion follows from the proposed model and is consistent with the experimental results.

The Ag_2O nucleation and growth peak has been observed in chronoamperometric transients above the potential of +240 mV (*vs.* Ag/AgCl). The height of this peak decreases as the convective diffusion is accelerated by the rotation speed of the RDE.

In case of the monolayer Ag_2O films, which can be obtained in the potential region of the first LSV peak (A_1), the surface concentration of Ag(I) in solution is lower than the equilibrium value corresponding to the reversible Ag/Ag(I) electrode, and the slope ($\delta E/\delta \log C_s$) is greater than 59.16 mV. The results of the LPSC measurements obtained on a stationary silver-disk electrode show a large unrecovered charge during the potential cycle (starting from the negative potential limit at the conditioning potential). The dependence of the peak currents A_1 and C_1 upon the potential scan rate is not linear. All these observations indicate a complex behavior of the system in the region of peak A_1 which cannot be simply described by the equilibrium silver dissolution with the formation of a reversible adsorption layer of Ag_2O .

Acknowledgment

This work was supported by the Office of Naval Research under Contract N00014-81-K-0339.

Manuscript submitted June 13, 1983; revised manuscript received Nov. 28, 1983.

The City University of New York assisted in meeting the publication costs of this article.

REFERENCES

1. S. U. Falk and A. J. Salkind, "Alkaline Storage Batteries," John Wiley and Sons, New York (1969).
2. P. O'D. Offenhardt and G. L. Holleck, *This Journal*, **127**, 1213 (1980).
3. R. Serenyi, Abstract 260, p. 417, The Electrochemical Society Extended Abstracts, Vol. 82-2, Detroit, MI, Oct. 17-21, 1982.
4. H. A. Frank, W. L. Long, and A. A. Uchiyama, *This Journal*, **123**, 1 (1976).
5. R. D. Giles and J. A. Harrison, *J. Electroanal. Chem.*, **27**, 161 (1970).
6. R. D. Giles, J. A. Harrison, and H. R. Thirsk, *ibid.*, **22**, 357 (1969).
7. M. Brezina, J. Koryta, and M. Musilová, *Collect. Czech. Chem. Commun.*, **33**, 3397 (1968).
8. J. M. M. Droog, P. T. Alderliesten, and G. A. Bootsma, *J. Electroanal. Chem.*, **99**, 173 (1979).
9. B. V. Tilak, R. S. Perkins, H. A. Kozłowska, and B. E. Conway, *Electrochim. Acta*, **17**, 1447 (1972).
10. R. S. Perkins, B. V. Tilak, B. E. Conway, and H. A. Kozłowska, *ibid.*, **17**, 1471 (1972).
11. P. Stonehart, *ibid.*, **13**, 1789 (1968).
12. T. P. Dirkse and D. B. de Vries, *J. Phys. Chem.*, **63**, 107 (1959).
13. T. G. Clarke, N. A. Hampson, J. B. Lee, J. R. Morley, and B. Scanlon, *Can. J. Chem.*, **46**, 3437 (1968).
14. T. G. Clarke, N. A. Hampson, J. B. Lee, J. R. Morley, and B. Scanlon, *Ber. Bunsenges. Phys. Chem.*, **73**, 279 (1969).
15. J. Ambrose and R. G. Barradas, *Electrochim. Acta*, **19**, 781 (1974).
16. B. Miller, *This Journal*, **117**, 491 (1970).
17. N. A. Hampson, K. I. MacDonald, and J. B. Lee, *J. Electroanal. Chem.*, **45**, 149 (1973).
18. R. Memming, F. Möllers, and G. Neumann, *This Journal*, **117**, 451 (1970).
19. M. L. Teijelo, J. R. Vilche, and A. J. Arvia, *J. Electroanal. Chem.*, **131**, 331 (1982).
20. M. Fleischmann, D. J. Lax, and H. R. Thirsk, *Trans. Faraday Soc.*, **64**, 3137 (1968).
21. M. Fleischmann, D. J. Lax, and H. R. Thirsk, *ibid.*, **64**, 3128 (1968).
22. E. J. Casey and W. J. Moroz, *Can. J. Chem.*, **43**, 1199 (1965).
23. B. E. Conway and M. A. Sattar, *Electrochim. Acta*, **14**, 695 (1969).
24. P. Stonehart and F. P. Portante, *ibid.*, **13**, 1805 (1968).
25. B. G. Pound, D. D. Macdonald, and Y. W. Tomlinson, *ibid.*, **24**, 929 (1979).
26. B. G. Pound, D. D. Macdonald, and Y. W. Tomlinson, *ibid.*, **25**, 563 (1980).
27. B. G. Pound, D. D. Macdonald, and Y. W. Tomlinson, *ibid.*, **25**, 1293 (1980).
28. B. G. Pound, D. D. Macdonald, and Y. W. Tomlinson, *ibid.*, **27**, 1489 (1982).
29. B. D. Cahan, Y. B. Ockerman, R. F. Amlie, and P. Rüetschi, *This Journal*, **107**, 725 (1960).
30. Y. A. McMillan, *Chem. Rev.*, **62**, 65 (1962).
31. Yu. S. Gorodetskii, *Elektrokhimiya*, **1**, 681 (1965).
32. Yu. S. V. Pleskov, *Dokl. Akad. Nauk SSSR*, **117**, 645 (1957).
33. M. J. Dignam, H. M. Barrett, and C. D. Nagy, *Can. J. Chem.*, **47**, 4253 (1969).
34. B. N. Kabanov and D. I. Leikis, *Z. Elektrochem.*, **62**, 660 (1958).
35. L. Young, *Trans. Faraday Soc.*, **51**, 1250 (1955).
36. B. D. Cahan and Chia-Tien Chen, *This Journal*, **129**, 921 (1982).
37. A. A. Yakovleva, T. I. Borisova, and V. I. Veselovskii, *Russ. J. Phys. Chem.*, **36**, 763 (1962).
38. G. Bush, *Usp. Fiz. Nauk*, **47**, 2 (1952).
39. L. Bergman and J. Hansler, *Z. Phys.*, **1-2**, 100 (1936).

Application of a Magnetohydrodynamic Generator-Detector Electrode to Hydrodynamic Voltammetry

Ryoichi Aogoki*

Department of Chemistry, The Institute of Vocational Training, 1960, Aihara, Sagami-hara, 229, Japan

Kazuo Fueki*

Department of Industrial Chemistry, Faculty of Engineering, University of Tokyo, Hongo, Bunkyo-ku, Tokyo, Japan

ABSTRACT

Utilizing a fluid motion induced by electromagnetic force, a new method of voltammetry under forced convection was developed. The electrolytic cell was composed of two pairs of electrodes, *viz.*, generator and detector pairs embedded on the bottom and top innerwalls of a rectangular channel. An intermediate produced on the surface of one of the first generator pair of the electrodes was swept downstream by the induced liquid flow to the neighboring electrode of the second detector pair and measured as a current. Examination of the mechanism between the induced flow of the electrolyte solution and the diffusion process of the intermediate permitted deriving the several expressions of electrolytic current for each pair of the electrodes as functions of bulk concentration of reacting species and externally applied magnetic field. It was also predicted that the detecting current interacts with the generating current, which can be depicted in terms of the collection efficiency of the intermediate. Observed results in experiments were in good agreement with these predictions.

It has been known that when a magnetic field is externally imposed on an electrolytic cell system, electromagnetic force is induced to move the solution and thus promotes the mass-transport process (1-4). Such a liquid motion becomes laminar flow in viscous or boundary layer mode for well-defined electrode cell geometry. The kinetics of the diffusion current in the viscous and boundary layer flows of electrolyte solution have already been established (5-7). The characteristics of the phenomenon are essentially attributable to the fact that the electrode itself acts as a kind of fluid pump. Thus, as a consequence of the coupling of electrolytic current and magnetic field, the electrolyte solution acquires fluid motion along the electrode surface. Therefore, in view of the application to studying the kinetics of electrochemical reactions, the electrode system has some advantages in contrast to other static electrode systems containing mechanical moving parts (8), *i.e.*, the cell dimension becomes stable and compact, and the whole system is easy to seal under arbitrary atmospheres. In this paper, we will aim at the application of this electrode system to voltammetry under forced convection, as represented by the rotating ring-disk electrode (RRDE), important for studying intermediates of electrode reactions.

The experimental setup of this magnetohydrodynamic generator-detector electrode system is two neighboring pairs of parallel electrodes; the first, a generator pair (one being a working electrode and the other its counterelectrode) yields intermediates and acts as a pump to carry the species downstream to the neighboring electrode, which is the working electrode of the second detector pair, capturing the intermediates in the form of electrolytic current.

In order to establish this method, it is important to know the mechanism between the generating and detecting currents and to obtain the expression for the collection efficiency of the detector electrode. We will, therefore, examine the behavior of the flowing of electrolyte solution induced by electromagnetic force, and then deduce the expressions of the diffusion currents at the generator and detector working electrodes as functions of the bulk concentration of reactants, the external magnetic flux density, and the collection efficiency. Finally, the predicted expressions are verified in experiments by comparing them with the observed results for the redox reaction in aqueous CuCl_2 solutions containing KCl as a supporting electrolyte.

*Electrochemical Society Active Member.

Key words: magnetic property, magnetohydrodynamic effect, voltammetry.

Theoretical

Figure 1 shows the schematic configuration of the electrolytic cell used for this study. The cell is made of a relatively short channel with two open ends. Inside the channel, two pairs of electrodes are embedded in the top and bottom innerwalls; the first pair comprises the working and counterelectrodes to generate reaction intermediates, and the second pair is the working and counter-electrodes for detecting the intermediates. Each electrode of the same pair possesses equal area. Consequently, the electrolytic cell is characterized by the following five zones: the first zone is the inactive entrance section, $0 \leq x < x_1$; the second zone is the region of generator electrode pair, $x_1 \leq x < x_2$; the third zone is the inactive gap, $x_2 \leq x < x_3$; the fourth zone is the region of detector electrode pair, $x_3 \leq x < x_4$; and the fifth zone is the inactive exit section, $x_4 \leq x \leq l$. The reference electrodes, as mentioned in the

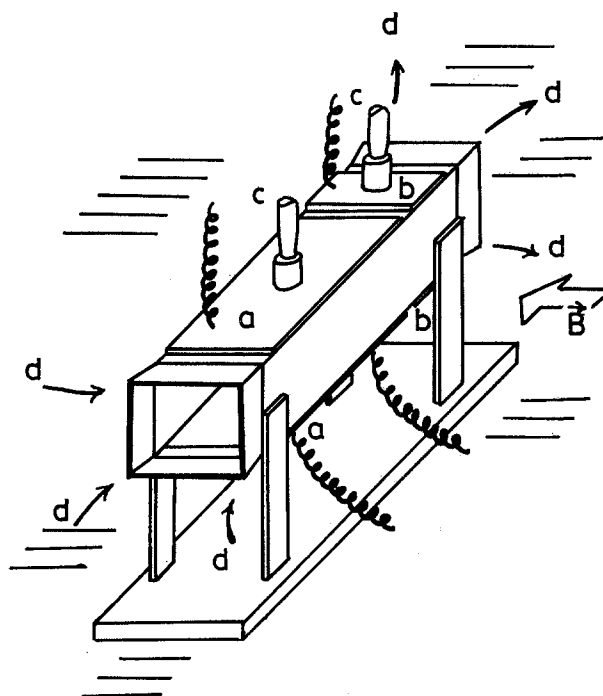


Fig. 1. Electrolysis cell. Magnetic flux density \vec{B} is applied vertically to the electrolytic currents, and the cell is placed horizontally in a large vessel. (a) Generating electrode section, (b) detecting electrode section, (c) Luggin capillary, and (d) streamline.

previous papers (5-7), are inserted into small holes drilled behind the working electrodes through conical Luggin capillaries so that the tips of the capillaries come to the levels of the electrode surfaces. The whole electrode cell is horizontally immersed in a large vessel ($25 \times 30 \times 5$ cm) filled with an electrolyte solution. When a dc current flows between the first generator electrode pair in the y -direction, the motion of the electrolyte solution is produced in the channel in the x -direction due to the electromagnetic force. Simultaneously, the reaction intermediate formed at the generator working electrode is conveyed downstream to the neighboring detector working electrode for measurement. As a result of the fluid motion, friction exerted over the whole channel walls by the liquid entering the channel gives rise to hydrodynamic boundary layers which develop with the distance from the inlet section. With assumptions of small channel length and/or comparatively large Reynolds number ($\gg 1$) referring to the channel width, the boundary layers do not fully develop. Thus, the fluid motion consists of two types of flows, *viz.*, main and thin boundary layer flows (14). Within the layer, another type of thin diffusion layer is occurring as a consequence of the mass transfer of active ionic species accompanying the electrode reactions. This was actually observed by means of laser interferometry (9). Figure 2 schematically illustrates the characteristics of the relation mentioned above.

The main flow part of the electrolyte solution is regarded as nonviscous and incompressible. It is essentially the same as in the previous paper (5); the main flow velocity, U , in the channel is given by

$$U = \sqrt{\frac{2\gamma B(I_g + I_d)}{\rho w}} \quad [1]$$

where γ is the cell constant of value nearly equal to unity (5), I_g is total generating current, I_d is total detecting current, w is the electrode width, B is the magnetic flux density, and ρ is the fluid density.

Then, the x and y components of the velocity in the boundary layer can be expressed as (6)

$$v_x = \frac{1.33}{4} \frac{U^{3/2}}{\nu^{1/2} x^{3/2}} y \quad [2]$$

and

$$v_y = \frac{1.33}{16} \frac{U^{3/2}}{\nu^{1/2} x^{3/2}} y^2 \quad [3]$$

where ν is the kinematic viscosity.

Diffusion current for active species reacting on the generator working electrode.—As the electrolytic current flows between the working and counter-electrodes of the generator section, the intermediate is formed on the surface of the generator working electrode following an electrode reaction represented by



where S_1 and S_2 are the species participating in the electrode reaction and n_1 is the number of electrons exchanged in the reaction. The transport of the active species will take place through the diffusion layer, which is due to the motion of the species entrained by the fluid motion induced by the electromagnetic force and to the diffusion of the species resulting from the concentration gradient, since any migration contribution is negligible owing to a large excess of an inert electrolyte. The diffusional equation for convective diffusion of species S_1 in steady state is simplified in consideration of sufficiently small thickness of the diffusion layer compared with the representative length of the electrode, *i.e.*, channel width (6). Subsequently, the equation is written as

$$v_x \frac{\partial C}{\partial x} + v_y \frac{\partial C}{\partial y} = D_1 \frac{\partial^2 C}{\partial y^2} \quad [5]$$

The diffusion problem for the species S_1 at the generator working electrode ($x_1 \leq x \leq x_2$) is solved with the following boundary conditions; (i) $C_1 = C_1^s$ (surface concentration) at $y = 0$, and (ii) $C_1 = C_1^0$ (bulk concentration) as $y \rightarrow \infty$.

The total generating current I_g solved in the same manner as before (6), is expressed as

$$I_g = 0.68 n_1 F D_1 (C_1^0 - C_1^s) \left(\frac{\nu}{D_1}\right)^{1/3} \left(\frac{U}{\nu}\right)^{1/2} (\sqrt{x_2} - \sqrt{x_1}) w \quad [6]$$

where D_1 is the diffusion coefficient of S_1 .

Detecting current and collection efficiency.—The intermediate S_2 formed on the surface of the generator working electrode is carried downstream to the neighboring detector working electrode surface by the resulting fluid flow. The reaction product S_2 is afterwards reduced or oxidized at the detector electrode section, yielding the species S_3 according to the reaction



where n_2 is the number of the electrons participating in the reaction. In the case when the intermediate S_2 can be regarded stable enough not to be decomposed on the way

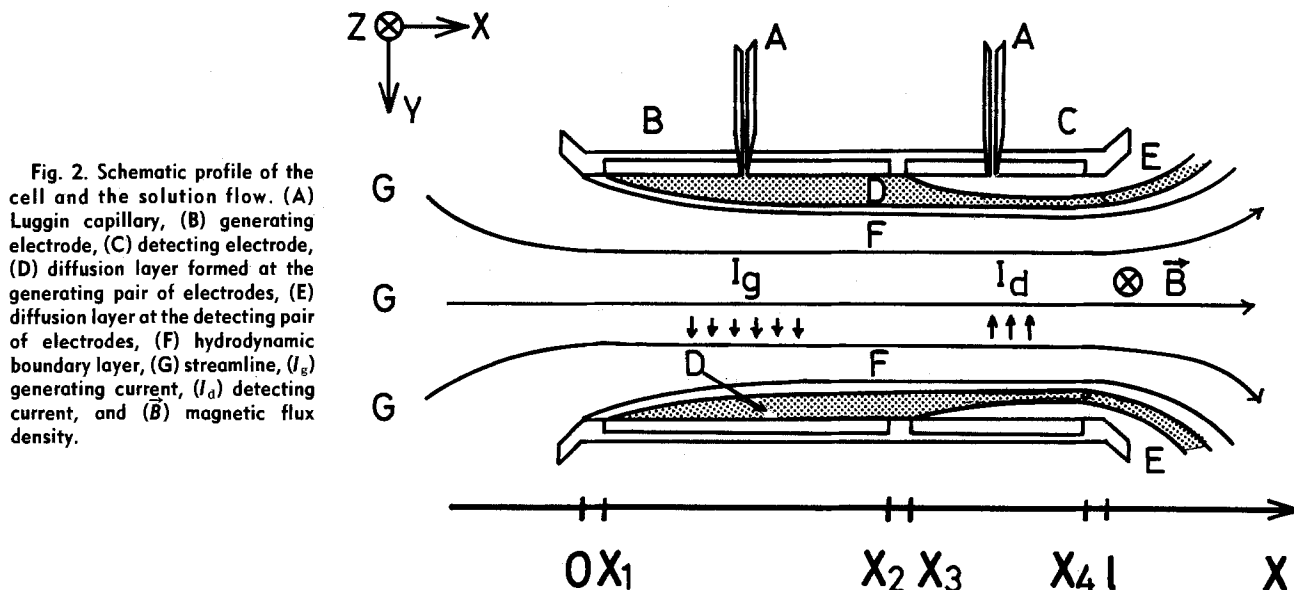


Fig. 2. Schematic profile of the cell and the solution flow. (A) Luggin capillary, (B) generating electrode, (C) detecting electrode, (D) diffusion layer formed at the generating pair of electrodes, (E) diffusion layer at the detecting pair of electrodes, (F) hydrodynamic boundary layer, (G) streamline, (I_g) generating current, (I_d) detecting current, and (B) magnetic flux density.

to the detector working electrode, it can be collected with a certain collection efficiency as will be mentioned later. The collection efficiency is defined according to Matsuda (13) as the absolute ratio of the total generating current to the total detecting current, N

$$N = \left| \frac{I_d}{I_g(\text{DE on})} \right| \quad [8]$$

or as the absolute ratio of the mass flux at the generator working electrode to the amount reaching the detector working electrode, N' , as follows (16)

$$N' = \left| \frac{J_d}{J_g(\text{DE on})} \right| \quad [9]$$

where $I_g(\text{DE on})$ and $J_g(\text{DE on})$ denote the total generating current and mass flux of S_1 , respectively, when the detector electrode pair is employed, and I_d and J_d are the total detecting current and mass flux of S_2 , respectively. N and N' have a relation of $N = (n_2/n_1)N'$, where N' should be a function of only electrode geometry in consideration of the equation, Eq. [10] below.

For the double-channel electrode comprising two neighboring rectangular electrodes, the diffusion problem of the intermediate S_2 with a half-life long enough for it to be carried by the liquid flow to the detector working electrode surface is solved from Eq. [5] with the following boundary conditions; (i) the amount of the product S_2 leaving from the surface of the generator working electrode per unit time is equal to that of the species S_1 entering from the bulk per unit time, i.e., $D_2(\partial C_2/\partial y)_{y=0} = -D_1(\partial C_1/\partial y)_{y=0}$ for $x_1 \leq x < x_2$. (ii) The product S_2 does not react at the inactive gap, $D_2(\partial C_2/\partial y)_{y=0} = 0$ for $x_2 \leq x < x_3$. (iii) S_2 is detected as a limiting current at the detector working electrode, $C_2 = 0$ at $y = 0$ for $x_3 \leq x < x_4$. (iv) S_2 does not exist in the bulk of the solution, i.e., $C_2 \rightarrow 0$ as $y \rightarrow \infty$ for all zones.

These boundary conditions correspond to those already treated for geometric systems such as a rotating ring-disk electrode (12). According to Matsuda (13), the collection efficiency expression for the two neighboring plane electrodes exposed to the solution flow with two-dimensional boundary layer and the conditions mentioned above is

$$N = \frac{n_2}{n_1} \left\{ \left(\frac{x_4^{3/4} - x_3^{3/4}}{x_2^{3/4} - x_1^{3/4}} \right)^{2/3} G \left(\frac{x_2^{3/4} - x_1^{3/4}}{x_3^{3/4} - x_2^{3/4}} \right) + G \left(\frac{x_3^{3/4} - x_2^{3/4}}{x_4^{3/4} - x_3^{3/4}} \right) - \left(\frac{x_4^{3/4} - x_1^{3/4}}{x_2^{3/4} - x_1^{3/4}} \right)^{2/3} G \left(\frac{x_2^{3/4} - x_1^{3/4}}{x_4^{3/4} - x_1^{3/4}} \cdot \frac{x_4^{3/4} - x_3^{3/4}}{x_3^{3/4} - x_2^{3/4}} \right) \right\} \quad [10]$$

where

$$G(\theta) = \frac{\sqrt{3}}{4\pi} \ln \left\{ \frac{(1 + \theta^{1/3})^3}{1 + \theta} \right\} + \frac{3}{2\pi} \arctan \left(\frac{2\theta^{1/3} - 1}{\sqrt{3}} \right) + \frac{1}{4} \quad [11]$$

Interference effect and diffusion currents.—The total diffusion currents, I_g and I_d , in Eq. [6] and [8] are identified with the electrolytic currents coupled with the external magnetic field in Eq. [1]. Therefore, the following two experimental conditions are considered.

1. The case when the detecting current does not flow ($I_d = 0$).

This situation is furthermore divided into two cases; the first is that no intermediate collected by the detector working electrode is formed at the generator working electrode, and the second is that from the beginning, the detector electrode pair is not employed. In these cases, the usual diffusional generating current flows at the generator section according to the equation in the previous report (6). Namely, in view of $I_d = 0$, elimination of the main flow velocity from Eq. [1] and [6] leads to the following equation

$$I_g(\text{DE off}) = H(C_1^0 - C_1^s)^{4/3} B^{1/3} \quad [12]$$

where

$$H = 0.753(n_1 F D_1)^{4/3} (\nu/D_1)^{4/9} \nu^{-2/3} \rho^{-1/3} \gamma^{1/3} \omega (\sqrt{x_2} - \sqrt{x_1})^{4/3} \quad [13]$$

2. The case when the detecting current flows ($I_d \neq 0$).

When an intermediate is formed on the generator working electrode surface, it diffuses into the solution to be carried downstream by convection to the detector working electrode. At the electrode surface, the species reacts immediately, and, simultaneously, a detecting current flows between the working and counterelectrodes of detector section. Since both generating and detecting currents participate in the formation of the electromagnetical force inducing fluid motion, they become dependent on each other, and are obtained by eliminating the variable, U , from Eq. [1], [6], and [8]

$$I_g(\text{DE on}) = (1 - N)^{1/3} H(C_1^0 - C_1^s)^{4/3} B^{1/3} \quad [14]$$

$$I_d = -N(1 - N)^{1/3} H(C_1^0 - C_1^s)^{4/3} B^{1/3} \quad [15]$$

where the sign of the current is determined according to the direction of the electrolytic current. Consequently, the generating current $I_g(\text{DE on})$ is influenced by the detecting current, decreasing in comparison with $I_g(\text{DE off})$ in the case of $I_d \neq 0$. Such an interference effect is introduced through the collection efficiency of the intermediate, N . The electromagnetical forces induced by $I_g(\text{DE on})$ and I_d are opposite in sign, so that the blocking effect of I_d on fluid flow increases with increasing N , which implies that the large value of N is not applicable to actual systems because the fluid motion slows down with increasing N . In the extreme case, viz., $N = 1.0$, as derived from Eq. [14] and [15], $I_g(\text{DE on})$ and I_d become zero since the fluid is prevented from flowing by the two electromagnetical forces which are equal in quantity but opposite in sign; thus, the thickness of the diffusion layer increases toward infinity.

Experimental

Theoretical Eq. [12], [14], and [15] were experimentally examined by measuring the relation of the limiting diffusion current corresponding to $C_1^s = 0$ against the concentration of active species in the bulk of the solution and the externally applied magnetic field. Moreover, the collection efficiencies observed for the electrode cells with several dimensions were compared with the values calculated by the theoretical equations, Eq. [10] and [11]. The detailed dimensions of the cells are described in Table I.

The working electrodes for generation and detection were made of Pt sheets and each counterelectrode was a copper sheet with the same area as its corresponding working electrode. The solutions used in the experiments were aqueous CuCl_2 solutions containing 1M KCl which is one of the conventional electrolyte systems to measure the collection efficiency of RRDE (12). Figure 3 represents the current-potential curves for the cell 4 in which cupric ion was reduced under a uniform magnetic flux density of 0.6 Wbm^{-2} , and SCE was used as a reference electrode. When increasing potential was at first applied to the generator working electrode, the reduction, $\text{Cu}^{2+} + e \rightarrow \text{Cu}^+$, started on the surface and at the same time, the generating current $I_g(\text{DE off})$, when the detector electrode pair was not employed, began to flow between the working and counterelectrodes of the generator pair. As soon as the detecting electrodes were switched on, the detecting current, I_d , began to flow in the opposite direction of I_g , corresponding to the oxidation, $\text{Cu}^+ \rightarrow \text{Cu}^{2+} + e$. As a result, the generating current $I_g(\text{DE on})$ in the case of $I_d \neq 0$ decreased in contrast to the initial value, $I_g(\text{DE off})$ by the interaction of I_d . Therefore, in this area, three different curves emerged.

Further, as the potential was increased, eventually copper metal deposition, $\text{Cu}^{2+} + 2e \rightarrow \text{Cu}$, took place and the generating current rose on the second wave, as shown in Fig. 3. In this region, since the reaction product was deposited as an insoluble substance, the detecting current

Table I. Dimensions of the electrolysis cell (unit: m)

Cell no.	x_1	x_2	x_3	x_4	l
1	2.9×10^{-3}	5.365×10^{-2}	5.464×10^{-2}	6.454×10^{-2}	6.654×10^{-2}
2	2.8×10^{-3}	5.28×10^{-2}	5.342×10^{-2}	7.342×10^{-2}	7.542×10^{-2}
3	1.0×10^{-3}	5.10×10^{-2}	5.262×10^{-2}	8.262×10^{-2}	8.462×10^{-2}
4	1.0×10^{-3}	5.10×10^{-2}	5.306×10^{-2}	1.0306×10^{-1}	1.0306×10^{-1}

channel height, $h = 5.0 \times 10^{-2}$ m
channel width, $w = 1.0 \times 10^{-2}$ m

ceased. Thus, the generating current was no longer affected and $I_g(\text{DE on})$ was the same as $I_g(\text{DE off})$, the separated curves becoming one. In addition, referring to the reactions occurring in the two regions, the ratio of the second limiting value of $I_g(\text{DE off})$ to the first current value of $I_g(\text{DE off})$ was $32 \text{ mA}/89 \text{ mA} = 0.36$, which is caused by the change of electrons transferred from 1 to 2. This is nearly equal to the value, $1/2^{4/3} = 0.4$, theoretically predicted. The usual RRDE method gives the theoretical ratio, $1/2 = 0.5$ to this CuCl_2 system. The experimental data by Nekrasov and Berezina (15) give it as $46 \mu\text{A}/102 \mu\text{A} = 0.44$.

Then, the experiments to measure the three total limiting currents, $I_g(\text{DE off})$, $I_g(\text{DE on})$, and I_d were carried out with the cell 3. Each observed value is plotted in Fig. 4 against various magnetic flux densities in an aqueous $7.14 \times 10^{-2} \text{ M}$ CuCl_2 - 1 M KCl solution. The plot of each current vs. the $1/3$ -power of magnetic flux density follows a good straight line. Figure 5 shows the results obtained by observing I_d against various concentrations of CuCl_2 in the bulk at a fixed magnetic flux density. Good linearity can be seen between the current and the $4/3$ -power of the concentration.

Finally, the dependence of the collection efficiency N for the cell dimensions listed in Table I was investigated. The experimental data of N were then compared with the

Table II. Collection efficiency of detecting electrode (N_{obs} : observed value, N_{pred} : theoretical prediction)

Cell no.	N_{obs}	N_{pred}
1	0.185	0.184
2	0.261	0.263
3	0.309	0.302
4	0.395	0.368

calculations as shown in Table II. For cells 1-4, the observed and theoretical values of the collection efficiency fall, except for cell 4, within a limiting error of about 2%: cell 1, $N_{\text{obs}} = 0.185$ and $N_{\text{pred}} = 0.184$; cell 2, $N_{\text{obs}} = 0.261$ and $N_{\text{pred}} = 0.263$; and cell 3, $N_{\text{obs}} = 0.309$ and $N_{\text{pred}} = 0.302$, where N_{obs} and N_{pred} are the observed and predicted collection efficiencies, respectively. The disagreement between the evaluated and measured values, that is, the evaluated value 0.368 and the observed value 0.395, for cell 4 may be because the relatively long channel, in comparison with the other cells makes the flow mode more viscous-like (7).

The interference effect between the generating and detecting currents is illustrated in Fig. 6. In the figure, solid lines indicate the theoretical results deduced from Eq. [14] and [15], and circles are experimentally observed data; here $I_g(\text{DE on})$ and I_d are divided by $I_g(\text{DE off})$ for normalization. Observed values are in good agreement with the theoretical curve. However, the whole range of the collection efficiency theoretically predicted cannot be realized in the actual situations. For the range nearly equal to 1.0, it is difficult to carry out the experiments. In the extreme case of $N = 1.0$, where $I_g(\text{DE on})$ and I_d have the same magnitude and opposite signs in direction, the net flow of the solution falls to zero, and this device be-

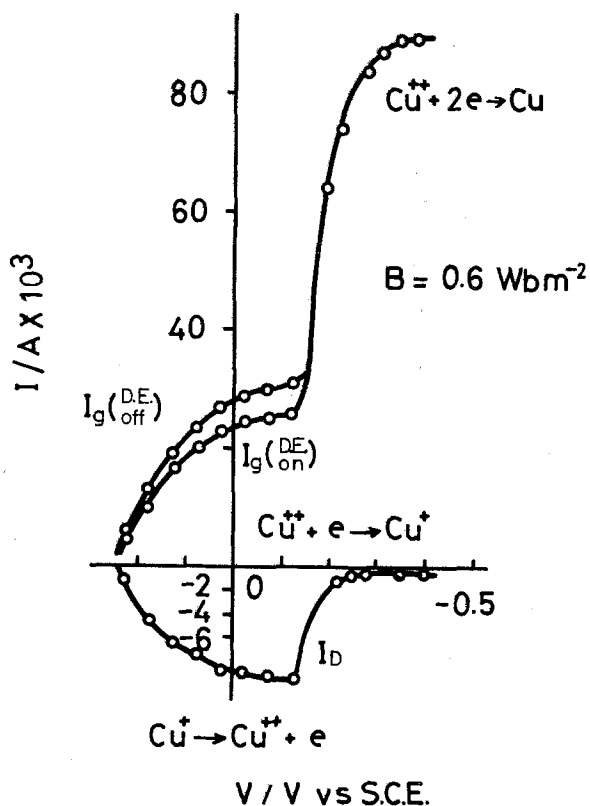


Fig. 3. Current-potential curves measured with cell 4 at 20°C in the aqueous solution of $8.21 \times 10 \text{ mol m}^{-3}$ CuCl_2 with 10^3 mol m^{-3} KCl as a supporting electrolyte. Imposed magnetic flux density is 0.6 Wbm^{-2} . $I_g(\text{DE}_{\text{off}})$: total generating limiting current when $I_d = 0$; $I_g(\text{DE}_{\text{on}})$: total generating limiting current when $I_d \neq 0$; I_d : total detecting current.

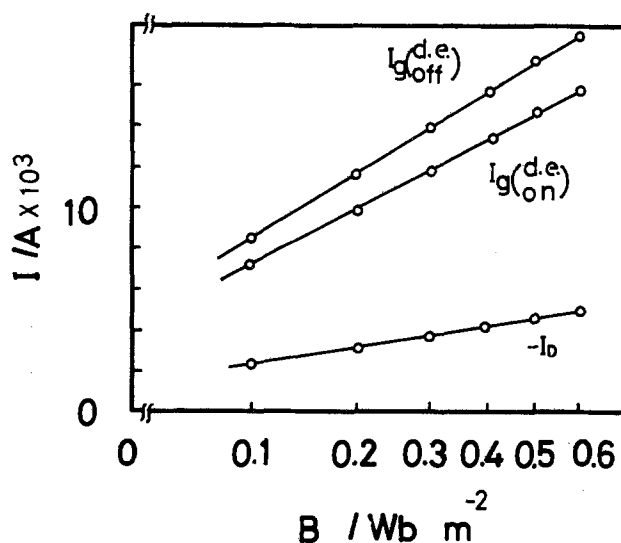


Fig. 4. Dependence of the total limiting current on the external magnetic flux density with cell 3. Electrode reaction is $\text{Cu}^{2+} + e \rightleftharpoons \text{Cu}^+$ at 20°C in $7.14 \times 10 \text{ mol m}^{-3}$ CuCl_2 + 10^3 mol m^{-3} KCl aqueous solution. $I_g(\text{DE}_{\text{off}})$: total generating limiting current in the case of $I_d = 0$; $I_g(\text{DE}_{\text{on}})$: total generating limiting current in the case of $I_d \neq 0$; I_d : total detecting limiting current.

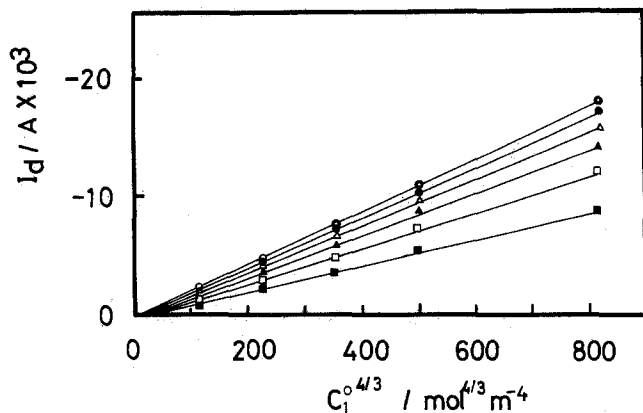


Fig. 5. Plots of I_d vs. the $4/3$ -power of the bulk concentration of CuCl_2 at the fixed magnetic flux density with cell 3. Electrode reaction in $\text{Cu} \rightarrow \text{Cu}^{2+} + e$ at 20°C . \circ : $B = 0.6 \text{ Wbm}^{-2}$; \bullet : $B = 0.5 \text{ Wbm}^{-2}$; \triangle : $B = 0.4 \text{ Wbm}^{-2}$; \blacktriangle : $B = 0.3 \text{ Wbm}^{-2}$; \square : $B = 0.2 \text{ Wbm}^{-2}$; \blacksquare : $B = 0.1 \text{ Wbm}^{-2}$.

comes useless for studying electrode kinetics. In most cases of RRDE geometry, efficiencies ranging from about 0.2 to 0.4 are employed (17). For this electrode system, the same range of the efficiency is also available for operation.

Discussion

The strength of the magnetic field we used was unfortunately not high enough to have the flow velocity induced by the electromagnetical force very high. The magnitude of the main flow velocity can be easily estimated by Eq. [1], i.e., $U \sim \sqrt{2\gamma B I_d / \rho w}$. Using the data, $\gamma \sim 1$, $B \sim 0.5 \text{ Wbm}^{-2}$, $I_d \sim 10^{-2} \text{ A}$, $\rho \sim 10^3 \text{ kg m}^{-3}$, and $w \sim 10^{-2} \text{ m}$, we can obtain $U \sim 3 \times 10^{-2} \text{ ms}^{-1}$. Thus, the Reynolds number in this case becomes $\text{Re} = Uw/\nu \sim 3 \times 10^2$. Therefore, the induced flow is concluded to be laminar, not turbulent. The sensitivity to detect unstable intermediates is chiefly limited by the main flow velocity. But, in the case of rectangular electrode, it is comparatively easy to make the gap between the generator and detector electrode sections quite narrow up to the order of magnitude of 10^{-4} m . The time for the intermediates to reach the detector working electrode from the generator working electrode is estimated as about $10^{-4} \text{ m} / 10^{-2} \text{ ms}^{-1} = 10^{-2} \text{ s}$. Hence, we can approximately say that the species of which lifetime is up to 10 ms can be detectable under usual laboratory conditions. This situation can be improved if we use a stronger magnet such as a superconducting magnet with a magnetic flux density of the order of 10 Wb m^{-2} . Species having a lifetime up to 0.1 ms will then be detectable. Such a strong magnet will also make available a much wider range of flow velocities for this device.

Another limitation may exist in the approximate nature of the fluid flow, which is based on the built-in assumptions, not only that the current distributions are uniform on both the generator and detector electrodes but also that the externally applied magnetic field is homogeneous in the whole region of the electrodes. Such uniformities may not be completely realized since the edge effect of electrolytic current at the ends of electrode cannot be neglected. However, this difficulty can be modified by introducing the cell constant γ as shown in Eq. [1], which can be easily obtained according to the experimental procedures in the preceding papers (5, 6). The introduction of γ gives satisfactory results supported by the good agreement between the observed and predicted values of the collection efficiency in Table II.

The relative advantages of this method may be stressed in the following; there is no mechanical moving part so that the cell dimension is stable and compact, and the whole cell system can be completely sealed under arbitrary atmospheres. This suggests that some troubles associated with nonaqueous or fused salt systems will be reduced. In addition, one should bear in mind that the range of application of this device can be extended not

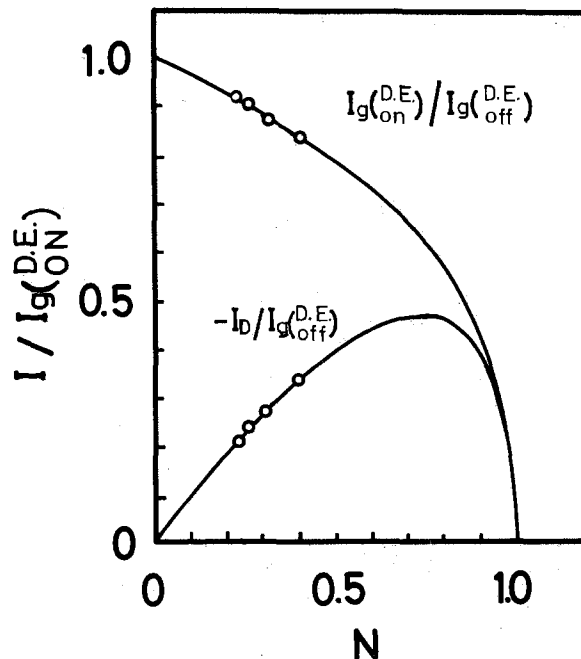


Fig. 6. Interference effect between the generating and the detecting currents, $I_g(\text{ON})$ and I_d , for the cells listed in Table I. Each current is divided by $I_g(\text{OFF})$ for normalization. Solid lines denote the results of calculation while circles are the results of observation.

only to boundary layer flow discussed in this paper, but also to other flow modes like viscous flow. This fact seems to indicate the possibility of the application to quite small electrode geometries. The multiple possibilities concerning practical applications are likely to bring bright prospects to this kind of voltammetry. From another point of view, this system may be the most useful when the effect of magnetic field on electrochemical reactions is investigated.

Acknowledgment

The authors thank Mr. T. Makino for helpful discussions in the course of this work.

Manuscript submitted Feb. 4, 1983; revised manuscript received Feb. 3, 1984.

The University of Tokyo assisted in meeting the publication costs of this article.

REFERENCES

1. A. V. Leont'ev and A. G. Smirnov, *Vopr. Magnith. Gidrodinam.*, **3**, 357 (1963).
2. N. I. Pekhteleva and A. G. Smirnov, *ibid.*, **2**, 89 (1965).
3. S. Mohanta and T. Z. Fahidy, *Can. J. Chem. Eng.*, **50**, 248 (1972).
4. T. Z. Fahidy, *Electrochim. Acta*, **18**, 607 (1973).
5. R. Aogaki, K. Fueki, and T. Mukaibo, *Denki Kagaku*, **43**, 504 (1975).
6. R. Aogaki, K. Fueki, and T. Mukaibo, *ibid.*, **43**, 509 (1975).
7. R. Aogaki, K. Fueki, and T. Mukaibo, *ibid.*, **44**, 89 (1976).
8. A. J. Arvia and S. L. Marchiano, in "Modern Aspects of Electrochemistry," No. 6, J. O'M. Bockris and B. E. Conway, Editors, p. 188, Plenum Press, New York (1971).
9. R. N. O'Brien and K. S. V. Santhanam, *This Journal*, **129**, 1266 (1982).
10. V. G. Levich, "Physicochemical Hydrodynamics," Sec. 3, p. 14, Prentice-Hall, New York (1962).
11. V. G. Levich, "Physicochemical Hydrodynamics," Sec. 15, p. 87, Prentice-Hall, New York (1962).
12. W. H. Albery and M. L. Hitchman, "Ring-Disc Electrodes," p. 19, Oxford University Press, New York (1971).
13. H. Matsuda, *J. Electroanal. Chem.*, **16**, 153 (1968).
14. H. Schlichting, "Boundary-Layer Theory," 6th ed., p.

- 125, McGraw-Hill Book Co., New York (1968).
 15. L. N. Nekrasov and N. P. Berezina, *Dokl. Akad. Nauk SSSR*, **142**, 855 (1962).
 16. A. J. Arvia and S. L. Marchiano, "Modern Aspects of Electrochemistry," No. 6, J. O'M Bockris and B. E.

- Conway, Editors, p. 219, Plenum Press, New York (1971).
 17. W. J. Albery and M. L. Hitchman, "Ring-Disc Electrodes," p. 23, Oxford University Press, New York (1971).

Photointercalation and Photodeposition of Copper in P-Type Lamellar InSe

C. Levy-Clement* and B. Theys

Laboratoire de Physique des Solides, CNRS, 92195 Meudon France

ABSTRACT

We report here, as an example of actual photointercalation, the light-induced intercalation of copper into p-type InSe from an organic medium ($\text{CH}_3\text{CN} + 0.1\text{M TBA-BF}_4 + 0.1\text{M CuCl}$). The two types of InSe electrodes used had their exposed surfaces parallel or perpendicular to the cleavage surface [(001) plane]. From the photovoltages, short-circuit currents, current *vs.* potential characteristics, photocurrent spectra, and SIMS measurements, it is shown that metallic copper is photoelectrodeposited on the cleavage surface whereas copper is photointercalated when the surface perpendicular to the cleavage face is in contact with the electrolyte. Deintercalation of copper does not take place spontaneously in the dark.

One of many photoelectrochemical effects that can occur at the semiconductor-electrolyte interface (1) is photointercalation. This effect has been theoretically predicted (2), but no experimental evidence has been published. In a classical semiconductor-liquid Schottky barrier, photogenerated minority carriers are ejected from the semiconductor to the electrolyte where they react with the redox system in solution. Majority carriers flow through the semiconductor and the external load to the counterelectrode. In a p-type photocathode whose crystal structure allows the insertion of guest atoms, oxidized species of the redox couple may penetrate into the semiconductor and trap *in situ* the photogenerated electrons, while holes flow to the counterelectrode. This process, is known as photointercalation. Lamellar compounds are very suitable materials, because of the existence of weak Van der Waals bonds between some adjacent planes. The layers are easily separated and a variety of atoms or organic molecules can be intercalated into the Van der Waals gaps (3). This process will occur spontaneously when thermodynamically favorable. When the intercalated species is a cation (M^+) and an electron is provided by the lamellar compound (Lc) the following reaction may proceed: $x\text{M}^+ + xe^- + \text{Lc} \rightarrow (\text{M})_x\text{Lc}$. When the lamellar compound is a metal or an n-type semiconductor the electrons can be introduced electrochemically (4-5) (Fig. 1a). Such a reaction cannot proceed in a p-type semiconductor in the dark because of the lack of electrons. The electrons can however be photogenerated (Fig. 1b).

For photointercalation to take place, one must find a suitable semiconductor plus cation pair. The p-type semiconductor must meet following conditions: (i) adequate carrier mobility, (ii) favorable thermodynamics for reaction of the reduced species with the lattice, (iii) fast diffusion of the reduced species in the lattice, (iv) stability against corrosion and photocorrosion, and (v) the redox potential of the intercalated cation must be located inside the bandgap of the semiconductor.

Indium selenide InSe is a III-VI lamellar semiconductor which meets the criteria for photointercalation. Depending on the growth conditions and on doping, this material exhibits n or p-type behavior (6). From a preliminary photoelectrochemical study of InSe in aqueous electrolytes, the position of the bandedges was estimated as -0.45V vs. NHE for the conduction band and as $+0.75\text{V vs. NHE}$ for the valence band (7-9). Copper (I) with a

Cu^+/Cu^0 redox potential at -0.38V vs. NHE in acetonitrile (10) is very suitable for intercalation. One can also easily see when it is reduced to red metallic copper (0). InSe has two crystalline surfaces exhibiting very different physical properties. One, the cleavage surface perpendicular to the \vec{c} axis, consists of selenium atoms bonded together with covalent forces. The other surface, parallel to the \vec{c} axis, is made of selenium and indium atoms, the selenium atoms of adjacent layers being bonded by Van der Waals forces (Fig. 2).

We report an example of demonstrated photointercalation, the light-induced topotactic reaction with p-type InSe and show how the structure of the surface in contact with the electrolyte plays a major role in this effect.

Experimental

Preparation of the electrodes.—p-type InSe single crystal was grown by the Bridgman-Stockbarger method (6) and has 500 ppm zinc doping. In the direction perpendicular to the \vec{c} axis, the bulk resistivity was $240 \Omega\text{-cm}$ and the mobility $40 \text{ cm}^2\text{v}^{-1}\text{s}^{-1}$. The number of carriers was $6.8 \cdot 10^{14}\text{cm}^{-3}$, assuming a one carrier model. Two types of

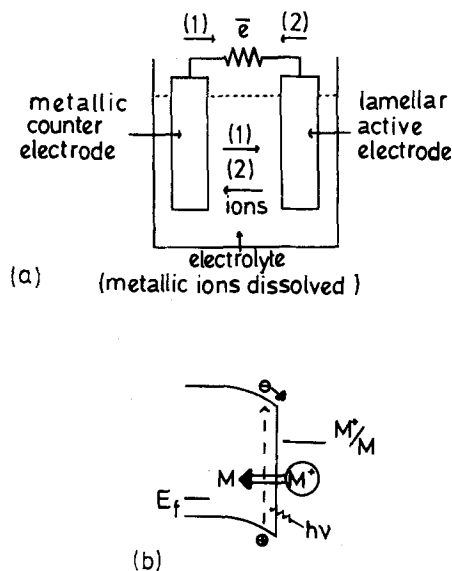


Fig. 1. (a) Schematic representation of the electrochemical (de)intercalation process [(1) \rightarrow intercalation, (2) \rightarrow deintercalation]. (b) Schema of the photointercalation process for a p-type semiconductor.

* Electrochemical Society Active Member.

Key words: photointercalation, photodeposition, p-type InSe, layered semiconductor.

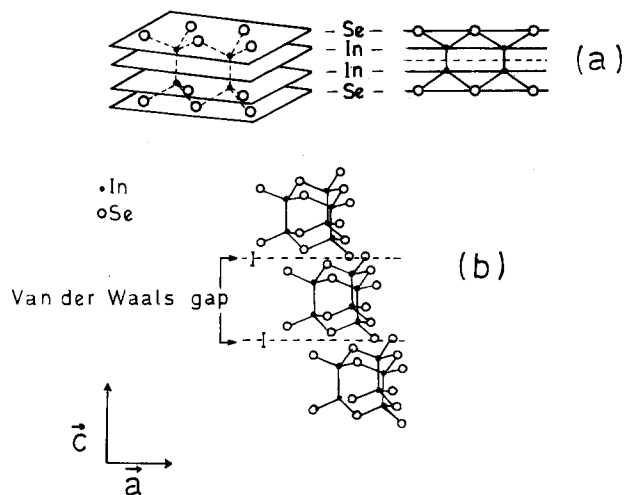


Fig. 2. Crystal structure of a polytype for InSe (a) packing of the layers, (b) perspective view, the unit cell extends over three layers.

crystalline surfaces were used. Crystals were cleaved perpendicular to the *c* axis or carefully cut parallel to the *c* axis. The electrode was named \perp electrode when the cleavage surface was exposed to the solution and \parallel electrode when the surface parallel to the *c* axis was exposed. The two surfaces were used without pretreatment. Optical properties of InSe are well known (11). In the direction \perp to the *c* axis there is an indirect gap of 1.187 eV and a direct gap, weakly allowed by spin-orbit coupling in the valence band, at 1.352 eV. In the direction \parallel to the *c* axis there is only the direct transition gap. Ohmic contacts at the back of crystals were made with conductive silver paint. Crystals were encapsulated in resin (Epoxy-patch, the Dexter Corporation) with only the chosen surface left exposed to the electrolyte.

Choice of the electrolyte.—The redox couple Cu^+/Cu^0 is not stable in noncomplexing aqueous solutions; therefore an organic electrolyte was used. The electrolyte was highly pure and dry acetonitrile in which 0.1M tetrabutylammonium tetrafluoroborate (TBA- BF_4 , Sigman Chemical Company) supporting electrolyte was dissolved with 0.1M CuCl (Johnson Matthey). TBA- BF_4 and CuCl were dehydrated under a 10^{-6} torr vacuum at 150° and 110°C, respectively, for 24 hr. The electrolyte was kept out of the light to avoid the photo-oxidation of copper (I).

Measurements.—A special cell was built with a Pyrex optical flat window and three watertight passages. A three electrode system was used. The counterelectrode was a copper wire and the reference electrode was Ag/0.1M AgNO_3 (dissolved in CH_3CN). Details of the photovoltage, short-circuit current, current/voltage characteristics [I-V] in the dark and under illumination, photocurrent spectroscopy measurements and the electronic equipment have been reported previously (12). The electrode was illuminated by a 6.5 mW 632.8 nm helium neon laser, or by a 250-W tungsten-iodine lamp; white light and laser light had comparable incident intensities in milliwatts per square centimeter. Either direct or chopped white light or monochromatic chopped light was used.

Results

The redox system.—The oxidation-reduction potentials of Cu^+/Cu^0 and $\text{Cu}^{2+}/\text{Cu}^+$ in $\text{CH}_3\text{CN} + 0.1\text{M TBA-BF}_4$ electrolyte were deduced from the cyclic voltammetric characteristics, obtained using two platinum electrodes. In Fig. 3 two oxidation-reduction waves are visible. The reduction of Cu^+ starts at -290 mV vs. Ag/AgNO₃ and the oxidation of Cu^0 takes place at $+600$ mV. The large peak that appears when the potential is scanned negative to positive corresponds to the oxidation of metallic Cu^0 deposited on the surface of the platinum cathode.

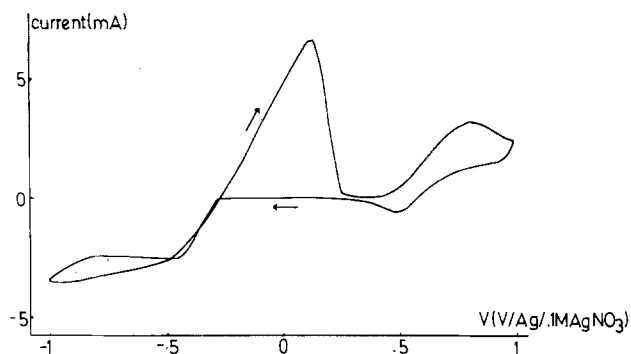


Fig. 3. Voltammetric behavior at Pt electrodes of CuCl in CH_3CN containing 0.1M TBA- BF_4 .

Photoelectrochemical experiments are done with either a \perp or \parallel electrode in contact with the electrolyte containing Cu^+ .

Behavior of the \perp electrode.—Figure 4 shows the variation of the open-circuit voltage of the \perp InSe photocathode vs. the reference electrode. In the dark the open-circuit voltage is -210 mV. Under the laser illumination it increases promptly to $+180$ mV and reaches $+250$ mV after 1 min. When the illumination is discontinued the open-circuit voltage drops rapidly to $+70$ mV, then slowly over a period of 20 min, to the initial value of -220 mV. Similar results are obtained under white light illumination. The very long period necessary for the open-circuit voltage to reach back the initial value is an indication of an important modification of the InSe surface under illumination. Further information will be obtained under short-circuit conditions.

Figure 5 shows the variation of the short-circuit current between \perp InSe and the counterelectrode in the dark and under the laser illumination. The current equals $0.1 \mu\text{A}/\text{cm}^2$ in the dark. Under the laser illumination, the current rises rapidly to $4 \text{ mA}/\text{cm}^2$ then starts to decline. When the illumination is discontinued, the current drops instantaneously to the background level. After a 5 min illumination the photocurrent drops to a quarter of the initial value and a copper spot, the shape of the laser illuminated area, appears. When the entire surface is illuminated with the white light the photocathode is completely

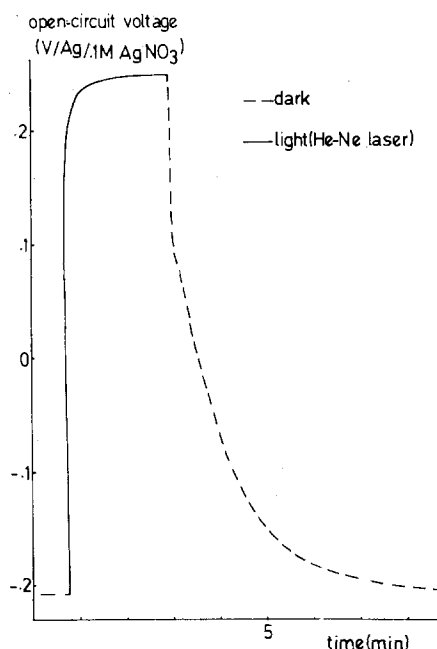


Fig. 4. Variation of the open-circuit voltage of \perp InSe cathode vs. the Ag/Ag⁺ reference electrode in the electrolyte. ----- In the dark, — under He-Ne laser illumination.

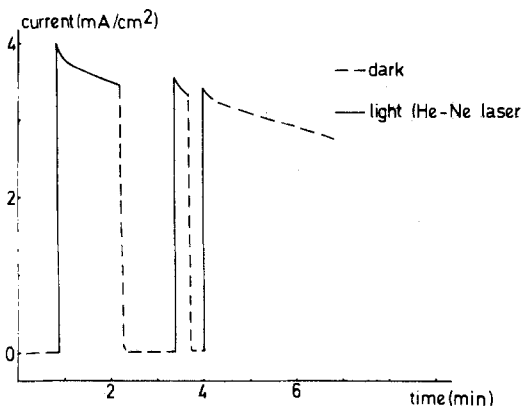


Fig. 5. Variation of the short-circuit current between \perp InSe and the copper counterelectrode in the electrolyte. ----- In the dark, — under He-Ne laser illumination.

covered with a metallic layer of copper. The very fast variation of the current between dark and light conditions shows that the photoelectrochemical effect at the semiconductor/electrolyte interface (photoelectrodeposition of copper 0) occurs with, or stops instantaneously without, the light.

Figure 6 shows the I-V characteristics. In the dark \perp InSe shows the expected p-type diode behavior (curve a). Under white light illumination a cathodic photocurrent appears, corresponding to the reduction of the copper (I). A residual photocurrent of 0.05 mA/cm^2 maintained under anodic polarization up to 1V is due to the presence of an InSe/Cu⁰ Schottky junction formed by the photodeposition of the metallic copper (curve b). When a +0.7V bias is applied for 5 min, the copper deposited at the surface of the photocathode is oxidized; as it is dissolved, a thin yellow film appears at the surface and the residual photocurrent disappears.

Figure 7 shows the photocurrent spectrum of the \perp InSe electrode with the copper deposited at the surface after 10 min white light illumination at -1V vs. Ag/Ag^+ . The photoresponse is in agreement with the photocurrent spectrum of p-type InSe in contact with aqueous solutions (7).

Behavior of the // electrode.—Figure 8 shows in the dark and under the laser illumination the variation of the open-circuit voltage of the // InSe photocathode vs. the reference electrode. In the dark the open-circuit voltage equals -305 mV and under the laser illumination it increases to -200 mV in 30s. Three minutes later it reaches an equilibrium value of -100 mV . When the illumination is discontinued, the open-circuit voltage declines slowly

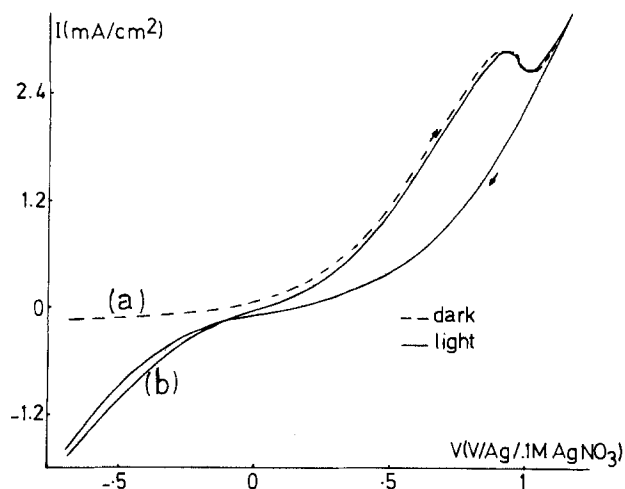


Fig. 6. Current voltage characteristics of \perp InSe electrode in the electrolyte. ----- Curve a in the dark, — curve b under direct white light. Light source, 250W tungsten-iodine.

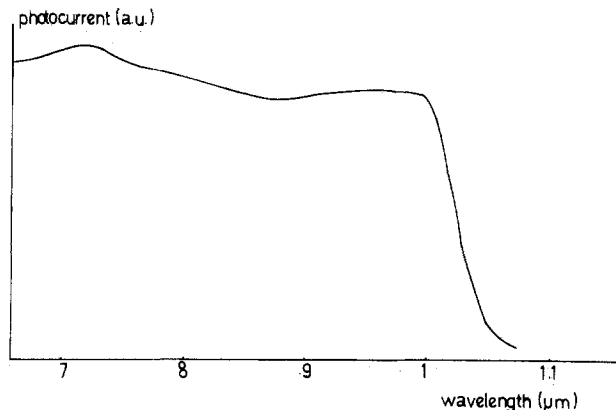


Fig. 7. Photocurrent spectrum of \perp InSe electrode, in the electrolyte at $-1\text{V vs. Ag/0.1 AgNO}_3$.

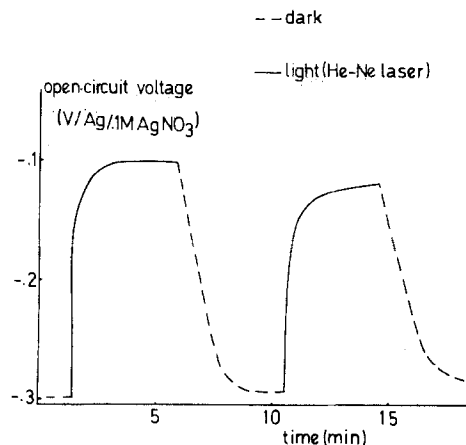


Fig. 8. Variation with time of the open-circuit voltage of // InSe electrode vs. the reference electrode in the electrolyte. ----- In the dark, — under He-Ne laser illumination.

and regularly over a period of 2 min to the initial value. Identical results are obtained under white light illumination and the value of the photovoltage is the same. When the experiment is repeated, the photovoltage value decreases, and, on successive trials, the photovoltage continues to decrease.

Figure 9 shows the variation of the short-circuit current between InSe and the counterelectrode in the dark and under the laser illumination. The dark current is $1.7 \mu\text{A/cm}^2$. Under the laser illumination it increases slowly and regularly; it takes 4 min to reach the steady-state value at $90 \mu\text{A/cm}^2$. The value of the photocurrent stays stable for at least half an hour. When the illumination is discontinued, the intensity of the current decreases regularly and after 2 min is back to its initial value. The same steady-state value for the photocurrent is obtained under direct white light illumination. Even after a 2h illumination period, no metallic copper was visible at the surface of the photocathode. The shapes of the photopotential and the short-circuit photocurrent vs. time curves are an indication that the effect occurring at the semiconductor-

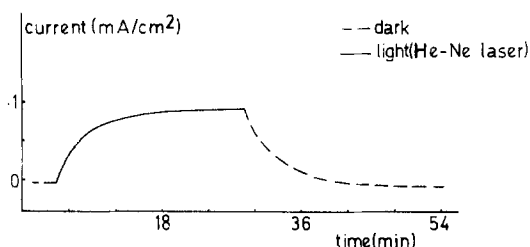


Fig. 9. Variation with time of the short-circuit current between // InSe electrode and the counterelectrode in the electrolyte. ----- In the dark, — under He-Ne laser illumination.

electrolyte interface is diffusive in nature. The intercalation effect is such an effect. We believe that under short-circuit conditions, the intercalation of copper (I) is photoinduced.

Figure 10 shows the current/voltage characteristics using the three electrode system. After a previous white light illumination under short-circuit conditions for 10 min, InSe no longer shows p-type diode behavior in the dark (curve a). Strong hysteresis of the curve depending on the scan direction is observed. Under direct white light illumination both anodic and cathodic photocurrent are observable (curve b). This effect is more readily visible on curve c where the photocurrent is measured with a lock-in amplifier, the white light being chopped, after a 3h white light illumination period, under a $-0.7V$ bias. Both dark current and photocurrent curves indicate that the \parallel electrode InSe is no longer a simple p-type semiconductor but has now n and p domains, coexisting on the same surface. A similar coexistence has been reported for the tungsten diselenide photoelectrode (13). The intercalation of copper is believed to be responsible for the appearance of the n-type domains.

Figure 11 shows the photocurrent spectra of the \parallel InSe electrode. Curve (a) corresponds to the beginning of the photointercalation when InSe is biased at $-1V$ vs. $Ag/AgNO_3$. Spectrum (b) also obtained with a $-1V$ bias applied to this InSe electrode (but after a previous 3h white light illumination period at a $-1V$ bias) corresponds to an advanced step of the photointercalation. Curve b indicates that the intercalated copper introduces recombination centers in the semiconductor. From the fact that the maximum of the photocurrent spectrum is at 1030 nm, one can deduce that less copper is intercalated in the bulk than near the surface of the semiconductor.

Figure 12 shows the concentration profile of copper in InSe after a 20h white light illumination period at a $0.15V$ vs. Ag/Ag^+ bias. The measurement was made with an IMS 300 CAMECA measuring the $126Cu_2^+$ and the $78Se^+$ peaks. The copper was detected to a depth of $55\mu m$.

Discussion

The results reveal drastically different photoelectrochemical behavior for the \perp face and the \parallel face of InSe in contact with the organic electrolyte. Previously we have shown that in $0.1M H_2SO_4$ the photopotentials of \perp and \parallel electrodes are limited to 280 and 230 mV, respectively, by the presence of states which pin the surface Fermi level. These values decrease by less than 50 mV when the pH is increased from 1 to 12 (14). In acetonitrile, the photopotential of the \perp electrode is no longer limited by surface states and a photopotential of 450 mV is developed. Such

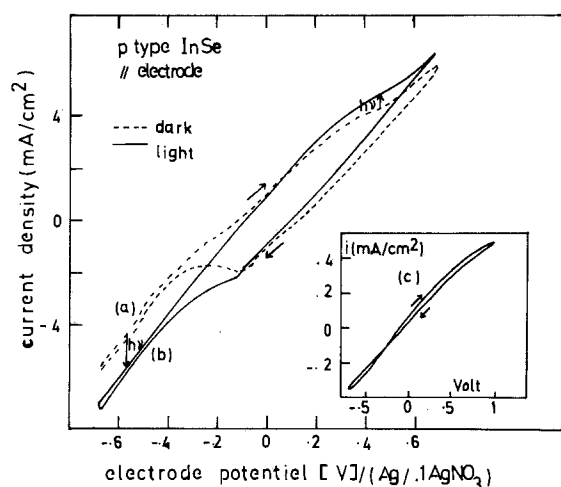


Fig. 10. I-V curve of \parallel InSe in the electrolyte. Curves a and b after a 10 min white light illumination under short-circuit conditions. ----- In the dark, — under direct white light. — Curve c under white chopped illumination and after a 3h white light illumination period at $0.7V$.

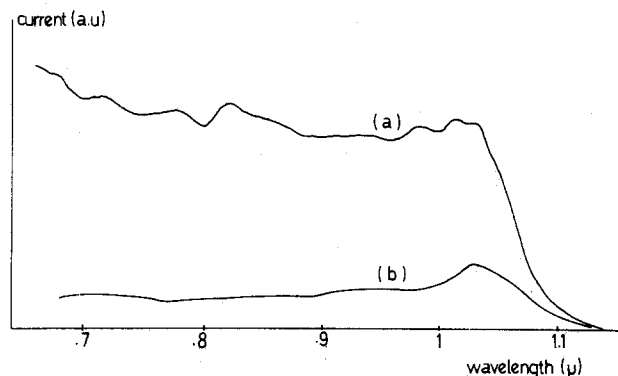


Fig. 11. Photocurrent intercalation spectra of \parallel InSe electrode, in contact with the electrolyte at $-1V$ vs. $Ag/0.1M AgNO_3$. Curve (a) corresponds to the beginning of the photointercalation. Curve (b) after a 3h white light illumination period at $-1V$ bias, corresponds to an advanced step of the photointercalation.

a high photopotential, however, cannot be reached even in acetonitrile with the \parallel electrode.

Under illumination, metallic copper is electrodeposited at the \perp surface whereas it is intercalated in the \parallel electrode. In both cases photogenerated electrons reduce the Cu^+ at the surfaces of the electrodes. Because intercalation of Cu^+ in InSe is a thermodynamically downhill process, less energy is needed to intercalate the metal than to deposit it at the surface. Since Cu^+ (or Cu^{2+}) cannot diffuse in a direction perpendicular to the Van der Waals plane, intercalation can physically take place only when the Van der Waals gaps are in contact with the electrolyte. Because the potential for intercalation is less negative than the potential for electrodeposition, no electrodeposition takes place as long as copper is being intercalated. Indeed, at the \parallel electrode, intercalation of copper occurs spontaneously under short-circuit condition. After a half-hour illumination period, the $90\mu A/cm^2$ maximum photocurrent starts to decrease and, after 20h, it drops to half of its initial value. At the \perp electrode where intercalation cannot take place even under illumination, Cu^+ is simply photodeposited on the surface. After 5 min illumination at short circuit, a metal (Cu^+)-semiconductor (p-type InSe) Schottky junction is formed. Figure 6 shows the I-V characteristics of this Schottky junction when immersed in the organic electrolyte. The small photocurrent that persists under anodic polarization is the leakage current across the Schottky barrier.

Both dark and light I-V characteristics of the \parallel electrode indicate that, upon photointercalation of copper, the p-InSe acquires n-type regions, with both n- and p-type regions coexisting on the same surface.

The observed decrease in photocurrent with time is due both to photodeposition and photointercalation of copper. Photodeposited copper absorbs the light and, as its thickness grows, the photocurrent declines. Photointerca-

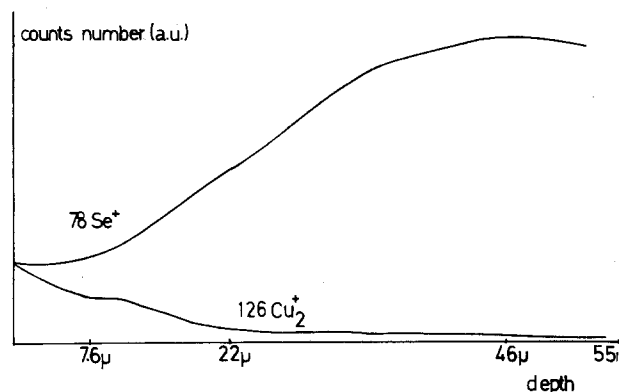


Fig. 12. SIMS measurement. Concentration profile of copper in \parallel InSe electrode after a previous 20h white light illumination period at $-0.15V$ bias in the electrolyte.

lation of copper in InSe does not prevent photons from being absorbed but introduces electron-hole recombination centers. These also cause the photocurrent to decline.

Copper photodeposited at the surface of the cleavage face can be anodically oxidized at +1V vs. Ag/Ag⁺, becoming a thin yellow film visible at the surface of the electrode.

Intercalation is a reversible reaction. From the theoretical study (2) it has been predicted that if intercalation of cations occurs by photoelectrochemical process, the deintercalation of these cations should take place spontaneously in the dark, while electrons flow to the counterelectrode, giving an external current of direction inverse to the one observed during photointercalation. Such a behavior is not observed in Fig. 9. We conclude that in our experiment the deintercalation of copper does not take place spontaneously in the dark.

In a classical lithium layered chalcogenide cell the host material is deintercalated upon charging the cell, *i.e.*, by driving electrons from the host to the metal electrode where lithium is electroplated. Similar deintercalation should be observed in InSe/Cu when an anodic bias is applied. Our results do not allow us, however, to conclude at this time that under anodic polarization copper is indeed deintercalated. More experiments have to be done in this direction with new p-type semiconductors, considering the important implication of the deintercalation process for *in situ* energy storage.

Conclusion

Evidence for the photointercalation of a metal into a layered semiconductor is presented. Under illumination copper is intercalated into p-type InSe only when the Van der Waals gaps are in contact with the electrolyte. This phenomenon occurs at more positive potential than the deposition potential of copper at the surface because intercalation is a thermodynamically favored process. For this reason deintercalation of copper does not occur spontaneously in the dark under short-circuit conditions. On the cleavage face only the photoelectrodeposition of metallic copper occurs.

Acknowledgments

Part of this work was supported by the European Community (project no. ESD-028-F).

Special thanks go to O. Gorochov whose contribution to this paper has been extensive and invaluable. The authors would like to thank D. M. Schleich for helpful discussions. They are grateful to A. Chevy for providing the crystal and to J. Rioux and C. Grattepain for the SIMS measurements. C. L. C. thanks W. R. McKinnon and J. R. Dahn for comments on intercalation.

Manuscript submitted Aug. 1, 1983; revised manuscript received Nov. 25, 1983.

REFERENCES

1. A. J. Nozik, Editor, "Photoeffects at Semiconductor-Electrolyte Interfaces," ACS Symposium Series, Vol. 146 (1981).
2. H. Tributsch, *Appl. Phys.*, **23**, 61 (1980).
3. M. S. Whittingham, *Progr. Solid State Chem.*, **12**, 41 (1978).
4. M. S. Whittingham, *Mater. Res. Bull.*, **9**, 1681 (1974).
5. G. V. Subba Rao and J. C. Tsang, *ibid.*, **9**, 921 (1974).
6. A. Chevy, Thèse d'Etat, Paris (1981).
7. C. Levy-Clement, N. Le Nagard, and O. Gorochov, "Proc. 4th Internation. Conf. on Photochemical Conversion and Storage of Solar Energy," Jerusalem Israël, Aug. 8-13, 1982.
8. B. Fotouhi, O. Gorochov, A. Katty, N. Le Nagard, C. Levy-Clement, D. Schleich, B. Theys, and H. Tributsch, "Photochemical, Photoelectrochemical and Photobiological Processes." Series D, Vol. 2. D. Reidel Publishing Company, EC Contractor's Meeting, pp. 78-85., Dec. 6-8, 1982.
9. C. Levy-Clement, N. Le Nagard, O. Gorochov, and A. Chevy, *This Journal*, **131**, 790 (1984).
10. A. J. Bard, Editor, "Encyclopedia of Electrochemistry of the Elements," Marcel Dekker Inc., Vol. 2, p. 395 (1974).
11. N. Piccioli, R. Le Toullec, F. Bertrand, and J. C. Chervin, *J. Phys.*, **42**, 1129 (1981).
12. O. Gorochov, A. Katty, N. Le Nagard, C. Levy-Clement, and D. M. Schleich, *Mater. Res. Bull.*, **18**, 111, 1983.
13. S. Menezes, L. F. Schneemeyer, and H. J. Lewerenz, *Appl. Phys. Lett.*, **38**, 949 (1981).
14. B. Theys and C. Levy-Clement, To be published.

Selectivity Changes in Electrochemical Reaction Sequences by Modulated Potential Control

Peter S. Fedkiw* and William D. Scott, Jr.

Department of Chemical Engineering, North Carolina State University, Raleigh, North Carolina 27695

ABSTRACT

Electro-organic reactions typically involve the electrochemical generation of a reactive intermediate which may participate in further chemical or electrochemical reactions. It is possible to effect the product distribution in such branched reaction networks by modulating the electrode potential. Reaction rate calculations under electrokinetic-controlled conditions for four reaction mechanisms, each involving an electrogenerated intermediate, are presented for step- and sinusoidal-potential modulation. The results show that reactor operating conditions unobtainable under steady potential control are possible. The cycle-averaged selectivity and yield of selected products may be significantly increased at the stationary state in comparison to those at an identical production rate but under dc conditions. The effect of modulation is frequency dependent; for some reaction sequences, the reaction trend at low frequency may be opposite than that at high frequency. The relative rates of a chemical reaction in parallel with an electrochemical reaction, both involving the intermediate, are more sensitive to potential modulation than either two parallel chemical or electrochemical reactions. Mass transfer limitations dampen the results of modulation. Reactor performance increases under modulated potential (or current) control possibly may be significant enough to make an electrochemical processing route economically viable.

In a branched-reaction sequence involving both chemical and electrochemical steps, the electrochemical reaction rates may be modified by a change in the electrode potential during the course of the reaction. Thus, it is conceivable to manipulate, by modulation of the potential,

*Electrochemical Society Active Member.

the outcome of a reaction to enhance the formation of desired products and simultaneously retard the formation of undesired products. The yield (percent of reactant consumed to form the desired product) and selectivity (ratio of desired product to all other side products) may be favorably increased by modulated potential control such

that an otherwise inefficient reaction may possibly become economically viable due to decreased capital costs (yield improvement) and reduced separation costs (selectivity increase).

The possible beneficial effects of modulated potential control have been qualitatively noted in the literature (1), but quantitative guidelines as to when modulated potential may be useful have not been presented. This paper presents calculated yields and selectivities of several branched-reaction sequences, typical of electro-organic processes, under two modes of potential control: sinusoidal and step modulation. Simple kinetic expressions and isotherms have been used to focus the results on the modulation effect. In this vein, the discussion is directed mainly at electrokinetic-controlled reactions occurring on electrodes with a uniform secondary-current distribution. It is shown that modulation can significantly enhance the selectivity of some products or can be detrimental to other products or even entire reaction sequences.

A brief review of modulated control of a chemical reactor and the use of modulated potential (or current) in electrochemical reactors is presented first. The example reaction sequences used in the calculations and their kinetic expressions are presented next, followed by the results and discussion.

Periodic Control of Reaction Rates

Chemical reactions.—It has been recognized that reaction rates and selectivities may be significantly effected in ordinary chemical reactors by periodic control of some external forcing function. Theoretical and experimental studies of both homogeneous and heterogeneous reactions have been performed. Temperature (2-6), reactant concentration (7-16), and heat-addition rate (17) have been modulated and have been shown to change the reaction rate and yield from that at the cycle-averaged value. Depending upon the particular reaction sequence under consideration, periodic control may be better or worse than steady-state operation. Reviews of periodic control for ordinary chemical reactors are available (18, 19). It is not very practical in an industrial context to modulate the reactant concentration into a reactor. In addition, the large thermal inertia associated with the reactor wall, catalyst support, and solvent can significantly dampen temperature fluctuations. Consequently, periodic forcing control of a reactor has not been practiced by the chemical industry.

Inorganic electrochemical reactions.—Periodic reaction control has been recognized to be of benefit by the inorganic electrochemical industry. In particular, electroplating characteristics may be significantly altered by periodic reaction control (20). The morphology of an electrodeposit may be controlled under periodic potential or current manipulation (21-28), and electrodeposited alloy composition may be changed by periodic reaction control (29-31). Electrodeposition under periodic reaction control at mass-transfer-limited conditions has also received attention (32-37). In addition, it has been shown that electrodisolution efficiency may be increased under periodic current control (38, 39) and corrosion characteristics may be modified (40, 41).

Electro-organic reactions.—Electro-organic reactions should be particularly sensitive to potential or current modulation, since they typically involve a sequence of electrochemical and chemical steps in a parallel or series arrangement. Electrolysis of organic substrates under periodic current modulation was first studied by Ghosh (42). Modulation of potential and current has been used mainly to ascertain reaction mechanisms in electro-organic-reaction sequences. Most studies on ac electrolysis are concerned with the determination of current efficiency and its dependence on frequency and do not explicitly consider the most interesting aspect of ac control, which is the ability of periodic operation to alter the course of complex reactions and the nature of the resulting products.

Wilson and Lippincott (43) used step current modulation to study the oxidation of propionic acid and acetate. They found the production of ethylene from oxidation of propionic acid decreased sharply with increasing frequency, while only a slight decrease in ethane formation from the oxidation of acetate was observed. They reasoned that the first reaction was second order in an adsorbed intermediate, while the second was first order. The realization that the pulse frequency has different effects on reactions of different orders has important consequences for reaction sequences in which competing reactions are of different order. Fleischmann *et al.* (44) studied the kinetics of the Kolbe electro-synthesis of ethane on Pt from aqueous acetate solutions under pulse-potential control. They observed that with short pulses acetate ions were completely oxidized to carbon dioxide; however, with increasing pulse time, the formation of ethane increased to its steady-state value. Hickling and Wilkins (45) investigate the anodic electrolysis of aqueous potassium ethyl malonate solutions and acetate solutions using step current modulation. By applying small cathodic currents between the anodic pulses, they observed a sharp minimum in current efficiency at a characteristic frequency. This frequency corresponded to the passage of a critical quantity of charge sufficient to destroy conditions for dimerization, thereby permitting oxygen evolution to become an effective side reaction. Fleischmann and Goodridge (46) and Atherton *et al.* (47) studied the decarboxylation kinetics of acetate ions in alkaline solution using square-wave potential modulation. Cycle time, amplitude, and duty ratio of the potential pulse were varied. Production of methanol, ethane, methane, and oxygen were measured. Oxygen evolution exhibited a maximum with pulse duration, while both ethane and methanol yields decreased. The ratios of ethane and methanol production to oxygen production (and, to some extent, ethane production to methanol production) were changed by varying the pulse length while holding the amplitude and duty ratio constant. Fleischmann *et al.* (1, 48) studied the reduction of nitrobenzene and the Kolbe synthesis of ethane under pulse potential control. They concluded that for the reduction of nitrobenzene, the product distribution could be altered by pulsing the electrode potential. Their work is the first clear qualitative statement that periodic control can selectively produce certain reaction products in cases where there are competitive reactions. Nadebaum and Fahidy (49, 50) developed a model for the reaction kinetics in the Kolbe synthesis and were able to predict the observed maximum production of oxygen with varying pulse time as seen by Fleischmann *et al.* Scrivastava and Shukla (51) studied the ac electrolysis of sodium salts of aliphatic acids. The reaction products were the same for both constant current and ac, but the relative distribution of the products exhibited a marked dependence on current density and frequency. Bhadani (52) studied the electropolymerization of styrene under ac control and noted that the yield and molecular weight of the resulting polymer decreased with frequency. Alkire and Tsai (53) examined the alternating current electrolysis of propylene oxide and reported a decrease in current efficiency with increasing frequency.

Electro-Organic Reaction Sequences

In electro-organic reactions an intermediate species is usually generated by a one- or two-electron transfer. This intermediate may then participate in further chemical or electrochemical reactions. Table I illustrates the reaction sequences which were studied in this work. [Other, more complex reactions have been discussed by Scott (54).] The intermediate concentration may be manipulated by modulation of the initial electrochemical-reaction rate, and, hence, any reaction which depends upon its concentration. Consider the E-C,E reaction sequence shown in Table I. If the electrode potential is modulated between a high driving force for the production of R_1 and a low value where this rate is negligible, the production of R_2 and R_3 will consequently vary periodically. The questions

Table I. Coupled electrochemical-chemical reaction sequences

Reaction designation	Mechanism
E-C,E	$R_0 \xrightarrow[K1R_0 \exp(-a_1fE)]{E} R_1 \begin{cases} \xrightarrow{K2R_1} C \rightarrow R_2 \\ \xrightarrow{E} R_3 \\ \xrightarrow{K3R_1 \exp(-a_3fE)} R_3 \end{cases}$
E-C ² ,E	$R_0 \xrightarrow[K1R_0 \exp(-a_1fE)]{E} R_1 \begin{cases} \xrightarrow{K2R_1^2} C^2 \rightarrow R_2 \\ \xrightarrow{E} R_3 \\ \xrightarrow{K3R_1 \exp(-a_3fE)} R_3 \end{cases}$
E-C,C ²	$R_0 \xrightarrow[K1R_0 \exp(-a_1fE)]{E} R_1 \begin{cases} \xrightarrow{K2R_1} C \rightarrow R_2 \\ \xrightarrow{C^2} R_3 \\ \xrightarrow{K3R_1^2} R_3 \end{cases}$
E-E,E	$R_0 \xrightarrow[K1R_0 \exp(-a_1fE)]{E} R_1 \begin{cases} \xrightarrow{K2R_1 \exp(-a_2fE)} E \rightarrow R_2 \\ \xrightarrow{E} R_3 \\ \xrightarrow{K3R_1 \exp(-a_3fE)} R_3 \end{cases}$

E = electrochemical reaction.
 C = first-order chemical reaction.
 C² = second-order chemical reaction.

addressed here are: how does the cycle-averaged production of R_2 or R_3 or their ratio (selectivity) increase or decrease under the modulated conditions, and what is the basis for this decision; what are the control conditions (e.g., frequency, modulation waveform, etc.) which result in higher production rates and reaction selectivity?

Electrode kinetics.—Since the focus of this work is the effect of modulated electrode potential on the outcome of reaction sequences, simple, yet representative kinetic expressions have been used in the calculations and are shown in Table I. The rate expressions used are consistent with those given by Sakellaropoulos (55). For presentation purposes, all electrochemical reactions are assumed to be reductions. No side reactions (such as solvent electrolysis) take place, and the electrode-electrolyte potential difference is assumed to be spatially uniform. Furthermore, for the majority of the calculations, mass-transfer limitations are neglected; i.e., electrokinetic-controlled reaction conditions exist. Additional assumptions are listed below.

1. All concentrations appearing in Table I are on an area basis, and the adsorbed species are assumed to follow a linear adsorption isotherm. (Scott has also presented calculations for a Langmuir isotherm.) The concentration of the intermediate R_1 in the bulk solution is assumed to be zero, and the net rates of all chemical and electrochemical reactions which consume R_1 are assumed to occur at a large enough value such that no R_1 escapes the vicinity of the electrode.

2. The electrochemical reactions are assumed to be irreversible, first order in the concentration of their reactant, and obedient to Tafel behavior with potential. The potential is assumed to be displaced sufficiently from the open-circuit potential of the initial electrochemical reaction and any follow-up electrochemical reaction.

Within the limitations of the above assumptions, the rates of reaction, for example, in the E-C,E reaction sequence, are written as

$$\begin{aligned} r_1 &= K1R_0 \exp(-a_1fE) \\ r_2 &= K2R_1 \\ r_3 &= K3R_1 \exp(-a_3fE) \end{aligned}$$

where the rate constants $K1$ are independent of the potential E , which is measured with an arbitrary reference electrode, a_1 is a cathodic transfer coefficient, and $f = F/RT$.

Solution Procedure

Production rates for the products R_2 and R_3 in the various reaction schemes shown in Table I were calculated by solving the governing equation for the intermediate concentration $R_1(t)$ and substituting into the appropriate rate expression. The Appendix shows the differential equation which governs the intermediate concentration for the various reaction sequences. The solution depends upon the waveform of the imposed voltage, $E(t)$; sinusoidal and step potential modulation as shown in Fig. 1 were used. Since the differential equation cannot be solved analytically, a numerical integration scheme useful

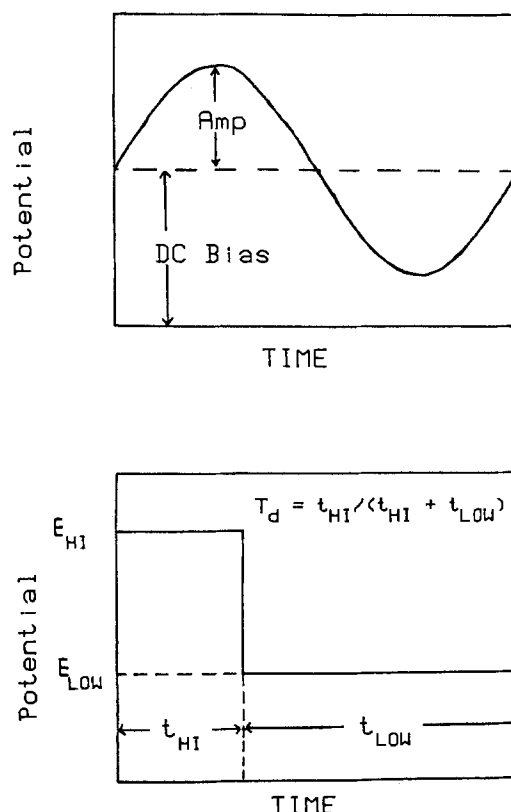


Fig. 1. Electrode potential waveforms used in calculations (a) sinusoidal (b) step. The definition of duty cycle is indicated in Fig. 1b.

for stiff ordinary differential equations was used (56). The integration was continued until the stationary state of the intermediate concentration was found. The reaction rates were then averaged over a period; only cycle-averaged quantities are reported here. The yield and selectivity of the reaction are of interest, and it is only necessary to report one of the two, since they are related for the reactions shown in Table I; for example, in the E-C,E reaction, the yield, Y , of the chemical product R_2 ($Y = \langle r_2 \rangle / \langle r_0 \rangle$) is related to its selectivity, S ($S = \langle r_2 \rangle / \langle r_3 \rangle$), as $Y = S/(1 + S)$, where $\langle \rangle$ designates a cycle-averaged quantity.

Results and Discussion

Basis of comparison.—At the stationary state, the cycle-averaged production rate and selectivity should be compared to some reference values to determine if the reaction modulation is beneficial. The dc reaction rates evaluated at the average potential of the modulation appear to be a logical choice, but are inappropriate bases, however, for two reasons. The first is a practical limitation due to the nature of the kinetic expressions used in the calculations. Step potential manipulation when the electrochemical reactions are completely eliminated during the “off” cycle is a limiting case of interest. Since the reactions are assumed irreversible, an infinite positive voltage, fE_{Low} , will be required to eliminate completely the electrochemical reactions. Hence, in this case, an average potential for a step potential manipulation has no meaning. The second objection is more fundamental. Because the electrochemical reactions depend exponentially upon the electrode potential, the cycle-averaged reaction rates under sinusoidal modulation will always be greater than that of a steady-state reaction evaluated at the cycle-averaged potential. It can be argued that, if the goal is larger production rates, then the reaction need only be operated at a higher, steady polarization instead of modulating the potential.

A given product-production rate is the basis chosen in this work for comparison of the modulated to steady-state reactor. It is assumed that there is a given requirement of the desired product, e.g., Z kg/hr of R_2 . At this given production rate, selectivities are calculated under steady-state and stationary-state conditions. With the results presented in this manner, it is clear if cyclic operation is beneficial or harmful to the net outcome of a reaction sequence.

E-C,E reaction sequence.—There are four intrinsic dimensionless variables which effect the outcome of the E-C,E reaction sequence: a_1 , a_2 , $K1/K2$, and $K3/K2$. In addition, the results depend upon the waveform of the imposed potential. For step potential modulation, the characteristics of the waveform are the duty cycle, T_d , the most cathodic and least cathodic voltage, fE_{Hi} and fE_{Low} , respectively, and the cycle time or frequency, w . Under sinusoidal potential modulation the control variables are the frequency, amplitude, $f\Delta E$, and bias voltage, fE_{dc} .

Calculations have been performed for a range of the rate constants (54). The magnitude of the reaction rates at any potential will, of course, depend upon the value of the rate constants; however, the trend of either increased or decreased selectivity under modulated potential control was found to be independent of the rate constants examined. The results are much more sensitive to the value of the transfer coefficients. Consequently, one set of reasonable values of the rate constants are used in the calculations presented, with emphasis placed on the effect of the transfer coefficients.

Figure 2a presents the cycle-averaged selectivity of the chemical product R_2 as a function of its dimensionless cycle-averaged production rate for constant and step potential modulation. Figure 2b presents analogous results for sinusoidal modulation with both figures calculated with $a_1 > a_3$. The center curves in Fig. 2a and 2b, labeled with “+,” are the selectivity under steady potential control. The potential becomes increasingly cathodic as more

of the product R_2 is produced, and three values of the steady-state potential are indicated in Fig. 2a and 2b.

The limiting case of $fE_{Low} = +\infty$ is used for step potential modulation. Under this polarization condition, all electrochemical steps are eliminated during the “off” portion of the cycle; hence, the intermediate may decay only via the chemical-reaction pathway. The largest selectivity for the chemical product can be anticipated under these conditions.

The asymptotic behavior for low and high frequency is shown on each figure for three fE_{Hi} for step potential modulation and three fE_{dc} for sinusoidal potential control. Each point on the modulated potential control curves in Fig. 2a represents operation at a different duty cycle. All curves originate on the dc line on which the duty cycle is one. Table II is an index for the duty-cycle value for all results graphically reported; e.g., the fourth symbol from the dc curve at any frequency represents a 50% duty cycle. Under sinusoidal potential control, the amplitude is varied at any frequency, and Table II also presents an index for all these results; e.g., the third point from the dc curve represents a dimensionless voltage amplitude of 5 imposed upon the dc bias.

The results show that selectivities not obtainable under dc operation are possible with modulated potential control, and an improvement in reactor performance is possible. Both an increase or decrease in selectivity is obtainable for both waveforms at any given production rate of R_2 depending upon the frequency; high frequency improves selectivity, while low frequency always decreases it for sinusoidal operation and, except at very low duty cycles, also for step potential control. Figure 3a and 3b show results at a number of intermediate frequencies for step and sinusoidal control, respectively. The dependence on frequency may be understood by examining the behavior of the intermediate concentration R_1 over a cycle. Under sinusoidal control at low frequency, a pseudo-steady state is obtained, and the intermediate concentration is maintained at a high value, which is effectively consumed by the electrochemical reaction during the potential oscillation. At high frequency, however, the intermediate concentration cannot follow the potential oscillations and is maintained at a lower value than that expected from the average calculated under steady conditions at the cycle-extreme potentials. Under step potential control at low frequency, the intermediate concentration and, hence, selectivity depend upon the duty cycle. A pseudo-steady state in the intermediate concentration during the “on” cycle may be obtained at low frequency. Since the intermediate concentration is its largest value then, the selectivity decreases because of its consumption in the electrochemical reaction. However, if the duty cycle is decreased to a small enough value, a pseudo-steady state of R_1 will not be obtained, and the selectivity will increase as T_d is decreased further, since the intermediate is consumed only by the chemical reaction during the “off” period.

The sign of the slope of the modulated-potential-control curves in Fig. 2 is different for the step and sinusoidal

Table II. Notation index for selectivity-production rate curves under modulated potential control

Number of symbol from dc curve	Step potential control	Sinusoidal potential control
	Duty cycle T_d	Amplitude $f\Delta E$
0	1	0
1	0.8	1
2	0.7	3
3	0.6	5
4	0.5	8
5	0.4	10
6	0.3	
7	0.2	
8	0.1	
9	0.05	
10	0.01	
11	0.005	

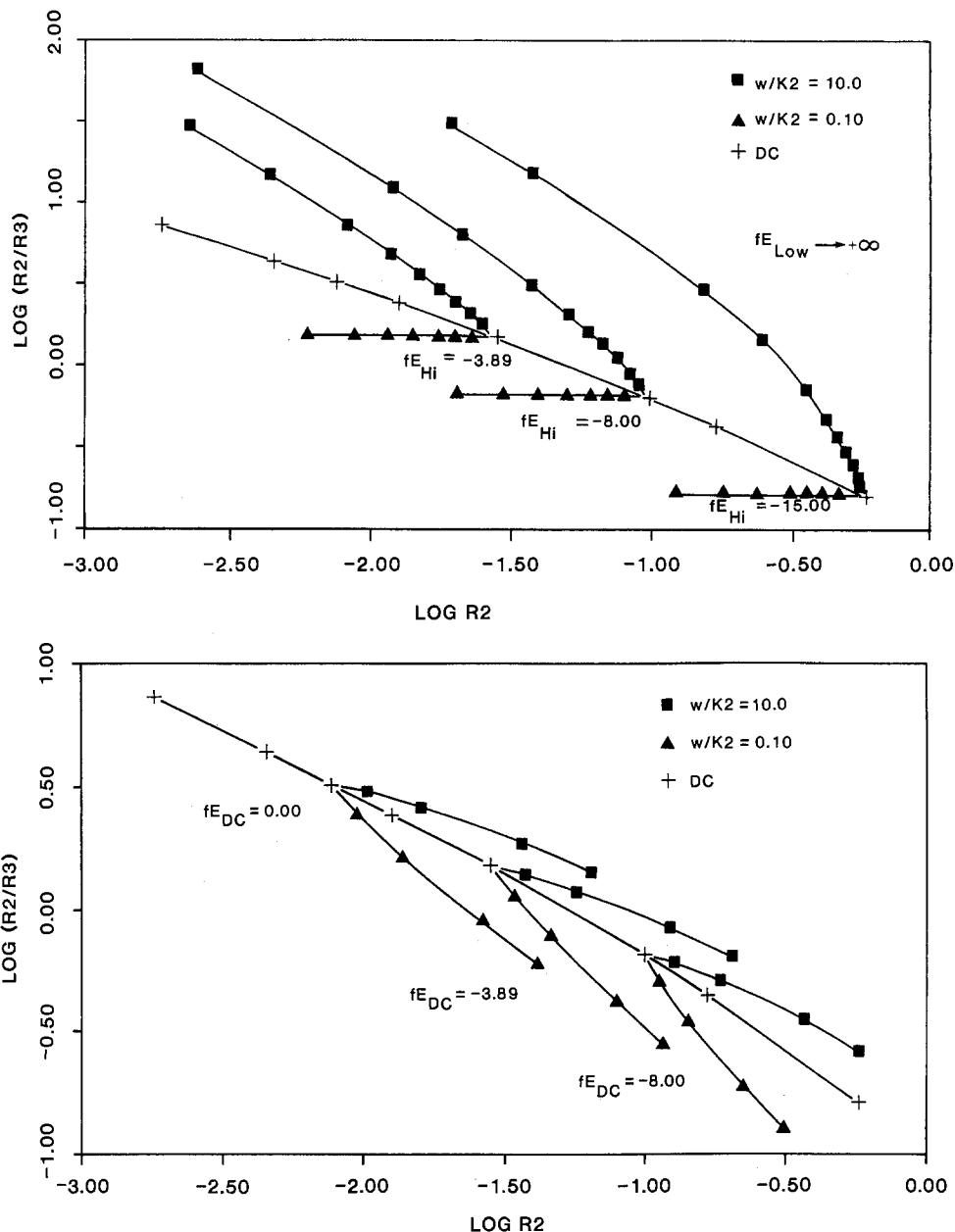


Fig. 2. Selectivity of the chemical product of the E-C,E reaction sequence as a function of its dimensionless production rate ($R_2 = r_2 K_2 R_0$): $a_1 = 0.4$, $a_3 = 0.2$, $K_1/K_2 = 0.01$, and $K_3/K_2 = 0.3$. A, top: step potential modulation. B, bottom: sinusoidal modulation.

waveform. This is due to the exponential dependence of the electrochemical reactions on potential. Under sinusoidal modulation the cycle-averaged production of R_1 increases with amplitude; hence, the curves slope downward to higher R_2 -production rates. Under step potential modulation, however, the cycle-averaged production of R_1 decreases with a drop in the duty cycle, and, hence, the opposite behavior is observed. Examination of Fig. 2 shows that the step potential modulation is a better control strategy in that larger increases in selectivity can be obtained than with sinusoidal control.

If fE_{Low} for step potential control is set to a less anodic value than that used in the calculations in Fig. 2, the increase in selectivity as T_D is lowered, with all other conditions remaining constant, goes through a maximum since the selectivity approaches the steady-state value at $fE_{Low} \rightarrow 0$.

The dramatically different behavior when the transfer coefficient of the second electrochemical step is larger than that of the first is shown in Fig. 4. In this situation at constant potential control of the reactor, a maximum in the production rate of the chemical product is observed. At low cathodic polarizations R_1 is generated at a rate sufficient to supply both the electrochemical- and chemical-follow-up reaction. As the potential becomes more cathodic, however, the second electrochemical reac-

tion effectively consumes more of R_1 than the chemical step and, eventually, consumes all of the R_1 produced. In this case, neither step or sinusoidal potential modulation was beneficial; either a decrease in selectivity was observed under varying potential or a steady potential existed which would meet the given production-rate requirement and yet result in a higher selectivity. (The case in which $a_1 = a_2$ was also examined, and the same conclusions may be stated.)

E-C²,E reaction sequence.—There are four intrinsic dimensionless variables which govern the outcome of this reaction sequence: K_1/K_2R_0 , K_3/K_2R_0 , a_1 , and a_3 . Calculations are presented for one set of rate constants, since the trend of increasing or decreasing reaction selectivity was found to be insensitive to these parameters. The relative values of the transfer coefficients effect whether there is a positive or negative result of the potential modulation. Four cases arise: (i) $a_1 = 2a_3$, (ii) $a_1 > 2a_3$, (iii) $2a_3 > a_1 > a_3$, and (iv) $a_1 < a_3$. Case (i) is a degenerate case in that the dc selectivity is independent of potential. Both high and low frequency modulation enhance the selectivity at any given production rate of the chemical product for both waveforms; the enhancement is more pronounced at the higher frequency. For case (ii), the dc selectivity increases with an increase in the production rate of the chemical product, while for case (iii) the dc selectivity decreases.

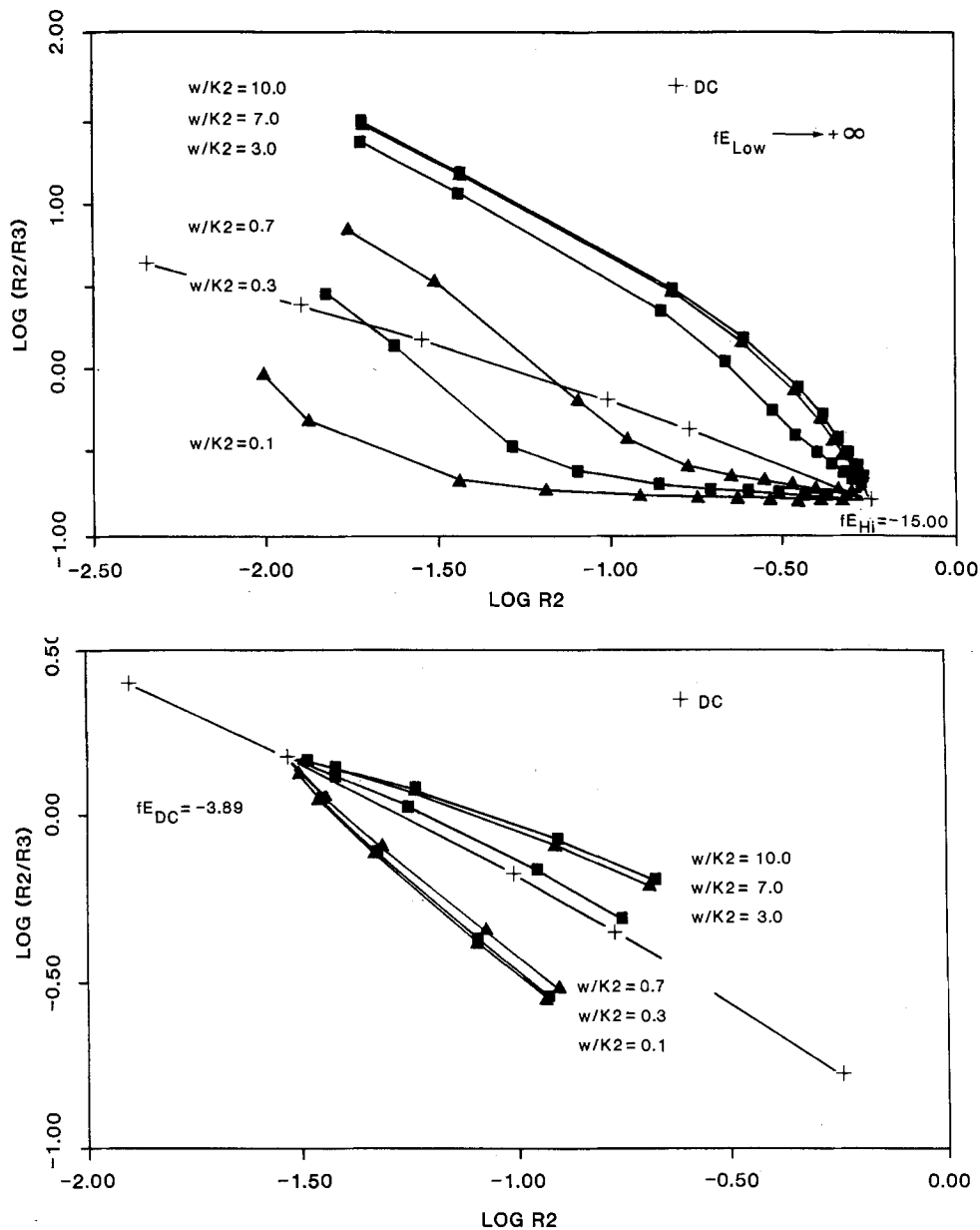


Fig. 3. Effect of frequency on the selectivity of the chemical product of the E-C,E reaction sequence as a function of its dimensionless production rate ($R2 = r_2 K2 R_0$): $\alpha_1 = 0.4$, $\alpha_3 = 0.2$, $K1/K2 = 0.01$, and $K3/K2 = 0.3$. A, top: step potential modulation. B, bottom: sinusoidal potential modulation.

Figure 5a and 5b and 6a and 6b illustrate the effect of step and sinusoidal potential modulation for cases (ii) and (iii), respectively. Again, ranges of reactor operation are possible which cannot be obtained under steady-state condi-

tions. The modulation effect on the selectivity for case (iii) in Fig. 6 is much like that for the first case discussed of the E-C,E mechanism: high frequency increases the selectivity, while low frequency decreases it. For case (ii),

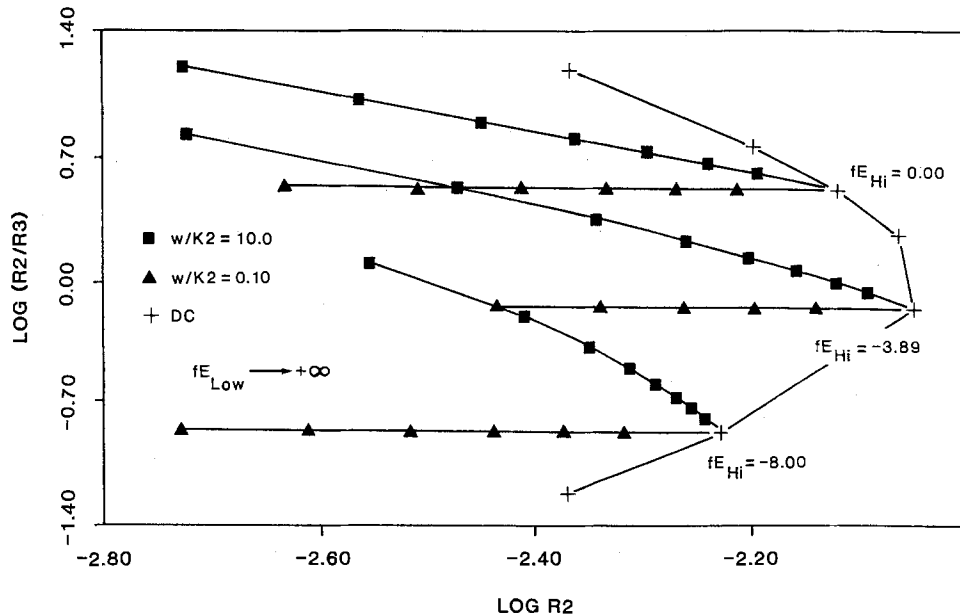


Fig. 4. Selectivity of the chemical product of the E-C,E reaction sequence as a function of its dimensionless production rate under step potential modulation ($R2 = r_2/K2 R_0$): $\alpha_1 = 0.2$, $\alpha_3 = 0.4$, $K1/K2 = 0.01$, and $K3/K2 = 0.3$.

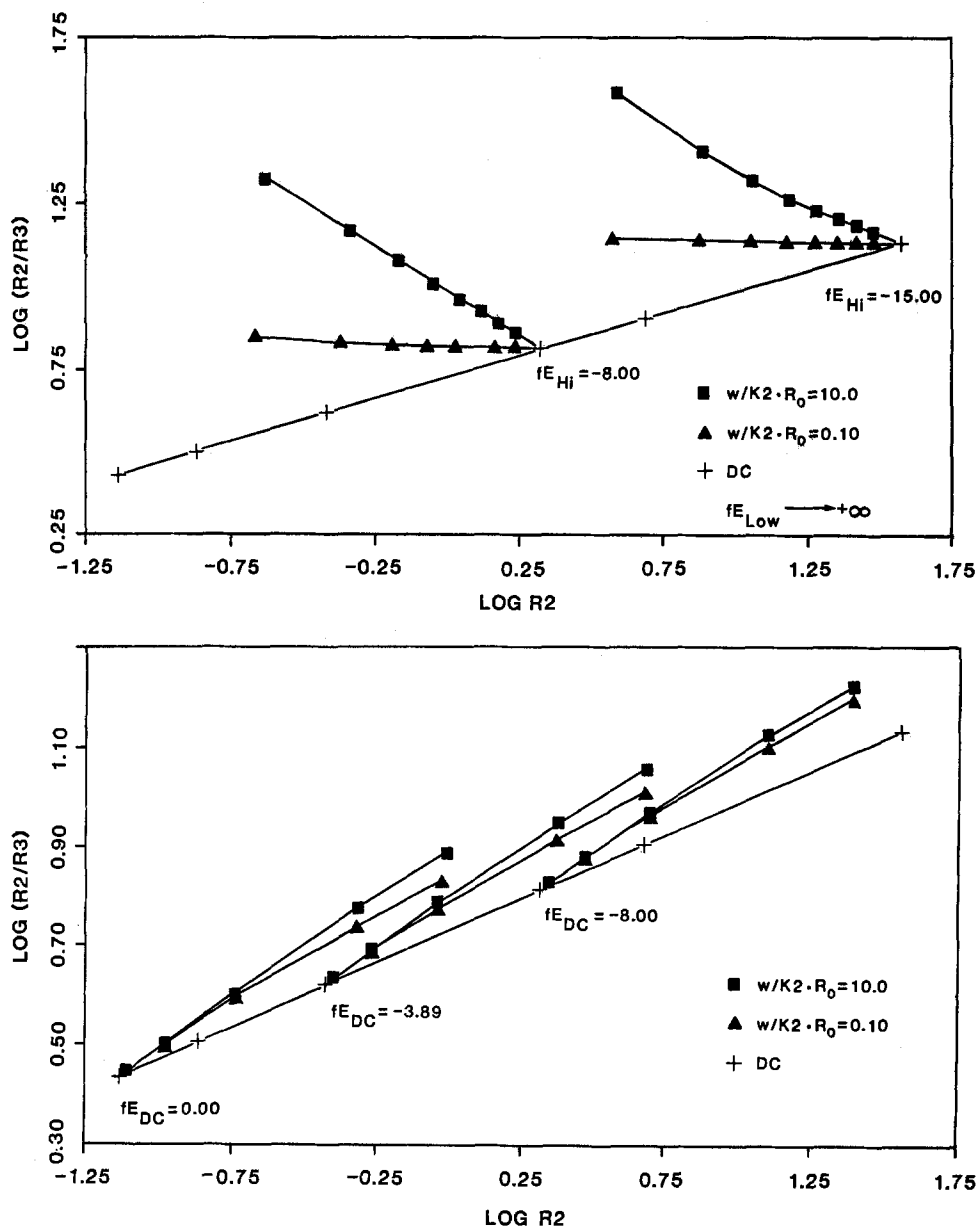


Fig. 5. Selectivity of the second-order chemical reaction product of the E-C²,E reaction sequence as a function of its dimensionless production rate ($R2 = r_2/K_2R_0^2$): $a_1 = 0.4$, $a_3 = 0.1$, $K_1/K_2R_0 = 0.1$, and $K_3/K_2R_0 = 0.1$. A, top: step potential modulation. B, bottom: sinusoidal potential modulation.

both high and low frequency modulation increase the selectivity. This may be attributed to the higher sensitivity of the second-order chemical reaction to the intermediate concentration than the first-order electrochemical reaction. In case (iv), a maximum-production rate of the chemical product is obtained under dc conditions as seen in Fig. 7, which shows the results of step potential modulation. No advantage of either step or sinusoidal potential control over steady potential control was found in this case. As in the E-C,E sequence, the step potential waveform appears to be better than sinusoidal when modulation is beneficial.

E-C,C² reaction sequence.—There are three dimensionless parameters which effect the outcome of this reaction sequence: K_1/K_2 , K_3R_0/K_2 , and a_1 . Figures 8a and 8b illustrate typical results for the selectivity of the second-order chemical product as a function of its production rate for step and sinusoidal potential modulation, respectively. Reactor operating conditions are again possible at the stationary state which are unobtainable at the steady state. The results at high frequency modulation approach those of dc operation; however, the low frequency modulation results for both waveforms illustrate an increase in selectivity at any given production rate of R_0 . At the low frequency, an increase in the intermediate concentration is obtained over that at higher frequencies; thus, the second-order chemical reaction is favored. The selectivity

of the first-order product is decreased by potential modulation.

E-E,E reaction sequence.—Five dimensionless kinetic parameters determine the outcome of this reaction sequence: K_1/K_2 , K_3/K_2 , a_1 , a_2 , and a_3 . Under dc conditions, the steady-state selectivity of the product with the smaller transfer coefficient decreased with an increase in its production rate, while the selectivity of the product with the larger transfer coefficient increased with its production rate. Modulation always decreased the selectivity in the first case and always increased it in the second case. Figures 9a and 9b illustrate typical results under step and sinusoidal potential control. Results using two different values of the lower potential, fE_{Low} , are shown in Fig. 9a. High frequency is better than low frequency in increasing selectivity for both waveforms, but note that the increase above the dc selectivity is considerably smaller for this reaction sequence than those for the previous three.

Comments.—Clearly, orders of magnitude increase in reaction selectivity can be obtained by modulation of the potential for some of the reaction sequences studied. The calculations have shown that modulation is most effective when a chemical-reaction step competes in parallel with an electrochemical step for the same intermediate. Such large increases in selectivity and yield may make an elec-

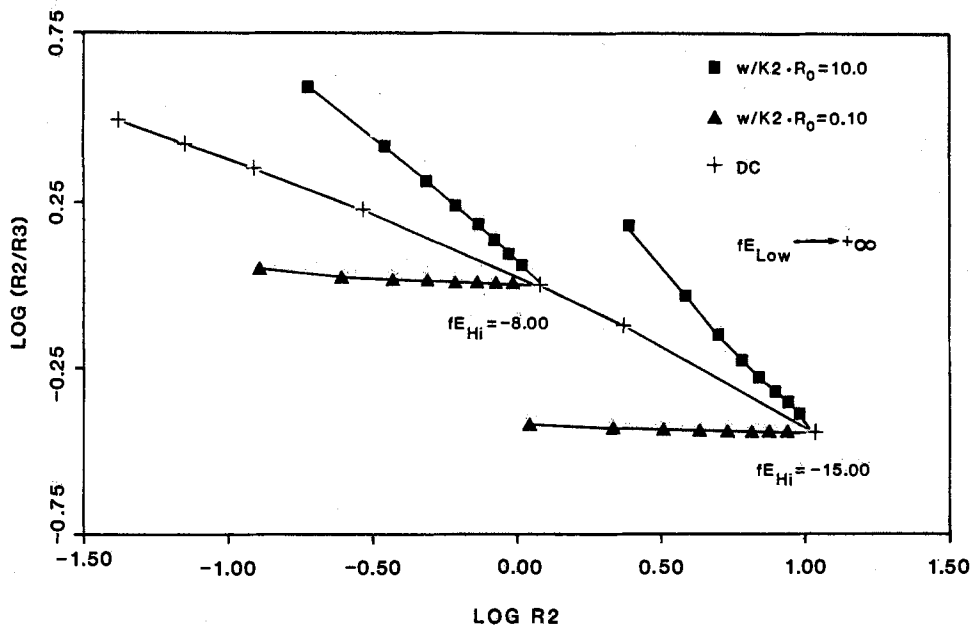
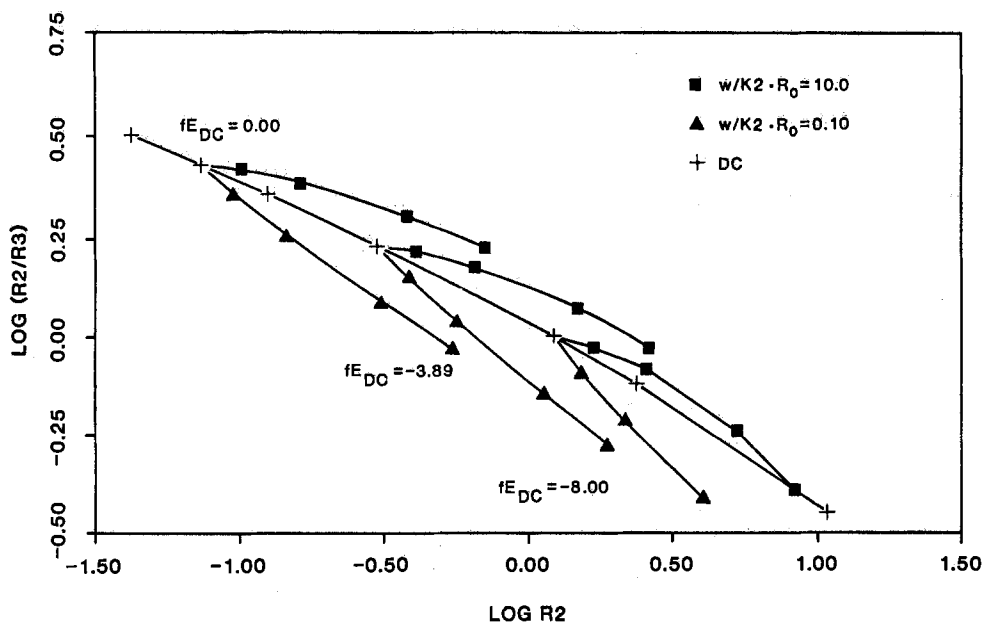


Fig. 6. Selectivity of the second-order chemical reaction product of the E-C²,E reaction sequence as a function of its dimensionless production rate ($R2 = r_2/K2R_0^2$): $a_1 = 0.4$, $a_3 = 0.3$, $K1/K2R_0 = 0.1$, and $K3/K2R_0 = 0.1$. A, top: step potential modulation. B, bottom: sinusoidal potential modulation.



trochemical processing step competitive with alternative chemical processing schemes. Of course, an increased energy cost must be paid if the potential is modulated. Capacitive double-layer charging, which was not considered

here, would be an energy loss which could become important for large-surface-area reactors. There is no reason to expect that either step or sinusoidal potential modulation is the best waveform. On the contrary, if an objective

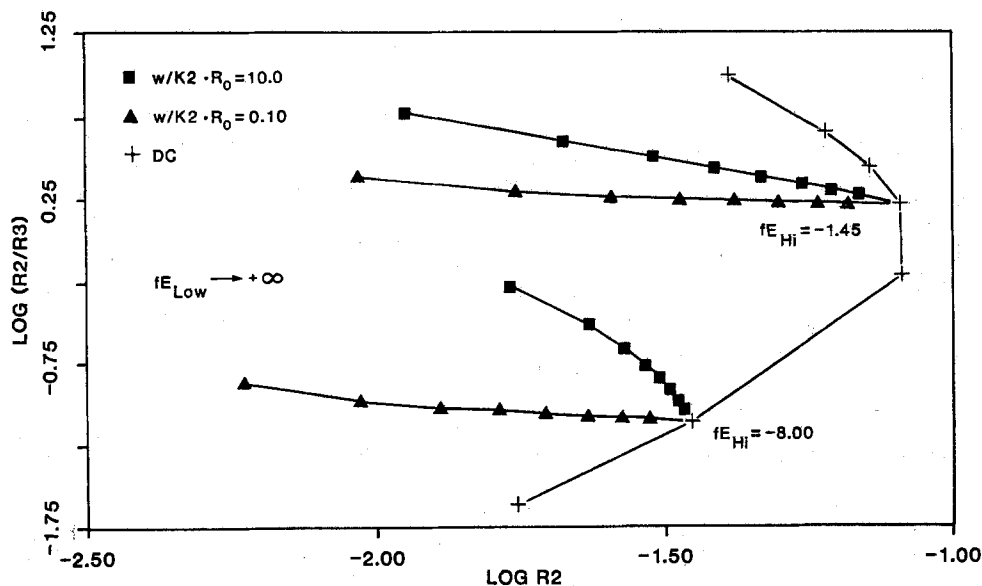


Fig. 7. Selectivity of the second-order chemical reaction product of the E-C²,E reaction sequence as a function of its dimensionless production rate under step potential modulation ($R2 = r_2/K2R_0^2$): $a_1 = 0.2$, $a_3 = 0.4$, $K1/K2R_0 = 0.1$, and $K3/K2R_0 = 0.1$.

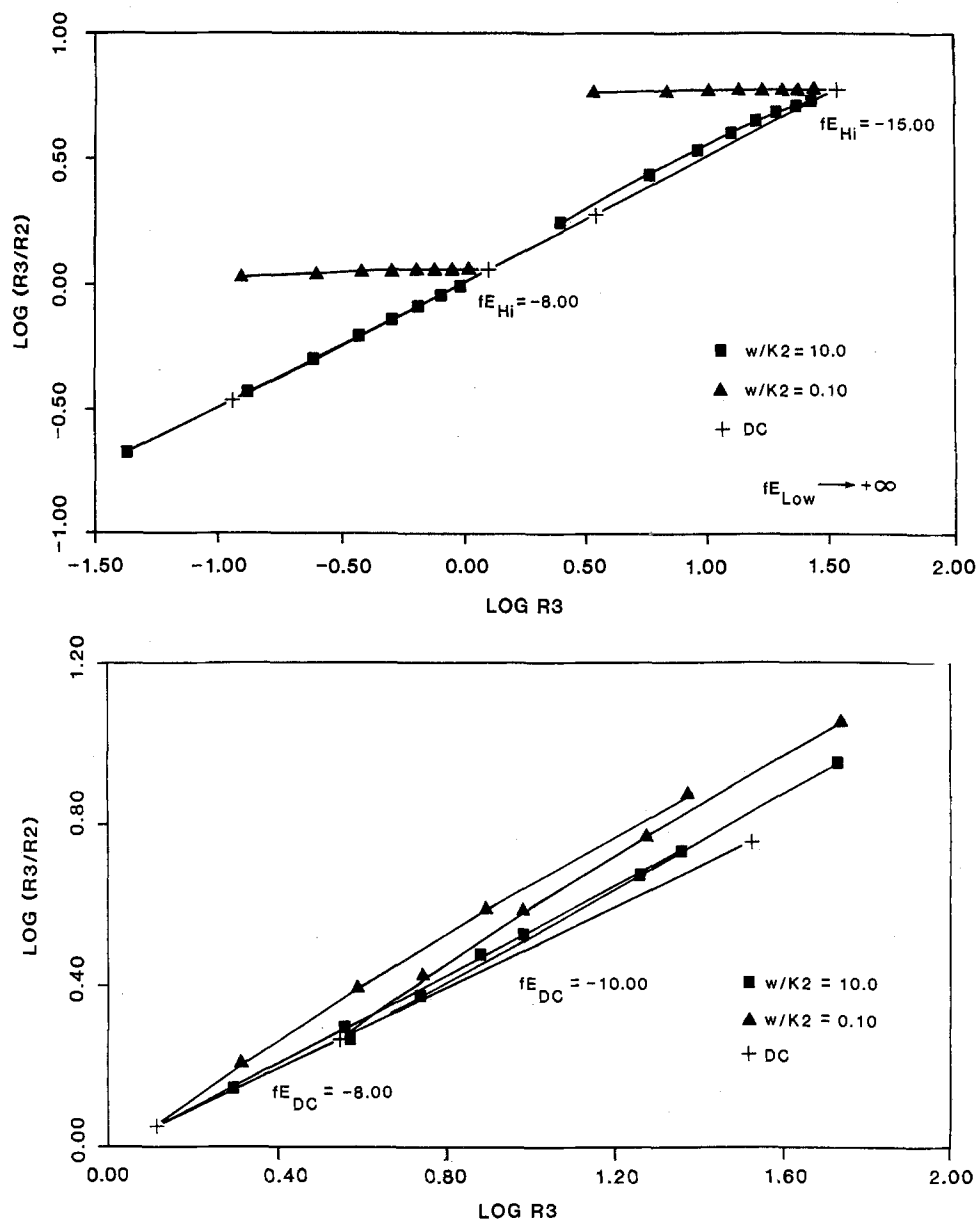


Fig. 8. Selectivity of the second-order chemical reaction product of the E-C, C² reaction sequence as a function of its dimensionless production rate ($R3 = r_3/K3R_0^2$): $\alpha_1 = 0.4$, $K1/K2 = 0.1$, and $K3R_0/K2 = 1.0$. A, top: step potential modulation. B, bottom: sinusoidal potential modulation.

function can be defined, mathematical techniques developed in control theory (57, 58) can be used to construct the optimal waveform to establish the maximum or minimum of the objective function.

If mass-transfer limitations are present, the degree to which the modulated potential changes the outcome of the reaction sequence is dampened. This can be expected, since mass transport is independent of potential in a well-supported electrolyte. Indeed, Scott has shown that a maximum production rate exists for some of the products in the reaction sequences of Table I when the mass-transfer rate of the initial reactant R_0 to the electrode becomes important. Figure 10 illustrates this effect for the E-C,E sequence at three values of the mass-transfer coefficient KM . Thus, the calculations presented here may be thought of as the "best case" example for the positive effect of potential modulation on reaction outcome. A simulation of an actual operating reactor must also consider the effect of nonuniform potential distribution, as well as possible mass-transfer limitations.

If the intermediate R_1 is soluble in the bulk solution, the beneficial effect of potential modulation may be either increased or decreased, depending upon the desired product and reaction sequence involved. For example, if the follow-up chemical reaction may occur homogeneously in the E-C,E reaction sequence, the increase in selectivity under modulated reaction control should be greater than that calculated here. This would be expected, since the

competing electrochemical reaction is heterogeneous and cannot consume that R_1 , which enters the bulk electrolyte. However, the selectivity of the second-order product in the E-C, C² reaction sequence if both chemical reactions occur homogeneously will be lower than that calculated here. This occurs because of the dilution effect and the higher sensitivity of the second-order chemical reaction to concentration than the first-order reaction.

The detailed understanding of reaction sequences and their characterization by appropriate rate expressions may limit the utilization of modulated potential control of a reactor. The results show how dramatically different the effect of modulation is on a reaction product depending upon how that product is formed. The waveform of the imposed potential strongly affects the reaction outcome. If experiments are performed on the wrong reaction system, or with the wrong waveform, or at the wrong frequency, the unfortunate conclusion may be drawn that modulation is not effective in enhancing reactor performance.

Finally, current to the reactor may be modulated instead of the potential. The outcome will be consistent with some periodic modulation of the potential but with a different waveform from that of the current. Care must be taken, if the reactor is operated in this mode, that the potential does not oscillate into secondary reaction regimes such as solvent electrolysis.

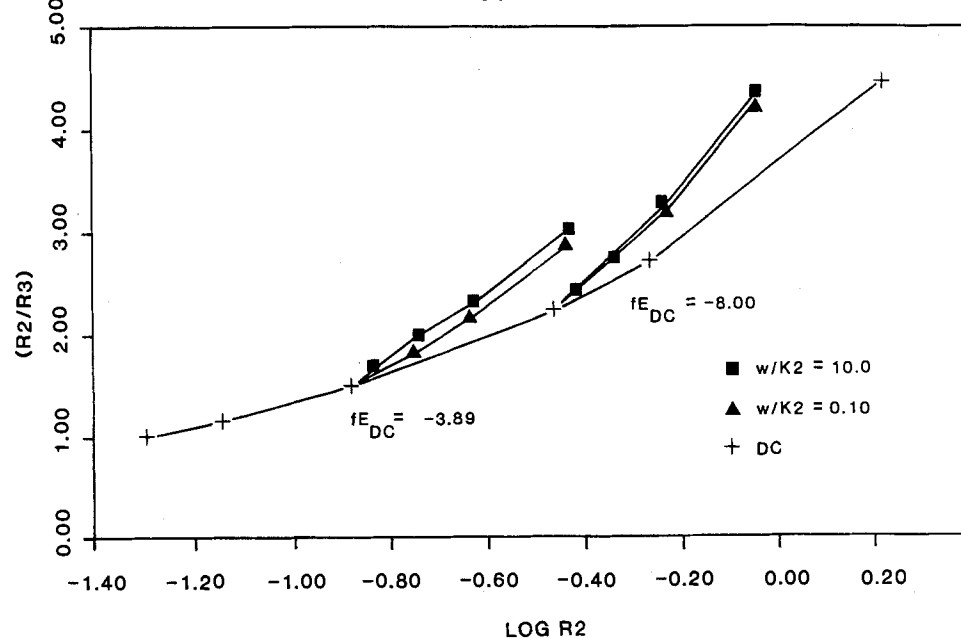
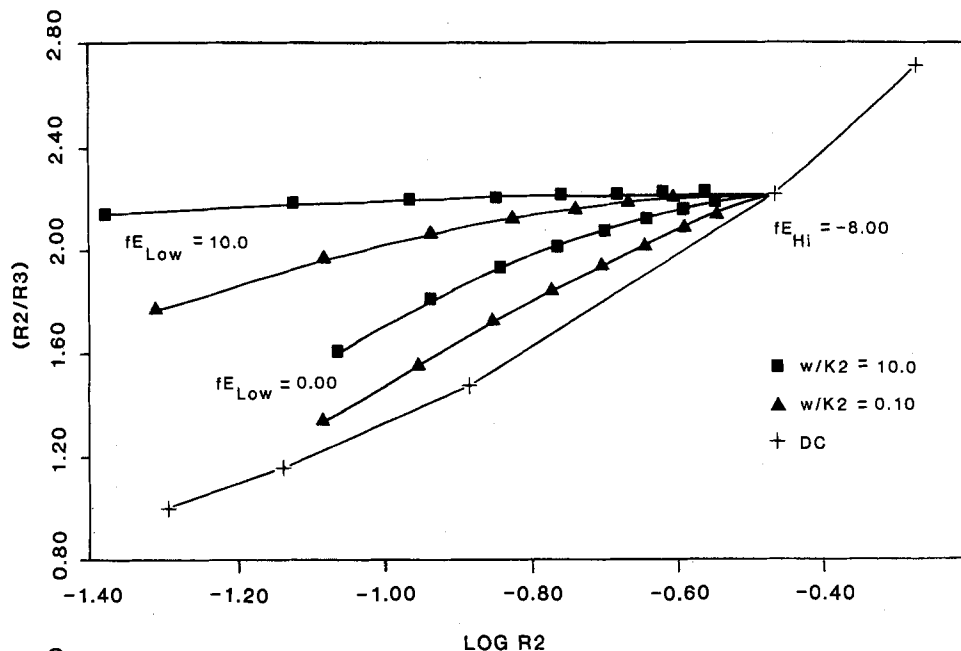


Fig. 9. Selectivity of the product with the larger transfer coefficient for the E-E reaction sequence as a function of its dimensionless production rate ($R_2 = r_2/K_2R_0$): $\alpha_1 = 0.2$, $\alpha_2 = 0.4$, $\alpha_3 = 0.3$, $K_1/K_2 = 0.1$, and $K_3/K_2 = 1.0$. A, top: step potential modulation. B, bottom: sinusoidal potential modulation.

Summary

Under electrokinetic-controlled conditions for the simple reaction sequences shown in Table I and subject to

the assumed rate expressions, substantial increases in reaction selectivity are possible by modulation of the electrode potential in comparison to steady-state operation. Step potential modulation was found to be more effective

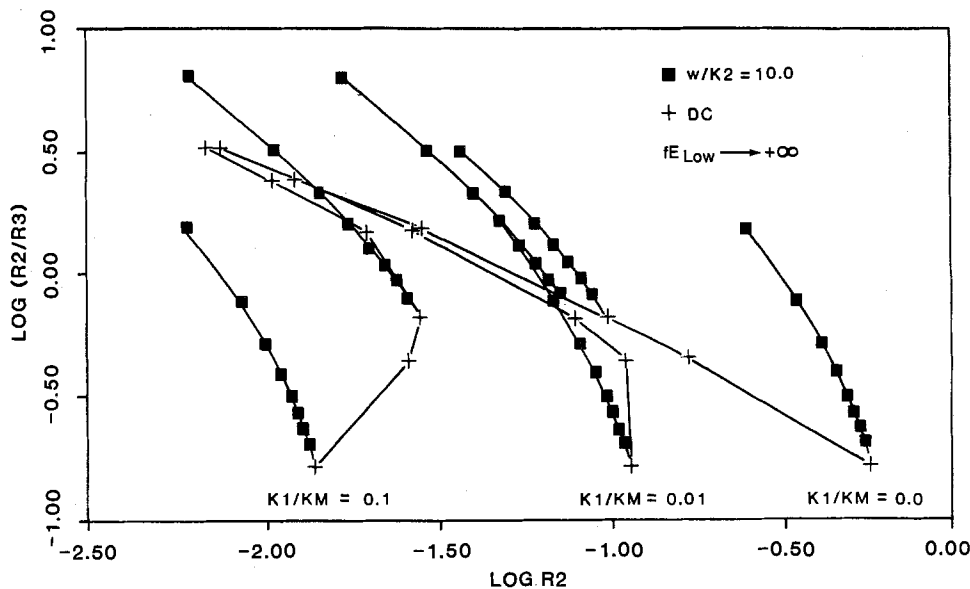


Fig. 10. Selectivity of the chemical reaction product of the E-C,E reaction sequence as a function of its dimensionless production rate in the presence of mass-transfer resistance under step potential modulation ($R_2 = r_2/K_2R_0$): $\alpha_1 = 0.4$, $\alpha_3 = 0.2$, $K_1/K_2 = 0.01$, and $K_3/K_2 = 0.3$.

Table A-1. Dimensionless intermediate concentration equations

Mechanism	Governing equation for intermediate
E-C ² ,E	$\frac{dI}{d\tau} = \frac{K_2 \cdot R_0}{w} \frac{K_1}{K_2 \cdot R_0} \exp(-a_1 fE) - \frac{K_2 \cdot R_0}{w} I^2 - \frac{K_3}{K_2 \cdot R_0} \frac{K_2 \cdot R_0}{w} I \exp(-a_3 fE)$
E-C, C ²	$\frac{dI}{d\tau} = \frac{K_1}{K_2} \frac{K_2}{w} \exp(-a_1 fE) - \frac{K_2}{w} I - \frac{K_3 \cdot R_0}{K_2} \frac{K_2}{w} I^2$
E-E,E	$\frac{dI}{d\tau} = \frac{K_1}{K_2} \frac{K_2}{w} \exp(-a_1 fE) - \frac{K_2}{w} I \exp(-a_2 fE) - \frac{K_3}{K_2} \frac{K_2}{w} I \exp(-a_3 fE)$

than sinusoidal modulation, although neither of the two is necessarily the best waveform. The effect is highly frequency dependent; the reaction outcome may show opposite behavior at low vs. high frequency. Mass transfer effects dampen any changes in reaction outcome caused by modulating the potential. By operating an electrolysis reactor in a modulated control mode, the combination of decreased capital cost for the reactor (increased yield) and decreased operating cost of downstream mass-separation devices (increased selectivity) may possibly make an electrolytic production route economically favorable.

Acknowledgment

This work was supported by the National Science Foundation under Grant no. CPE-8006703.

Manuscript submitted Aug. 1, 1983; revised manuscript received Dec. 21, 1983.

APPENDIX

In the E-C,E reaction sequence, the intermediate concentration R_1 is governed by the rate equation

$$\frac{d}{dt} R_1 = r_1 - r_2 - r_3$$

The transport rate of the initial reactant from the bulk solution to the electrode surface may be characterized by a pseudo-mass-transfer coefficient, KM , times the concentration difference between the surface and bulk concentration. The concentration driving force must be expressed on a surface concentration to be consistent with Table I. After simple manipulations and nondimensionalization of the resulting equation, the following equation which governs the dimensionless intermediate concentration $I (R_1/R_0)$ may be derived

$$\frac{dI}{d\tau} = \frac{(K_1/K_2)(K_2/w)\exp(-a_1 fE)}{1 + (K_1/KM)\exp(-a_1 fE)} - (K_2/w)I - (K_3/K_2)(K_2/w)I\exp(-a_3 fE)$$

where $\tau = wt$, w is the fundamental frequency of the potential oscillation ($w = 2\pi \cdot \text{cycle time}$), and R_0 is the surface concentration of the initial reactant.

Similar equations in the absence of mass-transfer limitations may also be derived for the other reaction mechanisms and are shown in Table A-1.

REFERENCES

- M. Fleischmann, I. N. Petrov, and W. F. K. Wynne-Jones, in "Proceedings of the First Australian Conference on Electrochemistry," Pergamon Press, New York (1965).
- F. J. M. Horn and R. C. Lin, *Ind. Eng. Chem., Prod. Res. Dev.*, **6**, 21 (1967).
- G. H. Denis and R. L. Kabel, *Chem. Eng. Sci.*, **25**, 1057 (1970).
- M. Matsubara, Y. Nishimura, and N. Takahashi, *ibid.*, **28**, 1369 (1973).
- M. Matsubara, Y. Nishimura, and N. Takahashi, *ibid.*, **28**, 1379 (1973).
- H. K. Abdul-Kareem, R. R. Hudgins, and P. L. Silveston, *ibid.*, **35**, 2085 (1980).
- R. L. Laurence and G. Vasudevan, *Ind. Eng. Chem., Prod. Res. Dev.*, **7**, 427 (1968).
- W. H. Ray, *ibid.*, **7**, 422 (1968).
- J. E. Bailey and F. J. M. Horn, *Chem. Eng. Sci.*, **27**, 109 (1972).
- A. Renken, *ibid.*, **27**, 1925 (1972).
- M. P. Unni, R. R. Hudgins, and J. Silveston, *Can. J. Chem. Eng.*, **51**, 623 (1973).
- C. K. Lee and J. E. Bailey, *Chem. Eng. Sci.*, **29**, 1157 (1974).
- M. B. Cutlip, *AIChE J.*, **25**, 502 (1979).
- H. K. Abdul-Kareem, P. L. Silveston, and R. R. Hudgins, *Chem. Eng. Sci.*, **35**, 2085 (1980).
- R. D. Skeirik and A. L. Devera, *ibid.*, **37**, 1015 (1982).
- H. D. Wilson and R. G. Rinker, *ibid.*, **37**, 343 (1982).
- J. E. Bailey, F. J. M. Horn, and R. C. Lin, *AIChE J.*, **17**, 818 (1971).
- J. E. Bailey, *Chem. Eng. Commun.*, **1**, 111 (1973).
- J. E. Bailey, in "Chemical Reactor Theory: A Review," L. Lapidus and N. Amundson, Editors, Prentice Hall, Inc., Englewood Cliffs, NJ (1977).
- A. J. Avila and M. J. Brown, *Plating*, **57**, 1105 (1970).
- K. I. Popov, M. D. Maksimovic, M. G. Paulovic, and G. R. Ostojic, *J. Appl. Electrochem.*, **7**, 331 (1977).
- K. I. Popov, D. N. Keca, and D. A. Draskovic, *ibid.*, **6**, 155 (1976).
- K. I. Popov, D. N. Keca, and S. I. Vidoskovic, *ibid.*, **6**, 365 (1976).
- K. I. Popov, D. N. Keca, and M. D. Maksimovic, *ibid.*, **7**, 77 (1977).
- K. I. Popov, D. N. Keca, and B. I. Vulsanovic, *ibid.*, **7**, 185 (1977).
- J. N. Jovicevic, D. M. Drazic, and A. R. Despic, *Electrochim. Acta*, **22**, 589 (1977).
- M. G. Pavolic, M. D. Maksimovic, and K. I. Popov, *J. Appl. Electrochem.*, **8**, 61 (1978).
- D-T. Chin and S. Venkatesh, *This Journal*, **128**, 1439 (1981).
- Z. Kovac, *ibid.*, **118**, 521 (1971).
- E. S. Chen and F. K. Sautter, *Plat. Surf. Finish.*, **63**, 28 (1976).
- M. H. Gelchinski, L. Gal-Or, and J. Yakalom, *This Journal*, **129**, 2433 (1982).
- H. Y. Cheh, *ibid.*, **118**, 551 (1971).
- S. Viswanathan, M. A. Farrel-Epstein, and H. Y. Cheh, *ibid.*, **125**, 1772 (1978).
- S. Viswanathan and H. Y. Cheh, *ibid.*, **126**, 398 (1979).
- S. Viswanathan and H. Y. Cheh, *J. Appl. Electrochem.*, **10**, 37 (1980).
- S. Viswanathan, M. A. Farrel-Epstein, and H. Y. Cheh, *This Journal*, **127**, 2383 (1980).
- T. Z. Fahidy and M. S. E. Abdo, *J. Appl. Electrochem.*, **11**, 691 (1981).
- K. Deo, S. G. Mehendale, and S. Venkatachalam, *ibid.*, **6**, 37 (1976).
- M. Datta and D. Landolt, *Electrochim. Acta*, **27**, 385 (1982).
- D-T. Chin and S. Venkatesh, *This Journal*, **126**, 1908 (1979).
- S. Venkatesh and D-T. Chin, *Isr. J. Chem.*, **18**, 56 (1979).
- J. C. Ghosh, *J. Am. Chem. Soc.*, **36**, 2333 (1914).
- C. L. Wilson and W. T. Lippincott, *ibid.*, **78**, 4290 (1956).
- M. J. Fleischmann, J. R. Mansfield, and W. F. K. Wynne-Jones, *J. Electroanal. Chem.*, **10**, 522 (1965).
- A. Hickling and R. Wilkins, *Discuss. Faraday Soc.*, **45**, 261 (1968).
- M. Fleischmann and F. Goodridge, *ibid.*, **45**, 254 (1968).
- G. M. Atherton, M. Fleischmann, and F. Goodridge, *Trans. Faraday Soc.*, **63**, 1468 (1967).
- M. Fleischmann, J. R. Mansfield, H. R. Thirsk, H. G. E. Wilson, and W. F. K. Wynne-Jones, *Electrochim. Acta*, **12**, 967 (1967).
- P. R. Nadebaum and T. Z. Fahidy, in "Symposium on Electrochemical Engineering," J. D. Thornton, Editor, Institute of Chemical Engineering (1971).
- P. R. Nadebaum and T. Z. Fahidy, *Electrochim. Acta*, **17**, 1659 (1972).
- S. C. Srivastava and S. N. Shukla, *ibid.*, **12**, 1049 (1967).
- S. N. Bhandani, *Ind. J. Technol.*, **12**, 570 (1974).

53. R. C. Alkire and J. E. Tsai, *This Journal*, **129** 1157 (1982).
54. W. D. Scott, M. S. Thesis, North Carolina State University, Raleigh, NC (1983).
55. G. P. Sakellaropoulos, *Adv. Catal.*, **30**, 217 (1981).
56. J. Villadsen and M. L. Michelsen, "Solution of Differential Equation Models by Polynomial Approximation." Prentice Hall, Englewood Cliffs, NJ (1978).
57. M. M. Denn, "Optimization by Variational Methods," McGraw-Hill, New York (1969).
58. W. H. Ray, "Advanced Process Control," McGraw-Hill, New York (1981).

Formation and Reduction of Anodic Sulfide Films on Antimony Electrodes

Alfred Viehbeck^{*1} and Norman Hackerman^{**}

Department of Chemistry, Rice University, Houston, Texas 77251

ABSTRACT

The growth and reduction of anodic Sb_2S_3 films on antimony electrodes in alkaline sulfide solutions has been investigated using potentiodynamic, galvanostatic, and potentiostatic techniques. The sulfidation mechanism and the efficiency of charge storage in the sulfide film are dependent on the electrode potential and current density. The initial stages of film formation follow a high field growth process involving ionic transport through the sulfide film. The growth of thicker films is controlled by coupled electrochemical and chemical reactions involving mass transport and nucleation. Metal dissolution accompanies film formation under most growth conditions. The anodic and cathodic behavior of these films is consistent with their rectification or n-type semiconductor properties.

The formation and reduction of anodic surface films has a major influence on the overall electrochemical reactivity of a metal. The growth of an anodic film usually occurs by the migration of cations or anions (or both) through the film phase and across the interfaces and is often described using either Verwey's (1) or Cabrera-Mott's (2) high field model. Recently, Chao *et al.* (3) proposed a point-defect model for the growth of a passive layer. While most of the information concerning anodic film growth and the basic mechanistic models have been derived from studies of oxide formation on metals, the development and behavior of anodic sulfide films has received relatively little attention (4, 5).

The growth of some metal sulfides was examined by Miller and Heller (6) in connection with their possible use as photoanodes. Peter (7, 8) has correlated the anodic formation of CdS and Bi_2S_3 to a high field process and on Hg electrodes examined the initial underpotential deposition of a sulfide monolayer (9). Anodic Ag_2S formation reportedly occurs in a manner similar to the mercury system (10). Recently, the anodic oxidation of sulfide on a Pt electrode in alkaline solutions was found to result in the formation of a sulfide containing surface layer that passivated the electrode (11). Preliminary investigations have also demonstrated the semiconductor properties of anodically formed antimony sulfide films (12).

In the work reported here we discuss the growth and reduction of anodic sulfide films on polycrystalline antimony electrodes (13). The electrode behavior and kinetic parameters determined experimentally have been used to correlate various growth models to this system. The results of ESCA analysis of the anodic films are discussed.

Experimental

All experiments were carried out in 0.1M Na_2S + 1.0M NaHCO_3 (pH 9.0) solutions, prepared using conductivity water (resistivity $> 5 \times 10^6 \Omega\text{-cm}$) and reagent-grade chemicals. Antimony electrodes were made from disks cut from a polycrystalline rod (6.615 g/cm³) having a purity of 99.998% (Alfa Products). These were cemented to nickel wire and mounted in epoxide resin. The electrode surface was polished to 0.05 μm alumina finish.

The electrochemical cell was a conventional three-compartment Pyrex design. The reference electrode was

* Electrochemical Society Active Member.

** Electrochemical Society Honorary Member.

¹ Present address: SumX Corporation, Austin, Texas, 78761.

Key words: antimony sulfide, anodic films, sulfidation, Sb_2S_3 film reduction.

a mercury/mercuric sulfide (red) slurry in contact with the sulfide solution (-0.513V vs. NHE) to which all potentials are referred.

The electrochemical measurements were carried out under an N_2 atmosphere on fresh electrodes that were first cathodically polarized (-1.00V) in the sulfide solution to remove any reducible surface films. Current densities were determined using a roughness factor of 1.7 as estimated from capacitance measurements (13).

Results and Discussion

Potentiodynamic conditions.—A typical current vs. potential (*i/E*) curve for an antimony electrode in the solution described and subjected to a triangular potential scan is shown in Fig. 1. The polarization profile is strongly dependent on the electrode surface preparation, solution composition, scan rate (ν), and the number of previous scanning cycles. With a fresh electrode, a positive potential scan usually exhibits four major anodic peaks which are represented as Peaks I, II, III, and IV (Fig. 1). The electrode surface also becomes yellow near the onset of Peak III turning to an orange color as the sulfide film thickens at higher potentials. The multiple anodic peaks are interpreted as the nucleation and spreading of successive sulfide layers where the overall surface process can be summarized by the following reaction

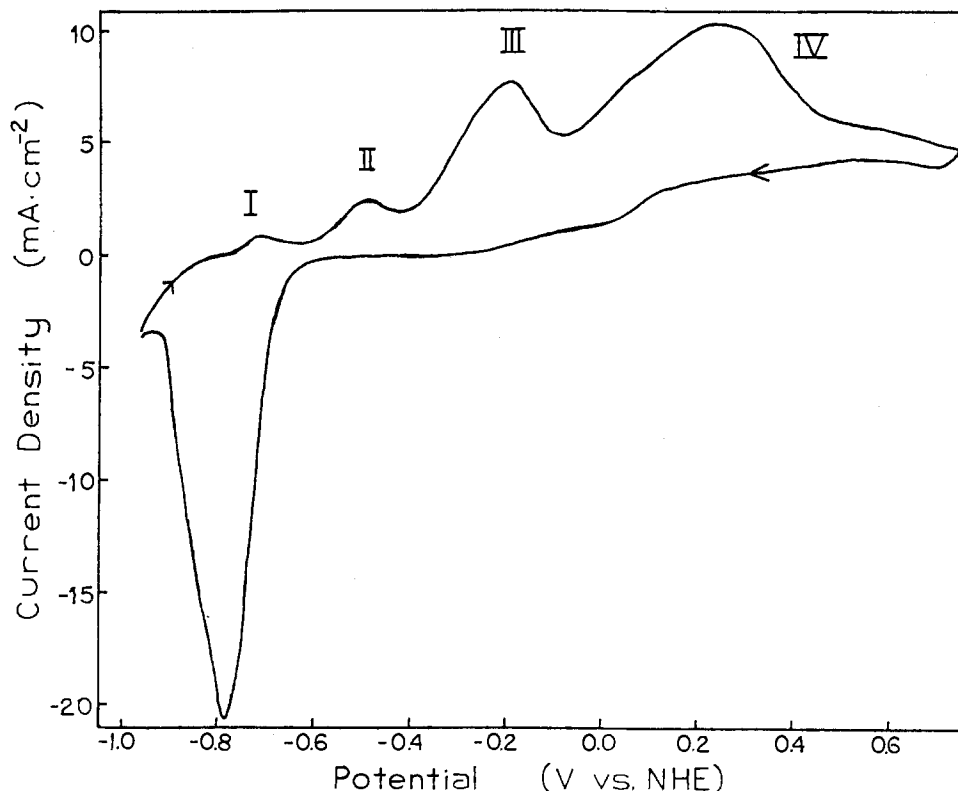


Similar *i/E* behavior has been seen for oxide nuclei spreading on an electrode surface (14, 15). Oxygen evolution does not occur even at potentials to +4.00V.

On the return negative (cathodic) scan there is a net anodic current response throughout most of the potential region of film formation. Depending on the sweep rate an anodic current peak is seen in the region 0.60 to 0.10V. This behavior might be due to the time dependent dissolution of some outer surface phase (*e.g.*, a sulfur layer) that is formed at the more noble potentials, thus reactivating the electrode to further sulfidation or metal dissolution. Surface film reduction on the Sb electrode occurs between -0.70 and -1.00V with a loss of the yellow-orange coloration.

The "development" of the surface is demonstrated in the *i/E* profiles in Fig. 2, made by repetitive triangular potential scans (RTPS). In each successive cycle, the anodic potential limit ($E_{\lambda,a}$) was progressively increased. As $E_{\lambda,a}$ is made more positive, the corresponding reduction charge increases, and there is a negative shift in the reduction

Fig. 1. Current vs. potential profile for an Sb electrode in a 0.1M Na₂S + 1.0M NaHCO₃ solution. $\nu = 20$ mV/s.



peak potential. This negative shift in the reduction peak with an increase in $E_{\lambda,a}$ might be associated with an increase in film stability due to a field-assisted growth process in which the free energy of the phase increases with potential, thus requiring a larger cathodic overvoltage to reduce the phase (16).

From coulometric measurements of the RTPS above (Fig. 3) the charge associated with Peak I is calculated to

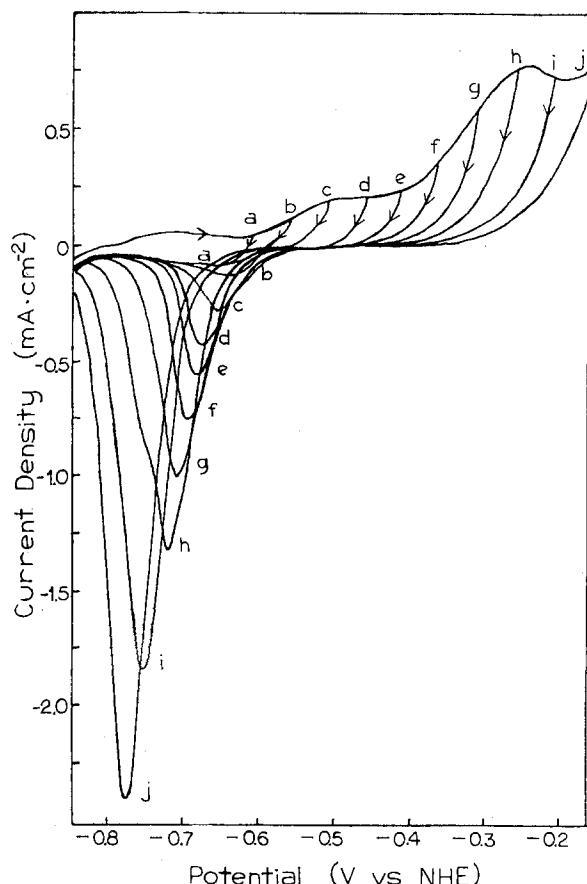


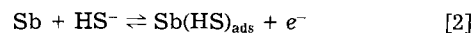
Fig. 2. Repetitive triangular potential scans for an Sb electrode in the sulfide solution with varied $E_{\lambda,a}$ at $\nu = 20$ mV/s.

be ≈ 0.30 mC/cm². Taking the sulfide film density (ρ) as that of bulk Sb₂S₃ (4.12 g/cm³) this charge value corresponds to approximately a monolayer of film with an estimated thickness of 0.52 nm. The charge passed in Peak II accounts for approximately two monolayers, while in Peak III the film grows to above 15 nm. However, the efficiency of anodic charge stored as film (*i.e.*, the ratio between Q_c and Q_a in Fig. 3) rapidly decreases for potentials positive of -0.30 V.

The current response under RTPS in the potential region between -1.00 and -0.20 V displayed an overall current increase with each successive cycle. This behavior is due to an increase in surface area by roughening. The reduction of the sulfide film leads to the formation of a porous layer of Sb metal, since the Sb₂S₃ phase occupies nearly twice the volume than the Sb metal from which it forms (17).

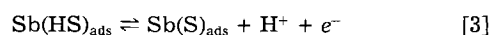
The sweep rate (ν) data for some of the anodic peak current maxima (i_m) and anodic peak potentials (E_m) are plotted in Fig. 4 and 5. The kinetic parameters derived from the voltammetric experiments are summarized in Table 1.

The potential of Peak I ($E_m = -0.74$ V or reversible potential, E^0) is not dependent on ν , while i_m and ν are linearly related (Fig. 4a). This is consistent with a deposition process involving a one-electron transfer, assuming Langmuir adsorption conditions and negligible solution diffusion effects (18). The initial reaction is considered to involve the adsorption of hydrosulfide ions (HS⁻) to form a monolayer deposit as in Eq. [2]



A similar process yielding an adsorbed sulfide intermediate prior to bulk sulfide film formation has been discussed for the sulfidation of Hg (9), Ag (10), and Pt (11).

The sweep-rate characteristics of Peak II (Fig. 4a and 5) correspond to a multistep consecutive mechanism in which the initial electron-transfer reaction is followed by a chemical reaction (19). A proposed scheme for the processes represented by Peak II is



yielding a hydro-sulfo Sb complex as an intermediate.

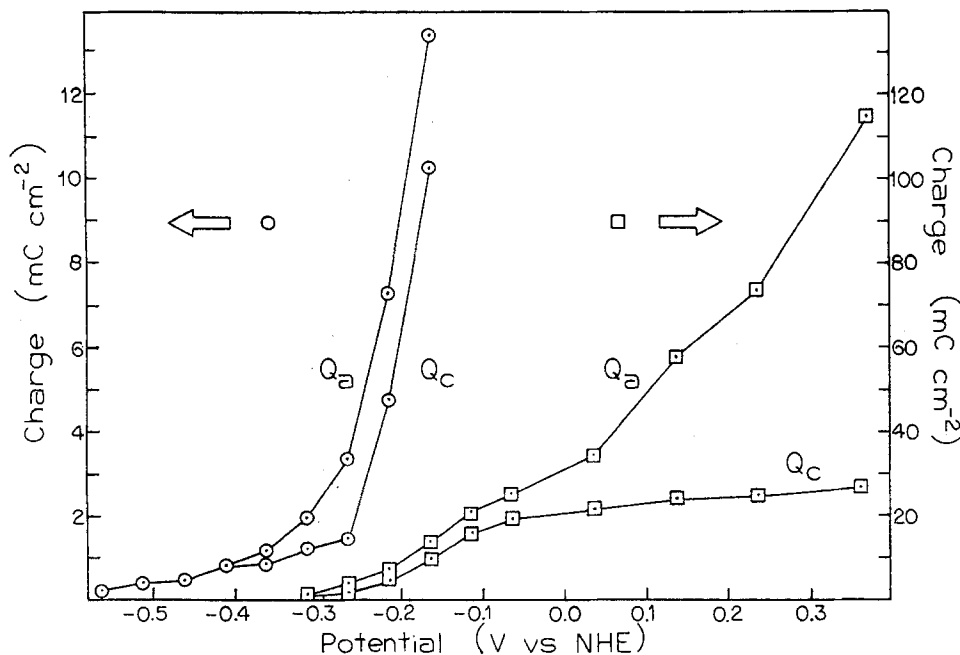
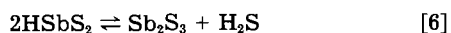
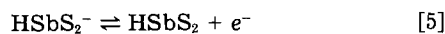


Fig. 3. Measured anodic (Q_a) and cathodic (Q_c) charge vs. $E_{\lambda,a}$.

This complex could then either dissolve or participate in a rapid electron-transfer reaction resulting in bulk antimony sulfide film formation



A similar mechanism has been proposed for the anodic formation of an oxide film on antimony (20, 21). It was re-

ported that the current efficiency for oxide formation is nearly 100% in acidic media, whereas extensive metal dissolution occurs during oxidation in alkaline solutions.

In the proposed sulfide film formation process, Eq. [4] is taken as the rate-determining step (RDS). The quasi-equilibrium hypothesis assumes that for an activation controlled process, all steps prior to the RDS are in equilibrium (18). Under potentiodynamic conditions (*i.e.*, $E = E_i + \nu t$, where E_i is the initial potential) the resulting expressions for the peak current and potential maximum as a function of ν are

$$i_m = Q_f(1 - \theta_m)(F/RT)\nu \quad [7]$$

$$E_m = G + 2.303(RT/F) \log \nu \quad [8]$$

where Q_f is the total film charge, θ_m is the fraction of surface covered by $(\text{HS})_{\text{ads}}$ at the maximum peak response, G is a constant, and R , T , and F have their usual meanings (22). These equations demonstrate the linear i_m vs. ν and ca. 59 mV/decade E_m vs. ν relations found for Peak II.

The effect of ν on Peak III (Fig. 4b and 5) corresponds to an irreversible process involving both an electrochemical and chemical reaction under diffusion control (23, 24). According to Delahay (23), the expressions for the peak current and potential as a function of ν are given by

$$i_m = (3.01 \times 10^5) n(\alpha N_a D_a \nu)^{1/2} C_0 \quad [9]$$

$$E_m = E^\circ + (RT/\alpha N_a F) [0.78 - \ln(K_0/D_a^{1/2}) + 0.5 \ln(\alpha N_a F \nu / RT)] \quad [10]$$

where α is the transfer coefficient, N_a is the number of electrons in the rds, n is the total number of electrons transferred in the sequence, C_0 is the concentration of diffusing species, and K_0 is the electrochemical rate con-

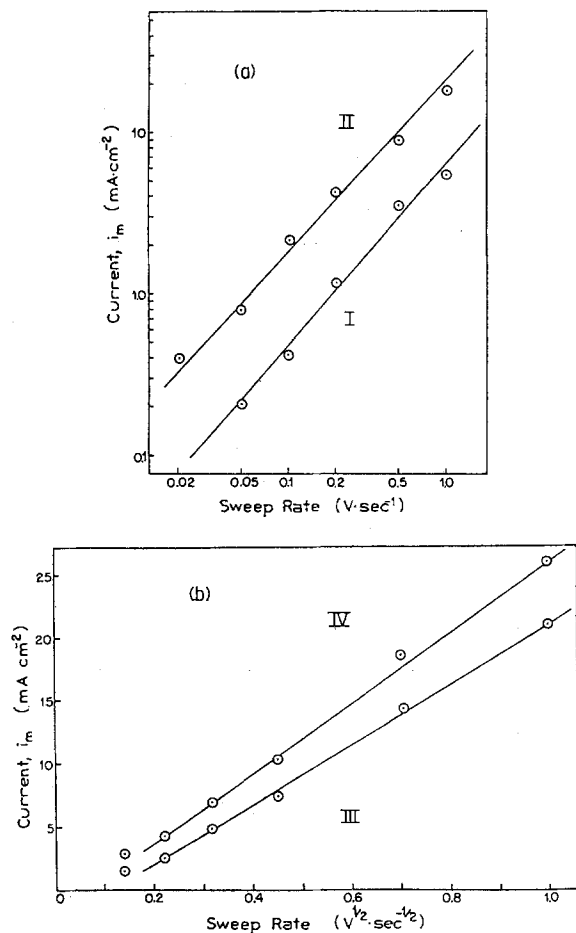
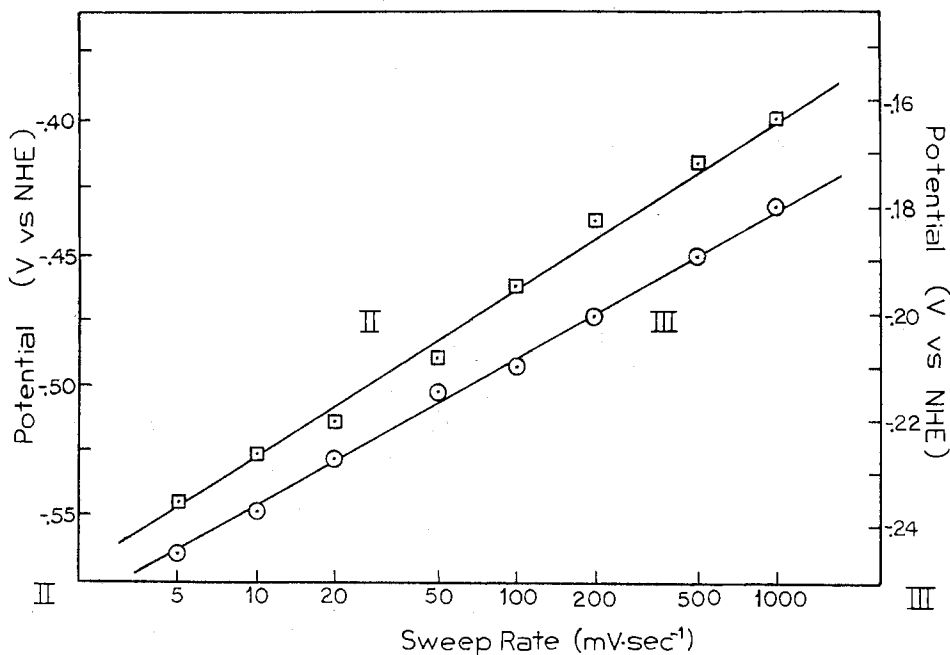


Fig. 4. A, top: sweep rate dependence of the current maximum for Peaks I and II. B, bottom: sweep rate dependence of the current maximum for Peaks III and IV.

Table I. Experimental kinetic parameters for anodic peaks

Peak I	$(\partial \log i_m / \partial \log \nu) = 0.88 \pm 0.01$ $(\partial E_m / \partial \log \nu) = 0$ $E_{1,\nu}^\circ = -0.74\text{V}$
Peak II	$(\partial \log i_m / \partial \log \nu) = 1.19 \pm 0.10$ $(\partial E_m / \partial \log \nu) = 55 \text{ mV/decade}$ $E_{2,\nu}^\circ = -0.57\text{V}$
Peak III	$(\partial \log i_m / \partial \log \nu) = 0.63 \pm 0.02$ $(\partial E_m / \partial \log \nu) = 28 \text{ mV/decade}$ $E_{3,\nu}^\circ = -0.31\text{V}$
Peak IV	$(\partial \log i_m / \partial \log \nu) = 0.57 \pm 0.05$ $E_{4,\nu}^\circ = +0.20 \text{ to } +0.40\text{V}$

Fig. 5. Sweep rate dependence of the potential for Peaks II and III



stant. Thus, the slope of the experimental E_m vs. $\log \nu$ plot yields a value that is one-half of the Tafel slope, which in this case gives a 56 mV/decade value for Peak III, and therefore $\alpha N_a = 1$. The value of the diffusion coefficient (D_a) as calculated from the i_m vs. $\nu^{1/2}$ plot, and Eq. [9] is 5.4×10^{-7} cm²/s, assuming HS⁻ as the diffusing species. This value is lower than expected for such a solution process, which is usually 2×10^{-5} cm²/s. This discrepancy suggests that the presence of sulfide film influences the charge transport kinetics. Similar deviations have also been found for the anodic growth of metal oxides and sulfides (10, 11, 25). Since the quantity of charge represented by Peak III is much greater than the charge in Peak II, this process is not merely due to the transformation of the Sb₂S₃ phase to a higher oxidation state; rather, it involves additional oxidation of Sb metal to Sb (III).

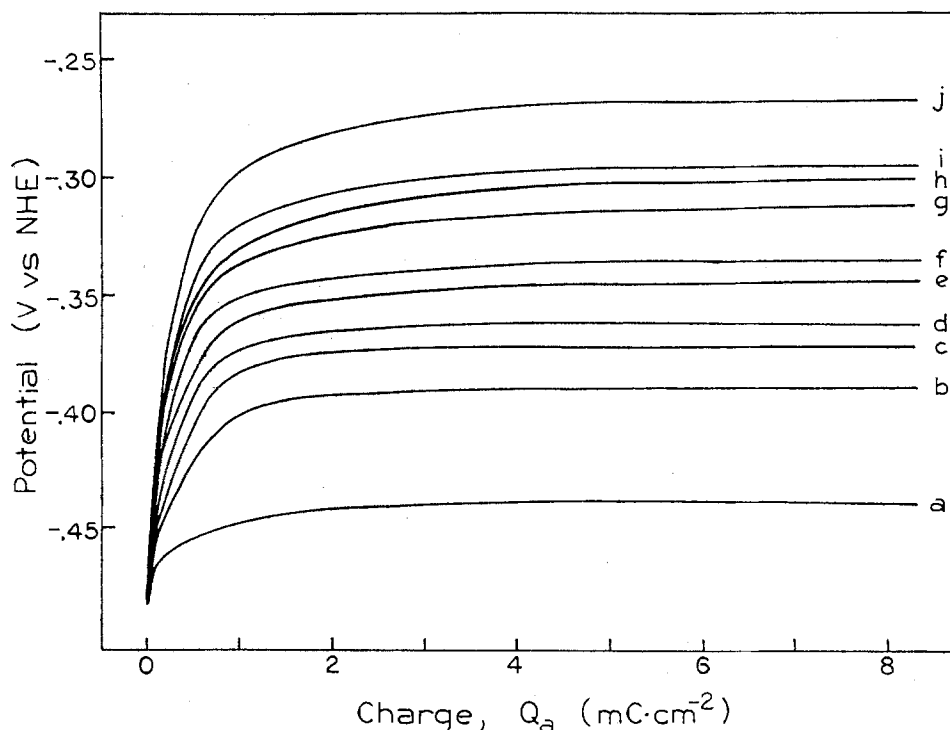
The current maximum of Peak IV (Fig. 4b) is linear with respect to $\nu^{1/2}$, which again indicates a mechanism having a diffusion-controlled rds. However, the dependence of the Peak IV potential on ν was difficult to establish due to the broad current response.

Although neglected in the above scheme, the anodic sulfidation process probably involves hydration effects, and at the more positive potentials oxide (hydroxide) incorporation into the sulfide film. Miller *et al.* (26) demonstrated the influence of sulfide film breakdown and hydroxide incorporation on the photoelectrochemical activity of anodic CdS and Bi₂S₃ films.

Galvanostatic conditions.—Under a controlled anodic current density (i_a), the electrode potential must compensate for the rate of film formation and dissolution. In Fig. 6, the potential vs. anodic charge (E/Q_a) transients are shown for the initial passage of 8 mC/cm² under different i_a . Within the first few tenths of a millicoulomb, there is a rapid potential increase which approaches a nearly constant value after ≈ 3 mC/cm². The constant potential represents a stationary state, when the anodic current is no longer consumed by film formation (*i.e.*, constant film thickness) (27).

Figure 7 shows plots of $\log i_a$ vs. E at various constant anodic charge. The resulting Tafel slopes exhibit an in-

Fig. 6. Dependence of electrode potential on the anodic charge under galvanostatic conditions. Curves a through j: 8, 20, 40, 50, 75, 100, 150, 200, 250, and 500 μ A/cm², respectively.



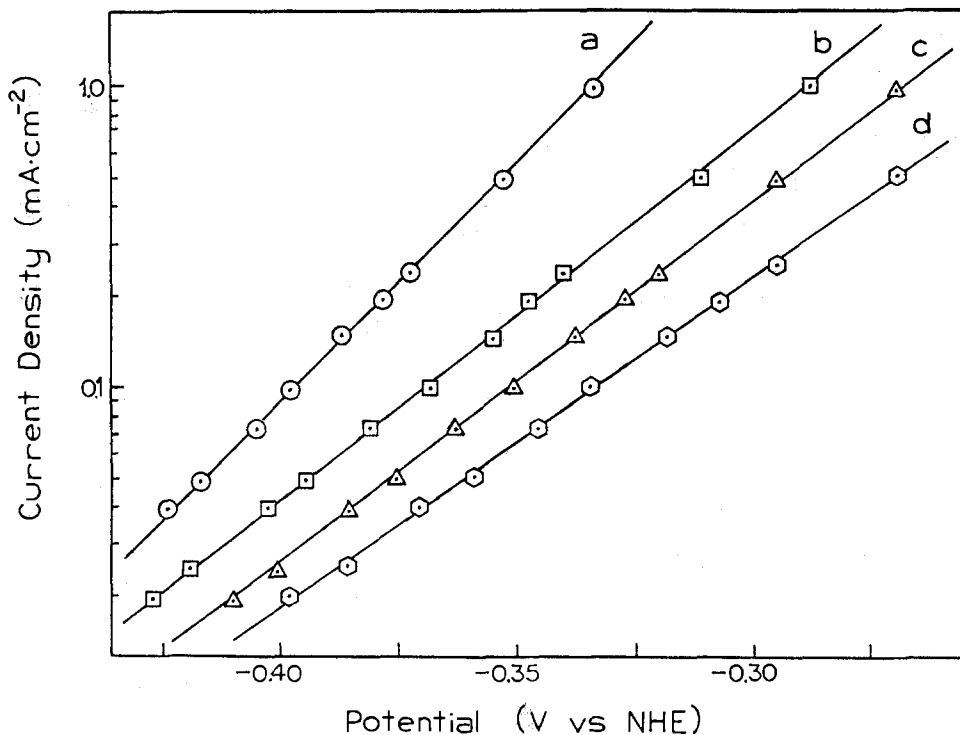


Fig. 7. Tafel plots of data in Fig. 6 at constant charge. a: 0.25. b: 0.5. c: 1.0. d: 5.0 mC/cm².

crease with film thickness and are consistent with the values determined from the scan-rate dependence of Peaks I and II. This behavior indicates that a constant potential drop is maintained across the film during its growth. The growth of an anodic film involving ionic charge transport is described by an exponential function of the field strength, H , given by

$$i = A_0 \exp(BH) \quad [11]$$

where A_0 and B are electrolytic parameters and negligible ionic movement in the direction opposite the field is assumed (1, 2, 28).

The (E/t) transients for sulfidation show an extended initial linear response and lower slopes with a lower i_a . The slopes of the charging curves are related to the rate of film formation where the film thickness is represented by the following expression (29)

$$L = L_0 + mi(t - t_0)/r \quad [12]$$

where L_0 is the initial film thickness, m is the coulometric volume of Sb_2S_3 ($m = 2.85 \times 10^{-4} \text{ cm}^3/\text{C}$), and r is the roughness factor. Extrapolating the linear potential traces to $t = 0$ gives an intercept at $E_f^0 = -0.55\text{V}$, which is the minimum potential required for film formation. This value corresponds to the potentiodynamic film-formation potential E_{f0}^0 . The minimum current necessary for initiation of film growth is estimated to be $i_0 = 10 \mu\text{A}/\text{cm}^2$ for $dE/dt = 0$ and E_f^0 .

The slopes (log) of the linear charging transients are plotted vs. i_a (log) in Fig. 8. The steady-state rate of sulfidation is related to i_a by the empirical equation

$$(dE/dt) = a(i)^b \quad [13]$$

where a is the formation rate at unit current density. From the slope of the plot in Fig. 8, b has a value of 1.29, which compares favorably with values reported for the anodization of other value metals (29, 30).

Under a fixed i , the potential drop across the film (E_f) can be considered constant with a field strength

$$H = E_f/L \quad [14]$$

Using the high field approximation and Eq. [12] and [14], the electrode potential can be expressed as

$$E = \phi + (L_0/B) \ln(i/A_0) + (mi/rB) \ln(i/A_0) \quad [15]$$

and the film formation rate by

$$(dE/dt)_i = (Mi/rB) \ln(i/A_0) \quad [16]$$

where ϕ is the sum of the potential differences at all the interfaces. In a limited range the $\log(i/A_0)$ term in Eq. [16] is insignificant, which is in agreement with the experimentally observed linearity in Fig. 8. Using Eq. [16], the calculated values for B are between $2.11 \times 10^{-6} \text{ cm/V}$ and $4.78 \times 10^{-6} \text{ cm/V}$. The activation or "half-jump" distance (γ) can be obtained from the relation

$$B = \frac{Z\gamma F}{RT} \quad [17]$$

where Z is the charge of the migrating ion. The value calculated for γ ranges between 0.18 and 0.41 nm. The estimated electric field strength varies from $3.2 \times 10^5 \text{ V/cm}$ for the lowest currents to $6.4 \times 10^5 \text{ V/cm}$ for the highest currents applied. This variation in the field strength with current illustrates the effect of the film-

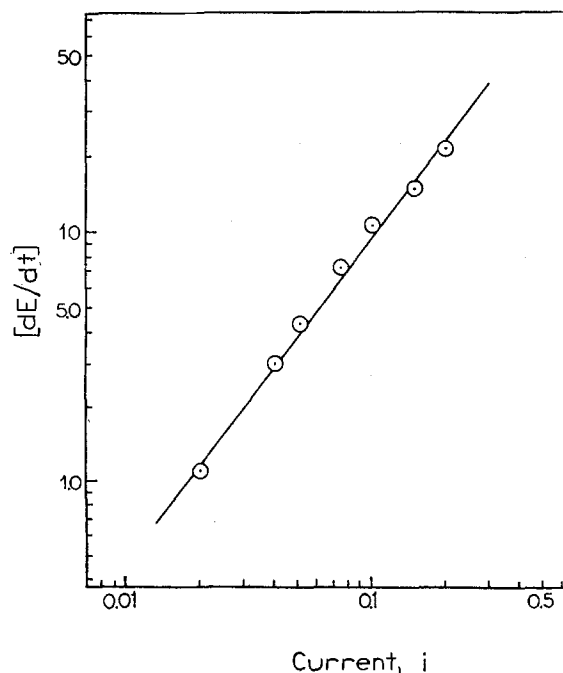


Fig. 8. Plot of sulfidation rate vs. current density.

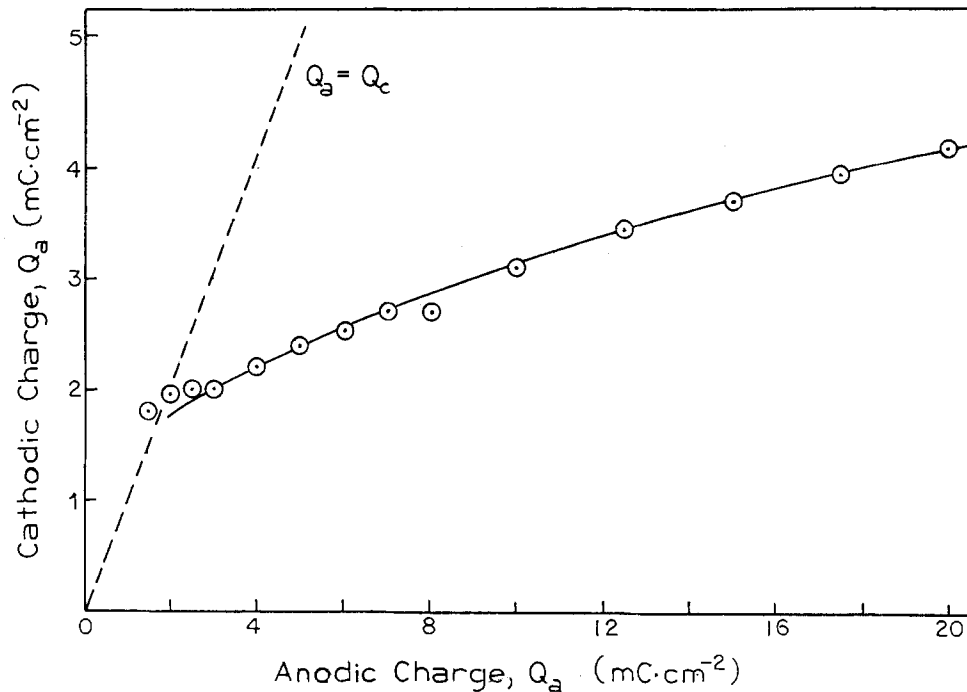


Fig. 9. Dependence of cathodic charge on anodic charge under the galvanostatic condition $i = 50 \mu\text{A}/\text{cm}^2$.

formation potential under the applied current. The film-growth parameters determined above correlate reasonably well with the growth model based on a field-assisted ionic conduction, in spite of the fact that the following have not been accounted for: (i) the small changes in potential during film growth, (ii) not all anodic charge is stored as film, and (iii) the polycrystalline and nonstoichiometric nature of the sulfide film.

Figure 9 illustrates the relation between the anodic charge and corresponding cathodic reduction charge under a constant $50 \mu\text{A}/\text{cm}^2$. The quantity of charge stored as film or Q_c was determined as the amount of charge consumed while at the reduction potential under chronopotentiometric conditions. The results of the galvanostatic measurements coincide with the potentiodynamic results which indicate a $<100\%$ anodic film-production efficiency (i.e., charge-storage efficiency) after the passage of $\approx 2 \text{ mC}/\text{cm}^2$. Atomic absorption analysis of the electrolyte solution for Sb ions confirmed that more than 95% of the charge not residing in the film is due to film dissolution. This observation supports a cationic migration scheme according to the Cabrera-Mott model for film growth.

The amount of charge stored in the film, plotted as reciprocal Q_c vs. $\log t$ is linear, as shown in Fig. 10. During galvanostatic sulfidation, the electrode potential is taken as nearly constant, and thus the growth process follows the Cabrera-Mott model, where the integrated form of the rate equation yields the inverse logarithmic rate law

$$\frac{1}{L} = C - D \ln t \quad [18]$$

where C is a constant and $D = RT/Z\gamma F E_t$ (2).

Figure 11a shows a typical E/t transient for an Sb electrode at $250 \mu\text{A}/\text{cm}^2$. Two potential steps are exhibited with the second arrest having an initial potential peak. Discontinuing the current at any time in either step results in a potential drop to the same open-circuit potential ($E_{oc} = -0.45 \pm 0.01 \text{ V}$). The peak prior to the second arrest is attributed to a fast nucleation process in the solution phase involving a dissolution/precipitation mechanism (31). The inflection between the transition from the first to second potential arrest, and the peak is produced when a species such as a hydro-sulfo antimony complex (e.g., HSbS_2) in reversible equilibrium is consumed by nucleation and deposition, causing a lowering of the concentra-

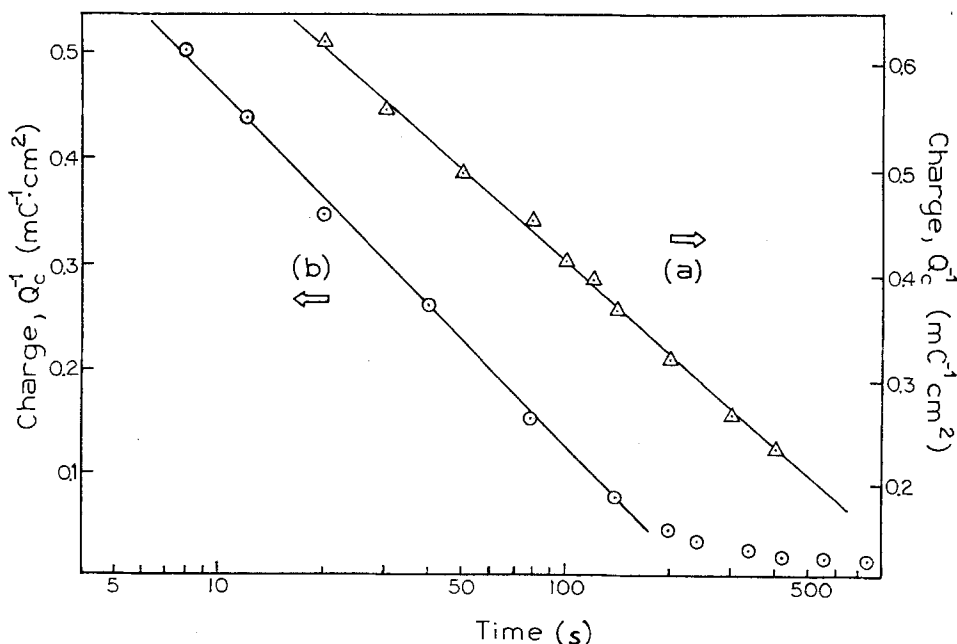


Fig. 10. Dependence of sulfide film charge on growth time under (a) $50 \mu\text{A}/\text{cm}^2$ and (b) $250 \mu\text{A}/\text{cm}^2$.

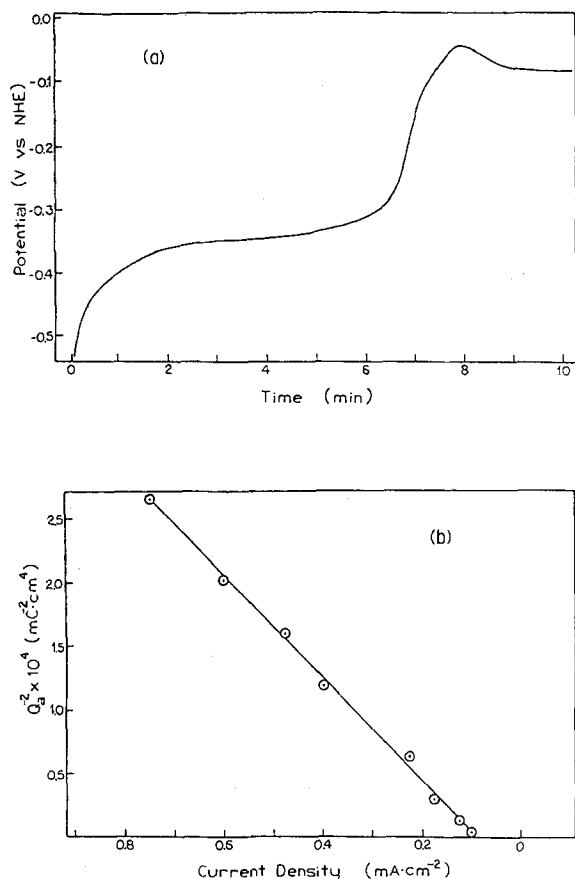


Fig. 11. A, top: potential transient under constant anodic current, $i = 250 \mu\text{A}/\text{cm}^2$. B, bottom: relation between anodic charge passed as $(1/Q_a^2)$ at the time of the potential inflection and current density.

tion polarization until a steady-state condition is reached. This diffusion-controlled process is also consistent with the results from the potential-scan experiments. In addition, processes involving sulfide film breakdown and oxide formation are also possible (26).

The transition from the first to second potential arrest assumed to be a change from a solid-state to a diffusion-limited growth process is dependent on the applied current density and the potential acquired. The quantity of charge required to induce the transition shown in Fig. 11b is represented by

$$1/Q_a^2 = i_{\min} + i_a \quad [19]$$

where i_{\min} is the minimum current needed to initiate the transitions. As extrapolated from the plot (Fig. 11b) $i_{\min} = 90 \mu\text{A}/\text{cm}^2$ at infinite time. In the equilibrium condition, the film thickness remains constant while the anodic current flow is consumed by film or metal dissolution.

ESCA analysis was used to further investigate the anodic sulfide films. The spectra ($\theta = 8^\circ$ and $\theta = 58^\circ$) of a film grown at $250 \mu\text{A}/\text{cm}^2$ to the second potential-arrest region revealed the presence of both a hydrated Sb_2O_3 outer layer and sulfide. The S_{2p} response showed two sets of doublets corresponding to S_2^{-2} and S^{-2} species. From the sulfur ratios, the structure of the sulfide component at the outer surface is a sulfide-polysulfide $\text{Sb}_2(\text{S}_2)_2\text{S}$ or Sb_2S_5 . The trend for the outer 30 Å of film indicates a compositional increase toward Sb_2S_3 and decrease in the Sb_2S_5 and hydrated Sb_2O_3 away from the outer surface.

From these results, it is inferred that the bulk of the film is present as Sb_2S_3 . The existence of polysulfide units in Sb_2S_3 is manifested by previous Mössbauer studies showing Sb in Sb_2S_3 exists only in the Sb (III) state (32, 33). Thus, the sulfidation at higher potentials probably results in the additional oxidation of sulfide to polysulfide during film growth and oxide (hydroxide) incorporation without oxidation of Sb to the (+5) state.

Photoelectrochemical spectral measurements of these semiconducting sulfide films gave the same bandgap for films grown at low and high potentials. The value of 1.7 eV is consistent with that of bulk crystalline Sb_2S_3 (12).

Potentiostatic conditions.—Analysis of the time dependence of the current response to a potential step can be used to investigate film-formation processes. Current transients (i/t) for an electrode subjected to a positive potential pulse exhibit high currents during the initial few milliseconds due to the charging of the double layer. The current decay thereafter is in response to the buildup of film on the surface until a steady-state condition is reached. Under potentiostatic conditions, the expression which relates the current to the charge accumulated in the film (Q_f) is given by

$$i = K \exp(cE - Q_f/d) \quad [20]$$

where K , c , and d are potential-independent constants (28). In this model, it is assumed that film growth occurs through a cation/anion place exchange in the film where the activation energy for growth increases linearly with film thickness. Integrating Eq. [20] yields the following equation relating i , t , and E

$$1/i = (t/d) + (1/K) \exp[(Q_0/d) - cE] \quad [21]$$

where Q_0 is the charge associated with the film at the time of the potential step. The integrated form of Eq. [21] gives a direct logarithmic growth-rate law.

For antimony sulfide film formation, the initial state of electrode surface is taken as film free or $Q_0 = 0$ at $t = 0$. Figure 12 shows the resultant current transients at different potentials plotted as reciprocal i vs. t . In the plots shown, the zero-time intercept decreases with E , as predicted by Eq. [21]. The value of d as determined from the slopes depends exponentially on E with a 195 mV/decade gradient. However, the parameter d is supposedly related to the chemical-activation energy and is therefore only a function of temperature. Such a dependency of d on E has also been found for the growth of oxides on Sn (29) and Fe (30), and is still a matter for debate.

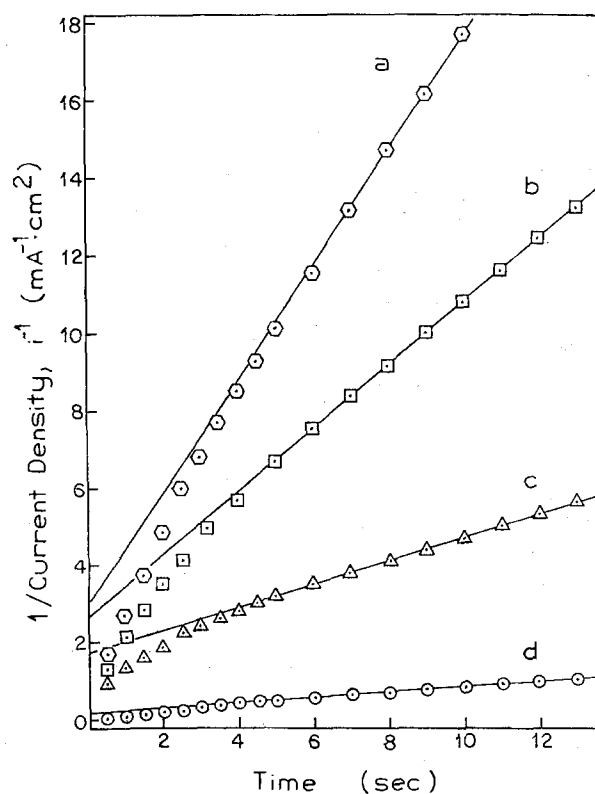


Fig. 12. Relation between reciprocal current and time under the potential steps. a through d: -0.43 , -0.39 , -0.34 , and -0.14V , respectively.

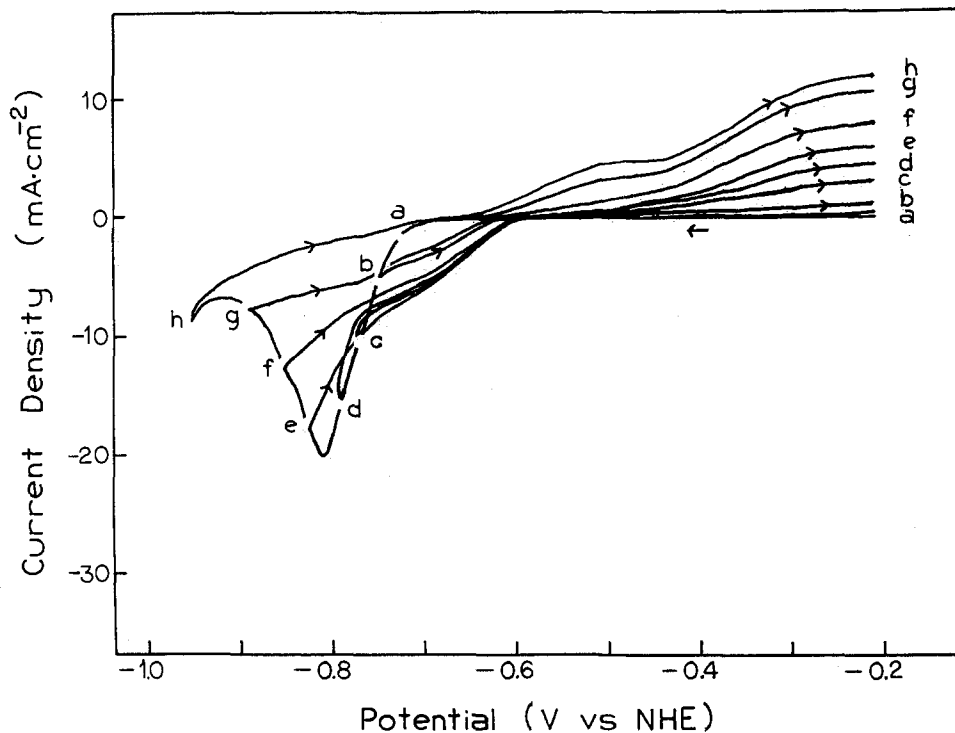


Fig. 13. Repetitive triangular potential scans with varied $E_{\lambda,c}$ at $\nu = 20$ mV/s. $E_{\lambda,a} = -0.20$ V.

The plots in Fig. 12 also deviate from linearity in the initial few seconds. The current is linearly related to $t^{-1/2}$ at short times. One explanation for this behavior is that since d is a time-independent constant, the initial deviation is due to the exponential term in Eq. [21] where $c = F/2\Phi RT$ cannot be assumed constant. In other words, the term $(1/K) \exp(-cE)$ must initially decrease with time until it reaches the value at the $1/i$ vs. t intercept. This can be explained on the basis that Φ , representing the ratio between the occurrence of the rate-determining step to that of the overall reaction, might be comparatively small when there is little or no film on the surface, but then increases with time until a steady-state value is attained.

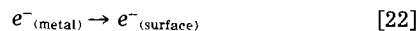
The potentiostatic film-growth data can also be successfully described using the "point-defect model" (3). In this model, the initial current transient associated with very thin films varies inversely with the square root of time. At longer times, the current varies inversely with time, leading to a logarithmic rate law for film growth. The model also assumes that the migration of anion vacancies through the film results in film growth, while the migration of cation vacancies results in metal dissolution. The metal cations at the film/solution interface are also considered to be in equilibrium and can result in film growth through reprecipitation.

Potentiodynamic film reduction.—Further information concerning the growth and properties of the sulfide films can be obtained by studying voltammetric film-reduction behavior. The influence of the cathodic scan potential limit ($E_{\lambda,c}$) on the anodic current profile is shown in Fig. 13. In each case, the potential is first held at -0.20 V for 30 s then scanned in the negative direction. On the positive going return scans, the anodic response is negligible for $E_{\lambda,c} > -0.68$ V. As $E_{\lambda,c}$ is made more negative, the subsequent positive scans exhibit anodic current over much of the same potential region, and with increased film removal the magnitude of the response is greater.

The most commonly used reduction model involves the transport of cations through the film and reduction at the metal/film interface (34). This model is the reverse of the high field anodic-growth mechanism. According to the ionic conduction mechanism, the anodic-

current response during a positive potential scan for the case where there is some film present on the electrode should remain small until the anodic field across the film can support ionic transport (35).

The reanodization profiles in Fig. 13 suggest that sulfidation and growth proceeds at potentials positive of the critical formation potential at a reduced rate on a partially removed film. Therefore, it is assumed that reduction to Sb metal occurs at the outer surface, as opposed to being formed at the metal/film interface. Instead of an ionic mechanism, the reduction can be expressed as an electronic migration process, where



It is further assumed that electron injection occurs over a low energy barrier at the metal/film interface (35). This mechanism is in agreement with the rectification properties (n-type semiconductor) of these anodic films, in which electronic current is not easily passed under anodic conditions, but can readily flow under cathodic bias (12).

The reduction of the anodic Sb_2S_3 films is usually observed as a single cathodic peak prior to H_2 evolution. The reduction response is dependent on both film thickness and sweep rate. Figure 14 illustrates the influence of scan rate on the reduction response for both a thin film (curve a) and a thick film (curve b). The thin sulfide films ($\approx 10 \text{ \AA}$) were potentiodynamically grown at 20 mV/s to -0.40 V, while the thicker films ($\approx 500 \text{ \AA}$) were formed at 100 mV/s to $+0.65$ V.

The sweep-rate effect on the reduction-peak parameters for the thin film case is depicted by the plots in Fig. 15a. The linear relations, i_m vs. ν and E_m vs. $\log \nu$ (25 mV/decade slope) are consistent with a reduction mechanism involving consecutive electrochemical reactions in which the third electron-transfer step is rate determining. Accordingly, the Sb ions in the thin film grown to -0.40 V are reduced from the (+3) state to Sb metal. The results correlate with the proposed mechanism involving the formation of an Sb_2S_3 phase at Peak II.

Figure 15b shows the $\nu^{1/2}$ dependence of the reduction-peak parameters for a thicker sulfide film. These characteristics for the peak parameters can be explained by a dissolution/precipitation process under ohmic-resistance control (36, 37). Assuming that the Sb_2S_3 film

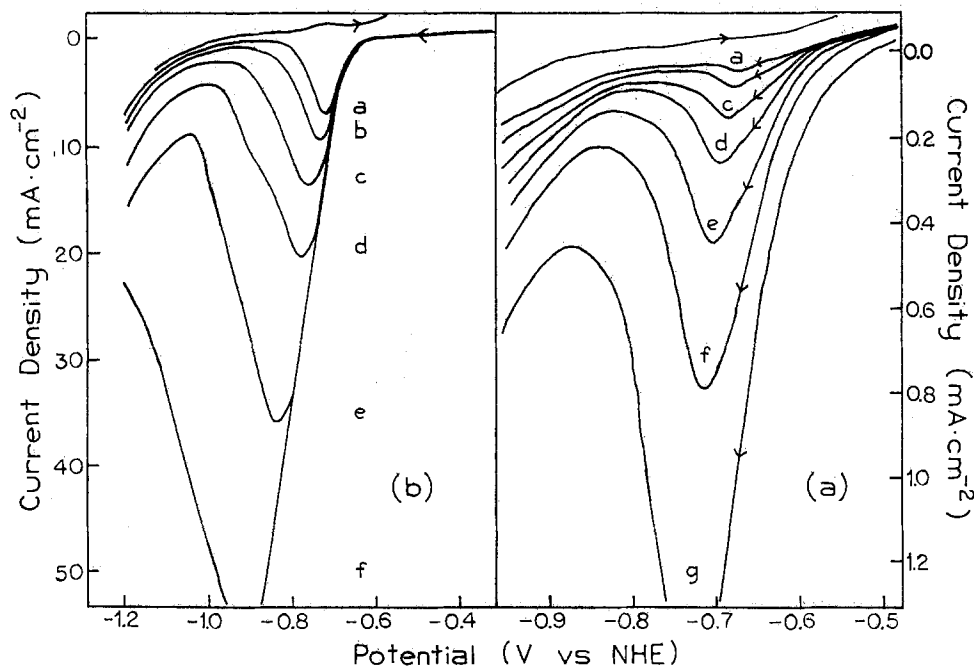


Fig. 14. Potentiodynamic reduction profiles for (a, right) thin sulfide film and (b, left) thick sulfide film

reduction occurs through electronic transport from the underlying metal to the film/solution interface, metal from the freshly reduced film would initially appear at discrete surface positions where electrons are likely to be trapped, e.g., anion vacancies. Such centers could act as nucleation sites which collect the Sb atoms diffusing across the surface. The newly formed Sb deposit occupies less volume than the sulfide. Thus, as the sulfide phase continues to be reduced at discrete locations, the reduction process can be envisaged as resulting in the development of channels in a dendrite fashion extending through the film to the metal substrate, where now the newly formed Sb metal accumulates at the base of the channels (35). This concept is substantiated by the

voltammetric-reduction results discussed above, where the current flow upon resulfidation of a partially reduced film depends mainly on the area of the film removed, rather than showing a threshold-voltage dependence, which would prevail for a uniform thinning of film.

It is believed that in the latter stages of film reduction the fresh metal deposits grow and spread to cover the base substrate. The reduction of the thicker films is then limited by the resistance in the pores between the Sb deposits given by

$$R = L_d/\delta A(1 - \theta) \quad [23]$$

where L_d is the deposit thickness, δ is the specific conductivity of the solution, A the surface area, and θ is the fraction of surface occupied by the newly deposited metal. Under potentiodynamic conditions, the following equations describe the sweep rate dependence of the peak maxima

$$i_m = (nF\rho\delta/M)^{1/2} A(1 - \theta_m)\nu^{1/2} \quad [24]$$

$$E_m = (nF\rho\delta/M)^{1/2} [(L_d/\delta) + R_s A(1 - \theta_m)]\nu^{1/2} \quad [25]$$

where R_s is the bulk solution resistance, θ_m is the coverage at the peak maximum, and M is the molecular weight of Sb (36, 37). Using Eq. [24], θ_m from Fig. 15b was estimated to be 0.9991, assuming the physical properties for Sb metal. This θ_m value is in good agreement with the model, which assumes that the layer-pore resistance is relatively small until the surface is beyond 99% covered (36).

Conclusions

The electrochemical investigation of antimony in alkaline sulfide solutions has demonstrated that anodization results in the formation of an antimony (III) sulfide film. The first anodic process possibly involves the adsorption of hydrosulfide onto the surface, followed by the nucleation of an Sb_2S_3 phase and its lateral spread across the electrode. The growth kinetics follow different rate laws, depending on whether film growth is produced by an applied current or an applied potential. However, considering the approximations made in the inverse and direct logarithmic rate models, they are nearly equivalent when considering small changes in the film thickness such as the situation during initiation of film formation.

The initial stage of film thickening has been interpreted as a high field-assisted ionic-migration process with, possibly, the rate-limiting energy barrier being at

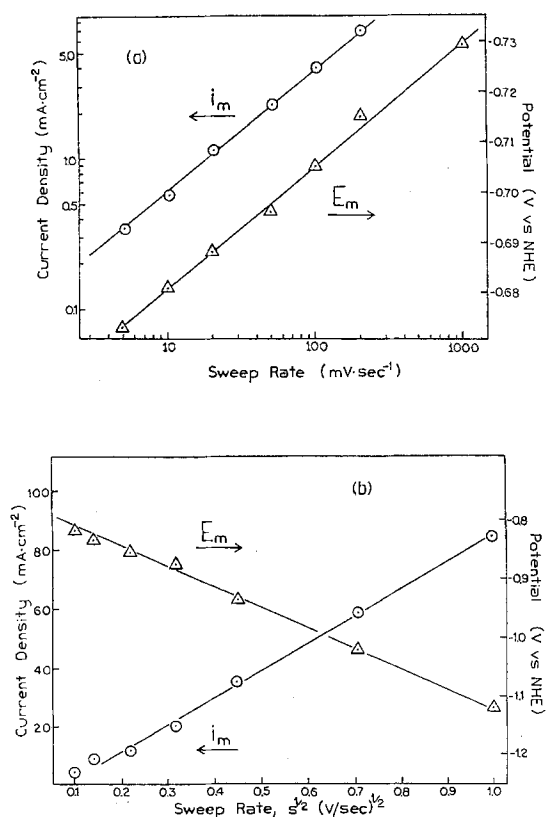


Fig. 15. Dependence of the reduction peak i/E maxima on ν for the (a, top) thin film and (b, bottom) thick film

the film/solution interface. The nature of the films is nonstoichiometric, which might be due to the differences in the cationic and anionic conductivities. A simple electrostatic approach has been taken in discussing the anodic films. Under anodic conditions, the films exhibit resistance to electronic transport, in accordance with their n-type semiconductor properties (12). For thicker films grown positive of -0.40V , the growth mechanism is controlled by a dissolution/precipitation process resulting in a porous antimony sulfide layer with some hydrated oxide incorporated into the film.

The reduction behavior of the sulfide ($E^\circ = -0.76\text{V}$) has been found to be dependent on the film thickness and sweep rate. For films a few monolayers thick, reduction proceeds through three consecutive electron transfers from Sb(III) to Sb(0). The reduction of thicker films is limited by resistance in the pores between the deposited-metal sites. Under cathodic conditions, charge transport through the films is predominantly due to electronic conductivity. Reduction occurring at the film/solution interface results in the deposition of a porous metal surface layer.

Acknowledgments

Financial support of this research by the Robert A. Welch Foundation, Houston, Texas, is gratefully acknowledged. The authors wish to thank Dr. Sergio Kapusta and Dr. S. Mark Wilhelm for helpful suggestions and discussions concerning this work. The ESCA surface analysis by Dr. Vaneica Young (Texas A&M University) is gratefully appreciated. The authors would also like to thank Dr. David W. DeBerry for his critical review of the manuscript.

Manuscript submitted Nov. 2, 1983; revised manuscript received Dec. 20, 1983.

Rice University assisted in meeting the publication costs of this article.

LIST OF SYMBOLS

A	electrode surface area
A_0	electrolytic parameter
a	film formation rate at unit current density
B	electrolytic parameter, defined in Eq. [17]
b	empirical constant, Eq. [13]
C	constant, Eq. [18]
C_0	Concentration of diffusing species
c	potential independent constant, Eq. [20]
D	potential dependent function, Eq. [18]
D_a	diffusion coefficient
d	potential independent constant, Eq. [20]
E	electrode potential referred to NHE
E°	reversible potential
E_f°	minimum film-formation potential
E_t	potential drop across film
E_i	initial electrode potential
E_m	potential at i/E peak maximum
E_{oc}	open-circuit potential
$E_{\lambda,a}$	anodic potential scan limit
$E_{\lambda,c}$	cathodic potential scan limit
G	constant, Eq. [8]
H	electric field strength
i	current density (per cm^2)
i_0	minimum film-formation current
i_a	anodic current
i_m	current at i/E peak maximum
i_{min}	minimum current for galvanostatic transition
K	potential independent constant
K_0	electrochemical rate constant
L	film thickness
L_0	initial film thickness
L_d	Sb deposit thickness
m	coulometric volume
n	total number of transferred electrons
N_a	number of electrons in rds
Q_0	initial film charge
Q_a	anodic charge
Q_c	cathodic charge
Q_t	total film charge

R_s	bulk solution resistance
rds	rate-determining step
r	roughness factor
t	time
Z	charge of migrating ions

Greek Symbols

α	transfer coefficient
γ	activation distance
δ	solution specific conductivity
θ	fraction of surface covered by Sb deposit
θ_m	fraction of surface covered at i/E peak maximum
ν	potential scan rate
ρ	density
Φ	ratio of the rds to overall reaction occurrence
ϕ	sum of all interfacial potential differences

REFERENCES

- E. J. W. Verwey, *Physica*, **2**, 1059 (1935).
- N. Cabrera and N. F. Mott, *Rep. Prog. Phys.*, **12**, 163 (1948-1949).
- C. Y. Chao, L. F. Lin, and D. D. Macdonald, *This Journal*, **128**, 1187 (1981).
- L. Young, "Anodic Oxide Films," Academic Press, New York (1961).
- M. J. Dignam, in "Oxides and Oxide Films," Vol. 1, J. W. Diggle, editor, Marcel Dekker, New York (1972).
- B. Miller and A. Heller, *Nature (London)*, **261**, 403 (1976).
- L. M. Peter, *Electrochim. Acta*, **23**, 165 (1978).
- L. M. Peter, *J. Electroanal. Chem.*, **98**, 49 (1979).
- L. M. Peter, J. D. Reid, and B. R. Scharifker, *ibid.*, **119**, 73 (1981).
- V. I. Birss and G. A. Wright, *Electrochim. Acta*, **27**, 1 (1982).
- S. Kapusta, A. Viehbeck, S. M. Wilhelm, and N. Hackerman, *J. Electroanal. Chem.*, **153**, 157 (1983).
- A. Viehbeck and N. Hackerman, in "Photoelectrochemistry: Fundamental Processes and Measurement Techniques," W. L. Wallace, A. J. Nozik, S. K. Deb, and R. H. Wilson, Editors, p. 478, The Electrochemical Society Softbound Proceedings Series, Pennington, NJ (1982).
- A. Viehbeck, Ph.D. thesis, Rice University, Houston, TX (1982).
- A. Bewick, M. Fleischmann, and H. R. Thirsk, *Trans. Faraday Soc.*, **58**, 2200 (1962).
- A. J. Arvia, A. J. Calandra, and M. E. Martins, *Electrochim. Acta*, **17**, 741 (1972).
- J. W. Schultze and M. M. Lohrengel, *Ber. Bunsenges. Phys. Chem.*, **8**, 552 (1976).
- D. E. Williams and G. A. Wright, *Electrochim. Acta*, **21**, 1009 (1976).
- B. E. Conway, "Theory and Principles of Electrode Processes," p. 109, Ronald Press, New York (1965).
- R. S. Schreiber Guzman, J. R. Vilche, and A. J. Arvia, *Corros. Sci.*, **18**, 765 (1978).
- I. A. Ammar and A. Saad, *J. Electroanal. Chem.*, **30**, 395 (1971).
- I. A. Ammar and A. Saad, *ibid.*, **34**, 159 (1972).
- S. Srinivasan and E. Gileadi, *Electrochim. Acta*, **11**, 321 (1966).
- P. Delahay, *J. Am. Chem. Soc.*, **75**, 1190 (1953).
- R. S. Nicholson and I. Shain, *Anal. Chem.*, **36**, 706 (1964).
- J. Ambrose, R. G. Barradas, and D. W. Shoesmith, *J. Electroanal. Chem.*, **47**, 47 (1973).
- B. Miller, S. Menezes, and A. Heller, *ibid.*, **94**, 85 (1978).
- K. J. Vetter, *Electrochim. Acta*, **16**, 1923 (1971).
- N. Sato and M. Cohen, *This Journal*, **111**, 512 (1964).
- H. A. Johansen, G. B. Adams, and P. Van Rysselberghe, *ibid.*, **104**, 339 (1957).
- I. A. Ammar and I. Kamel, *Electrochim. Acta*, **16**, 1601 (1971).
- P. Selinger, *Electrochim. Acta*, **21**, 637 (1976).
- G. G. Long, J. G. Stevens, and L. H. Bowen, *Inorg. Nucl. Chem. Lett.*, **5**, 21 (1969).
- T. Birchall and B. Della Valle, *Chem. Commun.*, 675 (1970).
- B. V. Tilak, R. S. Perkins, H. A. Kozlowska, and B. E. Conway, *Electrochim. Acta*, **17**, 1447 (1972).
- D. E. Williams, *ibid.*, **21**, 1097 (1976).
- A. J. Calandra, N. R. DeTacconi, R. Pereiri, and A. J. Arvia, *ibid.*, **19**, 901 (1974).
- W. J. Mueller, *Trans. Faraday Soc.*, **27**, 757 (1931).

An Ionized Air Reference Electrode

I. Principles of Operation

F. R. Foulkes,* W. F. Graydon, and M. Garamszeghy

Department of Chemical Engineering and Applied Chemistry, University of Toronto, Toronto, Ontario, Canada M5S 1A4

ABSTRACT

A novel ionized air electrode (IAE) has been investigated for use as a reference electrode in electrochemical systems. The IAE employs a low level source of ionizing radiation (Am-241) to ionize an air gap, thereby establishing electrical contact with the electrolyte of an electrochemical system without introducing a liquid junction potential and its associated uncertainties, such as contamination of the test solution. Other advantages of the IAE include operation over an extremely large temperature range, long life, high durability, low cost, simple design, and freedom from maintenance. Studies of the effects on electrode behavior of factors such as electrode configuration and materials of construction are presented. Preliminary measurements indicate that it may be possible to use the IAE to replace conventional reference electrodes, such as the saturated calomel electrode, in electrochemical measurements such as the electrometric determination of pH.

Commonly used reference electrodes, such as the saturated calomel electrode, suffer from limitations resulting from the direct physical contact made with the test solution by way of a liquid junction. Diffusion contamination of the test solution and the internal solution of the reference electrode is troublesome. In addition, the liquid junction potential (LJP) is often difficult to evaluate. In aqueous solutions, such LJP's generally are in the order of ± 10 mV (1). Ionic activities in nonaqueous media can vary so much from the values in aqueous solutions that LJP's between aqueous and nonaqueous solutions can be as large as several hundred millivolts. In such cases, commonly used reference electrodes often do not function very well because the unknown LJP can comprise a large fraction of the total measured electrode-potential difference. Furthermore, because of hysteresis effects, thermal disproportionation reactions, decomposition reactions, and the presence of a volatile aqueous phase, familiar reference electrodes such as the calomel electrode or the Ag/AgCl electrode are not very amenable to use at elevated temperatures.

In view of the above problems, a reference electrode that functions through a mechanism that differs from those encountered in the above-mentioned conventional systems might, under certain circumstances, serve as a useful alternative that suffers from fewer, or less severe, limitations. In the present paper, we describe a secondary reference electrode that is based on the use of an ionized air gap to contact the surface of the test solution (2-4). Such an electrode eliminates ionic contamination and permits use over a wide temperature range, including use with molten salts.

Ionized air electrodes (IAE) have been used in conjunction with standard reference electrodes since 1924 as indicator electrodes to study the surface potentials (χ) of solutions (5-7). The technique employed by all the early workers suffered from the major drawback of the very short half-life (138 days) of the Po-210 that was used to ionize the air. This required the frequent preparation of fresh electrodes from a stock solution of radium bromide. In 1960, Kamienski and co-workers (8) began using plutonium-239 as the ionizing source. Pu-239 has a much longer half-life than Po-210 (24,000 yr vs. 138 days), and decays with mono-energetic alpha particles of an energy about equal to that of Po-210 alpha particles. Using a 2 μ Ci source above a 0.1M potassium chloride solution, it was found that the time required to attain a steady potential varied from about 3 to 25 min. In 1964, Kamienski and Czarnecki (9) greatly reduced the time required to obtain a steady potential by increasing the activity of the alpha particle source to 20 μ Ci, permitting the use of electrode-solution separations of up to 1.5 cm to protect the elec-

trode from wetting. In more recent work americium-241 has been used as the ionizing source by Volthardt and Wustneck (10) and by Costa and co-workers (11, 12).

In spite of the previous use of the IAE as an indicator electrode to measure solution surface potentials, it would appear that, prior to the present work, such an electrode has not seriously been tried as a reference electrode. Possibly this oversight has resulted from concern about the variation of the surface potential from solution to solution or from concern about the reproducibility of the surface potential in seemingly identical solutions.

The magnitude of the surface potential that exists at a pure water/air interface is believed to be of the order of 0.13 ± 0.02 V, as a consequence of a net alignment of water molecules in the first few monolayers of the liquid phase (12-16). Experiments have demonstrated that the aqueous phase is positive relative to the air, indicating that the hydrogen ends of the water dipoles are directed inwards towards the bulk of the liquid phase (17-21). Insofar as this surface potential is reproducible and constant, it poses no impediment to the use of the IAE as a reference electrode. Unfortunately, the surface potential of water is shifted by the presence of dissolved solutes, so that such a variation poses a limitation on the use of an IAE as a reference electrode. Conversely, the LJP that is established between most conventional reference electrodes and a test solution also varies from solution to solution, giving rise to a similar limitation on the reproducibility and constancy of the reference potential.

In general, simple electrolytes such as the alkaline metal hydroxides, fluorides, chlorides, and sulfates exert only a small effect ($\Delta\chi$) on the surface potential of water (22, 23). At 0.1M concentration, aqueous solutions of the majority of common electrolytes exhibit surface potentials within ± 2 mV from the value for pure water. Furthermore, except in the presence of surface-active agents [which can alter the surface potential drastically (19, 20)], or at very high concentrations of solute, the shifts from the value for pure water are seldom greater than ± 10 mV (12, 22-24).

Similarly, the effect of solution pH on the surface potential of an aqueous solution does not seem to be significantly worse than the corresponding effect on a LJP. Kamienski (25), for example, has shown that dilute hydrochloric acid exerts negligible effect on solution surface potential over the pH range of 2 to 12. He also has shown that over the pH range of about 6 to 10 even certain surface active agents such as 0.025M p-hydroxybenzoic acid do not change the surface potential of the solution by more than about 10 mV (20). Admittedly, as is evident from Table I, in more concentrated acid solutions, the surface potential does change quite significantly from the value for pure water (22). However, as can be seen from Table II (1), LJP's also undergo large changes at extreme values of pH.

* Electrochemical Society Active Member.
Key words: electrode, nuclear particles pH, EMF.

Table I. Effect of HCl concentration on the surface potential (χ) of aqueous solution at 25°C (22)

HCl molality	$\Delta\chi^*$ (mV)
0.01	-2.0
0.05	-3.0
0.1	-3.5
0.2	-2.0
0.5	+4.6
1.0	+18.3
2.0	+46.4
3.0	+74.0

* $\Delta\chi = \chi(\text{solution}) - \chi(\text{pure water})$

Table II. Liquid junction potentials at 25°C between saturated KCl solution and solutions of various pH (1)

Solution composition	pH	LJP* (mV)
1M HCl	0.1	+14.1
0.1M HCl	1.1	+26.9**
0.1M HCl	1.1	+4.6
0.05M KH_2PO_4	1.68	+3.3
0.01M HCl	2.0	+9.1**
0.01M HCl	2.0	+3.0
0.5M KH-phthalate	4.00	+2.6
0.025M KH_2PO_4 + 0.025M Na_2HPO_4	6.86	+1.9
0.01M NaOH	12.0	+2.3
0.05M NaOH	12.7	+0.7
0.1M KOH	13.0	-0.1
0.1M NaOH	13.0	-0.4
1.0M KOH	14.0	-6.9
1.0M NaOH	14.0	-8.6

* The sign denotes the sign of the KCl side of the junction.

** Using 0.1M KCl instead of saturated KCl.

A preliminary design for an ionized air reference electrode employed a single element consisting of a 100 μCi source of americium foil, which served both as ionizing source and current collector (2). The element was kept suspended about 1 cm above the liquid in a shielded glass tube. This electrode was used to replace the SCE as reference electrode in a series of glass-electrode pH measurements in aqueous solutions of widely varying pH and ionic strength and in methanol-water systems.

Although this preliminary reference electrode performed well, producing pH measurements of good quality, the time required to reach a steady-state potential was long (10 ~ 15 min) and a slow potential drift about $5 \text{ mV} \cdot \text{h}^{-1}$ was observed. In the present study, the electrode design has been modified to reduce the response time and potential drift by using the Am-241 foil only as an ionizing source and by providing a separate, electrically isolated collector element.

In order to determine the suitability of the IAE for various proposed applications, design parameters such as ionization build-up time, potential, and resistance, as functions of source height, composition of ionized gas, and composition of collector metal have been studied.

Experimental

Electrode construction.—The design of the Am-241 ionized air reference electrode (IAE) is shown in Fig. 1. The electrode housing (B) is constructed in two parts, the upper containing the source (A) and the lower containing the collector (D). The upper housing is a double layer of Pyrex glass tubing closed at the top with the layers being separated by 0.002 cm thick lead foil, which serves as an electrostatic shield around the ionized air. The lower housing is constructed of a single layer of Pyrex glass tubing. Five lower housings were constructed, each with a different collector metal. The gas inlet (C) is 5 mm id glass tubing that connects directly to the gas supply via a short length of Tygon tubing. The two-part housing was constructed to allow the source-to-collector spacing to be easily varied from about 0.5 to 6.0 cm and to facilitate the use of the same Am-241 source for each of the different collectors.

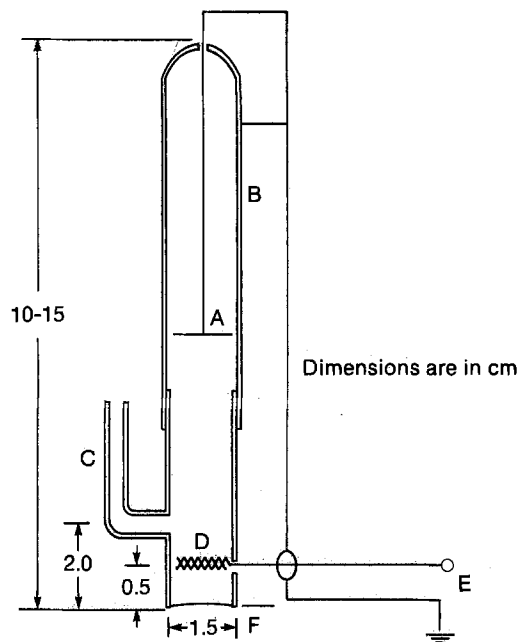


Fig. 1. Details of Am-241 ionized air reference electrode. A = Am-241 source; B = housing; C = gas inlet; D = collector electrode; E = connection to electrometer; F = surface of electrolyte.

The americium-241 alpha-particle source (A) is a disk (approximately 0.83 cm diam) of 100 $\mu\text{Ci}/\text{cm}^2$ Am-241 foil with an activity of approximately 57 μCi . Am-241 has a half-life of 433 yr and emits alpha particles at an energy of 5.5 MeV. The 2 μm thick gold covering on the foil, required to keep structural integrity of the Am-241 layer, somewhat reduces the average alpha particle energy.

The collector element (D) is constructed of 50-mesh screen and is of approximately 1 cm diam. Collectors were constructed from platinum, copper, nickel, iron, and brass. Electrical connection to the collector is by the center conductor of RG 58/U coaxial cable with the braid connected to the Am-241 source and the internal shield of the upper housing.

Measurements.—Voltage measurements were made using a Keithley 610 C electrometer. A Keithley 370 strip chart recorder was used with the electrometer for the measurement of voltage-time behavior. A Corning Model 7 pH meter was used in the millivolt mode for pH measurements. The conventional electrodes employed consisted of a Beckman Model 40498 glass electrode and a Fisher Model 13-639 saturated calomel reference electrode, both of which were new at the start of the work.

Reagents and materials.—Reagent grade chemicals dissolved in doubly distilled water were used for all aqueous solutions. Fisher Certified Buffer Solutions of pH 1, 2, 4, 6, 8, and 10 were used in the pH measurements. Laboratory grade gases (H_2 , He, Ne, Ar, CO_2 , CH_4 , O_2 , and air) supplied from gas cylinders were used without further purification in the experiments dealing with the electrode performance in different gaseous environments.

Temperature regulation.—The temperature was held constant using a water bath controlled by a Philadelphia Roto-Set adjustable mercury-switch temperature controller, which was connected to a 50W electric immersion heater through an electronic relay. Temperatures below 25°C were obtained by adding ice to the water bath to stabilize the heater at the lower temperatures. To reduce the possibility of electrical interference, the water bath was circulated around the experimental electrode assembly from outside the Faraday cage used to contain the cell, using a $50 \text{ ml} \cdot \text{s}^{-1}$ pump. For each experiment, an equilibration time of about 2h was allowed to ensure that the test assembly was at the desired temperature.

Experimental Results and Discussion

Potential gradient profiles.—If the americium ionized air electrode (IAE) is to be used in applications such as voltammetry, which involve making measurements in an applied electric potential field, the electrode must maintain a constant potential in the applied field. This property of the electrode was tested by constructing the device shown in Fig. 2. By passing a constant current through the platinum electrodes in the aqueous KCl solution, a potential gradient is established between the electrodes that is linear over most of the separation distance. By recording the potential of the test electrode (T) vs. the stationary electrode (R) at various distances (x) along the slider, the voltage-distance profile in the KCl solution can be obtained. If the profile is linear with a slope equal to the product of the solution current density and the solution resistivity, then the potential of the test electrode is constant in the applied electric field.

Figure 3 shows the results of such an experiment, during which an applied potential difference of 3.0V was placed across the two Pt electrodes (spaced 20 cm apart in 0.1M KCl at 22°C), driving a constant current of 1.3 mA through the cell. With an electrolyte resistivity of $78 \pm 2 \Omega\text{-cm}$ and an electrolyte cross-sectional area of $3.8 \pm 0.2 \text{ cm}^2$, the theoretical slope of the profile is $26.5 \pm 2 \text{ mV} \cdot \text{cm}^{-1}$ (95% confidence limits). Using a SCE as the stationary reference electrode (R), the lower line shows the profile obtained using a SCE as test electrode ($24.9 \pm 2.5 \text{ mV} \cdot \text{cm}^{-1}$), while the upper line shows the profile obtained using the IAE as test electrode ($24.5 \pm 2.2 \text{ mV} \cdot \text{cm}^{-1}$). The IAE employed a Pt collector at 0.5 cm above the solution with a 57 μCi source at 4.0 cm above the collector.

Both experimental slopes deviate by less than 10% from the theoretical value and by less than 2% from each other. A statistical test at the 97% confidence level indicates no significant difference between the theoretical and experimental slopes.

Response time.—In measuring the potential developed between a SCE previously placed in 0.1M KCl solution at 22°C and the IAE, the initial rise time of the IAE, *i.e.*, the time taken to fully build up the ionized air gap from $t = 0$ when the glass shell of the IAE is first placed adjacent to the solution surface, is in the order of 20 ~ 60s. When used in conjunction with a glass electrode in a pH meter application, the effect of this response time is unimportant, since it is less than the time required for the glass electrode to stabilize in the solution. If desired, the response time probably could be shortened by narrowing the tip of the IAE, possibly to capillary dimensions, thereby better maintaining trapped ionized air within the electrode shell.

The longer time-response stability of the potential developed by the IAE over pH 4.00 buffer solution at 25°C also was determined. The drift in the potential difference between the IAE and the SCE over a period of 8h was only $1.5 \cdot 10^{-4} \text{ V} \cdot \text{h}^{-1}$. In the same solution the drift in the potential difference between the IAE and the glass elec-

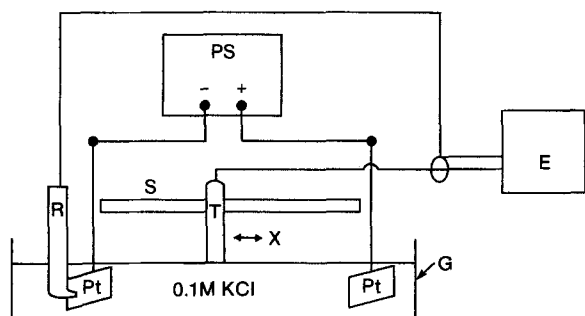


Fig. 2. Experimental assembly for measuring IR profile. E = electrometer; PS = dc power supply; Pt = platinum screen electrodes; R = stationary SCE reference electrode; S = slider; T = moving Am-241 test electrode; G = glass trough.

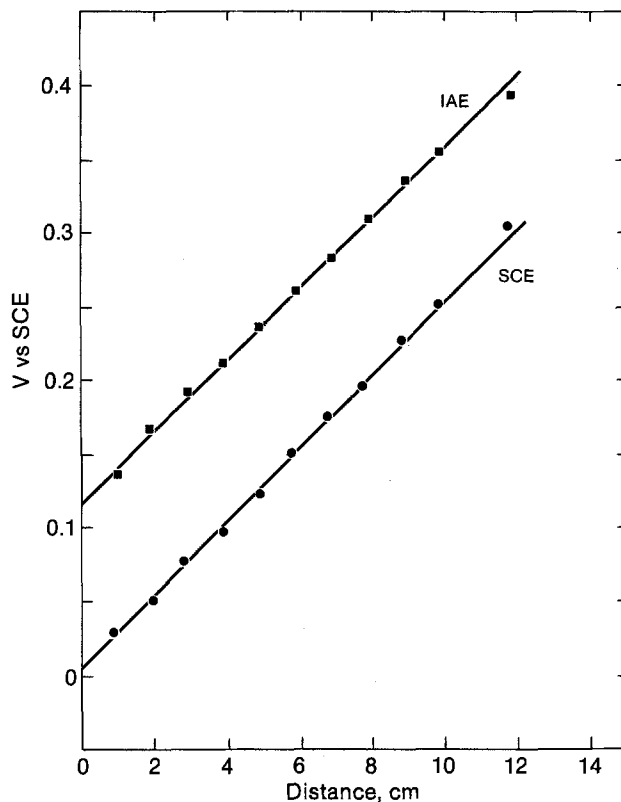


Fig. 3. IR profile test results. Potential profile through 0.1M KCl at 22°C. Cell electrodes 20 cm apart. Cell voltage 3.0V; current 1.3 mA. (●) using SCE as test electrode; (■) using Am-241 IAE as test electrode.

trode was equivalent to approximately 0.15 pH units over the same 8h period. An analogous study using a SCE vs. a glass electrode showed a drift similar to that using the IAE vs. glass electrode system, indicating either that the drift was attributable primarily to the particular glass electrode used or that the IAE and SCE used both exhibited about the same amount of drift.

Electrode resistances.—The IAE consists of two parallel conduction paths: collector to ground via the source (R_s), and collector to ground via the solution and external circuitry (R_g). Unless the resistance of the collector-to-source path is much higher than that of the collector-to-solution path, its presence can cause an error in the IAE potential measurements. A source-to-collector resistance of 100 times that of the collector-to-solution path can be expected to produce a measured error of about 1%.

The electrical resistances R_s and R_g were measured using the Keithley electrometer in the high impedance ohmmeter mode. As can be seen from Fig. 4, R_s increased rapidly with increasing source-to-collector separation (h). R_g was measured with the collector at a height of 0.5 cm above the 0.1M KCl solution. Electrical connection to the solution was made via a platinum wire with the end placed in the solution approximately 1 cm directly below the collector. The resistance of the 0.1M KCl solution was negligible compared with that of the air gap.

The high magnitude of R_g ($10^{10} \sim 10^{11} \Omega$) indicates the need for a very high impedance voltmeter to be used with the IAE. Electrometers and good-quality pH meters have comparable and suitable input impedances in the order of $10^{14} \Omega$.

Alpha particles of 5.5 MeV energy that are emitted into air ionize the air, producing a maximum number of ion pairs per centimeter at a distance of about 4 cm from the source, with the rate of ionization decreasing rapidly at distances greater than this (26). As discussed below, the metal collector interacts with these ionized air particles; therefore, it was deemed optimal to locate the collector at a distance of $h = 4$ cm from the Am-241 source. With regard to the collector-to-solution distance, it was found

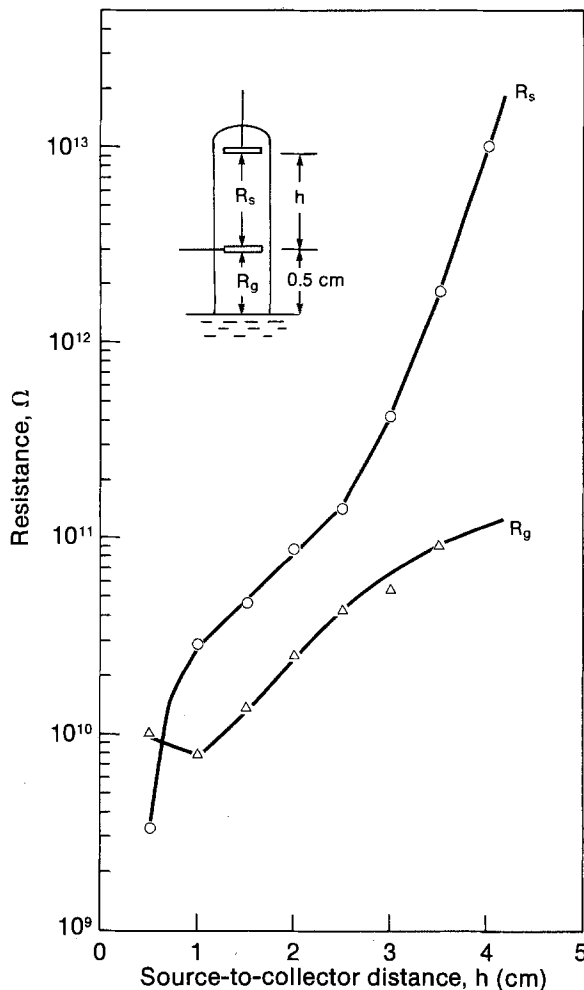


Fig. 4. Variation of source-to-collector resistance (R_s) and collector-to-solution resistance (R_g) with source-to-collector separation distance (h). 0.1M KCl solution.

that when this distance was made less than 0.5 cm, the reproducibility of the IAE was hampered by the condensation of water vapor on the surface of the collector. Conversely, if the collector-to-solution distance was increased to beyond 0.5 cm, in order to maintain a sufficiently high ratio of R_s to R_g it would have become necessary to increase the collector-to-source distance (h) to greater than 4 cm, which was considered undesirable. For these reasons, a collector-to-solution distance of 0.5 cm was considered to be the optimum practical distance. Consequently, most of the subsequent experimental work was performed with the collector 0.5 cm above the solution and the source 4.0 cm above the collector. Under these conditions the collector-to-solution resistance is about $10^{11}\Omega$, and the error in the measured voltages due to the voltage drop across the voltmeter is about $10^{11}/10^{14}$ or 0.1%. The R_s/R_g ratio of approximately 100 leads to a measurement error of less than 1%.

IAE potential vs. source height.—In Fig. 5, the potential of the IAE is plotted as a function of the source-to-collector distance, the platinum collector being fixed at a height of 0.5 cm above the 0.1M KCl solution. It can be seen that the potential becomes more positive as the source height is increased, indicating that it is possible to change the potential of the IAE by altering the source height. The practicality of this change is, however, limited by the restrictions on the electrode resistances discussed in the previous section.

Influence of the gas used for ionization.—It has been known since 1897 (27) that the voltage generated at an ionized gas electrode is affected by the nature of the gas ionized. To investigate this design parameter an experimental cell consisting of an ionized gas electrode, an

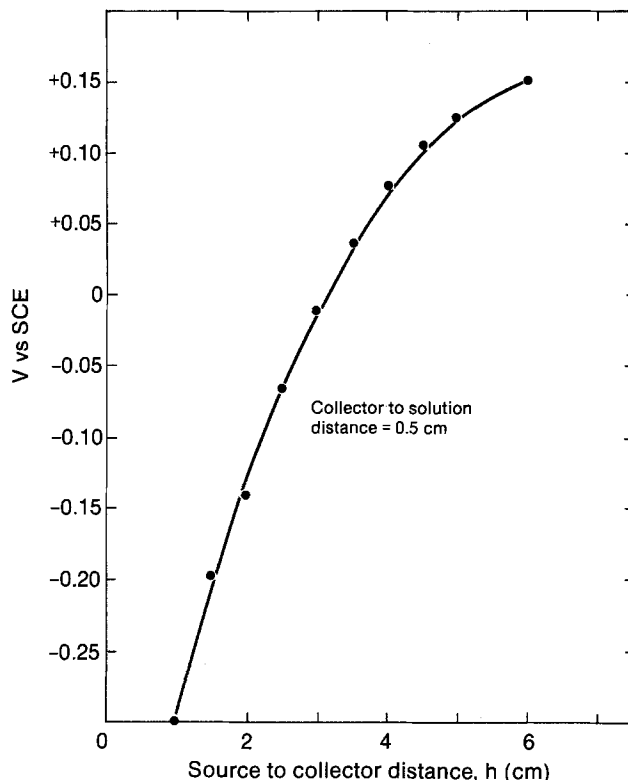


Fig. 5. Potential of IAE vs. source-to-collector separation distance (h). 0.1M KCl solution.

aqueous 0.1M solution of KCl, and a SCE was used with various gases as the absorbing medium. The results, shown in Fig. 6, indicate that a wide variation in the voltage of the IAE results from variation in the gas ionized and that the molecular weight of the gas is a property of major influence.

Alpha particle energy loss occurs mainly through ionization and excitation of the absorbing medium. Inelastic collisions of α -particles with loosely bound outer elec-

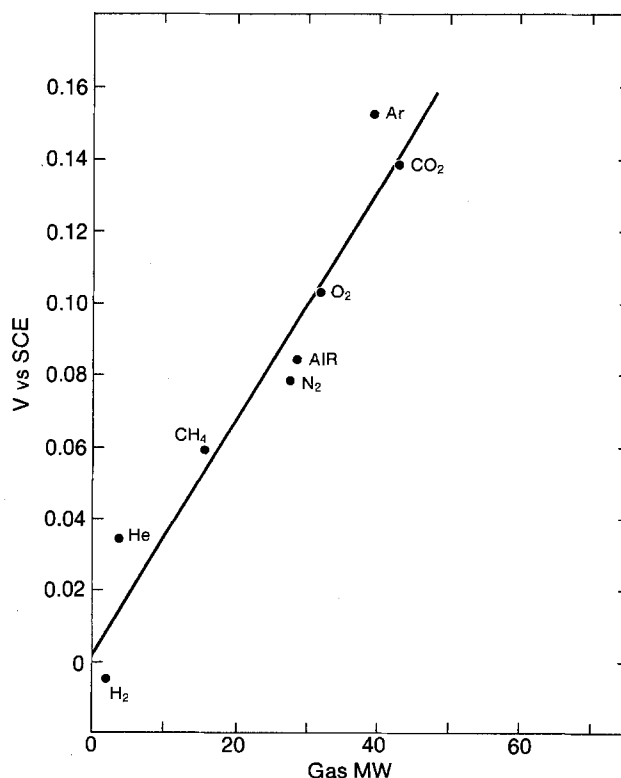


Fig. 6. Potential of IAE vs. molecular weight of gas used for ionizing medium. 0.1M KCl solution. Source-to-collector distance = 4 cm; collector-to-solution distance = 0.5 cm.

trons in the atoms or molecules of the absorbing gas result in the ejection of the struck electrons, *i.e.*, primary ionization of the atoms or molecules (28). The ejected electrons (delta particles) may possess sufficient kinetic energy to cause secondary ionization of the gas molecules, with the result that the total ionization may be several times larger than the primary ionization (29). A simple calculation (see Appendix) for the IAE used in the present study indicates that, when the absorbing medium is air, the steady-state concentration of ions will be about 2×10^8 ions/cm³.

To explain the effect of different gases, it appeared reasonable to postulate that the potential established at the IAE might be related to the average specific ionization of a given gas, *i.e.*, the average total number of ions produced by an α -particle per unit path length traversed. This is given by

$$-\frac{(dE/dx)_{AV}}{W} \quad [1]$$

where $(-dE/dx)_{AV}$ is the average rate of α -particle energy loss with distance and W is the mean energy expended to form an ion pair in a given gas. Since W is constant over a wide energy interval, the average specific ionization is approximately proportional to the average rate of energy loss (28). This, in turn, is related to the properties of the gaseous medium through the terms N , Z , and I in the well-known Bethe equation (28-33), which, when expressed in SI units takes the form

$$-\frac{dE}{dx} = \frac{e^4 z^2 N Z}{4\pi\epsilon_0^2 m_e v^2} \ln \left(\frac{2m_e v^2}{I} \right) \quad [2]$$

where E = energy of the α -particle (J), x = distance (m), e = electronic charge (C), z = valence of the α -particle ($2 \geq z \geq 0$), N = number of atoms in the absorbing medium (m⁻³), Z = atomic number of the absorbing medium, ϵ_0 = permittivity of free space (C · V⁻¹ · m⁻¹), m_e = rest mass of the electron (kg), v = velocity of the α -particle (m · s⁻¹), and I = effective ionization potential of the absorbing medium (J).

The valence, z , of an α -particle is a function of its (kinetic) energy, ranging from $z = 2$ at energies greater than

3 MeV (4.8×10^{-13} J) to $z = 0$ (corresponding to a neutral helium atom) when the particle essentially has been "stopped" by the absorbing medium. By substituting an expression for $z = f(E)$ (34) into the Bethe equation, the equation can be numerically integrated for each gaseous medium [the Bragg Additivity Rule (35) being used for compound gases] to yield a reasonably accurate value for the average "stopping power" $(-dE/dx)_{AV}$ for each gas

$$(-dE/dx)_{AV} = E_0/l \quad [3]$$

where E_0 is the initial energy of the α -particle and l is its range in the given medium, given by

$$l = \int_0^{E_0} \left(-\frac{dE}{dx} \right)^{-1} dE \quad [4]$$

Figure 7 shows a plot of the voltage of the ionized gas electrode *vs.* the average specific ionization for each gas, as calculated using Eq. [1]-[4]. It is evident that, with the exception of argon and helium, the correlation is somewhat better than that obtained by plotting the voltage *vs.* the molecular weight (*cf.* Fig. 6). The deviations for helium and argon are readily explained by the so-called "Jesse Effect" (36), which refers to the marked increase in the total amount of ionization of noble gases when very small amounts of certain other gases are added. Thus, when less than 1% of nitrogen is added to helium, the value of W drops from 46 eV/ion pair to about 30 eV/ion pair, resulting in a 50% increase in specific ionization. Similarly, in argon, the presence of small amounts of carbon dioxide, for example, greatly increases the specific ionization of the argon. These marked increases in the observed ionization of noble gases, which may be brought about by only a few hundred parts per million of various gases, can be explained in terms of the transfer of excitation energy from the main gas component to the minor gas component. Since only cylinder-grade gases were used and no special precautions were taken to exclude small amounts of contaminant gases, it is likely that the actual values for the specific ionization of argon and helium are much greater than indicated by the calculated values shown in Fig. 7, which would have the effect of

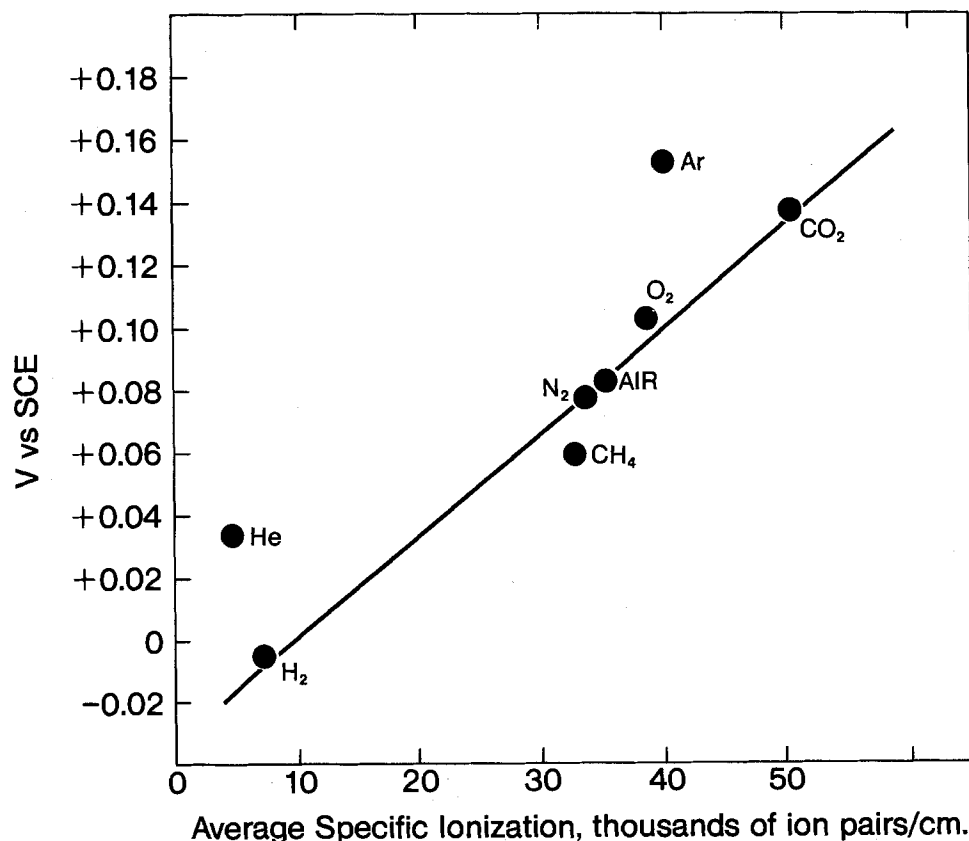


Fig. 7. Potential of IAE vs. average specific ionization. 0.1M KCl solution. Source-to-collector distance = 4 cm; collector-to-solution distance = 0.5 cm.

shifting the relevant data points to the right to fall in line with the behavior of the other gases.

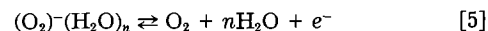
The results shown in Fig. 7 indicate that the mechanism by which a potential is generated at the IAE depends more on the number of ions present in the ionized gas than it does on the particular gas ionized. This might mean that the potential-determining ionized species is the same for all the gases employed. In pure air, for example, it is known that initially almost all the species are ionized with equal probability; but that within nanoseconds these ions transform into certain dominant species (37). In air, the dominant positive ions are $(\text{H}_3\text{O})^+(\text{H}_2\text{O})_n$ and $(\text{NH}_4)^+(\text{NH}_3) \cdot (\text{H}_2\text{O})_n$, whereas the dominant negative ions are $(\text{O}_2)^-(\text{H}_2\text{O})_n$ and $(\text{CO}_4)^-(\text{H}_2\text{O})_n$, with n ranging from 2 to 6. A common species present in all the gases employed was water, present to the extent of about 3% (assuming saturation at 25°C from the aqueous electrolyte). This implies that the ions $(\text{H}_3\text{O})^+(\text{H}_2\text{O})_n$ and/or $(\text{O}_2)^-(\text{H}_2\text{O})_n$ might be the potential-determining species.

Although air is preferred because of the simplicity of the electrode system, other gases may be useful under special circumstances.

Influence of the collector metal.—It also has long been known that the potential of an IAE is influenced by the metal chosen for the collector element (27). To investigate this aspect, collector screens made from several different metals were used with air as the ionizing gas in a configuration similar to that used for the previous section. As can be seen from Fig. 8, the potential generated by the IAE increases linearly with an increase in the electronic work function (Φ) of the metal used for the collector element (38). This dependence confirms that the voltage-determining mechanism involves electron exchange at the collector/gas interface. A metal with a high electronic work function has a strong affinity for electrons. This means that it has more electron energy states than does a metal with a low electronic-work function, so that electrons are readily accepted without conferring a negative charge to the surface of the metal. Conversely, a metal with a low electronic-work function accepts electrons with an accompanying tendency to acquire a nega-

tive surface charge. The above reasoning accounts for the variation of potential with Φ . The data plotted in Fig. 8 also confirm the constancy and reproducibility of the surface potential at the electrolyte/air interface, since, if any variation in this quantity from experiment to experiment were greater than a few millivolts, such variation would show up in Fig. 8 as additional scatter.

With regard to the potential-determining species at the collector/air interface, early work by Townsend (39) proved that negatively charged ions in air not only were more mobile than positively charged ions, but also had a greater affinity for water. It is thus suggested that the potential-determining reaction for the IAE might be



Use in pH measurements.—In order to test the IAE as a reference electrode for practical pH measurements, measurements were made under a variety of conditions using a commercial glass electrode pH meter with the SCE reference electrode replaced by the IAE. The IAE used for this practical application consisted of a 57 μCi source set at 4.0 cm above a 50-mesh Pt collector in air, the collector in turn being 0.5 cm from the solution surface. The IAE system was found to give a relatively rapid response and to be reasonably free from drift or instability, although it was somewhat less rapid and stable than the SCE reference system. In general, the values of pH measured in aqueous solutions at room temperature were indistinguishable from the values obtained using a SCE reference both in magnitude and precision as shown, for example, in Fig. 9, plot A. Plot B illustrates the magnitude of the errors introduced by the use of a small source-to-collector distance. The slope of the $h = 4.0$ cm line (plot A) is -0.059 ± 0.002 V/pH unit while that of the $h = 2.0$ cm line (plot B) is -0.0185 ± 0.003 V/pH unit, both by least squares linear regression. The theoretical slope of these lines at 25°C is -0.05915 V/pH unit. For plot A, the resistance ratio is $R_s/R_g = 100$. Therefore there is negligible error caused by the parallel conduction path error. For plot

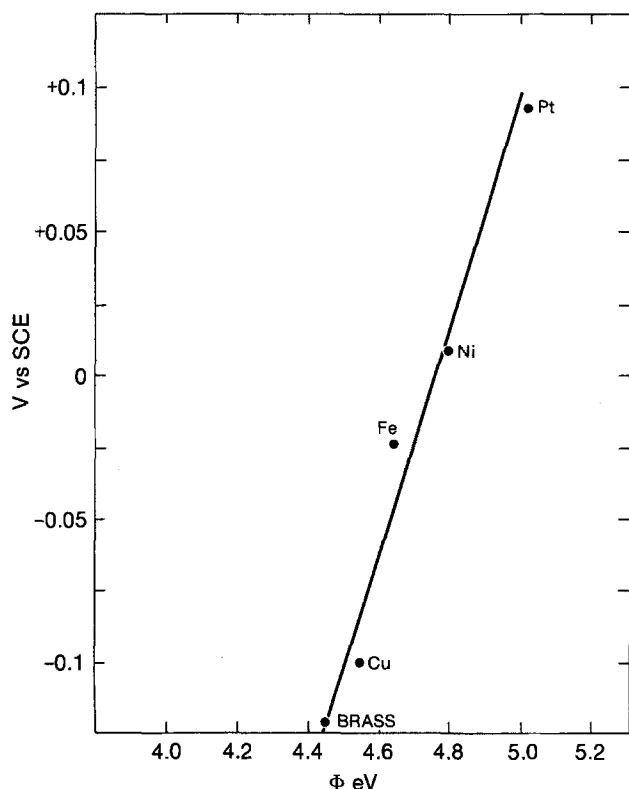


Fig. 8. Potential of IAE vs. work function of collector metal. 0.1M KCl solution. Source-to-collector distance = 4 cm; collector-to-solution distance = 0.5 cm.

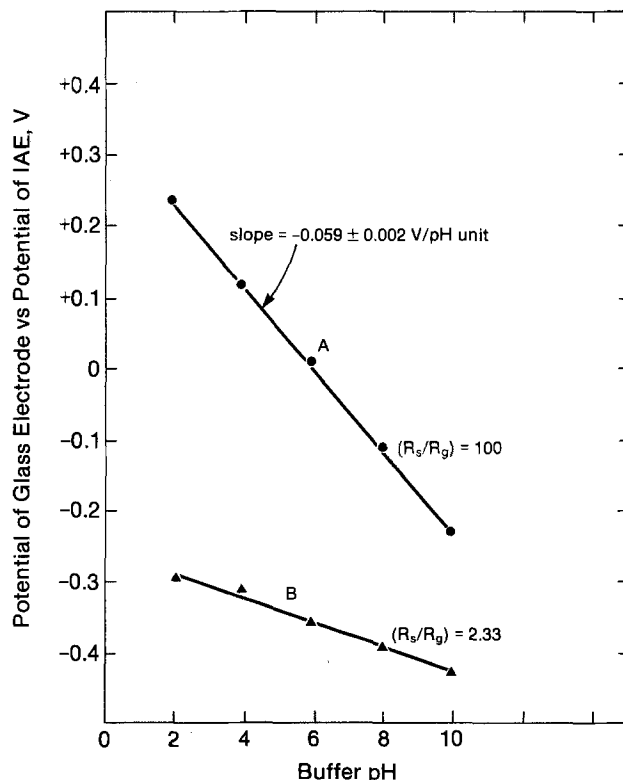


Fig. 9. pH response: use of IAE in combination with a glass electrode and a pH meter. 25°C. (●) Source-to-collector distance = 4.0 cm, (▲) Source-to-collector distance = 2.0 cm. Collector-to-solution distance = 0.5 cm.

B, $R_s/R_g = 2.33$. The large error caused by this low ratio was as expected. This error could be reduced by increasing the source-to-collector distance, but this also would cause an increase in the electrode response time. A suitable trade-off among these factors has to be established for a given application and incorporated into the electrode design. The 0.5 cm collector height combined with the 4.0 cm source-to-collector separation was found to be practical for the experimental work reported here.

Similar satisfactory results were obtained at various temperatures in the range 10°-50°C. Preliminary pH measurements in methanol-water systems using the IAE reference electrode also were without significant difference from SCE measurements. These, and other practical applications of the IAE will be reported in detail in the subsequent paper.

Areas for further study.—One problem area encountered with the IAE is the great care required in providing adequate electrical shielding to the system. To achieve reproducible measurement, it was found necessary not only to provide electrical shielding to both the IAE and all the leads, but also to place the complete assembly (cell, electrometer, temperature bath, etc.) in a Faraday cage and to stand back from the assembly while taking readings. Apparently, capacitance effects from the human body are strong enough to influence the electrometer readings.

A second problem is voltage drift from what appears to be moisture condensation on the collector element. This was encountered if the collector was closer than about 0.5 cm from the surface of the aqueous test solution or if the air temperature was permitted to drop several degrees over a short period of time. Methods of circumventing this problem might be the provision of a small heating element in the electrode casing, continuous flushing with relatively dry ionizing gas, or the provision of a hydrophobic microporous plastic cap over the tip of the IAE. This problem is unlikely to occur in nonaqueous or high temperature applications.

A third concern, more of theoretical than practical significance, is how to correlate the potential of the IAE with the Standard Hydrogen Scale. The data plotted in Fig. 3, for example, indicate that the potential of the IAE is +0.108V vs. that of the SCE, which gives a "standard" value of +0.35V on the Standard Hydrogen Scale. As discussed earlier, however, the potential of the IAE depends on a number of factors, such as the composition of the ionizing gas, the collector material, the placement of the electrode elements, the source strength, and the composition of the electrolyte. For any given set of values for the above parameters, the potential of the IAE appears to be constant and reproducible; hence, the electrode can be calibrated against a conventional reference electrode, making it a type of secondary reference electrode, albeit at the present time one for which the mechanism of operation is not completely understood. This in no way detracts from its usefulness in measuring things such as electrode polarization or as a monitor electrode in various difficult environments. Furthermore, as discussed earlier, the potentials of even conventional electrodes such as the Ag/AgCl electrode or the calomel electrode involve uncertainties owing to liquid junction potentials (especially in nonaqueous media), disproportionation and/or oxidation reactions, hysteresis, heat effects, aging, and contamination (1).

In conclusion, although it is unlikely in the near future that the IAE is going to displace more conventional electrochemical reference electrodes, it would appear possible that with more development it could play a valuable role as a secondary reference electrode for use in special situations for which conventional reference electrodes with liquid junctions are inappropriate. Applications that come to mind include high temperature corrosion monitoring, use with fused-salt or solid-electrolyte systems, contaminant-sensitive systems, situations involving long-term storage with only intermittent use, and embedded *in situ* systems that are not readily accessible for servicing.

Acknowledgments

The authors wish to acknowledge their gratitude to Dr. P. Sivenas and Professor F. Beales of the Department of Geology, University of Toronto, and to Professor S. N. Flengas of the Department of Metallurgy and Materials Science, University of Toronto, for early discussions that led to the development of the ionized air reference electrode. Financial assistance from the Natural Sciences and Engineering Research Council of Canada is gratefully acknowledged.

Manuscript submitted Feb. 7, 1983; revised manuscript received Jan. 30, 1984.

APPENDIX

Calculation of Extent of Air Ionization

Strength of ionizing source

$$= 57 \mu\text{Ci}$$

$$= (57 \times 10^{-6} \text{ Ci})(3.7 \times 10^{10} \text{ s}^{-1} \cdot \text{Ci}^{-1})$$

$$= 2.109 \times 10^6 \alpha\text{-particles/s}$$

$$\text{Volume of contained air} = (4.5)(\pi \times 0.75^2) = 7.952 \text{ cm}^3$$

Number of air molecules present at 25°C and 1 atm

$$= \frac{PVN_A}{RT} = \frac{(1.013 \times 10^5)(7.952 \times 10^{-6})(6.022 \times 10^{23})}{(8.314)(298.15)}$$

$$= 1.957 \times 10^{20}$$

E_0 = Total energy of each α -particle at point of emission = 5.48 MeV

Number of ion pairs formed per α -particle

$$= \frac{E_0}{W} = \frac{5.48 \times 10^6 \text{ eV}}{35 \text{ eV/pair}} = 1.565 \times 10^5$$

Total number of ion pairs formed per second

$$= (1.565 \times 10^5)(2.109 \times 10^6) = 3.302 \times 10^{11}$$

Total number of ions formed per second

$$= (2)(3.302 \times 10^{11}) = 6.604 \times 10^{11}$$

Rutherford (40) showed that for the irradiation of air with α -particles, the rate of recombination of the ionized particles is given by

$$\frac{dn}{dt} = -\alpha n^2 = -1.60 \times 10^{-6} n^2 \quad [\text{A-1}]$$

where n is the number of ions/cm³ and t is seconds.

If N_0 is the constant rate of ion production, then

$$N_0 = \frac{6.604 \times 10^{11}}{7.952} = 8.305 \times 10^{10} \text{ ions} \cdot \text{s}^{-1} \cdot \text{cm}^{-3}$$

and

$$\frac{dn}{dt} = N_0 - \alpha n^2$$

i.e.

$$n = (N_0 - \alpha n^2)t$$

$$\alpha n^2 + n - N_0 t = 0 \quad [\text{A-2}]$$

Solving Eq. [A-2] gives

$$n = (-1 + \sqrt{1 + 4\alpha N_0 t^2})/2\alpha t$$

For large t

$$n = \sqrt{\frac{N_0}{\alpha}} \quad [\text{A-3}]$$

Therefore, from Eq. [A-3], the steady-state concentration of ions is $\sqrt{8.305 \times 10^{10}/1.60 \times 10^{-6}} = 2.278 \times 10^8 \text{ ions/cm}^3$, and the total number of ions present is $(2.278 \times 10^8 \text{ ions/cm}^3)(7.952 \text{ cm}^3) = 1.812 \times 10^9$.

Percentage of air molecules ionized

$$= \frac{1.812 \times 10^9}{1.957 \times 10^{20}} \times 100\% = 9.26 \times 10^{-10}\%$$

REFERENCES

- R. G. Bates, "Determination of pH: Theory and Practice," John Wiley and Sons, Inc., New York (1964).
- M. Garamszeghy, BA Sci. Thesis, University of Toronto, Toronto, Ont., Canada (1980).
- M. Garamszeghy, MA Sci. Thesis, University of Toronto, Toronto, Ont., Canada (1981).
- F. R. Foulkes, U.S. Pat. application, filed May 21, 1981.
- J. Guyot, *Ann. Phys.*, **2**, 506 (1924).
- J. H. Schulman and E. K. Rideal, *Proc. R. Soc. London, Ser. A*, **130**, 259 (1931).
- W. D. Harkins and E. K. Fischer, *J. Chem. Phys.*, **1**, 852 (1933).
- B. Kamienski, J. Mikulski, J. Pawelek, and I. Stronski, *Bull. Acad. Pol. Sci., Ser. Sci. Chim.*, **8**, 685 (1960).
- B. Kamienski, and J. Czarnecki, *ibid.*, **12**, 407 (1964).
- D. Volthardt and R. Wustneck, *Kolloidn. Zh.* **36**, 1116 (1974).
- M. Costa, A. Faviani, and S. Bordi, *J. Electroanal. Chem.*, **47**, 147 (1973); M. Costa, L. Priami, and S. Bordi, *ibid.*, **70**, 229 (1975).
- A. N. Frumkin, Z. A. Iofa, and M. A. Gerovich, *Zh. Fiz. Khim.*, **30**, 1455 (1956).
- J. E. B. Randles and D. J. Schiffrin, *J. Electroanal. Chem.*, **10**, 480 (1965).
- S. Trasatti, *J. Electroanal. Chem. Interfacial Electrochem.*, **52**, 313 (1974).
- S. Trasatti, *J. Chem. Soc. Faraday Trans. 1*, **70**, 1752 (1974).
- A. N. Frumkin, B. Damaskin, I. Bagotskaya, and N. Grigoryev, *Electrochim. Acta*, **19**, 75 (1974).
- W. A. Weyl, *J. Colloid. Sci.*, **6**, 389 (1951).
- R. J. Good, *J. Phys. Chem.*, **61**, 810 (1957).
- B. Kamienski, *Electrochim. Acta*, **1**, 272 (1959).
- B. Kamienski, *ibid.*, **3**, 208 (1960).
- N. H. Fletcher, *Philos. Mag.*, **7**, 255 (1962).
- V. A. Rabinovich and T. E. Alekseeva, *Elektrokhimiya*, **10**, 521 (1974).
- J. E. B. Randles, *Discuss. Faraday Soc.*, **24**, 194 (1957).
- N. L. Jarvis and M. A. Scheiman, *J. Phys. Chem.*, **72**, 74 (1968).
- B. Kamienski and J. Inglot, *Bull. Int. Acad. Pol. Sci., Classe III, Ser. A*, 255 (1936).
- W. E. Stephens and T. Hurlimann, in "The Handbook of Physics," 2nd ed., E. U. Condon and H. Odishaw, Editors, Chap. 4, McGraw-Hill, New York (1967).
- Lord Kelvin, *Edin. Roy. Soc. Proc.*, **21**, 417 (1897).
- M. Mladjenovic, "Radioisotope and Radiation Physics," Chap. 4, 5, Academic Press, New York (1973).
- H. Bischel, "American Institute of Physics Handbook," 3rd ed., pp. 8-142, McGraw-Hill, New York (1972).
- National Academy of Sciences-National Research Council, "Penetration of Charged Particles in Matter," Nuclear Science Series no. 29, NRC Pub. 752, Washington, DC (1960).
- L. C. Northcliffe, *Ann. Rev. Nucl. Sci.*, **13**, Chap. 2 (1963).
- National Academy of Sciences-National Council, "Studies in the Penetration of Charged Particles in Matter," Nuclear Science Series, no. 39, NRC Pub. 1133, Washington, DC (1964).
- W. E. Meyerhof, "Elements of Nuclear Physics," Chap. 3, McGraw-Hill, New York (1967).
- G. H. Miley, "Direct Conversion of Nuclear Radiation Energy," 90, American Nuclear Society (1970).
- G. J. Hine and G. L. Brownell, Editors, "Radiation Dosimetry," Chap. 2, 14, Academic Press, New York (1956).
- G. S. Hurst and T. K. Strikler, in "Radiation Dosimetry," C. J. Hine and G. L. Brownell, Editors, pp. 134-143, Academic Press, New York (1956).
- R. C. Weast, Editor, "Handbook of Chemistry and Physics," 59th ed., pp. F-206, F-212, CRC Press, Boca Raton, FL (1978).
- H. Dolezalek, "Handbook of Chemistry and Physics," 61st ed., F-214, CRC Press, Boca Raton, FL (1980).
- Townsend, *Phil. Trans. R. Soc.*, **A193**, 129 (1899); reported in E. Rutherford, "Radioactive Substances and Their Radiations," pp. 53-54, Cambridge University Press, Cambridge, England (1913).
- E. Rutherford, "Radioactive Substances and Their Radiations," pp. 38-41, Cambridge University Press, Cambridge, England (1913).

An Ionized Air Reference Electrode

II. Applications

D. W. Kirk* and F. R. Foulkes*

Department of Chemical Engineering and Applied Chemistry, University of Toronto, Toronto, Ontario, Canada M5S 1A4

ABSTRACT

A novel ionized air electrode (IAE) that utilizes a low level source of ionizing radiation (Am-241) to ionize an air gap in order to establish electrical contact with an electrolyte was tested for use as a reference electrode in a number of electrochemical measuring systems. Experimental results indicated that it may be possible to use the IAE to advantage to replace conventional reference electrodes, such as the saturated calomel electrode, for use in pH meters. This use was shown to be especially promising in the case of pH measurements made in nonaqueous solvents such as methanol. The IAE also was tested in a binary molten carbonate electrolyte at 525°C and was found to give results comparable with those obtained using a platinum-wire reference electrode.

An ionized air reference electrode (IAE) has been described in a previous report (1). This reference electrode has a number of features that would be useful particularly for applications in which temperature, contamination, corrosion, or ill-defined liquid junction potentials create difficulties for conventional reference electrodes. An essential feature of the ionized air reference electrode is that contact with the electrolyte is achieved through an ionized air gap. Thus, contamination and liquid junctions are eliminated, while corrosion problems are much reduced. The details of the operation and design of this electrode have been discussed in Part I of this work (1).

All reference electrodes have the function of providing a stable reference voltage against which voltage changes at another electrode may be measured. Difficulties in the use of reference electrodes arise in a number of ways. Dif-

ferences in the electrolytes surrounding the reference electrode and working electrode cause liquid junction potentials to be set up, as well as causing cross-contamination problems. This is particularly serious for nonaqueous electrolytes where liquid junction potentials of several hundred millivolts can be generated. In high temperature work, reference electrodes with aqueous electrolytes are unsuitable, so that bare silver or platinum wires frequently are used (2). Corrosion and the build up of corrosion products on the electrode surface often severely limit the useful life of these electrodes. In the case of a solid electrolyte, no satisfactory reference electrode has been found.

The ionized air reference electrode makes contact with the electrolyte only through an air gap. With the use of suitable materials for the collector and housing, potential measurements can be made at almost any temperature and with any electrolyte. Although liquid junction poten-

* Electrochemical Society Active Member.

Key words: electrode, fused salts, organic, pH.

tials are eliminated with this arrangement, surface potentials are generated. In most cases, the magnitude of the surface potential will be comparable with that of the liquid junction potential. For most inorganic electrolytes in aqueous solutions, the surface potential is within the range ± 15 mV from that of pure water (3) and is not very dependent on electrolyte concentration at concentrations of less than one molar (3-6). In organic electrolytes, liquid junction potentials are often as large as 100 mV (7), and in most cases are difficult to calculate because of the lack of activity and conductivity data for these electrolytes. In contrast, the corresponding surface potentials may be small, and may not pose a problem in operating with an ionized air electrode. In this study, the use of the ionized air electrode will be compared with that of the saturated calomel electrode in aqueous and nonaqueous electrolytes and with a platinum wire in a molten salt electrolyte.

Experimental

A detailed description of the electrode design and the arrangement of the measuring system for use with aqueous systems has been given previously (1). For the high temperature work, the electrode housing was constructed of high temperature vycor glass (structurally stable to $\sim 1000^\circ\text{C}$). An americium-241 foil of strength $100 \mu\text{Ci} \cdot \text{cm}^{-2}$ was used as the ionization source. The collector element was a 50-mesh platinum screen placed 4 cm from the americium source. Platinum wire was used to make electrical connections to the collector and to ground the source. Nickel foil was wrapped around the electrode to serve as an electrostatic shield. Asbestos tape was used for insulating the wire leads within the furnace. A Keithley electrometer (Model 610 C) was used for all the measurements. A schematic of the arrangement is shown in Fig. 1.

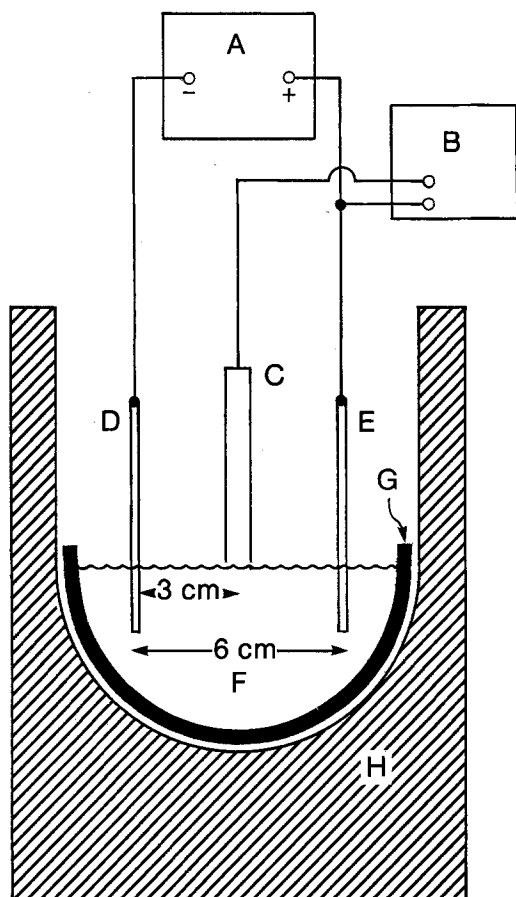


Fig. 1. Schematic arrangement of molten carbonate measuring system. A: dc power supply; B: electrometer; C: ionized air electrode; D: Pt wire cathode; E: Pt wire anode; F: binary carbonate melt; G: ceramic dish; H: electric furnace.

Results and Discussion

Aqueous measurements.—The ionized air reference electrode (IAE) was first tested as a reference electrode for pH measurements. Buffered solutions were prepared with pH values from 2 to 10. At room temperature, the theoretical voltage response of the glass electrode with a standard reference electrode such as the saturated calomel electrode (SCE) is -0.059V per pH unit, with the absolute voltage being standardized at a particular pH. The voltage response of the IAE depends on the ratio of the resistance between the source and the collector (R_s) to that between the collector and the solution (R_g). With a source-to-collector distance of 4 cm and a source-to-solution distance of 4.5 cm, $R_s/R_g = 100$. With $R_s/R_g = 100$, the slope of the line is $-0.059 \pm 0.002\text{V}$ per pH unit, as reported earlier (1).

The effect of temperature on the potential response of a reference electrode is an important operating characteristic of the electrode. Large potential variation is undesirable, since this creates more stringent requirements for accurate temperature control and the measured voltage must be corrected for the potential change. If the reference electrode has an isopotential point with the glass electrode (*i.e.*, a potential at which the glass/reference electrode couple does not change with temperature), then automatic temperature compensators can be used. Most pH meters using a glass/SCE electrode couple have this feature.

The changes in potential measured at three temperatures for the glass/IAE couple and the glass/SCE couple are shown in Fig. 2 as a function of pH. The rate of change of potential with pH is greater with increase in temperature for both electrode couples. Both the glass/SCE and the glass/IAE electrode couples have well-defined isopotential points.

In Table I, the theoretical and measured potential/pH responses for the glass/SCE and glass/IAE electrode couples are given for 10° , 25° , and 50°C . The deviation of either electrode pair is less than 1% from the theoretical value.

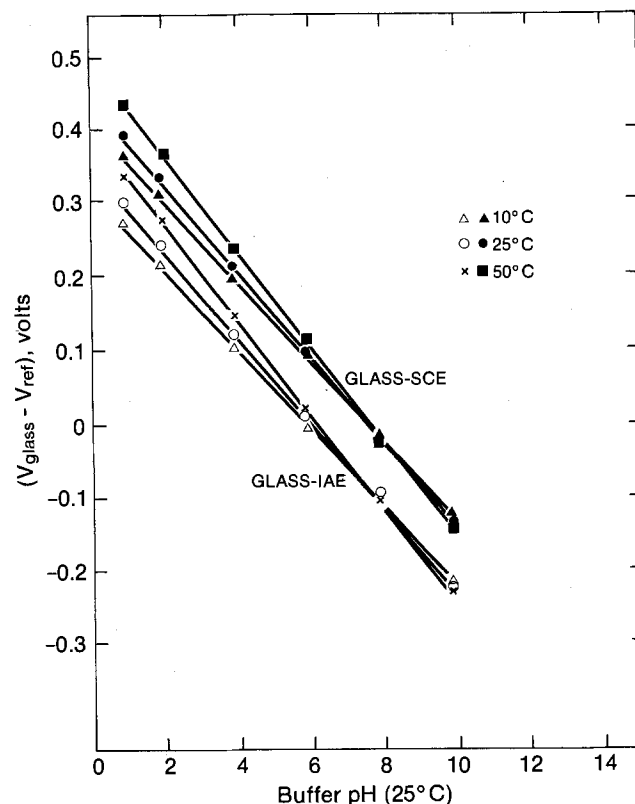


Fig. 2. Variation of pH response with temperature. $V(\text{glass}) - V(\text{IAE})$: $\Delta = 10^\circ\text{C}$; $\circ = 25^\circ\text{C}$; $\times = 50^\circ\text{C}$. $V(\text{glass}) - V(\text{SCE})$: $\blacktriangle = 10^\circ\text{C}$; $\bullet = 25^\circ\text{C}$; $\blacksquare = 50^\circ\text{C}$.

Table I. pH response vs. temperature for glass/reference electrode couples

Temperature (°C)	Slope, V/pH unit		
	Theoretical (8)	Glass vs. SCE	Glass vs. IAE
10	-0.05618	-0.0563 ± 0.0015*	-0.0560 ± 0.0014
25	-0.05916	-0.0592 ± 0.0018	-0.0591 ± 0.0015
50	-0.06412	-0.0643 ± 0.0012	-0.0642 ± 0.0017

* 95% confidence interval.

A plot of the electrode voltage vs. that of the SHE as a function of temperature is shown in Fig. 3. Data for the SCE were taken from Dobos (9), whereas the points for the IAE represent averages over the pH range 2-10, taken from the experimental data. The temperature coefficient for the SCE is $-0.51 \text{ mV} \cdot ^\circ\text{C}^{-1}$, while the experimentally determined temperature coefficient for the IAE was $-0.75 \pm 0.15 \text{ mV} \cdot ^\circ\text{C}^{-1}$. The temperature coefficient for the IAE is sufficiently close to that of the SCE that the IAE could be substituted for the SCE in pH measurements without recalibration over the temperature range $0^\circ\text{-}50^\circ\text{C}$.

Some pH measurements could be more accurate with the IAE. Polybasic acid electrolytes generate liquid junction potentials with the SCE of 30-40 mV (3), which is equivalent to over 0.5 pH units at 25°C . In many cases, the surface potential error for the IAE for these solutions is smaller and more constant (3-6).

Organic electrolytes.—The effect of organic electrolytes on the magnitude of the liquid junction potential can be difficult to estimate because of the lack of activity and conductivity data. One electrolyte solution for which data are available for the calculation of liquid junction potentials with the SCE is aqueous methanol (7). Therefore, methanol, water, and sodium citrate/citric acid combinations were used to study the behavior of the IAE relative to that of the SCE. For these solutions the liquid junction potential is $\approx 5 \text{ mV}$ (7)

A plot of measured potentials for the glass/SCE and the glass/IAE electrode couples as a function of the percent of methanol is given in Fig. 4. Both electrode pairs show

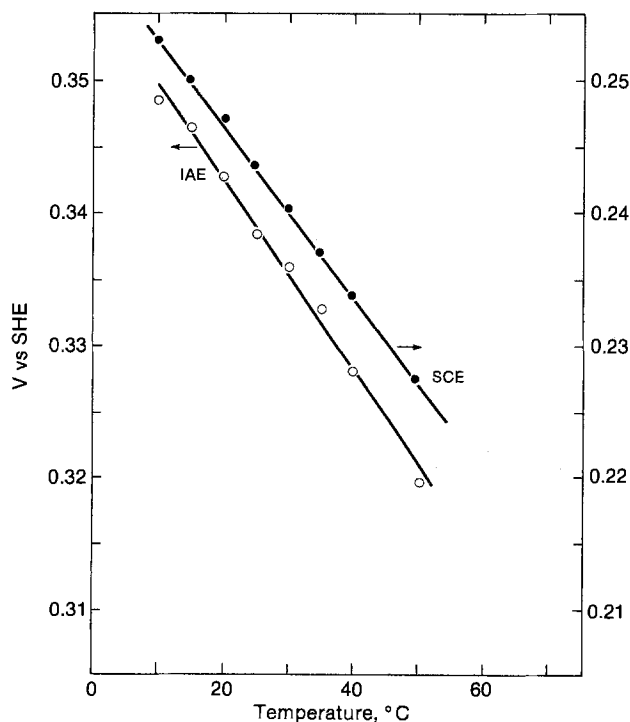


Fig. 3. Temperature variation of electrode potential vs. SHE. \circ = IAE; \bullet = SCE.

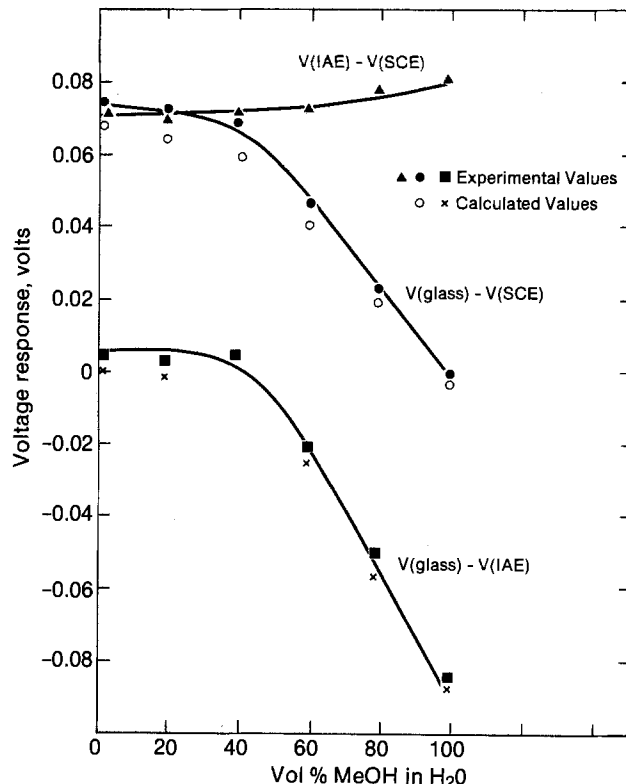


Fig. 4. Voltage response of the glass/IAE and glass/SCE electrode couples in aqueous methanol solutions. 25°C . $V(\text{glass}) - V(\text{IAE})$: \blacksquare = experimental, \times = calculated. $V(\text{glass}) - V(\text{SCE})$: \bullet = experimental, \circ = calculated. $V(\text{IAE}) - V(\text{SCE})$: \blacktriangle = experimental.

very similar behavior. With increase in methanol concentration, the measured potential decreases. In aqueous electrolytes, this potential decrease would correspond to an increase in alkalinity. With organic electrolytes, the pH scale ceases to be well defined. The prerequisite that pK for water = $-\log [\text{H}^+][\text{OH}^-] = 14$ at 25°C is no longer appropriate. Thus, for methanol $\text{pK} = 16.7$. A method of calculating the pK value for a methanol-water mixture has been given by Ohtaki and Tanaka (7). These values have been converted to the voltage scale and plotted in Fig. 4. The calculated values have the same voltage trends as the measured values. The differences between the experimental and calculated values can be attributed to liquid junction potentials in the case of the SCE and to surface potentials in the case of the IAE. In both cases the measured values are $\approx 5 \text{ mV}$ more positive than the calculated values. The differences between the two electrode couples also are plotted in Fig. 4, and reflect the effect of the solvent on the two half-cell potentials of the SCE and IAE without the effect of the glass electrode. Both electrodes either are not affected greatly by the change in methanol concentration or change in a similar manner.

The behavior of the glass/SCE and the glass/IAE electrode couples also was studied with the addition of citric acid or sodium hydroxide to various methanol-water mixtures. The results are shown in Fig. 5. At a concentration of 0.1 M citric acid, the measured potentials of both electrode couples decrease with increase in methanol concentration. The effect is similar to that of the methanol-water behavior in Fig. 4. The total potential change from pure water to pure methanol is about -0.088 V , while with 0.1 M citric acid the total change is about -0.080 V . In the case of the addition of a strong base (0.1 M NaOH), also shown in Fig. 5, the potential of both glass/reference electrode couples remains constant. The activity of the hydroxide ion apparently remains constant and dominates the response of the glass/reference electrode couple. The difference between the glass/SCE and the glass/IAE remains constant over the entire methanol concentration range for both weak acid and strong base additions. Thus, the IAE functions as a well-behaved reference electrode in these

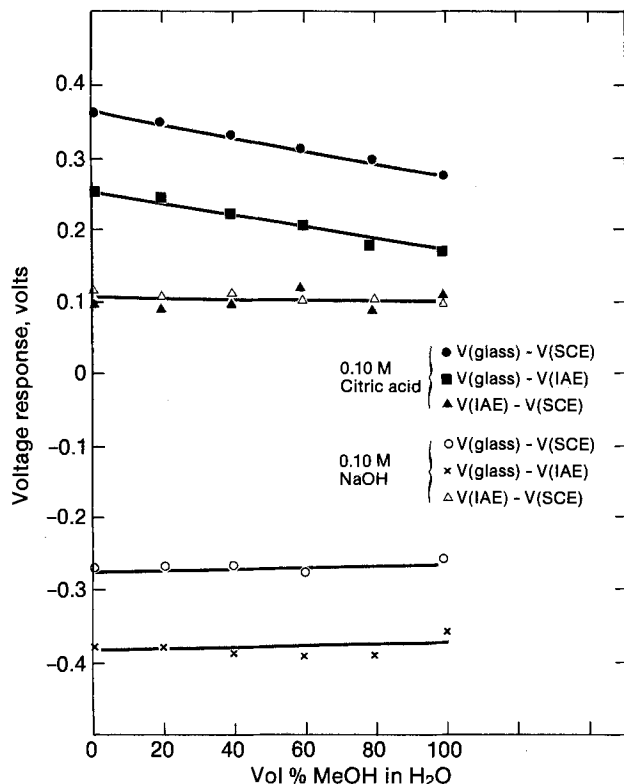


Fig. 5. Electrode response to aqueous methanol solutions containing 0.10M citric acid or 0.10M sodium hydroxide. 25°C. 0.10M citric acid: ● = $V(\text{glass}) - V(\text{SCE})$, ■ = $V(\text{glass}) - V(\text{IAE})$, ▲ = $V(\text{IAE}) - V(\text{SCE})$; 0.10M NaOH: ○ = $V(\text{glass}) - V(\text{SCE})$, × = $V(\text{glass}) - V(\text{IAE})$, △ = $V(\text{IAE}) - V(\text{SCE})$.

solutions, and the surface potential effects do not pose a serious problem to the operation of the electrode.

Molten salt electrolyte.—High temperature measurements were conducted at 525°C using a binary molten carbonate electrolyte consisting of 62 mol percent (m/o) Li_2CO_3 and 38 m/o K_2CO_3 , having a melting point of 500°C. A constant current was passed through the melt via two platinum working electrodes spaced 6 cm apart. The potentials of each working electrode were recorded relative to the reference electrode (IAE or Pt wire) situated 3 cm from either electrode.

Initial measurements with the IAE partially inside the furnace gave poor reproducibility. The cause of the problem was traced to two effects. First, the cooler surfaces of the IAE not in the furnace were subject to condensation of the melt vapors. Second, the temperature gradient affected the ionization of the air gap in the IAE and was difficult to control. By inserting the IAE completely into the furnace and increasing the collector-to-solution distance to 1 cm, reproducible readings were obtained.

In order to obtain an estimate of the ionization rise time and the stability of the potential generated at the IAE, the electrolysis cell was run at a steady cell voltage and cell current of 2.15V and 15 mA, respectively. At $t = 0$, the IAE was brought adjacent to the melt surface, and its potential vs. the anode and cathode monitored as a function of time. The results, shown in Fig. 6, indicate that the behavior of the IAE stabilizes after about 1 min. Similar measurements made using a Pt wire reference electrode stabilized within a few seconds.

The change of potential of both the IAE and the platinum wire reference electrode is shown in Fig. 7 as a function of cell current. Both reference electrodes show essentially the same potential change with current in the measurement of the cell anodic and cathodic polarization, although it is evident that there is somewhat more scatter with the IAE than with the platinum wire reference electrode. The cause of this scatter has not yet been determined, but may be related to CO_2 gas from the cell reaction mixing with the ionized air in the IAE housing and

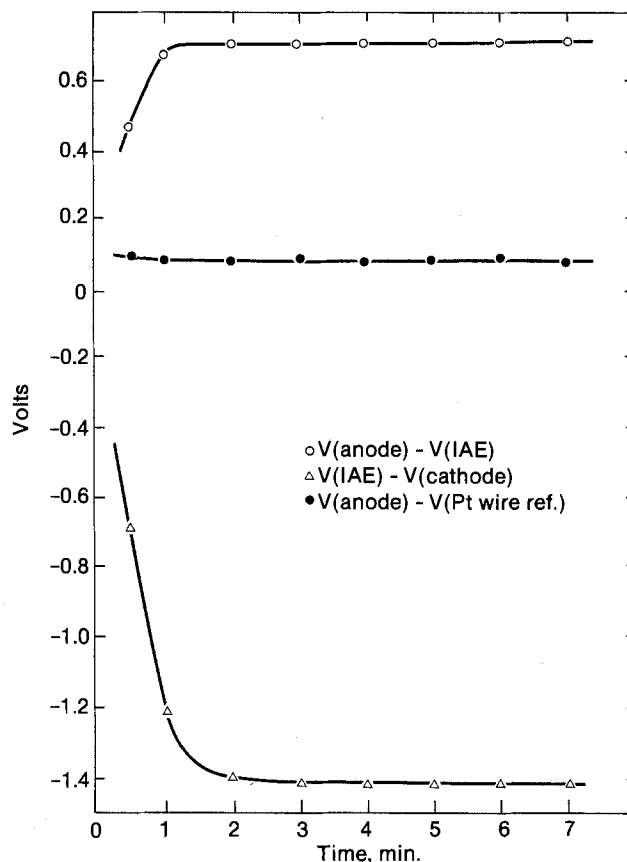


Fig. 6. Electrode potential vs. time. Molten carbonate electrolyte, 525°C. Cell voltage = 2.15V, cell current = 15 mA. ○ = $V(\text{anode}) - V(\text{IAE})$; △ = $V(\text{IAE}) - V(\text{cathode})$; ● = $V(\text{anode}) - V(\text{Pt wire reference electrode})$.

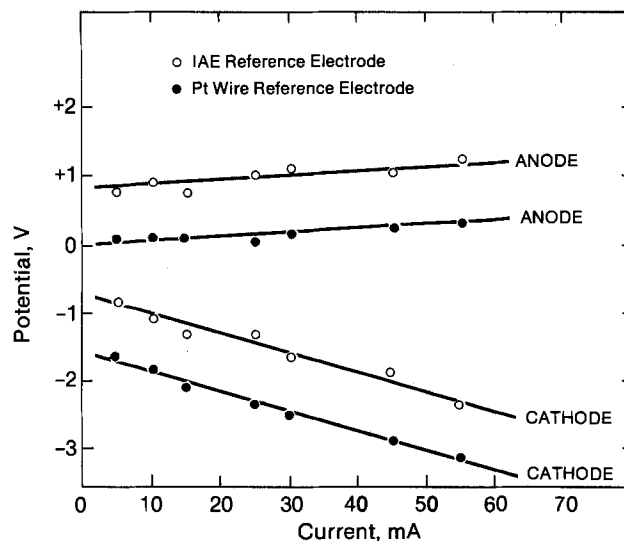


Fig. 7. Electrolysis cell steady-state polarization curve. Molten carbonate electrolyte, 525°C. ○ = $V(\text{anode}) - V(\text{IAE})$ or $V(\text{IAE}) - V(\text{cathode})$; ● = $V(\text{anode}) - V(\text{Pt wire reference})$ or $V(\text{Pt wire reference}) - V(\text{cathode})$.

affecting the ionization process. Regression analysis of the data shows that there is no statistical significance at the 95% confidence level between the anode and cathode slopes obtained using either the IAE or the Pt wire reference electrode. It is clear that the IAE can operate as a reference electrode in molten salt electrolytes. The response time is relatively rapid (1 min) and direct contact of the electrode with the melt is avoided. Further work is being carried out to demonstrate the application of the IAE with solid electrolytes.

Acknowledgments

Financial assistance from the Natural Sciences and Engineering Research Council of Canada is gratefully acknowledged.

Manuscript submitted Feb. 7, 1983; revised manuscript received Jan. 20, 1984.

REFERENCES

1. F. R. Foulkes, W. F. Graydon, and M. Garamszeghy, *This Journal*, **131**, 1325 (1984).
2. G. J. Janz, "Molten Salts Handbook," Academic Press, New York (1967).

3. V. A. Rabinovich and T. E. Alekseeva, *Elektrokhimiya*, **10**, 521 (1974).
4. B. Kamienski, *Electrochim. Acta*, **1**, 272 (1959).
5. B. Kamienski, *ibid.*, **3**, 208 (1960).
6. N. L. Jarvis and M. A. Scheiman, *J. Phys. Chem.*, **72**, 74 (1968).
7. H. Ohtaki and N. Tanaka, *ibid.*, **75**, 90 (1971).
8. R. G. Bates, "Determination of pH: Theory and Practice," pp. 327-330, John Wiley and Sons, Inc., New York (1964).
9. D. Dobos, "Electrochemical Data," p. 264, Elsevier Scientific Publishing Co., New York (1975).

Some Results on the Electrochemical and Thermal Oxidation and the Electrochemical Oxygen Evolution at Ti_xCu_{1-x} Alloys

G. G. Scherer, P. Brüesch, H. Devantay, K. Müller, and S. Stucki

Brown Boveri Research Center, CH-5405 Baden, Switzerland

ABSTRACT

The anodic behavior of polycrystalline, some deliberately oxidized, and amorphous Ti_xCu_{1-x} alloys has been investigated in 1N H_2SO_4 (0-2.5V SCE). In addition, some of the polycrystalline electrodes were characterized by means of ESCA before and after electrochemical treatment. Two types of alloys exist: Ti-rich alloys ($Ti \geq 0.84$) which passivate and behave like pure Ti, and Cu-rich alloys ($Cu \geq 0.33$) which corrode and show oxygen evolution. Nonpassivation behavior of the electrodes is related to a stationary copper concentration (≥ 0.01) at the surface.

The interest in the electrochemistry of titanium has grown during the last years due to the electrochemical properties of titanium and the potential applications of the metal (1). The discovery of photoelectrochemical water splitting at the TiO_2 /electrolyte interface (2) has prompted a great number of investigations about doped and undoped titanium oxide electrodes prepared mainly by thermal or anodic oxidation of a titanium substrate (3). The electrochemistry of titanium alloys, to the contrary, is hardly established except for some Ti alloys with Pd and Pt (1). Corrosion of Ti_xCu_{1-x} (x up to 0.33), for example, has only been investigated in detail in 1N H_2SO_4 between -600 and -10 mV (SCE) (4).

It was our idea to use the stability of TiO_2 layers in preparing an electronically conducting, noncorroding surface layer which could sustain the current densities of technical electrolysis processes (e.g., 250 mA/cm²). Such layers should be prepared by anodic or thermal treatment of a titanium alloy, for which we chose Ti_xCu_{1-x} with different compositions. Results, to be presented below, show that for our experimental conditions, two types of alloys exist: type I, with low Cu content, passivating like pure titanium; and type II, with higher Cu content, not forming an electrically blocking film, but corroding. Interestingly, strong oxygen evolution is observed at the type II alloys, a feature not found for the pure constituents. But our more detailed investigations showed that surface layers with the desired properties could not be prepared from TiCu alloys by the applied methods.

Experimental

Alloy preparation and characterization.—Polycrystalline Ti_xCu_{1-x} alloys were prepared by arc melting the respective mixtures of metal powders (reagent grade) in argon atmosphere. For homogeneity, the alloy buttons were remelted two times. After cutting, the samples were polished to a mirror finish.

The microstructure of each alloy was investigated using optical microscopy after a chemical etching process and scanning electron microscopy after electrochemical treatment. X-ray powder diffraction patterns were recorded in a Guinier camera with Cu $K\alpha$ radiation. The phases deter-

Key words: alloy, electrode, ESCA, oxidation.

mined, which are shown in Table I, are in agreement with the recently published phase diagram (5). The hexagonal solid solution of Ti_2Cu in α -Ti is present in the samples containing 92 and 84 atomic percent (a/o) Ti. Alloys $Ti_{0.67}Cu_{0.33}$ and $Ti_{0.50}Cu_{0.50}$ are essentially single phases of Ti_2Cu and TiCu, respectively. Both of these intermetallic compounds have been formed congruently. The microstructure of $Ti_{0.50}Cu_{0.50}$ is shown in Fig. 1. Alloy $Ti_{0.25}Cu_{0.75}$ consists mainly of the $TiCu_3$ phase.

Samples of $Ti_{0.92}Cu_{0.08}$ and $Ti_{0.50}Cu_{0.50}$ were also oxidized for 1h at 350°C in air, and samples of $Ti_{0.67}Cu_{0.33}$ were oxidized at the same temperature for 1h and 16h, to see the influence of thermal pretreatment on electrochemical behavior.

Amorphous Ti_xCu_{1-x} alloys with $x = 0.46, 0.57,$ and 0.67 were prepared by melt spinning.¹ These samples were 0.05 mm thick, 1 cm wide, and self-supporting.

Electrochemical measurements.—Electrochemical measurements were performed with a Princeton Applied Research Electrochemical System in standard electrochemical cells. Nonde-aerated 1N H_2SO_4 was used as electrolyte at room temperature (20°C). All potentials refer to the saturated calomel electrode (SCE).

Potentiodynamic scans were run between 0 and 2.5V (SCE) with scan rates of 2 mV/s. Galvanostatic measurements were conducted at 250 mA/cm².

The surface of some anodically oxidized samples was characterized by XPS. After electrochemical treatment under specific conditions, the samples were cleaned with distilled water, dried with purified nitrogen, and immediately introduced into the vacuum system.

XPS measurements.—XPS measurements were carried out in a Kratos ES 300 Electron Spectrometer with an overall resolution of ~1.3 eV. Binding energies have been measured using a gold standard. Polycrystalline Ti_xCu_{1-x} samples ($x = 0.25, 0.67,$ and 0.92) have been investigated. Samples polished outside the XPS machine could not be used for reference spectra owing to the formation of oxide films of various thicknesses. Therefore, samples were ground *in situ* in ultrahigh vacuum ($p < 10^{-8}$ torr) within

¹We thank Professor Günterodt, University of Basel, for kindly supplying these alloys.

Table I. Composition and x-ray analysis

Composition a/o	Structure
Ti _{0.92} Cu _{0.08}	Ti(α) and other weak lines
Ti _{0.84} Cu _{0.16}	Ti(α) + Ti ₂ Cu
Ti _{0.67} Cu _{0.33}	Ti ₂ Cu
Ti _{0.50} Cu _{0.50}	TiCu and other weak lines
Ti _{0.25} Cu _{0.75}	TiCu ₃ and other weak lines

the preparation chamber by allowing the tip of the rotating diamond end mill to abrade the sample in such a way as to clean the area that would be illuminated by the x-ray during analysis (6). The spectra of the samples ground *in situ* can be considered as reference spectra which, for large take-off angles of the electrons, reflect the composition of the bulk material.

In separate experiments, samples ground *in situ* were thermally oxidized in the preparation chamber at different temperatures and an oxygen pressure of 5×10^{-5} torr. After thermal oxidation, qualitative depth profiles have been obtained by sputtering with Ar ions (4 keV, 16 μ A/cm²). Samples with a surface area of 3×16 mm² were used in order to guarantee an approximately uniform sputter efficiency over the sample surface. These areas had been determined by sputter experiments of opaque films on glass substrates; they are also approximately uniformly illuminated by the x-ray beam. Sputter rates of TiO₂ and Ti_{0.67}Cu_{0.33} have been calibrated with films of known thickness deposited on glass by reactive sputtering in a Balzers Sputron RF/DC machine. Thicknesses have been measured by an Alpha-Step Tencon instrument. The sputter yield was about 30 Å/min for Ti_{0.67}Cu_{0.33} and 27 Å/min for TiO₂. From these calibration measurements, the thickness of the oxide layer on the bulk sample of Ti_{0.67}Cu_{0.33} prepared by *in situ* thermal oxidation has been estimated.

Some information about the depth profile of Cu, Ti, and O within the information depth of XPS (~20Å) has also been obtained by measuring the angular dependence of the intensities (7-9).

Results

Electrochemical measurements.—Polycrystalline alloys.—During the first anodic scan the corrosion current at potentials lower than 1.6V is always approximately one order of magnitude higher than for the second and the following scans, probably because of preferential copper dissolution from the surface (see XPS results) and oxidation of Ti. Cycling (2 mV/s) the electrodes between 0 and 2.5V for 2h leads to the voltage-log current plots displayed in Fig. 2.

In analogy to Ti, the current in the oxygen evolution region of the alloys Ti_{0.92}Cu_{0.08} and Ti_{0.84}Cu_{0.16} is slightly lower in each consecutive scan even after 2h. The oppo-

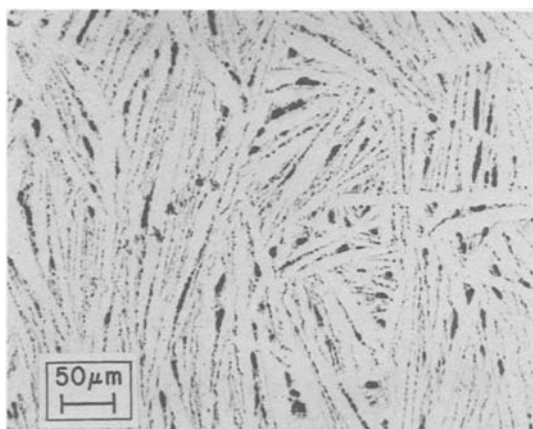


Fig. 1. Microstructure of an arc-melted Ti_{0.50}Cu_{0.50} sample. The structure contains only congruently formed TiCu with traces of other phases at the grain boundaries.

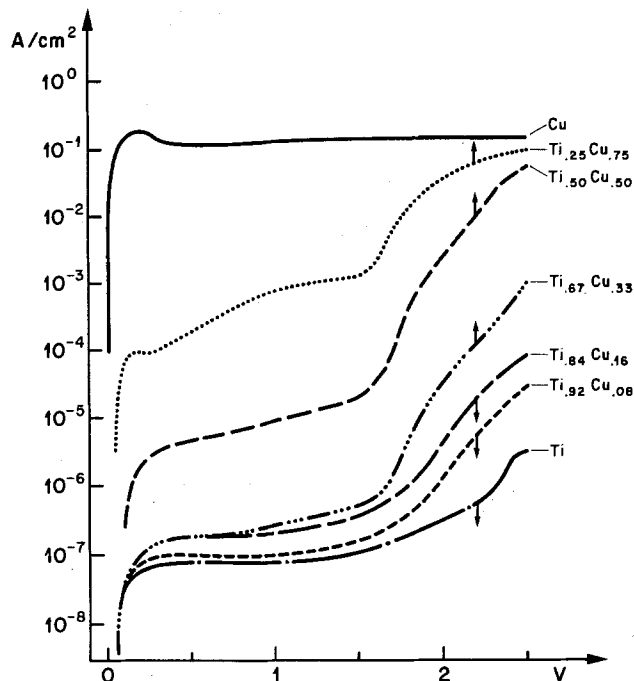


Fig. 2. Potentiodynamic (2 mV/s) voltage-log current plots for Ti_xCu_{1-x} electrodes recorded after 2h cycling in 1N H₂SO₄.

site is observed with the other three alloys on account of an increase in surface area because of copper and titanium corrosion. This can be seen in Fig. 3 for Ti_{0.50}Cu_{0.50} (galvanostatically polarized), where corrosion occurs preferentially at the grain boundaries. Copper redeposition at the counterelectrode is seen after some time. Titanium can be detected in solution by the specific yellow color produced when adding H₂O₂.

Common features are observed for all five alloys. First, the corrosion starts at approximately +50 mV in non-deaerated 1N H₂SO₄. Second, the current increases only slightly in the voltage range from 200 mV to 1.6V. Third, a steep increase in slope in the log current-potential plot is observed starting at approximately 1.6V; it is due to oxygen evolution. Generally, while the shape of the curves remains more or less the same, the currents increase with increasing copper content of the alloy.

The curves for Ti and Cu are also sketched in Fig. 2 for comparison. While Ti is totally passivated after a few cycles, Cu is corroding with a constant current density within the investigated potential range. It is interesting to note that neither of the two metals alone shows oxygen evolution.

Potentiodynamic current-voltage curves were also measured under the same conditions with deliberately ox-

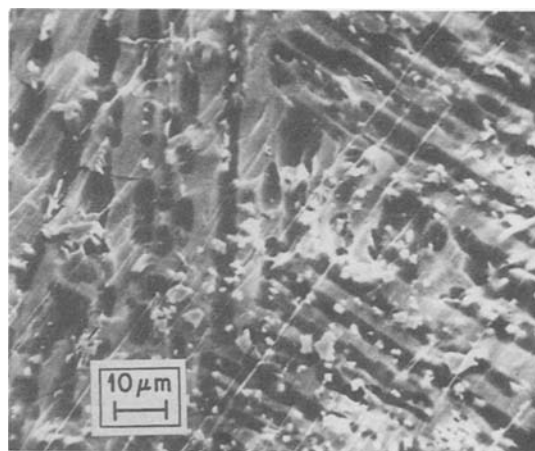


Fig. 3. SEM micrograph of an anodically polarized Ti_{0.50}Cu_{0.50} sample (1h, 250 mA).

dized samples of $Ti_{0.92}Cu_{0.08}$, $Ti_{0.67}Cu_{0.33}$, and $Ti_{0.50}Cu_{0.50}$ in order to see the influence of an oxidized surface on the electrochemical performance. Oxidation at $350^{\circ}C$ for 1h in air causes only minor changes in the electrochemical behavior. Oxidation of $Ti_{0.67}Cu_{0.33}$ for 16h leads to significant changes. The corrosion current (0.2-1.6V) decreases by a factor of five, and the current at 2.5V drops by more than two orders of magnitude.

Under galvanostatic conditions (250 mA/cm^2), alloys with $x = 0.92$ and 0.84 passivate within a few seconds, the potential rising up to 50V (limited by the power supply) and the current dropping to $\sim 5\text{-}10\text{ mA}$. Alloys with $x < 0.67$ exhibit strong oxygen evolution and corrosion of the two alloy components at steady state. No reasonable correlation of the corrosion potential at 250 mA/cm^2 with composition could be observed. A gravimetric determination of the dissolved copper from $Ti_{0.50}Cu_{0.50}$ showed that less than 1% of the total current is consumed for copper corrosion, oxygen evolution being the predominant electrode reaction.

As mentioned above, corrosion of alloys with $x < 0.67$ leads to a strong roughening of the surface (Fig. 3). Alloys with $x = 0.92$ and 0.84 on the contrary, show a smooth surface (SEM) after electrochemical treatment.

Amorphous alloys.—Potentiodynamic voltage-log current plots for amorphous Ti_xCu_{1-x} with $x = 0.46, 0.57,$ and 0.67 are shown in Fig. 4. The shape of the anodic curves is very similar to the ones of the polycrystalline alloys. Within the entire potential range, the currents are shifted to higher values with decreasing Ti concentration. A characteristic difference exists between the polycrystalline and amorphous $Ti_{0.67}Cu_{0.33}$ sample, the current of the amorphous sample being approximately one order of magnitude higher within the entire potential range. This result is in contrast to the anodic behavior reported for an amorphous and a polycrystalline $Ti_{0.50}Cu_{0.50}$ alloy (10). However, the preparation conditions may play an important role in corrosion behavior, as could be shown with differently prepared TiCu alloys (11).

Contrary to what was seen with the polycrystalline alloys, a nice linear dependence of the potentials at 250 mA/cm^2 on alloy concentration is observed for these three amorphous samples. This very probably reflects the single-phase behavior of these alloys (12).

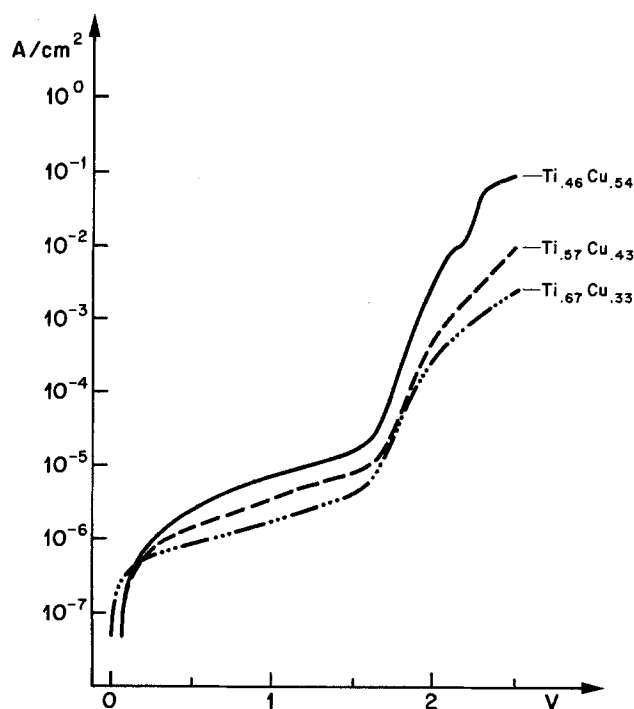


Fig. 4. Potentiodynamic (2 mV/s) voltage-log current plots for amorphous Ti_xCu_{1-x} electrodes in $1N\text{ H}_2\text{SO}_4$.

XPS.—An XPS spectrum of an *in situ* ground $Ti_{0.67}Cu_{0.33}$ sample is displayed in Fig. 5a. The residual oxygen level of the alloy is reflected by the O1s line observed near 950 eV kinetic energy and is at least four times lower than at the surface of an air exposed sample. This demonstrates the necessity of *in situ* preparation of a "clean" surface to characterize the true bulk composition of these samples.

Anodic polarization of the sample for 1h at 250 mA/cm^2 changes the surface composition of the alloy. These changes are shown in Fig. 5b. Electrochemical treatment increases the intensity of the O1s line more than four times while decreasing the copper lines (see below). In addition, three weak sulfur lines near 1258 eV ($S2s_{1/2}$), 1322 eV ($S2p_{1/2}$), and 1323 eV ($S2p_{3/2}$) appear which very probably originate from the electrolyte.

The Ti2p doublet of the same sample is shown in more detail in Fig. 6. That for the air-exposed sample is displayed in Fig. 6a, that for the *in situ* ground in Fig. 6b. The differences emphasize the statement about surface preparation made above. The air-exposed sample contains metallic Ti and TiO_2 . The binding energies of metallic $Ti2p_{1/2}$ and $Ti2p_{3/2}$ are 461.0 and 454.9 eV, respectively, while the corresponding energies for TiO_2 are 464.7 and 458.9 eV (13, 14). Thus, the chemical shift component of $Ti2p_{3/2}$ overlaps with the $Ti2p_{1/2}$ line. Grinding the sample *in situ* removes the TiO_2 layer (Fig. 6b). After anodic polarization, TiO_2 is the only detectable Ti species at the surface (Fig. 6c).

The influence of anodic polarization on superficial copper concentration is shown in Fig. 7 with the Cu2p doublet. After anodic oxidation, the intensities decrease by a factor of 40 ($\sim 1\text{ a/o Cu}$). The chemical shifts and the satellite structures indicate the presence of CuO and possibly Cu_2O (15).

The big difference between the air exposed and the *in*

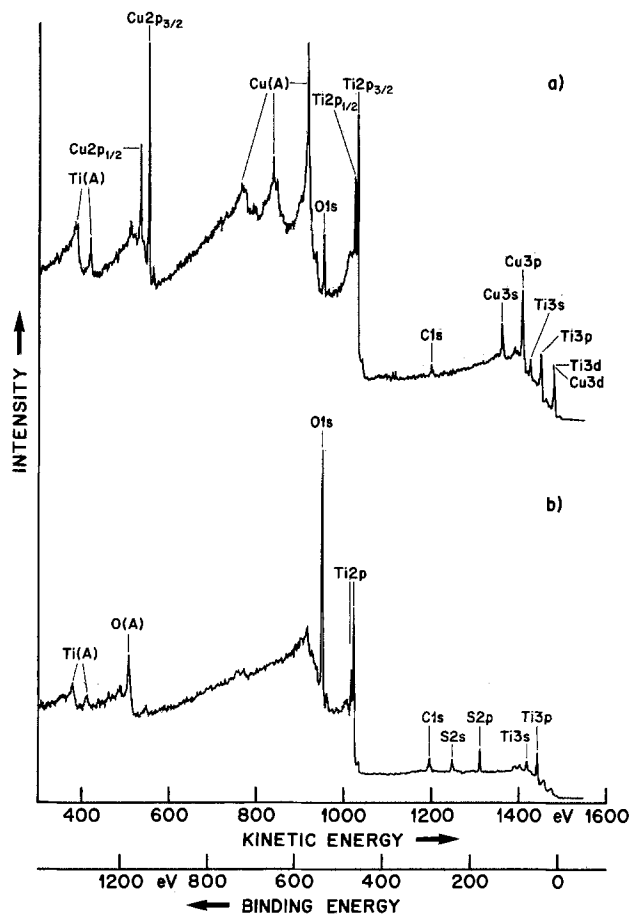


Fig. 5. XPS spectrum of $Ti_{0.67}Cu_{0.33}$. (a) Sample ground *in situ* (Al 75W, 10^4 Hz); and (b) after anodic polarization during 1h at 250 mA/cm^2 (Al 90W, 10^3 Hz).

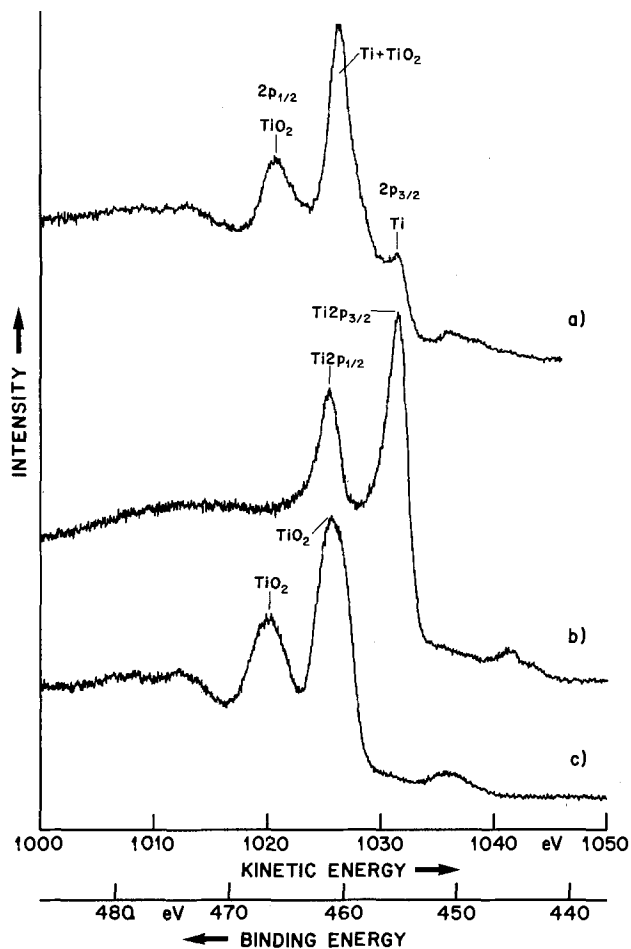


Fig. 6. XPS spectrum of $Ti2p_{1/2}$ and $Ti2p_{3/2}$ lines of $Ti_{0.67}Cu_{0.33}$. (a) Sample as received (Al 120W, 10^4 Hz); (b) sample ground *in situ* (Al 105W, 10^4 Hz); and (c) after anodic polarization during 1h at 250 mA/cm² (Al 125W, 10^4 Hz).

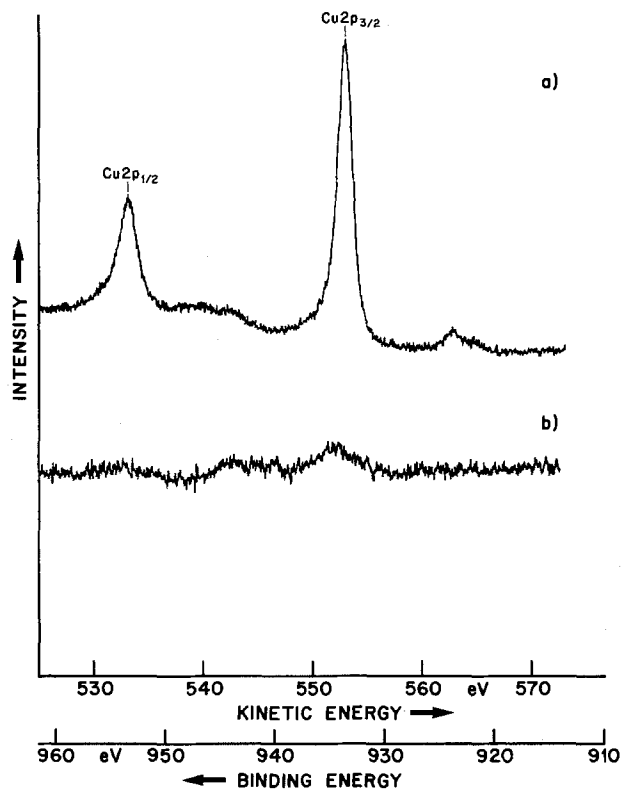


Fig. 7. XPS spectrum of $Cu2p_{1/2}$ and $Cu2p_{3/2}$ lines of $Ti_{0.67}Cu_{0.33}$. (a) Ground *in situ* (Al 75W, 10^4 Hz); and (b) after anodic polarization during 1h at 250 mA/cm².

situ ground sample was also observed with $Ti_{0.92}Cu_{0.08}$. Anodic oxidation leads to total conversion of the surface to TiO_2 . In contrast to $Ti_{0.67}Cu_{0.33}$, very little copper (< 0.2 a/o Cu) can be detected at the surface of this alloy after electrochemical treatment (10 mA/cm² for 2h). Anodizing the sample with 250 mA/cm² leads to immediate passivation. (Limited by the voltage output (50V) of the power supply, ~10 mA/cm² can be passed through the electrode.) Hence, the XPS results demonstrate that, within the information depth, very little copper or copper oxide is present at the surface of a passivating Ti_xCu_{1-x} alloy, the surface consisting essentially of pure TiO_2 .

The contrasting result for a corroding and heavily oxygen evolving alloy is displayed in terms of the Cu2p doublet for $Ti_{0.25}Cu_{0.75}$ (Fig. 8). Anodic oxidation (250 mA, 1h) again leads to a decrease in the copper concentration by a factor of 25 (Fig. 8b) compared to the copper surface concentration of the *in situ* ground sample (Fig. 8a). As with the $Ti_{0.67}Cu_{0.33}$ sample, the chemical shifts and satellite structures indicate the presence of CuO and possibly Cu_2O . After electrochemical treatment, Ti again is completely converted to TiO_2 , as with type I alloys.

The electrochemical results for oxidized Ti_xCu_{1-x} demonstrate that oxidation for 1h at 350°C in air did not significantly change the anodic behavior. To characterize the surface of oxidized Ti_xCu_{1-x} alloys, *in situ* ground surfaces of $Ti_{0.92}Cu_{0.08}$ and $Ti_{0.67}Cu_{0.33}$ were exposed for 10 min to an oxygen pressure of 5×10^{-3} torr at 350°C. The result for $Ti_{0.67}Cu_{0.33}$ is shown in Fig. 9 for the two Cu2p lines. The intensity decreased by a factor of about 12. The corresponding factor for $Ti_{0.92}Cu_{0.08}$ is more than 20. Additional oxidation of the former sample leads to a gradual increase in intensity of the O1s line and a further decrease in the intensities of the Cu lines. After 160 min of oxidation, the surface consists essentially of TiO_2 as can be judged from the chemical shifts of the Ti2p lines. Very small amounts of copper can, however, still be detected, indicating that the segregation between Ti and Cu is not complete. In contrast to anodic oxidation (Fig. 7), thermal oxidation leaves copper predominantly in its metallic state beneath the TiO_2 film; this is indicated by the binding energies of the Cu2p lines (Fig. 9). It should be mentioned, however, that the Cu3p line does show a chemical shift component in the form of a weak shoulder, indicating small amounts of CuO and/or Cu_2O .

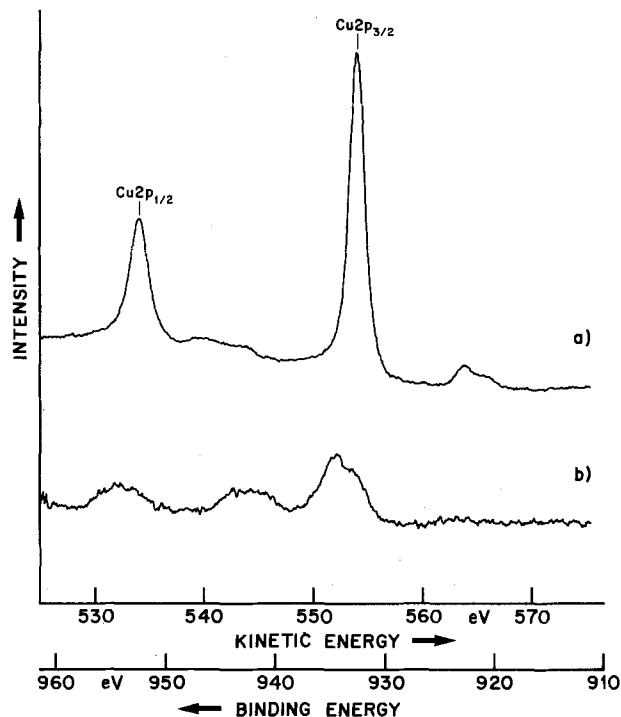


Fig. 8. XPS spectrum of $Cu2p_{1/2}$ and $Cu2p_{3/2}$ lines of $Ti_{0.25}Cu_{0.75}$. (a) Sample ground *in situ* (Al 75W, 10^4 Hz); and (b) after anodic polarization (Al 105W, 3×10^3 Hz).

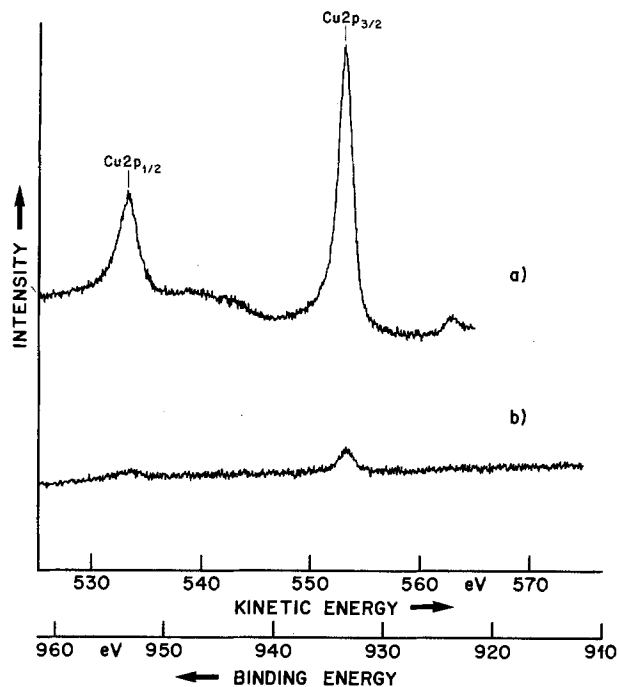


Fig. 9. XPS spectrum of $\text{Cu}2p_{1/2}$ and $\text{Cu}2p_{3/2}$ lines of $\text{Ti}_{0.67}\text{Cu}_{0.33}$. (a) Sample ground *in situ* (Al 130W, 10^4 Hz); and (b) after thermal oxidation during 10 min at 350°C and $p(\text{O}_2) = 5 \times 10^{-5}$ torr (Al 120W, 10^4 Hz).

A similar result is obtained when the depth profile of such an oxide film is determined by angular resolved XPS. Here the surface sensitivity can be considerably enhanced by measuring the spectra at small take-off angles θ of the photoelectrons (insert of Fig. 10) (7-9). Thin oxide films of less than 50Å have been formed by exposing a $\text{Ti}_{0.67}\text{Cu}_{0.33}$ sample first ground *in situ* to oxygen at $p = 5 \times 10^{-5}$ torr for 8 min at room temperature in the preparation chamber of the XPS system. Figure 10 shows the angular variation of the intensity ratios $R_1 = I(\text{O}1s)/I(\text{Cu}2p_{3/2}, \text{met.})$, $R_2 = I(\text{Ti}2p_{1/2}, \text{oxide})/I(\text{Cu}2p_{3/2}, \text{met.})$, and $R_3 = I(\text{Ti}2p_{3/2}, \text{met.})/I(\text{Cu}2p_{3/2}, \text{met.})$. The strong angular variation of the $R_1(\theta)$ and $R_2(\theta)$ curves suggests that the first surface layers consist of pure TiO_2 . On the other hand, the small variation of $R_3(\theta)$ confirms the fact that both metallic Cu and Ti exist below the oxide film.

The depth profile obtained by argon sputtering of the $\text{Ti}_{0.67}\text{Cu}_{0.33}$ sample after 160 min of oxidation is shown in Fig. 11. The intensity of the $\text{Cu}2p_{3/2}$ line increases continuously and reaches a maximum near $t \approx 30$ min corresponding to a film thickness of about 900Å. The concentration of oxygen decreases, as can be seen from the intensity of the O1s peak. Steady-state values are reached after about 70 min sputtering time. The origin of the weak oscillations in the copper and oxygen intensities is not known; we believe, however, that they do not reflect the true concentration profile but are, rather, sputter-induced effects.

Discussion

Anodic passivation behavior.—The potentiodynamic and galvanostatic measurements demonstrate that with respect to anodic corrosion two types of $\text{Ti}_x\text{Cu}_{1-x}$ alloy exist: type I, Ti-rich, with Cu concentrations going up to at least 16 a/o, which passivate and behave like pure Ti electrodes; type II, Cu-rich, with Cu concentrations going down to at least 33 a/o, which do not passivate but corrode and exhibit rather strong oxygen evolution.

The anodic passivation mechanism of titanium in H_2SO_4 has been carefully investigated (16, 17). Passivation starts with the growth of discrete patches of titanium oxide-hydroxide, which coalesce (17). Depending on the final applied voltage, two different passivation layers occur. Below 50V, the passivation film shows a quasi-amorphous structure, and above 50V, the layer is poly-

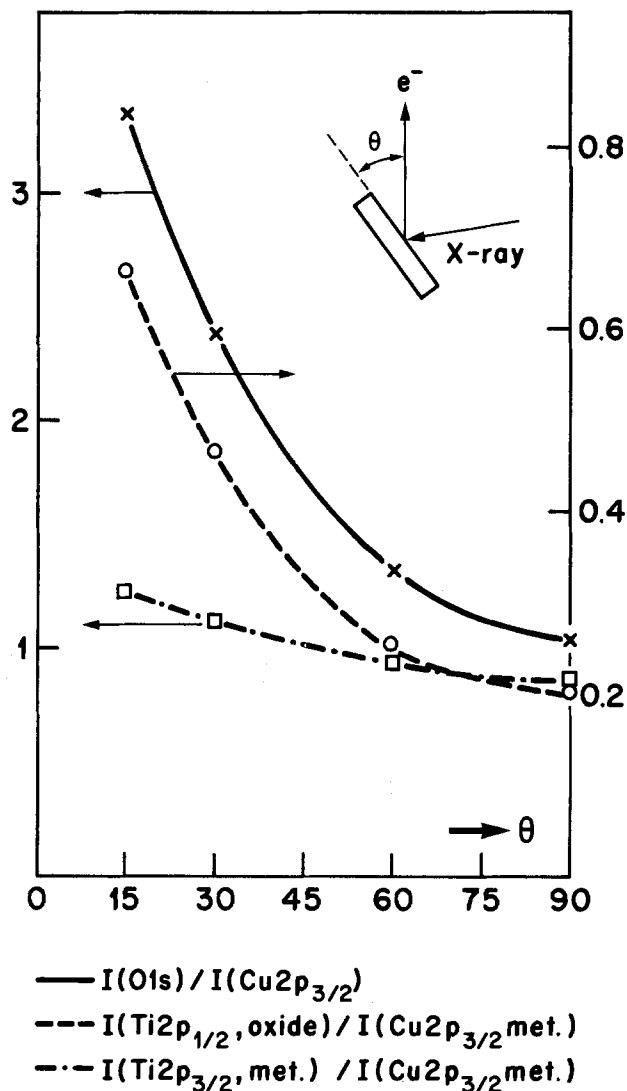


Fig. 10. Ratios of the intensities $I(\text{O}1s)/I(\text{Cu}2p_{3/2})$, $I(\text{Ti}2p_{1/2}, \text{oxide})/I(\text{Cu}2p_{3/2}, \text{met.})$, and $I(\text{Ti}2p_{3/2}, \text{met.})/I(\text{Cu}2p_{3/2}, \text{met.})$ as a function of the emission angle θ for the $\text{Ti}_{0.67}\text{Cu}_{0.33}$ sample. The dashed curve refers to the left-hand scale.

crystalline and of anatase modification. For both voltage ranges, a characteristic value of 25 Å/V has been determined (16). Auger measurements combined with noble gas ion sputtering showed a rather constant Ti/O ratio within the film and a relative sharp transition of the oxygen concentration at the metal oxide/metal interface (18).

XPS measurements of $\text{Ti}_{0.92}\text{Cu}_{0.08}$ after galvanostatic treatment demonstrated that the surface consists of more or less pure TiO_2 . Copper has been preferentially dissolved from the alloy (4). Considering the anodic passivation of $\text{Ti}_{0.84}\text{Cu}_{0.16}$ the same may be expected for this alloy. Both alloys essentially consist of $\text{Ti}(\alpha)$ with some amount of Ti_2Cu (Table I). The influence of foreign atoms on the passivation of Ti has been discussed as distortion of the TiO_2 lattice (19). Hence, a certain concentration of foreign component is necessary to bring about this distortion and hinder the build up of a "long range" order of TiO_2 . For the two investigated alloys, this would imply that bulk concentrations of 8 or 16% Cu are not enough to sustain the required surface concentration (at least > 0.2 a/o) which is balanced by preferential dissolution and bulk diffusion of Cu within the alloy, and necessary for preventing the formation of the passivation layer. For the surface of $\text{Ti}_{0.975}\text{Cu}_{0.025}$ passivated for 1 or 10 min, it has been found that the setting up of a long-range order is shifted from $\sim 50\text{V}$ (the value for pure Ti) to higher voltages (19). Also, from the appearance of a quadratic term in the growth law, it had been concluded that these films do not behave as barrier films.

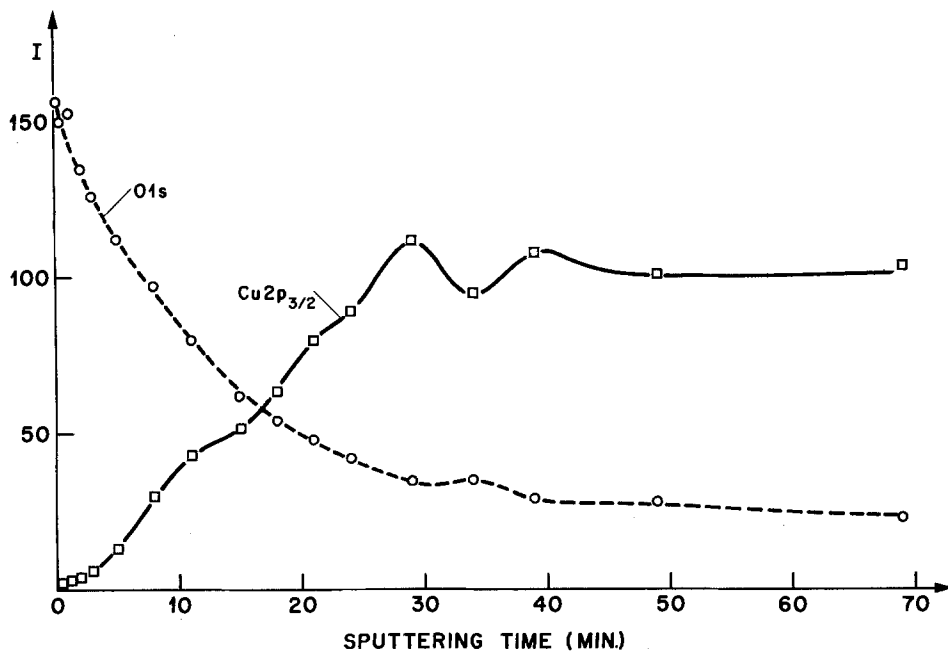


Fig. 11. Depth profile obtained by Ar ion sputtering of Ti_{0.67}Cu_{0.33} after thermal oxidation during 160 min at 350°C and $p(\text{O}_2) = 5 \times 10^{-5}$ torr. (Beam voltage 4 keV, ion current density 10 $\mu\text{A}/\text{cm}^2$, sputter yield $\approx 30 \text{ \AA}/\text{min}$.)

These qualitative assumptions about the influence of Cu on the passivation behavior of Ti are in agreement with the observations made with type II alloys. After anodic treatment, a stationary copper concentration can be detected at the surface for type II with the highest Ti concentration (Ti_{0.67}Cu_{0.33}).

The surface concentration of copper is reduced to approximately 1% through the preferential dissolution process. Hence 1% of copper at the surface is enough to prevent passivation. A similar result has been obtained with Ti_{0.25}Cu_{0.75}, where, after anodic treatment, a surface concentration of 3% Cu has been measured. In both cases, Ti is completely oxidized to TiO₂, no metallic-titanium peaks are observed.

The question remains how high the copper surface concentration has to be to start preventing passivation behavior. The metallographic results show that the two type I alloys are essentially two-phase alloys containing (Ti(α) and Ti₂Cu. Alloy Ti_{0.67}Cu_{0.33}, more or less 100% a single phase of Ti₂Cu, already belongs to type II. Therefore, nonpassivating behavior has to start at the particular Ti₂Cu/Ti(α) ratio where the surface portion of "Ti₂Cu" (taking into account the surface depletion of Cu) is large enough to prevent the coalescence of passivating TiO₂ patches. It would be interesting to determine the exact concentration where the break in passivation behavior occurs, and relate it to a model as done for Ti6Al4V (20).

The polarization behavior of the deliberately oxidized samples (1h 350°C, air) was not significantly different from that of the nonoxidized samples, except for Ti_{0.50}Cu_{0.50} oxidized for 16h. Even if the conditions for the two oxidation procedures were different (a stronger oxidation may be expected in air than at 5×10^{-5} torr O₂), the XPS results for the oxidized samples should give some information useful to understand the polarization behavior of the air-oxidized alloys. XPS shows that preferential oxidation of Ti to TiO₂ occurs and that Cu segregates towards the bulk. But after 160 min of oxidation, Cu still can be detected within the information depth of XPS in Ti_{0.67}Cu_{0.33} samples. In contrast to anodic oxidation, Cu is not oxidized at these temperatures but remains in the metallic state, which can be explained by the different standard free energies of oxide formation for the two metals (21). This is also confirmed by angle-resolved XPS of Ti_{0.67}Cu_{0.33} oxidized for only 8 min (Fig. 10). Only a very few surface layers of this sample consist of essentially pure TiO₂, leaving metallic Ti and Cu beneath. Hence oxidation under these conditions produces a few angstroms thin TiO₂ layer on top of a mixture of Ti oxide and metallic Cu (see also below). For the electrochemical behavior

it may be concluded that at least for the chosen oxidation conditions (1h, 350°C, air), the TiO₂ layer is not thick enough to behave passivating. In other words, the Cu concentration beneath this TiO₂ layer is high enough to still distort the TiO₂ layer under electrochemical conditions. An effect of the metallic state of Cu below this TiO₂ layer on the diffusion properties of Cu in TiO₂ may be speculated to be present. The fact that anodic oxidation leads to anatase while thermal oxidation yields a mixture of anatase and rutile may also have some influence.

The distribution of Cu within the Ti oxide layer can also be seen from the sputter profile² of the Ti_{0.67}Cu_{0.33} sample oxidized for 160 min (Fig. 11). The Cu concentration systematically increases from the surface to the bulk. The thickness of the mixed Ti oxide-Cu layer is estimated to be about 900 \AA . This value is much higher than the value for an oxide layer of pure TiO₂ prepared under comparable oxidation conditions ($\sim 200\text{\AA}$) (22). This is in qualitative agreement with results obtained from marker experiments, where Au doping of the Ti surface impedes the dissolution process of the oxide layer into the bulk and therefore causes an increase in oxide layer thickness (23).

Oxygen evolution.—An interesting feature of type II Ti_xCu_{1-x} alloys is the strong oxygen evolution starting at around 1.65V (Fig. 2). This is even more surprising because neither of the two components show oxygen evolution at these potentials. At 2.5V, for example, a current density on the order of 10^{-5} to 10^{-6} A/cm² can be passed through a passivated Ti electrode. On the other hand, Cu exhibits a constant corrosion current (~ 0.1 A/cm²) with no oxygen evolution up to potentials of at least 10V. This potential-independent current in H₂SO₄ comes about owing to a surface layer of CuOH which impedes passivation

² It is interesting to compare the intensity ratios $R(\text{Ti}/\text{O}) = I(\text{Ti}2p_{3/2})/I(\text{O}1s)$ and $R(\text{Ti}/\text{Cu}) = I(\text{Ti}3p)/I(\text{Cu}3p)$ observed at steady state with the corresponding bulk ratios. The latter values have been obtained from independent measurements with the same sample ground *in situ* before sputtering. We find $R(\text{Ti}/\text{O}) = 1.60$ after sputtering and $R(\text{Ti}/\text{O}) = 1.1$ for the bulk, indicating a rather strong preferential sputtering of the residual oxygen compared with Ti. For $R(\text{Ti}/\text{Cu})$, we find a value of 0.42 after sputtering and 0.51 for the bulk, reflecting a slight sputter-induced enrichment of Cu. This observation is in agreement with the general result obtained for many binary alloys; that the target develops a surface layer enriched in the heavier constituent, copper in our case (24, 25). Using the relation for the steady-state concentration ratio (25) we estimate a sputter yield ratio $S_{\text{Cu}}/S_{\text{Ti}}$ of about 1.1 for the alloy in the steady state. On the other hand, the corresponding ratio for the individual elements is about 3.2 at 1 keV (26). This demonstrates that the preferential sputtering behavior of the alloy cannot be predicted according to the sputter yields of the individual elements, a fact which has also been established for other alloys such as Al/Pd and Si/Pd (27).

as well as oxygen evolution, as could be demonstrated with freshly scratched copper electrodes (28).

Obviously, oxygen evolution at these electrodes is correlated to nonpassivation. The surface sites of the electrode where oxygen evolution occurs remain a matter of speculation. We could see above that nonpassivation is due to a stationary Cu surface concentration causing Cu, and some Ti, corrosion. Hence, a more or less fresh surface composed of Cu oxide and Ti oxide is exposed to the electrolyte under steady-state conditions. One can assume that the Cu component in the alloy should behave like a pure Cu electrode, implying that O₂ evolution does not take place on Cu sites. Oxygen evolution rather should take place at the titanium part of the electrode. It is tentatively assumed that at type II alloys, Ti is oxidized to TiO₂ only within the first layers. It has been shown that surface layers do not alter electrode behavior as long as they are less than 20Å thick (29). Furthermore, fresh titanium electrodes exhibit an activity orders of magnitudes higher than electrodes already passivated (30).

Conclusions

Our results demonstrate that passivation of Ti_xCu_{1-x} alloys is related to a critical copper surface concentration. Alloys either passivate or corrode, hence the desired properties of a stable and conducting surface layer could not be obtained. Nevertheless, Ti_xCu_{1-x} seems to be an interesting system to study passivation of titanium and should deserve further attention.

Acknowledgments

We like to thank R. Loitzl, W. Foditsch, and E.P.R.M. Killer for skillful technical assistance.

Manuscript submitted June 20, 1983; revised manuscript received Jan. 20, 1984. This was Paper 44 presented at the Minneapolis, Minnesota, Meeting of the Society May 10-15, 1981.

BBC Brown, Boveri & Company, Limited assisted in meeting the publication costs of this article.

REFERENCES

1. E. J. Kelly, in "Modern Aspects of Electrochemistry No. 14," J. O'M. Bockris, B. E. Conway, and R. E. White, Editors, p. 319, Plenum Press, New York (1982).
2. A. Fujishima and K. Honda, *Nature*, **238**, 37 (1972).
3. Y. Matsumoto, T. Shimizu, and E. Sato, *Electrochim. Acta*, **27**, 419 (1982); A. Monnier and J. Augustynski, *This Journal*, **127**, 1576 (1980), and references therein.
4. J. A. Petit, P. Lafarque, L. Porte, and T. M. Duc, *Electrochim. Acta*, **24**, 1023 (1979); *J. Less-Common Met.*, **69**, 19 (1980); P. Lafarque, J. A. Petit, and F. Dabosi, *ibid.*, **56**, 233 (1977).
5. W. G. Mofatt, "The Handbook of Binary Phase Diagrams," General Electric Company, Corp. Research and Development, Schenectady, NY (1981).
6. R. J. Colton and J. W. Rabalais, *J. Electron Spectrosc. Relat. Phenom.*, **7**, 359 (1975).
7. C. S. Fadley, *ibid.*, **5**, 725 (1974).
8. W. A. Fraser, J. V. Florio, W. N. Delgass, and W. D. Robertson, *Surf. Sci.*, **36**, 661 (1973).
9. H. Iwasahi, R. Nishitani, and S. Nakamura, *Jpn. J. Appl. Phys.*, **17**, 1519 (1978).
10. M. Naka, K. Hashimoto, and T. Masumoto, *J. Non-Cryst. Solids*, **30**, 29 (1978).
11. G. G. Scherer, P. Brüesch, K. Müller, and S. Stucki, Abstract 44, p. 133, Electrochemical Society Extended Abstracts, Vol. 81-1, Minneapolis, MN, May 10-15, 1981.
12. D. E. Polk, A. Calka, and B. C. Giessen, *Acta Metall.*, **26**, 1097 (1978).
13. "Photoemission in Solids I, Topics in Applied Physics," Vol. 26, M. Cardona and L. Ley, Editors, Springer, Berlin.
14. S. K. Sen, J. Riga, and J. Verbist, *Chem. Phys. Lett.*, **39**, 560 (1979).
15. A. Rosencwaig and G. K. Wertheim, *J. Electron Spectrosc. Relat. Phenom.*, **1**, 493 (1973).
16. G. Blondeau, M. Froelicher, M. Froment, A. Hugot-Le Goff, M. Brien, R. Calson, and P. Larroque, *J. Microsc. Spectrosc. Electron.*, **2**, 27 (1977); G. Blondeau, M. Froelicher, M. Froment, and A. Hugot-Le Goff, *Thin Solid Films*, **42**, 147 (1977).
17. J. C. Pesant and P. Vennereau, *J. Electroanal. Chem.*, **106**, 103 (1980); *J. Less-Common Met.*, **69**, 63 (1980).
18. H. J. Mathieu, J. B. Mathieu, D. E. McClure, and D. Landolt, *J. Vac. Sci. Technol.*, **14**, 1023 (1977).
19. G. Blondeau, M. Froelicher, M. Froment, A. Hugot-Le Goff, and J. Zerbino, *This Journal*, **126**, 1592 (1979).
20. H. J. Rätzer-Scheibe and H. Buhl, *Werkst. Korros.*, **30**, 846 (1979).
21. F. D. Richardson and J. H. E. Jeffes, *J. Iron Steel Inst.*, **160**, 216 (1984).
22. T. Fukuzuka, K. Shimogori, H. Satoh, and F. Kamikubo, in "Titanium 80, Proceedings of the Fourth International Conference on Titanium," p. 2783, The Metallurgical Society of AIME, Kyoto, Japan (1980); D. David, P. Cremery, E. A. Garcia, and G. Beranger, in "Titanium 80, Proceedings of the Fourth International Conference on Titanium," p. 2811, The Metallurgical Society of AIME, Kyoto, Japan (1980).
23. T. Smith, *Surf. Sci.*, **38**, 292 (1973).
24. P. K. Haff, *Appl. Phys. Lett.*, **31**, 259 (1977).
25. P. S. Ho, J. E. Lewis, and W. K. Chu, *Surf. Sci.*, **85**, 19 (1979).
26. H. Oechsner, *Appl. Phys. Lett.*, **8**, 185 (1975).
27. D. R. Penn, *J. Electron Spectrosc. Relat. Phenom.*, **9**, 29 (1976).
28. G. T. Burstein and R. C. Newman, *This Journal*, **128**, 2270 (1981).
29. W. Schmickler and J. Ulstrup, *Chem. Phys.*, **19**, 217 (1977).
30. E. Brauer and B. Schurich, *Ber. Bunsenges. Phys. Chem.*, **85**, 313 (1981).



Effect of Nonstoichiometry and Solvent on Discharge Property of Li/TiS₂ Battery

T. Yamamoto,^{*,1} S. Kikkawa, and M. Koizumi

The Institute of Scientific and Industrial Research, Osaka University, Osaka 567, Japan

Intercalation into TiS₂ has been extensively investigated and was applied as cathode reaction of lithium secondary battery (1). There have been many publications on this topic (1). However, it was not easy to obtain stoichiometric TiS₂ due to its variable compositional range and the presence of higher sulfide, TiS₃ (2). Thompson *et al.* verified the existence of stoichiometric TiS₂ (3). Its fine powder was then prepared from a titanium sponge between 450° and 600°C in a temperature gradient which fixed the sulfur pressure (4). Nonstoichiometry affects the discharge property of lithium battery. Winn *et al.* prepared single crystals of Ti_xS₂ ($x = 1.002, 1.01, 1.02$) and electro-intercalated lithium and sodium in propylene carbonate (5). They measured open-circuit voltages and chemical diffusion coefficients of alkali metals as a function of alkali content. Whittingham reported discharge curves of lithium battery in 70% tetrahydrofuran and 30% dimethoxyethane mixed solution using TiS₂ and Ti_{1.1}S₂ as cathodes (6). They also found that excess titanium reduced the diffusibility of intercalated lithium (6). Selection of solvent is important for the development of an ambient temperature secondary battery. 2-Methyltetrahydrofuran-LiAsF₆ was found to be superior to the electrolytes based on propylene carbonate, methyl acetate and tetrahydrofuran for the lithium electrode cycling efficiencies (7). However, the effect of solvents has not yet been comparatively investigated on intercalation battery using TiS₂ having various Ti/S ratios.

In the present study, samples having compositions of Ti_xS₂ ($1.00 \leq x \leq 1.13$) were prepared and the discharge properties of lithium batteries were galvanostatically investigated using lithium perchlorate as the electrolyte in several kinds of organic solvent. The discharged products were characterized using powder x-ray diffractometry.

Titanium sulfides were prepared by heating mixtures of titanium and sulfur having various mixing ratios at temperatures of 500°, 600°, and 800°C for several days in evacuated silica tubes. The tubes were 8 mm in diam and 10 cm long. The temperature gradient was within 3°C/cm in the furnace. The products were characterized by x-ray diffractometry and thermogravimetry. They had compositions of Ti_{1.00}S₂, Ti_{1.03}S₂, Ti_{1.06}S₂, and Ti_{1.13}S₂. Average particle sizes were ca. 13 μm for Ti_{1.00}S₂ and 9 μm for the others. Electrochemical properties were investigated several times on the sample belonging to the same batch. The samples of ca. 2 mg were pressed to disks of 5 mm diam at 700 MPa. Lithium perchlorate was dried in vacuum at 150°C. Tetrahydrofuran (THF), dimethylsulfoxide (DMSO), formamide (FA), and propylene carbonate (PC) were dried using 3Å molecular sieves. 1M solutions of LiClO₄ were prepared using the respective solvents. Bottle-type lithium batteries were set up using these electrolytes and discharged in He atmosphere. The Hokuto Denko Limited HJ-201 charge/discharge testing system was used for the galvanostatic discharge. The discharged

products were sealed in a capillary, and they were investigated by x-ray diffractometry using CuKα radiation.

Discharge properties were investigated using THF, DMSO, FA, and PC as the respective solvents of electrolyte on the sample having composition of Ti_{1.03}S₂. Galvanostatic discharge curves at 1.5 mA/cm² were presented in Fig. 1. The utilization in the figure was calculated as a quantity of discharged electricity from Li/TiS₂ cell against the amount of TiS₂ used as cathode. 100% utilization means that the discharged electricity corresponds to the amount necessary to obtain LiTiS₂ by lithium intercalation into TiS₂. Cell EMF was ca. 2.2V at the beginning. It gradually decreased to 1.5V with the discharge. Utilizations were 80% in DMSO, 75% in THF, 55% in FA, and 45% in PC when 1.5V of cell EMF was attained. Thereafter, the potentials rapidly decreased with the discharge in the solvents of THF, DMSO, and PC. However a plateau was observed at about 1.2V on the discharge curve in FA.

The discharged products were investigated using powder x-ray diffractometry. The cathode materials were taken out from the following two points; (i) 1.5V of cell EMF was attained, and (ii) the rapid potential decrease was finished. They were sealed in capillary tubes to prevent reactions with humidity. The diffraction results are summarized in Table I. The products discharged in THF showed only the basal spacing of about 6.2Å, which was the value of lithium intercalated TiS₂ (1). The products in DMSO or PC had the same spacing of 6.2Å and additionally very weak diffraction lines around 8.8Å, which could be assigned as the basal reflection of hydrated lithium intercalated phase by a monolayer of water (8). A small amount of water might remain in these solvents even after the drying on molecular sieves. The assignment is difficult for the spacing of 13.6Å observed in DMSO. This phase may correspond to the one detected on TaS₂ intercalated alkali ions solvated by DMSO (8). Basal spacing of ca. 13.2Å was observed on the discharged products in FA with 6.2Å phase. The intensity of x-ray diffraction lines

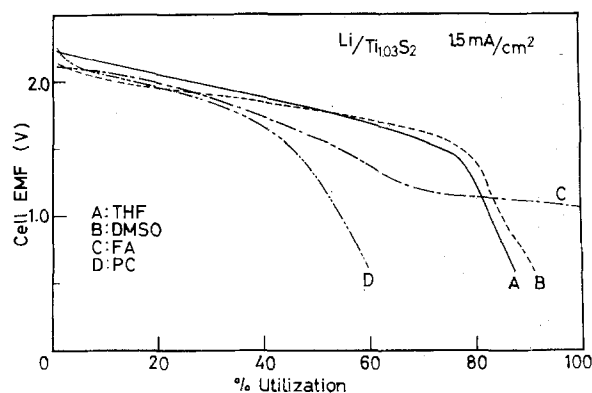


Fig. 1. Effect of solvents on discharge of Li/Ti_{1.03}S₂ cell with 1M LiClO₄. Current density was 1.5 mA/cm².

*Electrochemical Society Active Member.

¹Permanent address: Research Laboratory, Osaka Cement Company Limited, Minamiokajima, Osaka 551, Japan.

Table I. X-ray diffractions of the discharged cathodes in $\text{Li}/\text{Ti}_{1.03}\text{S}_2$ at $1.5 \text{ mA}/\text{cm}^2$

Solvent	Utilization (%) (final voltage, V)	Basal spacings (Å) of the additional phases observed with Li_xTiS_2 having 6.2Å spacing
THF	70 (1.7)	—
	94 (0.2)	—
DMSO	68 (1.6)	13.6, 8.8
	95 (0.2)	13.6, 8.8
FA	49 (1.6)	13.2
	100 (0.9)	13.5
PC	45 (1.6)	8.8
	69 (0.2)	8.8

for 13.2Å phase was comparably strong as that for 6.2Å. Spacings of 13Å had been reported for FA intercalated complexes of metal disulfides (9). Thus the 13.2Å spacing was estimated as that of the intercalated TiS_2 with lithium ions solvated by FA. Cointercalation of solvent reduced the amount of lithium which can be intercalated into TiS_2 .

It may be associated with solvation energy whether lithium alone is intercalated or incorporated with solvent molecules. According to Born's model, solvation energy ΔG can generally be related to the dielectric constant of solvent as follows

$$\Delta G = - \frac{L(Ze)^2}{8\pi\epsilon_0\gamma} \left(1 - \frac{1}{\epsilon} \right)$$

where L is Avogadro's number, Z is the number of ionic charge, ϵ_0 and ϵ are dielectric constants of vacuum and of solvent, and γ is ionic radius. Dielectric constants are 7.39 for THF, 48.9 for DMSO, 64.4 for PC, 78.5 for water, and 111.5 for FA (10). THF probably has the smallest solvation energy because of the smallest dielectric constant in these solvents. Thus, cointercalation of solvent was not observed in THF. THF might be the most favorable solvent in the present study.

Current pulse technique (11) was applied to investigate whether the solvent effect simply be due to ionic conductivity and/or lithium ion transport in the solution phase. 0.05 ~ 0.3 mA current was supplied to the batteries using $\text{Ti}_{1.03}\text{S}_2$ for the periods of 15s. The variation of the transient voltage (ΔE) with time (t) was plotted against $t^{-1/2}$. The linear region was observed in the period of 2 ~ 400s when THF was used as the solvent. The initial nonlinearity which was attributed to an "electrolyte effect" (11) was not observed for the duration less than 2s. Diffusivity around $2.5 \times 10^{-8} \text{ cm}^2/\text{s}$ was calculated from the slope of the linear region. The value is comparable to lithium diffusivity (11), but it changed with the amount of intercalated Li. In the case of PC, two kinds of slope were observed when more than 10% utilization was attained. The diffusivity calculated from the slope for the period between 2 and 25s was about $2.5 \times 10^{-8} \text{ cm}^2/\text{s}$. Much smaller values of $4 \times 10^{-9} \text{ cm}^2/\text{s}$ was obtained from the slope in the period between 25-400s. It may correspond to the diffusivity of hydrated lithium. Intercalation using FA as solvent showed linear region in ΔE vs. $t^{-1/2}$ plot in the utilization above 20%. The calculated diffusivity was about $1 \times 10^{-9} \text{ cm}^2/\text{s}$, which was probably the value for Li solvated with FA molecules. Thus, the ionic conductivities of lithium itself and/or of solvated lithium are apparently important for the observed solvent effect. The electrolyte effect can probably be observed in the initial period until 2s. Our equipment does not have enough capacity to resolve such transient phenomena.

Discharge properties were studied on the samples having various compositions, $\text{Ti}_{1.00}\text{S}_2$, $\text{Ti}_{1.03}\text{S}_2$, $\text{Ti}_{1.06}\text{S}_2$, and

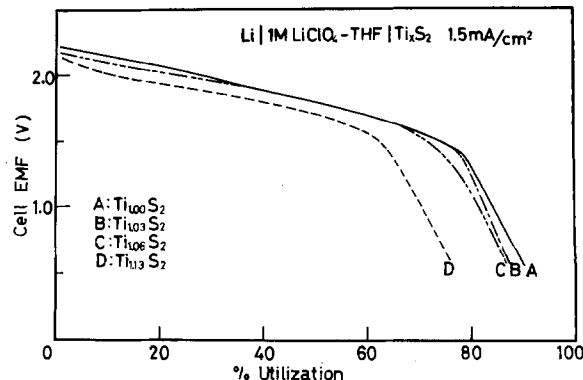


Fig. 2. Effect of nonstoichiometry on discharge of $\text{Li}/1\text{M LiClO}_4\text{-THF}/\text{TiS}_2$ cells at $1.5 \text{ mA}/\text{cm}^2$.

$\text{Ti}_{1.13}\text{S}_2$ at the constant current density of $1.5 \text{ mA}/\text{cm}^2$ in THF. Excess titanium reduces the discharge rate as previously reported (6). The utilizations at 1.5V were 75% for $\text{Ti}_{1.00}\text{S}_2$ and $\text{Ti}_{1.03}\text{S}_2$, and 71% for $\text{Ti}_{1.06}\text{S}_2$ and 62% for $\text{Ti}_{1.13}\text{S}_2$, as shown in Fig. 2. Summations of the amount of excess titanium and the utilization percent were about 75% for all samples. Excess titanium probably sits in the site which the intercalated lithium should occupy. It reduces the number of sites which can accommodate the intercalated lithium.

Intercalation of lithium into TiS_2 reduces the anisotropy of thermal expansion in the TiS_2 lattice (12). Excess titanium in the interlayer region also plays similar role to the intercalated lithium and binds the host TiS_2 layers to each other. Thus, the diffusion constant of about $10^{-7} \text{ cm}^2/\text{s}$ was reported for sodium in $\text{Na}_x\text{Ti}_{1.00}\text{S}_2$, but it was only about $10^{-9} \text{ cm}^2/\text{s}$ in $\text{Na}_x\text{Ti}_{1.02}\text{S}_2$. The present discharged products of $\text{Ti}_{1.06}\text{S}_2$ and $\text{Ti}_{1.13}\text{S}_2$ in THF showed only the basal spacing of 6.2Å, which is the same as that for Li_xTiS_2 , as shown in Table II. However, the discharged product of stoichiometric TiS_2 was accompanied by a small amount of 12.8 and 8.8Å phases. These two spacings probably correspond to those of the hydrated phases having bi- and monolayers of water (1). The stoichiometric TiS_2 partially intercalated the bulky hydrated lithium due to its weak bonding between the TiS_2 layers.

Discharge curves in FA are given in Fig. 3. $\text{Ti}_{1.00}\text{S}_2$ showed the initial voltage of 2.5V. The voltage rapidly decreased at around 25% of utilization. Only the expanded basal spacing of 13.2Å was observed just before and after

Table II. X-ray diffractions of the discharged cathodes in lithium battery at $1.5 \text{ mA}/\text{cm}^2$ prepared by using various compositional titanium disulfides

Solvent	Cathode	Utilization (%) (final voltage, V)	Basal spacings (Å) of the additional phases observed with Li_xTiS_2 having 6.2Å spacing
THF	$\text{Ti}_{1.00}\text{S}_2$	96 (0.2)	12.8, 8.8
	$\text{Ti}_{1.06}\text{S}_2$	95 (0.2)	—
	$\text{Ti}_{1.13}\text{S}_2$	80 (0.2)	—
FA	$\text{Ti}_{1.00}\text{S}_2$	26 (2.0)	13.2*
	$\text{Ti}_{1.00}\text{S}_2$	49 (1.0)	13.2*
	$\text{Ti}_{1.06}\text{S}_2$	100 (0.9)	8.8
	$\text{Ti}_{1.13}\text{S}_2$	100 (0.8)	8.8
PC	$\text{Ti}_{1.00}\text{S}_2$	80 (0.6)	8.8
	$\text{Ti}_{1.13}\text{S}_2$	55 (0.1)	8.8

* Diffraction lines of Li_xTiS_2 having 6.2Å spacing were not observed.

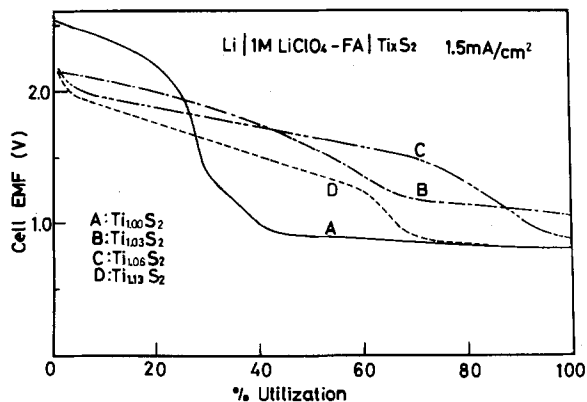


Fig. 3. Effect of nonstoichiometry on discharge of Li/1M LiClO₄-FA/TiS₂ cells at 1.5 mA/cm².

the rapid decrease of potential. The discharged product of Ti_{1.03}S₂ also showed the expanded spacing of FA cointercalated phase. However, the discharged products of Ti_{1.06}S₂ and Ti_{1.13}S₂ showed the spacing of ca. 6.2Å accompanied by a very weak 8.8Å line of the hydrated phase as shown in Table II. The variation of discharge property seems to suggest that the interlayer bonding of TiS₂ is strengthened with nonstoichiometry as observed on the discharge in THF. The final discharge voltage is ca. 1.0V, which is quite different from the value observed in other solvents. This peculiar behavior may correspond to the formation of formamide complexes with titanium sulfides whatever their nonstoichiometries are.

The utilizations at 1.5V in PC was seriously decreased with the degree of nonstoichiometry as illustrated in Fig. 4. The values were 55% for Ti_{1.00}S₂, 45% for Ti_{1.03}S₂, 38% for Ti_{1.06}S₂, and 28% for Ti_{1.13}S₂. Only the discharged product of Ti_{1.00}S₂ to 100% utilization showed a basal spacing of 18.8Å which might be a PC-cointercalated phase (1). The expanded basal spacing could not be observed on other discharged products.

In summary, excess titanium reduced the utilization of Li/TiS₂ battery due to the reduction of available interlayer sites for lithium as reported earlier (6). However, it is effective for pinning TiS₂ layers to each other to prevent the cointercalations of solvents. Polar solvent was sometimes cointercalated and this reduced the cell utilization for stoichiometric TiS₂. In this respect, THF was the most favorable solvent in the present research.

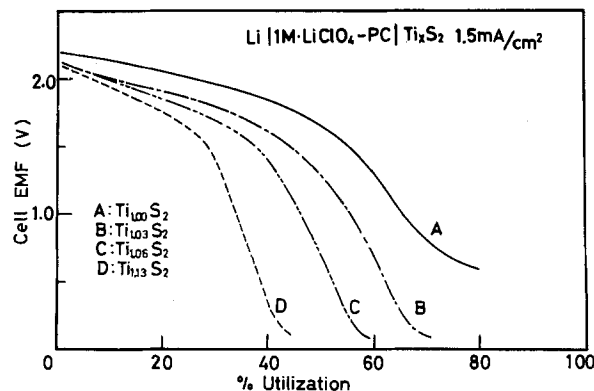


Fig. 4. Effect of nonstoichiometry on discharge of Li/1M LiClO₄-PC/TiS₂ cells at 1.5 mA/cm².

Acknowledgment

This research was partly supported by Grant-in-Aid for Scientific Research from the Ministry of Education and also by a grant from the research project in ISIR on new materials for efficient energy conversion.

Manuscript submitted May 13, 1983; revised manuscript received Jan. 2, 1984.

REFERENCES

1. M. S. Whittingham, *Prog. Solid State Chem.*, **12**, 41 (1978).
2. M. S. Whittingham and J. A. Panella, *Mater. Res. Bull.*, **16**, 37 (1981).
3. A. H. Thompson, F. R. Gamble, and C. R. Symon, *ibid.*, **10**, 915 (1975).
4. A. H. Thompson and F. R. Gamble, U.S. Pat. 3,980,761 (1976).
5. D. A. Winn, J. M. Shemilt, and B. C. H. Steele, *Mater. Res. Bull.*, **11**, 559 (1976).
6. M. S. Whittingham, U.S. Pat. 4,007,055 (1975).
7. V. R. Koch and J. H. Young, *Science*, **204**, 499 (1979).
8. A. Lurf and R. Schöllhorn, *Inorg. Chem.*, **16**, 2950 (1977).
9. R. Schöllhorn and A. Weiss, *Z. Naturforsch., Teil B*, **28**, 172 (1973).
10. G. J. Janz and R. P. T. Tomkins, "Nonaqueous Electrolytes Handbook," Vol. 1, pp. 3-82, Academic Press, New York (1972).
11. S. Basu and W. L. Worrell, in "Fast Ion Transport in Solids," P. Vashishta, J. N. Mundy and G. K. Shenoy, Editors, p. 149, Elsevier North Holland Inc., Amsterdam (1979).
12. M. S. Whittingham and A. H. Thompson, *J. Chem. Phys.*, **62**, 1588 (1975).

Composition of Chromate Passivation Films on Aluminum-Zinc Alloy-Coated Sheet Steel

H. E. Townsend and R. G. Hart

Bethlehem Steel Corporation, Sheet Steels and Coated Products Division, Research Department, Bethlehem, Pennsylvania 18016

Galvanized coatings, that is, zinc coatings applied by a hot-dip process, are widely used to protect steel against corrosion (1). Even greater protection is afforded by a new coating comprising (by weight percent): 55 Al, 43.5 Zn, and 1.5 Si (2, 3). Steel sheet with the Al-Zn alloy coating is marketed in the United States under Bethlehem Steel Corporation's trademark Galvalume. The Al-Zn alloy coating generally provides greater than two times the life of a zinc coating of equivalent thickness.

Although Zn and Al-Zn coatings have good durability during bold atmospheric exposure, both are susceptible

Key words: x-ray photoelectron spectroscopy, wet storage stain, galvanized.

to accelerated attack when exposed to moisture in the crevice-like conditions which are created when sheet is stored in coiled or stacked form. This attack is known as wet-storage staining, and its effects vary from mere superficial discoloration of the surface to total destruction of the coating.

Chromate passivation is the usual method of providing temporary protection against wet-storage stain during shipment and storage of Zn- and Al-Zn-coated sheet. This passivation treatment typically involves immersion of the sheet in an acid chromate bath to deposit a thin film containing roughly 6-25 mg of chromium per square meter. In an earlier study, we found that the degree of protection

against wet-storage stain imparted by a given amount of chromium deposited during chromate passivation is greater for the Al-Zn coating than for the Zn coating (4). The present study was conducted to determine whether differences exist in the passivation films that could account for the difference in performance.

Experimental

Al-Zn- and Zn-coated steel sheets were produced on commercial continuous hot-dip coating lines. The usual mill-applied chromate treatments were omitted to enable surface analyses before and after chromate treatment, which was done in the laboratory. For comparative purposes, we also studied wrought zinc (99.9%) sheet and Al-clad 3003 aluminum sheet.

Materials were passivated in the laboratory according to the following procedure: (i) vapor degrease, (ii) heat to 66°C, (iii) immerse in a chromate bath at 66°C for 5s, (iv) rubber roll squeegee to remove excess solution, and (v) dry in 52°C air. The chromate bath was a 3 v/o solution of Iridite 9L6, a proprietary fluoboric acid-activated chromate passivation treatment supplied by the Richardson Company, Des Plaines, Illinois. In the case of the zinc sheet, we found it necessary to abrade the surface prior to chromating in order to ensure uniform reaction in the chromate bath.

To remove most of the water soluble, unreacted portion of the film remaining on the sheet after passivation and thus facilitate spectroscopic analyses, the chromate-treated materials were washed in distilled water at 91°C for 1 min. Water-insoluble chromium on the surface after washing (Table I) was determined by stripping the remaining film in dilute phosphoric and sulfuric acids and analyzing the solution by atomic absorption.

X-ray photoelectron spectroscopy (XPS) analyses were performed in a Perkin-Elmer, Physical Electronics Model 548 spectrometer at pressures generally less than 10^{-9} torr. A magnesium x-ray source was used to excite photoelectrons which were detected over an area of 4 mm² with a pass energy of 50 eV. X-ray excited photoelectrons used in these analyses are listed in Table II. Depth profiles were obtained by argon ion (5 keV) sputtering. The ion beam was rastered over a 25 mm² area to give a Ta₂O₅ sputtering rate of 2 nm per min.

Results and Discussion

XPS provides information on the identity of elements present, relative quantities, and oxidation states. In Fig. 1-3, we give depth profiles for cationic species present in the film, expressed in atomic percent of cations. Oxygen and a small amount of fluorine also present in the films are omitted for simplicity. In general, oxygen was detected in direct proportion to the amount of trivalent cation.

Prior to chromating, the surface of the Al-Zn coating is covered with a thin layer of trivalent aluminum oxide (Fig. 1a). We attribute the paucity of zinc in the oxide

Table I. Materials and chromium content of passivation films

Material	Chromium in film (mg/m ²)
55% Aluminum-zinc-coated sheet steel	8
Zinc sheet	24
Aluminum sheet	7

Table II. Peaks used for XPS analyses

Element	Shell or Auger transition for XPS analyses
O	1S
Al	2P
Cr	2P
Zn	2P, L ₃ M ₄₅ M ₄₅

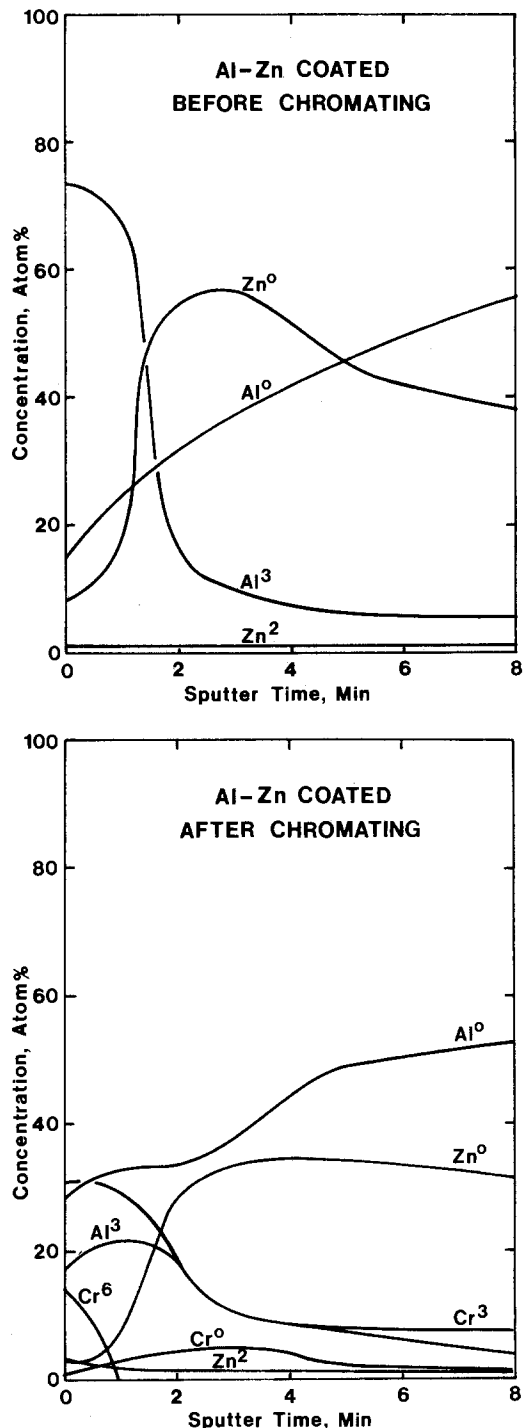


Fig. 1. XPS analysis of Al-Zn alloy-coated sheet steel. a, top: before chromating. b, bottom: after chromating.

film to preferential oxidation of the more active aluminum component during solidification of the hot-dip coating in air.

After chromating (Fig. 1b), a passivation film is observed that comprises chromium in three oxidation states. At the outer surface of the film, chromium is present in the hexavalent form that we associate with a thin residue of the wet film that was dragged out of the chromate bath during processing, dried on the surface, and incompletely removed during subsequent working. Following sputter removal of the hexavalent chromium, the major components of the film are trivalent oxides of aluminum and chromium. With continued sputtering, the trivalent components diminish, and a peak in metallic chromium occurs. Thus, in simplest terms we can picture the passivation film on the Al-Zn surface as consisting of three layers as shown in Fig. 5.

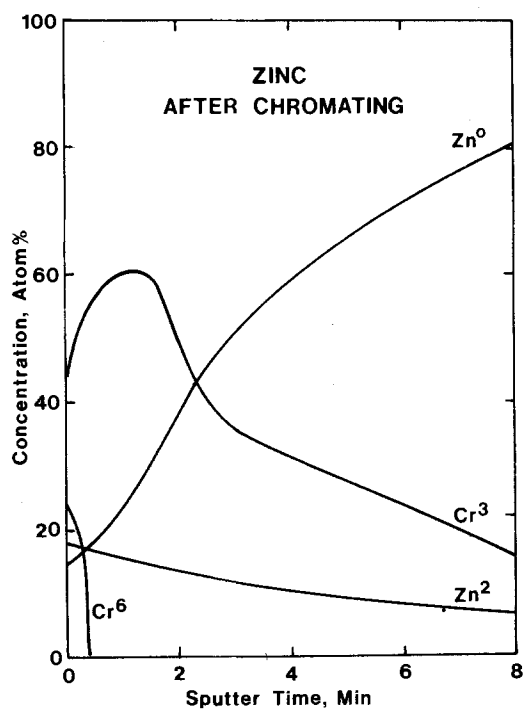
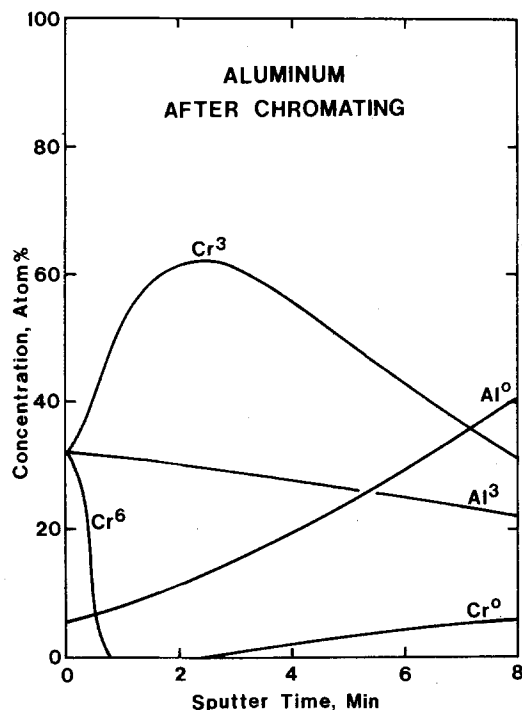
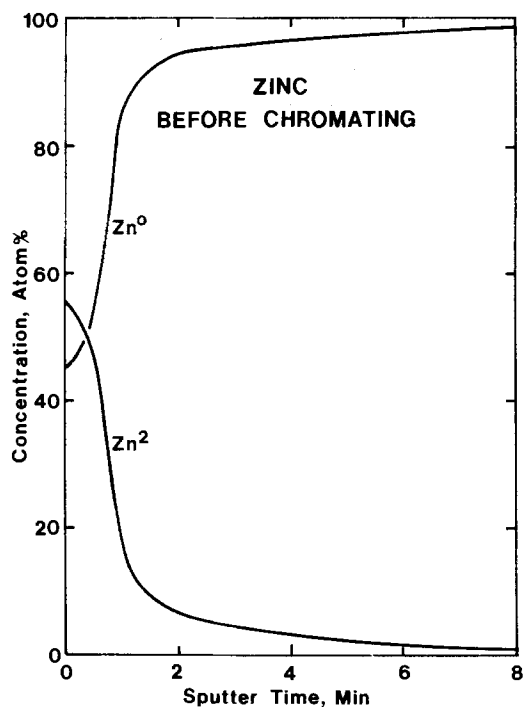
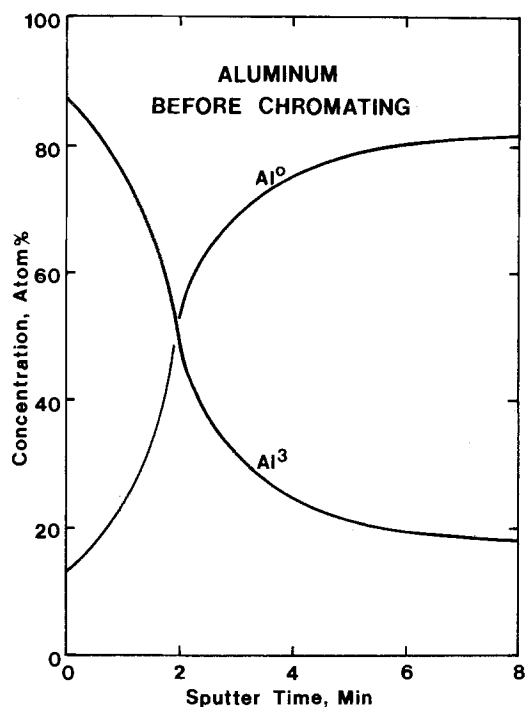


Fig. 2. XPS analysis of aluminum sheet. a, top: before chromating. b, bottom: after chromating.

Fig. 3. XPS analysis of zinc sheet. a, top: before chromating. b, bottom: after chromating.

Analysis of aluminum sheets prior to chromating (Fig. 2a) shows the surface is initially covered with an aluminum oxide film. After chromating (Fig. 2b), a three-layer film is observed that, except for the lack of zinc, is qualitatively similar to that formed on the Al-Zn coating.

Corresponding analyses of the zinc surface before chromate treatment (Fig. 3a) show an initial film of zinc oxide. After chromating (Fig. 3b), we see only two chromium containing layers: an outer layer of hexavalent chromium and an inner layer of trivalent chromium oxide.

Additional XPS analyses comparing galvanized and Al-Zn-coated sheet steel, typified in Fig. 4, confirm the absence of metallic chromium on the zinc-coated sheet.

The above results, which we summarized schematically in Fig. 5, indicate that the chromate passivation films formed on the Al-Zn alloy and aluminum differ from that

on zinc in two significant ways. They exhibit: (i) an intermediate layer containing aluminum oxide and (ii) an inner layer of metallic chromium. Either or both of these additional features could account for the greater degree of protection afforded by chromate passivation to Al-Zn coatings as compared to zinc coatings.

Our results for zinc surfaces are in reasonably good agreement with those of earlier work (7). However, our results differ from those of earlier studies of aluminum (8, 11) and aluminum-zinc coated steel (9) in that metallic chromium was not reported in the previous work. A probable explanation for the difference between our results and those of Ref. (8) and (9) is that we used ion sputtering to remove the outer layers of the passivation film and thus we were able to detect the underlying metallic chromium. Ion sputtering was employed in the work reported in Ref. (11), and, while the authors do not explicitly note

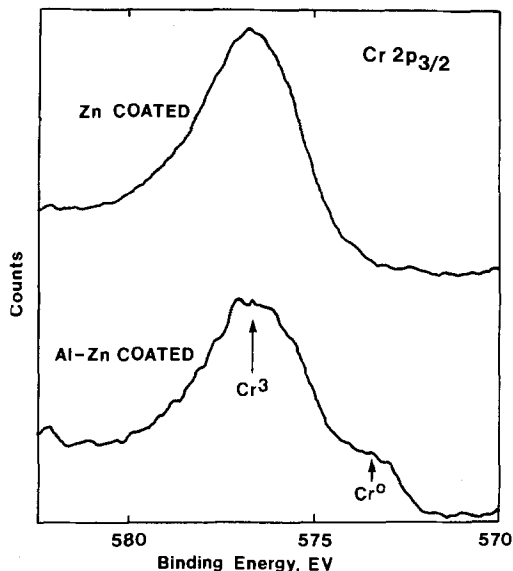


Fig. 4. XPS chromium spectrum comparing zinc-coated (upper curve) and Al-Zn alloy-coated (lower curve) sheet steel.

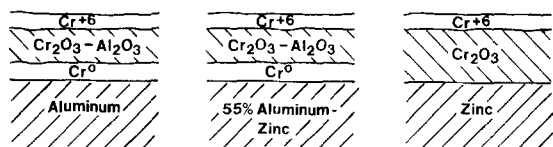


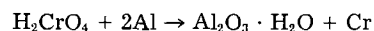
Fig. 5. Schematic of chromate passivation film on 55% Al-Zn-coated steel sheet.

it, there may be evidence in these results [compare Fig. 5 of our work to Fig. 7 of Ref. (11)] of chromium metal.

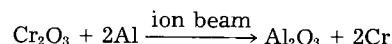
Aluminum oxide is thermodynamically more stable than chromium oxide. Greater thickness or stability of the aluminum containing oxide is suggested by the fact that twice the sputtering time was needed to remove the passivation film on aluminum even though the amount of chromium deposited on the zinc was over three times greater. For a given amount of chromium, an oxide film containing both aluminum and chromium should be a thicker or more dense barrier than one containing only chromium.

A layer of metallic chromium could also provide additional barrier protection. Indeed, metallic chromium found in the passivation film on CDC (cathodic deposited chromate) treated tinplate is believed to enhance re-

sistance to tarnishing (5, 6). In the case of aluminum and Al-Zn-coated steel, the metallic chromium may result from complete reduction of chromic acid in the passivation bath according to



Another explanation is that the metallic chromium detected in our work is a sputtering artifact. Although it has been reported that chromium oxide is not reduced by argon-ion bombardment in the vacuum of a spectrometer (10), we cannot rule out the possibility that aluminum may reduce chromium oxide when activated by an ion beam according to



Acknowledgments

We express thanks to M. J. Joosten for pioneering studies conducted during summer employment and E. J. McNerney and D. H. Van Billiard for skilled technical assistance.

Manuscript submitted June 5, 1983; revised manuscript received Jan. 17, 1984. This was Paper 69 presented at the San Francisco, California, Meeting of the Society, May 8-13, 1983.

Bethlehem Steel Corporation assisted in meeting the publication costs of this article.

REFERENCES

1. R. M. Burns and W. W. Bradley, "Protective Coatings For Metals," Reinhold Publishing, New York (1967).
2. J. C. Zoccola, H. E. Townsend, A. R. Borzillo, and J. B. Horton, in "Atmospheric Factors Affecting the Corrosion of Engineering Materials, STP646," pp. 165-184. ASTM, Philadelphia (1978).
3. H. E. Townsend and J. C. Zoccola, *Mater. Perform.* **18**, 13 (1979).
4. H. E. Townsend and J. C. Zoccola, *This Journal*, **125**, 1290 (1978).
5. S. E. Rauch and R. N. Steinbicker, *ibid.*, **120**, 735 (1973).
6. D. R. Gabe, *Surf. Technol.*, **5**, 463 (1977).
7. J. R. Duncan, *ibid.*, **16**, 163 (1982).
8. M. Koudelkova, J. Augustynski, and H. Berthou, *This Journal*, **124**, 1165 (1977).
9. J. A. Kramer and L. Salvati, Jr., in "Proceedings of the National Coil Coaters Association Technical Meeting, October 1982," pp. 23-32, National Coil Coaters Association, Philadelphia (1982).
10. K. S. Kim, W. E. Baitinger, J. W. Amy, and N. Winograd, *J. Electron Spectros. Relat. Phenom.*, **5**, 351 (1974).
11. J. A. Treverton and N. C. Davies, *J. Met.*, **44**, 480 (1977).

Metal/Flame-Sprayed-Aluminum Interface as Studied by Emission Mössbauer Spectroscopy

Henry Leidheiser, Jr.,* Svetozar Musić, and Attila Vértes

Department of Chemistry and Center for Surface and Coatings Research, Lehigh University, Bethlehem, Pennsylvania 18015

Herbert Herman and R. A. Zatorski

Department of Materials Science, State University of New York, Stony Brook, New York 11794

Two of the authors of this article (H. L. and H. H.) served on a National Academy of Sciences Committee to review the application of flame-sprayed aluminum to corrosion protection of components of naval vessels. A report on this subject has recently been issued by the Acad-

emy (1). As a result of the discussions of the committee, it became apparent that the type of bonding between a steel substrate and the aluminum was not known, although the low bonding strength, typically 2000-4000 lb/in², and the necessity of having the proper degree of roughness of the

Table I. Mössbauer parameter of thin electrodeposit after exposure to the atmosphere

Component	Chemical shift* (mm/s)	Quadrupole splitting (mm/s)	Magnetic hyperfine splitting (kOe)	Half-width at half max (mm/s)	Area fraction
Metallic	+0.394	0.00	337	1.03	56%
Divalent species**	-0.658	2.80	—	1.13	7%
Trivalent species**	+0.009	0.754	—	0.94	37%

* With respect to potassium ferrocyanide.

** Gamma ray emission is from Fe-57 species. There is not necessarily a 1:1 relationship between the originating Co-57 species and the Fe-57 atom that emits the gamma ray.

substrate, suggested that the adherence was primarily mechanical in nature. The following model experiments were carried out in order to explore this point.

The technique selected-emission Mössbauer spectroscopy has been used previously in studies of the interfacial region between a cobalt substrate and a polybutadiene coating (2). The method requires the use of cobalt because Co-57 is the precursor for the excited state of Fe-57, which actually emits the gamma ray that is detected by the Doppler effect conventionally utilized to obtain a Mössbauer spectrum. The method is very simple in concept. Metallic cobalt is electrocoated with a very thin deposit of cobalt containing Co-57. A reference Mössbauer spectrum is obtained. The cobalt is spray coated with aluminum, and another spectrum is obtained. Differences in the spectrum before and after spray coating with aluminum are indicative of chemical changes at the interface. A description of the experimental details will now be given.

The cobalt sheet in the form of a square, approximately 2 cm on a side, was sandblasted, scrubbed gently with a nylon brush under running distilled water, and immediately immersed in a plating bath containing $\text{CoSO}_4 \cdot 7\text{H}_2\text{O}$ doped with Co-57, 0.31 g/l; $\text{MgSO}_4 \cdot 7\text{H}_2\text{O}$ 100 g/l; H_3BO_3 30 g/l; pH = 4.0. A current density of 0.01 A/cm² was used. Two samples were prepared. One deposit was estimated to be approximately 5 nm thick, and the other was estimated to be approximately 10 nm thick. The resulting cobalt electrodeposit consisted of an ionic component (presumably the surface oxide) and a ferromagnetic metallic

component (the unoxidized metal). A computer evaluation of the spectrum of the thicker deposit is given in Table I, in which it is noted that the metallic component composed 56% and the ionic component composed 44% under the assumption that the recoil fraction was the same for all components.

After the original spectra had been obtained, the samples were maintained in a desiccator for approximately 2 weeks before being transported to Stony Brook for the flame spraying process. Both samples retained their clean appearance between the time of preparation and flame spraying. The samples were maintained in a vertical position through use of a magnetic holder and were flame sprayed in two passes with the gun pointing in a direction normal to the specimen surface. The resulting coating was approximately 0.01 cm thick. Adherence of the coating was poor at the edges, but the coating on the major fraction of the surface exhibited satisfactory adherence. The adherence was not measured quantitatively because of the difficulty in working with a radioactive sample.

The spectra for the thicker electrodeposit are given in Fig. 1 for the cobalt surface immediately after preparation and in Fig. 2 for the sample after the application of the aluminum. Superposition of the two spectra indicated that they were identical in all respects. The following conclusions can be drawn.

1. The amount of oxide film on cobalt remained constant before and after flame spraying. Thus, aluminum did not reduce the oxide film, and the oxide film did not thicken.

2. There was no evidence of a change in the chemical nature of the oxide film on cobalt. The 37:7 ratio of the trivalent:divalent species was the same before and after flame spraying.

In summary, it can be concluded that a flame-sprayed aluminum coating has no significant effect on the chemical nature of a cobalt surface such as normally exists during exposure to air at room temperature. The bonding between cobalt and flame-sprayed aluminum does not involve a chemical reaction and is largely, or perhaps exclusively, mechanical in nature. It appears reasonable that this conclusion in the case of cobalt can be extended to steel because there are many similarities in the chemical behaviors of the surface oxides on cobalt and iron.

Acknowledgment

This research was partially supported by a grant from the Office of Naval Research, to whom we are grateful.

Manuscript submitted Jan. 7, 1983; revised manuscript received Nov. 7, 1983.

Lehigh University assisted in meeting the publication costs of this article.

REFERENCES

1. R. A. Perkins, N. N. Ault, H. Herman, F. J. Hermanek, H. Leidheiser, Jr., F. W. Longo, W. G. Smith, R. Summitt, and M. L. Thorpe, Natl. Materials Advisory Board Report no. 409, National Academy Press, Washington, DC (1983).
2. H. Leidheiser, Jr., S. Musicic, and G. W. Simmons, *Nature*, **297**, 667 (1982).

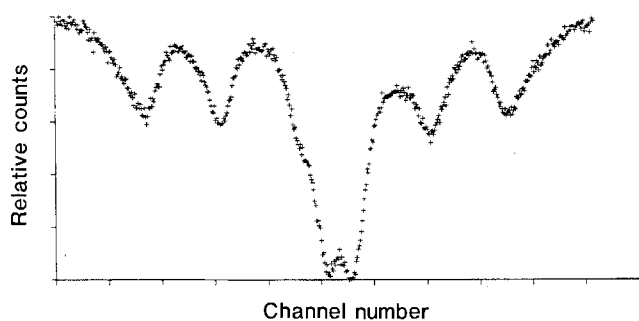


Fig. 1. Mössbauer emission spectrum of a cobalt electrodeposit doped with Co-57

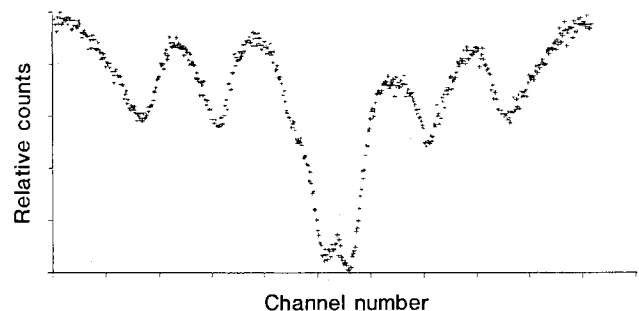


Fig. 2. Mössbauer emission spectrum of the same cobalt sample used in Fig. 1 after coating with flame-sprayed aluminum

Solubility Characteristics of Perfluorinated Polymers with Sulfonyl Fluoride Functionality

G. H. McCain and M. J. Covitch¹

Diamond Shamrock Corporation, T. R. Evans Research Center, Painesville, Ohio 44077

Functionalized perfluorocarbon polymers such as Nafion (E. I. du Pont de Nemours & Company) are of significant commercial importance as membranes in brine electrolysis cells (1), as well as fuel cells. The excellent chemical and thermal stability of these materials in the presence of harsh oxidizing electrolytes, such as chlorinated brine, make this class of polymers uniquely suited for electrochemical applications. A number of other electrochemical processes and components have utilized functionalized perfluorocarbon polymers including, for example, novel-coated electrodes (2) and water electrolysis cells (3).

Membranes are fabricated into sheet form by extrusion of the sulfonyl fluoride (or alkylcarboxylate) form. They are then saponified (4) in caustic to generate the hydrophilic sulfonate form which, unlike the sulfonyl fluoride precursor, swells in aqueous electrolytes and exhibits transport behavior typical of a cation exchange membrane. This fabrication method applies only to the manufacture of sheet and tube membranes (or other geometries of constant cross-sectional area). Martin *et al.* (5) published the first procedure to solubilize commercially available perfluorosulfonate polymers having equivalent weights of 1100-1200 for use in preparing chemically modified electrodes. Their procedure involves heating the polymer (presumably in the potassium sulfonate form) in an alcohol/water solution up to 250°C in a stirred pressure reactor. Stable solutions are obtained up to solid concentrations of 1 weight/volume percent (w/v). Above this concentration, the polymer can be well dispersed, but it partially settles out with time (6). Thus, this method is particularly useful for the preparation of very thin (<20 μm) film structures. Baczek and McCain (7) reported another procedure for solution processing of these materials. They found that solutions of up to 20 weight percent (w/o) solids can be prepared by dissolving the sulfonyl fluoride precursor form of the polymer in perhalogenated solvents at temperatures in excess of 220°C at atmospheric pressure. For the preparation of thick solvent cast separators (>100 μm thick) such as those which are useful as stand-alone membranes for many electrochemical processes, the latter procedure provides a fabrication method which is both convenient and suitable for the preparation of membranes with complex geometries. This paper describes the solubility characteristics of sulfonyl fluoride-type perfluorinated polymers in detail, including several new solvents which are useful for dissolving the polymer at temperatures as low as 143°C.

Experimental

The 1100 equivalent weight (EW) perfluorinated sulfonyl fluoride polymer was prepared from Nafion 511 or Nafion 117 by the following procedure. The as-received polymer has converted to the sulfonic acid form by continuous extraction with 18% HCl under reflux for 16h followed by thorough water washing and finally vacuum drying at 80°C for 24h. The polymer was then contacted with SF₆ and HF at 30°-50°C under autogenous pressure in either a 1-liter Monel bomb mounted on a shaker rack or a 1-liter stirred Parr Monel reactor according to the procedure described elsewhere (8). The reaction product was stirred in methanol for several hours and vacuum dried at 40°-60°C for 24h. 1200 EW sulfonyl fluoride polymer was prepared as above from Nafion 501.

¹Present address: The Lubrizol Corporation, Wickliffe, Ohio 44092.

Key words: membrane, solvents, separators, solvation.

All solvents were used as-received from commercial suppliers without further purification. Polymer dissolution was performed in Pyrex (Corning Glass Works) vessels under a blanket of dry nitrogen. The vessel was heated in either an oil or a sand bath and was periodically removed and shaken to promote dissolution.

Swelling measurements were performed on the sulfonyl fluoride form of Nafion 117. The dry membrane was submerged in a given liquid at 20°-24°C and removed, blotted, and weighed daily until it reached constant weight. Reported weight gain values represent averages of at least three days' equilibrium data. Cloud point measurements were made as follows: the sulfonyl fluoride polymer and a 50/50 mixture by weight of Halocarbon Oils 11-14 and 11-21 (Halocarbon Products Corporation) were heated in a test tube to 250°C in an oil bath until dissolution occurred. The test tube was then allowed to cool in ambient air, and the temperature (measured by a thermocouple probe inserted in the solution) at which the solution first became turbid was recorded as the cloud point temperature.

Results and Discussion

Ambient temperature swelling studies.—A number of organic liquids varying in solubility parameter² from 6.8-12.1 Hb were chosen as swelling agents in order to provide clues which would lead to the identification of a suitable solvent for the sulfonyl fluoride fluoropolymer. This solubility parameter range was suggested by Yeo (10) to include the solubility parameter of the "organic part" of the "Nafion precursor" (SO₂F form). The results of these swelling experiments are summarized in Table I and Fig. 1. The only significant weight increase is observed in the solubility parameter range from 7.3-9.1 Hb, which is within the lower range of Yeo's "envelope I" (10). There does not appear to be a good correlation between hydrogen bonding strength of the swelling agent and polymer weight gain since there are examples of high weight gain for both poorly and strongly hydrogen bonding solvents.

Within the class of poorly hydrogen bonding solvents, the perhalogenated compounds all induce polymer weight gains greater than 1.5%, whereas the nonhalogenated liquids swell the polymer to less than 0.7%. Among the perhalogenated liquids, there are two suggested trends. First, as the relative volatility (defined as the ratio of the temperature of the experiment to the boiling point in K) of the solvent increases, the weight gain increases (see Table II). Second, within the solubility parameter window of higher polymer weight gain (7.3-9.1 Hb), fluorinated liquids are more effective swelling agents than chlorinated compounds. Within the class of strongly hydrogen bonding liquids, all of the amines act as effective swelling agents. Piperidine, a secondary amine, may have reacted with the sulfonyl fluoride group of the polymer; thus, the weight gain of 27.45% in piperidine may be misleadingly high. The two tertiary amines probably are not quaternized by the sulfonyl fluoride group under the conditions of this experiment; thus, the weight gain values in these liquids are considered to be representative of the sulfonyl fluoride fluoropolymer *per se*. As was the

²The solubility parameter (δ) is defined as $(\Delta E/V)^{1/2}$ where ΔE is the energy of vaporization to infinite molecular separation and V is the molar volume. The dimension of the solubility parameter used in this paper is the Hildebrand, where 1 Hb = 1 (cal/cm³)^{1/2}. When the solubility parameters of the solvent and solute are very close in value, mutual solubility is thermodynamically favored.

Table I. Swelling data for Nafion 117 (SO₂F form) in various liquids grouped according to hydrogen bonding strength

Swelling agent	Solubility parameter, Hb	Weight gain of Nafion 117 (SO ₂ F) at 20°C, %
Poorly hydrogen bonding		
n-pentane	7.0	0.65
1,1,2-trichloro-2,2,1-trifluoroethane (TCTFE)	7.3	27.08
n-heptane	7.4	0.40
Halocarbon Oil (HO)	8.0 ^a	1.92
Cl(CFCICF ₂) _n Cl		
Cyclohexane	8.2	0.62
Carbon tetrachloride (CTC)	8.6	2.83
Toluene	8.9	0.35
Acetonitrile	11.9	0.18
Moderately hydrogen bonding		
Diethylether	7.4	0.73
Dibutylether	7.8	0.33
n-butylacetate	8.5	0.31
Tetrahydrofuran (THF)	9.1	11.63
1,4-dioxane	10.0	0.52
Dimethylsulfoxide	12.0	0.05
N,N'-dimethylformamide	12.1	0.13
Strongly hydrogen bonding		
Triethylamine (TEA)	7.4	20.74
Tributylamine (TBA)	7.7	9.99
Lauryl alcohol	8.1	0.23
Piperidine (PD)	8.7	27.45

^a Estimated according to Small's method (11) using a value of $G = 122$ for F and $n = 6$.

Table II. Relationship between swelling agent relative volatility* and polymer swelling for poorly and strongly hydrogen bonding solvents

Swelling agent	Relative volatility	Weight gain, %
Poorly hydrogen bonding		
1,1,2-trichloro-2,2,1-trifluoroethane	0.918	27.08
Carbon tetrachloride	0.837	2.83
Halocarbon Oil	0.555	1.92
Strongly hydrogen bonding		
Triethylamine	0.807	20.74
Tributylamine	0.598	9.99
Lauryl alcohol	0.551	0.23

* See text.

case of the poorly hydrogen bonding solvents, the relative volatility of these strongly hydrogen bonding liquids correlates with polymer weight gain (Table II).

Note that triethylamine swells the fluoropolymer more than tributylamine by a factor of two. Since the tertiary nitrogen is less shielded by the alkyl component in triethylamine than in tributylamine, the tertiary nitrogen group may play a significant role in polymer swelling.

Tetrahydrofuran is the only moderately hydrogen bonding liquid that swells the sulfonyl fluoride fluoropolymer to any great extent. This may be due to its high relative volatility (0.867), although diethylether has a larger relative volatility (0.951) but is far less effective as a swelling agent.

In summary, the room temperature swelling experiments suggest that compounds with high relative volatility, fluorine atoms, tertiary nitrogens, and/or cyclic ether oxygens may prove to be effective solvents for the sulfonyl fluoride fluoropolymer.

Polymer solubility.—As pointed out by Gierke (12) and Starkweather (13), these fluoropolymers are partially crystalline at equivalent weights greater than about 910. Therefore, dissolution of the fluoropolymer may be impeded by the presence of crystallinity. It is known (14) that these polymers are soluble in polar organic liquids such as alcohols below about 950 EW but are insoluble in these same solvents above 1000 EW except at elevated pressure (5). This is an analogous situation to the dissolution of other semicrystalline polymers such as polyethylene which require heat to break up the crystalline domains by solvent action. Therefore, compounds with high boiling temperatures which contain the chemical constit-

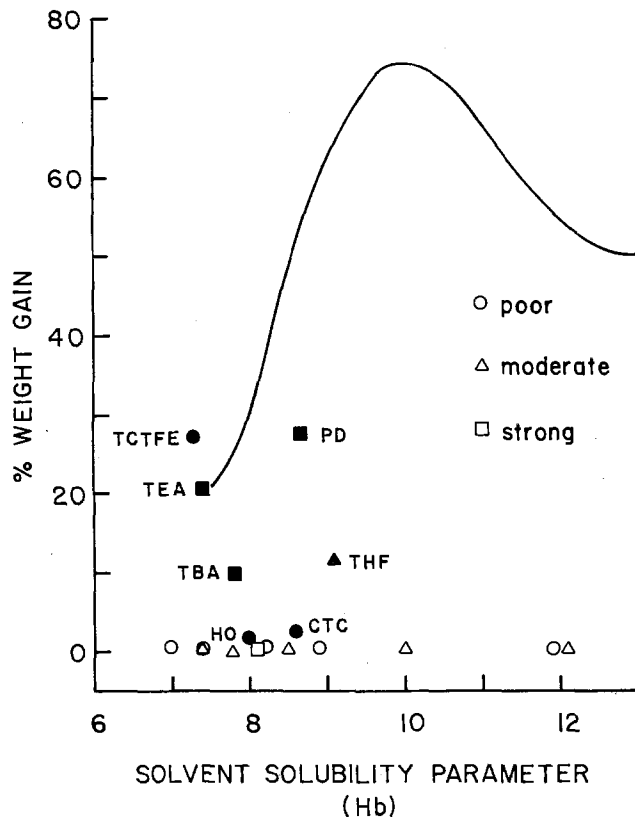


Fig. 1. Swelling data for Nafion 117 (SO₂F form) in various liquids grouped according to hydrogen bonding strength (see Table I for data). Solid line represents Yeo's "envelope I" (10).

uents suggested by the swelling experiments were chosen for study as potential solvents for the fluoropolymer. In order to maximize the possibility for dissolution in a given compound, the dissolution temperature was chosen to be within 10°C of the boiling temperature of the solvent.

A list of compounds which were successful in dissolving 1100 and 1200 EW Nafion sulfonyl fluoride fluoropolymer is found in Table III. Although at room temperature Halocarbon Oil barely swells the fluoropolymer, at high relative volatility it completely dissolves the material, resulting in a clear free-flowing liquid. As this solution cools, it becomes turbid at a temperature which is dependent upon both equivalent weight and solids content

Table III. Solubility of the sulfonyl fluoride forms of Nafion 501 and 511 at solids concentrations >2 w/o

	Solvent boiling point °C	Appearance at 20°C
Complete solubility		
Halocarbon Oil (telomers of chlorotrifluoroethylene)	225-260	Translucent gel
Perfluorooctanoic acid	189	Solid
Perfluorodecanoic acid	218	Solid
Perfluorotributylamine	170-180	Clear gel
Fluorinert FC-70 (3M Co., perfluorotrialkylamine)	215	Clear gel
Pentafluorophenol	143	Clear gel
Pentafluorobenzoic acid	220	Solid
Perfluoro-1-methyldecalin	159	Clear gel
Decafluorobiphenyl	206	Solid
Partial solubility		
Ethylperfluorooctanoate	167	Cloudy gel
1H,1H,11H-eicosafuoro-1-undecanol	180	Solid
Poor solubility		
1H,1H,7H-dodecafluoro-1-heptanol	169	
Pentafluorobenzylalcohol	181	
1-fluoronaphthalene	216	
Trifluoromethanesulfonic acid	162	
Pentafluorobenzaldehyde		

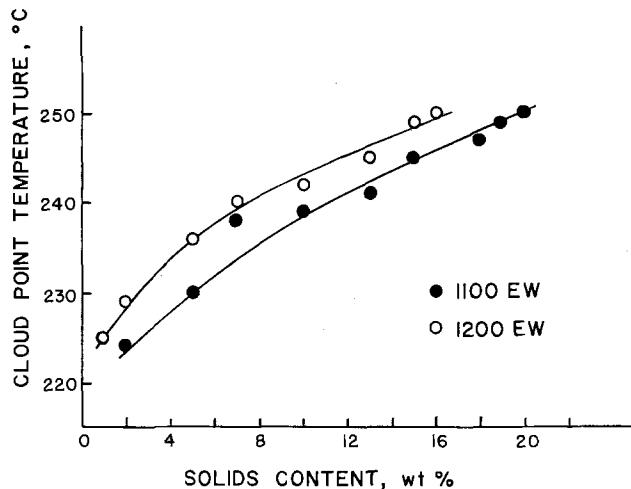


Fig. 2. Effect of solids content on cloud point temperature for fluoropolymer solutions in Halocarbon Oil.

(see Fig. 2). Below this temperature, the cloud point temperature, the polymer forms a translucent gel and exudes a portion of the solvent (syneresis). The other solvents also form gels as they cool, although most other gels are relatively transparent. The solutions which form solids at room temperature do so by virtue of the melting points of their respective solvents. The driving force for gelation during cooling is most probably related to the energy barrier for dissolution during heating, polymer crystallization.

Examination of Table III confirms several predictions which resulted from the room temperature swelling experiments. First, the solvent must be totally halogenated and preferably fluorinated. The only hydrogens which may be present are carboxylic acid and hydroxyl protons. Aliphatic, aromatic, aldehydic, and sulfonic acid hydrogens are undesirable. Second, the perfluorotertiary amines are good solvents for the sulfonyl fluoride fluoropolymer. Third, relative volatility seems to play a role in the solvation process since the temperature which is necessary for dissolution depends largely upon the boiling point of the solvent. For example, the 1100 EW sulfonyl fluoride fluoropolymer forms a clear 2 w/o solution in pentafluorophenol at 143°C; however, it does not go into solution in Halocarbon Oil at this concentration at temperatures less than 224°C.

Membrane formation from these solutions can be accomplished by standard casting techniques (7). Close control of the solution temperature, the substrate temperature, and the coating speed are required for reproducible results. Since these solutions form gels upon cooling, the solution must be maintained at a temperature within about 10°C of its boiling point during casting. If a cool substrate is dipped into the hot solution, a dense gel layer will form on the substrate. The solvent can then be extracted by leaching in a miscible liquid such as methylene chloride, or it can be driven off in a vented oven. It is often useful to fuse the membrane at 150°C for several hours following solvent extraction to ensure that the sep-

arator is free of pinholes or other imperfections. Flat sheets, thimbles with one closed end, fabric reinforced membranes, and complex shapes have all been formed by this process.

Now that the dissolution of sulfonyl fluoride containing perfluorocarbon polymers has been demonstrated, a number of fundamental investigations aimed at elucidating the molecular architecture of these materials are suggested. High temperature light scattering can reveal molecular weight and chain conformation information. Mechanisms of network formation (crystallinity, side chain aggregation?) could be elucidated by conducting x-ray diffraction and/or light scattering (clear gel systems only) experiments both above and below the gelation temperature. The dynamic mechanical and dielectric response of these gels as a function of temperature would complement similar studies (15) of these materials in the dry state and could provide direct evidence for dipole-dipole interactions between sulfonyl fluoride groups and/or the entire perfluoroether side chains. These are only several of a myriad of fundamental studies which are made possible by the identification of methods to solubilize sulfonyl fluoride containing fluoropolymers.

Acknowledgments

The authors are grateful to Diamond Shamrock Corporation for its generous support of this work and to Mr. Brian Peterson and Mr. Elvin Vauss for their help in the cloud point and swelling experiments, respectively.

Manuscript submitted June 3, 1983; revised manuscript received Nov. 16, 1983. This was Paper 565 presented at the San Francisco, CA, Meeting of the Society, May 8-13, 1983.

Diamond Shamrock Corporation assisted in meeting the publication costs of this article.

REFERENCES

- W. G. Grot, G. E. Munn, and P. N. Walmsley, Paper 154 presented at The Electrochemical Society Meeting, Houston, TX, May 7-11, 1972.
- T. P. Henning, H. S. White, and A. J. Bard, *J. Am. Chem. Soc.*, **104**, 5862 (1982).
- R. S. Yeo, J. McBreen, G. Kissel, F. Kulsea, and S. Srinivasan, *J. Appl. Electrochem.*, **10**, 741 (1980).
- W. G. Grot, U.S. Pat. 3,969,285 (1976).
- C. R. Martin, T. A. Rhoades, and J. A. Ferguson, *Anal. Chem.*, **54**, 1641 (1982).
- C. R. Martin, Personal communication.
- S. K. Baczek and G. H. McCain, U.S. Pat. 4,298,697 (1981).
- M. J. Covitch, U.S. Pat. 4,366,262 (1982).
- "Polymer Handbook," 2nd ed., J. Brandrup and E. H. Immergut, Editors, pp. IV-337, Wiley & Sons, New York (1975).
- R. S. Yeo, *Polymer*, **21**, 432 (1980).
- P. A. Small, *J. Appl. Chem.*, **3**, 71 (1953).
- T. D. Gierke, Abstract 438, p. 1139, The Electrochemical Society Extended Abstracts, Vol. 77-2, Atlanta, GA, Oct. 9-14, 1977.
- H. W. Starkweather, Jr., *Macromolecules*, **15**, 320 (1982).
- M. Suhara and K. Arai, U.S. Pat. 4,259,226 (1981); W. G. Grot, Can. Pat. 905,036 (1972); W. G. Grot, U.S. Pat. 3,692,569 (1972).
- I. M. Hodge and A. Eisenberg, *Macromolecules*, **11**, 289 (1978).



Application of Emission Spectroscopy for Profile Control during Oxygen RIE of Thick Photoresist

B. R. Soller*,¹ and R. F. Shuman¹

Sperry Research Center, Sudbury, Massachusetts 01776

and R. R. Ross

College of the Holy Cross, Worcester, Massachusetts 01610

ABSTRACT

Oxygen reactive ion etching of the planarizing photoresist layer in a three-layer resist system is described. The vertical and lateral etch rates of the thick resist layer, as well as the degree of isotropy of the resist profile, are reported as functions of RF power and oxygen pressure. The optical emission spectra are recorded and interpreted for oxygen plasmas used in etching, revealing the presence of oxygen atoms (O) and ionized oxygen molecules (O_2^+). It is demonstrated that trends in the degree of isotropy which occur with changes in RF power and oxygen pressure can be predicted by monitoring the O/O_2^+ emission intensity ratio.

A three-layer resist system has been developed for use in a variety of applications (1). Some of these applications, such as electron-beam lithography, require the planarizing resist to be etched with vertical walls. In the processing of GaAs devices, on the other hand, lift-off is used to define small metal features. A three-layer resist used for lift-off requires the planarizing layer to be undercut from the edge of the transfer layer. In order to achieve both vertical and undercut profiles reproducibly in the same material requires accurate control of the etch step. Reactive ion etching can be made reproducible when there is some understanding of the etching process. Emission spectroscopy is an unobtrusive technique for gaining information about the chemical species present in the plasma, as well as their relative concentrations. This paper describes how emission spectroscopy can be employed to study oxygen reactive ion etching of photoresist used as the planarization layer of a three-layer system. The spectral data are used to determine and monitor the chemical species in the plasma as functions of gas pressure and RF power. It is then demonstrated how emission spectroscopy can be used as a process development tool to predict and control the degree of isotropy in the profile of the planarization layer.

Experiments

The three-layer resist system developed at the Sperry Research Center employs positive photoresists and plasma deposited silicon nitride. Two micron thick AZ[®] 2430 is used as the planarizing layer, and one-tenth micron silicon nitride is plasma deposited over the resist, which has been hard-baked to prevent wrinkling. Details of this process are reported elsewhere (1). The imaging layer is generally 0.5 μm of a positive resist which can be either electron-beam or optically exposed and then developed. Once developed, the imaging resist acts as a mask for plasma etching the silicon nitride layer in CF_4/O_2 . The

patterned silicon nitride layer then serves as a mask for reactive ion etching of the AZ 2430 layer.

Etching of the AZ 2430 layer is accomplished with 13.56 MHz RF power applied to the bottom electrode of a planar system with a chamber volume of 13.5 liters. The input power to the 25.4 cm diameter electrode is varied between 50 and 450W. MOS purity oxygen is used as the etch gas and the flow of gas into the chamber is controlled by mass flowmeters. The chamber pressure is held constant by an automatic venetian blind valve controlled by a capacitance manometer, where pressures between 5 and 1000 mtorr are studied. During the etching both the top and bottom electrodes are maintained at 40°C.

Samples are etched for varying time periods but never long enough to completely remove the planarizing resist. After the specified etch time, the sample is cleaved and examined in the SEM, where measurements of the etch depth and the amount of undercut from the mask are made from SEM photographs. These data, taken from several locations on the sample, are used to calculate the average vertical and lateral etch rates. The lateral etch rate divided by the vertical etch rate is defined as the degree of isotropy, which is a quantitative way to describe the etched profile of the planarizing resist. The degree of isotropy is calculated for several oxygen pressures and RF input powers, and the average value is reported for each set of conditions.

Emission spectra are taken through a quartz window in the etching chamber using an optical multichannel analyzer. The spectrum between 300 and 800 nm is integrated on a 1024 channel linear diode array detector for 16s, which gives a good signal-to-noise ratio. The relative concentration of a species is determined by computing the area under the peak due to emission by that particular atom or molecule. These areas are corrected by subtracting the background spectra due to stray light and detector noise.

Results

The vertical etch rate of hard-baked AZ 2430 in an oxygen plasma is plotted in Fig. 1 for several values of the

*Electrochemical Society Active Member.

¹Present address: Digital Equipment Corporation, Hudson, Massachusetts 01749.

[®]Registered trademark of American Hoechst Corporation, Somerville, New Jersey, for their photoresist products.

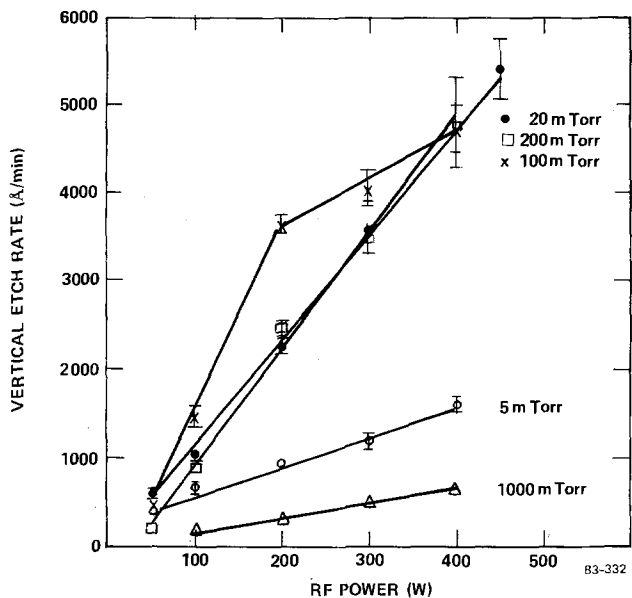


Fig. 1. Vertical etch rates for hard-baked AZ 2430 in an oxygen plasma. Etch rates as a function of RF power for several system pressures; error bars represent 1σ uncertainties.

machine parameters. Figure 1 shows the vertical etch rate as a function of RF power at constant pressure values. It can be seen that the etch rate increases linearly with increasing power when the oxygen pressure is 5, 20, 200, and 1000 mtorr. At a chamber pressure of 100 mtorr, the etch rate increases with increasing power, but the dependence is not linear.

The lateral etch rates for the same samples are plotted in Fig. 2 as a function of power at constant pressure. The power dependence of the lateral etch rate is similar to the power dependence of the vertical etch rate. Lateral etch rates increase with increasing power, the dependence being linear except for pressures near 100 mtorr.

Optical emission spectra are recorded of oxygen plasmas under the conditions used for etching. The spectra are recorded without wafers in the chamber to determine which chemical species are generated in the plasma and are available in the gas phase as possible etchants. Figure 3 shows the emission spectrum of a 20 mtorr oxygen

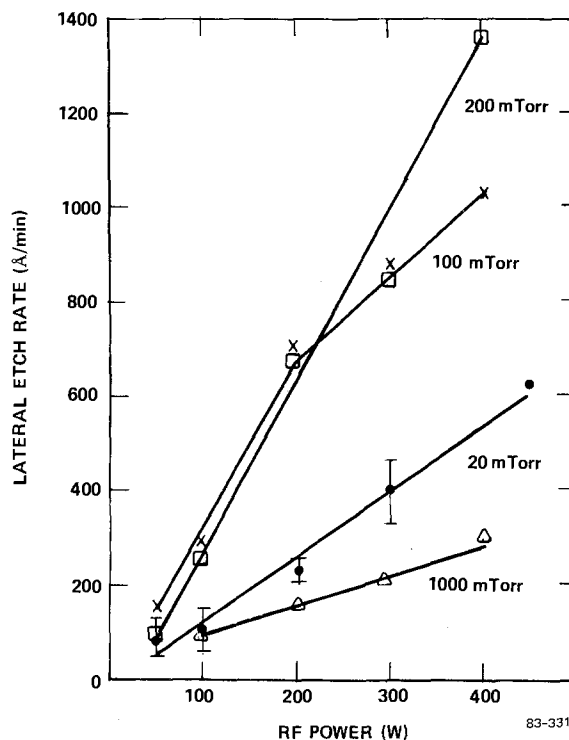


Fig. 2. Lateral etch rates for hard-baked AZ 2430 in an oxygen plasma. Etch rates as a function of RF power for several system pressures.

plasma excited at 300W. The wavelength of a peak or line in the spectrum is used to identify the chemical species responsible for the emission. Most of the emission peaks can be assigned to electronic transitions of oxygen atoms (O) and ionized oxygen molecules (O_2^+). The prominent oxygen atom lines are in the quintet and triplet systems (2). The oxygen molecular ion transitions observed are in the first negative $4\Sigma_g^- \rightarrow 4\Pi_u$ and second negative $2\Pi_u \rightarrow 2\Pi_g$ systems (3). Even though most of the gas in the system is molecular oxygen, the emission from O_2 is too weak to observe, a common occurrence in low pressure discharges (3).

Discussion

The electron-molecule reactions which occur in an oxygen discharge are listed in Table I. The number of ions or

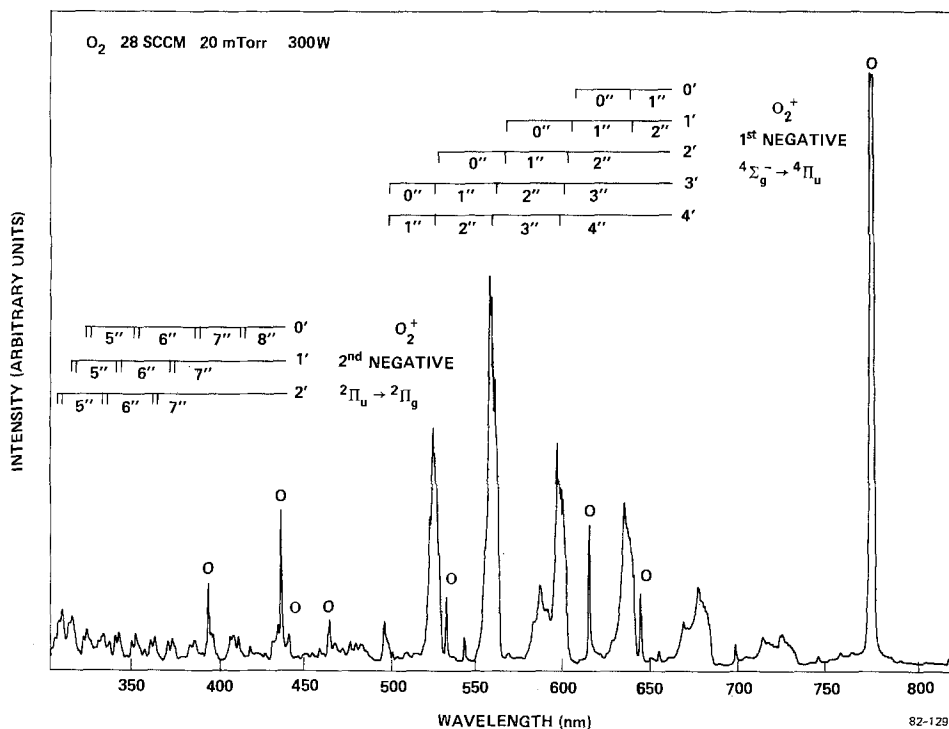


Fig. 3. Emission spectrum of 20 mtorr oxygen plasma excited at 300W. Emission peaks due to oxygen atoms and ionized oxygen molecules are identified.

Table I. Electron-molecule reactions occurring in an oxygen discharge (4)

Reaction	σ_{\max} (cm ²)
1. $e^- + O_2 \rightarrow O_2^+ + 2e^-$	2.72×10^{-18}
2. $e^- + O_2 \rightarrow O^+ + O + 2e^-$	1.0×10^{-18}
3. $e^- + O_2 \rightarrow 2O + e^-$	2.25×10^{-18}
4. $e^- + O_2 \rightarrow O^- + O$	1.41×10^{-18}
5. $e^- + O_2 \rightarrow O^- + O^+ + e^-$	4.85×10^{-19}
6. $e^- + O_2 \rightarrow O_2^+(\Delta_g) + e^-$	3.0×10^{-20}
7. $e^- + O \rightarrow O^+ + 2e^-$	1.5×10^{-18}

atoms produced from an electron-oxygen reaction depends on the density of oxygen, the cross section for the process (Table I), the number of electrons, and the electron energy distribution within the plasma. To dissociate O₂ into O atoms (reaction 3) requires an electron energy above 4.5 eV (5); ionization of O₂ to O₂⁺ (reaction 1) requires 12.2 eV (5); and ionization of O atoms to O⁺ (reaction 7) requires 13.6 eV (2). From other data it is expected that the electron energy distribution function peaks near 5 eV (6, 7), so to ionize O₂ and O requires electrons in the high-energy tail of the distribution. Other studies have found that oxygen atoms can make up approximately 10% of the plasma (8), but the degree of ionization of O₂ in the type of low temperature plasmas used for etching is of order 10⁻⁷ – 10⁻⁴ (9, 10). Spectral data of the plasmas studied in this work show emission from only O atoms and O₂⁺ ions. No emission is observed due to O⁺ ions, but since the lowest allowed transitions have excitation energies in excess of 25 eV, this does not preclude the presence of O⁺ (the highest energy O and O₂⁺ transitions observed are excited at less than 15 eV). However, Thompson reports that in the positive column of a DC discharge the O⁺/O₂⁺ ratio is equal to 1/70 (11). Therefore, the density of O⁺ is small enough that O⁺ can be neglected as an etchant. Oxygen is a very electronegative element, so electron attachment (reactions 4 and 5) is a likely reaction. However, the reverse of reaction 4 is very rapid (4), so any O⁻ formed would recombine quickly and very little O⁻ would be available for etching. In addition, O⁻ is negatively charged and would be repelled from the cathode, where etching is taking place.

Thus it can be concluded that there are three species present in the oxygen discharge which could possibly be responsible for the etching which occurs: O₂, O, and O₂⁺. It is known that O atoms will etch photoresist, but O₂ molecules will not etch photoresist under the same conditions (12). It is also likely that O₂⁺ ions will etch photoresist; these ions will be accelerated in a direction perpendicular to the wafer surface by the plasma sheath electric field. These ions may be directly responsible for etching photoresist in the vertical direction as proposed by Namatsu *et al.* (13), or these ions may participate in an ion-enhanced mechanism to promote vertical etching. In either case, the vertical etch rate would be proportional to the flux of O₂⁺ ions to the wafer surface. The O atoms produced in the oxygen plasma are unaffected by the sheath electric field, so the atoms will etch in both the lateral and vertical directions.

The degree of isotropy is defined to quantitatively compare etch profiles of the planarizing resist under different plasma conditions. This parameter is defined as the lateral etch rate divided by the vertical etch rate. For completely isotropic etching the degree of isotropy is one, while for anisotropic etching it equals zero. The degree of isotropy is plotted as a function of RF power and oxygen pressure in Fig. 4. The degree of isotropy is seen to increase with increasing pressure. At constant pressure, the degree of isotropy decreases for increasing RF power, but only at low values of power. At high RF power values the degree of isotropy remains constant as the power is increased. This information is valuable for process development. For completely anisotropic etching the oxygen pressure must be below 5 mtorr. Then any power value between 150 and 400W will yield anisotropic etching, but the power value determines the etch rate (Fig. 1). For

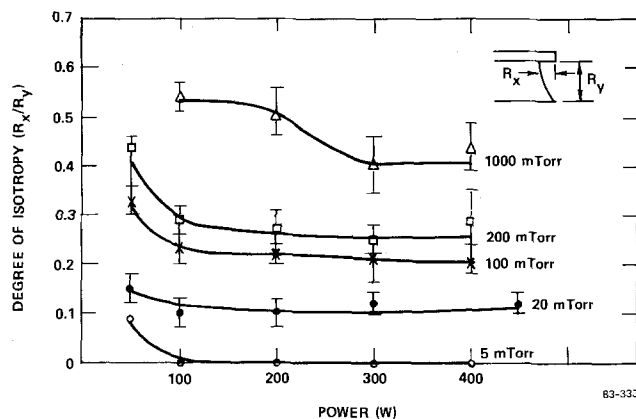


Fig. 4. Degree of isotropy of hard-baked AZ 2430 after oxygen RIE. The ratio of lateral to vertical etch rate is shown as a function of RF power for several system pressures. Error bars represent 1 σ uncertainties.

some processing techniques a controlled undercut is desired; this can be reproducibly achieved by using the etch rate and degree of isotropy data in Fig. 1 and 4 (1).

Assuming a model using first-order kinetics, both the vertical and lateral etch rates will be proportional to the density of the reactant species in the etching reaction. By this model the lateral etch rate will be proportional to the number of O atoms present in the plasma and the vertical etch rate will be proportional to the number of O₂⁺ ions. The oxygen atoms also contribute to the vertical etch rate, but at low pressures this contribution can be neglected because the lateral etch rate is small compared to the vertical etch rate (see Fig. 1 and 2). The emission intensities of these species can be used to monitor their relative concentrations in the plasma.

For an observed spectral line, the emission intensity has the form

$$I \propto n_e n_i f(\chi, T_e) \exp(-\chi/kT_e)$$

where n_e is the electron density, n_i is the density of the ions or atoms responsible for the emission, χ is the excitation energy to the upper state, and T_e is the electron temperature. The Boltzmann factor, $\exp(-\chi/kT_e)$, naturally appears in the rate of excitation due to electron collisions (14); the remaining temperature dependence has been written as $f(\chi, T_e)$. Since the Boltzmann factor dominates the temperature dependence for $kT_e \sim \chi$, the ratio of emission intensities for O atoms and O₂⁺ ions is given approximately by

$$\frac{I_o}{I_+} \propto \frac{n_o}{n_+} \exp(-\Delta\chi/kT_e)$$

Here n_o and n_+ are the densities of O and O₂⁺, respectively, while $\Delta\chi = \chi_o - \chi_+$ is the difference in excitation energies for the two spectral lines chosen.

Assuming that the degree of isotropy is proportional to the ratio n_o/n_+ , it is also proportional to I_o/I_+ multiplied by a temperature-dependent factor, $\exp(\Delta\chi/kT_e)$. This correction term is a decreasing function of electron temperature. At low temperatures ($kT_e < \Delta\chi$) corresponding to low power and high pressure in the plasma, the correction term is a strongly varying function. At high temperatures ($kT_e > \Delta\chi$) corresponding to high power and low pressure, this term varies slowly.

The intensity ratios of various oxygen atom lines to the 558 nm O₂⁺ band are plotted in Fig. 5. The ratios are plotted as a function of RF power for a 20 mtorr O₂ plasma. The ratio of oxygen atom lines at 394, 437, 533, 615, and 645 nm to the 558 nm O₂⁺ band changes very little as the power is increased. The ratio of the O atom lines at 777 and 844 nm (latter not shown in the spectrum or plot) to the O₂⁺ band decreases sharply as the power is increased. Similar plots have been made for plasmas produced at O₂ pressures of 5 and 100 mtorr; similar results are observed. The differences between the longer wave-

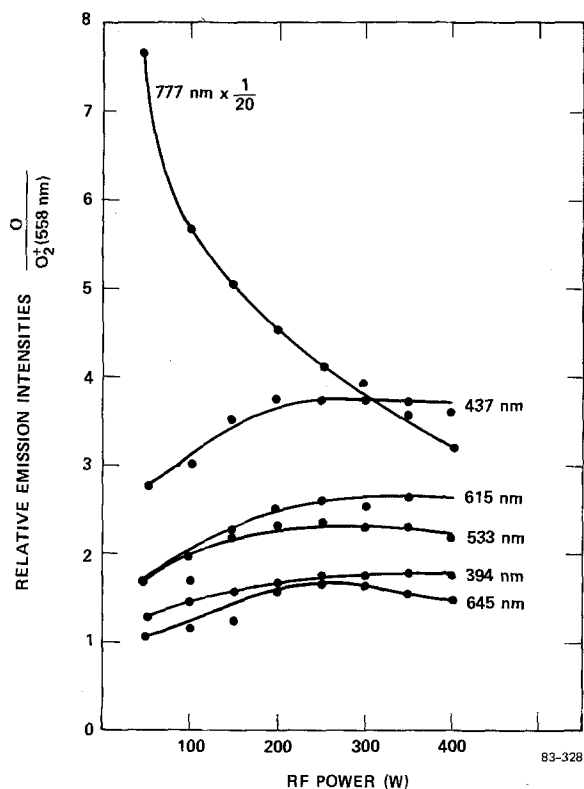


Fig. 5. Relative emission intensities of several oxygen atom lines compared to the O_2^+ band peaking at 558 nm. The intensity ratio of the 777 nm O line to the O_2^+ band is reduced by a factor of 20 in this plot. Chamber pressure is 20 mtorr.

length lines and the other five O atom lines are not presently understood but are being explored further. Spectra have also been compared to an O_2^+ band at 523 nm and a band in the second negative system of O_2^+ at 383 nm. All of these results show the same dependence of the ratios on machine parameters as observed in Fig. 5.

The ratio of the O atom emission line at 615 nm to the 558 nm O_2^+ band is plotted as a function of power at several values of oxygen pressure in Fig. 6. The ratio of the oxygen atom emission to the ionized oxygen molecule emission decreases as the pressure is lowered. At 5 and 20 mtorr chamber pressure, the ratio increases as the power is raised from 50 to 200W; between 200 and 400W the ratio of emission intensities is constant. For an oxygen pressure of 100 mtorr the curve of intensity ratios falls slightly as the power is raised over the range 50-400W. At oxygen pressures of 200 mtorr the emission curve falls sharply as the power increases.

The emission data in Fig. 6 and the degree of isotropy data in Fig. 4 show important similarities in their dependence on pressure and power. At a fixed pressure of 100 mtorr or below, both graphs flatten for powers above 200W. In addition, at a fixed power, decreasing the pressure decreases both the emission ratio and the degree of isotropy. The lowest degree of isotropy occurs at the lowest pressure, where the ratio of O/ O_2^+ emission is also at a minimum.

Application of the temperature correction term [$\exp(\Delta\lambda/kT_e)$] to the emission intensity data helps to understand the small differences between Fig. 4 and 6 at low power. Consider the data at fixed low pressure (5 or 20 mtorr) where the degree of isotropy is small. At high RF powers, the correction term varies slowly with power and the data shown in Fig. 4 and 6 are in substantial agreement. As the power is decreased, the electron tempera-

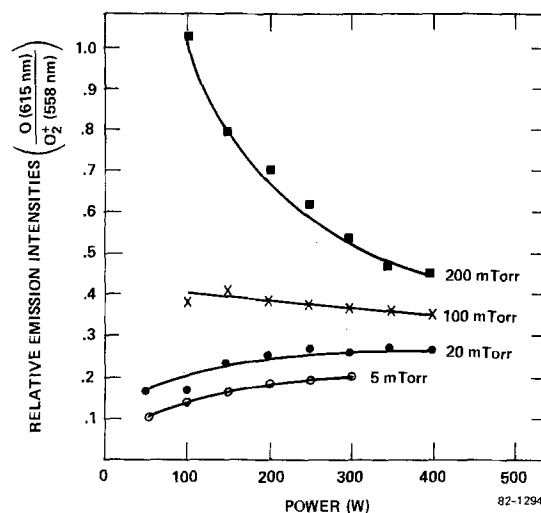


Fig. 6. Ratio of O emission at 615 nm to O_2^+ emission at 558 nm. This ratio is plotted against power for several pressures values.

ture decreases and the correction term increases, explaining the apparent discrepancy between the degree of isotropy and the emission data.

Conclusions

It has been shown that the degree of isotropy obtained in oxygen reactive ion etching of the planarizing layer of a three-layer resist system is a strong function of pressure, but a much weaker function of RF power. Emission spectra of oxygen plasmas revealed that O atoms and O_2^+ ions are present and available to etch photoresist. It was demonstrated that the parameter dependence of the degree of isotropy can be predicted by monitoring the O/ O_2^+ emission intensity ratios as functions of the same parameters. The effect that changes in the pressure and power have on the planarizing resist profile can be predicted from changes in the emission ratios.

Manuscript submitted June 29, 1983; revised manuscript received Feb. 9, 1984. This was paper 180 presented at the San Francisco, California, Meeting of the Society, May 8-13, 1983.

Sperry Corporation assisted in meeting the publication costs of this article.

REFERENCES

1. B. R. Soller, C. R. Snider, and R. F. Shuman, *This Journal*, In press.
2. S. Bashkin and J. O. Stoner, "Atomic Energy Levels and Grotrian Diagrams," p. 164, North Holland Publishing Co., Amsterdam (1975).
3. R. W. B. Pearse and A. G. Gaydon, "The Identification of Molecular Spectra," Chapman and Hall (1976).
4. J. R. Hollahan and A. T. Bell, "Techniques and Applications of Plasma Chemistry," John Wiley and Sons, New York (1974).
5. K. Masek, K. Rohlena, and L. Laska, *Pure Appl. Chem.*, **54**, 1181 (1982).
6. H. W. Rundle, D. R. Clark, and J. M. Deckers, *Can. J. Phys.*, **51**, 144 (1973).
7. B. Kralikova and J. Skala, *Proc. Int. Conf. Phenom. Ioniz. Gases 13th*, 103 (1977).
8. A. J. Bell and K. Kwong, *AIChE J.*, **18**, 990 (1972).
9. C. B. Zarwin, *This Journal*, **130**, 1144 (1983).
10. B. Chapman, "Glow Discharge Processes," John Wiley and Sons, New York (1980).
11. J. B. Thompson, *R. Soc. Proc.*, **262A**, 503 (1961).
12. J. F. Battey, *IEEE Trans. Electron. Devices*, **ed-24**, 140 (1977).
13. H. Namatsu, Y. Ozaki, and K. Hirata, *J. Vac. Sci. Technol.*, **21**, 672 (1982).
14. D. Mihalas, "Stellar Atmospheres," p. 142, W. H. Freeman and Co., San Francisco (1970).

Low Temperature Plasma-Enhanced Epitaxy of GaAs

K. P. Pande*

Bendix Advanced Technology Center, Columbia, Maryland 21045

A. C. Seabaugh

National Bureau of Standards, Semiconductor Materials and Processes Division, Washington, DC 20234

ABSTRACT

Low temperature ($\leq 450^\circ\text{C}$) deposition of single-crystal GaAs using a new plasma-enhanced MO-CVD technique is reported. In this technique, plasma is created by a dc potential and the substrate is not directly exposed to the plasma. Deposition of GaAs was achieved at extremely low plasma power ($0.3\text{--}0.5\text{ W/cm}^2$) using trimethylgallium (TMGa) and arsine (or trimethylarsenic) reactants. The resulting epitaxial films show excellent surface morphology and thickness uniformity over a large area substrate. A linear dependence of growth rate upon TMGa concentration was observed with a typical growth rate of $0.1\ \mu\text{m/min}$ for a TMGa flow rate of 15 ml/min . Undoped films were found to be n-type with a room temperature mobility in the range of $5200\text{ cm}^2\text{ V}^{-1}\cdot\text{s}^{-1}$. Measurements on Schottky barrier devices fabricated on n/n⁺ layers show uniform impurity doping profiles. Temperature dependence of the diode capacitance indicates a density of deep trapping centers as low as $6.2 \times 10^{13}\text{ cm}^{-3}$.

Significant advances have been made in the preparation of high purity GaAs for microwave and optoelectronic device applications using a number of epitaxial growth techniques (1). These techniques include liquid phase epitaxy (LPE), vapor phase epitaxy (VPE), metal-organic chemical vapor deposition (MO-CVD), and molecular beam epitaxy (MBE). With the exception of MBE, all of these techniques require high growth temperatures, typically $600^\circ\text{--}800^\circ\text{C}$. These high temperature growths can lead to thermally generated defects, interdiffusion, and autodoping in the epitaxial layer. While high quality MBE layers can be grown at lower temperatures ($\geq 500^\circ\text{C}$), this technique requires an expensive ultrahigh vacuum unit, and the epitaxial growth rate is extremely slow. Plasma-enhanced deposition offers the advantage (2) of low temperature growth with comparable or higher growth rates than those achieved with conventional epitaxial techniques. In addition, plasma-enhanced deposition should result in efficient utilization of reactant, high reactivity among constituent atoms, increase in the number of nucleation sites, residual impurity gettering, and high doping efficiency. This paper describes a novel growth system utilizing a plasma-enhanced MO-CVD process. In order to minimize any substrate damage due to radiation and ion bombardment, the substrate is not directly exposed to the plasma. Moreover, deposition of single-crystal GaAs is achieved at extremely low plasma power ($0.3\text{--}0.5\text{ W/cm}^2$) using metal-organic reactants. The use of metal-organic reactants facilitates the use of a simple one-zone reaction chamber, and the grown layers are highly uniform over a large area substrate (50 mm diam).

Experimental Details

Epitaxial GaAs layers were deposited using a reactor configuration shown schematically in Fig. 1. The T-shaped stainless steel pedestal was used as the active plasma electrode on which a dc bias was applied via an electrical feedthrough enclosed in a ceramic sheath. The substrate was placed on the top of the pedestal. The pedestal contains a resistive heater to heat the substrate and a thermocouple to monitor its temperature. The second plasma electrode (passive), placed approximately 2-3 in. below the pedestal, was made of a 1/4 in. diam stainless steel tube bent at 90° , as shown in Fig. 1. Arsine (AsH_3 , 10% in H_2) gas or trimethylarsenic ($[\text{CH}_3]_3\text{As}$) was introduced into the reaction chamber through a row of holes in the horizontal arm of this electrode. All the results reported here were obtained for epitaxial layers grown using arsine, since in using a trimethylarsenic source, high quality layers were not readily achieved. The passive

electrode was kept at ground potential, while a negative dc bias in the range of $300\text{--}350\text{V}$ was applied to the active pedestal electrode to create a plasma in the region shown in Fig. 1. This arrangement prevents the substrate from being directly exposed to the plasma.

For the deposition of epitaxial GaAs, trimethylgallium (TMGa) was introduced from the top of the reaction chamber by bubbling hydrogen through the TMGa source (at 0°C). Dopants [hydrogen sulfide (H_2S) or trimethylsilicon ($[\text{CH}_3]_3\text{Si}$)] can be introduced as needed through the TMGa port. Provisions were also made to etch the substrate *in situ* using gaseous HCl and to cover the substrate with a shutter (not shown in Fig. 1) during initial plasma excitation.

The epitaxial layers were deposited on highly polished Cr-doped GaAs substrates oriented 2° off the (100) direction, toward the (110) direction. Some samples were also

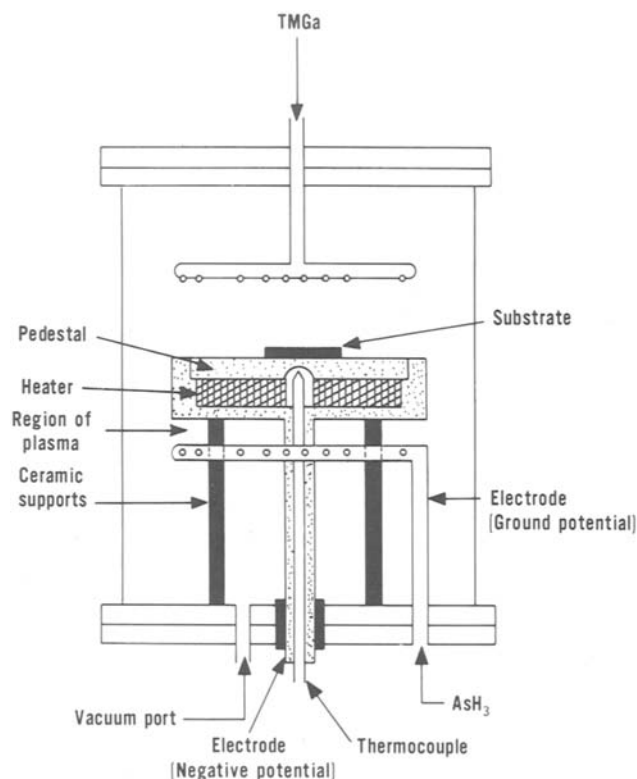


Fig. 1. Cross section of the plasma-enhanced MO-CVD reaction chamber.

*Electrochemical Society Active Member.

Key words: plasma CVD, MO-CVD, low temperature epitaxy, GaAs epitaxy.

grown on highly doped (n^+) GaAs substrates for device application. Prior to the growth, the substrates were cleaned in organic solvents and etched in $H_2SO_4:H_2O_2:H_2O$ (3:1:1 by volume) to remove the surface damage due to polishing.

Before a typical growth run, the system was evacuated to a few millitorr pressure and purged with nitrogen gas. This sequence was repeated at least three times. A plasma was then generated in argon or nitrogen gas to clean the reaction chamber. During this period, the substrate was covered with the shutter to minimize any hydrocarbon deposition on the substrate. After cleaning, the shutter was opened and the substrate was etched (3) *in situ* with gaseous HCl at 200°C (as desired) using a flow rate of 2 ml/min. As soon as the desired growth temperature was stabilized, the reactants were introduced to begin the epitaxial layer growth.

Results and Discussion

Materials.—Epitaxial growth was carried out over the temperature range 250°–500°C with TMGa flow rate varied between 5 and 35 ml/min at constant arsine flow rate of 15 ml/min. During the growth, the pressure in the reaction chamber was maintained between 0.8 and 1.5 torr. Typically, SEM micrographs of the epitaxial layers were highly uniform and featureless (4). Typical epitaxial layer thicknesses were between 1 and 10 μm . The films exhibit excellent thickness uniformity (within 3 to 4%, as measured in an SEM after cleaving and staining) over a large area (50 mm diam) substrate. Films can be grown at temperatures as low as 250°C, but films grown at such low temperatures show gallium inclusions (identified by energy dispersive x-ray analysis using an SEM) and hillock formations (4). By using an SEM in the specimen current mode, electron channeling patterns (ECP) (5) were recorded for films grown at 425°C. The electron channeling patterns for these layers are sharp with fine lines, angular details, and high band contrast (4), showing features very similar to those observed in high quality VPE layers.

To study the growth kinetics, the films were deposited at different TMGa flow rates at a constant arsine flow rate of 15 ml/min. Figure 2 is a plot of growth rate *vs.*

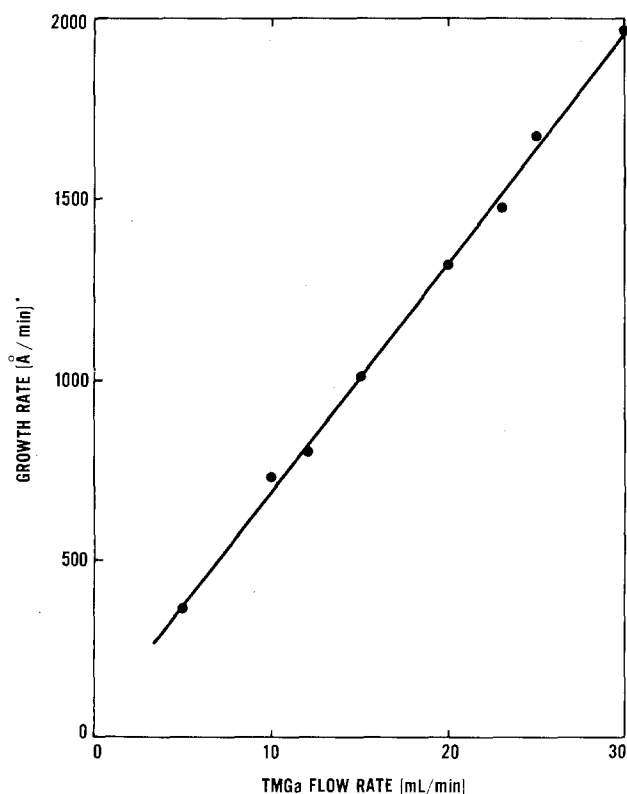


Fig. 2. Variation of growth rate with TMGa flow

TMGa flow. The linearity of the plot indicates that the growth is mass-transport-limited, as reported previously (6). The growth rate was found to be independent of growth temperature in the range 300°–500°C (Fig. 3), with all other deposition parameters constant. Note that below 300°C, the growth rate decreases rapidly, and a significant departure from linearity is observed. Below 300°C, incomplete growth, which may be caused by incomplete pyrolysis of the arsine, occurs.

Without intentional doping, all the epitaxial layers were found to be n -type. Net carrier concentration for undoped layers was found to decrease with decreasing growth temperature, as shown in Fig. 4. At a growth temperature of 350°C, the net impurity concentration derived from Hall-effect measurements was found to be $\sim 5 \times 10^{15} \text{ cm}^{-3}$. Undoped films grown at 400°C show a room temperature Hall mobility of $5200 \text{ cm}^2 \text{ V}^{-1} \cdot \text{s}^{-1}$ (Fig. 4). Films grown below 350°C show a decrease in mobility, which may be due to increased scattering as a result of hillock formation, as reported previously (7).

In order to assess the doping density in typical epitaxial layers, capacitance-voltage measurements were performed on Schottky-barrier diodes fabricated on two undoped n -type layers grown on (Te-doped) n^+ substrates. Both layers were grown at 425°C with a TMGa flow rate of 12 ml/min. Layer B1 was grown with an arsine flow rate of 15 ml/min, while layer B2 was grown with flow rate of 20 ml/min. Both of these layers showed a flat doping profile with net background impurity concentra-

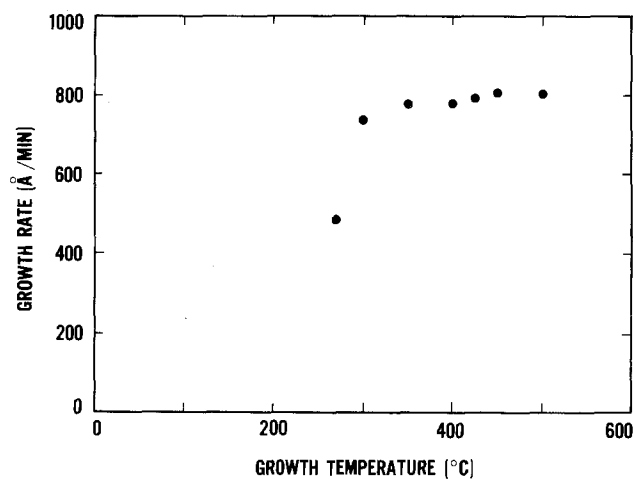


Fig. 3. Dependence of growth rate on growth temperature, with TMGa flow rate of 12 ml/min and AsH_3 (10% in H_2) flow rate of 152 ml/min.

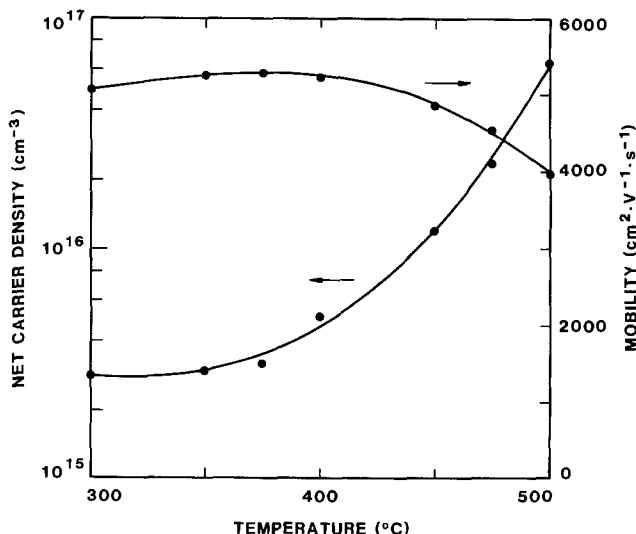


Fig. 4. Dependence of net room temperature carrier concentration and Hall mobility on growth temperature.

doping profile with net background impurity concentration of roughly $5 \times 10^{16} \text{ cm}^{-3}$ (layer B2 is shown, Fig. 5).

To estimate the trap concentration in these films, capacitance-temperature measurements were performed after the method of Sah *et al.* (8). The plots of measured reciprocal capacitance squared as a function of voltage at 77 K and room temperature are given in Fig. 6 for layers B1 and B2. Assuming all the deep traps are ionized at room temperature and deionized at 77 K, the difference in the ionized impurity concentration (measured from the slopes of the two lines) at these two temperatures is equal to the trap density. The lines drawn are least squares fits to the data points. The trap densities for layers B1 and B2 were 6.2×10^{13} and $3.0 \times 10^{14} \text{ cm}^{-3}$, respectively. It is not

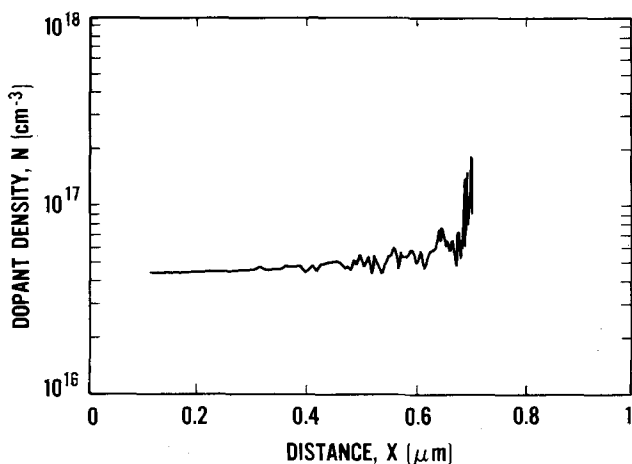


Fig. 5. Impurity profile of an n-type epitaxial layer on an n^+ substrate for a TMGa flow rate of 12 ml/min and growth temperature of 425°C.

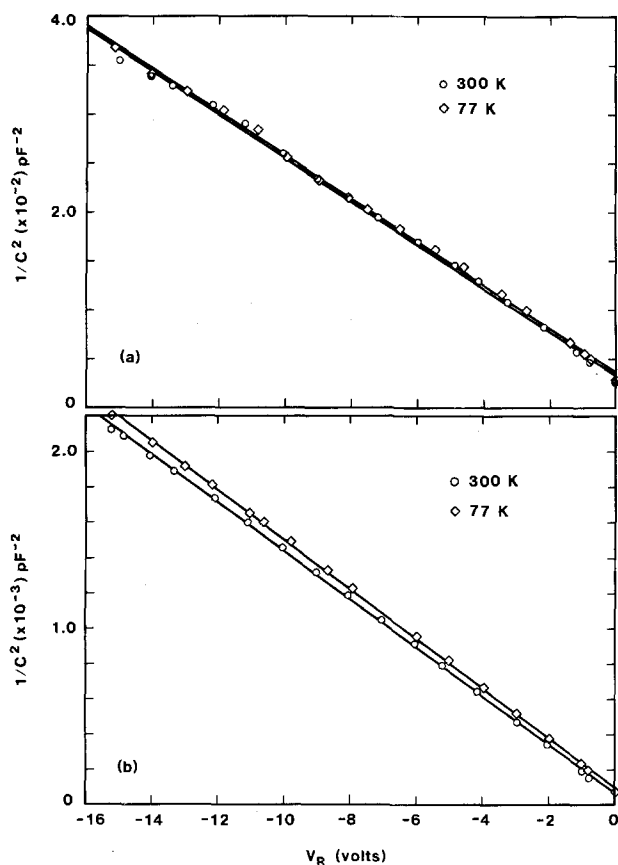


Fig. 6. Reciprocal capacitance squared vs. voltage at 77 and 300 K (a) for layer B1 and (b) for layer B2. Upper solid line corresponds to 77 K measurements.

known at present if low trap density in layer B1 is the result of reduced arsine flow rate during growth.

Devices.—The I-V characteristics of a Schottky-barrier device fabricated on an n/n^+ GaAs layer with gold as the rectifying contact exhibited 0.6V forward voltage drop and $\sim 55\text{V}$ reverse breakdown voltage (4). A device ideality factor of 1.02, indicating a thermionic emission transport mechanism, and a saturation current density in the range of 10^{-9} A/cm^2 were determined. A few Schottky-barrier solar cells were also fabricated by evaporating 7.5-10 nm of gold on the active n/n^+ layer. The response of the cells was measured under AM1 illumination. The photovoltaic response of these cells (4) without antireflective (AR) coatings showed an efficiency of 5.7% with high current collection (17.8 mA/cm^2) and fill factor (0.82), although open-circuit voltage was low (0.39V).

Conclusions

A new plasma-enhanced MO-CVD technique for the growth of epitaxial GaAs has been demonstrated. Using this technique, low temperature growth of device-quality GaAs layers with room temperature mobility of $5200 \text{ cm}^2 \text{ V}^{-1} \cdot \text{s}^{-1}$ has been achieved. The films show excellent surface morphology when grown between 350° and 500°C. It is the first time, to the authors' knowledge, that single-crystal epitaxial layers of GaAs have been grown at $\leq 400^\circ\text{C}$ with good electrical properties and device characteristics. Undoped n -on- n^+ epitaxial layers grown at 425°C showed a flat dopant profile with a shallow impurity concentration of approximately $5 \times 10^{15} \text{ cm}^{-3}$. The deep trap content in the epitaxial layers was in the range 6×10^{13} - $3 \times 10^{14} \text{ cm}^{-3}$. Schottky barrier devices show excellent performance with characteristics comparable to those fabricated on VPE- and MBE-grown samples. Solar cells without an AR coating showed an AM1 efficiency of over 5%. Optimization of this growth technique should lead to epitaxial layers with excellent electrical properties for high performance microwave and optoelectronic devices.

Acknowledgments

The authors would like to thank Dr. J. M. O'Connor and Dr. J. Coleman for helpful discussions, D. Ulrich for the SEM work, and Dr. G. P. Carver and Dr. R. A. Wachnik, National Bureau of Standards, for their assistance in the impurity profiling measurements.

Manuscript submitted Oct. 24, 1983; revised manuscript received Feb. 6, 1984.

The National Bureau of Standards assisted in meeting the publication costs of this article.

REFERENCES

1. L. Hollan, J. P. Hallais, and J. C. Brice, in "Current Topics in Material Science," Vol. 5., E. Kaldis, Editor, p. 1, North-Holland Publishing Co., New York (1980).
2. T. Hariu, K. Matsushita, Y. Komatsu, S. Shibuya, S. Igarashi, and Y. Shibata, in "GaAs and Related Compounds 1982," p. 141, Institute of Physics Conference Series, Institute of Physics, London.
3. K. P. Pande, D. Reep, A. Srivastava, S. Tiwari, J. M. Borrego, and S. K. Ghandhi, *This Journal*, **126**, 300 (1979).
4. K. P. Pande and A. C. Seabaugh, in "III-V Opto-Electronics and Device Related Processes," V. G. Keramidis and S. Mahajan, Editors, p. 201, The Electrochemical Society Softbound Proceedings Series, Pennington, NJ (1983).
5. D. C. Joy, D. E. Newbury, and D. L. Davidson, *J. Appl. Phys.*, **53**, R81 (1982).
6. J. P. Duchemin, M. Bonnet, F. Koelsch, and D. Huyghe, *This Journal*, **126**, 1134 (1979).
7. P. D. Dapkus, H. M. Manasevit, K. L. Hess, T. S. Low, and G. E. Stillman, *J. Cryst. Growth*, **55**, 10 (1981).
8. C. T. Sah, L. Forbes, L. L. Rosier, and A. F. Tasch, Jr., *Solid-State Electron.*, **13**, 759 (1970).

Fluorescence and Nonradiative Relaxations of Rare Earths in Amorphous Media and on High Surface Area Supports: A Review

Renata Reisfeld

Department of Inorganic and Analytical Chemistry, The Hebrew University of Jerusalem, Jerusalem, Israel 91904

ABSTRACT

The origins of the electronic levels of rare earths in the condensed phase and the influence of the glassy matrix on the position of the energy levels and factors responsible for radiative and nonradiative transitions are discussed. Examples are given of rare earth intensity parameters and nonradiative transitions in oxide, chalcogenide, and fluoride glasses. The spectral behavior of rare earth ions adsorbed or incorporated into high surface porous materials are discussed.

The main difference between optical spectra of inorganic ions in amorphous materials and crystalline media of comparable composition is the inhomogeneous broadening due to the variety of sites in the former (1, 2). This is due to the fact that the dopant ions in glasses reside in a variety of environments and experience different perturbing local fields. Thus, instead of identical electronic energy levels, there is a distribution of spectroscopic parameters which depend on the host glass composition and result in different radiative and nonradiative transition probabilities. These variations are evident in absorption and fluorescence spectra as inhomogeneously broadened lines when conventional light sources are used. The decay times of fluorescence from excited states of different sites normally exhibit a nonexponential behavior. However, if fast diffusion of excitation energy occurs among the different sites, then the decay will become exponential with the fastest time constant available among the sites.

Laser-induced fluorescence line narrowing (FLN) enables, in some cases, the excitation of a subset of ions having the same energies. In the absence of accidental coincidence of electronic levels, a tunable pulsed laser can be used for determining the electronic levels and transition probabilities of a selected subset of the total ensemble of sites. The intraconfigurational 4f-4f transitions of rare earth ions are especially suitable in this type of investigation because of small electron phonon coupling. The degree of selectivity of the FLN technique depends on the ratio of homogeneous to inhomogeneous widths (3), which is of the order of 10^{-3} for rare earths at low temperatures. Figure 1 (4) provides an example of FLN on Eu^{3+} in phosphotungstate glasses at 4 K, the excitation being performed into the ${}^5\text{D}_0$ level of the different sites. The three-line ${}^5\text{D}_0 \rightarrow {}^7\text{F}_1$ emission is shown as a function of excitation frequency of the ${}^7\text{D}_0 \rightarrow {}^5\text{D}_0$ transition and corresponds to the different sites.

Modeling the atomic arrangement in glass is often done using molecular dynamics. In this technique the position of the ions is calculated by numerical integration of Newton's equations of motion using a model interatomic potential function. This method so far has been applied to SiO_2 , B_2O_3 , BeF_2 , ZnCl_2 , and KCl and multicomponent sodium silicate, sodium borosilicate, and fluoroberyllate glasses (3). While the method is very elegant and promising, its validity is still being tested by comparison with experimentally measured physical properties such as thermodynamic and transport characteristics.

Radiative Transitions

For most practical purposes, the oscillator strengths and the connected radiative-transition probabilities obtained from the absorption spectra correspond to some average values due to the total number of sites. This is also true for the nonradiative-transition probabilities, which are obtained from the measured average lifetimes and average quantum efficiencies of fluorescence.

The positions of the spectra of the rare earth ions which are due to intraconfigurational f-f transitions in amor-

phous materials are only slightly dependent on the host. However, a small shift of the free-ion levels to lower energies, the nephelauxetic effect, can be observed as a result of covalency between the rare earths and the matrix. This is evident especially in chalcogenide glasses (5). The intensity of the transitions can be calculated to a good approximation by the Judd-Ofelt theory, in which the calculated matrix elements of the transition are combined with the experimentally obtained intensity parameters (6).

The optical transitions of rare earths in solids are predominantly of electric dipole character and their spectral intensities can be described using the treatment of Judd and Ofelt. In this approach, the line strength S of a transition between two J states is given by the sum of products of empirical intensity parameters Ω_t and matrix elements of tensor operators $U^{(t)}$ of the form

$$S(J, J') = \sum_{t=2,4,6} \Omega_t \left| \langle aJ || U^{(t)} || bJ' \rangle \right|^2 \quad [1]$$

The values of Ω_t are obtained from a least squares fit of measured and calculated absorption line strengths and typically have an experimental uncertainty of $\sim \pm 10\%$. The integrated intensities of the absorption bands yield Ω_t 's which are an effective average over the different rare earth environments in the glass.

The most significant factor determining the Ω values is the strength of the odd-order terms in the expansion of the local field at the rare earth site. These in turn are affected by the nearest neighbor anion(s) and cations. For a given glass, former systematic changes of Ω_t have been observed with changes in the size and charge of network modifier ions (7).

Intensity parameters of Nd^{3+} , Ho^{3+} , and Er^{3+} are given in Tables I, II, and III.

It has been shown recently (8) for Er^{3+} that the Judd-Ofelt parameters have also a physical meaning, so that the Ω_2 parameter is indicative of the amount of covalent bonding, while the Ω_6 parameter is related to the rigidity of the medium in which the ions are situated.

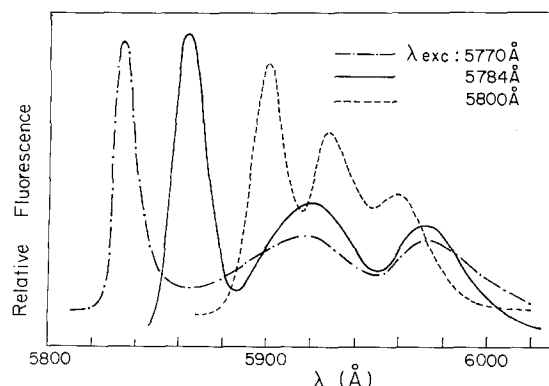


Fig. 1. Laser selective excitation of 2 w/o Eu^{3+} in phosphotungstate glasses at liquid helium temperature.

Table I. Intensity parameters of Nd³⁺ in various hosts

Host materials	Ω_2 10 ⁻²⁰ cm ²	Ω_4 10 ⁻²⁰ cm ²	Ω_6 10 ⁻²⁰ cm ²
3Al ₂ S ₃ · La ₂ S ₃ glass	9.45	4.84	6.54
3Ga ₂ S ₃ · La ₂ S ₃ glass	6.65	4.39	4.67
YAG crystal	0.20	2.70	5.00
Y ₂ O ₃ crystal	8.55	5.25	2.89
YAlO ₃ crystal	1.24	4.68	5.85
ED-2 glass	3.30	4.70	5.20
Borate glass	4.10	3.40	4.30
Silicate glass	4.00	3.30	2.50
Phosphate glass	3.50	3.90	5.80
Germanate glass	5.80	3.30	2.90

Table II. Intensity parameters of Ho³⁺ in various hosts

Host materials	Ω_2 10 ⁻²⁰ cm ²	Ω_4 10 ⁻²⁰ cm ²	Ω_6 10 ⁻²⁰ cm ²
3Al ₂ S ₃ · La ₂ S ₃ glass	8.09	3.85	1.40
3Ga ₂ S ₃ · La ₂ S ₃ glass	2.31	2.81	1.08
Phosphate glass	5.60	2.70	1.87
Calibo glass	6.83	3.15	2.53
Tellurite glass	6.92	2.81	1.42
LaF ₃	1.16	1.38	0.88

Table III. Ω_i parameters for erbium (III) in different environments (8)

System	Ω_2 (× 10 ⁻²⁰ cm ²)	Ω_4 (× 10 ⁻²⁰ cm ²)	Ω_6 (× 10 ⁻²⁰ cm ²)
46PbF ₂ -22ZnF ₂ -30GaF ₃ -2LaF ₃ glass	1.54	1.13	1.19
Er(III) hydrated ion solution	1.59	1.95	1.90
Y _{0.3} Zr _{0.5} O _{1.75} fluorite-type crystal	2.92	0.78	0.57
ErCl ₃ · 6H ₂ O in CH ₃ OH	3.2	3.2	0.8
2ErF ₂ -57ZrF ₄ -34BaF ₂ -4AlF ₃ -3LaF ₃ glass	3.26	1.85	1.14
3Al ₂ S ₃ -La ₂ S ₃ glass	3.74	4.33	0.90
Y ₂ O ₃ C-type crystal	4.59	1.21	0.48
NaPO ₃ glass	9.9	4.3	7
Borate glass	11.3	3.6	2.2
Molten LiNO ₃ + KNO ₃	15.8	1.8	1.4
ErCl ₃ (AlCl ₃) _r vapor	25.8	2.7	2.0

Nonradiative Transitions

Excited electronic levels of rare earths (RE) in solids decay nonradiatively by exciting lattice vibrations (phonons) (9). When the energy gap between the excited level and the next electronic level is larger than the phonon energy, several lattice phonons are emitted in order to bridge the energy gap. It was recognized that the most energetic vibrations are responsible for the nonradiative decay, since such a process can conserve energy in the lowest order. In glasses, the most energetic vibrations are the stretching vibrations of the glass-network polyhedra, and it was shown that these distinct vibrations are active in the multiphonon process (10) rather than the less energetic vibrations of the bond between the RE and its surrounding ligands. Later (11), it was demonstrated that these less energetic vibrations may participate in cases when the energy gap is not bridged totally by the high energy vibrations. The experimental results reveal that the logarithm of the multiphonon-decay rate decreases linearly with the energy gap, or the number of phonons bridging the gap. The theory of nonradiative decay by multiphonon mechanism was first proposed by

Kubo and Toyozawa (12), who proposed that the basic mechanism allowing such transitions is the correction in the Born-Oppenheimer (BO) approximation due to vibrational motion of ions which admixes the electronic wave function and causes transitions that represent stationary states in the zero-order BO approximation. For multiphonon processes, one has to proceed to higher order being $\Delta E/\hbar\omega$ to get real transitions between the electronic states (13). It should be noted that in contrast to the smallness of the radiative processes of high order, the nonradiative high order processes are quite high.

From the point of view of theoretical treatment, it is extremely difficult to calculate accurately the perturbation of a high order. However a considerable part of ΔH_{vibr} can be eliminated as a perturbation by including it exactly in the wave function by a "renormalization." The part of ΔH_{vibr} which still remains after renormalization is the non-adiabaticity of the BO correction operator. At the end of the calculation, an approximation is made of the interaction with only one phonon mode (14-18). For small coupling and low temperature, a Poisson-like function is obtained (17) for the distribution of the multiphonon relaxation rate with the number of phonons. The nonradiative transition probability W_p is given by

$$W_p = \exp(-S) S^p/p! \quad [2]$$

where S is the Huang-Rhys-Pekar number (13), and

$$S(T=0) = 1/2 \Delta^2 \quad [3]$$

(S is the measure of electron phonon coupling strength.)

The displacement Δ measures the horizontal shift of the electronic state potentials in units of the zero-point amplitude. In the case of an isolated RE ($S \ll 1$), S can be incorporated in the exponential formula of Dexter

$$W = \beta \exp(-\alpha \Delta E) \quad [4]$$

with

$$\alpha = (\hbar\omega)^{-1} [\ln(p/S) - 1] \text{ for low temperature} \quad [5]$$

and

$$\alpha = (\hbar\omega)^{-1} [\ln(p/S)(n+1) - 1] \text{ for } T > 0 \quad [6]$$

n being the phonon occupancy number or

$$n = (\exp(-\hbar\omega/kT) - 1)^{-1} \text{ as explained in Ref. (19)} \quad [7]$$

Application of the multiphonon theory to glasses requires the knowledge of the structural units forming the glass. Similar to the electronic spectra in glasses, the vibrational frequencies show inhomogeneous broadening due to the variation of sites. Table IV shows the average frequencies of the network formers. The vibrations involving the network modifiers are lower by a factor of 2 to 4. The lack of symmetry in a glass and the molecular character of the high energy vibration were taken into account by Layne *et al.* (20) in developing the theory of multiphonon relaxation in glass using higher order terms in the perturbation theory. The dependence of a multiphonon rate on the energy gap to be bridged results then from the ratio of p-phonon process to that for a p-1 phonon decay. Assuming the average matrix elements to be the same for p- and p-1-order processes, the ratio of W_p

Table IV. Parameters of nonradiative relaxations

Host	β s ⁻¹	α cm	$\hbar\omega$ cm ⁻¹	ϵ	Ref.
GLS, ALS glass	1 × 10 ⁶	2.9 × 10 ⁻³	350	0.36	(9)
Tellurite glass	6.3 × 10 ¹⁰	4.7 × 10 ⁻³	700	0.037	(9)
Germanate glass	3.4 × 10 ¹⁰	4.9 × 10 ⁻³	900	0.013	(9)
Phosphate glass	5.4 × 10 ¹²	4.7 × 10 ⁻³	1200	0.0037	(9)
Borate glass	2.9 × 10 ¹²	3.8 × 10 ⁻³	1400	0.0049	(9)
49BeF ₂ , 27KF, 14CaF ₂ , 10AlF ₃ glass	9 × 10 ¹¹	6.3 × 10 ⁻³	500	0.042	(43)
LaCl ₃ crystal	1.5 × 10 ¹⁰	13.0 × 10 ⁻³	260	0.037	(23)
LaBr ₃ crystal	1.2 × 10 ¹⁰	19.0 × 10 ⁻³	175	0.037	(23)
LaF ₃ crystal	6.6 × 10 ⁸	5.6 × 10 ⁻³	350	0.14	(23)
Y ₂ O ₃ crystal	2.7 × 10 ⁸	3.8 × 10 ⁻³	550	0.12	(23)
SrF ₂ crystal	3.1 × 10 ⁸	4.0 × 10 ⁻³	360	0.20	(23)
Y ₃ Al ₅ O ₁₂ crystal	9.7 × 10 ⁷	3.1 × 10 ⁻³	700	0.045	(23)
YAlO ₃ crystal	5 × 10 ⁹	4.6 × 10 ⁻³	600	0.063	(9)
LiYF ₄ crystal	3.5 × 10 ⁷	3.8 × 10 ⁻³	—	—	(9)

to W_{p-1} is

$$W_p/W_{p-1} = (\hbar/2M\omega) (n+1) 4m^2 | \langle a|V|b \rangle |^2 / (\hbar\omega)^2 \quad [8]$$

Since the perturbation is weak

$$W_p/W_{p-1} = \epsilon \ll 1 \quad [9]$$

This result leads to the following exponential dependence of the rate on the energy gap

$$W_p = W_0 \epsilon^p = W \exp [\ln(\epsilon)/\hbar\omega] \Delta E \quad [10]$$

Considering the dependence of W_p on the phonon occupation number from Eq. [7], the rate for a p-order multiphonon decay is at temperature $T > 0$

$$W_p = W_0 [n(T) + 1]^p \exp(-\alpha \Delta E) \quad [11]$$

where

$$\alpha = -\ln(\epsilon) \hbar\omega \quad [12]$$

and $W_0 = \beta$ of Eq. [4] is dependent on the host but independent of the specific electronic level of RE from which the decay occurs.

Struck and Fonger have treated the nonradiative decay processes by a numerical matrix method (21) and found that in the case of rare earth ions where there is a small offset in the configurational coordinates the multiphonon transition rate can be treated by the Kiel formula of the type which is consistent with Eq. [11] presented in Eq. [4], [10], and [11].

In calculating theoretically the multiphonon relaxation Siebrand (22) has used the Condon approximation in which the electronic matrix elements are separated from the vibrational ones and assuming that the transition is dominated by a small number of promoting modes which consume the energy $\hbar\omega$. The accepting modes provide only for the remaining energy difference $\Delta E_0 - \hbar\omega_{\max}$.

The theoretical results arising from this theory are

$$W_{NR} = \exp(-\Delta E_0 - 2\hbar\omega_{\max}) \alpha \quad [14]$$

By developing this theoretical expression further, van Dijk and Schuurmans (23) have shown that the pre-exponential factor in the nonradiative relaxation expression does not vary by more than one order of magnitude for the various compounds studied, and is due to the electronic factor.

The multiphonon decay rate from a given level to the next lower level decreases with the lowering of energy of the stretching frequencies of the glass former. Since a large number of phonons is needed in fluoride glasses and more so in chalcogenide glasses in order to reach the same energy gap, the nonradiative relaxations are smallest in these hosts. Dependence of the multiphonon transition rate on the number of phonons from the emitting to the next lower level for a number of glasses and crystal hosts are presented in Fig. 2.

The parameters α and β of Eq. [4] and ϵ of Eq. [12] of glasses and crystals are presented in Table IV together with the phonon frequencies.

Chalcogenide and Fluoride Glasses

Chalcogenide and fluoride glasses have been found to be highly efficient phosphors with several activators. These glasses have also low absorption in the infrared part of the spectrum because of the high order multiphonon absorption in this region, lower than that for the oxide glasses.

Rare earth sulfides with Ga_2S_3 and Al_2S_3 were prepared by Flahaut and his group, who have studied in detail the phase diagrams of these materials (24). The glass of composition $3Al_2S_3 \cdot La_2S_3$ (ALS) is transparent from 1,500-25,000 cm^{-1} , and the glass of composition $3Ga_2S_3 \cdot La_2S_3$ (GLS) from 1,500-20,000 cm^{-1} . These may prove important materials for fiber optical waveguides.

Laser emission cross sections of the 1077 and 1370 nm emissions of Nd^{3+} in $3Ga_2S_3 \cdot 0.85 La_2S_3 \cdot 0.15 Nd_2S_3$ (GLS) and $3Al_2S_3 \cdot 0.872 La_2S_3 \cdot 0.128 Nd_2S_3$ (ALS) were obtained from the calculated matrix elements in the glasses, exper-

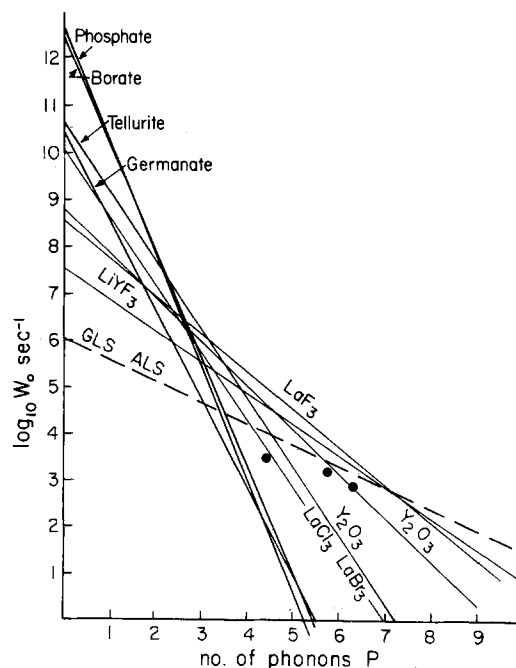


Fig. 2. Dependence of multiphonon transition rate on number of phonons in different glasses.

imentally measured intensity parameters, emission half-widths, and lifetimes. The laser threshold power for side-pumping in the chalcogenide glasses is much lower than for ED-2 glass.

The peak cross sections of Nd^{3+} in GLS are $7.95 \times 10^{20} cm^2$ at 1077 nm and $3.60 \times 10^{-20} cm^2$ at 1320 nm; $8.20 \times 10^{-20} cm^2$ at 1077 nm and $4.10 \times 10^{-20} cm^2$ at 1370 nm in ALS, as compared to $2.90 \times 10^{-20} cm^2$ at 1060 nm and $0.72 \times 10^{-20} cm^2$ at 1300 nm for ED-2 glass (25).

A new family of fluoride glasses was obtained in 1975 by Poulain *et al.* (26) in Rennes. They are called fluorozirconate glasses containing large amounts (above 50 mol percent [m/o]) of ZrF_4 (which can be replaced by HfF_4 or ThF_4) along with lesser amounts of alkaline-earth, rare earth, or uranium IV fluorides. Miranday *et al.* (27, 28) prepared another type of new fluoride glasses based on PbF_2 and 3d-group fluorides.

Because of the low relaxation of the rare earth luminescent ion in fluoride glasses, they can provide an ideal medium or host for various devices. The high infrared transmittance and good chemical stability makes them suitable for integrating the laser light source and the waveguide itself. The spectroscopic and fluorescent properties of Nd^{3+} containing fluorozirconate glasses have been reported by Weber in work with the Lucas-Poulain group in Rennes (29).

The low multiphonon relaxation in fluoride glasses is also evidenced by the luminescence arising from the 3D_3 , 5D_2 , and 5D_1 levels of Eu^{3+} in addition to the 5D_0 fluorescence in fluoride glasses (30). An example of such fluorescence is presented in Fig. 3 for Eu^{3+} in a glass of composition $57ZrF_4 \cdot 34BaF_2 \cdot 4AlF_3 \cdot 3LaF_3 \cdot 2EuF_3$.

The luminescence characteristics of Er^{3+} in fluoride glasses were studied recently (31). Because of low nonradiative relaxation, emission of Er^{3+} in these glasses can be observed from the first, second, fourth, and fifth electronic levels when excited into the $^2H_{11/2}$ level (see Fig. 4). In all these cases, the energy gap is lower than $2800 cm^{-1}$ to the next lower excited level.

Since the undoped materials are excellent candidates for fiber optic waveguides due to their high transmittance in the infrared and their chemical stability, it was suggested that erbium-doped materials having the desired laser emission wavelengths, which can be selected from Table V, be used as light sources for fiber optic systems. They could be integrated into the waveguide providing integrated fiber optic systems (31).

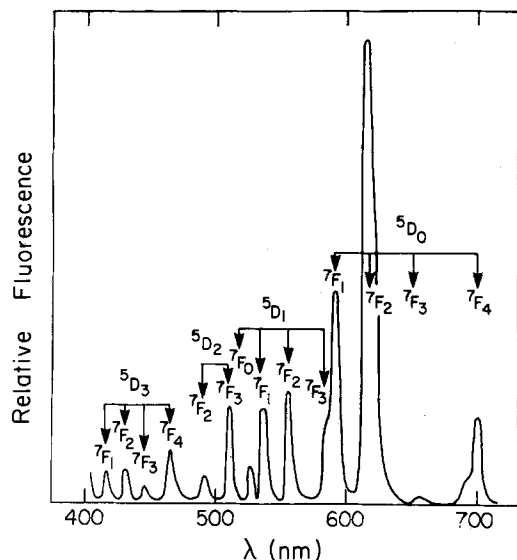


Fig. 3. Emission spectrum of Eu^{3+} in the glass $57\text{ZrF}_4:34\text{BaF}_2:4\text{AlF}_3:3\text{LaF}_3:2\text{EuF}_3$ under 395 nm excitation.

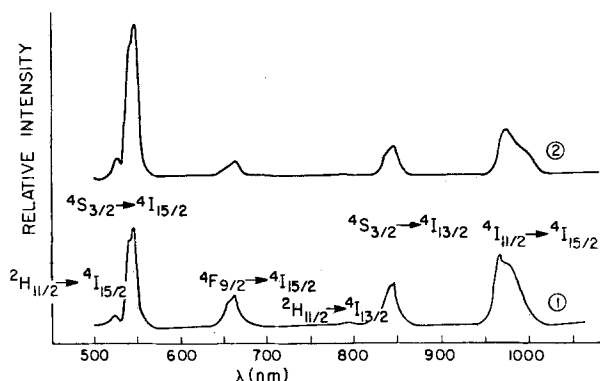


Fig. 4. Comparison of emission spectra of Er^{3+} in two fluoride glasses (1) 2.00 w/o $\text{ErF}_3:46\text{PbF}_2:22\text{ZnF}_2:30\text{GaF}_3:2\text{LaF}_3$ m/o, and (2) 2.66 w/o $\text{ErF}_3:57\text{ZrF}_4:34\text{BaF}_2:3\text{LaF}_3:4\text{AlF}_3$ m/o.

The emission of Er^{3+} in fluoride glasses can be additionally intensified by the process of energy transfer from Mn^{2+} to Er^{3+} (32).

Luminescence of Rare Earths Adsorbed on Porous Glasses

When porous glasses are dipped into a rare earth solution, the ions are adsorbed into the glass pores and exhibit fluorescence similar to that obtained for ions in the bulk of a glass (33).

Vycor porous glass, Corning no. 7930, has an average pore diameter of 40-70Å, sufficiently large for the penetration of rare earth ions or complexes. The surface area of such glasses is about 200 m²/g, as obtained by the nitro-

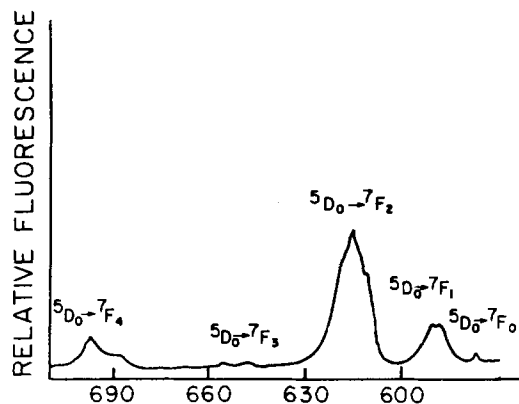


Fig. 5. Emission spectrum of Eu^{3+} adsorbed on Vycor

gen BET method. Also compressed pyrogenic silica gel Cab-O-Sil Aerosil, yields porous transparent disks (34). The disks are totally transparent in near-ultraviolet and visible light.

The relative intensities of fluorescence in the various rare earth ions adsorbed in Vycor and fumed silica disks are: $\text{Tb} > \text{Eu} > \text{Dy} > \text{Tm} > \text{Pr} > \text{Ho} > \text{Er}$ (35).

Figure 5 presents the fluorescence spectrum of Eu^{3+} adsorbed on Vycor. The hypersensitive transition $^5\text{D}_0 \rightarrow ^7\text{F}_2$ is much higher than the $^5\text{D}_0 \rightarrow ^7\text{F}_1$ transition due to magnetic dipole. Such a picture corresponds to the well-known behavior of the Eu ion in a low symmetry site.

We believe that a chemical bond is formed between Eu^{3+} and the glass support since the adsorbed ion cannot be washed out by liquids.

The ratio between the $^5\text{D}_0 \rightarrow ^7\text{F}_2$ transition to the $^5\text{D}_0 \rightarrow ^7\text{F}_1$ transition is even greater when Eu-benzoylacetonate is adsorbed on Vycor glass. The introduction of fluorescent complexes into porous glasses opens a possibility of using inorganic species with organic ligands, and thus increasing the luminescence by several orders of magnitude (36).

Energy transfer between dyes and rare earth ions can also be performed on various types of glass (37).

Application of Luminescence of Rare Earths in Luminescence Solar Concentrations

While the luminescence of rare earths for lasers (Nd-glass laser) and phosphors has been well established during the last two decades, their use in luminescent solar concentrators has been proposed only recently (38-40).

The first attempt to use neodymium ions for solar collectors was made by Levitt and Weber (41), who measured devices consisting of Owens-Illinois ED-2 Nd-doped laser glass. The efficiency of this glass for solar collection is rather low because of the low absorption of Nd^{3+} in this glass. The problem can be circumvented by incorporating Nd^{3+} into tellurite glass. Calculated plate efficiencies of Nd^{3+} in tellurite glass based on optical measurements of absorption and emission spectra and quantum efficiency

Table V. Selected possible laser transitions of erbium(III) in the glass $57\text{ZrF}_4:34\text{BaF}_2:3\text{LaF}_3:4\text{AlF}_3:2\text{ErF}_3$

Transition	Wavelength (nm)	Radiative transition probabilities $A(\text{s}^{-1})$	Branching ratio β_{12}	Peak cross section $\sigma_p(10^{-20} \text{ cm}^2)$
$^4\text{G}_{11/2} \rightarrow ^4\text{I}_{15/2}$	378	14,900	0.859	3.719
$^2\text{H}_{9/2} \rightarrow ^4\text{I}_{15/2}$	405	1,030	0.394	0.453
$^4\text{F}_{9/2} \rightarrow ^4\text{I}_{15/2}$	440	1,000	0.457	0.524
$^4\text{F}_{5/2} \rightarrow ^4\text{I}_{15/2}$	448	1,070	0.434	0.939
$^4\text{F}_{7/2} \rightarrow ^4\text{I}_{15/2}$	486	2,430	0.750	1.770
$^2\text{H}_{11/2} \rightarrow ^4\text{I}_{15/2}$	519	4,110	0.932	2.538
$^4\text{S}_{3/2} \rightarrow ^4\text{I}_{15/2}$	540	886	0.656	0.702
$^2\text{H}_{9/2} \rightarrow ^4\text{I}_{13/2}$	551	1,150	0.442	—
$^4\text{F}_{9/2} \rightarrow ^4\text{I}_{13/2}$	650	1,250	0.909	1.119
$^2\text{H}_{11/2} \rightarrow ^4\text{I}_{13/2}$	786	158	0.036	—
$^4\text{I}_{9/2} \rightarrow ^4\text{I}_{13/2}$	795	148	0.774	0.192
$^4\text{S}_{3/2} \rightarrow ^4\text{I}_{13/2}$	835	383	0.284	—
$^4\text{I}_{11/2} \rightarrow ^4\text{I}_{15/2}$	975	111	0.820	0.372
$^2\text{H}_{11/2} \rightarrow ^4\text{I}_{9/2}$	1495	640	0.014	—
$^4\text{I}_{9/2} \rightarrow ^4\text{I}_{15/2}$	1529	122	1.000	0.577
$^4\text{I}_{11/2} \rightarrow ^4\text{I}_{15/2}$	2691	24	0.180	—

of Nd^{3+} are 12%, which is three times higher than in conventional silicate glass (42).

Reisfeld and Kalisky have shown that a combination of UO_2^{2+} with Nd^{3+} or Ho^{3+} in glass (39) extends the spectral sensitivity range of luminescent solar concentrators due to efficient energy transfer from the $20,500\text{ cm}^{-1}$ excited level of the uranyl ion. Both energy transfer and direct excitation to the Nd^{3+} levels provide the well-known laser transition ${}^4\text{F}_{3/2} \rightarrow {}^4\text{I}_{11/2}$ (1060 nm) with a branching ratio around 0.5, as well as the transition to the ground state ${}^4\text{F}_{3/2} \rightarrow {}^4\text{I}_{9/2}$ (880 nm) (6). The latter transition is a resonant one and repopulates the ${}^4\text{F}_{3/2}$ level, and thus no appreciable amount of energy is lost by reabsorption. Both transitions lie in the spectral range in which silicon solar cells have high spectral sensitivity.

Acknowledgment

The author is deeply grateful to Mrs. E. Greenberg for her help in preparation of the manuscript.

Manuscript submitted Aug. 29, 1983; revised manuscript received ca. Dec. 7, 1983.

This was Paper 468 presented at the Montreal, Quebec, Canada, Meeting of the Society, May 9-14, 1982.

REFERENCES

- L. A. Riseberg, *Phys. Rev. A*, **7**, 671 (1973).
- M. J. Weber, in "Laser Spectroscopy of Solids," W. M. Yen and P. M. Selzer, Editors, pp. 189-239, Springer, Berlin (1981).
- M. J. Weber and S. A. Brawer, *J. Phys. (Paris)*, **43**, 291 (1982).
- F. D. Durville, G. Boulon, R. Reisfeld, H. Mack, and C. K. Jørgensen, *Chem. Phys. Lett.*, **102**, 393 (1983).
- R. Reisfeld, *Ann. Chim. Fr.*, **7**, 147 (1982).
- R. Reisfeld and C. K. Jørgensen, "Lasers and Excited States of Rare Earths," Springer, Berlin (1977).
- M. J. Weber, in "Proceedings of the International Conference on Lasers '82" New Orleans, LA, Dec. 13-17, 1982, proceedings to be published.
- C. K. Jørgensen and R. Reisfeld, *J. Less-Common Met.*, **93**, 107 (1983).
- R. Reisfeld, in "Radiationless Process," B. Di Bartolo and V. Goldberg, Editors, pp. 489-498, Plenum, New York (1980).
- R. Reisfeld and Y. Eckstein, *J. Chem. Phys.*, **63**, 4001 (1975).
- R. Reisfeld, J. Hormadaly, and A. Muranevich, *Chem. Phys. Lett.*, **38**, 188 (1976); J. Hormadaly and R. Reisfeld, *ibid.*, **45**, 436 (1977).
- Y. Toyozawa, in "Dynamical Processes in Solid State Optics," R. Kubo, Editor, p. 90, Benjamin (1976).
- R. Engman, "Nonradiative Decay of Ions and Molecules in Solids," North Holland, Amsterdam (1979).
- Y. E. Perlin, *Sov. Phys. Uspekhi*, **6**, 542 (1963).
- F. K. Fong, "Theory of Molecular Relaxation," John Wiley and Sons, New York (1975).
- R. Engman and J. Jortner, *Mol. Phys.*, **18**, 145 (1970).
- T. Miyakawa and D. L. Dexter, *Phys. Rev. B*, **1**, 2961 (1970).
- W. H. Fonger and C. W. Struck, *J. Lumin.*, **17**, 241 (1978).
- F. Auzel, in "Luminescence of Inorganic Solids," B. Di Bartolo, Editor, p. 67, Plenum Press, New York (1978).
- C. B. Layne, W. H. Lowdermilk, and M. J. Weber, *Phys. Rev. B*, **16**, 10 (1977).
- C. W. Struck and W. H. Fonger, *J. Lumin.*, **10**, 31 (1975).
- W. Siebrand, *J. Chem. Phys.*, **46**, 440 (1967).
- J. M. F. Van Dijk and M. F. H. Schuurmans, *ibid.*, **78**, 5317 (1983).
- J. Flahaut, in "Handbook in the Physics and Chemistry of Rare Earths," Vol. 4, K. A. Gschneidner, Jr. and L. Eyring, Editors, p. 31, North-Holland, Amsterdam (1979).
- R. Reisfeld, *J. Less-Common Met.*, **93**, 243 (1983).
- M. Poulain, M. Poulain, and J. Lucas, *Mater. Res. Bull.*, **10**, 243 (1975).
- J. P. Miranday, C. Jacoboni, and R. DePape, *J. Non-Cryst. Solids*, **43**, 393 (1981).
- J. P. Miranday, C. Jacoboni, and R. DePape, *Rev. Chim. Miner.*, **16**, 227 (1979).
- J. Lucas, M. Chanthanasinh, M. Poulain, M. Poulain, P. Brun, and M. J. Weber, *J. Non-Cryst. Solids*, **27**, 273 (1978).
- R. Reisfeld, E. Greenberg, R. N. Brown, M. G. Drexhage, and C. K. Jørgensen, *Chem. Phys. Lett.*, **95**, 91 (1983).
- R. Reisfeld, G. Katz, C. Jacoboni, R. DePape, M. G. Drexhage, R. N. Brown, and C. K. Jørgensen, *J. Solid State Chem.*, **48**, 323 (1983).
- R. Reisfeld, E. Greenberg, C. Jacoboni, R. DePape, and C. K. Jørgensen, *J. Solid State Chem.*, **53** (1984).
- H. Mack, D. Avnir, and R. Reisfeld, Abstract 472, p. 773, The Electrochemical Society Extended Abstracts, Vol. 82-1, Montreal, Quebec, Canada, May 9-14, 1982.
- R. Reisfeld, N. Manor, and D. Avnir, *Solar Energy Mater.*, **8**, 399 (1983).
- H. Mack, R. Reisfeld, and D. Avnir, *Chem. Phys. Lett.*, **99**, 238 (1983).
- D. Avnir, R. Reisfeld, and D. Levy, *Isr. Pat. Appl.* **69**, 794 (1983).
- R. Reisfeld, *Chem. Phys. Lett.*, **95**, 95 (1983).
- R. Reisfeld and S. Neuman, *Nature*, **274**, 144 (1978).
- R. Reisfeld and Y. Kalisky, *ibid.*, **283**, 281 (1980).
- R. Reisfeld and C. K. Jørgensen, *Struct. Bonding (Berlin)* **49**, 1 (1982).
- J. A. Levitt and W. H. Weber, *Appl. Opt.*, **16**, 2684 (1979).
- R. Reisfeld and A. Kisilev, Unpublished data.
- C. B. Layne and M. J. Weber, *Phys. Rev. B*, **16**, 3259 (1977).

Phosphor Depreciation by Ion Bombardment

Osamu Tada,* Kikuo Tominaga,* Toshiaki Kondo,* and Yoshihiro Kondo*

Tokushima University, Minamijosanjima, Tokushima 770, Japan

Keiji Ichinomiya

Nichia Chemical Industries, Limited, Anan, Tokushima 774, Japan

ABSTRACT

Phosphor depreciation due to physical damage has been studied. The effects of ion bombardment on luminescence, lattice disorder, and affinity for Hg atoms are investigated. The following results are obtained for $Zn_2SiO_4:Mn$ polycrystal: An amorphous layer of about 3000Å in depth is produced at the surface bombarded by Ar^+ ions with an energy of 200 eV. Hg atoms are adsorbed more easily at the ion bombarded surface than the nonbombarded surface. It is also found for 16 kinds of phosphor powders that the deterioration characteristic caused by ion bombardment is similar with that of lumen depreciation of a fluorescent lamp composed with the same phosphor. The possibility of the lumen depreciation of a fluorescent lamp arising from the ion bombardment is discussed.

Since the advent of the fluorescent lamp in the middle nineteen-thirties, many technical efforts have been expended for improvements in the fluorescent lamp. Nevertheless we have little information concerning the phosphor depreciation in a burning fluorescent lamp. In the investigation of the depreciation mechanism of a fluorescent lamp, the possibility of phosphor depreciation due to ion bombardment has not been denied completely. For example, Lehmann (1) proposed that phosphor depreciation is caused by energetic ion bombardment in the fluorescent lamp, although the generation mechanism of the energetic ions is not still clear. However, studies of the effects of ion bombardment on the properties of fluorescent phosphors are few. In this work we investigated the influence of ion bombardment on phosphor depreciation. First, physical damage of $Zn_2SiO_4:Mn$ polycrystal by ion bombardment is presented. An amorphous layer of about 3000Å in depth is produced at the surface bombarded by Ar^+ ions with an energy of 200 eV. The amorphous layer is nonluminescent under UV light excitement, but absorbs UV light. Hg atoms are adsorbed more easily at the amorphous layer than the nonbombarded polycrystal surface. Next ion bombardment test for phosphor powders and burning test for fluorescent lamps were carried out concerning 16 kinds of phosphors. The results show that the depreciation characteristic of phosphor powders induced by the ion bombardment is similar with that of lumen depreciation of fluorescent lamp. Finally the possibility of the lumen depreciation of fluorescent lamp arising from ion bombardment is discussed.

Experimental

Preparation of $Zn_2SiO_4:Mn$ polycrystalline disk.—To investigate the influence of ion bombardment on the properties of phosphor, it is desirable to use a large crystal surface rather than powders. Using the floating zone method (2), we prepared $Zn_2SiO_4:Mn$ polycrystals. Appearances of as-grown $Zn_2SiO_4:Mn$ polycrystal rod and its cross section (8 mm in diameter) normal to growth direction are shown in Fig. 1. The interior part of the cross section is composed of polycrystalline grains of about 0.5 mm in diameter, and the crystal axis [111] of each grain is uniquely parallel to the growth direction. The interior part was used for the experiment.

Apparatus for ion bombardment.—A schematic diagram of an apparatus used for the ion bombardment is shown in Fig. 2, which is a usual RF (radio frequency) diode sputtering apparatus. When RF voltage is applied on the target holder, glow discharge occurs and the phosphor placed on the target holder is bombarded by energetic positive ions. In the present experiment, the glow discharge was made in pure Ar or a mixed gas of Ar and

Hg vapor. Hg vapor was evaporated naturally from a glass vessel containing Hg. During the ion bombardment, gas pressure of Ar or Ar-Hg gas was maintained at 0.03 torr and the RF voltage was at 200 or 400V.

Phosphor powders used in this experiment.—An ion bombardment test for phosphor powders and a burning test for fluorescent lamps were carried out concerning the following 16 kinds of phosphors: (i) $(LaCe)PO_4:Tb$, (ii) $3.5MgO \cdot 0.5MgF_2 \cdot GeO_2:Mn$, (iii) $Y_2O_3:Eu$, (iv) $CaWO_4:Pb$, (v) $MgAl_{11}O_{14}:CeTb$, (vi) $CaO_{10}(PO_4)FCl:Eu$, (vii) $BaMg_2Al_{16}O_{27}:Eu$, (viii) $(SrCa)_5(PO_4)_3Cl:Eu$, (ix) $Y_2O_3:S:Eu$, (x) $Sr_5(PO_4)Cl:Eu$, (xi) $Sr_2P_2O_7:Sn$, (xii) $Y(PV)O_4:Eu$, (xiii) $Ba_2P_2O_7:Ti$, (xiv) $(SrMg)_3PO_4:Sn$, (xv) $YVO_4:Eu$, (xvi) $Zn_2SiO_4:Mn$. Correlation between the phosphor depreciation by ion bombardment and the lumen depreciation of fluorescent lamp was investigated.

Results and Discussion

Damage of phosphor surface by Ar^+ ion bombardment.—In the following experiments, we used the $Zn_2SiO_4:Mn$ polycrystalline disks indicated in Fig. 1, which were polished and etched by diluted HF solution. Then half the region of the disk surface was bombarded by Ar^+ ions with an energy of 200 eV using the apparatus illustrated in Fig. 2. Hg^+ ion bombardment gave a similar result, so we show only the results for the Ar^+ ion bombardment to make clear the influence of physical damage.

Amorphous layer by ion bombardment.—Residual damage on the $Zn_2SiO_4:Mn$ surface by the Ar^+ ion bombardment has been investigated by high energy electron diffraction (RHEED). The RHEED pattern for original nonbombarded surface is indicated in Fig. 3(a). Sixfold symmetry spots and extra spots are observed. But after the Ar^+ ion bombardment, all these spots vanished and the pattern changed to hollow pattern as shown in Fig. 3(b). This result indicates that most atoms at the $Zn_2SiO_4:Mn$ surface are microscopically displaced from the regular position, that is, the surface becomes amorphous by the ion bombardment.

Depth of amorphous (damaged) layer.—Depth of amorphous layer was estimated as follows. After the ion bombardment, a thin layer was removed chemically by diluted HF solution (0.03N), and cathodoluminescence was measured at each surface. In this case, the mean etch rate for $Zn_2SiO_4:Mn$ was determined to be 230 Å/min from the scanning microscope views of the cross sections of etched samples. Figure 4(a) shows the cathodoluminescence spectra at different etching time. Figure 4(b) indicates the peak intensities of the spectra as a function of the etching time or the etched depth. It is found that the defects which deteriorate the cathodoluminescence range to the depth of about 3000Å from the surface. At the surface there is a heavily damaged layer whose depth is be-

*Electrochemical Society Active Member.

Key words: amorphous, adsorption, fluorescence, damage.

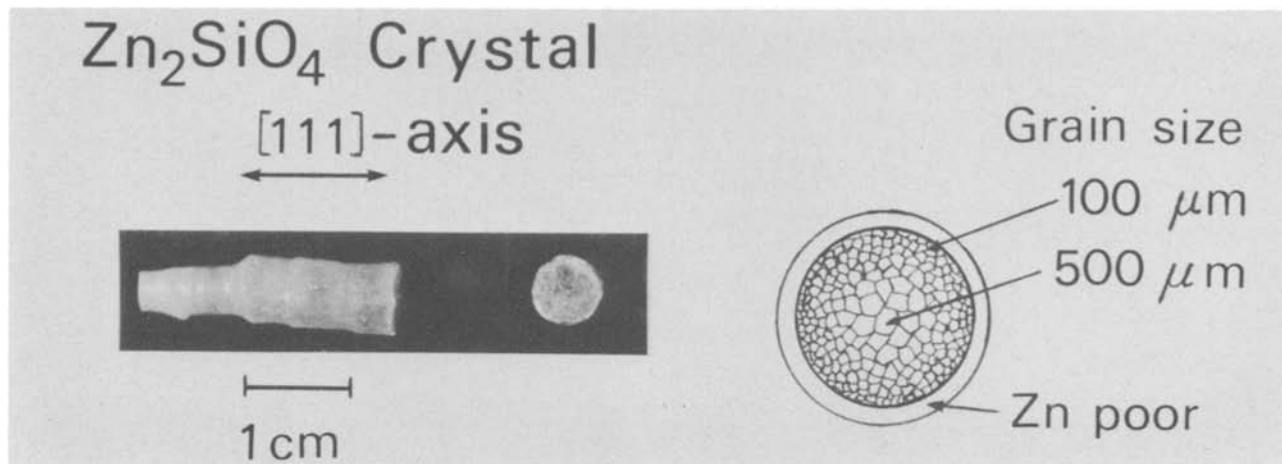


Fig. 1. Appearances of the as-grown $Zn_2SiO_4:Mn$ polycrystal rod and its cross section. The growth direction is parallel to the crystal axis [111]

low 100Å. Similar defect distribution monitored by photoluminescence intensity was obtained for ion-bombarded GaAs by Kawabe *et al.* (3). Since direct atom displacement by ion bombardment is thought to be much smaller than the depth of 3000Å, the heavily damaged layer will be the region corresponding to the direct atom displacement and the diffusion of defects will be responsible for the following damaged layer. The presence of this kind of diffused defects was assumed by Lehmann (1) in the investigation of phosphor depreciation. Our result confirms his assumption experimentally, although our bombarding ion energy (200 eV) is larger than that in Lehmann's report (100 eV).

Mercury adsorption on phosphor.—Fluorescent lamp phosphors originally have strong resistance against mercury adhesion. However ion bombardment changes this character. This will be understood from the following two experiments. The $Zn_2SiO_4:Mn$ polycrystalline disks were treated following processes (I), (II), and (III) indicated in Fig. 5(a), where process (I) is the bombardment by 200 eV Ar^+ ions, process (II) is the dipping process accompanying the stirring of Hg pool by ultrasonic vibrator, and process (III) is annealing at 400°C in air.

(i) Using electron probe microanalysis, we first measured the Hg signal on the $Zn_2SiO_4:Mn$ surface. In this

case, ion bombardment [process (I)] was carried out for only a part of the disk surface, and then the disk was dipped into Hg pool [process (II)]. The Hg signal at boundary area between the bombarded and nonbombarded parts is shown in Fig. 5(b). Almost all large signals are observed at the bombarded part. This result indicates that ion bombardment promotes the adsorption of Hg on the $Zn_2SiO_4:Mn$ phosphor.

(ii) To detect the adsorbed Hg atoms by another method, the samples were annealed abruptly at 400°C [process (III)]. In this case, the adsorbed Hg atoms will amalgamate with phosphor, and recovery of photoluminescence intensity will be hindered. Figure 5(c) shows the change in photoluminescence intensity during the above three processes. A curve (I-III) indicates that the ion bom-

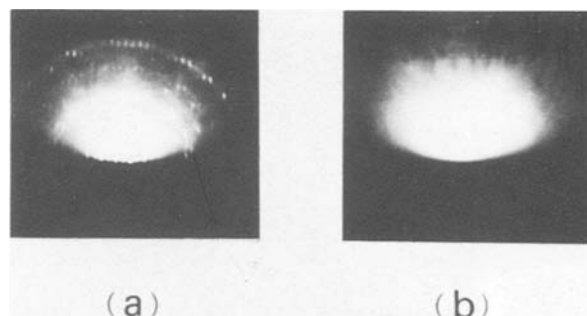


Fig. 3. Reflection high energy diffraction (RHEED) pattern for (a) nonbombarded and (b) bombarded $Zn_2SiO_4:Mn$ polycrystalline surface.

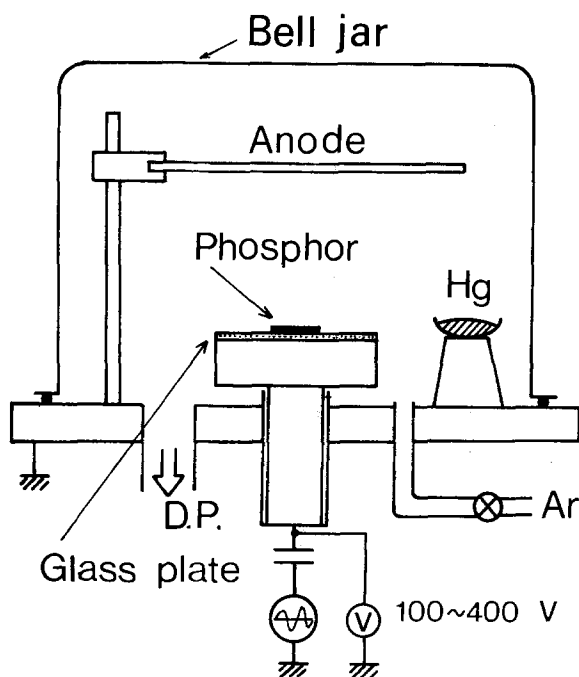


Fig. 2. Apparatus for the ion bombardment of phosphors (RF diode sputtering apparatus).

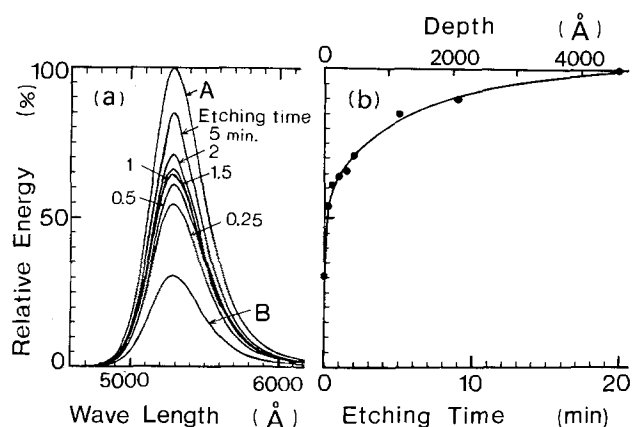


Fig. 4. (a) Cathodoluminescence spectra for etched $Zn_2SiO_4:Mn$ surfaces at different etching time. Curves A and B indicate the cathodoluminescence spectra for nonbombarded and bombarded $Zn_2SiO_4:Mn$. (b) Defect distribution monitored by cathodoluminescence intensity.

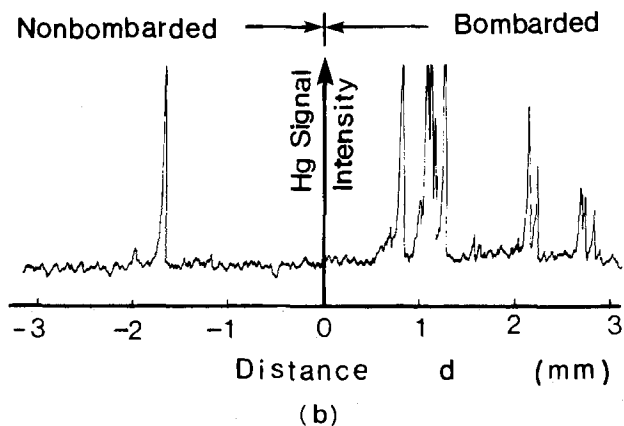
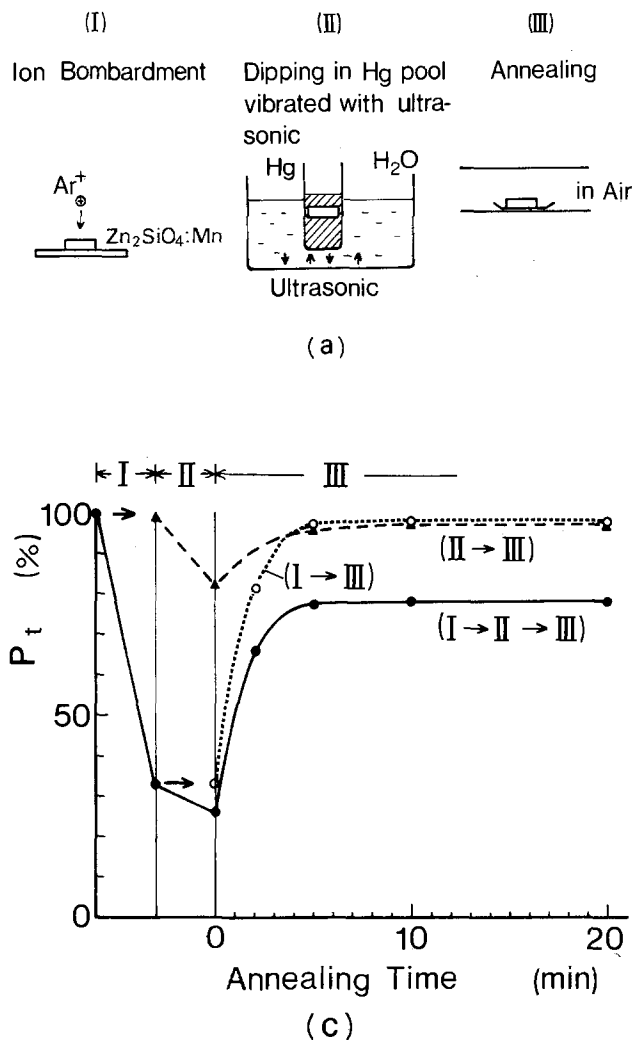


Fig. 5. (a) Treatment processes (I), (II), and (III) for $\text{Zn}_2\text{SiO}_4:\text{Mn}$ polycrystals. (b) Hg distributions on the bombarded and nonbombarded parts measured by electron probe microanalysis. (c) Photoluminescence intensity with respect to the above processes (I), (II), and (III).

bombarded sample is completely recovered by the annealing process (III). For the case of the nonbombarded sample, too, the photoluminescence intensity becomes 100% after the dipping and annealing processes as shown by a curve (II-III). However, when the bombarded sample is dipped into the Hg pool and then annealed, the photoluminescence intensity does not return to 100% as indicated by a curve (I-II-III). This depreciation is thought to be due to an amalgamation of the amorphous layer with Hg atoms, so we can say that Hg atoms are adsorbed mainly on the bombarded phosphor surface. This is the same result as that by electron probe microanalysis. Both results in Fig. 5(b) and (c) indicate that Hg adsorption is enhanced by ion bombardment, that is, the amorphous layer is more reactive in the adsorption of Hg atoms than crystalline surface.

Depreciation characteristic and annealing effect.—First we carried out the ion bombardment test for the $\text{Zn}_2\text{SiO}_4:\text{Mn}$ phosphor powder. The powder was put into a small stainless steel box and bombarded by Hg^+ or Ar^+ ions. Figure 6 shows the change in the logarithm of normalized photoluminescence intensity, $\ln P_t$, with respect to the square root of the bombarding time, \sqrt{t} . In both cases for the ion bombardments by Hg^+ and Ar^+ , the depreciation characteristic is the same. Data for 200 eV ion bombardment lie on a straight line as shown in Fig. 6, which indicates that P_t is expressed by an exponential function of \sqrt{t} . This time dependence is the same as that reported by Lehmann (1) for lower ion bombardment. Data for 400 eV ion bombardment are also indicated in Fig. 6. In this case, the data are approximately expressed by the two straight lines. At the initial stage of ion bombardment, the phosphor depreciates at a higher speed and thereafter the decreasing rate becomes slow. According to Lehmann's consideration (1), the photolumines-

cence intensity should be proportional to $\exp(-\alpha c \sqrt{t})$, where α is the optical absorption constant for UV light of the damaged layer, c is a constant, and I is the intensity of bombarding ion flux. The above expression explains the results in Fig. 6 at the initial stage at least, because the increase of RF voltage means the increase of the bombarding ion flux according to diode sputtering theory (4). Therefore we can understand the results in Fig. 6 by the same model mentioned by Lehmann (1), which assumes that the damaged (nonluminescent) layer opti-

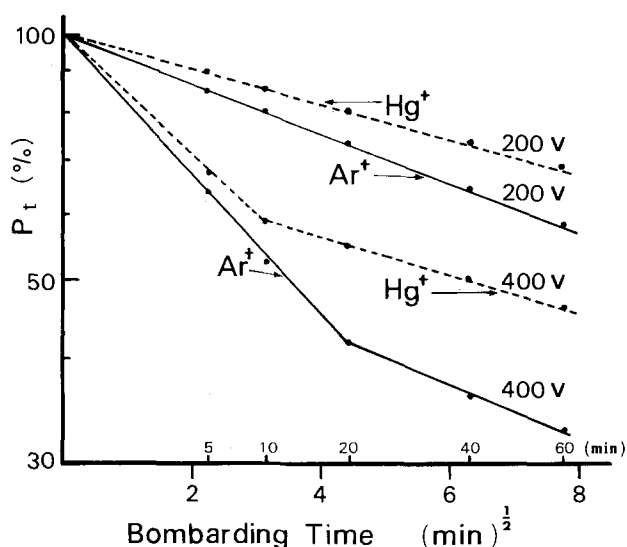


Fig. 6. Depreciation curves of the photoluminescence intensity P_t for ion-bombarded $\text{Zn}_2\text{SiO}_4:\text{Mn}$ powder at RF voltages of 200 and 400V.

cally absorbs exciting UV light and the thickness of damaged layer can be expressed by $c\sqrt{t}$.

Next we investigated the annealing effect on the photoluminescence after ion bombardment. Damage by ion bombardment vanishes by heating the sample. Figure 7 shows the recovery characteristic of photoluminescence by thermal annealing for $\text{Zn}_2\text{SiO}_4:\text{Mn}$ powder. The decreased photoluminescence by Ar^+ ion bombardment is perfectly recovered by annealing at a temperature of 400°C in air under atmospheric pressure. The same phenomenon was observed by annealing in H_2 gas, which indicates that the photoluminescence recovery is due to thermal rearrangement of the displaced atoms at the nonradiative layer, but not to some oxidation. However the damage by Hg^+ ion bombardment does not recover perfectly by the annealing. This residual damage is thought to be induced by the amalgamation of phosphor with Hg atoms.

The relatively low annealing temperature in this experiment is not so exceptional a condition. For example, in annealing experiments for ion-bombarded Ag, Ge, and GaAs, the annealing temperature ranged from 300° to 500°C , and sufficient annealing effect was obtained for the recovery of lattice disorder and luminescence (3, 5, 6). These low annealing temperatures react as follows; Defects generated by ion bombardment are easily movable at a room temperature as indicated in the diffusion of defects in Fig. 4, and so these defects conversely are removed by annealing at a relatively low temperature.

Relation between phosphor depreciation by ion bombardment and lumen output drop of fluorescent lamp.—Figure 8 shows lumen output L_t of fluorescent lamps of $(\text{LaCe})\text{PO}_4:\text{Tb}$ and $\text{Zn}_2\text{SiO}_4:\text{Mn}$ as a function of burning time t . The time dependence of L_t is the same as that of the photoluminescence intensity P_t in Fig. 6, although the scale of burning time in Fig. 8 is much longer than that of bombarding time in Fig. 6. Similar time dependence of L_t and P_t was observed for the remaining 14 kinds of phosphors. To investigate the relation between L_t and P_t , the intensities of L_t after 100, 500, and 1000h during the burning test run were plotted in Fig. 9(a), (b), and (c), respectively, with respect to the intensity of P_t after the Hg^+ ion bombardment for 1h. According to a regression analysis, a regression line of L_t on P_t is indicated as a solid line. In this case, the regression line was expressed by the relation $(100 - L_t) = \beta(100 - P_t)$, where β is the inclination of the line. Two dashed lines corresponding to two inclinations $\beta(1 \pm 0.3)$ are also described in Fig. 9. Most data points enter the region surrounded by the two dashed lines. These results indicate the tendency that the phosphor depreciated easily by ion bombardment also degrades rapidly in a fluorescent lamp during the burning test.

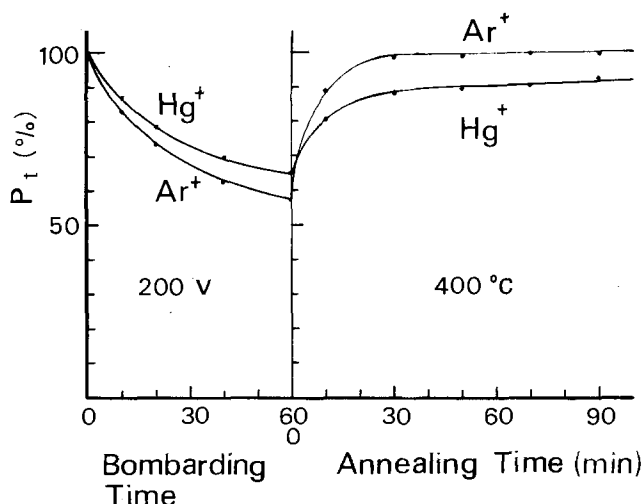


Fig. 7. Annealing characteristic of the photoluminescence of $\text{Zn}_2\text{SiO}_4:\text{Mn}$ powder bombarded by Ar^+ or Hg^+ ions.

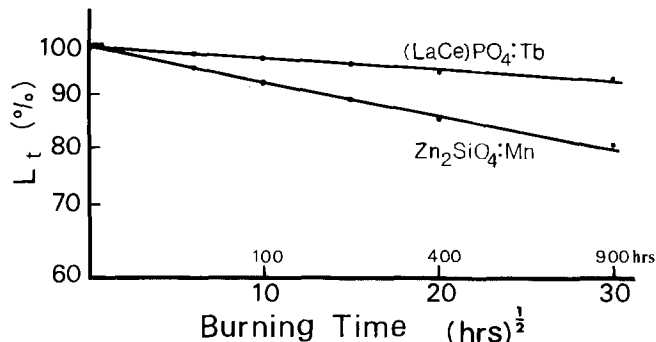


Fig. 8. Maintenance of two fluorescent lamps with thin coatings of phosphors, $(\text{LaCe})\text{PO}_4:\text{Tb}$ and $\text{Zn}_2\text{SiO}_4:\text{Mn}$.

It has been said that there is a correlation between Hg content in a depreciated lamp phosphor and lumen drop of its fluorescent lamp, and so the contamination of Hg atoms at the phosphor surface is responsible for the long-term depreciation of the lamp. For example, Froelich (7) proposed a photochemical depreciation process where the excited Hg atoms react with phosphor atoms such as oxygen. From this point of view, a criterion is deduced that a phosphor which has a long life in a burning lamp is the phosphor which resists the adsorption of Hg atoms. At the present stage, however, the content of Hg in the

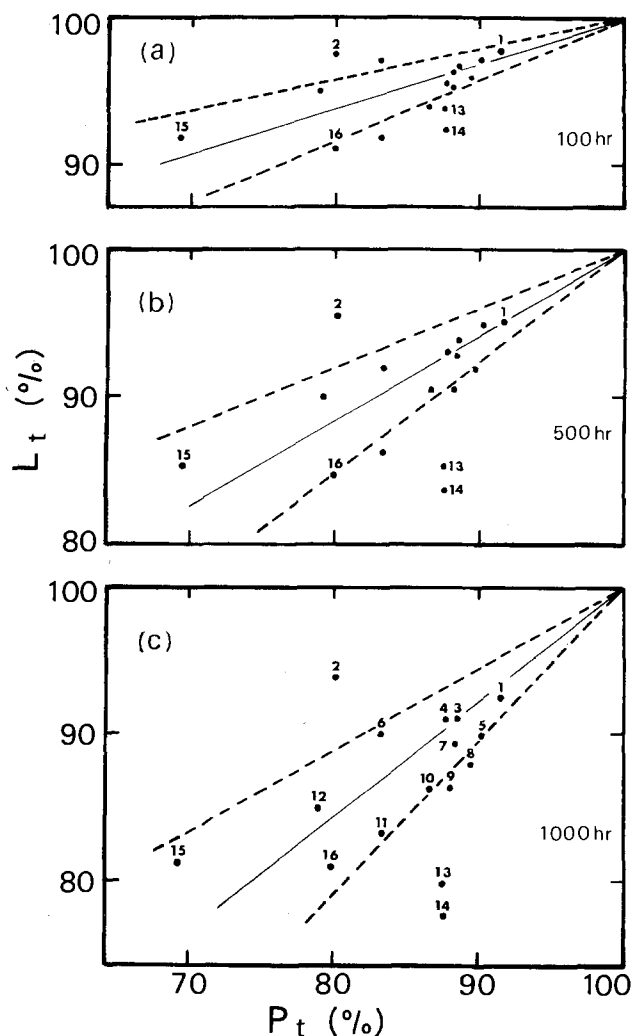


Fig. 9. Relation between the photoluminescence of the phosphors bombarded by Hg^+ ions for 1h and the lumen output of fluorescent lamp after the burning time for (a) 100, (b) 500, and (c) 1000h. The data for the 16 kinds of phosphor powders mentioned in the experiment are plotted. The solid line is a regression line which is expressed by the relation $(100 - L_t) = \beta(100 - P_t)$, where β is the inclination. Dashed lines are expressed by the relations $(100 - L_t) = \beta(1 \pm 0.3)(100 - P_t)$.

depreciated lamp phosphor depends on the different phosphors and the criterion to estimate the affinity of Hg atoms for phosphor is not known as pointed out by Narita (8). We can obtain another criterion to improve the phosphor maintenance. The results indicated in Fig. 6, 8, and 9 show that there is a close relation between the susceptibilities of the lumen drop of a fluorescent lamp and the phosphor depreciation by ion bombardment, and that the phosphor which has a long life in a fluorescent lamp is also stable for the Hg⁺ ion bombardment. Therefore the influence of ion bombardment on the phosphor depreciation by physical damage in a fluorescent lamp is supposed. However, for phosphor depreciation in a lamp, the presence of energetic ions to produce an amorphous layer is not demonstrated explicitly, so precise experimental works are necessary further for this point. Furthermore, taking into account that the adsorption of Hg atoms is enhanced by ion bombardment as indicated in Fig. 5, we think that the influence of ion bombardment on phosphor depreciation by Hg adsorption should be also taken into consideration for the depreciation mechanism of a fluorescent lamp.

Conclusions

In this experiment we obtained the following results:

1. Under energetic ion bombardment, the phosphor surface becomes amorphous. The depth of the amorphous layer is about 3000Å for ion bombardment by Ar⁺ ions with an energy of 200 eV. This amorphous layer is non-radiative under UV light excitement and absorbs UV light.
2. Adsorption of Hg atoms on the phosphor surface is enhanced by ion bombardment.
3. The depreciation characteristic of phosphor induced by ion bombardment is similar to that of lumen depreciation of a fluorescent lamp.

4. One of the criteria to produce the phosphor which has a long life is to prepare the phosphor which is strong for ion bombardment.

5. The results obtained in this experiment suggest that the influence of ion bombardment on phosphor depreciation should be taken into consideration for the lumen drop of a fluorescent lamp.

Acknowledgments

The authors would like to thank Mr. N. Ogawa, of Nichia Chemical Industries, Limited, for his encouragement of this experiment. They would also thank Professor I. Taniguchi of Doshisha University, and Dr. T. Shiosaki and Dr. M. Adachi of Kyoto University for the observation of RHEED pattern, and Mr. M. Morishita, Mr. H. Hagimori, Mr. T. Oka, and Mr. S. Koide for their assistance with the experiments.

Manuscript submitted April 25, 1983; revised manuscript received ca. Dec. 7, 1983.

Nichia Chemical Industries, Limited, assisted in meeting the publication costs of this article.

REFERENCES

1. W. Lehmann, *This Journal*, **130**, 426 (1983).
2. K. Nakanishi, T. Mori, Y. Shintani, and O. Tada, *Jpn. J. Appl. Phys.*, **14**, 1231 (1975).
3. M. Kawabe, N. Kanzaki, K. Masuda, and S. Namba, *Appl. Opt.*, **17**, 2556 (1978).
4. F. W. Aston, *Proc. R. Soc. London*, **A79**, 80 (1907).
5. G. J. Ogilvie and A. A. Thomson, *J. Phys. Chem. Solids*, **17**, 203 (1961).
6. R. L. Jacobson and G. K. Whener, *J. Appl. Phys.*, **36**, 2674 (1965).
7. H. C. Froelich, *ibid.*, **17**, 573 (1964).
8. K. Narita, *Electronic Ceramics*, 11(Winter), 23 (1980) (in Japanese).

A Simple Pre-Exposure Treatment to Improve Post-Develop Photoresist Step Coverage

Venkat Nagaswami

Zilog Incorporated, Technology Development Center, Cupertino, California 95014

Robert Carlson

Honeywell, Incorporated, Solid State Development Center, Plymouth, Minnesota 55441

ABSTRACT

In this study, a pre-exposure treatment to AZ-type photoresist that helps post-develop step coverage is reported. Using the present-day standard technique, the photoresist is coated and baked. This is followed by an immersion of the wafers in a dilute alkaline base such as 5:1 AZ351 developer for a short time. The wafers are then rinsed, dried, exposed, and developed using standard techniques. By this procedure, a significant improvement in step coverage has been observed. A possible reaction mechanism is proposed.

In semiconductor device fabrication, step heights of the order of 1 μm are not uncommon. Photoresist deposited on such surfaces by spin coating technique gives rise to nonuniform thickness of the photoresist layer in the vicinity of the steps. Postpatterning linewidth variation near the steps in the form of notching has been reported by several authors (1, 2). Nonuniform photoresist linewidths on metal layers result in nonuniform conductor linewidths, which in turn lead to electromigration failure and nonuniform electrode spacing in CCD. In extreme cases, discontinuities in the conductor due to poor step coverage have been observed. Increased usage of dry etching to produce small features adds to the step-

coverage problem by leaving vertical feature walls and cusped upper edges. The PCM technique (3) is one of the few solutions to this problem. In this study, a simple pre-exposure treatment has been investigated by the authors which gives improved step coverage without making the lithography process more complex.

Experimental

A pattern was etched in a 1.25 μm thick thermally grown SiO₂ layer on the wafer surface to produce steps of height about 1.25 μm . The wafers were primed with HMDS and coated with Shipley's AZ1350 photoresist to an average thickness of about 1.5 μm . After air drying for 10 min, the photoresist-coated wafers were baked at 90°C for 30 min in a convection-type bake oven. At this point,

Key words: photoresist step coverage, coupling reaction, dissolution rate of photoresist.

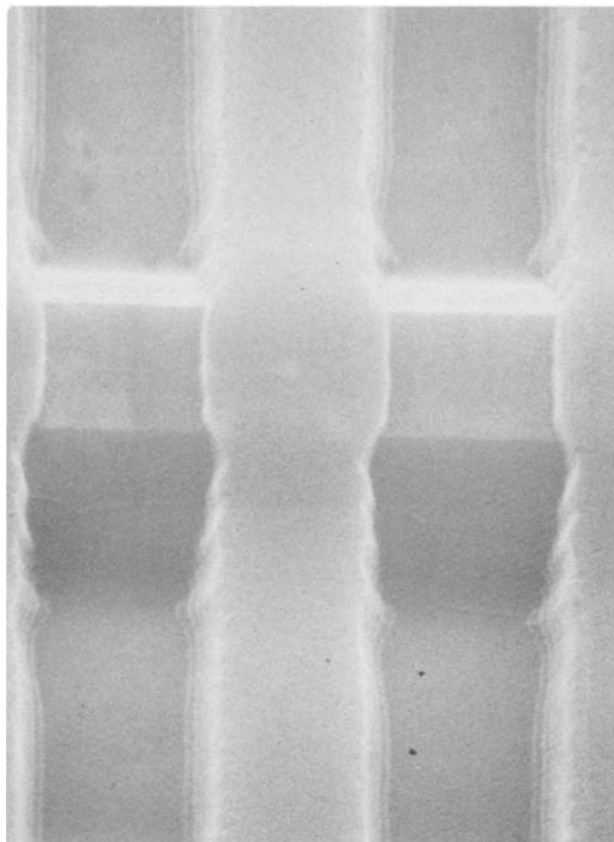


Fig. 1. Wafer processed with pre-exposure treatment

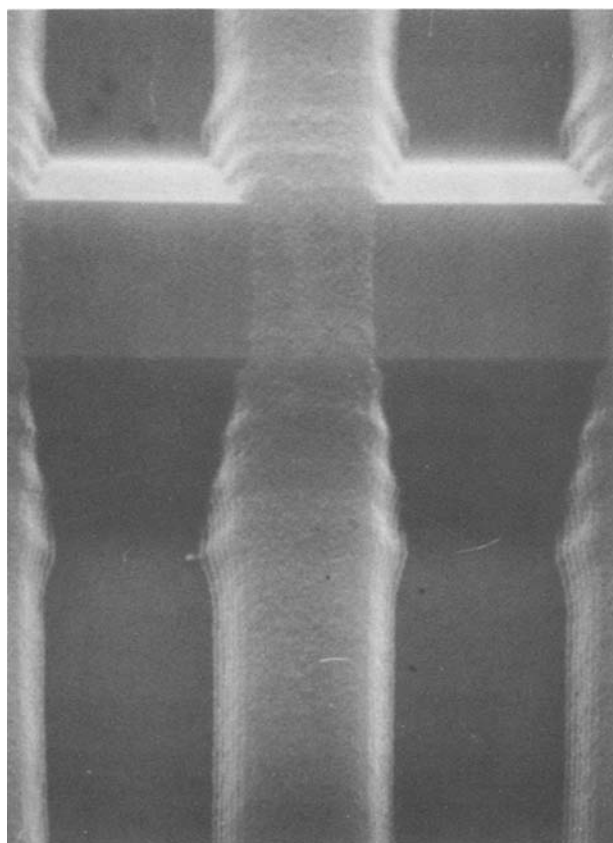


Fig. 2. Wafer processed by standard method. Note the resist line thinning over the step.

the wafers were divided into two groups. One group of wafers (Group A) were immersed in a 5:1 solution of AZ351 developer at room temperature for a short time

(typically 15-30s), rinsed in DI water for 10 min, spin dried, and sent on for exposure. The other group (Group B) went directly to exposure.

The projection aligner used was a Canon mask aligner which uses 405 and 436 nm wavelength UV light for exposure. After determining the optimum focus on a flat wafer, step exposure was performed on a test wafer from Group A and on one from Group B. The wafers were developed in 5:1 AZ351 developer for 60s. The minimum exposure required to clear a 4 μm pitch grating was determined in both cases. It was observed that the Group A wafers which went through the pre-exposure treatment required about 10% higher exposure than the Group B wafers. The wafers were then examined for the step coverage using the SEM.

Results

A remarkable increase in photoresist step coverage was observed in the case of the Group A wafers that went through the pre-exposure treatment. In the case of Group B wafers, the photoresist going over the 1.25 μm steps was found to thin down or disappear entirely. When the experiment was repeated using a new set of wafers and a different operator the results were the same.

The authors believe that the improved step coverage of the Group A wafers is the consequence of the dissolution rate of unexposed photoresist's being considerably lower than that of the conventional processing used in Group B. It was also observed that the surface of the photoresist of the pre-exposure-treated wafers was considerably smoother than that of Group B wafers. The image quality of Group A wafers were as good as that of Group B, if not better. The results are shown in SEM pictures (Fig. 1-6).

Explanation

The nature and chemistry of AZ-type positive resists has been extensively studied and reported by several authors (4-6). The AZ1350 formulation is composed primarily of PAC (Fig. 7) in a phenolic resin (Fig. 8). Imaging results from UV exposure of the resist in desired areas. The

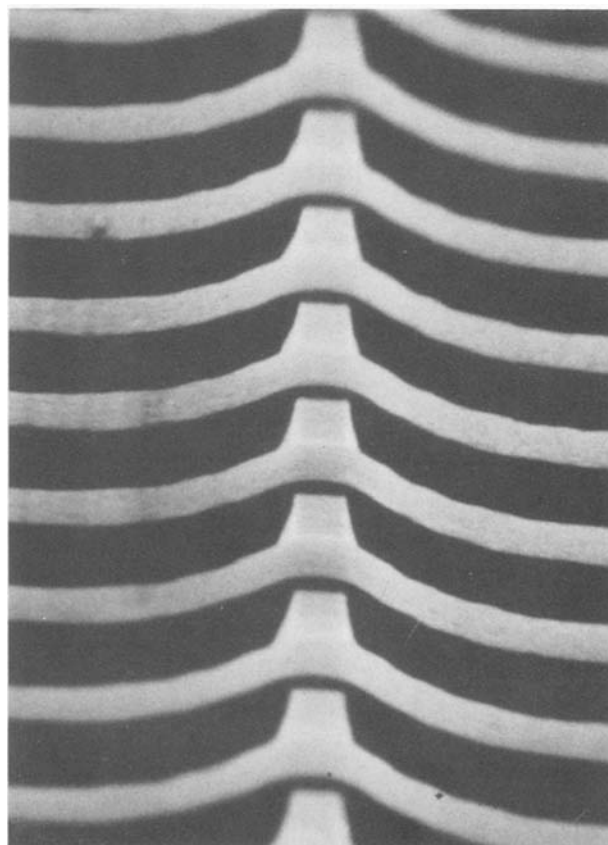


Fig. 3. Wafer processed with pre-exposure treatment

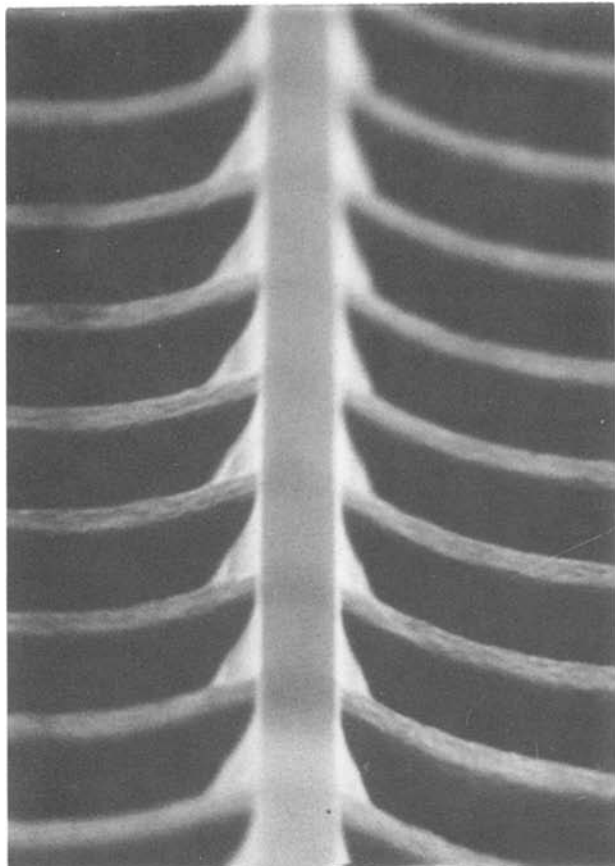


Fig. 4. Wafer processed by standard method. Note the discontinuity of the resist line over the step.

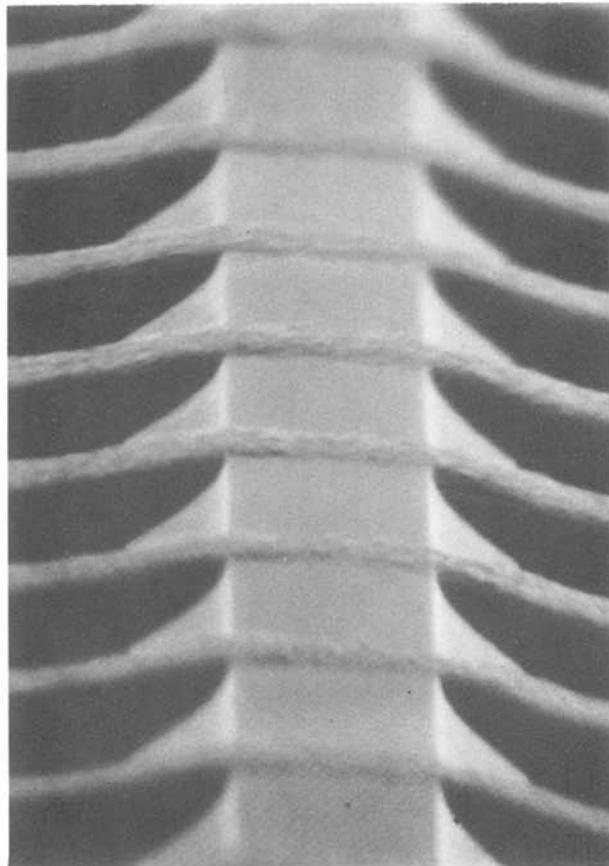


Fig. 6. Wafer processed by standard method. Note the resist line disappearing over the step.

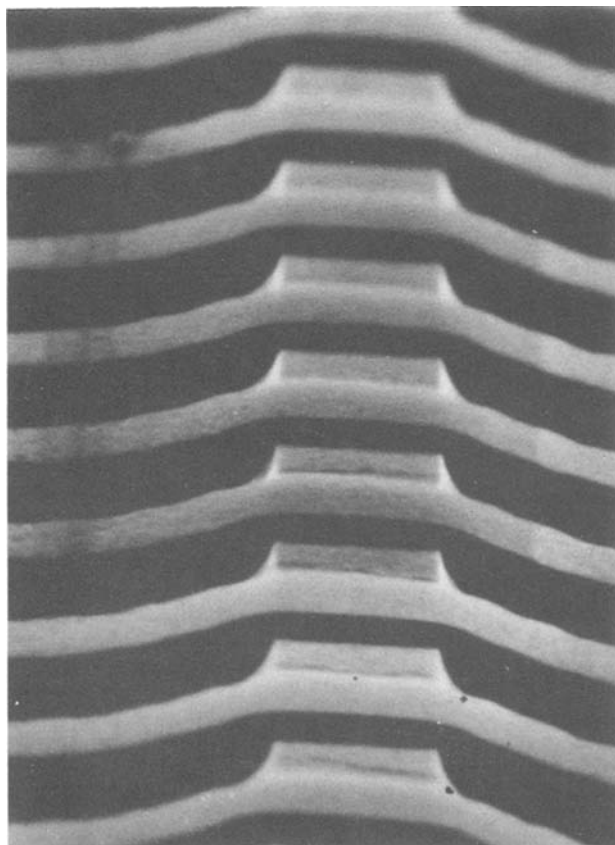


Fig. 5. Wafer processed with pre-exposure treatment

resulting photolysis mechanism (Fig. 9) was first proposed by Süs in 1944 and is now well recognized. The base-soluble material produced by UV exposure of PAC

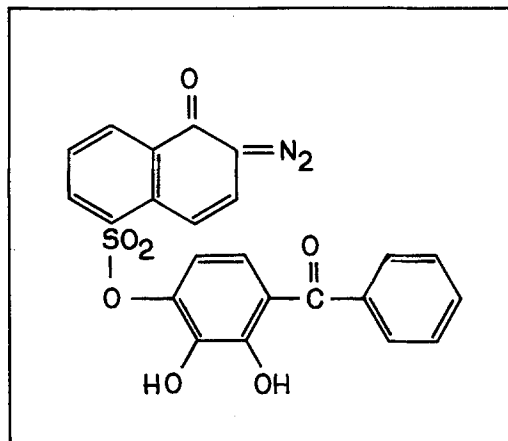


Fig. 7. Photoactive component in AZ1350 photoresist

has been presumed to be an indenecarboxylic acid formed from a reactive ketene intermediate. In the alkaline base, the exposed areas undergo the reaction shown in Fig. 10.

As the basic developer is also a solvent for the resin, the slower rate of dissolution in the unexposed area was postulated by DeForest (4) to result from a base-induced aZ_o coupling between the PAC and the resin (Fig. 11). It was proposed by DeForest that the coupling reaction takes place "instantaneously," producing a cross-linked structure that reduces the solubility of the unexposed region.

The observed slow dissolution rate of the unexposed photoresist of Group A wafers in the present study can be explained if we assume that coupling is a slow, diffusion-dependent reaction rather than an instantaneous reaction. The development and the coupling rates of resists depend on diffusion of the developer in the polymer film, the molecular configuration, and strain in the polymer film. At a given temperature, many parameters may affect the

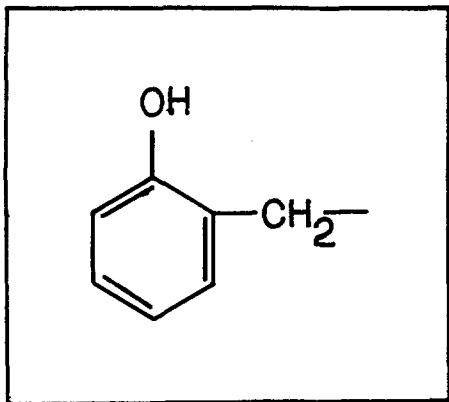


Fig. 8. Typical phenolic resin used in AZ1350 photoresist

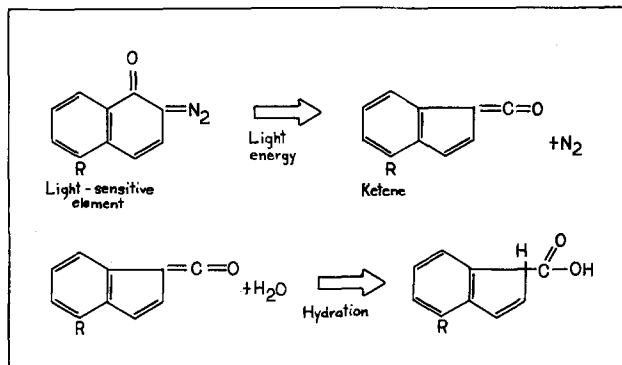


Fig. 9. Photolysis mechanism for photoactive component proposed by Süss in 1944.

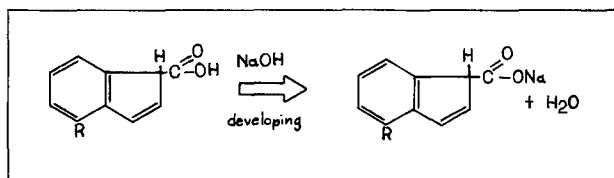


Fig. 10. Developing reaction of the exposed areas

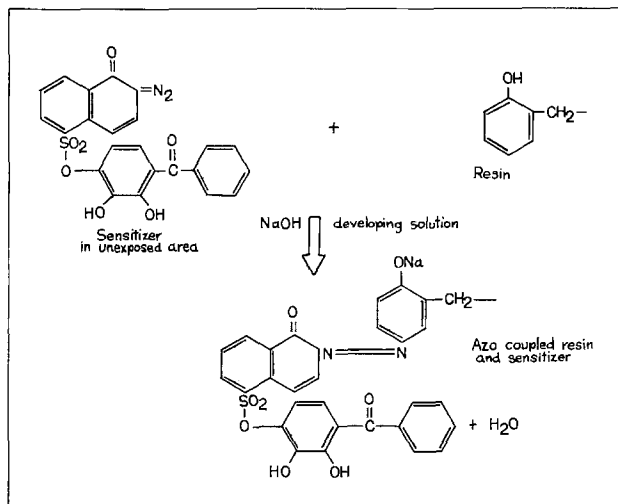


Fig. 11. Coupling reaction of sensitizer molecule with the resin in unexposed areas.

diffusion mechanism. Gel formation, free volume in the film, and solvent retention may all play a role in the developing of photoresist films (7). It is conceivable that in the conventional developing method, the coupling does not take place instantaneously to completion in the unexposed areas. Since the developer is amply used up in developing the exposed resist, fresh developer is not locally available to the unexposed resist in order that coupling may effectively take place.

In the method the authors have tried, the coupling takes place prior to exposure. Although this method desensitizes the resist a little bit, the compound is still photoactive. The study of Hiraoka and Pacansky (8) indicates that after development and rinsing there is some residual developer left in the resist. The authors believe that in their investigation, the residual developer has adequate time to be able to diffuse into the bulk of the resist and so the coupling reaction takes place to completion before the wafers go into the developer for the second time. The completion of the coupling reaction is responsible for preserving the photoresist thickness over the steps. In addition to inhibiting the dissolution rate of the unexposed portions of the resist, the authors believe that the pre-exposure treatment hardens the surface of the photoresist, which explains the smoother photoresist surface of Group A wafers as compared to Group B. This effect is similar to the technique used by Canavello *et al.* (9), in which the resist is soaked in chlorobenzene to alter the local development rate of the resist near the surface.

Summary

A simple pre-exposure treatment of wafers coated with AZ-type photoresist has been described. It improves the step coverage after development by inhibiting the dissolution rate of unexposed photoresist. The pre-exposure treatment involves immersing the photoresist-coated and baked wafers in a mild alkaline base such as 5:1 AZ351 developer for a short time. The phenomenon is explained as a consequence of the slow diffusion-dependant coupling reaction in which the diazo joins with other compounds to form aZ₀ linkage.

Acknowledgments

The authors wish to thank Helen Olson for her unique contribution to this project and Pam Mayernik for the meticulous care in running the experiments and quality SEM work.

Manuscript submitted Nov. 3, 1983; revised manuscript received Feb. 9, 1984.

Zilog Incorporated assisted in meeting the publication costs of this article.

REFERENCES

1. D. Widman and H. Binder, *IEEE Trans. Electron Devices*, **ed-22**, 467 (1975).
2. D. Buckley, "Microelectronic Manufacturing and Testing," pp. 15-17 (1982).
3. B. J. Lin, in "Proceedings of International Society for Optical Engineering," Vol. 174, p. 114 (1979).
4. W. S. DeForest, "Photoresist Materials and Processes," Chap. II, McGraw-Hill Book Co., Inc., New York (1975).
5. J. Pacansky and J. R. Lyerla, *IBM J. Res. Dev.*, **23**, 42 (1979).
6. Kenneth G. Clark, *Solid State Technol.*, 73 (1978).
7. J. M. Shaw and M. Hatzakis, *This Journal*, **126**, 2026 (1979).
8. H. Hiraoka and J. Pacansky, *ibid.*, **128**, 2645 (1981).
9. B. J. Canavello, M. Hatzakis, and J. M. Shaw, *IBM Tech. Discl. Bull.*, **19**, 4049 (1977).

Carrier Saturation in Tin-Doped InP Films Grown by Liquid Phase Epitaxy

B. H. Chin, R. E. Frahm, T. T. Sheng, and W. A. Bonner

AT&T Bell Laboratories, Murray Hill, New Jersey 07974

ABSTRACT

We have investigated tin doping at high concentrations in InP films grown on <100> InP by liquid phase epitaxy. Contrary to previously published work, our Hall measurements show that the carrier concentration saturates at $\sim 6 \times 10^{19}/\text{cm}^3$ for a mol fraction of tin in liquid ≥ 0.08 . Measurements of actual tin concentrations in the solid by secondary ion mass spectroscopy indicate that a solid solubility limit is reached. Transmission electron microscopy reveals no precipitate formation.

Liquid phase epitaxy (LPE) in InP from indium-rich solutions has become a major technique for the growth of optoelectronic device structures. When n-type layers are needed, tin is the usual dopant. Although there have been many studies (1-8) of tin doping in LPE InP, they have mainly concerned doping levels of $(N_D - N_A) \leq 5 \times 10^{19}/\text{cm}^3$, corresponding to a mol fraction of tin in solution of $\chi_{\text{Sn}}^l \leq 0.1$. Higher doping levels, however, have been less thoroughly investigated; furthermore, studies of doping in the $10^{19}/\text{cm}^3$ range have often involved atypical LPE growth conditions. Under the usual conditions for optoelectronic structures, *i.e.*, growth from indium solution on an InP substrate at 600°-700°C, we are aware of only two studies reporting doping levels in the $10^{19}/\text{cm}^3$ range. Rosztochy *et al.* (1) measured $(N_D - N_A) \approx 1.5 \times 10^{19}/\text{cm}^3$ at $\chi_{\text{Sn}}^l \approx 0.4$; Williams *et al.* (2) and Astles *et al.* (3) found $(N_D - N_A) \approx 8.5 \times 10^{19}/\text{cm}^3$ at $\chi_{\text{Sn}}^l \approx 0.5$. We would like to emphasize that, in both instances, only a single data point with $(N_D - N_A)$ in the $10^{19}/\text{cm}^3$ range was given. Other work reporting very high doping levels has utilized atypical growth conditions. Shay *et al.* (4) deposited an InP film on an InP substrate from a tin solution at $\sim 510^\circ\text{C}$; the resulting $(N_D - N_A)$ was $5 \times 10^{19}/\text{cm}^3$. Jacobs *et al.* (5, 6) studied doped, strongly lattice-mismatched layers of InP grown on GaAs substrates from either indium solution at 785°C or tin solution at 580°C. Values of $(N_D - N_A)$ as high as $9 \times 10^{19}/\text{cm}^3$ were measured.

In this study, we have grown InP, under typical LPE conditions, with χ_{Sn}^l up to 0.14. Contrary to previous work, we find that $(N_D - N_A)$ saturates at $\sim 6 \times 10^{19}/\text{cm}^3$ for $\chi_{\text{Sn}}^l \geq 0.08$. In addition to Hall measurements, the epitaxial layers were examined by secondary ion mass spectroscopy (SIMS) and transmission electron microscopy (TEM).

Crystal Growth

The epitaxial layers were grown on semi-insulating substrates from two-phase solutions (9); a graphite horizontal slider boat was used. The <100> oriented, Fe-doped InP wafers were first cut from a boule grown by liquid-encapsulated Czochralski (LEC) and then polished with bromine-methanol. Immediately prior to a LPE run, a substrate was freshly etched in 3 methanol:1 H_3PO_4 :1 H_2O_2 , rinsed successively in methanol and running DI water, and, finally, blown dry with high purity helium gas. During the period needed to homogenize the growth solution, the substrate was protected with an InP coverpiece (10) to reduce surface thermal decomposition.

To reduce variations in background doping levels, special precautions were observed for preparing the source materials—vacuum-baked indium rod (six 9's purity), tin shot (six 9's purity), and undoped $[(N_D - N_A) \approx 5 \times 10^{16}/\text{cm}^3]$ polycrystalline InP slices. The indium rod was first etched in 1 HNO_3 :1 H_2O , rinsed in running DI water, rinsed in methanol, and blown dry with helium. After the rod had been cut up into pieces weighing 5.00g, the pieces were loaded into the wells of the growth boat and baked

out overnight at 700°C in flowing hydrogen. The boat was then cooled, and the indium ingots were removed and stored for future use. Since high concentrations of tin are used in this study, impurities in the tin may be significant. Hence, the tin shot was also purified by the same procedure (except that concentrated HCl was the etchant). Just before a growth run, the source materials were freshly re-etched and weighed (the poly InP was also etched in concentrated HCl). Two melts were loaded into the boat: (i) a pure In "wash" melt (11) for *in situ* etching of the substrate surface and (ii) the growth melt, consisting of 5.000g In, the proper amount of Sn, and poly InP in excess of the solubility limit at the growth temperature.

An LPE run proceeded according to the following schedule. After the melts had been homogenized at 660°C for 1h, the furnace temperature was ramped down at 0.7°C/min. At 648°C, the substrate was pushed under the In "wash" melt for 10s and then pushed under the growth melt. Growth continued at a ramp rate of 0.7°C/min until 640°C was reached. The wafer was then wiped off, and the boat was rapidly cooled down. (Surface terraces became increasingly pronounced at high doping levels; however, clean wipe-off was achieved on all samples.) Since the distribution coefficient of tin may vary with temperature, the growth temperature was deliberately held to a narrow range (8°C). This growth interval was sufficient to produce a film thick enough ($\sim 5 \mu\text{m}$) for subsequent characterization.

Before discussing the characterization results, we must first clarify one point. Quantities will be plotted as a function of χ_{Sn}^l , the mol fraction of tin in liquid. Strictly

$$\chi_{\text{Sn}}^l = M_{\text{Sn}} / (M_{\text{In}}^0 + M_{\text{In}}^1 + M_{\text{P}} + M_{\text{Sn}}) \quad [1]$$

where M_{Sn} and M_{In}^0 are, respectively, the number of mols of pure Sn and In, whereas M_{In}^1 and M_{P} are the contributions from the dissolved InP. If

$$(M_{\text{In}}^1 + M_{\text{P}}) \ll (M_{\text{In}}^0 + M_{\text{Sn}}) \quad [2]$$

then

$$\chi_{\text{Sn}}^l \approx M_{\text{Sn}} / (M_{\text{In}}^0 + M_{\text{Sn}}) \quad [3]$$

We directly verified that condition (ii) was satisfied over the entire range of doping used in this study. The solubility of InP in the most highly doped melt was determined in the following way. A melt consisting of 5.000g In and 0.875g Sn was homogenized at 648°C. An InP wafer, which had been accurately weighed, was then slid under the melt. After a 1h homogenization, the wafer was pushed clear. From measurements of the weight gain in the melt and of the weight loss in the substrate, we determined the solubility to be 0.055g InP, a negligible amount compared to the initial 5.875g charge. Thus, Eq. [3] was used for χ_{Sn}^l .

Characterization

The epitaxial layers were characterized by Hall measurements, SIMS, and TEM. The net carrier concentra-

Key words: Hall measurements, secondary ion mass spectroscopy, transmission electron microscopy.

tion ($N_D - N_A$) was determined by Hall measurements in the van der Pauw configuration; a fully computer-controlled apparatus (12) was used for rapid and accurate measurements. To monitor the actual tin concentration, samples were analyzed by SIMS¹, a Cs ion source was used for depth profiling, and the mass 120 tin peak was monitored. Conversion of the SIMS signal levels to atomic concentrations was achieved by comparison with signals from ion-implanted standards. For TEM analysis, a 3 mm diam disk was ultrasonically cut from a wafer. After the substrate had been polished down to $\sim 25 \mu\text{m}$ with bromine-methanol, a number of small holes were opened up near the center of the disk with a jet polish of bromine-methanol.

Hall measurements of several nominally undoped layers gave a reproducible background doping level of ($N_D - N_A$) $\approx 1 \times 10^{17}/\text{cm}^3$, which was an order of magnitude less than the lowest intentional doping level. The values of ($N_D - N_A$) at room temperature as a function of χ_{Sn}^1 are plotted in Fig. 1. For $\chi_{\text{Sn}}^1 \lesssim 0.08$, there is a linear dependence of ($N_D - N_A$) on χ_{Sn}^1 ; in this regime, the calculated distribution coefficient is $k \approx 2.7 \times 10^{-3}$, in good agreement with values measured by other workers (8) [Two definitions of k exist (8); here, we use the common one: $k = (\text{mols Sn/gram of solid})/(\text{mols Sn/gram of liquid})$ (3, 8).] Contrary to previous work (1-3), however, we find that ($N_D - N_A$) saturates at $\sim 6 \times 10^{18}/\text{cm}^3$ for $\chi_{\text{Sn}}^1 > 0.08$.

Since Hall measurements yield only the net electrically active concentration, they do not unambiguously determine the doping behavior. Saturation of ($N_D - N_A$) as a function of χ_{Sn}^1 may be consistent with the following scenarios: (i) the mol fraction of tin in the solid, χ_{Sn}^s , saturates; i.e., a solubility limit of tin in the solid is reached. (ii) χ_{Sn}^s increases as a function of χ_{Sn}^1 with constant ($N_D - N_A$). In this case, some of the tin may be incorporated into neutral or acceptor sites. Alternatively, ($N_D - N_A$) may also remain constant if the concentration of acceptor impurities increases with χ_{Sn}^1 .

To clarify the situation, the concentration of tin in the solid, c_{Sn}^s (atoms/cm³), was determined by SIMS; the results are plotted in Fig. 1 as a function of χ_{Sn}^1 . Within the accuracy of the SIMS calibration (a factor of 2), the values of c_{Sn}^s measured by SIMS agree with the values of c_{Sn}^s expected from the Hall measurements (assuming that all tin is incorporated as ionized donors). We see clearly in Fig. 1 that c_{Sn}^s saturates; hence, a solid solubility limit is reached.

The following additional analyses were taken to support this result. The background doping of three samples, with $\chi_{\text{Sn}}^1 = 0, 0.06$, and 0.14 , respectively, was monitored by wide-field SIMS scans. Since the mass spectra of all three layers were essentially identical, there was no significant increase in background doping with increasing χ_{Sn}^1 . Furthermore, TEM analysis of the sample with $\chi_{\text{Sn}}^1 = 0.14$ revealed no precipitates (at a magnification of 50,000 \times), indicating that all tin was in solid solution.

Discussion

For $\chi_{\text{Sn}}^1 > 0.08$, we have shown that the carrier concentration in tin-doped InP saturates at ($N_D - N_A$) $\approx 6 \times 10^{18}/\text{cm}^3$; furthermore, the carrier saturation arises because a solubility limit of tin in the solid is attained. We emphasize that this result holds under the specific conditions employed, namely, growth from indium solution on a $\langle 100 \rangle$ -oriented InP substrate at 648°-640°C; however, these conditions are the common ones for optoelectronic device structures. Our results differ from those reported by Rosztochy *et al.* (1) and Astles *et al.* (2, 3), who found no evidence of carrier saturation. Although the exact rea-

¹SIMS analysis performed by C. A. Evans and Associates, San Mateo, California.

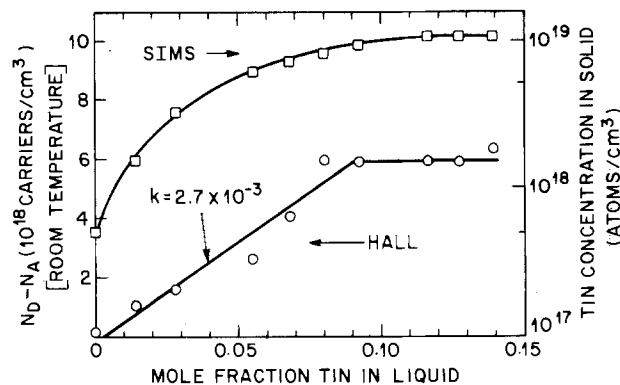


Fig. 1. Plot of room temperature carrier concentration and tin concentration as a function of mol fraction tin in liquid.

sons for this difference are not clear, there are two possibilities. First of all, dopant incorporation may depend on substrate orientation (13, 14) Rosztochy *et al.* used $\langle 111 \rangle \text{B}$ substrates throughout. In the case of Astles *et al.*, the situation is more vague because $\langle 111 \rangle \text{A}$, $\langle 111 \rangle \text{B}$, and $\langle 100 \rangle$ substrates were used. The authors mentioned that the doping behavior did not depend strongly on orientation; however, it is not clear whether the one very high value of ($N_D - N_A$) reported ($8.5 \times 10^{19}/\text{cm}^3$) was attained on all orientations. Secondly, at high χ_{Sn}^1 , impurities in the tin may be significant. Thus, the higher values of ($N_D - N_A$) measured by other workers may have been due to a strong donor impurity present in the tin. To resolve these issues, the incorporation of tin as a function of orientation and the presence of impurities in tin need further investigation.

Acknowledgments

The authors thank J. A. Lourenco for carrying out the LPE growth and R. H. Saul for helpful comments on the manuscript.

Manuscript submitted Aug. 19, 1983; revised manuscript received Dec. 9, 1983.

AT&T Bell Laboratories assisted in meeting the publication costs of this article.

REFERENCES

1. F. E. Rosztochy, G. A. Antypas, and C. J. Casau, in "1970 Symposium on GaAs and Related Compounds, Aachen," K. Paulus, Editor, p. 86, Institute of Physics Conference Series 9, Institute of Physics, London (1971).
2. E. W. Williams, W. Elder, M. G. Astles, M. Webb, J. B. Mullin, B. Straughan, and P. J. Tufton, *This Journal*, **120**, 1741 (1973).
3. M. G. Astles, F. G. H. Smith, and E. W. Williams, *ibid.*, **120**, 1750 (1973).
4. J. L. Shay, K. J. Bachmann, and E. Buehler, *Appl. Phys. Lett.*, **24**, 192 (1974).
5. B. Jacobs, E. Butter, and B. Dobner, *Krist. Tech.*, **13**, 383 (1978).
6. H. Neumann and B. Jacobs, *Phys. Status Solidi A*, **49**, K139 (1978).
7. E. B. Abrams, S. Sumski, W. A. Bonner, and J. J. Coleman, *J. Appl. Phys.*, **50**, 4469 (1979).
8. E. Kuphal, *J. Cryst. Growth*, **54**, 117 (1981).
9. M. A. Pollack, R. E. Nahory, J. C. DeWinter, and A. A. Ballman, *Appl. Phys. Lett.*, **33**, 314 (1978).
10. P. D. Wright, Y. G. Chai, and G. A. Antypas, *IEEE Trans. Electron Devices*, **ed-26**, 1220 (1979).
11. V. Wruck, G. J. Scilla, L. F. Eastman, R. L. Henry, and E. M. Swiggard, *Electron. Lett.*, **12**, 394 (1976).
12. R. E. Frahm, Unpublished data.
13. G. A. Antypas and L. Y. L. Shen, in "1976 Symposium on GaAs and Related Compounds, St. Louis," p. 96, L. F. Eastman, Editor, Institute of Physics Conference Series 336, Institute of Physics, London (1977).
14. K. Akita, A. Yamaguchi, K. Nakajima, and T. Takanohashi, *Electron. Lett.*, **24**, 921 (1981).

Effect of Heat-Treatment on Electrical Properties of Ion-Implanted Silicon on Sapphire

L. Jastrzebski,* R. K. Smeltzer,* and G. W. Cullen*

RCA Laboratories, Princeton, New Jersey 08540

J. Lagowski*

Massachusetts Institute of Technology, Cambridge, Massachusetts 02139

ABSTRACT

The electronic properties of silicon-on-sapphire were investigated as a function of selected heat-treatment sequences between 900° and 1100°C, similar to certain processing steps used in device fabrication. Employing photovoltage spectroscopy and laser scanning photovoltage microprofiling, it has been found that heat-treatments significantly change deep and shallow levels and the minority-carrier lifetimes. Detectable changes of the amorphization factor and of the magnitude of inhomogeneities were also observed, but only upon annealing at the highest temperature investigated (3h at 1100°C).

Silicon-on-sapphire (SOS) (1), in addition to bulk silicon (2), is a well-recognized material for applications in the electronic industry, especially for the fabrication of radiation hard devices. It has been previously demonstrated that macro- and microscopic electronic properties of as-grown SOS films are closely related to film crystallinity (3, 4), and that surface photovoltage spectroscopy can be used successfully to characterize their electronic properties (3-5). The properties of bulk silicon change during processing (6, 7). By analogy, it is anticipated that the electronic properties of as-grown SOS films also change during various heat-treatments, and that these changes are a strong function of the temperature of the processing steps. The various processing cycles used for the fabrication of conventional circuits and radiation-hard CMOS circuits could influence material characteristics differently, and could be reflected in circuit performance. In this work, we present systematic studies of ion-implanted and nonimplanted SOS films subjected to heat-treatments typical of the conventional CMOS fabrication and radiation hard processes. In addition, we also investigated the effects of a high temperature preannealing (which could be applied prior to processing) on the electronic characteristics of SOS films.

Experimental

Commercially available SOS wafers 0.6 μm thick were preselected according to their crystallographic quality (A type according to UV reflection) (8) and were subjected to processing treatments listed in Table I. Two processing sequences were used, one involving no ion implantation (sequence I), and another involving ion implantation as follows: $1 \times 10^{12}\text{cm}^{-2}$ boron implanted at 150 keV plus 1.1

$\times 10^{12}\text{cm}^{-2}$ boron implanted at 35 keV (sequence II). After implantation, the SOS films were oxidized in steam at 900°C for 23 min. The wafers were sectioned by cleaving. Sections A, B, and C were thermally treated according to a specification given in Table I. The processing temperatures used for the sequence A were typical for the radiation hard process, while those used for the sequence B are for the conventional process. The untreated section D was used as a reference.

The study of sections A, B, C, and D was carried out utilizing photovoltage-related techniques (5): (i) photovoltage spectroscopy measurements for determination of localized levels and the degree of amorphization, (ii) measurements of the temperature dependence of photovoltage for assessment of the role of trapping centers, and (iii) laser scanning photovoltage microprofiling for determination of the homogeneity of silicon-on-sapphire. A detailed description of these approaches and their application to silicon-on-sapphire was given elsewhere (5, 9).

Photovoltage measurements were carried out utilizing the metal-semiconductor (MS) configuration. Photovoltage generated by a chopped monochromatic light was measured between a semitransparent gold film and a second electric contact (made with a silver paste) which was kept in the dark. Two sets of samples ($3 \times 10\text{ mm}$), 1A, 1B, 1C, and 1D and 2A, 2B, 2C, and 2D, were cleaved from wafers treated according to process simulation sequence I and II, respectively (see Table I). They were simultaneously prepared for measurements (evaporation of gold and silver-paste contacts). Four samples (1A-1D and 2A-2D) were placed on the cold finger of the variable-temperature cryostat. They were simultaneously measured in an effort to optimize the reliability of comparative study.

*Electrochemical Society Active.

Table I. Process simulation sequences I and II

Processing	Section of the wafer			
	A	B	C	D
1.)				
2.)				
3.)				
4. No implantation		no implantation		sequence I
or				
Boron implant		$150\text{ keV}; 1 \times 10^{12} + 35\text{ keV}; 1.1 \times 10^{12}$		sequence II
5. 900°C steam,		all sections		
23 min				
6. Cleaning				
7.	900°C N ₂ ; 55'	1050°C N ₂ ; 35'	1100°C N ₂ ; 3h	—
8.	pull out	pull out	—	—
9.	950°C N ₂ ; 25'	950°C N ₂ ; 65'	—	—
10.	pull out	pull out	—	—
11.	850°C N ₂ ; 75'	1050°C N ₂ ; 20'	—	—
12.	450°C FG; 20'	450°C FG; 20'	450°C FG; 20'	—
	forming gas (FG)			
13. Strip oxide		all sections		

Table II. Magnitude of photovoltage at $h\nu \approx 2 \text{ eV}$, 220 K, photon flux $10^{16} \text{ cm}^{-2} \text{ s}^{-1}$

	Section of the wafer			
	A	B	C	D
Not implanted (Sequence I)	0.18 mV	0.480 mV	0.95 mV	0.12 mV
Implanted (Sequence II)	0.40 mV	1.2 mV	1.05 mV	0.33 mV

Note: Thermal treatment for sections A, B, C, and D as defined by Table I.

Results and Discussion

Magnitude of photovoltage.—The most significant quantitative difference between the various SOS films was in the magnitude of photovoltage in the region of intrinsic excitation ($h\nu > E_g$). As shown in Table II, the photovoltage was smallest for untreated film D and had higher values for films subjected to thermal treatments. This seems to be the observation for implanted and unimplanted films. The simplest interpretation of this effect is that it is associated with the enhancement of excess carrier lifetime. This would lead to a tentative conclusion that the highest temperature annealing steps (the heat-treatments B and C) are most beneficial in improving the lifetime value.

Temperature dependence of photovoltage.—In our previous studies, we utilized the temperature dependence of photovoltage as a means for the determination of thermal-activation energies of trapping centers (3-5). Such typical photovoltage vs. $1/T$ dependence is shown in Fig. 1. It exhibits, in the high temperature region, the photovoltage

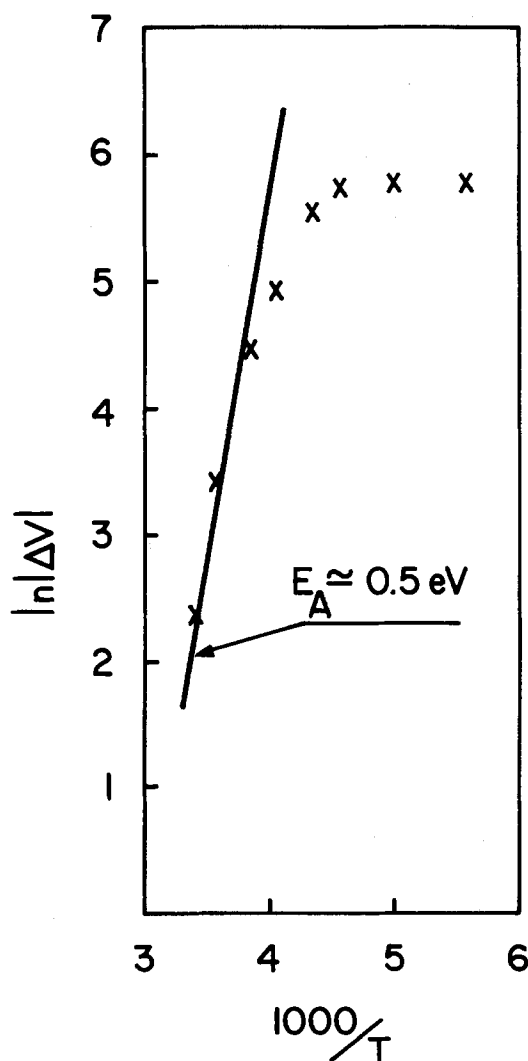


Fig. 1. Typical temperature dependence of the photovoltage of silicon-on-sapphire containing deep traps of thermal activation energy 0.5 eV.

quenching with a characteristic activation energy, $E_A \approx 0.5 \text{ eV}$, which has been observed in most of the SOS films studied previously (3-5). Exemption from this rule was observed only in films with the lowest density of deep levels, such as, for example, hydrogenated films of SOS (10).

The temperature dependence of photovoltage of the unimplanted films discussed here is only partially consistent with this tendency. As seen in Fig. 2, these films exhibit a photovoltage maximum at a temperature of about 220 K, and also photovoltage quenching with an activation energy approximately equal to 0.5 eV. However, this photovoltage quenching does not extend to room temperature. Instead, the photovoltage increases near room temperature for thermally treated films A, B, and C, and at a slightly lower temperature for the untreated film D. It is very likely that the differences, in comparison with previous results of Ref. (3) and (5), are due to surface effects. The SOS films discussed in Ref. (3) and (5) were covered with a protective SiO_2 layer (for example, 100 min steam oxidation at 900°C), while the films described here were subjected to oxide removal as the final preparation step. A silicon surface covered with a thin native oxide and with thermal oxide is known to exhibit different electrical properties (11).

Photovoltage vs. $1/T$ for a series of ion-implanted films treated according to process simulation sequence II is presented in Fig. 3. It is evident that all ion-implanted samples exhibit basically similar temperature dependence to the oxidized samples studied in Ref. (3) and (5). Thermal quenching with 0.5 eV activation energy is also clearly visible. The photovoltage quenching of unimplanted films did not extend up to room temperature, most likely because of surface effects. In ion-implanted material with much higher carrier concentration, the surface effects can generally be expected to be less pronounced; thus, the boron-implanted films analyzed in Fig. 3 did not show this surface-related effect.

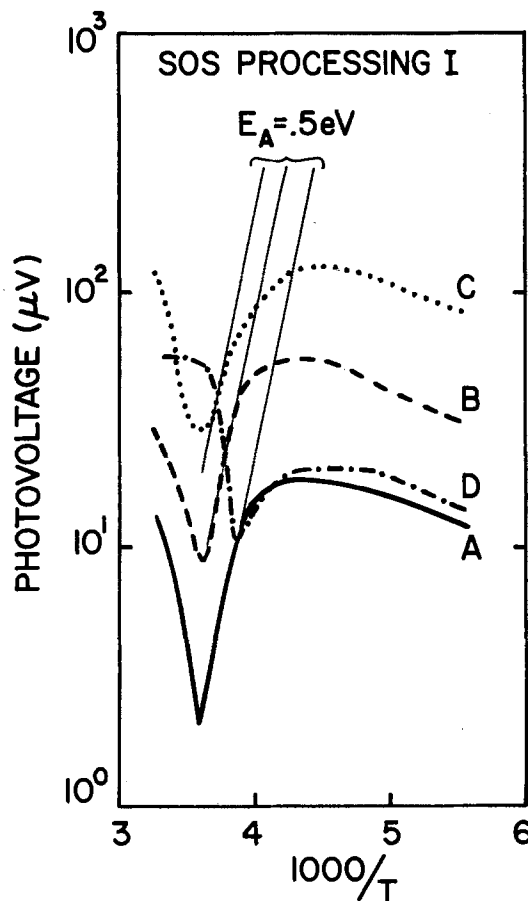


Fig. 2. Temperature dependences of the photovoltage of unimplanted silicon-on-sapphire heat-treated according to Table I (processing sequence I).

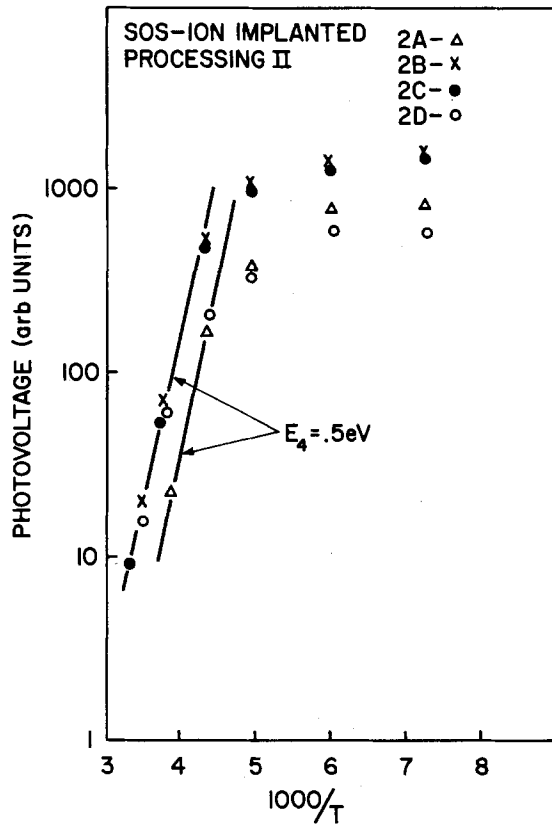


Fig. 3. Temperature dependences of the photovoltage of ion-implanted silicon-on-sapphire treated according to the processing sequence II (see Table I).

Spectral dependence of photovoltage.—The photovoltage spectra normalized to photovoltage values at $h\nu = 2.0$ eV are given in Fig. 4 for the two extremes of heat-treatments C and D. The normalization of photovoltage eliminates the differences in magnitude discussed above, and thus permits the observation of other differences occurring in particular spectral regions. Two regions, $h\nu < E_g$ and $h\nu \approx E_0$, are of primary importance here, as they correspond at lower energy to photoionization transitions involving localized levels and the higher energy reflect a degree of amorphization of SOS films (3)¹. It is seen from Fig. 4 that the heat-treatment at 1100°C suppresses both of them, although the effect is much stronger in the case of subbandgap photoionization transitions. The photovoltage spectra of films A and B, which received an intermediate heat-treatment (not shown in Fig. 4) also showed a noticeable suppression of deep level photoionization transitions in comparison with the untreated film D. However, no significant change was found for these films regarding the degree of amorphization (as judged from photovoltage increase around $h\nu \approx E_0$). It should be emphasized that the effects of heat-treatment were very similar for unimplanted and ion-implanted films (sequence 1 and 2).

For a quantitative analysis of the effect of heat-treatment on deep levels, we have attempted here a procedure discussed in Ref. (3) based on the subbandgap photoionization transitions in silicon-on-sapphire involving deep levels of energies, $E_1 \approx 0.6 - 0.7$ eV below the conduction band. The strength of this photoionization transition can be estimated from the photovoltage value normalized to the photovoltage value at the maximum (2 eV). As discussed in Ref. (3), they can be treated as a rough indication of the concentration of the deep levels. The relative concentration of deep levels E_1 in the processed samples, normalized to the concentration observed in as-grown samples (D), is given in Table III. The

¹Note that the amorphous-like shoulder at E_0 (Fig. 4) originates from defects in SOS affecting long-range interaction (dangling bonds and lattice strains), rather than from amorphous domains (12).

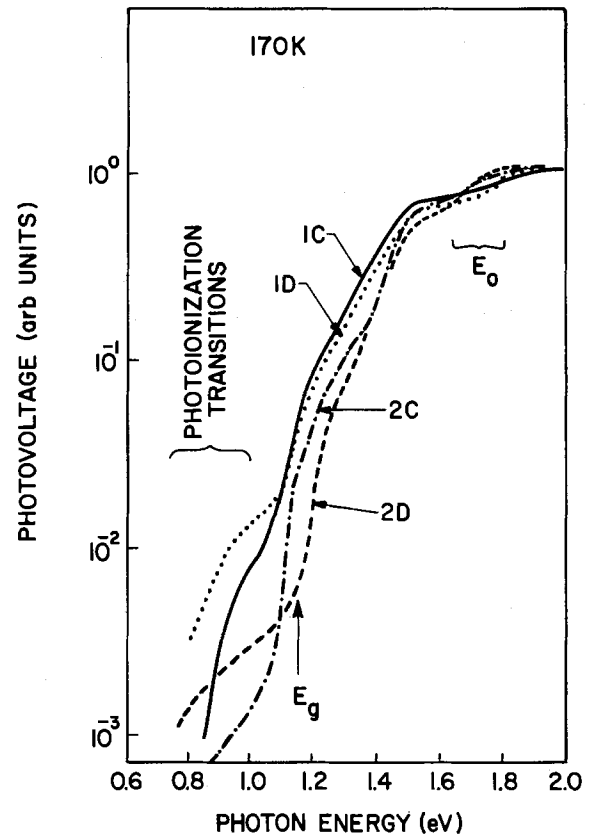


Fig. 4. 170 K photovoltage spectra (normalized to photovoltage value at $h\nu = 2.0$ eV) for unimplanted SOS films 1C and 1D and ion-implanted films 2C and 2D. Spectra were averaged in order to eliminate interference extrema.

lowest concentration of deep level E_1 is consistently observed in sample C, which received the highest temperature heat-treatment (1100°C); the highest concentration of E_1 levels is in the unannealed sample D.

A degree of amorphization can be conveniently analyzed by introducing the amorphization factor η (3)

$$\eta = \frac{\Delta V}{V} \cdot \frac{\alpha}{\Delta \alpha} - 1$$

where $\Delta V/V$ is the relative photovoltage increase taking place in the vicinity of $h\nu = E_0$, and $\Delta \alpha/\alpha$ is the corresponding change of the absorption coefficient of the bulk (single-crystalline) silicon. Estimated values of η normalized to values observed in the unannealed films D are listed in Table III for all films under study. It seems that only the films annealed at 1100°C show a systematic reduction in the value of the amorphization factor η , compared to the as-grown films D. Also, the value of the minority-carrier lifetime, determined from the photovoltage magnitude and normalized to values obtained from as-grown films D, is shown in Table III. The largest improvement is also observed in the films 1C and 2C, which were exposed to the highest temperatures.

Comments on Deposit Homogeneity

As discussed in Ref. (9), the laser scanning photovoltage in the MS configuration provides an effective means for revealing the electrical inhomogeneities of a thin semiconducting film. The relative change of the magnitude of photovoltage, ΔV , with respect to an average photovoltage signal, V_{av} , was used in our previous study as a quantitative measure of the homogeneity of silicon-on-sapphire. The central portion of the best SOS films analyzed by this technique exhibited $\Delta V/V_{av}$ as low as $\pm 3\%$, while the inferior quality films of D-F category exhibited $\Delta V/V_{av}$ even as high as $\pm 50\%$ (9, 10). Values of $\Delta V/V_{av}$ for the presently studied unimplanted films, with the exception of the edge of the wafers, were estimated to be between $\pm 10\%$ and $\pm 15\%$. The lowest value corresponds to film C,

Table III. The effect of heat-treatment on electrical properties of SOS

Property	Processing schedule							
	Implant	A		B		C		D*
		No implant	Implant	No implant	Implant	No implant	No implant	As grown
Relative concentration of deep levels E_1	1.0	0.4	0.7	0.3	0.2	0.2		1
Amorphization factor	1.2	1.0	1.0	1.2	0.7	0.7		1
Excess** carrier lifetime	1.2	1.5	4	4	3	8		1

* Note that all properties are referred to corresponding property of silicon-on-sapphire film not subjected to thermal annealing.

** Estimated from the magnitude of photovoltage under intrinsic excitation ($h\nu = 2$ eV), which at low temperature minimizes effects of surface recombination.

which received the highest temperature heat-treatment, and the highest value to the as-grown film D. Typical He-Ne laser photovoltage scans along the radial direction for a short distance in the central portion of the films 1D and 1C are shown in Fig. 5. The homogeneity of films 1A and 1B seems to fall between those of films 1C and 1D; however, the differences were too small for unambiguous correlation of homogeneity with a given heat-treatment. The peripheral regions of the films exhibited large inhomogeneities (photovoltage changes by as much as a factor of 3) confined within about 1 cm from an edge of the wafer.

Ion implanted wafers exhibited measurable inhomogeneities only in peripheral regions. It should be noted that the presence of inhomogeneous peripheral regions, and improvement of homogeneity upon ion implantation, is consistent with our previous study of silicon-on-sapphire (4, 9, 10). This indicates that a uniform implant of shallow ionized impurities tends to overshadow electrical inhomogeneities present in as-grown films with localized potential barriers.

Summary

It has been shown that the electronic properties of SOS films are affected by high temperature annealing. Improvement of the lifetime, a decrease of deep level concentration, and reduction of inhomogeneities have been observed in both ion-implanted and nonimplanted SOS

films after annealing. The annealing was designed to simulate processing steps used in the fabrication of radiation-hard and conventional SOS circuits. The largest improvement in electronic properties has been observed for SOS films subjected to the highest temperature treatment: 1100°C for 3h. These SOS samples also showed a reduction in the degree of amorphization. It seems that the smallest improvement of electronic properties has been observed for simulation of the radiation-hard process which has the lowest processing temperatures. Very similar changes in electrical properties have been observed for ion-implanted and nonimplanted samples.

It can be speculated that an increase of the minority-carrier lifetime is caused by a decrease in the deep level concentration, which is caused by the gettering action of the interfacial region between the silicon film and the sapphire substrate.

The efficiency of gettering introduced by interfacial strain should increase with increasing temperature due to the increase of strain and the mobility of defects. Therefore, one can expect that the defect density will be lower for the highest processing temperature. It can be speculated that high temperature annealing could also affect redistribution of aluminum near the silicon-sapphire interface, which could be reflected in the reduction of amorphization and interfacial inhomogeneities, as observed in the photovoltage scans.

Acknowledgments

The authors would like to thank M. T. Duffy and R. A. Soltis for supplying them with SOS samples selected according to crystallinity, and R. Soydan for his assistance.

Manuscript submitted June 6, 1983; revised manuscript received Dec. 3, 1983.

RCA Corporation assisted in meeting the publication costs of this article.

REFERENCES

1. L. S. Napoli, R. K. Smeltzer, J. Yeh, and W. F. Heagerty, *IEEE Trans. Nucl. Sci.*, **ns-29**, 1707 (1982).
2. L. S. Napoli, R. K. Smeltzer, R. Donnelly, and J. Yeh, *RCA Rev.*, **43**, 458 (1982).
3. L. Jastrzebski, M. T. Duffy, J. F. Corboy, G. W. Cullen, and J. Lagowski, *J. Cryst. Growth*, **58**, 37 (1982).
4. G. W. Cullen, M. S. Abrahams, J. F. Corboy, M. T. Duffy, W. E. Ham, L. Jastrzebski, R. T. Smith, M. Blumenfeld, G. Harbeke, and J. Lagowski, *ibid.*, **56**, 281 (1982).
5. J. Lagowski, L. Jastrzebski, and G. W. Cullen, *This Journal*, **128**, 2665 (1981).
6. L. Jastrzebski, *IEEE Trans. Electron Devices*, **ed-29**, 475 (1982).
7. C. W. Pearce, in "Semiconductor Silicon 1981," H. R. Huff, R. J. Kriegler, and Y. Takeishi, Editors, p. 705, The Electrochemical Society Softbound Proceedings Series, Pennington, NJ (1981).
8. M. T. Duffy, J. F. Corboy, G. W. Cullen, R. T. Smith, R. A. Soltis, G. Harbeke, J. R. Sandercock, and M. Blumenfeld, *J. Cryst. Growth*, **58**, 10 (1982).
9. J. Lagowski, L. Jastrzebski, and G. W. Cullen, *This Journal*, **129**, 2609 (1982).
10. L. Jastrzebski, J. Lagowski, G. W. Cullen, and J. I. Pankove, *Appl. Phys. Lett.*, **40**, 713 (1983).
11. See, for example, B. E. Deal, in "Semiconductor Silicon 1977," H. R. Huff and E. Sirtl, Editors, p. 276, The Electrochemical Society Softbound Proceedings Series, Princeton, NJ (1977).
12. J. Lagowski, L. Jastrzebski, and G. W. Cullen, *This Journal*, **130**, 1744 (1983).

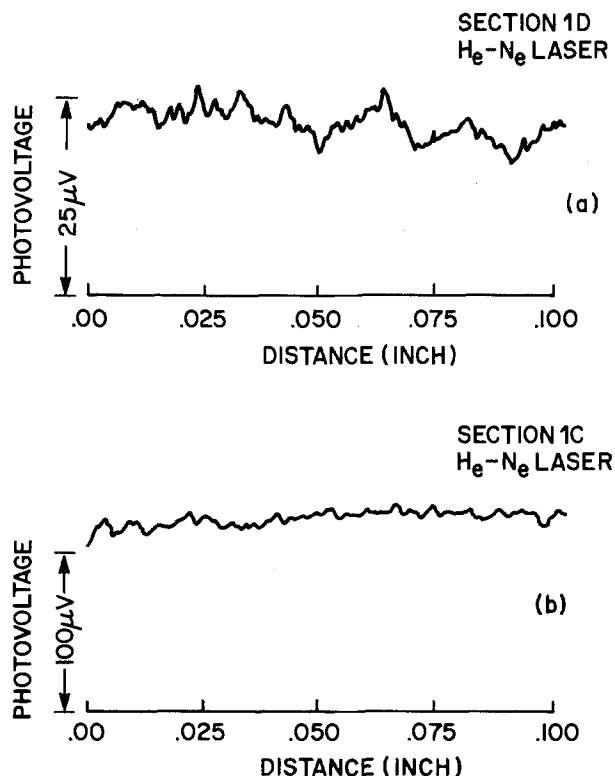


Fig. 5. Photovoltage scans of central portions of SOS wafers 1C and 1D. He-Ne laser excitation, MS configuration. Note that the magnitude of relative photovoltage changes $\Delta V/V_{avg}$ provides the measure of the magnitude of inhomogeneities.

Application of Low Angle Beveling for Thin Film Thickness Measurement by SEM or AES

G. Riga*¹ and B. Horblit²

Fairchild Camera & Instrument Corporation, Mountain View, California 94039

ABSTRACT

The feasibility of measuring the thickness of very thin films (<1000Å) by using a low angle beveling technique in conjunction with a scanning electron microscope (SEM) or an Auger electron spectroscopy (AES) has been demonstrated. The thin film thickness has been magnified in two steps, 200 times with low angle beveling, and an additional 5000 times with the SEM or AES. The accuracies of measurements performed on two SiO₂ films having thicknesses of 740 and 194Å were found to be 4.2% and 13.4%, respectively, when compared to ellipsometric measurements. This technique has also been used on MOS gate oxide and Si-Cr thin film resistor samples. With better control of the variables involved, it is reasonable to expect that films on the order of 20Å could be measured.

In many cases, conventional techniques cannot be used to measure the thickness of very thin films. This is because the required accuracies cannot be achieved under the restrictions imposed by sample size and structure (1-3). By using a combination of angle beveling with scanning electron microscopy (SEM) or Auger electron spectroscopy (AES), it is possible to measure the thickness of a large number of thin films in a wide variety of structures. In the case of insufficient SEM image contrast, the AES provided spatial and chemical resolution to determine the film boundaries.

Description of the Technique

A technique that uses two stages of magnification has been employed to measure the thicknesses of very thin films. The first magnification is obtained by beveling the sample at a small angle (4, 5, 9). The second is provided by the SEM or AES (6).

The technique consists of the following steps: (i) sample preparation; that is, mounting and beveling, (ii) measurements of bevel angle, film thickness by SEM or AES, and film width on the photo, and (iii) calculation of the film thickness.

The sample is mounted on a beveled mounting block using a low temperature melting wax. The block consists of a metallic disk that has the top surface precision machined at a known small angle with respect to the bottom surface of the disk. The beveling is achieved by polishing the specimen on a frosted-glass plate. The final polishing medium is a 0.1 μm diamond particle in oil. The surface of the specimen is cleaned with trichloroethylene (TCE). The bevel angle is then measured using the small angle measurement (SAM) technique (7).

The SAM technique requires a microscope in which the rotation of the specimen can be accurately determined. The detection of the layer can be accomplished by using the SEM or AES. The SEM can be used in all cases where the secondary or backscattered electrons provide sufficient material contrast to distinguish the edges of the layer. The AES can be used for all specimens, and is particularly useful in distinguishing layers that differ only

slightly in composition. The image obtained is in the form of an Auger elemental map (8). It is important to note that the minimum detection limit of the AES is about 1 weight percent (w/o). In either case—SEM or AES—care must be taken that the sample is mounted perpendicular to the electron beam. After the image of the layer is obtained, the width of the layer is measured from the photomicrograph and the actual layer thickness is calculated using

$$T = A \cdot \sin \alpha \cdot M^{-1}$$

where T is the actual film thickness, A the film width measured from the photomicrograph, α the bevel angle, and M the photomicrograph magnification.

Test to Determine Accuracy

The accuracy of the technique described above has been determined by comparison to ellipsometric measurements. Silicon dioxide films of about 200 and 700Å were thermally grown on silicon wafers. The films were carefully measured with an ellipsometer. The averages and ranges of the measurements are reported in Table I.

The thin oxide films were covered with 2500Å of polysilicon for edge delineation and simulation of typical device structure. After the samples were beveled, an SEM photomicrograph and an AES elemental dot map of the SiO₂ films were obtained (Fig. 1-4). The width of the layer measured from the photomicrograph is reported in Table I along with the calculated film thickness. The error with respect to the thickness value obtained from the ellipsometric measurement is 4.2% and 13.4% for the 700 and 200Å samples, respectively.

Source of Errors

Three orders of errors have been identified. Errors of first order include (i) edge definition of the film, (ii) determination of the bevel angle, and (iii) SEM or AES magnification. Errors of second order include (i) length measurements from the photomicrographs, and (ii) sample position in the SEM or AES. The error of third order is spatial resolution of the SEM or AES.

The sharpness of the interface between the film and the surrounding material determines how well the edge of the film can be defined and therefore how well its width can be measured. The edge definition of the film is a strong function of the quality of the beveled surface,

Table I. Summary of experimental data

Sample id	T_{ref} (Å) avg/range	Sin α	M (1000×)	A (mm)		T (Å)		ϵ %	
				SEM	AES	SEM	AES	SEM	AES
700	740/2	0.0094	5	38	41	714	771	-3.5	+4.2
200	194/7	0.0044	4	20	20	220	220	+13.4	+13.4
SiO ₂ gate	NA	0.0100	6	41	42	683	700	—	—
SiCr resistor	NA	0.0083	2	*	24	—	996	—	—

* Difficult to measure.

T_{ref} = thickness from ellipsometric measurements.

ϵ (%) = $(T - T_{ref}/T_{ref}) \cdot 100$.

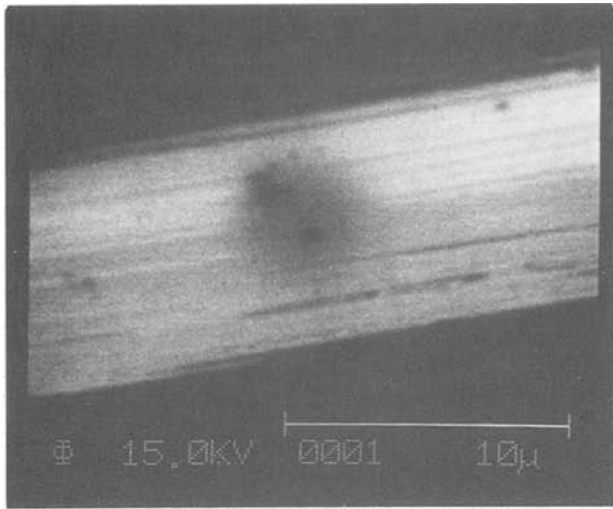


Fig. 1. SEM photomicrograph of 700Å SiO₂ film at 5000×

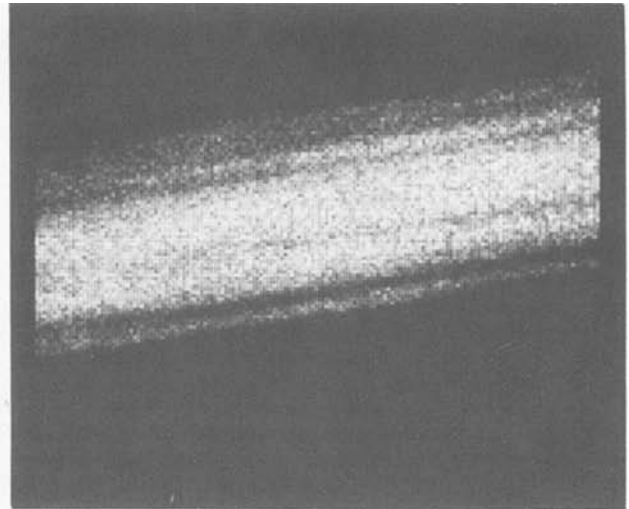


Fig. 4. AES oxygen dot map of sample shown in Fig. 3 at 5000×

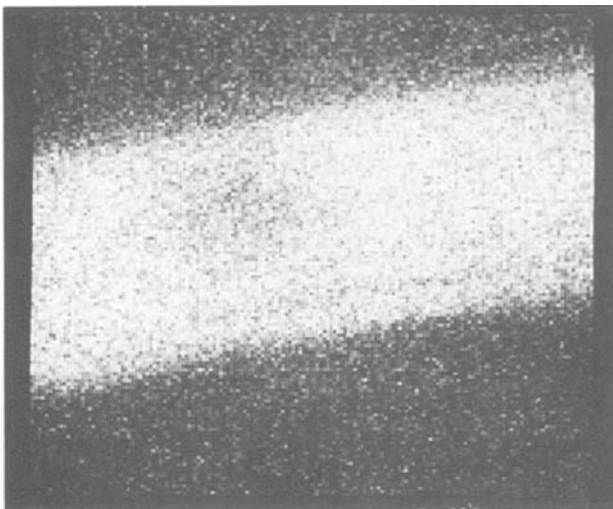


Fig. 2. AES oxygen dot map of sample shown in Fig. 1 at 5000×

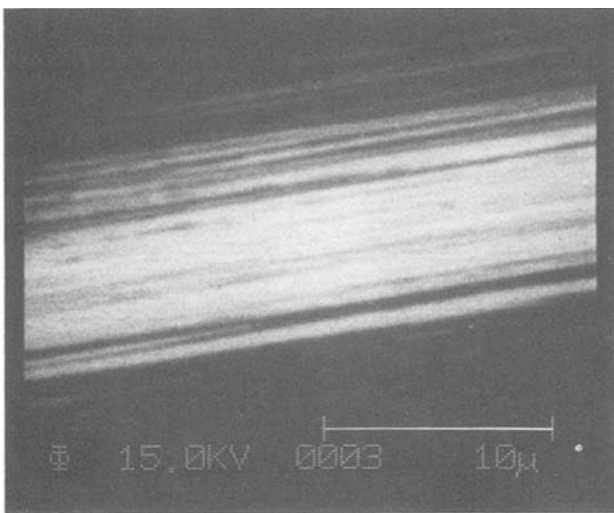


Fig. 3. SEM photomicrograph of 200Å SiO₂ film at 5000×

which is influenced by the particular lapping technique used. For the 200Å film, the edge definition was the main source of error in the determination of thickness.

The error introduced by the measurement of the bevel angle which was performed by the small angle measurement technique is on the order of $\pm 5\%$, and it can be further reduced if an interferometric technique is used.

The SEM or AES magnification error, which directly influences the width of the film observed from the photomicrograph, is generally less than 10%. The error can be reduced to less than 3% with the use of appropriate calibration standards.

After the edges of the film are defined on the photomicrograph, the error introduced in measuring the film width is on the order of ± 0.5 mm. The error in percent is therefore a function of the film width on the photomicrograph.

Applications

To demonstrate the applicability of the technique to a device structure characterization, the gate oxide of a MOS transistor and a Si-Cr thin film resistor have been measured (see Fig. 5-8). The film thicknesses have been found to be 700 and 996Å.

The Cr dot map of the Si-Cr film illustrates the effectiveness of the AES in delineating the film boundaries in cases of low material contrast. The Si-Cr resistor lies on and is covered by silicon dioxide.

Conclusions

It has been demonstrated that very thin films can be measured by appropriately combining the well-known techniques of angle beveling with scanning electron microscopy or Auger electron spectroscopy. Regardless of the film nature (*e.g.*, conductor or insulator), this technique can be used and is limited only by the AES detection limit.

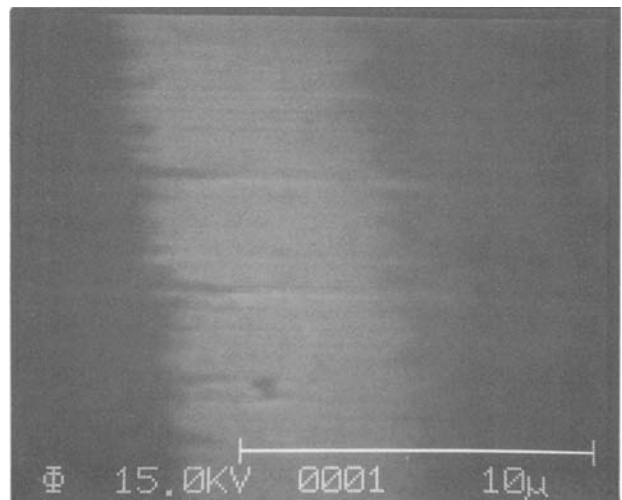


Fig. 5. SEM photomicrograph of a SiO₂ gate at 6000×

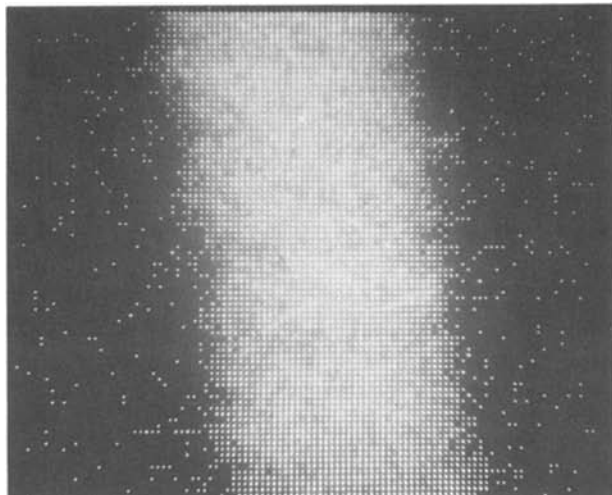


Fig. 6. AES oxygen dot map of sample shown in Fig. 5 at 6000 \times

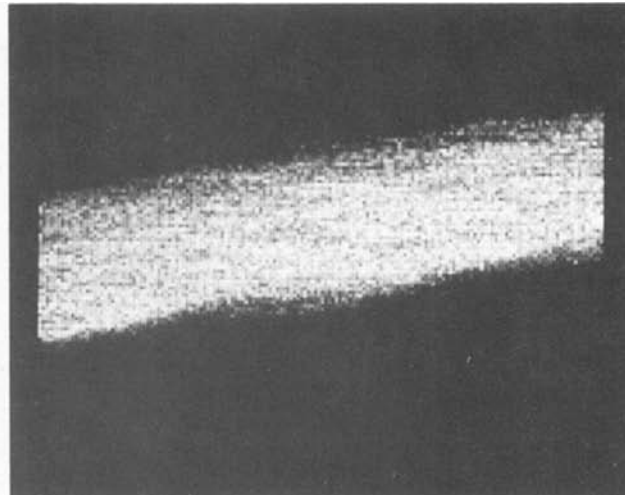


Fig. 8. AES chromium dot map of sample shown in Fig. 7 at 2000 \times

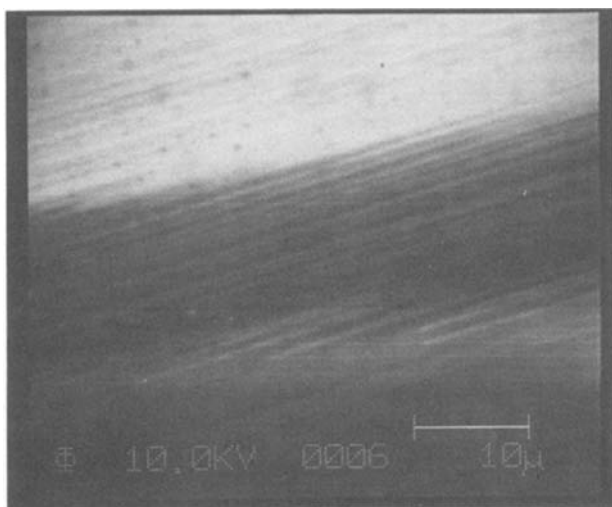


Fig. 7. SEM photomicrograph of Si Cr resistor at 2000 \times

By improving the beveling techniques (smoother surface) and increasing the accuracy in determining the bevel angle (by interferometry), it is reasonable to expect that films on the order of 20 \AA thick and covering small areas (e.g., $1 \times 10 \mu\text{m}$) might be measured (9, 10).

Acknowledgments

The authors express their appreciation to R. Razouk, M. Sklar, and B. Cairns of Fairchild Advanced Research and Development Laboratory for the help received in preparing the standards, and to W. Jansen of Perkin Elmer Physical Electronic Laboratories for the AES analysis.

Our thanks are also extended to Mr. R. Smith, General Manager of Fairchild Linear Division, for giving us permission to publish this paper.

Manuscript submitted June 1, 1983; revised manuscript received Jan. 11, 1984. This was Paper 324 presented at the Washington, DC, Meeting of the Society, Oct. 9-14, 1983.

Riga Analytical Lab, Incorporated assisted in meeting the publication costs of this article.

REFERENCES

1. J. W. Coburn, *J. Vac. Soc. Technol.*, **13**, 1037 (1976).
2. H. H. Andersen, *Appl. Phys.*, **18**, 131 (1979).
3. T. A. Whatley, D. J. Comaford, J. Colby, and P. Miller, in "Surface Analysis Techniques for Metallurgical Applications," pp. 114-125, ASTM STP 596, American Society for Testing and Materials, Philadelphia, PA (1976).
4. D. C. D'Avanzo, R. D. Rung, and R. W. Dutton, Technical Report no. 5013-2, Integrated Circuits Laboratory, Stanford Electronics Laboratory, Stanford University, Stanford, CA (1977).
5. P. J. Severin, in "Semiconductor Measurement Technology: Spreading Resistance Symposium," p. 99, NBS Special Publication 400-10, Washington, DC (1974).
6. A. Joshi, L. E. Davis, and P. W. Palmberg in "Methods of Surface Analysis," A. W. Czandara, Editor, Chap. 5, Elsevier, New York (1975).
7. A. H. Tong, E. F. Gorey, and C. P. Schneider, *Rev. Sci. Instrum.*, **43**, 320 (1972).
8. R. R. Olsen and D. F. Paul, in "Auger Chemical State Mapping," Physical Electronics Applications Note no. 8101, Perkin-Elmer Physical Electronics Division, Eden Prairie, MN (1982).
9. A. Meyer and S. Schwartzman, in "Semiconductor Measurement Technology: Spreading Resistance Symposium," p. 123, NBS Special Publication 400-10, Washington, DC (1974).
10. D. C. D'Avanzo, C. Clare, and C. Dell'Oca, *This Journal*, **127**, 2704 (1980).

The Thermodynamic Effects of Using an Inert Gas in the Hydride VPE Growth of InP

C. W. Tu and K. A. Jones*

Department of Electrical Engineering, Colorado State University, Fort Collins, Colorado 80523

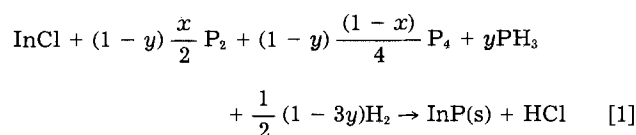
ABSTRACT

Substituting an inert gas for hydrogen as the carrier gas in the VPE growth of InP and other III-V compounds has the negative effects of reducing the growth rate and the HCl concentration in the growth zone. This results from a decrease in the supersaturation for the deposition reaction. These effects are quantified for the hydride growth of InP under equilibrium conditions. The thermodynamic growth rate and the equilibrium InCl, HCl, P₂, P₄, and PH₃ partial pressures are computed as a function of the inert gas/inert gas + H₂ pressures.

Hydrogen is an excellent carrier gas because it can be highly purified at a relatively low cost using a hydrogen purifier. It also getters oxygen. Recently, some people have suggested using N₂ as the carrier gas because it can be highly purified by first liquifying it (1), and because it suppresses the silicon contamination and reduces the degree of compensation (2). One should consider the possibility of forming nitrides if he chooses to use N₂, but he should also consider how substituting an inert gas for the H₂ affects the thermodynamics of the growth process. The latter consideration is the topic of this paper.

The parameters considered in this paper are the thermodynamic growth rate and the equilibrium PH₃ and HCl concentrations in the growth zone. Clearly, reducing the H₂ partial pressure will reduce the PH₃ pressure. This is important since it has been suggested that the growth rate is higher when more PH₃ is present due to the fact that InCl more readily reacts with PH₃ than with P₂ or P₄ (3). [It should be noted that PH₃ decomposes rather slowly (4), so that more PH₃ is present in the growth zone than is computed from thermodynamic data. Thus, the calculations that follow can only be used to indicate the trends.] The HCl concentration is important because it is thought that increasing the HCl concentration reduces the activity of silicon in the quartz reactor (5).

From the deposition reaction



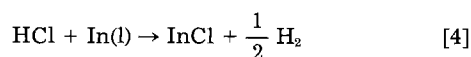
one can see that reducing the H₂ pressure will reduce the deposition rate, and this, in turn, will reduce the HCl partial pressure, since it is formed during the deposition reaction. In this equation, x is the ratio of the amount of phosphorus in the P₂ form to the amount of phosphorus in the P₂ and P₄ form and is given by the equation

$$x = \frac{P_{\text{P}_2}}{P_{\text{P}_2} + 2P_{\text{P}_4}} \quad [2]$$

y is the fraction of the phosphorus in PH₃ and is given by

$$y = \frac{P_{\text{PH}_3}}{P_{\text{PH}_3} + xP_{\text{P}_2} + (1-x)P_{\text{P}_4}} \quad [3]$$

First, the output pressures from the source zone, designated by the superscript 1, must be determined for the source zone reaction



The output InCl pressure is, from a chlorine balance

$$P_{\text{InCl}^1} = P_{\text{HCl}^0} - P_{\text{HCl}^1} \quad [5]$$

where P_{HCl^0} is the input HCl pressure. P_{HCl^1} can be found from the equation

$$P_{\text{HCl}^1} = \frac{P_{\text{HCl}^0} (1 - P_{\text{HCl}^0})^{1/2}}{(1 - P_{\text{HCl}^0})^{1/2} + K_5} \quad [6]$$

where K_n is the equilibrium constant for the reaction in equation n .

$$P_{\text{H}_2} = 1 - P_{\text{HCl}^0} \quad [7]$$

was used in deriving Eq. [6].

For the deposition zone, first a value of P_{P_4} is assumed, and then it is used to determine P_{P_2} after the equilibrium constant for the reaction



has been found. P_{PH_3} can be found from the phosphorus balance

$$P_{\text{PH}_3} = P_{\text{PH}_3^0} - 2P_{\text{P}_2} - 4P_{\text{P}_4} - (P_{\text{HCl}} - P_{\text{HCl}^1}) \quad [9]$$

where $P_{\text{PH}_3^0}$ is the input phosphine pressure and $P_{\text{HCl}} - P_{\text{HCl}^1}$ is the amount of phosphorus consumed by the deposition of InP. Again, P_{InCl} is found from the chlorine balance

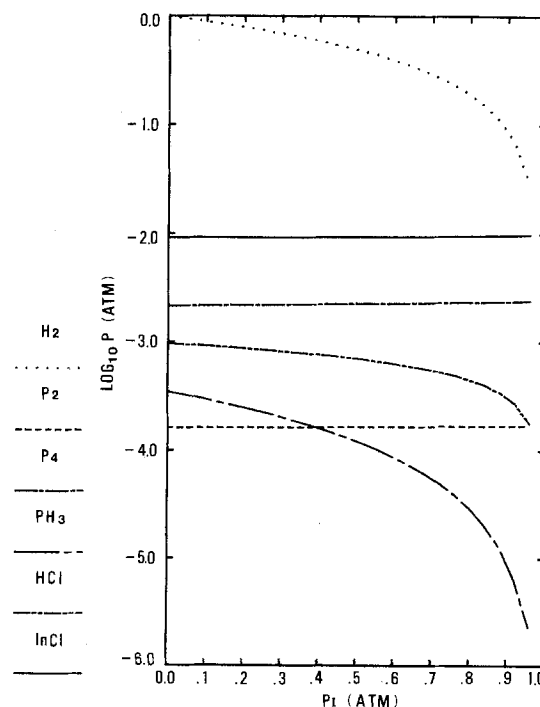


Fig. 1. The equilibrium HCl, PH₃, P₂, P₄, InCl, and H₂ partial pressures in the deposition zone plotted as a function of the inert gas partial pressure when $P_{\text{HCl}^0} = P_{\text{PH}_3^0} = 0.01$ atm, $T_s = 750^\circ\text{C}$, and $T_D = 650^\circ\text{C}$.

*Electrochemical Society Active Member.

Table I. The equilibrium HCl and PH₃ partial pressures for the P_{HCl}^o/P_{PH₃^o ratios of 0.01/3/0.01, 0.01/0.01, 0.03/0.01, 0.01/0.01/3, and 0.01/0.03, and for T_D = 600°, 650°, and 700°C}

P _i (atm)	0	0.1	0.2	0.3	0.4	0.5	0.6	0.7	0.8	0.9
$\frac{P_{HCl}^o}{P_{PH_3}^o}$										
P _{HCl} × 10 ⁴ atm	0.01/3/0.01	3.23	3.08	2.93	2.76	2.57	2.36	2.13	1.86	1.53
	0.01/0.01	9.53	9.10	8.64	8.13	7.59	6.97	6.28	5.47	4.48
	0.03/0.01	27.10	25.92	24.63	23.23	21.67	19.92	17.91	15.52	12.52
	0.01/0.01/3	7.08	6.78	6.45	6.10	5.70	5.25	4.74	4.14	3.40
	0.01/0.03	12.38	11.82	11.22	10.56	9.85	9.05	8.15	7.09	5.78
P _{PH₃} × 10 ⁴ atm	0.01/3/0.01	3.55	3.04	2.55	2.08	1.65	1.26	0.896	0.578	0.311
	0.01/0.01	3.46	2.96	2.48	2.03	1.61	1.22	0.864	0.554	0.292
	0.03/0.01	3.20	2.73	2.28	1.86	1.47	1.10	0.775	0.484	0.242
	0.01/0.01/3	2.51	2.16	1.81	1.49	1.19	0.903	0.683	0.416	0.221
	0.01/0.03	4.62	3.94	3.29	2.68	2.12	1.00	1.13	0.717	0.372
P _{HCl} × 10 ⁴ atm	T _D									
	600	18.81	18.07	17.26	16.37	15.38	14.26	12.97	11.42	9.48
	650	9.53	9.10	8.64	8.13	7.59	6.97	6.28	5.47	4.48
P _{PH₃} × 10 ⁴ atm	700	4.87	4.63	4.38	4.12	3.82	3.45	3.14	2.72	2.21
	600	3.84	3.28	2.75	2.26	1.79	1.36	0.967	0.621	0.329
	650	3.46	2.96	2.48	2.03	1.61	1.22	0.864	0.554	0.292
700	3.10	2.64	2.21	1.81	1.43	1.08	0.769	0.492	0.260	

$$P_{InCl} = P_{InCl}^I + P_{HCl}^I - P_{HCl} = C_1 - P_{HCl} \quad [10]$$

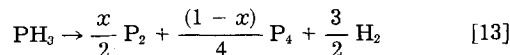
The total pressure is 1 atm, so that

$$\begin{aligned} P_{H_2} &= 1 - P_{InCl} - P_{P_2} - P_{P_4} - P_{PH_3} - P_I - P_{HCl} \\ &= 1 - P_{InCl}^I - 2P_{HCl}^I + P_{P_2} + 3P_{P_4} - P_{PH_3}^o - P_I + P_{HCl} \\ &= C_2 + P_{HCl} \approx C_2 \end{aligned} \quad [11]$$

where P_I is the partial pressure of the inert gas. Now, P_{PH₃} can be computed from

$$P_{PH_3} = P_{P_2}^{x/2} P_{P_4}^{(1-x)/4} P_{H_2}^{3/2} / K_{13} \quad [12]$$

where K₁₃ is the equilibrium constant for the dissociation reaction



P_{HCl} can be calculated from

$$P_{HCl} = \frac{C_1 K_1 Q}{1 + K_1 Q} \quad [14]$$

where

$$Q = P_{P_2}^{(1-y)x/2} P_{P_4}^{(1-y)(1-x)/4} P_{PH_3}^y P_{H_2}^{1/2(1-3y)} \quad [15]$$

K₁ is the equilibrium constant for the deposition reaction, and R is defined in Eq. [10]. Finally, P_{PH₃} computed from Eq. [9] is compared with the value found from Eq. [13]. If they are not the same, a new value of P_{P₂} is assumed. The process is repeated until the two P_{PH₃} values are equal.

The thermodynamic growth rate, R, is

$$R = \frac{P_{InCl}^I - P_{InCl}}{P_{InCl}^I} \times \frac{\text{no. of InCl}^I \text{ atoms crossing unit area per unit time}}{\text{no. of In atoms per unit volume in InP}}$$

Therefore

$$R \propto P_{InCl}^I - P_{InCl} \quad [16]$$

Using the thermodynamic data collected by Shaw (6), the equilibrium partial pressures of HCl, PH₃, H₂, P₂, P₄, and InCl were computed and are plotted as a function of the inert gas partial pressure in Fig. 1, and there it is seen that the growth rates are qualitatively similar to the experimental curves of Ihara *et al.* (1). For these calculations, the source temperature was, T_S = 750°C, the deposition temperature was, T_D = 650°C, and both P_{HCl}^o and P_{PH₃}^o were 0.01 atm. P_{HCl} decreases by about a factor of 10 as P_I increases from 0 to 0.98 atm. This reduction is due to less hydrogen being available to form HCl during the deposition reaction. Because there is less InP deposited with in-

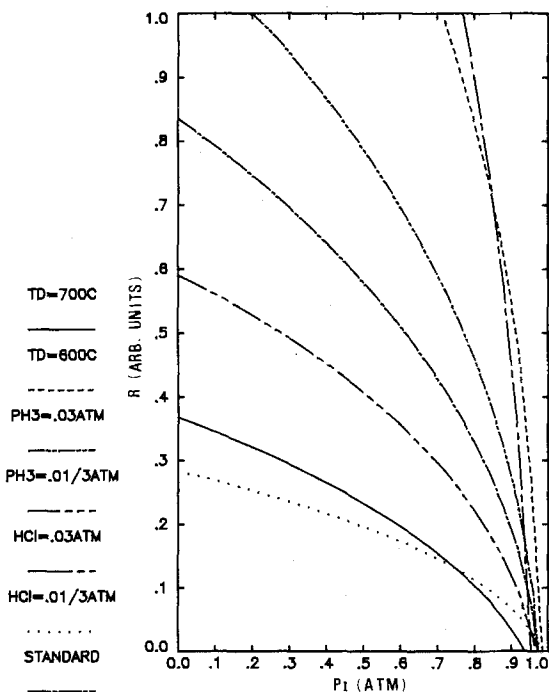


Fig. 2. The thermodynamic growth rate plotted as a function of the inert gas pressure for (a) the standard conditions, (b) P_{HCl}^o = 0.01/3, (c) P_{HCl}^o = 0.03, (d) P_{PH₃}^o = 0.01/3, (e) P_{PH₃}^o = 0.03, (d) T_D = 600°C, and (e) T_D = 700°C.

creasing P_1 , P_{InCl} increases. P_{PH_3} decreases two orders of magnitude over the range of P_1 , since there is less hydrogen available, and, as a result, P_{P_2} and P_{P_4} increase. They also increase because there is less InP deposited.

That there is less deposition when P_1 increases is shown in Fig. 2 where the ideal growth rate is plotted vs. P_1 . R decreases continuously until at $P_1 = 0.975$ atm there is no deposition. The effects on the growth rate of decreasing P_{HCl^0} or $P_{\text{PH}_3^0}$ by one third, increasing P_{HCl^0} or $P_{\text{PH}_3^0}$ by a factor of three, or increasing or decreasing T_D by 50°C are also shown in Fig. 2. The effects are largest when $P_1 = 0$, and all of the curves tend to converge on the point $R = 0$ and $P_1 = 0.97$.

Reducing P_{HCl^0} by one-third reduces the initial growth rate by one-third, and tripling P_{HCl^0} triples the initial growth rate. $R \propto P_{\text{HCl}^0}$ in this range, because $P_{\text{InCl}^1} \propto P_{\text{HCl}^0}$ and $R \propto P_{\text{InCl}^1}$. The effect of tripling or tripling $P_{\text{PH}_3^0}$ is smaller, as it only changes the initial growth rate by 30%. Adding to or reducing the PH_3^0 concentration has a smaller effect because the free-energy change for the deposition reaction is much more sensitive to the HCl concentration. Lowering the deposition temperature by 50°C doubles the initial growth rate, and raising it by 50°C halves the growth rate. These effects reflect the temperature dependence for the deposition reaction.

How changing HCl^0 , PH_3^0 , and T_D affects the equilibrium HCl and PH_3 concentrations for different values of P_1 is illustrated in Table I.

That decreasing the hydrogen partial pressure decreases the growth rate has been verified experimentally for the chloride growth of GaAs, InAs, GaP, and InP (7). The investigators also found that there were kinetic, as well as thermodynamic, effects, such as the growth rate being reduced more by a heavier inert gas.

Manuscript submitted Dec. 6, 1982; revised manuscript received Nov. 31, 1983.

REFERENCES

1. M. Ihara, R. Dazai, and O. Ryuzan, *J. Appl. Phys.*, **45**, 528 (1974).
2. L. Y. Lin, Y. W. Lin, X. R. Zhong, Y. Y. Zhang, and H. L. Li, *J. Cryst. Growth*, **56**, 344 (1982).
3. K. Fairhurst, D. Lee, D. S. Robertson, H. T. Parfitt, and W. H. E. Wilgoss, *J. Mater. Sci.*, **16**, 1013 (1981).
4. V. M. Connelly and R. F. Karlicek, *J. Appl. Phys.*, **53**, 6399 (1982).
5. J. W. DiLorenzo, *J. Cryst. Growth*, **17**, 189 (1972).
6. D. W. Shaw, *J. Phys. Chem. Solids*, **36**, 111 (1975).
7. O. Mizuno and H. Watanabe, *J. Cryst. Growth*, **30**, 240 (1975).

Chemical Vapor-Deposited Boron Nitride Film on Silicon as a Boron Diffusion Source

Chol Kim,* Byung-Ki Sohn,¹ and Katsufusa Shono**

Faculty of Science and Technology, Sophia University, Tokyo 102, Japan

ABSTRACT

CVD-BN films deposited onto silicon have been investigated as a diffusion source. The concentration ratio of boron to nitrogen C_B/C_N in the as-deposited BN film could be controlled in the range from 1.4 to 2.5 by changing the depositing temperature with the $\text{B}_2\text{H}_6/\text{NH}_3$ ratio of 1/140. The boron concentration at the silicon surface depends mainly on the concentration ratio C_B/C_N and remains constant during the heat-treatment for diffusion, but decreases with diffusion temperature. The concentration ratio of boron nitride to excess boron $C_{\text{BN}}/C_{\text{Bx}}$ in the film has been empirically formulated in the Boltzmann form as a function of the deposition temperature. The boron surface concentration has also been described in the Boltzmann form, in terms of the diffusion temperature and the concentration ratio $C_{\text{BN}}/C_{\text{Bx}}$. The excess boron atoms in the BN film cause boron diffusion into the silicon. The activation energy for excess boron diffusion in the BN film is approximately proportional to the concentration ratio $C_{\text{BN}}/C_{\text{Bx}}$.

A chemical vapor-deposited boron nitride (CVD-BN) film² has been used as a solid source of boron for diffusion into a silicon crystal (1). The encapsulation over the BN surface with a thin Si_3N_4 film very effectively produces good uniformity and good reproducibility of the sheet resistance of the boron-diffused layer.

The chemical and physical properties of the CVD-BN films are strongly dependent on the deposition parameters, such as the flow rates of the reactant and carrier gases, the flow-rate ratio of reactant gases, and the substrate temperature during the deposition (2). An example is that the electrical resistivity of the BN film deposited in the temperature range from 400° to 600°C under a fixed gas-flow condition increases from 10^{11} to 10^{15} Ω-cm with increasing deposition temperature (3). The strong dependence of the properties of BN film on the deposition parameters is mainly attributed to the composition and structure of the BN layer.

In this paper, the chemical composition of BN films is analyzed as a function of the deposition temperature. The

boron concentration at the silicon surface is discussed as a function of the film composition and the heat-treatment temperature for diffusion.

Experimental

BN and Si_3N_4 films were deposited with the CVD system described in a previous paper (4). The fused silica reaction chamber was 35 mm wide, 400 mm long, and 20 mm high. A graphite plate, 30 mm wide, 50 mm long, and 5 mm thick, was used as the susceptor with RF heating. The reactant gases used were 1% B_2H_6 in N_2 , 5% SiH_4 in N_2 and NH_3 , and the carrier gas was nitrogen.

Phosphorous-doped silicon wafers, having the resistivity of 3-5 Ω-cm and (100) orientation, were used as the substrate. The BN films were deposited under the gas-flow conditions: 50 cm^3/min of 1% B_2H_6 , 70 cm^3/min of NH_3 , and 2000 cm^3/min of nitrogen carrier gas. The volume ratio of B_2H_6 to NH_3 was kept constant at 1/140. The above conditions were maintained constant for all deposited films. The deposition temperature was varied from 440° to 830°C. The resultant thickness of the BN films grown over the silicon surface was about 1000Å. An Si_3N_4 film was successively deposited over the surface of the BN under the gas-flow conditions: 70 cm^3/min of NH_3 , 20 cm^3/min of 5% SiH_4 , and 2000 cm^3/min of nitrogen carrier gas, and a substrate temperature of 720°C. The thickness of the Si_3N_4 film was approximately 300Å.

*Electrochemical Society Student Member.

**Electrochemical Society Active Member.

¹On leave from Department of Electronics, Kyungpook National University, Daegu 635, Korea.

Key words: CVD, solubility, and integrated circuits.

²In this study and in the work of Ref. (2), the obtained film is nonstoichiometric. We customarily call the film "BN," which involves excess boron in boron nitride.

Boron diffusion into silicon from the BN film was carried out by heat-treatment performed in the temperature range from 1050° to 1200°C for 15-400 min in a nitrogen atmosphere. After the heat-treatment, the Si_3N_4 was removed in HF and the BN film in hot H_3PO_4 (1).

The boron diffusion depth was measured by spherical drilling and staining, and the sheet resistance with a four-point probe. The boron diffusion profile was obtained by use of spreading resistance. In obtaining the profile for the surface region, there were some errors which probably arose from using the angle lapping technique, or the corrective function to calculate the boron concentration from spreading resistance (5). Therefore, the surface concentration and the profile in the surface region were determined by the differential conductivity technique. The chemical composition of the BN film was determined by Auger electron spectroscopy (AES).

Results

Composition of the CVD-BN film.—The boron concentration C_B in the as-deposited CVD-BN film as a function of the deposition temperature T_D is shown in Fig. 1. For increasing deposition temperatures from 440° to 830°C, the boron concentration C_B decreased from 2.25×10^{22} to $1.05 \times 10^{22} \text{ cm}^{-3}$.

Figure 2 shows the concentration ratio of boron to nitrogen C_B/C_N in the as-deposited BN film as a function of the deposition temperature T_D . Under the gas-flow conditions, the concentration ratio C_B/C_N decreased from 2.5 to 1.4 with increasing deposition temperature in the temperature range from 440° to 830°C. In all the cases investigated, the as-deposited BN films were boron-rich and had an amorphous form, which was confirmed by observing reflection electron diffractor patterns.

Boron concentration at the silicon surface.—The boron profiles in silicon are shown in Fig. 3, where the deposition temperature T_D was (a) 440°C, (b) 600°C, and (c) 720°C, the diffusion temperature T_H was 1200°C, and the diffusion times were 15, 30, and 60 min. As the deposition temperature increased, the boron surface concentration C_s at silicon decreased. The BN films deposited at 440°, 600°, and 720°C gave boron surface concentrations of (a) 2×10^{20} , (b) 5.6×10^{19} , and (c) $0.9\text{--}1.2 \times 10^{19} \text{ cm}^{-3}$, respectively. These were kept constant during the heat-treatment for boron diffusion.

The boron surface concentration as a function of the deposition temperature is shown in Fig. 4 for the diffusion temperatures of 1050°, 1100°, and 1200°C. The maximum boron surface concentration, which was obtained for the BN deposited at temperatures lower than 500°C,

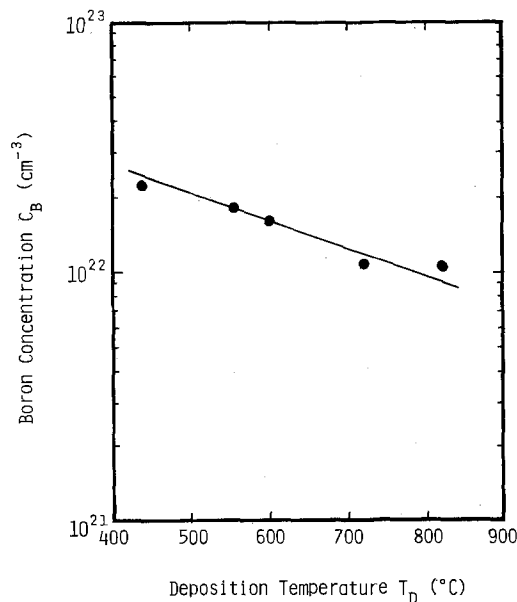


Fig. 1. Boron concentration of the as-deposited BN film vs. deposition temperature.

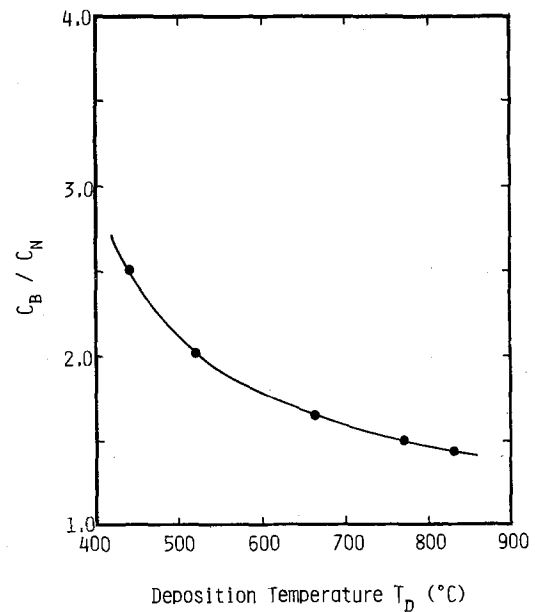


Fig. 2. C_B/C_N ratio of the as-deposited BN film vs. deposition temperature.

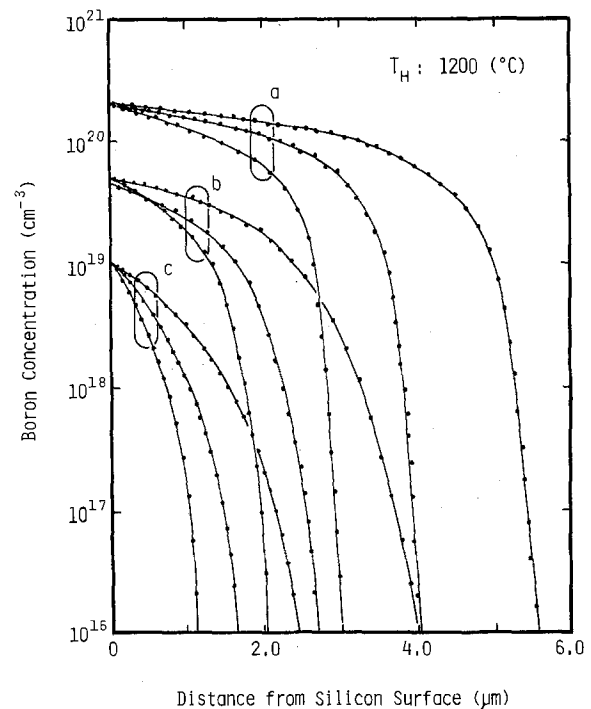


Fig. 3. Boron profiles in the silicon. The groups a, b, and c show the profiles for the deposition temperature 440°, 600°, and 720°C, respectively. The three curves in each group stand for the three different diffusion times 15, 30, and 60 min.

was $2.2 \times 10^{20} \text{ cm}^{-3}$. The boron surface concentration C_s decreases from 2.2×10^{20} to $2 \times 10^{18} \text{ cm}^{-3}$ with increasing deposition temperature T_D from 500° to 800°C and with decreasing the diffusion temperature T_H .

Discussion

As a result of the study of the deposition rate and the composition of BN films as a function of the flow rate and the flow-rate ratio of reactant gases, Murarka *et al.* concluded that, during the deposition, two nearly independent reactions occurred, leading to the simultaneous deposition of boron nitride and boron. They also concluded that the resulting films contained both BN and B in an intimate amorphous mixture (2). In other words, they concluded that the properties of the as-deposited BN films depend on the composition in terms of the concentration ratio of boron nitride to excess boron $C_{\text{BN}}/C_{\text{Bx}}$ in

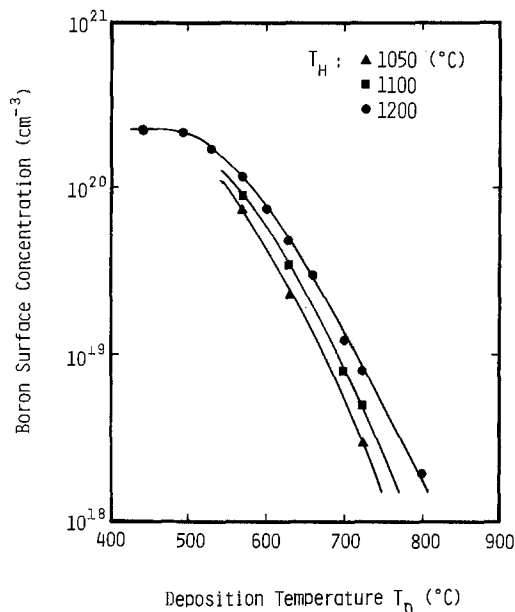


Fig. 4. Boron surface concentration vs. deposition temperature

the film, where C_{BN} is the BN concentration defined as equal to C_N , and C_{Bx} is the excess boron concentration given by $C_{Bx} = C_B - C_N$.

From the results shown in Fig. 2, the concentration ratio of boron nitride to excess boron C_{BN}/C_{Bx} in the as-deposited CVD-BN film can be plotted in Fig. 5 as a function of the reciprocal of the deposition temperature T_D . In the range of deposition temperature, given in Fig. 5, the concentration ratio C_{BN}/C_{Bx} can be written as

$$\frac{C_{BN}}{C_{Bx}} = R_0 \exp\left(-\frac{\Delta E}{k T_D}\right) \quad [1]$$

where $R_0 = 24.40$, $\Delta E = 0.225$ eV, and k is the Boltzmann constant. If the concentration ratio C_{BN}/C_{Bx} corresponds to the deposition rate ratio of BN to B, ΔE may stand for the difference between the activation energies for the simultaneous deposition of BN and B. Under the conditions in this investigation, both the reference concentration and the activation energy for the formation of the BN are larger than those for the B.

From Fig. 4 and Fig. 5, the boron surface concentration C_s can be plotted, as shown in Fig. 6, as a function of the

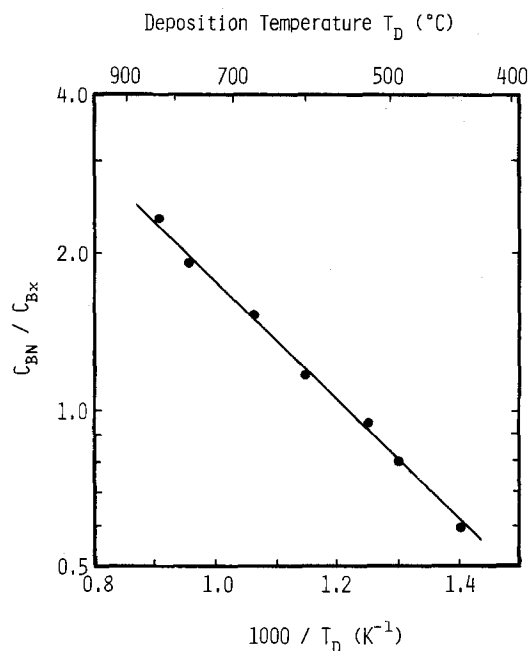


Fig. 5. C_{BN}/C_{Bx} ratio vs. the reciprocal of deposition temperature

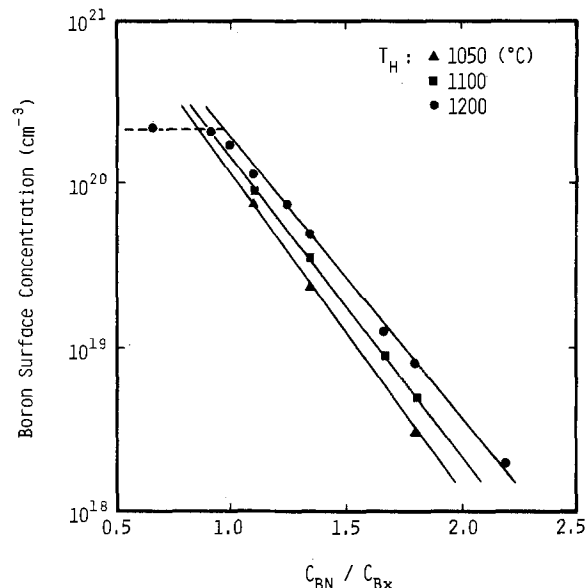


Fig. 6. Boron surface concentration vs. C_{BN}/C_{Bx} ratio

concentration ratio C_{BN}/C_{Bx} of the as-deposited BN film. The boron surface concentration C_s is an exponential function of the concentration ratio C_{BN}/C_{Bx} , and the slope β of the straight line on the semilogarithm graph varied approximately linearly with the diffusion temperature T_H , as shown in Fig. 7. The slope β is thus seen to be

$$\beta = 1 + \frac{E_0}{k T_H} \quad [2]$$

where $E_0 = 0.38$ eV. Then, the boron surface concentration C_s can be written, in Boltzmann form, as

$$C_s = C_x \exp\left(\frac{E_x}{k T_H}\right) \quad [3]$$

where

$$C_x = C_0 \exp\left(-\frac{C_{BN}}{C_{Bx}}\right) \quad [4]$$

$$E_x = E_0 \frac{C_{BN}}{C_{Bx}} \quad [5]$$

where $C_0 = 9.5 \times 10^{21}$ cm⁻³. E_x , the activation energy, is a function of the concentration ratio C_{BN}/C_{Bx} and increases

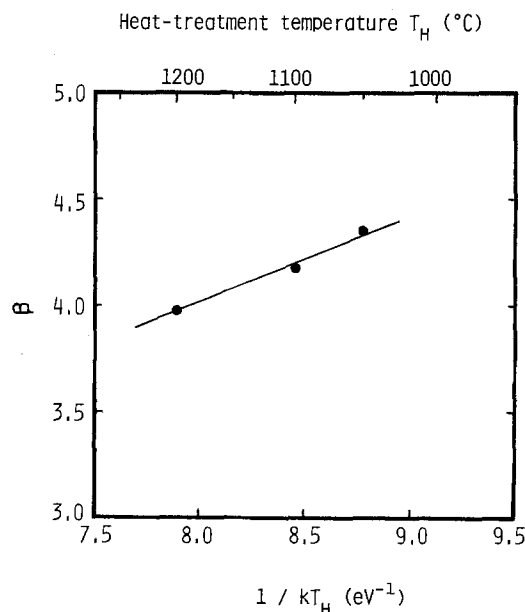


Fig. 7. β vs. the reciprocal of heat-treatment temperature

linearly from 0.25 to 0.95 eV with an increase of $C_{\text{BN}}/C_{\text{Bx}}$ over the range from 0.6 to 2.5.

The excess boron concentration C_{Bx} in the as-deposited BN film, which was shown as a function of the deposition temperature T_{D} in Fig. 1 and 2, is compared in Fig. 8 with the reference concentration C_{x} in Eq. [3]. The solid line in Fig. 8 is 2.6 times the value of C_{x} which was calculated from Eq. [1] and [4]. It closely fits the curve for C_{Bx} , the excess boron concentration. This means that, in the temperature range considered, the excess boron concentration C_{Bx} is approximately equal to 2.6 times C_{x} . The boron surface concentration C_{s} increases with the increasing excess boron concentration C_{Bx} , and must be zero if there are no excess boron atoms in the BN film. This formulation leads to the conclusion that only the excess boron atoms in the BN films act as a boron diffusant into the silicon.

According to Eq. [3], the boron surface concentration C_{s} in silicon should increase exponentially with the decreasing concentration ratio $C_{\text{BN}}/C_{\text{Bx}}$ and finally reach the value C_{v} . However, in the region at deposition temperatures lower than 500°C in Fig. 3 or at concentration ratios $C_{\text{BN}}/C_{\text{Bx}}$ less than 1.0 in Fig. 5, the experimental results do not agree with the trend of Eq. [3], but for a diffusion temperature of 1200°C, the boron surface concentration C_{s} is limited to $2.2 \times 10^{20} \text{ cm}^{-3}$, which corresponds to the solid solubility of boron in silicon (6).

A general description of impurity diffusion from a thin film source into a semi-infinite sink has been presented by Barry and Olofson (7). In their model, when the film thickness is larger than the diffusion length of impurity in the film, the impurity concentration at silicon surface C_{s} is independent of diffusion time but depends on an initial concentration of the impurity C_{i} in the film, a ratio of the impurity diffusivity D_{x} in the film to that D_{B} in the silicon, and a segregation coefficient m of the impurity. The relation is given as

$$C_{\text{s}} = \frac{C_{\text{i}} \sqrt{D_{\text{x}}/C_{\text{B}}}}{1 + \sqrt{D_{\text{x}}/D_{\text{B}}}} \quad [6]$$

The experimental results of Ref. (1) give the excess boron diffusivity D_{x} in the BN film less than $10^{-16} \text{ cm}^2/\text{s}$ at the diffusion temperature of 1200°C, which is much smaller than the boron diffusivity D_{B} in silicon. Therefore, Eq. [6] can be simplified as

$$C_{\text{s}} = C_{\text{Bx}} \sqrt{D_{\text{x}}/D_{\text{B}}} \quad [7]$$

where the initial impurity concentration C_{i} was replaced by the initial concentration of excess boron C_{Bx} in the

film. It can be found that the activation energy E_{x} of Eq. [3] is a difference of the activation energy for the excess boron diffusion in the film and for the boron diffusion in silicon. The former is approximately proportional to the concentration ratio $C_{\text{BN}}/C_{\text{Bx}}$ and the latter is still constant. The exponential relation of the surface concentration C_{s} on the concentration ratio $C_{\text{BN}}/C_{\text{Bx}}$ can be referred to the exponential dependence of the excess boron diffusivity D_{x} on the concentration ratio $C_{\text{BN}}/C_{\text{Bx}}$.

The boron profiles of Fig. 3 show significant characteristics. For the boron surface concentration $C_{\text{s}} = 2 \times 10^{20} \text{ cm}^{-3}$, the boron concentration in the silicon decreases linearly with increasing distance from the silicon surface. The diffusion profiles for the boron surface concentration $C_{\text{s}} = 0.9$ to $1.2 \times 10^{19} \text{ cm}^{-3}$ fit well on the complementary error function curve without the tail region where the boron diffusion was retarded. The detailed analysis of this will not be discussed here.

The boron diffusion technique presented has been employed in source and drain formation for PMOS IC fabrication and in the simultaneous formation of base and isolation regions in bipolar IC's. After the deposition of the BN, the film thickness has been inspected by the ellipsometric technique and the refractive index of the film calculated.

The refractive index of CVD-BN is shown in Fig. 9 as a function of the reciprocal of deposition temperature. The refractive index n can be written as

$$n = n_0 \exp\left(\frac{\Delta E'}{k T_{\text{D}}}\right) \quad [8]$$

where $n_0 = 1.17$ and $\Delta E' = 0.032 \text{ eV}$. By combining Eq. [1] and [8], an empirical relation between the concentration ratio $C_{\text{BN}}/C_{\text{Bx}}$ and the refractive index n can be written as

$$\frac{n}{n_0} = \left(R_0 \frac{C_{\text{Bx}}}{C_{\text{BN}}}\right)^{\Delta E'/\Delta E} \quad [9]$$

or

$$n = 1.83 \left(\frac{C_{\text{Bx}}}{C_{\text{BN}}}\right)^{0.14} \quad [10]$$

Equation [10] shows that the refractive index n depends only weakly on the concentration ratio $C_{\text{BN}}/C_{\text{Bx}}$ and that incorporation of boron into the films leads to a higher refractive index.

Using the relation of Eq. [10], the concentration ratio $C_{\text{BN}}/C_{\text{Bx}}$ can be determined from the refractive index n , instead of by direct measurement of the composition using the AES technique. This provides a convenient way of checking the boron diffusion source during the process.

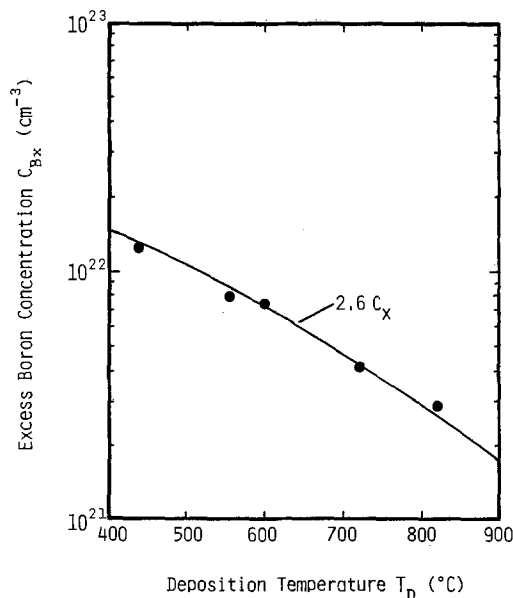


Fig. 8. Excess boron concentration vs. deposition temperature

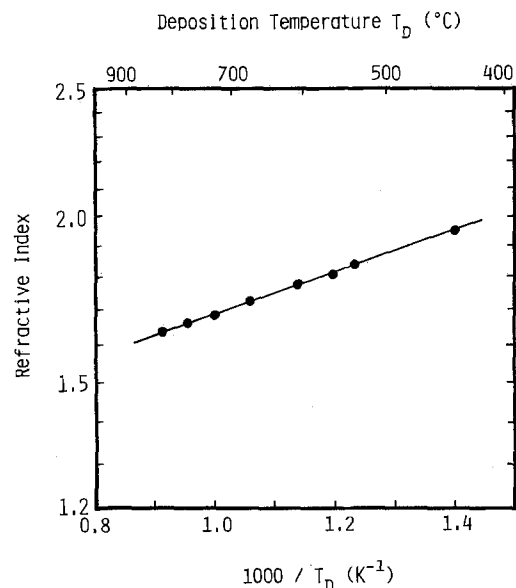


Fig. 9. Refractive index vs. the reciprocal of deposition temperature

Conclusions

Boron-rich BN films were deposited on silicon by CVD with the B_2H_6/NH_3 ratio of 1/140. When the deposition temperature increased from 440° to 830°C, the concentration ratio of boron to nitrogen C_B/C_N in the as-deposited film decreased from 2.5 to 1.4. The CVD-BN films deposited over the silicon wafer can be effectively used as a boron diffusion source. For diffusion heat-treatment at 1200°C, the boron surface concentration decreased over a range from 2.2×10^{20} to 2×10^{18} cm^{-3} as the deposition temperature of the BN film was increased from 440° to 830°C. The surface concentration remained constant during the diffusion heat-treatment, but decreased with decreasing heat-treatment temperature.

The concentration ratio of boron nitride to excess boron C_{BN}/C_{Bx} in the film was empirically formulated in the Boltzmann form as a function of the deposition temperature. The boron surface concentration has also been described in the Boltzmann form, in terms of the diffusion temperature and the concentration ratio C_{BN}/C_{Bx} . The excess boron atoms in the BN film constitute a source of boron diffusion into silicon. The activation energy for excess boron diffusion in the BN film is approximately proportional to the concentration ratio C_{BN}/C_{Bx} .

Acknowledgment

For the Auger analysis of BN films, the authors would like to thank Dr. S. Nishino of the NASA Lewis Research Center, who is now in the College of Engineering, Kyoto University, Kyoto, Japan.

Manuscript submitted May 13, 1983; revised manuscript received Feb. 29, 1984. This was Paper 205 presented at the Montreal, Quebec, Canada, Meeting of the Society, May 9-14, 1982.

Sophia University assisted in meeting the publication costs of this article.

REFERENCES

1. K. Shono, T. Kim, and C. Kim, *This Journal*, **127**, 1546 (1980).
2. S. P. Murarka, C. C. Chang, D. N. K. Wang, and T. E. Smith, *ibid.*, **126**, 1951 (1979).
3. C. Kim and K. Shono, *Jpn. J. Appl. Phys.*, **20**, 1901 (1981).
4. M. Hirayama and K. Shono, *This Journal*, **122**, 1671 (1975).
5. G. A. Lee, in "Proceedings of Spreading Resistance Symposium," p. 75, Gaithersburg, MD (1974).
6. G. L. Vick and K. M. Whittle, *This Journal*, **116**, 1142 (1969).
7. M. L. Barry and P. Olofsen, *ibid.*, **116**, 854 (1969).

Characterization of Metallic Precipitates in Epitaxial Si by Means of Preferential Etching and TEM

C. J. Werkhoven,^{*,1} C. W. T. Bulle-Lieuwma, B. J. H. Leunissen, and M. P. A. Vieggers

Philips Research Laboratories, 5600 JA Eindhoven, The Netherlands

ABSTRACT

Microdefects in epitaxial silicon have been studied by means of preferential etching and transmission electron microscopy. Wafers with a high density of etch pits contained a high density of very small (≤ 10 nm) defect clusters, as revealed by transmission electron microscopy. A good correlation between defect clusters and etch pits could be established. In a larger type of defect, occurring at lower density, the precipitating material was identified as being Cu. In wafers showing a low etch pit density, only a low density of another type of larger defects was found containing Fe or Ti. Processing conditions and gettering treatments only affected the density of the smallest and the Cu containing particles.

Preferential etching is widely used as a rapid method to characterize defects in semiconductor materials. Among the many etching features of silicon, the so-called shallow etch pits or S-pits (1) have been attributed to microdefects which usually develop after high temperature treatments, and which have been correlated with precipitates of transition metals (2). At high etch pit densities, *i.e.*, about 10^6 cm^{-2} , the appearance of the wafer surface is referred to as "haze."

At various instances, the characterization of microdefects was reported. Cullis and Katz (3) found relatively large (~ 2 μm) rod-like $FeSi_2$ precipitates, sometimes associated with Cu. Ward (4) observed iron disilicide precipitates in the emitter regions of ion-implanted bipolar transistors. Gleichmann *et al.* (5) found large precipitates in power devices after prolonged high temperature processing. Augustus (6) reported small precipitates in epitaxial silicon wafers, which were shown to contain either Ni or Fe. In wafers with gross contamination, larger Ni-containing defects were identified and it was concluded that Ni precipitated as $NiSi_2$. Earlier, Augustus *et al.* (7) reported the contamination of bipolar transistors with large rod-like precipitates of α -Fe, which were found in the boron diffused base regions. Stacy *et al.* (8) identified Ni as an impurity decorating oxidation-in-

duced stacking faults in wafers contaminated by metallic tools, and Cu as an impurity precipitating in nonintentionally contaminated wafers. Recently, Pearce and Kannon (9) reported precipitation phenomena of various metallic and nonmetallic impurities after high temperature processing.

The present work is part of a study on microdefects in nonintentionally contaminated epitaxial layers. In the first part (10), the characterization of a larger type of defect observed in wafers processed in an RF-heated reactor was described. The precipitated impurities were identified as Fe and Ti, which, as radioactive tracer experiments showed, originated from the susceptor. The present report focuses on a smaller type of defect which was unidentified at that time, and which appears to have a good correlation with preferential etching features.

Experimental Procedures

Epitaxial layers were grown in a radiantly heated barrel-type reactor at 1080°C using dichlorosilane as the Si source material. A prebake at 1150°C in H_2 was used to remove the native oxide. The substrate wafers were of 3 in. diam, boron-doped in the range 7-21 Ωcm , and of (111) orientation. Prior to high temperature processing, the wafers were cleaned in H_2O_2 - H_2SO_4 for 10 min at 110°C.

Defect characterization of the near front surface region was performed by preferential etching and transmission electron microscopy (TEM). In the former case, the wafers were immersed in the Wright etchant for 1 min at

*Electrochemical Society Active Member.

¹Present address: Philips Research Laboratories Sunnyvale, c/o Signetics Corporation, Sunnyvale, California 94086.

Key words: semiconductor, defects, epitaxy, contamination.

room temperature. The etching features were examined by optical microscopy and scanning electron microscopy (SEM). For TEM investigations, samples of the wafers were thinned from the rear side surface to a thickness of 300 nm by wet chemical etching. The specimens were studied in a 120 kV Philips EM400T microscope, equipped with an energy-dispersive x-ray spectrometer. The TEM work was done on the part of the wafer which was not preferentially etched. Some samples were also prepared with wafers which were etched for only 15s in order to investigate the development of etch pits at defect sites.

Preferential Etching

The density of etch pits as observed by optical microscopy ranged between 10^3 and 10^7 cm^{-2} . An accurate figure in the low density regime was difficult to obtain because of the small size and the shallowness of the etch pits. Even in the SEM, good contrast was not readily achieved in most cases. At higher densities the etch pits tended to be larger and deeper. A first indication of the density and the distribution of etch pits across the wafer surface could be obtained by visual observation using high intensity light.

A SEM micrograph of an etched wafer surface showing a high density of etch pits is presented in Fig. 1. The typical triangular-shaped pits vary in size from almost indistinguishable to about $1 \mu\text{m}$. It is evident that optical microscopy can significantly underestimate the defect density. A reduction of the etch-pit density by more than an order of magnitude was noticed after removal of a thin (200-300 nm) surface layer, indicating the presence of a near surface region significantly enriched with defects. The size distribution of etch pits as visible in Fig. 1 probably represents the depth distribution of the corresponding defects (about 700 nm is etched off during 1 min preferential etching).

In anticipation of the TEM investigations, we wish to remark that the lateral distribution of defects even on a submicron scale could be very inhomogeneous (see Fig. 1). Hence, large variations in defect density from one area to the other can be expected in high magnification TEM micrographs.

Transmission Electron Microscopy

The samples investigated by TEM were selected according to the etch pit density observed on separate parts of the wafers. Two extreme cases were considered, *viz.* a very high density of etch pits (10^6 - 10^7 cm^{-2}) and a low density of etch pits (10^3 - 10^4 cm^{-2}). In addition, we examined wafers whose initially high etch pit density was reduced to a low value by means of a phosphorus-diffusion gettering treatment at the rear side of the wafers from a POCl_3 source (3).

In samples with a high density of etch pits, three types of defects could be distinguished:

Type 1: very small defects, which were not resolved under dynamical two-beam imaging conditions. They

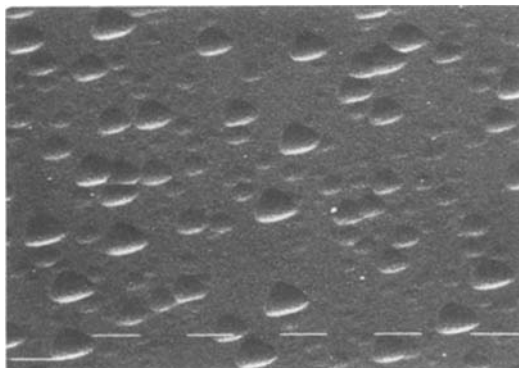


Fig. 1. SEM micrograph of a preferentially etched epitaxial wafer showing a high etch pit density. Scale mark is $1 \mu\text{m}$.

showed only a spherically symmetric tensile strain field typically extending about 10-nm. Faceting could be observed on somewhat larger defects. X-ray analysis failed to yield reliable results, probably owing to the small dimensions. The density varied markedly within a given sample and could be locally as high as 10^{10} cm^{-2} . A detailed study of the contrast phenomena (11) indicated increasing density towards the surface. A typical micrograph is shown in Fig. 2.

Type 2: faceting features similar to those present on the type 1 defects were also observed on a larger type of defect ranging in size between 30 and 200 nm. Many of these particles showed fringe contrast (see also Fig. 2), which indicates a specific orientation and misfit of the defect lattice in the Si matrix. Locally, the density could be 10^7 cm^{-2} (larger defects), but it could also be as low as 10^4 cm^{-2} (larger defects). The larger particles were accessible to x-ray microanalysis, showing Cu significantly above the background signal of the microscope. Attempts for a microdiffraction analysis were unsuccessful, due to the very small volume of the particles involved.

Type 3: the largest type of defect, with dimensions between 100 and 200 nm and densities between 10^4 and 10^5 cm^{-2} . These precipitates had a characteristic elongated or spherical shape and contained either Fe or Ti, respectively [see Fig. 3 and Ref. (10)]. The low densities involved hampered a reliable estimate of differences in density between different samples. In the earlier report (10), we related these defects with impurities in the susceptor.

Considering the TEM results on wafers with a low etch pit density, the absence of type 1 and 2 defects can be seen as a striking difference in comparison to wafers with a high etch pit density. The same applies to the wafers which received the gettering treatment. We therefore conclude that the smallest type 1 defects also leave distinct etch pits in the surface upon preferential etching. This was verified by examination of slightly etched (15s) wafers in the transmission electron microscope. As illustrated in Fig. 4, well-defined etch pits were observed, which showed a black, a white, or a black-and-white fringe contrast, depending on their depth. Under some

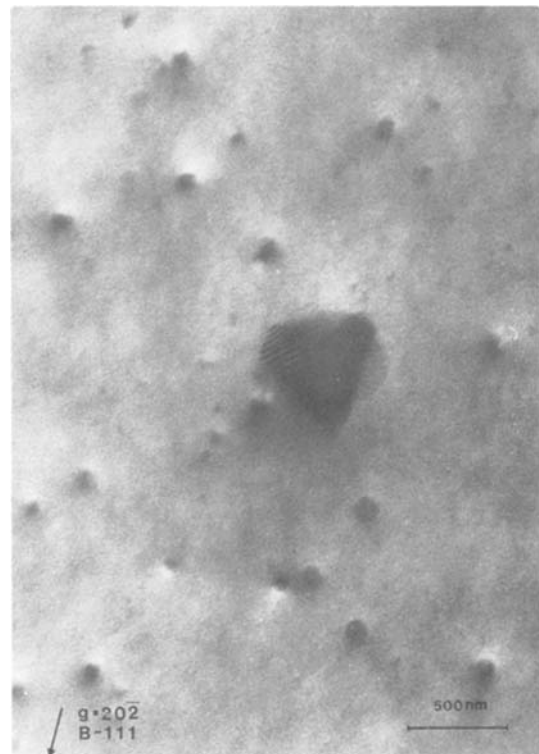


Fig. 2. Bright field TEM micrograph showing dynamical diffraction contrast of a higher density of small type 1 defects and one larger, type 2 defect containing Cu. The operative reflection: $g = 220$.

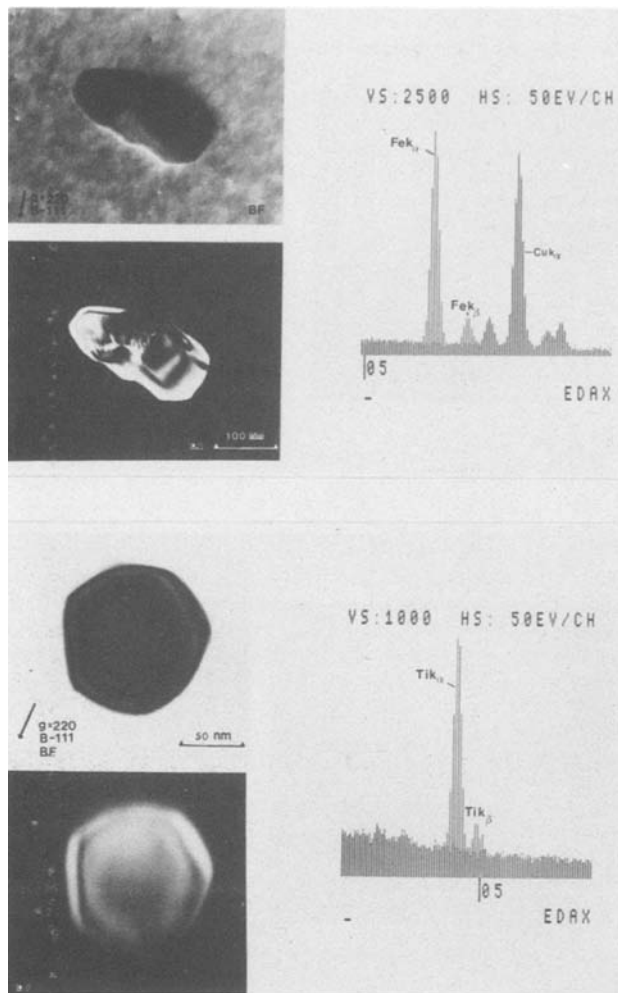


Fig. 3. TEM micrographs and x-ray spectra of type 3 defects containing Fe and Ti.

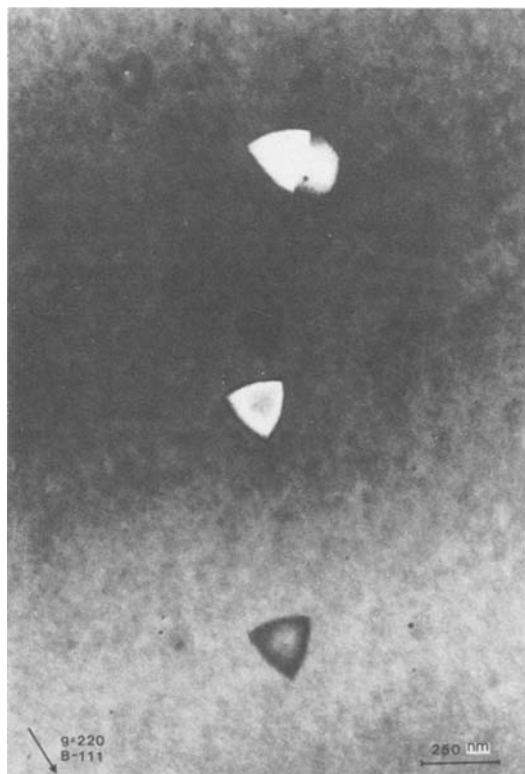


Fig. 4. Dark field TEM micrograph of a slightly etched wafer showing the various stages of development of etch pits at defect sites. The operative diffraction vector: $g = 220$.

etch pits, showing very weak contrast, a small type 1 defect was still present. Other defects, situated at a larger distance below the surface, had not yet developed etch pits with sufficient depth to cause a noticeable contrast effect. Larger and less regular contrast features were also observed, and because of their much lower density, we attributed these etch pits to type 2 and 3 defects.

In relation to the impurities identified in some of the defects, it is of interest to note the difference in sensitivity to the gettering treatment between type 1 and 2 defects on one hand and type 3 defects on the other. The trend observed here is in good agreement with the RBS results of Buck *et al.* (12), *i.e.*, rapid gettering of Cu with respect to Fe, and suggests that the type 1 defects, like the type 2 defects, also contain Cu. Some morphological resemblance between types 1 and 2 supports this as well.

Regarding the source of the metallic contamination, we have already mentioned (10) the role of the susceptor in the case of Fe and Ti. The same report also pointed out that Cu was consistently detected in substrate wafers by means of neutron activation analysis and confirmed earlier results obtained by the same technique (13). As reported by Stacy *et al.* (8), Cu is a major background impurity decorating oxidation-induced stacking faults. Hence, there are strong indications for suspecting the substrate wafer of being a source of the Cu on the defects observed after various high temperature processes.

A general phenomenon of Cu appears to be its tendency to form a high density of very small precipitates (3). In contrast with most transition metals, Cu has a relatively high solid solubility, so that supersaturation is reached at relatively low temperatures. The limited range of diffusion at low temperatures favors the formation of a high density of nuclei. The extremely weak x-ray signals obtained from the precipitates containing Cu point to a low metal content, suggesting a heterogeneous nucleation mechanism which may involve intrinsic point defects.

Summary

Depending on process conditions, preferential etching of (111)-oriented epitaxial wafers revealed a wide range of etch pit densities. When a high density of etch pits was found, TEM showed a high density of very small isolated defects which are not accessible for x-ray microanalysis. A good correlation was established between these defects and the etch pits. In addition, two types of larger precipitates containing Cu and Fe or Ti, respectively, were present in much lower densities. Apart from the etch pit density, only the density of the smallest defects and that of the somewhat larger precipitates containing Cu varied with deposition conditions and postgrowth gettering treatments. Both the etch pit density and the defect density decreased rapidly below the surface.

Acknowledgment

We appreciate the valuable discussions with A. J. R. de Kock and M. J. J. Theunissen.

Manuscript submitted Oct. 24, 1983; revised manuscript received Nov. 14, 1983.

Philips Research Laboratories assisted in meeting the publication costs of this article.

REFERENCES

1. G. A. Rozgonyi, R. P. Deysher, and C. W. Pearce, *This Journal*, **123**, 1910 (1976).
2. C. W. Pearce and R. G. McMahon, *J. Vac. Sci. Technol.*, **14**, 40 (1977).
3. A. G. Cullis and L. E. Katz, *Philos. Mag.*, **30**, 1419 (1974).
4. P. J. Ward, *This Journal*, **129**, 2573 (1982).
5. R. Gleichmann, U. Mohr, and K. Jegerlehner, *Cryst. Res. Technol.*, **18**, 297 (1983).
6. P. D. Augustus, in "Proceedings of the 3rd Oxford Conference on Microscopy of Semiconducting Materials," A. G. Cullis, S. M. Davidson, and G. R. Booker, Editors, p. 229, Institute of Physics, Oxford (1983).
7. P. D. Augustus, J. Knights, and L. W. Kennedy, *J. Microsc. (Oxford)*, **118**, 315 (1980).

8. W. Stacy, D. F. Allison, and T.-C. Wu, in "Semiconductor Silicon 1981," H. R. Huff, R. J. Kriegler, and Y. Takeishi, Editors, p. 344, The Electrochemical Society Softbound Proceedings Series, Pennington, NJ (1981).
9. C. W. Pearce and V. C. Kannon, Abstract 307, p. 478, The Electrochemical Society Extended Abstracts, Vol. 83-1, San Francisco, CA, May 8-13, 1983.
10. C. J. Werkhoven, in "Aggregation Phenomena of Point Defects in Silicon," E. Sirtl and J. Goorissen, Editors, p. 144, The Electrochemical Society Softbound Proceedings Series, Pennington, NJ (1983).
11. C. W. T. Bulle-Lieuwma, To be published.
12. T. M. Buck, J. M. Poate, K. A. Pickar, and C.-M. Hsieh, *Surf. Sci.*, **35**, 362 (1973).
13. M. J. J. Theunissen and G. S. Gruintjes, Abstract S81, ESSDERC/SSSDT, Toulouse, 1981.

Reduction of Electron-Beam-Induced Damage in MOS Devices Using Three-Layer Resist with Heavy Metal Interlayer

Masakazu Shimaya, Osake Nakajima, Chisato Hashimoto, and Yutaka Sakakibara

Nippon Telegraph and Telephone Public Corporation, Atsugi Electrical Communication Laboratory, Kanagawa, 243-01, Japan

ABSTRACT

A three-layer resist with a heavy metal interlayer is proposed to remove the electron-beam-induced damage in MOS devices. The three-layer resist with 280 nm thick platinum interlayer can decrease positive charge and neutral traps in the gate oxide to about one-fifth of those for direct exposure. This effect is equivalent to reducing exposure dosage about two orders of magnitude. The saturation effect of damage reduction is found with increasing the Pt interlayer thickness to above 280 nm, due to the damage generation by secondary electrons or x-ray. The dissipation energy calculation by Monte Carlo technique indicates that the saturation threshold for damage removal corresponds to about 1×10^{21} eV/cm³ dissipation energy in the gate oxide. This critical value for the dissipation energy provides an optimum metal interlayer thickness T_m in the three-layer resist, which is given as $T_m = 30E^{1.75}/\rho$ (nm), where E is the electron energy (keV) and ρ is the metal mass density (g/cm³). Considering the restriction of interlayer thickness and the dry etching capability in the lithography and patterning process, tungsten is suitable for the metal interlayer in the three-layer resist.

Direct writing electron-beam lithography provides the high resolution pattern delineation necessary to fabricate high density and high performance VLSI's. However, energetic electrons can create radiation damage in the gate oxide in MOS devices, due to the fact that they ionize materials as they pass through the surface layer. The radiation-induced positive charge and neutral traps in the oxide and interface traps at the Si-SiO₂ interface degrade MOSFET characteristics severely (1). Therefore, the radiation damage in the gate oxide has been studied extensively (2, 3). Of particular importance is the annealability of that damage with the temperature-time limits imposed by the device processing. The most restricted annealing process is postmetallization annealing, in which annealing temperatures are limited by either metal penetration or contact resistance degradation problems associated with the contact metallurgy. Typical postannealing at 400°-450°C in N₂ or forming gas, however, is not sufficient to remove positive oxide charge and neutral traps. Above 700°C, annealing has been reported necessary to remove these traps completely (4). Therefore, more efficient postmetallization annealing procedures have been investigated recently to remove radiation damage, such as annealing in pure hydrogen gas ambient (5), annealing in high pressure (50 atom) forming gas (6), and in the RF plasma (7). These methods are effective to some extent, compared to conventional forming gas annealing, but are not sufficient to remove radiation damage completely.

In this paper, the approach proposed is the suppressing or stopping of electron penetration into the gate oxide in the lithography step, using three-layer resist (8) with a heavy metal interlayer. We have evaluated residual damage in the gate oxide after electron-beam exposure and after annealing in N₂ at 450°C, as a function of the thickness of platinum interlayer in the three-layer resist. We also compare the experimental results with the dissipation energy in the gate oxide, calculated by Monte Carlo simulation. The optimum metal interlayer thickness is determined for some heavy metals, according to the electron energy.

Key words: radiation damage, neutral trap, MOS devices, three-layer resist, dissipation energy.

Experimental Procedure

MOS devices used in this work were polysilicon gate MOS capacitors fabricated on p-type (100) silicon substrate with a resistivity of 0.1-0.2 Ω · cm. All MOS capacitors were fabricated with conventional photolithography and chemical etching. After forming thick field oxides and removing oxides in the 2.5×10^{-3} cm² gate area, a 30 nm thick gate oxide was grown in dry oxygen at 950°C. Phosphorous-doped polysilicon electrodes 450 nm thick were fabricated by CVD, followed by annealing in dry N₂ at 1000°C so as to reduce the resistivity. After etching off polysilicon outside the gate area, CVD SiO₂ was deposited for surface passivation, followed by contact hole etching. Finally, the capacitors were annealed in a forming gas ambient at 450°C for 30 min.

The three-layer resist was formed as follows. AZ® resist 1.0 μm thick was spun on MOS capacitors and baked at 200°C for an hour. A platinum interlayer, 0-500 nm thick, was deposited on the AZ resist by RF sputtering. Finally, an electron-beam-exposed resist CMS 400 nm thick was spun on the Pt interlayer.

Electron-beam exposure to some capacitors in a wafer was carried out through the three-layer resist by an electron-beam lithography system (9). The gate area for individual capacitors was scanned by a 20 keV electron-beam. Dosages were between 2 and 2000 μC/cm². Annealing was carried out at 450°C in an N₂ ambient for 30 min after electron-beam exposure and taking off the three-layer resist.

High frequency C-V curves were measured to determine the radiation-induced flatband voltage shift. The density of neutral traps, as well as positively charged traps, were determined by avalanche injection technique, which injects hot electrons from the silicon substrate to gate oxides and measures the flatband voltage shift (10). By analyzing the characteristics of flatband voltage shift vs. the number of injected electrons, the effective density and the cross section of electron traps can be obtained.

Results and Discussion

Radiation damage after exposure.—Figure 1 shows the relation of the V_{FB} shifts vs. Pt interlayer thickness in

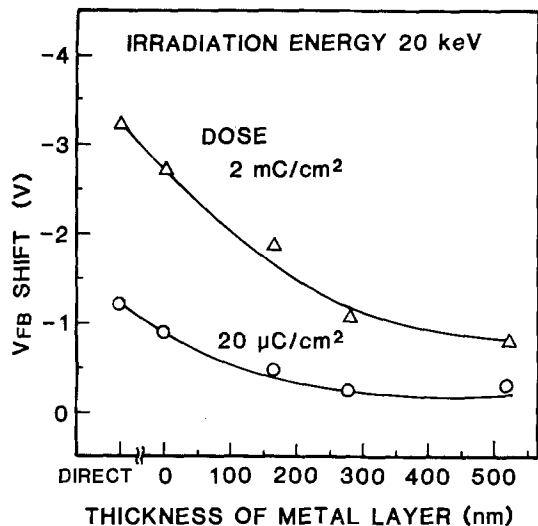


Fig. 1. Flatband voltage shift from pre-irradiation state for electron-beam-irradiated MOS capacitors as a function of Pt interlayer thickness in the three-layer resist.

three-layer resist after electron-beam exposure. Negative V_{FB} shift, indicating positive charge buildup in the oxide, decreases with an increase in the metal thickness, and tends to become constant when Pt layer is more than 280 nm thick. The V_{FB} shift for capacitors on which a three-layer resist was applied with 280 nm thick Pt interlayer decreases drastically to about one-fifth of that for direct exposure. This indicates that the application of three-layer resist in the lithography step is very effective in reducing radiation damage, and equivalent to reducing exposure dosages by about two orders of magnitude.

Figure 2 shows the results of electron injection measurements for MOS capacitors exposed at $20 \mu\text{C}/\text{cm}^2$. In this figure, the change in V_{FB} , which occurs as injected electrons are captured, is plotted against the number of injected electrons per unit gate area. This clearly shows that electron beam exposure substantially increases the trapping in the oxide and that the three-layer resist is very efficient to reduce the traps in the oxide. For unexposed capacitors, V_{FB} shift occurs after injecting above $10^{16}/\text{cm}^2$ electrons. This V_{FB} shift is thought to be due to electron trapping by water-related defects in the oxide (11), which exist in as-made state. Analysis of the curve for capacitors exposed directly, without the three layer resist, shows that two distinct kinds of traps are being filled as electron injected. The first kind of trap is positively charged and is completely filled after $10^{14}/\text{cm}^2$ electrons have been injected. This saturated V_{FB} shift coincides to the negative V_{FB} shift in the magnitude, observed after electron beam exposure, as shown in Fig. 1. The

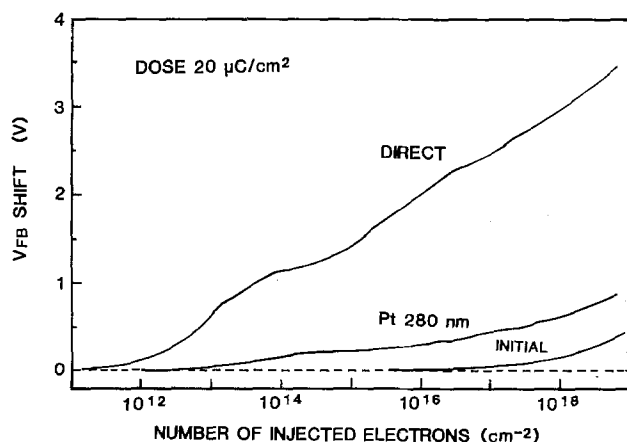


Fig. 2. Flatband voltage shift due to avalanche hot electron injection into the gate oxide for irradiated MOS capacitors.

electron capture cross section for positively charged traps is 10^{-13} - 10^{-14} cm^2 . The additional V_{FB} shift, observed after saturation of positively charged traps, is due to filling of neutral electron traps introduced by electron beam exposure. Its capture cross section is 10^{-15} - 10^{-16} cm^2 .

Noticeably, application of the three-layer resist is very effective in reducing neutral traps, as well as positively charged trap. The V_{FB} shift for capacitors with 280 nm Pt interlayer thickness after injection of $2 \times 10^{16}/\text{cm}^2$ electrons is only 330 mV and about one-seventh of that for direct exposure, where this injection level corresponds to the filling of positively charged traps and neutral traps. This damage reduction effect is accounted for by the suppression of electron penetration in the oxide through the three-layer resist. However, the decrease in positively charged traps and neutral traps is found to be constant with increasing interlayer thickness to above 280 nm. This constant phenomenon is believed to be due to the damage generation by secondary electrons or x-ray, which is produced by electron scattering within a high density metal layer in the three-layer resist.

Residual radiation damage after annealing.—Figure 3 shows V_{FB} shifts after annealing in a N_2 ambient at 450°C , as a function of Pt layer thickness. V_{FB} shift decreases extremely with increasing metal thickness. When exposure dosage is $20 \mu\text{C}/\text{cm}^2$, V_{FB} shift for capacitors with a 280 nm thick Pt interlayer is about 40 mV and is one-ninth of that for direct exposure. This ratio is smaller than that before annealing. When exposure dosage is $2 \text{ mC}/\text{cm}^2$, V_{FB} shift for capacitors with 280 nm Pt interlayer thickness is about 0.2V. This shift is smaller than the V_{FB} shift for direct exposure with $20 \mu\text{C}/\text{cm}^2$ exposure dosage. This result indicates that, after annealing in N_2 at 450°C , the application of three layer resist is equivalent to reducing exposure dosage more than two orders of magnitude.

Figure 4 shows the electron injection measurement results for capacitors annealed in N_2 at 450°C . The V_{FB} shift after injecting $2 \times 10^{16}/\text{cm}^2$ electrons is only 90 mV for capacitors with 280 nm thick Pt interlayer. The V_{FB} shift due to filling of neutral traps is approximately 50 mV. Neutral traps as well as positive charge are found to be removed sufficiently by annealing in N_2 at 450°C for capacitors with 280 nm Pt interlayer thickness.

These experimental results show that three-layer resist application with a heavy metal layer suppresses the generation of damages and furthermore enhances the removal efficiency of positive charge by low temperature annealing.

Dissipation energy in gate oxide.—The dissipation energy in the gate oxide is calculated and compared with the experimentally observed radiation damage.

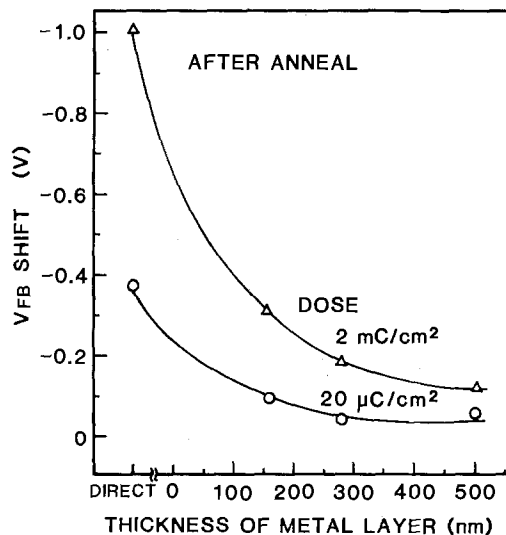


Fig. 3. Flatband voltage shift from pre-irradiation state for annealed MOS capacitors after EB exposure, as a function of Pt interlayer thickness.

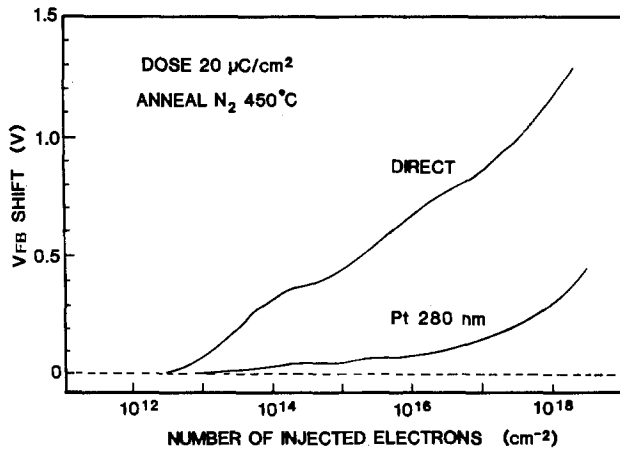


Fig. 4. Flatband voltage shift due to avalanche hot electron injection into the gate oxide for annealed MOS capacitors after EB exposure.

The Monte Carlo technique for the electron trajectories calculation has been applied by several authors to study the backscattered electrons, energy dissipation, and secondary electron emission (12, 13). We also use this method to calculate the dissipation energy in each layer of the multilayered structure.

In electron free path calculation, a few free path model is used, which takes into account not only the scattering probability in the layer involving the initial scattering point, but also that in other layers along the scattering direction (14). The multilayered structure shown in Fig. 5 is employed to calculate dissipation energy, where point electron beam is exposed. For detailed dissipation energy calculation, the multiple layer is divided into 50 layers. The calculation is accomplished for 10,000 electrons in order to obtain meaningful results.

The AZ resist thickness (0.4 μm) in Fig. 5 is thinner than that used in the experiment (1 μm). This is caused by the restriction in calculation depth. However, an estimated error in the dissipation energy in the gate oxide due to inadequate AZ resist thickness is negligible, since the density of AZ resist is low.

Figures 6a and 6b show examples of the dissipation energy profile for the multilayer structure, where metal interlayers are formed by 320 nm thick platinum and 600 nm thick platinum, respectively. In Fig. 6a, the dissipation energy in SiO_2 is about 3×10^{20} eV/cm³, which indicates that incident electrons penetrate the three-layer resist and reach the gate oxide. In Fig. 6b, the dissipation energy decreases drastically in the Pt layer and the dissipation energy in SiO_2 cannot be estimated. This result shows that incident electrons cannot penetrate the three-layer resist with 600 nm thick Pt interlayer.

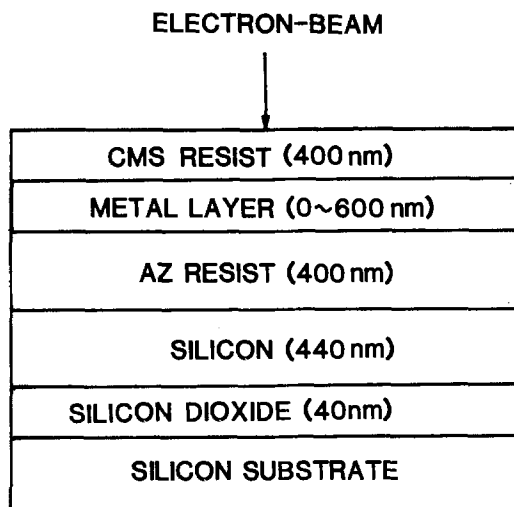


Fig. 5. Multilayered structure for dissipation energy calculation

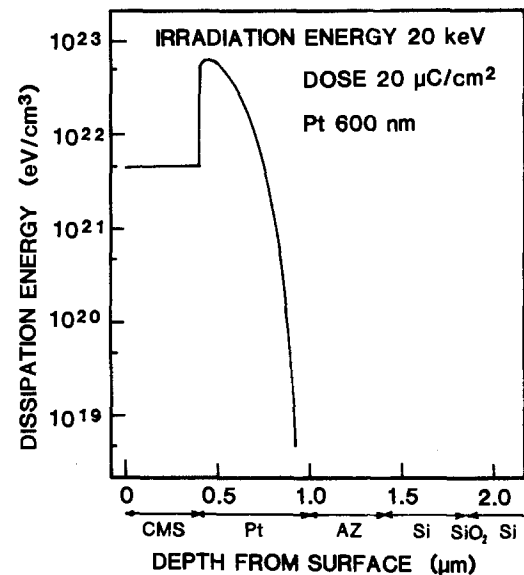
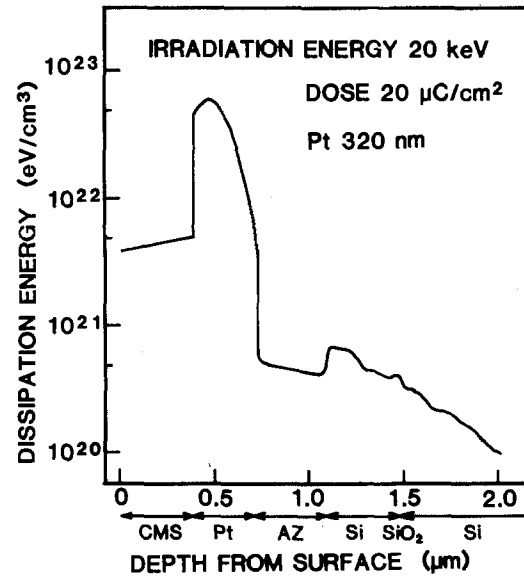


Fig. 6. An example of dissipation energy profile for the multilayered structure. (a, top) Platinum layer is 320 nm thick. (b, bottom) Platinum layer is 600 nm thick.

Optimum metal layer thickness.—Figure 7 shows the relation of the experimentally observed effective density for the positive oxide charge after electron-beam exposure and the calculated average dissipation energy in SiO_2 . As shown in the experiment, radiation damage cannot be reduced to less than a certain level, which will be determined by secondary electron or x-ray, even if the metal interlayer in the three-layer resist is sufficiently thick. A thinner metal interlayer is better with regard to the dry etching process. In Fig. 7, the effective positive charge density is found to become constant with a decrease in the dissipation energy below 1×10^{21} eV/cm³. Therefore, the optimum thickness of metal interlayer can be determined to be a thickness where the dissipation energy in the gate oxide is about 1×10^{21} eV/cm³.

Figure 8 shows the dissipation energy in the gate oxide as a function of several kinds of metal interlayer. The thickness corresponding to the 1×10^{21} eV/cm³ dissipation energy is about 260 nm for Pt, about 280 nm for W, and about 570 nm for Mo. These thicknesses correspond to about 65% of the experimental penetration distance for the metal layer, called gruen range R_G (15), which is represented by

$$R_G (\text{nm}) = 46 E^{1.75} / \rho \quad [1]$$

where E is electron energy (keV) and ρ (g/cm^3) is the den-

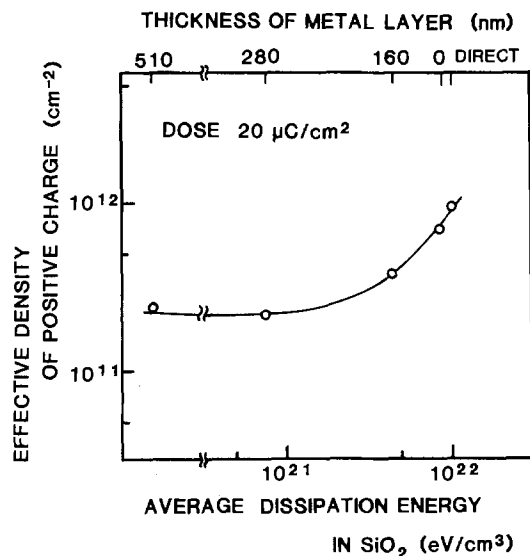


Fig. 7. Relation between effective density of radiation-induced positive charge and the average dissipation energy in the gate oxide.

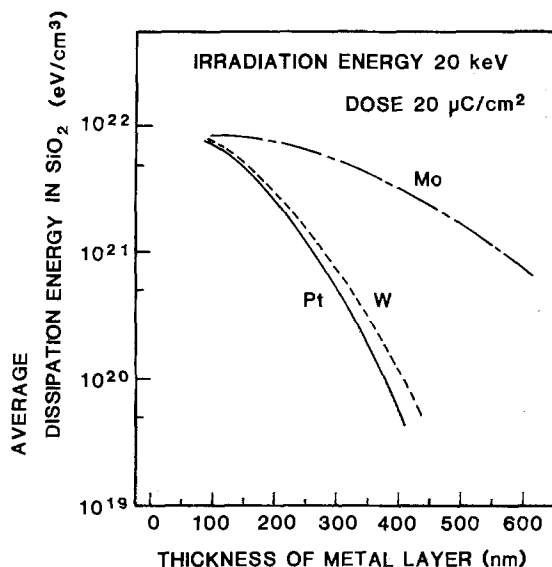


Fig. 8. Average dissipation energy in the gate oxide for various kinds of metal, as a function of metal interlayer thickness in the three-layer resist.

sity of metal. Thus, the optimum metal interlayer thickness in three-layer resist (T_m) can be given by a simple formula

$$T_m \text{ (nm)} = 30 E^{1.75}/\rho \quad [2]$$

Using this formula, the metal interlayer thickness is easily estimated without the complicated calculation of the dissipation energy. In Table I, T_m values are shown for various metals as a function of electron energy. For the three-layer resist technology, the metal interlayer thickness is restricted by dry etching tolerance of electron-exposed resist. Its thickness is normally less than 600 nm. When electron energy is 20 keV and metal thickness is assumed to be 600 nm, required metal density is calculated to be more than 9.5 g/cm³, using Eq. [2]. Considering this condition and the dry etching process, tungsten ($\rho = 19.3$ g/cm³) is suitable for the metal interlayer in the three-layer resist.

On the other hand, it seems that the use of the three-layer resist with a heavy metal interlayer may degrade the patterning resolution, because of the increase in the backscattered electrons. However, after careful consideration, no degradation in patterning resolution was obtained by thinning the electron-beam-exposed resist and selecting the appropriate exposure dosage. Moreover, the

Table I. Optimum thickness (nm) of metal interlayer for reducing damage.

METAL	ELECTRON-BEAM ENERGY (keV)		
	10	20	50
Mo	164	550	2743
Ta	102	342	1700
W	87	294	1461
Pt	78	265	1318

use of this resist has several advantages, for instance, the reduction in irradiation dosage. The work relating the patterning characteristics for the three-layer resist with a heavy metal interlayer will be published in detail elsewhere.

Although a three-layer resist with heavy metal interlayer has been discussed here, there is another scheme, such as a thick monolayer resist and a two-layer resist with the thick bottom layer for blocking incident electrons. These schemes are usually done by applying an organic material which has an excellent step coverage and high RIE resistance. However, a thickness of more than 5 μ m needs 20 keV electrons for blocking. Using such a thick resist, it is not easy to get a high pattern resolution. Therefore, the three-layer resist with heavy metal interlayer is a better technique than other resist schemes, with regard to the damage reduction and the high patterning resolution.

Conclusion

The three-layer resist with a heavy metal interlayer in the electron beam exposure step has been proposed to reduce electron-beam-induced damages in MOS devices.

Applying this resist with a 280 nm thick Pt interlayer, damages decreased drastically to about one-fifth of that for direct exposure and were removed sufficiently by annealing in N₂ at 450°C. The application of three-layer resist with 280 nm Pt interlayer is equivalent to reducing exposure dosages about two orders of magnitude. However, the decrease in damages is found to become constant with increasing Pt interlayer thickness to above 280 nm, because of the damage generation by secondary electrons or x-ray.

Applying the Monte Carlo method to the dissipation energy calculation, it is clear that the constant phenomenon for the damage decrease begins when the dissipation energy in the gate oxide is about 1×10^{21} eV/cm³. According to these results, the optimum metal interlayer thickness in the three-layer resist can be extracted by $T_m = 30E^{1.75}/\rho$. Tungsten is suitable as the interlayer metal in the three layer resist, because of its high mass density and its dry etching capability.

Acknowledgment

The authors would like to thank Dr. T. Matsumoto, Dr. E. Arai, and Dr. T. Kitayama for their advice and encouragement. They are also indebted to members of the High Density Integration Section and the Patterning Technology Section for sample preparation.

Manuscript submitted Nov. 2, 1983; revised manuscript received Feb. 20, 1984.

Nippon Telegraph & Telephone Public Corporation assisted in meeting the publication costs of this article.

REFERENCES

1. J. M. Aitken, *IEEE Trans. Electron Devices*, **ed-26**, 372 (1979).
2. J. M. Aitken, D. J. DiMaria, and D. R. Young, *IEEE Trans. Nucl. Sci.*, **ns-23**, 1526 (1976).
3. J. M. Aitken, D. R. Young, and K. Pan, *J. Appl. Phys.*, **49**, 3386 (1978).
4. M. Shimaya, N. Shiono, O. Nakajima, C. Hashimoto, and Y. Sakakibara, *This Journal*, **130**, 945 (1983).
5. J. M. Aitken and C. Y. Ting, in "International Electron Device Meeting, Washington," pp. 50-53 (1981).

6. A. Reisman, J. M. Aitken, A. K. Ray, M. Berkenblit, C. T. Merz, and R. P. Havreluk, *This Journal*, **128**, 1616 (1981).
7. T. P. Ma and M. R. Chin, *Appl. Phys. Lett.*, **36**, 81 (1980).
8. J. M. Moran and D. Maydan, *Bell Syst. Tech. J.*, **58**, 1027 (1979).
9. Y. Sakakibara, T. Ogawa, S. Moriya, M. Kobayashi, and T. Kobayashi, *IEEE Trans. Electron Devices*, **ed-28**, 1279 (1981).
10. E. H. Nicollian and C. N. Berglund, *J. Appl. Phys.*, **41**, 3052 (1970).
11. E. H. Nicollian, C. N. Berglund, P. F. Schmidt, and J. M. Andrews, *ibid.*, **42**, 5654 (1971).
12. R. J. Howryluk, *ibid.*, **45**, 2551 (1974).
13. R. Shimizu and K. Murata, *ibid.*, **42**, 337 (1971).
14. S. Horiguchi, M. Suzuki, T. Kobayashi, H. Yoshino, and Y. Sakakibara, *Appl. Phys. Lett.*, **39**, 512 (1981).
15. T. E. Everhart and P. H. Hott, *J. Appl. Phys.*, **42**, 5837 (1971).

Effects of Laser Back-Side Damage upon Mechanical Properties of Silicon

Dennis Elwell*

Center for Materials Research, Stanford University, Stanford, California 94305

Sookap Hahn*

Siltec Corporation, Mountain View, California 94043

ABSTRACT

The warpage of laser-damaged P-type (111) and (100) silicon wafers subject to thermal cycles which simulate processing sequences was found to be less than that produced by mechanical abrasion damage. Both warpage and laser damage depth in wafers from the tail-end of crystals were found to be different from that in wafers from the middle or seed-end. These differences cannot be explained on the basis of the total interstitial oxygen content in the wafer and suggest that the state of the oxygen has an important influence on the mechanical properties of silicon.

In recent years, one of the major aims of VLSI technology has been the fabrication of large area devices free of lattice defects. For this reason, efforts have been concentrated on the suppression of process-induced defects in silicon. The effectiveness of back-side damage gettering in the reduction of process-induced defects has been widely investigated and reported in the open literature (1-3). Back-side damage gettering uses a dislocation network on high stress regions created on the wafer back surface, which acts as an effective source of vacancies or a sink of interstitials. This dislocation network also acts as a sink of fast-diffusing metallic impurities and reduces their decoration on oxidation-induced stacking faults near the front surface, which is an important cause of structure-related device failure in silicon devices.

*Electrochemical Society Active Member.

Key words: semiconductor, integrated circuit, warpage, gettering.

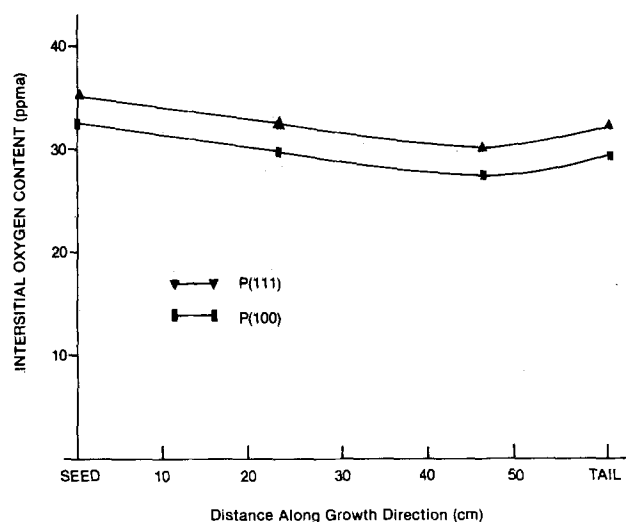


Fig. 1. Axial oxygen concentration distribution of two ingots used for this investigation.

Although various other methods of inducing back-side damage for gettering have been studied, for example lapping, sandblasting, phosphorous diffusion, ion implantation, Si_3N_4 deposition, polycrystalline silicon deposition, and laser irradiation, laser damage gettering has many advantages and has received some attention from a number of research groups (4, 5). Laser damage gettering utilizes laser irradiation to generate gettering sites where a variety of point defects, such as impurities and interstitials, gather. The technological advantages of this method are (i) the damage is induced at room temperature, (ii) the damage can be precisely controlled, and (iii) the damage is more permanent during common IC fabrication thermal cycles. Laser back-side damage gettering has the additional advantages that it is a clean and reproducible process, and throughput rates are compatible with wafer fabrication requirements.

One of the major obstacles to the development of a laser back-side damage gettering process is wafer distortion due to lattice damage generated by high power pulsed laser irradiation (6). Warped wafers are difficult to handle in automatic processing equipment. The generation of complex circuit patterns by photolithography on a warped or bowed wafer is difficult to perform due to a

Table I. Typical interstitial oxygen radial distributions for two ingots used for this investigation
(Unit = ppma, conversion factor = 9.63)

Type		P			P		
Orientation		111			100		
Radial	Axial	Seed-end	Mid	Tail-end	Seed-end	Mid	Tail-end
	R*	35.7	33.8	33.2	31.3	29.0	27.8
	(Center)						
	R/2*	33.8	33.1	32.5	30.4	29.0	27.9
	R/4*	31.2	32.7	32.2	28.5	28.0	27.7
	R/8*	26.5	31.9	31.0	26.9	27.1	27.2

*Distance from the periphery of the wafer.

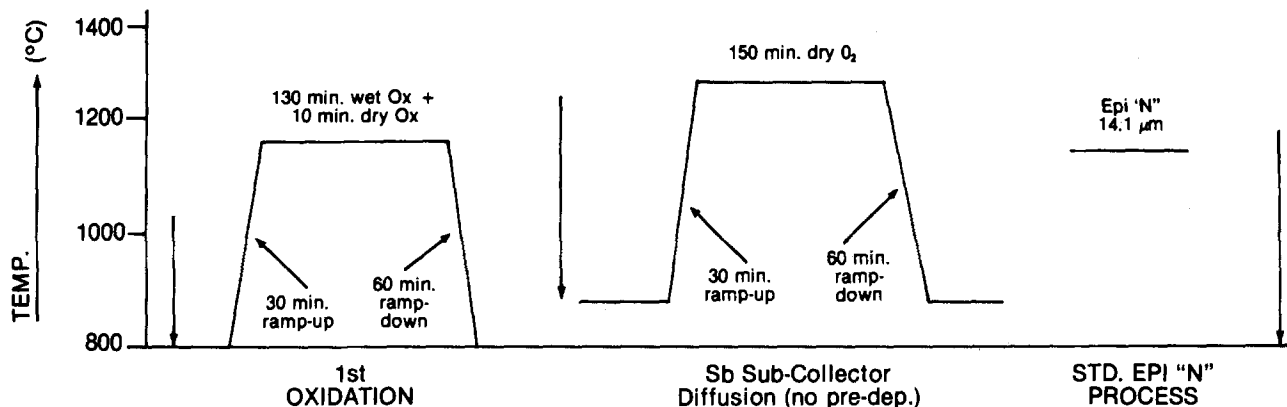


Fig. 2. Simulated high temperature cycles of the bipolar device process used for P(111) wafer warpage studies. Arrows indicate points of warpage measurements.

varying focal plane. This problem is especially serious with projection printing, during which wafer flatness is no longer improved by the application of mechanical pressure to a wafer with a mask, as occurs during contact

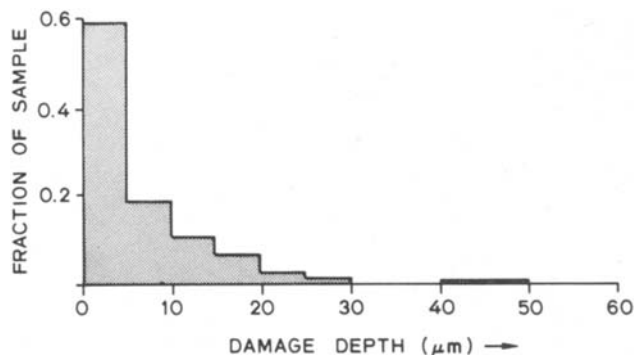


Fig. 3. Typical histogram showing distribution of depth of high power pulsed laser induced damage for a large number of dislocations.

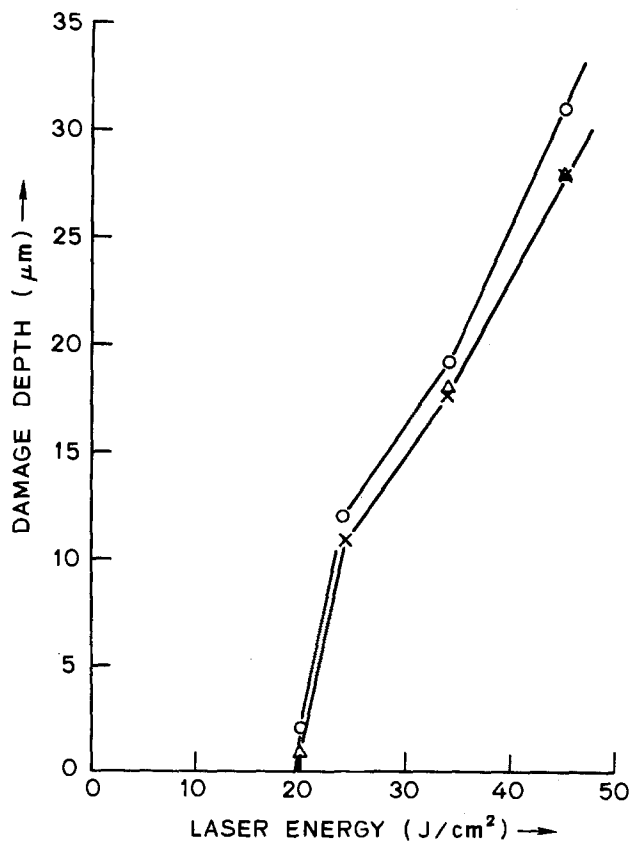


Fig. 4. Variation of depth of damage obtained from tail of histogram with laser energy (Δ seed end; X middle of crystal; O tail end).

printing. In addition to wafer handling and photolithographic problems, warpage can also affect the electrical characteristics of devices and circuits. Dislocations introduced into processed wafers as a result of plastic deformation are known to cause excessive leakage currents in processed circuits when located in the active device volume. Due to a change of lateral dimensions on the wafer by warpage, an exact device geometry (e.g., a channel length) cannot be realized due to the misalignment which can cause degradation of device characteristics.

The purpose of the present work is to examine how the lattice damage caused by laser irradiation affects the mechanical properties of silicon wafers during simulated high temperature device processing. In addition, an attempt is made to quantify the laser damage from measurements of the depth of damage using etching of polished sections.

Experimental

P(111)¹ (7-21 Ω-cm) and P(100)¹ (10-20 Ω-cm) wafers grown by the Czochralski method were used for this in-

¹In this paper, P(111) and P(100) wafers mean P-type (111)-oriented and P-type (100)-oriented wafers, respectively.

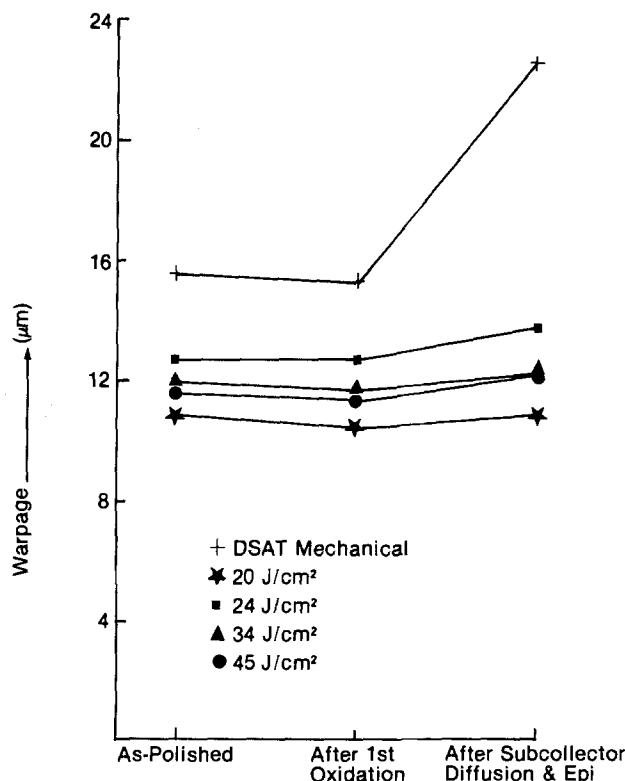


Fig. 5. Warpage for laser back-side damaged and mechanically back-side damage P(111) wafers based upon thermal cycles shown in Fig. 2.

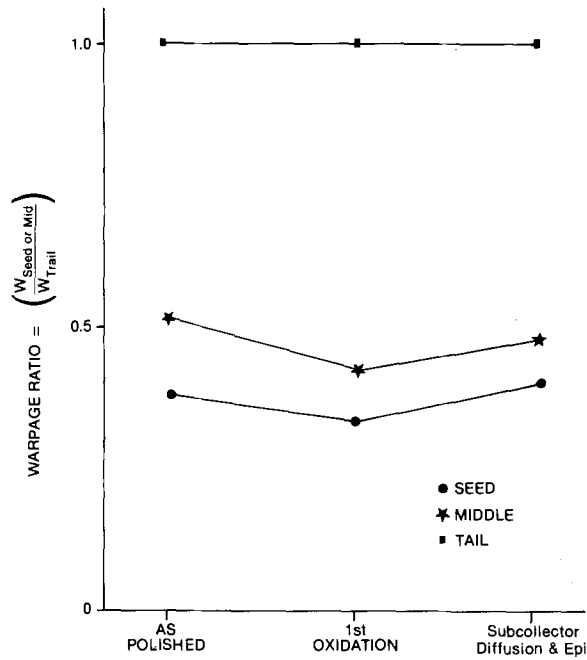


Fig. 6. Warpage ratio of 20 J/cm² laser back-side damaged P(111) wafers from seed-ends or middle section over those from tail-ends.

vestigation. The P(111) silicon crystal was grown under the following conditions: flat top shoulder, pull speed during body growth 3-3½ in./hr, seed rotation 15 rpm CCW, crucible rotation 8 rpm CW with a 3-phase ac powered Siltec 860D furnace. The growth parameters for the P(100) crystal were: slow shoulder, pull speed during body growth 3 1/2-4 in./hr, seed rotation 20 rpm CCW, crucible rotation 7 rpm CW with 3-phase ac powered Siltec 860D furnace. Both ingots had the same size of 100 mm diameter and 580 mm effective length and were doped with boron. 50 wafers of 625 μm thickness were cut from

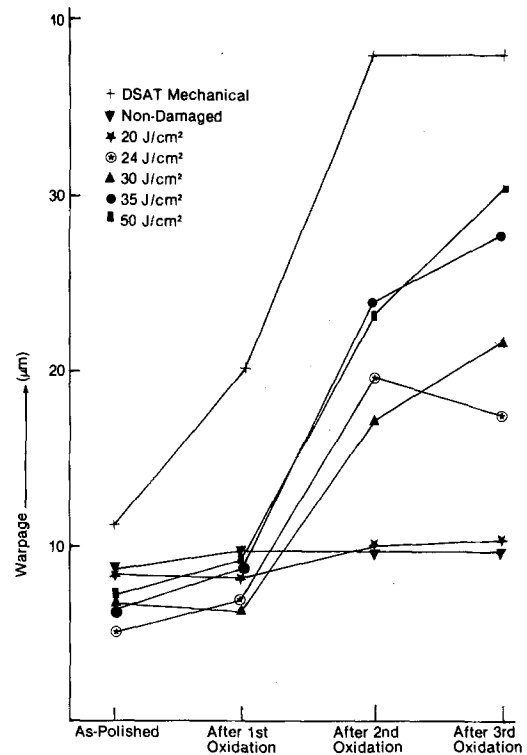


Fig. 8. Warpage of nondamaged, mechanically back-side damaged, and laser damaged P(100) wafers based upon multiple oxidation cycles with ramp-up and ramp-down schedules.

three portions (namely, seed-end, middle, and tail-end) of an ingot and were called P(100)-SEED, -MID, and -TAIL and P(111)-SEED, -MID, and -TAIL. The interstitial oxygen content, [O_i] and substitutional carbon were measured by a Nicolet MX-1 Fourier transform infrared spectrophotometer. The conversion factor for the deter-

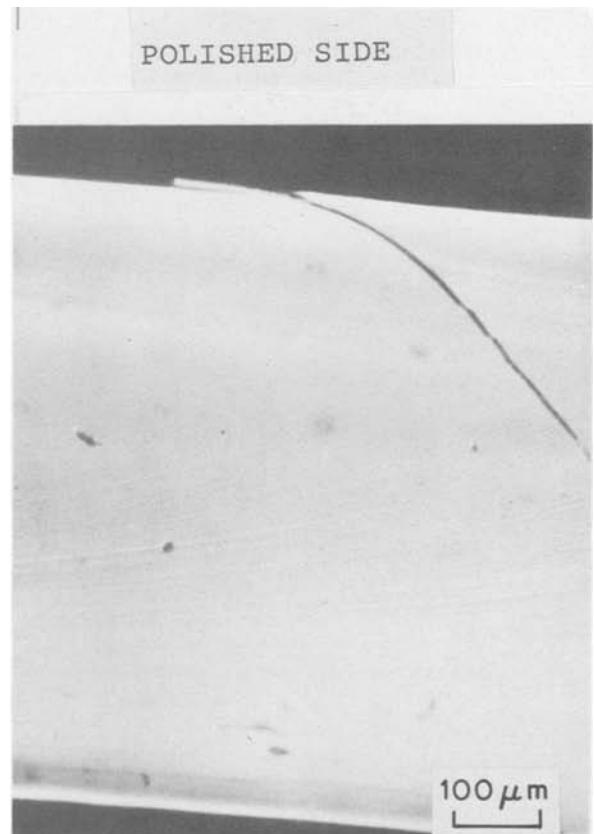
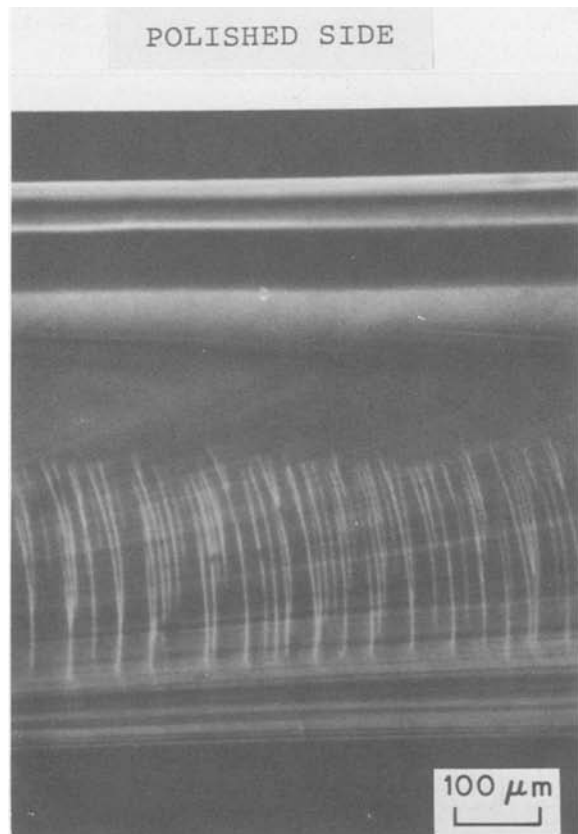


Fig. 7. Cross-section optical micrographs of P(111) wafer (a, above left) mechanically back-side damaged and (b, above right) laser back-side damaged ($E_d = 45 \text{ J/cm}^2$) after simulated high temperature bipolar thermal cycles. Stained by Sirtl etchant for 5 min (magnification: 110X).

mination of interstitial oxygen contents was 9.63 from ASTM F121-79. The longitudinal distribution of $[O_i]$ along the pulling direction for both crystals is shown in Fig. 1. The radial distribution of $[O_i]$ from three portions for both crystals is summarized in Table I. Carbon contents ranged from less than 0.05 ppm to 1.0 ppm for both crystals.

Laser damage was induced on the rear surface of the caustic-etched wafers by a Quantronix 610 Epitherm Q-switched Nd:YAG laser system. Various levels of energy density were used for back-side damage gettering as follows: 20, 24, 34, and 45 J/cm² for P(111) and 20, 24, 30, 35, and 50 J/cm² for P(100) wafers. The dot spacing of 150 μ m and row spacing of 250 μ m were fixed for all the different laser parameters. The pulse repetition rate varied between 0.9 and 8.5 kHz (which depends upon the desired energy density). The pulse duration time was 150 nsec, and the focused 1/e spot size of the pulses was about 65 μ m. The mechanical back-side damage process was carried out by a direct surface abrasion technique (DSAT). In this process, the wafer was rotated on a vacuum chuck, and an abrasive-coated paper (grit size 400), placed in line contact with the wafer, was moved radially, leaving a series of concentric damage sites. Simulated multiple high temperature thermal cycles used for P(111) warpage studies are shown in Fig. 2. Three multiple oxidation cycles at 1000°C for 3 hr with or without ramp-up and ramp-down schedules were used for P(100) warpage studies. For these experiments the wafers were stacked in the vertical position in a boat with 2.5 mm distance between wafers with at least five "dummy" wafers at both ends to ensure the same cooling kinetics for all the test wafers. Warpage during simulated thermal cycles was measured by an ADE 3046A gauge.

For measurements of laser damage depth, the wafers were cleaved and polished, initially with diamond grit and then with three different submicron alumina powders with appropriate felt pads. The polished surfaces were then Sirtl etched.

Results and Discussion

Laser damage depth measurements were made only on P(111) wafers. This method of characterizing the damage was suggested by Yang and Schwuttke (7) who used P(100) wafers and reported that the threshold energy density for Nd:YAG laser irradiation was about 6 J/cm².

Each laser spot gives rise to a bundle of dislocations, and the resulting pits were observed on Sirtl etching points where each dislocation (or similar defect) intersected the polished surface. The distance from the silicon surface to the center of the etch pit was measured for a number of etch pits. The depth of damage was then taken

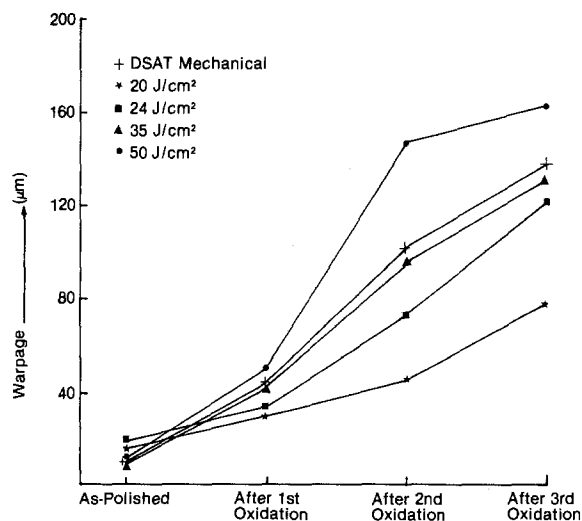


Fig. 9. Warpage of laser back-side damaged and mechanically back-side damaged P(100) wafers during multiple oxidation cycles without ramping.

as the tail of the resulting histogram of the number of pits observed at a certain distance from the wafer surface vs. that distance. A typical histogram is shown in Fig. 3; this was obtained for 232 individual damage depth counts.

It can be seen that occasional etch pits appear well beyond the normal tail of the distribution plot. These have been ignored in calculating the depth of damage, although they may be important in practice. The laser damage depth obtained as the mean of the cluster of data points at the tail of the distribution is plotted in Fig. 4 for the series of samples investigated. The accuracy of measurement is about $\pm 10\%$ but error bars have been omitted for clarity.

The damage depth for a laser beam intensity of 20 J/cm² was found to be only 1-2 μ m so the threshold intensity for detectable damage is 19 ± 1 J/cm². This value depends on the surface roughness as well as on the orientation. The dependence of damage depth on laser intensity has been indicated by joining up the data points in Fig. 4; the real behavior may be on a curve or show a step, but more data points would be necessary to resolve this question.

Within experimental error the damage depth is the same for wafers taken from the seed end and from the middle of a crystal. However, the average damage depth in wafers cut from the tail end is consistently a little higher than from the other regions.

Warpage

Due to rather subtle differences of warpage variation and related phenomena between P(100) and P(111) type materials during simulated multiple high temperature thermal cycles, we believe they warrant a separate discussion in this section.

P(111) materials.—The warpage of various energy density laser damaged and mechanical back-side damaged P(111) wafers is shown in Fig. 5. These data clearly demonstrate that back-side damage generated by pulse laser irradiation of energy densities less than 45 J/cm² have shown no adverse effects on warpage during subsequent oxidation cycles, compared with that of mechanical back-side damaged wafers. Based on the depth of damage measurements, the warpage of wafers damaged at 20 J/cm² is expected to be similar to that of undamaged wafers.

During the course of this investigation it was observed that P(111) materials from the seed-ends of the ingot generally exhibit higher resistance to warpage, regardless of the back-side damage techniques applied (mechanical or laser). A typical example is shown in Fig. 6. Recently,

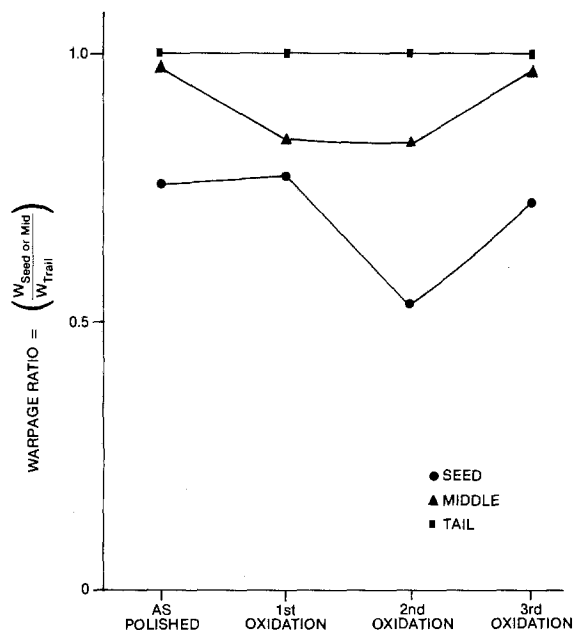


Fig. 10. Warpage ratio of 20 J/cm² laser back-side damaged P(100) wafers from seed-ends or middle section over those from tail-ends.

Eggermont *et al.* (8) have demonstrated that as-irradiated P(111) materials show a dramatically lower fracture strength than virgin wafers. It also has been reported by Schwuttke (9) that silicon materials from the seed-end are

stronger than those from the tail-end. As shown in Fig. 1, interstitial oxygen content differences between seed-end and tail-end materials are about 5 ppma, at the most. Also, oxygen diffusivity at room temperature is so low that it is

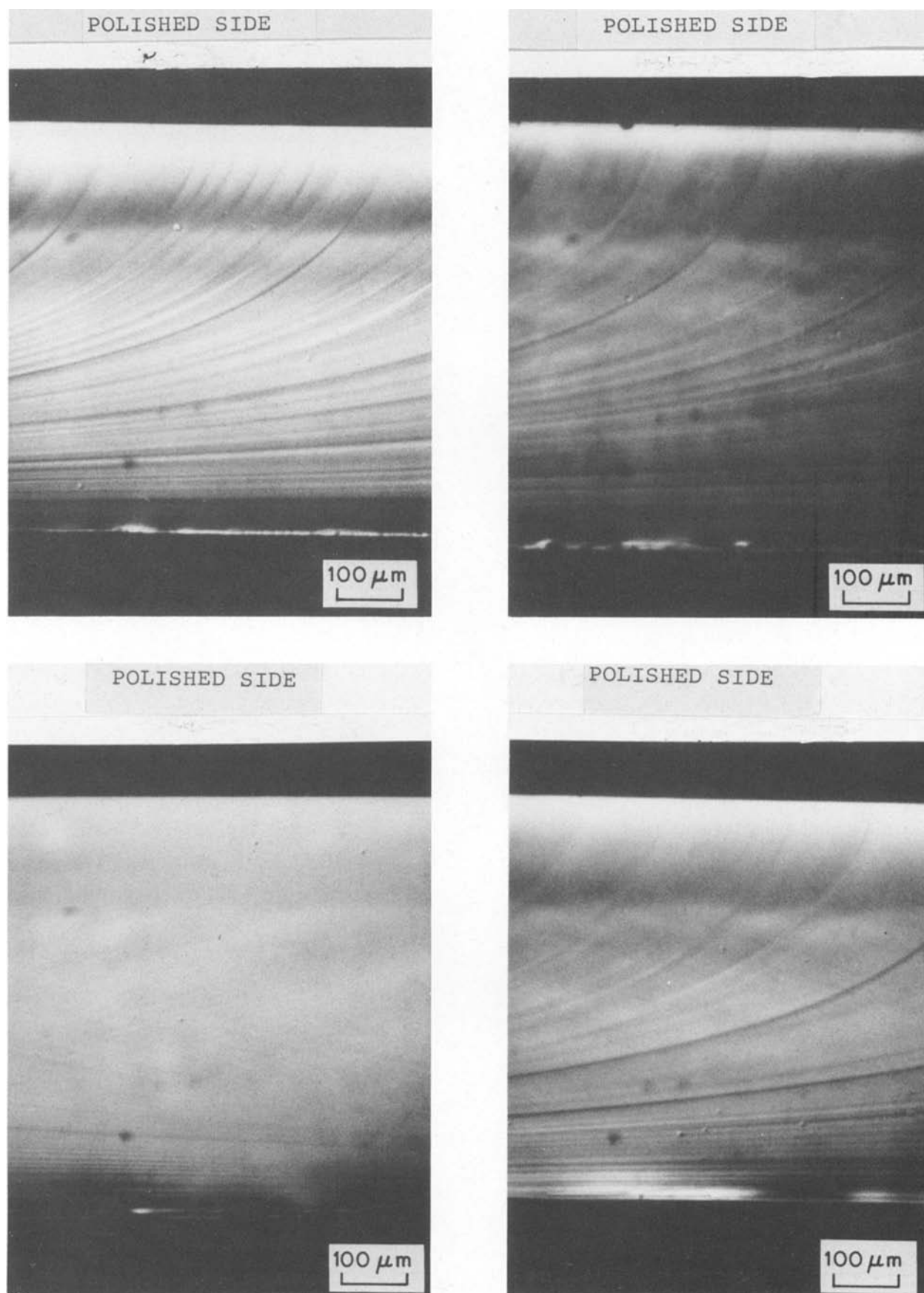


Fig. 11. Cross-section optical micrograph of (a, top left) nondamaged (b, top right) mechanically back-side damaged (c, bottom left) and (d, bottom right) laser back-side damaged ($E_d = 30$ and 50 J/cm^2) P(100) wafers after multiple oxidation cycles with ramp-up and ramp-down schedules. Stained by Wright etchant for 5 min. (magnification: 110X).

highly unlikely for oxygen impurities inside the bulk to interact with laser-irradiated defects. Therefore, we believe that this phenomenon cannot be explained by interstitial oxygen content differences alone.

The state of oxygen that gives the dislocation pinning effect is of technical importance. Hu and Patrick (10) established that precipitates are not the cause of pinning and proposed that clusters were. Other explanations (such as Cottrell atmospheres) fit the known data. Since, inside the Czochralski crystal pullers currently available, materials from seed-ends have been known to experience much faster cooling rates ($\sim 100^\circ\text{C/hr}$) than those from tail-ends, it can be expected that the state of oxygen from seed-ends might differ from that near tail-ends. The complexing of oxygen with carbon and other impurities could also vary from seed-end to tail-end. It should be pointed out that the difference in mechanical properties between material from the seed- and tail-end of a crystal could be associated with microcracks (or "microsplittings") as suggested by Schwuttke (9). He found more saw damage in wafers cut from the tail-end, and this residual damage is not completely removed from the back surface by the etching procedure. Recently, Eggermont *et al.* (8) have proposed that back surface laser damage depends strongly on the presence of microcracks and the seed- vs. tail-end microcrack concentration would explain the differences seen in Fig. 4 and 6.

It has been also reported that the presence of the oxygen precipitation induced by heat-treatment can increase the amount of nucleation sites for dislocations and decrease the upper yield point (11). The first half of the final thermal cycles used for P(111) material testing involved a Sb subcollector diffusion drive-in step (no predeposition) for about 3 hr at 1270°C under dry oxygen ambient. It has been well recognized that 1270°C is a sufficiently high temperature to dissolve grown-in micro-precipitates and process-induced oxide precipitates during the first oxidation cycle (1150°C) shown in Fig. 2. Therefore, we should not expect any significant contribution toward overall warpage variations due to the oxygen precipitation. Optical microscopic analysis of cleaved but unpolished laser back-damaged wafers by Sirtl etchant revealed that there were, in fact, very few precipitates inside the bulk of the finished wafers [Fig. 7 (a) and (b)]. These pictures also clearly demonstrate that damage generated by conventional mechanical means tends to propagate much deeper towards the front surface than that produced by laser irradiation of energy density less than 45 J/cm^2 during the high temperature thermal cycles used, and this leads to more pronounced warpage degradation.

P(100) materials.—Warpage data for P(100) materials based upon simulated multiple high temperature thermal cycles with or without ramp-up and ramp-down schedules are displayed in Fig. 8 and 9. The data clearly demonstrate that warpage variations of the wafers subjected to pulsed laser irradiation processes with energy density less than 35 J/cm^2 , regardless of the thermal cycles used, compare very favorably to those produced by the mechanical damage process. As in the case of (111) wafers, irradiation at 20 J/cm^2 appears to produce very little damage. Materials from seed-ends and middle sections were found to be more resistant to warpage than those from the tail-ends. This phenomenon is more pronounced under the thermal cycles without the ramping schedule. A typical example is shown in Fig. 10. Since interstitial oxygen concentration differences between seed-ends and tail-ends are less than 4 ppm, interstitial oxygen differences are not enough to explain this phenomenon, as in the case of P(111) wafers.

One interesting aspect of P(100) materials is that the laser irradiation process does not degrade warpage characteristics of materials from tail-ends significantly, whereas the opposite is true for P(111) materials. Why this rather subtle difference in warpage behavior between wa-

fers of the two different orientations occurs under high energy density pulsed laser irradiation is not obvious at the present time.

The finished wafers were cleaved and decorated by Wright etchant. Cross-section optical micrographs shown in Fig. 11 (a)-(d) reveal very limited numbers of noticeable precipitates. This is another clear indication of the rather insignificant role that oxygen precipitation plays in explaining the overall warpage variation phenomena observed during the course of this investigation.

Conclusions

Etching of polished sections to reveal the point of emergence of dislocation etch pits is a simple method of quantifying the initial back-side damage produced by laser irradiation. The damage threshold for P(111) silicon is $19 \pm 1\text{ J/cm}^2$.

From warpage variation studies of laser back-side damaged P(100) and P(111) material subjected to simulated bipolar and n-MOS high temperature thermal cycles, the following conclusions were reached:

1. Laser irradiation with energy density less than 45 J/cm^2 for P(111) materials and energy density up to 35 J/cm^2 for P(100) materials has shown no adverse effect on warpage variations during their respective simulated bipolar and n-MOS high temperature thermal cycles, compared with a conventional mechanical back-side damage process.
2. Materials from seed-ends are generally more resistant to warpage than those from tail-ends. This phenomenon cannot be explained by the total interstitial oxygen content alone. The state of the oxygen, which is a strong function of thermal history inside the Czochralski crystal puller, should be considered in addition to the total oxygen content.

Acknowledgments

The authors thank R. Koch and M. M. Simkins at Stanford University and I. James, D. Gaspar, and D. Suess at Siltec Corporation, for their experimental assistance. One of us (DE) wishes to acknowledge partial financial support from the National Science Foundation MRL Program through the Stanford University Center for Materials Research.

Manuscript submitted Aug. 16, 1983; revised manuscript received Feb. 11, 1983.

Siltec Corporation assisted in meeting the publication costs of this article.

REFERENCES

1. G. A. Rozgonyi, R. P. Deysher, and C. W. Pearce, *This Journal*, **123**, 1910 (1976).
2. A. Eder and C. Werner, in ASTM STP 712, 93 (1980).
3. Y. Ichida, T. Yanada, and S. Kawado, *ibid.*, 107 (1980).
4. Y. Hayafuji, T. Yanada, and Y. Aoki, *This Journal*, **128**, 1975 (1981).
5. C. W. Pearce and V. J. Zaleckas, *ibid.*, **126**, 961 (1980).
6. B. Leroy and C. Plougonven, *ibid.*, **127**, 961 (1980).
7. K. H. Yang and G. H. Schwuttke, *Phys. Status Solidi (A)*, **58**, 127 (1980).
8. G. E. J. Eggermont, D. F. Allison, S. A. Gee, K. N. Ritz, R. J. Falster, and J. F. Gibbons, in "Laser and Electron Beam Interactions with Solids," Vol. 4, B. R. Appleton and G. K. Celler, Editors, p. 615, North Holland Publishing Co., New York (1982).
9. G. H. Schwuttke, in Technical Report No. 3, Contract No. DAHC 15-72-C-0274, January 1974.
10. S. M. Hu and W. J. Patrick, *J. Appl. Phys.*, **46**, 1869 (1975).
11. K. Sumino, in "Semiconductor Silicon 1981," H. R. Huff, Y. Takeishi, and R. J. Kriegler, Editors, p. 208, The Electrochemical Society Softbound Proceedings Series, Pennington, NJ (1981).

Ion Bombarded-Enhanced Etching of Indium Phosphide

T. Inada,* S. Taka,¹ and K. Kodama

College of Engineering, Hosei University, Kajino-cho, Koganei, Tokyo 184, Japan

ABSTRACT

The effect of ion bombardment on the enhancement of the etch rate of InP has been investigated. The damage creation in InP due to ion bombardment has also been examined by Rutherford backscattering techniques. It has been shown that a highly enhanced etch rate of 800 Å/min in an HF solution is obtained from the ion bombardment-induced amorphous InP layer, which can be easily produced by room temperature ion bombardment with light mass ions such as Mg ions. The experimental results obtained have shown that the ion bombardment-enhanced etching can be used as a rapid precise tool for selective sectioning of InP.

Recently, there have been increasing requirements for the development of a precise tool for sectioning Si and compound semiconductors. Ion bombardment-enhanced (IBE) etching would be one of the most promising tools because this etching process can be characterized by ion species, incident ion energy, and ion dose used. In addition, this technique has a potential advantage of maskless selective etching of semiconductors if combined with a fine ion beam technology.

The possibility of the IBE etching for Si has been reported by Gianola (1) and then clearly demonstrated by Mazey *et al.* (2) and by Gibbons *et al.* (3). No report, however, has been published on the IBE etching of III-V compound semiconductors. This paper will present the results on the IBE etching of InP. We have investigated the introduction of lattice damage into InP, bombarded with Mg ions, using Rutherford backscattering techniques. Etch rates of InP bombarded under various conditions have been measured. Results clearly indicated the etch rate in an HF solution is highly enhanced for ion-bombarded amorphous InP layers.

Experimental

The substrates used in the present work were (100)-oriented, Fe-doped semi-insulating commercially available InP wafers. The substrates were degreased in several organic solvents, dipped in an HF solution, rinsed in deionized water, and then dried in an N₂ flow. The substrates were bombarded with Mg ions at room temperature and at incident energies in a range from 40 to 200 keV. During ion bombardment, the substrate was tilted by 7° from the incident ion beam to reduce channeling effects. The incident ions were scanned along the X- and Y-directions to introduce uniformly distributed damage in the InP substrate. A part of every sample was masked from the incident ion beam with a metal plate to get an unbombarded area on the sample. For some of the substrates, a mask of SiO₂ with various configurations was formed on the substrate prior to ion bombardment by a chemical vapor deposition technique combined with a conventional photoresist technique. Note that no damage was introduced in the InP surface layer during the SiO₂ deposition process within the detection limits of the Rutherford backscattering system used. The thickness of the SiO₂ mask was chosen so that almost all of the incident ions stop within the mask film. After ion bombardment, the mask patterns were printed in the InP substrate surface layer in a form of damage. If the etch rate of the ion-bombarded area is enhanced as compared with that of the unbombarded area, the printed mask patterns will be developed after etching. Such surface structures as developed by selective IBE etching were examined with a scanning electron microscope (SEM).

The damage incorporated into InP substrates due to ion bombardment was examined by Rutherford backscattering techniques using a collimated beam of 1.5 MeV He

ions from the Van de Graaff accelerator of Hosei University. The scattering angle used in the Rutherford backscattering measurement was 150°. Chemical etching of ion-bombarded InP was carried out by dipping the substrates into solutions with different HF contents. The etching time ranged from 40 to 10,000s. The variation of the thickness of the damaged surface layer with etch time was examined by successive Rutherford backscattering measurements followed by the chemical etching process. The height of a step, which appeared after etching between the ion-bombarded and unbombarded areas on the sample, was also measured using either an interferometer or a step-meter.

Results and Discussion

Figure 1 shows the Rutherford backscattering spectra obtained from an InP sample before and after ion bombardment with 200 keV Mg ions to a dose of $5 \times 10^{14}/\text{cm}^2$

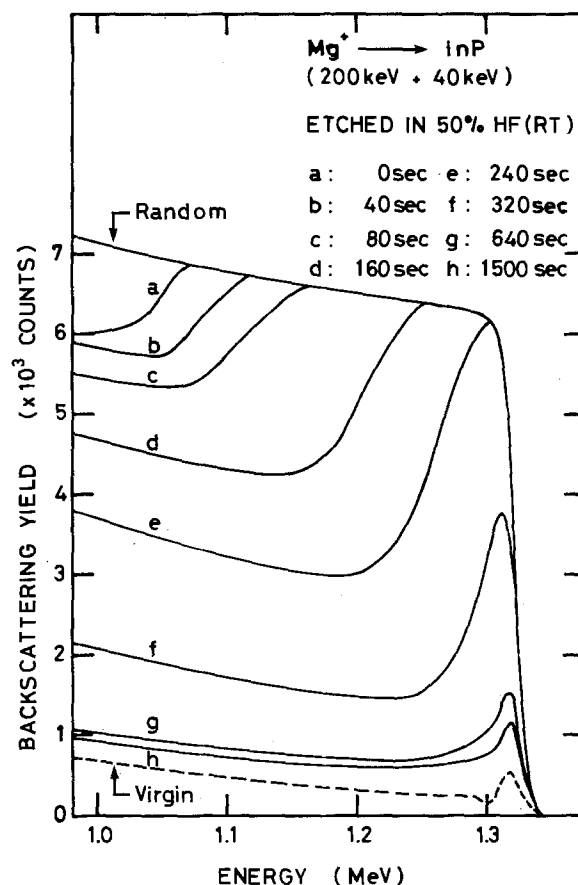


Fig. 1. Rutherford backscattering spectra obtained from an InP sample, bombarded with Mg ions to a total dose of $7 \times 10^{14}/\text{cm}^2$ ($200 \text{ keV } 5 \times 10^{14} + 40 \text{ keV } 2 \times 10^{14}/\text{cm}^2$), before (curve a) and after successive etching in an HF (50%) solution at room temperature (curve b-h). The curve (virgin) was obtained from an unbombarded area of the InP sample.

*Electrochemical Society Active Member.

¹Present address: Semiconductor Division, Toshiba Corporation, Kawasaki 210, Japan.

Key words: InP, ion-assisted etching, ion bombardment damage.

at room temperature. The sample was additionally bombarded with 40 keV to a dose of $2 \times 10^{14}/\text{cm}^2$ to achieve a uniformly distributed damage profile. The curves (virgin) and (a) in Fig. 1 show the channeling spectra from an InP sample before and after ion bombardment, respectively. The channeling yields reached the random levels after ion bombardment, indicating that the surface layer was transformed to an amorphous state. The thickness of the amorphous layer formed was estimated to be about $0.38 \mu\text{m}$ as calculated from the channeling data shown with the curve (a). After ion bombardment, the sample was successively dipped in an HF (50%) solution at room temperature. The curves (b)-(h) were obtained from the sample after each etch step. These channeling data clearly show that the thickness of the amorphous layer remaining after etching was decreased with increasing etch time. After etching for 320s, the entire amorphous layer was removed from the substrate, as indicated with the curve (f) in Fig. 1. The channeling yields of this sample were found to be still higher than those from the un-bombarded area, indicating that there was a transition layer which contained a high concentration of damage between the ion-bombarded amorphous layer and the underlying single-crystal substrate. It was also found that the thickness of the transition layer was decreased with increasing etch time as shown with the curves (f)-(h) in Fig. 1. These results showed that the etching still proceeded in the transition layer.

The thickness of the InP layer removed at each etching step is potted in Fig. 2 as a function of etch time, which is calculated from the channeling data shown in Fig. 1. In Fig. 2, the etched depths are also given, which were measured using either an interferometer or a step-meter. The etched depth was defined as a height of a step which appeared after etching between the ion-bombarded and un-bombarded areas on the sample, as illustrated with the insertion in Fig. 2. Note that there was a good coincidence between the data of the etched depth obtained by the channeling and step measurements within the experi-

mental errors, indicating that the etching proceeded only in the damaged region and not in the unbombarded area of the InP sample. This is based upon the idea that if the unbombarded area was stripped in the etchant used, the thickness of the removed InP layer in the bombarded area obtained by the step measurement should be thinner than that by the channeling measurement. From these results it was concluded that the etch rate of InP in the HF solution was enhanced by the introduction of damage in the substrate by ion bombardment.

As shown in Fig. 2, the etched depths were monotonically increased with increasing etch time in a range from 40 to 320s. The enhanced etch rate, defined as the inclination of the depth vs. etch time curve, was estimated to be about $800 \text{ \AA}/\text{min}$ in the ion-bombarded amorphous layer. It was also found that the etch rate was still enhanced in the highly damaged (not amorphous) InP layer but it was much reduced as compared with that of the amorphous layer.

The IBE etch rate was found to depend on both the concentration of HF in the etchant and its temperature. Figure 3 shows an etched depth vs. etch time curve, where etching was carried out on an ion-bombarded amorphous InP sample using a low HF content (25%) etchant. In addition, the etchant was cooled at 0°C during etching procedure. In this case, a reduced IBE etch rate of $45 \text{ \AA}/\text{min}$ was measured. This rate is a factor of 17 slower than that for the etching in the high HF content solution at room temperature. These results showed that the IBE etching is a thermally activated process. Figure 4 shows the dependence of the thickness of InP, removed after etching in the high HF content (50%) solution, on bombardment energy. The etching was done at room temperature for a given time, 1500s. The solid line in this figure shows the energy dependence of the sum of $(Rp + \Delta Rp)$ for Mg ions in InP, calculated from the LSS range-energy theory (4), where the Rp and ΔRp are the projected peak range and standard deviation, respectively. As can be seen in Fig. 4, there is a clear relationship between the

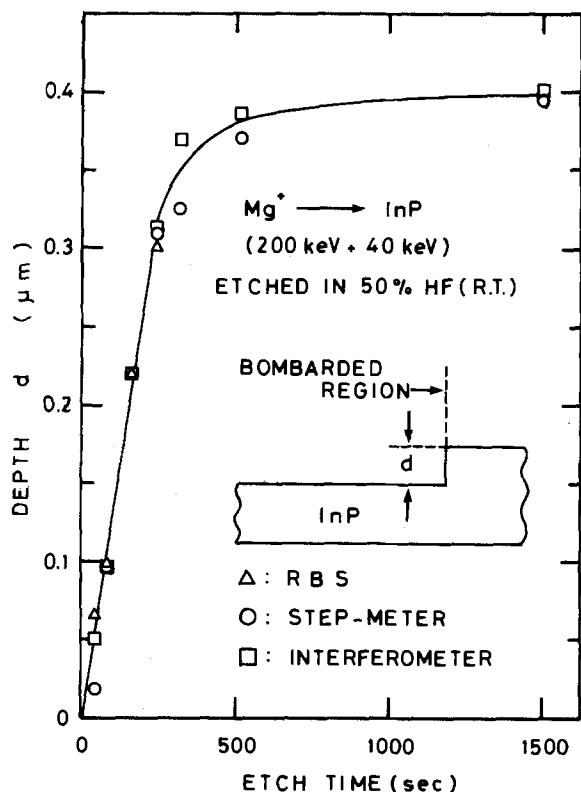


Fig. 2. The thickness of InP layers removed after etching in an HF solution as a function of etch time, calculated from the Rutherford backscattering data shown in Fig. 1. The data shown with open circles and squares reveal the height of steps, appeared after etching, as determined by a step-meter and an interferometer, respectively.

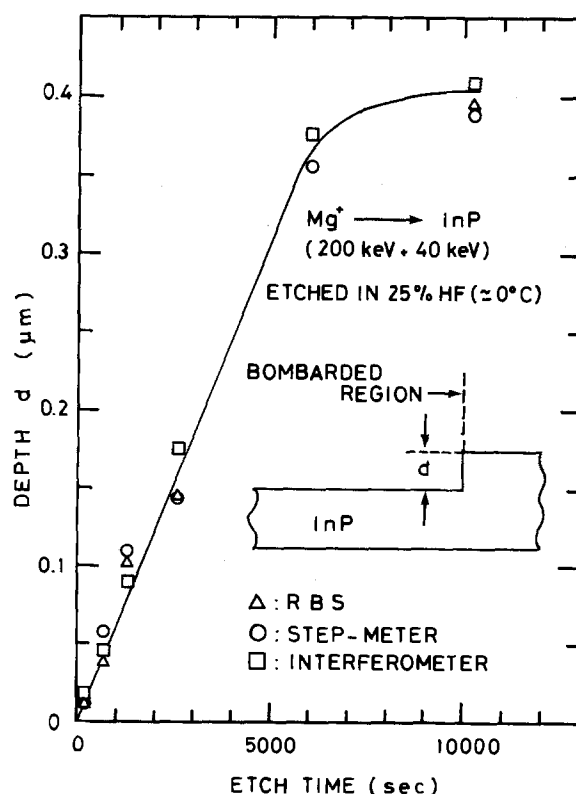


Fig. 3. The thickness of InP layers removed after etching in low HF content (25%) solution held at about 0°C as a function of etch time, calculated from Rutherford backscattering spectra. The data shown with open circles and squares reveal the height of steps, appeared after etching, as determined by a step-meter and an interferometer, respectively.

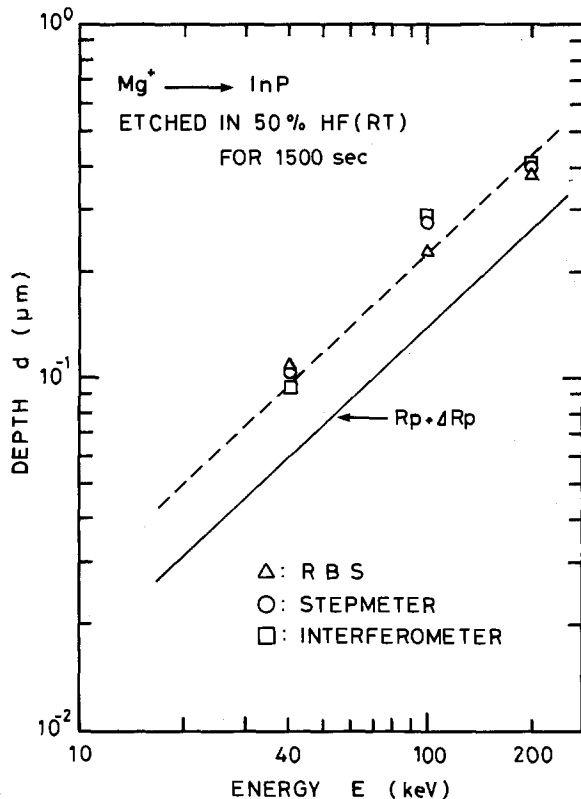


Fig. 4. Relationship between ion energy and the thickness of InP layers that can be removed after Mg ion bombardment at room temperature and dipping them in an HF (50%) solution for 1500s.

thickness of InP that can be removed by the IBE etching and the incident ion energy. This result shows that the depth of the region to be etched off from an InP substrate can be determined by incident ion energy rather than etch time, which is the striking feature of the IBE etching.

About $2 \mu\text{m}$ width SiO_2 strips were formed on InP substrates and used as a mask against the incident ion beam for achieving selective ion bombardment. These samples were bombarded at room temperature with 200 keV Mg ions to a dose of $5 \times 10^{14}/\text{cm}^2$ and then additionally with 40 keV Mg ions to a dose of $2 \times 10^{14}/\text{cm}^2$. After ion bombardment, these samples were submerged in the high HF content (50%) solution. As a result, steps were developed on the surface of the sample. Figure 5 is a SEM photograph showing a typical side view of the step developed by the IBE etching. The side of the step was found to be very sharp as shown in Fig. 5. We believe that this is due to the fact that the boundary between the ion-induced

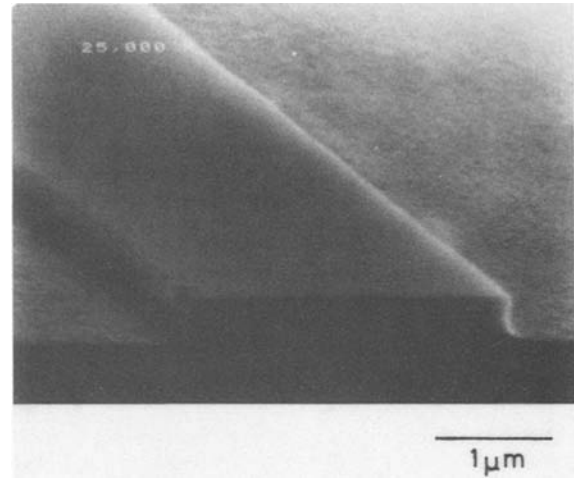


Fig. 5. SEM photograph showing the surface structure of InP, formed by selective ion bombardment-enhanced etching.

amorphous region and the unbombarded single-crystal region is clearly defined not only at the surface but also inside of the substrate, and the IBE etching stops at the boundary. These results indicate that the IBE etching is useful as a precise sectioning technique for submicron InP devices.

Summary

In summary, it has been demonstrated that the etch rate of InP in an HF solution is enhanced by the introduction of damage in the substrate by ion bombardment. The results obtained clearly show that the IBE etching of InP is controlled by physical parameters such as ion energy and dose. The highest rate of 800 Å/min is obtained in ion-induced amorphous InP layers. This etch rate is sufficiently high enough for the practical use of sectioning fine structures of InP devices. Such fundamental characteristics of the IBE etching as revealed in InP might be applied to other III-V compound semiconductors. Similar experiments on GaAs are now in progress and the results will be reported in the near future.

Manuscript submitted Oct. 3, 1983; revised manuscript received Feb. 7, 1984.

REFERENCES

1. U. F. Gianola, *J. Appl. Phys.*, **28**, 9 (1975).
2. D. J. Mazey, R. S. Nelson, and R. S. Barnes, *Philos. Mag.*, **17**, 1145 (1968).
3. J. F. Gibbons, E. O. Hechtl, and T. Tsurushima, *Appl. Phys. Lett.*, **15**, 117 (1969).
4. J. F. Gibbons, W. J. Johnson, and S. W. Mylroie, "Projected Range Statistic," Dowden, Hutchinson, and Rose, Stroudsburg, PA (1975).

Low Energy X-Ray and Electron Damage to IGFET Gate Insulators

A. Reisman*

Microelectronics Center of North Carolina, Research Triangle Park, North Carolina 27709
and
North Carolina State University, Raleigh, North Carolina 27650

C. J. Merz,* J. R. Maldonado, and W. W. Molzen, Jr.

IBM Corporation, Thomas J. Watson Research Center, Yorktown Heights, New York 10598

ABSTRACT

Radiation damage to 35 nm gate insulators of n-channel silicon IGFET's was investigated using direct exposure by x-rays from aluminum and copper targets in the dose range 10^4 - 10^8 rads (SiO_2). In addition, direct electron-beam damage at 3×10^6 rads (SiO_2) and 3×10^7 rads (SiO_2) was studied using an electron-beam direct write exposure system at 10 keV accelerating voltage, and incident electron doses of 20 and 200 $\mu\text{C}/\text{cm}^2$. The extent of damage was estimated using hot electron trapping in conjunction with device threshold determination via source-drain current-voltage measurements. It was found that the extent of x-ray induced damage is essentially the same for Al K α and Cu K α irradiation, and that the damage levels were the same when different dose rates at a constant total dose was employed. Positive charge levels were observed to begin leveling off above 10^6 rads, while neutral trap levels continued to increase monotonically. These levels at 10^8 rads are of the order of 2.3V positive charge threshold equivalent, and 4.2V of neutral traps using Al K α irradiation. Electron damage appears to be considerably higher at equivalent dosages. Apparent negative charge generation by x-rays is low, even at 10^7 rads, and appears to become significant (ca. 0.4V) at 10^8 rads. Apparent negative charge generation by electrons is noticeably greater, ca. 0.3V at 3×10^6 rads and 1.1V at 3×10^7 rads. The above, together with the results of an earlier report, indicate that it is important to keep ionizing radiation insulator dosage levels at 10^6 rads or less in processing steps. This can be best accomplished by using the lowest energy radiation possible to increase energy absorption in the films overlaying the gate insulator.

A variety of fabrication and analytical processes of potential, use in semiconductor chip manufacturing, subject the devices to low energy ionizing radiation in the range ≤ 25 keV. These processes include x-ray or E-beam lithography, E-beam metallization, plasma-assisted etching and deposition, plasma-assisted oxidation, and scanning electron microscope voltage contrast testing, to name several. The primary impinging radiation can, in turn, generate secondary ionizing radiation. Because of its lower energy, the absorption of this secondary radiation may be greater per unit of film thickness than that of the primary radiation.

This will, in fact, be the case if either the type of the secondary emission is of the same kind as that of the primary impinging radiation, e.g., primary x-rays give rise to secondary x-rays, or if photon primary radiation gives rise to electron secondary radiation. If electron primary radiation gives rise to secondary x-radiation of similar energy, this secondary radiation may penetrate more deeply than would the primary radiation (1). As a result of ionizing radiation exposure, it is also known that the gate insulator of an insulated gate field effect transistor, IGFET, may exhibit damage in the form of fixed positive charge and interface states immediately following irradiation (2, 3). In addition, so-called neutral traps are simultaneously generated during exposure to such radiation (4, 5). In the as-fabricated device, such neutral traps are not electrically active. The fixed positive charge and interface states can alter the time zero threshold and transconductance, respectively, of the IGFET, while as a function of time, all three of these defect types can be either annihilated or trap charge, thereby affecting the longer term device threshold stability. If electrons are captured, the instability is evidenced by an upward drift of the threshold voltage. These defects can, in large measure, be removed in all stages of device fabrication up to the device metallization step by elevated temperature annealing. If they are introduced during the metallization process via the use of E-beam metal deposition, x-ray or E-beam lithography, or plasma-based etching techniques, they cannot be removed completely using conventional annealing procedures. This is because metallized shallow junctions (0.5 μm or less) cannot be subjected to temperatures much in

excess of 400°C for time intervals much in excess of 30 min without incurring the possibility of metal penetration through the junctions. At atmospheric pressure, it has been found that in ambient atmospheres containing hydrogen, temperatures in excess of 550°C are required to remove neutral traps and fixed positive charge, while interface states can be removed at somewhat lower temperatures (5, 6). In nitrogen, it has been reported that fixed positive charge and neutral traps require temperatures in excess of 700°C, while the interface states can be eliminated at 450°C (7). It is argued in Ref. (7) that when the gate insulator is cyclically damaged and reannealed, it becomes more difficult to remove the damage with each successive damage cycle. This result is, however, debatable, since it has been shown that inert gas is not effective in removing fixed positive charge and neutral traps (8). When such removal is observed to a degree, it appears to be due to the presence of water vapor present as a contaminant in the inert gas.

In two recent studies (8, 9), it has been reported that essentially all of the generated fixed positive charge, almost all of the excess neutral traps, and all of the interface states and apparent negative charge can be removed by annealing at 50 atm and 400°C in a 10% H_2 -90% Ar ambient atmosphere. For these elevated pressure annealing studies, damage was introduced via a simulated E-beam metallization process using 10 keV electrons to evaporate aluminum from a hearth. First, the IGFET wafers were fabricated via a conventional polygate process using nonionizing radiative processing. The completed metallized patterned wafers were then coated with photoresist, and E-beam-evaporated aluminum was deposited on the photoresist as described in Ref. (8, 9). During this blanket metal deposition, the surface of the photoresist-covered wafer was bombarded by reflected primary electrons, secondary electrons from the aluminum melt, aluminum K α , and white radiation, as well as additional secondary electrons and x-rays when the hearth radiation impacted the device wafer surface. At the conclusion of the process, the photoresist and deposited aluminum were stripped off, and the devices were analyzed. Using 10 keV primary radiation, it is obvious that the energy range of the bombarding radiation, E , lies in the interval $0 < E \leq 10$ keV. The dosage range examined was approximately 10^4 - 10^7 rads (SiO_2). As a reference point, for the metallization sys-

*Electrochemical Society Active Member.

Key words: x-rays, electrons, MOSFET's, gate insulators.

tem employed, a 10 min evaporation at 0.5A beam current, during which 50 nm of aluminum was deposited, resulted in a composite x-ray/electron dose of about 5×10^6 rads (SiO_2).

It was found that the damage process resulted in the generation of fixed positive charge and neutral traps, as expected. What was unexpected were the observations that the fixed positive charge level saturated with increasing dose, and that "apparent" negative charge was generated. This apparent negative charge could be due to interface state generation as defined by the Deal Committee (3), or to an analog of fixed positive charge. The latter is believed to be the more likely explanation, since very little transconductance degradation was detected from I-V measurements. Recently, such fixed negative charge was observed as a result of hot carrier injection in encapsulated IGFET's (10). It is proposed in Ref. (10) that such fixed negative charge is due to the formation of SiO^- bonds.

Ning (11) had examined IGFET damage following E-beam metallization at 6.8 keV and 210 mA for 100s in a nonscanned hearth which deposited 1.2 μm of Al. Ning did note differences between ΔV_T (threshold shifts) and ΔV_{FB} (flatband shifts) which he attributed to interface states. He did not, however, verify this speculation, and this effect may be similar to the one we have attributed to fixed negative charge. Further, as he used only a single aluminum thickness, he could not have observed the fixed positive charge saturation effect we reported on.

The present study was stimulated by a desire to understand better (i) the radiation(s) responsible for the negative charge, (ii) whether the fixed positive charge saturation phenomenon can be generated using a single type of radiation, (iii) what the effects are of varying photon energy at fixed total dose, (iv) what the effects are of varying photon flux for a fixed total dose, (v) what the effects are of a large variation in electron dose with electron energies in the 10 keV range, and (vi) the similarities and differences between photon and electron damage.

Experimental Procedure

Devices.—The devices examined in the present study were 350 nm thick polysilicon electroded IGFET's fabricated as described in Ref. (8). They employed a lift-off Ti contact metallurgy, Al-3% Si interconnection metallurgy, 35 nm gate insulators, and 0.5 μm phosphorous junctions. The threshold of these devices, fabricated in 0.5 Ωcm Si, was $1.2 \pm 0.1\text{V}$ using -1V substrate bias. The specific devices employed in the present study were 20:1 width/length ratio devices with 50m channel lengths and gate insulator areas of $5.0 \times 10^{-4} \text{cm}^2$. This gate area is suitable for precise measurement of injected electron trapping by positively charged and neutral traps. As in the early study (8), only traps with cross sections $\geq 10^{-15} \text{cm}^2$ were examined since these are of greatest interest. The devices were examined using the hot electron injection technique of Ning (11) as used in Ref. (8).

X-ray damage.—Because of the nature of the process, in the simulated E-beam metal evaporation process employed in Ref. (8), the IGFET's were exposed to all x-ray wavelengths up to 10 keV. Because normal x-ray sources employ beryllium windows, they do not provide much energy less than 1 keV. Consequently, using an aluminum target x-ray source, as we did in the present study, is not a complete representation of the aluminum radiation experienced by a device wafer in an E-beam metallization process. What we could do, however, was to compare radiation of different energies to see if, at constant total dose, qualitative or quantitative differences in damage could be detected. This would give some indication of wavelength effects pending studies in the ≤ 1 keV range via other means. Such a comparison was run between aluminum $K\alpha$ radiation (1.49 keV) and copper $K\alpha$ radiation (8.03 keV). In addition, these two energies span the white radiation range encountered in the E-beam metallization process in question. While the present approach to exposure

with aluminum radiation does not fully duplicate conditions in an E-beam metallization system, it does approximate exposure conditions from a synchrotron ring source. The latter offers potential in x-ray lithography applications, and the energy range employed would be in the 1-2 keV vicinity. For a given target, the photon output above and below the characteristic wavelength range is small. For example, measurements of the high output aluminum target x-ray source available to us showed an aluminum $K\alpha$ photon output/total photon output at 15 kV of 0.8. Because of this, dosages were calculated based only on the $K\alpha$ output. For example, if it is assumed that the average wavelength of the white radiation centered near the $K\alpha$ value, the maximum energy error would be 20%. If it centered at higher wavelengths, the error would be much less since the absorption of this higher wavelength in a given film thickness would be roughly proportional to the cube of the energy ratios. Comparing the $K\alpha$ with an average energy of white radiation of 5 keV, for example, leads to the conclusion that the absorption in a unit of film thickness is given approximately by the ratio $(1.5/5)^3 = 0.03$. Thus, only $0.03 \times 0.20 = 0.006$ of the white radiation photons are absorbed in the same film thickness as is the characteristic radiation, a negligible amount. The calibrated aluminum $K\alpha$ x-ray source was operated at 15 keV for all exposures. The target was 40 cm from the sample providing uniform radiation over a 1 in. diam. Five of six pie wedge-shaped sections on each of two device wafers were irradiated using a 1.02 mm thick stainless steel template as a mask. The sixth wedge was used as a control. During irradiation, calculated Si rad dosages absorbed in the insulator, target beam current, and exposure times, respectively, were: 10^4 rads 10 mA 36s; 10^5 rads 100 mA 36s; 10^6 rads 200 mA 3 min; 10^7 rads 200 mA 30 min; and 10^8 rads 200 mA 300 min. The wafers were unbiased, as would be the case during device processing. The same experiment was repeated on a wafer overcoated with 0.4 μm photoresist and on another wafer overcoated with 0.4 μm of photoresist and 30 nm of aluminum to examine the effects of these coatings, since such layers could be present in a metal lift-off process and were present in the studies described in Ref. (8, 9). On an additional device wafer, the effect of dose rate at constant total dose was examined since the above-described exposures were made at different dose rates for practical reasons. In addition to a control wedge, one wedge was irradiated at 3.3 krad/min and another at 330 krad/min, both to a total insulator dose of 1.5×10^6 rads (SiO_2).

Copper radiation exposures were conducted somewhat differently than those with aluminum to assess the effects of photon energy, and to see if differences in target spectral content at different excitation voltages would affect defect generation levels. The yield of characteristic radiation is known to increase markedly with excitation voltage. For example, the output from a copper target increases in the ratio 1:2:10 (12) when the excitation voltage is increased from 15 to 20 to 40 kV, based on extrapolation of the data in Ref. (12) for a 15 kV target operating at 200 mA and a target to sample distance of 40 cm. The copper $K\alpha$ 20 kV irradiations, all at 50 mA, and a sample to source distance of 36 cm were conducted at: 10^4 rads 118s; 10^5 rads 19 min 46s; 10^6 rads 3h 17 min; and 2×10^7 rads 64h 48 min. The 40 kV exposures all at 100 mA were at: 10^4 rads 12s; 10^5 rads 119s; 10^6 rads 19 min 46s; 10^7 rads 3h 17 min; 7.2×10^7 rads 24h. The copper source, of course, had a similar low energy cutoff problem as did the aluminum source, because of the presence of a beryllium window.

Al $K\alpha$ x-ray dosages were calculated assuming mass absorption coefficients for SiO_2 and Si of 1.268×10^3 and $0.5428 \times 10^3 \text{cm}^2/\text{g}$, respectively. Copper $K\alpha$ x-ray dosages were calculated assuming mass absorption coefficients for SiO_2 and Si of 28 and 48 cm^2/g , respectively. The absorption in the SiO_2 was calculated at an incident flux of 2.8 $\text{mJ}/\text{cm}^2/\text{min}$. For 10 and 100 mA, rates were assumed to vary linearly. Thus, at 200 mA and 15 kV, the SiO_2 rad

rate was $0.33 \times 10^6/\text{min}$; at 100 mA and 15 kV, it was $0.165 \times 10^6/\text{min}$, etc. For copper, the data were calculated at 200 mA target current, then recomputed for 50 mA at 20 kV and 100 mA at 40 kV using the data in Ref. (12).

Electron damage.—Electron irradiation was conducted in an electron-beam lithography system. Chen *et al.* (13) had reported on E-beam lithography damage to 38 nm gate insulators in submicron IGFET's. They did not specify their device layer thicknesses, nor beam accelerating voltages, and they did not quantify defect concentrations using electron injection methods, but simply measured threshold shifts at rad doses up to 10^4 . This made it impossible for us to compare our results with theirs. For the present study, the E-beam system was operated at 10 keV to simulate the process being examined. The damage introduced at 20 and 200 $\mu\text{C}/\text{cm}^2$ incident fluxes was examined. The maximum penetration depth for these electrons was calculated using the Terrill equation (14). This equation, Eq. [1], is reported to be applicable to electrons with accelerating potentials in the range 10^3 – 10^5V . For the calculations

$$X_e = \frac{2.5 \times 10^{-12} V^2}{\sigma} \quad [1]$$

where V is in volts, σ is the density in g/cm^3 , and X_e is in cm. σ was assumed to be $2.32 \text{ g}/\text{cm}^3$ which approximates the values for SiO_2 ($2.32 \text{ g}/\text{cm}^3$) and Si ($2.33 \text{ g}/\text{cm}^3$). The dosage in the gate insulator was then calculated assuming (i) the penetration depth was 1.08 μm , (ii) the absorption is essentially linear, and (iii) none of the incident electrons is reflected. Based on these assumptions and the incident electron flux of 20 and 200 $\mu\text{C}/\text{cm}^2$, the dosages were calculated to be approximately 3×10^6 rads (SiO_2) and 3×10^7 rads (SiO_2), respectively. For the electron-beam studies, 15–18 devices were measured for each experimental condition.

Experimental Results and Discussion

Aluminum and copper $K\alpha$ irradiation.—Table I shows for an uncoated wafer and 15 kV target voltage, the threshold voltages, V_T , of devices before and after irradiation following injection of $2.5 \times 10^{13} \text{ e}/\text{cm}^2$ to annihilate positive charge and $1.25 \times 10^{16} \text{ e}/\text{cm}^2$ to label neutral traps. Positive charge, neutral trap, and apparent negative charge concentrations in terms of volts of threshold shift are also given in Table I. The thresholds were all measured at a substrate bias of -1.0V and a source drain voltage of 0.1V . An average of five devices were injected and measured on each pie wedge.

It is seen from Table I that the control wedge was unaffected by the irradiation sequence and the device thresholds varied by less than 0.05V for the 30 or so unirradiated devices measured on the different wedges. On all wedges, the same devices were measured before and after irradiation. The effects at $\leq 10^5$ rads are small with no negative charge detected, positive charge showing about a 0.2V shift, and generated neutral trap content at only 0.06V or thereabouts. At 10^6 rad dosages, the positive charge generation rate appears to begin slowing down while the neutral trap concentration rises dramatically. For the first time, a small quantity of negative charge appears to have been generated at the 10^7 rad dosage level. At 10^8 rads, which is a greater dosage than used in Ref. (8), the positive charge generation rate is slowing down further while the neutral trap generation rate continues to increase.

Negative charge increases significantly but is still at a lower value than observed in Ref. (8) at lower doses.

From the above, we may conclude that the negative charge observed in Ref. (8) is not due to the Al $K\alpha$ radiation, at least not when it is the sole type of ionizing radiation. Further, while the positive charge level does not saturate, its rate of generation on a percentage basis decreases markedly with increasing dose. The most important conclusions that can be drawn from Table I relate to the neutral trap picture, because these traps are the most difficult to remove. It is seen that their concentration does not become significant until a dose of 10^6 rads is absorbed. In Ref. (8) it was pointed out that unlike positive charge, neutral trap removal is related directly to its concentration before annealing; the larger the concentration, the more that will remain following annealing. Thus, it would argue for tailoring process steps, when possible, to keep the absorbed dose in the gate insulator to $\leq 10^6$ rads (SiO_2).

In an E-beam metallization process, for example, it would indicate that the hearth (the target in effect) should be kept as small as possible and that the molten scanned region should be as small as possible to keep the energy as localized as possible to obtain the maximum amount of evaporation in the shortest time. As we shall see below in discussions of negative charge generation due to electron damage, this would argue for using magnetic or electrostatic removal of reflected or secondary electrons from the hearth before they can impinge on the sample. In x-ray lithography, it would argue for employing the longest wavelengths possible to minimize penetration depth. This would require working in the energy range 0.5–1 keV, rather than using radiation in the 1–2 keV range since the absorption would be greater by approximately the cube of the ratios, e.g., $0.5^3/1.0^3 X$, where X is the absorption depth of a 1 keV photon. This is about 12.5% of X . Further, as the incident energy is confined to a thinner layer, it is very likely that much smaller incident doses would be required for exposure.

This raises another question as to whether traps are created during irradiation or merely made visible. It could be argued, for example, that the 2.30V equivalent of positive charge seen at a dosage of 10^8 rads in Table I was present in the insulator, prior to irradiation, and that the traps were electrically inactive because they had been annihilated by electrons, that all irradiation did was to empty these traps of their electrons. It would, however, be difficult to advance such an argument in the case of neutral traps for the following reason. The neutral traps are not visible electrically before or after irradiation. If the quantities seen after irradiation were already present before irradiation, they would have been detected in the neutral trap measurements of the control samples prior to irradiation. However, they are not seen and, therefore, they could not have been present initially. It is not unlikely that positive and negative charge defects are also created, and not simply made visible during the irradiation process.

Tables II and III represent the results obtained when device wafers were employed to simulate an E-beam metallization process using only the aluminum $K\alpha$ photon output of a hearth in such a process. Thus, in Table II, the data were obtained when the wafer was coated first with 0.4 μm of a positive photoresist; in Table III the data are those obtained when the wafer was coated with a bottom

Table I. Al $K\alpha$ x-radiation damage in 35 nm SiO_2 gate insulators at 15 kV target voltage, uncoated wafer

Rads (SiO_2)	V_T before irradiation (control wedge)	V_T after irradiation	Volts positive charge	Volts neutral traps	Volts negative charge
0	1.10 \pm 0.02	1.09 \pm 0.02	0.00	0.06 \pm 0.01	0.00
10^4	1.07 \pm 0.02	1.05 \pm 0.03	0.03 \pm 0.01	0.06 \pm 0.01	0.00
10^5	1.07 \pm 0.03	0.90 \pm 0.05	0.19 \pm 0.00	0.10 \pm 0.00	0.00
10^6	1.07 \pm 0.02	0.04 \pm 0.02	1.07 \pm 0.01	0.35 \pm 0.01	0.00
10^7	1.07 \pm 0.02	-0.61 \pm 0.01	1.77 \pm 0.01	1.72 \pm 0.04	0.08 \pm 0.01
10^8	1.12 \pm 0.02	-0.78 \pm 0.03	2.30 \pm 0.02	4.18 \pm 0.06	0.36 \pm 0.05

Table II. Al K α x-radiation damage in 35 nm SiO₂ gate insulators at 15 kV target voltage, wafer coated with 0.4 μ m positive photoresist

Rads (SiO ₂)	V _T before irradiation (control wedge)	V _T after irradiation	Volts positive charge	Volts neutral traps	Volts negative charge
0	1.05 ± 0.02	1.05 ± 0.02	0.00	0.06 ± 0.02	0.00
10 ⁴	1.07 ± 0.01	1.04 ± 0.01	0.03 ± 0.01	0.05 ± 0.01	0.00
10 ⁵	1.05 ± 0.02	0.88 ± 0.02	0.17 ± 0.01	0.08 ± 0.01	0.00
10 ⁶	1.03 ± 0.02	0.09 ± 0.01	0.94 ± 0.01	0.29 ± 0.02	0.00
10 ⁷	1.03 ± 0.01	-0.69 ± 0.02	1.82 ± 0.03	1.60 ± 0.03	0.10 ± 0.02
10 ⁸	1.04 ± 0.02	-0.81 ± 0.02	2.22 ± 0.01	3.87 ± 0.04	0.37 ± 0.02

Table III. Al K α x-radiation damage in 35 nm SiO₂ gate insulators at 15 kV target voltage, wafer coated with 0.4 μ m positive photoresist plus 30 nm Al

Rads (SiO ₂)	V _T before irradiation (control wedge)	V _T after irradiation	Volts positive charge	Volts neutral traps	Volts negative charge
0	1.08 ± 0.03	1.08 ± 0.03	0.00	0.06 ± 0.02	0.00
10 ⁴	1.08 ± 0.02	1.07 ± 0.02	0.02 ± 0.01	0.04 ± 0.02	0.00
10 ⁵	1.10 ± 0.03	0.95 ± 0.02	0.23 ± 0.02	0.14 ± 0.01	0.07 ± 0.02
10 ⁶			Not measured		
10 ⁷	1.11 ± 0.01	-0.65 ± 0.08	1.99 ± 0.04	1.81 ± 0.06	0.19 ± 0.05
10 ⁸	1.08 ± 0.01	-0.56 ± 0.15	2.19 ± 0.11	3.78 ± 0.41	0.62 ± 0.12

layer of 0.4 μ m of photoresist, and a top layer of 30 nm of aluminum was then deposited by resistance heating. To a first approximation, the results are, within experimental limits, identical to those shown in Table I. This indicates that no cooperative phenomena occur that affect the damage behavior induced by the low energy aluminum K α radiation due to the presence of these films. No absorption corrections were made in arriving at the total dose experienced by the gate insulator due to absorption in these top coatings.

Table IV shows the results obtained when the device gate insulators absorbed the same aluminum K α dose, 1.5×10^6 rads (SiO₂) at two different rates: 3.3 krad/min and 330 krad/min. It is seen that the results are the same for the two cases and consistent with the results shown in Tables II and III. This demonstrates that the insulator damage is reasonably independent of the dose rate and a function only of the total dose. It also indicates that the damage arises as a function of microscopic interaction of the ionizing radiation, e.g., bond-radiation interaction as opposed to a macroscopic effect, e.g., macroscopic heating. These data, obtained at doses of 1.5×10^6 rads, together with the data of Table I show the rapid increase in damage when the dosage reaches the 10^6 rad range. It indicates again, the necessity of keeping the insulator dosage below this value in processing. From a practical point of view, e.g., in a lithographic exposure using x-rays, or in an E-beam metal evaporation, it indicates that there is no advantage in reducing the dose rate of ionizing radiation in order to minimize damage; that as long as the total insulator dose is the same, the damage will be the same.

Tables V and VI show the effects of Cu K α radiation at constant total dose based on K α content, when the spec-

tral output from the target was varied significantly by employing 20 and 40 kV target beam accelerating voltages. Within experimental limits, the results are the same, indicating that basing the energy content calculation on K α output is a reasonable one. As with the Al K α exposures, the primary damage introduced appears to be in the form of positive charge and neutral traps. Thus, at the 10^6 - 10^7 rad levels, while volts of positive charge and neutral traps are detected, only tenths of volts of negative charge is in evidence.

The data in Tables I-VI are depicted graphically in Fig. 1 and 2. Figure 1 shows the positive charge situation, while Fig. 2 depicts the neutral trap behavior for Al and Cu x-ray damage. The graphs need no further discussion.

Electron beam irradiation.—Table VII shows the damage levels obtained at 3×10^6 rads (SiO₂) and 3×10^7 rads SiO₂ using 20 μ C/cm² and 200 μ C/cm² incident electron doses, respectively, at 10 keV accelerating voltage. Positive charge levels appear to be somewhat higher than obtained using x-rays as can be seen in Fig. 1, e.g., 1.8V vs. 1.3V at the 20 μ C level, and 2.9V vs. <2V at the 200 μ C level. By comparing the results of the present work to those obtained in Ref. (8), it can be seen that the positive charge level due to x-rays alone is lower than the combined x-ray and electron damage obtained in the earlier study in the 10^6 - 10^7 total rad dosage range, while the positive charge level due to electrons alone in the same dosage range is greater. This appears to be reasonable.

Neutral trap differences are even more pronounced than positive charge effects. At 3×10^6 rads electron dose, about 3.5V of threshold equivalent are generated, while x-rays at the same dose generate only 1V of equivalent

Table IV. Al K α x-radiation damage in 35 nm SiO₂ gate insulators at 15 kV target voltage, wafer uncoated. Two different exposure rates

Rads (SiO ₂)	V _T before irradiation (control wedge)	V _T after irradiation	Volts positive charge	Volts neutral traps	Volts negative charge
0	1.10 ± 0.03	1.11 ± 0.02	0.00	0.06 ± 0.02	0.00
1.5 × 10 ⁶ 3.3 krad/min	1.07 ± 0.02	-0.01 ± 0.02	1.12 ± 0.03	0.49 ± 0.02	0.04 ± 0.01
1.5 × 10 ⁶ 330 krad/min	1.09 ± 0.03	-0.14 ± 0.02	1.26 ± 0.02	0.47 ± 0.03	0.03 ± 0.01

Table V. Cu K α x-radiation damage in 35 nm SiO₂ gate insulators at 20 kV target voltage, wafer uncoated

Rads (SiO ₂)	V _T before irradiation (control wedge)	V _T after irradiation	Volts positive charge	Volts neutral traps	Volts negative charge
0	1.07 ± 0.04	1.06 ± 0.03	0.00	0.06 ± 0.01	0.00
10 ⁴	1.10 ± 0.02	1.03 ± 0.02	0.07 ± 0.01	0.06 ± 0.01	0.00
10 ⁵	1.10 ± 0.03	0.63 ± 0.02	0.48 ± 0.01	0.15 ± 0.03	0.00
10 ⁶	1.10 ± 0.03	-0.02 ± 0.04	1.14 ± 0.02	0.76 ± 0.04	0.03 ± 0.02
2 × 10 ⁷	1.07 ± 0.02	-0.15 ± 0.03	1.53 ± 0.06	3.62 ± 0.08	0.31 ± 0.03

Table VI. Cu K α x-radiation damage in 35 nm SiO $_2$ gate insulators at 40 kV target voltage, wafer uncoated

Rads (SiO $_2$)	V $_T$ before irradiation (control wedge)	V $_T$ after irradiation	Volts positive charge	Volts neutral traps	Volts negative charge
0	1.10 \pm 0.03	1.10 \pm 0.03	0.00	0.06 \pm 0.01	0.00
10 4	1.10 \pm 0.03	1.03 \pm 0.02	0.05 \pm 0.01	0.06 \pm 0.01	0.00
10 5	1.08 \pm 0.02	0.69 \pm 0.02	0.39 \pm 0.01	0.12 \pm 0.01	0.00
10 6	1.07 \pm 0.02	-0.11 \pm 0.08	1.28 \pm 0.03	0.59 \pm 0.04	0.03 \pm 0.01
10 7	1.07 \pm 0.02	-0.40 \pm 0.05	1.65 \pm 0.04	2.51 \pm 0.13	0.18 \pm 0.01
7.2 \times 10 7	1.10 \pm 0.03	-0.36 \pm 0.08	2.00 \pm 0.07	4.46 \pm 0.09	0.48 \pm 0.03

Table VII. Electron radiation damage at 3 \times 10 6 rads (20 μ C/cm 2) and 3 \times 10 7 rads (200 μ C/cm 2) using 10 keV electrons

Rads (SiO $_2$)	V $_T$ before irradiation (control wedge)	V $_T$ after irradiation	Volts positive charge	Volts neutral traps	Volts negative charge
0.00	1.16 \pm 0.02	1.16 \pm 0.01	0.00	0.06 \pm 0.01	0.00
3 \times 10 6	1.19 \pm 0.02	-0.32 \pm 0.03	1.76 \pm 0.03	3.53 \pm 0.05	0.25 \pm 0.04
0.00	1.16 \pm 0.01	1.14 \pm 0.01		Not measured	
3 \times 10 7	1.18 \pm 0.02	-0.55 \pm 0.10	2.85 \pm 0.10	>5.0V	1.08 \pm 0.03

threshold voltage. With the 3 \times 10 7 rad electron dosage, > 5V are generated. The limit of our measuring capability for V $_T$ is 5V. The comparable x-ray figure is 4V. Apparent negative charge generation for the electrons at 3 \times 10 6 rads is some three times greater than that generated by x-rays at the 10 7 level. Similarly, at the 3 \times 10 7 electron dose level, approximately three times as much negative charge is generated than that at the 10 8 level for x-rays.

Conclusions

Based on the results of studies of gate insulator damage in IGFET's due to x-rays alone, or electrons alone, it appears that apparent negative charge observed in earlier work (8) is due almost entirely to electrons, with x-rays

yielding low levels of such damage until the 10 8 rad (SiO $_2$) range is reached. It was found also that when using different x-ray dose rates, the extent of damage at constant total dosage is essentially the same. It also appears that the damage level with x-rays is relatively insensitive to the x-ray energy employed using aluminum and copper radiation, again the total dose being the determining factor. The positive charge saturation effect observed in the earlier work appeared to occur using x-rays alone, at about the same total dosage level as in the earlier study. However, even at the 10 8 dosage level, there is still some increase in positive charge level observed. A possible explanation is that positive charge saturation is coupled in some way to the simultaneous generation of apparent negative charge, such charge requiring electron irradiation for generation at lower dosage levels.

While x-rays and electrons appear qualitatively to generate the same type of damage, electrons are much more effective, *i.e.*, at given dosages, the concentrations of the generated defects are considerably greater with electrons than with x-rays. The effect is most obvious with negative charge formation.

With x-ray exposure, the damage to the gate insulator, in the form of both positive charge and neutral traps is relatively minor at the 10 4 rad (SiO $_2$) level, but becomes significant in the 10 5 -10 6 range. In fact, the rate of damage increase of neutral traps is considerably greater above 10 6 rads than below it. An opposite effect is observed in positive charge formation. However, as the rate of positive charge generation is greater below 10 5 rads and smaller above this value, positive charge and neutral traps achieve similar damage levels around the 10 6 rad value.

Since high levels of neutral traps are difficult to remove, it appears that processes involving ionizing radiation should be adjusted to keep dosage levels below 10 6 rads (SiO $_2$). In a lithographic process, for example, this can be done by using lower x-ray or electron energies for photoresist exposure. If this is done, then two effects will lead to lower damage levels being introduced into gate insulators of IGFET's. First, since absorption will be greater in the photoresist, penetration to underlying films will be less. Second, since absorption in the desired layer is more efficient, lower incident doses will be required to achieve the desired dose in the photoresist.

Acknowledgments

The authors are indebted to T. H. Ning and J. Aitken of IBM for their many stimulating discussions, to R. F. Boehme for conducting the copper irradiations, and to T. P. Donohue for conducting the electron-beam exposures. They also wish to thank C. K. Williams of North Carolina State University for computer plotting the data.

Manuscript submitted Nov. 10, 1983; revised manuscript received Jan. 12, 1984.

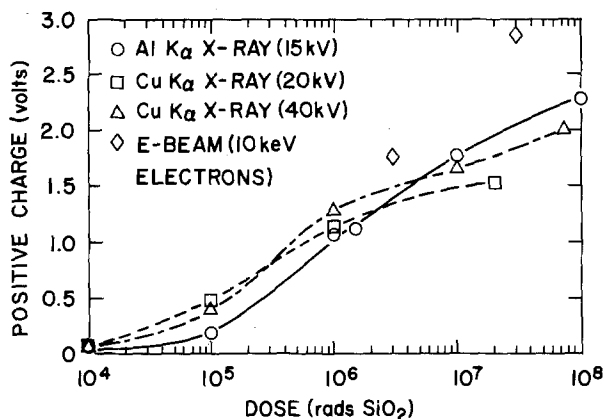


Fig. 1. Defect concentration in volts of threshold shift as a function of dosage, rads (SiO $_2$) for x-rays, positive charge.

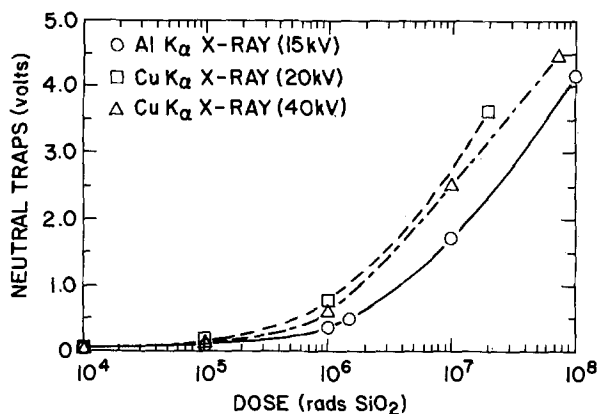


Fig. 2. Defect concentration in volts of threshold shift as a function of dosage, rads (SiO $_2$) for x-rays, neutral traps.

Microelectronics Center of North Carolina assisted in meeting the publication costs of this article.

REFERENCES

1. L. R. Tocci, M. J. McNott, and R. E. Johnson, *IEEE Electron Devices Lett.*, **ed14-6**, 175 (1983).
2. E. H. Snow, A. S. Grove, and D. J. Fitzgerald, *Proc. IEEE*, **55**, 1168 (1967).
3. B. E. Deal, *IEEE Trans. Electron Devices*, **ed-27**, 606 (1980).
4. J. M. Aitken and D. R. Young, *J. Appl. Phys.*, **47**, 1196 (1976).
5. J. M. Aitken, D. R. Young, and K. Pan, *ibid.*, **49**, 3386 (1978).
6. J. M. Aitken, *J. Electron. Mater.*, **9**, 639 (1980).
7. M. Shimaya, N. Shiono, D. Nakajima, C. Hashimoto, and Y. Sakakibara, *This Journal*, **130**, 945 (1983).
8. A. Reisman and C. J. Merz, *ibid.*, **130**, 1384 (1983).
9. A. Reisman, J. M. Aitken, A. K. Ray, M. Berkenblit, C. J. Merz, and R. P. Havreluk, *ibid.*, **123**, 1616 (1981).
10. W. G. Meyer and R. B. Fair, *IEEE Trans. Electron Devices*, **ed-30**, 96 (1983).
11. T. H. Ning, *J. Appl. Phys.*, **49**, 4077 (1978).
12. M. Green and V. E. Cosslett, *J. Phys. D.*, **1**, 425 (1968).
13. J. Y. Chen, R. C. Henderson, D. O. Patterson, and R. Martin, *IEEE Electron Devices Lett.*, **ed1-3**, 13 (1982).
14. H. W. Leverenz, "An Introduction to Luminescence of Solids," p. 158, Dover Publications, Inc., New York (1968). See also, T. E. Everhart and P. H. Hoff, *J. Appl. Phys.*, **42**, 5837 (1971); and H. M. Terrill, *Phys. Rev.*, **22**, 101 (1923).

Implantation and Annealing Studies of Laterally Seeded Recrystallized Silicon on Silicon Dioxide

S. K. Banerjee, R. Y. Tong, B. Lee, and R. Y. DeJule

Coordinated Science Laboratory, and Department of Electrical Engineering, University of Illinois at Urbana-Champaign, Urbana, Illinois 61801

B. G. Streetman*

Department of Electrical Engineering, University of Texas at Austin, Austin, Texas 78712

H. W. Lam

Texas Instruments, Incorporated, Central Research Laboratories, Dallas, Texas 75265

ABSTRACT

Phosphorus and boron implantation studies of laterally seeded silicon on silicon dioxide recrystallized by a scanning graphite strip heater are presented. Hall profiling has been used to obtain carrier concentration and mobility as a function of depth. The recrystallized silicon layer contains subgrain boundaries which slightly reduce dopant activation and carrier mobilities compared with bulk silicon values.

Composite structures consisting of laterally seeded recrystallized polysilicon films on insulating layers such as silicon dioxide grown on bulk silicon substrates have a tremendous potential in device applications. Such structures may, in principle, be used to make three-dimensional integrated circuits, dielectrically isolated high speed devices, solar cells, and other thin film devices. These films have certain advantages over silicon-on-sapphire (SOS) or conventional dielectrically isolated silicon. This technology is potentially less expensive than traditional dielectric isolation methods. Compared with SOS or silicon-on-quartz, these silicon-on-insulator (SOI) films are under less mechanical stress, which commonly results in a high density of stacking faults and in drastically altered carrier mobilities. Various directed energy sources such as scanned laser and electron beams have been employed to recrystallize the silicon films on insulating substrates (1). A particularly simple alternative is the use of a thin heated graphite strip swept mechanically across the surface (2).

Ion implantation is an extremely important method of selectively doping these films, as required in forming the source and drain regions in MOS transistors, for example. Although some structural and electrical properties of SOI layers have been reported (3), there have been few studies of ion implantation into such regrown films. The electrical activation and carrier mobilities for phosphorus and boron implants into silicon films regrown by a scanning graphite strip system are reported here as a function of dopant concentration and isochronal furnace anneal temperature. It is found that electrical activation and carrier

mobilities are comparable to those in bulk silicon and are much superior to those in the unrecrystallized films. Transmission electron microscopy (TEM) and selected area electron diffraction studies have been performed on the as-implanted and furnace annealed films. Residual implantation damage is observed, including dislocation loops and defect clusters. Segregation of implanted atoms along the subgrain boundaries is also observed.

Experimental Procedure

A recessed oxide 9100Å thick was grown on (100) Czochralski silicon wafers, with windows in the oxide exposing the underlying single crystal silicon. This step employed a modified LOCOS technique, which avoids "bird-beaking." An essentially planar surface of oxide and exposed crystalline silicon resulted, which was then covered by a 5000Å layer of polycrystalline silicon in a low pressure chemical vapor deposition (CVD) system (4).

The recrystallization technique is essentially the same as that described by Fan *et al.* (2). The samples were covered by a composite encapsulation layer to improve the stability of the liquid zone during zone melting and recrystallization. The cap consisted of a 500Å thermal oxide layer, covered by a 2 μm atmospheric pressure CVD silicon dioxide layer, and a final covering by 500Å of RF plasma-deposited silicon nitride. The thermally grown oxide appears to provide a smooth interface between the cap and the polysilicon and thereby improves the smoothness of the regrown film. The samples were placed on a stationary graphite strip which was resistively heated in a flowing argon ambient to approximately 1300°C in about 30s. A narrow graphite strip about 1 mm wide, placed 0.5 mm above the sample, was then heated

*Electrochemical Society Active Member.

up to produce a narrow molten region in the polycrystalline film over one of the "window" regions. The upper strip was then scanned over the sample surface at 1 mm/s using a motor driven system. In this procedure, the polysilicon over the window region is recrystallized first, with the underlying single crystal silicon substrate acting as a seed. This recrystallized region then assists in the lateral seeding of the silicon film as the melt zone is propagated over the silicon dioxide layer.

After completion of the recrystallization step, the encapsulant was removed using 1HF: 1H₂O. Electron channeling patterns using a scanning electron microscope (SEM) and selected area electron diffraction spot patterns using a TEM showed that the regrown films were (100) single crystal silicon. The surfaces were studied using SEM and Nomarski contrast optical microscopy. The roughness of the regrown films is about 200Å. The films contain large single crystal grains about 1 mm wide and extending indefinitely along the scan direction. There are a few small protrusions along some of the grain boundaries. The crystal grains contain low angle grain boundaries at about 25 μm intervals (5). These subgrain boundaries have been delineated by Seeco etching and have been examined by Nomarski optical microscopy. Cross-sectional SEM pictures were obtained to verify that the integrity of the underlying isolation oxide was maintained after the recrystallization of the polysilicon films.

Room temperature ³¹P+ (¹¹B+) implants were performed at 150 keV (70 keV) with the samples tilted 7° with respect to the ion beam normal to reduce channeling effects. The LSS peak for P (B) lies at 1888Å (2188Å) which is near the center of the 4500Å Si film. The amorphization threshold for P (B) room temperature implants is 6 × 10¹⁴ cm⁻² (8 × 10¹⁶ cm⁻²) (6). To study the concentration dependence of annealing, low (10¹³ cm⁻²), medium (10¹⁴ cm⁻²), and high (10¹⁵ cm⁻²) dose implants were studied. The 10¹⁵ cm⁻² ³¹P+ dose produces a surface amorphous layer (~3000Å) as determined by etching experiments (7). Thirty-minute conventional furnace anneals of the implanted samples were performed at various temperatures to study the temperature dependence of annealing. The anneals were performed in flowing forming gas (4% H₂, 96% N₂), using a 1000Å Si₃N₄ encapsulant layer to inhibit impurity out-diffusion during annealing.

Differential resistivity and ac Hall effect measurements in conjunction with successive layer removal were used to obtain the electrically active dopant profile and the carrier mobility variation with depth (8). Au-Sb (Au-B) contacts were deposited in a Van der Pauw geometry by evaporation and alloyed at 370°C for 10s in flowing hydrogen to produce ohmic contacts for these measurements. The layer removal was accomplished by chemical etching (750 HNO₃: 250 CH₃COOH: 1HF), providing an etch rate of ~300Å/min. The layer thicknesses removed were measured by a Sloan Dektak profilometer. For comparison, similar studies were performed on the unrecrystallized polysilicon films, and on bulk single crystal silicon. Secondary ion mass spectrometry (SIMS) was used to obtain the atomic profiles.

TEM and selected area electron diffraction studies were performed on the as-implanted and the annealed samples after thinning by chemical etching from the back of the wafers. Residual implantation defects and grain boundary segregation effects were studied in order to compare the structural information with the electrical data. For P, anneals at 500°, 700°, 900°, and 1000°C cover the entire range of temperatures for which there is significant annealing without appreciable redistribution of the P atoms (9).

Isochronal furnace annealing studies of B-implanted bulk Si by Seidel and MacRae (10) reveal three annealing temperature ranges. Below 500°C, activation increases because of annealing out of compensating damage centers, the fraction of substitutional B atoms remaining fixed, and mobilities being low. Between 500° and 600°C, a reverse annealing effect is observed with substitutional B atoms being replaced by Si interstitials, thereby improv-

ing hole mobilities. There is a high temperature annealing range between 700° and 1000°C where B atoms occupy substitutional sites by a mechanism involving the creation of Si vacancies and the movement of these vacancies to combine with B interstitials. In the present study, 30 min isochronal furnace anneals have been performed at 700°, 800°, 900°, and 1000°C for each dose to cover the high temperature annealing range described by Seidel and MacRae (10).

Results and Discussion

Temperature and dose dependence.—The donor concentration profiles and the electron mobility variation with depth in the recrystallized SOI layers are shown in Fig. 1-3 for P fluences in the range 10¹³-10¹⁵ cm⁻². The theoretical Irvin mobility (11) curve corresponding to a donor concentration profile after a 900°C, 30 min anneal is also shown. The sheet carrier concentrations for the various P doses and anneal temperatures are shown in Fig. 4. For low doses and slight lattice damage, there is appreciable activation even at 500°C, but for higher doses and lattice damage there is a considerable increase in electrical activation between 500° and 900°C. The greater redistribution for the higher doses, especially at 900° and 1000°C (Fig. 2 and 3), is consistent with the concentration and defect dependence of P diffusion observed in bulk Si implantation (12). A notable feature is that the electrical profile extends throughout the regrown film thickness, thereby attesting to the excellent crystalline quality of the regrown film even near the Si-SiO₂ interface. From the sheet concentration data in Fig. 4, the peak activation for the 10¹³ cm⁻² dose is seen to be at 700°C, while for the higher doses a 900°C anneal appears to be optimum. Also, the peak electrical activation for the 10¹⁴ cm⁻² dose is less than for a lower (10¹³ cm⁻²) or a higher (10¹⁵ cm⁻²) dose.

The mobility profiles are consistent with the electrical activation data. In ion-implanted Si, there is mobility degradation due to residual damage after annealing. There is a dip in the mobility profile corresponding to the peak of the electrical profile due to ionized impurity scattering, as seen from the Irvin curves. However, residual damage is also apparent in that the measured mobilities are lower than the Irvin mobilities. This discrepancy is greater for higher doses and for lower anneal temperatures, as expected. For donor concentrations of about 5 × 10¹⁶ cm⁻³, electron mobilities as high as 600 cm²/V-s are observed.

Similar studies have been performed for B with doses between 10¹³-10¹⁵ cm⁻² and anneal temperatures between 700°-1000°C. The results are essentially similar to those for P implants. The electrical profiles for a 10¹⁵ cm⁻² implant are shown in Fig. 5, and the sheet carrier concentration data are summarized in Fig. 6. The annealing and redistribution of B implants in bulk silicon have been extensively discussed by Hofker (13). The redistribution of B during annealing in Fig. 5 can be explained using the three-stream diffusion model of Chu and Gibbons (14). The model is valid for ion fluences below 10¹⁵ cm⁻² and anneal temperatures above 900°C. The model considers substitutional, electrically active B which diffuses slowly, B-vacancy pairs which are electrically inactive but diffuse fast, and positively charged vacancies. It may be noted that 100% activation is never achieved. This is consistent with observations in bulk Si, where amorphization is a prerequisite for complete activation of B. Tsai and Streetman (15) have shown that complete B activation in bulk Si is achieved by annealing at low temperature (550°C) if the Si is pre-amorphized by Si self-implants. This involves solid phase epitaxial regrowth from the underlying single crystal Si substrate. In order to examine if a similar technique could be applied to the SOI films, the recrystallized films were amorphized by low temperature (-110°C) multiple Si implants (4 × 10¹⁵ cm⁻² at 200 keV, 2 × 10¹⁵ cm⁻² at 150 keV, 1 × 10¹⁵ cm⁻² at 100 keV, 6 × 10¹⁴ cm⁻² at 50 keV) to produce a continuous 3500Å amorphous layer in a 4500Å thick regrown film. A 60 min 550°C anneal for a 70 keV, 10¹⁵ cm⁻² B implanted sample resulted in 100% activation with a sheet carrier mobility

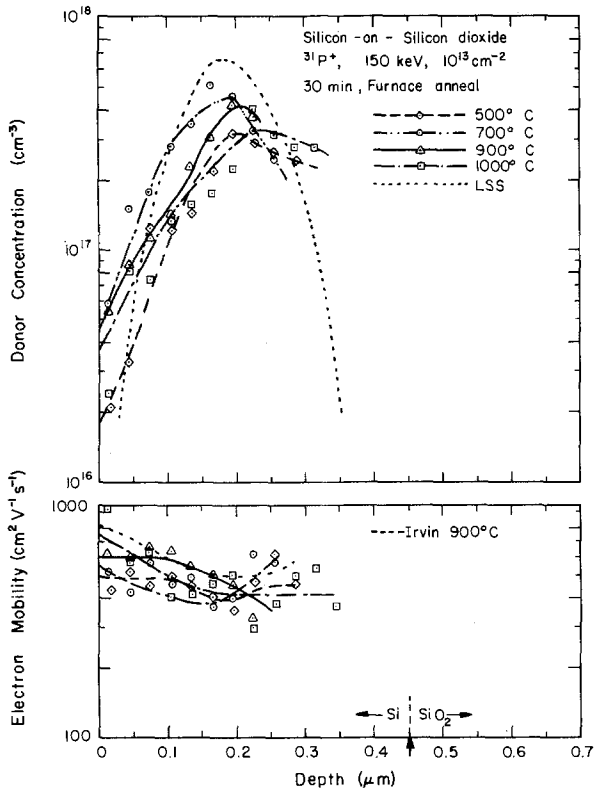


Fig. 1. Net donor concentration and electron mobility profiles obtained from differential sheet resistivity and Hall effect measurements for $^{31}\text{P}^+$ (10^{13} cm^{-2}) implanted silicon-on-oxide, after various isochronal anneals. The LSS distribution for the as-implanted $^{31}\text{P}^+$ is shown. The theoretical Irvin mobility profile in bulk Si is shown for the donor distribution measured after a 900°C anneal.

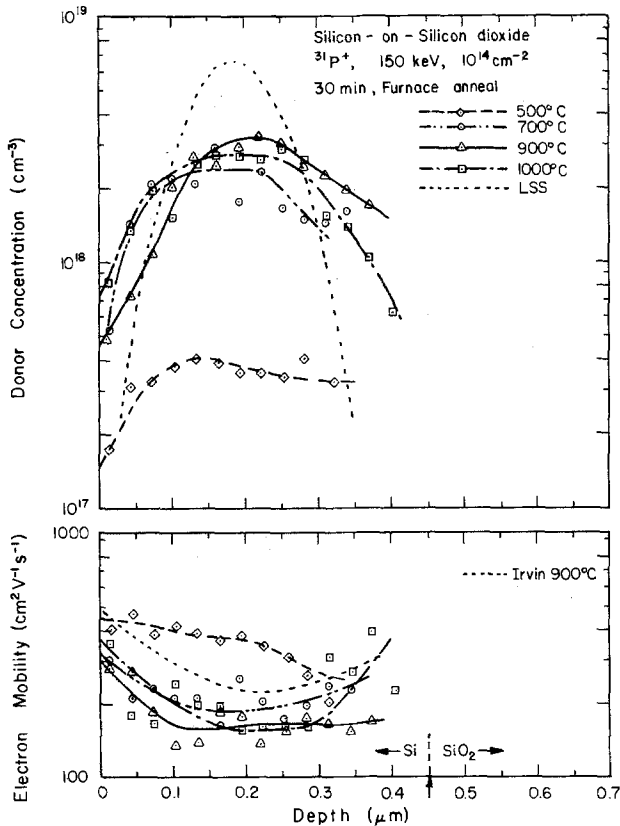


Fig. 2. Net donor concentration and electron mobility profiles for isochronal furnace annealed 10^{14} cm^{-2} , $^{31}\text{P}^+$ implanted silicon-on-oxide.

of $57 \text{ cm}^2/\text{V}\cdot\text{s}$. There is solid phase epitaxial regrowth from the underlying 1000Å thick single crystal Si layer accompanied by activation of the implanted B.

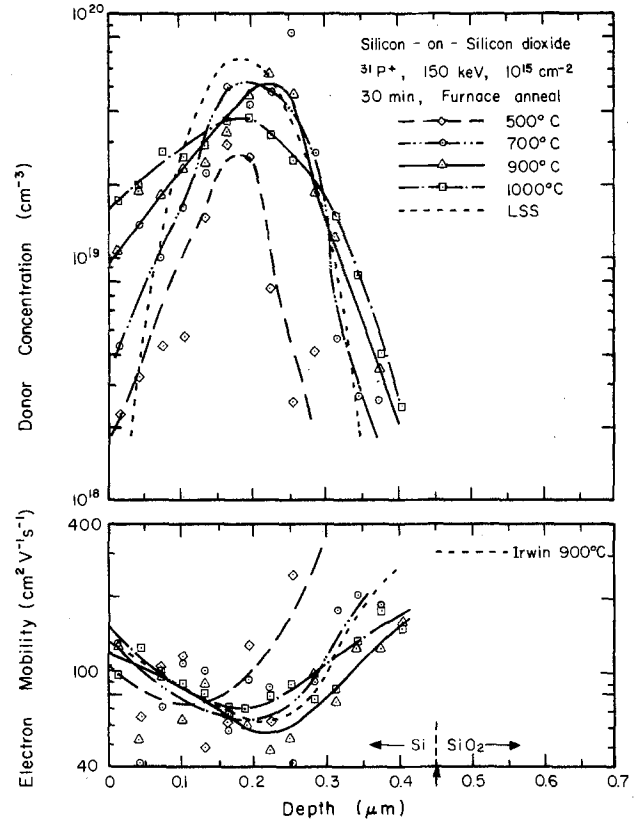


Fig. 3. Net donor concentration and electron mobility profiles for isochronal furnace annealed 10^{15} cm^{-2} , $^{31}\text{P}^+$ implanted silicon-on-oxide.

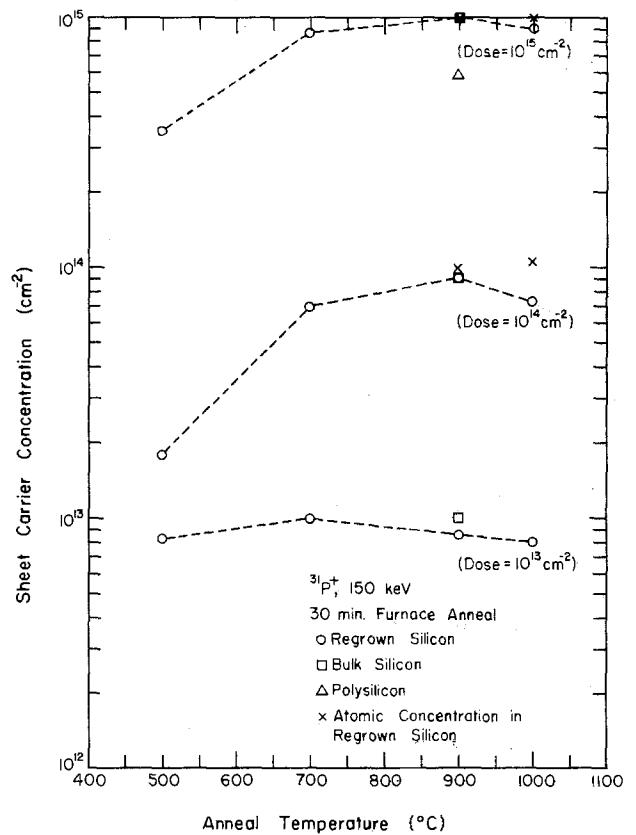


Fig. 4. Sheet carrier concentration for $^{31}\text{P}^+$ implanted silicon-on-oxide, bulk silicon, and polysilicon for 30 min furnace anneals. The doses are as indicated in parentheses. The x marks indicate the total $^{31}\text{P}^+$ atomic concentration in the films as determined by SIMS.

The mobility results suggest that the films are relatively free of stress. For example, compressive strain in the regrown silicon would lead to electron mobility degra-

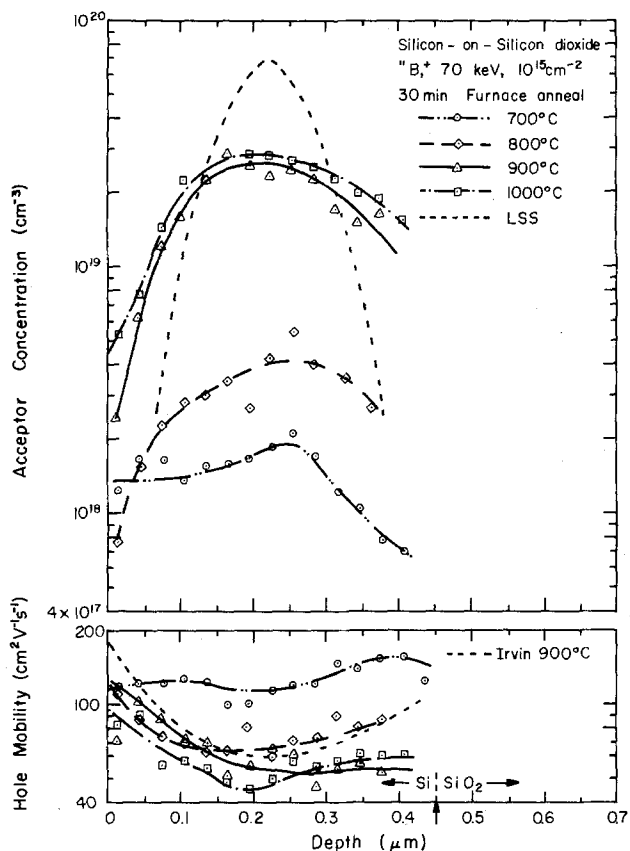


Fig. 5. Net acceptor concentration and hole mobility profiles for isochronal furnace annealed, $10^{15} \text{ cm}^{-2} \text{ }^{11}\text{B}^+$ implanted silicon-on-oxide.

dation and enhancement of hole mobilities (16). Conversely, a tensile stress in the films would cause electron mobility enhancement and a decrease of hole mobility. Since no such effects are observed, we conclude that the films are essentially stress-free. It may be noted that SOS films are under tremendous compressive stress, which causes a large density of stacking faults. Conversely,

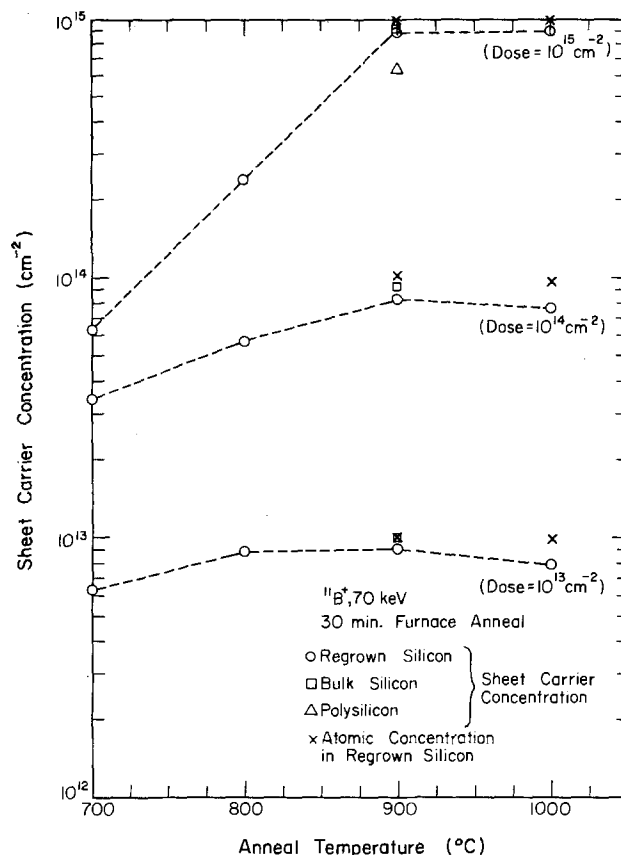


Fig. 6. Sheet carrier concentrations for $^{11}\text{B}^+$ implanted silicon-on-oxide, bulk silicon, and polysilicon for 30 min furnace anneals. The doses are as indicated in parentheses. The x marks indicate the total $^{11}\text{B}^+$ atomic concentration in the films as determined by SIMS.

silicon-on-quartz films are under tensile stress, which tends to cause cracking. In contrast, relatively stress-free films such as silicon-on-oxide have a high potential for device applications.

Structural properties of implanted SOI.—TEM and SEM studies of the P implanted films have been used to

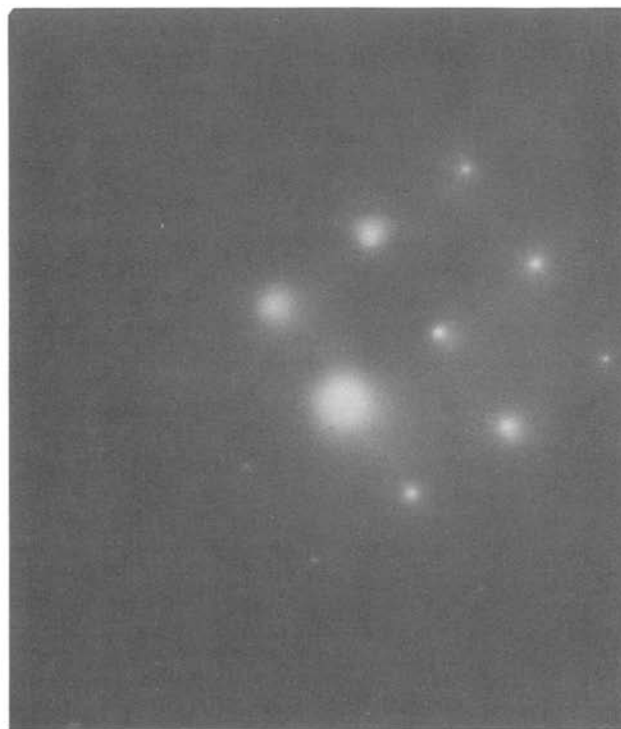
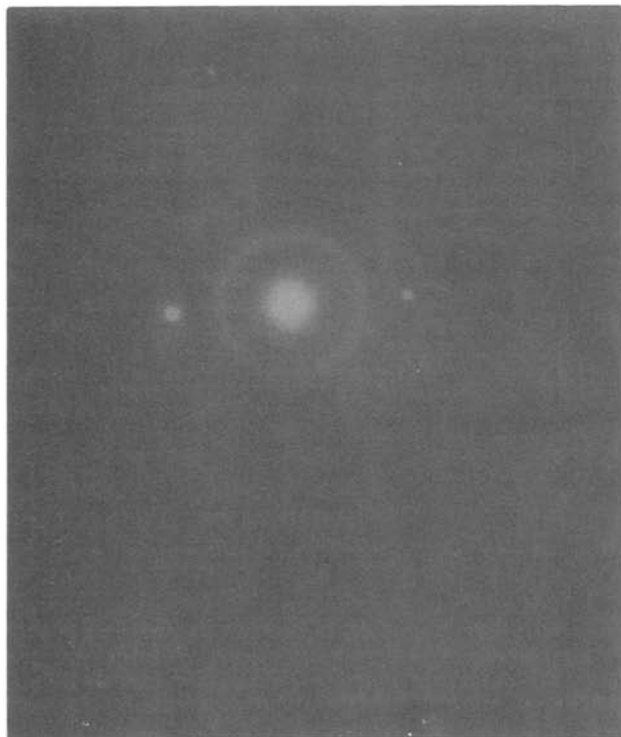


Fig. 7. Selected area electron diffraction pattern from as-implanted (10^{15} cm^{-2} , 150 keV, $^{31}\text{P}^+$) SOI film (left) and after a 30 min, 900°C furnace anneal (right).

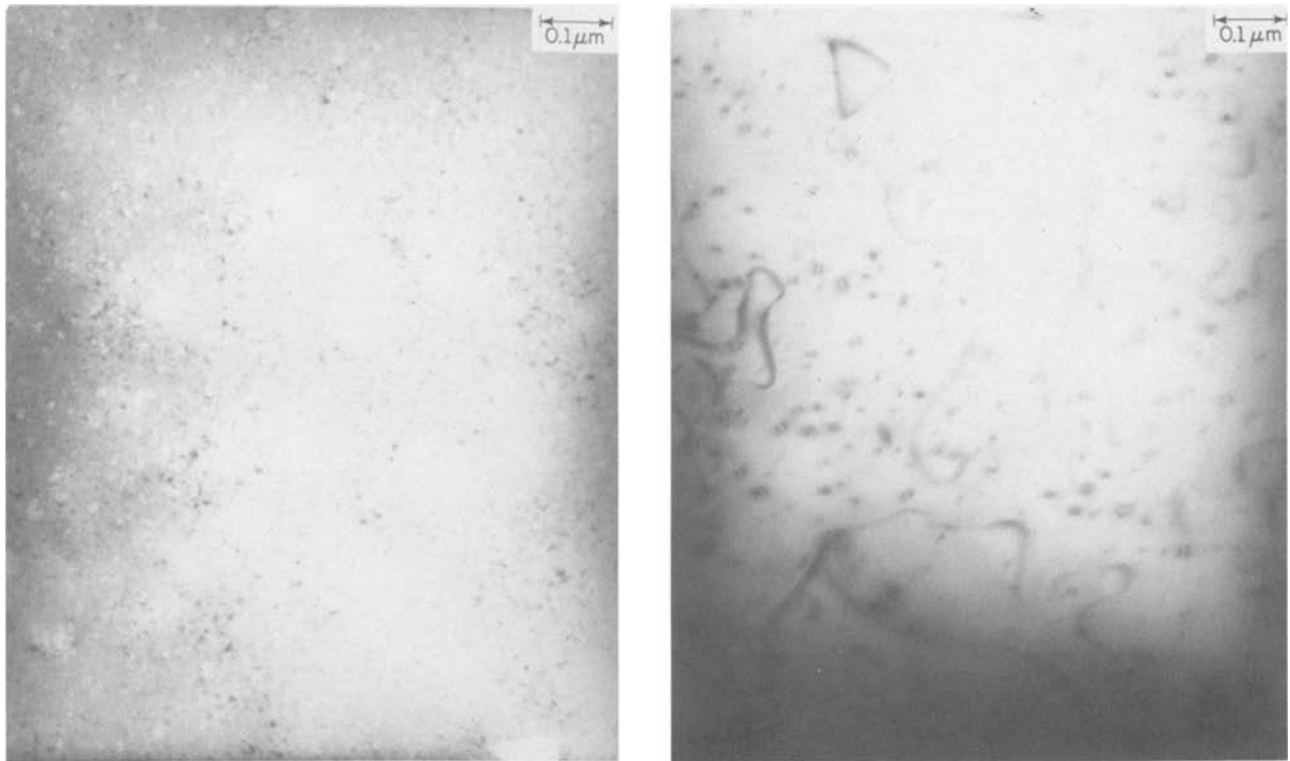


Fig. 8. Transmission electron micrograph of as-implanted (10^{15} cm^{-2} , 150 keV, $^{31}\text{P}^+$) SOI film (left) and after a 30 min, 900°C furnace anneal (right)

correlate their structural and electrical properties. For a 10^{14} cm^{-2} implant, electron channeling patterns can be observed in the as-implanted samples, indicating that the single crystal structure of the regrown films is retained. In contrast, for the 10^{15} cm^{-2} implant channeling patterns are not obtained from the as-implanted sample. However, upon annealing at 900°C for 30 min, the channeling pattern reappears. Selected area electron diffraction patterns obtained from the 10^{15} cm^{-2} implanted sample before and after annealing are shown in Fig. 7. For the as-implanted (10^{15} cm^{-2}) sample, the diffraction pattern is a superposition of a single crystal spot pattern and a diffuse ring pat-

tern, which indicates the presence of a highly damaged amorphous layer. Upon annealing, the ring pattern disappears, and the spot pattern alone is seen. There is solid phase epitaxial regrowth of the top amorphous layer from the underlying damaged but single crystal Si. TEM micrographs of an as-implanted and an annealed sample are shown in Fig. 8. Implanted P ions produce defect complexes and clusters during room temperature implantation. Upon annealing at high temperatures, these clusters coalesce into dislocation loops and networks. These residual defects cause the mobilities to be lower than would be expected from the Irvin mobilities. Since similar results

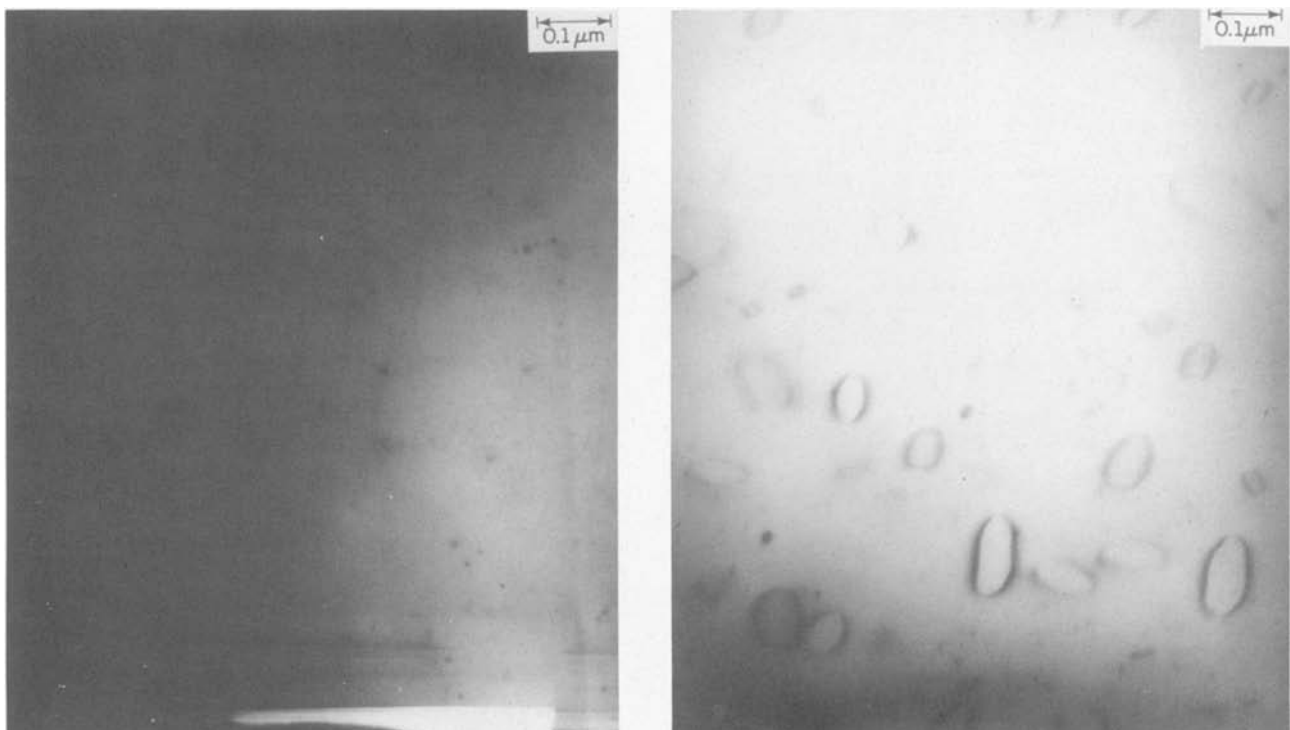


Fig. 9. Transmission electron micrograph of as-implanted (10^{15} cm^{-2} , 70 keV, $^{11}\text{B}^+$) SOI film (left) and after a 30 min, 1000°C furnace anneal (right)

have been observed in bulk silicon (7), the observed mobility degradation is apparently due to the implantation and annealing process and not because of the crystal growth technique. For 10^{13} cm $^{-2}$ implants, there is so little lattice damage that complete activation can be achieved at 700°C. For 10^{15} cm $^{-2}$ implants, complete activation is again achievable, although at a higher temperature because the epitaxial recrystallization of amorphized Si is accompanied by activation of the P in the regrown layer. It is for the intermediate dose (10^{14} cm $^{-2}$), which is insufficient to cause amorphization, that the residual defect density after annealing is rather high, leading to incomplete activation.

The B implantation produces point defects in Si such as vacancies and self-interstitials which have a high mobility at room temperature. Room temperature annealing causes these Frenkel type defects to coalesce into defect complexes including clusters such as those seen in Fig. 9 for a 10^{15} cm $^{-2}$ implant into the regrown Si. However, since B is a very light atom, the amorphization threshold for room temperature implants is very high (8×10^{16} cm $^{-2}$). The electron channeling pattern obtained from the as-implanted (10^{15} cm $^{-2}$) sample shows that the film is still single crystal. The defect clusters produced during a 10^{15} cm $^{-2}$ implant coalesce to form dislocation loops which remain even after annealing at 1000°C (Fig. 9). For anneals at 700° and 800°C, B precipitates along these dislocation networks, thereby leading to extremely poor activation, especially for the higher doses (Fig. 6). At higher temperatures, precipitated B atoms are released from the dislocation loops and occupy substitutional sites.

Comparison with bulk Si and polysilicon.—Since a 900°C anneal is optimal for implantation into the regrown Si, 900°C anneals were also performed for implanted polysilicon and bulk Si. For polysilicon, no profiles could be obtained for the 10^{13} cm $^{-2}$ and 10^{14} cm $^{-2}$ doses because of

the extremely high resistivity of the samples. Typical electrical profiles for 10^{15} cm $^{-2}$ P and B implants are shown in Fig. 10 and 11, respectively. SIMS atomic profiles are also shown for comparison. The sheet carrier concentration data for bulk Si and polysilicon are shown in Fig. 4 and 6 for P and B implants, respectively. B and P activation in the regrown Si films approaches bulk Si values for all doses. There is good agreement between the atomic and electrical profiles. At high anneal temperatures there is substantial dopant redistribution in the regrown Si films, accompanied by segregation effects along the subgrain boundaries (18). This becomes apparent in Fig. 12, which shows a typical subgrain boundary before and after a 1000°C, 30 min furnace anneal of a 10^{15} cm $^{-2}$ B implant. The subgrain boundaries become broader and darker after annealing, presumably because of B segregation along these boundaries. For the as-deposited polysilicon, the density of grain boundaries is so large that the electrical profiles lie significantly below those in bulk Si and recrystallized Si (Fig. 10 and 11). Trapping of carriers in a disordered region near the grain boundary can also contribute to lowering the sheet carrier concentration (18).

The variation of sheet carrier concentration with temperature in the regrown films can be understood in terms of two dominant mechanisms. Ion implantation damage is annealed out better at higher temperatures, leading to increased electrical activation. However, the increased redistribution at higher temperatures causes increased segregation at grain boundaries. This explains why for the 10^{14} cm $^{-2}$ and 10^{15} cm $^{-2}$ implants, the sheet carrier concentration is lower after annealing at 1000° than at 900°C. For the 10^{13} cm $^{-2}$ implant, the peak concentration occurs at a lower temperature (700°C) because the implantation damage is more easily annealed out. It is unlikely that the decrease in sheet carrier concentration after 1000°C anneals,

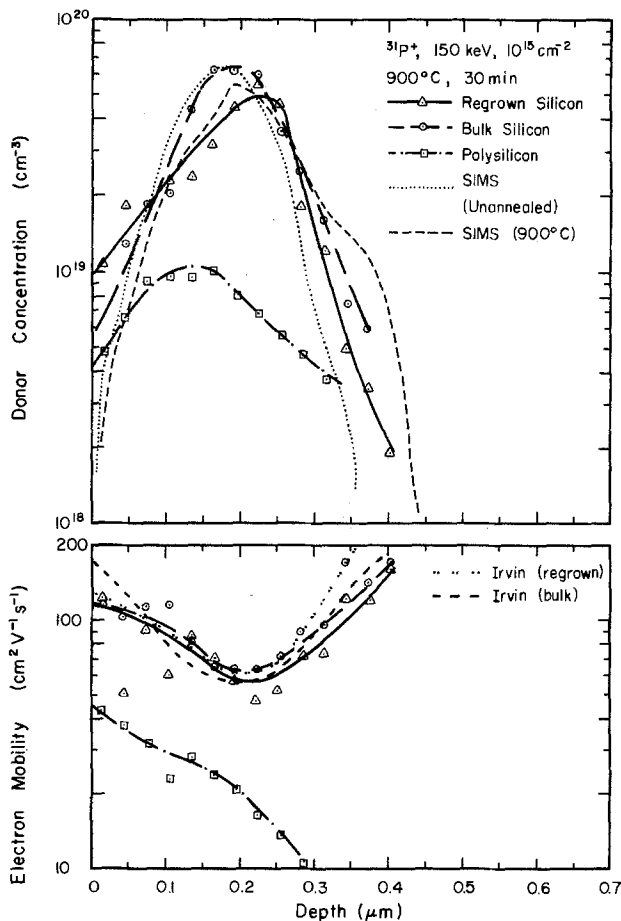


Fig. 10. Net donor concentration and electron mobility profiles in silicon-on-oxide, in bulk silicon, and in polysilicon for 10^{15} cm $^{-2}$ $^{31}\text{P}^+$ implants. SIMS atomic profiles are shown for comparison.

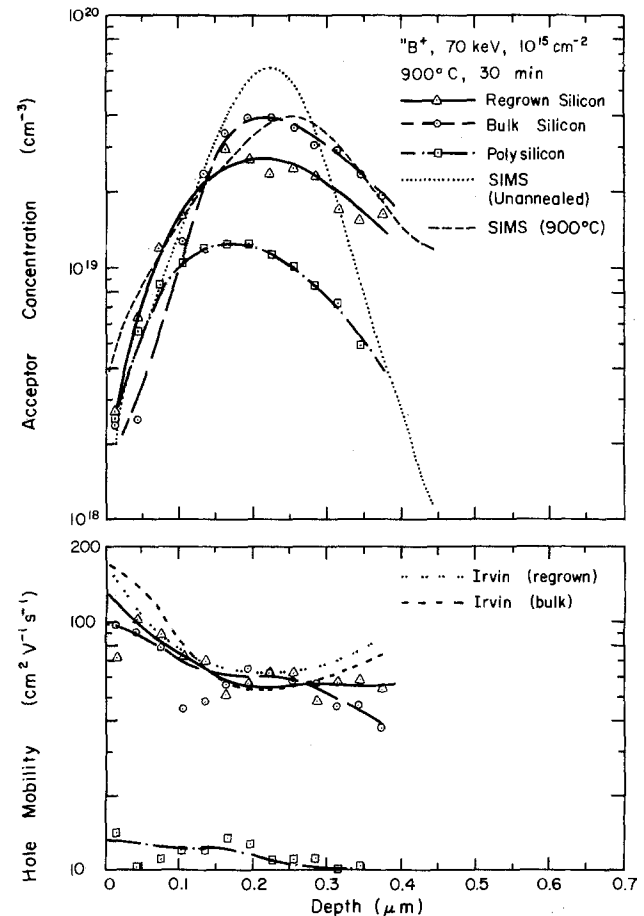


Fig. 11. Net acceptor concentration and hole mobility profiles in silicon-on-oxide, in bulk silicon, and in polysilicon for 10^{15} cm $^{-2}$ $^{11}\text{B}^+$ implants. SIMS atomic profiles are shown for comparison.

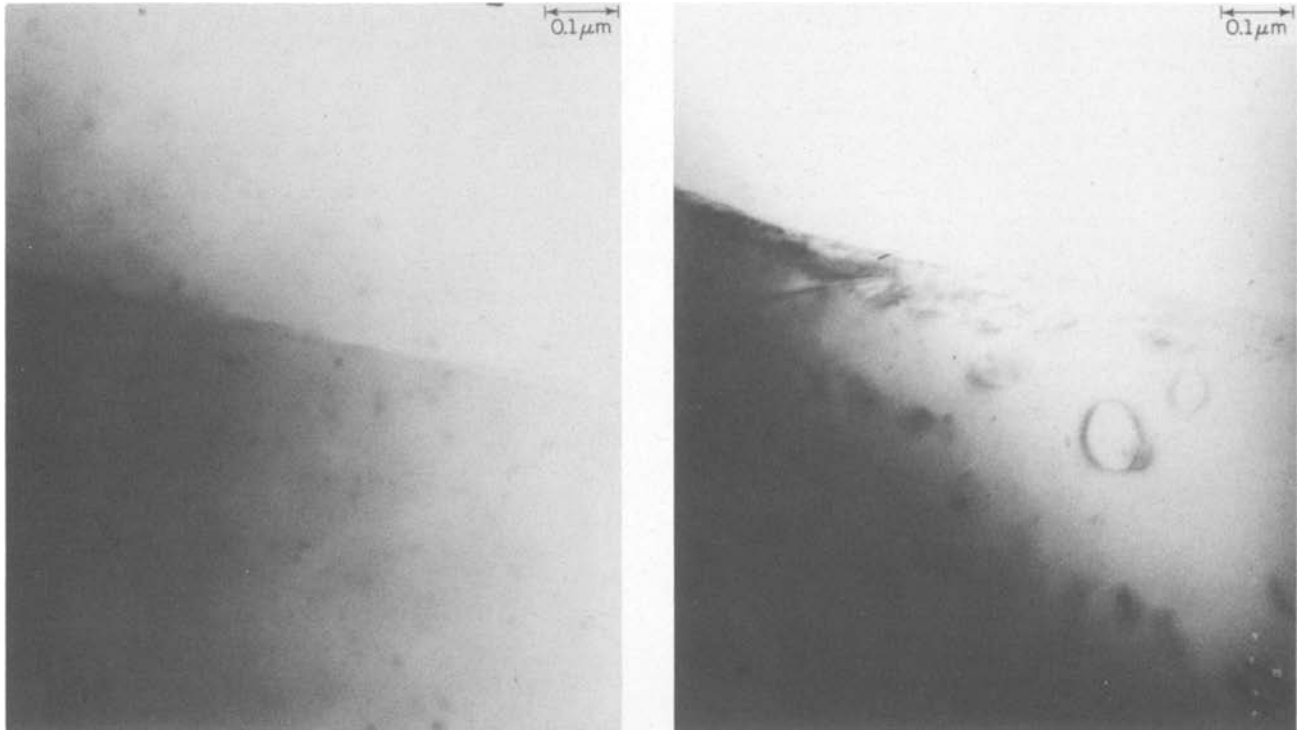


Fig. 12. TEM micrograph of a subgrain boundary in a 10^{15} cm^{-2} , 70 keV, $^{11}\text{B}^+$ implanted SOI sample before (left) and after (right) a 1000°C , 30 min furnace anneal.

relative to the 900°C anneals, is due to outdiffusion of impurities into the SiO_2 because the integrated SIMS atomic profiles indicate that there is little loss of dopants even at 1000°C .

The mobility profiles in Fig. 10 and 11 exhibit the general trend that mobilities are highest in bulk Si and extremely poor in the unrecrystallized polysilicon. A conduction model has recently been proposed by Wu and Yang (19) for polysilicon which includes scattering of majority carriers by grain boundaries and subgrain boundaries. In this model a potential barrier is created at grain boundaries along with a depletion region because of trapped charge and this causes majority carrier scattering. Such scattering at subgrain boundaries is apparently responsible for lower mobility in the recrystallized Si than in bulk Si. One can write the mobility in these SOI films, μ_{SOI} , as

$$\mu_{\text{SOI}}^{-1} = \mu_{\text{B}}^{-1} + \mu_{\text{GB}}^{-1} \quad [1]$$

where μ_{B} is the mobility in implanted bulk Si and μ_{GB} is the contribution of subgrain boundary scattering. The difference in mobility values for the regrown Si and bulk Si is most pronounced for the lowest dose, where ionized impurity scattering is least significant. Figure 13 shows the B electrical profiles for a 10^{13} cm^{-2} implant in recrystallized SOI and bulk Si. The acceptor concentrations at 1200Å are the same in bulk and regrown Si. Therefore, we expect the same ionized impurity scattering. We observe $\mu_{\text{B}} = 240 \text{ cm}^2/\text{V}\cdot\text{s}$ and $\mu_{\text{SOI}} = 180 \text{ cm}^2/\text{V}\cdot\text{s}$. Therefore, the subgrain boundary contribution to mobility is found to be $\mu_{\text{GB}} = 720 \text{ cm}^2/\text{V}\cdot\text{s}$. In polysilicon, the hole mobilities are extremely poor because of the high density of grain boundaries. The further degradation of mobilities close to the Si-SiO₂ interface (Fig. 10 and 11) is attributable to a high density of defects near the interface in the as-deposited films.

Summary

Lateral epitaxy by seeded solidification using a moving graphite strip heater has been used to produce single crystal silicon films on silicon dioxide. Electron channeling patterns, TEM micrographs, and selected area electron diffraction patterns all show that the regrown films are single crystal. However, the films contain low angle

grain boundaries, as determined by SEM and Seeco etch techniques. Donor concentrations and electron mobilities measured as a function of depth by the double ac Hall effect method show that a 30 min furnace anneal at 700°C is optimum for low (10^{13} cm^{-2}) phosphorus doses, while for

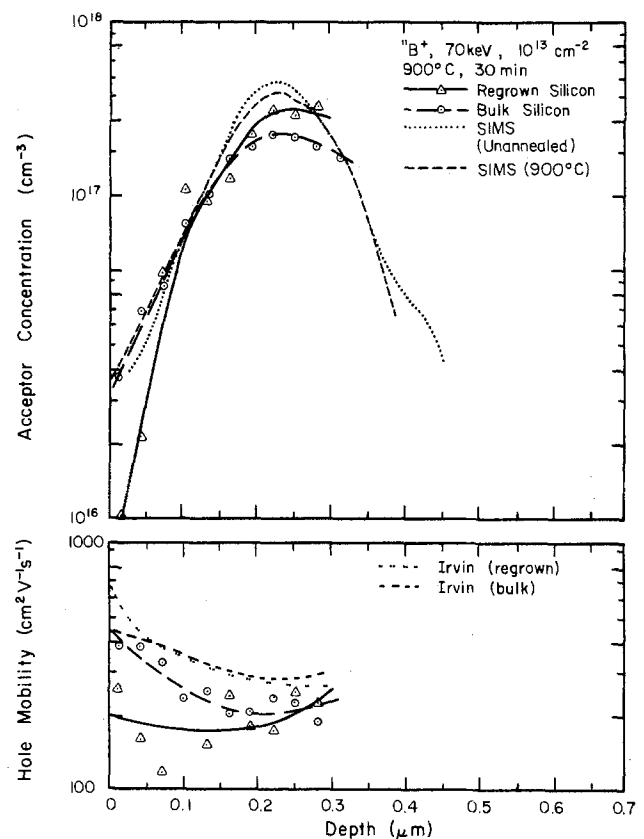


Fig. 13. Net acceptor concentration and mobility profiles in silicon-on-oxide and in bulk silicon for 10^{13} cm^{-2} $^{11}\text{B}^+$ implants. The theoretical Irvin mobilities in bulk silicon are shown corresponding to the acceptor distributions in the regrown silicon films and in bulk silicon. SIMS atomic profiles are shown for comparison.

higher doses, a 900°C anneal gives the highest activation. Phosphorus atoms are activated throughout the entire film thickness, with no mobility degradation near the silicon-silicon dioxide interface. TEM micrographs reveal the presence of residual implantation damage such as dislocation loops even after annealing at 900°C. These recrystallized films have electrical activation and mobilities comparable to bulk silicon, and are considerably superior to that in unrecrystallized polysilicon films. The slightly lower activation in the recrystallized films compared to that in bulk silicon is apparently due to phosphorus segregation and carrier trapping effects at subgrain boundaries in the regrown films, and grain boundary scattering causes slightly lower electron mobilities in these films compared with bulk silicon. Thus the subgrain boundaries in the silicon on silicon dioxide films have a slightly deleterious effect on carrier transport and electrical activation.

The annealing behavior of boron acceptor implants into silicon-on-insulator films recrystallized by seeded lateral epitaxy has been studied for doses of 10^{13} - 10^{15} cm⁻². A 30 min furnace anneal at 900°C is optimum. Complete activation at low temperatures (550°C) is achievable if the boron profile lies in an amorphized layer not extending throughout the entire regrown film thickness. In all cases electrical activation is observed throughout the entire regrown film thickness. TEM studies reveal clusters and dislocation loops as residual implantation damage even after annealing at 1000°C. This residual damage leads to mobility degradation and incomplete activation. The presence of subgrain boundaries in the regrown silicon films decreases carrier mobilities by introducing grain boundary scattering, and reduces sheet carrier concentrations by causing impurity segregation and carrier trapping. However, the effect of the residual subgrain boundaries on mobility is not severe, indicating that relatively stress-free device quality films are obtained. Hole mobilities and electrical activation values in the regrown film approach bulk silicon values. In the as-deposited polysilicon films, by contrast, electrical activation and hole mobilities are extremely poor.

Acknowledgments

This work was supported by the Office of Naval Research under Contract N00014-81-K-0431, and by the Joint Services Electronics Program (U.S. Army, U.S. Navy, U.S. Air Force) under Contract N00014-79-C-0424.

Manuscript submitted June 6, 1983; revised manuscript received Feb. 21, 1984.

The University of Texas at Austin assisted in meeting the publication costs of this article.

REFERENCES

- The following are representative of several different approaches: K. F. Lee, J. F. Gibbons, K. C. Saraswat, and T. I. Kamins, *Appl. Phys. Lett.*, **35**, 173 (1979); J. A. Knapp, S. T. Picraux, K. Lee, J. F. Gibbons, T. O. Sedgwick, and S. W. Depp, *Proc. Mater. Res. Soc. (1981)*, H. W. Lam, A. F. Tasch, T. C. Holloway, K. F. Lee, and J. F. Gibbons, *IEEE Electron Dev. Lett.*, **ed1-1**, 99 (1980).
- J. C. C. Fan, M. W. Geis, and B-Y. Tsaur, *Appl. Phys. Lett.*, **38**, 365 (1981); B-Y. Tsaur, J. C. C. Fan, M. W. Geis, D. J. Silversmith, and R. W. Mountain, *ibid.*, **39**, 561 (1981); J. C. C. Fan, B-Y. Tsaur, R. L. Chapman, and M. W. Geis, *ibid.*, **41**, 186 (1982).
- R. F. Pinizzotto, H. W. Lam, and B. L. Vaandrager, *ibid.*, **40**, 388 (1982); E. W. Maby, and D. A. Antoniadis, *ibid.*, **40**, 691 (1982); B-Y. Tsaur, J. C. C. Fan, and M. W. Geis, *ibid.*, **41**, 83 (1982).
- The initial sample preparation was done at Texas Instruments, Inc., Dallas.
- M. W. Geis, H. I. Smith, B-Y. Tsaur, J. C. C. Fan, E. W. Maby, and D. A. Antoniadis, *Appl. Phys. Lett.*, **40**, 158 (1982).
- F. F. Morehead, B. L. Crowder, and R. S. Title, *J. Appl. Phys.*, **43**, 1112 (1972).
- M. Y. Tsai, University of Illinois, CSL Report R-824.
- W. V. McLevige, P. K. Chatterjee, and B. G. Streetman, *J. Phys. E.*, **10**, 335 (1977).
- K. Uda and M. Kamoshida, *J. Appl. Phys.*, **48**, 18 (1977).
- T. E. Seidel and A. V. MacRae, in "Ion Implantation in Semiconductors," F. H. Eisen and L. F. Chadderton, Editors, pp. 149-154, Gordon and Breach, London (1971).
- J. C. Irvin, *Bell Syst. Tech. J.*, **41**, 387 (1962).
- T. Hirao, K. Inoue, S. Takayanagi, and Y. Yaegashi, in "Ion Implantation in Semiconductors," F. Chernow, J. A. Borders, and D. K. Brice, Editors, pp. 711-726, Plenum Press, New York (1976).
- W. K. Hofker, *Philips Res. Rept.*, Suppl. 8, 1 (1975).
- A. Chu and J. F. Gibbons, in "Ion Implantation in Semiconductors," F. Chernow, J. A. Borders, and D. K. Brice, Editors, pp. 1-9, Plenum Press, New York (1976).
- M. Y. Tsai and B. G. Streetman, *J. Appl. Phys.*, **50**, 183 (1979).
- B-Y. Tsaur, J. C. C. Fan, and M. W. Geis, *Appl. Phys. Lett.*, **40**, 322 (1982).
- F. Cembali, R. Galloni, M. Servidori, and F. Zignani, in "Ion Implantation in Semiconductors," F. Chernow, J. A. Borders, and D. K. Brice, Editors, pp. 471-482, Plenum Press, New York (1976).
- J. Murota and T. Sawai, *J. Appl. Phys.*, **53**, 3702 (1982).
- C. M. Wu and E. S. Yang, *Appl. Phys. Lett.*, **40**, 49 (1982).

Crystal Damage during CV Profiling

J. van de Ven

Faculty of Science, R.I.M., Department of Solid State III, Catholic University, Toernooiveld, 6525 ED Nijmegen, The Netherlands

ABSTRACT

After CV measurements of GaAs and highly doped Si, using mercury as a Schottky contact, crystal damage on the diode electrode sometimes occurs as can be made visible by selective etching techniques. The presence of this damage appears to be related to the magnitude of the applied bias voltage and to a slight contamination of the mercury with dust particles. The penetration depth has been observed to be in the order of a few hundred nanometers.

CV measurement of semiconductor structures has become a very important technique for fast profiling of carrier concentrations. It has been shown by various authors that for silicon and gallium arsenide mercury can be applied as cathodic as well as anodic Schottky contact (1-3). This method always has been considered as being nondestructive, but the present results point out that care has to be taken as to this assumption because it appeared rather

easy to create surface damage on the crystal during the CV measurement. This is not evident by normal inspection, but by using sensitive defect revealing methods the damage can be made visible.

Experimental

Measurements were mainly performed on n-type Si-doped GaAs with doping levels ranging from 5×10^{16} to 2

$\times 10^{18} \text{ cm}^{-3}$, but also some Sb- and P-doped Si samples were used. Various surface pretreatments were used: For GaAs, anodic polishing followed by a 4 w/o HCl/H₂O dip (4) or a H₂SO₄/H₂O₂/H₂O (vol. 3:1:1)-etch. Si crystals received a final 10 w/o HF dip. After CV measurement the samples were also cleaned in different ways, e.g., with a HCl or HF dip, ultrasonic acetone bath, etc.

The CV measurements themselves were performed using either the Hg-1 single mercury probe from MSI-electronics or a homemade double mercury probe. In both cases contact with the crystal was made by evacuating the vacuum channels on the probe head. The mercury used was "suprapur" from Merck and was regularly refreshed.

To reveal possible defects on the crystal surface DS and DSL etchants (5) have been used as well as anodic dissolution in EDTA electrolyte of pH ~ 8.5 (6).

Results and Discussion

It was found in several cases after CV measurements of GaAs and Si, that the reverse-biased diode contact could be made visible by selective etching methods. Usually this crystal damage appeared in the form of a ring on the surface, whereas inside as well as outside the ring the surface morphology was similar (Fig. 1). As revealed with a step profiler, the ring appears as an elevation on the surface after DSL or anodic defect revealing, but as a depression after DS etching. The formation of the ring has been observed on GaAs samples, Si doped in the range 5×10^{16} - $2 \times 10^{18} \text{ cm}^{-3}$, and on some heavily doped n-type Si samples. A condition for this turned out to be that the maximum applied bias voltage during profiling should at least have approached the breakdown voltage for the anodic diode contact. It was found that for highly doped material the ring could be revealed more easily. After using the double mercury probe, the large contact could only be made visible when the voltage was reversed during the CV measurement, thereby actually turning this contact into the reverse-biased diode contact. Similar results were obtained when a thin, $\sim 100\text{\AA}$, oxide layer on top of the GaAs sample was present. In some cases it was also noticed that after etching, the reverse-biased diode showed up as a rough area delimited by a ring, but this

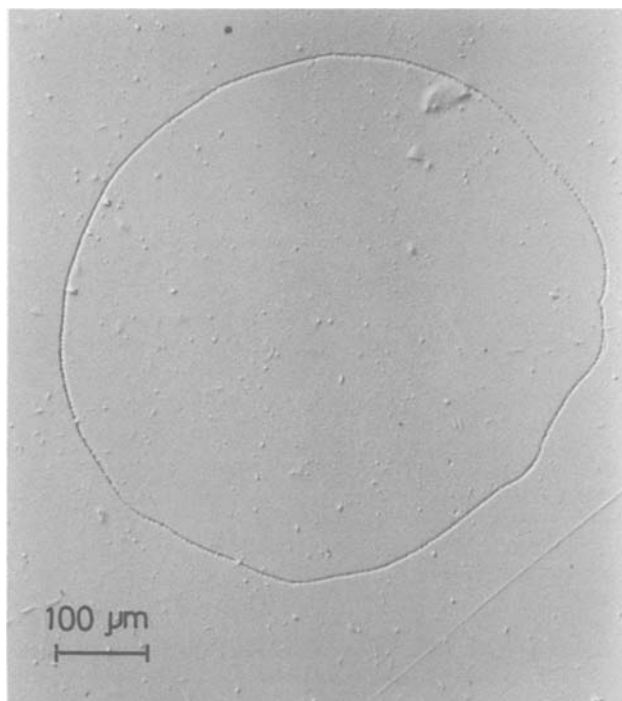


Fig. 1. Nomarski interference microscopy picture of the diode ring after CV measurements on 10^{18} cm^{-3} Si-doped GaAs. Selective etching has been performed with $D_{1:4}S_{1/1}$ [notation defined in Ref. (5)], etch depth $\sim 2 \mu\text{m}$. The ring is a depression of 500-1000 \AA .

kind of damage could be attributed to incomplete cleaning of the sample after CV measurement. Recommended in this respect is an ultrasonic acetone bath followed by a 4 w/o HCl dip and extensive rinsing with water.

In order to study the penetration depth of the crystal damage, electrochemical sequence etching on GaAs was performed. First thin layers of the sample were anodically polished off, followed by anodic defect revealing (6). For a 10^{18} cm^{-3} Si-doped GaAs sample which had been at the breakdown voltage of $\sim 2\text{V}$ for about 30s (which in itself is no extreme condition), the rim of the reverse-biased diode could still be observed after removal of $0.2 \mu\text{m}$ of material, but it had disappeared after anodically polishing off $0.5 \mu\text{m}$ of material. This shows that in this case the penetration depth of the effect is at least several tenths of microns, which lies in the same order of magnitude as the depletion width at breakdown for this sample.

Closer inspection of the ring, produced after anodic defect etching, with SEM showed a twisted structure (Fig. 2). This structure corresponds with the microstructure of the (perspex) probe head.

Careful inspection of the contacts showed that small dust particles contaminate the mercury and gather at the contact edges when vacuum is applied. These contaminations cannot be removed by simply replacing the mercury, but require extensive cleaning of the entire probe head. After such cleaning they will rapidly gather again, however, even when working under dust poor conditions. The presence of these particles proved to be a critical factor in the appearance of the ring.

From the former observations we can conclude about the origin of the crystal damage, that:

1. It is not merely mechanical, for then the applied bias voltage would not be critical and defects should be seen directly on the surface without defect etching,
2. It is not a simple matter of an amalgamating reaction, for then it cannot be explained (i) that only the edge of the contact would be visible, (ii) that when a thin oxide layer is left on the surface it looks undamaged after profiling, whereas on the crystal itself the reverse-biased diode ring can be made visible, and (iii) that the damage could not be seen on the polished surface before defect revealing. In addition, neither Si nor As have any tendency to dissolve in Hg, whereas pure elementary Ga only dissolves slightly (7, 8),
3. It is related to the presence of dust particles at the surface of the mercury diode biased up to breakdown conditions.

Therefore the conclusion is that at breakdown voltages an "avalanche effect" takes place at the diode edge, most probably supported by the presence of dust particles. The precise nature of the defect is unknown. It may be either caused by local introduction of impurities from the contact into the crystal lattice, possibly supported by a local heating up during the avalanche period, or it can be

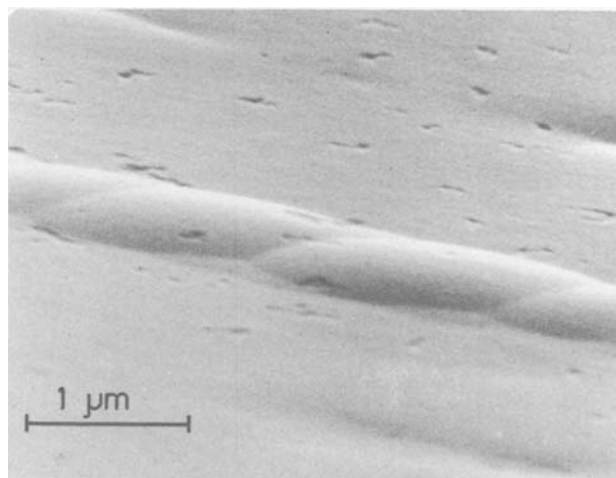


Fig. 2. Detail of Fig. 1; SEM photograph

formed by a local disordering of the lattice under the avalanche conditions. Anyhow, the appearance of an elevated ring on GaAs after DSL and anodical defect etching indicates an increased recombination center density in the damage region. The fact that a depression is found after DS etching indicates that a strong change in chemical potential has also taken place, because otherwise this defect revealing method would be expected to produce an elevation on the defect as well.

Summary

As under normal working conditions voltages may easily approach breakdown values and because small contamination of the mercury contacts will normally appear as well, crystal damage during CV profiling always may occur, especially when dealing with higher doped samples. Therefore, special attention to this effect should be given when dealing with highly doped epilayers which have to be used for further processing. As a positive side effect it can be mentioned that the contact surface area of the reverse-biased diode contact can be evaluated accurately after measurement. It should be stressed here that the CV results themselves are not influenced noticeably by the crystal damage.

Acknowledgments

The author wants to thank Dr. J. L. Weyher for assistance in performing and evaluating the DSL etching. Thanks are also due to Prof. Dr. J. Bloem and Dr. L. J.

Giling for critical reading of the manuscript and helpful suggestions.

This work is part of the research program of the *Stichting voor Fundamenteel Onderzoek der Materie* (Foundation for Fundamental Research on Matter) and was made possible by financial support from the *Nederlandse Organisatie voor Zuiver-Wetenschappelijk Onderzoek* (Netherlands Organization for the Advancement of Pure Research).

Manuscript submitted June 6, 1983; revised manuscript received Dec. 28, 1983.

Catholic University assisted in meeting the publication costs of this article.

REFERENCES

1. P. J. Severin and G. J. Poedt, *This Journal*, **119**, 1384 (1972).
2. M. Binet, *Electron. Lett.*, **11**, 580 (1975).
3. M. Binet, *Acta Electron.*, **23**, 53 (1980).
4. C. R. Elliot and J. C. Regnault, *This Journal*, **127**, 1557 (1980).
5. J. L. Weyher and J. van de Ven, *J. Cryst. Growth*, **63**, 285 (1983).
6. A. Yamamoto and S. Yano, *This Journal*, **122**, 260 (1975).
7. M. Hansen, Editor, "Constitution of Binary Alloys," pp. 166, 744, 836, McGraw-Hill Book Co., New York (1958).
8. R. P. Elliot, Editor, "Constitution of Binary Alloys," First Supplement, p. 447, McGraw-Hill Book Co., New York (1965).

The Influence of High Pressure Oxidation on Boron Redistribution in LOCOS Structures

P. Deroux-Dauphin

Thomson-EFCIS, BP 217, 38019 Grenoble Cedex, France

J. P. Gonchond

CNET-CNS, Chemin du Vieux Chêne, BP 98, 38243 Meylan, France

ABSTRACT

As device dimensions approach 1 μm , narrow channel effects are becoming more and more critical. In a LOCOS structure, these effects are essentially due to lateral diffusion of the field threshold implant during oxidation. EBIC, SIMS, and preferential chemical etching have been used to investigate the effects of high pressure oxidation on lateral and in-depth diffusion of boron. It has been found that lateral and vertical diffusion of boron is reduced by 0.20 and 0.33 μm , respectively, when the pressure increases from 1 to 20 bar. For a 3 μm linewidth test device, the observed reduction of the lateral diffusion of boron with increased pressure is shown to correspond to a 22% increase in the width of the active regions. The actual shape of the boron-doped region under the bird's beak has been deduced from EBIC measurements and preferential chemical etching within 0.06 μm accuracy. In addition, the boron segregation coefficient at the Si/SiO₂ interface is given as a function of pressure.

MOS devices in integrated circuits are becoming ever smaller in an aim to achieve higher device density and lower cost. However, many difficulties have arisen from the reduction of device size (1). One of these difficulties emanates from lateral diffusion of boron, which is used as a channel-stop implant in coplanar structures (2). Redistribution of the boron field implant plays an important role in narrow-channel effects (3) and influences the capacitance value between the n⁺ sidewall region and the P region at the field edge (4). Circuit designers require knowledge of such phenomena to draw up valid design rules.

Lee and Dutton have presented a 2-D approach to boron impurity profiles after oxidation at atmospheric pressure (5).

This paper presents measurements of the actual extent, both lateral and vertical, of the boron-doped region under

Key words: bird's beak, electron beam induced current, secondary ion mass spectroscopy.

the bird's beak in samples oxidized under high pressure. Test devices were fabricated, and three main characterization techniques used: electron-beam-induced conductivity (EBIC), secondary ion mass spectroscopy (SIMS), and preferential chemical etching. According to our measurements, lateral diffusion of the boron implant is reduced by 0.20 μm and vertical diffusion by 0.33 μm when the pressure is increased from 1 to 20 bar. The segregation coefficient of boron at the Si/SiO₂ interface has also been investigated as a function of pressure.

Experimental

Sample preparation.—Test devices for determining the lateral diffusion of boron were fabricated according to the classical coplanar process outlined in Fig. 1. CZ, n-type <100> silicon wafers of 10 $\Omega \cdot \text{cm}$ resistivity were used. The wafers were oxidized at 950°C in dry ambient to grow a 0.025 μm pad oxide. A silicon nitride film, 0.1 μm thick, was deposited by LPCVD. The wafers were subsequently

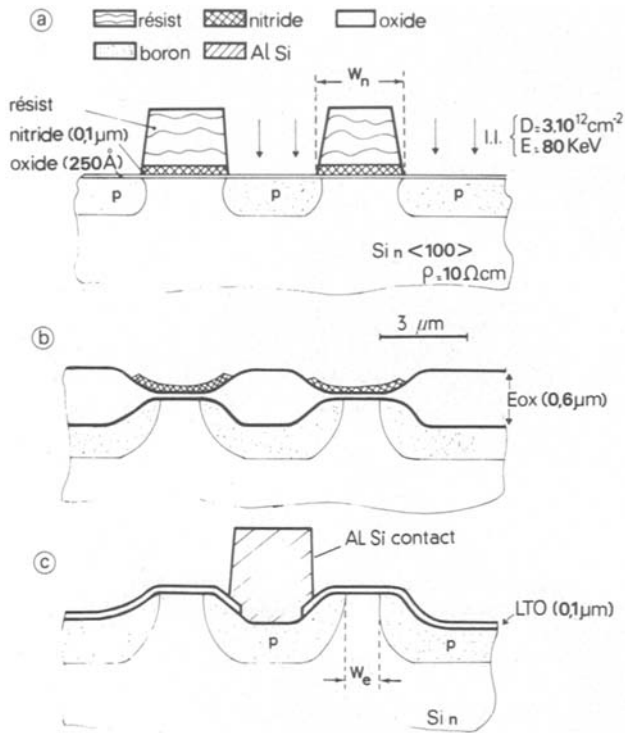


Fig. 1. Fabrication sequence of the test device investigated in this work

coated with photoresist, and the nitride film was selectively plasma etched so that a repetitive pattern of nitride stripes of width W_n was obtained (see Fig. 1a).

The samples were then implanted with boron at a dose of $3 \cdot 10^{12} \text{ cm}^{-2}$ and an energy of 80 keV. The photoresist was removed, and, after cleaning, the wafers were oxidized in a wet O_2 ambient at a constant temperature of 920°C and under various time-pressure conditions, as summarized in Table I.

For each pressure, P_{ox} , the corresponding oxidation time, t_{ox} , was chosen so that a $0.6 \mu\text{m}$ thick SiO_2 layer was grown. The nitride film was then etched off in orthophosphoric acid at 180°C , and the thick oxide was completely removed in buffered HF. Following that, a $0.1 \mu\text{m}$ film of low temperature oxide (LTO) was deposited, intended to reduce the reverse current of p-n junctions. Finally, aluminum electrodes were defined, yielding the structure shown in Fig. 1c.

Experimental details.—The distances to be measured were W_n (see Fig. 1a) and W_e (see Fig. 1c). The lateral diffusion of boron is then deduced from these measurements using the relation

$$X_{j1} = \frac{1}{2} (W_n - W_e) \quad [1]$$

In other words, our X_{j1} measurements are based on the exact values for W_n and W_e derived according to the methods described below.

SEM measurement of W_n .—Special precautions had to be taken in this measurement. First, we must point out that W_n represents the actual width of the nitride stripes, as shown in Fig. 1a, and not the width of the photomask used for etching the resist. Thus, W_n was measured just after etching of the resist film. Second, we had to be sure that W_n and W_e referred to the same nitride stripe on our test devices; otherwise, confusion could result from possible fluctuations of W_n on a given chip or from chip to chip. To get around this problem, a linewidth optical sys-

Table I. Time (t_{ox}) and pressure (P_{ox}) conditions used in our oxidation process

P_{ox} (bar)	1	5	10	15	20
t_{ox} (min)	290	56	32	25	19

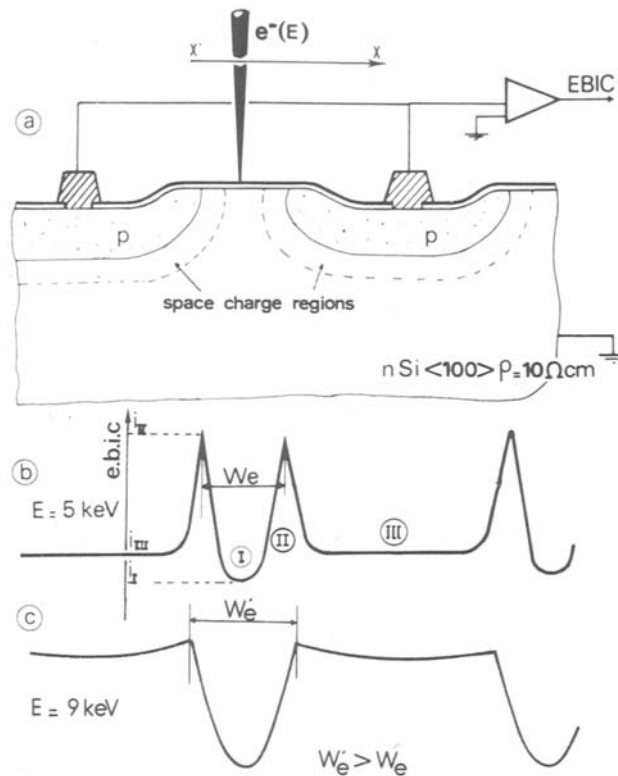


Fig. 2. a: Cross-sectional drawing of the sample structure investigated by EBIC. b and c: EBIC signal induced by the electron beam swept along $x'x$ in Fig. 2a and corresponding to beam energies of 5 and 10 keV, respectively.

tem measurement from Leitz was used to delineate an area on each wafer in which variations in linewidth are less than $0.05 \mu\text{m}$. The wafers were then cleared in this area and subsequently observed in a calibrated scanning electron microscope to check the optical measurement.

EBIC measurement of W_e .—The width W_e was measured using the EBIC technique in a Jeol 35C microscope operated in the line-scan mode. As shown in Fig. 2a, an electron beam of energy E is swept along $x'x$ perpendicular to the surface of the sample. The current induced by the electron beam in the p-n junctions is collected in an external circuit via a 10^7 - 10^8 V/A preamplifier.

Figure 2b shows the EBIC response of the p-n junctions at a beam energy of 5 keV. This signal exhibits three distinct areas.

Area I.—This is located between two adjacent p-type regions, i.e., outside the space-charge regions, and gives rise to a low induced current i_I corresponding to the diffusion part of the EBIC signal.

Area II.—This is characterized by a maximum induced current i_{II} and corresponds to the nearly vertical space-charge region at the edge of the p-n junctions.

Area III.—This corresponds to the EBIC response i_{III} in the p-n horizontal junction.

In order to explain the dependence of the EBIC signal on the beam energy E , we shall consider both the range of electrons in silicon given by (6)

$$R = 0.01837 E^{1.75} \frac{R(\mu\text{m})}{E(\text{keV})} \quad [2]$$

and the junction depth X_{jv} , equivalent to a few tenths of a micrometer, as will be seen below.

In Fig. 2b, the beam energy is set so that $R \approx X_{jv}$, i.e., the limited excitation volume and the very small diffusion length for minority carriers in the p^+ region produce a low i_{III} intensity. The EBIC signal is maximum in area II, where the space-charge region comes up to the sample surface (Fig. 2a).

The distance W_e between two adjacent boron-doped regions can then be deduced from the distance between two EBIC peaks, as shown in Fig. 2b. If E is now increased (case c in Fig. 2), the electron-hole pairs will be mainly generated in the horizontal space-charge region of the junction (area III), thereby increasing both i_{III} and W_e . Indeed, this increase in W_e can be accounted for by the curve of the space-charge regions as drawn in Fig. 2a. Relation [1] can then be written as

$$X_{ji}(E) = \frac{1}{2} \{W_n - W_e(E)\} \quad [3]$$

or, in terms of R , given by [2]

$$X_{ji}(R) = \frac{1}{2} \{W_n - W_e(R)\} \quad [4]$$

Finally, after measuring W_n and $W_e(R)$, we plot $X_{ji}(R)$ given by Eq. [4] to obtain a 2-D representation of the p-n junction. We have measured $W_e(E)$ by varying E from 3 to 9 keV and using electron-beam intensities from 2 to 20 pA. Low intensities were deliberately chosen to avoid fast charge effects in the top oxide layer. The following experimental procedures were likewise introduced: (i) to enhance the EBIC signal, the background level was counterbalanced by injecting an adjustable opposite dc current in the preamplifier, and (ii) to improve the accuracy of measurement, the EBIC signal was recorded on a plotter monitored by the line scan mode of the SEM.

SIMS analysis.—To complete our EBIC results, we used a Cameca IMS 300 ion microprobe for SIMS measurements of boron depth profiles in our samples. From these profiles, the segregation coefficient of boron at the Si/SiO₂ interface was deduced. Flat-bottomed, sharp-edged craters were created by using a large defocused primary beam (7).

The in-depth resolution obtained in these craters was better than 5 nm. To obtain the same secondary ion yield for boron in both silicon dioxide and silicon, an oxygen flow was set to saturate the surface with respect to our uniform sputtering rate (0.2 nm s⁻¹).

Preferential chemical etching.—Preferential chemical etching of silicon was used to reveal the p-n junctions in the LOCOS structure. The test devices were cleaned, preferentially etched in a 1:3:20 HF/HNO₃/CH₃COOH solution (9) and subsequently observed in a SEM.

Results

Bird's beak measurement.—Figure 3 is an SEM cross-sectional view of the LOCOS structure obtained at $P_{ox} = 15$ bar. In this micrograph, the bird's beak and the edge of the Si₃N₄ mask are clearly delineated. The lateral bird's beak parameter (L_{BB}) is defined as the distance between

the edge of the nitride mask and the tip of the bird's beak. SEM examination showed that L_{BB} is equal to 0.70 ± 0.003 μm for all the sample conditions given in Table I, i.e., L_{BB} is constant within the accuracy of our measurements. The ratio L_{BB}/E_{ox} where E_{ox} is the oxide thickness, is found to be 1.16 in each case. Therefore, high pressure oxidation has no significant effect on the shape of the bird's beak.

Two-dimensional representation of p-n junction, as deduced by SEM-EBIC.—Figure 4 shows the plots of $X_{ji}(R)$ derived from relation [4] for $P_{ox} = 1, 10,$ and 20 bar, and Fig. 5 gives those for $P_{ox} = 1, 5,$ and 15 bar. In these figures, the bird's beak, as seen in the micrograph in Fig. 3, has been drawn for purposes of clarity. The experimental points have been determined with an uncertainty of ± 0.06 μm, which is mainly due to the difficulty in determining the EBIC maxima.

Figures 4 and 5 illustrate that: (i) the reductions of X_{ji} and X_{iv} are about 0.2 μm and 0.33 μm, respectively, when P_{ox} increases from 1 to 20 bar, and (ii) the junction profile does not vary significantly between 10 and 20 bar oxidation pressure. In the case of our 3 μm linewidth test device and taking into account the lateral extension of the bird's beak, this reduction of X_{ji} with pressure leads to a relative increase of the width of the active regions of about 22%.

Also given in Fig. 4 and 5 (lower left-hand corner) are the junction depths X_{iv} for each P_{ox} as deduced from SIMS measurements. These values satisfactorily fit the $X_{ji}(R)$ plots. Finally, our EBIC measurements suggest a modification in the curvature of the junction profile beneath the bird's beak. The solid lines of the $X_{ji}(R)$ plots represent the actual shape of the junction, and the dashed lines those which might be expected. This surprising result is also found in the following.

Junction delineation by preferential chemical etching.—Figures 6a and 6b show our results for $P_{ox} = 1$ bar and 15 bar, respectively. For both pressures, the junction has been revealed. The junctions are drawn schematically in Fig. 6c. A reduction of X_{ji} and X_{iv} occurs when P_{ox} is increased. However, quantitative measurements can not be made by direct comparison of Fig. 6a and 6b. The sample structures in these figures issued from two distinct areas of the wafer. Hence, variations may exist in the linewidth measurement W_n not taken into account in this experiment. Nevertheless, the modification of the curvature of the junction profile under the bird's beak, as revealed by EBIC, appears again here. This result will be discussed next.

SIMS results.—The boron depth profiles measured by SIMS are plotted in Fig. 7 for $P_{ox} = 1, 10,$ and 20 bar. The

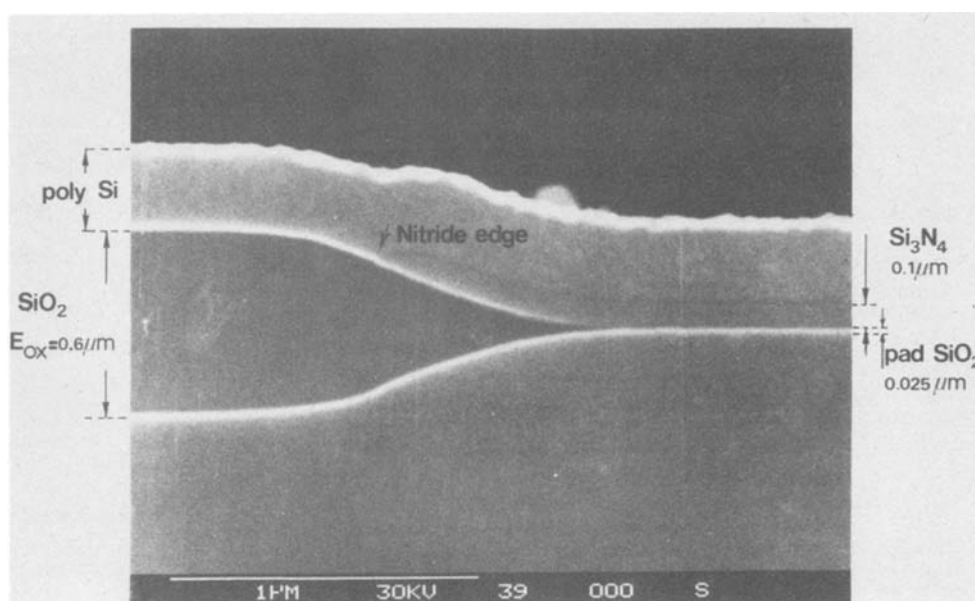


Fig. 3. Cross-sectional SEM micrograph of the LOCOS structure. Oxidation was performed at 920°C at pressures of 1, 10, and 20 bar.

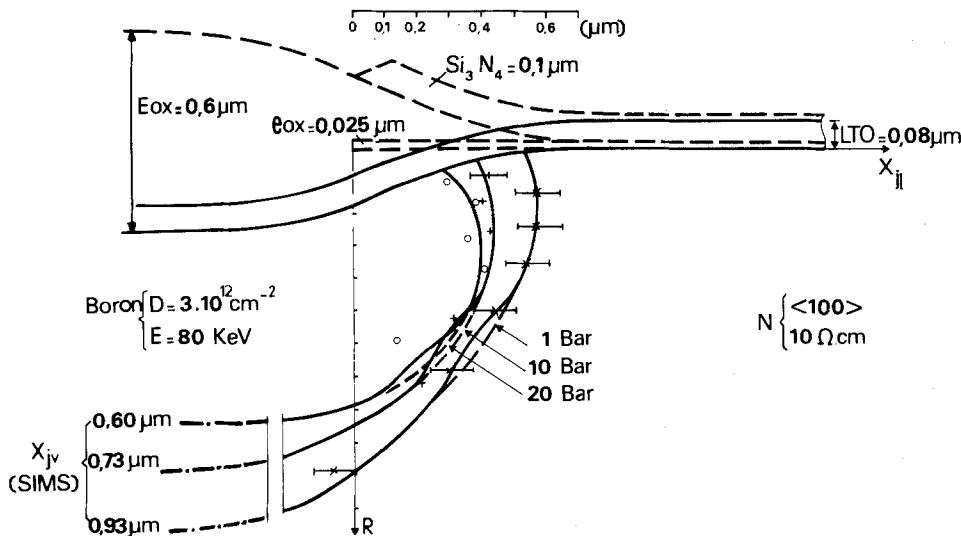


Fig. 4. Two-dimensional representation of the dopant profiles obtained after oxidation and deduced from EBIC measurements. Oxidation was performed at 920°C at pressures of 1, 10, and 20 bar.

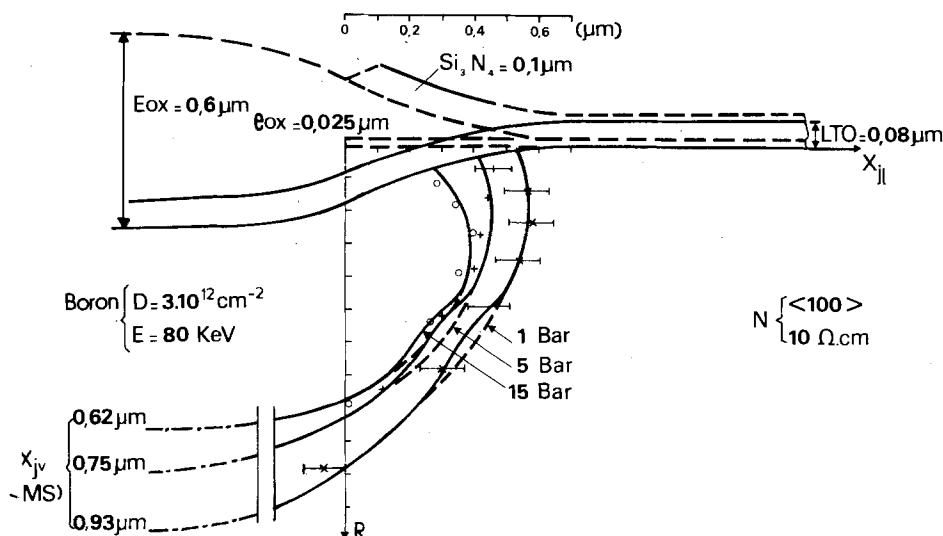


Fig. 5. Two-dimensional representation of the dopant profiles obtained after oxidation and deduced from EBIC measurements. Oxidation was performed at 920°C at pressures of 1, 5, and 15 bar.

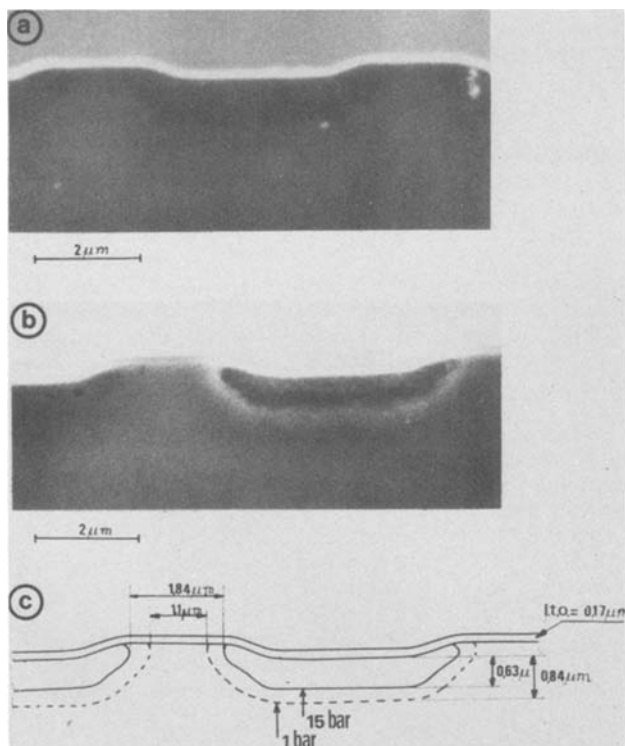


Fig. 6. a and b: Cross-sectional SEM micrographs showing preferential chemical etching of the channel-stop diffusion obtained at $P_{ox} = 1$ and 15 bar, respectively. c: a schematic representation of cases a and b.

as-implanted profile prior to oxidation is given for comparison purposes (dashed line). The data are summarized in Table II.

When P_{ox} increases from 1 to 20 bar, the following can be observed: (i) the in-depth diffusion of boron decreases from 0.47 to 0.14 μm , (ii) the surface concentration C_s increases by a factor of 2, and (iii) the maximum concentration C_{max} also increases and is located close to the Si/SiO₂ interface.

The segregation coefficient of boron at the Si/SiO₂ interface, defined by

$$m = \frac{\text{concentration of B in Si}}{\text{concentration of B in SiO}_2}$$

was determined from SIMS profiles, as shown in Fig. 8a and 8b. Results of these calculations are given in Fig. 8c. The accuracy of measurement is 5%. m increases from 0.3 to 1 bar to 0.92 at 20 bar, i.e., the surface concentration in silicon at 20 bar is 2.5 times greater than at 1 bar. This result is in good agreement with the findings of Fuoss *et al.* (10), who recently reported a ratio of 2.48 between 1 and 10 bar at $T_{ox} = 850^\circ\text{C}$.

Table II. Boron profile data deduced by SIMS

	As-implanted*	1 bar**	5 bar	10 bar	15 bar	20 bar
X_{jv} (μm)	0.72	0.93	0.75	0.73	0.62	0.60
C_s (10^{15} at./cm ⁻³)	15	8	21	24	26	21
$C_{s,max}$ (10^{15} at./cm ⁻³)	120	26	37	40	38	40
Depth at $C_{s,max}$ (μm)	0.28	0.2	0.12	0.08	0.08	0.08

* X_{jv} values calculated from the original surface of Si.
 ** X_{jv} values calculated from the Si/SiO₂ interface.

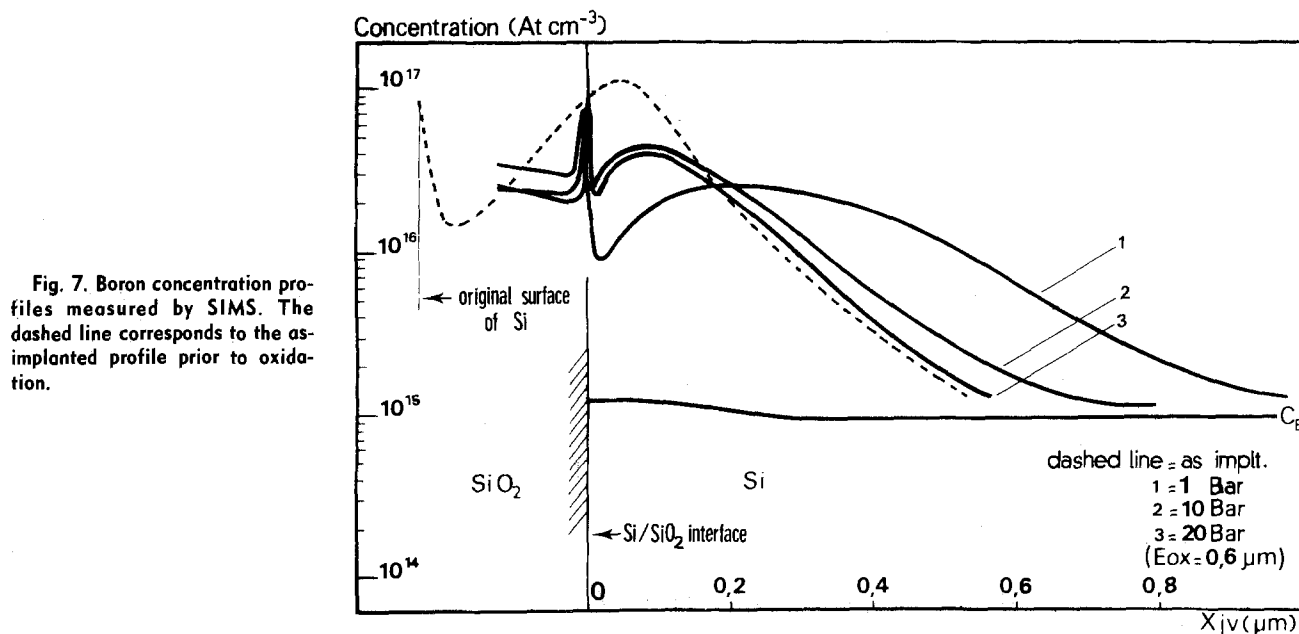


Fig. 7. Boron concentration profiles measured by SIMS. The dashed line corresponds to the as-implanted profile prior to oxidation.

Discussion

Our investigations show that the shape of the bird's beak and, in particular, its lateral extension L_{BB} are independent of oxidation pressure. This corroborates the results of Wu *et al.* (11), who noticed a 30 nm increase in L_{BB} at 10 bar compared to that at 1 bar. This increase is within the accuracy of our SEM measurements.

In this work, we have used the EBIC signal obtained at a single-line scan of the electron beam to determine the 2-D redistribution of boron. To our knowledge, this is the first use of EBIC for such purposes. Crucial to our study were the choice of a test device composed of a repetitive line pattern and the use of SIMS data to correctly cali-

brate the depth axis of the 2-D plots. In Fig. 4 and 5, we have plotted X_{j1} as a function of the electron range R , as the $X_{j1}(R)$ curves correctly fit the X_{jv} values deduced from SIMS. The low energies used, *i.e.*, $E \leq 10$ keV, further justify our choice of R . Indeed, the relationship between the collection efficiency of our junctions and E is nearly linear. This indicates that the generation mechanism of the electron-hole pairs is mainly limited by the surface recombination velocity.

Thus, according to a simple model of charge-collection (12) the depth of maximum collection shifts towards R , *i.e.*, the maximum depth of penetration. At any rate, our 2-D determination of the junction profiles was carried out merely to compare the different boron redistributions after oxidation.

The modification of the curvature of the junction delineation under the bird's beak revealed by both EBIC and preferential chemical etching was a surprising result. This particular shape may be accounted for as follows: the bird's beak is a region in which local stress within the oxide is likely to slow down growth of SiO_2 (13). According to Hu's model (14), the injection of Si interstitials from the Si/SiO₂ interface will also be reduced, making the oxidation enhanced diffusion (OED) of boron less effective in this area (15).

As outlined in Table I, the main advantage of a high pressure process is a reduction of the oxidation time t_{ox} . Our results further indicate that the shallowness of the junction depth x_{jv} under increasing pressure may be directly accounted for by the reduction of t_{ox} . Our SIMS results served as a first check of the $t_{ox}^{1/2}$ relationship of the in-depth diffusion of boron after heat-treatment. This time behavior suggests that, during high pressure oxidation, boron diffusion may be described using a classical model.

So far, apparently little research has been reported on the segregation mechanism of boron during high pressure oxidation. Recently, Charitat (16) developed the thermodynamic aspect of boron segregation on the basis of Fair's model (17). Assuming that the pressure is much lower in Si than in SiO₂, Charitat stated the thermodynamic equilibrium of boron by adding terms proportional to pressure to the chemical potentials. Therefore, in his model, he obtained an exponential relationship of the segregation coefficient, m vs. P_{ox} . Our results, especially between 5 and 20 bar, are in good agreement with Charitat's prediction.

Conclusions

In summary, we have drawn the following conclusions.
1. High pressure oxidation is not only useful for reducing time. It also appears very attractive for reducing

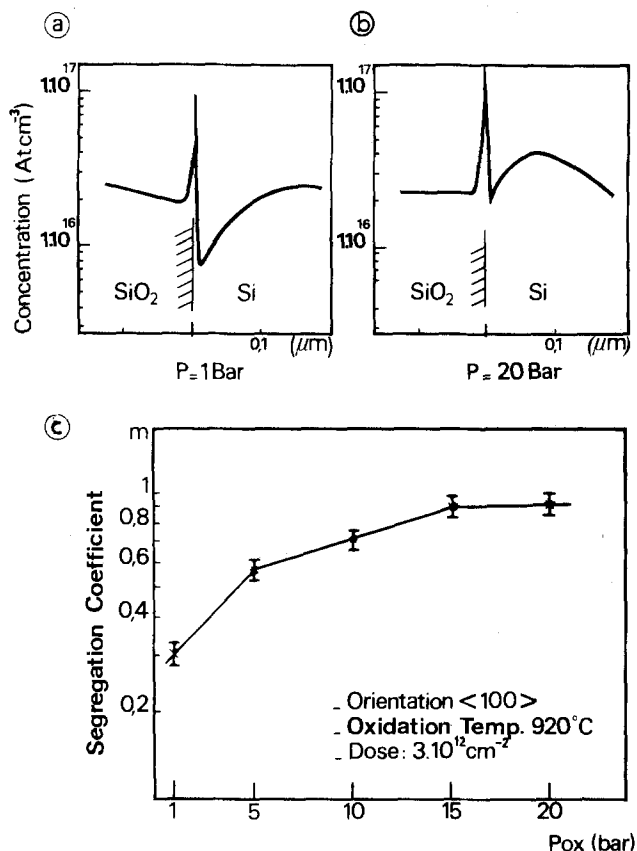


Fig. 8. a and b: SIMS profiles of the boron redistribution in the vicinity of the Si/SiO₂ interface after oxidation at 1 and 20 bar, respectively. c: segregation coefficient m vs. oxidation pressure.

the lateral diffusion of boron in LOCOS structures. For a 3 μm oxide-isolated device, this effect corresponds to a 22% increase in the active regions. With dimensions scaled down to 1 μm , this relative increase will be proportionally greater.

2. Under increasing oxidation pressure, a reduction in the junction depth together with an increase in the surface concentration of boron has been observed. These effects could have interesting implications, e.g., choice of the implant dose for precise adjustment of the threshold voltage of a device would be more straightforward.

3. A modification of the curvature of the p-n junction has been revealed under the bird's beak. This phenomenon is considered to be related to stress effects in the oxide.

4. The pumping of boron within the oxide is reduced in a high pressure process. This effect is correlated with the increase in the surface concentration of boron in silicon.

Acknowledgments

The authors would like to thank Mr. Montier, Dr. Bois, and Dr. Trilhe for their encouragement during this study. Dr. Demoulin, Dr. Mathiot, and Ms. Dargent are also thanked for their critical reading of the manuscript, and Mr. Paillet, Dr. Blanchard and Dr. Payo-Casares for their technical assistance in this work.

Manuscript submitted Nov. 14, 1983; revised manuscript received Jan. 25, 1984.

Thomson EFCIS and CNET-CNS assisted in meeting the publication costs of this article.

REFERENCES

1. R. H. Dennard, F. H. Gaensslen, E. J. Walker, and P. W. Cook, *IEEE Trans. Electron Devices*, **ed-26**, 325 (1979).
2. P. P. Wang, *ibid.*, **ed-25**, 779 (1978).
3. K. E. Kroell and G. K. Ackermann, *Solid-State Electron.*, **19**, 77 (1976).
4. H. Iwai and K. Taniguchi, *IEEE Trans. Electron Devices*, **ed-29**, 625 (1982).
5. H. G. Lee and R. W. Dutton, *ibid.*, **ed-28**, 1136 (1981).
6. T. E. Everhart and P. H. Hoff, *J. Appl. Phys.*, **42**, 5837 (1971).
7. B. Blanchard, *Int. J. Mass Spectrom. Ion Phys.*, **45**, 35 (1982).
8. B. Blanchard, N. Hilleret, and J. B. Quoirin, *J. Radioanal. Chem.*, **12**, 85 (1972).
9. E. S. Meieran and T. I. Kamins, *Solid-State Electron.*, **16**, 545 (1973).
10. D. Fuoss and J. A. Topich, *Appl. Phys. Lett.*, **36**, 275 (1980).
11. T. C. Wu, W. T. Stacy, and K. N. Ritz, *This Journal*, **130**, 1563 (1983).
12. G. E. Possin and C. G. Kirkpatrick, *J. Microsc.*, **118**, 291 (1980).
13. R. B. Marcus and T. T. Sheng, *This Journal*, **129**, 1278 (1982).
14. S. M. Hu, *J. Appl. Phys.*, **45**, 1567 (1974).
15. D. A. Antoniadis and I. Moskowitz, *ibid.*, **53**, 6788 (1982).
16. G. Charitat, Ph.D. Thesis INSA, Lyon, France (1982).
17. R. B. Fair and J. C. C. Tsai, *This Journal*, **125**, 2050 (1978).

An AES Investigation into the Phase Distribution of Ion-Implanted Oxygen in Silicon N-Channel Devices

C. G. Tuppen and G. J. Davies

British Telecom Research Laboratories, Ipswich, IP5 7RE, England

ABSTRACT

The buried oxide layer formed by high dose ion implantation has been shown, by Auger depth profiling, to be stoichiometric SiO_2 . A detailed examination of the Si KLL Auger transition suggested that regions corresponding to the tails of the implant profile contained oxygen randomly distributed in the silicon lattice. A model has been produced which accounts for the observed Auger spectrum associated with such a distribution. Ion beam-induced mixing and broadening effects are assessed, and the minimum detectable size of SiO_2 particles is calculated.

A number of recent communications have described the successful fabrication of LSI circuits on silicon-on-insulator (SOI) substrates prepared using ion-implantation techniques (1-3). The good electrical characteristics of these circuits have established SOI as a viable alternative to the established silicon-on-sapphire (SOS) technology. The insulating layer is prepared by high energy oxygen ion implantation with a sufficiently high dose to form a buried oxide layer. The near-surface silicon retains its crystalline properties (4), and, following a high temperature anneal, can be overgrown with good quality epitaxial silicon (4).

A number of analysis techniques have been used to study the implantation process and subsequent device-fabrication steps. These have included cross section transmission electron microscopy (TEM) (2, 4, 5-7). Rutherford backscattering spectroscopy (RBS) (2, 7-8), secondary ion mass spectrometry (SIMS) (7), x-ray photoelectron spectroscopy (XPS) (6-7), and Auger electron spectroscopy (AES) (2, 4, 6, 7, 9). Previously, AES has been used, qualitatively, to determine the shape of the implanted oxygen profile (6, 7), but not for accurate quantitative analysis.

This paper describes an AES investigation into the distribution, dose, and chemistry of the implanted layers.

Particular attention has been paid to the chemical form of the oxygen/silicon interaction both in the main body of the implant and more particularly in the interface region. The discussion includes a section on two alternative, theoretical models which describe different oxide phase distributions. The effect of sputter-cascade mixing is also considered.

Experimental

Substrates for implantation were 17-23 $\Omega\text{-cm}$, boron-doped, p-type silicon of (100) orientation. The buried oxide structures were prepared using an electrostatically scanned, 400 keV, molecular O_2^+ ion beam¹. All doses have been converted to equivalent 200 keV, atomic O^+ doses. Specimens were implanted through a 2 \times 2 cm silicon mask, and were supported on silicon points to reduce conductive heat loss, thus allowing a higher implantation temperature to be attained. Typical ion beam currents were in the range 40-52 μA , resulting in substrate temperatures in the range 450°-500°C.

Following implantation, the substrates were capped with CVD silica and annealed in nitrogen at 1150°C for 2h. A thin epitaxial Si layer (0.02 μm) was grown by CVD

¹ Courtesy of Dr. P. L. F. Hemment, Surrey University, Guildford, England.

from SiCl_4/H_2 at 1170°C for 75s. Devices were then fabricated using the standard $5\ \mu\text{m}$ n-MOS process.

AES was performed on a VG Scientific MA500 scanning Auger microscope fitted with a 5 keV argon ion gun. The spectrometer was controlled by an HP1000 minicomputer, which stored all the spectra on disk. This allowed detailed postprofiling examination of peak energy shifts and was also used for computer simulations of Auger spectra.

A series of samples was studied with doses ranging from 1.1×10^{18} to $3.3 \times 10^{18}\ \text{O}^+\ \text{cm}^{-2}$. Some were analyzed "as implanted," while others were profiled following various stages of the circuit fabrication process.

Results

Auger depth profiles were recorded by multiplexing the Si KLL, Si LVV, and O KLL transitions. Sputter depth scales were calibrated from a combination of ball-lapped craters and Dektak II surface-profile measurements. Quantification of Auger peak heights was complicated by changes in the relative atomic sensitivity of silicon. In the transition from elemental Si to stoichiometric SiO_2 , the relative sensitivity increased by a factor of 3.4. In view of this large matrix effect, all calculations were based on the oxygen peak heights, which were taken as directly representative of the oxygen concentration. Calibration of oxygen concentrations in the implanted region was based on spectra obtained during the same profile from silica capping layers and, in the case of device structures, silica gate oxides.

The Auger depth profile through a polysilicon capacitor fabricated on a $2.0 \times 10^{18}\ \text{ions cm}^{-2}$ implanted substrate is shown in Fig. 1. In this case, quantification of the silicon concentration was achieved using the relative sensitivity of silicon in silica, and so the profile is only truly valid in areas of stoichiometric SiO_2 . It does, however, show that the implant saturates at stoichiometric SiO_2 and also demonstrates the good depth resolution obtained during this work. Taken from the surface, this profile clearly displays the following layers: $0.8\ \mu\text{m}$ SiO_2 passivation, $0.3\ \mu\text{m}$ polysilicon, $0.05\ \mu\text{m}$ gate oxide, $0.02\ \mu\text{m}$ epitaxial silicon, and, finally, the ion-implanted oxygen.

Figure 2 shows how the shape of the oxygen profile changed as the dose was increased from 1.1×10^{18} to $3.3 \times 10^{18}\ \text{ions cm}^{-2}$. For doses below $1.8 \times 10^{18}\ \text{ions cm}^{-2}$, the implant failed to reach stoichiometric SiO_2 , and the profile shape follows a distorted gaussian curve with the leading edge of the profile displaying a steeper gradient than the trailing edge. The $1.8 \times 10^{18}\ \text{ions cm}^{-2}$ profile shows a well-formed, flat-topped SiO_2 region with very steep sides. As the dose was increased still further, the flat-topped region widened and the leading edge of the implant approached the surface of the substrate. Profiles

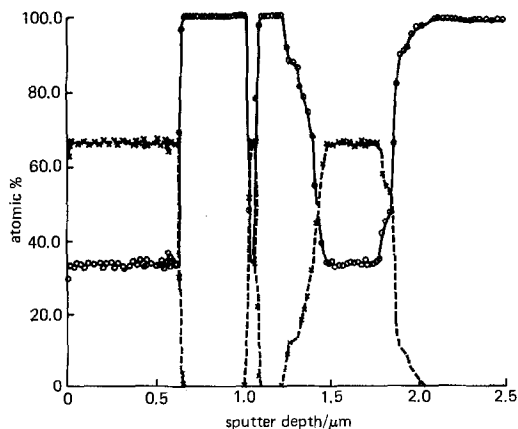


Fig. 1. Quantitative Auger depth profile of silicon (O) and oxygen (X) through a polysilicon capacitor fabricated on a $2.0 \times 10^{18}\ \text{ions cm}^{-2}$ implanted substrate.

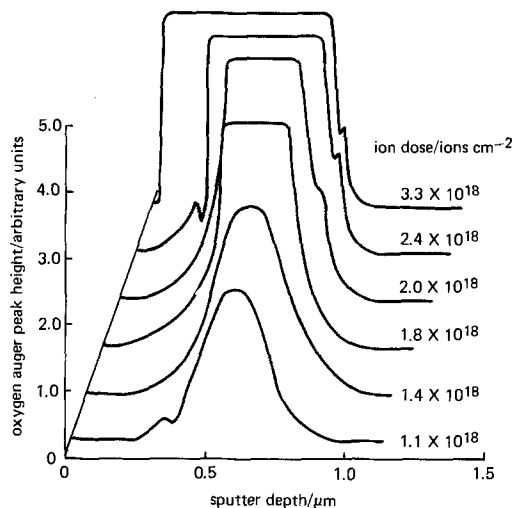


Fig. 2. A series of oxygen Auger depth profiles for implants in the range $1.1\text{--}3.3 \times 10^{18}\ \text{ions cm}^{-2}$.

from annealed specimens frequently displayed significant structure in the wings of the implant, e.g., the $2.4 \times 10^{18}\ \text{ions cm}^{-2}$ profile in Fig. 2. These findings are in accord with those of other workers (10, 11) and have been explained in terms of preferential nucleation centers (11).

Depth scales were determined using a series of ball laps on the $1.8 \times 10^{18}\ \text{ions cm}^{-2}$ implant. Penetration of the implanted layer by the ball lap was confirmed using Auger line scans, and accurate depths were then established using a surface profiler. Measurements gave an average implant depth of $4000 \pm 200\ \text{\AA}$ and a layer thickness of $2100 \pm 200\ \text{\AA}$.

An implant dose could then be calculated from the integrated area under the oxygen Auger depth profile, assuming the following.

1. The O atomic density in the stoichiometric SiO_2 layer was $5.33 \times 10^{22}\ \text{atomic cm}^{-3}$ (12). A high silica density value is considered appropriate, as the oxide would have been under severe compression during growth.
2. The sputter rate was constant throughout the implanted material.
3. Interference fringe errors in the ball-lap measurements were minimal.

Using the derived $1.8 \times 10^{18}\ \text{ions cm}^{-2}$ implant data, a plot of calculated dose vs. measured dose for the full range of profiles is shown in Fig. 3. The points all lie on a straight line with a slope of ~ 1 .

The Si KLL peak energy was monitored for all profiles and confirmed the assigned SiO_2 stoichiometry in the

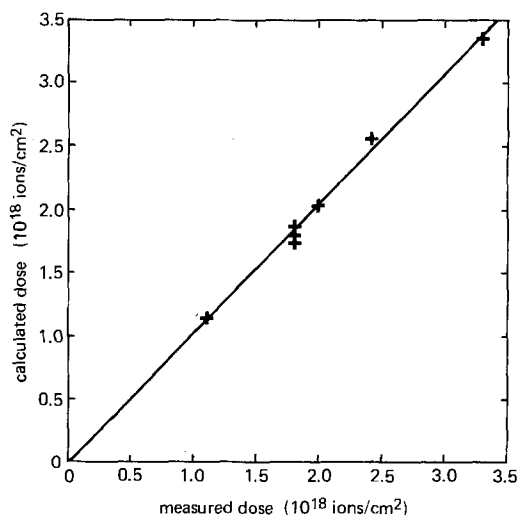


Fig. 3. Plot of implant dose calculated from the integrated area under oxygen Auger depth profiles vs. the dose measured during ion implantation.

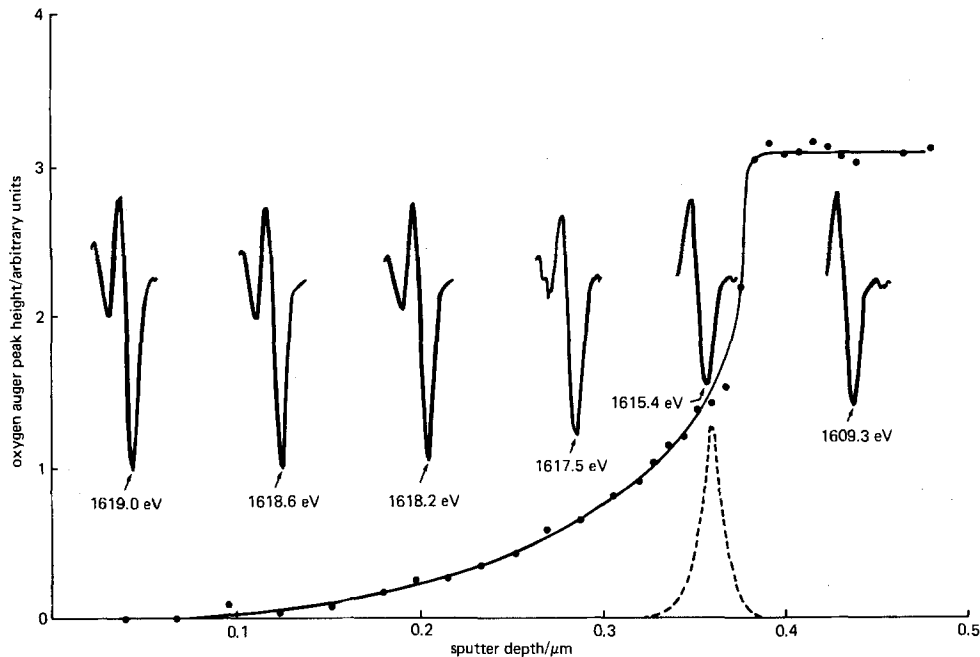


Fig. 4. A combination plot of the leading edge of the oxygen Auger depth profile for an unannealed 1.8×10^{18} ions cm^{-2} implant, together with the Si KLL spectrum at various points on the profile. The negative excursion of each spectrum is in line with the appropriate sputter depth. The dashed line represents the maximum sputter broadening contribution at a fractional oxygen concentration of 0.5 when compared to SiO_2 .

flat-topped regions. Concentrating on the near surface tail of the unannealed 1.8×10^{18} ions cm^{-2} implant profile, the Si peak showed a gradual transition from the elemental spectrum to a fully oxidized spectrum (Fig. 4). In line with a recent XPS study (13), the integrity of the silica, both in the implants and capping layers, was found to be unaffected by ion bombardment. Also, electron-beam irradiation was kept to a minimum, and, therefore, subsequent reduction of the oxide was also minimized.

Analysis of Results

The close agreement shown earlier between calculated and measured doses suggests that the Auger profiles are a good representation of the implanted-oxygen distribution. A theoretical model of the implantation process has already been produced and used to simulate these Auger profiles. A preliminary report of this model has been described elsewhere (14); a more complete description will be published shortly.

The shape and energy of the Si KLL peak can be used as an indication of the phase distribution of oxygen in the lattice. Although it has been shown that silicon is present as stoichiometric SiO_2 in the majority of the implant region, the spectra recorded in the near surface tail (Fig. 4) need to be discussed in terms of the oxygen phase distribution.

Two independent models have been proposed for the phase distribution of oxygen in nonstoichiometric silicon oxides; the microscopic-mixture model and the random bonding model (15, 16). In the microscopic-mixture model, the oxide is assumed to be composed of a mixture of discrete regions of SiO_2 in the Si lattice. In the random bonding model, the oxygen is considered to be randomly distributed in the Si lattice, giving a mixture of atomically localized oxides. These take the form of highly distorted tetrahedra with the general formula $\text{Si}(\text{Si}_x\text{O}_{4-x})$ where $0 \leq x \leq 4$.

The microscopic-mixture model.—Spectra can be theoretically simulated using the microscopic-mixture model, by forming a theoretical matrix of Si and SiO_2 peaks (17). This technique was confirmed by Auger analysis of a specially prepared silicon substrate partially covered by a silica layer. The electron beam was kept at a fixed raster size and moved stepwise across the Si/ SiO_2 boundary. Using this method, intermediate spectra were recorded, ranging from elemental silicon to stoichiometric silica. The peak shapes and energies established in this way were found to mirror those derived by computer simulation. These showed a distinct double peak, unlike the Au-

ger spectra recorded from ion-implanted material (Fig. 5), and gave incorrect energy shifts. A summary of experimental and calculated peak energies is given in Fig. 6.

A possible cause of the discrepancy mentioned above could be a loss of resolution in spectra recorded during a depth profile due to sputter broadening. At any given

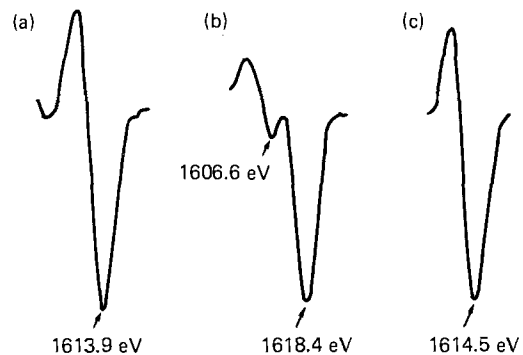


Fig. 5. KLL Si Auger spectra at a fractional oxygen concentration of 0.65 compared to SiO_2 . Curve a: recorded during depth profile. Curve b: simulated using the microscopic-mixture model. Curve c: simulated using the random bonding model.

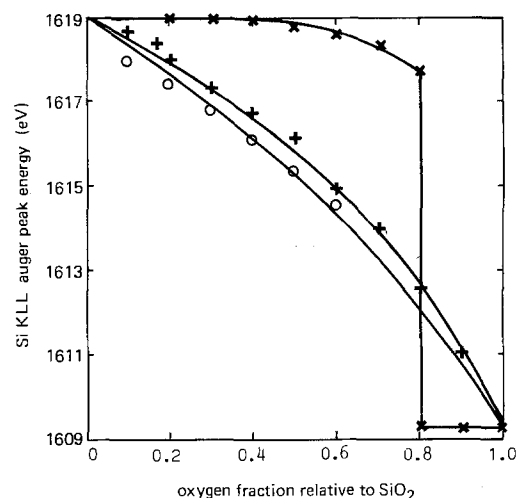


Fig. 6. Plot of Si KLL peak energies vs. effective SiO_2 concentration for spectra recorded during depth profiles (O), spectra simulated using the microscopic-mixture model (X), and spectra simulated using the random bonding model (+).

point on the profile curve shown in Fig. 4, spectra will contain components due to Si/SiO₂ ratios distributed about that point and described by a gaussian sputter broadening distribution function. Such a function is included in Fig. 4 and has been calculated on a worst possible case based on the broadening equation derived by Hofmann (18). After taking account of such a distribution in the theoretical microscopic-mixture model, a second set of simulations significantly failed to alter the results already described. The double-peak structure remained intact, and the peak energies showed only minor changes.

The random bonding model.—The random bonding model can be described in terms of a simple statistical distribution of oxygen in the silicon lattice (15). This model assumes that each tetrahedrally coordinated silicon atom can be surrounded by any number of oxygen atoms, up to a maximum of four. Each of the five possible tetrahedral oxide structures are assumed to be equally probable. The actual distribution varies according to the fractional oxygen concentration relative to SiO₂. In addition, the original model has been modified to take account of the change in density between silicon and silica (Fig. 7). This distribution was then used to simulate the Si KLL Auger spectrum for various oxygen concentrations.

A recent communication (19) has shown that chemical shifts of the Si KLL transition in stoichiometric binary compounds is linearly related to the difference in electronegativities between Si and its partner. This is supportive evidence for the assumption made by Johansson *et al.* (17) that the chemical shift for each of the five possible tetrahedral oxide coordinations will follow a linear relationship.

The simulation was based on an elemental silicon Auger peak, and chemical shifts were calculated from a linear scale. Taking account of the change in relative atomic sensitivity in the transition from Si to SiO₂, a spectrum was produced for each of the five possible oxide coordinations. Following the distribution shown in Fig. 7, the peak shape and energy of the Si KLL transition was then calculated for the full range of oxygen concentrations. In line with the implant profiles, the peaks showed a gradual transition from Si to SiO₂ with no evidence of the double peak predicted by the microscopic-mixture model, (Fig. 5). A plot of simulated peak energies *vs.* the fractional oxygen concentration relative to SiO₂ (Fig. 6) shows that the random bonding model comes very close to predicting the experimentally observed results.

Finally, effects due to ion beam mixing have to be considered. During low energy ion etching, some of the energy of the incident ion beam is distributed amongst the near-surface lattice atoms. This causes random scattering

and collision processes, which disrupt the local order of the lattice. The sputter broadening of interfaces is, in part, attributable to this effect and has been modeled by Anderson (20) in terms of a fixed-step diffusion process. Under the sputtering conditions used in this work, Anderson's equation gives a value for the sputter broadening of 100Å. To a first approximation, this value can be taken as the smallest size of discrete SiO₂ particles detectable during the set of depth profiles reported here and places a rider on the comparison between the oxygen-distribution models discussed above. Any silica particles distributed in the silicon lattice that were much less than 100Å in size would have been "randomized" by the cascade mixing process and would thus be indistinguishable from the random bonding model.

Discussion

The exact phase distribution of oxygen in single-crystal silicon has been the subject of much discussion. This has centered mainly on low concentrations of oxygen (< 10¹⁸ at. cm⁻³) dissolved in Czochralski-grown ingots (21-24). After extended high temperature annealing (650°-1000°C) precipitation of the dissolved interstitial oxygen was found. The rate of precipitation and resultant size of the precipitates has been shown to depend on the initial oxygen concentration, the number of lattice defects, the annealing time, and temperature.

The unannealed 1.8 × 10¹⁸ ions cm⁻² sample described in Fig. 4 was implanted with a substrate temperature of 500°C. The mobility of interstitial oxygen at this temperature is likely to be small, and we would, therefore, expect the majority of implanted oxygen to remain in the interstitial form. Interstitial oxygen would be described by the random bonding model and corresponds to the phase measured by Auger analysis. TEM micrographs of this sample have been published elsewhere (4), and preliminary interpretations showed no evidence of SiO₂ precipitates > 200Å.

One final parameter that should be considered is the local lattice temperature at the end of the implant pathway. This could be considerably higher than that of the surrounding bulk material and may give rise to localized precipitation effects. The magnitude and precise physical meaning of an increase in local temperature is very difficult to define, as the exact mechanisms and range of energy loss at termination of the implant process are not clearly understood. However, Shimura (25) has demonstrated redissolution of precipitates during 1230°C anneals of Czochralski silicon. Therefore, if the local temperature exceeded ~ 1200°C precipitate formation would not be expected.

The results presented in this paper represent the first stage of a detailed AES investigation into device-quality oxygen ion-implanted layers. A subsequent report will consider, in detail, the affects of annealing the implants and discuss the formation of structure in the wings of the profile. In addition, lower energy ion beam sputtering will be employed to decrease the minimum detectable particle size in proportion to the square root of the ratioed energies, thus reducing areas of uncertainty.

Conclusions

1. Auger depth profiles have been recorded for oxygen ion implants in the range 1.1-3.3 × 10¹⁸ ions cm⁻². The profile distributions have been used to model the implantation process theoretically.
2. Implant doses calculated from Auger profiles accurately matched values measured during implantation.
3. The oxygen Auger depth profiles for doses > 1.4 × 10¹⁸ ions cm⁻² displayed flat-topped plateaus which corresponded to an implanted stoichiometric SiO₂ layer.
4. An initial study of the Si KLL Auger peak shape has suggested that oxygen in the near-surface tail of the implant profile was present as a mixture of atomically random oxide species. The alternative microscopic-mixture model has been discounted for silica particles > 100Å in

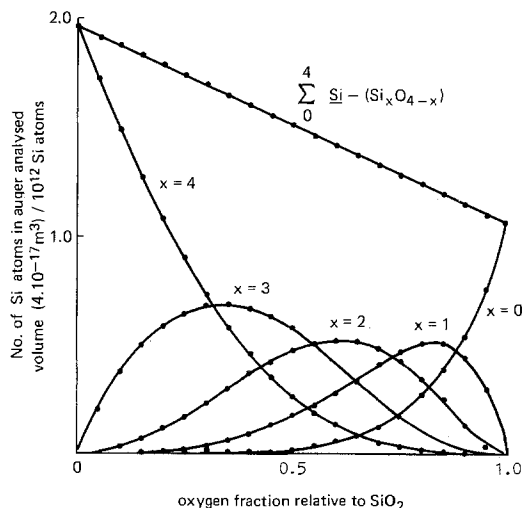


Fig. 7. The statistical distribution of silicon atoms in the nonstoichiometric oxides described by the random bonding model. The silicon atoms are present in the form of highly distorted tetrahedra with the general formula Si-(Si_xO_{4-x}).

size. Future work at lower ion beam energies will reduce the value of this minimum detectable particle size.

Acknowledgments

Acknowledgment is made to the Director of Research, British Telecom, for permission to publish this paper. In addition, thanks go to P. L. F. Hemment, R. P. Arrowsmith, and R. M. Dobson for the preparation of material and many useful discussions.

Manuscript submitted Nov. 7, 1983; revised manuscript received Nov. 23, 1983. This was Paper 223 presented at the Washington, DC, Meeting of the Society, Oct. 9-11, 1983.

British Telecom Research Laboratories assisted in meeting the publication costs of this article.

REFERENCES

1. R. P. Arrowsmith, A. E. Glaccum, P. L. F. Hemment, M. R. Taylor, and C. G. Tuppen, Paper to be presented at the IEEE SOS/SOI Technology Workshop, Wyoming, Oct. 1983.
2. R. F. Pinizzotto, B. L. Vaandrager, S. Matteson, H. W. Lam, S. D. S. Malhi, A. H. Handi, and F. D. McDaniel, *IEEE Trans. Nucl. Sci.*, **ns-30**, 1718 (1983).
3. H. W. Lam, R. F. Pinizzotto, H. T. Yuan, and D. W. Bellavance, *Electron. Lett.*, **17**, 356 (1981).
4. M. R. Taylor, C. G. Tupper, R. P. Arrowsmith, R. M. Dobson, A. E. Glaccum, M. C. Wilson, G. R. Booker, and P. Hemment, in "Institute of Physics Conference Series no. 67," A. G. Cullis, S. M. Davidson, and G. R. Booker, Editors, p. 485, Institute of Physics, London (1983).
5. D. Fathy, O. L. Krivanek, R. W. Carpenter, and S. R. Wilson, in "Institute of Physics Conference Series no. 67," A. G. Cullis, S. M. Davidson, and G. R. Booker, Editors, p. 479, Institute of Physics, London (1983).
6. T. Hayashi, S. Maeyama, and S. Yoshii, *Jpn. J. Appl. Phys.*, **19**, 1111 (1980).
7. P. L. F. Hemment, E. Maydell-Ondrusz, K. G. Stephens, J. Butcher, J. Ioannov, and J. Alderman, Paper 811 presented at Ion Beam Modification of Materials, European Physical Society, Grenoble, France, Sept. 1982.
8. U. Kreissig, E. Hensel, W. Skorupa, and H. Johansen, *Thin Solid Films*, **98**, 229 (1982).
9. K. Izumi, M. Doken, and H. Ariyoshi, *Electron. Lett.*, **14**, 593 (1978).
10. T. Hayashi, H. Okamoto, and Y. Homma, in "Institute of Physics Conference Series no. 59," p. 533, R. R. Hasiguti, Editor, Institute of Physics, London (1981).
11. P. L. F. Hemment, E. Maydell-Ondrusz, K. G. Stephens, R. P. Arrowsmith, A. E. Glaccum, J. A. Kilner, M. C. Wilson, and G. R. Booker, Paper 16 AD 7 presented at The Symposium on Ion Sources and Ion Assisted Technology and The 4th International Conference on Ion and Plasma Assisted Techniques, Institute of Electrical Engineers of Japan, Kyoto, Japan, Sept. 1983.
12. "Handbook of Chemistry and Physics," 53rd ed., p. B-133, CRC Press, Cleveland, OH (1972).
13. S. Hofmann and J. H. Thomas III, *J. Vac. Sci. Technol. B*, **1**, 43 (1983).
14. R. M. Dobson, R. P. Arrowsmith, and P. Hemment, *J. Vac. Sci. Technol. B*, **1**, 1331 (1983).
15. R. J. Temkin, *J. Non-Cryst. Solids*, **17**, 215 (1975).
16. H. R. Phillip, *ibid.*, **8**, 627 (1972).
17. J. S. Johannessen, W. E. Spicer, and Y. E. Strausser, *Appl. Phys. Lett.*, **27**, 452 (1975).
18. S. Hofmann, *Appl. Phys.*, **13**, 205 (1977).
19. R. Fellenberg, P. Streubel, and A. Meisel, *Phys. Status Solidi B*, **112**, 55 (1982).
20. H. H. Anderson, *Appl. Phys.*, **18**, 131 (1979).
21. J. C. Mikkelsen, Jr., *ibid.*, **42**, 695 (1983).
22. M. J. Binns, W. P. Brown, J. G. Wilkes, R. C. Newman, F. M. Livingston, S. Messolaras, and R. J. Stewart, *ibid.*, **42**, 525 (1983).
23. R. B. Fair, *J. Appl. Phys.*, **54**, 388 (1983).
24. F. Shimura and H. Tsuya, *This Journal*, **129**, 1062 (1982).
25. F. Shimura, *Appl. Phys. Lett.*, **39**, 987 (1981).

Selective Low Pressure Chemical Vapor Deposition of Tungsten

E. K. Broadbent*

Philips Research Laboratories, Signetics Corporation, Sunnyvale, California 94086

C. L. Ramiller¹

Applied Materials, Incorporated, Santa Clara, California 95051

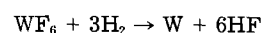
ABSTRACT

We have examined the kinetics of low pressure chemical vapor deposition of tungsten by the hydrogen and silicon reduction of WF_6 within a pressure range of 0.1-5 torr and a temperature range of 250°-500°C. The rate-limiting mechanism for the hydrogen reduction system was determined to be the dissociation of H_2 adsorbed on the surface, with an activation energy of 0.71 eV. A self-limiting deposit results from the WF_6 -Si reaction, the thickness and structure of which are dependent upon the initial native oxide characteristics. Deposition occurs selectively on materials that react directly with WF_6 or yield monatomic hydrogen. In the presence of hydrogen, the degree of selectivity is a function of temperature, substrate material, and surface cleanliness.

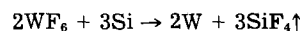
A number of potential integrated-circuit applications exist for selectively deposited tungsten thin films. Gargini and Beinglass (1, 2) have demonstrated that selectively deposited tungsten (1000-1500Å) on polysilicon and monosilicon surfaces within MOS device structures can serve as an interconnect shunt material and contact diffusion barrier, respectively. By selective deposition it is meant that tungsten is deposited only onto certain materials on the substrate while the surrounding regions remain essentially free of any deposit. Low pressure chemical vapor deposition (LPCVD) processing provides several distinct advantages over atmospheric CVD techniques. These advantages include increased control over the dep-

osition ambient, large load-size throughput, lower reactant gas flows, high purity deposits, and excellent deposit thickness uniformities and conformities.

Tungsten hexafluoride is well suited as a source gas for tungsten deposition on integrated-circuit substrates since it can be reduced by interactions with either hydrogen or directly with silicon. Chemical vapor deposition of tungsten has been reported by the hydrogen reduction of WF_6 (3-8) and by the silicon reduction of WF_6 (9-12) according to the reactions



and



As will be shown, it becomes advantageous to utilize both

*Electrochemical Society Active Member.

¹Present address: Tetron, Incorporated, Fremont, California 94539.

reduction reactions to selectively deposit tungsten films of an appreciable thickness onto monocrystalline or polycrystalline silicon surfaces.

A significant amount of work has been devoted to explain the reduction mechanism of WF_6 in the presence of hydrogen. In particular, Bryant (13) performed an exhaustive investigation of all previously available deposition rate data for the hydrogen reduction of WF_6 under experimental conditions in which gas-phase diffusion-controlled limitations were absent. His conclusions agree with the model presented earlier by Cheung (14), which states that the dissociation of H_2 molecules adsorbed on the substrate was the rate-limiting mechanism under surface-controlled reaction conditions. Since surface control of a chemical vapor deposition reaction is favored in relatively low pressure and temperature regimes, it was anticipated that the kinetic evaluation of low temperature LPCVD of tungsten by hydrogen reduction would yield data in agreement with the findings of Cheung and Bryant.

Much less effort has been committed to explain the reduction mechanism of WF_6 by interactions directly with silicon. Morosanu and Soltuz (15) reported a linear dependence between the tungsten deposit thickness and the reaction time for thin tungsten films ($\leq 10,000\text{\AA}$) deposited in an atmospheric CVD flow system. Melliar-Smith *et al.* (11) noted a limiting tungsten thickness of 300-400\text{\AA} was reached when WF_6 was reduced at a surface within an inert atmosphere. Sauermann and Wahl (12) also observed a limiting tungsten deposit thickness which displayed a dependence on the deposition temperature under high flow atmospheric conditions.

The purpose of this study was to examine the reaction mechanisms involved in low temperature (250°-500°C) low pressure (0.1-5 torr) CVD of tungsten. This particular regime is of practical interest for use in the fabrication of integrated circuits where both lower tungsten deposition rates and selective deposition is required. Both the hydrogen and the silicon reduction of WF_6 were evaluated. Experiments were designed to isolate and study each reduction reaction uniquely, without complicating interactions from the other. An explanation of the two-stage tungsten growth sequence that occurs on silicon in the presence of hydrogen was formulated and experimentally verified. A discussion of the two separate reduction systems as well as the mechanism for selective deposition is presented.

Experimental Procedure

The tungsten film depositions were carried out in a low pressure CVD system using a three-zone resistance-heated horizontal furnace 165 cm long. A quartz furnace tube 203 cm long with an inner diameter of 126 mm was centrally positioned within the furnace and served as the reaction chamber. A quartz boat was used to position the substrates vertically within the tube. The chamber interior is evacuated with a series combination of a 164 c.f.m. Roots blower and a 36 c.f.m. (at 1 atm) rotary-vane mechanical pump. Gas injection ports located in a load door assembly allowed for introduction of the processing gases into the chamber. Total chamber pressure was controlled by adjusting the speed of the Roots blower pump together with the gas flow rate into the tube. Gases used in the experiments were tungsten hexafluoride (99.8% WF_6), hydrogen, and argon (99.9998% Ar). The hydrogen was purified using an in-line palladium diffuser element.

All gas flows were controlled using valves and automatic mass flow controllers linked to a microprocessor. The WF_6 exists as a liquid source, and, hence, a resistance heating jacket was placed around the source bottle and adjusted to obtain the desired inlet gas line pressure. The WF_6 gas lines and mass flow controller were heated to avoid condensation of the source gas upon interior flow surfaces. Temperature within the three heated zones of the chamber was monitored with a three-position thermocouple array placed in close proximity to the wafer substrates. The temperature was controlled to within $\pm 2^\circ\text{C}$ of the desired value within the deposition zone. Pressure

was monitored with a capacitance manometer positioned within the chamber. The vacuum integrity of the system was ensured with helium leak detection techniques. Exhaust and by-product gases were handled by an exhaust hood and water scrubber apparatus. A schematic diagram of the system is shown in Fig. 1.

The deposition substrates were 100 mm diam 7-21 $\Omega\text{-cm}$ p-type <111>-oriented single-crystal silicon wafers. Three types of substrates were used: bare silicon, patterned oxide-coated, and patterned aluminum-coated. For the oxide-coated substrates, a 3000\text{\AA} layer of undoped SiO_2 was thermally grown on the Si and patterned into a simple repetitive bar structure by conventional photolithographic techniques. The aluminum-coated samples were prepared by depositing a 1500\text{\AA} evaporated Al layer atop 3000\text{\AA} of thermally grown SiO_2 . Both the bare and oxide-patterned Si substrates received a 2 min dilute hydrofluoric acid preclean prior to deposit, followed by a deionized water rinse and spin dry. The aluminum-coated samples received no pretreatment prior to deposition. Tungsten deposition thickness was determined using β -backscatter and stylus profilometer measurement techniques. The amount of silicon thickness consumed during tungsten deposition was determined by step height measurements and transmission electron microscopy.

The tungsten is deposited according to the following sequence. The substrates are cleaned by a wet chemical pretreatment technique. The loaded reactor tube is evacuated to a base pressure of less than 0.02 torr. The tube is then purged with hydrogen or argon, typically at a flow of 1500 cm^3/min and a system pressure of 0.3 torr. After the substrates reach the desired processing temperature, the chamber is again evacuated and metered flows of the processing gases are introduced into the chamber. Steady flow and pressure conditions are maintained for the deposition time period, after which the tube is evacuated. Dry nitrogen is used to backfill the chamber to atmospheric pressure. The samples are then cooled and removed.

The chemical vapor deposition of tungsten was performed in a low pressure regime of 0.1-5 torr for a temperature range of 250°-500°C. During the course of our experiments, the gas flow rates of WF_6 , hydrogen, and argon ranged between 20-200, 200-2000, and 200-2000 cm^3/min , respectively. The hydrogen reduction of WF_6 was studied using H_2 and WF_6 gases. Aluminum-coated samples served as the deposition substrates. Deposition times for tungsten on aluminum ranged from 1 to 180 min. The silicon reduction of WF_6 was examined using a hydrogen-free mixture of WF_6 and argon gases. The deposition substrates were either bare or oxide-patterned monosilicon wafers. Deposition times for tungsten on silicon ranged from 0.1 to 90 min.

Results and Discussion

Hydrogen reduction of WF_6 .—It was observed early in our studies that an adherent tungsten deposition could be readily initiated and sustained on aluminum surfaces. The use of aluminum-coated substrates with WF_6 and H_2 reactant gases enabled us to study uniquely the hydrogen

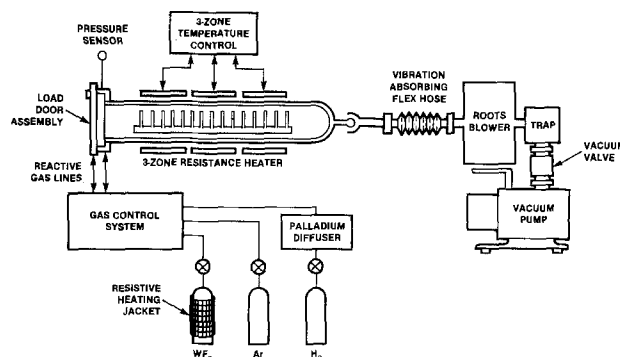


Fig. 1. Schematic diagram of the tungsten-deposition apparatus

reduction system without any additional complicating effects from WF_6 -silicon interactions.

The deposition rate of tungsten was examined as a function of the substrate temperature between 250° and 500°C. The growth rate of tungsten was found to be constant with respect to time. Arrhenius plots were assembled from the temperature-rate data for several total reaction pressures (Fig. 2). The H_2/WF_6 mass flow ratio was held constant throughout the course of experiments for each total pressure system. The plots display a constant slope throughout the temperature and pressure ranges evaluated, giving evidence of a consistent rate-limiting reaction mechanism. From the Arrhenius plots an activation energy, E_a , of 0.71 eV/atom (69,000 J/mol) was calculated.

A pressure dependence of the tungsten deposition rate is apparent in Fig. 2. This dependence was displayed more clearly by plotting the growth rate as a function of total pressure (Fig. 3) for the same data comprising the previous figure. As mentioned earlier, the H_2/WF_6 molar ratio remained essentially constant throughout these experiments. The deposition rate is seen to display a square root dependence on the total pressure ($R \propto P^{1/2}$).

Further experiments were performed to examine the reaction order of the WF_6 - H_2 system with respect to each individual reactant. A correlation between the deposition rate and changes in the H_2 partial pressure was first obtained. Shown in Fig. 4 is the rate as a function of the H_2 partial pressure component. During these depositions, the WF_6 partial pressure was maintained constant. Data were obtained for substrate temperatures between 270° and 475°C. The growth rate clearly displays a square root dependence on changes in the H_2 partial pressure ($R \propto P_H^{1/2}$). Similarly, the correlation between deposition rate and the WF_6 partial pressure was obtained while maintaining the H_2 partial component constant (Fig. 5). The tungsten growth rate displays no dependence on changes in the WF_6 partial pressure ($R \propto P_{WF_6}^0$). The reaction order for this system with respect to hydrogen and tungsten hexafluoride was thus determined to be one-half and zero, respectively, under the stated conditions.

Both the temperature and pressure dependence of the reaction rate suggest H_2 dissociation as the rate-limiting surface mechanism. The calculated activation energy (0.71 eV/atom) from the data represented in Fig. 2 is in close agreement with the reported value of 67,000 J/mol (0.69 eV/atom) for H_2 surface diffusion on tungsten (16, 17). According to Cheung (14), H_2 dissociation is con-

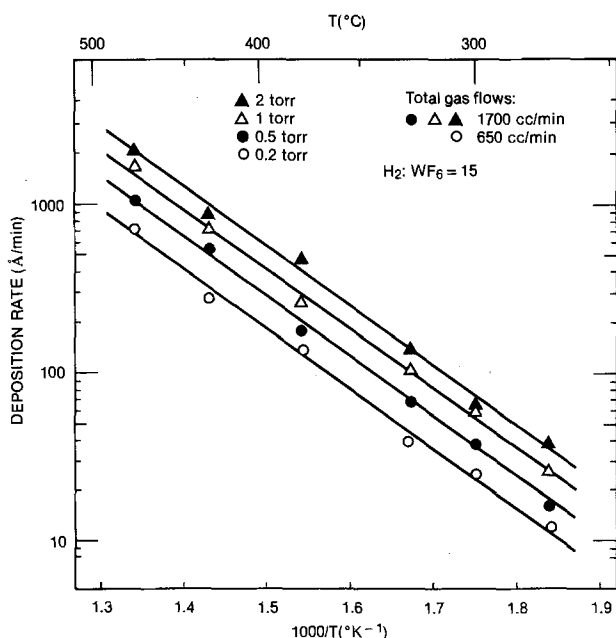


Fig. 2. Temperature dependence of tungsten deposition rate for several pressures (WF_6 - H_2 system).

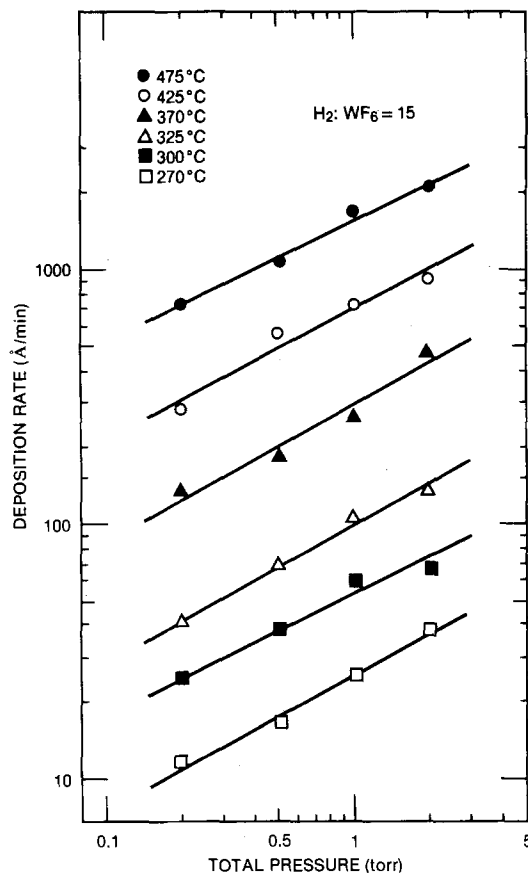


Fig. 3. Total pressure dependence of tungsten deposition rate for several temperatures (WF_6 - H_2 system).

trolled by the jumping of one of the H atoms to a neighboring site. The calculated E_a value is also in excellent agreement with the value of 16,000 cal/mol (0.69 eV/atom)

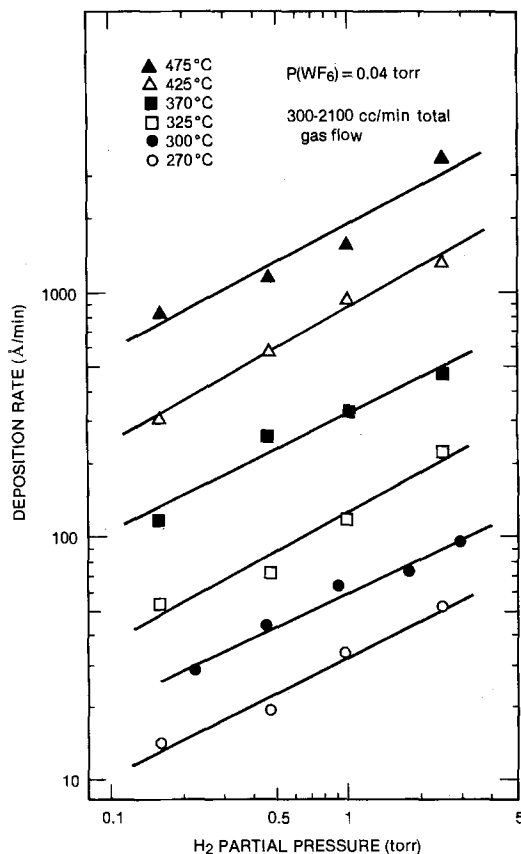


Fig. 4. Deposition rate as a function of H_2 partial pressure for several temperatures (WF_6 - H_2 system).

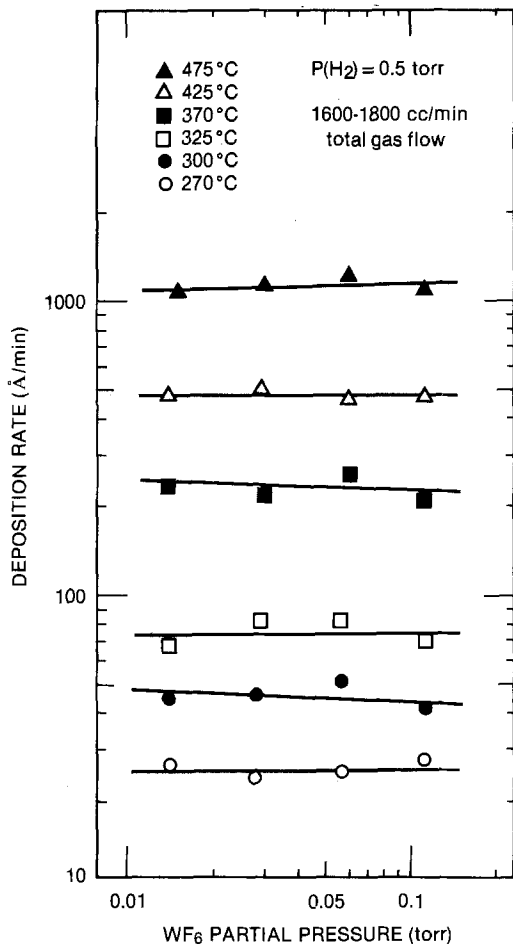


Fig. 5. Deposition rate as a function of WF_6 partial pressure for several temperatures (WF_6 - H_2 system).

obtained by Holman and Huegel (5) for a surface-controlled WF_6 - H_2 reaction.

The assessed reaction order of the WF_6 - H_2 system with respect to total and partial pressures provides further evidence for H_2 dissociation as the rate-controlling mechanism. Cheung (14) noted that either H_2 dissociation or HF desorption could be consistent rate-limiting processes under certain conditions for the surface-controlled reduction of tungsten hexafluoride. He proposed that the effect of total pressure on the reaction rate would provide the most critical test of the controlling mechanism. For a constant feed-gas composition, the deposition rate should vary as the square root of the total pressure if the rate-limiting mechanism were that of H_2 dissociation. This was indeed the case demonstrated in our experiments (Fig. 3). The square root total pressure dependence of the tungsten growth rate was further deciphered by examination of the rate with respect to individual reactant pressure (Fig. 4 and 5). The reaction orders derived for CVD tungsten formation kinetics indicate that only the rate-limiting kinetic step of H_2 dissociation would yield the observed dependences (13).

Silicon reduction of WF_6 .—The deposition rate of tungsten on silicon was examined for several substrate temperatures using WF_6 and Ar gases. The tungsten growth rate on Si is not linear with respect to time. The reduction reaction between WF_6 and Si proceeds rapidly until a limiting deposit thickness is reached. Once this limiting layer is achieved, no further deposition was observed to take place (Fig. 6). It is to be noted that the limiting deposit thickness was observed within the shortest controllable deposit time of 0.1 min (6s), and that this thickness appears relatively independent of the temperatures examined. The consistent results shown in Fig. 6 were obtained by loading all substrates into a reactor tube cooled to room temperature, and then ramping up to tempera-

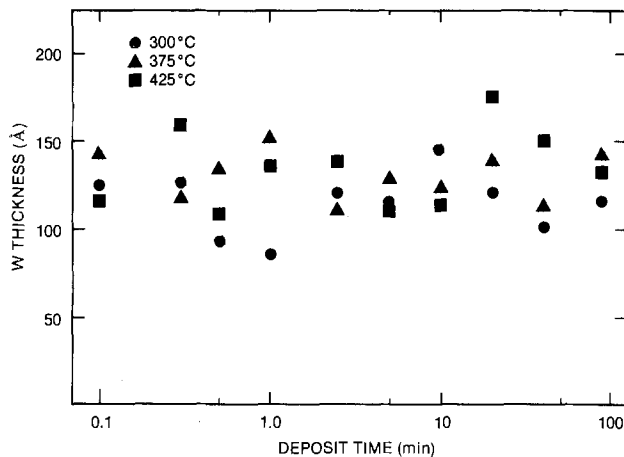


Fig. 6. Thickness of tungsten deposit on silicon as a function of deposition time (Ar: WF_6 flow = 10, 1250 cm^3/min total flow, 0.5 torr).

ture with an inert ambient prior to performing the deposition.

The deposition of tungsten resulting from WF_6 -Si reactions occurs at a rate of at least 1000 Å/min until the limiting deposit thickness is reached. Our findings with respect to a limiting deposit thickness of 100-150 Å for the temperature range of 270°-450°C are in accord with the results reported by Melliar-Smith *et al.* (11). They observed a limiting tungsten thickness of 300-400 Å when tungsten hexafluoride was reduced by silicon in an inert atmosphere between 420° and 880°C. Under no conditions did we observe a linear dependence of tungsten deposit thickness on reaction time, as reported by Morosanu and Soltuz (15).

The thickness and physical structure of the deposit layer were found to be extremely dependent upon the initial silicon surface preparation, and hence the native oxide characteristics. Evidence of this is seen in Fig. 7, where the limiting deposit thickness is recorded for two different load/preparation techniques. Substrates receiving either no pretreatment or an inadequate wet chemical cleaning treatment often displayed visible "streaking" across the deposit layer. This streaked appearance is a result of nonuniformities existing in the deposit thickness and surface roughness across a substrate. A very smooth surface is typical of tungsten deposit regions where a limiting thickness of less than a few hundred angstroms has been reached (Fig. 8). These regions appear very specular under optical light inspection. Film regions possessing a greater limiting deposit thickness display an increasing surface roughness, appearing cloudy or milky-white under optical inspection.

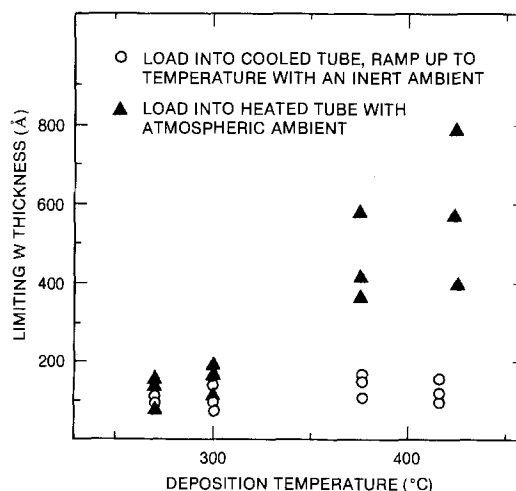


Fig. 7. Limiting tungsten deposit on Si as a function of temperature for two deposition loading techniques (Ar: WF_6 flow = 10, 1250 cm^3/min total flow, 0.5 torr, 10 min deposit time).

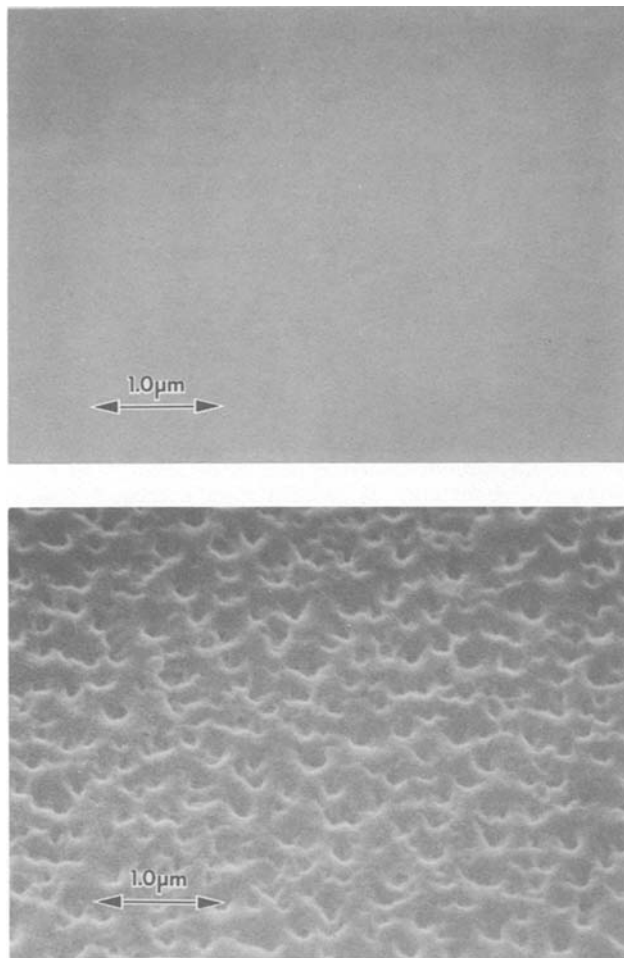


Fig. 8. SEM micrographs showing surface roughness for a limiting tungsten deposit of (a, top) 120 Å and (b, bottom) 800 Å.

The surface roughness of the deposited-tungsten layer was found to correlate with the tungsten-to-silicon interface roughness. Cross-sectional profiles of the W-to-Si interface were obtained using a stylus profilometer after removing the deposited layer in a solution of hydrogen peroxide. Thin deposits display both a very smooth W surface and a very even W-to-Si interface profile. Deposits that possess a greater limiting deposit thickness display an extreme W surface roughness ($\approx 400\text{-}800\text{Å}$) and a very uneven W-to-Si interface (Fig. 9). These observations were also confirmed using transmission electron microscopy (TEM) analysis of several prepared cross-sectional sample specimens (18).

No evidence of continued WF_6 -Si reactions exists after a limiting deposit layer is formed. The data of Fig. 6 do not suggest a diffusion-controlled transport mechanism of WF_6 through the deposit layer to the W-Si interface exists after the initial reaction stage. Scanning transmission

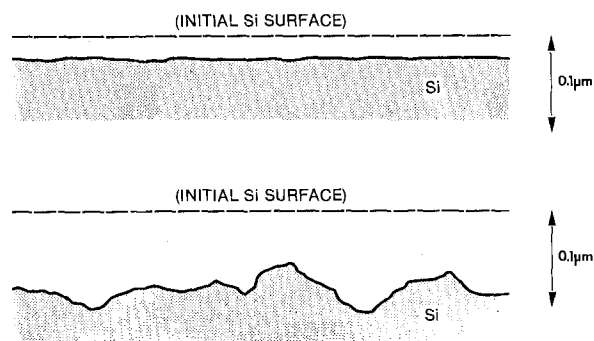


Fig. 9. Profile cross section of the exposed W-to-Si interface for a limiting deposit of (a) 120 Å and (b) 800 Å, after removal of tungsten material.

electron microscopy/energy dispersive x-ray analysis (STEM/EDX) and electron diffraction analysis of deposits obtained at 300° and 425°C show the tungsten films to be comprised of monocrystalline W grains, containing no large (> 1 atom percent [a/o]) amounts of Si. An abrupt interface exists between the tungsten grain structure and the silicon lattice. At higher processing temperatures, the underlying silicon can be expected to react with tungsten in the formation of WSi_2 . WF_6 species will react only with exposed regions of silicon until a continuous tungsten product layer is formed.

It can be argued that a more homogeneous rate of reaction between WF_6 and Si across a surface would result in a continuous limiting layer being formed with a minimal amount of silicon consumption. The presence of an oxide layer on the silicon surface can act as a barrier to the WF_6 -Si reaction. Where nonuniformities in the thickness and structure (e.g., pinhole density) of the oxide occur, the reaction will first initiate at preferred sites where the WF_6 can penetrate the barrier. Lateral tungsten growth from locally adjacent sites contributes to the formation of a continuous layer. As the density and uniformity of reaction sites increases, a continuous product layer is formed earlier, the resultant W-Si interface is more even and less consumption of silicon is required to yield the passivating layer. Where silicon surfaces have been exposed to higher temperatures in the presence of an oxidizing ambient, limiting deposits possessing both a greater thickness (Fig. 7) and a greater W-to-Si interface roughness (Fig. 9b) have resulted. As the thickness of the initial surface oxide layer continues to increase, discontinuous layers of islandlike growths, as well as no tungsten growth at all, were observed.

The thickness of silicon consumed during deposit was measured for the sample group prepared at 300°C using a number of deposit times. The ratio of silicon depth consumed to tungsten thickness deposited was observed to be approximately 2:1. Considering the stoichiometry of the WF_6 -Si reaction, calculations predict that 1.9 Å of silicon would be consumed for each 1 Å of tungsten deposited. This corresponds well to our observed 2:1 ratio.

Growth sequence on Si in presence of hydrogen.—A problem arises in using only the silicon reduction of WF_6 to perform depositions on silicon because only a limiting tungsten layer is achievable. Thus, if controllable deposition thicknesses of greater than several hundred angstroms are desired with minimal Si consumption, it becomes necessary to use both the silicon and hydrogen reduction reactions to result in thicker deposit layers. On the basis of separate examination of the reaction mechanisms of the WF_6 -Si and WF_6 - H_2 systems, a model was proposed and verified for the growth sequence that occurs on silicon in the presence of both WF_6 and hydrogen.

Examination of the growth sequence on silicon substrates suggests the following steps result (Fig. 10). The precleaned substrates are introduced into the reactor, and a deposition cycle is accomplished in which both WF_6 and H_2 gases are present. The exposed regions of silicon rapidly react with and reduce WF_6 , yielding a thin limiting

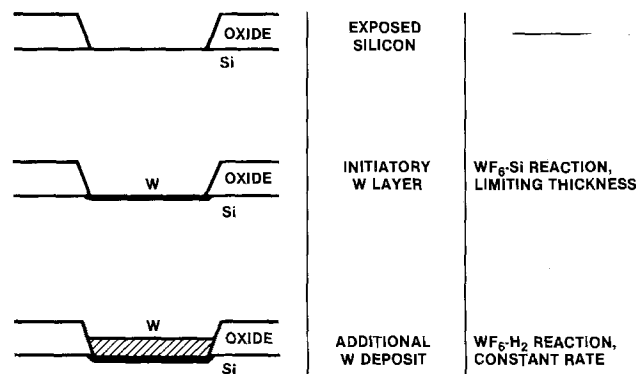


Fig. 10. Sequence of selective growth on Si in presence of hydrogen

tungsten deposit. As this reaction involves direct Si consumption, the ensuing growth and deposit occurs internal to the original silicon bulk structure. Once continuous, however, the limiting deposit layer passivates the WF_6 -Si reaction and provides an initiatory metal layer now capable of sustaining hydrogen dissociation. As dissociation occurs, the WF_6 - H_2 reaction results in additional amounts of tungsten deposit at a constant growth rate. This phase of growth thus continues until the desired final deposit thickness is achieved. To verify the existence of a two-stage growth sequence, tungsten films were deposited at lower substrate temperatures of 270°, 300°, 325°, and 350°C onto silicon substrates in the presence of WF_6 and H_2 . Thickness measurements performed after various deposit times demonstrate clearly the occurrence of a two-stage growth sequence (Fig. 11).

Selective deposition.—Tungsten was deposited on a number of additional samples prepared by patterning various materials on silicon substrates. These samples provided information as to the selective nature of low pressure CVD of tungsten. In the presence of tungsten hexafluoride and argon, selective limiting deposits of tungsten were observed on both monocrystalline and polycrystalline silicon surfaces within the entire temperature and pressure ranges examined. These areas of exposed silicon were immediately adjacent to areas of both silicon dioxide and silicon nitride on the substrate. Rutherford backscattering (RBS) analysis resolved the amount of residue accrued on such adjacent dielectric surfaces to be much less than one atomic monolayer (10^{15} atom/cm²) of tungsten, while also confirming the absence of tungsten within the bulk material. The surface of the quartz reaction chamber and substrate holder remain visibly free of any tungsten deposit when using WF_6 and Ar gases only, even after many hours of accumulated processing time.

In the presence of tungsten hexafluoride and hydrogen, selective deposition was observed to be dependent upon temperature, the local chemical composition of the surface, and surface cleanliness. As discussed previously, the initiation of a tungsten deposit on a particular material depends on the ability of this material to either (i) re-

duce directly the hexafluoride species, as in the case of silicon, or (ii) yield monatomic hydrogen. Certain materials act as nucleating surfaces throughout the entire 250°-500°C temperature range examined. Other materials, however, such as silicon dioxide, were seen to be both nucleating and non-nucleating, depending on the specific preparation of the oxide layer and conditions of the deposit. In general, increasing temperature leads to a loss of selectivity and deposition results on all materials present. Surface cleanliness also plays a role in the selective nature of the deposition, as contamination can locally retard or enhance the ability of a surface to initiate a deposit.

Cuomo and Laff (19) reported the ability to selectively deposit tungsten onto certain desired nucleating surfaces by chemically ablating the remaining portions of the substrate surface area. Such ablation is a consequence of attack by either the hexafluoride metal compound or hydrogen fluoride by-product, and is facilitated by high vapor concentrations as well as high reactor temperatures. Using low pressure CVD of tungsten, an ablative mechanism is not required in order to achieve selective deposition. Typically, for pressures below 1 torr, less than 20Å of SiO_2 is eroded in depositing 2000Å of tungsten selectively. The specific mechanism for selective deposition using low temperature-low pressure CVD techniques appears directly linked to free silicon and hydrogen surface interactions, and remains the focus of continuing studies.

Conclusions

The lower temperature-pressure conditions examined in the chemical vapor deposition of tungsten yield surface-controlled reactions for both the hydrogen and silicon reduction of WF_6 . The rate-limiting mechanism in the WF_6 - H_2 system was found to be the dissociation of hydrogen on the substrate. An activation energy of 0.71 eV/atom (69,000 J/mol) was found for this reaction. The deposition rate displays a square root dependence on the H_2 partial pressure. Observed deposition rates range from 10 to 3500 Å/min.

For the WF_6 -Si system, limited deposits of a controlled thickness (100-150Å) were formed on monocrystalline Si at all temperatures examined. The resultant surface roughness and film thickness are dependent upon native oxide characteristics, and hence the Si surface preparation. In the presence of hydrogen, a two-stage tungsten growth sequence occurs on silicon. Within a patterned substrate, an ablation mechanism is not necessary for selective deposition, as less than 20Å of SiO_2 is eroded in depositing 2000Å of tungsten.

Acknowledgments

Special acknowledgment is given to E. van de Ven for suggesting this topic and for his support throughout the experimental work. The authors wish to thank C. Vorst, G. de Groot, and S. Turner for sample preparation; and G. Delgado for experimental assistance. Appreciation is expressed to W. Stacy for the TEM, STEM/EDX, and electron diffraction analyses; and Y. Tamminga for the RBS analyses. Helpful discussions with E. Sabin are also acknowledged.

Manuscript submitted July 18, 1983; revised manuscript received Jan. 11, 1984. This was Paper 420 presented at the San Francisco, California, Meeting of the Society, May 8-13, 1983.

Philips Research Laboratories assisted in meeting the publication costs of this article.

REFERENCES

1. P. Gargini and I. Beinglass, Abstract 381, p. 924, The Electrochemical Society Extended Abstracts, Vol. 81-2, Denver, Colorado, Oct. 11-16, 1981.
2. P. Gargini and I. Beinglass, in "IEEE International Electron Devices Meeting," p. 54 (1981).

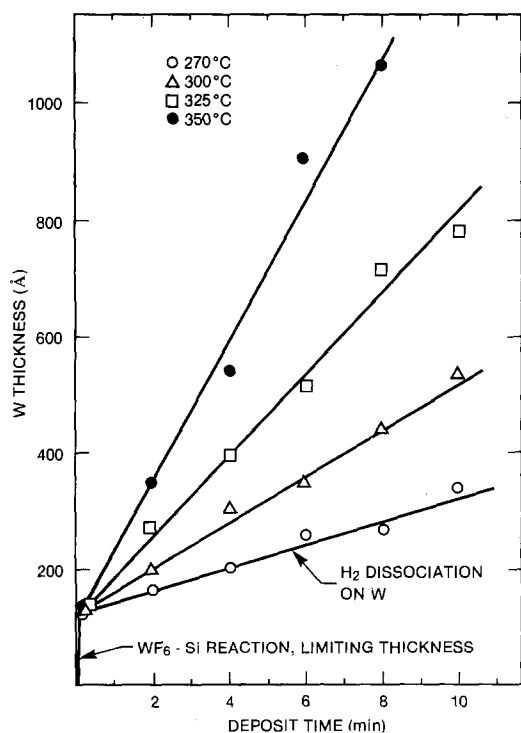


Fig. 11. Thickness of tungsten deposit on Si as a function of time in the presence of hydrogen (H_2 : WF_6 flow = 15g, 1700 cm³/min total flow, 0.5 torr).

3. A. Miller and G. D. Barnett, *This Journal*, **109**, 973 (1962).
4. J. F. Berkeley, A. Brenner, and W. E. Reid, Jr., *ibid.*, **114**, 561 (1967).
5. W. R. Holman and F. J. Huegel, in "Proceedings of the Conference on Chemical Vapor Deposition of Refractory Metals, Alloys and Compounds," A. C. Schaffhauser, Editor, p. 127, The American Nuclear Society, Hinsdale, IL (1967).
6. W. A. Bryant and G. H. Meier, *This Journal*, **120**, 559 (1973).
7. G. Wahl and P. Batzies, in "Chemical Vapor Deposition," G. F. Wakefield and J. M. Blocher, Jr., Editors, p. 425, The Electrochemical Society Softbound Proceedings Series, Princeton, NJ (1973).
8. N. Miller and I. Beinglass, *Solid State Technol.*, **23**, 79 (1980).
9. C. Crowell, J. Savace, and S. Sze, *Trans. Metal. Soc. AIME*, **233**, 478 (1965).
10. J. M. Shaw and J. A. Amick, *RCA Rev.*, **31**, 306 (1970).
11. C. M. Melliar-Smith, A. C. Adams, R. H. Kaiser, and R. A. Kushner, *This Journal*, **121**, 298 (1974).
12. H. Sauermann and M. Wahl, *Valvo Berichte*, Band 20, Heft 2, p. 62, Hamburg, Germany (1977).
13. W. A. Bryant, *This Journal*, **125**, 1534 (1978).
14. H. Cheung, in "The Third International Conference on Chemical Vapor Deposition," F. A. Glaski, Editor, p. 136, The American Nuclear Society, Hinsdale, IL (1972).
15. C.-E. Morosanu and V. Soltuz, *Thin Solid Films*, **52**, 181 (1974).
16. G. Ehrlich, in "Metal Surfaces," p. 236, The American Society for Metals, Metals Park, OH (1963).
17. R. Gomer, R. Wostman, and R. Lundy, *J. Chem. Phys.*, **26**, 1147 (1957).
18. W. T. Stacy and E. K. Broadbent, submitted to *This Journal*.
19. J. J. Cuomo and R. A. Laff, Br. Pat. 1,330,720 (1971).

Modeling of Sulfur Incorporation during Low Pressure CVD of GaAs (100) in the Ga-HCl-AsH₃-H₂-H₂S System

J. Korec, D. Grundmann, and M. Heyen

Institute of Semiconductor Electronics, Technical University Aachen, D-5100 Aachen, Germany

ABSTRACT

An extension is presented of an earlier model of the epitaxial growth of GaAs (100) under reduced pressure to include sulfur incorporation. In describing the growth of doped crystals, the dopant is treated in the same manner as the lattice components. Its incorporation flux is obtained from a dynamic balance between diffusion of the gaseous reactants towards the substrate and a sequence of surface processes. In the case of sulfur doping, the process is described as first leading to the formation of GaS which subsequently yields a regular solution GaAs_{1-x}S_x. The molar ratio x is determined by the ratio of the incorporation flux of the dopant and the growth rate of GaAs. Model calculations show quantitative agreement with the experimental data for the Ga-HCl-AsH₃-H₂-H₂S system at various H₂ pressures.

Reduction of the total pressure in the deposition system leads to improved uniformity of the thickness and dopant concentration of epitaxial films. For this reason, the low pressure technique has gained considerable importance in the technology of semiconductor devices.

The growth and doping of GaAs deposited under reduced H₂ pressures have been the subjects of recent investigations in our laboratory (1, 2). The topic of the present study is the analysis of the kinetics of the dopant incorporation for the case of the Ga-HCl-AsH₃-H₂-H₂S system at low H₂ pressures. As in the modeling of the growth process, a description of dopant incorporation requires taking into account the complete series of kinetic steps of diffusion in the gas-phase, adsorption, chemical reaction, and surface diffusion (3). To this end we will extend the model of GaAs growth on (100) surfaces for atmospheric (4) and reduced total pressures (5) to include sulfur incorporation. The model considerations will be focused on the experimental results published by Veuhoff *et al.* (2).

Model of Dopant Incorporation

Following Stringfellow (6), the sulfur incorporation in GaAs will be treated as the formation of GaS and its dissolution into GaAs to give a regular solution GaAs_{1-x}S_x. The diffusion of H₂S through the gas phase towards the growth surface should obey the mass-balance equation for sulfur atoms

$$k_{d,H_2S} (p_{H_2S}^0 - p_{H_2S}) = J_{GaS} \quad [1]$$

with

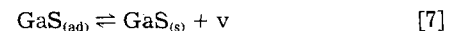
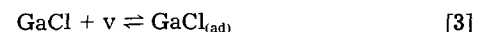
$$k_{d,H_2S} = \left(\frac{D_{0,H_2S}}{D_{0,HCl}} \right)^{2/3} k_{d,HCl} \sqrt{\frac{V}{P}} \quad [2]$$

where k_{d,H_2S} is the mass-transfer coefficient, $p_{H_2S}^0$ the input

Key words: doping, gas phase epitaxy, growth kinetics.

partial pressure of H₂S, p_{H_2S} the H₂S pressure near the substrate surface, J_{GaS} the formation flux of the GaS in the solid mixture, D_{0,H_2S} and $D_{0,HCl}$ the gas-phase diffusion coefficients for H₂S and HCl in H₂ at 273 K, V the linear gas velocity, and P the total pressure. We will put the latter quantity equal to the H₂ pressure in the reactor. The ratio of D_{0,H_2S} and $D_{0,HCl}$ is estimated to be 1.057; the value of $k_{d,HCl}^0$ is known from our growth calculations to be $7 \cdot 10^4 \mu\text{m h}^{-1} \text{bar}^{-1}$ (5).

The mass transport in the gas phase is followed by adsorption of the species and chemical reaction at the substrate surface



where v denotes a surface site of the arsenic sublattice; these adsorption sites were assumed to be the same in the doping and growth processes (4). Reaction [7] includes a surface diffusion step. However, in the growth model, the effect of surface diffusion was neglected for the (100) substrate orientation, and the same will be done here. The rate-limiting step on the surface is assumed to be reaction [5] leading to formation of GaS. Following the earlier study (3), the rate of this reaction is described in terms of the activated complex theory

$$J_{GaS} = \sigma \cdot \mathcal{H} \cdot \frac{k \cdot T}{h} \cdot z^* (\lambda_{\text{GaCl}(ad)} \cdot \lambda_{\text{H}_2\text{S}(ad)} - \lambda_{\text{GaS}(ad)} \cdot \lambda_{\text{HCl}} \cdot \lambda_{\text{H}} \cdot \lambda_v) \quad [8]$$

where σ is the thickness of the absorbed layer, \mathcal{H} the transmission coefficient, k Boltzmann's constant, T the

substrate temperature, h Planck's constant, z^* the partition function of the activated complex $\text{GaCl}\cdot\text{H}_2\text{S}^*_{(\text{ad})}$, and λ_i the absolute activity of the species i .

Assuming the equilibrium state for the reactions [3], [4], [6], and [7], we obtain (see Appendix)

$$\lambda_{\text{GaCl}(\text{ad})} = \lambda_{\text{GaCl}} \cdot \lambda_v \quad [9]$$

$$\lambda_{\text{H}_2\text{S}(\text{ad})} = \lambda_{\text{H}_2\text{S}} \cdot \lambda_v \quad [10]$$

$$\lambda_{\text{H}} = \lambda_{\text{H}_2}^{1/2} \quad [11]$$

$$\lambda_{\text{GaS}(\text{ad})} = \lambda_{\text{GaS}(\text{s})} \cdot \lambda_v \quad [12]$$

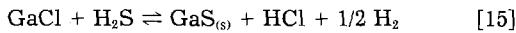
By expressing the absolute activities λ_i in terms of the absolute activities in the standard state λ_i° and activities of the species i , we can rearrange Eq. [8] to the form

$$J_{\text{GaS}} = C \cdot \theta_v^2 (P_{\text{GaCl}} \cdot p_{\text{H}_2\text{S}} - a_{\text{GaS}(\text{s})} P_{\text{HCl}} P_{\text{H}_2}^{1/2}/K) \quad [13]$$

with

$$C = \sigma \cdot \mathcal{K} \frac{k \cdot T}{h} z^* \cdot \lambda_{\text{GaCl}}^\circ \cdot \lambda_{\text{H}_2\text{S}}^\circ (\lambda_v^\circ)^2 \quad [14]$$

Since at typical H_2S pressures, the effect of S containing species on the fraction of free adsorption sites θ_v is negligible, we will use the value of θ_v calculated from the growth model in absence of H_2S (4). The equilibrium constant K in Eq. [13] is the equilibrium constant of the overall reaction, which may be obtained by addition of the reactions [3] through [7]



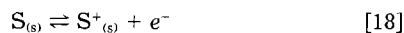
The activity $a_{\text{GaS}(\text{s})}$ appearing in Eq. [13] can be expressed in the form

$$a_{\text{GaS}(\text{s})} = x_{(\text{s})} \exp \left[\frac{(1 - x_{(\text{s})})^2 E}{k \cdot T} \right] \quad [16]$$

where $x_{(\text{s})}$ is the molar ratio of GaS incorporated in the solid at the semiconductor surface and E the interaction energy between GaAs and GaS. Taking into account that the molar ratio x has values between 10^{-6} and 10^{-3} , we see that the activity of the GaAs phase remains close to unity also in doped samples and simplify Eq. [16] to

$$a_{\text{GaS}(\text{s})} = x_{(\text{s})} \exp \left(\frac{E}{kT} \right) \quad [17]$$

The flux J_{GaS} discussed above (Eq. [13]) describes the incorporation of neutral S atoms into the substrate surface. In a next step, they are ionized, possibly after being covered by the next grown monolayer



As one can expect, different binding energies of dopant atoms near the surface and in the bulk of the crystal, the concentration of ionized S atoms in the volume $[\text{S}^+_{(\text{b})}]$ can differ from that at the surface $[\text{S}^+_{(\text{s})}]$. At given growth conditions, the volume concentration should be adjusted accordingly

$$\text{S}^+_{(\text{s})} \rightleftharpoons \text{S}^+_{(\text{b})} \quad [19]$$

If the total process of S uptake takes place at near equilibrium conditions, one could expect for $[\text{S}^+_{(\text{b})}] < n_i$

$$[\text{S}^+_{(\text{b})}]_{\text{eq}} \sim \frac{p_{\text{H}_2\text{S}}}{n_i} \quad [20]$$

and for $[\text{S}^+_{(\text{b})}] = n < n_i$

$$[\text{S}^+_{(\text{b})}]_{\text{eq}} \sim p^{1/2}_{\text{H}_2\text{S}} \quad [21]$$

where n_i is the intrinsic electron concentration at growth temperature ($5 \times 10^{16} \text{ cm}^{-3}$ at 1000 K). However, it was observed that the carrier concentration depends linearly on the H_2S pressure for sulfur concentrations corresponding to the entire accessible range of electron concentrations, namely, up to $3 \times 10^{18} \text{ cm}^{-3}$ (7). Hurle (8) explained this apparent discrepancy by postulating the existence of a high concentration of donor-type As vacancies fixing the

Fermi level at growth temperature for all sulfur concentrations. However, Veuhoff *et al.* (9) could show that the sulfur uptake continues linearly beyond the saturation level of the electron concentration, namely, up to approximately $5 \times 10^{19} \text{ cm}^{-3}$. It seems unlikely that the vacancies in a CVD-grown material could reach concentrations as great as 10^{20} cm^{-3} .

A second possible explanation was given by Zschauer and Vogel (10) and Casey and Panish (11) for LPE of GaAs. These authors postulate a pinning of the Fermi level at the surface due to a large density of acceptor-like surface states. Following this hypothesis, the linear uptake of the dopant can be explained provided that the growth rate is higher than the rate of exchange of dopant atoms between the surface region and the volume of the film. Assuming that in this case equilibrium exists between the gas phase and the substrate surface one obtains

$$[\text{S}^+_{(\text{b})}] = [\text{S}^+_{(\text{s})}]_{\text{eq}} \sim \frac{P_{\text{H}_2\text{S}}}{n_{(\text{s})}} \quad [22]$$

where the surface electron concentration $n_{(\text{s})}$ does not depend on the doping level. It has been observed in UHV experiments at room temperature that the adsorption of hydrogen atoms on clean n-type (110) GaAs causes acceptor-like defects which lead to a depletion of the surface (12). However, it should be mentioned that there is no direct experimental evidence for the pinning of the Fermi level under growth conditions.

The same qualitative results concerning the doping in CVD systems can be obtained by simply assuming different binding energies for neutral dopant atoms at the interface and in the volume of the semiconductor. Also in this case, for growth rates larger than some critical value, the dopant atoms incorporated in the surface are trapped by the growing layer. At smaller growth rates, the trapped dopant atoms have the possibility of adjusting their concentration in the volume in accordance to the constraints of equilibrium thermodynamics. For all cases mentioned above, the molar ratio of dopant in the volume $x_{(\text{b})}$ will be adjusted to the surface conditions ($x_{(\text{s})}$); the level of adjustment is determined by the ratio of diffusion rate and the rate of motion of the growing surface (13)

$$k_r = \frac{x_{(\text{b})}}{x_{(\text{s})}} = k_{\text{eq}} + (1 - k_{\text{eq}}) \exp(-r_c/r) \quad [23]$$

with

$$k_{\text{eq}} = \left(\frac{x_{(\text{b})}}{x_{(\text{s})}} \right)_{\text{eq}} \quad [24]$$

$$r_c = D_s/d \quad [25]$$

$$r = \Omega_{\text{GaAs}} J_{\text{GaAs}} \quad [26]$$

where k_{eq} is the equilibrium value of the distribution coefficient k_r , r_c is the critical growth rate determined by the ratio of the diffusion coefficient of sulfur D_s in GaAs and the width of the region over which the dopant gradient at the interface extends, and r is the actual growth rate related to J_{GaAs} by the molecular volume of GaAs in the solid Ω_{GaAs} .

Consideration of dopant redistribution in the solid requires an estimation of two parameters, k_{eq} and r_c . The values of these parameters can differ for the various models discussed above, but the formal description on this phenomena by Eq [23]-[26] should remain valid.

An immediate consequence of the mass balance for sulfur atoms, is that the net diffusion flux of sulfur containing species in the gas phase (Eq. [1]) equals the incorporation flux of GaS (Eq. [13]). The molar fraction of GaS incorporated in the bulk of the growing film is given by

$$x_{(\text{b})} = \frac{J_{\text{GaS}}}{J_{\text{GaS}} + J_{\text{GaAs}}} \approx \frac{J_{\text{GaS}}}{J_{\text{GaAs}}} \quad [27]$$

Introducing Eq. [13], [17] and [23] in Eq. [27] yields

$$x_{(\text{b})} = \frac{C \theta_v^2}{J_{\text{GaAs}}} (p_{\text{GaCl}} p_{\text{H}_2\text{S}} - x_{(\text{b})} p_{\text{HCl}} p_{\text{H}_2}^{1/2} K_{\text{eq}}/k_r) \quad [28]$$

with

$$K_{eq} = \exp(E/kT)/K \quad [29]$$

For p_{H_2S} follows from Eq. [1] and [27]

$$p_{H_2S} = p^{\circ}_{H_2S} - x_{(b)}J_{GaAs}/k_{d,H_2S} \quad [30]$$

Substituting p_{H_2S} in Eq. [28] using Eq. [30], we obtain

$$x_{(b)} = \frac{p^{\circ}_{H_2S}}{J_{GaAs} \left(\frac{1}{C\theta_v^2 p_{GaCl}} + \frac{1}{k_{d,H_2S}} \right) + \frac{K_{eq} p_{HCl} p^{1/2}_{H_2}}{k_r p_{GaCl}}} \quad [31]$$

Assuming negligible effect of the doping process on the mass transport balances for GaCl, HCl, and H_2 and on the surface coverage factors for adsorbed species resulting from the growth of GaAs (because $p^{\circ}_{H_2S} \ll p^{\circ}_{HCl}, p^{\circ}_{AsH_3}$), the quantities J_{GaAs} , θ_v , p_{GaCl} , p_{HCl} , and p_{H_2} (Eq. [31]) can be taken from the growth calculations (4, 5). Thus, after estimating the factors C , K_{eq} , r_c and k_{eq} , we can use Eq [31], [2], and [23] to calculate the dependence of the molar ratio $x_{(b)}$ on such technological parameters as $p^{\circ}_{H_2S}$, T , V , P , p°_{HCl} , and $p^{\circ}_{AsH_3}$.

In order to determine the contribution of the different process steps to the overall kinetics of dopant incorporation, we rewrite Eq. [31] as follows

$$x_{(b)} = \frac{p^{\circ}_{H_2S}}{A \cdot r + B \cdot r + E/k_r} \quad [32]$$

where

$$A = 1/(\Omega_{GaAs} i k_{d,H_2S}) \quad [33]$$

$$B = 1/(\Omega_{GaAs} \cdot C\theta_v^2 \cdot p_{GaCl}) \quad [34]$$

$$E = p_{HCl} \cdot p^{1/2}_{H_2} K_{eq}/p_{GaCl} \quad [35]$$

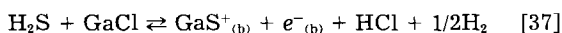
The terms $A \cdot r$, $B \cdot r$, and E/k_r appearing in Eq. [32] represent the contributions of the three limiting factors discussed above: mass transport in the gas phase, kinetics of the surface reactions, and thermodynamics of the incorporation reaction. The largest term is the "bottle neck" factor which dominates and controls the rate of the incorporation process.

Equation [32] implies three possible regimes of control of the dopant-incorporation process. The first one appears when the dopant incorporation is governed by the thermodynamics of the overall reaction [15], so that

$$x_{(b)} = k_r p^{\circ}_{H_2S}/E \quad [36]$$

This situation arises when the kinetic barriers presented by the mass transport in the gas phase and by the surface process have no significant effect on the kinetics of the overall process, e.g., at high deposition temperatures and low total pressures, and/or low growth rates of the host material. It can be seen that only under conditions of thermodynamic control can the process of dopant incorporation be affected by the variable distribution coefficient k_r .

The dependence of the actual distribution coefficient k_r (Eq. [23]) on the growth rate r is shown in the Fig. 1. At low growth rates ($r < 0.1r_c$), the dopant incorporation takes place in equilibrium with the bulk of the solid and the actual distribution coefficient k_r equaling its equilibrium value k_{eq} . This value can be determined from the equilibrium state of the overall reaction



with

$$[GaS^+_{(b)}] = \frac{p_{H_2S} p_{GaCl}}{n_{(b)} p_{HCl} p^{1/2}_{H_2}} \cdot K' \quad [38]$$

From a comparison of Eq. [38] with Eq [35] and [36] follows

$$(k_r)_r < 0.1r_c = k_{eq} = \frac{K_{eq} K'}{n_{(b)} [GaAs]} \quad [39]$$

In the case of extrinsic conditions ($n_i < [GaS^+_{(b)}] = n_{(b)}$) the

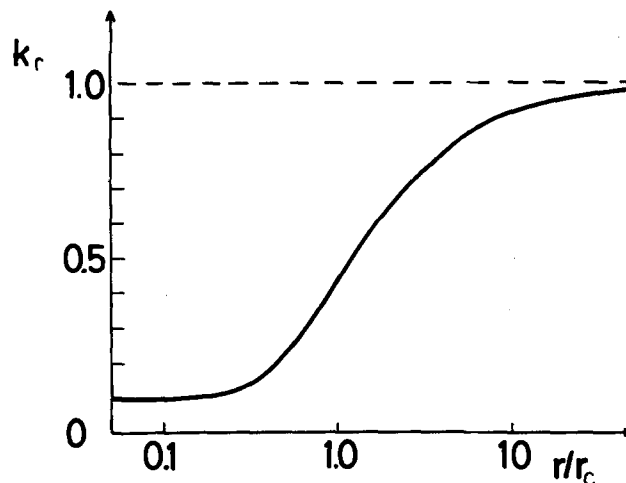


Fig. 1. Calculated dependence of distribution coefficient on growth rate of film r . r_c is critical value of the growth rate. $k_{eq} = 0.1$.

equilibrium-distribution coefficient (Eq. [39]) depends on the dopant concentration in the bulk of the film

$$k_{eq} = k^{\circ}_{eq}/x_{(b)} \quad [40]$$

Introducing Eq. [40] in Eq. [36], we obtain the square root dependence expected for the conditions of thermodynamic equilibrium

$$x_{(b)} = \left(\frac{k^{\circ}_{eq} p^{\circ}_{H_2S}}{E} \right)^{1/2} \quad [41]$$

At higher growth rates ($k_r \approx 1$), the equilibrium can only exist between gas phase and surface of the growing film, and the doping kinetics shows a linear dependence on $p^{\circ}_{H_2S}$ (Eq. [36]). Upon further increase of the growth rate, the dopant incorporation will be controlled by one of the kinetic barriers present in the system, that is, mass transport in the gas phase

$$x_{(b)} = p^{\circ}_{H_2S}/A \cdot r \quad [42]$$

or kinetics of reaction [5]

$$x_{(b)} = p^{\circ}_{H_2S}/B \cdot r \quad [43]$$

The diffusive control (Eq. [42]) should be particularly observed at atmospheric pressure, and the kinetic type of the dopant-incorporation control (Eq. [43]) should make itself particularly felt at low pressures and low deposition temperatures.

Comparison with Experiments

The above model was used to describe the experimental data by Veuhoff *et al.* (2). The concentration of the dopant incorporated in the GaAs film was assumed to be equal to the measured electron concentration. Since the data were obtained for a substrate temperature of 1023 K, the values of the model parameters were estimated for this particular substrate temperature only.

The calculated values appear to depend only weakly on the values of r_c and k°_{eq} (Eq. [23] and [40]), but are strongly affected by the values of C and K_{eq} (Eq. [31]). The experimental data could be reasonably reproduced if the values of $5 \mu\text{m/h}$ and 2×10^{-7} were chosen for r_c and k°_{eq} , respectively. Such values would pertain, if pinning of the Fermi level would occur (11). However, as mentioned before, there is no experimental proof that this model is correct. The numerical fitting of the calculated electron concentration to the data presented in Fig. 2 allowed us to determine the values of the factors C and K_{eq} at 1023 K to be $1.5 \times 10^8 \mu\text{m h}^{-1} \text{bar}^{-2}$ and $0.07 \text{bar}^{1/2}$, respectively. These values of the model parameters were used in all subsequent calculations performed in this study.

In Fig. 3, the terms $A \cdot r$, $B \cdot r$, and E/k_r are plotted as functions of the HCl input pressure for the experimental conditions from Fig. 2. It may be seen that the mass transport in the gas phase (term $A \cdot r$) does not present a

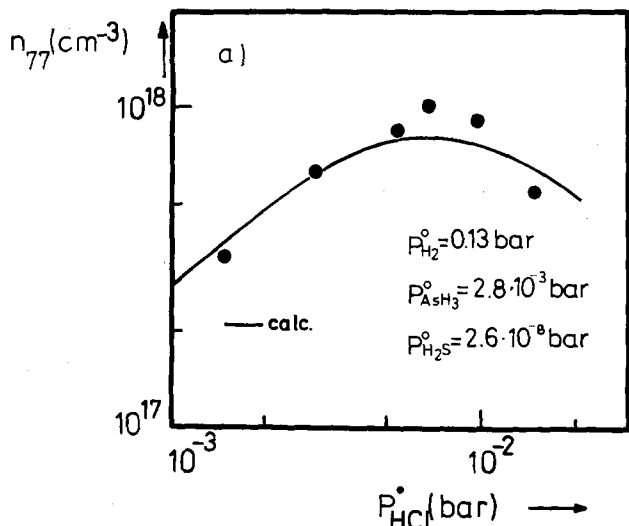


Fig. 2. Dependence of electron concentration resulting from sulfur doping on input HCl pressure ($p_{\text{HCl}}^0 = p_{\text{GaCl}}^0$). Curve: fit to Eq. [31]. Experimental points: Ref. (2).

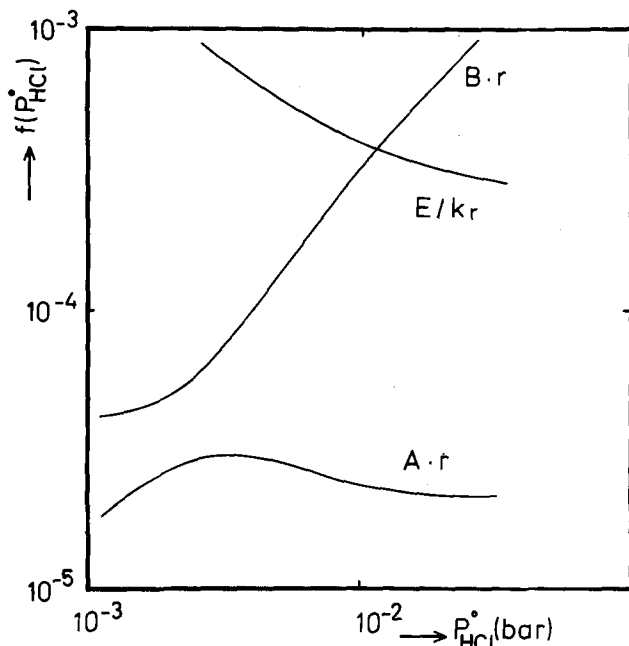


Fig. 3. Dependence of terms in Eq. [32] on input HCl pressure for experimental conditions of Fig. 2.

significant kinetic barrier at low total pressure. Since A does not depend on p_{HCl} , the plot of $A \cdot r$ against p_{HCl}^0 represents the behavior of the deposition rate of GaAs (5), which is roughly constant and amounts $6 \pm 1.5 \mu\text{m/h}$. This growth rate is comparable to the assumed critical growth rate of $5 \mu\text{m/h}$, which implies that $k_r = 0.45 \pm 0.1$. The equilibrium value of $k_r(k_{\text{eq}})$ would be 0.01 for a dopant concentration of 10^{18} cm^{-3} . This means that for thermodynamic control, as obtained for low HCl input pressures (i.e., $<10^{-2}$ bar), under the assumption of this model, the growing film would incorporate about fifty times more dopant atoms than would be obtained if equilibrium with the bulk of the semiconductor would pertain, but about half of the concentration expected for a complete freeze-in of the surface concentration. However, the redistribution effect does not play any role at high input HCl pressures ($>10^{-2}$ bar), where the dopant incorporation process is governed by the kinetics of the surface reactions [3]-[5]. At these conditions, the surface adsorption sites are blocked by the species taking part in the GaAs deposition process, which suppresses the supply of H_2S to the surface.

A comparison of the calculated electron-concentration dependence on the H_2 input pressure with the experimental results is presented in Fig. 4. The corresponding behavior of the terms $A \cdot r$, $B \cdot r$, and E/k_r is plotted in Fig. 5a. For the entire range of the experimental conditions used here, the dopant incorporation process appears to be controlled by the thermodynamics of the incorporation reactions [5]-[7] (term E/k_r). The increase of the H_2 pressure causes an almost linear increase of the GaAs growth rate from $1 \mu\text{m/h}$ at 0.02 bar to $27 \mu\text{m}$ at 0.64 bar. The critical growth rate r_c is reached at about 0.1 bar causing a strong modulation of the thermodynamic term E/k_r by the trapping effect (Fig. 1) in this pressure range. The dependences of the terms A , B , and E on the H_2 pressure are plotted in Fig. 5b. Comparing Fig. 5a and 5b we can see the strong influence of the trapping effect on the behavior of the thermodynamic term E/k_r .

The decrease of the growth rate below the critical value, around a H_2 pressure of 0.1 bar, causes extension of the equilibrium between gas phase and interface into the volume of the solid; the effect of trapping is reduced and the value of k_r decreases with decreasing growth rate. Under these conditions, the dopant uptake does not increase by further lowering $p_{\text{H}_2}^0$. This behavior is indeed observed experimentally. The expected decrease and saturation of the electron concentration at lower H_2 pressures (lower GaAs growth rates) needs further experimental investigation.

The experimentally observed linear dependence of the electron concentration on the input H_2S pressure is obtained also in model calculations, as shown in Fig. 6. The incorporation kinetics appears to be controlled by the equilibrium of reactions [5]-[7]. At the growth rates used in this experiment, $3.5 \mu\text{m/h}$ at total pressure of 0.065 bar and $15.5 \mu\text{m/h}$ at 0.33 bar, the equilibrium state is shifted to the surface conditions and the function k_r has a nearly constant value.

It was experimentally observed that the linear uptake of S atoms from the gas phase continues beyond the saturation value of the electron density appearing in Fig. 6 (9). However, also for the dopant uptake a saturation limit at $5 \times 10^{19} \text{ cm}^{-3}$ was found, which is not considered in our model. For such a high dopant concentration, the regular solution model assumed here loses its validity.

It should be interesting to study this dependence at low GaAs growth rates, where the calculations indicate a sublinear dependence of the dopant concentration in the film on the vapor pressure of H_2S . Thus, at low growth rates (as compared to the critical value) and under equilibrium conditions, the dopant incorporation should take place in equilibrium with the bulk of the semiconductor, and the dependence of $x_{(b)}$ on $p_{\text{H}_2\text{S}}^0$ should approach the square root relationship of Eq. [41].

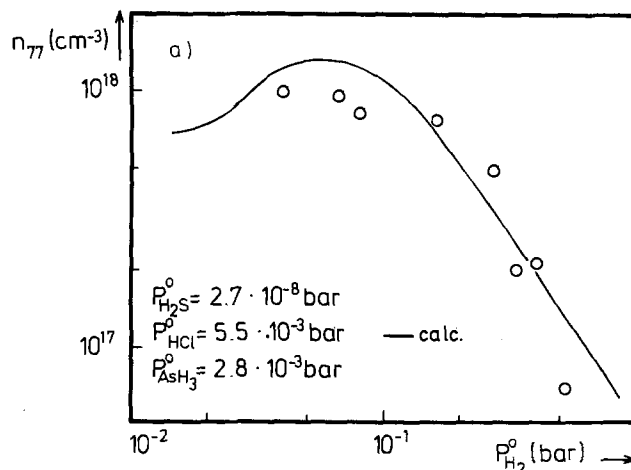


Fig. 4. Dependence of electron concentration resulting from doping on H_2 pressure. Curve: calculated; Experimental points: Ref. (2).

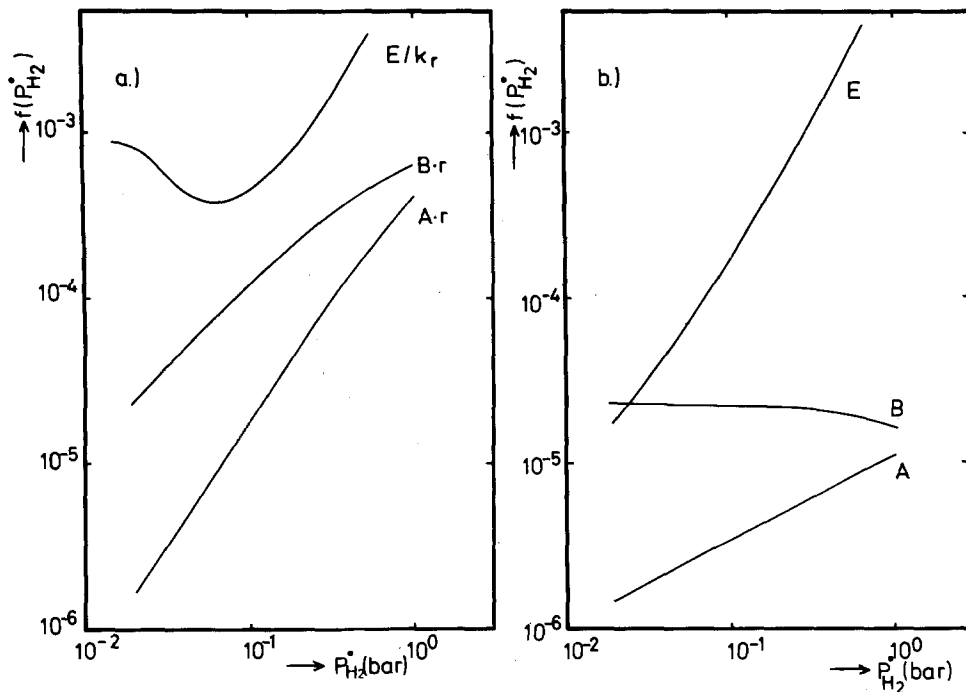


Fig. 5. a: dependence of terms appearing in Eq. [32] on H₂ pressure for experimental conditions of Fig. 4. b: dependence of terms defined by Eq. [33-35] on H₂ pressure for the same conditions.

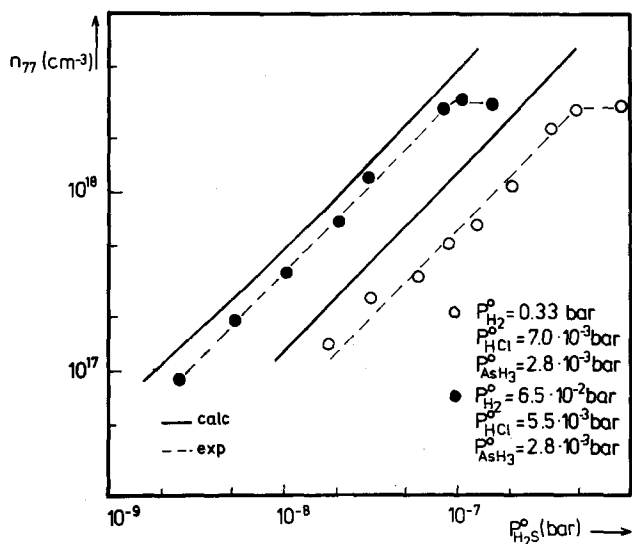


Fig. 6. Dependence of electron concentration on H₂S pressure. Calculated: full lines. Experimental: dotted lines Ref. (2).

Conclusions

The method of modeling the CVD processes proposed in an earlier paper (3) can be successfully adopted to describe the incorporation of dopants. Depending on the experimental conditions, the sulfur uptake during the epitaxial growth of GaAs on (100)-oriented substrates in a halide transport system is controlled by the kinetics of the surface reactions [3]-[5] or by the thermodynamics of the dopant incorporation [5]-[7]. The growth rate of the host material is one of the major parameters governing the incorporation process. A reduction of the total pressure in the Tietjen system causes a shift of the deposition conditions from thermodynamics to kinetic control (Fig. 5b) which is well known for the CVD of GaAs. However, the simultaneous decrease of the growth rate of the host material allows the dopant atoms to reach equilibrium concentrations, first at the surface, and next at very low growth rates, within the bulk of the deposited semiconductor film (Fig. 5a). The agreement between model calculations and experimental data may be considered to be an indication of the effect of the redistribution of dopant atoms between the interface and the bulk of the film.

Acknowledgments

The authors are indebted to Professor P. Balk for critical discussions. The contribution of J. Korec to this study was made possible by a fellowship granted him by the Alexander von Humboldt Foundation.

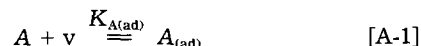
Manuscript submitted May 24, 1983; revised manuscript received Jan. 10, 1984.

The Technical University Aachen assisted in meeting the publication costs of this article.

APPENDIX

Description of Adsorption Reaction in Terms of Absolute Activities

Following the discussion published earlier (3), we proposed to describe an adsorption reaction of the type



in terms of activities of participating species, as commonly done in the description of the kinetics of homogeneous chemical reactions (14). The absolute activity λ_i of a species i is defined as

$$\lambda_i = \exp(\mu_i/kT) \quad [A-2]$$

where μ_i is the chemical potential (Gibbs free energy per molecule). Introducing a standard state for species i , one can express the absolute activity λ_i by means of an activity a_i of this species

$$\lambda_i = \lambda_i^\circ \cdot a_i \quad [A-3]$$

The absolute activity of the species i in the standard state λ_i° can be calculated using the method of statistical thermodynamics (3, 14). For an ideal gas, the activity a_i of species i in the gas phase is

$$a_i = \frac{p_i}{P^\circ} \quad [A-4]$$

where P° is the standard pressure (10⁵ Pa). The activity of an adsorbed species i has been proposed to be defined as (3)

$$a_{i(ad)} = \theta_i = C_{i(ad)}/C_s^\circ \quad [A-5]$$

where θ_i is the surface-coverage factor, $C_{i(ad)}$ the concentration of species i adsorbed at the surface, and C_s° the concentration of surface sites available for adsorption.

The condition for equilibrium state of reaction [A-1] can be expressed as follows

$$\lambda_A \cdot \lambda_v = \lambda_{A(ad)} \quad [A-6]$$

Substituting Eq. [A-3] in [A-6] and considering [A-4] and [A-5], we obtain for the equilibrium constant of the reaction [A-1]

$$K_{A(\text{ad})} = \frac{\lambda_v^{\circ} \lambda_A^{\circ}}{\lambda_{A(\text{ad})}^{\circ}} = \frac{\theta_A}{\theta_v(p_A/P^{\circ})} \quad [\text{A-7}]$$

REFERENCES

- N. Pütz, E. Veuhoff, K. H. Bachem, P. Balk, and H. Lüth, *This Journal*, **128**, 2202 (1981).
- E. Veuhoff, A. Sauerbrey, N. Pütz, M. Heyen, and P. Balk, *J. Phys. (Paris)*, **43**, C5 (1982).
- J. Korec and M. Heyen, *J. Cryst. Growth*, **60**, 286 (1982).
- J. Korec and M. Heyen, *ibid.*, **60**, 297 (1982).
- E. Veuhoff, N. Pütz, J. Korec, M. Heyen, and P. Balk, *J. Electron. Mater.*, **12**, 235 (1983).
- G. B. Stringfellow, *J. Phys. Chem. Solids*, **35**, 775 (1974).
- M. Heyen, H. Bruch, K.-H. Bachem, and P. Balk, *J. Cryst. Growth*, **24**, 127 (1977).
- D. T. J. Hurle, *J. Phys. Chem. Solids*, **40**, 627 (1979).
- E. Veuhoff, M. Maier, K.-H. Bachem, and P. Balk, *J. Cryst. Growth*, **53**, 598 (1981).
- K. H. Zschauer and A. Vogel, in "GaAs: 1970 Symposium Proceedings," p. 100, Institute of Physics, London (1971).
- H. C. Casey and M. B. Panish, *J. Cryst. Growth*, **13/14**, 818 (1972).
- R. Matz and H. Lüth, *Phys. Rev. Lett.*, **46**, 500 (1981).
- R. N. Hall, *Phys. Rev.*, **88**, 139 (1962).
- W. J. Moore, "Physical Chemistry," Longmans, London (1972).

Technical Notes



The Elimination of Devitrification Defects in Antimony Buried-Layer Diffusions

A. R. Alvarez and F. Pintchovski

Motorola Semiconductor, Incorporated, Mesa, Arizona 85202

Doped silicate glasses are widely used as diffusion sources for buried layers in bipolar technology. Thermal oxide is commonly used as a diffusion mask in these processes. More recently, the use of silicon nitride/silicon dioxide as a diffusion barrier for this application has been reported (1).

During the diffusion of boron, phosphorus, arsenic, and antimony from doped glass sources, a common type of glass damage occurs, devitrification, and this damage propagates into the silicon substrate (2). Devitrification can be defined as a phase transformation in which amorphous silica changes to a crystalline form, either cristoballite or trypidite. In this note, a composite $\text{Si}_3\text{N}_4/\text{SiO}_2$ diffusion mask is described. This mask was found to greatly decrease the levels of devitrification damage induced by antimony diffusions from a doped glass source. The reduction in defect density at buried layer led to improved breakdown characteristics in NPN transistors and a concomitant increase in functional circuit yields.

Experimental

Thermal SiO_2 and $\text{SiO}_2/\text{Si}_3\text{N}_4$ composites were evaluated as diffusion masks for antimony. The thermal oxide was grown in steam at 1200°C to a thickness of 1500 nm. A number of $\text{SiO}_2/\text{Si}_3\text{N}_4$ thickness combinations (Table I) were used. For the composite layer, SiO_2 was steam grown at 1000°C , while the Si_3N_4 was deposited by LPCVD at 780°C using ammonia and dichlorosilane as source gases (Fig. 1). An LPCVD antimony-doped SiO_2 glass was used as a diffusion source (3). Diffusions were carried out at 1250°C in an N_2/O_2 atmosphere.

Defect densities were obtained by averaging measurement taken at five points on a wafer. The measurements were performed using a microscope equipped with Nomarski interference contrast. Each measurement involved defect counting over a 0.0085 cm^2 area. A typical devitrification defect produced during the Sb buried-layer diffusion is shown in Fig. 2. Breakdown measure-

Key words: antimony, devitrification, buried layer, $\text{SiO}_2/\text{Si}_3\text{N}_4$ mask.

Table I. Devitrification vs. mask composition

T_{ox} (nm)	T_{NIT} (nm)	Devitrification density (cm^{-2})
200	20	0-90
200	40	0-40
200	100	0
1500	—	150-400

Buried layer: $\rho_s = 15-17 \Omega/\square$, $X_1 = 9 \mu\text{m}$.

ments of the collector-substrate diode formed in standard junction isolated bipolar integrated circuits were used to evaluate the electrical consequences of the defects.

Results and Discussion

Defect characterization of the Sb buried-layer process using SiO_2 as the diffusion mask indicated a very high defect density. The defect density vs. sheet resistance of the buried layer is plotted in Fig. 3. Microprobe analysis (EDAX) confirmed the presence of Sb at the defect sites in the silicon after glass removal. Examination of p-n

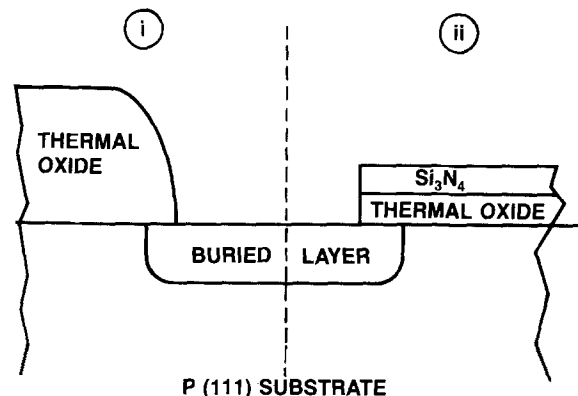


Fig. 1. Schematic representation of test structures: (i) thermal oxide diffusion mask, (ii) $\text{SiO}_2/\text{Si}_3\text{N}_4$ composite diffusion mask.

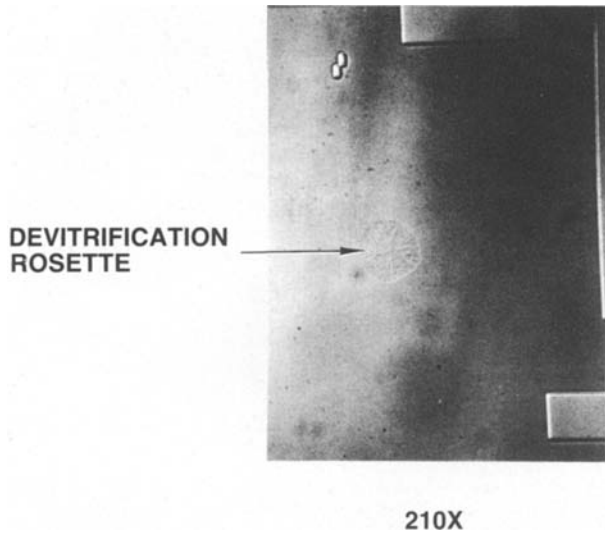


Fig. 2. Devitrification defect on thermal oxide diffusion mask

junction I-V characteristics verified the electrical activity of the defects. The Sb defects degraded collector-substrate breakdowns (BV_{CSO}) on fully processed NPN transistors. The resultant BV_{CSO} distribution was multimodal, since the breakdown voltage was dependent on the location of the defect (Fig. 4a). A simple heuristic argument is proposed to explain the distribution. Depending on the location of the defect, the avalanche breakdown voltage is determined by dopant concentration or is thickness limited by lateral depletion spread (Fig. 5). In the thickness-limited situation, breakdown is probably degraded further by the asperity of the defects'

configuration. When no defect is present, BV_{CSO} is nominally 200V. If the Sb defect overlaps the isolation diffusion, BV_{CSO} is reduced to approximately 35V. When the defect is located between the normal buried-layer pattern and the isolation diffusion, BV_{CSO} is again degraded, 110V being the dominant mode in this experiment.

From the defect density data, a first-order yield analysis was performed in order to estimate the effect of defect density on yield. The area subject to Sb defect-induced failure is from the edge of the buried-layer pattern to the center of the isolation pattern. Using this definition of "active" area, the yield model

$$\text{Yield} = \exp(-DA) \quad [1]$$

where D = effective defect density and A = critical area, was fitted to existing data. Equation [1] does not take into account defect clustering or a nonrandom distribution of defects across a wafer. Even so, it correlated well with observed yields, confirming devitrification as a dominant failure mode in the particular class of circuits studied.

Devitrification of SiO_2 during Sb and As diffusions is well documented (3, 4). It was felt that the suppression of SiO_2 devitrification would greatly reduce the defect density at the buried layer. During the course of experimentation, it was observed that besides being an effective diffusion barrier, an SiO_2/Si_3N_4 composite eliminated the devitrification problem. Defect density data vs. composite mask structure is given in Table I. Devitrification defects were not observed for nitride thicknesses greater than 100 nm. It follows that the devitrification-defect density is independent of the buried-layer sheet rho for nitride thicknesses greater than 100 nm. The composite mask exhibited similar results when a spin-on antimony solution was substituted for the LPCVD predeposition

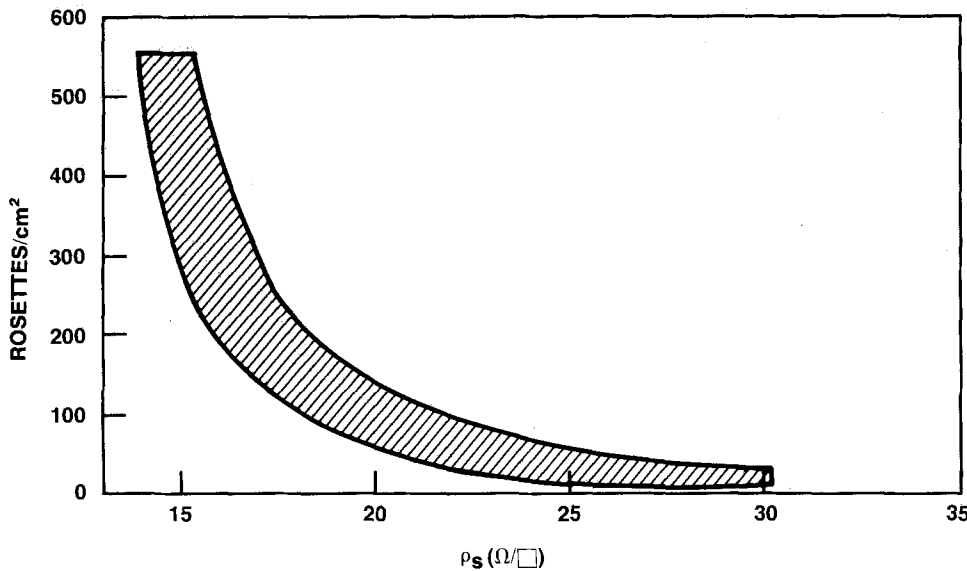


Fig. 3. Devitrification defect density vs. buried layer sheet resistance.

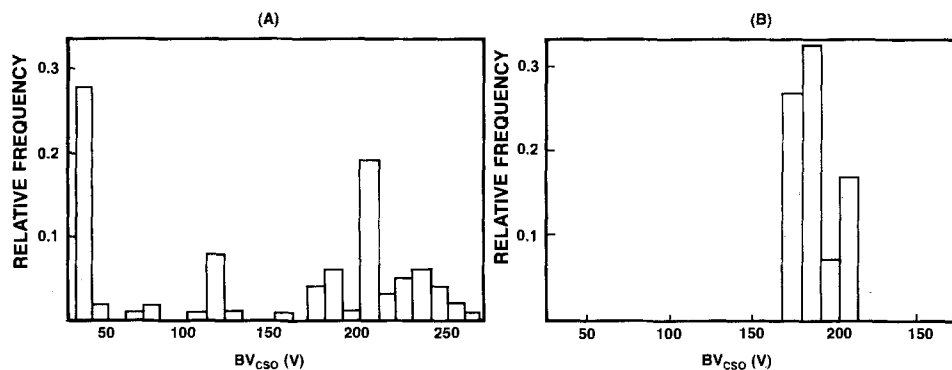


Fig. 4. Relative frequency vs. breakdown voltage: (A) thermal oxide diffusion mask, (B) SiO_2/Si_3N_4 composite diffusion mask.

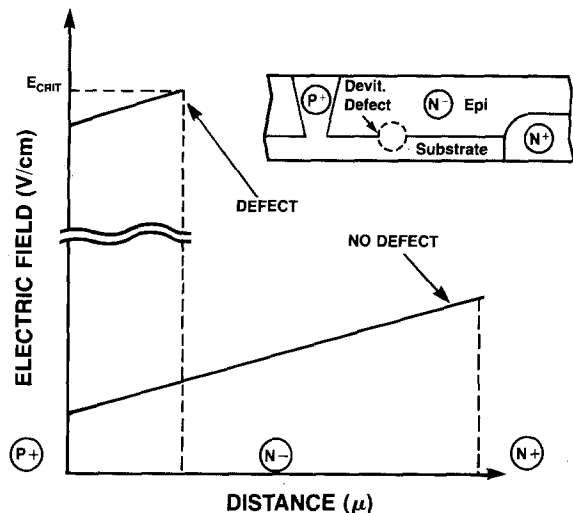


Fig. 5. Electric field vs. distance with and without devitrification defect

(5). An additional benefit of the composite is the elimination of the very long oxidation process previously required when an oxide mask alone was used.

Because of the reduction in defect density at the buried-layer step, utilization of the composite mask resulted in higher yields to the BV_{CSO} test. Breakdown data for NPN transistors processed with the composite mask exhibited a single mode centered at 190V (Fig. 4b).

Conclusion

An SiO_2/Si_3N_4 composite was found to essentially eliminate devitrification defects commonly associated with oxide-masked antimony buried-layer diffusions. The reduction in defect density significantly increased the yield of NPN transistors with 200V BV_{CSO} . The composite mask makes it possible to fabricate low sheet rho Sb buried layers with negligible yield loss due to diffusion-mask devitrification.

Acknowledgments

The authors wish to acknowledge K. Drozdowicz for first documenting the problem, R. Roop, J. B. Price, and P. J. Tobin for their guidance, and J. Featheringham, T. Duvall, and P. Wheeler for their assistance in carrying out the experiments.

Manuscript submitted Nov. 7, 1983; revised manuscript received Feb. 24, 1984.

Motorola Semiconductor, Incorporated assisted in meeting the publication costs of this article.

REFERENCES

1. A. Dixit, C. S. Chen, and C. E. Volk, *This Journal*, **127**, 2239 (1980).
2. E. Arai and Y. Terunuma, *Jpn. J. Appl. Phys.*, **9**, 691 (1970).
3. F. Pintchovski, P. J. Tobin, and J. B. Price, Abstract 418, p. 654, *The Electrochemical Society Extended Abstracts*, Vol. 83-1, San Francisco, California, May 8-11, 1983.
4. M. Ghezzi and D. M. Brown, *This Journal*, **120**, 110 (1973).
5. S. Wu, *ibid.*, **128**, 1804 (1981).

Improved Techniques for Orientation of (100) InP and GaAs Wafers

E. A. Caridi and T. Y. Chang

AT&T Bell Laboratories, Holmdel, New Jersey 07733

The distinction between $[011]$ and $[0\bar{1}\bar{1}]$ directions on (100) InP and GaAs substrates is often of crucial importance in epitaxial growth and device fabrication. In molecular beam epitaxy (MBE), the interpretation of the reflection high energy electron diffraction (RHEED) pattern depends on along which of these two directions the electron beam is directed (1). For the fabrication of various stripe geometry lasers (2) and etched mirror lasers (3), the identification of these two directions is essential since their etching properties are very different. The properties of FET's fabricated on (100) substrates have also been found to be orientation dependent due to the piezoelectric effect (4). It has been common practice to identify the $[011]$ and $[0\bar{1}\bar{1}]$ directions by patterning and etching mesas or orthogonal grooves on the substrate followed by an inspection of the cleaved cross section (5). This procedure is both tedious and wasteful of material. Recently, a simpler method based on the inspection of natural etch patterns on cleaved $\langle 011 \rangle$ surfaces has been introduced (6). This latter method minimizes the waste of material. However, the contrast between different etch patterns is relatively weak and easily confused. We describe in this paper novel techniques that are simple, unambiguous, and applicable to polished and unpolished substrates. By preparing the substrate in a prescribed manner, the orientations can always be ascertained almost instantly without wasting any material.

We find that the orientations on saw cut (100) surfaces of InP wafers can be most effectively revealed by removing 30 μm or more of the material per surface by

free etching in a 1:1:1 mixture of 96% H_2SO_4 :30% H_2O_2 : H_2O (7). Large wafers may be placed in a rack made of inert material (*e.g.*, Ta) and immersed in the solution for treatment. To obtain the desired result, it is essential that the solution be mixed immediately before use. The effectiveness of the mixture diminishes rapidly within a few minutes. For about 400 ml of solution, the temperature will remain at 85° to 90°C due to the exothermic nature of the solution. The appropriate etch time in such a case is 5 min. For treating small test pieces using less than about 200 ml of solution, it is necessary to preheat the beaker and maintain the solution temperature at about 80°C on a hot plate. In this latter case, the appropriate etch time is 20 min. A photomicrograph of the resulting surface is shown in Fig. 1. Greatly elongated parallel etch pits are clearly evident. In the case of a (100) saw cut GaAs surface, etching in a solution of 1:8:8 H_2SO_4 : H_2O_2 : H_2O (8) at a temperature of 55°C for 3 min produced features as shown in Fig. 2. The amount of material removed per surface is about 50 μm .

Similar preferential etching characteristics can be revealed on a polished surface of InP or GaAs. In this case, it becomes necessary to produce some etch pits on the surface first and then develop them into distinct orientation dependent features by using the 1:1:1 sulfuric etch for InP and the 1:8:8 sulfuric etch for GaAs.

A standard technique used to reveal the crystalline defects on InP single crystal is the Hubers etch (9) which is a solution of H_3PO_4 :HBr in a 2:1 ratio. Figure 3a shows the characteristically symmetric etch pits produced after 2 min in the Hubers etch. These pits can be preferentially etched to produce the elongated features similar to those

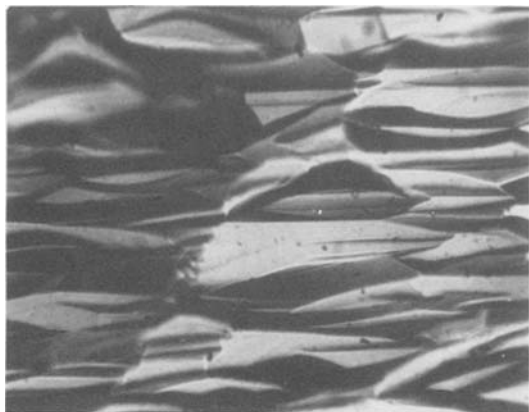


Fig. 1. Saw cut (100) surface of InP after etching for 20 min in 1:1:1 $\text{H}_2\text{SO}_4:\text{H}_2\text{O}_2:\text{H}_2\text{O}$ at a temperature of 80°C . The area of the figure is about $90\ \mu\text{m}$ by $60\ \mu\text{m}$.

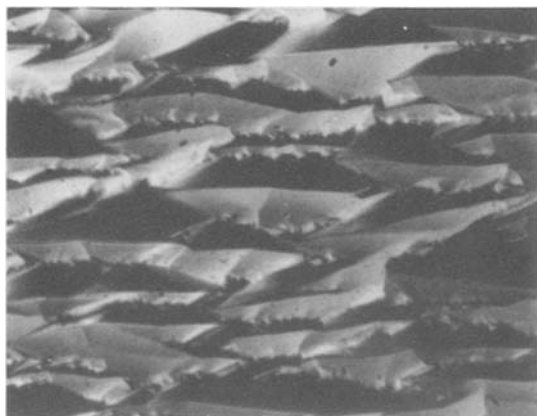


Fig. 2. Saw cut (100) GaAs surface after a 3 min etch in 1:8:8 $\text{H}_2\text{SO}_4:\text{H}_2\text{O}_2:\text{H}_2\text{O}$ at a temperature of 55°C . The area of the figure is about $90\ \mu\text{m}$ by $60\ \mu\text{m}$.

on the saw cut surface (Fig. 1 and 2) with the 1:1:1 sulfuric etch. Figure 3b shows the same area as Fig. 3a after being etched in the 1:1:1 sulfuric system at 80°C for 5 min.

A polished (100) GaAs surface can be suitably roughened by etching for 5 to 10 min in a 1:1:1 solution of 38% $\text{HCl}:\text{H}_2\text{O}_2:\text{H}_2\text{O}$. When this is followed by a 3 min etch using a 1:8:8 solution of $\text{H}_2\text{SO}_4:\text{H}_2\text{O}_2:\text{H}_2\text{O}$, one obtains a characteristically elongated etch pattern similar to that shown in Fig. 2, but the scale is an order of magnitude finer.

It has been determined by comparison with known etching characteristics of GaAs (10) and InP (7) that in all the above cases the pits are preferentially etched in the $[01\bar{1}]$ direction. This has been confirmed by the observed RHEED pattern taken in an MBE chamber when the crystal is put through the temperature cycle (1).

In all the above discussions, the designation of $[011]$ and $[01\bar{1}]$ directions are surface specific in that the substrate surface of interest (the front surface) is always defined as the (100) surface. To examine the properties of the back surface, which is the $(\bar{1}00)$ surface in the initial definition, one must redefine the back surface as (100). Simultaneously, in order to preserve the right-handedness of the coordinate system, one must reverse one more coordinate (say the third coordinate). As a result, the orientations of $[011]$ and $[01\bar{1}]$ on the back surface are rotated 90° from those on the front surface. Consistent with such a surface specific definition, we find that all the etch patterns described above are rotated 90° on the back surface of the substrate. This phenomenon of 90° rotation can be understood macroscopically from the 90° rotation of the relative locations of intervening $\{111\}$ facets of type A [Group III surface] and type B [Group V sur-

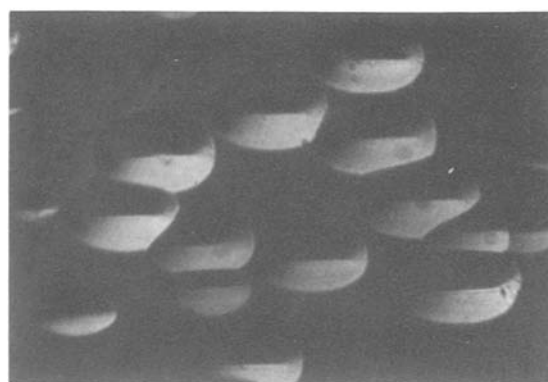
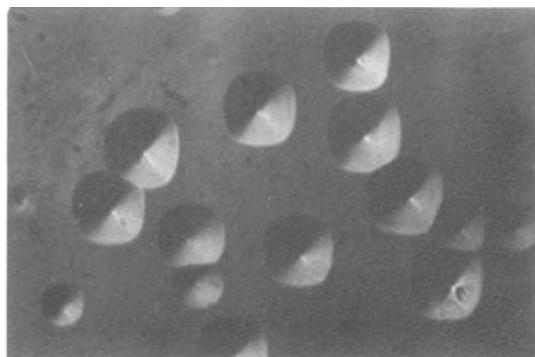


Fig. 3. (a, top) A polished (100) surface of InP is shown after 2 min in an Hubers etch. (b, bottom) Same area as (a) after etching with 1:1:1 $\text{H}_2\text{SO}_4:\text{H}_2\text{O}_2:\text{H}_2\text{O}$ for 5 min. The area of each figure is about $120\ \mu\text{m}$ by $90\ \mu\text{m}$.

face] (11) on opposite substrate surfaces (6). It can also be understood microscopically from the 180° reversal of the surface atomic arrangement as one goes from (011) surface to $(01\bar{1})$ surface, as well as from the 90° rotation of surface bonds on opposite surfaces of the substrate (assuming both Group III stabilized or both Group V stabilized).

We find the most convenient way to keep track of the substrate orientation is to develop the etch patterns on both sides of an unpolished wafer and then polish one side for epitaxial growth and processing. The orientation can always be ascertained simply by inspecting the back surface while keeping in mind the 90° rotation between front and back surfaces. This method is simple, unambiguous, and incurs no waste of material. The removal of saw cut damages by the etching process should also be beneficial to epitaxial growth.

Manuscript submitted Oct. 19, 1983; revised manuscript received Feb. 1, 1983.

AT&T Bell Laboratories assisted in meeting the publication costs of this article.

REFERENCES

1. A. Y. Cho, *J. Appl. Phys.*, **47**, 2841 (1976).
2. H. C. Casey, Jr. and M. B. Panish, "Heterostructure Lasers," B., Chap. 7, Academic Press, New York (1978).
3. K. Iga and B. I. Miller, *IEEE J. Quantum Electron.*, **18**, 22 (1982).
4. P. M. Asbeck, C. P. Lee, R. Vahrenkamp, and M. J. Sheets, Paper A-7 presented at the 25th Electronic Materials Conference, Burlington, Vermont, 1983.
5. T. Kambayash, C. Kitahara, and K. Iga, *Jpn. J. Appl. Phys.*, **19**, 79 (1980).
6. L. W. Stulz and L. A. Coldren, *This Journal*, **130**, 1628 (1983).
7. S. Adachi and H. Kawaguchi, *ibid.*, **128**, 1342 (1981).
8. C. Y. Chen and S. Wang, *J. Appl. Phys.*, **51**, 1802 (1980).
9. A. Huber and N. T. Linh, *J. Cryst. Growth*, **29**, 80 (1975).
10. S. Iida and K. Ito, *This Journal*, **118**, 768 (1971).
11. H. C. Gatos and M. C. Lavine, *ibid.*, **107**, 427 (1960).

Cadmium Selenide Interface States Studied by Electrochemical Photocapacitance Spectroscopy

Ron Haak* and Dennis Tench*

Rockwell International Science Center, Thousand Oaks, California 91360

With time and the efforts of many workers, it has become increasingly clear that surface oxides play a key role in determining the electrical properties of the II-VI materials. For n-CdSe, recent literature reports indicate that oxygen chemisorbs on the semiconductor surface to produce a negatively charged interface state (1), which dominates the performance of electronic devices based on this material (2). In view of the obviously important implications of such findings, additional work in this area is certainly warranted.

In the present work, the electrochemical photocapacitance spectroscopy (EPS) method (3, 4), which involves measuring the differential capacitance for the reverse-biased semiconductor in an electrolyte as a function of incident subbandgap light, was applied to further elucidate the nature of interface states on n-CdSe. This method has been shown to be an unusually sensitive means for characterization of deep levels in various semiconductor materials (4). In aqueous electrolytes, the interfacial oxide structure might be expected to be similar to that formed in the ambient atmosphere. A key goal in the present work was to establish unequivocally the location of the state associated with oxygen adsorption. Note that an alternate interpretation for previous data was that the observed states actually resided in the bulk and were rendered detectable by the enhanced thickness of the semiconductor space-charge layer resulting from the negative surface charge associated with adsorbed oxygen.

Experimental Details

The electrochemical photocapacitance spectroscopy (EPS) method, apparatus, and procedures have been described in detail previously (4). Electrolytes used in the present studies were 0.5M aqueous KOH and 0.1M tetraethylammonium perchlorate/acetonitrile. The reference electrode was a double-junction Ag/AgCl in the former electrolyte and a Ag/Ag⁺ (0.1M AgNO₃, 0.1M tetraethylammonium perchlorate-acetonitrile) in the latter. All potentials are reported relative to the flatband potential (U_{FB}), which was determined by ac impedance measurements to be -0.9V vs. Ag/AgCl in the aqueous solution and -0.9V vs. Ag/Ag⁺ in the acetonitrile electrolyte. The wavelength scan rate in nanometers per second is given in the figure captions.

The n-CdSe electrodes (0.2 cm² × 0.1 cm thick) were cut perpendicular the Z-axis from rods obtained from Cleveland Crystals, Incorporated (Cleveland, Ohio), and had charge carrier concentrations in the 10¹⁷/cm³ range. Ohmic contacts were made with In-Ga alloy. After attachment of a wire lead via silver epoxy, the electrode was sealed in Torr Seal[®] resin (Varian Associates, Palo Alto, California). Electrodes were polished on aqueous alumina powder slurries, to 1 μm particle size, unless otherwise noted. Chemically etched electrodes were immersed in 50 volume percent (v/o) HNO₃ for about 10s, then dipped in aqueous polysulfide solution (1.0M S + 2.5M Na₂S + 1.0M KOH) to remove excess Se from the surface. Photoetching was performed in an aqueous basic ferricyanide solution.

Results and Discussion

Figure 1 shows an EPS spectrum for a photoetched single crystal of n-CdSe in a basic aqueous electrolyte. Three capacitance increases/plateaus, associated with

*Electrochemical Society Active Member.

Key words: cadmium selenide, surface states, oxygen adsorption.

transitions from donor states at 1.04, 1.21, and 1.34 eV (onset values) to the conduction band, are evident. A capacitance decrease near the bandedge (at 1.60 eV), corresponding to a transition from the valence band to a donor state ~ 0.2 eV below the conduction bandedge, is also resolved. Note that, as might be expected, the onset energies for these phototransitions are found to depend on the solvent, and the observed or apparent values are affected by the concentration of the state in question and by interference from energetically adjacent states as their concentrations vary. Since such shifts in onset energy are sufficiently small so that there is little doubt concerning the identity of the different states, they are referred to below by the onset energies given here, but the spectra are labeled with the actually observed values, which are also given in parentheses in the text.

The probable origin of these levels can be ascertained by comparison of the EPS results with the vacuum surface photovoltage data for single-crystal n-CdSe reported by Brillson (1). Figure 2 shows an EPS spectrum for chemically etched single-crystal n-CdSe (curve 1), and surface photovoltage spectra for oxygen-adsorbed¹ (curve 2) and vacuum-cleaved (curve 3) surfaces. Note that the observed onset for the 1.21 eV state is somewhat higher in energy (1.28 eV) in this case, presumably because of interference from a large concentration of the 1.04 eV state. It is evident that the surface photovoltage spectrum for the oxygen-adsorbed surface and the EPS spectrum are very similar, indicating that the same bandgap states are involved. The 1.04 eV transition, and possibly the transition

¹Such a surface gave results very similar to those for an etched surface and might be expected to be comparable to that in an aqueous solution.

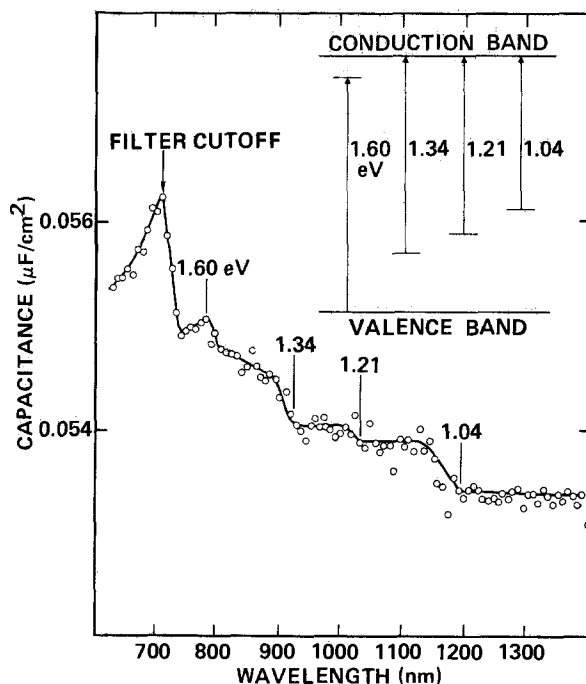


Fig. 1. EPS spectrum (5 kHz, 1.0 nm/s) and associated energy levels/phototransitions for a photoetched n-CdSe single crystal (0.9V vs. U_{FB}) in aqueous 0.5M KOH solution.

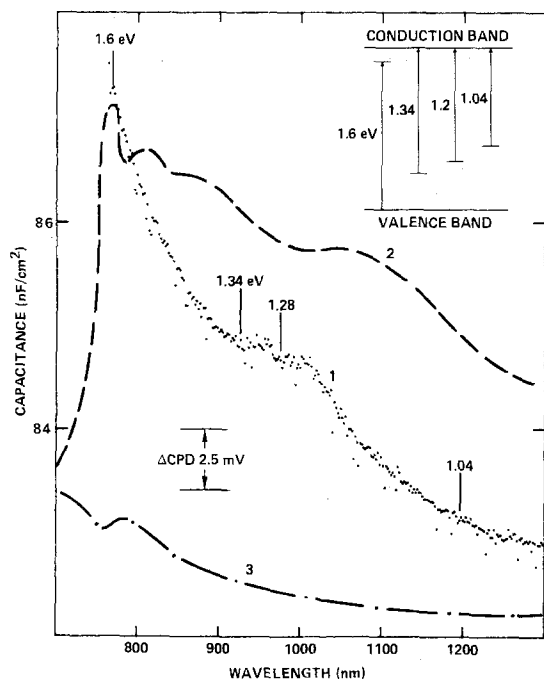


Fig. 2. Comparison of an EPS spectrum (5 kHz, 0.1 nm/s) for chemically etched single-crystal CdSe (0.7V vs. U_{FB}) in 0.5M KOH solution (curve 1) with surface photovoltage spectra reported in Ref. (1) for (curve 2) oxygen-adsorbed (70% coverage) and (curve 3) vacuum-cleaned (LEED-ordered) single-crystal n-CdSe.

at 1.21 eV (not resolved by the vacuum technique), must involve interface states associated with oxygen adsorption, since no change in surface photovoltage was observed for the vacuum-cleaved CdSe (curve 3) in this energy range. The densities of these states, calculated from the capacitance changes (4), are $5 \times 10^{12}/\text{cm}^2$ and $4 \times 10^{11}/\text{cm}^2$, respectively. The 1.34 eV transition is apparently intrinsic to CdSe since it was detected by Brillson for both vacuum-cleaved and oxygen-adsorbed CdSe crystals.

Although the capacitance decrease occurring just below the bandedge (at ~ 1.6 eV) is not always clearly resolved in EPS spectra because of interference from band-tailing, the state responsible (~ 0.2 eV below the conduction bandedge) always seems to be present in CdSe, at least in small concentrations, and is noteworthy. Brillson (1) found that argon-bombardment enhances the corresponding feature in surface photovoltage spectra, indicating that the state involved is associated with a lattice defect. EPS studies, which will be the subject of a future publication, have shown that this state is a donor-type interface state which is present in large concentrations in polycrystalline material prepared under some conditions.

EPS data for n-CdSe in aqueous solutions also correlate extremely well with other solid-state literature data for oxygen-adsorbed surfaces (2, 5-10). Another example is given in Fig. 3, which shows the EPS spectrum from Fig. 2 on the same graph with photocapacitance data reported by Ture *et al.* (2) for an aged Au-CdSe Schottky barrier device. Again, the similarities in the two spectra are striking; the apparent differences in the relative concentrations of the various states (as reflected in the relative magnitude of the associated capacitance changes) and the small shifts in onset energies are not surprising, considering the differences in environment at the two interfaces. It is important to note that these solid-state workers showed that the aging process for their devices involved conversion of the CdSe surface from its normal hexagonal structure to a cubic form, which readily chemisorbs oxygen. It was found that the aging process could be greatly accelerated by polishing the crystal, which produces a cubic surface layer.

Figure 4 shows EPS spectra in 0.5M KOH for a single-crystal n-CdSe after polishing on 1 μm grit without subse-

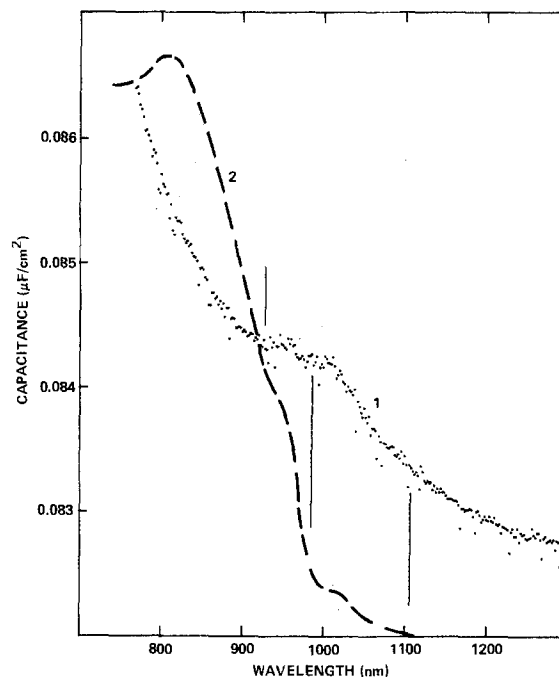


Fig. 3. Comparison of the EPS spectrum (curve 1) from Fig. 2 with a photocapacitance spectrum (curve 2) for an aged Au-CdSe Schottky-barrier device [after Ref. (2)].

quent etching. Although the onset energies are shifted slightly, it is evident that the 1.04 (1.05), 1.21 (1.26), and 1.6 (1.65) eV transitions observed for the etched surfaces also occur for the polished surfaces, although the corresponding states are present in larger concentrations. That all of these states reside at the interface is supported by the insensitivity of the corresponding capacitance changes to the electrode potential (Fig. 4), which is also observed for etched electrodes. Presumably, the 1.34 eV state is not resolved because of interference from a large concentration of the 1.21 eV state.

Figure 5 shows EPS spectra measured in acetonitrile solution for photoetched n-CdSe single crystals from two different batches of material. From spectrum no. 1 (same material as for studies discussed above), it is evident that the same principal interface states, although shifted

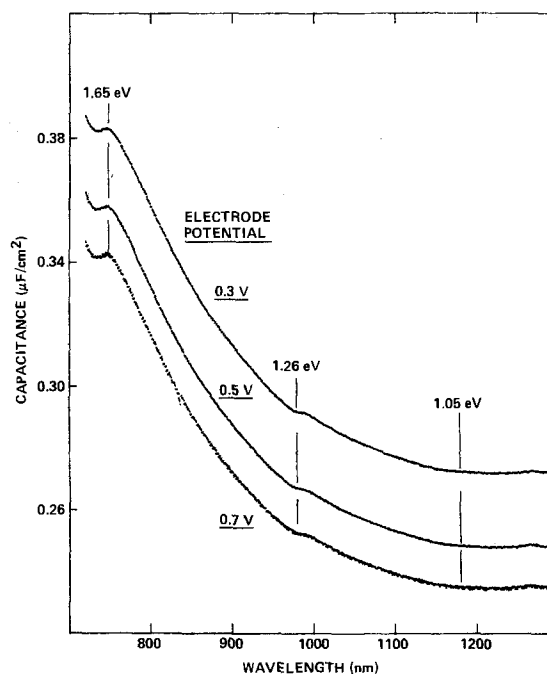


Fig. 4. EPS spectra (5 kHz, 0.3 nm/s) for a polished (1 μm) n-CdSe single crystal at various bias voltages in 0.5M KOH.

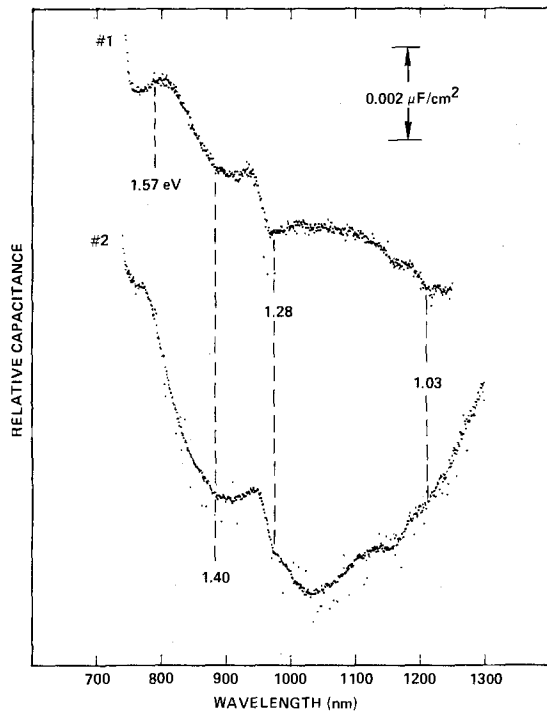


Fig. 5. EPS spectra (7 kHz, 2.0 nm/s) in acetonitrile (0.1M Et_4NClO_4) for photoetched n-CdSe single crystals from two batches of material (1.1V vs. U_{EB}).

slightly in energy in some cases, are also present in the nonaqueous solvent. This indicates that the CdSe surface structure formed by etching in aqueous solutions, including the chemisorbed oxygen, is reasonably stable in the nonaqueous solvent. In acetonitrile, however, some "peaking" generally occurs in the plateau regions for both the 1.04 (1.03) and 1.21 (1.28) eV states. Transitions from the valence band to bandgap states (which would bring about capacitance decreases) could produce such effects, but would require the introduction of two acceptor states at specific energies, which is highly unlikely. It is much more probable that the surface oxide structure, which is responsible for these states, is somewhat electrically decoupled from the conduction band in the acetonitrile environment so that the associated phototransitions are more localized, *i.e.*, involve an excited-state intermediate and thermal activation of the electron into the conduction band (4).

For material no. 2 (Fig. 5), the 1.40 eV transition is apparently enhanced, and a capacitance decrease, corresponding to a transition from the valence band to a bandgap state, is evident at longer wavelengths; the observed "tail" is superimposed on the normal 1.04 eV transition. This long wavelength tail is also observed for material no. 2 in aqueous solvents and is apparently associated with excess selenium in the crystal, since photoetching in aqueous sodium sulfate solutions, which is known to produce a selenium layer on CdSe surfaces, greatly enhances the magnitude of the long wavelength capacitance decrease.

At less positive potentials, significant CdSe surface reactions do occur in acetonitrile solution. This is illustrated in Fig. 6, which shows EPS spectra for an n-CdSe single crystal as a function of electrode potential. Normal spectra are observed at more positive potentials. As the electrode potential is decreased, however, the 1.21 (1.26) eV transition slowly disappears and the 1.04 eV transition

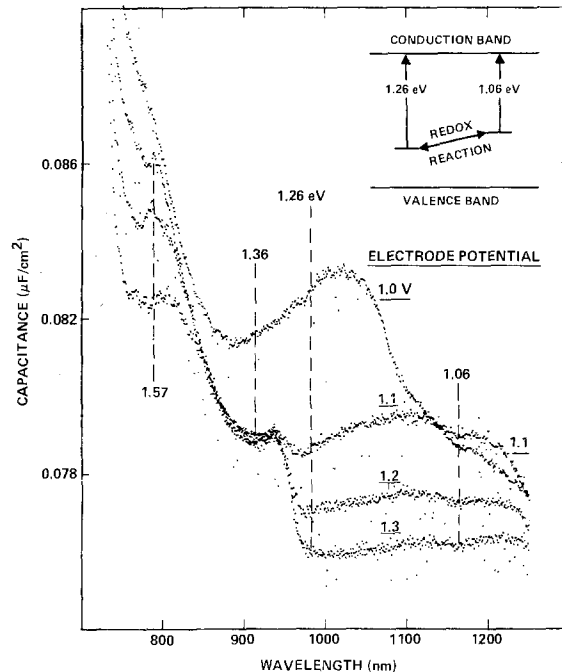


Fig. 6. EPS spectra (7 kHz, 0.3 nm/s) in acetonitrile (0.1M Et_4NClO_4) for a photoetched n-CdSe single crystal as a function of electrode potential.

becomes more pronounced. Apparently, the oxide structure associated with the 1.21 (1.26) eV state is electrochemically reduced to that corresponding to the 1.04 eV state, a process which to some extent is reversible. As might be expected, although the qualitative features are consistent, the quantitative aspects of EPS spectra for CdSe in acetonitrile are very difficult to reproduce, which, apparently, is a consequence of the instability of the surface oxide in this media.

Acknowledgments

This work was partially supported by the Solar Energy Research Institute (SERI) under subcontract no. XE-2-02126-01. The surface photovoltage data in Fig. 2 and the solid-state photocapacitance data in Fig. 3 were reproduced with permission of the publisher, North Holland Publishing Company, Amsterdam.

Manuscript submitted Oct. 24, 1984; revised manuscript received Jan. 6, 1984.

Rockwell International assisted in meeting the publication costs of this article.

REFERENCES

1. L. J. Brillson, *Surf. Sci.*, **69**, 62 (1977).
2. J. E. Ture, G. J. Russell, and J. Woods, *J. Cryst. Growth*, **59**, 223 (1982).
3. R. Haak, C. Ogden, and D. Tench, *This Journal*, **129**, 891 (1982).
4. R. Haak and D. Tench, *ibid.*, **131**, 275 (1984).
5. C. Manfredotti, A. Rizzo, L. Uasanelli, S. Galassini, and L. Ruggiero, *J. Appl. Phys.*, **44**, 4563 (1973).
6. E. Guesne, C. Sebenne, and M. Balkanski, *Surf. Sci.*, **24**, 18 (1971).
7. R. L. Consigny and J. R. Madigan, *Solid-State Electron.*, **13**, 113 (1970).
8. B. A. Kulp, *J. Appl. Phys.*, **37**, 4936 (1966).
9. R. H. Bube and L. A. Barton, *J. Chem. Phys.*, **29**, 128 (1958).
10. J. Reichman and M. A. Russak, *This Journal*, **128**, 2025 (1981).

Solid Solutions and Phase Transformations in the System ZnS-CdS under Hydrothermal Conditions

Shoji Kaneko, Hideo Aoki, Yuji Kawahara, and Fumio Imoto

Department of Industrial Chemistry, Faculty of Engineering, Shizuoka University, Johoku, Hamamatsu 432, Japan

Koichi Matsumoto

Research Institute of Electronics, Shizuoka University, Johoku, Hamamatsu 432, Japan

Zinc sulfide (ZnS) and cadmium sulfide (CdS) have the same two crystal structures, the cubic zinc-blende form transforming to the hexagonal wurtzite form as temperature is increased (1). Solid solubilities and phase transformations in the ZnS-CdS system were investigated using powder compacts heated in He, HCl, or H₂S (2, 3), and in single crystals grown by the chemical transport method (4, 5) or the Bridgman method (6). The ZnS-CdS phase relationships in hydrothermally processed samples have not been investigated except for a brief description of solid solution formation by Kremheller *et al.* (7).

In previous papers, we suggested that hydrothermal reaction was a useful synthesis method for inorganic powder materials (8-11). We further found that solid solution formation and phase transformations in the ZnS-MnS system were promoted by hydrothermal treatments (12). The present investigation was undertaken to elucidate the phase relationships in hydrothermally treated ZnS-CdS mixtures.

Experimental

High purity ZnS and CdS [> 99.99 weight percent (w/o)] for luminescent applications (Dai Nippon Painting Company, Limited) were used as starting materials. After combining the two powders in an agate mortar with ethyl alcohol, the mixture was dried overnight in an oven at 90°C and sealed, together with a 50% water charge, in a test-tube type autoclave (ca. 8 cm³ volume). The autoclave was heated in an electric furnace controlled to $\pm 2^\circ\text{C}$. Samples containing 0-100 mol percent (m/o) CdS at 10 m/o intervals were held in the furnace at 200°-400°C for 24h. After this treatment, the autoclave was rapidly removed from the furnace and submersed in ice water.

The phases present and the extent of solid solution formation were confirmed from x-ray diffraction patterns using a Rigaku Geigerflex Model D-2 with Ni-filtered CuK α radiation, and high purity silicon was used as an internal standard.

Results and Discussion

Crystalline phases.—It is well known that the cubic \rightarrow hexagonal transformation in ZnS takes place at 1020°C in a dry process (13). In the present hydrothermal study, the pressure was varied from 16 atm (1.6 MPa) at 200°C to 200 atm (20 MPa) at 400°C, depending on the treatment temperature, because of the constant 50% water charge (14). The phase transformation to hexagonal ZnS was not observed even at 400°C and 200 atm pressure. The transformation temperature of CdS in a dry process has not been well established, although it is known that the cubic \rightarrow hexagonal transformation is complete at 600°C in well-purified N₂ or Ar atmospheres. The phase transformation of CdS started to occur at 250°C using the present hydrothermal treatment, proceeded gradually above this temperature, and was completed at 300°C (Fig. 1). Increased pressure alone does not depress the transformation temperature this far until it has reached several hundred atmospheres (15, 16). Consequently, it is probable that the phase transformation observed under hydrothermal conditions has been facilitated by interaction with

Key words: inorganic, crystallography, solubility, system ZnS-CdS, hydrothermal treatment.

the included water (17) rather than by the pressure alone (14). Phase boundaries in the ZnS-CdS system under hydrothermal conditions are shown in Fig. 1. A complete ZnS-CdS solid solution was not formed by the hydrothermal treatment over the temperature and pressure ranges investigated. The solubility of ZnS in CdS increases and the solubility of CdS in ZnS decreases with increasing temperature. Adding ZnS to CdS under hydrothermal conditions decreases the cubic \rightarrow hexagonal transformation temperature. The solubility of ZnS in CdS is ca. 50 m/o and that of CdS in ZnS ca. 10 m/o at 400°C, suggesting that the zinc ion, which has a smaller ionic radius (0.74Å), was easily incorporated into the CdS lattice, but that the cadmium ion, which has a larger ionic radius (0.97Å), was not so easily incorporated into the ZnS lattice.

No intermediate compounds such as hydroxides, sulfates, or oxysulfates were identified from the x-ray diffraction patterns. Thus, although the effect of hydrothermal conditions on the phase relationships is important, its precise role is not clear.

Lattice constants of the solid solutions.—Figure 2 shows the lattice constants of solid solutions in the system ZnS-CdS calculated from the x-ray diffraction data by Cohen's least squares method (18). The lattice constant (a) of the cubic ZnS solid solution (ss) increased with increasing CdS content according to Vegard's law. Cubic ZnS ss was identified in the x-ray pattern of the 400°C sample up to 50 m/o CdS, but the lattice constant could not accurately be determined beyond 20 m/o CdS owing to the weakness of the ZnS x-ray peaks. A similar effect in the hexagonal CdS ss limited lattice parameter determination to ≤ 50 m/o ZnS (Fig. 2). The lattice constants a and c of hexagonal CdS decreased with increasing ZnS content.

Hume-Rothery's rules are almost satisfied between the hexagonal forms ZnS and CdS, so that a complete range of solid solution should be formed between the two sul-

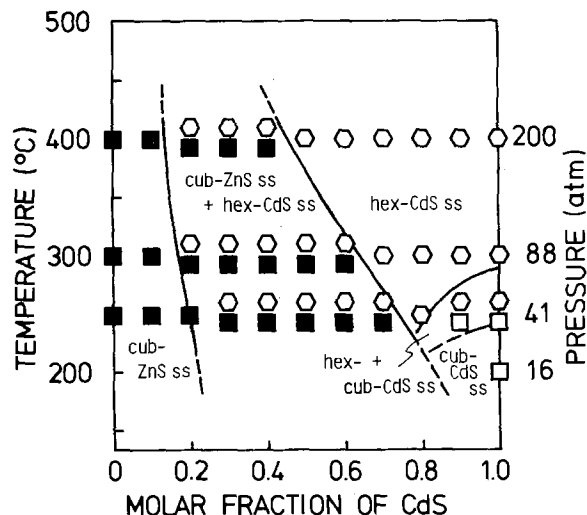


Fig. 1. Phase diagram of the system ZnS-CdS under hydrothermal conditions. ■: cubic-ZnS ss, □: cubic-CdS ss, ○: hexagonal-CdS ss.

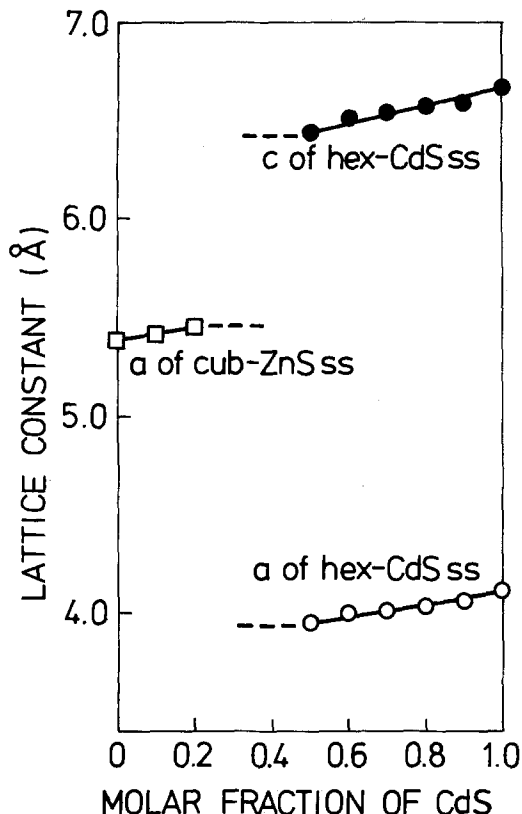


Fig. 2. Variation of lattice constants with composition in ZnS-CdS solid solutions treated hydrothermally at 400°C.

vides. The fact that two-phase regions existed in the system ZnS-CdS presumably stems from slight differences in the planar stacking of the two phases; cubic ZnS and hexagonal CdS formed under hydrothermal conditions, as previously observed in the system ZnS-MnS (12).

Summary

The cubic→hexagonal transformation of ZnS did not occur under hydrothermal conditions up to 400°C, while that of CdS was shifted to lower temperatures by hydro-

thermal treatments and additions of ZnS in solid solution. The cubic→hexagonal transformation of CdS ss was complete at 300°C. The formation of ZnS-CdS solid solutions was verified by variation of the lattice constants as a function of composition. In the system ZnS-CdS, the plots of the lattice constants of ZnS- and CdS-rich solid solutions vs. composition followed Vegard's law. The solid solubility of ZnS in CdS increased with an increase in temperature, while that of CdS in ZnS decreased with increasing temperature.

Manuscript submitted July 11, 1983; revised manuscript received Jan. 30, 1984.

REFERENCES

1. A. F. Wells, "Structural Inorganic Chemistry," 4th ed., p. 606, Oxford University Press, London (1975).
2. M. Sakaguchi, M. Ohta, M. Satoh, and T. Hirabayashi, *This Journal*, **124**, 550 (1977).
3. M. Satoh and M. Sakaguchi, *Denki Kagaku*, **47**, 544 (1979).
4. P. Cherin, E. L. Lind, and E. A. Davis, *This Journal*, **117**, 233 (1970).
5. W. Palosz, M. J. Kozielski, and B. Palosz, *J. Cryst. Growth*, **58**, 186 (1982).
6. M. J. Kozielski, *ibid.*, **30**, 86 (1975).
7. A. Kremheller, A. K. Levine, and G. Gashurov, *This Journal*, **107**, 12 (1960).
8. F. Imoto and S. Kaneko, *Kogyo Kagaku Zasshi*, **74**, 591 (1971).
9. S. Kaneko and F. Imoto, *Nippon Kagaku Kaishi*, 985 (1975).
10. S. Kaneko and F. Imoto, *Bull. Chem. Soc. Jpn.*, **51**, 1739 (1978).
11. S. Kaneko, K. Matsumoto, T. Sugiyama, and F. Imoto, "Proceedings of the 1st International Symposium on Hydrothermal Reactions," p. 760, Gakujutsu Bunken Fukyu Kai, Tokyo (1983).
12. S. Kaneko, H. Aoki, I. Nonaka, F. Imoto, and K. Matsumoto, *This Journal*, **130**, 2487 (1983).
13. F. A. Kröger, *Z. Kristallogr.*, **120**, 136 (1939).
14. G. C. Kennedy, *Am. J. Sci.*, **248**, 540 (1950).
15. F. W. Vahldiek, *J. Less-Common Met.*, **11**, 99 (1966).
16. W. L. Roth, in "Physics and Chemistry of II-VI Compounds," M. Aven and J. S. Prener, Editors, p. 134, North-Holland Publishing Co., Amsterdam (1967).
17. G. W. Morey, *J. Am. Ceram. Soc.*, **36**, 279 (1953).
18. H. P. Klug and L. E. Alexander, "X-Ray Diffraction Procedures for Polycrystalline and Amorphous Materials," 2nd ed., p. 597, John Wiley & Sons, New York (1974).

Electrodeposition of Nickel and Cobalt Oxides onto Platinum and Graphite Electrodes for Alkaline Water Electrolysis

Yih-Wen D. Chen and Rommel N. Noufi*

Solar Energy Research Institute, Golden, Colorado 80401

ABSTRACT

Smooth, compact, and bright films of nickel and cobalt oxides were prepared from 0.5M acetate aqueous solutions and electrodeposited onto platinum and graphite electrodes. Oxygen evolution potentials in 1M NaOH at room temperature were about 150-170 mV lower on nickel(III) oxide [NiO(OH)] and cobalt(III) oxide (Co₂O₃)-coated anodes than on bare anodes. Scanning electron micrographs of NiO(OH) deposits showed no morphological change after extensive electrolysis, and electrocatalytic activity was stable in long-term controlled-potential coulometric electrolysis. However, the electrocatalytic activity of Co₂O₃ showed initial decay followed by a fairly constant behavior. No visible change in the surface of the Co₂O₃ deposit was observed after extensive electrolysis.

The electrochemical properties of metal oxide electrodes have attracted interest over several decades. Early work was oriented toward understanding thick films relevant to battery development (1). The objective of more recent studies has been to develop a fundamental understanding of the redox processes in these films (2, 3). Since hydrogen has recently been considered one of the clean fuels for energy storage (4-6), its production by various methods (7-9) has been proposed. Splitting water to hydrogen and oxygen by electrolysis remains the simplest and most economical method. One drawback in alkaline water electrolysis is the high overvoltage of the oxygen evolution on anodes.

Although metal anodes have been conventionally used for water electrolysis (10-12), their use is not feasible because these anodes [especially nickel anodes (13)] tend to form a nonconducting oxide film, causing oxygen evolution to deteriorate with time. Metal oxides that can provide a catalytic path for oxygen evolution have been recognized (2). Most of the anodic metal oxides studied were formed by anodization of the bare substrates in alkaline solution (14-17). In this paper, we investigate electrodeposition of thin films of nickel and cobalt oxides on platinum and graphite to study an inexpensive method to prepare and characterize these very thin film electrocatalysts. The objective of the above task is to apply the results to semiconductor photoelectrodes in order to bring about or facilitate the photoelectrolysis of water.

Experimental

Reagents.—Sodium acetate and sodium hydroxide are Baker-analyzed reagents. Nickel(II) sulfate was obtained from Johnson Matthey Chemical, Limited, and cobalt(II) acetate was obtained from Alfa Products. All of the reagents were reagent grade and were used without further treatment.

Electrodes.—Rotating platinum disk and graphite disk electrodes (area = 0.20 cm²) were obtained from Pine Instrument Company. The electrodes were polished with 1, 0.3, and finally with 0.05 μm aluminum oxide.

Cells.—All measurements and electrodeposition were performed in a three-electrode cell and are compared with the saturated calomel electrode (SCE) results. The cell assembly is simply a beaker with 250 ml capacity and a Teflon cap with four holes for the rotating disk electrode, reference electrode, counterelectrode, and gas dispersing tube. To keep the reference electrode from contaminating the electrolyte, a Beckman junction tube (no. 531041) was used to fill the support-

ing electrolyte. All experiments were conducted at room temperature and under argon atmosphere.

Apparatus.—A PAR Model 173 potentiostat with Model 175 Universal programmer and Model 179 Digital coulometer was used to control potential electrodeposition, cyclic voltammetric measurements, and potential coulometric electrolysis of water. A Houston Model 200 X-Y recorder registered the data.

Analysis of the film.—The nickel and cobalt contents in the film were determined by dissolving the metal oxides in 1% HNO₃ and measuring by atomic absorption.

Results and Discussion

Electrodeposition of nickel(III) oxide on platinum and graphite electrodes.—The nickel(III) oxide, NiO(OH), was previously formed when nickel(II) oxide was electrochemically oxidized to the +3 oxidation state (14-16). In this investigation, NiO(OH) was prepared directly from 0.5M sodium acetate aqueous solution with 0.05M NiSO₄. Figure 1 illustrates the cyclic voltammogram for the oxidation of nickel(II) ion onto platinum. On the first anodic scan, no obvious anodic peak was observed; however, on the subsequent cycles, anodic peaks were easily identified. Upon scan reversal, reduction waves of the oxide were observed. The increase in redox peaks with each cycle indicates the

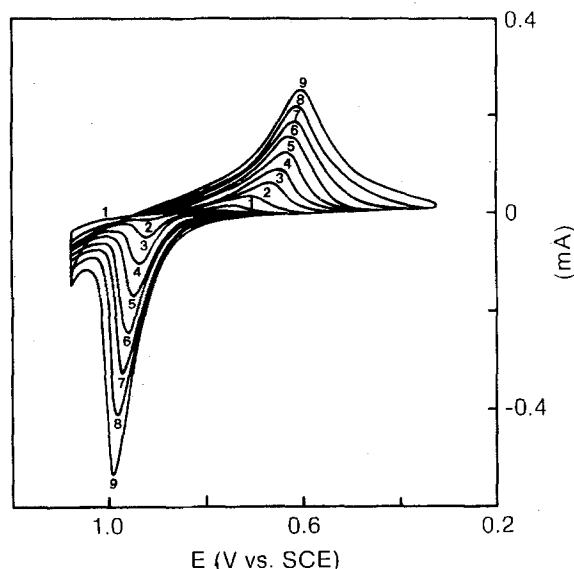


Fig. 1. Cyclic voltammograms at 50 mV/s for a rotating (900 rpm) platinum disk electrode (0.20 cm²) in an aqueous solution containing 0.05M NiSO₄ and 0.5M sodium acetate.

* Electrochemical Society Active Member.

Key words: electrocatalytic activity, morphology, stability.

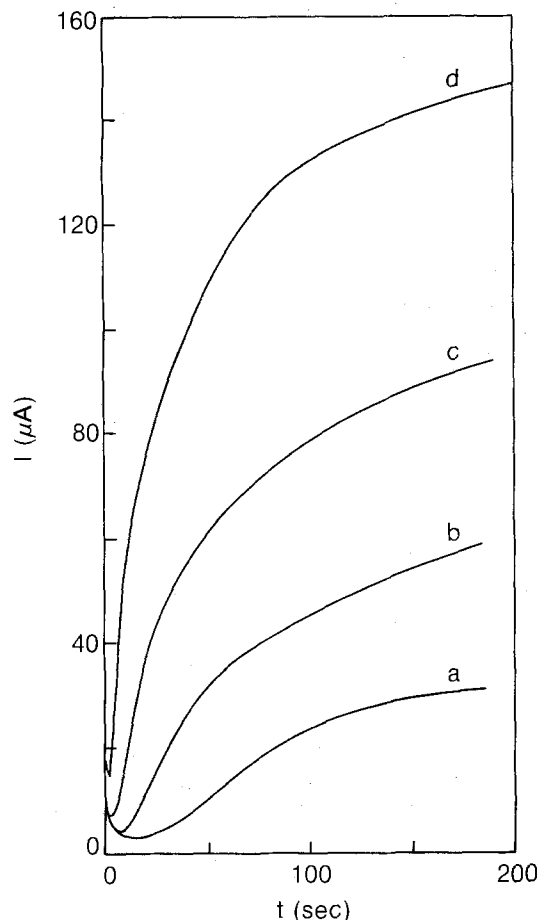


Fig. 2. Controlled potential coulometric electrodeposition of NiO(OH) on rotating (900 rpm) platinum disk electrode (0.20 cm^2) in aqueous solution containing 0.05 M NiSO_4 and 0.5 M sodium acetate at (a) 1.025 V , (b) 1.050 V , (c) 1.075 V , and (d) 1.100 V vs. SCE.

growth of the deposit. At potentials $>1.0 \text{ V}$, anodic currents [the result of electrocatalytic evolution of oxygen at the NiO(OH) film] increase with each cycle. This increase is seen again in Fig. 2, which illustrates controlled potential coulometric electrodeposition at different anodic limits. At each anodic limit, the anodic current decreases initially until $\sim 0.06 \text{ mC}$ had passed, which is the estimated quantity needed for monolayer deposition ($\sim 0.30 \text{ mC/cm}^2$) (18). After monolayer formation, the current density increases during the extensive electrodeposition because of electrocatalytic

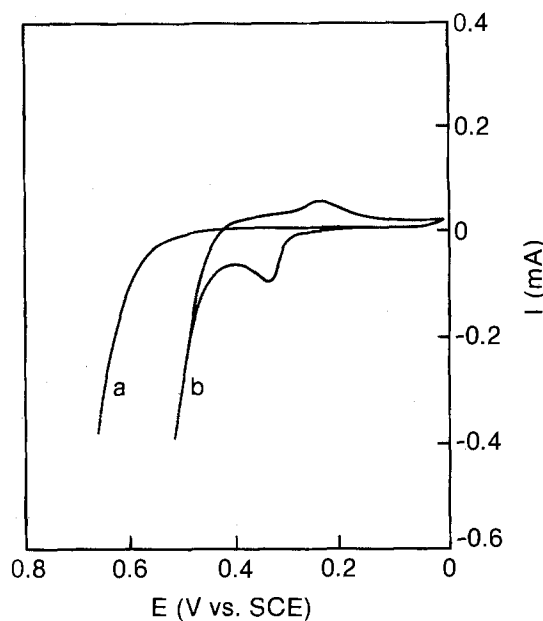


Fig. 4. Cyclic voltammograms at 50 mV/s for a rotating (900 rpm) platinum disk electrode (0.20 cm^2) in 1 M NaOH aqueous solution. Curve a: uncoated platinum electrode. Curve b: NiO(OH)-coated platinum electrode electrodeposited at $+1.10 \text{ V}$ with 15 mC passed, on rotating (900 rpm) platinum disk electrode, in an aqueous solution containing 0.05 M NiSO_4 and 0.5 M sodium acetate.

oxidation of water. Through x-ray photoelectron spectroscopy (XPS), the deposition product was identified as predominantly NiO(OH) (see Fig. 3), which is similar to the results obtained from the anodic oxidation of the Ni(OH)₂ film (14-16). Therefore, the NiO(OH) species seems essentially responsible for the catalyzed oxygen evolution. The oxygen evolution occurring with the anodic electrodeposition of NiO(OH) film is also evident from the analysis of the nickel content in the film (measured by atomic absorption, as shown in Table I). The coulometric efficiency of the deposition decreases with increase in applied potential.

The controlled potential coulometric electrodeposition of NiO(OH) on platinum and graphite electrodes yields reproducible, compact, and smooth films. With this method, thick conducting films can be deposited over 1 C/cm^2 . In comparison, passive oxide films were normally grown on nickel electrodes with limited thickness (19-21).

The electrocatalytic evolution of oxygen was also observed in 1 M NaOH aqueous solution, where the

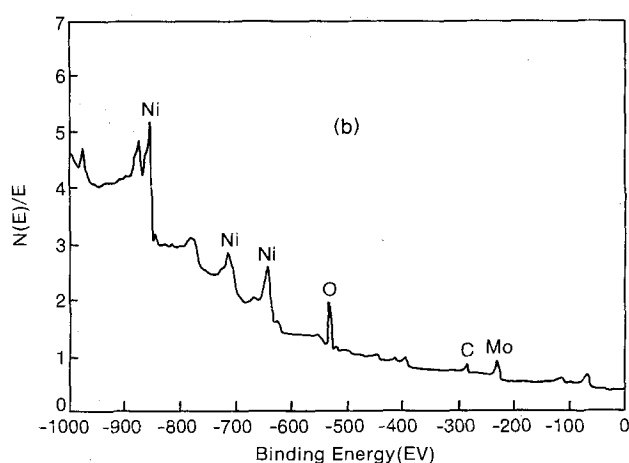
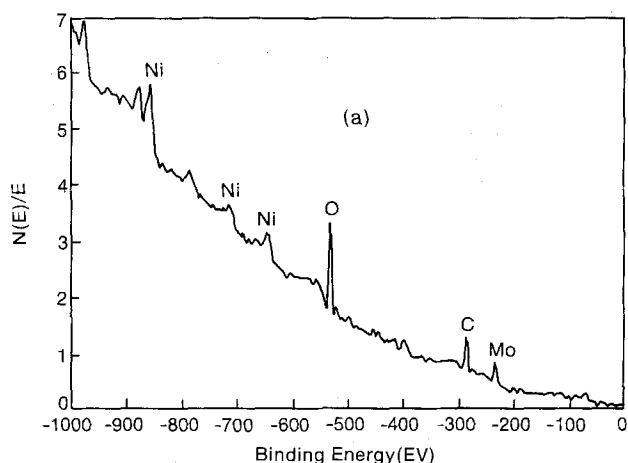


Fig. 3. XPS spectra of NiO(OH) electrodeposited on platinum (0.25 cm^2) at a potential, $E_a = 1.10 \text{ V}$ with $Q = 3.7 \text{ mC}$ in an aqueous solution containing 0.5 M sodium acetate and 0.05 M NiSO_4 . A, left: XPS spectrum of the immediate surface. B, right: XPS spectrum of the bulk.

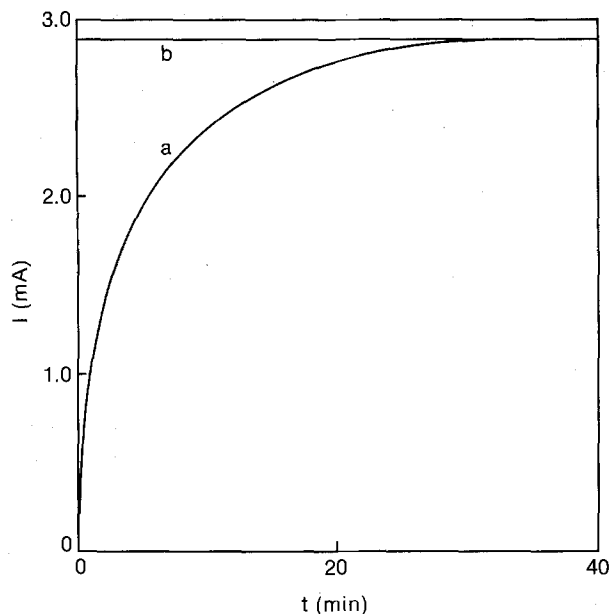


Fig. 5. Oxygen evolution at NiO(OH)-coated platinum electrode (0.20 cm^2) at $+0.55 \text{ V}$ in 1 M NaOH aqueous solution. Curve a: current-time curve for initial electrolysis. Curve b: current-time curve for continuous electrolysis after 3 days. The NiO(OH)-coated anode was prepared by electrodeposition on rotating (900 rpm) platinum disk electrode (0.20 cm^2) at $+1.0 \text{ V}$ with 10 mC passed in an aqueous solution containing 0.05 M NiSO_4 and 0.5 M sodium acetate.

oxygen evolution potential was about 150 mV lower on the NiO(OH) electrode than on the platinum anode (as shown in Fig. 4). The long-term stability of oxygen evolution on NiO(OH) film was tested in 1 M NaOH , and the film showed good stability. Initially, the catalytic current increased sharply, and then reached steady state after a few minutes (Fig. 5). The electrolysis continued for 3 days with no decay in current. Therefore, no passive oxide film formed, and there was also no morphological change in the NiO(OH) film (Fig. 6).

Electrodeposition of cobalt(III) oxide onto platinum and graphite electrodes.—Cobalt(III) oxide films were prepared by electrodeposition onto platinum and

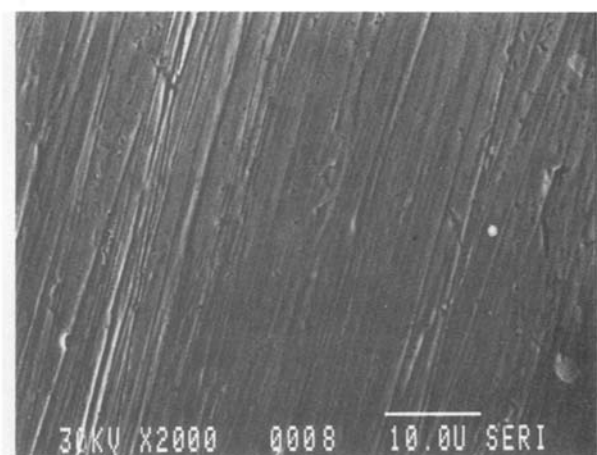
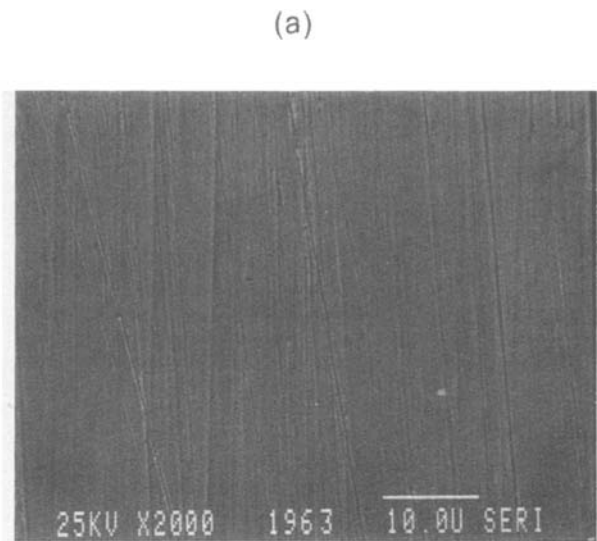


Fig. 6. Scanning electron micrographs of NiO(OH)-coated platinum electrode (times 2000) for (a, top) before and (b, bottom) after oxygen evolution in 1 M NaOH aqueous solution.

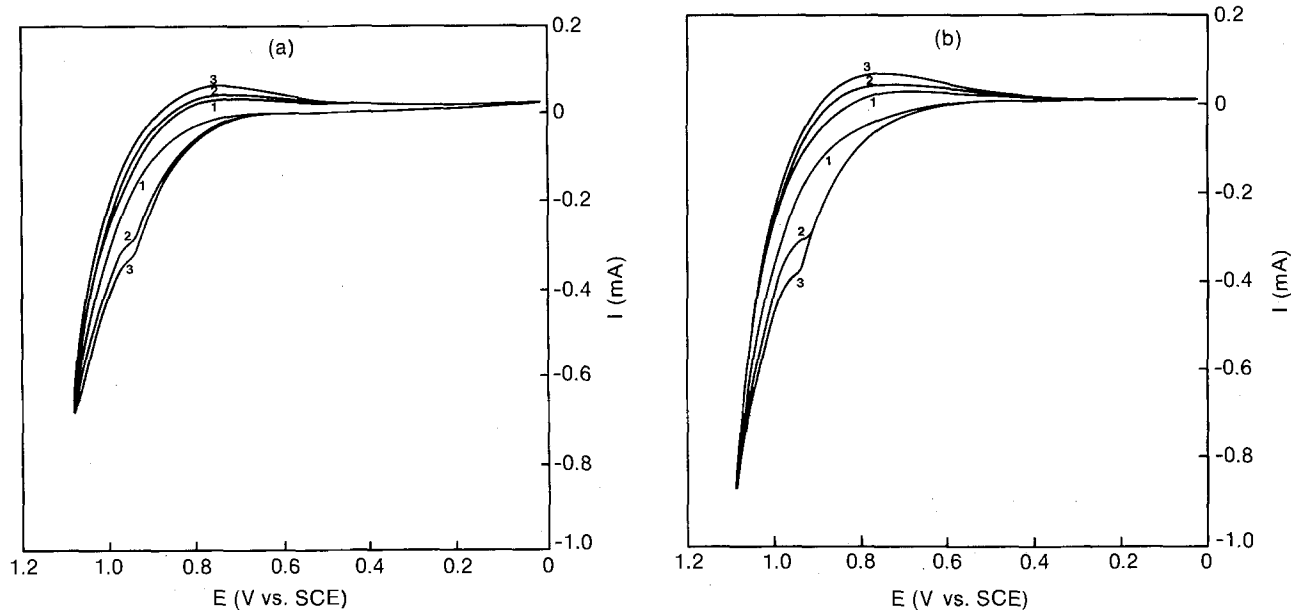


Fig. 7. Cyclic voltammograms at 50 mV/s for a (a, left) rotating (900 rpm) platinum disk electrode (0.20 cm^2) and (b, right) rotating (900 rpm) graphite disk electrode (0.20 cm^2) in aqueous solution containing 0.05 M Co(OAc)_2 and 0.5 M sodium acetate.

graphite electrodes in essentially the same way as the NiO(OH)-coated electrodes. Cyclic voltammograms of the oxidation of cobalt(II) ion onto platinum and graphite electrodes were basically the same for both electrodes (Fig. 7). On the first anodic scan, no obvious anodic peak was observed; however, on the subsequent cycles, anodic peaks were observed. On the scan reversal, broad and relatively small reduction waves were observed. The increase in peak height with each cycle indicates the growth of the film. The oxidation currents at the anodic limit increase while the film is continuously deposited, indicating the electrocatalytic evolution of oxygen. However, the catalytic effect by the cobalt oxide is not as clear as it is with NiO(OH); a more complicated film growth behavior is observed (Fig. 8). At each anodic limit, the oxidation current decreases initially until ~ 0.10 mC had passed, which is the estimated quantity (~ 0.5 mC/cm²) required for

monolayer deposition (21). After the monolayer formation, the current density increases and then decreases during bulk electrodeposition. The increase in the current density might indicate catalytic oxygen evolution, followed by a decrease in current density due to the less conducting character of the film. The electrodeposited film was not stable in air. The orange film gradually changes to green on the surface and becomes soluble in 1M NaOH. However, the underlayer of the green film stays orange and stable in 1M NaOH. XPS measurements were not sensitive enough to distinguish between the binding energies of Co₂O₃, Co₃O₄, and CoO (Fig. 9). However, Co₂O₃ is most likely the cobalt oxide deposited because the stoichiometry fits the analytical results of coulometric efficiency of the electrodeposition at lower applied anodic potential (Table I). At the lower potential, over 90% coulometric efficiency based on Co₂O₃ film formation is observed.

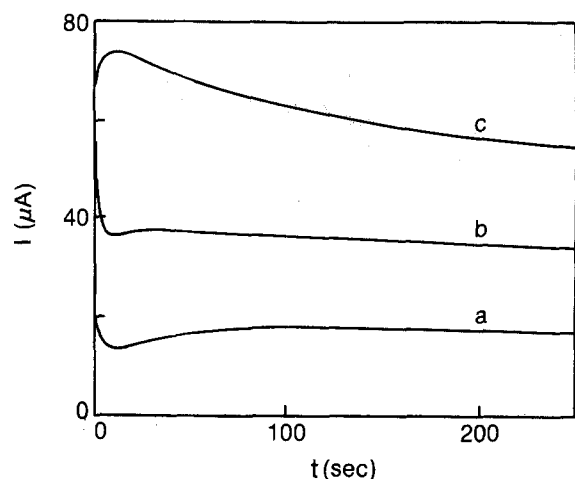


Fig. 8. Controlled potential coulometric electrodeposition of cobalt(III) oxide on rotating (900 rpm) platinum disk electrode (0.20 cm²) in an aqueous solution containing 0.05M Co(OAc)₂ and 0.5M sodium acetate at (a) 0.80V, (b) 0.85V, and (c) 0.90V vs. SCE.

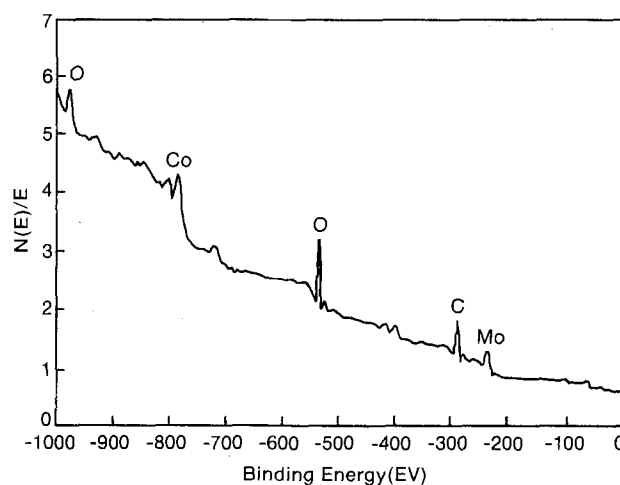


Fig. 9. XPS spectrum of cobalt oxide electrodeposited on platinum (0.25 cm²) at +0.80V with 2 mC passed in an aqueous solution containing 0.05M Co(OAc)₂ and 0.5M sodium acetate.

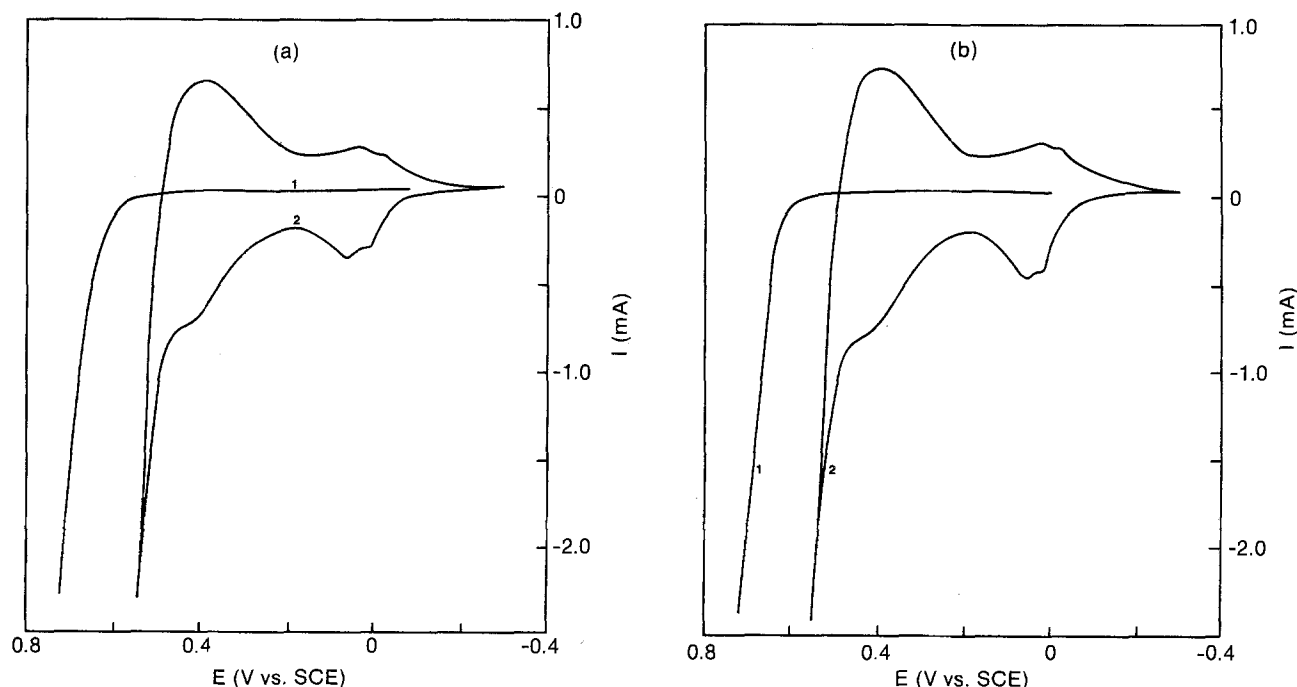


Fig. 10. Cyclic voltammograms at 50 mV/s for a (a, left) rotating (900 rpm) platinum disk electrode (0.20 cm²), and (b, right) rotating (900 rpm) graphite disk electrode (0.20 cm²), in 1M NaOH aqueous solution. Curves 1: uncoated platinum or graphite electrode. Curves 2: cobalt(III) oxide-coated platinum or graphite electrode at +0.80V with 10 mC passed from an aqueous solution containing 0.05M Co(OAc)₂ and 0.50M sodium acetate.

Table I. Coulometric efficiency of electrodeposition of nickel(III) and cobalt(III) oxides^a

Sample number	Metal analyzed	Q _a ^b (mC)	E _a ^c (V)	C ^d (ppm)	Coulometric efficiency (%)
1	Ni	30	1.10	0.47	28
2	Ni	30	1.07	0.55	32
3	Ni	30	1.00	0.62	36
4	Co	30	0.80	1.65	93
5	Co	30	0.90	1.55	88
6	Co	30	1.05	1.32	75
7	Co	30	1.10	1.12	63

^a An aqueous solution of 0.5M sodium acetate and 0.05M NiSO₄ was used to electrodeposit NiO(OH) on a rotating (900 rpm) platinum disk electrode. An aqueous solution of 0.5M sodium acetate and 0.05M Co(OAc)₂ was used to electrodeposit cobalt(III) oxide on a rotating (900 rpm) graphite disk electrode.

^b The number of coulombs applied for electrodeposition.

^c The constant anodic potential applied for electrodeposition.

^d Metal oxides were dissolved in 10 ml 1% HNO₃ and were measured by atomic absorption.

^e Coulometric efficiency is based on NiO(OH) and Co₂O₃ formation.

The electrocatalytic evolution of oxygen was evident in 1M NaOH aqueous solution where the oxygen evolution potential was about 170 mV lower on Co₂O₃ than uncoated anodes (see Fig. 10). The long-term stability of oxygen evolution on Co₂O₃ film was tested in 1M NaOH, and this film also showed good stability (Fig. 11). Contrary to NiO(OH), the catalytic current initially decreases sharply and stays fairly constant during extensive electrolysis. Initially, the catalytic current of Co₂O₃ is larger than that of NiO(OH). However, after extensive electrolysis, the catalytic current of Co₂O₃ becomes less than that of NiO(OH). Essentially, no visible change in the cobalt(III) oxide film was observed after long-term oxygen evolution experiment.

Acknowledgments

The authors wish to thank Rick Matson for preparing the scanning electron micrographs, and Bob Fischer for performing XPS. This work was carried out under a grant from the Director's Development Fund program at the Solar Energy Research Institute under Contract EG-77-C01-4042 to the Department of Energy.

Manuscript submitted July 11, 1983; revised manuscript received Dec. 5, 1983.

The Solar Energy Research Institute assisted in meeting the publication costs of this article.

REFERENCES

1. P. C. Milner and U. B. Thomas, in "Advances in Electrochemistry and Electrochemical Engineering," C. W. Tobias, Editor, Vol. 5, p. 1, John Wiley and Sons, New York (1967).
2. G. W. D. Briggs, "Electrochemistry: Specialist Periodical Reports," Vol. 4, Chemical Society, Washington, DC (1974).
3. A. Damjanovic and A. J. Ward, in "International Reviews of Science, Electrochemistry, Physical Chemistry Series Two," Vol. 6, J. O'M. Bockris, Editor, Butterworths, London (1976).
4. A. J. Bard, *J. Photochem.*, **10**, 59 (1979); *Science*, **207**, 139 (1980); *J. Phys. Chem.*, **86**, 172 (1982).
5. J. O'M. Bockris, in "Environmental Chemistry," J. O'M. Bockris, Editor, Plenum Press, New York (1977).
6. T. N. Vitzroglu and W. Seifritz, Editors, "Hydrogen Energy Systems," Proceedings of the 2nd World Hydrogen Energy Conference, International Association of Hydrogen Energy (1978).
7. J. Kiwi, K. Kalyanasundaram, and M. Gratzel, *Struct. Bonding*, **49**, 37 (1982).
8. J. O'M. Bockris, in "Trends in Electrochemistry," J. O'M. Bockris, D. A. J. Rand, and B. J. Welch, Editors, p. 79, Plenum Press, New York (1977).
9. B. D. McNicol, *Catalysis*, **2**, 243 (1978).
10. P. H. Smith, in "Industrial Electrochemical Processes," A. J. Kuhn, Editor, Elsevier, New York (1971).
11. E. A. Chapman, *Chem. Process Eng.*, **46**, 387 (1965).
12. R. L. Costa and P. G. Grimes, *Chem. Eng. Prog.*, **63**, 56 (1967).
13. H. Vandenberg and R. Leysen, in "International Society of Electrochemistry, 31st Meeting Proceedings," E. Vecchi, Editor, p. 315, Venice, Italy (1980).
14. B. MacDougall and M. J. Graham, *This Journal*, **128**, 2321 (1981).
15. J. L. Ord, J. C. Clayton, and D. J. DeSmet, *ibid.*, **124**, 1714 (1977).
16. P. W. T. Lu and S. Srinivasan, *ibid.*, **125**, 1416 (1978).
17. G. Bronoel and J. Reby, *Electrochim. Acta*, **25**, 973 (1979).
18. D. M. Kolb, *Adv. Electrochem. and Electrochem. Eng.*, **11**, 125 (1978).
19. T. Dickinson, A. T. Povey, and P. M. A. Sherwood, *J. Chem. Soc., Faraday Trans. 1*, **73**, 327 (1977).
20. B. MacDougall, D. F. Mitchell, and M. J. Graham, *Isr. J. Chem.*, **18**, 125 (1979).
21. B. MacDougall and M. Cohen, *This Journal*, **124**, 1185 (1977).

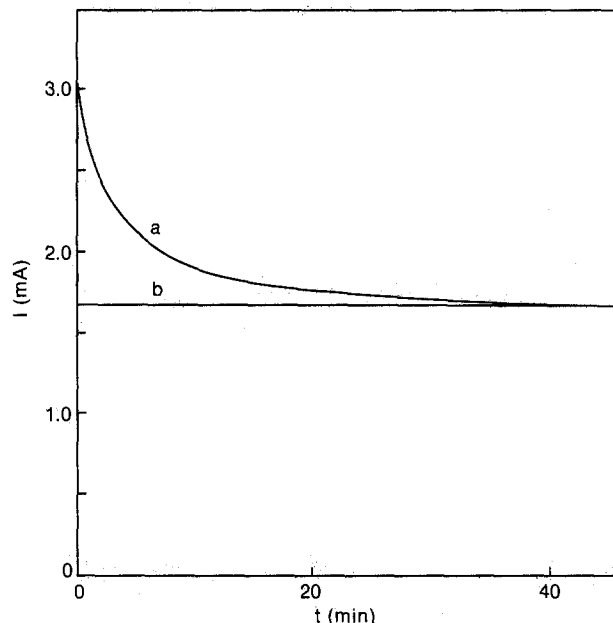


Fig. 11. Oxygen evolution at cobalt(III) oxide-coated graphite electrode (0.20 cm²) at +0.55V in 1M NaOH aqueous solution. Curve a: current-time curve for initial electrolysis. Curve b: current-time curve after electrolysis for 3 days. The cobalt(III) oxide-coated anode was prepared by electrodeposition on rotating (900 rpm) graphite disk electrode (0.20 cm²) at +0.80V with 10 mC passed from an aqueous solution containing 0.05M Co(OAc)₂ and 0.5M sodium acetate.

Electroactive Properties of Polyaromatic Molecules

Robert J. Waltman, A. F. Diaz,* and Joachim Bargon¹

IBM Research Laboratory, San Jose, California 95193

ABSTRACT

Electroactive and electrochromic films of electropolymerized polyazulene and polythiophene have been found to be surprisingly insensitive to common solvents and temperature. As electrodes in all-organic batteries these thin polymeric films allow current densities of 2 mA/cm² at open-circuit voltages of 2.3V. The electrochromic properties suggest application in electro-optical displays.

The variety of compounds which have been found to undergo electrochemical polymerization have demonstrated the facility of the electrochemical approach to synthesis of electrically conducting polymeric films. Such films have been prepared from molecules which represent all pertinent classes of aromatic compounds. They include the heterocyclic pyrroles (1, 2), thiophenes (3-5), furan (5), carbazoles (6, 7), the polynuclear aromatic hydrocarbons pyrene or fluorene (8), and even the nonbenzenoid aromatic hydrocarbon azulene (9). When in the oxidized form, all of these polymers are semiconducting (10^{-6} - $10^2 \Omega^{-1} \text{cm}^{-1}$), with polypyrrole exhibiting the highest conductivities of $10^2 \Omega^{-1} \text{cm}^{-1}$. Thin films from polypyrrole, polythiophene, and polyazulene which are supported by a Pt surface are also attractive, because they exhibit electroactive and electrochromic properties. Thus, electrically conducting polymers become suitable for application in electro-optic display devices (10) or as electrode materials (11). Successful application in the latter has been demonstrated by the fabrication of a lightweight, rechargeable battery employing a polyacetylene electrode, whereby large power and energy densities were obtained (12). The fact that electrochemically prepared polymers, such as polythiophene or polyazulene, have similar properties, points to their potential application in energy technology as well. Accordingly, we report herein some properties of these materials relevant to their applications in battery technology.

Experimental

All compounds were obtained from commercial sources. Polythiophene and poly- β -substituted thiophenes were prepared by the electrochemical oxidation of the appropriate thiophene monomers in a three-electrode, single- or two-compartment cell. Platinum, gold, and sodium chloride calomel (SSCE) were used as the working, counter, and reference electrodes, respectively. The solutions were typically 10^{-4} - 10^{-3}M in monomer, in a 0.1M electrolyte/acetonitrile solution. The electrolyte, usually tetraethylammonium tetrafluoroborate (TEAFB), was recrystallized from alcohol-ethyl acetate and dried under vacuum. The acetonitrile (Burdick and Jackson, spectrometric grade) was used directly without further purification. The solutions were bubbled with argon for 5-10 min, and protected by an argon blanket. Cyclic voltammograms of polymer films were measured in electrolyte solutions containing no other electroactive species. All electrochemical measurements were performed with an IBM EC225 Voltammetric Analyzer.

Results and Discussion

Electrochemical data.—Cyclic voltammetric data for some thiophene monomers and their corresponding polymers are given in Table I. All of the monomers show irreversible oxidation peaks and give rise to colored solutions upon electro-oxidation. The value of n for the oxidation reaction was estimated from the

* Electrochemical Society Active Member.

¹ Institut für Physikalische Chemie, Bonn-1, Germany.

Table I. Cyclic voltammetric data for thiophenes: monomer concentration 8.9-23.0 $\mu\text{mol cm}^{-3}$ in 0.1M TEAFB/CH₃CN with sweep rate 50 mV s⁻¹

Compound	Monomer				Polymer E_{on} (V)
	E_{pa} (V)	$i/AC\nu^{1/2}$ (A cm mol ⁻¹ s ^{1/2} V ^{-1/2})	$10^2 n^{3/2} D^{1/2}$ (cm s ^{1/2})	n	
thiophene	2.06	3791	1.4	2.7	0.96
3-methylthiophene	1.86	3203	1.2	2.4	0.72
3-iodothiophene	2.03	2362	0.9	2.0	
3-bromothiophene	2.10	3085	1.1	2.3	1.06
3-thiopheneacetonitrile	2.22	2725	1.0	2.2	1.12
3-thiophenecarboxylic acid	2.28	1031	0.4	1.2	
3-cyanothiophene	2.46	2260	0.8	1.9	
3-nitrothiophene	2.69	2476	0.9	2.0	
2,5-dimethylthiophene	1.77	1134	0.4	1.2	

Nicholson and Shain treatment for a totally irreversible electron-transfer process which provides $n^{3/2} D^{1/2}$, where D was assumed equal to $10^{-5} \text{cm}^2 \text{s}^{-1}$. In general, the reaction of compounds which produce polymer films occurs on the electrode surface and has n values between 2 and 3, as estimated from cyclic voltammetry. From elemental analysis, n values between 2.07 and 2.17 are obtained for some of these polymers. The reaction of compounds which produce soluble products and, therefore, occur away from the electrode, has n values between 1 and 2, depending upon whether monomeric ($n = 2$) or dimeric ($n = 1$) products are formed (13). Accordingly, the α, α' -blocked 2,5-dimethylthiophene has an n value of 1.2, similar to 2,5-dimethylpyrrole (13).

Whereas low molecular weight products are obtained from α -substituted heterocycles, polymeric films are indeed obtained from certain β -substituted monomers. The cyclic voltammogram of a typical 60 nm thin film of polythiophene on a Pt surface obtained from the electropolymerization of 2,2'-bithiophene is shown in Fig. 1.

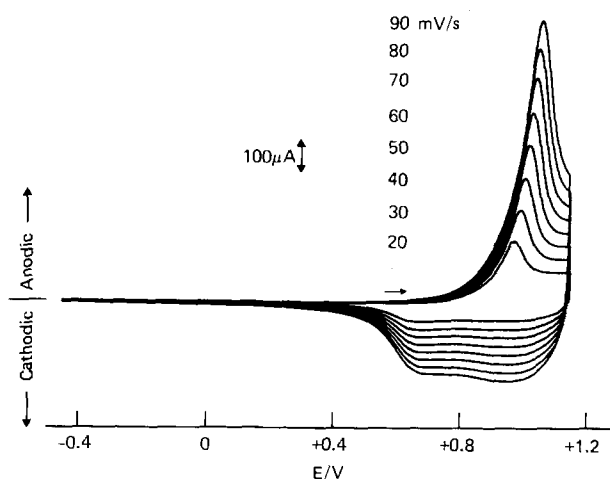


Fig. 1. Cyclic voltammogram of [Pt]-polythiophene-BF₄ film in 0.1M TEAFB/CH₃CN solution.

The details of the electroactive properties of these films have been previously considered (4), and no reiteration is necessary here. However, it is important to point out that these films can be cycled repeatedly between the oxidized, conducting state and the neutral, nonconducting state, an event which is accompanied by a reversible color change from green-back to a pale-copper color, respectively. The cycling behavior is observed for polythiophene films derived from either the monomer or the 2,2'-dimer. The anodic peaks obtained from the dimer derived polymer films, however, are noticeably sharper with peak widths at half height (PWHH) of ca. 90 mV for 60 nm films, while monomer derived films of the same thickness have PWHH of ca. 300-350 mV. Since it is known that the oxidation and reduction reaction is controlled by the diffusion of counteranions into and out of the surface-localized film, diffusion of ions through the dimer-derived film is less limiting. This may also reflect the more regularly α,α' -linked monomer units in the dimer-derived film. The sensitivity of the electrical properties of polythiophene to linkages between monomer units other than α,α' -bonds has been pointed out by Sanechika *et al.* (14). In particular, they found that the electrical conductivity of polythiophene decreases with increasing β -linkages introduced between monomer units.

Figure 1 also shows that the peak oxidation potential of polythiophene occurs at +1.0V. This is far anodic of the peak oxidation potential of polypyrrole (-0.15V), with the important consequence that polythiophene films are much more stable, especially to the presence of oxygen. Thus, unlike polypyrrole, neutral or electrochemically oxidized polythiophene films can be exposed to air, or even passed under a stream of oxygen, yet when put back into an electrolyte solution and cycled electrochemically, they retain their switching capabilities. However, ESCA studies of the neutral films reveal the presence of bonded oxygen at the surface of these materials. For neutral polythiophene films exposed to air for 24h, the C:S:O ratio is 4.0:0.55:1.0, respectively, while a 14 day exposure reveals a C:S:O ratio of 4.0:0:5.1, respectively (15). However, the surface properties are not representative of the bulk properties of the film, as is evidenced by its ability to retain electrochemical switching.

The electrochemical behavior of polyazulene films is similar to that of polythiophene films insofar that they too are electroactive and electrochromic (Fig. 2). The peak oxidation potential of the polymer film occurs at +0.650V, *i.e.*, lower than the polythiophene counterpart but still anodic of polypyrrole.

Stability of films.—For successful performance of these materials in various applications, such as in batteries, apart from the desirable electroactivity of the films, their stability under different conditions becomes of paramount importance. Thus, thicker films from polythiophene and polyazulene can be peeled off from the Pt anode. These are flexible, continuous, free standing films which are electrically conducting to the extent of $1 \Omega^{-1} \text{ cm}^{-1}$. The oxidized, conducting forms of these polymer films are also remarkably stable under different conditions. They are insoluble in strong acids, bases, or common organic solvents. For example, when oxidized films are placed in 6M HCl or NaOH, or in a solvent such as dichloromethane for 1h, they retain their electroactive properties when subsequently electrochemically cycled. The thicker films are also thermally stable to heating at 80°C for several hours. When kept for 3h at this temperature, polyazulene and polythiophene show a decrease in conductivity from 0.4 to 0.2 $\Omega^{-1} \text{ cm}^{-1}$, and from 0.1 to 0.04 $\Omega^{-1} \text{ cm}^{-1}$, respectively, while heating for 20h results in a ten-fold decrease in their conductivities. Whereas the thick films show moderate stability to heating, the thin films display a sensitivity of the switching behavior to changes in temperature. Thin films were

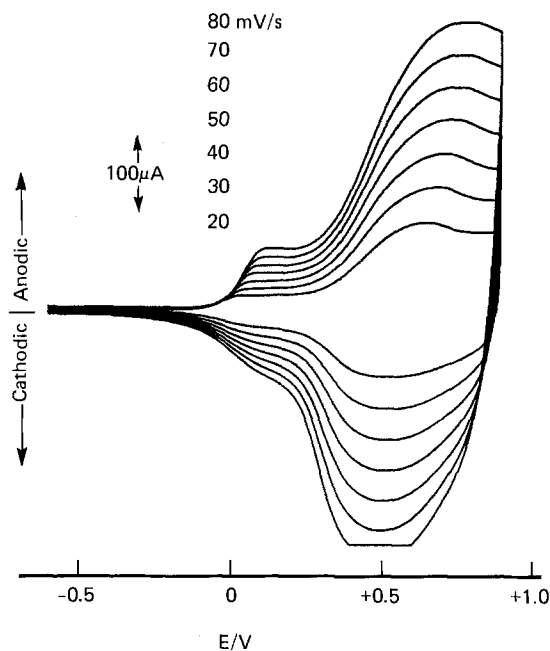


Fig. 2. Cyclic voltammogram of [Pt]-polyazulene- BF_4 film in 0.1M TEAFB/ CH_3CN solution.

cycled repeatedly in the temperature range between 0.0° and 80°C, and were found to be stable under these conditions for at least several hours. The electroactive properties are still retained (Fig. 3), and the peak oxidation potential shifts cathodically by 0.88 mV deg^{-1} with increasing temperature (Fig. 4). The 70 mV shift in the oxidation potential is reversible in this range, and a noticeable sharpening of the anodic peak is observed at higher temperatures (Fig. 3).

Apart from the demonstrated temperature stability, these data also allow information concerning the energetics of the switching reaction in this temperature range. The reaction is electrochemically irreversible and thus the relation $dG = -nFE$ cannot be applied. However, the dE/dT dependence is real and can be related to $d(dG)/dT$, which provides $-dS$. Thus, $dS = nF(dE/dT) = -3.4 \text{ cal deg}^{-1}$, whereby $n = 0.17$, *i.e.*, the amount of charge consumed in the partial oxidation of the film, as can be derived from elemental analysis data. This change of state also involves a change in composition where anions are incorporated into the film in order to balance the positive charges along the polymer chain. The sign and magnitude for the entropy term dS is consistent with what is characteristic for molecular complex formation (16). The sign for dS suggests that as the film switches from the neutral to the oxidized state, accommodation of counteranions (which is necessary to balance the positive charge induced in the polymer chain) results in a structure more rigid than in the neutral state of the film.

Substituent effects.—The eventual application of these materials in energy technology or in other fields will demand some chemical modifications in order to meet particular criteria. For example, we have demonstrated previously that the conductivity of polythiophene can be increased 100-fold with the introduction of a single β substituent (4). The fraction of counteranions in the film can also vary depending on which substituent is introduced into the parent polymer. Correspondingly, an investigation of polythiophene films with appropriate β substituents showed that when the peak oxidation potential of some β -substituted monomers are plotted against their respective Hammett substituent constants, a linear correlation is obtained (Fig. 5). The shift in the peak oxidation potentials of the series of β -substituted thiophenes is de-

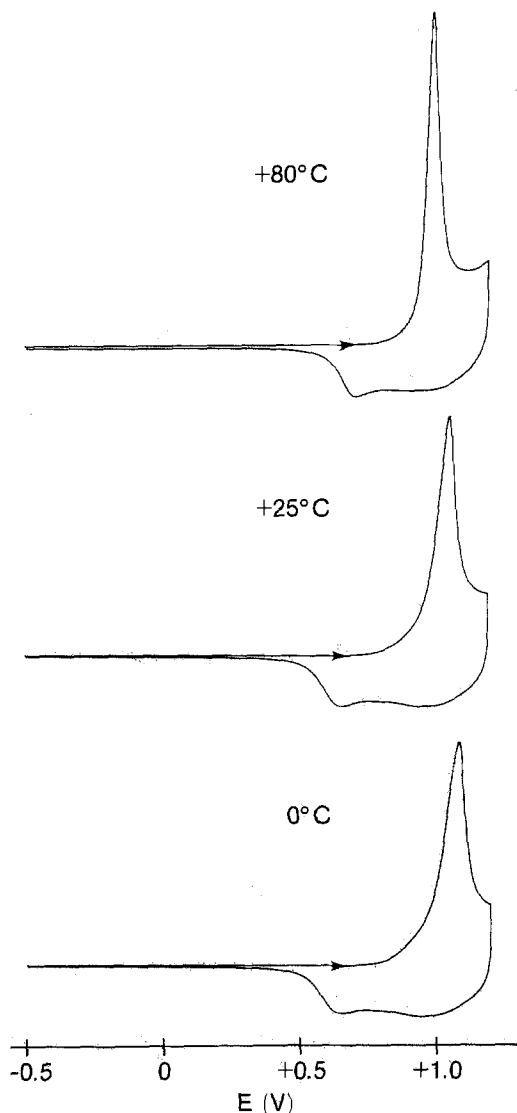


Fig. 3. Cyclic voltammograms of [Pt]-polythiophene-BF₄ as a function of temperature in 0.1M TEAFB/CH₃CN.

pendent on three parameters: namely, their polar, steric, and mesomeric effects, which are exerted by the substituents (17). This behavior can be described by the usual Hammett-Taft

$$E = \rho_{\pi}\sigma + S$$

equation where $\rho_{\pi}\sigma$ describes the polar-mesomeric

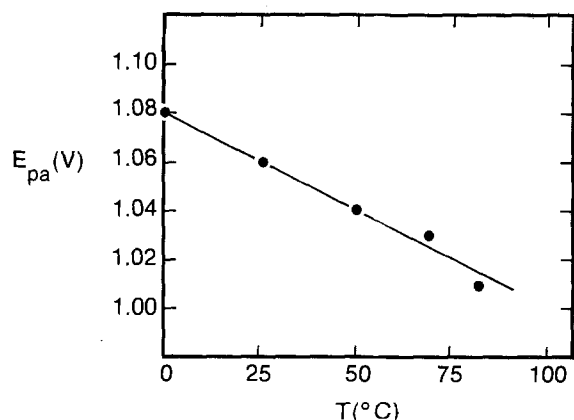


Fig. 4. The shift in the peak oxidation potential of polythiophene as a function of temperature.

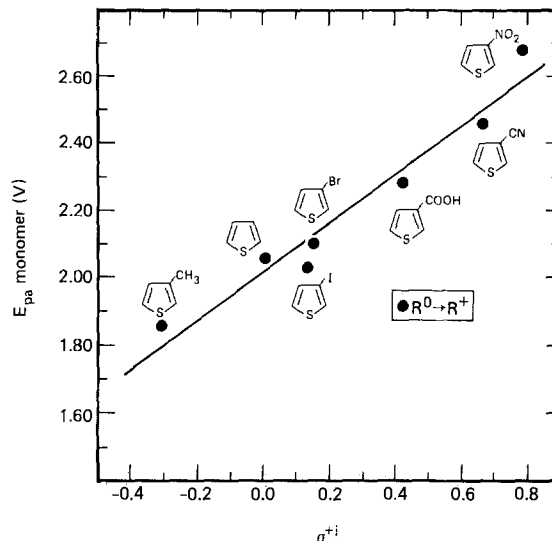


Fig. 5. Electrochemical peak oxidation potential of thiophene monomers vs. their respective Hammett substituent constants.

parameters, and S accounts for the steric factor (17). Accordingly, Fig. 5 allows three conclusions to be drawn. First, the straight-line fit indicates that all of the monomers are oxidized by the same mechanism, i.e., electro-oxidation results in the removal of a π electron from the thiophene ring. Second, the positive sign for the substituent constant ρ_{π} reveals that as the substituents take on more electrophilic character, the oxidation of the corresponding thiophenes proceed more difficultly. Finally, the steric term S appears to be minimal since for the substituents chosen here, a straight-line fit is obtained. Thus, the primary effect exerted by the β substituents is electronic and described by the $\rho_{\pi}\sigma$ term. One possible interpretation of these facts (Fig. 5) suggests that there is an optimum potential range, i.e., reactivity of the radical cation intermediate, which favors radical cation coupling in the follow-up reaction to yield polymeric films. Thus, under these conditions, polymerization occurs only for the parent thiophene, and the methyl-, bromo-, and iodo-substituted thiophenes. The latter two monomers yield poorly conducting films, while the other two polymers, polythiophene and poly(3-methylthiophene), have conductivities of ca. 10^{-2} - 10^{-1} , and $1 \Omega^{-1} \text{ cm}^{-1}$, respectively. 3-Thiophene carboxylic acid, 3-cyano-, and 3-nitro-thiophene yield no polymers on electro-oxidation under these conditions. Several reasons may be attributed to the lack of polymers obtained from the latter three monomers. One interpretation postulates that the stability (or reactivity) of these monomers is affected by the β substituents. Thus, as the reactivity of the radical cation intermediates increases, as reflected in their increasing oxidation potentials (Fig. 5), the more reactive these intermediates become with respect to nucleophiles, or they undergo other "escape" reactions, e.g., with the solvent or other nucleophilic species in the vicinity of the Pt surface. Thus, one possible effect of these strongly electron withdrawing groups is to destabilize the radical cation intermediate to the extent that radical cation coupling reactions become unfavorable when compared with other reaction pathways. Another reason for their failure to promote electropolymerization may be due to a breakdown of the solvent, since the anodic potentials applied become rather high for the nitro- and cyano-substituted monomers (Table I).

While steric factors do not seem to play any appreciable role in the primary electro-oxidation of the monomer (Fig. 5), their subsequent follow-up reactions (radical cation polymerization) are more susceptible to steric effects, which, therefore, may well play a role in deciding whether polymerization can compete favor-

ably with other potential follow-up reactions, such as with nucleophiles. This may explain the overall inferior quality of the polymer films derived from the 3-bromo- and 3-iodo-thiophenes, even though their oxidation potentials do not differ greatly from that of the parent thiophene monomer. It is, however, interesting to note that while a bulky substituent, such as iodo, allows polymerization (albeit of poor quality), a sterically smaller cyano group does not.

Another example of a property-structure correlation between thiophene monomers and their corresponding polymers is reflected in Fig. 6, where the peak oxidation potentials of some thiophene monomers are plotted against their respective polymers. The straight-line fit suggests that β -substituted monomers and their respective polymers are made up of a related system of π electrons, i.e., the electronic structures of the monomers and their corresponding polymers must be alike. This is consistent with the fact that polythiophene (and polypyrrole) consists primarily of α,α' -linked monomer units (3, 4).

Battery applications.—The stability of polythiophene and polyazulene films as described above suggests application of these materials as battery electrodes. Of particular importance is the high extent of counteranions which can be incorporated into these polymer films, especially into polyazulene, whereby one counteranion is shared by four azulene monomer units (Table II). Polythiophenes are additionally attractive from the standpoint that their film properties are readily altered via substituent groups. Thus, a simple battery cell (as shown in Fig. 7) was assembled utilizing oxidized and neutral polymer films adhered onto Pt as the two terminals. The films were typically 1×2 cm² with a thickness of ca. 10^{-3} cm, corresponding to a film weight of about 1-2 mg. These were immersed into a 0.1M TEAFB acetonitrile solution containing no other electroactive species. The arrows in Fig. 7 indicate the direction of electron flow. A polyazulene battery yielded a maximal open-circuit voltage of ca. 2.3V and an optimal initial short-circuit current of 4 mA. These data are summarized in Table II for both polyazulene and polythiophene batteries. These preliminary results for polyazulene are taken from five such batteries, while those for polythiophene (monomer derived) are based upon a single battery test. Polythiophene batteries derived from the dimer may conceivably yield higher values since they can store more charge (six monomer units share one charge) than the monomer-derived films. The batteries tested so far could be recharged at constant current, e.g., at 1 mA, to yield similar values in the regenerated cells.

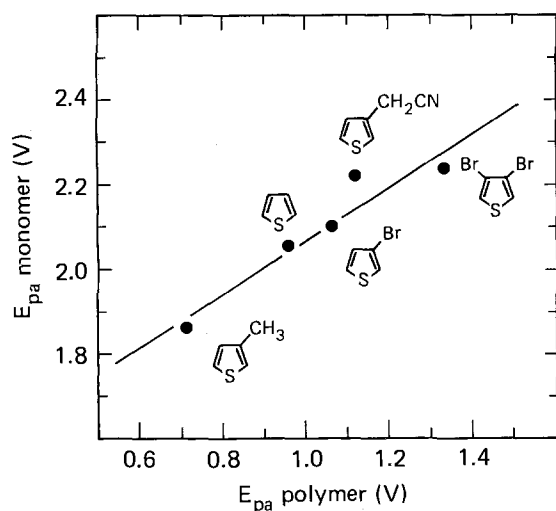


Fig. 6. Peak oxidation potential of thiophene monomers vs. their respective polymers in 0.1M TEAFB/CH₃CN.

Table II. Batteries from polyazulene and polythiophene

	Polyazulene	Polythiophene
Elemental composition	(AZ) ₄ ⁺ · BF ₄ ⁻	(TH) ₁₄ ⁺ · BF ₄ ⁻
Current density	0.4-2.2 mA/cm ²	0.02 mA/cm ²
Voltage	0.5-2.3V	0.5V

Our values are actually quite similar to the "all polymer" polyacetylene batteries of MacDiarmid *et al.* (18). However, unlike polyacetylene, which is known to be air sensitive, polyazulene batteries can be open to the air, at least short-term (days) tests revealed no apparent effect of air on the stability of the batteries. However, the long-term effect of oxygen on the rechargeability of polyazulene batteries has not been investigated thus far. Figure 8 shows the voltage change during a constant current discharge of 0.15 mA for a polyazulene cell in 0.1M TEAFB acetonitrile. More work is in progress.¹

¹ After this work was completed, data characterizing the electrochromic behavior of polythiophenes was reported by Garnier *et al.* (19).

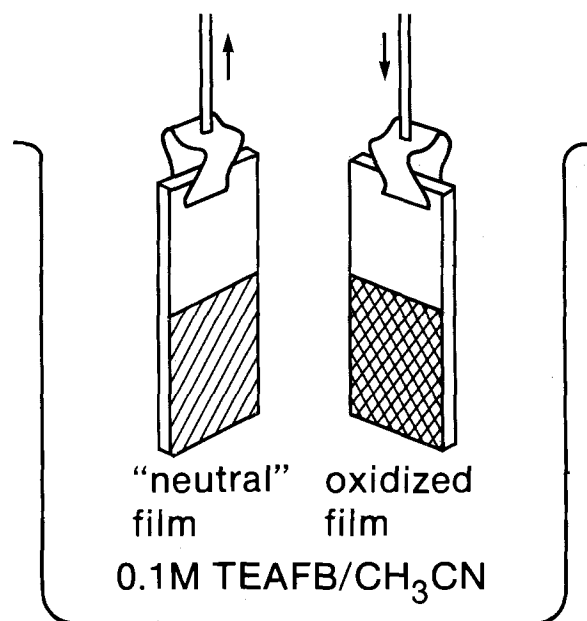


Fig. 7. A simple "all polymer" battery cell

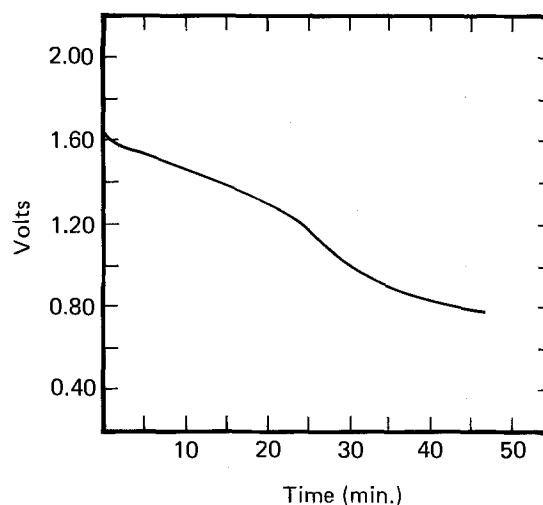


Fig. 8. A typical voltage change during 0.15 mA constant-current discharge of a polyazulene battery cell.

Manuscript received Aug. 25, 1983. This was Paper 546 presented at the San Francisco, California, Meeting of the Society, May 8-13, 1983.

IBM Corporation assisted in meeting the publication costs of this article.

REFERENCES

1. A. Dall'Olio, Y. Dascola, V. Varacca, and V. Bocchi, *Acad. Sci. Ser. C*, **267**, 433 (1968).
2. A. F. Diaz, K. K. Kanazawa, and G. P. Gardini, *J. Chem. Soc., Chem. Commun.*, 635 (1979); A. F. Diaz and J. I. Castillo, *ibid.*, 397 (1980); K. K. Kanazawa, A. F. Diaz, W. D. Gill, P. M. Grant, G. B. Street, G. P. Gardini, and J. F. Kwak, *Synthetic Metals*, **1**, 329 (1979/1980).
3. A. F. Diaz, *Chem. Scr.*, **17**, 145 (1981).
4. R. J. Waltman, J. Bargon, and A. F. Diaz, *J. Phys. Chem.*, **87**, 1459 (1983).
5. G. Tourillon and F. Garnier, *J. Electroanal. Chem.*, **135**, 173 (1982).
6. J. F. Ambrose and R. F. Nelson, *This Journal*, **115**, 1159 (1968).
7. J. Bargon, M. Mohmand, and R. J. Waltman, *IBM J. Res. Develop.*, **27**, 330 (1983).
8. R. J. Waltman and J. Bargon, Unpublished results.
9. J. Bargon, S. Mohmand, and R. J. Waltman, *Mol. Cryst. Liq. Cryst.*, **93**, 279 (1983).
10. A. F. Diaz and K. K. Kanazawa, in "Extended Linear Chain Compounds," Vol. 3, J. S. Miller, Editor, p. 417, Plenum Press, New York (1982).
11. A. F. Diaz, J. M. Vasquez Vallejo, and A. Martinez Duran, *IBM J. Res. Develop.*, **25**, 42 (1981).
12. P. J. Nigrey, A. G. MacDiarmid, and A. J. Heeger, *Mol. Cryst. Liq. Cryst.*, **83**, 309 (1982).
13. A. F. Diaz, A. Martinez, K. K. Kanazawa, and M. Salmon, *J. Electroanal. Chem.*, **130**, 181 (1981).
14. K. Sanechika, T. Yamamoto, and A. Yamamoto, *J. Polym. Sci., Polym. Lett. Ed.*, **20**, 365 (1982).
15. A. F. Diaz, R. Hernandez, R. J. Waltman, and J. Bargon, *J. Phys. Chem.*, To be published.
16. J. E. Leffler and E. Grunwald, "Rates and Equilibria of Organic Reactions," John Wiley and Sons, Inc., New York (1963).
17. P. Zuman, "Substituent Effects in Organic Polarography," Plenum Press, New York (1967), and references therein.
18. A. G. MacDiarmid, M. Aldissi, R. B. Kaner, M. Maxfield, and R. J. Mammone, Abstract 558, p. 843, The Electrochemical Society Extended Abstracts, Vol. 83-1, Washington, DC, Oct. 9-14, 1983.
19. F. Garnier, G. Tourillon, M. Gazard, and J. C. DuBois, *J. Electroanal. Chem.*, **148**, 299 (1983).



Application of Activated Carbon Fiber Fabrics to Electrodes of Rechargeable Battery and Organic Electrolyte Capacitor

M. Nawa, T. Nogami, and H. Mikawa

Department of Applied Chemistry, Faculty of Engineering, Osaka University, Yamada-Kami, Suita, Osaka 565, Japan

Since the energy crisis, a new energy storage system which does not waste precious raw materials has been required. Graphite intercalation compounds appear to have good prospects as electrode materials in batteries.¹ One product has already been marketed² and it is likely that its importance will grow in the near future. Carbon black with extremely large specific surface area has recently been used as a electric double layer capacitor³ with extremely large specific capacity. It is expected to find a great demand for back-up power source of computer memory. Most of these batteries and capacitors require some treatments to keep the electrode's stiffness. In a search for other electrode materials useful for the batteries and capacitors, we noticed that a special kind of activated carbon fiber (ACF) made from phenolic resin has the following attractive properties as an electrode material:⁴ (1) It has a quite large specific surface area (1500-2500 m²/g), and thereby it is expected to store a large amount of electricity; (2) it has a high electrical conductivity of 60 S cm⁻¹; (3) various types of ACF, such as felt, fiber, cloth and paper sheet can be obtained commercially. Thus, ACF can be directly used as electrodes without any treatment; (4) It is a quite stable material; (5) it has a small bulk density of 0.01 g/cm³ for a cloth; (6) it is a flexible material.

We have made an organic electrolyte capacitor by use of a p-doped ACF as a cathode and a n-doped ACF as an anode.⁵ We have also made a rechargeable battery by use of a p-doped ACF as a cathode and a lithium metal as an anode.⁵

ORGANIC ELECTROLYTE CAPACITOR

Two cloths of ACF (each 3.0 cm², 29

mg), type CH-25 available from Kuraray Chemical Co. Ltd., were separated with a glass fiber filter of 0.25 mm thickness. They were then placed in a glass vessel containing a 1 mol dm⁻³ solution of LiClO₄ in γ -butyrolactone (γ -BL) in an argon atmosphere. Platinum wires were attached to both of the ACF electrodes. After passing 7.1 C, the cell configuration was (ACF^{a-})Li^{a+} | LiClO₄ in γ -BL | (ACF^{a+})(ClO₄⁻)_a. The molar ratio of the dopant to carbon atom was estimated to be $a = 0.0315$ at this stage.⁶ The Voc and Isc were 3.0 V and 975 mA, respectively. The plot of the quantity of electricity recovered against the cell voltage is shown in Fig. 1. The plot deviates from a linear relation more and more significantly as the increase in the cell voltage. The upward deviation from a straight line is due to the co-existence of a capacitive contribution and a contribution from a galvanic cell. The capacitive contribution arises from an electric double layer formed over extremely large surface area of ACF. In view of the high electrical conductivity

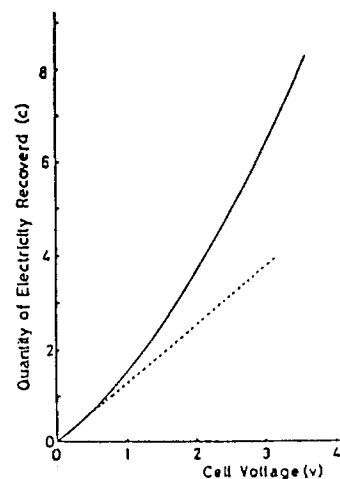


Fig. 1. Relation between the quantity of electricity recovered and the cell voltage.

Keywords: activated carbon fiber, organic electrolyte capacitor, rechargeable battery, supecific surface area.

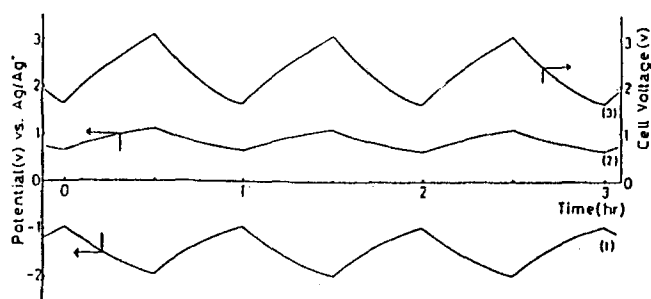


Fig. 2. The changes of the electrode potential vs. Ag/Ag^+ and cell voltage in charge-discharge cycles (charge current: 1.2 mA , discharge load: $2\text{ k}\Omega$). (1) negative electrode; (2) positive electrode; (3) cell voltage.

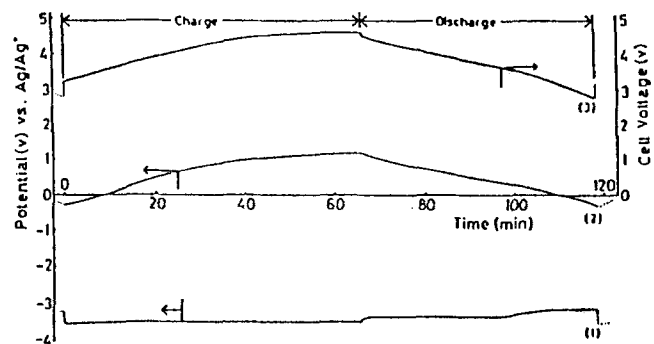


Fig. 3. The changes of the electrode potentials vs. Ag/Ag^+ and cell voltage in charge-discharge cycle under constant current of $1\text{ mA}/\text{cm}^2$. (1) Li electrode; (2) ACF electrode; (3) cell voltage.

of ACF, graphite structure is assumed to be contained in ACF. The contribution of the galvanic cell arises from the intercalation of Li^+ and ClO_4^- into the ACF lattice. Fig. 2 shows charge-discharge characteristics of the cell between 3.08 V and 1.65 V ($Q_{\text{in}} = 2.16\text{ C}$, $Q_{\text{out}} = 2.08\text{ C}$; 96 % efficiency), and the changes of the electrode potentials vs. Ag/Ag^+ . The change of the potential of $(\text{ACF}^{\text{a}-})\text{Li}^{\text{a}+}$ was about two times as large as that of $(\text{ACF}^{\text{a}+})\text{ClO}_4^{\text{a}-}$. The cycles were reproducible for more than 130 cycles. Although the contribution from galvanic cell is present in this system, its operation resemble the organic electrolyte capacitor. The maximum power density, energy density, and specific capacity were estimated to be $11.1\text{ kW}/\text{kg}$, $36.2\text{ WH}/\text{kg}$, and $36.5\text{ F}/(1\text{ g of ACF})$, respectively, based on V_{oc} , I_{sc} , quantity of electricity recovered and the weights of ACF and LiClO_4 consumed. If the cell is charged and then allowed to stand for one day, 40 - 50 % of charge initially inserted can no longer be recovered on discharge. However, it may be useful for a back-up power source because of the stability of the charge-discharge cycles and of extremely large specific capacity.

RECHARGEABLE BATTERY

A cloth of ACF (38.4 mg , 3.8 cm^2), and a strip of lithium were separated by a glass fiber filter of 0.25 mm thickness. They were then placed in a glass vessel containing a 1 mol dm^{-3} solution of LiClO_4 in $\gamma\text{-BL}$ in an argon atmosphere. Platinum wires attached to the ACF and lithium were connected to the positive

and negative terminals of D.C. power source, respectively. After passing 14.91 C , the battery at the charged state is expressed as $\text{bLi} | \text{LiClO}_4$ in $\gamma\text{-BL} | (\text{ACF}^{\text{b}+})(\text{ClO}_4^{\text{b}-})_{\text{b}}$. The molar ratio of dopant to a carbon atom was estimated to be $b=0.0503$ at this stage.⁶ The V_{oc} of 4.61 V and the I_{sc} of 696 mA were obtained, which correspond to a maximum power density of $14.8\text{ kW}/\text{kg}$, based on the weights of ACF and LiClO_4 consumed. Fig. 3 shows the changes of the electrode potentials vs. Ag/Ag^+ and the change of the cell voltage under a constant current of $1\text{ mA}/\text{cm}^2$ both in charge and discharge processes. Flat voltage could not be obtained, because of the presence of capacitive contribution of the ACF electrode. The present system is basically similar to the Li-graphite battery reported.⁷ However, the capacitive contribution in the Li-ACF battery is much larger than in Li-graphite battery. The theoretical energy density was estimated to $358\text{ WH}/\text{kg}$ based on V_{oc} , quantity of electricity passed and the weights of ACF and LiClO_4 consumed. The energy density in the present system is about 3.5 times as large as that of Li-graphite battery reported.⁷ The present system can store electricity more than three times as large as the Li-graphite battery. A partial charge-discharge cycle between $4.5\text{--}3.6\text{ V}$ ($Q_{\text{in}}=6.84\text{ C}$, $Q_{\text{out}}=5.7\text{ C}$, 83 % of the stored charge) was reproducible for more than 50 cycles. If the cell is charged and then allowed to stand for four days, 60 % of the charge originally inserted can no longer be recovered on discharge. However, the

self-discharge was very little after four days.

Since ACF is a flexible material, we can make a capacitor and a battery with flexibility.

ACKNOWLEDGMENTS

We are grateful to Drs. Hiroshi Fukusaki, Yoshiro Aoki, Kazuo Yamazaki, Michihide Yamauchi, and Hiroshi Yashima, Kao Corporation Wakayama Research Laboratory, for their helpful discussion.

REFERENCES

1. S. Flandrois, *Syn. Metals*, 4, 255 (1982).
2. A. Morita, T. Iijima, T. Fujii, and H. Ogawa, *J. Power Sources*, 5, 111 (1980).
3. S. Sekido, T. Muranaka, Y. Yoshino, and H. Mori, *National Technical Report*, 26, 220 (1980).
4. T. Kihata, T. Fukuda, N. Ishizaki, S. Ohmori, and H. Komagata, *Kagaku Kogyo*, 44, 343 (1980).
5. T. Nogami, M. Nawa, and H. Mikawa, *J. Chem. Soc., Chem. Commun.*, 1158 (1982).
6. Estimated from the elemental analysis of ACF: C, 96.38; H, 0.54; O, 3.03 %.
7. T. Ohzuku, Z. Takehara, and S. Yoshizawa, *Denki Kagaku*, 46, 438 (1978).

Manuscript submitted Oct. 1, 1982;
revised manuscript received March 15, 1983.

Osaka University assisted in meeting the publication costs of this article.

The Importance of Alkali Metal Cations in Acid Environments in Contact with Corrosion-Protective Organic Coatings

Henry Leidheiser, Jr.,* Hyacinth Vedage, Richard D. Granata,* and Malcolm L. White

Department of Chemistry and Center for Surface and Coatings Research, Lehigh University, Bethlehem, Pennsylvania 18015

It has previously been shown that the rate at which polybutadiene coatings delaminate from a steel surface, radially from a defect, upon cathodic polarization is a function of the cation present in the medium (1). The rate of delamination in the presence of different cations decreases in the order, Cs^+ , K^+ , Na^+ , and Li^+ . This same order of relative activity has been observed with other metallic substrates and with alkyd, epoxy and photoactive polymer systems. Our experience to date is that this alkali metal ion effect is ubiquitous and that it probably results from the relative rates of migration of the ions either through the coating or in the liquid layer at the interface under the potential gradient which exists when a cathodic potential is applied. We have recently observed another alkali metal ion effect which we have not yet explained but which effect may possibly be put to a useful purpose in certain situations. A description of this effect is given below.

All investigations have been conducted on a formulated epoxy/polyamideamine. The coating was applied to steel by a doctor blade technique to a thickness of 500 μm , a thickness for use with aggressive environments which is less than that recommended by the formulator. Exposure of coated steel to 0.1M H_2SO_4 at 60°C resulted in the formation in two days or less of blisters. Application of the coating to the as-received, rolled surface after solvent cleaning resulted in the formation of a single large blister that covered the entire 3.2 cm diameter exposed area after 2 days. Sandblasted steel surfaces treated similarly developed many isolated blisters that did not merge in two days. The results were reproducible.

Alkali metal ions were introduced into the sulfuric acid as the sulfate to a concentration of 0.5M, i.e., in a 5/1 ratio of metal

cation to hydrogen ion. The rate of blister formation was remarkably reduced. Small isolated blisters were detected after an average of 5 days in the case of Li^+ ion additions, after an average of 7 days in the case of Na^+ ion additions, and after an average of 10 days for K^+ ion additions.

The following experiment suggests that the alkali metal ions reduce the rate of collection of H^+ ions at the substrate/coating interface. A strip of pH sensitive paper was placed on a piece of glass and was overcoated with a 500 μm thick layer of the epoxy coating. The coated glass was exposed to 0.1M H_2SO_4 at 60°C for two days. The paper indicated the pH at the interface was very low. A similar sample exposed to 0.1M H_2SO_4 - 0.5M Na_2SO_4 for the same length of time yielded no change in color of the pH paper, suggestive of the fact that no significant concentration of H^+ ions had collected at the interface. The results obtained with the pH sensitive paper were also reflected in the coating itself. This coating changes from a black to tan color upon exposure to H_2SO_4 under the conditions of our experiments. The sample immersed in 0.1M H_2SO_4 exhibited this color change both at the top surface in contact with the electrolyte and the bottom surface as viewed through the glass. The sample immersed in the H_2SO_4 - Na_2SO_4 mixture exhibited the color change at the top surface but the bottom surface as viewed through the glass exhibited no change in color. The observations suggest that the alkali metal ion interferes with the transport of the hydrogen ions through the coating.

We have no completely satisfactory explanation for the effect at the present time. Osmotic behavior offers a possible explanation since the amount of water migration through the coating would be expected to decrease with increase in the ionic concentration of the electrolyte. However, it is hard to explain the big differences observed with the different alkali metal ions. The most appealing explanation is that the alkali

*Electrochemical Society Active Member

Key words: acid, coating, corrosion, protection

metal ions compete with the H^+ ions for simple diffusion or electromigration through the coating. The ions also may form strong bonds with the water molecules present in the coating and may reduce the rate at which an aqueous phase develops at the metal/coating interface. The aqueous phase is essential for the corrosion process to occur and consequently the rate of blistering is reduced. The bonding of water by the cations may also change the rate at which the coating swells during exposure to the acid.

ACKNOWLEDGEMENT

Appreciation is expressed to the Electric Power Research Institute who provided support for this research.

Hydrogen Evolution at p-InP Photocathodes in Alkaline Electrolyte

P. G. P. Ang^{1*} and A. F. Sammells*

Eltron Research, Incorporated, Naperville, Illinois 60540

ABSTRACT

The photoelectrochemical (PEC) performance of p-InP single crystal, surface modified by the sequential deposition of cobalt and platinum, has been investigated in 6N KOH. Efficiencies of 14.2% were realized from the photocathode for the electrical power savings obtained compared to a platinum cathode, operating at the same current density. A variety of definitions of efficiency for the conversion of light to hydrogen are discussed.

RESULTS AND DISCUSSION

Several approaches have been discussed previously for improving the performance of photoelectrodes by surface modification procedures. These have been discussed in several PEC review articles (1-4). The role of platinum for improving the performance of iron-oxide photoanodes was discussed by us some time ago to assist the photoelectrochemical oxygen-evolution reaction (5). Improving the performance of p-InP in both acid (6,7,8) and alkaline electrolyte (9) for specific photoelectrochemical reactions has also been observed. We wish to report on the enhanced performance of p-InP photocathodes realized by the sequential deposition of Co and Pt on its surface.

The p-InP single crystals (Zn-doped, carrier density $10^{16}/\text{cm}^3$, $\langle 111 \rangle$ surface, obtained from Crysta Comm Inc.) were used in the course of this work. Ohmic contact to the crystal was made by the sequential deposition of Au-Zn-Au followed by sintering at 475°C for 20 seconds. Current collection was via a nickel wire to the ohmic contact using silver epoxy which was then cured at 150°C for one hour. After encapsulation of this current collector and the semiconductor edges, the photocathode surface was etched with concentrated HCl for 10 seconds, during which time gas evolution was observed. Surface modification of

the p-InP surface was performed by the local electrodeposition of cobalt from a 1M CoCl_2 solution at low current density ($1 \text{ mA}/\text{cm}^2$).

The cobalt if electrodeposited uniformly would correspond to a thickness of 200 \AA . However, it is likely that the cobalt becomes deposited at preferred sites (probably defect) on the p-InP surface. Because of this, estimation of light blockage caused by this coating is difficult. Some surface characterization is however presently underway using Raman spectroscopic techniques and will be reported on later (10).

Curve A of Figure 1 shows the initial performance of the unmodified p-InP electrode in 6N KOH under $100 \text{ mW}/\text{cm}^2$ ELH quartz halogen illumination. Here the open-circuit potential vs SCE changed from -500 mV to -350 mV after illumination. Rather small photocurrents ($4 \text{ mA}/\text{cm}^2$ at -800 mV vs SCE) and poor fill factors ($\text{FF} = 0.23$) were characteristic of this electrode. After cobalt deposition, the initial open-circuit potential under illumination became more positive (-300 mV). The photocurrent density at -0.8 V vs SCE increased to $13 \text{ mA}/\text{cm}^2$ and gave a fill factor of 0.48, as shown in curve B of Figure 1.

The p-InP was further modified by placing 1 drop of a 0.01 M chloroplatinic acid solution onto the cobalt-treated surface, followed immediately by rinsing with distilled water. The initial performance of this electrode is shown in curve C of Figure 1, where the photocurrent density at -800 mV increased nominally to $14 \text{ mA}/\text{cm}^2$ with the initial open-circuit potential becoming -200 mV vs SCE. Here the fill-factor remained at 0.48. The electrode potential is about 900mV positive of the reversible hydrogen potential in alkaline electrolyte.

The series of curves A-C in Figure 1 are shown to indicate the incremental improvement in PEC performance that can be achieved by the sequential deposition of Co and Pt. However, greatest PEC performance enhancements on p-InP in alkaline electrolytes were achieved by completing the above sequential

*Electrochemical Society Active Member.

Key words: p-InP, Hydrogen Production, Photoelectrocatalysis

surface modification procedures prior to taking any current-potential measurements. This is shown using a second p-InP electrode prepared in a similar manner. With all p-InP electrodes fabricated, the initial V_{OC} of -200 mV vs SCE gradually drifted to more negative values (≈ 10 mins) and typically equilibrated between -300 and -400 mV. The current-potential curve for this second photocathode is shown in Figure 2. The enhanced performance observed for hydrogen evolution is probably an electrocatalytic effect. For comparison the current-potential curve scans for platinum during both hydrogen (left-hand side of Figure 2) and oxygen evolution (right-hand side of Figure 2) are shown. At the point of maximum power conversion efficiency, the p-InP photocathode gave a photopotential of -0.65 V vs SCE. The fill factor for this electrode was 0.58. At the same current density, the potential of the platinum electrode during hydrogen evolution was -1.24 V vs SCE. Here the cell voltage saving realized by substitution of a platinum electrode for the illuminated p-InP photocathode was 0.59 V. At 24 mA/cm² this corresponds to a power savings of 0.59 V x 24 mA/cm² = 14.2 mW/cm². With an incident illumination of approximately 100 mW/cm² unfiltered quartz halogen lamp (General Electric ELH bulb), the efficiency of solar to chemical conversion can be realized in terms of power saving (6,7), which is defined as

$$\eta = (i \times \Delta V) / I_{\text{light}}, \text{ or } \eta_1 = 14.2\%$$

It is appropriate at this time to compare the various alternative approaches available which have recently been discussed for calculating the efficiency of photoelectrodes. One other approach (6) for calculating the efficiency of such photoelectrodes is to compare the potential (V), at which hydrogen evolution occurs at the optimum power for the photocathode, with the reversible thermodynamic potential of hydrogen ($V_{H_2, \text{rev}}$) in an ideal fuel cell anode (-1.1 V vs SCE). Here it is assumed that overpotential losses at the hydrogen anode and at the oxygen cathode during operation is neglected. This second definition can be written as

$$\eta_2 = \frac{i \times (V - V_{H_2, \text{rev}})}{I_{\text{light}}}$$

With reference to Figure 2, this will give a value of

$$\eta_2 = \frac{24 \text{ mA/cm}^2 \times (-0.65 + 1.1) \text{ V}}{100 \text{ mW/cm}^2} = 10.8\%$$

This value obtained in 6N KOH by us compare to values of 13.3% for p-InP (Rh-H alloy) and 11.4% for p-InP (Pt-H alloy) in

1M HClO₄ electrolyte obtained by others (6). It should be noted, however that direct comparison of such efficiency values may in fact be a little erroneous since different light sources were used by each group.

It should be noted that if direct photoelectrolysis of water is the eventual goal for this work, there are significant advantages to the use of alkaline electrolytes where not only greater stabilities might be realized from photoanodes (or anodes) used with p-InP but oxygen evolution kinetics are well documented to be more rapid.

The efficiency of a PEC process can also be calculated as the power (P) ratio (11)

$$\eta_3 = \frac{P_{\text{stored}}}{I_{\text{light}} + P_{\text{bias}}}$$

from which we obtain an efficiency of

$$\eta_3 = \frac{1.23 \text{ V} \times 24 \text{ mA/cm}^2}{100 \text{ mW/cm}^2 + 1.25 \text{ V} \times 24 \text{ mA/cm}^2} = 22.7\%$$

1.23 V is the thermodynamic voltage of a hydrogen/oxygen fuel cell. The bias voltage of 1.25 V is the voltage between the p-InP and an oxygen-evolving platinum electrode at 24 mA/cm². It should be noted that this definition of efficiency is somewhat insensitive to the magnitude of the bias voltage applied. Although this definition gives a relatively large efficiency value, one should be aware that for water electrolysis between two platinum electrodes under a bias voltage without light, the corresponding efficiency will be larger:

$$\eta_3 = \frac{1.23 \text{ V} \times 24 \text{ mA/cm}^2}{1.84 \text{ V} \times 24 \text{ mA/cm}^2} = 66.8\%$$

Other ways are also available for calculating practical efficiency, including

$$\eta_4 = \frac{P_{\text{stored}} - P_{\text{bias}}}{I_{\text{light}}}$$

which for biased photoelectrodes can give decidedly pessimistic values. In our case we have $\eta_4 =$

$$\frac{1.23 \text{ V} \times 24 \text{ mA/cm}^2 - 1.25 \text{ V} \times 24 \text{ mA/cm}^2}{100 \text{ mW/cm}^2} = -0.48\%$$

A fifth definition of efficiency is to take the high heating value of hydrogen ($\Delta H = 1.47 \text{ eV}$) instead of using the Gibbs free energy $\Delta C = 1.23 \text{ eV}$. One assumption here is that all electrical current in the p-InP is used to make hydrogen under 100% Faradaic efficiency, i.e. no corrosion or other simultaneous side reaction occurs. Thus we can write:

$$\eta_5 = \frac{P_{\text{stored}} \text{ (using } \Delta H) - P_{\text{bias}}}{I_{\text{light}}}$$

or $\eta_5 =$

$$\frac{1.47\text{V} \times 24\text{mA/cm}^2 - 1.25\text{V} \times 24\text{ mA/cm}^2}{100\text{ mW/cm}^2} = 5.3\%$$

We have shown that a variety of efficiency values can be obtained from one electrode, depending upon the definition used. In short, care must be taken when comparing the "efficiencies" of fuel-producing PEC cells as reported by different laboratories.

The PEC performance discussed here for p-InP in alkaline electrolyte gives us the opportunity to design cells which have a high reversibility towards oxygen evolution at the counter electrode and possess good stability and corrosion resistance for the electrode components.

Manuscript submitted July 26, 1983; revised manuscript received April 2, 1984.

ACKNOWLEDGEMENTS

The authors are grateful to Drs. K. Krist and R. V. Serauskas of the Gas Research Institute for valuable discussion on comparative PEC efficiency calculations. This work was funded by the Gas Research Institute under contract #5082-260-0671.

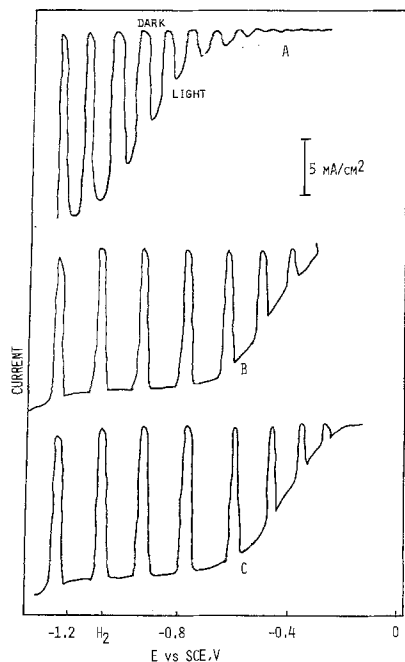


Fig. 1. Current-potential characteristics of single-crystal p-InP in 6N KOH under chopped 100 mW/cm² ELH illumination. A: acid-etched surface. B: after CoCl₂ treatment. C: after CoCl₂ treatment followed by H₂PtCl₆.

Eltron Research, Inc. assisted in meeting the publication costs of this article.

REFERENCES

1. A. J. Nozik, *Ann. Rev. Phys. Chem.*, **29**, 189 (1978).
 2. R. Memming, *Electrochim. Acta*, **25**, 77 (1980).
 3. A. Heller and B. Miller, *Electrochim. Acta*, **25**, 29 (1980).
 4. A. J. Bard, *J. Photochem.*, **10**, 59 (1979).
 5. A. F. Sammells and P. G. P. Ang, *This Journal*, **126**, 1831 (1979).
 6. E. Aharon-Shalom and A. Heller, *This Journal*, **129**, 2865 (1982).
 7. A. Heller, *Solar Energy*, **29**, 153 (1982).
 8. A. Heller, *Proc. 4th International Conf. on Photochemical Conversion and Storage of Solar Energy*, J. Rabani, Editor, Jerusalem, Isreal, Aug. 8-13, 1982.
 9. C. J. Liu, P. G. P. Ang, and A. F. Sammells, *This Journal*, **129**, 1387 (1982).
 10. P. G. P. Ang, T. M. Cotton and A. F. Sammells, *Fifth World Hydrogen Conf.*, Toronto, Canada, July 1984.
 11. O. J. Murphy and J. O'M. Bockris, *Abstract 248, Fall Electrochemical Society Meeting, Detroit, 1982.*
- ¹Present address: Technotronics, Inc., Woodridge, Illinois 60517.

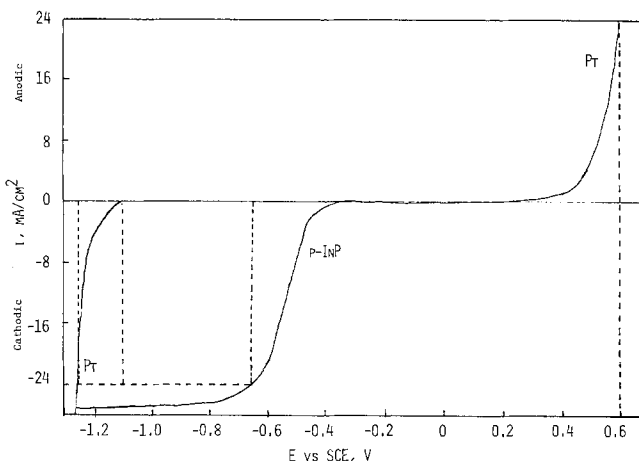


Fig. 2. Current potential curve on 6N KOH of hydrogen evolving p-InP single crystal (100 mW/cm² illumination, of hydrogen evolving Pt (left) and of oxygen evolving Pt (right) at 21°C.



A Model for the Anodic Dissolution of Zinc in Alkaline Electrolyte

Kinetics of Initial Dissolution

Yu-Chi Chang* and Geoffrey Prentice**

Department of Chemical Engineering, The Johns Hopkins University, Baltimore, Maryland 21218

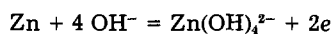
ABSTRACT

We propose a three-step mechanism to describe the kinetics of the initial dissolution of zinc in alkaline electrolyte. The rate-determining step is postulated to be a reversible reaction where a monovalent zinc hydroxide is converted to a soluble zincate. The surface reactions are assumed to occur on activated sites, where Langmuir adsorption is assumed. The reaction scheme is shown to be consistent with experimental quantities such as Tafel slope and reaction order for data obtained near room temperature in approximately 1N hydroxide electrolyte. The thermodynamic consistency of each elementary step is demonstrated from an analysis of available free energy data.

The zinc electrode in alkaline electrolyte is used in currently available battery systems and is a prime candidate for incorporation in advanced energy storage devices (1, 2). Consequently, many investigations have been conducted to determine the kinetic and thermodynamic characteristics of this electrode system. Extensive bibliographies of this work appear in Ref. (3-5). The overall kinetic characteristics (reaction orders, Tafel slopes, etc.) have been determined in numerous studies; however, fewer investigations regarding the elementary phenomena comprising the dissolution process have been conducted. A notable exception is the quantitative treatment presented by Bockris *et al.* (6).

Slow potentiodynamic sweeps on a rotating-disk electrode reveal four characteristic regions on a typical current-potential curve (Fig. 1): (i) an initial dissolution region where the current increases exponentially with potential, (ii) an active dissolution region where the current density increases rapidly with potential in a linear fashion, (iii) a prepasive region where a high level of current is maintained but is not a strong function of potential, and (iv) a passive region where little current flows, irrespective of potential. In the present investigation, we are concerned primarily with the initial dissolution region. In 1N KOH the proposed model is valid in a range near -1.23V vs. NHE.

Spectroscopic and potentiometric studies (7, 8) have demonstrated that the soluble reaction product is a zincate ion; the overall reaction can be represented by



Ranges of the kinetic parameters for this reaction obtained by various investigators are summarized by Bockris *et al.* (6).

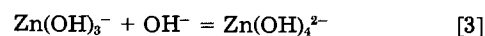
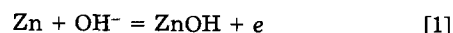
Kato *et al.* (9) observed a decrease in collection efficiency with rotation rate for the anodic dissolution of zinc on a rotating ring-disk electrode. This phenomenon has been confirmed by other investigators (4), and variations in collection efficiency with bulk zincate have also been observed.

In this study, we present a detailed analysis of our model and compare the derived results with corresponding experimental quantities and with the results derived from other proposed mechanisms.

* Electrochemical Society Student Member.
 ** Electrochemical Society Active Member.

Proposed Model

Reaction mechanism.—We are proposing the following three-step mechanism for the anodic dissolution of zinc in the initial stages



Our postulates are that the rate-determining step controls the overall reaction rate and that dynamic equilibria are rapidly established in the other two elementary steps. Although stable monovalent zinc compounds have not been isolated, evidence exists of their presence as short-lived species (10, 11). Reactions involving zinc and the monovalent hydroxide species are assumed to occur on the electrode surface. The third reaction, which involves only a soluble zincate species, is assumed to be a homogeneous reaction occurring in the electrolyte.

Analysis of rate expressions.—We treat the adsorbed species in accordance with Langmuir's hypotheses and

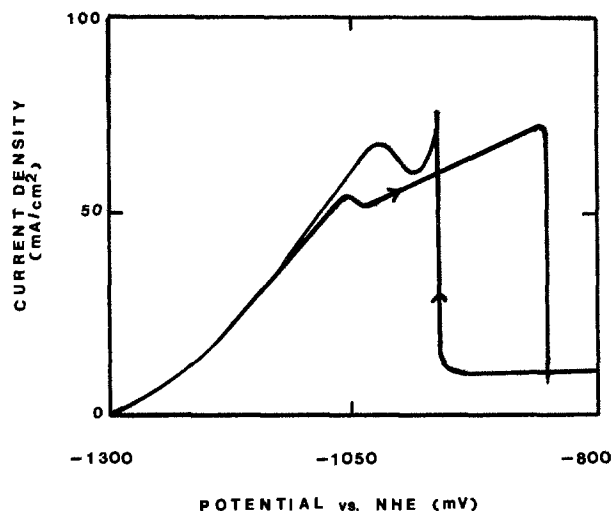


Fig. 1. Typical potentiodynamic sweep on a zinc RDE. 1.0N KOH, 300 rpm, 4 mV/s sweep rate, 25°C.

express the reaction rates in terms of species concentrations and electrode potential

$$r_1 = i_1/F = k_{a1}c_{OH^-} (1 - \theta) \exp[(1 - \beta_1)FV/RT] - k_{c1}\theta \exp(-\beta_1FV/RT) \quad [4]$$

$$r_2 = i_2/F = k_{a2}c_{OH^-}^2 \exp[(1 - \beta_2)FV/RT] - k_{c2}(1 - \theta) c_{Zn(OH)_3^-} \exp(-\beta_2FV/RT) \quad \text{rds} \quad [5]$$

$$r_3 = k_{a3}c_{Zn(OH)_3^-}c_{OH^-} - k_{c3}c_{Zn(OH)_4^{2-}} \quad [6]$$

where θ represents the fractional surface coverage by the ZnOH species.

At steady state, all the reactions proceed at the same rate; the net current density is given by

$$i = 2i_1 = 2i_2 \quad [7]$$

Since reaction [1] is assumed to be fast and essentially at equilibrium, the fractional surface coverage can be obtained from Eq. [4]

$$\theta = k_{a1}c_{OH^-}/[k_{a1}c_{OH^-} + k_{c1} \exp(-FV/RT)] \quad [8]$$

Substitution of Eq. [8] into Eq. [5] yields

$$i_2/F = i/(2F) = k_{a2}k_{a1}c_{OH^-}^3 \exp[(2 - \beta_2)FV/RT] \frac{[(H + 1)k_{c1}] - k_{c2}k_{c3}c_{Zn(OH)_4^{2-}} \exp(-\beta_2FV/RT)}{[(H + 1)k_{a3}c_{OH^-}]} \quad [9]$$

where

$$H = k_{a1}c_{OH^-}/[k_{c1} \exp(-FV/RT)] \quad [10]$$

The equilibrium potential, determined from Eq. [9], is

$$V^0 = RT/(2F) \ln[k_{c1}k_{c2}k_{c3}c_{Zn(OH)_4^{2-}}/k_{a1}k_{a2}k_{a3}c_{OH^-}^4] \quad [11]$$

and the exchange current density is

$$i_0 = 2Fk_{c2}[k_{a1}k_{a2}/(k_{c1}k_{c2})]^{1/2} (k_{c3}/k_{a3})^{(2-\beta_2)/2} c_{OH^-}^{2\beta_2-1} c_{Zn(OH)_4^{2-}}^{(2-\beta_2)/2} (H^0 + 1) \quad [12]$$

where H^0 is the variable H evaluated at the equilibrium potential V^0 . The overpotential represents the departure from the equilibrium potential and can be expressed as

$$\eta = V - V^0 \quad [13]$$

Equation [9], cast in the standard Butler-Volmer form, becomes

$$i = i_0^* [\exp(\alpha_a F \eta / RT) - \exp(-\alpha_c F \eta / RT)] \quad [14]$$

where $\alpha_a = 2 - \beta_2$, $\alpha_c = \beta_2$, and $i_0^* = i_0/[H^0 + 1]/(H + 1)$.

Results and Discussion

In order to calculate the current density as a function of potential, a value for the symmetry factor, a rate constant for reaction [2], and equilibrium constants for reactions [1] and [3] must be determined. The free energies of formation of the reacting species in reaction [3] are known; however, the free energy of reaction for the first two reactions cannot be determined, as they involve the unstable monovalent species for which thermodynamic data are unavailable. As an estimate for the free energy of formation of ZnOH, we chose a value of -65.8 kcal/mol, which corresponds to an equilibrium constant that is consistent with current density-potential data; moreover, this value is close to the free energy of formation of ZnO (-76.6 kcal/mol), as we expect from group contribution considerations. The forward rate constant for reaction [2] was also chosen to be compatible with current-potential data. A summary of kinetic and thermodynamic parameters appears in Table I.

Quantities such as Tafel slope and variation of the exchange current density with concentration are dependent on the choice of symmetry factor in the rate-determining

Table I. Summary of kinetic and thermodynamic quantities

Species	Standard free energy of formation (kcal/mol)	
ZnOH	-65.8	
OH ⁻	-37.6	
Zn(OH) ₃ ⁻	-166.0 to -167.6	
Zn(OH) ₄ ²⁻	205.2 to -206.2	
Reaction	Standard free energy of reaction (kcal)	Kinetic rate constant cm ⁴ /(s mol)
[1]	-28.2	9.3 × 10 ⁹
[2]	-25.0 to -26.6	
[3]	-2.6 to 0	

Thermodynamic quantities were obtained (or derived) from data found in Ref. (7, 12, 13). The free energy of formation of ZnOH and the rate constant were estimated (see Results and Discussion section).

step. The Tafel slopes are obtained directly from Eq. [14]; the anodic Tafel slope is

$$\partial V / \partial \log i_a = 2.3RT / [(2 - \beta_2)F - HF / (H + 1)] \quad [15]$$

and the cathodic Tafel slope is

$$\partial V / \partial \log i_c = 2.3RT / [\beta_2 F + HF / (H + 1)] \quad [16]$$

The variations in the exchange current density with concentration are obtained from Eq. [12]

$$\partial \ln i_0 / \partial \ln c_{OH^-} = 2\beta_2 - 1 - H^0 / (1 + H^0) \quad [17]$$

$$\partial \ln i_0 / \partial \ln c_{Zn(OH)_4^{2-}} = (2 - \beta_2) / 2 \quad [18]$$

Equation [17] indicates that the variation in the logarithm of the exchange current density with pH is dependent on pH. If we choose $\beta_2 = 0.5$ and $V = -1.240$ vs. NHE, $\partial \ln i_0 / \partial \ln c_{OH^-} = -0.33$ when evaluated at $[OH^-] = 1M$; at $[OH^-] = 2M$, $\partial \ln i_0 / \partial \ln c_{OH^-}$ is equal to -0.5 .

The value of the exchange current density calculated from Eq. [12] is 10 mA/cm², which is in agreement with the experimentally determined value at $1M$ KOH and $10^{-2}M$ Zn(OH)₄²⁻. The experimental value is affected by the surface roughness of the electrode, as the true surface area may be 2 or 3 times larger than the geometric area (14). A far more important consideration is the sensitivity of the calculated value to the choice of the symmetry factor. Data for many electrochemical reactions indicate that the symmetry factor is generally near 0.5 (15), and we have chosen this value in calculating i_0 . Because the symmetry factor appears as an exponent in the exchange current density expression Eq. [12], i_0 is extremely sensitive to the value of β_2 . A difference of 0.2 in β_2 causes a change of several orders of magnitude in i_0 ; by contrast, surface area effects are negligible. The quantities that depend on β_2 and the sensitivity of those quantities to changes in β_2 are summarized in Table II.

Table II. Quantities that depend on the symmetry factor

Quantity	Calculated value		Experimental value
	$\beta = 0.5$	$\beta = 0.7$	
α_a	1.5	1.3	1.0-1.6
α_c	0.5	0.7	0.4-0.7
Anodic Tafel slope (mV/decade)	50	70	30-60
Cathodic Tafel slope (mV/decade)	100	70	85-145
$\partial \log i_0 / \partial \log c_{OH^-}$	-0.33	0.07	0.14-0.45
$\partial \log i_0 / \partial \log c_{Zn(OH)_4^{2-}}$	0.75	0.65	0-0.67
i_0 (mA/cm ²)	10	2 × 10 ⁵	10-100

The experimental values are from the summary provided by Bockris *et al.* (6). Exchange current density is based on a zincate concentration of $0.0065M$ as in Ref. (6).

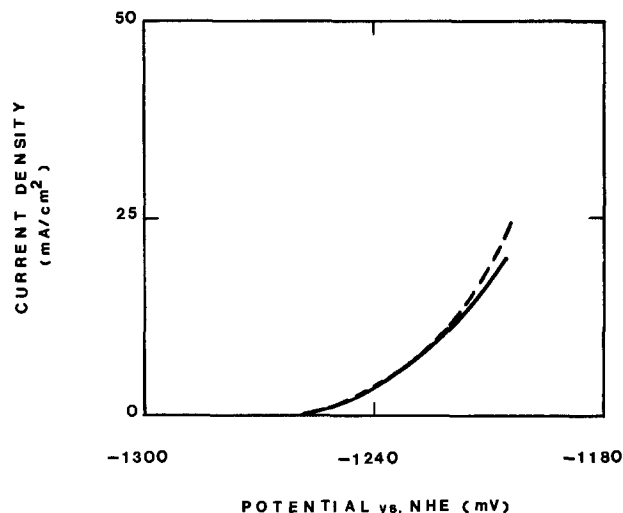


Fig. 2. Current density vs. potential for RDE. Solid line represents experimental data: 1N KOH, 25°C, 800 rpm, from Ref. (5). Dashed line calculated from Eq. [9].

The relation between current density and potential can be calculated from Eq. [9]. Comparison with the experimental data shows the narrow range, near -1.23V vs. NHE, over which the model is valid (Fig. 2). At more anodic potentials, it is likely that reactions involving species such as $\text{Zn}(\text{OH})_2$ and ZnO become more important and would need to be considered in a model for that region.

The reaction orders and the equilibrium potential are not dependent on the choice of symmetry factor. The anodic reaction orders are

$$\partial \ln i_a / \partial \ln c_{\text{OH}^-} = 3 - H / (H + 1) \quad [19]$$

$$\partial \ln i_a / \partial \ln c_{\text{Zn}(\text{OH})_4^{2-}} = 0 \quad [20]$$

and the cathodic reaction orders are

$$\partial \ln i_c / \partial \ln c_{\text{OH}^-} = -1 - H / (H + 1) \quad [21]$$

$$\partial \ln i_c / \partial \ln c_{\text{Zn}(\text{OH})_4^{2-}} = 1 \quad [22]$$

Since H is proportional to hydroxide concentration, the reaction orders vary with pH. A comparison of calculated and experimental reaction orders appears in Table III. All of the calculated values agree with the experimental determinations within the error of the experiment.

Several additional experimental observations are consistent with the proposed mechanism. Armstrong and Bulman (16) performed anodic dissolution studies on a rotating disk electrode. They obtained a linear plot of $1/i$ vs. $1/\omega^{1/2}$ at constant potential. Their analysis showed that the finite slope of this curve was evidence of the reversibility of the overall reaction. This observation is in agreement with our assumption that the rate-determining step is reversible. Armstrong and Bell (17) carried out impedance experiments, which indicated the presence of a single adsorbed intermediate. Their assumption that this intermediate is a monovalent zinc species is in agreement with our model. These investigators also determined the anodic Tafel slope from steady-state measurements. Their results show that the Tafel slope is 44 mV/decade at $V = -1.34\text{V}$ (Hg/HgO) and 120 mV/decade at $V = -1.31\text{V}$. We can evaluate the anodic Tafel slope from Eq. [15] at potentials corresponding to the values where Armstrong and Bell obtained their data. Since the variable H in that equation is potential dependent, the calculated Tafel slope is potential dependent. The Tafel slopes are 50 and 70 mV/decade, respectively. Both the experimental and calculated results show that the Tafel slope increases at more anodic potentials.

The four-step mechanism proposed by Bockris *et al.* (6) yields results that are generally similar to our results; however, there are several distinguishing features. In the

Table III. Comparison of experimental and calculated thermodynamic and kinetic parameters

Quantity	Calculated value	Experimental value
V^0 (V)	-1.26	-1.26
$\partial \ln i_a / \partial \ln c_{\text{OH}^-}$	~2.7	2.6 to 3.5
$\partial \ln i_c / \partial \ln c_{\text{Zn}(\text{OH})_4^{2-}}$	1	0.75 to 1.05

Calculated values are based on $\beta_2 = 0.5$. Experimental values from Ref. (6, 16).

Bockris model there are two adsorbed species, ZnOH and $\text{Zn}(\text{OH})_2^-$; in our model only the former species is considered as an adsorbed species. The reaction order with respect to hydroxide is somewhat different. Although direct comparisons are theoretically possible, the thermodynamic data on which to base a comparison are not available. For example, in the Bockris model $\partial \ln i_a / \partial \ln c_{\text{OH}^-} = 3 - (H + 2K_2 H c_{\text{OH}^-}) / (1 + H + K_2 H c_{\text{OH}^-})$, where K_2 is the equilibrium constant for the reaction $\text{ZnOH} + \text{OH}^- = \text{Zn}(\text{OH})_2^-$. This expression could be compared directly to Eq. [19] if free energy data were available for ZnOH and $\text{Zn}(\text{OH})_2^-$.

In further work, we plan to extend the model to more anodic regions and study the effects of mass transport on dissolution rates.

Acknowledgment

This material is based upon work supported by the National Science Foundation under Grant no. CPE-8202725.

Manuscript submitted Sept. 21, 1983; revised manuscript received Dec. 29, 1983. This was Paper 9 presented at the Washington, DC, Meeting of the Society, Oct. 9-14, 1983.

The National Science Foundation assisted in meeting the publication costs of this article.

LIST OF SYMBOLS

c	concentration, mol/cm ³
F	Faraday's constant, 96,500 C/eq
H	special variable, see Eq. [10]
i	current density, A/cm ²
i_0	exchange current density, A/cm ²
k	kinetic rate constant, cm ⁴ /(s mol) for reaction [2]
K	equilibrium constant, ratio of rate constants
p	reaction order with respect to soluble species
r	reaction rate, mol/s cm ²
R	gas constant, 8.31 J/mol K
T	temperature, K
V	potential with respect to a given electrode, V

Greek Symbols

α	transfer coefficient
β	symmetry factor
η	overpotential, V
θ	fractional surface coverage
ω	rotation rate, rad/s

Subscripts

a	anodic
c	cathodic
1, 2, 3	number of reaction, see Eq. [1]-[3]

Superscript

o	equilibrium condition
-----	-----------------------

REFERENCES

1. A. Fleischer and J. J. Lander, Editors, "Zinc-Silver Oxide Batteries," John Wiley and Sons, New York (1971).
2. C. Chakkaravarthy, A. K. Abdul Waheed, and H. V. K. Udupa, *J. Power Sources*, **6**, 203 (1981).
3. J. McBreen and E. J. Cairns, in "Advances in Electrochemistry and Electrochemical Engineering," H. Gerischer and C. W. Tobias, Editors, Vol. 11, p. 273, Wiley-Interscience, New York (1978).
4. M. C. H. McKubre and D. D. Macdonald, *This Journal*, **128**, 524 (1981).
5. R. D. Armstrong and M. F. Bell, in "Electrochemis-

- try," Vol. 4, p. 1, Specialist Periodical Reports, The Chemical Society, London (1974).
6. J. O'M. Bockris, Z. Nagy, and A. Damjanovic, *This Journal*, **119**, 285 (1972).
 7. T. P. Dirkse, *ibid.*, **101**, 328 (1954).
 8. J. S. Fordyce and R. L. Baum, *J. Phys. Chem.*, **43**, 843 (1965).
 9. H. Kato, T. Yoshimura, and M. Yamashita, *Nippon Kagaku Kaishu*, **12**, 1811 (1977).
 10. G. Bianchi, F. Mazza, and S. Trasatti, in "Proceedings of the Second International Congress on Metallic Corrosion," p. 905, New York (1963).
 11. D. Meyerstein and W. A. Mulac, *J. Phys. Chem.*, **72**, 784 (1968).
 12. J. A. Dean, Editor, "Lang's Handbook of Chemistry," 12th ed., Table 9-1, McGraw-Hill, New York (1979).
 13. R. C. Weast, Editor, "Handbook of Chemistry and Physics," 63rd ed., p. D-94, CRC Press, Cleveland (1982).
 14. T. I. Popova, G. L. Vidovich, N. I. Simonova, and B. N. Kabanov, *Sov. Electrochem.*, **3**, 860 (1967).
 15. J. O'M. Bockris and A. K. Reddy, "Modern Electrochemistry," p. 918, Plenum Press, New York (1970).
 16. R. D. Armstrong and G. M. Bulman, *J. Electroanal. Chem.*, **25**, 121 (1970).
 17. R. D. Armstrong and M. F. Bell, *ibid.*, **55**, 201 (1974).

A Model of the Structure of the Positive Lead-Acid Battery Active Mass

D. Pavlov* and E. Bashtavelova

Central Laboratory of Electrochemical Power Sources, Bulgarian Academy of Sciences, Sofia 1040, Bulgaria

ABSTRACT

A general model for the organization of the structure of the positive active mass is proposed based on SEM observations of samples, obtained from PAM and pastes with different phase compositions and crystal morphology. The structure is built up of two levels: a first-level microstructure, which consists of small crystals with the form of grains, prisms, plates, and needles organized in porous agglomerate, and a second-level macrostructure. The individual agglomerates (with a screw-like, spherical, prismatic or rock-like shape) are linked in a macroporous skeleton, which supports mechanically the active material, conducts the electric current, and serves as memory, where the conditions for the preparation of the paste, the curing, and the formation of the active material are coded. For convenience, two limiting structures are designated: (i) the "agglomerate type," when the agglomerate structure determines the properties and the cycle life of the plate; and (ii) the "crystalline type," when the microstructure determines the energy performance and the stability of the plate. The "agglomerate-type" structure is obtained from low sulfatized and dense pastes. During cycling, some irreversible processes occur, whereby the "agglomerate" structure is transformed into the "crystalline-type" structure, which in turn is dispersed to individual crystallites. This leads to softening and shedding of the active material and finally to cell failure. The proposed general model reveals the relationships between the performance of the positive plate and the technology of its production.

There are two groups of problems associated with the structure of the positive active mass. The first one treats of the formation of the structure and the conditions upon which it depends, as well as the structure organization. The second group of problems deals with the disruption of the structure during the battery operation. A great variety of structures has been presented in literature. Nevertheless, there is a general agreement concerning their principal functions: part of the PbO_2 serves as a mechanical support and electric conductor, while the rest takes part in the charge-discharge processes. Usually, these two functions have been associated with different structures of the PbO_2 crystals. Thus, Simon and Jones (1) found out that the active material is composed of needlelike or prismatic crystals and of small polyhedrons of nearly equal size. They ascribe the role of a mechanical support to the former, while the latter determine the plate capacity. The reason for this difference in morphology these authors related to the α - and β -modifications of PbO_2 (1). Very soon, however, this relation was experimentally rejected.

It was established that the structure of the PbO_2 active material depends upon two processes, as mentioned below.

Phase composition and the morphology of the crystals in the paste.—Burbank (2), Pierson (3), and Biagetti and Weeks (4) established that in many cases the morphology of the paste crystals is transformed to the structure of the positive active mass by metasomatic processes during formation.

Processes during plate formation.—Pavlov *et al.* (5) revealed that the formation occurs in two stages. During the first, only a part of the paste is oxidized to PbO_2 , while

* Electrochemical Society Active Member.

Key words: lead-acid battery, PbO_2 active mass structure, PbO_2 active mass shedding, agglomerate-type PbO_2 structure, crystalline-type PbO_2 structure.

the rest is converted to PbSO_4 . During the second stage, PbSO_4 is oxidized to β - PbO_2 . Yarnell and Weeks (6) and Butler *et al.* (7) showed that the 4PbOPbSO_4 crystals are oxidized by a solid phase reaction, as a result of which their morphology is acquired by the PbO_2 crystals. The PbSO_4 crystals, however, are oxidized by a dissolution-precipitation mechanism, whereby the morphology of the paste crystals is lost during the formation process. It was also established that the morphology of the PbO_2 crystals at the surface and in the interior of the positive plates is different (8).

The purpose of the present paper is to reveal the general organization of the positive active mass structure, as well as to establish some of the factors which influence this structure during its formation and destruction.

Experimental

Method

The principles upon which the present investigation is based are: (i) the preparation of a large number of structures of the PAM (positive active mass) and the revelation of their common building elements and organization; (ii) on the basis of this organization, to compose a general model of the structure of the PAM; and (iii) to study the relationship between the capacity and cycle life of the positive plate and the type of structure.

Types of Pastes

The variety of structures of the PAM was achieved by preparation of pastes with various phase compositions, while the formation conditions were kept constant. As established by Pavlov and Papazov (9) and Iliev and Pavlov (10), pastes with definite phase compositions and morphology of the crystals can be prepared by varying the ratio between H_2SO_4 and the oxidized lead powder (lead

oxide) H_2SO_4/PbO and the temperature during paste preparation.

In Table I are presented the pastes which were prepared using commercial leady oxide, oxidized to 63% tet-PbO.

Preparation of the Pastes and Plates

3 kg leady oxide was mixed in succession with calculated quantities of water and H_2SO_4 solution s.g. 1.4 in a laboratory mixer at a constant temperature. The mixing continued for 1h. The paste was applied manually on SLI battery grids of a lead alloy containing 6% Sb, 0.1% As, and 0.1% Sn. The applied amount of the paste was similar for all plates. The calculated capacity of a plate was 11 Ah at a 50% efficiency of the PAM.

The plates were cured in a chamber first for 48h at 30°C and 100% relative humidity (RH) and then for 24h at 40°C and 60-70% (RH). After curing, the content of metallic lead did not exceed 1%.

Formation

Elements were assembled of 3 positive and 4 negative plates. The formation was performed in H_2SO_4 (s.g. 1.05) at c.d. 5 mA/cm² and 30°C for 22h. The elements were then cycled in a H_2SO_4 solution (s.g. 1.28) for 5 cycles: 7h charge at 2A and 5h discharge at 2A.

Analysis

First, the morphology of the crystals and structure of the inner parts of the plates were studied by a JEOL T 200 SEM at two magnifications: small for the structure of the active mass and large for the crystal morphology. Second, the phase composition was determined by a TUR M 62 x-ray diffractometer using a Cu K_α cathode. The samples were collected from five different places on the plate. Finally, the pore volume and pore-site distribution were determined by a Carlo Erba 1500 Hg porosimeter. The samples were collected from five different places on the plate.

Electrochemical Performance

Five cells were assembled from each type of paste with three positive and four negative plates. They were tested for: (i) capacity at 20h rate of discharge and 25°C and (ii) cycle life charging for 5h at 1.32A, discharging for 1h with 5.5A (four cycles per day). The capacity was checked every 25 cycles. Every 50 cycles, samples were taken for structural, porometric, and phase investigations. All micrographs of the crystals and structure were taken after full charge of the plate only.

Results and Discussion

Model of Basic Building Elements and Levels of the Structure of the PAM

Figure 1 presents SEM micrographs of PAM from paste "c" containing 4PbOPbSO₄ and tet-PbO.

From the micrographs, it is seen that the smallest elements in the structure of the PAM are the individual crystals.

Table I. Pastes prepared using commercial leady oxide, oxidized to 63% tet-PbO

Phase composition	H_2SO_4/PbO (%)	Density of paste (g/cm ³)	(°C)
A. tet-PbO with small amounts of 3PbOPbSO ₄ · H ₂ O	1	4.3	30
B. 3PbOPbSO ₄ · H ₂ O with small amounts of tet-PbO and orthoromb. PbO	6	4.2	30
C. 4PbOPbSO ₄ with small amounts of tet-PbO and orthoromb. PbO	6	4.3	80
D. PbOPbSO ₄ , 3PbOPbSO ₄ , H ₂ O with small amounts of tet-PbO	12	4.2	30

They have different morphology. The pictures in Fig. 1a and 1b illustrate two different types of morphology of these crystals.

Needlelike and prismatic.—As seen in Fig. 1a, these have grown mainly along the C axis and have a common basis. A large number of the crystals are connected together in an agglomerate. For the case of Fig. 1a, the agglomerates are round.

Platelike crystals.—As seen in Fig. 1b, these have grown along the A and B axes and are connected by sharing the A-B planes. The crystals of this type are so ordered that they form screw agglomerates.

One can observe micropores between the crystals in each agglomerate. The number and volume of these pores depend on the morphology of the crystals. The combination of the crystals and micropores in the agglomerate will be denoted as microstructure of the active mass, which is the first structure level.

Figure 1c shows the SEM micrograph of the same active material with a low magnification. It is seen that the agglomerates have various forms, size, and microstructure and are linked in a branched skeleton (framework). The agglomerates enclose macropores, which are connected in channels, which in turn pierce the plate. The combination of the skeleton of agglomerates with the macropores forms the macrostructure of PAM and presents the second structure level.

It may be supposed that these two structure levels have different functions. In order that the charge-discharge reaction



should proceed at a spot, located deeply in the plate, the following transport processes must occur: (i) flows of H⁺ ions and H₂SO₄ should reach this spot coming from the bulk of the electrolyte, while H₂O should move in the opposite direction. The lowest resistance for these flows is along the macropores, which play the role of an ionic transport system. The micropores produce a large active surface area, and, consequently, they determine the capacity of the plate. (ii) The electrons taking part in the charge-discharge reactions at the above-mentioned spot have to be transported freely in the macrostructure. The agglomerates have the largest cross section, and therefore, low resistance. Hence, the macrostructure serves as a mechanical framework, which conducts the current, forms the ionic transport system, and holds together the microstructures of the individual agglomerates. The microstructures on their part provide the electric charge, which the active mass can yield without its disintegration.

Effect of the Phase Composition of the Paste on the Structure of the Active Material

PAM from 1% H₂SO₄/PbO paste.—Figure 2 presents the structure of a paste and the active mass formed from it.

From Fig. 2b, one can see that only a few of the crystals from the first structural level have clearly expressed prismatic form, while a large part of them appears as grains, which are so tightly linked that it is very difficult to distinguish them. In this case, the agglomerates have a compact granular microstructure. It can be assumed that this morphology of the crystals is related to the high rate of PbO₂ nucleation on the surface of the paste crystals and low rate of PbO₂ crystal growth during formation. PbO₂ has by 4% larger molar volume, as compared to that of PbO. It can be supposed that the PbO₂ grains cover the surface of the paste crystals and some of its inner parts will remain unchanged. As a result, the PbO₂ agglomerates will have a lower microporosity.

Figure 2c shows that the macrostructure is composed of large, shapeless continuously interconnected agglomerates with a rocklike appearance. It is quite similar to the paste structure shown in Fig. 2a. The compactness of the agglomerates, their low microporosity, and their strong

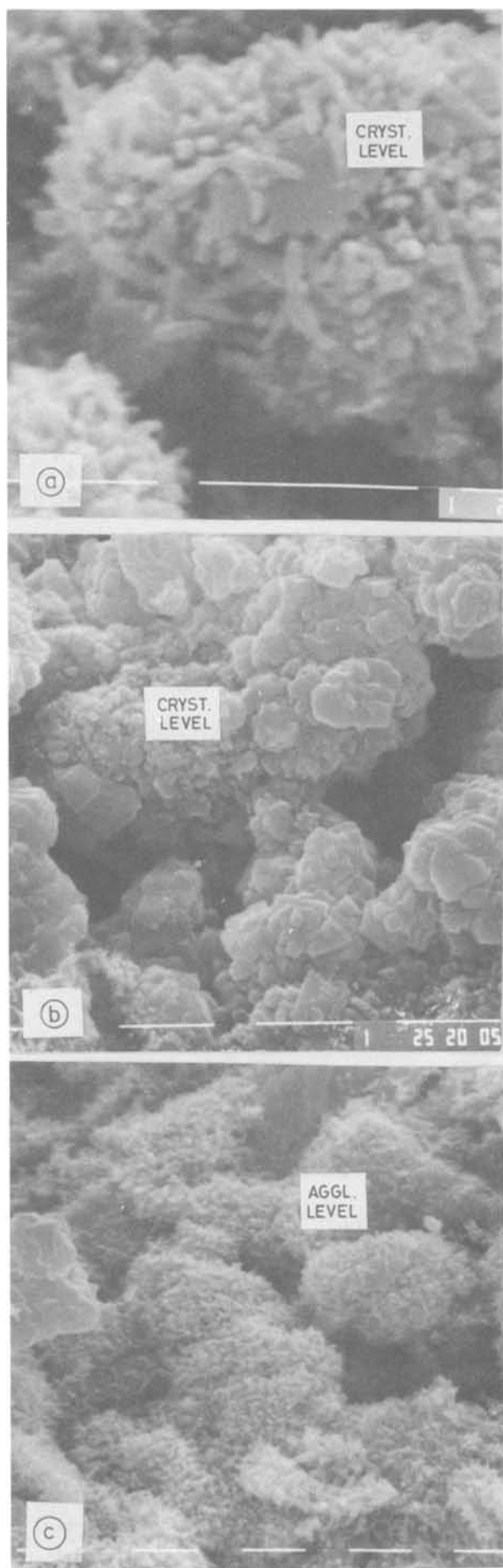


Fig. 1. SEM micrographs of PAM obtained from a $4\text{PbOPbSO}_4 + \text{tet-PbO} + \text{orthoromb. PbO}$ paste. The white lines correspond to $1 \mu\text{m}$.

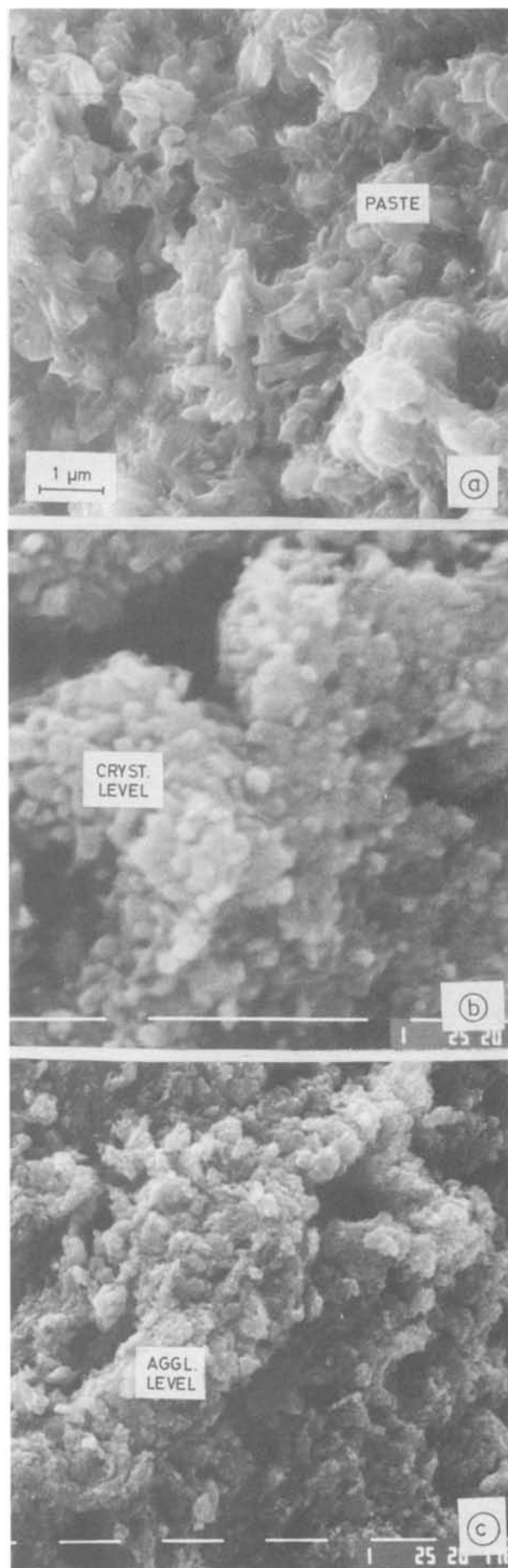


Fig. 2. SEM micrographs of: (a) $1\% \text{H}_2\text{SO}_4/\text{PbO}$ paste, (b) and (c) PAM obtained from it. The white lines correspond to $1 \mu\text{m}$.

adhesion make this macrostructure very rigid. The role of the microstructure of the agglomerates is strongly suppressed. Consequently, this type of PAM structure can be conventionally denoted as an "agglomerate type."

PAM from 12% H_2SO_4/PbO paste.—Figure 3a presents the structure of the paste and Fig. 3b and 3c that of the active mass.

Figure 3b shows that PAM consists of well-grown and clearcut prismatic crystals. The paste composition is characterized by a high degree of sulfatization. A comparison of Fig. 3a and 3c shows that the shape of the paste crystals is different from that of PAM. This supports the idea that the high sulfatized paste crystals are oxidized by dissolution-precipitation mechanism (6). The regular shape of the crystals implies that the rate of their growth is significant and they polygonize well.

The agglomerates are highly porous, which makes difficult their identification (Fig. 3b). This type of structure will evidently have a large surface area and pore volume, but also a mechanically weak macrostructure. The properties of the active mass will be determined mainly by the features of the individual PbO_2 crystals and the mode of their linking, *i.e.*, by the microstructure level. Thus we could designate conventionally this type of structure as "crystal type."

PAM from 6% H_2SO_4/PbO , 80°C paste.—The micrographs of the crystal and the agglomerate levels of the PAM were presented on Fig. 1. Here, Fig. 4a presents the SEM picture of the structure of the paste and Fig. 4b that of the agglomerate level of PAM.

The $4PbOPbSO_4$ crystals are 15-20 μm long and 2-4 μm wide (Fig. 4a). During formation, this morphology determined the size and shape of the agglomerates (Fig. 1c and 4b), *i.e.*, the second level of the active material structure. Many authors treated the agglomerates as PbO_2 crystals, and, especially Burbank (2), proposed a model according to which the metasomatic processes transform every $4PbOPbSO_4$ crystal into a PbO_2 crystal. According to the model of two-level structure, proposed here, the $4PbOPbSO_4$ crystal is the basic substance upon which the oxidation reaction proceeds, at a vast number of active sites. At these sites, the PbO_2 nuclei are formed which grow, fed by the oxidation reaction. The conversion of $4PbOPbSO_4$ crystal to PbO_2 decreases the volume of the solid phase by 15.38% per gram atom of Pb. As a result of this, micropores are formed between the PbO_2 crystals, through which the reaction is propagated deeply inside the $4PbOPbSO_4$ crystal. This type of structure has a well-built-up transport system of macropores. Its formation occurs during paste preparation and curing. The micropores are built up in the agglomerate structure during the formation.

PAM from 6% H_2SO_4/PbO , 30°C paste.—Figure 5a shows the structure of the paste, and Fig. 5b and 5c that of the PAM.

The paste contains shapeless $3PbOPbSO_4 \cdot H_2O$ crystals, which are well connected to each other (Fig. 5a). When they are oxidized to PbO_2 , the volume of the solid phase decreases by 34% per gram atom of Pb in the compound. Figures 5c and 5b show that both levels—macro- and microstructures—are well developed. The agglomerates have a round shape and are built up of individual crystals with a highly developed system of micropores.

Effect of the Paste Density on the Structure of PAM

This dependence was studied with active materials prepared from pastes obtained at 30°C and a 6% H_2SO_4/PbO ratio, using the following densities, obtained by varying the ratio liquid/oxide (9): (i) $d = 3.70 \text{ g/cm}^3$, with a structure shown in Fig. 6a and 6b, (ii) $d = 4.75$, with a structure shown in Fig. 7a and 7b, and (iii) $d = 4.2$, with a structure shown in Fig. 5b and 5c.

These figures demonstrate that the density of the paste exerts an exceptionally strong influence on both levels (the microstructure and the macrostructure of the active mass).



Fig. 3. SEM micrographs of: (a) 12% H_2SO_4/PbO paste, (b) and (c) PAM obtained from it. The white lines correspond to 1 μm .

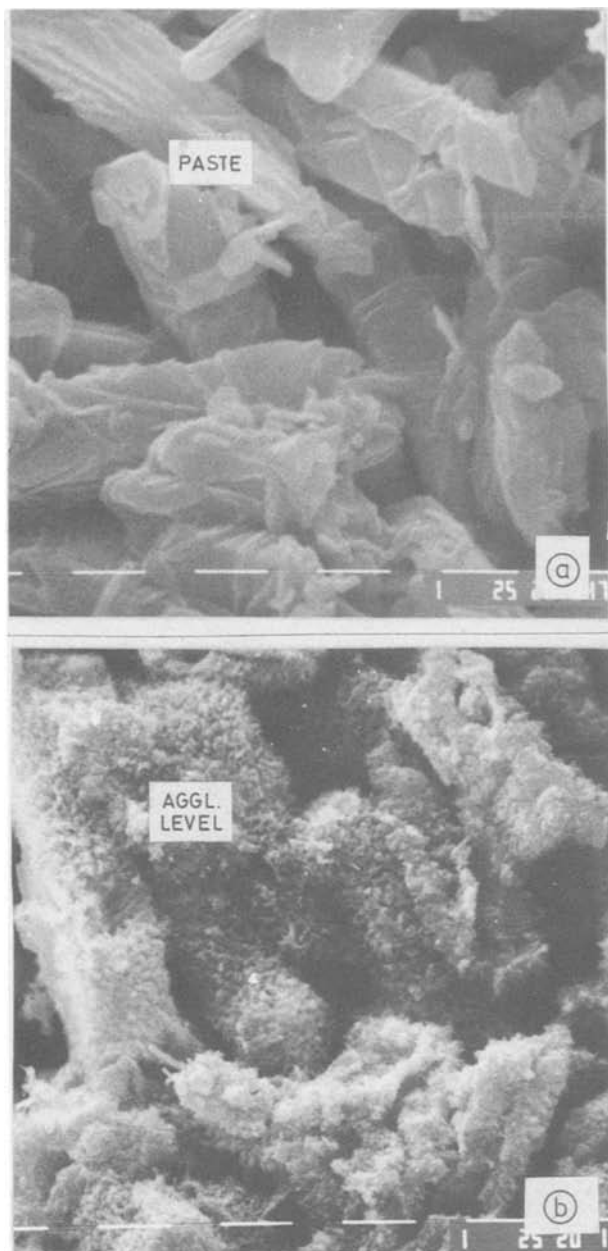


Fig. 4. SEM micrographs of: (a) 6% $\text{H}_2\text{SO}_4/\text{PbO}$ 80°C paste, and (b) PAM obtained from it. The white lines correspond to 1 μm .

At a low density of the paste (Fig. 6a and 6b), the agglomerates are built up of individual needlelike and prismatic crystals with a highly developed system of micropores, *i.e.*, we have a "crystal-type" structure. Evidently, this type of structure is produced during the formation of the plates. At lower densities of the paste, the rate of sulfatization processes is very high, and a considerable part of the active material is produced by oxidation of PbSO_4 , obtained during formation.

The active material obtained from dense pastes (Fig. 7a and 7b) has an "agglomerate-type" structure composed of screwlike ordered crystals.

Agglomerates with shapeless grains were observed on some isolated sites. The cured paste was probably not macrohomogenous enough. On the other places, where the active material contained a system of large macropores, the agglomerates consisted of numerous small prismatic crystals. This implies that both the micro- and macrostructure depend on the access of the H_2SO_4 and H^+ fluxes to the layer where the reactions of the plate formation occur. It can be expected that during formation of low density pastes the pH in the reaction layer will be low, in contrast to the case when high density pastes are

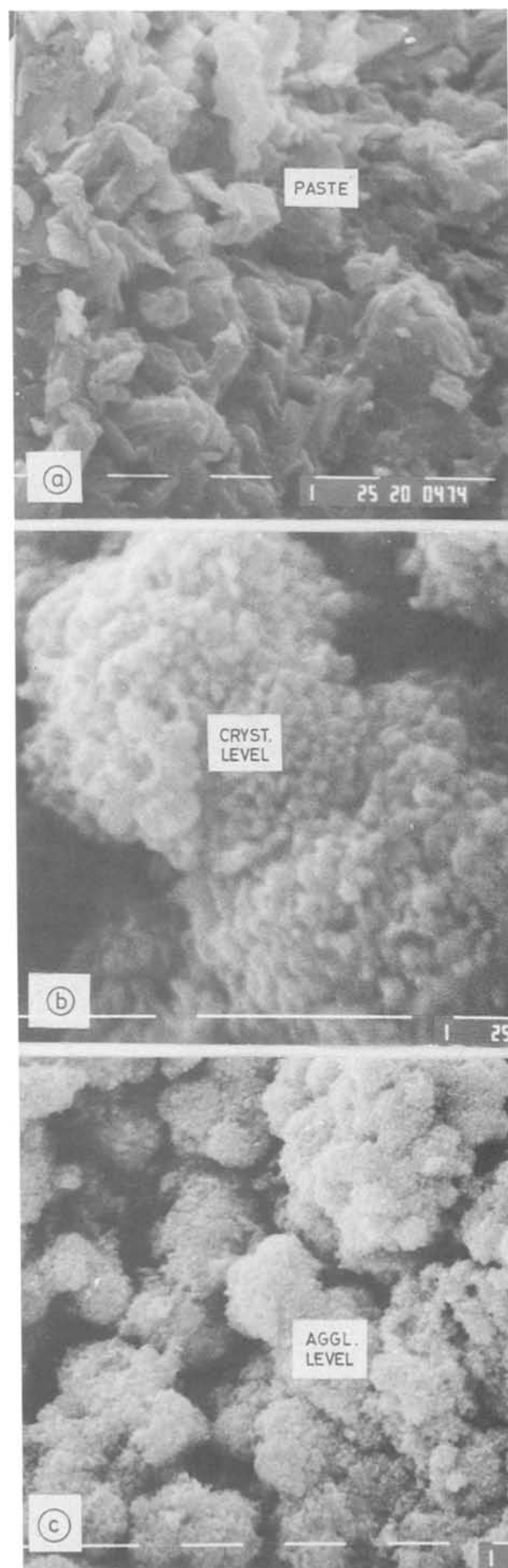


Fig. 5. SEM micrographs of: (a) 6% $\text{H}_2\text{SO}_4/\text{PbO}$ 30°C paste, (b), and (c) PAM obtained from it. The white lines correspond to 1 μm .

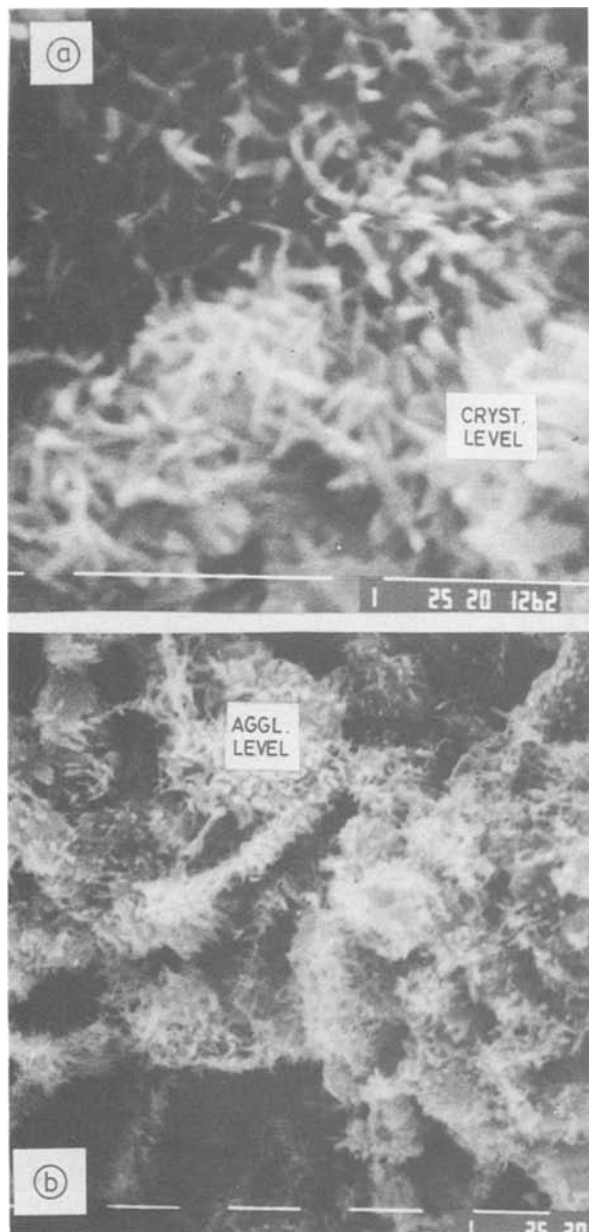


Fig. 6. SEM micrographs of PAM obtained from 6% $\text{H}_2\text{SO}_4/\text{PbO}$ paste with $d = 3.70 \text{ g/cm}^3$. The white lines correspond to $1 \mu\text{m}$.

formed. This will lead naturally to different oxidation mechanisms and, consequently, to different macro- and microstructures.

Porosity, Pore-Size Distribution and Specific Surface Area

Figure 8 displays the pore distribution graphs of the types of PAM mentioned above.

It is seen that the structures of PAM obtained from a low density paste ($d = 3.70 \text{ g} \cdot \text{cm}^{-3}$) or a higher degree of sulfatization (12% $\text{H}_2\text{SO}_4/\text{PbO}$) have a larger pore volume than those obtained from dense ($d = 4.75 \text{ g} \cdot \text{cm}^{-3}$) or low sulfatized pastes (1% $\text{H}_2\text{SO}_4/\text{PbO}$ ratio).

PAM structure obtained from the paste with $3\text{PbOPbSO}_4 \cdot \text{H}_2\text{O}$ has a larger pore volume than that obtained from 4PbOPbSO_4 paste.

In Table II, the specific surface areas of the above investigated PAM are presented.

Table II shows that the PAM structures obtained from the pastes with low density of high degree of sulfatization have larger active surface areas than those obtained from dense or low sulfatized pastes. The PAM structure obtained from the paste with $3\text{PbOPbSO}_4 \cdot \text{H}_2\text{O}$ has larger active surface than that obtained from 4PbOPbSO_4 paste. The results are in good agreement with the SEM structure observations (Fig. 1-7) and with

the results obtained from the porosity measurements (Fig. 8).

Phase Composition of the Active Material

The ratio of $\alpha/\beta\text{-PbO}_2$ revealed the following trends in the above PAM's: (i) the active mass prepared from the paste with a 1% $\text{H}_2\text{SO}_4/\text{PbO}$ ratio contains significant amounts of $\alpha\text{-PbO}_2$, whereas that obtained from the paste with a 12% $\text{H}_2\text{SO}_4/\text{PbO}$ ratio has practically no $\alpha\text{-PbO}_2$. (ii) PAM prepared from pastes containing $3\text{PbOPbSO}_4 \cdot \text{H}_2\text{O}$ or $4\text{PbOPbSO}_4 \cdot \text{H}_2\text{O}$ at an equal density have a very similar $\alpha/\beta\text{-PbO}_2$ ratio, despite the fact that their micro- and macrostructures are quite different.

These trends reveal the parallelism in the relationships of the $\alpha/\beta\text{-PbO}_2$ ratio and the type of the crystal structure of the active material on the oxidation mechanism of the crystals in the paste. The high sulfatized pastes maintain a low pH value on the reaction layer during the plate formation (5, 11), which leads to the dissolution-precipitation mechanism and formation of a large amount of $\beta\text{-PbO}_2$, as well as to a predominantly "crystal-type" structure. For the low sulfatized pastes, it is just the reverse case.

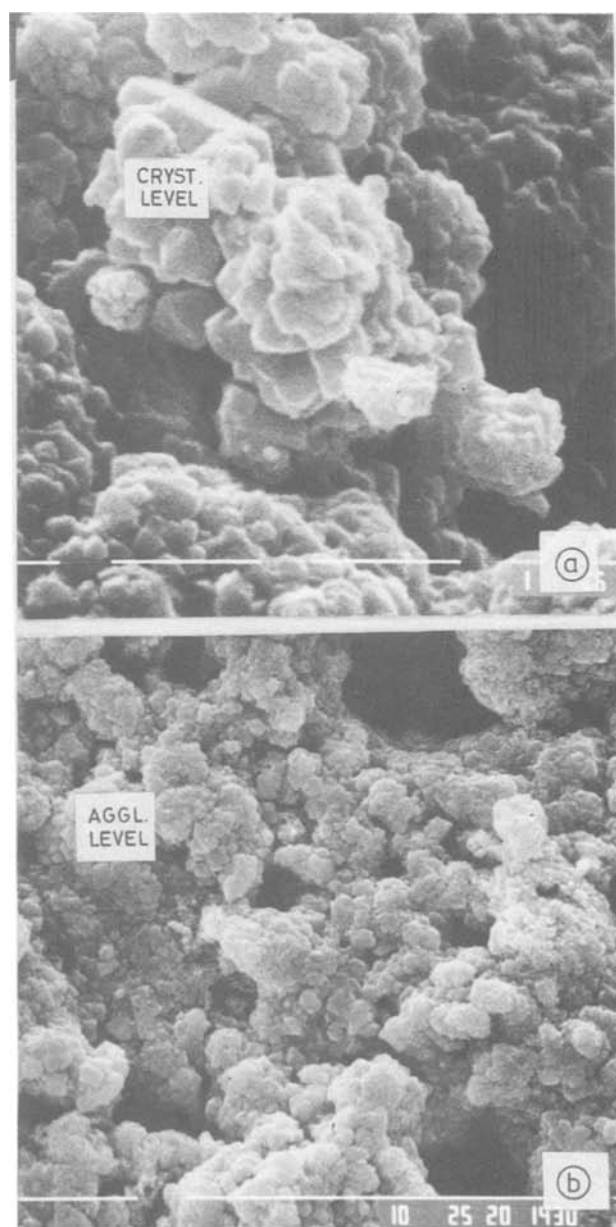


Fig. 7. SEM micrographs of PAM obtained from 6% $\text{H}_2\text{SO}_4/\text{PbO}$, $d = 4.75 \text{ g/cm}^3$. The white lines correspond to: (a) $1 \mu\text{m}$ and (b) $10 \mu\text{m}$.

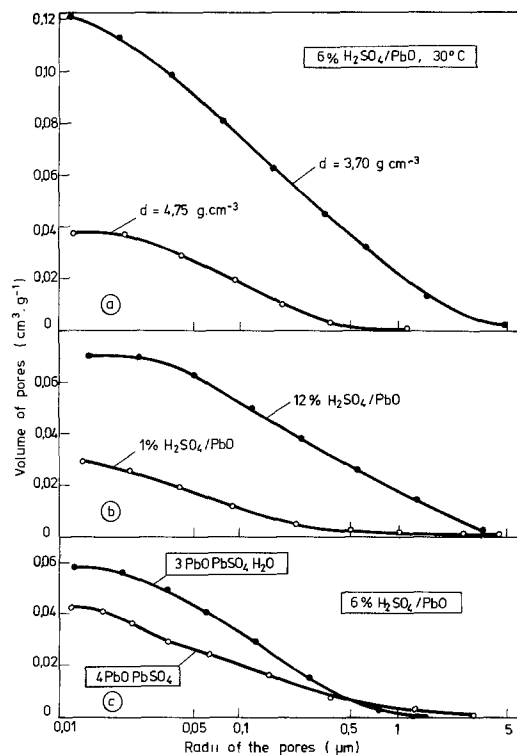


Fig. 8. Pore size distribution curves of six different PAM's obtained from the marked pastes.

Evolution of the Capacity and Structure of the Active Mass during Cycling of the Battery

Capacity and cycle life of the cells.—The initial capacity and the number of the charge-discharge cycles to 80% C_{20} at a 50% depth of discharge and 20% overcharge are shown in Table III.

Figure 9 reflects the evolution of the capacity during cycling. The reason for failure of the cells is shown on the respective curves.

From the results in Table III and Fig. 9, the following conclusions can be drawn. The "agglomerate-type" structure has generally low initial capacity and long life, which depends on the type of the agglomerates. Thus the agglomerates of the PAM prepared from $4\text{PbO}\cdot\text{PbSO}_4$ is more resistant to cycling than that of the active mass prepared from $3\text{PbO}\cdot\text{PbSO}_4 \cdot \text{H}_2\text{O}$ paste. The most resistant, probably, is the structure of the active mass obtained from tet-PbO (1% $\text{H}_2\text{SO}_4/\text{PbO}$) paste, but the capacity is below 80%—the lowest permissible limit. The low capacity of some of the "agglomerate-type" structures is probably due to the incomplete formation of the paste crystals, as well as to the low microstructure porosity and the active

Table II. PAM specific surface areas

Type of PAM	$S_{\text{BET}} \text{ m}^2 \cdot \text{g}^{-1}$
1% $\text{H}_2\text{SO}_4/\text{PbO}$	3.53
12% $\text{H}_2\text{SO}_4/\text{PbO}$	6.76
6% $\text{H}_2\text{SO}_4/\text{PbO}$, 80°C	4.41
6% $\text{H}_2\text{SO}_4/\text{PbO}$, 30°C	5.71
6% $\text{H}_2\text{SO}_4/\text{PbO}$, 30°C	
$d = 3.70 \text{ g} \cdot \text{cm}^{-3}$	8.16
$d = 4.75 \text{ g} \cdot \text{cm}^{-3}$	3.47

Table III. Initial capacity and cycle lives for cells tested

Active material prepared from paste containing	Capacity C/C_0 , %	Cycle life
1% $\text{H}_2\text{SO}_4/\text{PbO}$, 30°C	71	—
6% $\text{H}_2\text{SO}_4/\text{PbO}$, 30°C	101	140
6% $\text{H}_2\text{SO}_4/\text{PbO}$, 80°C	83	215
12% $\text{H}_2\text{SO}_4/\text{PbO}$, 30°C	110	90

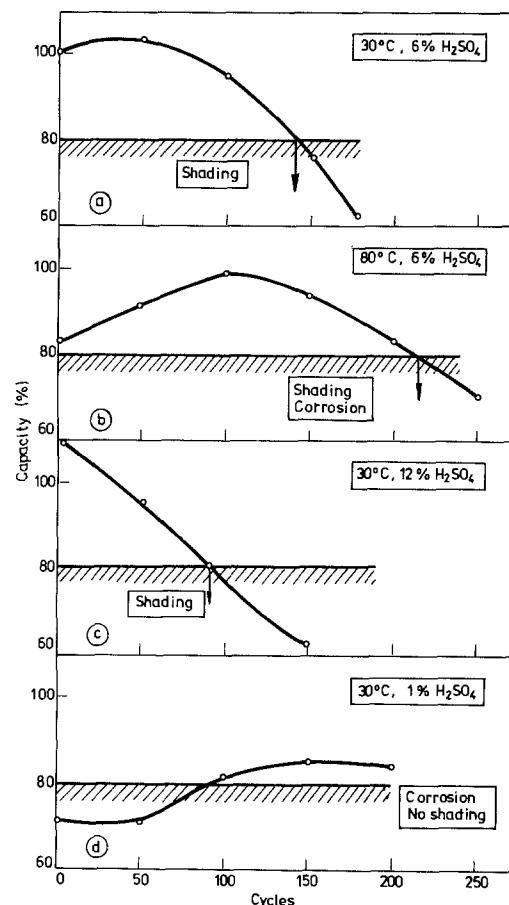


Fig. 9. Evolution of cell capacity during cycling of four types of PAM

surface area. During cycling, the residual PbO is oxidized, the porosity and active surface area grow, and the capacity increases.

The active mass with a "crystal-type" structure obtained from a 12% $\text{H}_2\text{SO}_4/\text{PbO}$ paste has a very high initial capacity, which continuously drops during cycling, due to shedding of the active mass.

Evolution of the structure of the active material during cycling.—The structure of the charged active mass obtained from a 1% $\text{H}_2\text{SO}_4/\text{PbO}$ paste after 150 cycles is displayed in Fig. 10.

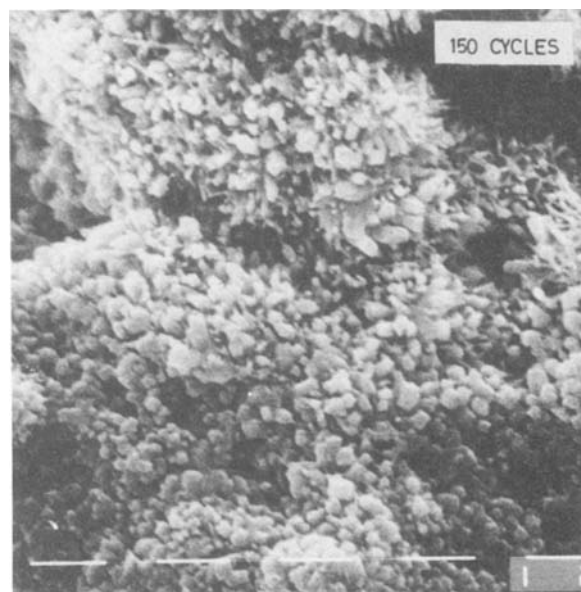


Fig. 10. SEM picture of PAM obtained from 1% $\text{H}_2\text{SO}_4/\text{PbO}$ paste after 150 cycles.

One can clearly see the tightly linked large agglomerates (Fig. 10) covered by well-shaped prismatic crystals. The juxtaposition of Fig. 2 and 10 reveals that the morphology of the crystals is strongly improved during cycling.

Figure 11 presents the structure of the charged active mass obtained from the 12% H_2SO_4/PbO paste after 100 cycles.

During cycling, the macrostructure is dispersed in well-shaped, not very tightly linked, needlelike, and prismatic crystals.

Figure 12 presents the pictures of the structure of the charged active mass, obtained from a $3PbOPbSO_4 \cdot H_2O$ paste after 100 and 150 charge-discharge cycles.

At 100 cycles (Fig. 12a), the microporosity of the agglomerates has increased during the cycling. At 150 cycles, the agglomerate level of the structure is completely dispersed and transformed into a crystalline structure.

Figure 13 presents the structure of the charged active mass obtained from a $4PbOPbSO_4$ paste.

At 150 cycles, it is still possible to distinguish the agglomerates which have retained the morphology of the $4PbOPbSO_4$ crystals. Besides this, the microstructural level has developed considerably. At 250 cycles, the agglomerate level of the structure is completely dispersed to a highly branched, weakly linked "crystal-type" structure.

Change of porosity during cycling.—Porosity evolution of the above PAM's during cycling is presented in Fig. 14.

Let us accept, conventionally, that the edge of the macro- and micropores is about $0.13 \mu m$ radii of the pores. From the change of porosity with the number of the cycles, the following trends of the structure evolution can be established.

PAM, 1% H_2SO_4/PbO paste.—At the above PAM (Fig. 14), the macro- and micropore systems are not well developed. During cycling, the plate works toward eliminating this deficiency. The PAM first develops the ionic transport system of macropores. As a result, the capacity of the cell rises slightly (Fig. 9a). The corrosion of the grid makes it impossible to follow the further evolution of the structure.

PAM, 12% H_2SO_4/PbO .—During cycling at this type of structure, first the number and volume of the micropores increase. The weakly expressed skeleton of agglomerates (Fig. 3) is dispersed to crystals and branches of crystals of the first structure level. During discharge, part of these

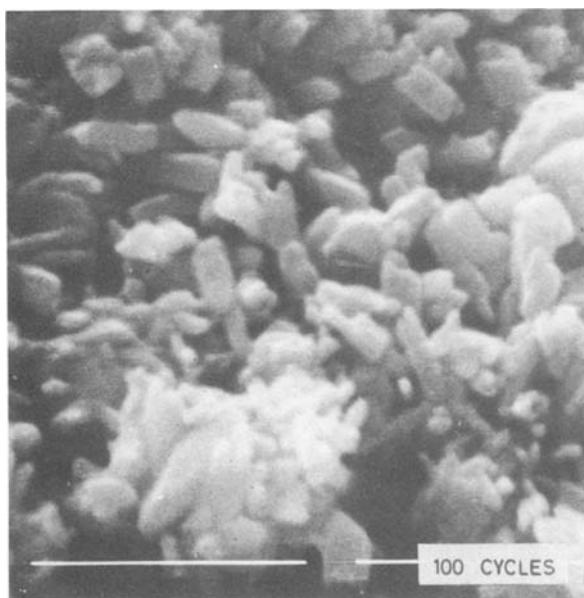


Fig. 11. SEM picture of the structure of PAM obtained from 12% H_2SO_4/PbO paste after 100 cycles.

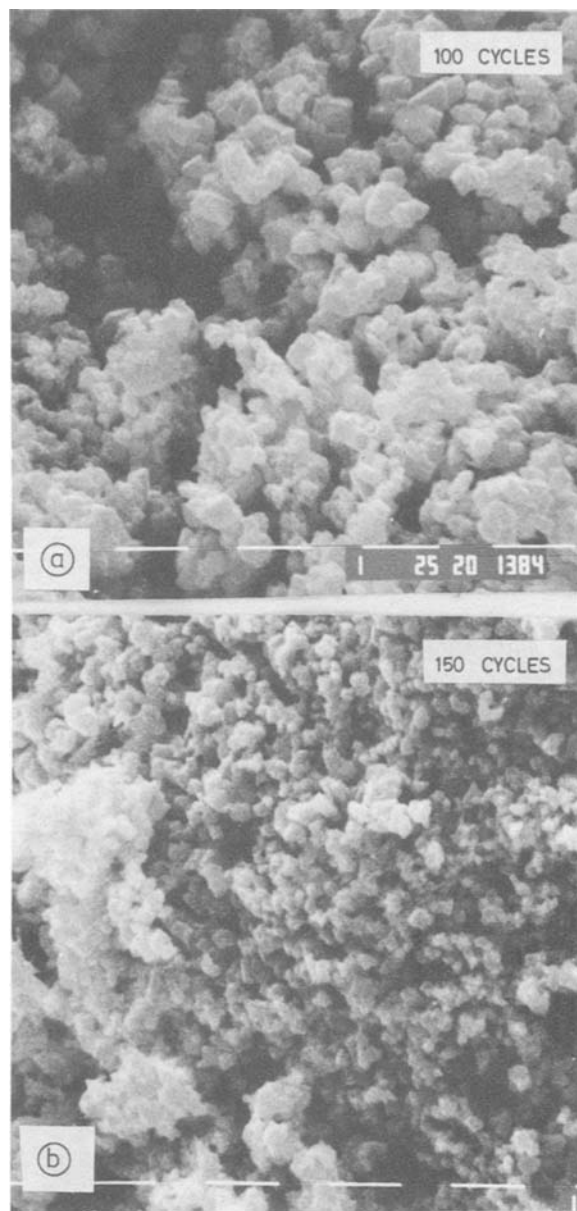


Fig. 12. SEM pictures of the structure of PAM obtained from 6% H_2SO_4/PbO at $30^\circ C$ paste after: (a) 100 cycles and (b) 150 cycles.

crystals is transformed into $PbSO_4$. It can be supposed that during charge the PbO_2 crystals or branches are formed in new places in the volume of the plate and the volume of macropores increases. Thus, a very weak structure is formed and the PAM softens and sheds. This process is described by Rand *et al.* (12).

PAM, 6% H_2SO_4/PbO , 30° and $80^\circ C$.—During the first 50 cycles, both structural levels of the PAM formed from $4PbOPbSO_4$ paste are reproduced completely. A similar process takes place with PAM formed from $3PbOPbSO_4 \cdot H_2O$ paste. After this period, the number of the micropores begins to increase slowly, which leads to dispersion of the agglomerate level of the structure, which accelerates the shedding of the active mass, which limits the cycle life of the battery.

Summary

In general, it can be stated that during cycling the agglomerate level of the structure evolves through the growth of the individual crystals and their chains, whereby the volume of micropores increases. Part of the crystals and their chains are disrupted due to the mechanical effect of O_2 bubbles, electrolyte convection, or mechanical vibrations.

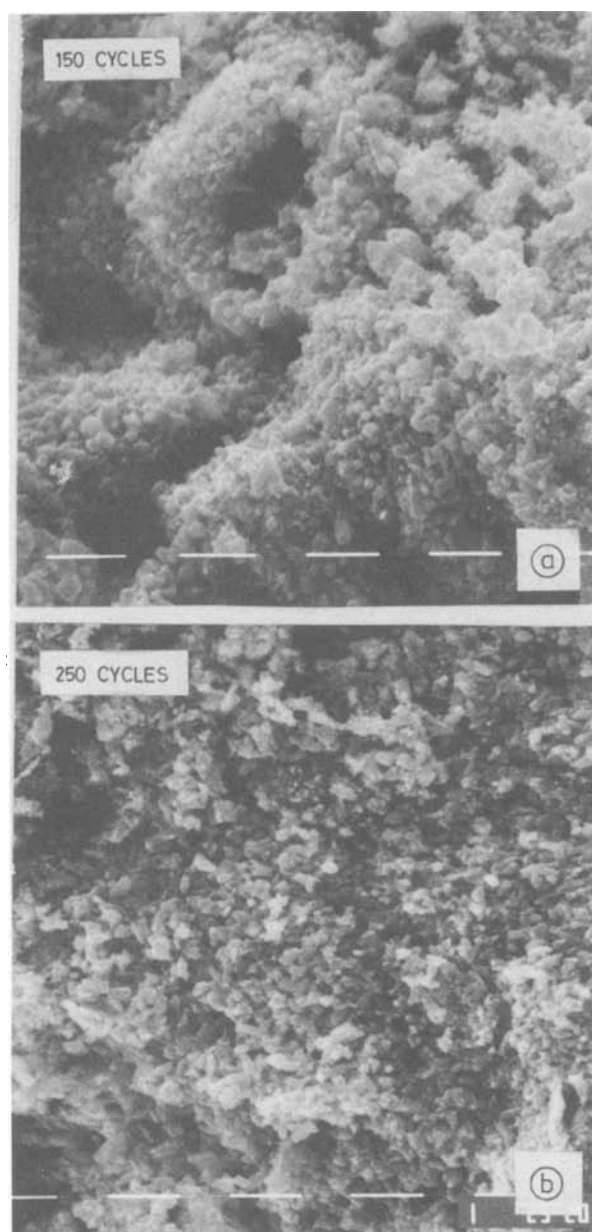


Fig. 13 SEM pictures of the structure of PAM obtained from a 6% $\text{H}_2\text{SO}_4/\text{PbO}$ paste at 80°C after: (a) 150 cycles and (b) 250 cycles.

Initially, the structure is composed of thick agglomerates, and at the end of cycling of thin crystal branches. The electric network of the active mass raises its ohmic resistance due to deteriorated contacts between the crystals, and the polarization of the plate increases. This evolution of the structure is not uniform over the plate cross section. Hollows can be formed in separate regions, and can grow to large dimensions. Simon and Caulder (13) have investigated these processes. This brings about a deterioration in the ionic transport system of the plate, which also increases its polarization.

The dispersion of the macrostructure depends on the type of the agglomerate skeleton. And as emphasized earlier, the shape of the skeleton level is determined by the phase composition, the structure and density of the paste, and the conditions during plate formation. Conse-

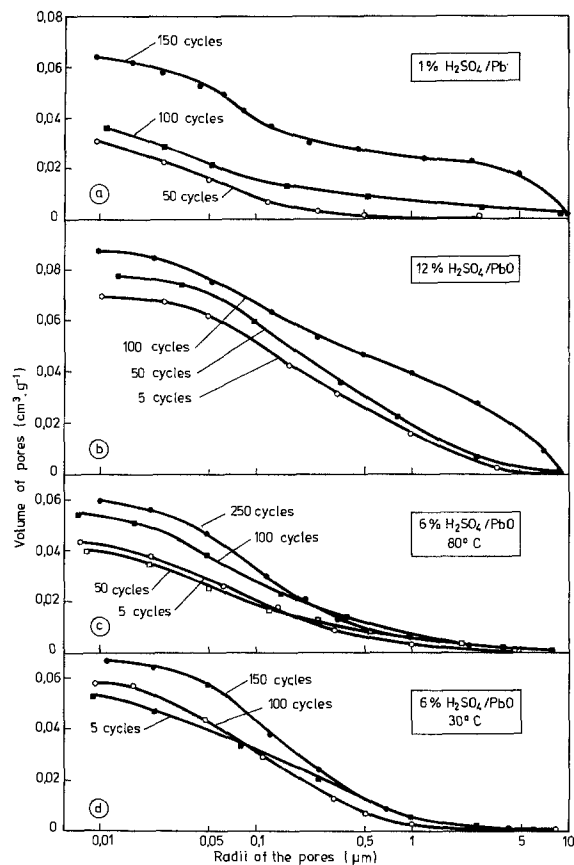


Fig. 14. Evolution of pore size distribution during cycling.

quently, the second structural level, the agglomerate skeleton, is the memory substrate, where the conditions of the technological processes during the plate production are coded.

Acknowledgments

Our thanks go to K. Stambolska, V. Stoyanova, and N. Zlatkova for the technical assistance and to M. Iosifova and A. Dimitrova for the SEM work.

Manuscript submitted Aug. 16, 1983; revised manuscript received Feb. 3, 1984.

REFERENCES

1. A. C. Simon and E. L. Jones, *This Journal*, **109**, 760 (1962).
2. J. Burbank, *ibid.*, **111**, 765 (1964); *ibid.*, **113**, 10 (1966).
3. J. R. Pierson, Report Globe Union, Inc., Milwaukee, WI (1966).
4. R. V. Biagetti and M. C. Weeks, *Bell Syst. Tech. J.*, **49**, 1305 (1970).
5. D. Pavlov, G. Papazov, and V. Iliev, *This Journal*, **119**, 8 (1972).
6. C. F. Jarnell and M. C. Weeks, *ibid.*, **126**, 7 (1979).
7. W. O. Butler, C. J. Venuto, and D. V. Visler, *ibid.*, **117**, 1339 (1970).
8. H. Bode, "Lead-Acid Batteries," R. J. Brodd and K. V. Kordesch, Translators, p. 252-255, The Electrochemical Society Series, John Wiley & Sons, New York (1977).
9. D. Pavlov and G. Papazov, *J. Appl. Electrochem.*, **6**, 339 (1976).
10. V. Iliev and D. Pavlov, *ibid.*, **9**, 555 (1979).
11. D. Pavlov and G. Papazov, *This Journal*, **127**, 2104 (1980).
12. K. Harris, R. J. Hill, and D. A. J. Rand, *J. Power Sources*, **8**, 175 (1982).
13. A. C. Simon and S. M. Caulder, *This Journal*, **118**, 659 (1971).

Electrochemical Calorimetry of the Zinc and Bromine Electrodes in Zinc-Bromine and Zinc-Air Batteries

V. Subrahmanyam Donepudi and B. E. Conway*

Department of Chemistry, University of Ottawa, Ottawa K1N 9B4, Ontario, Canada

ABSTRACT

Direct calorimetric measurements are reported on three half-cell reactions of interest in zinc battery thermodynamics: the Zn/Zn²⁺ reaction in aqueous Br⁻ solution; the Br₂/Br⁻ reaction at Pt and the Zn/ZnO-ZnO₂²⁻ reaction in alkali. An experimental procedure is described for determining the single reaction heats, observable as $T\Delta S$ quantities, in both directions of the above reactions, thus providing a method for eliminating, by difference, the Joule heating effects which are unavoidable in the course of measurements at finite currents. Corrections for entropies of transport are made and discussed. Under certain conditions, where Zn corrosion can occur with evolution of H₂, the $T\Delta S$ heat change for that process is also determinable. Some heat changes for overall cell reactions are also determined.

While enthalpy changes for reversible electrochemical reactions can be obtained from EMF measurements and their temperature coefficients by means of the Nernst equation through the Gibbs-Helmholtz relation, such values are necessarily for the overall, two-electrode reaction. Direct calorimetric measurements, subject to some corrections for ionic entropies of transport, can be applied to evaluation of the heat changes that are associated with the electrochemical reactions at the electrodes of a cell. Such directly measurable heats are, however, associated with the " $T\Delta S$ " quantity for the cell reaction, rather than the ΔH .

It is of interest to recall that the actual enthalpy change, ΔH , for an electrode reaction is not measurable calorimetrically like it would be for a corresponding overall chemical reaction. This is because the ΔH normally constitutes the main component of the ΔG value determining the EMF of the cell. From measurements of the latter at various temperatures, ΔH can, of course, be determined using a form of the Gibbs-Helmholtz equation.

Direct calorimetric measurements made at a suitably designed electrode configuration with an appropriately arranged thermal detection probe, and separated anode and cathode compartments, can also give information on the $T\Delta S$ quantity for single electrode processes which are of interest in a general way in electrochemical thermodynamics and ionic solution electrochemistry. In some papers (1-3), these $T\Delta S$ quantities have been referred to as electrolytic Peltier heats, and values for several redox reactions at electrodes have been reported (4-5). The first reliable work of this kind was done by Lange and Hesse (6) and Lange and Monheim (7) some years ago, but, for many years since that time up until several years ago, few other papers have appeared on this topic.

Renewed interest in electrochemical calorimetry has arisen on account of the importance of measurements of overall and component heat changes in battery processes. Such measurements are essential for understanding the thermochemistry of battery reactions and in assessing practical energy efficiencies as well as evaluating heat changes associated with various contributions to irreversibility in battery charge and discharge cycles.

Significant improvements have been made in experimental technique over that employed in older measurements, e.g., by arranging suitable thermal detection configurations at the electrodes together with modern temperature-sensitive devices of low thermal capacity such as thermistors (8-11b) and Pt/Pt-13% Rh hemisphere probes (11c) used in conjunction with a thermistor bridge and an adiabatic calorimeter vessel. By means of calorimetry, the following types of electrochemical phenomena have been previously studied: (i) electrochemical processes involving adsorbed enzymes at a Hg electrode

(8), (ii) photo-assisted electrochemical reactions (9), (iii) processes in electrodeposition and corrosion (10-11), and (iv) behavior of alkaline cells under load (12) and thermal characterization of internal power losses in Pace Maker batteries (13).

Among various systems employing Zn as the anode material, the Zn/Br₂ (14-19), the alkaline Zn/air (O₂), and the alkaline Zn/NiOOH or Zn/AgO batteries (21) have received much attention in both basic research and in the direction of modern battery technology with the aim of developing mechanically rechargeable batteries, especially for automotive transportation. Various problems that arise with Zn battery systems are well known and have been extensively discussed in the literature (e.g., 16, 20).

In comparison with Zn/halogen batteries, alkaline Zn batteries with air or another oxidizing agent as cathode material have been developed and used over many years (e.g., the Drumm battery, using a combination of Zn with nickel oxide in alkaline medium, was used on the Irish railways in the '30's).

The present paper describes the results of calorimetric measurements carried out on Zn/Zn²⁺ and Br⁻/Br₂ (at Pt) couples in a variety of electrolytes that can be used in the Zn/Br₂ battery. From the results, the $-T\Delta S$ quantities for the electrode reactions have been evaluated, taking into account entropies and heats of ionic transport, and the unavoidable Joule heating effects that are associated with " iR " drop in operating cells.

Comparative experiments were also carried out on the Zn/ZnO-ZnO₂²⁻ reactions in alkaline solutions.

The experimental objective of this study, as mentioned earlier, was to investigate a method for practical evaluation of heat changes in electrode processes and energy efficiencies, as well to establish some individual electrode reaction thermodynamic quantities by means of direct calorimetry.

Experimental

General.—The heat changes accompanying the Zn/Zn²⁺ reaction in bromide solutions or of Zn/ZnO-ZnO₂²⁻ in alkaline solutions were measured under galvanostatic polarization conditions at pure Zn rod electrodes 3.0 mm in diameter. For study of the Br⁻/Br₂ reaction, a black platinumized platinum mesh electrode was used.

The experiments were conducted in an all-glass adiabatic calorimeter mounted in a thermostat, which maintained the temperature around the calorimeter constant to ± 0.01 K. A description of the calorimeter and the associated thermistor bridge is given below, together with the experimental procedure and conditions. Calorimetric measurements were made both in the anodic and cathodic current directions at the same current densities to enable " i^2R " Joule heating effects to be canceled out in the measurements (see below), a procedure that, surprisingly, was not employed previously by most investiga-

* Electrochemical Society Active Member.

Key words: Peltier heats; zinc/bromine, zinc/air batteries, entropy of electrode reactions.

tors, with the significant exception (11d, 11e) of the use of both anodic and cathodic voltammetry scans to provide an approach to isothermal conditions while effecting a calorimetric calibration by means of anodic or cathodic currents passed through an embedded Peltier thermocouple junction.

Calorimeter.—The design of the calorimeter is shown schematically in Fig. 1a. The calorimeter vessel is made from two interconnecting tubular compartments completely sealed within a silvered evacuated jacket in the form of a special Dewar flask. The cathode and anode, and corresponding catholyte and anolyte, were thus separated with a common electrolytic bridge at the top of the two tubes. The maximum distance of separation between the two compartments was ca. 9 cm along the tubes, each of which was 2 cm in diameter. A more constricted bridge region at the top of the cell was avoided in order to minimize electrolytic Joule heating.

Three inlets to the cell were provided: a central one for a N_2 purging tube; a second one for the working elec-

trode, the reference electrode with its Luggin probe, and the thermistor probe; and a third for the counterelectrode. The electrode mounting tubes of glass, were held in the calorimeter inlet ports (Fig. 1a) by means of Teflon tape wound around the boundary region. This provided the opportunity for successive mounting and demounting of various electrode materials, as well as for positional adjustment.

Thermistor bridge.—The thermistor bridge circuit is shown in Fig. 1b. The circuit consists of a 2.5 k Ω type YSI-641 thermistor probe for making the temperature change measurements, together with matching resistances and a 5 k Ω variable resistance. A 0.356V, 1 kHz sinusoidal signal derived from a Servomex signal generator was applied to the bridge as well as to the reference input of a lock-in analyzer (PAR Model 5204). The output signal from the bridge is processed by the lock-in analyzer and becomes amplified when an appropriate sensitivity range is chosen on the analyzer. Prior to the commencement of an experiment, the bridge was balanced and the subsequent off-balance signals due to the exo- or endothermal energy changes, caused by passage of controlled current at a density of $\pm i$ A cm $^{-2}$, were measured and recorded on a Y-time recorder.

The bridge was calibrated by passing known currents, 0.1, 0.2, and 0.3 mA, successively through a 102 k Ω calibration resistor (R_{cal}) mounted adjacent to the thermistor in a similar geometry to that corresponding to the position of the electrode *vis-a-vis* the thermistor. Between each passage of current, time for cooling to the initial temperature was allowed. The calibration sequence was repeated several times for each calorimetric run. Calibration heats were therefore measured with similar sensitivity to that for the electrochemically generated heats at the working electrode. This was achieved by packing the calibration resistor (dimensions approximately 1.5 \times 5 mm) and the thermistor together in a reproducible geometry such that the distance or clearance between the resistance and the thermistor was maintained almost identical with the distance between the working electrode and the thermistor. During actual electrochemical runs, the calibration resistor was removed from the calorimeter to minimize possibility of corrosion.

A calibration line was plotted by relating a series of Joule heating rates, $i^2 R_{cal}$, expressed in mW *vs.* the out-of-balance thermistor signal. Figure 2 shows such a calibration plot; it is satisfactorily linear as anticipated.

Electrodes.—For studies of reactions at Zn, rods of this metal 3 mm in diameter were shaped into small coils having about four turns and apparent geometric areas in the range 17-20 cm 2 . The other ends of each of the rods were abraded to reduce the diameter and soldered to a 0.63 mm copper wire. The electrode was finally sealed to a glass tube holder with Araldite, which was cured overnight at room temperature. As shown in Fig. 1c, the thermistor probe was positioned inside the electrode coil, making close contact with the surface of that electrode. A Ag/AgBr reference electrode was inserted through the side opening tube of the T29/42 female joint (Fig. 1c) and positioned close to the working electrode. The working and reference electrodes, together with the thermistor probe, were held in position by wrapping them with Teflon tape at some distance from their active surfaces.

Solutions.—The heat changes due to the Zn/Zn $^{2+}$ reaction at a zinc electrode in Br $^-$ salt solutions were measured in the following bromide-containing solutions: (i) 0.1, 0.5, 1.0, 2.0, 3.0, and 4.0M ZnBr $_2$; (ii) 1.0M KBr, 1.0M KBr + 0.14M Br $_2$; and (iii) 1.0M ZnBr $_2$ containing 1.0M and 2.0M KBr.

A 1.0M KBr solution containing dissolved bromine at 0.18M was used for studying the Br $^-$ /Br $_2$ reaction at the platinum electrode.

ZnO dissolved in 8.0M KOH solution to a concentration of 1.0M was used for studying the alkaline Zn/ZnO system under simulated battery conditions.

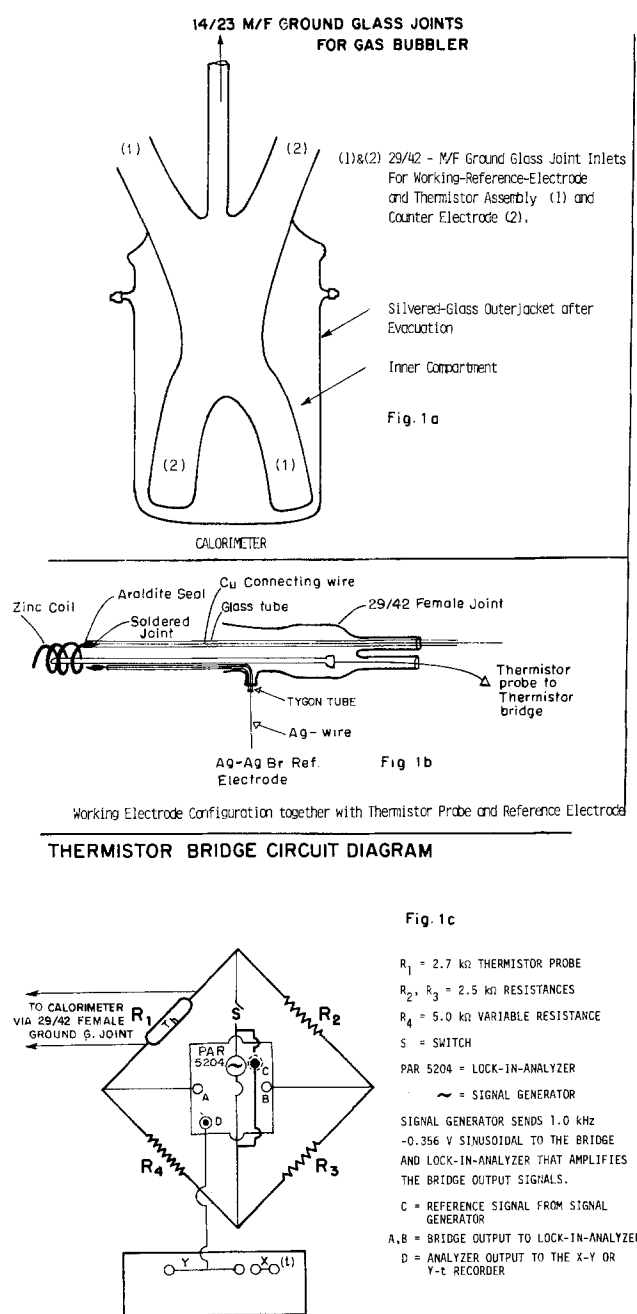


Fig. 1. Experimental arrangement for the calorimetric and electrochemical measurements. a (top): Calorimeter (schematic diagram). b (middle): Electrode configuration. c (bottom): Thermistor bridge.

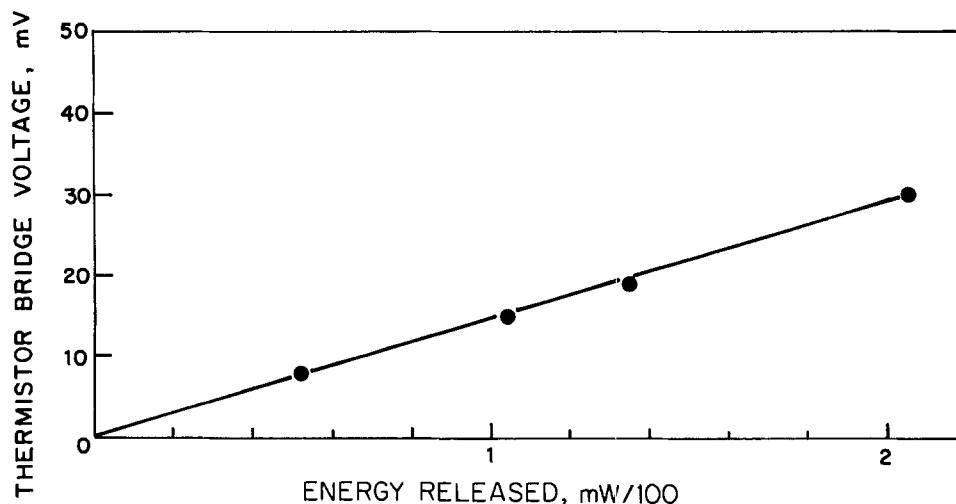


Fig. 2. Calibration line showing Joule heating rates generated by passage of controlled currents through a standard resistor vs. the off-balance thermistor bridge signal. Currents were applied to a 102 k Ω resistor.

The zinc content in the solutions was analyzed by the EDTA titration procedure and the dissolved bromine by the usual iodometric procedure.

Procedure.—In a typical experiment, the calorimeter containing the electrodes and thermistor probe, together with 100 cm³ of the required electrolyte solution, was completely immersed in the water thermostat at 299.4 \pm 0.01 K and allowed to attain thermal equilibrium overnight.

The solution resistance, pH, and the electrode potentials were then measured. Prior to the commencement of polarization experiments, the thermistor bridge was balanced. A Wenking potentiostat was used in the galvanostatic mode, and a series of constant currents between 10 and 40 mA were applied to the cell in 5 mA steps; the resulting thermal transients were recorded over a period of 100s. Prior to current reversal or a change in current, the thermal transient was allowed to reach a reasonably steady state. Usually, this was assisted by passing a few bubbles of nitrogen through the solution while making sure that the solution was not undercooled by evaporation of water from the solution. This procedure avoided prolonged waiting periods for thermal equilibrium to be attained between successive polarizations at different currents. Passage of the controlled currents for the controlled 100s polarization time gave the charges in coulombs, C, passed in the experiments and, hence, with the measured heat change, the electrochemical rate of heating or cooling in J s⁻¹ C⁻¹.

Results

Heat changes.—The Zn/Zn²⁺ reaction in bromide electrolyte solutions.—Polarization of the zinc electrodes in zinc bromide solutions at applied currents between 10 and 40 mA caused the initially balanced thermistor bridge to go out of balance with signals in the positive (exothermic) direction for the anodic and in the negative (endothermic) direction for the cathodic currents. The signal (mV) vs. time traces shown in Fig. 3 were obtained for polarization in 4M aqueous zinc bromide solutions; the responses exemplified in this figure are typical of the heat change behavior of the zinc electrode in all the ZnBr₂ solutions, the ZnBr₂ + KBr solutions and the KBr + Br₂ solutions.

The rate of heat release, $d(-Q)/dt$, expressed in mJ s⁻¹ at each applied current I , was obtained: (i) by correcting the bridge signals for the joule (I^2R) heating by obtaining the difference between the anodic and cathodic signals (e.g., see Fig. 4) and averaging, (ii) knowing the corresponding heat change from a calibration curve such as that in Fig. 2, and (iii) dividing Q by the time period for which the signal was measured. The slope of the straight line shown in Fig. 4, i.e., $d(-Q)/dt \times (1/I)$ was 0.23 J C⁻¹ or, when multiplied by 2F, is -44.4 kJ mol⁻¹, thus corresponding to the $T\Delta S$ term within which is included any heat of ionic transport associated with the Zn/Zn²⁺ reaction at the particular concentration involved. The $T\Delta S$ values for other concentrations of ZnBr₂ from 0.1M up-

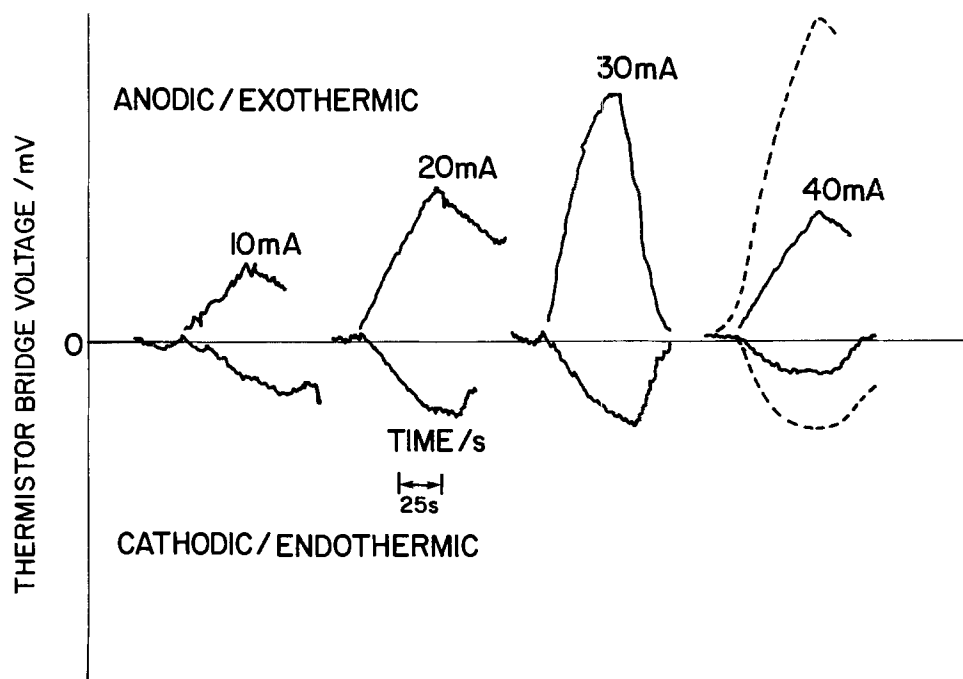


Fig. 3. Thermistor bridge voltage vs. time traces for galvanostatic polarization of a zinc electrode in 4M ZnBr₂ solution. Conditions: temperature 299.4 K; unstirred solution. Scale: X-axis 10 s cm⁻¹; Y-axis 10 mV cm⁻¹ for currents up to 40 mA. At 40 mA, Y-axis = 25 mV cm⁻¹. Dashed line shows a replot of the original transient.

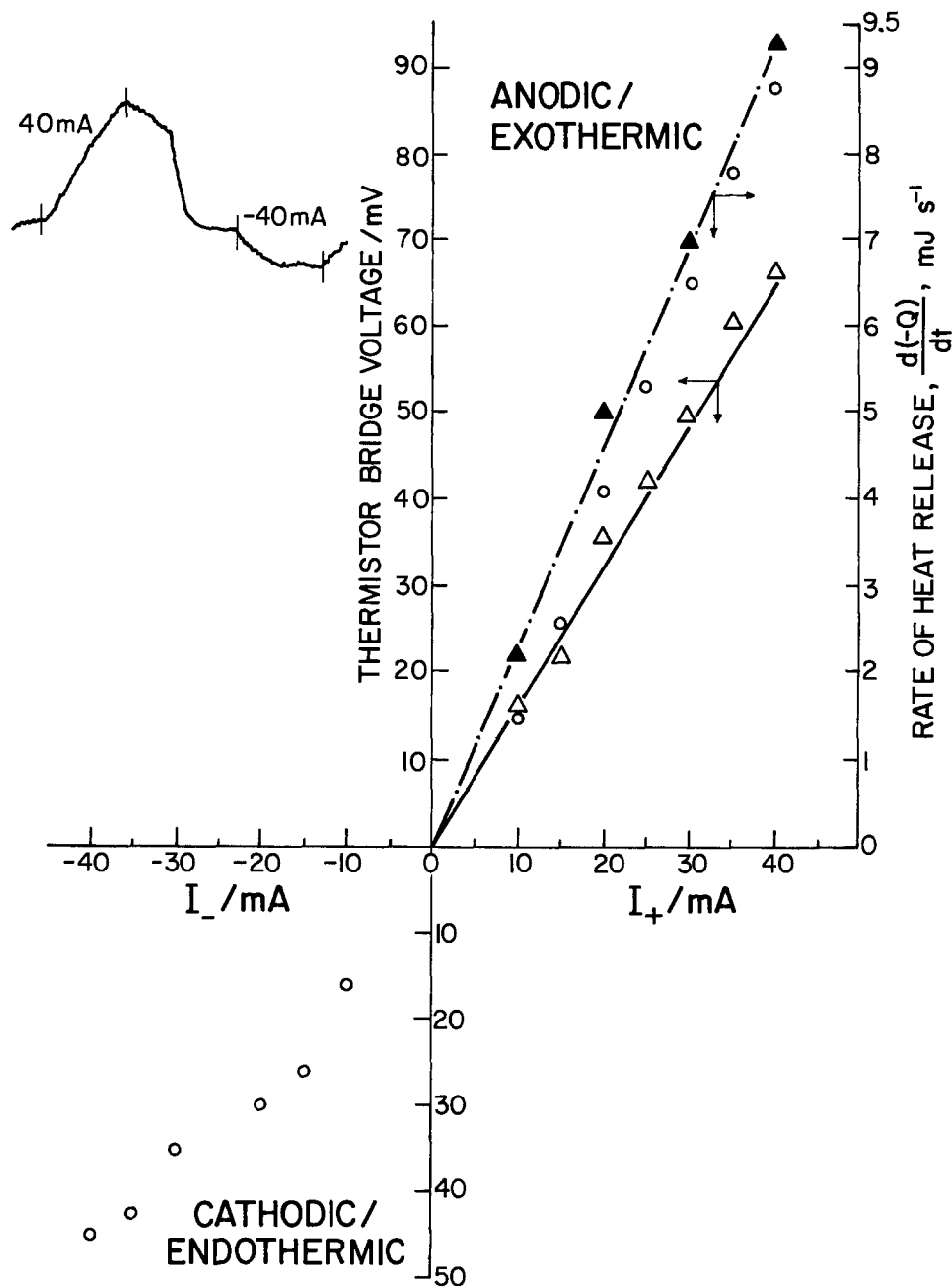


Fig. 4. Variation of bridge voltage and rate of heat release with applied current. Conditions as in Fig. 3. Typical thermistor bridge voltage (Y-axis; 25 mV cm⁻¹) vs. time (X-axis; 25 s cm⁻¹) is shown in the inset to illustrate the polarization effect. Differences of the anodic and cathodic extents of heat evolution in Fig. 3 and 4 give the basis for evaluation of the Joule heat contributions to the measured overall reaction heat charges at finite currents.

wards were calculated and are listed in Table I. Also included in this table are data for the effects of KBr additions, *i.e.*, for increase in the Br⁻/Zn²⁺ ratio, and for polarization effects in aq. KBr with and without dissolved Br₂ present.

The 0.1M ZnBr₂ solutions were somewhat unstable, owing to a small but significant degree of hydrolysis. However, addition of a trace of HBr prevented this problem, and a stable solution having an apparent solution resistance of 77.0Ω and a pH of 1.65 resulted. The $T\Delta S$ value was the same as that for a 4M solution, but there was an increase (see Table 1) upon addition of NaClO₄, to give a 1M concentration; this was added to improve the conductivity (apparent solution resistance then = 11.0Ω). There was a slight change in the $T\Delta S$ value when the electrode was polarized in ZnBr₂ solutions containing 1 and 2M KBr, *i.e.*, for an increase in the Br⁻ to Zn²⁺ ratio. However, cathodic polarization in 1M KBr solution was associated with an exothermic reaction (a shift in the bridge signal to the positive direction, see Fig. 5), corresponding to H₂ evolution at Zn. In this case, the cathodic and anodic bridge voltage signals were corrected for the Joule heat component by subtracting the I^2R values that were obtained while polarizing the zinc electrode in bromide solutions of the same ohmic resistance. The heat of the

anodic reaction was the same as for the ZnBr₂ case, while the cathodic reaction heat was around -132 kJ mol⁻¹ (Fig. 5). However, a normal trend was observed when the above solution contained 0.14M dissolved Br₂. This behavior corresponds to the reaction $Zn + Br_2 \rightleftharpoons ZnBr_2$ having the anodic Zn/Zn²⁺ and cathodic Br₂/Br⁻ components, respectively. Visual observations and chemical analyses showed the presence of brownish film adhering to the electrode surface and brown material in solution, with a depletion of the bromine concentration. The calorimetric observations showed evidence that this reaction was assisted by light (observation of discoloration of the solution when a zinc electrode was exposed to aerated as well as deaerated solutions).

The Zn/ZnO-ZnO₂²⁻ reaction in aq. KOH-ZnO solutions.—The results for this system were obtained in a similar way to those for the Zn/Zn²⁺ reaction in Br⁻ solutions described above. The reaction heats were -0.4~-0.5 kJ mol⁻¹ for the Zn/ZnO reaction in 1M Zn(II) solutions in 8M KOH solution, *i.e.*, potassium zincate solutions. These heats are much smaller than those for the Zn/Zn²⁺ reaction in Br⁻ solution.

The Br⁻/Br₂ reaction.—As mentioned previously, the Br⁻/Br₂ reaction was studied at black-platinized platinum mesh electrodes polarized in 1M KBr solution containing

Table I. $-T\Delta S$ values, i.e., "molar Peltier heats" of Zn/Zn²⁺ and Zn/ZnO-ZnO²⁻ processes at the zinc electrode, and of Br⁻/Br₂ at black-platinized platinum electrodes

Solution, conc. (M)	$-T\Delta S$ (kJ mol ⁻¹)
Zinc electrode/ZnBr ₂ solution	
1. 0.1	44.4
2. 0.1 + 1.0 NaClO ₄	65.6
3. 0.5	28.9
4. 1.0	49.5
5. 2.0	42.5
6. 4.0	44.4
7. 1.0 + 1.0 KBr; Br ⁻ :Zn ²⁺ = 3	38.6
8. 1.0 + 2.0 KBr; Br ⁻ :Zn ²⁺ = 4	44.4
9. ZnBr ₂ = 0; KBr = 1.0; Br ₂ = 0.14	49.2*
10. ZnBr ₂ = 0; KBr = 1.0	131.6**
Zinc electrode/ZnO + 8M KOH	
9. 0.25 ZnO	0.9
10. 1.00 ZnO	0.4
Black-platinized platinum	
11. KBr + 0.18 Br ₂ (Br ⁻ /Br ₂)	81.1

Solution volume 100 cm³; unstirred solutions; temperature of thermostat bath: 299.4 K. Measured heats include heats of ionic transport.

* From anodic signals.

** From cathodic signals.

0.18M Br₂ over the range of currents defined above. The $T\Delta S$ value for this reaction, as calculated from the line in Fig. 6, is -81.1 kJ mol⁻¹.

Polarization behavior.—When electrochemical reactions are driven to a condition of irreversibility, corresponding to a total overpotential η at a current density i , the irreversible heat production associated with kinetic effects is $i\eta$ J s⁻¹ cm⁻²; this is always an exothermic heat like the i^2R Joule heat. In order to make corrections when necessary for the $i\eta$ heating effect, polarization measurements were made on the electrode reactions under the same conditions as those employed in the calorimetry experiments. Here only the trends of the polarization behavior will be referred to. In several cases, the anodic and cathodic overpotentials at a given I were approximately equal, so the $i\eta$ heating almost canceled when the heat changes for the cathodic and anodic directions of the electrode reaction, conducted at the same current density, were compared. Here the same principle is used as that referred to earlier for compensating out the I^2R ohmic heating effects. It might be mentioned that compensating out the I^2R and $I\eta$ or $i\eta$ heating effects has not been referred to in most of the previous papers on electrochemical calorimetry except in Scherfey and Brenner's (4, 5) and in Graves's work (11d, 11e); in that of Lange (6, 7), extrapolations to zero I were made to eliminate these effects.

The potentials of unpolarized and polarized zinc electrodes were measured in various bromide solutions and in potassium zincate solution. Similarly, the potentials of platinized platinum-black electrodes in the solutions containing 1M KBr and 0.18M Br₂ were recorded. These values are listed in Table II. The cathodic and anodic polarization was high during polarization in 0.1M ZnBr₂ solution and diminished with increase in the ZnBr₂ concentration. The high cathodic polarization values of -1.19 V vs. Ag/AgBr are typical of the hydrogen evolution or oxygen reduction reactions. The open-circuit potentials of the zinc electrode in the bromide solutions corresponded nearly to the reversible half-cell potential of the zinc electrode, i.e., -0.76 V vs. H₂. However, in alkaline solutions, the measured potential of -1.6 V vs. the Ag/AgBr electrode roughly corresponds to a -0.059×16 mV decrement in the potential due to the pH effect. The potential of the platinum electrode in Br⁻/Br₂ solutions corresponded to the reversible potential of the Br₂/Br⁻ couple. The extents of polarization for anodic and cathodic currents at 40 mA cm⁻² were similar (± 120 mV) in this case but for the Zn electrode in aq. KBr solution, the cathodic polarization was much higher, corresponding to the known H₂ overvoltage behavior at Zn. The significance of the open-circuit potentials will be discussed later.

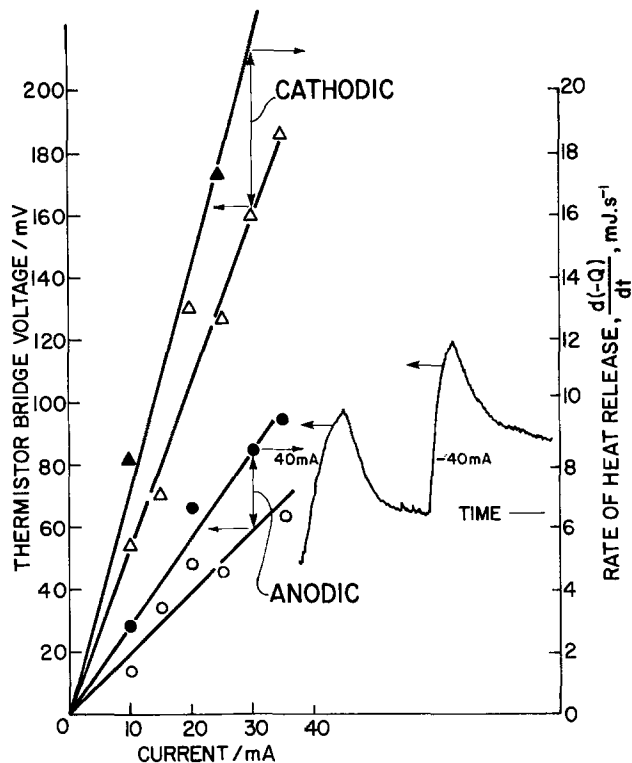


Fig. 5. Current vs. thermistor bridge voltage and rate of heat release plots for a polarized zinc electrode in 1M aq. KBr solution. Time (X-axis; 25 s cm⁻¹) vs. the thermistor bridge voltage (Y-axis; 10 mV cm⁻¹) traces are shown in the inset of this figure. The cathodic trace illustrates the exothermic response for cathodic current.

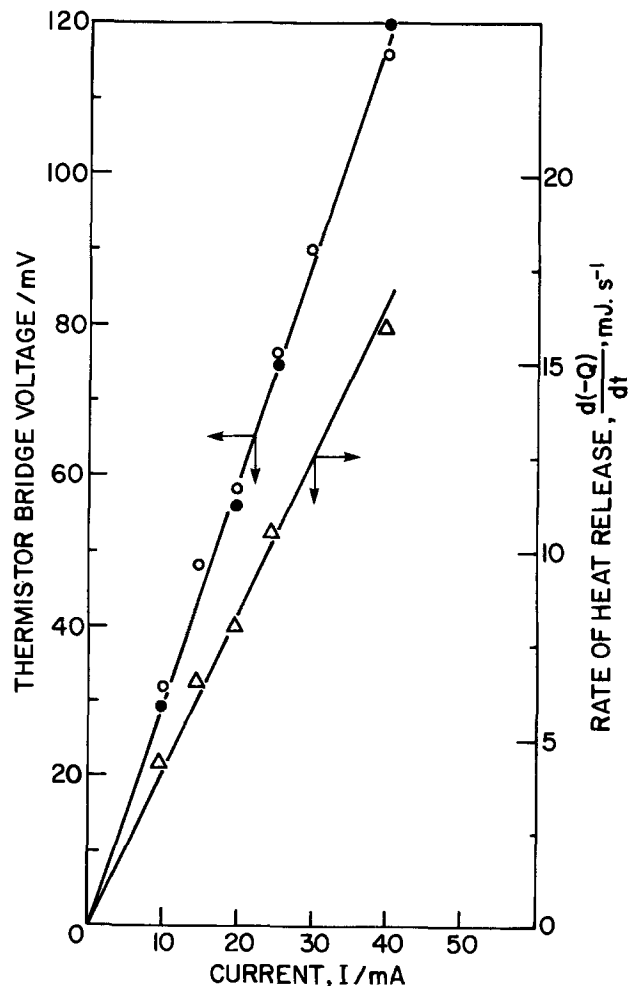


Fig. 6. Current vs. bridge voltage and rate of heat release lines for the Br⁻/Br₂ reaction at a black-platinized platinum electrode in 1.0M KBr + 0.18M Br₂ solution. ●: Duplicate data.

Table II. Potentials of zinc in bromide and zincate, and of platinum electrode in bromide + bromine solutions

No.	Solution	Current (mA)					Remarks
		0	10	20	30	40	
Zinc							
1.	0.1M ZnBr ₂ + 1.0M NaClO ₄	0.84	0.78 0.93	0.78 0.96	0.76 0.97	0.74 1.00	R _{app} = 21.2Ω pH initial = 5.60 adjusted to 3.34
2.	0.1M ZnBr ₂	0.86	0.70 0.99	0.65 1.06	0.62 1.12	0.56 1.19	R _{app} = 77.5Ω pH = 1.65
3.	1.0M ZnBr ₂	0.84	0.82 0.86	0.80 0.88	0.79 0.89	0.78 0.90	R _{app} = 25.2Ω pH = 4.90
4.	4.0M ZnBr ₂	0.78	0.75 0.80	0.75 —	0.74 0.82	0.73 0.83	R _{app} = 39.2Ω pH = 3.00
5.	1.0M KBr	0.94	0.86 —	0.88 1.52	0.88 1.62	0.86 1.66	R _{app} = 26.8Ω pH = 5.60
6.	≈8.0M KOH + ≈1.0M ZnO	1.60	1.58 1.63	1.55 1.61	1.55 1.66	1.53 1.67	R _{app} = 16.4Ω beyond pH range > 14.0
Platinum							
7.	1.0M KBr + 0.18M Br ₂	0.94	0.97 0.90	1.00 —	1.02 0.84	1.06 0.82	R _{app} = 24.0Ω

All the potentials are referred to Ag/AgBr reference electrode. The potentials are negative for zinc and positive for platinum electrodes. At each concentration, the values in first and second rows are for anodic and cathodic polarization, respectively.

Discussion

Interpretation of the experimental TΔS values.—The measured TΔS values, otherwise known as electrolytic Peltier heats, are defined as the heats that must be transferred at any junction in order to keep its temperature constant when F coulombs flow from one side of the junction to another, or when a flow of 1 mol of electrons takes place. Originally, the Peltier heat-change phenomenon referred to the transfer of electrons from one metal to another at a bimetallic junction. Electrochemical Peltier heats obviously involve more complex phenomena, including changes of solvation state of an ion or molecule and change of its charge, as well as the exit or entry of an electron from/to the Fermi level of the metal across the double layer.

When the electrochemical Peltier heat is divided by the temperature T, the value of the entropy \bar{S} transported across the electrode/solution boundary can be obtained. This value is the sum of the entropy changes due to the ionic entropy, the metal entropy, and the metal electron entropy contributions to the entropy change, ΔS, of the reversible electrode reaction and also the entropy changes arising as a consequence of ion transport as the cell reaction proceeds, i.e., the so-called Eastman ionic entropies of transport (22-23), S*. Using known electrochemical and thermodynamic quantities from the literature, Ozeiki *et al.* (2), Tamamushi (3), and Holmes and Joncich (10) have calculated the Peltier heats for the Cu/Cu²⁺ and Ag/Ag⁺ single-electrode reactions and compared them with the observed values. Problems associated with evaluation of Eastman entropies of transport and related quantities have been discussed in the previously published review article by Conway and Bockris (24), and in papers by Agar (1) and Tyrell and Hollis (25). However, for most ions in aqueous medium, except H⁺, the S* quantities are relatively small.

Calculation of the molar Peltier heat for the Zn \rightleftharpoons Zn²⁺ reaction, e.g., for 0.1M ZnBr₂ solution.—We recall that the electrochemical Peltier heat is defined in terms of the component entropy quantities, as follows

$$T \cdot \bar{S} = \text{II, (Molar Peltier heat)} = \left\{ \begin{array}{l} \text{(Net Entropy change } (\Delta S) \text{ due to the reaction)} \\ + \\ \text{(Entropy change due to ionic transport East-} \\ \text{man entropy } (\bar{S}^e)) \end{array} \right\} \times T \quad [1]$$

where T is the temperature (298 K) and \bar{S} is the entropy transported across the interface.

Net entropy change, ΔS, due to the reaction.—ΔS is given by

$$\Delta S = S_i + zS_e - S_M \quad [2]$$

for a reaction of metal M going to ions i and z electrons.

Normally S_e, the entropy of metal electrons, can be neglected relative to the other entropy terms in Eq. [2]. This question has been discussed in Ref. (11d). The basis of the assumption regarding the neglect of S_e is the known small electronic specific heat of metals relative to the Dulong and Petit value for the solid metal lattice at room temperature. C_{p,e} is the ca. 1% of the latter specific heat. The S_e is then correspondingly small. In the case of reaction of zinc, S^o_{Zn} = 41.6 J K⁻¹ mol⁻¹.

The partial g_i ionic entropy is

$$\bar{S}_i = \bar{S}_i^o - R \ln a_i - RT d \ln a_i/dT \quad [3]$$

for an ionic activity a_i. Introducing the molal activity coefficient γ and the molal concentration m_i,

$$\bar{S}_i = \bar{S}_i^o - R \ln m_i - R \ln \gamma - RT d \ln \gamma/dT \quad [4]$$

$$= \bar{S}_i^o - R \ln m_i + S_i^E \quad [5]$$

where S^E_i is the excess entropy of ion i at its concentration m_i.

In dealing with the problem of individual electrode heat changes, it is seen that the individual ionic excess entropies are required in addition to the individual \bar{S}_i^o quantities. The latter are quite reliably known for most simple ions from extra-thermodynamic procedures (1, 22, 23) but the S^E_i values, which are not negligible at appreciable concentrations, are not so easily evaluated in a reliable way. Recourse may be had to data calculated from the Debye-Hückel theory, based on Kielland's work (26), for dilute solutions, but for elevated concentrations where ion size and hydration effects become important (27) in determining γ_i, the required derivative d ln γ_i/dT is difficult to evaluate.

Activity coefficient data for aq. ZnBr₂ have been determined by Gibbard (18) over the temperature range 273-309 K for the concentration range 0.1-4.0M and provide, in principle, the required quantities but in terms of the mean ionic activity coefficient. However, anomalous activity behavior is indicated for this system as a function of concentration as shown in Fig. 7a (18). This is due to the well-known autocomplexation that occurs in zinc halide solutions as indicated by EMF, thermal and Raman spectroscopic experiments (18, 23, 28). Thus, Shchukarev *et al.* (29) reported widely different TΔS values for the formation of ZnBr⁺, ZnBr₂, ZnBr₃⁻, and ZnBr₄²⁻ complex ions.

Using the data of Gibbard, referred to above, and from Kielland (26), we have calculated the S^E_i for Zn²⁺ ion in 0.1M aq. ZnBr₂ assuming that at this concentration it is mainly uncomplexed as follows from the known (21) association constant. K₁ = 10^{-0.6}; S^E_i is found to be 11.4 J K⁻¹ mol⁻¹, so that $\bar{S}_i = -127.7 \text{ J K}^{-1} \text{ mol}^{-1}$ taking the conven-

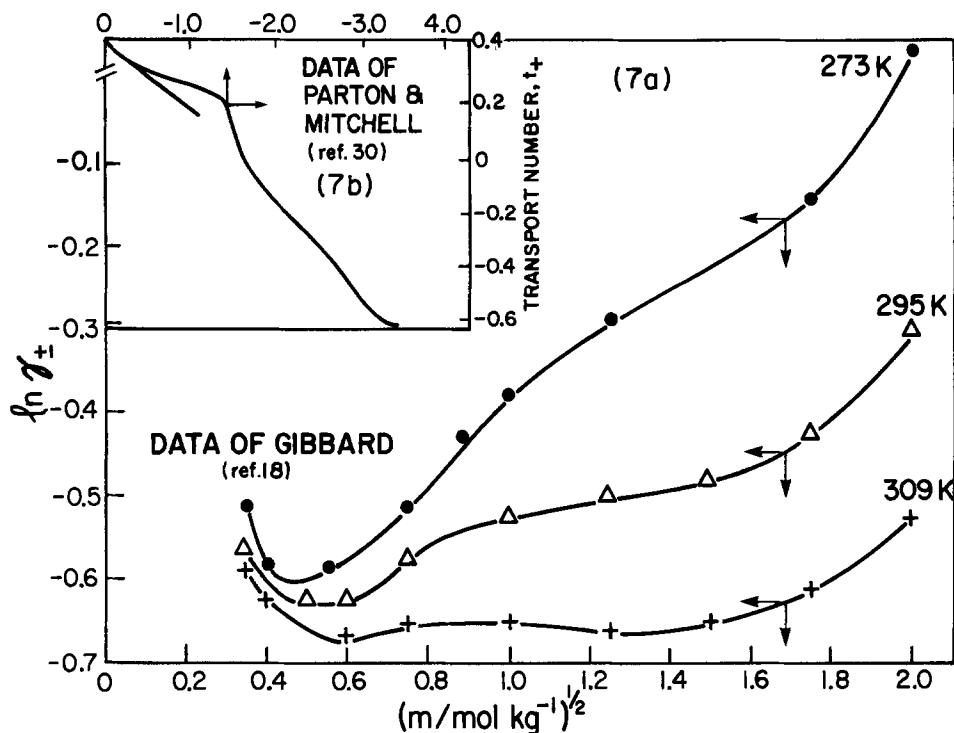


Fig. 7. Dependence of mean activity coefficients (a) and transport numbers (b) of zinc bromide solution at different concentrations and temperatures.

tional \bar{S}_i° for Zn²⁺ as $-106.5\ J\ K^{-1}\ mol^{-1}$ (23), noting that the corresponding absolute value of \bar{S}_i for Zn²⁺ will be $-152.6\ J\ K^{-1}\ mol^{-1}$, taking $2\bar{S}_{H^+}^\circ = -45.6\ J\ K^{-1}\ mol^{-1}$ (1, 23). It is not possible to evaluate \bar{S}_i for Zn²⁺ at higher concentrations owing to the autocomplexation and lack of corresponding activity coefficient data.

Calculation of the Eastman entropy change due to ion transport— \bar{S} is defined as

$$\bar{S} = (t_{Zn^{2+}} \cdot S^*_{Zn^{2+}} - 2 t_{Br^-} \cdot S^*_{Br^-}) \quad [6]$$

where S^* quantities are the entropies of transport for the species indicated and t the corresponding transport numbers.

The Eastman entropies of Zn²⁺ and Br⁻ ions are 18.8 and $2.5\ J\ K^{-1}\ mol^{-1}$, respectively. The value for the Zn²⁺ ion was obtained from the difference between the transported entropy of hydration and the entropy of hydration itself, $\bar{S}_h - S_h$ (23). The value for the Br⁻ ion is available from Agar (1). The transport numbers for Zn²⁺ and Br⁻ in 0.1M solution where autocomplexation is not appreciable are 0.37 and 0.63, respectively, from the work of Parton and Mitchell (30). At higher ZnBr₂ concentrations, $> 1.0M$, the cation transference number becomes negative, confirming autocomplexation (see Fig. 7b).

Substituting these t values into Eq. [6] gives a value of $\bar{S} = 3.8\ J\ K^{-1}\ mol^{-1}$.

Calculation of the resulting Peltier heat.—From the definition of the Peltier heat, Π , we can now calculate this quantity for the 0.1M ZnBr₂ solution as

$$T \cdot \bar{S} = (-127.7 - 41.6 + 3.8) \times 300 \quad [7]$$

$$= -49.7\ kJ\ mol^{-1}$$

The experimentally observed value from the calorimetric measurements with which the calculated value may be compared is $-44.4\ kJ\ mol^{-1}$ at a concentration 0.1M in ZnBr₂. Other observed data are as follows at the concentrations indicated

$$1.0M\ ZnBr_2 \quad -49.5\ kJ\ mol^{-1}$$

$$4.0M\ ZnBr_2 \quad -44.5\ kJ\ mol^{-1}$$

These differences are outside the experimental errors and are therefore likely to be due to irreversibility effects in the kinetic behavior of the zinc electrode.

The thermoelectrochemical results obtained here for the anodic and cathodic directions of the Zn $\xrightleftharpoons{\pm 2e} Zn^{2+}$

reaction gave rather concentration-independent values of $T\Delta S$ (Table I), except for the 0.5M ZnBr₂ solution. This result is a little surprising in relation to the sequence of $T\Delta S$ values for complexation of Zn²⁺ by Br⁻ to give ZnBr⁺, ZnBr₂, ZnBr₃⁻, and ZnBr₄²⁻ species where formation of the ZnBr₃⁻ complex has an unusually high $T\Delta S$ value of $+101\ kJ\ mol^{-1}$, while $T\Delta S$ for formation of the other ions is small and negative (29). Possible structures of "ZnBr₃⁻" in terms of an aquo-bromo complex have been discussed in Ref. (31). The results (Table I) found in the present work, which were checked in several separate runs, may be rationalized in terms of the situation which actually obtains in a solution of given ZnBr₂ at an appreciable concentration. It is known (28) that all complexes except ZnBr⁺ and the free aquo-ion are present together at appreciable and comparable concentrations, when total [ZnBr₂] is appreciable, so the $T\Delta S$ measured in the discharge of Zn is an overall value, which may not be very sensitive to the component of discharge current from ZnBr₃⁻ and hence to its anomalous entropy of formation from free ions (29).

Peltier heats in other bromide-ion containing and alkaline zincate solutions.—In 1M potassium bromide solutions, polarization is expected to cause zinc dissolution in the anodic and possible hydrogen evolution in the cathodic directions. In these solutions, there can, however, be a certain concentration of zinc ions owing to dissolution of the zinc electrode on open circuit. The approximate concentration can be estimated from the polarization curves where the anodic and cathodic branches can be extrapolated to open circuit. Of course, there can be a slight buildup of zinc ions also during the constant current polarization experiments. Separate polarization measurements made outside the calorimeter show that the zinc concentration in solution due to free corrosion of the zinc electrode can become around 5 mM, corresponding to a corrosion current of 0.9 mA passing during an overnight period (14h). At this concentration, the value of $R\ ln\ c$ is $-52.5\ J\ K^{-1}\ mol^{-1}$.

Using the transport number and Eastman entropy values for K⁺ and Br⁻ ions ($t_{K^+} = 0.51$; $S^*_{K^+} = 7.1\ J\ K^{-1}\ mol^{-1}$; $t_{Br^-} = 0.49$; $S^*_{Br^-} = 2.5\ J\ K^{-1}\ mol^{-1}$), one can obtain the entropy of transport for KBr = $2.4\ J\ K^{-1}\ mol^{-1}$. The molar Peltier heat, upon substitution of S_{Zn} , $S_{Zn^{2+}}$, and S_{KBr} into Eq. [1] and [2], is $-43.2\ kJ\ mol^{-1}$, which can be compared with the experimental value of $-49.2\ kJ\ mol^{-1}$. A polarization in the cathodic direction should cause H₂ ev-

olution to take place when the current exceeds that for the diffusion-controlled reductive deposition of any residual Zn^{2+} ions in solution, depending on their concentration. For a solution at pH 6, the estimated Peltier heat is $-69.4 \text{ kJ mol}^{-1}$. The appropriate values of quantities used in this calculation are given below

$$S_{H_2} = 130.5 \text{ kJ mol}^{-1}; 2\bar{S}_{H^+} = -45.6 \text{ J K}^{-1} \text{ mol}^{-1}$$

$$S_{H^+}^* = 43.1 \text{ J K}^{-1} \text{ mol}^{-1}; S_{OH^-}^* = 58.1 \text{ J K}^{-1} \text{ mol}^{-1}$$

together with

$$t_{H^+} = 0.64 \text{ and } t_{OH^-} = 0.36$$

for the aqueous solutions.

The experimental value is $-132.0 \text{ kJ mol}^{-1}$, so that the excess of $-63.0 \text{ kJ mol}^{-1}$ is due to the ηI term corresponding to the overvoltage of ca. 700 mV that is observed during the polarization (see Table II).

In alkaline solutions, the predicted molar Peltier heat for the Zn/ZnO reaction is 0.6 kJ mol^{-1} ($S_{Zn}^0 = 41.5 \text{ J K}^{-1} \text{ mol}^{-1}$; $S_{ZnO}^0 = 43.5 \text{ J K}^{-1} \text{ mol}^{-1}$). The difference between this and the experimental value is about 1 kJ mol^{-1} ; any explanation to account for this difference will be rather speculative, since the parallel reaction of Zn to form $Zn(OH)_2$ through the pores of the oxide film is well known, and the overall heat change is very small.

Peltier heat of the Br^-/Br_2 reaction at a platinum black surface.—The partial molar entropy of Br^- ion on the absolute scale is $103.7 \text{ J K}^{-1} \text{ mol}^{-1}$ (23). The ionic activity coefficient for Br^- ion at 1.0M concentration, 0.65, was obtained by extrapolating the straight line plot between $\log c_{Br^-}$ and activity coefficient to 1.0M [Kielland, Ref. (26)]. Further, the entropy of aqueous bromine solution (0.18M) was calculated from the known ΔG_f° (3.93 kJ mol^{-1}) and ΔH_f° ($-2.59 \text{ kJ mol}^{-1}$) values (32). The value of $S_{Br_2}^0$ obtained by this procedure is $-21.7 \text{ J K}^{-1} \text{ mol}^{-1}$. The total entropy of ionic procedure, \bar{S}_{KBr} , is already known ($2.4 \text{ J K}^{-1} \text{ mol}^{-1}$) for 1M KBr. As illustrated by the calculation given below, a value of $-74.8 \text{ kJ mol}^{-1}$ is obtained for the molar Peltier heat for this reaction, thus comparing reasonably well with the experimental value of $-81.0 \text{ kJ mol}^{-1}$.

Reaction term

$$\Pi = T\Delta\bar{S} = 300 \left[\frac{(S_{Br_2}^0 - 2\bar{S}_{Br^-} - 2R \ln C_{Br^-} - 2R \ln \gamma_{Br^-} + R \ln C_{Br_2}) - (S_{KBr})}{R} \right] \quad [8]$$

↑
Ionic transport term

where

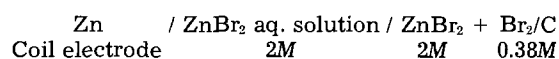
$$R \ln C_{Br^-} = 0 \text{ when } C_{Br^-} = 1.0M; R \ln C_{Br_2} = -14.2 \text{ J K}^{-1} \text{ mol}^{-1}$$

when

$$C_{Br_2} = 0.18M.$$

Heat changes in the overall Zn/Br₂ cell reaction and energy efficiency evaluation.—While individual electrode heat changes, as $T\Delta S$ quantities, can be measured with reasonable reliability, as we have shown earlier in this paper, it is not possible to obtain from the calorimetric measurements the corresponding enthalpy change, ΔH , for individual electrode reactions, as this would require knowledge of the free energy change for a half-cell reaction or the corresponding absolute half-cell interfacial potential. While such quantities have been discussed frequently, and at length in a recent paper (33), no estimate of a half-cell free energy change can be made with a reliability better than $\pm \text{ca. } 30 \text{ kJ mol}^{-1}$. Thus, energy efficiencies for half-cell processes have little quantitative meaning. However, overall cell efficiency quantities [cf. Ref. (34)] can be determined.

For calorimetric measurement of the overall heat effect associated with the Zn/Br₂ cell reaction, the cell



was set up in the calorimeter and the system allowed to reach thermal equilibrium overnight. The cell potential

was measured, and then the cell was discharged via the measuring resistance, 1.27Ω of the ammeter, where the net current due to zinc oxidation coupled with Br_2 reduction was measured. The thermistor bridge voltage vs. time (trace I) and current vs. time curves (trace II) are shown in Fig. 8. The inflection in the bridge-voltage trace corresponded to the fast current decay which takes place initially and the subsequent attainment of a steady state after 25s. From the bridge signal in the steady state, and based on a previous calibration, the ratio of rate heat release to i yielded a value of 73.4 kJ mol^{-1} , for the total heat quantity $-T\Delta S - I^2R - I\eta$, all exothermic heat changes being taken as nominally negative in the usual way.

For prolonged equilibration times prior to the cell discharges, i.e., 48 and 72h, the $-T\Delta S - I^2R - I\eta$ decreased, possibly because of intermixing and/or consumption of the Br_2 reactant. The values were 50 and 42 kJ mol^{-1} for 48 and 72h equilibration periods, respectively.

As with the individual electrode experiments, calorimetric measurements were made in both directions of the overall cell reaction, i.e., on discharge and charge. This allowed the I^2R component of the heat change to be estimated. At the current of 34 mA (see Fig. 8, curve III), its value was 10.4 mJ s^{-1} or $0.5 \text{ mJ s}^{-1} \text{ cm}^{-2}$, i.e., about 16% of the measured $T\Delta S$ heat or a substantially smaller fraction of the total enthalpy change. The I^2R component is, however, retained in the overall estimate of free energy efficiency given below.

The observed cell EMF was $1.775 \pm 0.015V$, so that the free energy change for the overall reaction is -343 kJ mol^{-1} . From the above value of the observed heat change, ΔH is obtained as -416 kJ mol^{-1} . This gives a "free energy efficiency" of 82% for the overall cell reaction as conducted in the experiment (obviously I^2R depends on solution concentration and cell geometry, and $I\eta$ on current density at a steady current of 34 mA, ca. 1.7 mA cm^{-2}). This value is to be compared with the "thermodynamic" efficiency value, $\Delta G/\Delta H$, of 91% predicted by Gibbard (19). Of course, in practical battery designs, I^2R energy losses can be relatively larger depending on choice of separators and geometries, while η is minimized by maximizing electrode real area, especially at the C cathode.

Conclusions

1. By means of direct calorimetric measurements carried out during the passage of net anodic or cathodic currents under galvanostatic conditions, it was possible to measure the electrolytic Peltier heats, i.e., the $T\Delta S$ values for the following individual, i.e., half-cell, electrode

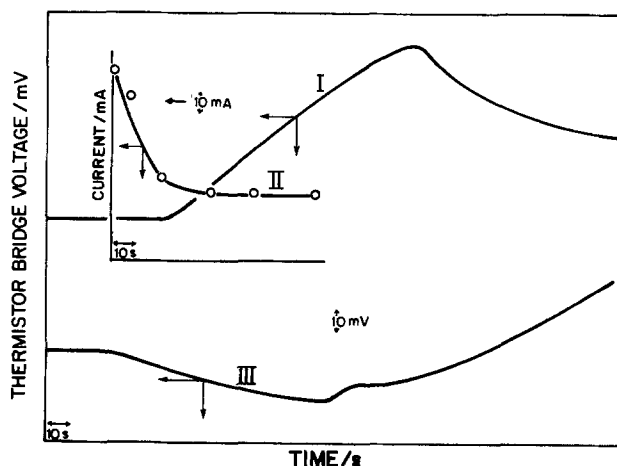


Fig. 8. Discharge characteristics of the cell Zn/2M ZnBr₂/2M ZnBr₂, 0.38M Br₂/C. Curve I: uncontrolled discharge, i.e., discharge via the resistance of the current measuring resistor. Curve II: current decay with time. Curve III: charge and discharge behavior of the above cell when polarized. X-axis: time = 10 s cm^{-1} for all curves. Y-axis: for curves I and III, bridge voltage = 10 mV cm^{-1} , for curve II, current = 10 mA cm^{-1} .

couples: Zn/Zn^{2+} (in aqueous Br^- solutions) and $Zn/ZnO-ZnO_2^{2-}$ processes at Zn electrodes and the Br^-/Br_2 process at black-platinized platinum electrodes.

2. The experimentally determined Peltier heat ($T\Delta S$) quantities for the above processes, corrected for i^2R Joule heating effects by a compensation measurement involving differences of anodic and cathodic heat effects, and for ionic entropies of transport, compare quite well with values that can be calculated from the relevant thermodynamic and extra-thermodynamic data for the species involved in the above half-cell reaction processes.

3. Polarization measurements gave useful complementary information on deviations from reversibility in the reaction processes studied, in relation to the components of heat change associated with overvoltages at net currents.

4. Calorimetric measurements in the overall reaction in the cell $Zn/2M ZnBr_2, aq./2M ZnBr_2 + 0.38M Br_2/C$ under conditions of free discharge at a steady-state current yielded information on the practical "free-energy efficiency" of the overall cell reaction under conditions where $i\eta + i^2R$ (or $i\eta$ alone) components of irreversible heat production were included. The efficiency thus determined under the experimental condition employed was 82%, which is to be compared with the thermodynamically derivable value of 91% for a Zn/Br_2 battery system behaving reversibly.

Acknowledgments

Grateful acknowledgment is made to the Natural Sciences and Engineering Research Council of Canada for support of this work on a Strategic Grant. One of us (B. E. C.) acknowledges the award of a Killam Senior Research Fellowship of the Canada Council.

Manuscript submitted Sept. 23, 1983; revised manuscript received Jan. 3, 1984. This was Paper 105 presented at the Washington, DC, Meeting of the Society, Oct. 9-14, 1983.

The University of Ottawa assisted in meeting the publication costs of this article.

REFERENCES

- J. N. Agar, in "Advances in Electrochemistry and Electrochemical Engineering," Vol. 3, P. Delahay and C. W. Tobias, Editors, p. 32, Interscience, New York (1963).
- T. Ozeki, N. Ogawa, K. Aikawa, I. Watanabe, and S. Ikeda, *J. Electroanal. Interfacial Electrochem.*, **145**, 53 (1983).
- R. Tamamushi, *ibid.*, **45**, 500 (1973); *ibid.*, **65**, 263 (1975).
- J. M. Scherfey, *This Journal*, **110**, 213 (1963).
- J. M. Scherfey and A. Brenner, *ibid.*, **105**, 665 (1958).
- E. Lange and Th. Hesse, *Z. Electrochem.*, **38**, 428 (1932); *ibid.*, **39**, 374 (1933).
- E. Lange and J. Monheim, *Z. Phys. Chem. A*, **150**, 177 (1930); see also in "Handbuch der Experimental Physik," Band 12, p.327, Akademische Verlag. m.b.h. Leipzig (1933).
- K. S. V. Santhanam, N. Jespersen, and A. J. Bard, *J. Am. Chem. Soc.*, **99**, 274 (1977).
- A. Fujishima, Y. Maeda, K. Honda, G. H. Brilmyer, and A. J. Bard, *This Journal*, **127**, 840 (1980).
- H. F. Holmes and M. J. Joncich, *Anal. Chem.*, **32**, 1251 (1960).
- a. B. B. Graves, *ibid.*, **44**, 993 (1972); b. S. L. Cooke, Jr. and B. B. Graves, *Chem. Instrum.*, **1**, 119 (1968); c. B. B. Graves, *Rev. Sci. Instrum.*, **44**, 571 (1973); d. B. B. Graves, in "Electrocatalysis," M. W. Breiter, Editor, p. 365, The Electrochemical Society Softbound Proceedings Series, Princeton, NJ (1974); e. B. B. Graves, Abstract 27, Physical and Surface Section, First Chemical Congress of the North American Continent, Mexico City (1975).
- F. B. Tudron, *This Journal*, **128**, 516 (1981).
- L. D. Hansen and R. M. Hart, *ibid.*, **125**, 842 (1978).
- C. S. Bradley, U.S. Pat. 312,802 (1885); U.S. Pat. 409,448 (1889).
- S. Barnartt and R. A. Forjet, *This Journal*, **111**, 1201 (1964).
- H. S. Lim, A. M. Lackner, and R. C. Knechtli, *ibid.*, **124**, 1154 (1977).
- P. C. Butler and D. W. Miller, Abstract 24, p. 38, The Electrochemical Society Extended Abstracts, Vol. 83-1, San Francisco, CA, May 8-13, 1983; K. R. Newby, R. J. Bellows, H. Einstein, P. G. Grimes, E. Kantner, and P. A. Malachuk, Abstract 25, p. 40, *ibid.*; M. Eisenberg, Abstract 44, p. 66, *ibid.*; H. F. Gibbard, Abstract 828, p. 1229, *ibid.*; H. F. Gibbard, Abstract 829, p. 1230, *ibid.*.
- H. F. Gibbard, *J. Solution Chem.*, **10**, 611 (1981).
- H. F. Gibbard, *This Journal*, **125**, 353 (1978).
- D. J. Eustace, *ibid.*, **127**, 528 (1980).
- J. McBreen and E. J. Cairns, "The Zinc Electrode," Advances in Electrochemistry and Electrochemical Engineering, Vol. 11, H. Gerischer and C. W. Tobias, Editors, Interscience, New York (1978).
- J. D. Eastman, *J. Am. Chem. Soc.*, **50**, 283, 292 (1928).
- W. G. Breck and J. Lin, *Trans. Faraday Soc.*, **61**, 2223 (1965).
- B. E. Conway and J. O'M. Bockris, in "Modern Aspects of Electrochemistry," Vol. 1, J. O'M. Bockris, Editor, Chap. 2, Butterworths, London (1954).
- H. J. V. Tyrrell and G. L. Hollis, *Trans. Faraday Soc.*, **48**, 893 (1952).
- J. Kielland, *J. Am. Chem. Soc.*, **59**, 1675 (1937).
- R. H. Stokes and R. H. Robinson, *ibid.*, **70**, 1870 (1948); see also B. E. Conway, "Ionic Hydration in Chemistry and Biophysics," Chap. 18, Elsevier, Amsterdam (1981).
- W. Yellin and R. A. Plane, *J. Am. Chem. Soc.*, **83**, 2448 (1961); see also J. W. Macklin and R. A. Plane, *J. Inorg. Chem.*, **9**, 821 (1970).
- S. A. Shchukarev, L. S. Lilich, and V. A. Latysheva, *Russ. J. Inorg. Chem.*, **1**, 36 (1956).
- H. N. Parton and J. W. Mitchell, *Trans. Faraday Soc.*, **35**, 758 (1939).
- D. F. C. Morris, E. L. Short, and D. N. Waters, *J. Inorg. Nucl. Chem.*, **25**, 975 (1963).
- L. G. Sillen, "Selected Thermodynamic Values," p. 31, N.B.S. Circular of U.S. Bureau of Standards, Washington DC (1963).
- S. Trasatti, *J. Electroanal. Chem. Interfacial Electrochem.*, **139**, 1 (1982).
- J. O'M. Bockris and S. Srinivasan, "Fuel Cells: Their Electrochemistry," McGraw-Hill, New York (1969).

Structural Parameters of β -PbO₂ and Their Relationship to the Hydrogen-Loss Concept of Lead-Acid Battery Failure

R. J. Hill and I. C. Madsen

CSIRO Division of Mineral Chemistry, Port Melbourne, Victoria, Australia 3207

ABSTRACT

Full-profile, Rietveld-type, x-ray powder diffraction studies have been performed on β -PbO₂ samples either prepared chemically or obtained from batteries operated under simulated electric vehicle service at 25° and 50°C. After a sharp initial decrease, the unit cell volume and cell edge ratio of battery β -PbO₂ assume relatively stable values which are both independent of the battery capacity and indistinguishable from those of chemically prepared material. A comparison of the observed unit cell volumes with values calculated for given levels of O²⁻/(OH)⁻, Pb⁴⁺/Pb²⁺ coupled substitution in the β -PbO₂ structure indicates that the maximum amount of this substitution is about 0.01 atoms of hydrogen per formula unit. These results suggest that the decline in battery capacity is not a function of the loss of a hydrogen species from the crystal structure of electrochemically active β -PbO₂. Estimates of the changes in PbO₂ crystallite size as a function of battery cycling history show that batteries began service with β -PbO₂ crystallite sizes of around 250Å, irrespective of the temperature of operation, but increased to values of about 700 and 900Å at 25° and 50°C, respectively. Since this increase in crystallite size occurred well before battery failure, the loss in battery capacity with cycling cannot be correlated with the changes in crystallite size and, therefore, with changes in the degree of structural order of the active material.

The decline in performance and eventual failure of lead-acid batteries applied in electric vehicle service is usually associated with a decline in the efficiency of utilization of the lead dioxide in the charged positive plate. This dioxide is primarily present as the tetragonal, or β -PbO₂, modification, although variable amounts of the orthorhombic, or α -PbO₂, form can also occur (1, 2). In addition, significant quantities of amorphous and/or very poorly crystallized and disordered PbO₂ in battery plates have been documented by x-ray diffraction (3-8), thermal decomposition (9, 10), and transmission electron microscopy (11, 12).

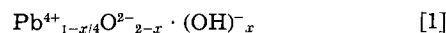
Among the more important reasons for the loss of battery capacity may be included: (i) a decrease in the degree of electrical contact between the PbO₂ particles themselves in the plate and between the particles and the current collector (grid), (ii) a decrease in the effective surface area of the particles, and (iii) softening and eventual shedding of material from the plate. However, a further recent suggestion (9, 10, 13-16) is that an electrochemically inactive form of β -PbO₂ develops in increasing amounts during charge/discharge cycling and that the loss of activity, and perhaps tendency toward active material shedding, is related (i) to the loss of a hydrogen species from the crystal structure of the active dioxide material and/or (ii) to an increase in the degree of structural order in the crystals.

In the latter proposed mode of battery failure, the electrochemically active PbO₂ containing the hydrogen species and/or a significant degree of structural disorder is said to progressively change to a more stoichiometric, defect-free variety resembling the chemically prepared product, which has traditionally been considered to be inactive and to contain fewer hydrogen ions. This mechanism has, however, been disputed in regard to the proposed loss of intrinsic PbO₂ activity (17, 18), and also in the claim that chemically prepared PbO₂ is electrochemically inactive (19).

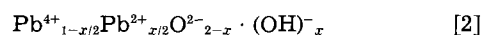
Chemical analyses of bulk samples of electrochemically prepared α -PbO₂ and β -PbO₂ (1, 20, 21) are usually consistent with the general formula PbO_{1.80-1.98}(OH)_{0.04-0.26}, which suggests the presence of a significant amount of hydrogen in the PbO₂ structure. These observations are supported by nuclear magnetic resonance (13), thermogravimetric analysis (9, 10), x-ray photoelectron spectroscopy (22), and inelastic neutron diffraction (11, 12). However, coherent (elastic) neutron diffraction studies of crystalline PbO₂ have been unable to locate ordered sites for the proposed hydrogen atoms and, in addition, have demonstrated that the traditional view of PbO₂ as substantially oxygen deficient is probably incorrect (23-26). Indeed,

Key words: x-rays, protons, crystallography, stoichiometry.

rather than indicating the presence of oxygen vacancies, the neutron diffraction results consistently show a slight deficiency of lead atoms relative to oxygen. The number of lead vacancies has been observed to be in the range 1%-5%, with the balance of positive charges presumed (23) to be achieved by the incorporation of hydrogen ions into the β -PbO₂ lattice, according to the formula



Note that with this model the range of lead vacancies is sufficient to account for the observed range of hydrogen atom contents. However, the validity of these departures from stoichiometry remains in some doubt, since they are, at most, only a few times the estimated standard deviations of the measurements. Furthermore, the amount of hydrogen present in β -PbO₂ samples has been found (11) to correlate with the difference between the total Pb and Pb⁴⁺ content of the material measured by chemical analysis. It has, therefore, been suggested (11, 26) that a more likely mechanism for the incorporation of large amounts of hydrogen atoms may involve the substitution of Pb²⁺ ions for Pb⁴⁺, leading to a formula of the kind



In this model, the presence of hydrogen atoms is not dependent on the presence of either lead or oxygen vacancies in the β -PbO₂ structure.

Since the unit cell volume of rutile-type oxides is a sensitive and predictable function of the ionic radii of the cations present (27), precise measurements of the unit cell dimensions of β -PbO₂ should show a systematic decrease in unit cell volume as the hydrogen atoms (and accompanying Pb²⁺ ions) are lost during cycling of a battery. Furthermore, if chemically prepared PbO₂ contains less hydrogen (and by implication is therefore electrochemically inactive), then the unit cell volume of β -PbO₂ from a failed battery should approach the value for chemically prepared material.

In the present study, we have tested the proposal of the presence of hydrogen species in β -PbO₂ and its relationship with battery capacity by undertaking full-profile Rietveld-type x-ray powder diffraction structure refinements (28) of β -PbO₂ samples prepared chemically and ones taken from batteries operated at 25° and 50°C. The use of a profile-refinement method incorporating the simultaneous analysis of two phases (29) is necessary for this application because of the presence of both α -PbO₂ and β -PbO₂ components in the battery material and the resultant high level of diffraction peak overlap. Moreover, the refinement method has the capability of producing unusually precise lattice parameters because of the

Table I. Proportion of operational life, relative capacity, and quantitative phase composition of the battery samples used for Rietveld structure refinement

Battery	Cycle number of sample	Proportion of battery operational cycle life (%)*	Relative Ah capacity (%)	Phase composition (w/o) (31)			
				β -PbO ₂	α -PbO ₂	PbSO ₄	Amorphous
B25**	0	0	100	38.1	31.2	0.3	30.3
	19	16	90	53.8	19.4	4.5	22.2
	44	38	100	51.6	23.2	2.7	22.5
	67	58	89	62.5	15.0	3.8	18.8
	90	78	83	71.4	8.9	2.3	17.4
	118	102	72	66.3	9.1	8.3	16.4
	145	125	49	63.3	12.3	7.1	17.3
B50†	0	0	100	35.7	34.8	2.0	27.4
	19	8	123	73.2	6.2	0.7	20.0
	59	24	105	74.2	8.3	3.2	14.3
	101	41	101	67.5	6.3	5.4	20.8
	143	58	100	64.3	8.3	1.4	26.0
	185	75	99	65.5	7.3	0.6	26.6
	228	93	92	58.9	9.6	2.2	29.4
	290	118	45	61.5	7.6	5.8	25.2

* Defined as the ratio of the number of charge/discharge cycles completed at the time of sampling to the total number at the time of failure (75% of the initial battery capacity).

** Battery operated at 25°C: failed after 116 charge/discharge cycles (2621 km).

† Battery operated at 50°C: failed after 246 charge/discharge cycles (7690 km).

requirement that the calculated and observed peak profiles match all along their steep sides as well as at the peak center. As a by-product of the refinement, accurate estimates were also obtained for the changes in crystallite size with battery cycling, which could then be related to changes in crystal structure order/disorder.

Experimental

Origin of β -PbO₂ samples.—After preliminary x-ray screening for phase purity, Univar PbO₂ (batch no. 11409) manufactured by Ajax Chemicals, and Analar PbO₂ (batch no. 81037 B210556) made by Hopkins and Williams, were chosen to represent chemically prepared β -PbO₂.

The battery samples were obtained at regular intervals from the charged positive plates of two 12V, 60 Ah lead-acid batteries operated at 25° and 50°C, respectively, and subjected to charge/discharge cycles that simulated electric vehicle service in an urban environment. Details of the test station design, cell construction, charge/discharge characteristics, sampling procedure, and operational results have been reported in detail elsewhere (8, 30, 31, and references therein). The end of useful battery life was taken as the point at which the discharge capacity, converted to the 20h rate, had fallen to 75% of the nominal rate at 25°C. At failure, the battery cycled at 25°C (B25) completed 116 charge/discharge cycles (2621 km of equivalent distance traveled) and was sampled a total of five times, whereas the battery cycled at 50°C (B50) completed 245 cycles (7690 km) and was sampled seven times (Table I). Both batteries were also sampled at least once in their postfailure period.

X-ray diffraction data collection.—All samples were back-pressed into standard aluminum holders and mounted in a Philips PW1050 diffractometer equipped with a PW1710 automatic step scanning system and a diffracted-beam curved graphite monochromator. Intensity measurements were made at intervals of 0.04° over the 2θ range 22°–117° using CuK α radiation and a step counting time of 5s. The x-ray tube was operated at 45 kV and 26 mA, with 1° divergence and receiving slits. These conditions allowed the collection of profile data for a total of 43 and 121 unique Bragg reflections for β -PbO₂ and (when present) α -PbO₂, respectively.¹ Dead-time corrections were applied automatically during data collection.

Structure Refinement Method

The least squares structure refinements were undertaken with the full-profile Rietveld-type program DBW 3.2 (28, 29), modified to include the application of a Pearson VII diffraction peak profile shape function (32). This

¹A complete listing of the step scan diffraction data for all of the samples is available from the authors upon request.

program can simultaneously refine the structures of two phases using x-ray data obtained from a conventional diffractometer, since it allows for the presence of two wavelengths (*i.e.*, CuK α_1 and α_2). Details of the refinement procedure have been described elsewhere (24, 29, 33). Starting values for the profile parameters were obtained by inspection of the observed diffraction pattern, and those for the atomic structure were taken from the literature (24).

Silicon calibration.—Before applying the Rietveld method to the β -PbO₂ samples, a coarsely crystalline sample of silicon was studied as a calibration standard. This step was required (*i*) to ascertain the potential accuracy, as well as precision, of the unit cell dimension determination, (*ii*) for the experimental determination of the graphite monochromator polarization ratio correction and of the intensity ratio of the CuK α_1 and α_2 reflection pair, and (*iii*) to define the instrumental contribution to diffraction peak broadening during the determination of crystallite size.

The results of the refinement of the Si data using the empirically determined polarization and CuK α_2/α_1 radiation intensity ratios, 0.91 and 0.5, respectively, are given in Table II. The unit cell parameter $a = 5.43113(9)\text{\AA}$ is less than three combined standard deviations larger than the value 5.43083(1) \AA generally accepted as the best absolute estimate of the cell dimension of crystalline Si (34). The application of the Rietveld method to the present problem is, therefore, capable of producing unit cell measurements of acceptable accuracy and precision. Furthermore, the unit cell parameter (and radiation intensity ratio) was found to be statistically invariant for refinements of Si data collected at regular intervals during the course of the study.

The mean dimension of the crystallites in the β -PbO₂ samples was determined from the Scherrer (35) and Warren (36) equations by comparing the values of peak width calculated at a constant 2θ value of 60° (37).

Battery samples.—Depending upon the stage of battery operational life at which sampling took place, the battery samples contained between 6 and 35 weight percent (w/o) of α -PbO₂ (Table I). Rather than exclude these α -PbO₂ "contaminating" peaks from the diffraction profile refinement, they were treated similarly to those of β -PbO₂ by incorporating the α -PbO₂ as a second phase (29). However, details of the α -PbO₂ pattern could only be refined for those samples in which the amount of α -PbO₂ was greater than 15 w/o (Table I), and even then, only the scale factor and a single peak width parameter (for crystallite-size measurements) could be released. No such complication arose for the samples of chemically prepared β -PbO₂, since these were single phase.

Table II. Rietveld crystal structure refinement results for silicon and the β -PbO₂ samples analyzed in the present study

Sample	Proportion of battery operational life (%) [*]	Rwp†	a(Å)	c(Å)	Unit cell volume (Å ³)	c/a	β -PbO ₂		α -PbO ₂	
							Peak FWHM at 60° 2 θ (°) ^{**}	Crystallite size (Å) ^{††}	Peak FWHM at 29° 2 θ (°)	Crystallite size (Å) ^{††}
Silicon		14.20	5.43113(9)				0.132			
Ajax β -PbO ₂		11.16	4.95602(11)	3.38646(9)	83.179(6)	0.68330(3)	0.239	460		
Hopkins & Williams β -PbO ₂		12.78	4.95865(7)	3.38814(6)	83.308(4)	0.68328(2)	0.163	965		
B25 cycle	0	16.04	4.96023(47)	3.38896(39)	83.382(25)	0.68323(14)	0.440	219	0.314(17)	143
	19	11.19	4.96283(18)	3.38603(14)	83.397(9)	0.68228(5)	0.257	417	0.300(13)	154
	44	12.07	4.95540(14)	3.38137(12)	83.033(8)	0.68236(4)	0.200	613	0.207(8)	188
	67	10.88	4.95710(11)	3.38199(9)	83.105(6)	0.68225(3)	0.188	688	0.248(12)	171
	90	11.98	4.95854(11)	3.38252(9)	83.166(6)	0.68216(3)	0.186	697		
	118	12.48	4.95751(11)	3.38150(9)	83.107(6)	0.68210(3)	0.174	806		
	145	12.02	4.96089(12)	3.38445(9)	83.293(6)	0.68223(3)	0.182	732		
B50 cycle	0	15.30	4.95949(42)	3.38858(35)	83.347(23)	0.68325(13)	0.404	240	0.249(12)	156
	19	12.60	4.95521(9)	3.38053(8)	83.006(5)	0.68222(3)	0.173	821		
	59	12.62	4.95497(9)	3.38087(7)	83.006(5)	0.68232(3)	0.160	1014		
	101	12.99	4.95327(8)	3.37992(7)	82.926(4)	0.68236(3)	0.152	1236		
	143	12.78	4.95570(10)	3.38076(9)	83.028(6)	0.68220(3)	0.171	842		
	185	13.18	4.95348(9)	3.37969(8)	82.927(5)	0.68229(3)	0.161	993		
	228	12.84	4.95540(11)	3.38084(9)	83.020(5)	0.68225(3)	0.184	713		
	290	12.59	4.95397(10)	3.37993(8)	82.950(5)	0.68227(3)	0.169	869		

^{*} Defined as in Table I.

[†] Conventional Rietveld refinement agreement index (28).

^{**} Obtained from a peak full-width at half maximum (FWHM) relationship fitted to the entire pattern (28, 29).

^{††} Obtained from the Scherrer equation (35) using silicon as the calibration standard.

Final values of all refined structural and profile parameters relevant to the present study are summarized in Table II: the full list of parameters may be obtained from the authors on request.

Results and Discussion

Unit cell volume.—Values for the unit cell volume of the β -PbO₂ crystal structure were calculated from the refined values of the unit cell dimensions (Table II) and are plotted in Fig. 1 against the proportion of battery operational life at the time of sampling (Table I). The unit cell volumes of the two chemically prepared samples are plotted, for convenience, at the 100% position on the battery life scale, along with published values (38-42) of the cell volumes obtained from eight very precise x-ray studies of chemical and natural β -PbO₂. Literature values for β -PbO₂ unit cell volumes determined by neutron diffraction were not considered because of a degree of uncertainty about the exact value of the neutron wavelength used (26).

The most obvious feature of the data plotted for batteries B25 and B50 is that the unit cell volume of the β -PbO₂ component starts service with a high value (about 83.36 Å³), which declines sharply during the first stage of battery operational life. The reason for this sudden drop in cell volume at a time when the capacity of the batteries (and therefore the electrochemical activity of their β -PbO₂) is equal to, or indeed, higher than the initial value at the commencement of service (Table I) is unclear. However, as discussed below, the early stages of the operational life of the batteries are marked by a dramatic increase in the size of the β -PbO₂ crystallites. Moreover, the initial values for the ratio of the unit cell dimensions (see below) are also atypical of the values encountered throughout the remainder of battery service. Both of these observations suggest that the physical properties of the very small crystals present in the very early stages of battery operation are not representative of the better crystallized material which results from charge/discharge treatment. The sharper decline in the unit cell volume of B50 relative to B25 is probably related to the fact that electrolyte diffusion, and charge/discharge reaction rates in general, are more rapid and more uniform at the higher operating temperature of this battery (8, 31).

After the initial "settling in" period, the unit cell volume of the β -PbO₂ in B50 remains fairly constant, while that of B25 tends to increase back towards its starting value. These variations are statistically significant when

compared to the error bars on the data points Fig. 1, but, since each sample taken from the operating battery is of necessity small (in order not to disrupt battery performance), the variations probably reflect small differences in the relative proportions of used and unused β -PbO₂ in the samples between and within individual plates. For B50, the fluctuations in cell volume are less severe than for B25, since the plate material is more uniform in composition and utilization at higher temperature.

In addition, the B50 β -PbO₂ unit cell volume is consistently smaller than that of B25. This observation is also likely to be a function of operating temperature, since a significantly higher proportion (about 45%) of the available β -PbO₂ present in the battery plates takes part in the charge/discharge reaction at higher temperature (9, 31).

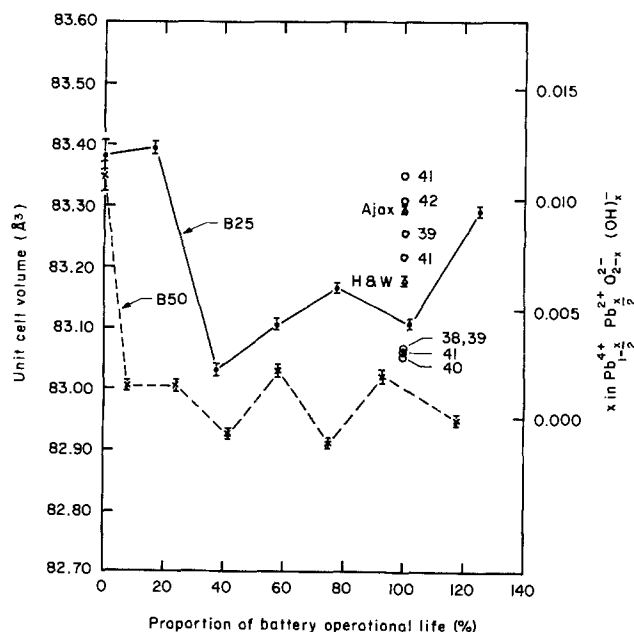


Fig. 1. Unit cell volume of the β -PbO₂ crystals in the two batteries B25 (●) and B50 (x) and two chemical preparations (Δ) plotted against the proportion of battery operational life at which sampling took place. The values were calculated from the least squares derived unit cell dimensions and are included along with their associated estimated standard deviations. Also plotted are the unit cell volumes of eight chemical β -PbO₂ samples (○) identified by their literature reference numbers.

Therefore, less of the unreacted, large cell volume β -PbO₂ remains to contribute to the bulk measurement.

The rise in the B25 β -PbO₂ unit cell volume in the post battery failure period (Fig. 1) probably arises from a similar effect, since the rate of "shedding" of the positive plate material is some 50% higher for this battery than for B50, and it is the heavily used material in the outer portions of the plate which is preferentially shed during battery operation (8, 43).

When allowance is made for the atypical nature of the β -PbO₂ present in the very early stages of battery operation, the unit cell volume of the dioxide is either constant (B50) or increases slightly (B25) for the period during which 50% of the capacity of the battery is lost. Even when the unit cell volumes at the beginning of battery operation are included, the total range of volumes exhibited by the battery material, whether healthy (active) or failed (inactive), is not much greater than the range of unit cell volumes observed for chemically prepared varieties of β -PbO₂ (Fig. 1). Behavior of this kind is not consistent with the suggestion that battery capacity declines as a result of the loss of a hydrogen species (and Pb²⁺ ions) from the β -PbO₂ structure, nor with the suggestion that chemically prepared β -PbO₂ is somehow more akin to inactive β -PbO₂ than to active β -PbO₂ (9, 10, 13-16). However, it is clear that comparisons between one or two isolated samples of battery and chemical β -PbO₂ (23, 26) could lead to conclusions in contradiction with the trends displayed by the larger number of samples used in the present study.

In Fig. 2, the unit cell volumes of 12 well-characterized rutile-type oxides (44-53) have been plotted against the cube of the corresponding cation radii. The data all fall close (correlation coefficient = 0.993) to the line

$$\text{Volume} = 41.8987 + 88.2806 (\text{radius})^3 \quad [3]$$

Using the accepted (54) value of 0.775Å for the radius of Pb⁴⁺, the unit cell volume predicted for stoichiometric PbO₂ with regression Eq. [3] is 82.949 Å³. This value has been plotted as the "x = 0.0" point in Fig. 1 and 2, and lies at the lower end of the range of determinations on both electrolytic and chemical β -PbO₂ given in Table II and Fig. 1 (82.926-83.397 Å³). All of the β -PbO₂ samples have unit cell volumes which are, therefore, either equal to, or only slightly larger than, the predicted value for stoichiometric β -PbO₂.

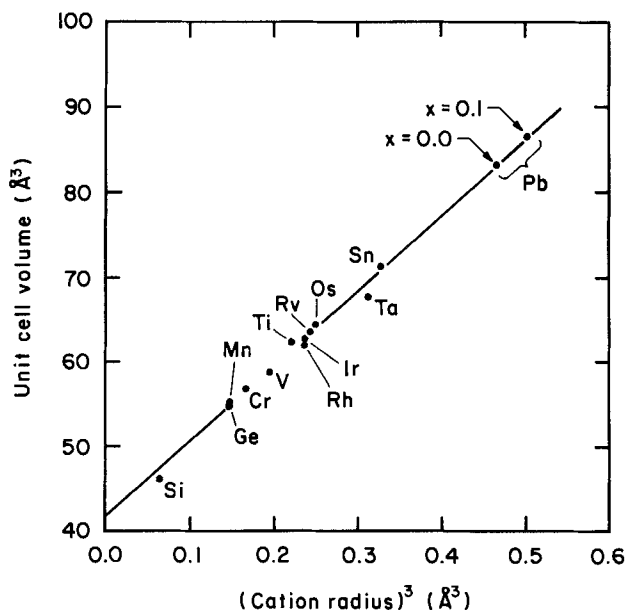


Fig. 2. Variation of the unit cell volume of 12 rutile-type oxides MO₂ with the cube of the radius of the cation M. The line is the least squares regression relation between the two quantities plotted. The two points labeled x = 0.0 and 0.1 represent the predicted volume of lead dioxide with the formulas PbO₂ and Pb⁴⁺_{0.95}Pb²⁺_{0.05}O_{1.9}(OH)⁻_{0.1} respectively.

The Pb²⁺ ion has a radius of 1.19Å in six-fold coordination, significantly different from the Pb⁴⁺ radius of 0.775Å, whereas the O²⁻ and (OH)⁻ radii are very similar with values of 1.36 and 1.34Å, respectively (54). Changes in unit cell volume as a result of the coupled substitution of O²⁻/(OH)⁻ and Pb⁴⁺/Pb²⁺ according to the formula [2] may, therefore, be reduced merely to the effect of the Pb⁴⁺/Pb²⁺ pair on the radius of the octahedral site. The predicted unit cell volume for a given degree of substitution, x, can then be determined by calculating a weighted mean cation radius for the octahedral site and inserting this in the regression Eq. [3].

A comparison (Fig. 1) of the range of observed unit cell volumes (82.926-83.397Å³) with the values calculated from the regression equation suggests that the maximum amount of (OH)⁻ substitution is likely to be of the order of x = 0.01. Hydroxyl contents of up to 25% quoted in the literature (1, 20, 21, 41) for chemical analysis of bulk battery positive plate material cannot relate entirely to substitution in the β -PbO₂ structure, since this would produce unit cell volumes vastly in excess of observed values (Fig. 2). A large proportion of the hydroxyl must, therefore, be present in surface layers and/or noncrystalline fractions of the samples. X-ray photoelectron (22) and infrared (55) spectroscopic studies of chemically and electrochemically prepared lead dioxide, and the related (rutile) oxide TiO₂, respectively, are in support of this conclusion.

c/a ratio.—By taking the ratio of the unit cell dimensions, c/a, rather than their individual values or the product, a²c (the unit cell volume), the effects of some possible systematic experimental errors in the determinations (e.g., 2θ zero error, sample eccentricity, wavelength uncertainty, etc.) are eliminated or reduced. Moreover, information is obtained about the relative changes (distortions) in unit cell dimensions which may otherwise cancel out in a volume calculation.

The c/a ratios for the B25, B50, and chemical preparations of β -PbO₂ have been plotted against the appropriate proportion of battery operational life in Fig. 3. The most notable feature of the data is the rapid decrease in c/a ratio during the first 15% of battery life. As in the case of the variation in β -PbO₂ unit cell volume discussed above, the very early stage of battery operation is atypical of the

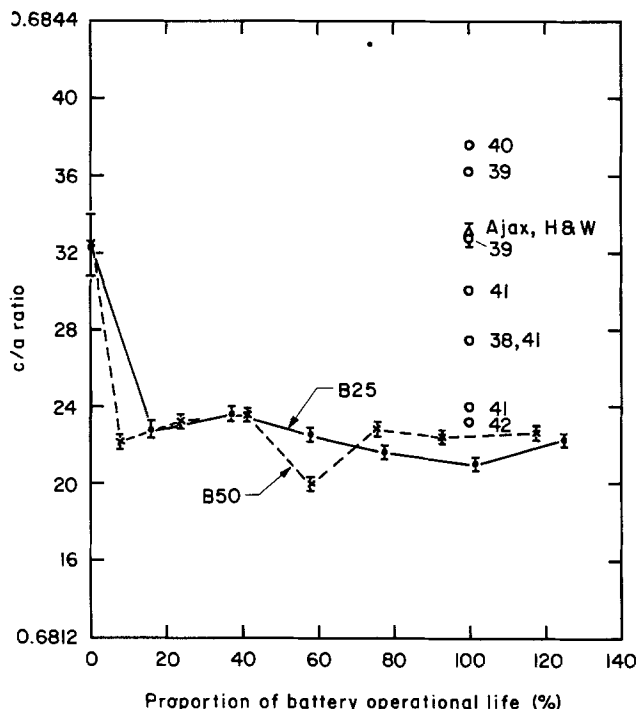


Fig. 3. Variation of the β -PbO₂ unit cell edge ratio c/a with the proportion of battery operational life at which the samples were collected. The data are plotted for the same samples and presented in the same manner as in Fig. 1.

remainder of the life of the battery for which the c/a ratio remains very uniform and equal for each battery. This suggests that the β - PbO_2 crystal structure suffers no observable distortion during the period for which more than 50% of the battery capacity is lost.

The c/a ratios determined for the two chemically prepared samples of β - PbO_2 in the present study are significantly higher than the middle- and late-stage battery sample values, but lie well within the range of values obtained from the literature for chemical β - PbO_2 . Indeed, some of the chemical preparations have c/a ratios close to those of the uncycled β - PbO_2 , whereas others have ratios more akin to those of heavily cycled material. As deduced from unit cell volume measurements, therefore, there appears to be no systematic distinction between β - PbO_2 from a failed and a healthy battery, or between electrolytic β - PbO_2 and at least some of the chemical preparations. This is only the case, however, when the trends exhibited by a number of samples are collected together.

As expected, similar conclusions apply when the variations of the two individual unit cell dimensions are analyzed as a function of battery capacity (Table II): like the cell volume and c/a ratio, the a and c values are again high during the early stages of charge/discharge cycling, but they quickly settle down to relatively constant values for the remainder of battery operational life. Moreover, the total range of unit cell sizes for the battery β - PbO_2 is approximately equal to that observed for chemically prepared material. There is no evidence that the a parameter in battery β - PbO_2 is significantly greater than that of chemical samples, as reported by Antonio *et al.* (26) for a more limited number of samples.

Crystallite size.—The mean dimension of the crystallites in the samples analyzed in the present study are plotted against proportion of battery operational life in Fig. 4. Both the 25° and 50°C batteries begin service with β - PbO_2 crystallite sizes of around 250Å, and both experience a substantial increase in size as the batteries are cycled, in agreement with earlier work (3, 5, 10, 41, 56).

For B50, a crystallite size of around 900Å is reached after only 10% of its operational life has been completed, whereas for B25, the rise to its stable value of around 700Å is only reached after 60% of its life. In the postfailure pe-

riod, the size of the β - PbO_2 crystallites in both batteries is around 800Å, approximately halfway between the values obtained for the two chemically prepared β - PbO_2 samples. Once again, therefore, it is clear that chemical preparations are not immediately distinguishable from the electrolytic samples.

The broadening of diffraction peaks can, however, be a result of nonuniform lattice strain brought about by the presence of nonstoichiometry and/or defects in the crystal structure of the material examined, rather than of a real decrease in crystallite size (41). With this possibility in mind, it has been suggested that the decrease in peak width as β - PbO_2 is cycled in a battery represents a change in the β - PbO_2 crystal structure towards a more stoichiometric, defect-free variety which is less reactive electrochemically (9, 10, 13-16).

The results presented for the B25 samples in Fig. 4 are consistent with this idea in that the effective crystallite size increases more or less steadily as the battery capacity declines towards failure. However, for B50 the crystallite size of the β - PbO_2 increased to its battery failure value after only 10% of the operational life passed. Therefore, while the increase in crystallite size for both batteries may well represent an increase in structural order, especially during the first few cycles, it is difficult to attach a consistent relationship between particle size/structural order and the capacity changes observed for both batteries. Moreover, one of the chemically prepared β - PbO_2 samples has a crystallite size which is not much greater than fresh battery material, yet this material is claimed to be defect-free and inactive (2).

During the limited period over which α - PbO_2 was present in sufficient quantities for its crystallite size to be determined, its size was found to remain constant at around 150Å. This very small crystallite dimension is consistent with the results of neutron powder diffraction (24, 26) and transmission electron microscope (12) studies of α - PbO_2 , which suggest that the crystal structure of this phase is highly disordered. In fact, the α - PbO_2 content of the battery samples decreases with charge/discharge cycling (Table I) because it does not reform from the PbSO_4 discharge product (8, 31). The α - PbO_2 measured in the present study is, therefore, material which has not discharged, and its crystallite size is unaltered from that present in fresh battery plates.

Summary and Conclusions

After an initial short period of charge/discharge cycling, the unit cell volume and c/a cell edge ratio of β - PbO_2 reach fairly stable values which are independent of the battery capacity and are indistinguishable from the values obtained from chemically prepared material. The suggestion that battery capacity declines as a result of gradual loss of a hydrogen species from the β - PbO_2 crystal structure, therefore, seems unlikely.

A comparison of the observed unit cell volumes with values calculated for a given level of $\text{O}^{2-}/(\text{OH}^-)$, $\text{Pb}^{4+}/\text{Pb}^{2+}$ coupled substitution in the β - $\text{PbO}_2 \cdot x\text{H}$ formula suggests that the maximum value of x is about 0.01, *i.e.*, little different from stoichiometric β - PbO_2 . Under the constraints of this model of hydrogen atom incorporation, measured (OH^-) contents of up to 25% quoted in the literature for analyses of bulk (crystalline plus noncrystalline) active material must, therefore, relate to the (OH^-) content of surface layers and/or the noncrystalline fractions of the samples, rather than to the β - PbO_2 crystal structure itself. Whether or not hydrogen atoms located in the β - PbO_2 surface layers and/or amorphous material play a role in the electrochemical activity of the positive plate remains to be determined. Furthermore, an alternative model in which hydrogen atoms substitute into the β - PbO_2 structure to compensate for lead atom vacancies may also yet prove to be relevant to the decline in battery capacity.

Batteries operated at both 25° and 50°C begin service with β - PbO_2 crystallite sizes of around 250Å; and experience an increase in size with cycling. However, in the case of the 50°C battery a crystallite size of around 900Å is

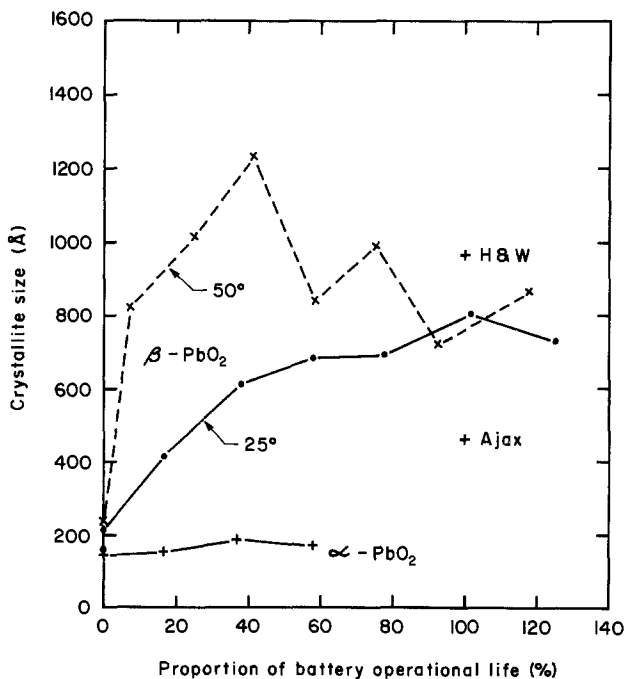


Fig. 4. Mean crystallite dimension of battery β - PbO_2 and α - PbO_2 plotted against the proportion of battery operational life at which samples were collected. The data are plotted for the same samples (minus the literature chemical preparations) and presented in the same manner (minus the error bars) as in Fig. 1.

reached after only 10% of its operational life has been completed. The gradual loss of battery capacity with cycle life cannot, therefore, be correlated with the observed relatively sudden increase in crystallite size and/or structural order during the early stages of operation.

Acknowledgments

We are indebted to Dunlop Batteries Australia for supplying battery materials and to the International Lead Zinc Research Organization for their joint support and for permission to publish this work. We also thank K. Harris and D. C. Constable for assistance with sample preparation and battery test rig operation. An early version of the manuscript benefited greatly from constructive reviews by Dr. S. Fletcher, Dr. I. E. Grey, and Dr. D. A. J. Rand.

Manuscript submitted Oct. 19, 1983, revised manuscript received Jan. 20, 1984.

CSIRO Division of Mineral Chemistry assisted in meeting the publication costs of this article.

REFERENCES

- J. Burbank, A. C. Simon, and E. Willihnganz, in "Advances in Electrochemistry and Electrochemical Engineering," P. Delahay and C. W. Tobias, Editors, p. 157, Wiley-Interscience, New York (1971).
- J. Perkins, *Mater. Sci. Eng.*, **28**, 167 (1977).
- D. Kordes, *Chem. Ing. Tech.*, **38**, 638 (1966).
- K. Weisener, W. Hoffman, and O. Rademacher, *Electrochim. Acta*, **18**, 913 (1973).
- K. Weisener and P. Reinhardt, *Z. Phys. Chem.*, **256**, 285 (1975).
- P. R. Skidmore and R. R. Schwarz, *Analyst*, **104**, 952 (1979).
- H. Nguyen Cong, A. Ejjenne, J. Brenet, and P. Faber, *J. Appl. Electrochem.*, **11**, 373 (1981).
- K. Harris, R. J. Hill, and D. A. J. Rand, *This Journal*, **131**, 474 (1984).
- S. M. Caulder and A. C. Simon, *ibid.*, **121**, 1546 (1974).
- J. D. Dawson, M. E. Rana, B. Munasiri, and J. McWhinnie, in "Power Sources, Vol. 7," J. Thompson, Editor, p. 1, Academic Press, London (1979).
- P. T. Moseley, J. L. Hutchison, C. J. Wright, M. A. M. Bourke, R. I. Hill, and V. S. Rainey, *This Journal*, **130**, 829 (1983).
- P. T. Moseley, J. L. Hutchison, and M. A. M. Bourke, *ibid.*, **129**, 876 (1982).
- S. M. Caulder, J. S. Murday, and A. C. Simon, *ibid.*, **120**, 1515 (1973).
- A. C. Simon, S. M. Caulder, and J. T. Stemmler, *ibid.*, **122**, 461 (1975).
- A. C. Simon, S. M. Caulder, and J. T. Stemmler, *ibid.*, **122**, 1640 (1975).
- P. Faber, *Electrochim. Acta*, **26**, 1435 (1981).
- B. Burrows and H. Giess, *This Journal*, **122**, 1640 (1975).
- J. Bouet and J. P. Pompon, *Electrochim. Acta*, **26**, 1477 (1981).
- E. J. Taylor, G. A. Shia, and D. T. Peters, Abstract 37, p. 58, The Electrochemical Society Extended Abstracts, Vol. 83-1, San Francisco, CA, May 8-13, 1983.
- N. E. Bagshaw, R. L. Clarke, and B. Halliwell, *J. Appl. Chem.*, **16**, 180 (1966).
- J. A. Duisman and W. F. Giaugue, *J. Phys. Chem.*, **72**, 562 (1968).
- K. S. Kim, T. J. O'Leary, and N. Winograd, *Anal. Chem.*, **45**, 2214 (1973).
- J. D. Jorgensen, R. Varma, F. J. Rotella, G. Cook, and N. P. Yao, *This Journal*, **129**, 1678 (1982).
- R. J. Hill, *Mater. Res. Bull.*, **17**, 769 (1982).
- P. D'Antonio and A. Santoro, *Acta Crystallogr.*, **B36**, 2394 (1980).
- A. Santoro, P. D'Antonio, and S. M. Caulder, *This Journal*, **130**, 1451 (1983).
- R. D. Shannon and C. T. Prewitt, *Acta Crystallogr.*, **B25**, 925 (1969).
- H. M. Rietveld, *J. Appl. Crystallogr.*, **2**, 65 (1969).
- D. B. Wiles and R. A. Young, *ibid.*, **14**, 149 (1981).
- D. Barrett, M. T. Frost, J. A. Hamilton, K. Harris, I. R. Harrowfield, J. F. Moresby, and D. A. J. Rand, *J. Electroanal. Chem.*, **118**, 131 (1981).
- D. C. Constable, J. R. Gardner, K. Harris, R. J. Hill, D. A. J. Rand, S. Swan, and L. B. Zalzman, ILZRO Project no. LE-290, Progress Report 7 (1982).
- M. M. Hall, V. G. Veeraraghavan, H. Rubin, and P. G. Winchell, *J. Appl. Crystallogr.*, **10**, 66 (1977).
- R. J. Hill, Submitted to *Am. Mineral.*
- C. R. Hubbard, *J. Appl. Crystallogr.*, **16**, 285 (1983).
- P. Scherrer, *Göttinger Nachrichten*, **2**, 98 (1918).
- B. E. Warren, *J. Appl. Phys.*, **12**, 375 (1941).
- H. P. Klug and L. E. Alexander, "X-ray Diffraction Procedures for Polycrystalline and Amorphous Materials," 2nd ed., p. 591, Wiley, New York (1974).
- T. Katz, *Ann. Chim.*, **5**, 5 (1950).
- G. Butler and J. L. Copp, *J. Chem. Soc.*, **1956**, 725 (1956).
- J. S. White, *Mineral Rec.*, **1**, 75 (1970).
- M. I. Gillibrand and B. Halliwell, *J. Inorg. Nucl. Chem.*, **34**, 1143 (1972).
- H. Harada, Y. Sasa, and M. Uda, *J. Appl. Crystallogr.*, **14**, 141 (1981).
- D. C. Constable, J. R. Gardner, J. A. Hamilton, K. Harris, R. J. Hill, D. A. J. Rand, S. Swan, and L. B. Zalzman, ILZRO Project no. LE-290, Progress Report 6 (1982).
- N. Schönberg, *Acta Chem. Scand.*, **8**, 240 (1954).
- K. V. Krishna Rao, S. V. Naidu, and L. Ivengar, *J. Phys. Soc. Jpn.*, **23**, 1380 (1967).
- R. D. Shannon, *Solid State Commun.*, **6**, 139 (1968).
- D. B. Rogers, R. D. Shannon, A. W. Sleight, and J. L. Gillson, *Inorg. Chem.*, **8**, 841 (1969).
- C. E. Boman, *Acta Chem. Scand.*, **24**, 116, 123 (1970).
- S. C. Abrahams and J. L. Bernstein, *J. Chem. Phys.*, **55**, 3206 (1971).
- W. H. Baur and A. A. Kahn, *Acta Crystallogr.*, **B27**, 2133 (1971).
- P. Porta, M. Marezio, J. P. Remeika, and P. D. Dernier, *Mater. Res. Bull.*, **7**, 157, 355 (1972).
- W. H. Baur, *Acta Crystallogr.*, **B32**, 2200 (1976).
- R. J. Hill, M. D. Newton, and G. V. Gibbs, *J. Solid State Chem.*, **47**, 185 (1983).
- R. D. Shannon, *Acta Crystallogr.*, **A32**, 751 (1976).
- M. Primet, P. Pichat, and M. V. Mathieu, *J. Phys. Chem.*, **75**, 1216 (1971).
- S. Ikari, S. Yoshizawa, and S. Okada, *J. Electrochem. Soc. Jpn. (Eng. Transl.)*, **27**, E186 (1959).

Determination of the Reliability of Aerospace Ni-Cd Batteries from Survival Data on Cells Fabricated Between 1964 and 1977

A. S. Jordan * and T. D. O'Sullivan

AT&T Bell Laboratories, Murray Hill, New Jersey 07974

ABSTRACT

We have performed a reliability analysis on Ni-Cd cells manufactured between 1964 and 1977 and aged by NASA ("CRANE") in simulated low earth and geosynchronous orbits. Similar cells are used in the construction of Ni-Cd batteries that serve as the energy storage medium in communications satellites. The statistical treatment of cell aging data conforms to techniques applied to semiconductor devices. In low earth orbit, the failure distribution by shorts is lognormal with standard deviation (s) of 1.06, median life (t_m) of 128,000h and activation energy of 0.29 eV. In geosynchronous orbit, the additional failure mode of capacity degradation leads to a bimodal lognormal distribution characterized by t_m of 283,000 and 122,000h and s of 1.14 and 0.27 for short and degradation, respectively. We have also deduced the probability of battery-survival and battery-failure rate, respectively. The inclusion of cell redundancy is a key feature of the analysis. It is shown that enhanced redundancy is a major factor in assuring long-term battery performance.

In view of the high initial cost and impossibility of repair at the present state of the art, no communication system requires a higher degree of long-term reliability than satellite communications. In geosynchronous orbit, the electronic system of transponders is powered by reliable solar cells at all times except during solar eclipses, when the energy storage system that frequently employs two rechargeable Ni-Cd batteries takes over. Each year, the satellite is exposed to two eclipse seasons, each lasting 44 days. During these seasons, the eclipse time varies from 4 to 70 min in a predictable manner. Then, unless the spacecraft's batteries deliver sufficient power above a specified voltage to the transponders, the operating loads must be reduced and the mission's objectives can only be partially met.

In general, solid-state devices, such as solar cells and transponders comprising semiconductor components (1), enjoy a greater reputation for reliability than batteries. Indeed, conventional Ni-Cd batteries exhibit a time-dependent decrease in voltage due to cell degradation as well as cell shorting (2). Since at present the batteries on geosynchronous satellites may well be the life limiting component (2), a study of their reliability is a vital prerequisite in guaranteeing a successful mission of, say, 10 yr duration. The most exhaustive source for life-test data on aerospace Ni-Cd batteries originates from the Naval Weapons Support Center, Weapons Quality Engineering Center at Crane, Indiana (CRANE) (3). The major objective of the current investigation is to determine by means of a large-scale statistical study the reliability of Ni-Cd cells and batteries tested by CRANE. Although these conventional cells are of an early vintage with respect to the date of design and manufacturing, it is considered that their statistical treatment would provide a "benchmark" to compare with more modern cell designs. Moreover, since the battery is but one component of the satellite's communication system, it is thought to be necessary to develop a technique of reliability analysis for batteries consistent with that for solid-state components on board.

Bearing in mind these objectives, in the first part of the paper we briefly describe the structure of conventional Ni-Cd cells and the aging experiments performed at CRANE to assess their reliability. Second, we present an outline of the statistical methodology employed to obtain the cumulative failure function for a large sample when the life testing of the survivors is occasionally terminated. Then, we determine the failure distribution for shorts in Ni-Cd cells aged at three temperatures and deduce the activation energy for the shorting process. In addition, for cells exercised in a simulated geosynchronous orbit, the data, which include both degradation failures and shorts, are analyzed.

At any time of service, the behavior of Ni-Cd cells is directly predictable from the parameters of the failure dis-

tribution. Subsequent, probabilistic reasoning combined with cell parameters leads to equations that forecast the long-term performance of the battery subsystem of any redundant configuration. The two measures of successful mission employed in the calculations are probability of battery survival and battery failure rate, the latter being a quantity preferred by designers of electronic systems. Finally, two alternatives are suggested to assure 10 yr of failure-free battery operation. These are (i) enhanced redundancy using conventional cells and/or (ii) longer median life, potentially achievable in improved designs.

Experimental Data

Ni-Cd cell and battery structure.—This investigation is restricted to the evaluation of reliability data on prismatic Ni-Cd cells (2, 3) manufactured by General Electric between 1964 and 1977. Though some of these cells on test are over a decade old, they are by and large similar to those in use today. The electrodes in these Ni-Cd cells are chemically deposited and have nylon separators; the electrolyte is KOH. The battery under consideration comprises a string of 32 cells, of which at least 29 or 30 must operate to deliver 29V, the minimum required in this realistic example for full power transponder operation. There are two identical batteries on board.

Aging program at CRANE.—The prismatic Ni-Cd cells made by General Electric (GE) were tested at CRANE (3). This facility has been running real-time tests for over 17 yr under NASA supervision. The data base to be treated here is extracted from the annual reports of CRANE. It should be emphasized at the outset that the CRANE testing program includes, besides prismatic cells, cylindrical cells, as well as products of manufacturers other than General Electric. In addition to real-time tests in both low earth and geosynchronous orbits, aging experiments were also performed under accelerated conditions such as different temperatures and charge/discharge rates. This paper focuses on the treatment of real-time data, modified only by moderate temperature acceleration, on prismatic GE cells.

Table I summarizes the total number of suitable cells tested at CRANE and the actual numbers acceptable in our statistical analysis, separated with respect to nominal capacity. The cells excluded were either exercised in a nonstandard orbit or tested only for a few hundred hours before termination. Moreover, some cells were disqualified because at several aging temperatures the sample size was too small to establish the failure distribution with a reasonable degree of confidence.

The cells were tested in groups of five held at the nominal aging temperatures 0°, 22.5°, and 40°C within less than ±2°C. Each pack of five had its own dc power supply for charging and discharging. In low earth orbit, cells at 0°, 22.5°, and 40°C were cycled every 1.5h at 15%, 25%, and

*Electrochemical Society Active Member.

Table I. Cells tested by CRANE and number used in analysis, by nominal capacity

Nominal capacity (Ah)	Total no. of cells	No. of cells used
6	220	128
8	20	20
12	229	148
20	61	48
26.5	10	0
40	10	0
50	12	0

40% depths of discharge. There was essentially continuous monitoring for shorts, detected by a precipitous drop in voltage.

The second mode of orbit simulation is the geosynchronous one, which virtually imitates the operation of a communication satellite. During the two eclipse seasons, each lasting 44 days, the cells were repeatedly charged and discharged for the appropriate length of time, which was controlled by a computer. Aging tests were conducted at 40%, 60%, and 80% depths of discharge, and at 0° and 22.5°C. As was the case in low earth simulations, the shorts were automatically recorded. In addition, the cells exercised in geosynchronous orbit were completely discharged to reveal their remaining capacity. In this manner, the time dependence of the degradation in actual average capacity for a pack of five cells could be determined. It should be emphasized that with the small degree of cell redundancy in series (29 or 30 from 32 must function) feasible on some spacecraft, each cell must retain at least 60% (7.2 Ah) of its nominal capacity (12 Ah) to a 1V cutoff per cell, because otherwise the voltage delivered to the transponders is insufficient for full-power operations. The fraction 7.2 Ah/12 Ah is the nominal depth of discharge. If actual capacities were used, it becomes 7.2 Ah/16.7 Ah = 43%, where 16.7 Ah is the average initial capacity taken from the CRANE data. Any cell can be treated by this method as long as the actual capacity is known.

Statistical Methodology

Previous reliability assessments based on the CRANE data base concentrated exclusively on accelerated tests, especially with regard to charge/discharge rates and depth of discharge. For example, Fedors *et al.* (5) applied the Griffith theory of crack formation in solids to construct a fractional order reaction-rate model of "flaw" propagation in cells to describe failure due to degradation. In contrast, when dealing with real-time aging of cells, one has to consider shorts and degradation. By invoking the well-known lognormal probability distribution to account for both modes, we intend to treat the experimental results in a unified manner. Furthermore, a key feature of our technique is the consistent analysis of failed and terminated cells. Clearly, on the relatively short time-scale of accelerated testing the need to discontinue is reduced.

Life testing of components, such as cells and semiconductor devices, serves two important interrelated functions. One purpose is to unravel, if possible, the major failure mechanisms. The other objective is to lay the experimental foundation for predicting and assuring reliability in operating systems. It has been previously shown that without a large sample size the forecasting of future behavior with a high degree of confidence is impossible (6). Therefore, in analyzing the aging data on shorts from CRANE, an extended sample had to be constructed. In doing so, though, we paid particular attention to unique features of the testing procedure.

Cells were put on test in packs of five at different times. When rack space was needed, experiments were discontinued before all cells in the pack failed. Since shorts represent catastrophic events without a forewarning or precursor, no information can be derived about the time to failure of the terminated survivors. Hence, the statistical treatment employed in describing

the failure distribution must be such that it allows (i) the combination of the testing results on many packs with cells of common characteristics regardless of chronology and (ii) taking into account the removal of operating survivors. Similar conditions have been encountered in the acquisition and analysis of burn-out failure of GaAs power FET's (4). Moreover, appropriate precedents for the necessary statistical reasoning are available, for instance, from medically oriented investigations. Therefore, a brief outline of the technique used to construct the failure distribution for shorts will be sufficient.

In the absence of terminations the cumulative failure function (CFF) corresponding to a given time to failure is usually obtained by evaluating the so-called plotting points (6). If the initial number of cells in the sample is N , and at any time between t_{j-1} and t_j , the number of failed cells is d_j , then at $t_p \geq t_j$ the simplest choice of plotting positions for the CFF is

$$\text{CFF}(t_p) = \sum_{j=1}^p \frac{d_j}{N+1} \quad [1a]$$

The reliability function (7) $R(t_p)$, is then given by

$$R(t_p) = \frac{N - \sum_{j=1}^p d_j + 1}{N+1} \quad [1b]$$

where putting $N+1$ instead of N in the denominator prevents the CFF ever reaching unity, a value that cannot be accommodated in probability plotting.

If, however, at time t_j , r_j cells are removed prior to failure, the above procedure must be altered. Kaplan and Meier were among the first to formulate and solve the problem of the distribution of survival times when completing the measurements is either inconvenient or impossible (8). A maximum likelihood estimate of the survival probability was derived, which can be interpreted by the following appeal to intuition: suppose after 2 yr of testing a group of ten cells, two of them short, and after an additional year one more of the eight survivors fails. Then, imagine another group of five cells, of which one shorts after 2 yr and the remaining four are immediately terminated. The probability of survival or reliability at two years for the joint sample, R_j , is

$$R_j(2) = \frac{12}{15} = 0.80$$

To obtain the reliability of 3 yr $R_j(3)$, one first estimates the conditional probability for 3 yr given survival for 2 yr. Based on the first sample, we find

$$\frac{R(3)}{R(2)} = \frac{8-1}{8} = 0.875$$

Hence, we can write

$$R_j(3) = \frac{R(3)}{R(2)} R_j(2) = 0.70$$

The generalized result of Kaplan and Meier (8) is in the form of the following chain rule

$$R(t_p) = \frac{N_1 - d_1}{N_1} \times \frac{N_2 - d_2}{N_2} \times \frac{N_3 - d_3}{N_3} \times \dots \times \frac{N_p - d_p}{N_p} \quad [2]$$

However, in order to be consistent with Eq. [1b], Herd's version of Eq. [2], where unity is added to both numerator and denominator, was chosen (9, 10). Accordingly, the reliability function and CFF which take into account failures as well as removals are of the form

$$R(t_p) = \prod_{j=1}^p \frac{N_j - d_j + 1}{N_j + 1} \quad [3a]$$

$$\text{CFF} = 1 - R(t_p) \quad [3b]$$

where

$$N_j = N - \sum_{i=0}^{j-1} (d_i + r_i)$$

In general, initially $d_0 = 0$; thus after some algebra it can be shown that if there are no terminations Eq. [3] reduce to Eq. [1].

Results

Failure distribution in low earth orbit.—The CRANE data for shorts on conventional Ni-Cd cells aged in a simulated low earth orbit at 0°, 22.5°, and 40°C were analyzed by means of Eq. [3]. In order to avoid statistical uncertainties due to a reduced sample size, no subdivision with respect to nominal capacity was introduced. In Fig. 1, 2, and 3, we have plotted on lognormal graph paper the time to induce a short at 0°, 22.5°, 40°C, respectively. At each of these temperatures, the course of the data points suggests that the failure distribution for shorts is approximately lognormal (7). By least squares treatment (7), we obtained the best values for the median lives, t_m , and standard deviations, s , which are listed in Table II. The fact that the correlation coefficients (see Table II) are above 0.97 at all temperatures is an indication of the reasonableness of the lognormal failure model for shorts. However, some scatter can be discerned among the standard deviations. But, when their upper and lower limits for the population at the 90% confidence level (7) are compared, a considerable overlap is observed, implying that a common, nearly temperature-independent standard deviation characterizes the distribution.

In order to improve the precision of the calculations by using a larger data base and to determine the activation energy for shorts, we have reduced the results at 40° and 22.5° to 0°C and combined them with the actual data at 0°C. In this fashion, the scatter due to sample size seen at the separate temperatures is minimized. The higher temperature times to failure were adjusted by an acceleration factor based on the Arrhenius law but with a variable activation energy, E_a . Then, the joint sample was repeatedly treated by means of Eq. [3] and that E_a was finally accepted, which led to the smallest root-mean-square difference between the median lives at given aging temperatures (see Table II) and the ones

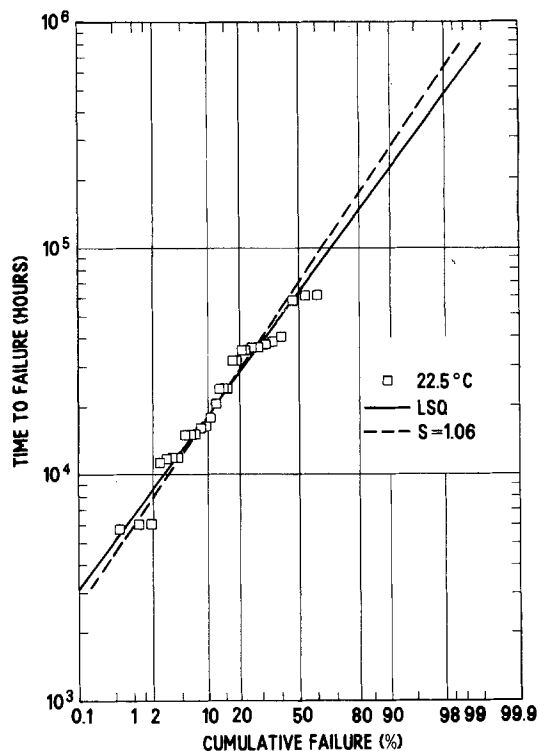


Fig. 2. The lognormal projection of time to failure by shorts as a function of cumulative failure percentage for Ni-Cd cells aged in low earth orbit at 22.5°C. The solid line was computed from the appropriate least squares estimates listed in Table II. The dashed line is based on a single parameter linear regression, taking $s = 1.06$ from that of the combined sample.

projected to the same temperatures from the median life determined for the total combination at 0°C. In this manner, an E_a of 0.29 eV was evaluated, which corresponds to a root-mean-square difference of 5323h.

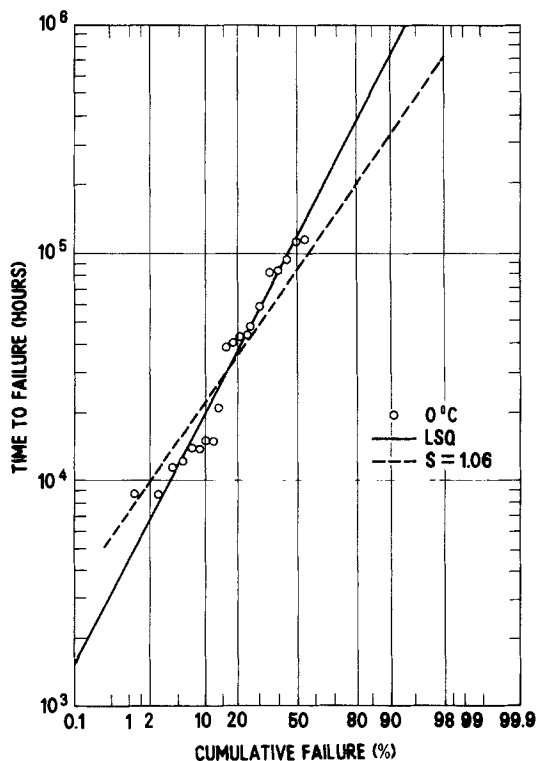


Fig. 1. The lognormal projection of time to failure by shorts as a function of cumulative failure percentage for Ni-Cd cells aged in low earth orbit at 0°C. The solid line was computed from the appropriate least squares estimates listed in Table II. The dashed line is based on a single parameter linear regression, taking $s = 1.06$ from that of the combined sample.

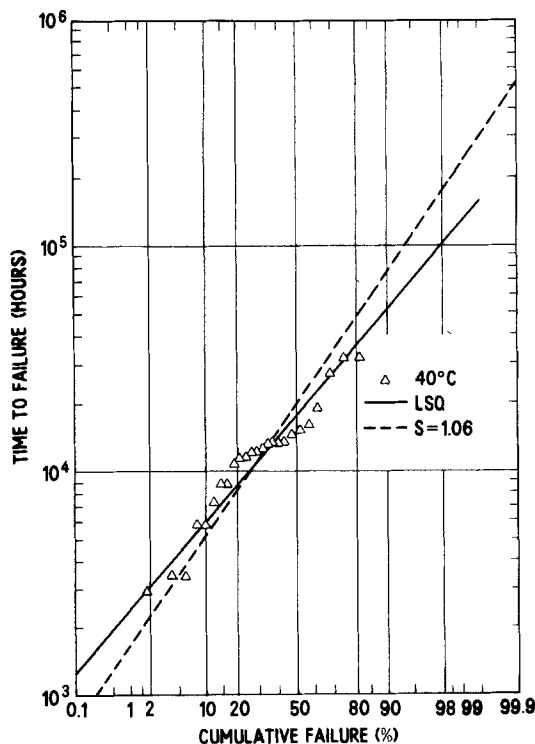


Fig. 3. The lognormal projection of time to failure by shorts as a function of cumulative failure percentage for Ni-Cd cells aged in low earth orbit at 40°C. The solid line was computed from the appropriate least squares estimates listed in Table II. The dashed line is based on a single parameter linear regression, taking $s = 1.06$ from that of the combined sample.

Table II. Lognormal parameters for Ni-Cd cells in low earth orbit

Temp (°C)	Shorted cells							Correlation coefficient
	Total no. of cells	t_{mpu} (h)	t_m	t_{mpi}	σ_u	s	σ_l	
40	25/50	22,960	17,770	13,740	1.06	0.86	0.72	0.9701
22.5	29/171	77,420	63,740	52,500	1.16	0.98	0.85	0.9799
0	20/83	181,570	123,660	83,700	1.74	1.42	1.20	0.9722
0 [combined sample]	74/304	148,020	127,640	110,120	1.16	1.06	0.98	0.9833

Confidence level = 90%.

In Fig. 4, we present the time to failure by shorts *vs.* CFF for the joint sample at 0°C. The improved description of the failure data by means of the lognormal distribution is immediately obvious when the total sample is used. Further support for this qualitative viewpoint is found in comparing the increase in the correlation coefficient (0.983) with the average value of the coefficients at the different aging temperatures (0.974). In addition, by blending the data using 0.29 eV, temperature-dependent clustering could be avoided. We have observed such clustering at large assigned activation energies.

In Table II, we have also listed the lognormal parameters and confidence limits of the joint sample. Concentrating on the standard deviation, we find that there is a good overlap between the bounds for the combined sample and those observed at the different aging temperatures. A marginal discrepancy of 0.04 standard deviation units exists between the lower limit of the 0°C sample and the upper limit of the combined one. To be sure, one may attach significance to the apparent temperature-dependent variation in s values in Table II. Without more aging data, this is not statistically warranted for the error bounds were taken at the 90% confidence level. At the 95% level, the overlap becomes acceptable. That the standard deviation of 1.06 obtained for the total sample is satisfactory to describe the data at all three temperatures is demonstrated in Fig. 1, 2, and 3, where the dashed lines represent least squares lines with a fixed slope ($s = 1.06$) and variable intercepts.

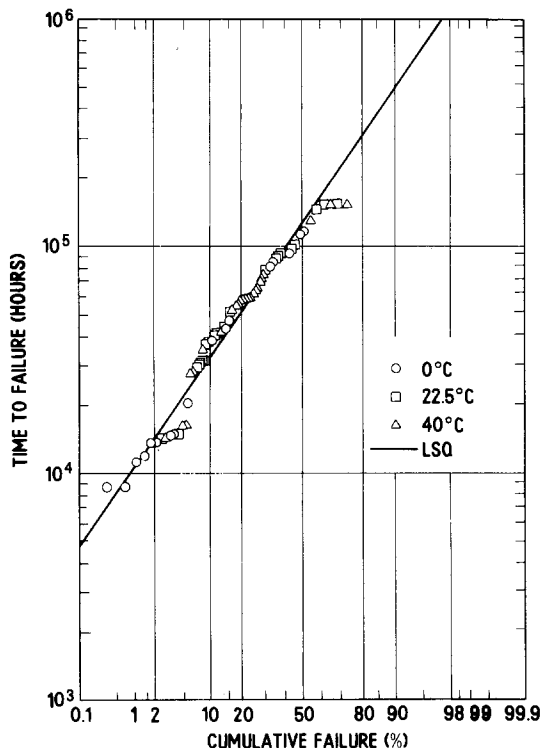


Fig. 4. The lognormal projection of time to failure by shorts as a function of cumulative failure percentage for Ni-Cd cells aged in low earth orbit at 0°, 22.5°, and 40°C. Before combination of the total data, the high temperature values were reduced to 0°C using an activation energy of 0.29 eV (see text). The solid line was computed from the appropriate least squares estimates in Table II.

Taking into account the confidence limits, in Fig. 5 we show on an Arrhenius plot that the combined data base in conjunction with the 0.29 eV activation energy provides temperature-dependent median lives consistent with the median lives determined at separate aging temperatures.¹ Therefore, to predict the behavior of conventional Ni-Cd cells operating in low earth orbit which fail predominantly by shorts, we recommend the use of lognormal parameters obtained by treating the total sample reduced to 0°C.

Failure distribution in geosynchronous orbit.—As we have already established, employing the extended data base, that the failure distribution for shorts of conventional Ni-Cd cells exercised in low earth orbit is lognormal, the proposition that cells aged in simulated geosynchronous orbit behave similarly is eminently plausible. Following the previously used computational techniques, we have analyzed the meager CRANE data for shorts arising in geosynchronous orbit (3) and plotted the results in the usual lognormal projection in Fig. 6. The results of the least squares regression for the parameters (7) are listed in Table III. Due to the limited sample size, the evidence for lognormality is not as strong here as in low earth orbit. This is indicated by inspection of the data in Fig. 6, and corroborated by the magnitude of the correlation coefficient. The noteworthy features of the derived parameters are the significant enhancement of t_m in geosynchronous orbit and the gratifying insensitivity of s to the test conditions (1.14 *vs.* 1.06).

In addition to shorts, cells in geosynchronous orbit also exhibited time-dependent degradation in their capacity. Since the degradation process is not catastrophic, the time to failure could be estimated, and thus there is no need in this case to invoke the analysis developed for sudden failure with terminations. Hence, Eq. [1a] and [1b] can be directly used in treating degradation data.

¹Treating the discrete median lives by a conventional least squares technique would give equal weight to each of the three temperatures and not to each failure. The corresponding E_a is 0.34 ± 0.05 eV, which is in reasonable accord with the preferred value of 0.29 eV.

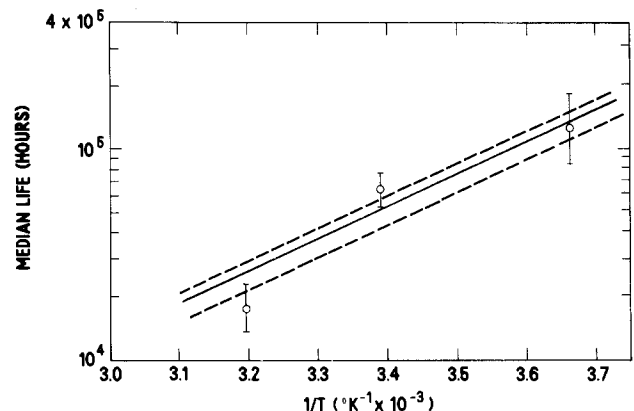


Fig. 5. Logarithm of median life *vs.* reciprocal aging temperature for shorts of Ni-Cd cells aged in low earth orbit (Arrhenius plot). The solid line is based on the t_m of the total sample and $E_a = 0.29$ eV. The discrete points are the median lives obtained at the different aging temperatures and listed in Table II. The error bars and the dashed lines represent the confidence limits on t_m at the 90% confidence level.

Table III. Lognormal parameters for Ni-Cd cells in geosynchronous orbit

Failure mode	Failed cells		t_{mpu} (h)	t_m	t_{mpi}	σ_u	s	σ_1	Correlation coefficient
	Total no. of cells								
Shorts	9/40		439,810	283,400	182,530	1.57	1.14	0.91	0.9184
Capacity degradation	29/29		132,640	122,280	112,690	0.35	0.27	0.22	0.9694

Avg. temp: 11°C.
Confidence level = 90%.

From the CRANE data collection, the variation of the average capacity with time could be extracted for packs of five cells. Due to the meager data base, no temperature-dependent trends were observed between capacity degradation tests conducted at 0° and 22.5°C. In full operation, the design of the transponders on the spacecraft demand at least 60% of the rated capacity (12 Ah) of any cell or 7.2 Ah. As mentioned earlier, in view of the fact that the actual initial capacity of the cells was well above the rated one, namely, averaging 16.7 Ah, the time to failure by degradation was defined as the time at which the capacity is depleted to 43% of its original value. In cases when the time to failure had not yet been reached, a linear extrapolation of the degradation data was employed. This can be generalized for any spacecraft, since the power required is known and the actual capacity of the cells can be measured.

In Fig. 6, we present the time to failure by degradation as a function of CFF in lognormal projection. The number of cells plotted at a given time indicates the cells surviving in a pack of five, i.e., not removed on account of shorts or other defects. The least squares line through the data, together with the relatively high correlation coefficient, suggests that the lognormal distribution provides a good description of capacity degradation failure in Ni-Cd cells. Compared to the failure by shorts, there is a significant reduction in t_m and s in the case of the degradation process. Nevertheless, as is shown later, when redundancy on the spacecraft is taken into account, shorting is much more likely to cause battery failure than degradation. Summing up, Ni-Cd cells aged in

simulated geosynchronous orbits demonstrate a bimodal lognormal distribution, initially by shorts, and then by capacity degradation.

Discussion

Comparison with field experience.—Telemetric information received from Intelsat IV, a communication satellite managed by Comsat, indicates shorts in three cells from a total of 150, the last failure occurring at 6.7 years (2). Evidently, one cannot perform credible statistical analysis on three data points, especially when the largest CFF is only 2%. Nonetheless, linear extrapolation of $\log t$ vs. CFF at $s = 1.1$ yields $t \approx 600,000$ h with at least $\pm 300,000$ h uncertainty. This estimated median life in the field shows a considerable overlap with the one obtained from the CRANE results for shorts aged under geosynchronous conditions (see Table III). Therefore, we conclude that with regard to shorts the long-term behavior in a simulated geosynchronous orbit is in no apparent conflict with actual operating experience on board a spacecraft.

Probability of survival and failure rate of a battery.—For a systems designer, perhaps the most important information involving component reliability is its failure rate (4, 7, 10). At any service life, t , the instantaneous failure rate, $f(t)$, can be calculated from the defining equation

$$f(t) = -\frac{d \ln R}{dt} \quad [4]$$

which in the case of the lognormal distribution is of the form (7)

$$f(t) = \frac{\sqrt{2} \exp\left[-\frac{1}{2s^2} (\ln t/t_m)^2\right]}{\sqrt{\pi}ts \operatorname{erfc} \frac{1}{\sqrt{2}s} \ln t/t_m} \quad [5]$$

In Fig. 7, we have plotted $f(t)$ as a function of service life for cells using $s = 1.1$ and parametrizing t_m between 300,000 and 800,000h. It can be seen that beyond 7 yr of service t_m must be at least 500,000h if it is desired to keep f below 1000 FIT's (1 FIT is defined as one failure in 10^6 h), a value easily surpassed by semiconductor components (1) which may be parts of a transponder.

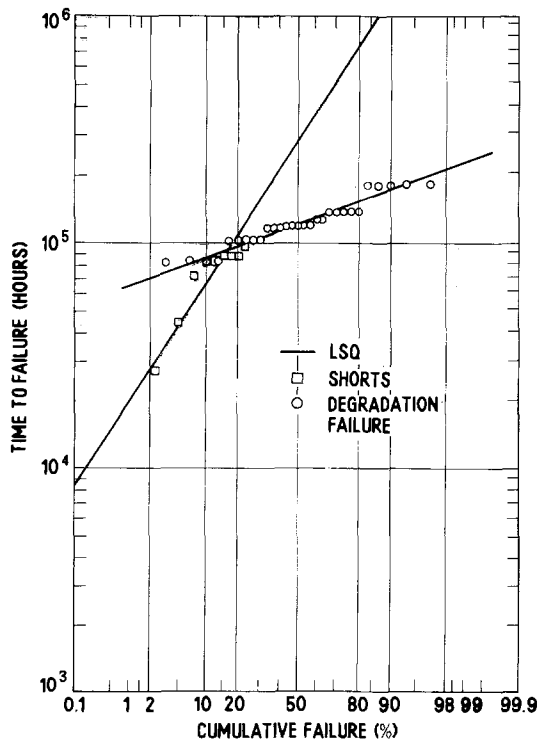


Fig. 6. The lognormal projection of time to failure by shorts and capacity degradation as a function of cumulative failure percentage for Ni-Cd cells aged in geosynchronous orbit. The solid lines were computed from the appropriate least squares parameters listed in Table III.

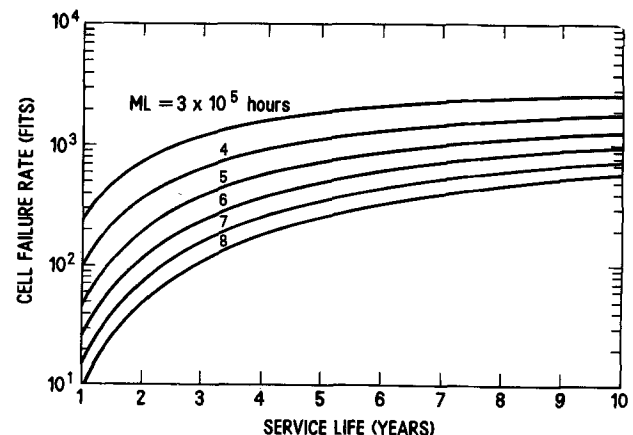


Fig. 7. The failure rate for shorts in Ni-Cd cells as a function of service life. The lines were computed from Eq. [5] using a standard deviation of 1.1.

As mentioned earlier, the Ni-Cd battery in reality is a subsystem comprising a fixed number of cells, most of which must be functional at the end of mission to achieve completely successful transponder operations. If the total number of identical cells in a battery is n and at least m cells provide failure-free performance at time, t , with reliability, R , then the probability of subsystem survival, R_s , can be directly obtained from the binomial distribution in the form (10)

$$R_s(x \geq m, n, t) = \sum_{x=m}^n \frac{n!}{x!(n-x)!} [R(t)]^x [1 - R(t)]^{n-x} \quad [6]$$

A typical Ni-Cd battery in a satellite is designed as a string containing, for example, $n = 32$ cells; $m = 30$ or perhaps 29 of these must deliver voltage to the transponders at 10 yr of service. We can conceive $\delta = (n - m)/(n - 1)$ as the degree of redundancy. On the one hand, if $n = m$, then $\delta = 0$ and the design is nonredundant; on the other hand, if $m = 1$, then $\delta = 1$, which is the ultimate in safety. An increase in δ is accompanied by an increase in R_s .

To evaluate the battery failure rate, f_s , from the cell failure rate, we apply the chain rule of differentiation to the general expression equivalent to Eq. [4]. Accordingly

$$f_s(t) = \frac{-d \ln R_s}{dt} = - \frac{d \ln R_s}{dR_s} \frac{dR_s}{dR} \frac{dR}{dt} \quad [7]$$

Substituting the cell failure rate f into Eq. [7], we have

$$f_s(t) = \frac{R}{R_s} \frac{dR_s}{dR} f(t) \quad [8]$$

Performing the differentiation required by Eq. [8] on Eq. [6] provides the battery failure rate in terms of $f(t)$ as

$$f_s(t) = \frac{f(t)}{R_s} \sum_{x=m}^n \frac{n!}{x!(n-x)!} \{x[R(t)]^x [1 - R(t)]^{n-x} - (n-x)[R(t)]^{x+1} [1 - R(t)]^{n-x-1}\} \quad [9]$$

where $f(t)$ and R_s are given by Eq. [5] and [6], respectively.

Clearly, if the lognormal distribution holds and the Arrhenius law is obeyed the method developed herein should be useful in the extrapolation of temperature-accelerated data. However, it provides no guide in relating tests with accelerated charge/discharge rates to real-time results.

Long-term performance of Ni-Cd batteries.—In Fig. 8 and 9, we present the survival probability (Eq. [6]) and failure rate (Eq. [9]) of a Ni-Cd battery as a function of service life. Since in geosynchronous orbit the failure distribution for cells is bimodal, reflecting shorts as well as degradation, the calculations for a battery take into account both mechanisms. The respective standard deviations for shorts and degradation are rounded to 1.1 and 0.3, in accord with the values listed in Table III. For shorts, t_m is a parameter incremented in 100,000h steps between 300,000 and 800,000h, while it is postulated that t_m for degradation is an invariant fraction of that for shorts. Based on Table III, the ratio of t_m 's between shorts and degradation is ~ 2.4 . The assumption invoked implies that any improvement in eliminating shorts as a cause of failure will also lead to a proportionate reduction in degradation. One can observe in Fig. 8 and 9 that capacity degradation is of no concern above a median life of 400,000h.

If one wants to assure the probability of battery survival at no less than 90%, then from Fig. 8, employing the CRANE geosynchronous results ($t_m \approx 300,000$ h), we find the longest allowable service lives of 4.7 and 7.2 yr, respectively, for $m = 30/n = 32$ and 28/32 configurations. To be on the safe side, at 10 yr the 30/32 and 28/32 configurations require median lives of 650,000 and 425,000h, respectively. Clearly, a small increase in the degree of redundancy, δ , extends assured service life more effectively than a minor design-related improvement in t_m . Indeed,

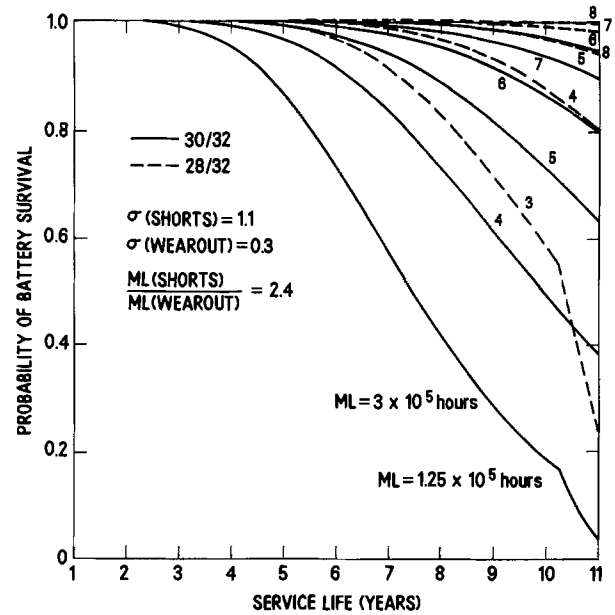


Fig. 8. Probability of Ni-Cd battery survival as a function of service life and cell redundancy. The curves were calculated from Eq. [6]. Probability for both shorts and degradation are shown. Each one of the lines is labeled by the cell median life for shorts and degradation, where applicable; the cell standard deviation is 1.1 and 0.3 for shorts and degradation failures, respectively.

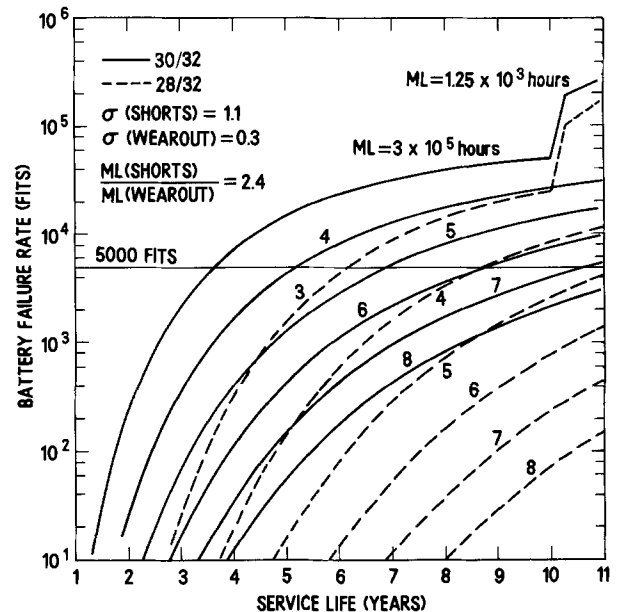


Fig. 9. Failure rate for Ni-Cd battery as a function of service life and cell redundancy. The curves were calculated from Eq. [9]. Failure rates for both shorts and degradation are shown. Each one of the lines is labeled by the cell median life for shorts and degradation, where applicable; the cell standard deviation is 1.1 and 0.3 for shorts and degradation failures, respectively.

the conventional cells tested at CRANE would be acceptable if a δ corresponding to 30/36 were permissible. To be sure, overall weight limitations on a spacecraft make this an unrealistic option for the present generation.

An examination of the battery failure rate reinforces the previous conclusions. Conservatively, we selected 5000 FIT's as the largest permissible failure rate.² This is not quite arbitrary for $f_s = 5000$ FIT's implies one battery failure per 20 yr of service, which seems safe, as it is at least twice the life expectancy of current communications satellites. The cells in the CRANE compilation guarantee battery failure rates in geosynchronous orbit below 5000

²This translates into a survival probability of slightly over 90%.

FIT's at service lives less than 3.6 and 6.2 hr for 30/32 and 28/32 configurations, respectively. Again, without excess redundancy (30/32), t_m of ~650,000h is necessary, while for a more redundant design (28/32), t_m ~450,000 would be sufficient at 10 yr of service. Of course, perhaps we have a low estimate for t_m , and its true population value may be near the upper limit given in Table III (~440,000h). Consequently, a battery service life over 6 yr could be assured in the standard (30/32) configuration. Nonetheless, one should not infer that Ni-Cd cells in the 30/32 mode do not perform satisfactorily at 10 yr of service because the state of the art in cell fabrication has advanced beyond the technology of the 1964-1977 period.

Acknowledgments

This paper is respectfully dedicated to the memory of James W. Nielsen.

We are grateful to D. W. Maurer and the late J. W. Nielsen for their interest in this work and for a critical reading of the paper. We also appreciate helpful suggestions by W. B. Grupen and J. V. DiLorenzo in the preparation of the manuscript.

Manuscript submitted Sept. 15, 1983; revised manuscript received Feb. 10, 1984. This was Paper 863 RNP presented at the San Francisco, California, Meeting of the Society, May 8-13, 1983.

AT&T Bell Laboratories assisted in meeting the publication costs of this article.

REFERENCES

1. H. Fukui, S. H. Wemple, J. C. Irvin, W. C. Niehaus, J. C. M. Hwang, H. M. Cox, W. O. Schlosser, and J. V. DiLorenzo, in "18th Annual Proceedings on Reliability Physics (IEEE)," p. 151, IEEE, New York (1980).
2. J. D. Dunlop, M. W. Earl, F. W. Weber, and D. B. Cooper, in "Proceedings of the 28th Power Sources Conference," Atlantic City, NJ, June 12-15, 1978, The Electrochemical Society, Inc., p. 113 (1979).
3. J. D. Harkness *et al.*, "17th Annual Report of Cycle Life Test," NAVWPNSUPPCEN Crane Document no. WQEC/C 81-1 (1981); J. D. Harkness *et al.*, "Synchronous Orbit Testing of Sealed Ni-Cd Cells," NAVWPNSUPPCEN Crane Document no WQEC/C 77-134 (1977); J. D. Harkness, Personal communication.
4. A. S. Jordan, J. C. Irvin, and W. O. Schlosser, in "18th Annual Proceedings on Reliability Physics (IEEE)," p. 123, IEEE, New York (1980).
5. R. F. Fedors, M. Cizmecioglu, S. D. Hong, A. Gupta, and J. Moacanin, Abstract 122, p. 331, The Electrochemical Society Extended Abstracts, Vol. 80-2, Hollywood, FL, Oct. 5-10, 1980; *J. Power Sources*, **8**, 369 (1982).
6. M. O. Locks, "Reliability, Maintainability, and Availability Assessment," Hayden Book Co., Rochelle Park, NJ (1973).
7. A. S. Jordan, *Microelectron. Reliab.*, **18**, 267 (1978).
8. E. L. Kaplan and P. Meier, *J. Am. Stat. Assoc.*, **53**, 457 (1958).
9. G. R. Herd, in "Proceedings of the 6th National Symposium on Reliability and Quality Control," p. 217 (1960).
10. W. H. Von Alven, Editor, "Reliability Engineering," ARINC Research Corp., Prentice Hall, Englewood Cliffs, NJ (1965).

Electrochemical Behavior of Solid Cathode Materials in Organic Electrolyte Lithium Batteries: Copper Sulfides

F. Bonino, M. Lazzari, and B. Rivolta

Dipartimento di Chimica Fisica Applicata, Polytechnic of Milan, Milan, Italy

B. Scrosati*

Dipartimento di Chimica, University of Rome, Rome, Italy

ABSTRACT

The characteristics of copper sulfide cathodes have been evaluated in typical organic electrolyte lithium batteries. The behavior of α -Cu₂S (chalcocite), Cu_{1.76}S (digenite), and CuS (covellite) is discussed in terms of mechanism of reaction, discharge properties, and energy content. In view of possible use in primary, voltage-compatible lithium batteries, Cu₂S shows the most interesting performance, both in terms of constancy of the operational voltage and in terms of discharge rates.

Within a research program on the relationship between electrochemical behavior and structure of solid materials which can be used as cathodes in primary and secondary lithium organic electrolyte batteries (1-5), the following copper sulfides have been studied in this work: α -Cu₂S (chalcocite), Cu_{1.76}S (digenite), and CuS (covellite).

The behavior of these materials has been examined by determining the mechanism of the electrochemical reaction, the discharge properties, and the energy content.

Experimental

The copper sulfides have been synthesized from the elements using powdered Cu and S (reagent grade chemicals, dried under vacuum prior to use).

Chalcocite, α -Cu₂S, has been prepared in a two-compartment glass envelope. The two starting elements, *e.g.*, Cu and S, were separately placed in each compartment. After sealing under vacuum, the envelope was heated,

*Electrochemical Society Active Member.

maintaining the Cu compartment at 475°C and the S compartment at 350°C, respectively. After annealing for two days, the envelope was cooled still keeping a temperature gradient between the two compartments.

Digenite, Cu_{1.76}S, has been prepared by heating in air a compressed pellet of a Cu-S mixture (with a slight excess of S). Covellite, CuS, has been obtained by annealing a stoichiometric amount of Cu and S in an evacuated glass ampul for six days at 480°C.

The structure of the final compound was in all cases controlled and characterized by x-ray analysis.

The solvents used, *e.g.*, propylene carbonate (PC) and γ -butyrolactone (BL), pure commercial products, were further purified by fractional distillation. All the lithium salts, *e.g.*, LiClO₄, LiAsF₆, and LiCF₃SO₃ were reagent grade chemicals.

Typical two electrode, button-type laboratory cells were used for the discharge tests. The structure of these cells has been described previously (2, 4, 5).

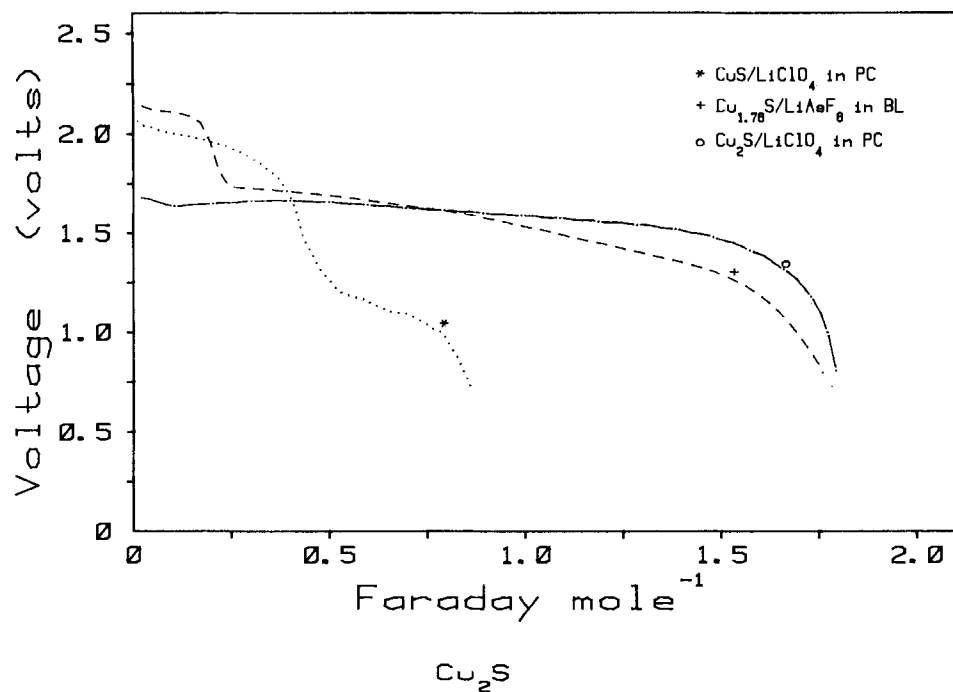


Fig. 1. Typical discharge curves at 0.5 mA/cm² of lithium organic electrolyte cells with CuS, Cu_{1.76}S, and Cu₂S, respectively, cathodes.

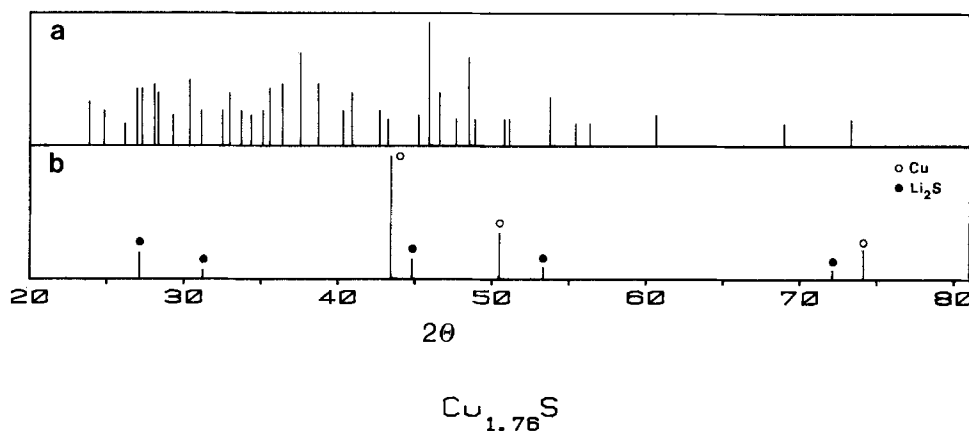


Fig. 2. X-ray spectra of the Cu₂S cathodic material before (a) and after (b) discharge in a lithium organic electrolyte cell (CuKα).

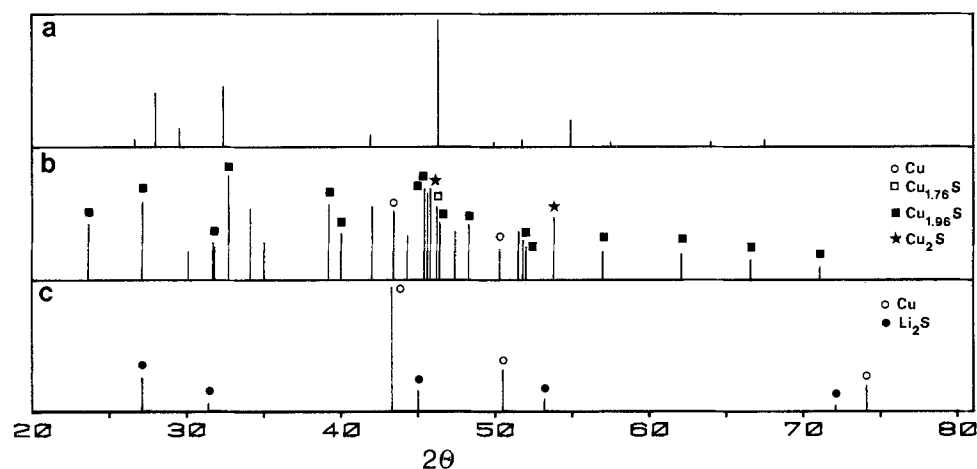


Fig. 3. X-ray spectra of the Cu_{1.76}S cathodic material before discharge (a), after 0.25 F/mol discharge (b), and at the end of the discharge (c) in a lithium organic electrolyte cell (CuKα).

The discharge curves and cell characteristics were controlled and analyzed by a computer system on line with the potentiostat.

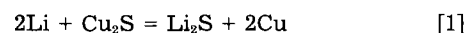
Results and Discussion

Typical 0.5 mA/cm² constant current discharge curves of lithium organic electrolyte cells using the three copper sulfide cathodes are shown in Fig. 1.

The reduction of Cu₂S is a single process consuming 2F/mol of sulfide. After the complete discharge, the cathodic mass was analyzed by x-rays.

The spectrum, reported in Fig. 2b, revealed only the presence of metallic copper and of lithium sulfide. Comparison with the spectrum of the starting Cu₂S, shown in Fig. 2a, indicates that the electrochemical reaction had proceeded to completion.

The discharge reaction of the Li/Cu₂S cell may then be safely identified as



The formation of copper during discharge is a favorable event. The metal gives the cathodic mass sufficient elec-

CuS

Fig. 4. X-ray spectra of the CuS cathodic material before discharge (a), after 0.4 F/mol discharge (b), and at the end of the discharge (c), in a lithium organic electrolyte cell (CuK α).

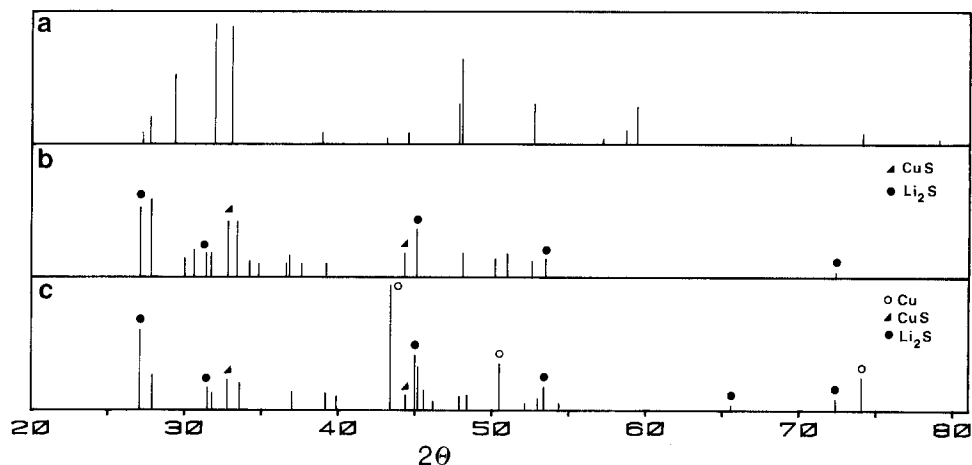
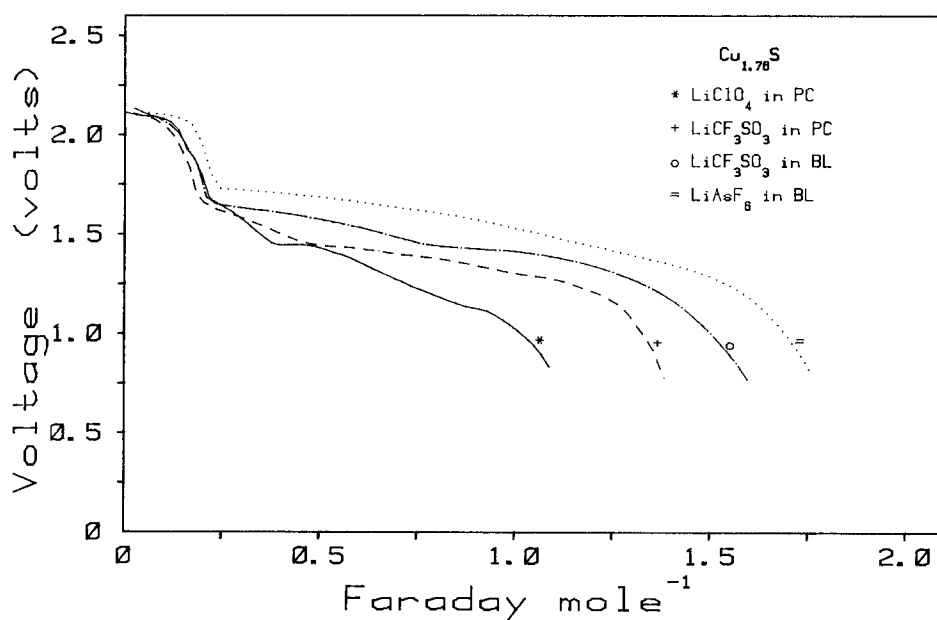


Fig. 5. Typical discharge curves at 0.5 mA/cm² of the Li/Cu_{1.76}S couple in various electrolytes.

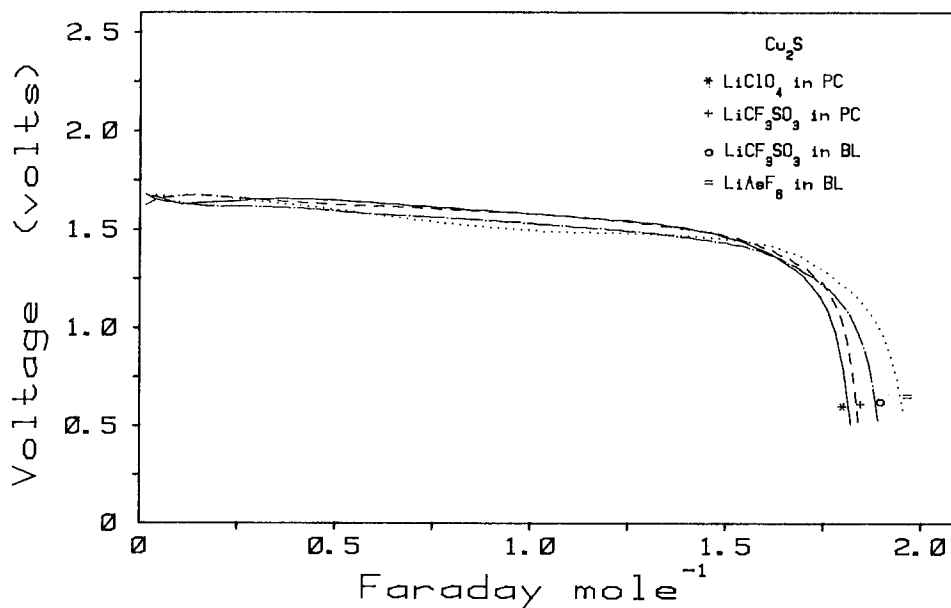


tronic conductivity to be used without additives (such as graphite), and this is beneficial in terms of overall energy density. Furthermore, the exceptionally flat discharge curve shown in Fig. 1 is a direct result of the production

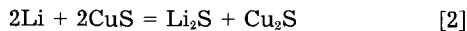
of finely dispersed copper which keeps the resistance of the cathodic mass low throughout cell life.

Digenite, Cu_{1.76}S, shows a more complex, two-stage discharge process. The first starting at 2.1V (vs. Li) and

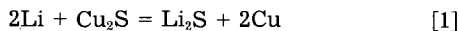
Fig. 6. Typical discharge curves at 0.5 mA/cm² of the Li/Cu₂S couple in various electrolytes.



about 0.25 F/mol deep, and the second starting at 1.6V (*vs.* Li) and up to about 1.8 F/mol (see Fig. 1). In an attempt to clarify the discharge mechanism, x-ray analyses were done on cathodic masses after a discharge of 0.25 F/mol and at the end of the discharge (Fig. 3). In the first case, a very complex spectrum was found in which all the reflections of the starting material ($\text{Cu}_{1.76}\text{S}$) had disappeared, indicating that radical structure modifications had followed the first reduction step. In contrast, at the end of the discharge, the spectrum was well defined and showed only the reflections of Cu and of Li_2S . Since digenite may be considered a solid solution of 20% CuS and 80% Cu_2S , the discharge data shown in Fig. 1 and the x-ray analysis suggest that the first stage of discharge was due to the reduction of the CuS fraction via the reaction



and the second was due to the reduction of the residual Cu_2S fraction via the reaction



Several experimental results confirm this hypothesis. They are: (i) Some reflections of Cu_2S could be identified in the complex x-ray spectrum after the first plateau (see Fig. 2). (ii) The coulombic ratio between the first plateau (0.25 F/mol) and the second plateau (1.55 F/mol) approaches the ratio between CuS (20%) and Cu_2S (80%) in the $\text{Cu}_{1.76}\text{S}$ compound (see Fig. 1). (iii) The second discharge plateau of the Li/ $\text{Cu}_{1.76}\text{S}$ cell approaches that of the Li/ Cu_2S cell (see Fig. 1).

As in the case of digenite, the discharge of covellite, CuS, also seems to follow a two-step route, with a first plateau around 2V (*vs.* Li) extending for 0.4 F/mol and a second at about 1.1V (*vs.* Li) extending for 0.9 F/mol. X-ray analyses at various discharge depths are shown in Fig. 4. At 0.4 F/mol, reflections of CuS, Cu_2S , and Li_2S are present while no reflections of Cu are observed (Fig. 4b). After complete discharge (0.9 F/mol), reflections of Cu, Li_2S , residual CuS, and several others including $\text{Cu}_{1.96}\text{S}$ and Cu_2S , could be identified (Fig. 4c). The mechanism of reduction is then very complex, as has been pointed out by Dampier (6) and by Gabano *et al.* (7), who originally investigated the characteristics of the Li/CuS couple in organic electrolyte cells.

The complexity of the discharge mechanism and the poor coulombic efficiency (see Fig. 1) suggest that CuS is not a very promising cathode material for lithium batteries. From this point of view, $\text{Cu}_{1.76}\text{S}$ and particularly

Table I. Characteristics of Li/ $\text{Cu}_{1.76}\text{S}$ and of Li/ Cu_2S , organic electrolyte batteries at room temperature

Current density (mA/cm ²)	Average voltage (V)	Depth of discharge (F/mol)	Specific capacity (Ah/kg)	Specific energy (Wh/kg)
$\text{Li}/\text{Cu}_{1.76}\text{S}$				
0.1	1.64	1.8	333	548
0.3	1.62	1.75	315	510
0.5	1.58	1.75	311	494
1.0	1.52	1.3	229	349
$\text{Li}/\text{Cu}_2\text{S}$				
0.1	1.62	1.9	313	508
0.3	1.61	1.9	309	497
0.5	1.57	1.8	295	462
1.0	1.54	1.7	280	431
2.0	1.49	1.4	220	327
4.0	1.42	1.1	189	268

Cu_2S show much more interesting performance. Therefore, this study has been concentrated on these two sulfides.

The influence of the electrolyte on the discharge characteristics of Li/ $\text{Cu}_{1.76}\text{S}$ and of Li/ Cu_2S cells is shown in Fig. 5 and 6, respectively, where discharge curves at 0.5 mA/cm² are compared in various electrolytes. For the Li/ $\text{Cu}_{1.76}\text{S}$ system, there are some differences between electrolytes with the LiAsF₆-BL electrolyte appearing to be the most efficient (Fig. 5). For the Li/ Cu_2S cell, all the electrolytes tested behaved satisfactorily (Fig. 6). Note the exceptional flatness of the discharge curves for the Li/ Cu_2S system at an operational voltage of about 1.5V.

The superior behavior of the Li/ Cu_2S cell is also confirmed by the results of Fig. 7 which illustrates the discharge behavior at various rates: the discharge curves remain flat even at very high current densities.

The discharge characteristics of the two copper sulfide cathodes examined in this study are summarized in Table I.

The values of the operational voltages and of the energy densities make these sulfides, and Cu_2S in particular, very promising cathodic materials for voltage compatible ambient temperature lithium batteries.

Finally, the reversibility of the electrochemical reaction in the Li/ Cu_2S system has been investigated in view of possible applications as a rechargeable system. Cu_2S discharged down to 1.5 F/mol at 0.5 mA/cm², can indeed recover more than 90% of the capacity during the first recharge at the same current density. However, the x-ray

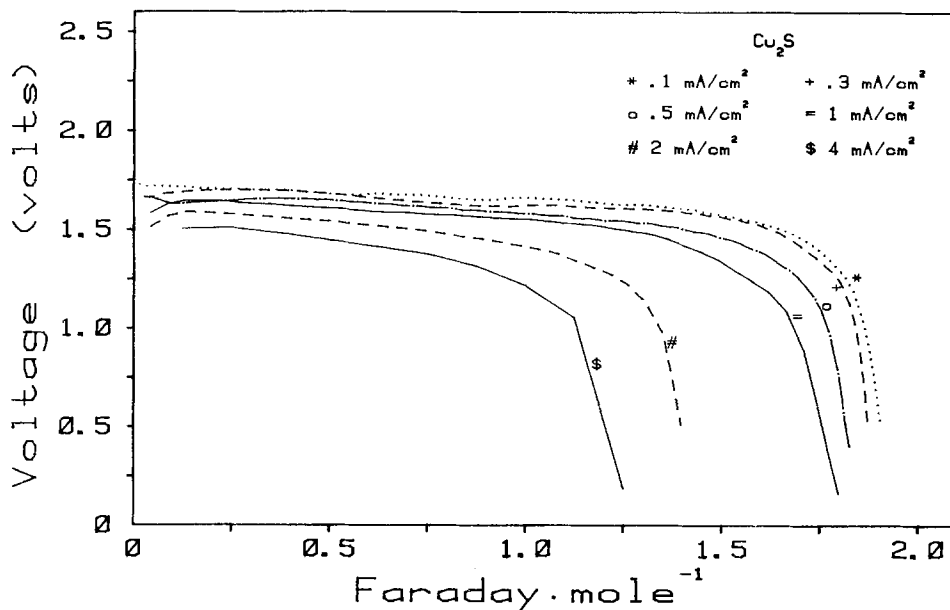


Fig. 7. Typical discharge curves of the Li/LiClO₄-PC/ Cu_2S battery at various rates and at room temperature.

analysis, run at various stages of the recharge process, showed a progressive attenuation of the Cu and Li_2S reflections, followed by the formation of a complex mixture of sulfides (e.g., $\text{Cu}_{1.96}\text{S}$, Cu_2S , $\text{Cu}_{1.8}\text{S}$, CuS).

The rather complicated oxidation mechanism for the $\text{Li}/\text{Cu}_2\text{S}$ system excludes any immediate application of this system in secondary lithium batteries.

Acknowledgments

We acknowledge the support of the Consiglio Nazionale delle Ricerche (CNR) for this research.

Manuscript submitted Oct. 14, 1983; revised manuscript received Nov. 2, 1983. This was Paper 75 presented at the Washington, DC, Meeting of the Society, Oct. 9-14, 1983.

The University of Rome assisted in meeting the publication costs of this article.

REFERENCES

1. B. Scrosati, B. Di Pietro, F. Bonino, M. Lazzari, and G. Razzini in "Power Sources for Biomedical Implantable Applications and Ambient Temperature Lithium Batteries," B. B. Owens and N. Margalit, Editors, Vol. 80-4, p. 276, The Electrochemical Society Softbound Proceedings Series, Pennington, NJ (1980).
2. F. Bonino, L. Busani, M. Lazzari, M. Manstretta, B. Rivolta, and B. Scrosati, *J. Power Sources*, **6**, 261 (1981).
3. M. Lazzari, G. Razzini, B. Rivolta, F. Alessandrini, and B. Scrosati in "Lithium Batteries," H. V. Venkatesetty, Editor, Vol. 81-4, p. 21, The Electrochemical Society Softbound Proceedings Series, Pennington, NJ (1981).
4. M. Boccoli, F. Bonino, M. Lazzari, and B. Rivolta, *Solid State Ionics*, **7**, 65 (1982).
5. F. Bonino, M. Lazzari, and B. Scrosati, *This Journal*, In press.
6. F. W. Dampier, *ibid.*, **121**, 656 (1974).
7. J. P. Gabano, V. Dechenaux, G. Gerbier, and J. Jamat, *ibid.*, **119**, 459 (1972).

Electron Microscopy Study of Formation of Thick Oxide Films on Ir and Ru Electrodes

V. Birss,^{*,1} R. Myers, H. Angerstein-Kozłowska, and B. E. Conway*

Department of Chemistry, University of Ottawa, Ottawa K1N 9B4, Ontario, Canada

ABSTRACT

The thick (5-60 μm) oxide films that can be formed electrochemically at Ir and Ru electrodes are examined by scanning and transmission electron microscopy. Their morphologies are discussed in relation to the remarkable reversibility of redox processes associated with the thick films and the enhancement of apparent electrocatalytic effectiveness of the oxide films, which is found for anodic Cl_2 and O_2 evolution processes to increasing extents with growth of the oxide film. The latter effects are much larger at Ir than at Ru. This difference is likely to be associated with the different morphologies of electrochemically grown oxide films that are observable on these two metals. In the case of Ir, the apparent enhancement of electrocatalysis for anodic Cl_2 or O_2 evolution seems to be associated with development of a hyperextended, microporous, hydrous oxide film that is accessible to H_2O and Cl^- ions. Comparisons are made with thermally formed oxide films generated by decomposition of RuCl_3 coatings.

The formation of oxide films on noble metals has been the subject of a large number of papers on account of the interest of this topic for (i) electrocatalysis of organic molecule oxidations (1-3), anodic Cl_2 evolution (4-6), and O_2 reduction (7), and (ii) as a model-type system for studying the transition from monolayer oxide film formation to development of multilayer oxide phases (8-10) on metals. The states of thick oxide films on Ir and Ru, where the oxides are principally IrO_2 and RuO_2 , respectively, are of particular interest in relation to electrocatalysis for Cl_2 evolution as treated in previous papers from this and other laboratories.

Much of the earlier work was concerned with the mechanisms and characteristics of formation of monolayer films of OH and O species on Pt and Au, and the resolution of the reversible from the irreversible stages of the oxide film formation processes at the submonolayer level of coverage. [For review, see Ref. (3).]

The growth law for potentiostatic oxide film extension at Pt was established by Gilroy and Conway (11) as the direct logarithmic one in time, even at submonolayer levels of surface oxide formation, and a possible mechanism for this behavior was treated by Gilroy (12). Applications of the Mott-Cabrera "high field" growth mechanism (13), which applies to development of thicker insulating dielectric films, were made by Ord and Ho (8), by Damjanović *et al.* (9, 10), and in related ways by Vetter and Schultze (14).

The first indication that the oxide film formation and growth process at Ir is different from that at Pt or Au was

given in the work of Stonehart *et al.* (15), who showed that surface oxide formation and reduction at Ir behaves as a reversible process which can also be observed as optically (16) reversible. Subsequently, a number of papers appeared characterizing this "reversible" type of oxide film behavior; in particular, Gottesfeld *et al.* (17) showed that the reversible behavior is not associated with metal oxidation and reduction of oxide back to the metal, but rather the oxide remains on the surface throughout a cyclic variation of potential between 0.0 and 1.4 E_{H} , but a redox process takes place within the film. The transition between true OH/O monolayer formation and reduction at Ir and development of thicker films was recently studied by Mozota and Conway (18).

Following the work on Ir (15, 18, 19, 20), similar behavior was found at Ru by Hadži-Jordanov *et al.* (21) in this laboratory and by Rand *et al.* (22), and the transition from monolayer oxide formation and reduction to reversible redox behavior at oxide films formed at Ru either thermally or by potential cycling was demonstrated in the work of Hadži-Jordanov *et al.* (21). Since that time, Burke (23) has shown that similar behavior can be generated at several other metals, even Rh and Pt, by a potential cycling regime.

By extensive cycling at Ir and Ru, optically and electron optically visible oxide films can be generated and their morphologies examined and related to their electrochemical behavior, e.g., electrocatalysis for Cl_2 (24) or O_2 (25, 26) evolution reactions. This paper reports scanning electron microscopy studies on such oxide films. Elsewhere (30), we report XPS results on the electronic states of Ir and O in electrochemically formed oxide films at Ir.

^{*}Electrochemical Society Active Member.

¹Present address: Department of Chemistry, University of Calgary, Calgary, Alberta, Canada.

Experimental

Electrodes.—High purity-grade (Materials Research and Engelhard) Ir rod or wires were employed as the Ir electrode materials. The 4 mm diam rod was cut into 0.5 mm thick circular sections and spot-welded to an Ir wire that was presealed into a soft-glass tube as electrode holder. Ir wire electrodes were spot-welded to a very short length of fine Pt wires presealed into glass tubes. The purpose of this procedure is to avoid preoxidation of Ir, which can occur under flame treatment. Zone-refined Ru rods were also obtained from Materials Research Company, cut, and similarly mounted or directly sealed into glass tubes. Ru wire was not obtainable.

Solutions.—1.0 or 0.5M aqueous H_2SO_4 solutions used in the work were prepared from Cl⁻-free BDH Aristar grade sulfuric acid; in our experience, this is the best grade of this acid available from the point of view of purity. Pyrodistilled water (27) was used for preparation of all solutions, and high purity techniques were employed in all the electrochemical experiments, as reported elsewhere (18, 24, 27).

Types of experiments.—Oxide films were generated on Ru and Ir electrodes by a potential-cycling regime [cf. Ref. (18-21)] using an anodic potential limit of at least +1.4V and a cathodic limit of +0.05V E_H . Potentials were referred to that of an H_2 reversible electrode in the same solution (scale designated " E_H , V"), but in a separate compartment of a three-compartment cell. The potential cycling regime was established by means of a cyclic voltammetry setup employing a Wenking potentiostat and a function generator in the usual way. The counterelectrodes were always made of the same metal, Ru or Ir, as that used as the respective test electrode in order to avoid contamination by a foreign metal, e.g., from a Pt counter-electrode by dissolution [cf. Ref. (28)].

In some experiments, potentiostatic oxide film formation was investigated. As found previously (15), the oxide film on Ir cannot be grown in time by holding the potential constant at an appropriate value, 1.4 ~ 1.6V E_H ; only under a cyclic-potential program does it grow. However, the oxide film at Ru can be grown either by the cycling regime or under constant potential conditions, viz., at > 1.45V, E_H , with the growth rate increasing with higher anodic potentials.

During the course of the growth of the film on Ir, the now well-known electrochromic effect (29) is observed, provided the extent of oxide film thickening is not too great (18), when the film becomes black at all potentials. Ru also showed some electrochromic effect in alkaline solution, but this is less marked than that at Ir.

During the oxide film-formation process, either at Ir or Ru, some dissolution of the metals occurs giving brownish solutions after prolonged cycling. The dissolution (at Ru) is greater under cycling conditions [cf. Ref. (28)] than under steady anodic polarization.

In another set of experiments, growth of the oxide was carried out at Ru under constant current conditions or under the influence of a program in which the current was increased from 0.1 to 5 mA cm^{-2} over 4h. The extent of growth of the oxide film under constant current conditions for 4 ~ 5h was found to be equivalent to that under potential cycling (0.05 to 1.45V, E_H) over a period of 3 ~ 4 days. Of course, in a potential cycling regime, the fraction of time spent in each half-cycle over the potential range where oxide growth rate is significant, will only be ca. 20%. Under controlled current conditions, however, O_2 gas is evolved so that the film growth partial current is a small fraction of the overall current passing. If O_2 , rather than Cl_2 [cf. Ref. (24)], is evolved at oxidized Ir electrodes, the oxide film suffers mechanical degradation. This does not occur when Cl_2 is evolved.

Scanning electron and optical microscopy.—A "Semco" Nanolab 7 scanning electron microscope was employed to study the morphology of the oxide films up to high magnifications using a LaB₆ filament. Photomicrographs

were taken at various tilt angles which illustrated three-dimensional aspects of morphologies. The oxides of Ir or Ru generated in these experiments did not require coating by C or Au as they were already quite conducting.

Optical microscopy observations were also made using a Nomarski interference microscope.

X-ray emission analyses.—The SEM was fitted with Microspec wavelength and KeveX energy dispersive x-ray analyzer systems, which enabled elemental compositions of materials to be monitored during SEM.

O:Ru and O:Ir ratios were evaluated using the x-ray spectrometers attached to the SEM. The oxygen:metal ratios were determined on various samples of oxidized Ru or Ir by reference to thermally formed bulk standard materials (RuO_2 and IrO_2). The Ru count rate was determined on the electrochemically formed oxide film at Ru and compared with that from the RuO_2 standard. Similar measurements were made on oxidized Ir electrodes.

Morphology and electrochemical history.—Photomicrographs were taken on oxide films grown to various thicknesses. Each sample was characterized by a cyclic voltammogram taken just before the electrode was transferred, after a brief wash in pyrodistilled water, to the SEM chamber. With some electrodes, a cyclic voltammogram was taken also immediately after the electron microscopy to check if any irreversible changes had occurred on account of the electron microscopy observations, e.g., due to vacuum drying or electron-beam reduction. The cyclic voltammograms for Ru were hardly changed after exposure of the oxide films in the SEM.

The optical microscopy was done on electrodes transferred in the wet state to the microscope stage so that artifact structures that could result from drying at an elevated temperature were avoided.

Several micrographs were made by transmission electron microscopy (TEM) after making replicas by means of collodion treatment. This procedure gave highest levels of magnification up to 25 nm per cm of the printed photographs. In the TEM instrument, electron diffraction characterization of the actual object material could also be made.

"Electrochemical" film thickness.—By means of the cyclic voltammetry measurements, the electrochemically determined apparent film thickness of the oxide films was determined in terms of the ratio, CEF, of the charge under the cyclic voltammogram, $i dt = i/s \cdot dV$, for a sweep-rate $s = dV/dt$, for a given oxide film to that for initial true monolayer² formation or reduction (18). This ratio was termed the "charge enhancement factor" (CEF) in previous publications (18, 24).

Results and Discussion

Electrochemical characterization of oxide films at Ir and Ru.—Typical cyclic voltammograms showing the transition from monolayer to multilayer oxide film formation at Ir and Ru are shown in Fig. 1 and 2, and illustrate the major difference between the behavior of the two-dimensional surface monolayer processes, which are irreversible, and the reversible behavior of the multilayer films having CEF values up to several hundred (18). The variation in the shapes of the cyclic voltammograms with potential for oxide films formed at Ir (Fig. 1) is principally due to the change of conductivity (31) of the oxide film at Ir as it is reduced from IrO_2 to Ir_2O_3 (29) at potentials < ca. 0.65V E_H . In the case of the ruthenium oxide film (Fig. 2), good conductivity is retained throughout the potential range 0.05-1.4V E_H , i.e., down to the H_2 re-

²Care must be exercised at Ir or Ru in the evaluation of the true oxide monolayer formation and reduction cyclic voltammogram (18); thus, it is easy for multilayer oxide formation to begin unless the potential limits of the cyclic voltammogram are carefully controlled and appropriately limited (18). Such effects are seen in some previously published work (30) where monolayer behavior was referred to, but, in fact, the currents correspond to some multilayer redox component processes.

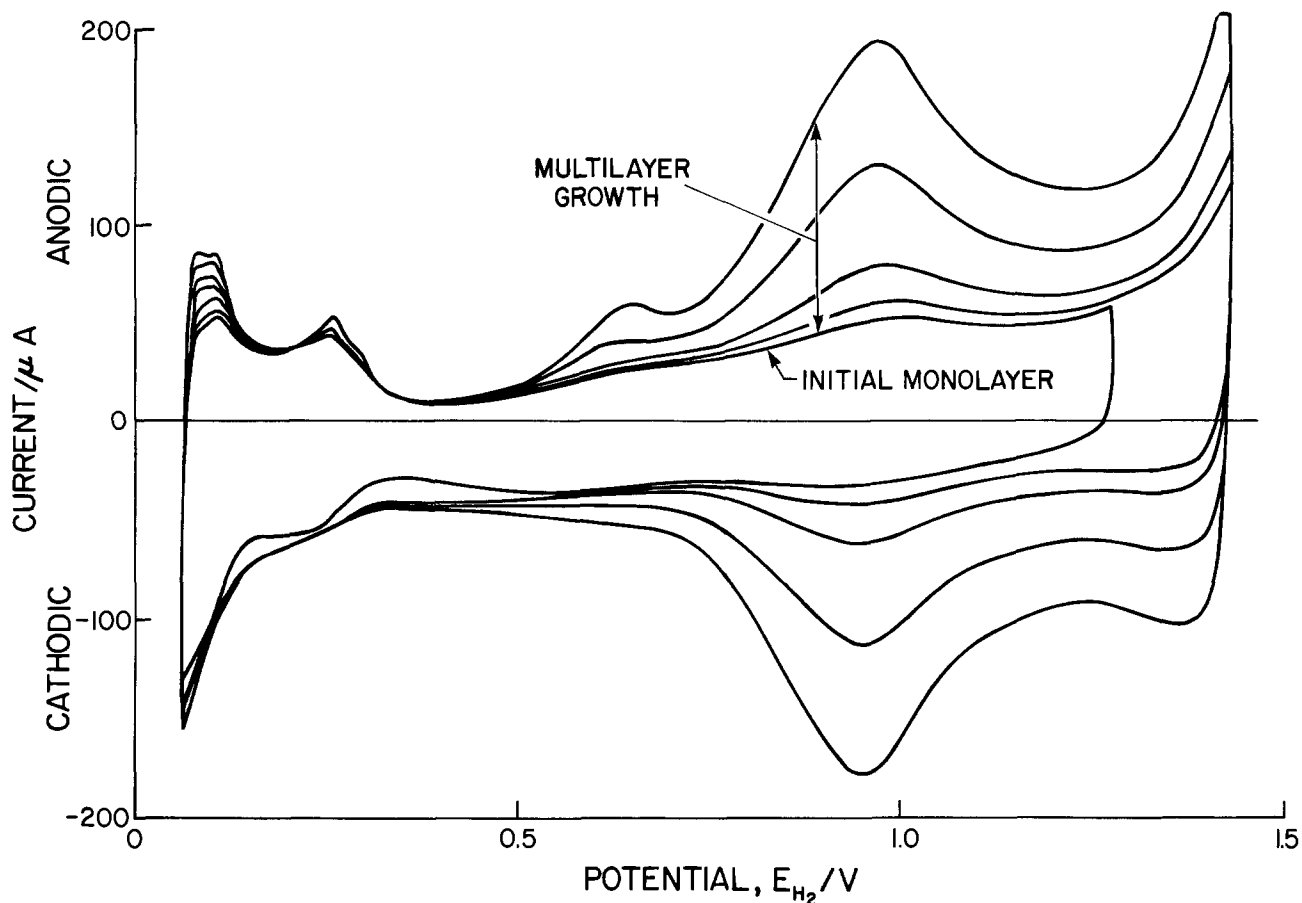


Fig. 1. Cyclic voltammograms for Ir electrode at 295 K showing transition from monolayer oxide film formation and reduction to development of multilayer oxide films with reversible oxidation-reduction region after cycling.

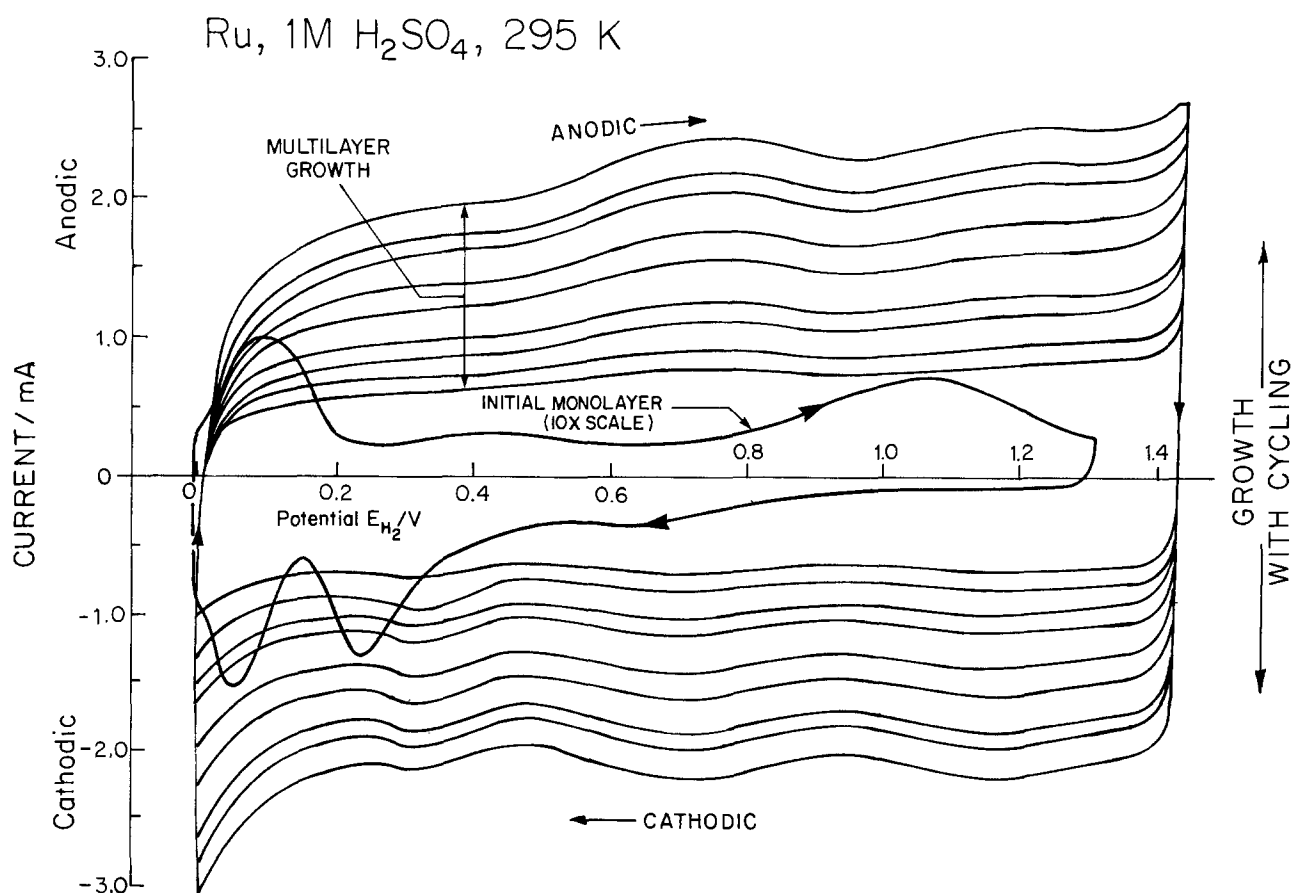


Fig. 2. Cyclic voltammograms for Ru electrode showing monolayer to multilayer oxide film transition, as with Ir shown in Fig. 1

versible potential in the "reduced" state as well as in the oxidized state.

The thicknesses of oxide films estimated from CEF values (based on 0.3 nm per layer, corresponding to passage of charge of $220 \mu\text{C cm}^{-2}$) are substantially smaller than are indicated from the dimensions of edges of cracked films that are observed in SEM pictures (see below). A comparison of normalized currents at a given potential ($0.8V E_H$) in the cyclic voltammograms for Ru and Ir during the growth under cycling conditions, with the film thicknesses observed in the SEM, is shown in Fig. 3. These lines give an approximate idea of the relationship between the effective "electrochemical" thickness of the films and the apparent (*i.e.*, allowing for porosity in the structures) geometrical thickness. The discrepancy is by a factor of *ca.* 10 or more for Ir oxide films and 50-100 for Ru oxide films grown electrochemically. These discrepancy factors may be due to (i) microporosity in the hydrous oxide films, and/or (ii) limited electrochemical accessibility of the material inside the films, or (iii) to electrochemical redox activity being restricted only to the surfaces of pores; that is, the charging/discharging processes observed in cyclic-voltammetry experiments may arise quasi-two-dimensionally at the surface of a hyperextended microporous structure.

Optical interference microscopy observations.—The first microscopic observations of the oxide film on cycled Ru electrodes were made by means of a Nomarski optical interference microscope, with the electrodes still in a wet or damp state. Two photographs of the oxide film developed after *ca.* 200 cycles of potential change from 0.05 to 1.4V E_H are shown in Fig. 4a. This photo

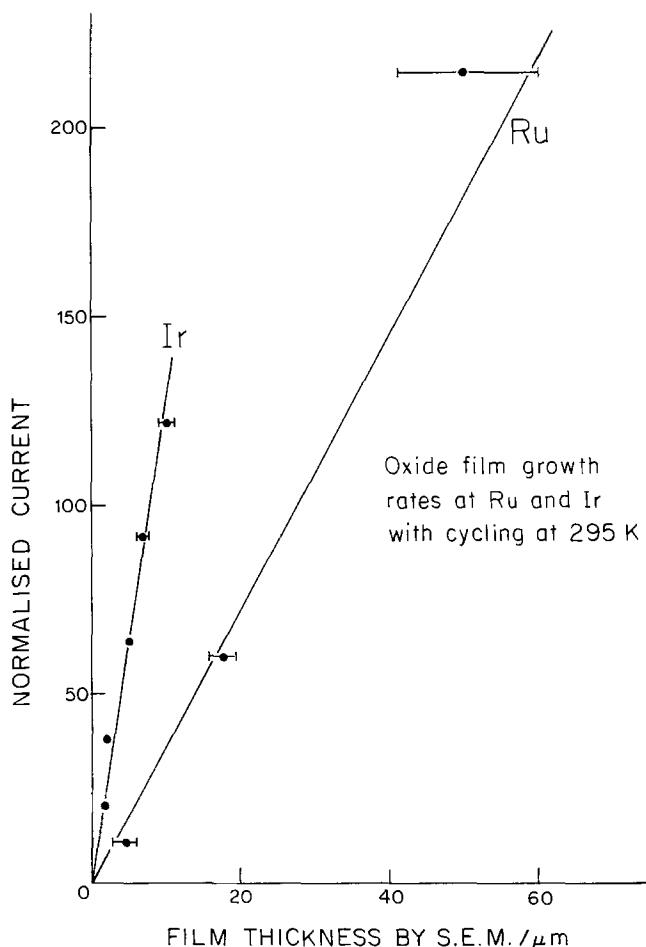


Fig. 3. Relation of normalized currents at 0.8V E_H for Ru and 1.0V for Ir in cyclic voltammograms taken during the oxide film growth during cycling, to film thickness determined by SEM observations. (Normalized currents are approximately proportional to CEF's.) Conditions: 0.5M H_2SO_4 , 298 K, cycling between 0.0 and 1.5V E_H , at 0.1 V s^{-1} .

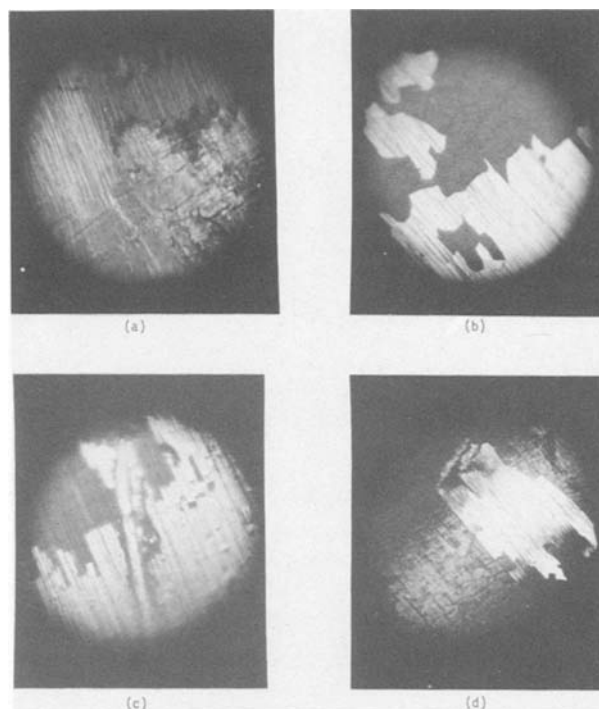


Fig. 4. Nomarski optical microscope photos of the hard shell layer that develops on Ru electrodes as they are oxidized in a potential cycling program. Original photos are Kodachrome showing interference contrast colors of various regions of the surface. a (top left): initial stage of film formation, *ca.* 50 nm. b (top right), c (bottom left), and d (bottom right): thicker films peeling off electrode, *ca.* 5 μm .

shows that the oxidized Ru electrode has a smooth shiny outer surface layer, but the underlying thick film formation cannot be observed in the SEM (see below). After thick film formation has occurred, this smooth outer layer seems to overlay some looser oxide material underneath it (Fig. 4b). The smooth outer layer is extremely hard, as was indicated by its resistance to attempts to probe into it with a steel needle. However, by means of the needle or a scalpel, flakes of this hard oxide layer can be separated off from the underlying bulk Ru oxide or the metal, revealing a looser material beneath. At Ir, such a layer is not observed.

An interesting aspect of the development of the oxide films on Ru is that if the original metal surface is scratched, or otherwise retains some polishing lines, the scratch marks are retained on the outside of the electrochemically grown oxide film. The outer surface of the oxide film, referred to above, has an appearance shown in Fig. 4a and 4b. The retention of the scratch marks indicates that the oxide film grows by migration of OH or O ions into the film rather than the reverse process of metal ion formation and migration outwards (*cf.*, the radioisotope marking procedure of Davies (32) for studying O or metal ion migration processes in oxide-film formation at base metals) coupled with provision of OH⁻ or O²⁻ species from H₂O at the oxide/solution interface.

More detailed indications of the structure of the oxide films at Ru and Ir are given by the electron microscopic observations to be described next.

Scanning electron microscopy observations.—In this section, we shall describe, first, the general morphology of the oxide films at Ru and Ir as seen with the SEM and then refer more specifically to certain aspects of the morphology of the oxide films, *e.g.*, the presence of columnar structures and the identification of rather small scale porosity.

General morphological features.—The appearance in the SEM of the hard outer layer material, referred to above, is shown in Fig. 5. The persistence of the original scratch marks on the metal, now on the outer surface of

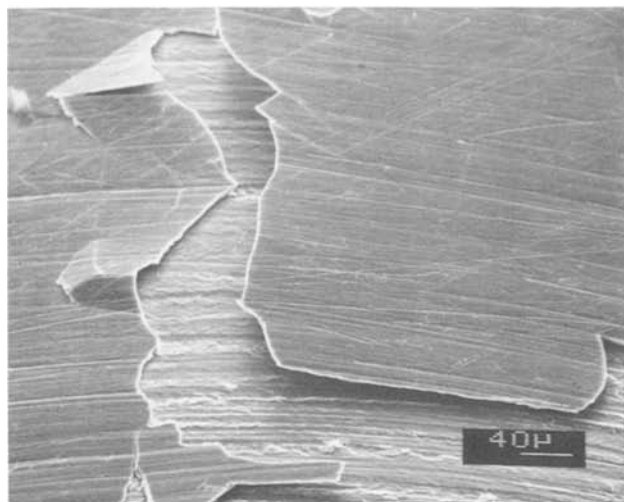


Fig. 5. SEM photos of the hard outer shell layer at an electrochemically oxidized Ru electrode (cf. Fig. 4a and 4b). Note retention of scratch marks.

the oxide film, is seen again. At higher magnification, the general appearance of the film is shown in Fig. 6, where the scratch marks are again clearly seen on the outside of the film. Figure 6 shows the structure of the film at a still higher magnification ("4.0 μm " scale) looking into its edge.

Figure 8 shows a region where some oxide has broken away, exposing an underlying oxide or the substrate Ru metal itself. (Compare the optical photomicrographs in section 2, Fig. 4a and 4b). The CEF values for the oxide films shown in the above figures are ca. 400. The depth of the depression in Fig. 8 is ca. 6 μm , indicating an oxide thickness of at least this magnitude. The CEF was 400 which would correspond only to an "electrochemical thickness" of ca. 0.12 μm . This verifies the deduction that the electrochemical charge associated with a change of oxidation state of the film in cyclic voltammetry experiments corresponds to only a small fraction of the oxide film material actually generated by the potential cycling procedure. Alternatively, the film is highly porous or the reversible electrochemical activity originates only at the outer regions of a porous structure.

The oxidation behavior of Ir appears to be significantly different from that of Ru in the following ways. Although a thick oxide film can also be formed, as at Ru, it is only generated by potential cycling, not under constant potential or constant current conditions where

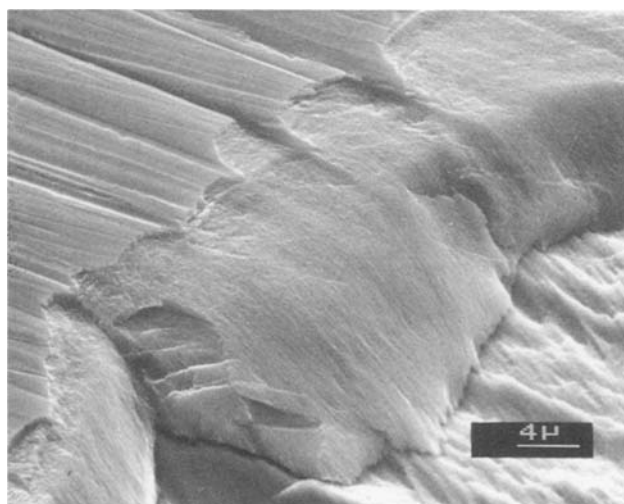


Fig. 6. General appearance of the oxide film at a Ru electrode at higher magnification than that of Fig. 5. Note retention of scratch marks.

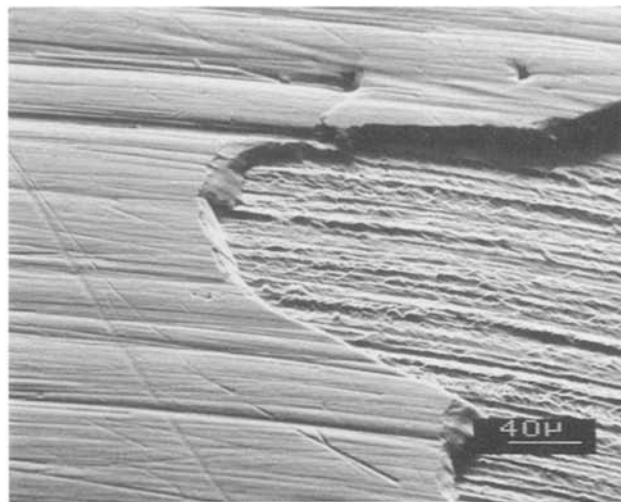


Fig. 7. SEM photo of the oxide film at Ru at high magnification showing edge of a fractured region.

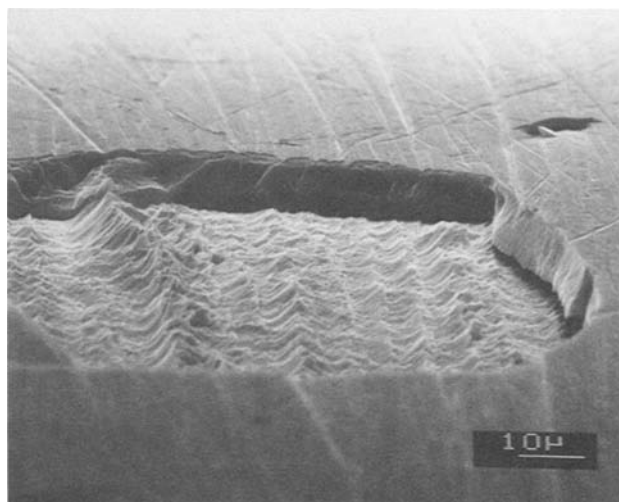


Fig. 8. SEM photo of the oxide layer at Ru showing a region where the film has broken away exposing underlying material.

Ru will form a thick oxide film. Also, very little dissolution of Ir is detectable, even after several hundred growth cycles; hence Ir oxide film growth is not connected with a dissolution redeposition cycle. This is demonstrated by the independence of growth rate upon electrode rotation (Fig. 9) (0 or 4000 rpm) using an Ir rotating disk electrode. At Ru, by contrast, appreciable metal dissolution takes place during the oxide forming process, as can be seen visually from the gradual coloration of the solutions which became brown.

Figures 10a, 10b, and 10c show the structure of an electrochemically formed oxide film at Ir with a CEF of 180. Again, the thicknesses of the films are substantially greater than corresponds to the CEF value. A cracked structure, similar to dried-out mud, is seen, and, although the oxide film appears to be peeling off in some photos, it was found that electrochemically oxidized Ir electrodes are mechanically stable to Cl_2 evolution for extended periods of time at 100 mA cm^{-2} . Thus, a given electrode does not suffer diminution of CEF by this treatment, though the stability to O_2 evolution is not as good as to Cl_2 evolution.

The "tubular" pore structures found at oxidized Ru (Fig. 11 below) are not observed at Ir although the apparent electrocatalytic behavior (24) for Cl_2 evolution does suggest the presence of a microporous, hyperextended large area structure.

Specific morphological features.—Under certain conditions and/or at high magnifications, several special fea-

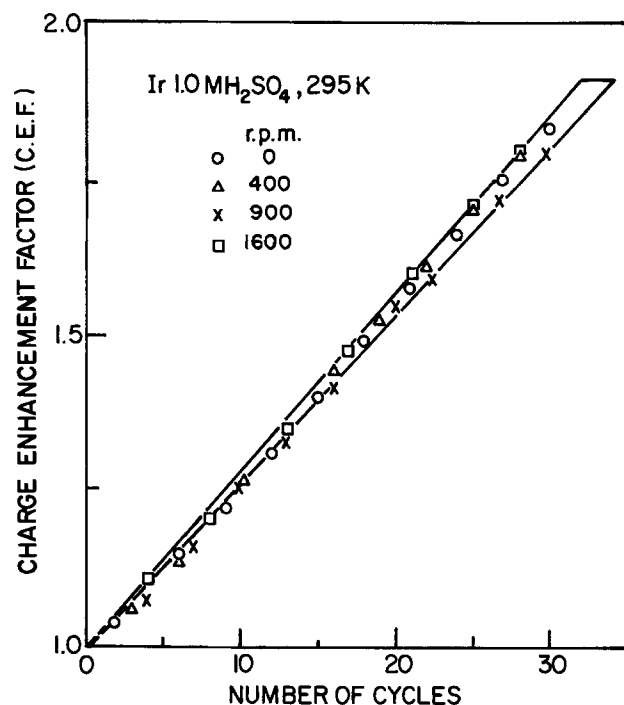


Fig. 9. Independence of anodic currents in cyclic voltammograms for oxidation processes at Ir electrode on electrode rotation rate. CEF's are independent of rotation rate. (Outer lines show breadth of errors; differences at various rotation rates are less than these errors.)

tures of the structure of the oxide films formed on Ru can be observed.

First, Fig. 11 shows the remarkable columnar structure that is seen in a fracture section across the oxide film grown at a fast cycling rate (1 V s^{-1}) to a CEF of ca. 200. The photo in Fig. 12 shows this columnar structure at a higher magnification together with top ends of the parallel columns. The orientations of the columnar structures seem to depend on the grain orientation of the original metal or else specific orientations of grains of oxide are developed during the oxide growth, as shown in Fig. 13. As will be discussed later, these columnar structures may result from anodic etching with concurrent oxide film formation at the etched regions, *i.e.*, involving a nonpassivating oxide layer.

An oxide film that has been formed at a Ru electrode by constant-current oxidation or by a programmed change of current (Fig. 14), in both cases with concomitant O_2 evolution, does not show the columnar structures illustrated above. The structure is more amorphous and is associated with a higher O:Ru ratio, determined in the x-ray spectrometry experiments, than is found at the cycled material. However, these experiments always gave substantially lower O:Ru ratios than correspond to the nominal stoichiometric composition " RuO_2 " taken for a thermally prepared RuO_2 specimen as standard. At electrochemically oxidized Ir, the corresponding O:Ir ratios were larger and closer to the expected " IrO_2 " stoichiometry for an IrO_2 standard.

Pore structures.—Attempts were made at high SEM magnifications to detect a pore structure that might account for the large oxidation/reduction charge associated with the electrochemical behavior of oxide films developed on Ir and Ru to appreciable thicknesses (CEF values of 200-500). The columnar structures developed at Ru under certain conditions (*cf.*, Fig. 11, 12, and 13) indicate the possibility of extended pores down or between the columns. However, direct high magnification observations in the SEM were unable to distinguish fine-scale roughness from possible entrances to pores in the surface, *e.g.*, in Fig. 6. Because of this problem, several observations were made at very high magnifications by means of TEM which are described below.

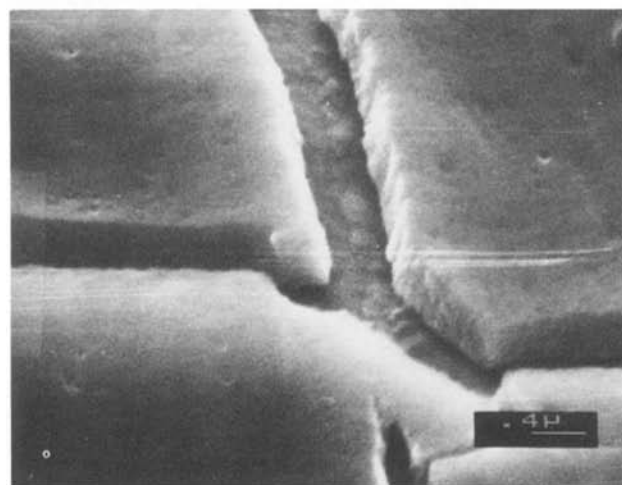
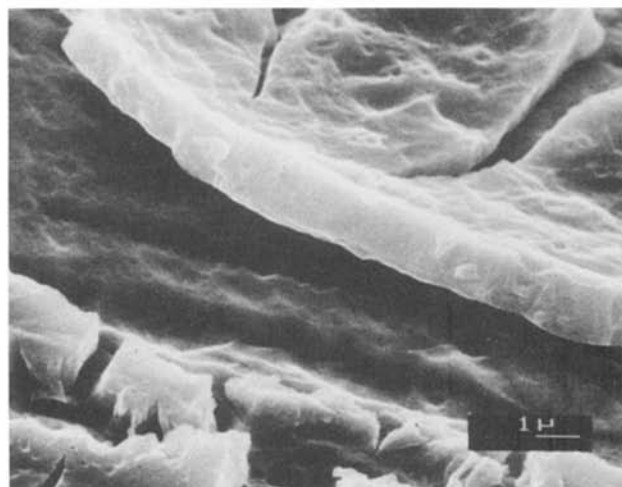
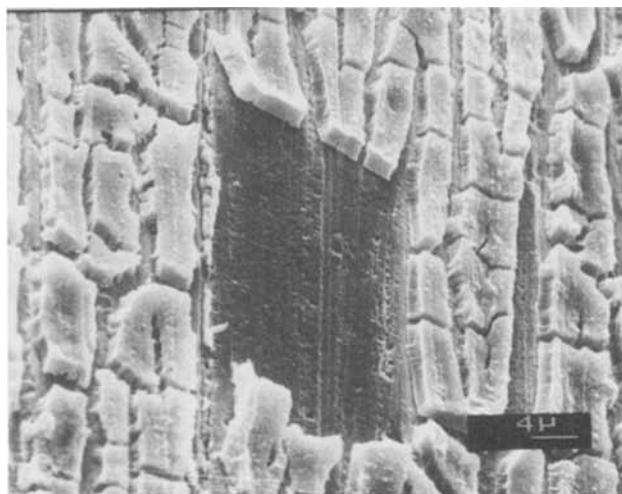


Fig. 10. SEM photos of the structure of electrochemically formed thick oxide films at an Ir electrode. (Note cracked structures not seen at Ru, and absence of outer shell layer.)

Morphologies of other deposits.—Comparison with oxide films formed in other ways is of some interest. Figure 15a shows the morphology of an RuO_2 oxide film formed thermally from a RuCl_3 -coated electrode (Ti substrate, as with a DSA-type electrode). Figure 15b shows an oxide film developed by the cycling procedure from Ru electroplated on Au. Compared with features developed in the oxidation of bulk Ru, the oxide structure seems to be influenced mainly by the morphology of the electroplated Ru metal substrate.

Transmission electron microscopy.—During the SEM studies of the oxide films formed at Ru by potential cy-

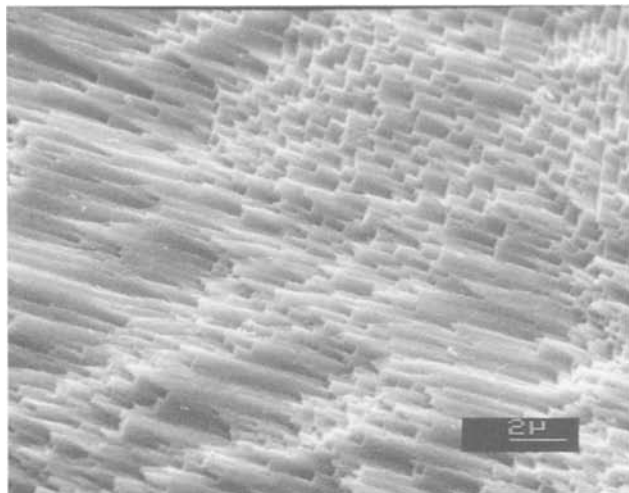


Fig. 11. SEM photo showing columnar and apparently tubular structure at electrochemically oxidized Ru electrode. Region is a fracture section.

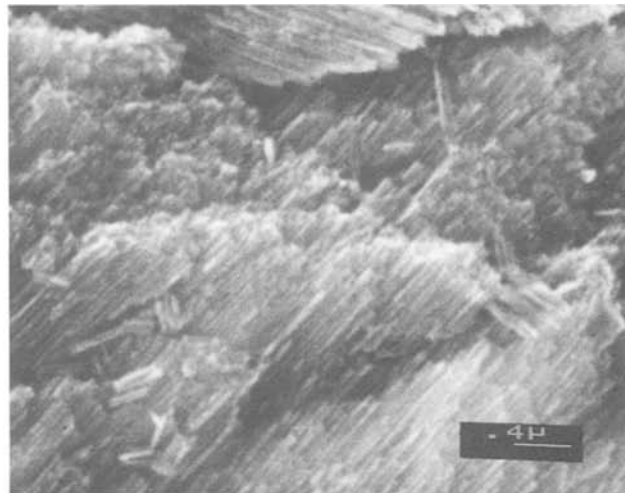


Fig. 13. Columnar structures of oxidized Ru electrode developed in relation to different grain orientations. Note detached pieces.

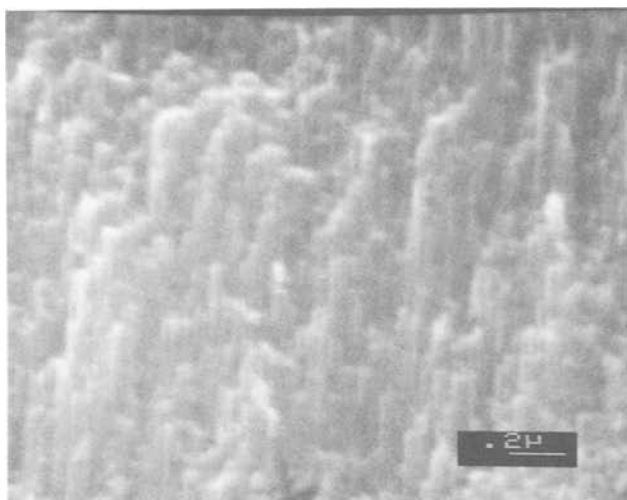


Fig. 12. Another SEM photo of the columnar structure of the oxidized Ru electrode at higher magnification and at an 86° tilt.

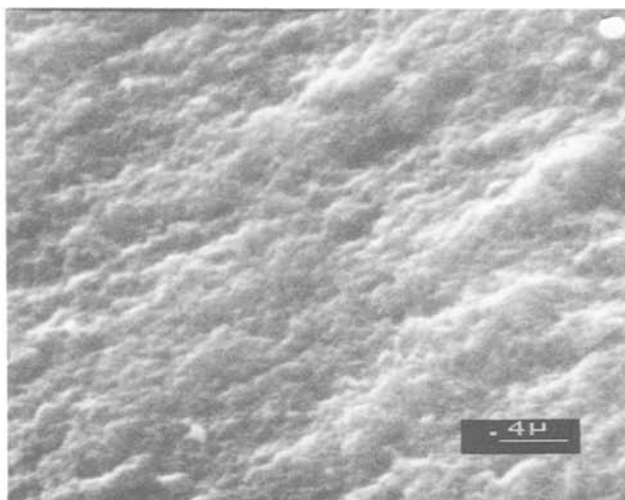


Fig. 14. SEM photo of amorphous oxide film formed at Ru under constant current oxide film formation conditions.

cling, it had been noticed that columnar structures develop in the latter material (see Fig. 5 and 11-13). It was possible to replicate the oxide surface with Formvar and, in so doing, to include some fragments of the oxide layer formed at Ru by the cycling procedure in the Formvar replica. These replicas were then examined by transmission electron microscopy. (Fig. 16a and 16b).

Figure 16a shows a TEM photograph of such a replica of the surface of the columnar film on Ru. At these high magnifications (scale of original photo 60 nm per cm), the oxide material is seen to be made up of remarkable parallel cylindrical bodies ca. 30 nm in diameter. Some are seen to have become separated and apparently bent around on top of other material. Details at a level of res-

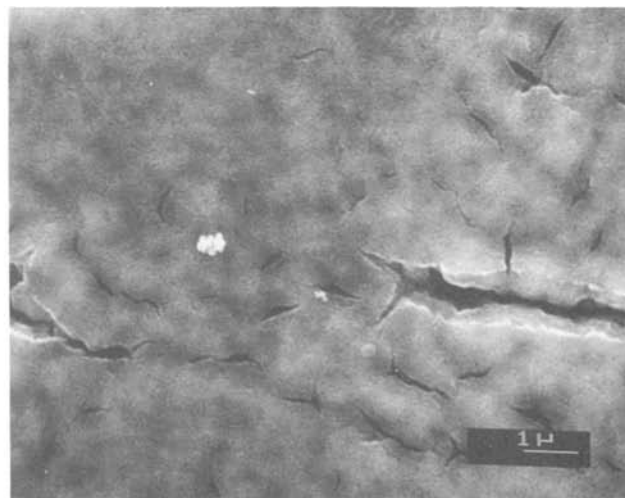


Fig. 15. a, left: SEM photo of oxide film at Ru formed thermally by decomposition of RuCl_3 coatings. b, right: Oxide film on Ru electroplated on Au. Film developed by the electrochemical cycling procedure.

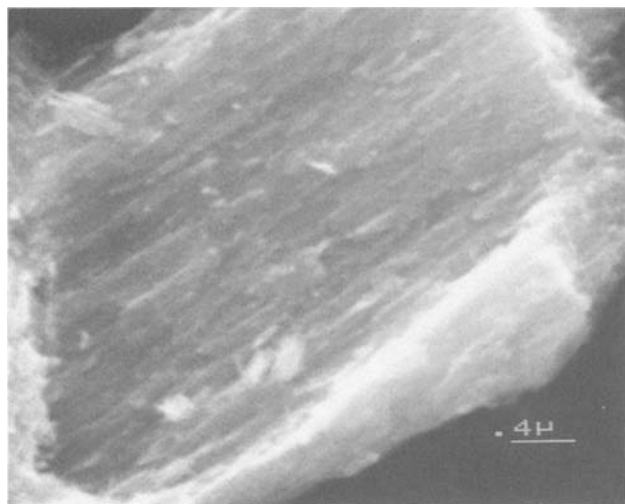
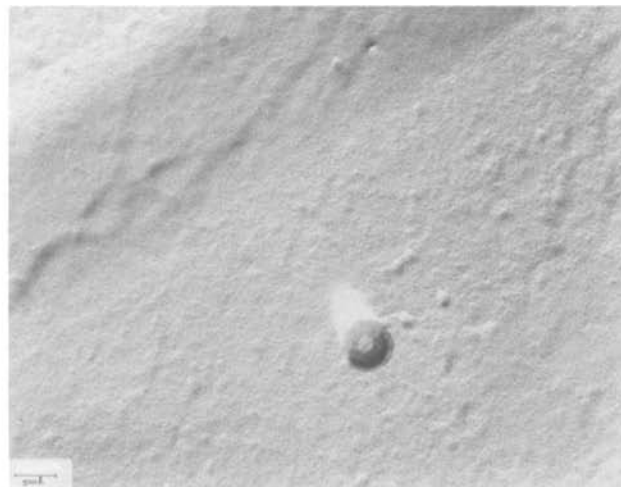
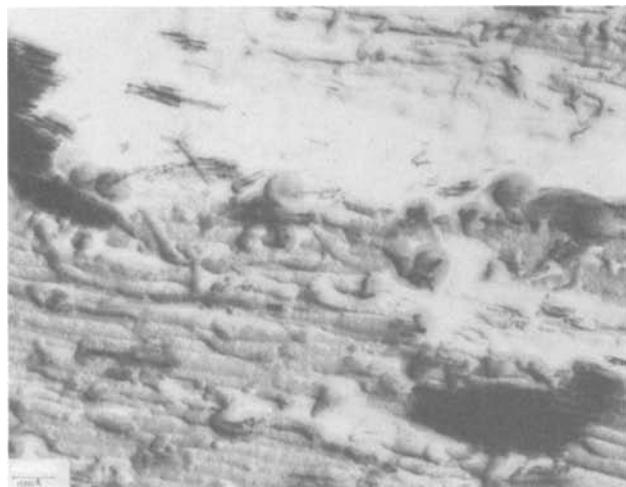


Fig. 16. a, top left: TEM photograph of the columnar structures developed at electrochemically oxidized Ru electrodes. b, top right: TEM photo of outer region of oxide film at Ru. c, left: SEM photo of a region of an actual oxide fragment trapped in the replica; see part of the TEM photo in Fig. 16a at the bottom right-hand side. In b, the circular microfeatures are clearer in the original photomicrographs than in this reproduction.

olution of < 5 nm can be detected in this photo. An SEM picture of the actual replica of the columnar material is shown in Fig. 16c.

Since the TEM photo shows the image of a replica, it is to be noted that the apparent topology is a negative of that of the actual sample fragment.³

The small pieces of oxide which were extracted into the replica from this region appear as the very dark areas of the TEM photograph in Fig. 16a at the lower right. The fact that the tiny oxide fragments exhibit the same columnar structure as in the replica material (*cf.* Fig. 16a) confirms the interpretation of the photomicrographs that highly oriented pores are an intrinsic part of the oxide structure. It should also be noted that the outer walls of the pores in the oxide pieces align well with the observed column edges on the remainder of the replica, demonstrating the accuracy of the replication procedure and the homogeneity of the structure. Figure 16a shows also that the channels or pores of this oxide region are of approximately 10-15 nm diam. Figure 16b is another TEM photo of a different replica of the oxidized Ru surface taken from an area where the outer layer of the oxide was still completely intact (*cf.* Fig. 4a, 4b, and 5), so that this photo shows the actual outer surface of the oxide. This photo shows many circular features having a diameter of *ca.* 10 nm. It is possible that these features are the exposed ends of some of the pores in the oxide film. The background has a fine structure on the order of 1 nm in dimensions, probably due to carbon coating the replicas.

³It is also to be noted that Formvar replicas of a smooth substrate surface are themselves entirely structureless, so the columnar features in Fig. 16a are not artifacts of the replication procedure. In any case, the columnar structures are seen directly under the SEM (Fig. 11-13).

An SEM photo of the oxide fragment shown in Fig. 16a is reproduced in Fig. 16c. Once again, the columnar structure is clearly seen.

In the case of Ir oxide films, these columnar structures could not be detected, and the fine structure at high magnifications seems generally like that of an amorphous material. Presumably, the apparent high area indicated by the proportionality of electrocatalytic activity for anodic Cl_2 evolution (24) to film thickness (CEF) is associated with a highly microporous structure with dimensions below those resolvable in the SEM. We refer to this as a hyperextended material.

Comparison of oxide films at Ir and Ru.—These results lend credence to the view that the high capacity for acceptance of electrochemical charge exhibited by the hydrous oxide type of materials that can be generated on Ir, Ru, and other metals [*cf.* Burke (23)] is connected with a high area pore structure which provides access for electrolyte ions and passages or chemical water channels for migration of the protons required in the oxide redox processes; these are of a remarkably reversible kind.

From an electrochemical point of view, the striking feature (18, 19, 21) of these anodically formed thick oxide films is that they exhibit a charge *vs.* potential relationship of the same kind as that of an electrochemical two-dimensional surface process, *e.g.*, submonolayer surface oxidation of Pt or underpotential deposition of metal monolayers on Au, and yet the material is demonstrably present in bulk form. In particular, for any given fractional degree of oxidation or reduction of the material, there is a corresponding reversible potential, as with an electrosorption isotherm (33) or with a three-dimensional redox system, as in the case of a redox titra-

tion. For a normal bulk phase oxide, on the contrary, there is: (i) an almost unique (theoretically, actually unique) single-valued potential for the formation or reduction of the oxide, and (ii) in a cyclic voltammetry experiment, the current *vs.* potential profiles in anodic and cathodic directions are never mirror images of each other, but correspond to processes requiring an overpotential in either direction for significant currents to pass; hence, the anodic and cathodic *i vs. V* profiles are completely asymmetric with respect to one another for other solid bulk phase materials.

While the electrochemical behavior of Ir and Ru is in some ways similar with respect to the development of thick oxide films upon potential cycling which exhibit reversible redox behavior over a wide range of potentials (wider at Ru than at Ir due to loss of conductivity (18, 31) in Ir oxide films below ca. 0.65V E_H , associated with reduction to a lower valence state of the Ir ions), the present work demonstrates important structural and some significant chemical differences in the films.

The principal structure difference is the development of the columnar features in the case of oxidized Ru and the retention of a hard surface on the exterior of the electrochemically generated oxide films at Ru. At Ir, neither of these features is observed and the oxide appears structurally more homogeneous (amorphous) apart from "mud cracks." Also, with Ir, no hard outer surface is retained. It may be suggested that the structures developed at Ru are the result of anodic etching accompanied by formation of a thin layer of oxide on the structures resulting from etching. This would be consistent with the appearance of substantial quantities of dissolved Ru species in solution during the film formation process under cycling or dc polarization conditions. An oxidized etched structure would also be consistent with the low O:Ru ratios found in comparison with the higher O:Ir ratios found at Ir, where the oxide film structure is visibly different. Thus, at Ru, the x-ray signals may originate relatively more from unoxidized metal contained in the film than is the case at Ir. However, the electrochemically accessible surface at the Ru material is certainly in an oxidized state, as indicated by the "reversible" cyclic voltammogram and the associated increase of CEF with cycling (Fig. 2), as well as by the difference of the features of the cyclic voltammogram compared with that for monolayer oxide formation and reduction [see Ref. (21)]

Other electrochemical differences in the properties of the films at Ru and Ir can be summarized as follows: (i) failure of oxide films to grow at Ir under dc potentiostatic conditions while they do grow at Ru under constant current or constant potential polarization, as well as by cycling; (ii) progressive increase of anodic Cl_2 or O_2 currents with oxide film thickness (CEF) at Ir but noticeably less at Ru electrodes, and (iii) dissolution of soluble species during oxide film formation at Ru but not significantly at Ir. Also, the change of conductivity of oxide films at Ir with potential (18, 31), referred to earlier, is to be noted.

The thick oxide film at Ir seems to be developed as a hyperextended hydrous oxide layer in which redox processes involving the Ir itself can proceed reversibly⁴ and in which, through a microporous structure, other faradaic reactions, such as oxidation of Cl^- , can also occur at currents proportional to CEF (24) and hence probably to real electrochemically accessible area. However, at Ru, while similar redox processes involving some ionic states (Ru II, Ru III, Ru IV) of Ru itself can evidently take place reversibly, the body of the film structure remains inaccessible for other faradaic reactions, such as Cl_2 evolution. This, we suggest, may be due to the presence of the impervious outer layer of oxide which is seen to exist at Ru but not at Ir electrodes.

⁴Very recently, photos of thick films that can also be formed on Pt (34) have been published (35). However, the films do not show reversible redox behavior like that at Ru or Ir.

Acknowledgments

We are grateful to Mr. Dwight Craig for perceptive discussions throughout the conduct of this work. Grateful acknowledgment is also made to Continental Group, Incorporated for support of this work and for provision of an electron microscope and associated x-ray spectrometry facilities at the University of Ottawa. We are also indebted to Mr. M. Shevalier for the SEM measurements of film thicknesses on Ir at various CEF's.

Manuscript submitted Sept. 12, 1983; revised manuscript received Feb. 1, 1984. This was Paper 845 presented at the San Francisco, California, Meeting of the Society, May 8-13, 1983.

The University of Ottawa assisted in meeting the publication costs of this article.

REFERENCES

1. S. Gilman, *J. Phys. Chem.*, **67**, 1898 (1963); *ibid.*, **68**, 70 (1964).
2. V. S. Bagotzky and Y. B. Vassil'yev, *Electrochim. Acta*, **9**, 869 (1964).
3. B. E. Conway, in "Electrochemistry of Conductive Metal Oxides," Vol. B, S. Trasatti, Editor, Elsevier, Amsterdam (1980).
4. E. L. Littauer and L. L. Shrier, *Electrochim. Acta*, **11**, 127 (1966).
5. B. E. Conway and D. M. Novak, *J. Electroanal. Chem.*, **99**, 133 (1979).
6. B. E. Conway and D. M. Novak, *J. Chem. Soc., Faraday Trans. 1*, **77**, 2341 (1981); *ibid.*, **75**, 2454 (1979).
7. A. Damjanović and J. O'M. Bockris, *Electrochim. Acta*, **11**, 376 (1966).
8. J. Ord and F. C. Ho, *This Journal*, **118**, 46 (1971).
9. A. Damjanović, L. S. R. Yeh, and J. F. Wolf, *ibid.*, **127**, 874 (1980); *ibid.*, **127**, 1951 (1980).
10. A. Damjanović and L. S. R. Yeh, *ibid.*, **126**, 555 (1979).
11. D. Gilroy and B. E. Conway, *Can. J. Chem.*, **46**, 875 (1968).
12. D. Gilroy, *J. Electroanal. Chem.*, **71**, 257 (1976).
13. H. Cabrera and N. F. Mott, *Rpt. Prog. Phys.*, **12**, 163 (1948-1949).
14. K. J. Vetter and J. W. Schultz, *J. Electroanal. Chem.*, **34**, 131 (1972); *ibid.*, **34**, 141 (1972).
15. P. Stonehart, H. A. Kozłowska, and B. E. Conway, *Proc. R. Soc. London, Ser. A*, **310**, 541 (1969).
16. S. Gottesfeld and B. E. Conway, *J. Chem. Soc. Faraday Trans. 1*, **69**, 1090 (1973).
17. S. Gottesfeld, *This Journal*, **127**, 1922 (1980).
18. J. Mozota and B. E. Conway, *Electrochim. Acta*, **28**, 1 (1983); *ibid.*, **28**, 9 (1983).
19. A. Capon and R. Parsons, *J. Electroanal. Chem.*, **39**, 275 (1972).
20. J. M. Otten and W. Visscher, *ibid.*, **55**, 1 (1974); *ibid.*, **55**, 13 (1974).
21. S. Hadzi-Jordanov, H. Angerstein-Kozłowska, M. Vuković, and B. E. Conway, *This Journal*, **125**, 1473 (1978).
22. D. Mitchell, D. A. J. Rand, and R. Woods, *J. Electroanal. Chem.*, **89**, 11 (1978).
23. D. N. Buckley and L. D. Burke, *J. Chem. Soc. Faraday Trans. 1*, **71**, 1447 (1975); *ibid.*, **72**, 2431 (1976).
24. B. E. Conway and J. Mozota, *This Journal*, **128**, 2142 (1981).
25. J. Vuković, H. Angerstein-Kozłowska, and B. E. Conway, *J. Appl. Electrochem.*, **12**, 193 (1982).
26. S. Gottesfeld and S. Srinivasan, *J. Electroanal. Chem.*, **86**, 89 (1978).
27. B. E. Conway, H. Angerstein-Kozłowska, W. B. A. Sharp, and E. Criddle, *Anal. Chem.*, **45**, 1331 (1973).
28. D. A. J. Rand and R. Woods, *J. Electroanal. Chem.*, **35**, 209 (1972); *ibid.*, **55**, 375 (1974).
29. J. D. McIntyre and S. Gottesfeld, *This Journal*, **126**, 742 (1979).
30. J. Augustynski, M. Koudelka, B. Sanchez, and B. E. Conway, *J. Electroanal. Chem.*, **160**, 233 (1984).
31. S. H. Glarum and J. H. Marshall, *This Journal*, **127**, 1467 (1980); see also L. D. Burke and D. P. Whelan, *J. Electroanal. Chem.*, **124**, 333 (1981).
32. J. W. Davies, J. P. S. Pringle, R. L. Graham, and F. Brown, *This Journal*, **109**, 999 (1962).
33. B. E. Conway and E. Gileadi, *Trans. Faraday Soc.*, **58**, 2493 (1962).
34. S. Shibata and M. P. Sumino, *Electrochim. Acta*, **20**, 739 (1975); see also *J. Electroanal. Chem.*, **89**, 37 (1978).
35. A. C. Chialvo, W. E. Triaca, and A. J. Arvia, *ibid.*, **146**, 93 (1983).

Carbon Dioxide Reduction at a Metal Phthalocyanine Catalyzed Carbon Electrode

S. Kapusta* and N. Hackerman**

Department of Chemistry, Rice University, Houston, Texas 77251

ABSTRACT

Metal phthalocyanines (metal = Co, Ni) deposited on carbon electrodes have been found to catalyze the electroreduction of carbon dioxide to formic acid in acid solutions ($pH = 3-7$). The overpotential for CO_2 reduction on cobalt phthalocyanine is approximately 200 mV lower than on the best metal cathodes at currents up to 10 mA/cm^2 . The main reaction product in long-term electrolysis is the formate ion at $pH > 5$. Methanol is also produced at lower pH values. The phthalocyanine becomes inactive in the less acid solutions once a fairly negative potential is imposed, probably due to an irreversible reduction of the catalyst.

Even though the activity of metal phthalocyanines towards the reduction of oxygen in aqueous solutions has been extensively studied [(1-3) and references therein], their use as electrocatalysts for the reduction of carbon dioxide has attracted much less attention. The only results available (4, 5), corresponding to cobalt and nickel phthalocyanines adsorbed on amalgamated platinum electrodes, show a single reduction step preceded by the formation of a CO_2 complex. The activity of the electrode decreases sharply once a fairly negative potential is reached. These results prompted us to repeat these experiments in order to obtain a better understanding of the kinetics and mechanism of the reaction. In particular, we concentrated on the effect of the central metal ion and the supporting electrode material on the activity of the metal phthalocyanines. The results of long-term electrolysis have also been analyzed.

Experimental

All measurements were performed in a standard three-compartment cell at $23^\circ \pm 0.2^\circ C$. The working electrode was a glassy carbon rod (Atomergic Corporation, Plainview, New York) having a 0.07 cm^2 cross section and mounted on either a Teflon or a Pyrex glass support. The electrode was polished using $0.05 \mu\text{m}$ alumina and ultrasonically cleaned prior to depositing the catalyst. The metal phthalocyanines were prepared as described in (6). They were deposited on the polished carbon surface from a concentrated sulfuric acid solution by diluting the solution with water. By this method, approximately $10 \mu\text{g/cm}^2$ of metal phthalocyanine was deposited on the carbon surface (1). The catalyst is probably not deposited uniformly but rather forms islands of different thicknesses.

Solutions were prepared from analytical-grade reagents and conductivity water. Both N_2 and CO_2 gases were purified by passing them through hot copper turnings and then through a wash bottle containing an acid solution of chromium (III) sulfate and amalgamated zinc granules. The analysis of the solution after long-term electrolysis was performed using a GC fitted with a flame ionization detector. The actual conditions are described in Ref. (7).

Standard potentiostatic and potentiodynamic techniques were used for the electrochemical experiments. Current densities have been calculated on the basis of the apparent area of the electrode. All potentials are referred to the saturated calomel electrode (SCE).

Results and Discussion

Figure 1 shows current vs. potential curves obtained under potentiodynamic conditions on phthalocyanine-modified carbon electrodes. Regardless of the pH value of the solution, CO_2 is not reduced on bare carbon electrodes. The current due to hydrogen evolution under these conditions is practically zero up to about -1.6V .

*Electrochemical Society Active Member.

**Electrochemical Society Honorary Member.

The activity of the catalyst towards the reduction of CO_2 is judged from both the potential at which an increase in current with respect to background (*i.e.*, bare carbon) is noted and from the shape of the reduction curve (*i.e.*, whether or not a diffusion-limited current is observed). The overall effectiveness of the phthalocyanines for catalyzing the CO_2 reduction reaction depends markedly on the central metal ion. The relative order of activity was found to be $Co^{2+} > Ni^{2+} \gg Fe^{2+} = Cu^{2+} > Cr^{3+}, Sn^{2+}$, etc. This order is quite different from that usually reported for the oxygen-reduction reactions (7), especially regarding the relative activity of the iron phthalocyanine. In all following experiments, only cobalt (CoPc) and nickel (NiPc) phthalocyanines were used.

Two current peaks can be observed in the potentiodynamic traces of curve 1 in Fig. 1. Similar but smaller peaks were also observed in CO_2 -free solutions and attributed to the reduction of the CoPc with formation of mono- and dianions, respectively (4). The ability of the catalyst to reduce CO_2 is therefore closely associated with

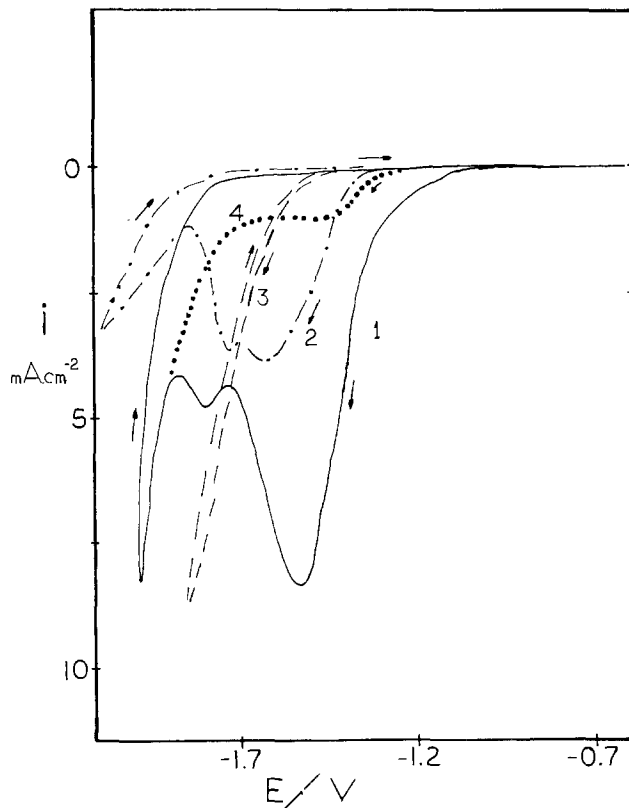


Fig. 1. Potentiodynamic i vs. E curves measured on glassy carbon electrodes covered with metal phthalocyanines. Curve 1: (—) cobalt. Curve 2: (---) nickel. Curve 3: (- · -) iron or copper. Curve 4: (· · ·) bare carbon electrode. $0.5M Na_2SO_4 + 0.1M NaHCO_3$ solution, saturated with CO_2 at normal pressure. Sweep rate: 0.05 V/s .

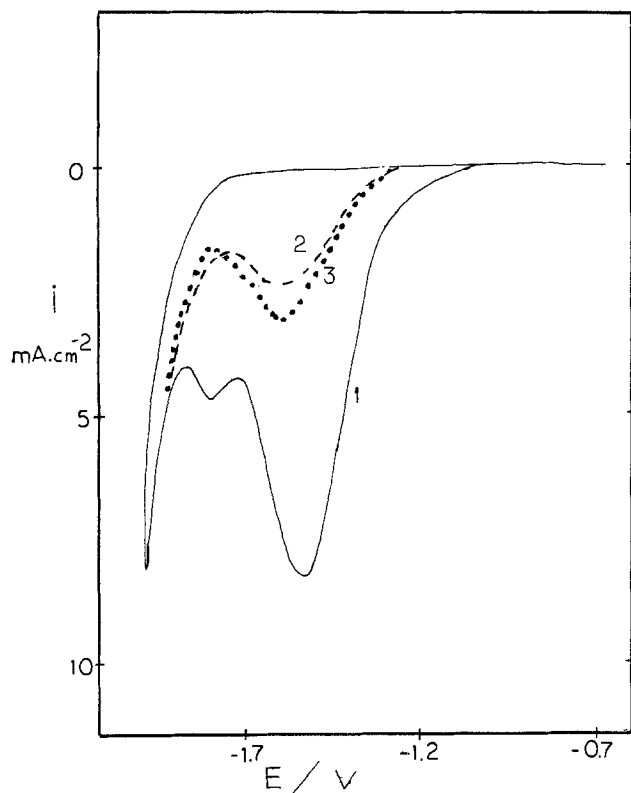


Fig. 2. Potentiodynamic i - E curves measured on glassy carbon electrodes covered with CoPc. Curve 1: (—) first sweep. Curve 2: (---) second sweep. Curve 3: (· · ·) third sweep following activation at 1.0V for 1 min. Similar conditions as in Fig. 1.

its oxidation state, as is also the case for oxygen (8). The i - E curve can be cycled several times with very little hysteresis and good reproducibility as long as the cathodic switching potential is kept positive to the first current peak (about -1.55 V). In neutral and slightly acid solutions (pH 5-7), the loss of activity of the phthalocyanines for CO_2 reduction is noted once this limit is exceeded. The current is then much lower for the second i - E curve than for the initial sweep. In fact, the activity of the modified electrode is reduced to that of a bare carbon electrode after a few cycles to -1.6 V or an extended voltage excursion

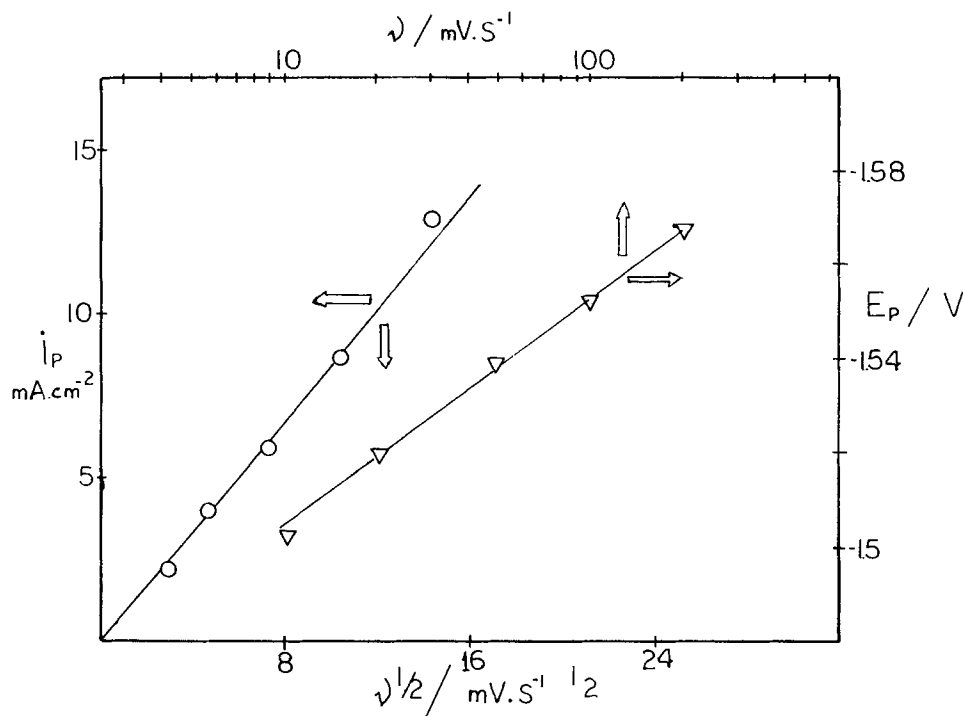
to -1.9 V. This effect can be observed by comparing the results shown in Fig. 2 with curve 4 in Fig. 1. Polarizing the electrode at about 1.0V for a few minutes partially restores the activity of the catalyst. The highest reduction currents obtained on these "restored" electrodes is about 40% of those measured initially. The mechanism of deactivation is not yet understood, although it probably involves either poisoning of the electrode by a reaction intermediate or the irreversible reduction of the catalyst.

The magnitude of the cathodic current peaks increases linearly with the concentration of CO_2 . The sweep-rate dependence of the peak current and peak potential, shown in Fig. 3, are consistent with a diffusion-limited irreversible electron transfer having a Tafel slope of -110 ± 10 mV (9). The diffusion coefficient of CO_2 can be estimated from the slope of the i_p vs. $v^{1/2}$ plot to be about 1×10^{-5} cm^2/s . Diffusion-limited currents have been observed on metal electrodes only at potentials 200 mV more negative than on CoPc modified electrodes. Figure 4 shows cathodic Tafel plots measured on both CoPc and NiPc under potentiostatic conditions. The results obtained on tin cathodes (10) are shown for comparison. The slopes of the linear portions (*i.e.*, -120 mV/decade), are consistent with the results of the potentiodynamic experiments and indicate that transfer of the first electron to a CO_2 molecule is the rate-determining step of the reaction.

Limiting currents are reached on both CoPc and NiPc at about the same potential, although the magnitude of these currents is quite different. Of course, no difference should be expected if these were diffusion-limited currents. We believe that deactivation of the NiPc occurs before the diffusion limit is reached, although kinetic complications (*i.e.*, a difference in reaction mechanism) could also explain the lower currents. The total cathodic charge measured on PcCo during a single sweep between -0.6 and -1.4 V is about 30 mC/cm^2 . This large value, compared with about 0.2 mC/cm^2 expected for a unit turnover ratio, confirms the catalytic nature of the process.

At $pH < 6$, the i - E profile shows a new reduction peak at a potential of about -1.2 V, in addition to the main peak at -1.55 V (Fig. 5). The ratio of the peak currents is about 2.5 to 1, and depends very slightly on pH . We have not yet been able to identify the processes associated with each peak, although we expect to gain a better understanding from ring-disk electrode experiments currently under way. We suspect, however, that the presence of two re-

Fig. 3. Sweep rate dependence of the cathodic peak current, i_p , and peak potential, E_p , measured on a CoPc covered carbon electrode. Same solution as in Fig. 1, CO_2 saturated.



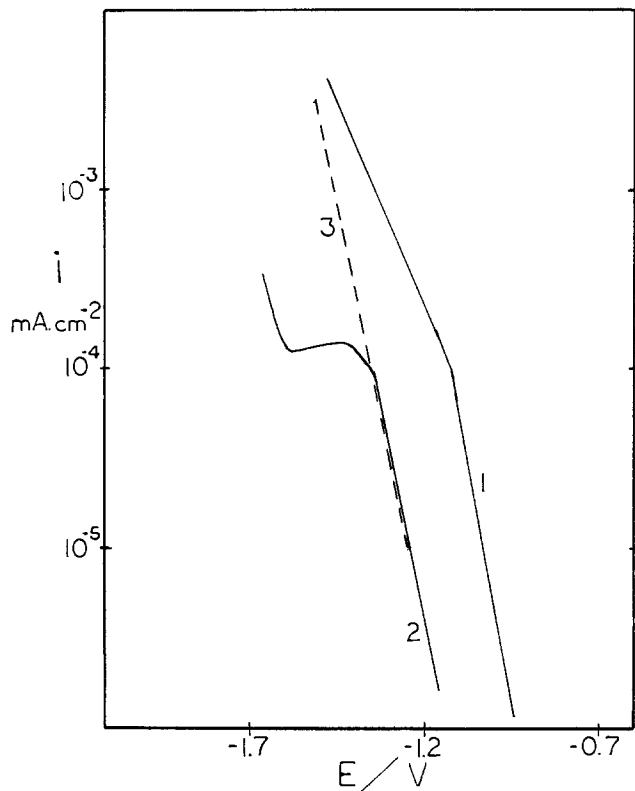


Fig. 4. Potentiostatic Tafel plots measured on CoPc-(1) and NiPc-(2) covered carbon electrodes. Results for tin (3) taken from Ref. (11). Similar conditions as in Fig. 1.

duction peaks is related to the reduction of CO_2 beyond the formate stage. In fact, the amount of methanol produced in long-term electrolysis of CO_2 solutions increases on lowering the pH in the range 7-3, although it never reaches a current efficiency larger than 5%. The main reaction product is in all cases the formate ion.

Previous reports (5) indicated that the shape of the i - E plot depended on the time the electrode was held at potentials more positive than about -1.0V , due to the formation of a CO_2 -phthalocyanine complex. We found no evi-

dence for this process. It seems likely that the reported effect was caused by a time-dependent coverage of the electrode with water-soluble phthalocyanines, and not by a slow complex formation reaction.

The substrate has a strong influence on the activity of the metal phthalocyanines towards the reduction of CO_2 . Graphite and glassy carbon seem to be specific in their ability to utilize phthalocyanines as catalysts. As mentioned earlier, the overpotential for this reaction on CoPc deposited on glassy carbon is about 200 mV lower than on the best metal cathodes. Some activity was also observed using high overpotential metals (Hg, Pb) as supports. On other electrodes, *e.g.*, Pt and Au, the phthalocyanines have essentially no catalytic activity towards CO_2 reduction. These results agree with those obtained for the reduction of oxygen (11), and suggest that the bonding between the substrate and the catalyst determines the electrode activity.

The limiting potential at which the catalyst retains its activity becomes more negative on lowering the pH of the solution. To test the short-term stability of the phthalocyanines, a CoPc electrode was operated continuously for 72h at potentials between -1.4 and -1.2V and current densities of about 1 mA/cm^2 in a 0.1M NaHCO_3 solution saturated with CO_2 . The cathodic charge was equivalent to 260 C/cm^2 . No significant loss of activity was observed. The solution was analyzed after this electrolysis using the GC technique described earlier. The main reaction product was the formate ion formed with a current efficiency of about 60%. Methanol was produced only in those solutions having a pH value lower than 4, indicating that formic acid (rather than the formate ion) is the reacting species for the second reduction process. The maximum current efficiency for methanol formation was about 5% at pH = 3.

Further information about the system can be obtained from measuring the electrode impedance. Figure 6 shows the potential dependence of the differential capacitance of a CoPc-covered carbon electrode in solutions saturated with N_2 and CO_2 . The capacitance measured at 1 kHz is in good agreement with the double layer capacitance determined from complex plane analysis ("Cole-Cole" plots). The difference between both curves in Fig. 6 can be attributed to a difference in the pH value of the solutions. Therefore, the capacitance maximum is not associated with the formation of a CO_2 complex, as previously sug-

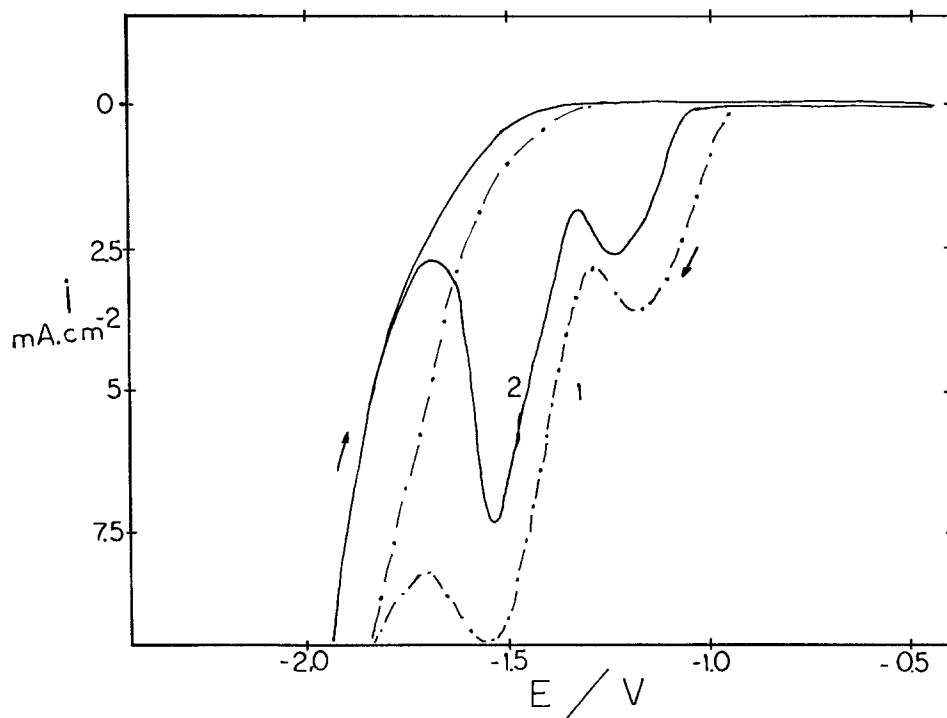
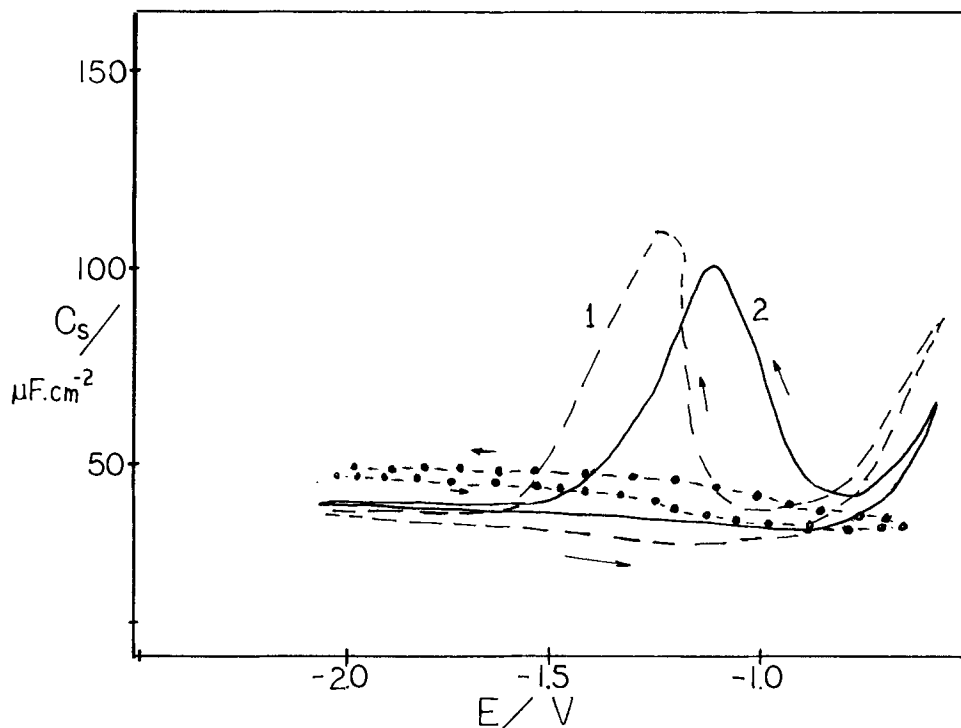


Fig. 5. Potentiodynamic i - E profiles measured on CoPc-covered carbon electrodes in solutions saturated with CO_2 . Curve 1 (---) $\text{Na}_2\text{HPO}_4/\text{NaH}_2\text{PO}_4$ buffer at pH = 5.8. Curve 2: (—) acetate buffer or phosphate buffer at pH = 4. Sweep rate = 50 mV/s .

Fig. 6. Potential dependence of the differential capacitance measured on CoPc-covered carbon electrodes. Same solution as in Fig. 1. Curve 1: (---) nitrogen saturated. Curve 2: (—) CO₂ saturated. Curve 3: (- · -) bare carbon electrode in CO₂-saturated solution. Frequency = 1 kHz. Sweep rate = 0.01 V/s.



gested (5). It is more likely due to a change in the oxidation state of the central ion. The potential at the maximum (-1.1V in CO₂-saturated solutions) corresponds either to the foot of the first current peak in the *i*-*E* plots (Fig. 1), or to the first current peak at pH < 6. In any case, we think that there is a close relationship between the oxidation state of the central ion, the catalytic activity of the electrode, and its differential capacity.

In conclusion, metal phthalocyanines are promising electrocatalysts for the electroreduction of CO₂ in aqueous solutions. The reaction product in nearly neutral solutions is the formate ion, although methanol is also obtained in more acid solutions. Future work will be directed towards an understanding of the mechanism of the reaction and the deactivation of the catalyst in order to increase its long-term stability.

Acknowledgment

The financial support of this investigation by the Robert A. Welch Foundation of Houston, Texas, is gratefully acknowledged.

Manuscript submitted Sept. 12, 1983; revised manuscript received Nov. 23, 1983.

Rice University assisted in meeting the publication costs of this article.

REFERENCES

1. R. Brodd, V. Leger, R. Scarr, and A. Kozawa, in "Electrocatalysis on Non-Metallic Surfaces," NBS STP No. 455, p. 253, U.S. Department of Commerce, Washington, DC (1976).
2. M. Savy, C. Bernard, and G. Magner, *Electrochim. Acta*, **20**, 383 (1975).
3. J. Appleby, J. Fleisch, and M. Savy, *J. Catal.*, **44**, 281 (1976).
4. S. Meshitsuka, M. Ichikawa, and K. Tamaru, *J. Chem. Soc. Chem. Commun.*, 158 (1974).
5. K. Hiratsuka, K. Takahashi, H. Sasaki, and S. Toshima, *Chem. Lett.*, 1137 (1977).
6. F. H. Moser and A. L. Thomas, "Phthalocyanine Compounds," Reinhold, New York (1963).
7. I. Sekine, H. Ohkawa, and T. Handa, *Corros. Sci.*, **22**, 1113 (1982).
8. A. Wolberg and J. Manassen, *J. Am. Chem. Soc.*, **92**, 2982 (1970).
9. P. Delahay, "New Instrumental Methods in Electrochemistry," p. 183, Interscience, New York (1954).
10. S. Kapusta and N. Hackerman, *This Journal*, **130**, 590 (1983).
11. A. Kozawa, V. Zilioni, and R. Brodd, *ibid.*, **117**, 1469 (1970).

Kinetics of Repassivation of Nickel/Copper Alloys in Alkaline Solution

R. D. K. Misra* and G. T. Burstein

Department of Metallurgy and Materials Science, University of Cambridge, Cambridge CB2 3QZ, England

ABSTRACT

Data have been obtained for the rate of repassivation of nickel and binary nickel/copper alloys at pH 14. The fresh metal surfaces, which are created *in situ*, react initially to produce a monolayer of oxide. This monolayer is formed by random oxidation of exposed metal atoms at a rate which is unaffected by the copper content of the material. Subsequent film thickening occurs by ion migration through the film under high electric field. The copper content of the alloy affects this process only to a small extent, the reaction being largely controlled by the nickel component. The rate constants are given.

Growth of anodic oxide films on nickel in alkaline solutions has been investigated in some detail owing to the use of the metal as an electrode material in nickel/iron and nickel/cadmium batteries (1-11). Film growth is also of importance in the maintenance of passivity of nickel and alloys containing nickel.

It is now commonly accepted that anodic oxidation of nickel in alkaline solutions leads initially to the formation of a film of $\text{Ni}(\text{OH})_2$ (1-11). Ellipsometry has shown that this film is $\beta\text{-Ni}(\text{OH})_2$ (4) although it may be formed from $\alpha\text{-Ni}(\text{OH})_2$ (7, 8, 10). Recent experiments have shown that when $\beta\text{-Ni}(\text{OH})_2$ is formed, it cannot readily be reduced electrochemically (10). At higher potentials this film is converted to $\beta\text{-NiOOH}$ (2, 6, 7, 10) although little is known about the kinetics and mechanisms of growth of, and transformations between these oxide phases. For the $\text{Ni}(\text{OH})_2$ layer, formed anodically from the metal both dissolution followed by precipitation (9, 12) and direct solid-state surface oxidation (6, 9) have been proposed. Thickening of the $\beta\text{-Ni}(\text{OH})_2$ film has been shown to follow the Cabrera-Mott (13) formalism of high field-assisted ion transport (10, 11).

Pourbaix' thermodynamic calculations for equilibrium of nickel with aqueous solutions of pH 14 (14) provide data for additional oxides of nickel, including Ni_3O_4 and NiO_2 , but no consideration of the NiOOH phase was made.

Anodic oxide films on Ni-Cu alloys have received less attention although oxidation in dry oxygen and steam environments has been characterized (15-17). The anodic oxidation of Monel 400 (70% Ni, 30% Cu) in LiOH solution is found to approximate most closely to the oxidation of the major component of the alloy (12). In an earlier paper (18) we established that passivity of a range of Ni-Cu alloys in 1M H_2SO_4 solution was due to oxide film growth by ion migration under high electric field. The rate-controlling parameters are a function of the copper content of the alloy, but the alloys largely follow the kinetics of film growth associated with pure nickel. It was concluded that the film was fundamentally a nickel oxide, containing varying amounts of copper ions depending upon the alloy composition.

In this paper we establish the oxide growth parameters for Ni, Ni-30%Cu, Ni-50%Cu, and Ni-70%Cu in 1.0M KOH, pH 14, using the scratched electrode in order that film growth could be studied starting from the bare metal surface. The technique is useful in this case owing to the apparent irreducibility of the nickel oxide film (10). Alloys of the above compositions are all single phase homogeneous solid solutions, and the data obtained are not complicated by varying metallurgical microstructures.

Experimental

The scratched rotating disk electrode technique was used to investigate the repassivation of nickel and binary

alloys of nickel and copper in 1.0M KOH. The technique has been described extensively in previous papers (19-26).

The electrodes were made from 99.999% pure metals. Alloys were synthesized by arc melting followed by homogenization. The electrolyte was AR grade KOH made to 1.0M with doubly distilled water; it was purged with pure nitrogen before and during use.

Scratches are generated on the electrode disk (~0.5 cm diam) rotating at 100 Hz. A stylus contact time of ~1.5 ms produced a scratch ~0.15 cm long by ~40 μm wide by ~3 μm deep. The electrode was held at constant potential with respect to a saturated calomel reference electrode. The current transient consequent upon generation of the scratch was recorded superimposed onto the steady-state background current flowing from the whole electrode surface. A typical anodic current transient is shown in Fig. 1. Parameters taken from each transient are given by the maximum observed bare surface current density i_s , the current density flowing from the scratch at time t after scratching, $i(t)$, and the charge density that has flowed from the scratch at time t , $q(t)$. These are quantified by

$$i_s = \frac{1}{2\pi r \omega y} \frac{dI}{dt} \quad [1]$$

$$i(t) = \frac{1}{2\pi r \omega y t_c} [I(t) - I_b] \quad [2]$$

$$q(t) = \frac{1}{2\pi r \omega y t_c} \int_0^t [I(t) - I_b] dt \quad [3]$$

where dI is the increase in current on the scratch in time dt during scratching, $I(t)$ is the total current flowing from the whole electrode at time t after scratching, I_b is the base current flowing from the whole electrode before scratching, t_c is the contact time of the stylus, y is the scratch width, r is its distance from the center of rotation and ω is the electrode rotation rate.

Current transients were quantified as a function of electrode potential E (presented on the normal hydrogen electrode scale). The metals used were pure Ni, Ni-30Cu, Ni-50Cu, and Ni-70Cu where the amount of copper is expressed in weight percent. All experiments were performed at ambient temperature of $(19^\circ \pm 2^\circ)\text{C}$.

Results

The magnitude of the rate of reaction of the freshly bared metal surface is given by i_s . Although i_s is a differential quantity (see Eq. [1]), when its value is high it probably does not give a measure of the true bare surface reaction rate. Nevertheless, it provides a guideline for the bare surface reactivity of the material when plotted as a function of electrode potential.

The "bare surface polarization curve" for pure nickel in 1.0M KOH is shown in Fig. 2. It shows a unique potential, E_{ms} , at which zero net current flows from the scratch. For

* Electrochemical Society Student Member.

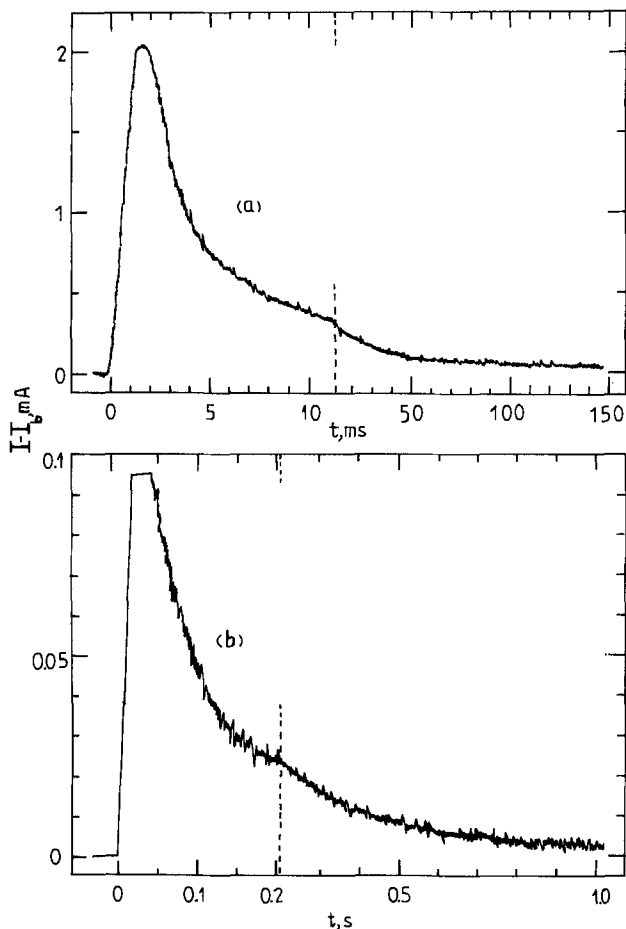


Fig. 1. Current transient recorded on scratched nickel immersed in 1.0M KOH, pH 0 at -105 mV (NHE). (a) and (b) depict the output from two transient recorders, and dashed lines represent changes of time scales.

potentials negative with respect to this bare surface mixed potential the net current flowing from the scratch is negative. At all potentials positive with respect to E_{ms} the current flowing from the scratch is positive. The first

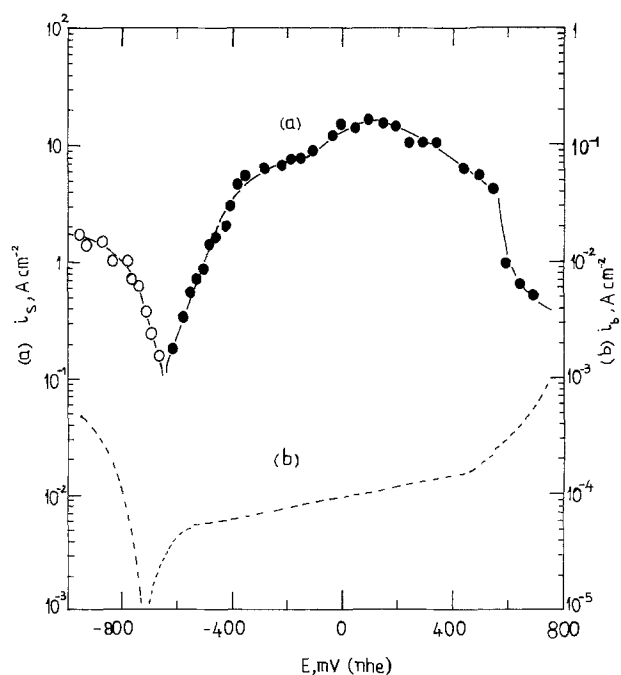


Fig. 2. Bare surface current density, i_s (\circ , \bullet) and steady-state current density, i_b (broken line) as a function of potential for nickel in 1.0M KOH. White points cathodic, black points anodic.

250 mV of the anodic branch shows linear behavior ($\log i_s \propto E$) and therefore obeys Tafel's law. For potentials higher than this the current continues to increase with E , but at a slower rate, until a peak bare surface current density of ~ 15 A cm^{-2} , and this is followed by a steady decrease in i_s for continuing increase in E . For comparison, the steady-state current density (i_b) flowing from an unscratched nickel electrode is also shown. The values of i_s lie up to 5 orders of magnitude higher than i_b . Bare surface polarization curves for the three Ni-Cu alloys were similar to that of nickel, each showing a small linear anodic Tafel region over 1-2 decades in i_s . Values of the bare surface mixed potential and the anodic Tafel slope (in i_s) are given in Table I. The anodic Tafel slope, $\partial E / \partial \log i_s$, is 149 ± 4 mV and is invariant with the alloy composition, at least when the mole fraction of nickel, $X_{Ni} > 0.3$. The value of E_{ms} is a function of X_{Ni} (also given in Table I) although the dependence is small. Such data can be fitted to a logarithmic plot in X_{Ni} which gives the empirical relationship

$$E_{ms} \text{ (mV, NHE)} = -639 - 92 \log X_{Ni} \quad [4]$$

The rate of decay of current density on the scratch can be analyzed in a number of ways. The simplest of these is a plot of $\log i(t)$ against $\log t$. Such a plot is shown for current decay on scratched nickel in Fig. 3 for a range of potentials. At low potentials these plots are curved and show a progressively increasing rate of current decay as the decay proceeds. At higher potentials, however, the plots are linear except for data taken at very short times after scratching. In this connection it is important to bear in mind that because the scratch is not created instantaneously, but requires a finite time to be formed ($t_c \approx 1.5$ ms) the position $t = 0$ is rather arbitrarily defined as that point at which the scratch is half of its final length. This creates an error in the time scale for short times after scratching and contributes to the curvature of the lines in Fig. 3 in that region. The high potential transients show linearity however, for $t \geq 4$ ms, and this linearity covers almost three decades in $i(t)$ and t . The slopes, $\partial \log i(t) / \partial \log t$ of these graphs were found to be independent of potential and alloy composition for all four materials. They give a mean, $\partial \log i(t) / \partial \log t = -0.97 \pm 0.01$, independent of potential and alloy composition. Plots of the type shown in Fig. 3 are by nature empirical and do not directly provide the mechanism of film growth as has been described earlier (18, 23, 26). Detailed information on the kinetics and mechanism of the process can, however, be obtained by describing $i(t)$ as a function of $q(t)$, the total charge density passed on the scratch at time t .

Two kinetically distinct processes can be defined from the data, depending upon potential. At low potentials (but still positive with respect to E_{ms}) a range exists where $i(t)$ is linearly related to $q(t)$. This region corresponds to the data which show curvature in Fig. 3 ($\log i(t) / \log t$ plots). The data are presented in Fig. 4 for a number of electrode potentials for all four materials. The current density $i(t)$ decays linearly with the charge density passed, $q(t)$, up to a maximum of $q(t) \approx 530 \mu\text{C cm}^{-2}$. The current decay plots are representative of those occurring at low anodic charge densities.

At higher potentials Fig. 3 shows that the decay of $i(t)$ with respect to $q(t)$ should be different from that described by Fig. 4, and this is indeed the case. Data for the Ni-30Cu alloy are presented in Fig. 5 as a function of E . The graphs show that $\log i(t)$ decreases linearly as $q(t)^{-1}$ decreases for at least two decades in $i(t)$, although for high values of $q(t)^{-1}$ the graphs are curved. The same be-

Table I. Bare surface mixed potential E_{ms} , anodic Tafel slope in i_s ($\partial E / \partial \log i_s$) and anodic Tafel slope from Eq. [9] ($\partial E / \partial \log i(0)$)

Metal	E_{ms} (mV, NHE)	$\partial E / \partial \log i_s$ (mV)	$\partial E / \partial \log i(0)$ (mV)
Ni	-643	149	93
Ni-30 Cu	-650	155	94
Ni-50 Cu	-665	145	92
Ni-70 Cu	-690	146	94

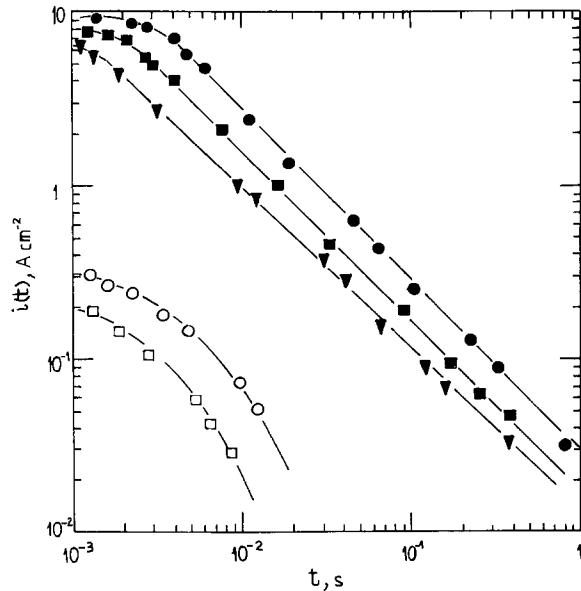


Fig. 3. Decay of current density with time for repassivation of scratched nickel in 1.0M KOH at potentials of \square : -605 mV (NHE), \circ : -580 mV (NHE), ∇ : -105 mV (NHE), \blacksquare : -5 mV (NHE), \bullet : $+70$ mV (NHE).

havior was shown for all four metals at potentials above those described by Fig. 4. The kinetics and mechanism are described quantitatively below.

Discussion

The enormous acceleration in electrochemical reaction rate produced by scratching the electrodes is a direct consequence of removal of the existing surface oxide films. The depth of the scratch (ca. $3 \mu\text{m}$) is far greater than the thickness of the pre-existing film and its creation thus involves exposure of bare metal surface to the electrolyte. The work that is put into the metal surface by the machining action has itself been shown to be of relatively little consequence on the rate of reaction for similar experiments on silver (21) and bismuth (25) electrodes, and it is reasonable to assume the same to be true for the data presented here.

The cathodic branch of the bare surface polarization curve observed at low potentials (see Fig. 2) is undoubtedly a consequence of accelerated hydrogen evolution on the scratch surface, since water is the only reducible species of any significant concentration. It should be noted that E_{ms} is positive with respect to both the observed steady-state mixed potential as well as the equilibrium hydrogen potential ($E_o = -827$ mV (NHE) at pH 14 and 1 atm H_2). It is therefore evident that water is reduced on the scratch surface at an underpotential with respect to E_o . This cathodic current represents the nonsteady-state reaction $\text{H}_2\text{O} + e^- \rightarrow \text{H}_{ads} + \text{OH}^-$ on the bare metal surface. Interpretation of the kinetics of this reaction are, however, hampered by the presence of even trace amounts of oxygen or dissolved metal ions in the electrolyte. Because of the very high electrode rotation speed used for these experiments ($\omega = 100$ Hz) trace amounts of reducible species provide detectable cathodic base currents which may then be perturbed by the scratching process. It is not yet known whether this would provide a significant error in E_{ms} although the fact that E_{ms} is a systematic function of X_{Ni} (see Eq. [4]) implies that the error is small.

Polarization Curves

In a previous paper (18) describing the behavior of nickel and nickel/copper alloys in acid solutions it was found that the bare metal surfaces reacted anodically at potentials below those expected from the thermodynamic potentials for nickel and for copper, equilibrating with their oxides. Although anodic dissolution was still thermodynamically possible the fact that a transient was observed at all means that a film had been scraped away

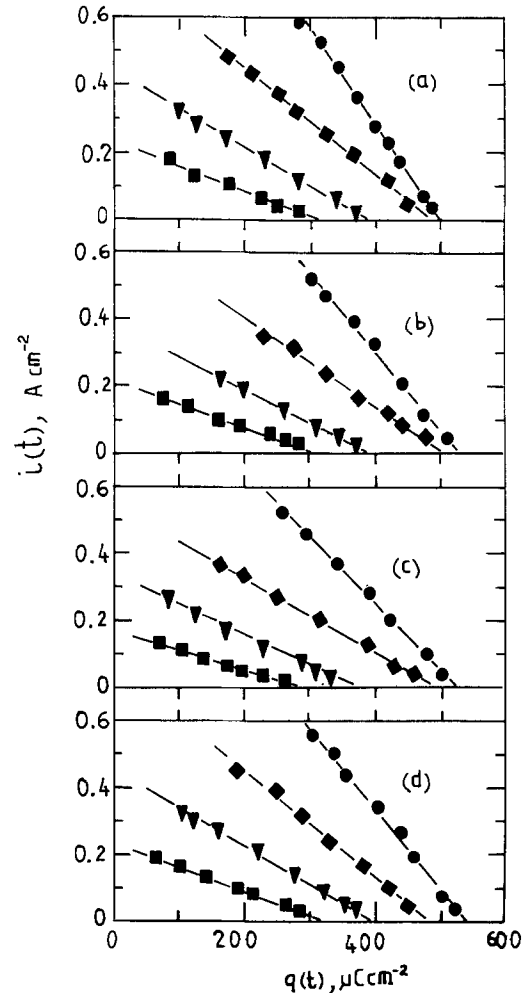


Fig. 4. Decay of current density as a function of charge density passed in 1.0M KOH at potentials of \blacksquare : -605 mV (NHE), ∇ : -580 mV (NHE), \blacklozenge : -555 mV (NHE), \bullet : -530 mV (NHE). (a) Ni, (b) Ni-30 Cu, (c) Ni-50 Cu, (d) Ni-70 Cu.

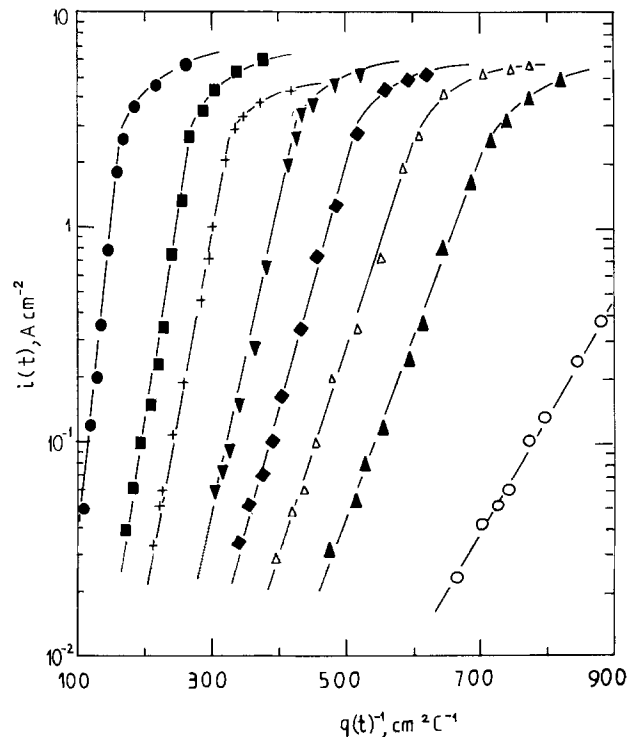


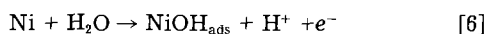
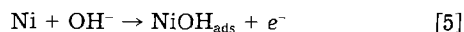
Fig. 5. Decay of current density according to Eq. [13] for scratched Ni-30Cu in 1.0M KOH. \circ : -380 mV (NHE), \triangle : -255 mV (NHE), \diamond : -105 mV (NHE), \blacklozenge : -5 mV (NHE), \blacktriangledown : 45 mV (NHE), $+$: $+95$ mV (NHE), \blacksquare : $+145$ mV (NHE), \bullet : $+195$ mV (NHE).

and analysis of the anodic charge densities involved showed that the film existing at potentials below the Ni/NiO equilibrium potential is of the order of a monolayer in thickness.

Formation of an oxide monolayer at a thermodynamic underpotential with respect to that required for a bulk oxide was not observed in the present results taken at pH 14. The value of E_{ms} for pure nickel, which is the potential below which anodic activity on the scratch is not observed, (see Table I) is in fact 74 mV more positive than the Ni/NiO equilibrium potential [-717 mV (NHE)] (27), and the data provide no evidence of underpotential anodic activity. The same is true of the nickel/copper alloys (Eq. [4], Table I), although these materials all display an E_{ms} value well below the equilibrium potential for the Cu/Cu₂O reaction [-356 mV (NHE)] (27), even where the mole fraction of Ni, $X_{Ni} = 0.3$. It is, of course, possible that nickel does possess such underpotential anodic activity as shown at pH 0 (18), but its observation is masked by the accelerated cathodic reaction on the scratch (see Fig. 2). Indeed, copper itself has been shown to be anodically active at potentials well below -356 mV (NHE) at pH 14 (22). The fact that the cathodic reaction is more strongly accelerated on scratched nickel than on scratched copper surfaces is seen clearly by inspection of the cathodic branches of the bare surface polarization curves for either metal. Thus, for example, at $E = -1000$ mV (NHE), pure Ni gives $i_s \approx 2$ A cm⁻² (Fig. 2) while pure Cu at the same potential and pH gives $i_s \approx 0.1$ A cm⁻² (22), both being cathodic values.

It is a curious consequence of this, that although copper is thermodynamically more noble than nickel when equilibrated with water (27) the E_{ms} values imply that the freshly generated nickel surface is apparently more noble than that of copper, and this can be seen to hold true for the alloys as well (Eq. [4]). It is not yet known whether this order of bare surface reactivity would be observed in the absence of the bare surface cathodic curve or not. All the anodic values of i_s for the 4 metals (see Fig. 2 and Eq. [4]) are, however, measured at a thermodynamic overpotential for Ni in equilibrium with NiO [or Ni(OH)₂].

The anodic Tafel slope, $\partial E/\partial \log i_s$ (see Table I) is 149 ± 4 mV and is indicative of the first electron transfer step being rate determining. We can write this for pure Ni as a pH dependent or independent reaction as



The solubility of Ni(II) is negligible at this pH and thus reaction [5] or [6] must be followed by rapid formation of the first monolayer of Ni(II) oxide (either NiO or Ni(OH)₂). Using reaction 6 we can write

$$i_s = k_6 \exp\left(\frac{\beta FE}{RT}\right) \quad [7]$$

where k_6 is the potential independent rate constant for reaction [6] and $\beta = 0.4$, and this equation will hold only for the initial reaction rate at which no charge has yet flowed. This can only be true where the actual value of i_s is relatively low. For higher values of i_s , significant quantities of charge flow in the period required to measure i_s ; thus i_s is itself underestimated by virtue of the growing film (see below).

It is also possible to investigate the current density flowing from the scratch at zero charge density (and therefore, by definition, zero time) by extrapolation of plots of $i(t)$, and this is considered below.

Film Growth at Low Overpotentials

At low anodic overpotentials, within the Tafel regions of the bare surface polarization curves (see Fig. 2) the $\log i(t)/\log t$ plots for nickel and the three alloys are all curved. The decay of current density obeys the linear relationship between $i(t)$ and $q(t)$ demonstrated in Fig. 4. In the absence of dissolution these kinetics are best seen as

the lateral growth of film over the scratch surface with negligible film thickening. One would expect this to occur during the growth of the first monolayer of oxide. For the process to follow the kinetics indicated by Fig. 4 the oxidation process must be totally random involving no nucleation and growth stages. Thus the observed rate of reaction at time t after scratching is simply the current flowing from that portion of the surface not yet covered by film at that instant. We can thus write for constant potential

$$i(t) = i(0) \left[1 - \frac{q(t)}{q_m} \right] \quad [8]$$

where $i(0)$ is the potential dependent rate constant defined by $i(t)$ at $q(t) = 0$ and therefore at $t = 0$, and q_m is the charge density associated with generation of the completed monolayer. Assuming reaction [6] to be rate controlling, we can replace Eq. [7] by

$$i(0) = k_6 \exp\left(\frac{\beta FE}{RT}\right) \quad [9]$$

Equation [8] is obeyed by the data in Fig. 4 for all four metals. The real bare surface current density in the absence of any film is $i(0)$ and this was obtained by extrapolation of plots of the type shown in Fig. 4. Such a plot is shown in Fig. 6. The graph is short in its range of potentials owing to the relatively short range over which linear $i(t)$ vs. $q(t)$ behavior is observed. The Tafel slopes are listed in Table I alongside those taken from the i_s data. They are independent of the metal composition and have a mean value $\partial E/\partial \log i(0) = 93 + 1$ mV. From these data it is not quite so obvious that reaction [5] or [6] is rate controlling although Eq. [9] may still be applicable, with $\beta = 0.64$. Nevertheless, the rate constant is provided as a function of potential and its value is high. Furthermore, there is no significant dependence of $i(0)$ on the Cu content of the material, demonstrating that it is the oxidation of Ni which controls the rate of oxidation of the alloys, even where $X_{Ni} = 0.3$. Presumably, the oxide monolayer actually contains oxidized Cu since Cu is capable of oxidizing to the extent of a monolayer at these potentials, (22). As such reaction [6] is more accurately written for the alloys as

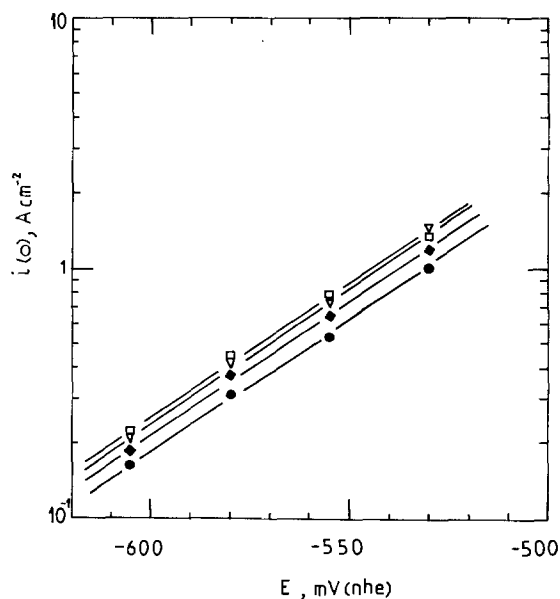
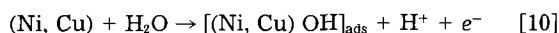


Fig. 6. Maximum bare surface current density, $i(0)$ (Eq. [9]) as a function of potential for scratched nickel and nickel-copper alloys. ∇ : Ni, \bullet : Ni-30 Cu, \bullet : Ni-50 Cu, \square : Ni-70 Cu.

the product of which is then oxidized to a monolayer containing a mixed NiO/Cu₂O lattice.

Although one cannot define the equilibrium potential for monolayer formation, it is possible to extrapolate the lines in Fig. 6 to the potential for Ni equilibrating with bulk NiO and produce the exchange current density $i_0(0)$ for $q(t) = 0$. The value is independent of the metal composition and provides for the four metals $i_0(0) = 0.013 \pm 0.002 \text{ A cm}^{-2}$.

The values of q_m , the anodic charge density passed in order to complete the monolayer (but in the absence of film thickening), can also be obtained from Fig. 4. It is the value of $q(t)$ when $i(t) = 0$, (Eq. [8]) and is seen to be independent of the metal composition but shows a small increase with increasing potential. The data are shown in Fig. 7. Measured values of q_m range between ~ 0.3 and 0.53 mC cm^{-2} and there is linear dependence upon potential. The lowest of these values is what might be expected from oxidation of surface Ni atoms, each by two electrons, to produce a monolayer of oxide film, in line with similar measurements made on other materials (20, 22, 24, 25, 28-30). It is also in line with the Ni(I) monolayer proposed for underpotential oxidation of Ni in acid solutions, where the mean charge density involved is $\sim 0.16 \text{ mC cm}^{-2}$ (18). The monolayer in the present case can be envisaged as a simple lattice of alternate Ni²⁺ and O²⁻ ions of 1 atom thickness produced by oxidation of about half the original surface Ni atoms, in line with previous work (24). Oxidation of the complete surface layer of metal atoms would then produce a monolayer of oxide of 2 atoms thickness with the same structure. Formation of such a monolayer would involve evolution of $\sim 0.6 \text{ mC cm}^{-2}$ of anodic charge density and this is close to the observed values at the highest potential of Fig. 7. Such behavior is not inconsistent with the fact that these reaction rates are all measured at an overpotential for NiO [or Ni(OH)₂] formation.

The line presented in Fig. 7 is that produced by linear regression of all the data for the four metals and it is interesting to note that extrapolation of the line to $q_m = 0$ pro-

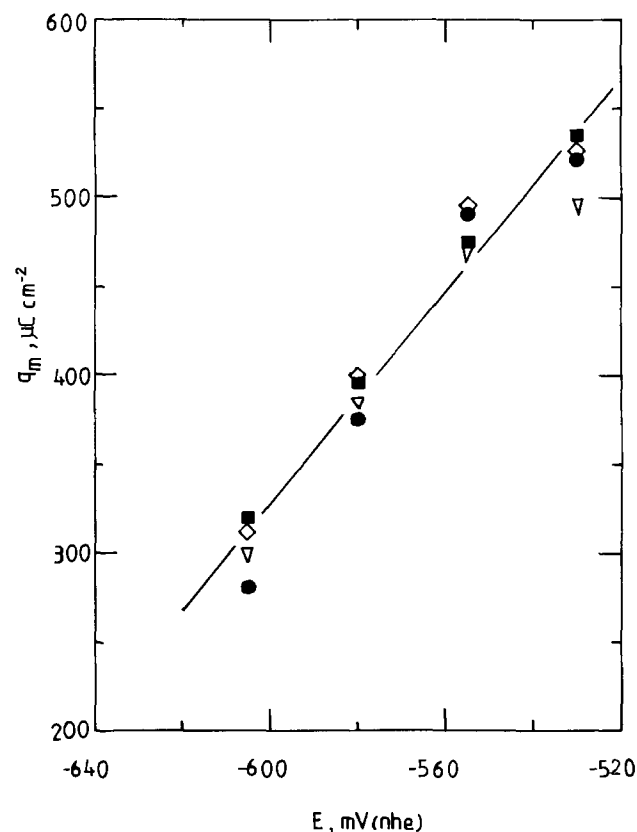


Fig. 7. Maximum bare surface charge density, q_m , as a function of potential for scratched nickel and nickel-copper alloys, ▽: Ni, ◇: Ni-30 Cu, ●: Ni-50 Cu, ■: Ni-70 Cu.

duces an intercept of $E = -710 \text{ mV (NHE)}$. This is extremely close to the equilibrium potentials (E_0) between Ni and NiO or Ni(OH)₂ [-717 and -711 mV (NHE) , respectively] (27) at pH 14, with the implication that below E_0 the metal carries no Ni(II) oxide at all. It is also indicative of the fact that it is the oxidation of Ni itself which controls oxidation of the alloys at these potentials. However, extrapolation of Fig. 7 is open to question since the reasons for potential dependence of q_m are not yet known.

It should be noted that if film thickening were to occur at a significant rate at these potentials then the data shown in Fig. 4 would be expected to show deviation from linearity, particularly at the lower values of $i(t)$.

Film Growth at High Overpotentials

At higher anodic overpotentials the $\log i(t)/\log t$ plots are linear (Fig. 3) for Ni and the Ni/Cu alloys. The charge densities involved in the decay of $i(t)$ are now significantly higher and certainly well in excess of that required for formation of a monolayer of film (see Fig. 5). This means that the equivalent monolayer charge density has been exceeded in a short time compared with the stylus contact time, and the decay in scratch current density is due to film thickening. By assuming that the rate of reaction at time t is controlled by ion migration under high electric field through that thickness of film already reformed, $x(t)$, we can write the classical film growth equation

$$i(t) = A \exp \left[\frac{BV}{x(t)} \right] \quad [11]$$

where V is the constant applied voltage. If all the anodic charge density passed on the scratch goes towards film growth then $x(t)$ is related to $q(t)$ by

$$x(t) = \frac{Mq(t)}{zF\rho} \quad [12]$$

where M is the molecular weight of the film, ρ is its density, and z is the charge number of the metal cation. When all the applied potential difference lies across the film then $V = E - E_g$ where E_g is the potential at which the field is zero. Thus

$$i(t) = A \exp \left[\frac{BzF\rho (E - E_g)}{Mq(t)} \right] \quad [13]$$

Equation [13] in logarithmic form is seen to be obeyed in Fig. 5 for repassivation of Ni-30Cu and is also obeyed for the remaining materials where $i(t) < 3$ to 4 A cm^{-2} ; the equation is followed for at least 2 decades in $i(t)$ for all 4 materials.

The rate constant, A , from Eq. [13] was calculated from the intercept of the $\log i(t)/q(t)^{-1}$ curves at $q(t) = \infty$, and values are listed in Table II. There is no variation of A with electrode potential and no significant variation with alloy composition. The mean value is $\log (A/\text{A cm}^{-2}) = -5.4 \pm 0.5$. Differentiation of Eq. [13] gives

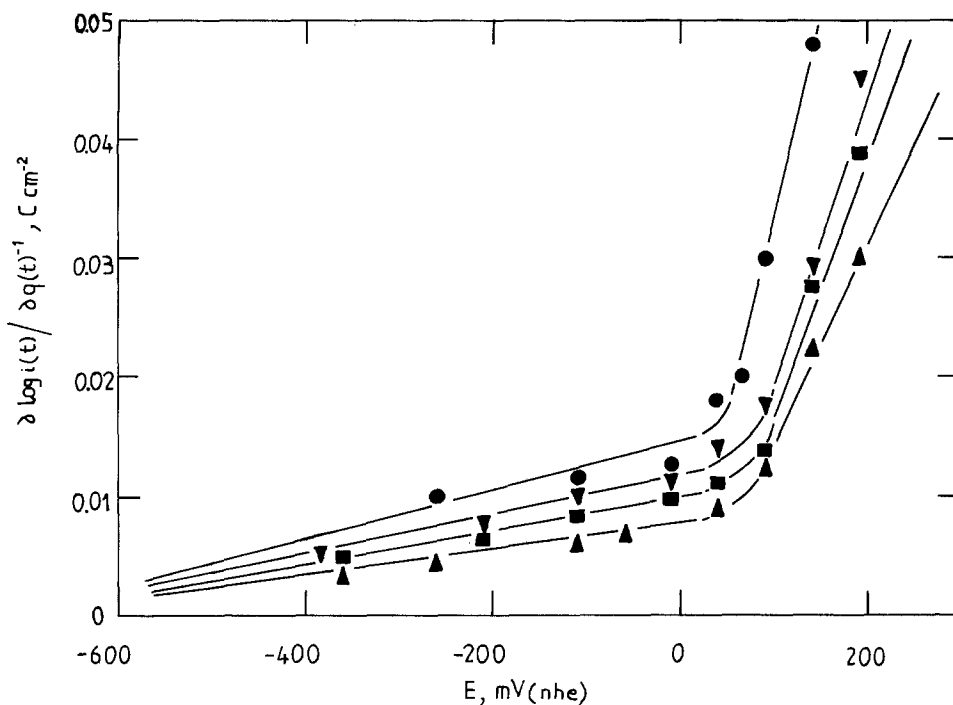
$$\frac{\partial \log i(t)}{\partial q(t)^{-1}} = \frac{BzF\rho (E - E_g)}{2.3M} \quad [14]$$

and the high field gradient should therefore be linearly related to the applied potential. This graph is shown for the four materials in Fig. 8. The data for each metal describe two regions of film growth, depending upon potential and both regions can be fitted to Eq. [14]. Transition from the low potential region of Fig. 8 to the high potential region is observed at $\sim +40 \text{ mV (NHE)}$. The data are described by the gradient of Eq. [14] as

$$\frac{\partial}{\partial E} \left[\frac{\partial \log i(t)}{\partial q(t)^{-1}} \right] = \frac{BzF\rho}{2.3M} \quad [15]$$

and the intercept, E_g , where $\partial \log i(t)/\partial q(t)^{-1} = 0$. These parameters are listed in Table II for the two regions of $E < 40 \text{ mV (NHE)}$ and $E > 40 \text{ mV (NHE)}$.

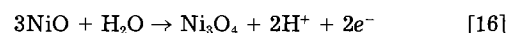
Fig. 8. Gradient of high field current decay on scratched nickel and nickel-copper alloys in 1.0M KOH as a function of potential ●: Ni, ▼: Ni-30 Cu, ■: Ni-50 Cu, ▲: Ni-70 Cu.



Values of E_g are independent of the alloy composition. The mean values are $E_g = -694$ mV (NHE) for $E < 40$ mV (NHE) and $E_g = +18$ mV (NHE) for $E > 40$ mV (NHE). The lower value is very close to the equilibrium potential (E_0) between Ni and NiO [or Ni(OH)₂] (*loc. cit.*) and to the intercept of Fig. 7; it is clear that the growing film is one of the Ni(II) oxides from the moment of inception of the oxide on the newly generated metal surface and that its occurrence is in complete accord with equilibrium thermodynamics. This means that for the alloys copper plays no significant thermodynamic part in the reaction. Since equilibrium between Cu and its oxides occurs at a significantly more noble potential its electrochemical ac-

tivity in the alloys must be enhanced to that of nickel simply by virtue of the presence of Ni.

The measured value of E_g for the higher potential region [+ 18 mV (NHE)] can be interpreted in terms of oxidation of the nickel to one of its higher oxides. According to Pourbaix (27) this could be



with

$$E_0 [\text{mV (NHE)}] = 897 - 59.1 \text{ pH} \quad [17]$$

or

$$E_0 [\text{mV (NHE)}] = 876 - 59.1 \text{ pH} \quad [18]$$

Table II. Measured parameters for film growth under high electric field (Eq. [11], [13]-[15], [19], [20]) for Ni/Cu alloys in 1.0M KOH

Metal	Potential (mV, NHE)	log (A/A cm ⁻²)	$\partial \log i(t) / \partial q(t)^{-1}$ C cm ⁻²	$\frac{\partial^2 \log i(t)}{\partial q(t)^{-1} \partial E}$ C cm ⁻² V ⁻¹			
				E_g (mV, NHE)		E_g (mV, NHE)	
				$E < 40$ mV (NHE)	$E > 40$ mV (NHE)	$E < 40$ mV (NHE)	$E > 40$ mV (NHE)
Ni	-255	-5.6	0.0100				
	-105	-5.3	0.0115				
	-5	-5.6	0.0125				
	+45	-6.1	0.0170	0.021	0.334	-705	+10
	+70	-6.0	0.0210				
	+95	-6.5	0.0303				
	+145	-6.4	0.0490				
Ni-30 Cu	-380	-5.3	0.0050				
	-205	-5.5	0.0076				
	-105	-5.4	0.0096				
	-5	-5.5	0.0115				
	+45	-5.5	0.0140	0.017	0.243	-690	+20
	+95	-5.4	0.0175				
	+145	-5.5	0.0286				
Ni-50 Cu	+195	-5.9	0.0454				
	-355	-5.2	0.0050				
	-205	-5.3	0.0060				
	-105	-5.4	0.0084				
	-5	-5.7	0.0098				
	+45	-5.7	0.0110	0.014	0.218	-695	+25
	+95	-5.3	0.0139				
Ni-70 Cu	+145	-5.4	0.0278				
	+195	-5.5	0.0385				
	-355	-4.1	0.0036				
	-255	-4.0	0.0044				
	-105	-5.2	0.0062				
	-5	-5.2	0.0070				
	+45	-5.3	0.0090	0.011	0.169	-685	+15
+95	-5.0	0.0135					
+145	-5.2	0.0222					
+195	-5.3	0.0303					

This observation is consistent with previous work by more conventional electrochemical experiments as well as ellipsometric measurements (4), although the phase formed at higher potentials may be β -NiOOH (2, 6, 7, 10), not considered by Pourbaix.

The gradient given by Eq. [15] (see Table II) is, now, a function of the alloy composition. For each material, its value at higher potentials [$E > 18$ mV (NHE)] is some 15 times that at lower potentials [$E < 18$ mV (NHE)]. The data are plotted in Fig. 9 as a function of the alloy composition. The relationship is approximately linear in mol fraction of Cu and gives empirically

$$\frac{\partial^2 \log i(t)}{\partial q(t)^{-1} \partial E} (\text{C cm}^{-2} \text{V}^{-1}) = 0.021 - 0.015X_{\text{Cu}} \quad [19]$$

for $E < 18$ mV (NHE), and

$$\frac{\partial^2 \log i(t)}{\partial q(t)^{-1} \partial E} (\text{C cm}^{-2} \text{V}^{-1}) = 0.325 - 0.220X_{\text{Cu}} \quad [20]$$

for $E > 18$ mV (NHE). Equation [19] is quantitatively comparable with that for film growth at low current densities on the same materials in acid solutions (18), where

$$\frac{\partial^2 \log i(t)}{\partial q(t)^{-1} \partial E} (\text{C cm}^{-2} \text{V}^{-1}) = 0.023 - 0.014X_{\text{Cu}} \quad [21]$$

The quantity described by Eq. [15] and [19]-[21] is a property of the film only, and by Eq. [15] can be used to define B , provided values for z , ρ , and M are assumed. For NiO growing on pure Ni we have $z = 2$, $\rho = 6.7 \text{ g cm}^{-3}$ and $M = 74.6 \text{ g mol}^{-1}$. From Eq. [19] $B = 2.8 \times 10^{-6} \text{ cm V}^{-1}$. If the oxide is $\text{Ni}(\text{OH})_2$, as described by others (1-11) then $\rho \approx 3.9 \text{ g cm}^{-3}$ (31) and $M = 92.7 \text{ g mol}^{-1}$, whence $B = 6.1 \times 10^{-6} \text{ cm V}^{-1}$. The value of B can be interpreted, as previously (18), in terms of the half-width (b) of the energy barrier towards migration of the cations through the oxide. Thus

$$b = \frac{BkT}{ez} \quad [22]$$

where k is the Boltzmann constant, T the temperature, e the electronic charge, and z the charge number. For pure NiO or $\text{Ni}(\text{OH})_2$ growing on pure Ni we obtain $b = 0.35 \text{ nm}$

or 0.76 nm , respectively, and the values are reasonable in terms of approximate lattice spacings. Variation of B with copper content of the alloy can then be interpreted in terms of changes in the parameters associated with ion migration in the film. Inspection of Eq. [15] and [22] shows that such variation (shown in Fig. 9) occurs in the parameter $bz^2\rho/M$ as the film composition, and perhaps structure, change with the incorporation of Cu cations, either as Cu^+ or as Cu^{2+} . While it is not possible to determine which of the film constants individually are changing, it is clear that the growing film is based on the nickel oxide lattice, and not copper oxide, both in terms of the thermodynamic as well as the kinetic parameters. It is also clear that there are no abrupt changes in these properties with copper content, at least up to 70% Cu in the alloy (and therefore in the film as well); the oxidized copper must thus form a uniform homogeneous solid solution in the nickel oxide lattice. The same deduction can be made for passive films grown on these materials in acid solutions (18).

The film growth parameters under conditions of high applied potential [$E > 18$ mV (NHE)] are more difficult to explain. The value of A is the same as that for lower potentials but the value of B for pure Ni as determined from Eq. [15] and [20] (see Fig. 9) are considerably larger, no matter which stoichiometry one assigns the oxide. Thus, for Ni_3O_4 , which we now write as $\text{NiO}_{1.3}$, $\rho = 3.6 \text{ g cm}^{-3}$, $M = 79.5 \text{ g mol}^{-1}$ (of $\text{NiO}_{1.3}$) and z has a mean value of 2.7. This gives $B = 6.5 \times 10^{-5} \text{ cm V}^{-1}$ and $b = 6.2 \text{ nm}$. The latter value is too large to be associated with a simple energy barrier in the oxide. It is possible that this film is duplex or even multiplex in nature with a more complex field distribution through its thickness. Nevertheless, the effects of copper on the process are exactly analogous to those effects observed with the lower potential film, as is seen in Fig. 9. In both regions of potential the nucleation and growth of the passivating film is controlled by nickel oxide; only the field strength across the films is modified by the presence of copper, and this is true for alloys of composition $0.3 \leq X_{\text{Ni}} \leq 1$.

The parameters described above for film growth under high electric field (A , B , and E_0) for $E < 18$ mV (NHE) are fully consistent with those describing repassivation of these materials in acid solution (18). The early kinetic region in acid solutions, which is described by a high value of A (18), was not, however, observed at pH 14.

Conclusions

1. The initial step in the repassivation of a freshly generated nickel surface in alkaline solution is the formation of a monolayer of NiO or $\text{Ni}(\text{OH})_2$. The reaction occurs with an apparent bare surface exchange current density of 13 mA cm^{-2} and an anodic Tafel slope of 93 mV . The mechanism of formation of this monolayer does not involve separate nucleation and lateral growth steps but consists of random oxidation of exposed metal atoms. No evidence has been found for nickel reacting anodically at potentials below the Ni/Ni (II) equilibrium potential although this has been observed for repassivation in acid solutions. The measured anodic charge required to complete the monolayer is a function of the applied potential.

2. The initial step in the repassivation of freshly generated surfaces of nickel/copper alloys containing up to 70% Cu is quantitatively similar to that described above for pure nickel. No effects of copper, either thermodynamic or kinetic, can be observed on the growth of the first monolayer of oxide.

3. Thickening of the Ni(II) oxide passive film on nickel in alkaline solution (pH 14) beyond the first monolayer coverage obeys the equation relating the rate of reaction to the high electric field across the film (Eq. [13]). For potentials below +18 mV (NHE) this occurs with $A = 4 \times 10^{-6} \text{ A cm}^{-2}$, $B = 6 \times 10^{-6} \text{ cm V}^{-1}$, and $E_0 = -694 \text{ mV}$ (NHE). For potentials above +18 mV (NHE) the film is oxidized to a higher oxide and growth of the film occurs with the same value of A , but with $B = 6.5 \times 10^{-5} \text{ cm V}^{-1}$ and $E_0 = +18 \text{ mV}$ (NHE).

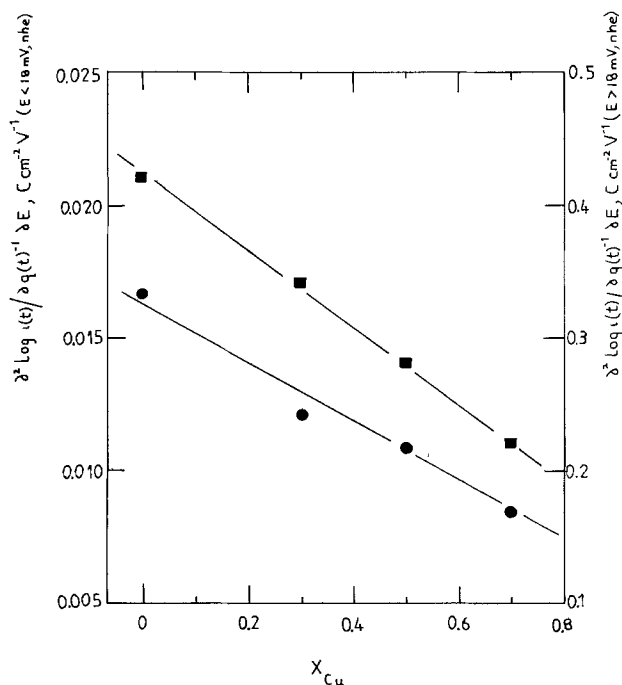


Fig. 9. $\partial/\partial E [\partial \log i(t)/\partial q(t)^{-1}]$ as a function of the mol-fraction of copper. ■: $E < 18$ mV (NHE), left-hand ordinate. ●: $E > 18$ mV (NHE), right-hand ordinate.

4. Oxide film thickening during repassivation of nickel/copper alloys containing up to 70% Cu obeys Eq. [13] with A and E_0 values similar to those described for Ni. The high field gradient (and therefore the B value) however, decreases with increase in the copper content of the alloy for both film growth regions ($E < \text{and} > +18$ mV (NHE)).

Acknowledgments

We are grateful to the Ernest Oppenheimer Foundation for the financial support of R. D. K. M. and to Professor R. W. K. Honeycombe for the provision of laboratory facilities.

Manuscript submitted Aug. 22, 1983; revised manuscript received Feb. 2, 1984.

REFERENCES

- J. L. Weininger and M. W. Breiter, *This Journal*, **110**, 484 (1963).
- J. L. Weininger and M. W. Breiter, *ibid.*, **111**, 707 (1964).
- D. E. Davies and W. Barker, *Corrosion*, **20**, 47t (1964).
- H. Bode, K. Dehmelt, and J. Wilte, *Electrochim. Acta*, **11**, 1079 (1966).
- D. M. MacArthur, *This Journal*, **117**, 422 (1970).
- J. A. Hopper and J. L. Ord, *ibid.*, **120**, 183 (1973).
- W. Visscher and A. Damjanovic, Extended Abstracts 27th Meeting, I.S.E., Zurich (1976).
- R. S. Schreiber Guzman, J. R. Vilche, and A. J. Arvia, *This Journal*, **125**, 1578 (1978).
- W. Visscher and E. Barendrecht, *Electrochim. Acta*, **25**, 651 (1980).
- J. F. Wolf, L-S. R. Yeh, and A. Damjanovic, *ibid.*, **26**, 409 (1981).
- J. F. Wolf, L-S. R. Yeh, and A. Damjanovic, *ibid.*, **26**, 811 (1981).
- D. D. Macdonald, *ibid.*, **21**, 169 (1976).
- N. Cabrera and N. F. Mott, *Rep. Prog. Phys.*, **12**, 163 (1949).
- M. Pourbaix, N. de Zoubov, and E. Deltombe, CITCE VII, Lindau, 193 (1955).
- J. E. Castle, J. T. Harrison, and H. G. Masterson, "Proc. 2nd Int. Conf. Met. Corr.," p. 822, NACE, New York (1963).
- C. Moore and D. Bindley, *ibid.*, p. 391.
- P. J. Boden, *Corros. Sci.*, **11**, 363 (1971).
- R. D. K. Misra and G. T. Burstein, *ibid.*, **24**, 305 (1984).
- F. P. Ford, G. T. Burstein, and T. P. Hoar, *This Journal*, **127**, 1325 (1980).
- G. T. Burstein and D. H. Davies, *ibid.*, **128**, 33 (1980).
- G. T. Burstein and R. C. Newman, *Electrochim. Acta*, **25**, 1009 (1980).
- G. T. Burstein and R. C. Newman, *This Journal*, **128**, 2270 (1981).
- G. T. Burstein and P. I. Marshall, *Corros. Sci.*, **23**, 125 (1983).
- G. T. Burstein and R. D. K. Misra, *Electrochim. Acta*, **28**, 363 (1983).
- G. T. Burstein and G. W. Ashley, *Corrosion*, **39**, 241 (1983).
- G. T. Burstein and R. D. K. Misra, *Electrochim. Acta*, **20**, 825 (1983).
- M. Pourbaix, "Atlas of Electrochemical Equilibria in Aqueous Solutions," pp. 332, 386, Pergamon Press, Oxford (1966).
- G. T. Burstein and R. D. K. Misra, *Electrochim. Acta*, **28**, 371 (1983).
- R. C. Newman and G. T. Burstein, *J. Electroanal. Chem.*, **129**, 343 (1981).
- G. T. Burstein and R. C. Newman, *Electrochim. Acta*, **26**, 1143 (1981).
- "Handbook of Physics and Chemistry," R. W. Weast, Editor, pp. B-135, B-136, CRC Press, Cleveland (1976).
- T. P. Hoar in "Modern Aspects of Electrochemistry," No. 2, J. O'M. Bockris, Editor, p. 262, Butterworths, London (1959).

Structure Investigations of Electrodeposited Nickel

I. X-Ray Diffraction and Mössbauer Spectroscopic Measurements

A. Vértes, I. Czakó-Nagy, and M. Lakatos-Varsányi

Department of Physical Chemistry and Radiology, Eötvös Loránd University, H-1088 Budapest, Hungary

L. Csordás

Department of Solid State Physics, Eötvös Loránd University, H-1088 Budapest, Hungary

H. Leidheiser, Jr.*

Department of Chemistry and Center for Surface and Coatings Research, Lehigh University, Bethlehem, Pennsylvania 18015

ABSTRACT

Nickel was electrodeposited on copper substrates from sulfamate-sulfite, sulfamate, chloride, and chloride-sulfate electrolytes. The crystalline orientation was determined by x-ray diffraction, the magnetic orientation by Mössbauer spectroscopy of Co-57-doped deposits, and the stress by electrode deflection. The stress level was correlated with the relative intensity of the lines in the Mössbauer emission pattern in the case of deposits with a (100) preferred orientation.

The stress developed in nickel electrodeposits has been of interest for many years because of concern that internal stress may reduce corrosion resistance and also may lead to deformation of the substrate when the substrate is thin. The goal of the studies reported herein was an exploration of techniques based on Mössbauer spectroscopy that might be utilized for qualitative or quantitative measurements of the stress level in nickel electrodeposits. This goal has not yet been totally achieved but partial success has been obtained in the case of deposits with a (100) preferred orientation.

We report in this and the following paper the results of studies of nickel electrodeposits utilizing x-ray diffraction, Mössbauer emission spectroscopy of deposits doped

* Electrochemical Society Active Member.

with Co-57, and positron annihilation spectroscopy. For convenience in presenting the results, the first paper deals with the measurements related to stress in the deposits and the second paper deals with measurements related to structural imperfections.

Experimental

The test samples were prepared by electrodeposition of nickel on copper substrates from four different plating solutions: sulfamate-sulfite, sulfamate, chloride-sulfate, and chloride. The copper substrates were 0.2 mm thick and were surfaced prior to electroplating by abrasion with pumice, etching in dilute HNO_3 , and washing in distilled water. The experimental conditions for the forma-

Table I. Composition of the plating solutions and deposition conditions

Sample identification	Composition of plating baths	Electrolyte concentration (g/l)	Current density (A/dm ²)	pH	Temp. (°C)
1	Sulfamate-sulfite		2.75	4.0	50
	Ni sulfamate	330			
	H ₃ BO ₃	30			
	Na lauryl sulfate	1			
2	Sulfamate		2.75	4.0	50
	Ni sulfamate	330			
	H ₃ BO ₃	30			
	Na lauryl sulfate	1			
3	Chloride-sulfate		5.0	5.6	45
	NiSO ₄ · 7H ₂ O	170			
	NiCl ₂ · 6H ₂ O	35			
	H ₃ BO ₃	35			
4	Chloride		5.0	2.0	60
	NiCl ₂ · 6H ₂ O	300			
	H ₃ BO ₃	30			
	Na lauryl sulfate	0.5			
5	Chloride		5.0	2.0	60
	NiCl ₂ · 6H ₂ O	300			
	H ₃ BO ₃	30			
	Na lauryl sulfate	0.5			
6	Chloride		10.0	2.0	60
	NiCl ₂ · 6H ₂ O	300			
	H ₃ BO ₃	30			
	Na lauryl sulfate	0.5			
7	Chloride		10.0	2.0	60
	NiCl ₂ · 6H ₂ O	300			
	H ₃ BO ₃	30			
	Na lauryl sulfate	0.5			
8	Chloride		15.0	2.0	60
	NiCl ₂ · 6H ₂ O	300			
	H ₃ BO ₃	30			

tion of the deposits are summarized in Table I. Deposits from the chloride-sulfate bath were prepared over a temperature range of 20°-60°C. The surface active agent, sodium lauryl sulfate, was added in three cases to minimize pitting. The deposit thickness was 250 μm in the case of the panels utilized for the x-ray diffraction studies and was 30 μm in the case of the panels utilized in the Mössbauer studies. In the latter case, a small amount of Co-57 in the form of the chloride was added to the plating bath in order to yield an electrodeposit that was doped with Co-57. The stress in the deposit was measured in four cases using the deflection of the cathode as developed by Hoar and Arrowsmith (1). One side of the cathode was coated with a commercial epoxy-polyamide coating known as "Abdeck" so as to limit the electrodeposit to one side of the cathode. It is not felt that stresses due to water uptake by the coating were significant since the stress measurement was made within 10 min of immersion in the plating bath.

X-ray diffraction data were accumulated using a DRON-3 diffractometer and the K_α radiation of molybdenum. The emission Mössbauer spectra were obtained using a spectrometer manufactured by Ranger Electronics. The absorber was K₄Fe(CN)₆·3H₂O, and all chemical shifts are given relative to this standard. The spectra were fitted by Lorentzian functions.

Results

Stress measurements.—The measured values of the stress are tabulated for four electrodeposits and literature

Table II. Residual stresses in nickel electrodeposits

Sample	Residual stress (N/mm ²)		Reference
	Our results	Results taken from the literature	
1		-130	(2)
2	15	17.5	(2)
3	170	260	(3)
4		410	(4)
5		410	(4)
6	260	490	(4)
7	280	490	(4)
8		580	(4)

values are cited for deposits prepared under all eight conditions in Table II. It will be noted that our measured values are lower than those taken from the literature.

X-ray diffraction measurements.—The results of the x-ray diffraction measurements are given in Table III. Data are also given for rolled nickel and the values for powdered nickel from the ASTM standard card file are given at the end of the table.

The deposit from the sulfate-chloride bath exhibited very strong (100) preferred orientation as has been reported previously (5, 6). Samples 1 and 2 exhibited a weak (100) preferred orientation and samples 4-8 exhibited a weak (110) preferred orientation.

The x-ray diffraction characteristics of plating bath 3 were also studied as a function of temperature over the range of 20°-60°C. The strong (100) preferred orientation was maintained over the temperature range, 30°-55°C.

Thermal treatment of sample 3 at 500° for 1h in an argon atmosphere did not change the crystalline orientation, and the sample maintained the strong (100) preferred orientation.

Mössbauer spectroscopic measurements.—Mössbauer data for 13 nickel deposits doped with ⁵⁷Co are summarized in Table IV. The isomer shift, the quadrupole splitting, and the effective magnetic field values are those characteristic for ⁵⁷Co atomically dispersed in nickel. The only parameter that exhibited significant differences for deposits formed under different experimental conditions was the relative line intensities, given as *R* in the table. This parameter is determined by the magnetic orientation

Table III. X-ray diffraction data

Sample	Reflection (Miller indexes)	I _{rel}	Orientation	Lattice parameter <i>a</i> (nm)
1a	(111)	100	Weak (100)	0.3512
	(200)	94		
	(220)	1		
1b	(111)	100	Weak (100)	0.3511
	(200)	90		
	(220)	0.8		
2a	(111)	100	Weak (100)	0.3507
	(200)	74		
	(220)	2		
2b	(111)	100	Weak (100)	0.3506
	(200)	77		
	(220)	1.5		
3a	(111)	2.1	Strong (100)	0.3524
	(200)	100		
	(220)	0.2		
3b	(111)	2.4	Strong (100)	0.3518
	(200)	100		
	(220)	0.2		
4a	(111)	100	Weak (110)	0.3513
	(200)	39		
	(220)	44		
4b	(111)	100	Weak (110)	0.3515
	(200)	35		
	(220)	41		
5	(111)	100	Weak (110)	0.3514
	(200)	40		
	(220)	40		
6	(111)	100	Weak (110)	0.3526
	(200)	40		
	(220)	42		
7	(111)	100	Weak (110)	0.3513
	(200)	37		
	(220)	34		
8a	(111)	100	Weak (110)	0.3517
	(200)	39		
	(220)	42		
8b	(111)	100	Weak (110)	0.3518
	(200)	40		
	(220)	37		
Rolled	(111)	100		
	(200)	99		
	(220)	24		
Nickel ASTM Standard Powdered Nickel	(111)	100		
	(200)	42		
	(220)	21		

a and b refer to parallel measurements of different samples deposited from the same solution.

Table IV. Mössbauer parameters of the ^{57}Co -doped Ni-electrodeposits

Sample	Isomer shift δ^* (mms $^{-1}$)	Quadrupole splitting ΔE_Q (mms $^{-1}$)	Effective magnetic field H_{eff} (Tesla)	Half-width at the half-maximum Γ (mms $^{-1}$)	$R = \frac{A_1 + A_6^{**}}{A_2 + A_5}$	3/R
1a	-0.042	-0.003	26.50	0.320	3.31***	0.90
1b	-0.033	-0.003	26.73	0.326	3.00	1.00
2a	-0.038	-0.003	26.84	0.300	2.33	1.28
2b	-0.037	-0.002	26.58	0.300	2.02	1.48
2c	-0.040	+0.001	26.68	0.306	2.10	1.43
3a	-0.042	-0.005	27.00	0.320	7.50	0.40
3b	-0.041	-0.007	26.71	0.323	7.35	0.41
4	-0.039	+0.013	27.50	0.295	4.06	0.74
5	-0.046	+0.016	26.55	0.296	2.76	1.09
7	-0.045	+0.010	26.05	0.288	2.86	1.05
8a	-0.044	+0.010	26.81	0.318	3.73	0.80
8b	-0.035	-0.001	26.68	0.307	3.64	0.82
8c	-0.042	+0.011	26.67	0.319	3.67	0.82

* Relative to $\text{K}_4\text{Fe}(\text{CN})_6 \cdot 3\text{H}_2\text{O}$ absorbent.

** A_i is the area of the i th line.

*** An aging for three months at room temperature did not change the results.
(a, b, and c stand for the parallel electrodepositions.)

of the domains in the nickel electrodeposit, and it is affected by the crystalline orientation and by the internal stress (7, 8). Representative spectra are shown in Fig. 1. The ratio of lines 3 to 1 should be unaffected by changes in orientation, and the spectra shown in Fig. 1 do indeed indicate that this ratio is a constant.

Discussion

Previously, it has been predicted (9) that the stress level in nickel electrodeposits can be determined from Mössbauer emission spectra provided that the orientation of the deposit is (100). The reasoning behind this conclusion will be briefly stated, but the original publication should be consulted for a more detailed summary.

The easy directions of magnetization in a magnetic material are determined by the magnetocrystalline anisotropy and the mechanical stress brought about by magnetostriction. These easy directions are the possible directions for domain magnetization. The relative abundance of the various easy directions is determined by the requirement that the magnetostatic energy should be a minimum. The domain structure, and especially the domain sizes, are related to the necessity for the presence of domain walls where spins out of the easy direction exist. In a magnetic metal, all these effects are coupled and the domain pattern is determined by a local minimum of the sum of the magnetocrystalline, magnetoelastic, elastic, magnetostatic, and domain wall energies.

The magnetic orientation of the sample relative to the spatial orientation of the sample can be determined by measurement of the relative areas of the first and sixth lines in the Mössbauer emission pattern to the second and fifth lines

$$R = \frac{A_1 + A_6}{A_2 + A_5} = \frac{3/4 (1 + \cos^2 \theta)}{\sin^2 \theta} \quad [1]$$

where A_i is the area of the i th line of the Mössbauer spectrum and θ is the angle between the directions of the propagation of the gamma rays and the magnetization (10).

It was suggested that stress in the electrodeposit changes the easy direction of magnetization from the normal (111) direction to the (110) direction in those cases where the (100) plane lies parallel to the metal surface. The magnitude of the stress is assumed to determine the fraction of the domains which have a (110) direction of magnetization. The fraction shows up in the ratio of the line intensities as given in the above equation.

The predicted relationship (9) between the value of 3/R and the stress level in nickel electrodeposits with a (100) preferred orientation is given in Fig. 2. Experimental points determined in this study for samples 1-3, the only ones of the set with a (100) preferred orientation, are also included in the figure. The point for sample 2, in which the stress level was low, falls on the theoretical curve, whereas the points for samples 1 and 3 are seriously off the curve. The zero stress level value is an assumed value taken from the sample heated at 500°C in argon.

A strong (100) orientation is maintained over the temperature range of 30°-50°C in the case of the panels plated from the sulfate-chloride bath. Mössbauer measurements on similar samples indicated that the 3/R values increased approximately 20% for each 10°C increase in bath temperature. Data given by Brugger (11) and Croly (12), as summarized by Safranek (4), indicate that the stress level in deposits from the sulfate-chloride

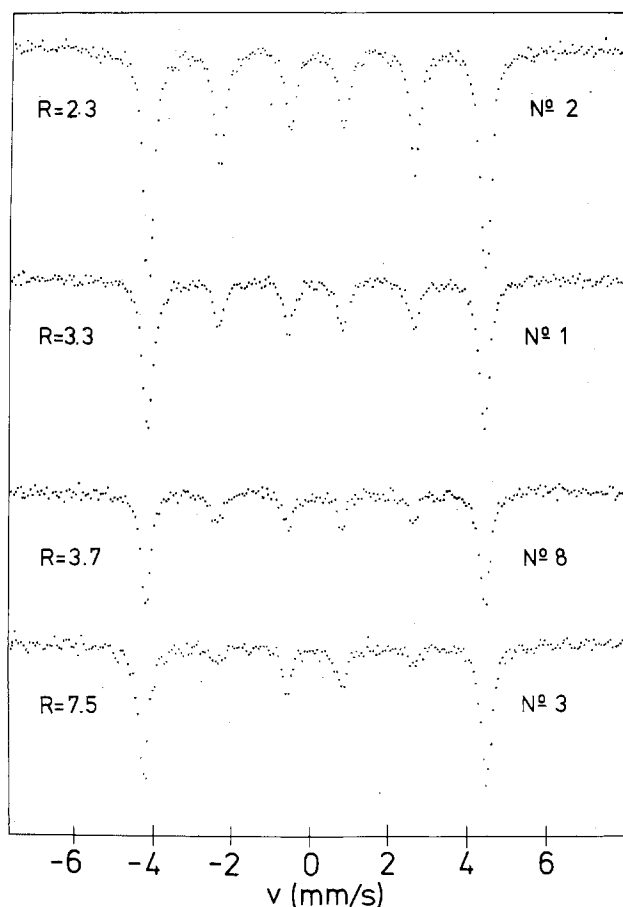


Fig. 1. Representative Mössbauer emission spectra from nickel electrodeposits doped with Co-57.

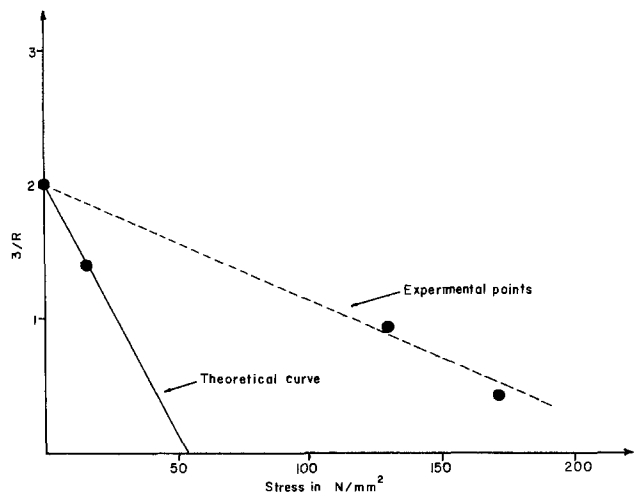


Fig. 2. Comparison between the theoretical curve developed in Ref. (9) and the experimental values for electrodeposits with a (100) preferred orientation. The point at 130 N/mm² represents the literature value for a sample with compressive stress.

bath decreases over the temperature range of interest, namely, 30°-50°C. Thus, these data also support the prediction that deposits with a (100) preferred orientation exhibit a Mössbauer hyperfine split pattern whose character is related to the stress level in the deposit.

One other piece of information supports in a qualitative way the relationship between $3/R$ and the stress level in (100) oriented nickel electrodeposits. Sample 3 was heated at 500°C in an argon atmosphere for 6h and the $3/R$ value was determined after slowly cooling the sample to room temperature. The $3/R$ value increased from its original value of 0.4 to approximately 2, a value characteristic of a very low stress level in the deposit. Concurrently with the change in relative intensity of the lines in the hyperfine split spectrum, the measured effective magnetic field increased to 29.2T from its original value of 26.8. The probable explanation for this increase in the effective magnetic field is the aggregation of cobalt atoms within the nickel matrix.

The measurement of stress, or changes in stress level on thermal treatment by the emission Mössbauer technique, is not practical for routine commercial applications because of the necessity to use the radioactive isotope ⁵⁷Co. However, the method may have application in laboratory studies or in the development of a process. Also, presently the method appears applicable only to deposits with a (100) preferred orientation. This limitation does not seem to be unduly restrictive since deposits made from the sulfate-chloride bath under common conditions of current density and temperature in the absence of organic addition agents ordinarily exhibit a strong (100) preferred orientation.

It does appear that there is a relationship between the ratio of lines 1 and 2 in the Mössbauer spectra and the stress for nickel deposits with a (100) preferred orientation. The chief difficulty is that the line ratio is much less sensitive to stress than the theoretical conclusions in Ref. (9) suggest. Refinements in the theoretical treatment are warranted.

Manuscript submitted May 13, 1983; revised manuscript received Feb. 10, 1984.

REFERENCES

1. T. P. Hoar and D. J. Arrowsmith, *Trans. Inst. Met. Finish.*, **36**, 1 (1958).
2. J. L. Marti, *Plating*, **53**, 61 (1966).
3. A. Brenner, V. Zentner, and C. W. Jennings, *ibid.*, **39**, 865, 899, 933 (1952).
4. W. H. Safraneck, "The Properties of Electrodeposited Metals and Alloys," pp. 261-274, American Elsevier Publishing Co., New York (1974).
5. H. Leidheiser, Jr. and A. T. Gwathmey, *This Journal*, **98**, 225 (1951).
6. F. Denise and H. Leidheiser, Jr., *ibid.*, **100**, 490 (1953).
7. L. D. Lafleur, *Phys. Rev. B*, **20**, 2581 (1979).
8. J. H. Kjeldgaard and G. Trumpy, *Appl. Phys.*, **21**, 361 (1980).
9. L. Takács, A. Vértes, and H. Leidheiser, Jr., *Phys. Status Solidi A*, **74**, K45 (1982).
10. A. Vértes, L. Korecz, and K. Burger, "Mössbauer Spectroscopy," p. 44, Elsevier, Amsterdam (1979).
11. R. Brugger, "Nickel Plating: Bright and Semi-Bright Nickel Plating, Corrosion Resistance, Heavy Nickel Plating and Electroforming," Leuze Verlag, Saulgau, Germany (1967).
12. P. B. Croly, *Print. Plates Mag.*, **50**, 3 (1964).

Structure Studies of Nickel Electrodeposits

II. Positron Lifetime Measurements

A. Vértes and Cs. Szeles

Department of Physical Chemistry and Radiology, Eötvös Loránd University, H-1088 Budapest, Hungary

Zs. Kajcsos

Central Research Institute for Physics of the Hungarian Academy of Sciences, Budapest, Hungary

H. Leidheiser, Jr.*

Center for Surface and Coatings Research, Lehigh University, Bethlehem, Pennsylvania 18015

ABSTRACT

Positron lifetime measurements were made on nickel electrodeposits. The shapes of the lifetime spectra depended on the conditions of the electrodeposition. The defect structure of the crystal lattice of the electrodeposits was analyzed on the basis of the parameters of the positron annihilation measurements. The effect of heat-treatment on the lifetime spectra was studied and the hydrogen concentration in the electrodeposited nickel was estimated.

Positron annihilation measurements have proven very useful in studies of the defect structure in metals. Such measurements are made by injecting positrons generated during the radioactive transition in ^{22}Na . The positrons are thermalized on a time scale which is short compared to their lifetimes. The annihilation rate of a positron-electron pair is a function of the electron density sampled by the positrons at the time of annihilation. In condensed media, most of the positrons annihilate with an electron into two gamma quanta, each with an energy of 511 keV, in the center of the mass frame of the annihilating positron-electron pair. The momentum of the positron after thermalization can be neglected in first order and the electron momentum is assumed by the gamma quanta. This fact results in deviations from the 180° angular difference between the two gamma quanta as well as in a Doppler broadening of the 511 keV annihilation radiation in the laboratory framework. The three major parameters that arise from positron annihilation experiments in metals are: positron lifetime, angle between the two gamma quanta formed, and the Doppler broadening of the gamma quanta. Measurements in this report are limited to positron lifetimes.

Positrons may be trapped in vacancies, dislocations, vacancy clusters, voids, and in almost any type of structural disorder. The annihilation of positrons in a trapping site results in a longer lifetime and in a narrower angular or energy distribution of annihilation gamma quanta than values measured for untrapped positrons. Annihilation of positrons in a specific type of trapping site results in specific parameters for the annihilation process. Consequently, the positron lifetime spectra contain information about the shape and concentration of the defects in crystalline materials (1).

The data generated in the positron lifetime measurements yield a plot of positron lifetime *vs.* number of events associated with that lifetime. The spectrum was analyzed to obtain the following information: average lifetime ($\bar{\tau}$), lifetime of major components of spectrum (τ_1 and τ_2), and their intensity (I_i).

The measurements reported herein represent positron lifetime measurements on the nickel electrodeposits studied by x-ray diffraction and Mössbauer spectroscopy in the preceding paper (2).

Experimental

The samples were prepared by electrodeposition of nickel on copper substrates. The experimental conditions for deposition are given in the preceding paper (2).

*Electrochemical Society Active Member.

Positron lifetime measurements were performed using a lifetime spectrometer based on NE 111 plastic scintillators, XP 1021 photomultipliers, and ORTEC electronics with double-energy gating (3) with a self-resolution of ~ 320 ps as determined by ^{60}Co . A sandwich-type sample-source arrangement was applied with the ^{22}Na positron source in the $(4-6)\times 10^5$ Bq activity range; the source holder was a ~ 1 mg/cm² thick Mylar foil.

The lifetime spectra were deconvoluted with the POSITRONFIT EXTENDED (4) program, taking into account the source correction given by Bisi *et al.* (5), the intensity of which was around 7%. The results of the two-component unconstrained evaluations were the most reliable and resulted in a variance in the 1.0-1.3 range for all the spectra. The error bars in the figures are all one standard deviation of the values given by the computer. Selected spectra were accumulated repeatedly. The extracted parameters of the independent measurements fell within one standard deviation. The average lifetime $\bar{\tau} = \sum I_i \tau_i$ was calculated for all spectra (where τ_i is the lifetime of positrons annihilating in the *i*th state, and I_i is the intensity of the *i*th component). This value was rather insensitive to the type of evaluation and was within ± 2 ps the same value independent of the number of terms in the evaluation.

Isothermal heat-treatments were performed *in vacuo*. The samples were maintained at the given temperature for 1h. They were then allowed to cool slowly to room temperature. All measurements were taken at room temperature.

Results

The average lifetime values for all the as-deposited samples are shown in Fig. 1 as a function of the literature values for the stress in such deposits. It is likely that the longer positron lifetimes are associated with higher stress levels and that shorter positron lifetimes are associated with lower stress levels, but the chemical effect cannot adequately be evaluated because all the high stress deposits were formed in baths containing chloride.

The effect of current density on the average positron lifetime is shown in Fig. 2 where it will be noted that the short lifetimes are associated with deposits formed at low current densities and the longer lifetimes are associated with deposits formed at higher current densities.

Figure 3 gives data on samples deposited from the sulfate-chloride bath over a temperature range of 20° - 60°C . The solid points in the figure represent measurements made on the same samples after aging at room temperature for 6 months. The arrows indicate the direction in

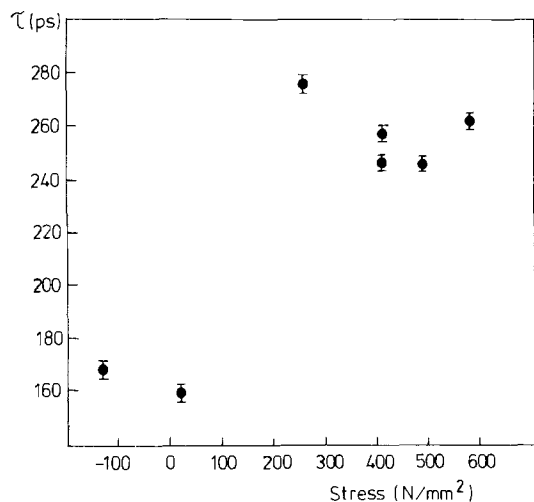


Fig. 1. The average positron lifetime for all unannealed samples plotted as a function of stress in the deposit. Literature stress values are used in this representation.

which the data changed. The summation of the effects indicated that the concentration of the long lifetime component increased during the aging.

Figures 4 and 5 summarize data for samples 1, 2, 3, and 8 as a function of the temperature to which the deposit was heated. It will be noted that the average lifetime of the positrons in samples 1 and 2 was approximately 160 ps for annealing temperatures below 300°C and was in the range of 250-290 ps for samples 3 and 8 for annealing temperatures of 200°C and below. The value of $\bar{\tau} = 160$ ps indicates the presence of a substantial concentration of structural imperfections such as vacancies, dislocations, and other defects in the as-deposited state in samples 1 and 2. The average lifetime of the as-deposited samples 3 and 8 is significantly above the lifetime value of 180 ps characteristic of the saturation lifetime for single vacancies in nickel (6). The presence of more extended defects in the as-deposited state of samples 3 and 8 is indicated.

Discussion

The average lifetime of the positron in electrodeposited nickel is related to the internal stress as shown in Fig. 1 and to the current density utilized in the deposition process as shown in Fig. 2. Samples prepared at low current density and with low internal stress had positron average

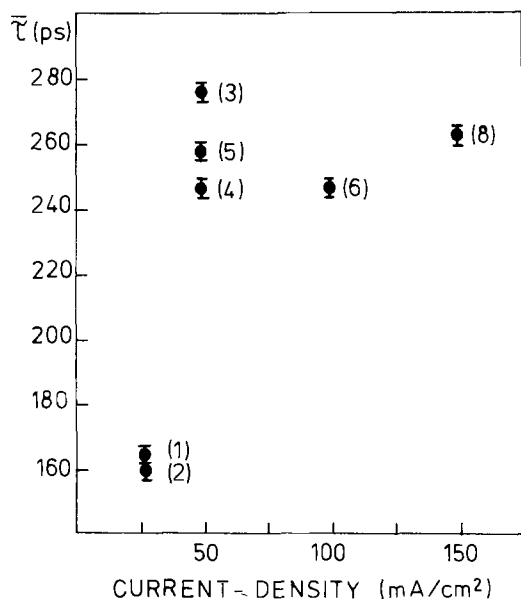


Fig. 2. The average positron lifetime for all samples plotted as a function of the current density utilized in the deposition process.

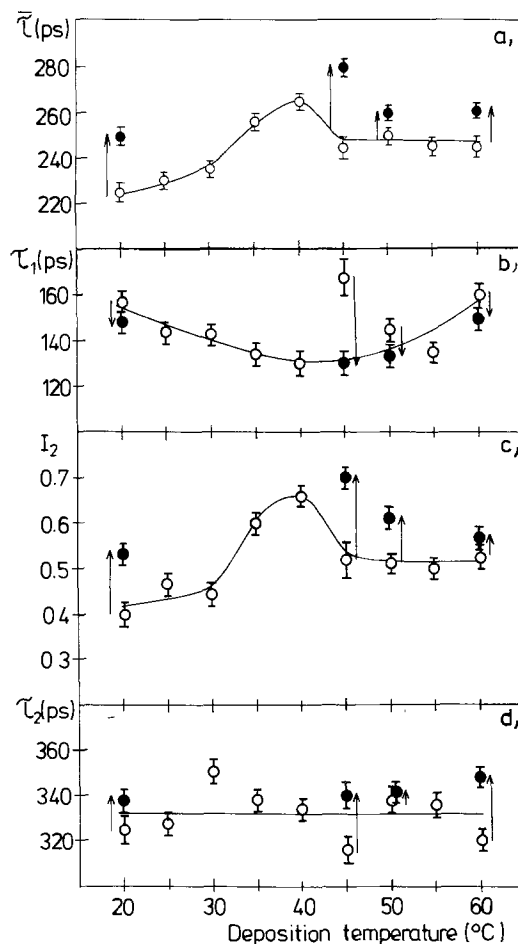


Fig. 3. Positron lifetime data for deposits formed in the sulfate-chloride bath over a temperature range of 20°-60°C. The solid points are measurements made after aging at room temperature for 6 months. The arrows indicate the direction of change.

lifetimes of the order of 160 ps, whereas the samples formed at higher current density and with high internal stress had positron average lifetimes of the order of 260 ps. These early results led us to believe that the positron average lifetime might be used to determine quantitatively the stress level in the deposit nondestructively. However, the measurements shown in Fig. 3 lead us to believe that a simple relationship between stress level and positron average lifetime does not exist. It is well known that an increase in the temperature of deposition in the case of the sulfate-chloride bath results in a decrease in the internal stress (7), yet the positron average lifetime of sample 3 increased slightly with an increase in deposition temperature in the range of 20°-60°C. In fact, the value of τ_1 exhibited a minimum at a plating temperature of 40°C while the value of I_2 was a maximum at the same plating temperature. It is apparent that the magnitude of I_2 , which is related to the three-dimensional defect concentration, determines, to a major extent, the value of the positron average lifetime. The value of τ_2 was not a function of the temperature of deposition and was in the range of 320-350 ps.

Aging of the samples for 6 months resulted in a slight decrease in the value of τ_1 and a slight increase in the value of τ_2 . The large increase in I_2 suggests that the defect pattern within the deposit changes over time with a trend towards larger volume defects and a corresponding diminution in the number of dislocations and vacancies. These changes in the positron lifetime parameters are consistent with the vacancy clustering model which will be discussed later.

Isochronal annealing studies.—In earlier publications dealing with positron annihilation in electrodeposited nickel, it was conjectured that the trapping centers could

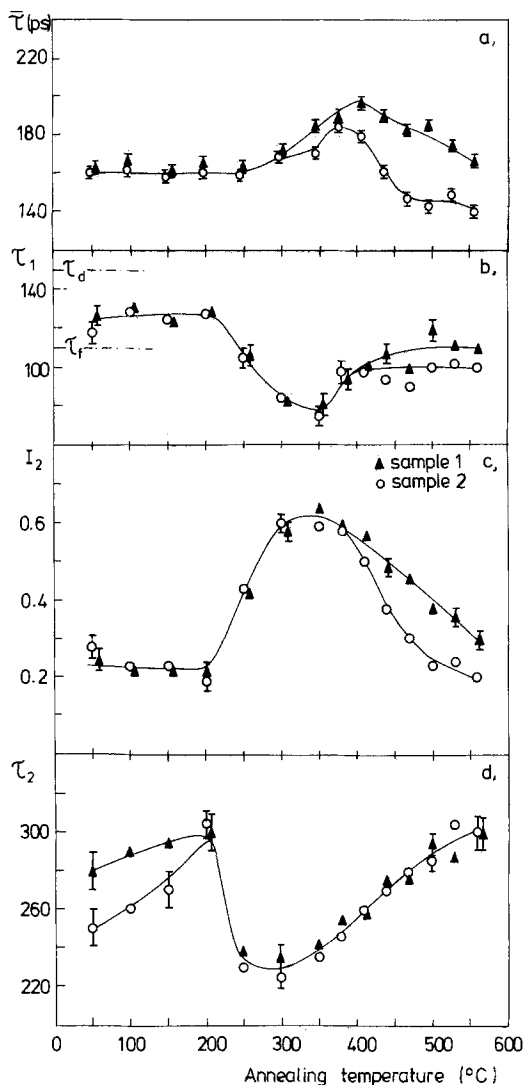


Fig. 4. Positron lifetime data for samples 1 and 2 after annealing at elevated temperatures.

be interpreted in terms of single vacancies and vacancy clusters (8, 9). Data obtained following heat-treatment have yielded evidence that the defect structure of electro-deposited nickel is more complex than originally supposed.

Let us consider first the behavior of the positron lifetime parameters during isochronal annealing of samples containing a relatively small number of lattice defects in the as-deposited state, such as those found in samples 1 and 2. The values of $\bar{\tau}$, τ_1 , τ_2 , and I_2 as a function of annealing temperature are summarized in Fig. 4. It is clear that at least two types of defects are created during deposition. One of them, with $\tau_2 = 250$ - 280 ps and $I_2 = 0.22$, is associated with divacancies by analogy with the known value for τ_{2v} for divacancies in bulk nickel, namely, 250 ps (6). We thus attribute this component to small three-dimensional microvoids having, on average, the volume of a divacancy. The value of the shorter lifetime component, $\tau_1 = 125$ ps, is slightly greater than the characteristic lifetime for annihilation in bulk nickel, namely, 110 ps (6). Thus, it appears that the shorter lifetime is an average value for annihilation of positrons in the untrapped state and a lifetime characterizing annihilation in weak traps such as vacancies and dislocations. The fact that the τ_1 and I_2 parameters are not significantly changed by annealing at 200°C suggests that the weaker traps are dislocations since vacancies are mobile at 80°C in nickel. Dislocations, on the other hand, start to decrease in number when annealing is carried out above 200°C , as inferred from previous positron annihilation experiments (6).

The high value of τ_2 at the highest annealing temperature of 500°C suggests that the deeper traps are micro-

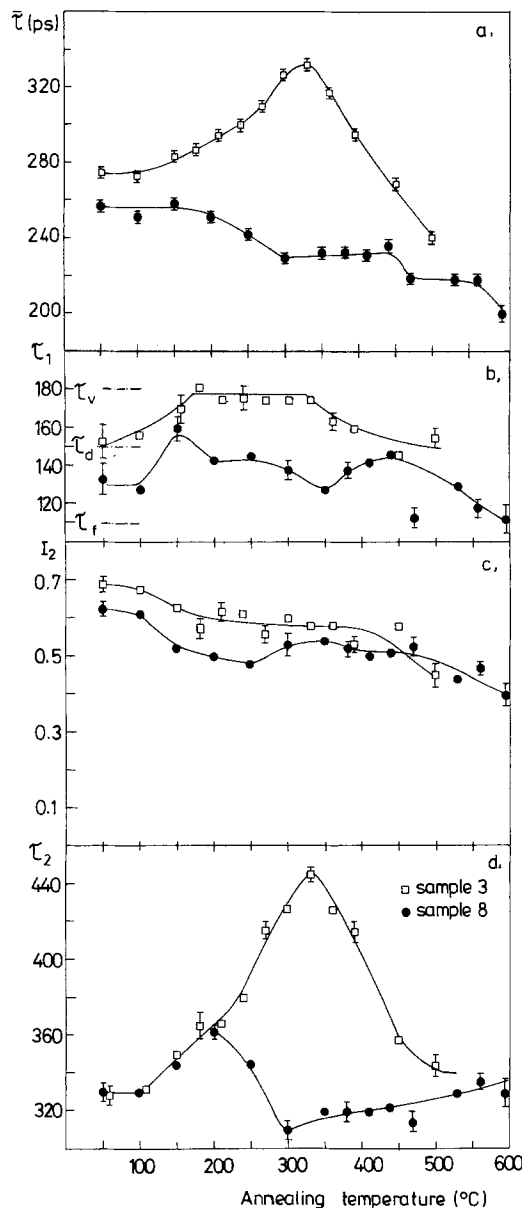


Fig. 5. Positron lifetime data for samples 3 and 8 after annealing at elevated temperatures.

voids of size equivalent to trivacancies or greater. It is tentatively suggested that these traps represent trivacancies formed on (111) planes, perhaps during growth or perhaps during the annealing treatment.

The annihilation parameters changed dramatically when the annealing temperature exceeded 200°C . A decrease in the values of τ_1 and τ_2 was accompanied by a large increase in I_2 as a consequence of an increase in the number of small three-dimensional defects. The value of τ_2 is much less for the samples annealed at 250 - 500°C than for the sample annealed at 200°C . It is conjectured that these values are representative of a defect volume less than that characteristic of a trivacancy, possibly single vacancies.

The decrease of τ_1 is simply a consequence of the increase in trap density since the increase means a higher escape rate from the "free" state of positrons, *i.e.*, a higher trapping rate in defects.

The increase in the value of I_2 for samples annealed above 200°C is attributed to the increase in the trap density because of vacancy generation by dislocation climb (10). Once vacancies are generated, they migrate to sinks such as dislocations and grain boundaries and condense to small vacancy clusters both at grain boundaries and within the interior of the grains. The decrease in I_2 and the increase in τ_2 in samples annealed above 350°C sug-

gests such an intragrain vacancy clustering mechanism. As the vacancies aggregate to divacancies, trivacancies, and higher order vacancy agglomerates, the number of small trapping centers decreases while their average size increases. Such a process has been detected previously in deformed nickel containing a small amount of antimony impurity which served as a nucleation center for vacancy clusters (6).

Samples annealed at 550°C yield positron parameters that approximate the unannealed deposit. This fact suggests that there is a highly stable configuration of small three-dimensional defects which are resistant to heat-treatment. As vacancy clusters and dislocations are known to anneal out of nickel totally at 450°C by recrystallization, it is proposed that these open volume defects are associated with grain boundaries.

Let us consider next the heat-treatment of samples 3 and 8 with the high values of internal stress. These data are summarized in Fig. 5. In the case of sample 3, the values of τ_1 and τ_2 increase at annealing temperatures of 200°C and below. In the 200°-330°C range, τ_2 increases further while τ_1 remains constant and is practically equal to the saturation lifetime of positrons trapped at single vacancies, namely, 180 ps (6). Annealing above 300°C caused both lifetimes to decrease with an increase in temperature until they reached values at 500°C approximately the same as those of the as-deposited samples. The value of I_2 decreases from 0.7 to 0.45 as the annealing temperature is increased from the as-deposited temperature to 500°C.

The values for τ_1 in the as-deposited state were sufficiently high that it appears that there is very little annihilation from the "free" state. The positrons presumably are rapidly localized after thermalization and the subsequent annihilation takes place in dislocations or microvoids. In the annealing range of 170°-330°C, the value of τ_1 is approximately 180 ps, a value characteristic of single vacancies.

The nature of positron traps in nickel electrodeposits.—We will now offer suggestions concerning the nature of the positron traps in nickel electrodeposits. Ample evidence exists for the presence of hydrogen in metals and the association of this hydrogen with a defect structure in the metal. For example, hydrogen embrittlement of metals is attributed to the segregation of hydrogen at dislocations and grain boundaries and the subsequent development of voids and microcracks along such imperfections (11). The clustering of hydrogen atoms in dislocations is presumed to be responsible for the increase in hydrogen absorption by steel during cold working (12). The high activation energy of hydrogen diffusion in iron near room temperature was explained by the excess energy required to free hydrogen from dislocations (13). Observations have been made of the precipitation of hydrogen into bubbles and the nucleation of bubbles preferentially at dislocations and grain boundaries in the case of hydrogen-loaded copper (14). Hydrogen embrittlement occurs in nickel at temperatures and strain rates at which hydrogen atoms can segregate to moving dislocations. Grain boundary cracks have been detected by TEM in hydrogen-charged nickel, which exhibited intercrystalline brittle fracture (15).

The migration energy of hydrogen in nickel is $E_m = 0.38$ eV (15), which is low in comparison with the migration energy of monovacancies $E_{1v} = 1.2$ eV (6) and the activation energy of self-diffusion $Q_{1v} = 2.88$ eV (16). These values indicate that the diffusion of hydrogen atoms in nickel takes place via interstitial sites. It is also clear from the value of the migration energy that the hydrogen is mobile below room temperature in nickel and that the hydrogen rapidly precipitates at dislocations and grain boundaries. The typical values of the hydrogen content of electrodeposited nickel of 10-200 ppm indicates that considerable hydrogen is to be expected in the nickel deposits used in this study (17). The precipitation of hydrogen at dislocations and grain boundaries and the subsequent formation of molecular hydrogen in dislocation cores pro-

duce local distortion of the lattice. The net effect of this distortion is a diminution in the nickel ion core electrons and a local decrease of electron density within this region. Such imperfections are possible traps for positrons.

The long lifetime component in the unannealed samples is attributed to the annihilation of positrons in hydrogen bubbles formed along grain boundaries. These hydrogen bubbles remain as free volume after heat-treatment and the diffusion of hydrogen out of the sample. The effect of dissolved oxygen in the electrodeposited nickel is probably less than that of dissolved hydrogen because the oxygen is probably present as nickel oxide or as an occluded salt containing oxygen. Migration of oxygen is hindered by the compound formation.

A second consideration in appraising the positron traps is the character of the trapped hydrogen. When hydrogen enters a metal such as nickel, it yields its electron to the conduction bands of the metal and exists in the lattice as a proton (18). Vacancies, microvoids, and dislocations have effective attractive potentials for positively charged particles such as hydrogen ions and positrons, and these particles are thus attracted to such sites. It has been suggested by Alex *et al.* (19) that proton trapping at these defects could reduce the attractive potential between the defects and the positrons. This reduction is probably more effective than in the case of hydrogen bubbles. In the case of vacancies, total trapping inhibition is possible.

The release of protons from vacancies and protons or hydrogen molecules from hydrogen precipitates at grain boundaries increases both the trapping probability and consequently, the positron lifetimes.

The increase of τ_1 upon annealing at moderate temperatures, as shown in sample 3 of Fig. 5, may be explained in terms of irreversible thermally activated proton detrapping from initially screened vacancies which then become effective positron traps. The initial increase in the value of τ_2 with an increase in annealing temperature in the case of sample 3 shown in Fig. 5 is illustrative of the reduction of electron density in more extended imperfections which, in turn, is explained by the release of protons or hydrogen. A similar increase in τ_2 was observed in the case of samples 1 and 2 shown in Fig. 4. The release of hydrogen molecules from grain boundary segregates may proceed by short cut diffusion along dislocations which are known to form dense tangles around such imperfections (14). Another possible explanation for the initial increase in τ_2 at low annealing temperatures is the migration of vacancies to grain boundary hydrogen precipitates with resultant increase in defect size.

The available data permit an estimate of the amount of hydrogen released from vacancies during thermal treatment under certain assumptions. The assumptions are the following: (i) only a single proton or hydrogen atom is trapped in every vacancy, (ii) saturation trapping occurs in dislocations in the as-deposited state, (iii) a simple three-state trapping model reasonably approximates the real condition. The annihilation channels in the trapping model are: "free," dislocation-, and vacancy-bound state annihilation. The lifetime spectrum is then

$$S(t) = \lambda_1 I_1 \exp(-\lambda_1 t) + \lambda_d I_2 \exp(-\lambda_d t) + \lambda_{1v} I_3 \exp(-\lambda_{1v} t) \quad [1]$$

where $\lambda_i = \lambda_f + K_d + K_{1v}$, K_d , and K_{1v} are trapping rates to dislocations and vacancies; $I_i = K_i/\lambda_i - \lambda_i$, as $i = 2$ or 3 on the left side, i must be replaced by d or $1v$ on the right; $I_1 = 1 - I_2 - I_3$; λ_f , λ_d , and λ_{1v} are the annihilation rates of different positron states; and $\lambda_i = \tau_i^{-1}$, if $i = f, d$, or $1v$.

The average lifetime is then

$$\bar{\tau} = I_1 \tau_1 + I_2 \tau_2 + I_3 \tau_3 \quad [2]$$

$$= (1 + \tau_d K_d + \tau_{1v} K_{1v}) / (\lambda_f + K_d + K_{1v})$$

This gives a linear relation between K_{1v} and K_d

$$K_{1v} = [K_d(\bar{\tau} - \tau_d) + \bar{\tau}\lambda_f - 1] / (\tau_{1v} - \bar{\tau}) \quad [3]$$

The trapping rates are proportional to defect concentra-

tions $K_i = \mu_i \times C_i \cdot C_i$ is the trap concentration and μ_i is the specific trapping rate to the i th type defect.

Utilizing a simple two-state trapping model (20), we give an estimate for the dislocation density in sample 3. For this purpose, we set $K_{1v} = 0$ in the above formulas, and from Eq. [2] we find that the dislocation density is given by

$$\rho_d = \frac{1}{\mu_d \cdot \tau_f} \cdot \frac{\bar{\tau} - \tau_f}{\tau_d - \bar{\tau}} \quad [4]$$

where $\bar{\tau}$ is the mean lifetime, $\tau_f = 110$ ps, $\tau_d = 150$ ps, and $\mu_d = 1.2 \text{ cm}^2 \text{ s}^{-1}$ is the trapping rate per unit dislocation concentration (21). Taking the statistical uncertainties of our data into account and presuming that only dislocations contribute to τ_1 , insertion of $\bar{\tau} = \tau_1$ into Eq. [4] gives $\rho_d = 5 \times 10^{10} \text{ cm}^{-3}$ as an estimate for the dislocation density in sample 3.

Let us use this estimate, which is equivalent to $K_d = 6 \times 10^{10} \text{ s}^{-1}$, and apply Eq. [3] for $\tau_1 = \bar{\tau}$ [$\tau_{1v} = 180$ ps (9)]. The trapping rate to single vacancies, which causes saturation trapping in such defects, is then $K_{1v} = 4.2 \times 10^{11} \text{ s}^{-1}$. This value corresponds to $C_{1v} \cong 190$ ppm vacancy concentration and, under our assumption, to the same hydrogen concentration as well. This value is a lower limit for the hydrogen content of sample 3 as it does not count the precipitated hydrogen at grain boundaries.

The slight decrease of I_2 below 200°C (Fig. 5c) is simply the consequence of the increase in the trapping rate to weaker traps (dislocations and vacancies in this case), $K_w = \mu_w \times C_w$; that is, to the increase of weaker trap concentration. (K_w = trapping rate, μ_w = specific trapping rate, and C_w = the concentration of weaker traps.) In the case of saturation trapping at two types of defects, the intensity ratio of the two lifetime components in the lifetime spectra is equal to the trapping rate ratio

$$\frac{I_2}{I_1} = \frac{K_b}{K_w} \quad [5]$$

Since we believe that annihilation of positrons localized at hydrogen bubbles gives rise to the long lifetime component, K_b is the trapping rate to hydrogen bubbles. As K_w changes strongly compared with K_b , the intensity ratio changes accordingly.

Using Eq. [5], we obtain an estimate for the lower limit of the concentration of precipitated hydrogen. We replace K_w by $K_{1v} = 4.2 \times 10^{11} \text{ s}^{-1}$ and take $I_1 = 0.4$ and $I_2 = 0.6$ from Fig. 5c. The trapping rate to bubbles is then $K_b = 6.3 \times 10^{11} \text{ s}^{-1}$. The trapping rate is proportional to the bubble concentration $K_b = \mu_b \times C_b$, where μ_b is the specific trapping rate or trapping rate per unit trap concentration. Calculations show that the specific trapping rate for small spherical microvoids is proportional to the number of vacancies building up the microvoid $\mu = nX\mu_{1v}$ (22). μ_{1v} is the specific trapping rate to single vacancies and n is the number of vacancies which have the same total volume as the void. It has been calculated (23) that the positron lifetime is a slowly varying function of the void volume if $n > 5$ and $\tau_{\text{void}} = f(nXV_0)$, where V_0 is the volume of a vacancy in nickel. Utilizing this relationship, one could, in principle, estimate n and μ . In our case, we must replace n by $n_{\text{eff}} = \eta X n$, where η accounts for the screening effect of hydrogen inside the void. At $\tau_2 \cong 360$ ps, $n_{\text{eff}} \cong 6-7$ (6), and employing $\mu_{1v} = 2.2 \times 10^{15} \text{ s}^{-1}$ (21), we get $C_b \cong 40$ ppm for the lower limit of bubble concentration. From the estimated hydrogen density in such bubbles, $\sim 0.1 \text{ g/cm}^3$ (14), and from the estimated volume of the bubbles $V_b = n_{\text{eff}}XV_0$, it follows that, on average, every defect could accommodate two hydrogen molecules. We reach an estimate of the precipitated hydrogen concentration: $C_{\text{H}_2} \cong 80$ ppm. The total H_2 content of our sample is then at least $C_{\text{H}_2} = 175$ ppm.

Vacancy clustering is observable in sample 3 as a steep increase of τ_2 above 200°C, despite the near-saturation behavior of I_2 and the absence of a peak in this parameter around 350°C. It is noteworthy, however, that the minimum in τ_2 coincides with the peak in I_2 for samples 1 and

2, a fact which also supports the vacancy clustering picture. The decrease of τ_2 observed between 200° and 300°C in the case of samples 1 and 2 was not observed for sample 3, because the high concentration of single vacancies in sample 3 leads to the appearance of a separate vacancy component in the deconvoluted lifetime spectrum as $\tau_1 \cong \tau_{1v} = 180$ ps. The interpretation is that only higher vacancy agglomerates contribute to τ_2 .

Above 330°C, all the positron parameters decrease, indicating the disappearance of defects.

The behavior of positron parameters of sample 8 is the most complicated. The behavior of I_2 (Fig. 5c) is similar to that of sample 3. τ_2 increases in the same way as for sample 3 up to 200°C, whereas the subsequent behavior is similar to that of samples 1 and 2 (Fig. 5d). The evolution of τ_1 in Fig. 5 resembles that in Fig. 4b.

Conclusions

During the course of deposition, at least three different types of structural defects which are effective trapping centers for positrons are created in nickel. These are dislocations, lattice vacancies, and more extended three-dimensional imperfections having at least the volume of three vacancies. The latter defects are probably hydrogen segregations at grain boundaries.

The concentration of defects is highly dependent on the plating conditions (2).

Some of the defects are filled with hydrogen ions. The release of protons takes place at ambient temperatures.

The stability of some more-extended defects against high temperature heat-treatments indicates that these lattice distortions are associated with grain boundaries.

The annealing of deposits takes place as a result of vacancy-migration above 200°C and intracrystalline agglomeration to vacancy clusters.

Manuscript submitted June 1, 1983; revised manuscript received Feb. 10, 1984.

REFERENCES

1. "Positrons in Solids," P. Hautojärvi, Editor, Springer, Berlin (1979); "Positron Annihilation," P. G. Coleman, S. C. Sharma, and L. M. Diana, Editors, North-Holland, Amsterdam (1982).
2. A. Vértes, I. Czako-Nagy, M. Lakatos-Varsányi, L. Csordás, and H. Leidheiser, Jr., *This Journal*, **131**, 1522 (1984).
3. Zs. Kajcsos, J. Ch. Abbe, J. Oberlin, G. Serény, A. Haessler, Report CRN/CNPA 75-25.
4. P. Kirkegaard and M. Eldrup, *Comp. Phys. Comm.*, **7**, 401 (1974).
5. A. Bisi, G. Gambarini, and L. Zappa, *Nuovo Cimento Soc. Ital. Fis. B*, **53** 428 (1979).
6. G. Dlubek, O. Brümmer, N. Meyendorf, P. Hautojärvi, A. Vehanen, and J. Yli-Kaupilla, *J. Phys. F*, **9** 1961 (1979).
7. D. J. Evans, *Trans. Faraday Soc.*, **54**, 1086 (1958).
8. A. Vértes, Zs. Kajcsos, I. Czako-Nagy, M. Lakatos-Varsányi, G. Brauer, and H. Leidheiser, Jr., *Nucl. Instrum. Methods*, **199**, 353 (1982).
9. A. Vértes, Zs. Kajcsos, Cs. Szeles, I. Czako-Nagy, M. Lakatos-Varsányi, and H. Leidheiser, Jr., in "Positron Annihilation," P. G. Coleman, S. C. Sharma, and L. M. Diana, Editors, p. 224, North-Holland, Amsterdam (1982).
10. P. B. Hirsch, *Philos. Mag.*, **7**, 67 (1962); G. Saada, *Acta Metall.*, **9**, 166, 965 (1965); and I. Kovács, *ibid.*, **15**, 1731 (1967).
11. P. Cotterill, "The Hydrogen Embrittlement of Metals," Pergamon, Oxford (1961).
12. L. S. Darken, *Trans. AIME*, **221**, 654 (1961).
13. R. W. Lee, B. E. Sevets, and R. G. Frank, *Mem. Sci. Ser. Met.*, **58**, 130 (1961).
14. W. R. Wampler, T. Schober, and B. Lengeler, *Philos. Mag.*, **34**, 129 (1976).
15. T. Boniszewski and G. C. Smith, *Acta Metall.*, **11**, 165 (1963).
16. K. Maier, H. Mehrer, E. Lessman, and W. Schüle, *Phys. Status Solidi B*, **78**, 689 (1976).
17. S. Nakahara and E. C. Felder, *This Journal*, **129**, 45 (1982).

18. G. K. Wertheim and D. N. E. Buchanan, *J. Phys. Chem. Solids*, **28**, 225 (1967).
19. F. Alex, T. D. Hadnagy, K. G. Lynn, and J. G. Byrne, in "Proceedings of the International Conference on Effect of Hydrogen on Behaviour of Metals," p. 642, The Metallurgical Society of AIME, (1975).
20. D. C. Connors and R. N. West, *Phys. Lett. A*, **30**, 24 (1969).
21. G. Dlubek, O. Brümmer, and E. Hensel, *Phys. Status Solidi A*, **34**, 737 (1976).
22. R. M. Nieminen and J. Laakkonen, *Appl. Phys. Lett.*, **20**, 181 (1976).
23. P. Hautojärvi, J. Heiniö, M. Manninen, and R. M. Nieminen, *Philos. Mag.*, **35**, 973 (1977).

Diffusion-Controlled Multisweep Cyclic Voltammetry

III. Deposition of Silver on Stationary and Rotating-Disk Electrodes

P. C. Andricacos* and P. N. Ross, Jr.*

Materials and Molecular Research Division, Lawrence Berkeley Laboratory, University of California, Berkeley, California 94720

ABSTRACT

An experimental study of diffusion-controlled silver electrodeposition has been carried out in order to investigate the applicability of the model for reversible metal deposition during multisweep cyclic voltammetry. For a stationary planar electrode, excellent agreement between theory and experiment has been obtained for the position of the cathodic current maxima on the potential axis, as well as for the dependence of their magnitude on parameters such as sweep rate, cathodic reversal potential, and number of applied sweeps. Anodic currents measured at the foot of the wave deviated from theoretical predictions as a consequence of the small but uncompensated resistance of the electrolyte. In an effort to predict and therefore control the amount of deposit, integral charges associated with each sweep have been measured and successfully correlated with the parameters of the experiment. It has been found that at millimolar concentrations, deposit thicknesses of the order of up to 20 monolayers can be formed with quantitative control. Experiments with a rotating-disk electrode have demonstrated that a periodic current response is obtained upon multiple sweeping, as predicted by theory. First sweep and periodic currents normalized with respect to the limiting current could be correlated with the dimensionless sweep rate in accordance with the theoretical predictions. Contrary to previous investigations, the diffusion coefficient of the silver ion was determined by limiting current measurements, and the value thus obtained was subsequently used to successfully correlate stationary electrode cyclic voltammetry data. During limiting current measurements with very slow sweeps, the development of surface roughness was observed as a significant increase of the current from the constant value obtained at faster sweeps. Based on the dimensionless sweep rate, a semiempirical criterion was developed for the optimal conditions for the potentiodynamic determination of steady-state limiting currents, the use of which may eliminate errors arising from both transient effects and surface area increase due to roughness.

In previous communications (1, 2), we presented calculations for diffusion-controlled cyclic voltammetry (CV) for both a stationary planar and a rotating-disk electrode (RDE) for reversible depositions at unit deposit activity. These represented extensions to previous linear sweep voltammetry (LSV) analysis for the stationary electrode (3) and the RDE (4), and were carried out in order to predict the effects of multiple sweeping on the deposition current and charge. For an experimental investigation of the theoretical predictions, we chose the electrodeposition of Ag. This was for several reasons. The kinetics of this reaction are very fast, so the reaction can be considered reversible and controlled by diffusion, as required by the theory. The equilibrium potential is sufficiently anodic to allow for a wide selection of values for the potential at which the sweep is reversed (other reversible systems such as Sn^{2+}/Sn do not allow for this possibility due to the onset of H_2 evolution). Since Ag deposits are usually rough and the amount of deposit is quantitatively related to sweep rate, manipulation of sweep rate values can be used to induce electrochemically noticeable roughness, thereby contributing to a quantification and possibly an elucidation of this phenomenon. Previous investigation (5, 6) of the Ag system by LSV have shown agreement between theory and experiment for stationary electrodes, but the value of the diffusion coefficient of the Ag^+ ion used by Mamantov *et al.* (5) originated from a non-electrochemical measurement by Stackelberg *et al.* (7). However, Bachmann and Dohrmann (6) obtained their diffusivity value by essentially fitting the Delahay LSV model (3). In the present investigation, consistency is sought by measuring diffusivity from limiting currents and using the value thus obtained to correlate stationary

electrode and RDE single-sweep and multisweep voltammetry data. Also, in limiting current measurements by Kraichman and Hogge (8), as well as in a previous LSV-RDE study by Andricacos and Cheh (4), gelatin was used in the electrolyte as a leveling agent, but as we are interested in this study in the effects of roughness on multisweep voltammetry, no leveling agents were employed.

Experimental

Experiments were performed in a glass three-compartment cell. Silver wires were used for both reference and counterelectrodes. The working electrode was a Pine Instruments Au RDE with a geometrical area 0.46 cm^2 polished to a mirror finish. When rotating, it was driven by a Pine Instruments Analytical Rotator assembly. The electrolyte composition was $1.1(2) \times 10^{-3} \text{ AgNO}_3$ in 1M HClO_4 ; it was prepared from reagent-grade AgNO_3 (Allied Chemical), electronic-grade HClO_4 (Apache Chemicals), and pure H_2O (Harleco). No further purification was attempted. The electrode potential was controlled with a PAR potentiostat (Model 173D) connected to a PAR Universal Programmer (Model 175). The potentiostat was equipped with a digital coulometer (PAR Model 379), and both current and integral charge were recorded either with an X-Y recorder or an oscilloscope depending on the sweep rate.

The Au RDE at zero rotation speed served as a stationary planar electrode. It was preferred relative to other possibilities because its configuration minimized possible natural convection complications, *i.e.*, downward facing with the density increasing from top to bottom (9). An inert substrate was chosen instead of Ag to avoid repeated polishing and subsequent irreproducibilities in the initial condition of the surface.

The Au RDE was initially immersed in the O_2 free electrolyte at a potential of 0.200V anodic to that of the refer-

*Electrochemical Society Active Member.

Key words: electrode, deposition, mass transport, voltammetry, silver.

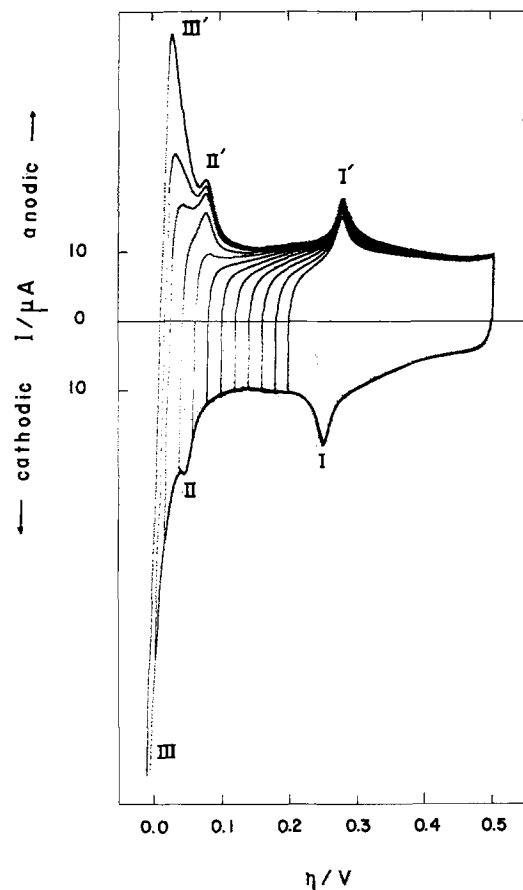


Fig. 1. Cyclic voltammogram of a stationary Au disk electrode immersed in $1.1 \times 10^{-3} \text{ M AgNO}_3 + 1 \text{ M HClO}_4$. Sweep rate: $0.050 \text{ V} \cdot \text{s}^{-1}$. The potential region is anodic to a Ag wire reference electrode in the same electrolyte.

ence Ag wire and was subsequently cycled in the UPD region. Figure 1 shows a typical voltammogram obtained at 0.050 Vs^{-1} . Peaks I, I' represent underpotential deposition and stripping, whereas peaks II, II' probably originate from an alloying state (10). These peaks were invariant with rotation speed, whereas peaks III, III' were rotation dependent and were taken as bulk deposition. Bulk deposition occurred at potentials slightly anodic to zero *vs.* Ag wire, since the Nernstian potential is apparently not established at monolayer coverages. If the cathodic sweep is extended well into the bulk-deposition region, the resulting diffusion-controlled peak is of lower magnitude

and appears at more cathodic potentials compared to an electrode initially covered with Ag. A simple excursion into the UPD region is thus not sufficient to establish the Nernstian equilibrium potential of Ag corresponding to unit activity at the surface. Unit activity was achieved by preplating the RDE surface at -0.025 V and 1600 rpm until a deposit equivalent to a charge of $\text{ca. } 10^{-2} \text{ C cm}^{-2}$ had accumulated on the surface. The potential of the preplating was chosen sufficiently away from the limiting current to avoid powder formation (9). Upon open circuiting, the RDE potential was within 0.001 V relative to the Ag wire and remained constant for at least 15 min . The potentiostat was reconnected and the electrode potential adjusted so that exactly zero current passed as judged by the digital coulometer registering less than 10^{-7} C for at least 1 min . This procedure guaranteed that the anodic reversal potential was exactly the equilibrium at unit surface activity. After this initial preparation, the cathodic reversal potential was chosen, and multisweep measurements were taken. Upon completion of the measurements, the electrode potential was swept into the anodic region again, and the deposited Ag was stripped at $+0.020 \text{ V}$. After some time, the anodic current dropped to $\text{ca. } 0$, leaving residual Ag at a surface activity consistent with an equilibrium potential of 0.020 V . Slow sweeping at 0.001 Vs^{-1} in the anodic direction resulted in stripping of all deposited Ag both during preplating and CV measurement. For each sweep rate, the procedure was repeated and yielded results reproducible to better than 1%. For the limiting current measurements the preplating step was omitted.

Results and Discussion

Cyclic voltammetry on a stationary planar electrode.—Figure 2a shows a typical multisweep voltammogram for Ag deposition on the Ag-preplated Au horizontal disk electrode. The same voltammogram unfolded in time appears in Fig. 2b. The second representation is better if the emphasis is on the measurement of current peak heights. Figure 2c is the corresponding charge/potential diagram. Since such diagrams have not appeared in the literature before, a brief qualitative description will be given here. The curve 0-a-b-c in Fig. 2c corresponds to the charge in the first complete sweep, including both cathodic and anodic portions. Point a is the value of the charge at the end of the first cathodic sweep, *i.e.*, at the cathodic reversal potential. During the reverse sweep, the charge continues to increase in the cathodic direction until it reaches an extremum at point b; this corresponds to the potential at which the current changes from cathodic to anodic. Since the current remains anodic until the end of the reverse sweep, the cathodic

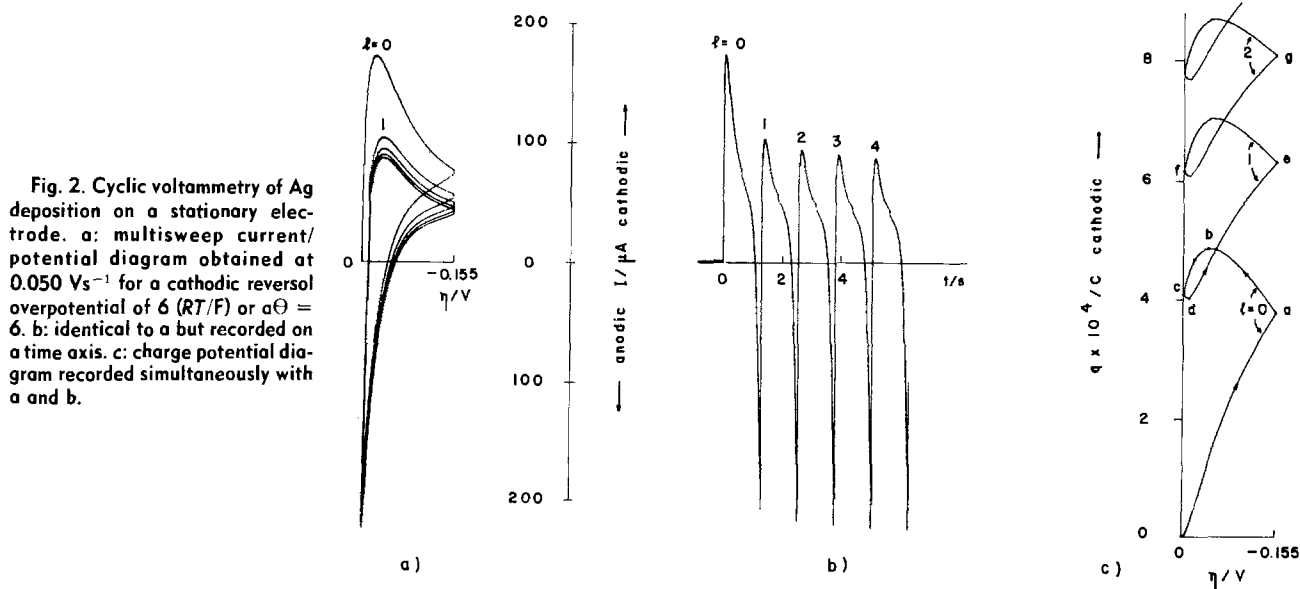


Fig. 2. Cyclic voltammetry of Ag deposition on a stationary electrode. a: multisweep current/potential diagram obtained at 0.050 Vs^{-1} for a cathodic reversal overpotential of $6 (RT/F)$ or $\alpha\Theta = 6$. b: identical to a but recorded on a time axis. c: charge potential diagram recorded simultaneously with a and b.

charge decreases from point b to c. For a very short time after c, the decrease continues corresponding to that interval during the second sweep that the current is anodic. At point d, the current becomes cathodic, and the cathodic charge starts increasing again. The general features of the charge-potential diagram are retained as the number of applied sweeps is increased. However, relative magnitudes change, and the quantitative aspects of this change will be discussed below.

Peak potentials.—The overpotential at which the cathodic current maximum is observed is predicted (3) to be equal to $0.854 (RT/nF) = 0.022V$ for $l = 0$ ($T = 25^\circ C$, $n = 1$) and increases (2) to at most $1.3 (RT/nF) = 0.033V$ upon multiple sweeping; it is independent of the sweep rate, diffusivity, and bulk concentration for reversible depositions at unit deposit activity. These predictions were verified to within 0.003V.

Cathodic current maxima.—The theoretical analysis predicts cathodic current maxima given by the relations (2)

$$i_{c,max}^l [(at_c)_{max}^l; a\theta] = A c^b v^{1/2} I_{c,max}^l [(at_c)_{max}^l; a\theta] \quad [1]$$

$$\text{and } A = (nF)^{3/2} (RT)^{-1/2} D^{1/2}$$

where l is the number of already applied complete sweeps, v the dimensional sweep rate, c^b the bulk concentration of Ag^+ , $a = (nF/RT)v$, $(at_c)_{max}^l$ is the dimensionless peak overpotential in multiples of RT/nF , θ the time duration of each anodic or cathodic part of the sweep, and $a\theta$ is the dimensionless reversal overpotential in multiples of RT/nF . $I_{c,max}^l$ is the maximum value within a sweep of the cathodic current-density function, the values of which can be computed from the equations given in Ref. (2).

Experiments were performed at three cathodic reversal overpotentials: 0.104, 0.155, and 0.411V, corresponding to $a\theta = 4, 6$, and 16, respectively. The anodic reversal potential was always at the equilibrium value. Values of the current function necessary for the calculations are given in Table I. Plots of $i_{c,max}^l$ vs. $v^{1/2}$ are shown in Fig. 3. The solid lines in these figures correspond to the theoretical predictions of Eq. [1] and agree very well with the experimental data. Since this is the case, a value for D_{Ag^+} can be extracted from the multisweep CV data and Eq. [1], as was done by Bachmann and Dohrmann (6) using the Delahay model (3) predictions for LSV ($l = 0$). The value extracted from the CV data was $1.4 (2) \times 10^{-5} \text{ cm}^2\text{s}^{-1}$, which is also consistent with the value calculated from the RDE limiting current measurements to be described.

The value of the potential at which the sweep is reversed is immaterial for the current maximum during the first sweep ($l = 0$). However, it significantly affects its magnitude during subsequent sweeps. As $a\theta$ increases, the height of the second ($l = 1$) maximum decreases. Furthermore, the differences between sweeps for $l > 1$ decrease with increasing $a\theta$. This is in agreement with the computational observation (2) that in the limit $a\theta \rightarrow \infty$, the

Table I. Computed values of the dimensionless current and charge density functions for multisweep cyclic voltammetry (reversible deposition at unit deposit activity on a stationary planar electrode)

	$a\theta$	$I_{c,max}^l$	$I_{a,max}^l$	$Q_c^l(a\theta)$	$Q_a^l(a\theta)$
0	4	0.610*	0.785	1.917	1.982
	6	0.610	0.829	2.505	2.738
	16	0.610	0.899	4.368	5.282
1	4	0.390	0.829	1.163	0.993
	6	0.355	0.868	1.439	1.345
	16	0.294	0.926	2.171	2.475
2	4	0.353	0.848	1.026	1.764
	6	0.320	0.886	1.253	1.035
	16	0.268	0.938	1.827	1.901
10	4	0.299	0.890	0.873	0.372
	6	0.270	0.923	0.964	0.503
	16	0.232	0.964	1.296	0.924

* Independent of $a\theta$; computed in Ref. (3).

current becomes periodic. It is interesting to note that even after ten sweeps the cathodic current density maxima computed on the basis of the geometrical area of the electrode are still described by Eq. [1].

Anodic current maxima.—Anodic current maxima are the anodic currents measured at the end of the l th anodic or the beginning of the $l + 1$ cathodic sweep, i.e., they are the currents measured at the equilibrium potential for $l > 0$. They are described by an equation identical to Eq. [1], the only difference being in the values of the current function

$$i_{a,max}^l = A c^b v^{1/2} I_{a,max}^l \quad [2]$$

$I_{a,max}^l$ values relevant to the experimental conditions of the present study are given in Table I. Figure 4 shows a comparison between the predictions of Eq. [2] (solid lines) and the experimental points.

It is observed that the measured currents are lower than those predicted by Eq. [2]; the deviations are more pronounced at the higher sweep rates and the lower values of $a\theta$. Such deviations would be expected from a small iR effect since the current variation near the equilibrium potential is very steep and it becomes steeper the faster the sweep rate and the smaller the $a\theta$ value. An alternative effect with a similar pattern of deviation with sweep rate, and $a\theta$ can be thought of as arising from finite kinetics of the dissolution reaction. However, no additional evidence of kinetic limitations was observed. It should be noted that anodic current deviations are not expected to propagate with l since they occur over very short time intervals. Maximum anodic currents do not exhibit a strong dependence on either the number of cycles or the reversal potential. Generally, they increase with l and $a\theta$, and this behavior is not difficult to rationalize in terms of the computed concentration profiles (1).

¹Equivalently, $I_e^{l+1}(0; a\theta)$.

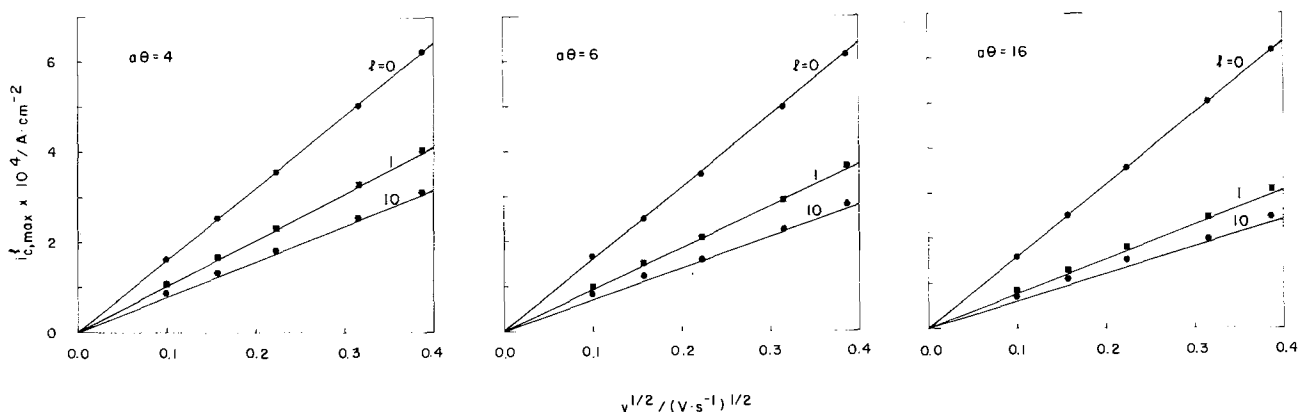


Fig. 3. Dependence of the cathodic peak current density on the square root of the sweep rate, the number of applied sweeps, and reversal potential. Solid lines are predictions of Eq. [1] (stationary electrode cyclic voltammetry).

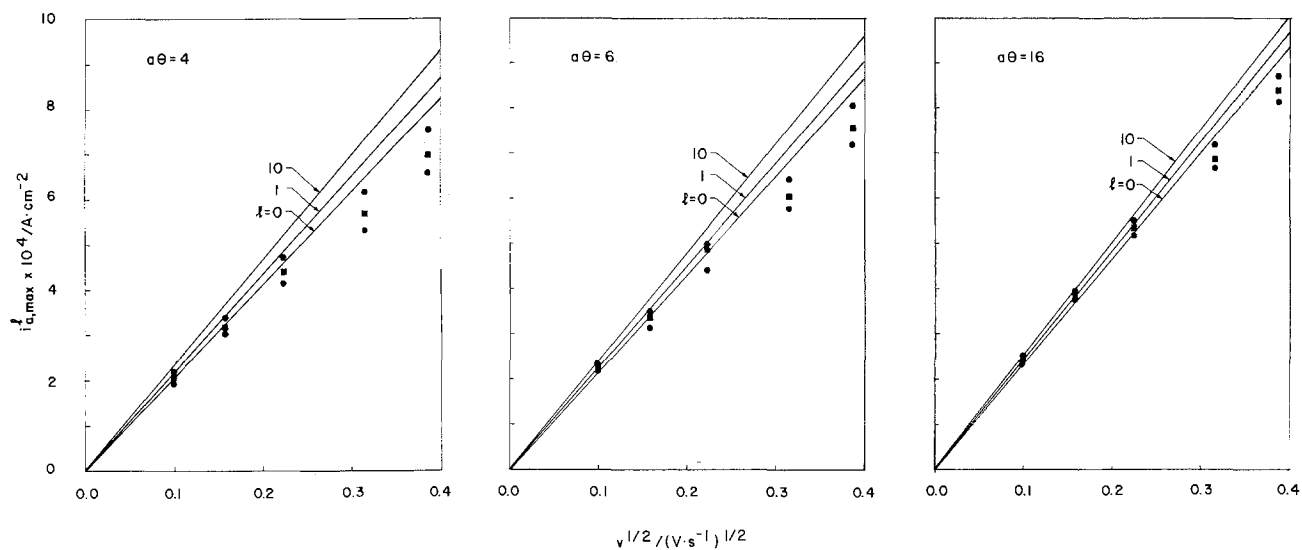


Fig. 4. Dependence of the maximum anodic current on the square root of sweep rate, the number of applied sweeps, and reversal overpotential. Solid lines are predictions of Eq. [2] (stationary electrode cyclic voltammetry).

Cathodic charges.—Integral cathodic charges as functions of l and $\alpha\theta$ are shown in Fig. 5 and 6. In Fig. 5, the quantity q_c is the amount of charge accumulated during the $l + 1$ cathodic sweep; its value can be read off easily from a charge/potential diagram such as the one appearing in Fig. 2c. For instance, for $l = 0$, q_c^0 is the value at point a; for $l = 1$, q_c^1 , i.e., the charge during the second cathodic sweep, is the difference between points e and c; for $l = 2$, q_c^2 is the difference between points g and f, and so on.

Charge has a linear dependence on the inverse of the square root of the sweep rate (2) as shown by

$$q_c^l(\alpha\theta) = Bc^b v^{-1/2} Q_c^l(\alpha\theta) \quad [3]$$

and $B = (nFRTD)^{1/2}$

where Q_c^l is the charge density function, values of which are given in Table I, computed from the equations of Ref. (2). Good agreement between Eq. [3] and experiment can be seen in Fig. 5, except in the case for $\alpha\theta = 16$ and $l > 0$ in the low sweep-rate range. The charge deviations under these conditions are not accounted for by the anodic current deviations in Fig. 4. Although one would expect that lower measured anodic currents would yield higher cathodic charges, the time duration over which these lower anodic currents are measured is too small to account for the deviations appearing in Fig. 5. We attribute these deviations to a roughness effect. Although it may not affect the value of the current density at any given potential, its effect is enhanced when one integrates over the entire current curve. This explanation is consistent with deviations appearing at conditions that produce high total change, e.g., low sweep rates, high reversal potentials, and values of l greater than 0.

As can be seen from Fig. 5, the amount of deposit accumulated even after multiple potential sweeps is very small. Assuming that the formation of a Ag monolayer requires $2 \times 10^{-4} \text{ C cm}^{-2}$, it is seen that the largest value ($\alpha\theta = 16$, $v = 0.010 \text{ Vs}^{-1}$) measured on the first sweep corresponds to about 15 monolayers. During the reverse sweep, the charge remains almost constant (e.g., points a and d on Fig. 2c) and increases by about ten more monolayers during the second cathodic sweep ($l = 1$). Although the net amount is only of the order of the order of 20 monolayers, a roughness effect is detectable from the deviations of the charge from that predicted by the theory. It should be noted that if the roughness originated from preplating, it should manifest itself during the $l = 0$ sweep; however, the $l = 0$ results agree with Eq. [3], in which the geometrical area of the electrode has been used.

A plot of the dimensionless net charge density function, Q_n^l , is shown in Fig. 6. Theoretical predictions (2) are given in Table I, whereas experimental values are obtained from

$$Q_n^l(\alpha\theta) = q_n^l(\alpha\theta)/Bc^b v^{-1/2} \quad [4]$$

where q_n^l is the value of the charge at the equilibrium potential. For instance, with reference to Fig. 2c, q_n^0 corresponds to point c, q_n^1 to the difference between points f and c, and so on. Q_n^l depends only on l and $\alpha\theta$, and not on the sweep rate. Therefore, for fixed l and $\alpha\theta$, q_n^l should be the same, irrespective of which pair of q_n^l and v values is used. Results in Fig. 6 have been computed for $v = 0.150 \text{ Vs}^{-1}$ and the corresponding q_n^l values; however, if data for 0.010 Vs^{-1} were used, the deviations observed for $\alpha\theta = 16$ and $l = 1, 2$ appear in Q_n^l as values higher than the ones obtained for $v = 0.150 \text{ Vs}^{-1}$.

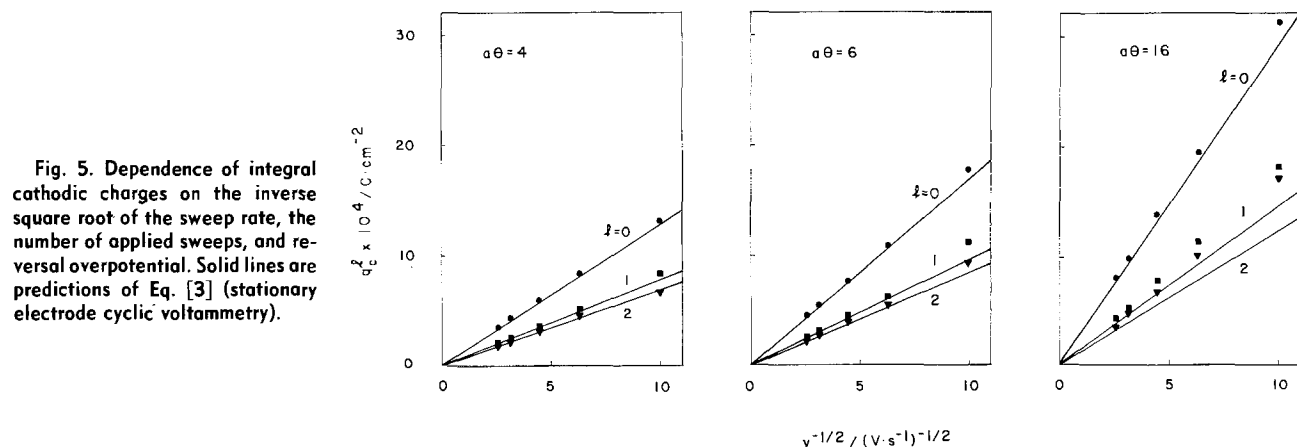


Fig. 5. Dependence of integral cathodic charges on the inverse square root of the sweep rate, the number of applied sweeps, and reversal overpotential. Solid lines are predictions of Eq. [3] (stationary electrode cyclic voltammetry).

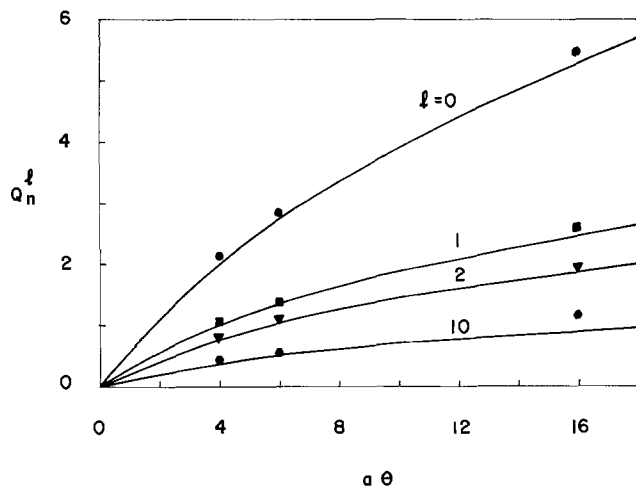


Fig. 6. Dependence of the net charge density function on reversal overpotential. Solid lines are theoretical predictions and points are experimental results correlated by Eq. [4] (stationary electrode cyclic voltammetry).

Figure 6 indicates that potential sweeping from the equilibrium to some reversal value and back always results in the formation of a net deposit on the surface. The amount is maximum for the first sweep, but decreases considerably upon multiple sweeping. In the limit $l \rightarrow \infty$, the hypothetical charge density during the complete sweep is predicted (2) to be 0, and this trend appears in Fig. 6.

Cyclic voltammetry on a rotating-disk electrode.—Experiments were performed at two rotation speeds, 80 and 400 rpm, and at sweep rates varying from 0.050 to 10 Vs^{-1} , corresponding to a variation in the dimensionless sweep rate, σ ; between 5 and 215. Double layer currents were corrected for with a constant value of $50 \mu\text{f cm}^{-2}$ measured by the method of Bachmann and Dohrmann (6). Since the double layer capacitance is a potential-dependent quantity, errors are introduced especially at sweep rates higher than 2Vs^{-1} , at which double layer currents are a significant portion of the measured total.

A representative RDE voltammogram appears in Fig. 7a, obtained at 0.1Vs^{-1} and a rotation speed of 80 rpm. The value of the dimensionless sweep rate

$$\sigma = \frac{nF}{RT} v \frac{\delta^2}{D} \quad [5]$$

(where δ is the thickness of the Nernst diffusion layer computed from the Levich theory) is ca. 11 at this sweep rate and rotation speed. Since $\sigma > 3$, a peak of magnitude $i_{c,\text{max}}^0$ should appear on the first sweep (1, 4), as was observed. For $\sigma > 4$, this peak is the same as if the electrode were stationary. If ω is increased to 400 rpm, the $\sigma > 3$ condition is not satisfied and no current peak should appear; such a peak was not observed when ω was increased to 400 rpm. The sweep in Fig. 7a was reversed at an overpotential of 0.300V , where a limiting current was observed. Since the characteristic time of the RDE, δ^2/D , was approximately 2.8s and the duration, Θ , of each sweep 3s, the periodicity criterion (1) requiring $\Theta > \delta^2/D$ was strictly satisfied. It is then expected (1) that the current response during the second cathodic sweep be periodic, i.e., not change during multiple sweeping. This behavior is confirmed in Fig. 7a; the height of the periodic cathodic current maximum, $i_{c,\text{max}}$, is lower than $i_{c,\text{max}}^0$ and does not change upon multiple sweeping.² Similarly, the magnitude of the anodic current, i_a , at the foot of the wave is always constant, provided that the periodicity criterion is satisfied. It should be noted here that it is not always possible to meet the periodicity requirement exactly. For

²Errors arising from double layer capacitance corrections are more significant in the value of the periodic current maximum, since $i_{c,\text{max}} < i_{c,\text{max}}^0$, and their difference increases with increasing σ .

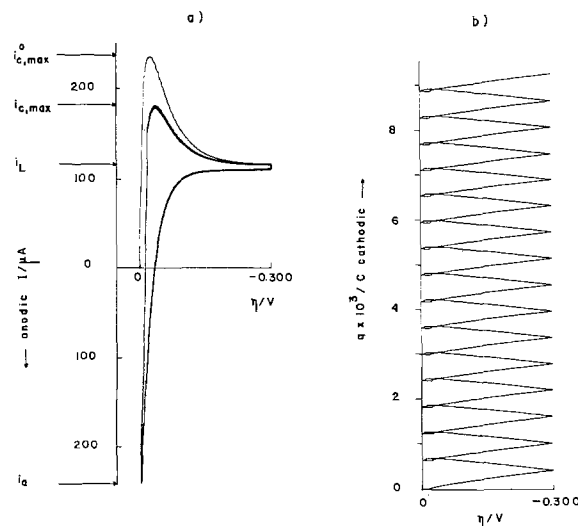


Fig. 7. Cyclic voltammetry of Ag deposition on a rotating disk electrode. a: multisweep current/potential diagram obtained at 0.100Vs^{-1} and $\omega = 80 \text{rpm}$ showing the first sweep and periodic current responses. b: charge/potential diagram recorded simultaneously with a.

instance, with a characteristic time of 2.8s (80 rpm) and a sweep rate of 1Vs^{-1} , 2.8V of potential range are required. However, even for $\Theta > 0.1 (\delta^2/D)$ the deviation of the current from that for the exact periodic state is not experimentally significant, as was confirmed by the observed voltammetry.

Figure 7b is the charge/potential diagram corresponding to the RDE voltammogram of Fig. 7a. Due to the electrode rotation, more deposit is accumulated on the RDE than on the stationary electrode at the same conditions. The amount of deposit, and equivalent charge, is mostly defined by Θ and the limiting current, i_L . Since the electrode current is near i_L for most of the time, and since the excess cathodic charge in the cathodic current peak is partially counterbalanced by the anodic charge near the equilibrium potential, the charge/potential diagrams have a much simpler (nearly linear) appearance than the stationary electrode diagrams (Fig. 2c).

LSV current functions are related to σ by (1, 4)

$$J_{c,\text{max}} = \frac{i_{c,\text{max}}^0}{i_L} = 0.61 \sigma^{1/2}, \sigma > 4 \quad [6]$$

It should be noted that an experimental investigation of Eq. [6] does not require knowledge of the bulk concentration of the reactant or the electrode area as long as it remains constant during the performance of the experiment. Due to the dimensionless nature of Eq. [5], it is possible that different combinations of rotation speed and sweep rate yield the same value of σ . However, the measured peak currents when normalized with respect to the appropriate i_L , should yield the same J . This was, in fact, observed, as shown by the results of Fig. 8.

The periodic current maxima correlation (1)

$$J_{c,\text{max}} = \frac{i_{c,\text{max}}}{i_L} = 0.88 \sigma^{0.251}, \sigma > 9 \quad [7]$$

is seen (Fig. 9) to agree well with the experimental data. Again $J_{c,\text{max}}$ is independent of electrode area and reactant bulk concentration. In addition, its value for a particular δ does not depend on the particular combination of ω and v that gives rise to this value of σ . The dependence of $J_{c,\text{max}}$ on σ is weak and requires a large range of sweep rates for its experimental determination. However, if low rotation speeds are used, this is not a significant disadvantage. At low rotation speeds, a periodic state is established, unlike the l dependence of a stationary electrode response, and can be retained for longer times since deposit accumulation is also lower.

Figure 10 shows the dependence of the periodic dimensionless anodic current function maximum on σ , which is

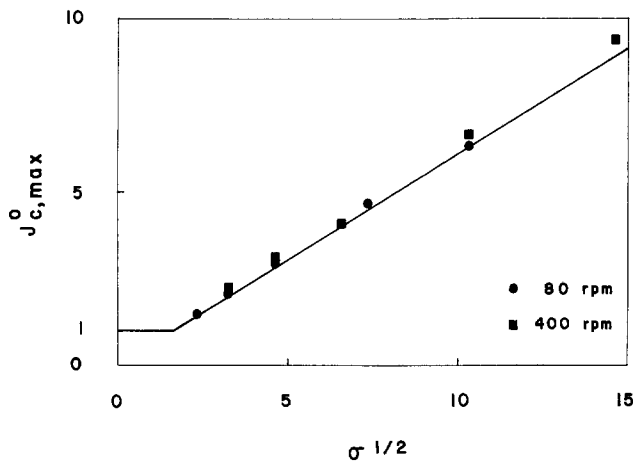


Fig. 8. Dependence of the first sweep cathodic current maximum on the dimensionless sweep rate. Solid line is the prediction of Eq. [6] (RDE cyclic voltammetry).

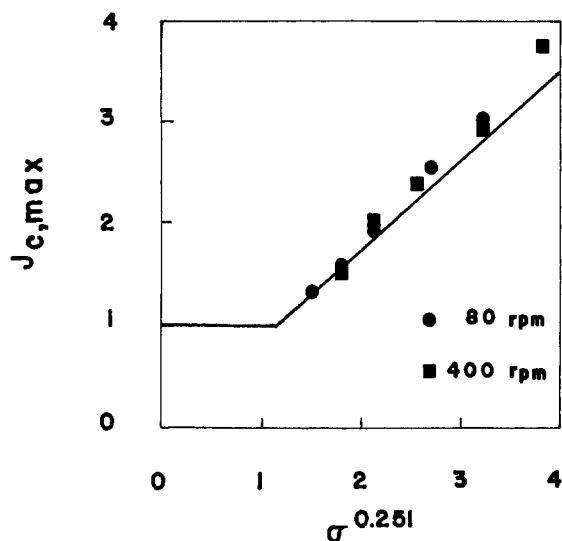


Fig. 9. Dependence of the periodic cathodic current maximum on the dimensionless sweep rate. Solid line is the prediction of Eq. [7] (RDE cyclic voltammetry).

predicted (1) to be

$$J_a = \frac{i_a}{i_L} = 1 - \sigma^{1/2}, \sigma > 9 \quad [8]$$

The experimental observations deviate from the predictions of Eq. [8] in a manner analogous to the i_a for the stationary electrode. The deviation is higher at the higher rotation speed, and this is consistent with an iR effect, since at higher rotation speeds anodic current variations are steeper near the equilibrium potential.

Limiting current measurements.—Limiting currents were measured potentiodynamically in the rotation speed range 100–6400 rpm and were found to depend linearly on $\omega^{1/2}$ with zero intercept. Based on the geometrical area of the electrode, the extracted value for D_{Ag^+} was $1.4 (2) \times 10^{-5} \text{ cm}^2\text{s}^{-1}$, in excellent agreement with the one reported by Bachmann and Dohrmann (6), and consistent with the value obtained from the CV data analysis above.

The possible errors associated with the determination of limiting currents by potential sweeping have been the subject of some discussion in the literature (11). It is believed that if the sweep rate is very high the resulting mass-transfer situation is transient and does not yield an accurate measurement of mass-transfer coefficients in

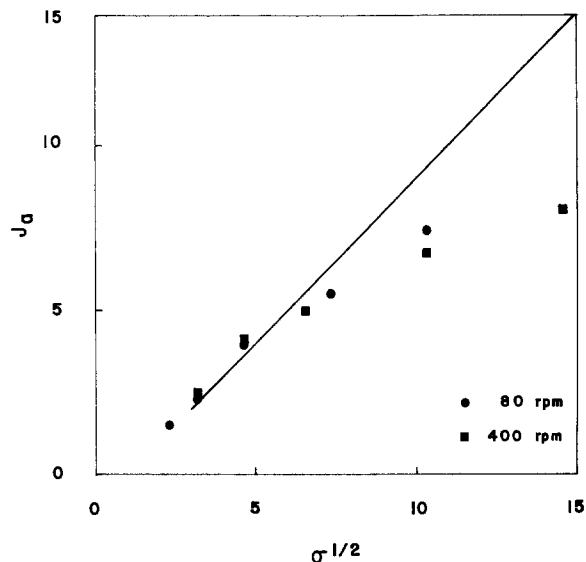


Fig. 10. Dependence of the periodic anodic current maximum on the dimensionless sweep rate. Solid line is the prediction of Eq. [8] (RDE cyclic voltammetry).

the steady state. However, if the sweep rate is very low, and the reaction under study is electrodeposition, the onset of surface roughness with characteristic size similar to the diffusion layer thickness may also yield an erroneous limiting current measurement.

The fact that the potentiodynamically measured limiting currents yielded a value of D_{Ag^+} that is consistent with other literature indicates these objections to the potentiodynamic method require qualification. The more serious limitation is related to the control of the total amount of deposit during the time period required for limiting current measurements. Potentiodynamically, the amount of deposit is not controlled directly, but indirectly by choice of rotation speed and sweep rate. The choice of these two parameters must be made judiciously to obtain true limiting current measurements that are relatively unaffected by surface roughness. For the combination of rotation speed and sweep rate such that $\sigma > 3$, as in Fig. 7, the limiting current can be measured with the deposition of less than $1 \text{ mC} \cdot \text{cm}^{-2}$. There may be circumstances where i_L measurement using $\sigma > 3$ is not possible, due to very high sweep rates or to insufficient potential range (competing reactions). However, when $\sigma > 3$, and for reactions which are not kinetically limited, the current increases more sharply to i_L (1), so that the measurement can be made in a narrower potential region, but the quantity of deposit will be much larger, and the possibility of roughness effects much greater. Roughness effects were clearly evident for some combinations of rotation rate and sweep rate, as shown in Fig. 11.

For very low values of the sweep rate (0.002 and 0.005 Vs^{-1} , Fig. 11) there appear to be well-defined conditions at which the current increases beyond the i_L value. Since the electrode potential is such that no other reactions besides Ag deposition can occur, this increase must be attributed to an increase of the effective surface area of the electrode through the formation of irregularities of characteristic dimension comparable to the thickness of the diffusion layer. It is also possible that these irregularities once formed may further enhance mass transfer through their effect on the hydrodynamics of the system. Table II shows results obtained at different sweep rates and rotation speeds for the potential and the integral charge at which the measured current becomes greater than the limiting current. Several features of these results should be noted: at the same rotation speed, less deposit and more overpotential is required at increasing sweep rates; at the same sweep rate, the critical over-potential in-

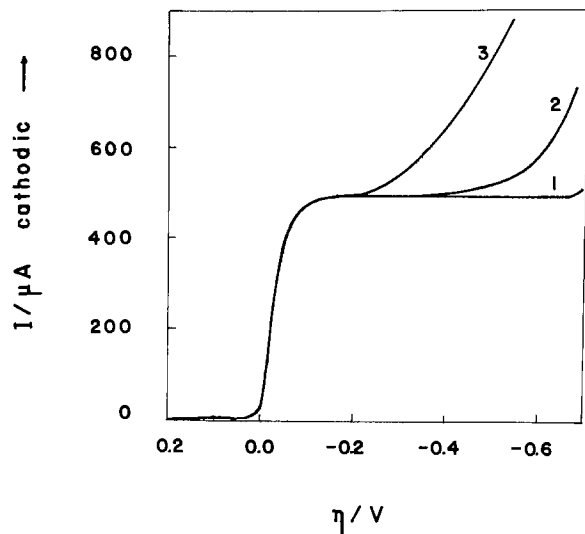


Fig. 11. Potentiodynamic limiting current determination at 1600 rpm and 0.025 Vs⁻¹ (curve 1), 0.005 Vs⁻¹ (curve 2), and 0.002 Vs⁻¹ (curve 3).

creases with increasing rotation speed; assuming uniform deposition, the height of the deposit at the onset is at least 100 times smaller than the boundary layer thickness.

It should be noted also that the characteristic amounts of Ag deposited in Table II are approximately 10-100 times greater than in the other CV curves which were used to test the RDE theory. Collectively, these observations indicate that the irregularities are confined to a very small (e.g., 1%) fraction of the total surface, possibly at the very edge of the disk. We do not, however, offer a definitive physical interpretation of the surface roughness.

Conclusions

An experimental investigation of Ag deposition by multisweep cyclic voltammetry has shown excellent agreement between experiment and a model assuming reversible kinetics at unit activity of the deposit. The anodic reversal potential was set to equal the equilibrium potential of the electrode, while sweep rate, number of applied sweeps, and cathodic reversal potential were treated as parameters.

For the stationary electrode, cathodic current maxima (peaks) were observed that continuously decreased in magnitude with increasing number of applied sweeps, while the peak potential shifted in the cathodic direction. Peak heights were a linear function of the square root of the sweep rate with slopes which depend on the value of the current function at a given cathodic reversal potential as well as on the diffusion coefficient of the ion, its bulk concentration, and the area of the electrode. Although each complete sweep results in the formation of a net deposit, the electrode geometrical or projected area could be

Table II. Characteristic values for the potential and integral charge at which deviation from the limiting current occurs

ω (rpm)	v (V · s ⁻¹)	$-\eta^a$ (V)	$q \times 10^2{}^b$ (C · cm ⁻²)	$\delta \times 10^3{}^c$ (cm)	$l \times 10^6{}^d$ (cm)	δ/l
3600	0.005	0.250	7.0	0.9	7.4	125
	0.010	0.350	5.2		5.5	169
	0.020	0.400	3.0		3.2	286
2500	0.002	0.175	10.1	1.1	11	104
	0.005	0.300	7.3		7.8	142
	0.010	0.425	5.3		5.6	198
1600	0.002	0.200	9.4	1.4	10	139
	0.005	0.350	6.9		7.4	189

^a Cathodic overpotential at which deviation occurs.

^b Integral charge at η .

^c Thickness of the Levich diffusion layer.

^d Deposit thickness equivalent to q ; deposit assumed uniform with a density of 10.5 g · cm⁻³.

used to compute current densities at millimolar concentrations even after the application of ten complete sweeps at 0.010 Vs⁻¹ extending for 0.411V in the cathodic potential region. The integral charges associated with each potential sweep on the stationary electrode followed a linear dependence on the inverse of the square root of the sweep rate. As the number of applied sweeps increases, less deposit is formed during a cathodic sweep. However, even at deposit thicknesses of the order of 20 monolayers, a surface roughness effect was observed as a deviation of the measured charge density from the value computed on the basis of the geometrical area of the electrode.

Cyclic voltammetry experiments performed on the RDE verified the prediction that a periodic current response is obtained during the second and subsequent potential sweeps. In addition, current maxima were obtained when the dimensionless sweep rate exceeded 3, in agreement with theoretical predictions.

When the magnitudes of the cathodic current maxima were normalized with respect to the limiting current at a particular rotation speed, the resulting dimensionless quantity was correlated to the dimensionless sweep rate. For $\sigma > 9$, the periodic dimensionless current was shown to vary linearly with $\sigma^{1/4}$. It was concluded that cyclic voltammetry on the RDE should be performed at low rotation speeds to avoid excessive deposit accumulation and the need for high sweep rates. At these rotation speeds, the limiting current as well as the first and periodic current maxima are well defined, and the RDE correlations can be subsequently used for diagnostic purposes without accurate knowledge of the value of the electrode surface area or the bulk concentration of the reacting species.

In correlating cyclic voltammetry data for both stationary and rotating-disk electrodes, knowledge of the diffusion coefficient of the reacting ion is required. In this investigation a diffusivity value for D_{Ag^+} was obtained by RDE potentiodynamic limiting current measurements. At moderate sweep rates, a limiting current plateau was obtained which was accurately described by the Levich equation. However, at much lower sweep rates, nonuniform deposit accumulation caused the limiting current to increase above its previously determined value. In order to avoid surface roughness and transient effects and also in order to maximize the potential range over which the limiting current is observed, it is concluded that the optimal value of the sweep rate is the one just before the appearance of the cyclic voltammetry current peak. For reversible deposition reactions, this value can be found from the requirement that the dimensionless sweep rate be equal to 3.

Acknowledgment

This work was supported by the Assistant Secretary for Conservation and Renewable Energy, Office of Energy Systems Research, Energy Storage Division of the U.S. Department of Energy under Contract no. DE-AC03-76SF00098.

Manuscript submitted Sept. 7, 1983; revised manuscript received ca. Feb. 9, 1984.

The University of California assisted in meeting the publication costs of this article.

REFERENCES

- P. C. Andricacos and P. N. Ross, Jr., *This Journal*, **130**, 1340 (1983).
- P. C. Andricacos and P. N. Ross, Jr., *ibid.*, **130**, 1353 (1983).
- T. Berzins and P. Delahay, *J. Am. Chem. Soc.*, **75**, 555 (1953).
- P. C. Andricacos and H. Y. Cheh, *This Journal*, **127**, 2153 (1980).
- G. Mamantov, D. L. Manning, and J. M. Dale, *J. Electroanal. Chem.*, **9**, 253 (1965).
- K. J. Bachmann and J. K. Dohrmann, *ibid.*, **21**, 311 (1969).
- M. V. Stackelberg, H. Pilgram, and V. Toome, *Z. Electrochem.*, **57**, 352 (1953).

8. M. B. Kraichman and E. A. Hogge, *J. Phys. Chem.*, **59**, 986 (1955).
9. N. Ibl, in "Advances in Electrochemistry and Electrochemical Engineering," Vol. 2, P. Delahay and C. W. Tobias, Editors, pp. 49-143, John Wiley and Sons, New York (1962).
10. E. Schmidt and S. Stucki, *J. Electroanal. Chem.*, **39**, 63 (1972).
11. J. R. Selman and C. W. Tobias, *ibid.*, **65**, 67 (1975).

Sulfur Chemistry in Equimolar NaOH-H₂O Melt

I. Electrochemical Oxidation of Sodium Sulfide

M. N. Moscardo-Levelut and V. Plichon

Laboratoire de Chimie Analytique des Milieux Réactionnels, ESPCI, 75231 Paris Cedex 05, France

ABSTRACT

Both anodic steps of sulfide oxidation at a gold electrode have been studied in the equimolar NaOH-H₂O melt at 100° and 140°C by voltammetric techniques and electrolysis associated with UV spectrophotometry. The first step leads to S₂²⁻, S₃²⁻, and molecular sulfur following the time scale of the techniques, and the second one to sulfite anion. The influence of temperature is discussed. Application to analytical characteristics of polysulfides is given. The most interesting feature is the distinction between di- and tri-sulfide with the help of their anodic waves and UV spectrum.

This and the following paper are devoted to the study of the sulfur compounds from sulfur disproportionation in strongly basic media. This reaction plays an important role in the utilization of this abundant raw material because it leads to polysulfides, which are used as intermediates in organic or inorganic synthesis (1). This disproportionation reaction is quite complex and is not rigorously controlled, partly because of a lack of convenient analytical tools. Better control could be expected via the spectrophotometric or the electrochemical properties of the relevant species, but a survey of the literature (2) reveals a lack of knowledge about the nature and the properties of the ions, which must be considered in the strongly alkaline and high temperature conditions in which the reaction generally starts (liquid sulfur with sodium hydroxide at temperatures above 120°C).

In view of these arguments, we investigated the electrochemical and UV behavior of the various species from the sulfur disproportionation, *i.e.*, sulfide, polysulfides, and sulfur oxyanions in the equimolar melt NaOH-H₂O at temperatures between 100° and 140°C. Relevant properties of water-NaOH mixtures have been studied and reviewed largely by Tremillion *et al.* (3). These melts are ionic liquids and transparent in the near-UV down to 310 nm. Their acidity is characterized by the pH₂O or by the related pHO⁻ or pO²⁻ function. But except around the pure components composition, the pH₂O is quite buffered in a given melt, depending on the H₂O/HO⁻ ratio, so that the pH₂O need not be regarded as an important parameter in the equimolar melt, contrary to the analogue pH in water. On the other hand, the potential can be varied over a wide range, allowing use of electrochemical techniques. The melting temperature of the equimolar melt is 64.5°C (4, 5).

This first paper deals with the electrochemical oxidation of sodium sulfide. Only a few works in the literature are concerned with strongly basic solutions. The first electrochemical studies date from the beginning of this century. Among them, we can mention Fetzner's (6) works in 4M sodium hydroxide. This author has shown by controlled current electrolysis that oxidation of concentrated sulfide solutions leads at low current density to polysulfides, and at high density to sulfate and dithionate.

By controlled potential electrolysis, Bohnholtzer and Heinrich (7) distinguished sulfur formation and its dissolution into polysulfides, then, at a more oxidizing potential, the formation of sulfate and dithionate. For his part, Gerischer (8) showed that the predominant species are in

turn polysulfide, thiosulfate, and sulfate. Allen and Hickling (9), studying the mechanism and the kinetics of the oxidation, concluded that the first oxidation step of sulfide ion in 1M NaOH solution on platinum or gold electrode leads to polysulfides.

Redox potentials of polysulfides have been calculated (10) or measured (9, 11, 12) in weakly alkaline conditions. Though severe discrepancies exist in the values, the redox potentials of polysulfides fall within very narrow limits in water; thus when they exist, they will be necessarily present simultaneously.

As all these results were obtained in solutions not concentrated enough in NaOH to be extrapolated to the equimolar melt, we undertook investigations on the electrochemical oxidation of sulfide by means of steady-state voltammetry, cyclic voltammetry, chronoamperometry, and controlled potential coulometry.

Experimental

Cells.—Two kinds of materials were used, Pyrex for experiments at 100°C, and Teflon at 140°C. Unexpected absence of corrosion of Pyrex and quartz at 100°C allowed us to use a conventional Pyrex cell with five exits and a thermostated jacket. The cell remains unattacked during more than one year. At 140°C, attack was fast, and a Teflon cell, similar to the conventional Pyrex one, was used. Silicone oil was circulated inside the jacket in order to control the temperature at ±1°C.

Spectrophotometric measurements could be performed only at 100°C because of the attack of silica at higher temperatures. The Pyrex electrochemical cell was for this purpose supplied with two horizontal grindings, through which ran two silica optic fibers with polished faces. Both fibers were directly dipped into the melt, with no protection, and no attack occurred. The optical path was the distance between both polished plane ends of the lined-up fibers (generally 0.315 cm measured by a calibrated wedge clock).

Electrodes.—The working electrode was either a gold disk electrode ($\phi = 0.5$ or 1.0 mm) sealed into Pyrex glass or Teflon according to the temperature, or a cylindrical gold gauze for electrolysis.

All potentials are referred to the system Ag/Ag(I) saturated with Ag₂O (13). We checked its reversibility and its stability in our melt. The reference electrode was a silver wire dipped into the melt saturated with Ag₂O contained in a compartment made either of a Pyrex tube thinned at one end or of porous Teflon to ensure sufficient electrical junction. For cyclic voltammetry and step chronoamperometry, a Pt wire was used as quasireference electrode because the impedance of the thinned tube was

much too high for fast experiments (14). The auxiliary electrode was a platinum wire separated from the bulk of the melt by a glass frit or a Nafion membrane (du Pont) mounted in a Teflon cylindrical holder. The glass frit, of medium porosity, was slightly attacked by the melt and had to be changed often.

Instrumentation.—Electrochemical instrumentation was standard and entirely commercial (Tacussel). The spectrophotometer was an apparatus running in single-beam mode. The light beam issued from a xenon arc (XBO 75W Osram) associated to a monochromator (H 20 Jobin-Yvon) and was focused on the first quartz fiber (Quartex) which dipped into the solution. The light beam went through the solution and was sent with another quartz fiber exactly aligned on the first one to a photomultiplier (R 212 Hamamatsu), which detected the transmitted light. Normalization of the signal, *i.e.*, correction of the signal for variation of the incident flux of the PM response with wavelength was achieved by point-to-point division of the signal by a reference one. Stability with time of the light flux was frequently checked during experiments by measuring the signal at a wavelength where sulfur compounds do not absorb.

Reagents.—All reagents were Prolabo quality RP Normapur used without further purification. Hygroscopic Na₂S 9H₂O was periodically titrated by standard procedures. Nitrogen employed to maintain an inert atmosphere above the melt was saturated with H₂O by a bubbler which contained water at the same vapor pressure as the 1.1 melt.

Results and Discussion

Current-voltage curves of sulfide oxidation at a gold electrode are shown in Fig. 1 for voltammetry at a rotating electrode, in Fig. 2 for potential step chronoamperometry, and in Fig. 3 for cyclic voltammetry. They show that oxidation of Na₂S occurs in two main steps for

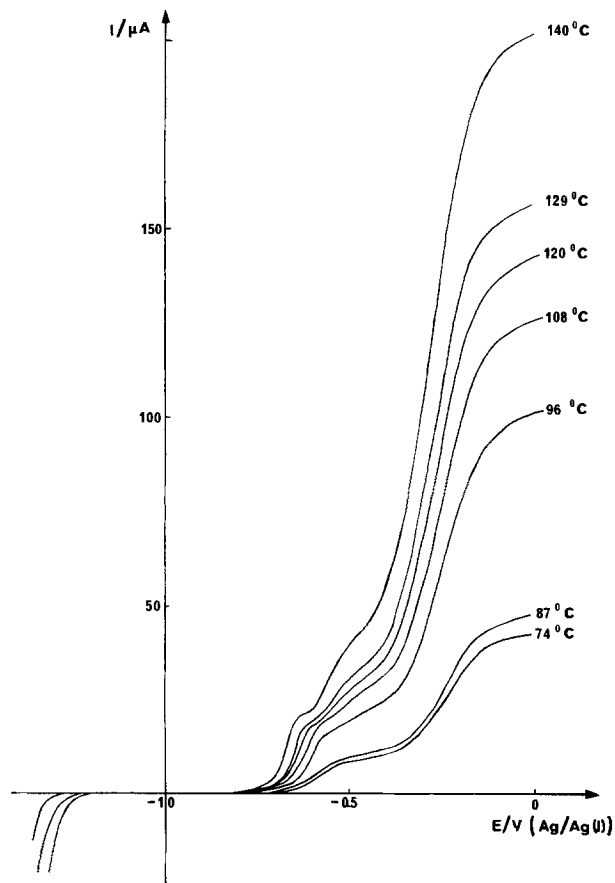


Fig. 1. Sulfide oxidation at a rotating gold electrode in NaOH-H₂O (1-1) melt at various temperatures. S²⁻ = 10⁻²M. Rotation speed: 1600 rev. min⁻¹. Electrode area: 0.785 mm². Scanning rate: 10 mV s⁻¹.

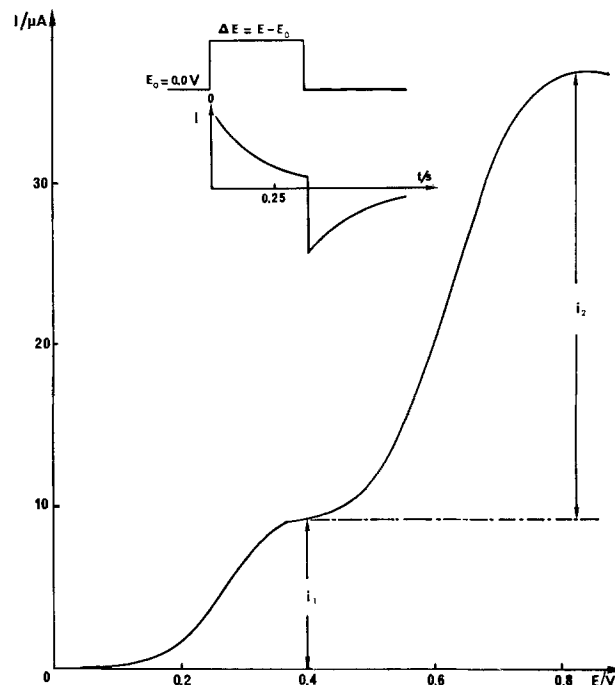


Fig. 2. Potential step chronoamperometry for 1.57 10⁻²M sulfide in NaOH-H₂O (1-1) melt at 100°C. Curve calculated from current measurement at $t = 0.25$ s stepping from the rest potential. Gold electrode area: 0.20 mm². Quasireference electrode: platinum wire.

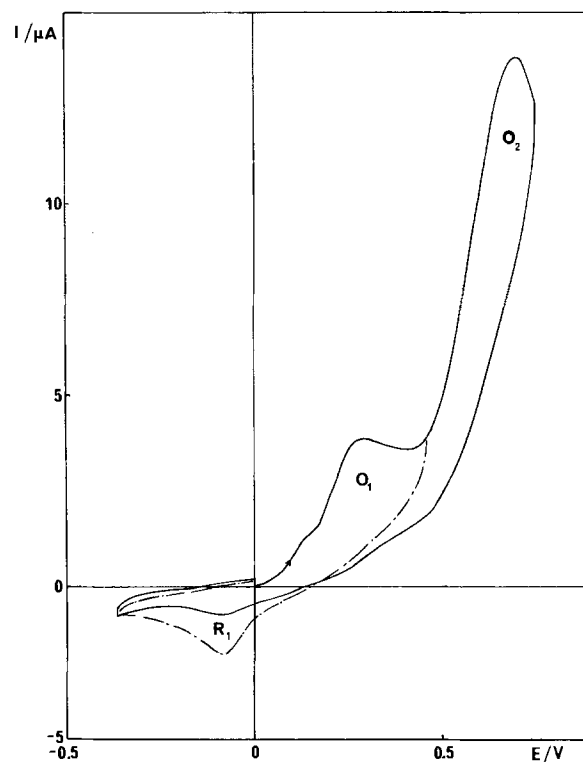


Fig. 3. Cyclic voltammetry of 10⁻²M sulfide solution in NaOH-H₂O (1-1) melt at 100°C. Gold electrode area: 0.20 mm². Scanning rate: 0.1 V s⁻¹. Quasireference electrode: platinum wire.

all temperatures between 75° and 150°C. Electrochemical characteristics are given for 100°C in Table I. The two waves are proportional to the concentration of sulfide ion. A prewave is sometimes observed. As its presence does not affect the characteristics of the two main waves, this prewave has not been studied in more detail.

A priori, three main species must be considered as the final products of the oxidation steps, *viz.*, polysulfides S_x²⁻, molecular sulfur, or oxyanions S_xO_y²⁻. Oxyanions were ruled out for the first wave because more than

Table I. Electrochemical data of the two anodic steps of S^{2-} in $NaOH-H_2O$ (1-1) at $100^\circ C$. $Na_2S = 10^{-2} M$; E vs. $Ag/Ag(I)$; i = limit current at 1000 rpm or peak current at $0.1 V s^{-1}$ or diffusion current 0.25s after a 0.4V step from the rest potential to the plateau; n = electron number

	First step			Second step			i_2/i_1
	$E_{1/2}/V$	$i_p/mA cm^{-2}$	n_1	$E_{1/2}/V$	$i_p/mA cm^{-2}$	n_2	
Rotating electrode	-0.62	3.04	2	-0.27	11.2	?	3.7
Cyclic voltammetry		1.9	4/3 or 2*		5.6	4	2.95
Step chronoamperometry		3.02	4/3		9.0	4	3.0

* For scan rate $> 2 V s^{-1}$.

$2e^-/S^{2-}$ would result in the unrealistic value of more than $6e^-/S^{2-}$ for the second wave, according to their relative height. Confirmation was carried on by controlled-potential electrolysis on the first plateau (less than $2e^-/S^{2-}$, see below). But, polysulfides or sulfur could not be ruled out, since their occurrence is now well established in molten salts. Before we investigate this problem in more detail, we shall first comment on the nature of the polysulfides which exist in the 1-1 melt, the di- and tri-sulfide S_2^{2-} and S_3^{2-} . The two classic ways of polysulfide preparation in a basic medium are addition of S_8 to a sulfide solution and S_8 disproportionation. Very simple experiments show that, depending on the method, two different polysulfides, both yellow colored, are obtained in this melt: (i) for case a, by addition of sulfur to sulfide in excess, a UV peak appears at $\lambda_{max} = 365 nm$, i.e., with higher absorption at 365 nm than at any other wavelength, for instance, the arbitrarily chosen value $\lambda = 330 nm$ ($A_{365} > A_{330}$). The first oxidation wave of S^{2-} does not decrease with S addition, which means that the obtained S_x^{2-} is electro-oxidizable at the same potential as S^{2-} . (ii) For case b, by disproportionation of S_8 in a sulfide-free melt, a UV band appears, but with $A_{365} < A_{330}$. No oxidation wave corresponding to the first wave of S^{2-} is observed, which indicates that this polysulfide is not electro-oxidizable in that potential range.

In both cases, a reduction wave of polysulfides appears roughly at the same potential. Since the well-known stability order of polysulfides is (15, 16) in basic media $S_2^{2-} > S_3^{2-} > S_4^{2-}$, etc., the simplest and most logical assignment is the following. In presence of S^{2-} in excess (case a), the less sulfur containing species is obtained, i.e., S_2^{2-} . The wavelength of its maximum absorption agrees with the published value for S_2^{2-} (16). In the disproportionation case b, the polysulfide which follows in the stability order, that is, S_3^{2-} , can be assumed. This assignment has been proved by electrolysis experiments, described in the next paragraph. In these experiments, a polysulfide with the same characteristics ($A_{365} < A_{330}$, no oxidation wave at the potential of the first S^{2-} wave) is obtained for $1.23e^-/S^{2-}$ to be compared to 1.0 for S_2^{2-} , 1.33 for S_3^{2-} , and 1.5 for S_4^{2-} .

Details of the electrochemical and spectrophotometric properties of these polysulfides are reported in the last paragraph. No other polysulfide has been detected, and the distinction between S_2^{2-} and S_3^{2-} can be clearly achieved via criteria a and b mentioned above.

First Oxidation Step

Main features of the wave.—Wave and peak were analyzed according to the usual procedure. Linear plots of the wave height or of the peak current vs. the square root of the electrode rotation speed or of the potential sweep rate indicate a process limited by the sulfide diffusion. The diffusion coefficient D of the sulfide ion has been deduced from chronoamperometry measurements on the plateau of the wave. On the time scale of experiments (1s-10 ms), linear decrease of current vs. $t^{-1/2}$ is observed according to Cottrell's equation valid on the diffusion plateau whatever the reversibility of the process (17)

$$D = \frac{i^2 \pi t}{(n FAC)^2}$$

where n , F , A , and C are the number of electrons, the Faraday constant, the electrode area, and the sulfide concentration, respectively. At $100^\circ C$, we obtain a value of D equal to $4.3 \cdot 10^{-6} cm^2 s^{-1}$, assuming a value of $n = 4/3$ (see below). This low value can be explained by the high viscosity (18) of the medium ($\eta = 8 cP$).

Wave analysis gives straight lines of E vs. $\log i/(i_1 - i)$ plot with a slope of 90 mV. Compared to a slope of 74 mV for a one-electron reversible system at $100^\circ C$, the electrode reaction appears to be irreversible, in agreement with the large anodic and cathodic peak separation observed in cyclic voltammetry (Fig. 3).

Controlled potential electrolysis.—Controlled potential electrolysis of Na_2S at a cylindrical gauze electrode has been performed on the plateau of the first oxidation step of sulfide [$-0.5V$ vs. $Ag/Ag(I)$]. The yellow color developed meanwhile provides obvious evidence of the formation of polysulfides during the electrolysis, and their appearance has been followed by simultaneous recording at regular periods of their UV spectrum (Fig. 4) and their voltammetric waves at a rotating gold electrode (Fig. 5).

If the oxidation process was a simple one: $Red \rightarrow Ox$, the electrolysis current I should vary as the concentration of Red, i.e., in inverse proportion to the number F/S^{2-} of Faraday exchanged per mole of sulfide (linear plot of I vs. F/S^{2-}), and the absorbance should increase in direct proportion to F/S^{2-} whatever the wavelength in the absorption band of Ox. The break observed for 1.3 F/S^{2-} and the discrepancies between the curve A_{365} and A_{330} vs. the number of Faraday per mol of sulfide (Fig. 6) show that the oxidation of sulfide cannot be assigned to a simple reaction. Three main parts must be considered in the course of the electrolysis.

First part: $F/S^{2-} < 0.5$.—During this first part, A_{365} increases at a higher rate than A_{330} , which indicates the prevailing formation of S_2^{2-}

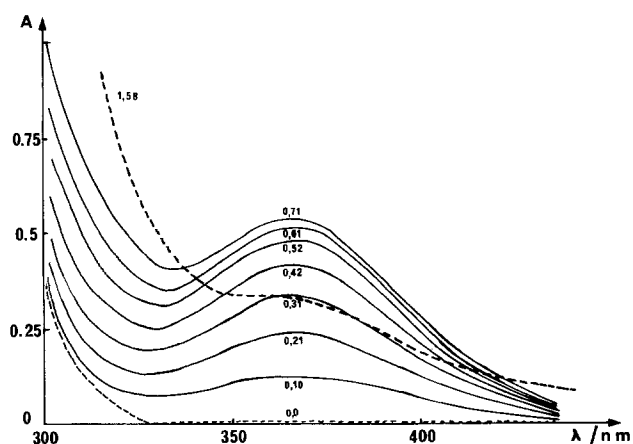
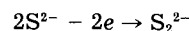


Fig. 4. UV spectra recorded during the electrolysis at $E = -0.5V$ of a $9.1 \cdot 10^{-3} M S^{2-}$ solution in $NaOH-H_2O$ (1-1) melt at $100^\circ C$. Number of Faradays per sulfide mole are indicated on each curve. Optic path: 0.315 cm.

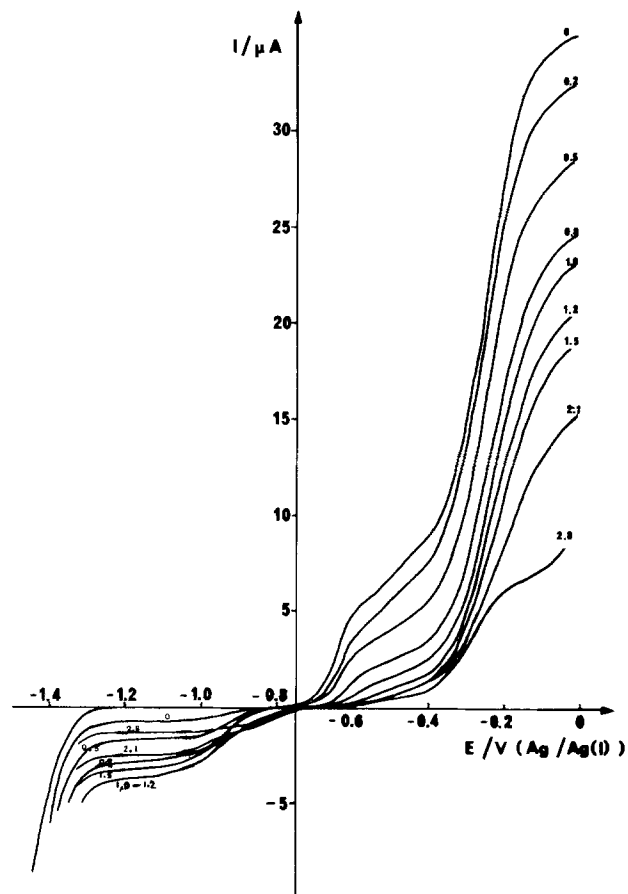
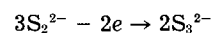
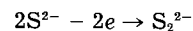


Fig. 5. Voltammetric curves at a rotating gold electrode ($S = 0.20 \text{ mm}^2$) recorded during the electrolysis at $E = -0.5 \text{ V}$ of a $9.2 \cdot 10^{-3} \text{ M S}^{2-}$ solution in NaOH-H₂O (1-1) melt at 100°C . Number of Faradays per sulfide mole is indicated on each curve.

This reaction is not quantitative as shown by the non-linear increase above 0.2 F/S^{2-} of the absorption at 365 nm and by the maximum value of 0.8 F/S^{2-} instead of 1 required for complete oxidation. Above 0.2 F/S^{2-} , the less absorbing trisulfide S_3^{2-} must begin to appear, though there is no clear proof. This short range does not allow any significant extrapolation to zero of the electrolysis current to get the number of exchanged electrons and make a distinction between S_2^{2-} and S_3^{2-} .

Though S_2^{2-} has the same first anodic wave as S^{2-} , the limiting current of the first wave decreases (Fig. 5) because two sulfides lead to only one S_2^{2-} , which involves a 50% decrease in concentration of electroactive species.

Second part: $0.5 < \text{F/S}^{2-} < 1.3$.—If electrolysis is carried out beyond 0.5 F/S^{2-} , the remaining sulfide and the disulfide which is electro-oxidizable at the same potential as sulfide are oxidized into trisulfide, as shown by the lower increase rate, or even decrease above 0.8 F/S^{2-} , of A_{365} compared to A_{330}



Both sulfides clearly coexist during a certain time, but the presence of S_3^{2-} becomes obvious at $\text{F/S}^{2-} > 1$, since $A_{330} > A_{365}$ and the current of the anodic first wave falls to a small value. Extrapolation of the electrolysis current indicates that it would be zero for consumption of $1.23 \pm 0.05 \text{ F/S}^{2-}$ at 100° and 140°C . Compared to the theoretical values of 1 needed for oxidation of S^{2-} into S_2^{2-} , 1.33 into S_3^{2-} , and 1.5 into S_4^{2-} , this experimental value attests the formation of the trisulfide and not the tetrasulfide S_4^{2-} . This result shows also that S_3^{2-} cannot be produced by disproportionation of sulfur obtained as a transitory species in the mechanism described below because, in that case, extrapolation to zero current would lead to a value of 2 F/S^{2-} .

Third part: $\text{F/S}^{2-} > 1.3$.—It is fundamental to realize that the time scale of the last part of the electrolysis is widely different: hours instead of 40 min (see time axis of Fig. 6). During this period, one observes the simultaneous disappearance of the yellow color, of the UV band, and of the anodic and cathodic voltammetric curves. These concordant observations mean that the trisulfide ion disappears via a process which is too slow to be mass-transport limited. We supposed that S_3^{2-} is unstable and slowly disproportionates into an oxyanion $\text{S}_x\text{O}_y^{2-}$ and an electroactive species S^{2-} or S_2^{2-} , which is again oxidized in S_3^{2-} . The hypothesis explains the slow decrease of the electrolysis current (Fig. 6). Because of the low value of the current and of the long time required for the electrolysis, no significant extrapolation of the I - F plot of Fig. 6 could be performed to gain information on the disproportionation reaction. Electrolysis must end when sulfide and polysulfide are completely changed into a more stable oxyanion.

Evolution of the anodic and cathodic limiting current at the rotating gold electrode recorded during the elec-

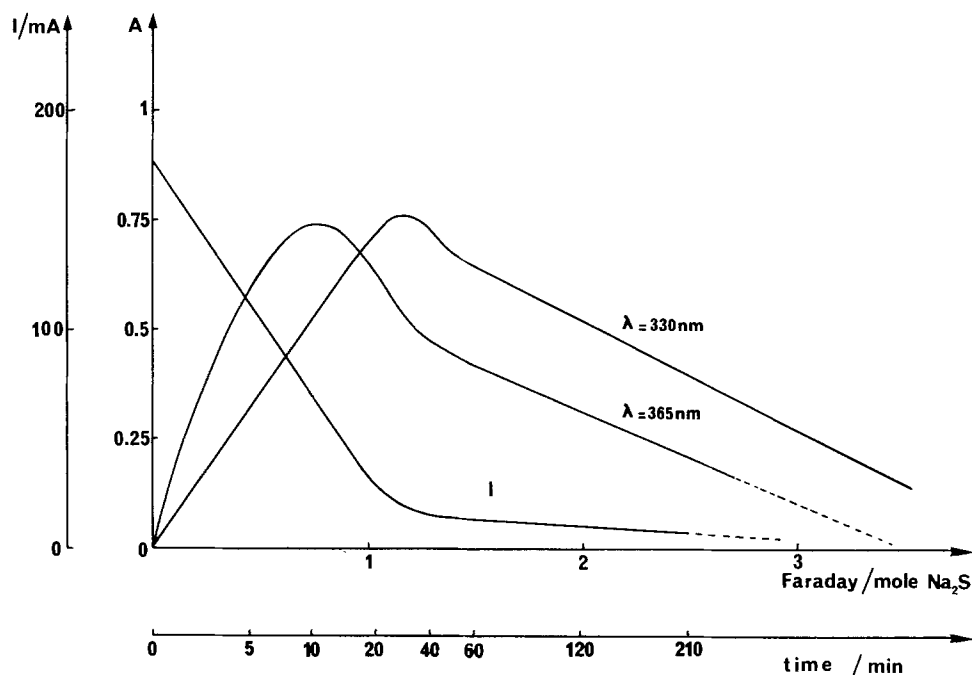
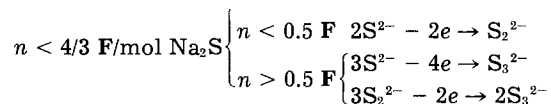


Fig. 6. Variations of A_{330} , A_{365} , and I (electrolysis current) during the electrolysis of sulfide on the first plateau. Experimental conditions same as Fig. 4 and 5.

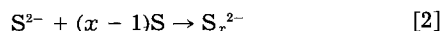
trolysis (Fig. 5) agrees qualitatively with the appearance of polysulfides. Nevertheless, quantitative analysis did not allow a clear distinction between the di- and trisulfide formation (19).

We can sum up the first step of Na_2S electrolysis with the following scheme



$n > 4/3 \text{ F/mol Na}_2\text{S}$: slow disproportionation of S_3^{2-}

Number of electrons involved at voltammetric time scale.— In the classic scheme of formation of polysulfides via an EC mechanism, molecular sulfur is supposed to be first obtained



We shall now consider which compound among the possible S_2^{2-} , S_3^{2-} , or S and species is obtained at the time scale of voltammetric experiments, widely different from the time scale of controlled-potential electrolysis.

A distinction between insoluble molecular sulfur and soluble polysulfides was achieved via cyclic voltammetry experiments. At medium sweep rate ($v < 2 \text{ V s}^{-1}$), Fig. 3 shows the reduction peak associated with the first oxidation peak. Both its diffusive shape [linear i_p vs. $v^{1/2}$ plot, slow decrease to zero instead of the sharp fall observed when reduction of sulfur deposit occurs as, for example, in $\text{PbCl}_2\text{-KCl}$ melt (20)] and its potential (the same as the reduction potential of a polysulfide solution prepared by disproportionation of sulfur into the melt) ruled out molecular sulfur deposit. Reaction [2] prevails at low sweep rate. The polysulfide must be S_3^{2-} and not S_2^{2-} , since S_2^{2-} is anodically oxidized at the potential of the first wave. S_3^{2-} can be seen only at the beginning of large-scale electrolysis when a chemical reaction between the anodically produced trisulfide and the remaining sulfide in large excess can occur in the bulk of the cell.

When scanning the potential at a sweep rate higher than 2 V s^{-1} , in addition to the oxidation and reduction peaks observed at slower sweep rate, a new reduction peak appears at less negative potential than the former (Fig. 7). This peak was attributed to the intermediate formation of sulfur via reaction [1].

As this reduction peak is ill-shaped and merges into the main one with increasing potential sweep rate, a quantitative diagnostic was tried only on the anodic peak i_A . In diffusive conditions, $i_A v^{-1/2}$ is proportional to the number of exchanged electrons and should increase from less than $2e^-/\text{S}^{2-}$ at low sweep rate (minimum $1e^-/\text{S}^{2-}$ for S_2^{2-} , $4/3$ for S_3^{2-} , 1.5 for S_4^{2-} , etc.) to $2e^-/\text{S}^{2-}$ at higher sweep rate, that is a twofold maximum increase.

A plot of $i_A v^{-1/2}$ vs. $\log v$ is shown on Fig. 8. The constant value of $i_A v^{-1/2}$ when $v < 2 \text{ V s}^{-1}$ agrees with a single diffusive step (oxidation in S_3^{2-}), but at a higher sweep rate, much more than a twofold increase was observed without apparent limit. For want of something better, we supposed that sulfur forms a deposit on the electrode which artificially increases its area. Since an $i_A v^{-1/2}$ plot has no simple meaning in those conditions, no kinetic study could be performed.

In cyclic voltammetry experiments, we have shown that a polysulfide is obtained with probably $n = 4/3$ except at high sweep rate ($v > 2 \text{ V s}^{-1}$) where sulfur was detected ($n = 2$). Only polysulfide was observed in double-step chronoamperometry at the time scale of our apparatus ($1\text{s} < t < 0.01\text{s}$): the backward cathodic reaction is diffusion controlled (linear i_c vs. $t^{-1/2}$ plot) which excluded a deposit of insoluble sulfur during the forward anodic step (Fig. 2). As in cyclic voltammetry at low sweep rates and for the same reason, S_3^{2-} must be considered as the most probable final species ($n = 4/3$).

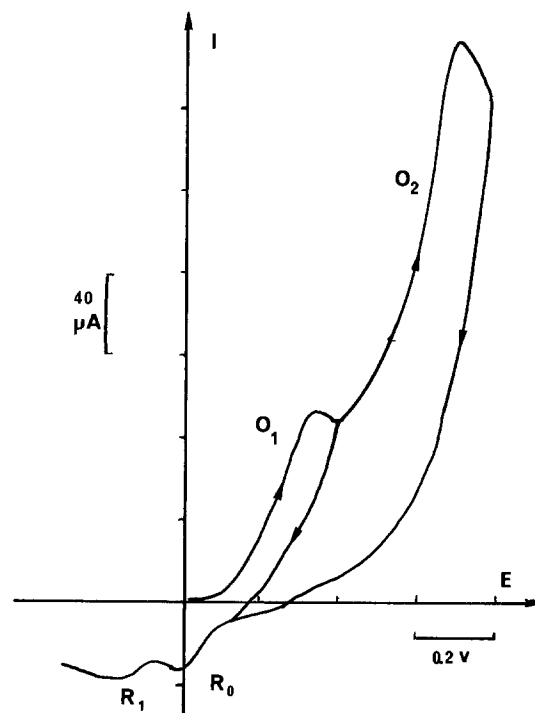


Fig. 7. Cyclic voltammetry of a $1.6 \cdot 10^{-2} \text{ M}$ solution of sulfide in $\text{NaOH-H}_2\text{O}$ (1-1) melt at 100°C at a gold electrode (area: 0.20 mm^2). Scanning rate: 20 V s^{-1} . Quosireference electrode: Pt wire.

On the contrary, at a rotating gold electrode, several arguments are in favor of a sulfur deposit when current potential curves are slowly recorded (2 mV s^{-1}). The first one is explained in the second paper (21), where it is shown that disulfide and sulfide are oxidized with the same number of electrons which is necessarily two, and which agrees with reaction [1]. The second reason is that polysulfides react with sulfite (21). Since anodic curves of sulfide recorded at a rotating electrode are not influenced by the presence of sulfite in solution, it may be supposed that sulfur is obtained instead of polysulfide. The third reason is the curious influence of temperature on the anodic wave detailed below and easily explained by a sulfur deposit. The last proof comes from the value of the ratio of limiting currents of the two anodic steps, which does not agree with chronoamperometry and cyclic voltammetry results (Table I) and can be still explained by a sulfur deposit.

From all these reasons, we believe that molecular sulfur and not polysulfide is obtained at a rotating gold electrode. As this deposit modifies the electrode sur-

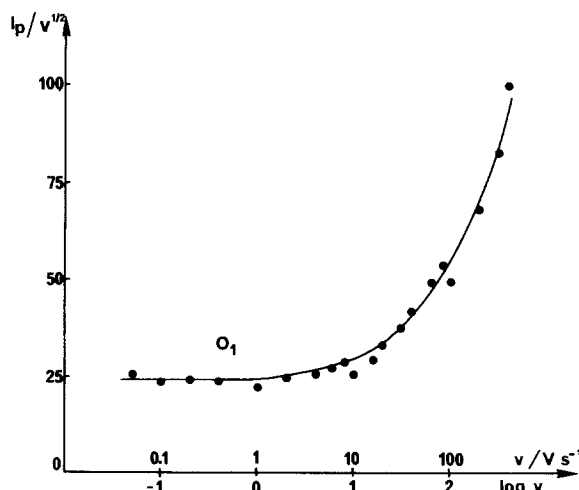


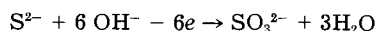
Fig. 8. $i_A v^{-1/2}$ vs. $\log v$ plot for the first oxidation peak of a $2.25 \cdot 10^{-2} \text{ M}$ sulfide solution.

face, quantitative measurements required for the determination of the diffusion coefficient or the number of electrons involved in the second step have only been performed via chronoamperometry experiments, since sulfide is oxidized to the S(IV) state without going through the intermediate S(0) state.

Second Oxidation Step

The second oxidation wave, proportional to sulfide concentration, was found to be controlled by diffusion of the sulfide ion as proved by the straight lines of limiting or peak current plot *vs.* the square root of electrode rotation speed or potential sweep rate. The electrochemical process involved is irreversible, as indicated by the absence of a reduction peak in cyclic voltammetry, even at high potential-sweep rate (Fig. 7). The number of electrons exchanged during this second step has been calculated by two different means: comparison of heights of the two anodic waves and electrolysis on the second plateau. The ratio of the limiting current deduced from chronoamperometry measurements or cyclic voltammetry (Table I) leads to $n = 4$ (4.0 and 3.9, respectively), that is, for the total electron number of the two waves a value of 5.3. This result is not far from the value of 5.8 obtained by electrolysis of a S²⁻ solution directly on the second plateau. No polysulfides are formed during the course of electrolysis since no UV band has been transitively detected.

It may be concluded that the oxidation of sulfide leads to S(IV). Since the only known sulfur compounds in high alkaline hydroxide solution are oxyanions, the second oxidation step of sulfide would lead to sulfite ion, according to the reaction



Influence of Temperature

Stationary voltammetric curves at a rotating gold electrode have been recorded for temperatures between 74° and 146°C (Fig. 1). Both waves increase in the same way, but the limiting current *vs.* temperature plot presents two discontinuities around 90°/100° and 140°C (Fig. 9). If variations of current are due to a change of physical properties of solvent, the current should be consistent with the Levich equation (17) and proportional to $\eta^{-5/6} \rho^{7/6}$ (η = kinematic viscosity, ρ = density), which is not verified experimentally. No discontinuity is observed in any physical properties of the solvent in that temperature range (18, 22). It is more credible to attribute such current discontinuities to changes of physical properties of sulfur (23). The first discontinuity between 90° and 100°C might be due to the transition between the two solid phases αS_8

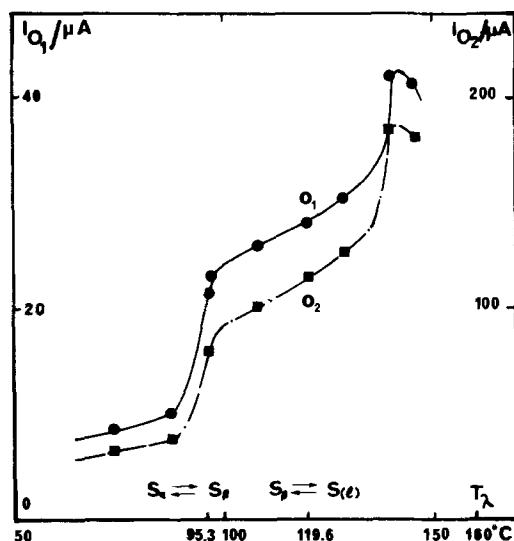


Fig. 9. Variation of limiting currents i_1 and i_2 *vs.* temperature (data from Fig. 1).

$\approx \beta\text{S}_8$ and the second one around 140°C to the polymerization of liquid sulfur. The variations of the electrical conductivity, resistivity, and viscosity of sulfur *vs.* temperature are similar to the one that we observed for wave heights beyond 120°C. This conductivity increases beyond the sulfur melting point to reach a maximum around 160°C before decreasing. Considering the electrical resistivity, it varies from $10^{12} \Omega\text{cm}^{-1}$ at 115°C to $2 \cdot 10^{10} \Omega\text{cm}^{-1}$ at 130°C. A sudden change is noticed for the viscosity which decreases to 6 cP at 150°C, then increases quickly to reach 43 cP at 170°C.

Although unproved, this explanation would support the sulfur deposit hypothesis put forward to explain the curious value of the limiting currents at a rotating gold electrode, or the unexpected increase of the $i_{A0}^{-1/2}$ function in cyclic voltammetry.

Controlled potential electrolyses at 140°C on the first or the second plateau do not display any change relative to 100°C results except for the rate of reactions. At 100° and 140°C, the oxidation mechanisms must be the same, only the kinetics are different, as the time scale recorded on Fig. 10 shows. Reactions become faster when temperature is increased. That is true not only for the formation of trisulfide, but also for its disproportionation.

Properties of S₂²⁻ and S₃²⁻

The disulfide is quite stable over 2h at 100° and 140°C in oxygen-free atmosphere. On the contrary, the trisulfide slowly decomposes at 100°, and more rapidly at 140°C. These results agree with previous observations in less basic media: the stability of polysulfide ions decreases when temperature, length of the chain, and alkalinity increase (15, 24-26).

We have not studied the decomposition reaction of S₃²⁻ because of a lack of analytical tools for oxyanions and because of the crossed reactions between the possible products of the reaction (21). We can only state that a mixture of disulfide (very slight increase of A_{365}) and monosulfide (increase of the first anodic wave, decrease of the reduction wave) appears without any other information about the presence of oxyanion. A steady state seems slowly reached at 100°C, and more quickly at 140°C, which could correspond to the equilibrium between S²⁻, S₂²⁻, S₂O₃²⁻, and SO₃²⁻ studied in the second paper (21).

The disulfide has a band located at 365 nm, in agreement with published values (16, 27, 28). For the trisulfide,

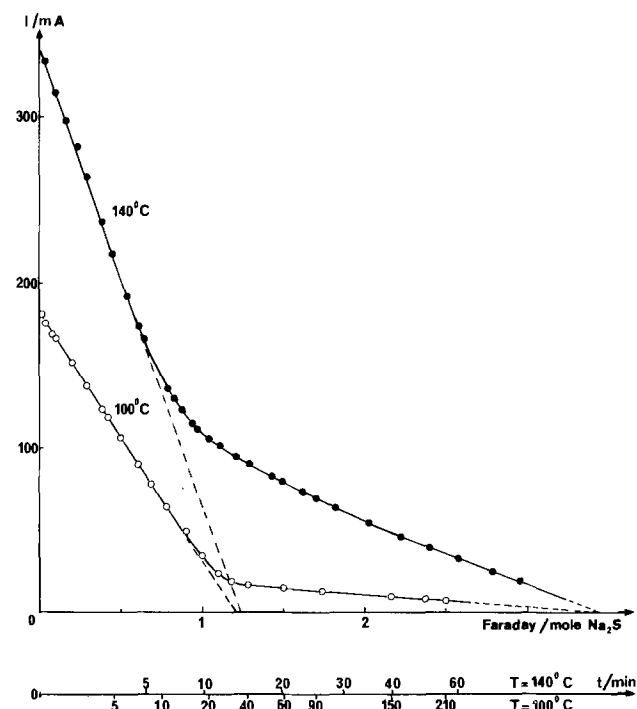


Fig. 10. Electrolysis current on the first anodic step ($E = -0.5\text{V}$) of a $1.1 \cdot 10^{-2}\text{M}$ solution of S²⁻ in NaOH-H₂O (1-1) melt at 100° and 140°C.

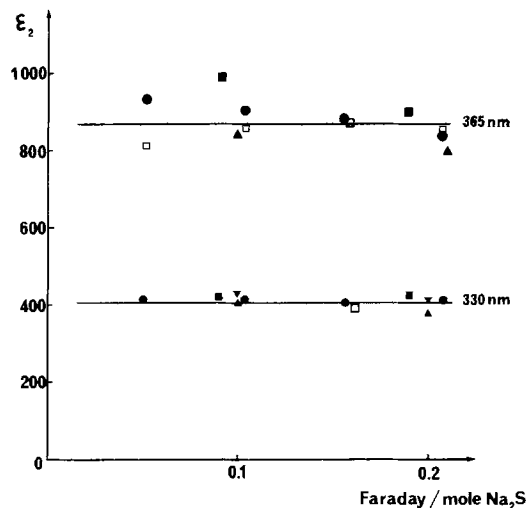


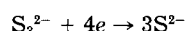
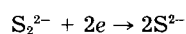
Fig. 11. Determination of the molar absorptivity at 330 and 365 nm of S_2^{2-} in NaOH- H_2O (1-1) melt at $100^\circ C$. Initial concentration of S_2^{2-} : $0.91 \cdot 10^{-2} M$ (\blacktriangle); $1.35 \cdot 10^{-2} M$ (\square); $1.70 \cdot 10^{-2} M$ (\bullet); and $2.09 \cdot 10^{-2} M$ (∇ and \blacksquare).

the maximum at 303 nm could not be observed because of the melt absorption below 310 nm, and the visible band at 416 nm noticed by Giggenbach (16) was not detected.

Molar absorptivities, ϵ , were measured by application of the Beer-Lambert law to solutions of sulfide electrolyzed at less than $0.2 F/S_2^{2-}$ and $1.2 F/S_2^{2-}$ assuming a 100% yield for the oxidation into S_2^{2-} in the first case and into S_3^{2-} in the second case. Due to experimental difficulties of spectrophotometry in molten salts, a 5% reproducibility was obtained (Fig. 11). Results are detailed in Table II.

Good agreement with published values is obtained for S_2^{2-} , but some discrepancies arise for S_3^{2-} . Because of the slow degradation of S_3^{2-} into S_2^{2-} , our value at 330 nm could be slightly low and the one at 365 nm slightly high, which is not in opposition with the work of Giggenbach. However, we do not believe that it could explain a variation of a factor of almost two. Besides differences in temperature and solvent, we would like to point out that results of Ref. (16) should be treated with caution because each individual spectrum of polysulfides was calculated using for HS^- a pK_A value of 17.1 (29) which has been criticized (30) instead of 13, the value generally accepted (30-32), except recently (33).

Both polysulfides can be oxidized or reduced at a rotating gold electrode, as has been shown in Fig. 5. Figure 12 shows typical cyclic voltammometric experiments at a stationary gold electrode recorded for disulfide in presence of sulfide and for trisulfide. Both polysulfide ions are reducible at the same potential. This peak is diffusive (linear plot of i_p vs. $v^{1/2}$ when $v < 1 V s^{-1}$) and irreversible. It leads to sulfide: electrolysis at $-1.15V$ allows the recovery of S^{2-} characteristic voltammometric curves and ends up after $1.9 \pm 0.2 F/S_2^{2-}$ and $4.2 \pm 0.2 F/S_3^{2-}$ according to the following reactions



This reduction step characterizes the presence of polysulfides in solution, but does not allow a distinction between them. This distinction is achieved via the anodic waves: the disulfide is oxidized in two steps, the trisulfide in only one. These waves have not been studied in more detail but by analogy with sulfide, since half-

Table II. Molar absorptivity of S_2^{2-} and S_3^{2-} (ϵ in $M^{-1} cm^{-1}$)

	This work	After Ref. (16)
S_2^{2-}	$\epsilon_{330} = 405 \pm 25$	260
S_2^{2-}	$\epsilon_{365} = 870 \pm 50$ (max)	850
S_3^{2-}	$\epsilon_{330} \approx 580$	1020
S_3^{2-}	$\epsilon_{365} \approx 380$	130

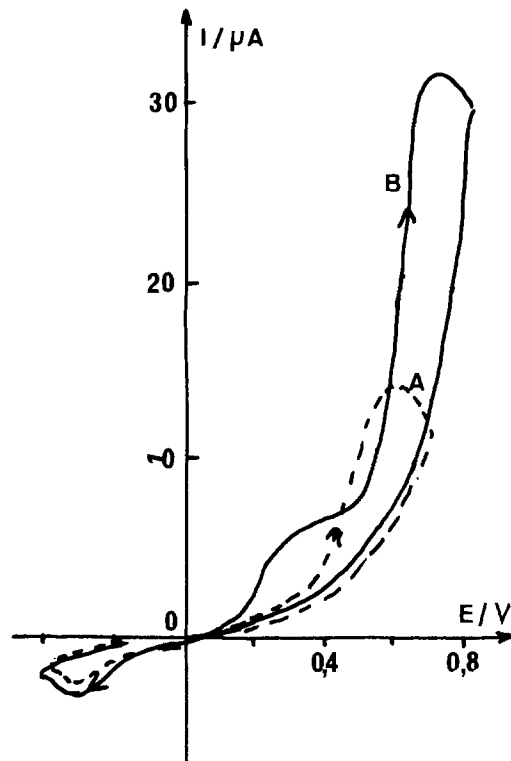


Fig. 12. Cyclic voltammetry on a stationary gold electrode ($v = 0.2 V s^{-1}$) in NaOH- H_2O (1-1) melt at $100^\circ C$. Curve A: S_3^{2-} ($3.8 \cdot 10^{-3} M$). Curve B: S_2^{2-} ($3.4 \cdot 10^{-3} M$) + S^{2-} ($1.4 \cdot 10^{-2} M$).

wave potentials are similar, one can suppose that the same reactions occur.

The voltammetric curves and the UV spectra of the sulfur compounds can be used as an analytical tool to characterize their presence in the NaOH- H_2O melt and to measure their concentration. It will be applied in the second paper (21) to study the crossed reactions between sulfur compounds.

Manuscript submitted June 17, 1983; revised manuscript received March 2, 1984.

ESPCI assisted in meeting the publication costs of this article.

REFERENCES

- B. Meyer, in "Sulfur, Energy and Environment," Chap. 13, Elsevier, Amsterdam (1977).
- V. Plichon, A. de Guibert, and M. N. Moscardo-Levelut, in "Ionic Liquids," D. Inman and D. Lovering, Editors, Chap. 18, Plenum Press, New York (1981).
- B. Tremillon and R. G. Doisneau, *J. Chim. Phys.*, **71**, 1379, 1445 (1974).
- R. Cohen-Adad, A. Tranquard, R. Peronne, P. Negri, and A. P. Rollet, *C. R. Acad. Sci. Ser. C*, **251**, 2035 (1960).
- A. P. Rollet and R. Cohen-Adad, *Rev. Chim. Min.*, **1**, 451 (1964).
- W. R. Fetzer, *J. Phys. Chem.*, **32**, 1787 (1928).
- W. Bohnholtzer and F. Heinrich, *Z. Electrochem.*, **39**, 939 (1933).
- H. Gerischer, *ibid.*, **54**, 540 (1950).
- P. L. Allen and A. Hickling, *Trans. Faraday Soc.*, **63**, 1626 (1957).
- W. M. Latimer, "Oxidation Potentials," p. 66, Prentice-Hall, New York (1938).
- D. Peschenski, *C. R. Acad. Sci. Ser. C*, **227**, 770 (1948); D. Peschanski and G. Valensi, *ibid.*, **227**, 845 (1948); *J. Chim. Phys.*, **46**, 602 (1949).
- G. Maronny, *J. Chim. Phys.*, **18**, 140, 202 (1959); **25**, 214 (1959).
- M. Maurice, L. Lacourcelle, and J. Royon, *Electrochim. Acta*, **14**, 1061 (1969).
- C. C. Herrmann, G. G. Perrault, and A. A. Pilla, *Anal. Chem.*, **40**, 1173 (1968).
- L. Gustafsson and A. Teder, *Svensk Papperstidn.*, **72**, 249 (1969).
- W. Giggenbach, *Inorg. Chem.*, **11**, 1201 (1972).
- A. J. Bard and L. R. Faulkner, "Electrochemical Meth-

- ods. Fundamental and Applications," Chap. 5, John Wiley and Sons, Inc., New York (1980).
18. M. A. Klochko and M. M. Godneva, *Rus. J. Inorg. Chem.*, **4**, 964 (1959); after *C.A.*, **54**, 11653h.
 19. M. N. Moscardo-Levelut, these de doctorat, Université de Paris VI, Paris (1981).
 20. A. De Guibert and V. Plichon, *J. Electroanal. Chem.*, **90**, 399 (1978).
 21. M. N. Moscardo-Levelut and V. Plichon, *This Journal*, **131**, 1545 (1984).
 22. I. A. Dibrov, V. P. Mashovets, and R. P. Matveeva, *Zh. Prikl. Khim.*, **37**, 29 (1964); after *C. A.*, **60**, 9941h.
 23. B. Meyer, *Chem. Rev.*, **76**, 367 (1976).
 24. W. Giggenbach, *Inorg. Chem.*, **13**, 1724 (1974).
 25. W. Giggenbach, *ibid.*, **13**, 1730 (1974).
 26. N. Hartler, J. Libert, and G. Akerlund, *Svensk Papperstidn.*, **75**, 673 (1972).
 27. G. Schwdrzenbach and A. Fischer, *Helv. Chim. Acta*, **43**, 1365 (1960).
 28. A. Teder, *Svensk Papperstidn.*, **70**, 197 (1967).
 29. W. Giggenbach, *Inorg. Chem.*, **10**, 1333 (1971).
 30. S. Ramachandra-Rao and L. G. Hepler, *Hydrometall.*, **2**, 293 (1977).
 31. L. G. Sillen, "Stability Constants of Metal Ions Complexes," Vol. 17, p. 128, The Chemical Society, Burlington House, London (1964); *ibid.*, Vol. 25 (1971).
 32. I.U.P.A.C., "Dissociation Constants of Inorganic Acids and Bases in Aqueous Solutions," p. 53, Butterworths, London (1969).
 33. B. Meyer, K. Ward, K. Koshlap, and L. Peter, *Inorg. Chem.*, **22**, 2345 (1983).

Sulfur Chemistry in Equimolar NaOH-H₂O Melt

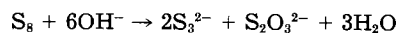
II. Chemical Reactions Between Sulfur, Sulfide, Polysulfides, and Oxyanions

N. M. Moscardo-Levelut and V. Plichon

Laboratoire de Chimie Analytique des Milieux Réactionnels (ERA 953), ESPCI, 75231 Paris Cedex 05, France

ABSTRACT

Chemical reactions of sulfur compounds have been studied in equimolar NaOH-H₂O melt at 100°C by voltammetry and UV spectrophotometry. Disproportionation of sulfur is fast and quantitative according to



On the contrary, addition of sulfur to sulfide is not quantitative and gives S₂²⁻ besides prevailing sulfur disproportionation. SO₃²⁻ reacts with S₂²⁻ and S₃²⁻, while S₂O₃²⁻ decomposes S²⁻. A pseudo-equilibrium is observed: S²⁻ + S₂O₃²⁻ ⇌ S₂²⁻ + SO₃²⁻ with concentration quotient Q = 10^{-0.8}.

This paper is devoted to the chemical reactions which occur in the equimolar NaOH-H₂O melt at 100°C and 140°C between the following sulfur compounds: molecular sulfur, sulfide, polysulfides S_x²⁻, and oxyanions S_xO_y²⁻. Though most of these reactions are qualitatively known or simply widely accepted sometimes without definite publication to support them, some discrepancies still arise in the literature.

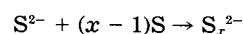
We shall focus first on the disproportionation reaction of molecular sulfur. Dissolution of sulfur in basic aqueous solution is industrially used to prepare polysulfide solutions. It has been shown since the beginning of the century that sulfur dissolution leads to polysulfides and oxyanions, according to a disproportionation reaction. Resulting compounds are not clearly known: sulfite or thiosulfate on the one hand, or mono-, di-, tri-, or tetrasulfide on the other.

Polysulfides S_x²⁻ have been recognized in numerous reports (1-3), with mean rank, *x*, from 2.5 to 4 according to the conditions of NaOH concentration and temperature (3). A complex mixture is generally assumed. However, both sulfite and thiosulfate have been claimed by Calcagni (1) in 66 weight percent (w/o) NaOH. Thiosulfate has been suggested by Schulek *et al.* (2) at 100°C and Ugorets *et al.* (3) up to 200°C. However, it is known that a precipitate of sulfite is obtained in industrial conditions.

The rate of the disproportionation reaction strongly depends on the conditions of temperature and NaOH concentration. It increases with both parameters (1, 4). For instance, at room temperature, no reaction occurs in 0.1M NaOH, while 1 month is required in 1M and only 24h in 5M. At 100°C, reaction is not yet observed in 0.1M, while a few hours in 1M, and, as we shall see, a few minutes in the equimolar melt, are quite enough to achieve sulfur dissolution.

When sulfur is dissolved in sulfide containing solutions, addition reactions may compete with the disproportionation

Keywords: sulfur, polysulfides, sulfur oxyanions, hydroxide-water melt.

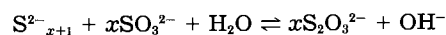


There has been research directed at determining what polysulfides can be produced. In reviewing the literature, one finds conflicting reports as to the nature of the polysulfide species because of the difficulty of distinguishing between mixtures and pure compounds.

In aqueous alkaline solutions, Schwarzenbach and Fischer (5) concluded that disulfide and trisulfide were not present. They showed that only the polysulfides of highest rank, such as S₄²⁻ and most likely S₅²⁻, are obtained, contrary to the old study of Peschanski and Valensi (6), who suggested that S₂²⁻, S₃²⁻, S₄²⁻, and S₅²⁻ are present and depend upon the pH and the amount of sulfur added to sulfide solution.

For high pH ranges (OH⁻ concentration up to 18M), Giggenbach (7) has calculated the equilibrium distribution of the various species at 25°C as a function of OH⁻ concentration. An increase of sodium hydroxide concentration displaces equilibria towards smaller polysulfide ions.

All these complex equilibria are disturbed by the presence of oxyanions. Ahlgren and Lemon (8) and then Giggenbach (9, 10) have shown that in neutral medium, SO₃²⁻ reacts with polysulfides according to



This reaction is used for the titration of polysulfides (11, 12) though it is slow and quantitative only above 50°C and in presence of sulfite in excess. At higher temperatures, the compounds obtained react to form new polysulfides: Giggenbach (9, 10) observes that at high temperatures addition of sulfite to polysulfides leads first to an increase of the polysulfide concentration before the usual decrease. Values of *x* are unknown because various mixtures probably result.

Disproportionation of oxyanions must also be taken into account; however, disproportionation constants of

sulfite and thiosulfate have been published only for a weakly basic medium, assuming S^{2-} and SO_4^{2-} as final products (13, 15).

Two reasons, among others, may explain discrepancies about the nature of the compounds formed in these reactions, and particularly from the sulfur disproportionation. The first one supposes a change in the nature of the prevailing reaction (e.g., the disproportionation reaction) with the solvent composition, since published information has been obtained in a wide range of solvent composition and temperature. The second one assumes a permanency of the initial step (e.g., disproportionation) and explains changes in final products by variations in stability of the initial ones with experimental conditions. For instance, it has not been proved if the industrially obtained sulfite is directly formed by disproportionation of molecular sulfur or results from a further disproportionation of, for example, trisulfide or thiosulfate in the very high concentration conditions generally used.

We did not attempt to observe the influence of the solvent. All the reactions we speak about were studied in the same experimental conditions. In this paper, we shall try to give an answer, valid for the equimolar NaOH-H₂O melt at 100°C or 140°C, to the following questions: what is the nature of the disproportionation reaction of sulfur? Is there any competition between disproportionation, fast in this melt, and addition reaction when molecular sulfur is added to a sulfide containing solution? What is the influence of the oxyanions? We were helped by the fact that only two polysulfides exist in the melt, S_2^{2-} and S_3^{2-} , which have different voltammetric and UV characteristics (16).

Experimental

Methods of preparation of polysulfide solution.—Several methods of preparation exist, but none gives pure solutions of polysulfides. Generally, a mixture of polysulfides and/or oxyanions is obtained, the proportion depending on the ratio of reagents, on the temperature, and on the reaction time. Three methods will be specially discussed: disproportionation of sulfur, addition of sulfur to sulfide, and electrochemical oxidation of sulfide.

Disproportionation of sulfur.—The dissolution of sulfur directly into the melt, an industrial method, is perhaps the simplest. As we shall see, it leads to S_3^{2-} initially free of S_2^{2-} , but thiosulfate is present. This method offers two advantages: it is a very simple one, and the concentration of S_3^{2-} can be easily calculated, though it is valid only just after the dissolution of sulfur, since S_3^{2-} is unstable. Its disadvantages come from the presence of thiosulfate and later of the degradation products of both S_3^{2-} and $S_2O_3^{2-}$ (SO_4^{2-} , SO_3^{2-} , S_2^{2-} , S^{2-}). Because the nature of the reaction was still debated at the beginning of this study, we could not use it to determine the polysulfide properties.

Addition of sulfur to sulfide.—The products of the reaction of S_8 with sulfide solutions strongly depend on the proportion of the reagents and on the temperature since two reactions are competing, the disproportionation reaction and the addition reaction. Without strictly controlled conditions, a complex mixture of S_2^{2-} , S_3^{2-} , SO_3^{2-} , and $S_2O_3^{2-}$ results. When sulfide is in large excess compared to sulfur, solution of S_2^{2-} free of oxyanion is obtained in presence of S^{2-} and traces of S_3^{2-} . However, we did not use this method because it was less quantitative than the electrochemical preparation.

Electrochemical oxidation of sulfide.—As shown in earlier (16), electrochemical oxidation of sulfide leads to S_2^{2-} solution when the electrolysis is stopped before 0.2 F/ S^{2-} and to S_3^{2-} after exchange of about 4/3 F/ S^{2-} . This method of preparation offers two important advantages: in each case, the polysulfide is obtained free of the other polysulfides and of oxyanions (but S^{2-} is present in the first case), and its concentration can be easily calculated. However, caution must be taken to get fast electrolysis because of the instability of S_3^{2-} . The obvious disadvan-

tage of this method is the complication of any electrochemical synthesis.

Unless otherwise mentioned, we used only the electrochemical preparation for the above reasons. Experimental details have been described elsewhere (16).

Other solutions.—Starting solutions of sulfide are prepared by adding to the NaOH-H₂O melt various amounts of solid Na₂S, recently titrated. Concentrated solutions of oxygenated compounds are prepared in water and added to the hydroxide melt, with a microsyringe to avoid volume correction. Experiments are carried out under nitrogen atmosphere.

Results and Discussion

Voltammetric properties of sulfur oxyanions.—Sodium sulfate and sulfite are neither oxidized nor reduced in the potential range accessible at a gold electrode in the equimolar NaOH-H₂O melt at 100°C or at 140°C. Thiosulfate presents no reduction wave, but can be oxidized at -0.05V, which is near the potential of oxidation of the gold electrode. This wave has not been studied further. Over a period of 2h or more, sulfite and sulfate solutions are stable, but thiosulfate decomposes even in an inert atmosphere, slowly at 100°C (less than 10% per hour) and more rapidly at 140°C. None of these compounds absorb in the UV range accessible in the melt.

UV spectra and voltammetric curves of sulfide, polysulfides (16), and oxyanions can be used as analytical tools to prove the presence of these species in the melt and measure their concentration. Qualitative criteria are gathered in Table I and can be summarized as follows: the presence of disulfide S_2^{2-} is shown by a higher absorption at 365 nm than at the arbitrarily chosen value 330 nm, and by the presence of two anodic waves. The trisulfide S_3^{2-} is obtained when absorption at 365 nm is lower than at 330 nm and only one anodic wave is present. In uncolored melt, one anodic wave means the presence of thiosulfate, and two anodic waves the presence of sulfide.

Reactions between polysulfides and oxyanions.—The general methodology includes preparation of polysulfide solutions via electrochemical oxidation of sulfide in order to get solutions free of oxyanions, then addition of various quantities of sodium thiosulfate, sulfite, or sulfate. Occurrence of a reaction is shown by the appearance or the disappearance of the sulfur compounds, which can be observed according to the analytical criteria of Table I. (Results are summarized in Table III.)

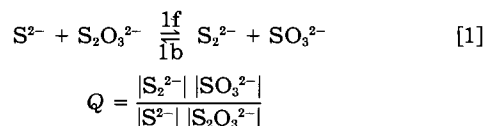
Cases of no reaction.—No other modifications of spectra or voltammetric curves than those due to instability (S_3^{2-} and $S_2O_3^{2-}$) are observed in the following cases: $S^{2-} + SO_3^{2-}$; $S_2^{2-} + SO_4^{2-}$; $S_3^{2-} + SO_4^{2-}$; $S^{2-} + SO_3^{2-}$; $S_2^{2-} + S_2O_3^{2-}$; $S_3^{2-} + S_2O_3^{2-}$. These results are easily proved except for the $S_2^{2-} + S_2O_3^{2-}$ reaction, because S_2^{2-} solution necessarily contains a five-fold excess of sulfide, which reacts with $S_2O_3^{2-}$ as detailed below. However, quantitative measurements at 365 nm or on the reduction wave of S_2^{2-} show that for equal initial S^{2-} concentrations, the same quantities of disulfide appear whether S_2^{2-} is initially present or not. Besides, the first anodic wave remains constant, which means that the total concentration in $S^{2-} + S_2^{2-}$ keeps a constant value. One can conclude that $S_2O_3^{2-}$ reacts with excess of S^{2-} , but not with S_2^{2-} .

Table I. Analytical characteristics of sulfur compounds in NaOH-H₂O equimolar melt at 100° or 140°C

	UV absorption	Anodic wave (below -0.2V)	Cathodic wave
S^{2-}	—	two	—
S_3^{2-}	$A_{365} > A_{330}$	two	one
S_2^{2-}	$A_{365} < A_{330}$	one	one
$S_2O_3^{2-}$	—	one	—
SO_3^{2-}	—	—	—
SO_4^{2-}	—	—	—

Consequently, in all the cases mentioned, we have been able to conclude that no reaction occurs.

Equilibrium between S^{2-} , S_2^{2-} , $S_2O_3^{2-}$, and SO_3^{2-} .—There exists an equilibrium between S^{2-} and $S_2O_3^{2-}$ on the one hand, and S_2^{2-} and $S_2O_3^{2-}$ on the other (it would be more exact to say: pseudoequilibrium, since three of the components are thermodynamically unstable)



This equilibrium has been proved by showing that the forward (1f) and backward (1b) reactions do exist and lead to the same proportion of components.

Backward reaction.—Arguments to assess the backward reaction are the following. Addition of sulfite to a disulfide solution leads to a decrease of the reduction wave (Fig. 1) and of the UV band at 365 nm (Fig. 2), which proves that S_2^{2-} disappears. At the same time, the first anodic wave keeps a constant value (Fig. 3), which proves that the concentration of $S_2^{2-} + S^{2-}$ remains constant: one S_2^{2-} is transformed into one S^{2-} .

The presence of $S_2O_3^{2-}$ is not simple to show because its anodic wave merges into the second anodic wave of S_2^{2-} and S^{2-} in excess. The reduction wave and absorption at 365 nm do not entirely disappear, even in presence of sulfite in excess.

Forward reaction.—Thiosulfate added to a sulfide solution leads to S_2^{2-} , as proved by the three following observations: appearance of yellow color with $A_{365} > A_{330}$, appearance of a reduction wave, and no decrease of the first anodic wave (Fig. 3). This last observation involves the substitution of one S^{2-} by one S_2^{2-} . No analytical method allows sulfite detection. Quantitative measurements show that the reaction is not total, even with $S_2O_3^{2-}$ in excess.

Reaction quotient.—The pseudoreaction quotient Q , defined above, has been determined by measuring the limiting current i of the reduction wave or the absorption A at 365 nm vs. the ratio $|S_2O_3^{2-}|/|S^{2-}|_i$ for the forward reaction and $|SO_3^{2-}|/|S_2^{2-}|_i$ for the backward reaction, the subscript i referring to the initial conditions. An example is given on Fig. 3.

Let x be either the absorption at 365 nm or the limiting current. Assuming that $x = x_T$ for a totally shifted forward

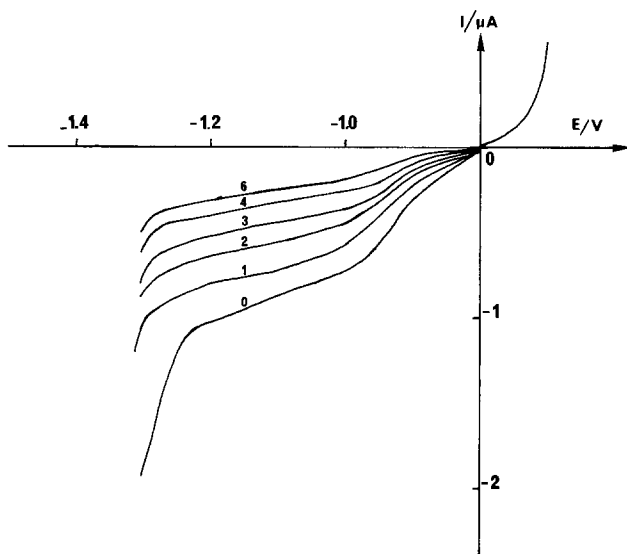


Fig. 1. Voltammetric curves at a rotating gold electrode during the addition of a $10^{-1}M$ sulfite solution to a S_2^{2-} solution in NaOH-H₂O (1-1) melt at 100°C in presence of sulfide in excess. Initial conditions: $S^{2-} = 2.2 \cdot 10^{-2}M$ electrolyzed up to 0.2 F/S²⁻. $SO_3^{2-}/S_2^{2-} = 0$ (curve 0), 0.5 (curve 1), 1.25 (curve 2), 3.75 (curve 4), 4.35 (curve 5), and 5.0 (curve 6).

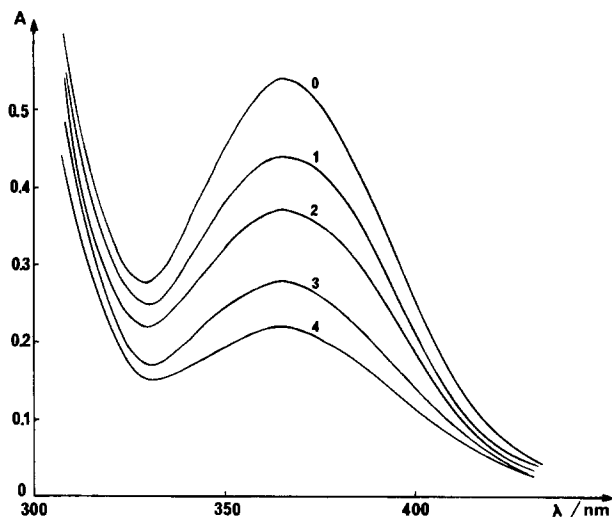


Fig. 2. UV spectrum during the addition of a $10^{-1}M$ sulfite solution to a S_2^{2-} solution in presence of sulfide in excess. Initial conditions: $S^{2-} = 2.2 \cdot 10^{-2}M$ electrolyzed up to 0.2 F/S²⁻. $SO_3^{2-}/S_2^{2-} = 0$ (curve 0), 0.5 (curve 1), 1.0 (curve 2), 2.0 (curve 3), and 2.8 (curve 4).

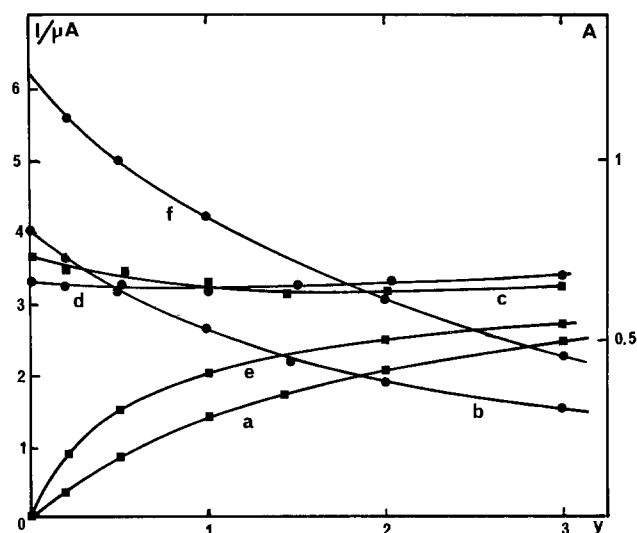


Fig. 3. Intensity of the reduction wave (a, b), of the first anodic wave (c, d) and of the absorption at 365 nm (e, f) vs. the ratio y of the reagents. (Curve d: scale $\times 10$.) Curves a, c, and e: $y = |S_2O_3^{2-}| / |S^{2-}|_i$ with $|S^{2-}|_i = 5 \cdot 10^{-3}M$. Curves b, d, and f: $y = |SO_3^{2-}| / |S_2^{2-}|_i$ with $|S_2^{2-}|_i = 5 \cdot 10^{-3}M + |S^{2-}|_i = 4 \cdot 10^{-2}M$.

reaction, one easily calculates from balance equations that Q is given by

$$Q = \frac{x^2}{(x_T - x)(ax_T - x)}$$

For the backward equation, taking into account that S_2^{2-} is prepared in the presence of excess sulfide ($|S^{2-}|_i = 8|S_2^{2-}|_i$), one easily calculates

$$Q = \frac{x[ax_1 - (x_1 - x)]}{8x_1 + (x_1 - x)(x_1 - x)}$$

Results are given in Table II. Good agreement is obtained, whatever the reaction (forward or backward), the techniques or the ratio of the components (from 0.2 to 3). The mean value of $pQ = -\log Q$ is 0.8 ± 0.1 at 100°C.

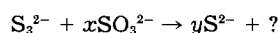
Reaction of SO_3^{2-} on S_3^{2-} .—When sulfite is added to a S_3^{2-} solution, the reduction wave (Fig. 4) and the absorption at 330 nm (Fig. 5) characteristic of S_3^{2-} decrease in too large proportion to be simply explained by S_3^{2-} instability. After addition of a four-fold excess of sulfite, A_{330} does not yet equal zero, but is higher than A_{365} . It can be concluded that S^{2-} and not S_2^{2-} is finally obtained, but not

Table II. pQ at 100°C of the pseudoequilibrium [1]

Reaction	Method	$y = 0.2$	$y = 0.5$	$y = 1$	$y = 2$	$y = 3$
(1b)	spectrophotometry	0.94	0.77	0.75	0.76	0.80
	voltammetry	0.95	0.83	0.81	0.83	0.76
(1f)	spectrophotometry	0.44	0.68	0.70	0.85	0.97

Conditions for (1f): $y = |\text{S}_2\text{O}_3^{2-}|/|\text{S}_2^{2-}|$ and $|\text{S}_2^{2-}|_i = 5 \cdot 10^{-3}\text{M}$.
 Conditions for (1b): $y = |\text{SO}_3^{2-}|/|\text{S}_2^{2-}|$ and $|\text{S}_2^{2-}|_i = 5 \cdot 10^{-3}\text{M} + |\text{S}_2^{2-}|_i = 4 \cdot 10^{-2}\text{M}$.

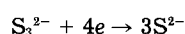
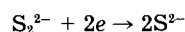
quantitatively



It must be noticed that a minor concentration of S_2^{2-} seems present at the beginning of sulfite addition, since A_{365} remains constant or decreases less than A_{330} up to a ratio $|\text{SO}_3^{2-}|/|\text{S}_3^{2-}|$ equal to 0.5. The disulfide S_2^{2-} disappears further.

All reactions between polysulfides and sulfur oxyanions have been summarized in Table III.

Sulfur disproportionation.—Sulfur rapidly dissolves into the melt while a yellow color, characteristic of polysulfides, appears. Possible disproportionation reactions are given in Table IV (except for the less probable disproportionations into $\text{S}_2\text{O}_3^{2-}$, $\text{S}_2\text{O}_4^{2-}$, and $\text{S}_4\text{O}_6^{2-}$, which have not been taken into account). We have also given the recognition criteria based on the analytical properties of the polysulfides and the number of Faraday per sulfur atom required to reduce into S^{2-} the resulting polysulfides according to these reactions



If recorded shortly after the dissolution, voltammetric curves show at 100°C and 140°C a cathodic and only one anodic wave (Fig. 6, curve 0), while in the UV spectrum at 100°C, absorption at 330 nm is higher than at 365 nm (Fig. 7, curve 0). Limiting currents and UV absorption are proportional to the quantity of added sulfur. The UV absorption and the absence of the first anodic wave of S^{2-} or S_2^{2-} support the fact that the disproportionation of sulfur

Table III. Crossed reactions between polysulfides and sulfur oxyanions in NaOH-H₂O (1-1) melt at 100°C

	$\text{S}_2\text{O}_3^{2-}$	SO_3^{2-}	SO_4^{2-}
S^{2-}	$\text{S}^{2-} + \text{S}_2\text{O}_3^{2-} \rightleftharpoons \text{S}_2^{2-} + \text{SO}_3^{2-}$	none	none
S_2^{2-}	none	$\text{S}_2^{2-} + \text{SO}_3^{2-} \rightleftharpoons \text{S}^{2-} + \text{S}_2\text{O}_3^{2-}$	none
S_3^{2-}	none	$\text{S}_3^{2-} + x\text{SO}_3^{2-} \rightarrow y\text{S}^{2-} + ?$	none

Table IV. Recognition criteria of the disproportionation reaction of S_y : number of Faraday (F) per S atom required to reduce into S^{2-} the obtained polysulfide, presence (+) or absence (-) of the first anodic wave, and UV absorption with $A_{330} > A_{365}$ (+) or $A_{330} < A_{365}$ (-)

Reaction	F/S	Anodic wave	UV
[2] $6\text{S} + 6\text{HO}^- \rightarrow 2\text{S}_2^{2-} + \text{S}_2\text{O}_3^{2-} + 3\text{H}_2\text{O}$	0.67	+	-
[3] $5\text{S} + 6\text{HO}^- \rightarrow 2\text{S}_2^{2-} + \text{SO}_3^{2-} + 3\text{H}_2\text{O}$	0.80	+	-
[4] $7\text{S} + 8\text{HO}^- \rightarrow 3\text{S}_2^{2-} + \text{SO}_3^{2-} + 4\text{H}_2\text{O}$	0.86	+	-
[5] $8\text{S} + 6\text{HO}^- \rightarrow 2\text{S}_3^{2-} + \text{S}_2\text{O}_3^{2-} + 3\text{H}_2\text{O}$	1.00	-	+
[6] $7\text{S} + 6\text{HO}^- \rightarrow 2\text{S}_3^{2-} + \text{SO}_3^{2-} + 3\text{H}_2\text{O}$	1.14	-	+
[7] $10\text{S} + 8\text{HO}^- \rightarrow 3\text{S}_3^{2-} + \text{SO}_4^{2-} + 4\text{H}_2\text{O}$	1.50	-	+
Experimental:	1.1 ± 0.1	-	+

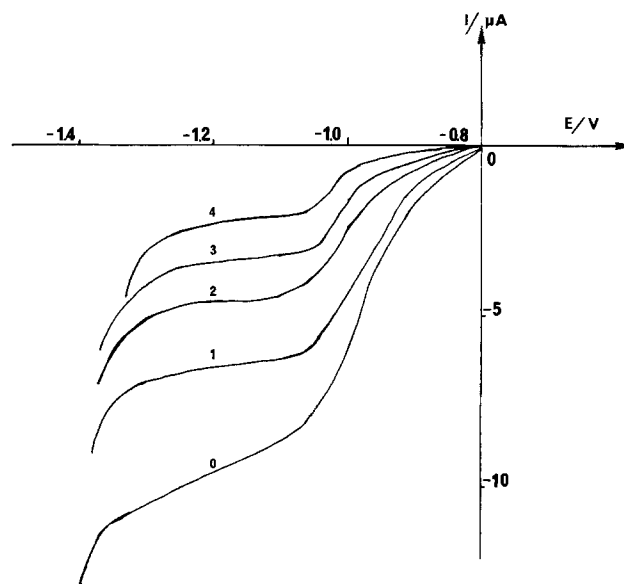


Fig. 4. Voltammetric curves at a rotating gold electrode during the addition of a 0.5M sulfite solution to a $6.8 \cdot 10^{-3}\text{M}$ S_3^{2-} solution in NaOH-H₂O (1-1) melt at 100°C. $\text{SO}_3^{2-}/\text{S}_3^{2-} = 0$ (curve 0), 0.55 (curve 1), 1.1 (curve 2), 1.7 (curve 3), and 3.0 (curve 4).

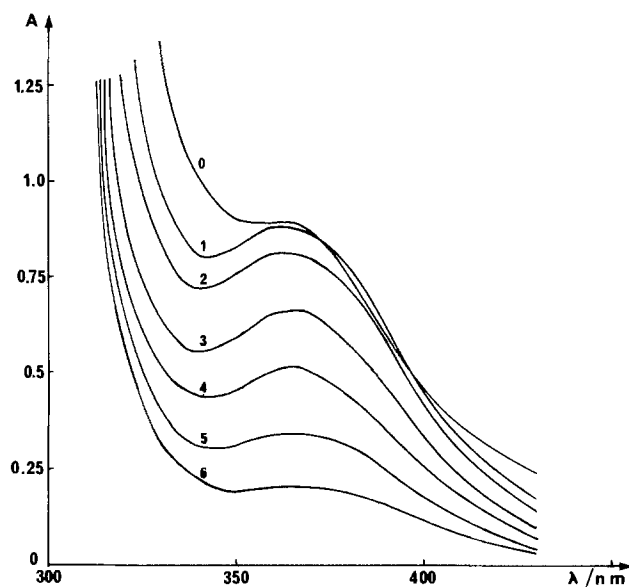


Fig. 5. UV spectrum during the addition of a 0.5M sulfite solution to a $6.7 \cdot 10^{-3}\text{M}$ S_3^{2-} solution in NaOH-H₂O (1-1) melt at 100°C. $\text{SO}_3^{2-}/\text{S}_3^{2-} = 0$ (curve 0), 0.38 (curve 1), 0.57 (curve 2), 0.95 (curve 3), 1.33 (curve 4), 1.90 (curve 5), and 2.85 (curve 6).

leads first to trisulfide free of disulfide (S_2^{2-} begins to appear later on, after 1h at 100°C and a few minutes at 140°C because of the instability of S_3^{2-} and $\text{S}_2\text{O}_3^{2-}$). Reactions [2], [3], and [4] are ruled out.

The determination of the reaction has been accomplished via an electrolysis on the plateau of the cathodic wave at -1.15V, corresponding to the reduction of the polysulfide into sulfide. The number of Faradays per sulfur atom required for complete disappearance of the cathodic wave of a solution of dissolved sulfur has been experimentally found to be between 1.0 and 1.15 at 100°C.

This value excludes all the reactions of Table IV except for [5] and [6]. Reaction [6] may be eliminated because it has been seen above that S_3^{2-} reacts on sulfite to give S_2^{2-} : this anion is not detected just after the dissolution. Therefore, the disproportionation reaction of sulfur in the equimolar NaOH-H₂O melt at 100° and 140°C is reaction [5].

This reaction is also the most probable if one considers that it is the only one which agrees for its stoichiometry

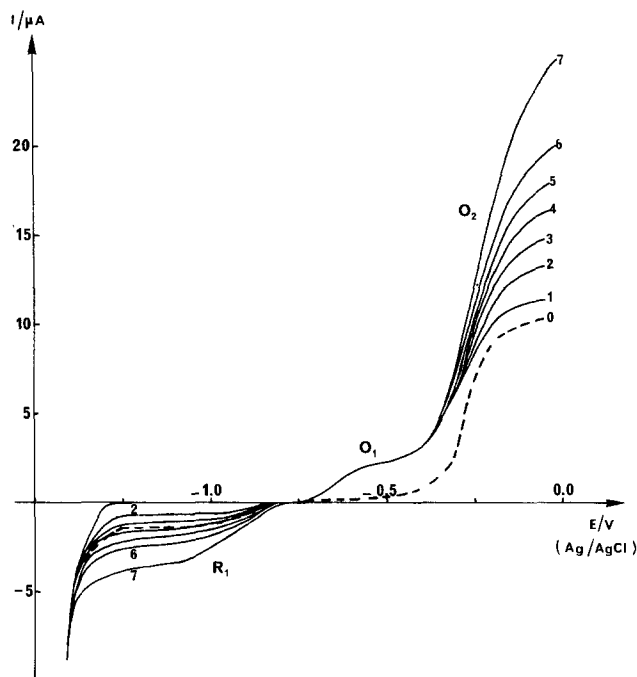
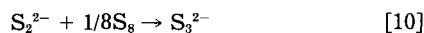
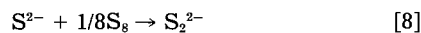


Fig. 6. Voltammetric curves at a rotating gold electrode during the addition of sulfur to the NaOH-H₂O (1-1) melt in absence (curve 0) or in presence (curves 1-7) of $4.3 \cdot 10^{-3} M$ Na₂S. $S/S_i^{2-} = 0$ (curve 1), 0.46 (curve 2), 0.80 (curve 3), 1.15 (curve 4), 1.53 (curve 5), 1.93 (curve 6), and 3.14 (curve 7).

with the eight atoms of the sulfur ring. The disproportionation is fast since 95% is achieved in 2 min at 140°C. The rate is probably limited simply by agitation speed and diffusion into the bulk.

Addition of sulfur to sulfide.—Since the disproportionation reaction is fast in this melt, four reactions can compete when molecular S₈ is added to a S²⁻ solution, three addition reactions, and the S₈ disproportionation reaction



We shall show that when too little sulfur is added (typically $y = S/S_i^{2-} < 0.1$ in our conditions) reaction [8] does occur though not exclusively, while if addition is continued up to an excess of sulfur (typically $y > 2$), disproportionation reaction [5] is exclusively observed. In the intermediate range, both S₂²⁻ and S₃²⁻ are obtained via competition between reaction [8] and reaction [5], the prevailing reaction as S/S_i^{2-} increases.

Figures 6 and 7 show typical voltammetric curves and UV spectra recorded for successive additions of sulfur to sulfide solution. Plots of limiting currents or absorption at 365 nm vs. the quantity of added sulfur are given in Fig. 8 and 9. When $y < 0.1$, addition of sulfur leads to the onset of the reduction wave and the UV absorption of polysulfides, but the curves differ, depending on whether sulfide is present or not. Obviously, a reaction occurs with sulfide, which differs from the S₈ disproportionation obtained in its absence. Whatever the sulfide concentration, it leads to S₂²⁻, since $A_{365} > A_{330}$, whence it can be concluded that reaction [8] occurs.

When S₈ is added in excess ($y > 2$), variations of limiting currents and absorption are similar to the variations in absence of sulfide. It means that the disproportionation reaction [5] occurs, which is quite expected.

Completeness of the addition reaction.—Reaction [8] is not quantitative. As displayed in Fig. 8 and 9, the UV absorption is proportional to sulfur addition only for low values of y , and the reduction current does not increase with the

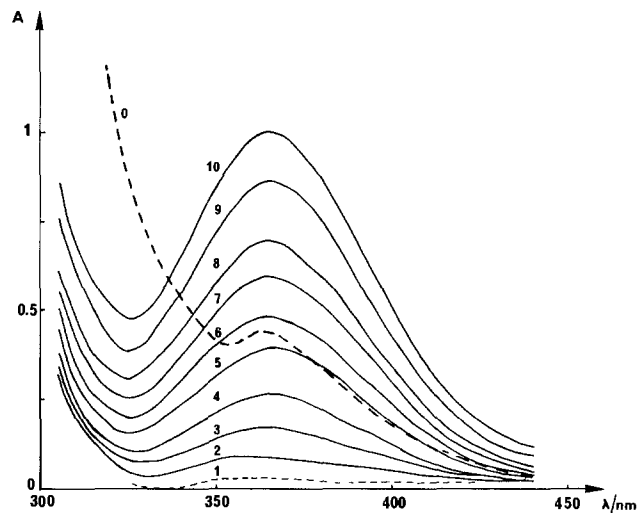


Fig. 7. UV spectra during the addition of sulfur to the NaOH-H₂O (1-1) melt in absence (curve 0) or in presence (curves 1-8) of $1.5 \cdot 10^{-2} M$ Na₂S. $S/S_i^{2-} = 0$ (curve 1), 0.02 (curve 2), 0.05 (curve 3), 0.09 (curve 4), 0.15 (curve 5), 0.19 (curve 6), 0.24 (curve 7), 0.30 (curve 8), 0.39 (curve 9), and 0.47 (curve 10).

theoretical slope. A clear break point is not observed on curves for $y = 1$, corresponding to the end of the addition and the beginning of the disproportionation.

When $y < 2$, disulfide and trisulfide are simultaneously formed, and for S₃²⁻ the question is by which reaction: [9], [10], or [5]? It is easily seen that reactions [9] and [10] do not occur. If they did, an increase in y would result in a decrease of the first anodic wave because of the substitution of the oxidizable S²⁻ by the electroinactive S₃²⁻, while the reduction wave would increase at the same rate as for $y < 0.2$ (reduction of x mol of S₂²⁻ via $2e$ of $x/2$ mol of S₃²⁻ via $4e$ leads to the same limiting current). Experiments are inconsistent with these conditions.

Reaction [10] is also ruled out by spectrophotometric measurements, since we do not arrive at a situation where $A_{365} \geq A_{330}$, as would be expected if S₂²⁻ were substituted by S₃²⁻ [cf. electrolysis experiments in Ref. (16) for valuable comparison].

It can be concluded that when $0.1 < y < 2$, competition between reactions [8] and [5] does occur, rather than reactions [9] or [10].

Quantitative measurements have not been performed to calculate the relative amounts of the two reactions because it depends on too many experimental parameters (initial concentration in sulfide, y value, temperature, etc.). Besides, quantitative measurements on S₃²⁻ concentration are difficult because of its instability (16). For instance, curves of Fig. 8 require hours to be performed in molten salt experiments, and the decomposition of the nonoxidizable S₃²⁻ into S₂²⁻ and S²⁻ explains the slight increase of the current of the first anodic wave observed for high values of y .

We shall just add that even for the smallest value of y which could be used with a convenient experimental precision ($[S^{2-}] = 1.5 \cdot 10^{-2} M$; $y = 0.07$), reaction [8] represents only 70% of the sulfur dissolution, using ϵ values determined in Ref. (16). Obviously, solid flowers of sulfur do not have the same structure and the same properties as the transitory electrogenerated *in situ* sulfur (16).

In our melt, sulfur disproportionation is fast and widely challenges the addition reaction on sulfide. Dissolution of sulfur is not accelerated by sulfide, especially as the rate-limiting step seems to be agitation speed and diffusion into the bulk. This would not be the case at lower temperatures or OH⁻ concentrations.

An important consequence results from the consideration of the first anodic wave shown on Fig. 6 and detailed on Fig. 8. If one does not take into account the slight decrease in the current (probably due to a smaller diffusion coefficient of S₂²⁻ as compared to S²⁻), these curves show

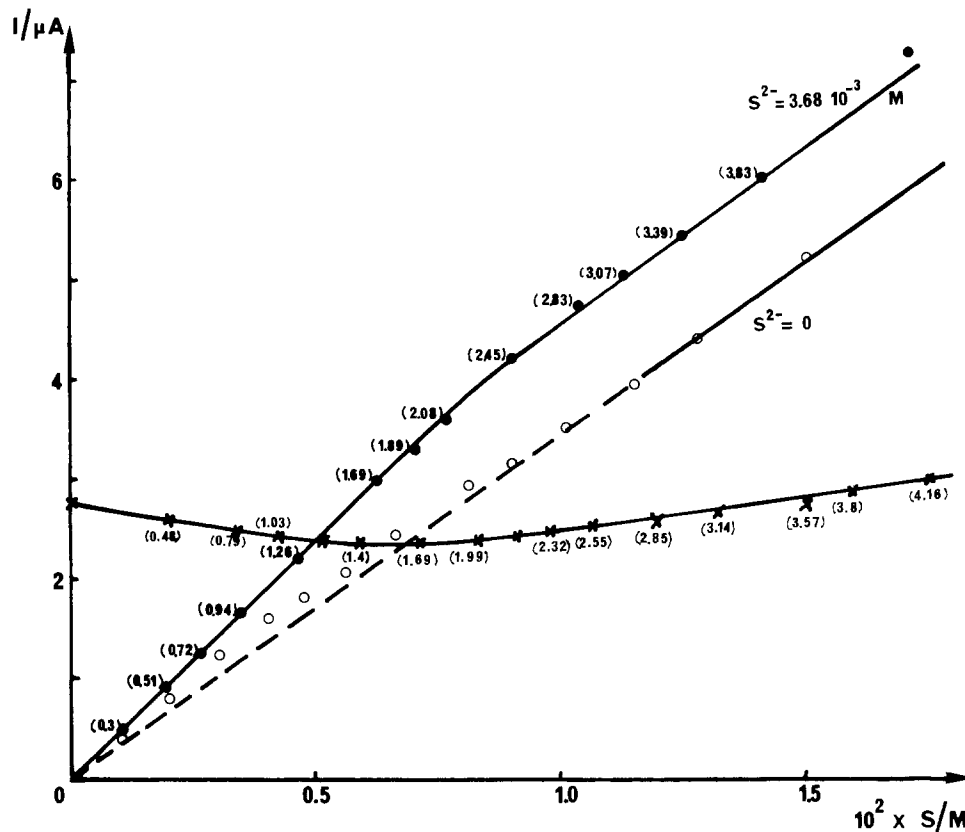


Fig. 8. Plot of the limiting current of the first anodic wave (X) and of the reduction wave vs. the amount of dissolved sulfur (in S atom l^{-1}) in absence (○) or in presence (●) of $3.68 \cdot 10^{-3} M S^{2-}$. Numbers on curve are the ratio $y = S/S_1^{2-}$.

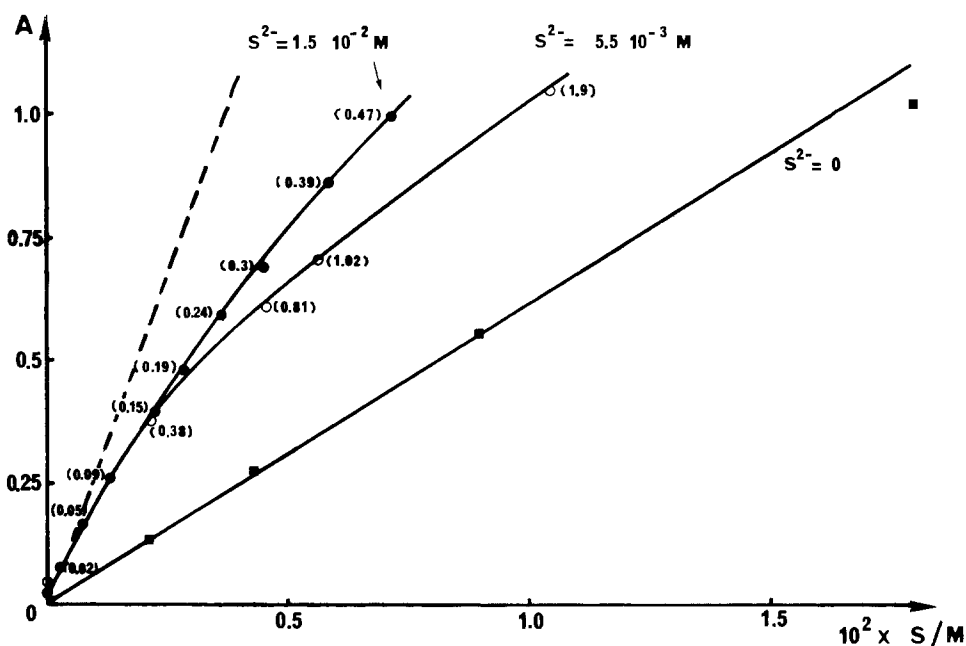


Fig. 9. Plot of A_{365} vs. the amount of dissolved sulfur (in S atom l^{-1}) in absence (■) or in presence of $S^{2-} = 5.5 \cdot 10^{-3} M$ (○) and $1.5 \cdot 10^{-2} M$ (●). y values are indicated on each curve. Dotted line: theoretical curve assuming that reaction [8] is quantitative.

that the half-wave potential and limiting current remain roughly constant, as long as $y < 0.5$. Since one sulfide is substituted by one disulfide according to reaction [8], it means that S_2^{2-} is electro-oxidizable at the same potential as S^{2-} , and in the case of a rotating gold electrode with the same number of exchanged electrons.

This last assessment is inconsistent with an oxidation into S_3^{2-} , which requires $4/3$ electrons per sulfide against $2/3$ per disulfide. It does agree well with an oxidation in molecular sulfur (2 electrons in both cases). This fact has already been noted in Ref. (16).

Conclusion

When coupled with spectrophotometry, electrochemistry is a powerful tool for the study of chemical reactions in solution. With these two techniques, we obtained the

following results on the sulfur compounds in the equimolar NaOH- H_2O melt at 100° or $140^\circ C$.

1. Only two polysulfides exist in this melt: the disulfide S_2^{2-} and the trisulfide S_3^{2-} .
2. Voltammetric and spectroscopic characteristics of S_2^{2-} and S_3^{2-} have been described. They were used as analytical criteria allowing a distinction between S_2^{2-} and S_3^{2-} via UV absorption and presence of a first anodic wave.
3. There exist two anodic steps for sulfide oxidation at a gold electrode: the first one leads to S_2^{2-} , S_3^{2-} , or molecular sulfur depending on the time scale of the techniques, and the second to sulfite.
4. Disproportionation of sulfur is fast and quantitative. It leads to S_3^{2-} and $S_2O_3^{2-}$. On the contrary, addition of sulfur on sulfide to form S_2^{2-} is only partial.

5. Sulfite, thiosulfate, sulfide, and disulfide are related by a pseudoequilibrium.

Acknowledgment

This research, including that reported in Ref. (16), has been partly supported by Société Nationale Elf Aquitaine, which is gratefully acknowledged, especially for a grant to M.N.M. We wish to express our sincere gratitude to Dr. J. Badoz-Lambling, Director of ERA 953, for the fruitful discussions and helpful advice, and to C. Thibaut and M. Labat from SNEA for stimulating discussions and helpful suggestions.

Manuscript submitted June 17, 1983; revised manuscript received March 2, 1984.

ESPCI assisted in meeting the publications costs of this article.

REFERENCES

- G. Calcagni, *Gazz. Ital.*, **50**, 331 (1920).
- E. Schulek, E. Koros, and L. Marcos, *Acta Chim. Acad. Sci. Hung.*, **10**, 291 (1956).
- M. Z. Ugorets, K. T. Rustembekov, K. M. Akhmetov, and E. A. Buketov, *Tr. Khim. Metall. Inst. Akad. Nauk Kaz. SSR.*, **17**, 77 (1972), after C.A., **81**, 20380Z.
- M. Z. Ugorets, K. T. Rustembekov, K. M. Akhmetov, and O. I. Semina, *ibid.*, **22**, 21 (1973), after C.A., **81**, 69003T.
- G. Schwarzenbach and A. Fischer, *Helv. Chim. Acta*, **43**, 1365 (1960).
- D. Peschanski, *C. R. Acad. Sci. Ser. C*, **227**, 770 (1948); D. Peschanski and G. Valensi, *ibid.*, **227**, 845 (1948); *J. Chim. Phys.*, **46**, 602 (1949).
- W. Giggenbach, *Inorg. Chem.*, **11**, 1201 (1972).
- P. Ahlgren and S. Lemon, *Svensk Papperstidn.*, **5**, 160 (1967).
- W. Giggenbach, *Inorg. Chem.*, **13**, 1724 (1974).
- W. Giggenbach, *ibid.*, **13**, 1730 (1974).
- W. Sack, *Z. Anal. Chem.*, **131**, 199 (1950).
- D. N. Fogg and N. T. Wilkinson, *J. Appl. Chem.*, **2**, 357 (1952).
- G. Valensi, *Rapp. Tech., Cent. Belge Etude Corros.*, **207**, 1 (1973); *C. R. Acad. Sci. Ser. C*, **221**, 352 (1945); *ibid.*, **223**, 455 (1946); *Bull. Soc. Chim. (France)*, **12**, 642 (1945).
- I. B. D'Yachkova, I. L. Khodakovskiy, and V. I. Vernadskiy, in "Transactions of Geokhimiya II," p. 1358 (1968).
- W. A. Pryor, *J. Am. Chem. Soc.*, **82**, 4794 (1960).
- M. N. Moscardo-Levelut and V. Plichon, *This Journal*, **131**, 1538 (1984).

Chemical, Electrochemical, and Technological Aspects of Sodium Chlorate Manufacture

K. Viswanathan* and B. V. Tilak*

Occidental Chemical Corporation, Hooker Research Center, Grand Island, New York 14072

ABSTRACT

A critical review of the chemistry, electrochemistry, and engineering principles involved in the production of sodium chlorate is presented. Various chlorate manufacturing technologies were discussed, with emphasis on materials of construction, and trends towards developing cost and energy effective methods for producing sodium chlorate.

One of the energy intensive electrolytic industries is the electrochemical production of sodium chlorate, wherein approximately 4500-5500 kWh of electricity is required to produce 1 short ton of sodium chlorate which may be compared to a value of 2700-2800 kWh/ton of chlorine using OCC's H-4 cells with DSA® anodes¹ and asbestos diaphragm (see Table I) (1). Electrosynthesis of chlorate dates back to 1802, when Hisinger and Berzelius (2) prepared sodium chlorate by electrolysis of sodium chloride. It was confirmed by Kolbe (3) who also prepared chloric acid from hypochlorous acid electrolytically.

Presently, about one million tons of sodium chlorate are produced annually, the U.S. share being about 0.25 MM tons. These figures may be compared to the annual chlorine production capacity of 30 MM tons, the U.S. production level being about 11 million tons. The anticipated growth of the chlorate industry is about 4%-5% per year, in contrast to the growth rate of 2%-2.5% for the chlor-alkali industry. These opportunities for growth in the chlorate industry appear promising in view of the following considerations: (i) environmental regulations arising from the formation of chlorinated organics may mandate the replacement of chlorine for bleaching purposes with alternate bleaching chemicals, such as ClO₂, for which NaClO₃ is the precursor. About 20%-25% of the paper mills appear likely to change their bleaching process to chlorine dioxide. (ii) Oxygen bleaching, which is now attracting commercial attention in pulp and paper industry, also uses ClO₂ and, hence, would require greater chlorate production.

* Electrochemical Society Active Member.

Keywords: chlorate formation, role of dichromate, unit operations, cathodes, chlorate manufacturing technologies.

¹ DSA is a registered trademark of Diamond Shamrock Technologies, S. A., of Geneva, Switzerland.

The end-use profile of NaClO₃ shows that approximately 82% of sodium chlorate is consumed by the pulp and paper industry. Other uses of sodium chlorate are in the agricultural industry as a defoliant and herbicide, as an oxidizer in uranium milling, and in perchlorate production.

The purpose of this article is to review the chemistry and electrochemistry involved in the production of chlorate, and outline the various technologies with emphasis on (i) the materials of construction and (ii) the trends towards developing cost-effective and energy-efficient sodium chlorate technology by improving current efficiency, lowering cell voltage, and minimizing capital costs.

Chemistry and Electrochemistry Involved in Chlorate Formation

Nature of the Overall Process

Sodium chlorate is produced by the electrolysis of NaCl and can be described by the overall chemical reaction

Table I. Comparison of chlorate and chlor-alkali industry

	Chlorate	Chlor-alkali
Power consumption (kWh/ton)	4500-5500	2700-2800
World production capacity (MM ton)	1	30
U.S. production capacity (MM ton)	0.25	15
Anticipated growth rate (%)	4-5*	2-2.5*

* Projected growth rates in 1983.



which requires 6 Faradays to produce 1 g mol of chlorate or 685 Ah/lb of chlorate (at 100% efficiency.)

Reaction [1] is endothermic (4), the overall heat of the reaction (ΔH) being 224 kcal/g mol (3745 BTU/lb; 1.1 kWh/lb) of chlorate. Therefore, the thermoneutral voltage, i.e., the voltage at which heat is neither required by the system nor lost by the system to the surroundings, would be $\sim 1.62\text{V}$, as calculated from Eq. [2]

$$-nFE = \Delta H \quad [2]$$

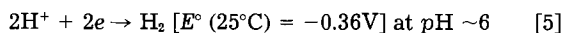
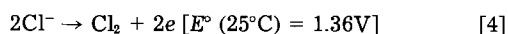
However, in practice, chlorate cells operate in the voltage range 3-4V, at an average current efficiency (CE) of $\sim 95\%$. This results in heat generation (q) to the extent of

$$q = \left[\left(\frac{100}{\text{CE}} \right) (138.36) E \right] - \Delta H (\text{cal/g mol}) \quad [3]$$

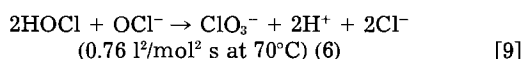
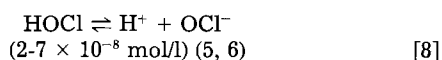
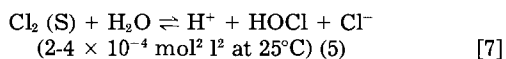
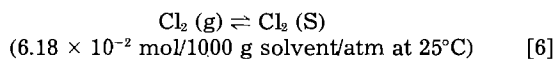
which, for a chlorate electrolyzer operating at 95% efficiency and 3.3V, would be ~ 250 kcal/g mol or 4250 BTU/lb of NaClO_3 . This heat, generated in cells operating at voltages $> 1.62\text{V}$, must be removed.

Reactions Involved in Chlorate Formation

The primary electrochemical reactions occurring in a chlorate cell are the discharge of chloride ions and H^+ ions to form H_2 and Cl_2 , respectively

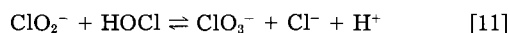
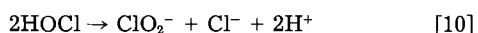


Chlorine evolved at the anode dissolves in the boundary layer and hydrolyzes to form HOCl and OCl^- which, in turn, react in the bulk of the electrolyte to form chlorate. This series of reactions is shown in Eq. [6]-[9] with the equilibrium constants stated in parenthesis for Eq. [6]-[8] and rate constant for Eq. [9]



Reaction [9], which results in chlorate formation, proceeds very slowly with an optimal rate (7), when $[\text{HOCl}] = 2[\text{OCl}^-]$, which occurs at a pH value equal to $pK - \log 2$, where $pK = -\log$ (equilibrium constant) for reaction [8]. Thus, the pH values in industrial cells are controlled in the range of 5.9-6.7.

Kinetics of chlorate formation.—Two mechanisms are proposed in the literature to describe the formation of chlorate. The reaction sequence, proposed by Foerster (8) and confirmed by many others (6, 9, 10), is a third-order reaction involving 2 mol HOCl and 1 mol OCl^- , as represented by Eq. [9]. However, according to Lister (11), who examined the decomposition kinetics of hypochlorite in alkaline solutions, chlorate formation follows a bimolecular sequence



Eq. [10] being the slower of the above reactions.

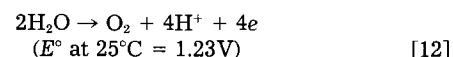
Recent studies (12) addressed this controversy and showed the mechanism to conform with that proposed by Foerster. The apparent inconsistency in Lister's analysis (11) was traced to his method of determining the HOCl concentration which was subsequently used in the evaluation of the rate constant. Thus, the chlorate formation reaction is an apparent third order involving 2 mol HOCl

and 1 mol OCl^- , the third-order rate constant being $0.025 \text{ l}^2 \cdot \text{mol}^{-2} \cdot \text{s}^{-1}$ at 25°C in $4M$ NaCl solutions. The rate of chlorate formation is proportional to $[\text{HOCl}]^2 [\text{OCl}^-] V$ where V refers to the volume of the reactor, and, hence, as the concentration of $\text{OCl}^- + \text{HOCl}$ decreases, the rate falls significantly necessitating the use of large volumes (and therefore large retention times) to carry out the reaction.

Parasitic reactions affecting efficiency.—While reaction [9] leads to the formation of chlorate, several parallel reactions occur at the electrodes and within the cell, lowering the overall efficiency for ClO_3^- formation.

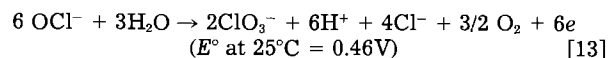
Anodic parasitic reactions.—Prior to the advent of metal anodes, the preferred anode material was graphite [see, however, Ref. (13) for historical details], which led to a chlorate efficiency of 80%-85% due to the oxidation of C to CO_2 and the lower overpotential for O_2 evolution compared to Cl_2 evolution on graphite. However, since the commercialization of metal anodes based on Pt-Ir and RuO_2 coatings on Ti substrates, the current efficiencies have increased to 93%-95%. This loss in current efficiency of 5%-7% can be traced to the chemical decomposition of HOCl and OCl^- to O_2 and Cl^- (which will be described below). The reactions described below are thermodynamically favored at potentials where Cl_2 is generated and can markedly lower the efficiency.

O_2 evolution.—Oxygen evolution reaction, represented by Eq. [12], is dependent



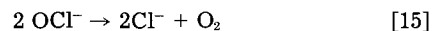
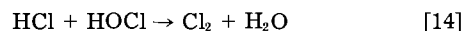
on the nature of the anode material and the pH of the medium. Typically, the current efficiency values for the O_2 evolution reaction vary from about 1% to 3% on noble metal based electrodes in the pH range 5.5-6.5.

Oxidation of OCl^- to ClO_3^- .—This reaction



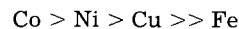
under some conditions can occur lowering (14) the current efficiency for ClO_3^- formation to 66.67%.

Bulk parasitic reactions.—There are two reactions occurring in the bulk which can decompose the OCl^- essential for chlorate formation. These are represented by Eq. [14] and [15]



Addition of acid results in the release of Cl_2 and, hence, lowered cell efficiency. Another reaction favored at pH values less than 1 is the decomposition of chlorate to form chlorine dioxide (14).

Lister (15) made a careful study of the kinetics of O_2 evolution from solutions containing hypochlorite and found the mechanism of O_2 evolution to be of second order. The hypochlorite decomposition reaction proceeds at a rate of 1×10^{-5} g mol/l min at 40°C in pure solutions, and is greatly accelerated by Co, Ni, Fe, Cu, and Mn ions in the electrolyte in the following order



and also by light.

For current efficiency calculations, chlorate industries use the following formula (16)

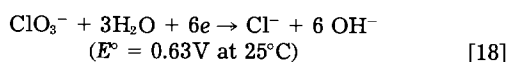
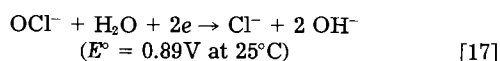
$$\text{Chlorate efficiency} = \frac{100 - 3\% \text{ O}_2 - 2\% \text{ Cl}_2}{100 - \% \text{ O}_2 - \% \text{ Cl}_2} \quad [16]^a$$

by analyzing the exit gas stream. Material balance calculations show that Eq. [16] is adequate to describe the performance of a typical chlorate cell. However, implicit in

^a Uguine-Kuhlman uses the formula: chlorate efficiency = $100\% - 2\% \text{ O}_2 - \% \text{ Cl}_2$, with $\% \text{ Cl}_2 = 0.3-0.5$ and $\% \text{ O}_2 = 2-2.5$, which can be derived from Eq. [16] by simple binomial expansion.

the derivation of Eq. [16] are the following considerations: (i) 1 mol of O_2 generated corresponds to a loss of 4 Faradays of electricity, and (ii) 1 mol of Cl_2 escaped corresponds to a loss of 2 Faradays of electricity. Very often, the cell gas is scrubbed with caustic, and the scrubber liquor is recycled to the cell again.

Cathodic parasitic reactions—role of sodium dichromate during chlorate electrolysis.—The primary reaction at the cathode is the discharge of H^+ ions to form H_2 . However, thermodynamic and kinetic considerations favor OCl^- and ClO_3^- reduction reactions (Eq. [17] and [18])



The rates of these reactions are believed to be suppressed by the addition of sodium dichromate (in the 1-5 g/l range) during electrolysis.

Sodium dichromate is a conventional and multifunctional additive used routinely in the commercial production of sodium chlorate. Several roles are attributed to chrome, which include: (i) suppressing the corrosion of the Fe cathode (17-20), (ii) buffering (9, 21) the electrolyte in the pH range 5-7, where the chlorate formation rate is optimum, (iii) preventing the cathodic reduction of OCl^- and ClO_3^- ions by the " Cr_2O_3 " film formed by chromate reduction (22, 23), and (iv) inhibiting the O_2 evolution reaction at the anode (24, 25). It is of interest to note that the fluoride ion (26) is believed to play a similar role as dichromate during chlorate electrolysis with PbO_2 anodes. The relative importance of these functions is critically discussed in this section.

Inhibition of corrosion of steel cathode.—Cathodes made of steel are generally used in electrolytic chlorate cells, the electrolyte under operating conditions analyzing 450 g/l $NaClO_3$, 150 g/l $NaCl$, 4-5 g/l OCl^- , and 2-3 g/l $Na_2Cr_2O_7$ at $70^\circ C$ (pH \sim 5.9-6.7). If the role of dichromate is indeed one of suppressing the corrosion of steel under open-circuit conditions, then the open-circuit potential (E_{ocp}) should show significant differences in the presence and absence of dichromate. However, experimental measurements in the above solutions show the E_{ocp} to be -0.30 to $-0.32V$ vs. SCE in the presence and absence of dichromate, suggesting that the major role of $Cr_2O_7^{--}$ is not one of offering protection to steel from corrosion.

Enhancement of buffer capacity.—It was mentioned earlier that the preferred pH range of operation of a typical chlorate cell is in the range 5.9-6.7 to achieve optimal conversion of hypochlorite to chlorate. The system has a natural buffer capacity in this range due to HOC/OCl^- equilibrium represented by Eq. [8]. Taniguchi and Sekine (9) mentioned that chrome addition enhances the buffer capacity in this critical pH range due to the equilibrium reaction



pH titration data obtained in the presence of dichromate in solutions containing 150 g/l $NaCl$ and 450 g/l $NaClO_3$, at $70^\circ C$, in the absence of OCl^- , showed (12) that dichromate indeed buffers in the pH range 5.9-6.7. In the presence of OCl^- and $Cr_2O_7^{--}$, the buffer capacity was found to be directly proportional to the concentration of OCl^- and $Cr_2O_7^{--}$ and equal to the sum of the individual contributions from OCl^- and $Cr_2O_7^{--}$. Thus, it is definitively established (12) that dichromate enhances the buffer capacity in the pH region 5-7.

Inhibition of oxygen evolution.—One of the parasitic anodic reactions during chlorate electrolysis is oxygen evolution from either the discharge of water molecules (Eq. [12]) or the oxidation of OCl^- to ClO_3^- (Eq. [13]). It was stated in the literature (24, 25) that $Cr_2O_7^{--}$ suppresses the amount of oxygen generated during chlorate electrolysis. While one may rationalize this observation in terms of

blocking of sites for oxygen evolution by dichromate and/or complexation of hypochlorite decomposing catalysts (e.g., Fe, Co, Ni) by $Cr_2O_7^{--}$ (and/or CrO_4^{--}), further investigations are needed to understand the mechanistic aspects involved in this phenomenon.

Suppression of parasitic cathodic reactions.—In an electrolytic chlorate cell, there are two parasitic cathodic reactions (Eq. [17] and [18]) arising from the cathodic reduction of negatively charged ions, OCl^- and ClO_3^- . If these negatively charged ions are to be reduced cathodically, they have to approach the cathode by diffusion and convection against an adverse potential gradient. If the solution contains a large excess of supporting electrolyte, the adverse potential gradient is small and the transport of anions is affected only slightly. However, if an inert porous diaphragm is formed on the cathode that greatly counteracts the effect of convection, the approximate material balance equation for the species may be written as

$$N_i = -Z_i U_i F C_i \nabla \phi - D_i \nabla C_i \quad [20]$$

where N_i refers to the flux of species i , Z_i to the valence of the species, U_i to mobility, C_i to concentration, $\nabla \phi$ to the potential gradient, and D_i to the diffusivity of species i .

The first term on the right-hand side of Eq. [20] accounts for transport by migration (away from the cathode surface for anions) and the second term to the contribution from diffusion. If the potential gradient term is increased by increasing the local current density, then the transport of anions to a cathode can be completely suppressed. This may be achieved by forming an inert film with low porosity on the cathode. These facts were clearly expounded in a paper by Wagner (23). [See Ref. (27) for a historical perspective on the role of chromate during chlorate electrolysis.]

Dichromate is known to be cathodically reduced to form a " Cr_2O_3 " film on the cathode surface, which creates an adverse potential gradient that prevents the reduction of OCl^- and ClO_3^- ions. Polarization and mass-balance studies performed in the presence and absence of dichromate using steel and Pt cathodes clearly demonstrated (12) that the primary role of chromate is in the suppression of cathodic reduction of OCl^- and ClO_3^- via the establishment of an adverse potential gradient. Wagner's film theory is further substantiated using steel cathodes coated with Kalgard and Cr_2O_3 films in chlorate solutions, and by rotating disk electrode studies wherein $Fe(CN)_6^{3-}$ reduction was hindered by 0.1 g/l $Cr_2O_7^{--}$, while Fe^{3+} reduction was unaffected.

It is of interest to note that the limiting current density for $Fe(CN)_6^{3-}$ reduction is independent of rotation speed in the presence of $Cr_2O_7^{--}$, in contrast to the linear dependence as a function of square root of the rotation speed observed in the absence of $Cr_2O_7^{--}$. This suggests that the surface film dampens the convection effects significantly, resulting in the suppression of mass-transfer rates by a factor of $\gg 100$. To a first approximation, these effects may be expressed (28) by the relationship

$$Sh = 1.05 [Re/(1 + ld\epsilon)]^{0.93} \quad [21]$$

where l refers to the thickness of the porous film, d to the pore diameter and ϵ to the porosity, as shown by Roberston *et al.* (28). These results unequivocally suggest that the flow velocity in chlorate cells can at best only minimize the solution ohmic drop arising from void fraction of H_2 bubbles and in no way influences the kinetics of the hydrogen evolution reaction occurring via the discharge of H_2O molecules at pH values > 12 even though the bulk pH is ~ 6 and discharge of H_2 from H^+ ions is mass-transfer controlled at this pH value.

Energy Consumption and Components of Cell Voltage

Energy consumption (P) of a chlorate cell is a function of current efficiency (CE expressed as a fraction) and cell voltage (V in volts) as

$$P \text{ (kWh/ton)} = \frac{1372 \times V}{\text{CE}} \quad [22]$$

Current efficiency is a function of operating characteristics (*e. g.*, flow rate, pH, temperature, etc.) and cell design (*e. g.*, monopolar or bipolar), and is generally in the range 90%-95% for metal electrode cells. However, cell voltage is governed by the polarization characteristics of the anode and the cathode and conductivity characteristics of the electrolyte + gas mixture and can be expressed as

$$V = (\text{thermodynamic decomposition of the anode and the cathode}) + (\text{anodic overvoltage}) + (\text{cathodic overvoltage}) + (\text{ohmic drop between the anode and cathode due to the gas/electrolyte mixture}) + \text{ohmic drop across the hardware}$$

Typical energy requirements and components of a chlorate cell voltage are shown in Table II [see Ref. (1)].

Unit Operations in Chlorate Technology

The very nature of the formation of chlorate dictates the need for several unit operations for chlorate production as noted below.

Electrolysis zone.—In the electrolysis zone, the electrochemical reactions (Eq. [4] and [5]) take place along with the hydrolysis of Cl_2 . Escape of chlorine due to incomplete hydrolysis results in an imbalance of pH, and HCl has to be added to maintain the pH at the optimal value required for chlorate formation. (Pennwalt uses chlorine to maintain pH balance.)

Reaction zone.—Since a relatively large volume is required to carry out reaction [9], a reaction zone is needed.

Cooling zone.—Reaction [9] is exothermic, and the energy supplied to the cell exceeds the heat required to carry out the overall reaction [1], and hence a cooling zone is needed to remove the excess heat and control the operating temperature.

Circulation zone and means.—This is usually carried out by either a gas lift mechanism or by external pumping.

Acknowledging the need for the above, various manufacturers have developed their technologies judiciously by either separating or aggregating the four essential zones in their overall designs. Thus, while the chemistry and electrochemistry involved in chlorate formation appear relatively simple, eight to ten cleverly engineered technologies, distinctly different from each other, were developed during the past several years (see Table III). In spite of the distinguishing differences among the various technologies, emerged (i) as a consequence of the various permutations and combinations of patterns available to construct the cell circuits and (ii) as a result of patentability and economic considerations, there are several common features in these cell designs. In this sec-

Table II. Typical requirement of electrical energy for a chlorate cell (using steel cathodes and Pt-Ir anodes)*

Current density	1.9 A/in ²
Current efficiency	94%
Cell voltage components	
Thermodynamic decomposition voltage	1.71V
Anode overvoltage	0.05V
Cathode overvoltage	0.94V
Ohmic drops	0.80V (A/C gap: 3-5 mm)
Average cell voltage	3.50V
Electrical energy requirement	5100 kWh/ton chlorate
Operating conditions	
Temperature	80°C
Solution composition (g/l)	NaCl: 150. NaClO ₃ : 450 NaOCl: 3-5. Na ₂ Cr ₂ O ₇ : 2-5

From Ref. (1).

Table III. Chlorate cell technologies

Technologies	Ref.
Canoxy-Squamish*	(29)
Chemetics/Solvay	(30)
Chemwest	(31)
DeNora	(32)
Huron	(34)
Kemanord	(35)
Krebs	(25, 36)
Krebskosmo	(37)
Pennwalt	(38)
Ugine Kuhlmann	(39)
OCC**	(33)
Oulu	(50)
Eltech Systems	(51)

* Presently licensed by Chemetics International Company.

** Occidental Chemical Company (formerly Hooker Chemical Company) is a wholly owned subsidiary of Occidental Petroleum Corporation. This technology is presently licensed by Kemanord.

tion, an attempt is made to rationalize these differences showing the commonality among them in terms of system and electrode configurations.

System Configurations

The basic requirement in any chlorate cell operation is the need for four zones for achieving high efficiency and low cost. However, by judicious engineering, one can combine these unit operations to make the overall system cost effective, as shown in Fig. 1. Thus, DeNora, Eltech, OCC, Huron, and Canoxy-Squamish employ a single-vessel system wherein electrolysis, reaction, heat removal, and pumping by gas-lift are accomplished. Krebs, on the other hand, prefers to use a two-vessel system in which electrolysis is carried out in a separate vessel and the cell liquor is pumped by gas-lift to an external reactor to remove the heat and to allow the reaction to proceed to completion. Pennwalt, Ugine-Kuhlmann, Kemanord, and Krebskosmo designed their cell circuits in a classical fashion by using three separate vessel zones with liquor circulating from cell tank, to reactor, to circulating pump through the heat exchanger back to the cell bank. Chemetics, instead, pumps the electrolyte only through the heat exchanger and employs gas-lift to circulate liquor from the cell to the reactor. It may be pointed out here that Canoxy-Squamish technology is presently licensed by Chemetics.

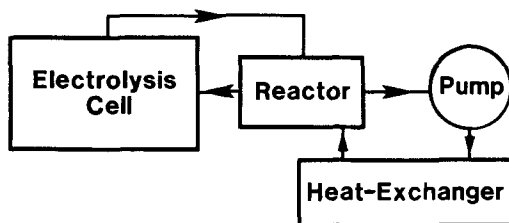
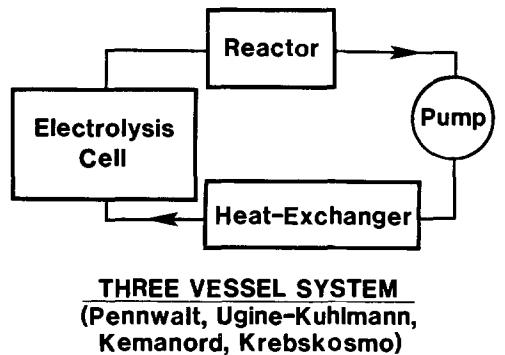
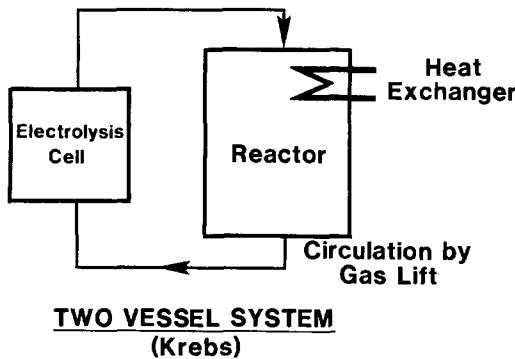
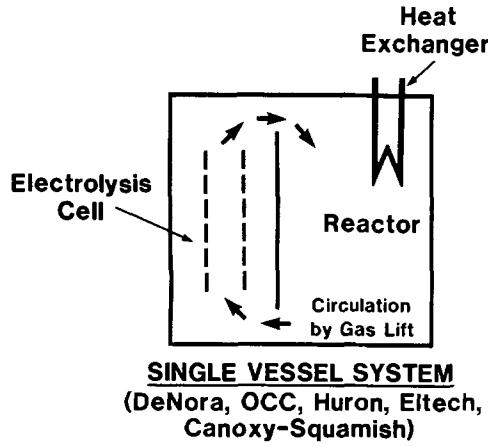
Electrode Configurations

Monopolar cells.—The basic design (see Fig. 2) in monopolar chlorate cells is the parallel plate configuration, the cathode plates being solid sheets in the case of OCC, Chemetics, and Krebs, and perforated in the case of Ugine-Kuhlmann and Pennwalt who claim lower cell voltage by this cathode design.

Bipolar cells.—Four different electrode designs are presently employed in bipolar cells, as shown in Fig. 3a and 3b. The simplest design is that of the OCC's D-cells at Columbus, which consists of parallel solid graphite plates. Improvements in the concept are introduced in the Eltech and Huron cells by employing bipolar plates of titanium cathodes and DSA anodes in electrical contact at the plastic partition at the top and bottom of the stack to separate the individual cells. The plastic used by Huron is PVC, and Eltech uses a fluoro polymer. Circulation is achieved in this design by gases generated during electrolysis flowing through the perforations. A similar design is used by Canoxy-Squamish, the differences being that the bipolar units are solid plates of Ti anode and Fe cathode bolted together and arranged vertically with spacers in between the bipolar elements.

DeNora achieves efficient gas-lift circulation in the cell by stacking the solid Ti-0.2% Pd cathodes/DSA anode bipolar elements vertically. Thus, cell height appears to provide high circulation rates in this design.

While, the OCC "D" at Columbus, Eltech, Huron, DeNora, and Canoxy-Squamish cell designs are truly bi-



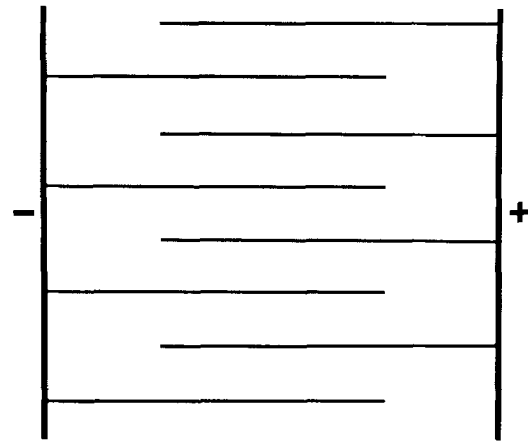
(Chemetics pumps liquor only through the heat exchanger)

Fig. 1. System configuration

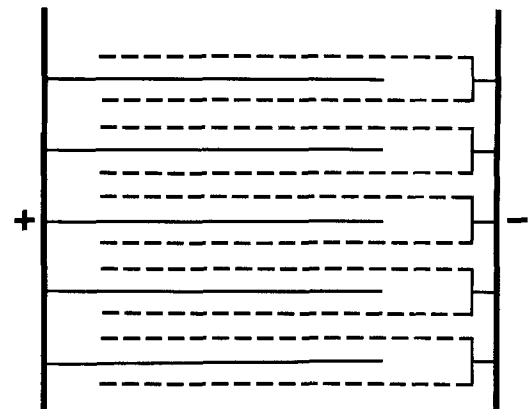
polar in character, the Kemanord design may be classified as a "pseudobipolar" system, since the bipolar stacks constituted of a Ti-Ag layer-steel composite sandwich provide current to the monopolar electrodes in between them (see Fig. 3a). [For details related to these technologies see Ref. (29-40).]

Materials of Construction

An overview of the materials of construction used in the chlorate industry presented in Tables IV and V shows that the materials used range from plastics (e.g., Huron) to exotic materials, such as Teflon and Ti, used by DeNora.



SOLID PARALLEL PLATES
(OCC [hollow cathodes], Chemetics, Krebs)



PERFORATED PARALLEL PLATES
(Ugine-Kuhlmann, Pennwalt)

Fig. 2. Electrode configurations for monopolar cells (sectional plan views).

The operating and capital costs of chlorate cell technologies differ from each other mainly because of the differences arising from system and electrode configurations and materials of construction of electrodes and cells. The differences in system and electrode configuration are reflected in power consumption, cell voltage, and overall cell efficiency variations. The differences in the nature of the materials of construction, system, and electrode configurations are presumably reflected in the capital cost variations among these cell technologies.

From the materials of construction point of view, the various chlorate technologies fall into three broad categories: (i) those which rely very heavily on plastics (e.g., Eltech, Huron, Chemetics). (ii) those which rely very heavily on Ti and Fe (e.g., Kregs, Pennwalt, Ugine-Kuhlmann, OCC at Taft), and (iii) those which attempt to find an economic medium (e.g. DeNora, Canoxy-Squamish, Kemanord).

The use of plastics (generally PVC or CPVC) limits the operating temperature and leads to high maintenance, whereas the use of Ti and Teflon increases the capital costs with low maintenance operations. Some of these aspects related to materials of construction in chlorate cells are addressed in the following sections.

Anodes (41, 42).—Graphite was extensively used as an electrode 80 to 90 years ago in monopolar and bipolar cells. However, it is not a satisfactory material because it is disintegrated by anodic oxidation and mechanical attri-

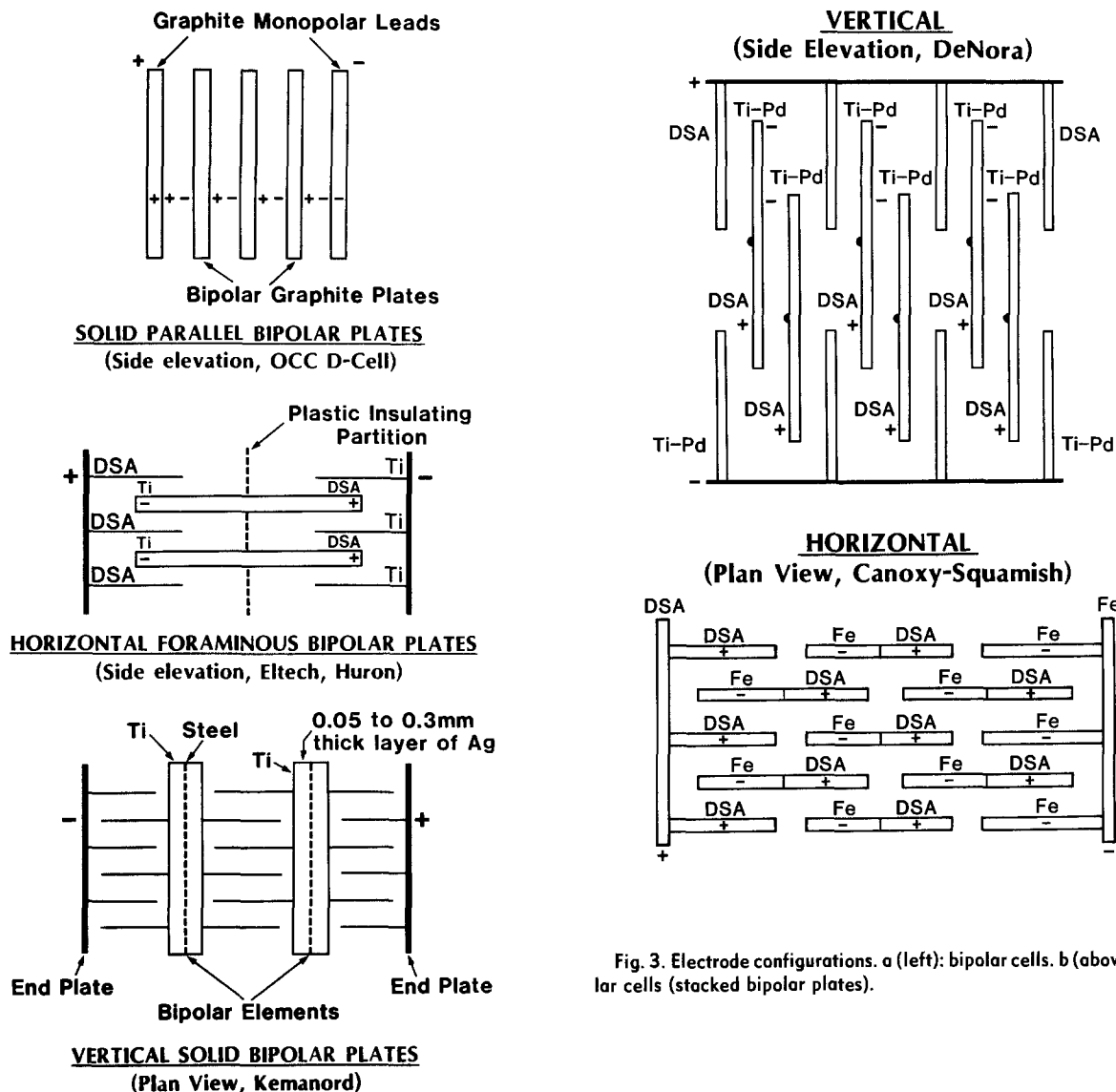


Fig. 3. Electrode configurations. a (left): bipolar cells. b (above): bipolar cells (stacked bipolar plates).

tion. As the electrodes wear away, the gap between the electrodes widens, resulting in an increase in the solution ohmic drop and, hence, the cell voltage. Furthermore, graphite imposes restrictions on the operating temperature of the electrolytic cell due to its rapid disintegration at elevated temperatures. An important development in recent years has been the use of metal anodes, which are essentially precious metal alloy or precious metal oxide coatings on valve metals. Titanium is the most commonly used substrate material, and the noble metal coatings are based on Pt, Ir, and Ru. These electrodes do not deteriorate like graphite electrodes, and are therefore termed dimensionally stable. In contrast to graphite electrodes, metal anodes can be operated at higher temperatures (70°-95°C) and higher current densities (2-4 A/in²) with high current efficiencies (90%-95%). These dimensionally

stable anodes operate close to the thermodynamic decomposition voltage for the Cl⁻ to Cl₂ reaction, thus resulting in significant energy savings with minimal maintenance and have, in a way, revolutionized the electrolytic chlor-alkali and chlorate operations making inroads into other electrochemical industries.

Cathodes.—Cathodes are most often Fe based, and many chlorate cells use steel cathodes, with the possible exception of DeNora cells, which employ Ti-0.2% Pd alloy, and Huron and Eltech cells, which use Ti cathodes. However, iron is a moderately good electrocatalyst for the hydrogen-evolution reaction, the activation overvoltage being 220-400 mV in the current density range 1.5-2.5 A/in². However, the hydrogen overvoltage on titanium is much higher than on Fe.

Chlorate cell liquor, which typically contains 450 g/l NaClO₃, 150 g/l NaCl, and 2-5 g/l NaOCl (at 70°-90°C) is one of the worst corrosive media since OCl⁻ to Cl⁻ is a thermodynamically favored reaction, with sufficient free energy to drive the oxidation of most metals below their reversible potentials under open-circuit conditions. The only metals that might withstand oxidation are probably noble metals which tend to establish the Nernstian potential for the OCl⁻/Cl⁻ and/or ClO₃⁻/Cl⁻ couple. While valve metals are also stable in this medium under open-circuit conditions, they tend to hydride easily during electrolysis, resulting in the loss of mechanical integrity due to lattice expansion and subsequent distortion.

Because of aforementioned limitations, chlorate cell technology is predominantly monopolar although there

Table IV. Materials of construction

Materials	Company
Plastics (PVC, Siliglas®* FRP, TFE-lined FRP)	Chemetics/Solvay, Huron, Eltech
Metal (Ti, steel)	Pennwalt, Krebs, OCC, Ugine-Kuhlmann Chemetics/Solvay
Mixture of plastics (Teflon) and metals (steel, Ti)	DeNora, Canoxy-Squamish, Kemanord, Chemetics/ Solvay

* Registered trademark of Huron Chemicals, Limited.

Table V. Summary of materials of construction and assembly techniques and operating parameters

Company	Anode	Cathode	Cell body	Cell cover	Reactor	Major assembly techniques	Temp (°C)	Current density (A/in ²)	Cell voltage (V)	DC power consumption (kWh/ton)
Canoxy Squamish ¹	Coated Titanium	Steel	Titanium support cradle only for electrodes	FRP hood	Titanium-lined FRP	FRP layout over titanium liner, and bolting			N.A.	
Chemetics/Solvay	Coated Titanium	Steel	PVC-lined FRP. Teflon-lined fiber-glass and steel, titanium	—	PVC-lined FRP, titanium, Teflon-lined FRP	Explosion cladding on electrodes, plastic and metal welding, FRP layout, and bolting	60-85	0.66-2.59	2.6 and up	3700 and up
Chemwest	Coated Titanium	Titanium	Teflon-lined FRP	Teflon-lined FRP	Titanium	FRP layout over Teflon liner, welding, and bolting			N.A.	
DeNora	Coated titanium	Titanium (Ti-0.2% Pd alloy)	Teflon-lined steel	Rubber (as explosion hatch)	Teflon-lined steel	Welding and bolting	90	1.42	3.2	4700
Eltech	Coated Titanium	Titanium	Teflon-lined FRP	Teflon-lined FRP	Teflon-lined FRP	FRP over Teflon liner bolted assembly	65	1.6	3.2	4625
Huron	Coated Titanium	Titanium	PVC	Siliglas® FRP	Siliglas® FRP	PVC welding, Siliglas® assembly	65	1.68-2.08	3.22-3.4	4650-4950
Kemanord	Coated Titanium	Steel	Rubber-lined steel	Rubber-lined steel	Rubber-lined steel	Explosion cladding on electrodes, welding, cementing of linings, and bolting	50	1.55	3.3	5000
Krebs	Coated Titanium	Steel	Steel, with titanium anode cover plate	Titanium inlet and outlet reducer connections	Titanium	Welding and bolting	80	1.6	2.9	4180
Krebskosmo	Coated Titanium	Steel	Frames of PVDF	End plates of steel	Titanium	Spot welding, explosion cladded titanium Fe sheets, rivet fastening, sealing by insertion of gaskets into grooves, bolting Ti anode and Fe cathode	N.A.	N.A.	3.3	4550-5230 (at 80% to 120% of nominal current rating 4000)
OCC	Coated Titanium	Steel	Steel bottom, titanium top	Titanium	Titanium	Welding and bolting	90	1.49	2.76	
Oulu	Coated Titanium	Steel	Steel	Steel	Titanium	Welding	80	1.61	2.9	4250
Pennwalt	Coated Titanium	Steel	Steel	Steel	Titanium	Welding and bolting	85	1.8	3.5	5000
Ugine-Kuhlmann	Coated Titanium	Steel	Steel bottom, titanium top	Rubber (as explosion hatch)	Titanium	Welding and bolting	70	1.3	3.0	4850

¹ Presently licensed by Chemetics/Solvay. N.A. refers to nonavailability of data from the manufacturer.

are few bipolar cells, such as the ones used by Huron, DeNora, and Eltech. Thus, whenever steel cathodes are used, there is a need for cathodic protection to protect steel from corrosion during open-circuit conditions (or cell shutdown). The magnitude of the cathodic protection current should be so chosen that the potential of steel is well below the mixed potential set up by the hypochlorite reduction and the metal oxidation reactions.

Reactor.—The nature of the material chosen for the reactor should not only be stable to the “oxidative” chlorate cell liquor, but should also be able to withstand the temperature at which the cells are operated. For high temperatures of operation, the choice seems to be restricted to titanium or Teflon-lined materials. Krebs, Pennwalt, Ugine-Kuhlmann, and OCC use Ti reactors. DeNora, Eltech, and Chemetics/Solvay have experimented with Teflon-lined steel and Teflon-lined fiber glass, and Huron and Chemetics use plastics such as CPVC, Siliglas®, and FRP. These may however restrict the operating temperature of the cells. (Huron, however claims that Siliglas is suitable up to 65°-85°C.)

Cell cover and cell body.—Choice of cell cover includes: FRP, Teflon-lined FRP, rubber, titanium and Siliglas. The considerations involved in selection are very similar to that of the reactor. Cell body is typically steel in most cases and should be protected by making it cathodic under all conditions. Criteria for the selection of cell body material are similar to those involved for the reactors; this requires no further elaboration.

Energy Conservation in Chlorate Industry: Future Developments

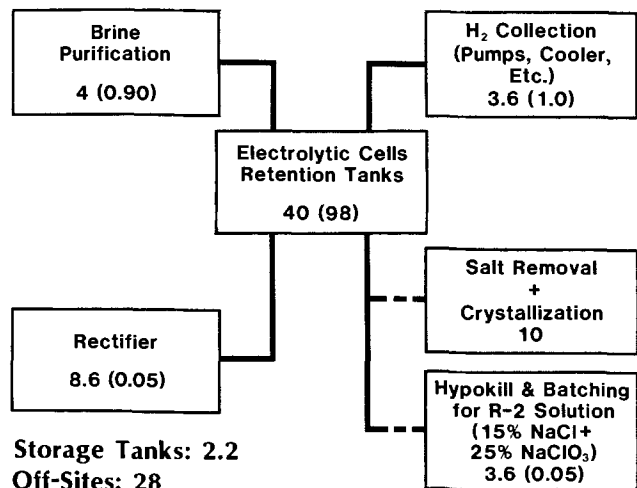
The opportunities to achieve energy savings in the chlorate industry can be generated by examining the flow sheet (1) describing the various unit operations involved in chlorate production. Figure 4 illustrates the general layout in a chlorate plant and shows the electrolytic stage to be the most capital and energy consuming unit in chlorate manufacture.

A closer look at the energy consumption requirements indicates that the majority of energy losses in electrolytic chlorate production are associated with (i) thermodynamic decomposition voltage and (ii) cathode potential. Some of these and other aspects related to the future developments in chlorate technology are discussed below.

Materials of construction.—It is pertinent to address the issue of why chlor-alkali diaphragm cells have certain characteristics different from those of chlorate cells. The reason for this primarily stems from the need to separate the anolyte from the catholyte via a diaphragm which re-

stricts major design variations. Removal of this constraint in chlorate cells has permitted development of a plethora of cell designs. If one now corrects for the effects of operating temperature, electrode gaps, and current densities, and compares them on a common basis, it can be safely assumed that there is little to choose among these different chlorate technologies even though each design is different (40) - the process conditions being mainly limited by the nature of the materials of construction. The development of a superior technology depends to a significant degree on finding cheaper materials of construction which will withstand the chlorate cell environment. This is elaborated upon in the following discussion.

In the chlorate industry, approximately 50% of the production costs are associated with the electrical energy and 30% in capital. To reduce the power consumption, one has to operate the cells at high temperatures to reduce the cell voltage, and this presently demands the use of expensive materials of construction. The dilemma now lies in increased capital cost, which demands higher current densities (and hence higher cell voltages) or increased product output. For operation at high temperatures, titanium is the preferred material of cell construction. However, its price in today's market is volatile. An economic replacement for the expensive titanium metal is needed, and possibilities exist, for example, via a more extensive usage of cathodically protected steel or



Storage Tanks: 2.2
Off-Sites: 28

Fig. 4. Approximate capital and power requirements (expressed as percentage of total) for a 20,000 TPY chlorate plant using Krebs technology. Total power: 275,000 kWh/day. (Power requirements are stated in parenthesis for a solution (R-2) plant [from Ref. (1)].

cheaper stable coatings on metals. (For example, DeNora has examined Teflon-coated steel, and Huron proposed the usage of Siliglas®-lined steel.) Another advantage of using expensive metals like titanium lies in decreased downtime and maintenance of the cells. Use of plastics in this regard may be unsatisfactory with the possible exception of polyvinylidene difluoride (PVDF) or Teflon, which are also relatively expensive. Presently, no "low-cost" materials of construction capable of withstanding the corrosive environment of a chlorate cell have been identified.

Reduction in thermodynamic decomposition voltage.—Voltage savings of approximately 1V can be accomplished by using air-depolarized cathodes (43, 44) instead of the conventional H₂ cathodes. While this is not yet a commercial reality, a quantum leap in this area would be a significant technological advance (49). However, its impact on capital and operating costs require critical evaluation.

Cathode overpotential.—The cathode overpotential is presently about 1.0-1.2V, of which the contribution from the activation overpotential is about 0.3-0.4. The remainder is associated with the concentration overpotential and IR drop in the "chrome film." While the concentration overpotential cannot be reduced unless the mass-transfer coefficient in the cells surpasses an impossible value 10⁹ (see above), the activation overvoltage can be reduced by using "activated" cathodes (45, 46). However, one of the problems with steel-based cathodes is the corrosion of Fe-based materials, under open-circuit conditions due to OCl⁻ ion reduction; the conjugate reaction is the metal oxidation reaction. This imposes a serious restriction on the catalytic coatings (on steel) which provide the required high surface area for achieving low overvoltage. Thus, the search and/or development of materials exhibiting stability in OCl⁻ containing electrolytes in the pH region of 4-6 is the "slow-step" in the development of catalytic cathodes.

Ti cathodes, however, are stable in chlorate media but suffer from hydrogen embrittlement due to permeation of H₂ into the metal lattice, formation of TiH₂, and subsequent lattice distortion and degradation. While alloys of Ti containing 0.2% Pd (32) and rare-earth metals (47) and Ag-coated Ti (48) have been suggested to surmount the hydriding problem, the performance characteristics of these electrodes have not been firmly established. Moreover, an "understanding" of the factors involved in H₂ permeation kinetics into Ti during chlorate electrolysis and hydrogen embrittlement, required for the development of criteria for preventing and/or minimizing hydrogen entry, is presently lacking. A theoretical analysis of the nature and mechanism of H₂ entry into and discharge on Ti and other materials such as Ag, Pt, Au, etc., in chlorate solutions could provide a lead in developing non-hydrogen embrittling Ti-based cathodes. Nevertheless, it is a monumental task to develop materials that would replace steel.

Hydrogen recovery.—Except the Kemanord, Pennwalt, and Krebs locations which recover the hydrogen from chlorate cells for hydrogenation and NH₃ synthesis, respectively, all chlorate-recovered H₂ is presently used as a boiler fuel. Chemetics/Solvay also recover hydrogen for bottling purposes. While detailed economic information is not available at the present time, it appears worthwhile considering the fuel cell route for H₂ utilization, thus recovering some of the energy put into the electrolytic cells.

Acknowledgments

The authors wish to thank Occidental Chemical Company for permission to publish this paper. Our special thanks are due to Mr. L. Allais of Krebs, Dr. E. Hausmann of Krebskosmo, Mr. J. R. Hodges of Pennwalt Corporation, Dr. V. Tulkki of Oulu, Dr. J. Cormier of Ugine-Kuhlmann, Mr. D. Owens of Huron Chemicals Limited, Dr. R. Backstrom of Chemetics International Company, and Mr. L. C. Curlin of Eltech Systems Corporation for

critically reviewing the article, supplying technical information, and for permission to publish the data provided by them.

Manuscript submitted Oct. 4, 1983; revised manuscript received Jan. 9, 1984.

Occidental Chemical Corporation assisted in meeting the publication costs of this article.

REFERENCES

1. T. V. Bommaraju, E. M. Spore, and J. C. Hanson, Paper presented at the Electrolytic Technology Committee Ad-hoc Meeting, U. S. Dept. of Energy and Argonne National Laboratory, Washington, DC, March 12-13, 1979.
2. W. Von Hisinger and J. Berzelius, *Neues Allg. J. Chem.*, **1**, 115 (1803).
3. H. Kolbe, *J. Prakt. Chem.*, **41**, 137 (1847).
4. Yu-Ren Chin, SRI Report no. 112, March 1977.
5. G. H. Kelsall, U.S. Department of Commerce, *NTIS PB*, **277**, 430 (1977).
6. D. Kokoulina and L. I. Khristalik, *Sov. Electrochem.*, **7**, 346 (1971).
7. M. M. Jaksic, *This Journal*, **121**, 70 (1974).
8. F. Foerster and E. Muller, *Z. Electrochem.*, **9**, 171 (1903); F. Foerster, *Trans. Electrochem. Soc.*, **46**, 23 (1924); *J. Prakt. Chem.*, **59**, 53 (1899).
9. I. Taniguchi and T. Sekine, *Denki Kagaku*, **43**, 715 (1975).
10. H. Imagawa, *ibid.*, **21**, 520 (1953).
11. M. W. Lister, *Can. J. Chem.*, **30**, 879 (1952).
12. B. V. Tilak, K. Viswanathan, and C. G. Rader, *This Journal*, **128**, 1228 (1981).
13. N. Ibl and H. Vogt, "Comprehensive Treatise of Electrochemistry," Vol. 2, p. 167, J. O'M. Bockris, B. E. Conway, E. Yeager, and R. E. White, Editors, Plenum Press, New York (1981).
14. M. M. Jaksic, *Electrochim. Acta*, **21**, 1127 (1976).
15. M. W. Lister, *Can. J. Chem.*, **34**, 479 (1956).
16. M. M. Jaksic, A. R. Despic, I. M. Csonka, and B. Z. Nikolic, *This Journal*, **116**, 1316 (1969).
17. D. M. Brasher and A. D. Mercer, *Trans. Faraday Soc.*, **61**, 803 (1965).
18. H. Kerst, *Corrosion*, **16**, 523t (1960).
19. H. Oranowska, and Z. Szklarska-Smizlowska, *Zasch. Metal.*, **8**, 523 (1972).
20. S. Kowamura, N. Tanaka, and M. Nagayama, *Boshoku Gijutsu*, **22**, 500 (1973).
21. M. J. Jaksic, A. R. Despic, and B. Z. Nikolic, *Sov. Electrochem.*, **8**, 1533 (1972).
22. I. E. Veselovskaya, E. M. Kuchinskii, and L. V. Morochko, *J. Appl. Chem. USSR*, **37**, 76 (1964).
23. C. Wagner, *This Journal*, **101**, 181 (1954).
24. J. Cormier, in "Proceedings of the Oronzio DeNora Symposium: Chlorine Technology": Oronzio DeNora, Editor, p. 237, Oronzio DeNora Impianti, Elettrochimici S. p. A., Milan, Italy (1979).
25. F. Griedelinger, *ibid.*, p. 261 (1979).
26. A. T. Kuhn, "Industrial Electrochemical Processes," p. 525, Elsevier Publishing Co., Amsterdam (1971).
27. H. Vogt, *This Journal*, **128**, 29C (1981).
28. P. M. Robertson, D. Matic, and N. Ibl, "Extended Abstracts of the 157th Electrochemical Society Meeting at St. Louis, Missouri, May 11-16, 1980," Abstract 387, Vol. 80-1, p. 961 (1980).
29. G. O. Westerlund, Canadian Pat. 933,488 (1973).
30. G. O. Westerlund, U.S. Pat. 3,766,044 (1973).
31. a: G. O. Westerlund, U.S. Pat. 4,101,406 (1978); b: Brochure from Chemwest, Vancouver, BC, Canada, titled "Sodium Chlorate Production" (1976).
32. a: DeNora commercial brochure titled "Oronzio DeNora S.P.A. NaClO₃, KClO₃," b: P. M. Spazianti, in "Proceedings of the Oronzio DeNora Symposium: Chlorine Technology," Oronzio DeNora, Editor, p. 284 (1979), c: O. DeNora, V. DeNora, and P. M. Spazianti, U.S. Pat. 4,046,653 (1977).
33. a: C. J. Harke, J. C. Parkinson, and J. E. Currey, U.S. Pat. 3,732,153 (1973); C. R. Nowrok, U.S. Pat. 4,039,420 (1977); C. R. Nowrok, U.S. Pat. 4,218,293 (1982); E. M. Spore, U.S. Pat. 4,332,648 (1982); E. M. Spore, U.S. Pat. 4,332,659 (1982); b: C. G. Rader, E. M. Spore, and J. C. DeLong, in "Modern Chlor-Alkali Technology," Vol. 2, C. Jackson, Editor, p. 305, Society of Chemical Industry, London (1983).
34. a: Huron Chemicals commercial brochure, sheets A-E, I-XI, 1978 revisions; b: J. V. Casson, J. S. Bennett, and R. E. Loftfield, U.S. Pat. 3,819,503 (1974), G. J. Crane, U.S. Pat. 3,503,858 (1970), G. J. Crane, U.S. Pat. 3,518,173 (1970), J. V. Casson, R. E. Loftfield, and B. Kindl, U.S. Pat. 3,997,414 (1976), J. V. Casson and R. E. Loftfield, U.S. Pat. 4,087,344 (1978).

35. K. Larsson, U.S. Pat. 3,759,815 (1973), 3,992,279 (1976).
36. a: J. Fleck, U.S. Pat. 3,539,486 (1970); b: J. Fleck, *Chem. Ing. Chem.*, **43**, 173 (1971); c: *Inf. Chem.*, **17** (July/Aug. 1970); d: F. Greiveldinger, Abstract 445, p. 1114, The Electrochemical Society Extended Abstracts, Vol. 78-1, Seattle, WA, May 21-26, 1978.
37. a: Krebskosmo commercial brochure title "Sodium Chlorate Electrolysis;" b: E. Hausmann, H. Will, and A. Belloni, in "Proceedings of the Oronzio DeNora Symposium: Chlorine Technology," O. DeNora, Editor, p. 69 (1949); c: Symposium on Chlorine Technology, India, Feb. 1980.
38. a: Pennwalt commercial brochure titled "The Pennwalt Electrochemical Sodium Chlorate Process," Philadelphia, PA; b: J. R. Hodges, Abstract 447A, p. 1122, The Electrochemical Society Extended Abstracts, Vol. 78-1, Seattle, WA, May 21-26, 1978; c: J. R. Hodges, U.S. Pat. 4,075,077 (1977).
39. a: Uguine Kuhlmann commercial brochure titled "Manufacture of Sodium Chlorate by Electrolysis, PCUK Process;" b: M. Bakes, J. Cormier, and R. Scalliet, Abstract 442, p. 1108, The Electrochemical Society Extended Abstracts, Vol. 78-1, Seattle, WA, May 21-26, 1978; c: J. Cormier, in "Proceedings of the Oronzio DeNora Symposium: Chlorine Technology," O. DeNora, Editor, p. 237 (1979); d: D. Fournier and J. Bourgeois, U.S. Pat. 4,060,475 (1977).
40. J. E. Coleman, in "Tutorial Lectures in Electrochemical Engineering and Technology," Vol. 77, R. Alkire and T. Beck, Editors, A.I.Ch.E. Symp. Ser. 204, p. 244, Institute of Chemical Engineers, New York (1981).
41. D. M. Novak, B. V. Tilak, and B. E. Conway, in "Modern Aspects of Electrochemistry," Vol. 14, J. O'M. Bockris and B. E. Conway, Editors, p. 195, Plenum Press, New York (1982).
42. H. S. Holden and J. M. Kolb, "Encyclopedia of Chemical Technology," p. 172, John Wiley and Sons, New York (1981).
43. P. P. Anthony *et al.*, Br. Pat. 991,079 (1965).
44. M. G. DuBellay, *et al.*, U.S. Pat. 3,527,690 (1970).
45. M. Kobayashi, M. Onuma, and T. Kawakami, Japan Kokai, 7,877,900 (1978).
46. H. Westerlund, U.S. Pat. 4,098,671 (1978); 4,089,771 (1978).
47. D. W. DuBois and W. B. Darlington, U.S. Pat. 4,075,070 (1978).
48. R. C. Langley, U.S. Pat. 4,186,066.
49. A. Kaufman, A. Stawsky, and A. T. Perretta, DOE Report. no. SAN/1240-1 (1978).
50. V. S. Tulkki and T. K. Suonpera, in "Proceedings of the Oronzio DeNora Symposium: Chlorine Technology," O. DeNora, Editor, p. 246 (1979).
51. Eltech Commercial brochure titled "5KA Chlorate Cell," Eltech Systems Corporation, Chardon, OH.

Decomposition of Benzoate Ester Radical Anions

John H. Wagenknecht,* Richard D. Goodin,* Patrick J. Kinlen, and F. E. Woodard

Monsanto Company, Corporate Research Laboratories, St. Louis, Missouri 63167

ABSTRACT

The electrochemical reduction of benzoate esters in aprotic media leads to relatively stable radical anions. The radical anions decompose to electroinactive products in an initial EC mechanism. At long-time scales and/or higher concentrations, the benzoate esters begin to exhibit more complicated mechanistic behavior. The initial rates of decomposition of several benzoate ester radical anions have been determined by digital simulations of cyclic voltammograms, double potential step experiments, and rotating ring-disk techniques. On short-time scales, the reduction of *t*-butyl *p*-toluate is a good example of pure EC mechanistic behavior. The final decomposition products are many and complex for most of the esters studied, but *t*-butyl benzoate cleanly gives benzoate anion and *t*-butyl *p*-*t*-butyl benzoate.

The electrochemical reduction of benzoate esters has been studied by many workers. Coleman (1) recently reviewed the area and work is described in Baizer's (2) and Weinberg's (3) books. Horner (4) has reported the results of reduction of benzoate esters in aqueous medium. In aprotic media, benzoate esters may be reduced to radical anions which have been studied by ESR (5). Isolable products of the reduction of benzoate esters in aprotic media have been described by various workers. The reduction of phenylbenzoate led to cleavage of the carbonyl carbon-oxygen bond to form phenate and the dianion of benzil (6). Similar benzoate ester cleavage has been reported by Mairanovsky (7). Another example of cleavage of the same bond was reported in the reduction of methylbenzoate in acetonitrile to form benzoylacetonitrile (8). On the other hand, Gul'tyai has recently reported (9) that the reduction of methylbenzoate in dimethylformamide leads quantitatively to benzoate, *i.e.*, cleavage of the oxygen-methyl bond. Gul'tyai's report prompted us to report our results concerning the reduction of benzoate esters, which confirms that oxygen-alkyl bond cleavage is the major pathway of decomposition of benzoate ester radical anions in aprotic media.

Experimental

Methyl, ethyl (Eastman), *i*-propyl, and *t*-butyl benzoates (ICN Pharmaceuticals) were used as received. *t*-Butyl-*p*-toluate (bp 90°C at 3.2 torr) and *t*-butyl-*p*-*t*-butylbenzoate (bp 80°C at 0.1 torr) were prepared from the corresponding acid chlorides (Aldrich) and *t*-butyl alcohol. Tetraethylammonium perchlorate (Aldrich) was recrystallized from methanol before use. Tetraethylammonium fluoroborate (Southwestern Analytical) was used as received. Acetonitrile (Burdick & Jackson distilled in glass) was dried (10) over alumina (ICN Nutritional Biochemicals W 200 Neutral Activity grade Super 1).

*Electrochemical Society Active Member.

Coulometry was performed using a Princeton Applied Research Model 173 potentiostat with a Model 179 coulometer. GC analyses were performed with a Varian (Varian Associates, Incorporated) 3700 chromatograph with a 6 ft × 1/8 in. column packed with 10% OV-17 on 80/100 mesh Chromasorb W-AW. GC-mass spectral analyses were performed on a Finnigan-TSG GC-mass spectrometer.

Coulometry was performed in a 2.5 cm diam Nafion® 117 (E. I. du Pont de Nemours and Company) divided H cell with a 3 cm diam Hg pool cathode and 1 cm² Pt foil anode. The anolyte and catholyte were 50 ml of CH₃CN containing 0.1M Et₄N⁺ClO₄⁻. The catholyte contained ~0.5g of benzoate ester and 0.5g of phenetole (internal standard for chromatography). Electrolyses were run at -2.3V vs. SCE. The SCE was sheathed in a tube separated from the catholyte by a porous ceramic plug to minimize contamination of the catholyte with water and KCl.

At each 25C interval, a small catholyte sample was removed, treated with CH₃I, warmed a few minutes, and then analyzed by gas chromatography for remaining substrate and methylbenzoate.

The catholyte from the *t*-butyl benzoate reduction after 250C was analyzed by GC and found to contain a 35% yield of *t*-butyl-*p*-*t*-butylbenzoate, which was identified by comparison of the GC retention time and mass spectrum with an authentic sample. (Mass spectrum *M/e*(%): 163(100), 179(30), 161(18), 164(6.7), 57(5.4), 135(5.3), 178(5.2), and 91(4.1).)

All rotating ring-disk experiments were performed with a DT6 electrode from Pine Instrument Company with a platinum disk and platinum ring. The calculated collection efficiency (*N*) of this electrode is 0.176 (12). Digital simulation gives a value of 0.173. Using ferrocene as a model system, the experimental *N* value was found to be 0.173. Rotation was provided by a Pine Instrument ASR Rotator and potential control by a Tacussel (Ryaby Asso-

ciates) Bipotentiostat. The reductions were carried out in DMF, which was 0.1M in Bu_4NClO_4 and dried over activated neutral alumina. Kinetic rate constants for the decomposition of the anion radicals were determined from a working curve generated by finite difference digital simulation techniques assuming an EC mechanism (12).

The voltammetric cell was the same as the design of Buchta and Evans (13). All potentials are given with respect to a silver reference electrode (IBM Instruments) containing a filling solution of a 0.1M AgNO_3 in acetonitrile.

The hanging mercury drop electrode was of a design similar to that described by Evans *et al.* (14), while the planar platinum electrode (0.465 cm diam) was obtained from IBM Instruments.

A mercury-plated planar platinum electrode (0.290 cm diam, used for voltammetry of *i*-propyl benzoate) was prepared by alternatively oxidizing and reducing the platinum electrode above a pool of mercury. After five or six cycles at 0.1A, the negatively polarized platinum electrode was dipped into the mercury pool for approximately 5 min. The electrode was then removed from the pool while the negative potential on the electrode was maintained. Excess mercury was wiped carefully from the surface with a paper tissue. The electrode surface was renewed in this manner before each set of experiments.

The computer-controlled cyclic voltammetric apparatus consisted of an Apple II Plus[®] microcomputer (Apple Computer Incorporated), an ISAAC 9/A (Cyborg Corporation) data acquisition and control system, and an IBM Model EC/225 voltammetric analyzer. Standard IR compensation techniques were used. Figure 1 shows a

schematic diagram of the ISAAC/IBM interface. Binary outputs from the ISAAC are used to *reset* and start the voltammetric scans. The SWEEP/SWEEP signal from the IBM indicates the cyclic scan has started and triggers the ISAAC data acquisition. The fastest time interval for data acquisition is 1 ms, which matches the time constant for the IBM potentiostat. Current and potential outputs of the IBM are measured by the ISAAC in the differential mode. The potential ("X") output of the IBM is referenced to the initial potential. The gain of the A/D converters on the ISAAC is selected to optimize the full scale range of the current and voltage outputs (16). Normally, the current A/D range is $\pm 5\text{V}$, while the potential A/D range is $\pm 5\text{V}$ or $\pm 500\text{mV}$.

The double potential step experiments were performed using a microcomputer and data acquisition system developed at the University of North Carolina (15). The high speed potentiostat (constructed in-house) and electrochemical cell used in these experiments are described elsewhere (16). The electrodes were prepared by attaching a mercury drop to a Pt disk using a method reported by Bellamy (17). The excess mercury was then removed by shaking the electrode, leaving a thin mercury film.

Results and Discussion

Initial voltammetric studies of a series of benzoate esters showed the relative stability of the radical anions to be from most stable to least stable: ethyl \approx isopropyl, *t*-butyl (Fig. 2). Initial attempts to calculate the rate of decomposition of the radical anions using the technique of Nicholson and Shain (18) gave values for k_f , which varied

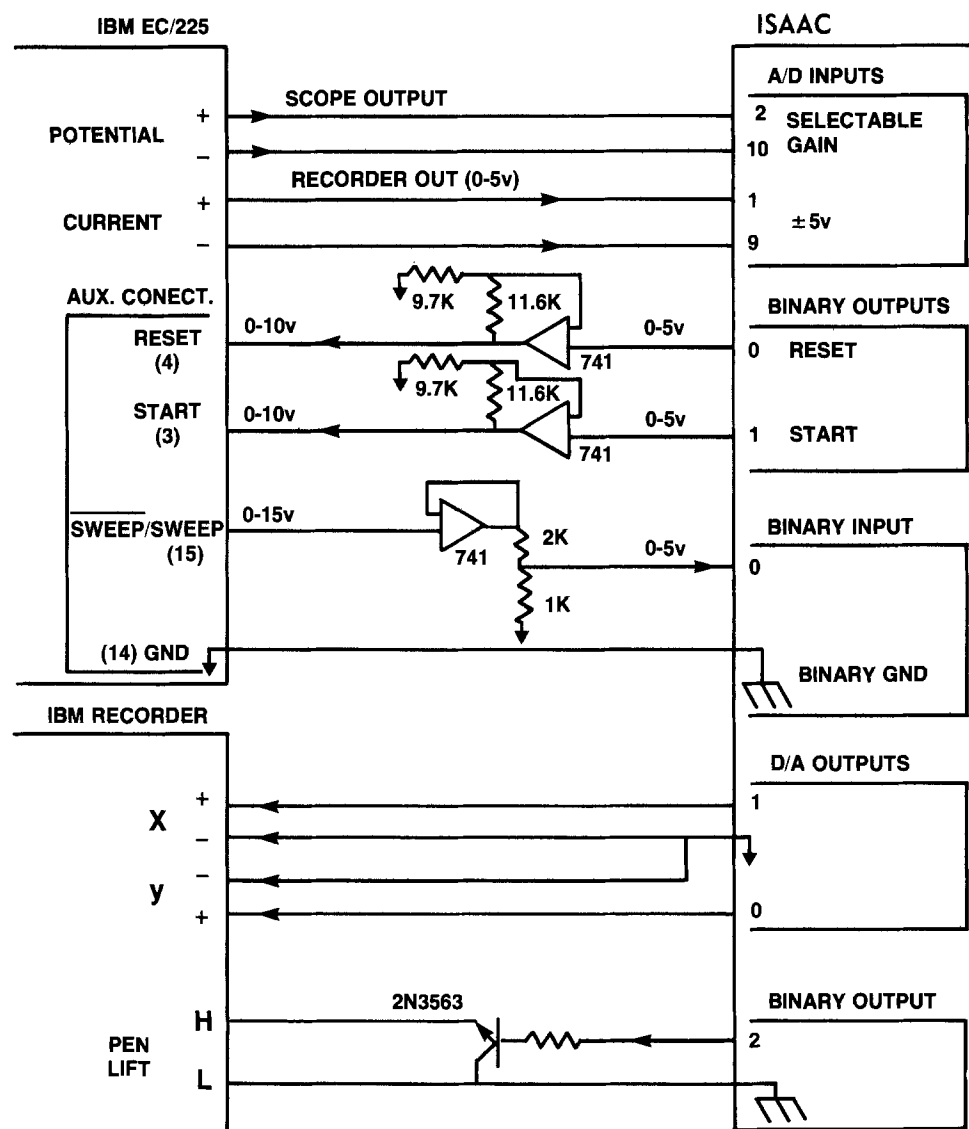


Fig. 1. Schematic diagram of the ISAAC 9/A—IBM EC/225 interface.

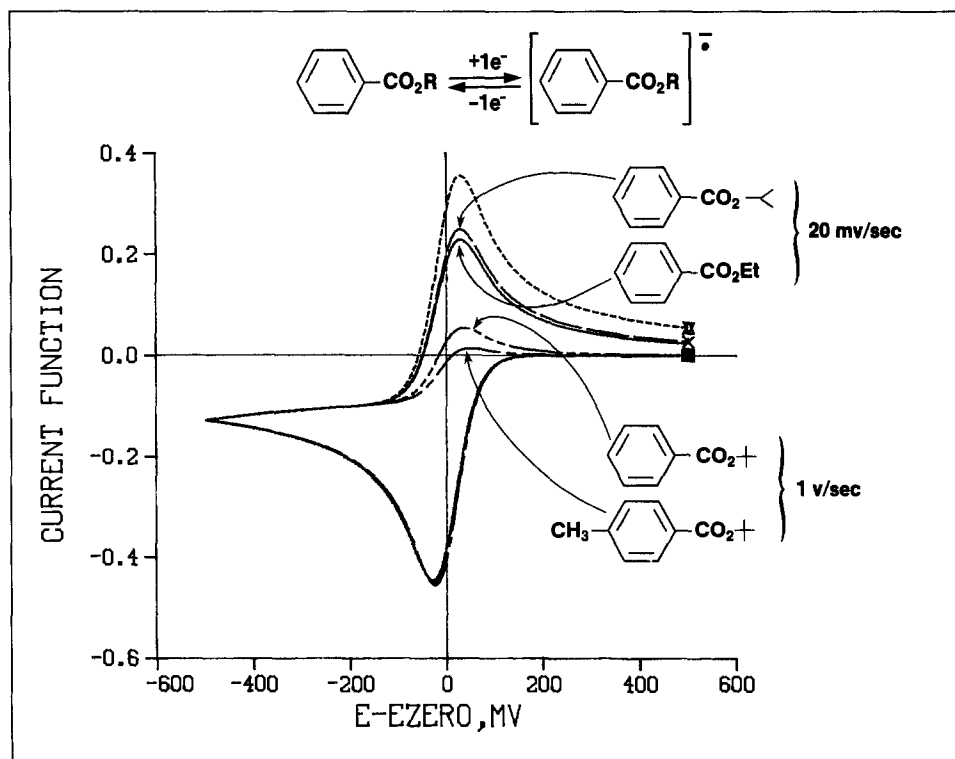
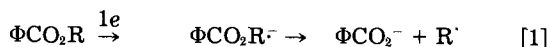


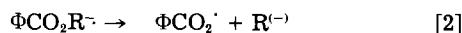
Fig. 2. Superimposed voltammograms of the reduction of various benzoate esters. The dashed line represents a total reversible system.

with sweep rate. This is thought to be due to the fact that the return peak current is difficult to measure accurately when the decomposition rate is fast.

The relative rates of decomposition of the radical anions were significant in that they suggest the following decomposition pathway



The reasoning is that the relative rates of decomposition of the radical anions are in the same order as the stability of the cleaved alkyl radical. If the cleavage led to benzoyloxy radical and alkyl anion



then the relative rates of cleavage ought to be reversed; *i.e.*, ethyl anion is a lower energy species than *t*-butyl anion and, therefore, the *t*-butyl ester radical anion should have been most stable.

Coulometric analyses of the electroreductions of *i*-propyl benzoate and *t*-butyl benzoate and *t*-butyl *p*-toluate were carried out with solution analysis at regular intervals during the electrolyses. Catholyte samples were removed, treated with methyl iodide, and analyzed by GC. By that method, the disappearance of starting ester and appearance of benzoate anion (analyzed as the methyl ester) were monitored. The results are shown in Fig. 3-5. Least squares plot of the ester concentration show 1.12 and 1.18 F/mol reduction, respectively, for the *i*-propyl benzoate and *t*-butyl benzoate.

Benzoate ion is formed at a yield much lower than the proposed mechanism would require. In the case of *i*-propyl benzoate, the yield of benzoate ion is only 25%. A complex mixture of other products is formed. A similar result was obtained in the reduction of methyl benzoate in DMF or acetonitrile. Again, only about a 30% yield of benzoate ion was obtained [as opposed to the 100% reported by Gul'tyai (9)], and a complex mixture of products was observed by gas chromatography. We were unable to detect benzoylacetonitrile in the reduction of methylbenzoate in CH_3CN as reported previously (8).

t-Butylbenzoate was better behaved, cleanly yielding about 65% of benzoate ion and about 35% of *t*-butyl *p*-*t*-butylbenzoate. A pathway for the formation of those products is shown in Fig. 6. The initially formed ester radical anion cleaves to form benzoate ion and *t*-butyl radi-

cal. In addition to other reaction pathways for *t*-butyl radical, it may attack unreduced ester. By some means, that initially formed adduct must lose a hydrogen and add an electron to give the observed product and allow for the observed 1F/mol disappearance of initial ester.

There are several possible means of meeting both requirements. The initial adduct radical may lose the 4-hydrogen atom to an acceptor, which is subsequently reduced at the electrode or by the ester radical anion. Another possibility is that the radical adduct is reduced to the corresponding anion, which could lose hydride to an

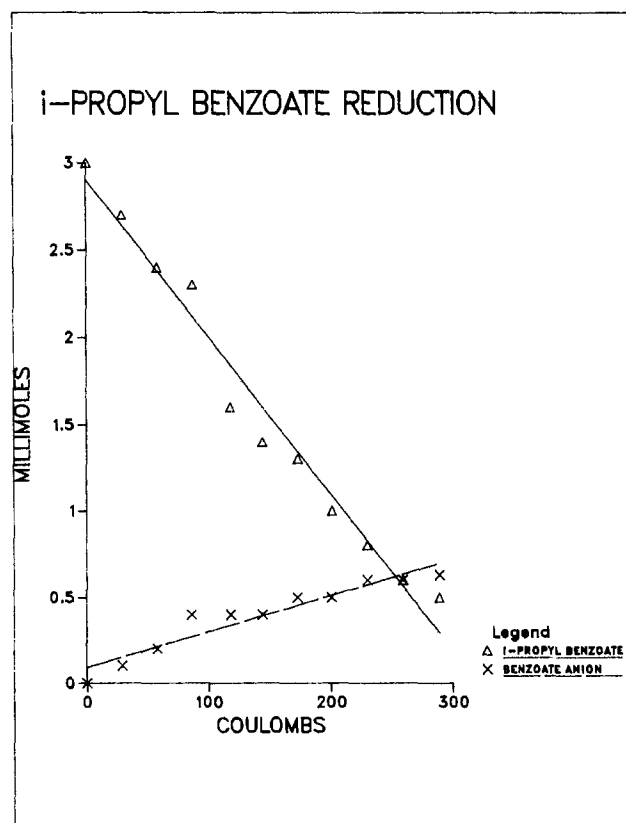
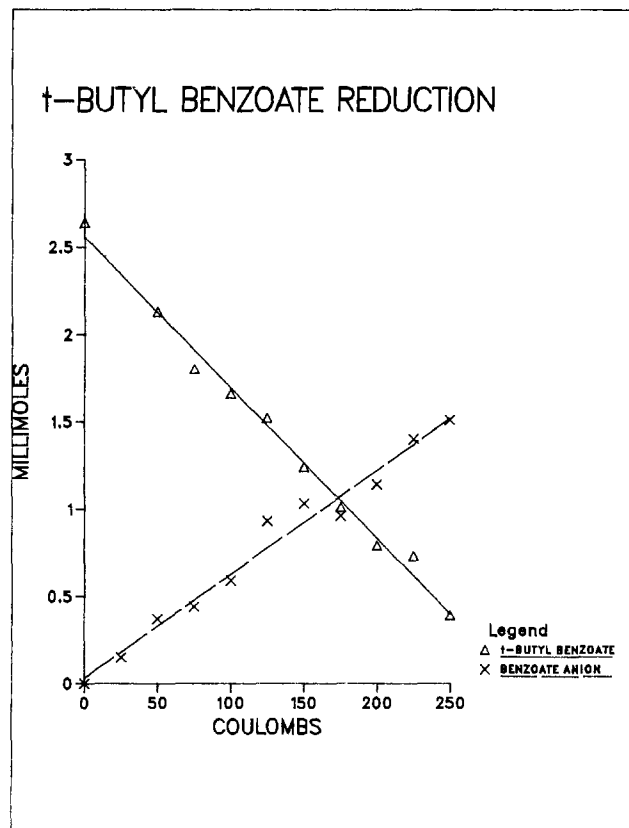
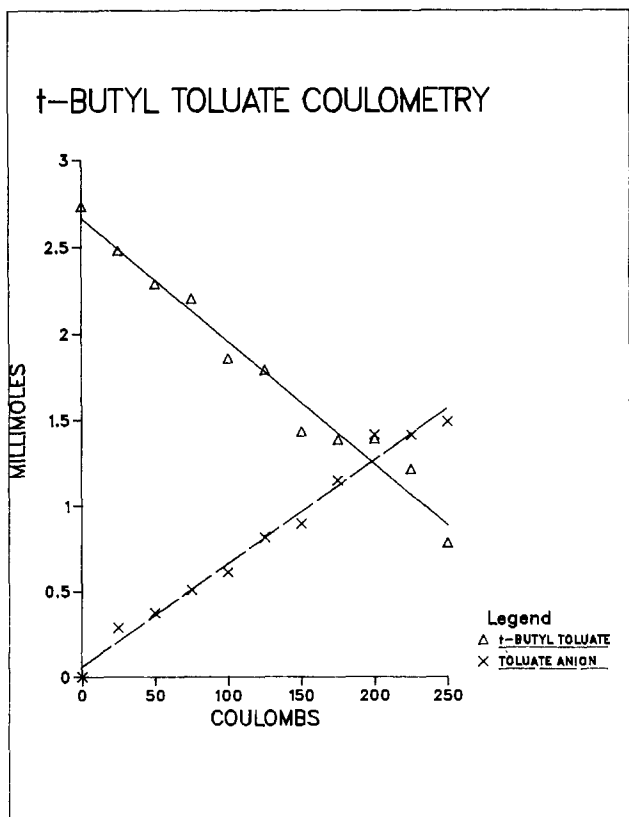
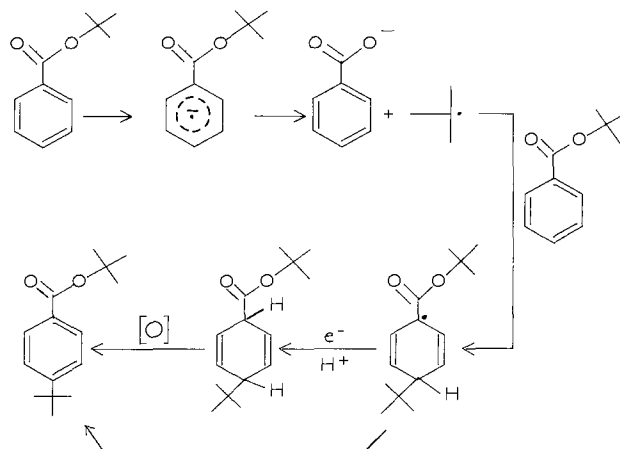


Fig. 3. Coulometry of *i*-propyl benzoate

Fig. 4. Coulometry of *t*-butyl benzoate

acceptor forming the product ester, or be protonated to the dihydro derivative shown. The dihydro compound might be oxidized on workup or in the gas chromatograph to the observed product, although we consider that quite unlikely.

Another possible reaction pathway is the reaction of the benzoate radical anion with *t*-butyl radical to form the ad-

Fig. 5. Coulometry of *t*-butyl *p*-toluateFig. 6. Reduction pathway for *t*-butylbenzoate

duct anion, which might be protonated to the dihydro derivative or electron transfer to substrate, forming the adduct radical.

As will be indicated later, *t*-butyl *p*-toluate is the best example of a simple EC mechanism by electroanalytical techniques at 1 mM concentration. The coulometry at 50 mM concentration is not as clean, giving 1.31 F/mol. This indicates reactions after radical anion cleavage, which lead to products that are also reduced. As shown in Fig. 5, the yield of *p*-toluate ion is only 65%.

Our first attempt at improving (compared to crude cyclic voltammetry) the kinetic data for benzoate ester radical anion decomposition was to use the rotating ring-disk technique. For *t*-butyl-*p*-toluate, a plot for disk diffusion limited current ($i_{D,1}$) vs. $\omega^{1/2}$ was linear at rotation rates of 500-3200 rpm with a correlation coefficient of 0.99996. Constant current was applied to the disk at levels corresponding to various points on the rising portion of the voltammetric wave. The collection efficiency at 1000 rpm was fairly constant (0.086 ± 0.0002) at $i_p/i_{D,1}$ ratios from 0.30 to 0.92. This behavior is indicative of a first order EC mechanism (19).

The collection efficiency was measured with the disk potential held on the limiting plateau at rotation rates of 500-3000 rpm. The rate constant for anion radical decomposition as determined from digital simulation working curves was $0.34 \pm 0.05 \text{ s}^{-1}$. For *t*-butylbenzoate, the rate constant for anion radical decomposition was determined in a similar manner to the toluate and found to be $(9.8 \pm 0.4) \times 10^{-2} \text{ s}^{-1}$.

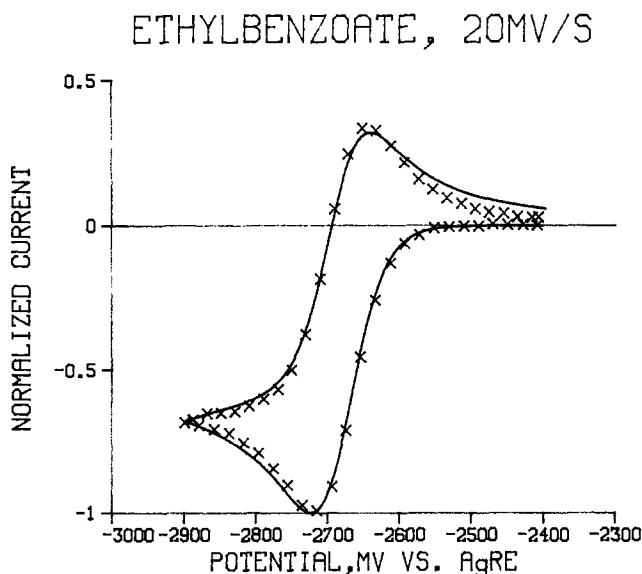


Fig. 7. Voltammogram (XXX) and digital simulation (—) for ethyl benzoate.

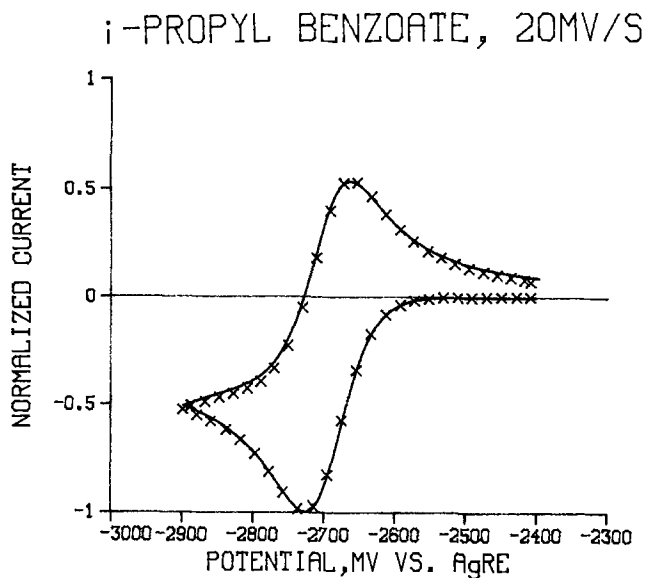


Fig. 8. Voltammogram (XXX) and digital simulation (—) for *i*-propyl benzoate.

The rate constants determined by the rotating ring-disk method are significantly lower than those determined by electrochemical techniques described later. This may be due to an artifact which results from the necessity of using rigorously anhydrous solvents and very negative potentials to study these compounds. The Teflon shroud housing the electrode assembly showed darkly colored areas on the surface radiating outward from the electrode. We believe that this is due to reduction of the Teflon by the anion radicals. Reduction of polytetrafluoroethylene is known to yield surface carbon layers which can have appreciable conductivity in the reduced form (20). Reduction of the surface of the insulating spacer between the disk and ring electrodes could conceivably produce a resistive current leakage pathway, which could make the ring currents higher than expected and, thus, result in lower rate constants. This technique was abandoned for this application.

We then turned to digital simulation of cyclic voltammetry (22), carried out under more rigorously controlled conditions than had been done previously.

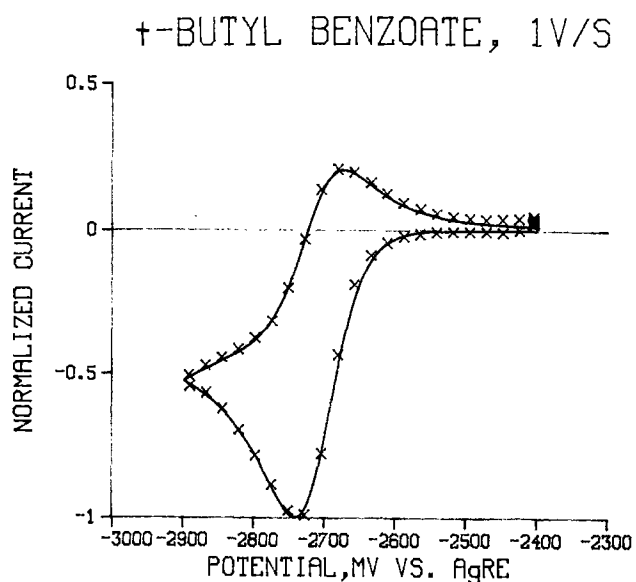


Fig. 9. Voltammogram (XXX) and digital simulation (—) for *t*-butyl benzoate.

Digital simulations were run assuming quasi-reversible electron transfer followed by a first-order chemical step. (Incorporation of slow electron transfer was required to obtain good fits for *t*-butyl benzoate and *t*-butyl-*p*-toluate.) Best fits were obtained visually, the important kinetic parameter being k_f/a , where k_f is the rate constant for the chemical step and a is related to the sweep rate, ν , by the expression $a = nF\nu/RT$.

The cyclic voltammograms for various esters and the digital simulation curves are shown in Fig. 7-10. For ethyl and *i*-propyl benzoate, scan rates of 50 mV/s or less were required to detect the effect of the chemical reaction of the reverse peak. At these low scan rates, spherical diffusion equations were required in the simulation to obtain good fits when using the HMDE. These are quite good fits, verifying that the reduction of benzoate esters involves a simple EC mechanism. The values of k_f are shown in Table I.

The results of the preparative experiments show that since *t*-butyl *p*-*t*-butylbenzoate is formed in the reduction of *t*-butyl benzoate, the reaction is not simply EC but

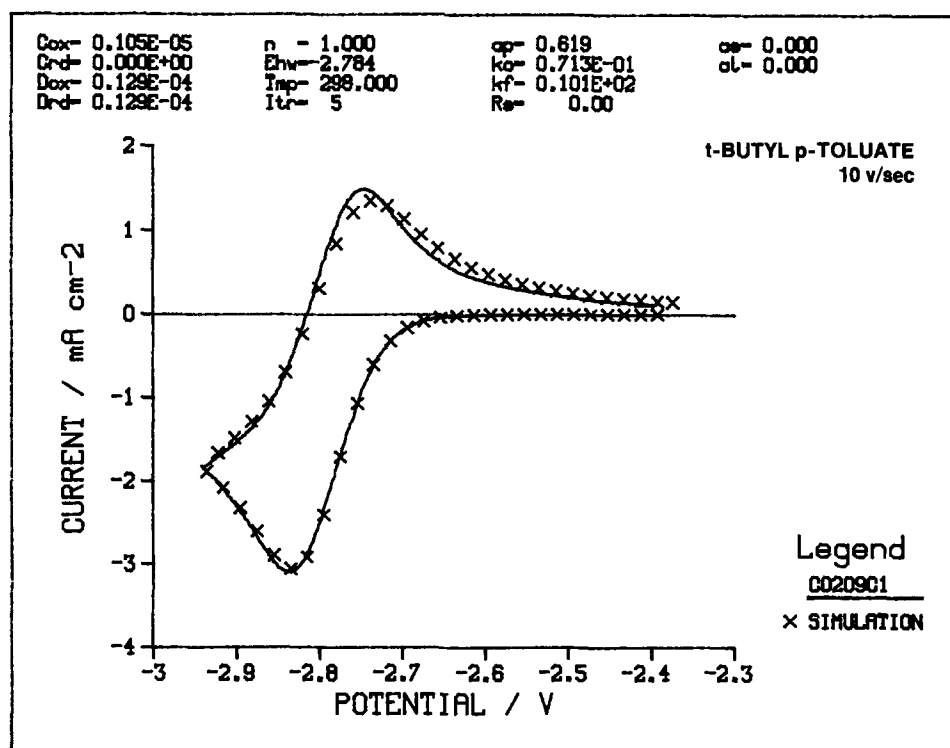


Fig. 10. Voltammogram (—) and digital simulation (XXX) for *t*-butyl-*p*-toluate.

Table I.

Benzoate ester	$E_{1/2}^a$	k_f (s^{-1})	Min. ^b scan rate
Ethyl benzoate	-2683	0.015 ± 0.002^c	<10
Isopropyl benzoate	-2710	0.012 ± 0.002	<10
<i>t</i> -butyl benzoate	-2710	4.3 ± 0.2	200
<i>t</i> -butyl <i>p</i> -toluate	-2784	10.1 ± 0.2	1000

^a MV vs. Ag/0.1M AgNO₃/acetonitrile reference electrode (AgRE).

^b Minimum scan rate (mV/s) required to see a return peak.

^c Variation required to see a deviation from "best fit" curve.

complicated by side reactions. It seems likely that the difference in results between preparative experiments and electroanalytical experiments may be explained by the large difference in concentration of the two types of experiments (50 mM for coulometry vs. 1 mM for electroanalytical experiments).

t-Butyl radical has been reported (23) to reduce in other systems between -2.8 and -3.0V (corrected to our Ag ref-

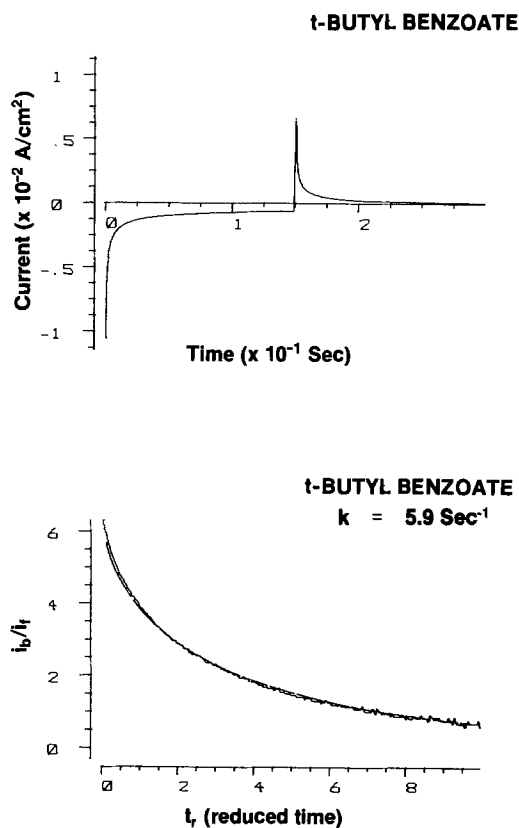
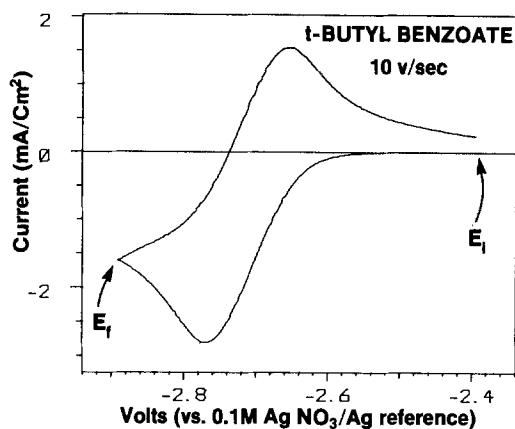


Fig. 11. (Top) Voltammogram of *t*-butylbenzoate showing E_i and E_f used in the double potential step equipment. (Center) Current/time trace from the double potential step experiment. (Bottom) Current ratio vs. reduced time. (Jagged line) data, (smooth line) least squares fit.

erence electrode). We see no evidence of this in our system either directly or as an ECE component. We have not reexamined the previous substrates in our system as a control; however, the absence of direct electrochemical evidence for *t*-butyl radical reduction, considering the modest reaction rates for our cleavage reactions, is not particularly disconcerting.

Double potential step experiments (15) were carried out to obtain independent verification of the EC mechanism and radical anion decomposition rate constants. Each potential step experiment was done both with and without the redox couple (i.e., the benzoate ester) present. This allowed the current/time profiles to be corrected for double layer charging and background faradaic processes.

The relaxation currents measured during double potential step experiments were analyzed by a method similar to that of Schwarz and Shain (21). The homogeneous rate constant was determined from a nonlinear least squares fit of the dimensionless current ratio (i.e., the current flowing after the forward step (I_f) divided by the reverse step current (I_b) at corresponding times after each step) plotted as a function of the reduced time (i.e., the time after each step divided by the duration of the forward step). Our method, which will be described in detail in a later paper, is an improvement over the method used by Schwarz and Shain in that the entire curve is used rather than just a single point. The nonlinear least squares fitting procedure, which was done on the UNC microcomputer, was complete in several minutes. A graphic display of the fit obtained during successive iterations was provided.

Figure 11 shows graphically the series of steps involved in obtaining the rate constant for *t*-butyl benzoate. Figure 12 shows the data and digital simulation fit for *t*-butyl *p*-toluate. The rate constants obtained were 5.9 and 10.0 s^{-1} , respectively, which were very near the results obtained for those two compounds by digital simulation of the cyclic voltammetry.

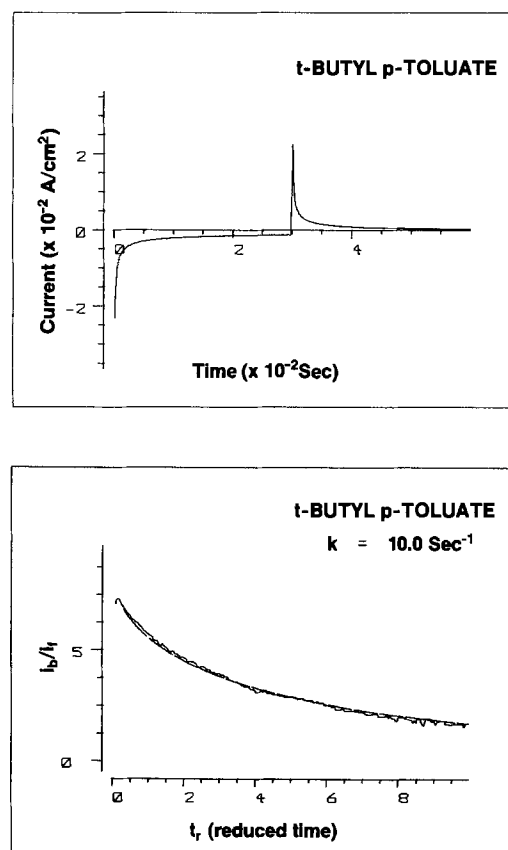


Fig. 12. (Top) Current/time trace from double potential step experiment with *t*-butyl-*p*-toluate. (Bottom) Current ratio vs. reduced time. (Jagged line) data, (smooth line) least squares fit.

The double potential step method is particularly attractive for measuring the homogeneous rate constant for EC systems because the number of variables used for fitting can be reduced to one. By stepping to a sufficiently forcing potential, the electrochemical reaction becomes diffusion controlled, and thus the charge transfer rate parameters have no influence on the relaxation currents. The dependence on electrode area as well as the dependence on the concentration and diffusion coefficient of the electroactive species is removed by using the ratio of the forward and reverse currents.

In conclusion, we have demonstrated by several methods (voltammetry, double potential step experiments, coulometry, and product isolation) that the reduction of benzoate esters in dilute (1 mM) nonaqueous medium involves an EC mechanism. The system becomes more complex at higher concentrations. The initially formed radical anion cleaves to form benzoate ion and alkyl radical. This is one of a very few examples of the reduction of organic compounds by an EC mechanism.

Manuscript submitted Aug. 12, 1983; revised manuscript received Dec. 22, 1983. This was Paper 641 presented at the San Francisco, California, Meeting of the Society, May 8-13, 1983.

Monsanto Company assisted in meeting the publication costs of this article.

REFERENCES

- J. P. Coleman, in "Chemistry of Acid Derivatives," Saul Patai, Editor, Chap. 13, John Wiley & Sons, New York (1979).
- L. Ebersson, in "Organic Electrochemistry," M. M. Baizer, Editor, Chap. X, Marcel Dekker, Inc., New York (1973).
- M. R. Rifi, "Technique of Electroorganic Synthesis," Part II, N. L. Weinberg, Editor, Chap. VIII, John Wiley & Sons, New York (1975).
- L. Horner and H. Honl, *Liebigs Ann. Chem.*, **2036** (1977).
- M. Hirayama, *Bull. Chem. Soc. Jpn.*, **40**, 1822 (1967).
- R. Seeber, F. Mango, G. Bontempelli, and A. Mazzocchin, *J. Electroanal. Chem. Interfacial Electrochem.*, **72**, 219 (1976).
- V. G. Mairanovsky, *Angew. Chem.*, **15**, 281 (1976).
- L. Kistenbrugger, P. Mischke, J. Voss, and G. Wiegand, *Liebigs Ann. Chem.*, 461 (1980).
- V. P. Gul'tyai, T. Ya. Rubinskaya, and L. M. Korotaeva, *Bull. Acad. Pol. Sci. Ser. Sci. Chem.*, 1499 (1982).
- O. Hammerich and V. D. Parker, *Electrochim. Acta*, **18**, 537 (1973).
- K. B. Prater and A. J. Bard, *This Journal*, **117**, 335 (1970).
- W. J. Albery and S. Bruckenstein, *Trans. Faraday Soc.*, **62**, 1920 (1966).
- R. C. Buchta and D. H. Evans, *Anal. Chem.*, **40**, 2181 (1968).
- P. E. Whitson, H. W. Vandenberg, and D. H. Evans, *ibid.*, **45**, 1298 (1973).
- F. E. Woodard, W. S. Woodward, and C. N. Reilly, *ibid.*, **53**, 1251A (1981); F. E. Woodward, R. D. Goodin, P. J. Kinlen, and J. H. Wagenknecht, *ibid.*, Submitted for publication.
- F. E. Woodard, Ph.D. Dissertation, University of North Carolina, Chapel Hill, NC (1982).
- A. J. Bellamy, *Anal. Chem.*, **52**, 607 (1980).
- R. S. Nicholson and I. Shain, *ibid.*, **36**, 706 (1964).
- V. J. Puglisi and A. J. Bard, *This Journal*, **119**, 833 (1972).
- D. J. Barker, D. M. Brewis, R. H. Dahm, and L. R. J. Hoy, *Electrochim. Acta*, **23**, 1107 (1978).
- W. M. Schwartz and I. Shain, *J. Phys. Chem.*, **69**, 30 (1965).
- S. W. Feldberg, "Electroanalytical Chemistry," Vol. 3, pp. 199-296, Marcel Dekker, New York (1969).
- R. Breslow and R. Goodin, *J. Am. Chem. Soc.*, **98**, 6076 (1976), and references therein.

Rotating Ring-Disk Electrode Study of Competitive Photo-oxidation at α -Fe₂O₃ Photoanodes in Aqueous Solution

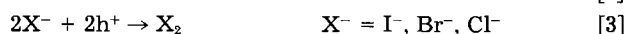
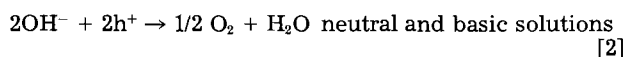
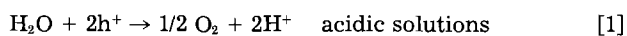
Menahem Anderman* and John H. Kennedy

Department of Chemistry, University of California, Santa Barbara, California 93106

ABSTRACT

Competition reactions at α -Fe₂O₃ photoanodes were studied using the RRDE technique. It was found that iodide, bromide, and chloride ions were photo-oxidized in preference to water in acidic solutions. The competition ratio was measured as a function of halide-ion concentration, halide-ion flux, light intensity, electrode potential, and solution pH. A direct correlation between the disk photocurrent and the competition ratio at a given halide flux was demonstrated. A lack in selectivity for the dark current was also observed.

Photogenerated holes (h⁺) at an *n*-type semiconductor electrode/aqueous electrolyte interface are capable of oxidizing halide ions, as well as water and other reducing agents. The general scheme for such reactions is



Such reactions have been studied previously using bulk electrolysis (1, 2) as well as rotating ring-disk electrode (RRDE) techniques (3-6). General trends that have been observed include: (i) X⁻ is photo-oxidized in preference to water in acidic solutions, and (ii) the percentage of X⁻ oxidation (ϕ_{X_2}) decreases with increasing pH and decreasing X⁻ concentration. The only attempt to correlate competitive photo-oxidation with the disk electrode current was

carried out by Kobayashi *et al.* on an *n*-TiO₂ electrode (6).

We report here RRDE measurements of competitive photo-oxidation at α -Fe₂O₃ electrodes. In addition to testing the general trend described above for the α -Fe₂O₃ case, we have quantitatively correlated the disk current with the flux of X⁻ to the electrode surface. Questions probed were: (i) Does such a correlation exist? (ii) Can a simple kinetics scheme account for all available data? (iii) Do other parameters such as electrode potential or light intensity influence the competition, or is it only the overall availability of holes at the electrode surface that determines the competition at a given X⁻ flux? (iv) Does the dark current show the same competition characteristics as the photocurrent?

Experimental

Polycrystalline pellets of α -Fe₂O₃ (1 atom percent [a/o] SiC doped) were prepared as described previously (7). The procedure for assembling these disks into the RRDE has also been described in a previous publication (8). The

* Electrochemical Society Active Member.

Key words: α -Fe₂O₃ photoanode, competition reactions, photo-electrochemistry, rotating ring-disk electrode.

Pt ring was pretreated by polishing with fine alumina powder and washing with deionized water in an ultrasonic bath. Before taking measurements, the ring was cycled between the potentials for oxygen evolution and hydrogen evolution until reproducible I-V curves were obtained. The measured collection efficiency for the $\alpha\text{-Fe}_2\text{O}_3$ -disk/Pt-ring was $N_0 = 0.134 \pm 0.003$, while the collection efficiency for a Pt-disk/Pt-ring of the same size was 0.135. These values show fair agreement with the calculated collection efficiency of 0.143 using the formula of Albery and Bruckenstein (9). The disk area was 0.307 cm^2 .

It should be noted that the $\alpha\text{-Fe}_2\text{O}_3$ disk was somewhat porous and was not polished to avoid deleterious surface defects (8, 10). This created some operating limitations as follows:

1. Collection efficiency dropped at high rotation speeds, $\omega > 1000 \text{ rpm}$. Therefore, all quantitative studies were carried out at $\omega \leq 470 \text{ rpm}$, which was well within the satisfactory operating region.

2. At disk current densities above 2 mA/cm^2 , oxygen bubbles were adsorbed on the surface and disturbed solution flow to the ring, resulting in a drop in ring current.

3. Some I_2 , Br_2 , and Cl_2 apparently diffused into the $\alpha\text{-Fe}_2\text{O}_3$ pores. A few seconds of induction time were required before steady-state collection currents were observed. This problem was especially severe for iodine, which has been reported before (11).

The electrochemical cell was a 200 ml all-quartz cylinder, covered with a teflon lid. The cell included a SCE reference, Pt-wire counterelectrode separated from the main compartment by fritted glass, and gas entry tubes.

The electrochemical cell was a 200 ml all-quartz cylinder, covered with a Teflon lid. The cell included a SCE with two X-Y recorders to monitor both ring and disk currents. All experiments were conducted at ionic strength equal to 1.0, which was adjusted with NaClO_4 as the supporting electrolyte. Experiments in the pH range 2.0-6.4 were carried out in phosphate buffers (0.02-1M). It should be noted that carboxylic acid-based buffers can be oxidized at $\alpha\text{-Fe}_2\text{O}_3$ (12) and, therefore, are not suitable. Full light intensity of the 150W xenon lamp, filtered by an IR filter and focused with a quartz lens, was 500 mW/cm^2 at the electrode surface. Neutral density filters were used to reduce this intensity when desired.

Ring current-ring potential (I_R - V_R) scans were taken at a rate of 33 mV/s at constant disk potential (and constant disk current). Disk current-disk potential/ring current

scans (I_D - V_D/I_R) were taken at a rate of 2 mV/s at a predetermined ring potential. Alternatively, some I_D/I_R data were obtained pointwise with the disk potential stepped in 50 mV intervals.

Results

Bromide oxidation in 1M acid.—Ring current-ring potential (I_R - V_R) curves in $0.2M \text{ HBr}/0.8M \text{ HClO}_4$ solution are shown in Fig. 1 (curves 1-3). Curve 1 was recorded for an oxygen-free solution in the dark with zero disk current. Curve 2 was recorded for the same solution in the light with a disk current of $1000 \mu\text{A}$ ($1V$ vs. SCE). A diffusion-limited plateau for the collection of Br_2 at the ring is evident. The plateau extended from $+0.35V$ vs. SCE to $-0.15V$ vs. SCE, at which point reduction of water begins. Efficiency of bromine production at the disk is given by Eq. [4]

$$\phi_{\text{Br}_2} = \frac{I_D(2\text{Br}^- \rightarrow \text{Br}_2)}{I_{D,\text{total}}} = \frac{I_R(\text{Br}_2 \rightarrow 2\text{Br}^-)}{N_0 I_{D,\text{total}}} \quad [4]$$

Curve 3 of Fig. 1 is the I_R - V_R curve for an oxygen-saturated solution when $I_D = 0$. Oxygen detection at the ring begins at $+0.2V$ vs. SCE. Thus it is possible to detect both O_2 and Br_2 when they are produced simultaneously at the disk electrode, as shown in curve 4 of Fig. 1.

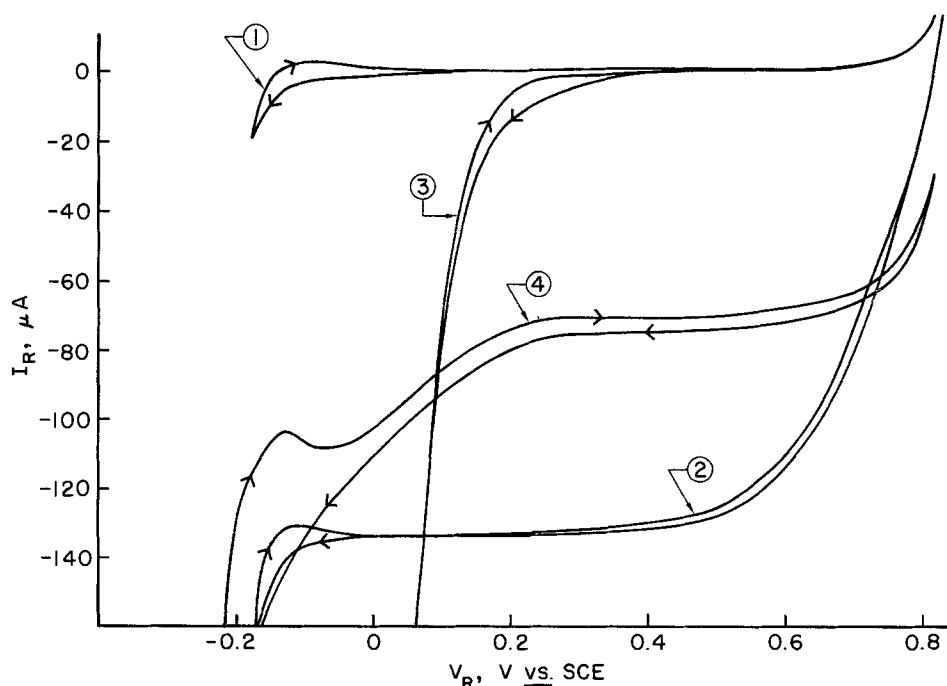
Bromine production efficiency was 100% for a $0.1M \text{ HBr}/0.9M \text{ HClO}_4$ solution at all light intensities studied (33 - 500 mW/cm^2) and for disk potentials of 0.3 - $1.4V$ vs. SCE.

Bromine production efficiency (ϕ_{Br_2}) as a function of disk photocurrent for a $0.01M \text{ KBr}/1M \text{ HClO}_4$ solution is shown in Fig. 2. It is clearly seen that production efficiency drops at high disk currents. The flux of Br^- to the disk electrode may be calculated by the well-known Levich equation

$$\text{Flux} = I_D^{\text{dl}} = 0.62 nAFD^{2/3} \nu^{1/6} C_b \omega^{1/2} \quad [5]$$

where I_D^{dl} is the diffusion limited current (mA), n is the number of electrons transferred in the reaction, F is the Faraday constant, A is the electrode area (cm^2), D is the diffusion coefficient (cm^2/s), ν is the kinematic viscosity (cm^2/s), ω is the angular velocity (rad/s), and C_b is the concentration of the diffusing species (M) in the bulk solution. At the Br^- concentration shown in Fig. 2, the calculated flux is $1920 \mu\text{A}$. For all disk currents below $1920 \mu\text{A}$, one would expect $\phi_{\text{Br}_2} = 100\%$ if flux of Br^- to the disk electrode is the controlling factor. Above $1920 \mu\text{A}$ the efficiency should be given by Eq. [6]

Fig. 1. Ring current-ring potential for $0.2M \text{ HBr}/0.8M \text{ HClO}_4$ (curves 1-3); and for $2 \times 10^{-3} \text{ HBr}/1M \text{ HClO}_4$ (curve 4). Rotation frequency = 470 rpm . Curve 1: oxygen-free solution, $I_D = 0 \mu\text{A}$. Curve 2: oxygen-free solution, $I_D = 1000 \mu\text{A}$. Curve 3: oxygen-saturated solution, $I_D = 0 \mu\text{A}$. Curve 4: oxygen-free solution, $[\text{Br}^-] = 2 \times 10^{-3}M$, $I_D = 1000 \mu\text{A}$.



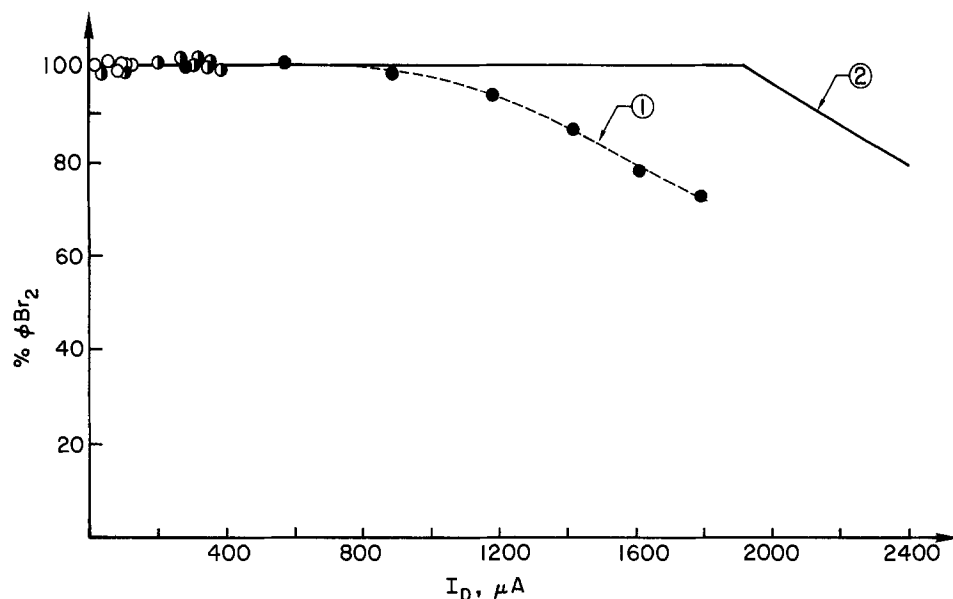


Fig. 2. Bromine production efficiency as a function of disk current (I_D) for 0.01M KBr/1M HClO_4 . Curve 1: experimental data; \bullet full light, \circ 18% of full light, and \circ 6.7% of full light. Curve 2: calculated for 100% oxidation of Br^- flux.

$$\phi_{\text{Br}_2} = \frac{\text{Flux}(\text{Br}^-)}{I_D} \quad [6]$$

The calculated production efficiency is shown as curve 2 in Fig. 2.

The influence of mass transfer is more clearly seen in Fig. 3. Here, disk current-disk potential/ring current (I_D - V_D / I_R) curves are shown for a 10^{-3}M KBr/1M HClO_4 solution. At low current density at the disk, the ring collection current follows the disk current closely with $\phi_{\text{Br}_2} > 95\%$. At higher disk currents, the ring current tends to plateau. The Br^- flux for this solution calculated by Eq. [5] is 192 μA and the maximum ring current would be $0.134 \times 192 = 26 \mu\text{A}$. This compares well with the experimental value of 22 μA shown in Fig. 3.

The possible influence of light intensity and electrode potential on bromine production efficiency was checked with I_D - V_D / I_R curves taken at three different light intensities and shown in Fig. 4. It is apparent that neither light

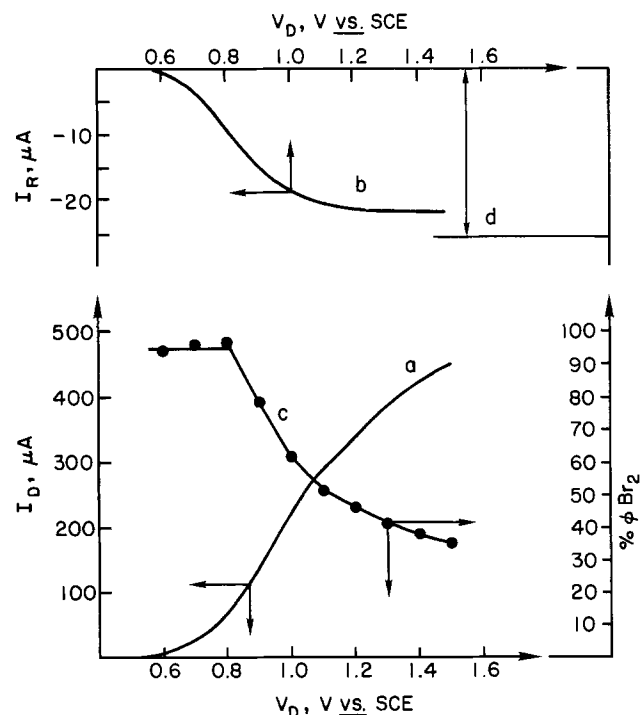


Fig. 3. Disk current-ring current/disk potential for 10^{-3}M KBr/1M HClO_4 , 18% of full light. a: disk current. b: ring current. c: bromine production efficiency, ϕ_{Br_2} . d: calculated diffusion-limited plateau value for detection of Br_2 at the ring.

intensity nor electrode potential has any effect on the electrode reaction. Only the availability of holes at the surface (*i.e.*, the current density) will determine the competition ratio at a given Br^- flux. The solid line in Fig. 4 was calculated using Eq. [6], and the agreement with experiment is excellent.

Bromide oxidation at higher pH.— I_R - V_D / I_D curves for 0.02M KBr at pH 2.0 (phosphoric acid buffer) are given in Fig. 5. At low disk current, *i.e.*, 200 μA , $>95\%$ of production efficiency for bromine was observed (curve 2). Production efficiency dropped to 90% when I_D was 400 μA (curve 3) and to 60% when I_D was 900 μA (curve 4). For the last case, oxygen was also detected at the ring.

Bromine production efficiency as a function of disk current for various weakly acidic solutions is shown in Fig. 6. At pH 2.0, essentially the same results were obtained for the three different light intensities investigated. However, the Br^- flux to the disk for these conditions was 3840 μA , considerably higher than the maximum disk current at which ϕ_{Br_2} was still nearly 100%. The same qualitative picture was obtained at higher pH (curve b in Fig. 6) with ϕ_{Br_2} decreasing with increasing pH, as observed previously (3, 5).

For solutions containing 1M KBr ϕ_{Br_2} was 100% even at pH's as high as 4.2. Only at pH 6.4 was a decrease in ϕ_{Br_2} to 92% (curve c in Fig. 6) observed. Although this drop was small, it was outside experimental uncertainty, and, in addition, oxygen was detected at the ring.

At pH 12.2 no trace of Br^- oxidation was observed even for a 0.5M KBr solution. The I_R - V_D / I_D curves were not affected by the addition of Br^- to the solution. Plateau currents for oxygen reduction at the ring were observed (Fig. 7) with $\phi_{\text{O}_2} > 95\%$.

Chloride oxidation.—Photo-oxidation of chloride at $\alpha\text{-Fe}_2\text{O}_3$ electrodes competes effectively with water in strongly acidic solutions, as can be seen in Fig. 8 (curves 1 and 2). The production efficiency for Cl_2 in 1M HCl remained $> 95\%$ at all disk currents studied, but a small drop was seen at high current levels for 0.1M HCl/0.9M HClO_4 solutions (curve 2). This drop in efficiency was more pronounced when the concentration of chloride was decreased to 0.01M (curve 4). Also, ring voltammograms exhibited 3-4 reduction waves. For solutions containing $2 \times 10^{-3}\text{M}$ HCl/1M HClO_4 , in which chloride flux to the surface was equivalent to 330 μA , the dependence of ϕ_{Cl_2} on I_D was strong even at low disk current levels (curve 5).

As expected, ϕ_{Cl_2} dropped considerably as the pH was increased with efficiency values of 70-80% at pH 2.0 (curve 3 of Fig. 8) and $< 30\%$ and 200 μA at pH 4.0 (curve 6). No dependence on light intensity or electrode poten-

Fig. 4. Bromine production efficiency as a function of disk current (I_D) for $10^{-3}M$ KBr/ $1M$ HClO₄. Broken line: experimental; ● full light, ○ ▲ 18% of full light (two samples), and ○ 6.7% of full light. Solid line: calculated for 100% oxidation of Br⁻ flux.

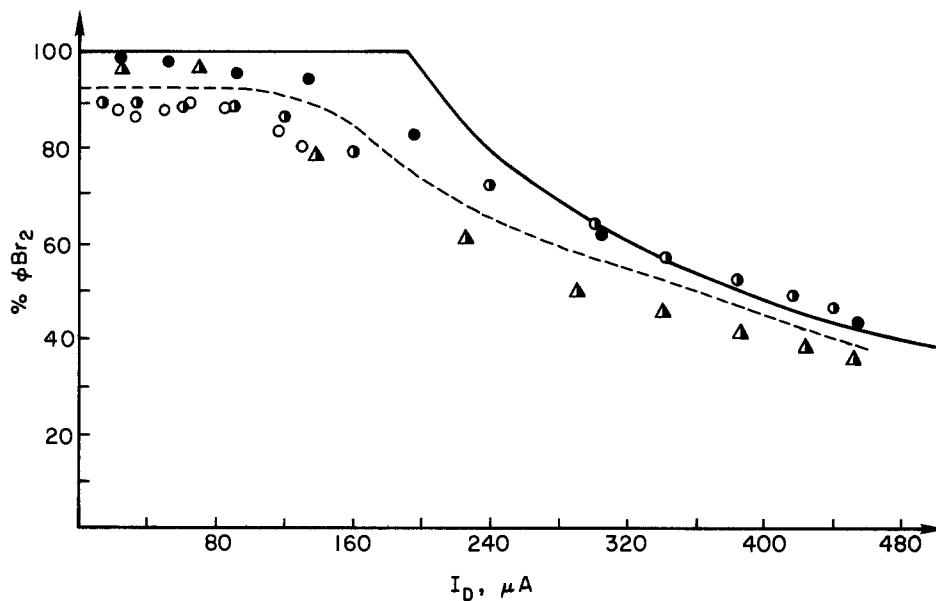


Fig. 5. Ring current-ring potential/disk current for 0.02M KBr, pH 2.0 (phosphoric acid buffer), oxygen-free, full light. Curve 1: $I_D = 0 \mu A$. Curve 2: $I_D = 200 \mu A$. Curve 3: $I_D = 400 \mu A$. Curve 4: $I_D = 900 \mu A$.

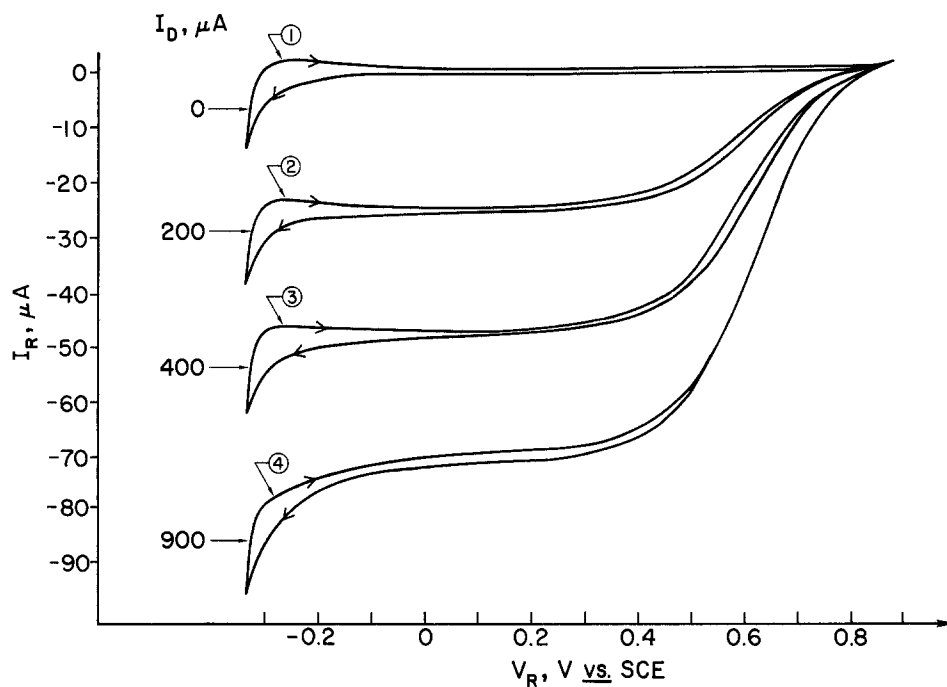
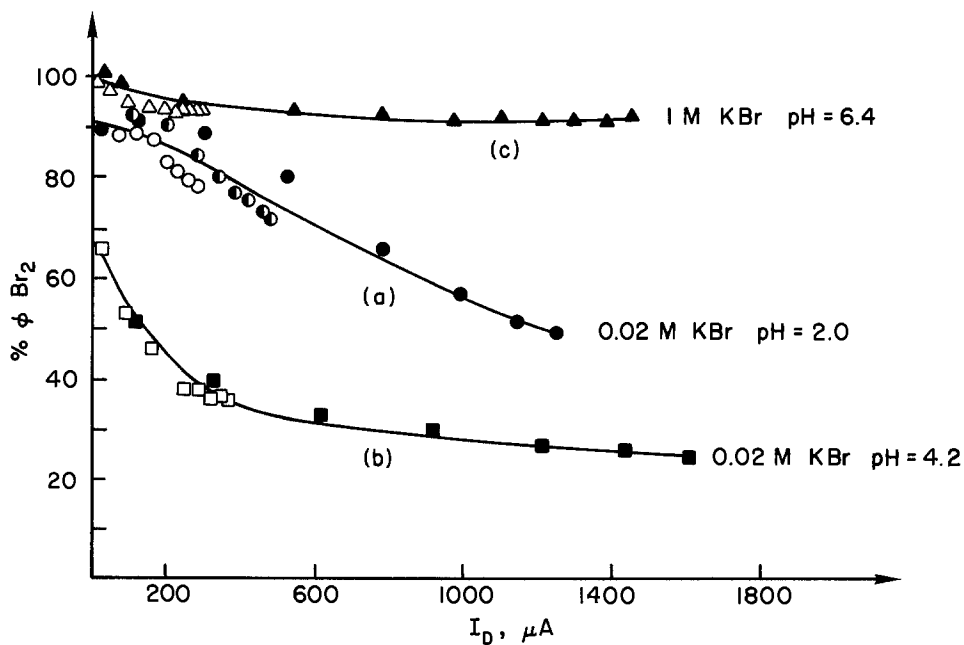


Fig. 6. Bromine production efficiency for weakly acidic solutions. ●▲ full light, ○△□ 18% full light, and ○ 6.7% of full light.



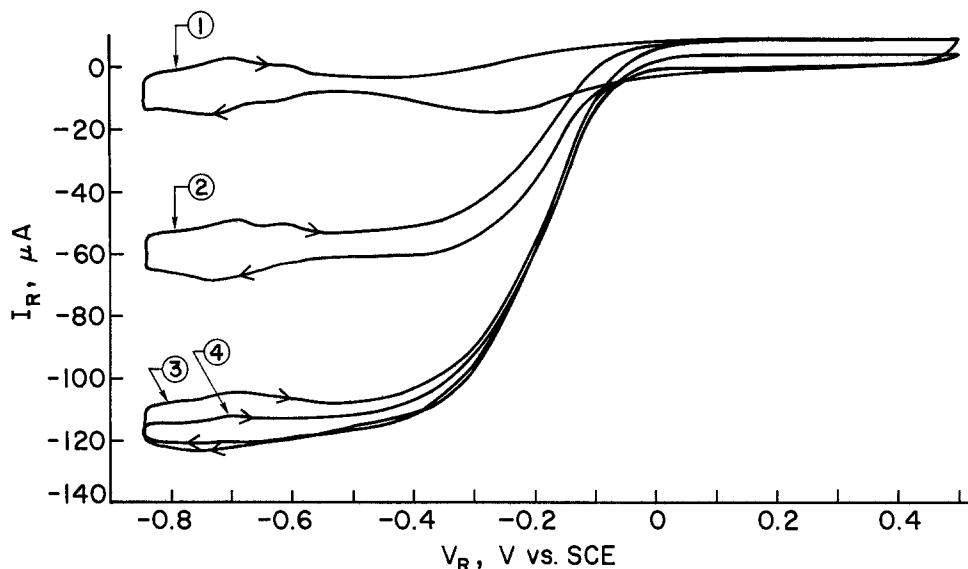


Fig. 7. Ring current-ring potential/disk current for 0.5M KBr, 0.02M NaOH (pH 12.2). Curve 1: oxygen-free solution, $I_D = 0 \mu\text{A}$. Curve 2: initially oxygen-free solution, $I_D = 500 \mu\text{A}$. Curve 3: air-saturated solution, $I_D = 0 \mu\text{A}$. Curve 4: initially oxygen-free solution, $I_D = 1000 \mu\text{A}$.

tial was observed. The I_R - V_R curve for 1M NaCl at pH 4.0 (Fig. 9, curve 2) shows the presence of O₂ as well as Cl₂, similar to the results presented earlier for bromide solutions.

Iodide oxidation.—Adsorption of iodine on the electrode surface (8) and possible diffusion of iodine into the bulk electrode along grain boundaries (11), complicated the RRDE measurements. By allowing time for the system to reach a steady state, it appeared, within experimental uncertainty, that 100% of the iodide flux could be oxidized to iodine at the disk in acidic solutions. No oxygen was detected at the ring as long as the iodide flux was higher than the disk current.

Dark currents.—At potentials $> 1.5\text{V vs. SCE}$, dark currents were observed at the α -Fe₂O₃ electrodes. Above 2.0V vs. SCE, the dark currents rose sharply as the semiconductor was driven to inversion. It was demonstrated previously (7) that oxygen was generated with 100% efficiency in the dark for 1M HClO₄ solutions. Addition of 0.1M Br⁻ or 0.1M Cl⁻ to the electrolyte was made, and electrolysis was carried out at 1.8-2.0V vs. SCE. For 0.1M KBr/1M HClO₄, production efficiency for Br₂ was $< 50\%$, and the ring currents were time dependent. Also, additional reduction waves were observed. It appears that both Br₂ and O₂ are produced in the dark along with at least one more product (such as HBrO or BrO₃⁻). Production efficiency for Cl₂ in the dark for solutions containing 0.1M KCl/1M ClO₄ was $< 50\%$, and the ring voltammograms were also complex.

Discussion

The competition reactions reported here at α -Fe₂O₃ electrodes follow the same general trend that has been observed at TiO₂ electrodes. The halides (I⁻, Br⁻, and Cl⁻) are oxidized in preference to water in acidic solution. However, because OH⁻ oxidation is kinetically favored over halide oxidation, the production efficiency for halogen decreases as the pH increases.

In Fig. 2-4, it was demonstrated that all Br⁻ reaching the electrode surface will be oxidized in preference to water in acidic solution. This is not true for Cl⁻ and for both Cl⁻ and Br⁻ in more basic solution.

A simple first-order kinetics scheme can be envisaged for the competition between halide and hydroxide ions. The halogen production efficiency is given by

$$\phi_{X_2} = \frac{k_X[X^-]}{k_X[X^-] + k_{OH^-}[OH^-]} \quad [7]$$

where k_X and k_{OH^-} are first-order rate constants for the oxidation of X⁻ and OH⁻, respectively. If we define a competition ratio: $k' = k_{OH^-}/k_X$, then Eq. [7] can be written as

$$\phi_{X_2} = \frac{[X^-]}{[X^-] + k'[OH^-]}$$

or

$$k' = \frac{[X^-] - \phi_{X_2}[X^-]}{\phi_{X_2}[OH^-]} \quad [8]$$

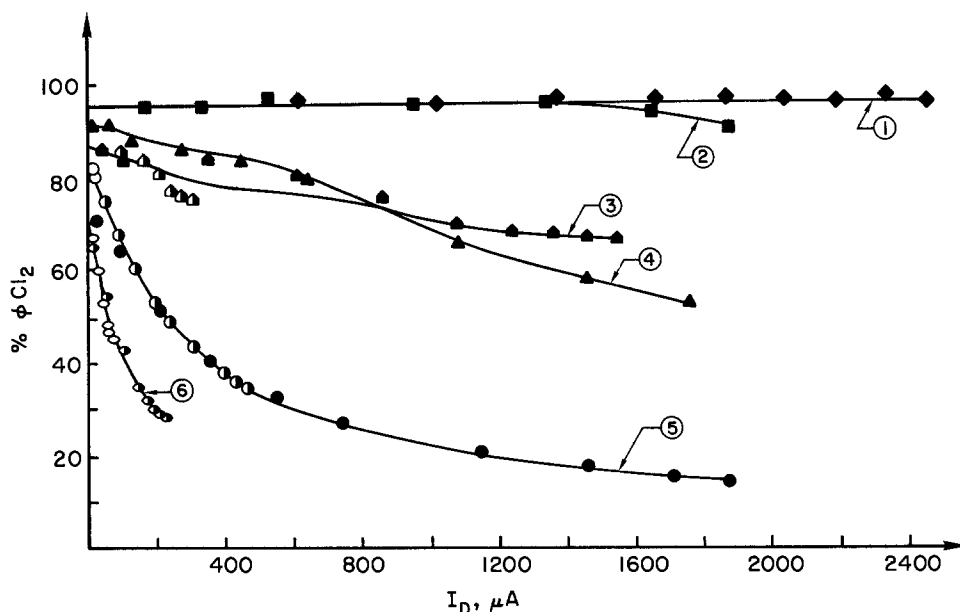


Fig. 8. Chlorine production efficiency as a function of disk current (I_D) for various chloride containing solutions. Curve 1: 1M HCl. Curve 2: 0.1M HCl/0.9M HClO₄. Curve 3: 1M NaCl, pH 2.0 (phosphoric acid buffer). Curve 4: 0.01M HCl/1M HClO₄. Curve 5: 0.002M NaCl/1M HClO₄. Curve 6: 1M NaCl, pH 4.0 (phosphate buffer). ■, ◆, ▲, △, ○: full light. ●, ▲, ○: 18% of full light. ○: 6.7% of full light.

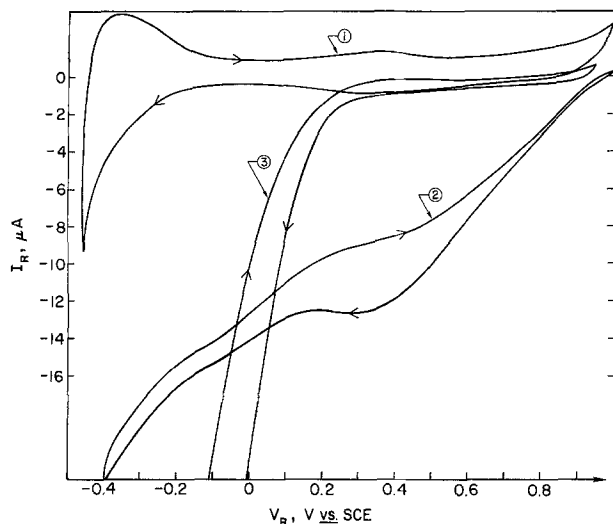


Fig. 9. Ring current-ring potential/disk current for 1M NaCl, pH 4.0 (phosphate buffer). Curve 1: oxygen-free solution, $I_D = 0 \mu\text{A}$. Curve 2: initially oxygen-free solution, 18% of full light, $I_D = 200 \mu\text{A}$. Curve 3: oxygen-saturated solution, $I_D = 0 \mu\text{A}$.

A simple test for the validity of Eq. [8] is if the same value of k' is obtained for various concentrations of X^- and OH^- . Such information is available from Fig. 6 for bromine production and from Fig. 8 for chlorine production. For the bromine case ($I_D = 700 \mu\text{A}$) the following values for k' are calculated: 9×10^9 (curve a), 4×10^8 (curve b), and 4×10^8 (curve c). For the chlorine case ($I_D = 200 \mu\text{A}$), k' values are: 3×10^{11} (curve 3), 1×10^{11} (curve 4), and 3×10^{10} (curve 6). Thus, the true kinetics is somewhat more complicated than this simplistic picture, but to an order of magnitude it is clear that $k'_{\text{Br}} \sim 10^8$ and $k'_{\text{Cl}} \sim 10^{11}$, which means that $k_{\text{Br}}/k_{\text{Cl}} \sim 10^3$.

It was demonstrated that the crucial parameter that determines the production efficiency in acidic solution is the ratio: flux X^-/I_D , relating the rate at which halide ions reach the electrode surface compared to the availability of holes at the electrode surface. Concentration of X^- , light intensity, and electrode potential only affect the production efficiency by their effect on this important ratio. In this respect, earlier publications (3-5) are somewhat misleading in that they disregarded this flux argument.

The complicated nature of these semiconductor electrodes is further demonstrated by the investigation of dark currents. The selectivity seen when $\alpha\text{-Fe}_2\text{O}_3$ is a photoanode is lost when operating in the dark. In fact, the behavior of $\alpha\text{-Fe}_2\text{O}_3$ in the dark resembles that of a metallic electrode. That is, mixtures of oxidation products for Br^- and Cl^- oxidation at high anodic potentials have been observed at metal electrodes (13). This similarity is not

too surprising when one recalls that the $\alpha\text{-Fe}_2\text{O}_3$ was driven to inversion to observe dark currents.

Conclusions

The following conclusions can be drawn from the observations reported here:

1. The general trends regarding competitive photo-oxidation at n -type semiconductor electrodes have been confirmed for $\alpha\text{-Fe}_2\text{O}_3$.

2. Quantitative agreement between the flux of Br^- reaching the electrode surface and the efficiency of Br_2 production has been demonstrated in acidic solution.

3. The critical factor in determining the competition ratio at a given pH is the flux $X^-/\text{disk current ratio}$.

4. A simple kinetics scheme does not fully account for the experimental data, but apparently Br^- is about 10^3 times more effective than Cl^- at capturing holes at the $\alpha\text{-Fe}_2\text{O}_3$ electrode surface, while OH^- is considerably more effective than either halide.

5. The dark current selectivity is considerably different than the photocurrent selectivity, with the $\alpha\text{-Fe}_2\text{O}_3$ electrode exhibiting more metallic-like behavior.

Acknowledgment

This work is supported by the Division on Chemical Sciences, Office of Basic Energy Sciences, U.S. Department of Energy.

Manuscript submitted Aug. 15, 1983; revised manuscript received Jan. 30, 1984.

The University of California assisted in meeting the publication costs of this article.

REFERENCES

1. S. N. Frank and A. J. Bard, *J. Am. Chem. Soc.*, **99**, 4667 (1977).
2. R. Shinar and J. H. Kennedy, *This Journal*, **130**, 860 (1983).
3. A. Fujishima, T. Inoue, and K. Honda, *J. Am. Chem. Soc.*, **101**, 5582 (1979).
4. K. Hirano and A. J. Bard, *This Journal*, **127**, 1056 (1980).
5. T. Inoue, T. Watanabe, A. Fujishima, and K. Honda, *Chem. Lett.*, 1073 (1977).
6. T. Kobayashi, H. Yoneyama, and H. Tamura, *J. Electroanal. Chem.*, **122**, 133 (1981).
7. J. H. Kennedy and M. Anderman, *This Journal*, **130**, 848 (1983).
8. M. Anderman and J. H. Kennedy, *ibid.*, **131**, 21 (1984).
9. W. J. Albery and S. Bruckenstein, *Trans. Faraday Soc.*, **60**, 1920 (1966).
10. T. Kobayashi, H. Yoneyama, and H. Tamura, *J. Electroanal. Chem.*, **138**, 105 (1982).
11. J. H. Kennedy, R. Shinar, and J. P. Ziegler, *This Journal*, **127**, 2307 (1980).
12. J. H. Kennedy and D. Dünwald, *ibid.*, **130**, 2013 (1983).
13. T. Mussini and G. Faiva, in "Encyclopedia of Electrochemistry of the Elements," A. J. Bard, Editor, Vol. 1, Chap. 1, 2, Marcel Dekker Inc., New York (1973).

Photoelectrochemical Behavior of Iron Oxide/*n*-Si Heterojunction Electrodes with an Outer Pd Layer

Tetsuya Osaka,* Kiyomi Ejiri, and Naruya Hirota

Department of Applied Chemistry, School of Science and Engineering, Waseda University, Okubo, Shinjuku-ku, Tokyo 160 Japan

ABSTRACT

Iron oxide/*n*-Si heterojunction electrodes modified by an outer Pd layer were studied for its utility as an efficient photoanode. The addition of an evaporated Pd layer on the electrode greatly enhanced the photocurrent and shifted the onset potential from 0.5V (Hg-HgO) to the more cathodic side in a 0.2M KOH solution. A 100Å Pd layer showed the most cathodic onset potential of -0.36V (Hg-HgO). The unmodified iron oxide/*n*-Si electrode gave a relatively broad spectral photoresponse with the maximum region lying between 550 and 700 nm. With the addition of the Pd layer the quantum efficiency of spectral photoresponse from 400 to 800 nm became 20% higher. The addition of methanol enhanced the photocurrent up to 1.25 times at 0.6M concentration on the unmodified electrode, whereas on the Pd-modified electrode, the photocurrent decreased slightly by the addition of methanol. These phenomena are discussed in terms of various mechanisms for methanol oxidation.

A large number of oxide semiconductors have been investigated as photoanode materials because of their stability in the harsh conditions of oxygen evolution. Almost all oxide semiconductors have a large bandgap and even those with smaller bandgaps have been found to possess an unsatisfactory photocurrent onset potential (1). One of the oxide semiconductors, α -Fe₂O₃, has not been reported to show high energy conversion efficiency (2-9). An α -Fe₂O₃/*n*-Si electrode was reported to have stabilized *n*-Si semiconductor, and the heterojunction electrode showed broad spectral region of photoresponse (10-16). The photocurrent onset potential of α -Fe₂O₃/*n*-Si, however, is insufficiently cathodic. This paper reports the photoelectrochemical characteristics of Pd-modified iron oxide/*n*-Si electrodes for the purpose of improving the onset potential, as well as the effect of methanol on the electrodes with and without the Pd layer.

Experimental

Electrode preparation.—Single crystal *n*-Si semiconductors made by Shin-Etsu Chemical and possessing 0.85~1.15 Ωcm resistivity were used as substrates. A 400Å iron film was first vacuum-evaporated using a Hitachi electron beam evaporator onto a (100) plane *n*-Si substrate. The iron oxide was formed by heating in a vacuum furnace in an O₂ atmosphere of 0.1 torr at 400°C for 1.0h. The final thickness of iron oxide film was ca. 750Å, which was measured by a stylus technique (Rank-Taylor-Hobson Talystep I). The composition of the iron oxide was confirmed to be Fe₂O₃ by RBS (Rutherford backscattering spectroscopy) and XPS (x-ray photoelectron spectroscopy) methods, the data of which are to be published shortly (17). Pd layers were formed by two different methods: vacuum evaporation and the conventional Sn-Pd two-step activation wet process for electroless plating.

Photoelectrochemical measurements.—Electrochemical measurements were made potentiodynamically at 0.1 V·s⁻¹ in a 0.2M KOH solution in a purified Ar atmosphere at 25°C. Hg-HgO electrode in the same solution was used as a reference electrode. The photocurrent was measured using a 500W xenon lamp from Ushio Electric with an infrared filter. The spectral response of the photocurrent was measured between 400 and 800 nm using various spectral filters from Toshiba Glass. The total light intensity of the lamp, measured by a Tektronix radiant flux meter, was 0.085 W·cm⁻². The intensity at each wavelength was normalized for the spectral photoresponse. The differential capacitance of the semiconductor electrode was measured potentiodynamically at 5 mV·s⁻¹ by using a phase-sensitive impedance meter from Fuso-Seisakusho. Products of methanol oxidation on the

electrodes were qualitatively checked by a Hitachi gas chromatograph. Formaldehyde and oxygen gas were detected by using column packings of PEG 1000 and WG 100 (Gasukuro Kogyo Incorporated), respectively. The reproducibility was confirmed by using more than three electrodes for one matter. The stability of the electrodes was checked for about a one week term experiment.

Results and Discussion

Photoresponse of Fe₂O₃/*n*-Si heterojunction electrodes with Pd layer.—Figure 1 shows the characteristics of photocurrents for Fe₂O₃/*n*-Si electrodes with and without a 100Å layer of vacuum evaporated Pd in a 0.2M KOH solution. Photocurrent is greatly enhanced by the Pd layer. The photocurrent saturation point was observed at the region more anodic than 2.2V both with and without the Pd layer, but, the photocurrent of the Pd-modified electrode at the saturated photocurrent region is ca. 2.4 times larger than that of the unmodified electrode. A shift of the onset potential to the cathodic side was also observed as a result of Pd modification. Figure 2 shows the onset potential for electrodes with various thicknesses of Pd prepared by the two processes in a 0.2M KOH solution. With addition of a Pd layer, the photocurrent increased greatly and the onset potential also became more cathodic. In the case of the adsorbed layer of Pd prepared by the wet process, which may consist of adsorbed Pd particles of several tens of angstroms (18), the onset potential was not greatly improved. In the case of a Pd layer formed by vacuum evaporation, however, the photocurrent was significantly improved, especially at the low bias region, and the increase in photocurrent depends on the thickness of the Pd layer. The 100Å Pd layer gave the best improvement of onset potential (-0.36V) as can be seen in Fig. 2.

The relation between quantum yield (η) and the wavelength for the two cases, with and without a Pd layer, is plotted in Fig. 3. The spectral photoresponse for the Fe₂O₃/*n*-Si electrode shown in Fig. 3 shows the broad photoresponse between 400 and 800 nm, and the maximum photoresponse lies between 550 and 700 nm. The increase in the spectral photoresponse in the maximum response region may be caused by effective hole-injection from the Si to the electrode surface across the Fe₂O₃ film. The photoresponse of Fe₂O₃/*n*-Si heterojunction electrodes has been reported by Yazawa *et al.* (10-12), and they report that it has a broad photoresponse between 480 and 850 nm. There appears to be a slight difference between the spectral photoresponse obtained by Yazawa *et al.* (10) and ours. Since the characteristics of the photocurrent of the Fe₂O₃/*n*-Si depend strongly on the iron oxide states (16), the difference in spectral photoresponse may be due to the difference of the oxidized states of iron oxides which are formed by the differ-

*Electrochemical Society Active Member.

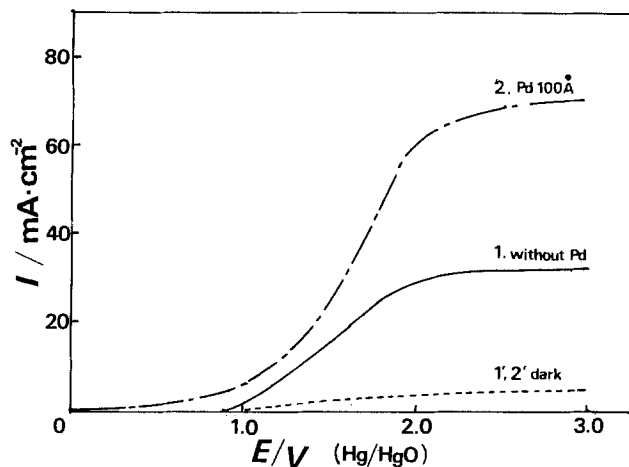


Fig. 1. Current-potential curves for Pd-modified $\text{Fe}_2\text{O}_3/n\text{-Si}$ electrodes in 0.2M KOH at $0.1\text{ V} \cdot \text{s}^{-1}$. 1,2: illuminated, 1',2': dark.

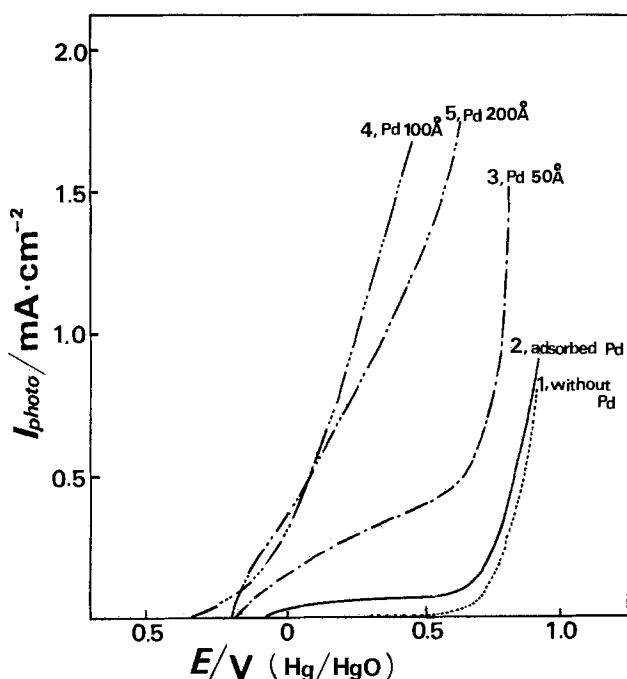


Fig. 2. Photocurrent-potential curves for Pd-modified $\text{Fe}_2\text{O}_3/n\text{-Si}$ electrodes in 0.2M KOH at $0.1\text{ V} \cdot \text{s}^{-1}$. Pd preparation, 2: wet process, 3,4,5: vacuum evaporation.

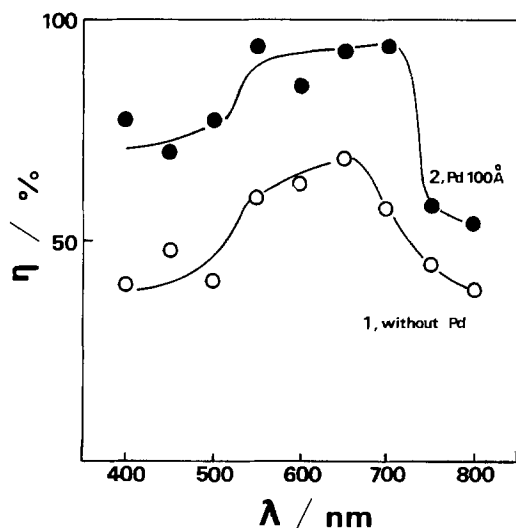


Fig. 3. Spectral dependence of quantum efficiency of anodic photocurrents for $\text{Fe}_2\text{O}_3/n\text{-Si}$ electrodes both with and without Pd layer in 0.2M KOH in the saturated photocurrent region.

ent methods. The Pd-modified heterojunction electrode has almost the same response shape as $\text{Fe}_2\text{O}_3/n\text{-Si}$, but the quantum yield is about 20% higher, and at the maximum response region the quantum yield approaches 100%.

Figure 4a presents the capacitance behavior (C - E curves) at 1 kHz for $\text{Fe}_2\text{O}_3/n\text{-Si}$ electrodes with and without Pd layer. The Mott-Schottky plots (Fig. 4b) were constructed from these curves in order to obtain flatband potentials and estimate band structure, though the Mott-Schottky plot which assumes a simple Schottky barrier does not necessarily give information about the exact flatband potential for such multilayered heterostructures. The plots in Fig. 4b indicate that the flatband potentials are apparently very close for two cases with and without the Pd layer. We assume that the introduction of the Pd layer results in a Schottky barrier electrode structure increasing its current collection efficiency, and that the increase in current collection efficiency due to Pd layer alters the onset potential in spite of the apparently closed flatband potentials. A relatively large extension of spectral range for photoresponse, improved by an outer metal layer, has been reported for $p\text{-GaP}$ (19, 20) and SrTiO_3 (21). Since the spectral photoresponse of the semiconductor itself, such as $p\text{-GaP}$ or SrTiO_3 , is in contrast with this heterojunction electrode, limited to shorter wavelengths, the introduction of surface metal layer is considered to effectively improve spectral photoresponse at longer wavelengths.

Effect of methanol on photocurrent in heterojunction electrodes with and without Pd layer.—Figure 5 shows the photocurrent vs. potential curves on the unmodified $\text{Fe}_2\text{O}_3/n\text{-Si}$ electrode in a 0.2M KOH solution with various methanol concentrations. On this electrode the addition of methanol obviously causes an increase in photocurrent, but no shift in the onset potential. This effect with the unmodified electrode, well-known as "current doubling," was not observed on the Pd-modified electrode. The photocurrent ratio I_p/I_a vs. methanol concentration plots at 1.2V are shown in Fig. 6 for both electrodes, where I_p and I_a represent the photocurrents in the presence and absence of methanol in the solution. On the unmodified electrode, the photocurrent clearly increased with the addition of methanol and shows the maximum I_p/I_a ratio of 1.25 at 0.6M methanol, whereas on the Pd modified electrode, the photocurrent decreased slightly with an increase in methanol concentration. The photoelectrochemical oxidation of alcohols on $\alpha\text{-Fe}_2\text{O}_3$ was discussed by Miyoshi *et al.* (22), who claimed

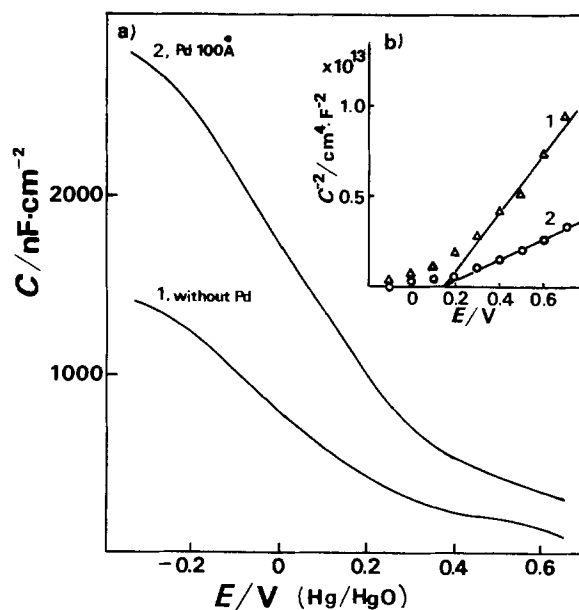


Fig. 4. Capacitance behavior for $\text{Fe}_2\text{O}_3/n\text{-Si}$ electrodes both with and without Pd layer in 0.2M KOH at 1 kHz . (a) Capacitance-potential curves and (b) Mott-Schottky plots.

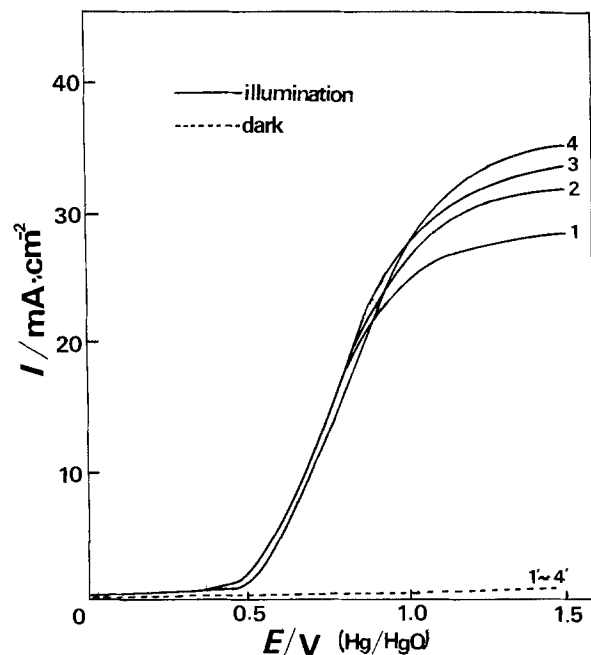


Fig. 5. Effect of methanol on photocurrent of $\text{Fe}_2\text{O}_3/n\text{-Si}$ electrode in 0.2M KOH at $0.1\text{ V} \cdot \text{s}^{-1}$. Methanol concentration, 1: 0M , 2: 0.08M , 3: 0.18M , 4: 0.45M .

that the addition of methanol did not cause an increase in the photocurrent despite their finding that the methanol was photoelectrochemically oxidized on the illuminated Fe_2O_3 . Accordingly, there is a large difference between Fe_2O_3 and $\text{Fe}_2\text{O}_3/n\text{-Si}$ electrodes with regard to the effect of methanol on photocurrent. Moreover on the Pd-modified electrode, the current doubling effect of methanol was not observed.

In order to determine whether the methanol is photoelectrochemically oxidized on $\text{Fe}_2\text{O}_3/n\text{-Si}$ electrodes with and without Pd layer, potentiostatic electrolysis at the saturated photocurrent region of 3.0V was performed for 10h in a 0.2M KOH solution under illumination. Gas chromatographic analysis showed that the main product of methanol in the solution on illuminated electrodes with and without Pd layer is formaldehyde and that the gas product is almost entirely O_2 . No production of CO_2 could be detected because CO_2 is absorbed by the KOH solution. Therefore, the methanol is concluded to be oxidized photoelectrochemically on the electrodes both with and without the Pd layer. It is generally accepted that the photoelectrochemical oxidation of methanol proceeds through a two-step mechanism for the case of accompanying the current doubling effect (22, 23)

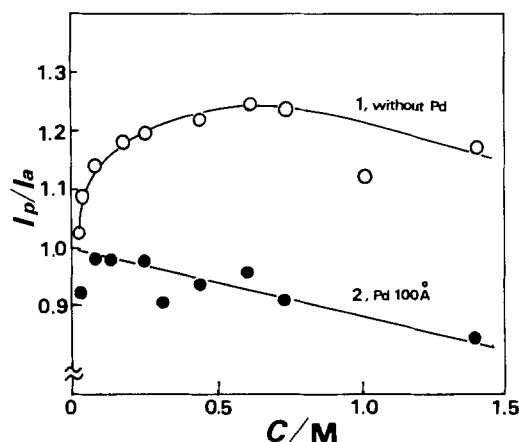
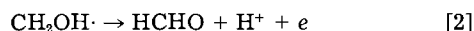


Fig. 6. Plots of I_p/I_a vs. methanol concentration for $\text{Fe}_2\text{O}_3/n\text{-Si}$ electrodes both with and without Pd layer in 0.2M KOH at 1.2V (Hg/HgO).

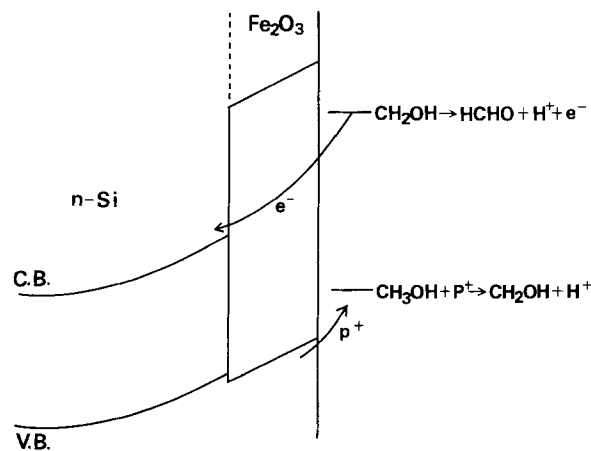


Fig. 7. Schematic diagram of current doubling process of methanol for $\text{Fe}_2\text{O}_3/n\text{-Si}$ electrode.

The photoelectrochemical oxidation of organic compounds showing current doubling effect can be explained by electron-injection of the intermediate radical into the conduction band (Eq. [2]). Figure 7 shows a schematic diagram of the current doubling process, based on a tentative model of a possible energy diagram for the $\text{Fe}_2\text{O}_3/n\text{-Si}$ electrode, proposed by Yazawa *et al.* (11, 12). The tentative model is assumed on the basis of efficient hole-injection that may be produced by the nice fit of the valence bandedge between outer and inner semiconductors. Miyoshi *et al.* (22) explained the oxidation of methanol on $\alpha\text{-Fe}_2\text{O}_3$ electrode by the assumption that the intermediate radical of methanol, produced by oxidation due to photogenerated holes, is further oxidized by the photogenerated holes instead of injecting the electron of the intermediate radical into the conduction band, since the energy level of intermediate radical is situated at the level lower than that of conduction band of Fe_2O_3 . On the unmodified $\text{Fe}_2\text{O}_3/n\text{-Si}$ electrode, however, current doubling occurs, and furthermore this effect disappears on the Pd modified electrode. The following consideration is suggested in order to explain these results. On the unmodified $\text{Fe}_2\text{O}_3/n\text{-Si}$ electrode, methanol is first oxidized to an intermediate radical by the photogenerated holes in the valence band as shown in Eq. [1], and further oxidation of the intermediate proceeds by electron-injection into the conduction band by the tunneling effect as shown in Fig. 7. The assumption of a tunneling effect, which is needed to explain the opposite results obtained from the Fe_2O_3 and $\text{Fe}_2\text{O}_3/n\text{-Si}$ electrodes, may be supported by the finding that the increase of photocurrent is merely 1.25 times. On the Pd-modified electrode, the intermediate radical, after the initial oxidation of Eq. [1], is further oxidized by the hole in the valence band as shown in Eq. [3]



since the hole density in the valence band becomes higher due to the effective hole generation by Pd layer.

Conclusion

The addition of a Pd layer on top of an $\text{Fe}_2\text{O}_3/n\text{-Si}$ heterojunction electrode caused quantum yield *ca.* 20% higher for the photoresponse between 400 and 800 nm, and made the onset potential more cathodic in a 0.2M KOH solution. The effect of methanol on photocurrent was studied, and the results obtained with and without the Pd layer were opposite. The characteristics of photoresponse and the mechanism of methanol oxidation for $\text{Fe}_2\text{O}_3/n\text{-Si}$ heterojunction electrodes both with and without Pd layer were discussed.

Manuscript submitted June 7, 1983; revised manuscript received Feb. 7, 1984.

Waseda University assisted in meeting the publication costs of this article.

REFERENCES

1. D. E. Scaife, *Sol. Energy*, **25**, 41 (1980).
2. K. L. Hardee and A. J. Bard, *This Journal*, **123**, 1024 (1976).
3. K. L. Hardee and A. J. Bard, *ibid.*, **124**, 215 (1977).
4. R. A. Fredleim and A. J. Bard, *ibid.*, **126**, 1892 (1979).
5. J. H. Kennedy and K. W. Frese, *ibid.*, **125**, 709 (1978).
6. J. H. Kennedy and K. W. Frese, *ibid.*, **125**, 723 (1978).
7. J. H. Kennedy, N. Anderson, and R. Shinar, *ibid.*, **128**, 2371 (1981).
8. L. S. R. Yeh and N. Hackerman, *ibid.*, **124**, 833 (1977).
9. R. M. Candea, *Electrochim. Acta*, **26**, 1803 (1981).
10. H. Morisaki, H. Ono, H. Dohkoshi, and K. Yazawa, *Jpn. J. Appl. Phys.*, **19**, L148 (1980).
11. H. Morisaki, H. Ono, H. Dohkoshi, and K. Yazawa, *ibid.*, **20**, 777 (1981).
12. K. Yazawa, *Denki Kagaku*, **49**, 418 (1981).
13. G. Nogami, S. Shibata, N. Terasaki, and H. Hayashi, *ibid.*, **49**, 251 (1981).
14. G. Nogami, *ibid.*, **49**, 235 (1981).
15. G. Nogami, *ibid.*, **50**, 309 (1982).
16. H. Kitayama, F. Sugawara, K. Ejiri, and T. Osaka, *ibid.*, **51**, 322 (1983).
17. T. Osaka, H. Kitayama, N. Hirota, and S. S. Eskildsen, *Electrochim. Acta*, to be published.
18. T. Osaka, H. Takematsu, and K. Nihei, *This Journal*, **127**, 1021 (1980).
19. H. Yoneyama, S. Mayumi, and H. Tamura, *ibid.*, **125**, 68 (1979).
20. H. Uchida, H. Yoneyama, and H. Tamura, *ibid.*, **127**, 99 (1980).
21. I. Watanabe, Y. Matsumoto, and E. Sato, *J. Electroanal. Chem.*, **133**, 359 (1982).
22. S. Miyoshi and A. Kunugi, *Denki Kagaku*, **48**, 476 (1980).
23. M. Miyake, H. Yoneyama, and H. Taumua, *Chem. Lett.*, 635 (1976).

Dye Sensitization of Cuprous Thiocyanate Photocathode in Aqueous KCNS

Kirthi Tennakone, Mahendra Kahanda, Cyril Kasige, and Parakrama Abeysooriya

Department of Physics, Ruhuna University College, Matara, Sri Lanka

Ranmuthu H. Wijayanayaka and Padmananda Kaviratna

Department of Chemistry, Ruhuna University College, Matara, Sri Lanka

ABSTRACT

Cuprous thiocyanate (p-type semiconductor) is found to adsorb thiocyanated cationic dyes to yield high photoresponses in aqueous KCNS. The method of preparation and the performance of dye-sensitized CuCNS photocathodes are discussed.

Electrolytic photocells with semiconductor electrodes are attracting attention as economical devices for the conversion of solar energy (1-8). The additional advantage of these systems is the possibility of extending the spectral response by sensitization with dyes (9-13). It is also known that the dye-sensitized (DS) photocurrent is rather insensitive to impurities and defects in the semiconductor (14, 15); polycrystalline and amorphous materials with large bandgaps when sensitized yield high photocurrents. The sensitization is effective only if the dye is absorbed at the semiconductor surface (9-13). Thus, to produce practically useful DS cells, it is necessary to search for systems where the dye adsorption is optimized. We have found that cuprous thiocyanate (a p-type semiconductor) (16-17) readily adsorbs cationic dyes when CNS^- is the anionic ligand. In this paper, we describe our observations on DS CuCNS electrodes in aqueous KCNS.

Experimental

CuCNS photocathode is made by the following method. A copper plate 5×5 cm is anodically polished in 10% H_2SO_4 . An acidic solution of KCNS (0.25 mol l^{-1} in KCNS, 0.7 mol l^{-1} in acetic acid, solution pH ~ 3.5) is electrolyzed with the copper plate as the anode. The current density is kept at ≈ 2.5 mA cm^{-2} , and the plating is continued for ≈ 30 min. CuCNS deposits on the anode as a hard white layer firmly affixed to the copper substrate. (Unless a large excess of acetic acid is used, there is no risk of liberation of HCN in this process.)

To obtain an unbroken uniform coating, it is essential that the surface is free from patches of grease. The addition of 1-2 ml or propan-2-ol to 100 ml of the electrolyte enhances even deposition by removing grease. The dyes used in this investigation are mostly triarylmethane chlorides (BDH grade). CuCNS readily adsorbs these dyes

when Cl^- is replaced by CNS^- . The thiocyanated dyes (TD's) are prepared by the following method. A solution of the commercial dye in alcoholic KCNS (concentration > 2.5 mol l^{-1}) is boiled until most of the alcohol is expelled. The TD recrystallizes when the solution is cooled to room temperature (30°C). The crystals are separated by filtration, washed with KCNS solution, and dried at 80°C. CuCNS electrodes are made to adsorb the TD's by immersing them in the dye solution (0.1g per liter of water containing 10% ethanol, solution pH has no effect on the degree of adsorption) for 30 min. Rapid adsorption takes place, and the electrode acquires colors characteristic of the dyes (bluish-green, green, red for methyl violet, malachite green, and rosaniline). It is found that the best photoresponse is obtained when $\sim 10^{16}$ molecules of the dye/ cm^2 is adsorbed to form almost a monolayer (the amount of adsorbed dye is determined by extraction of the absorbed dye with ethanol and colorimetric estimation).

The absorption spectra of the dyes (in aqueous solution and adsorbed on solid CuCNS) are measured using Unicamp SP 500 Series 11 spectrophotometer. The light sources used in all experiments were tungsten filament lamps. Capacitance measurements indicate the flatband potential of CuCNS in aqueous KCNS is $\sim +0.2$ vs. SCE.

As they all perform better in the backwall mode, the anode used is a brass frame (same dimensions as the cathode) coated with copper sulfide. To obtain reproducible dark open-circuit voltages (≈ 0), it is prepared by the following procedure. The electrode is immersed in dilute HNO_3 (0.05 mol l^{-1}), H_2S is bubbled for about 10 min and kept in contact with the solution for 24h.

The electrolyte is an aqueous solution of KCNS (0.1 mol l^{-1}) containing $\sim 10^{-3}$ mol l^{-1} of thiocyanogen. Thiocyanogen is prepared by mixing a solution of Br_2 in diethyl ether with excess AgCNS (18). When the ethereal

solution of $(\text{CNS})_2$ is shaken, and aqueous KCNS and ether are allowed to evaporate, $(\text{CNS})_2$ passes into the aqueous medium. Thiocyanogen in aqueous solution undergoes partial decomposition and polymerization (19). However, in the presence of KCNS, a weak solution of $(\text{CNS})_2$ is almost completely stabilized (20) due to formation of $(\text{CNS})_2^-$. The presence of this ion can be easily demonstrated by its characteristic absorption peak at 475 nm (21). In fact, the oxidation of CNS^- by atmospheric oxygen always produces detectable quantities of $(\text{CNS})_2^-$ in aqueous solutions of KCNS.

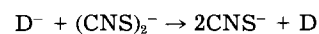
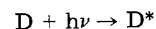
Unlike in other DS cells, the dye does not diffuse into the electrolyte, and the solubilities of TD's are suppressed by the CNS^- ions.

Results and Discussion

The thiocyanates of Cu(I) and Ag show semiconduction at the optical absorption edge near 335 nm (see Fig. 1.) In the absence of sensitizers, a feeble photoresponse is seen

in the UV region (the material is completely photostable in aqueous KCN in the presence or absence of dyes). When the dyes are adsorbed, the photocurrent is enhanced by a factor more than 100, and the peak of the spectral response shifts towards the long wavelength region (Fig. 2, curve 3 gives the action spectrum of the cell in the optical region in the absence of UV component). The mechanism of dye sensitization is widely discussed in literature (4, 9-13). When these ideas are applied to the present system, the photoreaction occurring at the electrodes can be expressed as follows.

Photocathode



where D denotes a dye molecule, D^* an excited dye mole-

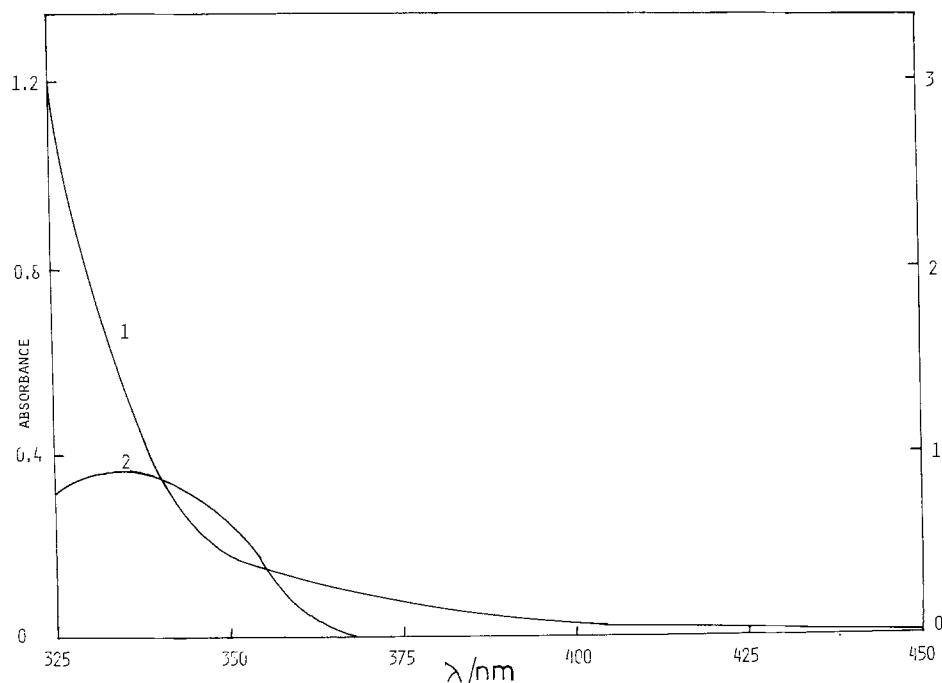


Fig. 1. Curve 1: diffuse reflectance spectrum of solid CuCNS. Curve 2: action spectrum when the photocathode is unsensitized.

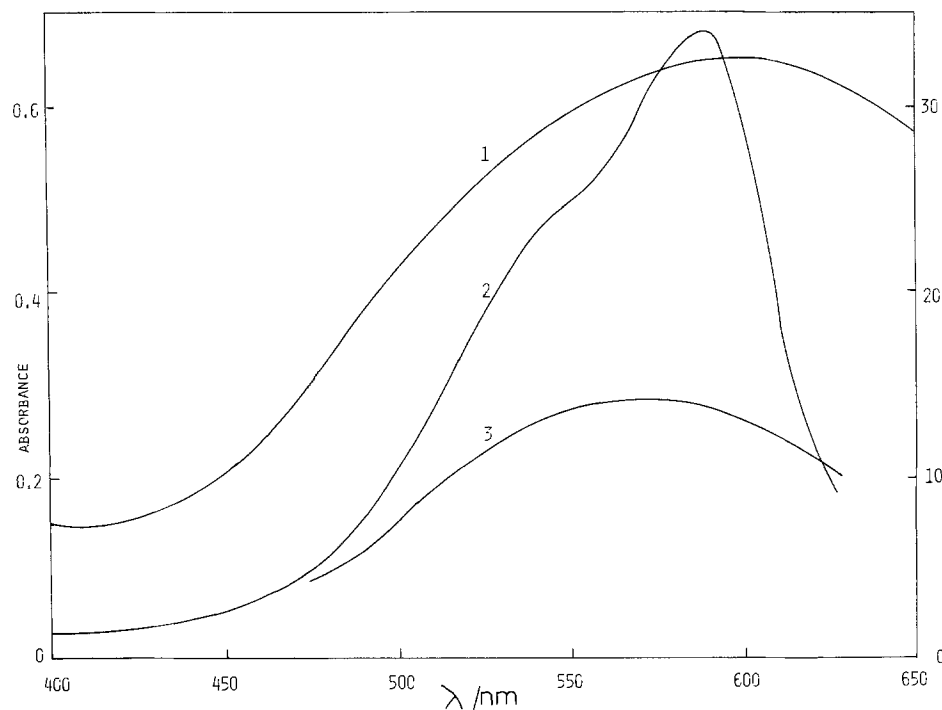
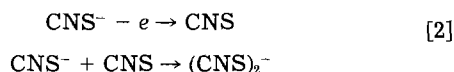


Fig. 2. Curve 1: diffuse reflectance spectrum of methyl violet adsorbed in CuCNS. Curve 2: absorption spectrum of an aqueous solution of methyl violet ($\approx 0.1 \text{ g dm}^{-3}$, cm cell). Curve 3: action spectrum when the photocathode is sensitized with methyl violet.

cule, and D^- a dye molecule that has lost one electron. The hole generated is transferred into the valance band.

Anode.—Near the anode, CNS^- ions discharge electrons yielding CNS free radicals, which combine with CNS^- ions in the solution to regenerate $(CNS)_2^-$ ions, *i.e.*



Thus, in principle, the cell is regenerative, because of the presence of the redox couple $CNS^-/(CNS)_2^-$ ($\sim +0.29$ vs. SCE).

It is interesting to note the close resemblance of the action spectrum of the photocurrent to the diffuse reflectance spectrum of the dye adsorbed on $CuCNS$ (Fig. 2). However, this is different from the absorption spectrum of the dye in aqueous solution. In the former spectrum,

the absorption peak is broader—a factor acting favorably on the performance of the cell. Compared to other DS systems, the efficiency of the cell (power produced/light energy incident per second) obtained from the plots of I vs. V and IV vs. V (Fig. 3 and 4) is high. The highest value, 2.8% (light source tungsten filament lamp at intensity of illumination 40 W m^{-2}), is obtained with methyl violet. The corresponding quantum yield, *i.e.*, number of electrons passed per second/number of incident photons per second in the wavelength region 450–600 nm (intensity distribution of the lamp is estimated using a bolometer coupled to a spectrometer), is $\sim 27\%$; other triarylmethane TD's give slightly lower efficiencies (Table I). The stability is also good and $CuCNS$ remains completely photostable; however, the dyes photodegrade slowly, decreasing the photocurrent at a rate $\approx 0.1 \mu\text{A cm}^{-2} \text{ h}^{-1}$ (Fig. 5). After about 48h of operation (light intensity 40 W m^{-2}), the dye degenerates, possibly because of the formation of re-

Fig. 3. I vs. V curve for a methyl violet-sensitized cell.

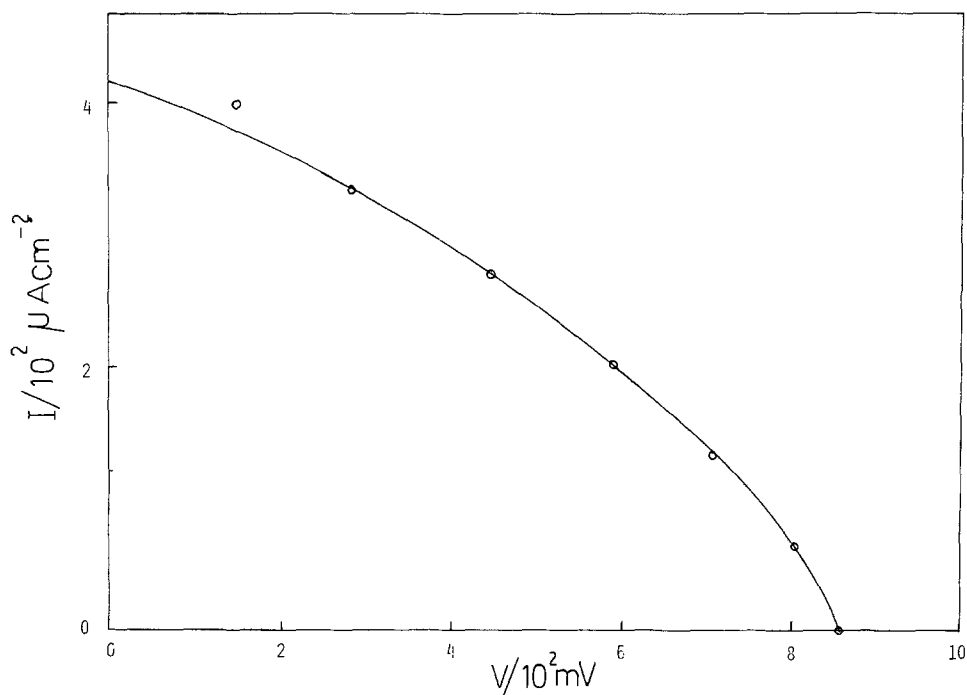
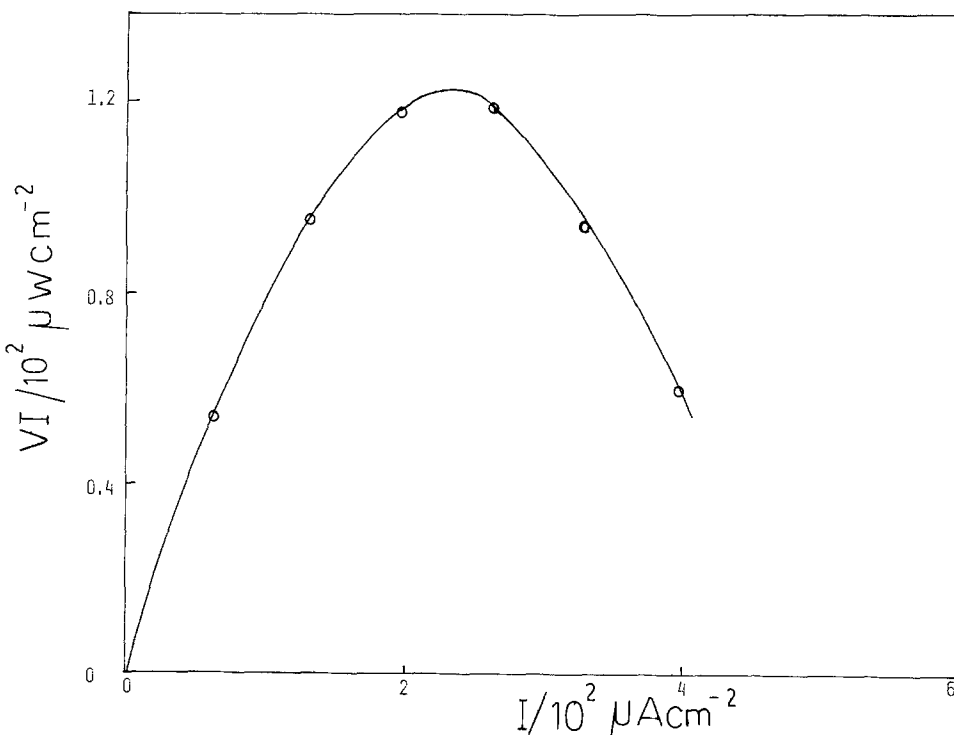


Fig. 4. IV vs. I curve for a methyl violet-sensitized cell (intensity of illumination 40 W m^{-2}).



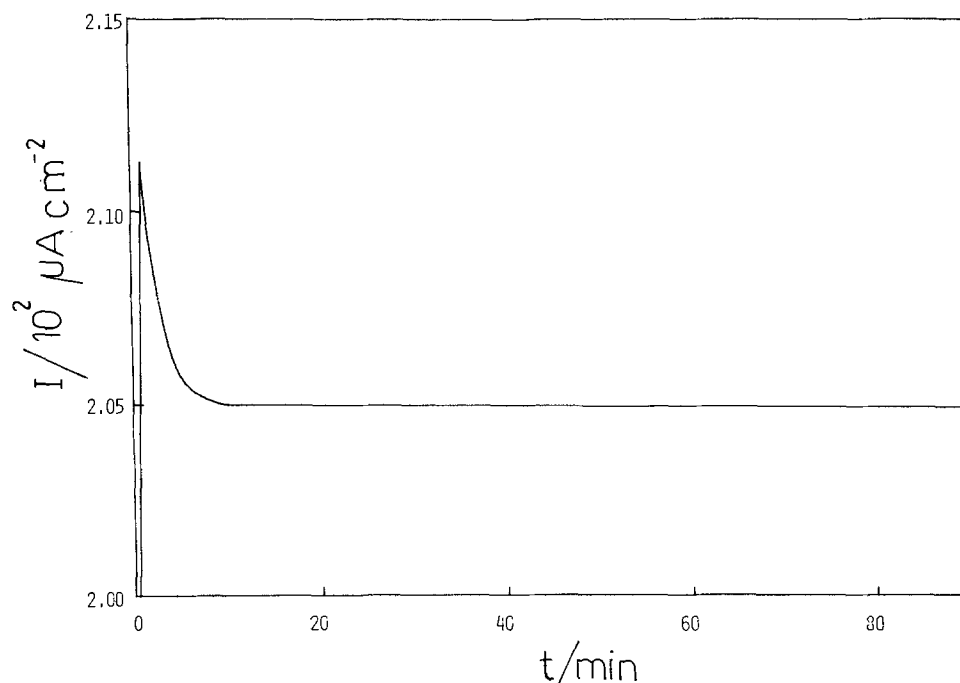
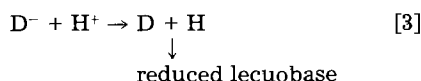


Fig. 5. The time development of the photocurrent of a methyl violet-sensitized cell set near the maximum power point (intensity of illumination $\approx 40 \text{ W m}^{-2}$).

duced leuco-compounds. This is supported by the fact that when oxidizing agents are added, the photocathode regains the original color and photoresponse. The photo-reduction of the dyes could result from presence of the reaction.



in addition to reaction [1]. We have not succeeded in finding better redox electrolytes that do not react with the TD's. Apart from the triarylmethanes, other classes of cationic dyes (e.g., rhodamines, acridines) also show good adsorption. Unfortunately, they also suffer from the same defect.

Another interesting feature of the cell is the high open-circuit voltage (V_{oc}). Most dyes give a $V_{oc} \sim 800 \text{ mV}$ when the intensity of illumination is 40 W m^{-2} (Table I).

Although the efficiency of the system is comparable or slightly better than most efficient DS cells reported in the literature (13), the system in the present form does not have any practical value. Nevertheless, our investigations show that if methods are found for affixing dyes into high bandgap materials to optimize the photoresponse, DS cells would turn out to be practically useful systems (absorption of the dye is not the only criterion determining the performance of a DS cell, the stability of the dye towards repeated oxidation and reduction, the presence of an intense absorption band, and good electrical conductivity are also deciding factors). The V_{oc} of a photoelectrochemical cell depends on the bandgap of the material. The short-circuit photocurrent (I_{sc}) is determined by the number of photons converted into electron-hole pairs without recombinations (23). Thus, theoretically, DS cells

could have high efficiencies because I_{sc} can be controlled by the use of dyes, relevant to the desired spectral region.

Manuscript submitted Aug. 23, 1983; revised manuscript received Jan. 15, 1984.

REFERENCES

1. J. R. Bolton and D. O. Hall, *Ann. Rev. Energy*, **4**, 353 (1979).
2. H. Tsubomura, M. Matsumura, K. Nakatani, K. Yamamoto, and K. Meda, *Sol. Energy*, **21**, 93 (1978).
3. A. J. Bard and M. S. Wrighton, *This Journal*, **124**, 1706 (1977).
4. W. J. Albery, A. W. Foulds, K. J. Hall, R. Hillman, K. G. Eydell, and A. F. Orchard, *Nature*, **282**, 793 (1979).
5. A. Heller, *Acc. Chem. Res.*, **14**, 154 (1981).
6. L. A. Harris and R. H. Wilson, *Ann. Rev. Mater. Sci.*, **8**, 99 (1978).
7. M. Tomkiewicz and H. Fay, *Appl. Phys.*, **18**, 1 (1979).
8. D. Cahen, J. Manassen, and G. Hodes, *Sol. Energy Mater.*, **1**, 343 (1979).
9. H. Gerischer, *Photochem. Photobiol.*, **16**, 243 (1972).
10. H. Tributsch and H. Gerischer, *Ber. Bunsenges. Phys. Chem.*, **73**, 251 (1969).
11. K. Hauffe, H. Danzmann, H. Pusch, J. Range, and H. Voltz, *This Journal*, **117**, 993 (1970).
12. R. Memming, *Photochem. Photobiol.*, **16**, 325 (1972).
13. H. Tsubomura, M. Matsumura, Y. Nomura, and T. Amamia, *Nature*, **261**, 402 (1979).
14. M. Matsumura, Y. Nomura, and H. Tsubomura, *Bull. Chem. Soc. Jpn.*, **52**, 1559 (1979).
15. M. Matsumura, S. Matsudaira, and H. Tsubomura, *Ind. Eng. Chem. Prod. Res. Dev.*, **19**, 415 (1980).
16. K. Tennakone, *J. Phys. D.*, **16**, L5 (1983).
17. K. Tennakone and W. M. Ariyasinghe, *J. Chem. Phys.*, **72**, 5 (1980).
18. I. L. Finar, "Organic Chemistry," Vol. 1, 5th ed., p. 404, Longman (1975).
19. Cotton and Wilkinson, "Advanced Inorganic Chemistry," 3rd ed., p. 301, John Wiley & Sons, New York (1972).
20. M. Schonhofer, G. Beck, and A. Henglein, *Chem. Ber.*, **74**, 1011 (1970).
21. J. H. Baxendale and D. A. Stott, *Chem. Commun.*, **67**, 699 (1967).
22. K. Tennakone, W. G. D. Dharmaratne, and S. C. Jayawardena, *J. Chem. Soc. Faraday Trans. 1*, **78**, 2279 (1982).
23. D. Bonnet, in "Photoconductivity and Related Phenomena," J. Mort and D. M. Pai, Editors, p. 187, Elsevier, Amsterdam (1976).

Table I. Open-circuit voltage (full spectral range of a W filament lamp at $\sim 40 \text{ W m}^{-2}$)

Dye	V_{oc} (mV)	Efficiency (%)
Methyl violet	850	2.8
Crystal violet	830	2.6
Malachite green	760	2.0
Radamine B	550	—

Methods to Improve Electrochemical Reversibility at Carbon Electrodes

R. Mark Wightman, Mark R. Deakin,* Paul M. Kovach,* Werner G. Kuhr, and Kenneth J. Stutts

Department of Chemistry, Indiana University, Bloomington, Indiana 47405

ABSTRACT

Carbon electrodes are frequently used for electroanalytical studies of oxidizable compounds. However, for many compounds, heterogeneous charge-transfer rates are very slow at carbon electrodes, leading to ill-defined voltammograms. Ascorbic acid (vitamin C) is perhaps one of the best examples of such phenomena, with a peak potential that is approximately 350 mV more positive at most carbon surfaces than at mercury electrodes. Ferricyanide also exhibits voltammetry at carbon electrodes that is less reversible than at noble metal electrodes. Various electrode surface treatments have been employed to accelerate the rates of ascorbate and ferricyanide electrolysis. Pretreatment of carbon fiber electrodes with a high current density results in a significant shift of the voltammetric waves for both compounds to potentials where they are more easily electrolyzed. Similar results are obtained with glassy carbon surfaces that have been heated at 500°C under reduced pressure. An alternate method to increase reversibility is the judicious use of polishing procedures. Thus, it appears that the surface properties of carbon electrodes can have profound effects on the observed voltammetry.

Carbon electrodes are widely used in electroanalytical applications because of the very low residual current over the large potential range accessible in aqueous solution. Several different types of carbon have been employed, including wax impregnated graphite rods (1), carbon powder bound with an inert, viscous liquid [carbon paste, Ref. (2)], glassy carbon (3), pyrolytic graphite (4), and carbon fibers (5). These electrodes have been used in applications as diverse as measuring diffusion coefficients, understanding oxidation mechanisms of organic compounds, and trace analysis (6).

At all of these types of carbon electrodes, very few molecules show diffusion-controlled electrochemical behavior in aqueous solutions, even at the relatively slow scan rates usually employed in voltammetry with conventional X-Y recorders (less than 500 mV s⁻¹). Therefore, the various factors that control charge-transfer processes at carbon electrodes must be considered. In addition to the inherent electron-transfer rates of the molecules being considered, it is also necessary to recognize that the surface of carbon has a rich chemistry of its own (7) that may well affect the observed electrochemistry (8). Charge-transfer rates at the basal plane of cleaved, highly oriented graphite are impaired for several redox couples (8-10). Since microscopic sites of basal orientation may occur on isotropic carbons, the effect of these sites could be convoluted with the observed electrochemistry. At carbon paste electrodes, a decrease in the apparent electrochemical reversibility is observed with an increase in concentration of the pasting liquid. This decrease in reversibility has been attributed to a decrease in sites for electron transfer at the electrode surface (11, 12). An equally important parameter appears to be the degree of oxidation of the carbon surface (13).

In this paper, the relative rates of electron transfer at carbon and metallic electrodes are compared for two different redox systems. The systems studied are ferricyanide, a one-electron, outer-sphere reduction, that has been well characterized previously, and ascorbate, a two-electron oxidation that also involves a proton transfer. It will be shown qualitatively that the rates of these processes are much slower at many forms of carbon than at metallic electrodes, but that these rates can be accelerated by a variety of surface treatments. Faster rates of electron transfer result in well-defined voltammetric behavior. This leads to greater resolution of voltammetric waves, an advantageous feature for chemical analysis.

Experimental

Reagents.—All chemicals were reagent grade and used as received from commercial sources. Ascorbic acid was

*Electrochemical Society Student Member.

Key words: carbon electrodes, carbon fibers, oriented graphite, glassy carbon.

studied in a buffer containing citrate and phosphate (9.2 mM, 181.6 mM, pH 7.4). The reduction of ferricyanide was studied in 0.5M K₂SO₄ or KCl solutions that were adjusted to neutral pH. All solutions were prepared with water distilled in glass from alkaline permanganate and were purged thoroughly with nitrogen before use.

Electrodes and instrumentation.—Carbon paste was prepared by thoroughly mixing carbon powder (UCP-1-M, Ultra Carbon, Bay City, Michigan) with Nujol (20% by weight). The electrode was formed by press fitting a copper rod through a Teflon tube, and packing the well at the end with the carbon paste. Vapor-deposited, pyrolytic graphite-coated disks (1 mm thick) also were obtained from Ultra-Carbon. The disks were fabricated into electrodes with the use of heat-shrinkable Teflon so that only the face of the disk was exposed to the solution. The surfaces were not polished. Electrical connection was made with mercury on the interior of the electrode assembly.

Electrodes fabricated from low-modulus carbon fibers (AS4-6K, Hercules) were constructed by inserting a single carbon fiber in a glass capillary, tapering the glass around the fiber with a commercial pipet-puller (David Kopf Instruments), and sealing the fiber to the glass by carefully placing a drop of epoxy at the end of the glass so that it entered the tube by capillary action. This was done so that the carbon fiber that extends beyond the glass was not coated. Electrodes prepared in this manner have the geometry of a cylinder of micrometer dimensions. Because of their geometry and very small size, voltammograms exhibit a significant contribution from cylindrical diffusion effects.

Experiments which employed carbon-fiber, carbon-paste, and pyrolytic graphite electrodes were conducted in an electrochemical cell fabricated from a 25 ml beaker. All experiments employed a commercial potentiostat (Model 174A, Princeton Applied Research Corporation).

Pressure annealed pyrolytic graphite (PAPG), a highly oriented graphite, was a gift from Union Carbide. This material is sufficiently well oriented that a new basal plane can be exposed by removing the existing one with adhesive tape. Glassy carbon (GC-20, Tokai, Japan) was polished successively with 5.0, 3.0, and 0.05 μm alumina until a mirror finish was obtained. Sheets of the PAPG and the glassy carbon were cut into 2.5 × 0.8 cm rectangles. The rectangles were used as the floor of a cell fabricated from plexiglass and the area (0.0381 cm²) of the electrode exposed to the solution was defined by a polyethylene gasket between the plexiglass and carbon. The upper part of the cell contained the auxiliary and reference electrodes.

Results

Reduction of Fe(CN)₆³⁻ at different forms of carbon.—The negatively charged ion, Fe(CN)₆³⁻, is reduced

in an outer-sphere mechanism. Several investigators have studied its heterogeneous electrochemistry (14-21), and the reaction rate has been found to depend on the electrolyte composition. The reaction rate is greatest in solutions containing potassium ions (17), and the effect of anions on the rate is rather small (18). The results presented here for the reduction of $\text{Fe}(\text{CN})_6^{3-}$ have been obtained in 0.5M K_2SO_4 in order to optimize the solution conditions. Under these conditions, the peak separation for the cathodic and anodic scans (ΔE_p , a measure of the rate of the heterogeneous reaction) at platinum is approximately 70 mV for the cyclic voltammograms of $\text{Fe}(\text{CN})_6^{3-}$. However, increased peak separations are observed at glassy carbon (170 mV), the edge plane of PAPG (190 mV), and carbon paste (380 mV) (Fig. 1). These results were obtained at neutral pH, where differences between platinum and carbon electrodes are more pronounced than in acidic solutions. The greatest peak separation is obtained at the basal plane of PAPG (710 mV). Thus, at all of the unmodified carbon surfaces, the reduction of $\text{Fe}(\text{CN})_6^{3-}$ is significantly slower than at platinum with the slowest rate obtained at the basal plane of PAPG.

Oxidation of ascorbate at carbon electrodes.—The oxidation mechanisms of ascorbic acid and its optical isomer, d-araboascorbic acid, have been studied extensively at gold and mercury electrodes (22-25). At pH 7.4 the oxidation involves the loss of two electrons and one proton. Although the oxidation is chemically irreversible (the oxidized form is rapidly hydrated), the oxidation process is not kinetically hindered at mercury electrodes (Fig. 2). In contrast, the oxidation of ascorbate at glassy carbon is electrochemically less reversible, as characterized by a very drawn-out oxidation wave whose peak is found approximately 350 mV more positive than that observed on mercury. At carbon paste, low-modulus carbon fibers, and the edge orientation of PAPG, the voltammetric peak for the oxidation of ascorbate lies at similar potentials as that of glassy carbon. At pyrolytic graphite the oxidation of ascorbate is even more electrochemically irreversible.

Effects of electrochemical treatments.—Electrochemical treatments can be used to improve the electrochemical reversibility at carbon electrodes (9, 26, 27). For example, electrolysis of the basal plane of PAPG causes an increase

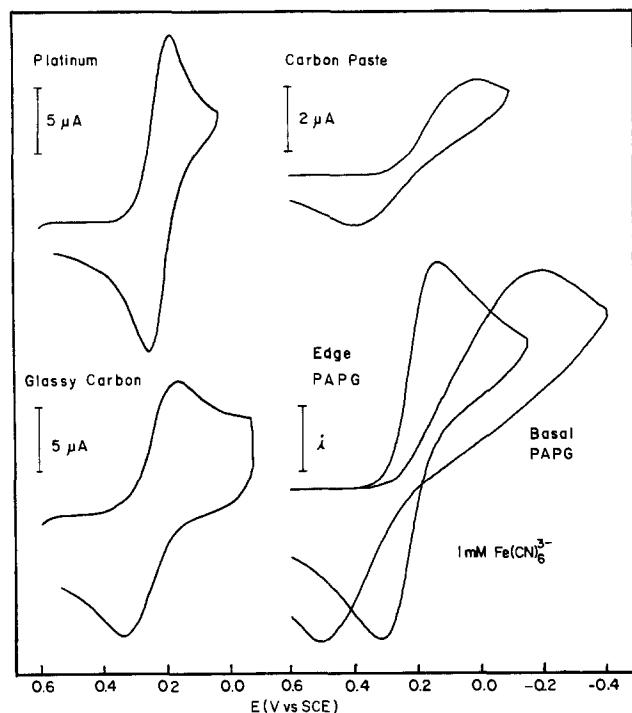


Fig. 1. Cyclic voltammograms of ferricyanide at platinum, carbon paste (20% Nujol), glassy carbon (Tokai GC-20), and pressure-annealed pyrolytic graphite (PAPG, Union Carbide). Conditions: scan rate 0.100 V s^{-1} , $1 \text{ mM Fe}(\text{CN})_6^{3-}$, and $0.5 \text{ M K}_2\text{SO}_4$ neutral solution.

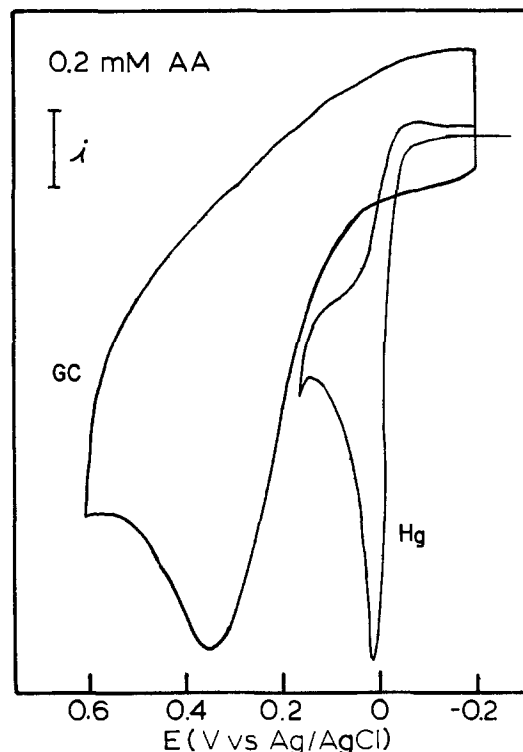


Fig. 2. Cyclic voltammograms of ascorbic acid (AA) at mercury and glassy carbon electrodes. Conditions: scan rate 0.100 V s^{-1} , 0.2 mM AA in pH 7.4 buffer (phosphate).

in the degree of electrochemical reversibility for the reduction of $\text{Fe}(\text{CN})_6^{3-}$ (Fig. 3) and the oxidation of ascorbic acid (Fig. 4). The electrolysis treatment used in this case is relatively mild ($E_{\text{app}} = +1.4 \text{ V vs. SCE}$ in citrate buffer, pH 5.2, 8 mA cm^{-2} current density, 20 min). Background scans of the treated electrodes have not shown peaks near 0.2V, usually attributed to quinone functional groups on the surface. This method has been used to fabricate an electrode surface that is useful as an amperometric liquid chromatography detector (10). Identical electrochemical reversibility is obtained with pyrolytic graphite disks after they have been exposed to a RF plasma (28), a treatment that has been shown to shift ascorbate oxidation to that observed on the edge orientation. However, with the basal plane of PAPG or with pyrolytic graphite, these

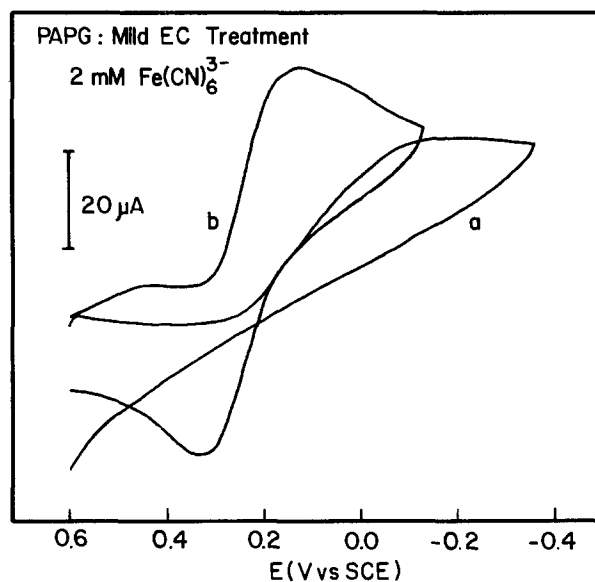


Fig. 3. Cyclic voltammograms of ferricyanide at the basal plane of PAPG (curve a) fresh surface (curve b) after 15 min electrolysis at $+1.5 \text{ V}$. Conditions: scan rate 0.100 V s^{-1} , $2 \text{ mM Fe}(\text{CN})_6^{3-}$, $0.5 \text{ M K}_2\text{SO}_4$, pH 3.0.

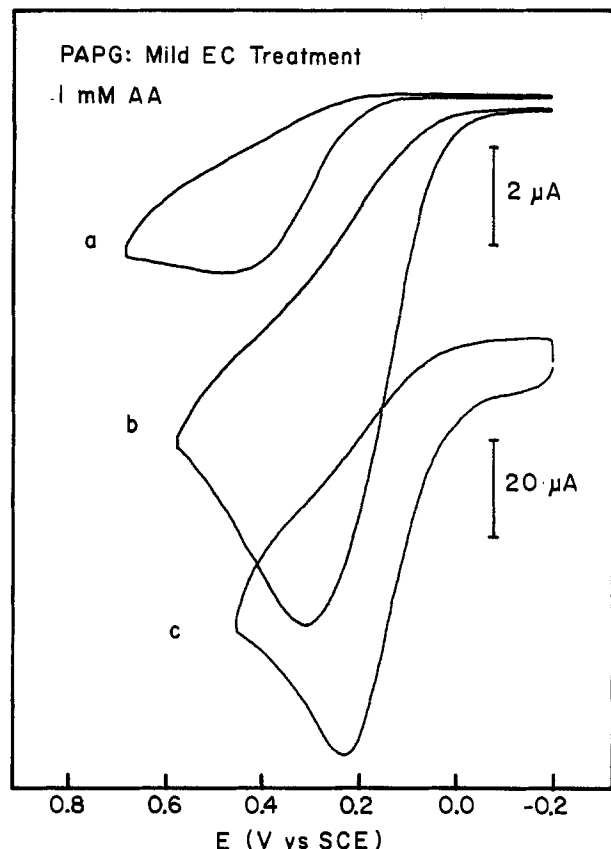


Fig. 4. Cyclic voltammetry of ascorbic acid (AA) at pressure-annealed pyrolytic graphite (PAPG) (curve a) at the basal plane before electrolysis (curve b) at the basal plane after 20 min electrolysis at +1.4V, and (curve c) at edge-oriented PAPG. Conditions: scan rate 0.100 V s^{-1} , 1.0 mM AA , $\text{pH } 7.4$.

mild surface treatments are only able to give electrochemical reversibility that is comparable to that observed at carbon paste or the edge orientation of PAPG. Both the plasma and electrochemical treatments on these types of carbon give an increased amount of surface roughness (10, 13, 29), and thus an increased amount of edge orientation exposed to the solution.

The small surface area of carbon fibers permits much greater current densities to be applied to these electrodes. Exposure to high current densities (2 A/cm^2) leads to an increase in surface functionalities (30), and a decrease in the interior order of the fibers (31). However, this type of treatment has been shown to increase the electrochemical reversibility of several compounds, including the catecholamines (32). The voltammetric wave for the oxidation of ascorbate is shifted to the potential where it occurs on mercury electrodes (Fig. 5). This treatment also causes an increase in the electrochemical reversibility for the reduction of $\text{Fe}(\text{CN})_6^{3-}$ (Fig. 5). The change in shape of the voltammogram from sigmoidal to peaked is either a reflection of the greatly altered microscopic area of the electrode or an increase in the amount of adsorption.

Effect of polishing procedures.—Carbon materials, such as low-modulus carbon fibers, the basal plane of PAPG, and pyrolytic graphite, can be used without preparation of the surface. Thus, electrochemistry at these surfaces reflects the properties of the carbon that were determined during its manufacture. In contrast, the response obtained at glassy carbon surfaces is highly dependent on the manner in which the surface is prepared (3). Most investigators polish the surface to a mirror-like surface using a fine grade of alumina. A highly polished surface is found to have low residual current, resulting in a more usable electrode for analytical applications. However, surface analysis has shown that the polishing material may be embedded in the surface (33), and this may affect the electrochemical results.

Previously, it has been shown that certain polishing procedures can provide more reversible electrochemical

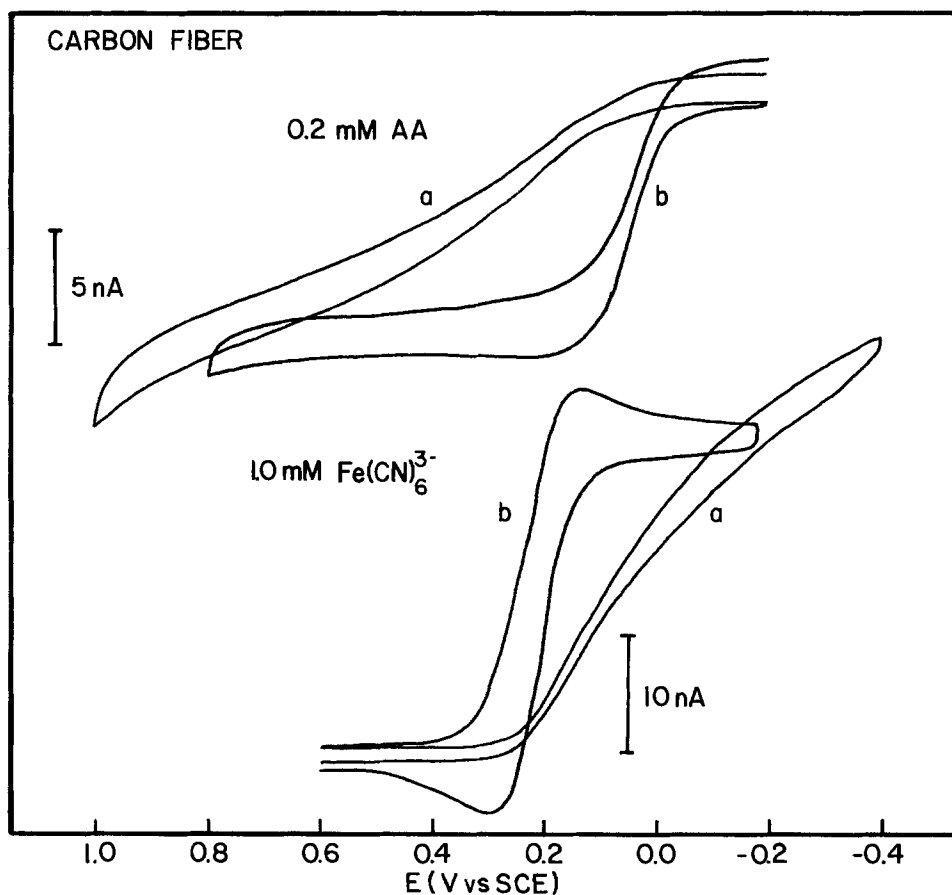


Fig. 5. Cyclic voltammetry of ascorbic acid (above) and ferricyanide (below) at low-modulus carbon fiber (curves a) untreated carbon fiber (curves b) electrolyzed carbon fiber ($0 - +3.0\text{V}$, 70 Hz , 20s , $+1.5\text{V } 20\text{s}$). Conditions: scan rate 0.100 V s^{-1} , 0.2 mM AA , $1 \text{ mM Fe}(\text{CN})_6^{3-}$, $\text{pH } 7.4$.

behavior. For example, glassy carbon electrodes prepared by polishing the electrode with α -alumina (1 μm particle size) exhibit a shift in the oxidation wave for ascorbate in pH 7.0 buffer to the potential observed on mercury (34). X-ray photoelectron spectroscopic and electron microscopic examination of the surface show that this treatment embeds the alumina on the surface. This alumina-coated surface is highly efficient at adsorbing organic species which leads to the observed increase reversibility of oxidation. The rate of reduction of $\text{Fe}(\text{CN})_6^{3-}$ at glassy carbon electrodes can be increased by polishing with alumina using high rotation speeds [1500 rpm, Ref. (35)].

The effects of polishing procedures can be minimized if the electrode surface is carefully cleaned before use. The use of ultrasonic cleaning (34) or soxhlet extraction of the electrode surface have been found to be effective. For glassy carbon that has been hand polished with 0.05 μm alumina, no change is observed in the reduction of $\text{Fe}(\text{CN})_6^{3-}$ on freshly polished surfaces or surfaces that have been polished and extracted in toluene ($\Delta E_p = 160$ mV at 100 mV/s scan rate, 0.5M K_2SO_4 , pH 7.4). Electrochemistry at surfaces prepared in this manner is very similar to that obtained at the edge orientation. Soxhlet extraction of glassy carbon electrodes in a more active solvent does affect the reversibility: the use of methanol results in a large increase in the reversibility of $\text{Fe}(\text{CN})_6^{3-}$. Thus, for voltammetric studies with glassy carbon, the electrode has been refluxed in toluene subsequent to surface polishing with 0.05 μm alumina, and this has been used as the control surface with which comparisons of reversibility can be made with carbon surfaces treated by alternate means.

Recent investigations in our laboratory have shown that increased rates can be obtained at glassy carbon surfaces that have been polished with diamond paste and subsequently soxhlet extracted with toluene. The reversibility of both $\text{Fe}(\text{CN})_6^{3-}$ and ascorbate is improved over that obtained at the control electrode (Fig. 6). A large shift is seen for the oxidation of ascorbate, but the effect on $\text{Fe}(\text{CN})_6^{3-}$ is less pronounced. Adsorption is not evidenced for the compounds tested. The surface gives reproducible behavior for repeated scans.

Heat-treated carbon surfaces.—Heat-treatment of glassy carbon surfaces (36) or carbon fibers significantly improves the observed electrochemical reversibility. The carbon to be treated is heated to 500°C under 1 torr of vacuum for two or more hours. As with the electrodes pol-

ished with diamond paste, a drastic improvement in reversibility is observed. This is illustrated for the oxidation of ascorbate at a carbon fiber electrode in Fig. 7.

The heat-treatment produces identical results at glassy carbon. The heat-treatment only involves a surface change since abrading the carbon surface eliminates the effects of heat-treatment. The effects of the heat-treatment are long lasting both in solution and when exposed to the laboratory atmosphere. Surface analysis of heat-treated glassy carbon using x-ray photoelectron spectroscopy shows only a small change in the C_{1s} region of the spectrum (Fig. 8). These changes presumably reflect a change in oxygen binding to the surface; however, they are too small for quantitative information. Examination of the surface with electron microscopy reveals no change in the surface morphology.

Discussion

The data in this paper clearly show that the degree of electrochemical reversibility for the compounds tested at carbon electrodes is highly dependent on the surface state of the carbon. Differences are very profound between the edge and basal plane of PAPG. Mild electrochemical treatment of the basal plane results in a surface that yields electrochemistry comparable to the edge orientation. Slow rates are also found at the pyrolytic disks; however, the rates can be accelerated by electrochemical or RF etching procedures. Since all of these treatments roughen the surface, with a corresponding increase in edge orientation, the data suggest that charge transfer is severely impaired at the basal plane, and that the presence of sites of edge orientation is necessary for electron transfer to occur. The slow rate of electron transfer at the basal plane may have several different origins. One that has been proposed is that the basal surface is hydrophobic, and thus wetting of the electrode by aqueous solutions is impaired (37). The edge orientation is formed by cleaving carbon-carbon bonds. If this is done in air or aqueous solutions, oxygen containing functional groups can be formed on the surface, resulting in a more polar surface than the basal plane (8).

Isotropic carbons such as carbon paste, low-modulus carbon fibers, and glassy carbon all show electrochemistry that is similar in degree of reversibility to that obtained at the edge orientation. With carbon paste, the interpretation of the results is complicated, since the degree of reversibility is affected by the pasting composition (12).

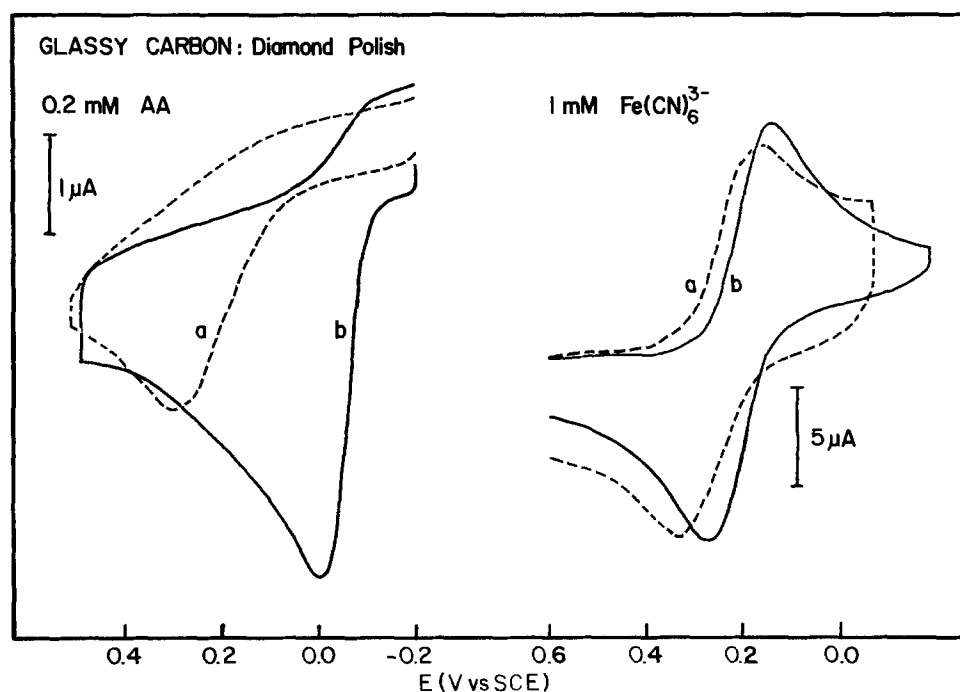


Fig. 6. Cyclic voltammetry of ascorbic acid (left) and ferricyanide (right) at glassy carbon. Curves a: control. Curves b: after polishing with 1 μm diamond paste and extracting in toluene 2h. Conditions: scan rate 0.100 V s^{-1} , 0.2 mM AA, 1 mM $\text{Fe}(\text{CN})_6^{3-}$, pH 7.4.

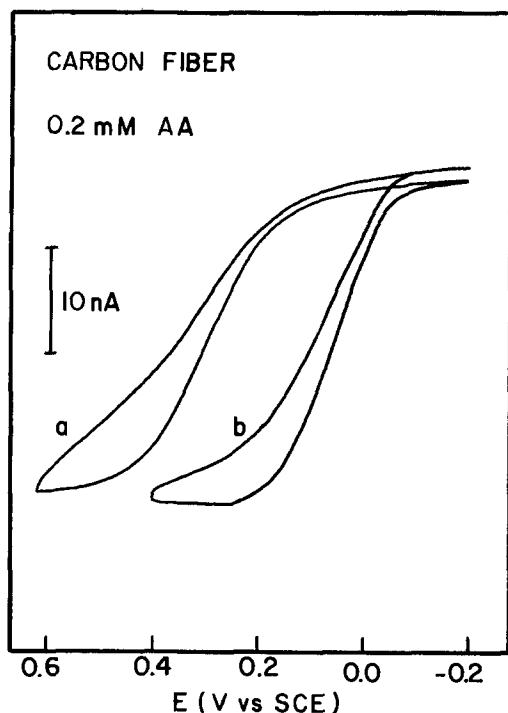


Fig. 7. Oxidation of ascorbic acid at carbon fiber. Curve a: untreated carbon fiber. Curve b: after 4.5h heat-treatment at 540°C under reduced pressure, cooled in air. Conditions: scan rate 0.100 V s⁻¹, 0.20 mM AA, pH 7.4.

However, even with a dry paste, the rate for Fe(CN)₆³⁻ reduction is much slower than that observed at platinum electrodes (13, 35). Mild electrochemical treatments, which accelerate the observed rates on the basal plane of PAPG and on pyrolytic graphite, do not affect the rates at glassy carbon. Rather, it appears that the mild electrochemical treatments simply alter the morphology of the basal plane so that electrochemical results are obtained which are similar to the isotropic carbons. Electrochemical rates are found to be slower on the cylindrical axis of high modulus carbon fibers when compared to low-modulus carbon fibers (data not shown). This may arise because high modulus fibers have a greater degree of basal character on the cylindrical axis than the low modulus fibers.

Thus, to increase electrochemical reversibility at carbon, it appears that an important step is to increase the

availability of edge orientation. However, this approach reaches a limit, defined by the nature of edge orientation. The rates observed at edge-oriented carbon are slower than at metal electrodes for both of the compounds tested, which have very different electrolysis mechanisms. As shown, other changes which favorably affect the electrochemistry can also be accomplished, at least for the compounds examined here. Heat-treatment, high current density, and certain polishing techniques all significantly increase the rates that are observed at carbon electrodes. Rates at some treated surfaces approach those observed on metal electrodes. Polishing and the application of a high current density both evolve heat. Thus, these results may have a common origin. It is established that these surface treatments alter the chemical nature of the functional groups on the surface (31, 38). This may be the cause of the increased reversibility. For example, the removal of carboxyl groups would be expected to enhance the rate of the negatively charged compounds examined in this study. Surface spectroscopy (Fig. 8) does not indicate a loss of oxygen functionalities. However, spectral resolution of surface oxides in this experiment is poor. Alteration of surface sites would certainly produce changes in the double layer structure. These variations which can affect surface hydrophobicity or the double layer potential could play a dominant role in the variation of observed rate constants at carbon surfaces. Future studies of the nature of the physical and chemical nature of the surface of these carbon materials will be required to understand the origin of these results.

Acknowledgments

This work was supported by NSF and the U.S. Army Research Office (CHE 81-21422). R. M. W. is an Alfred P. Sloan Fellow and the recipient of a Research Career Development Award (KO4-NS-356).

Manuscript submitted Sept. 26, 1983; revised manuscript received Dec. 5, 1983.

Indiana University assisted in meeting the publication costs of this article.

REFERENCES

1. P. J. Elving and D. L. Smith, *Anal. Chem.*, **32**, 1849 (1960).
2. R. N. Adams, *ibid.*, **30**, 1576 (1958).
3. W. E. Vander Linden and J. W. Dieker, *Anal. Chim. Acta*, **119**, 1 (1980).
4. H. A. Laitinen and D. R. Rhodes, *This Journal*, **109**, 413 (1962).
5. M. A. Dayton, J. C. Brown, K. J. Stutts, and R. M. Wightman, *Anal. Chem.*, **52**, 946 (1980).
6. R. N. Adams, "Electrochemistry at Solid Electrodes," Marcel Dekker, New York (1969).

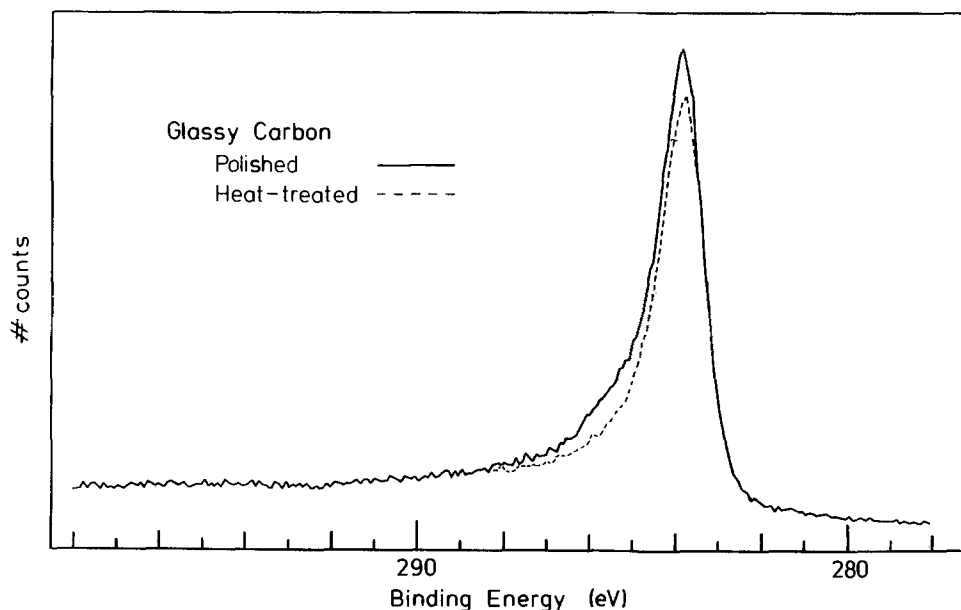


Fig. 8. X-ray photoelectron spectrum of C_{1s} peak of glassy carbon. Solid line: control. Broken line: after 4h heat-treatment at 540°C under reduced pressure and cooled in air.

7. R. E. Panzer and P. J. Elving, *Electrochim. Acta*, **20**, 635 (1975).
8. R. E. Panzer and P. J. Elving, *This Journal*, **119**, 864 (1972).
9. I. Morcos and E. Yeager, *Electrochim. Acta*, **15**, 953 (1970).
10. R. M. Wightman, E. C. Paik, S. Borman, and M. A. Dayton, *Anal. Chem.*, **50**, 1410 (1978).
11. R. Neeb, I. Kiehnast, and A. Narayanan, *Z. Anal. Chem.*, **262**, 339 (1972).
12. M. E. Rice, Z. Galus, and R. N. Adams, *J. Electroanal. Chem.*, **143**, 89 (1983).
13. J. F. Evans and T. Kuwana, *Anal. Chem.*, **49**, 1632 (1977).
14. Z. Galus and R. N. Adams, *J. Phys. Chem.*, **67**, 866 (1963).
15. A. N. Frumkin, O. A. Petry, and N. V. Nikolaeva-fedorovich, *Electrochim. Acta*, **8**, 177 (1963).
16. D. H. Angell and T. Dickinson, *J. Electroanal. Chem.*, **35**, 55 (1972).
17. L. M. Peter, W. Durr, P. Binora, and H. Gerischer, *ibid.*, **71**, 31 (1976).
18. P. Kulesza, T. Jedral, and Z. Galus, *ibid.*, **109**, 141 (1980).
19. J. Kuta and E. Yeager, *ibid.*, **59**, 110 (1975).
20. L. Muller and S. Dietzsch, *ibid.*, **121**, 255 (1981).
21. T. J. Meyer and H. Taube, *Inorg. Chem.*, **7**, 2369 (1968).
22. R. Brdicka and P. Zuman, *Coll. Czech. Chem. Commun.*, **15**, 766 (1950).
23. M. Rueda, A. Aldaz, and F. Sanchez-Burgos, *Electrochim. Acta*, **23**, 419 (1978).
24. A. Aldaz and A. M. Alquie, *J. Electroanal. Chem.*, **47**, 532 (1973).
25. C. Acerete, L. Garrigos, J. Guillime, E. Diez, and A. Aldaz, *Electrochim. Acta*, **26**, 1041 (1981).
26. W. J. Blaedel and R. A. Jenkins, *Anal. Chem.*, **47**, 1337 (1975).
27. R. C. Engstrom, *ibid.*, **54**, 2310 (1982).
28. J. F. Evans, T. Kuwana, M. T. Henne, and G. P. Royer, *J. Electroanal. Chem.*, **80**, 409 (1977).
29. H. J. Wieck, R. F. Antrim, A. M. Yacynych, and V. A. Greenhut, *Analyst*, **107**, 951 (1982).
30. A. Proctor and P. M. A. Sherwood, *Carbon*, **21**, 53 (1983).
31. E. Theodoridou, J. O. Besenhard, and H. P. Fritz, *J. Electroanal. Chem.*, **122**, 67 (1981).
32. F. G. Gonon, C. M. Fombarlet, M. J. Buda, and J. F. Buda, *Anal. Chem.*, **53**, 1386 (1981).
33. J. F. Evans and T. Kuwana, *ibid.*, **51**, 358 (1979).
34. J. Zak and T. Kuwana, *J. Am. Chem. Soc.*, **104**, 5514 (1982).
35. J. Jordan, Abstract 502, p. 52, Pittsburgh Conference on Analytical and Applied Spectroscopy, Pittsburgh, PA., March 8-12, 1982.
36. K. J. Stutts, P. M. Kovach, W. G. Kuhr, and R. M. Wightman, *Anal. Chem.*, **55**, 1632 (1983).
37. I. Morcos, *J. Chem. Phys.*, **57**, 1801 (1972).
38. A. Proctor and P. M. A. Sherwood, *J. Elect. Spectrosc. Relat. Phenom.*, **27**, 39 (1982).

Deposition and Stripping of Mercury at Gold Electrodes in Acidic Media

I. Voltammetric Studies

Lois A. Schadewald, Timothy R. Lindstrom,¹ Wedad Hussein,² Eric E. Evenson,³ and Dennis C. Johnson*

Department of Chemistry and Ames Laboratory - U.S. Department of Energy,⁴ Iowa State University, Ames, Iowa 50011

ABSTRACT

The maximum quantity of bulk Hg(0) which can exist on the surface of a gold electrode in acidic media corresponds to a coverage of $\theta_{\text{Hg}(0)} = 1$. Deposited Hg(0) in excess of this quantity diffuses into the Au substrate to form a bulk Au-Hg alloy; however, no alloy is formed until $\theta_{\text{Hg}(0)} = 1$. The potential for the stripping peak of the Au-Hg alloy is positive of the peak potential for the stripping of bulk Hg(0) by ca. 0.4V. The diffusion rate for Hg in the Au-Hg alloy is sufficiently slow so that the alloyed Hg is never totally stripped under the usual condition of cyclic voltammetry. Evidence is also given for the formation of Hg(I) adions during the underpotential deposition process for which $n_{\text{app}} = 1.6 \text{ eq mol}^{-1}$.

The underpotential deposition and stripping (UPD and UPS) of the equivalent of up to a monolayer of Hg adatoms/ions at Au electrodes in acidic media has been studied by Sherwood and Bruckenstein (1) and Lindstrom (2). The apparent number of electrons, n_{app} , involved in the formation of the adlayer was determined from ring-disk experiments to be 1.8 eq mol^{-1} (1). Several anodic peaks are observed for the UPS of the complete adlayer of Hg, which is consistent with the conclusion that more than one surface state exists for the deposited Hg, even in the first single adlayer. For a very small quantity of UPD Hg, e. g., $\theta_{\text{Hg}} < 0.1$, a single, sharp, anodic stripping peak is obtained at a potential difference (ΔE) of approximately 0.5V with respect to the stripping peak for bulk Hg(0). The value of n_{app} for $\theta_{\text{Hg}} < 0.1$ was determined in our laboratory by flow-injection coulometry to be 1.6 eq mol^{-1} (3), which is in reasonable agreement with the

value reported for the full ad layer by Sherwood and Bruckenstein (1). The energy of stabilization for the initial UPD of Hg on Au, i. e., $\Delta G_{\text{stab}} = -n_{\text{app}} F(\Delta E)$, is estimated to be $18.4 \text{ kcal mol}^{-1}$ for $n_{\text{app}} = 1.6$. The value of $n_{\text{app}} = 1.6$ corresponds approximately to a closest-packed model for the product of UPD in which Hg(I) is coadsorbed with Hg(0) in the ratio 1:2 (3). Accordingly, each Hg(I) is bound in a cluster with six Hg(0) adatoms and each Hg(0) is bound to three Hg(I) adions and three other Hg(0) adatoms. The UPD of Hg clusters having mixed oxidation states for $\theta_{\text{Hg}} < 0.1$ has not been proved; however, evidence for the existence of Hg(I) adions as proposed in this model is presented here. The UPD and UPS of Hg in the adlayer at low surface coverage has been the basis of quantitative determinations of Hg(II) at the ppb level and below (4-6).

The area under the combined anodic peaks for the UPS of Hg at a freshly polished Au rotating-disk electrode (Au RDE), on which bulk Hg(0) is deposited under conditions of cyclic voltammetry, is observed to increase with scan number. Furthermore, the ratio of the integrated anodic and cathodic charges (Q_a/Q_c) becomes constant only after many successive triangular potential scans; however, the ratio is always less than 1.0. We report here the results of a study of this phenomenon by cyclic voltammetry at an Au RDE and an Au, coulometric, flow-through electrode.

*Electrochemical Society Active Member.

¹ Present address: E. I. du Pont de Nemours and Company, Parkersburg, West Virginia.

² Present address: Department of Chemistry, Jackson State University, Jackson, Mississippi.

³ Present address: Control Laboratory, Eli Lilly and Company, Indianapolis, Indiana

⁴ Operated for the U.S. Department of Energy by Iowa State University under Contract no. W-7504-ENG-82.

Experimental

Instrumentation.—The Au ring-disk electrode (Model DT6; R_1 , R_2 , and $R_3 = 0.382$, 0.399 , and 0.422 cm respectively; $\beta^{2/3} = 0.352$; $N = 0.177$) and a Model MSR rotator were from Pine Instrument Company, Grove City, Pennsylvania. The electrode was polished according to customary metallographic procedures using $1.0 \mu\text{m}$ alumina on Buehler microcloth. The electrolysis cell was of a conventional design with a miniature calomel reference electrode (no. 476017), Corning Scientific Instruments, and a Pt-wire counterelectrode. All potentials are given with respect to this reference electrode (V vs. SCE). Nitrogen was dispersed through the solutions in the cell to remove dissolved O_2 prior to voltammetric studies, and an inert atmosphere was maintained over the solution during experimentation. The potentiostats (Models RDE-2 and RDE-3) were from Pine Instrument Company, and the X-Y recorder (Model 7035B) was from Hewlett Packard Instruments. The Au flow-through electrode for flow-injection coulometry has been described previously (3). All work with this electrode was performed under O_2 -free conditions within a dry box which was flushed with N_2 for 24h prior to experimentation.

Chemicals.—All chemicals were Analytical Reagents from Mallinckrodt, Incorporated, or Fisher Scientific Company. The supporting electrolyte was 2.0M HNO_3 , 1.0M H_2SO_4 , or 0.1M HClO_4 . Standard solutions of Hg(II) were prepared by slow dissolution of the triply distilled metal in warm nitric acid, followed by stepwise dilutions with supporting electrolyte. All water was triply distilled with demineralization after the first distillation; the second distillation was from an alkaline solution of KMnO_4 .

Results and Discussion

Cyclic voltammetry at the Au RDE.—Results were virtually identical for the three acidic solutions investigated, and only representative data are shown. Current-potential (I-E) curves obtained at the Au disk of the RRDE and shown in Fig. 1 are characteristic of the changes in voltammetric response observed for a freshly polished Au electrode with consecutive triangular scans of applied potential in $1.0 \times 10^{-4}\text{M}$ Hg(II) . Bulk Hg(0) is stripped from the electrode on the positive sweep at 0.4V (peak A) by the reaction $\text{Hg(0)} \rightarrow \text{Hg(I)} + e$, i.e., $n = 1$ (1, 2). The anodic current observed in the range $0.45\text{--}1.00\text{V}$ for the UPS corresponds to stripping of Hg stabilized by interaction with the Au substrate to produce Hg(II) , i.e., $n = 2$ (1, 2). The cumulative area of the stripping peaks in the range $0.45\text{--}1.00\text{V}$ increases for successive triangular scans, finally becoming constant after 10-20 scans. Whereas several anodic peaks can be observed for UPS of the complete adlayer, i.e., $\theta_{\text{Hg}} \cong 1$ (1-3), these peaks cannot be discerned in comparison to the very large single peak (B) when bulk Hg(0) has been deposited.

The majority of the current for peak B is tentatively concluded to correspond to the stripping of Hg from a bulk Au-Hg alloy, which is formed within the electrode following deposition of a large quantity of bulk Hg(0) at $E < 0.4\text{V}$. When the I-E curves obtained for the Au RDE had become reproducible (ca. 20 triangular scans) the electrode was electrochemically stripped of deposited mercury by application of the triangular waveform of applied potential for approximately 15 min in a solution of supporting electrolyte without added Hg(II) . The electrode was then returned to the solution used for producing Fig. 1 and successive I-E curves were recorded. The curve for the first scan contained peak B with an area nearly equivalent to the reproducible value obtained after 20 scans in the previous experiment which produced Fig. 1. If the electrode was polished after stripping in the supporting electrolyte, the area of peak B in the succeeding I-E curves obtained for the Hg(II) solution was again slow to be reestablished, as shown in Fig. 1. We conclude that a significant fraction of the Hg(0) deposited at $E < 0.4\text{V}$ under these conditions diffuses into the Au electrode, per-

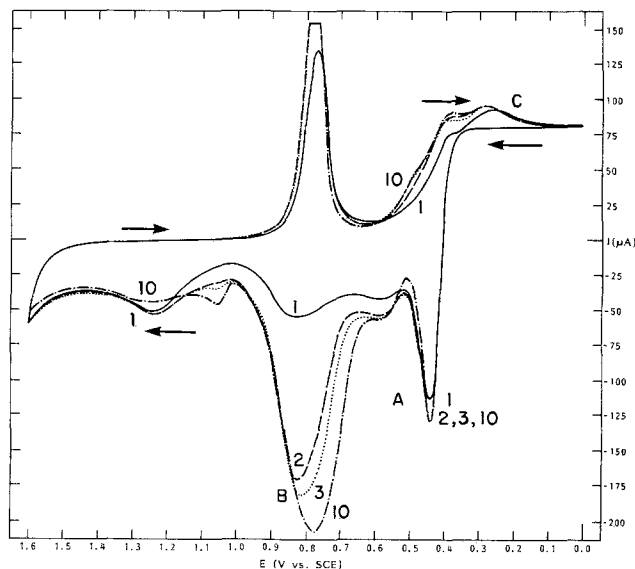


Fig. 1. I-E curves for Hg(II) at a Au RDE in 0.1M HClO_4 . Conditions: $C^b_{\text{Hg(II)}} = 1.0 \times 10^{-4}\text{M}$ Hg(II) , $W = 3600 \text{ rev min}^{-1}$, $\phi = 2.0 \text{ V min}^{-1}$. Scan number given in figure.

haps along grain boundaries, to form a bulk Au-Hg alloy. The Hg in the alloy very near the surface of the electrode is quickly oxidized by the UPS process; however, the Hg which has diffused to a significant depth within the Au is not completely stripped during the time in which the potential is in the region of UPS during the positive potential scan. Such behavior can be interpreted on the basis of differences in the solid-state diffusion rates of Hg for the deposition and stripping processes. Diffusion is the direct result of an activity gradient, and the gradient resulting from the deposition of bulk Hg(0) having an activity of 1.0 will be significantly higher than that corresponding to the stripping process, where, even for a large concentration of the Au-Hg alloy, the activity of Hg in the alloy is much less than 1.0. For $E > 1.0\text{V}$, the oxide formed on the Au surface might serve also as a barrier against diffusion of Hg from the bulk alloy to the electrode surface. When the oxide has been cathodically removed from the Au surface on the negative potential scan to ca. 0.7V , the electrode potential is more negative than required for complete anodic stripping of the Au-Hg alloy. Hence, a significant quantity of Hg can be trapped within the Au electrode under the voltammetric conditions typically used in these studies. X-ray analysis of Au electrodes previously plated with bulk Hg(0) and then stripped at 1.6V confirmed the retention of Hg in Au electrodes. Those results will be reported in the future.

Based on the results of Fig. 1 and the general knowledge that Au is extensively amalgamated when placed in contact with liquid Hg(0) , it was anticipated that the area of peak B could be varied substantially by altering the quantity of bulk Hg(0) deposited at $E < 0.4\text{V}$ without significant change in area of peak A for stripping of bulk Hg(0) . This was confirmed, and typical data are shown in Fig. 2. The triangular sweep of the electrode potential was interrupted on the negative scan at 0.00V for time periods increased by 5s intervals from 0-20s on successive triangular scans. The area of peak A, for anodic stripping of bulk Hg(0) , did not change; only peak B increased, for stripping the Au-Hg alloy. For other experiments in solutions of higher concentration of Hg(II) than used for Fig. 2, the area of peak B was several times larger than shown in Fig. 2 without an increase in peak A. The area of peak A in Fig. 2 was determined with a planimeter, based on the triangular approximation shown in Fig. 2, to correspond to $235 \mu\text{C}$ for the stripping of bulk Hg(0) , i.e., $n = 1$ (1, 2). Using $20 \mu\text{F cm}^{-2}$ (7, 8) as the double layer capacity for polycrystalline Au, the roughness factor was estimated from the charging current at 0.0V vs. SCE to be ca. 2.5 for the Au electrode polished with $1.0 \mu\text{m}$ alumina.

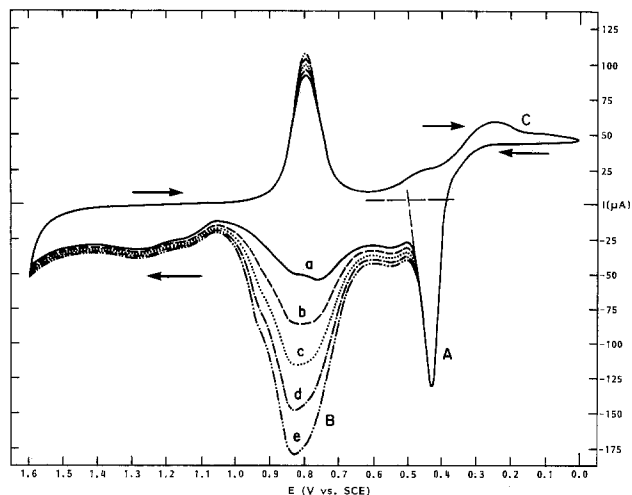


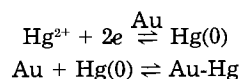
Fig. 2. I-E curves for Hg(II) at a Au RDE in 0.1M HClO₄. Conditions: $C_{\text{Hg(II)}}^b = 5.0 \times 10^{-5} \text{M}$, $W = 3600 \text{ rev min}^{-1}$, $\phi = 2.0 \text{ V min}^{-1}$. Time delay at 0.0V: curve a = 0s, curve b = 5s, curve c = 10s, curve d = 15s, and curve e = 20s.

Furthermore, based on a packing density of 1.5×10^{15} at. cm^{-2} for pure Au, the limiting area of peak A is calculated to correspond to the equivalent of 0.85 atomic layer of bulk Hg(0). Since the triangular approximation of peak A will underestimate the true area, we conclude the limiting coverage corresponds to $\theta_{\text{Hg(0)}} = 1$.

A slight increase in surface roughness of the Au electrode is a result of the deposition and stripping process. The area of the cathodic peak for reduction of the surface oxide on the negative scan (ca. 0.9V) is observed to increase slightly, and the anodic current for formation of the surface oxide is observed also to increase with each successive scan, as shown in Fig. 2. The increased cathodic charge for oxide reduction is not, however, as large as the increased anodic charge for $E > 1.0\text{V}$. We conclude that Hg which has diffused into the interior of the Au during deposition of bulk Hg(0) continues to be stripped for $E > 1.0\text{V}$ at a rate controlled by the solid-state diffusion of Hg. As peak B is increased, corresponding to the formation of larger quantities of alloy, a greater amount of Hg remains within the Au after the alloy near the surface is stripped and the anodic current for $E > 1.0\text{V}$ is increased. The gold oxide, therefore, is not a totally effective barrier against diffusion of Hg from the interior of the electrode to the electrode-solution interface.

The Au electrode was polished after obtaining the data in Fig. 2 and returned to a solution of $2.0 \times 10^{-4} \text{M}$ Hg(II). The I-E curves for 40 consecutive triangular scans of electrode potential were recorded on a stripchart recorder. The areas corresponding to deposition and stripping of bulk Hg(0) and the Hg-Au alloy were determined by a planimeter; representative values of the ratio Q_a/Q_c are plotted in Fig. 3 as a function of scan number. The increase in the ratio after scan 15 is barely perceptible in Fig. 3. The average for scans 15-40 is $Q_a/Q_c = 0.81$ with a standard deviation of 0.03. The triangular potential scans were continued, and the I-E curves recorded for scans 71 and 72, for which the charge ratio had the values 0.83 and 0.85, respectively. One factor contributing to the observation of values of the charge ratio less than unity is that bulk Hg(0) is deposited with $n = 2$, whereas it is stripped (peak A) with $n = 1$ (1, 2). The charge ratio for scan 72 was adjusted for this fact by integrating twice the triangular approximation of peak A (as indicated in Fig. 2) in the computation of Q_a . The adjusted value for Q_a/Q_c is 0.91. Indeed, the Hg deposited even for scan 72 apparently is not totally stripped during the subsequent positive potential sweep, and the quantity of the Au-Hg alloy continues to increase slowly even after so large a number of consecutive triangular potential sweeps.

The formation of the Au-Hg alloy requires the prior deposition of bulk Hg(0) in the equivalent of $\theta_{\text{Hg(0)}} = 1$, even when the Hg-Au alloy has been formed on previous scans for $E < 0.4\text{V}$, but only partially stripped during the positive scan for $E > 0.4\text{V}$



This was demonstrated when the negative potential scan for the Au RDE in $1.0 \times 10^{-4} \text{M}$ Hg(II) was interrupted for 1.0 min at 0.45V. The subsequent positive sweep from 0.45V resulted in an I-E curve with the virtual absence of peak B, even though 0.45V is substantially negative of the peak potential (0.8V) for stripping of the Au-Hg alloy. No bulk Hg(0) is deposited at 0.45V, and, consequently, no alloy was formed. Clearly, the formation of the Au-Hg alloy can only occur if an activity gradient for Hg(0) exists which can bring about diffusional mass transport into the Au substrate. As described above, this diffusional transport ceases when the quantity of bulk Hg(0) has decreased to the equivalent of $\theta_{\text{Hg(0)}} = 1$.

Cyclic voltammetry at the Au RDE.—A cathodic peak (peaks C in Fig. 1 and 2) is obtained on the limiting current plateau for deposition of Hg(0) during the negative

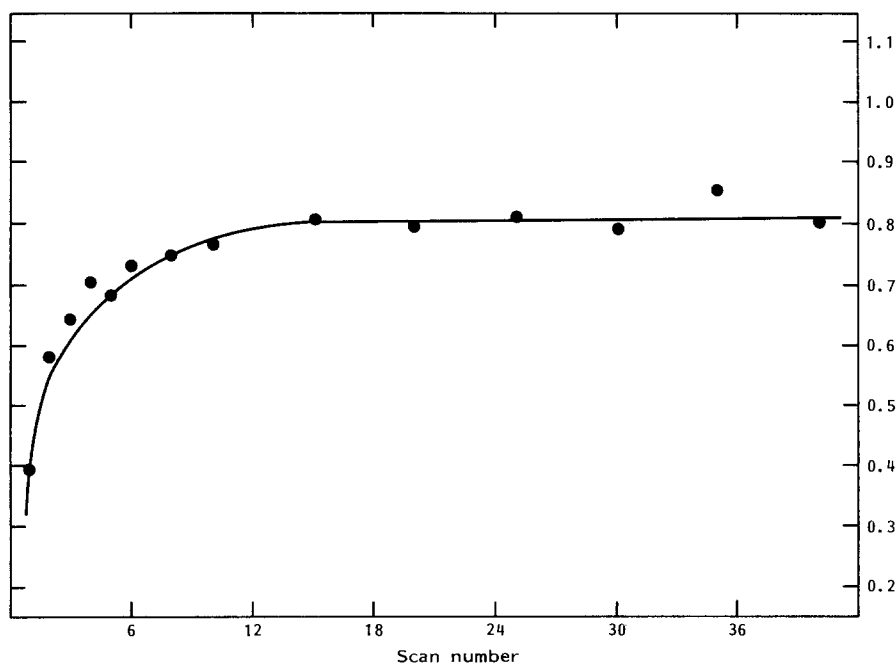


Fig. 3. Q_a/Q_c vs. scan number for Hg(II) at Au RDE in 0.1M HClO₄. Conditions: $C_{\text{Hg(II)}}^b = 5.0 \times 10^{-5} \text{M}$, $W = 3600 \text{ rev min}^{-1}$, $\phi = 2.0 \text{ V min}^{-1}$.

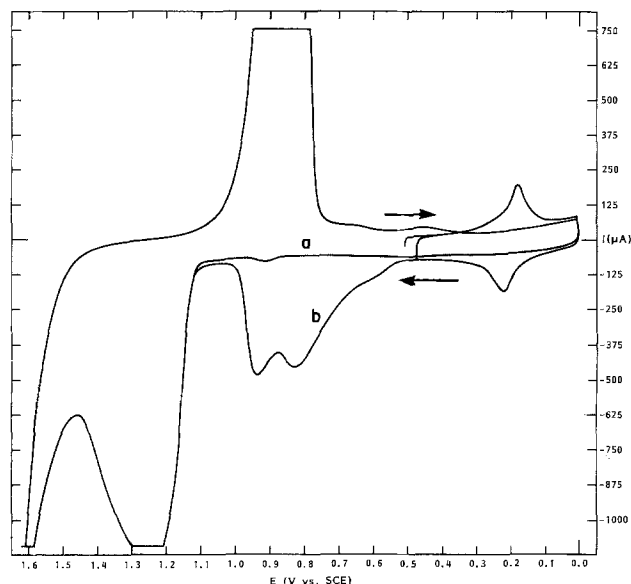


Fig. 4. I-E curves for a Au coulometric electrode. Conditions: $C_{\text{Hg(II)}}^b = 1.28 \times 10^{-4} \text{M}$, $V_s = 193 \mu\text{l}$, Carrier stream: $1.0 \text{M H}_2\text{SO}_4$, $v_f = 0.5 \text{ ml min}^{-1}$. Curve: o = blank, b = following deposition of Hg at 0.5V.

potential scan for $E \sim 0.3 \text{V}$. This peak current is in excess of the mass-transport-limited value for Hg(II) and is concluded tentatively to correspond to the reduction of Hg(I) adions produced on the Au surface for $E > 0.40 \text{V}$. Shielding and collection experiments with the Au ring-disk electrode confirmed the absence of any soluble species produced or consumed at the disk electrode corresponding to peak C (2). The area of peak C for scan 1 in Fig. 1 was determined to be $40 \mu\text{C cm}^{-2}$, which corresponds to an estimated surface coverage of 0.17 for Hg(I). This value is compared to that of 0.33 for the cluster model of the adlayer produced by UPD containing Hg(I) and Hg(0) in the ratio of 1:2 (3).

Flow-injection coulometry and voltammetry.—Determination of n_{app} by flow-injection coulometry, as reported by Lindstrom and Johnson (3), was repeated with the apparatus housed completely within a dry box purged for 24h with N_2 to eliminate interference by cathodic detection of dissolved O_2 . Injections consisted of $193 \mu\text{l}$ aliquots of $2.066 \times 10^{-5} \text{M Hg(II)}$. The deposited Hg was voltammetrically stripped from the electrode after the

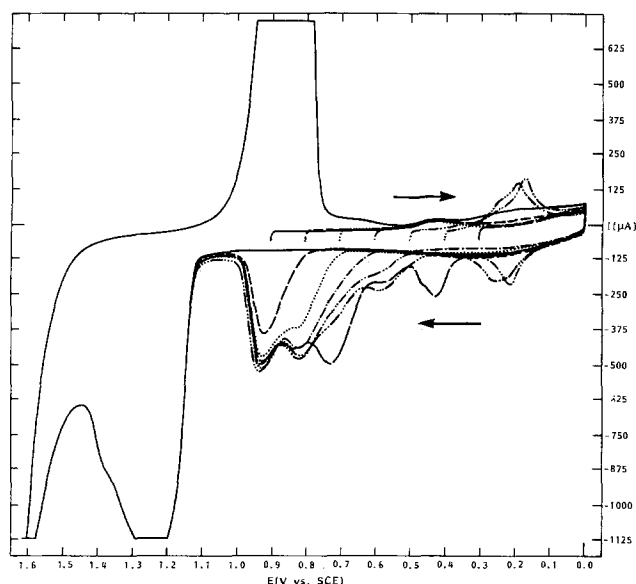


Fig. 5. I-E curves for a Au coulometric electrode. Conditions: $C_{\text{Hg(II)}}^b = 1.28 \times 10^{-4} \text{M}$, $V_s = 193 \mu\text{l}$, $\phi = 2.0 \text{ V min}^{-1}$, Carrier stream: $1.0 \text{M H}_2\text{SO}_4$, $v_f = 0.5 \text{ ml min}^{-1}$. E_{dep} (V vs. SCE): — 0.9, - - - 0.8, ····· 0.7, - · - · 0.6, - - - - 0.5, - · - · - · 0.4, blank also shown (—).

Table I. Evaluation of n_{app} for deposition of Hg(II) by flow-injection coulometry

E (V)	Injection no.	$10^4 Q$ (C)	n_{app}
0.45	1	4.606	1.59
	2	4.652	1.61
	3	4.615	1.60
	4	4.791	1.66
	5	4.606	1.59
	6	4.615	1.60
	average	4.648	1.61
0.00	1	5.631	1.95
	2	5.705	1.97
	3	5.668	1.96
	4	5.779	2.00
	5	5.834	2.02
	6	5.723	1.98
	average	5.723	1.98

Conditions: $C_{\text{Hg(II)}}^b = 2.066 \times 10^{-5} \text{M}$, $V_s = 193 \mu\text{l}$.
Carrier stream: 0.1M HCO_3^- , $v_f = 0.5 \text{ ml min}^{-1}$.

peak for each injection had been produced. Hence, deposition of bulk Hg(0) was negligible, and formation of the Au-Hg alloy was avoided. Results for n_{app} are reported in Table I for the cathodic reactions at $E = 0.45$ and 0.00V . The averages of six determinations are $n_{\text{app}} = 1.61 \pm 0.01 \text{ eq mol}^{-1}$ at 0.45V and $1.98 \pm 0.02 \text{ eq mol}^{-1}$ at 0.00V . These results are in agreement with the cluster model for UPD of Hg at $E > 0.45 \text{V}$ as proposed by Lindstrom and Johnson (2), as well as the evidence presented above (Fig. 1 and 2) that the Hg(I) adions are reduced to Hg(0) at $E < 0.3 \text{V}$.

In a separate study, a $193 \mu\text{l}$ aliquot of $1.28 \times 10^{-4} \text{M Hg(II)}$ was injected for an electrode potential of 0.50V . Following passage of the sample aliquot through the electrode, I-E curves were recorded for triangular potential scans between the limits of 0.45 and 0.00V with the continuing flow of supporting electrolyte through the electrode. Reproducible cathodic and anodic peaks were obtained in the region 0.2 - 0.3V (Fig. 4), which did not diminish in size during the repeated triangular potential scans. Hence, both oxidation states of Hg in the half-reaction involved are strongly adsorbed to the Au surface. The reaction is concluded to correspond to $\text{Hg(I)}_{\text{ads}} + e = \text{Hg(0)}_{\text{ads}}$. On the last positive scan, the potential was allowed to increase to 1.2V ; the I-E curves recorded are included in Fig. 4. The large anodic peaks obtained are from oxidative stripping of the Hg(0) adatoms and Hg(I) adions as Hg(II).

It can be observed in Fig. 1 and 2 that no anodic peak is obtained at ca. 0.3V for the positive potential scan at the Au RDE. This is easily explained, since, for the conditions of Fig. 1 and 2, the Au electrode is covered with bulk Hg(0) when the positive potential scan reaches 0.3V and adsorbed Hg(I) cannot form because of the absence of any exposed Au metal, which is necessary for the stabilization of Hg(I) adions.

Current-potential curves were recorded following injections of $193 \mu\text{l}$ aliquots of $1.28 \times 10^{-4} \text{M Hg(II)}$ as a function of variation in the deposition potential in the range 0.9 - 0.3V ; the corresponding curves are shown in Fig. 5, together with a residual I-E curve. The cathodic peak at 0.2V attributed above to the reduction of Hg(I) adions is observed only for $E_{\text{dep}} = 0.4$ and 0.5V . We conclude that the presence of Hg(I) adions and the validity of the cluster model pertain only to regions of the electrode surface for which the UPD process results in the nearly complete development of the adlayer of Hg.

The question remains unanswered as to the nature of the product of the UPD process for $0.9 > E_{\text{dep}} > 0.5 \text{V}$, for which $n_{\text{app}} = 1.6$, but the adlayer is not completely filled.

Acknowledgment

This work was partially supported by the Office of Basic Energy Sciences.

Manuscript submitted Aug. 9, 1983; revised manuscript received Jan. 3, 1984.

Iowa State University assisted in meeting the publication costs of this article.

REFERENCES

1. W. G. Sherwood and S. Bruckenstein, *This Journal*, **125**, 1098 (1975).
2. T. R. Lindstrom, Ph.D. Thesis, Iowa State University, Ames, IA (1980).
3. T. R. Lindstrom and D. C. Johnson, *Anal. Chem.*, **53**, 1855 (1981).
4. R. W. Andrews, J. H. Larochele, and D. C. Johnson, *ibid.*, **48**, 212 (1976).
5. R. E. Allen and D. C. Johnson, *Talanta*, **20**, 799 (1973).
6. K. W. Pratt, Jr., Ph.D. Thesis, Iowa State University, Ames, IA (1981).
7. C. Hinnen, N. V. Huong, A. Rousseau, and J. P. Dalbera, *J. Electroanal. Chem.*, **95**, 131 (1979).
8. S. Trasatti, *ibid.*, **150**, 1 (1983).

Transient Photocurrents in WSe₂ and MoSe₂ Photoanodes

Stan Prybyla and Walter S. Struve

Department of Chemistry, Iowa State University, Ames, Iowa 50011

B. A. Parkinson*

Solar Energy Research Institute, Photoconversion Research Branch, Golden, Colorado 80401

ABSTRACT

Transient photocurrents induced by short laser pulses at WSe₂ and MoSe₂ photoanodes were studied as a function of electrode morphology, solution redox species, incident laser power and power density, concentration of redox species, and added load resistance. Dual exponential current decay transients were observed in most cases, and a speculative qualitative model is proposed to explain the shape of the transients. The pitfalls associated with such measurements are discussed, and suggestions are made for improved measurement techniques.

Most of the recent research in photoelectrochemistry has been focused on increasing the efficiency and stability of cells for the production of chemicals or electricity. Much of the more fundamental research has been directed at understanding the energetics of the semiconductor/electrolyte interface (1-4). There has been relatively little investigation of the dynamics of charge transport and equilibration across the semiconductor/electrolyte interface. One method of studying such dynamics would be to examine the currents, voltages, and luminescence produced by ultrashort laser pulses impinging on the interface. Perone and Richardson *et al.* have investigated photopotential transients at TiO₂ (5) and CdS (6) electrodes in the submicrosecond time domain with a "coulostatic flash" technique. A similar technique was employed by Kamat and Fox (7) to study native and chemically modified TiO₂ electrodes in acetonitrile solutions. Frippiat *et al.* (8) studied the dye sensitization of SnO₂ with rhodamine B using a similar method.

The "coulostatic flash" technique involves studying the open-circuit potential change of a semiconductor electrode in response to a short (~10 ns) laser pulse of photons with energies above the bandgap. Recently, Gottsfeld and Feldberg (9) have done a theoretical analysis of the photopotential transients obtained in such experiments. They considered both surface and bulk recombination and back diffusion of carriers to derive mathematical expressions to describe the decay of photopotential as a function of time and pertinent semiconductor parameters. The decay of photopotential may provide some information on carrier lifetimes, surface and bulk recombination mechanisms, the role of traps, and sensitization by adsorbed dyes. However, it provides no information about net electron transfer to the solution. The fact that the experiment is performed at open circuit necessitates that any electron transfer to the solution must be compensated by an equal and opposite charge transfer to the semiconductor in order to maintain charge neutrality in the electrode. This is in contrast to conventional couloustatics where the charge is injected into the double

layers of the working and counterelectrodes before the potential decay of the working electrode is followed at open circuit.

There have also been several studies of photocurrent transients induced by short laser pulse illumination of a semiconductor/electrolyte interface which is at a potential near short circuit. Harzion *et al.* (10) have studied the fast photocurrent transients in CdSe cells with a sulfide/poly-sulfide redox electrolyte. They have also recently extended their measurements to the time resolved luminescence at the interface induced by the fast light pulses (11). Kawai *et al.* (12) investigated photocurrent transients at the MoSe₂ electrode immersed in iodide electrolytes. They studied the dependence of the photocurrent transients on light intensity, bias voltage, and electrolyte concentration, and observed transients with two current peaks, which were explained as charge carrier generation in the solid followed by electron transfer across the interface. The extreme stability of the Group VI semiconducting diselenide electrode materials in halide electrolytes and the high efficiencies obtained for the conversion of sunlight to electricity or stored chemical energy, make them of interest in various energy conversion schemes (13-16). A more detailed investigation of photocurrent transients produced by short laser light pulses impinging upon these materials seemed worthwhile, and the results of our study are reported herein.

Experimental

The MoSe₂ and WSe₂ crystals were grown and mounted as described previously (13). The doping level of these crystals is between 10¹⁶ and 10¹⁷ cm⁻³. In the cases when the van der Waals surfaces were exposed to the solution, the crystals were carefully cleaved with transparent tape before mounting in Torr-Seal epoxy. Figure 1 shows a diagram of the experimental apparatus with an insert giving the detail of the electrochemical cell. The leads connected to the cell were kept as short as possible to minimize stray capacitance and inductance. A platinum electrode with an area very large in comparison to the semiconductor was used to prevent any counterelectrode process from controlling the current flow in the cell. The cell was enclosed within a metal Faraday cage to reduce

* Electrochemical Society Active Member.

Key words: photoelectrochemistry, WSe₂, MoSe₂, transient photocurrents.

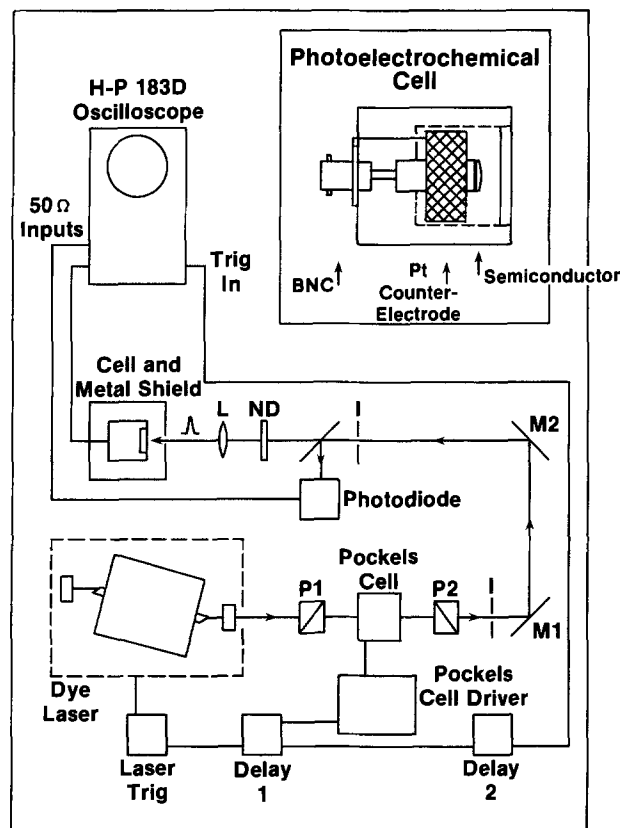


Fig. 1. Configuration of experimental apparatus showing laser and cell. Insert shows photoelectrochemical cell configuration.

noise and remove RF interference generated by the flash lamp.

The semiconductor and counterelectrode leads were connected directly to the 50 Ω signal input and ground return of a Hewlett Packard Model 1830A dual channel vertical amplifier situated within a HP 183D oscilloscope mainframe. For the load resistance studies with $R_L > 50\Omega$, a Tektronix Model 7704 oscilloscope was used with a 7A18 dual trace amplifier plug-in (input impedance 1 M Ω). The light source was a flashlamp-pumped dye laser operating at 607 nm (rhodamine 6G). Short light pulses were generated with a Pockels cell and had a full width at half maximum of 5 ns (see Fig. 2C). A HP 4220 PIN photo-

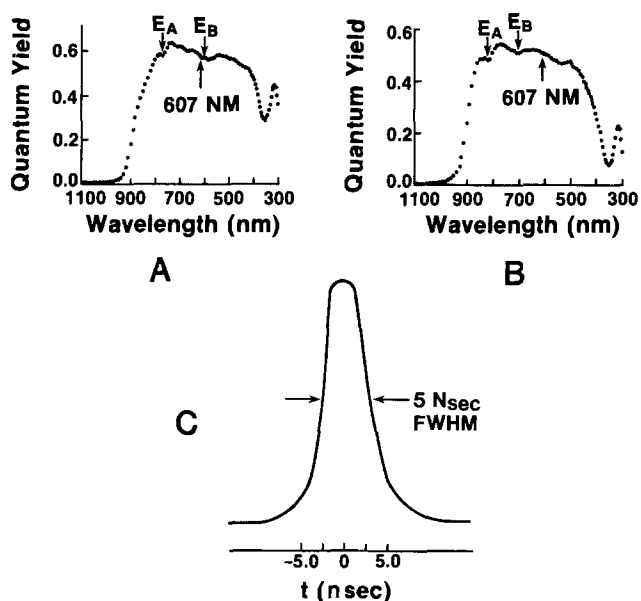


Fig. 2. (A) WSe₂ photocurrent spectrum showing laser excitation wavelength. (B) MoSe₂ photocurrent spectrum showing laser excitation wavelength. (C) Laser excitation pulse.

diode was used to measure the pulse energies, which were varied by insertion of neutral density filters into the light path. The power density impinging on the sample was varied by using a lens to focus or defocus the laser spot onto the semiconductor at a fixed power. The size of the laser spot on the sample was measured by exposing Polaroid film at the position where the crystal was mounted. The photocurrent transients were recorded directly from the oscilloscope onto Polaroid film. The area of the spot varied from 0.108 to 0.0038 cm², and in combination with neutral density filters resulted in power densities from 8 to 21,000 W/cm². The electrolytes were prepared from reagent grade chemicals which were used without further purification. Measurement of dark cell resistances and capacitances were made using a Hewlett Packard vector impedance meter model 4815A or by Mott-Schottky techniques using a lock-in amplifier.

Results

The photocurrent spectra for WSe₂ and MoSe₂ are shown in Fig. 2A and 2B. Structural features in the spectra, which are indicated with arrows, reveal the position of excitonic transitions in the material, a phenomenon which was described previously (18). The wavelength of the excitation pulse, with respect to the photoresponse of the crystals, is also indicated. The 607 nm wavelength is well above the bandgap of both materials, and so the absorption coefficient is about 10⁵ cm⁻¹ at this wavelength. The high absorption coefficient dictates that the light is absorbed within 200 nm of the semiconductor/electrolyte interface. The current-voltage curves in the dark and under illumination for various crystals whose transient behavior was investigated are shown in Fig. 3. The strong correlation between the surface perfection of the crystal and the dark currents, photocurrents, and photovoltage obtained in a regenerative photovoltaic cell is evident in the figure. This relation between surface morphology and junction properties of the cell has been discussed extensively in the literature (19-21). The edge-mounted crystal (Fig. 3C) and the crystal with many exposed non-van der Waals surfaces show much lower fill factors and photocurrents than the carefully cleaved van der Waals surfaces of the crystals in Fig. 3A and 3B. The iodide/triiodide electrolyte has been demonstrated to give the best photoresponse with this class of semiconductors due to the adsorption of the triiodide ion on the surface of the electrode (22) and the favorable redox potential. The iron(II)/iron(III) redox system was also studied although the steady-state current-voltage behavior is less ideal with this redox system, resulting in a lower light to electrical energy conversion efficiency.

Figure 4 shows the transient photocurrent response produced with laser pulses of the same energy for a WSe₂ electrode with a smooth van der Waals surface in both iodide and iron redox electrolytes. The transients are characterized by a rapid rise followed by a decay of the current which lasts until about 1 μ s. The peak photocurrent in the iodide solution is considerably higher than in the iron electrolyte.

Figure 5 shows the photocurrent transients for samples with a lower degree of surface perfection than the WSe₂ sample in Fig. 4. The sample in Fig. 5A is the same MoSe₂ sample as that whose current-voltage behavior was shown in Fig. 3D. Although the pulse energy is more than twice that of the WSe₂ sample in Fig. 4, the peak photocurrent is much less, and the peak quickly decays to a weaker component, which itself decays with a timescale on the order of 100 ns. A more extreme example of the surface structure controlling the transient is shown in Fig. 5B. The WSe₂ sample in this case was mounted edge-on such that no van der Waals surfaces were in contact with the solution. The transient photocurrent is more than ten times less than the corresponding peak current on the well cleaved surface, even though the laser power was more than 50 times higher. The current transient in this case virtually follows the laser pulse in that the

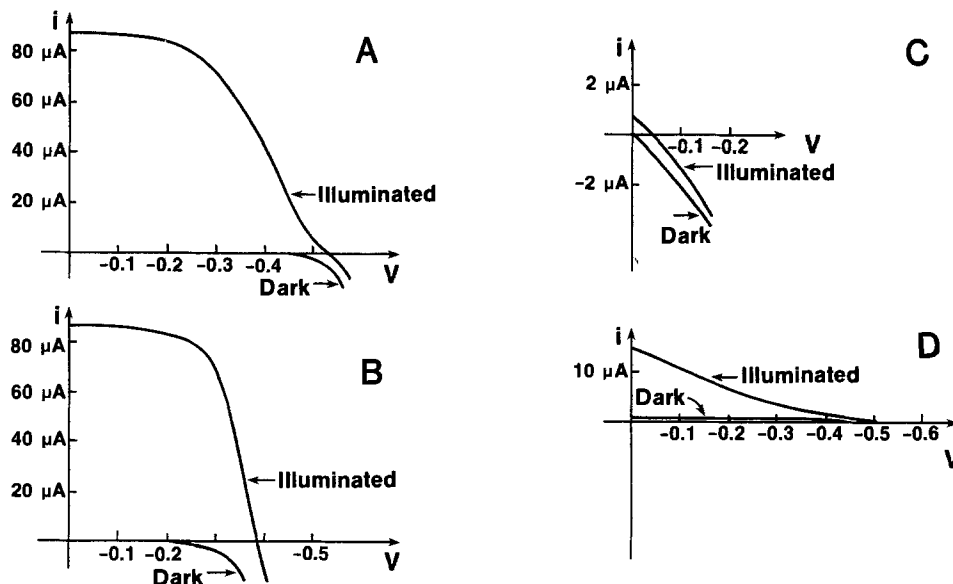


Fig. 3. Current-voltage curves for various semiconductor samples under CW illumination of 632.8 nm (1.87 mW/cm^2). All samples in $5.0 \text{ M KI}/10^{-2} \text{ M I}_2$. (A) WSe_2 50-4. (B) MoSe_2 33-2. (C) WSe_2 50-1 (edge-mount). (D) MoSe_2 2 (concave surface).

FWHM is less than 10 ns. Figure 5C shows a frequently observed behavior for short-time scales with samples that have primarily van der Waals surfaces exposed to the solution. This behavior is characterized by an increase in the photocurrent occurring about 30 ns after the initial risetime and preceded by a small decay or plateau region. Transients of this nature were also observed on MoSe_2 by Kawai *et al.* (12).

Figure 6 shows the risetime to the peak photoresponse for WSe_2 electrodes in both iodide and iron electrolytes. The risetime is dependent on both the laser power and the laser power density in a complex fashion. At low laser power densities, the risetimes are shorter than at the higher power densities. The risetimes tend to be constant at about 50 ns for the intermediate power densities while for the higher power densities, an initial increase followed

by a decrease in the risetime is observed for the iodide solutions. The risetimes always decrease with increasing laser power for the iron solutions.

Figure 7 shows the natural logarithm of the normalized peak photocurrent for a typical transient obtained with a WSe_2 sample in both iodide and iron(II)/iron(III) electrolytes. For all transients, this analysis reveals two linear

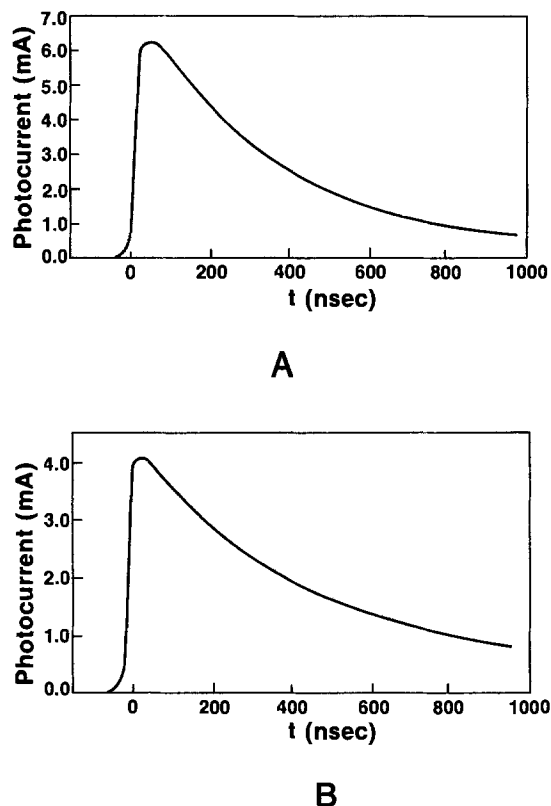


Fig. 4. Photocurrent transients for sample with high fill factor and high efficiency (WSe_2 50-4). Incident pulse energy 80.3 nJ (750 nJ cm^{-2}). (A) $5.0 \text{ M KI}/10^{-2} \text{ M I}_2$. (B) $0.5 \text{ M Fe}^{2+}/0.05 \text{ M Fe}^{3+}$.

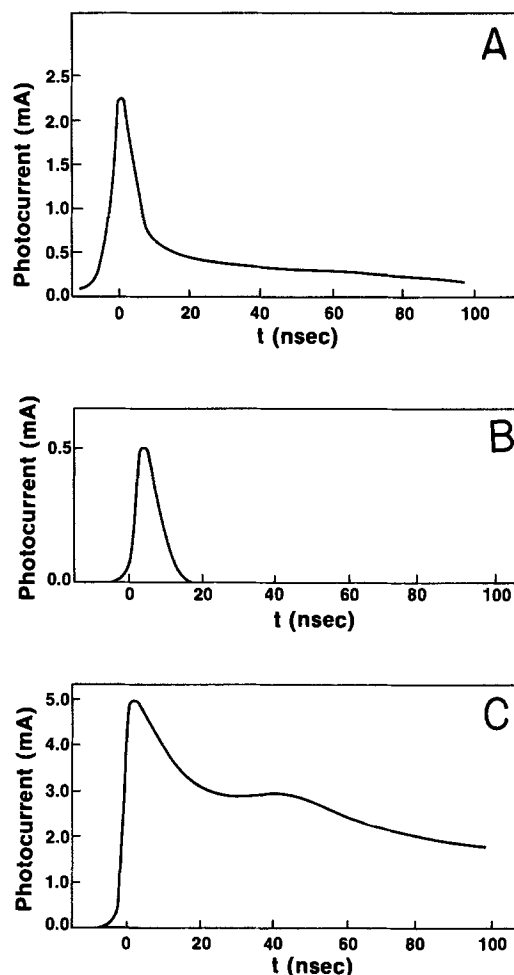


Fig. 5. (A) Photocurrent transient for sample with low efficiency (MoSe_2 2). Incident pulse energy 179 nJ $5.0 \text{ M KI}/10^{-2} \text{ M I}_2$. (B) Photocurrent transients for edge-mounted sample WSe_2 50-1. (Illumination 1 to C-axis). Incident pulse energy 4300 nJ $5.0 \text{ M KI}/10^{-2} \text{ M I}_2$. (C) Photocurrent transient of sample with visible steps on surface (WSe_2 50-3). Incident pulse energy 4300 nJ $5.0 \text{ M KI}/10^{-2} \text{ M I}_2$.

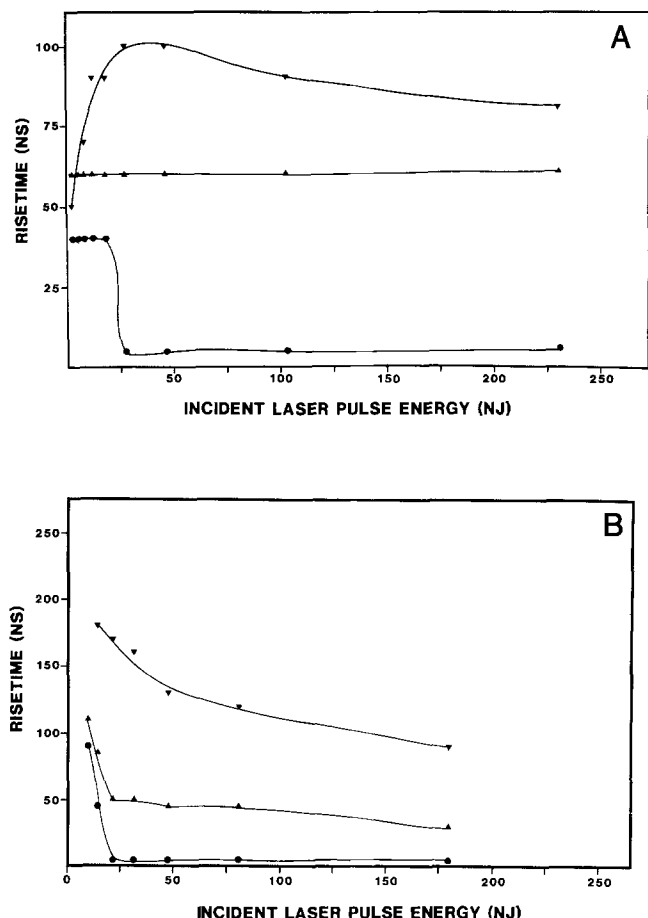


Fig. 6. Risettime to peak photoresponse for WSe_2 50-4 in (A) $5\text{M KI}/10^{-2}\text{M I}_2^-$; (B) $0.5\text{M Fe}^{2+}/0.05\text{M Fe}^{3+}$ for various powers (nJ) and power densities. ∇ , 0.015 cm^2 spot; \blacktriangle , 0.042 cm^2 spot; and \bullet , 0.107 cm^2 spot.

segments with a transition occurring at about 400-600 ns. At low laser power densities in iodide solutions, the transition comes at slightly less than 400 ns. Less than ideal crystal surfaces yielded very fast decays possibly limited by the RC time constant of the cell. These fast transients could not be analyzed using a dual exponential fit.

The decay times for WSe_2 sample 50-4, which followed the dual exponential discussed above, were analyzed by fitting the transients to a function of the form

$$I = A[\exp(-t/\tau_1)] + B[\exp(-t/\tau_2)] \quad [1]$$

τ_1 is this expression, which corresponds to the first decay, was found to be approximately constant at about 120

$\pm 25\text{ ns}$ independent of pulse energy, energy density, or redox couple. However, at low power and power densities in the iodide electrolyte, a significant decrease in τ_1 was noted as a value between 40 and 80 ns. A systematic trend in the τ_2 values was observed, as is shown in Fig. 8. This second decay time increased with increasing laser power and laser power density, and significantly longer decay times were measured in the iron electrolytes.

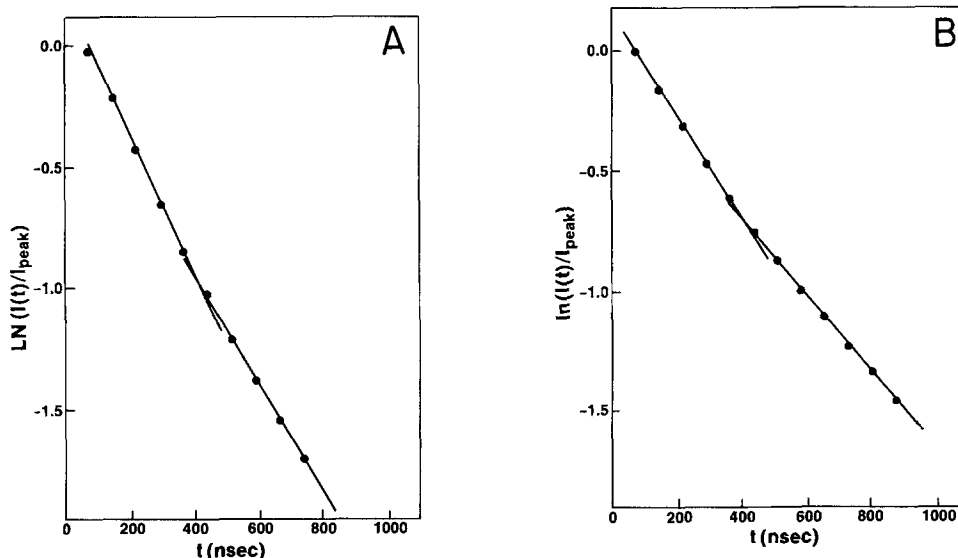
Figure 9 shows the dependence of the peak photocurrent on the incident pulse energy at four different power densities for the iodide and iron electrolytes, respectively. In both cases, the photocurrent saturates at pulse energies above 100 nJ, although the peak current is higher in the iodide solution. It is also apparent from the figures that, for a given pulse energy, the peak is higher for the transients with the lower energy or power density. It should be reemphasized that the power densities are many times the power density of solar photons ($\sim 100\text{ mW/cm}^2$).

The quantum yields for charge transfer can be obtained from the integration of the photocurrent time transients, to obtain the charge which has passed through the interface, and dividing it by the number of incident photons. Figure 10 shows that the quantum yields rapidly diminish with increasingly pulse energy. The largest quantum yields, which are observed at the lowest power densities, are still well below the quantum yields which are measured at even lower intensities with either chopped or CW radiation [see Fig. 2 and Ref. (18)].

The quantum yield for electron transfer was also measured as a function of the concentration of triiodide in the electrolyte. Triiodide concentration was varied because it can be either oxidized to iodine, or reduced to iodide, enabling the counterelectrode reaction to proceed. Figure 11 shows the results of this experiment. The quantum yield is increased by a factor of almost two by changing the I^- concentration from 3×10^{-5} to 10^{-2}M . The solution was maintained at a constant ionic strength of 3.16 by adding KCl to the solution. The ionic strength was maintained at this high level to assure that the solution resistance was kept relatively low and constant and that no ion migration effects were controlling the response of the system. It is unknown exactly what the residual quantum yield is due to at low iodide concentration, but chloride oxidation has been shown to occur on these electrodes (16).

The time resolved photocurrents were also studied as a function of added load resistance. This type of study was also done by Harzion *et al.* (10). The load resistance was connected directly between the semiconductor and counterelectrode. The overall load resistance was calculated from the parallel combination of the added load resistance and the $50\ \Omega$ input impedance of the oscilloscope. For this study, the transient was fit to the best single ex-

Fig. 7. (A) Normalized natural log of photocurrent response as a function of time for WSe_2 50-4 using I^-/I_3^- redox couple (B) Normalized natural log of photocurrent response as a function of time for WSe_2 50-4 using $\text{Fe}^{2+}/\text{Fe}^{3+}$ redox couple. The peak photocurrents were 6.2 mA for the I^-/I_3^- and 4.1 mA for $\text{Fe}^{2+}/\text{Fe}^{3+}$.



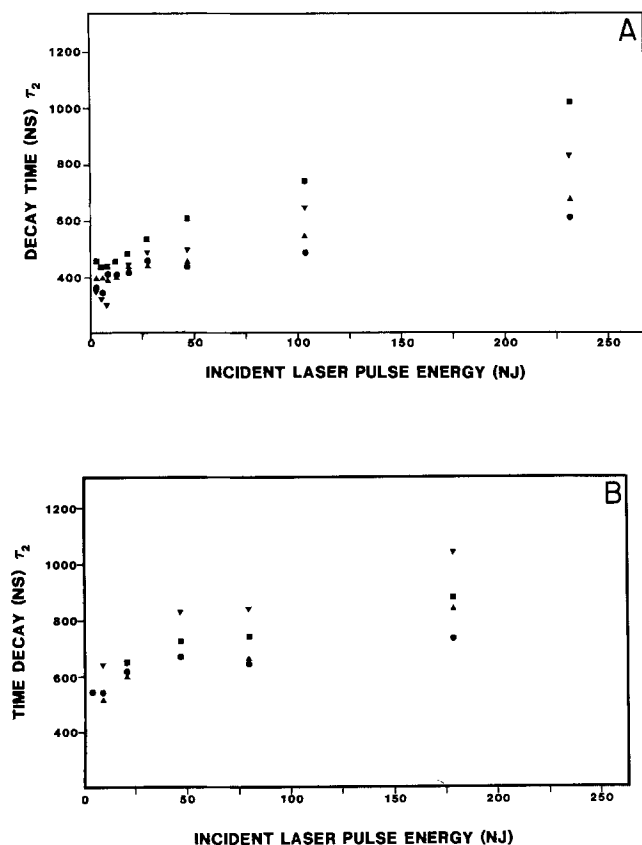


Fig. 8. Dependence of second decay time constant (τ_2) on incident laser power (nJ) and power density for WSe_2 50-4 in (A) $5.0\text{M KI}/10^{-2}\text{M I}_2$, and (B) $0.5\text{M Fe}^{2+}/0.05\text{M Fe}^{3+}$. \bullet , 0.107 cm^2 spot; \blacktriangle , 0.042 cm^2 spot; \blacktriangledown , 0.015 cm^2 spot; and \blacksquare , 0.0038 cm^2 spot.

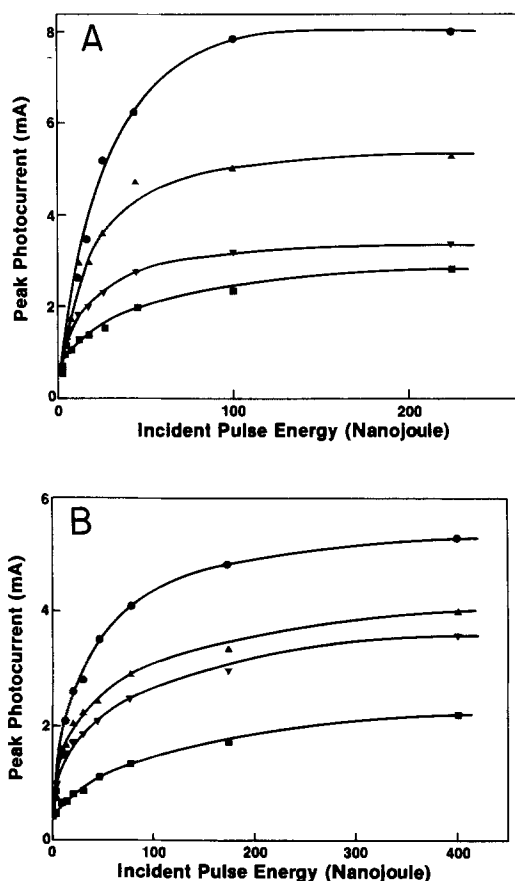


Fig. 9. (A) Peak photocurrent response as a function of incident pulse energy for WSe_2 50-4 in $5.0\text{M KI}/10^{-2}\text{M I}_2$. (B) Peak photocurrent response as a function of incident pulse energy for WSe_2 in $0.5\text{M Fe}^{2+}/0.05\text{M Fe}^{3+}$. The symbols are the same as Fig. 8.

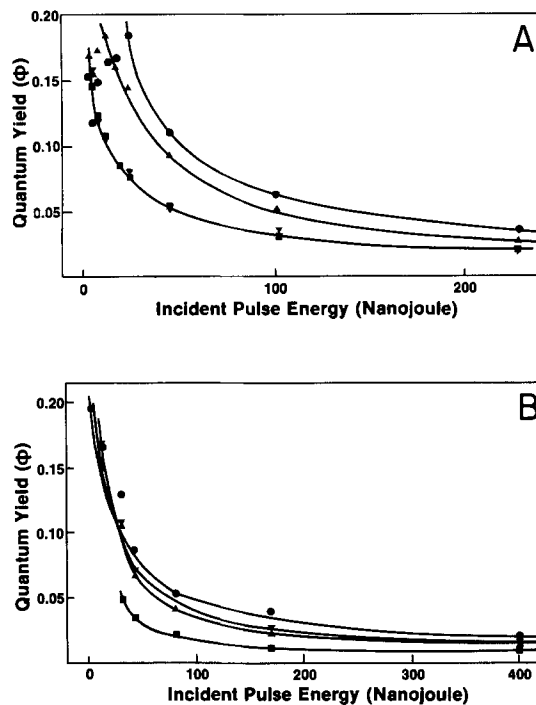


Fig. 10. (A) Quantum yield of charge transfer as a function of incident pulse energy for WSe_2 50-4 in $5.0\text{M KI}/10^{-2}\text{M I}_2$. (B) Quantum yield of charge transfer as a function of incident pulse energy for WSe_2 50-4 in $0.5\text{M Fe}^{2+}/0.05\text{M Fe}^{3+}$. The symbols are the same as Fig. 8.

ponential decay (τ). Figure 12B shows the decay time constant (τ) plotted against the overall load resistance for the cell in the low resistance region. A linear behavior is observed much like that reported by the Israeli group for CdSe (10).

Figure 12A shows the influence on the decay time (τ) of adding substantial resistance to the cell and using a high impedance scope input. In this case, the decay times can be as long as a millisecond for a load resistance of $1\text{ M}\Omega$. The high resistance measurements approach the open-circuit experiments of the type reported by Perone *et al.* (5, 6) and Kamat and Fox (7). Figure 13 shows the effect that increasing the load resistance has on the quantum yield for electron flow. At low resistances, the quantum yield remains constant but begins to diminish at resistances above about $5\text{ k}\Omega$. This curve is exactly analogous to the load curve of a photovoltaic cell in that it progresses from a high quantum yield at short circuit (at zero load) to virtually no photocurrent at very high loads (near the open-circuit potential).

Discussion

It will be helpful to establish some boundary conditions which may be controlling the transient currents in these

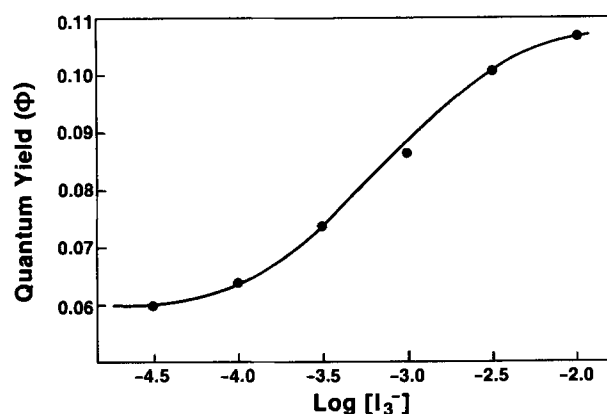


Fig. 11. Quantum yield as a function of the log of the triiodide concentration for the WSe_2 50-4 electrode with a constant pulse energy of 80 nJ and an ionic strength held constant at 3.16 with KCl.

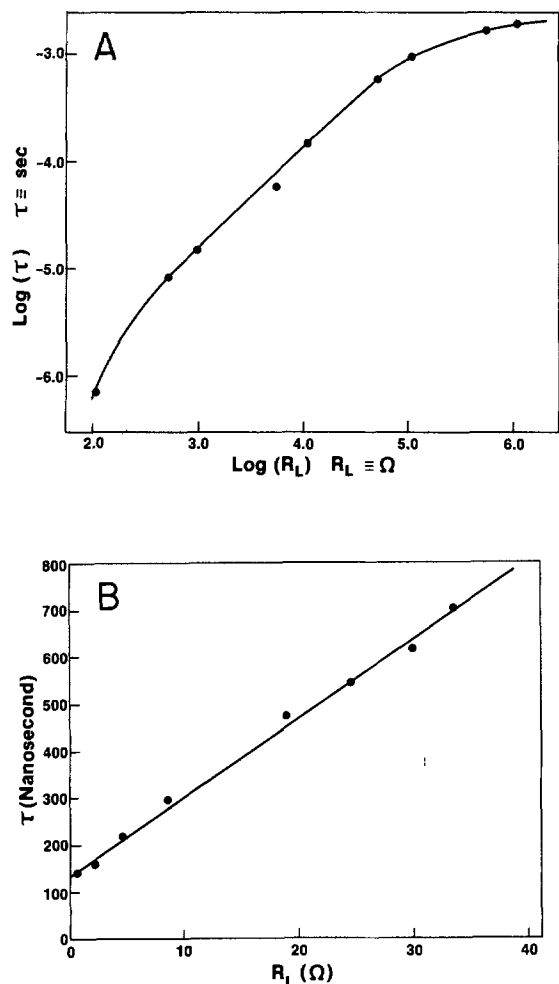


Fig. 12. (A) $\text{Log} \tau$ (transient decay time constant) as a function of $\text{log} R_L$, MoSe_2 33-2 in $5.0\text{M KI}/10^{-2}\text{M I}_2$, incident pulse energy 227 nJ, and $100\Omega < R_L < 1\text{M}\Omega$. (B) τ (transient decay time constant) as a function of load resistance R_L , MoSe_2 33-2 in $5.0\text{M KI}/10^{-2}\text{M I}_2$, incident pulse energy 227 nJ, and $\sim 1\Omega < R_L < 50\Omega$.

systems. The diffusion of electroactive species to the electrode surface can be shown to be unimportant to the shape of the current transient in several ways. First, the time decay of the photocurrent does not follow a $t^{-1/2}$ decay which would be expected for the case of semi-infinite linear diffusion of the electroactive species to the in-

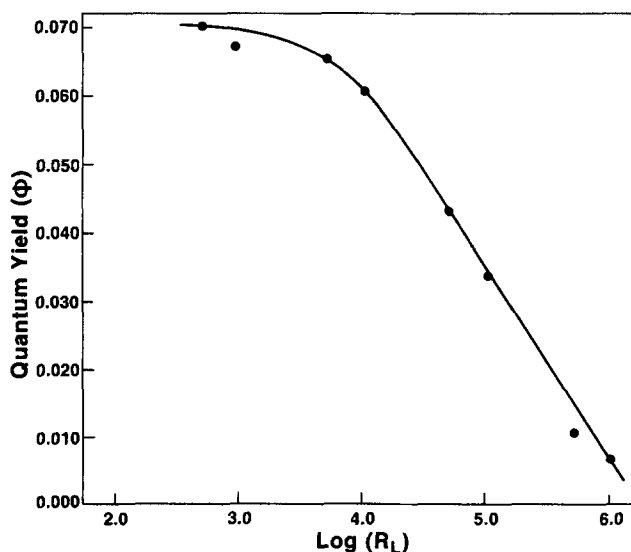


Fig. 13. Quantum yield of charge transfer as a function of $\text{log} R_L$, MoSe_2 33-2 in $5.0\text{M KI}/10^{-2}\text{M I}_2$, and incident pulse energy 227 nJ.

terface. The decay also does not follow a $t^{-2/3}$ dependence as was observed over limited time scales for TiO_2 and CdS under open-circuit conditions (5, 6). Other workers have reported complex shapes of photopotential decays under open-circuit conditions (11).

Secondly, although the quantum yield is influenced by the concentration of redox species in the electrolyte, the biexponential nature of the transients is not. Furthermore, the quantum yield is not a linear function of concentration of redox species. Thirdly, a calculation of the diffusion length of iodide or iron(II) during the duration of the laser pulse (5 ns) reveals that only in the case of the 0.5M iron(II) solution at the smallest spot size (highest power density) does the number of photons in the pulse approach the number of redox atoms within the diffusion length of the electrode on this timescale. Triiodide can also be adsorbed on the surface, and, thus, there will be no need for these molecules to diffuse to the surface. The result is that despite the high power laser pulses the shortness of the light pulse renders the total charge injected into the semiconductor insufficient to induce concentration polarization.

A second question is whether the RC time constant of the cell is limiting the current flow in the system as a result of the inherent resistance in the semiconductor and electrolyte and the capacitance associated with the semiconductor space charge layer, Helmholtz layer, and associated electronic components. Our data support the point of view that processes other than the cell resistance and capacitance also influence the temporal current flow in the system. The cell RC constant can be measured independently by measuring both the total resistance of the cell [5.5Ω for WSe_2 (sample 50-4) and 6.1Ω for MoSe_2 (sample 33-2)] and the total cell capacitance (7 nF for WSe_2 and 11 nF for MoSe_2), and results in calculated cell time constants of from 35 to 75 ns. The time scale in which we are making measurements are, with the exception of the fastest risetimes, much longer than this. Furthermore, semiconductor samples with many surface imperfections show decays which are much shorter than samples with more perfect surfaces, even though the resistivity of the samples are nearly identical and the capacitance associated with the imperfect surfaces is much larger. In summary, we believe that, although the RC components of the cell and measurement electronics have some influence on the decay transient, information about other effects, including charge transfer and recombination, is also contained in the transient.

Lateral minority carrier transport can be shown to be unimportant, even for small spot sizes, from the measured diffusion length of minority carriers in these crystals (23). The maximum minority carrier diffusion length (L_p) measured in these materials is around $3\mu\text{m}$, negligible compared to the 350μ radius of the smallest spot. An anisotropy factor of 10 to 20, due to the fact that L_p was measured perpendicular to the layers, would only increase the effective radius of the charge transfer area 8-17%. However, the saturation of recombination centers, by the large hole flux, could increase the effective diffusion length. Since such effects are unknown in these samples, they were neglected. Majority carriers, which have much higher mobilities (23), were assumed to be quickly separated by the space charge and removed into the bulk of the crystal.

The risetime to the peak photocurrent shown in Fig. 6 for WSe_2 in iodide and iron electrolytes can be as fast as 5 ns. No explanation is offered for the dependence of the risetime on laser pulse energy or energy density. Intuitively, one might expect that a smaller illuminated area would produce a transient current with a faster rise due to the lower capacitance associated with the smaller portion of the photoanode through which current flows. The data, on the other hand, show a trend opposite to this expectation. Because of the unusual behavior of the risetimes (MoSe_2 in iodide/triiodide electrolytes behaves similarly to WSe_2 in this electrolyte), most of the discus-

sion in this paper will be concerned with the decay transients.

The double hump in the photocurrent decay shown in Fig. 5C was also observed by previous workers (12). These workers attributed the two peaks to electron hole separation followed by charge transfer. We think this is unlikely because electron hole separation occurs on a picosecond time scale, much faster than any of the measurements reported here. A simple calculation of the transit time for electrons across a distance equal to the width of the depletion layer, without field assistance but based only on the measured mobility of electrons in these crystals, yields a value of about 30 ps. Feldberg and Gottesfeld (9) also arrive at the conclusion that electron hole separation cannot be directly observed on the time scale of our experiments.

A possible explanation of the effect is that undissociated excitons can be dissociated by the return of the space charge field, which was temporarily eliminated by the large concentration of electron hole pairs created by the intense laser pulse. Recent experiments on WS_2 crystals where the excitation energy was tuned from below the first excitonic transition to above the exciton energy showed no difference in the shape of the transients with energy (24). The result of this experiment makes excitonic effects unlikely as an explanation for the double hump. Back diffusion of majority carriers, due to the flattening of the bands at the surface, may also be an explanation for the double hump. These effects have been considered for photovoltage transients (9) but should be less significant when a conduction path is available for the separation of the charges.

A recent theoretical model based on the interaction of the capacitive and resistive elements in the cell predicts that, under some conditions, a reversal of the current can be seen after the light pulse (25). Preliminary experiments at an InP electrode have actually revealed such an effect (24). The suggestion is that the dip between the two humps may be caused by a small temporary reinjection of holes back into the semiconductor. The back injection of holes could be the result of a surface state which fills when the Fermi level is driven past the state by the large influx of photogenerated carriers. When the Fermi level relaxes back to the original energy position, some of the photo-oxidized triiodide at the surface will be reduced by the electrons in the surface states, causing a temporary dip in the transient response.

A large photon flux is likely to cause the movement of the bandedges of the semiconductor. Even much smaller levels of illumination have been shown to cause the movement of the semiconductor bands with respect to the solution levels (26). The movement of the bands would be expected to have a dramatic effect on the electron or hole transfer rate from the semiconductor to the solution. We propose that the dual exponential observed for the decay of the photocurrent is the result of band movement. The initial fast decay can be attributed to the relaxation of the bandedges back to their original energy position while the slower decay is due to the kinetic limitations of hole transfer to the solution from long-lived traps near the valence band. Long-lived traps were postulated (by previous workers) to explain the long photovoltage decay transients lasting 20 ms (5-7). Another explanation given in Ref. (9 and 11) for long photovoltage transients is the back-diffusion following charge separation of majority carriers to the surface to recombine with the minority carriers or oxidized solution species.

The low quantum yields observed, relative to the steady-state quantum yields, indicate that the dominant process in all cases is recombination. High recombination rates are not surprising due to the large concentrations of electrons and holes produced by the intense laser pulse. Recombination rates are dominant for samples with only edge sites exposed to the solution

(Fig. 3C and 5B), and result in only small transient currents and quantum yields. Band movement is not important in this case due to the large concentration of surface states which effectively pin the Fermi level. Similar results are also seen for another sample whose van der Waals surface has a large concentration of edge sites (Fig. 3D and 5A).

The difference in the behavior of the two redox electrolytes employed in this study can be understood from the differences in the electron transfer rate constants between the two couples and also to the different band bending in the semiconductor. The faster electron transfer rate for the iodide couple, along with the fact that there is adsorption at high triiodide concentrations (22), results in a higher peak current for this system and a faster decay for the second component. The longer-lived τ_2 component of the transients in iron solutions compensates for the higher peak currents in the iodide case, which results in similar quantum yields for the two systems. However, at very high power densities, the quantum yields in iodide are significantly higher, suggesting that the adsorbed charge may help sustain more charge transfer under these conditions. τ_2 is also a function of the triiodide concentration in the electrolyte, whereas τ_1 is virtually independent of the donor concentration. τ_2 increases from about 700 ns at triiodide concentrations of $3 \times 10^{-4}M$ to over 1000 ns at concentrations of 0.1M. The sigmoidal shape of quantum yield as a function of concentration parallels the "isotherm" for the adsorption of triiodide on a WSe_2 electrode, recently measured by chronocoulometry (22). The adsorption maximum was reached at a concentration of 0.1M as determined by this electrochemical technique which directly measures the surface excess of an electroactive species. The quantum yield also reaches a maximum near this concentration.

The differences in the band bending in the semiconductor in either of the redox electrolytes is expected to be within several hundred millivolts. The 236 mV difference in the standard redox potentials (E°) for the two systems (0.771 for Fe(II)/Fe(III) and 0.535 for I^-/I_3^-) is more than compensated by the shift in flatband potential caused by the adsorption of I_3^- (22). Flatband shifts of up to 500 mV were observed on $MoSe_2$ electrodes resulting from the addition of I_3^- to I^- solutions. Regenerative cells with $MoSe_2$ photoanodes show open-circuit photovoltages which at high light intensities are several hundred millivolts higher for the iodide electrolytes than the iron electrolytes (27). At low intensities, the photovoltage for the iron system was greater by 150 mV (27). Power conversion efficiencies and fill factors, both of which are strongly influenced by the kinetics of interfacial charge transfer, are much smaller in the cells with the iron redox systems due mainly to the slower charge transfer rate constant for this system. The band bending in the semiconductor may influence the measured peak photocurrents and quantum yields, but we believe the interfacial charge transfer is also very important.

In summary, the entire decay transient is described as follows and depicted schematically in Fig. 14. The initial light pulse creates a large number of carriers which drives up the Fermi level and flattens the bands (Fig. 14B). In this process, the Fermi level passes a surface state near the conduction band, resulting in a small flow of electrons into this state and producing a dip in the anodic photocurrent at between 20 and 40 ns. The charge accumulated on the surface state causes the bands to move (Fig. 14C). After about 60 ns (depending on the laser power and power density), recombination and charge transport have removed enough carriers to permit the bands to move back towards the equilibrium position, removing the electrons from the surface level and accounting for the temporary increase in anodic current. The discharging of the surface state continues for the duration of the first transient, allowing the

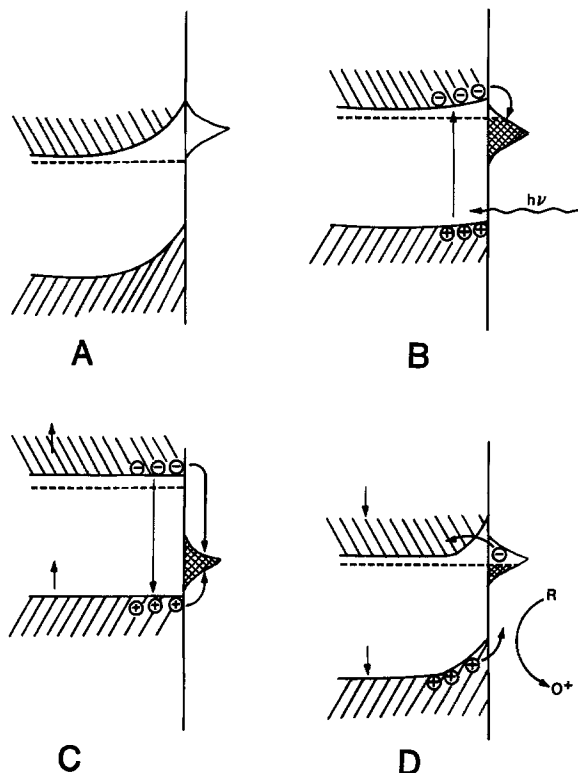


Fig. 14. Band diagram showing the position of the semiconductor bands in response to the light pulse. A full description appears in the text.

bands to return to their initial position (Fig. 14A). The holes in the long-lived (up to 1000 ns) traps then transfer to the electrolyte. The latter charge transfer is sensitive to such variables as electron transfer rate and solution donor concentration. The surface state is in communication with the solution rather than the bulk of the semiconductor, which is why its position remains fixed while the band edges move. These surface states are also responsible for the dark current at these junctions (28).

Conclusion

It is obvious from this report that the temporal behavior of the photocurrent and photovoltage at a semiconductor/electrolyte interface is very complex. The complexity arises from the interaction of semiconductor parameters (carrier lifetimes, dielectric constants, bulk and surface states, band structure, carrier mobilities, doping level, etc.), electrolyte parameters (concentration, standard potential and standard rate constant of any redox species, solution resistance, adsorption and diffusion of redox species and counterions, etc.), and external electronic parameters (noise, stray capacitance and inductance, impedance matches, etc.). In order to gain a more complete understanding of the light pulse-induced photocurrents, it will be necessary to further isolate these various parameters to examine their importance. We have begun experiments with more well characterized III-V materials in order to get a handle on the influence of the semiconductor properties. The electrolyte properties are rather easily controlled by proper selection and variation of the redox and electrolyte ions. The external electronic parameters are difficult but not impossible to sort out, as long as the time scale is not too short and the effect of the RC components can be deconvoluted. Time resolved luminescence may be able to provide complementary information about radiative recombination without interference from the equivalent electrical circuit elements of the cell itself (11).

Another refinement that can be made is to reduce the intensity of the incident laser pulses. One could hope to reduce the amount of band movement and recombination, prevalent at high laser powers, and probe the electron transfer events more directly. The difficulty is that

the small signal-to-noise ratio at the very low laser intensities necessitates the use of signal averaging techniques.

Acknowledgment

The authors wish to thank John Turner for helpful discussions and experimental expertise, and Ron Wilson, Steve Feldberg, Shimshon Gottesfeld, Sam Perone, and Laurie Peter for helpful discussions and providing preprints of their work. Phil Afenrud performed some useful experiments and provided many helpful comments and discussions. This work was supported by the Office of Energy Research, Department of Energy, under Contract EG-77-C-01-4042 for work done at SERI and under contract no. W-7405-ENG-82 for work done at Ames Laboratory.

Manuscript submitted Sept. 2, 1983; revised manuscript received Jan. 17, 1984.

Solar Energy Research Institute assisted in meeting the publication costs of this article.

REFERENCES

- H. Gerischer, *Top. Appl. Phys.*, **31**, 115 (1979).
- A. J. Nozik, *Annu. Rev. Phys. Chem.*, **29**, 189 (1978).
- A. J. Bard, A. B. Bocarsly, F. R. F. Fan, E. G. Walton, and M. S. Wrighton, *J. Am. Chem. Soc.*, **102**, 3671 (1980).
- J. A. Turner and A. J. Nozik, *Appl. Phys. Lett.*, **41**, 101 (1982).
- S. P. Perone, J. H. Richardson, S. B. Deutscher, J. Rosenthal, and J. N. Ziemer, *This Journal*, **127**, 2580 (1980); S. P. Perone, J. H. Richardson, S. B. Deutscher, J. Rosenthal, and J. N. Ziemer, *Faraday Discuss. Chem. Soc.*, **70**, 35 (1980).
- J. H. Richardson, S. P. Perone, and S. B. Deutscher, *J. Phys. Chem.*, **85**, 341 (1981).
- P. V. Kamat and M. A. Fox, *ibid.*, **87**, 59 (1983).
- A. Fripiat, A. Kirsch-De Mesmaeker, and J. Nasielski, *This Journal*, **130**, 239 (1983).
- S. Gottesfeld and S. W. Feldberg, *J. Electroanal. Chem. Interfacial Electrochem.*, **146**, 47 (1983).
- Z. Harzion, N. Croitoru, and S. Gottesfeld, *This Journal*, **128**, 551 (1981).
- Z. Harzion, D. Huppert, N. Croitoru, and S. Gottesfeld, *J. Electroanal. Chem. Interfacial Electrochem.*, **150**, 571 (1983).
- T. Kawai, H. Tributsch, and T. Sakata, *Chem. Phys. Lett.*, **69**, 336 (1980).
- G. Kline, K. Kam, D. Canfield, and B. A. Parkinson, *Sol. Energy Mat.*, **4**, 301 (1981).
- G. Kline, K. Kam, R. Ziegler, and B. A. Parkinson, *ibid.*, **6**, 337 (1982).
- C. Levy-Clement, A. Heller, W. A. Bonner, and B. A. Parkinson, *This Journal*, **129**, 1701 (1982).
- L. F. Schneemeyer, M. S. Wrighton, A. Stacy, and M. J. Sienko, *Appl. Phys. Lett.*, **36**, 710 (1980).
- F. R. F. Fan, H. S. White, B. Wheeler, and A. J. Bard, *This Journal*, **127**, 518 (1980).
- K. Kam and B. A. Parkinson, *J. Phys. Chem.*, **86**, 463 (1982).
- H. J. Levensz, A. Heller, and F. J. DiSalvo, *J. Am. Chem. Soc.*, **102**, 1877 (1980).
- D. Canfield, T. Furtak, and B. A. Parkinson, *J. Appl. Phys.*, **51**, 6018 (1980).
- W. Kautek, J. Gobrecht, and H. Gerischer, *Ber. Bunsenges. Phys. Chem.*, **84**, 1034 (1980).
- J. A. Turner and B. A. Parkinson, *J. Electroanal. Chem.*, **150**, 611 (1983).
- K. Kam, D. L. Rath, and B. A. Parkinson, in "Photoelectrochemistry: Fundamental Processes and Measurement Techniques," W. L. Wallace, A. J. Nozik, S. K. Deb, and R. H. Wilson, Editors, p. 532, The Electrochemical Society Softbound Proceedings Series, Pennington, NJ (1982).
- P. Afenrud and B. A. Parkinson, Unpublished experiments.
- R. H. Wilson, presentation at U.S./Japan Photoelectrochemistry Meeting, San Diego, CA, March 1983.
- G. Cooper, J. Turner, B. A. Parkinson, and A. J. Nozik, *J. Appl. Phys.*, In press.
- H. Tributsch, *Sol. Energy Mat.*, **1**, 257 (1979).
- B. A. Parkinson, T. E. Furtak, D. Canfield, K. K. Kam, and G. Kline, *Discuss. Faraday Soc.*, **790**, 233 (1980).
- J. M. Martin and S. P. Perone, Private communication.

Electrocatalytic Oxidation of As(III)

I. Voltammetric Studies at Pt Electrodes in 0.5M HClO₄

Tim D. Cabelka¹, Deborah S. Austin, and Dennis C. Johnson

Department of Chemistry and Ames Laboratory—U.S. Department of Energy,² Iowa State University, Ames, Iowa 50011

ABSTRACT

Hydrodynamic voltammetry and hydrodynamically modulated voltammetry at a disk electrode, and shielding experiments at a ring-disk electrode, were applied in a study of the electrochemical response of As(III). The adsorption of As(III) occurs at Pt electrodes with partial charge transfer. The adsorption isotherm was determined and a maximum coverage is established for $C_{As(III)}^b > 6 \times 10^{-5} M$. The oxidation of As(III) is electrocatalyzed dramatically by formation of PtOH on the electrode, but is slow for a surface covered by a well developed layer of PtO. The rate-determining step (rds) for As(III) oxidation at the PtO-covered electrode does not involve charge transfer in the region $E = 0.9 - 1.2V$ vs. SCE. The log of the rate constant for the rds measured at 1.1V decreases linearly with the increasing charge equivalent to the surface oxide. The oxidation of As(III) at an oxide-covered electrode is catalyzed by evolution of O₂(g). The electrocatalysis is concluded to be the result of ·OH generated at the electrode surface.

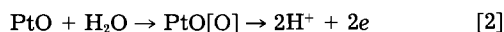
The majority of publications on the electrochemical reactions of As(III) pertain to cathodic studies at Hg electrodes; key reviews and recent studies are cited (1-5). Significant studies of the cathodic reaction of As(III) at solid electrodes have been described (6-10), and applications for trace analysis have utilized the anodic peak for voltammetric stripping of the electrodeposited As(0). The earliest anodic studies of As(III) at solid electrodes were motivated by the application for the industrial preparation of arsenates (11-15), and alkaline media were used almost exclusively. MacNevin and Martin (16) found that the current efficiency could be as high as 100% at Pt electrodes in concentrated acid solutions, but the efficiency was significantly lower for pH > 3. No evidence was found for oxidation of As(III) by dissolved O₂(g) in acidic solutions, nor was there evidence for anodic production of the intermediate oxidation state As(IV). A large decrease was observed in the anodic current at $E \approx 1.0V$ vs. SCE under constant conditions of mass transport when the Pt electrode had been prepolarized at $E \gg 1.0V$ to generate the surface oxide. The anodic signal was restored following cathodic polarization to reduce the surface oxide. The oxide was found to be removed slowly by exposure of the electrode to the As(III) solution under open-circuit conditions.

Catherino (17) analyzed Tafel plots of *i*-*E* data for As(III) at a Pt electrode in the potential region where concentration polarization can be ignored. The results were consistent with a mechanism involving two consecutive one-electron transfer steps. The results were interpreted on the basis of As(IV) as the intermediate product in agreement with previous conclusions from kinetic studies of the homogeneous oxidation of As(III) (18-19). The possible involvement of surface oxide was not considered.

Zakharov and Songina (20) reported briefly on the oxidation of As(III) at a Pt anode. They observed that As(III) is oxidized simultaneously with the formation of the oxide layer on the electrode surface and concluded that the oxide participates in the mechanism as a donor of oxygen atoms as indicated by the reaction



Accordingly, the faradaic current results from the regeneration of the surface oxygen by the reaction



A similar mechanism involving adsorbed ·OH was proposed more recently by Zakharov *et al.* (21) for oxidation of As(III) at Au electrodes. We have chosen the anodic ox-

idation of As(III) as one of several model systems for the study of electrocatalysis by surface oxides at solid metal electrodes in anodic reactions where oxygen is transferred from the aqueous solvent to the reaction product. In a recent paper (22), the oxidation of I⁻ to IO₃⁻ at a Pt anode was concluded to be catalyzed by formation of the surface oxide and by the evolution of O₂(g). In the present series, we describe our voltammetric studies of As(III).

Because of the apparent catalytic involvement of the surface oxide on Pt electrodes with many anodic oxidation reactions, including that of As(III), a brief review concerning pertinent aspects of the present status of thinking regarding formation of the oxide in acidic media is appropriate. An excellent summary of the older literature is given by Gilman (23). More recently, Angerstein-Kozłowska, Conway and co-workers (24-26) demonstrated that the anodic wave for oxide formation can be deconvoluted into three peaks corresponding to the stepwise formation of the lower surface oxides with empirical surface stoichiometries of Pt₄OH (ca. 0.89V vs. NHE), Pt₂OH (ca. 0.95V vs. NHE), and PtOH (ca. 1.05V vs. NHE). In potentiodynamic experiments at a scan rate of 100 mV/s, the equivalent of a monolayer of PtOH (*i.e.*, $\theta = 1$) is generated on the positive scan to $E = 1.1V$ vs. NHE (0.85V vs. SCE). With the continued positive scan, PtOH is converted fully to PtO (*i.e.*, $\theta = 2$) at $E = 1.4V$ vs. NHE (1.15V vs. SCE). Reversal of the positive scan at potential values for which $\theta \ll 1$ produces a cathodic peak for reduction of PtOH, which is in support of the conclusion that the reaction $Pt + H_2O = PtOH + H^+ + e$ is reversible for $\theta \ll 1$. When the PtOH ($\theta \ll 1$) is allowed to age, or for increased values of the positive scan limit for which $\theta \rightarrow 1$, the cathodic peak for reduction of the surface oxide is shifted to more negative values. This is concluded to result from induced surface rearrangement of PtOH, the so-called "place exchange," to yield a thermodynamically more stable product designated "HOPT". Shibata found that the diffraction pattern obtained by LEED for an electrode polarized at $E > 1.15V$ vs. NHE, followed by reduction of the oxide, was identical to the pattern for Pt black. It is at a potential of 1.15V where place exchange is concluded to become significant.

Vetter (28) and Vetter and Schultze (29) investigated the growth mechanism of the surface oxide on Pt electrodes. The accumulated anodic charge (Q_{ox}) corresponding to formation of the oxide at $1.0 < E < 2.0V$ increases linearly with $\log t$ for $t = 2 \text{ ms} - 1000s$. At a fixed value of t , Q_{ox} increases as a linear function of E . They concluded that only a phase oxide exists at the electrode surface which increases in thickness with increasing time and potential. The growth mechanism was concluded to include the field-assisted place exchange of Pt²⁺ and O²⁻ ions to produce the phase oxide lattice. Such a mechanism had been proposed by Visscher and Devanathan (30) and Ord and Ho (31). For low surface coverage, the rate-determining

¹Present address: Dow Chemical Company, Midland, Michigan 48640

²Operated for the U.S. Department of Energy by Iowa State University under Contract no W-7405-ENG-82.

Key words: platinum oxide, modulated voltammetry, anode, ring-disk electrode.

step (rds) is that between the Pt^{2+} at the electrode surface and O^{2-} in the inner Helmholtz plane. At high coverages, the place-exchange mechanism is still operative, but the rds cannot unambiguously be assigned as occurring at the metal-metal oxide interface or the metal oxide-inner Helmholtz interface.

The anodic signal for As(III) at an oxide-covered Pt electrode can decrease significantly below the theoretical transport-limited value, and yet the current is essentially independent of potential over a significant range (32). Hence, the rds does not involve charge transfer, nor is inhibition the result of iR-loss across a poorly conducting oxide layer. Faradaic reactions at rotating disk electrodes (RDE) under mixed control by mass transport and kinetics produce electrode currents (33) which are smaller than the transport-limited value, as described by

$$i = \frac{nFA DC^b}{\delta + K} \quad [3]$$

where n , F , A , D , and C^b have their usual electrochemical significance. The thickness (δ) of the diffusion layer at the electrode-solution interface is

$$\delta = 1.62 D^{1/3} \omega^{-1/2} \nu^{1/6} \quad [4]$$

where ω is the angular velocity (rad/s) of electrode rotation and ν is the kinetic viscosity (cm^2/s) of the solution. The parameter K in Eq. [3] is of a form dependent on the nature of the kinetic mechanisms involved. For mixed control involving a slow chemical step at the electrode surface, $K = D/k$ where k is a potential-independent rate constant. For slow electron-transfer kinetics, k is potential dependent. The numerical value of K is easily calculated from the intercept of a plot of i^{-1} vs. $\omega^{-1/2}$. The slope of such a plot is identical to that for the transport-limited case (i.e., $K = 0$) for which the intercept is zero.

Experimental

Instrumentation.—Disk and ring-disk electrodes were from Pine Instrument Company, Grove City, Pennsylvania. These included: a Model DD20 Pt RDE (area = 0.455 cm^2), a Model DT06 Pt-Pt RRDE (disk area = 0.459 cm^2 , $\beta^{2/3} = 0.368$, and $N = 0.178$), and a Model AFMD18 (area = 0.166 cm^2). The electrodes were polished according to the usual metallographic procedures with $1 \mu\text{m}$ alumina on microcloth for the final step. The Model ASR-2 and Model MSR rotators were from Pine Instrument Company. The MSR rotator is designed for hydrodynamically modulated voltammetry and can accelerate from 1000 to 4000 rev/min in 22 ms. The potentiostat was a Model RDE3, Pine Instrument Company, or a Model 173, EG&G Princeton Applied Research, Princeton, New Jersey, equipped with a Model 176 current-to-voltage converter. Voltage waveforms generated by a Model 175 Universal Programmer, EG&G Princeton Applied Research, were used occasionally. The Model RDE3 bipotentiostat was used for all ring-disk studies. The reference electrode was a miniature saturated calomel electrode (SCE), Corning Scientific Instruments, Corning, New York. Current-potential (i-E) curves were recorded on an Omnigraphic Series 100 X-Y recorder, Houston Instruments, Austin, Texas. Instrumentation for square wave hydrodynamically modulated voltammetry has been described elsewhere (22).

Chemicals.—All chemicals were reagent grade from Baker Chemical Company. Solutions of As(III) were prepared by dissolving As_2O_3 in a minimal volume of a concentrated solution of NaOH with subsequent dilution by H_2O . All H_2O was triply distilled; demineralization followed the first distillation, the second distillation was from alkaline permanganate solution (ca. 0.1M KMnO_4 , 0.1M KOH), and the final distillation was from $1\text{M H}_2\text{SO}_4$. Dissolved O_2 was removed by dispersed N_2 .

Procedures.—The technique of square wave modulated hydrodynamic voltammetry (22, 34) is based on the measurement of the component of total electrode current

which is coupled to the frequency of a square wave variation of the rotational velocity during application of a slow, staircase potential waveform. The modulated signal is free of contributions from surface controlled processes, e.g., double layer charging, oxide formation, and solvent breakdown. The experimental conditions were similar to those used previously (22): $t_d = 150 \text{ ms}$, $N = 10$, $\Delta E = 5 \text{ mV}$, and $\phi = 0.15 \text{ V/min}$.

Results and Discussion

Voltammetric study of As(III) as a function of concentration.—Current-potential (i_d - E_d) curves obtained at the Pt RDE are shown in Fig. 1. A residual curve is included for comparison. In the absence of As(III), the surface oxide is formed during positive scan of potential for $E_d > 0.55 \text{ V}$; this oxide is reduced on the subsequent negative scan to produce peak D at $E_p = 0.48 \text{ V}$. Faradaic formation and subsequent dissolution of adsorbed atomic hydrogen occurs for $0.1 > E_d > -0.2 \text{ V}$, and evolution of $\text{H}_2(\text{g})$ occurs for $E_d < -0.2 \text{ V}$. The adsorption of As(III) results in suppression by ca. 150 mV of the anodic formation of surface oxide; and the large peak-shaped wave (C) with $E_p = 0.85 \text{ V}$ corresponds to the simultaneous processes of (i) oxide formation, (ii) oxidation of adsorbed As(III), and (iii) oxidation of As(III) transported to the electrode surface by the convective-diffusional process. The total anodic current decreases steadily during the continuing positive scan of $E_d > 0.85 \text{ V}$, until the onset of $\text{O}_2(\text{g})$ evolution at $E_d > 1.25 \text{ V}$. The predominant cause of the decay for this high rate of potential scan ($\phi = 6.0 \text{ V/min}$) is the loss of the contribution from oxidation of the adsorbed As(III). A current plateau (i.e., potential-independent current) is observed for As(III) oxidation during the negative scan in the region $1.2 > E_d > 0.7 \text{ V}$. Oxidation of As(III) ceases with reduction of the surface oxide to produce peak D. Because oxidation of As(III) can occur during the negative scan at the oxide-covered surface at least to $E_d = 0.6 \text{ V}$, whereas oxidation of As(III) at the oxide-free surface does not commence on the positive scan until $E_d > 0.7 \text{ V}$, it is concluded that oxidation of As(III) is catalyzed by the surface oxide, in agreement with the conclusion of Zakharov and Songina (20). Because of the similarity of the height for peak D in the presence and absence of As(III), it is concluded to a first approximation that the extent of oxide formation for $E_d > \text{ca. } 1.0 \text{ V}$ is unaffected by the presence of As(III). The nature of the faradaic process generating peak E will be discussed later.

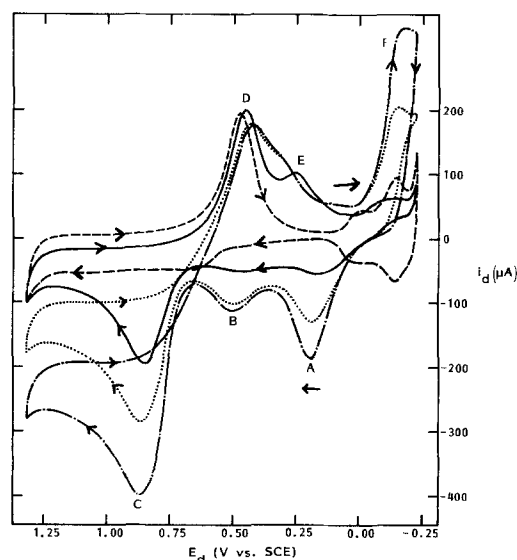


Fig. 1. Current-potential curves for Pt RDE as a function of $C^b_{\text{As(III)}}$. Electrode: DD20 Pt RDE. Conditions: $\omega = 104.7 \text{ rad/s}$, $\phi = 6.0 \text{ V/min}$, 0.50M HClO_4 . (---) residual, (—) $4.01 \times 10^{-5}\text{M As(III)}$, (---) $1.97 \times 10^{-4}\text{M As(III)}$, (— · —) $3.83 \times 10^{-4}\text{M As(III)}$.

Variation of scan limits.—Wave F on the negative scan for $E_d < 0.0V$ in Fig. 1, and peaks A and B on the subsequent positive scan, correspond to cathodic deposition and oxidation of As(0), respectively. Peaks A and B are not obtained when the cathodic (*i.e.*, negative) scan limit (E_c) is $\geq 0.0V$. When the quantity of deposited As(0) is increased beyond that for Fig. 1, accomplished by use of higher concentrations of As(III) or by cessation of the potential scan at $E_c < -0.2V$, the area of peak A continues to grow in proportion to the amount of deposited As(0); however, the area of peak B reaches a limiting value. Peak A is concluded to correspond to the anodic stripping of bulk As(0), which is not stabilized by interaction with the Pt substrate, and peak B is concluded to correspond to oxidation of As(0) adatoms. The potential for onset of $H_2(g)$ evolution (*ca.* $-0.25V$) does not change with As(0) deposition.

Current-potential curves were recorded as a function of the anodic (*i.e.*, positive) scan limit (E_a) for $E_c = 0.7-1.4V$. For $E_a = 0.8V$, only a slight quantity of oxide is formed, and the cathodic peak for oxide reduction is barely perceptible on the negative scan. Clearly, the quantity of oxide increases substantially for $E_a > 0.8V$ and E_p for peak D is shifted to more negative values, as is observed for the absence of As(III) (23-26). Although accurate integration of peak D is not possible as a function of the variation in E_a , due to interference by peak E, the height of peak D is approximately the same in the presence and absence of As(III) for all values $E_a \geq 1.0V$. This is consistent with the conclusion made above that the presence of As(III) has minimal effect on the quantity of oxide produced on the time scale of the cyclic voltammetry, provided the adsorbed As(III) has been totally oxidized to soluble As(V) during the positive scan.

Variation of rotational velocity (ω).—The effect of variation of ω on the i_d-E_d curve for As(III) is shown in Fig. 2. As ω is increased, the anodic current for any value $E_d > 0.8V$ also is increased because of the increased flux of As(III) from the bulk solution to the electrode surface. The observation of a plateau current on the negative scan in the region $1.2 > E_d > 0.8V$ could be easily mistaken as diagnostic evidence that the corresponding electrode reaction is mass-transport limited. Accordingly, a plot of i_d vs. $\omega^{1/2}$ would be expected to be linear (see Eq. [3] and [4] for $K = 0$) with a slope of $0.62nFAD^{2/3}\nu^{-1/6}C^b$, as predicted by Levich (33, 35). For the oxidation of As(III) with $\phi =$

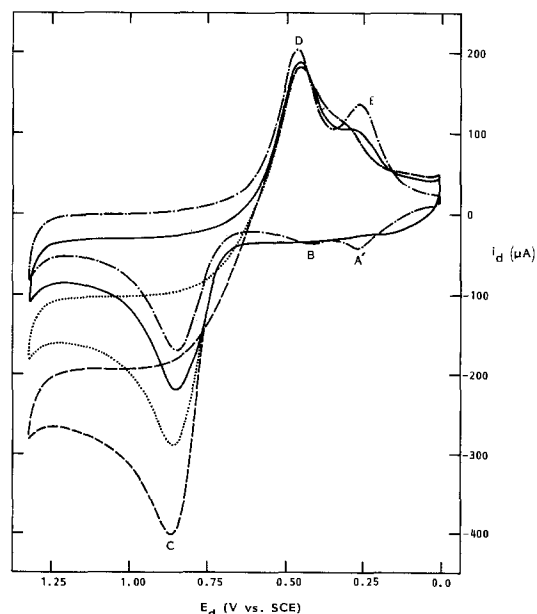


Fig. 2. Current-potential curves for As(III) as a function of ω . Electrode: DD20 Pt RDE. Conditions: $\phi = 6.0 V/min$, $1.97 \times 10^{-4}M$ As(III) in $0.50M$ $HClO_4$, ω (rad/s): (—) 0.00, (—) 10.47, (---) 104.7, (----) 418.9.

$6.0 V/min$, such a plot deviates severely from linearity and the expected slope, and is indicative of mixed control.

There is a dramatic difference between the features of the i_d-E_d curves for $\omega = 0$ rad/s and those for $\omega > 0$ rad/s. Peak E is made very prominent, and peaks A and B appear distinctly for the absence of rotational velocity. For $\omega = 0$ rad/s, the As(V) produced anodically for $E_d > 0.8V$ remains in the diffusion layer during the time in which E_d is scanned to E_c . It is concluded that As(V) is deposited as As(0) at underpotential in the region of peak E and subsequent oxidation of the deposition product yields peaks A' and B. The lesser peak E observed for $\omega > 0$ rad/s is concluded to result from As(V) adsorbed on the oxide-covered surface.

Voltammetric study of As(V).—While the electrochemistry of As(V) is not of primary interest here, it is informative to consider the voltammetric response of As(V) as it relates to our understanding of the As(III)-As(V) half-reaction. Arsenic(V) is generally considered to be electroinactive without the benefit of extensive coordination by ligands other than water. Several i_d-E_d curves are shown in Fig. 3 for As(V) as a function of E_c ; a residual curve is included for comparison. Peak E, concluded to result in part from the underpotential deposition of As(V), is clearly visible, as are peak A', B, and C. Since the potential of peak A' (0.25V) for As(V) in Fig. 3 is slightly different than the potential of peak A (0.20V) in Fig. 1 observed when an extensive quantity of bulk As(0) is deposited from a solution of As(III), the stability of the As(0) adatoms producing peak A' is concluded to be slightly greater than that of bulk As(0). We conclude that peaks A' and B represent oxidation of As(0) adatoms to As(III) adions on the polycrystalline surface. The As(III) adions produced by anodic processes yielding peaks A' and B are oxidized to soluble As(V) by the process producing peak C. The combined area of peaks A', B, and C, measured by a planimeter with respect to the residual curve, was found to be within *ca.* 10% of the area for peak E. This is in excellent agreement with the proposed mechanism for production of these peaks, in view of the probable error in the assumption that the residual curve shown accurately represents the background signal in the presence of As(V). Although a clear distinction is made here between peak A' for As(V) (see Fig. 3) and peak A for As(III) (see Fig. 1), oxidation of As(0) adatoms at 0.25V certainly contributes to the larger peak A obtained for stripping of bulk As(0).

Ring-disk studies.—The rotating ring-disk electrode (RRDE) is recognized as a valuable tool for the investigation of electrode reactions (35, 36). Since As(V) does not exhibit continuous electroactivity at a constant electrode potential, meaningful collection experiments cannot be performed for solutions of As(III) with detection of As(V) at the ring electrode. The use of a Pt ring electrode for

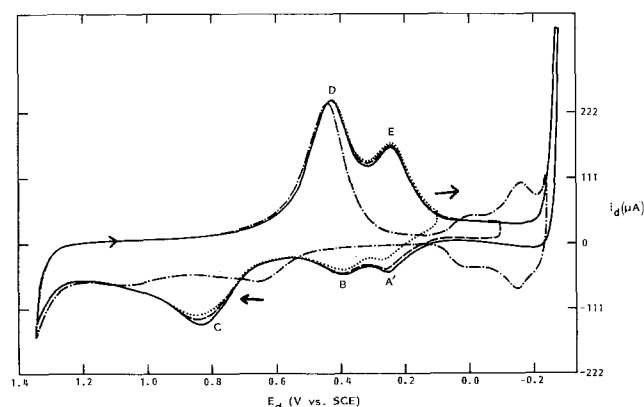


Fig. 3. Current-potential curves for As(V) as a function of E_c . Electrode: DD20 Pt RDE. Conditions: $\omega = 100.0$ rad/s, $\phi = 6.0 V/min$, $1.41 \times 10^{-4}M$ As(V) in $0.50M$ $HClO_4$, E_c (vs. SCE): (---) 0.10, (----) -0.10, (—) -0.28, (—) -0.25 (Pt residual).

shielding experiments was not satisfactory because of the continual decay of activity of the Pt electrode for anodic detection of As(III) caused by buildup of surface oxide at the detection potential. The oxidation of As(III) at a Au electrode occurs at a transport-limited rate (18), and the Pt ring of the RRDE was electroplated with Au. The i_d - E_d and i_r - E_d curves for $E_r = 1.0V$ are shown in Fig. 4 for a solution of 0.098 mM As(III). The ring current at $E_d = 0.0V$ is slightly less than the predicted value of 22.2 μA , for this value of $C^b_{As(III)}$; however, i_r increases slightly beyond the predicted value as E_d is scanned positive. This phenomenon is concluded to result from the potential-dependent adsorption and desorption of As(III) at the disk electrode for $E_d < 0.6V$. If the scan of E_d was halted at any value in the region $0.0 < E_d < 0.6V$, the value of I_r quickly drifted to the theoretical limiting value. At $E_d = 0.65V$ on the positive scan, the oxidation commences for As(III) from the bulk solution, and i_r decreases accordingly (*i.e.*, the ring electrode is shielded). The value of i_r measured at $E_d = 0.85V$ on the positive scan is 11.1 μA for $\phi = 6.0$ V/min, in excellent agreement with the predicted value of 11.4 μA for a transport-limited reaction at the disk electrode. For $E_a > 1.3V$, at the scan rate used here, the value of i_r measured in the region $0.8 < E_d < 1.2V$ during the negative scan is slightly greater than that predicted for the mass-transport-controlled oxidation of As(III) at the disk electrode. This observation is in agreement with the conclusion based on the plot of i_d vs. $\omega^{1/2}$ that oxidation of As(III) at an oxide-covered surface is under mixed control, *i.e.*, the value of i_d is less than the transport-limited value. Shielding of the As(III) flux to the ring electrode during the negative scan of E_d continues to ca. 0.7V, in agreement with the previous observation (see Fig. 1) that oxidation of As(III) at a Pt electrode is made more reversible by the presence of the surface oxide.

Shielding of the ring electrode decreases as the oxide at the disk electrode is cathodically reduced ($E_p \approx 0.4V$), but then increases again for E_d in the region of peak E (see Fig. 1). We conclude that As(III) is adsorbed at the disk electrode in the region of peak E with partial charge transfer. Loucka (38) concluded that As(III) is adsorbed from 0.5M H_2SO_4 with electrodeposition as As(0) for $E < 0.7V$ vs. NHE. We are hesitant to agree with Loucka's conclusion because of the absence of distinct anodic peaks in the region $0.1 < E_d < 0.6V$ during the subsequent positive scan for oxidation of the As(0) adatoms. The adsorption of As(III) at the disk electrode is complete for $E_d \approx 0.05V$, and i_r increases to the unshielded value.

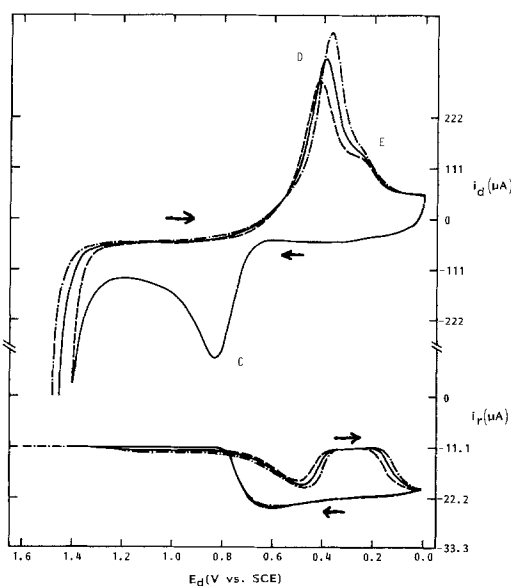


Fig. 4. Current-potential curves for As(III) at RRDE. Electrode: DT06 Pt-Pt RRDE. Conditions: $\omega = 100.0$ rad/s, $\phi = 6.0$ V/min, $9.8 \times 10^{-5}M$ As(III) in 0.50M $HClO_4$, $E_r = 1.00V$ vs. SCE. E_a for disk electrode (vs. SCE): (---) 1.40V, (—) 1.50V, (- · -) 1.60V.

The ring-disk experiment was repeated with variation of E_a and E_c , and the i_d - E_d and i_r - E_d curves are shown in Fig. 5 for 0.524 mM As(III). Of greatest interest is the case of $E_c = -0.2V$, in which bulk As(0) is deposited at the disk electrode. Anodic peaks A and B for the i_d - E_d curve, previously concluded to correspond to oxidation of bulk As(0) (peak A) and As(0) adatoms (peaks A' and B'), result in production of some soluble As(III), which is subsequently detected at the ring electrode. (Note: the oxidation of As(0) at the disk electrode involves 3 eq/mol, whereas the detection of As(III) at the ring electrode involves 2 eq/mol.) The value of the peak current at $E_d = 0.2V$ on the i_r - E_d curve is $70 \pm 10\%$ of the value expected if all As(III) produced for peak A in the i_d - E_d curve is soluble, whereas the peak current at $E_d = 0.5V$ on the i_r - E_d curve is $90 \pm 10\%$ of the theoretical for peak B in the i_d - E_d curve. Hence, a significant stripping fraction of the As(III) produced by the anodic stripping of bulk As(0) remains adsorbed at the electrode surface. The possibility that oxidation of As(0) to As(V) could occur at the disk electrode for $E_d < 0.7V$ is not likely, given the value of 0.132V vs. SCE for the standard reduction potential of the As(V)-As(0) couple, which is 0.125V positive of the standard reduction potential for the As(III)-As(0) couple.

It is important to observe that the area of peak C in the i_d - E_d curve, resulting from oxidation of adsorbed As(III) adions to As(V), is not increased substantially if bulk As(0) is deposited for $E_c < 0.0V$ (compare the i_d - E_d curves for $E_c = 0.0$ and $-0.2V$). Apparently, the surface coverage by As(III) is fixed by the adsorption isotherm and the bulk concentration for As(III) whether or not As(0) has been deposited previously on the electrode. The adsorption isotherm for As(III) was determined from transient ring-disk experiments as a function of $C^b_{As(III)}$ in the manner reported previously for I^- at Pt (37). In essence, the quantity of As(III) adsorbed was calculated from the integrated area of the shielding wave in the i_r -time curves recorded following a step of E_d from 1.2 to 0.2V and to 0.0V. The isotherms, shown in Fig. 6, are virtually the same for both experiments. The limiting surface coverage by adsorbed As(III) is produced for $C^b_{As(III)} > 6 \times 10^{-5}M$ and corresponds to 2.3×10^{-9} mol/cm² or 1.38×10^{15} at./cm². The approximate surface density of Pt atoms for a perfectly smooth polycrystalline electrode is 1.35×10^{15} at./cm². There was no effort to determine the surface roughness of

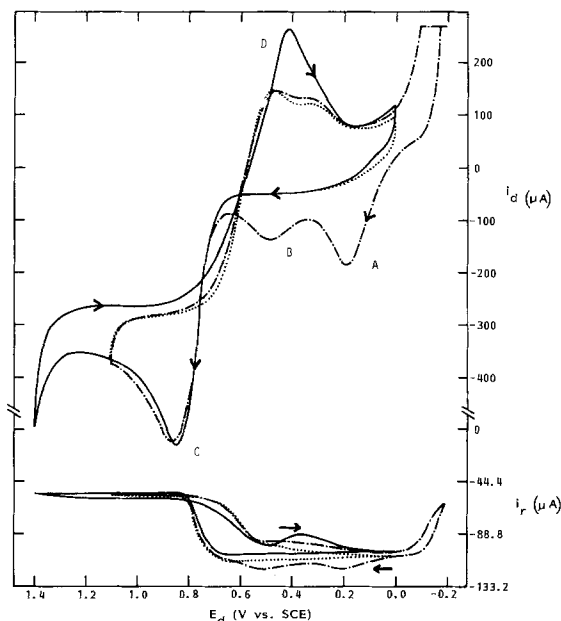


Fig. 5. Current-potential curves for As(III) at RRDE. Electrode: DT06 Pt-Pt RRDE. Conditions: $\omega = 100.0$ rad/s, $\phi = 6.0$ V/min, $5.24 \times 10^{-4}M$ As(III) in 0.50M $HClO_4$, $E_r = 1.00V$ vs. SCE. Scan limits for disk electrode (vs. SCE): (---) $E_a = +1.10V$, $E_c = -0.20V$; (····) $E_a = +1.10V$, $E_c = 0.00V$; (—) $E_a = +1.40V$, $E_c = 0.00V$.

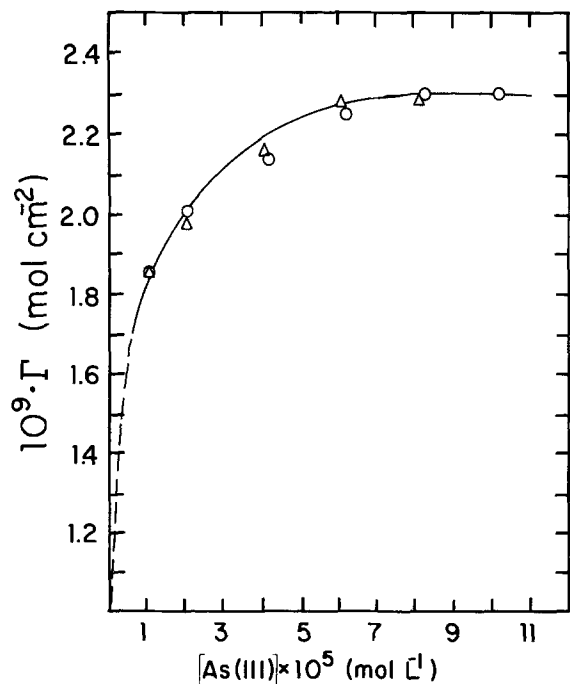


Fig. 6. Adsorption isotherm for As(III) at Pt RDE. Electrode: DD20 Pt RDE. Conditions: $\omega = 100.0$ rad/s, $0.50M$ $HClO_4$. Curves: (○) E_d stepped from 1.10 to 0.00V, (△) E_s stepped from 1.40 to 0.20V.

the electrode; however, if a roughness factor of 2 is reasonable, a 1:2 correspondence exists for As(III): Pt.

Variation of potential-scan rate (ϕ).—The effects of increasing ϕ on the i_a - E_d curve for As(III) were observed. As expected for the surface-controlled reactions contributing to peaks C and D, these peaks increase with increasing ϕ in the range $\phi = 1-6$ V/min. Of greater interest, however, are the large, cathodic, surface-controlled currents observed during the negative scan in the region $0.4 > E_d > 0.0V$ and the anodic current during the positive scan for $0.0 < E_d < 0.7V$ (see Fig. 2 for $\omega > 0$ rad/s). Peak E has been assigned on the basis of ring-disk studies (Fig. 4 and 5) to the adsorption of As(III) with partial charge transfer. Given the absence of a sharp anodic peak on the subsequent positive scan, we conclude tentatively that As(0) adatoms, as a discreet oxidation state, are not involved. The double layer capacitance for a Pt electrode in

a pure acidic electrolyte is ca. $40 \mu fd/cm^2$. Estimates of the apparent capacitance from the observed currents as a function of ϕ yielded values of $1050 \mu fd/cm^2$ at 1.0 V/min and $856 \mu fd/cm^2$ at 10.0 V/min. The anomalously large capacitance calculated for an adsorption process accompanied by partial charge transfer to produce adions having an intermediate oxidation state is described as "pseudocapacitance" (39-42). The arsenic adions, in whatever oxidation state integral or fractional, are probably reduced to As(0) for $E_d < 0.0V$ (see Fig. 1), and the subsequent voltammetric oxidation of As(0) yields distinct anodic peaks (A and B in Fig. 1). The underpotential deposition of As(V) as As(0) adatoms in the region of peak E eliminates the appearance of the pseudocapacitance for the region $0.0 \leq E_d \leq 0.15V$ (Fig. 2).

We rationalize the adsorption of As(III) with partial charge transfer on the basis of π bonding. It is known for some compounds containing arsenic that if the atom to which arsenic has donated electrons also has an orbital of the same symmetry as the empty d orbitals of arsenic, back-donation can occur resulting in overall multiple-bond character (43). While it may be meaningless to discuss Pt d orbitals on the surface of a polycrystalline metal which is not perfectly smooth, there is solid evidence of Pt contributing to $d\pi$ - $d\pi$ bonding in CO adsorption (44). Such back-donation implies a specific preferred orientation of the adsorbed species on the electrode surface. The conclusion of specific binding of arsenic adions to Pt atoms is not contradicted by any voltammetric observations.

Square wave hydrodynamically modulated voltammetry (QHMV).—The total anodic current observed for As(III) at $E_d > 0.8V$ on the positive scan is the result of two surface-controlled processes plus the oxidation of As(III) from the bulk solution under mixed transport-kinetic control. The application of QHMV has been described for distinguishing the transport-controlled component of electrode currents (22, 34) in the presence of surface-controlled reactions. The modulated technique ignores the surface-controlled currents from double layer charging, faradaic reaction of adsorbed species, formation and dissolution of surface oxides, and the evolution of $O_2(g)$ and $H_2(g)$ by breakdown of the solvent.

In Fig. 7 are shown Δi_a - E_d curves obtained by QHMV for 2.0 mM As(III). The residual response is not shown because Δi_a remained at zero for virtually the entire range of E_d shown. The value of Δi_a measured on the positive scan is at a maximum for $0.8 < E_d < 0.9V$, which is concluded to correspond to an appreciable surface coverage by

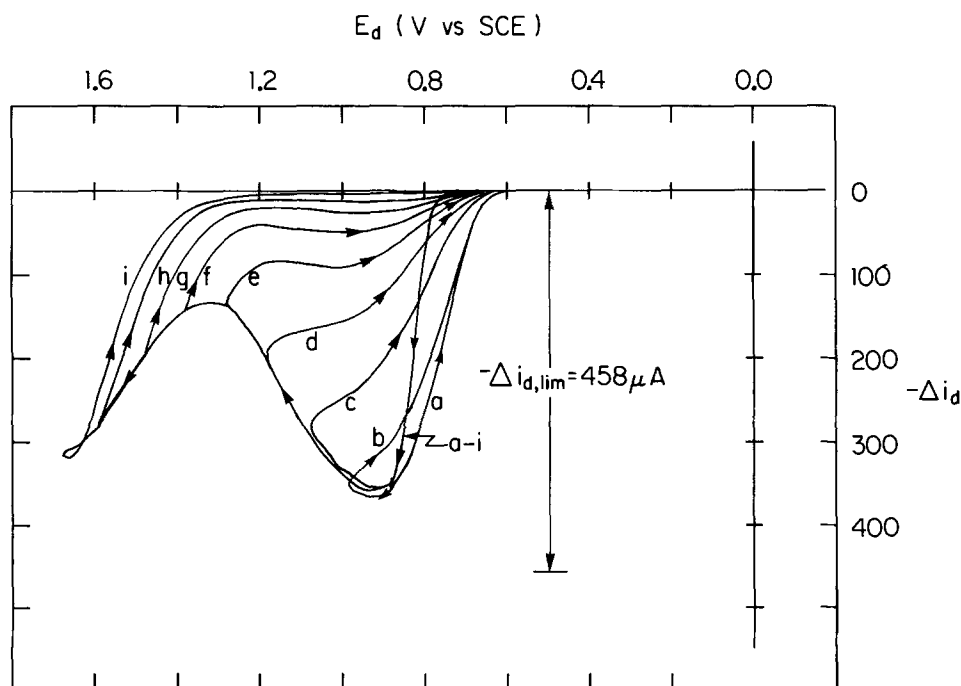


Fig. 7. Current-potential curves by square-wave hydrodynamically modulated voltammetry for As(III) at RDE. Electrode: AFMD18 Pt RDE. Conditions: $\Delta\omega^{1/2} = 20.47-10.23$ (rad/s) $^{1/2} = 10.23$ (rad/s) $^{1/2}$; $\phi = 0.15$ V/min; 2.0 mM As(III) in $0.50M$ $HClO_4$. E_d (vs. SCE): (a) 0.90V, (b) 1.00V, (c) 1.10V, (d) 1.20V, (e) 1.30V, (f) 1.40V, (g) 1.50V, (h) 1.60V, (i) 1.70V.

PtOH ($\theta \ll 1$). The Δi signal gradually decreases as the positive scan of E_d continues. When the scan is reversed for $E_a > 1.2V$, Δi_d drops significantly below the maximum value to a value which is, to a good approximation, independent of E_d for $0.9 < E_d < 1.2V$. Hence, the rate-determining step does not involve charge transfer and is concluded to involve a slow chemical transfer of oxygen to As(III) from the oxide-covered surface. The value of Δi_d measured at $E_d = 1.00V$ on the negative scan decreases significantly as E_a , for the preceding positive scan, is increased beyond 1.2V. It should be noted that the slow scan rate used allows a greater amount of surface oxide to be formed for $E_d > 1.2V$ as compared with the high scan rate used for Fig. 1. This undoubtedly corresponds to oxide coverage beyond the equivalent of a monolayer of PtO (i.e., $\theta > 2$). Even for an extensive layer of surface oxide (e.g., $E_d = 1.6V$), oxidation of As(III) in the region $E_d \gg 1.2V$ occurs at a rate nearly equal to the maximum value observed for the highly active PtOH surface. We note with enthusiasm that evolution of $O_2(g)$ ceases at ca. 1.2V on the negative scan (see residual curve of Fig. 1) which is the potential at which Δi has decreased to its minimum value during the negative scan. In a separate experiment, the negative scan from $E_a = 1.50V$, was reversed at $E_c = 1.0V$; Δi_d increased again to the value shown in Fig. 7 for $E = 1.50V$. We conclude that the oxidation of As(III) at the oxide-covered surface is catalyzed by the evolution of $O_2(g)$. Since the homogeneous oxidation of As(III) by $O_2(g)$ occurs at a negligible rate in acidic media (16), we conclude the catalytic mechanism occurs by way of adsorbed $\cdot OH$ generated as the first step in the mechanism for evolution of $O_2(g)$ (45, 46).

The role of the formation of surface oxide, starting at $E_d = ca. 0.8V$ on the positive scan, in the electrocatalysis of the oxidation of As(III) is amplified further by a wave analysis performed for the rising part of the Δi_d - E_d curve in the vicinity of $E_{1/2}$. The value of $E_{2/3} - E_{1/3}$ is ca. 20 mV in comparison to the value 17.8 mV expected for a reversible process ($n = 2$) without electrocatalytic involvement of the electrode surface. This apparent "reversibility," in spite of the fact that the value of $E_{1/2} = 0.78V$ is ca. 0.46V positive of the value of E° for the As(V)-As(III) half-reaction in this medium (0.32V), is further diagnostic evidence of electrocatalysis in which the value of $E_{1/2}$ is determined by the potential dependence of the catalytic surface state rather than the standard reduction potential of the electroactive species in the solution. The value of $E_{1/2}$ for the electrocatalyzed-oxidation of As(III) observed on the negative scan for $E_a = 0.90$ is 0.65V, which is ca. 0.13V negative of the value observed for the positive scan. The loss of electrocatalytic activity on the negative scan is the result of the reduction of the surface oxide to produce peak D (see Fig. 1).

Effect of variation of E_a .—The catalytic benefit of the formation of the surface oxide for oxidation of As(III) at Pt electrodes is clearly indicated, although the maximum transport-coupled signal is less than the theoretical. Yet, the formation of oxide beyond the equivalent of $\theta = 1$ ($E_a > 1.0V$) results in a decrease of the anodic current for As(III) well below the transport-limited value, and for $\theta > 2$ ($E_a > 1.3V$) the current is severely inhibited (see Fig. 7). The involvement of the surface oxide in the reaction mechanism was characterized further by the determination of the rate constant (k) for the mixed control from current measurements made at $E_d = 1.0V$ following anodic polarization of the electrode to values of $E_a > 1.1V$. Accordingly E_d was cycled at $\phi = 6.0$ V/min between $E_c = 0.0V$ and the designated value of E_a . After several cyclic scans to insure the reproducibility of the i - E response, the scan of E_d was halted at 1.0V on the negative scan and i_d was obtained as a function of ω within a time period of ca. 50s. The rate of oxide growth at 1.0V is minimal under these conditions when $E_a > 1.1V$, and the quantity of oxide was presumed constant during the time in which the i_d - ω data was recorded. The corresponding value of k for each value of E_a was calculated from the intercept of plots

of i^{-1} vs. $\omega^{-1/2}$. The resulting plot of $\ln k$ vs. E_a is linear, as shown in Fig. 8 (curve on right).

The area (Q_{ox}) under the reduction peak for the surface oxide (peak C in the residual curve of Fig. 1) was measured as a function of E_a in the absence of As(III). The values of Q_{ox} were determined to be a linear function of E_a as represented by

$$Q_{ox} = (546 \mu C/V) (E_a - 0.79) \quad [5]$$

The quantity ($E_a - 0.79$) in Eq. [5] represents the effective overpotential observed for oxide formation (η_{ox}). The linear correspondence of Q_{ox} and E_a has already been noted (23, 28, 29). Continuing with our conclusion made earlier that Q_{ox} for $E \geq 1.0V$ is the same for the presence or absence of As(III), the values of $\ln k$ were replotted as a function of Q_{ox} , and the result is shown in Fig. 8 (curve on left). The equations of the linear plots in Fig. 8 are as follows: for $\log k$ vs. E_a

$$\log k = 1.77 - 2.46 E_a$$

and for $\log k$ vs. Q_{ox}

$$\log k = -0.174 - (4.48 \times 10^{-3}) Q_{ox}$$

In the equations above, k has dimensions in centimeters per second and Q_{ox} is in microcoulombs. Alternately

$$k = M \cdot \exp \{ -E_a/E_0 \} \quad [6]$$

and

$$k = N \cdot \exp \{ -Q_{ox}/Q_0 \} \quad [7]$$

where $M = 58.9$, $E_0 = 0.177V$ vs. SCE, $N = 0.670$, and $Q_0 = 97.0 \mu C$.

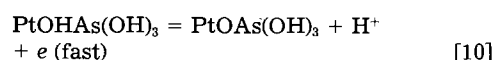
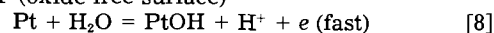
Conclusions

We conclude that oxygen from adsorbed $\cdot OH$ (i.e., PtOH) generated as the first step in the formation of surface oxide at a Pt electrode, and in the evolution of $O_2(g)$, is rapidly transferred to As(OH)₃ in the electrocatalyzed production of OAs(OH)₃. The rate of the surface reaction between adsorbed $\cdot OH$ and As(OH)₃ can be sufficiently rapid (i.e., $\theta \rightarrow 1$) so that the faradaic current for As(III) is nearly equal to the transport-limited value for low ω .

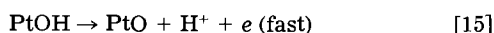
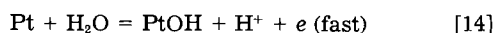
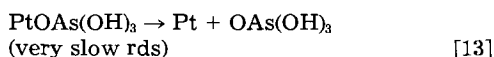
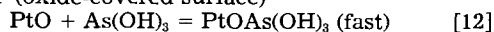
Results reported here for Pt electrodes bearing extended layers of PtO (i.e., $\theta > 2$) do not rule out the possibility of oxygen abstraction by As(OH)₃ directly from the PtO as well; however, the abstraction reaction is very slow, is independent of potential for a constant oxide coverage, and decreases with increases in the quantity of oxide (Q_{ox}). The $O_2(g)$ evolution reaction on oxide-covered Pt electrodes has been reported also to occur at a rate which decreases with increases in the oxide coverage (45, 46).

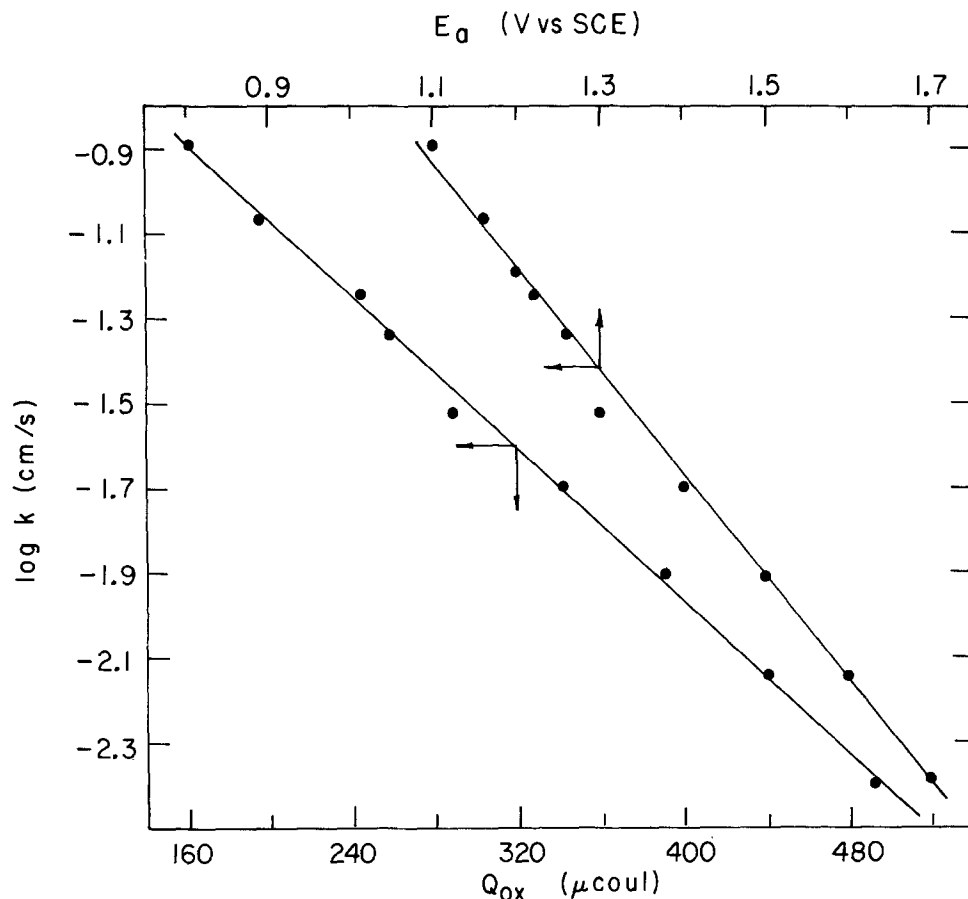
Mechanisms are proposed below for the electrocatalyzed oxidation of As(III) at an oxide-free Pt electrode initiated by discharge of adsorbed $\cdot OH$ (Scheme I) and the possibility of the much slower oxygen abstraction from an oxide-covered surface (Scheme II). The variant of Scheme I involving $\cdot OH$ adsorbed at an oxide-covered surface is self-evident.

Scheme I (oxide-free surface)



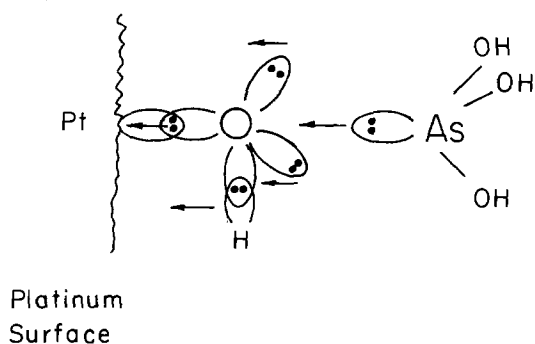
Scheme II (oxide-covered surface)



Fig. 8. Plot of $\log k$ vs. E_a and Q_{ox} .

The product of the reaction in Eq. [10] can be viewed simply as the activated state in a mechanism analogous to a bimolecular substitution reaction. Accordingly, the approach of the lone electron pair of As(III) toward the antibonding orbital of the surface oxygen results in a shift of electron density, as illustrated below. Ultimately, the surface oxygen is released from the Pt, and formation of $\text{OAs}(\text{OH})_3$ is complete.

Adsorbed As(III) at an oxide-free Pt surface reacts rapidly with $\cdot\text{OH}$ discharged at adjacent surface sites; however, there is no evidence yet that adsorption of As(III) at sites adjacent to the oxygen bearing site is a prerequisite to reactivity. If adsorption of As(III) at oxide-free Pt sites is indeed a prerequisite to oxidation, a seemingly convenient explanation of the loss activity for a surface covered by an extended layer of PtO (*i.e.*, $\theta > 2$) could be based on the consequential decrease in the surface density of Pt adsorption sites. Such an electrode surface would not be uniformly accessible, and the observed limiting current would be much less than the theoretical transport-limited current (*i.e.*, the "Levich current") for a uniformly accessible electrode. The response of nonuniform electrodes has been considered by Nagy *et al.* (47), and by Landsberg and Thiel (48). This explanation of the mixed control observed for oxidation of As(III) will be tested in Part II of this work. Also in Part II, the results of kinetic studies of the electrocatalyzed oxidation of As(III) at Pt electrodes will be presented.



Acknowledgments

This work was supported by the Office of Basic Energy Sciences. One of the authors (T.D.C.) gratefully acknowledges the financial support of The Electrochemical Society, Incorporated, through a Colin Garfield Fink Summer Fellowship for 1982.

Manuscript submitted Sept. 16, 1983; revised manuscript received Dec. 23, 1983.

Iowa State University assisted in meeting the publication costs of this article.

REFERENCES

1. J. P. Arnold and D. M. Johnson, *Talanta*, **16**, 1191 (1969).
2. H. V. Susic and M. G. Pjescic, *J. Electroanal. Chem.*, **34**, 535 (1972).
3. D. J. Myers and J. Osteryoung, *Anal. Chem.*, **45**, 267 (1973).
4. A. P. Tomilov and N. E. Chromutov, in "Encyclopedia of Electrochemistry of the Elements," Vol. II, A. J. Bard, Editor, Chap. 2, Marcel Dekker, New York (1974).
5. A. Watson, in "Polarography of Molecules of Biological Significance," W. F. Smyth, Editor, Chap. 10, Academic Press, London (1979).
6. L. F. Trushina and A. A. Kaplin, *Zh. Anal. Khim.*, **25**, 1616 (1970).
7. A. A. Kaplin, N. A. Veits, and A. G. Stromberg, *ibid.*, **28**, 2192 (1973).
8. G. Forsberg, J. W. O'Laughlin, R. G. Megargle, and S. R. Koirtiyohan, *Anal. Chem.*, **47**, 1586 (1975).
9. A. A. Kaplan, N. A. Veits, N. M. Mordvinova, and G. G. Glukhov, *Zh. Anal. Khim.*, **32**, 687 (1977).
10. A. A. Kaplin, N. A. Veits, and N. M. Mordinov, *Elektrokhimiya*, **14**, 227 (1978).
11. D. Aleksyeev, *J. Rus. Phys. Chem. Soc.*, **41**, 1155 (1909).
12. S. J. Lloyd and A. M. Kennedy, *Trans. Am. Inst. Chem. Engrs.*, **16**, 29 (1924).
13. S. J. Lloyd and A. M. Kennedy, *Chem. Met. Eng.*, **32**, 624 (1925).
14. O. A. Essin, *Z. Electrochem.*, **35**, 234 (1929).
15. O. W. Brown, J. E. Hatfield, and J. M. Church, *Trans. Electrochem. Soc.*, **70**, 323 (1936).
16. W. M. MacNevin and G. L. Martin, *J. Am. Chem. Soc.*, **71**, 204 (1949).

17. H. A. Catherino, *J. Phys. Chem.*, **71**, 268 (1967).
18. M. Daniels, *ibid.*, **7**, 1338 (1966).
19. R. Woods, I. M. Kolthoff, and E. J. Meehan, *J. Am. Chem. Soc.*, **86**, 1698 (1964).
20. V. A. Zakharov, and O. A. Songina, *Rus. J. Phys. Chem.*, **38**, 412 (1964).
21. V. A. Zakharov, O. A. Songina, and L. P. Kal'nitskaya, *Elektrokhimiya*, **7**, 1702 (1971).
22. D. S. Austin and D. C. Johnson, *Anal. Chem.*, **55**, 2222 (1983).
23. S. Gilman, in "Electroanalytical Chemistry," Vol. 2, A. J. Bard, Editor, Marcel Dekker, New York (1967).
24. H. Angerstein-Kozłowska, B. E. Conway, and W. B. A. Sharp, *J. Electroanal. Chem.*, **43**, 9 (1973).
25. B. V. Tilak, B. E. Conway and H. Angerstein-Kozłowska, *ibid.*, **48**, 1 (1973).
26. B. E. Conway and S. Gottesfeld, *J. Chem. Soc. Faraday Trans. 1*, **69**, 1090 (1973).
27. S. Shibata, *Electrochim. Acta*, **17**, 395 (1972).
28. J. W. Schultze, *Z. Phys. Chem. N.F.*, **73**, 29 (1970).
29. K. J. Vetter and J. W. Schultze, *J. Electroanal. Chem.*, **34**, 131, 141 (1972).
30. W. Visscher and M. A. Devanathan, *ibid.*, **8**, 127 (1964).
31. J. L. Ord and F. C. Ho, *This Journal*, **118**, 46 (1971).
32. J. A. Lown and D. C. Johnson, *Anal. Chim. Acta*, **116**, 41 (1980).
33. Yu. V. Pleskov and V. Yu. Filinovskii, "The Rotating Disc Electrode," Chap. 3, Consultants Bureau, New York (1976).
34. J. Wang, *Talanta*, **28**, 369 (1981).
35. V. G. Levich, "Physicochemical Hydrodynamics," p. 69, Prentice-Hall, Inc., Englewood Cliffs, NJ (1962).
36. W. J. Albery and M. L. Hitchman, "Ring Disc Electrodes," Clarendon Press (1971).
37. D. C. Johnson, *This Journal*, **119**, 331 (1972).
38. T. Loucka, *J. Electroanal. Chem.*, **47**, 103 (1973).
39. D. C. Grahame, *Chem. Rev.*, **41**, 441 (1947).
40. E. Gileadi and B. E. Conway, in "Modern Aspects of Electrochemistry," Vol. 3, J. O'M. Bockris and B. E. Conway, Editors, Butterworths, London (1964).
41. B. E. Conway, "Theory and Principles of Electrode Processes," Ronald Press, New York (1965).
42. M. A. Habib and J. O'M. Bockris, in "Comprehensive Treatise of Electrochemistry," Vol. 1, J. O'M. Bockris, B. E. Conway, and E. Yeager, Editors, Plenum, New York (1980).
43. F. A. Cotton and G. Wilkinson, "Advanced Inorganic Chemistry," 4th ed., p. 440, John Wiley and Sons, New York (1980).
44. D. A. Seanor and C. H. Ambery, *J. Chem. Phys.*, **42**, 2967 (1965).
45. A. Damjanovic and B. Jovanovic, *This Journal*, **123**, 374 (1976).
46. A. Damjanovic and A. T. Ward, in "Electrochemistry: The Past Thirty and the Next Thirty Years," H. Bloom and F. Gutman, Editors, Chap. 6, Plenum Press, New York (1977).
47. F. Nagy, G. Horanyi, and G. Verzea, *Acta Chim. Acad. Sci. Hung.*, **34**, 35 (1962).
48. R. Landsberg and R. Thiele, *Electrochim. Acta*, **11**, 1243 (1966).

Reactivity of Anthracene in Liquid SbCl₃-AlCl₃-N-(1-Butyl)Pyridinium Chloride Mixtures

S. P. Zingg, A. S. Dworkin, Morten Sørli¹, D. M. Chapman,² A. C. Buchanan, III, and G. Pedro Smith

Oak Ridge National Laboratory, Chemistry Division, Oak Ridge, Tennessee 37830

ABSTRACT

Mixtures of SbCl₃ and N-(1-butyl)pyridinium chloride (BPCl) containing 75-87 m/o (mole percent) SbCl₃ and SbCl₃-AlCl₃-BPCl mixtures containing 60 m/o SbCl₃ and 16-23 m/o AlCl₃ were found to be liquid at 25°C. Dilute solutions of anthracene were stable in ternary mixtures containing 18 m/o AlCl₃, but in mixtures containing 22-24 m/o AlCl₃, anthracene reacted under the influence of the solvent, which behaved as both oxidant and H-transfer catalyst. The oxidized product was protonated anthracene, which was stable in this melt. The source of protons was provided by hydrogen liberating Scholl condensations combined with the reduction of Sb(III). A part of the hydrogen from Scholl reactions reacted with anthracene to form 9,10-dihydroanthracene. By contrast, a liquid mixture without SbCl₃, AlCl₃-BPCl (2:1 mole ratio) proved to be a much less active H-transfer catalyst than the SbCl₃-rich liquids even though it is a stronger Lewis acid, and it did not induce protonation beyond a trace attributable to protic impurities. The role of impurities in these mixtures was investigated with results that are relevant to earlier investigations of liquid AlCl₃-BPCl mixtures. An improved procedure for purifying BPCl is described.

Studies of polycyclic aromatic hydrocarbons and hydroaromatics in anhydrous SbCl₃-based melts have shown these melts to be extremely active solvent-catalysts for a variety of hydrogen redistribution reactions at surprisingly low temperatures, 80°-130°C (1-5). Under certain conditions, these melts can also act as oxidizing reagents toward arenes, and some of the resulting reactions are of unusual types (4, 5). The melts investigated previously have either been pure SbCl₃ or SbCl₃ with 1-10 m/o (mole percent) of added chloride ion donor, such as KCl, or chloride ion acceptor, such as AlCl₃. The added chloride ion donor reduces the oxidizing power of the melt while the added acceptor increases it.

The development by Osteryoung *et al.* (6) of low-melting chloroaluminate systems by replacing the usual alkali-metal cations with N-(1-butyl)pyridinium cations (BP⁺) led us to investigate the possibility of preparing

SbCl₃-rich mixtures that are molten at ambient temperatures by adding moderate amounts of BPCl or BPAICl₄ to SbCl₃. We felt these mixtures might retain the useful properties of the higher melting salts and, at the same time, have the convenience of being liquid under ambient conditions. We found that SbCl₃-BPCl mixtures containing 75-87 m/o SbCl₃ and SbCl₃-BPAICl₄ mixtures containing 75 m/o SbCl₃ are liquid at 25°C. In the latter mixtures, BPAICl₄ is formed *in situ* by adding BPCl and AlCl₃ in equal amounts to SbCl₃. The SbCl₃-BPAICl₄ mixture was of particular interest to us because of the possibility of varying the melt acidity and oxidizing power over substantial ranges by adding relatively small amounts of the base BPCl, or generating acidic SbCl₂⁺ ions by adding AlCl₃, which reacts with SbCl₃ to form SbCl₂⁺ and AlCl₄⁻ (see below). Although we made no attempt to establish the solubility limits of those additions, we showed that systems formed by mixing 60 m/o SbCl₃, 17-24 m/o BPCl, and the balance, AlCl₃, are liquid at 25°C.

Having established the occurrence of these low-melting SbCl₃-rich melts, we wished to determine to what extent SbCl₃ diluted by 25 m/o BPAICl₄ at ambient temperature retains the catalytic properties that SbCl₃ displays at ele-

¹ Visiting scientist from the University of Tennessee, Knoxville, Tennessee 37919.

² Graduate student, University of Tennessee, Knoxville, Tennessee 37919.

Key words: catalysis, organic, spectra.

ated temperatures. For this purpose, we chose anthracene as the hydrogen-transfer substrate because of the extensive research (1, 3-5) on its reactivity in SbCl_3 -rich high-melting mixtures. The results of this investigation are given here.

It is important to recognize that the solvent-catalyst properties of SbCl_3 - BPAICl_4 with added AlCl_3 are fundamentally different from those of ambient temperature chloroaluminate melts. In the SbCl_3 -rich melts, SbCl_2^+ is the Lewis acid and has an additional redox functionality, whereas, in the chloroaluminate melts, the Lewis acidity resides in Al_2Cl_7^- , which has no redox functionality. In this paper, we demonstrate the consequences of these differences.

A final and by no means trivial item considered here is our discovery that BPCl purified by the procedures conventional in studies of ambient temperature chloroaluminate melts is contaminated by water and ethyl acetate to a degree that has serious consequences for investigations of the chemistry of dilute solutions of organics both in SbCl_3 -rich and in chloroaluminate melts.

Experimental Section

Materials.—Antimony(III) chloride (Alfa, 99% minimum) was purified by the following procedure. It was first melted under argon and mixed with Sb metal in order to reduce any Sb(V) and with Sb_2O_3 to remove volatile chloride impurities. This was followed by two sublimations under dynamic vacuum and then zone refining a minimum of thirty passes. The resultant colorless crystals melted to give a clear colorless liquid.

Aluminum chloride (Fluka, puriss.), to which 1 w/o (weight percent) purified NaCl was added, was refluxed over high purity aluminum (Alfa, M6N) for 3 days in sealed quartz ampuls, and then distilled away from the NaAlCl_4 phase. This procedure was repeated twice and the resulting AlCl_3 crystals were then vacuum sublimed through a fine porosity Pyrex frit. The purified AlCl_3 crystals were colorless and melted to form a colorless liquid. The NaCl used in this procedure was prepared from reagent grade material, purified by vacuum drying in the solid state followed by melting and bubbling first HCl and then argon (both high purity grades) through the melt.

BPCl was prepared from pyridine (Fisher, certified ACS) and 1-butylchloride (Matheson, Coleman, and Bell, >98%). The starting materials were further purified by distillation from P_2O_5 under argon. The synthetic procedure given by Robinson and Osteryoung (8) was followed. As an added precaution, each step was carried out under argon because BPCl is exceedingly hygroscopic. The product was recrystallized five times under argon from acetonitrile (Fisher, certified ACS), which had been distilled under argon from P_2O_5 . In the original procedure (8), ethyl acetate was used in recrystallizing the final product but we omitted this material because we were unable to remove it completely from crystalline BPCl even after prolonged heating under vacuum at 110°C . The BPCl was dried under vacuum in the presence of P_2O_5 in a drying pistol at 110°C and the drying pistol was transferred to the glove box while still under vacuum. During preparation and all subsequent handling, BPCl was shielded from exposure to light. The water content of the final product was determined by Karl Fischer analysis (Galbraith Laboratories) to be $\leq 0.2\%$. The elemental analysis (Galbraith Laboratories) showed 62.75% C, 8.06% H, 8.34% N, 20.59% Cl, and 0.14% O (calculated values: C 62.97; H 8.22; N 8.16; Cl 20.65). The BPCl was further analyzed for organic impurities by dissolving a 1g sample in a small amount of water and then extracting with three 30 ml aliquots of methylene chloride. After drying with CaSO_4 and reducing the volume to 5 ml, the methylene chloride was analyzed using a Hewlett Packard Model 5880 gas chromatograph equipped with a flame ionization detector and an OV-101, 12m capillary column. No measurable levels of organic impurities were found in BPCl that had been purified without the use of ethyl ace-

tate. The melting point of the final product was $132.3^\circ\text{--}133.1^\circ\text{C}$ (corr.).

Anthracene (Eastman, scintillation grade) was recrystallized from acetic acid and then toluene before sublimation. Analysis by HPLC and GC showed less than 0.1% impurities.

9H-anthracenium heptachlorodialuminate ($\text{C}_{14}\text{H}_{11}\text{Al}_7\text{Cl}_7$) **1** was prepared in Schlenk-ware according to the procedure of Koptuyug (9). Thereafter, it was stored and handled in a glove box. The 200 MHz $^1\text{H-NMR}$ spectrum of a solution of this compound in molten SbCl_3 -10 m/o AlCl_3 was that of the 9H-anthracenium **2** (the cation of compound **1**, shown in Fig. 1) ion without extraneous peaks.

2-Ethylanthracene (Aldrich, 98%) was recrystallized twice from ethanol. No impurities were detected by GC or HPLC analysis.

Preparation of solvents and solutions.—All handling of salts (including weighing on an analytical balance) was carried out in an argon atmosphere glove box in which both water vapor and oxygen were monitored instrumentally and kept below 1 ppm by continuous circulation of the atmosphere through a purification train. In preparing SbCl_3 - AlCl_3 - BPCl melts, SbCl_3 and BPCl were mixed to form a binary liquid to which AlCl_3 was slowly added. This procedure allowed dissipation of the heat generated by the AlCl_3 - BPCl reaction so that the rise in temperature was only slight. In the preparation of AlCl_3 - BPCl melts, a substantial temperature rise could not be avoided.

The formal compositions of melts are specified here in terms of mole percentages of the three constituents in the order SbCl_3 - AlCl_3 - BPCl . Melts for which the mole ratio AlCl_3 : BPCl exceeded unity are referred to as acidic, while those for which this ratio was less than unity are termed basic.

For the preparation of solutions, anthracene and 2-ethylanthracene were weighed on a microbalance outside of the glove box while compound **1** was weighed on an analytical balance in the glove box. The quantity of solvent (SbCl_3 - AlCl_3 - BPCl) was determined by analytical weighing in the glove box. Solvent volume was calculated from density values (7). Values for other compositions were determined by linear extrapolation.

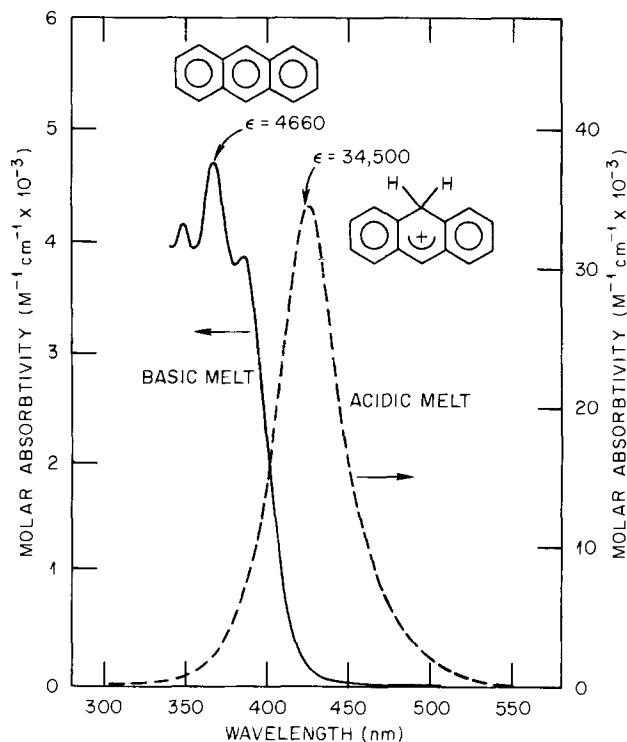


Fig. 1. Spectra of anthracene and the 9H-anthracenium ion in SbCl_3 - AlCl_3 - BPCl melts with compositions of 60:18:22 and 60:22:18, respectively.

Decomposition reactions.—The decomposition of anthracene in acidic ternary melts was initiated by mixing a solution of anthracene in a basic 60:19:21 melt with an appropriate amount of an acidic melt. For anthracene solutions at the 150 mM concentration level, the extent of reaction was measured by quench and separation at the end of a given reaction period. The same quench and separation procedures were followed as those used previously to study the decomposition of anthracene in SbCl_3 -rich melts at elevated temperatures (1). These solutions contained 160–200 mg of solute. Product analysis included antimony metal as well as organics.

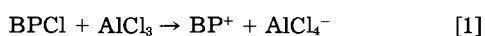
Studies of solutions at the 30 mM level included *in situ* optical spectroscopy (see below) in addition to quench and separation. Product analysis did not include antimony metal because of the small amounts of material involved. After a solution had been prepared, it was divided into two portions. One portion was weighed and left in the glove box for quench and separation at the end of the reaction period. This portion contained 10 mg or more of solute. The other portion (~1 ml) was loaded into an optical cell (see below) which was then sealed, removed from the glove box, and placed in the spectrophotometer. In several runs, a second 1 ml spectroscopy sample was withdrawn from the quench-and-separation portion after 23h. The spectrum of this second sample was the same as the 23h spectrum of the sample that had been removed at the beginning of the run.

Optical spectroscopy.—Optical absorption spectra were measured either with a Cary 14 or a Cary 219 spectrophotometer. The optical cell, shown in Fig. 2, consisted of a 1 cm pathlength quartz glass cuvette attached by means of a graded seal to a 100 cm long Pyrex glass neck with a 15 Ace threaded glass joint at the top. A quartz glass insert, to which an eyelet was attached, could be lowered into the cell by means of a glass rod with a hook on the end. A Teflon bushing and O-ring provided an airtight seal. The quartz insert could be rotated so that two different optical pathlengths of about 60 and 110 μm were obtainable. The sample compartments of both spectrophotometers were modified to accommodate these cells. Pathlengths of cells with inserts in place were calibrated using the 373 nm band of K_2CrO_4 solutions in aqueous 0.05N KOH [$\epsilon = 4842 \text{ M}^{-1} \text{ cm}^{-2}$ (10)]. Measurements were made with at least four independently prepared concentrations of dichromate for each calibration, and the results were reproducible to within 0.5%.

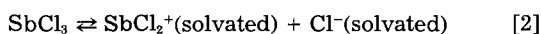
ESR spectroscopy.—The spectrometer, sample tubes, and experimental procedures have been described previously (11). All material transfers were performed in a dry box. The loaded sample tubes were sealed under argon a vacuum line. Concentration of anthracene in the melts was ~5 mM. ESR spectra were obtained at ambient temperatures (22°–23°C).

Results and Discussion

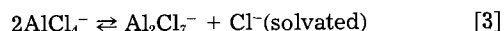
Reactions among solvent components.—The SbCl_3 - AlCl_3 -BPCl mixtures considered here have formal compositions with the following mole fractions: 0.60 SbCl_3 , (0.20 + a) AlCl_3 , and (0.20 - a) BPCl, where $-0.04 \leq a \leq 0.03$. Since these components vary enormously in chloride donor/acceptor strength, extensive chloride-exchange chemistry occurs on mixing. Aluminum trichloride is a strong chloride ion acceptor while SbCl_3 is a much weaker chloride ion acceptor, and BPCl is a chloride ion donor. Therefore, the dominant chloride exchange reaction is



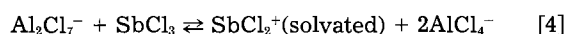
Since the AlCl_3 :BPCl is close to unity for all melts, the liquid may be regarded as consisting of the binary mixture SbCl_3 -25 m/o BP(AlCl_3) with relatively small additions of AlCl_3 or BPCl. Pure molten SbCl_3 is very slightly ionized as shown in Eq. [2] (12)



It is plausible to suppose that the same equilibrium occurs in our low-melting mixtures and is displaced strongly to the left. Likewise, it has been shown that in liquid BPCl- AlCl_3 mixtures at ambient temperatures, the AlCl_4^- ion is in equilibrium with Al_2Cl_7^- and Cl^- ions (13). In our mixtures, a similar equilibrium must occur as shown in Eq. [3]



where Cl^- is solvated by SbCl_3 molecules. Since Al_2Cl_7^- is a much stronger chloride ion acceptor than SbCl_3 , the equilibrium in Eq. [3] is strongly displaced to the left. The Al_2Cl_7^- anion should also be a stronger chloride ion acceptor than $\text{SbCl}_2^+(\text{solvated})$ so that the equilibrium in Eq. [4]



should be displaced to the right. This also appears to be the case in SbCl_3 - AlCl_3 mixtures at elevated temperatures (12). Thus, when AlCl_3 is added to liquid SbCl_3 -BP(AlCl_3), the dominant acidic species should be $\text{SbCl}_2^+(\text{solvated})$ rather than Al_2Cl_7^- . On the other hand, BPCl is expected to dissolve in SbCl_3 -BPCl to form BP^+ cations and $\text{Cl}^-(\text{solvated})$ anions with the concomitant suppression of the formation of $\text{SbCl}_2^+(\text{solvated})$, according to Eq. [2].

In summary, for all of the SbCl_3 - AlCl_3 -BPCl compositions considered here, the primary constituents are SbCl_3 molecules and the spectator ions BP^+ and AlCl_4^- . Secondary constituents are $\text{SbCl}_2^+(\text{solvated})$ and $\text{Cl}^-(\text{solvated})$. When the formal mole ratio AlCl_3 :BPCl exceeds unity to a significant degree, the concentration of $\text{SbCl}_2^+(\text{solvated})$ is correspondingly increased, while that of $\text{Cl}^-(\text{solvated})$ is greatly suppressed. This situation is reversed when the AlCl_3 :BPCl ratio is significantly less than unity. The Al_2Cl_7^- anion is at most no more than a minor constituent in the melts considered here.

Optical spectra.—During the decomposition of anthracene, the principal species observed by optical spectroscopy are unreacted anthracene and the anthracenium ion. Therefore, for purposes of both identification and quantification, the spectra of these species were measured in SbCl_3 - AlCl_3 -BPCl melts under nonreactive conditions.

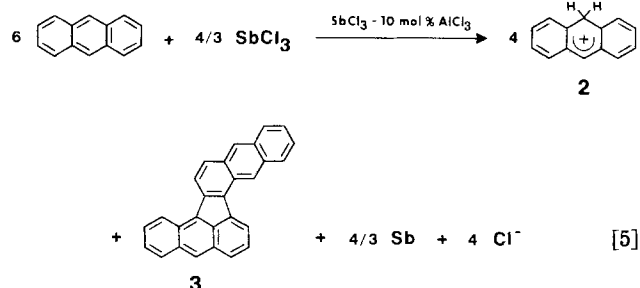
Figure 2 shows the spectrum of a 31.1 mM solution of anthracene in a basic 60:18:22 melt, and that of a 9.75 mM solution of 9H-anthracenium heptachlorodialuminate 1 in an acidic 60:22:18 melt. The positions and molar absorptivities of the three maxima in the anthracene spectrum are as follows: 347 nm, $4130 \text{ M}^{-1} \text{ cm}^{-1}$; 366 nm, $4660 \text{ M}^{-1} \text{ cm}^{-1}$; and 384 nm, $3830 \text{ M}^{-1} \text{ cm}^{-1}$. We attribute these bands to vibronic components of the $^1\text{L}_a \leftarrow ^1\text{A}$ electronic transition (14). By comparison, we found that the corresponding bands for anthracene in methanol have as coordinates the following: 339 nm, $5447 \text{ M}^{-1} \text{ cm}^{-1}$, 356 nm, $8130 \text{ M}^{-1} \text{ cm}^{-1}$; 375 nm, $7967 \text{ M}^{-1} \text{ cm}^{-1}$. Other bands in this group that we shall make use of later have maxima at 309 and 323 nm. The vibrational spacing for all five bands is close to $0.14 \mu\text{m}^{-1}$. The bands of anthracene in the molten salt are much broader than those of anthracene in methanol so that the band areas and oscillator strengths are more nearly comparable than are the molar absorptivities.

The spectrum of the solution of compound 1 in Fig. 2 consists of an intense band with maximum at 424 nm and molar absorptivity of $34,500 \text{ M}^{-1} \text{ cm}^{-1}$. This is plausibly attributed to the 9H-anthracenium cation 2, the structure of which is shown in the figure. The spectrum of this ion in anhydrous HF at 25°C (15) has a similar band at 408 nm ($37,400 \text{ M}^{-1} \text{ cm}^{-1}$), while in concentrated H_2SO_4 at 25°C (16) the band maximum is at 424 nm (ca. $30,000 \text{ M}^{-1} \text{ cm}^{-1}$).

Spectral data and the results of analysis by hydrolysis and separation show that both the solution of anthracene in the basic melt and that of compound 1 in the acidic melt are stable. Their spectra remained unchanged after 24h. Following hydrolysis of the anthracene solution, the starting material was recovered and no decomposition products were found. Hydrolysis of the solution of com-

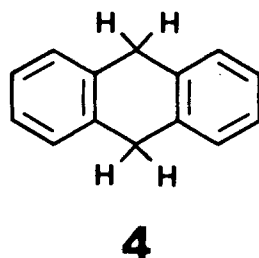
compound 1 resulted principally in the deprotonation of compound 1 and led to recovery of anthracene equivalent to 85% of the starting material. A similar recovery factor was found when solutions of anthracene in SbCl_3 -10 m/o AlCl_3 were hydrolyzed by the procedure used here.

Anthracene decomposition reaction.—We found that the reactions by which anthracene decomposes in acidic SbCl_3 - AlCl_3 - BPCl mixtures at 28° - 40°C are closely related to those that occur in SbCl_3 -rich melts at 80° - 175°C . These elevated temperature reactions are of two types. First, in SbCl_3 -10 m/o AlCl_3 , anthracene reacts rapidly and completely with the solvent in a redox process that is schematically illustrated in Eq. [5] (4)



The oxidized product is the 9H-anthracenium ion 2, produced in 55-65% yields. The source of protons for this product is a combination of Scholl-type condensation-dehydrogenation reactions and the reduction of Sb(III) . The dominant condensed product is anthra[2,1-a]aceanthrylene 3, produced in yields of ~ 20 w/o of the starting anthracene. The remaining organic material (~ 15 - 25 w/o) consists of a variety of condensed compounds. The accompanying reduction reaction converts Sb(III) into a lower oxidation state, which, when hydrolyzed, disproportionates into Sb metal and Sb(III) (17). Stoichiometry requires that the mole ratio compound 2: Sb(metal) be 3:1.

The second type of reaction occurs when anthracene is dissolved in SbCl_3 without AlCl_3 . This reaction is a relatively slow catalytic hydrogen-transfer with the melt serving as solvent/catalyst (1). Part of the anthracene is hydrogenated to form mostly 9,10-dihydroanthracene 4, and the source of hydrogen is Scholl-type condensation-dehydrogenation reactions



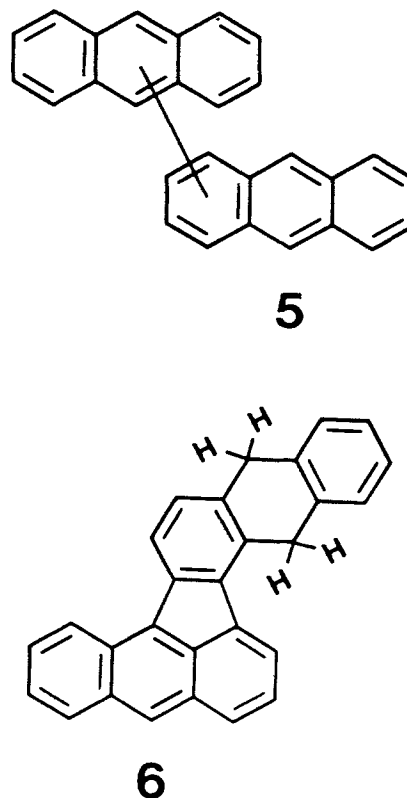
A wide variety of condensed products is formed, including compound 3, but no single product predominates.

In the present study, we find that both of the above types of reactions occur simultaneously for anthracene in acidic SbCl_3 - AlCl_3 - BPCl mixtures at 28° - 40°C . Evidence regarding the formation of compound 2 comes from the optical spectroscopic measurements. As noted earlier, this cation is destroyed by hydrolysis so that its presence in the melt cannot be established by quench and separation. The spectra in Fig. 3 are typical of those obtained when ~ 30 mM anthracene reacts in the acidic melt during a 23h run at 28° - 30°C . These spectra are referenced to air and can be converted to absorbance by subtracting the curve labeled solvent. The solvent melt was quite transparent except at the shortest wavelengths so that, over most of the wavelength range in Fig. 3, the apparent absorption of the solvent consists of light losses due to reflections at cell windows.

After 20 min reaction time, the concentration of anthracene fell to $\sim 95\%$ of its starting value of 34.4 mM. A shoulder at ~ 420 nm is attributed to compound 2 at a concen-

tration estimated to be 1-2 mM. Bands at 510 and 530 nm are due to unidentified reaction products. With increasing time, absorption due to anthracene slowly decreased, while that due to compound 2 slowly increased along with bands due to other reaction products at longer wavelengths. At the end of 1380 min (23h), some anthracene remained but the concentration could not be evaluated accurately because of interference from the band of compound 2. The concentration of compound 2 reached ~ 7.5 mM, which is 22% of the initial anthracene concentration.

Identified substances obtained from quench and separation were the following: anthracene (partly unreacted starting material and partly from the hydrolysis of compound 2), compound 3, compound 4, four isomers of bianthracene grouped together here as compound 5 (2, 9'-isomer produced in highest yield), a dihydroanthraaceanthrylene 6, (not identified as to isomer), and antimony metal (recovered only for runs at the 150 mM concentration level)



In addition, small quantities of unidentified products (usually ~ 5 w/o of the initial anthracene) were obtained, and when the HPLC column was washed with CH_2Cl_2 , some highly condensed material came off.

Quench and separation was performed for eight runs, each terminated after 23h. Five of these runs were made with 60:22:18 melts at 28° - 30°C and used initial anthracene concentrations of 31, 34, 34, 141, and 157 mM. One run was made with a 60:22:18 melt at 40°C and an initial concentration of 31 mM, while 2 runs were made with slightly more acidic 60:23:17 melts at 28° - 30°C and initial concentrations of 28 and 139 mM. The only substantial differences in the relative amounts of substances recovered from these runs was between those with initial concentrations of 28-34 mM and those with initial concentrations of 139-157 mM. Table I summarizes the five runs made with 60:22:18 melts at 28° - 30°C . In this table, the amounts of substances are given as w/o of the initial weight of anthracene. Results for the three runs with initial concentrations of 31, 34, and 34 mM are averaged under the column headed ~ 30 mM, and those with initial concentrations of 141 and 157 mM are averaged under ~ 150 mM. Typical of deviations about the average values were those for anthracene, namely: 57-67% and 27-30%, respectively. The amounts of anthracenium ion for runs with initial concentrations of

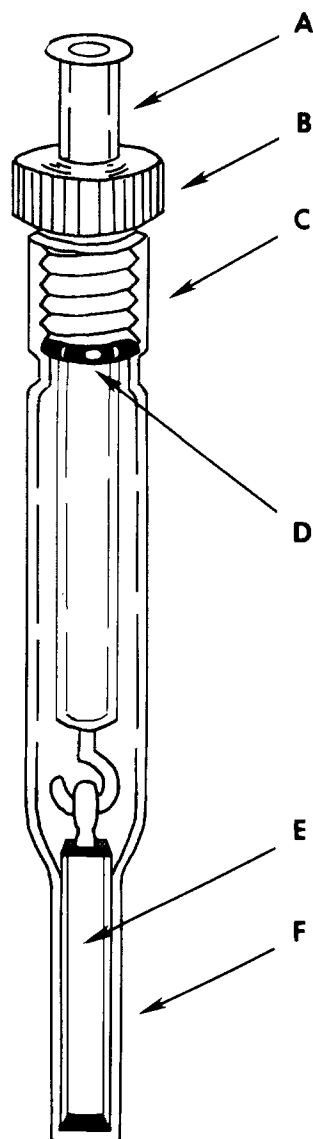


Fig. 2. Optical cell. (A) Pyrex glass rod with hook, (B) threaded Teflon bushing, (C) threaded Pyrex glass joint, (D) FETFE O-ring, (E) quartz glass insert, and (F) quartz glass optical cell.

~30 mM were obtained from optical spectra, and those for the other runs were calculated from the amounts of Sb metal recovered from quench and separation (moles of anthracenium = $3 \times$ moles of Sb).

The anthracene recovered from quench and separation consisted of unreacted starting material plus that regenerated from hydrolysis of the anthracenium ion. We estimate a recovery factor of 85% for hydrolysis, hence the amounts of unreacted anthracene were on the order of 43-47% and 15-18% for initial concentrations of ~30 mM and ~150 mM, respectively. Identified products typically accounted for ~80% of the starting material for the former and ~70% for the latter concentration. In both cases, an additional amount of material (~5%) consisted of small amounts of various unidentified products observed during chromatography. The highly condensed material accounted for an appreciable part of the remainder in runs with initial concentrations of ~150 mM, but very little of this material was found for runs with initial concentrations of ~30 mM.

These results show that a part of the hydrogen lost in forming condensed products was consumed in forming hydroarenes, while the rest was consumed in protonating anthracene. The same reactions occurred in melts with initial anthracene concentrations of 31-157 mM. At the higher concentrations, the conversion of anthracene was greater, and relatively less protonated product 2 formed than at the lower initial concentration. Thus, the decom-

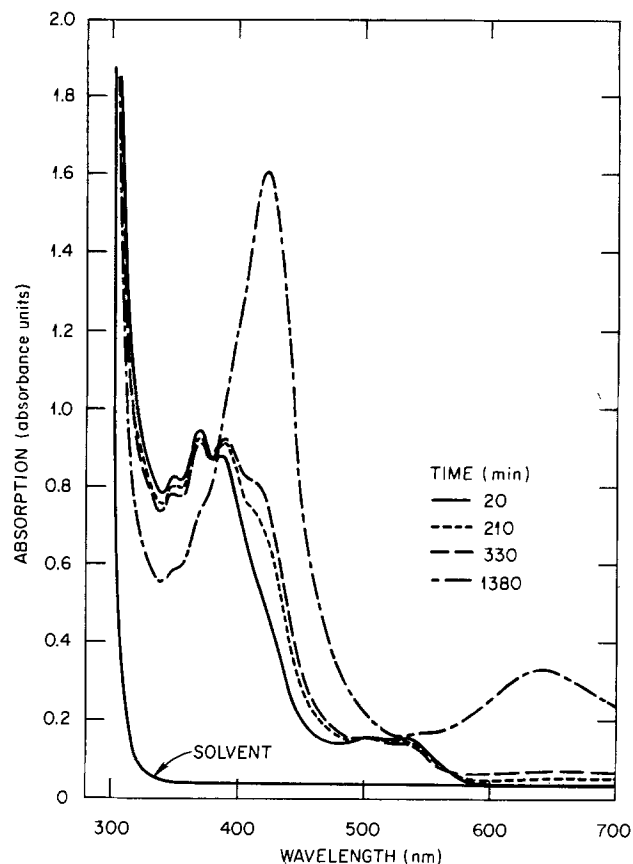


Fig. 3. Spectra measured during the decomposition of anthracene in an $\text{SbCl}_3\text{-AlCl}_3\text{-BPCI}$ (60:22:18) melt at 30°C together with the spectrum of the solvent. All spectra referenced against air.

position of anthracene in acidic $\text{SbCl}_3\text{-AlCl}_3\text{-BPCI}$ melts proceeded by a combination of the same types of reactions found at elevated temperatures in $\text{SbCl}_3\text{-10 m/o AlCl}_3$ and in SbCl_3 alone. It is as though the low-melting mixtures were intermediate in oxidizing power to SbCl_3 with and without 10 m/o AlCl_3 . Further evidence that this is, in fact, the case is provided by the ESR studies described below and the EMF studies in the following paper (7). The reactions in the low-melting mixtures at $28^\circ\text{-}40^\circ\text{C}$ were very much slower than those at higher temperatures in SbCl_3 and $\text{SbCl}_3\text{-10% AlCl}_3$.

ESR spectra.—The fact that Sb(III) in acidic $\text{SbCl}_3\text{-AlCl}_3\text{-BPCI}$ melts acts as a mild oxidizing agent toward anthracene was established by the recovery of Sb metal. It is interesting, therefore, that we were also able to identify the presence of the anthracene radical cation in these solutions by means of ESR spectroscopy. Dilute solutions (~5 mM) of anthracene in two acidic melts, 60:22:18 and 60:21:19, were examined by ESR at ambient temperatures ($22^\circ\text{-}23^\circ\text{C}$). In both cases, the ESR spectrum of the anthracene radical cation was observed, and the measured pro-

Table I. Substances recovered from anthracene decomposition in liquid $\text{SbCl}_3\text{-AlCl}_3\text{-BPCI}$ (60:22:18) after 23h at $28^\circ\text{-}30^\circ\text{C}$

Substance	Amount (w/o)	
	~30 mM	~150 mM
Anthracene	63	29
Dihydroanthracene 4	4	10
Bianthracenes 5	11	11
Anthra[2,1- α]aceanthrylene 3	3	4
Dihydroanthraaceanthrylene 6	2	13
Anthracenium ion 2	20	14
Highly condensed material	trace	large

ton hyperfine coupling constants ($a_1 = 3.05$, $a_2 = 1.37$, and $a_3 = 6.47\text{G}$) were similar to those measured in $\text{SbCl}_3\text{-}8\text{ m/o AlCl}_3$ at elevated temperatures (11). However, these spectra were much less intense than the corresponding anthracene radical cation spectrum observed in $\text{SbCl}_3\text{-}8\text{ m/o AlCl}_3$, suggesting that the $\text{SbCl}_3\text{-AlCl}_3\text{-BPCl}$ melts are weaker oxidants. EMF studies presented in the following paper support this conclusion (7). Thus, the acidic $\text{SbCl}_3\text{-AlCl}_3\text{-BPCl}$ melts can act as oxidants toward anthracene, producing radical cations that may be key reactive intermediates in the protonation-condensation reaction as previously proposed for arenes in $\text{SbCl}_3\text{-}10\text{ m/o AlCl}_3$ (4).

Anthracene in $\text{AlCl}_3\text{-BPCl}$ (2:1).—The important role that SbCl_3 played in the anthracene decomposition reactions in acidic $\text{SbCl}_3\text{-AlCl}_3\text{-BPCl}$ melts is emphasized by comparison with the behavior of this solute in a solvent containing only AlCl_3 and BPCl . For this comparison, we chose the formal composition $\text{AlCl}_3\text{-BPCl}$ (2:1), which is, in fact, the liquid compound $\text{N-(1-butyl)pyridinium heptachlorodialuminate BPA}_2\text{Cl}_7$ (13). This is a very strong Lewis acid, and if Lewis acidity in combination with such protonic impurities as our melts may contain is sufficient to catalyze the decomposition of anthracene, then the 2:1 melt should be a very active catalyst.

Studies using optical spectroscopy and quench and separation were carried out on a 35 mM solution of anthracene in the 2:1 melt and followed the same general procedures used with acidic $\text{SbCl}_3\text{-AlCl}_3\text{-BPCl}$ melts in so far as possible. The calculation of concentrations was based on the value 1.33 g cm^{-3} for the density of the melt (19). The reaction temperature was 30°C , the time to quench was 24h, and optical spectra were measured at intervals from 0.5 to 29h after mixing and included a spectrum taken at the time of quench.

After quench and separation, the only substances found in more than trace amounts were anthracene (78 w/o), compound 4 (2 w/o), and compound 5 (6 w/o). No more than a trace of highly condensed material was found when the HPLC column was washed with CH_2Cl_2 .

Spectra measured after 0.5 and 24h are shown in Fig. 4. These are referenced to air and can be converted to solute absorbance by subtracting the curve labeled solvent. In between 0.5 and 24h, the spectra changed slowly and progressively, never exceeding the extremes shown in the figure. The spectrum measured at 29h was almost indistinguishable from that measured at 24h.

The $\text{AlCl}_3\text{-BPCl}$ solvent melt transmitted further into the ultraviolet than did $\text{SbCl}_3\text{-AlCl}_3\text{-BPCl}$ mixtures so that, for the anthracene solution, five vibronic bands of the ${}^1L_a \leftarrow {}^1A$ electronic transition were exposed at 312 (sh), 328, 344, 362, and 381 nm, with a $0.14\text{ }\mu\text{m}^{-1}$ vibra-

tional spacing. These are slightly red-shifted with respect to the corresponding bands of anthracene in methanol (see above), and the 344, 362, and 381 nm bands are very close to the corresponding bands for anthracene in $\text{SbCl}_3\text{-AlCl}_3\text{-BPCl}$. Assuming the concentration of anthracene after 0.5h to be 35 mM or slightly less, the molar absorptivity of the 362 nm band is calculated to be about $6 \times 10^3\text{ M}^{-1}\text{ cm}^{-1}$. This value is intermediate to those for anthracene in methanol and in $\text{SbCl}_3\text{-AlCl}_3\text{-BPCl}$, respectively, which is in keeping with the fact that the band widths for anthracene in the 2:1 melt are likewise intermediate.

The only absorption in the 0.5h spectrum not attributable to anthracene was a band at $\sim 420\text{ nm}$ that we attribute to compound 2. Assuming that the molar absorptivity of compound 2 has a value similar to that for compound 2 in $\text{SbCl}_3\text{-AlCl}_3\text{-BPCl}$, we estimate that its concentration in $\text{AlCl}_3\text{-BPCl}$ was $\sim 1\text{ mM}$. This small amount of compound 2 probably came from impurity proton sources. With increasing time, the concentration of compound 2 diminished although a small amount persisted after 24h.

The only product absorption (other than compound 2) found after 24h was a very broad band centered near 640 nm. This does not correspond to either of the major products found on quench and separation; the bands of compound 4 should lie well out of range in the UV, and those of compound 5 should lie in the same general region as the anthracene bands. The most reasonable source of the 640 nm absorption is a trace of a highly condensed arene in a protonated or oxidized form. Such cations usually have intense absorptions in the visible range, and the parent arenes are usually more easily protonated and oxidized than anthracene, compound 4, or compound 5.

The long wavelength absorption bands of bianthracenes in methanol were found to be very similar to those of anthracene in the same solvent. Among other small differences, they were somewhat red-shifted. Assuming that a similar state of affairs holds in the 2:1 melt, the absorption in the 300-400 nm region of the spectrum after 24h was what one would expect for a mixture of anthracene and compound 5 in the ratio found on quench and separation with an anthracene concentration reduced to roughly 80% of its initial value.

Thus, we find that the 2:1 melt, unlike the acidic $\text{SbCl}_3\text{-AlCl}_3\text{-BPCl}$ melt, did not promote the oxidative protonation of anthracene to an appreciable extent. It did catalyze the Scholl condensation-dehydrogenation reaction (to form compound 5) accompanied by a partial hydrogenation of the substrate (to form compound 4), but even for these reactions the 2:1 melt was not nearly as active a catalyst as the less acidic melts containing SbCl_3 .

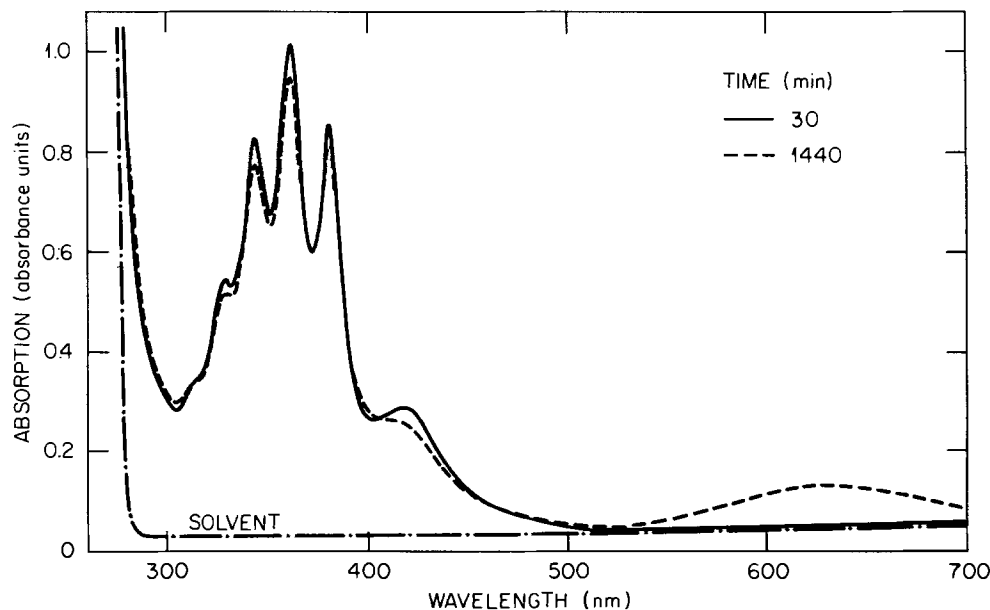


Fig. 4. Spectra measured during the decomposition of anthracene in an $\text{AlCl}_3\text{-BPCl}$ (2:1) melt at 30°C together with the spectrum of the solvent. All spectra referenced against air.

Effects of impurities.—Because of the low concentration of anthracene used in the spectrometric studies, we found it necessary to pay close attention to the effects of impurities. Thus, it was not until water and ethylacetate were identified and eliminated as impurities in BPCI that we obtained consistently reproducible results. Since BPCI is a widely used constituent in low-melting salt mixtures and since studies of the spectroscopy and electrochemistry of solutes in these melts is commonly done at low concentrations, we describe what we learned about impurity effects.

We found that when BPCI was dried by a less rigorous procedure than that described above and then used to prepare acidic $\text{SbCl}_3\text{-AlCl}_3\text{-BPCI}$ melts, solute anthracene was protonated at a much faster rate, and the concentration of compound 2 reached a much higher level than it did in the reactions described above. When BPCI was dried under vacuum over P_2O_5 at 110°C for progressively longer times, the amounts of compound 2 diminished. The concentration level for promptly formed compound 2 achieved after prolonged drying was about 1-2 mM, and this we attribute to impurities (not necessarily water).

In the literature procedure (8) for the preparation of BPCI, ethyl acetate is used as a cosolvent along with acetonitrile in the recrystallization of the product. In our initial experiments, which followed this procedure, an unknown product was observed in 16% yield from the reaction in an acidic room temperature melt containing 11 mM anthracene. This product was identified by GC-MS as three isomeric ethylantracenes. The ethyl group could not have come from the fragmentation of anthracene since no other fragments of the parent arene were found. It is well known (18) that esters will alkylate arenes in organic solvents with a Lewis acid present as catalyst. Analysis of the BPCI showed that the small ethyl acetate content of the sample could account for all of the ethylantracene found in the reaction of anthracene in the acidic $\text{SbCl}_3\text{-AlCl}_3\text{-BPCI}$ mixture. Vacuum drying of the BPCI crystals resulted in a decrease in the ethyl acetate content and thus in the yield of ethylantracene. However, traces of ethyl acetate remained even after a week of drying. To determine whether the presence of ethyl acetate and thus ethylantracene would significantly effect our results, the reaction of 2-ethylantracene was followed spectroscopically in the acidic room temperature melts under the same conditions utilized for the reaction of anthracene. Protonated ethylantracene was formed and found to absorb at 424 nm (the same wavelength observed for the anthracenium ion). In addition, ethylantracene reacted more rapidly than anthracene, probably because ethylantracene is more easily oxidized and protonated than anthracene. Since the presence of ethylantracene would obviously interfere with the investigation of the anthracene reaction, all subsequent purifications of BPCI excluded the use of ethyl acetate.

In a study published after the present paper was submitted, Sahami and Osteryoung (20) reported an electrochemical procedure for determining water in liquid $\text{AlCl}_3\text{-BPCI}$ mixtures containing excess BPCI. They found 7.5-20 mM residual water initially present in their melts. In agreement with our findings, they concluded that this water originated as an impurity in the highly hygroscopic BPCI from which the melts were made. They also showed that water in liquid $\text{AlCl}_3\text{-BPCI}$ mixtures of all compositions reacts with chloroaluminate ions to form HCl, which has appreciable solubility in these melts. This result supports our observation that water in $\text{AlCl}_3\text{-BPCI}$ containing excess AlCl_3 acts as a strong proton source capable of protonating anthracene.

In a pioneering investigation of aromatic hydrocarbons in liquid $\text{AlCl}_3\text{-BPCI}$ mixtures, Robinson and Osteryoung

(8) reported that when these hydrocarbons were added to acidic melts, colored solutions were formed that could be reversibly decolorized by making the melt basic, and the UV-visible spectra of these colored solutions were similar to those of arene σ complexes. In the case of anthracene, they reported a band maximum at 417 nm, very close to the position of the intense visible band of the 9H-anthracenium ion in liquid BPAl_2Cl_7 , as reported here. At the time that Robinson and Osteryoung reported their findings, $\text{AlCl}_3\text{-BPCI}$ melts were generally believed to be anhydrous; therefore, these authors proposed that the σ complexes they observed were of the $\text{AlCl}_3\text{-arene}$ type formed in an equilibrium such as $\text{arene} + \text{Al}_2\text{Cl}_7^- = \text{AlCl}_3\text{-arene} + \text{AlCl}_4^-$. In view of our results and those of Sahami and Osteryoung (20), it is most likely that the σ complexes were of the $\text{H}^+\text{-arene}$ type, i.e., arenium ions, since HCl in the presence of acidic chloroaluminates has long been known to be an exceedingly strong protonating agent, and chloroaluminates cannot displace H^+ from the resulting complexes (note compound 1, above).

Acknowledgment

This research was sponsored by the Division of Chemical Sciences, Office of Basic Energy Sciences, U.S. Department of Energy under contract W-7405-eng-26 with the Union Carbide Corporation. M. Sørli is grateful for financial assistance from Norges Teknisk-Naturvitenskapelige Forskningsråd and for a travel grant from Norges Almenvitenskapelige Forskningsråd.

Manuscript submitted Sept. 23, 1983; revised manuscript received ca. Feb. 13, 1984. This was Paper 757 presented at the San Francisco, CA, Meeting of the Society, May 8-13, 1983.

Oak Ridge National Laboratory assisted in meeting the publication costs of this article.

REFERENCES

1. A. S. Dworkin, M. L. Poutsma, J. Brynestad, L. L. Brown, L. O. Gilpatrick, and G. P. Smith, *J. Am. Chem. Soc.*, **101**, 5299 (1979).
2. A. C. Buchanan, III, A. S. Dworkin, G. P. Smith, M. V. Buchanan, and G. Olerich, *Fuel*, **60**, 694 (1981).
3. A. C. Buchanan, III, A. S. Dworkin, and G. P. Smith, *J. Org. Chem.*, **47**, 603 (1982).
4. A. C. Buchanan, III, A. S. Dworkin, and G. P. Smith, *J. Am. Chem. Soc.*, **102**, 5262 (1980).
5. A. C. Buchanan, III, A. S. Dworkin, and G. P. Smith, *J. Org. Chem.*, **46**, 471 (1981).
6. C. Nanjundiah, K. Smimizu, and R. A. Osteryoung, *This Journal*, **129**, 2474 (1982).
7. D. M. Chapman, G. P. Smith, M. Sørli, C. Petrovic, and G. Mamantov, *ibid.*, **131**, 1609 (1984).
8. J. Robinson and R. A. Osteryoung, *J. Am. Chem. Soc.*, **101**, 323 (1979).
9. V. A. Koptug, J. S. Isaev, and A. I. Rezvukhin, *Tetrahedron Lett.*, **823** (1967).
10. G. W. Haupt, *J. Res. Natl. Bur. Stds.*, **48**, 414 (1952).
11. A. C. Buchanan, III, R. Livingston, A. S. Dworkin, and G. P. Smith, *J. Phys. Chem.*, **84**, 423 (1980).
12. C. Petrovic, G. Mamantov, M. Sørli, M. H. Lietzke, and G. P. Smith, *J. Phys. Chem.*, **86**, 4598 (1982).
13. J. Schoebrechts and B. Gilbert, *This Journal*, **128**, 2679 (1981).
14. H. B. Klevens and J. R. Platt, *J. Chem. Phys.*, **17**, 470 (1949).
15. G. Dallinga, E. L. Makor, and A. A. Verrijn Stuart, *Mol. Phys.*, **1**, 123 (1958).
16. V. Gold and F. L. Tye, *J. Chem. Soc.*, 2172 (1952).
17. M. Sørli and G. P. Smith, *J. Inorg. Nucl. Chem.*, **43**, 931 (1981).
18. G. A. Olah, in "Friedel-Crafts and Related Reactions," Vol. 1, G. A. Olah, Editor p. 49, Interscience, New York (1963).
19. J. Robinson, R. C. Bugle, D. Koran, and R. A. Osteryoung, *J. Am. Chem. Soc.*, **101**, 3776 (1979).
20. S. Sahami and R. A. Osteryoung, *Anal. Chem.*, **55**, 1970 (1983).

Electrochemical Properties of the Solvent $\text{SbCl}_3\text{-AlCl}_3\text{-N-}$ (1-Butyl)Pyridinium Chloride and Electrochemical and Spectroelectrochemical Studies of Arene Solutes

D. M. Chapman,¹ G. P. Smith, M. Sørlie,² C. Petrovic,³ and G. Mamantov^{*,3}

Oak Ridge National Laboratory, Chemistry Division, Oak Ridge, Tennessee 37830

ABSTRACT

Physical and electrochemical properties are reported for $\text{SbCl}_3\text{-AlCl}_3\text{-N-}$ (1-butyl)pyridinium chloride (BPCI) mixtures that are liquid at ambient temperatures, and studies of the electrogeneration and open-circuit decay of some arene radical cations, both in this medium and in $\text{SbCl}_3\text{-KCl}$ at elevated temperatures, are described. Specific conductivities, densities, and viscosities of the compositions [m/o (mole percent)] 60:19:21 (basic) and 60:21:19 (acidic) $\text{SbCl}_3\text{-AlCl}_3\text{-BPCI}$ were measured over the temperature range 24°-100°C. For a potentiometric titration between the compositions 60:18:22 and 60:22:18 with SbCl_3 fixed at 60 m/o, the potential of the Sb(III)/Sb(0) couple increased by 0.43V at 27°C. Electrochemical studies showed that perylene (Per), 9,10-dimethylantracene (DMA), and 9,10-diphenylantracene (DPA) can be reversibly oxidized to their radical cations in a 60:19:21 melt, whereas the oxidation of anthracene (Ant) is irreversible. Spectroelectrochemical studies showed that Per radical cations were stable in this melt, those of DPA decayed very slowly, those of DMA decayed somewhat faster, and those of Ant were too transient to be observed optically. Similar degrees of stability were found for these radical cations in SbCl_3 containing 1M KCl at elevated temperatures, and transient spectra of Ant radical cations were observed in this solvent.

Molten SbCl_3 has proven to be a remarkable reaction medium for arenes (1-7). In some cases, these hydrocarbons undergo solvent-catalyzed hydrogen transfer chemistry, while in others the solvent acts as an oxidizing agent, and the primary reaction products include solvent-stabilized carbocations, either arenium ions or arene radical cations. To a great extent, reaction rates and even the type of reaction can be markedly altered by adding relatively small amounts of a chloride ion donor (e.g., KCl) which makes the melt less active, or a strong chloride ion acceptor (e.g., AlCl_3) which increases the oxidizing power of Sb(III) as well as the Lewis acidity of the melt.

When used as a reaction medium, SbCl_3 has the disadvantage of an elevated melting point, 73°C. Therefore, it was interesting to learn that when SbCl_3 is diluted with 25 m/o (mole percent) N-(1-butyl)pyridinium tetrachloroaluminate ($\text{BP[AlCl}_4\text{]}$), the mixture is liquid at 25°C, and anthracene, dissolved in this liquid, displays some of the same chemistry as in SbCl_3 at elevated temperatures (8). As a next step toward utilizing $\text{SbCl}_3\text{-BP[AlCl}_4\text{]}$ mixtures to study the oxidative chemistry of arenes, we explored the possibilities and problems of applying electrochemical and spectroelectrochemical tools to this medium, with results that are reported here.

The importance of electrochemical and spectroscopic methods for the study of arene chemistry in SbCl_3 -rich liquids deserves special emphasis. Since very reactive carbocations occur as solvent-stabilized primary products in many of these reactions, conventional quench and separation procedures often do not give adequate information and, in fact, can be misleading. Spectroscopic methods (NMR, ESR, and optical) applied *in situ* are required to identify the carbocations and to calibrate quench and separation procedures for purposes of quantification. Furthermore, since these carbocations, whether they be radical cations or arenium ions, are products of reactions in which the solvent acts as an oxidant, it is essential to establish the relative oxidizing power of the solvent as a function of added chloride ion donors and acceptors, and the relative oxidizability of the solutes.

Finally, there is the question of whether radical cations that are relatively stable in inorganic SbCl_3 -rich melts will have a similar degree of stability in $\text{SbCl}_3\text{-BP[AlCl}_4\text{]}$,

where they have a greater opportunity of being scavenged by adventitious nucleophiles or, possibly, by BP^+ ion via hydrogen abstraction. To answer this question, we compared the persistence of a series of different arene radical cations in $\text{SbCl}_3\text{-BP[AlCl}_4\text{]}$ with their persistence in molten $\text{SbCl}_3\text{-KCl}$.

As a practical matter, the solvent is prepared by mixing SbCl_3 , AlCl_3 , and BPCI. For this reason, the solvent compositions are, throughout this paper, expressed in mole percentages of these formal constituents in the above order. It should, however, be kept in mind that the chemically active species are chloroantimony species and not chloroaluminate ions. (See Ref. (8) for a discussion of the reactions among melt components.)

Materials.—Purification of the melt constituents has been described (8). 9,10-Dimethylantracene (Aldrich, >99%) and anthracene (Reilly Tar and Chemical Corporation, Scintillation Grade) were used without further purification. Perylene (Aldrich, 99%, Gold Label) and 9,10-diphenylantracene (Aldrich, 99%) were recrystallized from toluene. Antimony metal (Bradley Mining Company, 99.99%) was vacuum cast into 3 mm diam single crystals that were drilled and threaded to serve as electrodes.

Cells and electrodes.—The spectroelectrochemical (SE) cell, electrodes, and fittings have been described (9), except that tungsten (Alfa, 99.98%) was substituted for platinum wire as a working electrode material, and the reference electrode was fitted with a Pyrex screw joint, FETFE O-ring, and Teflon bushing (Ace Glass) for easy assembly. The electrolyte in the reference electrode was a binary $\text{SbCl}_3\text{-BPCI}$ melt saturated with solid SbCl_3 . This reference electrode is designated $\text{SbCl}_3\text{-BPCI(l)}$, $\text{SbCl}_3\text{(solid)/Sb}$. The indicator electrode for the EMF measurements was an Sb metal rod which was machined to expose a fresh surface and cleaned with methanol. The acid-base titration was performed by pipetting a known volume of acidic melt into a known volume of basic melt. For measurements using $\text{SbCl}_3\text{-KCl}$ melts, the spectroelectrochemical cell and reference electrode, as well as the purification procedure for KCl, were the same as described previously (9). The conductivity cells, instrumentation, and experimental procedures were the same as described previously (10).

Density and viscosity measurements.—Density measurements were made with a picnometer which consisted of a Pyrex bulb (~8 ml in volume) to which two Pyrex precision-bore graduated tubes (Aceglass, 2 mm id, grad-

* Electrochemical Society Active Member.

¹ Graduate Student, University of Tennessee, Knoxville, Tennessee 37919.

² Visiting scientist from the University of Tennessee, Knoxville, Tennessee 37919.

³ Present address: Department of Chemistry, University of Tennessee, Knoxville, Tennessee 37919.

Key words: EMF, voltammetry, organic.

uated in mm) were fused vertically, parallel to each other. The tubes were joined via a bridging tube at the top to allow for pressure equalization in each arm. An extension of tubing above the bridge allowed for addition of melt and seal-off. After addition of melt, the apparatus was sealed off under ~ 0.8 atm of argon. The densitometer was submerged vertically in a water bath controlled to $\pm 0.03^\circ\text{C}$ by a Lauda Model K2-R circulator. The graduations on the arms of the picnometer were calibrated using accurately weighed amounts of Hg. Temperature was measured with a Pt resistance thermometer using a Minco RTB 8078 bridge, whose calibration is traceable to NBS standards. For this experimental configuration, the error in density values is estimated to be less than 0.2% over the temperature range $25^\circ\text{--}100^\circ\text{C}$.

Viscosity measurements were made in a glove box using a Sargent-Welch Model S-83400D falling ball viscosimeter. Calibration of the viscosimeter (cell constant = $4.07 \pm 0.01 \times 10^{-4} \text{ cm}^2 \text{ s}^{-2}$) was accomplished as described in the literature (11). The tube fitted snugly into a bored-out 1 in. diam aluminum rod wound with coaxial heating element. Temperature was controlled by a Leeds and Northrup controller to $\pm 0.5^\circ\text{C}$ and was measured with a copper/constantan thermocouple calibrated against a Pt resistance thermometer. Three or more determinations were made at each temperature.

Instrumentation.—The electrochemical instrumentation consisted of a Princeton Applied Research Model 174A Polarographic Analyzer, a Model 173 Potentiostat/Galvanostat equipped with a Model 179 Digital Coulometer, and a Model 175 Waveform Generator. Data were recorded with either a Hewlett-Packard Model 7045A X-Y recorder or a Nicolet Model 2090-III digital storage oscilloscope.

Absorption spectra for the spectroelectrochemical (SE) experiments were measured in the visible region with the following equipment. Radiation from a 10W tungsten/quartz/halogen lamp was filtered with neutral density filters to control intensity and a long pass filter to eliminate second-order light. An image of the filament was focused on a square aperture to crop the edges, and a 4×4 mm image of the aperture was focused on the optical cell, which had a 1 mm path length and contained an optically transparent electrode (OTE). Light transmitted through the cell was focused on the entrance slit (0.025 mm) of a flat field 0.32m spectrograph (Instruments SA, Incorporated Model HR-320) equipped with a $152.5 \text{ grooves mm}^{-1}$ grating. Dispersed light was focused on the face of a solid state multichannel detector, which constituted the front end of an optical multichannel analyzer (Princeton Applied Research OMA-2 system). Two types of detectors were used. One was a Vidicon (Princeton Applied Research Model 1216 detector controller. This detector provided 500 optical channels over a spectral window ~ 260 nm wide to give a resolution of ~ 0.5 nm. The window could be positioned anywhere in the range 420–800 nm. The other type of detector was a Reticon (Princeton Applied Research Model 1412) with a linear silicon photodiode array thermoelectrically cooled to -20°C and operated by Princeton Applied Research Model 1412 detector controller. This detector provided 1022 optical channels over a spectral window ~ 505 nm wide to give a resolution of about ~ 0.5 nm. This window could be positioned in the range 420–1000 nm. The system processor was Princeton Applied Research Model 1215 with extended memory. Operation of the detectors was monitored with a Tektronix 604A oscilloscope, and hard copy was obtained with a Hewlett-Packard 9872B plotter and a Data Access Systems Model 360 line printer. Wavelength calibration and resolution verification were performed with Hg, Ne, Ar, and Xe atomic lamps. For the spectra reported here, the time used to measure a spectrum, including signal integration to improve S/N, was negligibly small compared with the time interval between spectra. The spectra were corrected for dark current and lamp intensity drift. Two

optical references were used in SE measurements. One reference was the spectrum of the solution prior to electrolysis while the other contained only corrections for light losses at the OTE and due to reflections at the cell windows. Cary Models 14 and 219 spectrophotometers were used for nonspectroelectrochemical optical measurements.

Experimental procedures.—All material transfers were performed in an argon-filled glove box where O_2 and H_2O were continuously monitored and kept below 1 ppm by circulation of the atmosphere through a purification train. Weighings were performed on an analytical balance in the glove box. Positive feedback circuitry was employed during voltammetric measurements to compensate for solution resistance. In order to remove gas bubbles trapped in the OTE, the SE cell was partially evacuated for a short period prior to the experiment and refilled with argon.

All temperatures (unless otherwise noted) were measured with copper/constantan thermocouples, which were calibrated against the platinum resistance thermometer described above.

Results and Discussion

Physical properties.—The electrical conductivities of the $\text{SbCl}_3\text{-AlCl}_3\text{-BPCl}$ 60:19:21 (basic) and 60:21:19 (acidic) melts were measured over the temperature range $24^\circ\text{--}100^\circ\text{C}$ with results that are shown in Fig. 1. The specific conductivities of the two ternary mixtures are almost equal at ambient temperatures, but at higher temperatures the basic melt becomes more conducting. The conductivities are comparable to those reported for binary $\text{AlCl}_3\text{-MCl}$ (2:1) ambient temperature liquids (12), but are about one order of magnitude less than the conductivities reported for acidic alkali metal chloroaluminate melts at slightly higher temperatures (13). For comparison with $\text{SbCl}_3\text{-AlCl}_3$ melts, we have included in Fig. 1 the conductivity of the binary melt whose composition most closely resembles the $\text{SbCl}_3\text{-AlCl}_3$ ratio in the ternary melts (10).

The densities of a 60:19:21 melt and a 60:21:19 melt were measured over the temperature range $25^\circ\text{--}100^\circ\text{C}$. The data were fitted to the equation $\rho = mT + b$, where ρ is the density (g cm^{-3}) and T is the temperature ($^\circ\text{C}$). For the 60:19:21 melt, $m = -1.3595 \times 10^{-3}$, $b = 2.0637$, and the correlation coefficient is $r = 0.99991$. For the 60:21:19 melt,

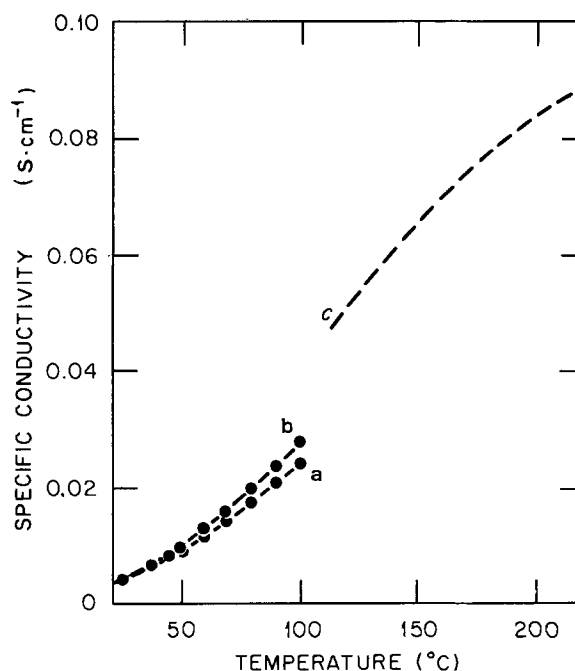


Fig. 1. Specific conductivities of (a) $\text{SbCl}_3\text{-AlCl}_3\text{-BPCl}$ (60:21:19); (b) $\text{SbCl}_3\text{-AlCl}_3\text{-BPCl}$ (60:19:21); and (c) $\text{SbCl}_3\text{-AlCl}_3$ (3:1) [Ref. (10)].

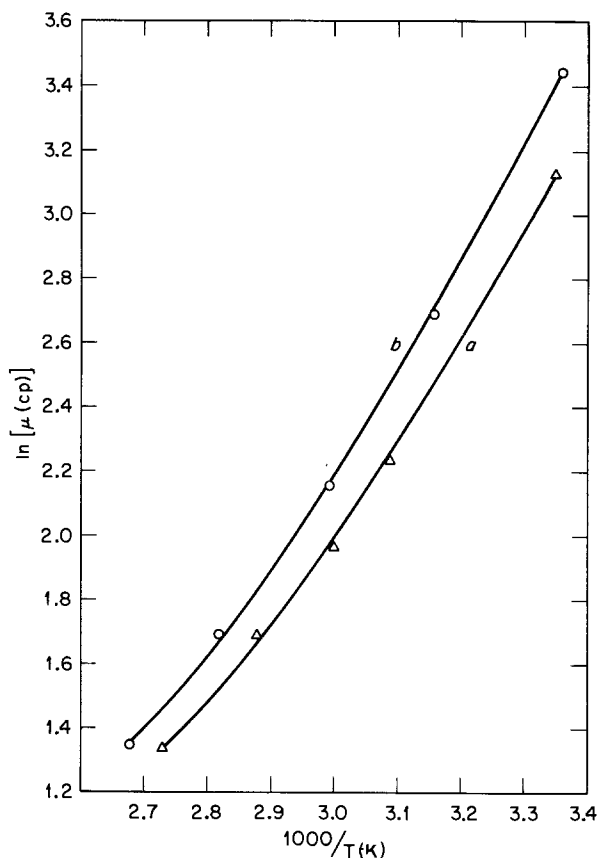


Fig. 2. Arrhenius plots of the viscosities (μ) of (a) 60:21:19 melt; and (b) 60:19:21 melt.

$m = -1.4236 \times 10^{-3}$, $b = 2.0813$, and $r = 0.99983$. The density of a 60:16:24 melt was determined by pycnometric weighing in the glove box at 28°C to be $1.998 \pm 0.002 \text{ g cm}^{-3}$.

The viscosities of these two melts were also measured over the temperature range 25°–100°C, and Arrhenius plots are shown in Fig. 2. These viscosities are comparable to those measured for chloroaluminate mixtures molten at ambient temperatures (12).

Sb(III)/Sb(0) couple.—For reasons given in the Introduction, the reduction of Sb(III) plays a key role in the chemistry of arenes in SbCl₃-rich melts. Therefore, a knowledge of the composition dependence of the Sb(III)/Sb(0) couple is very useful in elucidating the composition dependence of arene reactions. However, before trying to measure the potential of this couple, we felt it prudent to check for the electrochemical reversibility of the Sb(III)/Sb(0) couple in an acidic 60:21:19 melt by means of current-overvoltage (i - η) curves. The anodic branch of $\log i$ vs. η plots displayed Tafel behavior, and the apparent exchange current density was $13 \mu\text{A cm}^{-2}$. The cathodic branch did not display Tafel behavior, and previous measurements have shown that the reduction of Sb(III) to Sb(0) is a complex process (14, 15). The magnitude of the apparent exchange current density indicates that the redox couple behaves reversibly for potentiometry performed with high impedance circuitry (as is the case in the present investigation). Thus, the following EMF data are thermodynamic values and the Sb(III)/Sb(0) couple is suitable for use as a reference electrode.

The change in the potential of an antimony electrode resulting from changes in melt composition was measured using the following concentration cell



where $x:y$ varied from 22:18 to 18:22. The lack of information regarding the transference numbers of charge carriers prevented a calculation of the junction potential.

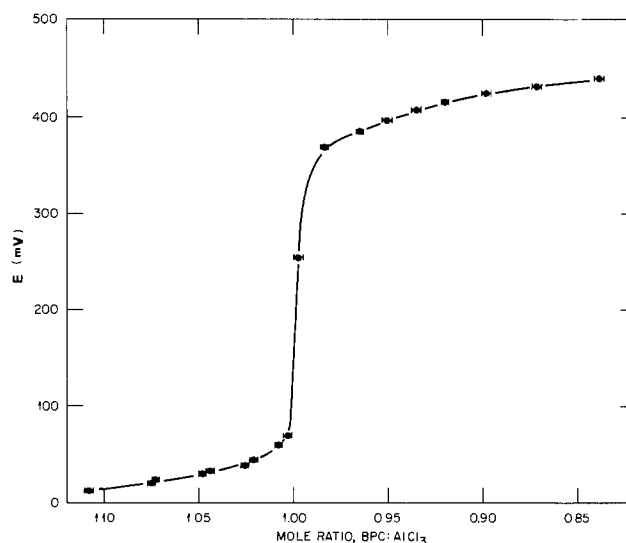


Fig. 3. EMF of Sb(III)/Sb(0) couple at 27°C for SbCl₃-AlCl₃-BPCl = 60:18:22 to 60:22:18 m/o. Sb metal working electrode.

The EMF data are shown in Fig. 3 and demonstrate that the potential of the Sb(III)/Sb(0) couple may be tuned over a range of 0.43V for the compositions indicated. For comparison, at 99°C the variation in potential across the composition range 98:2 m/o SbCl₃-KCl to 98:2 m/o SbCl₃-AlCl₃ is 0.48V (14).

The marked concentration dependence of the EMF is understood qualitatively. It arises from a combination of the dependence of SbCl₃ reduction on Cl⁻ activity and the large changes in this quantity that occur when excess BPCl is titrated with AlCl₃. However, attempts to model this behavior in terms of simple reactions such as $\text{AlCl}_3 + \text{SbCl}_3 \rightarrow \text{SbCl}_2^+ + \text{AlCl}_4^-$ combined with $\text{SbCl}_3 \rightleftharpoons \text{SbCl}_2^+ + \text{Cl}^-$ were not fruitful, and this is not surprising. SbCl₃ is an associated molecular liquid with a moderate dielectric constant in which ion pairing and complex ion solvation processes are known to occur (10, 16-19). Nevertheless, these EMF values have the same utility when applied to problems in arene chemistry as would values calculated for a suitably elaborate model of Cl⁻ activity.

Voltammetry and chronocoulometry.—In this section we describe the application of several electrochemical methods to studies of the oxidation of 9,10-dimethylanthracene (DMA) in 60:19:21 melts. Also, as a preliminary to the spectroelectrochemical studies in the next section, we report $E_{1/2}$ values for the oxidation of perylene (Per) and 9,10-diphenylanthracene (DPA), and the potential at which the irreversible oxidation of anthracene (Ant) begins.

The available electrochemical window in the SbCl₃-AlCl₃-BPCl mixtures (Fig. 4) is somewhat larger than that reported for SbCl₃-CsCl and SbCl₃-AlCl₃ (>90 m/o SbCl₃) melts at 100°C (9). The potential span for both the 60:21:19 and 60:19:21 compositions is about 1.8V, compared to 1.4V for the binary melts. The negative potential limit in the ternary melts is the reduction of Sb(III) to Sb metal. As can be seen in Fig. 4 in comparison to Fig. 3, overpotentials for the reduction process at an inert electrode exist for both ternary melts. The anodic limit for the liquids is the oxidation of Sb(III) to Sb(V).

DMA, Per, and DPA are sparingly soluble in a 60:19:21 melt and the dissolution rate is slow. Solutions were prepared by adding the arene to the melt and heating to 80°–100°C with stirring in a closed container for a period of about 1h.

Voltammetry of DMA solutions in basic melts yielded data summarized in Table I. Scan rates up to 20 V s^{-1} revealed no significant shift in the anodic peak potential, and the half-wave potentials determined by differential pulse polarography (21) (avg = 0.47V) corresponded well to the values obtained from the voltammetric results.

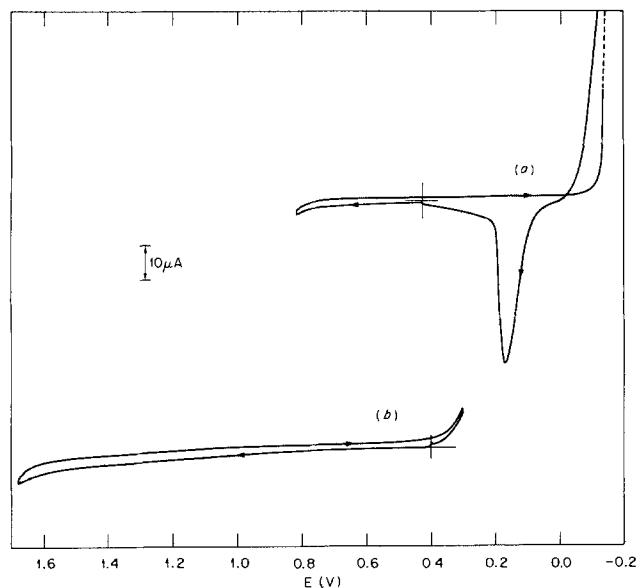


Fig. 4. Background cyclic voltammograms of (a) $\text{SbCl}_3\text{-AlCl}_3\text{-BPCl}$ (60:19:21); (b) $\text{SbCl}_3\text{-AlCl}_3\text{-BPCl}$ (60:21:19). Glassy carbon electrode, area = 0.071 cm^2 . Sweep rate = 100 mV/s , temp = 20°C .

The integrated Cottrell equation (22) predicts that for diffusion-controlled electrode reactions, a linear relationship holds between the charge (Q) and the square root of time ($t^{1/2}$). Figure 5 is a plot of Q vs. $t^{1/2}$ for times up to 20s; it is clearly linear. The intercept of the plot yields a value of the apparent double layer capacitance of approximately $5 \mu\text{F cm}^{-2}$, while the slope (uncorrected for impurities) gives an upper limit on the diffusion coefficient of neutral DMA of $2.5 \times 10^{-7} \text{ cm}^2 \text{ s}^{-1}$. Finally, the technique of double potential step chronocoulometry (22) demonstrated that the charge consumed around a square potential cycle obeys theoretical predictions ($Q_{2s}/Q_{10s} = 0.414$) (23) for 10 and 20s pulse widths. Thus, there is no significant reaction of the DMA radical cation on a voltammetric time scale.

Cyclic voltammograms of Per and DPA in 60:19:21 melts at 20°C corresponded to those expected for simple reversible behavior for scan rates up to 0.5 V s^{-1} , demonstrating that the radical cations of both are unreactive on a voltammetric time scale. An $E_{1/2}$ of 0.43V was obtained for Per while the $E_{1/2}$ of DPA was 0.54V . The oxidation of Ant was quite irreversible. For a voltammogram measured at a sweep rate of 0.2 V s^{-1} on a 8.7 mM solution of Ant at 19°C , the onset of oxidation occurred at about 0.6V .

These results for the 60:19:21 melt are similar to those reported by Bauer *et al.* (14, 24) and by Texier (25) in voltammetric studies of arene oxidation at 99°C in molten SbCl_3 with 0.1M KCl. Relative to a SbCl_3 saturated with KCl/Sb electrode, $E_{1/2}$ values of 0.24 , 0.31 , 0.39 , and 0.51V for Per, DMA, DPA, and Ant, respectively, are reported with mention that the anthracene radical cation is unstable.

Table I. Electrochemical parameters for a 1.2 mM solution of DMA in a 60:19:21 melt at 27°C . Glassy carbon working electrode area = 0.071 cm^2

ν (mV/s)	E_{p_a} (V) ¹	E_{p_c} (V) ¹	ΔE_p (mV) ²	$E_{p/2a}$ (V)	$E_{1/2a}$ (V) ³	n ⁴
10	0.505	0.440	65	0.445	0.473	0.95
20	0.500	0.440	60	0.443	0.471	0.95
50	0.503	0.440	63	0.443	0.471	1.0
100	0.503	0.443	60	0.445	0.473	0.98
200	0.505	0.445	60	0.447	0.477	0.98

¹ All potentials relative to liq. $\text{SbCl}_3\text{-BPCl}$ (l), sat. SbCl_3/Sb .

² Theory = 60 mV (20).

³ Calculated from $E_{1/2} = E_{p/2} + 1.09 RT/nF$ (20).

⁴ Calculated from $|E_p - E_{p/2}| = 2.2 RT/nF$ (20).

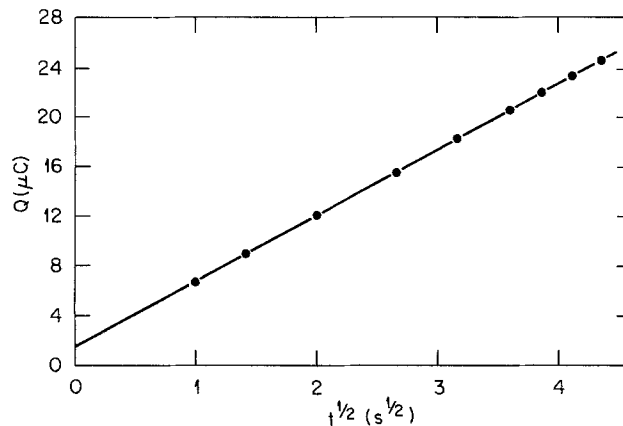


Fig. 5. Charge-time^{1/2} plot for a 1.4 mM solution of DMA in $\text{SbCl}_3\text{-AlCl}_3\text{-BPCl}$ (60:19:21). Potential step: $+0.35$ to $+0.65\text{V}$. Glassy carbon electrode area = 0.071 cm^2 , temp = 27°C .

It is noteworthy that SbCl_3 containing 0.1M ($\sim 1 \text{ m/o}$) KCl at 99°C is a significantly stronger oxidizing medium with respect to Per, DPA, and DMA than is the 60:19:21 melt at ambient temperatures. In particular, the difference between $E_{1/2}$ and $E(\text{Sb(III)/Sb})$ for Per, DMA, and DPA in $\text{SbCl}_3\text{-KCl}$ at 99° (14 , 24 , 25) is $0.16 \pm 0.03\text{V}$ less than the same difference for these arenes in the 60:19:21 melt at ambient temperatures.

Spectroelectrochemical studies.—Measurements of absorption spectra at an OTE during electrolysis and subsequent open-circuit decay provide further information about the relative stabilities of Per, DMA, DPA, and Ant radical cations in 60:19:21 melts and allow us to compare these stabilities with those in molten SbCl_3 containing 1M KCl at elevated temperatures. In a previous SE study (9), the Per radical cation was shown to be exceedingly stable following its electrochemical generation at 100°C in SbCl_3 containing 1M KCl. No optical spectroscopic measurements have been reported for the Ant, DPA, and DMA radical cations in SbCl_3 at elevated temperatures. The results of such measurements are described here.

The absorption spectrum of a dilute solution of Per in a 60:19:21 melt was measured over the range $350\text{-}1000 \text{ nm}$ at 20°C . It consisted of a complex vibronic band with a profile similar to that for Per in 95% ethanol (26). In the 60:19:21 melt, this band is somewhat red-shifted with respect to that in 95% ethanol (longest wavelength peak: 451 nm , melt: $\sim 434 \text{ nm}$, ethanol). There is also a very weak band at 548 nm in the melt spectrum due to a trace of the Per radical cation (*vide infra*), probably formed by an oxidizing impurity.

SE measurements were made on a 0.34 mM solution of Per in the 60:19:21 melt at 26°C with a Vidicon detector covering the range $430\text{-}690 \text{ nm}$. Spectra were measured at 1 min intervals during electrolysis at $+0.65\text{V}$ and during a subsequent period with the circuit open. As electrolysis proceeded, the 451 nm band of Per diminished while the 548 nm band of Per^+ grew in. The presence of a well-defined isosbestic point where the Per and Per^+ spectra cross and the absence of bands due to anything, except these two species, are strong evidence that Per^+ was the only electrolysis product and that it did not react further. After 35 min of electrolysis, 26% of the Per had been oxidized. At this point, the circuit was opened and the spectrum of the Per/ Per^+ mixture did not change during another 30 min of observation. Measurements of the spectrum of electrogenerated Per^+ in a 60:19:21 melt out to 1000 nm with a Cary 14 spectrophotometer showed it to be closely similar to the spectrum of Per^+ in $\text{SbCl}_3\text{-KCl}$ and $\text{SbCl}_3\text{-AlCl}_3$ melts (9).

Electrogenerated DMA^+ , in contrast with Per^+ , reacted at a moderate rate, both in a 60:19:21 melt at ambient temperatures and in $\text{SbCl}_3\text{-KCl}$ at elevated temperatures. SE measurements were made with a Reticon de-

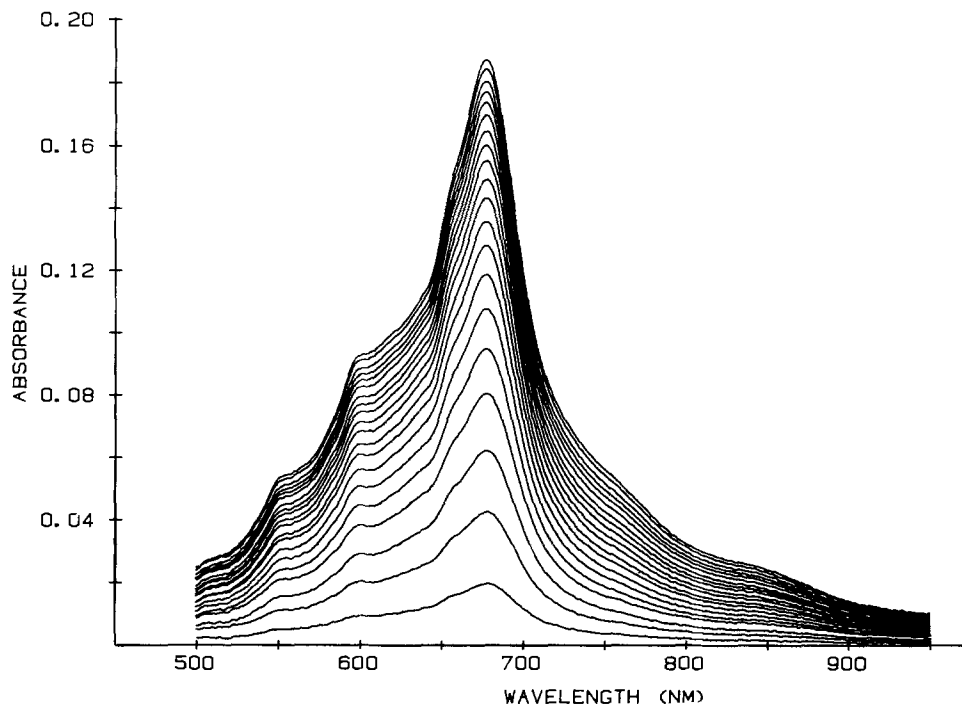


Fig. 6. Spectra measured every 60s during 20 min electrolysis at 0.65V of 1.2 mM DMA in a 60:19:21 melt. Pre-electrolysis spectrum used as reference. Pt-screen OTE and 1.0 mm path-length.

tector on a ~ 1 mM solution of DMA in a 60:19:21 melt, with results show in Fig. 6 and 7. To within experimental uncertainty, these spectra have the same profiles reported for transient DMA⁺ in benzonitrile at a much lower optical resolution than that reported here (27). Bands assigned to DMA⁺ are at 550, 600, ~ 656 (sh), and 678 (max) nm. Weak broad shoulders at about 620, 760 and 850 nm are attributed to subsequent reaction products because they develop at a much slower rate during electrolysis and are more persistent under open-circuit conditions than those assigned to DMA.

Similar SE measurements were made on 1.0-2.7 mM solutions of DMA in SbCl₃ containing 1M KCl at 75° and 100°C and gave similar results. The profile of the DMA⁺ spectrum (540-800 nm) in these melts did not differ in any important respect from that shown in Fig. 6 and 7. At 75°C, the DMA⁺ band positions were 549, 596, ~ 660 (sh), and 677 (max) nm. Weak broad shoulders at about

624 and 760 nm were observed and attributed to subsequent reaction products for the reasons cited above. Also, after prolonged electrolysis a broad band grew in with a peak at ~ 600 nm, and during open-circuit decay, this band continued to grow while the DMA⁺ bands diminished. Decay rates at the elevated temperatures were about an order of magnitude faster than at ambient temperature. This difference in rates may not be entirely due to the temperature difference since the DMA⁺ concentrations during open-circuit decay were higher in the elevated temperature runs than in the ambient temperature runs.

From the value of $E_{1/2}$ for DMA and the formal potential of the Sb(III)/Sb(0) couple in the 60:21:19 melt at 25°C, it is estimated that DMA should be partially oxidized with the simultaneous reduction of Sb(III) in this medium. The optical spectrum of DMA in the acidic melt revealed weak absorption bands due to DMA⁺, but

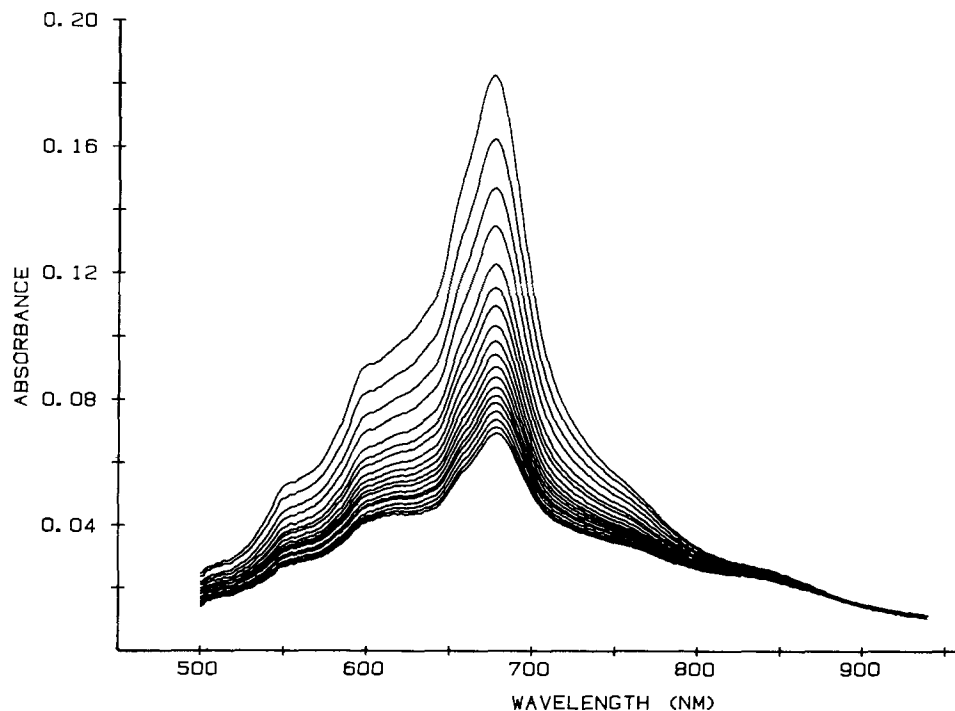


Fig. 7. Spectra measured every 180s during 57 min open-circuit decay following electrolysis in Fig. 6. Reference same as in Fig. 6.

the lack of accurate values for the molar absorptivities of the optical transitions prevented a quantitative determination of the concentration.

The absorption spectrum of a 4.1 mM solution of DPA in a 60:19:21 melt was measured at 31°C over the range 340-1000 nm with a Cary 14 spectrophotometer. The only absorption was due to the near-UV electronic band of the neutral molecule for which the longest wavelength vibronic maxima were found at 385 and 405 nm, slightly red-shifted from their positions in acetonitrile (28).

SE measurements were made on a 4.1 mM solution of DPA electrolyzed at +0.73V in a 60:19:21 melt. Spectra, taken with a Vidicon detector covering the range 530-790 nm, were measured at 1 min intervals during 30 min of electrolysis and a subsequent 40 min of open-circuit decay. The spectral profile of the resulting DPA⁺ cation was about the same as in acetonitrile (28) with bands at 559 (shoulder), 598, 658, and 734 nm. When the spectra obtained in the molten salt were normalized and compared, no absorption attributable to anything other than DPA⁺ was found. During open-circuit decay the time required for the DPA⁺ concentration to decrease by 10% was 22 min.

Similar SE measurements were made on a 0.49 mM solution of DPA in SbCl₃ containing 1M KCl at 100°C. Spectra taken with a Vidicon detector over 490-750 nm were measured at 0.5 min intervals during 17.5 min of electrolysis at 0.55V and during a subsequent 15 min of open-circuit decay. The DPA⁺ bands at 562 (shoulder), 599, 660, and 736 nm were not significantly displaced from their positions in the 60:19:21 melt. The decrease in absorbance during open-circuit decay was approximately logarithmic with a half-life of 20 min so that the time required for the DPA⁺ concentration to decrease by 10% was about 3 min.

SE studies of the electrolysis of Ant in a 60:19:21 melt at 26° and in SbCl₃ containing 1M KCl at 75°C showed that Ant⁺ is very reactive in both cases. During the initial stages of electrolysis in SbCl₃-KCl, a very weak spectrum, closely similar to that of Ant⁺ in other media (29), occurred but was soon obscured by a similar but red-shifted spectrum. The latter is reasonably attributable to the radical cation of a bianthracene or a substituted anthracene, both of which are possible products of Ant⁺ decay reactions. During electrolysis in the 60:19:21 melt, the Ant⁺ spectrum was not observed. Presumably Ant⁺ reacted so rapidly that its concentration remained extremely low.

These SE experiments provide comparative data on the stabilities of arene radical cations in the 60:19:21 melt and in molten SbCl₃-KCl. The examples chosen cover a very wide range of stabilities. Per⁺ is stable in both types of melts while Ant⁺ is very reactive in both. DPA⁺ and DMA⁺ show intermediate stabilities with DPA⁺ being the more persistent in both kinds of melts, even though the $E_{1/2}$ of DPA is more positive than the $E_{1/2}$ of DMA. The observed rates of decay of the latter two cations were slower in the 60:19:21 melt. This effect need not be due entirely to the lower temperature since the concentrations of the cations and their neutral precursors are also likely to be important rate determining factors.

Acknowledgment

This research was sponsored by the Division of Chemical Sciences, Office of Basic Energy Sciences, U.S. Department of Energy under contract W-7405-eng-26 with the Union Carbide Corporation. M. Sørli is grateful for

financial assistance from Norges Teknisk-Naturvitenskapelige Forskningsråd and for a travel grant from Norges Almenvitenskapelige Forskningsråd. D. M. Chapman and G. P. Smith gratefully acknowledge helpful discussions with Dr. A. C. Buchanan, III.

Manuscript submitted Sept. 23, 1983; revised manuscript received ca. Feb. 13, 1984. This was paper 754 presented at the San Francisco, CA, Meeting of the Society, May 8-13, 1983.

Oak Ridge National Laboratory assisted in meeting the publication costs of this article.

REFERENCES

1. A. S. Dworkin, M. L. Poutsma, J. Brynstad, L. L. Brown, L. O. Gilpatrick, and G. P. Smith, *J. Am. Chem. Soc.*, **101**, 5299 (1979).
2. A. C. Buchanan, III, A. S. Dworkin, J. Brynstad, L. O. Gilpatrick, M. L. Poutsma, and G. P. Smith, *ibid.*, **101**, 5430 (1979).
3. A. C. Buchanan, III, A. S. Dworkin, and G. P. Smith, *ibid.*, **102**, 5262 (1980).
4. A. C. Buchanan, III, A. S. Dworkin, G. P. Smith, M. V. Buchanan, and G. Olerich, *Fuel*, **60**, 694 (1981).
5. A. C. Buchanan, III, A. S. Dworkin, and G. P. Smith, *J. Org. Chem.*, **46**, 471 (1981).
6. A. C. Buchanan, III, A. S. Dworkin, and G. P. Smith, *ibid.*, **47**, 603 (1982).
7. A. C. Buchanan, III, R. Livingston, A. S. Dworkin, and G. P. Smith, *J. Phys. Chem.*, **84**, 423 (1980).
8. S. P. Zingg, A. S. Dworkin, M. Sørli, D. M. Chapman, A. C. Buchanan, III, and G. P. Smith, *This Journal*, **131**, 1602 (1984).
9. M. Sørli, G. P. Smith, V. E. Norvell, G. Mamantov, and L. N. Klatt, *ibid.*, **128**, 333 (1981).
10. C. Petrovic, G. Mamantov, M. Sørli, M. H. Lietzke, and G. P. Smith, *J. Phys. Chem.*, **86**, 4598 (1982).
11. C. Nanjundiah, K. Shimizu, and R. A. Osteryoung, *This Journal*, **129**, 2474 (1982).
12. R. A. Carpio, L. A. King, R. E. Lindstrom, J. C. Nardi, and C. L. Hussey, *ibid.*, **126**, 1614 (1979).
13. R. A. Carpio, L. A. King, F. C. Kibler, Jr., and A. A. Fannin, Jr., *ibid.*, **126**, 1650 (1979).
14. D. Bauer and P. Texier, *C. R. Acad. Sci., Ser. C*, **266**, 503 (1968).
15. G. Mamantov and C. Petrovic, Report No. AFWAL-PR-83-2032, Aeropropulsion Laboratory, Wright-Patterson Air Force Base, Ohio, April (1983).
16. F. Aliotta, G. Maisano, N. Micali, P. Migliardo, C. Vasi, F. Wanderlingh, R. Triolo, and G. P. Smith, *J. Chem. Phys.*, **76**, 3987 (1982).
17. E. Johnson, A. H. Narten, W. E. Thiessen, and R. Triolo, *Faraday Discuss. Chem. Soc.*, **66**, 287 (1978).
18. L. Pazsitka and Bertram, *J. Electroanal. Chem. Interfacial Electrochem.*, **28**, 119 (1970).
19. G. B. Porter and E. C. Baughan, *J. Chem. Soc.*, 744 (1958).
20. R. S. Nicholson and I. Shain, *Anal. Chem.*, **36**, 706 (1964).
21. E. P. Parry and R. A. Osteryoung, *ibid.*, **37**, 1634 (1965).
22. J. H. Christie, R. A. Osteryoung, and F. C. Anson, *J. Electroanal. Chem. Interfacial Electrochem.*, **13**, 236 (1967).
23. J. H. Christie, *ibid.*, **13**, 79 (1967).
24. D. Bauer, J.-P. Beck, and P. Texier, *Collect. Czech. Chem. Commun.*, **36**, 940 (1971).
25. P. Texier, *Bull. Soc. Chim. Fr.*, 4315 (1968).
26. R. A. Friedel and M. Orchin, "Ultraviolet Spectra of Aromatic Compounds," Spectrum 563, John Wiley & Sons, Inc., New York (1951).
27. A. Kira, S. Arai, and M. Imamura, *J. Phys. Chem.*, **76**, 1119 (1972).
28. R. E. Sioda, *J. Chem. Phys.*, **72**, 2322 (1968).
29. D. Distler and G. Hahlneicher, *Ber. Bunsenges. Phys. Chem.*, **74**, 960 (1970).

The Effect of Cyanide on the Oxidation of Formaldehyde on Au, Cu, and Pd Electrodes

Jean Horkans*

IBM, Thomas J. Watson Research Center, Yorktown Heights, New York 10598

ABSTRACT

The effect of the CN^- ion on the formaldehyde electro-oxidation reaction has been examined in basic EDTA solutions at 75°C on Au, Pd, and Cu electrodes. The results are compared with the cyclic voltammetry of these three metals in HCHO-free EDTA solutions. The cyanide ion poisons HCHO electro-oxidation on Au and Pd; on Cu, however, substantially higher HCHO-oxidation currents can be sustained in the presence of cyanide. The poisoning on Au and Pd is related to the suppression of dissolution of the metal by the formation of a sparingly soluble metal cyanide on the surface. Metal dissolution is apparently also suppressed on Cu electrodes, but the greatest promoting effect of CN^- occurs in a potential range in which CN^- adsorbs on the unoxidized Cu surface.

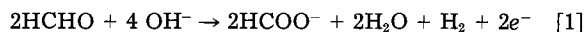
The electro-oxidation of formaldehyde is a reaction of considerable technological importance. Formaldehyde can serve as a fuel in fuel cells. It is also used as the reducing agent in electroless deposition of metals, particularly Cu. There is thus ample incentive to gain a better understanding of its electrochemistry. Nonetheless, formaldehyde oxidation has been studied much less extensively than the oxidation of methanol or formic acid, and little work has been done under the high pH conditions of electroless deposition.

Formaldehyde is known to interact strongly with polar solvents (1). It is present in dilute aqueous solution primarily as methylene glycol, $\text{H}_2\text{C}(\text{OH})_2$, which will be ionized to the methylene glycolate ion at high pH. In dilute solutions, polymer formation is insignificant. For the sake of convenience, formaldehyde will be designated as HCHO throughout this paper.

The cyclic voltammetry for the oxidation of HCHO has a similar shape on a variety of electrodes and in solutions of various compositions (2-10). Buck and Griffith (2) studied this reaction on Pt electrodes in acidic and basic electrolytes. They found a Tafel behavior only in a narrow potential range where oxidation current just begins to flow in the anodic sweep. The HCHO-oxidation current does not attain its diffusion-limited value, but rather reaches a peak at a potential determined by oxide formation on the Pt surface. Formaldehyde oxidation continues on the oxidized surface, but at a slower rate than on clean Pt. When the platinum oxide is reduced in the cathodic sweep, the HCHO-oxidation current increases suddenly. There is considerable structure in the curves, and the details in the shape depend on pH. A two-electron reaction to formate was found to occur above pH 11.5. In the pH range 7-10, a three-to-four-electron reaction occurs.

The involvement of the surface oxide of Pt in the HCHO-oxidation reaction is also discussed by Kuliev *et al.* (3).

In basic solutions, HCHO is oxidized to the formate ion. van den Meerakker (4) examined a number of electrode materials and showed that the reaction could proceed by either of the following two stoichiometries



or



On Pt and Pd, the reaction proceeds according to [2]. It largely does so on Au as well, depending on the electrode potential. On Cu electrodes, HCHO is oxidized according to [1].

Conway (5) has discussed the mechanism of the oxidation of organic substances on noble metal electrodes, but does not specifically treat formaldehyde. He points out

*Electrochemical Society Active Member.

Key words: metal oxidation, electroless deposition, cyclic voltammetry, catalysis.

that there is a clear relationship between the currents for the oxidation of the organic species and those for surface oxidation and reduction, but that this is complicated by inhibition and catalytic effects. Dissociative adsorption is generally the first step of the reaction. The adsorbed species can then react with adsorbed oxygen or hydroxide, which may be in a form not yet incorporated into the stable surface oxide film. Strongly bound intermediates can form, however, and serve to poison the reaction.

Gold shows a behavior qualitatively similar to that of Pt (6, 7). The catalysis of HCHO oxidation by the UPD of foreign metal adatoms on noble metal electrodes has been examined by Adzic *et al.* (6, 7) and by Motoo and Shibata (10).

In industrial electrochemical processes using formaldehyde, the electrolyte may include other components that can influence the HCHO-oxidation reaction. Electroless plating baths contain a particularly large number of chemical species. One of the more common of these is the cyanide ion, which is often used to stabilize the Cu(I) that is produced as an intermediate in electroless Cu deposition (11), or which can be released as a by-product during the electroless deposition of metals from their cyanide complexes.

Molenaar (12) has considered the effect of the cyanide ion on the electroless plating of Au-Cu alloys. Gold cannot be plated from its cyanide complex using HCHO as the reducing agent, but Au-Cu alloys can be plated over a wide composition range. It has been proposed (12) that the CN^- poisons the HCHO-oxidation reaction on Au electrodes but not on Cu.

The present work examines the effect of cyanide ion concentration on the HCHO-oxidation reaction on Au, Pd, and Cu electrodes. The measurements were made in EDTA solutions at elevated temperatures under conditions approaching those used in real electroless-deposition processes. The results are related to oxide formation processes on these metals in HCHO-free solutions.

Experimental

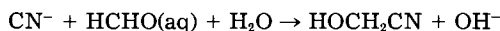
The electrodes were thin metal foils. The Pd and Au were cleaned in concentrated HNO_3 before use. Copper foils were cleaned by a brief etch in 10% HNO_3 ; they were discarded after one use.

The solutions were prepared from reagent-grade chemicals and deionized H_2O that had then been distilled under O_2 and passed over a hot Pt filament. The pH of the solutions was adjusted with NaOH. No measures were taken to purify the formaldehyde, but bottles of formaldehyde were discarded when they showed significant polymer formation at the bottom. To minimize the extent of any possible homogeneous reactions of HCHO, it was not added to the solution until just prior to the measurement. As received, the HCHO contains CH_3OH as a stabilizer. It was verified that CH_3OH oxidation does not interfere with the results by running experiments in HCHO-free

solutions containing an equivalent amount of CH_3OH ; no significant methanol-oxidation currents were observed.

Solutions were thoroughly deaerated with N_2 before the measurements were made. During the measurement, the solution was blanketed with N_2 .

Formaldehyde reacts with the cyanide ion to form formaldehyde cyanohydrin according to the following reaction (1)



The formaldehyde cyanohydrin can then react further; hydrolysis can occur with ammonia evolution and a variety of other products can form. Thus, in the presence of HCHO , CN^- is consumed. This fact makes it very difficult to control the $[\text{CN}^-]$ during the measurement. Studies that assume a $[\text{CN}^-]$ from the amount added to the solution can be grossly in error. In the present work, an aliquot of the solution was removed immediately after the electrochemical measurement and cooled to room temperature. The $[\text{CN}^-]$ was then determined using a specific ion electrode. The range of concentrations studied was limited by the consumption of CN^- . At nominal free NaCN concentrations on the order of 150 ppm, the resulting $[\text{NaCN}]$ as determined with the CN^- electrode at the time of the measurement was <20 ppm.

The working electrode was mounted horizontally (facing down) in a Teflon holder. The counterelectrode was a Pt screen parallel to the working electrode at the bottom of the cell. The reference electrode was a $\text{Hg}/\text{Hg}_2\text{SO}_4$, sat. K_2SO_4 electrode in a separate compartment at room temperature. Potentials are quoted *vs.* the mercury sulfate electrode (MSE) at room temperature, which has a potential of 0.68V *vs.* NHE. A Luggin capillary probed the potential near the surface of the working electrode. The jacketed cell was made of Pyrex; circulating water maintained the solution in the cell at 75°C .

Results

All data were obtained at both room temperature and 75°C . To avoid an excessive number of figures, only the 75°C data will be given here; the room temperature data show the same trends and lead to the same general conclusions. The trends are emphasized at the higher temperature, however, since HCHO oxidation and metal dissolution are faster. In addition, the technologies employing HCHO oxidation often proceed at elevated temperatures, and it is informative to study the reaction near the temperature at which it is used.

Since the HCHO -oxidation reaction has such a strong relationship to oxide formation on the electrode surface, the cyclic voltammetry characteristic of HCHO oxidation will be compared to that in HCHO -free solution at a similar value of the $[\text{CN}^-]$. Such a comparison assumes that the surface-oxidation processes are the same in the presence and the absence of the adsorbed organic species. Kalcheva *et al.* (13) believe this to be true. Conway (5) also discusses this subject.

In the presence of CN^- , which reacts with HCHO , there may be electroactive species other than the methylene glycolate ion. The CN^- is present in trace amounts, however, and the concentration of methylene glycolate ion in solution should be much greater than that of either formaldehyde, cyanohydrin or any of the products of cyanohydrin reactions.

Au.—Figure 1b shows the cyclic voltammetry of a Au foil electrode in a solution of 0.12M EDTA, pH 11.7, at 75°C . During the initial stages of the oxidation of the Au surface, significant dissolution can occur. Thus, the charge under the oxidation peak in the anodic scan is substantially greater than that necessary to form an oxide film of monolayer dimensions. At sufficiently positive potentials, the surface becomes passivated by a protective oxide film. The situation is analogous to that described by Frankenthal and Siconolfi (14) for concentrated Cl^- solutions. In the cathodic sweep, the electrode remains passive until the oxide film begins to be reduced. Reduction of the oxide depassivates the Au, and dissolution

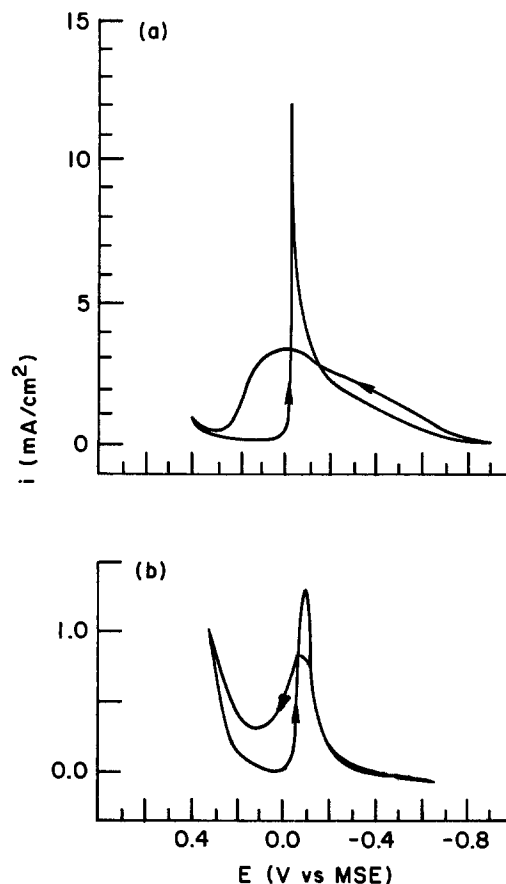


Fig. 1. Cyclic voltammetry of a Au foil electrode in 0.12M EDTA, pH 11.7, 75°C , (a) with 0.03M HCHO , and (b) with no HCHO . The sweep speed was 20 mV/s .

again occurs; this sequence of events results in an oxidation peak in the cathodic sweep.

The result of adding 0.03M HCHO to the EDTA solution is shown in Fig. 1a. Formaldehyde oxidation begins at $\sim -0.7\text{V}$ in the anodic sweep, and the current rises gradually as the potential is made more positive. A maximum current is reached at $\sim 0\text{V}$ in the anodic sweep, the same general potential region in which the electrode passivates in HCHO -free solution. In the cathodic sweep, the current remains low until $\sim 0.0\text{V}$, where a large spike of oxidation current occurs. Thereafter, the curve more or less retraces the anodic sweep. The spike in the cathodic sweep occurs at the potential at which the gold oxide film begins to be reduced and bare Au sites are once again exposed on the surface.

Low concentrations of CN^- influence the behavior of Au electrodes in HCHO containing and HCHO -free solutions. Representative curves for the highest NaCN concentration studied are given in Fig. 2. (A NaCN concentration of 1 ppm is $2 \times 10^{-5}\text{M}$.) Addition of CN^- to HCHO -free solutions suppresses the dissolution of the Au electrode, as evidenced by a reduction in the peak heights in both the anodic and cathodic sweeps (Fig. 2b). In HCHO solutions (Fig. 2a), addition of CN^- shifts the HCHO -oxidation currents in the anodic sweep to more positive potentials and the spike in the cathodic sweep to more negative potentials. The curves show features not observed in the absence of CN^- , but these are not clearly related to features in the curves in HCHO -free solutions (in Fig. 2b).

The effect of CN^- concentration is summarized in Fig. 3. The maximum currents in both the anodic sweep (solid circles) and the cathodic sweep (open circles) are plotted as a function of $[\text{NaCN}]$. Information about potential shifts is, of course, lost in such a representation.

In HCHO -free solution (Fig. 3b), the peak height in both sweep directions is substantially reduced by CN^- ion. Although the gold cyanide complex is highly soluble, the

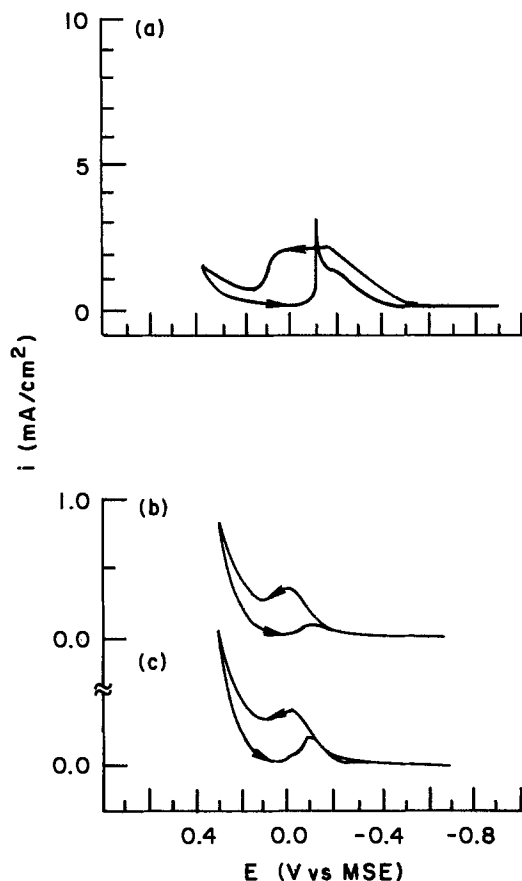


Fig. 2. Cyclic voltammetry of a Au foil electrode in 0.12M EDTA, pH 11.7, 75°C, (a) with 0.03M HCHO and 6.6 ppm NaCN, (b) with no HCHO and 12.2 ppm NaCN, and (c) with no HCHO and 4.3 ppm NaCN. The sweep speed was 20 mV/s.

cyanide ion is present at low concentration and is in insufficient supply to form significant amounts of soluble $\text{Au}(\text{CN})_2^-$ ions. Instead, when the electrode is oxidized, compounds such as AuCN , which are less soluble than the gold-EDTA complex, probably form on the surface. The suppression of the dissolution current is pronounced at $[\text{NaCN}] = 1.9$ ppm and increases with $[\text{CN}^-]$ in the concentration range studied. Dissolution of gold as the EDTA complex still occurs, as evidenced by the magnitude of the currents flowing and by the continued presence of an anodic peak in the cathodic sweep.

The currents due to HCHO oxidation (Fig. 3a), are increased slightly at the lowest CN^- levels, but thereafter decrease monotonically with CN^- . Thus it appears that the adsorption of CN^- to form sparingly soluble gold compounds decreases the catalytic activity of Au for HCHO oxidation in EDTA solution, possibly through a reduction in the number of surface sites on which adsorption of formaldehyde can occur.

Pd.—The cyclic voltammetry of a Pd electrode in CN^- -free EDTA solution at 75°C is shown in Fig. 4b. The sorption of hydrogen just begins at the negative limit of the sweep; significant hydrogen sorption does not occur in the same potential range as HCHO oxidation on Pd. Both oxide formation and Pd dissolution occur in this potential range, as evidenced by the anodic peak that appears once oxide reduction begins in the cathodic sweep. The magnitude of the currents is generally smaller than for Au in the same solution.

Upon addition of HCHO to the solution, the behavior shown in Fig. 4a is obtained. Current begins to flow at $\sim -0.8\text{V}$ in the anodic sweep, increasing to a peak value at $\sim -0.3\text{V}$. The potential of the maximum current is slightly positive to the first peak in the cyclic voltammetry in HCHO-free solution. The simultaneous occurrence of palladium oxidation and dissolution make it impossible to

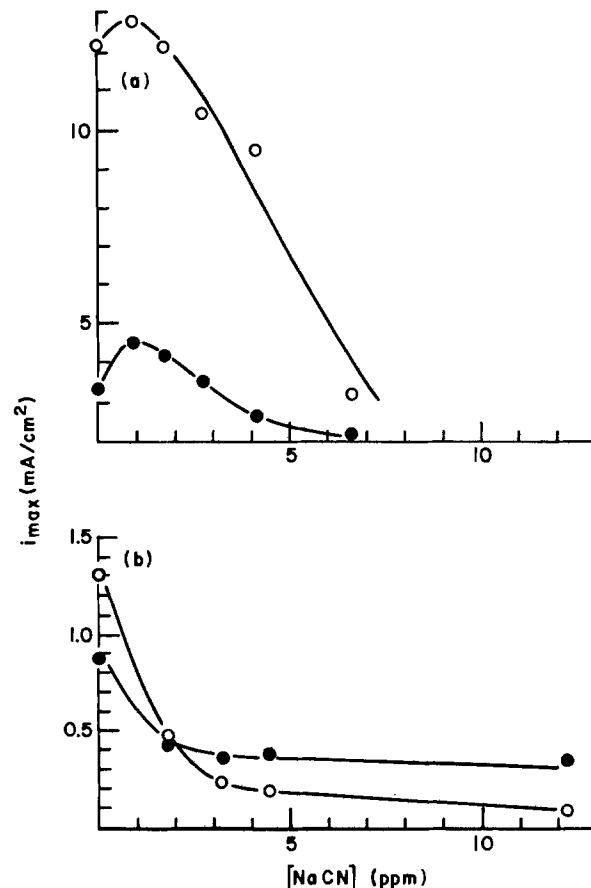


Fig. 3. The dependence of the peak current on CN^- concentration for a Au foil electrode in 0.12M EDTA, pH 11.7, 75°C, (a) with 0.03M HCHO, and (b) with no HCHO. The closed circles are the anodic sweep, the open circles the cathodic sweep.

relate the HCHO-oxidation peak to the state of oxidation of the electrode, but it appears that the HCHO current begins to drop when the Pd electrode becomes covered with an oxide or hydroxide film, perhaps a monolayer in thickness. Formaldehyde oxidation proceeds at a lower but significant rate during the cathodic sweep; the structural details in this region are not clearly related to any structure in the curve of Fig. 4b. As soon as the reduction of the Pd oxide begins in the cathodic sweep and free Pd sites are once again available on the surface, a sharp HCHO-oxidation spike appears.

In the presence of ~ 6 ppm NaCN, the behavior of Fig. 5 is obtained. In HCHO-free solution, the Pd dissolution reaction is suppressed, Fig. 5b. The onset of palladium oxidation in the anodic sweep is shifted to more positive potentials. Oxidation currents (due to Pd dissolution) are no longer observed in the cathodic sweep. In HCHO solution, 5.5 ppm of NaCN has depressed the peak in the anodic sweep and shifted it to a slightly more positive potential. The peak in the cathodic sweep, which has almost disappeared, has shifted to a more negative potential. The cathodic sweep in the presence of CN^- shows none of the structure that appears in CN^- -free solution.

The CN^- -dependence of the peak currents is shown in Fig. 6. In HCHO-free solution, Fig. 6b, the peak current in the anodic sweep is not very dependent on $[\text{NaCN}]$. The total oxidation charge is lower in the presence of CN^- , however, because of the shift in the onset of oxidation to more positive potentials. The shift occurs even at the lowest CN^- concentrations and has little concentration dependence. A more dramatic effect of CN^- is seen in the cathodic sweep. At $[\text{NaCN}] = 1.3$ ppm, a reduction peak is followed by a small oxidation peak. At higher concentrations, oxidation currents are no longer observed in the cathodic sweep.

The dependence of HCHO oxidation of $[\text{CN}^-]$ is complicated, as shown in Fig. 6a. Low levels of CN^- somewhat

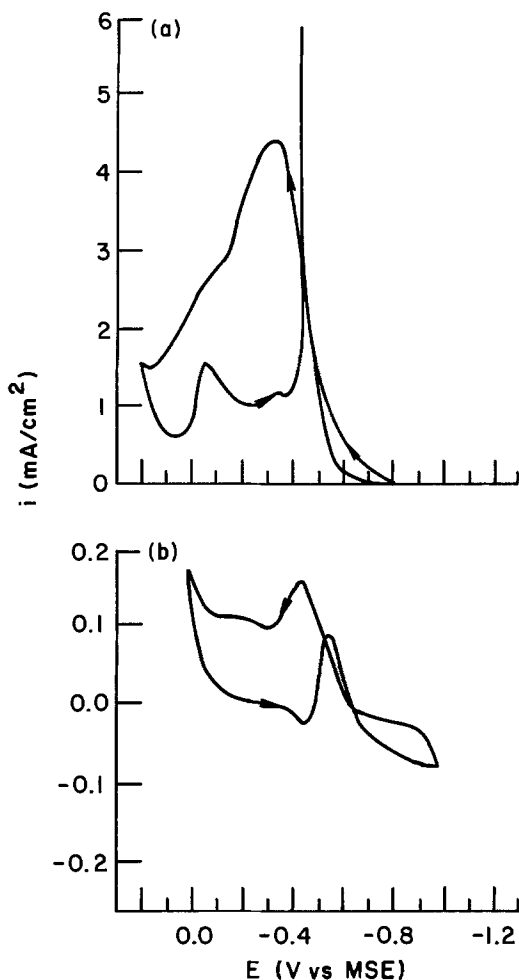


Fig. 4. Cyclic voltammetry of a Pd foil electrode in 0.12M EDTA, pH 11.7, 75°C, (a) with 0.03M HCHO, and (b) with no HCHO. The sweep speed was 20 mV/s.

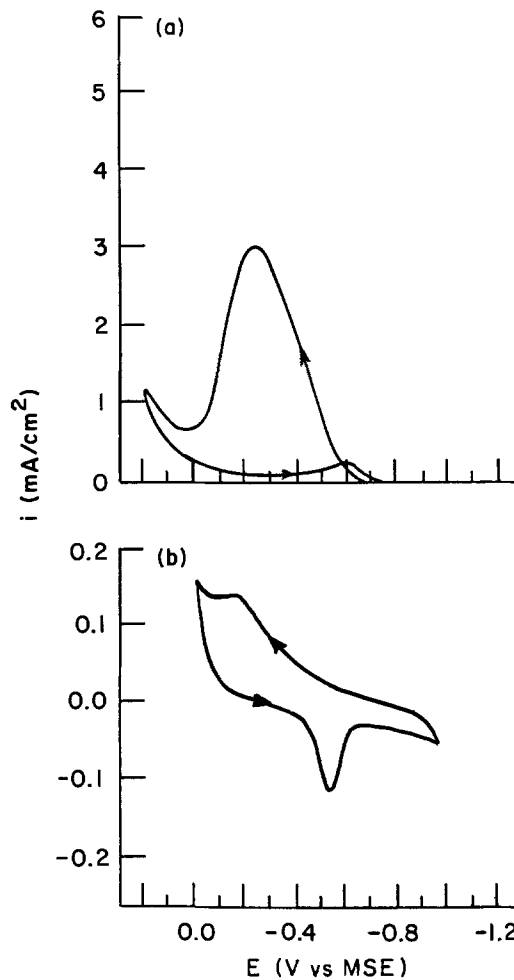


Fig. 5. Cyclic voltammetry of a Pd foil electrode in 0.12M EDTA, pH 11.7, 75°C, (a) with 0.03M HCHO and 6.0 ppm NaCN, and (b) with no HCHO and 5.5 ppm NaCN. The sweep speed was 20 mV/s.

reduce the peak currents in both the anodic and cathodic sweeps. Further addition of CN^- causes a maximum in the peak height. Sufficiently high $[\text{NaCN}]$ suppresses HCHO oxidation on Pd.

Cu.—Copper is a less noble metal than either Pd or Au, and EDTA strongly complexes Cu(II) ions. In addition, the stoichiometry of the HCHO-oxidation reaction is different on Cu than on Pd and Au (4). Thus, HCHO oxidation is studied in a different potential region on Cu than on the other metals of this investigation.

Figure 7b shows the cyclic voltammetry of Cu in the pH 11.7 EDTA solution at 75°C. In this potential range, only one redox couple, presumably Cu/Cu₂O, is observed. (Pourbaix diagrams (15), calculated at room temperature and in the absence of complexing anions, are not very helpful in assigning oxidation states in this system. The cyclic voltammetry of Cu in 0.4M Na₂SO₄ solution at pH 11.7 and 75°C has also been studied, however. In that solution, there are two pairs of peaks, due to Cu/Cu₂O and Cu₂O/Cu(OH)₂. In Na₂SO₄ the Cu/Cu₂O peaks appear in the same potential region as the pair of peaks in the EDTA solution. This observation gives some confidence to the assignment of the peaks in Fig. 7b to the Cu/Cu₂O couple).

The charge under the anodic peak (Fig. 7b) is several times that under the cathodic peak. This discrepancy may be the result of some copper ions leaving the surface as dissolved species. Unlike Au and Pd, however, Cu does not show an oxidation peak in the cathodic sweep.

On Au and Pd electrodes, the currents measured in HCHO solution are much larger than those due to the reactions of the metal in HCHO-free solution. Figure 7a shows that this is not the case on Cu electrodes. In the

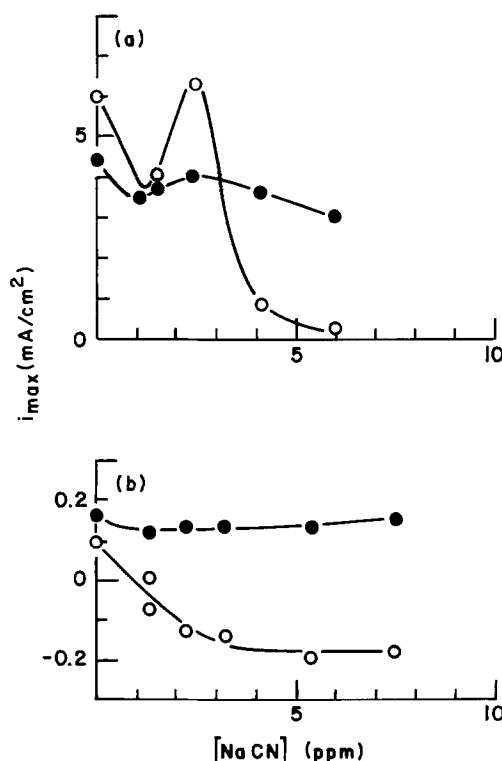


Fig. 6. The dependence of the peak current on CN^- concentration for a Pd foil electrode in 0.12M EDTA, pH 11.7, 75°C, (a) with 0.03M HCHO, and (b) with no HCHO. The closed circles are the anodic sweep, the open circles the cathodic sweep.

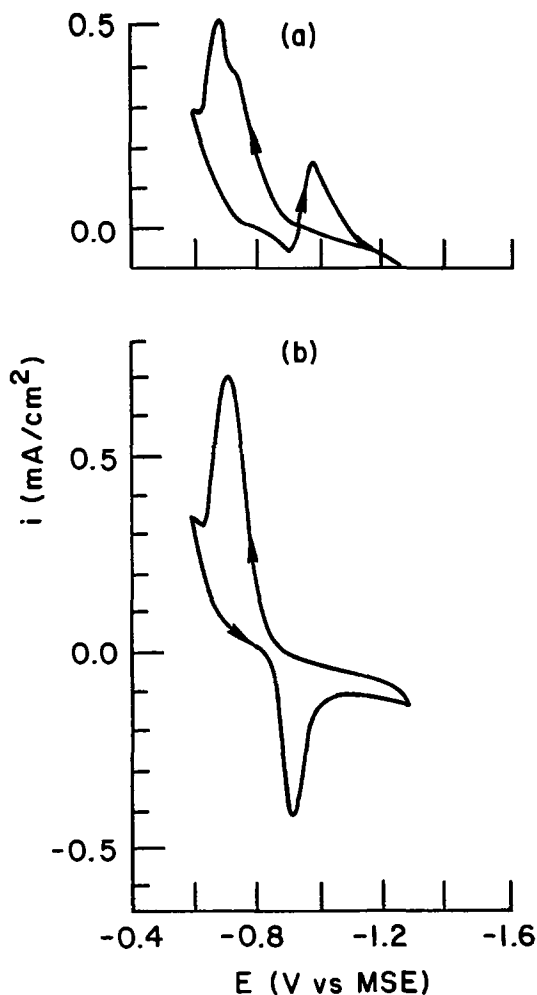


Fig. 7. Cyclic voltammetry of a Cu foil electrode in 0.12M EDTA, pH 11.7, 75°C, (a) with 0.03M HCHO, and (b) with no HCHO. The sweep speed was 20 mV/s.

anodic sweep, there is a narrow potential range (between $\sim -1.0\text{V}$ and $\sim -0.8\text{V}$) in which a very slightly higher current flows in the presence of HCHO; otherwise, the observed currents are actually higher in HCHO-free solution. Formaldehyde oxidation does occur on this electrode, however, as evidenced by the anodic peak that appears in the cathodic sweep as soon as the Cu_2O reduction begins.

The lower current in the presence of HCHO can be explained by a complex interaction of the processes of copper oxidation, copper dissolution, and HCHO oxidation. The adsorption of HCHO on the Cu electrode can suppress the Cu dissolution reaction. In other words

$$i_{\text{Cu diss.}} + i_{\text{HCHO ox.}} + i_{\text{Cu ox.}}$$

in the presence of adsorbed HCHO is lower than

$$i'_{\text{Cu diss.}} + i'_{\text{Cu ox.}}$$

in the HCHO-free solution because adsorbed HCHO suppresses Cu dissolution, and

$$i_{\text{Cu diss.}} < i'_{\text{Cu diss.}}$$

Nonetheless, the HCHO oxidation currents must be of the order of or less than the currents due to the other processes occurring on the surface.

Figure 8 shows the effect of CN^- on Cu oxidation and the electro-oxidation of HCHO. The cyclic voltammetry of Cu in CN^- containing EDTA solution (Fig. 8b) exhibits increased currents in the potential range negative to the $\text{Cu}/\text{Cu}_2\text{O}$ couple. Formaldehyde oxidation in the presence of CN^- proceeds at a higher rate than in its absence. (Compare Fig. 7a and 8a). An especially large enhancement in the current is observed in the same potential

range as the increased currents in Fig. 8b (*i.e.*, negative to the Cu_2O peak).

The effect of CN^- concentration is shown in Fig. 9. Cyanide has a smaller effect on the cyclic voltammetry of Cu in EDTA solution (Fig. 9b) than on that of Au or Pd. Sodium cyanide concentrations of up to 2.7 ppm result in virtually no change in the curve. At higher $[\text{NaCN}]$, the Cu_2O reduction peak is somewhat reduced in magnitude and has a shoulder on the negative side. This shoulder at potentials negative to the $\text{Cu}/\text{Cu}_2\text{O}$ couple is probably due to adsorption of the cyanide ion.

Formaldehyde electro-oxidation is highly dependent on the CN^- concentration (Fig. 9a). Addition of 1.2 ppm

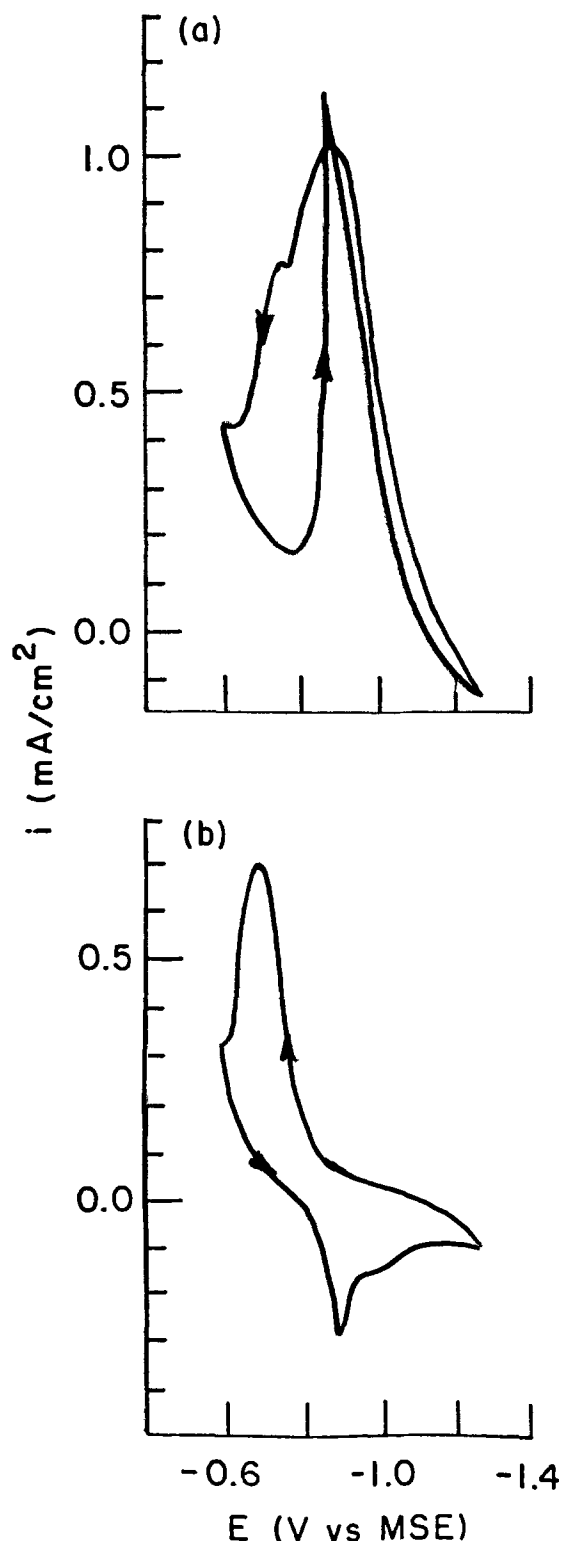


Fig. 8. Cyclic voltammetry of a Cu foil electrode in 0.12M EDTA, pH 11.7, 75°C, (a) with 0.03M HCHO and 8.7 ppm NaCN, and (b) with no HCHO and 9.4 ppm NaCN. The sweep speed was 20 mV/s.

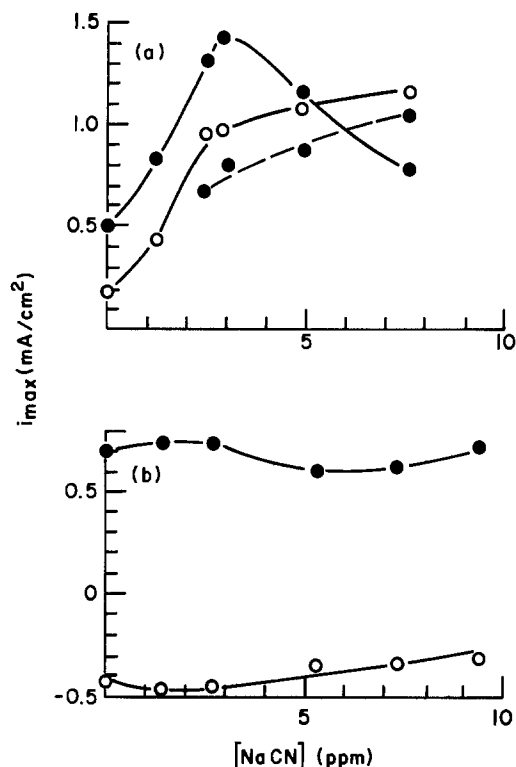


Fig. 9. The dependence of the peak current on CN^- concentration for a Cu foil electrode in 0.12M EDTA, pH 11.7, 75°C, (a) with 0.03M HCHO. The open circles represent the peak in the cathodic sweep. The closed circles represent the two peaks in the anodic sweep: the solid line the peak at $\sim -0.75\text{V}$ and the dashed line the peak at $\sim -0.9\text{V}$. (b) The same solution with no HCHO. The closed circles are the anodic sweep, the open circles the cathodic sweep.

NaCN increases the currents over the entire potential range. Further increase in the current occurs at $[\text{NaCN}] = 2.5$ ppm, and a second major peak in the anodic sweep appears at more negative potentials ($\sim -0.9\text{V}$). As $[\text{NaCN}]$ increases further, the peak at -0.75V in the anodic sweep goes through a maximum, and the -0.9V peak in the anodic sweep continues to increase in height. The oxidation peak in the cathodic sweep increases with $[\text{CN}^-]$ and shifts to more positive potentials in the range of concentrations studied. The substantial increase in the magnitude of the HCHO-oxidation currents caused by the addition of CN^- contrasts to the behavior on Au and Pd, for which the HCHO oxidation reaction becomes poisoned at fairly low cyanide concentrations.

Discussion

The HCHO-oxidation reaction requires rather specific surface conditions for the electrode material on which it proceeds. Information about the state of the surface can be gained by comparing the cyclic voltammetry in HCHO-free solution with that in HCHO containing solutions. Such a comparison leads to the conclusion that HCHO oxidation requires the availability of bare metallic sites on the surface; complete oxide coverage effectively impedes the reaction.

The effect of CN^- on HCHO oxidation on Au and Pd electrodes can be interpreted in light of this model. Cyanide was found to suppress the dissolution of these two metals in EDTA solution. At low cyanide levels, slightly soluble metal cyanide may form on the electrode surface. The surface population of bare metal sites would then be reduced, suppressing the rate of HCHO oxidation.

The situation is apparently somewhat more complex on Pd than on Au electrodes, as reflected in the fact that the HCHO-oxidation peaks go through a maximum as a function of the cyanide concentration. The maximum may result from the separate effects of the CN^- ion on the adsorption of hydrogen and the adsorption of the formaldehyde fragment on the Pd electrode. In the absence of further experimental evidence, however, such a model remains speculative.

The electrochemistry of Cu in EDTA solutions is quite different from that of Au or Pd. Whereas Au and Pd in CN^- -free solution sustain HCHO-oxidation currents that are significantly larger than the currents due to surface processes (oxidation and dissolution), Cu does not. The effect of CN^- on HCHO oxidation on Cu depends on the electrode potential. In the potential region of Cu_2O formation, the effect is much the same as on Pd: the size of the peak goes through a maximum as a function of $[\text{CN}^-]$. At more negative potentials, where CN^- adsorption is indicated from the cyclic voltammetry in HCHO-free solution, the HCHO oxidation current increases with $[\text{CN}^-]$ in the concentration range studied. Unlike Au and Pd, which show poisoning of HCHO electro-oxidation by CN^- , Cu can sustain substantially higher HCHO-oxidation currents in the presence of CN^- .

The uniqueness of the effect of CN^- on HCHO oxidation on Cu is related to the fact that the reaction proceeds by a different stoichiometry and in a different potential range than on Au or Pd. On Cu, formaldehyde oxidation occurs in a potential range in which cyanide adsorption is the dominant process, and thus cyanide can strongly influence this reaction.

Acknowledgments

The author gratefully acknowledges the contributions of H. C. McGrath, who provided experimental assistance during this study, and L. T. Romankiw, whose discussions stimulated the direction of the work.

Manuscript submitted Aug. 29, 1983; revised manuscript received ca. Dec. 14, 1983.

IBM Corporation assisted in meeting the publication costs of this article.

REFERENCES

1. J. F. Walker, "Formaldehyde," p. 52, Reinhold, New York (1964).
2. R. P. Buck and L. R. Griffith, *This Journal*, **109**, 1005 (1962).
3. S. A. Kuliev, N. V. Osetrova, V. A. Bagotskii, and Yu. B. Vasil'ev, *Sov. Electrochem.*, **16**, 921 (1980).
4. J. E. A. M. van den Meerakker, *J. Appl. Electrochem.*, **11**, 387 (1981).
5. B. E. Conway, in "Electrodes of Conductive Metallic Oxides," Vol. B, p. 433, S. Trasatti, Editor, Elsevier, New York (1980).
6. M. D. Spasojevic, R. R. Adzic, and A. R. Despic, *J. Electroanal. Chem.*, **109**, 261 (1980).
7. R. R. Adzic and M. L. Avramov-Ivic, *ibid.*, **134**, 177 (1982).
8. B. J. Podlovchenko, O. A. Petry, A. N. Frumkin, and H. Lal, *ibid.*, **11**, 12 (1966).
9. T. Loucka and J. Weber, *ibid.*, **21**, 329 (1969).
10. S. Motoo and M. Shibata, *ibid.*, **133**, 119 (1982).
11. E. B. Saubestre, *Plating*, **59**, 563 (1972).
12. A. Molenaar, *This Journal*, **129**, 1917 (1982).
13. S. V. Kalcheva, M. V. Christov, E. I. Sokolova, and S. N. Raicheva, *J. Electroanal. Chem.*, **55**, 223 (1974).
14. R. P. Frankenthal and D. J. Siconolfi, *This Journal*, **129**, 1192 (1982).
15. M. Pourbaix, "Atlas of Electrochemical Equilibria," p. 382, Pergamon Press, Inc., Oxford, England (1966).

Transport Numbers in Molten Acidic Aluminum Chloride-1-Methyl-3-Ethylimidazolium Chloride

Their Relationship to EMF Measurements in Chloroaluminate Melts

Charles L. Hussey*

Department of Chemistry, University of Mississippi, University, Mississippi 38677

Harald A. Øye*

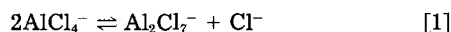
Institutt for Uorganisk Kjemi, Norges Tekniske Høgskole, Universitetet i Trondheim, N7034 Trondheim, Norway

ABSTRACT

External and internal transport numbers were determined for the aluminum chloride-1-methyl-3-ethylimidazolium chloride room-temperature ionic liquid in the range of aluminum chloride mole fractions, $0.50 < x_{\text{AlCl}_3} < 0.67$. The 1-methyl-3-ethylimidazolium cation external transport number was found to be 0.71, while the internal transport number was found to be 1.00. The latter result may be of a general nature for all chloroaluminate melts and provides justification for using simplified formulas to represent the relationships between the EMF of concentration cells and the chemical potentials of chloroaluminate melts.

Molten mixtures of aluminum chloride and 1-methyl-3-ethylimidazolium chloride (MEIC) have been found to be useful solvents for electrochemistry and spectroscopy (1). Attractive features of this molten salt system are its low melting temperature, which is 20°C or less over the range of AlCl_3 mole fractions extending from 0.35 to 0.66 (2), and its wide range of Lewis acidity (1). AlCl_3 -MEIC mixtures are very similar in all respects to another much-studied low temperature chloroaluminate melt, the aluminum chloride-1-(n-butyl)pyridinium chloride (BPC) system. However, MEIC is easier to synthesize and purify than BPC, and AlCl_3 -MEIC melts exhibit significantly lower melting temperatures.

Both the AlCl_3 -MEIC and AlCl_3 -BPC systems have been studied using ^{27}Al NMR spectroscopy (3, 4). In addition, the latter has been investigated using Raman spectroscopy (5). From these studies it was established that AlCl_4^- and Al_2Cl_7^- are the principal anionic constituents of acidic (AlCl_3 -rich) melts in the range of AlCl_3 mole fractions, $0.50 < x_{\text{AlCl}_3} < 0.67$, while AlCl_4^- and Cl^- are the anionic constituents of basic melts. Potentiometric studies indicate that the acid-base properties of these melts can be represented by an equilibrium with Al_2Cl_7^- , AlCl_4^- , and Cl^- (1, 6-8)



Molecular AlCl_3 or Al_2Cl_6 appear to be absent from acidic AlCl_3 -MEIC and AlCl_3 -BPC in the range $0.50 < x_{\text{AlCl}_3} < 0.67$, unlike acidic AlCl_3 -alkali chloride melts, since aluminum chloride vapor pressures above the organic salt-based systems are negligible at elevated temperatures.

Concentration cells with aluminum electrodes have been used extensively to obtain potentiometric data in chloroaluminate melts (1, 6-11). However, the use of these cells to obtain thermodynamic data presupposes a knowledge of the transport numbers of the ionic components of the melt. It has been generally assumed in these studies that the external transport number of the melt cation is unity. This assumption has been questioned, especially for chloroaluminate melts with organic cations where the ionic radius of the cation may be comparable to or even larger than that of the prevalent anions, e.g., AlCl_4^- and Al_2Cl_7^- (12). However, no comprehensive study of transport numbers in chloroaluminate melts has appeared in the literature.

Basic Principles

In order to gain insight into ionic transport in chloroaluminate melts with organic cations, the transference experiment depicted in Fig. 1 was conducted. In this experi-

* Electrochemical Society Active Member.

ment current was passed between aluminum electrodes in a three-compartment cell. Before the start of the experiment, the three compartments, separated from one another by porous disks, were filled with AlCl_3 -MEIC melt of the same composition. Then, a known charge, Q , was passed through the cell and the concentration and weight changes in the catholyte and anolyte were determined.

The experimental arrangement is similar to a Hittorf cell, but the experiments permit the calculation of external transport numbers (relative to the porous membranes) as well as internal transport numbers (relative to a chosen reference, e.g., chloride ion). The first type of transport numbers give information about cooperative movements relative to the membranes. However, only the internal transport numbers are needed for the calculation of the EMF of concentration cells, although the more detailed external transport numbers also can be used. The pertinent equations for calculation of transport numbers and specific relationships between the various types of transport numbers are delineated below.

Transport numbers relative to an external reference.—If it is assumed formalistically that the melt is composed of 1-methyl-3-ethylimidazolium cation, R^+ , aluminum ion, Al^{3+} , and chloride ion, Cl^- , then the number of moles of these ions, n_{R} , n_{Al} , and n_{Cl} , respectively, in a sample of melt with weight, w , are given by

$$n_{\text{Al}} = \frac{x_{\text{Al}}w}{x_{\text{Al}}M_{\text{AlCl}_3} + (1 - x_{\text{Al}})M_{\text{RCI}}} \quad [2]$$

$$n_{\text{R}} = \frac{(1 - x_{\text{Al}})w}{x_{\text{Al}}M_{\text{AlCl}_3} + (1 - x_{\text{Al}})M_{\text{RCI}}} \quad [3]$$

$$n_{\text{Cl}} = n_{\text{R}} + 3n_{\text{Al}} = \frac{(2x_{\text{Al}} + 1)w}{x_{\text{Al}}M_{\text{AlCl}_3} + (1 - x_{\text{Al}})M_{\text{RCI}}} \quad [4]$$

where M is the molecular weight of the designated component, and x_{Al} the mole fraction of AlCl_3 . The external transport number for R^+ , t_{R} , can be calculated directly

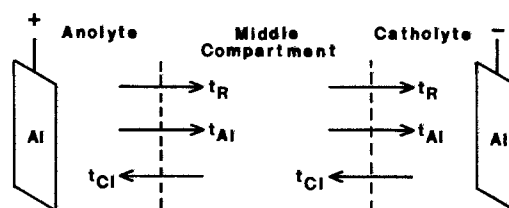


Fig. 1. Schematic diagram of the transference experiment and definition of the formal external transport numbers.

from the expression shown below and an analogous equation written for the anode compartment

$$t_R \cdot \frac{Q}{F} = \frac{(1 - x_{Al}^c)w^c}{x_{Al}^c M_{AlCl_3} + (1 - x_{Al}^c)M_{RCl}} \quad [5]$$

$$- \frac{(1 - x_{Al}^o)w^o}{x_{Al}^o M_{AlCl_3} + (1 - x_{Al}^o)M_{RCl}}$$

The charge passed, Q , is given in coulombs, and F is Faraday's constant. The superscript o denotes the condition before the experiment, and the superscript c indicates the condition in the cathode compartment after passing current.

The moles of Al^{3+} transported into the catholyte, corrected for the loss or gain of Al^{3+} due to the electrode reactions, is given by Eq. [6]

$$(t_{Al} - 1) \cdot \frac{Q}{3F} = \frac{x_{Al}^c w^c}{x_{Al}^c M_{AlCl_3} + (1 - x_{Al}^c)M_{RCl}} \quad [6]$$

$$- \frac{x_{Al}^o w^o}{x_{Al}^o M_{AlCl_3} + (1 - x_{Al}^o)M_{RCl}}$$

An analogous expression can be written for the anode compartment. The external transport number for chloride ion can then be calculated from t_R and t_{Al}

$$t_{Cl} = 1 - t_R - t_{Al} \quad [7]$$

Transport numbers with chloride ion as the reference.—The amount of Cl^- is presumed constant in a compartment when internal transport numbers are calculated with Cl^- as the reference. By using Eq. [4] and considering the cathode compartment, the following condition must be fulfilled in which the number of moles of Cl^- ion in the compartment before and after electrolysis are equal

$$\frac{(2x_{Al}^o + 1)w^o}{x_{Al}^o M_{AlCl_3} + (1 - x_{Al}^o)M_{RCl}} = \frac{(2x_{Al}^c + 1)w^c}{x_{Al}^c M_{AlCl_3} + (1 - x_{Al}^c)M_{RCl}} \quad [8]$$

A similar expression can be written for the anode compartment.

Insertion of Eq. [8] into Eq. [5] so as to eliminate w_o and replacing t_R with t'_R , the internal transport number of R^+ , gives

$$t'_R = \frac{3Fw^c(x_{Al}^o - x_{Al}^c)}{Q[x_{Al}^c M_{AlCl_3} + (1 - x_{Al}^c)M_{RCl}](2x_{Al}^o + 1)} \quad [9a]$$

A similar expression can be written for the anode compartment

$$t'_R = \frac{3Fw^o(x_{Al}^a - x_{Al}^o)}{Q[x_{Al}^o M_{AlCl_3} + (1 - x_{Al}^o)M_{RCl}](2x_{Al}^a + 1)} \quad [9b]$$

The superscript a refers to the condition in the anode compartment following electrolysis. It should be noted that it is not necessary for w^c and w^a to correspond to the total amount of sample in each electrode compartment as used here. As in a Hittorf experiment, these weights must simply encompass the quantity of melt in which concentration changes occur. The definition that $t_{Cl} = 0$ gives the following relationship between internal transport numbers

$$t'_R + t'_{Al} = 1 \quad [10]$$

Relationships between external transport numbers.—In an acidic $AlCl_3$ - RCl ionic liquid, $0.50 < x_{AlCl_3} < 0.67$, the constituent ions have been shown to be R^+ , $AlCl_4^-$, and $Al_2Cl_7^-$ (5). As shown by Øye and King (12), the external transport numbers t_{Al} and t_{Cl} may be substituted by t_{AlCl_4} and $t_{Al_2Cl_7}$, i.e., the external transport numbers for the actual ionic constituents of the melt

$$t_{Al} = -3t_{AlCl_4} - 6t_{Al_2Cl_7} \quad [11]$$

$$t_{Cl} = 4t_{AlCl_4} + 7t_{Al_2Cl_7} \quad [12]$$

and therefore

$$t_R + t_{AlCl_4} + t_{Al_2Cl_7} = 1 \quad [13]$$

Combination of Eq. [11] and [12] and rearrangement gives the anion external transport numbers in terms of t_{Al} and t_{Cl}

$$t_{AlCl_4} = \frac{7t_{Al} + 6t_{Cl}}{3} \quad [14]$$

$$t_{Al_2Cl_7} = \frac{-4t_{Al} - 3t_{Cl}}{3} \quad [15]$$

Relationships between external and internal transport numbers.—The external and internal (relative to chloride ion) transport numbers are related to one another by stoichiometry, since movement of Cl^- is equivalent to movement of R^+ and Al^{3+} in the other direction, i.e., chloride transport is divided between the anions proportional to their equivalent fractions. Hence

$$t'_{Al} = t_{Al} + \frac{3n_{Al}}{3n_{Al} + n_R} t_{Cl} \quad [16]$$

or

$$t'_{Al} = t_{Al} + \frac{3x_{Al}^o}{2x_{Al}^o + 1} (1 - t_{Al} - t_R) \quad [17]$$

similarly

$$t'_R = t_R + \frac{n_R}{3n_{Al} + n_R} t_{Cl} \quad [18]$$

or

$$t'_R = t_R + \frac{1 - x_{Al}^o}{2x_{Al}^o + 1} (1 - t_{Al} - t_R) \quad [19]$$

The mole fraction of the original melt is used since no change in concentration near the membrane is assumed. The consistencies of these equations can be demonstrated by combining Eq. [19] with Eq. [5] and [6]. The result is Eq. [9a].

Cooperative movement of aluminum and chloride ions.—In the present experiments t_{Al} is found to be negative, indicating that aluminum is transported toward the anode and away from the cathode (*vide infra*). Cooperative movement of Cl^- and Al^{3+} can be defined as

$$C = \frac{t_{Cl}}{-1/3t_{Al}} = \frac{3(t_{Al} + t_R - 1)}{t_{Al}} \quad [20]$$

where C refers to the ratio of the number of moles of Cl^- and Al^{3+} transported to the anode or away from the cathode.

Experimental

Apparatus.—The preparation of melt and all subsequent transference experiments were conducted in a dry, oxygen-free nitrogen atmosphere inside a Kewaunee Scientific Engineering Corporation dry box system equipped with a Model 202500 30-cfm inert gas purifier. The quality of the atmosphere inside the dry box was tested by measuring the lifetime of a lighted 25W light bulb with a hole pierced in its glass envelope. The dry box atmosphere was found acceptable when the bulb remained lighted for 12h or more. Electrolysis experiments were conducted using a Hewlett Packard Model 6216A direct current power supply. The charge passed was determined via an AMEL Model 731 digital integrator.

Chemicals.—Anhydrous $AlCl_3$ (Fluka, A.G.) was sublimed under vacuum directly inside the dry box a minimum of three times. The organic salt, 1-methyl-3-ethylimidazolium chloride, was synthesized and purified according to the procedure of Wilkes *et al.* (1). The oxide content of the melt was determined using the procedure described by Stojek *et al.* (13). Melts that were 5 ppm or greater in oxide were discarded.

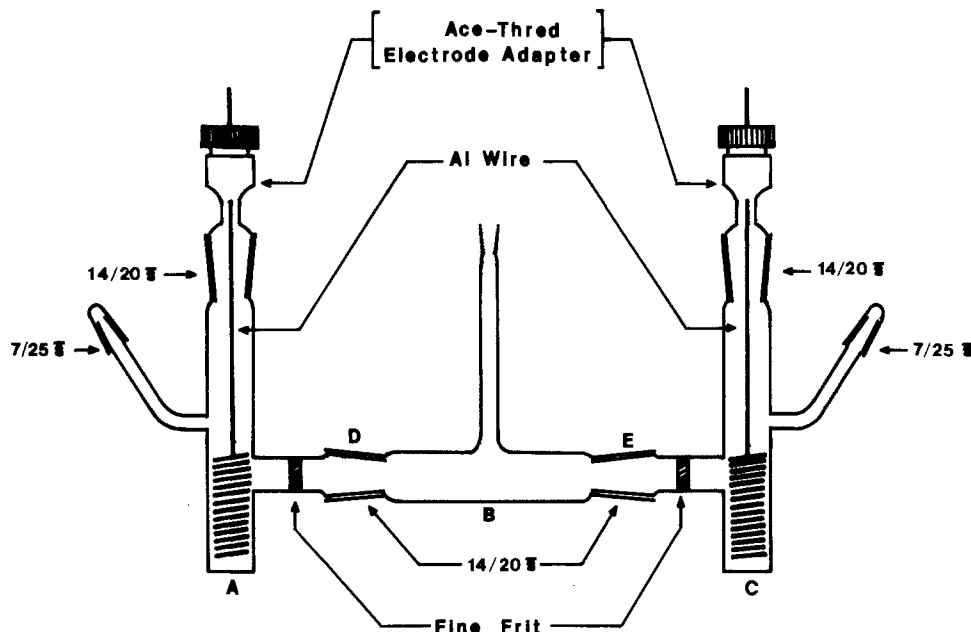


Fig. 2. Transference cell

Cell.—Transport data were obtained using a Hittorf-type cell (Fig. 2). The compartments in this cell were isolated by means of 10 mm diam fine porosity fritted disks. The porous areas of these disks were reduced by about 75% by heating them moderately with a glassblowing torch. The hydrostatic resistances of these disks were checked with melt, and it was determined that corrections for hydraulic flow were unnecessary under the experimental conditions employed. It should be noted in this regard that acidic AlCl_3 -MEIC melts are fairly viscous at room temperature compared to water and to ionic liquids used at elevated temperatures (2) and that only slight differences in the liquid levels in compartments A, B, and C (Fig. 2) arose during an experiment. The porous disks, prepared as above, were highly resistant to diffusional mixing also. A cell with melts of different composition, but with equal liquid levels in A, B, and C, was stored for several days without detectable changes in the composition of the melt in each compartment. The aluminum electrodes used in compartments A and C were fashioned from 80 cm of 1.0 mm diam wire (Alfa Products, m5N purity). Approximately 77 cm of the wire was immersed. The electrodes were pretreated by immersion in an aqueous etching solution that was 5% HF and 15% HNO_3 by volume and dried in an oven before use.

Analysis of melt.—The AlCl_3 -MEIC melt was analyzed using an absorption spectroscopic procedure. Figure 3 shows an absorption spectrum for the 1-methyl-3-ethylimidazolium cation dissolved in distilled water. The absorption maximum, λ_{max} , for the cation is observed at 211.5 nm with a molar absorptivity of $4.21 \times 10^3 \text{ M}^{-1} \text{ cm}^{-1}$. This species obeyed the Lambert-Beer law in very dilute solutions. Melt samples were analyzed by measuring the cation absorbance at λ_{max} for solutions of melt appropriately diluted with distilled water. (Caution: the addition of water to acidic melts results in a violent exothermic reaction!) UV analyses of these samples were conducted in 1.0 cm path length quartz cells using a Perkin-Elmer Hitachi 200 UV-vis spectrophotometer. This instrument is equipped with a digital display and could be read to 0.001 absorbance units. However, the stated photometric accuracy of the instrument was 0.002 absorbance units. The results obtained for triplicate analyses of known melt samples are listed in Table I. These results reflect both the accuracy and precision of this analytical procedure.

Procedure.—Melt was added to compartments A and C until equal levels were attained in both compartments. The cell was disassembled, and the weight of the melt in A and C was determined. The cell was reassembled, and compartment B was filled with melt until its liquid level

matched that in A and C. A current of 3.0 mA (0.12 mA cm^{-2}) was passed between the aluminum electrodes. After the desired period of electrolysis, the cell was again disassembled, excess melt was cleaned from the inside and outside of the male joints D and E, and compartments A and C were reweighed. The weight of melt in each compartment was corrected for the change in weight of the aluminum electrodes in the compartment. Triplicate samples of the original melt and melt in compartments A, B, and C after electrolysis were analyzed. No difference between the composition of melt in the original sample and that in compartment B after electrolysis was ever detected. All experiments were conducted at $28^\circ \pm 2^\circ\text{C}$, and compartments A, B, and C were open to the dry box atmosphere during electrolysis.

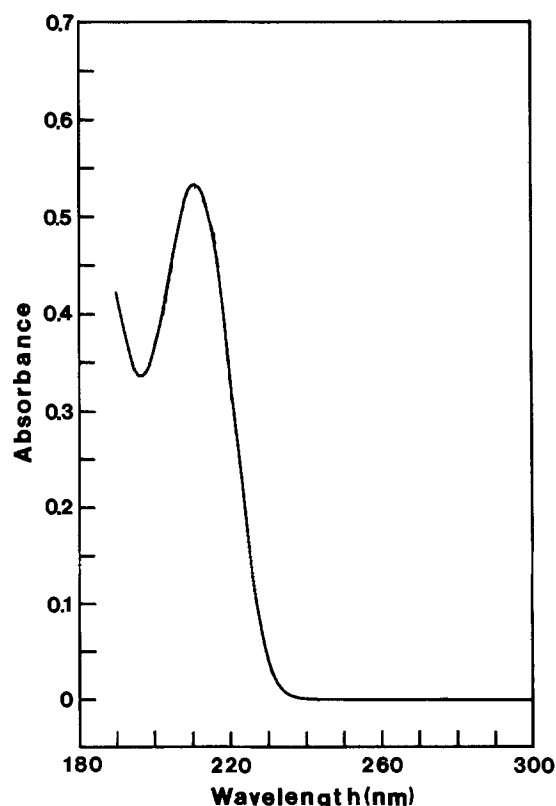
Fig. 3. Absorption spectrum for $2.4 \times 10^{-4} \text{ M}$ 1-methyl-3-ethylimidazolium chloride in distilled water.

Table I. Results for triplicate analysis of AlCl_3 -MEIC melt samples

x_{AlCl_3}		Relative error (%)
Calculated	Measured	
0.448	0.446 ± 0.002*	-0.45
0.554	0.555 ± 0.001*	+0.18
0.622	0.621 ± 0.001*	-0.16

* Average deviation from the mean.

Results and Discussion

Electrolysis experiments conducted in acidic melt indicated that aluminum could be efficiently stripped from the anode and deposited as shiny, moderately adherent dendrites at the cathode. No discoloration of the acidic melt was noted, and no new organic species were detected in the melt by NMR spectroscopy after electrolysis. The aluminum anode weight loss was about 3-5 weight percent (w/o) larger than predicted theoretically from the charge passed. Similar effects were noted by Robinson and Osteryoung (14) in acidic AlCl_3 -BPC and were attributed to corrosion of the electrode by impurities in the melt. Fortunately, corrosion of the anode has minimal effect on the transport numbers reported herein, since the analytical procedure used for determining melt composition is not based on analysis of the aluminum content of the melt. Therefore, the effects of this corrosion were neglected. Cathode efficiencies could not be calculated accurately because it was not possible to remove this electrode from the cell and clean it without disturbing the aluminum dendrites. The cathode efficiency was assumed to be 100%. Transference experiments were also attempted in basic melt. However, the melt in the cathode compartment became discolored, suggesting that the electrode reaction occurring at aluminum did not correspond to the expected deposition of aluminum metal. The transference experiments reported herein were restricted to acidic melts.

Experimental transference data are listed in Table II. The lower case letter following each run number indicates whether the data were taken from the anode compartment, a, or cathode compartment, c, of the cell. Identical run numbers denote experiments in which the data were taken from both the anode and cathode compartments during a single run. Runs 2a through 6c were made during the initial phase of this study and were single compartment runs. The precision with which the initial and final values of x_{Al} could be determined are based on the relative average deviation from the mean for triplicate samples.

Table II. Experimental transference data for acidic AlCl_3 -MEIC melt

Run no.	x_{Al}	$(X_{\text{Al}})^*$	w° (g)	w (g)	Charge (C)
2a	0.507 ± 0.002	0.570 ± 0.002	8.427	8.341	500
3a	0.515 ± 0.003	0.559 ± 0.002	8.706	8.593	436
4a	0.513 ± 0.001	0.570 ± 0.001	8.550	8.401	488
5a	0.537 ± 0.000	0.595 ± 0.002	8.464	8.338	500
6c	0.670 ± 0.001	0.620 ± 0.002	8.539	8.420	373
7a	0.577 ± 0.001	0.618 ± 0.001	8.128	8.112	310
7c	0.577 ± 0.001	0.543 ± 0.001	8.860	8.882	310
8a	0.555 ± 0.001	0.587 ± 0.001	9.123	9.039	283
8c	0.555 ± 0.001	0.521 ± 0.003	9.211	9.260	283
9a	0.615 ± 0.001	0.652 ± 0.000	9.431	9.426	337
9c	0.615 ± 0.001	0.577 ± 0.001	9.013	8.988	337
10a	0.621 ± 0.001	0.659 ± 0.001	8.589	8.634	292
10c	0.621 ± 0.001	0.583 ± 0.002	8.118	8.114	292
11a	0.591 ± 0.002	0.627 ± 0.001	9.073	9.076	272
11c	0.591 ± 0.002	0.560 ± 0.001	8.616	8.604	272
14a	0.605 ± 0.001	0.637 ± 0.002	9.157	9.170	291
14c	0.605 ± 0.001	0.567 ± 0.003	8.571	8.573	291

* Mole fraction of AlCl_3 in the anode or cathode compartment after electrolysis.

Calculated transport numbers as well as calculated values of the cooperative movement ratio, C , are recorded in Table III. Both t_{Al} and C vary with melt composition. However, significant variation of t_{r} and t'_{r} is more equivocal. Least squares analysis of the data for t_{r} and t'_{r} in Table III vs. x_{Al} yielded slopes of -0.30 ± 0.13 and 0.11 ± 0.22 , respectively, at the 95% confidence level. Thus, t_{r} appears to be statistically independent of melt composition with an average value of 1.01 ± 0.04 at the 95% confidence level. Values of t_{r} may decrease slightly as x_{Al} increases, but this result is questionable. The mean value of t_{r} is 0.71 ± 0.02 at the 95% confidence level. The standard deviations for t_{r} and t'_{r} are about 7%. This uncertainty is to be expected since the major source of error contributing to the precision with which these transport numbers may be calculated is the precision with which the melt could be analyzed. An uncertainty of ± 0.002 in x_{Al} translates to an uncertainty of ± 0.04 in the calculated value of the transport number. The mean value of t'_{r} calculated from anode data was 1.01 ± 0.06 at the 95% confidence level, while the mean value of t'_{r} estimated from cathode measurements was found to be 1.01 ± 0.07 . Thus, the experimental results appear to be independent of the electrode from which they were derived.

The negative values for t_{Al} (Table III) indicate that aluminum is transported toward the anode and away from the cathode during electrolysis. This implies that aluminum migrates in anionic complexes and that transport of aluminum by a naked aluminum ion, Al^{3+} , or cationic complex is unlikely. The result that t'_{r} is approximately 1.00 (strictly 1.01) can be used to provide straightforward structural interpretation in terms of ionic movements. For in this case, Eq. [17] reduces to

$$t_{\text{Al}} = \frac{-3x_{\text{Al}}}{2x_{\text{Al}} + 1} t_{\text{Cl}} \quad [21]$$

and the cooperative movement ratio is

$$C = \frac{2x_{\text{Al}} + 1}{x_{\text{Al}}} \quad [22]$$

Thus, if $x_{\text{Al}} = 0.50$, the melt stoichiometry corresponds to RAICl_4 and C is 4. Likewise, if $x_{\text{Al}} = 0.67$, the melt stoichiometry can be written as RAL_2Cl_7 , and C would have a value of 3.5. Thus, anionic transport corresponds to melt stoichiometry.

Numerical models for transport numbers.—The results obtained for the various transport numbers can be translated into the numerical models shown below by using Eq. [7], [17], and [19] as well as Eq. [13] to [15], if t_{r} and t'_{r} are presumed to be constant.

Table III. Calculated transport numbers in acidic AlCl_3 -MEIC melt

Run no.	X_{Al}	t_{r} (Eq. [5])	t_{Al} (Eq. [6])	C (Eq. [20])	t'_{r} (Eq. [9])
2a	0.507	0.754	-1.113	3.66	1.086
3a	0.515	0.660	-0.615	4.66	0.888
4a	0.515	0.729	-0.743	4.09	0.971
5a	0.537	0.724	-0.841	3.98	0.973
8a	0.555	0.772	-0.901	3.76	1.010
8c	0.555	0.789	-1.227	3.52	1.093
7a	0.577	0.733	-1.305	3.61	1.042
7c	0.577	0.668	-1.049	3.95	0.939
11a	0.591	0.802	-1.670	3.36	1.152
11c	0.591	0.641	-1.209	3.89	0.935
14a	0.605	0.666	-1.285	3.78	0.956
14c	0.605	0.732	-1.384	3.58	1.127
9a	0.616	0.682	-1.218	3.78	0.947
9c	0.616	0.676	-1.390	3.65	0.971
10a	0.621	0.717	-1.699	3.50	1.052
10c	0.621	0.703	-1.350	3.66	0.982
6c	0.670	0.688	-1.963	3.48	1.009

Mean value	0.714	1.008
Standard deviation	0.047	0.074

Internal transport numbers for R^+ , Al^{3+} , and Cl^-

$$t'_R = 1.00, t'_{Al} = 0, t'_{Cl} = 0 \quad [I]$$

External transport numbers for R^+ , Al^{3+} , and Cl^-

$$t_R = 0.71, t_{Al} = 0.29 \frac{-3x_{Al}^0}{1 - x_{Al}^0}, t_{Cl} = 0.29 \frac{1 + 2x_{Al}^0}{1 - x_{Al}^0} \quad [II]$$

External transport numbers with respect to the actual component ions for $0.50 \leq x_{Al}^0 \leq 0.67$

$$t_R = 0.71, t_{AlCl_4} = 0.29 \frac{2 - 3x_{Al}^0}{1 - x_{Al}^0}, t_{Al_2Cl_7} = 0.29 \frac{2x_{Al}^0 - 1}{1 - x_{Al}^0} \quad [IIIa]$$

If it is assumed that the reaction shown in Eq. [1] has a small equilibrium constant and that significant formation of Al_2Cl_6 does not occur in acidic melt in the range of x_{Al}^0 examined, then the anion fractions of $AlCl_4^-$ and $Al_2Cl_7^-$ are

$$x_{AlCl_4} = \frac{2 - 3x_{Al}^0}{1 - x_{Al}^0} \quad [23]$$

and

$$x_{Al_2Cl_7} = \frac{2x_{Al}^0 - 1}{1 - x_{Al}^0} \quad [24]$$

Hence

$$t_R = 0.71, t_{AlCl_4} = 0.29x_{AlCl_4}, t_{Al_2Cl_7} = 0.29x_{Al_2Cl_7} \quad [IIIb]$$

Applications to $AlCl_3$ - RCl concentration cells.—Oye and King (12) derived the following equation for the EMF of $AlCl_3$ - RCl concentration cells with aluminum electrodes and chlorine electrodes, respectively

$$Al: \quad -FdE = \frac{(1 - t_{Al})(1 - x_{Al}) + 3t_R x_{Al}}{3(1 - x_{Al})} d\mu_{AlCl_3} \quad [25]$$

$$Cl_2: \quad -FdE = \frac{-t_{Al}(1 - x_{Al}) + 3t_R x_{Al}}{3(1 - x_{Al})} d\mu_{AlCl_3} \quad [26]$$

Since the EMF calculated from these equations must be independent of the reference frame used for the transport numbers, these equations must be the same when using internal transport numbers. This can be seen by inserting Eq. [17] and [19] into Eq. [25] and [26]. The expressions obtained are

$$Al: \quad -FdE = \frac{(1 - t'_{Al})(1 - x_{Al}) + 3t'_R x_{Al}}{3(1 - x_{Al})} d\mu_{AlCl_3} \quad [27]$$

$$Cl_2: \quad -FdE = \frac{-t'_{Al}(1 - x_{Al}) + 3t'_R x_{Al}}{3(1 - x_{Al})} d\mu_{AlCl_3} \quad [28]$$

These equations can be reduced further by using the relationship $t'_R = 1 - t'_{Al}$

$$Al: \quad -FdE = \frac{t'_R(1 + 2x_{Al})}{3(1 - x_{Al})} d\mu_{AlCl_3} \quad [29]$$

$$Cl_2: \quad -FdE = \frac{t'_R(2x_{Al} + 1) + x_{Al} - 1}{3(1 - x_{Al})} d\mu_{AlCl_3} \quad [30]$$

The result that t'_R is approximately 1.00 and is independent of composition is of great significance from a thermodynamic viewpoint. Inserting this result into Eq. [29] and [30] gives the EMF of a concentration cell with aluminum electrodes, which is simply

$$Al: \quad -FdE = \frac{1 + 2x_{Al}}{3(1 - x_{Al})} d\mu_{AlCl_3} \quad [31]$$

while that for a concentration cell with chlorine electrodes is

$$Cl_2: \quad -FdE = \frac{x_{Al}}{1 - x_{Al}} d\mu_{AlCl_3} \quad [32]$$

As shown previously (12), Eq. [31] may also be given the alternate formulation

$$Al: \quad -FdE = \frac{1}{3} d\mu_{MAICl_4} - \frac{4}{3} d\mu_{MCl} \quad [33]$$

while Eq. [32] can be written as

$$Cl_2: \quad -FdE = 1/2d\mu_{Cl_2} - d\mu_{MCl} \quad [34]$$

Although the present study was limited to the acidic compositions of the aluminum chloride-1-methyl-3-ethylimidazolium chloride melt, some of the results obtained appear to be applicable to chloroaluminate melts in general. This is because the internal movement of Al^{3+} and Cl^- , which are bound in the complexes $AlCl_4^-$ and $Al_2Cl_7^-$, is probably insensitive to the nature of the cation. While t_R may be different for each system, the finding that t'_R is 1.00 may be a general result for chloroaluminate melts with alkali metal cations as well as organic cations. Actually, one would expect t'_R to be close to unity in the $AlCl_3$ - $NaCl$ system, since t_R for this melt is expected to be larger than found in the present system. Therefore, contributions due to anion transport would be smaller. The general use of Eq. [31]-[34] is therefore justified in the range $0.50 < x_{Al} < 0.67$. The applicability of these equations for $x_{Al} < 0.50$ is presently under investigation.

External transport numbers were obtained for the anions in the present work. The $AlCl_4^-$ and $Al_2Cl_7^-$ mobilities (t/x_i) were found to be equal, cf., [IIIb]. However, this does not necessarily indicate that the $AlCl_4^-$ and $Al_2Cl_7^-$ ions physically move in the melt with the same mobility. For example, a bridge exchange mechanism in which $AlCl_3$ is transferred between $AlCl_4^-$ and $Al_2Cl_7^-$ units may also account for the results that were observed.

Acknowledgments

CLH wishes to acknowledge the assistance of Mr. Towner B. Scheffler during the experimental portion of this study. This work was supported by the National Science Foundation through Grant No. CHE-8025235.

Manuscript submitted Oct. 18, 1983; revised manuscript received Dec. 13, 1983.

The University of Mississippi assisted in meeting the publication costs of this article.

REFERENCES

1. J. S. Wilkes, J. A. Levisky, R. A. Wilson, and C. L. Hussey, *Inorg. Chem.*, **21**, 1263 (1982).
2. A. A. Fannin, Jr., D. A. Floreani, L. A. King, J. S. Landers, B. J. Piersma, D. J. Stech, R. L. Vaughan, J. S. Wilkes, and J. L. Williams, *J. Phys. Chem.*, to be published.
3. J. L. Gray and G. E. Maciel, *J. Am. Chem. Soc.*, **103**, 7147 (1981).
4. J. S. Wilkes, G. F. Reynolds, and J. S. Frye, *Inorg. Chem.*, **22**, 3870 (1983).
5. R. J. Gale, B. Gilbert, and R. A. Osteryoung, *ibid.*, **17**, 2728 (1978).
6. R. J. Gale and R. A. Osteryoung, *ibid.*, **18**, 1603 (1979).
7. J. P. Schoebrechts and B. P. Gilbert, *This Journal*, **128**, 2679 (1981).
8. Z. J. Karpinski and R. A. Osteryoung, Submitted to *Inorg. Chem.*
9. G. Torsi and G. Mamantov, *ibid.*, **10**, 1900 (1971).
10. L. G. Boxall, H. L. Jones, and R. A. Osteryoung, *This Journal*, **120**, 223 (1973).
11. B. Gilbert, D. L. Brotherton, and G. Mamantov, *ibid.*, **121**, 773 (1974).
12. H. A. Oye and L. A. King, *Inorg. Nucl. Chem. Lett.*, **16**, 547 (1980).
13. Z. Stojek, H. Linga, and R. A. Osteryoung, *J. Electroanal. Chem. Interfacial Electrochem.*, **119**, 365 (1981).
14. J. Robinson and R. A. Osteryoung, *This Journal*, **127**, 122 (1980).

Electron Transfer Kinetics of Redox Centers Anchored to Metal Surfaces: Weak vs. Strong Overlap Reaction Pathways

S. W. Barr, K. L. Guyer, T. T.-T. Li, H. Y. Liu, and M. J. Weaver*

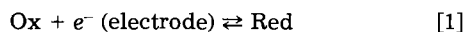
Department of Chemistry, Purdue University, West Lafayette, Indiana 47907

ABSTRACT

Unimolecular rate constants k_{et} are presented for the one-electron electroreduction of various $\text{Co}^{\text{III}}(\text{NH}_3)_5\text{X}$ complexes bound to mercury, platinum, and gold surfaces via either small inorganic or extended organic ligands X. These "surface intramolecular" rate parameters are compared with estimates of k_{et} for outer-sphere pathways obtained from homogeneous rate data in order to ascertain the consequences of reactant-surface binding upon the electron transfer energetics. Only small or moderate decreases in the elementary reorganization barrier ΔG^*_{et} occur upon surface attachment, suggesting the occurrence of weak overlap pathways. Aside from the dependence of k_{et} upon the bridging ligand X at a given electrode potential due to differences in thermodynamic driving force, the observed variations in k_{et} appear to be due in part to variations in the electronic transmission coefficient κ_{el} . Measurements of electrochemical frequency factors for reactants containing a series of thiophenecarboxylate bridges indicate that the substantial decreases in k_{et} observed upon interruption of ligand conjugation arise predominantly from decreases in κ_{el} .

Although electrode processes commonly occur via reaction pathways involving specifically adsorbed intermediates, our understanding of the manner and extent to which the reaction-electrode interactions influence the electron transfer energetics, *i. e.*, determine the degree of electrocatalysis, is still at a rudimentary level. A difficulty that has hampered the elucidation of such "surface environmental" effects is that the reactions often occur via complex and/or uncertain mechanisms. One approach is to select for detailed study electrode reactions where the reactant, or reaction intermediate, is sufficiently strongly adsorbed to enable unimolecular rate constants (s^{-1}) for the heterogeneous electron transfer step to be evaluated in addition to the usual rate constants ($\text{cm}^2 \text{s}^{-1}$) for the overall reaction (1-3). We have been interested in examining such systems that also are mechanistically simple, enabling detailed molecular-level interpretation of the rate data to be undertaken.

An especially tractable class of "model reactions" are one-electron transition metal redox couples



where the solution species Ox and Red are substitutionally inert and bind strongly to the surface via a suitable coordinated ligand (1-3). Such electrode reaction pathways can be labeled "inner sphere" by analogy with homogeneous electron transfer processes between a pair of metal ions bound via a common ligand. Providing that the electron transfer step is rate determining, the overall ("apparent") rate constant, k_{app}^{is} ($\text{cm}^2 \text{s}^{-1}$), for reaction [1] can be expressed simply as (2-6)

$$k_{app}^{is} = K_p^{is} k_{et}^{is} \quad [2]$$

where k_p^{is} is the stability constant for forming the adsorbed ("precursor") state from the bulk reactant, and k_{et}^{is} (s^{-1}) is the rate constant for the elementary electron transfer step involving the surface-attached intermediate. This "pre-equilibrium" treatment provides a convenient separation between electrocatalytic influences upon k_{app}^{is} arising from variations in the cross-sectional reactant concentration at the electrode surface contained in K_p^{is} , and those due to variations in the electron transfer energetics themselves, embodied in k_{et}^{is} .

Fundamental information on the surface environmental factors influencing k_{app}^{is} can therefore be obtained by separately examining the sensitivity of k_{et}^{is} as well as K_p^{is} to variations in the electrode composition and the structure of the bridging ligand (3-5). We have demonstrated that a number of cobalt(III) and chromium(III) complexes are sufficiently strongly adsorbed at several metal surfaces, especially mercury, silver, platinum, gold, and copper, to enable values of k_{et} to be obtained for the one-electron re-

duction of the surface-bound redox center (2, 3). These complexes contain a simple inorganic (Cl^- , Br^- , NCS^- , N_3^-) or an organic ligand (*e. g.*, pyrazine, 4, 4'-bipyridine, thiophenecarboxylates) featuring a halide, nitrogen, or sulfur lone pair as a surface "lead-in" group. These processes are closely analogous to the intramolecular reduction of Co(III) by homogeneous reducing centers such as Ru(II) and Fe(II) that have been extensively investigated in the last few years (7). Therefore, they can be perceived as "surface intramolecular" reactions.

In this paper, we shall examine some of our recent results, chiefly for reductions of pentaamminecobalt(III), in order to illustrate the virtues of such strategies for unraveling the structural factors influencing the kinetics of electrocatalytic reactions. More complete descriptions of these results along with the experimental details are available elsewhere (2, 3).

Rate Formulations

Rate constants for surface-bound as well as other "intramolecular" free energy for the elementary electron transfer step ΔG^*_{et} by (6, 8)

$$k_{et} = \kappa_{el} \Gamma_n \nu_n \exp(\Delta G^*_{et}/RT) \quad [3]$$

The nuclear frequency factor ν_n (s^{-1}) describes the effective frequency with which the configuration of the various nuclear coordinates appropriate for electron transfer is approached from the precursor state. The electronic transmission coefficient κ_{el} denotes the probability that electron transfer will occur once the transition state is reached. The nuclear tunneling factor Γ_n is a quantum mechanical correction which accounts for the contribution to the measured rate from molecules which react without entirely surmounting the classical free energy barrier (6, 8). Although ν_n is a composite term arising from a weighted mean of manifold frequencies associated with reactant vibration and solvent reorientation modes, it will be close to $1 \times 10^{13} \text{ s}^{-1}$ for reactions, such as those considered here, where inner-shell reorganization provides an important component of ΔG^*_{et} (6). The nuclear tunneling factor Γ_n is usually close to unity (*ca.* 1-4) at room temperature. However, κ_{el} may well be orders of magnitude below unity if the electronic coupling between the donor and acceptor orbitals is weak (*vide infra*).

The reorganization energy ΔG^*_{et} at a given electrode potential E can be separated into "intrinsic" and "thermodynamic" contributions (4)

$$\Delta G^*_{et} = \Delta G^*_{int} + \alpha_{et} [RT(\ln K_p - \ln K_s) + \mathbf{F}(E - E^\circ)] \quad (4)$$

Here, α_{et} is the transfer coefficient for the elementary step (≈ 0.5), K_s is the equilibrium constant for forming the successor state (*i. e.*, the ground state immediately follow-

* Electrochemical Society Active Member.

ing electron transfer) from the bulk product, and E° is the standard potential for the redox couple. The "intrinsic barrier" ΔG_{int}^* is the value of ΔG_{et}^* that remains when the free energies of the precursor and successor states are equal (4). It is of particular interest since it is the free energy barrier usually calculated from contemporary electron transfer theories. The first and second sets of terms in parentheses in Eq. [4] constitute "surface" and "bulk" components, respectively, of the thermodynamic driving force for the elementary electron transfer step.

Consequences of Surface Attachment Upon Electron Transfer Energetics

A central question in the examination of electrocatalytic reactions is to what extent the elementary barrier to electron transfer is modified by binding the reactant to the electrode surface. In view of Eq. [3], the rate constant k_{et} for passage over this barrier may well be increased by surface attachment as a result of an increase in κ_{el} as well as from a decrease in ΔG_{et}^* . Such variations in κ_{el} are characteristic of "weak overlap" reactions where the metal redox center is almost entirely insulated from the electron donor (or acceptor) site provided by the electrode surface. On the other hand, variations in ΔG_{et}^* , more specifically in ΔG_{int}^* , are characteristic of "strong overlap" reactions. Here, $\kappa_{\text{el}} \approx 1$ and the interaction with the electron donor (or acceptor) site is sufficient to significantly distort the reactant and product potential energy surfaces in the intersection region so that the net free energy barrier is "rounded off" (9), thereby decreasing ΔG_{int}^* and increasing k_{et} .

At first sight, the question of the influence of surface attachment upon k_{et} may seem hypothetical since values of k_{et} cannot usually be measured directly for unattached reactants. Nevertheless, the pre-equilibrium rate formalism embodied in Eq. [2] and [3] also applies to outer-sphere pathways (6); i. e., those where the reactant in the transition state is separated from the electrode surface by at least one layer of solvent molecules (10). For such processes, the precursor stability constant K_p^{os} can be estimated from (6)

$$K_p^{\text{os}} = \delta r \exp(-w_p/RT) \quad [5]$$

where w_p is the average work involved in transporting the reactant from the bulk solution to the reaction site (precursor state), and δr is the effective thickness of the reaction zone. The latter equals the effective distances from the plane of closest approach over which electron tunneling can occur with sufficient probability to contribute significantly to the observed rate. Although the typical values of δr are uncertain, it is probably within a factor of two of ca. 1×10^{-8} cm for structurally simple reactants (6). The average work term w_p can simply be estimated from $w_p = ZF\phi_r$, where Z is the reactant charge number and ϕ_r is the average potential at the reaction site. An essentially equivalent formalism to this "encounter pre-equilibrium" model has been employed recently for outer-sphere redox reactions in homogeneous solution (8). Besides their practical value, such treatments are fundamentally more correct than the gas phase collisional model which commonly has been employed for describing outer-sphere reactions (6).

Admittedly, electrode reactions usually follow rate dominating inner-, rather than outer-, sphere pathways for reactants featuring surface attachment sites. Consequently, apparent rate constants and hence, values of k_{et} for outer-sphere pathways, $k_{\text{et}}^{\text{os}}$, will be unobtainable, at least within the same surface environment for which values of k_{et} for inner-sphere pathways, $k_{\text{et}}^{\text{is}}$, are determined. Nevertheless, the desired estimates of $k_{\text{et}}^{\text{os}}$ can be obtained by several routes as follows:

Method I.—Suitable chemical modification of the electrode surface, such as the monolayer adsorption of iodide or an underpotential deposited (upd) metal, can eliminate the competing inner-sphere route, enabling $k_{\text{et}}^{\text{os}}$ to be obtained from the measured value of $k_{\text{app}}^{\text{os}}$, provided that

K_p^{os} can be estimated from double layer structural data (3a, 11).

Method II.—At least relative values of $k_{\text{et}}^{\text{os}}$ at a given electrode potential E for a series of structurally related reactants may be obtained directly from the corresponding second-order rate constants, k_{h} , for their homogeneous reduction (or oxidation) with a suitable reagent (e. g., $\text{Ru}(\text{NH}_3)_6^{2+}$) that constrains the reaction to occur by an outer-sphere pathway (3a). Thus, providing K_p^{os} is approximately the same for each reactant

$$(k_{\text{et},1}^{\text{os}}/k_{\text{et},2}^{\text{os}})_E = (k_{\text{h},1}/k_{\text{h},2})_R \quad [6]$$

where the subscripts 1 and 2 refer to a pair of reactants, and R refers to a fixed homogeneous coreactant. This relationship follows from the "weak overlap" model of Marcus and others (12), and has been shown to apply to a number of reactions involving transition metal complexes (11, 13, 14). Additionally, if one or more of the electrochemical rate constants is known to refer to an outer-sphere pathway, Eq. [6] can be utilized to obtain estimates of $k_{\text{et}}^{\text{os}}$ for the remaining members of the series.

Method III.—For reactants where the surface attachment site is relatively remote from the redox center, such as for extended organic bridges, $k_{\text{et}}^{\text{os}}$ may be identified approximately with that obtained for a related reactant containing a similar ligand that lacks the surface binding group (3c).

Methods II and III will be utilized here. Various illustrative kinetic data for the one-electron reduction of 15 $\text{Co}^{\text{III}}(\text{NH}_3)_5\text{X}$ complexes (RoX) are gathered in Tables IA and IB. With the exception of OH_2 , NH_3 , F^- , and acetate (OAc^-), all the ligands X feature a lone pair on a nitrogen, sulfur, or halide atom, which induces sufficiently strong binding at suitable metal surfaces to enable the extent of reactant adsorption, and, hence, $k_{\text{et}}^{\text{is}}$ to be measured. The values of $k_{\text{et}}^{\text{is}}$ given in Table I were obtained either from the corresponding apparent rate constants $k_{\text{app}}^{\text{is}}$ combined with K_p^{is} (Eq. [2]) or directly from the transient currents for reduction of the initially adsorbed species. Details are given elsewhere (2, 3). The precursor stability constant K_p^{is} was determined from $K_p^{\text{is}} = \Gamma_p/C_b$ (cm), where Γ_p is the surface concentration (mol cm^{-2}) in the precursor state at a given electrode potential, and C_b (mol cm^{-3}) is the corresponding bulk reactant concentration. Mercury-, platinum-, and gold-aqueous interfaces were selected for detailed study of these reactions. The polarizable potential range at platinum and gold extends to sufficiently positive values to enable kinetic data to be obtained even for the most reactive complexes. The mercury-aqueous interface provides an especially suitable surface with which to obtain outer-, as well as inner-, sphere rate data in view of its reproducibility and well-defined structure. The values of Γ_p were obtained primarily using rapid linear sweep voltammetry and, at mercury, by additionally using chronocoulometry (2, 3). The rate constants in Table I all refer to a common electrode potential, 0 mV vs. SCE. This choice, although somewhat arbitrary, was made to minimize the extent of data extrapolation that was involved. The relative values of k_{et} are approximately independent of the potential chosen.

Outer-sphere values of k_{et} , $k_{\text{et}}^{\text{os,Hg}}$, are listed in parentheses in Table I for the four $\text{Co}^{\text{III}}(\text{NH}_3)_5\text{X}$ reductions, $\text{X} = \text{OH}_2$, NH_3 , F^- , and OAc^- , expected to refer to outer-sphere electrochemical pathways at mercury electrodes. These were obtained from the apparent rate constants at mercury in NaClO_4 and/or KPF_6 electrolytes by using Eq. [3] with $\delta r = 1 \times 10^{-8}$ cm, w_p being estimated from the diffuse layer potentials, ϕ_r , as described in Ref. (15) and (16).

Values of $k_{\text{et}}^{\text{os}}$ are also given for most other reactions in Table I. These values, labeled $k_{\text{et}}^{\text{os,Ru}}$, $k_{\text{et}}^{\text{os,Cr}}$, and $k_{\text{et}}^{\text{os,Fe}}$, refer to the homogeneous reduction of a given $\text{Co}^{\text{III}}(\text{NH}_3)_5\text{X}$ complex by $\text{Ru}(\text{NH}_3)_6^{2+}$, $\text{Cr}(\text{bpy})_3^{2+}$ ($\text{bpy} = 2, 2'$ -bipyridine), and $\text{Fe}(\text{CN})_6^{4-}$, respectively. They were obtained from the corresponding second-order rate constants for reduction of each complex relative to that for $\text{Co}(\text{NH}_3)_5\text{OH}_2^{3+}$ reduction (Method II). The values of $k_{\text{et}}^{\text{os}}$ were derived by

Table IA. Unimolecular rate constants (s^{-1}) for reduction of $\text{Co}(\text{NH}_3)_5\text{X}$ complexes containing inorganic bridging ligands X at 0 mV vs. SCE in 0.1M NaClO_4

Reactant ^a	Electrochemical				Homogeneous			
	$k_{\text{app}}^{\text{Hg}^b}$ cm s ⁻¹	$k_{\text{et}}^{\text{Hg}^c}$	$k_{\text{et}}^{\text{is,Au}^d}$	$k_{\text{et}}^{\text{is,Pt}^e}$	$k_{\text{et}}^{\text{os,Ru}^f}$	$k_{\text{et}}^{\text{os,Cr}^g}$	$k_{\text{et}}^{\text{os,Fe}^h}$	$k_{\text{et}}^{\text{th}^i}$
RoOH_3^{3+}	5×10^{-4}	(2×10^3)			$[2 \times 10^3]$	$[2 \times 10^2]$	$[2 \times 10^2]$	$[2 \times 10^3]$
RoNH_3^{3+}	1.5×10^{-6}	(10)			6			~ 10
RoF^{2+}	2×10^{-6}	(1×10^2)			200			~ 100
RoAc^{2+}	2×10^{-6}	(80)			10	50	4	~ 50
RoNCS_-^{2+}	3×10^{-3}	25	30	1.5	5×10^2	4×10^2	50	~ 30
$\text{RoN}_3_-^{2+}$	3×10^{-4}	20			1×10^3	1.5×10^3	25	~ 30
		(~ 20)						
RoCl_-^{2+}	>0.1		6×10^3	3×10^3	2×10^3	3×10^4	3×10^2	$\sim 5 \times 10^2$
RoBr_-^{2+}	>0.1		8×10^3	1.5×10^3	1×10^3	2×10^3		$\sim 1 \times 10^3$

^a Ro = $\text{Co}^{\text{III}}(\text{NH}_3)_5$, OAc = acetate.

^b Apparent (measured) rate constant for overall reaction at mercury-aqueous interface measured using normal pulse or dc polarography.

^c Unimolecular rate constant at mercury-aqueous interface. Values without parentheses, $k_{\text{et}}^{\text{is}}$, refer to inner-sphere (ligand-bridged) pathway, measured either directly or indirectly from $k_{\text{app}}^{\text{is}}$ using Eq. [2]. Values within parentheses, $k_{\text{et}}^{\text{os}}$, refer to outer-sphere pathway at mercury, determined from $k_{\text{app}}^{\text{os}}$ using $k_{\text{et}}^{\text{os}} = k_{\text{app}}^{\text{os}}/K_p^{\text{os}}$, with K_p^{os} determined from Eq. [5] (see text).

^d Value of $k_{\text{et}}^{\text{is}}$ determined at gold-aqueous interface.

^e Value of $k_{\text{et}}^{\text{is}}$ determined at platinum-aqueous interface.

^f Value of $k_{\text{et}}^{\text{os}}$ for outer-sphere pathway, $k_{\text{et}}^{\text{os}}$, obtained from the value of $k_{\text{os}}^{\text{et}}$ ($2 \times 10^3 \text{ s}^{-1}$) obtained for $\text{Co}(\text{NH}_3)_5\text{OH}_2^{3+}$ reduction at mercury electrodes combined with relative rate constants for homogeneous reduction of $\text{Co}(\text{NH}_3)_5\text{X}$ and $\text{Co}(\text{NH}_3)_5\text{OH}_2^{3+}$ by $\text{Ru}(\text{NH}_3)_6^{2+}$ (Eq. [6]).

^g As for footnote f, but using $\text{Cr}(2,2'\text{-bipyridine})_3^{2+}$ as outer-sphere reductant.

^h As for footnote g, but using $\text{Fe}(\text{CN})_6^{4-}$ as outer-sphere reductant.

ⁱ Value of $k_{\text{et}}^{\text{th}}$ determined from $k_{\text{et}}^{\text{os}}$ for $\text{Co}(\text{NH}_3)_5\text{OH}_2^{3+}$ ($2 \times 10^3 \text{ s}^{-1}$) by correcting for changes in thermodynamic driving force ($E - E^\circ$) using Eq. [7], with K_{II} taken as 0.1 (see text).

All electrochemical rate data from Ref. (3). Homogeneous rate data for $\text{Ru}(\text{NH}_3)_6^{2+}$ reductions: X = OH_2 , NH_3 , Cl^- , and Br^- from Ref. (24); X = F^- from Ref. (25); X = NCS^- , N_3^- from Ref. (26); X = OAc and thiophene carboxylates from Ref. (3). Rate data for $\text{Cr}(2,2'\text{-bipyridine})_3^{2+}$ reductions from Ref. (27). Rate data for $\text{Fe}(\text{CN})_6^{4-}$ reductions from Ref. (28-30). Values of K_{III} for $\text{Co}^{\text{III}}(\text{NH}_3)_5\text{X}$ formation are from Ref. (31) except for $\text{Co}(\text{NH}_3)_5\text{OAc}^{2+}$, which was estimated from its equation rate relative to other $\text{Co}(\text{NH}_3)_5\text{X}$ complexes (3).

Table IB. Unimolecular rate constants (s^{-1}) for reduction of $\text{Co}(\text{NH}_3)_5\text{X}$ complexes containing thiophenecarboxylate bridging ligands X at 0 mV vs. SCE in 0.1M NaClO_4

Reactant ^a	Electrochemical			Homogeneous
	$k_{\text{app}}^{\text{Hg}^b}$ cm s ⁻¹	$k_{\text{et}}^{\text{Hg}^c}$	$k_{\text{et}}^{\text{is,Au}^d}$	$k_{\text{et}}^{\text{os,Ru}^f}$
RoOH_3^{3+}	5×10^{-4}	(2×10^3)		$[2 \times 10^3]$
RoAc^{2+}	2×10^{-6}	(80)		10
$\text{[S]}-\text{COORo}^{2+}$	2×10^{-3}	25	3	7
$\text{[S]}-\text{CH}_2\text{COORo}^{2+}$	4×10^{-4}	2.5	5	20
$\text{[S]}-(\text{CH}_2)_2\text{COORo}^{2+}$	6×10^{-4}	2.5	6	20
$\text{[S]}-(\text{CH}_2)_3\text{COORo}^{2+}$	3×10^{-4}	2	3	6
$\text{[S]}-\text{CH}=\text{CHCOORo}^{2+}$	3×10^{-3}	45	6	25
$\text{[S]}-\text{COORo}^{2+}$	5×10^{-4}	30	7	7
$\text{[S]}-\text{CH}_2\text{COORo}^{2+}$	5×10^{-4}	1.5	10	10

combining these relative values of $k_{\text{et}}^{\text{os}}$ with the estimate of $k_{\text{et}}^{\text{os, Hg}}$ for $\text{Co}(\text{NH}_3)_5\text{OH}_2^{3+}$ reduction, ca. $2 \times 10^3 \text{ s}^{-1}$, obtained at the mercury-aqueous interface at 0 mV vs. SCE. The validity of this procedure is supported by the approximate agreement (within ca. two fold) between the corresponding values of $k_{\text{et}}^{\text{os, Hg}}$, $k_{\text{et}}^{\text{os, Ru}}$, and $k_{\text{et}}^{\text{os, Cr}}$, although somewhat larger differences in these quantities are seen for $\text{Co}(\text{NH}_3)_5\text{OAc}^{2+}$ reduction (Table I).

Close examination of values of $k_{\text{et}}^{\text{is}}$ and $k_{\text{et}}^{\text{os}}$ reveals several interesting trends. Broadly speaking, the variations in k_{et} for the surface-attached reactants obtained by altering the bridging group X follow those for the corresponding values of k_{et} for outer-sphere homogeneous environments. This indicates that the reorganization barrier to electron transfer is not greatly altered by surface attachment via these bridging ligands. In other words, the substantially larger rate constants for the overall reaction at mercury, $k_{\text{app}}^{\text{Hg}}$, seen for reactions following ligand-bridged pathways (Table I) can be attributed in large part to the increases in K_p , i.e., the greater cross-sectional reactant concentrations at the electrode surface, brought about by reactant-surface bond formation.

Nevertheless, significant differences in k_{et} are seen for a number of reactants in the various reaction environments. Thus, for $\text{X}^- = \text{NCS}^-$, Br^- , and Cl^- , k_{et} differs by up to 100-fold between the corresponding values obtained for inner-sphere electrochemical, and outer-sphere homogeneous reaction environments. The values of $k_{\text{et}}^{\text{os}}$ are not expected to depend significantly upon the reaction environment. However, the homogeneous reductants $\text{Ru}(\text{NH}_3)_6^{2+}$ and $\text{Cr}(\text{bpy})_3^{2+}$ yield larger values of $k_{\text{et}}^{\text{os}}$, yet the reductant $\text{Fe}(\text{CN})_6^{4-}$ yields smaller values than those of $k_{\text{et}}^{\text{is}}$ obtained for the corresponding inner-sphere electrochemical pathway. Moreover, the ratios of $k_{\text{et}}^{\text{is}}$ for $\text{Co}(\text{NH}_3)_5\text{Cl}^{2+}$ relative

to those for $\text{Co}(\text{NH}_3)_5\text{NCS}^{2+}$ reduction at gold and platinum are 200 and 2×10^3 , respectively. Although comparable ratios of $k_{\text{et}}^{\text{os}}$ are seen for $\text{Ru}(\text{NH}_3)_6^{2+}$ and $\text{Cr}(\text{bpy})_3^{2+}$ (4×10^2 and 75, respectively), the corresponding $k_{\text{et}}^{\text{os}}$ ratio is only ca. 6 for reduction by $\text{Fe}(\text{CN})_6^{4-}$. These results suggest that the reactant orientation can have an important influence upon k_{et} . Thus, the anionic ligand NCS^- or Cl^- is anticipated to be oriented towards the cationic reductants $\text{Ru}(\text{NH}_3)_6^{2+}$ and $\text{Cr}(\text{bpy})_3^{2+}$, but away from the anionic reductant $\text{Fe}(\text{CN})_6^{4-}$. However, "strong overlap" pathways are very unlikely for outer-sphere reactions. Therefore, the much larger values of $k_{\text{et}}^{\text{is}}$ for $\text{Co}(\text{NH}_3)_5\text{Cl}^{2+}$ relative to $\text{Co}(\text{NH}_3)_5\text{NCS}^{2+}$ reduction at gold and platinum may well be associated with the necessary orientation of anionic ligands towards the electrode, rather than any diminution of the reorganization barrier caused by binding the reactant to the metal surface (3a). The origin of such orientation effects may lie in the increased orbital overlap, and hence, larger values of κ_{et} , brought about by interposing chloride (or bromide) ligands between the donor and acceptor orbitals located at the metal surface and $\text{Co}(\text{III})$, respectively.

In order to more fully understand the effects of varying the bridging ligand X upon the intramolecular reactivity, it is necessary to estimate the variations in the thermodynamic driving force term $[RT(\ln K_p - \ln K_s) + F(E - E^\circ)]$ in Eq. [4]. Although, to a first approximation, the "surface" component $RT(\ln K_p - \ln K_s)$ can be neglected since we expect that $K_p \approx K_s$, at a given electrode potential, the "bulk" driving force $F(E - E^\circ)$ may vary greatly, due to the dependence of the standard potential E° on the ligand structure. Although values of E° are largely unknown for the present $\text{Co}(\text{III})/\text{Co}(\text{II})$ couples, information on the likely variations in E° with X can be obtained as follows.

The variation in k_{et} relative to that for $\text{Co}(\text{NH}_3)_5\text{OH}_2^{3+}$ reduction, $k_{et}^{\text{OH}_2}$, caused by variations in the driving force term $F(E - E^\circ)$ can be expressed as

$$k_{et}^{\text{th}} = k_{et}^{\text{OH}_2}(K_{\text{II}}/K_{\text{III}})^{1/2} \quad [7]$$

where K_{III} is the equilibrium constant for $\text{Co}^{\text{III}}(\text{NH}_3)_5\text{OH}_2 + \text{X} \rightleftharpoons \text{Co}^{\text{III}}(\text{NH}_3)_5\text{X}$, and K_{II} is the equilibrium constant for formation of the corresponding Co(II) complex. Although values of K_{II} are unknown, they are expected to be, in most cases, smaller and markedly less dependent on X^- than are the values of K_{III} , in view of the difference in electronic configuration between Co(III) and Co(II) (t_{2g}^6 and $t_{2g}^5 e_g^2$, respectively). Therefore, an approximate (and probably limiting) estimate of the expected driving force effects upon k_{et} can be obtained by inserting the appropriate literature values of K_{III} into Eq. [7], along with the experimental value of $k_{et}^{\text{OH}_2}$, taking K_{II} as a constant.

The resulting "thermodynamic" estimates of k_{et} , k_{et}^{th} , are also listed in Table IA. (The sources of K_{III} are given in the footnote to Table I. The value of K_{II} was taken as $0.1 M^{-1}$; although somewhat arbitrary, this choice is intuitively reasonable given that Co(II) is expected to have some affinity for anionic ligands relative to H_2O , the value $K_{\text{II}} \approx 0.02 M^{-1}$ corresponding to an absence of such affinity). Comparison of the values of k_{et}^{os} and k_{et}^{is} with the corresponding estimates k_{et}^{th} shows that the observed variations of k_{et}^{is} as well as k_{et}^{os} with the nature of X are in large part accounted for by this "thermodynamic" component, although the values of k_{et} for $\text{Co}(\text{NH}_3)_5\text{Cl}^{2+}$ and $\text{Co}(\text{NH}_3)_5\text{Br}^{2+}$ reduction in electrochemical ligand-bridged and cationic outer-sphere environments are somewhat larger than expected on this basis. We therefore conclude that binding Co(III) to the electrode surface via simple halide or pseudohalide ligands produces only relatively minor changes in the elementary electron transfer barrier, although some "inner-sphere catalysis" does occur for chloride and bromide ligands at platinum and gold. The latter, nonetheless, may be due to increases in κ_{el} caused by more favorable electronic coupling rather than to diminutions in ΔG^*_{in} caused by the occurrence of "strong overlap" reaction pathways.

Turning now to the organic ligand-bridged reactions, comparison of k_{et} values for the seven thiophene-attached reactants in Table IB provide further evidence of the occurrence of electronic coupling effects. The k_{et}^{is} values at mercury for the reactants featuring uninterrupted conjugation between Co(III) and the sulfur surface binding site are relatively constant ($25\text{-}30 s^{-1}$) and close to k_{et}^{os} for $\text{Co}(\text{NH}_3)_5\text{OAc}^{2+}$ reduction. However, k_{et}^{is} for reactants containing one or more saturated carbons between the carboxylate group and the thiophene ring are 10- to 20-fold smaller (Table I). In contrast, k_{et}^{os} for $\text{Ru}(\text{NH}_3)_6^{2+}$ reduction of these complexes show only a relatively small dependence on the thiophenecarboxylate structure, the nonconjugated ligands yielding somewhat larger k_{et}^{os} values than the conjugated systems. This indicates that the smaller k_{et}^{is} values for the former systems at mercury are characteristic of the ligand-bridged mechanism itself, rather than to variations in the properties of the isolated Co(III) redox center, such as the E° values. The most likely explanation is that the electronic coupling between the Co(III) acceptor and surface donor orbitals is sufficiently weak for the conjugated ligands to yield smaller values of κ_{el} , and, hence, smaller k_{et}^{is} values (Eq. [3]), than for the conjugated ligands. This is supported by the activation parameter data discussed below. The absence of further decreases in k_{et}^{is} as the number of saturated carbons is increased from one to three may well be due to the involvement of an alternative reaction pathway where the electron tunnels "directly" between the surface and the Co(III) rather than via the bridging ligand. Interestingly, these ligand conjugation effects are absent for the reduction of the surface-bound thiophene complexes at gold, the relative values of k_{et}^{is} following instead the $k_{et}^{\text{os, Ru}}$ values (Table I). One explanation is that the mode of adsorption of the bridging ligand at gold differs from

that at mercury; the thiophene ring possibly lying flat or the carboxyl oxygen binding to the metal in the former case. This may enable reasonable electronic coupling to be maintained even in the absence of bridging ligand conjugation.

Activation Parameters for Surface-Bound Reactants

In addition to the evaluation of k_{et}^{is} at a single temperature, valuable information on the factors influencing the electron transfer energetics for surface-bound reactants may be obtained from measurements of electrochemical activation parameters. We have recently discussed their significance for surface-bound reactants (17). Since neither the standard potentials nor their temperature dependences are known with any accuracy for the present systems, so-called "ideal" activation enthalpies ΔH^*_i were determined from Arrhenius plots of $\ln k_{et}^{\text{is}}$ against $(1/T)$ at a constant cell potential using a nonisothermal cell arrangement. These measurements enable the frequency factor for the elementary electron transfer step, A_{et} ($= \nu_n \kappa_{el} \Gamma_n$, Eq. [3]), to be determined from

$$\ln A_{et} = \ln k_{et}^{\text{is}} + \Delta H^*/RT - \Delta S^*/R \quad [8]$$

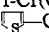
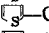
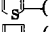
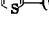
where ΔS^*_i is the "ideal" activation entropy. Although ΔS^*_i is not negligible, it can be estimated from $\Delta S^*_i = 0.5 \Delta S^*_{et}$, where ΔS^*_{et} is the entropic driving force ("reaction entropy") for the electron transfer step. For the present Co(III)/(II) couples, on the basis of the available reaction entropy data (18), ΔS^*_{et} is expected to lie in the range 20-30 cal/K · mol.

Values of ΔH^*_i and A_{et} for reduction of selected surface-bound reactants at mercury electrodes are summarized in Table II. Since the estimated values of ΔS^*_{et} have uncertainties in the range ca. 5-10 cal/K · mol, the resulting frequency factors A_{et} may be up to 3- to 10-fold in error. Nevertheless, the relative values of A_{et} , particularly for structurally similar reactants, are more reliable. The two Cr(III) reactants both yield values of A_{et} that are close to the value, $1 \times 10^{13} s^{-1}$, expected for adiabatic pathways ($\kappa_{el} \approx 1$) for which $A_{et} \approx \nu_n$. The A_{et} values for the two Co(III) reactants, $\text{Co}(\text{en})_2(\text{NCS})_2^+$ (I) and $\text{Co}(\text{NH}_3)_5(2\text{-thiophene acrylate})^{2+}$ (IV) (both $1 \times 10^{12} s^{-1}$), suggest that these reactions are also close to being adiabatic ($\kappa_{el} \approx 0.1$). However, the remaining thiophene complexes (V, VI, VII), which have interrupted conjugation, exhibit markedly (10^2 - to 10^3 -fold) smaller values of A_{et} as well as k_{et} . This supports the above suggestion that the smaller reactivity of these latter complexes arises from the weaker electronic coupling (i.e., smaller values of κ_{el}) brought about by the interposition of saturated carbon atoms between the donor and acceptor sites (3, 17).

Conclusions

The foregoing analyses indicate that attachment of Co(III) to mercury, platinum, and gold surfaces via either simple inorganic or organic bridging groups yields only small or moderate changes in the elementary reorganization barrier ΔG^*_{et} . Thus, the corresponding values of k_{et}^{is} and of k_{et}^{os} obtained either in other reaction environments or estimated from the reactivities of structurally similar reactants are typically within ca. 5- to 30-fold of each other. In addition to the influence of the bridging ligand upon k_{et} arising from variations in the thermodynamic driving force, the dependence of k_{et}^{is} on the nature of the bridging ligand appears to arise in part from alterations in κ_{el} as a result of changes in the degree of electronic coupling between the surface donor and Co(III) acceptor orbitals. These reactions can therefore be considered to involve weak rather than strong overlap electron transfer. The possible exceptions are halide bridges at platinum and gold, where the surface bonds are expected to be relatively covalent, thereby weakening the Co(III)-halide bonds and decreasing the component of ΔG^*_{in} and, hence, ΔG^*_{et} , associated with the inner-shell (metal-ligand) reorganization energy. However, the relatively large values of k_{et}^{is} observed for these reactions can be attributed in part

Table II. Electrochemical activation parameters for reduction of representative surface-bound Co(III) and Cr(III) reactants at mercury electrodes in 0.1M NaClO₄

Reactant	E mV vs. SCE	k_{et}^{is} s ⁻¹	$\Delta H^*_{1,b}$ kcal · mol ⁻¹	$\Delta S^*_{1,c}$ cal · deg ⁻¹ mol ⁻¹	A_{et}^d s ⁻¹
I. c-Co(en) ₂ (NCS) ₂ ⁺	-100	0.15	20.5	~10	~1 × 10 ¹²
II. c-Cr(OH) ₃ (NCS) ₂ ⁺	-600	70	20	~13	~3 × 10 ¹³
III. f-Cr(OH) ₃ (NCS) ₃	-600	70	16	~0	~3 × 10 ¹³
IV.  CH=CHCOORo ²⁺	-200	4 × 10 ³	15.6	~13	~1 × 10 ¹²
V.  CH ₂ COORo ²⁺	-200	260	14.1	~13	~1 × 10 ¹⁰
VI.  (CH ₂) ₂ COORo ²⁺	-200	290	14.8	~13	~3 × 10 ¹⁰
VII.  (CH ₂) ₃ COORo ²⁺	-200	230	13.2	~13	~1 × 10 ⁹

^a Unimolecular rate constant for reduction of surface-bound Co(III) or Cr(III) complex at stated electrode potential *E*.

^b "Ideal" activation enthalpy at stated value of *E*, determined from $\Delta H^*_1 = -R[\partial \ln k_{et} / \partial (1/T)]_E$ using a nonisothermal cell arrangement (17).

^c Estimated "ideal" activation entropy ΔS^*_1 (see text).

^d Frequency factor for elementary electron transfer reaction, determined from listed values of k_{et}^{is} , ΔH^*_1 , and ΔS^*_1 .

to increases in k_{et} arising from the enhanced electronic coupling provided by the interposition of the monatomic ligand between the donor and acceptor orbitals.

The experimental frequency factors for the surface intramolecular reactions at mercury, $A_{et} \approx 10^{10}$ - 10^{13} s⁻¹, suggest that κ_{et} lies in the region ca. 10^{-3} -1.0 (*i.e.*, nonadiabatic pathways occur), although κ_{et} probably approaches unity (*i.e.*, adiabaticity is achieved) only with small inorganic bridging ligands. These conclusions are similar to those from recent experimental and theoretical work for related homogeneous electron transfer processes. Thus, values of κ_{et} substantially below unity are predicted for some homogeneous outer-sphere reactions even at small internuclear separations (5-6Å) (19). Nonadiabatic pathways for homogeneous intramolecular Co(III) - Ru(II) reactions bridged by bipyridine ligands featuring interrupted conjugation are also evidenced by the values of A_{et} obtained for these processes (7), especially after correction for the entropic driving force (20).

It is interesting to compare this situation with the catalyses induced by the ligand-bridged reduction of Co^{III}(NH₃)₆X complexes by homogeneous reagents such as Cr²⁺, Eu²⁺, V²⁺, and Fe²⁺. The analysis of the reaction energetics is considerably more tenuous than for the electrochemical reactions since little information is available on the precursor complex stabilities K_p^{is} . Moreover, the comparison of rate constants for corresponding outer- and inner-sphere pathways is less straightforward for homogeneous reactions since cognizance must be taken of the contribution to the reorganization energy from the coreactant. This component will probably be different for the outer- and inner-sphere routes since the coreactant's coordination sphere will necessarily be altered in forming the precursor complex.

Nevertheless, some useful deductions can be made from the available rate data. The most remarkable ligand-bridged rate accelerations occur for reductions by Cr²⁺; for example, Co(NH₃)₅Cl²⁺ is reduced by Cr²⁺ nearly 10¹⁰-fold more rapidly than is Co(NH₃)₆³⁺ (21). The corresponding rate ratios for reduction by V²⁺ and Eu²⁺ are about 10⁴, similar to that for Ru(NH₃)₆²⁺ (Table I) (21). The Co(NH₃)₅Cl²⁺-Cr²⁺ reaction clearly follows an inner-sphere pathway, whereas the latter two processes may follow outer-sphere mechanisms. Although the binding constant of Cr²⁺ to Co(NH₃)₅Cl²⁺ is unknown, it would need to be ca. 10⁶-fold higher than for the other reagents to account for the additional rate acceleration, which is highly implausible. Therefore, this, and also other ligand-bridged Co^{III}(NH₃)₅X - Cr²⁺ reactions seem certain to occur via "strong overlap" pathways; *i.e.*, where the elementary electron transfer barrier ΔG^*_{et} is lowered substantially by electronic interactions between the redox centers (4).

There have been several recent discussions of the factors influencing such inner-sphere catalyses (22, 23). It suffices to note here that such rate enhancements appear to be dependent upon the symmetry of the donor and acceptor orbitals, the most dramatic rate accelera-

tions occurring for systems where both orbitals have e_g symmetry (22). For such systems, it has recently been suggested that the precursor formation and electron transfer steps are merged such that the bridge forms a "three-center" bond with the two metal cations (23). The absence of such dramatic catalyses for the electrochemical reduction reactions is probably related to the relatively weak electronic coupling expected between the surface and Co(III) e_g acceptor orbitals, although the donor orbitals at gold, and especially platinum, surfaces are expected to have some d orbital character. Nevertheless, strong overlap electron transfer may well occur for electrochemical processes involving adsorbed redox centers, such as oxygen, which bind directly to metal surfaces rather than via a bridging group.

The evaluation of electrochemical rate constants and activation parameters for surface-bound reactants, especially for a series of structurally related systems, clearly provides detailed information on the electron transfer energetics that are unavailable from measurements of electrochemical reactivities for bulk phase reactants. We anticipate that a wealth of hitherto unavailable information on the factors influencing the degree of adiabaticity of heterogeneous electron transfer reactions can be extracted from systematic studies of the dependence of A_{et} as well as k_{et} on the structure of the metal redox center, the metal surface, and the mediating group.

Acknowledgments

This work was supported in part by the Air Force Office of Scientific Research and the Office of Naval Research. M. J. W. gratefully acknowledges a fellowship from the Alfred P. Sloan Foundation.

Manuscript submitted Aug. 29, 1983; revised manuscript received Dec. 22, 1983. This was Paper 719 presented at the San Francisco, CA, Meeting of the Society, May 8-13, 1983.

REFERENCES

- M. J. Weaver and F. C. Anson, *J. Electroanal. Chem. Interfacial Electrochem.*, **58**, 95 (1975).
- K. L. Guyer, S. W. Barr, and M. J. Weaver, in "Electrocatalysis," W. E. O'Grady, P. N. Ross, Jr., and F. G. Will, Editors, p. 377, The Electrochemical Society Softbound Proceedings Series, Pennington, NJ (1982).
- S. W. Barr and M. J. Weaver, *Inorg. Chem.*, In press; K. L. Guyer and M. J. Weaver, *ibid.*, In press; and T. T.-T. Li, H. Y. Liu, and M. J. Weaver, *J. Am. Chem. Soc.*, In press.
- M. J. Weaver, *Inorg. Chem.*, **18**, 402 (1979).
- M. J. Weaver, *Isr. J. Chem.*, **18**, 35 (1979); V. Srinivasan, S. W. Barr, and M. J. Weaver, *Inorg. Chem.*, **21**, 3154 (1982).
- J. T. Hupp, and M. J. Weaver, *J. Electroanal. Chem. Interfacial Electrochem.*, **152**, 1 (1983).
- For reviews see, H. Taube, *Adv. Chem. Ser.*, **162**, 127 (1977); and H. Taube, in "Tunneling in Biological Systems," B. Chance, D. C. DeVault, H. Frauenfelder, R. A. Marcus, J. R., Schrieffer, and N. Sutin, Editors, p. 173, Academic Press, New York (1979).
- N. Sutin and B. S. Brunschwig, *ACS Symp. Ser.*, **198**, 105 (1982).

9. See for example, R. A. Marcus, *J. Phys. Chem.*, **72**, 891 (1968).
10. M. J. Weaver and T. L. Satterberg, *ibid.*, **81**, 1772 (1977).
11. K. L. Guyer, S. W. Barr, R. J. Cave, and M. J. Weaver, in "Electrode Processes," S. Bruckenstein, J. D. E. McIntyre, B. Miller, and E. Yeager, Editors, p. 390, The Electrochemical Society Softbound Proceedings Series, Princeton, NJ (1980).
12. R. A. Marcus, *J. Phys. Chem.*, **67**, 853 (1963); and R. A. Marcus, *ibid.*, **43**, 679 (1965).
13. T. L. Satterberg and M. J. Weaver, *ibid.*, **82**, 1784 (1978).
14. M. J. Weaver, *ibid.*, **84**, 568 (1980).
15. M. J. Weaver, *J. Electroanal. Chem. Interfacial Electrochem.*, **93**, 231 (1978).
16. P. D. Tyma and M. J. Weaver, *ibid.*, **111**, 195 (1980).
17. J. T. Hupp and M. J. Weaver, *ibid.*, **145**, 43 (1983); M. J. Weaver, *J. Phys. Chem.*, **83**, 1748 (1979); and T. T. Li, K. L. Guyer, S. W. Barr, and M. J. Weaver, *J. Electroanal. Chem. Interfacial Electrochem.*, **164**, 27 (1984).
18. E. L. Lee, R. J. Cave, K. L. Guyer, P. D. Tyma, and M. J. Weaver, *J. Am. Chem. Soc.*, **101**, 1131 (1979); and E. L. Yee and M. J. Weaver, *Inorg. Chem.*, **19**, 1077 (1980); J. T. Hupp and M. J. Weaver, *This Journal*, **131**, 619 (1984).
19. M. D. Newton, *Int. J. Quant. Chem. Symp.*, **14**, 363 (1980); M. D. Newton, *ACS Symp. Ser.*, **198**, 255 (1982).
20. J. T. Hupp and M. J. Weaver, *Inorg. Chem.*, **23**, 256 (1984).
21. For a convenient data tabulation see, R. G. Wilkins, "The Study of Kinetics and Mechanisms of Reactions of Transition-Metal Complexes," pp. 260-261, Allyn and Bacon, Inc., Boston (1974).
22. R. G. Linck, in "Inorganic Chemistry Series I," Vol. 9, p. 303, Butterworths, London (1972); and J. K. Burdett, *Inorg. Chem.*, **19**, 2537 (1978).
23. F. P. Rotzinger, K. Kumar, and J. F. Endicott, *Inorg. Chem.*, **21**, 4111 (1982).
24. J. F. Endicott and H. Taube, *J. Am. Chem. Soc.*, **86**, 1686 (1964).
25. R. C. Patel and J. F. Endicott, *ibid.*, **90**, 6364 (1968).
26. A. Adegite, M. Dosumu, and J. F. Ojo, *J. Chem. Soc., Dalton Trans.*, 630 (1977).
27. J. P. Candlin, J. Halpern, and D. L. Trimm, *J. Am. Chem. Soc.*, **86**, 1019 (1964).
28. D. Gaswick and A. Haim, *ibid.*, **93**, 7347 (1971).
29. A. Miralles, Ph.D. Thesis, State University of New York at Stony Brook (1974).
30. A. Haim, Personal communication.
31. N. Sutin, *Ann. Rev. Phys. Chem.*, **17**, 119 (1966.)

Technical Notes



Preliminary Results of *In Situ* Al₂S₃ Preparation in MgCl₂-NaCl-KCl Eutectic Melt

Chen C. Hsu*

Argonne National Laboratory, Chemical Technology Division, Argonne, Illinois 60439

Because of the rising cost of electrical energy, a number of industrial processes have been proposed (1) for saving energy in the production of aluminum. Three of these processes were evaluated for their energy saving potential; all three involve reduction of a compound containing aluminum: Al₂O₃, AlCl₃, or Al₂S₃. Theoretically, the energy required for direct Al₂S₃ electrolysis is less than that required for the reduction of the other two compounds (2); for AlCl₃ by 24% and Al₂O₃ by 34%. The energy needed for conventional high temperature preparation of Al₂S₃, however, is very high (3). Unless other methods requiring less energy can be used for Al₂S₃ preparation, there is little advantage to the use of the Al₂S₃ process in terms of the overall energy requirements. One obvious way to decrease the energy requirement is to reduce the reaction temperature for the Al₂S₃ preparation by using molten-salt media.

Molten salts have been used extensively as reaction media for both inorganic and organic chemical preparation (4-6). There are several advantages for the use of molten-salt solutions: (i) the intimate contact in either a homogeneous solution phase, or in heterogeneous systems where reactants are dispersed in the solution, enhances the reaction rate. (ii) Local overheating due to exothermic reaction or freezing due to endothermic reaction is minimized. The molten salt acts as a heat transfer medium, which results in a better process control. (iii) Ease of removal of the gas reaction products increases the reaction efficiency. (iv) Reaction thermodynamics are improved due to the inherent physicochemical properties of the

melt in regard to the acid-base, redox, and complexing ability. One of the disadvantages, however, is the difficulty of separating the products from the media. One

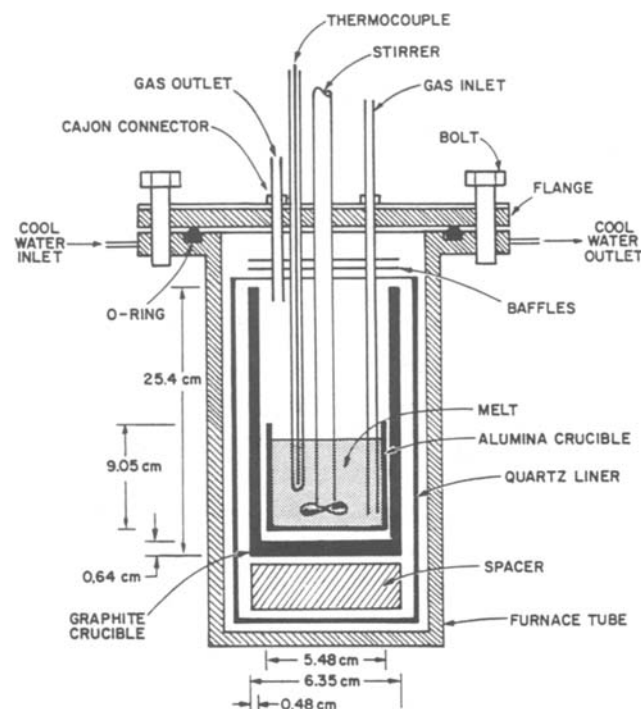


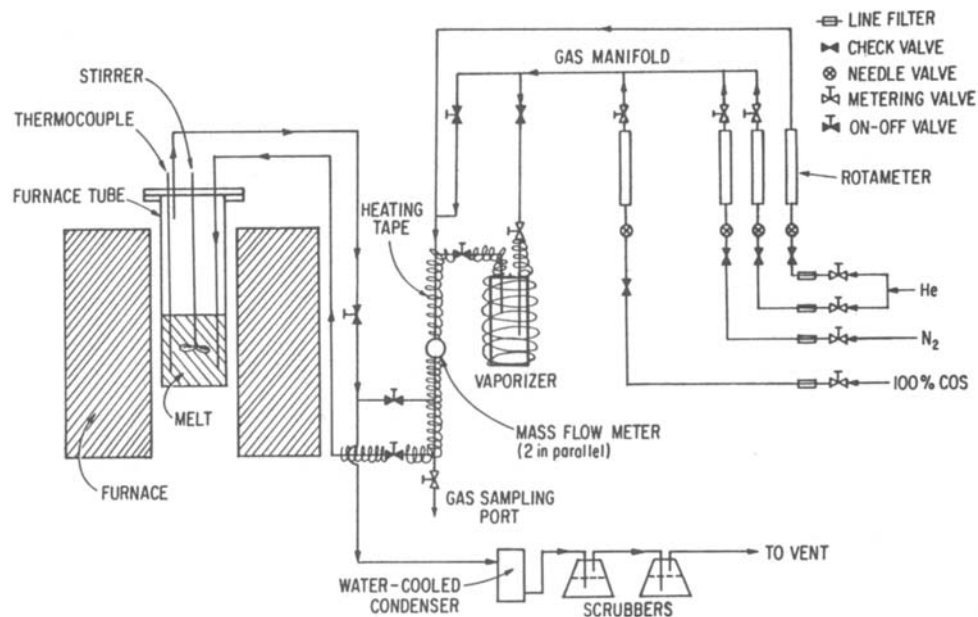
Fig. 1. Schematic diagram of the molten-salt reactor

* Electrochemical Society Active Member.

Present address: Department of the Army, Research Division, Chemical Research and Development Center, Aberdeen Proving Ground, Maryland 21010.

Key words: fused salts, voltammetry, synthesis.

Fig. 2. Schematic diagram of the apparatus for the molten-salt reaction.



possible solution in the case of Al_2S_3 reduction in a melt would be to prepare Al_2S_3 in the same melt used for electrolysis. Consequently, *in situ* Al_2S_3 preparation in a chloride melt was undertaken.

Experimental

Al_2S_3 preparation.—Chemicals used for this investigation are high purity $\text{MgCl}_2\text{:NaCl:KCl}$ eutectic salt [50:30:20 m/o (mole percent)] (Anderson Physics Laboratories), Al_2O_3 (Aluminum Company of America), and COS (Matheson Gas Company). All materials were used as received except for Al_2O_3 , which was further dehydrated in an oven at approximately 150°C for at least a week before use. All salts were stored inside a glove box under recirculating helium gas purified with charcoal embedded in a Dewar flask containing liquid nitrogen.

Alumina crucibles (Coors Company) with dimensions of 5.48 cm od, 5.16 cm id, and 9.05 cm high were baked overnight in a 250°C oven before being transferred to the glove box and filled with the reactants. After 55-65g of the chloride eutectic salt and 3-5g of Al_2O_3 were loaded into the crucible, the crucible was placed inside a larger covered graphite crucible filled with argon and transferred to a quartz-lined stainless steel furnace tube (see Fig. 1 and 2). The top of the furnace tube was closed immediately and the system was evacuated to a vacuum of approximately $5\ \mu\text{m}$, then backfilled with helium gas until a slightly positive pressure was produced in the furnace tube. As soon as the desired temperature was reached, the motor-driven stirrer was turned on and COS was passed through the melt. A platinum-10% rhodium + platinum thermocouple with a Trenderator (Omega Engi-

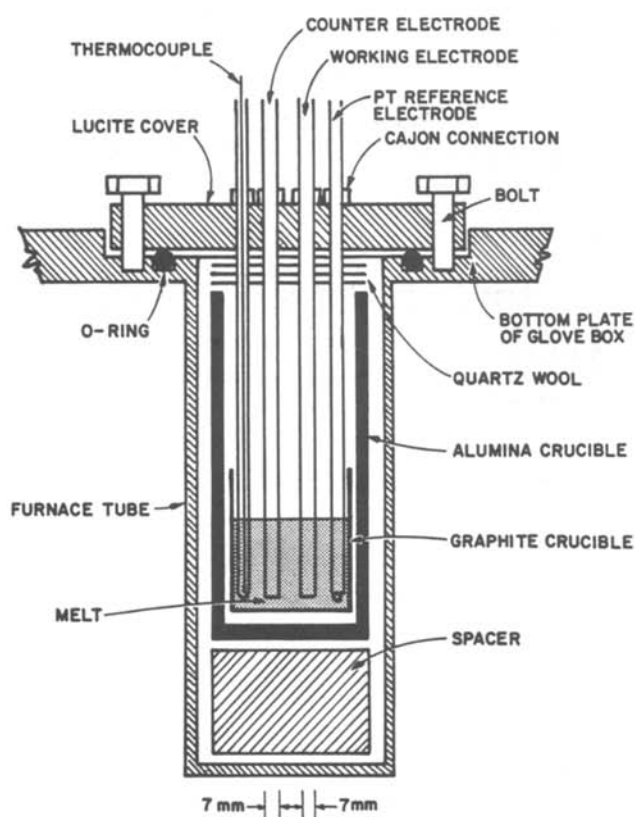


Fig. 3. Schematic diagram of the electrochemical cell for the cyclic voltammetric study.

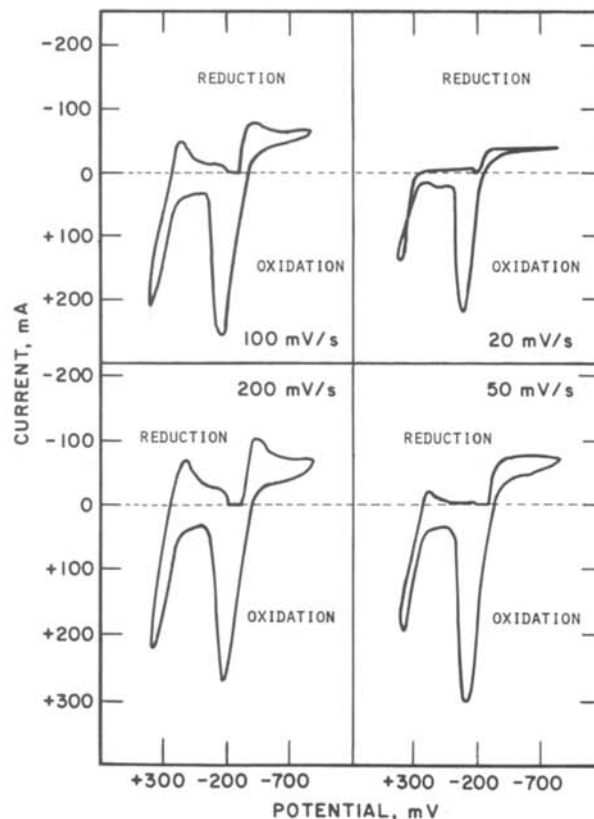


Fig. 4. Cyclic voltammograms of Al_2S_3 at concentration of $2.63 \times 10^{-2}\text{M}$ at 750°C with Pt as quasi-reference.

neering, Incorporated) was used to monitor the temperature, while a flow transducer with a digital display was used to show the mass flow rate of COS. The reaction conditions were as follows: a temperature of approximately 850°C , a COS flow rate of $68\text{--}135\text{ cm}^3/\text{min}$, and a reaction duration of $1.33\text{--}3.22\text{ h}$. At the end of each experiment, COS flow was stopped, and the furnace power and inlet and outlet tube valves were turned off. The graphite crucible was covered with aluminum foil and transferred back into the glove box for electrochemical analysis.

Electrochemical analysis of Al_2S_3 .—The apparatus for the electrochemical analysis, shown schematically in Fig. 3, consists of two 7 mm diam, high density, cylindrical graphite rods used as working and counterelectrodes, a Pt quasi-reference electrode, and a thermocouple for monitoring the temperature of the system. A Princeton Applied Research Model 175 Universal Programmer and Model 173 Potentiostat/Galvanostat along with a HP 7044A X-Y recorder were used to generate cyclic voltammograms (CV) in which the peak current was correlated with Al_2S_3 concentration. The peak currents of various Al_2S_3 concentrations were converted to peak current densities. The electrode areas in the melt varied from 2.31 to 4.05 cm^2 .

For qualitative and quantitative analysis of the synthesized Al_2S_3 with cyclic voltammetry technique, a correlation of peak current densities with various known Al_2S_3 concentrations in the chloride eutectic melt was carried out using the apparatus shown in Fig. 3.

Results and Discussion

The aluminum cation reduction peak in the cyclic voltammograms occurs at approximately -490 mV , while the sulfur anion oxidation occurs at around $+540\text{ mV}$ with a total peak-peak potential of 1.03 V vs. Pt quasi-reference at 750°C with the scan rate of 20 mV/s . Typical

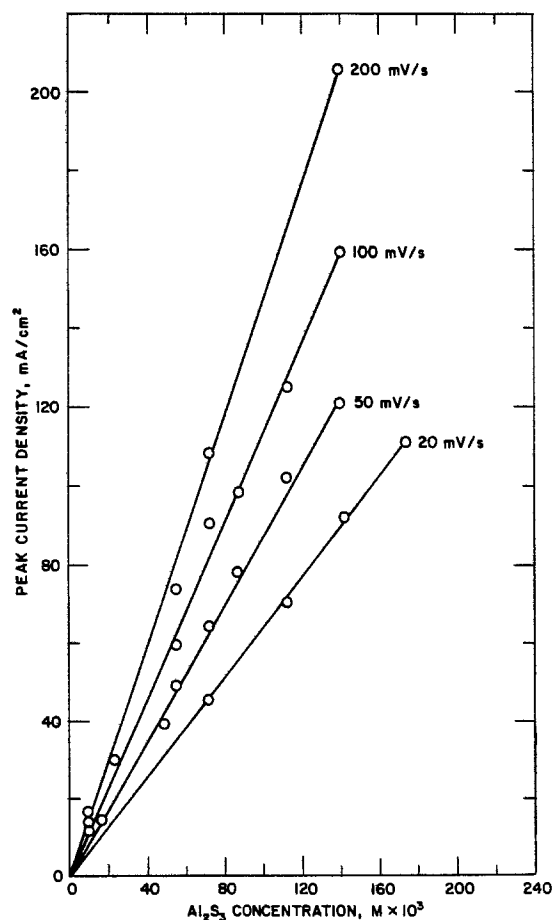


Fig. 5. Correlation of Al^{3+} reduction peak current density with Al_2S_3 concentration at 750°C .

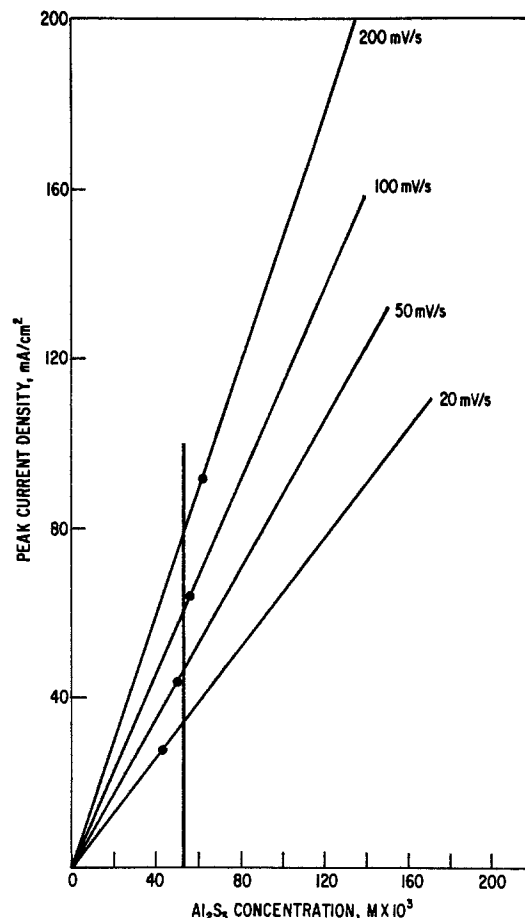
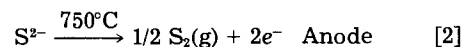
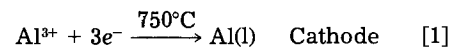
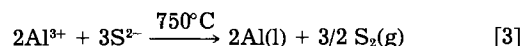


Fig. 6. Estimate for Al_2S_3 concentration of sample 7 from cyclic voltammograms.

cyclic voltammograms at 750°C using various scan rates are shown in Fig. 4. Only two peaks are obtained; one for aluminum cation reduction and the other for sulfur anion oxidation. The electrochemical reactions at the cathode and anode can be represented as follows (7)



The overall reaction can be shown as



The peak current of Al^{3+} was converted to peak current density for various Al_2S_3 concentrations at four different scan rates at 750°C , the temperature used for Al_2S_3 electrolysis. A plot of Al^{3+} reduction peak current density vs. Al_2S_3 concentration is shown in Fig. 5. This figure clearly shows the linear relationships between peak current density and Al_2S_3 concentration that exist at scan rates from 20 to 200 mV/s at 750°C . This correlation is the basis on which the analyses of the synthesized Al_2S_3 were performed.

Al_2S_3 formed in the molten salt reactor was analyzed in the glove box using the cyclic voltammetry method described above. Despite the concentration variations in synthesized Al_2S_3 , a reduction peak and an oxidation peak in a typical cyclic voltammogram of the sample occur at -490 and $+540\text{ mV}$, respectively. This information clearly indicates that conversion of Al_2O_3 to Al_2S_3 in the melt does occur. The peak current density of Al_2S_3 from the CV was used to estimate the Al_2S_3 concentration in the melt. A typical plot for this kind of estimate is shown in Fig. 6, where the heavy dots denote the synthesized Al_2S_3 at various scan rates. The Al_2S_3 concentration is taken to be the average value as shown in Fig. 6. Analyt-

Table I. Conditions of *in situ* Al₂S₃ preparation at 850°C and reaction product concentrations determined by analysis

	1	2	3	Sample 4	5	6	7
Weight of melt, ^a g	58.3698	65.1523	55.7496	63.4005	60.6638	62.3703	60.8763
Weight of Al ₂ O ₃ , g	2.9238	3.3127	3.5592	4.2507	3.4580	2.8850	2.7320
COS flow rate, cm ³ /min	135	102	108	68	134	105	81
Reaction time, h	1.333	2	1.50	2	2	3.22	1
Al ₂ S ₃ concentration in melt, w/o	0.13	0.19	0.22	0.07	0.13	0.20	0.40
Stirrer speed, rpm	150	300	220	300	200	300	300

^a Eutectic chloride salt mixture having the composition, MgCl₂:NaCl:KCl = 50:30:20 m/o.

ical results and reaction conditions are shown in Table I. A plot of Al₂S₃ concentration vs. COS flow rate shows that the yield of Al₂S₃ is not strongly dependent upon flow rate, Fig. 7. The best result so far obtained in terms of Al₂S₃ concentration is about 0.4 w/o (weight percent), as shown in Table I. Similar amounts of Al₂S₃ were formed for samples 2, 3, and 6, all of which had essentially the same COS flow rate but different reaction times. The smallest amount of Al₂O₃ conversion to Al₂S₃ is 0.07 w/o of

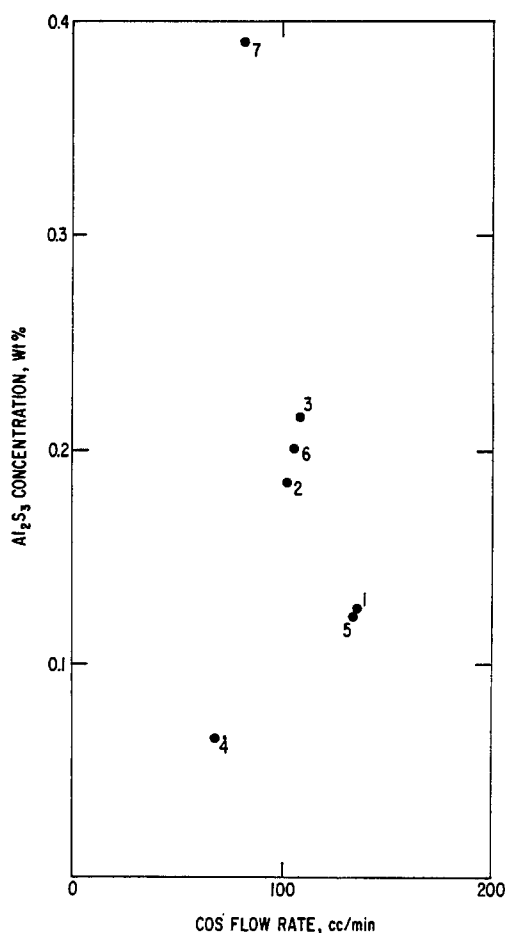


Fig. 7. Relation of the converted Al₂S₃ concentration with COS flow rate. The number by the dot is the sample number.

sample 4. The fact that the conversion is not dependent on reaction time suggests that equilibrium may be attained under the conditions used for samples 2, 3, and 6. If this is true, high temperatures will be needed for higher degrees of conversion. The Al₂O₃ concentration in the melt should not affect the results from electrochemical analyses since Al₂O₃ solubility in the melt is extremely low (8) (e.g., 0.0059 w/o at 901°C). It is interesting to note that the reaction of Al₂O₃ and COS in a gaseous environment requires a temperature of 1300°C (3, 9).

Further work is needed, particularly at a temperature higher than 850°C for kinetic and mechanistic studies to improve Al₂S₃ yield in this synthesis process. Obviously, at the present low Al₂S₃ concentration, it is not practical to use the aforementioned synthesis method for aluminum electrowinning purpose. Nevertheless, it has been demonstrated that *in situ* synthesis of Al₂S₃ can occur in the chloride eutectic melts, and that cyclic voltammetry is indeed a valid method for species identification and concentration determination.

Acknowledgments

This work was performed under the auspices of the U.S. Department of Energy, Division of Electrochemical Energy Systems.

Manuscript submitted April 20, 1982; revised manuscript received Jan. 19, 1984.

Argonne National Laboratory assisted in meeting the publication costs of this article.

REFERENCES

1. T. R. Beck, in "Proceedings of Workshop on Energy Conservation in Industrial Electrochemical Processes," Report of Argonne National Laboratory, ANL-OEPM-77-1, Argonne, IL (1976).
2. "A Survey of Potential Processes for the Manufacture of Aluminum," A. D. Little, Inc., Cambridge, MA, ANL-OEPM-79-4 (1979).
3. C. C. Hsu, Unpublished results (1982).
4. W. E. Haupin, J. A. Remper, and M. B. Dell, U.S. Pat. 4,039,648 (1977).
5. H. S. Blackmore, U.S. Pat. 605,812 (1898).
6. E. I. Zhluktenko, R. G. Rakitskaya, A. N. Fatiev, and E. S. Markritskii, U.S.S.R. Pat. 765,397 (1980).
7. N. Q. Minh, R. O. Loutfy, and N. P. Yao, *J. Electroanal. Chem.*, **131**, 229 (1982).
8. C. C. Hsu, Unpublished results (1982).
9. "Report of New Extractive Aluminum Techniques of Light Metals Society and Light Metals Refining Association," Chap. 4, pp. 1-12, Tokyo, Japan (1976).

Oxygen Evolution Study on Porous Molybdenum Naphthalocyanine Electrodes

H. Dieng, O. Contamin, and M. Savy*

Laboratoire d'Electrochimie Interfaciale du CNRS, 92195 Meudon Principal Cedex, France

In order to minimize the cathodic and anodic overvoltages taking place during water electrolysis in alkaline solution several authors have tried using as electrode catalysts oxides of the metals of the 3d series codeposited with molybdenum compounds (1-5). Among all the samples investigated, NiMoO₄ gave the best performances in endurance tests.

It has been employed for both oxygen and hydrogen evolution (4). By increasing the working temperature from 80° to 115°C one can observe a concomitant decrease of about 200 mV in the voltage between the anode and the cathode.

Cobalt oxide doped with lithium has also been reported recently (6) as offering relatively good performances for oxygen evolution at 70°C in KOH solutions. In the vicinity of ambient temperatures, molybdenum naphthalocyanine NPcMo loadings on carbon black (7) allow oxygen evolution at relatively small overvoltages (100 mV) but at current densities of only several hundred microamperes per square centimeter.

The aim of the present note is to determine whether in comparison with Mo oxides NPcMo can be employed with a certain degree of stability in electrolyzers at current densities of several hundred milliamperes per square centimeter and at working temperatures reaching 115°C or more and remain stable.

Experimental

The electrodes consisted of the carbon black powders ex CO or ex CH₄ (8) previously tested for their stability under anodic polarizations during more than 3000h. The carbon black powder was put into a sealed tube with an initial mixture of dicyanonaphthalene and ammonium paramolybdate. The thermal treatment conditions and the characterization of the final products by x-ray and XPS spectroscopy have been reported elsewhere (9). This impregnation was supported on a nickel-sintered electrode provided by Compagnie Générale d'Electricité. It presented a BET surface of 0.1 m²/g, 0.3 mm thickness, 70% porosity with 10μ diameter pores. The level of impregnation of NPcMo/C was 2.5 and 20% by weight. It must be noticed that in the present work the amount of Teflon deposited from the Soreflon suspension was relatively high, 56 mg for 50 mg of carbon black powder. This amount of Teflon turned out to be necessary to secure electrode cohesion. With large amounts the ohmic drop became too high. The charge of carbon black to the nickel support was about 50 mg/cm², and this corresponds to the maximum of activity.

From x-ray analysis (9) Mo oxides appear to be always associated with the naphthalocyanine. In order to distinguish between the oxide and the naphthalocyanine, several samples have been prepared varying the ratio dicyanonaphthalene/ammonium paramolybdate. Loadings of 2.5 and 20% have been chosen to reveal any possible kinetic factors in the synthesis able to modify the ratio Mo oxide/NPcMo. In order to appreciate the variations of activity or stability due to the amount of residual oxides, an extended washing with concentrated KOH has been carried out on several samples. In all cases the samples were prepared under deaerated conditions. They were washed with benzene, ethanol, 10% hydrochloric acid solutions, then distilled water and ethanol. In each case two samples were prepared to test the reproducibility of their performances.

*Electrochemical Society Active Member.

The nickel support covered with carbon black powder was mounted in an electrode carrier in Teflon inside a Teflon cell (Fig. 1). The anode compartment is separated from the cathode compartment by a porous Teflon membrane. The Hg/HgO reference electrode was placed inside the compartment of the working electrode. 8M KOH solutions were used. For voltammetric studies standard equipment was employed consisting of a signal generator Fabelle ST.1, a potentiostat Wenking 66TAI, and an X-Y recorder Ifelec M100. For transient studies the equipment was similar to that presented in Ref. (10). A galvanostatic pulse was sent to the cell, and the corresponding potential was measured through an oscilloscope and stored by a transient recorder (Biomation). The potential is related to the applied constant current i_0 by the equation

$$U(t) = Ri_0 + \frac{i_0 t}{C} \quad [1]$$

The slope yields the value for C and the intercept the value of R (see Table II). Corresponding frequencies f vary from $5 \cdot 10^{-7} > f > 5 \cdot 10^{-6}$.

Using current reversal it is possible to determine R and C separately, the circuit becoming equivalent to a resistance and a capacitance in series.

The impedance measurements have been performed after several cycles of polarizations but before the endurance tests for which a separator was used in the cell.

Results and Discussion

In Tables Ia and Ib, corresponding to temperatures of 25° and 80°C, respectively, are given the data obtained on the most active samples for a 2 day polarization at 560 mV Hg/HgO. The current densities are given in milliamperes per square centimeter (geometric).

In all cases the addition of catalytic material to the grid is accompanied by a corresponding increase in the current densities visible, even with the uncatalyzed carbon black samples. A modification in the order of activity at 25° and 80°C can be observed between samples containing molybdenum oxides and sample A (2.5% loading on carbon black carefully washed with concentrated KOH). At

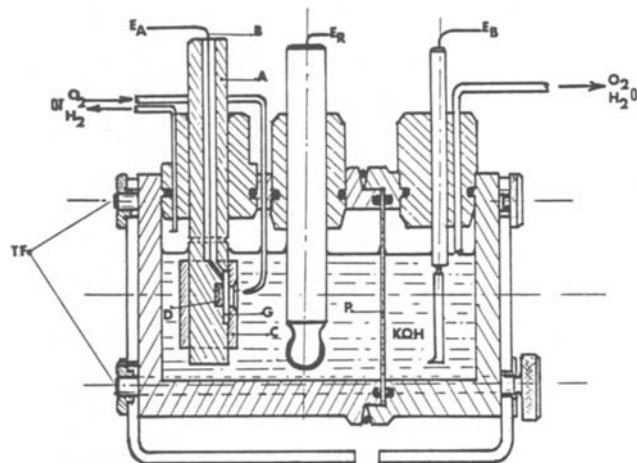


Fig. 1. Electrode holder and electrochemical cell. E_R, reference electrode; E_A, working electrode; E_B, counter-electrode; A, electrode carrier; B, wire connected to the nickel support; C, cover for sample tightening on the Ni support; D, investigated samples; P, porous Teflon separator; T_F, bolts for cell fixation.

Table Ia. Activities of the samples compared to the Ni support
 $T = 25^{\circ}\text{C}$
 50 mg/cm² loadings i mA/cm² $E = 560$ mV/Hg/HgO

Samples	i initial	$\Delta i = i$ initial - i support	i final	Δi final after 2 days polarization i sample - i support
Ni support	69.0		64.5	
C ex CO (27% Ni, BET 44 m ² /g) NPcMo	82.5	13.5	69.0	4.5
A 1 Mo for 4 DCN 2.5% loadings	72.5	3.5	72.5	8.0
B <i>Ibid.</i> A 20% loadings	112.5	43.5	106.5	42.0
C <i>Ibid.</i> B KOH washing	90.5	21.5	95.0	30.5
D 1 Mo for 1 DCN 20% loadings	82.5	13.5	95.0	30.5
E Ammonium molybdate BET 4.4 m ² /g	97.5	28.5	89.5	25.0
F C + DCN 20% loadings	inactive			

25°C the most active sample consisted of a 20% loading without any washing with KOH. With sample A only a weak increase in the activity was observed. The stability of NiMoO₄ can also be underscored.

In contrast at 80°C sample A presented the best activity and stability. It can be compared with the NiMoO₄ and ammonium molybdate sample E which have been investigated in Ref. (1-5).

The results of impedance measurements are given in Table II.

Table Ib. Activities of the samples compared to the Ni support
 $T = 80^{\circ}\text{C}$
 (Specifications the same as Table Ia)

Samples	i initial	Δi	i final	Δi final
Ni support	135.0		100.0	
ex CO	162.5	27.5	150.0	50.0
A	190.0	55.0	190.0	90.0
B	190.0	55.0	160.0	60.0
C	180.0	45.0	145.0	45.0
D	160.0	25.0	160.0	60.0
E	195.0	60.0	141.5	42.5
NiMoO ₄ BET 3.6 m ² /g	155.0	20.0	155.0	55.0

Table II. Resistances and capacitances deduced from Eq. [1] in absence of the separator

Samples	R/Ω cm ² (geom.)			$C/\mu\text{F}$ cm ⁻² (geom.)	
	25°C	80°C	110°C	25°C	80°C
Ni support	4.65	2.29	0.95	188.0	317.0
C ex CO	5.48	3.2		233.0	378.0
NiMoO ₄	4.75	2.6	1.2	653.0	1130.0
A	4.60	2.29	0.9	229.0	322.0
B	4.76	2.87		246.5	307.0
C	4.87	2.57		365.0	442.0
D	5.12	1.69		158.0	350.0
E	5.20	2.55		771.0	930.0
F	5.3	2.7		237.0	307.0

This table displays a relatively small variation of the resistivities between the different samples in the range of the temperatures investigated from 25° up to 115°C. For the samples which contain Mo naphthalocyanine (presence of DCN in the synthesis) there was only a small difference between the capacitances from 307 to 350 μF at 80°C. They remained lower than that of the support covered with carbon black but of the same order. For molybdenum oxide and NiMoO₄ an increase by about a factor of three was observed. Therefore the higher activity observed with the naphthalocyanine samples cannot be correlated with a difference in specific areas which increase as the capacitance increases. In contrast the increase in capacitances *vs.* temperature observed on all the samples may correspond to an increase of the surface in contact with the electrolyte due to improved wetting (capacitances becoming higher with the penetration of the electrolyte into the pores).

Cyclic voltammetry.—Typical results at 80°C are given in Fig. 2, with correction being made for the ohmic drop given in Table II. All samples containing NPcMo gave reproducible results, with oxygen evolution occurring be-

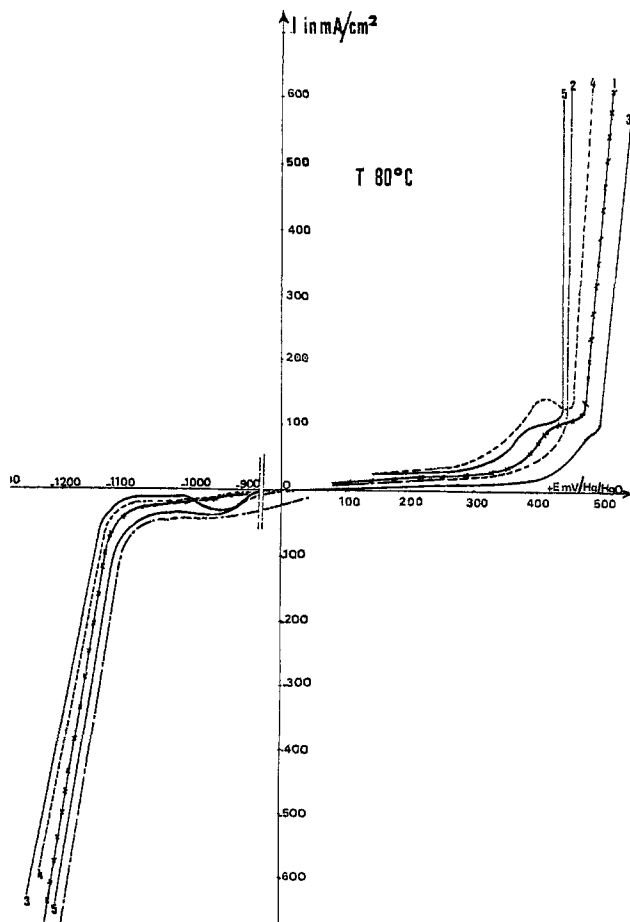


Fig. 2. i - E curves at 80°C KOH 8 mol initial. 1, Ni support; 2, carbon black; 3, NiMoO₄; 4, ammonium molybdate; 5, NPcMo sample A. Reference Hg/HgO scanning velocity 0.2 mV/s.

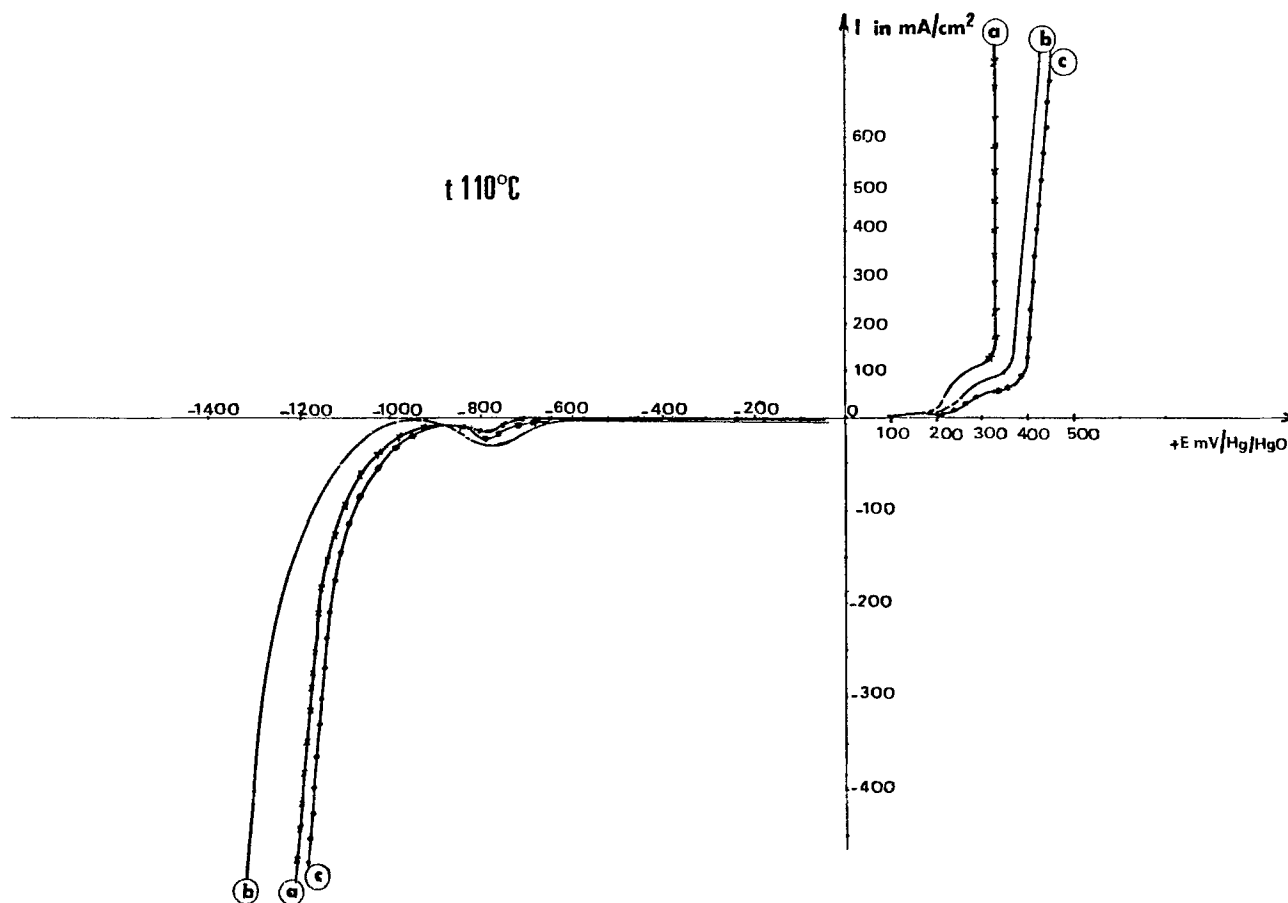


Fig. 3. *i-E* curves at 110°C KOH 8 mol initial. a, NPcMo sample A; b, NiMoO₄; c, Ni support. Same conditions as for Fig. 2.

tween 440 and 450 mV (Hg/HgO) at 300 mA/cm², the scanning velocity being fixed at 0.2 mV/s. At a current density of 300 mA/cm² the potential gain for NPcMo was about 80 and 40 mV compared with NiMoO₄ and MoO₃, respectively. Humps before O₂ evolution can be attributed to Ni²⁺/Ni³⁺ couple which is present in the carbon black structure ex CO (7) and also found with the nickel support. On the same figure data for hydrogen evolution are represented. The carbon black support yielded the same activity as NPcMo. It must be pointed out however from Table Ib that the carbon black samples without any loading were not as stable as NPcMo.

Data concerning the support NiMoO₄ and NPcMo at 110°C are represented in Fig. 3, with the scanning velocity being fixed at 0.2 mV/s. With correction being made for the ohmic drop, at a constant current density, the overvoltage for O₂ evolution on NPcMo sample A is about 100 mV lower than on NiMoO₄, which is roughly equivalent to the support. The variation of the O₂/4 OH⁻ reversible potential *vs.* temperature can be obtained from Eq. [58] and Fig. 6 of Ref. (11) (also see Appendix). It may be stressed that on the NPcMo sample, several hundred milliamperes per square centimeter are obtained at an overvoltage less than 125 mV from the theoretical potential of the O₂/4 OH⁻ couple. For H₂ evolution the support and NPcMo were equivalent and more active than NiMoO₄.

Results for a cell with a cathode and anode of the same material with a constant potential of 1.5V between the electrodes are represented in Fig. 4 as a function of time. The Teflon cell with a separator as given in Fig. 1 has been used. The absence of separator introduced a lack of stability in the electrode performances. Curve a refers to NPcMo sample A, curve b to NiMoO₄, and curve c to the support. It must be noted that good stability was obtained only with the NPcMo sample A and NiMoO₄. However in these conditions the current density with NPcMo sample A remained twice that observed with NiMoO₄.

Therefore the comparison between the Mo naphthalocyanine samples shows that there is greater stability in

the performance for both H₂ and O₂ evolution for the lowest ratios NPcMo/C. Thus, sample A had the best stability.

At 110°C the fact that the ohmic drop for both H₂ and O₂ evolution was of the same order for the support and

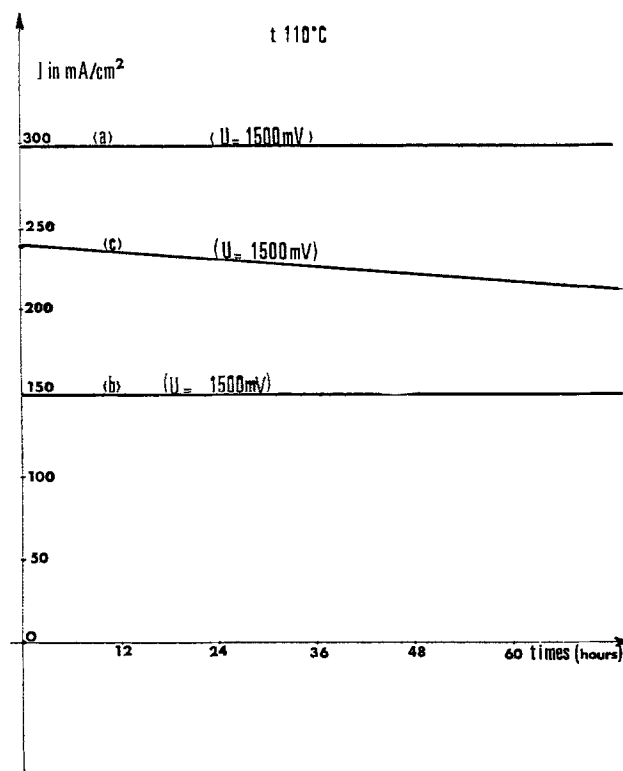


Fig. 4. Tests of stability at 110°C. $E = 1.500V$ (time in hours). (a) NPcMo sample A electrode, (b) NiMoO₄, (c) Ni support.

NPcMo sample A suggests that the residual resistivity can be attributed to the ohmic drop occurring in the pores of the support. Taking into account the stability of these materials for practical utilization in electrolyzers, one can choose the highest possible temperature (112°C or more). The performances obtained with this preparation can be compared with those described (1-6). In addition an important advantage of the stability at 110°C is that the porous separator can be operated under favorable conditions, since it has a high resistivity at temperatures below 110°C.

Acknowledgments

The authors wish to thank Professors Guerchais and Sala Pala for the synthesis of the samples, Dr. Roger Parsons for a critical reading of the manuscript, and the Direction d'Etudes et Recherches Techniques for its financial support.

Manuscript submitted April 4, 1983; revised manuscript received Aug. 3, 1983.

Laboratoire d'Electrochimie Interfaciale du CNRS assisted in meeting the publication costs of this article.

APPENDIX

The ΔG° vs. temperature is given for water by the Lewis and Randall (12) expression

$$\Delta G^\circ \text{ cal/mol} = -57,410 + 0.94T \log T + 0.00165T^2 - 3.7 \cdot 10^{-7}T^3 + 3.92T \quad [\text{A-1}]$$

which is related to the standard potential of the cell by the thermodynamic relation

$$E_o^T = - \frac{\Delta G^\circ}{2F} \quad [\text{A-2}]$$

because 2 electrons are needed for the formation of one water molecule.

At $T = 383$ K one obtains

$$E_o^T = 1.16V$$

Taking into account the partial pressure of oxygen

$$E_{eq} = E_o^T + \frac{RT}{4F} \ln \frac{P_{O_2} P_{H_2}^2}{P_{H_2O}^2} \quad [\text{A-3}]$$

Substituting the pressures by their values one obtains

$$E_{eq} = 1.26V$$

$$E_{o, eq} = 324 \text{ mV Hg/HgO in KOH } 8M$$

REFERENCES

1. D. Brown and N. Mahmood, European Pat. 0,004,169.
2. D. Brown and N. Mahmood, European Pat. 0,009,405.
3. A. J. Appleby and G. Crepy, French Pat. 2,362,945.
4. A. J. Appleby and G. Crepy, French Pat. 2,418,280.
5. A. J. Appleby and G. Crepy, French Pat. 2,418,281.
6. P. Rasiyah and A. C. C. Tseung, *This Journal*, **130**, 365 (1983).
7. G. Magner, M. Savy, G. Scarbeck, J. Riga, and J. J. Verbist, *ibid.*, **128**, 1674 (1981).
8. G. Magner, M. Savy, and G. Scarbeck, *ibid.*, **127**, 1076 (1980).
9. J. Riga, M. Savy, J. J. Verbist, J. E. Guerchais, and J. Sala Pala, *J. Chem. Soc., Faraday Trans. 1*, **78**, 2773 (1982).
10. O. Dupre La Tour, J. Farcy, E. Levart, P. Malaterre, and D. Schuhmann, *J. Electroanal. Chem.*, **39**, 241 (1972).
11. R. L. Leroy, C. T. Bowen, and D. J. Leroy, *This Journal*, **127**, 1954 (1980).
12. G. Lewis and M. Randall, "Thermodynamics and Free Energy of Chemical Substances," McGraw Hill, New York (1923).



Desorption Rates at Electrode/Electrolyte Interfaces

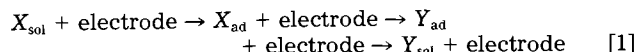
Yehuda Zeiri, Antonio Redondo, and William A. Goddard III

Arthur Amos Noyes Laboratory of Chemical Physics, California Institute of Technology, Pasadena, California 91125

ABSTRACT

A recently proposed theoretical approach using classical stochastic diffusion theory (CSDT) to predict desorption rates from solid surfaces is generalized to treat desorption of a particle from a solid surface into a liquid phase. Such systems are characterized by large friction constants resulting in a strong dependence of the desorption rate on the microscopic parameters of the liquid (e.g., solvent self-diffusion constant). The dependence of desorption on the different microscopic parameters of the system is examined. Based on these results, we propose electrochemical measurements which can be combined with the CSDT method to obtain microscopic information on the particle-surface interaction potentials at the solid/liquid interface.

The understanding of the microscopic details of processes occurring at metal and semiconductor electrodes have great importance in the design and improvement of electrochemical cells, fuel cells, etc., as well as in the fundamental study of solid/liquid interfaces. The basic and most important step in any system that contains a solid/liquid interface is the charge transfer process. Although a large amount of work has been devoted to the study of charge transfer at electrodes, relatively little is known about the detailed microscopic dynamics of these processes. The rate of charge transfer at an electrode can be regarded, in general, as a combination of the rates of three basic steps; (i) adsorption to the electrode surface, (ii) charge or atom transfer between the adsorbate and the electrode, and (iii) desorption of the newly formed adsorbate from the surface to the solvent. We can write these three steps in the following schematic form



where the subscripts sol and ad stand for solvated and adsorbed, respectively, and it was assumed that particle X was transformed into Y after the charge transfer takes place. In general, it is impossible to measure experimentally the individual rates of these three processes. Theoretical determination of the charge transfer rate, $X_{\text{ad}} + \text{electrode} \rightarrow Y_{\text{ad}} + \text{electrode}$, is possible provided that the adsorbate-electrode interaction potentials and the corresponding coupling terms are known. However, since the adsorption and desorption steps are complicated many-body processes that take place on a very long time scale compared to a molecular vibrational period, a theoretical estimate of the corresponding rates is very difficult.

Recently we have described a new method to evaluate rates of desorption for atoms and molecules adsorbed on solid surfaces, which is based on classical stochastic diffusion theory (CSDT) (1). Using the CSDT formalism (in the following we shall refer to Ref. (1b) as paper I), we have derived simple analytic expressions for atoms and molecules desorbing from solid surfaces (to vacuum), where the desorption rates were given in terms of the microscopic parameters of the system (e.g., D_e , the binding energy, Ω_0 , the stretching frequency of the adsorbate-surface interaction, k_r , the force constant for frustrated rotation, and T , the temperature). Similar expressions for the rate of desorption of both atoms (2) and molecules (3) from solid surfaces have also been obtained using transi-

tion state theory (TST). These rate expressions have the form

$$R = \frac{\Omega_0}{2\pi} f(T) \exp \left[- \frac{D_e}{kT} \right] \quad [2]$$

where $f(T) = 1$ for atomic adsorbate and $f(T) \propto k_r/kT$ for molecules. An interesting feature of Eq. [2] is that the desorption rate does not depend on the characteristics of the solid surface (e.g., Debye frequency) except through the adsorbate-surface interaction potential. This behavior is a result of the thermal averaging, incorporated in both the CSDT and TST methods, which suppresses the individual dynamical events occurring during the desorption process.

In this paper, we derive an expression for the rate of desorption of an atom (or ion) from an electrode surface into a condensed phase, namely, the solution. In so doing, we shall follow a derivation similar to the one employed in gas phase desorption (1). An expression for the desorption rate is derived below followed by the presentation and discussion of the results obtained for some model calculations. Finally, in the last part of the paper we outline some conclusions related to the calculated rates.

CSDT for Desorption from Electrode Surfaces

We shall start by considering a system composed of a desorbing particle (atom or ion), with mass M , interacting with a solid surface (electrode) and a number of solvent particles, with mass M_1 , as illustrated schematically in Fig. 1. For the description of the surface, we shall follow the ideas introduced by Adelman and Doll (4, 5) and divide the electrode atoms into two groups: (i) a small number of atoms which are strongly interacting with the adsorbed particle, this group will be called the primary zone, and (ii) the rest of the solid which is assumed to act as a heat bath. Without loss of generality we shall assume that the primary zone contains only one atom whose mass will be denoted by M_s . A further simplification is introduced by limiting both the desorbing particle and the primary zone atom to a one-dimensional motion normal to the solid surface. Thus, the motion of the adparticle will be described by a Newtonian equation of motion

$$M\ddot{R} = - \frac{\partial V(R, \zeta, \mathbf{Z})}{\partial R} \quad [3]$$

where ζ represents the displacement of the surface pri-

1555

mary zone atom from its lattice point. The vector \mathbf{Z} includes the displacement from equilibrium along the line connecting the centers of the adparticle and the solvent particles surrounding it. The total interaction potential, $V(R, \zeta, \mathbf{Z})$, felt by the adparticle is assumed to be given by a sum of pairwise interactions

$$V(R, \zeta, \mathbf{Z}) = V(R - \zeta) + \sum_{i=1}^{N(R)} V_i(R - \mathbf{Z}_i) \quad [4]$$

where $N(R)$ is the number of solvent particles surrounding the adsorbate at any given R . In the following, we shall use harmonic potentials to represent the interaction between the desorbing particle and the solvent

$$V_i(R - \mathbf{Z}_i) = 1/2 k_i [r - \mathbf{Z}_i]^2 \quad [5]$$

The interaction between the surface and the desorbing particle will be represented by a properly dissociating potential (e.g., Morse or Lennard-Jones) which is fitted with parabolic splines (see paper I)

$$V(R - \zeta) = \sum_i V_i(x) \quad [6]$$

where $x = R - \zeta$ and

$$V_i(x) = \begin{cases} 0 & x < x_i \\ A_i + B_i x + 1/2 C_i x^2 & x_i \leq x \leq x_{i+1} \\ 0 & x_{i+1} < x \end{cases} \quad [7]$$

x_i and x_{i+1} being the boundaries of the i th interval. The fit of Eq. [7] is performed in such a way that at any boundary point, x_i , the functions V_{i-1} and V_i and their first derivatives are continuous.

The motion of the surface primary zone atom as well as the motion of the solvent molecules will be described using the equivalent harmonic chain representation (EHCR) introduced by Adelman (6). We shall use this representation to construct model heat baths and employ the Markovian approximation in reducing the resulting generalized Langevin equations of motion to the corresponding Langevin equations (Appendix A). The introduction of the Markovian approximation is justified (see paper I) due to the large difference in the desorption time scale compared to a molecular vibrational period. Using the effective equation of motion derived in Appendix A to describe the motion of the primary zone surface atom, we have

$$M_s \ddot{\zeta} = -M_s \Omega_s^2 \zeta - M_s \beta_s \dot{\zeta} - \frac{\partial V(R, \zeta, \mathbf{Z})}{\partial \zeta} + f_s(t) \quad [8]$$

and similarly, the motion of the i th solvent particle is described by

$$M_i \ddot{\mathbf{Z}}_i = -M_i \Omega_i^2 \mathbf{Z}_i - M_i \beta_i \dot{\mathbf{Z}}_i - \frac{\partial V(R, \zeta, \mathbf{Z})}{\partial \mathbf{Z}_i} + f_i(t) \quad [9]$$

The effective frequencies and friction constants of Eq. [8] and [9] are given in terms of the EHCR parameters as discussed in Appendix A.

Next we substitute the potentials of Eq. [2]-[7] into Eq. [8] and [9] and solve them formally (using Laplace transforms). These solutions are then substituted into Eq. [3] to give

$$M \ddot{R} = \sum_{i=1}^{N(R)} \left[-k_i R + \frac{k_i^2}{M_i} \int_0^t \Theta_i(t-t') R(t') dt' + k_i f_i(t) \right] + \sum_{i=1}^n \left[-(B_i + C_i R) + C_0 \frac{C_i}{M_s} \int_0^t \Theta_s(t-t') R(t') dt' + C_i f_s(t) \right] \chi_i \quad [10]$$

where C_0 represents the force constant associated with the desorbing particle-surface interaction and χ_i is the characteristic function of the i th interval ($\chi_i = 1$ if R is in the i th interval and $\chi_i = 0$ otherwise). The memory kernels Θ_i and Θ_s in Eq. [10] are given by

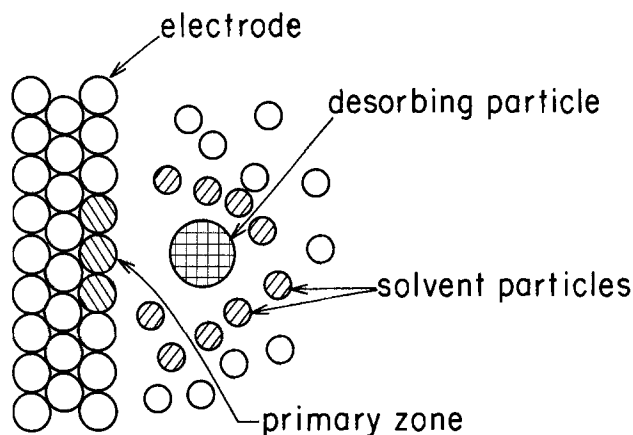


Fig. 1. Schematic description of the adsorbate at a solid/liquid interface.

$$\Theta_i(t) = \frac{1}{S_i} \left\{ \exp \left[-\frac{1}{2} (\beta_i - S_i) t \right] - \exp \left[-\frac{1}{2} (\beta_i + S_i) t \right] \right\} \quad [11]$$

where $S_i = [\beta_i^2 - 4\bar{\Omega}_i^2]^{1/2}$ and $\bar{\Omega}_i^2 = \Omega_i^2 + k_i/M_i$. Similarly

$$\Theta_s(t) = \frac{1}{S_s} \left\{ \exp \left[-\frac{1}{2} (\beta_s - S_s) t \right] - \exp \left[-\frac{1}{2} (\beta_s + S_s) t \right] \right\} \quad [12]$$

where $S_s = [\beta_s^2 - 4\bar{\Omega}_s^2]^{1/2}$ and $\bar{\Omega}_s^2 = \Omega_s^2 + C_0/M_s$.

Assuming that the adsorbate-solvent interaction has the same form for all the $N(R)$ solvent particles, we can eliminate the first summation in Eq. [10] and instead multiply each term by $N(R)$. Furthermore, we may also eliminate the second summation and replace C_i and B_i by $C(R)$ and $B(R)$. Integrating by parts the two convolution integrals in Eq. [10] and rearranging terms, we can rewrite the effective equation of motion for the desorbing particle as

$$M \ddot{R} = -\{[N(R)k_i - \Gamma_i(0)] + [C(R) - \Gamma_s(0)]\}R - B(R) - \int_0^t [\Gamma_i(t-t') + \Gamma_s(t-t')] \dot{R}(t') dt' - [\Gamma_i(t) + \Gamma_s(t)] R(0) + F(t) \quad [13]$$

where

$$\Gamma_i(t) = N(R) \frac{k_i^2}{M_i} \int_t^\infty \Theta_i(t') dt' \quad [14]$$

$$\Gamma_s(t) = \frac{C_0 C(R)}{M_s} \int_t^\infty \Theta_s(t') dt' \quad [15]$$

The term in braces in Eq. [13] represents the total potential felt by the desorbing particle. It includes the corrections due to the thermal motion of both the surface atoms and the solvent particles surrounding the desorbing particle; thus, this is the potential that one would obtain experimentally. In the following, we shall denote this total potential by $V_{\text{tot}}(R, \zeta, \mathbf{Z})$. Due to the large difference in time scales one may introduce the Markovian limit to Eq. [13] and obtain the corresponding Langevin equation

$$M \ddot{R} = -\frac{\partial V_{\text{tot}}(R, \zeta, \mathbf{Z})}{\partial R} - (\tilde{\beta}_i(R) + \tilde{\beta}_s(R)) \dot{R} + \tilde{F}(t) \quad [16]$$

where

$$\tilde{\beta}_i(R) = \frac{N(R)k_i^2\beta_i}{M_i\bar{\Omega}_i^4} \quad [17]$$

$$\tilde{\beta}_s(R) = \frac{C_0 C(R)\beta_s}{M_s\bar{\Omega}_s^4} \quad [18]$$

Equation [16] represents an effective equation of motion for the desorbing particle whose motion is coupled to a heat bath constituted by the electrode surface

and the solvent particles. Since $V_{tot}(R, \zeta, \mathbf{Z})$ is an anharmonic function, we may fit it by a parabolic spline fit of the form introduced in Eq. [4]-[7]

$$V_{tot}(R, \zeta, \mathbf{Z}) = \sum_i V_i(R) \quad [19]$$

$$V_i(R) = \begin{cases} 0 & R < R_i \\ A_i + \bar{B}_i R + \frac{1}{2} \bar{C}_i R^2 & R_i \leq R \leq R_{i+1} \\ 0 & R_{i+1} < R \end{cases} \quad [20]$$

To express $\bar{\beta}_1$ and $\bar{\beta}_s$ in terms of the microscopic parameters of the system, one should evaluate the effective frequencies and friction constants of Eq. [8] and [9]. One can use as an estimate of these quantities the expressions obtained in Appendix A (Eq. [A.7] and [A.9]) and rewrite β_1 and β_s in the form

$$\bar{\beta}_1 = \frac{N(R)kT\kappa_1^2}{D_1 M_1^2 \left(\Omega_{01}^2 + \frac{\kappa_1}{M_1} \right)^2} \quad [21]$$

where D_1 is the self-diffusion coefficient of the liquid, and

$$\bar{\beta}_s = \frac{0.52547 \omega_D C_0 C(R)}{M_s \left(0.33295 \omega_D^2 + \frac{C_0}{M_s} \right)^2} \quad [22]$$

Thus, the final effective equation of motion for the desorbing particle is given by

$$M\ddot{R} = -\bar{B}(R) - \bar{C}(R)R - \beta_{tot}(R)\dot{R} + \tilde{F}(t) \quad [23]$$

where $\bar{B}(R)$ and $\bar{C}(R)$ are the first and second derivatives of the total potential, V_{tot} , evaluated at the point R , and $\beta_{tot}(R) = \bar{\beta}_1(R) + \bar{\beta}_s(R)$.

As discussed above, Eq. [23] describes the motion of the desorbing particle in terms of a Brownian oscillator where the interaction with the heat bath is given in terms of the microscopic quantities of the system. The amplitude of the random force, $\tilde{F}(t)$, is defined by its relation to β_{tot} through the second fluctuation-dissipation theorem. To derive an expression for the rate of desorption, one should first evaluate the probability distribution function for the desorbing particle and use this to obtain the flux at any given point in space. In evaluating the expression for the flux, we shall closely follow the derivation in paper I. The steady-state probability distribution is the solution to the (time independent) generalized Liouville equation (1, 7) and is given by

$$W(R, U) = A_0 F(R, U) \exp \left[-\frac{MU^2}{2kT} - \frac{V_{tot}(R)}{kT} \right] = A_0 F(R, U) W_{MB}(R, U) \quad [24]$$

where A_0 is a normalization constant, U is the velocity of the desorbing particle, W_{MB} is the Maxwell-Boltzman distribution function, and

$$F(R, U) = \left[\frac{\alpha - \tilde{\beta}_{tot}}{2\pi q} \right]^{\frac{1}{2}} \int_0^\xi \exp \left[-\frac{(\alpha - \tilde{\beta}_{tot})\xi'^2}{2q} \right] d\xi' \quad [25]$$

where $\xi = U - \alpha R - b$, $q = kT\tilde{\beta}_{tot}$, $\tilde{\beta}_{tot} = \beta_{tot}/M$ and

$$\alpha = \frac{1}{2}[\tilde{\beta}_{tot} + (\tilde{\beta}_{tot}^2 - 4d_1)^{\frac{1}{2}}] \quad [26]$$

$$b = -\frac{2d_0}{\alpha - \tilde{\beta}_{tot}} \quad [27]$$

where $d_1 = \bar{C}(R)/M$ and $d_0 = \bar{B}(R)/M$. The functional form of $F(R, U)$ is such that $F(R, U) = 1$ for $R = 0$ while $F(R, U) \rightarrow 0$ as $R \rightarrow \infty$.

In order to obtain an expression for the rate of desorption, we will calculate the flux of desorbing particles at a given distance from the surface, R_0 . The calculated flux must take into account only those particles at R_0 which have sufficient kinetic energy (and the proper velocity direction) to escape. Thus, the expression for the flux at a given value of R_0 is

$$j(R_0, U_0) = \int_{U_0}^\infty W(R_0, U) U dU \quad [28]$$

where U_0 is the smallest (positive) velocity for which a particle at R_0 will desorb, i.e.

$$D_e = V_{tot}(R_0) + \frac{1}{2}MU_0^2 \quad [29]$$

and where D_e is the well depth of V_{tot} . Substitution of Eq. [24] and [25] into [28] gives

$$j(R_0, U_0) = A_0 \left(\frac{\alpha - \tilde{\beta}_{tot}}{2\pi q} \right)^{\frac{1}{2}} \exp \left[-\frac{V_{tot}(R_0)}{kT} \right] \times \int_{U_0}^\infty \exp \left[-\frac{MU^2}{2kT} \right] \int_0^\xi \exp \left[-\frac{(\alpha - \tilde{\beta}_{tot})\xi'^2}{2q} \right] d\xi' U dU \quad [30]$$

Integrating by parts and rearranging we obtain

$$j(R_0, U_0) = A_0 \frac{kT}{M} \exp \left\{ -\frac{[MU_0^2 + 2V_{tot}(R_0)]}{2kT} \right\} Y(T) \quad [31]$$

where

$$Y(T) = \Phi(\alpha_1) + \exp(-\eta) \left[\frac{\pi\beta_{tot}kT}{2Ma} \right]^{\frac{1}{2}} [1 - \Phi(\alpha_2)] \quad [32]$$

with $\alpha_1 = \left(\frac{M(\alpha - \beta_{tot})}{2kT\beta_{tot}} \right)^{\frac{1}{2}} [U_0 - (\alpha R_0 + b)] \quad [33]$

$$\alpha_2 = \left(\frac{Ma}{2kT\beta_{tot}} \right)^{\frac{1}{2}} [-\vartheta(\alpha R_0 + b) + U_0] \quad [34]$$

$$\vartheta = 1 - \beta_{tot}/\alpha \quad [35]$$

and

$$\eta = \vartheta\beta_{tot}(\alpha R_0 + b)^2/2q \quad [36]$$

The symbol $\Phi(\alpha)$ represents the error function (8). Substituting Eq. [29] into Eq. [31]-[32] leads to the final expressions for the flux

$$j(R_0, U_0) = A_0 \frac{kT}{M} Y(T) \exp \left[-\frac{D_e}{kT} \right] \quad [37]$$

The rate for a desorption process is given (1, 7) by the ratio of the flux (Eq. [31]-[32]) at R_0 to the number of particles, N_0 , at the surface. The distribution function of the particles in the neighborhood of the equilibrium distance, $R = 0$, is given by W_{MB} , Eq. [24], leading to

$$N_0 = A_0 \int_{-\infty}^\infty \int_{-\infty}^\infty \exp \left[-\frac{MU^2}{2kT} - \frac{V_{tot}(R)}{kT} \right] dR dU = A_0 \left[\frac{2\pi kT}{M} \right]^{\frac{1}{2}} \int_{-\infty}^\infty \exp \left[-\frac{V_{tot}(R)}{kT} \right] dR \quad [38]$$

where the limits in the integral over R have been taken from $-\infty$ to ∞ because the integrand becomes negligibly small for values of R far away from $R = 0$.

For experimentally interesting temperature ranges (where $kT \ll D_e$), one can approximate the interaction potential, $V_{tot}(R)$, by a harmonic potential to obtain

$$N_0 = A_0 \left(\frac{2\pi kT}{M\Omega_0} \right) \quad [39]$$

where Ω_0 is the stretch frequency associated with the bottom of the potential well, V_{tot} .

Combining Eq. [37] and [38] leads to a desorption rate of the form

$$R = \frac{j}{N_0} = \left[\frac{kT}{2\pi M} \right]^{\frac{1}{2}} Y(T) \left\{ \int_{-\infty}^\infty \exp \left[-\frac{V_{tot}(R)}{kT} \right] dR \right\}^{-1} \exp \left[-\frac{D_e}{kT} \right] \quad [40]$$

and using Eq. [39] for N_0 leads to

$$R = \frac{\Omega_0}{2\pi} Y(T) \exp \left[-\frac{D_e}{kT} \right] \quad [41]$$

as the final expression for the desorption rate of atoms from solid surfaces.

In concluding this section, it should be emphasized that the major assumptions in deriving the expressions for the desorption rate are the introduction of the Markovian limit in Eq. [30] and [A.4]. As discussed above, the justification for the use of this approximation is based on the large difference between the time scale for the process of interest (desorption) compared to the molecular time scale (the vibrational period). Namely, we have assumed that the long time behavior of the different motions is well described by the Langevin equation of motion. It should be noted that a similar derivation can be made for this case in which Eq. [30] and [A.4] are used without the introduction of the Markovian approximation. Such derivation is much more complicated, due to the algebraic complexity of the equations. At present, we are in the process of performing these calculations to check the validity of the use of the Markovian limit.

Results and Discussion

In this section, we shall discuss the dependence of the desorption rate on the different microscopic parameters of the system. One of the major difficulties in most microscopic theories of solid/liquid interfaces arises from the lack of reliable interaction potentials for such systems. In the present study, we have chosen a model potential of the Morse type. One of our main objectives will be the study of the relationship of desorption rates to the potential parameters (D_e and Ω_0). Moreover, in the calculations described below, we have introduced a further approximation, namely, we assumed that $\Omega_{0(1)}^2 \ll k_f/M_1$. Since $\Omega_{0(1)}$ corresponds to the low frequency limit (it is zero for the case of free diffusion), this assumption is valid for most systems (especially in the case where the adsorbate-solvent interaction is strong, e.g., for ions in polar solvents). Using this approximation, we can rewrite the friction due to the solvent (Eq. [21]) in the form

$$\tilde{\beta}_1 = \frac{N(R)kT}{D_1} \quad [42]$$

A comparison between the magnitudes of $\tilde{\beta}_1$ in Eq. [42] and $\tilde{\beta}_s$ of Eq. [22] for typical values of the different parameters show that $\tilde{\beta}_s$ is smaller than $\tilde{\beta}_1$ by about two to four orders of magnitude (for example, for $M_s = 50$, $\Omega_0 = 600 \text{ cm}^{-1}$, $D_1 = 1.0 \times 10^{-5} \text{ cm}^2 \text{ s}^{-1}$, $T = 300 \text{ K}$, $\omega_0 = 278 \text{ cm}^{-1}$, and $R = 6.0 \text{ bohr}$, we obtain $\tilde{\beta}_1 = 38.6 \text{ a.u.}$ and $\tilde{\beta}_s = 0.36 \text{ a.u.}$). As a result, one may neglect $\tilde{\beta}_s$ and write

$$\beta_{\text{tot}}(R) = \tilde{\beta}_1(R) \quad [43]$$

In obtaining Eq. [43], we have taken into account the fact that $C(R)$ at $R = R_0$ is smaller than C_0 by about two orders of magnitude.

In Fig. 2, we present the calculated desorption rate as a function of temperature for two different values of Ω_0 (all other parameters are kept constant). In both cases, the solid line represents the actual rate while the dashed line represents the rate that one would obtain by setting $Y(T) = 1$. It is clear from these results that $Y(T)$ is very sensitive to changes in the stretch frequency while its dependence on the variation in T is weak. Moreover, it is clear from the functional form of Y (Eq. [32]) that this quantity will tend to reduce the desorption rate into a liquid with respect to that into vacuum. Figure 3 shows the variation of $\log(Y)$ as a function of the mass of the adparticle for different frequencies and bond strength of the total potential. This figure shows that $Y(T)$ exhibits a strong dependence on M , Ω_0 , and D_s , while it is weakly dependent on both D_1 (in the physically meaningful range of the diffusion constant, $5 \times 10^{-6} - 5 \times 10^{-5}$) and T .

Under typical electrochemical experimental conditions, it is difficult to change the temperature in the controlled manner (temperature programmed desorption) so useful at the gas/solid interface, but systematic changes in the applied voltage are very easy to perform. To relate our theory to these conditions, we have calculated the varia-

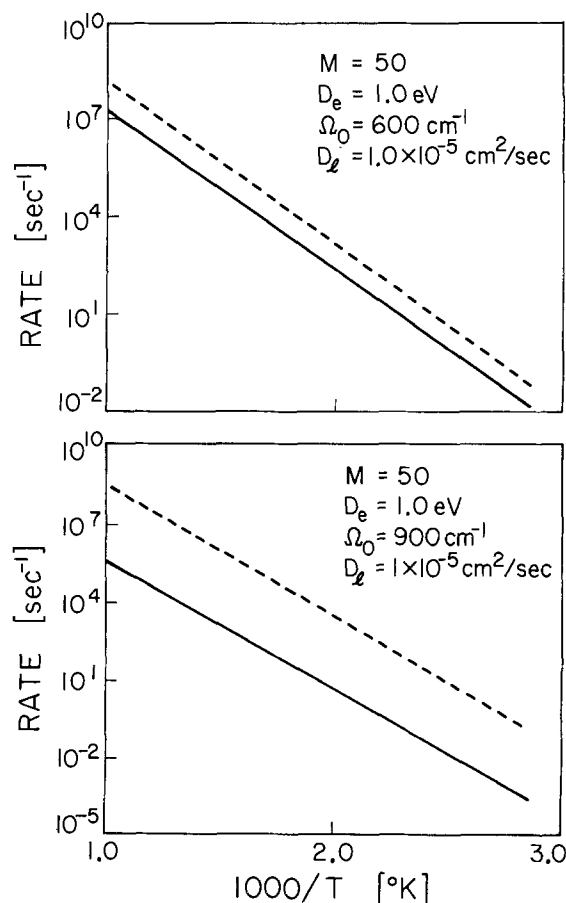


Fig. 2. Rates of desorption vs. temperature for two different stretch frequencies (a, top) $\Omega_0 = 600 \text{ cm}^{-1}$ and (b, bottom) $\Omega_0 = 900 \text{ cm}^{-1}$. The solid line corresponds to the calculated rate while the dashed line represents the rate that would be obtained by setting $Y(T) = 1$.

tion of the desorption rate as a function of the applied voltage. In the absence of an external field, the potential felt by the desorbing particle, V_{tot} , was assumed to have a Morse form. The potential profile due to the applied field through the diffuse layer was chosen to vary according the Gouy-Chapman (9) model

$$V_{\text{elec}}(X) = 2kT \{ \log(1 + A(V_0) \exp[-\alpha X]) - \log(1 - A(V_0) \exp[-\alpha X]) \} \quad [44]$$

where $1/\alpha = 30.4 \text{ \AA}$, X is the distance from the electrode and

$$A(V_0) = \tanh\left(\frac{V_0}{4kT}\right) \quad [45]$$

V_0 being the potential difference between the electrode and the bulk of the solution. We then assumed that the net potential felt by the adparticle (considered to be an ion in this case) is given by

$$V_{\text{net}} = V_{\text{tot}} + V_{\text{elec}} \quad [46]$$

Figure 4 shows the dependence of the desorption rate on the applied voltage. It is evident from these results that there is a large change in the rate (about three orders of magnitude) at low applied fields, and one obtains a saturation at voltages that are larger than 0.3V. This saturation is a result of the fast exponential decay of $V_{\text{elec}}(X)$ at high voltages. The increase in the rate is a consequence of our choice of the sign of the potential difference between the two electrodes. A decrease in the rate would be obtained if we would choose a reversed sign for this potential difference.

Conclusions

We have described in this paper a microscopic model which leads to analytic expressions for the desorption

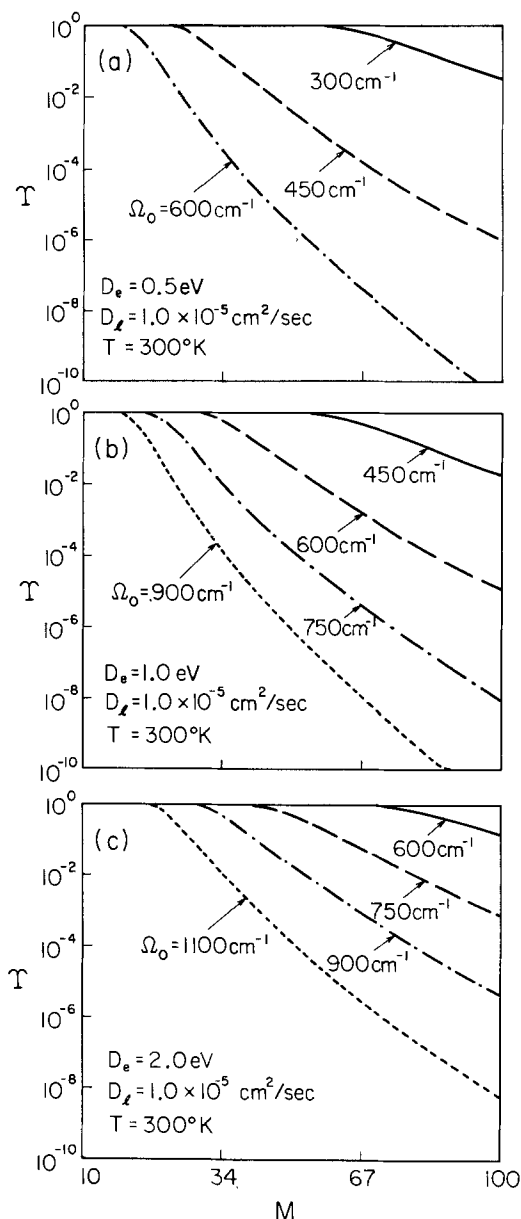


Fig. 3. Variation of $Y(T)$ with the adsorbate mass for different dissociation energies. (a, top) $D_e = 0.5$ eV; (b, middle) $D_e = 1.0$ eV; and (c, bottom) $D_e = 2.0$ eV.

rate of an adsorbate from an electrode into the solvent. These expressions are easy to implement, provided that the microscopic parameters of the system are known. We have also proposed a procedure to calculate the dependence of the desorption rate on an applied electric field. Unfortunately, the microscopic details of processes that occur at electrode/electrolyte interfaces are very difficult to obtain experimentally, and hence, it is necessary to link these microscopic quantities to experimentally measurable data. A possible example corresponds to the measurement of the equilibrium rate constant (ratio between adsorption and desorption rates), which can then be used to obtain estimates of the adparticle-electrode binding energy. For example, one could obtain the equilibrium rate constant from measurements of the variation of the flatband potential, $V_H(C_{tot})$, of semiconductor electrodes as a function of ion concentration, C_{tot} (10). Consider a parallel plate capacitor model of the interface. The surface charge density, $\sigma(C_{tot})$, can be obtained by using the Schottky model of a metal-semiconductor junction (11),

$$\sigma(C_{tot}) = [2e\epsilon N_D V_H(C_{tot})]^{1/2} \quad [47]$$

where e is the fundamental charge, ϵ is the dielectric constant, and N_D is the impurity concentration in the semiconductor. If one assumes that the change in flatband

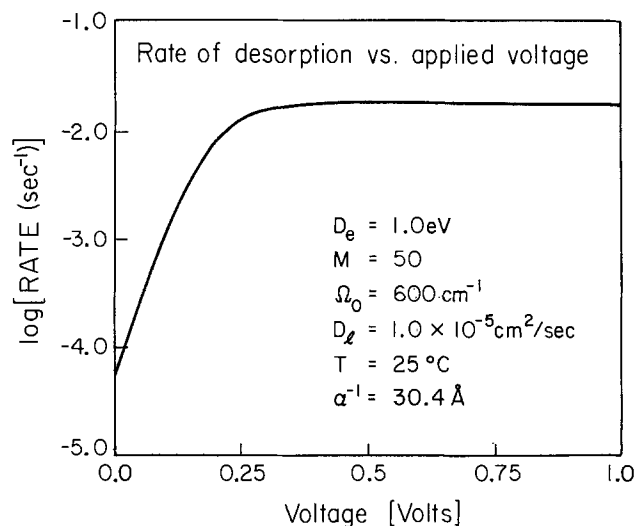


Fig. 4. Rate of desorption vs. applied voltage

potential as a function of the concentration of ions in the solution is mainly due to adsorption of ions on the electrode surface, then the adsorbate concentration in the Helmholtz layer, C_{ad} (number of particles per unit volume), is given by

$$C_{ad} = \frac{[\sigma^2(0) + 2e\epsilon N_D \Delta V_H]^{1/2} - \sigma(0)}{ed} \quad [48]$$

where d is the width of the Helmholtz layer, and $\sigma(0)$ corresponds to the surface charge density when $C_{tot} = 0$. In Eq. [48], we assumed that the adsorption of ion on the electrode surface does not change the initial surface charge density, that is

$$\sigma(C_{tot}) \approx edC_{ad} + \sigma(0) \quad [49]$$

This assumption should be particularly applicable at low coverages of the electrode surface. Equation [48] relates the measured change in flatband potential, ΔV_H , to C_{ad} . Assuming equilibrium conditions for a given C_{tot} , we have

$$C_{ad}k_d = (C_{tot} - C_{ad})k_{ad} \quad [50]$$

where k_d and k_{ad} are the rates for desorption and adsorption, respectively. Equations [48] and [50] provide a means to determine the equilibrium constant of the system, k_{ad}/k_d , from measurements of C_{tot} and ΔV_H , as a function of applied voltage.

Once the equilibrium constant is known, one could use the results of CSDT (Eq. [41]) to determine the adparticle-electrode binding energy, D_e , as follows. From a knowledge of the vibrational frequencies for the adsorbate-electrode system (e.g., from IR reflection experiments) and an independent determination of the adsorption rate, k_{ad} , (e.g., by using Langmuir adsorption-desorption kinetics), one would determine the binding energy from Eq. [50] and [41].

Acknowledgment

We acknowledge partial support of this work by the Department of Energy (Contract DE-AM03-76SF00767; Project Agreement DE-AT03-80ER10608).

Manuscript submitted Aug. 1, 1983.

APPENDIX A

In this appendix we shall outline the procedure by which the parameters of the Langevin equations of motion (Eq. [8] and [9]) can be evaluated. We start by describing the motion of the primary zone surface atom and the motion of a solvent particle using the equivalent harmonic chain representation introduced by Adelman (6). For simplicity, we shall use a two atom model heat bath chain

$$\begin{aligned} \ddot{Q}_0(t) &= -\omega_{e1}^2 Q_0(t) + \omega_{e1}^2 Q_1(t) \\ \ddot{Q}_1(t) &= -\Omega_1^2 Q_1(t) + \omega_{e1}^2 Q_0(t) - \beta_2 \dot{Q}_1(t) + f_2(t) \end{aligned} \quad [A-1]$$

where Q_0 is the actual position of the particle, and Q_1 is the position of a fictitious particle. The coefficients ω_{e0}^2 and ω_{c1}^2 represent the Einstein and coupling frequencies while Ω_1^2 and β_2 are the low frequency and friction constant, respectively. Reference (6) provides a description of the derivation and the relations between these parameters. We now solve formally (using Laplace transforms) the equation of motion for Q_1 and substitute the result in the equation for Q_0

$$\ddot{Q}_0(t) = -\omega_{e0}^2 Q_0(t) + \omega_{c1}^4 \int_0^t \Theta(t-t') Q_0(t') dt' + \tilde{f}(t) \quad [A-2]$$

where

$$\Theta(t) = \frac{1}{S} \{ \exp(-\frac{1}{2}(\beta_2 - S)t) - \exp[-\frac{1}{2}(\beta_2 + S)t] \} \quad [A-3]$$

and $S = [\beta_2^2 - 4\Omega_1^2]^{\frac{1}{2}}$. Integration by parts of the memory integral of Eq. [A-2] yields

$$\ddot{Q}_0(t) = -\omega_{e0}^2 Q_0(t) + \omega_{c1}^4 \beta(0) Q_0(t) - \omega_{c1}^4 \int_0^t \beta(t-t') \dot{Q}_0(t') dt' - \omega_{c1}^4 Q_0(0) \beta(t) + \tilde{f}(t) \quad [A-4]$$

where $\beta(t)$ is related to Θ by

$$\beta(t) = \int_t^\infty \Theta(t') dt' \quad [A-5]$$

We introduce now the Markovian limit to reduce Eq. [A-4] into a Langevin equation of the form

$$\ddot{Q}_0(t) = -\Omega_{\text{eff}}^2 Q_0(t) - \beta_0 \dot{Q}_0(t) + F(t) \quad [A-6]$$

where the frequency and friction constants are given by

$$\Omega_{\text{eff}}^2 = \omega_{e0}^2 - \frac{\omega_{c1}^4}{\Omega_1^2} \quad [A-7]$$

and

$$\beta_0 = \frac{\omega_{c1}^4 \beta_2}{\Omega_1^4} \quad [A-8]$$

Thus, Eq. [A-6] represents an effective equation of motion which governs the motion of both the primary zone surface atom and the solvent particle. The coefficients in these equations of motion are given in term of the equivalent harmonic chain representation parameters which for a Debye solid take the values (6): $\omega_{e0}^2 = 0.6 \omega_D^2$, $\omega_{c1}^2 = 0.262 \omega_D^2$, $\Omega_1 = 0.507 \omega_D$, and $\beta_2 = 0.161 \pi \omega_D$. Using these values for the EHCR parameters, we obtain that

$$\Omega_{\text{eff}}^2(\text{solid}) = 0.33295 \omega_D^2 \quad [A-9]$$

and

$$\beta_0(\text{solid}) = 0.52547 \omega_D \quad [A-10]$$

It is much more difficult to estimate the EHCR parameters for a liquid particle since a knowledge of the velocity autocorrelation function is required. However, we may use the relation (6)

$$\Omega_1^2 = \frac{\omega_{c1}^4}{\omega_{e0}^2 - \Omega_0^2} \quad [A-11]$$

and

$$\beta_2 = \beta_1 \frac{\Omega_1^2}{\omega_{e0}^2 - \Omega_0^2} \quad [A-12]$$

where we used the Einstein relation $\beta_1 = kT/M_1 D_1$ (k = Boltzmann factor, M_1 = solvent particle mass, and D_1 = self-diffusion constant of the solvent). One can use these relations to rewrite Ω_{eff}^2 and β_0 in the form

$$\Omega_{\text{eff}}^2 = \Omega_0^2 \quad [A-13]$$

and

$$\beta_0 = \beta_1 = \frac{kT}{M_1 D_1} \quad [A-14]$$

The low frequency constant, Ω_0^2 , is usually equal to zero for a freely diffusing particle (6), however, in our case, this frequency is nonzero since the solvent particles of interest are interacting strongly with both the electrode surface and the desorbing particle and hence, are not freely diffusing.

REFERENCES

- (a) A. Redondo, Y. Zeiri, and W. A. Goddard III, *Phys. Rev. Lett.*, **49**, 1847 (1982); (b) Y. Zeiri, A. Redondo, and W. A. Goddard III, *Surf. Sci.*, In press.
- B. J. Garrison and S. A. Adelman, *J. Chem. Phys.*, **67**, 2379 (1977).
- A. Redondo, Y. Zeiri, J. J. Low, and W. A. Goddard III, *J. Chem. Phys.*, Submitted for publication.
- S. A. Adelman and J. D. Doll, *ibid.*, **61**, 4242 (1974); S. A. Adelman, *ibid.*, **71**, 4471 (1979), and references cited therein.
- J. C. Tully, *Surf. Sci.*, **111**, 461 (1981); J. C. Tully, *Ann. Rev. Phys. Chem.*, **31**, 319 (1980), and references cited therein.
- S. A. Adelman, *J. Chem. Phys.*, **71**, 4471 (1979); S. A. Adelman, *ibid.*, **73**, 3145 (1980); M. Berkowitz, C. L. Brooks III, and S. A. Adelman, *ibid.*, **72**, 3889 (1980); and C. L. Brooks III, M. Berkowitz, and S. A. Adelman, *ibid.*, **73**, 4353 (1980).
- H. A. Kramers, *Physica*, **7**, 284 (1940); S. Chandrasekhar, *Ref. Mod. Phys.*, **15**, 1 (1943).
- M. Abramowitz and I. A. Stegun, "Handbook of Mathematical Functions," Dover, New York (1972).
- A. J. Bard and L. R. Faulkner, "Electrochemical Methods," p. 504, Wiley, New York (1980). This model is not entirely applicable in the present case because of the absence of solvent particles between the electrode and the desorbing particle. Although this model has been chosen here to provide an illustration of our theory, the method is not restricted to any particular type of electrostatic interaction between the adparticle and the electrode.
- See for example, T. Inoue, T. Watanabe, A. Fujishima, and K. Honda, *Bull. Chem. Soc. Jpn.*, **52**, 1243 (1979); S. Sumi, T. Watanabe, A. Fujishima, and K. Honda, *ibid.*, **53**, 2742 (1980).
- See for example, B. R. Gossick, "Potential Barriers in Semiconductors," p. 70, Academic, New York (1964).

Low Temperature Oxidation of Metals and Semiconductors

Francis P. Fehlner*

Corning Glass Works, Research and Development Division, Corning, New York 14831

ABSTRACT

The growth of oxide films on metals and semiconductors at low temperatures has been interpreted using the Cabrera-Mott theory which assumes a uniform oxide structure. Kinetic data taken from the literature were introduced into the Ghez integration of the Cabrera-Mott equation. Results were found to correlate with a division of oxides into network formers, intermediates, and modifiers. The network formers and intermediates were best fit by inverse logarithmic kinetics (Cabrera-Mott), while the modifiers appeared to follow direct logarithmic kinetics. Values of activation energy for ion movement, the number of potentially mobile ions, and the self-induced voltage across the oxide have been derived for the network forming and intermediate oxides. These values are compared with those obtained from other experiments.

The field of low temperature oxidation has been experimentally handicapped by a lack of extensive data on simple systems. Several reasons account for this paucity of data: the difficulty of measurements, poor reproducibility of metal samples, little control of impurities (especially water vapor), and incomplete characterization of the product oxide. Fortunately, this situation is changing as semiconductor techniques and surface analytical methods are applied to the problem. As a result, data over an extensive temperature and pressure range are becoming available.

Analysis and interpretation of such kinetic data is the next difficulty. Historically, linearity of a plot on graph paper has been taken to be indicative of a particular mechanism. However, it has become apparent that for low temperature oxidation, both direct logarithmic (x vs. $\log t$, where x is oxide thickness and t is time) and inverse logarithmic kinetics ($1/x$ vs. $\log t$) can often fit the same set of data.

One resolution of this dilemma is to examine the principles upon which each derived rate equation is based and calculate values for physical quantities which are measurable in other experiments. Many descriptive models of low temperature oxidation have been put forward, but the Cabrera-Mott theory (1) stands out as having proven validity. For this reason, it is emphasized here as the basis for interpreting kinetic data from low temperature oxidation.

The Cabrera-Mott approach (1) assumes a quasiequilibrium of electrons tunneling across the thin oxide. Some electrons are trapped on oxygen sites at the oxide-gas interface, setting up a spontaneous voltage which is taken to be constant. The resulting field aids cation incorporation at the metal-oxide interface. This process is assumed to be rate limiting. Fehlner and Mott (2) have applied these ideas to anion incorporation at the oxide-gas interface and conclude that the same equation may be applied to both anion and cation movement.

In experiments, oxide thickness x is measured as a function of time, t , while pressure P , temperature T , number of potentially mobile ions N , activation energy for ion movement W , voltage across the oxide V , ion-jump distance $2a$, frequency of vibration ν , and oxide volume per ion Ω are assumed to remain fixed. An oxide film with uniform properties is also assumed to exist.

Following the approach of Ghez (3), the Cabrera-Mott equation is expressed as

$$dx/dt = N\Omega\nu \exp \left[- \left(W - \frac{qaV}{x} \right) / kT \right] \quad [1]$$

where the field across the oxide is $E = V/x$. Equation [1] can (2) be integrated for $x \ll x_1$, to give

$$x_1/x = -\ln [(t + \tau)/x^2] - \ln(x_1, u) \quad [2]$$

where

*Electrochemical Society Active Member.

Key words: oxidation at low temperatures, vitreous oxide, kinetics.

$$u = N\Omega\nu \exp(-W/kT) \text{ (}\AA \text{ sec}^{-1}\text{)} \quad [3]$$

$$x_1 = |ZeaV/(kT)| \text{ (}\AA\text{)} \quad [4]$$

and τ is an adjustable parameter, related to initial oxide thickness x_0 . Compared to t , τ is often taken to be negligible. The absolute value is used for x_1 in Eq. [4] because dx/dt should be positive (4).

Experimental Procedure

Mainly data for dry oxidation have been included in this work and then only if the data were available over a sufficiently large span of temperature. In addition, the oxide formed had to be noncrystalline to x-ray diffraction, or microcrystalline at the worst.

A discussion of the degrees of perfection in a vitreous oxide has been presented by Revesz and Fehlner (5). Any long-range order in a vitreous oxide may be considered to be a defect, just as disorder in a single crystal is considered to be a defect. The implications of the noncrystalline state for low temperature oxidation are pointed out by Fehlner and Mott (2). The division of oxides into network formers and network modifiers is a key point.

In some cases, data analysis based on Eq. [1] was available in the literature. In other cases, data points were taken from the original curves in the literature by using a digitizing technique. Values of x and t at a particular temperature were converted into values of $1/x$ and $\log(t/x^2)$ (x in angstroms and t in seconds) using a computer program. These points were then plotted, and values of the slope m and intercept b determined based on a least squares analysis. Values of correlation coefficient R were also determined. A value of 1 indicated perfect correlation.

Continuing with the computer program, values of u and x_1 were calculated from m and b and plotted vs. $1/T$ according to Eq. [3] and [4]. The slope based on Eq. [3] was used to determine activation energy W , while the intercept gave a value of N . The vibrational frequency ν was taken to be 10^{12} s^{-1} , while Ω was derived from the density of the relevant oxide.

The value of $|V|$ was determined from Eq. [4] using the slope of x_1 vs. $1/T$. The value of $2a$ was assumed to be approximately equal to the ionic spacing in the crystalline oxide as obtained from x-ray diffraction data. This assumption is considered valid since short-range order is maintained in bulk vitreous oxides. It is expected to hold true for similar oxides formed as films during low temperature oxidation.

Results

Low temperature oxidation of semiconductors and metals analyzed in the present study are reported below. Low temperature is defined by the relative magnitude of thermal to electrostatic energy available to drive the reaction. Temperatures for transition from low to high temperature oxidation have been estimated from the Cabrera-Mott equation by Fehlner (6). For instance, for Al, it is $\sim 300^\circ\text{C}$, and for Si, $\sim 500^\circ\text{C}$ at 1 atm.

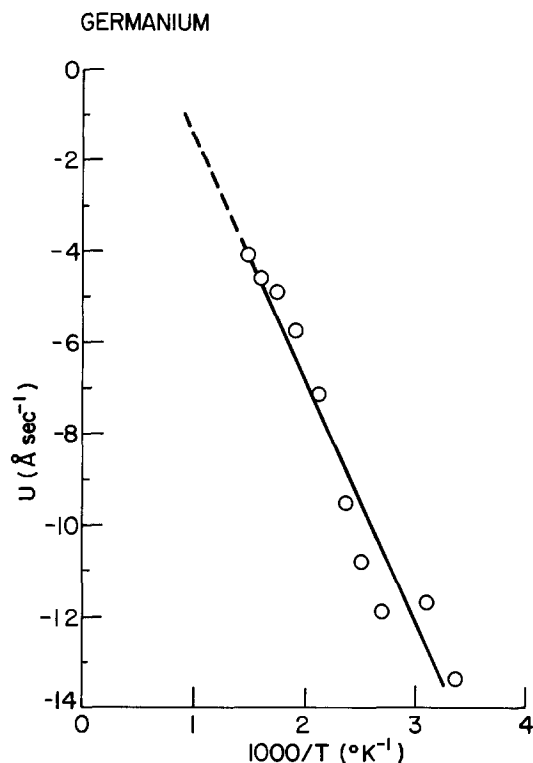


Fig. 1. Log u vs. $1/T$ for germanium

Values of W , N , and $|V|$ are reported and compared with values from the literature. The activation energy W is compared with values determined at high temperatures, although it is not altogether clear that either the parabolic or linear rate constants are directly relevant. The Cabrera-Mott equation assumes interface control through incorporation of the mobile ion, while the parabolic equation is based on control by diffusion in the bulk oxide. The linear rate constant depends on interface control, but at the reaction interface rather than the incorporation one. The comparison is therefore valid only if both the low and high temperature processes depend on the same key event such as breaking a metal-oxide or metal-metal bond.

The best comparison of W may be made with values reported for anodization (7). The similarity between anodization and low temperature oxidation lies in the fact that

Table I. Correlation coefficient R for germanium oxidation (8)

$T(^{\circ}\text{C})$	x vs. $\log t$	$1/x$ vs. $\log (t/x^2)$
25	0.985	-0.967
50	0.995	-0.988
100	0.991	-0.992
125	0.982	-0.990
150	0.981	-0.988
200	0.983	-0.993
250	0.991	-0.998
300	0.996	-0.997
350	0.996	-0.992
400	0.989	-0.997

both are field-driven processes. As a result, direct comparison between the two is possible. However, such results are scarce due to temperature restrictions and the limited ability of some metals to anodize.

Germanium.—Data for the low temperature oxidation of germanium were taken from the work of Ligenza (8). He measured the rate of dry oxidation for germanium powder at 75 torr between 25° and 400°C. The data were analyzed using the Ghez formulation of the Cabrera-Mott equation, $1/x$ vs. $\log (t/x^2)$, as well as with a plot of x vs. $\log t$. Table I gives the correlation coefficients for the two approaches, and it is evident that no choice can be made on this basis between the two kinetic expressions.

For the reason stated above, the data were further analyzed using the Cabrera-Mott expression. Hence, values of $\log u$ were plotted vs. $1/T$, as shown in Fig. 1. The correlation coefficient was 0.970. A value of $W = 1.1$ eV was calculated from the slope and a value of $N = 2 \times 10^6$ cm⁻² from the intercept taking $\Omega = 41\text{\AA}^3$ (hexagonal GeO₂). This value of W is difficult to compare with activation energies obtained at high temperatures because the volatility of the suboxide leads to linear kinetics (9). As a result, the activation energy obtained at high temperatures is not representative of ionic movement during diffusion as represented by parabolic kinetics.

It is interesting to note that the present analysis gives rise to a temperature independent activation energy for ion movement, as contrasted with Ligenza's analysis, where W was a function of T .

The plot of x_1 vs. $1/T$, shown in Fig. 2, produced a correlation coefficient of 0.736. Taking $Z = 2$ for anion conduction as discussed below and $2a = 3\text{\AA}$, $|V|$ was determined to be 0.2V. This magnitude is close to the surface potential value of -0.3V obtained by field emission for monolayer coverage of oxygen on germanium (10).

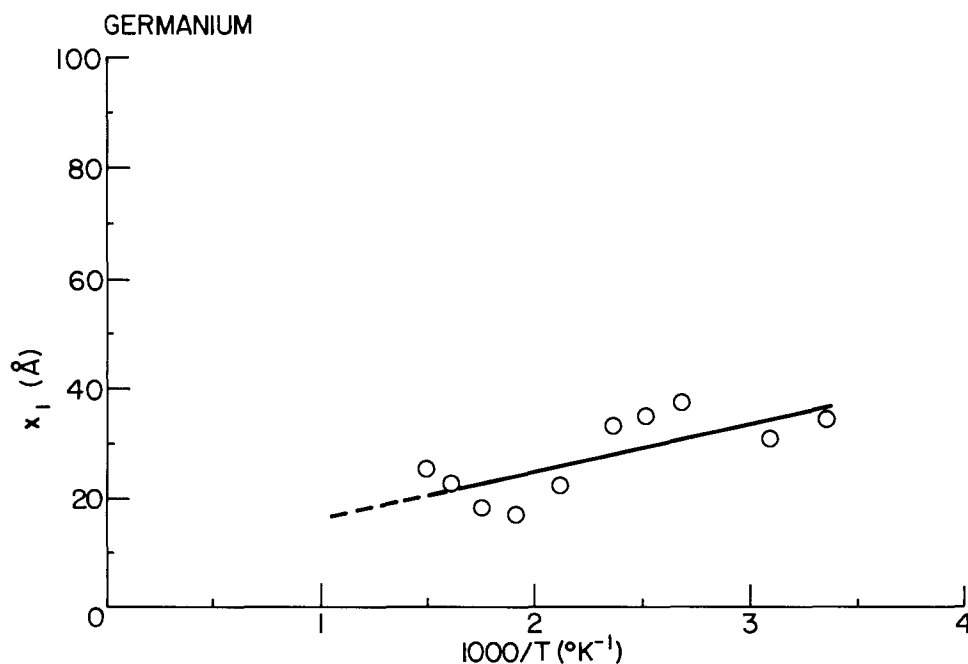


Fig. 2. x_1 vs. $1/T$ for germanium

Silicon.—The 1972 paper of Fehlner (6) summarized literature data for low temperature oxidation of single-crystal silicon at 25°, 400°, and 600°C, but these data were insufficient to define the kinetics. Kamigaki and Itoh (11) found that silicon oxidation between 950° and 1100°C followed Cabrera-Mott kinetics, provided that the oxygen partial pressure in an O₂/N₂ mixture held at 1 atm was less than 10⁻¹ atm. This agreed with curve fitting performed for the present work. As a result, the data at 10⁻² and 10⁻³ atm were analyzed along with the 1 atm data at 400° (6) and 600°C (12).

The results of Kamigaki and Itoh throw into question the ~500°C upper temperature limit for Cabrera-Mott kinetics. However, the explanation for the discrepancy may lie in the nature of the diffusing species. Field-driven oxidation at lower temperatures relies on ion movement (13), while oxygen molecules are the mobile species at higher temperatures (14-16). At 1 atm pressure of oxygen, the temperature of transition from ionic to molecular movement is estimated to be 500°C.

Oxygen solubility in SiO₂ varies directly with pressure. Thus, a pressure reduction to 10⁻² atm would decrease the O₂ concentration in SiO₂ by a factor of 100, and it might be expected that the temperature of transition from ionic to molecular movement would rise. As a result, the change in kinetics would occur at a higher temperature.

The correlation coefficients for the direct log and inverse log plots are compared in Table II. The Cabrera-Mott fit is slightly better in this case. The Ghez analysis of log *u* vs. 1/*T* in Fig. 3 yielded *R* = 0.959. The value of *W* was calculated to be 1.5 eV, which may be compared with the values of 1.8 and 1.4 eV found by Lie *et al.* (16) for parabolic oxidation from 800°-900°C and 900°-1000°C, respectively. They also found a value of 1.9 eV for linear oxidation over the same temperature range. The rate-limiting step in the parabolic oxidation is taken to be diffusion of a reactant through the oxide, while that for the linear oxidation is taken to be reaction at the silicon-oxide interface. The value for logarithmic kinetics falls between the two and may be compared with the Si-Si bond energy of 1.8 eV (17) and the O-O bond energy of 1.44 eV (18).

The value of *N* was calculated assuming Ω = 45 Å³ (vitreous silica). It was found to be 1 × 10⁶ cm⁻². Voltage was determined from the slope of *x_i* vs. 1/*T* in Fig. 4, where the correlation coefficient was 0.858. The value of |*V*| was 2.6V, taking *Z* = 2 and 2*a* = 3Å.

Lead.—A detailed study of lead oxidation has been carried out as part of the tunneling device investigation at IBM (19-21). Ellipsometry was used to follow the growth rate of PbO on a single-crystal lead film at temperatures between -90° and 150°C. Comparative oxide thicknesses determined by ellipsometry, x-ray absorption, and electron tunneling all agreed within an order of magnitude. A small dependence of PbO growth rate on oxygen pressure at 25°C was also determined for the range 4 × 10⁻² to 7.6 × 10² torr.

Eldridge and Dong (19, 20) had calculated values of *u* and *x_i*, but they applied them to an oxidation model based on piezoelectric effects. In the present approach, these values of *u* and *x_i* were analyzed using Eq. [2]-[4].

The plot of log *u* vs. 1/*T* (Fig. 5) gave a value of *W* = 0.44 eV. This may be compared with a value of 0.56 eV reported by Archbold and Grace (22) for parabolic oxida-

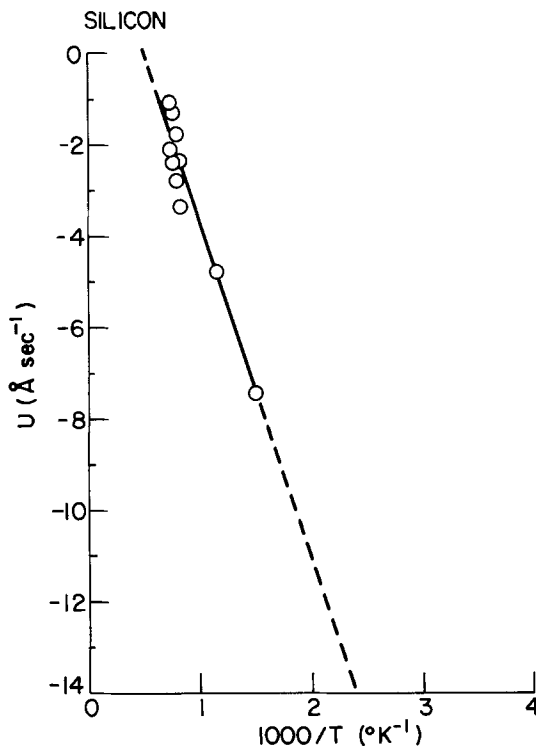


Fig. 3. Log *u* vs. 1/*T* for silicon

tion of molten lead (453°-643°C). However, Weber and Baldwin (23) report higher values, ~1.3 eV for molten lead (460°-700°C) and ~2.0 eV for solid lead (254°-321°C). It should be noted that the structural morphology of the oxide changes with temperature and can thus affect the kinetics of oxidation.

The value of *N* was found to be 7 × 10² cm⁻² based on Ω = 38.9 Å³ (tetragonal PbO). The plot for *x_i* vs. 1/*T* (Fig. 6) contained data points which were all bunched together. Since Eq. [4] implies an intercept of (0, 0), an estimate of the voltage was obtained by drawing a straight line through the origin and the center of the experimental points. A value of |*V*| = 1.5V was estimated for anion conductivity using 2*a* = 4Å and *Z* = 2. This may be compared with the surface potential value of +0.6V reported for oxygen adsorption on a lead film at 23°C and 6 × 10⁻³ torr (24).

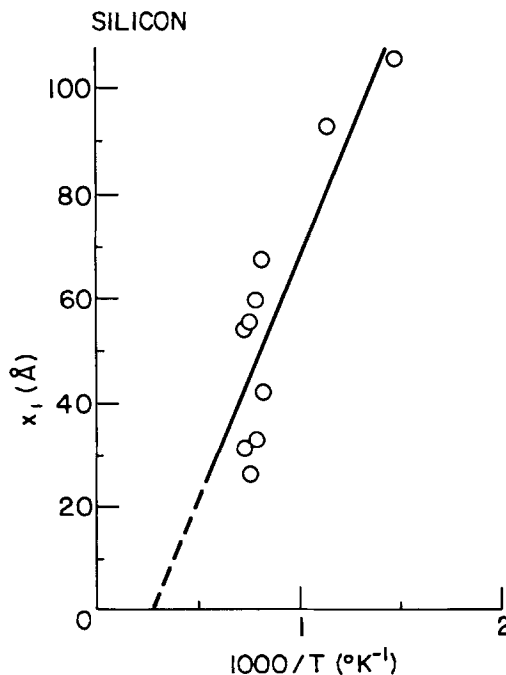
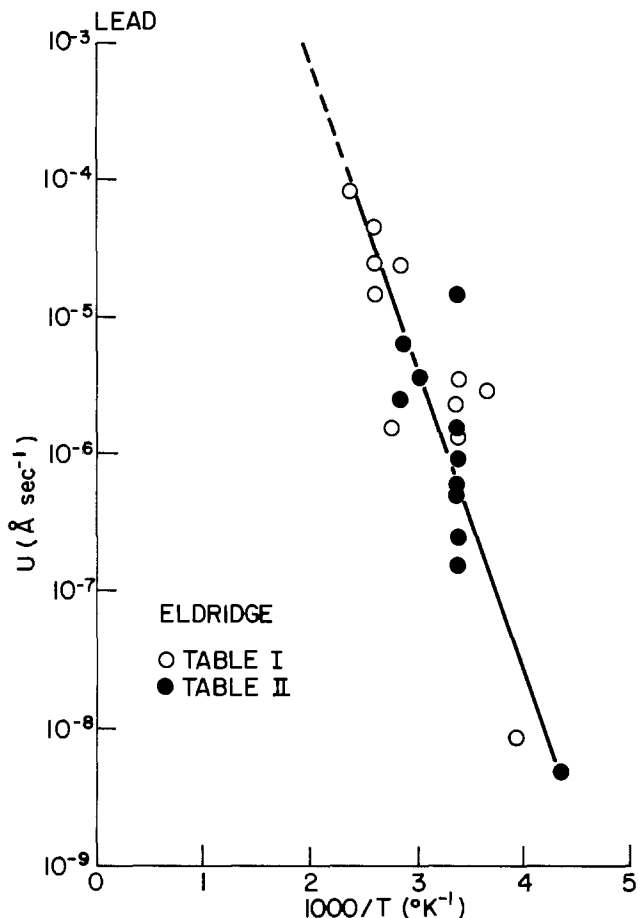


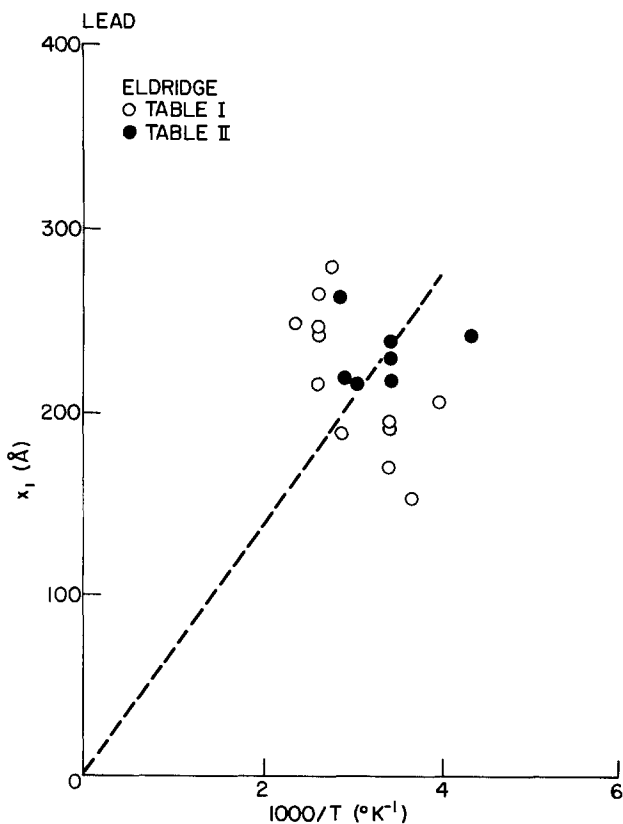
Fig. 4. *x_i* vs. 1/*T* for silicon

Table II. Correlation coefficient *R* for silicon oxidation

<i>T</i> (°C)	<i>P</i> _{O₂} (atm)	Ref.	<i>x</i> vs. log <i>t</i>	1/ <i>x</i> vs. log (<i>t</i> / <i>x</i> ²)
400	1	(6)	0.908	-0.945
600	1	(12)	0.961	-0.965
950	10 ⁻²	(11)	0.971	-0.983
1000	10 ⁻²	(11)	0.976	-0.992
1050	10 ⁻²	(11)	0.978	-0.993
1100	10 ⁻²	(11)	0.979	-0.994
950	10 ⁻³	(11)	0.984	-0.998
1000	10 ⁻³	(11)	0.981	-0.995
1050	10 ⁻³	(11)	0.982	-0.996
1100	10 ⁻³	(11)	0.981	-0.999

Fig. 5. Log u vs. $1/T$ for lead

Aluminum.—Dry oxidation of aluminum foil at 1 torr has been treated by Dignam *et al.* (25, 26) for the temperature range 250°–505°C. A time-temperature-dependent relationship was found for the transition from an “amor-

Fig. 6. x_1 vs. $1/T$ for lead

phous” oxide to γ -alumina crystallites. The sigmoidal kinetics characteristic of this process have been discussed in terms of oxide crystal nucleation and growth by Pryor (27), Bartlett (28), and others. The initial growth kinetics prior to crystal formation could be fitted by Dignam *et al.* only with an equation derived from the Cabrera-Mott theory using computer-aided procedures. Values for the constants were obtained as follows:

$$2\Omega\nu an = 2.5 \times 10^6 \text{ \AA sec}^{-1}$$

$$W = 1.60 \text{ eV}$$

$$2qaV = 8.2 e \text{ \AA V}$$

The value of W may be compared with 1.3 eV determined from anodization (7a). In the above, n is the volume concentration of the mobile species and Ω is the oxide volume per ion. For $\Omega = 45.6 \text{ \AA}^3$, $\nu = 10^{12} \text{ s}^{-1}$, and $2a = 5.6 \text{ \AA}$; $n = 9.8 \times 10^{15} \text{ cm}^{-3}$ ($N = 2an = 5.6 \times 10^8 \text{ cm}^{-2}$). Assuming $q = 3$ for Al^{3+} ion movement, $|V|$ equals 0.49V. If $q = 2$ for anion movement, then $|V| = 0.73\text{V}$. These values agree in general with the magnitude of values obtained through surface potential measurements. Both positive and negative surface potential values have been reported, depending upon whether polycrystalline rods (29) [+0.15V] or films (30) [−0.3 to −0.7V] were examined.

The pressure dependence of aluminum oxidation at low temperatures was reported to be dependent on the square root of oxygen pressure (31).

Grimblot and Eldridge (32) report on a study of aluminum film oxidation for conditions of 27°–427°C and 25–600 torr oxygen. They interpret their results in terms of the Cabrera-Mott equation. However, different values of the derived constants were found: W was 0.8–1.0 eV, $|V|$ was $\sim 3\text{V}$, and N can be calculated from their results to be $2 \times 10^3 \text{ cm}^{-2}$. The lack of agreement between their values and those of Dignam *et al.* (25, 26) reflect the fact that Grimblot and Eldridge (their Fig. 4) found larger values of oxide thickness at lower temperatures. The latter authors also report that the initial oxide formed is heavily doped with aluminum and is therefore not characteristic of Al_2O_3 .

Chromium.—Oxidation of chromium in dry oxygen at 300°–600°C has been reported by Young and Cohen (33) for a pressure of 4.0×10^{-3} torr. A transition from Cabrera-Mott to parabolic kinetics at $\sim 450^\circ\text{C}$ was found to be a function of both time and temperature. The transition could be correlated with a change in oxide structure from a flat, fine-grained, almost vitreous Cr_2O_3 to a strongly preferred fiber texture containing ridges and nodules. Since the activation energy for oxide growth in both regions was less than that self-diffusion of Cr in Cr_2O_3 (34), the rate-controlling process appeared to be transport via preferred pathways. Numerical integration of the Cabrera-Mott expression (35) led to two equations, one based on interstitial cations and the other on cation vacancies. The former depended on N , the number of surface metal atoms in sites suitable for movement into the oxide, while the latter depended on the number of adsorbed anions on the oxide. The major difference between the two kinetic expressions lies in a pre-exponential factor in $1/x$. The cation mechanism follows Eq. [1], while the vacancy mechanism adds the term $1/x$ to the right side of Eq. [1].

If cation interstitials were assumed, then $N = 5 \times 10^{13} \text{ cm}^{-2}$ and $W = (W_i + u) = 1.8 \text{ eV}$, based on $\Omega = 48.1 \text{ \AA}^3$. The activation energy for ion movement W was the sum of W_i , the heat of solution of an interstitial cation and u , the energy barrier to movement within the oxide.

Values of $|V| = 2.8\text{V}$ for cation interstitials and $|V| = 2.4\text{V}$ for vacancies were derived from the data. These may be compared with the values of −2.1 to −2.4V obtained from surface potential measurements (36, 37) at 25°C.

The vacancy mechanism gave an activation energy of $Q \approx 1.9 \text{ eV}$ for small x , where Q is the activation barrier to ion movement at the oxide-gas interface. The above values of activation energy may be compared with the high temperature values for Cr_2O_3 as obtained by Gulbransen

and Andrew (38) at 76 torr. For the first 5000Å of oxide growth, $W = 1.63$ eV, based on parabolic kinetics.

Iron.—Graham *et al.* (39) measured the rate of oxidation of iron from 24° to 200°C using a manometric technique. Starting pressure was 1.3×10^{-2} torr. Relative rates of oxidation were polycrystalline $> (110) > (112)$ at 24°C. The difference between (110) and (112) essentially disappeared at 200°C. Results were interpreted in terms of magnetite growth by a direct logarithmic rate law, although after 60 min, an inverse logarithmic rate law fit equally well. No particular mechanism was chosen as a result.

Data for the polycrystalline iron, for which there was the most data, were plotted according to inverse and direct logarithmic laws. In both cases, correlation coefficients were greater than 0.940, except for the direct log plot at 200°C. This had a value of 0.887. Hence, the indirect log plot appeared to be slightly better.

Values of the constants were found using $Z = 2$, $2a = 8.3\text{Å}$, and $\Omega = 25\text{Å}^3$ (cubic Fe_3O_4) in Eq. [2]-[4]. The activation energy was calculated to be 0.8 eV. This compares with a value of 1.39 eV found for the parabolic oxidation at 200°-400°C (39). The polycrystalline nature of the iron film and the polycrystalline oxide growing epitaxially on it may explain the difference in results. However, the amount of data is limited, making the results imprecise.

Values of N equal to 5×10^8 and $|V|$ equal to 0.1V were also found, the latter from the plot of x_1 vs. $1/T$. Unfortunately, the correlation coefficient for this plot was only 0.07, so that the value of voltage is unreliable. However, values of N and W were derived from the $\log u$ vs. $1/T$ plot, which had a correlation coefficient of 0.83.

Nickel.—Graham and Cohen (40) determined the oxidation rate of polycrystalline nickel sheet in dry oxygen. Pressures were 5×10^{-3} - 6×10^{-1} torr. Temperatures varied from 23° to 450°C. The results were interpreted in terms of an initial fast oxidation followed by a logarithmic rate for oxide thicknesses between 8 and 30Å. A parabolic rate law fit the data for thicker oxides. The oxides were polycrystalline, and diffusion occurred via easy diffusion paths for parabolic growth.

Two different sets of points were analyzed. The 23°-340°C data fit both direct and inverse logarithmic kinetics with equally high (>0.970) correlation coefficients. Further analysis of the inverse log data using $Z = 2$, $2a = 4.2\text{Å}$, and $\Omega = 16.6\text{Å}^3$ (cubic NiO) gave the following results: $W = 1.6$ eV, $N = 2 \times 10^{13}$ cm $^{-2}$, and $|V| = 2.6$ V. The correlation coefficient of x_1 was 0.957, and that of u was 0.998.

The data between 23° and 400°C were also analyzed. The 450°C curve was omitted, since it obviously did not fit the inverse log kinetics. Correlation coefficients were slightly higher for the inverse log (>0.970) than for the direct log (>0.910) kinetics. Analysis of inverse log results gave $W = 1.6$ eV, $N = 3 \times 10^{13}$ cm $^{-2}$, and $|V| = 2.3$ V. Correlation coefficients were 0.933 for x_1 and 0.998 for u . The value of W may be compared with that of 1.8 eV found by Graham and Cohen (40) when they analyzed the higher temperature results according to parabolic kinetics. Surface potential measurements (41) on a nickel film showed a change of -0.95 V when oxygen was adsorbed at 25°C and 10^{-2} torr.

Tantalum.—Vermilyea's (42) data for the anodization of tantalum between 150° and 300°C were utilized by Ghez (3) as his prime example illustrating the Cabrera-Mott law. Values of $W = 1.6$ eV and $N = 3 \times 10^{12}$ cm $^{-2}$ were derived from the data taking $\Omega = 84 \text{Å}^3$ (rhombohedral Ta_2O_5). The value of W may be compared with that obtained at higher temperatures, 1.1 eV, as found for the oxidation range 250°-450°C at 0.1 atm where parabolic oxidation yields an adherent oxide (43). Values of W equal to 0.71 eV (7b) and 2.185 eV (7c) were found through fitting of empirical rate equations for anodization.

Ghez calculated a value of $|V| = 1.79$ V using $z = 5$ and $a = 1.5\text{Å}$. However, assuming anion conductivity, z may be taken to be 2. With $2a = 4.38\text{Å}$, the value of $|V|$ becomes 1.5V.

Copper.—The data of Rhodin (44) were analyzed at four temperatures between -195° and 50°C as reported for the (100), (110), and (111) faces of a copper crystal. Isotherms had been recorded by Rhodin over the course of 1 month and included data for two typical runs made under each set of experimental conditions. No pressure dependence was noted in the range 10^{-2} - 10^2 torr O_2 . The relative oxidation rates were (100) $>$ (110) $>$ (111).

Plots of $(1/x)$ vs. $\log(t/x^2)$ had correlation coefficients ranging from 0.35 to 0.99. Much of the scatter was due to combining the dual runs. Unfortunately, no sensible values of W , N , or $|V|$ could be determined from this data.

Similar data of Young *et al.* (45) were also plotted. Isotherms for the oxidation of (100), (111), (110), and (311) faces of a copper single crystal had been reported for five temperatures between 70° and 178°C. The relative rates were (100) $>$ (111) $>$ (110) $>$ (311). Care had been taken to prepare a clean, strain-free copper surface, since contaminants greatly affected the (110) rate relative to the (111) rate.

Plots of both x vs. $\log t$ and $(1/x)$ vs. $\log(t/x^2)$ showed excellent correlation coefficients. On this basis, there would be little reason to choose one set of kinetics over the other.

Values of W and N calculated from the plots of $\log u$ vs. $1/T$ (correlation coefficients for the crystal faces varied between 0.77 and 0.96) are listed in Table III. All are reasonable for copper oxidation except the high value $N = 2 \times 10^{18}$ cm $^{-2}$ for (111) copper. This is greater than a monolayer. It is noteworthy that Young *et al.* fitted the data from 70° to 178°C to an inverse logarithmic plot for only the (311) and (110) faces. Their qualitative fit was not confirmed by more quantitative studies. The lack of agreement was ascribed to imperfections in the oxide.

Values of $|V|$ in Table III were too large and the correlation coefficients for x_1 vs. $1/T$ too small (0.29-0.46). Hence, $|V|$ is not considered to be correct for copper oxidation.

The data sets of Rhodin and Young *et al.* covered two different temperature ranges so that, despite the scatter in Rhodin's data, it seemed logical to try combining both sets of data. Figure 7 contains the combined result for $\log u$ vs. $1/T$, while Fig. 8 contains x_1 vs. $1/T$. In Fig. 7, the data for all crystal faces group together as a function of temperature except those obtained at -195°C .

The plot in Fig. 7 was used to obtain values of $W = 1.9$ eV and $N = 1 \times 10^{21}$ cm $^{-2}$, taking $\Omega = 39.6 \text{Å}^3$ (cubic Cu_2O). The value of W can be compared with those obtained for parabolic oxidation in air (46): 0.87 eV for 300°-550°C and 1.63 eV for 500°-900°C. Moisture tends to decrease the rate of copper oxidation (47), so the comparison is only approximate.

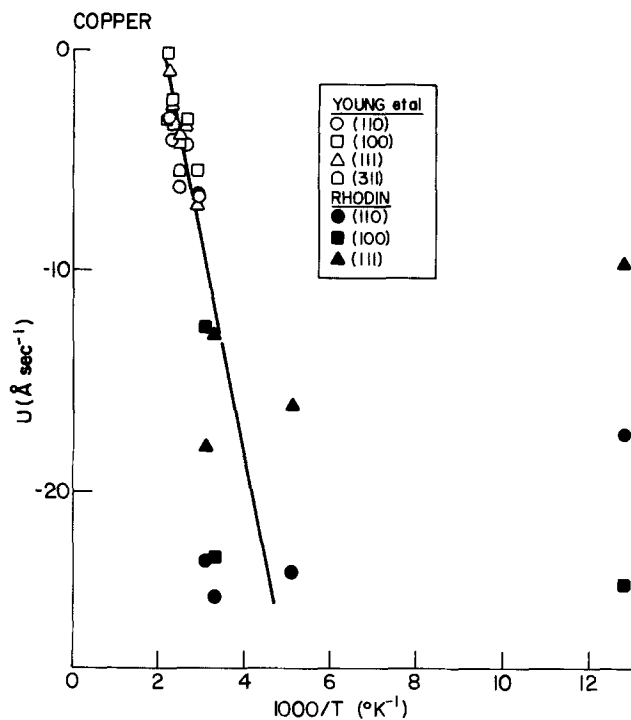
It is apparent that the value of N found by combining the data sets is too large, since the number of sites is $\sim 10^6$ times that of a monolayer.

A value for $|V|$ could not be obtained from Fig. 8 because the scatter in the points made it difficult, if not impossible, to define a straight line that would cut the Y-axis even when the points at -195°C were omitted. The implication is that the combined data for copper do not fit the Cabrera-Mott rate law.

Copper was investigated further by analyzing the data of Campbell and Thomas (47). They measured the rate of both wet and dry oxidation between 100° and 256°C. Oxygen pressure was 150 torr with 15 torr added moisture in the wet runs. They found that kinetics appeared to follow a cubic rate law.

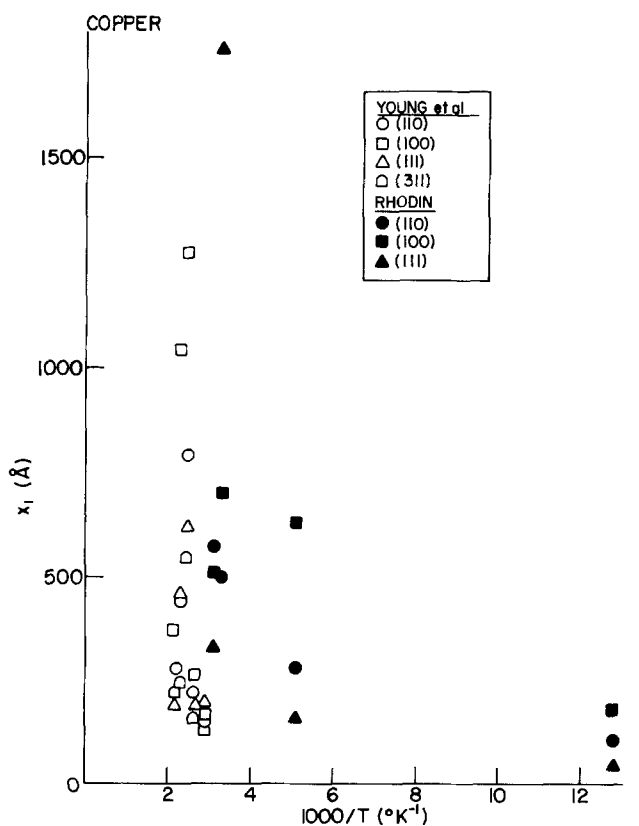
Table III. Results for copper (45)

Crystal face	N (cm $^{-2}$)	W (eV)	V (V)
(311)	4×10^9	0.93	-11.28
(110)	4×10^8	0.87	-19.55
(111)	2×10^{18}	1.53	-11.98
(100)	4×10^{15}	1.28	-49.54

Fig. 7. Log u vs. $1/T$ for copper

The data for dry oxidation were plotted according to both the direct and inverse logarithmic rate laws. While correlation coefficients were >0.920 in both cases, they were higher for the direct log plots. Even so, values of N and W were calculated. Values of voltage calculated from the inverse log data were too high. This was also true of wet oxidation between 100° and 169°C .

The overall conclusion from the three sets of data on copper oxidation is that direct rather than inverse logarithmic kinetics fit the low temperature data better.

Fig. 8. x_1 vs. $1/T$ for copper

Sodium.—The dry oxidation rate of sodium was measured between -79° and 48°C by Cathcart *et al.* (48). A manometric method was used at ~ 200 torr pressure. Carefully purified sodium films on glass formed the substrate. Oxide film structure was not determined, but logarithmic-type kinetics were followed.

Analysis according to the direct and inverse logarithmic kinetics gave good correlation coefficients for the direct log plot (>0.957 , except for -20°C , which was 0.885) but poor ones for the inverse log plot (>0.572 , except for 35°C , which was 0.821). Attempts to calculate values of W , N , and $|V|$ gave impossible results, as shown in Table IV. Values of $Z = 1$, $2a = 5\text{\AA}$, and $\Omega = 22.7\text{\AA}^3$ were used.

It was concluded that direct log kinetics are a better fit to the sodium data than inverse log kinetics.

Beryllium.—Fowler (49) under the guidance of Blakely, has measured the rate of oxidation of a Be (0001) crystal face. An ultrahigh vacuum apparatus was used in the temperature range 27° – 497°C at oxygen pressures of 3×10^{-8} to 2×10^{-6} torr. Adsorption of oxygen on the clean Be surface was followed by oxide island nucleation and growth. The islands coalesced into an oxide film which grew according to direct logarithmic kinetics. At high temperatures, BeO (0001) epitaxy on Be (0001) was found. As temperatures decreased, epitaxy became progressively poorer, being unobservable at 27°C .

Reconstruction of the BeO (0001) surface was observed at a critical thickness of 6–7 monolayers of oxide. This was attributed to intrinsic polarization of the wurtzite structure of BeO. Electron enhancement of oxidation by the Auger beam was found and minimized.

Data for two different maximum exposures ($1.05 \times 10^4\text{L}$ and $4.2 \times 10^3\text{L}$) were analyzed according to both the direct and inverse logarithmic rate laws. Pressure was 10^{-6} torr. In both cases, it was obvious that the direct log kinetics fit the data, while inverse did not. The former gave straight lines with good correlation coefficients (>0.99 , except for one 27°C curve, which was 0.867) while the latter produced L-shaped plots with poor correlation coefficients. No attempt was made to calculate values of W , N , and $|V|$ in view of this clearcut preference for direct log kinetics.

Discussion

The results of the above analyses are collected together in Table IV. The metals are arranged according to the cation group numbers of the periodic table. Values of N , W , and $|V|$ are included.

The first observation is that, in general, the results for the Group I and II metals appear impossible and should not be included in the table. For instance, the value of N for Cu is too large in one case, $|V|$ for Cu is too large in another, and N is too small for Na, beyond the limits of error which are estimated to be an order of magnitude for N . Beryllium is similar in that no values of N , W , or $|V|$ were even calculated. However, values of N , W , and $|V|$ for the other metals in Table IV are reasonable, and the applicability of the Cabrera-Mott model appears to be established.

Table IV. Values of N , W , and $|V|$ obtained from kinetic data for low temperature oxidation

Group no.	Element	Ref.	N (cm^{-2})	W (eV)	$ V $ (V)
IA	Na	(48)	1×10^{-8}	-0.2	0
IB	Cu	(44, 45)	1×10^{21}	1.9	?
IB	Cu	(47)	2×10^7	0.5	86
IIA	Be	(49)	?	?	?
IIIA	Al	(25, 26)	6×10^6	1.6	~ 0.6
IIIA	Al	(32)	2×10^3	-0.9	~ 3
IVA	Si	(6, 11, 12)	1×10^6	1.5	2.6
IVA	Ge	(8)	2×10^6	1.1	0.2
IVA	Pb	(19, 20)	7×10^2	0.4	1.5
VB	Ta	(3, 42)	3×10^{12}	1.6	1.5
VIB	Cr	(33)	5×10^{15}	1.8	2.8
VIII	Fe	(39)	5×10^8	0.8	?
VIII	Ni	(40)	3×10^{15}	1.6	2.3

A comparison of the various values of N (excluding Groups I and II) shows an interesting correlation. The values decrease from Group III to IV and then increase again for Groups V through VIII. Two exceptions are found, the second set of results for aluminum and the results for iron. Oxides of these metals are considered to be intermediate oxides in the sense that they can be incorporated into, as well as modify a network. Both anion and cation movement are expected in such oxides. This flexibility may allow such oxides to shift roles depending on the conditions of oxidation. Such a shift could affect the value of N .

The overall trend in N appears to correlate with ionic transport numbers for metal oxides, as listed in Table V, taken mainly from work on anodic oxides (58). Cation transport predominates for the Group I and II oxides, but quickly diminishes as the group number increases towards Group IV. Here, anion movement predominates. As the group number increases still further, cation movement again becomes significant.

Oxide structure is the key to understanding ion movement (2, 5). It is noteworthy that the oxides of Group I and II metals are classified as network modifiers, *i.e.*, they break up the three-dimensional network of a vitreous oxide. At room temperature and above, films of these oxides tend to be polycrystalline. The movement of small cations is favored by the presence of defects in the close-packed ionic solid.

The oxides of the elements in Group IV are classified as network formers. They are capable of bonding into a three-dimensional network which can change the mechanism of self-diffusion. The strong covalent bonding in the network promotes formation of holes and channels through which large anions or even oxygen molecules can pass. Cations, because of their high charge density, are less mobile in such a network structure.

Network-forming oxides tend to be vitreous at room temperature. The temperatures at which the oxide network remains stable to recrystallization are determined by the nature of the cation, the presence of impurities, and applied stresses. The best network forming oxide, SiO_2 , is stable even at 1200°C while growing on silicon.

Barr (59) studied the passivation in air of elemental metals using ESCA. His results could be divided into two general classes. In the first, passivation terminated with the outermost layer of metal oxide, *i.e.*, that exposed to air, in its highest oxidation state, but with the bulk of the metal oxide in a lower oxidation state. Such oxides were classed as modifiers.

The second class of oxides terminated in the same oxidation state throughout the oxide. These oxides were classed as network formers. The results were complicated by the presence of water, but the correlation with the present work is impressive. For example, his network formers were Si, Al, Zr, Sn, Mo, W, Y, La, and Rh while his modifiers were Ce, Pt, Pd, Fe, Co, Ni, and Cu. Intermediate oxides were not distinguished.

Fehlner and Mott (2) proposed that the Cabrera-Mott theory can be applied to low temperature oxidation where anions and/or cations are mobile in a uniform ox-

ide. It is noteworthy that in the case of cation movement, oxidation kinetics are affected much more by crystalline orientation of the metal substrate than by oxygen pressure. The converse is true for anion movement.

Let us turn once again to the results in Tables IV and V. The correlation based on N is significant, but the present work is only the first step in deriving values of N , W , and $|V|$ from curve fitting of data. The Ghez formulation of the Cabrera-Mott equation has been used to analyze all the results except the Al (25, 26) and Cr (33) cases. In these two examples, numerical analysis was used to directly fit the data to the Cabrera-Mott equation. This approach is expected to be at least as good as the approximations of Eq. [1]-[4]. However, the status of unknowns in the available experimental results, *e.g.*, the concentration of impurities such as water and the structure of the metal surface and oxide, argued against such detailed analysis at this time. Instead, the less rigorous Ghez integration of the Cabrera-Mott equation was favored so that results from a spectrum of metals could be compared.

The results for Group IV elements are particularly interesting. Given the network oxide structure and anion conductivity, it may not be surprising that N derived from the Cabrera-Mott expression is small. It is tempting to speculate that this is so because N no longer refers to the potentially mobile cation population at the metal-oxide interface. Instead, it refers to the number of potentially mobile anions at the oxide-gas interface, which in turn may relate to the number of paths available for ion movement through the oxide. It follows that where N is relatively small and W is > 1 eV, the rate of oxide growth is also small. Thus, the addition of alloying elements to base metals to promote network oxide formation can lead to protective oxide films and corrosion resistance, *e.g.*, Cr in stainless steel (60).

Conclusions

The present results are limited in scope, especially as regards modifying oxides. Nevertheless, it appears that oxidation according to the Cabrera-Mott theory occurs when a uniform, stable, three-dimensional oxide film is formed. This occurs at different temperatures dependent on the ability of the metal to form vitreous oxide.

Metals which form modifying oxides have a polycrystalline structure and do not appear to fit the Cabrera-Mott inverse logarithmic kinetics. No attempt has been made here to fit these results to another theory.

Values of W obtained from Cabrera-Mott analysis of data for network formers and intermediates are similar to values obtained from high temperature oxidation. This implies that a similar rate-limiting step, perhaps bond breaking, may control oxidation over the whole span of temperature.

Values of N appear to correlate with the structure and mode of ion transport in oxides. They are smallest for network formers, where anion movement predominates. A larger value is found for intermediates, where both anion and cation movement may occur.

Values of the absolute value of voltage V are reasonable for the network formers and intermediates. Comparison with values determined from surface potential measurements shows fairly good agreement.

Acknowledgments

Comments on this paper by A. G. Revesz, H. A. Schaeffer, and T. L. Barr are greatly appreciated.

Manuscript submitted Nov. 2, 1983; revised manuscript received Feb. 6, 1984.

Corning Glass Works assisted in meeting the publication costs of this article.

REFERENCES

1. N. Cabrera and N. F. Mott, *Rep. Prog. Phys.*, **12**, 163 (1948-1949).
2. F. P. Fehlner and N. F. Mott, *Oxid. Met.*, **2**, 59 (1970).
3. R. Ghez, *J. Chem. Phys.*, **58**, 1838 (1973).
4. R. Ghez, Private communication.

Table V. Ionic transport numbers for oxides

Metal group	Oxide	Cation	Anion	Ref.
I	$\text{Cu}_2\text{O}^\dagger$	~ 1	~ 0	(50, 51)
II	BeO^\dagger	0.75	0.25	(52)
III	Al_2O_3^*	0.6, 0.4	0.4, 0.6	(53, 54)
IV	ZrO_2^\dagger	< 0.05	> 0.95	(53)
	HfO_2^\dagger	< 0.05	> 0.95	(53)
	SiO_2	< 0.05	> 0.95	(55)
V	V_2O_5	0.28	0.72	(56)
	Nb_2O_5	0.24	0.76	(53)
	Ta_2O_5	0.24	0.76	(57)
VI	WO_3	0.37	0.63	(53)

* Transport number varies with current density and electrolyte used in anodization.

† Oxide was microcrystalline as formed.

5. A. G. Revesz and F. P. Fehlner, *Oxid. Met.*, **15**, 297 (1981).
6. F. P. Fehlner, *This Journal*, **119**, 1723 (1972).
7. L. Young, "Anodic Oxide Films," Academic Press, New York (1961); (a) p. 220, (b) p. 93, (c) p. 99.
8. J. R. Ligenza, *J. Phys. Chem.*, **64**, 1017 (1960).
9. O. Kubaschewski and B. E. Hopkins, "Oxidation of Metals and Alloys," 2nd ed., p. 259, Butterworths, London (1962).
10. N. V. Mileskina and R. Z. Bakhtizin, *Surf. Sci.*, **29**, 644 (1972).
11. Y. Kamigaki and Y. Itoh, *J. Appl. Phys.*, **48**, 2891 (1977).
12. A. M. Goodman and J. M. Breece, *This Journal*, **117**, 982 (1970).
13. P. J. Jorgensen, *J. Chem. Phys.*, **37**, 874 (1962).
14. B. E. Deal and A. S. Grove, *J. Appl. Phys.*, **36**, 3770 (1965).
15. A. G. Revesz and H. A. Schaeffer, *This Journal*, **129**, 357 (1982).
16. L. N. Lie, R. R. Razouk, and B. E. Deal, *ibid.*, **129**, 2828 (1982).
17. L. Pauling, "The Nature of the Chemical Bond," 3rd ed., p. 85, Cornell University Press, Ithaca, NY (1960), p. 85.
18. E. A. Irene and Y. J. van der Meulen, *This Journal*, **123**, 1380 (1976).
19. J. M. Eldridge and D. W. Dong, *Surf. Sci.*, **40**, 512 (1973).
20. J. M. Eldridge, *ibid.*, **40**, 531 (1973).
21. N. J. Chou, J. M. Eldridge, R. Hammer, and D. Dong, *J. Electron. Mater.*, **2**, 115 (1973).
22. T. F. Archbold and R. E. Grace, *Trans. Metall. Soc. AIME*, **212**, 658 (1958).
23. E. Weber and W. M. Baldwin, *J. Metals (New York)*, **4**, 854 (1952).
24. J. M. Saleh, B. R. Wells, and M. W. Roberts, *Trans. Faraday Soc.*, **60**, 1865 (1964).
25. M. J. Dignam, W. R. Fawcett, and H. Bohni, *This Journal*, **113**, 656 (1966).
26. M. J. Dignam, *ibid.*, **109**, 184, 192 (1962).
27. M. J. Pryor, *Oxid. Met.*, **3**, 271 (1971).
28. R. W. Bartlett, *This Journal*, **111**, 903 (1964).
29. R. L. Wells and T. Fort, Jr., *Surf. Sci.*, **33**, 172 (1972).
30. E. E. Huber, Jr. and C. T. Kirk, Jr., *ibid.*, **5**, 447 (1966); *ibid.*, **9**, 217 (1968).
31. G. L. Hunt and I. M. Ritchie, *J. Chem. Soc. Faraday Trans. 1*, **68**, 1413 (1972).
32. J. Grimblot and J. M. Eldridge, *This Journal*, **129**, 2369 (1982).
33. D. J. Young and M. Cohen, *ibid.*, **124**, 769, 775 (1977).
34. G. A. Hope and I. M. Ritchie, *Thin Solid Films*, **34**, 111 (1976).
35. D. J. Young and M. J. Dignam, *J. Phys. Chem. Solids*, **34**, 1235 (1973).
36. C. M. Quinn and M. W. Roberts, *Trans. Faraday Soc.*, **60**, 899 (1964).
37. W. A. Crossland and H. T. Roettgers, *Phys. Failure Electron.*, **5**, 158 (1966).
38. E. A. Gulbransen and K. F. Andrew, *This Journal*, **104**, 334 (1957).
39. M. J. Graham, S. I. Ali, and M. Cohen, *ibid.*, **117**, 513 (1970).
40. M. J. Graham and M. Cohen, *ibid.*, **119**, 879 (1972).
41. C. M. Quinn and M. W. Roberts, *Trans. Faraday Soc.*, **60**, 899 (1964).
42. D. A. Vermilyea, *Acta Metall.*, **6**, 166 (1958).
43. E. A. Gulbransen and K. F. Andrew, *J. Metals (New York)*, **2**, 586 (1950).
44. T. N. Rhodin, *J. Am. Chem. Soc.*, **72**, 5102 (1950); *ibid.*, **73**, 3143 (1951).
45. F. W. Young, J. V. Cathcart, and A. T. Gwathmey, *Acta Metall.*, **4**, 145 (1956).
46. G. Valensi, *Rev. Metall.*, **45**, 10 (1948).
47. W. E. Campbell and U. B. Thomas, *Trans. Electrochem. Soc.*, **91**, 623 (1947).
48. J. V. Cathcart, L. L. Hall, and G. P. Smith, *Acta Metall.*, **5**, 245 (1957).
49. D. E. Fowler, Ph.D. Thesis, Cornell University, Ithaca, NY (1983).
50. J. Bardeen, W. H. Brattain, and W. Shockley, *J. Chem. Phys.*, **14**, 714 (1946).
51. P. K. Krishnamoorthy and S. C. Sircar, *Acta Metall.*, **16**, 1461 (1968).
52. M. T. Shehata, C. J. Good-Zamin, and R. Kelly, in "Thin Film Phenomena-Interfaces and Interactions," J. E. E. Baglin, and J. M. Poate, Editors, p. 428, The Electrochemical Society Softbound Proceedings Series, Princeton, NJ (1978).
53. J. A. Davies, B. Domeij, J. P. S. Pringle, and F. Brown, *This Journal*, **112**, 675 (1965).
54. F. Brown and W. D. Mackintosh, *ibid.*, **120**, 1096 (1973).
55. W. D. Mackintosh and H. H. Plattner, *ibid.*, **124**, 396 (1977).
56. W. D. Mackintosh and H. H. Plattner, *ibid.*, **123**, 523 (1976).
57. J. P. S. Pringle, *ibid.*, **120**, 398 (1973).
58. J. P. S. Pringle, *Electrochim. Acta.*, **25**, 1423 (1980).
59. T. L. Barr, *J. Phys. Chem.*, **82**, 1801 (1978).
60. A. G. Revesz and J. Kruger, in "Passivity of Metals," R. P. Frankenthal and J. Kruger, Editors, p. 137, The Electrochemical Society Corrosion Monographs Series, Princeton, NJ (1978).

Chemical Properties and Film Casting of Radiation-Grafted Ion Containing Polymers

Marilyn N. Szentirmay and Charles R. Martin*

Department of Chemistry, Texas A&M University, College Station, Texas 77843

ABSTRACT

A series of radiation-grafted cation- and anion-exchange polymers have been studied with the intent of developing procedures for dissolving and film casting these polymers. Solvent swelling studies have shown that these polymers display two maxima in plots of solvent uptake *vs.* solvent solubility parameter. While similar behavior is shown by the ion-exchange polymer Nafion, the anion- and cation-exchange polymers studied here will not dissolve under conditions (developed by us) which dissolve Nafion. We believe that this insolubility results from covalent cross-links and/or enhanced crystallinity in the chain-material regions of these polymers. These polymers do, however, swell extensively in certain solvents at high temperatures, and suspensions may be prepared from the swollen polymer. We have cast films from these suspensions onto electrode surfaces and report initial results of electrochemical characterization of these films.

Ion containing polymer (ICP) (1, 2) membranes have been used as separators in chlor-alkali cells (3) and in cells for energy conversion (4, 5), and ICP film-based chemically modified electrodes show promise for use in electrochromics (6), electrocatalysis (7), photoelectro-

chemistry (8) and electroanalysis (9, 10). Further developments in these areas will require ICP's with better mechanical and dynamic properties (11) which can be produced at a lower price (12). Accordingly, this research group has been investigating the fundamental chemical and electrochemical properties of a variety of ICP's (13, 14) and studying possible new applications for these polymers (10, 15).

* Electrochemical Society Active Member.

Key words: ion containing polymers, film casting polymers, RAI pore membranes.

We report here results of studies of ICP's prepared by derivitizing, through radiation grafting, polyethylene (PE) and polytetrafluoroethylene (PFE) sheets (12, 16). Both cation-exchange polymers (sulfonated PE's and PFE's) and anion-exchange polymers (quaternized PE's and PFE's) were studied. These polymers are of interest because they may prove to have the desirable chemical and transport properties of Nafion, a highly successful perfluorosulfonate polymer (1, 13, 14), but can be produced at lower costs (12). The quaternized polymers are of particular interest to us because they may prove to be cationic versions of Nafion and thus be useful when anion exchange or transport is needed.

The purposes of the work described here were to use solvent swelling studies (12, 17) to develop procedures for film casting these radiation grafted ICP's and to use electrochemical methods for preliminary investigations of the physical and transport properties of the resulting films. Particular emphasis is placed on the quaternized polyethylene polymer.

Experimental

Materials.—The ICP's and polyethylene were obtained from RAI Research Corporation (Hauppauge, New York). The sulfonated polyethylene (PE-SS, 700 g/mol-SO₃H) and the sulfonated polytetrafluoroethylene (PFE-SS, 850 g/mol-SO₃H) are prepared by grafting styrene onto sheets of the polymer, followed by sulfonation of the styrene (12, 16). The quaternized polyethylene (PE-QA, 1100 g/mol N) and the quaternized polytetrafluoroethylene (PFE-QA, 1000 g/mol N) are prepared by grafting vinylbenzylchloride onto the polymers and quaternized with triethylamine (16). Membranes were converted to various counterionic forms by soaking in appropriate salt or acid solution.

Water was triply distilled or obtained from a Milli-Q water purification system (Millipore Corporation, Bedford, Massachusetts). 2-Ethylhexanol, 1-decanol, 2-ethylbutanol, 1-pentanol, ethylene glycol, sodium anthraquinone-2-sulfonate, disodium anthraquinone-2,6-disulfonate, and sodium hexafluorophosphate were obtained from Aldrich Chemical Company (Milwaukee, Wisconsin). Xylene was obtained from Center Chemical Company (Austin, Texas). Triethylamine was obtained from MCB (Cincinnati, Ohio). Hydroquinone was obtained from J. T. Baker Chemical Company (Phillipsburg, New Jersey). Trifluoroacetic acid (TFA) was obtained from Sigma Chemical Company (St. Louis, Missouri). Ru(NH₃)₆Cl₃ was obtained from Johnson Matthey, Incorporated (Winslow, New Jersey). 8-Hydroxy-1,3,6-pyrenetrisulfonic acid, trisodium salt was obtained from Eastman Kodak Company (Rochester, New York) and recrystallized twice from aqueous acetone. Ru(bpy)₃Cl₂ (bpy = 2,2'-bipyridine) was obtained from G. F. Smith. All other chemicals were reagent grade.

Solvent swelling measurements.—Studies similar to those described by Yeo *et al.* (12, 17) were done. The membranes (0.06-0.10g) were immersed in the desired solvent in a capped vial at room temperature for at least 2 days, then removed, blotted dry, and weighed immediately in a closed weighing bottle. The membranes were then replaced in the solvents and reweighed more than 1 day later to insure that no further solvent uptake had occurred. Each value of percentage increase in weight is the average of two or more experiments. In almost all cases, reproducibility was better than $\pm 5\%$.

Preparation of polymer suspensions.—Specific conditions used to soften the ion-exchange polymers are given in the Results and Discussion section. The pressure reactor (Parr Instrument Company, Moline, Illinois) was purged with N₂ before sealing. In some cases, N₂ was added after sealing to increase the pressure in the reactor. The contents of the reactor were stirred while heating. Prior to heating in the reactor, PFE-SS was ultrasonically cleaned in 50:50 ethanol-water to remove a pink color. The softened polymers were ground in a glass tissue

grinder driven by an overhead stirring motor. Titrations to check the manufacturer's listed value of the ion-exchange capacity of PE-QA (chloride form) were done by equilibrating a known weight of polymer with aqueous KNO₃ and titrating the Cl⁻ released with AgNO₃. Chlorofluorescein was used as the indicator.

Preparation of electrode films.—Glassy carbon (1/8 in. diam, Atomergic Chemetals Corporation, Plainview, New York) was polished as described previously (14). Films of PE-SS and PE-QA were cast onto glassy carbon electrodes from suspensions in propanol, PFE-QA from a suspension in 50:50 ethanol-water, and PFE-SS from a suspension in 50:50 ethylene glycol-ethanol. The electrodes were coated by syringing a measured amount of polymer suspension onto the electrode surface (14). After the solvent evaporated (in air), the polymer-coated electrodes were soaked at least 6h in supporting electrolyte before use. This served to both hydrate the film and wash out any residual solvent. Wet film thicknesses were measured with an Alpha-step surface profiler (Tencor Instruments, Mountain View, California).

Electrochemical measurements.—A PAR Model 173 potentiostat and Model 175 programmer (EG&G PAR, Princeton, New Jersey), an X-Y recorder (Houston Instruments, Austin, Texas), and a Nicolet 2090-3 digital oscilloscope (Nicolet Instrument Corporation, Madison, Wisconsin) were used for electrochemical experiments. A three-electrode cell with a saturated calomel reference electrode (SCE) and a Pt disk counterelectrode was employed. All electrochemical measurements were done in N₂-degassed solutions.

Results and Discussion

Solvent swelling studies.—Yeo *et al.* (12, 17) have found that Nafion and the sulfonated RAI membranes exhibit two maxima in plots of solvent uptake *vs.* solvent solubility parameter. We have shown that Nafion may be dissolved at high temperatures in binary solvent systems composed of a solvent which has a solubility parameter near the first swelling maximum and a solvent which has a solubility parameter near the second swelling maximum (13). It was of interest to us to see if a similar approach could be used to dissolve the various RAI membranes. If so, chemically modified electrodes based on films of these polymers could be prepared. Such electrodes allow for convenient evaluation of the charge transport properties (14) and the ion exchange thermodynamics (10) of ICP's.

Solvent swelling studies are also of interest because they can be used to deduce information about ICP morphology (*vide infra*). Solvent swelling data are already available for the sulfonated RAI polymers (12). We report results of swelling studies of PE-QA. Since the solvents used varied in hydrogen bonding ability, three component solubility parameters (δ) (18, 19) were used for these studies. The solvents and their solubility parameters are listed in Table I.

Results of the solvent swelling studies of PE-QA are shown in Fig. 1-3. In pure solvents, the Cl⁻ form of PE-QA exhibits two swelling maxima, one at approximately 10 Hb, the other a broad maximum in the range 15-20 Hb (Fig. 1). As noted above, similar results were obtained with Nafion (17), PFE-SS, and PE-SS (12). In propanol-water mixtures, PE-QA chloride exhibits solvent uptakes greater than those observed in either pure propanol or pure water (Fig. 2). Again, this type of behavior was also observed with Nafion (17). Finally, when PE-QA is converted from the Cl⁻ form to the PF₆⁻ form its solvent swelling characteristics change dramatically (Fig. 3). While nearly all of the solvents swell the PF₆⁻ form much less extensively, it is of particular interest to note that the low δ envelope is essentially completely wiped out.

It is now fairly well established that many ICP's are, on a microscopic level, biphasic (20). Yeo *et al.* (12, 17) have concluded that in Nafion, PFE-SS, and PE-SS, the high solubility parameter envelope results from interactions in

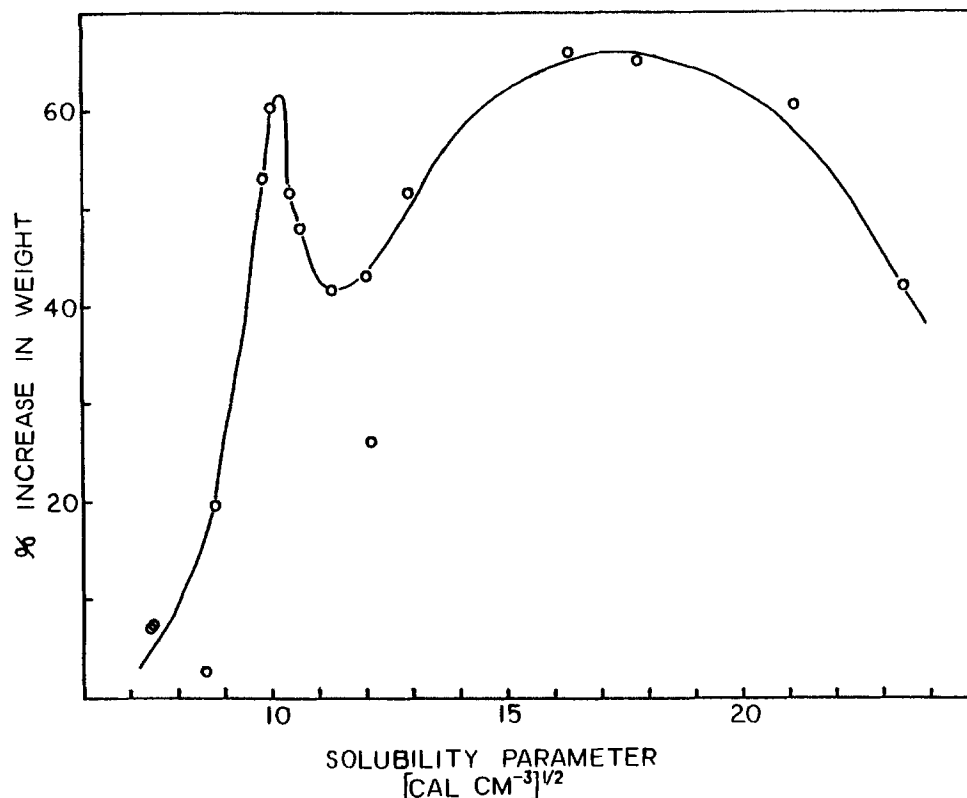


Fig. 1. Solvent uptake vs. solubility parameters of solvents for PE-QA, chloride form.

the ionic cluster phase (20) and the low solubility parameter envelope results from interactions with the organic chain-material phase or with the sidechains. The fact that two δ maxima are observed in PE-QA Cl⁻ suggests that this ICP is also biphasic. Because polyethylene (the chain material in PE-QA) has a δ of about 8 (21) and the first swelling maxima occurs at $\delta = 10$, it is reasonable to conclude that the low δ maximum in PE-QA results primarily from interactions with the sidechains. A comparison of solvent uptake data for PE-QA with data for the polyethylene used by RAI to make PE-QA (Table II) supports this conclusion. The solvents which produce the greatest swelling in PE-QA do not appreciably swell polyethylene.

That the low δ maximum is attributable to interactions with the sidechains is also supported by the PF₆⁻ swelling

data. It is generally accepted that counterions are localized in the ionic domains of ICP's and not in the surrounding chain material phase (20). Therefore, if the swelling maximum at 10 Hb were due primarily to interactions with the chain material, the tremendous sensitivity of swelling to the nature of the counterion would not be expected. Furthermore, by the same argument, since the sidechain interactions are very sensitive to counterion, it seems likely that the sidechains intrude into the ionic domains. This intrusion of organic sidechain explains why luminescence probe studies of these ICP's indicate that the cluster phase is rather hydrophobic (22, 23).

Polymer suspensions.—The swelling studies revealed several solvents and solvent systems which showed promise for dissolving PE-QA chloride (*e.g.*, 50:50 ethanol water and dimethylsulfoxide). However, PE-QA would not dissolve in any solvent or solvent system, even at high temperatures and pressures. The failure of PE-QA to dissolve is surprising, since a similar approach was successfully used to dissolve Nafion (13). Since cluster formation may be regarded as electrostatic cross-linking (24), it

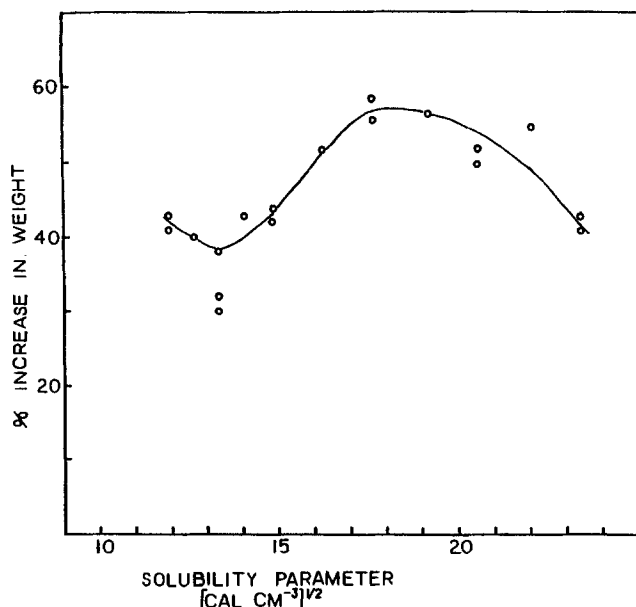


Fig. 2. Solvent uptake of PE-QA, chloride form vs. solubility parameters, δ_{mix} , of propanol-water mixtures. $\delta_{\text{mix}} = V_{\text{PROH}} \delta_{\text{PROH}} + V_{\text{H}_2\text{O}} \delta_{\text{H}_2\text{O}}$ (17), where V_{PROH} and $V_{\text{H}_2\text{O}}$ are volume fractions, and δ_{PROH} and $\delta_{\text{H}_2\text{O}}$ are solubility parameters, of propanol and water, respectively.

Table I. Solvents and solubility parameters

Solvent	Solubility parameter ^a (cal cm ⁻³) ^{1/2} , Hb
Triethylamine	7.4 ^b
Heptane	7.5 ^c
4-Methyl-2-pentanone	8.6
Xylene	8.8
2-Ethylhexanol	9.8
1-Decanol	10.0 ^c
2-Ethylbutanol	10.4
1-Pentanol	10.6
1-Butanol	11.3
1-Propanol	12.0
N,N-Dimethylformamide	12.1
Dimethylsulfoxide	12.9
Ethylene glycol	16.3
Formamide	17.8
Glycerol	21.1
Water	23.5

^aAll values from Ref. (19), except as noted.

^bValue from ref. (21).

^cValue calculated from Ref. (18).

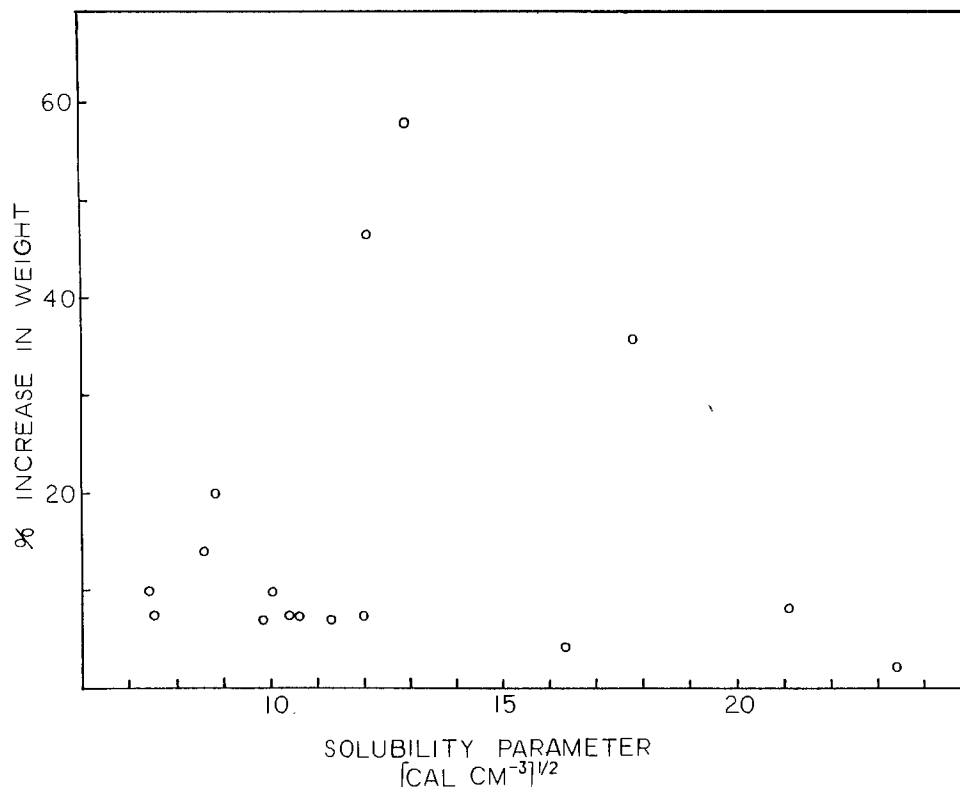


Fig. 3. Solvent uptake vs. solubility parameters of solvents for PE-QA, PF_6^- form.

seemed possible that the clusters might be responsible for the insolubility. To test this possibility, PE-QA chloride membranes were immersed for several hours in boiling xylene. This caused the charged sites to cleave from the membrane.¹ The uncharged membranes were then boiled in fresh xylene for several more hours. While boiling xylene will dissolve the polyethylene used to prepare PE-QA, it did not dissolve the decharged PE-QA. This shows that the presence of the charged groups (and, therefore, cluster formation) is not responsible for the insolubility. We believe that covalent cross-links are introduced during the radiating grafting procedure; even a minute amount of cross-linking would render this polymer insoluble in any solvent.

We were also unable to dissolve PE-SS, PFE-QA, and PFE-SS. PE-SS is probably also covalently cross-linked, but tetrafluoroethylene polymers show little tendency to cross-link when bombarded with radiation (16). The insolubility of these polymers in solvent systems which will dissolve Nafion may result from higher degrees of crystallinity in the starting PFE's than in Nafion. The Nafions which we successfully dissolved (13) by heating to 250°C have melting points around 210°C (25). The melting points of the polytetrafluoroethylenes are around 350°C (26). While in principle this indicates that PFE-QA and PFE-SS could be dissolved at higher temperatures, we have found that in the solvents studied here the charged sites begin to cleave from PFE-QA at temperatures above about 150°C and from PFE-SS at temperatures above about 300°C.

¹ When as-received membranes are immersed in an aqueous solution of the fluorescent anion 8-hydroxy-1,3,6-pyrenetrisulfonate, strong fluorescence from the cationic membrane is observed. After treatment in boiling xylene, and reimmersion in the fluorophore solution, no fluorescence can be detected from the membrane.

Table II. Solvent uptake measurements for polyethylene and PE-QA

Solvent	Percentage increase in weight	
	Polyethylene	PE-QA
Xylene	13	17
Decanol	2	60
Butanol	<1	42
DMSO	0	52
H ₂ O	0	42

In spite of their insolubility, we were able to cast films of all of these ICP's. This was accomplished by using the solvent swelling experiments to identify strongly swelling solvents, using these solvents in the high temperature reactor to soften the polymers, and then grinding the wet, softened polymer in a ground glass tissue grinder. Suspensions of the polymers resulted; these suspensions were filtered to remove the larger particles and then used to cast films. The conditions required to soften each polymer are shown in Table III. As noted above, temperatures high enough to soften PFE-QA also cleaved the charged sites. For this reason, we were forced to use lower than optimal temperatures, and poor softening resulted.

A comparison of the ion-exchange capacities of PE-QA chloride before treatment and after suspension showed that charged sites are not destroyed during the softening and grinding process. The ion exchange capacities were 0.95 meq/g for the as-received membranes and 0.94 meq/g after suspension.

Polymer-coated electrodes.—Films cast from the ICP suspensions were examined with a surface profilometer. These studies showed that while the entire electrode surface was covered, the coatings were uneven, as might be expected for films composed of small adhering particles. Thickness measurements on wet PE-QA films gave densities of 0.69 g/cm³; the density of the dry, as-received membrane is 0.65 g/cm³ (27). Figure 4, curve A shows background currents observed at a bare glassy carbon electrode. Figures 4B through 4E show analogous background currents for electrodes coated with the various RAI polymers. As would be expected (13), background currents do not change appreciably after coating.

Table III. Summary of conditions used to suspend RAI polymers

Polymer	Counterion	Solvent	T (°C)	P (psi)	t (h)
PE-QA	Cl ⁻	50:50 Propanol-Water	150	100	4
PE-SS	Li ⁺	Methanol	150	250	4
PFE-SS	Li ⁺	Ethylene Glycol	250	730	3
PFE-QA ^a	OH ⁻	50:50 Propanol-Water	150	100	4

^aVery little softening.

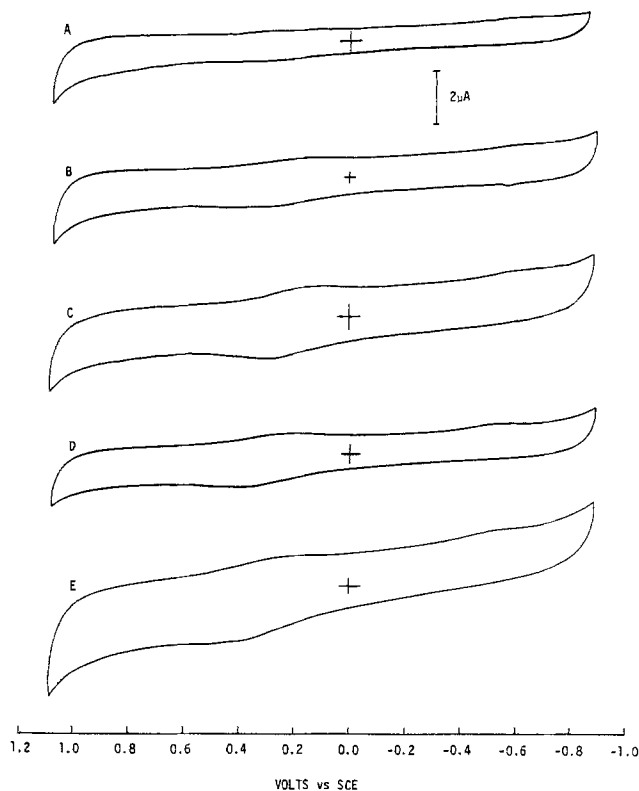
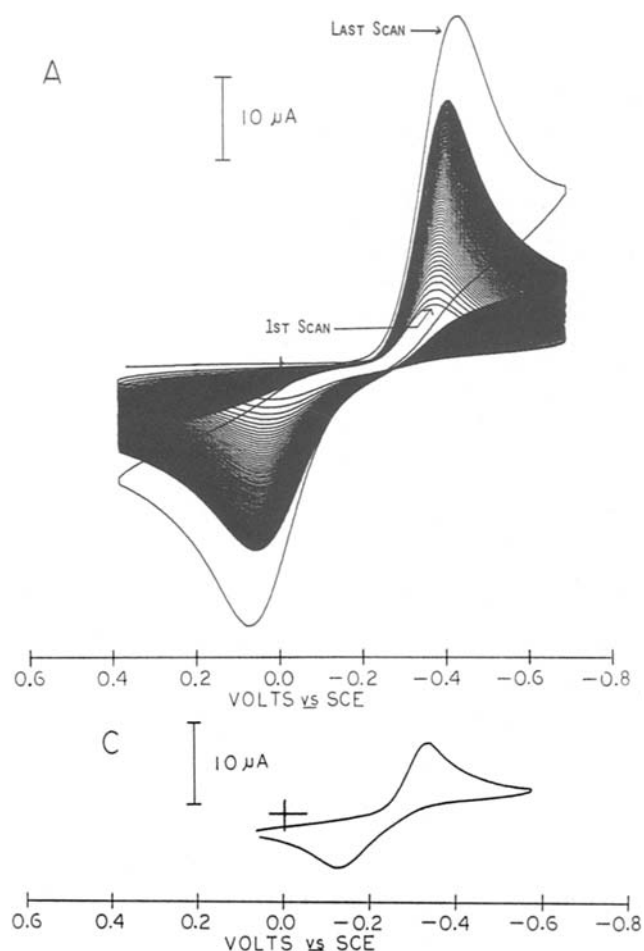


Fig. 4. Cyclic voltammograms recorded at 0.1 V/s. A. Uncoated glassy carbon electrode in 0.2M NaTFA, pH 3.0. Curves B to E are glassy carbon electrodes coated with the following. B: PFE-SS, $\sim 10^{-7}$ mol $\text{SO}_3^-/\text{cm}^2$ (0.2M NaTFA, pH 3.0). C: PE-SS, 4.5×10^{-7} mol $\text{SO}_3^-/\text{cm}^2$ (0.2M NaTFA, pH 3.0). D: PFE-QA, 6.3×10^{-7} mol quaternary ammonium sites/ cm^2 (0.1M TFA/0.1M NaTFA). E: PE-QA, 2.4×10^{-7} mol quaternary ammonium sites/ cm^2 (0.1M TFA/0.1M NaTFA).



As has been observed with other ICP-based chemically modified electrodes (13, 28, 29), the RAI films incorporate and retain electroactive counterions and allow for charge transport to and from these ions. For example, Fig. 5A shows a series of cyclic voltammograms recorded after a PE-QA-coated electrode was immersed in a solution of anthraquinone sulfonate (AQS). Current increased with time, eventually reaching a steady-state level (13, 28, 29). When the electrode was removed from solution, rinsed, and placed in supporting electrolyte, current due to the retained AQS was observed. The voltammogram in Fig. 5B was recorded 35 min after the coated electrode was placed in supporting electrolyte. While, when immersed in supporting electrolyte, AQS is slowly leached from the polymer, the film itself remained attached to the electrode and could be reloaded with AQS to the same voltammetric current level shown in the last scan in Fig. 5A. Analogous results were obtained with the other RAI polymers.

Preliminary investigations of the charge and mass-transport properties of PE-QA films at electrode surfaces were also carried out. Figure 6A shows that voltammetric peak currents, i_p , for polymer-bound AQS are proportional to the square root of scan rate. This is the expected (28) dependency in the thick (ca. 4 μm) films used here. Potential step chronocoulometry for AQS and anthraquinone-2,6-disulfonate (AQDS) in PE-QA films produced linear charge vs. $t^{1/2}$ plots (Fig. 6B). Apparent diffusion coefficients (14, 28) of about 1×10^{-9} cm^2/s were obtained, from such plots, for both the oxidized and reduced forms of AQS and AQDS.

Figures 5 and 6 show that PE-QA extracts and transports electroactive counterions. It was also of interest to evaluate the extent to which neutrals and coions permeate the film. We have found that small, neutral molecules (e.g., hydroquinone) readily penetrate films of PE-QA; in fact, peak currents for hydroquinone at coated electrodes are identical to those at uncoated electrodes. These molecules are not, however, retained by the film in that no trace of the hydroquinone voltammetric wave is observed when a PE-QA modified electrode is transferred from a hydroquinone solution to a solution containing only supporting electrolyte.

Coions (e.g., $\text{Ru}(\text{bpy})_3^{2+}$, $\text{Ru}(\text{NH}_3)_6^{3+}$) also penetrate PE-QA films. Peak currents for these ions are, however, reduced to less than about 25% of the peak currents observed for the same solution at an uncoated electrode. Coions are also not retained by these films. The ability of coions to penetrate the rather thick (4 μm) films used here suggests that there are pinholes or channels through the films. Again, this is not surprising, given the fact that these films are composed of adhering particles. We are

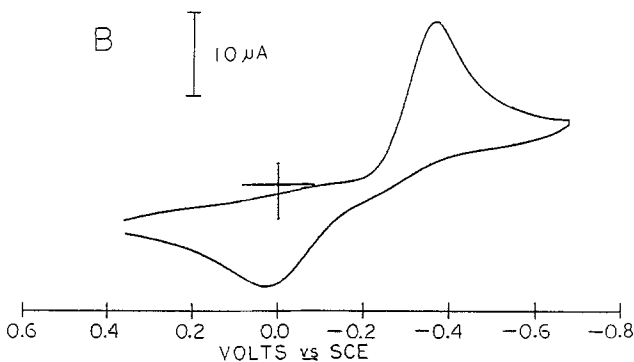


Fig. 5. Cyclic voltammograms of AQS recorded at a scan rate of 0.1 V/s. Supporting electrolyte = 0.2M NaTFA, pH 3.0. A: Loading of PE-QA film (4.5×10^{-7} mol quaternary ammonium sites/ cm^2 , 7 μm thick) from 2.3×10^{-4} M AQS. First scan recorded immediately after immersion. Last scan recorded 95 min later. B: Same PE-QA film after loading, rinsing, and soaking in supporting electrolyte for 35 min. C: Steady-state voltammogram of 2.3×10^{-4} M AQS on bare glassy carbon electrode.

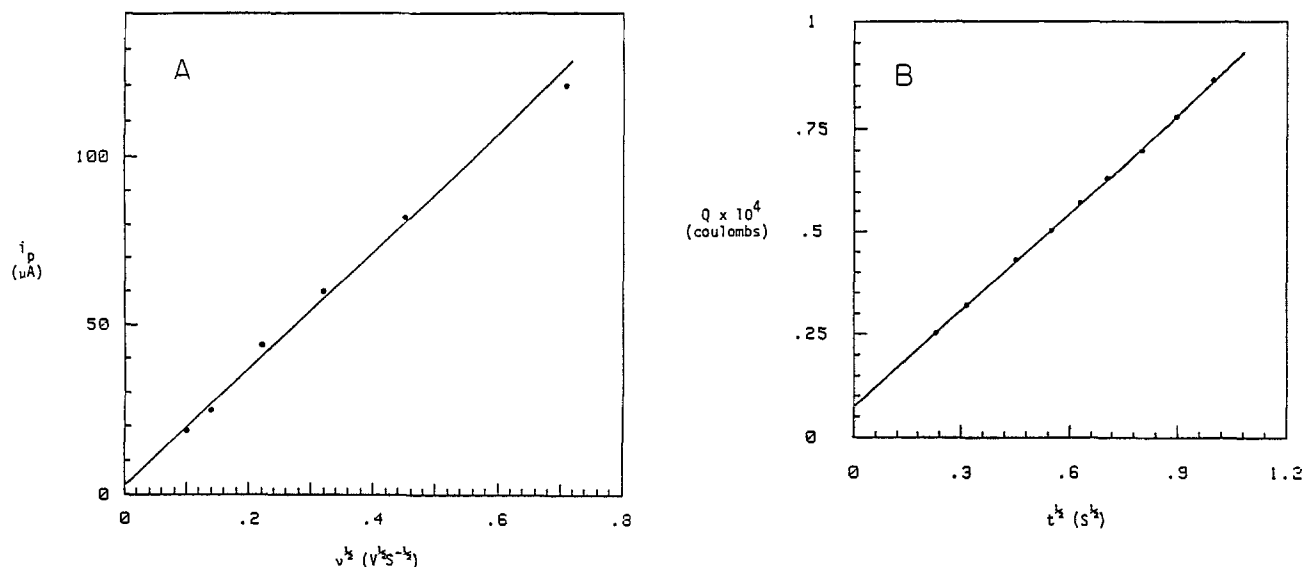


Fig. 6. A: Anodic peak current, i_p , vs. square root of scan rate, $v^{1/2}$, for AQS in a PE-QA film (2.4×10^{-7} mol quaternary ammonium sites/cm², 4 μm thick). Supporting electrolyte: 0.1M TFA/0.1M NaTFA. B: Chronocoulometric plot of charge (Q) vs. $t^{1/2}$ for reduction of AQS in PE-QA electrode described in Fig. 4, curve D. Supporting electrolyte: 0.2M NaTFA, pH 3.0.

currently investigating the possibility of using annealing procedures to reduce the void volumes of these films.

Conclusions

Solvent swelling studies have provided a method for film casting the RAI ICP's. While these polymers show solvent swelling characteristics very similar to Nafion, they will not dissolve in solvents which dissolve Nafion [e.g., 50:50 ethanol-water (13), dimethylsulfoxide (29), or propylene carbonate (30)]. We suggest that cross-linking introduced during the grafting procedure or enhanced crystallinity cause this lack of solubility. The solvent swelling studies have also provided information about the polymer-solvent interactions which produce swelling and about the morphology of PE-QA. More importantly, these studies have shown that the chemical properties of the PE-QA ionomer are strongly dependent on the nature of the counterion.

Because of the ability to cast films, charge-transport properties and ion-exchange thermodynamics of these polymers may now be conveniently evaluated. In previous studies, we have shown that Nafion preferentially binds hydrophobic counterions (10, 15, 28) and that hydrophobic interactions can influence rates of diffusion in Nafion films at electrode surfaces (14). It will be of interest to see if hydrophobic interactions are of importance to ion exchange and charge transport in films of the RAI polymers.

Acknowledgments

This work was supported by the Office of Naval Research and by the Robert A. Welch Foundation.

Manuscript submitted Nov. 10, 1983; revised manuscript received Feb. 28, 1984.

REFERENCES

- "Perfluorinated Ionomer Membranes," A. Eisenberg and H. L. Yeager, Editors, ACS Symposium Series no. 180, American Chemical Society, Washington, DC (1982).
- "Ions in Polymers," A. Eisenberg, Editor, ACS Advances in Chemistry Series no. 197, American Chemical Society, Washington, DC (1980).
- W. Grot, G. E. Munn, and P. M. Walmsley, Paper 154 presented at the Electrochemical Society Meeting, Houston, TX, May 7-11, 1972.
- F. G. Will, *This Journal*, **126**, 36 (1979).
- A. B. LaConti, A. R. Fragala, and J. R. Boyack, in "Electrode Material and Processes for Energy Conversion and Storage," J. D. E. McIntyre, S. Srinivasan, and F. G. Will, Editors, p. 354, The Electrochemical Society Softbound Proceedings Series, Princeton, NJ (1977).
- K. Itaya, H. Akahoshi, and S. Toshima, *This Journal*, **129**, 762 (1982).
- K. N. Kuo and R. W. Murray, *J. Electroanal. Chem.*, **131**, 37 (1982).
- N. Oyama, S. Yamaguchi, M. Kaneko, and A. Yamada, *ibid.*, **139**, 215 (1982).
- N. Oyama and F. C. Anson, *This Journal*, **127**, 247 (1980).
- M. N. Szentirmay and C. R. Martin, *Anal. Chem.*, to be published.
- B. R. Shaw, G. P. Haight, Jr., and L. R. Faulkner, *J. Electroanal. Chem.*, **140**, 147 (1982).
- R. S. Yeo, S. F. Chan, and J. Lee, *J. Memb. Sci.*, **9**, 273 (1981).
- C. R. Martin, T. A. Rhoades, and J. A. Ferguson, *Anal. Chem.*, **54**, 1639 (1982).
- C. R. Martin and K. A. Dollard, *J. Electroanal. Chem.*, **159**, 127 (1983).
- R. B. Moore, III, J. E. Wilkerson, and C. R. Martin, Submitted to *Anal. Chem.*
- V. D'Agostino, J. Lee, and E. Lu, in "Ion Exchange: Transport and Interfacial Properties," R. S. Yeo and R. P. Buck, Editors, p. 148, The Electrochemical Society Softbound Proceedings Series, Pennington, NJ (1981).
- R. S. Yeo, *Polymer*, **21**, 432 (1980).
- C. M. Hansen and A. Beerbower, in "Kirk-Othmer Encyclopedia of Chemical Technology," Suppl. Vol., 2nd ed., pp. 889-910, Wiley-Interscience, New York (1971).
- C. M. Hansen and K. Skaarup, *J. Paint Technol.*, **39**, 511 (1967).
- T. D. Gierke and W. Y. Hsu, in "Perfluorinated Ionomer Membranes," A. Eisenberg and H. L. Yeager, Editors, pp. 283-307, ACS Symposium Series no. 180, American Chemical Society, Washington, DC (1982).
- H. Burrell, in "Polymer Handbook," J. Brandup and E. H. Immergut, Editors, 2nd ed., Chap. 4, John Wiley and Sons, New York (1975).
- P. C. Lee and D. Meisel, *J. Am. Chem. Soc.*, **102**, 5477 (1980).
- N. E. Prieto and C. R. Martin, Unpublished data.
- S. C. Yeo and A. Eisenberg, *J. Appl. Polym. Sci.*, **21**, 875 (1977).
- H. W. Starkweather, Jr. and J. J. Craig, *Macromolec.*, **15**, 752 (1982).
- C. A. Sperati, in "Polymer Handbook," J. Brandup and E. H. Immergut, Editors, 2nd ed., p. V-32, John Wiley and Sons, New York (1975).
- M. N. Szentirmay and C. R. Martin, Unpublished data.
- C. R. Martin, I. Rubinstein, and A. J. Bard, *J. Am. Chem. Soc.*, **104**, 4817 (1982).
- N. Oyama, T. Ohsaka, K. Sato, and H. Yamamoto, *Anal. Chem.*, **55**, 1429 (1983).
- C. R. Martin, Unpublished data.

Gas-Phase-Functionalized Plasma-Developed Resists: Initial Concepts and Results for Electron-Beam Exposure

G. N. Taylor,* L. E. Stillwagon, and T. Venkatesan

AT&T Bell Laboratories, Murray Hill, New Jersey 07974

ABSTRACT

A resist method involving gas phase functionalization of exposed or unexposed resist by volatile inorganic compounds followed by pattern development using oxygen reactive ion etching is described for use in ion, photo, electron, and x-ray lithography. Negative or positive tones can be obtained in theory from a single exposure by employing selective reaction of either the exposed or unexposed regions with volatile reactive inorganic compounds that form *in situ* masks during plasma development (usually as refractory metal oxides). Near surface functionalization (top several thousand angstroms) is seen as having resolution advantages for electron and photolithography. It is envisioned as being controlled by either limited permeation or by selective near-surface exposure (*i. e.*, low voltage ion or electron exposures). In electron lithography, this could reduce the proximity effect in backscatter-limited thick resist films on high Z substrates. Consequently, we have studied materials and functionalizing reagents for electron lithography at 10 keV. The radiation-initiated reactions studied in the resist were the creation and destruction of unsaturation (olefins, etc.). The inorganic functionalizing reagent was diborane. Pattern development was achieved using O₂ reactive ion etching. Thin ($\leq 2000\text{\AA}$) 1 μm line and space patterns were obtained at 10-50 $\mu\text{C}/\text{cm}^2$ doses for materials which afforded negative and positive tones. These include chlorinated polyacrylates, polyisoprene, and copolymers containing unsaturation and chlorine functionality.

Recently, a report from our laboratory described plasma-developed ion-implanted resists having at least 2500 \AA resolution (1). These resists used implanted metal ions acting as *in situ* etch masks during O₂ reactive ion etch removal of the unexposed regions. Organic polymers were typically employed as resists using oxygen as the etch gas, although thin SiO₂ also was used with fluorocarbon etch gases. In both cases, In⁺ ions were first implanted at low potentials. Features as small as 1500 \AA wide and 1 μm high were fabricated by this technique using a 20 keV focused beam of In⁺ ions (2). Presently, resolution appears limited mainly by the beam size and shape. One of the problems of the scanning ion beam systems is the low penetration ($\sim 200\text{\AA}$) of the heavy ions in most polymer resist (3). A resist that can be patterned with a near surface exposure would be attractive for such systems. Yet, the metal-implanted resists are impractical for present-day scanning ion exposure, since they require excessive dose (10^{16} ions/cm²) even though the implanted-metal layer mask is only 2-4 monolayers thick. Clearly, higher sensitivity is needed given present-day metal ion exposure systems. Thus, we sought new resist materials and processes. One method would involve making use of the many chemical events which occur when each ion is implanted in a resist film. This would amplify the implantation process and hopefully improve sensitivity.

In this report, we describe some initial results for one of the approaches derived from the above considerations. We call resists utilizing this methodology gas-phase-functionalized plasma-developed resists. They are applicable to all four lithographic processes (ion, photo, electron, and x-ray lithography), but would appear to have primary use for ion and photolithography. In the next section, we outline the particular resist methodology and the advantages (both realized and hypothesized) for each application. Finally, we describe some initial results for electron resists in which both positive and negative tone images are produced from the same exposure by various gaseous and subsequent plasma treatments.

Methodology

We envision gas-phase-functionalized plasma-developed resists to behave according to the two routes outlined in Fig. 1. There we depict a resist with reactive groups A which upon irradiation form product groups P at the expense of A, which is depleted in the exposed regions. Next the exposed film is treated with a reactive gas MR containing reactive groups R and inorganic atoms

* Electrochemical Society Active Member.

M capable of forming nonvolatile compounds MY which are resistant to removal under reactive ion etching conditions using gas Y. Several situations are now possible. (i) If the metal containing gas does not diffuse into the film and/or does not react with either the exposed or unexposed areas, no functionalization will occur and no amplification upon development is expected. (ii) Conversely, if the metal compound diffuses everywhere and reacts with both A and P, no etching is likely to occur upon RIE development. (iii) If, however, gas diffusion occurs and reaction with either A or P occurs, selective functionalization results. Subsequent plasma development then can produce either negative tone images when the inorganic compound bonds selectively to P or positive tone images when it selectively bonds to A. Tone is thus dependent upon both the actinically generated species (radiation chemistry) and selective functionalization (organometallic and inorganic chemistry).

Some further considerations would also appear to be of importance. Since the functionalizing step is a gas-solid reaction, surface layers of the resist would be expected to react first if the reaction rate were much greater than the diffusion rate or if the major portion of the incident radiation were absorbed in the topmost ($\sim 1000\text{-}2000\text{\AA}$) layer of resist. For the first case, a reactive gas diffusing into a polymer film, the concentration of gaseous species C at a depth x (in centimeters) into a film from the film surface can be estimated from Eq. [1] where C_0 is the continuous gas concentration at the surface, D is the diffusion coefficient in square centimeters per second, and t is the diffusion time in seconds

$$C = C_0 \operatorname{erfc} \left(\frac{x}{2\sqrt{Dt}} \right) \quad [1]$$

This is the simplified plane sheet solution to the one-dimensional diffusion problem. For the present purposes, it is analytically convenient to calculate C/C_0 as a function of the variables x , D , and t . Some results are given in Table I for two polymers chosen for their structural analogies to systems investigated in this report. In all cases, both inert (O₂, Ar) and interactive (SF₆) gases diffuse more readily into rubbery poly(isoprene) PI than into glassy poly(ethyl methacrylate) PEM. In fact, for PI after treatment for 1s, the gas concentration is expected to be higher in a 1 μm film than in the gas phase for each gas listed. Only for PEM and large molecules (Ar, SF₆) are C/C_0 values < 1.0 found. With SF₆, a significant interaction with PEM ester carbonyl is expected. Consequently, D is very low and no gas penetrates even 1 μm deep for treatment times as long as 10s. At shallower depths, a gra-

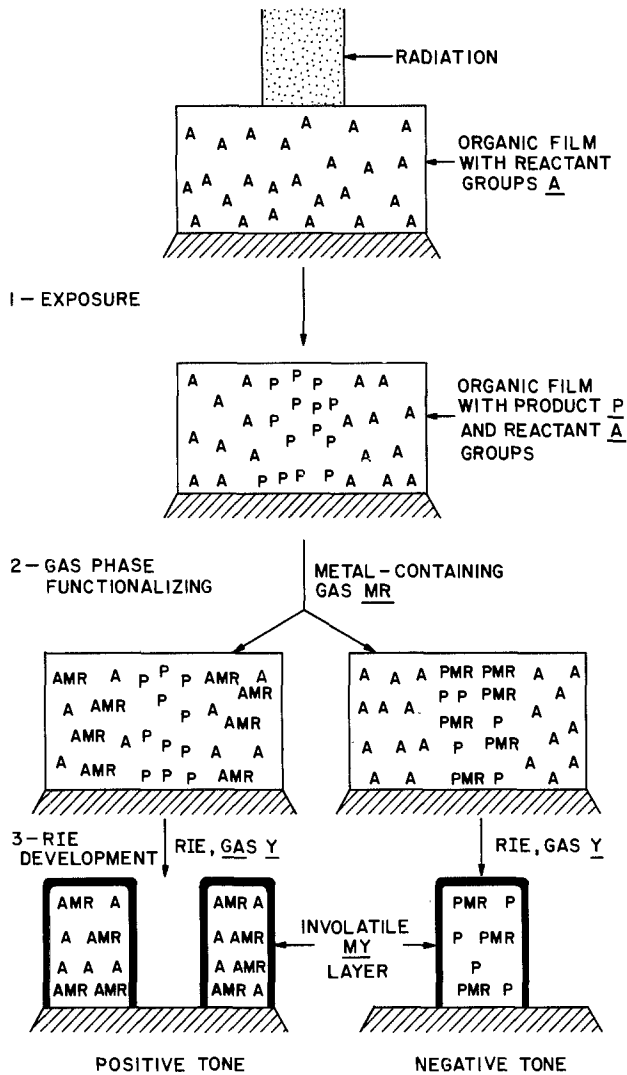


Fig. 1. Schematic representation of gas-phase-functionalized plasma developed resists showing (1) exposure of a material with reactive groups A (2) conversion of such groups to product groups P, and (3) selective functionalization of either A or P with metal containing reagent MR, where M is the metal and R are reactive or inert groups or atoms. (4) reactive ion etch development using gas Y forming nonvolatile compounds MY and volatile AY, PY, and host Y compounds.

dient of SF_6 is expected. Reaction in the near-surface top 2000Å region is clearly favored by short treatment times, low diffusion coefficients associated with large gas molecules, and glassy polymers. Figure 2 presents a representation of near-surface functionalization in this way.

Table I. Dependence of C/C_0 on polymer and gas diffusion properties and on processing properties^a at 25°C

Gas	D ($\text{cm}^2/\text{s} \times 10^6$)	t (s)	x (μm)	C/C_0
A. Poly(isoprene), $T_g = -73^\circ\text{C}$				
O_2	1.73	1.0	1.0	1.45
Ar	1.36	1.0	1.0	1.42
SF_6	0.115	1.0	1.0	1.03
B. Poly(ethyl methacrylate), $T_g = 65^\circ\text{C}$				
O_2	0.103	1.0	1.0	1.00
Ar	0.020	1.0	1.0	0.65
SF_6	0.00022	1.0	1.0	0.00
SF_6	0.00022	1.0	0.5	0.00
SF_6	0.00022	1.0	0.1	0.67
SF_6	0.00022	10.0	1.0	0.00
SF_6	0.00022	10.0	0.5	0.44
SF_6	0.00022	10.0	0.25	0.77
SF_6	0.00022	10.0	0.1	1.15

^aSource: "Polymer Handbook," 2nd ed., J. Brandrup and E. H. Immergut, Editors, John Wiley and Sons, New York (1975).

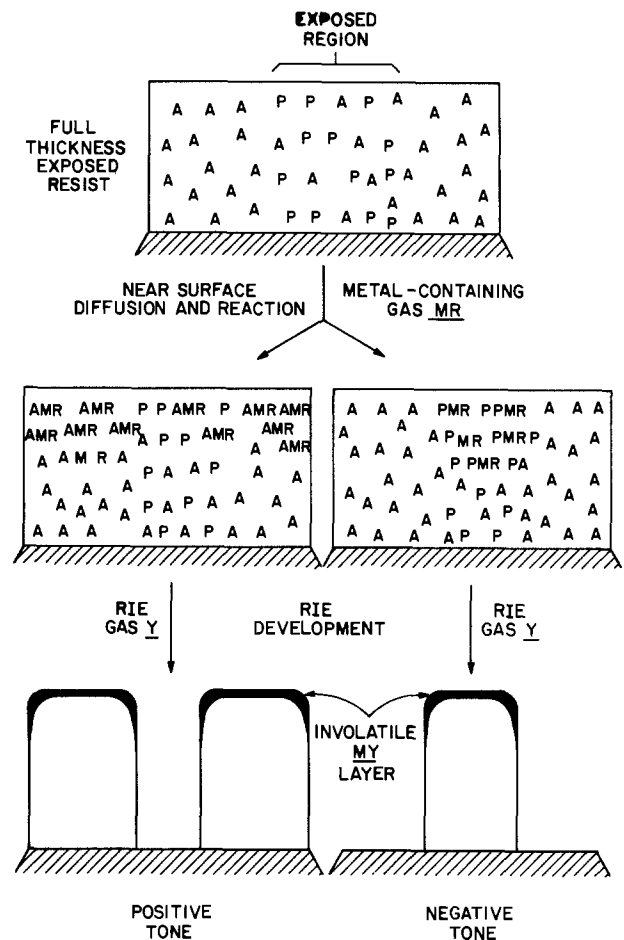


Fig. 2. Schematic representation as in Fig. 1 for the negative tone showing near-surface functionalization of product P by metallic reagent MR. In this case, the gradient shown in Fig. 3 for P is not achieved because of low absorption cross section. Near-surface functionalization is achieved by limited permeation of MR during the sample treatment time.

An alternative to diffusion-controlled reactions in the near-surface region is exposure of the resist selectively in the near-surface region, followed by gas phase functionalization and RIE development as above. This is represented schematically in Fig. 3 for the negative tone case. In the limit of complete diffusion of inorganic reagent MR throughout the film, only negative tone can be achieved in theory. Functionalizing original species A in this instance would result in reaction of subsurface layers as well, thus preventing development. The consequence would only be relief-image formation upon development rather than complete development. In the limit of restricted gas permeation to the near-surface regions, positive tone could be formed with advantages being derived from the near-surface exposure.

For the four lithography types, surface exposure can be achieved most readily with ion beam lithography and photolithography. Use of low energy (~ 20 -50 keV) high atomic number (Z) ions permits exposure of only the top 100-250Å of any organic resist because of the very rapid stopping of the ionic species. For UV and visible photons, resists containing 10 weight percent (w/o) of compounds having $\epsilon \geq 50,000$ l/mol-cm at the exposing wavelength absorb $\geq 90\%$ of the incident light in the topmost 2500Å and $\geq 40\%$ in the first 1000Å. In the vacuum UV ($\lambda < 190$ nm), many polymers have $\epsilon_{\text{values}} > 10^5$ l/mol-cm, while highly conjugated aromatic materials have similar absorbances in 190-700 nm regions. Materials which meet the high absorbance criteria are, therefore, readily available for ion or photon exposures. In the photon case, improved resolution should result, whereas for ions sensitivity should be enhanced.

The situation is considerably different for electron and x-ray lithography in their present forms. For the former,

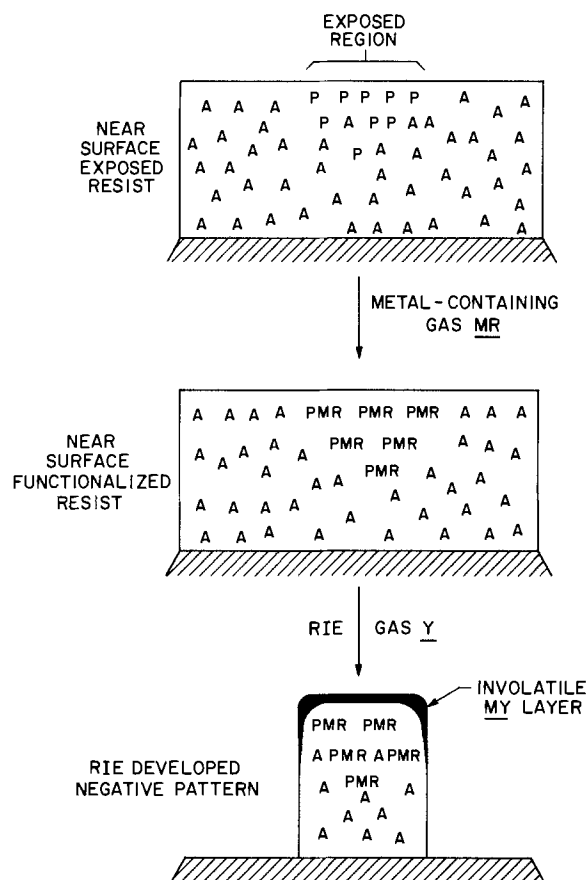


Fig. 3. Schematic representation as in Fig. 2, but only for negative tone showing a gradient of product P produced primarily in the near-surface region due to extremely high absorption cross section expected for ion beam and photon exposures.

high accelerating voltages (15-30 kV) are employed, and even higher ones are contemplated for production use in order to minimize the proximity effect caused by electrons backscattered from the substrate (3). At 20 kV, for example, with a typical low Z resist like PMMA, only about 5% of the incident dose is absorbed in a 1 μm film. The exposure contribution by electrons backscattered from the substrate is considerable and results in greater exposure near the substrate. Clearly, selective surface exposures are not achieved using present exposure voltages. However, if the permeation limited approach outlined in Fig. 2 were followed, one might expect improved resolution because surface functionalization would reduce the proximity effect normally encountered. Another alternative is to expose using very low energy electron beams (< 5 keV), the scheme shown in Fig. 3. These are being developed by Pease and his group at Stanford, but are only in the initial stages of investigation (4). Only permeation-limited functionalization would appear to have merit for electron lithography as we presently know it. However, since few exposure events occur in the near-surface region, such resists would appear to have very limited sensitivity.

X-ray lithography in its present forms likewise suffers from low absorption. For the Pd_L (4.37Å) to Cu_L (13.3Å) wavelength range generally in use today, a maximum of about 40% absorption per micrometer can be achieved using high Z absorbers in 1 μm thick polymeric films. Only about 5% absorption occurs in the top 1000Å. At much longer wavelengths, for which there are no currently available inexpensive high throughput exposure systems, high absorption in the top 1000Å can be achieved ($\lambda = 40 - 2000\text{Å}$). However, for the systems currently available, we again expect to be plagued by insensitivity.

We can now estimate the chances for this new type of resist for each of the lithographic technologies. Ion beam lithography appears to offer the best opportunity because

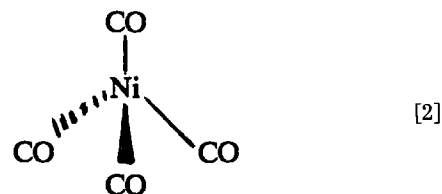
of extremely high absorbed doses in well-confined near-surface layers. But, for high resolution, conducting organic materials may be required (1). This would limit materials choices. Photolithography using very strong absorbers also is a very good candidate especially in the deep and vacuum UV regions. Use as an x-ray resist does not appear very promising, since sensitivity must be extremely high (weak sources), while absorbance is only moderate at best.

An analogous difficult application would be for E-beam resists. This results from an estimated operational dose range of 1-10 $\mu\text{C}/\text{cm}^2$ at 20 keV and 5% absorption in a 1 μm thick film. The near-surface (top 2000Å) absorbed dose would be less than 1% of the incident dose or about 4 mJ/cm^2 . For comparison, commercial photoresists require 40-100 mJ/cm^2 dose when used in microlithography. Sensitivity will once again be pushed to the limit in E-beam examples. Amplification upon development could help in achieving such a sensitivity.

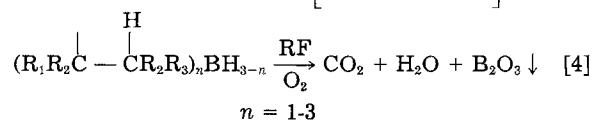
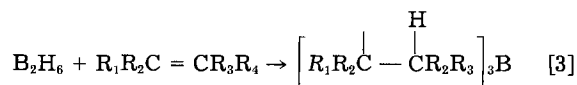
In electron lithography important benefits may be realized. These could result if the proximity effect, which distorts pattern size as a function of geometry in the 1-0.1 μm range, could be reduced. The proposed resist scheme (Fig. 2) has such a potential if only the near-surface layers can be selectively functionalized by etch resistant inorganic groups. It is for this reason that we chose to work first on E-beam-exposed samples.

Results and Discussion

In analyzing chemical systems which would be reactive enough to provide adequate sensitivity as an E-beam resist, we decided to study olefin forming and olefin destroying reactions. The olefinic group could then react with an appropriate inorganic compound. In this regard, the reagent of choice would be nickel carbonyl (2)

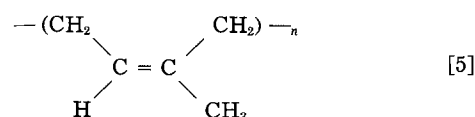


which reacts readily with substituted olefins to give olefin-Ni complexes. However, its extreme toxicity makes its use unacceptable. Another gaseous reagent, diborane B_2H_6 , also reacts readily with olefins especially in the presence of ether compounds according to a well-researched mechanism pioneered by Brown (6). Complete reaction occurs according to Eq. [3]. However, in the solid state



one might expect incomplete reaction to give organoboron hydrides shown at the left side of Eq. [4]. Upon plasma oxidation, these boron compounds would be expected to form B_2O_3 , which has a bp of about 1860°C and should act as a good *in situ* mask for protecting underlying resist.

Initial experiments focused on functionalizing poly(isoprene) [5] with B_2H_6 generated by reaction of BF_3 with NaBH_4 in diglyme solution. The product



diborane was carried by argon into a reaction vessel containing a silicon wafer coated with poly(isoprene). After treatment, samples were etched in a reactive ion etcher

Table II. Influence of process conditions on poly(isoprene) thickness after gas phase reaction and O₂ reactive ion etching^a

Run no.	Reagent gas	Carrier gas	Temp (°C)	Prereaction flush time (min) ^b	Reaction time (min) ^b	Postreaction flush time (min) ^b	NT _D ^c
1	B ₂ H ₆	Ar	25	5	0	0	0.0
2	B ₂ H ₆	Ar	25	5	5	0	0.06
3	B ₂ H ₆	Ar	50	5	5	0	0.18
4	B ₂ H ₆	Ar	80	5	5	0	0.31
5	B ₂ H ₆	Ar	110	5	5	0	0.40
6	B ₂ H ₆	Ar	80	5	5	5	0.05
7	B ₂ H ₆	Ar	80	5	20	5	0.77
8	B ₂ H ₆	Ar	80	5	40	5	0.83

^aEtch time just sufficient to clear the control sample in run 1. Poly(isoprene) etch rate was 1400 Å/min.

^bFlow was 300 ml/min or about a reactor volume/min.

^cNormalized thickness after RIE development along with a control sample which totally cleared.

for various times at 30W power, -250V bias, 10μ O₂ pressure, and approximately 30 sccm flow. The treatment sequence was, first, a flush of the reaction vessel with inert gas, reaction for a given time, temperature, gas, and flow, and, finally, a postreaction treatment. The latter usually consisted of an inert gas flush for a specified time.

Results from the first functionalization experiments using 4900Å initial poly(isoprene) thickness are summarized in Table II. Two sets of experiments are listed. One utilized no flush after reaction and varied the temperature. The second kept temperature constant, used a flush after reaction, and varied treatment time. The former (runs 1-5) shows the importance of temperature on boron incorporation. The etching rate was slowed by nearly a factor of 2 after a 110°C treatment, while low temperature treatment produced only slight changes in developed thickness from the untreated control sample. The majority of the boron incorporated was only sorbed and not reacted. This is indicated by comparing runs 4 and 6 conducted at 80°C for 5 min. Run 6 used a flush after reaction and exhibits a six-fold reduction in NT_D (see Table II), compared to run 4, which did not use a flush. Thus, without a flush sorbed B₂H₆ appeared to be locked into the film by reaction with O₂ upon exposure to air. This may also occur with run no. 6 but to a much reduced extent. Runs 7 and 8 for longer times suggest that reaction may contribute to boron locking, as evidenced by the high normalized thickness values, where a maximum value of 1.0 can be attained. However, can conditions such as those in runs 4, 7, and 8 provide enough selectivity for image formation after exposure and processing?



We first tried a potential negative tone producing polymer, poly(vinyl chloride) PVC (5). This material is known to efficiently evolve HCl upon exposure to ionizing radiation with the generation of polyene sequences (7). However, both Ga⁺ exposures at 6.5 and 10 keV electron exposures at 100 μC/cm² failed to give any change in the slight negative tone images observed for PVC without B₂H₆ treatment. At the latter dose, 0.5 μm lines and spaces were visible in only very thin (< 500Å) resist.

Electron exposures at 10 keV also were conducted with poly(isoprene) using doses from 1-100 μC/cm². At 100 μC/cm² and after B₂H₆ treatment, faint 500Å thick positive tone images were obtained. This is the tone expected for boron reaction and masking. Control exposures at 100 μC/cm² without B₂H₆ treatment gave negative tone images (1100Å). Thus poly(isoprene) appeared to afford some selective functionalization and thus provided the first example of this type of resist. However, such images are not useful because of the very thin final resist, resist flow during reaction, and excessive dose.

In addition, other disadvantages were encountered. The tone inversion was dependent on reaction temperature, with 70°-80°C being optimum. At higher temperatures (> 100°C) no appreciable film removal was observed during

development, while at < 60°C, the final developed image thickness disappeared (no patterns). Also, surface texture was very rough and reproducibility was fair at best.

Poor reproducibility could result from a variety of factors. One is the chemical generation of B₂H₆, which occurs in spurts and is extremely difficult to control adequately. Consequently, we tried 1% B₂H₆ in nitrogen at 76°C and found no reaction with poly(isoprene) under a wide variety of conditions as judged from the O₂ reactive ion etch rates. This was further confirmed by ESCA analysis for B_{1s} at 186 eV, done by Schwartz and Gualtieri. Addition of dimethylether to the B₂H₆ gas stream had no effect, although Brown had claimed it accelerated gas phase reactions of B₂H₆ (6). Treatment at 107°C did show slight evidence of reaction. However, selectivity and flow as expected were adversely affected at this temperature.

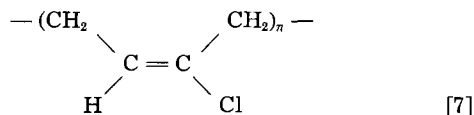
It seemed likely that the B₂H₆ concentration was too low in the 1% mixture used above. So, we experimented with 14.6% B₂H₆ in N₂, the maximum percentage available commercially. The etch rate of a control sample, untreated poly(isoprene) of 5600Å thickness, was compared to a variety of samples treated at 75°C using a 5 min N₂ flush before and after treatment. The etch rates in an oxygen plasma relative to the control sample are given in Table III. From Table III we see that treatment with B₂H₆ reduces the etch rate and that the degree of reduction is fairly independent of treatment time. The addition of dimethylether to B₂H₆ increases the etch rate. This is the behavior expected for a noncatalytic diluent, even though it was thought to enhance B₂H₆ reactions, according to early studies by Brown and co-workers (6).

Poor etching selectivity can result from three sources: (i) inefficient destruction or creation of reactive double bonds during the exposure step, (ii) inefficient reaction of the functionalizing inorganic reagent, or (iii) inadequate etch resistance of the incorporated inorganic species. To probe the first possibility, we studied other polymers which may be expected to be more reactive to the incident radiation. It is known, for example, that a synergism exists between halogens and olefinic groups leading to the more facile destruction of unsaturation upon electron irradiation of polymers containing both groups (8). A likely candidate for examination would appear to be poly(chloroprene) [7], but it is quite unreactive

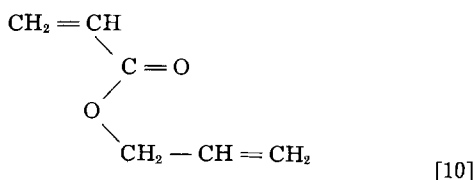
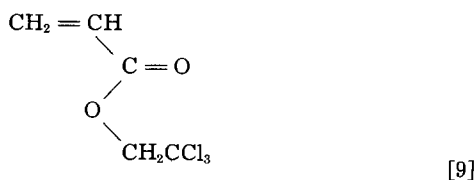
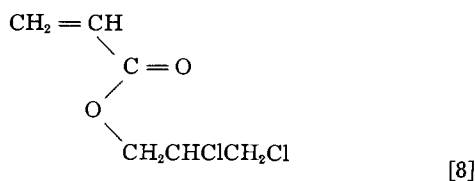
Table III. Relative O₂ RIE etch rates of poly(isoprene) reacted with 15% B₂H₆ in N₂ at various conditions

Run no.	Gas and composition (v/o)	Reaction time (min)	Second gas and composition (v/o)	Rel. etch rate
1	0	0	—	1.0*
2	B ₂ H ₆ -N ₂ , 100	5	—	0.64
3	B ₂ H ₆ -N ₂ , 100	30	—	0.75
4	—	—	—	—
5	B ₂ H ₆ -N ₂ , 50	5	DME, 50	0.86
6	B ₂ H ₆ -N ₂ , 50	30	DME, 50	0.80

*800 Å/min.



toward B_2H_6 because of the electron withdrawing properties of chlorine. As alternatives, we chose copolymers of 2, 3-dichloro-1-propyl acrylate [8] and 2, 2, 2-trichloroethyl acrylate [9] with



allyl acrylate [10] prepared by transesterifying the homopolymers of [8] and [9] with allyl alcohol. The copolymers designated at [8]-[10] and [9]-[10], respectively, contained 14.5 and 12.8 mole percent (m/o) allyl acrylate determined from elemental analysis. 0.5-1.1 μm thick films of the two copolymers were irradiated on EBES at 10 keV and five doses: 1, 5, 10, 50, and 100 $\mu\text{C}/\text{cm}^2$. Homopolymer films of monomers [8] and [9] were also irradiated and used as control materials. After exposure, the materials were either developed by O_2 RIE or treated with B_2H_6 under a variety of conditions and then developed as above. The baseline experiments for exposure only are summarized in Table IV. Here normalized thicknesses after development (NT_D) are listed at the five exposure doses. Since $NT_D = NT_{DE} - NT_{DU}$, where E and U designate the exposed and unexposed regions, negative values for NT_D imply positive tone. Samples were heated as indicated to mimic those heated later in a B_2H_6 atmosphere.

In each case, irradiation and plasma development gave weak positive tone images analogous to those found for poly(2, 3-dichloropropyl methacrylate) and poly(methyl methacrylate-co-oximinobutanedione methacrylate) by Taylor and Wolf (9). In those instances, lower doses were required, and the phenomenon was thought to result from cracking during exposure and post exposure heating. In the present instance, since most of the films were rubbery, cracking seemed unlikely. Rather, we believe the irradiated regions contract due to E-beam-induced cross-linking and gaseous product evolution. (All four materials behave as sensitive low contrast negative resists using solution development.) Even at the highest dose, none of the materials underwent enough chemical change

Table IV. NT_D Values as a function of dose for four chlorinated polymer films developed by O_2 RIE

Polymer	NT_D at				
	10 keV electron dose ($\mu\text{C}/\text{cm}^2$)	1	5	10	50
[8] DCPA ^a	0.0	trace	-0.04	-0.09	-0.11
[9] TCEA ^b	0.0	trace	-0.03	-0.06	-0.09
[8]-[10] Copolymer ^c	0.0	0.0	trace	-0.05	-0.07
[9]-[10] Copolymer ^d	0.0	0.0	-0.04	0.08	-0.10

^aHeated at 90°C for 30 min after exposure.

^bHeated at 70°C for 30 min after exposure.

^cHeated at 70°C for 30 min after exposure.

^dHeated at 40°C for 30 min after exposure.

to significantly influence the development (etch) rates. Thus, all give shallow positive tone images at doses > 10 $\mu\text{C}/\text{cm}^2$.

In contrast to this, samples reacted with B_2H_6 exhibit significant differences. The optimum results for each material are collected in Table V. In three of the four instances, addition of an equal amount of dimethyl ether gave better results than treatment with B_2H_6 alone. Treatments for times of less than 30 min were inferior, while longer times showed no additional improvement. Etching time to clear increased for all treated samples and was longer for longer treatment times (range of 4-11 min). For the two homopolymers treatment with B_2H_6 changed the resist tone from positive to negative (Fig. 4a, Table V). Best results were obtained with DCPA irradiated at 50 $\mu\text{C}/\text{cm}^2$ to give 0.21 normalized thickness at 1 μm line and space resolution. This is a change of 0.3 in normalized thickness from the control sample exhibiting positive tone. Note that a maximum was obtained at 50 $\mu\text{C}/\text{cm}^2$. Apparently, at higher doses the unsaturation generated by electron exposure is reduced by cross-linking processes. A similar but less dramatic trend was observed for TCEA. Both polymers exhibit the tone expected for reaction of B_2H_6 with unsaturation created in irradiated regions. Apparently either generation of olefinic unsaturation or reaction with B_2H_6 is less efficient for the glassy TCEA.

Results for the allyl acrylate copolymers show the opposite trend as expected for preferential B_2H_6 reaction in unirradiated regions (Fig. 4b, Table V). However, the changes are not as dramatic. The normalized thicknesses of the positive tone images in the control samples increased by a maximum of 0.13 for the [8]-[10] copolymer and only 0.08 for the [9]-[10] copolymer. High doses (50-100 $\mu\text{C}/\text{cm}^2$) were required, and final films were thin. This process is clearly less selective and less sensitive than the negative tone case using DCPA. All are inadequate for EBES and have not achieved the ideal condition of near-surface functionalization proposed in Fig. 2, since full resist thickness did not result. However, the effect has clearly been demonstrated, especially for DCPA, where the tone is inverted by gas phase reaction after exposure.

What factors are responsible for the low sensitivity and selectivity? Several could possibly contribute. The first is inefficient reaction of B_2H_6 with olefinic groups in the solid state. A second could be inefficient masking by boron due to facile sputtering of B_2O_3 (which seems unlikely) or removal during development as volatile organo-boron-oxygen compounds. A third possibility is too low

Table V. NT_D values as a function of B_2H_6 reaction and dose for four chlorinated polymer films

Polymer	Reagents	Temp (°C)	Treatment time (min)	NT_D at 10 keV electron dose ($\mu\text{C}/\text{cm}^2$)				
				1	5	10	50	100
[8] DCPA	B_2H_6	90	30	0	0.04	0.08	0.21	0.18
[9] TCEA	B_2H_6	70	30	0	trace	0.03	0.06	0.10
[8]-[10] Copolymer	DME	70	30	0	-0.05	-0.10	-0.18	-0.18
	B_2H_6							
[9]-[10] Copolymer	DME	40	30	-0.05	-0.07	-0.09	-0.16	-0.16
	B_2H_6							
	DME							

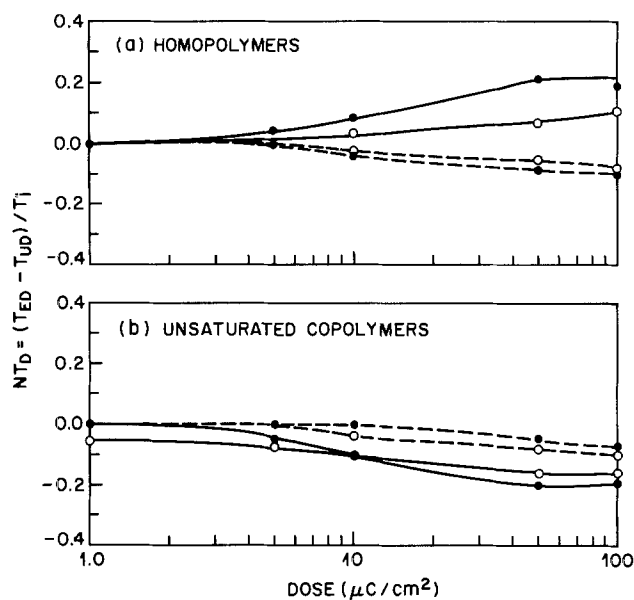


Fig. 4. Normalized thickness vs. log dose for: (a, top) DCPA (●) and TCEA (○) homopolymers treated (—) and untreated (---) with B_2H_6 and developed by O_2 RIE, and (b, bottom) analogously treated DCPA-co-AA (●) and TCEA-co-AA (○) samples which exhibit only positive tone.

conversion of unsaturated groups upon irradiation. A fourth is sorption outcompeting reaction and therefore minimizing etch rate differences.

Other reasons may undoubtedly contribute as well. The halving of removal rates by treatment with B_2H_6 for long times clearly suggests that boron incorporation reduces etch rates. But, how much is incorporated? From the work of Venkatesan and co-workers (1), we know that about four equivalent monolayers of metal forming a nonvolatile oxide are sufficient to reduce the etching rate by about a factor of 10. Assuming a linear relationship between metal content and relative etch rate, we would expect somewhat less than one monolayer of boron reacted preferentially in the film in the present case from the halved relative etch rate. But, it is dispersed throughout the film prior to O_2 RIE development. The latter would serve to concentrate the boron at the surface, much like SiO_2 is concentrated on the surface during O_2 RIE development of plasma-developed silicon containing x-ray resist (10).

To ascertain boron content, Schwartz and Gualtieri ran ESCA spectra of some of our samples before exposure and after B_2H_6 treatment and O_2 reactive ion etching. Rutherford backscattering analyses were not possible due to substrate interferences. In the case of the samples discussed in Tables IV and V, the chlorine present partially interferes with the boron 1s peak at 186 eV because of the strong Cl_{2p} absorption at 197.5 eV. Careful analysis, however, revealed no "boron shoulder" with the Cl_{2p} peak for untreated and boron-treated [8]-[10] copolymer. Other expected peaks (O_{1s} , C_{1s} , Cl_{2s} , and Cl_{1s}) also were observed. In the RIE-developed sample, a small shoulder on the low energy side of the Cl_{2p} peak was found; it seems likely that it is the B_{1s} peak. Comparison to other peaks and correction for differences in cross section provides a rough estimate that about 0.03 equivalent monolayers of boron were present. Since the film studied had 14.8 m/o unsaturation prior to irradiation (an ample amount for reaction), it seems likely that inefficient reaction with B_2H_6 in the solid state is partially responsible for the low sensitivity. Low normalized thickness after development, in spite of etch rates reduced by as much as a factor of 2, suggests that selectivity is poor and that sorbed material is not completely removed by flushing after reaction with B_2H_6 .

Fine patterns can nonetheless be obtained. Photomicrographs of positive and negative tone patterns are shown in Fig. 5. Figure 5a shows negative tone patterns obtained

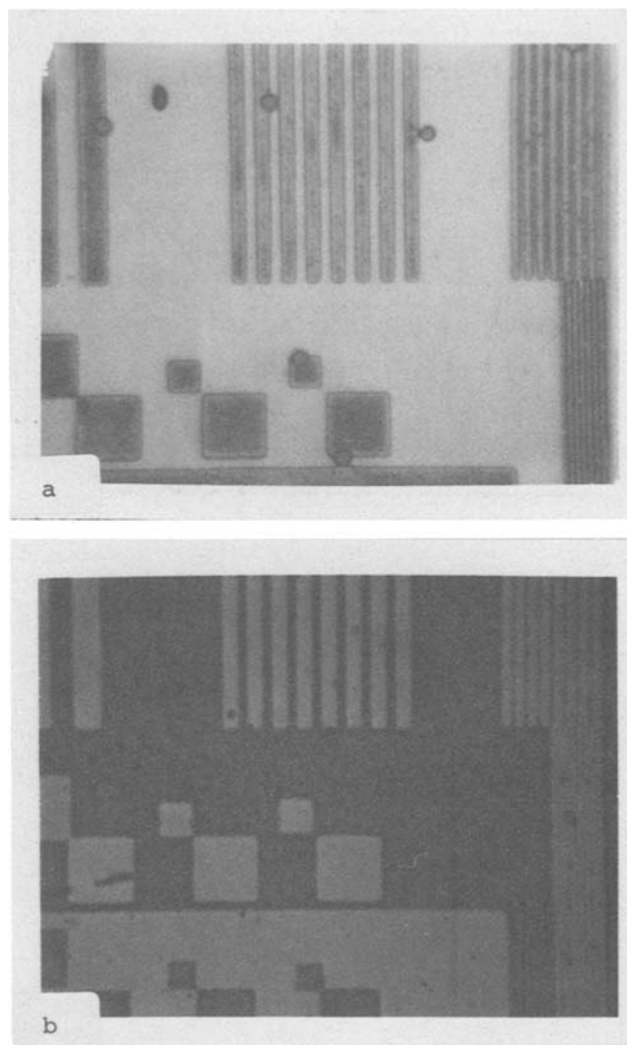


Fig. 5. Photomicrographs of O_2 RIE-developed images in (a) DCPA exposed to $50 \mu C/cm^2$ at 10 keV and reacted with B_2H_6 (final thickness 1800\AA) negative tone. (b) Copolymer of TCEA and AA exposed at $10 \mu C/cm^2$ and reacted with B_2H_6 (final thickness $\sim 800\text{\AA}$) positive tone. Finest lines and spaces are 0.5, 1.0, 2.0, and 4.0 μm .

in DCPA after a $50 \mu C/cm^2$ exposure, B_2H_6 treatment, and O_2 RIE development. In this instance, the development endpoint was easy to detect since most of the resist was selectively removed. $0.5 \mu m$ lines and spaces $0.18 \mu m$ thick are evident along with the larger 1, 2, and 4 μm lines and spaces. In Fig. 5b, positive tone images 800\AA thick are shown for the copolymer of TCEA and AA after exposure at $10 \mu C/cm^2$, B_2H_6 treatment, and O_2 RIE development. In this case, clearing of fine features was very difficult to gauge during development, and all fine features were overetched. Nonetheless, remnants of the 0.5, 1.0, and 2.0 μm lines are evident in the micrograph along with a very rough granular texture which is not as noticeable in the negative tone example. In most cases, we see a granular texture which is very similar to that observed with plasma-developed negative x-ray resists (11). In the latter instance, the granularity arises from the Si containing component and appears as small ($< 500\text{\AA}$) SiO_2 granules (11). In the present instance, it appears uniformly in the exposed and unexposed regions and for both tones. We believe it results from sorbed B_2H_6 , which continues to desorb slowly upon removal from the treatment cell. Upon diffusion to the surface, it probably reacts with O_2 to give B_2O_3 in trace amounts, which would act as a partial discontinuous mask in the development process.

Conclusions and Final Remarks

In this paper, we have outlined the principles of functionalizing organic resists by gas phase reaction with

inorganic or organometallic reagents, which selectively bind inorganic atoms to either exposed or unexposed resist regions. The reactive selection is amplified by plasma development, which converts the metal into a nonvolatile *in situ* mask. Two additional examples are already present in the literature. The first is grafting of dichloromethylvinyl silane to plasma-polymerized methyl methacrylate selectively in electron exposed regions, followed by O₂ plasma development to give negative tone patterns (12). Negative tone patterns were also obtained with electron-irradiated PMMA treated with dimethyl dichlorosilane and then water and developed by O₂ RIE (13). In this latter instance, a permeation, water-induced polymerization model was proposed. It differs from that which we discuss here. The radiation grafting example is a good example of the model which we outline here.

We have tested this new resist technique using 10 keV electron lithographic exposures from 1 to 100 $\mu\text{C}/\text{cm}^2$ and treatment with diborane, which efficiently reacts with electron-rich C-C double bonds to form organoboranes in solution. Pattern development was achieved with O₂ RIE at 10 μ pressure. Formation of both positive and negative tone patterns was achieved using chloroacrylate homopolymers or copolymers with allyl acrylate containing 12-15% unsaturation. Comparison to control samples not treated with diborane demonstrates selective functionalization in both instances. A maximum change of 0.30 in normalized thickness was realized for DCPA irradiated at 50 $\mu\text{C}/\text{cm}^2$. High resolution but thin final developed patterns were obtained. Sensitivity and resolution do not appear to be as high with the copolymer positive tone resists.

While these materials and processes demonstrate the principles of the technique, they are far from practical use. First, both sensitivity (50 $\mu\text{C}/\text{cm}^2$) and final thickness ($\sim 1500\text{\AA}$) are inadequate. This appears to result from two factors, poor reaction of diborane with unsaturation in the resist and competition from sorbed material, which desorbs at a slow rate and which can presumably form a skin on the resist surface upon exposure to air. ESCA

measurements appear to indicate that inefficient functionalization is the primary limitation.

Acknowledgments

We are indebted to G. P. Schwartz and G. A. Gualtieri for their careful and patient ESCA analyses. Also, we thank J. Frackowiak and R. K. Watts for the electron beam exposures and M. P. Bohrer for helpful discussions.

Manuscript submitted Sept. 7, 1983; revised manuscript received Jan. 5, 1984.

AT&T Bell Laboratories assisted in meeting the publication costs of this article.

REFERENCES

1. T. Venkatesan, G. N. Taylor, A. Wagner, B. Wilkens, and D. Barr, *J. Vac. Sci. Technol.*, **19**, 1379 (1981).
2. T. Venkatesan, G. N. Taylor, and B. Wilkens, Private communication.
3. G. S. Greeneich, *J. Vac. Sci. Technol.*, **19**, 1269 (1981), and references therein.
4. R. F. W. Pease, Paper 308 presented at The Electrochemical Society Meeting, Montreal, Quebec, Canada, May 9-14, 1982.
5. W. T. Lynch, Private communication.
6. H. C. Brown, "Hydroboration," Benjamin, Inc., New York (1962).
7. R. Salovey, in "The Radiation Chemistry of Macromolecules," Vol. 2, M. Dole, Editor, Academic Press, New York (1973).
8. S. M. Miller, M. W. Spindler, and R. L. Vale, *J. Polym. Sci.*, **A1**, 2537 (1963).
9. G. N. Taylor and T. M. Wolf, in "Proceedings of Microcircuit Engineering 81," pp. 381-385, Sept. 28-30, 1981, Lausanne, Switzerland.
10. R. F. Roberts and G. N. Taylor, Unpublished data.
11. G. N. Taylor, T. M. Wolf, and J. M. Moran, *J. Vac. Sci. Technol.*, **19**, 872 (1981).
12. M. Yamada, J. Tamano, K. Yaneda, S. Morita, and S. Hattori, in "Proceedings of the Dry Process Symposium," Paper IV-2, pp. 90-93, Tokyo, Japan, Nov. 18-19, 1982.
13. D. Follett, K. Weiss, J. A. Moore, A. J. Steckl, and W. T. Lui, Abstract 201, p. 321, The Electrochemical Society Extended Abstracts, Vol. 82-2, Washington, DC, Oct. 17-21, 1982.

The Scope and Mechanism of New Positive Tone Gas-Phase-Functionalized Plasma-Developed Resists

T. M. Wolf, G. N. Taylor,* T. Venkatesan, and R. T. Kraetsch

AT&T Bell Laboratories, Murray Hill, New Jersey 07974

ABSTRACT

A new type of plasma-developed positive acting photo and electron-beam resist is described. It is based upon the difference in functionalization occurring when exposed resists such as Waycoat IC-43 and Selectilux N-60 are treated with gaseous inorganic halides. Unexposed areas etch slowly during O₂ reactive ion etching. In these areas, azide-inorganic halide complexes are readily converted to a masking metal oxide layer. In the exposed areas, inorganic amino halides are converted to volatile organic and inorganic compounds. Thicknesses in excess of 5000 \AA result for 8s contact photoexposures at 366 nm followed by treatment with SiCl₄ and O₂ reactive ion etching. In addition, 0.6 μm resolution is attained. Electron beam exposures indicate resolution capabilities of less than 0.3 μm , with sensitivity on the order of 10-20 $\mu\text{C}/\text{cm}^2$ at 20 keV. A mechanism consistent with UV, infrared, Rutherford backscattering, ESCA, and kinetic data is presented.

In a previous paper (1), Taylor and co-workers described a new resist technology involving gas phase functionalization of an exposed resist with inorganic compounds. They envisioned selective reaction of the gaseous inorganic compounds in either the exposed or the unexposed regions of the resist. This selective reaction would optimally occur at or near the surface of the resist and would be controlled by either the limited permeation of the inorganic compounds, the near-surface exposure, or both. The selectivity would be further enhanced during pattern development using reactive ion etching, during

which the inorganic compound would be converted into a nonvolatile product. This nonvolatile product would act as an *in situ* mask, a concept previously used for plasma-developed x-ray resists (2) and ion-implantation resists (3). In the present instance, positive or negative tones could be obtained by controlling either the gas phase functionalization process or the type of etchants employed during the development process. Whichever the case, it is conceivable that either tone could be generated from the same exposure using appropriate methods.

Although this technique is applicable for use in ion, photo, electron, and x-ray lithography, Taylor and co-workers studied the method using 10 keV electron expo-

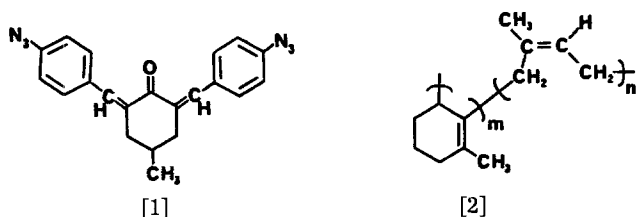
* Electrochemical Society Active Member.

sure of chlorine containing acrylic polymers and copolymers containing allylic ester groups. B_2H_6 was used as the functionalizing agent. Exposed and functionalized resists were developed using O_2 reactive ion etching. High resolution patterns were obtained ($\sim 1.0 \mu m$), but the final patterns were too thin ($< 2000 \text{ \AA}$) and were obtained only at high doses ($\sim 50\text{-}100 \mu C/cm^2$).

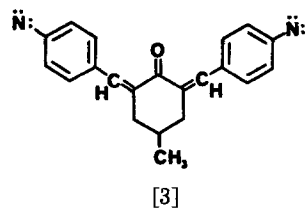
Herein, we describe some initial results obtained in a study of the gas phase functionalization of two negative acting photoresists, Waycoat IC-43 (Phillip A. Hunt Company) and Selectilux N-60 (E. Merck Incorporated), with various inorganic halogen compounds. Our goal was the development of a low dose, high resolution gas phase functionalized photo or electron resist. We wanted to utilize the photochemistry of the sensitizers in the resist to effect a means to selectively sorb a volatile inorganic halide. We also wanted a very high absorbed concentration of the inorganic halide. This would insure the formation of a thick metal oxide protecting layer during O_2 reactive ion etching. High values of normalized developed thickness, NT_D , in excess of 5000 \AA , should result. We also envisioned the difference in selectivity to be large enough to enable one to achieve resolution less than $1.0 \mu m$.

Methodology

Waycoat IC-43 and Selectilux N-60 are two commercially available negative-acting photoresists whose radiation chemistry is well documented (4). The resists consist of a bis-azide sensitizer [1] in a partially cyclized poly(isoprene) host [2]



Upon UV irradiation, the sensitizer loses two molecules of nitrogen to give the dinitrene intermediate [3]

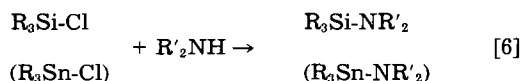


The dinitrene can add across a double bond to give an aziridine [4], or insert into a carbon-hydrogen bond to give a secondary amine [5]. The difunctionality of



the sensitizer affords cross-linking of the polymer host and the material functions as a negative solution-developed resist in conventional photolithography.

However, the transformation of the azide functionality to either an aziridine or amine can potentially be useful in the gas phase functionalization process. Inorganic halides, such as silicon tetrachloride ($SiCl_4$) and tin tetrachloride ($SnCl_4$), are known to react with secondary amines (5) to form tetrasubstituted silyl or stannyl amines [6]. On this basis we formulated



the lithographic process outlined in Fig. 1. Photolysis of the resist converts the azide A contained in the partially cyclized polyisoprene host into aziridines and amines B. Next, the exposed resist is treated with a gaseous inorganic halide MX. This is envisioned to functionalize the exposed areas via the reaction with the amines as depicted by BMX. Oxygen reactive ion etching would strip the unexposed, unfunctionalized areas. Etching would oxidize the inorganic-amine product to an inorganic oxide. This oxide would then act as an *in situ* masking layer, which would effectively prevent further etching in the exposed areas.

These processes were outlined (schematically) first by Taylor *et al.* (1) for negative resists. Since then, Follett and co-workers (6) and Hattori and co-workers (7) have described similar processes. Both used PMMA, which afforded negative tone patterns.

Both of these examples appear to be impractical. This paper describes materials and processes which bring gas phase functionalized plasma-developed resists closer to reality. In addition, a novel means for achieving positive tone is detailed.

Experimental

Prebaked $1 \mu m$ thick films of Waycoat IC-43 and Selectilux N-60 on Si were contact exposed on two different exposure tools. An Optical Associates Incorporated deep UV exposure light source (Model 29D) and intensity control system (Model 780) were employed using 250-300 nm optics. A Cobilt Model CA2020H Contact Printer at 366 nm was used for resolution studies.

The exposed coatings were functionalized using $SiCl_4$, $SnCl_4$, or Me_2SiCl_2 (Alfa Products). Gas phase functionalization took place in a reaction cell, the details of which will be discussed in a later paper. Treatment times were typically 1-60s.

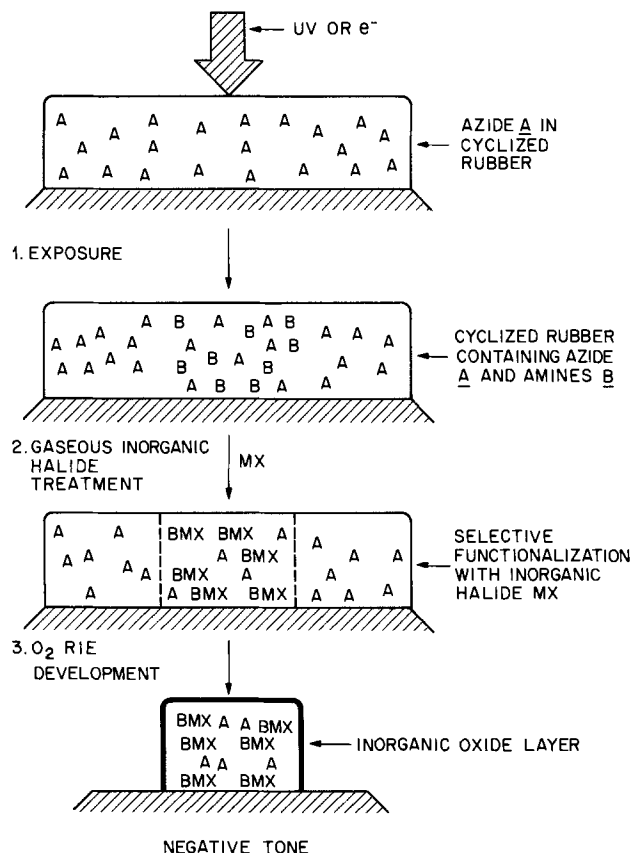


Fig. 1. Schematic showing the proposed mechanism for gas-phase functionalized resists. Azide A incorporated in a host polymer is radiologically converted to an amine B. Treatment with an inorganic halide MX gives an amine-inorganic halide BMX capable of conversion to a refractory nonvolatile oxide MO_2 during O_2 RIE.

Etching was done in a Cooke Vacuum Products reactive ion etcher, using oxygen as the sole etchant. The typical etching conditions were 20W, 10-20 mtorr, and an oxygen flow of 8-12 sccm.

Results and Discussion

The azide containing gas-phase-functionalized resists etched in a manner completely opposite the mechanism we envisioned (Fig. 1). The unexposed regions etched at a significantly lower rate than their exposed counterparts! Under the best processing conditions, a normalized developed thickness, NT_D , between 0.5 and 0.7 was obtained. Positive acting resist behavior resulted whenever we "successfully" functionalized the resist (Fig. 2). The term "successful" is used to indicate complete clearing of the substrate in the exposed areas upon reactive ion etching. Instances will be described later where only partial or even no clearing was obtained.

Waycoat IC-43 and Selectilux N-60 were successfully functionalized using SnCl_4 , SiCl_4 , and dimethyldichlorosilane $[(\text{CH}_3)_2\text{SiCl}_2]$. Figure 3 shows the results for the normalized developed thickness of SiCl_4 functionalized Selectilux N-60 as a function of exposure time and functionalization time. N-60 was contact exposed using the Cobilt CA2020H and then treated with SiCl_4 for various times. Two trends are noted. First, when SiCl_4 treatment time was varied (8, 16, or 32s) at constant exposure, NT_D passed through a maximum. At 3, 5, and 7s SiCl_4 treatments, patterns could be developed. However, at or above 10s treatment, neither the exposed nor the unexposed areas could be etched. Secondly, varying the exposure time while keeping the SiCl_4 treatment time constant (3, 5, 7, or 10s) afforded a maximum NT_D at a 16s exposure time. Coincident with decreasing NT_D at high doses or long treatment times was a decrease in the etch rate relative to the same etching rate for functionalized low dose exposures. A 10s SiCl_4 treatment always afforded resist films that could not be etched, regardless of exposure time.

These results indicate the possibility of two types of behavior depending on exposure and SiCl_4 treatment times.

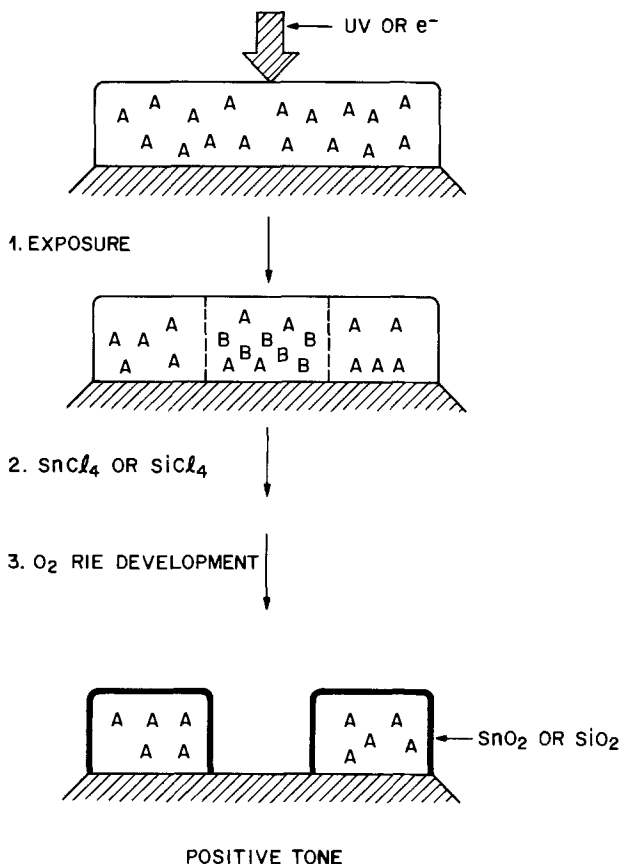


Fig. 2. Schematic depicting the observed pathway of gas phase-functionalized negative photoresists treated with SiCl_4 or SnCl_4 .

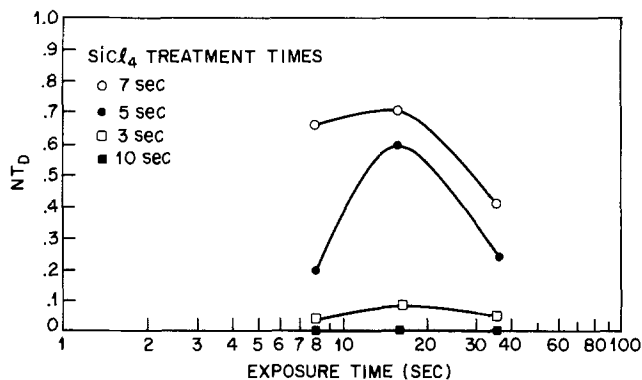


Fig. 3. Plots of the normalized developed thickness vs. exposure time for Selectilux N-60 treated with SiCl_4 for various times.

At low doses and low SiCl_4 treatment times, one can easily develop patterns. Etch time to clear the exposed regions and etch rate are constant and equivalent to that of an unfunctionalized resist (1250 Å/min) used as a control. It appears as if SiCl_4 were present only in the unexposed areas, contrary to our expectations. During RIE, the silicon present there is converted to SiO_2 , thus reducing the etch rate.

However, a much different picture is evident from an analogous study using SnCl_4 as the volatile inorganic halide and Waycoat IC-43 resist. Waycoat IC-43 has nearly identical components and structures to those in Selectilux N-60. 1 μm thick films of IC-43 on Si wafers were exposed to 250-300 nm UV radiation for 1, 3, 5, 10, 30, and 60s using the OAI exposure tool. Each sample was treated with SnCl_4 for 1 min. An analogously treated but unexposed sample of IC-43 was used as a control. In this case, the use of SnCl_4 permits the analysis of the depth distribution of the reagents (Sn and Cl) using Rutherford backscattering spectroscopy (RBS) (8). Figure 4 shows the spectra obtained for 3 samples: an unexposed control, a 3s exposure, and a 30s exposure.

The control spectrum reveals that SnCl_4 was uniformly distributed (sorbed) within the resist. This simulates the unexposed areas on a patterned wafer that etch at a slower rate than the exposed areas. Incredibly, Sn was present in the photoexposed wafers as well. Both the 3 and the 30s samples show a Sn background comparable to the control; that is, they both show a uniform distribution of Sn in the resist (1.2×10^{17} Sn at./cm²). In addition, the appearance of a new peak in the vicinity of channel no. 400 shows a build-up of Sn (1.8×10^{17} Sn at./cm²) in the near-surface region (upper 2500Å) of the resist. Tables I and II summarize the amounts of Sn and Cl sorbed for each exposure dose. Figure 5 shows a plot of the additional Sn concentration vs. exposure time using the data

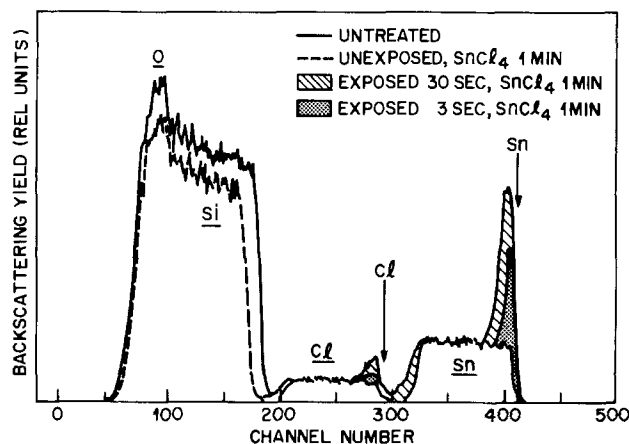


Fig. 4. Rutherford backscattering spectra for exposed and unexposed Waycoat IC-43 treated with SnCl_4 for 1 min showing the increase in Sn and Cl as a function of exposure time.

Table I. RBS results for photoexposed Waycoat IC-43 resist treated for 1 min with SnCl_4

Exposure time (s)	Sn (cts)	Cl (cts)	Cl/Sn ^a (total)	Cl/Sn ^a (excess)
0	23,365	8,561	3.17	0
1	27,739	9,591	2.99	0
3	31,490	10,026	2.75	1.14
5	31,445	10,207	2.80	1.48
10	34,693	11,057	2.76	1.42
30	37,822	11,652	2.66	1.54
60	40,329	12,229	2.62	1.36

^aCalculated using correction factors involving atomic numbers for Sn and Cl.

Table II. Increase in Sn as a function of photoexposure from the RBS data

Exposure time (s)	Total Sn (cts)	Total Sn (at. $\times 10^{17} \text{ cm}^{-2}$)	Near-surface Sn (cts)	Near-surface Sn (at. $\times 10^{16} \text{ cm}^{-2}$)
1	27,739	1.28	0	0
3	31,490	1.45	3,751	1.73
5	31,445	1.45	3,706	1.70
10	34,693	1.60	6,954	3.20
30	37,822	1.74	10,083	4.64
60	40,329	1.86	12,590	5.79

given in Table II. There appears to be a first-order dependence of excess Sn with respect to exposure time. IC-43 coated wafers exposed for 30s and treated with SnCl_4 contain 50% more Sn than the control sample. Moreover, it is this high Sn concentration area that is etched away in preference to the unexposed, but treated, control!

An examination of the data in Table I shows that the ratio of Cl to Sn in the background of all the samples is approximately 3.2 and is lower than the value of 4.0 for SnCl_4 itself. But, in the regions that correspond to the Sn build-up, this ratio decreases to 1.4. Clearly, Sn appears to be present in different forms in the exposed and the unexposed regions. One of these may be an amino-tin compound, as outlined earlier in this paper. The other appears to be SnO_2 overlying a SnCl_4 -sensitizer complex of undetermined form.

ESCA analysis supports the above hypothesis. Substantial differences for the surfaces of the exposed and unexposed samples of IC-43 treated with SnCl_4 were seen in the ^{3d}Sn and ^{1s}O peaks of the ESCA spectra (Fig. 6). In the unexposed region the signals are like those observed for SnO_2 (this region does not etch rapidly, as would be expected if SnO_2 were present). The exposed regions exhibit a Sn composition that is more representative of either an organotin oxychloride or an organotin amino chloride.

UV-visible spectroscopy gives additional clues to the mechanism of the gas-phase-functionalization process.

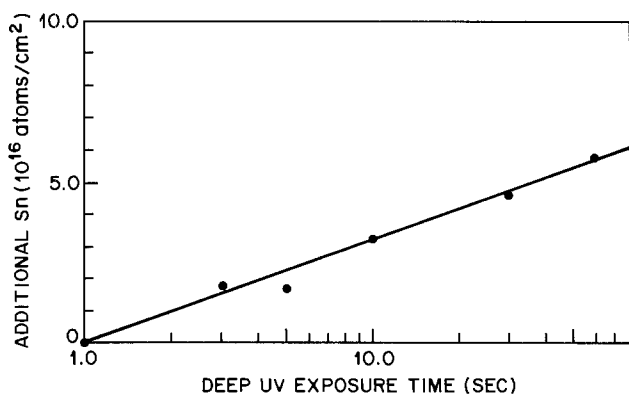


Fig. 5. Plot of the additional Sn absorbed (taken from the RBS data) during gas phase functionalization of $1 \mu\text{m}$ of Waycoat IC-43 treated with SnCl_4 as a function of deep UV exposure time.

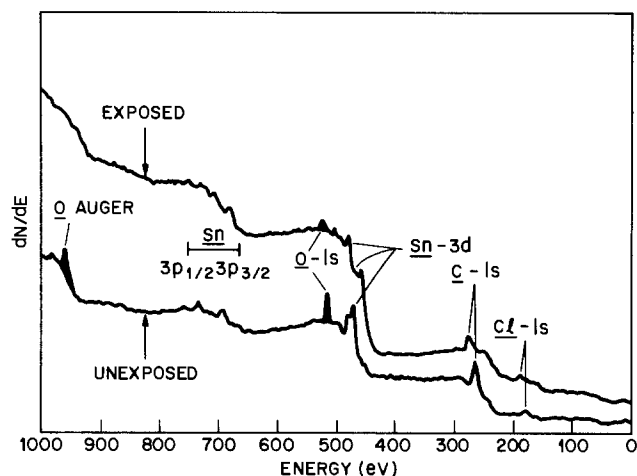


Fig. 6. ESCA spectra of $1 \mu\text{m}$ exposed and unexposed Waycoat IC-43 treated with SnCl_4 .

Figure 7 shows the spectra of an unexposed, $1 \mu\text{m}$ thick film of IC-43 before and after treatment with SnCl_4 . The original absorption band centered at 370 nm is slightly red shifted upon treatment. The intensity is also reduced. Unexposed Selectilux N-60 resist treated with SiCl_4 shows a similar behavior (Fig. 8). The changes in both these spectra suggest complexation of the inorganic halide with the azide sensitizer. However, for an exposed (60s) sample of N-60 treated with SiCl_4 , we see a complete disappearance of the 370 nm chromophore. This indicates the absence of this type of complexation and the occurrence of other chemical reactions in the exposed regions.

Complexation of the unexposed N-60 may occur with either of the three major functional groups present. These include the highly substituted double bonds of the host polymer (partially cyclized polyisoprene) and the azide ($-\text{N}_3$) and carbonyl ($-\text{C}=\text{O}$) groups of the sensitizer. A series of experiments was conducted to determine the complexing functionality. Various polymers were coated on Si wafers and treated with SiCl_4 . Then, they were reactive ion etched in oxygen along with an untreated control. Poly(*cis*-1,4-butadiene), poly(methyl methacrylate), and poly(methyl vinyl ketone) showed no difference in etch rate from the control. SiCl_4 complexation with the double bonds in poly(butadiene) or the carbonyl groups in the latter two polymers should have decreased the etch rate via the formation of an oxide layer. The carbonyl and olefinic groups do not appear to be involved in complexation.

The need for the azide group in the system is critical. It is further supported by another experiment. As we saw above, poly(*cis*-1,4-butadiene) was not functionalized. We

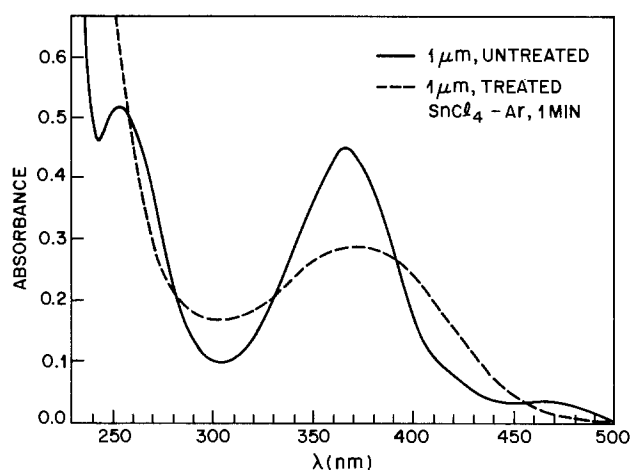


Fig. 7. UV-visible absorption spectra of $1 \mu\text{m}$ unexposed Waycoat IC-43 before and after 60s treatment with SnCl_4 .

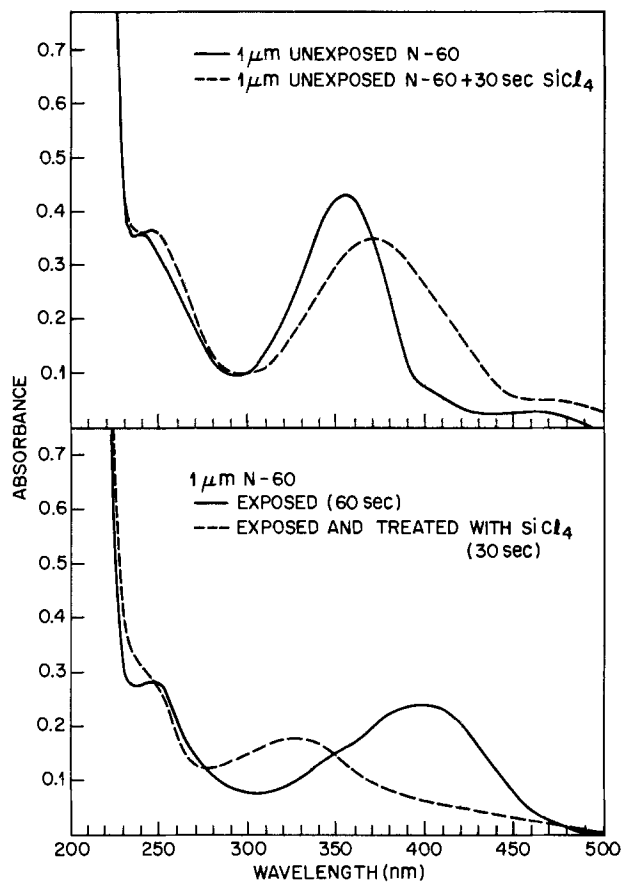
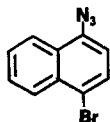


Fig. 8. UV-visible absorption spectra of exposed and unexposed Selectilux N-60 with a 30s SiCl_4 treatment and without a SiCl_4 treatment.

added 10 weight percent (w/o) 1-azido-4-bromo-naphthalene [7], which contains no carbonyl groups



[7]

to a solution of poly(cis-1,4-butadiene). The mixture was spun on a Si wafer, contact exposed with deep-UV radiation, and treated with SiCl_4 . Positive tone patterns ($NT_D \sim 0.2$) were obtained upon oxygen reactive ion etching, thus confirming azide complexation.

Mechanism.—The spectroscopic studies (RBS, ESCA, and UV-visible) and the previously described observations suggest the mechanism for gas-phase functionalization outlined in Fig. 9. Two types of inorganic halide functionalization appear to occur. In the unexposed regions, MCl_4 is quickly sorbed into the film. We presume the formation of an $\text{R-N}_3 \dots \text{MX}$ complex. In the presence of water this complex hydrolyzes to form inorganic oxide MO_2 . During O_2 RIE, some loss of MO_2 may occur due to sputtering of this protective masking layer. This metal oxide layer may be renewed during oxidative etching by converting unhydrolyzed inorganic compounds to MO_2 .

In the exposed regions, MX_4 also is sorbed quickly. From the infrared spectra, all azide groups having a strong absorbance at 2250 cm^{-1} disappear upon a 16s exposure at 366 nm with the formation of amine products. The inorganic halide then appears to react with the amine or aziridine groups generated during photo exposure.

These new products ($\text{R}'\text{-N-MCl}_x$) apparently hydrolyze more slowly than the complexed metal halides. Upon O_2 RIE, the compounds are removed as CO_2 , H_2O , NO_2 , and volatile inorganic compounds of unknown structure. At short MX treatment times, little oxide is formed to

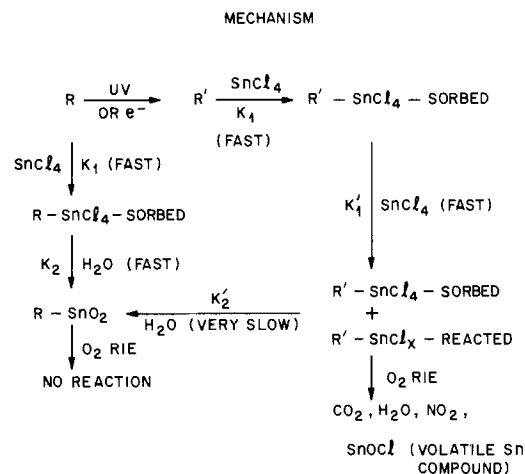


Fig. 9. Proposed mechanistic and kinetic scheme for the gas phase functionalization of negative azide containing photoresists with gaseous inorganic halides.

hinder removal of the exposed areas. However, a second mode of MX_4 sorption appears to occur at longer treatment times. MX_4 also is physically sorbed into the resist. The concentration of it quickly builds after all the photo-generated products have reacted. This second complex appears to be highly reactive toward water, thus forming a metal oxide layer which severely hinders removal of these areas during O_2 RIE. With very long MX treatment times, no etching is possible in either region.

This mechanism also is consistent with the failure to obtain patterned resists for films which were photoexposed and treated for short times ($< 8\text{s}$). Under these conditions, insufficient azide is photodecomposed, as evidenced by considerable residual IR absorbance at 2250 cm^{-1} . Substantial concentrations of $\text{R-N}_3\text{-MX}_4$ are present in both the exposed and unexposed areas of the resist. This highly reactive complex is readily converted to a metal oxide in the presence of water or during O_2 RIE. The net result is the inability to attain any significant differential etch rate during O_2 RIE. Complete photodecomposition of the bis-azide sensitizer appears to be necessary in order to optimize selectivity as judged from the IR analyses.

Pattern resolution.—The use of gas phase-functionalized IC-43 as an electron-beam resist gave us an indication of the resolution capabilities for this lithographic process and material. $1 \mu\text{m}$ of IC-43 was exposed to a 20 keV electron beam at doses of 1, 3, 6, 9, 12, 18, and $24 \mu\text{C}/\text{cm}^2$. The resist was then treated with SnCl_4 for 1 min. Figure 10 shows a scanning electron micrograph of underexposed $1 \mu\text{m}$ lines and spaces at $18 \mu\text{C}/\text{cm}^2$ developed using O_2 reactive ion etching. The exposed regions (represented by the trenches) contain a slight residue. A closer examination of the lines reveal that the field butting was misaligned by $\sim 0.15 \mu\text{m}$. This misalignment was resolved by the gas-phase-functionalized resist. The smallest gap width is about $0.3 \mu\text{m}$. Additional samples were not exposed by electron irradiation due to the low wafer throughput. Process development like that outlined below for contact photoexposures would be expected to afford improved E-beam images.

Cobilt contact exposures of N-60 reveal the resolution potential of these photolithographic gas phase-functionalized resists. A 16s photoexposed sample of N-60 was treated for 7s with SiCl_4 . Figure 11a shows the nominal $1 \mu\text{m}$ lines and spaces obtained after exposure, treatment, and O_2 RIE. The lines were $0.7 \mu\text{m}$ high and $0.6 \mu\text{m}$ wide; the spaces were $1.4 \mu\text{m}$ wide. This was independent of exposure from 3-16s. Thinner films were obtained at the shorter exposure times. A close examination of the mask used for these photoexposures revealed that the chrome lines measured about $0.6 \mu\text{m}$, with $1.4 \mu\text{m}$ gaps. It appears that in this exposure mode the mask dimensions were re-

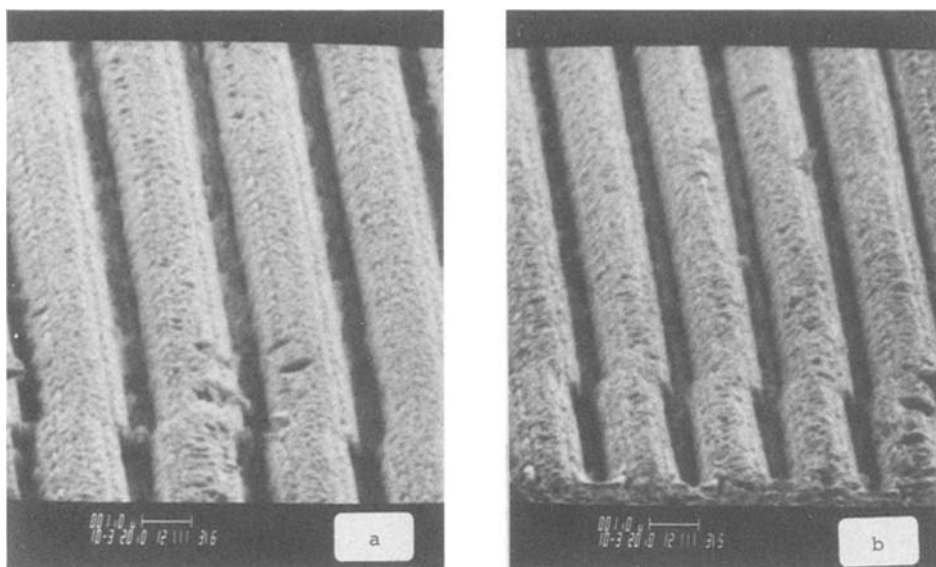


Fig. 10. Scanning electron micrographs of O_2 RIE-developed Waycoat IC-43 irradiated at 20 keV and $18 \mu C/cm^2$ and treated with $SnCl_4$. Fig. 10a and 10b depict underexposed $1 \mu m$ and $0.75 \mu m$ lines and spaces, respectively, in $0.80 \mu m$ thick resist. The $0.15 \mu m$ misaligned address structure is clearly seen.

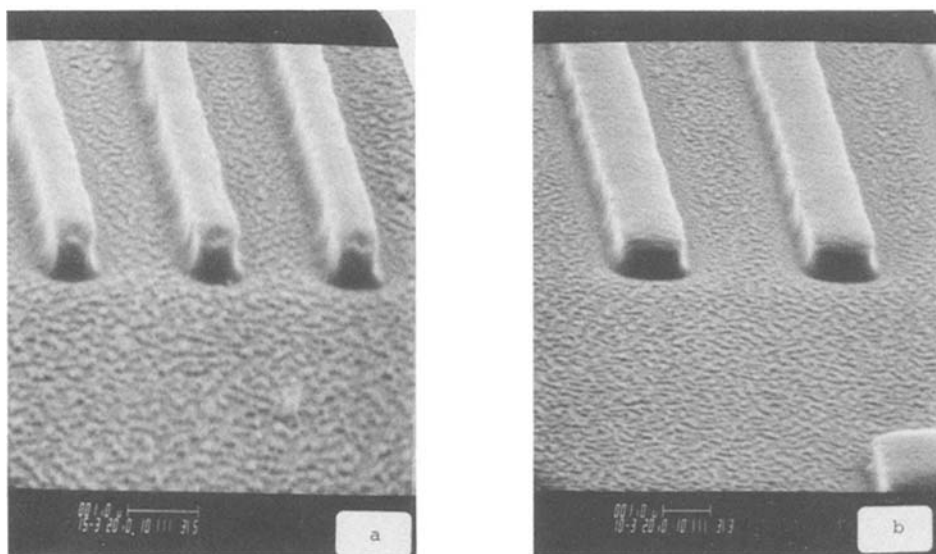


Fig. 11. Scanning electron micrographs of $0.6 \mu m$ lines and $1.4 \mu m$ spaces (Fig. 11a) and $1.4 \mu m$ lines and $2.6 \mu m$ spaces (Fig. 11b) obtained after O_2 RIE development of $1 \mu m$ Selectilux N-60 contact exposed for 16s with UV irradiation and treated with $SiCl_4$ for 7s. Final resist thickness is $0.7 \mu m$.

produced quite faithfully. In Fig. 11b, the $2.0 \mu m$ lines and spaces actually measured $1.4 \mu m$ and $2.6 \mu m$, respectively. These also correspond to the same dimensions found for corresponding features on the mask.

The presence of residue in the exposed regions of these samples and in the E-beam-exposed samples attests to the difficulties associated with excess $SiCl_4$ sorbed in the resist. This excess $SiCl_4$ may be hydrolyzed during handling to form traces of inorganic oxide. It also may be formed in the exposed area during O_2 RIE. The residue cannot be removed by sputtering during pattern development at high bias. If it is pure oxide, such as SiO_2 , it may be possible to remove it after development by brief RIE using CHF_3 gas or a freon-oxygen mixture similar to that used by Taylor and co-workers (9) for plasma-developed x-ray resists. These experiments are currently in progress.

Conclusions

A new type of plasma-developed, positive acting photo and electron-beam resist has been described. It is based upon the chemical differences induced by the gas-phase functionalization resulting when exposed samples of Waycoat IC-43 or Selectilux N-60 resists are treated with volatile inorganic halides such as $SiCl_4$ or $SnCl_4$. In the unexposed regions, the inorganic halide is uniformly distributed throughout the resist and complexes with the azide group of the sensitizer. This complex is readily con-

verted to a masking refractory oxide by either hydrolysis in the presence of water or by an oxidative process during oxygen reactive ion etching.

The functionalization that takes place in the exposed areas is quite different. The inorganic chloride-amino compounds that appear to be formed hydrolyze more slowly and are readily removed as volatile organic and inorganic compounds during O_2 reactive ion etching. These areas are removed at a much higher rate than their unexposed counterparts. Normalized developed thicknesses in excess of 5000 \AA can be obtained at 366 nm for Cobilt contact exposures between 8 and 24s upon O_2 RIE development.

Resolution in the vicinity of $0.6 \mu m$ can be obtained with $SiCl_4$ -functionalized contact photoexposure of Selectilux N-60. Smaller dimensions are possible with electron-beam exposures of Waycoat IC-43. With further development and extension to other materials and exposure sources, practical single-level plasma-developed gas phase-functionalized resists previously envisioned may be extended to H^+ ion beam and low voltage electron ($< 5 \text{ keV}$) and scanning metal ion beam ($< 4 \text{ keV}$). At a minimum, practical trilevel and perhaps even bilevel applications may be feasible, provided processes for residue removal are forthcoming.

Acknowledgments

We thank G. Gaultieri and G. P. Schwartz for the ESCA spectra and their interpretation, E. Reichmanis for use of

the OAI deep UV exposure tool, and B. J. Wilkens for experimental assistance with the RBS measurements.

Manuscript submitted Sept. 7, 1983; revised manuscript received March 3, 1984.

AT&T Bell Laboratories assisted in meeting the publication costs of this article.

REFERENCES

1. G. N. Taylor, L. E. Stillwagon, and T. Venkatesan, *J. Vac. Sci. Technol.*, To be published.
2. G. N. Taylor, T. M. Wolf, and J. M. Moran, *ibid.*, **19**, 872 (1981).
3. T. Venkatesan, G. N. Taylor, A. Wagner, B. Wilkens, and D. Barr, *ibid.*, **19**, 1379 (1981).
4. S. Shimizu and G. R. Bird, *This Journal*, **126**, 273 (1979) and references therein.
5. V. Bazant, V. Chralonsky, and J. Rothowsky, "Organosilicon Compounds," Academic Press, New York (1965); A. E. Purce, "Silylation of Organic Compounds," Purie Chemical Co., Rockford, IL (1968).
6. D. Follett, K. Weiss, J. A. Moore, A. J. Stechl, and W. T. Lui, Abstract 201, p. 321, The Electrochemical Society Extended Abstracts, Vol. 82-2, Detroit, MI, Oct. 17-21, 1982.
7. M. Yamada, J. Tamano, K. Yaneda, S. Morita, and S. Hattori, "Proceedings of Symposium on Dry Processes," Paper IV-2, pp. 90-93, Tokyo, Japan, Nov. 18-19 (1982).
8. W. Chu, J. W. Mayer, and M. A. Nicolet, "Backscattering Spectrometry," Academic Press, New York (1978).
9. G. N. Taylor, M. Y. Hellman, M. D. Feather, and W. E. Willenbrock, *Polym. Eng. Sci.*, **23**, 1029 (1983).

Hydrogen Plasma Etching of Organics

F. Y. Robb*

Motorola, Incorporated, Process Technology Laboratory, SRDL, Phoenix, Arizona 85008

ABSTRACT

The use of hydrogen plasmas for reactive ion etching of organic films has been characterized. It was found that anisotropic etching could be easily achieved, but with relatively slow etch rates ($< 300\text{\AA}/\text{min}$). The effect of variables (such as pressure, temperature, and power) and chemistry changes (such as the addition of O_2 and N_2) were studied and discussed. In addition, the applications of contact-hole etching and trilevel resist processing are considered.

The increasing complexity of integrated circuits has demanded technological changes in the areas of materials, lithography, and processing. The need for an anisotropic etch process for organic films is a result of both material and lithographic advancements. One new dielectric/passivant material which has recently gained acceptance in the semiconductor world is polyimide (1). An anisotropic etch process for polyimide will clearly be needed as device geometries shrink to the submicron regime. In the lithography area, the trilevel resist process outlined by Moran and Maydan (2), extends lithographic capabilities by first planarizing the wafer's surface with a thick organic layer. That thick layer is then patterned using a thin inorganic intermediate masking layer and very thin top layer of resist. This trilevel process requires an anisotropic organic etch to maintain good dimensional control.

Oxygen plasma attack of organic films is well known, as "ashing" of photoresist is quite common in the microelectronics industry (3). In addition, the use of oxygen for reactive ion etching of organics has been widely studied and applied (4-6). In order to achieve anisotropic etching of organic films with oxygen reactive ion etching, however, relatively low pressures (< 0.02 torr) are required (5).

Hydrogen plasmas are also capable of removing organic films under the proper conditions (7-8). In those studies, temperatures between 150° and 200°C were needed to promote etching, although only mild ion bombardment was present. (One investigator utilized a high frequency barrel etcher, while the other immersed the sample in the positive column of a dc discharge.) The subject of this paper is the characterization of organic etching in hydrogen plasmas under low temperature/higher ion bombardment conditions. The principle motivation behind this study was to develop an anisotropic organic etch process (for both trilevel masking and preohmic applications) at operating pressures above 0.10 torr, making sophisticated and costly vacuum equipment unnecessary.

Experimental

Figure 1 shows a schematic diagram of the experimental apparatus. The RF electrodes and reactor baseplate

*Electrochemical Society Active Member.

Key words: plasma etching, hydrogen discharges, semiconductor processing, organics.

were constructed of aluminum, and a Pyrex bell jar comprised the remainder of the vacuum chamber. The wafers were placed on the smaller powered electrode which had a surface area of approximately 500 cm^2 .

The system was operated at a RF frequency of 13.56 MHz, with the power variable from less than 0.1 to $0.6\text{ W}/\text{cm}^2$. The operating pressure, which was measured with a capacitance manometer (MKS Baratron), was varied by changing the input flow of process gas to the chamber. The gas was injected into the chamber via a single hole in the reactor baseplate. Gas flow was measured via Tylan mass flowmeters, which allowed mixtures of gases to be made. Flow rate restrictions and the 0.01 torr system base pressure limited usable etching to the above 0.1 torr regime. Temperature was varied by resistance heaters and monitored via a thermocouple, both positioned within the electrode support structure.

Various cathode covers were investigated in order to eliminate metallic contamination of the etching wafers. Contamination-free etching resulted only when all reactor surfaces were covered with an organic film. Both conventional photoresist coatings and du Pont Kapton sheet polyimide (affixed with a resist "glue") were successfully used, although the lifetime of the sheet polyimide was considerably longer. The test sample etch rates with organic reactor coatings were approximately 40% lower than with the bare aluminum cathode, presumably because of loading. Both the trilevel resist and contact resistance applications utilized a polyimide reactor coating.

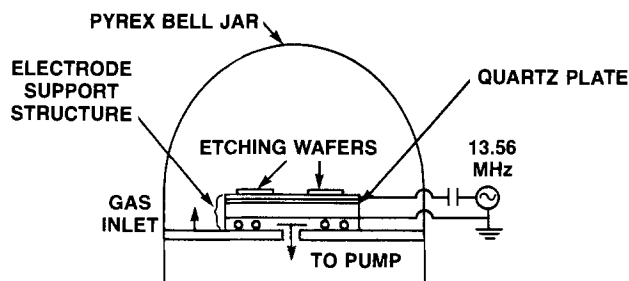


Fig. 1. Reactor utilized for organic etch studies

Oxidized silicon substrates, coated with from 1.0 to 2.0 μm of an organic film, were used. du Pont PI2545 polyimide was mainly used, although the etch rates of Hunt Chemical HR-100 negative and HPR-204 positive photoresists were also measured. The polyimide film was cured via multiple temperature bakes, ending with a 15 min 420°C N_2 bake. The HR-100 films were hardbaked for 30 min at 150°C in N_2 , while the HPR-204 films were given a 2h 200°C vacuum bake. For patterned samples, a thin intermediate masking layer of plasma nitride or oxide was next applied and patterned, with a resist mask, by reactive ion etching in CF_4 or CHF_3 .

Figures 2 through 6 plot the etch rates of PI2545, while Fig. 4 also includes the HR-100 and HPR-204 rates for comparison. In general, the photoresists' etch rates were virtually the same, with the polyimide etch rate being 10%-20% higher.

Etch data was measured for small loads with typically only one 3 in wafer per run. The etch uniformity (2σ) across a 3 in wafer was less than 5%. Error bars represent the maximum spread in etch rate measured over a several month period.

Various analysis techniques were used to characterize the etch process. Film-thickness and etch-depth measurements on patterned samples were made on the Tencor 10-00020 Alpha Step. For sheet organic films of HR-100 and HPR-204, the IBM 7840 Film Thickness Analyzer was used to make thickness measurements. The anisotropy of the etch and general etch quality were determined from scanning electron micrographs (SEM's) of samples given a 20% overetch.

The contact resistance measurements were made on p-type silicon to aluminum-Si contacts. The silicon substrates were BF_2 implanted with a thermal oxide mask, at $2 \times 10^{15}/\text{cm}^2$ and 40 keV. An 800°C , 10 min N_2 activation anneal followed the implant. A 6000\AA thick dielectric film of either du Pont's PI 2566 polyimide, fully cured to 450°C , or low pressure CVD phosphosilicate glass (PSG) was next applied/deposited, and preohmic holes patterned. All samples were given a 35s 75:1 HF (75 to 1 volume mixture of 49% HF and water) preclean before subsequent sputter deposition, at 150°C , of 8000\AA of aluminum-1.5% silicon. After a 30 min, 450°C N_2 anneal, the contact resistance was measured using a four-terminal Kelvin resistor test structure, which is more fully described elsewhere (9). The voltage was measured at two currents to confirm ohmic behavior. Contacts which showed diode-type behavior or opens were rejected. Specific contact resistance was calculated from SEM measurements of the etched preohmic openings.

Results and Discussions

Oxygen comparison study.—Since oxygen has become the industry standard for organic etching, a brief comparison of its etch characteristics to those of hydrogen was initially performed. The etch rate and anisotropy of polyimide films etched in both oxygen and hydrogen plasmas were characterized as function of pressure in the 0.1-0.5 torr range. Figure 2 shows that the etch rates in oxygen increased twofold, from about 500 $\text{\AA}/\text{min}$, as the pressure was lowered from 0.5 torr. The etch rate in hydrogen, however, varied little with pressure and was always less than 300 $\text{\AA}/\text{min}$. SEM's of patterned samples etched in oxygen with a 20% overetch showed definite undercutting at all pressures in this range. Samples patterned in hydrogen showed no undercutting, even when overetched more than 100%, when the etch pressure was below 0.4 torr.

The data suggest that both oxygen and hydrogen have two modes of etching. One mode, dominated by neutral radical etching, exists at high pressure and results in some horizontal etching. The second mode, one of ion-assisted etching, occurs at lower pressures and results in highly directional etching. The transition from the neutral to the ion-assisted etch mode occurs at different pressures for hydrogen and oxygen plasmas. The literature (4-6) suggests a transition pressure of about 0.02 torr for

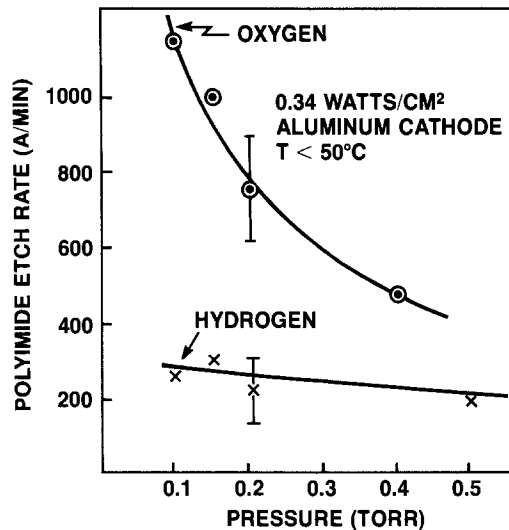


Fig. 2. Hydrogen and oxygen etch rates for polyimide as a function of pressure.

oxygen, while this study defines a much higher hydrogen transition pressure of about 0.4 torr. Anisotropic organic etching in hydrogen, therefore, eliminates the need for sophisticated and costly vacuum equipment.

Because the etch rates in hydrogen are quite slow compared with oxygen, however, several methods for increasing the rate were investigated and are discussed below.

Hydrogen process studies.—As a first attempt to increase organic etch rates in hydrogen, elevated temperature was investigated. Studies of the oxygen ashing of organics have shown as much as tenfold increase in oxidation rate as the temperature was increased from 60° to 130°C (10, 11). Figure 3 shows that the etch rate in hydrogen, however, varies little as the temperature is increased from 30° to 125°C . An earlier study (7) of hydrogen "ashing" indicated that the organic etch rate will increase dramatically with temperature, but only if the temperature is raised above 150°C . In this application, flowing of the top resist limited the temperature to below 130°C . An Arrhenius plot of the hydrogen data in Fig. 3 yields an activation energy of less than 0.9 kcal/mol. This is less than the literature value of 2.8 kcal/mol reported for oxygen organic etching in the same pressure/temperature regime (5) and suggests that ions, which have larger kinetic energy than radicals and are thus less affected by temperature, are the primary etching species in the hydrogen plasma.

Figure 4 shows that organic etch rates in hydrogen do increase as the power density is increased. However, even at the maximum system power density, the rate was only 300 $\text{\AA}/\text{min}$. The increasing rate with increasing power may be attributed to increased reactive species production

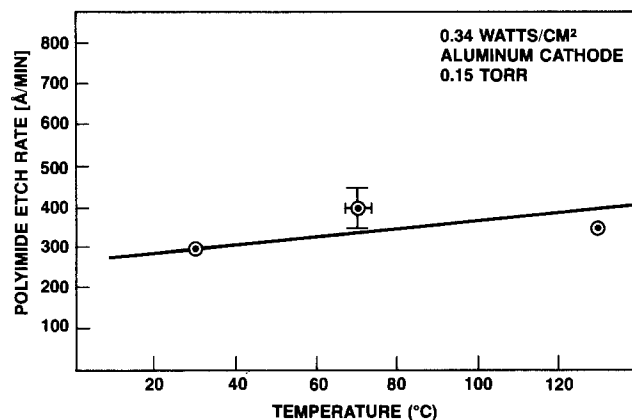
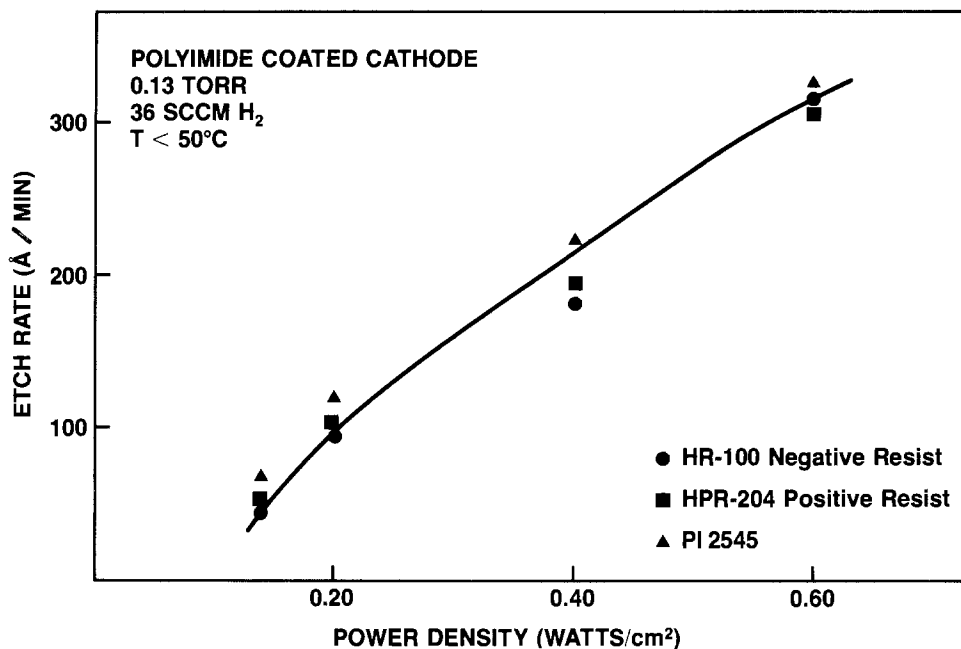


Fig. 3. Temperature dependence of the polyimide etch rate in a hydrogen plasma.

Fig. 4. Power density dependence of various organic etch rates in a hydrogen plasma.



and/or enhanced ion bombardment energies as power is increased. From the etch rate at maximum power, and assuming a simple CH_4 etch product, it can be estimated that a hydrogen atom flux to the surface of $1.0 \times 10^{16}/\text{cm}^2 \text{ s}$ is needed to sustain etching. This should be compared to a calculated hydrogen ion flux of $6.3 \times 10^{15}/\text{cm}^2 \text{ s}$, which assumes a fairly typical hydrogen ion density of $10^{11}/\text{cm}^3$ and a flux of $1/4 n \bar{v}$. The good agreement is consistent with an ion-assisted etch mechanism.

Finally, the addition of oxygen and nitrogen to the hydrogen plasma was investigated as a means of increasing the etch rate. Figure 5 shows a linear increase in etch rate is produced as increasing amounts of oxygen are added. Unfortunately, however, the amount of undercutting also increased linearly as the oxygen percentage increased, with even samples etched in 8% oxygen displaying slight undercutting. It appears that the mixed H_2/O_2 plasmas simply produce an additive result. The faster etching, free radical-dominated oxygen etch mode is superimposed on the slower etching, ion-assisted hydrogen etch mode, with the exact results controlled by the percentage of oxygen added.

Figure 6 displays the polyimide etch rate as a function of the amount of nitrogen added to hydrogen. Interest-

ingly, the etch rate in a N_2/H_2 mixture is higher than in either constituent alone. Figure 7 compares the etch profiles for a pure hydrogen and a 17% N_2/H_2 mixed plasma. Although a straight-walled profile is observed for pure hydrogen, retrograde undercutting (where the width of the top hard mask opening is smaller than the base of the etched feature) results in the mixed N_2/H_2 plasmas. In addition, samples etched in pure nitrogen displayed straight-walled profiles, although severe etch residues made pure nitrogen etching unusable.

The reason for the retrograde profile is not well understood. Since pure nitrogen profiles showed no retrograde, the nitrogen species by themselves cannot be the cause. Scattering of the small hydrogen ion by the relatively large nitrogen species [via the model proposed by Zarowin and Gelatt (12)] also seems unlikely, since no profile changes were observed when comparable amounts of argon were added to the hydrogen plasma. The presence of a new retrograde undercutting species in these N_2/H_2 plasmas was investigated by comparing emission spectra from the various plasmas, but no new species could be identified.

Finally, surface recombination may be modified when nitrogen is added. A change in the surface recombination

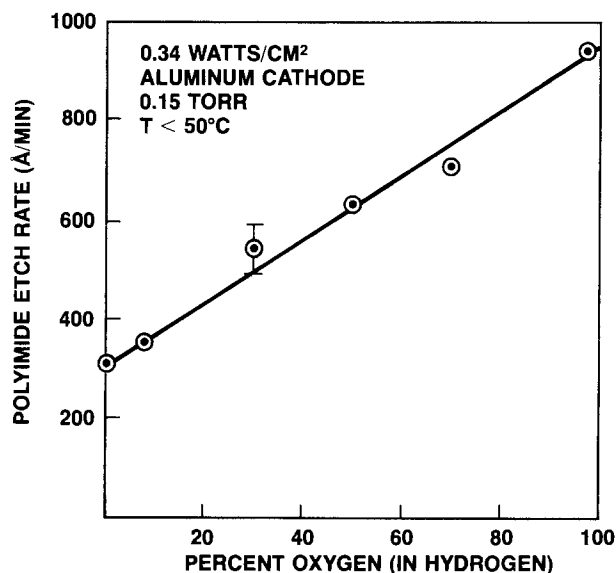


Fig. 5. Polyimide etch rate as a function of the oxygen concentration in hydrogen.

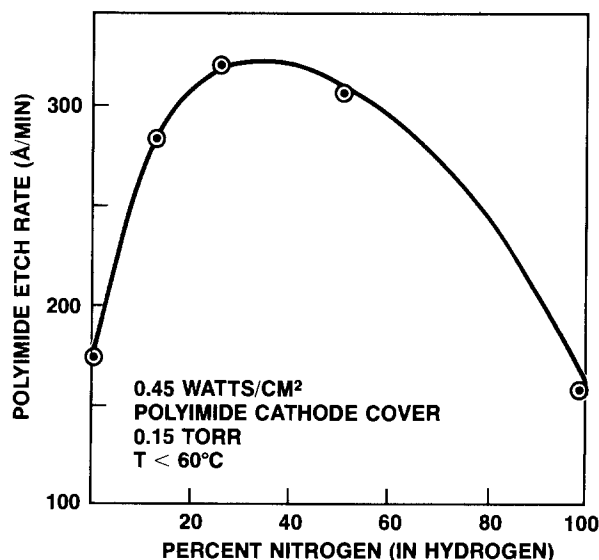


Fig. 6. Polyimide etch rate as a function of the nitrogen concentration in hydrogen.

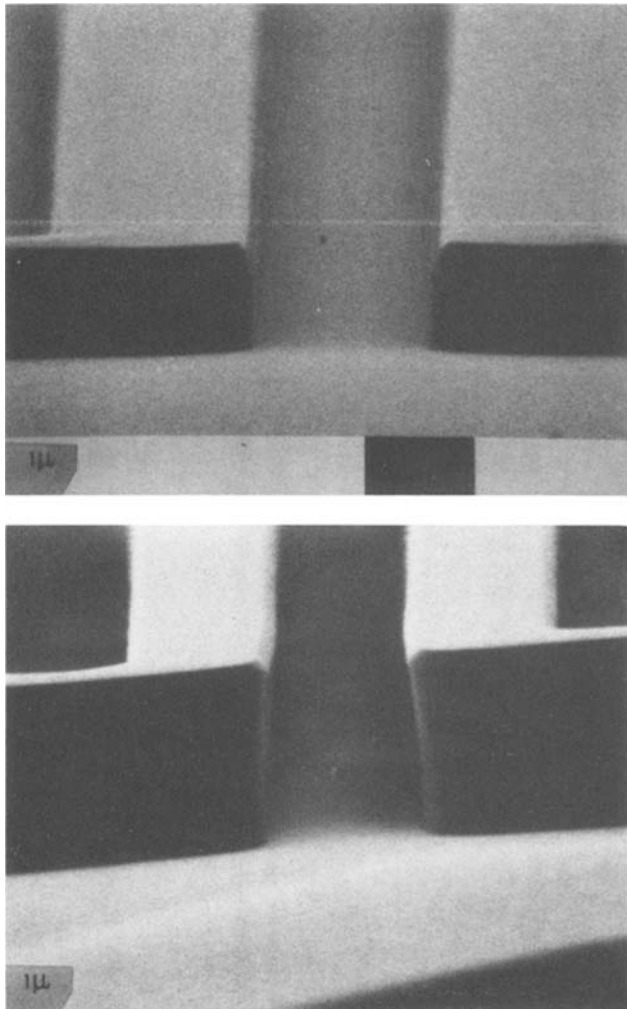


Fig. 7. Etch profiles of plasma oxide masked polyimide films patterned in a pure hydrogen (top) and 17% N_2/H_2 plasma (bottom). Both samples were given 50% overetch.

properties could result in higher surface concentrations and/or different surface diffusivities of etching species, producing retrograde undercutting. Similar "catalytic" effects, brought about by the addition of small amounts of impurities to hydrogen, have been previously reported (13).

Successful anisotropic organic etching with a hydrogen plasma involves several factors. Cathode-coupled wafer placement is essential because etching could not be initiated when substrates were placed on an anode surface. An organic coating must be placed over metallic reactor surfaces to eliminate contamination of the substrates. A pure hydrogen chemistry is required for nonretrograde anisotropic etch profiles. In the present study, 0.13 torr H_2 (which required 36 sccm) and 0.6 W/cm^2 (maximum power) gave the optimum results, yielding organic etch rates of approximately 300 \AA/min and selectivity over both thermal oxide and polysilicon of greater than 60/1. Under these conditions the etch rates of HR-100 negative and HPR-204 positive photoresist were virtually identical, with the PI2545 polyimide rate about 15% higher.

Applications.—Two applications of the hydrogen plasma etch process were investigated. In the first, a thin plasma oxide/thick polyimide (or HPR-204) structure was patterned, using an E-beam-sensitive top resist, to provide a thick organic mask for the subsequent etching of submicron polycide gate features. SEM measurements found linewidth changes of less than $0.1 \mu\text{m}$ between the top E-beam resist and the final polycide gates. No problems were encountered with the sequential etching processes themselves, although successful postetch mask removal required a brief wet etch for removal of sidewall

Table I. p-Type silicon to aluminum-Si contact resistance as a function of the interlayer dielectric and its etch technique. The total number of contacts possible on each wafer is 82

DIELECTRIC	DIELECTRIC ETCH	AFTER ETCH TREATMENT	R_s ($\Omega \mu\text{M}^2$)	STANDARD # DEVIATION	CONTACTS PER WAFER
PSG CONTROL	6:1 BHF	—	2.34	1.91	44
PSG CONTROL	6:1 BHF	IN SITU BACKSPUTTER	3.64	1.81	65
PSG CONTROL	6:1 BHF	H_2 PLASMA	3.24	2.31	62
POLYIMIDE	H_2 PLASMA	—	28.9	8.59	5
POLYIMIDE	H_2 PLASMA	IN SITU BACKSPUTTER	43.8	21.7	22

buildups. The sidewall build-up phenomenon is not unique to hydrogen organic etching; others have identified and similarly solved the problem for oxygen plasmas (14).

The second application involved the etching of preohmic openings in a polyimide dielectric and subsequent measurement of the silicon-to-aluminum contact resistance. Table I displays the specific contact resistance and number of ohmic contacts per wafer (out of 82 possible) for both hydrogen-etched polyimide and buffered HF-(BHF) etched PSG controls. It should be noted that alignment problems on the first PSG control accounted for its lower contact yield.

Although SEM inspection of the polyimide preohmic vias showed no obvious problems, Table I data show a definite degradation of these contacts. The contact resistance was an order of magnitude higher and the number of contacts much lower than for PSG control contacts. In addition, *in situ* premetal backspattering had little effect. The problem is a result of the polyimide dielectric rather than hydrogen plasma itself, as wet etched contacts exposed to the hydrogen plasma for 20 min (a typical overetch time) showed little degradation. Others (15, 16) have observed a similar problem for oxygen plasma etching of polyimide vias. The applicability of the oxygen-plasma solutions to hydrogen-etched contacts is currently being investigated.

Conclusions

The use of a hydrogen plasma for etching organic films has been investigated. Anisotropic etching was easily achieved, at pressures more than an order of magnitude higher than those required for equivalent anisotropic oxygen etching. A major drawback, however, is the relatively slow etch rate of less than 300 \AA/min . The hydrogen-etch temperature dependence, etch rate, and etch anisotropy are consistent with an ion-assisted etch mechanism. No unusual problems were encountered when using the hydrogen etch for trilevel patterning of a thick organic masking material. The specific contact resistance of test structures fabricated with hydrogen-etched polyimide vias, however, was much higher than wet-etched PSG controls.

Acknowledgments

The author wishes to thank Dr. Clarence Tracy for his helpful comments and suggestions during data taking, and for his careful review of this paper. Also, special thanks go to Linda Marcy for the typing of this report.

Manuscript submitted Aug. 29, 1983; revised manuscript received Jan. 23, 1984.

Motorola, Incorporated, assisted in meeting the publication costs of this article.

REFERENCES

- I. M. Gold, *Electron. News*, p. 39, Nov. 6, 1978.
- J. M. Moran and D. Maydan, *Bell Syst. Tech. J.*, **58**, 1027 (1979).
- R. W. Kirk, in "Techniques and Applications of Plasma Chemistry," J. R. Hollahan and A. T. Bell, Editors, p. 347, J. Wiley and Sons, New York (1974).
- E. Basseous, L. M. Ephrath, G. Pepper, and D. J. Mikalsen, *This Journal*, **130**, 478 (1983).

5. H. Namatsu, Y. Ozaki, and K. Hirata, *J. Vac. Sci. Technol.*, **21**, 672 (1982).
6. G. W. Ray, S. Peng, D. Burriesci, M. O'Toole, and E. Lieu, *This Journal*, **129**, 2152 (1982).
7. F. Robinson and C. Tracy, U.S. Pat. 4,201,579 (1980).
8. A. P. Webb, R. Brewer, H. Stuessi, and S. Veprek, *J. Nucl. Mater.*, **93/94**, 634 (1980).
9. R. M. Anderson and T. M. Reith, *This Journal*, **122**, 1337 (1975).
10. F. Robinson, Private communication.
11. J. F. Battey, *This Journal*, **124**, 437 (1977).
12. C. D. Gelatt and C. B. Zarowin, Paper 554 RNP presented at The Electrochemical Society Meeting, St. Louis, MO, May 11-16, 1980.
13. F. Kaufman, in "Chemical Reactions in Electrical Discharges," R. F. Gould, Editor, p. 29, American Chemical Society, Washington, DC (1969).
14. E. Kinsbron, W. E. Willenbrock, and H. J. Levinstein, in "VLSI Science and Technology/1982," C. J. Dell-Oca and W. M. Bullis, Editors, p. 116, The Electrochemical Society Softbound Proceedings Series, Pennington, NJ (1982).
15. D. R. Day and S. D. Senturia, *J. Electron. Mater.*, **11**, 441 (1982).
16. P. K. Smith, T. O. Herndon, R. L. Burke, D. R. Day, and S. D. Senturia, *This Journal*, **130**, 225 (1983).

The Effect of Various Encapsulants on the Electrical Properties of Implanted Layers in GaAs

V. B. Rao*,¹ and R. Y. Koyama

Tektronix, Incorporated, Semiconductor Research Department, Beaverton, Oregon 97077

ABSTRACT

Reactively sputtered silicon nitride, plasma-enhanced CVD silicon nitride, and silox have been investigated as dielectrics for the encapsulation of GaAs for the purpose of post-implantation anneal. The effect of several treatments on the GaAs surface prior to dielectric deposition was analyzed by Auger spectroscopy and ellipsometry to characterize the high temperature annealability of the encapsulated samples. An ammonium hydroxide-hydrogen peroxide etchant that leaves the surface clean and damage free was found to be the most suitable. After surface treatment and dielectric deposition, Van der Pauw devices were fabricated and carrier mobilities and sheet carrier concentrations for devices annealed at 800°C were compared. In specific cases, the electrical characteristics of devices annealed at higher temperatures (850° and 900°C) were also measured. Differences in the carrier mobilities and sheet carrier concentrations obtained, using the various dielectric films, have been explained in terms of the movement of a surface depletion layer edge closer to or away from the GaAs-dielectric interface.

Ion implantation is widely used for planar fabrication of a variety of gallium arsenide-integrated circuits (1, 2). The implantation process requires a high temperature anneal to restructure the lattice and electrically activate the implanted ions. However, the incongruent evaporation of Ga and As from GaAs at temperatures in excess of 600°C (3) makes it difficult to anneal without surface degradation. In order to inhibit decomposition of GaAs at high temperatures, it is necessary to encapsulate the GaAs samples in a suitable dielectric such as reactively sputtered silicon nitride (4), RF plasma CVD silicon nitride (5), or CVD silicon dioxide (6). Some investigations have shown that samples can also be annealed in a carefully controlled arsine overpressure (7), or by using a proximity cap (8).

Several investigations have compared the various dielectrics in terms of their effectiveness in the encapsulation of GaAs. It was found from backscattering measurements (9), low temperature photoluminescence and Auger electron spectroscopy (AES) measurements (10), and also from an XPS study on annealed SiO₂/GaAs interfaces (11) that SiO₂ films permit outdiffusion of Ga from GaAs. Such outdiffusion of Ga could result in nonstoichiometry near the GaAs-SiO₂ interface, and could significantly affect the activation of carriers during a post-implant anneal. It was also shown (9) that Ga outdiffusion through RF plasma-deposited CVD Si₃N₄ films was considerably lower than through SiO₂ films, provided that the Si₃N₄ films are relatively oxygen free. Thus, they concluded that oxygen contamination of the silicon nitride film was responsible for the pronounced Ga outdiffusion.

Most of these investigations reported on the effectiveness of the various dielectric films for encapsulation in order to maintain the chemical integrity of the GaAs substrates. However, relatively little has been reported on the

effect that these dielectrics have on the basic properties of carriers produced by the implanted ions, such as carrier mobilities (μ_n) and sheet carrier concentrations (N_s). In the present study, carrier concentrations and mobilities were measured on Van der Pauw devices, which were fabricated using reactively sputtered silicon nitride (sputtered nitride), plasma-enhanced CVD silicon nitride (plasma nitride), or CVD SiO₂ (silox). The properties of each dielectric film as an encapsulant and its influence on the activation and mobility of carriers are discussed.

The major limitation in the use of dielectric films for encapsulating GaAs is the temperature at which the samples can be annealed before they fail by cracking when the films are in tension, or blistering when they are in compression (12). During our initial annealing studies, it was observed that surface preparation of the GaAs substrates prior to plasma nitride deposition was extremely critical in preventing film failure. This suggested that, besides film stress, the high temperature annealability of these samples depended in some manner on the properties of the GaAs-dielectric interface. Therefore, a detailed characterization of several surface treatments was done using Auger spectroscopy and ellipsometry in conjunction with the annealing studies.

Experimental Procedures

Predielectric surface treatments.—The substrates used for the study were <100> oriented undoped semi-insulating LEC GaAs single-crystal wafers (2 in diam). All samples were initially degreased using trichloroethylene (boiling) and acetone, and followed by a light isopropyl alcohol scrub to dislodge any adhered particles. Each wafer was screened under an optical microscope (using dark field) for scratches and particles. They were then etched using either (i) 10 DIH₂O:1HCl followed by 100 DIH₂O:1HF; (ii) 10 DIH₂O:1NH₄OH; or (iii) 485DIH₂O:10 NH₄OH:3.5H₂O₂ as described in Table I. All etch cycles were followed by a 45s DIH₂O rinse.

*Electrochemical Society Active Member.

¹Present address: Cray Research Incorporated, Chippewa Falls, WI 54729.

Key words: semiconductor, circuits, mobility, ion implantation.

Table I Different surface treatments studied

Sample	Surface treatment	Depth etched
A	1HCl:10 DIH ₂ O; 15s 1HF:100 DIH ₂ O; 15s DIH ₂ O rinse; 45s	<10Å (21)
B	1NH ₄ OH:10 DIH ₂ O; 30s DIH ₂ O rinse; 45s	<10Å (21)
C	1NH ₄ OH:10 DIH ₂ O; 60s DIH ₂ O rinse; 45s	≤10Å (21)
D	485DIH ₂ O:10 NH ₄ OH: 3.5H ₂ O ₂ ; 5s DIH ₂ O rinse; 45s	≈150Å
E	485DIH ₂ O:10 NH ₄ OH: 3.5H ₂ O ₂ ; 166s DIH ₂ O rinse; 45s	≈5000Å

The samples from one-third of the wafers that were treated as described in Table I were immediately taken for AES measurements. In all cases, survey scans were made to determine all contaminating elements. Depth profiles were then taken by using Ar sputter etching in combination with AES. The excitation voltage of 5 kV and emission current of 400 nA was maintained constant for all samples. The base pressure inside the chamber prior to Ar sputtering was 5×10^{-10} torr, and during Ar sputtering and data collection the pressure was 5×10^{-8} torr. For the depth profiles, data were collected for about 1 min prior to sputtering to ascertain that a stable situation existed.

Samples from the next third of the wafers were studied by ellipsometry using a Gaertner Model L119. Samples were etched and measured immediately so as to minimize contamination and oxide growth on the freshly etched samples. All ellipsometric measurements were made in the dark at an angle of incidence of 70° and using a wavelength of 5461Å. A photomultiplier was used as the detector, and extinction was measured at two settings of the analyzer and polarizer. ψ and δ are, respectively, the amplitude ratio and the phase difference between the incident and reflected elliptically polarized light; these are calculated from the analyzer and polarizer settings using the equations for nonideal compensators (13).

From the values of ψ and δ , the thickness of the contaminating layer over GaAs can be calculated (14) by assuming the imaginary part of the refractive index ($k = 0.304$) for GaAs and the refractive index of the film ($n = 1.90$); the film on GaAs exposed to air is believed to be gallium oxide (15) with a refractive index of 1.90. Several investigations have used the extinction coefficient (k) as a measure of the extent of crystal damage in Si (16, 17) and GaAs (18) substrates. In this study, ψ and δ values were also used to calculate the extinction coefficient and hence, imply the extent of crystal damage remaining in GaAs substrates after the various surface treatments. These calculations assume that the film thickness (over GaAs) is small and hence, can be assumed to be zero.

The remainder of the samples after being etched were immediately placed in a plasma nitride reactor for nitride deposition. Plasma Si₃N₄ films were deposited at 400°C by the RF plasma-enhanced reaction between SiH₄ and NH₃ with Ar as the carrier gas. The SiH₄/NH₃ ratio in the mixture was maintained at 0.425. The total flow rate for all gases was about 180 sccm with SiH₄ being about 5% of the total. Deposition was started when a base pressure of 2 mtorr was reached, and the pressure during deposition was about 350 mtorr; 1000Å of plasma nitride was deposited on all of these wafers at a deposition rate of 90 Å/min. The wafers were then annealed in a forming gas atmosphere (90% N₂, 10% H₂) at various temperatures between 800° and 950°C for 20 min. After annealing, the wafers were inspected for film failure using an optical microscope.

Van der Pauw device preparation and measurement.—From the results of the cleaning experiments (to be dis-

cussed later), it became evident that plasma nitride films could be annealed favorably at the elevated temperatures if a 485DIH₂O:10 NH₄OH:3.5H₂O₂ etch was used. As noted from Table I, the 166s etch removes about 5000Å of GaAs material. After degreasing (as described in the previous section), GaAs wafers were treated with this etchant prior to dielectric deposition. Either plasma nitride (1000Å), sputtered nitride (1000Å), or silox (1250Å) was deposited. Plasma nitride was deposited as described earlier. Deposition of sputtered nitride was accomplished by reactive sputtering from a pure silicon target in the presence of pure nitrogen gas. Wafers were placed on a water-cooled substrate table; the actual wafer temperature during sputter deposition was determined to be no higher than 300°C. The chamber was pumped down to a pressure of 2×10^{-6} torr or better before commencement of deposition. After admitting nitrogen gas and initiating the plasma, a 20 min presputter was done to allow the target composition to stabilize, and also to react and pump away some of the residual impurities from the chamber. The deposition rate was approximately 45 Å/min at a power density of 0.93 W/cm². CVD silox films were deposited by a reaction between SiH₄ and O₂ in the presence of N₂. The deposition rate is around 400 Å/min at a deposition temperature of 420°C.

The silox, plasma nitride, and sputtered nitride films were characterized by Auger spectroscopy and ellipsometry. It was observed that the CVD silox films are very nearly stoichiometric (*i.e.*, they are SiO₂). The index of refraction for silox is found to be 1.46 ± 0.02 . For the plasma and sputtered nitride films, the ratio of atomic concentration of Si to N is 0.90 ± 0.05 . The atomic concentration of oxygen throughout the film thickness is less than 2-3 atom percent (*a/o*) for the nitride films. The index of refraction for both the plasma and sputtered nitride films is found to be 2.01 ± 0.02 . This result shows that these nitride films are to be differentiated from silicon oxynitride, whose index of refraction is typically between 1.45 and 2.00, depending on the oxygen content (19).

Following dielectric deposition, ion implantation of ²⁸Si⁺ into the GaAs wafers was carried out at room temperature through the dielectric films, using patterned photoresist as the implant mask. The thicknesses of plasma and sputtered nitrides (1000Å), and silox (1250Å) were chosen to ensure about the same stopping power for Si ions through these films (20) and also to adequately encapsulate the wafer during the post-implant anneal. Implantation was graded in rows on any given wafer with doses that ranged from 8×10^{11} to 1×10^{13} cm⁻². The implant energy was 140 keV and the beam was incident at an angle of 7° from the normal to the wafer surface to minimize channeling effects. After implantation, the samples were annealed in a forming gas atmosphere. In most cases, annealing was carried out at 800°C for 20 min, but in two cases, annealing was performed at 850° and 900°C as well. Finally, alloyed Au-Ge-Ni was used for the ohmic contacts.

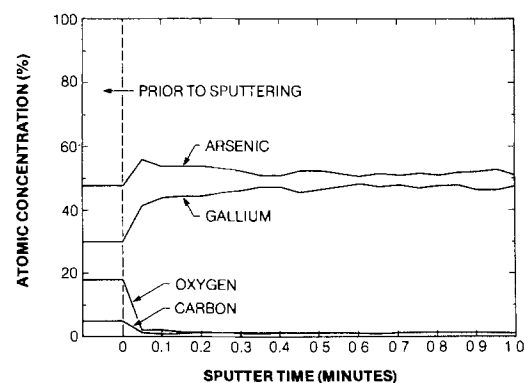


Fig. 1. Auger depth profile E (see Table I)

Sheet carrier concentrations (N_s) and Hall mobilities (μ_H) for the various implant doses were obtained from measurements made using a Hall apparatus, in which data collection and reduction was facilitated by computer control. The sheet carrier concentration (N_s), which is equal to the impurity concentration integrated over the depth of the impurity profile, was calculated from the sheet Hall coefficient. Hall mobilities were calculated from the sheet Hall coefficient and the sheet resistance. It should be pointed out that the Hall mobility measurement for an implanted layer results in an average mobility for the distributed profile. The strength of the magnetic field was 6000G. Each Van der Pauw die is 5 mm on a side, and on a 2 in. wafer there are between five and nine devices per row for each implant dose. This provides data for assessing the die-to-die uniformity of electrical properties across a wafer, for any given implant dose.

Results and Discussion

Cleaning procedures.—Table I shows the different surface preparation sequences performed on GaAs samples and the corresponding depth of material etched. The Auger spectroscopy, ellipsometry, and annealing results for each of these preparations are presented in Table II. From the Auger depth profiles for samples A through E, the a/o of C and O near the surface was obtained. It is seen from the table that the C concentration decreases consistently down the column to about 5 a/o for sample E. For sample E, the oxygen concentration near the surface was about 18 a/o. It was observed that the C on these samples was not present as a carbide, but was either elemental in nature or a hydrocarbon, as ascertained by the shape and position of the Auger peaks. In addition, this C may have been adsorbed on the surface from the atmosphere or from the cleaning solutions.

To confirm the above hypotheses, samples were exposed to an ultraviolet source (22) (in atmosphere) for about 3h, and quickly loaded into the Auger chamber. The Auger spectra did not show any traces of C. However, the oxygen concentration on the surface of these samples increased from between 17 and 20 a/o to about 37 a/o for all samples. This cleaning action by exposure to a UV source is believed to occur (22) by a complex reaction involving the interaction of surface species with photons and ozone. Certain wavelengths in the UV spectrum are absorbed by O (and causes the generation of ozone) and by hydrocarbons on the sample surface. When the C on the surface reacts and leaves, the surface becomes highly reactive and hence becomes oxidized. This explains the disappearance of C from the Auger spectra and the increase in the concentration of O. Hence, we conclude that C and O were present only on the surface of the wafers.

Figure 1 shows the Auger depth profile for the sample that had the lowest C and O concentrations on the surface (sample E). The rate of sputtering (of GaAs) for a sputtering voltage of 5 kV and an emission current density of $327 \mu\text{A}/\text{cm}^2$, was determined to be approximately $800 \text{ \AA}/\text{min}$. This rate is obviously too high to determine the thickness of the contaminating layer accurately. Since data collection was made between sputter intervals of 0.05 min, the first data point for C and O was at the surface and the next about 40 \AA below. Hence from Fig. 1, it is seen that the contaminating layer thickness is less than 40 \AA . Also, from this figure and from depth profiles for

samples A through D (not included here), the stoichiometry of GaAs near the surface of the sample is disturbed as a result of the surface treatments. There is excess As near the surface, consistent with previously reported data (23) on As "pile-up" at the interface due to HCl and NH_4OH cleaning solutions on GaAs. It should be noticed however, that below a depth of about 200 \AA , stoichiometry is again nearly restored.

From the ellipsometry data, the thickness of the contaminating film was determined as described earlier. From Table II, it is seen that the film thickness decreases consistently for samples A to E down to about 5 \AA for sample E. Although the thicknesses are approximate and could be in error (14) by $\pm 5 \text{ \AA}$, the errors are systematic. This means that the differences in the film thicknesses for the various samples are fairly precise. As noted earlier, the extinction coefficient (k) has been used as a measure of the surface damage in Si single-crystal substrates (16, 17), where the higher the extinction coefficient, the greater the degree of damage. It is seen from Table II that there is a systematic decrease in the value of the extinction coefficient for samples A through E. For sample E, the extinction coefficient of 0.329 is approaching the value of 0.304 for damage-free GaAs (24), measured at a wavelength of 5461 \AA . This is to be expected since the surface treatment used for sample E removes about $0.5 \mu\text{m}$ of material, and along with it, removes the surface damage remaining after the chem-mechanical polishing of the wafers.

From the annealing experiments, it is seen that only plasma nitride films deposited on sample E did not show any signs of failure by cracking or blistering in the temperature range of $800^\circ\text{--}950^\circ\text{C}$. All other films showed signs of failure (by blistering), although it was not possible to correlate the extent of failure with the various surface treatments. These results suggest that the combined effects of reduced surface contamination and an essentially damage-free surface (sample E) prior to plasma nitride deposition was responsible for its high temperature annealability.

Electrical measurements.—Annealing experiments on Si ion-implanted undoped semi-insulating GaAs wafers were carried out using different encapsulating dielectrics. This enabled a comparison of carrier mobilities and sheet carrier concentrations which resulted with the various dielectrics. For two specific cases, measurements were made with and without the dielectric present to understand what effect the dielectric had on the electrical properties of the devices.

Several experiments were performed with silox (1250 \AA), and plasma and sputtered nitride films (1000 \AA each) to compare the values of μ_H and N_s . As mentioned earlier, the film thickness was adjusted to achieve about the same stopping power with all films. Measurements were made with the dielectric layer remaining over the implanted layer. Figure 2 shows a comparison of the activation as a function of the implant dose for the various dielectrics. It should be pointed out that the actual scatter in the data was very small; the individual points shown in Fig. 2 average over five to nine devices for each implant dose. Also, these activations have neither been corrected for dose reduction due to implantation through the dielectric layer, nor for carrier loss due to the existence of

Table II Auger spectroscopy, ellipsometry, and annealing results for various surface treatments

Sample	Auger data a/o near surface		Ellipsometry data		Annealing results 1000Å plasma nitride cap 800°-950°C
	C	O	Thickness d(film) (14)	Ext. coefficient k(GaAs) (16)	
A	14	6	13A	0.440	Failed*
B	12	21	10A	0.419	Failed*
C	7	19	10A	0.408	Failed*
D	—	—	8A	0.386	Failed*
E	5	18	5A	0.329	Did not fail

* Failed by blistering.

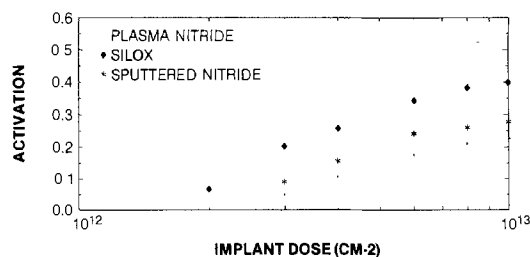


Fig. 2. A comparison of activations for Van der Pauw devices encapsulated and annealed at 800°C with plasma nitride, sputtered nitride, and silox.

the depletion layer. Nevertheless, relative comparisons between the activations for the three dielectric films are still possible, and we notice from Fig. 2 that there is a significant difference in activations. The activation (for a dose of $1 \times 10^{13} \text{ cm}^{-2}$) for silox is about 40% whereas it is 22% for plasma nitride and 28% for sputtered nitride. Figure 3 shows a comparison of mobilities for the same devices. The two curves for each dielectric film bound the scatter in the mobility data. It is seen that the highest mobilities are obtained with the plasma nitride film (4300 cm^2/Vs) and the lowest with sputtered nitride (3800 cm^2/Vs), with silox being intermediate (4100 cm^2/Vs). This clearly demonstrates that the electrical properties of the implanted layers are strongly dependent on the type of dielectric used.

Onuma *et al.* (25) found that for Si implantation into Cr-doped GaAs substrates, the carrier concentration (cm^{-3}) profiles were identical for samples encapsulated with CVD SiO_2 and CVD Si_3N_4 , and annealed at 800°C. However, for higher annealing temperatures (850°-900°C), the diffusion coefficient of Si in GaAs was one or two orders of magnitude higher for SiO_2 encapsulated samples when compared to Si_3N_4 encapsulated samples. In the preceding comparison of the present study, since all samples were annealed at 800°C, we could assume that differences in N_s and μ_H for the three dielectrics may not be due to enhanced Si diffusion. A likely explanation for higher activations with silox films compared to silicon nitride could be the creation of excess Ga vacancies near the GaAs-dielectric interface. It was shown (10) that Ga outdiffusion through SiO_2 films was more pronounced than through oxygen-free silicon nitride films. As mentioned earlier, the silicon nitride films studied in the present investigation are relatively oxygen-free. Since implanted Si becomes a donor by occupying Ga sites, the higher activations for silox samples compared to silicon nitride is reasonable to expect. This would suggest (from Fig. 2) that outdiffusion of Ga from plasma nitride would be more than from sputtered nitride samples, although this has not been verified experimentally. Another possible explanation for the differences in N_s and μ_H for the three dielectric films is the difference in the stress induced by these films at the interface.

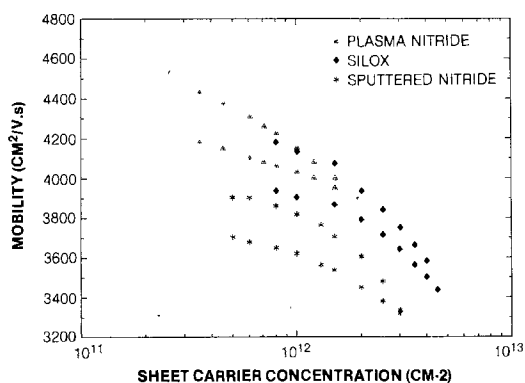


Fig. 3. A comparison of mobilities for Van der Pauw devices encapsulated and annealed at 800°C with plasma nitride, sputtered nitride, and silox.

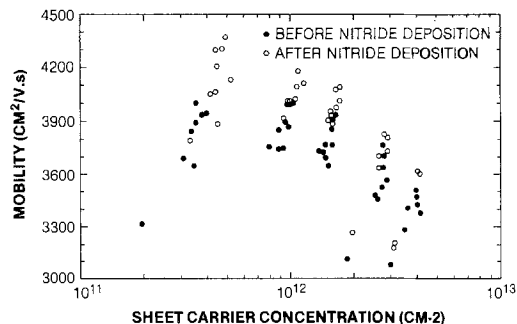


Fig. 4. Mobility vs. sheet carrier concentration for Van der Pauw devices with and without a plasma nitride passivation.

A separate experiment was performed to compare the properties of Van der Pauw devices with and without the dielectric present. Figure 4 shows a comparison of the carrier mobilities as a function of sheet carrier concentration (and hence implant dose) for Van der Pauw devices before and after plasma nitride deposition. Only for this case, we started with devices that were fabricated by a slightly different procedure, such that there was no dielectric film present over the completed devices. Measurements were first made on these Van der Pauw devices. Then 1000Å of plasma nitride was deposited over the wafer and etched to expose only the ohmic contacts, and a second set of measurements were made. It is seen that there is an appreciable difference in mobilities, especially for the lower implant doses. The peak (average) mobility increases from about 3900 cm^2/Vs before nitride deposition to about 4200 cm^2/Vs after nitride deposition. There is also an appreciable improvement in the apparent activation of carriers as indicated by the systematic shift of the "after nitride" data points to the right. Next, the plasma nitride (from the same wafer) was carefully stripped in a parallel plate plasma etch system (0.08 W/ cm^2 , 200 mtorr, 400 Å/min), removing about 800Å, and then completely removed in 1HF:1DIH₂O. This would ensure that there is essentially no damage introduced due to the stripping process. It was observed that the mobilities and activations returned to their original values. This suggests that the mere presence of the plasma nitride over the implanted layer increases both N_s and μ_H . We believe that this behavior may be suitably explained by the movement of the surface depletion layer edge closer to or away from the interface with the addition or removal of the nitride, respectively.

A somewhat similar experiment was also performed with the sputtered nitride dielectric film. Unlike our plasma nitride deposition process (which is fairly gentle), sputtered nitride deposition introduces radiation damage. Hence, we started with devices already fabricated with sputtered nitride, which was annealed following deposition and ion implantation. When the sputtered nitride layer was carefully removed, (under conditions described earlier, but with an etch rate of 250 Å/min), there was a degradation in activations and mobilities (as it was observed for the case of plasma nitride), for all implant doses considered. However, when 1000Å of sputtered nitride was redeposited, there was a further decrease in the activations and mobilities. This latter behavior could be due to radiation damage introduced in the implanted layer due to the sputtering process and consequent movement of the surface depletion layer edge away from the dielectric interface. Because of the presence of the alloyed ohmic contacts, no attempt was made to anneal this radiation damage.

Higher temperature (850° and 900°C) annealing experiments were also performed with sputtered and plasma nitride. Figure 5 shows the activation vs. implant dose data for samples annealed at 800° and 900°C using a sputtered nitride encapsulant. It is observed that the activations are higher at the higher temperature for all implant doses considered. In Fig. 6, the mobility data for the samples

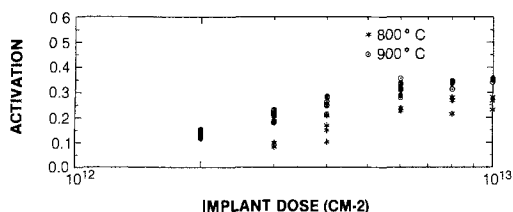


Fig. 5. A comparison of activations for Van der Pauw devices encapsulated with sputtered nitride and annealed at 800° and 900°C.

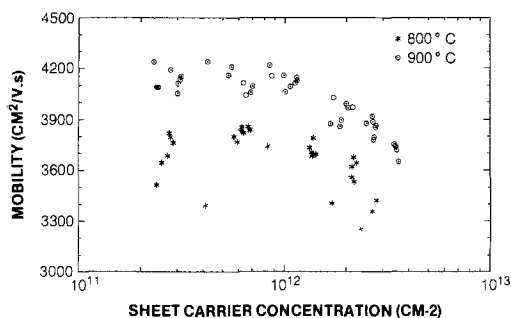


Fig. 6. A comparison of mobilities for Van der Pauw devices encapsulated with sputtered nitride and annealed at 800° and 900°C.

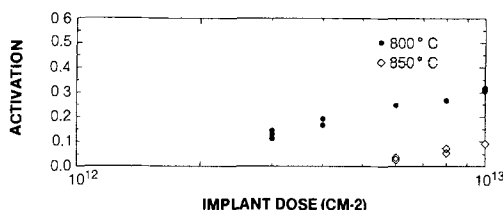


Fig. 7. A comparison of activations for Van der Pauw devices encapsulated with plasma nitride and annealed at 800° and 850°C.

are presented. Again, we see that the samples annealed at 900°C showed higher mobilities. The peak mobility increased from 3800 cm²/Vs at 800°C to about 4200 cm²/Vs at 900°C. When similar experiments were performed with plasma nitride, however, there was an opposite trend. From Fig. 7 we see that the activations were considerably lower for the 850°C anneal (compared to 800°C) and that for the lower implant doses (< 4 × 10¹² cm⁻²) there was no activation. There was very little difference in the mobility characteristics of the devices annealed at 800° and 850°C. When samples were annealed at 900°C, there was no activation even for the highest implant dose considered (1 × 10¹³ cm⁻²). This difference in behavior of the sputtered and plasma nitride encapsulants, it not clearly understood at the present time. However, a reasonable explanation could be based on outdiffusion of Ga or As from the interface at the elevated temperatures. In this case, the implanted Si ions could occupy either Ga or As sites, and this results in an increase or decrease in activation, respectively. Also, there may be differences in the stress induced by the dielectric films, which could lead to a difference in the enhanced diffusion of the implanted ions in the GaAs substrate.

Conclusions

It has been shown from AES and ellipsometry studies that surface preparation of GaAs samples prior to plasma nitride deposition is critical to their high temperature annealability, and that a clean and damage-free surface prior to deposition is essential. Hall measurements on devices which were encapsulated with plasma nitride, sputtered nitride, and silox, and annealed under the same con-

ditions resulted in different sheet carrier concentrations and mobilities for a given implant dose. This may be due to (i) interdiffusion of impurities, (ii) different stresses induced by the films, or (iii) different depletion layer thicknesses. A separate experiment and measurements show that the presence of plasma and sputtered nitride over the implanted layer improves the electrical characteristics of the devices. This behavior was explained in terms of the movement of a surface depletion layer edge closer to or away from the interface. Finally, we observed increased mobilities and activations with a sputtered nitride encapsulation at 900°C, when compared to 800°C. On the other hand, we saw decreased activations at 850°C for plasma nitride encapsulated samples and no activation at 900°C. This may be due to outdiffusion of Ga or As and excess compensation, or to differences in stresses.

Acknowledgments

The authors wish to thank S. Lane, I. Beers, J. Simmons, W. Vetanen, and B. Avrit for processing support, and the other members of our Semiconductor Research Department for many helpful discussions. Thanks are also due to D. Jones and C. Drosd of the Tektronix Materials Analysis Laboratory for the AES measurements.

Manuscript submitted Aug. 30, 1983; revised manuscript received Feb. 20, 1984.

Tektronix, Incorporated assisted in meeting the publication costs of this article.

REFERENCES

1. E. W. Strid and K. R. Gleason, *IEEE Trans. Microwave Theory Tech.*, **30**, 969 (1982).
2. G. McCormack, A. Rode, and E. Strid, *IEEE GaAs IC Symposium*, p. 25, New Orleans, LA, Nov. 9-11, 1982.
3. S. T. Picraux, in "Ion Implantation in Semiconductors and Other Materials," B. L. Crowder, Editor, p. 641, Plenum, New York (1973).
4. L. E. Bradley and J. R. Sites, *J. Vac. Sci. Technol.*, **16**, 189 (1979).
5. M. J. Helix, K. V. Vaidyanathan, B. G. Streetman, H. B. Dietrich, and P. K. Chatterjee, *Thin Solid Films*, **55**, 143 (1978).
6. A. G. Foyt, J. P. Donnelly, and W. T. Lindley, *Appl. Phys. Lett.*, **14**, 373 (1969).
7. J. Kasahara, M. Arai, and N. Watanabe, *J. Appl. Phys.*, **50**, 541 (1979).
8. B. Molnar, *Appl. Phys. Lett.*, **36**, 927 (1980).
9. J. Gyulai, J. W. Mayer, I. V. Mitchell, and V. Rodriguez, *ibid.*, **17**, 332 (1970).
10. K. V. Vaidyanathan, M. J. Helix, D. J. Wolford, B. G. Streetman, R. J. Blattner, and C. A. Evans, Jr., *This Journal*, **124**, 1781 (1977).
11. U. Lonig and E. Sasse, *ibid.*, **130**, 950 (1983).
12. A. K. Sinha, H. J. Levinstein, and T. E. Smith, *J. Appl. Phys.*, **49**, 2423 (1978).
13. R. J. Archer and C. V. Shank, *J. Opt. Soc. Am.*, **57**, 191 (1967).
14. A. C. Adams and B. R. Pruniac, *This Journal*, **120**, 408 (1973).
15. A. W. Laubengayer and H. R. Engle, *J. Am. Chem. Soc.*, **61**, 1210 (1939).
16. K. Watanabe, M. Miyao, I. Takemoto, and N. Hashimoto, *Appl. Phys. Lett.*, **34**, 518 (1979).
17. F. Ohira and M. Itakura, *Jpn. J. Appl. Phys.*, **21**, 42 (1982).
18. Q. Kim and Y. S. Park, *J. Appl. Phys.*, **51**, 2024 (1980).
19. D. M. Brown, P. V. Gray, F. K. Heumann, H. R. Phillip, and E. A. Taft, *This Journal*, **115**, 311 (1968).
20. J. F. Gibbons, W. S. Johnson, and S. M. Mylroie, "Projected Range Statistics," Dowden, Hutchinson, and Ross Stroudsburg, PA (1975).
21. T. H. Miers, *This Journal*, **129**, 1795 (1982).
22. W. L. Baun, *Appl. Surf. Sci.*, **6**, 39 (1980).
23. C. C. Chang, P. H. Citrin, and B. Schwartz, *J. Vac. Sci. Technol.*, **14**, 943 (1977).
24. F. Kukes, *Optik*, **31**, 83 (1970).
25. T. Onuma, T. Hirao, and T. Sugawa, *This Journal*, **129**, 837 (1982).

Interface States and Fixed Charges in MNOS Structures with APCVD and Plasma Silicon Nitride

R. Hezel, K. Blumenstock, and R. Schörner

Institut für Werkstoffwissenschaften VI, Universität Erlangen-Nürnberg, D-8520 Erlangen, Germany

ABSTRACT

The net positive charge density Q_N/q and the interface state density D_{IT} of MNOS structures on p-Si (100) with APCVD and plasma silicon nitride is studied as a function of the nitride deposition temperature and the postdeposition annealing temperature. For APCVD silicon nitride, a decrease of Q_N/q is accompanied by an increase of D_{IT} with increasing deposition and annealing temperature. Electron irradiation (30 keV and 5×10^{-5} C/cm² dosage) did not affect Q_N/q , whereas D_{IT} was increased for nitride films deposited below 800°C. For plasma silicon nitride, both Q_N/q and D_{IT} decreased with deposition and annealing temperature up to 450°C. Very low interface state densities (8×10^9 cm⁻² eV⁻¹) could be achieved. These low D_{IT} values are due to the influence of hydrogen incorporated in the PECVD silicon nitride films. Very high positive charge densities ($>10^{13}$ cm⁻²) could be obtained by cesium contamination of the plasma nitride films.

Pyrolytic chemical vapor deposited (CVD) silicon nitride films are widely used as active layers in microelectronics, e.g., as gate dielectric in nonvolatile memory elements. The performance of these metal-nitride-oxide-silicon (MNOS) devices is strongly dependent on the density of fast interface states and fixed insulator charges (1-3).

Plasma enhanced CVD (PECVD) silicon nitride films are almost exclusively applied for final passivation of semiconductor devices. There is, however, growing interest in using plasma Si nitride as an electrically active layer. It appears to be promising as dielectric for high efficiency silicon inversion layer solar cells (4, 5), as well as for amorphous silicon thin film transistors for application as switching elements in large area displays and imaging arrays (6, 7). In both cases, the properties of the plasma Si nitride/silicon interface, such as the fixed nitride charges and the fast interface states, are of great importance. However, no data about these quantities are available in the literature up to now. For the case of inversion layer solar cells, a high density of fixed positive insulator charges in conjunction with a low interface state density is required in order to obtain a highly conductive inversion layer (8, 9). In contrast to MOS devices, where a correlation between the fixed oxide charges and the interface states was found (10), for MNOS structures with atmospheric pressure CVD (APCVD) Si nitride, some data pointing to an inverse behavior were already reported by us (11, 12).

In the present work the grown-in fixed charges (density Q_N/q) and the fast surface states (density D_{IT}^* at midgap) have been investigated as a function of the nitride deposition temperature and after postdeposition heat-treatment in nitrogen.

The studies were performed on Al/Si nitride/thin Si oxide/p-Si (100) structures with APCVD as well as with PECVD Si nitride; the different behavior of these dielectric films will be outlined. Particularly for the case of plasma Si nitride on silicon, where very low interface state densities could be achieved, the crucial role of hydrogen is discussed. The effect of cesium contamination of the plasma Si nitride films on the interface properties, as well as the influence of electron irradiation, was also studied in this work.

Experimental

The MNOS structures were fabricated in the following way. Chemically mechanically polished (CZ) p-Si (100) 2 Ω cm substrates were cleaned in trichlorethylene, acetone, 1% HF, NH₄OH-H₂O₂, and HCl-H₂O₂ solutions. The thin oxide preparation was performed at 525°C for 15 min in a dry O₂/N₂ atmosphere resulting in a thickness of 1-1.3 nm, as measured by ellipsometry ($\lambda = 632.8$ nm). Oxides

Key words: plasma silicon nitride, MNOS, interface states, insulator charges.

prepared in this way are also used by us for tunnel MIS diodes (5), and an extensive characterization of these films is given elsewhere (13). Immediately after the oxide formation, the silicon nitride films of 1000 nm thickness were deposited either by APCVD or PECVD. The gases used in both cases were 2% SiH₄ (diluted in Ar) and 100% NH₃. APCVD films were deposited in a hot-wall reactor with a SiH₄/NH₃ ratio of 1:500 at temperatures ranging from 620° to 900°C. A capacitively coupled parallel-plate reactor with radial gas flow was used for the fabrication of the plasma nitride films. The RF (30 kHz) power was 11W, and the SiH₄/NH₃ ratio was 1:25 at a pressure of 1.2 mbar. The deposition temperature ranged from 210° to 270°C. Finally, aluminum contacts were evaporated from a heated tungsten boat.

The refractive index, measured by ellipsometry, was $n = 1.90 \pm 0.03$ for the APCVD Si nitride films and $n = 1.88 \pm 0.02$ for the PECVD Si nitride films. Electron irradiations at 30 keV and a dose of 5×10^{-5} C/cm² of the capacitors with APCVD Si nitride were performed in a scanning electron microscope. The cesium contamination was accomplished by spinning an alcoholic solution of CsCl (10^{-4} mol CsCl/l) onto the wafer prior to the nitride deposition. Good uniformity of the charge density across the wafer was obtained in this way. No special oxide was grown before the CsCl deposition.

High frequency and quasistatic C-V measurements were performed in order to determine the density of fixed insulator charges and interface states. The high frequency (1 MHz) capacitance (C_{HF}) and the low frequency capacitance (C_{LF}) were recorded simultaneously with a measurement system described elsewhere (14). The rate of the linearly increasing voltage ramp was between 5 and 50 mV/s. In order to avoid possible effects of charge injection from silicon into the Si nitride on the interface state density D_{IT}^* at midgap, the curves were recorded starting from inversion towards accumulation, since charge injection occurs only at voltages smaller than the flatband voltage.

Results and Discussion

APCVD silicon nitride.—In Fig. 1, the fixed charge density (graph a) and the midgap interface state density (graph b) of MNOS structures prepared by depositing APCVD Si nitride on the thin oxide on silicon is shown as a function of the nitride deposition temperature. The results obtained after a postdeposition heat-treatment at 900°C for 30 min in nitrogen as well as after electron irradiation with a beam energy of 30 keV and a dose of 5×10^{-5} C/cm² are also included in Fig. 1. As can be seen from Fig. 1a, the fixed charge density Q_N/q decreases with increasing nitride deposition temperature from 4.3×10^{12} cm⁻² at 620°C down to 5×10^{11} cm⁻² at 900°C. Almost the same low value of Q_N/q is obtained after annealing at 900°C of a nitride film deposited at 650°C. The insensitiv-

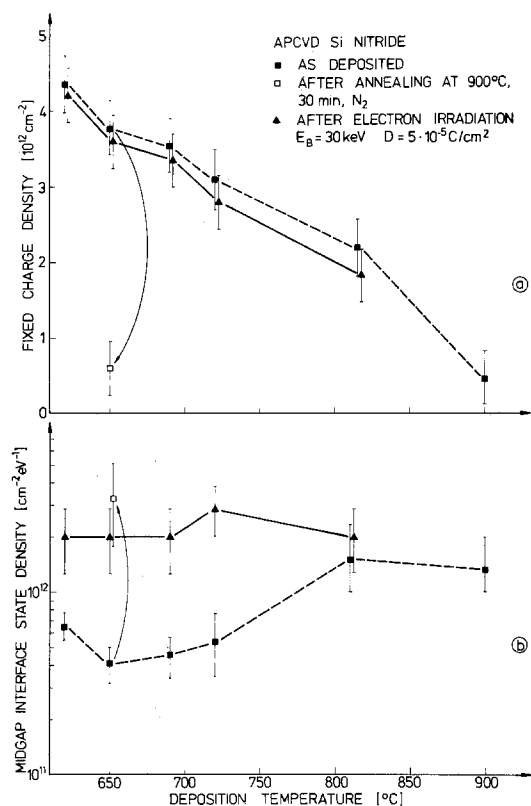


Fig. 1. Fixed charge density (a) and midgap interface state density (b) of MNOS structures [Al/100 nm APCVD Si nitride/native oxide/p-Si (100)] as a function of the deposition temperature. The effects of annealing at 900°C and irradiation with 30 keV electrons (dose $D = 5 \times 10^{-5} \text{ C/cm}^2$) are also shown.

ity of the fixed nitride charges against electron irradiation is clearly demonstrated for the whole deposition temperature range. This confirms earlier results obtained by us (12, 15). For the decrease of Q_N/q with deposition and annealing temperature, a correlation with the decomposition of Si-H and N-H bonds was found (3, 11).

The values of the interface state density (Fig. 1b) range from 4×10^{11} to $6 \times 10^{11} \text{ cm}^{-2} \text{ eV}^{-1}$ in the deposition temperature range 620°–720°C, whereas a remarkable increase of D^*_{IT} occurs at higher deposition temperatures. A drastic increase of D^*_{IT} is obtained after annealing a nitride film at 900°C which was deposited at 650°C. A nearly constant high value of the interface state density ($D^*_{IT} \sim 2 \times 10^{12} \text{ cm}^{-2} \text{ eV}^{-1}$) resulted after electron-beam irradiation of the MNOS structures with nitride films grown at different temperatures. Thus, as a main result in Fig. 1b, the

same high value of the interface state density is obtained in MNOS structures with APCVD Si nitride either by depositing the films at temperatures above 800°C or by annealing at high temperatures as well as by electron irradiation.

It is known that Si-H bonding, particularly, in APCVD Si nitride decreases considerably with increasing deposition temperature (16). The observed variation of the interface state density with deposition temperature may therefore be attributed to a loss of chemically bound hydrogen creating unsaturated silicon bonds. A similar decomposition of Si-H and N-H bonds (17) and the formation of dangling silicon bonds is made responsible for the observed increase of D^*_{IT} after annealing. The increase of D^*_{IT} after electron irradiation is attributed to bond breaking at the silicon/insulator interface.

Pyrolytic CVD Si nitride, and particularly Si oxynitride, is known to be resistant against ionizing radiation (18, 19). According to our results, this fact must be restricted to nitrides deposited or annealed at temperatures above 800°C. It is not clearly understood why the interface states but not the fixed charges of the low temperature APCVD Si nitrides are affected by electron irradiation. It should be noted in this context that the fixed grown-in charges in MNOS structures are located some nanometers away from the silicon surface in a region of Si nitride or Si oxynitride (12).

It was clearly established by depth profiling of a MNOS structure using a combination of Auger electron spectroscopy and low energy electron energy loss spectroscopy in our laboratory that the Si oxide, originally present at the silicon surface, was transformed into Si oxynitride during the Si nitride deposition at 800°C (12, 20).

From Fig. 1, the general conclusion can be drawn that no correlation exists between the fixed charges and the fast interface states in MNOS structures with APCVD Si nitride.

PECVD silicon nitride.—In MNOS structures with plasma Si nitride in the as-deposited state, charge injection occurs already at voltages slightly more negative than the flatband voltage. This is demonstrated in Fig. 2a by the high and low frequency C-V curves obtained for capacitors with plasma Si nitride films 100 nm thick deposited at 270°C. Even after recording the C-V curves up to -8.5 V , which is only 3.5V below the flatband voltage, a hysteresis of 1V is observed. In contrast to MNOS structures with APCVD Si nitride, the very poor charge retention properties of as-deposited plasma Si nitride are reflected, particularly in the different shapes of both the C_{HF} and C_{LF} curves measured before (solid lines) and after (broken lines) accumulation was reached. The interface state density was in all cases determined from the initial C-V curves (solid lines in Fig. 2a).

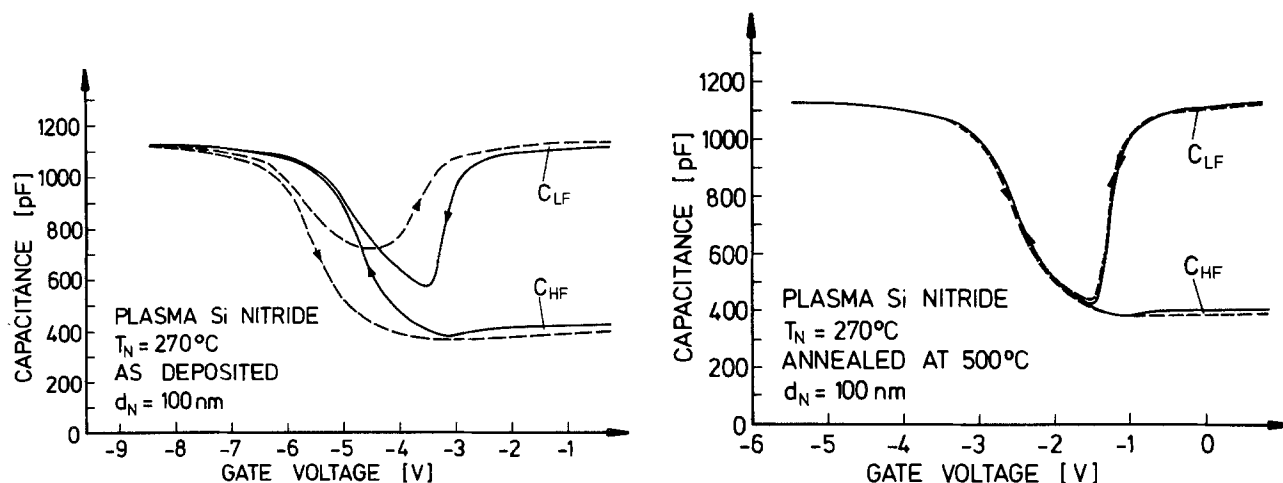


Fig. 2. High and low frequency C-V curves of MNOS structures [Al/100 nm PECVD Si nitride/1.2 nm Si oxide/p-Si (100)] of the as-deposited state (Fig. 2a, left) and after annealing at 500°C in N₂ (Fig. 2b, right). The plasma Si nitride was deposited at $T_N = 270^{\circ}\text{C}$.

Drastic changes of the interface properties were obtained after annealing the plasma nitride films at temperatures above their deposition temperature. The hysteresis is strongly reduced after annealing the samples above 450°C. This is demonstrated in Fig. 2b by the C-V curves of a MNOS structure with plasma Si nitride deposited at 270°C and annealed at 500°C. Lowering of both the fixed charge density and the interface state density occurring by annealing can also be seen from Fig. 2b. This important behavior was studied in more detail, and the results are presented in Fig. 3. The charge density (Fig. 3a) and the interface state density (Fig. 3b) are plotted as a function of the postdeposition annealing temperature. The films were deposited at 210°, 240°, and 270°C, respectively. As can be seen from Fig. 3a, the fixed charge density Q_N/q drops from 6.6×10^{12} to 2.8×10^{12} cm⁻² by increasing the deposition temperature from 240° to 270°C. By postdeposition annealing, the Q_N/q values are reduced. For annealing temperatures above 430°C, a nearly constant fixed charge density of about 1×10^{12} cm⁻² was obtained for all deposition temperatures.

For the midgap interface state density D_{IT}^* of the as-grown films, as shown in Fig. 3b, the same value of 2×10^{12} cm⁻² eV⁻¹ was obtained at deposition temperatures of 210° and 240°C, whereas $D_{IT}^* = 1.7 \times 10^{11}$ cm⁻² eV⁻¹ resulted for films grown at 270°C. By annealing these films at temperatures up to 500°C, a decrease of the interface state density by about two orders of magnitude occurred. At annealing temperatures between 450° and 500°C, minimum values of D_{IT}^* were obtained which increase with decreasing deposition temperature. Very low midgap interface state densities of 8×10^9 cm⁻² eV⁻¹ could be achieved for films deposited at 270°C and annealed at 500°C. A strong increase of D_{IT}^* up to 7×10^{11} cm⁻² eV⁻¹ occurred by annealing the plasma nitride films at temperatures up to 700°C.

For comparison, the interface state density of the MNOS structure with a plasma nitride film deposited at 270°C and annealed at 500°C was measured by CC-DLTS (21). As shown in Fig. 3b, $D_{IT}^* = 9 \times 10^9$ cm⁻² eV⁻¹ was obtained, which is in good agreement with the value determined by the quasistatic technique. In Fig. 4, the

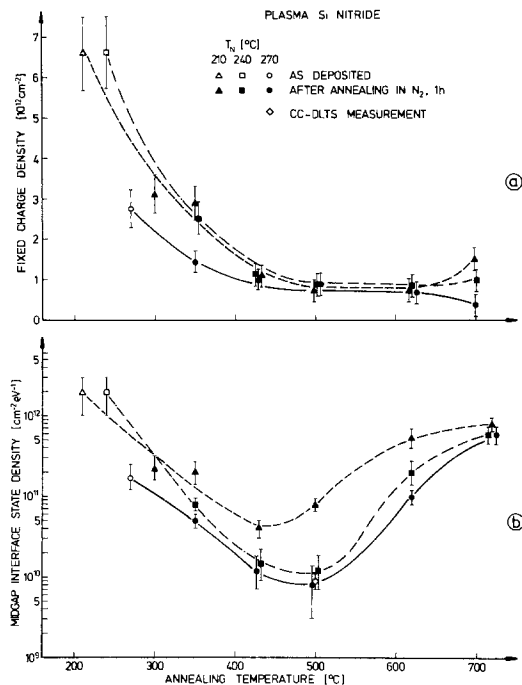


Fig. 3. Fixed charge density (a) and midgap interface-state density (b) of MNOS structures with plasma Si nitride as a function of the postdeposition annealing temperature. The nitride films were deposited at 210°, 240°, and 270°C. The midgap interface-state density of a MNOS sample ($T_N = 270^\circ\text{C}$, annealed at 500°C) was also determined by CC-DLTS.

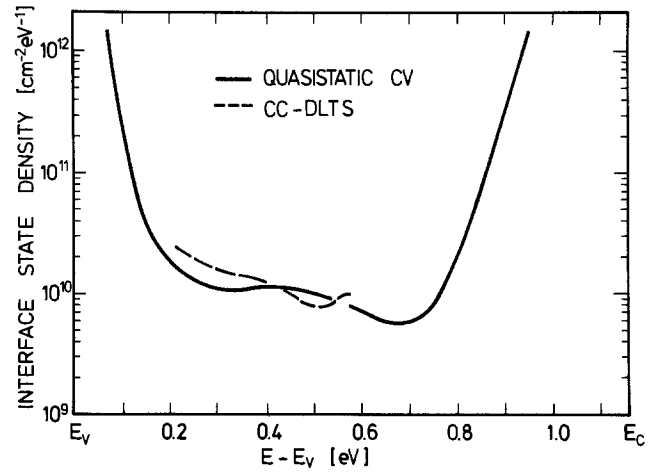


Fig. 4. Interface state density of a MNOS structure with plasma Si nitride as a function of the bandgap energy determined by the quasistatic C-V technique and CC-DLTS. The corresponding C-V curves are shown in Fig. 2b.

interface state density of this sample is shown as a function of the energy in the silicon bandgap, determined by the quasistatic C-V technique, as well as by CC-DLTS. As can be seen, the results obtained by the two techniques are in good agreement.

In the following, the results presented in Fig. 3 will be discussed. The high interface-state density of PECVD Si nitride films in the as-grown state (Fig. 3b) is attributed to unsaturated bonds at the silicon/insulator interface, resulting from incomplete bonding, which may be enhanced by electron and ion bombardment during the plasma-deposition process. It is known that a high amount of hydrogen is incorporated into the plasma Si nitride films (22). It is further known that annealing of the films in nitrogen at temperatures up to 500°C leads to a decomposition of N-H bonds, whereas the amount of Si-H bonds increases slightly. By heat-treatments at temperatures above 500°C, however, both N-H and Si-H centers are lost (23). It is reported for the Si/SiO₂ system that the formation of silane groups at the interface at annealing temperatures ranging from 300° to 500°C is responsible for the passivation of the interface states (24). Hence the strong decrease of the interface state density at annealing temperatures up to 500°C is attributed to the saturation of unsaturated bonds at the silicon surface by hydrogen originating from N-H bonds in plasma Si nitride. The loss of chemically bound hydrogen at annealing temperatures above 500°C is assumed to be responsible for the observed increase of the interface state density. This latter behavior is in analogy to that of APCVD Si nitride films, as discussed above.

About the nature of the fixed positive charges in plasma Si nitride, no information is available in the literature. Whereas for APCVD Si nitride a correlation between the charges and hydrogen bonding in the films was suggested (3, 11), the data presented in Fig. 3a for plasma nitride do not clearly indicate such a correlation. Although the decrease in N-H bonding (23) parallels a decrease in the fixed charge density after annealing at temperatures up to 500°C, a correlation of these two quantities cannot be established in the present state.

From the common decrease of the fixed charge density and the midgap interface state density with annealing temperatures of up to 450°C, as demonstrated in Fig. 3, at least in this temperature region some relationship between Q_N/q and D_{IT}^* may exist.

Cesium contamination of PECVD silicon nitride films.—It was demonstrated recently for APCVD Si nitride on silicon that the density of positive nitride charges can be drastically increased by the incorporation of alkaline ions (25). In order to obtain very high and stable positive charge densities in plasma Si nitride on silicon

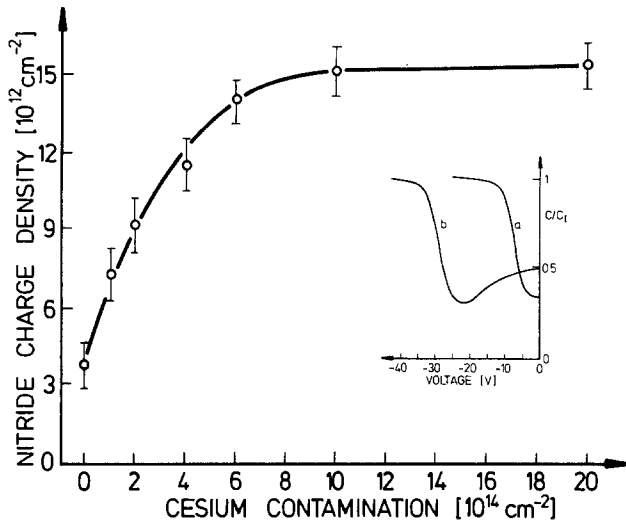


Fig. 5. Influence of cesium contamination of MNOS structures with plasma Si nitride upon the insulator charge density. The C-V curves before (curve a) and after (curve b) cesium contamination are shown in the insert.

in this work, the films were heavily contaminated with cesium by spinning an alcoholic solution of CsCl onto the native oxide on silicon prior to the nitride deposition. In Fig. 5, the nitride charge density is plotted as a function of the cesium concentration up to a level of $2 \times 10^{15} \text{ cm}^{-2}$. As can be seen, the insulator charge density increases with increasing cesium concentration until, at a contamination level of about $8 \times 10^{14} \text{ cm}^{-2}$, saturation is reached. In all cases, only a fraction of the amount of cesium deposited is electrically active as positive insulator charge. The saturation charge density was found to be dependent on the plasma-deposition parameters, but no systematic investigations have been performed. It could be shown that peak values of the nitride charge density up to $2.2 \times 10^{13} \text{ cm}^{-2}$ can be achieved for a cesium contamination level of $2 \times 10^{15} \text{ cm}^{-2}$.

In the insert in Fig. 5, the high frequency C-V curves of both the uncontaminated MNOS capacitor with plasma Si nitride (curve a, $V_{FB} = -7.7 \text{ V}$, $Q_N/q = 3.8 \times 10^{12} \text{ cm}^{-2}$, nitride thickness = 72 nm) and the corresponding one with a cesium contamination of $2 \times 10^{15} \text{ cm}^{-2}$ (curve b, $V_{FB} = -30.5 \text{ V}$, $Q_N/q = 1.5 \times 10^{13} \text{ cm}^{-2}$) are shown. No ion hysteresis was observed at room temperature for gate fields up to insulator breakdown, indicating that these charges are immobile in the nitride film. The interface state density of the Cs-doped samples could not be determined by the standard quasistatic C-V technique due to high leakage currents occurring as a consequence of the extremely high flatband voltages. However, it can be qualitatively deduced from the shape of the C-V curves that the additional charges introduced in the Si nitride film by the cesium contamination neither give rise to a significant amount of additional surface states nor cause large surface-potential fluctuations due to inhomogeneous charge distribution. This behavior is in contrast to that of alkaline ions in MOS structures. For comparison, corresponding samples with pyrolytic CVD Si oxide films deposited on silicon by the silane oxygen reaction at 650°C were coprocessed with the MNOS structures. Similar to the results obtained recently by us for sodium contamination (25), the C-V curves of the cesium-contaminated MOS samples were displaced towards negative voltages, and they were extremely distorted and showed a pronounced ion hysteresis at room temperature.

The thermal stability of the cesium-induced charges in plasma Si nitride was investigated by annealing the samples in a nitrogen ambient at temperatures up to 500°C . The results are shown in Fig. 6. At temperatures below the nitride deposition temperature of 260°C , no degradation of the charge density occurred. Above the

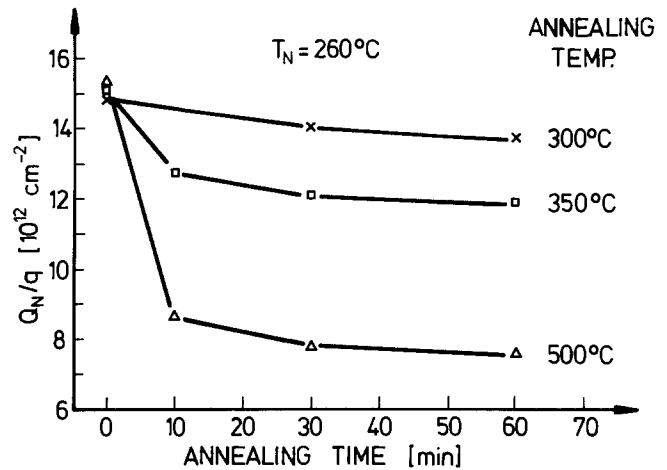


Fig. 6. Effect of N_2 annealing on the insulator charge density of plasma Si nitride MNOS structures contaminated with cesium.

deposition temperature, the charge density decreases with annealing time. Still, a charge density of about $8 \times 10^{12} \text{ cm}^{-2}$ was present in the contaminated structures after 1h annealing at 500°C . The shape of the C-V curves was not significantly changed by this heat-treatment.

It could be further verified that before and after annealing the charges were located near the silicon insulator interface and that no ion migration occurred during the heat-treatment (9). The charge decay is assumed to be either due to the neutralization of positive charges or to a partial compensation of the positive charges by the creation of negative charges (11).

Conclusions

In this work, MNOS structures with APCVD and plasma Si nitride have been investigated with respect to the fixed positive insulator charge density Q_N/q and the midgap interface state density D^*_{IT} . For APCVD Si nitride no correlation could be established between Q_N/q and D^*_{IT} , since with increasing nitride deposition temperature a decrease of Q_N/q and an increase of D^*_{IT} occurred. With plasma Si nitride for postdeposition annealing temperatures up to 450°C , a common decrease of Q_N/q and D^*_{IT} was found, whereas at higher temperatures D^*_{IT} increases again and Q_N/q remains constant. The origin of the fixed charges is unknown for both nitride films; only some correlations between Q_N/q and hydrogen bonding in these films are possible. The dependence of the interface state density upon deposition and annealing temperature, respectively, can be interpreted by the influence of hydrogen bonded to silicon and nitrogen. Due to hydrogen passivation of unsaturated silicon bonds, very low values of D^*_{IT} ($8 \times 10^6 \text{ cm}^{-2} \text{ eV}^{-1}$) could be achieved for plasma nitride films deposited at 270°C and annealed at 500°C . This low interface state density, together with a moderate fixed charge density, makes the low temperature plasma Si nitride films suitable for an application as active layers in semiconductor devices. For high efficiency inversion layer solar cells, extremely high charge densities can be obtained by cesium contamination of the plasma nitride layers.

Acknowledgments

The authors are grateful to K. Hofmann of the Institute for Applied Physics in Erlangen for performing the CC-DLTS measurements. This work was supported by the Bundesministerium für Forschung und Technologie of the Federal Republic of Germany.

Manuscript submitted June 1, 1983, revised manuscript received March 9, 1984. This was Paper 123 presented at the San Francisco, California, Meeting of the Society, May 8-13, 1983.

REFERENCES

1. H. Schauer, E. Arnold, and P. C. Mürau, *IEEE Trans. Electron. Devices*, **ed-25**, 1037 (1978).

2. L. Lundkvist, C. Svensson, and B. Hansson, *Solid-State Electron.*, **19**, 221 (1976).
3. R. Hezel and E. Hearn, *This Journal*, **125**, 1848 (1978).
4. R. Hezel and R. Schörner, *J. Appl. Phys.*, **52**, 3076 (1981).
5. R. Schörner and R. Hezel, *IEEE Trans. Electron. Devices*, **ed-28**, 1466 (1981).
6. H. C. Tuan, M. Y. Thompson, N. M. Johnson, and R. J. Lujan, *IEEE Electron. Devices Lett.*, **edl-3**, 357 (1982).
7. A. J. Snell, K. D. Mackenzie, W. E. Spear, P. G. LeComber, and A. J. Hughes, *J. Appl. Phys.*, **24**, 357 (1981).
8. G. C. Salter and R. E. Thomas, *Solid-State Electron.*, **20**, 95 (1977).
9. R. Hezel, in "Proceedings of the 16th IEEE Photovoltaic Specialists Conference," p. 1237, San Diego, Sept. 1982, IEEE, New York (1982).
10. E. Arnold, J. Ladell, and G. Abowitz, *Appl. Phys. Lett.*, **13**, 413 (1968).
11. R. Hezel, *J. Electron. Mater.*, **8**, 459 (1979).
12. R. Hezel, *Solid-State Electron.*, **24**, 863 (1981).
13. R. Hezel, T. Meisel, and W. Streb, *J. Appl. Phys.*, **27**, 5516 (1984).
14. K. Blumenstock, R. Schörner, and R. Hezel, in "Insulating Films on Semiconductors," J. F. Verweij and D. R. Wolters, Editors, Elsevier, Amsterdam (1983).
15. R. Hezel, *Solid-State Electron.*, **22**, 735 (1979).
16. H. J. Stein and V. A. Wells, Abstract 113, p. 303, The Electrochemical Society Extended Abstracts, Vol. 77-1, Philadelphia, PA, May 8-13, 1977.
17. H. J. Stein and H. A. Wegener, *This Journal*, **124**, 908 (1977).
18. P. F. Schmidt and J. D. Ashner, *IEEE Trans. Nucl. Sci.*, **ns-17**, 11 (1970).
19. R. Hezel, *Radiat. Eff.*, **65**, 101 (1982).
20. N. Lieske and R. Hezel, in "Insulating Films on Semiconductors 1979," p. 206, Institute of Physics Conference Series 50, Institute of Physics, London (1980).
21. M. Schulz and E. Klausmann, *Appl. Phys.*, **18**, 169 (1979).
22. W. A. Lanford and M. J. Rand, *ibid.*, **49**, 2473 (1978).
23. H. J. Stein, V. A. Wells, and R. E. Hampy, *This Journal*, **126**, 1750 (1979).
24. R. R. Razouk and B. E. Deal, *ibid.*, **129**, 806 (1982).
25. R. Hezel, in "Insulating Films on Semiconductors," M. Schulz and G. Pensl, Editors, p. 219, Springer Series in Electrophysics no. 7, Springer Verlag, Berlin (1981).

Rice Hulls as a Raw Material for Producing Silicon

L. P. Hunt,* J. P. Dismukes,* and J. A. Amick*

Exxon Research and Engineering Company, Clinton, New Jersey 08801

A. Schei* and K. Larsen

Elkem a/s, Research and Development Center, N-4620 Vaagsbygd, Norway

ABSTRACT

Rice hulls are a relatively high-volume, low-cost by-product commodity which contains the two basic components needed to produce silicon: silica and carbon. Impurity analyses have indicated that rice hulls from various sources are compositionally similar and that they have low concentrations (10-20 ppmw) of aluminum and iron, the major impurities in conventional raw materials used to prepare metallurgical silicon. The levels of the major impurities (Ca, K, Mg, and Mn) in rice hulls can be reduced by about a factor of 100 to around 20 ppmw by hot hydrochloric acid leaching. The doping impurities boron and phosphorus, important in silicon intended for solar cells, were less affected by acid leaching. Their concentrations were found to be 1 and 40 ppmw, respectively, in leached hulls. Coking of unpurified rice hulls produced a material with a C:SiO₂ ratio of about 4:1. An increase in concentrations of some impurities was noted since coking results in about a 67% loss in sample weight. The coked hulls were extruded with sucrose as a binder to produce 5 mm diam pellets with an average bulk density of about 800 g/l. The pellets gave favorable changes in bulk density and compression strength with increasing percentage sucrose. The abrasiveness of silica caused die wear in the extruder, resulting in roughly a doubling of the original concentration of iron in the coked hulls. Coked rice hull pellets showed excellent reactivity for producing silicon. Laboratory tests employing the reaction of silicon monoxide with carbon in the pellet showed very high reactivities for both purified and unpurified materials. A test in a small arc furnace of unpurified material showed energy consumption per unit weight of silicon to be about 15%-30% lower than normal. Unpurified rice hulls were used for these tests. Although the silicon produced in the arc furnace test was contaminated, estimates of silicon purity attainable from coked hulls, unpurified and purified, indicate their potential as raw materials for the production of MG-Si and solar-grade silicon.

The impetus for this work arose from the need to produce a grade of silicon pure enough for fabrication into solar cells and low enough in cost so that photovoltaic energy can be competitive with conventional energy sources. Metallurgical-grade silicon (MG-Si) of about 99% purity is produced by an arc-furnace process in the western world at an annual rate of about 400,000 tons (1). Even though MG-Si can be upgraded considerably during a series of purification steps (2), the concentration of boron cannot be substantially reduced while maintaining silicon in its elemental form. Since boron in excess of about 0.4 part per million by weight (ppmw) results in an unacceptable decrease in the conversion efficiency of silicon solar cells (3), various research programs have focused on reducing the level of impurities introduced into the arc furnaces through use of higher purity raw materials (2, 4, 5, 6).

This paper discusses the potential use of rice hulls, or rice husks, as they are also called, as a raw material

source for preparing silicon. As will be seen later, raw rice hulls could be of interest for the production of MG-Si, while purified rice hulls might be suitable for producing a higher quality of silicon such as a solar grade.

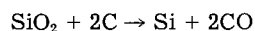
Numerous reports on the composition, properties, and intended uses of rice hulls have appeared since 1871. References (7) and (8) summarize the status of this by-product commodity, for which new markets are still being sought to utilize the annual production capacity. Because of this excess supply, rice hulls can be purchased at a large-volume cost of around \$22/ton. It has been calculated that the yearly U.S. harvest of rice, 2% of the world total, generates sufficient hulls for potential recovery of about 100,000 tons of silicon (9).

Burning of rice hulls leaves an ash that consists mainly of silica with about 5% impurity oxides. Singh and Dhindaw reported that the silica structure is not quartz, but is rather an active form of silica that might be more easily reduced to silicon (10). They proposed use of the ash as the silicon feed stock for an arc-furnace process for producing solar-grade silicon. However, since the rice

* Electrochemical Society Active Member.

hull contains only about 20% silica ash, the ash is not cost competitive with quartzite sources used for MG-Si production.

The purification of rice hulls using various acid leaching solutions has been reported previously (9, 11). Purified hulls were pyrolyzed (coked) to produce a product containing an atomic-to-molecular ratio of C:SiO₂ of about 4:1. It was suggested that this material, together with pure quartz, be used as feedstock for the carbothermic reduction process to produce silicon. Since the rice hull contains 15% fixed carbon, it is cost competitive with commercial reductants used to produce MG-Si. A method for adjusting the C:SiO₂ ratio to lower values by controlled combustion was also detailed. The procedure can provide carbon-free silica or a mixture having a 2:1 C:SiO₂ ratio required by the reaction



This paper reports on the leaching of rice hulls, their conversion into pellets, and the reactivity of these pellets. Suggestions are made for further investigations.

Raw Rice Hulls

Samples of raw rice hulls from different parts of the world were analyzed to determine whether or not significant differences in impurity concentrations exist. Good agreement was found between the results of the two analytical techniques that were used: optical-emission and spark-source mass spectrometry. Table I shows that rice hull samples from the U.S. (Arkansas and Louisiana), Japan, and Malaysia¹ are very similar in composition. Low variation of impurity composition with source has also been observed for tree wood (12). The unusually high concentrations reported in one case each of Al, Fe, P, and S may be attributable to the analytical technique, since these high values were not observed in samples of the same rice hulls that had been processed as indicated below. Table I also gives the average rice hull analysis for later comparison.

Rice Hull Purification

Compositional analysis has been reported for rice hulls leached with boiling solutions of concentrated hydrochloric acid and deionized (DI) water in HCl/H₂O ratios of 1:1 and 1:3 (9, 11). Anticipating material-of-construction problems in a pilot plant; acid leaching tests were carried out at a lower temperature and in more dilute acid solution. Raw rice hulls, ground to -20 +80 mesh, were acid leached under conditions indicated in Table II. The samples were subsequently washed with DI water, dried, and analyzed.

Leaching for 15 min under boiling conditions at a 1:10 HCl:H₂O ratio was just as effective for purification as leaching with more concentrated acid solutions. However, leaching for 5h at 50°C with a 1:10 solution did not reduce impurity concentrations to levels as low as those attained under boiling conditions.

¹ Samples courtesy of Rice Institute, Manila, Philippines.

Table I. Impurity concentrations in rice hulls from various sources

Impurity* (ppmw)	Source of hulls				
	Arkansas	Japan	Louisiana	Malaysia	Avg
Al	20	10	200**	10	10
B	2	1	2	1	2
Ca	1000	1000	1000	1000	1000
Fe	20	20	60**	20	20
K	4000	8000	2000	1200	3800
Mg	900	200	600	300	500
Mn	500	200	500	200	350
Na	20	50	10	20	25
P	>1000**	200	—	50	130
S	50	>1000**	—	20	40
Ti	2	0.5	10	1	3

*Other impurities <1 ppmw.

**Unusually high; not included in average.

Table II. Effect of acid leaching conditions on rice hull impurity concentrations

Impurity*	Concentration (ppmw)		
	0.25 1:3 Boil	0.25 1:10 Boil	5.0 1:10 50
Al	40	40	20
B	1	1	<1
Ca	30	20	150
Fe	4	4	15
K	5	5	200
Mg	15	5	90
Mn	5	3	50
Na	10	5	15
Ti	1	5	5

*Other impurities <1 ppmw.

Three of the raw rice hull samples from different sources (see Table I) were acid leached for 15 min in boiling 1:10 hydrochloric acid solution. As might be expected, the impurity levels in the acid leached hulls were similar (see Table III). Ca, K, Mg, and Mn were reduced by factors of 40-100 times, and Na, P, and S by factors of 3-8. Their average composition is given in Table III.

One commercial source of acid-leached rice hulls was investigated. Quaker Oats Company produces furfural by the acid extraction of rice hulls using H₃PO₄ and waste H₂SO₄. The waste by-products hulls, called "residue," are burned by Quaker Oats for their energy value. A sample of moist "residue" was washed with DI water, dried, and analyzed. The results in Table IV show that this product is more impure than the average leached hull sample listed in Table III. However, the impurities present at considerably higher concentrations are the ones that vaporize and are removed in exhaust gases during the arc-furnace production of silicon and its subsequent recrystallization. Therefore, this commercial by-product is a potential source of purified rice hulls for silicon production.

Rice Hull Coking

Ground rice hulls, unleached and leached, were coked in 1 liter (~400g) quantities in a quasifluidized-bed reac-

Table III. Purity of rice hulls from various sources leached for 15 min in boiling 1:10 concentrated hydrochloric acid/water solution

Impurity* (ppmw)	Source			
	Arkansas	Japan	Malaysia	Avg.
Al	20	5	10	10
B	1	1	1	1
Ca	50	20	5	25
Fe	50	5	10	20
K	50	20	20	30
Mg	10	10	6	10
Mn	5	20	1	3
Na	5	20	2	9
P	50	50	10	10
S	5	5	5	5
Ti	20	1	5	9

*Other impurities <1 ppmw.

Table IV. Comparison of purity of acid-leached rice hulls from a commercial process (Quaker Oats Company) to that prepared in this work

Impurity* (ppmw)	Quaker Oats by-product	Avg. this work (from Table III)
Al	20	10
B	2	1
Ca	200	25
Fe	50	20
K	200	30
Mg	150	10
Mn	10	3
P	100	40
S	100	5

*Other impurities <1 ppmw.

tor constructed from a 45 × 10 cm diam quartz tube. The reactor was continuously purged with nitrogen at ~1 l/min. The system was heated to 500°C until heavy smoke evolution, from the decomposition of organic compounds, began to decrease (~30 min). The reactor was then heated to 800°C, and coking was considered to be complete when smoke evolution was no longer visible (~15 min). A weight reduction to one-third of the original value was observed: approximately 65% of raw rice hulls are converted to volatiles during pyrolysis.

Samples of acid leached rice hulls from various sources (see Table I) were coked and analyzed. The results in Table V show that impurity concentrations in leached/coked hulls are, on the average, similar to those in their leached-only precursors. Five of the eleven measurable impurities increased in concentration (see Table VI for comparison). A three-fold increase is expected if all of an impurity remains, while the matrix weight decreases by a factor of three during coking. Of the only remaining impurities, the concentration of two remained the same (Ca and P), while that of B, Fe, and Ti actually decreased. When potassium is excluded from consideration, the maximum average of any impurity in the coked hulls does not exceed 50 ppmw. If one further excludes those impurities that are lost during subsequent high-temperature processing, the total impurity concentration is only about 100 ppmw. A further lowering of impurity concentrations has been reported when hydrogen chloride gas is used during coking (9, 11).

When no prior leaching was used, somewhat different results were obtained when comparing impurity concentrations of coked hulls to that of their precursor. Table VI shows that Al, Mg, and Mn concentrations increase by about the same amount as they did for the leached/coked hulls. However, an actual reversal was noted for B, Fe, and Ti, while a large decrease was observed for phosphorus. More in-depth investigations are required to explain these differences. It should be noted that raw rice hulls have a total impurity concentration about 30 times greater than that of leached hulls.

Table VI also provides a convenient comparison of the change in impurity concentrations going from raw → leached → coked rice hulls and from raw → coked hulls.

Table V. Impurities in leached coked rice hulls from various sources

Impurity*	Arkansas	Japan	Louisiana	Malaysia	Avg.
Al	75	50	10	60	50
B	1	1	0.5	0.5	0.7
Ca	20	20	50	13	20
Fe	20	8	5	13	10
K	100	100	50	75	90
Mg	50	55	50	20	40
Mn	35	13	20	13	20
Na	20	50	5	10	20
P	50	50	20	20	40
S	20	15	<1	20	20
Ti	5	1	<1	1	2

*Other impurities <1 ppmw.

Table VI. Comparison of impurities at various stages of rice hull processing

Impurity* (ppmw)	Average from preceding tables			Coked only
	Raw	Leached	Leached/ coked	
Al	10	10	50	50
B	2	1	0.7	10
Ca	1000	25	20	>1000
Fe	20	20	10	200
K	3800	30	90	>1000
Mg	500	10	40	1700
Mn	350	3	20	1000
Na	25	9	20	10
P	130	40	40	20
S	40	5	20	<1
Ti	3	9	2	10

*Other impurities <1 ppmw.

Pelletization of Coked Hulls

Raw materials used for the production of silicon in an arc furnace must have sufficient mass so as not to be entrained in the large by-product stream of gases leaving the surface of a furnace. Due to the small size and low bulk density of coked rice hulls, it is necessary to agglomerate them prior to smelting in an arc furnace.

Extrusion pelletization tests were carried out by California Pellet Mill Company in a Model CL Laboratory pellet mill with the goal of producing strong pellets of minimum density (Fig. 1). Strength is required to prevent premature pellet disintegration in an arc furnace, whereas low density is directly related to raw material reactivity for producing silicon. Coked rice hulls were mixed with water as a lubricant and sucrose as a binder. Sucrose was chosen because of its purity and its ability to enhance the reactivity of activated carbon and carbon black during smelting tests in a 100 kW arc furnace (4). Sucrose content of dry pellets was determined by heating them to 300°C under nitrogen and measuring the weight loss due to water evolution during the decomposition of sucrose. No change in pellet size due to sucrose decomposition could be measured. Table VII shows pellet density and relative strength as a function of sucrose content for 8 × 5 mm diam cylindrical pellets. Favorable changes in both physical properties occur with increasing sucrose content. Pellets containing 17% sucrose gave adequate strength at minimum sucrose cost. Bulk densities in the 800 g/l range were measured.

Pellet composition was measured to determine the effect of the abrasiveness of the silica in coked rice hulls upon the pelletizer die. Analysis showed an increase in iron concentration from 200 to 500 ppmw (see "Coked only" analysis in Table VI). No other change in impurity concentration was measurable.

Based upon the data above and upon laboratory reactivity measurements (see next section), approximately 100 kg of 13 × 10 mm diam pellets containing 17% sucrose were produced in a Model CM pellet mill at California Pellet Mill Company. Coked hulls were prepared by Exxon Enterprises, Materials Division (Greer, South Carolina) from -20 +80 mesh, unleached, Louisiana rice hulls. The reactivity of these pellets was tested in an arc furnace, as described in the next section.

Pellet Reactivity

Unleached/coked pellets, designated as CRP in Table VII, were tested by SINTEF (Trondheim, Norway) for their reactivity. The test, as originally devised, consists of passing a SiO/CO gas mixture of known composition through a bed of carbon and measuring the CO content of the exit gas (13). Reactivity of the carbon is measured in milliliters of SiO: a low volume of SiO exiting the bed implies that a large percentage of it reacted with the carbon reductant according to the reaction

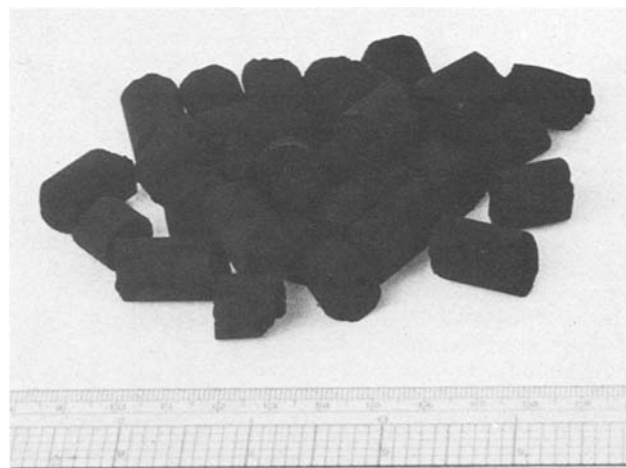


Fig. 1. Pellets prepared from coked rice hulls with sucrose binder.

Table VII. Density and strength of coked rice hull pellets with various sucrose contents

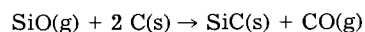
Sample no.	Sucrose (%)	Density	Relative strength
6	12	816*	Low
4	13	816*	Low
CRP-3	15	1.44**	Medium
7	17	784*	Medium
CRP-2	21	1.35**	High
CRP-1	32	1.17**	High

* Bulk (g/l).

** Actual (g/cm³).

Table VIII. Impurities in silicon projected from raw materials consisting of unleached and leached rice hulls (coked) based on commercially established recovery factors

Impurity	Conc. in silicon (ppmw)	
	Coked-only hulls	Leached/coked hulls
Al	40	40
B	7	0.5
Ca	>500	10
Fe	160	8
P	3	6
Ti	8	2



Since the rice hull pellets contain both carbon and silica, it was necessary to prereact the silica at 1500°C in a graphite cylinder purged with argon. Treatment was discontinued when carbon monoxide evolution was no longer appreciable due to reaction $\text{SiO}_2 + 3\text{C} \rightarrow \text{SiC} + 2\text{CO}$. The reactivity of the remaining carbon was then measured in the usual manner, as described above.

The reactivity of samples CRP-1, CRP-2, and CRP-3 were 272, 206, and 255 ml SiO, respectively. These are the lowest values ever measured by SINTEF. Similar results were obtained for purified coked hulls. As a comparison, the reactivity of typical commercial reductants for the production of MG-Si lie within the range 850-1600 ml SiO, while that of reactive charcoals varies from 300-1000 ml SiO.

The 100 kg batch of pellets, described in the previous section, was smelted in a 50 kW, one-electrode arc furnace (14). Since the analyzed pellets had an atomic-to-molecular ratio of $\text{C}:\text{SiO}_2 = 3.7$, the balance of the SiO_2 was supplied by adding chunks of pure quartz in order to adjust the total raw material ratio close to its stoichiometric value of 2.0. Furnace operation was excellent during the short 23h test, which produced 35 kg of silicon. Energy consumption of 20.9 kWh/kg was very low for this furnace. Energy utilization in the 50 kW furnace is normally 25-30 kWh/kg for commercial raw materials used to prepare MG-Si.

The arc-furnace experiment was performed primarily to test the reactivity of the coked pellets. Pure smelting conditions could not be used. However, an estimate of an impurity concentration in silicon can be made from its published recovery factor, which is the fraction of the impurity in the raw materials that ends up in silicon (15). Recovery factors, obtained from commercial-scale operation, were applied to the "Coked only" and "Leached/coked" analyses in Table VI to project impurity level as listed in Table VIII for two grades of silicon. "Coked only" hulls have the potential of producing silicon with impurities 1-2 orders of magnitude lower than those in commercial MG-Si. "Leached/coked" hulls are definitely of interest for solar-grade silicon. Since the P/B ratio exceeds 10, however, eventual fabrication of n/p solar cells would require development of a process to substantially reduce the concentration of phosphorus.

Conclusions

Extruded pellets of coked rice hulls, with sucrose as a binder, were shown by two techniques to be very reactive

raw materials for the production of silicon using submerged-electrode, arc-furnace technology. A short duration arc-furnace experiment using these pellets resulted in the lowest energy consumption ever measured in this furnace. Silicon from the experiment was contaminated, but projections indicate that the purity should far exceed that of commercially available MG-Si.

The coked hulls were pelletized in pilot-scale equipment for which commercial-size equipment already exists.

Acid leaching of rice hulls was demonstrated to produce a much purer coked material than that used in the furnace test just described. Although sufficient raw material was not available to make a smelting test, it can be projected that an acid-leached and coked product is of interest as a raw material for the production of solar-grade silicon. A source of suitably acid-leached hulls may be available as a by-product from a commercial process used by Quaker Oats Company. Their by-product analyzed to have a purity approaching that demonstrated in our laboratory leaching experiments.

Acknowledgments

Special thanks are expressed to M. Pope of ER&E for the acid leaching experiments and for expediting many phases of this study. Gratitude is also extended to J. Cook, M. Gust, and H. Schleckser of Exxon Enterprises' Materials Division for providing hulls in their raw and coked forms and for pilot-plant concepts for leaching rice hulls; to R. Robinson and G. Wendelin of California Pellet Mill Company for laboratory and pilot plant pelletizations; and to O. Raaness of SINTEF for providing SiO reactivity analyses.

Manuscript submitted Oct. 14, 1983; revised manuscript received Feb. 29, 1984.

Exxon Research and Engineering Company assisted in meeting the publication costs of this article.

REFERENCES

- "Economics of Silicon and Ferro-Silicon," 3rd ed., Roskill Information Services, London (1980).
- D. Helmreich, E. Sirtl, and J. Dietl, in "Crystals, Growth, Properties and Applications," Vol. 5, J. Grabmaier, Editor, Springer-Verlag, Berlin (1981).
- P. A. Iles and S. I. Soclof, in "Record of the 11th IEEE Photovoltaic Specialists Conference," p. 19, Institute of Electrical and Electronic Engineers, New York (1975).
- L. P. Hunt and V. D. Dosaj, Final Report, Dept. of Energy Report DOE/JPL/954559-78/7, DOE Technical Information Center, Springfield, VA (1979).
- S. Pizzini, in "Materials and New Processing Technologies for Photovoltaics," J. P. Dismukes, P. Rai-Choudury, E. Sirtl, and L. P. Hunt, Editors, p. 25, The Electrochemical Society Softbound Proceedings Series, Pennington, NJ (1982).
- H. A. Aulich, K.-H. Eisenrith, H.-P. Urbach, and J. C. Grabmaier, *ibid.*, p. 177.
- E. C. Beagle, "Rice-Husk Conversion to Energy," FAO Agricultural Services Bull. 31, Food and Agricultural Organization of the United Nations, Rome (1978).
- D. F. Houston, in "Rice, Chemistry and Technology," D. F. Houston, Editor, American Association of Cereal Chemists, St. Paul, MN (1972).
- J. A. Amick, *This Journal*, **129**, 864 (1982).
- R. Singh, and B. K. Dhindaw, in "Sun: Mankind's Future Source of Energy," Pergamon Press, New York (1978).
- J. A. Amick, J. V. Milewski, and F. J. Wright, U.S. Pat. 4,214,928 (1980).
- L. P. Hunt, V. D. Dosaj, and J. R. McCormick, Quarterly Report No. 4, Dept. of Energy Report DOE/JPL/954559-77/2 DOE Technical Information Center (1977).
- J. Kr. Tuset and O. Raaness, in "Proceedings of the 34th AIME Electric Furnace Conference," p. 101, Lew A. Cummings Co., Inc., Manchester, NH (1976).
- V. Dosaj, L. Hunt, and A. Schei, *J. Metals*, **30**, 8 (1978).
- L. P. Hunt, V. D. Dosaj, J. R. McCormick, and A. W. Rauchholtz, in "Record of the 13th IEEE Photovoltaic Specialists Conference," p. 333, Institute of Electrical and Electronic Engineers, New York (1978).

Fabrication of Low Dark-Current Planar Photodiodes Using an Open-Tube Method for Zn Diffusion into InP and $\text{In}_{0.53}\text{Ga}_{0.47}\text{As}$

I. Camlibel, A. K. Chin,* H. Guggenheim, S. Singh, L. G. Van Uitert, and G. J. Zydzik

AT&T Bell Laboratories, Murray Hill, New Jersey 07974

ABSTRACT

A novel process for fabricating planar low dark-current InP- and $\text{In}_{0.53}\text{Ga}_{0.47}\text{As}/\text{InP}$ -based photodetectors is described. The process utilizes a film of ZnF_2 as a source of Zn dopant and an encapsulating layer of either SiO_2 , borosilicate, or Al_2O_3 . Localized p-n junctions were fabricated using standard photolithography and diffusing in an open-tube air ambient. Dark currents as low as 5×10^{-12} and 3×10^{-10} A at 10V reverse bias voltage have been achieved in 75 μm diam unpassivated planar diodes of InP and $\text{In}_{0.53}\text{Ga}_{0.47}\text{As}$, respectively.

Thermal diffusion of an acceptor such as Zn plays an important role in the formation of p-n junctions in III-V semiconductor devices, e.g., photodiodes for use in long-wavelength lightwave communication systems. In the fabrication of such devices, the p-n junctions may be formed by diffusion from the gas phase in sealed ampuls (1-4), ion implantation (5), or open-tube diffusion from films deposited (6, 7) or spun-on (8) the semiconductor wafers. The diffusion from the gas phase requires accurate control of the partial pressures of the species involved to be reproducible, and necessitates the use of a sealed ampul. In order to confine the diffusion to a localized region of the wafer, a dopant-impermeable mask like Si_3N_4 is required. Ion implantation causes compensation and irradiation damage (5). This technique requires a subsequent high-temperature sealed-ampul or open-tube annealing step to activate the implanted dopant and to remove the damage. CVD deposited films require elaborate deposition apparatus (6, 7), and spin-on films still require a sealed ampul for optimum diffusion (8).

In this paper, we report on a novel process for fabricating low dark-current planar-photodiodes of InP or $\text{In}_{0.53}\text{Ga}_{0.47}\text{As}$. This process requires neither a sealed ampul nor a diffusion mask. The diffusion source consists of an initial film of ZnF_2 followed by a film of SiO_2 . These followed by a film of SiO_2 films are easily and reproducibly deposited by electron-beam evaporation. Standard photolithography and chemical etching is used to define the ZnF_2 film for planar photodiodes. After the $\text{ZnF}_2/\text{SiO}_2$ is defined, a layer of SiO_2 , borosilicate, or Al_2O_3 is deposited over the wafer surface to prevent loss of zinc and decomposition of the semiconductor surface during diffusion. The wafer is then annealed in an open tube to diffuse in the Zn.

Experimental

The $\langle 100 \rangle$ -oriented n-InP crystals used in this work were LEC grown. The crystals were chemical-mechanically polished to a mirror-like finish using a 1% Br_2 in CH_3OH solution. The carrier concentration ($N_D - N_A$) was in the range of $2\text{-}5 \times 10^{15} \text{ cm}^{-3}$. The $\text{In}_{0.53}\text{Ga}_{0.47}\text{As}$ samples with $(N_D - N_A) \approx 1 \times 10^{16} \text{ cm}^{-3}$ were undoped n-type LPE layers ($\sim 4 \mu\text{m}$ thick) grown lattice matched to InP substrates.

Prior to the deposition of the films, the samples were degreased in chloroform, acetone, and methanol. They were then etched in a 1:1 solution of hydrofluoric acid (HF) in deionized water for 1 min, thoroughly rinsed in deionized water, and blown dry with nitrogen gas. The sample was then immediately transferred to an E-beam evaporator. To form full surface p-n junctions 150Å of ZnF_2 followed by 600Å of SiO_2 or borosilicate film (BSG), or 3000Å of Al_2O_3 film were deposited at $\sim 2 \times 10^{-6}$ torr pressure. The ZnF_2 film acts as a source of the Zn dopant. The encapsulant, SiO_2 , BSG, or Al_2O_3 , prevents any thermal degradation of the sample surface during diffusion and also protects the ZnF_2 film (which is slightly

*Electrochemical Society Active Member.

Key words: diffusion, p-n junctions, III-V compounds.

hygroscopic) from atmospheric humidity, thus allowing storage of wafers for long periods of time ($>24\text{h}$).

To demonstrate the ability to form localized p-n junctions 75 μm diam islands of the ZnF_2 encapsulant film were defined using conventional photolithographic techniques. The unwanted portions of ZnF_2 and the encapsulant were then removed using a CF_4 plasma and a buffered HF solution etch, respectively. A final protective layer of 1.2 kÅ thick SiO_2 or BSG film was then E-beam evaporated over the full surface of the wafer.

The samples were then annealed in an air-ambient, open-tube three-zone furnace at temperatures and durations which were chosen to yield a junction depth of $x_j \approx 2 \mu\text{m}$. As determined from C-V probing of the epitaxial layers, this junction depth is sufficient to fully deplete the remaining n-InGaAs layer in the bias voltage of -10V . The conditions for obtaining such junction depths were inferred from the diffusion profiles of active Zn in a number of InP and $\text{In}_{0.53}\text{Ga}_{0.47}\text{As}$ samples (of varying carrier concentrations $N_D - N_A$), diffused for various times at several temperatures. The diffusion temperatures used for InP and $\text{In}_{0.53}\text{Ga}_{0.47}\text{As}$ were 500° and 550°C , respectively. For all samples the junction depth x_j was found to vary with \sqrt{t} , where t is the diffusion time. Junction depth was measured on (110) surfaces of cleaved samples after staining with an aqueous solution of $\text{K}_3\text{Fe}(\text{CN})_6$ and KOH under illumination.

Upon completion of the diffusion process, the sample was quenched to room temperature in about 1 min by simply removing it from the furnace. The samples were then etched in concentrated HF to remove the films. The cleaned samples did not show any surface deterioration. Unpassivated planar devices thus formed were ready for metallization and electrical measurements. For purposes of comparison, mesa-type diodes were also fabricated from each wafer using conventional photolithographic and etching techniques.

Results and Discussion

Measurements of dark current (I_d) and capacitance (C) as a function of voltage were performed on 10-15 devices from four InP and $\text{In}_{0.53}\text{Ga}_{0.47}\text{As}$ wafers. Figure 1 shows the room temperature reverse I-V characteristics of some typical planar InP diodes. The diodes typically exhibited

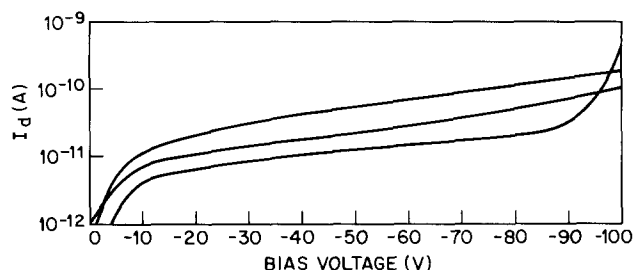


Fig. 1. Dark current-voltage characteristics of planar InP photodiodes at room temperature.

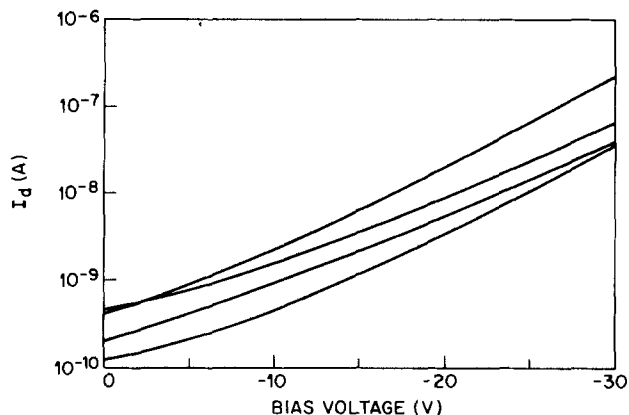


Fig. 2. Dark current-voltage characteristics of planar $\text{In}_{0.53}\text{Ga}_{0.47}\text{As}$ photodiodes at room temperature.

dark currents ranging from $\sim 3 \times 10^{-11}$ to 10^{-8} A at -10 V with very sharp breakdown voltages, V_b , varying between 70 and 150 V. The measurements repeated after a 30 s etch in 0.05% Br_2 in methanol solution showed slightly improved values of I_d and V_b , which now ranged from 5×10^{-12} to 10^{-8} A and 100 to 200 V, respectively. The capacitance for InP diodes was found to be < 0.1 pF at 0 V. (This was the lowest capacitance measurable in our measuring setup). The mesa-type devices yielded comparable electrical characteristics.

In Fig. 2, the dark current as a function of the reverse-bias voltage is shown for a number of planar $\text{In}_{0.53}\text{Ga}_{0.47}\text{As}$ diodes. The leakage currents in these devices ranged from $\sim 3 \times 10^{-10}$ to 3×10^{-8} A at a 10 V reverse bias with soft breakdowns ranging from 45 to 70 V. The capacitance values were 0.7 and 0.2 pF at 0 and 10 V, respectively. Similar I-V and C-V characteristics were obtained with mesa devices formed on the same wafer. It was confirmed by the C-V data that the background doping density of the $\text{In}_{0.53}\text{Ga}_{0.47}\text{As}$ wafer was indeed in the 10^{16} cm^{-3} range. Improved capacitance and possibly higher breakdown voltages can be expected from wafers with $N_b - N_A \leq 5 \times 10^{15} \text{ cm}^{-3}$.

The electrical performance of these p-n junctions formed by ZnF_2 diffusion is comparable state-of-the-art devices fabricated by other techniques (4, 8-10).

Summary and Conclusions

We have developed a novel process for p-n junction formation in the InP/InGaAs material system which overcomes some of the difficulties encountered in the more commonly employed p-n junction formation techniques, such as sealed-tube gas-phase diffusion, ion implantation, and diffusions from CVD-deposited or spun-on doped films. We have demonstrated the high selectivity and the simplicity with which the p-n junctions could be reproducibly formed. The devices thus fabricated exhibited state-of-the-art electrical performance (4, 8-10). Finally, the process shows the potential to be applicable to other material systems in which localized and reproducible p-n junctions are to be formed.

Acknowledgments

We are indebted to W. A. Bonner for supplying some of the InP substrates and D. D. Roccasceca for LPE $\text{In}_{0.53}\text{Ga}_{0.47}\text{As}$. Thanks are due to P. B. O'Connor and W. H. Grodkiewicz for borosilicate material. We appreciate the help of H. Wade in making electrical measurements.

Manuscript submitted Nov. 29, 1983; revised manuscript received Feb. 7, 1984.

AT&T Bell Laboratories assisted in meeting the publication costs of this article.

REFERENCES

1. Y. Matsushima, K. Sakai, S. Akiba, and T. Yamamoto, *Appl. Phys. Lett.*, **35**, 466 (1979).
2. N. Susa, H. Kanbe, H. Ando, and Y. Ohmachi, *Jpn. J. Appl. Phys.*, **19**, L675 (1980).
3. N. Susa, Y. Yamauchi, H. Ando, and H. Kanbe, *IEEE Electron Dev. Lett.*, **ed1-1**, 55 (1980).
4. S. R. Forrest, I. Camlibel, O. K. Kim, H. J. Stocker, and J. R. Zuber, *ibid.*, **ed1-2**, 283 (1981).
5. L. Vescan, J. Selder, H. Kräutle, W. Kutt, and H. Beneking, *Electron Lett.*, **18**, 533 (1982).
6. J. R. Shealy, B. J. Baliga, and S. K. Ghandi, *IEEE Electron Dev. Lett.*, **ed1-1**, 119 (1980).
7. R. J. Field and S. K. Ghandi, *This Journal*, **129**, 1567 (1982).
8. S. Aytac and A. Schlachetzki, *Solid-State Electron.*, **24**, 57 (1981).
9. L. Vescan, J. Selders, M. Maier, H. Kräutle, and H. Beneking, Paper 33 presented at the Second NATO Workshop on Materials Aspects of InP, Lancaster, England (1983).
10. P. P. Webb and G. H. Olssen, *IEEE Trans. Electron. Dev.*, **ed-30**, 395 (1983).

Stabilization of Mo-Gate MOS Structures Using H_2 Doping in Mo and High Temperature Forming Gas Annealing

Shin-ichi Ohfuji and Noboru Shiono

Nippon Telegraph and Telephone Public Corporation, Atsugi Electrical Communication Laboratory, 1839, Ono, Atsugi-shi, Kanagawa Prefecture 243-01, Japan

ABSTRACT

Mobile ionic charge-related instability in Mo-gate MOS devices has been successfully prevented by high temperature forming gas annealing ($\text{H}_2/\text{N}_2 = 1/10$) above 900°C , combined with H_2 -doped Mo or H_2 -doped Ta-Mo alloy gate electrodes. H_2 -doped films were deposited by RF sputtering in a mixed H_2 and Ar ambient. It is concluded that sodium diffusion from Mo-gate metal into the gate SiO_2 is prevented by forming gas annealing above 900°C , and that its effect is enhanced by H_2 -doping in Mo films. It is also revealed that, when Ta-Mo (7 atom percent Ta) alloy gate structures are used, high temperature forming gas annealing does not degrade other MOS characteristics and maintains good stability under short-term bias-temperature stress aging.

A refractory metal gate, in place of a conventional polysilicon gate, has been studied extensively in order to improve the gate-level conductivity for realizing high density and high performance MOS LSI's (1). However,

Key words: metals, integrated circuits, contamination, sputtering.

one of the problems in refractory metal-gate MOS structures is poor reliability, compared with polysilicon-gate MOS structures. The reasons are that pure refractory metal materials are difficult to prepare in the present technology, especially for sputtering target materials, and refractory metals do not have self-passivation effects like phosphorus-doped polysilicon on ionic contamination.

Several approaches have been investigated to avoid ionic contamination for metal-gate MOS structures. Phosphosilicate glass (PSG) coating on top of the thermally grown SiO_2 layer (2) or gate oxide grown in a dilute mixture of HCl and dry O_2 at high temperature ($>1100^\circ\text{C}$) (3) are widely used. However, when these methods are used, it is not easy to form a thin gate oxide less than 50 nm thick, which is the typical gate-oxide thickness for high density MOS devices, with good controllability. Another approach is CVD PSG deposition on patterned-Mo films followed by high temperature annealing (4), which tends to getter mobile ions along the perimeter of Mo-gate electrodes. However, this method is not effective for large area gate MOS structures. Recently, forming gas annealing after Mo patterning has been reported to be effective in reducing ionic contamination (5, 6). However, this method is not so effective when contamination level is high. The mechanism is also not clear yet.

In this work, the effects of high temperature forming gas annealing for intentionally H_2 -doped Mo and Ta-Mo alloy films have been examined to reduce ionic contamination in the gate SiO_2 . H_2 doping in the films was realized by reactive sputtering in a mixed H_2 and Ar ambient. The authors have found that high temperature forming gas annealing above 900°C for H_2 -doped Mo, especially H_2 -doped Ta-Mo gate structures, is very effective to reduce ionic contamination in the gate SiO_2 . Also, the basic mechanism of this effect was analyzed, and the stability of these structures was examined through short-term bias-temperature stress aging.

Experimental

Mo-gate MOS capacitors were fabricated on p-type (100) silicon wafers with 4-6 Ωcm resistivity. Thin gate SiO_2 was grown in a dry O_2 ambient at 950°C to a 40 nm thickness. Mo film was deposited by an RF planar magnetron sputtering equipment in Ar gas at 1 Pa pressure. H_2 -doped Mo films were prepared by sputtering in a mixed H_2 and Ar ambient, with varying H_2 partial pressure. Ta-Mo alloy films were deposited by cosputtering using two targets, Mo and Ta. Ta concentration in the films was 7 atom percent (a/o), to maintain high conductivity ($<3 \times 10^{-5} \Omega\text{cm}$, after 1000°C annealing) and process compatibility of Mo gate process. H_2 -doped Ta-Mo films were prepared in a mixed H_2 and Ar ambient, like H_2 -doped Mo films. Gate metal film thickness was 0.33 μm for all samples. Purity for both Mo and Ta targets was 99.95%.

MOS gate electrodes of $500 \times 500 \mu\text{m}$ were defined by conventional photolithography and chemical etching using $\text{H}_3\text{PO}_4\text{-HNO}_3$ solution. After Mo patterning, annealing was carried out in N_2 ambient or forming gas ambient ($\text{H}_2/\text{N}_2 = 1/10$) at various temperatures between 600° and 1000°C for 30 min. Such high temperature annealing is necessary to activate implanted impurity ions. For some samples, forming gas annealing at 450°C for 30 min was performed to reduce the fixed oxide-charge density and interface trap density at the Si-SiO_2 interface.

Mobile ionic charge density in the MOS structures was measured by triangular voltage sweep method (TVS) (7) with a 50 mV/s ramp rate at 270°C . Depth distribution profiles for sodium in the MOS structures were measured directly by SIMS (CAMECA, IMS-3F). Bias-temperature (BT) stress aging was made in order to examine slow trapping instability, as well as mobile ionic charge-related flatband voltage instability.

Results and Discussion

Effects of annealing ambient and temperature.—Figure 1 shows mobile ionic charge density N_m vs. annealing temperature as a function of annealing ambient for various gate-metal structures. High temperature forming gas annealing above 900°C is found to be effective for reducing mobile ionic charge density, especially for H_2 -doped Mo and H_2 -doped Ta-Mo gate structures. However, mobile ionic charge density increases drastically after N_2 annealing for all samples, irrespective of gate metal structures.

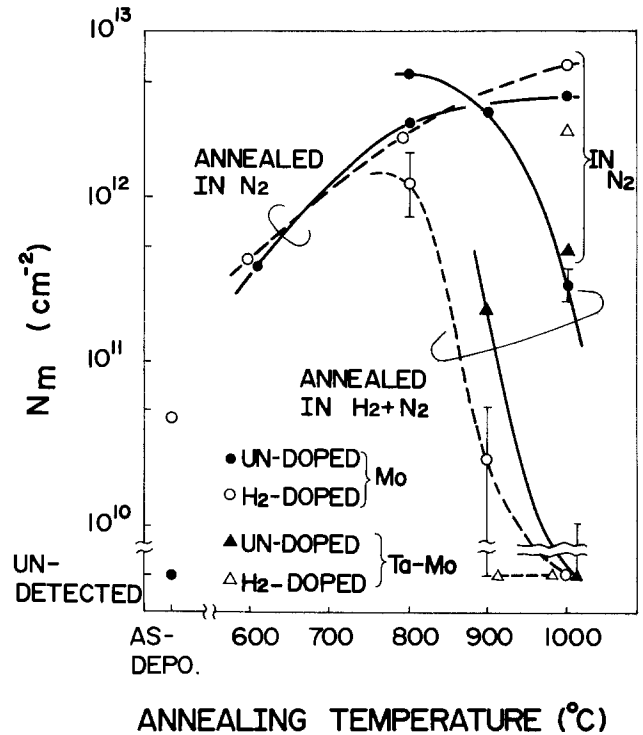


Fig. 1. Mobile ionic charge density N_m vs. annealing temperature in N_2 or forming gas ($\text{H}_2 + \text{N}_2$) for various gate metal structures.

The effect of H_2 -doping in the Mo films on the reduction of mobile ionic charge density N_m is shown in Fig. 2. In this figure, N_m vs. H_2 partial pressure in a sputtering gas ambient is shown as a function of annealing ambient at 1000°C . The N_m for as-deposited samples increases with H_2 partial pressure. The reason for this increase is not clearly understood. After forming gas annealing, mobile ionic charge density decreases below 10^{10} cm^{-2} , when H_2 partial pressure is higher than $8 \times 10^{-2} \text{ Pa}$. This indicates that H_2 doping in the Mo films enhances the reduction effect on mobile ionic charge density in forming gas annealing, although, in N_2 annealing, H_2 -doping is not effective.

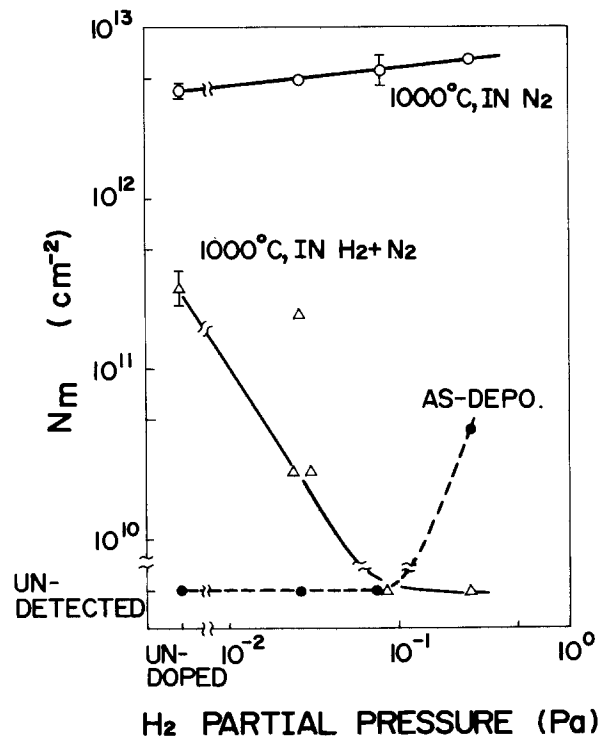


Fig. 2. Mobile ionic charge density N_m vs. H_2 partial pressure in sputtering gas ambient for as-deposited and annealed samples.

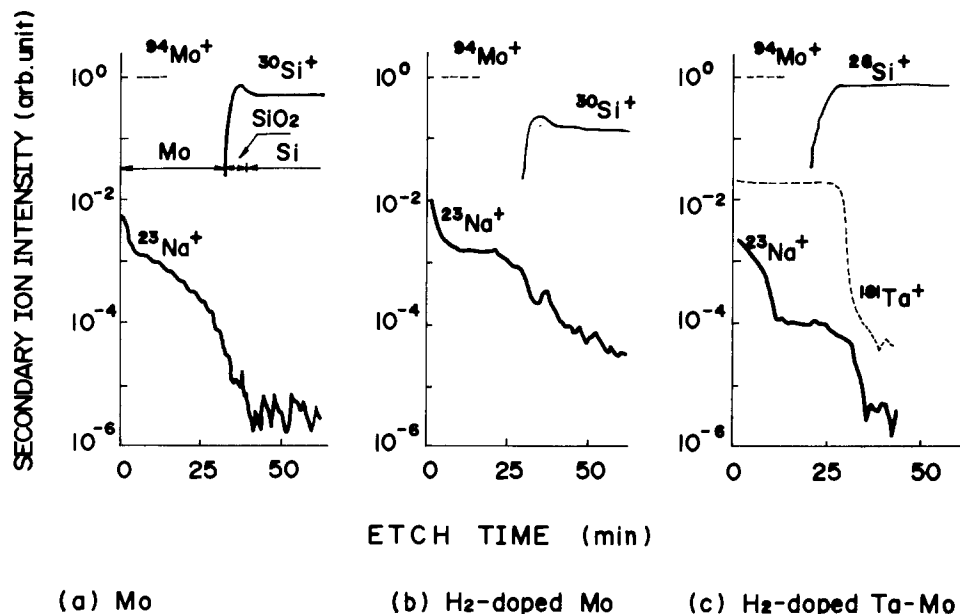


Fig. 3. Depth relative distribution profiles for sodium and silicon obtained by SIMS in as-deposited gate metal (0.3 μm)/gate SiO_2 (40 nm)/Si substrate structures. a: with Mo gate. b: with H_2 -doped Mo gate. c: with H_2 -doped Ta-Mo gate.

In the following sections, H_2 -doped Mo and H_2 -doped Ta-Mo films represent the films deposited in an H_2 partial pressure of 3×10^{-1} Pa.

Sodium concentration profiles in MOS structures.—A possible reduction mechanism for mobile ion contamination under high temperature forming gas annealing is sodium gettering in the SiO_2 , like PSG-coated gate SiO_2 or HCl oxides. To clarify this effect, sodium distribution profiles in the MOS structures were measured by SIMS. Figures 3, 4, and 5 show depth relative distribution profiles of sodium and silicon for as-deposited, annealed in N_2 , and annealed in forming gas at 1000°C samples, respectively. Ion intensities were normalized by $^{94}\text{Mo}^+$ ion intensities in gate electrodes. For as-deposited samples with Mo gate (Fig. 3a) and H_2 -doped Ta-Mo gate (Fig. 3c), sodium is detected only in the gate electrodes. The $^{23}\text{Na}^+$ ion intensity in the gate electrodes corresponds to the sodium concentration less than 1 ppm, which is quantitatively measured by a flameless atomic absorption analysis. At the metal- SiO_2 interface region, $^{23}\text{Na}^+$ ion intensity decreases rapidly. However, for as-deposited samples with H_2 -doped Mo gate (Fig. 3b), a slight increase in $^{23}\text{Na}^+$ intensity in the SiO_2 region is observed, which corresponds to the small amount of mobile ionic charge density measured by TVS, as shown in Fig. 1. In the case of N_2 annealing (Fig. 4), a clearly identified $^{23}\text{Na}^+$ intensity

peak in the SiO_2 region is detected for all samples. This indicates that sodium ions in the gate electrodes can diffuse into the gate SiO_2 layer during N_2 annealing and are responsible for the large amount of mobile ionic charge densities observed in the actual MOS structures. In the forming gas annealing (Fig. 5), the $^{23}\text{Na}^+$ intensity peak in the SiO_2 region almost disappears, and its intensity decreases abruptly, as it does for as-deposited samples. The decrease in $^{23}\text{Na}^+$ ion intensity in the SiO_2 region is drastic for H_2 -doped Mo and H_2 -doped Ta-Mo gate structures.

Figure 6 shows the correlation between ion intensity ratio $I(^{23}\text{Na}^+)/I(^{30}\text{Si}^+)$ in the gate SiO_2 region and the mobile ionic charge density N_m measured by TVS for Mo gate and H_2 -doped Mo gate capacitors. Here, $^{30}\text{Si}^+$ ion intensity in the gate SiO_2 region was chosen as the standard ion intensity. This result indicates that the SIMS-measured $^{23}\text{Na}^+$ ion intensities in the gate SiO_2 region correspond closely with the mobile ionic charge density measured by TVS.

These analytical results indicate that sodium diffusion from Mo films into the gate SiO_2 layer is enhanced by high temperature annealing in N_2 , whereas its diffusion is very slow or prevented in forming gas annealing above 900°C . The preventing effect under forming gas annealing is more apparent in H_2 -doped Mo and H_2 -doped Ta-Mo gate structures. This suggests that the H_2 doping into the Mo enhances the preventing effect on sodium diffusion

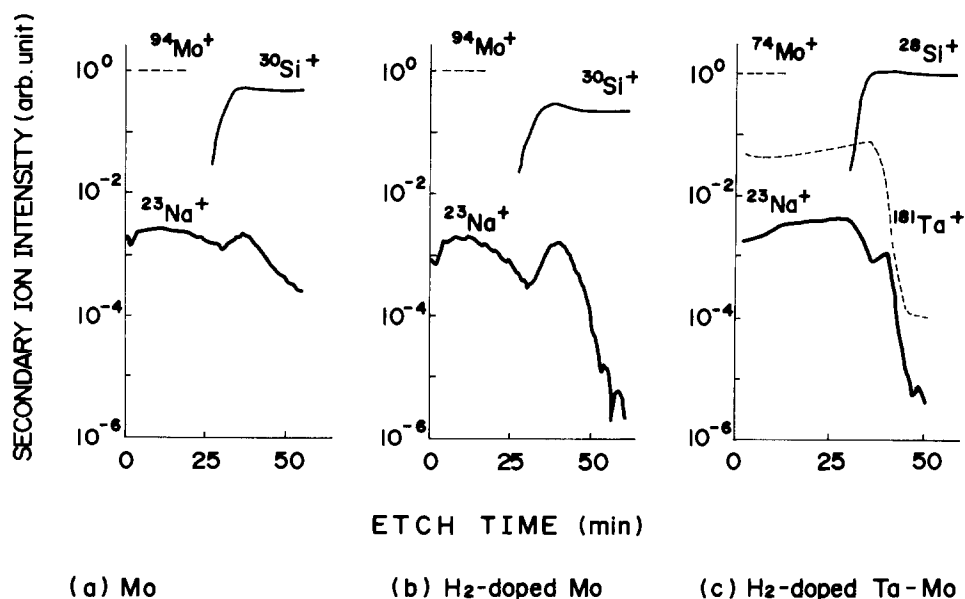


Fig. 4. Depth relative distribution profiles for sodium and silicon in 1000°C , N_2 -annealed MOS structures. a: with Mo gate. b: with H_2 -doped Mo gate. c: with H_2 -doped Ta-Mo gate.

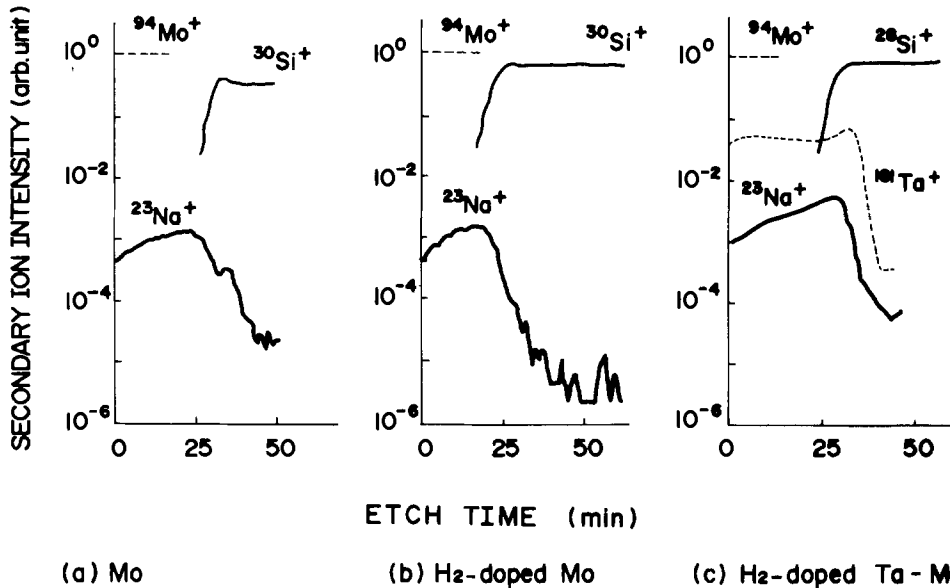


Fig. 5. Depth relative distribution profiles for sodium and silicon in 1000°C, forming gas annealed MOS structures. a: with Mo gate. b: with H₂-doped Mo gate. c: with H₂-doped Ta-Mo gate.

into the gate SiO₂ layer. Since Ta film has about 10⁴ times higher hydrogen absorption property (8), compared to Mo film, H₂-doped Ta-Mo film may contain a larger amount of hydrogen atoms in the film than H₂-doped Mo film. This explains that H₂-doped Ta-Mo gate structure has a superior ability to prevent sodium diffusion into the gate SiO₂.

It has been known that sodium diffusion in the SiO₂ is very rapid. The diffusion constant is $D = 5 \exp(-1.5(eV)/kT) \text{ cm}^2/\text{s}$ (9). In fact, rapid diffusion is observed during N₂ annealing. However, sodium diffusion is prevented in forming gas annealing above 900°C, as described above. This leads to a conclusion that the sodium-diffusion constant decreases drastically in forming gas ambient above 900°C, although the physical origin remains uncertain.

Leakage current characteristics.—Although high temperature forming gas annealing is found to be very effective for reducing mobile ion contamination in the gate SiO₂, such high temperature annealing may degrade other MOS characteristics, such as leakage currents and stability at the Si-SiO₂ interface. MOS leakage current characteristics were measured, and short-term stability under BT stress aging was examined.

Figure 7 shows leakage current vs. applied field characteristics for MOS capacitors with various gate metal struc-

tures annealed in forming gas at 1000°C. This shows that high temperature forming gas annealing results in significant leakage current increases and decrease in breakdown field for H₂-doped Mo-gate MOS capacitors. A slight leakage current increase is also observed for Mo-gate MOS capacitors. Ta-Mo and H₂-doped Ta-Mo gate MOS capacitors, however, can maintain low leakage current without breakdown-field degradation.

The leakage current increase due to forming gas annealing is probably attributed to local oxide defect creation caused by molybdenum silicide formation at the Mo-SiO₂ interface with the deoxidizing reaction of SiO₂. However, a stable Ta-Mo-SiO₂ interface, due to the presence of tantalum oxides at the interface, probably prevents interface reaction during high temperature forming gas annealing, for Ta-Mo and H₂-doped Ta-Mo gate structures.

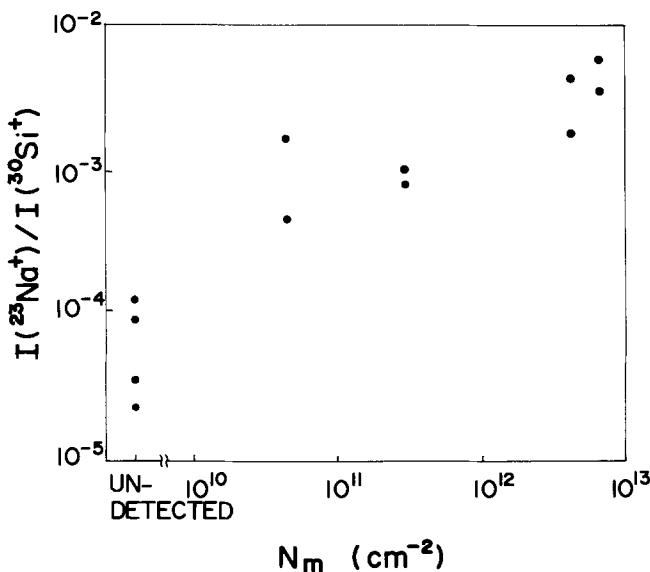


Fig. 6. SIMS-measured ion intensity ratio $I(^{23}\text{Na}^+)/I(^{30}\text{Si}^+)$ vs. TVS-measured mobile ionic charge density N_m for Mo-gate and H₂-doped Mo-gate capacitors.

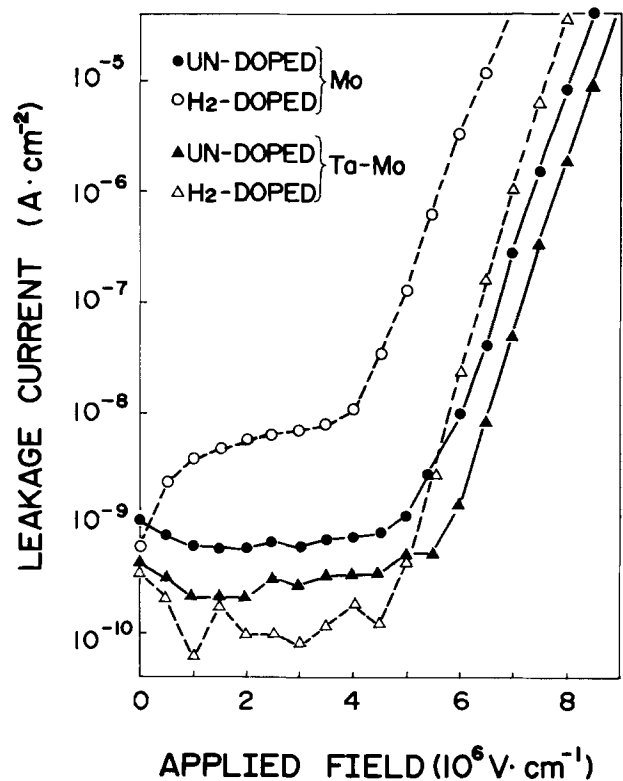


Fig. 7. Variation in leakage current as a function of applied field for Mo-gate and Ta-Mo gate MOS capacitors. Samples were annealed in forming gas at 1000°C for 30 min.

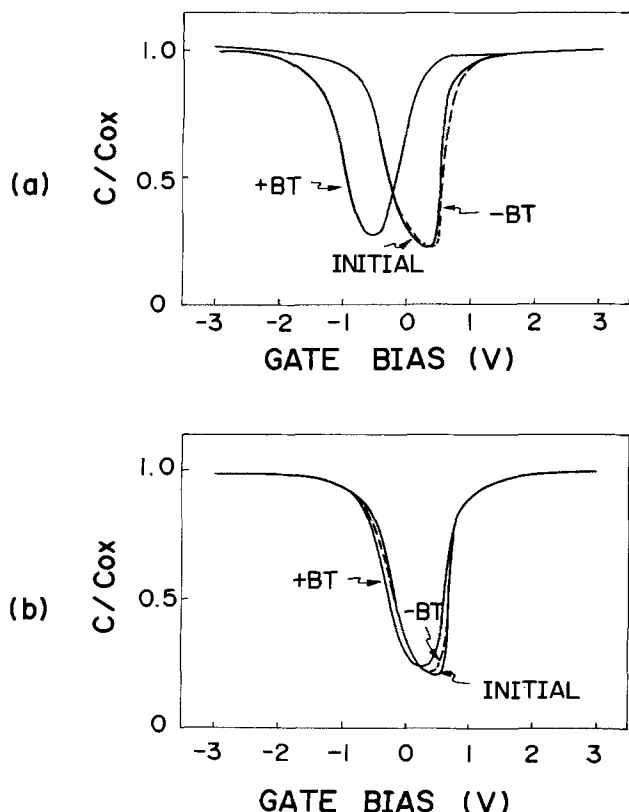


Fig. 8. Typical changes in quasistatic C-V characteristics under positive and negative BT stress aging. a (top): for Mo-gate MOS capacitors. b (bottom): for H₂-doped Ta-Mo gate MOS capacitors.

Short-term stability at Si-SiO₂ interface.—Short-term positive and negative bias-temperature (BT) stress aging was made for H₂-doped Mo and H₂-doped Ta-Mo gate structures annealed in forming gas at 1000°C. BT stress conditions were ± 5 V and ± 10 V gate bias at 270°C for 30 min. Under negative BT, the flatband voltage (V_{FB}) shift was small, less than 0.1V for all samples. This indicates that slow trapping instability is negligible. Under positive BT, a negative V_{FB} shift was measured within 0.1V, which was almost the expected shift from TVS measurement. From this result, low mobile ionic charge density is confirmed.

In addition to the V_{FB} shift, interface trap generation was estimated by quasistatic C-V measurement. Figure 8 shows typical changes in quasistatic C-V characteristics under positive and negative BT stress aging for (a) Mo gate and (b) H₂-doped Ta-Mo gate MOS capacitors annealed in forming gas at 1000°C. Here, for H₂-doped Mo gate structures, the quasistatic C-V curve could not be obtained because of large leakage current, as shown in Fig. 7. Interface trap density D_{it} at midgap is less than 2×10^{10} cm⁻² eV⁻¹ for all samples in the initial state, i.e., the as-made state. Under negative BT, a negligible amount of D_{it} generation is observed in both gate structures. However,

a slightly large D_{it} , about 5×10^{10} cm⁻² eV⁻¹ at midgap, is generated for Mo-gate structures associated with negative V_{FB} shift under positive BT. It is also noticeable that D_{it} increases mainly from midgap toward the conduction band edge for Mo-gate structure, which is extracted from large distortion of the C-V curve from depletion to inversion region, as shown in Fig. 8a. For H₂-doped Ta-Mo gate structures (Fig. 8b), the C-V curve distortion is small. These results show that high temperature forming gas annealing does not degrade the Si-SiO₂ interface stability for H₂-doped Ta-Mo gate MOS structures.

Conclusion

High temperature forming gas annealing above 900°C was found to be very effective for reducing mobile ionic charge density for Mo-gate MOS structures. This effect is enhanced by H₂ doping in the films in the deposition process. Depth distribution profiles for sodium in the gate SiO₂ layer, analyzed by SIMS, lead to a conclusion that high temperature forming gas annealing prevents sodium diffusion from Mo-gate metal layer into the gate SiO₂, although the physical origin of this effect remains uncertain. A disadvantage of high temperature forming gas annealing is leakage-current increase in the MOS structures. However, an addition of several percent Ta in Mo films can prevent the leakage current increase and assure good stability at the Si-SiO₂ interface under BT stress aging. The H₂-doped Ta-Mo gate MOS structure, combined with high temperature forming gas annealing above 900°C, is very promising as regards highly reliable refractory metal-gate MOS devices.

Acknowledgments

The authors wish to thank T. Matsumoto and C. Hashimoto for their advice and encouragement. They also would like to thank N. Honma for quantitative analysis, T. Amazawa for allowing the use of his TVS measurement system, and I. Kawashima for SIMS work.

Manuscript submitted Aug. 15, 1983; revised manuscript received Feb. 24, 1984.

Nippon Telegraph and Telephone Public Corporation assisted in meeting the publication costs of this article.

REFERENCES

1. T. Mano, K. Takeya, T. Watanabe, N. Ieda, K. Kiuchi, E. Arai, T. Ogawa, and K. Hirata, *IEEE J. Solid-State Circuits*, **sc-15**, 865 (1980).
2. D. R. Kerr, J. S. Logan, P. J. Burkhardt, and W. A. Pliskin, *IBM J. Res. Dev.*, **8**, 376 (1964).
3. R. J. Kriegler, Y. C. Cheng, and D. R. Colton, *This Journal*, **119**, 388 (1972).
4. T. Nozaki and H. Okabayashi, *ibid.*, **128**, 175 (1981).
5. H. Ishikawa, M. Yamamoto, H. Tokunaga, N. Toyokura, F. Yanagawa, K. Kiuchi, and M. Kondo, *IEEE Trans. Electron. Dev.*, **ed-27**, 1586 (1980).
6. F. Yanagawa, K. Kiuchi, T. Hosoya, T. Tsuchiya, T. Amazawa, and T. Mano, *ibid.*, **ed-27**, 1602 (1980).
7. N. J. Chou, *This Journal*, **118**, 601 (1971).
8. For a review of the subject, see T. Schober and H. Wenzl, "Hydrogen in Metals II," p. 11, G. Alefeld and J. Völkl, Editors, Springer-Verlag, Berlin (1978).
9. H. F. Wolf, "Semiconductors," p. 363, Wiley-Interscience, New York (1971).

Structural Perfection Testing of Films and Wafers by Means of Optical Scanner

E. F. Steigmeier and H. Auderset

Laboratories RCA Limited, CH-8048 Zurich, Switzerland

ABSTRACT

An alternative use of an optical scanner is presented for rapid structural perfection testing of films and wafers. Specific examples are given: (i) for silicon-on-sapphire quality, (ii) for structural perfection of low pressure chemical vapor deposited amorphous silicon, and (iii) for the distribution of precipitated oxygen in silicon wafers treated for internal gettering. Further, in phase transformable materials, the method permits the determination of the depositional phase (amorphous or crystalline) after film growth and after annealing.

In a previous paper, we reported on a laser scanner system for dust and defect detection on silicon wafers, thin films, and other surfaces (1).¹ The present work deals with an alternative and novel use of the above instrument, for testing the structural perfection of various materials and assessment of thin film quality (2). Specifically, we will describe the testing of silicon-on-sapphire (SOS) wafers, the qualification of low pressure chemical vapor deposited (LPCVD) amorphous silicon layers, and other materials. In addition to determining the structural quality of crystalline or amorphous material, a rapid acceptability characterization of phase-transformable material can be performed, *i.e.*, of a material which in a certain process can be deposited in either the amorphous or the crystalline phase, depending on the deposition conditions. This is exemplified for the case of as-deposited amorphous or crystalline LPCVD silicon. Moreover, the laser scanner system is capable of determining whether the film of subsequently annealed and thus crystallized material has resulted from an as-deposited amorphous layer, or from an as-deposited crystalline layer; this feature is important because silicon recrystallized from amorphous deposited films is found to be of superior quality in terms of device performance. Finally, it is shown that the method of structural perfection testing can be used to qualify the precipitated oxygen distribution in single-crystal silicon wafers in connection with treatment for internal gettering. In summary, the alternative use of the laser scanner in the quality-control mode is shown to be very effective in different fields of applications (IC technology, solar cells, thin films, and others).

Instrumental

The laser scanner used for this study has been described in detail elsewhere (1). As shown in Fig. 1, it consists of HeCd laser light (325 or 442 nm) of about 10 mW focused onto a spinning wafer while being translated. The scattered elastic light is collected in a coaxial arrangement, detected by a fast photodiode or a photomultiplier. After suitable amplification, the electrical signal is then mapped on a storage oscilloscope, making use of the polar-to-rectangular coordinate transformation sketched in the lower part of Fig. 1. The laser wavelength of 325 or 442 nm is selected according to the desired light penetration depth or film thickness. One laser scan takes about 6s for a 3 in. wafer.

In general, every material exhibits an intrinsic elastic light scattering due to temperature or entropy fluctuations (3). In addition, extrinsic elastic scattering is produced by all effects causing local changes of the dielectric constant or refractive index. These include all kinds of structural imperfections on a microscopic scale such as strain, mosaic misorientation of the lattice, stacking

Key words: semiconductor, crystallization, CVD, integrated circuits.

¹This laser scanner system is commercially available from Fluorocarbon Process Systems, Anaheim, California 92803, and is used in many places throughout the semiconductor industry.

faults, dislocations, twinning, grain boundaries, and, of course, microscopic variation of the material, as, for example, in an agglomerate. Surface irregularities (surface roughness, scratches, etc.) also contribute to this extrinsic light scattering. For all cases of practical relevance, however, and for the light wavelengths used here, the surfaces are sufficiently smooth that the volume effects dominate over the surface effects.

For the present paper, we limit ourselves to the "quality-control mode" use of the instrument (1). In this mode, all events originating from individual defects are disregarded. Instead, one deals with the large regions in between the individual events. These regions give rise to the background scattering level originating from the bulk. This is demonstrated in Fig. 2. For a good quality wafer (Fig. 2a), the background level of a signal, as taken along the spiral path, is very low, and a large dc shift is needed for the background level to reach the writing threshold of the storage scope. For a poor quality wafer (Fig. 2b), the background level is high, and a small dc shift is needed to reach the writing level. Thus, the dc shift can be used as a direct measure of structural quality. The scanner units, measuring the dc shift, can be considered as arbitrary rel-

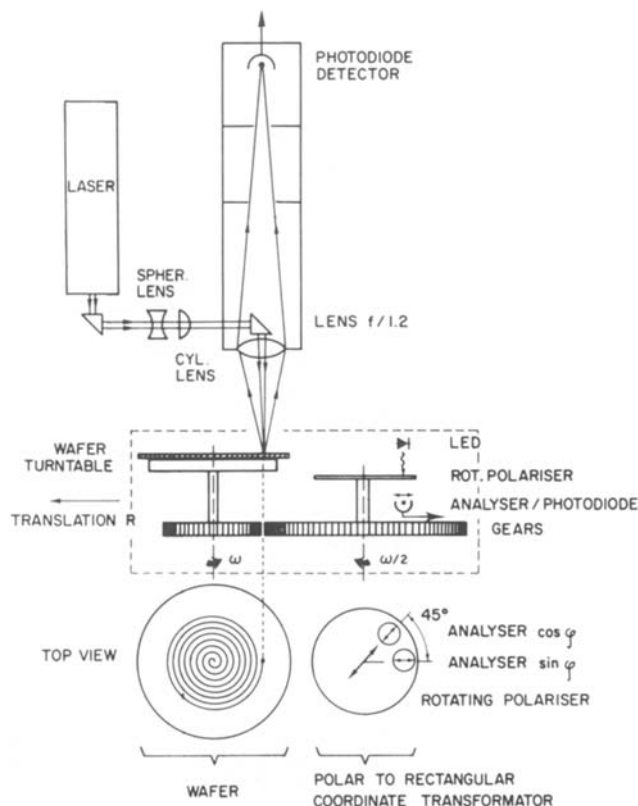


Fig. 1. Laser scanner measuring arrangement

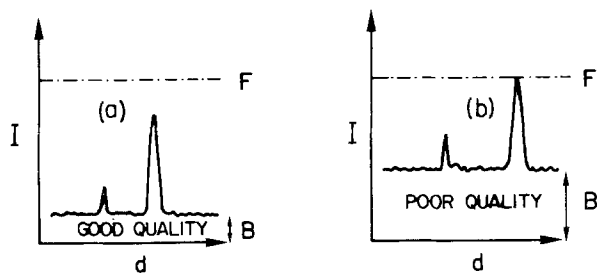


Fig. 2. Intensity signal I vs. distance d along the spiral path on the wafer. The dash-dotted line represents the writing (full) threshold F of the storage scope. (a): Good quality wafer with small background level B . (b): Poor quality level with large background level B . Individual defects or dust, which are not considered here, are indicated by the spikes.

ative units of quality, a high value indicating high quality of perfection.

It should be noted that the coaxial arrangement (Fig. 1) is of particular importance in using the quality-control mode, since it is essential for the sensitivity uniformity across a larger wafer area (1).

Results and Discussion

General.—An example for the use of the quality-control mode to qualify a wafer is presented in Fig. 3. This shows scanner mappings taken at various threshold settings for

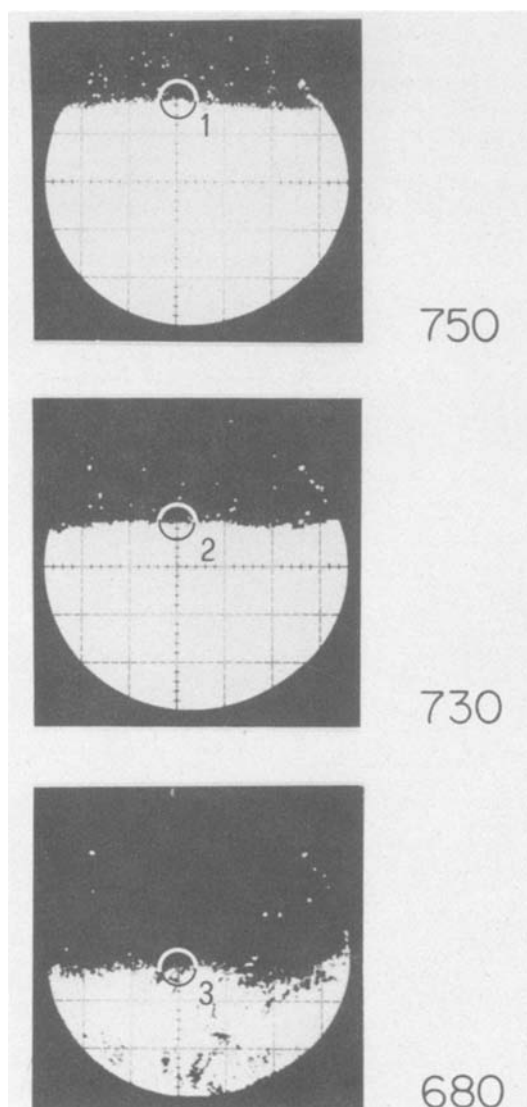


Fig. 3. Scanner mappings of a wafer exhibiting a structural quality variation along a vertical line. A (top): taken at threshold setting of 750 units. B (center): at 730 units. C (bottom): 680 units.

a wafer with a structural quality variation along a vertical line. Since the best material is found to produce full writing at the highest scanner unit setting (corresponding to largest dc shift), it is seen that point 1 is of the relative best, point 2 of medium, and point 3 of the poorest quality on this wafer.

Silicon-on-sapphire structural perfection testing.—For silicon-on-sapphire (SOS), it has been shown (4) that the crystalline perfection of the silicon layer is directly related to the final device performance. Imperfections may result (5) from the polishing quality of the sapphire substrate, from the thermal mismatch of sapphire and silicon lattice, and from details of the epitaxial deposition or growth process. It was shown (6) that the volume percentage (221) twins in the silicon layer is a good indicator of structural quality, since the microtwins represent the dominant crystallographic defect in SOS films (7). Several methods have been used (4, 8) to characterize the quality of near-surface SOS. Among them, UV reflectance measurement plays a particular role (9), since it is a most widely used simple method.² For this reason, the results of the scanner method can best be correlated (2) with the UV reflectance method, in addition to the (221) twinned density.

Figure 4 shows the result of the scanner method for SOS wafers plotted vs. UV reflectivity. The vertical scales show the scanner units, directly proportional to the dc offset, as mentioned above, for incident laser light of 325 nm. Note that a high number indicates good quality, i.e., a low elastic scattering background and vice versa. The horizontal scales give the UV reflectometer units R_{280} and R_{400} ; these units for 280 and 400 nm, respectively, represent the reflectance difference relative to the single-crystal standard. (One R_{280} unit corresponds to about 0.05% loss of absolute reflectance, and one R_{400} unit to 0.03% loss.) It is seen in Fig. 4 that the two measurements, elastic light scattering as determined by the scanner method and UV reflectivity, correlate extremely well. A typical high quality SOS wafer (category A) would be selected for a scanner threshold level of about 710 units or more.

It should be borne in mind that the light penetration depth varies considerably between 280 and 400 nm. Therefore, the UV reflectivity data plotted on the horizontal axis of Fig. 4, sample quite different near-surface regions of about 50Å for the left-hand part of Fig. 4, and of about 1000Å for the right-hand part. It is notable that the laser scanner results, sampling a surface depth of about 85Å, correlate with both of them.

Figure 5 shows the correlation of the laser scanner results with the UV reflectivity difference ΔR , defined by $R_{280} - R_{400}$, which is frequently used (9) to qualify the SOS wafers.

Also of interest, and shown in Fig. 6, is the correlation of the laser scanner units with the (221) twinning concentration as determined by x-ray (6). It is found that SOS films of category A, with a (221) twinning density of up to 4%, correspond to 710 laser scanner units and more, while films of category B, with a (221) density of 4 to 6.5%, are found between 680 and 710 laser scanner units.

To summarize the results on SOS:

1. The laser scanner used in the quality-control mode can determine the structural perfection of SOS films, in good correlation with UV reflectivity and twinning density.
2. The method permits one to continuously scan the whole SOS film and thus to provide a uniformity map of the structural perfection.
3. Due to its high speed, the optical-scanner method offers itself as an alternative for rapidly determining the structural perfection or acceptability of SOS films for device processing.

Quality characterization of amorphous silicon.—The scanner can also be used for determining the quality of

²The UV reflectometry method is presently used by all major manufacturers and users of SOS.

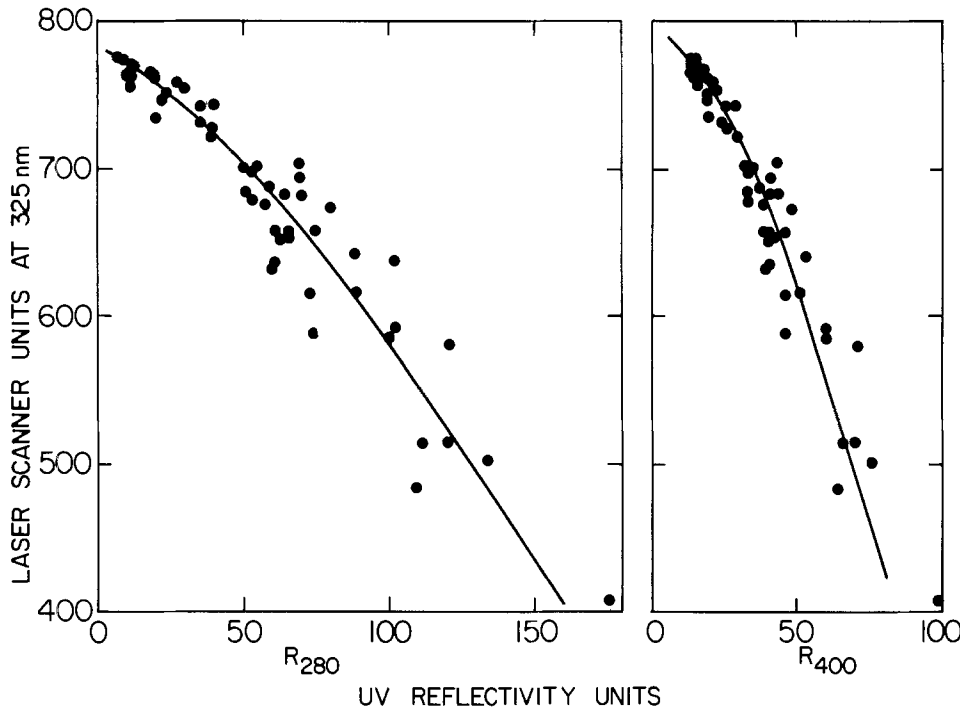


Fig. 4. Correlation between laser scanner units at 325 nm and UV reflectivity units at 280 and 400 nm, respectively, for SOS wafers of various quality.

amorphous silicon. The term “amorphous” in this context of light scattering denotes material in which the narrow crystalline Raman line of 522 cm^{-1} is completely absent in the Raman spectrum. Instead, a broad line is observed. This peaks at about 490 cm^{-1} . This is the result of breakdown of perfect lattice periodicity, which relaxes the selection rules and permits a multitude or all lattice modes to be excited by the light. It is known that in amorphous silicon some short-range order still prevails; only the long-range order is missing. In this sense, the structural perfection in amorphous silicon might be connected with the degree of spatial short-range order fluctuations. We have found that amorphous silicon produced by the different methods to obtain solar cell material, *e.g.*, evaporation, glow discharge, sputtering, LPCVD, etc., results in elastic light scattering results of the corresponding films that vary over several orders of magnitude. In addition to

the deposition method, the substrate temperature, geometry, gas species present, and other factors play an important role on the resultant structural perfection.

To demonstrate the influence of the substrate on the structural perfection of amorphous silicon, and the application of the scanner in the quality control mode, we present here some results on multilevel polysilicon depositions as relevant in the charge-coupled device (CCD) processing. As Fig. 7 shows, we have, in a controlled experiment, inspected amorphous silicon (I) as deposited on a thermally oxidized single-crystal substrate and compared it with amorphous silicon (II) as deposited on the “same” oxide, which, however, had been formed on top of a previously deposited amorphous poly-A, which subsequently had been POCl_3 doped, and annealed at 900°C . Figure 7 (middle part) shows that the scanner results

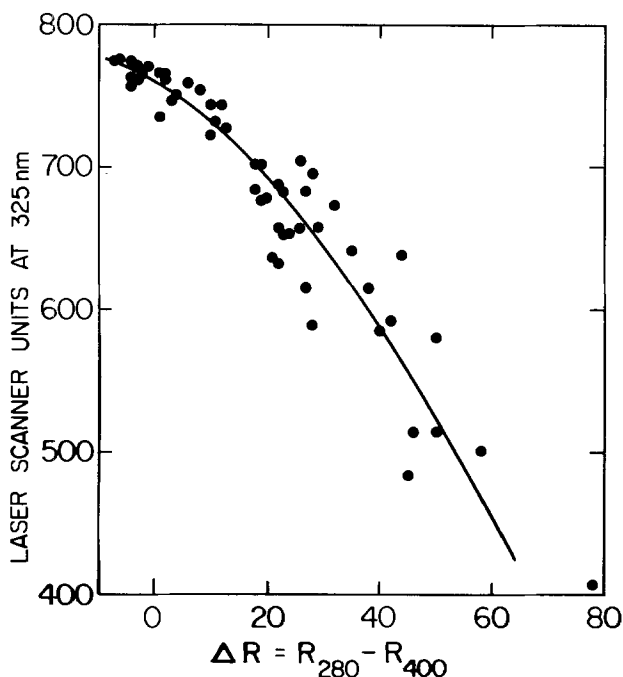


Fig. 5. Correlation between laser scanner units at 325 nm and UV reflectivity difference for SOS films.

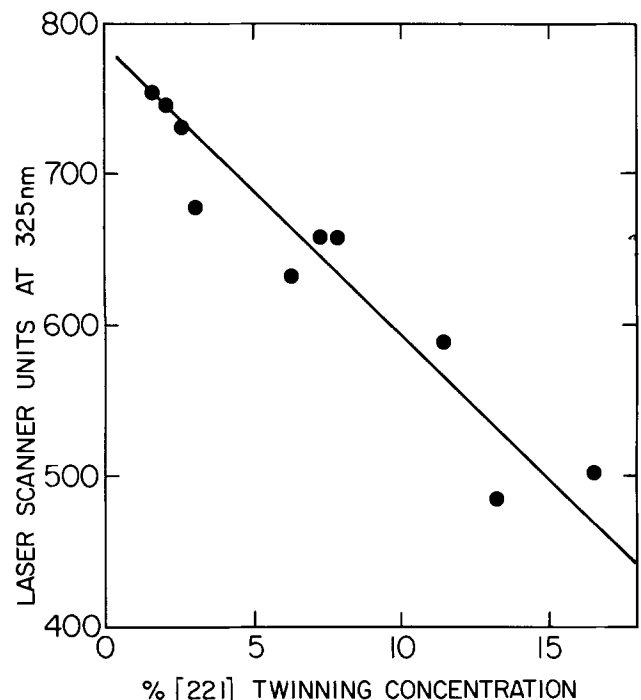


Fig. 6. Plot of laser scanner units at 325 nm vs. percent of (221) twinning concentration for SOS films.

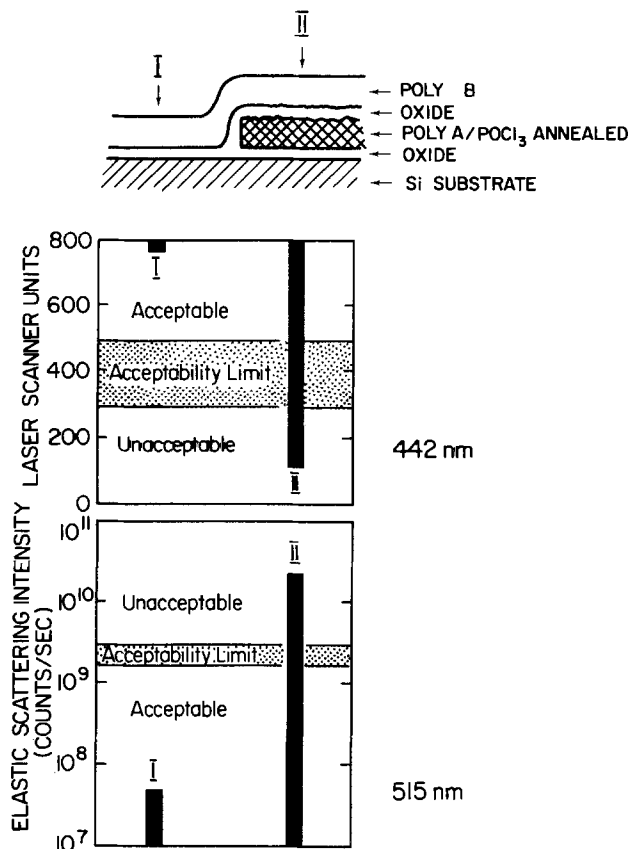


Fig. 7. Testing the structural perfection of amorphous silicon by means of laser scanner (middle part) for 10 mW (442 nm) focused onto a spot of $50 \times 220 \mu\text{m}$, and static elastic light scattering (bottom part) for 100 mW (515 nm) focused onto a spot of $40 \mu\text{m} \times 2 \text{mm}$.

show excellent structural perfection for layer I and poor structural perfection for layer II. In fact, the latter is indeed below the acceptability limit which we have established after extensive work with amorphous silicon layers. It should be emphasized that the whole poly-B layer, resulting in the two different regions I and II, was deposited in one and the same LPCVD process ($T_d = 566^\circ\text{C}$). The bottom part of Fig. 7 shows that the scanner results are confirmed by an independent measurement of the elastic light scattering with a static method: again, layer I is found to be very good and layer II to be very poor and unacceptable.

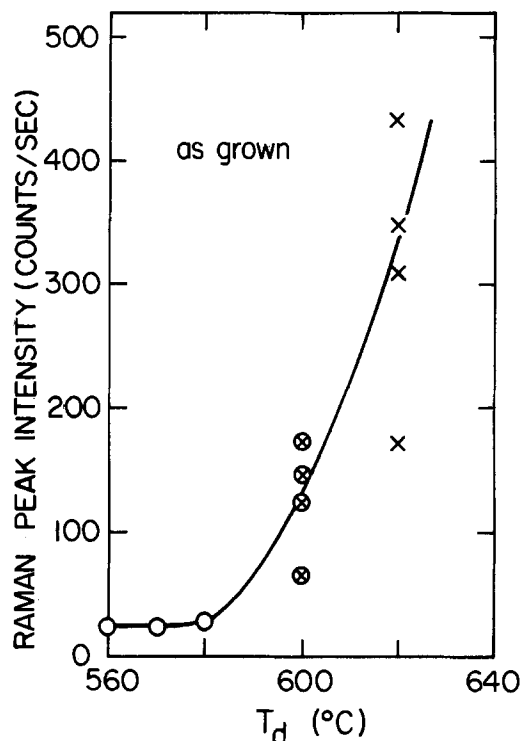


Fig. 9. Raman peak intensity for as-grown LPCVD silicon layers vs. deposition temperature. ○: amorphous. x: crystalline. ⊗: mixed.

In order to understand the exact nature of the difference between these two layers, we had them analyzed by cross-sectional transmission electron microscopy (TEM). The results are given in Fig. 8 (courtesy of J. McGinn). It is seen that both layers are indeed amorphous for TEM, at least for the scale of the light penetration depth (for $\lambda = 442 \text{ nm}$) of about 1000\AA . There is one striking difference between them, however: for layer I, the oxide top surface is very smooth (arrow a), while for layer II, the oxide top surface is rather rough (arrow b). We speculate that it is this rough surface II which has influenced the degree of spatial short-range order fluctuations, and thus the local refractive index, and the light scattering a few thousand angstroms further up in the amorphous silicon layer II. In any case, the rough oxide-to-silicon interfaces of region II are very undesirable for many devices, because they might induce electrical breakdown at much lower electrical fields than desired. Such unwanted conditions can be

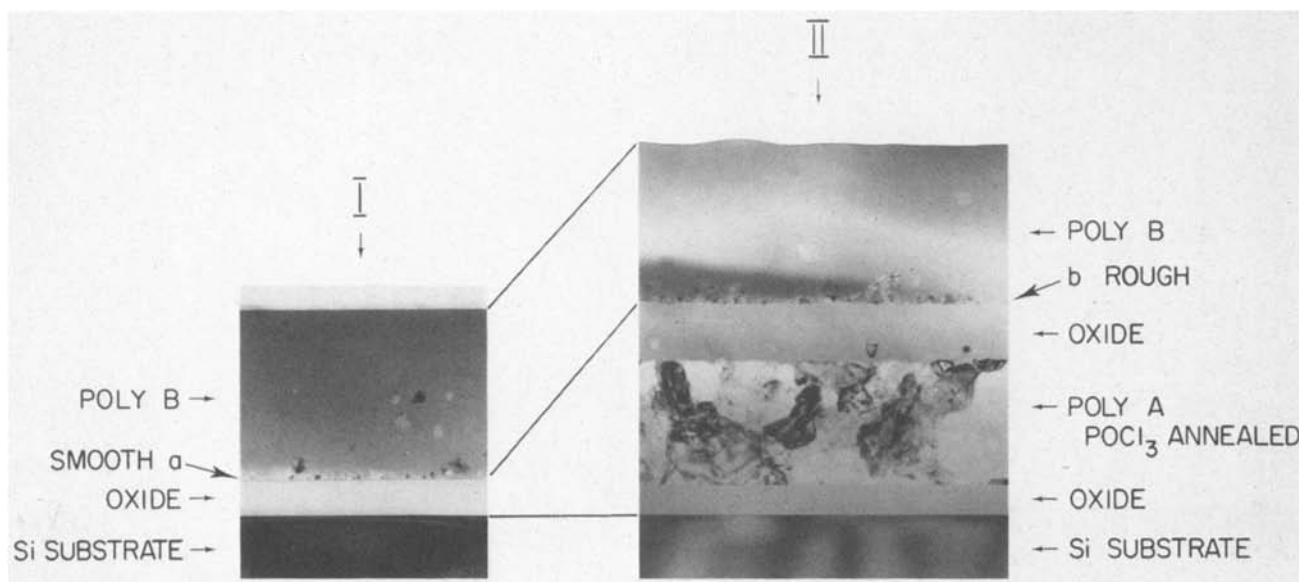


Fig. 8. Transmission electron microscopy (TEM) cross sections of layers I and II from Fig. 7 (courtesy of J. T. McGinn). Thickness of poly-B is 6600\AA in both region I and II, and thickness of poly-A is 5400\AA .

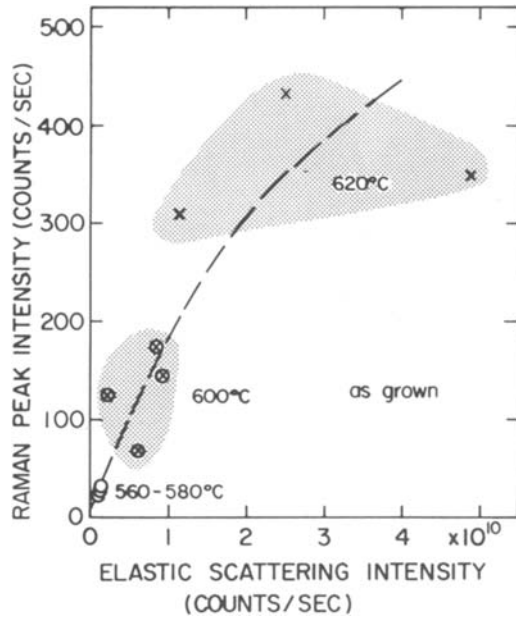


Fig. 10. Correlation between Raman peak and elastic intensity (100 mW/40 $\mu\text{m} \times 2 \text{ mm}$) for LPCVD silicon films of different deposition temperatures, as-grown. \circ : amorphous. \times : crystalline. \otimes : mixed.

revealed nondestructively by using the scanner in the quality-control mode.

Determining the crystallographic phase of a deposited layer.—Films of LPCVD silicon can be deposited in either one of the two phases, depending on the deposition temperature (T_d): for $560 \leq T_d \leq 580^\circ\text{C}$, the films are amorphous, for $T_d \geq 620^\circ\text{C}$, they are crystalline. The simplest and most rapid method to determine the crystallinity is by Raman scattering, as shown in Fig. 9. For convenience, we have plotted here the peak intensity of the Raman spectrum in the $490\text{--}530 \text{ cm}^{-1}$ region. Since the broad amorphous peak is much weaker (≈ 25 counts/s) than the crystalline peak ($\approx 100\text{--}400$ counts/s), the degree of crystallinity can simply be determined from the peak Raman intensity. Recent work on undoped (10, 11) and *in situ* phosphorus-doped (12) LPCVD polysilicon has demonstrated that only films deposited in the amorphous phase and subsequently crystallized by annealing have the high quality, in terms of structural perfection and surface roughness, which is required for critical device applications. The laser scanner has played an important role in the structural perfection characterization of the corresponding films. In the following, it will be shown in detail how the scanner, once calibrated for

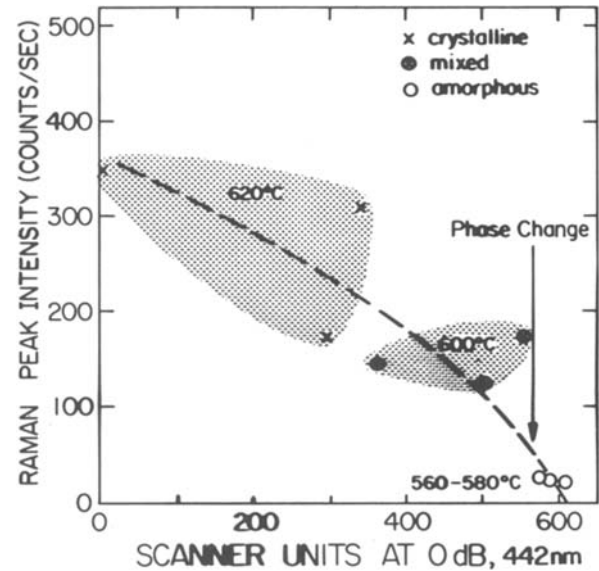


Fig. 11. Correlation between Raman peak intensity and laser scanner units for as-grown LPCVD silicon films, deposited at different deposition temperatures as indicated. \circ : amorphous. \times : crystalline. \otimes : mixed.

one system, e.g., LPCVD silicon, can be used very effectively for rapidly determining the crystallographic phase of a deposited film, a procedure for which x-ray measurements usually take at least 30 min. Moreover, it will be shown that even an annealed film can be identified whether it originates from a desirable, originally amorphous-deposited film or from a less desirable crystalline-deposited film. This permits rapid feedback in device processing.

Two detection methods have actually been used for testing with elastic light scattering: (i) the blue version of the laser scanner (442 nm) in the quality-control mode, and (ii) the static method (515 nm) with photomultiplier detection.

The former is more rapid and provides a map of the whole wafer area, while the latter is more sensitive. In principle, both methods give fully consistent results as will be seen.

Figure 10 shows the correlation between Raman peak intensity and elastic intensity, determined with the static method (b) for different deposition temperatures. It can be seen that the amorphous layers resulting from the LPCVD process always are of lowest elastic light scattering, the fully crystalline layers of highest, and the mixed amorphous-crystalline layers of intermediate. Figure 11 shows the corresponding results with the scanner method

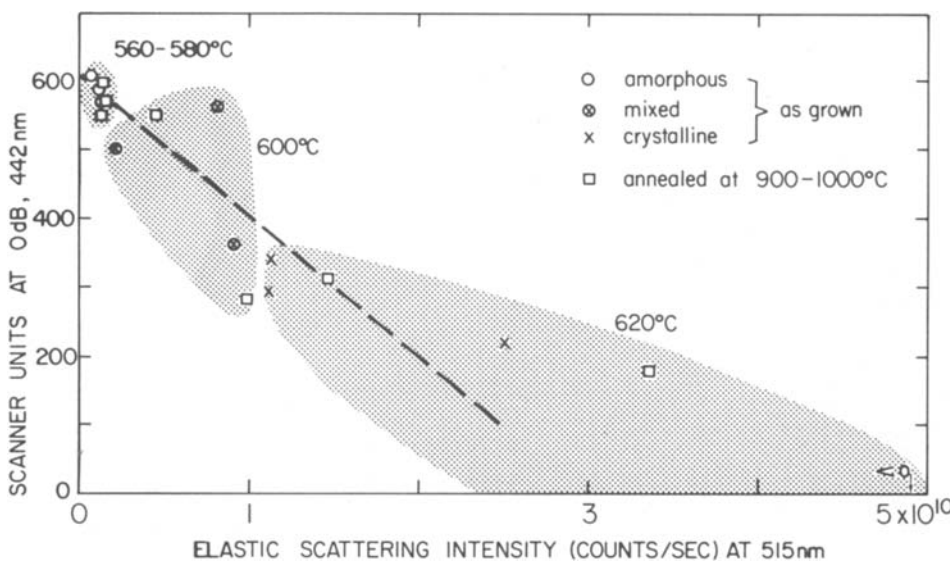
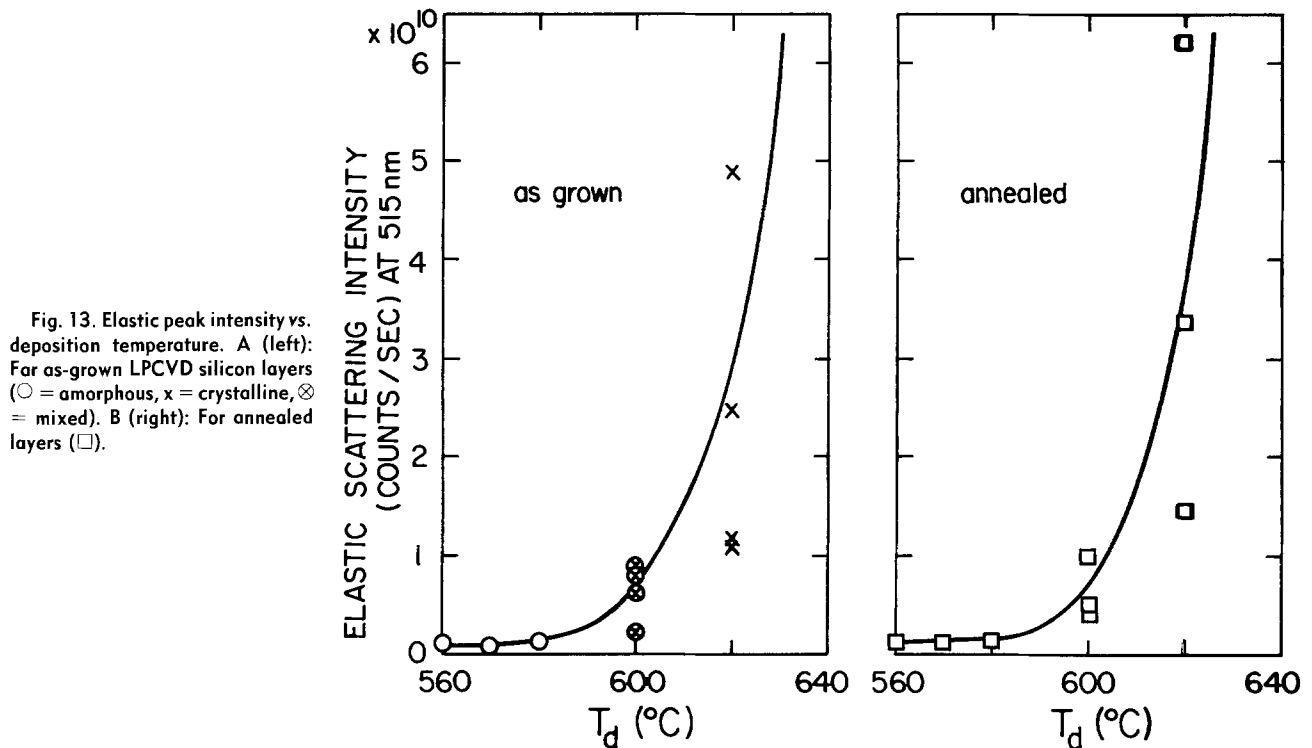


Fig. 12. Correlation between elastic scattering by scanner method (a) and by static method (b) for LPCVD silicon films, as-grown and annealed.



in the quality-control mode (a). The highest scanner units are observed for the amorphous layers, and the lowest for the less-desirable crystalline layers. In Fig. 12, the two methods are correlated with each other. It is seen that the correspondence is very good. Of considerable importance is the finding in Fig. 12 that the annealed films coincide well with the as-grown LPCVD films, particularly the ones which had been deposited in amorphous form. This is shown in more detail in Fig. 13 by using the static method. Thus, the elastic scattering of the films does not change with annealing, and it is possible to determine with the scanner (or the static method) whether an annealed film had been produced in the desirable amorphous form or in the less-desirable crystalline form. Since the amorphous deposition is preferred more and more for device processing, the acceptability assessment by the scanner of as-grown or annealed polysilicon layers is quite useful.

Internal gettering.—As device processing moves towards larger wafer size, the warpage of silicon wafers due to plastic deformation at elevated temperatures represents a more and more important problem to the IC industry (13). It is known that oxygen in small complexes improves the mechanical strength of silicon due to dislocation pinning. However, for many devices, lifetime is a limiting factor, and careful internal gettering is required to remove any impurities from the active device zone. For this purpose, one presently uses wafers with an oxygen-denuded zone in a shallow surface region, and with oxygen precipitates in the lower lying bulk part. Much work remains to be done in this field to reach a full understanding. We have studied the applicability of light scattering techniques for quantitatively assessing the structural perfection status of such wafers. For this, we have looked at bevel-polished wafers of the above kind (courtesy of Wacker Chemitronics, Burghausen, Germany) by means of the scanner in the quality-control mode and the static elastic scattering technique. The results appear very encouraging: both techniques can easily discriminate between the two regions and also show the crossover. Figure 14 presents the results on a beveled wafer. In the top part, the scanner map is reproduced as obtained in a few seconds. In the bottom part, the results of the static elastic light scattering are given. The agreement is obvious. Since the scanner method produces a whole map of the wafer, one can easily see if there are any radial

uniformities in the oxygen distribution. Judging from the top part of Fig. 14, this appears to be the case. It has been verified independently with the static method by studying along different lines across the wafer. At the present time, it is still unclear how much of the effect originates from the wafer and how much from a possible imperfect even polish. However, effects of the former type, namely,

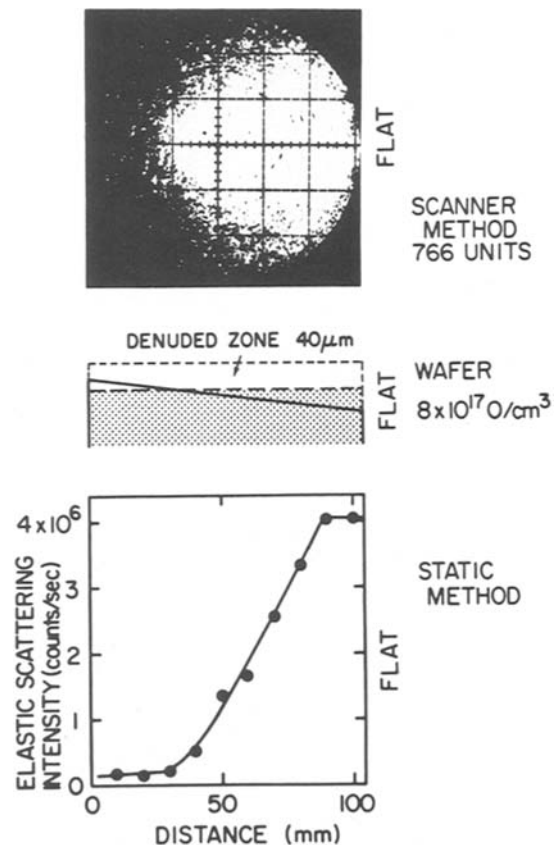


Fig. 14. Observation of transition from oxygen-denuded zone to precipitation zone on a beveled internal gettering silicon wafer. Top: Scanner method (442 nm), picture taken at 766 scanner units with 0 dB attenuation. Bottom: Static elastic scattering (515 nm).

a radial variation of the oxygen distribution, have been reported in the literature (14).

From these results, it appears that the scanner used in the quality-control mode can provide an important tool in studying the subtle details of oxygen distribution connected with internal gettering and warpage.

Acknowledgment

The authors gratefully acknowledge helpful and important contributions to this work: M. T. Duffy and R. Soltis, RCA Laboratories, Princeton, New Jersey, for supplying SOS wafers and determining the twin density; S. Vecrumba, RCA Laboratories, Lancaster, Pennsylvania, for providing a matrix of CCD process wafers; J. T. McGinn, RCA Laboratories, Princeton, New Jersey, for performing the TEM measurements; A. E. Widmer, Laboratories RCA, Limited, Zurich, for providing and annealing the LPCVD silicon films; and P. Stallhofer, Wacker Chemitronics, Burghausen, Germany, for providing the bevel-polished internal gettering wafers.

Manuscript submitted Nov. 27, 1983; revised manuscript received Feb. 13, 1984.

Laboratories RCA, Limited assisted in meeting the publication costs of this article.

REFERENCES

1. E. F. Steigmeier and H. Auderset, *RCA Rev.*, **44**, 5 (1983).
2. E. F. Steigmeier and H. Auderset, U.S. Pat. 4,391,524 (1983).

3. R. Wehner and R. Klein, *Physica*, **62**, 161 (1972), and references therein.
4. M. T. Duffy, P. J. Zanzuchi, W. E. Ham, J. F. Corboy, G. W. Cullen, and R. T. Smith, *J. Cryst. Growth*, **58**, 19 (1982).
5. G. W. Cullen, in "Heteroepitaxial Semiconductors for Electronic Devices," p. 21, Springer, New York (1978).
6. G. W. Cullen, M. S. Abrahams, J. F. Corboy, M. T. Duffy, W. E. Ham, L. Jastrzebski, R. T. Smith, M. Blumenfeld, G. Harbeke, and J. Lagowski, *J. Cryst. Growth*, **56**, 281 (1982).
7. M. S. Abrahams and C. J. Buiocchi, *Appl. Phys. Lett.*, **27**, 325 (1975); M. S. Abrahams, C. J. Buiocchi, R. T. Smith, J. F. Corboy, J. Blanc, and G. W. Cullen, *J. Appl. Phys.*, **47**, 5139 (1976).
8. L. Jastrzebski, M. T. Duffy, J. F. Corboy, G. W. Cullen, and J. Lagowski, *J. Cryst. Growth*, **58**, 37 (1982).
9. M. T. Duffy, J. F. Corboy, G. W. Cullen, R. T. Smith, R. A. Soltis, G. Harbeke, H. R. Sandercock, and M. Blumenfeld, *ibid.*, **58**, 10 (1982).
10. G. Harbeke, L. Krausbauer, E. F. Steigmeier, A. E. Widmer, H. F. Kappert, and G. Neugebauer, *Appl. Phys. Lett.*, **42**, 249 (1983).
11. G. Harbeke, L. Krausbauer, E. F. Steigmeier, A. E. Widmer, H. F. Kappert, and G. Neugebauer, *RCA Rev.*, **44**, 287 (1983).
12. G. Harbeke, L. Krausbauer, E. F. Steigmeier, A. E. Widmer, H. F. Kappert, and G. Neugebauer, *This Journal*, **131**, 675 (1984).
13. D. Thebault and L. Jastrzebski, *RCA Rev.*, **41**, 592 (1980); L. Jastrzebski, *IEEE Trans. Electron Devices*, **ed-29**, 475 (1982).
14. M. Ogino, T. Usami, M. Watanabe, H. Sekine, and T. Kawaguchi, *This Journal*, **130**, 1397 (1983).

Thermal Pulse Diffusion of Zn in GaAs from an Elemental Source

D. Dobkin¹ and J. F. Gibbons

Stanford Electronics Laboratories, Stanford University, Stanford, California 94305

ABSTRACT

We have studied Zn diffusion from an electroplated elemental source, using rapid thermal annealing techniques to investigate a range of diffusion times from 3 to 30s. Improved surface morphology is obtained by exploiting the high vapor pressure of Zn to remove excess source material, leaving only one to two monolayers of Zn tightly bound to the substrate. Resultant diffusions form shallow (0.1-0.2 μm) heavily doped ($1 \times 10^{20}/\text{cm}^3$)p⁺ regions. Junction properties are almost independent of diffusion time and linear in temperature over the range investigated.

Zinc is a common p-type dopant for GaAs. Diffused Zn layers are typically formed using sealed ampuls with a Zn-As compound as a dopant source (1, 2) or in open-tube diffusions with Zn-doped SiO₂ cap (3). We have investigated the diffusion of Zn into GaAs from an elemental Zn layer for short times (3-30s) using the technology developed for rapid annealing of implanted material (4).

Experimental Results

The rapid thermal annealer is designed so that only the sample in process is heated; thus, the incorporation of the Zn source directly on the wafer is advantageous. As a diffusion source, we have used a layer of elemental Zn, $\approx 100\text{\AA}$ thick, deposited by electroplating directly onto a GaAs surface after a pretreatment in a RuCl₃ solution. This process is described in more detail elsewhere (5).

In our initial studies, plated samples were placed in the rapid thermal annealer and covered by a silicon wafer to form a proximity cap. The chamber was evacuated by a mechanical pump/LN₂ trap and backfilled with a 90% Ar:10% H₂ mixture. Diffusions were performed for temperatures from 700° to 850°C and at 800°C for times from 4 to 30s (risetime was typically 5-7s). Samples were then characterized by Hall measurements and chemical stripping.

¹Also with Watkins-Johnson Company, Palo Alto, California.
Key words: semiconductor, diffusion, junctions, electrodeposition.

The doping profiles were found to be flat with a very abrupt drop-off. The plateau doping was typically $\approx 10^{20}/\text{cm}^3$. SIMS measurements verified this picture of the diffused profile (Fig. 1). The junction depth was found to be linear in temperature and almost independent of diffusion time (Fig. 2).

A disadvantage of this process was a degradation of surface morphology in the plated regions, evidenced as a clearly visible discoloration which was verified to be due to surface roughening using SEM observations. We speculate that this roughening is due to dissolution of GaAs into the Zn film once the temperature exceeds the Zn melting point (1).

To avoid this problem, we have exploited the high vapor pressure of Zn at moderate temperatures to remove the majority of the film before diffusion. The samples are loaded into the annealer without a top Si wafer and the chamber evacuated. Initial work was performed at a pressure of 50-100 mtorr using a mechanical pump. An oil diffusion pump with LN₂ trap was later added to the system, enabling operation at $\approx 3 \times 10^{-4}$ torr. (This pressure is far above the ultimate base pressure of the system, but is a compromise value chosen to minimize cycle time.) The sample is then raised to a temperature of 440°-520°C in vacuum for times of from 15 to 45s (most frequently 30s). The chamber is vented with forming gas and the sample covered with a Si wafer. Diffusion then proceeds as before. The plated regions are visually indistinguishable, at-

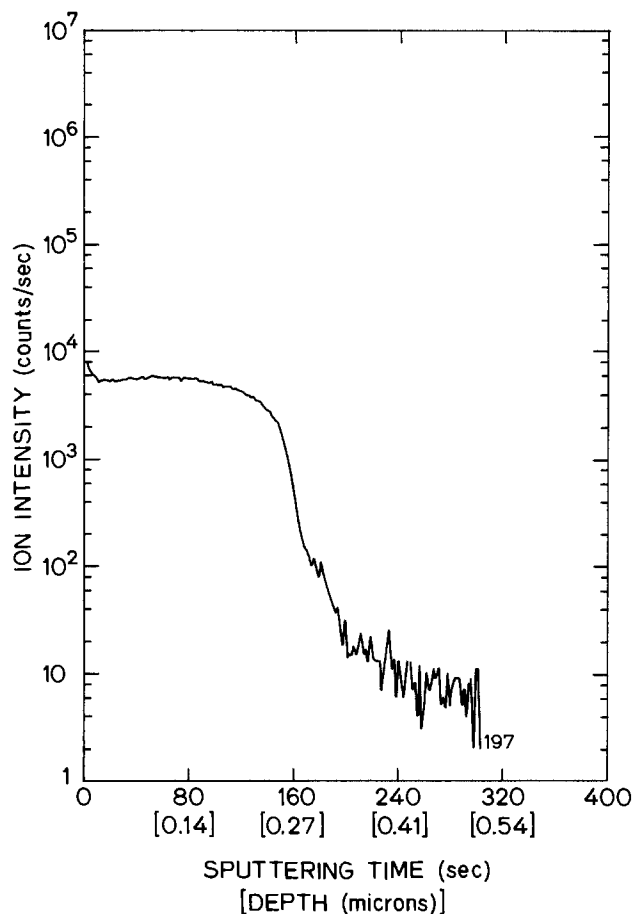


Fig. 1. SIMS profile of Zn diffusion: 10 sec at 800°C. (Depth scale estimated from Dektak measurement of sputtered crater.)

testing to undegraded surface morphology. Samples were characterized by Van der Pauw/Hall and four-point probe measurements combined with chemical stripping.

Electrical results are summarized in Fig. 3-6. Here sheet conductance is plotted as the dependent variable. It is found that the doping profiles were again flat with an abrupt edge, and that the peak doping ($\approx 1 \times 10^{20}/\text{cm}^3$) did not vary much with the various parameters explored. Thus, the variation in sheet conductance primarily represents variations in junction depth. The total dose corresponds to roughly one to two monolayers of Zn (5×10^{14} - $1.5 \times 10^{15}/\text{cm}^2$).

The data show that the junction depth decreases roughly linearly with increasing evaporation temperature, and increases linearly with increasing diffusion temperature. On the other hand, the junction properties seem substantially independent of the times used in either process, within the range explored.

To verify the usability of this process for device fabrication, junction GaAs FET's were produced. The starting material was liquid-phase epitaxial n-GaAs (doping $\approx 1 \times 10^{17}/\text{cm}^3$) on Cr-doped substrate without a buffer layer. Plating and evaporation/diffusion were performed as above to create a uniform p^+ region about $0.2 \mu\text{m}$ thick. Devices were isolated by chemical etching of mesas. Aluminum metal was patterned on the wafer by lift-off to form gate lines, which also acted as a mask for chemical removal of the p^+ layer from the remainder of the wafer. AuGeNi ohmic contacts were then patterned by lift-off and alloyed to complete the structure. Current voltage characteristics were measured on a curve tracer, with and without illumination from a microscope lamp; the results are shown in Fig. 7. The devices are seen to be well-behaved with illumination, but display hysteresis in the dark.

This hysteretic behavior was tentatively attributed to traps at the epi-substrate interface, possibly due to outdif-

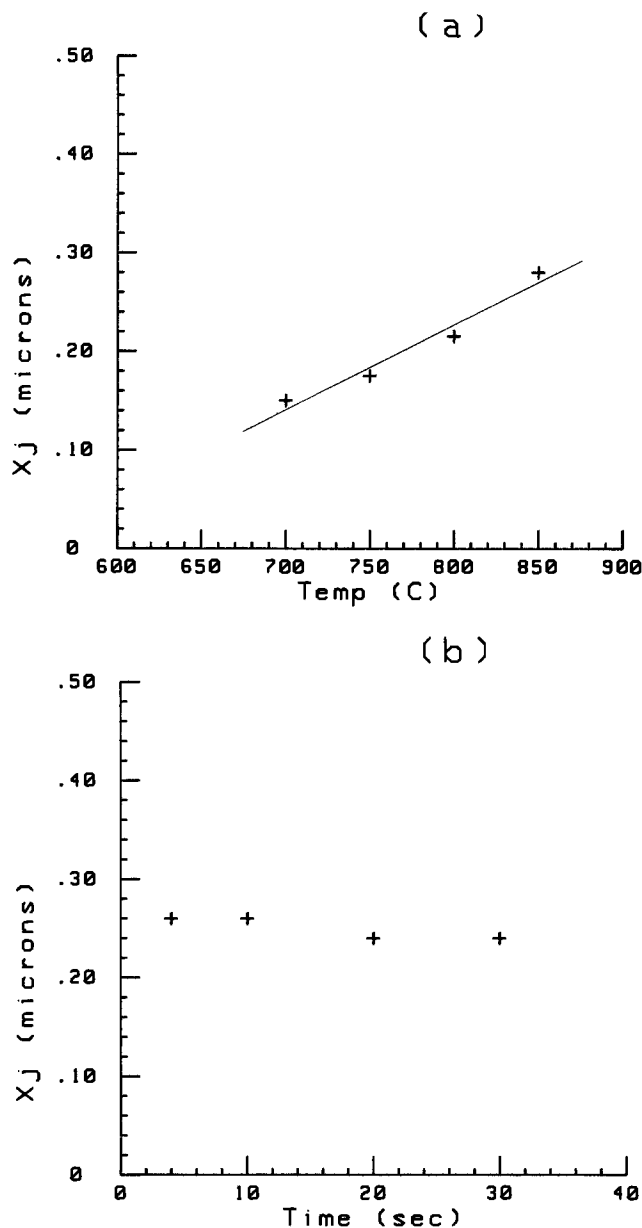


Fig. 2 (a, top) Junction depth vs. diffusion temperature (10s diffusion). The line is a least squares fit to the data; slope $1.0 \times 10^{-3} \mu\text{m}/^\circ\text{C}$; extrapolated to $x_j = 0$ at $T = 540$. (b, bottom) Junction depth vs. diffusion time (800°C).

fusion of impurities either during epitaxial growth or in the diffusion thermal processing. We found that a substrate bias of -50 to -60V would completely pinch off the device even at zero gate voltage; such behavior is considered to be due to deep impurities at the epi-substrate interface (6). To verify that this behavior was material-related rather than intrinsic to the Zn diffusion process, a second piece of the same wafer was processed in an identical fashion but without any zinc plating, to fabricate MESFET's of similar geometry. These devices displayed an identical "backgating" behavior.

Deep-level transient spectroscopy measurements were also made using a boxcar-integration scheme. A typical scan is shown in Fig. 8. The control sample was an aluminum Schottky barrier on n type ($10^{17}/\text{cm}^3$) bulk GaAs with a AuGe alloyed back contact; a second piece of the same wafer received an evaporation/diffusion to form a p^+ layer, followed by Al evaporation and chemical etching to form mesa diodes. The data show two electron trap levels in the control sample. The level of 150 K is completely absent in the diffused sample; the level at 370 K is just observable. (Hole traps were not investigated, as we do not at present have an optical DLTS capability.) The two

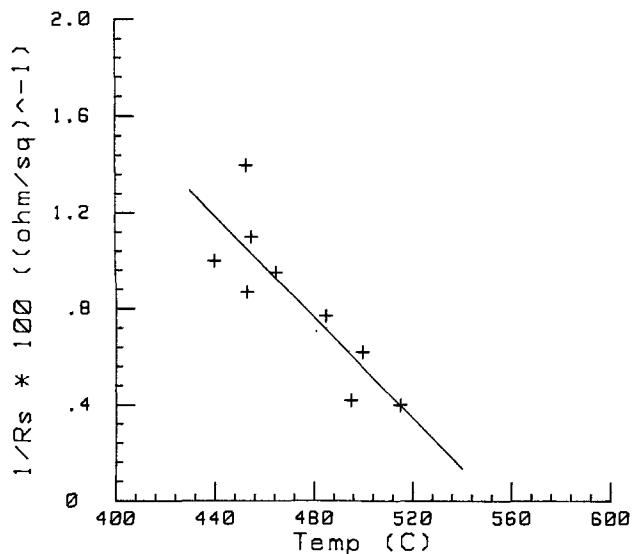


Fig. 3. Sheet conductance vs. Zn evaporation temperature. (Evaporation pressure 3×10^{-4} torr; diffusion 6s at 800°C .) Fitted line: slope $-1.06 \times 10^{-4} (\Omega \cdot ^\circ\text{C})^{-1}$; extrapolated to $\sigma = 0$ at $T = 550$.

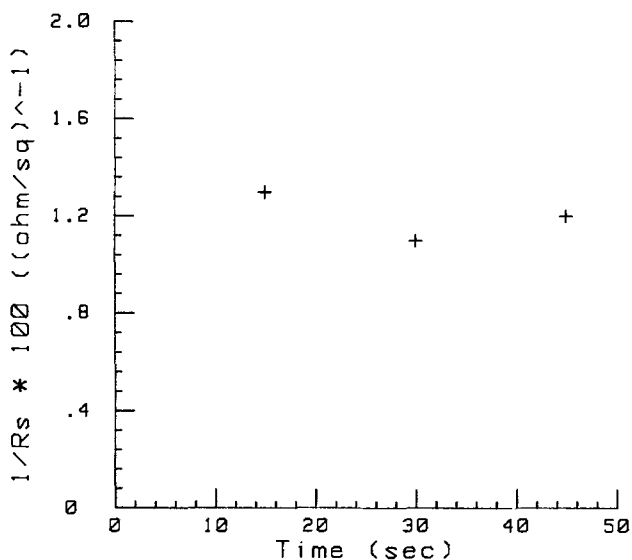


Fig. 4. Sheet conductance vs. Zn evaporation time. (Conditions as Fig. 3.)

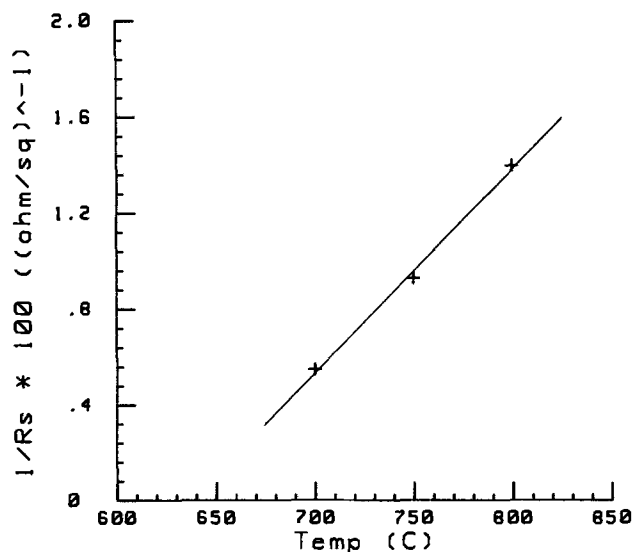


Fig. 5. Sheet conductance vs. diffusion temperature (evaporation 455°C , 30s; diffusion 6s). Fitted line: slope $= 8.5 \times 10^{-5} (\Omega \cdot ^\circ\text{C})^{-1}$; extrapolated to $\sigma = 0$ at $T = 640$.

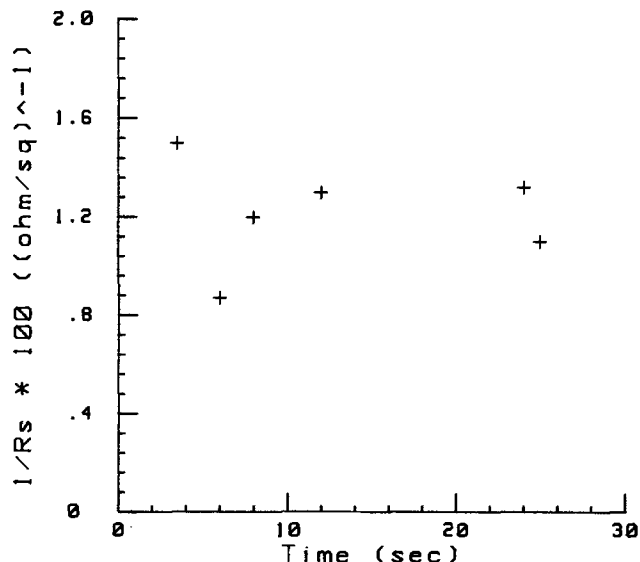


Fig. 6. Sheet conductance vs. diffusion time (evaporation as Fig. 5; diffusion at 800°C).

peaks are tentatively identified as EL7 and ET2, respectively (14), although due to the heavy doping and consequent high fields, precise characterization is difficult.

Discussion and Conclusions

The most interesting aspects of the dependence of p^+ region formation on the various experimental parameters are the weak (linear rather than exponential) dependence of junction depth on temperature of diffusion, the linear decrease of junction depth with increasing "evaporation" temperature, and the lack of any strong time dependence. These features contrast strongly with the typical behavior of diffusing species in semiconductors: diffusion constant $D \propto \exp[-E_a/kT]$ where E_a is several eV, and junction depth $x_j \propto \sqrt{t}$. The non-erfc/non-Gaussian diffusion profiles, on the other hand, are not surprising in view of the well-known concentration dependence of Zn diffusion (9).

The diffusion time independence of the p^+ region formation is reminiscent of the post-diffusion annealing results of Tuck and Houghton (10). In this work, junctions formed by conventional sealed ampul diffusion of Zn were annealed in a second Zn-free ampul at the same temperature as the diffusions. For temperatures less than 900°C , the anneal had essentially no effect on the diffused profiles. Zn diffusion is generally held to occur through either interstitial Zn (11) or interstitial Ga (12). The concentration of V_{Ga} , which controls the inclusion of Zn

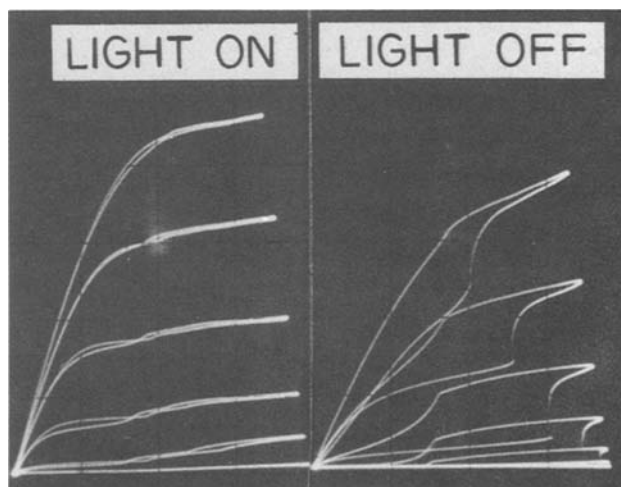


Fig. 7. I-V characteristic of JFET. Scales: 5 mA/div vertical, 1 V/div horizontal, 0.5 v/step. $W_g = 300 \mu\text{m}$.

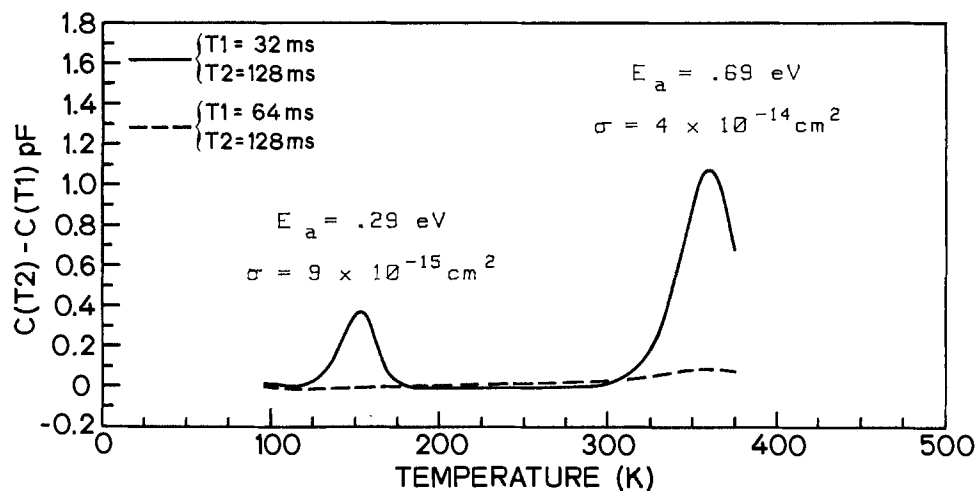


Fig. 8. DLTS scan of control (—) and Zn-diffused (---) samples. (Sample capacitance \approx 650 pfd.)

atoms in the lattice, is calculated by assuming equilibrium with As pressure at the surface, implying that the relevant defects are generated primarily at the surface. We must thus speculate that when a Zn source is not present, the driving force for defect creation at the surface is removed and diffusion then proceeds by a very slow substitutional mechanism. We have previously found that after "evaporation" Al Schottky barrier heights are modified, suggesting the presence of a very thin layer containing Zn at the surface (5). This layer may act as the finite source of Zn required by the model sketched above.

The independence of evaporation time may be explained by considering evaporation rates. The equilibrium Zn vapor pressure at 500°C of about 1.5 torr (13) gives an evaporation rate of about 3×10^5 monolayers/s assuming detailed balance and a unity sticking coefficient. Thus, all bulk Zn evaporates away in a very short time (\ll 1s), if retarding effects such as oxidation are negligible. After this time, only Zn atoms in an especially stable state, e.g., tightly bound to the substrate, remain, and these may be only weakly affected by further heat-treatment.

At present, we have no explanation for the temperature dependence of the diffusion process.

In conclusion, we have explored a new regime of Zn diffusion using rapid thermal processing and a plated elemental Zn source. We have characterized the dependence of junction formation on several process parameters. The use of an "evaporation" step to remove excess Zn results in preservation of surface morphology and a process suitable for device fabrication. The high doping levels obtained may make the process of interest for contact layer formation.

Acknowledgments

We would like to thank Mark Greiner for valuable discussions and technical assistance. We are grateful to the

Semiconductor Department of Watkins-Johnson Company, whose facilities were used extensively in this work. SIMS measurements were performed by C. Hopkins, J. Bertrand, and I. Ward of Charles Evans & Associates, San Mateo, California. This work was supported by AROD contract no. DAAG29-81-K-0061.

Manuscript submitted Jan. 24, 1984.

Stanford University assisted in meeting the publication costs of this article.

Note added in proof.—Hysteresis-free JFET's have been fabricated using vapor-phase epitaxial material with an unchopped buffer layer.

REFERENCES

1. K. Shih, *This Journal*, **123**, 1737 (1976).
2. A. Luque, J. Martin, and G. Aravjo, *ibid.*, **123**, 249 (1976).
3. R. Field and S. Gandhi, *ibid.*, **129**, 1567 (1982).
4. K. Conway, W. Opyd, J. Gibbons, T. Sigmon, and L. Bubulac, *Appl. Phys. Lett.*, **41**(8), 750 (1982).
5. D. Dobkin and J. Gibbons, *Appl. Phys. Lett.*, **44**, 884 (1984).
6. C. Kocot and C. Stolte, *IEEE Trans. Electron Devices*, **ed-29**, 1059 (1982).
7. D. Lang, *J. Appl. Phys.*, **45**, 3023 (1974).
8. G. Vincent, A. Chantre, and D. Bois, *ibid.*, **50**, 5484 (1979).
9. B. Tuck and M. Kadhim, *J. Mater. Sci.*, **7**, 581 (1972).
10. B. Tuck and A. Houghton, *J. Phys.*, **D14**, 2147 (1981).
11. H. Rupprecht and C. LeMay, *J. Appl. Phys.*, **35**, 1970 (1964).
12. D. Gosele and F. Morehead, *ibid.*, **52**, 4617 (1981).
13. J. O'Hanlon, "A User's Guide to Vacuum Technology," p. 371, Wiley, New York (1980).
14. G. Martin, A. Mitonneau, and A. Mircea, *Electron. Lett.*, **13**, 191 (1977).

Thermal Annealing of Proton-Bombarded GaAs and (Al, Ga)As

B. Schwartz,* L. A. Koszi,* P. J. Anthony,* and R. L. Hartman

AT&T Bell Laboratories, Murray Hill, New Jersey 07974

ABSTRACT

A study of the annealing of proton-bombarded, p-type GaAs and (Al,Ga)As revealed different electrical conductivity recovery effects, depending on the host crystal and the original dopant species and concentration level. It was found that the dopant dependence of the annealing temperatures was in the order $T_{Zn} < T_{Mg} < T_{Ge}$. In fact, whereas a Zn-doped binary system annealed completely at $\leq 570^\circ\text{C}$, Ge-doped samples, both binary and ternary, did not recover to better than within a factor of five of their original conductivities, even at temperatures as high as 700°C . The Mg-doped ternaries recovered at $\leq 570^\circ\text{C}$, while equivalently doped binaries acted similarly to the Ge cases in approaching only within a factor of five of their original values at 700°C . The ability to place juxtaposed regions of conducting and nonconducting layers in the "bulk" of a multilayered crystal structure was demonstrated. The potential for three-dimensional integration in compound semiconductors, utilizing these effects, is discussed.

The bombardment and penetration of a solid by an accelerated charged particle is an old field of study (1, 2) which became important in semiconductor technology with the fabrication of nuclear particle detectors by ion implantation (3). This technique has since become an integral part of silicon-integrated circuit fabrication (4) and is beginning to be used for the construction of compound semiconductor devices and circuits as well (5).

The recognition by Foyt *et al.* (6) that proton bombardment-induced damage in GaAs could be used to produce electrical isolation between adjacent devices, and the subsequent use of this technique by Dymant *et al.* (7) for the fabrication of stripe geometry double heterostructure lasers that would operate cw at 25°C , were two important steps in the development of optoelectronics. This technology depends on the ability to control the generation of regions of high resistivity material by bombardment-induced carrier removal (8). However, the use of this type of damage has been limited to the preparation of "tubs" (*i.e.*, regions from the near surface to the surface in restricted areas of the slice) of semi-insulating material. This is a direct consequence of the fact that the bombarding ions impinge on the surface from essentially a normal direction, with a patterned attenuator to define which areas of the semiconductor are exposed and which are protected. The result is a pseudo-three-dimensional technology.

We present observations that will enable the fabrication of more complex three-dimensional devices based on the interactive effects between the proton bombardment generation of high resistivity in GaAs and (Al, Ga)As, the dopants present in these materials, and a moderately high temperature anneal. We have found that proton-bombarded germanium-doped GaAs and/or (Al, Ga)As can be heated to 600°C and will maintain semi-insulating properties, while an identical treatment of Mg- or Zn-doped material will cause a return to a high conductivity state. In this paper, we shall show our preliminary results and mention a few of the many possible uses of this phenomenon in fabricating novel and improved devices.

Below is a description of the experimental procedures used in this study, followed by the experimental results and data analysis. Then we put this work in perspective and point out some possible technological applications, and we conclude with a summary.

Experimental Procedures

The experiment consisted of: (i) exposing the full surface of epitaxial samples of p-type GaAs and/or (Al, Ga)As to 300 keV protons at a dose of $3 \times 10^{15} \text{ cm}^{-2}$ [these bombardment conditions are known to render the surface region of this material semi-insulating to a depth of $\sim 3 \mu\text{m}$, with a resultant resistivity in the $10^5 \Omega\text{-cm}$ range (9)]; (ii) heating the samples at temperatures ranging from 450° to 700°C in an open-tube leaky-box "diffusion-type" furnace in a forming gas ambient for 30 min (estimated time at

maximum temperature being 15 min); and (iii) evaluation of the results using either a depth-profile conductance measurement (10) or a cleave-and-stain technique (11).

Two types of liquid phase epitaxial samples were prepared for this study. One set involved a single epitaxial layer containing the specific dopant of interest, and the other consisted of multiple epitaxial layers alternately doped with the impurity element of interest. Most of the single-layered samples were 1-2 μm thick GaAs or $\text{Al}_x\text{Ga}_{1-x}\text{As}$ ($x = 0.3$ or 0.4 films), containing either Mg or Ge, with a free carrier concentration from 2×10^{17} to $1 \times 10^{18} \text{ cm}^{-3}$, and were grown on (100) oriented, 10^{18} cm^{-3} , Si-doped n-type substrates. The multilayered samples were also grown on n-type Si-doped substrates, but they contained juxtaposed Mg- and Ge-doped layers, each about 0.2-0.6 μm thick and doped in the mid 10^{17} to low 10^{18} range; the total thickness of the epitaxial layers was $\sim 2 \mu\text{m}$.

The electrical measurements were done on the single-layer samples exclusively. After the bombardment and annealing sequences were completed, ohmic contacts of Au-Zn were evaporated onto the bombarded surface of the sample in the circular geometry shown in Fig. 1, at a deposition temperature of 140°C . As controls, unannealed samples, identically bombarded, were similarly metalized.

Layer resistivity was evaluated by applying a fixed bias of 0.1V between the inner dot contact and the outer ring and measuring the voltage drop across a suitably adjusted series sampling resistor (10). By etching the exposed semiconductor material in the annular ring in care-

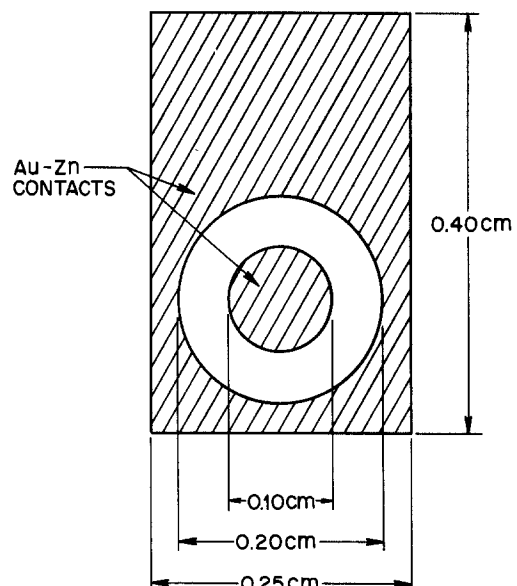


Fig. 1. The ring-dot configuration used to make the electrical measurements.

fully controlled steps, one can profile the conductivity of the bombarded regions; the sample resistivity is inversely proportional to the slope of the conductance *vs.* etching time plot. The low bias voltage limits the current to the p-type material above the n-type substrate. The current leakage across the junction and also through the $10^6 \Omega\text{-cm}$ deionized water used in the etching procedure places a $10^3 \Omega\text{-cm}$ upper bound on the resistivity that can ordinarily be measured.

Because of the large diffusion coefficient and high volatility of Zn, single epitaxial layers doped with Zn were not grown, and Zn-doped bulk GaAs was used instead. This altered the resistivity measurement geometry (*i.e.*, no p-n junction to isolate the measurements to the top 1-2 μm of material) and made interpretation of the measurements more difficult.

The cleave-and-stain measurements were done exclusively on LPE-grown multilayered samples containing alternately Ge and Mg as the p-dopants, in both the binary GaAs and the ternary (Al, Ga)As, also alternately juxtaposed. The epitaxial layers ranged in thickness from 0.15 to 0.6 μm , while the total of all layers was approximately 2 μm thick. The samples were not full surface bombarded with protons, but tungsten wire stripe masks were used to produce bombarded and unbombarded regions of the same slice. Subsequent to bombardment and anneal, the samples were cleaved on the (110) plane, stained in a solution of 5:1::H₂O:NH₄OH, and then photographed in a scanning electron microscope.

Experimental Results

Table I is a summary of the results of the electrical measurements performed on the bombarded and annealed single layer samples. All of the control samples examined without bombardment showed resistivities in the 10^{-2} to $10^{-1} \Omega\text{-cm}$ range. Because the evaluation technique used has an upper measurement limit of $10^4 \Omega\text{-cm}$, the largest normalized resistivity ratio (*i.e.*, the ratio of the resistivity after bombardment and anneal to that before bombardment) is listed as $> 10^4$; the value ~ 5 indicates that complete return to original resistivity was not achieved.

Samples 1-3 were Ge-doped epitaxial layers, samples 4-8 were Mg-doped epitaxial layers, and sample 9 was a Zn-doped bulk slice. As seen from column IV, the sample compositions ranged from the binary (samples 2, 3, 7-9) to 30 and 40% Al (samples 1, 4-6) in the ternary.

Three major trends can be discerned by examining the data in Table I. (i) In the ternary-based systems, proton-bombarded Mg-doped slices recovered their initial resistivity in the temperature range 575°-600°C, while the Ge-doped material continued to show high resistivity up to temperatures of 700°C. (ii) In the binary-based systems, except for the Zn-doped material, none of the samples completely annealed back to their original resistivity, coming only within a factor of about five of their initial value, even after annealing to temperatures of about 700°C. (iii) One can distinguish the influence of original dopant concentration on the recovery level by comparing the annealing results of samples 2 and 3, wherein a higher initial doping level yielded better recovery of conductivity.

Figure 2 is an example of the results of the cleave-and-stain experiments performed on the bombarded and annealed multilayered samples. The specimen displayed in Fig. 2 was a six-layered sample consisting of the following: starting with the n-type Si-doped substrate (layer 1), a 3-4 μm thick Te-doped buffer layer was grown first, then a thin (0.2 μm) Mg-doped, Al_{0.08}Ga_{0.92}As layer was grown (layer 3), then a 0.6 μm Ge-doped Al_{0.40}Ga_{0.60}As layer (layer 4), then a Mg-doped, 0.6 μm thick Al_{0.4}Ga_{0.6}As layer (layer 5), and finally a 0.15 μm heavily Ge-doped GaAs layer was deposited. A proton bombardment mask was used over the right-hand third of the sample shown, while the specimen was exposed to 300 keV protons at a dose of 3×10^{15} . The sample was annealed at 570°C for 15 min and then was metallized, cleaved, and stained in order to bring out the various layers.

Table I. Ratio of the sample resistivity after bombardment and anneal to resistivity before bombardment, at indicated temperatures

Sample	Dopant—	Approx. concentration	Epitaxial layer composition	Resistivity ratio	Anneal temp °C	Resistivity ratio	Anneal temp °C	Resistivity ratio	Anneal temp °C	Resistivity ratio	Anneal temp °C
1	Ge	2×10^{17}	40% Al	$> 10^4$	450	$> 10^4$	575	$> 10^4$	600	$\sim 10^3$	650
2	Ge	4×10^{17}	Binary	—	—	—	—	$> 10^4$	600	$\sim 10^3$	650
3	Ge	4×10^{18}	Binary	—	—	—	—	~ 5	600	~ 5	650
4	Mg	3×10^{17}	40% Al	$> 10^4$	450	$> 10^4$	550	~ 5	600	—	—
5	Mg	1×10^{18}	40% Al	$> 10^4$	450	$> 10^4$	500	1	600	—	—
6	Mg	1×10^{18}	30% Al	$> 10^4$	450	~ 10	570	1	600	—	—
7	Mg	1×10^{18}	Binary	—	—	1	570	~ 5	600	—	—
8	Mg	1×10^{18}	1% Sb	$> 10^4$	450	~ 5	570	~ 5	625	—	—
9	Zn	$> 1 \times 10^{18}$	Binary	$> 10^4$	450	1	570	—	650	—	—

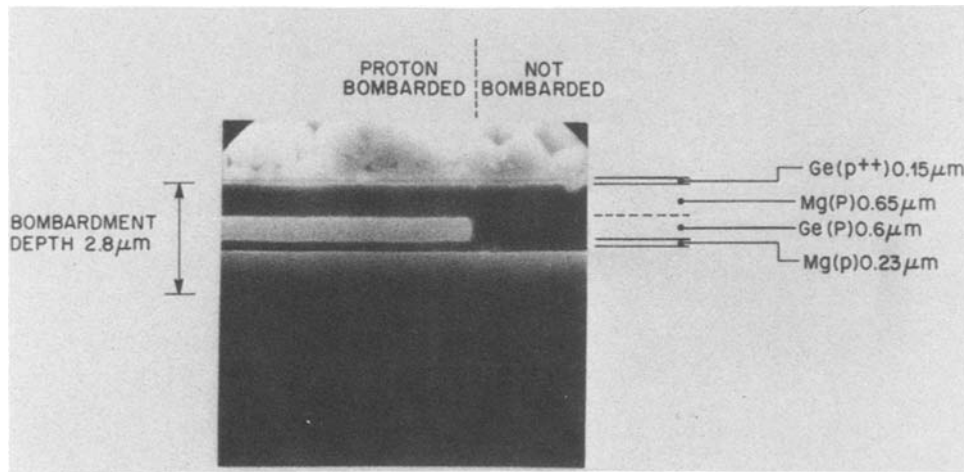


Fig. 2. An SEM photomicrograph of a stained cross section of a proton-bombarded and -annealed multilayer sample.

A number of interesting observations can be made from this photograph. First, all of the Mg-doped layers stained the same as the unbombarded region, including the protected area of the Ge-doped layer. On the other hand, the exposed Ge-doped layer did not stain the same as the unbombarded region of the Ge-doped layer. Although the protons penetrated the n-type Si-doped substrate and, in fact, the "end of range" for the protons was well into the substrate, there was no evidence of an etching delineation to indicate a change in conductivity in the substrate. Lastly, although the p-type binary cap layer was Ge-doped, it was very heavily doped, and some magnesium might even have been incorporated by melt carry-over from the p-type (Al, Ga)As layer below it to provide for a substantial recovery of conductivity.

Discussion

In spite of the fact that a large literature exists on radiation damage in solids (12-15), and semiconductors in particular (16-18), the mechanisms involved in the generation of high resistivity in GaAs by proton bombardment are not well understood. Very little theoretical work has been done on this subject, and most of the experimental studies have revolved around two basic points: carrier removal effects (8, 9, 19) and optical absorption as a function of bombardment conditions followed by heat-treatments of various kinds (9, 20, 21). In a few cases, measurements have been made to show the influence of annealing on the recovery of electrical conductivity (8, 22-25), including that of proton-bombarded (Al, Ga)As (26).

Under the conditions defined by Sakurai *et al.* (24), it was found that a proton bombardment dose of $6 \times 10^{12}/\text{cm}^2$ into n-type (originally 10^{16} cm^{-3} , Te-doped) GaAs did not respond to annealing at a temperature of 435°C for 35h. Favennac *et al.* (26) found that equivalently doped and bombarded (Al, Ga)As annealed extensively after 15 min at 550°C . Steeples *et al.* (25) have shown that the temperature required for the onset of annealing effects was both proton-dose and n-type dopant concentration dependent. However, Donnelly *et al.* (27) claimed that a multiple energy proton bombardment sequence into 4×10^{18} Si-doped GaAs "... combined with a post bombardment anneal ... (of up to 500°C) ... is superior to a single energy bombardment in creating high resistivity layers in n⁺-GaAs ...". Dymant *et al.* (9) showed that annealing results of heavily (*i.e.*, $\geq 10^{18} \text{ cm}^{-3}$) Zn-doped p-type GaAs after proton bombardment was both dose and time-temperature dependent.

In almost all of these studies, the question of the "onset" of annealing appeared to be most important, and the conditions required to recover to the prebombardment value of conductivity were not stressed; in a few studies, however, continued annealing was performed. Whereas Foyt *et al.* (6) noted that "... an overnight anneal of 700°C ... removed the high resistance layer and the entire sample returned to the substrate carrier concentration,"

they also observed that "... contact alloying at 500°C without removing the high resistance layer" was achieved. Favennac *et al.* (26) presented the only direct data to show that the normalized resistivity ratio returned to unity for a 10^{16} cm^{-3} Te-doped (Al, Ga)As layer that was bombarded with a dose of 7×10^{12} protons/ cm^2 and then annealed at 550°C for 15 min.

The data presented in this paper differ in two ways from most of the information obtained in previous studies. From the beginning, we were interested in determining the conditions required for reaching, if at all possible, the original conductivity of the prebombarded samples, and we were also concerned with obtaining information on the influence of specific dopants and host crystals on these recovery conditions. From the data shown in Table I, and analyzed above, it is clear that there are strong influences pertaining to all of these parameters. The major observations were: (i) the recovery-anneal temperatures, as a function of dopant, were $\text{Zn} < \text{Mg} < \text{Ge}$; (ii) total recovery was achievable in the ternary more readily than in the binary host; and (iii) the higher the background doping, the lower the temperature at which recovery started. This last point is totally consistent with the previously reported concepts of requiring larger proton doses and/or lower annealing temperatures for increased background doping in the host crystal. However, the first two points noted above are new and are potentially of scientific as well as technological interest.

As was stated earlier in this paper, the fundamental understanding of the mechanisms involved in rapid generation after proton bombardment, subsequent anneal, and dopant activation is minimal at best. Because of this, it is not possible to provide a definitive explanation for the effects we have just noted. However, a strong diffusion mechanism involvement, possibly defect-enhanced, is clearly suggested. It is known (28), for example, that p-type dopants diffuse more readily in the ternary than in the binary, and the known diffusion coefficients are in the order, $\text{Zn} > \text{Mg} > \text{Ge}$. This would be consistent with the annealing temperature dependence observed in this work. It is difficult to be more quantitative in this discussion because dopant diffusion in the Al-Ga-As system is not well understood, and many parameters influence the mechanism of diffusion (29, 30) (*e.g.*, arsenic vapor pressure and control thereof, dopant concentration effects (31), etc.). Couple this with the complications introduced by dealing with a severely defected material resulting from ion bombardment, and one can begin to appreciate the magnitude of the problem.

To determine the amount of damage introduced by bombarding GaAs with protons, we have calculated that approximately 50 atomic sites are affected by each of the incoming 300 keV protons (see Appendix). The ion dose used in these experiments was $3 \times 10^{15} \text{ cm}^{-2}$, which results in an "area" damaging effect of approximately $1.5 \times 10^{17} \text{ cm}^{-2}$. Knowing that at 300 keV the projected range for

protons in GaAs (33) is approximately $2.5 \mu\text{m}$, and assuming, for simplicity, that all of the displaced atomic sites are uniformly distributed, one finds a "damage" concentration level in the mid 10^{20} cm^{-3} as a result of this specific set of bombardment conditions. This damage level is not far from the conditions described by Wang *et al.* (34) for making GaAs amorphous; they determined a critical proton dose of approximately 10^{16} cm^{-2} at bombardment energies comparable to those used in our study. This means that, under all of the background doping conditions used in our experiments, there were at least two orders of magnitude higher defect densities generated by ion bombardment than the electrically active dopant present to compensate for these defects during annealing. Therefore, the strong influence of defect-enhanced diffusion is a very real possibility.

From a technological point of view, some very interesting and potentially novel device possibilities arise from the observations made in this study. For example, when two layers of GaAs and/or (Al, Ga)As are placed side by side but doped with different dopants, one can visualize, if the sample is properly proton-bombarded and annealed (schematically shown as T_a in Fig. 3), that one of the layers could be maintained in a high resistance condition, while the other layer could be made conducting again. An example of this effect in a more complicated structure is clearly shown in Fig. 2, where just such a set of conditions was achieved with the p-type dopants Mg and Ge in the multilayer sample. From the limited data of Steeples *et al.* (25), one might infer that similar disparate annealing effects should occur with n-type dopants. This leads to the very interesting speculation that by a judicious choice of host crystal (epitaxial layer), dopants, and processing conditions (*i.e.*, bombardment and anneal), one should be able to control the juxtaposition of conducting and non-conducting layers and/or parts of layers, either of the same or different initial conductivity type and/or bandgap, buried within the solid. This kind of capability opens entirely new vistas in the potential for three-dimensional integrated circuits in compound semiconductors; for example, planar-buried interconnects, buried blocking layers, buried active devices, and buried optical wave guides.

Another very striking piece of information should be considered with regard to three-dimensional integration. Examining the dose dependencies of high resistivity generation in p- and n-type GaAs by Dymont *et al.* (9) and Pruniaux *et al.* (8), respectively, one obtains the data in Fig. 4 which show that p- and n-type GaAs become highly resistive at different proton doses. Coupling this information with the ability to grow juxtaposed layers either n- or

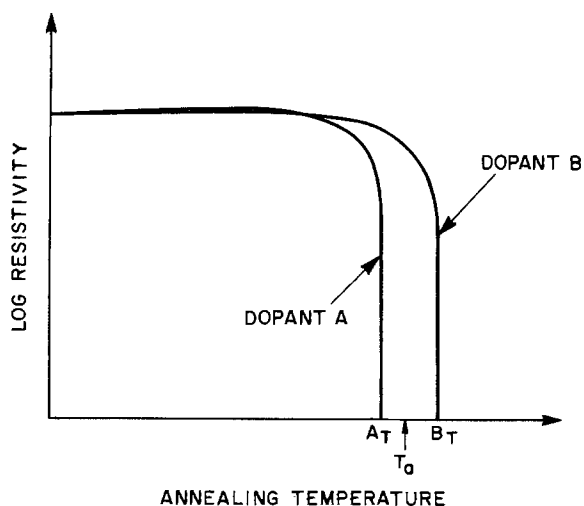


Fig. 3. A schematic showing annealing curves for two differently doped GaAs samples; T_A is a temperature where sample containing dopant A has recovered its conductivity and sample B is still highly resistive.

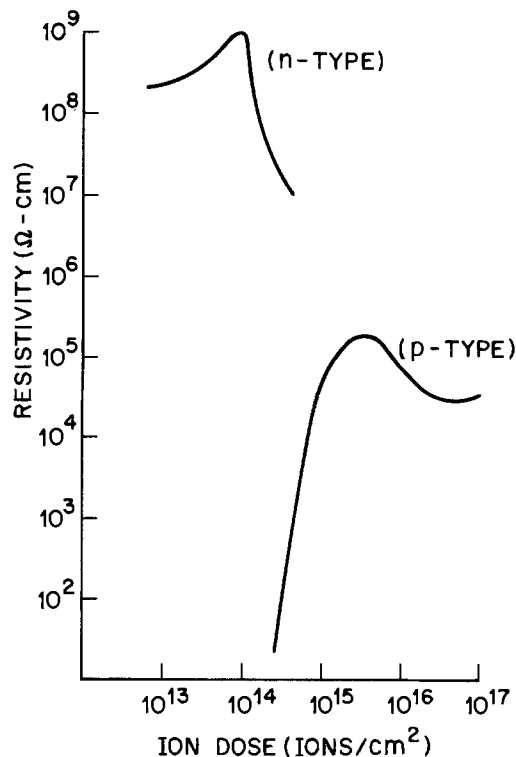


Fig. 4. Resistivity curves for proton-bombarded p- and n-type GaAs, as a function of proton dose, after Ref. (8, 9).

p-type with carefully chosen dopants, we see that countless possible permutations and combinations are available to the device designer for three-dimensional integrated optoelectronics.

Conclusion

It has been shown that the annealing characteristics of proton-bombarded p-type GaAs and (Al, Ga)As depend strongly on the dopant species and concentration, as well as on the host crystal used. Total recovery of electrical conductivity has been achieved more readily in the ternary than in the binary and with the higher diffusion coefficient dopants. Juxtaposing of buried conducting and nonconducting regions has been achieved by judiciously choosing the dopants, epitaxial layer compositions, and annealing conditions. On the basis of these observations, speculations have been presented about the possibilities of three-dimensional integration.

Acknowledgments

The authors would like to acknowledge the able assistance provided by the Lightwave Sources Models Laboratory and J. W. Lee in the fabrication of the samples used in this study. We would also like to thank F. Capasso, R. A. Logan, A. T. Macrander, M. B. Panish, M. W. Focht, and V. Swaminathan for stimulating discussions.

Manuscript submitted Sept. 26, 1983; revised manuscript received Jan. 11, 1984.

AT&T Bell Laboratories assisted in meeting the publication costs of this article.

APPENDIX

From Gibbons (32)

$$N_t = \{P(E_0 - E_c) + bE_c\}/Ed \quad [A-1]$$

where N_t is the total number of displaced atoms per incident ion, P is the probability factor $\approx 10^{-3}$, E_0 is the initial energy of projectile = 300 keV, E_c is the energy at which nuclear stopping power equals electronic stopping power $\approx 1 \text{ keV}$, E_d is the displacement energy for target atom $\approx 15 \text{ eV}$, and $b = 1/2$ if $E_b > E_c$, and $1/4$ if $E_b < E_c$.

$$E_b = \frac{\gamma E_A^2}{4E_d} \quad [A-2]$$

$$\gamma = \frac{4M_1M_2}{(M_1 + M_2)^2} \quad [\text{A-3}]$$

$$E_A = 2E_R Z_1 Z_2 (Z_1^{2/3} + Z_2^{2/3})^{1/2} (M_1 + M_2) / M_2 \quad [\text{A-4}]$$

where Z_1 and M_1 are the atomic number and mass of the projectile, Z_2 and M_2 are the atomic number and mass of the single element target atom, and E_R is the energy of projectile at which it is equal to the Coulomb interaction potential of the two nuclei separated by the sum of the radii of their screening clouds ≈ 13.5 eV.

For protons as the projectile, assuming the average mass and atomic number for GaAs (the target) to be that of Ge (*i.e.*, 73 and 32, respectively) by putting in the appropriate values, one obtains: $E_A \approx 3$ keV, $\gamma \approx 0.05$, and $E_b \approx 8$ keV. Therefore, by substituting the proper values in Eq. [A-1], $N_i \approx 50$ displaced atoms/incident proton. Considering a proton dose of 3×10^{15} cm⁻², then $N_{\text{total}} = 3 \times 10^{15} \times 0.5 \times 10^2$, or total atomic displacement $\approx 1.5 \times 10^{17}$ cm⁻².

REFERENCES

- G. Carter and W. A. Grant, "Ion Implantation of Semiconductors," Edward Arnold Publishers, Ltd., London (1976).
- J. F. Gibbons, *Proc. IEEE*, **56**, 295 (1968).
- T. Alvager and N. J. Hansen, *Rev. Sci. Instrum.*, **33**, 567 (1962).
- T. E. Seidel, in "VLSI Technology," S. M. Sze, Editor, p. 219, McGraw-Hill, New York (1983).
- D. V. Morgan, F. H. Eisen, and A. Ezis, *IEEE Proc.*, **1**, 128, 109 (1981).
- A. G. Foyt, W. T. Lindley, C. M. Wolfe, and J. P. Donnelly, *Solid-State Electron.*, **12**, 209 (1969).
- J. C. Dymant, L. A. D'Asaro, J. C. North, B. I. Miller, and J. E. Ripper, *Proc. IEEE*, **60**, 726 (1972).
- B. R. Pruniaux, J. C. North, and G. L. Miller, in "Proceedings of the Second International Conference, Ion Implantation in Semiconductors," I. Ruge and J. Graul, Editors, p. 212, Springer-Verlag, Berlin (1971).
- J. C. Dymant, J. C. North, and L. A. D'Asaro, *J. Appl. Phys.*, **44**, 207 (1973).
- J. L. Zilko and P. J. Anthony, *This Journal*, **128**, 871 (1981).
- L. I. Greene, Personal Communication, June 2, 1975.
- M. W. Thompson, "Defects and Radiation Damage in Metals," Cambridge University Press, Cambridge, MA (1969).
- L. T. Chadderton, "Radiation Damage in Crystals," John Wiley & Sons, New York (1965).
- "Radiation Damage in Solids," D. S. Billington, Editor, Academic Press, New York (1962).
- J. Gittus, "Irradiation Effects in Crystalline Solids," Applied Science Publishers, London (1978).
- "Radiation Effects in Semiconductors," F. L. Wook, Editor, Plenum Press, New York (1968).
- "Radiation Effects in Semiconductors—1976," N. B. Urli and J. W. Corbett, Editors, The Institute of Physics, Bristol, England (1977).
- "Defects and Radiation Effects in Semiconductors—1980," R. R. Hasiguti, Editor, The Institute of Physics, Bristol, England (1981).
- K. Wolleben and W. Beck, *Z. Naturforsch.*, **21a**, 1057 (1966).
- H. J. Stein, in "Ion Implantation in Semiconductors and Other Materials," B. L. Crowder, Editor, p. 39, Plenum Press, New York (1972).
- H. C. Snyman and J. H. Neathling, *J. Appl. Phys.*, **52**, 6637 (1981).
- L. W. Aukerman, P. W. Davis, R. D. Graft, and T. S. Shilliday, *ibid.*, **34**, 3590 (1963).
- J. D. Speight, P. O'Sullivan, P. A. Leigh, N. McIntyre, K. Cooper, and S. O'Hara, in "Gallium Arsenide and Related Compounds," C. Hilsum, Editor, p. 275, Institute of Physics, London (1977).
- T. Sakurai, Y. Bamba, and T. Furuya, *Fujitsu Sci. Tech. J.*, **71** (June, 1975).
- K. Steeples, I. J. Saunders, and J. G. Smith, *IEEE Electron Devices Lett.*, **ed1-1**, 72 (1980).
- P. N. Favennac and D. Diguët, *Appl. Phys. Lett.*, **23**, 546 (1973).
- J. P. Donnelly and F. J. Leonbarger, *Solid-State Electron.*, **20**, 183 (1977).
- V. Swaminathan, J. L. Zilko, W. T. Tsang, and W. R. Wagner, *J. Appl. Phys.*, **53**, 5163 (1982).
- M. B. Small, R. M. Potenski, W. Reuter, and R. Ghez, *Appl. Phys. Lett.*, **41**, 1068 (1982).
- D. L. Kendall, in "Semiconductors and Semimetals," Vol. 4, R. K. Willardson and A. C. Beer, Editors, p. 163, Academic Press, New York (1968).
- C. M. Wolfe and G. E. Stillman, *Appl. Phys. Lett.*, **27**, 564 (1975).
- J. F. Gibbons, *Proc. IEEE*, **60**, 1062 (1972).
- H. Matsumura, M. Nagatomo, S. Furukawa, and K. G. Stephens, *Radiat. Eff.*, **33**, 121 (1977).
- W. Wei-yuan, X. Jing-yang, N. Qi-min, T. Ru-huan, L. Yue-gin, and Q. Yue-ying, *Acta Phys. Sin.*, **28**, 685 (1979).

Topographic Imperfections in Zone Melting Recrystallized Si Films on SiO₂

C. K. Chen, M. W. Geis, B-Y. Tsaur, R. L. Chapman, and John C. C. Fan*

Lincoln Laboratory, Massachusetts Institute of Technology, Lexington, Massachusetts 02173-0073

ABSTRACT

The principal topographic imperfections in Si films recrystallized on SiO₂ by the graphite-strip-heater technique have been examined. Wafer warpage has been reduced to less than 4 μm for 2 in. diam samples. The protrusion density decreases with finer sub-boundary spacing; this correlation can be understood in terms of the thermal gradient present at the liquid-solid interface.

In recent years, substantial efforts have been directed toward the development of a technology for producing high-quality single-crystal Si films on insulating substrates (1-4). These efforts have been motivated by the potential of thin film devices for achieving higher packing density, speed, and radiation resistance than bulk devices, and by the potential of Si-on-insulator (SOI) structures for accomplishing the three-dimensional integration of electronic circuits. Of the several SOI approaches currently under investigation (5), one of the most promising is zone melting recrystallization (ZMR), in which the grain size of a polycrystalline Si film on an insulating

*Electrochemical Society Active Member.

substrate is greatly increased by the passage of a narrow molten zone. We have developed ZMR using graphite-strip heaters to the point where 2 and 3 in. diam wafers can be recrystallized over their entire surface (6-8), and we have used the recrystallized SOI material to fabricate majority carrier devices and integrated circuit chips with properties comparable to those of analogous bulk devices (9, 10). However, before the full potential of SOI technology using graphite-strip heaters can be realized, techniques must be developed to eliminate or minimize the remaining material problems: wafer warpage, protrusions, and low angle grain boundaries. The first two of these are topographic imperfections. In this paper, we

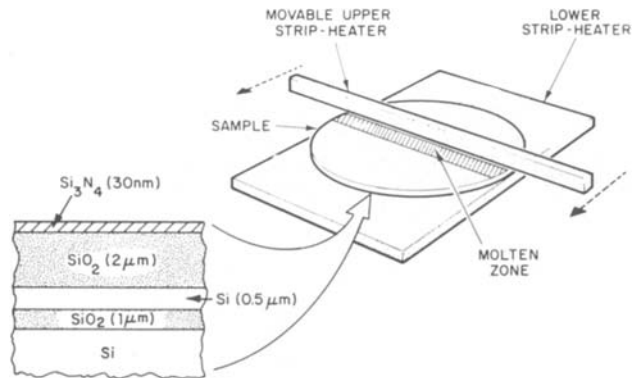


Fig. 1. Schematic diagram of a graphite-strip heater used for zone melting recrystallization of encapsulated Si films. The inset shows a cross section through a typical sample.

present the results of our investigation of these imperfections and discuss their dependence on thermal profiles present during the recrystallization process (11). In addition, we will briefly discuss our observation of voids, which are occasionally formed in the crystallized films because of contamination during wafer preparation.

ZMR by the Graphite-Strip-Heater Technique

The configuration of the graphite-strip-heater oven we use for ZMR of Si on SiO₂ is shown schematically in Fig. 1 (8). The sample, which is placed on the stationary lower heater, consists of a fine-grained Si film on an insulating substrate or layer, together with an encapsulation layer over the Si film. The inset of Fig. 1 shows a schematic cross section of a typical sample, prepared by coating a Si wafer 10-20 mil thick with a 1.0 μm thick thermally grown SiO₂ layer, a 0.5 μm poly-Si layer formed by low pressure chemical vapor deposition (LPCVD), a 2 μm layer of CVD SiO₂, and a 30 nm layer of sputtered Si-rich Si₃N₄. The lower strip heater is used to heat the sample to a base temperature of 1100°-1300°C, generally in a flowing Ar gas ambient at atmospheric pressure. Additional radiant energy, provided by the movable upper strip heater, is used to produce a narrow molten zone in the poly-Si layer (mp of Si = 1410°C). The molten zone is then translated across the sample by scanning the upper heater, typically at 1/2 mm/s, leaving a recrystallized Si film (7). The thicknesses of the SiO₂ and Si layers, the composition of the encapsulation layer, the molten zone speed, and the shape of the upper heater and its position relative to the sample all have a strong effect on the morphology and crystallography of the recrystallized films.

Topographic Imperfections

Warpage.—Zone melting recrystallized Si films exhibit several types of topographic imperfections. One type is wafer warpage, which must be minimized because of the

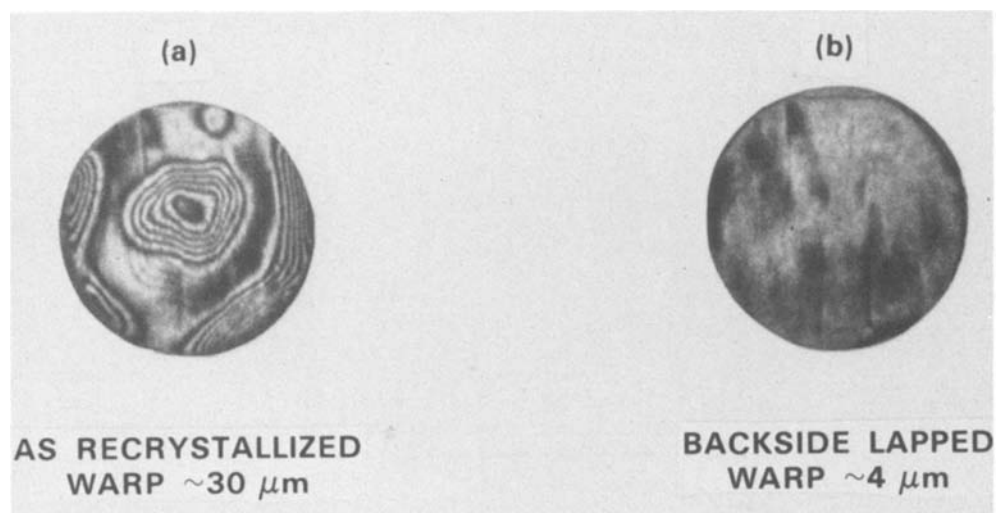
stringent flatness requirements imposed by photolithographic processes used in VLSI fabrication. Warpage was measured with a laser interferometer flatness monitor which gives a fringe pattern that provides a topographic map of the sample surface, with each fringe corresponding to a constant height contour. Before recrystallization, the overall warp, peak to valley, of a 2 in. diam sample placed on a vacuum chuck is typically 2-4 μm, a value comparable to that for a bulk Si wafer after processing. To maintain this degree of flatness for recrystallized samples, well-controlled heating rates and temperature profiles are necessary.

Uniform thermal contact between the sample and lower heater and a constant separation between the sample and moving upper heater are essential for recrystallization to be accomplished over the entire surface of 2 and 3 in. diam samples. Because Si has a lower emissivity than graphite, a radial temperature gradient will result if an SOI sample is placed on a uniformly heated lower heater. One can compensate for this effect by making a circular depression in the surface of the lower heater in order to reduce the resistive heating directly beneath the sample¹. For example, we have found that a 0.010 in. deep 2 in. diam well in a 0.040 in. thick lower heater (8) minimizes the radial temperature variation and allows uniform recrystallization of the entire surface of a 2 in. diam. sample in an Ar ambient.

Figure 2a shows an interference pattern obtained for an as-recrystallized 0.013 in. thick, 2 in. diam SOI sample that was placed on a vacuum chuck for measurement. The pattern shows that the sample was relatively flat over a large portion of the surface, but had several high points. We have determined that such high points, which are characteristic of as-recrystallized samples, result from imperfections that protrude from the back side of the samples (see Fig. 3) and prevent them from conforming to the flat surface of the vacuum chuck. Auger analysis shows that these imperfections are Si mounds that are coated with a thin surface layer (~100Å) of carbon. They are most likely caused by local melting of the Si substrate at hot spots on the graphite heater. The molten Si breaks through the SiO₂ coating on the back side of the substrate and beads up because of surface tension before it solidifies. These imperfections are readily removed by lapping the back side of the sample with 40 μm abrasive for 30s. By using this procedure, the measured overall warp was dramatically reduced from ~30 to ~4 μm, as shown in Fig. 2b. To simulate the effects of high temperature device processing, recrystallized samples with a total warp of ~4 μm were heated at a maximum ramping rate of 80°C/min and then annealed for 1h at 1000°C and then for 1h at 1100°C in a N₂ ambient. The overall flatness was actually slightly improved, probably as the result of elimination of stress in the Si substrate by the annealing. Simi-

¹For a similar technique, but relying upon reduced thermal contact between the sample and lower heater, see Ref. (12).

Fig. 2. Interference patterns, with a sensitivity of 5 μm per fringe, for a 2 in. diam SOI sample (a) as recrystallized and (b) following back-side lapping.



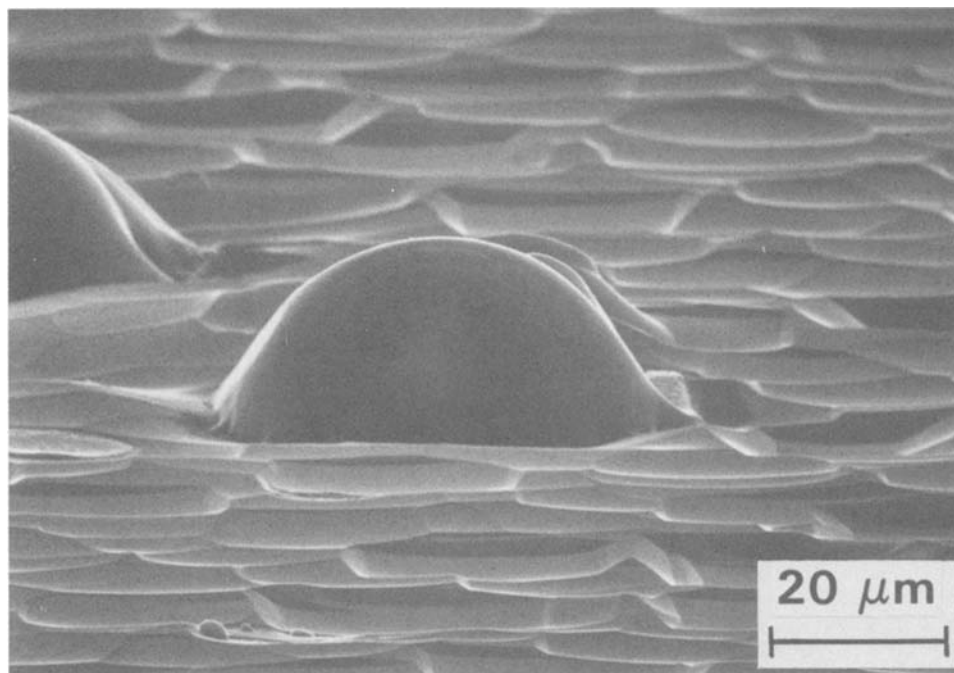


Fig. 3. Scanning electron micrograph showing an imperfection on the back side of an SOI wafer.

lar results have been obtained for 0.015 in. thick, 3 in. diam wafers, with total warp typically $\sim 10 \mu\text{m}$ and in the best case $6 \mu\text{m}$. (Slip occurs in the Si substrate, but not in the Si film during ZMR. However, the annealing experiments show that slip does not adversely affect the overall wafer flatness during subsequent high temperature processing.)

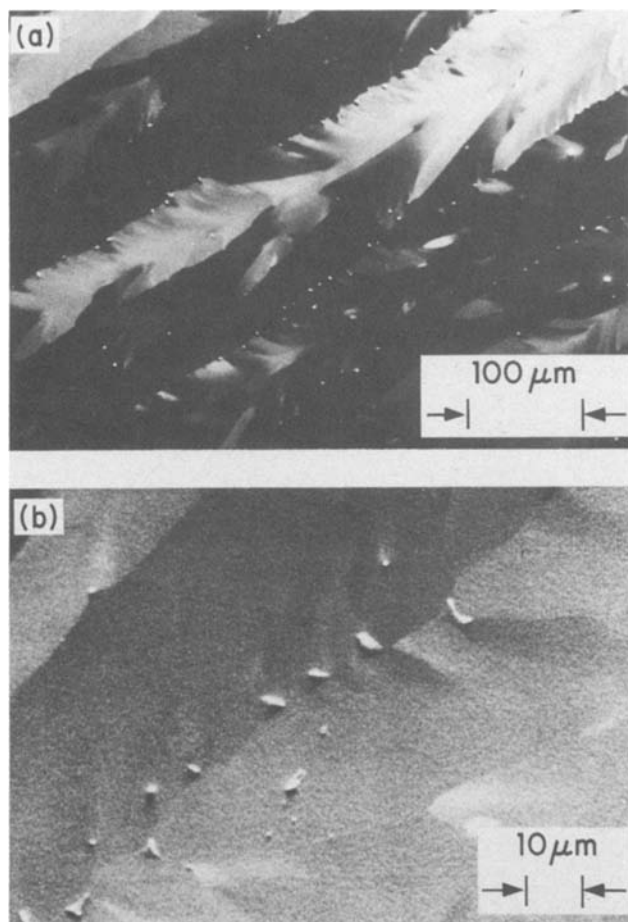


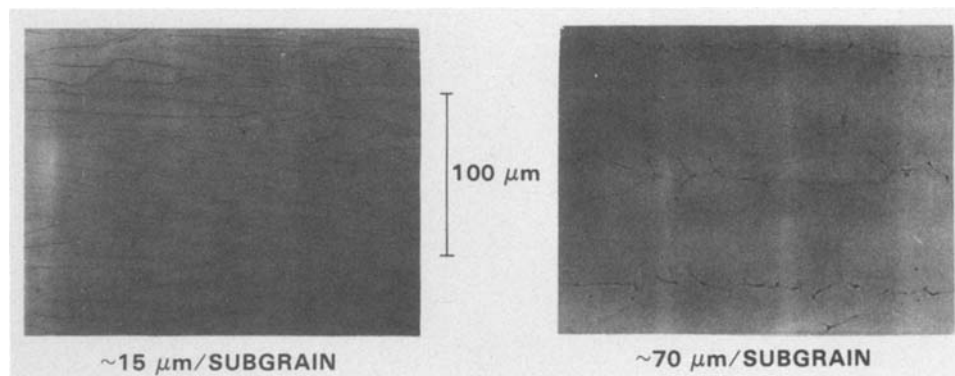
Fig. 4. (a): Micrograph of a recrystallized Si film taken with a scanning electron microscope operated in the backscattering mode. The Si₃N₄/SiO₂ cap has been removed. (b): Magnified view of a small area of the film showing protrusions.

Protrusions.—Figure 4 shows scanning electron micrographs of a recrystallized SOI film containing protrusions. These imperfections are believed to result from the volume expansion occurring during the solidification of liquid Si pools which remain after the liquid-solid interface has passed. According to Auger microprobe analysis, the protrusions consist predominantly of Si, and they do not differ significantly from the surrounding Si film in their impurity content. As shown in Fig. 4, the protrusions generally lie along low angle grain boundaries (sub-boundaries), suggesting some correlation between the two types of imperfections. By evaluating a large number of SOI samples, we have established a direct relation between protrusion density and sub-boundary spacing. The relationship is illustrated in Fig. 5, which shows optical micrographs of two recrystallized SOI samples that were etched in Secco etch (13) and diluted with an equal volume of water to delineate the defects. The sample on the right, which has a wider sub-boundary spacing, has many protrusions; the sample on the left, with more closely spaced sub-boundaries, has very few. In Fig. 6, the sub-boundary spacing is plotted vs. protrusion density; 85% of the data points fall in the shaded region, which shows a systematic decrease in protrusion density with decreasing sub-boundary spacing. This correlation can be understood in terms of the model developed earlier to explain sub-boundary formation (14). According to this model, the sub-boundary spacing decreases as the thermal gradient in the scanning direction is increased. As this gradient increases, the protrusion density should also decrease, since the liquid-solid interface becomes more stable and hence less susceptible to small thermal fluctuations which would give rise to protrusions.

A number of experimental procedures can be followed to increase the temperature gradient at the liquid-solid interface². These include reducing the scan speed (7), decreasing the thickness of the Si film to reduce the total heat of fusion to be dissipated (7), replacing the Ar gas with He (which has a higher thermal conductivity) to increase the rate of heat dissipation to the ambient, and reducing the thickness of the underlying SiO₂ layer or the base temperature of the sample in order to increase the rate of heat dissipation to the substrate. In all cases when such procedures have been followed, the result (if any was detected) was to reduce the sub-boundary spacing and protrusion density as expected for an increase in the temperature gradient.

²For a theoretical analysis of the recrystallization process, see Ref. (15).

Fig. 5. Photomicrographs of recrystallized Si films illustrating the correlation between protrusion density and sub-boundary spacing.



The temperature gradient is also affected by the shape of the upper strip heater and its separation from the sample. We have carried out calculations to investigate the effect of these parameters on the geometrical distribution of power from the upper heater that is incident on the sample. The calculations were made for the two heater cross sections shown schematically in Fig. 7, where D is the heater-sample separation and x is the position on the sample surface along the scan direction, with $x = 0$ located beneath the center of the heater. The heater was assumed to be an infinitely long blackbody. To obtain the relative power distribution, the incremental power originating from a small segment of the heater surface and incident at a position x was calculated from the angle subtended by the segment and the angle of incidence at x . This incremental power was then integrated over the region of the heater visible from x , yielding the relative incident power profile, $P(x)$

$$P(x) = \begin{cases} P_1(x) & 0 \leq x \leq \frac{W}{2} \\ P_1(x) + P_2(x) & x \geq \frac{W}{2} \end{cases}$$

where $P_1(x)$ and $P_2(x)$ are respectively the contributions to P from the bottom and side of the heater, as given by

$$P_1(x) = N \left\{ \frac{x + \frac{W}{2}}{\left[\left(x + \frac{W}{2} \right)^2 + D^2 \right]^{1/2}} - \frac{x - \frac{W}{2}}{\left[\left(x - \frac{W}{2} \right)^2 + D^2 \right]^{1/2}} \right\}$$

$$P_2(x) = N \left(x - \frac{W}{2} \right) \left\{ \frac{1}{\left[\left(x - \frac{W}{2} \right)^2 + D^2 \right]^{1/2}} - \frac{1}{\left[\left(x - \frac{W}{2} \right)^2 + (D + H)^2 \right]^{1/2}} \right\}$$

W is the width and H the height of the heater, and N is a factor normalizing the distribution to unity at $x = 0$. Normalized incident power profiles for several values of D and for the two heater shapes are shown in Fig. 7. The incident power profiles (and thus the temperature gradients) become sharper with decreasing heater-sample separation. Consistent with this result, lower protrusion densities have been observed for reduced separations. To achieve sharp incident power profiles experimentally, care must be taken to control or eliminate the bowing of the SOI sample, and of the upper and lower strip heaters as a result of thermal expansion upon heating. Such bowing could significantly alter the upper heater-sample sep-

aration. Note also that the temperature gradient at the liquid-solid interface depends on the position of the interface with respect to the upper heater (*i.e.*, on the width of the molten zone), since the gradient as well as the incident power varies with x .

Voids.—From time to time, we have found that recrystallized Si films from a particular batch of SOI wafers contain voids with densities as high as $5/\text{mm}^2$. Figure

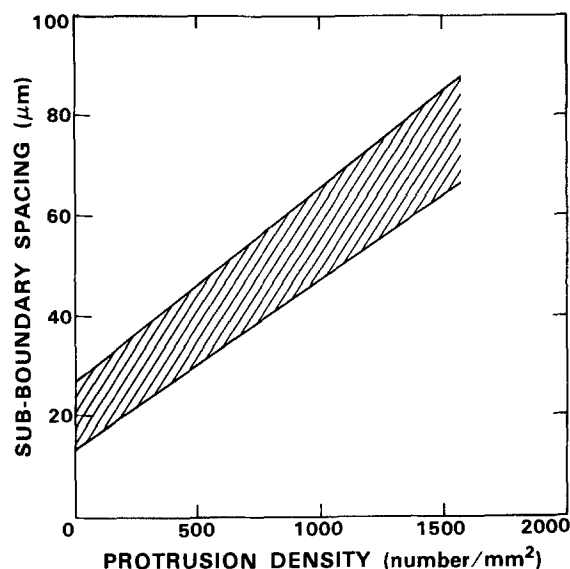


Fig. 6. Plot of sub-boundary spacing vs. protrusion density. Data points for 85% of the samples examined fall in the shaded region.

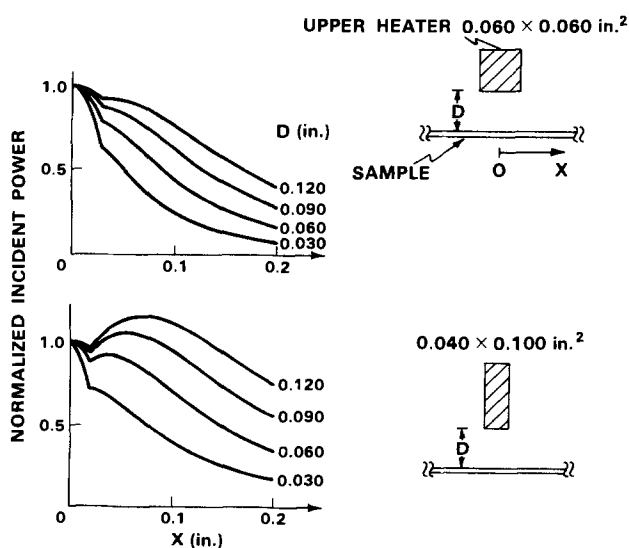


Fig. 7. Power incident on a sample from the upper strip heater as a function of position x along the sample surface. D is the heater-sample separation.

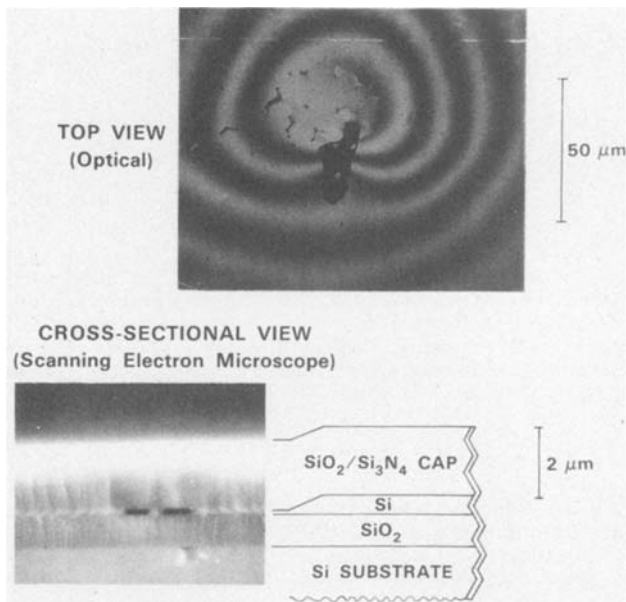


Fig. 8. Optical (Nomarski interference) and SEM micrographs of typical voids. The cross-section diagram shows the reduction in the thickness of the recrystallized Si film in the vicinity of the void.

8 shows optical and scanning electron microscope (SEM) micrographs of typical voids. The SEM cross-sectional view indicates that the voids result from the flow of molten Si, which leads to local thinning of the Si film, and in extreme cases to the absence of Si between the two oxide layers. Because void-free recrystallized Si films have often been produced immediately before and after the preparation of films with high void densities, these imperfections are believed to result from contamination introduced in the fabrication of the SOI structure. Although the precise mechanism of void formation is not known, we have found that reducing the scan speed from 1 mm/s to 0.5 mm/s significantly decreases the void density in films from contaminated batches. This improvement probably occurs because the lower rate produces a sharper temperature gradient, which stabilizes the liquid-solid interface.

Conclusion

We have discussed factors affecting the principal topographic imperfections in ZMR Si films. With suitable control of the heating rate and temperature profile, together with back-side lapping after recrystallization, total warp of less than 4 μm has been achieved for 2 in. diam SOI wafers on a vacuum chuck. This flatness approaches that needed for VLSI applications. Lower protrusion density has been correlated with finer sub-boundary spacing, and both can be attributed to a sharper thermal gradient at the growth front. Lower protrusion density can be achieved by reducing the thickness of the lower SiO₂ layer and the poly-Si film, the scan speed, and the upper heater-sample separation, and by using an ambient gas with higher thermal conductivity. 2 in. diam films nearly free of protrusions have been obtained. However, such films have a high density of sub-boundaries.

We are presently exploring two approaches to solve the problem of protrusions and sub-boundaries in recrystallized SOI films. First, we are investigating control of the sub-boundaries by means of entrainment (14). Second, we are attempting to suppress sub-boundary formation by

using sharper temperature gradients,³ repeated melting and regrowth, and periodic seeding (17). Because the protrusions lie along the sub-boundaries, success with either approach would yield SOI films with large areas free of both sub-boundaries and protrusions. We believe that the characteristics needed for employing large-area wafers will be achieved in the near future, making the ZMR process a practical technique for producing SOI materials for VLSI applications.

Acknowledgments

The authors acknowledge the expert technical assistance of M. J. Button, M. C. Finn, R. W. Mountain, and P. M. Nitishin, and helpful discussions with H. I. Smith and A. J. Strauss. This work was sponsored by the Department of the Air Force and the Defense Advanced Research Projects Agency.

Manuscript submitted Nov. 23, 1983; revised manuscript received March 9, 1984.

Massachusetts Institute of Technology assisted in meeting the publication costs of this article.

³As the temperature gradient increases, the sub-boundary density will also increase. However, if a sufficiently sharp gradient can be achieved, the formation of instabilities giving rise to sub-boundaries will be suppressed (16).

REFERENCES

1. "Laser and Electron Beam Processing of Materials," C. W. White and P. S. Peercy, Editors, Academic Press, New York (1980).
2. "Laser and Electron Beam-Solid Interactions and Material Processing," J. F. Gibbons, L. D. Hess, and T. W. Sigmon, Editors, North Holland, New York (1981).
3. "Laser and Electron Beam Interactions with Solids," B. R. Appleton and G. K. Celler, Editors, North Holland, New York (1982).
4. "Laser-Solid Interactions and Transient Thermal Processing of Materials," J. Narayan, W. L. Brown, and R. A. Lemons, Editors, North Holland, New York (1983).
5. See *J. Cryst. Growth* for an issue devoted to SOI technology, **63**, (1983).
6. J. C. C. Fan, M. W. Geis, and B-Y. Tsaur, *IEDM Technical Digest*, p. 845, Washington, DC (1980); M. W. Geis, H. I. Smith, D. A. Antoniadis, D. J. Silversmith, J. C. C. Fan, and B-Y. Tsaur, Paper H-1, AIME Electronic Materials Conference, San Diego, CA, June 24-26, 1981; and E. W. Maby, M. W. Geis, Y. L. LeCoz, D. J. Silversmith, R. W. Mountain, and D. A. Antoniadis, *IEEE Electron. Devices Lett.*, **ed1-2**, 241 (1981).
7. M. W. Geis, H. I. Smith, B-Y. Tsaur, J. C. C. Fan, D. J. Silversmith, and R. W. Mountain, *This Journal*, **129**, 2812 (1982).
8. J. C. C. Fan, B-Y. Tsaur, R. L. Chapman, and M. W. Geis, *Appl. Phys. Lett.*, **41**, 186 (1982), and references therein.
9. B-Y. Tsaur, M. W. Geis, J. C. C. Fan, D. J. Silversmith, and R. W. Mountain, *ibid.*, **39**, 909 (1981).
10. B-Y. Tsaur, J. C. C. Fan, R. L. Chapman, M. W. Geis, D. J. Silversmith, and R. W. Mountain, *IEEE Electron. Devices Lett.*, **ed1-3**, 398 (1982).
11. C. K. Chen, M. W. Geis, B-Y. Tsaur, R. L. Chapman, and J. C. C. Fan, Paper G-5, AIME Electronic Materials Conference, Burlington, VT, June 22-24, 1983.
12. McD. Robinson, C. C. Chang, R. B. Marcus, G. A. Rozgonyi, L. E. Katz, and C. L. Paulnack, *This Journal*, **129**, 2858 (1982).
13. F. Secco D'Aragnona, *ibid.*, **119**, 948 (1972).
14. M. W. Geis, H. I. Smith, D. J. Silversmith, and R. W. Mountain, *ibid.*, **130**, 1178 (1983).
15. H. E. Cline, *J. Appl. Phys.*, **54**, 2683 (1983).
16. D. E. Holmes and H. C. Gatos, *J. Appl. Phys.*, **52**, 2971 (1981).
17. J. C. C. Fan, M. W. Geis, and B-Y. Tsaur, *Appl. Phys. Lett.*, **38**, 365 (1981).

Characterization of RF Sputter-Deposited Ti-W Schottky Barrier Diodes in Boron-Doped Silicon

O. Paz,* F. D. Auret,¹ and J. F. White

IBM East Fishkill Laboratories, Hopewell Junction, New York 12533

ABSTRACT

The properties of defects introduced during RF sputter deposition of Ti-W contacts on p-Si were investigated using I-V, deep level transient spectroscopy (DLTS), and electron-beam-induced current (EBIC) techniques combined with isochronal and isothermal annealing. It was found that the barrier height decreased from 0.56V before annealing to 0.5V after isochronal annealing. DLTS measurements indicate the presence of several sputter-induced defect states. Annealing removed some of the defects, but second generation defects were still present after annealing at 500°C, now distributed deeper into the substrate. EBIC results showed that the diffusion length decreased with increasing annealing temperature. DLTS and EBIC results suggest that a hole trap at $E_v + 0.35$ eV is a strong recombination center. This hole trap is very likely the same defect as the one identified as the K center [V + O + C].

Sputtering, which allows deposition of both metals and insulators, is especially useful because of its ability to deposit compounds with good stoichiometric control. When sputtering metal contacts, they and the substrate underneath are subject to bombardment by energetic particles. These particles include low energy Ar ions from the plasma, sputtered metal atoms [with energies up to 20 eV (1)], high energy electrons, and neutral Ar atoms. It has been found that in silicon, the sputtering process creates an electrically active damaged layer in the substrate underneath the contact (2, 3).

Mullins and Brunnschweiler (2) suggested that during sputter deposition (on n-type silicon), high density donor-like traps are created near the surface. Berg *et al.* (3) proposed that the increasing surface-trap density causes electron tunneling through the barrier at an energy lower than the energy at the top. This leads to lowering of the effective barrier height. Not much has been published on the structural modification that this damage may cause in the surface layer. Ogilvie and Thomson (4) have shown that positive argon ions (at an energy of 130 eV) can introduce disoriented crystallites and stacking faults near the surface of single-crystal silver.

In this work, we investigate the damage induced in the substrate when Ti-W Schottky barrier diodes (SBD's) are RF sputter deposited. The effect of the damage on the properties of the rectifying junctions is obtained from I-V measurements, while the DLTS and EBIC techniques are employed to characterize the nature of the defects, and the extent to which they increase recombination.

Experimental

p-Type ($N_A = 1 \times 10^{16}$ cm⁻³), Czochralski-grown, <100> Si wafers (82 mm diam) were used. In order to form ohmic contacts, the wafers were chemically cleaned and Al deposited on their unpolished back sides. The wafers were subsequently annealed for 30 min at 450°C in forming gas. Prior to sputtering, the wafers were dipped in buffered HF for 10s to remove the residual surface oxide. After pumping the system to 10⁻⁶ torr, a 2000Å thick continuous layer of Ti-W (10% Ti, 90% W by weight) was sputter deposited at a power of 1 kW (800V) in an argon atmosphere of 8 × 10⁻³ torr. In order to define a dot pattern of SBD's, 0.5 mm Al dots were resistively deposited on the Ti-W film through a contact mask. The Ti-W film around the dots were then removed by chemical etching. This method of forming the SBD's prevented possible contamination of the wafer's surface due to contact with the contact mask.

I-V and DLTS measurements were taken on the devices without annealing them as well as after annealing for 10 min at 25° or 50°C intervals up to 500°C. EBIC measure-

ments were taken before annealing and after annealing for 20 min at 275° and 400°C. The longer annealing times approximately compensate for the fewer annealing cycles that were received by the latter devices. DLTS (5) analysis was performed by using the dual-gated, lock-in amplifier technique (6). Measurements were taken in the temperature range 83-300 K.

Diffusion lengths in the Si layer beneath the contact were determined using electron-beam excitation (EBIC mode). The diffusion lengths were measured at 18 kV and corrected for carriers generated by backscattered and secondary emitted electrons. In carrying out the correction due to backscattered electrons, the number of collected carriers at 8.6 kV (the energy spectrum of backscattered electrons with primary energy of 18 kV) was also measured. The model used to calculate the diffusion length is described in Ref. (7). Here we briefly outline some of the assumptions used in deriving it. Due to the normalization procedure (the collection current is divided by the specimen current (7), the diffusion length does not depend on the beam current (except for injection effects that can be reduced or taken into account). The acceleration voltage determines the generation volume and, therefore, the depth (we are using a one-dimensional model) of generation and collection. Because of the geometry, any variations in surface recombination velocity are not a problem. It is assumed that carriers are collected at the edge of the depletion layer with infinite collection velocity. In the depletion layer itself, no recombination is assumed. This constraint is less significant when the depletion layer depth is small compared to the generation volume.

When the beam electrons penetrate the metal layer, they lose part of their energy due to scattering, without generation of excess carriers. Therefore, the metal thickness, as well as the mass density and atomic weight, greatly influence charge collection. In order to correct the diffusion length readings for losses in the metal layer, charge collection *vs.* metal thickness was plotted for evaporated Mo contacts (on n-type wafers) in the thickness range 200-2700Å. For SEM beam energy of 18 kV, a linear fit produced the following relationship

[Loss of Excess Carriers]

(in carriers per incident electron) =

$$[0.919] \times [\text{layer thickness in angstroms of the Mo layer}] \quad [1]$$

For a Ti-W layer, the readings were further corrected by assuming that the effective layer thickness Y is proportional to the maximum penetration range R_{\max} [for R_{\max} , Kanaya and Okayama's (8) model was used]

$$\frac{Y_{\text{Mo}}}{Y_{\text{Ti-W}}} \approx \frac{R_{\max\text{Mo}}}{R_{\max\text{Ti-W}}} \quad [2]$$

* Electrochemical Society Active Member.

¹ Permanent address: Department of Physics, University of Port Elizabeth, Port Elizabeth 6000, South Africa.

Key words: films, plasma, SEM, sputtering.

Results

The barrier heights were extracted from the log (I)-V curves by using Beguwala and Crowell's three-point method (9). The influence of anneal temperature on these barrier heights is shown in Fig. 1. The devices were annealed for 10 min at 50°C intervals up to 500°C. A gradual decrease in the barrier height from 0.56V at room temperature to 0.5V at 500°C was observed. Isothermal annealing (400°C, 1h intervals) showed that the barrier height stabilized at 0.52V after 3h, and remained at that value even after 8h anneal at 400°C.

The activation energies and annealing characteristics of the DLTS defect states obtained from the DLTS spectra are summarized in Table I. Figure 2 shows typical DLTS spectra, taken before annealing and after 275°, 375°, and 450°C anneals. Before any annealing, three defect levels were observed: H(0.26), H(0.35), and H(0.45) (the H signifies that the defect is a hole trap and that the activation

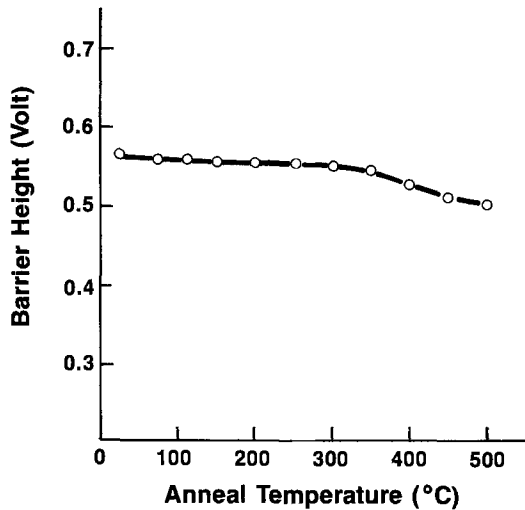


Fig. 1. The variation of barrier height, calculated from log (I)-V measurements, of RF-sputtered Ti-W SBD on p-Si, with isochronal (10 min) annealing temperature.

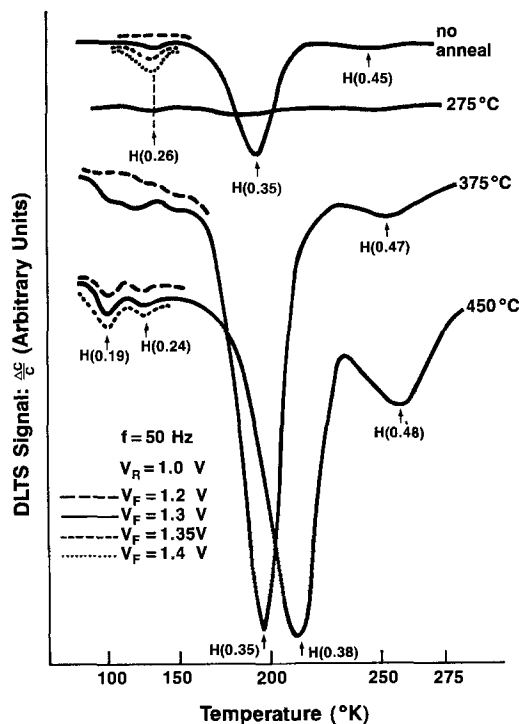


Fig. 2. DLTS spectra of RF sputter-induced damage below the Ti-W contact, taken before annealing and after 275°, 375°, and 450°C anneals. A bias of 1.0V was used. A variation of the DLTS signal with depth (by varying V_F) for some defects is shown.

Table I. Properties of defects induced in P-Si by RF sputtering

Defect	σ_p (cm ²)	Peak temp. at 11 ms, emission constant	Isochronal annealing T_{in} (°C)	T_{out} (°C)
H(0.17)	4×10^{-16}	106	325	>500
H(0.24)	2×10^{-16}	125	300	400
H(0.26)	6×10^{-16}	132	RT*	>350
H(0.29)	4×10^{-16}	139	400	>500
H(0.35)	1×10^{-15}	196	RT	225
H(0.35)	1×10^{-15}	196	275	450
H(0.38)	1×10^{-15}	213	400	>500
H(0.47)	2×10^{-15}	252	275	400
H(0.48)	2×10^{-15}	261	400	>500

* The symbol RT means that the defect was observed after deposition and without any annealing.

energy is measured from the valence band). At 275°C, almost no defects can be observed; however, annealing at higher temperatures again increased the defect concentration, as well as introduced new defects. A similar disappearance of the defects after 250°C, and reappearance after annealing at higher temperatures, was observed by us in ion beam sputter-deposited Mo contacts on n- and p-type Si (10). Figure 3 summarizes the results of depth profiling that was achieved by the fixed-bias variable pulse method (5). As the figure shows, the most prominent defect level observed before annealing H(0.35) was located very close ($\leq 1600\text{\AA}$) to the interface. This defect level merits a detailed discussion. Figure 4 plots the DLTS signal (that is proportional to the concentration of the defect states) vs. the isochronal annealing temperature (10 min, 25°C interval). The figure shows that defect H(0.35) follows the same trends as defect H(0.35) that was analyzed after ion beam deposition of Mo on p-type silicon (10). After a 200°C anneal, H(0.35) disappeared almost completely. Upon increasing the anneal temperature to 300°C, it reappeared only to be distributed much deeper ($< 4000\text{\AA}$, see Fig. 3) in the substrate. Its concentration reached a maximum after 350°C annealing, and it finally annealed out at approximately 450°C. Above 300°C, more defects were introduced. The most significant defect in this temperature range H(0.38) started to appear as H(0.35)

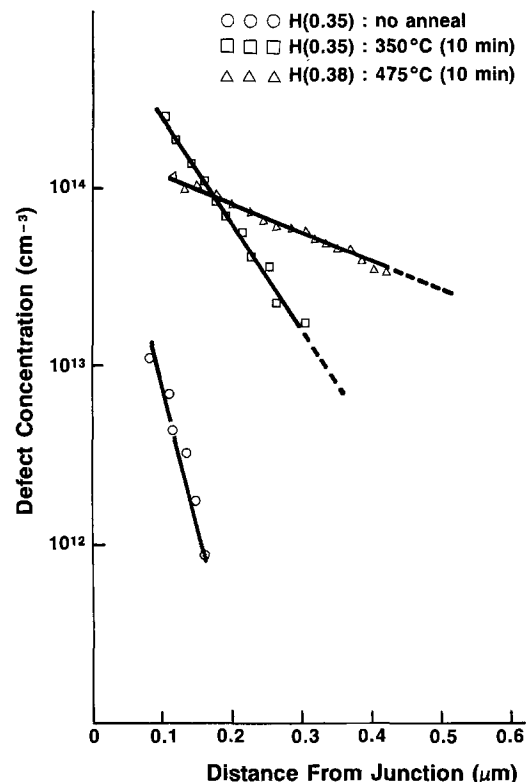


Fig. 3. Depth concentration profiles of H(0.35) and H(0.38) taken before and after annealing.

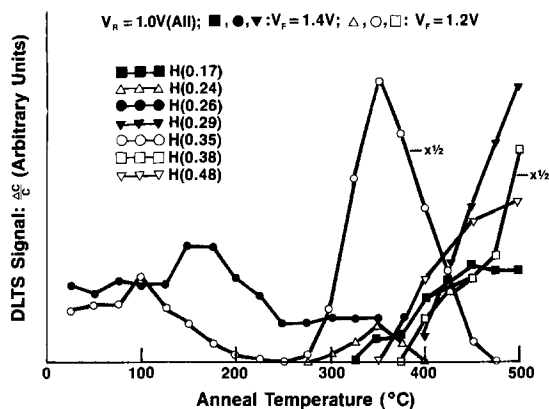


Fig. 4. Isochronal (10 min) annealing behavior of RF sputter-induced damage. The defects represented by dark symbols were only present very close to the surface.

began to anneal at 400°C. It was still present after annealing at 500°C, now observed even deeper into the Si substrate ($\leq 6000\text{\AA}$) than H(0.35). Figure 5 illustrates that isothermal annealing (400°C, 1h intervals) showed a gradual increase in the defect concentrations, especially of H(0.38) and H(0.29). Annealing, therefore, did not remove the process-induced defects, but only caused them to move deeper into the Si substrate.

Another related conclusion was that the defect H(0.35) exhibited the same annealing behavior as H(0.35), observed after irradiating similar wafers with 2 MeV electrons (Fig. 6). For the latter case, SBD's were formed on the irradiated wafers by resistive evaporation of Ti. Furthermore, it was recently found that defects H(0.35) and H(0.38) are present after electron-beam deposition of Mo, Hf, and Ti on p-type silicon, and all exhibit a similar annealing behavior (11). As discussed in more detail in Ref. (11), H(0.35) is very likely the same (12, 13) defect as the one identified as the K center [V + O + C]. The defect H(0.38) appears after H(0.35) anneals out. This strongly suggests that H(0.38) is formed from the dissociates of H(0.35).

Figure 7 illustrates the diffusion length results. At 18 kV, electron-hole pairs are produced within a 4.5 μm generation volume. Generation of excess carriers in the substrate can be approximated as an exponential that decays with increasing depth. Therefore, more excess carriers are generated within the surface portion of the generation volume than in the bulk portion. This means that, at 18 kV, the diffusion lengths measured are more representative of the damaged layer beneath the contact than the bulk. As the figure shows, the diffusion length decreases gradually from about 4.5 to 1.2 μm after annealing the samples at 275° and 400°C, respectively.

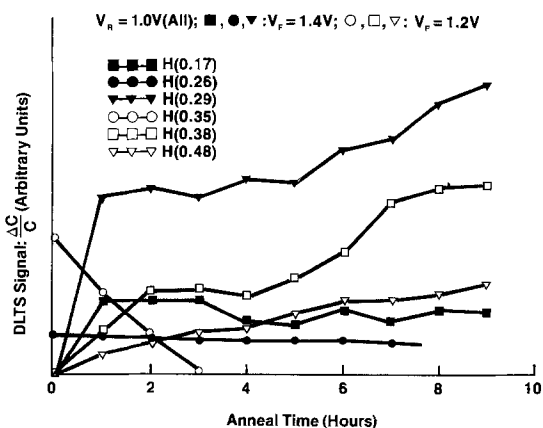


Fig. 5. Isothermal annealing (400°C, 1h intervals) behavior of RF sputter-induced defects. Defects represented by dark symbols were only present very close to the surface.

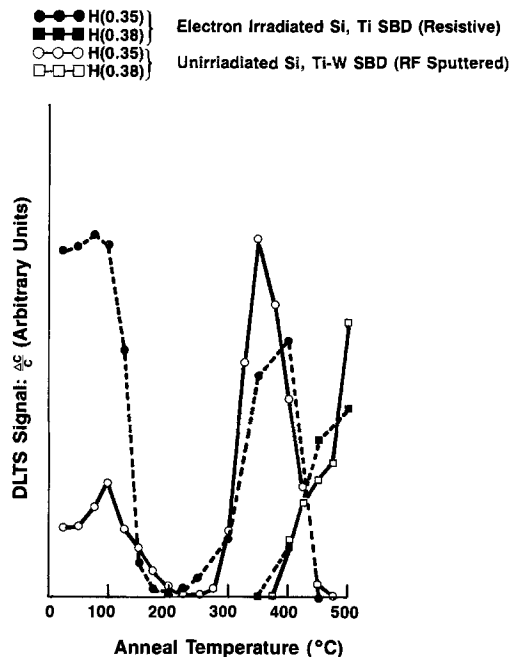


Fig. 6. Isochronal annealing behavior of H(0.35) and H(0.38) observed in 2 MeV electron-irradiated samples and in unirradiated, RF sputter-deposited samples.

Discussion

The decrease in barrier height that was observed in the present work after annealing is consistent with observations on ion beam sputter-deposited Mo contacts (on p-type silicon) (10). After RF or ion beam sputter deposition, the device barrier heights are modified: as reported for n-type silicon (10), the barrier heights are decreased, and they increase for p-type silicon. Mullins and Brunnschweiler (2) calculated the potential energy profile in n-type silicon assuming that donor-like traps are introduced due to the sputtering damage. They showed that, for traps that are distributed into the substrate as a decreasing exponential, the modified potential energy profile leads to narrowing of the barrier and increased tunneling. This is reflected in a lower effective barrier height. For p-type silicon, we can qualitatively reason out an increase in the effective barrier height as follows: if we assume donor-like traps, the positively charged traps will neutralize some of the negatively charged ionized acceptor impurities. This has the same effect as moving the Fermi level away from the valence band, which leads to widening of the barrier and a decrease in tunneling. Fonash *et al.* (14) suggested a similar effect for ion-beam-generated damage. The decrease in barrier height that we observed after annealing (Fig. 1) suggests that a decrease in defect concentration near the interface has taken place. However, the DLTS data suggests that as the defects mi-

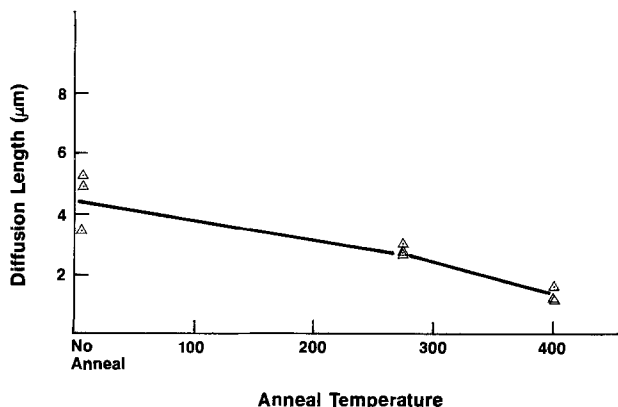
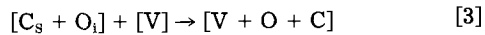


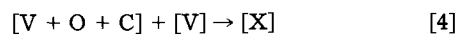
Fig. 7. Variation of minority carrier diffusion length, measured below the Ti-W SBD, with annealing temperature.

grated deeper into the substrate, their concentration increased (even as close to the interface as can be determined given the spatial resolution of the method). This is illustrated for trap H(0.35) in Fig. 3. The concentration of H(0.35) and its replacement H(0.38) is higher at 350° and 475°C than before annealing.

A comparison of the DLTS spectrum and the diffusion length results suggest that H(0.35) is a strong recombination center. The significant increase in the concentration of H(0.35) seen after 375° or 400°C anneal is accompanied by a factor of three reduction in diffusion length. Based on the annealing behavior we postulated that H(0.35) is the same defect as the vacancy-carbon-oxygen complex [V + C + O] that was identified, using the EPR technique, in irradiated p-type silicon (15). A possible mechanism for the formation of this defect is the following (12)



where [V] represents the vacancy and [C_s + O_i] represents a complex consisting of substitutional carbon and interstitial oxygen. The concentration of the [V + O + C] complex can be determined from the concentration of its constituents. Both substitutional carbon and interstitial oxygen are present in Czochralski-grown silicon. The vacancies are introduced due to the bombardment by Ar ions or neutral Ar atoms. After annealing, the vacancies will migrate deeper into the substrate producing even more [V + O + C] complexes, as we observed from both the DLTS and the diffusion length data. An argument can be made that the [V + O + C] complex was observed by several investigators that reported slightly different energy levels (12). This conclusion is based on an agreement on the location of the levels and their annealing behavior. More recently, Benton and Kimerling (16) reported a hole trap at $E_v = 0.36$ eV that has the same DLTS peak temperature as we report, after correcting for the different instrumentation time constants, although anneal data were not given. In still another work, conducted at our laboratory, H(0.35) and H(0.38) were observed after electron-beam deposition of Mo and Ti on p-type silicon (11). The preponderance of this defect after several processes and in a wide range of samples suggests a major defect in boron-doped silicon. The annealing behavior reported here for the [V + O + C] is somewhat different than the annealing behavior reported previously for the [V + O + C] complex (12). This difference may be due to the substrates used. The disappearance of the [V + O + C] after 275°C does signify, in our opinion, not that the defects were removed, but rather that a change of state took place. This conclusion is based on the diffusion length's remaining low. The change of state can occur due to two reasons. First, it can be due to a Fermi level shift that may result from dopant compensation. However, the oxygen thermal donor is not sufficiently activated at 275°C to cause this compensation. Second, the [V + O + C] complex can react with a vacancy to form a new complex [X] that can either be electrically inactive or have a state in the upper bandgap and, therefore, undetectable to us



the subsequent reappearance of the [V + O + C] complex at higher temperatures may be due to production of new [V + O + C] complexes upon further vacancy migration.

A recent paper reports that complexes involving oxygen are lifetime limiting (17). Dislocation-free Czochralski-grown Si crystals were used, doped with boron or phosphorus. The interstitial oxygen concentration in their samples (about 10^{18} cm⁻³) is comparable to ours, and the carbon concentration is relatively high (10^{17} cm⁻³).

The crystals were measured as grown without any heat-treatment. Since defect energy levels were not measured, we can only speculate that the reported defects may have been [V + O + C] complexes.

Conclusions

We have demonstrated that RF sputtering of Ti-W contacts introduces defects near the semiconductor interface. Log (I) vs. V results confirm an earlier observation that sputtering induced damage increases the barrier height in p-type silicon. Log (I) vs. V and DLTS measurements, taken after isochronal annealing, suggest that the defects move deeper into the substrate at temperatures above 275°C. Also, new defects are introduced and defects are present even after 500°C anneal. Isothermal annealing indicated that the total defect concentration at 400°C increased with anneal time. EBIC results indicate that annealing lowers the lifetime in the surface layer of the substrate (up to a depth of 4 μm). It also shows that some of the defects observed by DLTS, in particular H(0.35), are recombination centers.

Two of the defects observed after Ti-W sputtering, H(0.35) and H(0.38), have the same anneal characteristics as H(0.35) and H(0.38) observed by us on unspattered wafers that received 2 MeV electron irradiation. This suggests that H(0.35) is the same defect as the one identified as the K center, also present in p-type wafers that received 1.5 MeV electron irradiation.

Acknowledgments

We acknowledge Dr. T. Y. Tan for his encouragement and support, Mr. C. P. Schneider for technical assistance, and Mr. N. A. Bojarczuk and Dr. R. Kleinhenz for useful discussions.

Manuscript submitted Sept. 26, 1983; revised manuscript received Feb. 12, 1984. This was Paper 877 RNP presented at the San Francisco, California, meeting of the Society, May 8-13, 1983.

IBM Corporation assisted in meeting the publication costs of this article.

REFERENCES

1. E. Grusell, S. Berg, and L. P. Andersson, *This Journal*, **127**, 1573 (1980).
2. F. H. Mullins and A. B. Brunnschweiler, *Solid-State Electron.*, **19**, 47 (1976).
3. S. Berg, L. P. Andersson, H. Norstrom, and E. Grusell, *Vacuum*, **27**, 189 (1977).
4. G. J. Ogilvie and A. A. Thomson, *J. Phys. Chem. Solids*, **17**, 203 (1961).
5. G. L. Miller, D. V. Lang, and L. C. Kimerling, *Ann. Rev. Mater. Sci.*, **7**, 377 (1977).
6. D. Pons, P. M. Mooney, and J. C. Bourgoin, *J. Appl. Phys.*, **51**, 2038 (1980).
7. O. Paz and J. M. Borrego, *Appl. Phys. Lett.*, **42**, 958 (1983).
8. K. Kanaya and S. Okayama, *J. Phys. D*, **5**, 43 (1972).
9. M. Beguwala and C. R. Crowell, *J. Appl. Phys.*, **45**, 2792 (1974).
10. F. D. Auret, O. Paz, and N. A. Bojarczuk, *ibid.*, **55**, 1581 (1984).
11. F. D. Auret and P. M. Mooney, *ibid.*, **55**, 984 (1984).
12. P. M. Mooney, L. J. Cheng, M. Suli, J. D. Gerson, and J. W. Corbett, *Phys. Rev. B*, **15**, 3836 (1977).
13. Y. H. Lee, K. L. Wang, A. Jaworowski, P. M. Mooney, L. J. Cheng, and J. W. Corbett, *Phys. Status Solidi A*, **57**, 697 (1980).
14. S. J. Fonash, S. Ashok, and R. Singh, *Appl. Phys. Lett.*, **39**, 423 (1981).
15. Y. H. Lee, J. W. Corbett, and K. L. Brower, *Phys. Status Solidi A*, **41**, 637 (1977).
16. J. L. Benton and L. C. Kimerling, *This Journal*, **129**, 2098 (1982).
17. K. Nauka, H. C. Gatos, and J. Lagowski, *Appl. Phys. Lett.*, **43**, 241 (1983).

Free Carrier Reduction in Vacuum-Annealed S-, Sn-, and Ge-Doped (100) InP

G. P. Schwartz,* G. J. Gualtieri, L. H. Dubois, and W. A. Bonner

AT&T Bell Laboratories, Murray Hill, New Jersey 07974

A. A. Ballman

AT&T Bell Laboratories Holmdel, New Jersey 07733

ABSTRACT

Raman scattering has been utilized to examine variations in the free-carrier concentration of S-, Sn-, and Ge-doped (100) InP and Si-doped (100) GaAs induced by vacuum annealing the wafers at 500°-550°C for periods ranging from 30 to 60 min. Corrections for the concentration dependence of the conduction electron effective mass have been incorporated analytically. After annealing, reduction of the free-carrier concentration is observed in all cases; for InP, the magnitude of the reduction varied from ~20% for S-doped material annealed at 550°C for 30 min to 20%-50% for Sn- and Ge-doped samples annealed at 500°C for 1h. A 1h anneal of Si-doped GaAs at 500°C reduced the net free-carrier density by roughly a factor of 4. Our measurements indicate that if annealing induced dopant "pile up" occurs at the surface because of gettering or the dynamics of surface evaporation, then the dopants either (i) are not electrically active, (ii) have been compensated by defects generated during annealing, or (iii) are piled up within the space-charge depletion region.

The net doping level in the near-surface region of most compound semiconductors is known to be sensitive to the thermal history experienced by the sample. Some of the factors known to alter the surface free-carrier density include (i) dopant redistribution induced by gettering to surface defects, (ii) direct dopant volatilization, and (iii) generation and diffusion of defects related to surface substrate evaporation. The latter consideration is particularly important for a material like InP because it incongruently evaporates *in vacuo* at temperatures above 360°C. Other parameters, such as the gas ambient, are also critical in influencing the type of defects generated during substrate volatilization. As a consequence, reports can be found in the literature concerning InP in which varying the annealing ambient can either reduce (1) or enhance (2) the near-surface doping level relative to bulk values:

The present study concerns alterations of the near-surface free-carrier concentration induced by uncapped vacuum annealing of InP and GaAs wafers at 500°-550°C for periods varying from 30 to 60 min. The substrates studied were all degenerately n-doped in the range $0.5\text{-}2 \times 10^{18} \text{ cm}^{-3}$. In degenerately n-doped zinc blende materials, it is possible to obtain the net free-carrier density from a Raman measurement of the coupled plasmon-phonon mode frequencies. The technique is both contactless and nondestructive, with a penetration depth which depends on the excitation wavelength and the absorption coefficient of the substrate. The current study has examined free-carrier variations within the first 2000Å of the surface.

The remaining sections of the paper are organized as follows. "Experimental and Results" contains details of the experiments and the Raman spectra of S-, Sn-, and Ge-doped InP and Si-doped GaAs before and after vacuum annealing. "Theory" in the "Discussion" section presents the details of calculations pertinent to converting plasmon-phonon mode frequencies into net free-carrier densities, and "Free-carrier concentration" contains a comparison of our results with data previously reported in the literature.

Experimental and Results

Wafers of S-, Sn-, and Ge-doped (100) InP and Si-doped (100) GaAs were bromine-methanol polished, rinsed in methanol, and blown dry, and then inserted into quartz ampuls which were evacuated to $\sim 5 \times 10^{-6}$ torr and sealed. The ampuls were placed in a preheated furnace at 500°-550°C and removed after periods varying from 30 to

* Electrochemical Society Active Member.

60 min. Table I records the thermal history of each sample.

Raman measurements were carried out using the 5145Å line of an argon ion laser for excitation and a 1m double monochromator with holographic gratings for analysis of the scattered light. The instrument resolution was set at $6\text{-}8 \text{ cm}^{-1}$, and the incident power was typically 100-300 mW, which was dispersed in a line source of approximate length 5 mm. All measurements were performed at room temperature with the samples mounted in an argon-purged cell.

The resulting Raman spectra taken before and after annealing are presented in Fig. 1-4 for S-, Sn-, and Ge-doped (100) InP and Si-doped (100) GaAs, respectively. The lower spectrum in each figure represents the sample prior to annealing. The primary features of interest are the coupled plasmon-phonon modes labeled as ω_+ and ω_- . Since ω_- is only weakly concentration dependent in the free-carrier density range of interest, our analysis will emphasize only the shifts observed in ω_+ . These are summarized in Table I. In addition to these two modes, one also sees scattering from longitudinal optic (LO) phonons originating from the carrier-depleted space-charge layer in which there are no conduction electrons available for screening. In (100) n-InP with a nominal 10-20Å native oxide, the upward band bending is roughly 0.5 eV (3), whereas on n-GaAs it is closer to 0.8 eV (4). In the carrier

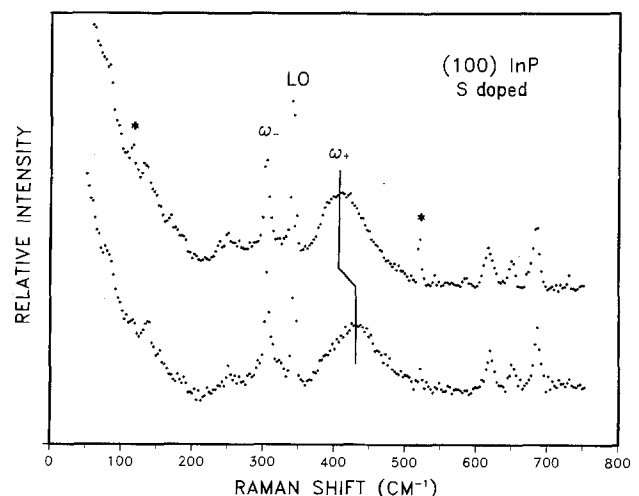


Fig. 1. Raman spectra for S-doped InP before (lower trace) and after (upper trace) a vacuum anneal at 550°C for 30 min.

Table I. Free-carrier concentration measurements

	Dopant	Anneal	ω_+ (cm ⁻¹)		N (carriers/cm ³)	
			No anneal	Annealed	No Anneal	Annealed
(100) InP	S	550°C 1/2h	431	407	1.0×10^{18}	7.8×10^{18}
	Sn	500°C 1h	376	358	0.47×10^{18}	0.25×10^{18}
	Ge	500°C 1h	555	481	2.2×10^{18}	1.5×10^{18}
(100) GaAs	Si	500°C 1h	511	332	1.7×10^{18}	0.43×10^{18}

concentration range between 5×10^{17} and 2×10^{18} cm⁻³, this represents a depletion zone of ~370-185Å for InP and 480-240Å for GaAs. The effective measurement depth in a surface reflection geometry for collection of 95% of the signal is $\approx 3 \times \lambda/4\pi k \times 1/2$ where λ is the excitation wavelength and k is the absorptive part of the index of refraction. These effective measurement depths are of order 1400 and 1700Å for InP and GaAs, respectively. The unscreened LO signal is fairly strong in our spectra because the space-charge depletion zone represents a sizable fraction of the effective measurement depth.

For frequencies lower than ω_- , additional structure is observed, which consists primarily of transverse acoustic overtones (5, 6). The three relatively strong peaks seen in the InP spectra between 600 and 700 cm⁻¹ are overtones and combination modes of the transverse and longitudinal optic phonons (2TO, LO + TO, 2LO in increasing cm⁻¹) (5, 6). Asterisks denote laser plasma lines at 116 and 520 cm⁻¹. These modes are peripheral to our interests and will not be considered further.

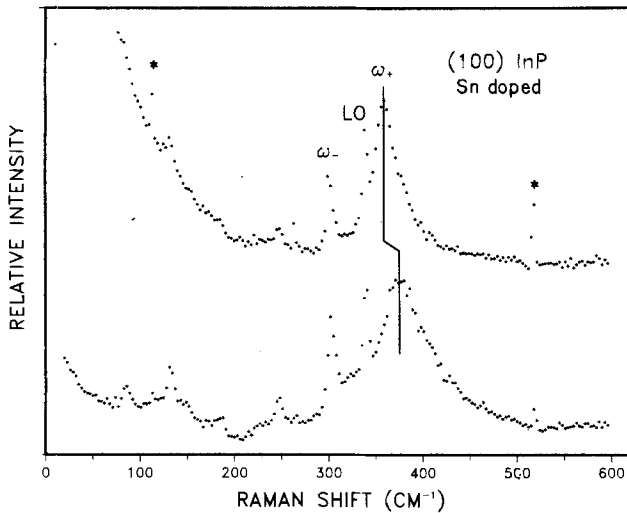


Fig. 2. Raman spectra for Sn-doped InP before (lower trace) and after (upper trace) a vacuum anneal at 500°C for 1h.

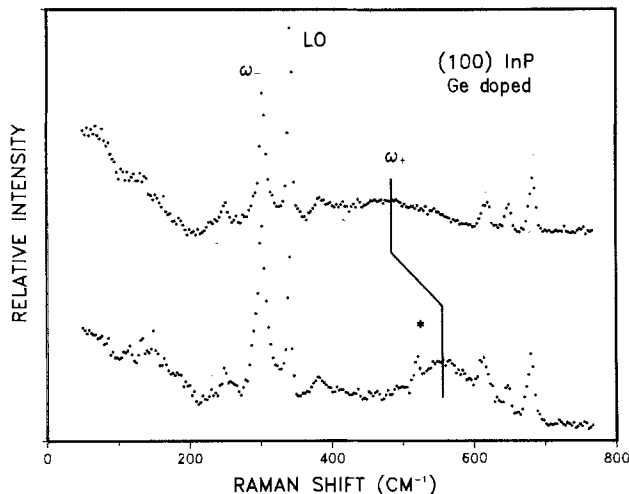


Fig. 3. Raman spectra for Ge-doped InP before (lower trace) and after (upper trace) a vacuum anneal at 500°C for 1h.

Discussion
Thermally induced variations in the net carrier concentration have been extensively studied by a variety of techniques including infrared reflectivity, capacitance-voltage profiling, sheet resistivity, etc. In this section, we present an outline of the theory necessary for converting the measured ω_+ frequency shifts into changes in free-carrier densities followed by a comparison and discussion of our results with other reports in the literature.

Theory.—The coupling of the conduction electron plasma oscillations to the vibrations of long wavelength longitudinal optic phonons in partially ionic semiconductors was treated theoretically in the early 1960's by Yokota (7) and later by Varga (8) and Singwi and Tosi (9). The zeroes of the dielectric response function for longitudinal waves yields the coupled plasmon-phonon modes ω_{\pm} , which are given in the long wavelength limit in the absence of phonon and plasmon damping by

$$\omega_{\pm}^2 = \frac{1}{2} (\omega_{LO}^2 + \omega_p^2) \pm \frac{1}{2} [(\omega_{LO}^2 + \omega_p^2)^2 - 4\omega_p^2\omega_{TO}^2]^{1/2} \quad [1]$$

In this expression ω_{LO} and ω_{TO} are the longitudinal and transverse optic phonon frequencies and ω_p is the bulk plasma frequency

$$\omega_p^2 = 4\pi N e^2/\epsilon_{\infty} m^* \quad [2]$$

N represents the net difference in donor and acceptor concentrations $N_d - N_a$, ϵ_{∞} is the high frequency dielectric constant, and m^* is the conduction electron effective mass. The plasma frequency in Eq. [2] must be corrected for finite values of the scattering wave vector q . The N - and q -dependent plasma frequency is given by (10)

$$\omega_p^2(N, q) = \omega_p^2(N) + \frac{3}{5} (qV_F)^2 \quad [3]$$

where V_F is the conduction electron Fermi velocity. The scattering q vector is determined from

$$q^2 = k_i^2 + k_s^2 - 2k_i k_s \cos \phi \quad [4]$$

I and S denote incident and scattered; k is the photon wave vector $2\pi n/\lambda$, where n is the real part of the substrate refractive index. Since the incident and scattered

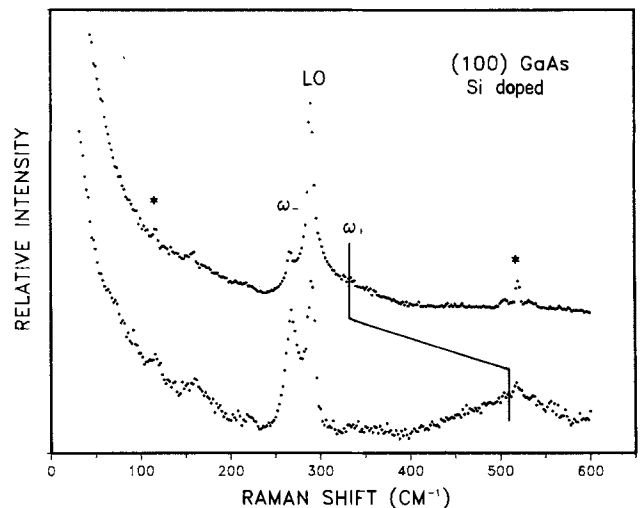


Fig. 4. Raman spectra for Si-doped GaAs before (lower trace) and after (upper trace) a thermal anneal at 500°C for 1h.

frequencies are very close ($k_i \sim k_s$), Eq. [4] reduces to $q \sim 4\pi n/\lambda$ for the surface reflection geometry ($\phi \sim 180^\circ$) employed. Data from Ref. (11) were interpolated to obtain the real part of the refractive index n at 5145Å. We obtain $q = 0.87$ and $1.05 \times 10^6 \text{ cm}^{-1}$ for InP and GaAs, respectively.

At high carrier-concentration levels one also anticipates that m^* will be concentration dependent (12) because both InP and GaAs have nonparabolic conduction bands. The carrier concentration dependence of m^* is not typically corrected for because experimental data for m^* vs. N have not been fit to some simple analytic equation. The correction is far from negligible however, as demonstrated by Chandrasekhar and Ramdas (13) in analyzing infrared reflectivity data on GaAs.

In order to obtain an analytic function for incorporating m^* corrections, the following procedures were followed. For GaAs, 18 data points were scaled from the smoothed curves found in Fig. 3 of Ref. (13) in the carrier concentration range $10^{16} - 10^{19} \text{ cm}^{-3}$. These 18 points were then fit to an equation of the form

$$m^*/m_0 = \sum_{j=0}^4 B_j [\ln N - \ln N_0]^j \quad [5]$$

where $N_0 = 1.0 \times 10^{16}$. For InP, m^*/m_0 values were taken from the raw data of Kesmanly *et al.* (14), except that all data were uniformly increased by 0.009 m^*/m_0 units in order to obtain a room temperature value of $m^*/m_0 = 0.0781$ in undoped material consistent with the recent magneto-phonon measurements of Eaves *et al.* (15). These data were plotted and a smooth curve drawn through them from which 18 points were taken and fit to Eq. [5]. The fits to the m^*/m_0 plots for InP and GaAs are shown as solid lines in Fig. 5. It should be emphasized that the open symbols do not represent the original published data, but rather values extracted from curves visually fit to the original data. This was necessary because the density of original points was too low to fit satisfactorily to Eq. [5]. The values of the fitting parameters B_j are tabulated for InP and GaAs in the upper section of Table II.

The coupled plasmon-phonon mode frequencies denoted by ω_{\pm} in Eq. [1] can now be solved analytically incorporating both finite q vector and concentration dependent m^* corrections. Figures 6 and 7 show the results of such calculations for InP and GaAs in the carrier concentration range $10^{16} - 10^{19} \text{ cm}^{-3}$. The materials parameters ω_{LO} , ω_{TO} , $q(5145\text{\AA})$, and ϵ_{∞} used in the calculations are listed in the second part of Table II.

Free-carrier concentration.—The results of the calculations presented in graphical form in Fig. 6 and 7 allow us

Table II. Fits and parameters for InP and GaAs

Fits to m^*/m_0 for InP and GaAs from Eq. [5]

j	InP	GaAs
	B_j	B_j
0	$+7.839 \times 10^{-2}$	$+7.224 \times 10^{-2}$
1	-2.133×10^{-3}	-2.096×10^{-3}
2	$+2.034 \times 10^{-3}$	$+2.135 \times 10^{-3}$
3	-5.595×10^{-4}	-6.286×10^{-4}
4	$+5.875 \times 10^{-5}$	$+6.306 \times 10^{-5}$
Materials parameters for calculating ω_{\pm}		
	InP	GaAs
$\omega_{LO} (\text{cm}^{-1})$	342.4	292.0
$\omega_{TO} (\text{cm}^{-1})$	304.0	269.0
$q (\text{cm}^{-1})$	8.73×10^5	1.045×10^6
ϵ_{∞}	9.55	10.91

to extract both the sign and magnitude of changes in the free-carrier density. From Table I, it is seen that the ω_{+} mode frequency decreases after annealing, *i. e.*, the free-carrier density is reduced relative to the unannealed sample in all cases. Two comments are in order. The first is that the observed sign (*i. e.*, free-carrier reduction rather than enhancement) is independent of whether one includes or excludes q vector and m^* corrections. The latter parameters influence the magnitude of the shift ΔN , but do not alter the sign of the shift. The second comment is that the measurements probe the region behind the space-charge depletion zone out to depths of $\sim 1400\text{\AA}$ for InP and 1700\AA for GaAs. The region examined in Raman scattering is similar to what is examined in C-V measurements, but it is not necessary to perform an extended analysis to account for the influence of deep traps (16). Other techniques such as sheet resistivity do not probe so sharply defined a spatial zone, nor is that technique easily applied to heavily doped materials (just as Raman scattering is not generally applicable at low carrier concentrations) (17).

The magnitude of the carrier density reduction ($\Delta N/N$) is $\sim 22\%$ for S-InP annealed at $550^\circ\text{C}/12\text{h}$, 47% for Sn-InP annealed at $500^\circ\text{C}/1\text{h}$, and 21% for Ge-InP annealed at $500^\circ\text{C}/1\text{h}$. The largest change occurred in the sample with the lowest initial doping, *i. e.*, Sn-doped InP with N initially around 4.7×10^{17} . The uncertainty in assigning a value to $\Delta N/N$ is larger in that case due to the small shift observed (18 cm^{-1}) and the intrinsic limitations associated with accurately locating the ω_{+} peak position. It is also likely that if carrier compensation related to drifting sur-

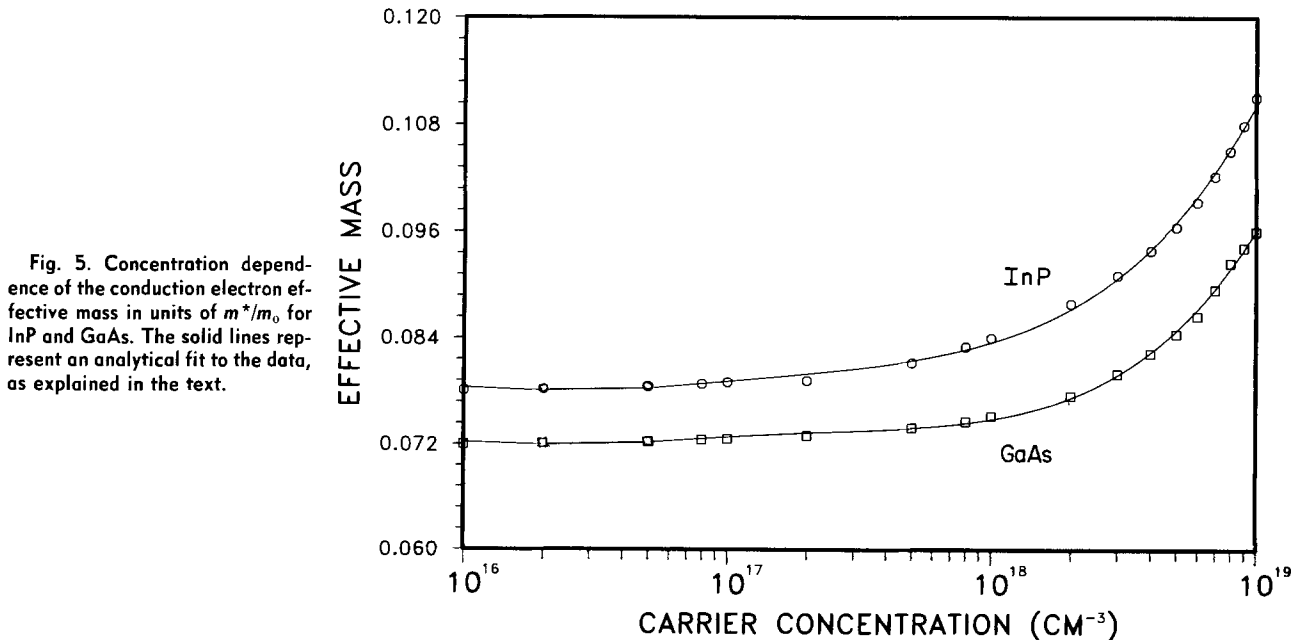


Fig. 5. Concentration dependence of the conduction electron effective mass in units of m^*/m_0 for InP and GaAs. The solid lines represent an analytical fit to the data, as explained in the text.

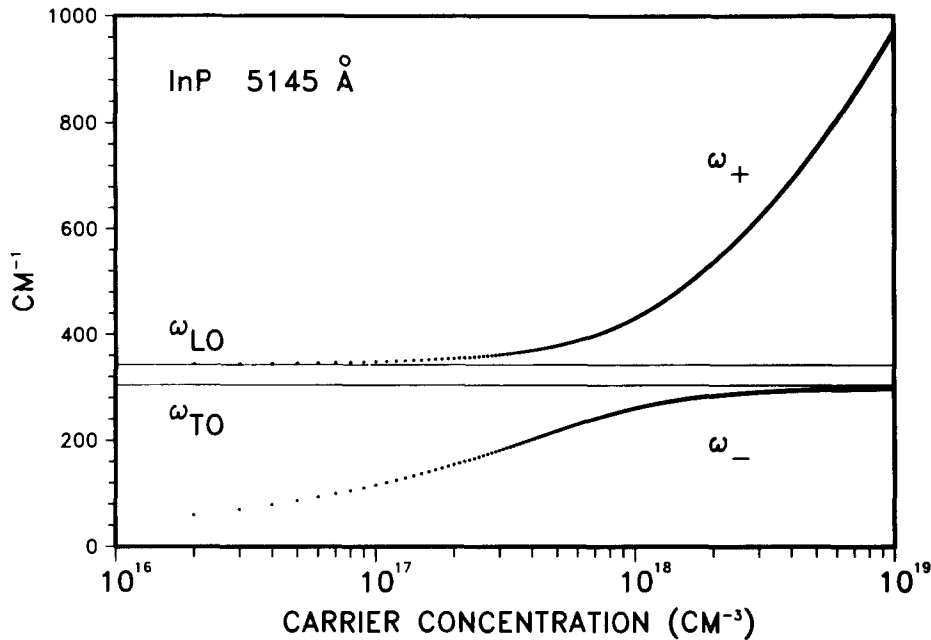


Fig. 6. Calculated plasmon-phonon mode frequencies ω_{\pm} vs. free-carrier concentration for Raman scattering from InP at 5145Å. The solid horizontal lines correspond to the bulk substrate LO and TO modes. The calculations have been corrected for finite q vector and concentration-dependent effective mass.

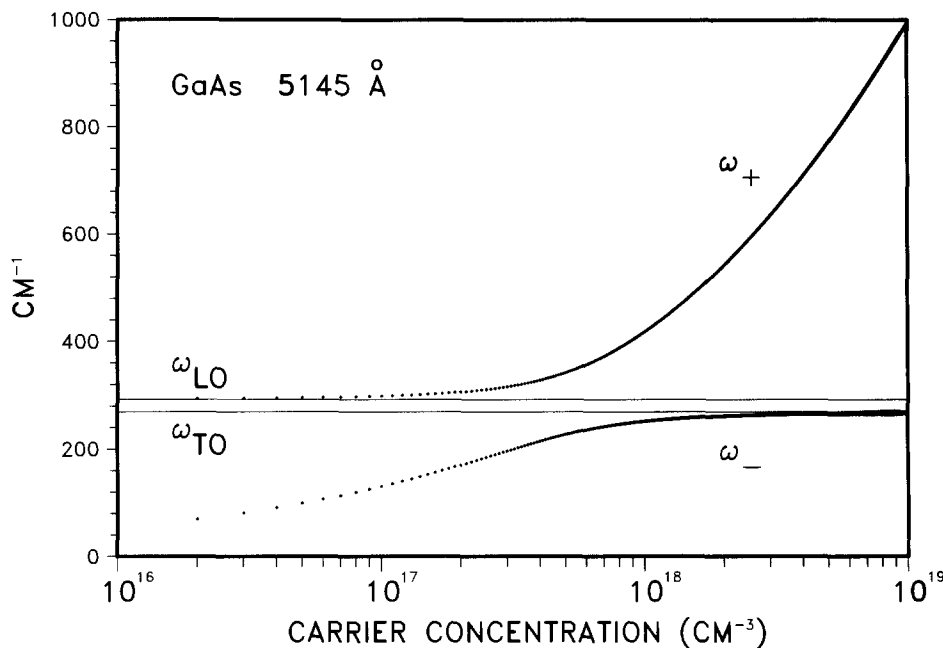


Fig. 7. Calculated plasmon-phonon mode frequencies ω_{\pm} vs. free-carrier concentration for Raman scattering from GaAs at 5145Å. The solid lines correspond to the bulk substrate LO and TO modes. The calculations have been corrected for finite q vector and concentration-dependent effective mass.

face generated defects is a dominant mechanism for free-carrier removal, then equivalent annealing conditions should affect the sample with the lowest initial carrier concentration the most. For Si-doped GaAs, we observe a reduction of $\sim 75\%$ in N after annealing. This value is similar to what was reported some years ago by Kung and Spitzer (18, 19) in their infrared reflectivity studies of Si-doped GaAs. They observed a reduction in N from ~ 8.5 to $4 \times 10^{18} \text{ cm}^{-3}$ after a 1h anneal at 600°C ($\Delta N/N \sim 53\%$). Our annealing cycles were not exactly comparable however because those authors subjected their samples to a 15 min preanneal at 1100°C in order to establish a common thermal history. Our results are qualitatively similar in view of these differences.

Thermally induced alterations of the free-carrier concentration in n-InP have been reported previously (1, 2, 20). The studies in Ref (1) and (2) involved low doped substrates ($N \sim 3 \times 10^{15} \text{ cm}^{-3}$) and annealing ambients of hydrogen or phosphorus vapor. Since their annealing ambients and doping levels differed from ours, a strict comparison of results is inappropriate.

The most comparable study has been the published results of Chin *et al.* (20), who examined vacuum-annealed (100) InP doped with S, Sn, Se, Zn, Mn, Fe, and undoped

annealed at 550°C for 1/2h. They interpreted their measurements (defect etching, cathodoluminescence, photoluminescence) in terms of rapid dopant out-diffusion for S, Sn, and Se, but they observed no measurable out-diffusion in Zn, Mn, Fe, and undoped materials. For S-doped InP, they estimated from the photoluminescence linewidth that the surface layer consisting of the top $5 \mu\text{m}$ was $\sim 50\%$ higher in carrier concentration relative to the bulk, whereas in an extended region ($\sim 200 \mu\text{m}$) behind this surface layer, the carrier concentration was approximately 10% lower than the bulk. Our own results show a reduction rather than an enhancement of the near-surface free-carrier density, but it should be noted that our reference point is the near-surface carrier density measured prior to annealing rather than the bulk density measured after annealing. Whether this difference in reference points is sufficient to account for the discrepancy in results remains to be seen.

Finally, it is probably worthwhile to comment that our observations of near-surface free-carrier reduction do not rule out the possibility that dopant redistribution with surface "pileup" has occurred. This phenomenon has been observed in secondary ion mass spectroscopy (SIMS) measurements of Fe- and Cr-doped InP (21) and

may well be a general artifact of thermal annealing due to surface gettering of impurities. The Raman measurements do not address the question of the actual dopant density; they only measure the net free-carrier concentration. SIMS measurements provide actual dopant profiles, but they do not specify whether the dopants are electrically active, *i.e.*, whether they contribute to the free-carrier density or not. It is not obvious *a priori* that dopants gettering at defects would be electrically active. In addition, if the dopant pileup were to occur sufficiently close to the surface that it was contained within the space-charge depletion zone, then Raman scattering would not detect any enhancement of the free-carrier density, since measurements of ω_+ only probe the region beyond the edge of the space-charge layer.

Summary

Raman scattering measurements of the coupled plasmon-phonon mode frequencies of S-, Sn-, and Ge-doped (100) InP and Si-doped (100) GaAs have been performed before and after vacuum anneals at 500°-550°C. A consistent reduction of the free-carrier density is observed in all cases within the near-surface region bounded by the edge of the depletion layer and a depth of 1400-1700Å. Numerical calculations of the ω_{\pm} frequencies incorporating an analytic correction for the carrier density dependence of m^* allow one to estimate the percentage reduction $\Delta N/N$ in the free-carrier density. For S- and Ge-doped ($1.2 \times 10^{18} \text{ cm}^{-3}$) InP, $\Delta N/N$ is $\sim 20\%$. For Sn-doped ($\sim 5 \times 10^{17} \text{ cm}^{-3}$) InP, $\Delta N/N \sim 50\%$. For Si-doped ($\sim 2 \times 10^{18} \text{ cm}^{-3}$) GaAs, $\Delta N/N \sim 75\%$.

Acknowledgments

One of us (GPS) wished to thank Bulusu Dutt for discussion of this work.

Manuscript received Nov. 28, 1983.

AT&T Bell Laboratories assisted in meeting the publication costs of this article.

REFERENCES

1. S. Guha and F. Hasegawa, *Solid-State Electron*, **20**, 27 (1977).
2. K. Tsubaki and K. Sugiyama, *Jpn. J. Appl. Phys.*, **19**, 1185 (1980).
3. P. W. Chye, I. A. Babalsla, T. Sukegawa, and W. E. Spicer, *Phys. Rev. B*, **13**, 4439 (1976).
4. W. E. Spicer, P. W. Chye, C. M. Garner, I. Lindau, and P. Pianetta, *Surf. Sci.*, **86**, 763 (1979).
5. M. M. Sushchinsky, V. S. Gorelik, and O. P. Maximov, *J. Raman Spectrosc C*, **7**, 26 (1978).
6. T. Sekine, K. Uchinokura, and E. Matsuura, *J. Phys. Chem. Solids*, **38**, 1091 (1977).
7. I. Yokota, *J. Phys. Soc. Jpn.*, **16**, 2075 (1961).
8. B. B. Uarga, *Phys. Rev. A*, **137**, 1896 (1965).
9. K. S. Singwi and M. P. Tosi, *Phys. Rev.*, **147**, 658 (1966).
10. D. Pines, "Elementary Excitations in Solids," W. A. Benjamin, New York (1963).
11. B. O. Seraphin and H. E. Bennett, in "Semiconductors and Semimetals, Vol. 3: Optical Properties of III-V Compounds," R. K. Willardson and A. C. Beer, Editors, pp. 449-543, Academic Press, New York (1967).
12. E. O. Kane, *J. Phys. Chem. Solids*, **1**, 249 (1957).
13. H. R. Chandrasekhar and A. K. Ramdas, *Phys. Rev. B*, **21**, 1511 (1980).
14. F. P. Kesmanly, D. N. Nasledov, A. Ya. Nashelskii, and V. A. Skripkin, *Sov. Phys. Semicond.*, **2**, 1221 (1969).
15. L. Eaves, R. A. Stradling, S. Askenazy, J. Leotin, J. C. Portal, and J. P. Ulmet, *J. Phys. C*, **4**, L42 (1971).
16. S. Loualiche, A. Nouailhat, and G. Guillot, *Solid-State Electron.*, **25**, 577 (1982).
17. G. Abstreiter, E. Bauser, A. Fisher, and K. Ploog, *Appl. Phys.*, **16**, 345 (1978).
18. J. K. Kung and W. G. Spitzer, *J. Appl. Phys.*, **44**, 912 (1973).
19. J. K. Kung and W. G. Spitzer, *ibid.*, **45**, 4477 (1974).
20. J. D. Oberstar, B. G. Streetman, J. E. Baker, and P. Williams, *This Journal*, **128**, 1814 (1981).
21. A. K. Chin, I. Camlibel, B. V. Dutt, V. Swaminathan, W. A. Bonner, and A. A. Ballman, *Appl. Phys. Lett.*, **42**, 901 (1983).

Low Field Recombination of Self-Activated Centers in II-VI DCEL Cells

M. S. Waite*

School of Materials Science and Physics, Thames Polytechnic, London SE18 6PF, England

ABSTRACT

Excitation of formed dc electroluminescent powder cells containing ZnS:Cl or ZnSe:Cl(Br) phosphors gives two peaks of recombination luminescence with respect to the applied voltage pulse. Peak A coincides with the leading edge of the voltage pulse, while the luminescence of peak B rises to a maximum at approximately 10 μs from the end of the voltage pulse. In both cases, the luminescence arises from DAP transitions of self-activated centers, $V_{\text{Zn}} - \text{Cl}_{\text{(Se)}}$ in the phosphors. However, the origins are different. Temperature and electrical measurements suggest that peak A corresponds to recombination involving carriers released from traps of activation energy $\sim 0.3 \text{ eV}$, by the applied voltage pulse. The profile of peak B is strongly influenced by the time constant $C \times R$, where C is the capacitance of the formed layer and R is the resistance of the unformed region. Electroluminescent efficiencies of 0.01% (4% duty cycle) were found for 465 nm emission from ZnS:Cl cells with thin insulating films on the anode, but much lower efficiencies, $\sim 10^{-3}\%$ without the insulating film.

Zinc sulfide activated with Mn is well established as the standard material for DCEL powder displays, providing an emission centered at 580 nm with a bandwidth of 60 nm (1-3). To increase the range of colors available without using filters, it is possible to modify the lattice, as in Zn(S,Te):Mn(4), or choose different activators for ZnS, such as the rare earths, Tb, Er, or Tm (5). These modifications have been found to be less efficient ($10^{-2}\%$) than ZnS:Mn ($10^{-1}\%$), and more efficient displays based on alkaline sulfide phosphors have been developed (6, 7). A

* Electrochemical Society Active Member.

Key words: dc electroluminescence, II-VI phosphors, self-activated centers.

common feature in these systems is the use of localized activators, Ce, Mn, and Tb, which are excited by impact with hot electrons rather than the use of donor-acceptor recombination processes as in powder DCEL devices based on Cu-doped ZnS.

During an investigation of the electroluminescence of undoped ZnS in conventional DCEL powder cells, it was noticed that under pulsed operation a narrow blue band at 467 nm replaced the very broad, relatively featureless emission seen with dc operation (8). The narrow band corresponded to the self-activated (SA) luminescence arising from the recombination of electrons on donor sites and holes localized at the A centers, $V_{\text{Zn}} - \text{Cl}_{\text{S}}$ complex centers

(9). The donor levels were presumed to be from chlorine present in the precipitated ZnS. Further preparation of ZnS phosphors with chlorine deliberately added also gave this emission band in a pulsed DCEL cell, while ZnS fired in H_2S and lacking the self-activated photoluminescence did not exhibit SA electroluminescence. In the following, the spectral and temperature dependence of emission from DCEL cells, made with zinc sulfide and zinc selenide self-activated phosphors, is described. The application of these processes to large screen displays technology in forming an alternative to impact excitation of characteristic activators is mentioned, with reference to parallel work being done on Ag-doped zinc cadmium sulfide phosphors (10).

Experimental

Preparation of phosphors.—Zinc sulfide, zinc selenide, and mixtures of the two were slurred with potassium chloride or bromide and fired in a stagnant atmosphere at 800°-950°C, depending on selenide content. The phosphor particles were washed in acetic acid to remove oxides and with sodium sulfite to dissolve excess selenium on the surface. A few samples of chloride slurred zinc sulfide were also fired in N_2 for comparison. These samples were also photoluminescent but have low intensities of SA electroluminescence. X-ray powder diffraction analysis of the phosphors indicated that both cubic and hexagonal phases were present in ZnS:Cl and the cubic phase in ZnSe:Br. Analysis of ZnS:Cl and ZnSe:Cl phosphors indicated a Cl content of 10 ppm, with less than 1 ppm of Cu, when prepared with an initial halide concentration of 1% w/w.

Construction of cells.—The phosphors were treated with $10^{-2}M$ $CuCl_2$ to provide the particles with a conducting Cu-rich surface and made into DCEL cells, as reported by Vecht *et al.* (1). After treatment in the copper solution, the phosphors were screened onto conducting glass substrates (Fig. 1), with thicknesses in the range 30-60 μm depending upon the particle size, phosphors with smaller particle size, ca. 2 μm diam, giving the thinner layers. The densities of the layers were in the range of $1.5-2.0 \times 10^3$ $kg\ m^{-3}$ compared to 4×10^3 $kg\ m^{-3}$ and 5.42×10^3 $kg\ m^{-3}$ for bulk ZnS and ZnSe, respectively. In addition to the electroluminescent cells prepared on conducting glass substrates, several were constructed using insulating layers 500-1000Å thick between the conducting substrate and

the layer of phosphor particles. Dielectrics used included SiO and YF_3 .

Forming and operation.—The cells were formed by the initial application of a dc field, and the spectra of the avalanche emission processes were obtained under dc operation at 100-150V. To observe the low field recombination emission, the cells are operated with short pulses (Fig. 2) for 5-500 μs , and at a frequency of 100 Hz-5 kHz. The recombination luminescence was also observed over a range of temperatures from room temperature to 100 K.

Results

Time dependence.—The emission from the formed panels appears at three characteristic points during the cycle of excitation and relaxation, as shown in Fig. 2 for the case of a self-activated phosphor, excited at the formed voltage with unipolar rectangular pulses at 100 Hz. Three separate features can be seen.

Peak A.—This appears on the leading edge of the voltage pulse. This leading edge has a slight slope to it, of 1 μs per 30V, as indicated in Fig. 2b and the maximum for peak A is seen before the pulse reaches the maximum or avalanche voltage at room temperature. This emission is only seen when pulsed excitation is used.

Peak B.—This follows the voltage pulse, rising to a maximum at a time interval from the end of the pulse of 10-50 μs , τ_B , depending upon the nature of the phosphor and the extent of forming. Typical values of τ_B at room temperature for formed panels are 5-20 μs .

Emission C.—This corresponds to the "on" phase of the rectangular pulse. The decay of this emission is rapid, ca. 200 ns, which is the limit of resolution of the present equipment. By analogy with similar emission in other semiconductors, this is termed "avalanche emission" and appears to have similar origins in intraband momentum loss and interband transfer. It has been investigated in electroluminescent diodes of II-VI materials under high fields (11) and in thin film and powder cells (12, 13). It is not directly useful in EL displays since the efficiency is low ($<10^{-6}$ photons/electron) even if the spectral characteristics of the emission were acceptable.

The luminescence of principal significance to displays is that represented by peaks A and B rather than the emission C, and it is the properties of peaks A and B which are of interest.

The values of τ_B have been found to be dependent on the forming process and can be related to the capacitance of the copper-depleted layer. Typically, values of 5-10 μs for ZnS:Cl are found in panels formed to voltages in the

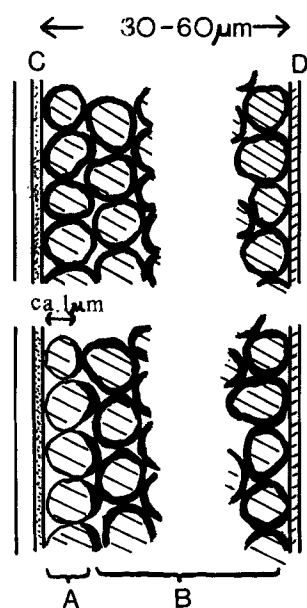


Fig. 1. Structure of DCEL powder cells. A: Cu-depleted layer. B: Unformed Cu-coated ZnS particles. C: Tin oxide or ITO layer. D: Al back electrode.

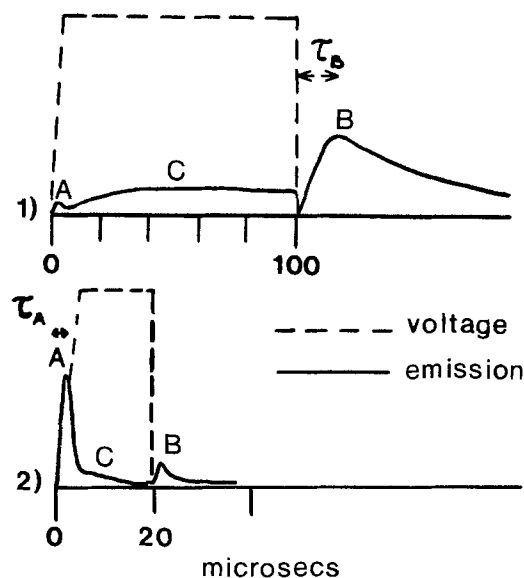


Fig. 2. Emission under pulsed excitation. 1: 100 Hz, 100 μs pulse width. 2: 1 kHz, 20 μs pulse width.

range 80-100V, with a capacitance of ca. $25 \mu\text{F m}^{-2}$. In a progressive forming experiment, the variation of τ_B was followed as a ZnS:Cl panel was formed from 60-110V. After an initial rapid decrease in τ_B , there is a steady decline with increasing values of $1/C$ (Fig. 3). As forming proceeds and the width of the Cu depleted zone (proportional to $1/C$) increases, the intensities of the recombination peaks A and B increase relative to the change in current (Fig. 3). The overall luminescence efficiency thus increases. The capacitance of unformed panels has values of $100\text{-}500 \mu\text{F m}^{-2}$, determined mainly by thin oxide layers underlying the deposited Al. Once forming has started and a resistive Cu depleted layer has begun to grow at the anode, the majority of the field is dropped across this region and the capacitance exhibits the sharp initial decrease seen in Fig. 3. The slower decline in $1/C$ can be seen as representing the gradual increase in the thickness of the Cu depleted layer which also occurs continually during use and which constitutes one of the principal failure mechanisms of DCEL powder cells.

These observations suggest that the post field peak B is determined, at least in part, by rate processes which involve the geometry of the Cu depleted layer rather than merely the kinetics of thermal release of carriers from traps and radiative decay. This conclusion is also reached by observations of the temperature dependence of τ_B .

Spectra of peaks A and B.—The spectral characteristics of the recombination luminescence are shown in Fig. 4 and 5 for ZnS:Cl, ZnSe:Cl, and ZnSe:Br with the spectra of avalanche emission obtained by continuous dc excitation for comparison. For ZnS:Cl the emission characteristics: a peak maximum of 2.67 eV (465 nm) and a bandwidth of 0.45 eV, correspond to the self-activated luminescence, the recombination between electrons at Cl donor sites and holes on $V_{\text{Zn}} - \text{Cl}$ neutral acceptors (14).

For ZnSe:Cl and ZnSe:Br the emission maximum is located at 1.98 eV (623 nm), close to the emission maximum of 1.99 eV determined by a recent ODMR study of ZnSe:Cl (15). The 1.98 eV peak was obtained at an excitation intensity equivalent to an input power of $2.5 \times 10^3 \text{ Wm}^{-2}$ while at higher intensities, $7.5 \times 10^3 \text{ Wm}^{-2}$, ZnSe:Br devices exhibited a shift in emission maximum to lower energies 1.95 eV (Fig. 5). The shift is in the opposite direction from that expected from the characteristics of DAP luminescence, where the emission maximum moves to higher energies with increased excitation intensity as distant pairs become saturated (16). Furthermore, in the experiments by Shionoya and colleagues on DAP luminescence in

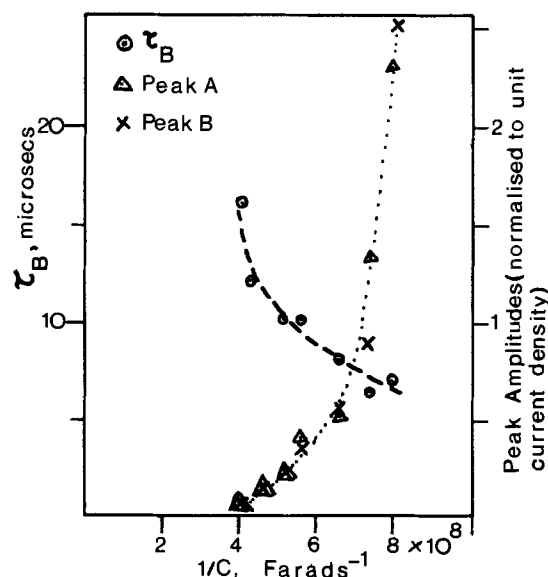


Fig. 3. Variation of device capacitance and amplitudes of recombination peaks A and B during initial stages of forming. ZnS: Cl panel, P8/80; area $0.2 \times 10^{-4} \text{ m}^2$.

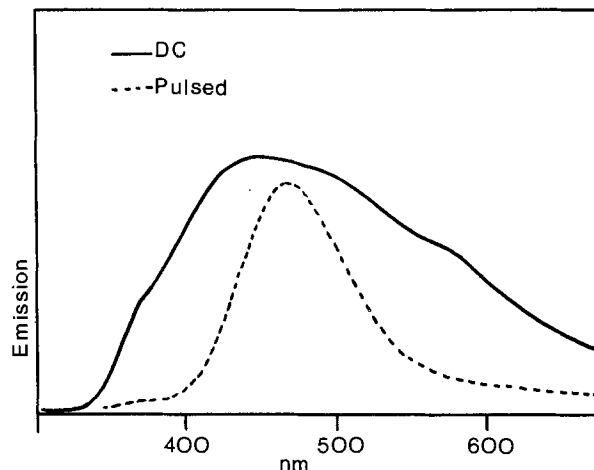


Fig. 4. Electroluminescent spectra of ZnS:Cl panels under dc and pulsed excitation.

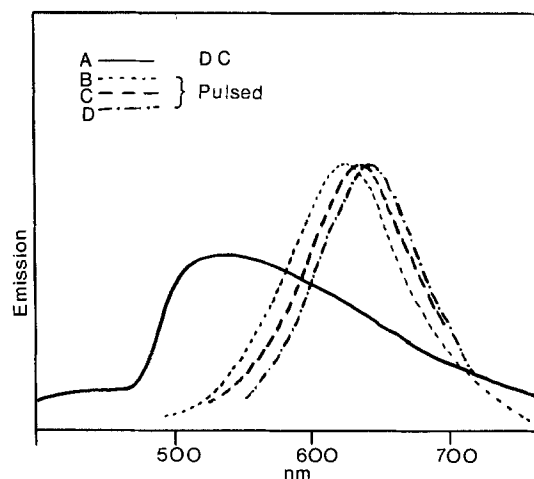


Fig. 5. Electroluminescent spectra of ZnSe: Cl, ZnSe:Br, and ZnSe:Cu under dc and pulsed excitation. Curve A: ZnSe: (Cl,Br): dc excitation. Curve B: ZnSe: Cl: pulsed excitation power: $2.5 \times 10^3 \text{ Wm}^{-2}$. Curve C: ZnSe: Cl: pulsed excitation power: $7.5 \times 10^3 \text{ Wm}^{-2}$. Curve D: ZnSe: Cu, pulsed excitation.

ZnS phosphors, the range of excitation intensity necessary to cause a significant spectral shift is much higher than that found here. There may, therefore, be two very broad emission bands in the ZnSe:Br spectrum whose relative intensity depends upon the excitation level. The obvious suspect is Cu contamination which has a broad emission band at 1.94 eV (17). DCEL cells with ZnSe:Cu (0.02) phosphors were prepared and after forming showed a recombination electroluminescence at 1.94 eV (640 nm) under pulsed excitation (Fig. 5). This suggests that the ZnSe:Cl,Br phosphors show both SA and Cu electroluminescence, with the relative contribution of the Cu emission increasing at higher excitation intensities.

Temperature dependence of recombination pulses.—The effect on peaks A and B of reducing the temperature has been examined for ZnS:Cl and ZnSe:Cl phosphors. The rise and decay times and the luminescent efficiencies are both affected. In particular, τ_B was seen to be strongly dependent on temperature, as seen in Fig. 6 for ZnS:Cl cell as the temperature is successively reduced from 300 to 100 K. From 300 to 220 K, τ_B fell from ca. $10 \mu\text{s}$ to ca. $4 \mu\text{s}$. In general, below 220 K the post-field emission is seen to consist of two components: (i) the broad peak for which the delay time τ_B gradually decreases and (ii) a fast rising spike (ca. $0.3 \mu\text{s}$) with a decay time of approximately $2 \mu\text{s}$. In some samples, the fast spike dominated the post-field emission at low temperatures (Fig. 7). The decay of this fast pulse should be compared with the values of 0.5 and $4 \mu\text{s}$ found by Shionoya and colleagues for the decay of

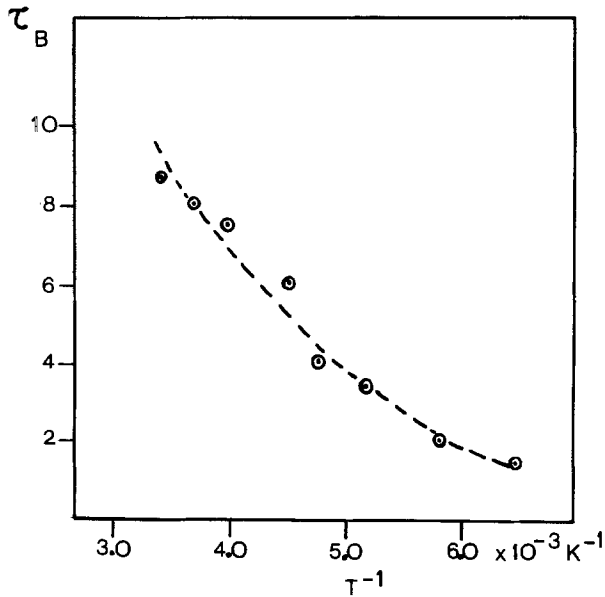


Fig. 6. Variation of τ_B with temperature: ZnS:Cl panel, P3/81: 100 μ s pulse width, 100 Hz excitation rate.

SA luminescence at 77 K (18). If the emission corresponding to peak B arises from the recombination of electrons thermally released from traps with holes at neutral acceptor centers, the emission might be expected to extend for a longer time at lower temperatures so that τ_B should increase. It may be that there are several closely overlapping components in the post-field recombination corresponding to different trap depths which are successively frozen in as the temperature is lowered. However, the change in τ_B seems to be too smooth for this explanation. The intensity of peak B does not appear to vary greatly with temperature.

The behavior of peak A with temperature is different from that of peak B. The intensity of peak A, as measured by the area of the oscilloscope trace and normalized to unit current densities, increases as the temperature is reduced and the delay time increases (Fig. 8). The variation in τ_A for ZnS:Cl is typically from 1.0 μ s at room temperature to ca. 4 μ s at 150 K. Since the time in which the field builds up to its maximum value is at least 3 μ s for applied voltages of 100V, the changes in τ_A indicate that a higher

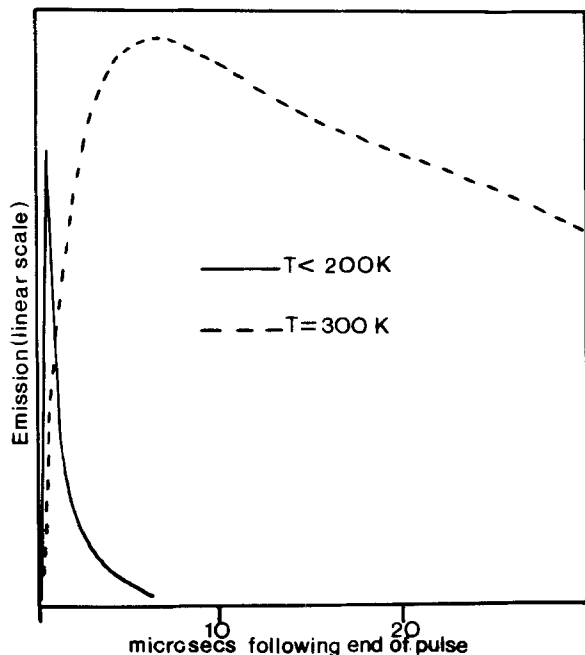


Fig. 7. Comparison of rise and decay of post-field recombination luminescence at and below room temperature for ZnS:Cl: P9/80.

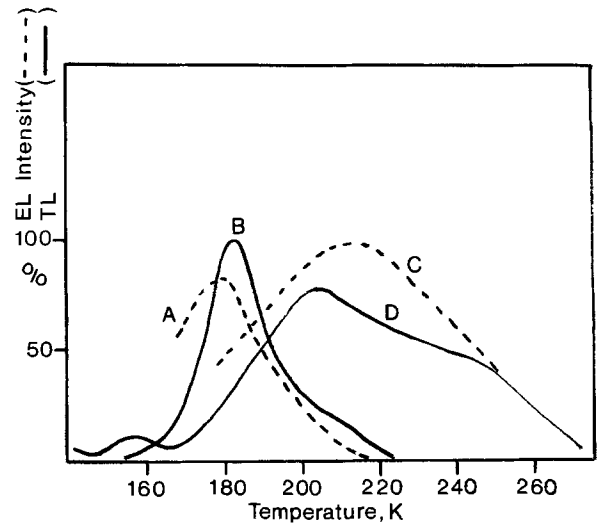


Fig. 8. Variation in electroluminescent efficiency of peak A and thermoluminescence for ZnS:Cl, and ZnS:Ag, 100 μ s pulse width, 100 Hz excitation rate [after Ref. (10)]. Curves A and B: ZnS:Cl, (P3/81). Curves C and D: ZnS,Ag, (ZA6/7).

field is needed at lower temperatures to promote the recombination. This is analogous to the luminescence induced by field detrapping in photoconductors as analyzed by Haering (19). If the recombination for ZnS:Cl represented by peak A depends upon the release of trapped carriers, the temperature dependence of the normalized area of this peak should parallel that of the thermoluminescence of the SA luminescence. In Fig. 8 [from Ref. (10)], the glow curve for ZnS:Cl is illustrated together with the area of peak A, normalized to unit current density. There is an approximate agreement between the two maxima at 180-183 K, and both are shifted relative to the maxima for the Ag-blue emission from ZnS:Ag, which also appears in the figure from Ref. (10).

Effect of pulse width on recombination efficiency.—The charging and discharging times of the displacement current in the devices at room temperature are of the order of 2 μ s, as judged from the current signal. However, with pulse widths as small as this, the panels have a very low efficiency because the total of trapped carriers per cycle is low. The effect upon brightness of the pulse width for a ZnS:Cl phosphor is soon in Fig. 9, where the peak heights of A and B have been plotted against the total charge passed per cycle. Although the curves are not completely coincidental, they both show a continued increase in output with charge

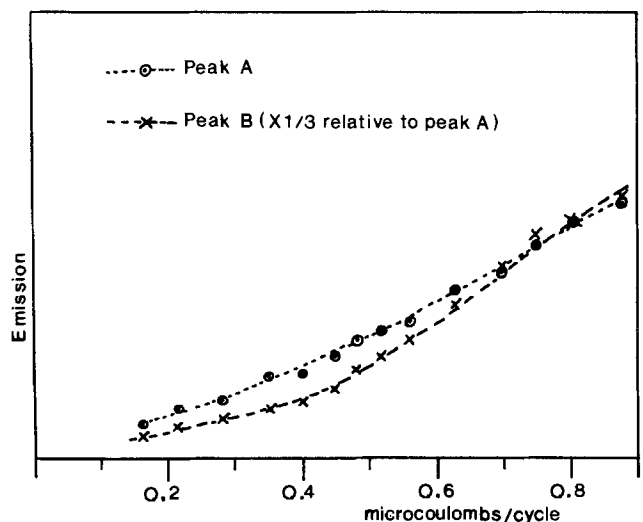


Fig. 9. Variation in recombination efficiency with the total charge passed per cycle, ZnS:Cl, (P8/80).

passed per cycle. Thus the more carriers that pass through the cells, the greater the concentration of trapped charges and the greater the luminescence output. The quantum efficiencies, combining the output of both peaks A and B, are approximately 10^{-3} photons per electron, leading to power efficiencies in the range 10^{-2} – $10^{-3}\%$ for ZnS:Cl and ZnSe:Br. There is little evidence for saturation of the post field peak B at higher charges in the phosphors with deliberate addition of donor impurity, in contrast to a previous observation with lower Cl concentrations (8). τ_A and τ_B are independent of pulse width, provided the extent of forming does not change.

Effect of other impurities.—The presence of oxygen has been found to be particularly important for low field recombination. In phosphors prepared by firing in N_2 with exclusion of oxygen, peaks A and B are not seen even when the phosphor has strong self-activated photoluminescence. This suggests that the presence of oxygen provides conditions for producing the traps for the space charge, although the identity of the traps is not known at present. The glow curves in Fig. 8 indicate a trap depth of ca. 0.3 in ZnS:Cl compared with a value of 0.27 eV found by Hoogenstraaten for oxygen in ZnS (20). A minimum estimate of $4 \times 10^{20} m^{-3}$ has been made for the trap density in ZnS:Cl from the intensity of the low field recombination luminescence, based on the assumption of unit quantum efficiency for the self-activated luminescence.

Li and Cd reduced or eliminated low field recombinations at SA sites in ZnS:Cl, and Cu concentrations as low as 5 ppm were found to reduce the SA electroluminescence without introducing copper-related luminescence, acting in effect as nonradiative centers. Shallow hole traps, producing nonradiative pathways, have been found by Tabei and Shionoya (21) in ZnS:Cu and Al at 50–300 eV from the valency band edge, and similar shallow traps may be present in the ZnS:Cl phosphors with low Cu concentrations. In ZnSe:Br, the effect of Cu is to increase overall red electroluminescence by an increase in the 1.94 eV emission, which corresponds to recombination via the Cu centers. Recent work by Robbins and others has shown that the Cu has a different role in the individual II-VI compounds (22). The significance of this work on the low field electroluminescence is discussed below.

Discussion

The DAP transitions observed do not occur under high field conditions, where only avalanche emission or localized transitions are seen (8). There is some similarity between the cells described here and conventional ac powder cells in that luminescence is the result of electron-hole recombination processes involving donor and acceptor centers rather than localized states of characteristic activators excited by electron impact. However, there are sufficient differences to make it advisable not to consider the dc power cells as merely planar versions of the ac powder cells. Field emission of electrons and holes from the ends of copper sulfide inclusions is considered to be part of the mechanism of the powder ACEL cells in the generally accepted Fischer model (23). According to this interpretation, substitutional Cu_{Zn} centers bind holes to form neutral acceptors adjacent to the inclusions, while the more mobile electrons travel to the boundaries of the ZnS particle. The primary light peak obtained on field reversal occurs as electrons are field emitted into the region containing neutral acceptors, while a secondary peak is produced as the displaced electrons return. The practical brightness depends on the displaced charge, and therefore on the capacitance of the powder layer and the applied voltage. This capacitive coupling limits the applications; although the overall efficiency of a green emitting (ZnS:Cu,Cl) panel can be high, up to 19 lm/W, considerably greater than that obtained in a ZnS:Mn DCEL powder panel (ca. 1 lm/W),

even allowing for the smaller lumen equivalent of the Mn emission.

In DCEL powder panels, the field across the Cu-depleted layer is of the order of $10^8 V m^{-1}$ (3), where impact ionization of ZnS can occur. The primary electrons injected into this high field region can generate further electron-hole pairs in an avalanche process. There is some evidence for this in the form of negative resistance in current-voltage characteristics of powder panels (3), and in ACEL thin film cells, the multiplication gain in ZnS:Mn films operating at similar fields has been determined by Venghaus (24). Carrier multiplication rates of $10^6 m^{-1}$ were obtained in fields of 0.8 to $1.2 \times 10^8 V m^{-1}$, rising rapidly in the region 1.2 – $1.5 \times 10^8 V m^{-1}$, where the threshold field for strong light emission was found. In principle, there are opportunities in dc systems for overcoming the limited brightness per cycle of ac powder devices while taking advantage of the high radiant efficiency of DAP processes in ZnS and ZnSe. The recombination processes described here, however, were only observed under certain conditions. These were (i) the presence of oxygen during the preparative stage of the self-activated phosphors, and (ii) in ZnS, the absence of copper impurities which distinguished these cells from conventional ac powder cells.

Origin of post-field recombination peaks.—Oxygen is believed to produce deep traps, of at least 0.3 eV (20), in self-activated ZnS, trapping a proportion of the excess electrons produced during a dc pulse. An explanation of the profile and temperature dependence of peaks A and B in ZnS:Cl and ZnS:Ag,Cl, by assuming that these peaks represent the recombinations of Cl donor bound electrons with the $(V_{Zn} - Cl)_0$ and Ag neutral acceptor centers as electrons are released from traps, predicts the wrong temperature dependence for τ_B . The value for the delay would be expected to increase as the temperature falls and the rate of electron release from traps slows. In practice, τ_B is found to decrease from typically 10–15 μs at 300 K to ca. 2 μs at 100 K. This characteristic appears to be general for powder DCEL panels since it is seen in Ag-doped phosphors as well as self-activated phosphors. Another characteristic which needs to be explained is the lack of dependence of the rise and decay of peak B on the excitation intensity as the current or the pulse length is increased. This suggests that bimolecular kinetics are not followed in the early stages of the recombination, implying that in the recombination zone the concentration of neutral acceptors or electrons (free or in shallow donors) is effectively constant.

Electrons are the more mobile carriers in compensated ZnS and, in an alternative mode for peak B outlined in Ref. (10) following removal of the applied field electrons, are considered as diffusing back to positive donor sites from shallow traps or surface sites concentrated at the anode. However, in order to reconcile diffusion over a distance of $10^{-6} m$ (the formed layer) with a recombination maximum of ca. $10^{-5} s$, the electron mobility must be lower than the literature value of ca. $10^{-2} m^2 V s^{-1}$ (25) by several orders of magnitude. Such a trap-limited value would again result in the wrong temperature dependence of τ_B .

Recent measurements of the tail of the decay curve of peak B in some ZnS:Cl cells do show a $t^{-1/2}$ dependence over part of the decay curve (Fig. 10), but it also appears that other processes are rate determining at different regions of the decay. This area is now receiving further study.

The recombination maximum of peak B is more closely coincident with the discharged capacitance spike as measured by a test resistor in series with the cell. The decay time of the discharging spike is of the order of $10^{-6} s$, and Abdalla has pointed out that a DCEL powder cell has a discharge time given by $C \times R$, where C is the capacitance of the formed layer and R is the resistance of the unformed Cu-coated ZnS, which acts as a distributed series resistance (26). Values obtained for C and R for test areas

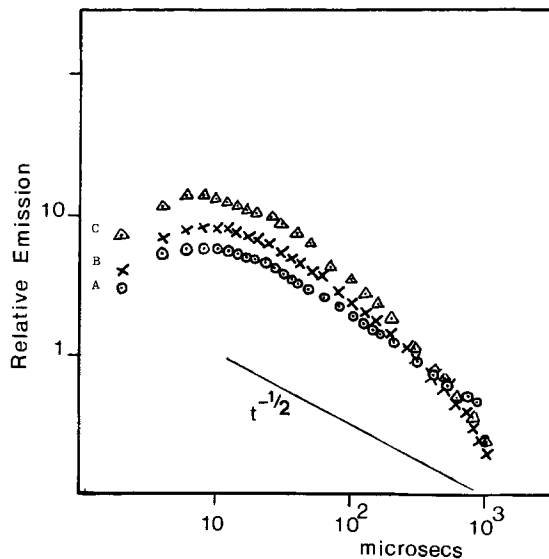


Fig. 10. Time dependence of the decay of electroluminescence in peak B, 100 μ s pulse width, ZnS:Cl, formed to 80V. Curve A: 65V applied voltage. Curve B: 80V applied voltage. Curve C: 100V applied voltage.

in ZnS:Cl and ZnSe:Br panels are typically 0.5-1.5 nF and 10^3 - $10^4\Omega$, respectively, giving capacitance spikes with decay times of the order of 0.5-15 μ s, so that the movement of shallow trapped electrons back to ionized donor levels as the polarization decays is dependent upon the distributed resistance of the unformed region of the cell. This gives better agreement with observed values of τ_B than the models given above. It would also explain the fall in τ_B as the capacitance of the Cu-depleted layer falls during the forming process. The formed zone gradually increases in width, reducing C , but without significantly affecting R , since the formed layer is only 3% of the total thickness of the powder layer. In Fig. 11, observed values τ_B are plotted against values of the product $C \times R$ taken from several ZnS:Cl and ZnSe:Br cells without anodic insulating films. This is a weak but apparent correlation with the $\tau_B = C \times R$ line acting as a boundary limit to the spread of results. The temperature dependence of R_s is complex,¹ but the initial decrease in R_s as the temperature is reduced below 300 K is consistent with the initial rapid fall shown in Fig. 6.

Peak A is not affected by the change in R_s and the temperature dependence observed, which is a move to greater τ_B values as T decreases, agrees with that expected if recombination follows the release of trapped carriers.

Role of copper centers.—The role of copper is also of interest for any eventual practical utilization of these effects. The low field recombination peaks, which are readily noticed in self-activated ZnS and ZnSe, are much less prominent in Cu-doped ZnS.

Another difference is that peak A is more prominent than peak B at room temperature in Cu-doped ZnS than in ZnSe:Cl. The efficiency of emission through the Cu center is much lower than that of the SA luminescence in ZnS, being $10^{-3}\%$ (power efficiency) compared to $2 \times 10^{-2}\%$ for the most efficient panels so far obtained with ZnS:Cl, whereas in ZnSe, recombination via Cu-red centers appears from preliminary observations to be more efficient than the self-activated luminescence. The resistivities of the unformed panels (corresponding to R_s) are generally lower for ZnS:Cu phosphor than for ZnS:Cl phosphor under the same processing conditions: this presumably accounts for the difference in τ_B . However, it does not explain directly the lower efficiency.

The nature of the deep Cu-related centers in II-VI's has

¹ The resistance of Cu-coated ZnS phosphor layers falls with decrease in temperature to reach a minimum at a temperature which varies between 150 K and room temperature, depending on the initial resistance and the degree of Cu uptake.

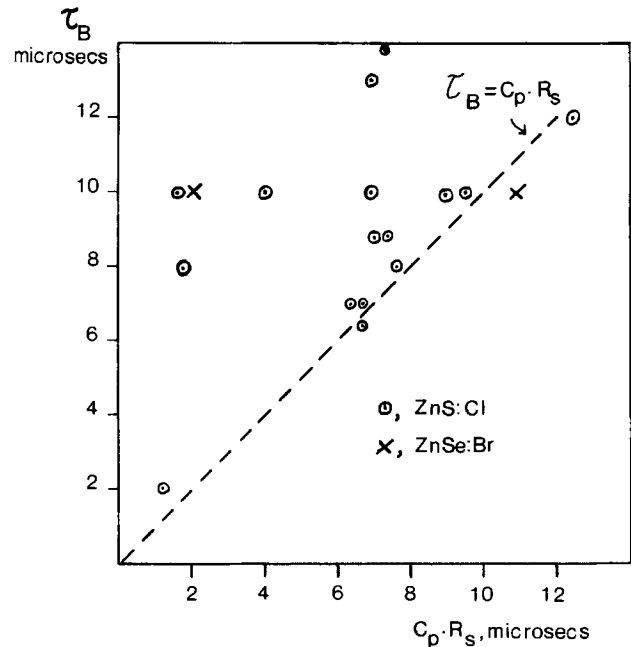


Fig. 11. τ_B as a function of the capacitance of the formed layer, C , and the small signal resistance of the informed layer, R . Results from several panels of ZnS:Cl and ZnSe:Br phosphors.

recently been the subject of several investigations (17, 22, 27), and Robbins (22) has pointed out differences in the Cu center among the various semiconductors of this group. For ZnS, the neutral acceptor involved in the G-Cu luminescence is the 2T_2 (d^9) state of Cu_{Zn}^{2+} with a shallow hole state at 0.35-0.4 eV from the vb edge due to the $^2E(d^9)$ state. In ZnSe, the Cu level in the gap has the configuration (d^{10})h, a hole bound to a filled d^{10} core. The lower efficiency of Cu-doped ZnS low field el compared to the SA el or the R-Cu luminescence of ZnSe may be related to the greater probability of electron recombination in ZnS via the $E(d^9)$ state. In ZnSe:Cu,Br the effect of copper is to increase overall red emission (620-650 nm) by recombination at the Cu center, and in these phosphors, the reported acceptor ionization energies of Cu and SA centers are similar, 0.6 eV (14, 28). The reduction in SA recombination luminescence by Li, which acts as a shallow acceptor in ZnS with an ionization energy of ca. 30 meV, may also involve a similar mechanism.

Practical output.—The highest power efficiency: $10^{-2}\%$, was found with Cl-doped ZnS, and corresponds to the lower range of efficiencies found in ZnS:Mn DCEL powder panels. In practical terms, a brightness of 20 Ft.L at 4% duty cycle for blue SA electroluminescence was found for a ZnS:Cl panel with a YF_3 insulating film on the anode. Generally, an improvement in efficiency was noted with the presence of an insulating film on the anode, but no systematic investigation has yet been carried out. In ac thin film panels, Marelllo and colleagues found that the blue luminescence of a ZnS:Ag film was much weaker than that of Mn emission (29), but it is not reported that the Ag-doped films were optimized. If the temporarily trapped charge can be held in the formed layer long enough for recombination to take place, then this type of excitation of phosphors should lead to multi-color el panels of similar design to the ZnS:Mn powder DCEL panels.

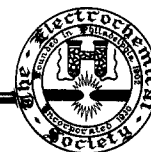
Manuscript submitted Nov. 28, 1983; revised manuscript received Feb. 6, 1984.

REFERENCES

1. A. Vecht, R. Ellis, N. J. Werring, and P. J. F. Smith, *J. Phys. D*, **2**, 953 (1969).
2. M. I. Abdalla, A. Godin, and J. P. Noblanc, *J. Lumin.*, **19/19**, 473 (1979).
3. C. J. Alder, A. F. Cattell, K. Dexter, M. Dixon, and J.

- Kirton, *Electron. Lett.*, **16**, 571 (1980).
4. A. Vecht, M. H. Higton, and N. R. Davis, Abstract 210, p. 546, The Electrochemical Society Extended Abstracts, Vol. 80-1, St. Louis, MO., May 11-16, 1980.
 5. M. S. Waite and A. Vecht, *Appl. Phys. Lett.*, **19**, 471 (1971).
 6. A. Vecht, M. H. Higton, J. W. Mayo, and J. M. Blackmore, *SID Tech. Digest*, 110 (1980).
 7. A. Vecht, M. S. Waite, M. H. Higton, and R. Ellis, *J. Lumin.*, **24/25**, 917 (1981).
 8. M. S. Waite and A. E. Thomas, *This Journal*, **127**, 509 (1980).
 9. J. E. Nicholls, J. J. Davies, B. C. Cavenett, J. R. James, and D. J. Dunstan, *J. Phys. B*, **12**, 361 (1979).
 10. M. S. Waite, *J. Lumin.*, **24/25**, 921 (1981).
 11. J. W. Allen, *ibid.*, **7**, 228 (1973).
 12. S. Tanaka, Y. Maruyama, H. Kobayashi, and H. Sasaki, *ibid.*, **12/13**, 911 (1976).
 13. M. S. Skolnick, *J. Phys. D*, **14**, 301 (1981).
 14. J. R. James, J. E. Nicholls, B. C. Cavenett, J. J. Davies, and D. J. Dunstan, *Solid-State Commun.*, **17**, 969 (1975).
 15. D. J. Dunstan, J. E. Nicholls, B. C. Cavenett, and J. J. Davies, *J. Phys. C*, **13**, 6409 (1980).
 16. K. Era, S. Shionoya, and Y. W. Washizawa, *J. Phys. Chem. Solids*, **29**, 1827 (1968).
 17. See for example, H. G. Grimmeiss, C. Ovren, and R. Mach, *J. Appl. Phys.*, **50**, 6328 (1979); P. J. Dean, *Czech. J. Phys.* **B30**, 272 (1980); R. N. Bhargava, *J. Cryst. Growth*, **59**, 15 (1982).
 18. T. Koda and S. Shionoya, *Phys. Rev. A*, **136**, 541 (1964).
 19. R. R. Haering, *Can. J. Phys.*, **37**, 1374 (1959).
 20. W. Hoogenstraaten, *This Journal*, **100**, 356 (1953).
 21. M. Tabei and S. Shionoya, *J. Lumin.*, **16**, 161 (1978).
 22. D. J. Robbins, *ibid.*, **24/25**, 137 (1981).
 23. A. G. Fischer, in "Luminescence of Inorganic Solids," P. Goldberg, Editor, Chap. 10, Academic Press, New York (1966).
 24. H. Venghaus, *J. Cryst. Growth*, **59**, 403 (1982).
 25. D. L. Rode, in "Semiconductors and Semimetals," Vol. 10, R. K. Willardson and A. C. Beer, Editors, p. 50, Academic Press, New York (1975).
 26. M. I. Abdalla, A. Godin, A. Brenac, and J-P. Noblanc, *IEEE Trans. Electron. Devices*, **ed-28**, 689 (1981).
 27. M. Godlewski, W. E. Lamb, and B. C. Cavenett, *J. Lumin.*, **24/25**, 173 (1981).
 28. G. A. Saumc, R. H. Glaenger, and J. E. Deuker, *J. Phys. Chem. Solids*, **30**, 2447 (1969).
 29. V. Mareello, L. Samuelson, and A. Onton, *J. Appl. Phys.*, **52**, 3590 (1981).

Technical Notes



Reproducible "Leaky Tube" Diffusion of Zinc into GaAs with Submicron Junction Depths

R. J. Roedel, J. L. Edwards, A. Righter, P. Holm, and H. Erkaya

Center for Solid State Electronics, Arizona State University, Tempe, Arizona 85287

The diffusion of zinc into GaAs and other III-V semiconductors to produce p-type layers remains a common procedure in compound semiconductor processing. It has been used in the fabrication of light-emitting diodes (1), injection lasers (2), optical waveguides (3), and other structures. In general, these devices require junction depths of the order of 1-5 μm , and the technique most often used to obtain these "deep" diffusions is the "closed tube" process, in which an evacuated quartz ampul containing the GaAs wafer and the zinc source is placed in the diffusion furnace. However, there are several applications in which very shallow ($<1 \mu\text{m}$) p⁺ layers are quite desirable. These include tunnel diode-transition regions in cascade solar cells, the emitter regions of GaAs photovoltaic devices, the gate regions of GaAs JFET structures, and ohmic contact areas. Ion implantation of Zn, Mg, or Be has been used to produce very shallow p-type layers in GaAs. Troeger *et al.* (4) have reported the fabrication of triply implanted E-JFET's in which both n-type implants and the p-type (Mg) implant are less than 1 μm deep. Kasahara *et al.* (5, 6) have used Zn ion implantation for the construction of shallow ($\sim 0.2 \mu\text{m}$) p-type gate regions of GaAs JFET's. However, problems have remained with p-type ion implantation into GaAs. The p-type implantation has been reported to produce p-i-n, rather than p-n, junctions by several authors (7, 8). Additional complications include low activation of the implanted species (5), drastic redistribution of the implanted ions during thermal annealing (6), and an incomplete knowledge of the residual lattice damage after annealing. However recent work by Taira *et al.* (9) and Kasahara *et al.* (10) shows that dual implantation of Zn and As can be used to produce Zn profiles that closely match those predicted by the LSS theory.

In this paper, we wish to report that thermal diffusion of Zn can be used to fabricate extremely shallow p⁺ layers in a very reproducible manner, with carrier concentrations as high as $1.8 \times 10^{20} \text{ cm}^{-3}$.

In our laboratory, we employ the so-called "leaky tube" diffusion technique, which is a variation of the the "box" diffusion process described by Tuck (11) and Springthorpe and Svilans (12). A schematic of the leaky tube diffusion system is shown in Fig. (1). The leaky tube apparatus consists of a normal open-tube furnace system that contains a quartz liner sealed at one end. Ultrapure helium can be passed through the outer open tube, or through the liner with the aid of a small purge tube. During diffusion, the He flow through the liner can be halted so that a stagnant, inert ambient can be established in the diffusion zone. The quartz boat holds GaAs samples horizontally and can accommodate four 2 in. wafers; in addition, it holds a quartz crucible containing 30g of elemental zinc of 6N purity. In the diffusion zone, a small temperature gradient ($\sim 4^\circ\text{C}$) is maintained along the boat to prevent Zn condensation on the wafers.

A series of n-type GaAs wafers [$N_D \sim 1 \times 10^{18} \text{ cm}^{-3}$, (001) orientation] were diffused for times varying between 5 and 30 min at a temperature of 600°C. Figure 2 shows the junction depth *vs.* square root time for these diffusions, and the linear form of this plot indicates that the diffusion is "well behaved," *i.e.*, predictable. The line does not go through the origin. This reflects an "incubation" period of approximately 1 min; before this time, diffusion does not take place. The junction depth was first determined by staining cleaved samples in a dilute solution of KOH and $\text{K}_3\text{Fe}(\text{CN})_6$ in water for 5s. None of the diffusion showed two diffusion "stain lines," but this was expected, as the intrinsic carrier concentration at the diffusion tem-

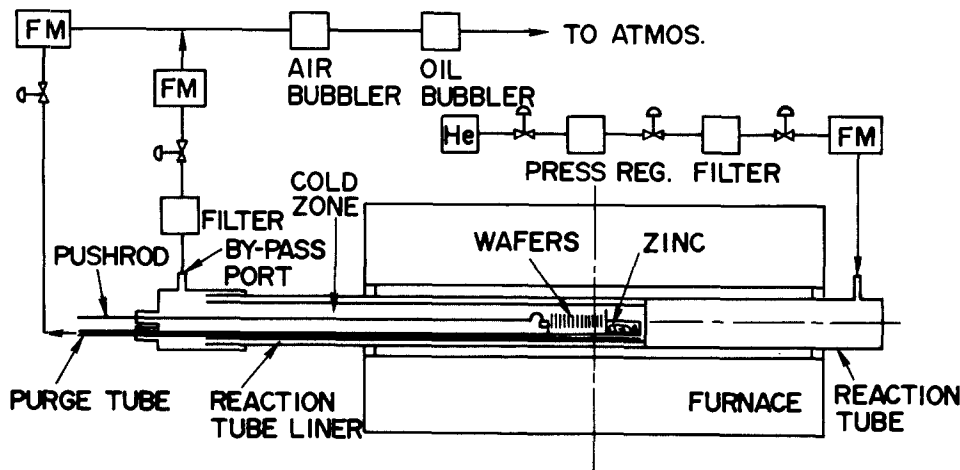


Fig. 1. Schematic of the leaky tube diffusion system.

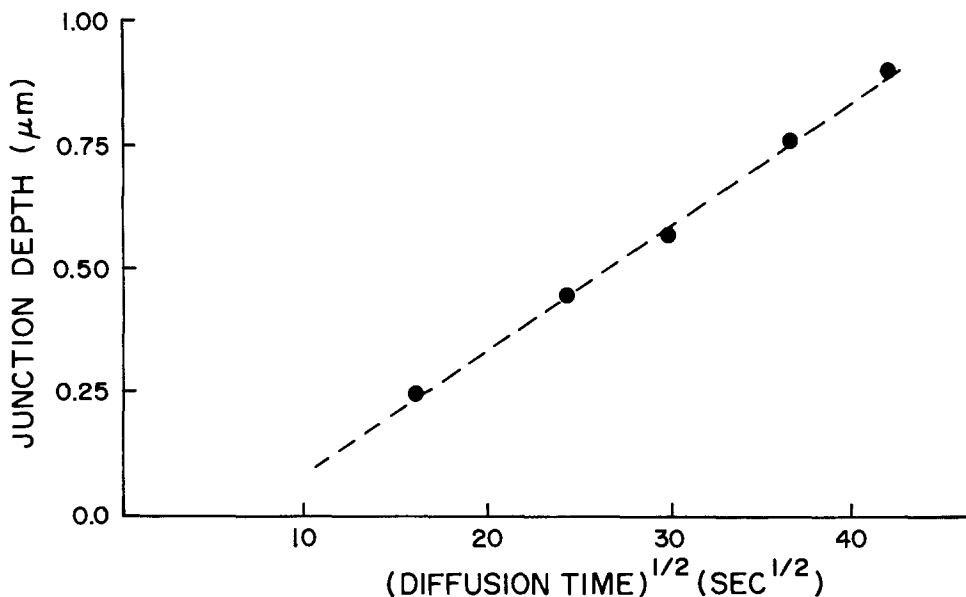


Fig. 2. Junction depth vs. square root of diffusion time for the leaky tube diffusion of zinc into (001) GaAs at 600°C.

perature ($n_i \sim 1.4 \times 10^{16} \text{ cm}^{-3}$) is lower than the background doping. These junction depths were confirmed independently using electrochemical profiling techniques. All of the diffused samples were coated with a 50Å sputtered-SiO₂ film prior to diffusion. As described elsewhere (14), the thin SiO₂ coating prevents the thermal decomposition of the substrates during diffusion, but allows the zinc to diffuse without attenuation.

Figure 3 contains photomicrographs of three typical cleaved and stained samples diffused with Zn at 600°C for 5, 10, and 15 min. The junction depth of each is 0.22, 0.44, and 0.56 μm, respectively. The uniformity of the junctions is quite noteworthy; across a 1.5 cm wafer, the deviation from planarity is not measurable. In a series of ten diffusions for 5 min at 600°C, the average junction depth was 0.22 μm with a standard deviation of less than 4%. We attribute this remarkable reproducibility to the inherent stability and repeatability of the leaky tube diffusion apparatus. It should be noted that we also performed short duration diffusions at 600°C on GaAs wafers without the 50Å SiO₂ layer. The junction depths of the bare wafers were identical to their coated counterparts, but the bare wafers subjected to diffusions longer than 15 min began to show signs of surface erosion.

After optical examination of the diffused substrates, electrical characterization was carried out. With a four-point probe, the sheet resistance of the 5, 10, and 15 min diffused layers was found to be 95.8, 63.6, and 55.4 Ω/□, respectively. These values correspond to average resistivities of 2.21×10^{-3} , 2.80×10^{-3} , and 3.10×10^{-3} Ω-cm, respectively. A modified electrochemical profiler (manufactured by Polaron Instruments) was then used to mea-

sure the electrically active zinc diffusion profiles. Figure 4 shows the profiles of three samples diffused for 5, 10, and 15 min which did not have a SiO₂ coating. It is very interesting to note that the 10 and 15 min samples show a carrier concentration peak near the surface, followed by a plateau-like region, and finally a steep drop in concentration as the junction is approached. The 5 min sample, however, shows only the peak and the steep drop-off, with the plateau region conspicuously absent. In fact, the slopes of the peak region and the drop-off region for all three samples are virtually identical. The appearance of the plateau region for diffusions 10 min or longer (and its absence beforehand) may indicate that a fundamental change in the zinc diffusion mechanism takes place in the first few minutes of diffusion.

The formation of a peak in carrier concentration near the surface is almost certainly effected by the leaky tube diffusion technique. At the end of the diffusion cycle, the samples are not quenched and brought quickly to room temperature. Rather, the boat is pulled to the cold end of the diffusion furnace and is cooled slowly with an external fan. Thus, the wafers remain in contact with a warm boat for an extended period, and out-diffusion of the Zn from the surface occurs. The profiles in Fig. 5 corroborate this explanation. Both samples in this figure were diffused for 5 min at 600°C, but sample of curve a was covered with 50Å of SiO₂, and the sample of curve b was bare. Both show the near-surface peak (in different locations but with the same height), and nearly identical drop-off regions. The presence of the SiO₂ film on the sample of curve a effectively impedes the out-diffusion, and as a result the carrier peak is closer to the surface.

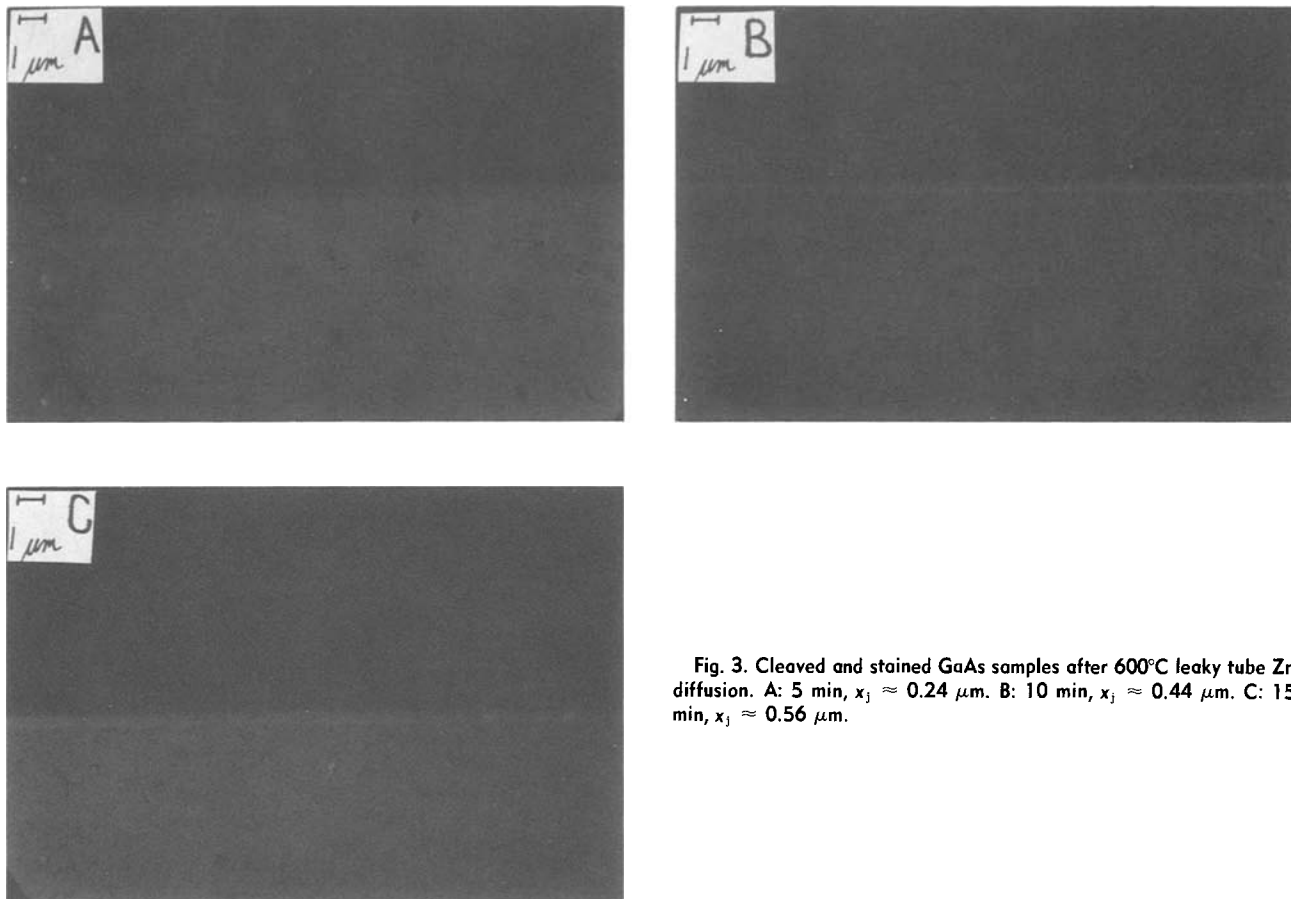


Fig. 3. Cleaved and stained GaAs samples after 600°C leaky tube Zn diffusion. A: 5 min, $x_j \approx 0.24 \mu\text{m}$. B: 10 min, $x_j \approx 0.44 \mu\text{m}$. C: 15 min, $x_j \approx 0.56 \mu\text{m}$.

The peak carrier concentration produced by our short diffusion cycles was as high as $1.8 \times 10^{20} \text{ cm}^{-3}$. To the authors' knowledge, this concentration is higher than any previously reported using either thermal diffusion or ion implantation. Although these high concentrations were not corroborated with another differential technique, such as differential Hall measurements, we have integrated the carrier concentrations from Fig. 4 in the formula

$$\bar{\rho} = \frac{x_j}{q \int_0^{x_j} p(x) \mu_p(x) dx}$$

to calculate the average resistivity. We find for these three samples, $\rho = 2.34 \times 10^{-3}$, 2.72×10^{-3} , and $3.06 \times 10^{-3} \Omega\text{-cm}$, for the 5, 10, and 15 min samples, respectively. These numbers are within 5% of the four-point probe measured values. We feel confident that the carrier con-

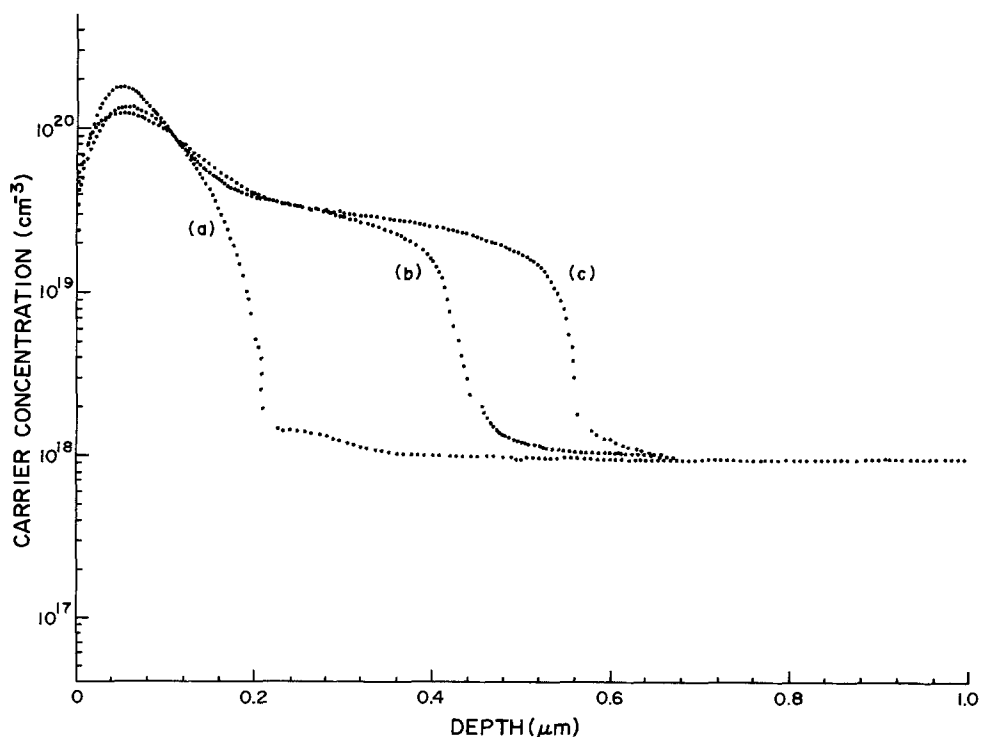


Fig. 4. Carrier concentration profiles for GaAs samples after Zn diffusion at 600°C. Curve a: 5 min. Curve b: 10 min. Curve c: 15 min. All samples were without an SiO_2 coating.

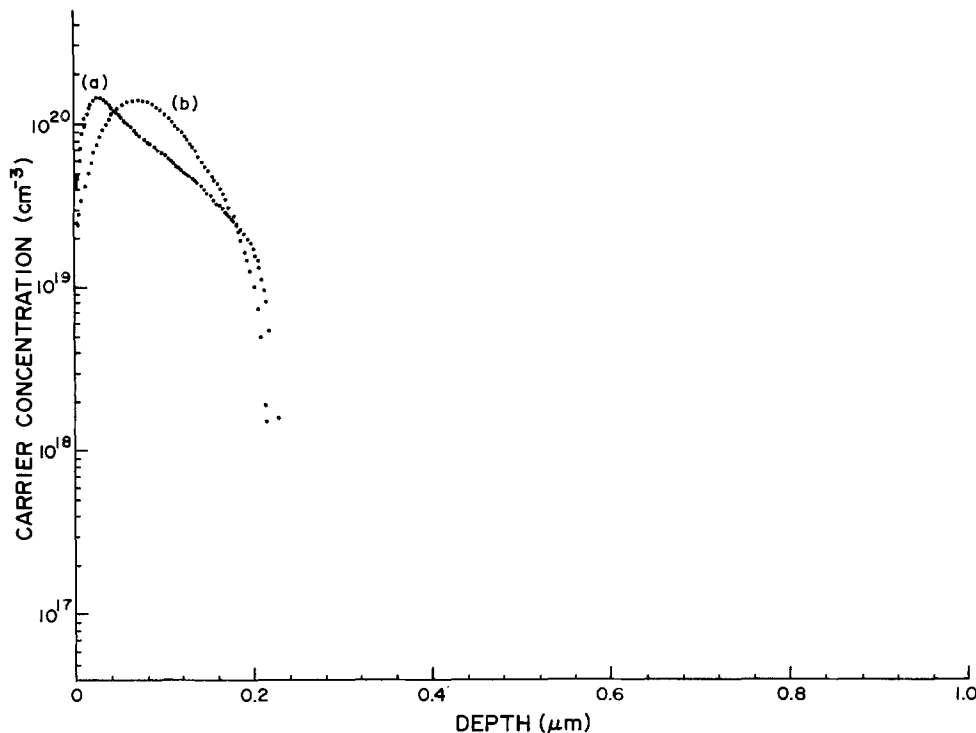


Fig. 5. Carrier concentration profiles for GaAs samples after 15 min Zn diffusion at 600°C. Curve a: with 50Å SiO₂ coating. Curve b: without SiO₂.

centrations, as measured by the Polaron apparatus, are accurate.

In summary, we report that the leaky tube diffusion technique can be utilized to produce very shallow, heavily doped p-type GaAs layers on an extremely reproducible basis. This repeatability is associated with the large quantity of source material and the stagnant ambient in the diffusion zone: a stable and consistent zinc vapor environment is readily achieved from run to run. We feel that even shallower diffusions are possible, but not by carrying out the diffusions at 600°C for durations less than 5 min. Rather, performing the diffusions at lower temperatures ($\approx 550^\circ\text{C}$) for short durations should restrict the Zn penetration to depths $\approx 0.1 \mu\text{m}$. Work is underway to examine the depths, profiles, and characteristics of these lower temperature Zn diffusions.

Acknowledgments

The authors would like to express their gratitude to S. Ageno for assistance with the diffusion, to G. Conrad for help with the doping profile determination, and to J. Marion and J. Martin for their able support in the laboratory. This work was supported in part by an Arizona State University Research Grant.

Manuscript submitted Nov. 7, 1983; revised manuscript received Feb. 13, 1984.

REFERENCES

1. C. Cognetti, M. Conti, and G. Chiaretti, *Solid-State Electron.*, **25**, 1093 (1982).
2. C. S. Hong, J. J. Coleman, P. D. Dapkus, and Y. Z. Liu, *Appl. Phys. Lett.*, **40**, 208 (1982).
3. K. Tada, T. Suzuki, and K. Yamane, *Thin Solid Films*, **83**, 289 (1981).
4. G. L. Troeger, A. J. Behle, P. E. Frieberthausen, K. L. Hu, and S. H. Watanabe, in "1979 International Electron Devices Meeting, Tech. Digest," pp. 497-500, (1979).
5. J. Kasahara, H. Sakurai, Y. Kato, and N. Watanabe, *Jpn. J. Appl. Phys.*, **21**, L103 (1982).
6. J. Kasahara and N. Watanabe, *Appl. Phys. Lett.*, **38**, 798 (1981).
7. R. G. Hunsperger and O. J. Marsh, *Metall. Trans.*, **1**, 603 (1970).
8. T. Itoh and Y. Kushiro, *J. Appl. Phys.*, **42**, 5120 (1971).
9. K. Taira, J. Kasahara, Y. Kato, M. Arai, and N. Watanabe, *IEEE Electron. Devices Lett.*, **ed1-4**, 314 (1983).
10. J. Kasahara, K. Taira, Y. Kato, M. Arai, and N. Watanabe, *Jpn. J. Appl. Phys.*, **22**, L373 (1983).
11. B. Tuck, "Introduction to Diffusion in Semiconductors," pp. 180-187, Peter Peregrinus Ltd., Stevenage, England (1974).
12. A. J. Springthorpe and M. N. Svilans, in "Institute of Physics Conference Series 65," Chap. 7, p. 589, Institute of Physics, London (1983).
13. W. Duebart, O. Hildebrand, H. W. Marten, and N. Arnold, *ibid.*, p. 597.
14. J. L. Edwards and R. J. Roedel, *Electron. Lett.*, **19**, 962 (1983).

Structure of Silver (100) and (111) Single-Crystal Surfaces Obtained by Chemical Polishing

Radoslav R. Adzic,¹ Michael E. Hanson,* and Ernest B. Yeager**

Case Center for Electrochemical Sciences and the Department of Chemistry, Case Western Reserve University, Cleveland, Ohio 44106

Interest has been increasing in the investigation of electrochemical reactions on single-crystal electrode surfaces [see, e.g., Ref. (1-7)]. Electrode processes having a pronounced dependence on the particular single-crystal surface include hydrogen adsorption (8-11), underpotential deposition of metals (4), oxidation of organic molecules (6), and oxygen reduction (7). Inadequately characterized single-crystal surfaces, however, may lead to misleading results. Atomically flat, well-ordered surfaces are needed in order to obtain meaningful data. Ultrahigh vacuum techniques such as low energy electron diffraction (LEED), Auger electron spectroscopy (AES), and x-ray photoelectron spectroscopy (XPS) can facilitate the characterization of such surfaces and verification of freedom from adsorbed impurities, but these techniques are *ex situ*. Elaborate systems (8-11) have been developed for preparing and characterizing single-crystal electrode surfaces in ultrahigh vacuum and then transferring them into the electrochemical environment and vice versa under conditions designed to minimize structural changes and contamination. Experiments with these transfer techniques, however, are very time consuming and impose substantial restraints on the types of electrochemical systems that can be studied because of factors such as the use of completely volatilizable electrolytic solutions and thin-layer cell configurations.

Some electrochemists, including one of the authors (R.A.), have prepared single-crystal surfaces of metals by chemical methods and then proceeded to examine the

electrochemical properties of these surfaces. This work, however, has left unanswered the question of the quality of the single-crystal surfaces. This paper presents results which demonstrate that chemical polishing in the instance of silver single-crystal electrodes can yield ordered (100) and (111) surfaces, as judged by LEED.

Single crystals of Ag, 99.99% pure, were obtained from Metal Crystals Limited, Cambridge, England. They were oriented to better than 1°, mechanically polished by standard metallographic techniques with diamond paste, gradually decreasing the size of the grit to 1 μm. The crystals were further polished chemically, using procedures similar to those already reported (12). An aqueous solution of 30 volume percent (v/o) of H₂O₂ and a solution of 21.5 g/l of NaCN were mixed in a 1:1 ratio for polishing the Ag(111) single-crystal surface. For the Ag(100) face, a lower concentration of 20 v/o of H₂O₂ was used. The crystals were held for 5s in these solutions, during which time vigorous gas evolution occurred. They were taken out, held in air for 3s, and transferred into a solution of 37.5 g/l NaCN, where gas evolution ceased. After washing, the procedure was repeated several times, in most instances in a fresh solution of H₂O₂ and NaCN until a highly reflecting surface was obtained. The electrode surface was then thoroughly washed in pure water. The surface obtained in this way was protected by a drop of pure water and transferred into the UHV preparation chamber of the LEED-AES-XPS system, which has been described in prior publications (8, 9). The water drop was then volatilized during the pump down.

Figure 1a shows the LEED pattern from the Ag(111) surface immediately after introduction into the UHV chamber at 10⁻¹⁰ torr. This LEED pattern was obtained without cleaning the surface in the vacuum chamber in any way. Neither argon-ion sputtering nor thermal an-

* Electrochemical Society Student Member.

** Electrochemical Society Honorary Member.

¹ Permanent address: Institute of Electrochemistry, ICTM and Center for Multidisciplinary Studies, University of Belgrade, Belgrade, Yugoslavia.

Key words: LEED, silver single crystals, chemical polishing.

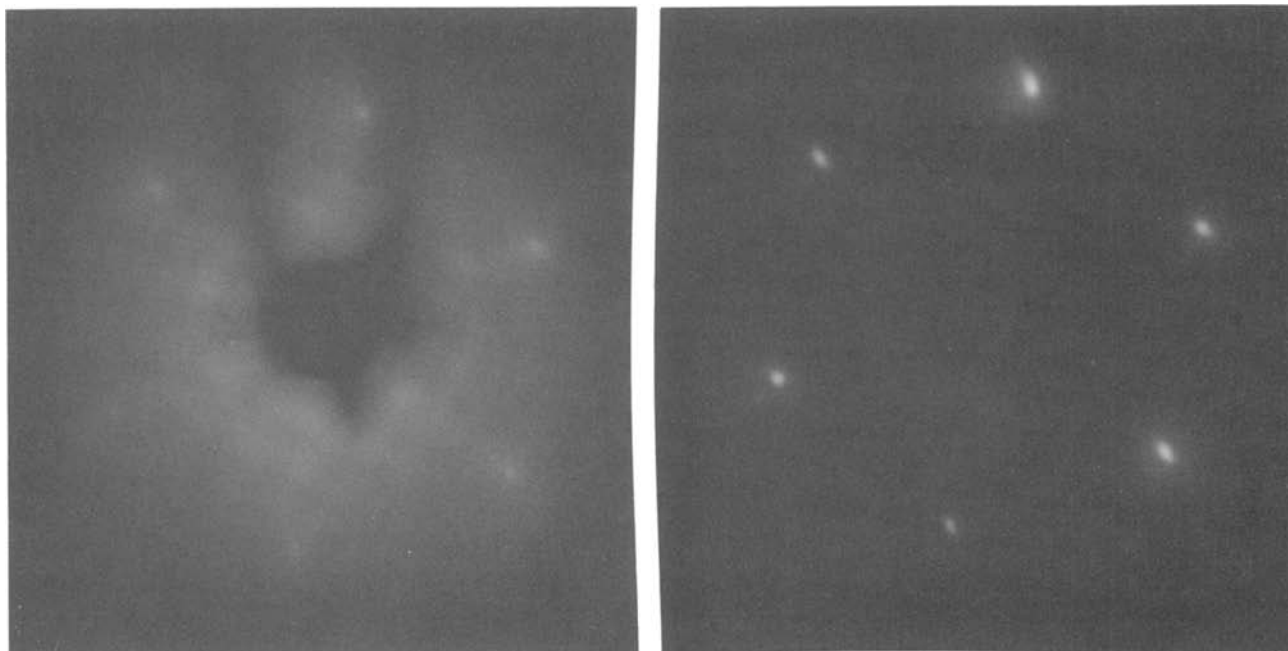


Fig. 1. A (left): LEED pattern of chemically polished Ag (111) immediately after introduction to the vacuum chamber (no sputtering or thermal annealing). Primary beam energy: 47 eV. Exposure time: 3 min. F-stop: 1.4, Kodak Panatomic X film for all exposures. B (right): same as A after sputtering at 1.5 kV for 3 min and thermally annealing at 600°C. Primary beam energy: 45 eV. Exposure time: 30s.

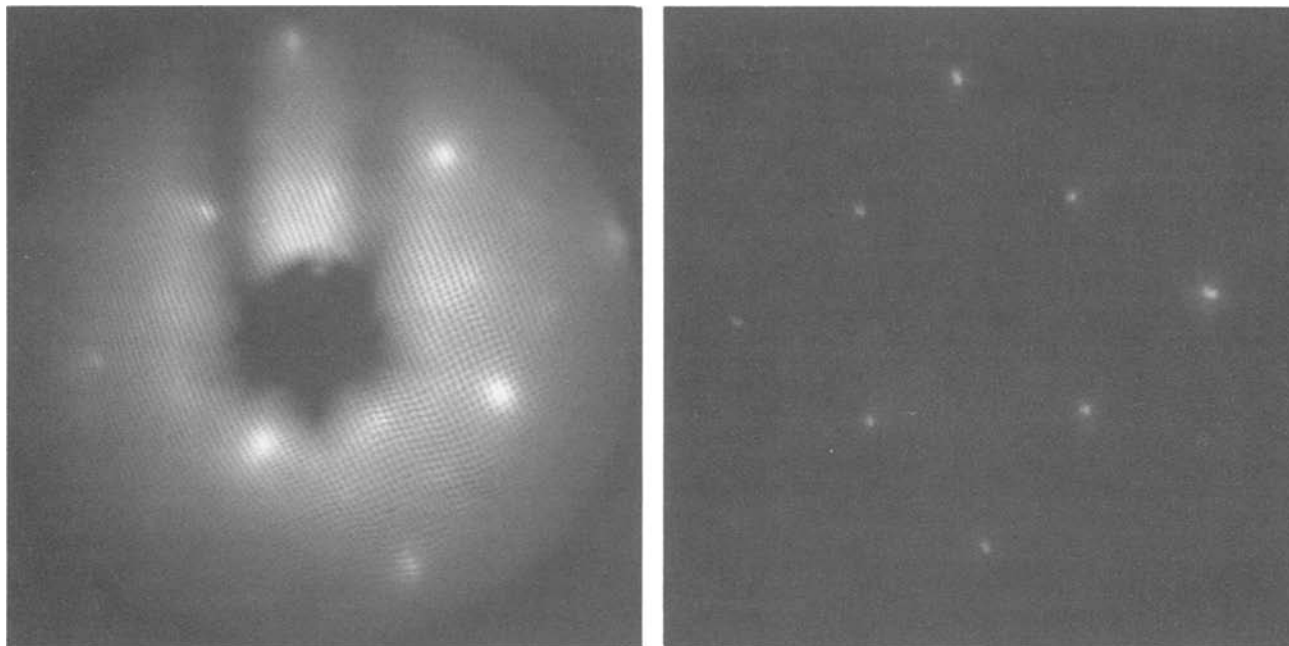


Fig. 2. A (left): LEED pattern of chemically polished Ag (100) immediately after introduction to the vacuum chamber (no sputtering or thermal annealing). Curvature of the pattern is due to the sample's protruding inside the radius of the screen because of its unusually large size for the system. Primary beam energy: 48 eV. B (right): same as A after sputtering at 1.5 kV for 3 min and thermally annealing at 600°C. Primary beam energy: 60 eV. Exposure time: 30s.

nealing was used. Figure 1b shows the LEED pattern of chemically polished Ag(111) after a single sputtering with an argon-ion gun (Varian Model 981-2043) for 3 min at 1.5 kV and subsequent radiative thermal annealing at approximately 600°C. The crystal reached this temperature in approximately 5 min and was allowed to cool to room temperature, which required about 20 min in vacuum. Analogously, Fig. 2a and 2b show LEED patterns of chemically polished Ag(100) before and after, respectively, UHV sputtering and annealing.

For both the (111) and (100) crystal faces before UHV sputter cleaning, highly diffuse background and weak fractional-order spots are present in the LEED pattern, probably due to random and ordered impurity adsorption during transfer to the vacuum chamber. Auger electron spectra before sputtering indicate the main impurity to be carbonaceous. No nitrogen was detected in the AES, indicating no substantial amount of CN^- remained on the surface. The LEED spots are surprisingly well defined, indicating a high two-dimensional periodicity, although not as ordered as the UHV-cleaned and annealed surfaces. Voltammetry curves were also obtained in 0.1M HF in a thin-layer cell using a special transfer techniques (8, 9). Over the potential range $-0.1-0.45\text{V vs. RHE}$, voltammetry curves were generally featureless.

These data demonstrate that chemical polishing can yield silver single-crystal surfaces of high enough quality to produce LEED patterns. This is of great importance for studies of these surfaces outside UHV systems.

Acknowledgments

This research has been supported by the Office of Naval Research and the Department of Energy. Grants have

also been received for equipment from General Motors and Union Carbide Corporation.

Manuscript submitted Dec. 2, 1983; revised manuscript received Jan. 19, 1984.

Case Center for Electrochemical Services assisted in meeting the publication costs of this article.

REFERENCES

1. J. M. Blakely and J. C. Shelton, in "Surface Physics of Materials," Vol. I, J. M. Blakely, Editor, pp. 189-239, Academic Press, New York (1975).
2. G. Somorjai, "Principles of Surface Chemistry," Prentice-Hall, Inc., Englewood Cliffs, NJ (1972).
3. A. Hamelin, T. Vitanov, E. Sevastyanov, and A. Popov, *J. Electroanal. Chem. Interfacial Electrochem.*, **145**, 225 (1983).
4. K. Juttner and J. W. Lorenz, *Z. Phys. Chem. N.F.*, **122**, 163 (1980).
5. R. R. Adzic, A. V. Tripkovic, and W. E. O'Grady, *Nature*, **296**, 137 (1982).
6. J. Clavilier, R. Parsons, R. Durand, C. Lamy, and J. M. Leger, *J. Electroanal. Chem. Interfacial Electrochem.*, **124**, 321 (1981).
7. R. R. Adzic and N. M. Markovic, *ibid.*, **138**, 443 (1982).
8. A. Homa, E. Yeager, and B. D. Cahan, *ibid.*, **150**, 181 (1983).
9. A. Homa, Ph.D. Thesis, Case Western Reserve University, Cleveland, OH (1981).
10. A. T. Hubbard, R. M. Ishikawa, and J. Katekaru, *J. Electroanal. Chem. Interfacial Electrochem.*, **86**, 271 (1978).
11. P. N. Ross Jr., *This Journal*, **126**, 1 (1979).
12. A. Bewick and B. Thomas, *J. Electroanal. Chem. Interfacial Electrochem.*, **65**, 911 (1975).



Redox Pathways

Applications in Catalysis

Thomas J. Meyer

Department of Chemistry, University of North Carolina, Chapel Hill, North Carolina 27514

ABSTRACT

Complex redox pathways, like H-atom transfer, hydride transfer, or O-atom transfer, appear in the chemistry of polypyridyl complexes of ruthenium and osmium. These pathways provide a basis for the known activities of the complexes as electrocatalysts in the oxidation of organics, the interconversion of nitrite and ammonia, the oxidation of water to oxygen, the oxidation of Cl^- to Cl_2 , and the interconversion of nitrate and nitrite.

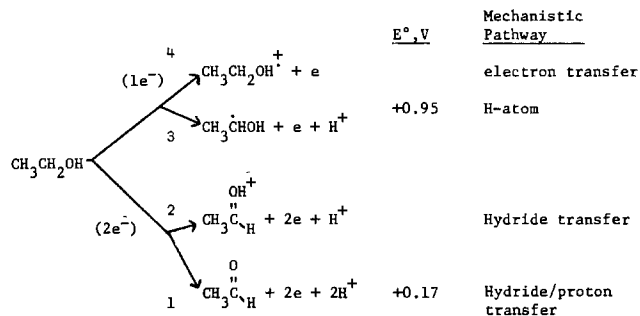
One-electron transfer processes, whether to or from an electrode surface, or between two reactants in solution, are becoming well-defined processes chemically (1, 2). An extensive theoretical background is available based on the pioneering work of Marcus (3), Levich and Dogonadze (4), and Hush (5b), and more recently based on quantum mechanics and time-dependent perturbation theory (6-10). The theoretical work has been extended to optical electron transfer (5). The successful interplay between theory and experiment in this area promises to lead to a series of advances in other areas; for example, to an understanding of electron transfer in biological systems, to an understanding of and ability to control photochemical and photophysical events, and to the possible design of devices based on the electron transfer properties of chemical sites in films or in polymers.

Notwithstanding our success at comprehending and manipulating one-electron transfer events, there are additional classes of redox pathways—hydrogen atom transfer, hydride transfer, O-atom transfer, etc.—which are far more complex and which present formidable challenges both from the mechanistic and theoretical points of view. Although more difficult to study, the potential rewards in learning to control such pathways are considerable. They appear to lie at the heart of some significant redox transformations in both organic and inorganic chemistry, and knowledge of their details could lead to the systematic development of new families of catalytic reagents.

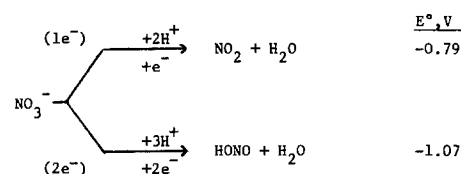
The themes here are to develop in preliminary detail some of the issues involved in complex redox pathways, to turn to identification of such pathways based on a closely related series of redox reagents, and, finally, to show how even at this early stage of development it is possible to use such findings to develop potentially useful catalytic reagents for carrying out redox transformations that are electrochemically driven.

Mechanistic Implications

In order to understand why complex redox pathways such as hydride transfer might appear and what factors could lead to the determination of which pathway provides the lowest energy alternative for a given transformation, it is useful to consider the energetics of two illustrative reactions, one organic and one inorganic. As summarized in Scheme 1, the first case considered is the oxidation of ethanol to acetaldehyde.



Scheme 1



Scheme 2

Four distinct pathways are considered in Scheme 1, and they are divided into one-electron (3 and 4) and two-electron (1 and 2) cases. Although other pathways could have been considered, the ones shown here have all been suggested to have an important role in the oxidation chemistry of ethanol, except perhaps for 1. Energetically, the most desirable pathways are those involving two-electron transfer steps and the immediate formation of the two-electron product. There is an additional advantage in that the two-electron pathways avoid high energy, one-electron intermediates. This is important from the synthetic point of view because one-electron, radical intermediates often have indiscriminate chemistries, which can lead to a lack of selectivity, and control of the reaction products can be lost if they appear.

From the mechanistic point of view, one-electron steps are appealing since the demands that they place on a chemical oxidant are relatively simple. The simplest case of all is outer-sphere electron transfer (reaction 4 in Scheme 1), which, although energetically costly, is relatively simple from the viewpoint of mechanistic demand. All that is required is electronic coupling between the chemical oxidant and the reducing agent and a reasona-

ble Boltzmann population of those vibrational levels which interconvert the reactant and product structures. Once formed, the ethanol radical cation would quickly undergo a series of proton-electron losses



to give the final product, acetaldehyde.

Although relatively easy to achieve from the mechanistic point of view, a simple one-electron transfer step has a costly energy demand. In order to achieve a significant reaction rate, a reasonably strong oxidizing agent is required because of the instability of the radical cationic intermediate.

Reaction 3 in Scheme 1 is a slightly more complex, but less energetically demanding pathway. It also involves one-electron transfer, but now with the simultaneous loss of both a proton and an electron from ethanol to give the intermediate radical with a proton complement fitting to the pH conditions of the medium. The mechanistic demands imposed by a hydrogen atom transfer pathway are more severe. Electronic coupling must occur between the reducing and oxidizing agents, and, in addition, there must be an acceptor site on the oxidant for the transferred proton. The combination of electronic and vibrational coupling needed to meet the demands of the pathway leads to a significant increase in molecular complexity.

The advantages of the two-electron steps are clear, but they are achieved at the cost of a further increase in molecular complexity. For the hydride transfer pathway, reaction 2 in Scheme 1, it is necessary to have not only an electron acceptor and a proton acceptor site on the oxidant at the same time, but, in addition, the acceptor must have a two-electron capability. The savings in energy and the gain in specificity can be had only at the cost of a greater challenge at the mechanistic level.

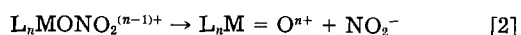
Perhaps the ideal pathway for carrying out the oxidation of ethanol is that shown in reaction 1 of Scheme 1, which involves a hybrid of both hydride transfer and proton transfer. The advantage of pathway 1 is that it creates the product in its equilibrium structure with regard to electron and proton content. However, the demands now placed on the oxidant are quite fancy indeed. In a concerted step, it must accept a coupled proton-electron pair (a hydride ion) and an additional proton. Impossible? We will, in a moment, find reagents which appear to come close.

The inorganic example shown in Scheme 2 is the reduction of nitrate ion to nitrite. Once again, there is a clear energetic advantage in favor of the two-electron step. However, as is often the case for inorganics when compared to organics, the advantage is far less dramatic because of a lesser relative instability for intermediate radicals. This is an important point mechanistically since facile one-electron pathways could appear for inorganic substrates: we will see just such a case later in the reduction of nitrite ion to ammonia.

Returning to Scheme 2, it is possible by inspection to begin to see mechanistic approaches for carrying out the reduction of nitrate. A traumatic change in structure must occur in that an oxide group must be lost on reduction. One approach to this problem mechanistically could involve an initial binding step

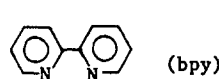


If the metal site has an accessible higher oxidation state, two electrons removed and stabilized by bonding to an oxo group, a concerted two-electron step could occur involving synchronous breakage of the MO-NO₂ bond and formation of the double bond component of the metal oxo link (M = O). The net two-electron reaction would be of the oxygen atom transfer type, as shown in Eq. [2]

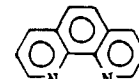


Higher Oxidation States of Polypyridyl Complexes of Ru and Os

Having presented the case for the implied importance of multiple electron steps both mechanistically and in catalysis, the most difficult task remains: the identification of chemical systems having appropriate reactivity properties. A likely place to look is in the polypyridyl chemistry of Ru and Os. An extensive background synthetic chemistry exists for these complexes, based on the ligands, 2,2'-bipyridine, 1,10-phenanthroline, and their derivatives



(bpy)



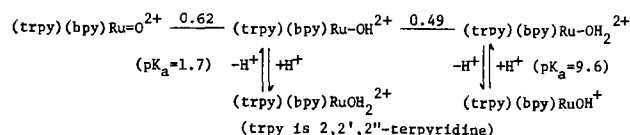
(phen)

2,2'-bipyridine

1,10-phenanthroline

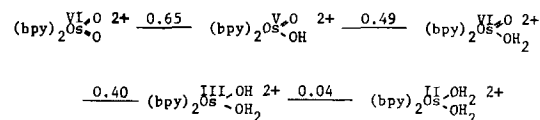
Typical complexes of ruthenium and osmium containing these ligands have a high stability toward loss of ligands in both oxidation states II and III, and it is interesting to note that complexes like Ru(bpy)₃²⁺ have found extensive use as photosensitizers in energy conversion applications (11-14).

A key feature in the redox chemistry of complexes of this type are cases where water is one of the bound ligands. For these complexes, the usual redox properties are complicated by the gain and loss of protons as shown by plots of $E_{1/2}$ vs. pH. As summarized in Scheme 3, the effect of oxidation of the aquo complex is enhanced acidity of the bound M-O-H protons, which accounts for the domains of pH-dependent redox behavior. Of more interest is the appearance in electrochemical

Scheme 3 (E° values in V vs. SCE at pH 7) (15, 16)

experiments of a higher oxidation state, Ru^{IV}. The potential of the Ru^{IV/III} couple also has a complex pH dependence, as suggested by Scheme 3. It is striking that the potentials for the Ru^{IV/III} and Ru^{III/II} couples are so close in value, since for related couples where there is no chance for proton gain or loss, e.g., Ru(bpy)₂Cl₂^{2+/+} - Ru(bpy)₂Cl₂⁺⁰, the difference in potentials exceeds 1.6V. Based on thermodynamic arguments, the key to the stabilization of the higher oxidation state is proton loss and donation of the freed p-II oxygen electron density to the metal to form the M = O double bond.

The accessibility of multiple higher oxidation states is a general feature of complexes of this type. It is important to realize that by making systematic variations in the ligands at the metal, a series of related redox reagents can be prepared and characterized where such features as reduction potentials can be varied systematically. An extreme example of such behavior is shown in Scheme 4, which is a

Scheme 4 (E° values in V vs. SCE at pH 4.0) (17)

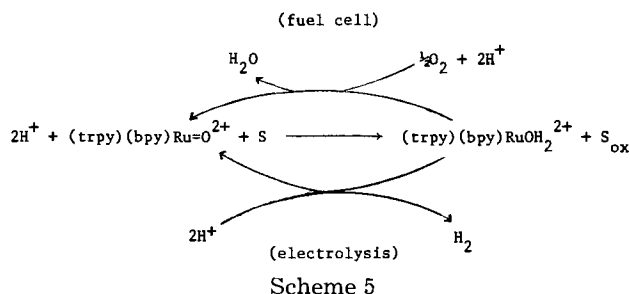
Latimer-type diagram interrelating oxidation states from Os(VI) to Os(II) in a coordination environment containing two bipyridine ligands. The redox potentials quoted in Scheme 4 are specified at pH 4 because there are complex variations in $E_{1/2}$ with pH for all of the couples. The data in Scheme 4 clearly open up the possibility of having a series of redox couples with an implied capacity for multiple electron changes. The importance of the oxo groups in stabilizing higher oxidation states is rather dramatic here, when it is realized that five different oxidation states of osmium, from II to VI, can exist over a potential range of ~ 0.6V.

The availability of higher oxidation states is striking in itself, but it also has important implications for mechanism and catalysis. The various oxidation states are reasonably stable; in fact, the Os(VI) dioxo complex, (bpy)₂Os(O)₂²⁺, has been isolated and characterized. The higher oxidation states also have some of the features that appear to be demanded by the mechanistic pathways mentioned above. One of these features is the existence of two-electron couples like the Ru(IV)/(II) couple in Scheme 3, which occur at potentials very near those for the component one-electron couples. The presence of the oxo group is important both in stabilizing higher oxidation states and mechanistically by providing an O atom transfer pathway, an initial lead-in site for attack on a substrate, or an acceptor site for a transferred proton in a hydride transfer.

Coordinative stability is essential for catalysis and for the Ru and Os complexes the primary coordination geometries stay intact in the different oxidation states. Critical structural changes occur only at the oxo "active site." This is in contrast to more typical oxidants like CrO₃ or MnO₄⁻, where reduction leads at some stage to changes in coordination number and composition (e.g., CrO₃/Cr(H₂O)₆³⁺), and it is usually quite difficult to make such systems catalytic.

Electrocatalysis

Before proceeding further into the chemical reactivity of the Ru and Os complexes, it is of value to consider how they might be used as catalysts in electrocatalytic applications. The principles involved are straightforward. They are illustrated in Scheme 5 for the hypothetical case where Ru(IV) is the active oxidant of a substrate S where the products of the reaction are S_{ox} and Ru(II)-OH₂. In the electrocatalytic schemes, the catalyst redox couple is oxidatively regenerated at the electrode in a net electrocatalytic "shuttle" mechanism. Two cases are shown in Scheme 5. One is an electrolysis cell, in which



the oxidation of the catalyst to its oxidized form is accompanied by reduction of water to hydrogen. From an energy balance point of view, it is important to note that H₂ is formed in the second cell compartment. Given the ready availability of oxygen in the air, electrocatalyses based on the Ru(IV)/Ru(II) couple in Scheme 5 occur with a near energy balance, assuming that the free energy stored in hydrogen as product could be recovered in an efficient hydrogen-oxygen fuel cell.

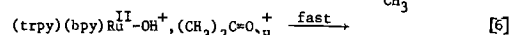
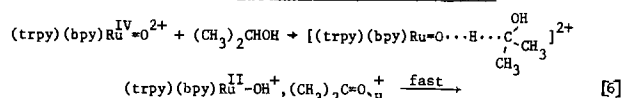
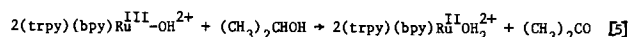
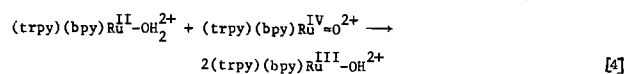
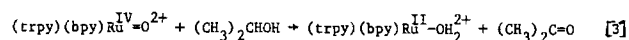
In the second approach, the catalytic regeneration is shown as running spontaneously by utilizing oxidizing equivalents from an O₂/H₂O electrode. Low overvoltage, high current density, practical O₂/H₂O electrodes are not available. If the technology does evolve, such cells could combine two functions and operate as chemical synthesis fuel cells, where either organic or inorganic transformations of interest could be carried out spontaneously with the production of an electrical current.

We have successfully operated electrolysis cells based on the shuttle mechanism, but an additional design feature must be taken into account. The shuttle mechanism has disadvantages arising from a requirement for relatively large amounts of catalytic material and from the difficulty of an added separation step at the end, one to recover the catalyst. A more sophisticated design feature involves the attachment of the redox sites directly to an electrode surface. In this configuration, catalyst demands

are greatly decreased and the possibility exists for flow-through design. There is an extensive background chemistry of this kind for the polypyridyl complexes, in which the electrode attachment is accomplished by adsorption of preformed polymers containing the redox sites, or by electropolymerization of appropriate complexes directly onto an electrode surface. This work has been reviewed elsewhere (18) and will not be of additional concern here.

Oxidation of Organics

The higher oxidation state oxo complexes of Ru mentioned above undergo rapid reactions with a variety of organic substrates. In some cases, the reactions have been investigated in detail either electrocatalytically or mechanistically, or both. A reaction which has been particularly well studied is the oxidation of isopropanol by Ru(IV)=O, as shown in Scheme 6. In the first step, a two-electron oxidation of isopropanol to acetone occurs along with the reduction of Ru(IV) to Ru(II) (19a). However, spectrophotometric studies show that (trpy)(bpy)-RuOH²⁺ is the initial product. It appears because the comproportionation reaction in Eq. [4] is rapid compared to the initial oxidation of isopropanol.



Scheme 6

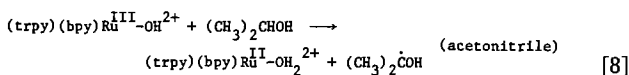
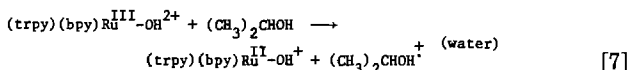
Following oxidation by Ru(IV), a slower reaction is observed in which isopropanol is oxidized by Ru(III) (Eq. [5]). The oxidation by Ru(III) is slower by ~ 400 at room temperature and occurs by an initial one-electron step to give the intermediate organic radical.

A variety of experimental facts are available for the oxidation of isopropanol by Ru(IV)=O: (i) The rate law is first order in both Ru(IV) and alcohol over a broad pH range with $k(25^\circ) = 0.07 \text{ M}^{-1}\text{s}^{-1}$. (ii) An isotopic labeling experiment shows that the oxo group is not transferred from Ru(IV) to the alcohol in the redox step. This is an important point for catalytic design, since it suggests that the mechanistic details of the reaction involve a template step in which substitution at the metal is not required. The importance of this point is that for inert second- and third-row transition metal complexes, overall catalytic rates are often controlled by substitutional steps. A template mechanism avoids such pitfalls. (iii) Comparing rate constants between (CH₃)₂CHOH and its perdeutero analog, (CD₃)₂CDOD, shows that the H/D kinetic isotope effect is $(k_{\text{H}}/k_{\text{D}}) \sim 18$. The majority of the effect (~ 6) comes from the C-H bond adjacent to the hydroxyl group, which is not surprising, since it is the bond that is oxidized in the net reaction.

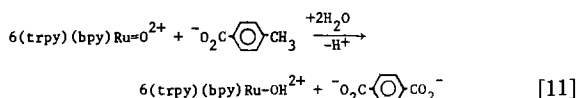
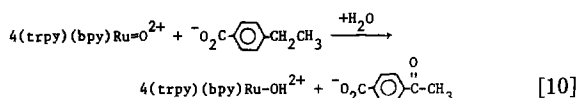
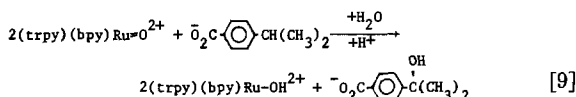
The results of a variety of experiments are consistent with the mechanism shown in Eq. [6], in which a concerted two-electron step occurs via a hydride transfer. It is interesting to note that even though Ru(IV)=O has apparently chosen to use a low energy, but complex, hydride transfer pathway, the initial products are formed with nonequilibrium proton contents, which is costly energetically. Following the redox step, proton equilibrium is achieved by rapid proton gain and loss steps to give the final products in their stable proton environments, which are determined by the pH of the solution. It is interesting to speculate that if an additional site were added to the complex as a proton acceptor site, at a structurally appropriate location, the proton composition dilemma might be

avoided, leading to the mechanism suggested by reaction [1] in Scheme 1, in which both two electrons and two protons are removed in a simultaneous step.

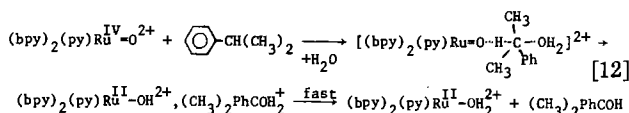
Without discussing the details, the oxidation of isopropanol by Ru^{III} also has some interesting features. From a combination of kinetic studies and kinetic isotope effects, it has been concluded that the oxidations occur by initial one-electron steps, as shown in Eq. [7] and [8], but that there is a change in mechanism between outer-sphere electron transfer in water to H atom transfer in acetonitrile



Detailed kinetic and mechanistic information is also available for the oxidation of C-H groups adjacent to aromatic rings by Ru(IV) = O. Typical reactions are shown in Eq. [9]-[11], where the examples shown are solubilized aromatic hydrocarbons, which were convenient for kinetic studies in water (19b). It is interesting to note that in contrast to Ru(IV)=O, Ru(III) no longer undergoes reactions at a measurable rate. This is not too surprising, since Ru^{III} is forced to behave as a one-electron oxidant, and the intermediate aromatic hydrocarbon radicals are far less stable than, for example, radicals of secondary alcohols. However, it clearly points out the value of the accessibility of two-electron pathways. Again, without elaborating on details, several interesting features have evolved from the aromatic oxidations: (i) the multiple electron reactions shown, for example, in Eq. [10] and [11] occur via a



series of consecutive two-electron steps. (ii) The example in Eq. [10] is illustrative of a clear element of selectivity in the preference for oxidation of C-H groups adjacent rather than remote to the aromatic ring. (iii) In the initial hydrocarbon oxidation step in Eq. [9], an oxygen atom must be derived from an external source in order to satisfy the compositional demands of the products. The results of kinetic and mechanistic studies suggest that the hydrocarbon oxidation occurs by a two-electron hydride transfer, Eq. [12], with the added feature that water or



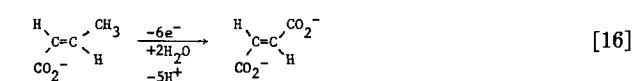
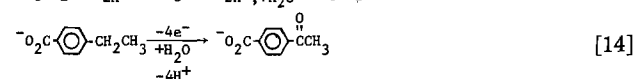
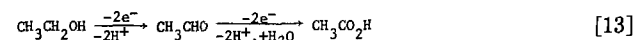
another nucleophile (Br⁻, t-BuOH) enters the rate law in a first-order fashion in acetonitrile (19b).

Once again, it is worth noting that the oxo complex has chosen a relatively sophisticated pathway to carry out an oxidation, but the demands of the reaction products are not fully met in that the proton contents of the initial products are not those at equilibrium. Here again, an improvement in catalyst design might be achieved by including a proton acceptor group at an appropriate site structurally.

One of the striking features to arise from the oxidation of aromatic hydrocarbons is the suggestion of an implied

functional group selectivity based on rate-constant data. As an example, under equivalent conditions, oxidation of the hydrocarbon in Eq. [9] is faster by 200 than oxidation of isopropanol. This is a surprising turnabout in reactivity and suggests the possibility of developing selective oxidants based on kinetic selectivity.

The major theme of the paragraphs above has been a discussion of mechanistic detail, but the same redox systems have proven to be of value in electrocatalysis. Examples of electrocatalytic oxidations based on the complex (trpy)(bpy)RuO²⁺ in water or in mixed organic solvent/water mixtures are shown in Eq. [13]-[16]. Some of the important

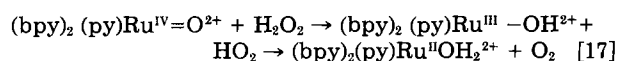


features to emerge from this work are the following: (i) The reactions are all carried out at or slightly above room temperature using the electrochemical shuttle procedure in Scheme 5. (ii) The reactions are notable for the fact that they appear to be quantitative within experimental error without the appearance of side-products. (iii) In multiple electron reactions like Eq. [14]-[16], the net processes involve a series of two-electron steps and in favorable cases intermediates, e.g., acetaldehyde in Eq. [13], build up, and, in fact, procedures can be developed for carrying out the selective oxidation of ethanol to acetaldehyde (20).

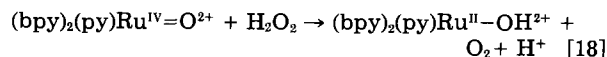
The Ru(IV) complex is not a universal catalyst. Under the relatively mild conditions of the electrocatalytic procedure no, or at least slow, reactions occur with a number of organics including acetate ion, tertiary alcohols, alkanes, or aromatic hydrocarbons. Finding that there are unreactive substrates represents a challenge to catalyst design. By preparing catalysts which are stronger oxidants and/or using more forcing conditions, it should be possible to find the conditions needed to oxidize any organic.

Inorganics

The Ru and Os complexes dealt with here have an equally interesting and revealing chemistry, both mechanistically and catalytically, in a series of important inorganic redox reactions. As a first example, consider the oxidation of hydrogen peroxide by (bpy)₂(py)Ru = O²⁺. The steps that occur in the net reaction are shown in Eq. [17]. One reason

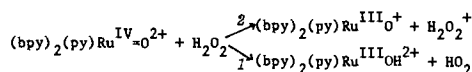


for studying the reaction was the possibility of finding a hydride transfer pathway for the oxidation of hydrogen peroxide to oxygen, Eq. [18], given the apparent propensity of Ru(IV)=O to undergo two-electron transfer steps. Although the reaction may not appear to be of consequence in its own right, it could have important implications for the



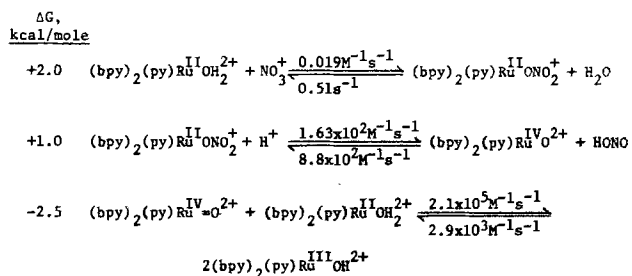
design of catalysts for the electrocatalytic reduction of oxygen to hydrogen peroxide based on microscopic reversibility. Nonetheless, it is clear from stopped-flow studies that the reaction occurs as shown in Eq. [17]-that is, through a series of two sequential one-electron steps. There is something quite extraordinary about the initial, relatively slow, one-electron step. At room temperature,

the rate constant for the reaction is $k = 2.1 M^{-1}s^{-1}$ (25° , $\mu = 0.1M$), and the H/D isotope effect is $(k_{H_2O}/k_{D_2O}) = 22.1 \pm 0.6$. The large H/D kinetic isotope effect indicates the existence of a complex pathway which can best be described as a hydrogen-atom transfer. The reason for the appearance of such an elaborate pathway in a reaction of this kind is obvious when one considers the possibilities shown below. One-electron



transfer by pathway 2, while mechanistically simple, necessarily gives the initial products with nonequilibrium proton compositions. The energetic demands associated with creating a Ru^{III} complex which is short a proton and a protonated perhydroxal radical are sufficient that this pathway is apparently noncompetitive. The large kinetic isotope effect signals the fact that pathway 2 is operative. The dilemma posed by proton composition in pathway 2 is avoided in pathway 1 by the simultaneous transferral of both an electron and a proton from hydrogen peroxide to the oxidizing agent in a net H-atom transfer.

Clear evidence has been obtained that the Ru redox couples can undergo multiple electron steps with inorganics. A case in point is the reversible interconversion of nitrate to nitrite. An initial experimental observation was that if $(bpy)_2(py)RuOH_2^{2+}$ is dissolved in nitric acid solution, it is unstable and with time is oxidized to $(bpy)_2(py)RuOH^{2+}$. The observation is remarkable when it is realized that a pH 1, $\Delta G^\circ \sim 0$ and that nitrate ion is commonly used as the anionic component of "inert electrolytes." Both the mechanistic and kinetic details of the interconversion between nitrate and nitrite have been investigated in detail and the facts as they are now known are presented in Scheme 7 (22).

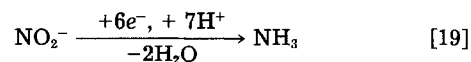


Scheme 7. ($\mu = 0.1M$; pH 2.0)

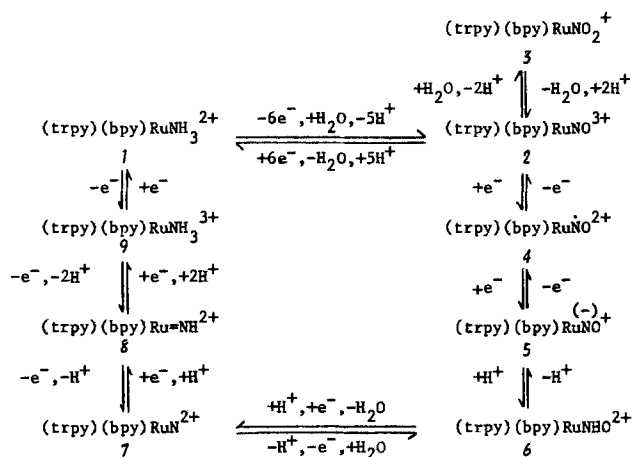
In the overall mechanism, the initial step involves a substitution in which NO_3^- displaces a water molecule in the inner coordination sphere to give an intermediate nitrate complex. The second step is the key one from the redox point of view, since in it the ion is literally stripped apart to give as products HONO and the Ru(IV)-oxo complex. Once again, the advantage of a multiple electron capability clearly emerges. In this case the pathway is O atom transfer, and its existence depends upon the accessibility of a higher oxidation state at the metal as well as the metal's ability to bind the oxide ion as it is removed from the bound nitrate. It is ironic that by far the slowest process in the overall scheme is the initial substitution step, a situation which is quite common for second- and third-row transition metal ions. With regard to the redox step, the rate constant for reduction of nitrate once bound is $160 M^{-1}s^{-1}$, showing that if the proper reactivity features are built into the redox reagent, nitrate can be reduced in a facile manner.

The overall reduction of nitrate to ammonia is an important process in plants. The nitrate to nitrite step described above is a mimic for a class of enzymes called nitrate reductases. The next step in plant metabolism, reduction of nitrite to ammonia, is carried out by the nitrite reductase enzymes. The reduction of nitrite to ammonia is a net six-electron step (Eq. [19]), and the reaction

demands are sufficiently formidable that at first glance it would seem unreasonable to think that a simple chemical reagent could carry out the net transformation. In fact, when bound in Os and Ru complexes, the interconversion

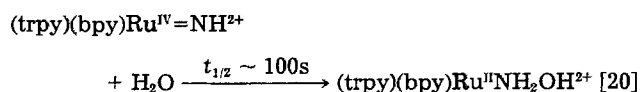


between nitrite and ammonia can be made reversible, and the results of a series of electrochemical studies have shown that the mechanism involves the one-electron steps, shown in Scheme 8 (23).



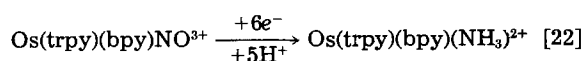
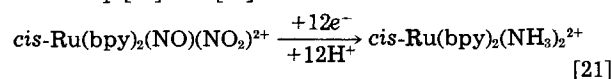
Scheme 8

The existence of the series of reactions depends on a closely matched balance of redox levels between the metal and coordinated ligands. In the reductive sense, the initial step is the interconversion of a metal nitro complex to the corresponding nitrosyl, which is well known chemically (24). Once the nitrosyl complex is formed, an initial one-electron reduction occurs at levels largely $\pi^*(NO)$ in character. The second step also involves a one-electron reduction at the ligand but is irreversible because of the subsequent addition of a proton to give a new intermediate in which an NHO group is bound to the metal. In the scheme, the consequences of the addition of a third electron are notable. According to the scheme, at this point there is a crossing of the sense of the redox orbitals involved, and the redox chemistry is carried out by orbitals largely metal-based in character, to give a nitrido complex $M(V)=N$ as intermediate. The rest of the scheme and the nitrido ammonia conversion are relatively straightforward. The four-electron intermediate, $Ru(IV)=NH$, contains a metal imine group and is an analog of the corresponding $Ru(IV)$ -oxo complex. The intermediate has not been isolated because it is inherently unstable in water, and reacts to give the corresponding hydroxylamine complex, with $t_{1/2} \sim 100s$ at $25^\circ C$ (Eq. [20]). Further reduction of the $Ru(IV)$ -NH intermediate leads



to isolable Ru(III) and finally to Ru(II) complexes, both of which contain coordinated ammonia. As suggested by the scheme, the reactions shown are reversible, at least for the complex shown, and can be driven in either direction, depending on whether the complexes are exposed to oxidizing or reducing conditions.

The chemistry suggested by the reactions in Scheme 8 appears to have general features as shown by the reactions in Eq. [21] and [22]



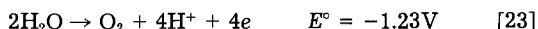
However, the catalytic interconversion of ammonia and nitrite based on the Ru and Os complexes suffers from the disadvantage of their being substitutionally inert. Once the redox chemistry occurs, the redox product is firmly bound.

It is possible to make the nitrite-to-ammonia interconversion catalytic. The key is to turn to the first-row transition metal congener, iron. Electrolysis of an aqueous solution containing nitrite in the presence of the water soluble iron tetraphenylporphine derivative, Fe(TPPS)(H₂O)₂²⁺, which contains -SO₃⁻ groups on the phenyl groups of the ligand, results in the electrocatalytic production of ammonia (23a). Although detailed mechanistic information is not available for the catalyzed reaction, it seems reasonable to expect that the mechanism is related to that in Scheme 8 and involves initial binding of NO₂⁻, acid-base equilibrium to give the nitrosyl, and reduction of the bound ligand. The advantage of the iron porphyrin complex in catalytic applications is that at the end of the reduction process, the complex is labile and exchange of ammonia for nitrite can occur. It is interesting to note that it is thought that the active redox sites in the enzymatic systems for nitrite reduction are also based on iron porphyrin groups. It is conceivable that much of the enzyme function is a redox apparatus designed to bring redox equivalents to the active iron porphyrin site.

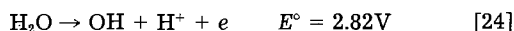
Oxidation of Water to Oxygen

It should be evident by now that the polypyridyl complexes of Ru and Os, with which we began, are extremely versatile in their redox properties. One of the most appealing features is the availability of varying redox potentials through systematic variations in structure. In the appropriate coordination environment, oxidizing complexes are accessible which have the thermodynamic ability to attack the problem of the electrocatalytic oxidation of water to oxygen or of chloride to chlorine. The problem of water oxidation is important to the possibility of developing photocatalytic systems for water splitting (H₂O → H₂ + 1/2 O₂) and also as the microscopic reverse of an extremely important fuel cell component, the reduction of O₂ to H₂O.

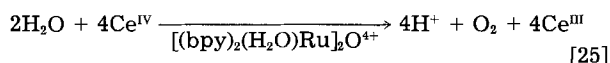
As can be seen from reaction [23], the mechanistic demands inherent in water oxidation are, once again, rather formidable. In order to



carry out the transformation at the thermodynamic potential for the H₂O/O₂ couple, a bond between two oxygens must be formed, and four protons and four electrons lost. There are severe energetic penalties if other pathways are chosen because of the instability of intermediate oxidation states of oxygen. For example, in 1M acid, the potential for the H₂O/OH couple is (25)

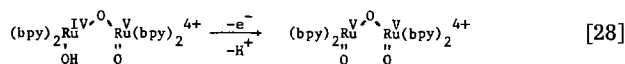
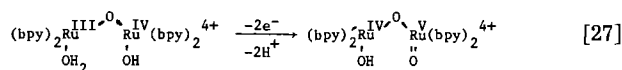
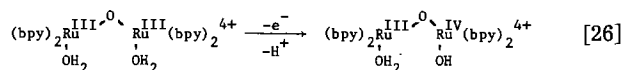


The approach we have taken to a water oxidation catalyst is to turn to a water oxidation catalytic dimeric structure, namely, (bpy)₂(H₂O)₂RuORu(H₂O)(bpy)₂⁴⁺. The structure of the dimer has been determined by x-ray crystallography. From the structure, the RuORu link is bent (165.4°) and the water molecules are slightly canted so that the water-water separation distance is ~ 4.7Å (26). The composition of the dimer is obviously promising for water oxidation in that it contains two linked metal sites and two bound water molecules held in close proximity. In fact, when more than four equivalents of a strong oxidant like Ce(IV) are added to aqueous solutions containing the dimer, the catalytic oxidation of water to oxygen occurs (Eq. [25] (27)). The system works effectively as a



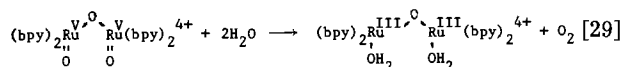
catalyst through many turnovers, although over an extended period of time, the catalytic properties of the system can be lost under certain conditions.

The redox properties of the dimer have been investigated by electrochemical techniques and are summarized in Scheme 9 (26). The actual proton compositions of the various dimers which appear there depend on pH, and the reaction shown are those which occur at pH 1.



Scheme 9

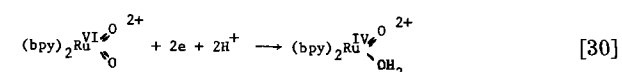
In the initial step, one electron and one proton are lost to give a formally Ru(III)-Ru(IV) dimer. The actual description of oxidation state in the dimers is complicated by the existence of strong electronic coupling through the bridging oxo group (29). The next stage is a two-electron, two-proton step giving a Ru(IV)-Ru(V) dimer. The appearance of a two-electron step shows that the Ru(IV)-Ru(IV) dimer is near to being or is actually unstable with respect to disproportionation. Under some pH conditions, an additional one-electron oxidation wave can be observed. Oxidation past that wave delivers the system to a state where the dimer presumably contains two chemically linked Ru(V) = O groups. Although information past this point is not yet available, we suspect that the Ru(V)-Ru(V) form is the active catalyst in the oxidation of water, perhaps by the four-electron step shown in Eq. [29]



It is illuminating to trace how the dimeric system appears to carry out the oxidation of water to oxygen. The net effect of Eq. [26]-[28] is the loss of the requisite numbers of electrons and protons to arrive at the structure, O=Ru(V)ORu(V)=O. In the structure, two oxo groups are held in close proximity in a dimeric unit where four redox equivalents are stored between the two metal sites. The water-to-oxygen interconversion appears to be quite rapid under certain conditions. Once again, the telling point here is that if transition metal redox reagents can be designed with the needs of a target reaction in mind, even reactions as complex as water oxidation and nitrite reduction can be carried out in a facile and potentially useful way.

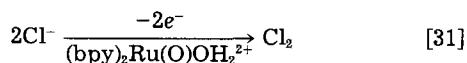
Oxidation of Chloride to Chlorine

The electrochemical oxidation of Cl⁻ to Cl₂ is a commercially important process which is carried out at carbon-based electrodes, which suffer from decomposition, or, more recently, at TiO₂ electrodes impregnated with Ru. RuO₂ containing electrodes are also efficient catalysts for the oxidation of water to oxygen, and given the structures of some of the metal complexes discussed here, extensions of the catalytic chemistry to the electrocatalytic oxidation of chloride to chlorine seem promising. In fact, we have found that a number of high oxidation state, Ru-oxo complexes do catalyze the oxidation of chloride to chlorine. Two such systems have been studied in detail: the dimeric system described in the previous section, and the Ru^{VI/IV} couple shown in Eq. [30] (28). The monomeric couple is part of a larger redox set, much like the one shown for the osmium analog in Scheme 4.



In the presence of either the Ru(IV) complex shown in Eq. [30] or the dimeric complex shown in Eq. [27], elec-

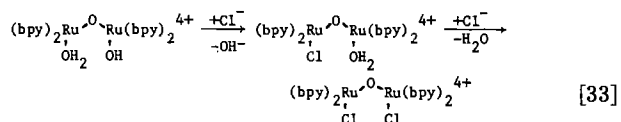
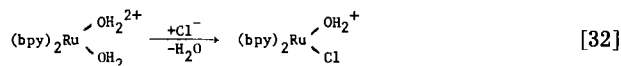
trollysis at carbon electrodes containing Cl^- leads to large catalytic currents and the production of chlorine, eq. [31]



or



The results of catalytic, electrochemical, and spectral experiments have revealed a number of details concerning the catalyzed oxidations and the way the catalysts operate: (i) for both catalysts, catalytic lifetimes are limited by slow replacement of water by chloride ion in the inner coordination spheres, Eq. [32], [33]. (ii) The monomeric



system has an additional instability arising from slow oxidation of water by $(\text{bpy})_2\text{Ru}(\text{O})_2^{2+}$, which occurs with the concomitant formation of an as-yet unidentified complex of Ru(III). (iii) It is clear from electrochemical studies that the active form of the dimer toward oxidation of chloride to chlorine is the Ru(IV)-Ru(V) dimer (Eq. [27]). This leads to an element of selectivity since electrolyses at potentials sufficient to oxidize the Ru(III)-Ru(IV) dimer to the Ru(IV)-Ru(V) dimer lead to the selective oxidation of Cl^- to Cl_2 without the appearance of oxygen. (iv) The catalyst couples are pH dependent in most pH regions, but the Cl_2/Cl^- couple is pH independent up to ~pH 3. As a consequence, it is possible to vary the overall driving force for the $\text{Cl}^- \rightarrow \text{Cl}_2$ oxidation by simply varying pH. (v) From pH variations, overvoltages for the catalyzed reactions are low since even when ΔG for the net reaction is as low as -0.07V , significant catalytic currents are still observed. (vi) A second point of note to arise from the pH dependence study is that in solutions more basic than pH 4, where chlorine exists largely as HOCl , or as OCl^- , the electrocatalytic reaction can be run in the reverse sense. Under these conditions, chlorine as HOCl rapidly oxidizes the Ru(III)-Ru(IV) dimer to Ru(IV)-Ru(V) or the Ru(IV) monomer to Ru(VI). For the dimer, this provides a route to use chlorine as the oxidant in the chemically catalyzed oxidation of water to oxygen.

Although the catalytic systems described here for the oxidation of chloride to chlorine have their faults, the net chemistry is successful. This appears to be a case where it should be possible to devise "ideal catalysts" which are reactive and long-lived and which can be attached to electrode surfaces.

A Mechanistic Summing-Up

Three interwoven themes have been developed here. The first was a consideration of complex redox events and the demands they place on a reagent if it is to be capable of carrying out complex redox transformations at reasonable rates. The second was the existence of complex redox pathways in real chemical systems, and the third was the incorporation of the chemical systems into operating electrocatalytic systems.

The chemical systems presented here are not, one would hope, the ultimate in catalyst design, but their properties are clearly encouraging. In the long run, these systems and others like them may fulfill a more important role in fundamental chemistry. They may allow a complete tally to be made of the reactivity patterns inherent in redox reactions. In the context of the speculations about chemical reactivity, it is interesting to note that even at this early stage at least six distinct redox pathways have been identified for the Ru complexes of interest here. Although the details of the various pathways may be debatable, all six are discernibly and

definably different based on H/D kinetic isotope effects, rate laws, activation parameters, etc. The six pathways and examples of them are illustrated in Scheme 10.

- Outer Sphere:
 $(\text{bpy})_2(\text{py})\text{Ru}^{\text{III}}\text{OH}^{2+} + (\text{CH}_3)_2\text{CHOH} \rightarrow (\text{bpy})_2(\text{py})\text{Ru}^{\text{II}}\text{OH}^+ + (\text{CH}_3)_2\text{CHOH}^+$
- H-atom Transfer:
 $(\text{bpy})_2(\text{py})\text{Ru}^{\text{IV}}=0^{2+} + \text{H}_2\text{O}_2 \rightarrow (\text{bpy})_2(\text{py})\text{Ru}^{\text{III}}-\text{OH}^{2+} + \text{HO}_2$
- Hydride Transfer:
 $(\text{bpy})_2(\text{py})\text{Ru}^{\text{IV}}=0^{2+} + (\text{CH}_3)_2\text{CHOH} \rightarrow (\text{bpy})_2(\text{py})\text{Ru}^{\text{II}}-\text{OH}^{2+} + (\text{CH}_3)_2\text{C}=\text{OH}^+$
- Hydride Transfer - Nucleophilic Addition:
 $(\text{bpy})_2(\text{py})\text{Ru}^{\text{IV}}=0^{2+} + \text{HCMe}_2\text{Ph} + \text{H}_2\text{O} \rightarrow (\text{bpy})_2(\text{py})\text{Ru}^{\text{II}}-\text{OH}^+ + \text{H}_2\text{OCMe}_2\text{Ph}$
- O-atom Transfer:
 $(\text{bpy})_2(\text{py})\text{Ru}^{\text{IV}}=0^{2+} + \text{NO}_2^- \rightarrow (\text{bpy})_2(\text{py})\text{Ru}^{\text{II}}-\text{O}-\text{NO}_2^+$
- Oxidative Coupling:
 $(\text{bpy})_2\text{Ru}^{\text{V}} \begin{array}{l} \text{O} \\ \text{O} \end{array} \text{Ru}(\text{bpy})_2 \begin{array}{l} 4+ \\ \text{OH}_2 \end{array} + 2\text{H}_2\text{O} \rightarrow (\text{bpy})_2\text{Ru}^{\text{III}} \begin{array}{l} \text{O} \\ \text{OH}_2 \end{array} \text{Ru}^{\text{III}} \begin{array}{l} \text{O} \\ \text{OH}_2 \end{array} (\text{bpy})_2 \begin{array}{l} 4+ \\ \text{OH}_2 \end{array} + \text{O}_2$

Scheme 10

It is without question that other redox pathways will appear for these reagents as additional substrates are investigated mechanistically. One of the most fascinating issues will be the attempt to unravel not only the details of the pathways, but to discover those factors leading to the most facile pathways for a given reaction. A combination of mechanistic studies with continued synthetic advances should lead to an extended family of catalysts for carrying out redox transformations in both organic and inorganic chemistry.

Acknowledgments

Acknowledgments are made to the National Science Foundation under grant no. CHE-8002433 and to the National Institutes of Health under grant no. GM15238-14 for support of this research.

Manuscript submitted June 27, 1983; revised manuscript received Feb. 24, 1984. This was Paper 705 presented at the San Francisco, California, Meeting of the Society, May 8-13, 1983.

The University of North Carolina assisted in meeting the publication costs of this article.

REFERENCES

- R. D. Cannon, "Electron Transfer Reactions," Butterworths, London (1980).
- J. Ulstrup, "Charge-Transfer Processes in Condensed Media," Springer-Verlag, Berlin (1979).
- R. A. Marcus, *Discuss. Faraday Soc.*, **29**, 21 (1960); *Annu. Rev. Chem.*, **15**, 155 (1964); *J. Chem. Phys.*, **43**, 679 (1965); *Electrochim. Acta*, **13**, 995 (1968).
- V. G. Levich, *Adv. Electrochem. Eng.*, **4**, 249 (1966).
- (a) R. S. Mulliken and W. B. Person, "Molecular Complexes," Wiley-Interscience, New York (1969); (b) N. S. Hush, *Prog. Inorg. Chem.*, **8**, 391 (1967); *Electrochim. Acta*, **13**, 1005 (1968).
- (a) R. Kubo and Y. Toyawaza, *Prog. Theor. Phys. Osaka*, **13**, 161 (1965); (b) M. Lax, *J. Chem. Phys.*, **20**, 1752 (1952); (c) K. Huang and A. Rhys, *Proc. Phys. Soc. Ser. A*, **204**, 413 (1951).
- (a) J. Ulstrup and J. Jortner, *J. Chem. Phys.*, **63**, 4258 (1975); (b) S. Efrima and M. Bixon, *Chem. Phys.*, **13**, 447 (1976); (c) R. P. Van Duyne and S. F. Fischer, *ibid.*, **5**, 183 (1974).
- T. Holstein, *Philos. Mag.*, **37**, 49 (1978); *Ann. Phys. Leipzig*, **8**, 343 (1959).
- N. R. Kestner, J. Logan, and J. Jortner, *J. Phys. Chem.*, **78**, 2148 (1974).
- E. D. German and A. M. Kuznetsov, *Electrochim. Acta*, **16**, 1595 (1981).
- V. Balzani, F. Bolletta, M. T. Gandolfi, and M. Maestri, *Top. Curr. Chem.*, **75**, 1 (1978).
- (a) N. Sutin and C. Creutz, *Pure Appl. Chem.*, **52**, 2717 (1980); (b) N. Sutin, *J. Photochem.*, **10**, 19 (1979).

13. T. J. Meyer, *Acc. Chem. Res.*, **11**, 94 (1978).
14. K. Kalyanasundaram, *Coord. Chem. Rev.*, **46**, 159 (1982).
15. B. A. Moyer and T. J. Meyer, *Inorg. Chem.*, **20**, 436 (1981).
16. K. J. Takeuchi, D. Pipes, and T. J. Meyer, *Inorg. Chem.*, To be published.
17. K. J. Takeuchi, S. W. Gersten, G. J. Samuels, and T. J. Meyer, *ibid.*, **22**, 1283 (1983).
18. H. D. Abruna, J. M. Calvert, P. Denisevich, C. D. Ellis, T. J. Meyer, W. R. Murphy, Jr., R. W. Murray, B. P. Sullivan, and J. L. Walsh, *ACS Symp. Ser.*, **192**, 133 (1982).
19. (a) M. S. Thompson and T. J. Meyer, *J. Am. Chem. Soc.*, **104**, 4106 (1982); (b) M. S. Thompson and T. J. Meyer, *ibid.*, **104**, 5070 (1982).
20. B. A. Moyer, M. S. Thompson, and T. J. Meyer, *ibid.*, **102**, 2310 (1980).
21. J. A. Gilbert, S. W. Gersten, and T. J. Meyer, *ibid.*, **104**, 6872 (1982).
22. (a) W. F. De Giovanni, J. A. Gilbert, and T. J. Meyer, Manuscript in preparation; (b) B. A. Moyer and T. J. Meyer, *J. Am. Chem. Soc.*, **101**, 1326 (1979).
23. (a) W. R. Murphy, Jr., K. J. Takeuchi, and T. J. Meyer, *ibid.*, **104**, 5817 (1982); (b) M. S. Thompson and T. J. Meyer, *ibid.*, **103**, 5577 (1981).
24. F. R. Keene, D. J. Salmon, J. L. Walsh, H. D. Abruna, and T. J. Meyer, *Inorg. Chem.*, **19**, 1896 (1980).
25. W. M. Latimer, "Oxidation Potentials," Prentice-Hall, Englewood Cliffs, NJ (1952).
26. J. A. Gilbert, W. R. Murphy, Jr., and T. J. Meyer, Manuscript in preparation.
27. S. W. Gersten, G. J. Samuels, and T. J. Meyer, *J. Am. Chem. Soc.*, **104**, 2049 (1982).
28. W. R. Murphy, Jr., J. A. Gilbert, C. D. Ellis, and T. J. Meyer, *J. Am. Chem. Soc.*, **105**, 4842 (1983).
29. T. R. Weaver, T. J. Meyer, S. A. Adeyemi, G. M. Brown, R. P. Eckberg, W. E. Hatfield, E. C. Johnson, R. W. Murray, and D. Untereker, *J. Am. Chem. Soc.*, **97**, 3039 (1975).

Molecular Ingredients of Heterogeneous Catalysis

G. A. Somorjai and R. C. Yeates

Materials and Molecular Research Division, Lawrence Berkeley Laboratory and Department of Chemistry, University of California, Berkeley, California, 94720

ABSTRACT

The purpose of this paper is to present a review and status report of the rapidly developing surface science of heterogeneous catalysis. We describe the experimental results that identified three molecular ingredients of catalysis: (i) structure (ii) carbonaceous deposit, and (iii) the oxidation state of surface atoms. The hydrogenation of ethylene at both the gas-solid and liquid-solid interfaces is described.

The explosively rapid development in surface science over the past 15 yr was concentrated on studies of the solid-gas and solid-vacuum interfaces. Electron, atom, and ion scattering techniques revealed the atomic structure and composition at the surface (1). Many of these techniques that are frequently used in surface studies are listed in Table I. The same techniques could not be used to probe the solid-liquid interface. The high elastic and inelastic scattering cross sections that make these probes surface sensitive render them ineffective in studies of interfaces between two phases of high atomic densities. As a result, studies of solid-liquid interfaces were pursued by the use of an ultrahigh vacuum-liquid cell that permitted *in situ* investigations of electrochemical reactions and then the direct transfer of the electrode surface into ultrahigh vacuum for analysis of the surface structure and composition (2). These cells are similar in design to the low pressure-high pressure cells developed in our laboratory (3) for combined low pressure surface science and high pressure catalysis studies, and have been most valuable in studies of platinum electrodes and electrocatalysis. More recently, high intensity electromagnetic radiation emanating from lasers (4) or from the synchrotron (5) has been employed increasingly for studies of the solid-liquid interface. Laser Raman spectroscopy, infrared ellipsometry, grazing angle x-ray scattering, and Fourier transform infrared techniques are among those that hold great promise for *in situ*, molecular-level analysis of the solid-liquid interface.

In this paper, we shall review what has been learned about the atomic structure and composition of clean surfaces from surface science studies of the solid-vacuum interface. We shall show the surface structures of a few organic molecules that have been determined by combined LEED and HREELS studies. We shall then describe the model of the working metal catalyst surface as revealed by single-crystal studies primarily using platinum surfaces. We shall correlate what is known about the hydrogenation of ethylene, C_2H_4 , that was studied over the Pt(111) crystal face, both at the solid-liquid and solid-gas

interfaces. Finally, we shall review what needs to be done, in our estimation, to accelerate the development of solid-liquid interface studies which are clearly at the frontier of surface science.

The Structure of Miller-Index Surfaces

The atomic structure of clean low Miller-index surfaces.—Low energy electron diffraction studies have revealed two important features of atomic surface structure: (i) relaxation and (ii) reconstruction. It has been found that for most solid surfaces, the spacing between the first and second layers is shortened as compared to the spacing between the second and third, which in turn is shortened as compared to the third and fourth, and so on. This contraction is larger for more open surfaces, that is, for surfaces having lower atomic density. For example, the contraction for the (110) surface of face-centered cubic metals is greater than that of the higher density (111) surface. In the surface plane (X-Y plane) the atoms maintain the structure of the projection of the bulk unit cell onto the surface. The contraction occurs in the Z direction, perpendicular to the surface. This phenomenon may be understood by considering the surface as an intermediate between a diatomic molecule and bulk crystal. The interatomic distance in diatomic molecules is much shorter than the interatomic distance in the solid crystal. The surface atoms, having fewer nearest neighbors than atoms in the crystal, exhibit a lattice parameter somewhere between these two extremes in order to compensate for the anisotropy of the forces (*i.e.*, having atoms on one side and vacuum or atoms of another type on the other side).

Reconstruction is also a consequence of surface atom relaxation. When atoms are placed in an anisotropic environment, such as the surface, there are many dangling bonds that would like to pair up in order to maximize the binding energy between surface atoms. As a result, the atoms at the surface seek a new equilibrium position, not only in the Z direction, but also in the surface (X-Y) plane. This massive dislocation of surface atoms leads to reconstruction, the ap-

Table I. Some of the frequently utilized surface characterization techniques to determine the structure and composition of solid surfaces. Adsorbed species present at concentrations of 1% of a monolayer can be readily detected.

Surface analysis method	Acronym	Physical basis	Type of information obtained
Low energy electron diffraction	LEED	Elastic backscattering of low energy electrons	Atomic surface structure of surfaces and of adsorbed gases
Auger electron spectroscopy	AES	Electron emission from surface atoms excited by electron x-ray or ion bombardment	Surface composition
High resolution electron energy loss spectroscopy	HREELS	Vibration excitation of surface atoms by inelastic reflection of low energy electrons	Structure and bonding of surface atoms and adsorbed species
Infrared spectroscopy	IRS	Vibrational excitation of surface atoms by absorption of infrared radiation	Structure and bonding of adsorbed gases
X-ray and ultraviolet photoelectron spectroscopy	XPS UPS	Electron emission from atoms	Electronic structure and oxidation state of surface atoms and adsorbed species
Ion scattering spectroscopy	ISS	Inelastic reflection of inert gas ions	Atomic structure and composition of solid surfaces
Secondary ion mass spectroscopy	SIMS	Ion beam induced ejection of surface atoms as positive and negative ions	Surface composition
Extended x-ray absorption fine structure analysis	EXAFS	Interference effects during x-ray emission	Atomic structure of surfaces and adsorbed gases
Thermal desorption spectroscopy	TDS	Thermally induced desorption or decomposition of adsorbed species	Adsorption energetics composition of adsorbed species

pearance of a new surface unit cell. Most semiconductors and many metal surfaces undergo these reconstructions (Fig. 1). Many of these structures have been analyzed by surface crystallography and the precise location of surface atoms has been determined (6).

The structure of high Miller-index surfaces.—Studies of high Miller-index surfaces by low energy electron diffraction have revealed that they are composed of low Miller-index surfaces in stepped and kinked configurations. Typical high Miller-index surfaces with various combinations of terraces and kinks are displayed in Fig. 2 and 3. By cutting crystals along a high Miller-index direction and suitable cleaning afterwards, one can obtain diffraction patterns from which the structure of these high Miller-index surfaces can be determined. Because of the periodicity of the steps and/or kinks, structure determination of diffraction is possible. Steps of monatomic height provide minimum surface free energies for these surfaces and therefore are prevalent on clean high Miller-index surfaces.

The Composition of Clean Surfaces

Because of differences in bonding at the surface and in the bulk, there is a considerable driving force for many impurities to segregate to the surface (7). Sulfur, carbon, boron, and silicon are often found to segregate to the surface upon heating. Although surface segregation of impurities is rather inconvenient when one would like to study the properties of clean surfaces, subsequent removal of the segregated impurity atoms provides a cleaning mechanism for many solids. For multicomponent systems, the surface free energy is minimized by placing that component which has the lowest free energy on the surface. As a

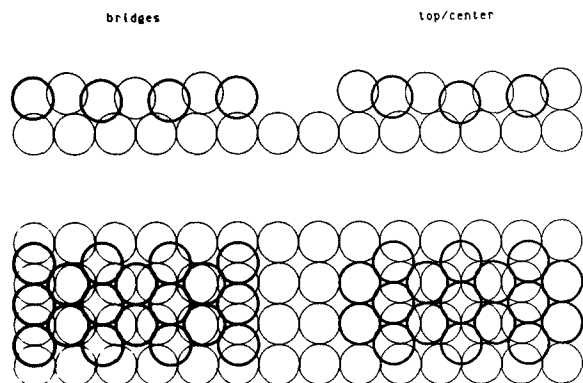


Fig. 1. Arrangement of atoms on the reconstructed (100) surface of platinum, gold, and iridium.

result, surface compositions are almost always different from the bulk composition for multicomponent systems (Fig. 4). This is particularly important for alloys because metals, having high surface energy in the range of thousands of ergs per square centimeter, provide a large thermodynamic driving force to segregate the component with the lowest surface energy to the surface, thus minimizing the total surface energy. Several thermodynamic models predict surface segregation in alloy surfaces (8).

It should be noted that the adsorption of gas atoms or molecules that form bonds of different strengths with a different alloy constituent can change the surface composition markedly. For example, copper is segregated to the surface of clean copper/nickel alloys (9). Upon adsorption of carbon monoxide, which forms a much stronger bond with nickel than with copper, nickel diffuses to the surface, altering the surface composition (10). When carbon monoxide is desorbed, the copper moves back onto the surface and provides a copper-rich alloy phase.

It should be noted that, in order to observe the surface segregation predicted by thermodynamic models, one needs to provide large enough diffusion rates to facilitate equilibration between the surface and bulk. At suffi-

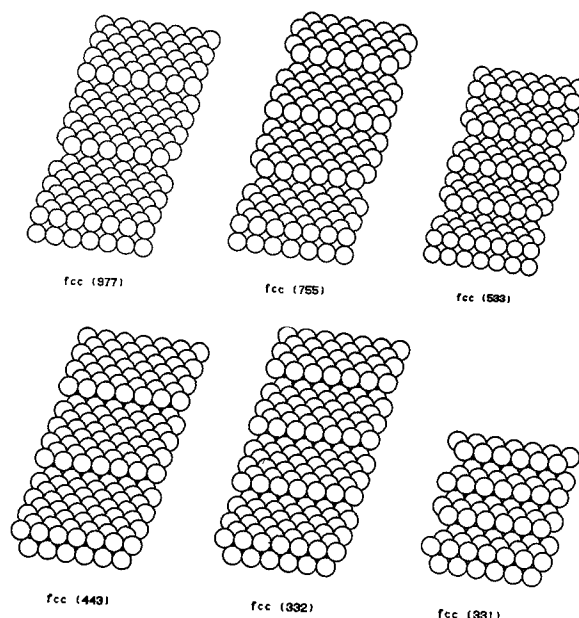
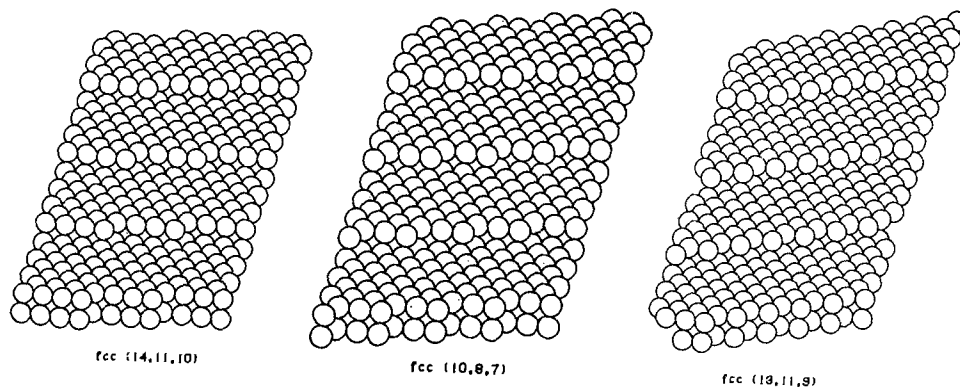


Fig. 2. Structure of several high Miller-index stepped surfaces with different terrace widths and orientation.

Fig. 3. Structure of several high Miller-index surfaces with different kink concentrations.



ciently low temperatures, one may freeze in metastable surface compositions. The surface segregation is minimized when the bulk lattice forces are strong enough to overcome any change due to the introduction of a surface. As a general rule, if the heat of mixing or the heat of compound formation is much greater than the surface energy differences of the components, surface segregation may be unimportant.

Structure of Alkenes and Benzene on Metal Surfaces

Our low energy electron diffraction and high resolution energy loss spectroscopy studies have been directed toward the determination of the molecular structure and bonding of hydrocarbons on platinum and rhodium surfaces. Figure 5 shows the stable structures of ethylene, propylene, and butene adsorbed on platinum and rhodium surfaces in our laboratory (11) and on palladium and nickel surfaces in other laboratories. The carbon-carbon bond closest to the metal surface is perpendicular to the surface plane, and is elongated to a single bond, 1.5Å. The carbon closest to the metal sits in a three-fold hollow site with a carbon-metal distance of 2.0Å, considerably shorter than the 2.2Å covalent bond length expected. This indicates a very strong multiple carbon-metal bond of carbene- or carbyne-like character. The methyl group or ethyl groups are away from the surface and are rotating rather freely. Only at high coverages will these side groups order to form new surface structures. These structures are called alkylidyne because of their similarity to several organometallic cluster compounds. Benzene lies flat on the (111) crystal face of these transition metals with the center of the benzene ring above the threefold hollow site (Fig. 6). The surface structure is highly symmetrical, as determined by both LEED and HREELS

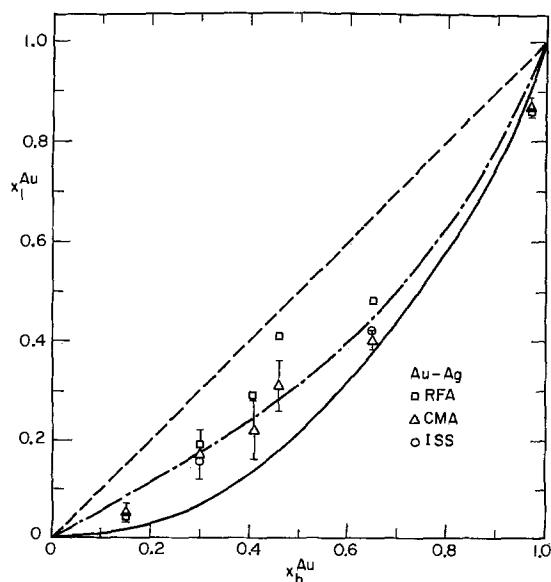
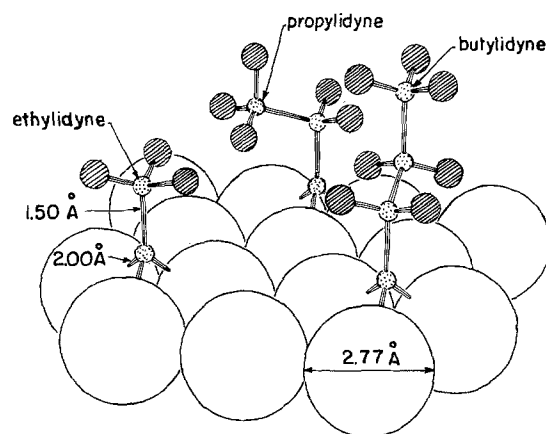


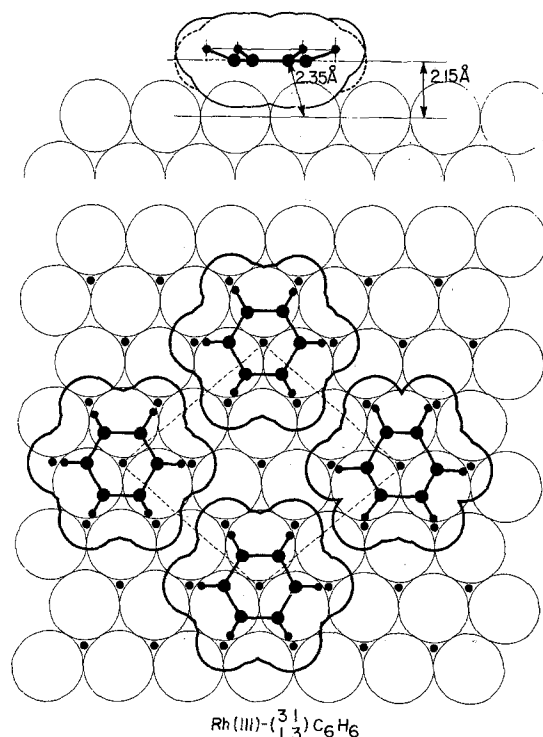
Fig. 4. Surface concentration of Au-Ag alloy plotted vs. the bulk concentration.

studies. As the temperature is increased, selective C-H and C-C bond breaking occurs and organic fragments, C_2 , C_2H , and CH , form on the surface. These fragments are very stable and seem to be present in the temperature range 140°-400°C (12), perhaps the most important temperatures for catalytic reactions. The hydrogen-deuterium exchange in these organic fragments is very facile. The



Pt(111) + ethylidyne, propylidyne and butylidyne

Fig. 5. Atomic surface structure of alkylidyne species adsorbed on Pt(111).



Rh(111)-(1/3, 1/3) C₆H₆

Fig. 6. Atomic surface structure of benzene adsorbed on Rh(111)

carbon atoms are strongly bound to the surface and stay on the surface for periods much longer than the turnover times of most catalytic reactions. The function of these fragments in a catalytic reaction appears to be one of hydrogen storage. They readily supply their hydrogen to incoming organic reactants and intermediates. Above 400°C, all the hydrogen desorbs and a graphitic overlayer forms. This layer poisons the transition metal surface for heterogeneous catalysis.

The Model of the Working Metal Catalyst during Hydrocarbon Conversion

Over the last ten years, studies of hydrocarbon conversion reactions using single-crystal surfaces have revealed the dominant molecular ingredients of hydrocarbon conversion catalysis. These are the atomic structure of the metal surface, its composition, and the oxidation state of the surface atoms. How does the reaction rate depend on the atomic structure of the catalyst surface? To answer this question, reaction rate studies using various flat, stepped and kinked single-crystal surfaces have been very useful indeed. For the important aromatization reaction of n-hexane to benzene and n-heptane to toluene, we discovered that the hexagonal platinum surface, where each surface atom is surrounded by six nearest neighbors, is three to seven times more active than the platinum surface with a square unit cell (13). Aromatization reaction rates increase further for stepped and kinked platinum surfaces (14). Reaction rate studies on more than ten different crystal surfaces with various terrace orientations and step and kink concentrations indicate that maximum aromatization activity is achieved on stepped surfaces with terraces of hexagonal orientation, about five atoms wide (Fig. 7).

The reactivity pattern of platinum crystal surfaces for alkane isomerization reactions is completely different than that for aromatization (15). Our studies revealed that maximum rates and selectivity (the rate of the desired reaction divided by the total rate) for butane isomerization reactions are obtained on the flat crystal face with the square unit cell. Isomerization rates for this surface are four to seven times higher than those for the hexagonal surface and are only increased slightly by surface irregularities (steps and kinks) on the platinum surface (Fig. 8). For the undesirable hydrogenolysis reactions that require C-C bond scission, we found that the two flat surfaces with the highest atomic density exhibit very similar reaction rates (15). However, the distribution of hydrogenolysis products varies sharply over these two surfaces. The hexagonal surface displays selectivity for scission of the terminal C-C bond, whereas the surface with the square unit cell always prefers cleavage of C-C bonds located in the center of the reactant molecule. The hydrogenolysis rate increases markedly (three- to fivefold) when kinks

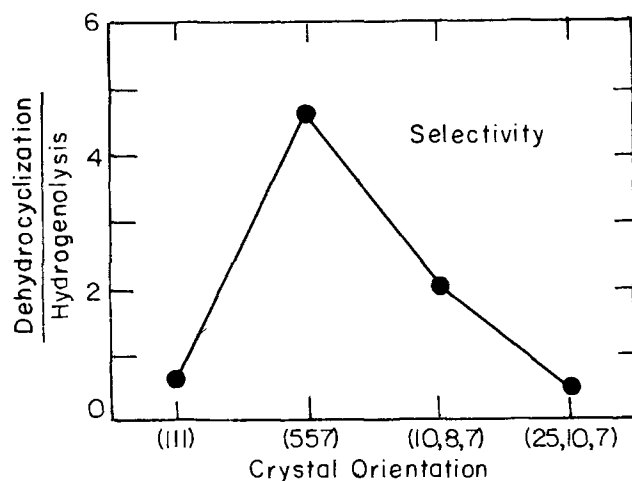


Fig. 7. The dependence of dehydrocyclization selectivities as a function of surface structure ($P_{n\text{-heptane}} = 15$ torr, $P_{H_2} = 480$ torr, and $T = 573$ K).

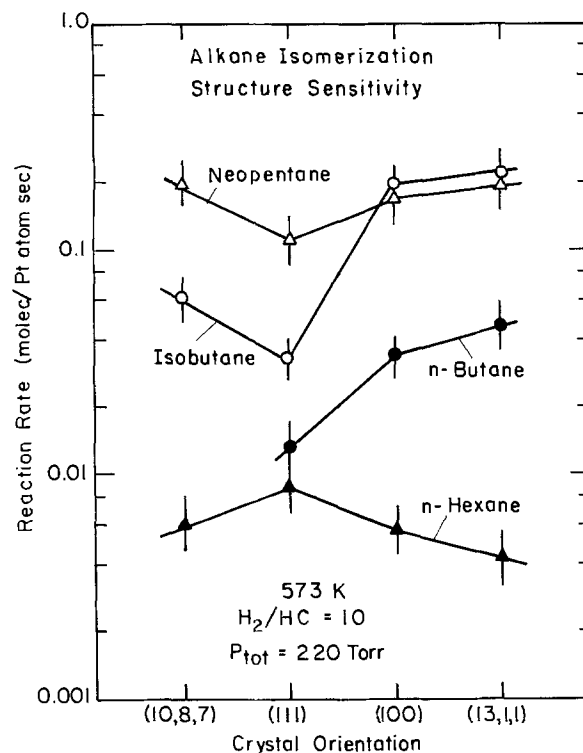


Fig. 8. The dependence of isomerization rate of various alkanes as a function of surface structure.

are present in high concentrations on the platinum surfaces.

Since different reactions are sensitive to different structural features of the catalyst surface, one must prepare the catalyst with an appropriate structure to obtain maximum activity and selectivity. As indicated, H-H and C-H bond breaking processes are more facile on stepped surfaces than on the flat crystal faces, while C-C bond scission is aided by kink sites.

What is the composition of the working metal catalyst surface? When the surface of platinum was examined after carrying out any one of the hydrocarbon conversion reactions, it was always covered by a near monolayer amount of carbonaceous deposit. Studies of carbon 14-labeled organic molecules and thermal desorption spectroscopy revealed that the turnover time of the carbon fragments was longer than the turnover times of the catalytic reactions (17). Deuterium exchange studies indicate rapid exchange of the hydrogen atoms between the adsorbing reactant molecules and the active, but irreversibly adsorbed carbon fragment deposits. The carbon atoms in this layer do not exchange. One important property of the carbonaceous deposit is its ability to store and exchange hydrogen. 10% and 15% of the surface remains uncovered, while the rest of the metal surface is covered by the organic deposit. The fraction of uncovered metal sites decreases slowly with increasing temperature (17). The structure of these uncovered metal islands is not very different from the structure of the initially clean metal surface.

The result of our catalytic hydrocarbon conversion reaction studies on platinum crystal surfaces was to develop a model (18) for the working platinum and other transition metal catalysts and is shown in Fig. 9. Between 80% and 95% of the catalyst surface is covered with an irreversibly adsorbed carbonaceous deposit that stays on the surface for times much longer than the reaction turnover time. The structure of these carbonaceous deposits vary continuously from two-dimensional to three-dimensional with increasing reaction temperature, and there are platinum patches that are not covered by this deposit. These metal sites can accept the reacting molecules and are responsible for the observed structure sensitivity and turnover rates. While there is evidence that the carbona-

MODEL FOR THE WORKING PLATINUM CATALYST

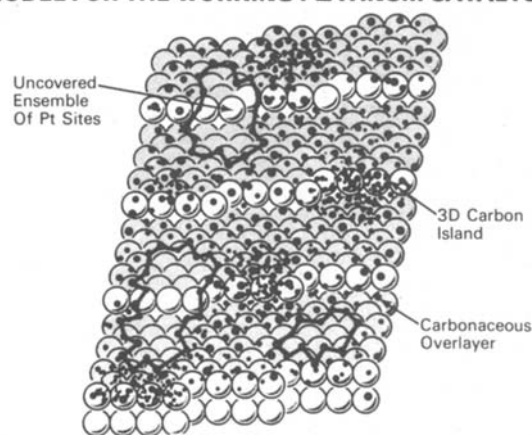


Fig. 9. Model for the working surface composition of a platinum reforming catalyst.

aceous deposit participates in some of the reactions by hydrogen transfer and by providing sites for rearrangement and desorption while remaining inactive in other reactions, its chemical role requires further exploration.

In other catalytic reactions, such as the hydrogenation of carbon monoxide, the oxidation state of the transition metal ions at the surface plays an important role in reaction selectivity. It was found that, using rhodium metal, carbon monoxide and hydrogen proceed to form methane (19) and nothing else (Fig. 10). When rhodium was used in the 3+ formal oxidation state as lanthanum rhodate (20) or rhodium oxide (21), oxygenated molecules such as acetic acid, ethanol, acetaldehyde, and methanol were produced. Changing the nature of adsorbed molecules by changing the oxidation state of the transition metal can drastically alter the reaction selectivity. In the case of the hydrogenation of carbon monoxide, the insertion of a carbon monoxide molecule into the growing organic chain can only occur in the presence of higher oxidation-state transition metal ions. In the presence of the metallic state, hydrogenation and CO dissociation predominate to produce mostly methane.

Ethylene Hydrogenation at the Solid-Liquid and Solid-Gas Interfaces of Pt(111)

One of the few reactions that has been studied at both the solid-liquid and solid-gas interfaces using combined low pressure surface science techniques and high pressure catalytic techniques is the hydrogenation of eth-

ylene. The research at the solid-liquid interface is being carried out by Hubbard (22) and his co-workers, and the hydrogenation of ethylene at the solid-gas interface was carried out in our laboratory (23). In both cases, the reaction exhibited an insensitivity to the surface structure and only depended on the number of surface platinum atoms.

When a clean platinum single-crystal surface was exposed to ethylene in the gas phase, a saturation coverage of ethylidyne formed with the structure shown in Fig. 5. The rate of hydrogenation of the ethylidyne molecules was much slower than the observed hydrogenation rate, indicating that the ethylidyne molecule is not a direct intermediate. Since the ethylidyne molecules block the metal atoms and prevent the direct adsorption of ethylene on the metal surface, the ethylene molecules adsorb on top of the ethylidyne layer and are hydrogenated by hydrogen transfer from the ethylidyne. This mechanism explains the structure insensitivity of this reaction. The hydrogenation reaction has an activation barrier of 10.8 kcal/mol (Fig. 11) with a reaction order of 1.3 for hydrogen and -0.60 for ethylene (Fig. 12).

When a clean platinum single-crystal surface was exposed to an aqueous ethylene solution, a strongly adsorbed ethylene layer formed. The structure of this adsorbed ethylene has not yet been determined. Two mechanisms appear to be important in the hydrogenation of ethylene at the solid-liquid interface. The adsorbed ethylene molecule can accept two electrons from the platinum electrode and subsequently react with two hydrogen ions in solution. Also, hydrogen ions can be reduced at the platinum surface. These adsorbed hydrogen atoms can then react with reversibly adsorbed ethylene to form ethane. The dependence of the reaction on temperature has not yet been determined.

Needs for Accelerated Development of Atomic-Scale Studies at the Solid-Liquid Interface

There is no doubt that the chemistry that occurs at the solid-liquid interface is at the frontier of modern surface science. Our challenge is to determine the atomic structure at the solid-liquid interface and the surface composition under adsorption and various reaction conditions. A molecular level understanding of many phenomena in electrochemistry and in biology depends on closer scrutiny of the solid-liquid interface. There are many new techniques that promise to open up this interface to closer scrutiny. The new high intensity photon scattering techniques are certainly among those that are likely to be used in these studies. Techniques that use high intensity, tunable synchrotron radiation and laser techniques are at

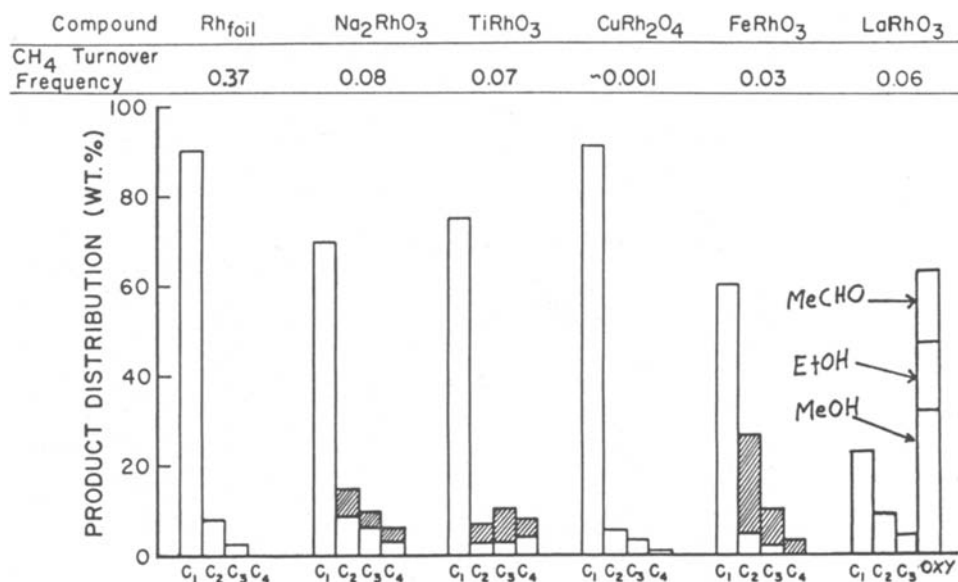


Fig. 10. The product distributions of the hydrogenation of carbon monoxide over rhodium and various rhodates.

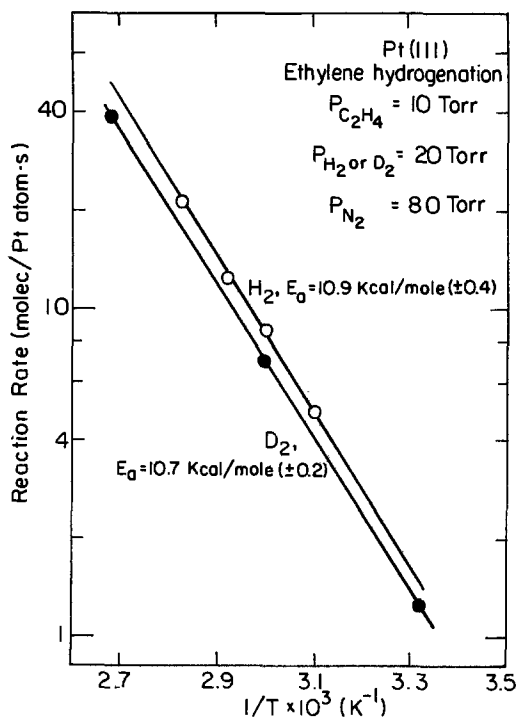


Fig. 11. Arrhenius plots for ethylene hydrogenation with H_2 and D_2 over Pt(111). $P_{C_2H_4} = 10$ torr, P_{H_2} or $P_{D_2} = 20$ torr, $P_{N_2} = 80$ torr.

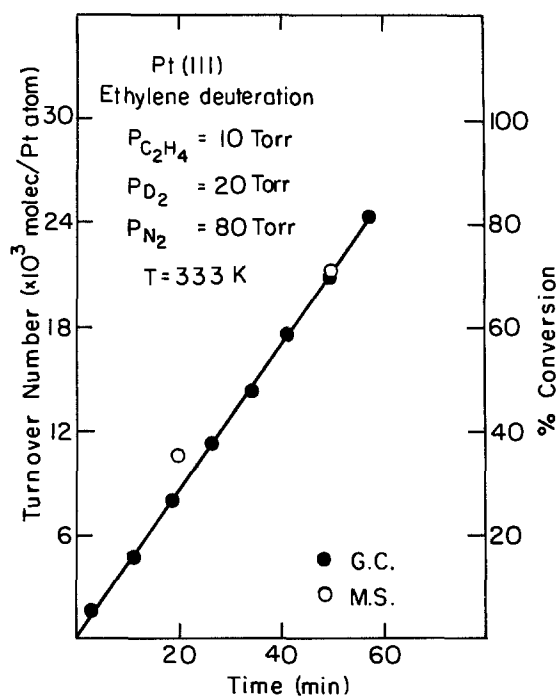


Fig. 12. Product accumulation curve as a function of time for ethylene hydrogenation over Pt(111). $T = 333$ K. The product was measured by mass spectrometry (\circ) and gas chromatography (\bullet).

the forefront of the promising technologies. It is our hope that the intensive use of these techniques and the development of new techniques will accelerate the understanding of solid-liquid interfaces at the atomic level.

We should emphasize the need for studies of chemisorption of the same atoms and molecules on the

same surface at both the solid-liquid and solid-gas interfaces. By detailed studies of both interfaces, one should be able to correlate the different phenomenon and perhaps use the tremendous amount of data available about solid-gas interfaces to aid in the understanding of the solid-liquid interface on the molecular scale.

It is equally important to study catalytic reactions at the solid-liquid and solid-gas interfaces on the same crystal face. Candidates, in addition to ethylene hydrogenation, are the oxidation of hydrogen and partial oxidation reactions of small molecules. It should be noted that, while temperature-dependence studies reveal kinetic parameters readily, temperature-dependent measurements are rarely made in solid-liquid interface studies.

Acknowledgment

We would like to thank the Division of Material Sciences and the Office of Basic Energy Sciences of the U.S. Department of Energy under Contract no. DE-AC03-76SF00098 for supporting this work.

Manuscript received Aug. 22, 1983. This was Paper 694 presented at the San Francisco, California, Meeting of the Society, May 8-13, 1983.

The University of California assisted in meeting the publication costs of this article.

REFERENCES

- G. A. Somorjai, "Chemistry in Two Dimensions: Surfaces," Cornell University Press, Ithaca, NY (1981).
- A. T. Hubbard, *Acc. Chem. Res.*, **13**, 177 (1980).
- D. R. Kahn, E. E. Petersen, and G. A. Somorjai, *J. Catal.*, **34**, 294 (1974).
- T. M. Cotton, S. G. Schultz, and R. P. VanDuyne, *J. Am. Chem. Soc.*, **104**, 6528 (1982).
- G. G. Long, J. Konger, D. R. Black, and M. Kuriyama, *This Journal*, **130**, 240 (1983).
- "The Chemical Physics of Solid Surfaces and Heterogeneous Catalysis," Vol. 1, D. A. King and D. P. Woodruff, Editors, Elsevier Scientific Publishing Co., New York (1982).
- J. Blakely and J. Shelton, "Surface Physics of Materials," Vol. 1, p. 199, Academic Press, New York (1975).
- S. H. Overbury, P. A. Bertrand, and G. A. Somorjai, *Chem. Rev.*, **75**, 547 (1975).
- H. H. Brongersma, M. J. Sparnay, and T. M. Buck, *Surf. Sci.*, **71**, 657 (1978).
- J. C. M. Harberts, A. F. Bourgonje, J. J. Stephan, and U. Ponc, *J. Catal.*, **47**, 92 (1977).
- G. A. Somorjai, in "Proceedings of the 9th International Conference on Atomic Spectroscopy, XXII CSI," Pure and Applied Chemistry, Tokyo, Sept. (1981).
- M. Salmeron and G. A. Somorjai, *J. Phys. Chem.*, **86**, 341 (1982).
- S. M. Davis, F. Zaera, and G. A. Somorjai, *J. Catal.*, **53**, (1983).
- W. D. Gillespie, R. K. Herz, E. E. Peterson, and G. A. Somorjai, *ibid.*, **70**, 147 (1981).
- S. M. Davis, F. Zaera, and G. A. Somorjai, *J. Am. Chem. Soc.*, **104**, 7453 (1982).
- S. M. Davis, B. E. Gordon, M. Press, and G. A. Somorjai, *J. Vac. Sci. Technol.*, **19**, 231 (1981).
- S. M. Davis and G. A. Somorjai, *J. Phys. Chem.*, **77**, 439 (1982).
- G. A. Somorjai and S. M. Davis, *Platinum Met. Rev.*, **17**, 54 (1983).
- D. G. Castner, R. L. Blackdar, and G. A. Somorjai, *J. Catal.*, **66**, 257 (1980).
- P. R. Watson and G. A. Somorjai, *ibid.*, **72**, 347 (1981).
- P. R. Watson and G. A. Somorjai, *ibid.*, **74**, 282 (1982).
- A. T. Hubbard, M. A. Young, and J. A. Schoeffel, *J. Electroanal. Chem.*, **114**, 273 (1980).
- F. Zaera and G. A. Somorjai, *J. Am. Chem. Soc.*, To be published.



Reduction of Voltage Delay in the Li/SOCl₂ System via Suitable Choice of Electrolyte Salts

N. A. Fleischer,^{*} S. M. Manske, and R. J. Ekern^{*}

RAYOVAC Corporation, Madison, Wisconsin 53711

ABSTRACT

New electrolyte salts based on the reaction between NbCl₅ and either Li₂S or Li₂O in SOCl₂ substantially reduce voltage delay in laboratory half-cells. The maximum effect was obtained with the NbCl₅/Li₂S combination. The conductivity of both electrolytes is 13.2×10^{-3} mho cm⁻¹ at 26°C. Observations with scanning electron microscopy (SEM) show that the anode film formed in the new electrolyte has a different morphology and appears less dense than the film formed in control LiAlCl₄ electrolyte. The anodic rate capability of Li is slightly greater, over a range of over-potentials, in the NbCl₅/Li₂S electrolyte than in LiAlCl₄. Atomic absorption, infrared, and x-ray photoelectron spectroscopy and electrochemical analysis suggest that the salt formed by reacting NbCl₅ with Li₂S in SOCl₂ is either Li₂Nb₂Cl₁₀S or Li₂Nb₂Cl₁₂. The mechanism for reducing voltage delay and affecting anode film morphology is thought to be associated with the nature of the salt's anion, or possibly the SO₂ produced when Li₂S is combined with the NbCl₅ in SOCl₂.

The Li/SOCl₂ system (1, 2) is attractive as a battery power source because of its high voltage and energy density, good shelf life, and broad operating temperature range. However, a major concern about its successful commercial application is voltage delay. Voltage delay is the excessive polarization of the anode (when a cell is first placed on load), which causes the cell voltage to temporarily drop below a predefined cutoff voltage.

According to the multilayer model of anodic film growth (3, 4), a primary passivating film of LiCl is rapidly formed upon contact of the Li with the SOCl₂ solvent. This primary film is dense and thin. Voltage delay is caused by the subsequent growth of a secondary, porous film on top of the primary film. The growth of the secondary film in LiAlCl₄ electrolytes is believed to be associated with the nature of the AlCl₄⁻ anion and its interaction with the primary film. LiAlCl₄ is widely used in cells as the electrolyte salt (5) because of its high conductivity. Other variables which might affect film growth include electrolyte purity, the chemical dissolution and ionic conductivity of the solid phase of the film, and temperature (3, 6).

Several different approaches have been developed for reducing voltage delay (7-12). The approach of this work is that voltage delay can be controlled by using an electrolyte salt which, as opposed to LiAlCl₄, would not appreciably interact with the primary LiCl film. However, the choice of alternate salts is limited by the low dielectric constant of SOCl₂ (9.25 at 20°C). Similar electrolyte approaches have been used by others. Schlaikjer (7) and Dey (13) have used clovoborate salts to successfully reduce voltage delay. These salts have very large anion structures which are considered to be inert towards the primary LiCl film. Gabano (8) and Bresson *et al.* (14) have studied various Lewis acid/base combinations as electrolytes.

In this paper, we report on the development of conductive, NbCl₅-based electrolytes (15). The effects of this electrolyte on voltage delay, anode film formation, and Li and SOCl₂ discharge were studied. A chemical analysis of the salt was performed.

^{*}Electrochemical Society Active Member.

¹ Present address: Tadirun, Lithium Primary Battery Plant, Rehovot 76100, Israel.

Key words: anode, inorganic, polarization, infrared.

Experimental

Electrolytes were prepared in an Ar-filled glove box (1-2 ppm H₂O, Vacuum Atmospheres Company). NbCl₅ (Aldrich, 99.8% Pure) was dissolved in distilled thionyl chloride at 70°C while being stirred for 60-90 min. The solution was allowed to cool and then was stirred for 1-2h. A secondary salt of Li₂S (98% Pure Anhydrous, Aldrich or 99% Pure Alfa), LiCl (Mallinckrodt AR Grade, dried under vacuum at 150°C), Li₂O (95% Pure, Alfa), or LiBr (Fisher certified, dried under vacuum at 178°C) was slowly added to the solution which was stirred for another 60 min. The electrolytes were decanted and filtered (Reeve Angel 934 AH, glass fiber). AlCl₃-(99% Pure, Fluka) based electrolytes were prepared with Li₂S or LiCl without heating.

The electrolyte concentration of Nb and Li were determined by atomic absorption analysis (Perkin-Elmer Model 603 Spectrophotometer). The concentration values have an accuracy of $\pm 0.05M$ for Nb and $\pm 0.012M$ for Li.

Conductance measurements were performed in the glove box with a Yellow Springs Instrument Model 31 Bridge at 1 kHz. The manufacturer states that the instrument has an accuracy of $\pm 1\%$. The conductivity cell with Pt electrodes was used in the inverted position, and the vent was sealed with Teflon tape.

Voltage delay measurements using galvanostatic steps were previously described in Ref. (25). The measurements and cell construction were performed inside the glove box. The cell apparatus consisted of a Teflon bottle with a Teflon screw cap. All electrodes were made from lithium (Foote Mineral Company). The working electrode was constructed by forcing a glass capillary tube (3 mm id) through 0.15 cm thick Li foil. The tube was then pulled from the lithium and excess material trimmed with a razor blade to form an electrode with a well-defined surface area. A Ni wire contacted the rear of the Li slug inside the tube for electrical contact. The other end of the Ni wire was force fitted through a small hole in the cell cap as a feed through. This construction prevented the Ni from contacting the electrolyte.

The counterelectrode was a flat Li ribbon positioned parallel to the face of the working electrode. The Li reference electrode was positioned close to the working electrode, but did not interfere with the current flow. Both the counter- and reference electrodes were connected to

Ni feed throughs well above the electrolyte level. The cyclic voltammetry experiments used the same instruments, but the working and counterelectrodes were both made from nickel foil. Tafel anodic polarization curves were run using the same instruments and used lithium as the working and counterelectrodes.

Scanning electron microscopy (SEM) of lithium anodes and x-ray photoelectron spectroscopy (ESCA) of dried salts were performed as in Ref. (26).

Infrared (IR) spectra of electrolyte samples were observed with a Perkin-Elmer 457A Grating IR Spectrophotometer. The IR cell has a path length of 0.025 mm and BaF₂ windows. Samples of evaporated electrolyte salt for IR analysis were prepared by forming them into KBr pellets.

Results

Solubility and conductivity.—The concentration and conductivities of various solutions are shown in Table I. The maximum solubility of NbCl₅ in SOCl₂ is 0.93-0.96M at room temperature. Heating the solution at 70°C for several hours or stirring at room temperature for several days in the presence of excess salt did not change this value. The conductivity of NbCl₅/SOCl₂ solution is very low. This has been noted for other Lewis acids in SOCl₂ (16). Li₂S, LiCl, LiBr, and Li₂O, which act as Lewis bases in SOCl₂, are basically insoluble in pure SOCl₂ (the maximum solubility of Li₂S was found to be 0.003M), but do dissolve in the NbCl₅ solution to form neutralized solutions with conductivities close to that of LiAlCl₄ electrolyte (Table I). 1.60M was used as the reference concentration for LiAlCl₄ electrolyte because at this concentration its conductivity is near its maximum (1).

The neutralization of the acid by a base with a single lithium ion is straightforward (*e.g.*, LiCl and AlCl₃ to form LiAlCl₄). The reaction is more complicated for bases with two lithiums in the stoichiometry such as Li₂S or Li₂O (8). We found that, in the case of the NbCl₅/Li₂S combination electrolyte, the concentration of the acid is equal to that of lithium, or, in other words, to twice that of the base. Reacting NbCl₅ in amounts ranging from 1.0 to 1.5M with Li₂S in the range 0.5-2.0M (these concentrations are assuming all of the amount added would have been soluble) yielded a constant concentration of 0.93-0.96M Nb and 0.94-1.00M Li (0.47-0.50M Li₂S). The reaction between NbCl₅ and Li₂S is discussed below in more detail.

The concentration and conductivity of the NbCl₅/Li₂S electrolyte can be increased by redissolving material from the evaporated solution. In this way, the concentration of Nb was raised to 1.42M with a corresponding increase in Li. The solution conductivity increased to 16.5 × 10⁻³ mho cm⁻¹ at 26°C.

Table I. Conductivities of electrolytes in SOCl₂ at the indicated concentration at 26°C and measured at 1 kHz

Electrolyte	Concentration (M)	Conductivity (mho cm ⁻¹ × 10 ³)
NbCl ₅	0.93	0.01
Li ₂ S + NbCl ₅	0.93	13.2
Li ₂ O + NbCl ₅	0.93	13.2
LiBr + NbCl ₅	0.93	13.9
LiCl + NbCl ₅	0.93	12.0
LiCl + AlCl ₃	1.60	19.7
Redissolved Li ₂ S + NbCl ₅	1.42	16.5

Voltage delay.—Figure 1 shows quite clearly that the NbCl₅/Li₂S combination electrolyte greatly reduced voltage delay in half-cells as compared to the control LiAlCl₄. Figure 2 shows that substituting Li₂O for Li₂S is also very effective in reducing voltage delay.

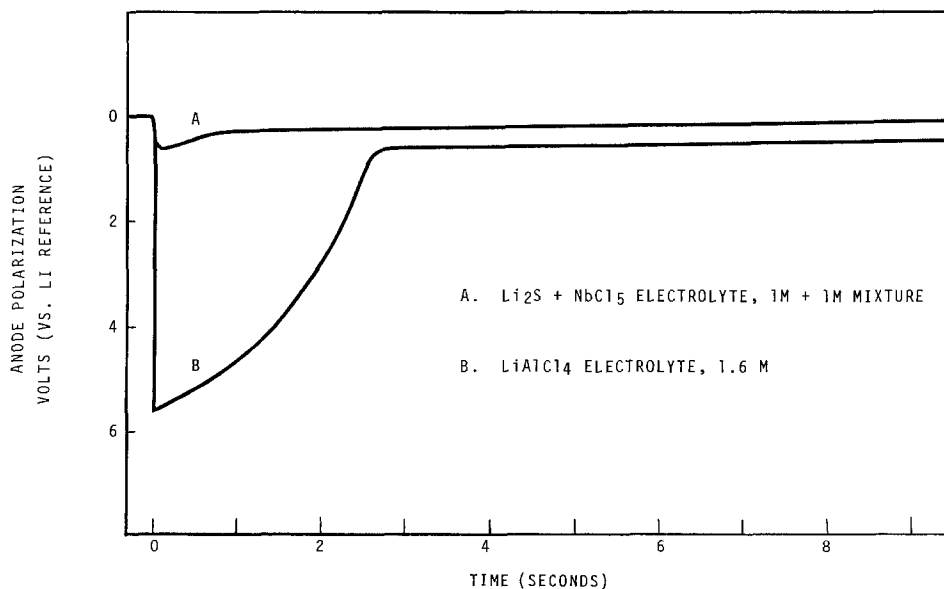
Anodes that were stored for 5 days at room temperature in an electrolyte of AlCl₃/Li₂S, as described in Ref. (8), had a maximum polarization in this type of experiment of almost three times the polarizations in the Nb-based electrolyte. Maximum polarization in the AlCl₃/Li₂S electrolyte (1M concentration) was typically about 0.930V *vs.* only 0.335V for the NbCl₅/Li₂S electrolyte.

NbCl₅ by itself does not reduce voltage delay. Anodes stored 5 days at room temperature in 0.93M NbCl₅/SOCl₂ had an average maximum polarization of 5.748V *vs.* 0.335V for the NbCl₅/Li₂S electrolyte. While the low conductivity of the NbCl₅/SOCl₂ electrolyte might affect its voltage delay polarization to some degree, it is clear from Fig. 6 that this electrolyte has a direct impact on the morphology of the anode passivating film.

The voltage delay polarization of anodes stored in 0.93M NbCl₅/LiCl and NbCl₅/LiBr electrolytes was excessive (maximum polarization greater than 9.530V after 5 days of room temperature storage) and did not show any improvements compared to the LiAlCl₄ control.

The magnitude of the polarization obtained in these tests for the LiAlCl₄ electrolyte is greater than expected, based on previous reports (27). Dey and Schlaikjer (27) report that a polarization maximum of about 6V *vs.* Li reference is obtained only after 11 days of storage at 55°C and at 15 mA/cm² anodic current. In this work, a polarization of almost 6V was obtained after 5 days of room temperature storage in the LiAlCl₄ electrolyte at 6 mA/cm². This difference might be due to a contaminant in the LiAlCl₄ electrolyte used here (even though it was carefully prepared and handled). The electrolyte typically contained less than 3 ppm Fe, and less than 130 ppm water, based on IR analysis of the OH absorption band. The data obtained with the Nb-based electrolytes is, of course, inde-

Fig. 1. Anode polarization at 6 mA/cm² after 5 days room temperature storage in various electrolytes.



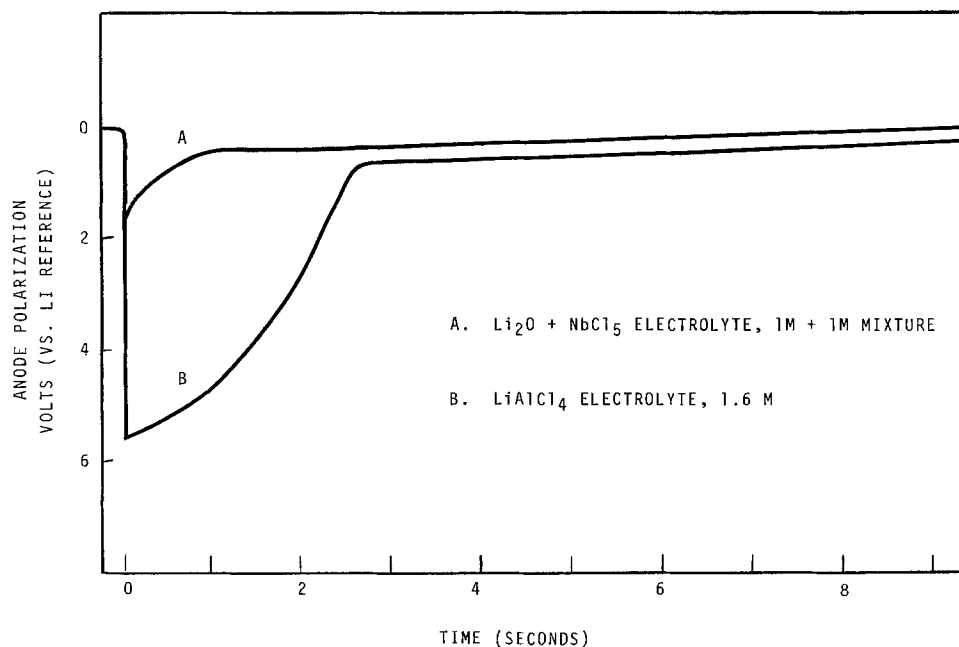


Fig. 2. Anode polarization at 6 mA/cm² after 5 days room temperature storage in various electrolytes.

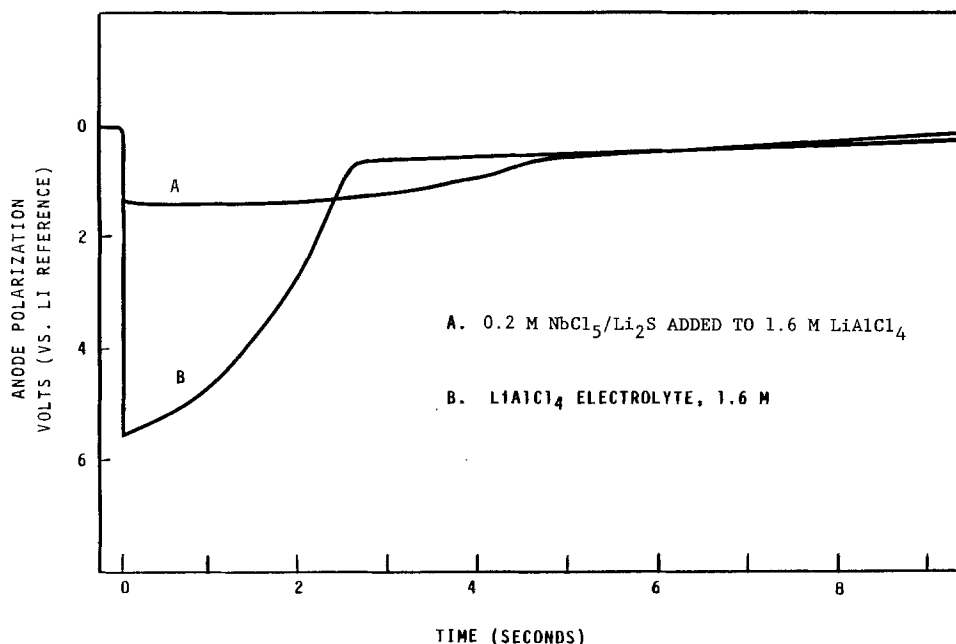


Fig. 3. Anode polarization at 6 mA/cm² after 5 days room temperature storage in various electrolytes.

pendent of the LiAlCl₄ measurements. The benefits of the Nb-based electrolyte are further illustrated in Fig. 3. NbCl₅/Li₂S used as a minor additive in the LiAlCl₄ electrolyte significantly reduces voltage delay. This occurs in spite of the greater than expected polarization found with the initial LiAlCl₄ electrolyte.

Extended storage of the Nb-based (and LiAlCl₄) electrolytes at room temperature did not alter their voltage delay polarization characteristics, concentration, or conductivity, indicating good solution stability.

Film morphology.—Anode film morphology was studied with SEM following immersion in various electrolytes for various times and temperatures. A comparison of Fig. 4 and 5 shows that the anode film formed in the NbCl₅/Li₂S electrolyte is less dense and of a different morphology than the one grown in LiAlCl₄. Figure 6 shows that the film formed in a solution of just NbCl₅/SOCl₂ under identical conditions is dense with bulky crystal growth. NbCl₅/Li₂S, as an additive to the LiAlCl₄ electrolyte, also changed the morphology of the anode film. The films in Fig. 4-6 all analyzed (SEM/EDAX) to be LiCl; essentially, no Nb was detected on the surface of the anodes stored in the Nb-based electrolytes.

These differences in LiCl film morphologies correlate very well with the corresponding half-cell polarization data of Fig. 1-3. The trend is for anodes covered by a dense, bulky appearing film to have greater voltage delay than those covered with less dense appearing films.

Rate capability.—The data in Table II show that the discharge rate of Li in the NbCl₅/Li₂S electrolyte is slightly greater over a range of overpotentials than in LiAlCl₄ solutions. The data were obtained by Tafel polarization curves at a 5 mV/s scan rate, and represent an average of four measurements. The half-cells were filled with electrolyte just prior to testing and were prepulsed at 6 mA/cm² for 5s to minimize film buildup.

Table II. Anodic rate capability of Li in various electrolytes at room temperature

Electrolyte	Current density (mA/cm ²)		
	400 mV vs. Li	200 mV vs. Li	50 mV vs. Li
1.60M LiAlCl ₄	13.48	6.41	1.03
0.93M NbCl ₅ /Li ₂ S	14.90	7.05	1.83

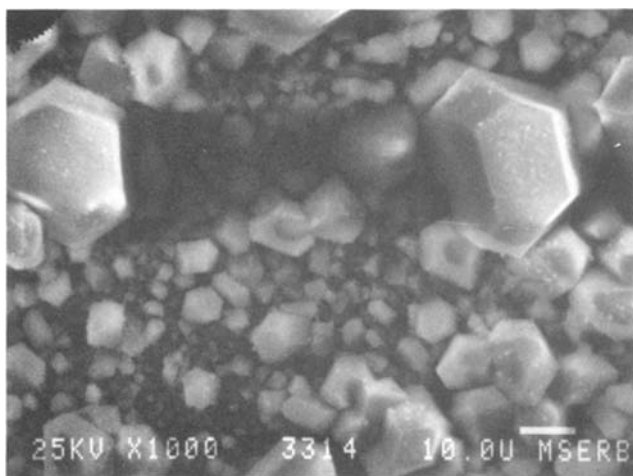


Fig. 4. Li sample stored in 1.6M LiAlCl₄ electrolyte for 5 days at 71°C. The white bar in the lower right corner represents a length of 10 μm.

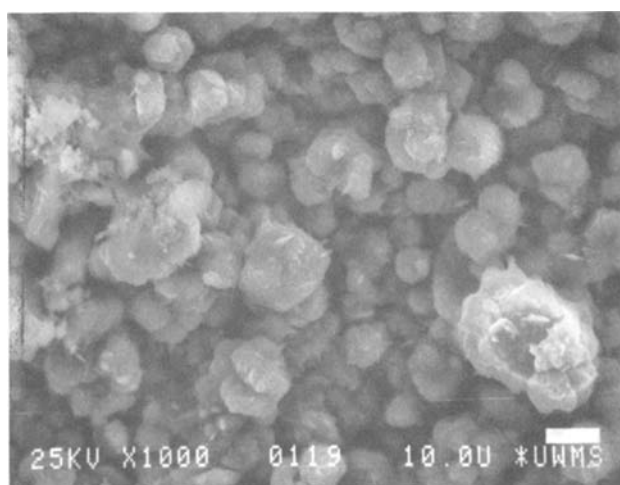


Fig. 6. Li sample stored in 0.93M NbCl₅ electrolyte for 5 days at 71°C. The white bar in the lower right corner represents a length of 10 μm.

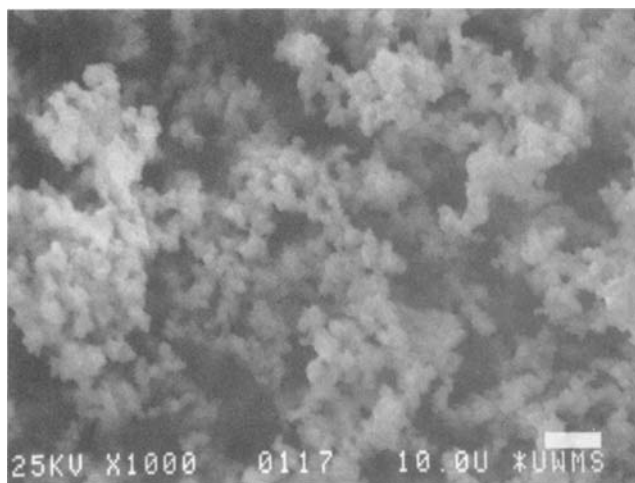


Fig. 5. Li sample stored in 0.93M NbCl₅/Li₂S electrolyte for 5 days at 71°C. The white bar in the lower right corner represents a length of 10 μm.

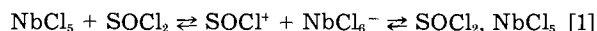
Cyclic voltammetry.—Typical cyclic voltammograms (Fig. 7) on Ni working electrodes in the NbCl₅/Li₂S combination electrolyte are very similar to those in LiAlCl₄ electrolyte (17, 18). Since the potential at which the reactions occur is the same in both electrolytes, the use of the NbCl₅/Li₂S should not affect the operating voltage in battery cells. The use of a Ni working electrode shifted the cathodic peaks to potentials lower than would be found on carbon substrates (17, 18).

At the start of the cathodic scan, a small peak (marked "A" in Fig. 7) appears at about 2.85V vs. the Li reference.

This peak has been observed in previous studies (17-20) and has been attributed (20) to the first step of a two-step reduction of SOCl₂ or to the reduction of oxidation products of SOCl₂ such as Cl₂ (5, 17, 19). The peak marked "B," occurring at 2.14V, can be assigned to the main reduction reaction of SOCl₂ (17-20). The decrease in current at potentials immediately cathodic to peak B is due to the passivation of the electrode surface by LiCl produced in the reaction. A weak peak (marked "C") occurs at about 0.79V. It has been attributed by others to the reduction of SOCl₂ reduction products as in LiAlCl₄ solutions (17-20).

The current rise at the end of the cathodic scan is due to the plating of lithium onto the Ni working electrode. The composition of the deposit, as determined by atomic absorption for Li and Nb, was essentially Li. Since both counter- and working electrodes in this test were Ni, the only source of the Li is the NbCl₅/Li₂S electrolyte. On the return anodic scan, the Li deposit is stripped off of the Ni and no other anodic peaks are observed at this current sensitivity.

Infrared spectroscopy.—The IR spectrum for pure SOCl₂ is distinguished by its single S-O stretch frequency at about 1229 cm⁻¹ (17, 21). The spectrum of a NbCl₅/SOCl₂ solution (Fig. 8) has two additional S-O species, appearing as shoulders at 1150 and 1106 cm⁻¹ on the SOCl₂ peak. Based on literature (22) describing similar solutions of metal chlorides in SOCl₂, the 1106 cm⁻¹ peak represents the product of the following reaction



The most likely form of the product is the 1:1 undissociated complex. This conclusion is based on a detailed report of similar solutions of AlCl₃ in SOCl₂ by Long and Bailey (21). They were able to isolate the 1:1 complex of

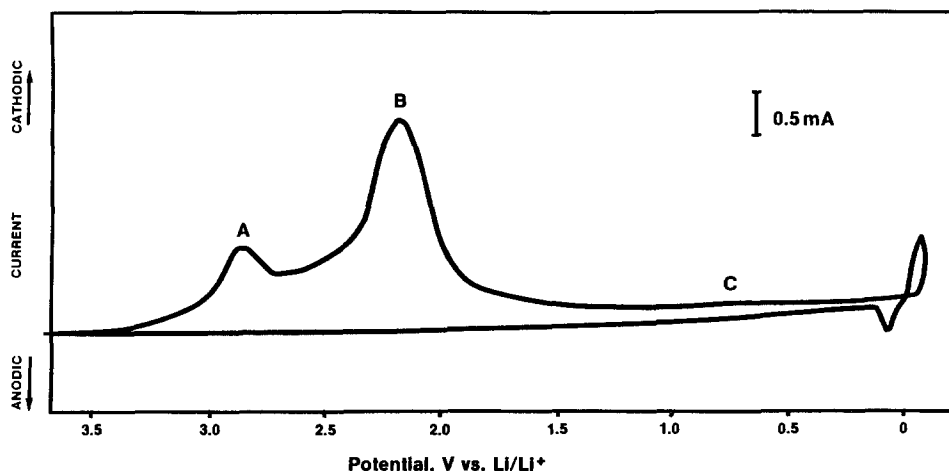


Fig. 7. Cyclic voltammogram of 0.93M NbCl₅/Li₂S in SOCl₂ on a Ni electrode. Scan rate is 10 mV/s.

SOCl₂, AlCl₃ in solid form and obtain its Raman spectrum. That spectrum was basically identical to the spectrum of the solution species. IR analysis of the same AlCl₃ solution in this lab yielded an absorption peak at a similar wave number of 1110 cm⁻¹. Thus, the analogy for solutions of NbCl₅ in SOCl₂ points to the existence of the 1:1 undissociated complex. However, Abraham and Mank (17) interpreted this and other data to mean that the product is in the ionic form.

NbCl₅ has a strong affinity for oxygen, and so a lengthening of the S-O bond in thionyl chloride due to the attached NbCl₅ would lower the S-O stretch frequency from 1229 to 1106 wave numbers. The other shoulder, the 1160 peak, is probably due to a 2:1 NbCl₅-SOCl₂ complex with the second NbCl₅ loosely attached to the first. Similar 2:1 complexes were also found in AlCl₃/SOCl₂ solutions (21). This second molecule of NbCl₅ would not decrease the primary S-O stretch frequency as much as the first, and so an intermediate peak between 1106 and 1229 wave numbers, the 1160 peak, is obtained. Since two peaks are observed, it may indicate that the 1:1 and 2:1 complexes are both present and in some sort of equilibrium.

Adding Li₂S to the NbCl₅/SOCl₂ solution to form the NbCl₅/Li₂S electrolyte eliminates the 1106 and 1160 cm⁻¹ peaks. A peak at 1332 cm⁻¹ representing SO₂ (23) appears, as shown in Fig. 9. Adding excess Li₂S to the NbCl₅/SOCl₂ did not increase the SO₂ peak height. No SO₂ peak was observed in the original SOCl₂ solvent, nor was one in the NbCl₅/SOCl₂ solution. Adding Li₂S alone to SOCl₂ does not produce an SO₂ peak either. The SO₂ peak also appears in spectra of solutions made by redissolving in pure SOCl₂ the evaporated material of the NbCl₅/Li₂S combination electrolyte. IR spectra in this lab of a previously reported electrolyte formulation (8) of AlCl₃/Li₂S also contained the SO₂ peak.

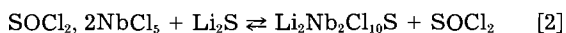
SO₂ dissolved in the electrolyte has been reported to reduce voltage delay (9). However, the optimum concentration cited was 5 weight percent (w/o). The amount of SO₂ produced here according to Eq. [2a] and [4] (see below) would be less than 1 w/o.

The IR spectra of powder samples of the evaporated material of the NbCl₅/Li₂S electrolyte showed peaks at 1595 and 812 wave numbers. The 1595 peak probably represents a Nb-Cl bond (24). The Nb-Cl bond was also indicated in ESCA measurements of the material. The ESCA results also suggest that the Nb is in the +5 oxidation state. The 812 cm⁻¹ peak could not be identified. Nb-S, Li-S, Nb-O, Li-O, Li-Cl, and S-Cl bonds all absorb at wave numbers other than 1595 and 812 cm⁻¹ (24).

Discussion

The analytical evidence for the composition of the NbCl₅/Li₂S electrolyte salt consists of several items: (i) the measured concentration of Nb and Li show that the stoichiometric balance of the two elements are the same, (ii) the cyclic voltammetry plating experiment determined that Li was the cation of the salt, (iii) IR spectroscopy and ESCA qualitatively identified Cl in the salt, that it was attached to the Nb, and that Nb was in the +5 oxidation state, and (iv) SO₂ is produced in the neutralization of NbCl₅/SOCl₂ solutions with Li₂S. A number of attempts to analyze for the sulfur content of the salt via a variety of analytical methods were all unsuccessful. The dried salt is very hygroscopic.

Based on the cited analytical evidence, possible reaction schemes for the neutralized electrolyte can be narrowed down to at least three possibilities. In Eq. [2], the 2:1 NbCl₅-SOCl₂ complex reacts with Li₂S. No SO₂ is produced, and S, a possible constituent, is contained in the neutralized electrolyte salt



Another possible reaction (which would produce SO₂), involving the 2:1 NbCl₅-SOCl₂ complex, has been suggested by one of the reviewers of this paper

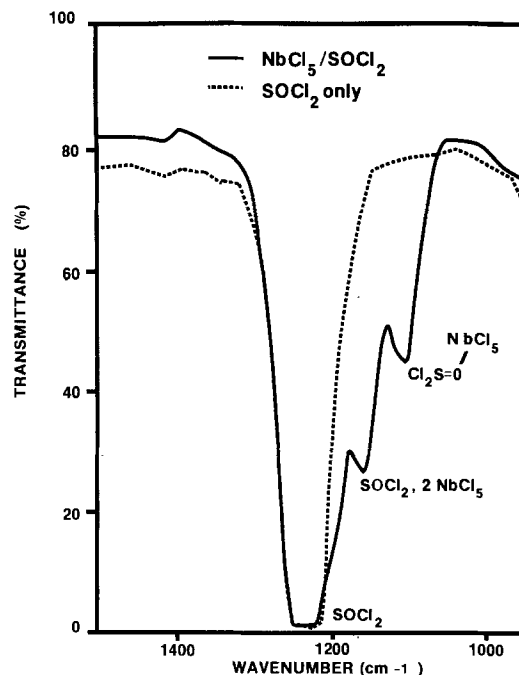
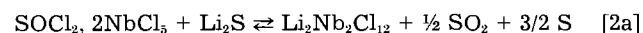


Fig. 8. Infrared spectra of NbCl₅ in SOCl₂ (—) and SOCl₂ alone (· · ·)

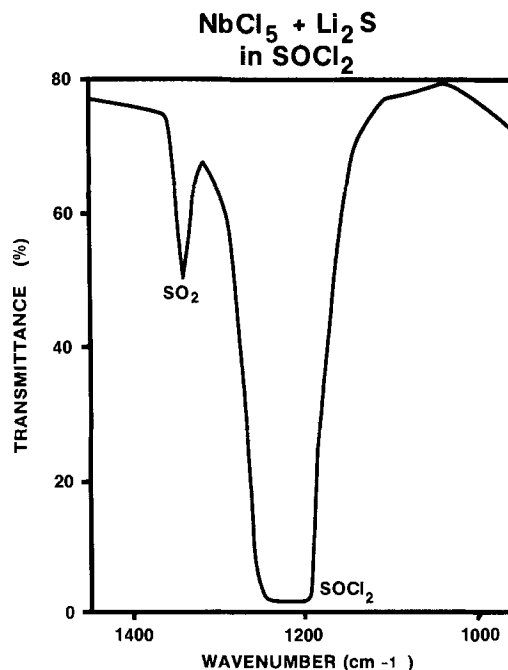
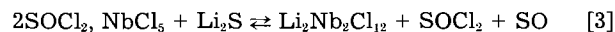


Fig. 9. Infrared spectrum of NbCl₅/Li₂S in SOCl₂

In the next scheme, Eq. [3] and [4], the 1:1 complex reacts to form the neutralized salt. The product does not contain any sulfur, but SO₂, as detected in the IR work, is produced



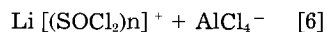
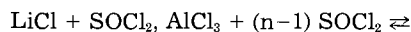
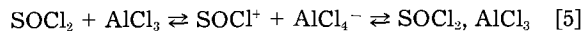
(The product Li₂Nb₂Cl₁₂ in Eq. [2a] and [3] could also conceivably be represented as 2LiNbCl₆.)

A definite test for S in the neutralized salt would help identify the correct scheme.

The anion of either of the products formed in Eq. [2] and [3] is quite different than tetrachloroaluminate, AlCl₄⁻. Some of the properties of the neutralized electrolyte can be explained in terms of the postulated anions. The large size of either anion, even with its divalent charge, would lead to a reduced anionic charge density. This would tend to favor dissociation of the salt, and

could lead to the higher electrolyte conductivity relative to that of plain $\text{NbCl}_5/\text{SOCl}_2$ solutions. However, these same factors could decrease the mobility of the anion relative to Li^+ or AlCl_4^- and so explain the lower overall electrolyte conductivity relative to LiAlCl_4 . Similar reasoning was applied to explain conductivity behavior of clovoborate electrolytes (7).

The growth of the LiCl anode film in LiAlCl_4 electrolyte is promoted by the relative instability of LiAlCl_4 in SOCl_2 and can be represented as



The dissociated LiAlCl_4 electrolyte in Eq. [6] can exchange with the LiCl anode film. But because of the nature of the anions postulated in Eq. [2] and [3], it is felt that no such exchange equilibrium exists between these anions and the LiCl film formed in the NbCl_5 -based electrolytes. Thus, growth of the voltage delay causing film is reduced.

Conclusions

1. Voltage delay in half-cells was reduced by using electrolyte formed by the neutralization in SOCl_2 of NbCl_5 with Li_2S , or NbCl_5 with Li_2O . The use of the $\text{NbCl}_5/\text{Li}_2\text{S}$ electrolyte as a minor additive to LiAlCl_4 was also effective in reducing voltage delay.

2. The conductivity of $\text{NbCl}_5/\text{Li}_2\text{X}$ ($\text{X} = \text{S}$ or O) electrolytes in SOCl_2 is slightly less than the corresponding LiAlCl_4 solutions.

3. The anode film formed in the $\text{NbCl}_5/\text{Li}_2\text{S}$ electrolyte has a different morphology and appears less dense than the film formed in LiAlCl_4 . The mechanism for the effect is thought to be due to the nature of the anion in $\text{NbCl}_5/\text{Li}_2\text{S}$ electrolyte and/or the SO_2 produced by the neutralization of NbCl_5 with Li_2S .

4. Anode rate capability is slightly higher in the $\text{NbCl}_5/\text{Li}_2\text{S}$ electrolyte than in LiAlCl_4 . The $\text{NbCl}_5/\text{Li}_2\text{S}$ electrolyte does not affect the cathodic discharge characteristics of SOCl_2 .

5. NbCl_5 by itself in SOCl_2 has low conductivity and promotes voltage delay.

Manuscript submitted Dec. 14, 1983; revised manuscript received Feb. 13, 1984. This was Paper 32 presented at the Washington, DC, Meeting of the Society, Oct. 9-14, 1983.

REFERENCES

1. J. J. Auburn, K. W. French, S. J. Lieberman, V. K. Shah, and A. Heller, *This Journal*, **120**, 1613 (1973).
2. W. K. Behl, J. Christopoulos, and S. Gilman, *ibid.*, **120**, 1619 (1973).

3. R. V. Moshtev, Y. Geronov, and B. Puresheva, *ibid.*, **128**, 1851 (1981).
4. E. Peled and H. Yamin, in "Proceedings of the 27th Power Sources Conference," Atlantic City, NJ, June 21-24, 1976, p. 237.
5. H. V. Venkatasetty and D. J. Saathoff, *This Journal*, **128**, 773 (1981).
6. E. Peled and H. Yamin, *Isr. J. Chem.*, **18**, 131 (1979); E. Peled, *This Journal*, **126**, 2047 (1979).
7. C. R. Schlaikjer and C. Young, in "Proceedings of the 29th Power Sources Conference," Atlantic City, NJ, June 9-12, 1980, The Electrochemical Society, Inc., p. 129 (1981); C. R. Schlaikjer, in "Proceedings of the 28th Power Sources Conference," Atlantic City, NJ, June 12-15, 1978, The Electrochemical Society, Inc., p. 241 (1979).
8. J. P. Gabano and G. Gelin, in "Power Sources 8," J. Thompson, Editor, pp. 3-15, Academic Press, London (1981).
9. D. L. Chua, W. C. Merz, and W. S. Bishop, in "Proceedings of the 27th Power Sources Conference," Atlantic City, NJ, June 21-24, 1976, p. 33.
10. T. Kalnoki-Kis, U.S. Pat. 3,993,501 (1976), 4,218,523 (1980).
11. J. R. Driscoll, U.S. Pat. 4,093,784 (1978).
12. V. O. Catanzarite, U.S. Pat. 4,170,693 (1979), 4,296,185 (1981).
13. A. N. Dey and J. Miller, *This Journal*, **126**, 1445 (1979).
14. J. Bresson, G. Feuillade, and R. Wiart, *ibid.*, **129**, 2649 (1982).
15. N. A. Fleischer and S. M. Manske, U.S. Pat. Appl. Serial no. 507,668, filed 1983.
16. V. Gutman, "Halogen Chemistry," Vol. 2, Chap. 5, Academic Press, New York (1967).
17. K. M. Abraham and R. M. Mank, *This Journal*, **127**, 2091 (1980).
18. G. L. Holleck and M. J. Turchan, in "Record of the 10th Intersociety Energy Conversion Engineering Conference," p. 449 (1975).
19. W. K. Behl, in "Proceedings of the 27th Power Sources Symposium, Atlantic City, NJ, June 21-24, 1976, p. 30.
20. H. V. Venkatasetty, *This Journal*, **127**, 2531 (1980).
21. D. A. Long and R. T. Bailey, *Trans. Faraday Soc.*, **59**, 594 (1963).
22. V. H. Spandau and E. Brunneck, *Z. Anorg. Chem.*, **270**, 201 (1952); *ibid.*, **278**, 197 (1955).
23. B. F. Martz and R. T. Lagemann, *J. Chem. Phys.*, **22**, 1193 (1954).
24. R. A. Nyquist and R. O. Kagel, "Infrared Spectra of Inorganic Compounds," Academic Press, New York (1971).
25. N. A. Fleischer, J. R. Thomas, and R. J. Ekern, in "Proceedings of the 30th Power Sources Conference, Atlantic City, NJ, June 7-12, 1982, The Electrochemical Society, Inc., p. 172 (1983).
26. N. A. Fleischer and R. J. Ekern, *J. Power Sources*, **10**, 179 (1983).
27. A. N. Dey and C. R. Schlaikjer, in "Proceedings of the 26th Power Sources Conference," Atlantic City, NJ, April 29-30, May 1-2, 1974, p. 47.

Thermogravimetry-Evolved Gas Analysis of Silver Oxide Cathode Material

W. A. Parkhurst,* S. Dallek,* and B. F. Larrick

Naval Surface Weapons Center, Electrochemistry Branch, Silver Spring, Maryland 20910

ABSTRACT

A new, rapid, and precise thermogravimetry-evolved gas analysis (TG-EGA) method has been developed for the determination of the AgO, Ag₂O, Ag, and Ag₂CO₃ content of silver oxide cathodes. Cathode samples were analyzed by the present method and by the commonly used wet chemical method. The analysis is being used to study the rates of change in chemical composition during storage of cathodes prepared by various manufacturers. The analysis results can be used to correlate the compositional changes with degradation in battery performance.

Batteries employing silver oxide cathodes are used in numerous military and commercial applications. The electrochemically prepared cathodes, used in high rate battery applications, contain various amounts of silver (II) oxide, silver (I) oxide, silver, and silver carbonate impurity. The change in chemical composition of these cathodes during storage remains a problem of serious concern. For example, AgO is thermodynamically unstable and decomposes to form an Ag₂O phase, having higher ohmic resistance (1), resulting in a voltage regulation problem. Ag₂O is also found to be formed (2) when solid AgO contacts solid Ag. In silver oxide/zinc cells, the zinc anode is a getter for the evolved O₂ from the AgO decomposition, resulting in a film of ZnO that can cause increased polarization after activation (3). Clearly, the capacity and performance of silver oxide batteries can be adversely affected by the degradation of the cathode material (4). Therefore, the need to determine the chemical composition of silver oxide cathodes after preparation and during storage under various conditions is of considerable importance. Methods reported for the analysis of this material involve lengthy gravimetric and titrimetric (5) or gasometric (6) procedures. An obvious need exists for a better analytical procedure for silver oxide electrodes.

Thermogravimetry (TG) techniques have been employed for a wide range of analytical determinations (7). Complex mixtures of substances can be rapidly analyzed by TG, provided that the substances decompose independently of one another, thus permitting the establishment of separate, measurable mass plateaus. Evolved gas analysis (EGA) is frequently used as a simultaneous complementary technique to TG. Attempts to analyze silver oxide cathodes by thermal analysis techniques have been reported (8, 9).

We report here the development and employment of a new, extremely rapid, precise thermogravimetry-evolved gas analysis (TG-EGA) analytical method for the determination of the AgO, Ag₂O, Ag, and Ag₂CO₃ content of silver oxide cathode material.

Experimental

Apparatus.—The TG studies were performed with a du Pont 1090 Thermal Analysis System and a 951 Thermogravimetric Analyzer (TGA). TG samples were run in platinum boats over a temperature range of 298 to 753 K (25°–550°C) at a heating rate of 20 K/min in a flowing atmosphere (50 cm³/min) of dry argon. Because the decomposition temperatures of AgO and Ag₂CO₃ overlap, neither can be determined in the presence of the other by TG alone (10, 11); therefore, an EGA method using a Hewlett-Packard 5710-A Gas Chromatograph (GC) was developed for determination of the evolved CO₂ from the Ag₂CO₃ decomposition. Samples for GC analysis were

placed in a specially designed Pyrex vessel (Fig. 1) fitted with a Teflon valve. The vessel was first evacuated ($p \leq 20\mu$ Hg), placed in the TGA furnace, heated over the same temperature range as in the TG run, and then connected to the GC for determination of the amount of evolved CO₂. The GC employed a thermal conductivity detector and a Carbosieve column. Pressures were measured with a Validyne Model DM56A digital manometer system with an AP10 absolute pressure transducer. The GC furnace temperature was maintained at 468 K. Helium purge gas was employed for maximum sensitivity. The tightness of all valves and connections was checked by monitoring the constancy of the digital manometer readings while the system was under vacuum and when pressurized.

The AgO, Ag₂O, Ag, and Ag₂CO₃ content of the cathode sample was determined from the TG mass loss plateaus and from the GC analysis of the evolved CO₂.

Samples.—Commercially obtained AgO (99.5%, Rayovac Corporation) (12), Ag₂O (99.6%, Metz Metallurgical Corporation), Ag (99.98%, Fischer Scientific Company), and Ag₂CO₃ (99.7%, Alfa Products) were studied initially to determine their thermal transition temperatures. Samples of active cathode material were obtained from several battery manufacturers either as powders or on silver current collectors from which the material was removed and powdered. Typically, a 100 mg sample was used for each TG and GC run.

Results

During the development of the present method, numerous TG experiments were run on chemically and electrochemically prepared silver oxide cathode material and on the individual components to establish the validity of the technique. Typical TG curves and their derivatives for pure AgO, Ag₂O, Ag₂CO₃, and silver oxide cathode material are shown in Fig. 2. In Fig. 2a, the three main decom-

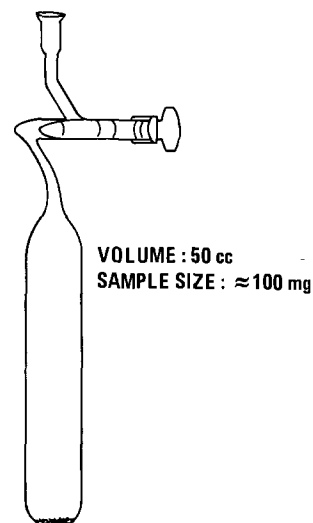


Fig. 1. Gas collection vessel for CO₂ analysis.

* Electrochemical Society Active Member.

Key words: battery, cathode, thermogravimetry, gas chromatography.

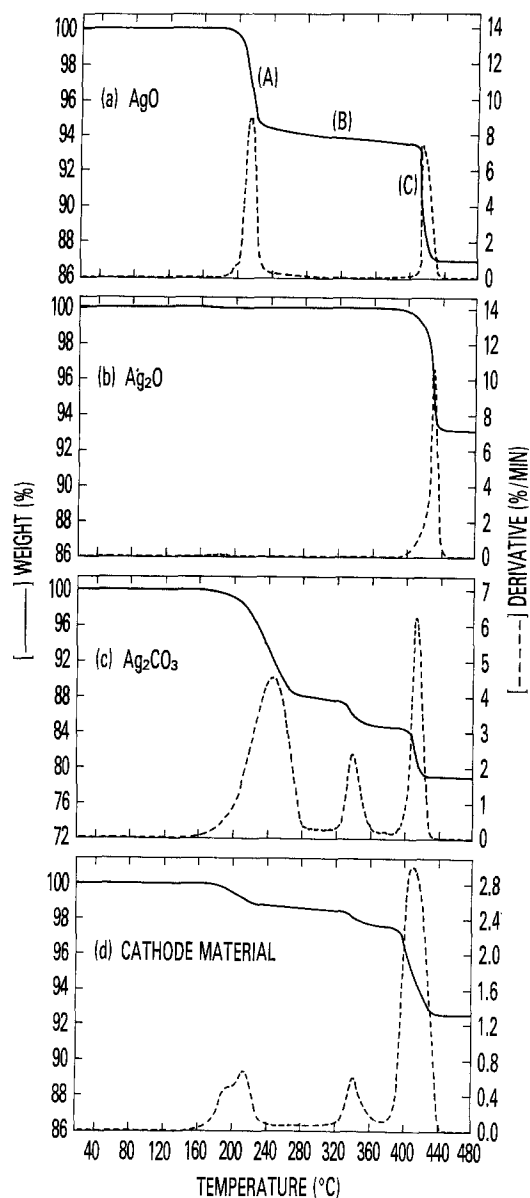


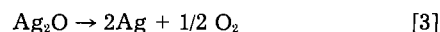
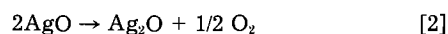
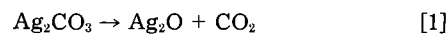
Fig. 2. TG curves of AgO, Ag₂O, Ag₂CO₃, and silver oxide cathode material. Heating rate: 20 K/min. Atmosphere: Ar, 50 cm³/min.

position processes of AgO can be seen: (i) an initial rapid decomposition of AgO to Ag₂O, (ii) a slow continuing decomposition of AgO, and (iii) a rapid decomposition of Ag₂O to Ag. The structure of AgO was established by neutron diffraction to be Ag₂O₃ · Ag₂O (13). X-ray photoelectron spectroscopy (XPS) studies (14) confirmed this structure and showed that the mass loss in process B (Fig. 2a) is caused by the decomposition of the Ag₂O₃ component of AgO. The decomposition curve of Ag₂O is shown in Fig. 2b. As seen in Fig. 2, there is the possibility that the decomposition of Ag₂O (Fig. 2b) may be initiated just prior to the completion of the AgO decomposition process near the very end of region (B) in Fig. 2a. However, as seen in the derivative curves in Fig. 2a and 2b, the rates of decomposition in this region are very small. We have determined that any overlap in this region has a negligible effect on the precision of the calculated composition. The shoulder on the derivative curve in Fig. 2a and the small derivative peak in Fig. 2b at about 433 K (160°C) are caused by the slight contamination of these samples by Ag₂CO₃. The decomposition curve of Ag₂CO₃ is shown in Fig. 2c. The evolution of CO₂ from the two "forms" of Ag₂CO₃ beginning at about 433 K (160°C) and 593 K (320°C) in Fig. 2c agrees with previously reported temperatures (15). Mass spectrometric analysis (14) of the evolved gas confirmed it to be CO₂ during both mass losses. The final mass loss on this curve is caused by the decomposi-

tion of the Ag₂O, as seen above. In Fig. 2d, a TG curve of a cathode sample containing a considerable amount of Ag₂CO₃ is shown.

The equations used to evaluate the TG-EGA data for silver oxide cathode material were derived, as follows, on the assumption that the sample initially consists of only Ag₂CO₃, AgO, Ag, and Ag₂O, having weight fractions A, B, C, and D, respectively.

The decomposition reactions are



Let W_1 equal the weight fraction remaining after reaction [1], W_2 equal the weight fraction remaining after reactions [1] and [2], and W_3 equal the weight fraction remaining after reactions [1], [2], and [3]. Using the appropriate gravimetric factors, the weight balance equations are

$$1 = A + B + C + D$$

$$W_1 = 0.8404A + B + C + D$$

$$W_2 = 0.8404A + 0.9354B + C + D$$

$$W_3 = 0.7824A + 0.8708B + C + 0.9310 D$$

The weight loss equations are

$$1 - W_1 = 0.1596A$$

$$W_1 - W_2 = 0.06458B$$

$$W_2 - W_3 = 0.07416 (W_3 - C)$$

Rearranging

$$A = 6.2657 (1 - W_1) = \text{weight fraction Ag}_2\text{CO}_3$$

$$B = 15.4838 (W_1 - W_2) = \text{weight fraction AgO}$$

$$C = W_3 - 13.4838 (W_2 - W_3) = \text{weight fraction Ag}$$

$$D = 1 - A - B - C = \text{weight fraction Ag}_2\text{O}$$

W_2 and W_3 are determined from the TG curves. W_1 is obtained from the GC analysis of the evolved CO₂ as follows

$$F = \frac{g \text{ CO}_2/44.011 \text{ g/mol}}{g \text{ CO}_2/44.011 \text{ g/mol} + g \text{ O}_2/32.00 \text{ g/mol}} = \text{mole fraction CO}_2 \text{ in the evolved gas}$$

$$g \text{ CO}_2 = (1 - W_1) (S) \text{ and } g \text{ O}_2 = [(1 - W_3) - (1 - W_1)] (S)$$

where S = total sample weight.

$$F = \frac{(1 - W_1)2.7507}{(1 - W_1)2.7507 + [(1 - W_3) - (1 - W_1)]/2}$$

$$W_1 = 1 - (2.7507)(1 - W_3)F/(0.7507F + 2)$$

In Fig. 3, the TG curve of the cathode sample shown in Fig. 2d has been enlarged and labeled with points W_2 and W_3 . The value of W_2 , at which point the decompositions of Ag₂CO₃ and AgO into Ag₂O are complete but prior to the onset of the decomposition of Ag₂O, is determined from the intersections of the extrapolated completion of the AgO decomposition and the onset of the Ag₂O decomposition processes. The derivative curve is used to locate the point more precisely. At the point W_3 , the sample is completely decomposed into Ag. The weight fraction, W_1 , remaining after the two-step loss of CO₂ from the decomposition of Ag₂CO₃ is determined by GC, as described above. Repeated CO₂ analyses, used in determining W_1 , resulted in Ag₂CO₃ determinations that agreed to within 0.01%.

Several cathode samples were analyzed by the present TG-GC method and by the commonly used Wagner method (5) combined with a standard gravimetric determination of the CO₂ from the Ag₂CO₃ component. The results are shown in Table I. Reasonable agreement was achieved between the two methods.

During the course of this work, samples of very pure, stable, chemically prepared AgO (99.5%, Rayovac Corpo-

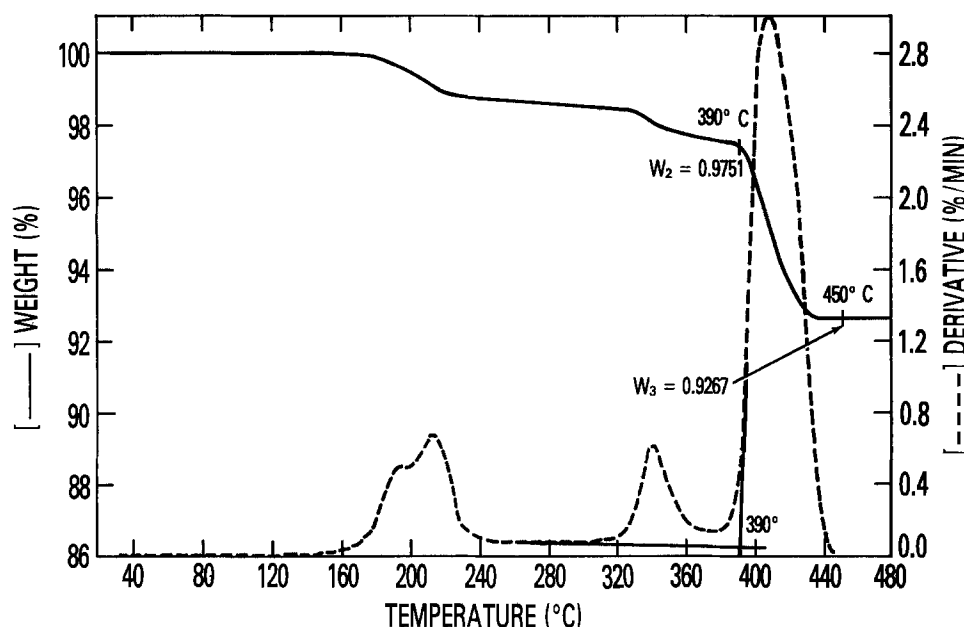


Fig. 3. TG curves of silver oxide cathode material showing points W_2 and W_3 . (W_1 is obtained from the GC analysis.)

ration) were run periodically to check the calibration of the TGA by determining the final mass plateau, W_3 . The results are given in Table II. The theoretical value of W_3 for the pure AgO is 0.8708, as compared with the average measured value of 0.8701 for these runs. The lower experimental values are a result of the slight contamination of the AgO with Ag_2CO_3 . GC analyses of the evolved CO_2 from this AgO material gave an average Ag_2CO_3 content of 0.75%. Using the average measured value of $W_3 = 0.8701$ and setting $B = (1 - A)$, $C = 0$, and $D = 0$, the derivation

equation may be solved to give $A = 0.0079$ (0.79% Ag_2CO_3), in excellent agreement with the 0.75% from the GC analysis. This result and the results shown in Table II demonstrate, respectively, the accuracy and precision obtained using the TG-EGA technique on this AgO material. The lack of suitable standard materials and analytical methods precluded the determination of accuracy for typical cathode material mixtures containing AgO, Ag_2O , Ag, and Ag_2CO_3 .

Discussion

A new, extremely rapid, precise analytical method has been developed using a combined TG-EGA technique to analyze the components of silver oxide cathode material. At a heating rate of 20 K/min, a TG run takes only about 20 min; a concurrent GC analysis is performed during the TG run on a separate sample. This analysis method requires minimal sample manipulation and eliminates the need to prepare and standardize chemical reagents. It relies only on the measurement of mass loss by an extremely accurate electrobalance coupled with a high speed microprocessor analyzer and on the analysis of the evolved CO_2 in the $CO_2 + O_2$ mixture by GC. In addition, the TG curve of a silver oxide sample provides a "fingerprint" that can be compared to subsequent curves to immediately discern aging trends.

This new analysis technique is being used to study rates of change in chemical composition during storage of silver oxide cathodes; in addition, correlations are possible between the compositional changes and the degradation in battery performance. The present technique is being developed further so that a simultaneous, rather than concurrent, TG-EGA determination can be performed on a single sample.

Manuscript submitted Oct. 27, 1983; revised manuscript received Feb. 27, 1984.

The Naval Surface Weapons Center assisted in meeting the publications costs of this article.

REFERENCES

1. T. P. Dirkse, in "Zinc-Silver Oxide Batteries," A. Fleischer and J. J. Lander, Editors, pp. 99-115, John Wiley and Sons, New York (1971).
2. B. D. Cahan, J. B. Ockerman, R. F. Amlie, and P. Ruetschi, *This Journal*, **107**, 725 (1960).
3. N. A. Hampson, in "Zinc-Silver Oxide Batteries," A. Fleischer and J. J. Lander, Editors, pp. 37-61, John Wiley and Sons, New York (1971).
4. F. M. Bowers and E. Gubner, in "Zinc-Silver Oxide Batteries," A. Fleischer and J. J. Lander, Editors, pp. 347-359, John Wiley and Sons, New York (1971).
5. R. D. Wagner, NOLTR 64-214, U.S. Naval Ordnance

Table I. Comparison of TG-EGA and Wagner (5) analyses of silver oxide cathode samples

Sample	Method	Ag_2CO_3 (w/o)	AgO (w/o)	Ag_2O (w/o)	Ag (w/o)
A**	TG-EGA	0.75	99.10	0.00	0.00
	Wagner*	1.02	98.26	0.00	0.03
B	TG-EGA	4.89	63.17	22.83	9.11
	Wagner	4.84	63.53	21.92	8.22
C	TG-EGA	6.14	73.70	18.31	1.85
	Wagner	6.09	71.44	19.96	2.58
D	TG-EGA	7.21	36.08	27.39	29.32
	Wagner	7.33	35.22	29.96	22.88
E	TG-EGA	9.08	60.70	28.72	1.50
	Wagner	8.09	61.94	26.67	0.02
F	TG-EGA	11.28	47.84	39.19	1.69
	Wagner	5.59	47.43	43.91	0.05
G	TG-EGA	5.39	35.15	33.27	26.19
	Wagner	4.32	37.60	36.06	20.88

* Wagner analyses performed at the Naval Weapons Support Center (Crane, IN).

** 99.5% AgO (Rayovac Corporation).

Table II. TG results for chemically prepared AgO*

Run no.	Heating rate (°C/min)	W_3
1	20.0	0.8703
2	20.0	0.8702
3	20.0	0.8698
4	20.0	0.8702
5	20.0	0.8700
6	2.0	0.8699
7	0.2	0.8703
		$\bar{X} = 0.8701$
		$\sigma = 0.0002$

* 99.5% AgO (Rayovac Corporation).

- Laboratory, Silver Spring, MD (1965).
6. T. Katan and R. R. Carlen, Paper 108 presented at The Electrochemical Society Meeting, Hollywood, FL, Oct. 5-10, 1980.
 7. W. W. Wendlandt, "Thermal Methods of Analysis," 2nd ed., pp. 99-133, John Wiley and Sons, New York (1972).
 8. J. J. Lander, W. C. Bourne, and J. W. Logsdon, AFAPL-POE-TM-76-19, Air Force Aero-Propulsion Laboratory, Wright-Patterson Air Force Base, OH (Aug. 1976).
 9. R. E. Klausmeier, Report no. QE/C 61-44, Quality Evaluation Laboratory, U.S. Naval Ammunition Depot, Crane, IN (1961).
 10. P. A. Barnes and E. Kirton, *Anal. Calorim.*, **3**, 57 (1974).
 11. P. A. Barnes and R. M. Tomlinson, *J. Thermal Anal.*, **7**, 469 (1975).
 12. S. A. Megahed, Private communication.
 13. V. Scatturin, P. L. Bellon, and A. J. Salkind, *This Journal*, **108**, 819 (1961).
 14. C. R. Anderson, S. Dallek, W. A. Parkhurst, and B. F. Larrick, Paper 83 presented at The Electrochemical Society Meeting, Washington, DC, Oct. 9-14, 1983.
 15. P. A. Barnes and F. S. Stone, *Thermochim. Acta*, **4**, 105 (1972).

The Corrosion of Carbon Black Anodes in Alkaline Electrolyte

I. Acetylene Black and the Effect of Cobalt Catalyzation

Philip N. Ross* and Harvey Sokol

Lawrence Berkeley Laboratory, Materials and Molecular Research Division, Berkeley, California 94720

ABSTRACT

¹⁴C labeling of acetylene black was used together with mass spectroscopic analysis of the gas evolved to determine the current efficiencies for oxygen evolution, carbon dissolution, and carbon gasification (to carbon monoxide). The current efficiencies were found to depend dramatically on potential, temperature, and the presence of an evolution catalyst like Co₃O₄. On uncatalyzed black, three regimes could be distinguished: (i) at potentials below 500 mV vs. Hg/HgO and temperatures below 50°C, carbon dissolution is the primary anodic process, (ii) at 500-600 mV and 50°C or lower, carbon dissolution and oxygen evolution occur at equivalent rates, and (iii) above ca. 600 mV or above ca. 60°C, oxygen evolution and gasification of the carbon to carbon monoxide are the dominant processes. Catalyzation with Co₃O₄ collapsed these regimes so that all three anodic processes are concurrent throughout the potential region of interest, and the overall rate of corrosion increased significantly. In addition, Co₃O₄ catalyzation caused the production of organic products (ca. 5% current efficiency) in a potential region where none is produced from acetylene black alone. The mechanism of action of Co₃O₄ on the acetylene black corrosion is not yet understood, but there is evidence that direct physical contact between the Co₃O₄ particles and carbon particles is not required to produce accelerated corrosion of the carbon.

With the advent of dimensionally stable metal oxide anodes for chlor-alkali cells, technological interest in the oxidation of carbon anodes (usually graphite) in caustic solution has waned. In the years when diaphragm cells with graphite anodes were the leading technology, there was a substantial body of literature produced concerning the corrosion of graphite accompanying chlorine evolution. This literature is reviewed in several places (1-4), the most recent being in the compilation of the electrochemistry of carbon by Randin (4). The literature on the corrosion of graphite anodes during oxygen evolution in chloride-free electrolyte is, in comparison, almost nonexistent. Most of the work on graphite anodes for oxygen evolution has been in acid solution, and it is known that the corrosion processes for graphite change as a function of pH (5). Current technological interest in the use of graphite and/or carbon blacks in alkaline battery positives has revived interest in the corrosion processes of these materials in strongly alkaline chloride-free solutions. Graphite powder is used as a current collector and dispersion substrate for nickel electrodes (6), and various types of carbon blacks are of interest for use as catalyst substrates for bifunctional air electrodes (7). Acetylene black is widely used in primary batteries of both the alkaline and nonaqueous type, and is being examined as a catalyst substrate for air electrodes for a number of fuel cell and metal-air battery technologies. In none of these battery applications is the acetylene black intended to act as an active material for oxygen evolution, and in the primary batteries oxygen evolution does not occur in normal use, so it is not surprising that very little research has been published on the corrosion of acetylene black in oxygen evolving electrodes. Yet the use of acetylene black in a bifunctional air electrode is technologically attractive because of its very low cost relative to metal oxide materi-

als. The principal question concerning its use is the corrosion resistance.

It is a difficult matter to measure corrosion rates accurately in gas evolving electrodes. Standard electrochemical methods are not useful by themselves because the gas evolution is generally the predominant anodic process; so, the observed current is not representative of the corrosion processes. Electrochemical methods must be combined with other analytical tools which discriminate between the different anodic processes, at the least between oxygen evolution and all other processes, and, ultimately, each anodic process is measured independently. Historically, analysis of the anode gas composition for oxygen, carbon monoxide, and carbon dioxide has been used together with standard electrochemical methods to obtain relative current yields for O₂, CO, and CO₂. Examples of this approach are seen in the reports by Kristalik *et al.* (8) on the corrosion of graphite anodes of the type used in chlor-alkali cells. The gas analysis method does not account for corrosion processes that produce solution-phase species (soluble or insoluble), surface oxides, or intercalation compounds like "graphite oxide" (9). Other work (10) on graphite anodes reported that the formation of water soluble products can be 30%-40% of the current yield, and the total current yield of all reaction products (solution plus gas phase) was less than 100%, leading to the conclusion that some current (10%-20%) passed in the formation of "graphite oxide." It is clear that if one is to determine the rate of corrosion processes by the rate of appearance of products the inventory of products must be complete. The prior work on graphite anodes suggests quantitative solution analysis is imperative, including organic compounds that are not well established. The approach we have taken in this work was to use ¹⁴C acetylene black and quantitative radiochemical techniques for analyzing the products in solution and a

* Electrochemical Society Active Member.

quadrupole mass spectrometer for analyzing products in the gas evolved. The ^{14}C technique has several advantages over conventional methods for the quantitative analysis of carbon in water: (i) the lower limit of detection is ppb vs. ppm, (ii) the quantitative determination is absolute and relatively free of matrix or solvent effects, (iii) different types of carbon in the electrode can be discriminated against. The ability to label certain physical parts of a carbon electrode with ^{14}C was particularly useful in examining corrosion in the presence of evolution catalysts. The disadvantage of the ^{14}C labeling technique is that acetylene black is probably the only industrial carbon black that is made from a relatively pure feedstock (acetylene) that can be labeled, so the technique cannot be extended to furnace blacks of technological interest. In order to make quantitative discriminations of inorganic (carbonate) from organic carbon in solution, we did develop a chromatographic procedure based on complete oxidation of organic to CO_2 . Our experience with this procedure indicated that with further development it is capable of making the quantitative determinations of the rate of production of carbonate ion and organics at the levels likely to be observed with industrial carbon blacks in future studies.

Experimental

^{14}C radiotracer.— ^{14}C labeled acetylene black was supplied by Nuclear Research Chemicals with a specific radioactivity of 1.625 mCi/mg. The ^{14}C acetylene black was produced using the same commercial procedure for Shawinigan Acetylene Black (Shawinigan Products Department, Gulf Oil Chemicals Company), but reduced to laboratory scale. Shawinigan Acetylene Black is made by continuous thermal decomposition of acetylene at 800°C in a retort. The retort is first heated to the decomposition temperature by burning the acetylene on introduction, then burning is discontinued, and the acetylene continues to flow into the retort in the absence of air. Thermal decomposition occurs resulting in a flocculent black with a bulk density of ca. 0.019 g/cm^3 . ^{14}C labeled acetylene black was produced by Nuclear Research Chemicals using the same procedure with ^{14}C labeled acetylene gas. Since the quantity of ^{14}C labeled acetylene black was quite small (2.59 mg), owing to its high cost and the fact that only a small amount is needed for radiotracer work, all the physical properties of the ^{14}C acetylene black could not be compared to those of commercial Shawinigan black. Examination of the particle size, aggregate morphology, and microstructure by transmission electron microscopy (TEM) was the principal tool used to determine that the ^{14}C labeled acetylene black was similar to Shawinigan acetylene black in its physical and chemical properties. The ^{14}C black was blended with Shawinigan black using a two-stage procedure. First, 0.59 mg ^{14}C was liquid blended with 100 mg of Shawinigan using isopropanol and ultrasonic agitation. Second, 10 mg of that blend was liquid blended with 100 mg of Shawinigan. The specific activity of the resulting blend was determined using an oxidizer method (Packard Model 306 Oxidizer) to be $1.4 \pm 0.05\text{ dpm/mg}$.

Catalyzation procedure.—Both the ^{14}C blend and the unlabeled Shawinigan black were catalyzed with cobalt oxide using an impregnation procedure. The cobalt content was prepared at a 20 weight percent (w/o) level assuming Co_3O_4 as the final form. $\text{Co}(\text{NO}_3)_2 \cdot 6\text{H}_2\text{O}$ was dissolved in 1:1 methanol:water; the carbon black was dispersed into the solution with ultrasonic agitation; ammonium hydroxide was added to pH 11 to precipitate cobalt hydroxide into the carbon black. The impregnated carbon black was filtered from solution and air dried at 120°C for 24h. Conversion of the cobalt to Co_3O_4 was confirmed by x-ray diffraction analysis, which showed only lines for this phase.

Cell and electrode design.—The electrochemical cell used in these studies is depicted in Fig. 1. It was essentially a standard glass H-cell modified for both gas

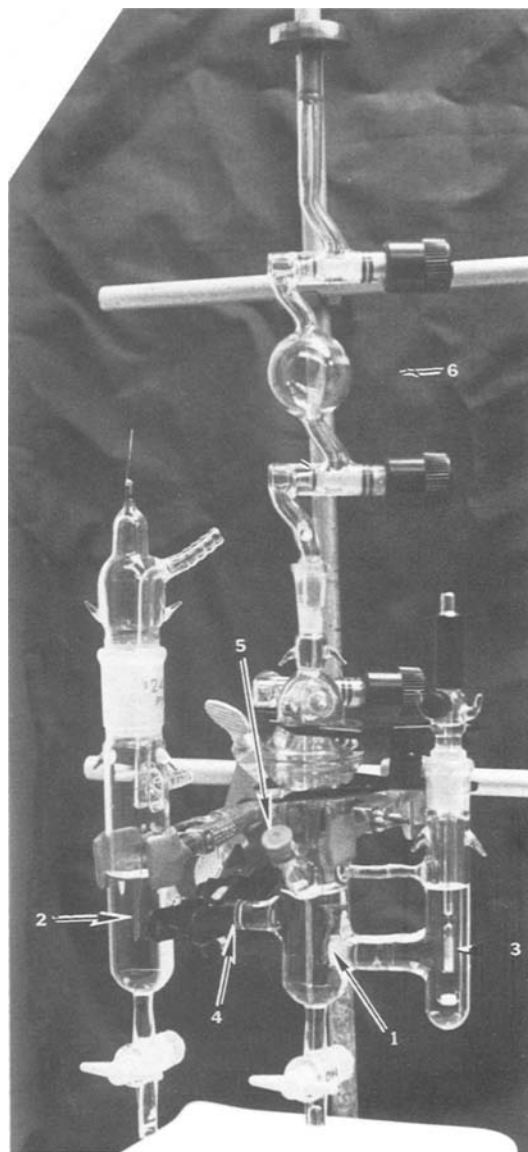


Fig. 1. Three-chambered corrosion cell. 1: test. 2: Ni counter-electrode. 3: Hg/HgO reference electrode. 4: Nafion membrane. 5: septum for liquid sampling. 6: gas sampling bulb.

and solution sampling and solution sampling. The solution in the working electrode compartment was isolated from exchange with solution in the counterelectrode compartment by cation-exchange membrane (du Pont Nafion 117) and from the solution in the reference by a thick ultrafine porous ceramic. Solution samples were drawn from the working electrode compartment through the rubber septum using a $100\ \mu\text{l}$ syringe. The reference electrode was Hg/HgO and the solution was 30 w/o KOH + 2 w/o LiOH. Some experiments were done without the lithium addition, and the presence of lithium did have an effect (increased precipitation of corrosion product within the pores of the electrode due to reduced solubility), so all the results reported here were obtained with the mixed electrolyte. The working electrode consisted of a carbon black-PTFE paste impregnated into a gold-plated tantalum mesh acting as the current collector. The paste contained 5 w/o PTFE solids (du Pont TFE-30B dispersion) mixed into the carbon black with 1:1 isopropanol:water, and was applied to the mesh by spatula followed by air curing at 320°C for 10 min. The typical loading of a working electrode was 40 mg (ca. 10 mg/cm^2) of carbon black or catalyzed black. The working electrodes were vacuum filled with electrolyte at room temperature prior to use in the cell. The internal electrolyte volume in the working electrode was determined gravimetrically after emersion

of the electrode and wiping the surface free of bulk electrolyte. The internal electrolyte volume was typically 2-3 $\mu\text{l}/\text{mg}$ initially, with an increase by as much as 100%-200% on use in the cell (after extensive oxidation).

Solution analysis.—100 μl aliquots were withdrawn from the working electrode compartment at periodic intervals (usually 30 min) and put immediately into 5 ml of scintillation solution (New England Nuclear Atomlight NEF-968) and counted in a commercial scintillation counter (Tracor). Stirring of the solution in the compartment was accomplished by bubbling with argon; results from stirred and unstirred solution did not agree when the corrosion rate was above a certain level, so all the results reported here are for stirred solutions. Because of the requirement for gas flow, gas sampling and solution sampling were not simultaneous. Conventional (*i.e.*, nonradiochemical) qualitative analysis of the solution was conducted to distinguish inorganic (carbonate) from organic corrosion products. The complete analysis procedure, shown in Fig. 2, was initially carried out in an apparatus built in our laboratory. However, it was found that the solutions did not contain any purgeable organic carbon, so the volatilization step was eliminated. Subsequently, the organic/inorganic determinations were made in a single apparatus, a Dohrmann DC-80 Total Carbon Analyzer. Under certain conditions, the KOH solution became colored, and these solutions were analyzed colorimetrically with a UV/VIS spectrophotometer. Attempts were made to isolate and to analyze the colored product by GC-MS and proton NMR, but, as described later in the text, these were largely unsuccessful.

Gas analysis.—Purified argon was used as the diluent gas. The gas evolving from the electrode was accumulated in the space over the KOH solution, then sampled into a 10 ml gas sampling bulb using vacuum withdrawal. The sampling bulb was then isolated and transferred to a quadrupole mass spectrometer (Balzers QMG112) for analysis. Quantitative determinations of the composition of the gas (absolute partial pressures) were made using the calibration procedures described in the Appendix. The only gases observed evolving from the solution were oxygen and carbon monoxide. All the carbon dioxide created anodically was apparently trapped in the electrolyte. The time required to accumulate an analyzable quantity of gas varied with potential, temperature, and whether the cobalt catalyst was present, *e.g.*, from as much as 15h to as little as 30 min. During this time, the electrode potential was controlled, and the total charge passed was measured using a digital coulometer (PAR 179). The rate of gas evolution was calculated as an average quantity from the total moles of gas evolved and the collection time.

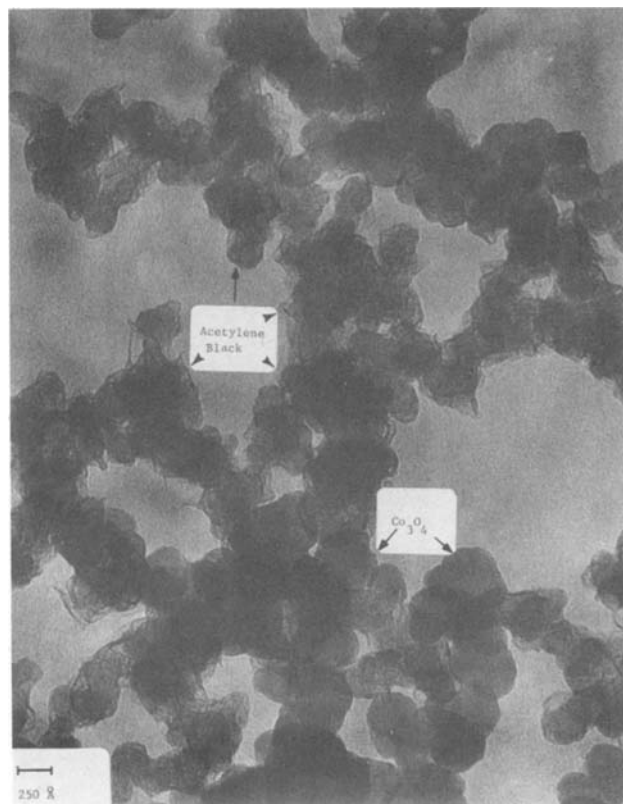


Fig. 3. TEM of cobalt oxide catalyzed acetylene black

Results

Microstructure analysis by TEM.—Classical texts (11, 12) on carbon chemistry refer to acetylene as having a "chainlike" structure and as more "crystalline" than most carbon blacks. At relatively low magnification, as shown in Fig. 3, acetylene black does appear to have a "chainlike" structure in that prime particles appear joined together in chainlike fashion so as to give a three-dimensional "fishnet" structure. However, at much higher magnification in a high resolution (<0.25 nm) TEM, the microstructure of acetylene black was seen to be very heterogeneous, and it is apparent that graphitic "chains" or "ribbons" characterize only a portion of the total structure present. Therefore, while the characterization of acetylene black as being more crystalline (graphitic) than most carbon blacks is essentially correct, it is also the case that acetylene black has a significant

ANALYSIS OF SOLUBLE CORROSION PRODUCTS

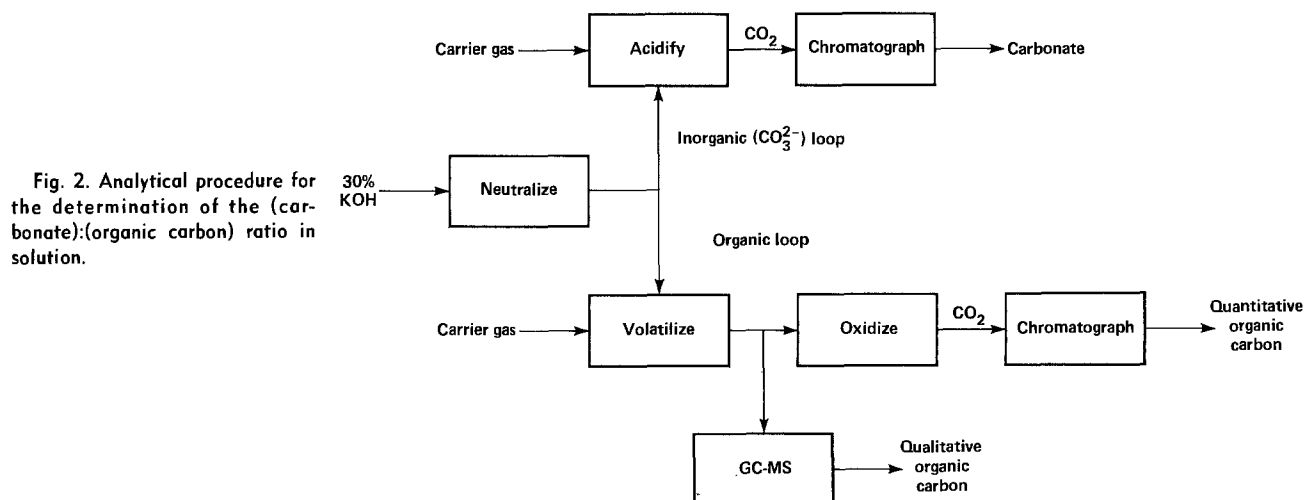


Fig. 2. Analytical procedure for the determination of the (carbonate):(organic carbon) ratio in solution.

portion of the carbon present in a disordered (lacking microcrystallinity) microstructure.

The ^{14}C labeled carbon black was indistinguishable from the Shawinigan acetylene black in terms of the microstructure observed by TEM.

TEM analysis also showed that the catalyzation of the acetylene black with Co_3O_4 resulted in macroscopically uniform dispersion of the oxide in the black, but there was evidence of microscopic "clustering" of the oxide. A typical illustration of this "clustering" is shown by Fig. 3, in which the oxide prime particles (200-300Å) have aggregated into certain regions of the black, leaving other regions of black without Co_3O_4 . The characteristic dimensions of the catalyzed and uncatalyzed regions of black are ca. $0.1\ \mu\text{m}$, so that on the scale of $1\ \mu\text{m}$ or more, the catalyzed black can be considered to be a homogeneous composite material.

Corrosion rates for acetylene black.—A characteristic curve for the amount of carbon lost from the electrode into KOH solution as a function of time and potential is shown in Fig. 4. These data were always obtained in the direction of increasing potential following an initial (new electrode) "aging" period of 48h at 45°C , 450 mV vs. Hg/HgO.¹ After obtaining data at one potential, the solution was drained and replaced with fresh solution before stepping the potential. The rate of weight loss to solution was calculated from the slope of the linear least squares fit of the data. In some cases, such as at higher temperatures, or with Co_3O_4 present, there was clear evidence of an "induction period," as seen from the data in Fig. 5. These induction periods appear to represent a memory in the carbon, as after a step to either higher potential or higher temperature the dissolution² rate remains for a period at the lower rate. Tafel plots of the dissolution rates are shown in Fig. 6. For the purposes of these plots, the dissolution rate was obtained from the steeper slope observed after the induction period. These data illustrate a further memory effect of much longer duration. The one set of rates was taken in the order of increasing potential and increasing temperature, then the temperature was reduced from 65° to 25°C , and the sequence was repeated. The second set of data showed a lasting displacement to higher dissolution rates for the same potential and temperature. These memory effects show clearly how sensitive the dissolution rate of acetylene black is to the pretreatment history, and makes it essentially impossible to determine an absolute (single-valued) dissolution rate

¹ All potentials in this paper are given vs. an Hg/HgO in the same electrolyte at room temperature.

² For compactness, the term "dissolution" refers to the oxidation of carbon to form dissolved species, or partially soluble or insoluble products which are solvent-extracted from within the electrode.

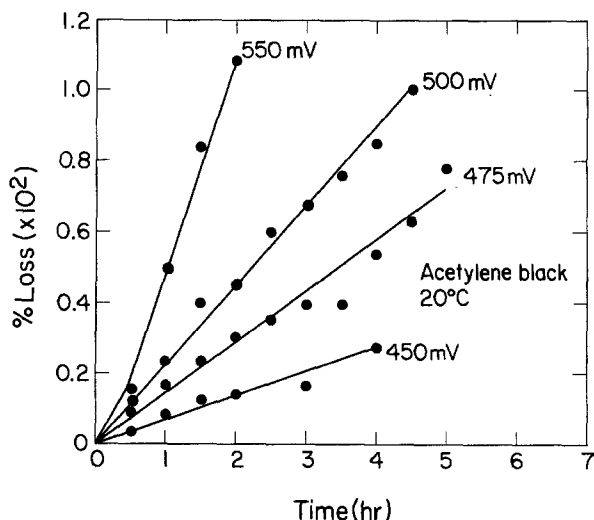


Fig. 4. Quantity of carbon appearing in solution, expressed as a percentage of carbon initially in the electrode, vs. time at a fixed potential.

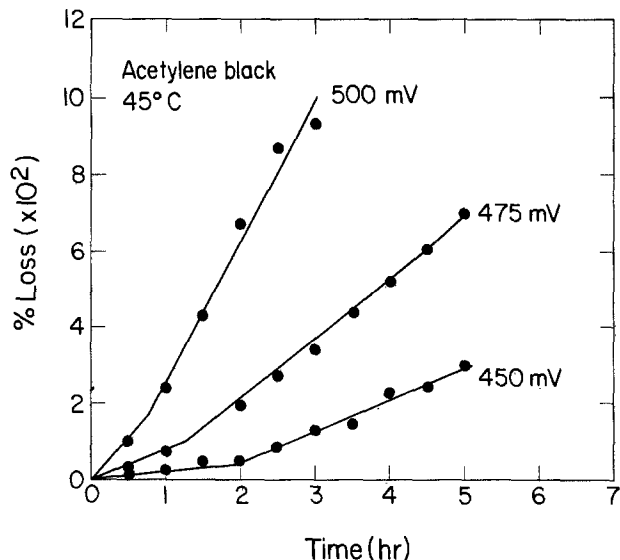


Fig. 5. Same plot as Fig. 4 at 45°C

for a particular potential and temperature. Therefore, the Tafel slopes in the plots in Fig. 6 probably do not have any significance relative to the mechanism for acetylene black dissolution. Rather, the potential dependence shown is the effect of increasing the potential on the quasi-steady-state dissolution rate.

The data shown in Fig. 6 are for the dissolution of the acetylene black into the bulk solution and do not contain the contributions from insoluble species or from partially soluble species that precipitate in the pores of the electrode, or from gaseous oxidation products. An extraction procedure was developed to analyze for precipitated product. After a run like that in Fig. 4 or 5, the cell was drained of KOH, replaced with an extraction solution, and left at open-circuit potential while sampling from the solution. Extraction of precipitated carbonate was obtained using 1M KOH solution, while extraction of organic was obtained using ethanol-water. Very little precipitated organic was extracted at any of the conditions in Fig. 6. Using the known solubility of $\text{KHCO}_3\text{-K}_2\text{CO}_3$ in KOH (13) and the measured internal electrolyte volume in

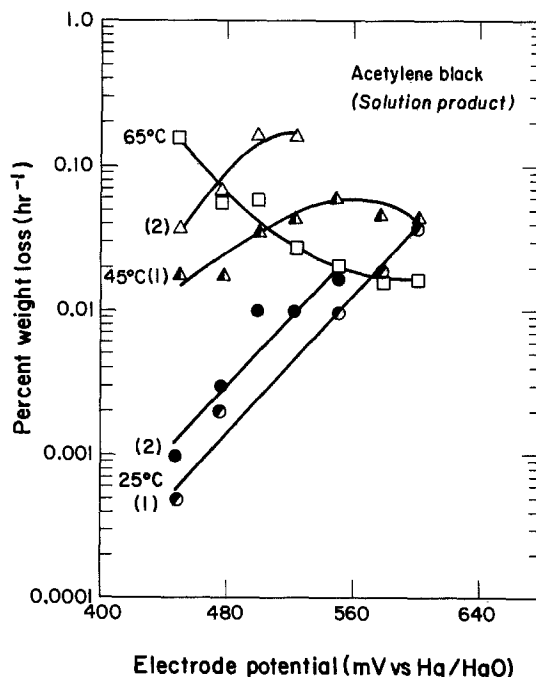


Fig. 6. Rate of appearance of carbon in solution as a function of potential and temperature for (curves 1) ascending temperature and (curves 2) descending temperature.

the electrode, one can calculate the amount of corrosion (as carbonate) required to cause precipitation in the electrode assuming no carbonate ion diffusion out of the internal region. The amount is surprisingly high: ca. 1 w/o loss is required to cause carbonate precipitation to occur, even in the absence of diffusion into bulk solution. Since the typical data collection time for the rates given in Fig. 6 was ca. 5h, only at the very highest dissolution rates ($>0.1\% \text{ h}^{-1}$) would one expect to see any precipitated product in the electrode, and this was in fact the case. The extraction analyses did indicate that there was precipitated carbonate internal to the electrode in the 45° and 65°C runs. The corrections to the dissolution rates for this contribution is shown in Fig. 7. Internal precipitation appears to account for the flattening of the potential dependence of dissolution rate in the 550-600 mV potential region at 45°C. It does not, however, entirely account for the negative potential dependence of the rates at 65°C.

Mass spectrometer analyses of the gas above the electrode indicated that only two gases were produced in significant quantity: oxygen and carbon monoxide. The CO_2 in equilibrium with the KOH solution in these experiments was at too low a partial pressure to be detected by our analyzer. There was no detectable evolution of CO at 25°C, but at 45°C, CO evolution was evident, and at 65°C, it was substantial, as shown by the data reported in Fig. 7. Above ca. 600 mV at 45°C, CO becomes the majority corrosion product, which accounts for the apparent maximum in the dissolution rate observed by analysis of the solution. At 65°C, CO becomes the majority corrosion product at about 100 mV lower potential than at 45°C. When the gas-phase and internal precipitate contributions are added to the solution-phase analysis, the resulting Tafel plot at 45°C from 550 to 625 mV continues with approximately the same slope (ca. 130 mV per decade) as the low potential portion where carbonate was the only product. Above 625 mV, the slope changes sharply due to the very different potential dependence for oxidation to CO than for dissolution to carbonate. The Tafel plot at 65°C after the gas phase and internal volume correction still shows behavior unlike that seen in the low temperature data. The relatively flat potential dependence of the total corrosion rate in the potential region of 400-500 mV may represent transport limitations, e.g., limiting diffusion of dissolved corrosion products out of the electrode and internal pH

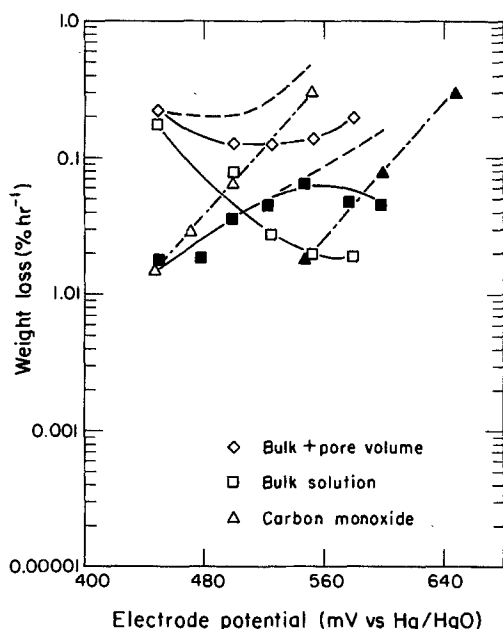


Fig. 7. Contribution of carbon monoxide production and pore volume precipitate to the total corrosion rate at 45° (closed symbols) and 65°C (open symbols). Dashed curves represent the total corrosion rates calculated from the gaseous and solution product rates.

change, rather than nearly potential independent kinetics.

Qualitative analysis of the solution by the procedures in Fig. 2 indicated there was no measurable quantity ($<10 \text{ ppm}$) of organic carbon in the solution at temperatures below 65°C. At 65°C, traces of organic carbon appeared at 550 and 575 mV, but the current efficiency for producing organic species was extremely low ($<<1\%$).

In the potential region of this study, there are three anodic processing occurring: oxygen evolution, carbon dissolution, and carbon surface oxide formation. The latter is a pseudocapacitance, while the former two are faradaic processes, so that, in principle, one can separate out the surface oxide formation from the other two by analysis of time dependence of the current response. The ¹⁴C labeling and the mass spectrometer analysis enable the carbon dissolution and oxygen evolution rates to be determined independently, and from the simultaneous measurement of the total anodic current the current efficiencies for each anodic process can be calculated. The results at 45°C are shown in Fig. 8 and in Table I. The anodic current equivalent to a given rate of appearance of carbon product was calculated from Faraday's law, assuming $4e^-$ per g-mol carbonate ion, $2e^-$ /g-mol carbon monoxide, and $1.5e^-$ /g-mol carbon in organic form. The latter assumes that mellitic acid is the model for organic carbon in solution. Under the potentiostatic conditions used, when the potential was stepped to a higher potential, the current increased sharply, then decreased to a steady-state potential and temperature. The time dependent current probably represents the surface oxidation process. Generally, the sum of the partial currents due to CO evolution, O₂ evolution, and carbon dissolution was very close to the steady-state current, so that the contribution of the oxide formation process to the steady-state current was usually very small ($<10\%$).

Corrosion rates for catalyzed acetylene black.—The effect of cobalt catalyzation on all the anodic partial currents was dramatic. The Tafel plots for the carbon dissolution rates are shown in Fig. 9. In comparison to the uncatalyzed results in Fig. 6, several changes due to catalyzation are apparent: (i) the rate of dissolution was much greater (factor of 2-3), (ii) the potential depend-

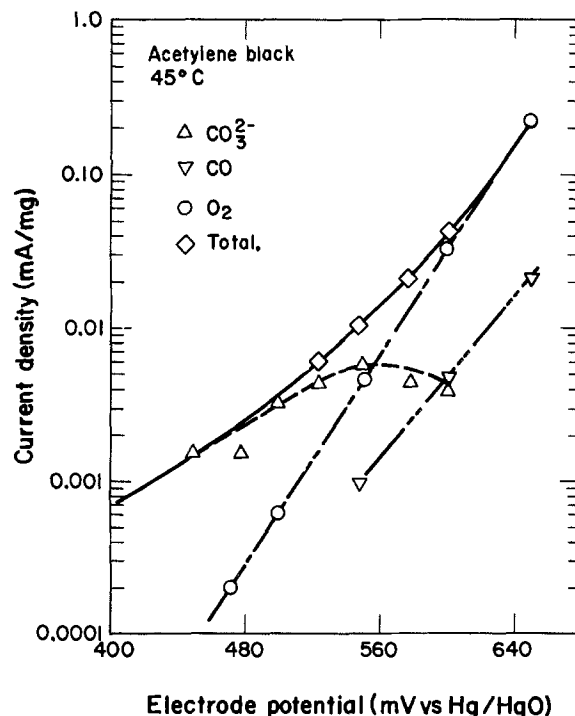


Fig. 8. Partial anodic currents for oxygen evolution, carbon monoxide evolution, and carbonate ion formation and the total anodic current at 45°C.

Table I. Current efficiencies* at 45°C

Potential	Acetylene black		O ₂	Organic
	CO	CO ₂ (CO ₃ ²⁻)		
480	≈8	80	13	≈0
550	10	55	35	0
600	10	10	80	0
Co ₃ O ₄ -catalyzed acetylene black				
480	18	18	64	≈0
550	6	15	74	5

* Based on the sum of the partial currents and not the observed total current.

ence at 25° and 45°C was about the same, and (iii) the potential dependence at 65°C was very different. The change in potential dependence at 65°C reflects the preferential acceleration by Co₃O₄ of carbon dissolution processes that produced highly soluble organic species, as observed by the organic/inorganic qualitative analysis of the solution. The increase in organic product was even intuitively apparent by dramatic coloration of the solution, producing deeply colored reddish-brown solutions. At 65°C with fresh KOH solution in the cell, dark brown streaks could be seen streaming from the electrode upon the imposition of a potential of 550 mV! Gas evolution rates from the electrode were also increased, as seen by a comparison of the curves in Fig. 10. The oxygen evolution rates increased by more than an order of magnitude; the lower potential dependence probably reflects oxygen transport limitations at these higher evolution rates. The rate of CO evolution at lower potentials (ca. 450 mV) was also increased by about an order of magnitude, but the rate at high potential (650 mV) was about the same. The nearly flat potential dependence of the CO evolution rate cannot be due entirely to transport limitations: the transport limitations on oxygen evolution (which is evolving at a higher rate than CO) did not produce such a flat potential dependence. It is more likely that there was a change in the distribution of

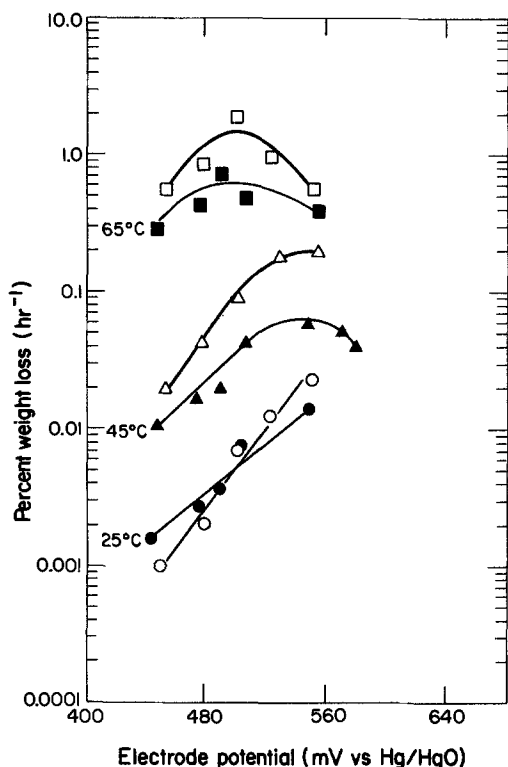


Fig. 9. Cobalt oxide-catalyzed acetylene black dissolution rate as a function of potential and temperature. Open symbols: ¹⁴C mixed into Co-impregnated ¹²C acetylene black. Closed symbols: Co-impregnated ¹⁴C acetylene black mixed into ¹²C acetylene black.

anodic processes that occurred with increasing potential. In particular, the dissolution of carbon to soluble organic products was found to increase suddenly when the potential was increased from 450 to 550 mV. This is reflected in the current efficiencies reported in Table I; at 450 mV there was essentially zero organic product, but at 550 mV the rate of dissolution to organic was nearly equal to the rate of oxidation to carbon monoxide.

The characterization studies of the structure of the catalyzed acetylene black had indicated that there was some clustering of the Co₃O₄ phase so that there are significant regions of the carbon that are not in contact with Co₃O₄. To learn more about the degree of direct contact between Co₃O₄ and carbon black required for the catalyzation of the carbon corrosion processes, an electrode was fabricated from a mechanical blend of uncatalyzed ¹⁴C acetylene black and unlabeled catalyzed acetylene black. Mechanical blending is unlikely to produce the degree of physical contact between the ¹⁴C aggregates and the Co₃O₄ clusters achieved by solution phase impregnation. Therefore, if direct physical contact between Co₃O₄ and the carbon black particles were required for catalyzed corrosion, the mechanical blend should yield lower dissolution rates as measured by the ¹⁴C method. As the comparison of results made in Fig. 9 indicates, this was not observed, since the dissolution rates observed with the mechanical blend were the same (within the ±50% deviation of values observed for identical electrodes) as with the solution impregnated electrode. It appears then that direct physical contact between the oxide phase and the carbon black aggregates is not required for enhancement of the corrosion process to occur.

Discussion

One of the objectives of this study was to determine the individual rates of all the anodic processes occurring in an acetylene black electrode in the 450-650 mV potential region. The approach was to measure the rate of appearance of products of the anodic processes using a variety of techniques, and there remains the question as to whether all the anodic processes occurring in the electrode were accounted for. Techniques were developed to analyze for gaseous products, soluble products in the KOH solution, and partially soluble or solvent extractable products within the electrode. There are well-known anodic processes which do not produce products that

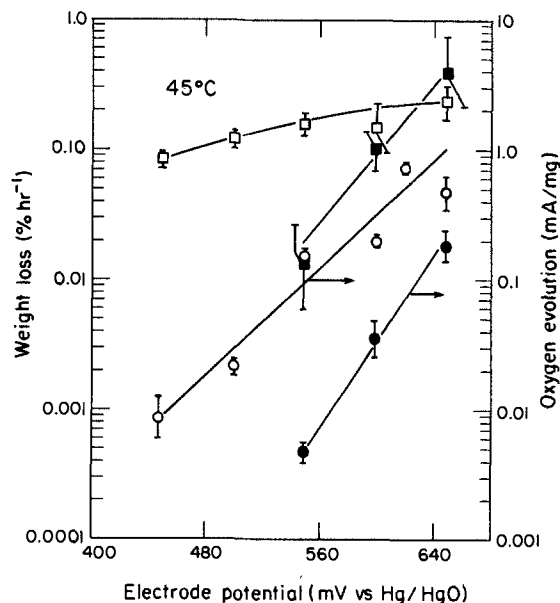


Fig. 10. Rates of gas evolution at 45°C as a function of potential for (open symbols) catalyzed acetylene black and (closed symbols) acetylene black. Error bars represent the range of values observed with repetitions with nominally identical electrodes.

would be seen by these techniques, in particular, the oxidation processes that form surface oxides or intercalation compounds like "graphite oxide" (14). An approximate measure of these processes can be obtained by comparison of the sum of the measured partial rates (as partial currents) with the observed total anodic current. This procedure has an inherent inaccuracy as the product evolution rates require a finite sampling time, whereas the anodic current is instantaneous and is changing during the sampling period. The resulting sums of the measured partial rates of oxygen evolution, carbon monoxide evolution, and carbon dissolution were generally less (ca. 90% of the total current) than the average values of the anodic currents observed over the time period for the partial rate determinations. But there are sufficient inaccuracies in the partial rate determinations that the relatively small differentials are probably not reliable measures of anodic processes like surface oxidation or "graphite oxide" formation. One can, however, reasonably conclude that these latter processes make a relatively minor (ca. 10%) contribution of the time-averaged anodic current observed under potentiostatic conditions.

Due to the different potential dependence of each anodic process, the predominant anodic process changes as a function of potential (at constant temperature) and, due to different activation energies, the predominant process changes as a function of temperature at any given potential. For uncatalyzed acetylene black at low (<50°C) temperature, three regimes can be distinguished: (i) in the low potential region (450-500 mV) the predominant process is dissolution of the acetylene black to carbonate ion, (ii) in the 500-600 mV region oxygen evolution and carbon dissolution occur at equivalent rates, and (iii) above 600 mV, oxygen evolution and carbon monoxide evolution are the dominant processes. Elevation of the temperature to 65°C, or catalyzation with Co_3O_4 preferentially accelerates the gas evolution reactions (for O_2 and CO) such that all three anodic processes occur at nearly equivalent rates even at low potential. Carbon monoxide production was always commensurate with oxygen evolution and was never observed in the absence of oxygen evolution, indicating that there is a good possibility that chemical oxidation of the carbon by evolving oxygen (or intermediates) may be occurring in addition to direct electrochemical oxidation. This was also indicated by the effect of Co_3O_4 on the CO evolution rate, particularly the results that showed that physical contact between Co_3O_4 and carbon was not necessary for enhanced oxidation. The results with the cobalt catalyzed acetylene black also suggest that CO evolution and organic formation are competing, and not parallel, reaction paths. This was evident from the observation that the appearance of significant quantities of organic product was always at conditions (potential and temperature) where the current efficiency for CO evolution was the lowest, e.g., Table I. It is not mechanistically obvious why oxidation to CO and dissolution to organic would be competing reacting paths.

While the anodic processes of oxygen and carbon monoxide evolution appear to be coupled, there is no apparent coupling between oxygen evolution and dissolution to organic products. This is clear by comparison of the data in Table I, where high current efficiency for oxygen was not accompanied by measurable organic dissolution product. Also, in the case of the 65°C experiments with uncatalyzed acetylene blacks, the absolute oxygen evolution rates were about the same as with the catalyzed black at 45°C, yet no measurable quantity of organic appeared in the absence of catalyst. It seems clear that oxygen evolution is not a sufficient condition for organic product formation, and that cobalt oxide has a selective catalytic effect for the dissolution process to organics. We did not perform experiments designed to determine whether physical contact of Co_3O_4 and carbon aggregates is required for this catalysis as we did for the carbonate ion reaction. This determination could have been made by using ^{14}C detectors on the chromatographs in the organic carbon analysis, but our apparatus was not equipped with

these detectors. Unfortunately, there are no results in this work that would help to elucidate the mechanism of the selective catalyzation of the dissolution of carbon to organic products.

We attempted some experiments designed to explore the relationship between the acetylene black microstructure and the corrosion rate, but these have not yet yielded definitive results. Because of the heterogeneous nature of the acetylene black microstructure, it might be expected that the corrosion rate might change (go down) with time as the more easily oxidized sites are used up. Also, if the different types of carbon in the black are removed at different rates, one might expect to see the microstructure change by TEM analysis of corroded samples. However, it was clear from the TEM analysis that the scale of heterogeneity is fairly large, and that the amount of carbon loss required to see a significant change in either the structure or the overall corrosion rate could be as much as 30%-40%. A ^{14}C acetylene black electrode was potentiostated in KOH solution at 550 mV, 45°C for 500h, which resulted in a total weight loss (determined gravimetrically) of ca. 30%. This electrode was placed in the corrosion cell of Fig. 1, and the rates of the anodic processes were measured. The absolute rates of all anodic processes were increased by factors of 1.5-2 times those for "new" acetylene black, but the current efficiencies were significantly changed, with the corrosion rates reduced relative to oxygen evolution. The TEM analysis on the corroded black was inconclusive in that we could not distinguish regions of the carbon that had been attacked preferentially. Apparently, the increase in surface area with carbon loss more than offsets the decrease in the rate per unit area, resulting in a net increase in corrosion rate. The same effect was seen in the temperature cycling experiments shown in Fig. 6. After the measurements at 65°C, which resulted in a weight loss of about 20%, the dissolution rates at the lower temperatures were about a factor of 2 higher than before the 65°C measurements. It would seem that the difference in corrosion rate (per unit area) between the different forms of carbon in acetylene black cannot be very large, perhaps only factors of 2-3.

We were not able to identify the organic products of acetylene black corrosion, and, in particular, the nature of the deep reddish-brown coloration of the KOH solution. There is a long and interesting history related to the observation and analysis of colored caustic solutions from the oxidation of graphite anodes in chlor-alkaline cells. Thiele (15) reviewed observations made in the 1930's on the oxidation of graphite in caustic solutions, and reported that a brown discoloration of the solution was observed with graphite oxidation, that "lampblack" carbon-colored solutions more intensely than graphite, and that the brown product was probably humic acid. In the early 1940's, Heller (16) did a thorough analytical study to identify the source of color in caustic from chlor-alkali diaphragm cells. He found that when graphite anodes from these cells were soaked in water a yellowish coloration developed, which left a dark brown residue upon drying. From this brown residue, Heller extracted a bright yellow crystalline compound which he concluded, from various property measurements, was pyromellitic acid chloroquinone. Janes and co-workers (17-18) at Union Carbide reported that caustic solutions prepared from the yellow crystalline material isolated by Heller had the same UV-Vis spectrophotometer spectra as chlor-alkali cell effluent, and concurred with Heller that this material was the source of color in caustic from diaphragm cells. They also reported that less graphitic raw materials for the anode like "lampblack" or "charcoal" gave increased coloration in cell effluent. However, further analytical study of Heller's yellow material by Wawzonek and Eftax (19) indicated this material was not a single compound but a mixture of mellitic acid, pentacarboxylchlorobenzene, tetracarboxylchlorobenzene, and a material of unknown structure that is actually the source of color! Since this active period sparked by Heller's work, there has been very little further work on this subject. Some Russian

work (10) reported isolating mellitic acid as one of the organic products from graphite anode oxidation in 0.01N Na_2SO_4 , but mellitic acid constituted only a fraction of the total organic product which was not otherwise identified. There appears to be no precedent in the literature for the specific catalyzation of the dissolution process to organic products, as we have observed in this work.

The practical consequences of the determinations of the partial rates of the anodic processes occurring in acetylene black electrodes made in this work could be significant with regard to the use of this material in alkaline batteries, but care must be taken in applying these partial rates directly to practical electrodes. The rates of oxygen evolution, the current efficiencies in Table I, and the total anodic currents measured at any potential are influenced by the rate of transport of products from within the porous mass of the electrode. The rates measured here were for fully submerged electrodes containing only enough PTFE to bind the acetylene black together. Experiments done with a floating electrode containing ca. 20% PTFE so as to approximate the practical "gas diffusion" type structure (20) indicated the rate of oxygen evolution from catalyzed acetylene black increased severalfold over that observed with the same material in a submerged electrode. This means the concentration of dissolved oxygen inside the submerged electrode was probably severalfold higher than in the high transport rate gas diffusion electrode, so that the corroding action of evolved oxygen may be accentuated due to the transport effect. Also, in PTFE-bonded gas diffusion electrodes, it is usually the case that all of the carbon is not wetted by electrolyte, so that the direct electrochemical corrosion rate will not be as high as for fully wetted carbon, but the oxygen evolved can react homogeneously with the dry catalyst to form gaseous carbon dioxide that may diffuse out of the electrode without being trapped in the electrolyte. The gas diffusion electrode might, therefore, be expected to give higher gaseous product to dissolved product ratios than reported here. However, due to the complexity of the interactions and the potentially compensating nature of some of these interactions, it is difficult to predict what the differences in the partial rates might be between a practical gas diffusion electrode and the fully submerged electrode used here.

Conclusions

1. Carbon dissolution to carbonate ion, gasification of carbon to carbon monoxide, and oxygen evolution are the predominant anodic processes in uncatalyzed acetylene black at 450-600 mV vs. Hg/HgO in concentrated KOH. No evidence for the formation of a "graphite oxide" intercalation compound was found. The potential and temperature dependence of these anodic processes is different, so that there are various combinations of the three processes that are dominant at different conditions: (i) at potentials below 500 mV and temperatures below 50°C, carbon dissolution is the primary anodic process, (ii) at 500-600 mV and 50°C or lower, carbon dissolution and oxygen evolution occur at equivalent rates, and (iii) above ca. 600 mV or above ca. 60°C at any potential above 450 mV, oxygen evolution and carbon gasification are the dominant anodic processes.

2. Below 500 mV and 50°C, the current efficiency for oxygen evolution from acetylene black is sufficiently small that the total anodic current is essentially the corrosion current.

3. In a cobalt oxide-catalyzed acetylene black electrode, the current efficiency for oxygen evolution is increased severalfold, but the rates of the corrosion processes are also accelerated relative to those for the uncatalyzed black. In addition, cobalt oxide causes organic products to form at significant rates at conditions where only trace amounts are observed for uncatalyzed black.

Acknowledgments

This work was supported by the Assistant Secretary for Conservation and Renewable Energy, Office of En-

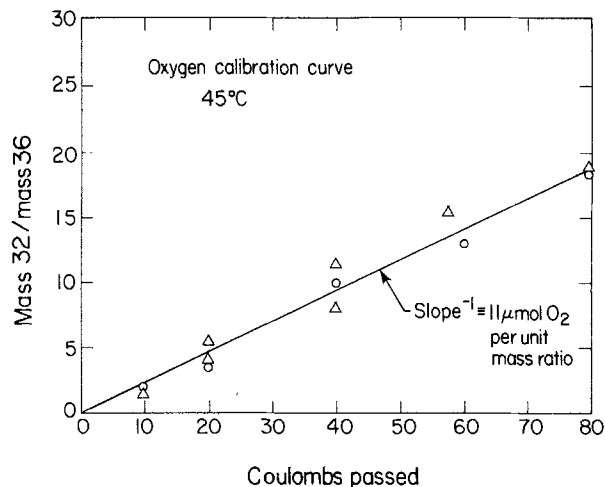


Fig. 11. Mass spectrometer calibration curve for absolute determination of oxygen in argon dilute gas above the electrolyte.

ergy Systems Research, Energy Storage Division of the U.S. Department of Energy under Contract no. DE-AC03-76SF00098. The authors acknowledge valuable discussions with Dr. Kim Kinoshita, who guided us to the interesting literature on colored caustic solutions from chlor-alkali cells.

Manuscript submitted Nov. 11, 1983; revised manuscript received March 12, 1984.

The University of California assisted in meeting the publication costs of this article.

APPENDIX

Mass Spectrometer Calibration

The calibration procedure was based on the electrolytic generation of oxygen from KOH solution into the gas space above the solution, whose volume is maintained at a constant value. A nickel Exmet® working electrode was used to evolve oxygen at a constant rate by use of a constant current power supply. The quantity of oxygen in the argon is therefore known precisely, and a calibration curve of mass spectrometer peak ratio (oxygen to argon) vs. quantity of oxygen (in coulombs) can be prepared, as shown in Fig. 11. Because oxygen is always present in low concentration relative to the argon, we chose the $M/e = 36$ peak of argon (the natural abundance of the 36 isotope is 0.337%) as the normalization factor. Water vapor in equilibrium with the KOH solution is present at partial pressures of 20-200 torr depending on temperature, so that the total pressure of the argon above the solution is a function of the solution temperature. A different calibration curve was therefore required for each solution temperature. The absolute calibration for carbon monoxide was obtained using the absolute oxygen calibration and observing the $M/e-28:M/e-32$ peak ratios for calibrated mixtures of oxygen and carbon monoxide (purchased from Matheson). As a check on this calibration, we computed the expected $M/e-28:M/e-32$ peak ratios from the quadrupole analyzer transmission function supplied by the manufacturer and tabulated ionization probabilities for O_2 and CO and found them to be in reasonable agreement ($\pm 5\%$) with the observed values.

REFERENCES

1. L. Vaaler, *Electrochem. Technol.*, **5**, 170 (1967).
2. C. Mantel, "Carbon and Graphite Handbook," pp. 378ff, Wiley Interscience, New York (1968).
3. A. Kuhn and P. Wright in "Industrial Electrochemical Processes," A. Kuhn, Editor, pp. 525ff, Elsevier, Amsterdam (1971).
4. J. Randin, "Encyclopedia of Electrochemistry of the Elements," Vol. VII, A. Bard, Editor, pp. 2-240, Marcel Dekker, New York (1976).
5. G. Kokhenov and N. Milova, *Elektrokhimiya*, **5**, 93 (1969).
6. R. Gunther, U.S. Pat. 4,130,696 (1978); W. Ferrando and R. Sutula, U.S. Pat. 4,215,190 (1980).

7. E. Buzzelli, Iron-Air Battery Development Final Report, Lawrence Livermore National Laboratory Report UCRL-15543 (1983).
8. N. Viet, D. Kokoulina, and L. Krishtalik, *Elektrokhimiya*, **8**, 221 (1972); *ibid.*, **8**, 225 (1972); *ibid.*, **8**, 384 (1972).
9. A. Ubbelohde and F. Lewis, "Graphite and Its Crystal Compounds," pp. 110ff, Oxford (Clarendon) Press (1960).
10. V. Sapunov, V. Shapranov, R. Bergman, and V. Shulika, *Khim. Tverd. Topliva*, **11**, 153 (1977).
11. "Kirk-Othmer Encyclopedia of Chemical Technology," 2nd ed., Volume 4, pp. 149-334, John Wiley and Sons, New York (1972).
12. W. Reynolds, "Physical Properties of Graphite," p. 37 ff, Elsevier, Amsterdam (1968).
13. E. Cairns and D. Macdonald, *Electrochem. Technol.*, **2**, 65 (1964).
14. R. Croft, *Quart. Rev.*, **14**, 1 (1960).
15. H. Thiele, *Trans. Faraday Soc.*, **34**, 1033 (1938).
16. H. Heller, *Trans. Electrochem. Soc.*, **87**, 501 (1945).
17. M. Janes, *ibid.*, **92**, 23 (1947).
18. M. Janes, N. Johnson, and E. Pilcher, *This Journal*, **102**, 474 (1955).
19. S. Wawzonck and D. Eftax, *ibid.*, **104**, 494 (1957).
20. H. Kunz and R. Gruver, *ibid.*, **122**, 1275 (1975).

The Cycling Efficiency of Lithium-Aluminum Electrodes in Nonaqueous Media

A. S. Baranski,* W. R. Fawcett,*¹ T. Krogulec, and M. Drogowska

Guelph-Waterloo Centre for Graduate Work in Chemistry (Guelph Campus), Department of Chemistry, University of Guelph, Guelph, Ontario, Canada N1G 2W1

ABSTRACT

The cycling efficiency of a lithium-aluminum electrode has been studied in a variety of aprotic systems and compared with that of pure lithium. It is shown that the efficiency of the alloy electrode is virtually independent of the nature of the electrolyte solution but that it depends somewhat on the amount of alloy deposited per unit area and current density used in the charging and discharging processes. The roles of the β - and α -phases of the alloy system in the operation of the electrode and in cracking and disintegration of the electrode are considered in detail. It is shown that the cycling efficiency could be improved significantly by mechanically stabilizing the alloy material on the surface of the electrode.

In recent years, substantial research effort has been directed to the development of rechargeable lithium and lithium alloy electrodes for batteries operating at room temperature in nonaqueous media (1, 2). In this connection, it has been shown that the charging efficiency of pure lithium electrodes can reach 96%-98% in a few carefully selected electrolyte solutions (3, 4). However, in order to achieve high efficiencies, complex and costly methods of solvent and electrolyte purification are necessary. The major problem limiting cycle life in experimental cells was found to be short circuits caused by the growth of lithium dendrites through the separator (2). One way of overcoming this problem is to alloy the lithium with aluminum. β -LiAl deposited on aluminum does not grow dendrites (5, 6) and exhibits high rechargeability in many aprotic solvents (5-7). The major disadvantages of the lithium-aluminum electrode are that the atomic weight of LiAl is 4.9 times greater than that of Li, and that the equilibrium potential is 0.38V more positive. If one estimates the change in energy density in a cell using a TiS_2 intercalation cathode with nature of the anode, one finds that the theoretical energy density of the LiAl/ TiS_2 system is only about 33% lower than that of the Li/ TiS_2 system. Thus, if higher cycle life is achieved, the lithium-aluminum anode is an attractive alternative for use in ambient temperature high energy density batteries. In a previous paper (8), a study of charge and mass-transfer processes occurring at a lithium-aluminum electrode in propylene carbonate (PC) was reported. The present paper is concerned with cycling studies in other media. In addition, the factors affecting the cycling efficiency have been examined in more detail, with a view to finding methods of improving the electrode's performance.

Experimental

The apparatus and electrochemical methods were the same as those used in the previous study (8). The active

material of the working electrode was electrodeposited at high purity aluminum or nickel wires, 2 mm diam, which were mounted in Teflon tubes. Electrodes of higher surface area used in some experiments were prepared from aluminum foil 0.4 mm thick. The counter- and reference electrodes were made of pure lithium, as described earlier (8). The experiments were carried out in a controlled atmosphere chamber under an atmosphere of purified argon.

Tetrahydrofuran (THF), 2-methyl-tetrahydrofuran (MTHF), and bis-(2-ethoxyethyl) ether (EEE), used as solvents, were purified by drying with LiAlH_4 and distilled under argon from a Vigreux column 1m high, only the middle fraction (60%) being collected. THF and MTHF were then distilled a second time under reduced pressure and temperature. N,N -dimethylformamide (DMF) and 1-methyl-2-pyrrolidone (MP) were dried over CaH_2 and then distilled under reduced pressure. In the case of PC and dimethylsulfoxide (DMSO), drying was carried out over 4Å molecular sieves for 24h before distilling at reduced pressure. The water content of the purified solvents was $\leq 0.01\%$. Three lithium salts were used to prepare the electrolyte solutions. Commercial LiAsF_6 from U.S. Agri-chemicals was used without drying or other purification. Reagent grade LiClO_4 and LiI were dried under vacuum at 120°C for 48h before use. The electrolyte solutions were prepared at low temperature in the controlled-atmosphere chamber.

Results and Discussion

A comparison of the cycling efficiencies of lithium-aluminum electrodes in various media.—In order to improve understanding of the influence of the medium on the rechargeability of lithium-aluminum anodes, experiments were performed in which the cycling efficiency of the lithium-aluminum was measured and compared with that for pure lithium. The lithium electrode (Li/Ni) was formed by electrodepositing lithium on a nickel wire, 2 mm diam, at a constant current density of 2.5 mA cm^{-2} for 1000s. Then, the deposit was completely oxidized at the same current density. This cycle was repeated five

* Electrochemical Society Active Member.

Key words: battery, electrode, alloy.

¹ Present address: Department of Chemistry, University of California, Davis, California 95616

times, and the ratio of the charge involved in the oxidation process for the last three cycles, Q_o , to that for the reduction process, Q_R , was used to estimate the average cycling efficiency. The lithium-aluminum electrode (LiAl/Al) was formed under the same conditions at an aluminum wire; the cycling conditions and method of estimating cycling efficiency were the same as for those for the Li/Ni system. Data for nine different electrolyte solutions are presented in Table I. The striking result is that the cycling efficiency of the Li/Ni system changes from 5% to 94% when the electrolyte solution is changed, whereas that of the LiAl/Al system is virtually constant and high (91%-95%) in all solutions. In other experiments, the influence of corrosive additives, namely, I_2 , H_2O , and SO_2 , on the cycling efficiency was examined (Table II). Again, it was found that the LiAl/Al electrode is much less sensitive to corrosion than the Li/Ni electrode. It is obvious that the major factors affecting the cycling efficiency of these systems are quite different. According to the generally accepted view, metallic lithium can be plated from many aprotic solvents with close to 100% coulombic efficiency (2). However, subsequent oxidation is much less efficient. Two models have been proposed to explain this result. According to Rauh and Brummer (2, 9), the surface grains on the lithium deposit react with the electrolyte solution, and are undercut by corrosion. Some of the grains become partially or completely isolated from the substrate. Thus, subsequent oxidation is not 100% efficient. The morphology of the residual lithium is seriously distorted in subsequent platings, and, cycle by cycle, the deposit becomes increasingly dendritic. In addition, as the deposit becomes more dendritic, it is more vulnerable to the corrosion and isolation process. An alternative model has been described by Peled (10), who interpreted the poor stripping efficiencies of alkali and alkaline earth metals in terms of the formation of a solid electrolyte interphase in which Li^+ ion is conductive. Excessive local heating and the high local electric field result in the formation of a short circuit through the solid interphase during the charging cycle. As a result, a parcel of lithium metal forms within the solid electrolyte out of

direct electrical contact with the substrate. The short circuit disappears after plating ceases, and, on subsequent discharge, the encapsulated parcel of lithium is unavailable for electro-oxidation.

In the case of the lithium-aluminum electrode, neither of the above mechanisms is applicable. For this system, four steps can be distinguished in the reduction process: (i) migration of Li^+ ions through the solid/electrolyte interphase, (ii) charge transfer, (iii) diffusion of lithium in β -LiAl, and (iv) reaction of lithium with aluminum. Because the mobility of aluminum in β -LiAl is negligible in comparison with that of lithium (11), the lithium-aluminum deposit is never dendritic, and, therefore, much less vulnerable to corrosion. The nondendritic character of the deposit was confirmed by scanning electron microscopy. However, even if the solution reacts efficiently with the grain boundaries of the alloy phase, one of the products, aluminum, may provide good electrical contact between the grains. Peled's model (10) does not apply to the LiAl/Al electrode because formation of the alloy occurs at a more positive potential than the potential necessary for deposition of metallic lithium. These differences explain why the cycling efficiency of the LiAl/Al electrode is relatively high and virtually independent of electrolyte nature. In addition, lithium-aluminum is thermodynamically less reactive than lithium. This factor seems to be less important because of the high cycling efficiency of the LiAl/Al electrode, even in the presence of sulfur dioxide.¹

On the basis of the present results, it is concluded that the cycling efficiency of the LiAl/Al electrode is much more determined by the properties of the alloy itself rather than by those of the electrolyte. It follows that changing the composition of the electrolyte or the method of purification is unlikely to improve cycling efficiency. In any case, the majority of experiments were conducted in THF and MTHF solutions of $LiAsF_6$, electrolyte solutions which are believed to be last reactive with lithium (3, 12).

Factors affecting the cycling efficiency of the lithium-aluminum electrode.—In order to determine the influence of various factors on the cycling efficiency of the LiAl/Al electrode, extensive galvanostatic cycling experiments were carried out in THF and MTHF solutions containing 1.5M $LiAsF_6$. In the first stage of the cycle, Li^+ ions were reduced at the electrode for a precisely measured period of time; then the direction of the current was changed and oxidation of Li from the previously formed alloy was carried out. During this procedure, the electrode potential was recorded. The final sharp rise of electrode potential to greater than + 2.0V was considered an indication that lithium was exhausted from the electrode. Since the absolute value of the current during the experiment was constant, the ratio of the oxidation time (τ_o) to the reduction time (τ_R) is equal to the cycling efficiency with respect to lithium, η_{Li} (8). In the first type of cycling experiment, the electrical charge involved in the reduction process, Q_R , was kept constant at 0.25 C cm^{-2} , and the current density was varied from 0.04 mA cm^{-2} to 25 mA cm^{-2} . Ten cycles were recorded at each current density, and the average cycling efficiency was calculated. From the dependence of average efficiency on current density (Fig. 1), the maximum efficiency is obtained for current densities in the range 1-5 mA cm^{-2} .

In other experiments, the current density was kept constant at 5 mA cm^{-2} and the charge density involved in one cycle varied from 0.1-50 C cm^{-2} . The results showing the average efficiency of ten identical cycles are shown in Fig. 2. A sharp decrease in efficiency for charge densities greater than 8 C cm^{-2} was observed in both THF and MTHF. It is important to notice that identical results were obtained earlier in PC (8). The influence of temperature on cycling efficiency was also studied in a 1.5M $LiAsF_6$ solution in MTHF. In agreement with results obtained in

¹ The standard potential for the reaction $2SO_2 + 2Li^+ + 2e \rightleftharpoons Li_2S_2O_4$ is 2.6V more positive than that for the reaction $Li^+ + Al + e \rightleftharpoons \beta$ -LiAl.

Table I. A comparison of the cycling efficiencies of lithium at the lithium-aluminum (LiAl/Al) and lithium (Li/Ni) electrodes in various aprotic media*

Electrolyte solution	Efficiency (%)	
	LiAl/Al	Li/Ni
THF, 1M $LiAsF_6$	94	94
THF, 1M LiI	94	34
MTHF, 1M $LiAsF_6$	95	88
EEE, 1M $LiClO_4$	94	55
EEE, 1M LiI	94	30
PC, 1M $LiAsF_6$	96	55
DMF, 1M $LiAsF_6$	91	78
DMSO, 1M $LiAsF_6$	93	85
MP, 1M $LiAsF_6$	93	>5

* The current density for deposition of Li^+ was 2.5 mA cm^{-2} and the deposition time 1000s, except for the DMF system, in which case the current density was 5 mA cm^{-2} .

Table II. The influence of corrosive additives on the cycling efficiencies of the lithium-aluminum and lithium electrodes

Electrolyte solution	Additive	Efficiency (%)	
		LiAl/Al	Li/Ni
THF, 1M $LiAsF_6$	$10^{-3}M I_2$	92	75
	$10^{-2}M I_2$	86	67
	$10^{-1}M I_2$	0	0
PC, 1M $LiAsF_6$	0.55M H_2O	82	24
	$10^{-2}M I_2$	93	70
	$10^{-2}M I_2$	88	55
	$10^{-1}M I_2$	67	62
	0.55M H_2O	89	74
	0.5M SO_2	95	—

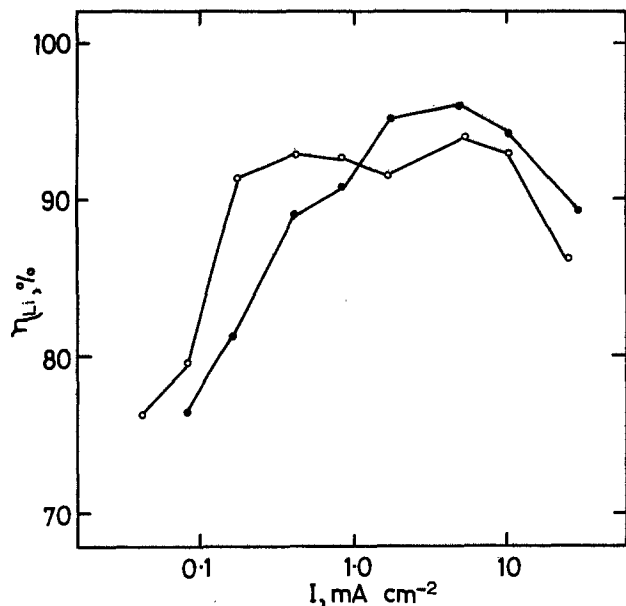


Fig. 1. The dependence of average cycling efficiency on current density at a lithium-aluminum electrode in THF (●) and MTHF (○) containing 1.5M LiAsF₆ with a constant charge density due to deposited lithium (0.25 C cm⁻²).

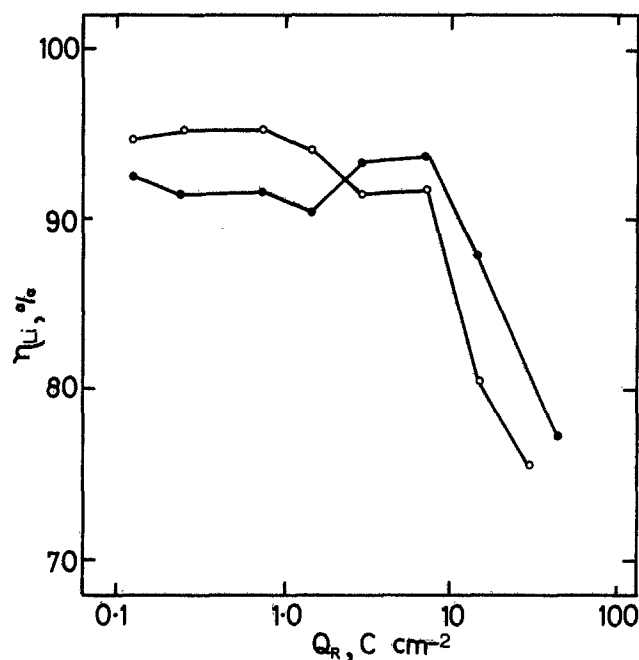


Fig. 2. The dependence of average cycling efficiency on charge density due to deposited lithium at a lithium-aluminum electrode in THF (●) and MTHF (○) containing 1.5M LiAsF₆ for a constant current density (5 mA cm⁻²).

PC (8), the efficiency decreases with decrease in temperature, the effect of temperature being greater at larger charge densities and currents (Table III). These results are further indication that the cycling efficiency of the lithium-aluminum electrode is more affected by the properties of the alloy phase than by the nature of the electrolyte or solvent. The reasons why the efficiency for this system is less than 100% are now considered in detail.

One reason for the observed efficiencies for the LiAl/Al could be the slow diffusion of lithium into the bulk of the aluminum phase. On the basis of the phase diagram for Li-Al(13), lithium can dissolve in aluminum to form the α -phase which contains up to 7 atom percent (a/o) Li and has a density close to that of pure aluminum. The loss of active lithium due to this process can be described by an integrated form of the Cottrell equation

Table III. Temperature dependence of the cycling efficiency of the lithium-aluminum electrode*

Temp (°C)	Efficiency (%)	
	$i = 5 \text{ mA cm}^{-2}$ $Q = 1.5 \text{ C cm}^{-2}$	$i = 15 \text{ mA cm}^{-2}$ $Q = 4.5 \text{ C cm}^{-2}$
-5	86	31
8	90	80
25	91	86
40	91	—

* The electrolyte solution contained 1.5M LiAsF₆ in MTHF.

$$\Delta Q = 2F c_{\alpha m} D_{\alpha}^{1/2} t^{1/2} / \pi^{1/2} \quad [1]$$

where ΔQ is the loss in charge density due to active lithium, $c_{\alpha m}$ the maximum concentration of lithium in the α -phase at the boundary with the β -phase ($c_{\alpha m} = 7 \times 10^{-3}$ mol cm⁻³), D_{α} the diffusion coefficient of lithium in the α -phase, t the time after formation of the β -phase by reduction of Li⁺ at aluminum, and the other symbols have their usual meanings. In order to assess the role of this process, a known amount of β -LiAl was deposited on an aluminum electrode, and the electrode was dried and stored under an argon atmosphere for varying periods of time. Then, the active lithium was electrochemically oxidized, and the loss in charge density due to storage determined. A plot of ΔQ against $t^{1/2}$ for two series of experiments is shown in Fig. 3. The value of D_{α} determined from the slope is 1.4×10^{-12} cm²s⁻¹. Melendres *et al.* (14) reported a value of 4×10^{-10} cm²s⁻¹ for D_{α} at 450°C, but no other values of this parameter were found in the literature. It is noted that D_{α} is much smaller than D_{β} , the diffusion coefficient of lithium in β -LiAl [$D_{\beta} = 7.7 \times 10^{-8}$ cm²s⁻¹ at 25°C (8)]. The diffusion of lithium from β -LiAl into pure aluminum may explain the decrease in cycling efficiency observed when small current and charge densities are involved (see Fig. 1), but this process has a negligible effect on observed efficiencies when the current density $i > 1 \text{ mA cm}^{-2}$ and $Q > 1 \text{ C cm}^{-2}$.

The decrease in efficiency observed at high current densities (Fig. 1) is probably due to blocking of the β -LiAl phase by rapidly formed α -phase. If this conclusion is correct, one may expect that when the deposit is oxidized under controlled-potential conditions instead of galvanostatic conditions, the blocking process will affect the current density, but the charge efficiency of the oxidation process will remain high, provided that the oxidation is carried out for a sufficiently long period of time. Current-

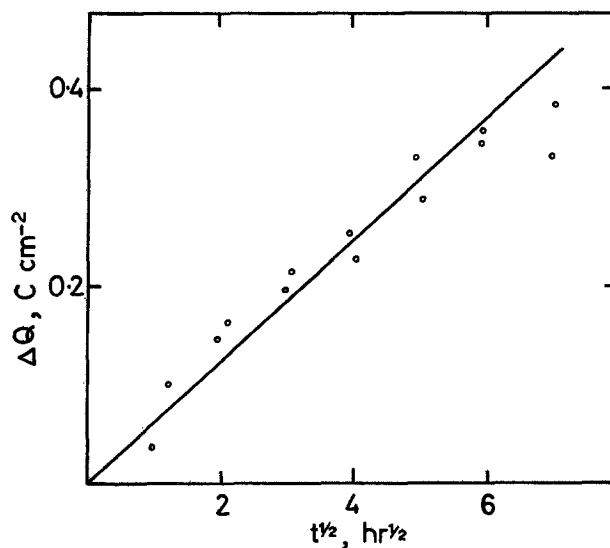


Fig. 3. The dependence of the decrease in oxidizable lithium, ΔQ on the square root of time $t^{1/2}$ for a lithium-aluminum electrode formed in THF.

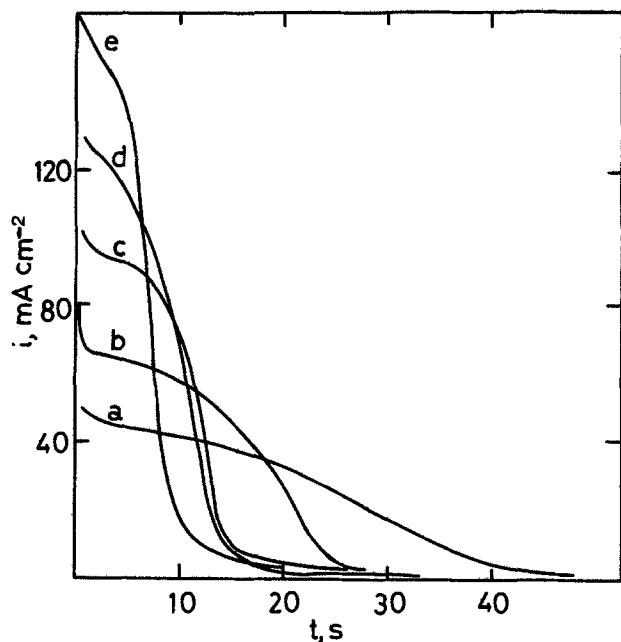


Fig. 4. Current density against time curves for the potentiostated oxidation of lithium from a LiAl/Al electrode covered with 1.5 C cm^{-2} of electrodeposited lithium in THF solution containing 1 M LiAsF_6 . The potentials at which oxidation was carried out against a Li/Li⁺ reference electrode were (a) 1.0V, (b) 1.2V, (c) 1.4V, (d) 1.7V, and (e) 2.0V.

time curves for the potentiostatic oxidation of the alloy electrode are shown in Fig. 4. By integrating these curves, it was shown that the charge efficiency of the oxidation process is about 95%, independent of the initial current density even when this exceeds 100 mA cm^{-2} . The blocking of β -LiAl by rapidly formed α -phase is likely to be more efficient at low temperature due to the decrease in the rate of diffusion. This fact may account for the decrease in cycling efficiency with decrease in temperature (Table III).

Conversion of the β -phase containing 47-56 a/o lithium to the α -phase containing up to 7 a/o lithium during oxidation of the active material of the electrode has additional significance with respect to cycling efficiency. Because of the low value of D_α , the lithium in the α -phase is not oxidized during the time scale of our experiments. The efficiency of the first cycle with respect to lithium at a fresh aluminum electrode may be estimated on the basis of the following argument. Assuming that the composition of the β -phase is 56 a/o Li, and that n_β mol of Li are deposited in m mol of Al on the surface of the electrode, then $n_\beta = 0.56m/0.44$. If the α -phase remaining on the surface after the oxidation step contains 7 a/o Li and n_α moles of Li are present in the same amount of Al, $n_\alpha = 0.07m/0.93$. It follows that the efficiency at the fresh electrode is $\eta_{Li} = 100 \cdot 100n_\beta/n_\alpha = 94\%$. In subsequent cycles, the efficiency rises according to the relationship

$$\eta_{Li} = 100 \left[1 - \left(\frac{7 \times 44}{93 \times 56} \right)^N \right] \quad [2]$$

where N is the number of cycles. Thus, one may account for the increase in efficiency observed with increase in number of cycles. However, η_{Li} should approach 100% according to Eq. [2]. This is not observed experimentally after long cycling.

Structural changes in the lithium-aluminum electrode during cycling.—According to the literature (6) and previous work in this laboratory (8), the main reason for the loss in efficiency of the lithium-aluminum system is cracking and disintegration of the electrode during cycling. Since the molar volume of the β -phase is 1.3 times greater than that of the α -phase, the aluminum lattice is destroyed when β -LiAl is formed, and particles of the β - and α -phases lose contact with one another. The development of cracks on the surface of the electrode with cycling was

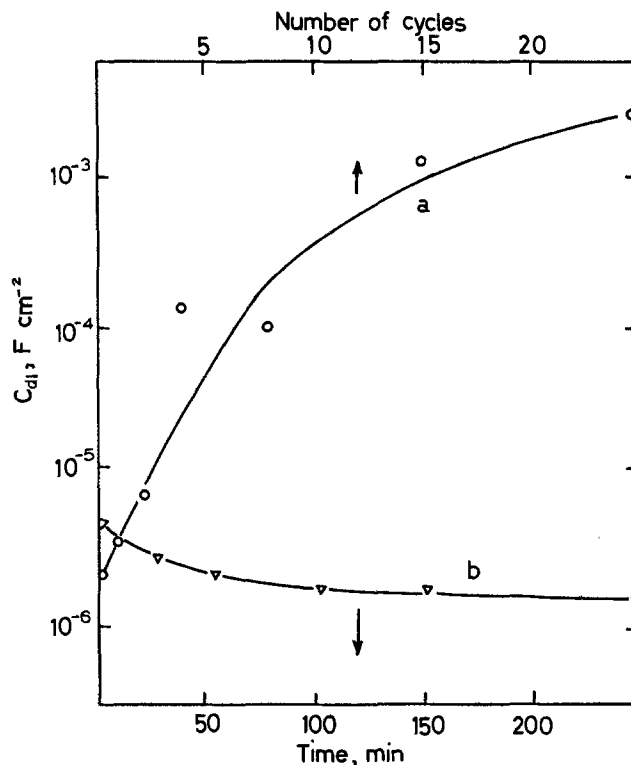


Fig. 5. Dependence of the specific double layer capacity at the lithium-aluminum electrode/solution interface on (a) the number of cycles and (b) time after lithium had been deposited. The electrolyte solution was 1 M LiAsF_6 in THF, the current density for cycling, 5 mA cm^{-2} , and the charge density due to deposited lithium, 3 C cm^{-2} . The specific capacity was estimated on the basis of the apparent electrode area.

clearly visible in electron micrographs. The disintegration process was studied at an aluminum electrode in a THF solution containing 1 M LiAsF_6 using the ac impedance technique. The electrode was charged and discharged with a lithium charge density of 3 C cm^{-2} at a current density of 2.5 mA cm^{-2} . After each charging cycle, the in-phase and out-of-phase components of the cell impedance were measured at various frequencies in the range 5-20,000 Hz. The double layer capacity C_{dl} was calculated as described previously (8) using the measured components of the impedance and solution resistance. This quantity calculated at 20 Hz is shown in Fig. 5 as a function of the number of cycles. A large increase in C_{dl} , almost by a factor of 1000, is apparent when the electrode is cycled 25 times. This is clearly connected with an increase in the active surface area of the electrode caused by cracking of the deposit. The change in C_{dl} with time for a free standing alloy electrode not involved in either the charging or discharging process is also shown in Fig. 5. The slight drop in C_{dl} over a period of several hours is probably due to an increase in the thickness of a passivation layer on the electrode.

The increase in the surface area of the electrode is also responsible for the appearance of new waves on the potential against time curves recorded during galvanostatic cycling. Curves for the first and fourteenth cycles at an alloy electrode are shown in Fig. 6. It is probable that the wave near +0.8V with respect to a Li/Li⁺ reference electrode is due to the process



The transition time associated with this wave is given by the equation

$$\tau_\alpha^{1/2} = \frac{\pi^{1/2} F A D_\alpha^{1/2} c_{\text{om}}}{2I} \quad [4]$$

where A is the true surface area of the electrode, and I the current. The change in electrode surface area estimated from Eq. [4] indicates that the area increased by a factor

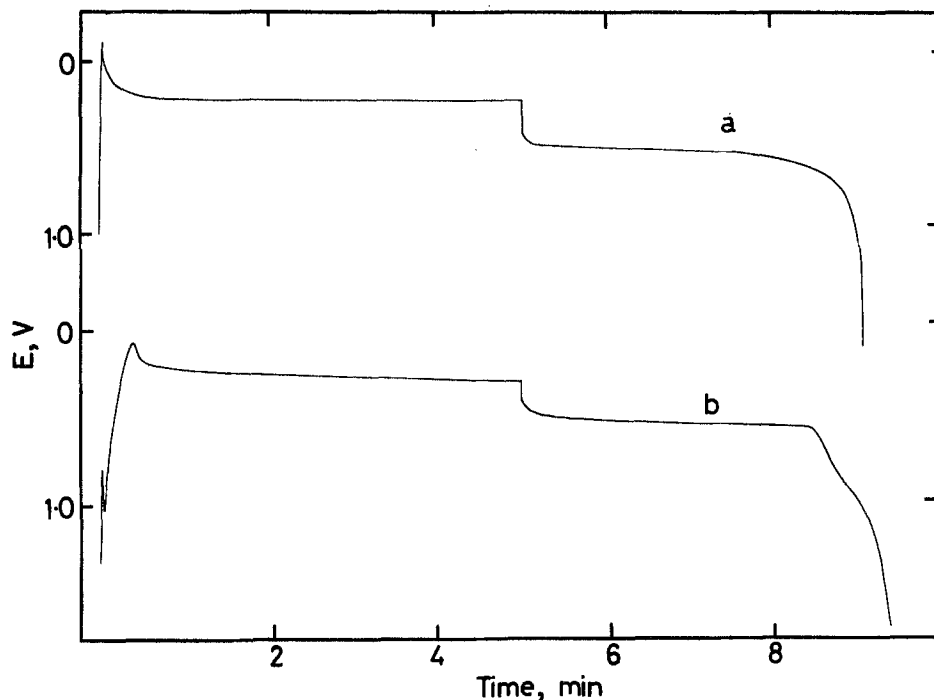


Fig. 6. Potential against time curves recorded galvanostatically during 5 min of reduction of Li^+ at a lithium-aluminum electrode and subsequent oxidation in THF solutions containing 1M LiAsF_6 . Curve a is for the first cycle, and curve b for the fourteenth.

of 10 after 12 cycles. This is much less than the area increase estimated on the basis of the double layer capacity (Fig. 5). However, one should keep in mind that the estimates of area changes based on C_{dl} or Eq. [4] are only qualitative, since the relationships used are not really applicable to very rough surfaces composed of particles with small grain size.

In another experiment, lithium was repeatedly transferred from one LiAl/Al electrode to another in a THF solution containing 1M LiAsF_6 . The initial amount of electrodeposited lithium corresponded to 5 C cm^{-2} and the apparent surface area was 20 cm^2 . Because the cycle efficiency is less than 100%, the active charge on the system decreased with the number of cycles, and, at the same time, a black powder fell off of the electrodes and accumulated on the bottom of the cell. When the charge dropped to 1% of its initial value, the experiment was stopped. The black deposit and the electrodes were separately dissolved in HCl, and the resulting solution analyzed

for Li^+ ion using atomic absorption spectroscopy. On the basis of three experiments, it was concluded that 20%-30% of the lithium lost during the cycling experiment remained on the electrodes in a nonactive form, presumably, as the α -phase, or as β - LiAl in particles which had lost electrical contact with the substrate. The remaining lithium was found in the black deposit.

It should be emphasized that the proposed mechanism in which β -phase particles are isolated from the electrode is different from the mechanism of lithium encapsulation proposed by Rauh and Brummer (9). The low efficiency observed with the lithium-aluminum electrode is a result of mechanical problems rather than chemical corrosion. It follows that the performance of the alloy electrode can be improved using mechanical methods.

Methods of improving the cycling efficiency of the alloy electrode.—On the basis of the above results, it was decided to attempt to improve the cycling efficiency of the

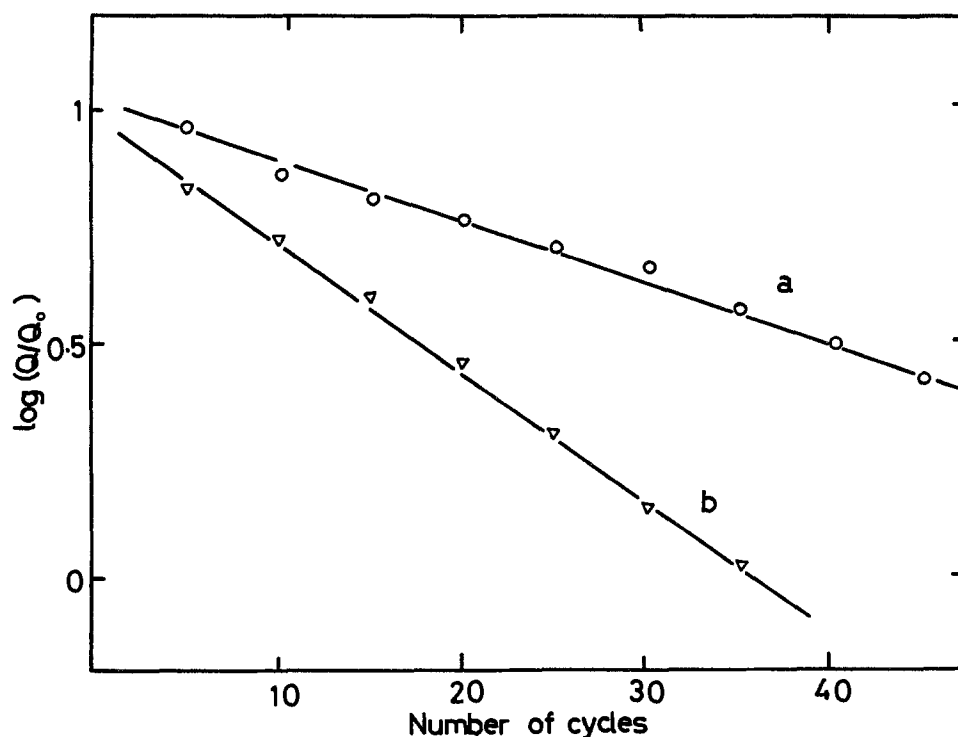


Fig. 7. The coverage of the alloy electrode with active lithium expressed as charge density Q against the number of cycles for (a) a LiAl/Al electrode pressed against a polypropylene separator soaked with a PC solution containing 1M LiAsF_6 , and (b) a free standing LiAl/Al electrode in the same electrolyte.

alloy system by pressing a separator against the electrode. By applying pressure, electrical contact between the grains should be improved and separation from the substrate prevented. In addition, since the LiAl deposit is not dendritic, shorting of the battery electrodes through the separator should not occur. To test the effect of pressure, two aluminum electrodes, one of which was covered with a known amount of alloy, were separated by two layers of polypropylene separator material (Kendall E-1452) soaked with a PC solution containing 1M LiAsF₆. The total system was compressed under a weight to achieve a pressure of 2.5 kg cm⁻². The active lithium was repeatedly cycled from one electrode to the other under galvanostatic conditions with a current of 1 mA cm⁻², and the charge associated with each cycle recorded. In a parallel experiment, the same initial amount of active lithium was cycled between two free standing electrodes in the same electrolyte. On the basis of the results presented in Fig. 7, it is clear that the performance of the system under pressure is much better than that for free standing electrodes; in the former case, the cycling efficiency over 40 cycles averaged 97%; in the latter, it averaged 94%. This aspect of the lithium-aluminum system certainly merits further investigation.

Conclusions

The results presented above demonstrate that the factors affecting rechargeability of the lithium-aluminum electrodes in nonaqueous media are different than those affecting the rechargeability of pure lithium. The cycling efficiency of the alloy electrode is much more determined by the properties of the alloy itself rather than by the properties of the electrolyte solution.

At the beginning of the cycling experiment, the charging efficiency of the LiAl/Al electrode is limited mostly by conversion of the β -phase into the less active α -phase either electrochemically in the oxidation cycle or as a result of reaction of the β -phase with the aluminum substrate. In addition, in the oxidation portion of the cycle, blocking of the β -phase by rapidly formed α -phase occurs, especially if large current or charge densities are involved. With increase in the number of cycles, these two effects become less important. However, due to the large difference in molar volumes between the β - and α -phases,

a process of disintegration of the electrode develops. The surface area of the alloy electrode increases, the deposit cracks and falls off the electrode, or remains on the electrode without electrical contact. Finally, the cycling efficiency can be significantly improved by pressing a separator against the electrode in order to prevent separation of the alloy phase and improve electrical contact between grains of the alloy phase.

Acknowledgment

This research was supported by the Department of National Defence, Ottawa, Canada, through Contract no. 05SU 47714-1-1054.

Manuscript submitted Nov. 7, 1983; revised manuscript received Feb. 23, 1984. This was Paper 540 presented at the San Francisco, California, Meeting of the Society, May 8-13, 1983.

The Department of National Defence, Ottawa assisted in meeting the publication costs of this article.

REFERENCES

1. J. O. Besenhard and G. Eichinger, *J. Electroanal. Chem.*, **68**, 1 (1976).
2. V. R. Koch, *J. Power Sources*, **6**, 357 (1981).
3. J. L. Goldman, R. M. Mank, J. H. Young, and V. R. Koch, *This Journal*, **127**, 1461 (1980).
4. V. R. Koch, J. L. Goldman, C. J. Mattos, and M. Mulvaney, *ibid.*, **129**, 1 (1982).
5. I. Epelboin, M. Froment, M. Garreau, J. Thevenin, and D. Warin, *ibid.*, **127**, 2100 (1980).
6. J. R. van Beck and P. J. Rommer, in "Power Sources 7," J. Thompson, Editor, p. 595, Academic Press, London (1979).
7. J. O. Besenhard, *J. Electroanal. Chem.*, **94**, 77 (1978).
8. A. S. Baranski and W. R. Fawcett, *This Journal*, **129**, 901 (1982).
9. R. D. Rauh and S. B. Brummer, *Electrochim. Acta*, **22**, 75 (1977).
10. E. Peled, *This Journal*, **126**, 2047 (1979).
11. H. E. Shone and W. D. Knight, *Acta Metall.*, **11**, 933 (1963).
12. V. R. Koch, *This Journal*, **126**, 181 (1979).
13. T. O. Brun, J. D. Jorgensen, M. Misawa, F. J. Rotella, and S. Susman, *ibid.*, **129**, 2509 (1982).
14. C. A. Melndres, S. Siegel, and J. Settle, *ibid.*, **125**, 1887 (1978).

Structural Changes of Positive Active Material in Lead-Acid Batteries in Deep-Discharge Cycling

T. G. Chang*

Cominco Limited, Product Research Centre, Sheridan Park, Mississauga, Ontario, Canada L5K 1B4

ABSTRACT

The positive active material of lead-acid cells under deep-discharge cycling conditions was studied. Morphological transformation and changes in surface area, density, pore-size distribution, and composition were recorded. The relationship of these parameters to discharge capacity and ultimate failure are discussed. It was found that pores can be classified in two categories, namely, macropores with diameters larger than 0.5 μm and micropores with smaller diameters. Macropores are responsible for mass transport to and from the reaction surface provided by the micropores. In order to sustain high capacity discharge performance, an optimum structure of active material must contain both kinds of pores appropriately distributed.

The utilization of the active material in the positive plates of lead-acid batteries is quite low, about 35% for traction and 50% for SLI batteries at 100% depth of discharge at the 5h rate.

In the course of our investigation (1) of positive active material made from various oxides, we found positive plates prepared from a finely divided oxide, Fume Lith-

arge (produced by NL Industries, Incorporated), gave a very high utilization of up to 65% at the 5h rate. However, this high utilization declined rapidly in the first ten deep-discharge cycles. After 24 cycles, the utilization was lowered to the level of active materials prepared from coarser oxides under similar conditions. A subsequent investigation was undertaken to identify and characterize the active material structures which contribute to high discharge capacity and the structural transformations which take place during deep-discharge cycling.

*Electrochemical Society Active Member.

Key words: electrode, charge, discharge, SEM.

The morphology of the active material in positive plates has been widely and quite intensively investigated (2-33). However, the failure of active material in deep cycling is not yet well understood. Simon *et al.* (12) found an association between the presence of a coralloid structure and active material failure. Although the advent of the coralloid structure was accompanied by a loss of capacity, they pointed out, on the basis of theoretical considerations, that the structure appeared ideal for a porous electrode. The structure has a dense PbO_2 core, which should provide strength and conductivity. The large voids in the convolutions should provide a free flow of electrolyte from the bulk to the reacting surface. Burrows and Giess (17) suggested that a decrease in surface area of the active material in cycling might be partly responsible for the loss of capacity. It was also suggested that failure of active material was associated with an increasing amount of amorphous lead dioxide (26) and "inactive" lead dioxide (34, 35). In this paper, we also explore the cause of active material failure.

Experimental

Lead oxides were made into pastes with the addition of water and sulfuric acid, and pasted on a $47 \times 75 \times 1.9$ mm book-mold grid (Pb-3%Sb alloy). The oxides were Fume Litharge (NL Industries, Incorporated), a finely divided orthorhombic lead monoxide, and Grenox (Canada Metal Company, Limited), a Barton pot leady oxide. The plates (3 mm thick) were cured at 40°C , formed in 1.05 sp gr H_2SO_4 for Fume Litharge plates (wet paste density 4.0 g/cm^3) and 1.10 sp gr H_2SO_4 for Grenox plates (wet paste density 4.4 g/cm^3). They were cycled in 600 ml beaker cells containing excess 1.25 sp gr H_2SO_4 at 30°C . Each cell contained a test (positive) plate with one counterelectrode on each side and a reference electrode capillary (connected to a room temperature reference electrode in a side compartment) within 1 mm of the test plate. No separator or other supports were used. The plates were discharged in successive cycles at 600, 900, 1200, 1200, 900, and 600 mA for the first through sixth cycles, respectively. This discharge pattern was repeated for subsequent cycles. The discharge was terminated when the potential of the test plate fell to 995 mV *vs.* $\text{Hg/Hg}_2\text{SO}_4$ (in 1.25 sp gr H_2SO_4). The plate was then charged at a constant potential of 1295 mV with a maximum current of 2A until the current fell to 150 mA, whereupon the plate was charged at this current until 115% of the ampere-hour capacity of the previous discharge was returned.

The surface area measurements were made by Micromeritics Instrument Corporation, Norcross, Georgia,

using the BET gas adsorption method. Pore volumes and pore-size distributions were determined by Micromeritics and by Quantachrome, Syosset, New York, using mercury porosimetry. The pore volumes and densities of active material were also determined in our laboratory using the water uptake and displacement method described by Fleischmann (36).

Specimens for optical or scanning electron microscopic examination were prepared by grinding and polishing samples impregnated with a polyester resin or by saturating the sample with water, which was then frozen, and microtomed. The second method has some advantage over the first: the sample preparation is much simpler and faster, and a much better view of the plate can be obtained where it is not obstructed by mounting material. This simple and convenient method to investigate active material in lead-acid batteries does not appear to have been used previously.

Results

The average discharge capacities for the positive plates prepared from the two oxides are presented in Fig. 1. In the first cycle, Fume Litharge plates gave a high utilization (over 60%) compared with Grenox plates (45%). However, the capacity of the Fume Litharge plates declined at a high rate, especially in the first ten cycles. After 24 cycles, it was on a level which was no longer extraordinarily high, considering the low density paste used in these plates. In contrast, plates prepared from Grenox did not have a high discharge capacity. The capacity only declined slightly in the first few cycles, and increased slowly to a maximum of 46% theoretical at the fiftieth cycle. The plates prepared from Fume Litharge failed at about the eighty-fifth cycle, whereas the plates from Grenox failed at about the one-hundred-fifth cycle.

Data for surface area, porosity, and density of the active materials are given in Table I. Some of the pore size distribution curves are presented in Fig. 2.

Morphological Changes in Cycling

Grenox was a rather coarse leady oxide which had a median particle size of about $4 \mu\text{m}$ diam, whereas the median size for Fume Litharge was about $1 \mu\text{m}$. After curing, all pastes were a mixture of residual oxide and tribasic lead sulfate ($3\text{PbO} \cdot \text{PbSO}_4 \cdot \text{H}_2\text{O}$) crystals. However, the tribasic crystals in Grenox plates had dimensions of about $0.5 \times 0.5 \times 2.5 \mu\text{m}$, whereas those in Fume Litharge plates were about $0.3 \times 0.3 \times 0.5 \mu\text{m}$.

As-formed active material.—In the surface layer of both types of formed plates (100-200 μm thick) the particles

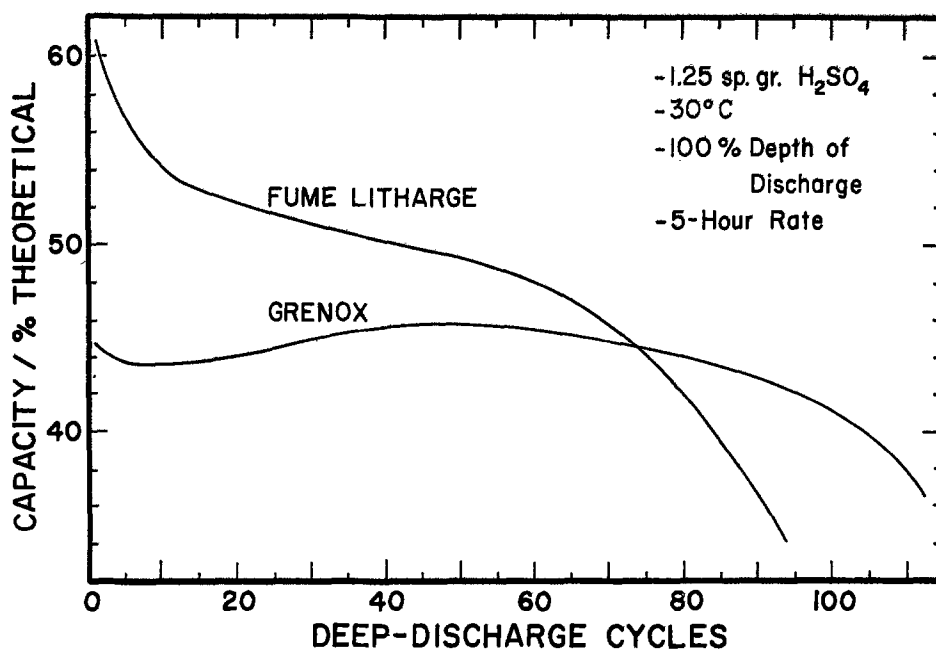


Fig. 1. Discharge capacities of positive plates prepared from Fume Litharge and Grenox in deep-discharge cycling.

Table I. Surface area, porosity, and density of the active material

Cycle no.	As-formed		1		12		24		50		102 (Failed)	126 (Failed)
	F	G	F	G	F	G	F	G	F	G	F	G
Surface area (m ² /g)	3.4	2.6	3.6	3.7	3.7	3.6	2.9	2.9	3.1	3.0	3.6	3.2
Pore volume (m ³ /g)	0.16	0.12	0.15	0.12	0.17	0.12	0.17	0.13	0.20	0.15	0.23	0.22
Porosity (%)	61	53	58	52	62	52	58	53	60	53	61	55
Apparent density (g/cm ³) (Water method)	3.73	4.29	3.69	4.29	3.67	4.20	3.56	4.01	3.22	3.62	—	—
Calculated true density (g/cm ³)												
Hg porosimeter	9.81	—	8.88	—	8.98	9.0	8.34	—	7.43	6.5	6.75	5.4
Water method	8.8	9.2	8.6	8.9	8.4	8.7	8.1	8.5	7.3	7.7	—	—

Note: F = Fume Litharge, G = Grenox.

were arranged in a whorl-like manner, as shown in Fig. 3. The same structure has been described by Simon and Caulder (11). This structure was also observed on the sides of cracks in the plates, but not elsewhere, suggesting that it was formed at locations which were heavily sulfated during soaking and forming. The active materials in the interior were very different, comparing plates prepared from the two oxides. The active material prepared from Grenox had mainly two types of particles: irregularly shaped ones formed from the residual oxide and cigar-shaped ones from tribasic sulfate crystals, as shown in Fig. 4. The interior active material prepared from Fume Litharge had a fine brain-coral structure, as shown in Fig. 5, in which lobes and branches had a diameter about 2-5 μm . The interlobar channels were very evenly distributed. The lobes were made up of submicron particles and were porous.

Active material after one cycle.—The structure of most of the active material was drastically changed by the first cycle. In the plates prepared from Grenox, the cigar-shaped particles were hollowed out; thus, a cellular network was formed, as shown in Fig. 6. The same process occurred in the plates prepared from Fume Litharge. The particles in the lobes were also hollowed out, and the material was redeposited over a larger volume. As shown in Fig. 7, the lobes and branches expanded and merged into one another. The interlobar channel nearly disappeared. The active material in the center of all plates, however, remained basically unchanged from their as-formed structure.

Active material after 12 cycles.—The surface layer containing the whorl-like structure had been completely transformed to a coralloid structure (12, 13) after 12 cycles. Under this surface layer, active material started to consolidate to form coralloid structure, which, in the initial stage (Fig. 8), had porous lobes with small interlobar channels of about 5-10 μm diam. In the center of the plate, 1/4 of the total thickness for Fume Litharge plates, and more than 1/3 of the total for Grenox plates, the fine-network structure predominated.

Active material after 24 cycles.—The active material in the surface layer had begun to disintegrate by 24 cycles.

Under it, the coralloid structure had spread inward. The active material at the center of the Fume Litharge plate entered the initial stage of coralloid structure development, characterized by porous lobes and small interlobar channels. The coralloid structure closest to the surface experienced a further consolidation: the lobes became much more densely packed, and the interlobar channels were enlarged to 10-20 μm diam, as shown in Fig. 9. In contrast, the coralloid structure in the Grenox plates was less well developed, and the network structure still dominated the center of the plates (about 1/3 of the total thickness).

Active material after 50 cycles.—The coralloid structure became completely established by 50 cycles, even in the center of Fume Litharge plates. Big pores with diameters larger than 25 μm were formed in the outer part of the plate (Fig. 10a). They had smooth walls and apparently were the result of the coalescence of smaller pores. The lobes associated with big pores were densely packed. In the center of the plate the coralloid structure was not in an advanced stage, *i.e.*, the lobes were still quite porous and interlobar channels were small. Big pores on the side of a grid wire facing the bulk electrolyte coalesced to form a gap of several hundred micrometers in length. The disintegration of the active material in this part was noticeable. Similar development, but to a lesser degree, also occurred in Grenox plates. In the center part, about 1/4-1/3 of the total thickness, the cellular-like network structure still dominated.

Active material cycled to failure.—The average cycle life of Fume Litharge plates was about 85 cycles, and that of Grenox plates about 110 cycles. The cross section of a failed Fume Litharge plate is presented in Fig. 10b. Big pores of diameters of up to 100 μm permeated the whole plate. The cross section of a failed Grenox plate was very similar to that of a Fume Litharge plate, showing no more of the network structure. Typical cross sections of coralloid structure in charged and discharged plates are shown in Fig. 11 and 12, respectively. In a discharged plate the lobes were surrounded by PbSO_4 crystals. Their cores appeared black under polarized light illumination, and the

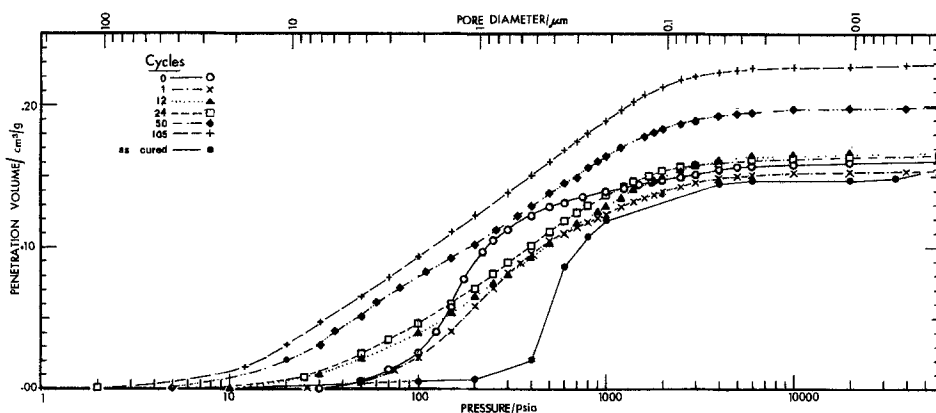


Fig. 2. Pore size distribution for active material prepared from Fume Litharge.



Fig. 3. Active material on the surface of an as-formed plate prepared from Fume Litharge.

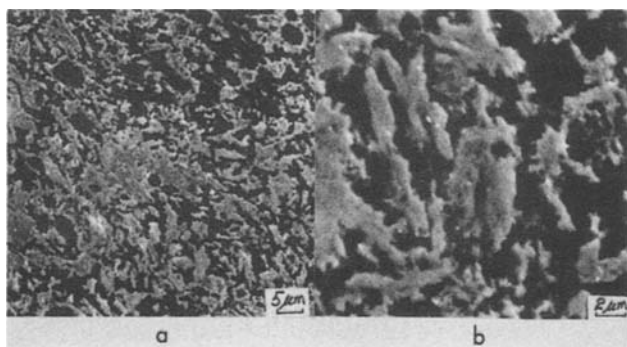


Fig. 4. As-formed active material prepared from Grenox

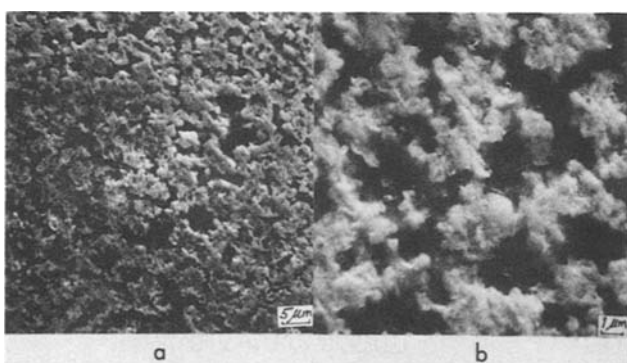


Fig. 5. As-formed active material prepared from Fume Litharge

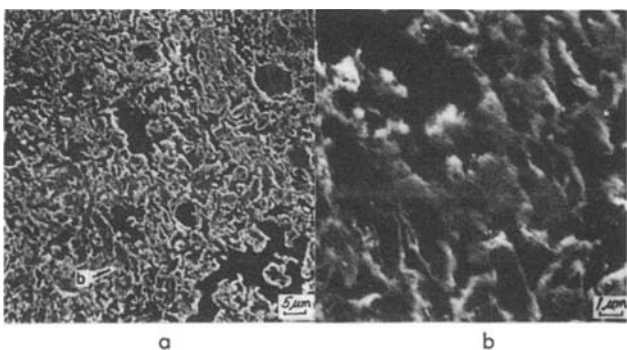


Fig. 6. One-cycle active material prepared from Grenox. b (right): Location as indicated by arrow in a (left).

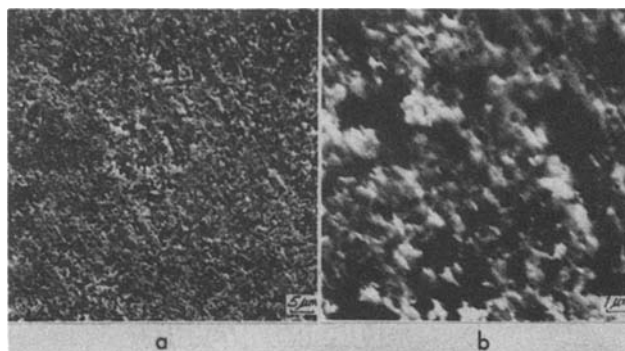


Fig. 7. One-cycle active material prepared from Fume Litharge

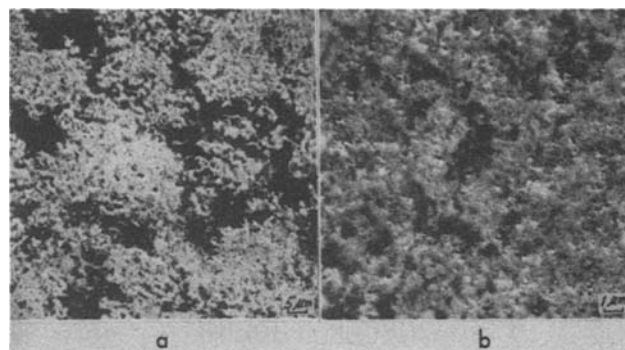


Fig. 8. 12-cycle active material prepared from Fume Litharge. b: core of a lobe.

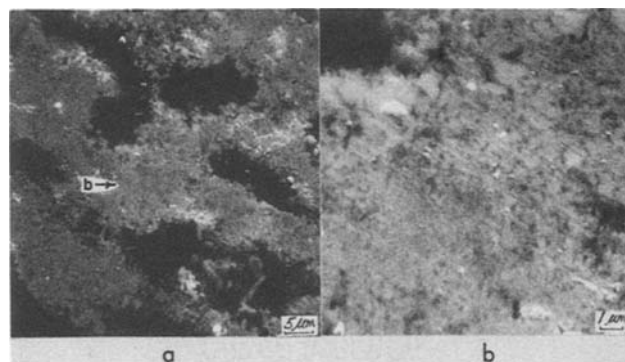


Fig. 9. 24-cycle active material prepared from Fume Litharge. b: core of a lobe, as indicated by the arrow in a.

x-ray diffractometric analysis showed that they were mainly β - PbO_2 with some PbSO_4 , i.e., the lobe interiors were not discharged. Figure 13 shows that little difference could be found between the active material inside a lobe of a discharged plate and that of a charged one. They all consisted of crystalline particles with dimensions of 0.2-0.5 μm .

As the coralloid structure became established at the core of the plate and large pores formed and grew, a dendritic growth was observed adjacent to the corrosion layer around the grid wire, as shown in Fig. 14. In a failed plate, the thickness of this dendritic layer could be as large as 100 μm . X-ray diffractometric analysis determined the dendrites to be β - PbO_2 in a charged plate and PbSO_4 in a discharged plate.

Discussion

Active material transformation.—The pore-size distribution curve for the as-formed active material retained the as-cured shape, but was displaced toward larger diameters, as shown in Fig. 2. This indicates that the structure in the cured plate was essentially unchanged by formation, as confirmed by the morphological study. The external forms of the basic lead sulfate crystals in the cured

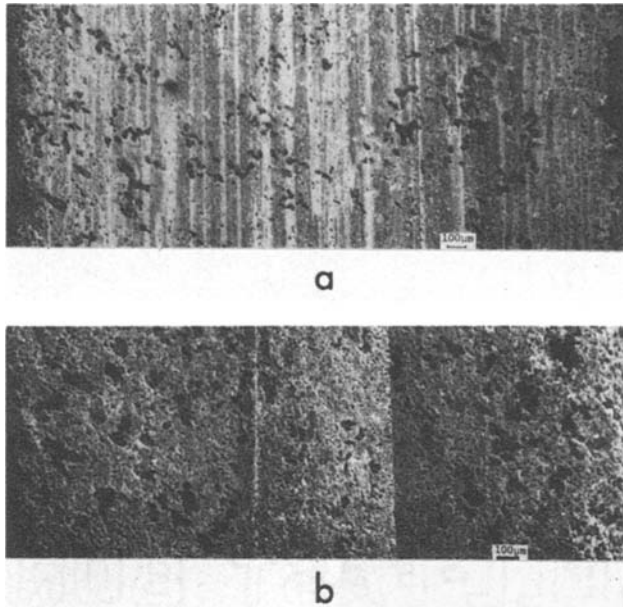


Fig. 10. Microtomed cross section of plates prepared from Fume Litharge. a: 50 cycles. b: 104 cycles (failed).

plate were preserved after their conversion to PbO_2 (shown in Fig. 4 and 5), in agreement with previous findings (2, 6, 12). Thus, uniformly sized fine particles in the cured plate prepared from finely divided Fume Litharge result in the fine brain-coral structure of the formed plate. In subsequent cycling, particles are hollowed out, leaving a cell-like form. Like the interlocking columnar basic sulfate crystals, these interconnected cells form a three-dimensional network. Further cycling consolidates the active material into a coralloid structure. Initially, the lobes and branches are porous, and the interlobar channels small. With further cycling, the lobes and branches

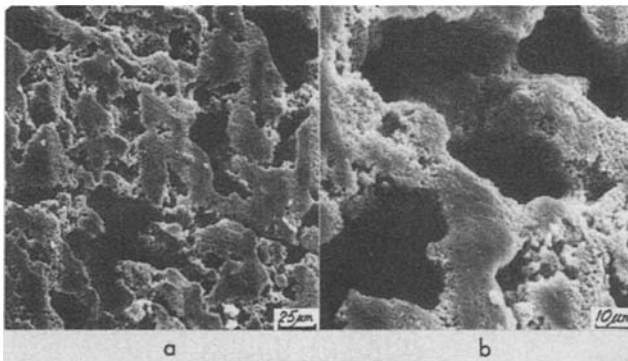


Fig. 11. Microtomed cross section of active material of a charged failed plate (121 cycles).

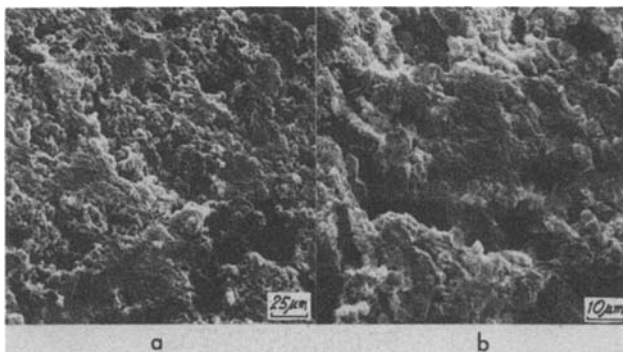


Fig. 12. Microtomed cross section of a discharged failed plate (92 cycles).

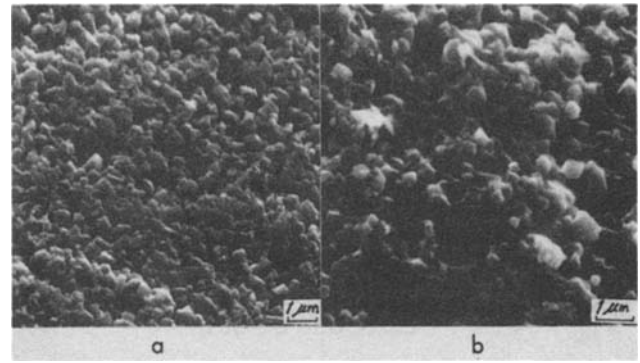


Fig. 13. Active material inside a lobe in a failed plate. a: charged. b: discharged.

become more densely packed and the pores grow to a diameter of 5-20 μm . More cycling brings about the coalescence of these pores to form pores with diameters as large as 100 μm . With the formation of large pores, the active material begins to disintegrate. When the large pores permeate the core, the plate fails.

The morphological changes do not occur uniformly throughout the plate. There is always a gradient in structure. During the initial period of cycling, the active material closer to the surface is discharged deeply, while that further inside the plate is less utilized. However, on further cycling, the active material in the outer part consolidates into the coralloid structure with large densely packed lobes and big interlobar pores, and its utilization decreases. This process does, however, open up the structure in the outer part, making the active material deeper inside the plate more accessible to the electrolyte and thereby increasing its utilization. This process continues until the active material in the core is transformed to the coralloid structure. From then on, the capacity of the plate must decrease with cycling, as there is no further reserve of high capacity active material to replace that with decreasing utilization.

Gas generation and the coralloid structure.—In 1971, Simon and Caulder (11) advanced a hypothesis that the formation of the coralloid structure was caused by the physical effect of gas generation within the structure during charging periods. Later, in 1975, they (12) modified this hypothesis, suggesting that the coralloid structure was not the result of gas action.

Our observations suggest that gas action is a major factor governing the development of the coralloid structure. With or without gas action, active material is bound to



Fig. 14. The dendritic growth around a grid wire in a plate being cycled to failure.

consolidate under deep-discharge cycling. In the initial consolidation stage, there is little contribution from gas action. Once the framework has formed, gas action becomes more important. During the charging period, especially towards its end, a large quantity of oxygen is generated, both on and inside the plate. To escape to the plate surface, the oxygen bubbles would follow the larger pores with the least resistance, and the escaping bubbles, which exert considerable pressure on the pore walls, would break off and carry out loosened particles. This may explain why the walls of bigger pores are so smooth. Furthermore, at high potential and low pH, PbO_2 may dissolve in the solution to form tetravalent ions (37, 38). The dissolved Pb^{4+} ions may be transported out of the plate and reprecipitate as a very fine PbO_2 .

Some existing walls between channels are broken down as the result of the bubble action. This is clearly shown by the microscopy. As the coralloid structure develops, pores coalesce forming bigger pores with smooth walls. As bigger pores, with dimensions larger than 50 μm , become more numerous and larger, the structure is evidently weakened, and disintegration is the final result. The gaps between the grid members and the active material, observed after prolonged cycling, may also be due to gas action.

It is generally known that by placing pressure on a plate, the cycle life of the plate is extended. Ando *et al.* (39) put a pressure of 40 kg/dm^2 on their plates with active material of low apparent density and achieved a lifetime of 1000 cycles (75% DOD at 5h rate). It is possible that pressure on the active material impedes the formation and growth of the large pores caused by gas action and thereby delays deterioration of the active material.

In summary, although gas generation does not initially create the coralloid structure, it plays an important role in its evolution and, finally, its destruction.

Density of active materials.—Dittman and Sams (40) found the apparent density of positive active material always decreases during service, especially if it is subjected to deep-discharge cycling. Fleischmann (36), using the water uptake and displacement method, found that the solid portion of a fully charged positive active material had a "true" density of $7.8 \pm 0.6 \text{ g}/\text{cm}^3$. By using gas pycnometry, he got a higher value, $8.5 \pm 0.4 \text{ g}/\text{cm}^3$. Micka *et al.* (41) measured the active material density in cycled positive plates pycnometrically in toluene, and obtained a mean value of $8.65 \text{ g}/\text{cm}^3$. Since these values are less than that for PbO_2 of $9.37 \text{ g}/\text{cm}^3$ (42), they postulated the existence of amorphous lead dioxide. More recently, Constable *et al.* (26), employing x-ray diffractometry, claimed to have found an increase in amorphous material after cycling and they suggested that this amorphous lead dioxide was electrochemically inactive.

In this work, using the water method, we also found that the active material expanded with cycling. The apparent density decreased with cycling (Table I), as the pore volume increased. The calculated true density also declined with cycling. For Grenox plates this density was $9.2 \text{ g}/\text{cm}^3$ in the as-formed plate and decreased to about $7.7 \text{ g}/\text{cm}^3$ after 50 cycles. The corresponding values for Fume Litharge plates were 8.8 and $7.3 \text{ g}/\text{cm}^3$. The data obtained by mercury porosimetry (Table I) were in very good agreement with those from the water method. The density of the active material from the failed Grenox plate was $5.4 \text{ g}/\text{cm}^3$ (126 cycles) and that with Fume Litharge $6.8 \text{ g}/\text{cm}^3$ (102 cycles). These data cannot be accounted for by the PbSO_4 content. Even in failed plates, the PbO_2 content determined titrimetrically was 92%-95%. Microscopy, both optical and electron, had also failed to reveal any appreciable amount of PbSO_4 crystals, which are usually easy to detect.

The existence of amorphous PbO_2 , the density of which is very low, and the hypothesis that the amount of this amorphous phase increases with cycling are not supported by microscopy or x-ray diffractometry. SEM microscopy showed that at the beginning of the cycling test

the crystal size was not uniform. The outlines of a large amount of the primary particles could not be clearly defined (at up to 10,000 \times magnification). As the cycling progressed, the crystal sizes became larger and more uniform. In the failed plates, the crystals were clearly seen to be polyhedral and had a diameter ranging from 0.2 to 0.5 μm (Fig. 13). X-ray diffractometry showed that the lines for α - and β - PbO_2 in the as-formed plates were broad, indicating small crystal size and/or crystals with defective structure, *i.e.*, lattice distortions. As the cycling proceeded, the α - PbO_2 / β - PbO_2 ratio became smaller, and the lines for both of them narrower, indicating higher crystallinity and/or larger crystal size. This was consistent with the evidence provided by the microscopy.

The evidence from x-ray diffractometry and other measurements suggests that the amount of amorphous PbO_2 (or crystals with lattice distortions) also decreases with cycling and may practically disappear within 24 cycles. Meanwhile, the coralloid structure is forming and developing with cycling. Within the lobes and branches of this structure, the pores become smaller, and the tortuosity factor larger. Consequently, it becomes difficult for mercury (at less than 60,000 psi, *i.e.*, $4.14 \times 10^6 \text{ kPa}$) and water (1 atm, *i.e.*, 101 kPa) to fill up all the micropores. Therefore, the measured density of the active material gradually decreases with cycling. The gas is able to penetrate all the pores, no matter how small they are. Therefore, the values obtained by gas pycnometry are higher than those obtained by mercury and water methods. In addition, there may be noncommunicating pores in the active material, which will lower the measured density.

Cause of failure of positive active material.—The loss of active material through sludging has been suggested as the reason for loss of capacity. Ikari and Yoshizawa (43) have shown that the loss of capacity exactly parallels the loss of active material due to sludging. The microscopy done in this investigation revealed that, in the first couple of cycles, the active material in the center of the plate, which constituted nearly 1/3 of the total, did not take part in the cycling. In later cycles, active material in this part did participate, as the outlying active material consolidated and opened up the plate. This did not increase the plate capacity, because unfavorable structural changes took place in the outlying active material and lowered its dischargeability. This means that the loss of at least 1/4 of the amount of active material (under the experimental conditions) should not have caused a loss in capacity, although the two may have occurred in parallel because of the structural degradation.

It has also been assumed that the loss of capacity is related to a decrease in total surface area due to consolidation of active material in cycling (17). This explanation of capacity loss is not borne out by our experimental data. The as-formed Grenox plate had a surface area of $2.6 \text{ m}^2/\text{g}$. After one cycle, the surface area increased markedly, to $3.7 \text{ m}^2/\text{g}$. Correspondingly, the capacity did not increase; actually, it decreased. In the 24-cycle plate, the surface area was found to be $2.9 \text{ m}^2/\text{g}$, but the capacity at that cycle was higher than in the previous cycles. The surface area remained at $3.0 \text{ m}^2/\text{g}$ for the rest of the cycling. Even plate failure did not reduce the surface area. Similarly, with Fume Litharge plates, there appeared to be no simple correlation between surface area and discharge capacity. The results from this work suggest that not only is a large surface area needed for the discharge process, but an appropriate surface area distribution is also necessary.

After all the active material has been transformed into the coralloid structure, the capacity declines at a higher rate. The enlargement of the pores on further cycling promotes electrolyte communication between the bulk and the lobe surfaces and the enlarged pores themselves are able to store more electrolyte. This, however, creates an optimum condition for deposits of PbSO_4 at the opening of the micropores. In a discharge, the sulfate ions in a micropore are quickly consumed, and the acidity in the pore is lowered, which in turn increases the solubility of

PbSO₄ and produces a higher Pb²⁺ concentration in the micropore. However, outside of the micropore, the acid concentration is still high, owing to the large diameters of the interlobar channels. This results in a fast deposition of PbSO₄ at the pore openings (44, 45) and consequent blocking of the pores. An alternative hypothesis is that advanced by Winsel *et al.* (46), who proposed that if the pores are very small, the reaction product PbSO₄ will fill the pores completely, thus limiting the discharge capacity. This is in accordance with our microscopic observation that in a discharged plate, on the walls of pores with a diameter larger than 50 μm, fewer and smaller PbSO₄ crystals were present. Furthermore, in a discharged plate, there were lobes and branches surrounded by light colored PbSO₄ crystals, but the cores still remained unconverted PbO₂. All the above appears to support the hypothesis that the loss of capacity is caused by the formation and development of the coralloid structure. The plates prepared from Fume Litharge had a higher initial capacity than those from Grenox. However, coralloid structure formed and developed in the former at a much higher rate, which caused a higher rate of capacity loss and a shorter cycle life.

Recently, some researchers have found that when plates were cycled towards failure, there was a buildup of PbSO₄ crystals around the grid member. This was found in plates of Pb-Sb grids (33, 47) and in nonantimonial grids (48-50). As discussed previously, we have observed the same buildup. The evidence obtained from our investigation suggests that the buildup of PbSO₄ crystals may be the result of the development of the coralloid structure. At the beginning of cycling, the active material is evenly distributed, and the pores are small. The active material at the center of the plate does not participate in the charge-discharge process. As the cycling proceeds, the coralloid structure forms and spreads inward. As the coralloid structure ages, the active material in it becomes less available for discharge. At the same time, the structure becomes more open due to enlarged interlobar channels, making the electrolyte much more available to the active material in the inner part of the plate, which includes the active material and the corrosion product around the grid members. Thus, towards the end of a plate's cycle life, the corrosion product around a grid member and the active material around it are subjected to a discharge of increasing depth. This is indicated by the growth of dendrites around the grid members. These rings of dendrites are fully converted to PbSO₄ crystals in the discharge period. In the process, the resistance around the grid members increases and finally insulates them from the active material. This, of course, lowers the utilization of the more distant active material. The appearance of the rings of dendrites foretold, and might also have contributed to, the final failure of the plate, but it should be emphasized that they were the result of the deterioration of the active material and, therefore, not the primary cause of failure.

Optimal active material structure for high discharge capacity.—It has been shown in the previous discussion that the unusually high discharge capacity of plates prepared from Fume Litharge disappeared with the disappearance of the fine brain-coral structures in cycling. The transformation of this structure began in the active material close to the plate surface and then advanced inward with cycling. After about ten cycles, this kind of structure was eliminated from the plate and a 10% capacity loss was recorded. There was no decrease in apparent density or in surface area accompanying the decrease in capacity (Table I). Therefore, the reasons for the capacity drop must be found in the structural changes.

The pores in the fine brain-coral structure in the as-formed plate can be divided into two classes: macropores and micropores. Macropores have a diameter larger than 0.5 μm and are essential for mass transport from the plate surface to the interior of the plate. Micropores are pores with diameters smaller than 0.5 μm; most were actually

much smaller. Although the volume of the micropores is only a fraction of the total void volume, the surface area contributed by them is larger than 90% of the total.

When mass transport is not the limiting factor, discharge capacity is proportional to the second power of the internal surface of the active material (46). As the surface area in the micropores accounts for almost all the total surface area of the active material, the mass transfer to and from them is critical in maintaining the discharge process.

If we assume that the depth of discharge is 60% of the theoretical value, the volume increase due to the conversion of PbO₂ to PbSO₄ is 0.120 cm³ per gram of active material. If this were spread evenly over the surface, it would be 0.0165 μm in thickness and the diameter of the pores would decrease by 0.033 μm. This rough calculation shows that, in order to keep the mass-transport channels open, the macropores which are responsible for it should have a minimum diameter of about 0.05 μm. Smaller pores would be plugged or filled during discharge, and, consequently, the mass transport through them would cease. The discharge of a plate usually starts in the active material closer to the plate surface and proceeds inward. Generally, the active material in the outer part of the plate is discharged to a greater depth than that in the interior. Thus, to make the active material in the interior accessible to the electrolyte, the pores responsible for mass transport must have a diameter much larger than 0.05 μm: perhaps, about 0.5 μm.

In the as-formed active material, the volume of the macropores, with diameters ranging from 0.5 to 2.0 μm, was 0.10 cm³ per gram of active material. After one cycle, this dropped to 0.077 cm³/g, a 23% decrease, equivalent to a 23% decrease in the number of macropores. After 12 cycles, the fine brain-coral structure had disappeared, and the volume of the macropores with diameters ranging from 0.5 to 2.0 μm had shrunk to 0.056 cm³/g, a 44% decrease. Although there was some (0.03 cm³) increase in pores with diameters larger than 3 μm, the length of the additional bigger macropores was less than 1% that of the smaller macropores they replaced.

In the first few cycles, the major change is the transformation of the fine brain-coral structure to a fine network structure with much fewer macropores. The loss of capacity may be mainly due to the increased hindrance in mass transport from the plate surface to the active material inside. After about eight cycles, the coralloid structure started to form, and pores with diameters larger than 5 μm became more numerous. As the big pores increased in number, the mass transport between the bulk electrolyte and the active material in the core was expedited such that it was no longer a capacity limiting factor. However, as the total length of the macropores was reduced, the distance between the active material in the micropores and a macropore became longer. As their diameters were so small, the micropores could be easily plugged and filled by the discharge product PbSO₄. Therefore, later in cycling, the mass transport between macropores and the active surface in the micropores became a capacity limiting step. This is clearly illustrated by the micrographs of the as-formed active material (Fig. 5) and that of a 24-cycle plate (Fig. 9). The longest distance between any PbO₂ in the as-formed plate to the nearest macropore was about 2 μm; the corresponding distance in the 24-cycle plate was about 10 μm.

In summary, not only are pore volume and surface area important in obtaining a high discharge capacity, but pore-size distribution is of equal importance. If the former two are constant, the latter becomes the determining factor. The unusually high initial capacity of the Fume Litharge plate came from the optimal pore-size distribution. There were adequate amounts of macropores for mass transport, which would not be plugged or filled by the discharge product during discharge. Besides facilitating the communication between bulk electrolyte and the inner parts of the plate and enhancing the utilization of the active material which resided deeper in the plate, a

larger number of macropores also shortens the length of individual micropores, promoting higher utilization for the active material around the micropores.

There are two necessary conditions for obtaining a very high utilization. First, there should be a sufficient amount of micropores to provide an adequate amount of specific surface area, e.g., 3.5 m²/g, for electrochemical reactions. Secondly, the length of each micropore should be sufficiently short. In other words, there should be an adequate number of macropores per unit volume of active material to furnish an unimpeded mass transport between the bulk electrolyte and the reacting surface. Therefore, using a coarser oxide than Fume Litharge, higher utilization can also be obtained. To achieve that, a low density paste (lower than 4 g/cm³) should be prepared to provide an adequate amount of macropores. Due to the larger particle size of the oxide, the specific area might still be too low after formation, i.e., the amount of micropores may still be too small. Therefore, the utilization in the first cycle could still be low. However, the following recharge will open up the structure, generating a cellular-like network structure with a much larger micropore density, and, hence, a much larger surface area. Therefore, in the subsequent cycles, the utilization should be high (about 60% theoretical at the 5h rate). This achievement would be lost, however, in the ensuing cycles as the coralloid structure forms and develops. This hypothesis has actually been demonstrated in this laboratory.

Acknowledgments

The technical assistance of N. A. Haneke, W. W. Gregory, and K. Cowan is gratefully acknowledged. Discussions with E. M. L. Valeriotte and J. A. Brown were very helpful to the author. The editorial assistance of E. M. L. Valeriotte is also gratefully recognized.

Manuscript submitted Dec. 27, 1983; revised manuscript received Jan. 5, 1984. This was Paper 79 presented at the Washington, DC, Meeting of the Society, Oct. 9-14, 1983.

Cominco, Limited assisted in meeting the publication costs of this article.

REFERENCES

1. T. G. Chang, "Evaluation of Battery Oxides," ILZRO Project LE-272, Progress Report no. 6, International Lead Zinc Research Organization, Inc., New York (1979).
2. J. R. Pierson, *Electrochem. Technol.*, **5**, 323 (1967).
3. G. Sterr, *Electrochim. Acta*, **15**, 1221 (1970).
4. N. E. Bagshaw and K. P. Wilson, *ibid.*, **10**, 867 (1965).
5. J. Burbank, *This Journal*, **111**, 765 (1964).
6. J. Burbank, *ibid.*, **113**, 10 (1966).
7. J. Burbank, NRL Report 7256, Washington, DC (1971).
8. J. Burbank, and E. J. Ritchie, *This Journal*, **116**, 125 (1969).
9. A. C. Simon and E. L. Jones, *ibid.*, **109**, 760 (1962).
10. A. C. Simon, C. P. Wales, and S. M. Caulder, *ibid.*, **117**, 987 (1970).
11. A. C. Simon and S. M. Caulder, *ibid.*, **118**, 659 (1971).
12. A. C. Simon, S. M. Caulder, and J. T. Stemmler, *ibid.*, **122**, 461 (1975).
13. A. C. Simon and S. M. Caulder, in "Power Sources 5," D. H. Collins, Editor, p. 109, Academic Press, London (1975).
14. C. P. Wales and A. C. Simon, *This Journal*, **128**, 2512 (1981).
15. J. L. Dawson, M. E. Rana, B. Munasiri, and J. McWhinnie, in "Power Sources 7," J. Thompson, Editor, p. 1, Academic Press, London (1979).
16. W. O. Butler, C. J. Venuto, and D. V. Wisler, *This Journal*, **117**, 1339 (1970).
17. B. Burrows and H. Giess, *ibid.*, **122**, 1640 (1975).
18. J. Perkins and M. T. Coyle, *ibid.*, **124**, 524 (1977).
19. K. Wiesener, W. Hoffmann, and O. Rademacher, *Electrochim. Acta*, **18**, 913 (1973).
20. K. Wiesener and P. Reinhardt, *Z. Phys. Chem.*, **256**, 285 (1975).
21. P. Reinhardt and K. Wiesener, *ibid.*, **257**, 193 (1976).
22. P. Reinhardt and K. Wiesener, *ibid.*, **257**, 412 (1976).
23. P. Reinhardt, M. Vogt, and K. Wiesener, *J. Power Sources*, **1**, 127 (1976/1977).
24. D. Barrett, M. T. Frost, J. A. Hamilton, K. Harris, I. R. Harrowfield, J. F. Moresby, and D. A. J. Rand, ILZRO Project LE-290 Report (June 1980).
25. M. T. Frost, J. A. Hamilton, K. Harris, I. R. Harrowfield, R. J. Hill, J. F. Moresby, and D. A. J. Rand, ILZRO Project LE-290 Progress Report no. 3 (1980).
26. D. C. Constable, J. R. Gardner, J. A. Hamilton, J. Harris, R. J. Hill, D. A. J. Rand, S. S. Wan, and L. B. Zalman, ILZRO Project LE-290 Progress Report no. 6 (1982).
27. D. Barrett, M. T. Frost, J. A. Hamilton, J. Harris, I. R. Harrowfield, J. F. Moresby, and D. A. J. Rand, *J. Electroanal. Chem.*, **118**, 131 (1981).
28. S. Hattori, M. Yamaura, M. Kono, M. Yamane, H. Nakashima, and J. Yamashita, ILZRO Project LE-197 Report (June 20, 1975).
29. S. Hattori, M. Yamaura, M. Kono, M. Yamane, H. Nakashima, and J. Yamashita, ILZRO Project LE-197 Report (Sept. 20, 1975).
30. S. Hattori, M. Yamaura, M. Kono, M. Yamane, H. Nakashima, and J. Yamashita, ILZRO Project LE-197 Report (Aug. 20, 1976).
31. S. Hattori, M. Yamane, and H. Nakashima, *Denki Kagaku*, **43**, 393 (1975).
32. S. Hattori, M. Yamaura, M. Kono, Y. Ohtani, M. Yamane, and H. Nakashima, in "Power Sources 5," D. H. Collins, Editor, p. 139, Academic Press, London (1975).
33. J. Perkins, *Mater. Sci. Eng.*, **28**, 167 (1977).
34. S. M. Caulder, J. S. Murday, and A. C. Simon, *This Journal*, **120**, 1515 (1973).
35. S. M. Caulder and A. C. Simon, *ibid.*, **121**, 1546 (1974).
36. C. W. Fleischmann, *ibid.*, **127**, 664 (1980).
37. P. Delahay, M. Pourbaix, and P. Van Rysselberghe, *ibid.*, **98**, 57 (1951).
38. P. C. Foller and C. W. Tobias, *ibid.*, **129**, 567 (1982).
39. K. Ando, K. Yonezu, M. Tsubota, K. Takahashi, and K. Nishida, Paper 7 presented at The Electrochemical Society Meeting, Detroit, MI, October 17-21, 1982.
40. J. F. Dittmann and J. F. Sams, *This Journal*, **105**, 553 (1958).
41. K. Micka, M. Svata, and V. Koudelka, *J. Power Sources*, **4**, 43 (1979).
42. Indian Lead Zinc Information Centre, "Lead-Acid Batteries, a Reference and Data Book," p. 39, Elsevier Sequoia S.A., Lausanne, Switzerland (1977).
43. S. Ikari and S. Yoshizawa, *J. Electrochem. Soc. Jpn.*, **27**, 613 (1959).
44. K. J. Vetter, *Chem.-Ing.-Tech.*, **45**, 213 (1973).
45. D. Pavlov, *Electrochim. Acta*, **13**, 2051 (1968).
46. A. Winsel, U. Hullmeine, and E. Voss, *J. Power Sources*, **2**, 369 (1977/1978).
47. K. Harris, R. J. Hill and D. A. J. Rand, *ibid.*, **8**, 175 (1982).
48. W. Kappus and A. Winsel, *ibid.*, **8**, 159 (1982).
49. I. K. Gibson, K. Peters, and F. Wilson in "Power Sources 8," J. Thompson, Editor, p. 565, Academic Press, London (1981).
50. S. Hattori, M. Yamaura, M. Kono, M. Yamane, H. Nakashima, and J. Yamashita, ILZRO Project LE-276, Progress Report no. 2 (1978).

Preparation and Open-Circuit Potentials of Silver-Intercalated 2H-TaS₂ and 1T-TiS₂

G. A. Scholz and R. F. Frindt

Physics Department, Simon Fraser University, Burnaby, British Columbia, Canada V5A 1S6

ABSTRACT

If 2H-TaS₂ or 1T-TiS₂ crystals are placed into an aqueous AgNO₃ electrolyte, a spontaneous intercalation/corrosion reaction of the host dichalcogenide is observed. The intercalation/corrosion reaction can be greatly reduced, or even eliminated, by using a dilute electrolyte or, even better, an organic solvent. The EMF of the Ag_xTaS₂/Ag⁺(glycerol)/Ag and Ag_xTiS₂/Ag⁺(glycerol)/Ag electrochemical cells are reported as a function of *x*, and the features observed are shown to correspond to the structural changes induced in the host lattice by the intercalating silver ions.

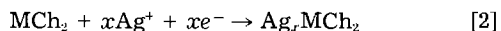
In a recent series of papers (1-7), we have reported some of the physical, structural, electronic, and optical properties observed in the Ag_xTaS₂ and Ag_xTiS₂ intercalation compounds. In this publication, we describe in detail their method of preparation and the EMF dependence of Ag_xTaS₂/Ag and Ag_xTiS₂/Ag electrochemical cells on the intercalated silver concentration.

Sample Preparation

Intercalation compounds can be prepared via thermal, electrochemical, or chemical methods. The Ag_xTaS₂ and Ag_xTiS₂ compounds have been prepared using all of these methods, depending on whichever method was more appropriate to the given experimental situation. X-ray diffraction studies (1) revealed no structural differences in the samples using the above methods of preparation.

Thermally, the intercalated dichalcogenides were prepared in a standard way (8) by placing the appropriate amounts of prereacted 2H-TaS₂ or 1T-TiS₂ and silver powders, including about 1 mg/cm³ of iodine to facilitate crystal growth, in one end of a well cleaned and evacuated 750 cm³ quartz transport tube. The tube was heated in a three zone furnace to about 1050 K, with a gradient of about 50 K in the central zone, for approximately 100h. Before removing the transport tube from the oven, it was first cooled slowly (about one day) to near 400 K. It was found that the intercalation process was severely impeded if traces of water vapor were present, and particular care in this regard was exercised. Thermally prepared Ag_xTaS₂ and Ag_xTiS₂ samples have the advantage of being homogeneously intercalated with a minimum of multiple phases.

The electrochemical intercalation cell is quite straightforward and consists of a silver anode in conjunction with either a 2H-TaS₂ or 1T-TiS₂ crystal (MCh₂) as the cathode. By completing the external circuit the anodic and cathodic half-cells



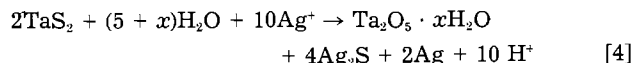
are able to proceed to give the desired net reaction



Since the EMF of the Ag/TaS₂ and Ag/TiS₂ cells is about +0.2 and +0.1V, respectively, if measured with respect to the silver anode (Ag/Ag⁺ ~ -0.8V), it implies that the intercalation half-cell (Eq. [2]) must have an EMF of about +1.0 and +0.9V, respectively. The increase in the negative free energy, which enables the intercalation reaction (Eq. [3]) to proceed spontaneously, is therefore provided by the intercalation of the silver ions into the host dichalcogenide (Eq. [2]). This is in marked contrast to other intercalation systems, such as Li/TiS₂, where it is the ionization of the lithium anode that provides the driving force for the intercalation reaction to proceed.

Uniform intercalation of the silver ions is an area of concern when the dichalcogenides are electrochemically intercalated and the use of small crystallites is a neces-

sity. It was found that crystallites up to a few millimeters in diameter and about 100 μm in thickness appear to intercalate quite well. Whereas the choice of salt used for the electrolyte fell naturally on AgNO₃, since it is one of the few soluble silver salts readily available, the solvent needs to be chosen with some care. The reason is that 2H-TaS₂ and 1T-TiS₂ will spontaneously intercalate silver by chemically reacting with the electrolyte if the solvent is aqueous. The vigor of the reaction is much more pronounced for 2H-TaS₂ than for 1T-TiS₂, and appears to be primarily controlled by both the AgNO₃ concentration and the crystal thickness. For example, after mixing about 30g of very fine 2H-TaS₂ powder with an aqueous solution saturated with AgNO₃, an extremely vigorous and exothermic reaction, during which the glass container became hot to touch, can be observed. The reaction is much less vigorous with 1T-TiS₂. After this reaction is complete, the 2H-TaS₂ and 1T-TiS₂ crystals have changed appearance from metallic looking platelets, having, respectively, a steel-blue and gold luster, to a material which, although still having the platelet shape, is now green-yellow in color and that will completely disintegrate when touched. Furthermore, the formation of some elemental sulfur and silver was observed, but sulfide odors were not noticed. Finally, in both cases it was observed that the electrolyte changed from being only slightly acidic to extremely acidic. For 2H-TaS₂, one could in addition to the above also observe the formation of a gelatinous substance which is slightly milky in color and is very likely tantalic acid, that is Ta₂O₅ · xH₂O. The creation of this hydrous pentoxide will likely correspond to the reaction shown in Eq. [4] below



The observed large decrease in the pH is strong evidence that 2H-TaS₂ undergoes a hydrolysis reaction and suggests that the similar, although less vigorous, reaction observed for 1T-TiS₂ is also a hydrolysis. After washing either of the green-yellow substances in distilled water, they changed their color to black. X-ray diffraction powder patterns revealed only a few weak lines, most of which were quite fuzzy, that did not correspond to any of the known structures, or simple variations thereof, of the silver intercalation compounds reported in previous work (1). Microprobe x-ray fluorescence analysis of the black powders were quite variable, but often indicated the presence of a large silver to tantalum or titanium ratios (in the order of 4:1). Consequently, the bulk of this new amorphous material likely corresponds to the complete decomposition of the dichalcogenides into a random mixture of a series of hydrated oxides of the transition metal along with Ag₂S plus elemental sulfur and silver (Eq. [4]).

If the aqueous AgNO₃ electrolyte is made more dilute, no vigorous reaction is observed with the dichalcogenide powders but, instead, we now find that silver intercalates. The degree of intercalation appears to be primarily controlled by the AgNO₃ concentration. For example, in a

0.1N aqueous AgNO_3 electrolyte the intercalation of silver into 2H-TaS_2 will proceed to a maximum mole fraction of $x \approx 1/3$ (i.e., $\text{Ag}_{1/3}\text{TaS}_2$) as determined from the lattice parameters (1), and for lower AgNO_3 concentrations, the degree of intercalation is correspondingly lower. If the AgNO_3 concentration is reduced to 0.1N when intercalating 1T-TiS_2 , which is generally much less reactive, no corrosion/intercalation reaction was observed. Judging from the x-ray powder patterns, the silver intercalation compounds prepared in this manner, that is by simply placing the dichalcogenide crystals into an aqueous AgNO_3 solutions, are indistinguishable from the thermally intercalated materials. Therefore, this chemical intercalation method provides a convenient means by which the host dichalcogenide can be intercalated to various degrees. This chemical intercalation of the host dichalcogenide must be accompanied by a simultaneous oxidation reaction so that a ready source of electrons is provided to balance the positive charge of the intercalating silver ions. One of the likely candidates for this oxidation reaction is the hydrolysis of the host dichalcogenide, as was readily observable when the dichalcogenides were placed into an aqueous solution saturated with AgNO_3 (Eq. [4]). In short, the chemical intercalation of the host dichalcogenide appears to be made possible by the simultaneous decomposition of part of the host crystal. In an effort to see if the effects of the self-intercalation of $\sim 1/3$ mole fraction of silver can be directly observed, an optically thin crystal of 2H-TaS_2 was observed under the microscope before and after 0.1N Ag^+ aqueous electrolyte was added. Even though the bulk of the dichalcogenide was relatively small, and a relatively large amount ($\sim 1/3$ mole fraction) of it should have corroded away (Eq. [4]), no obvious signs of corrosion (e.g., decrease in the crystal size, changes in color, dendrites, etc.) could be seen at the crystal edges where, one would think, the chemically active sites are likely to be. Therefore, since the corrosion of the host crystal is the only possible mechanism for supplying electrons to the intercalation process, it would appear that the basal planes are corroding away.

The problem of the parallel intercalation/corrosion reactions can be avoided altogether by using nonaqueous electrolytes. Although several choices for such a solvent exist, judging from experience, acetonitrile or glycerol appear to be best. Glycerol became the solvent of choice because it is much more convenient to use in practice. However, problems still exist when trying to restrict the intercalation/corrosion reactions to mole fractions below about $1/10$ for Ag_xTaS_2 unless special precautions, such as preparing the electrolyte and sample in a dry box, are taken. If any silver should precipitate and come into contact with the dichalcogenide, intercalation will of course occur. Therefore, in addition to the electrochemical cell having to be scrupulously clean and free of any reducing substances which might cause silver to precipitate, the electrolyte should also not be exposed to any intense light because of the photochemical nature of AgNO_3 . Using a solution of AgNO_3 in glycerol as electrolyte will allow the quantitative use of coulometry, as a parallel method to weighing, for measuring the intercalated mole fraction of silver ions.

In all of our work on the Ag_xTaS_2 and Ag_xTiS_2 systems, we have always used as electrolyte a solution of AgNO_3 in glycerol, which was often renewed, to avoid the corrosion/intercalation reactions described above. Furthermore, for reasons of standardization and convenience, the AgNO_3 /glycerol electrolyte was consistently made 0.1N for all measurements and crystal preparations. Note that Butz *et al.*'s (14) criticism of "massive self-intercalation" invalidating our optical measurements of the intercalation rate of silver into 2H-TaS_2 (2) is not valid because self-intercalation in 0.1N aqueous electrolyte is limited to $x < 1/3$, and it was the stage 1 front, which occurs reversibly for $x > 0.4$, that was monitored. Furthermore, as was pointed out in Ref. (2), these optical measurements were mostly performed with glycerol as the solvent.

EMF Measurements

The EMF of the $\text{Ag}_x\text{TaS}_2/\text{Ag}$ cells were determined by using thermally prepared powder samples of known composition, and by intercalating single 2H-TaS_2 crystals electrochemically. Both methods have drawbacks, but tend to be somewhat complementary. For reasons of convenience, the Ag_xTiS_2 samples for the EMF measurements were only prepared electrochemically. All EMF measurements were carried out with a PAR 173 potentiostat.

If the electrodes are thermally prepared, the EMF measurements of the $\text{Ag}_x\text{TaS}_2/\text{Ag}$ cells are sometimes hampered because the surface of the crystallites is easily contaminated with iodine, sulfur, silver, etc. Therefore, under the zero net current conditions at which EMF's are measured, various other equilibrium reactions can exist and will contribute to the net EMF. The degree to which the EMF's of the other equilibrium reactions are important is determined by the magnitude of their respective exchange current as compared to the exchange current for the equilibrium intercalation reaction. For the Ag_xTaS_2 samples, it was found by experience that whereas consistent EMF values could be obtained for thermally intercalated samples with $x \approx 1/3$, for samples with $x \geq 1/3$ the EMF's were sometimes erratic and often close to the Ag/Ag^+ potential. Closer inspection of these samples usually showed that not all of the silver had intercalated and that elemental silver was deposited on the crystal surface, thus making it possible for a large (EMF determining) Ag/Ag^+ exchange current to be established. The electrode construction for measuring the EMF of the thermally prepared powders is shown in Fig. 1. Quartz tubing was drawn to a very fine capillary at one end, the intercalated dichalcogenide powder along with a length of gold wire was inserted, tapped tight until good electrical contact resulted, and the whole assembly was then epoxied at the top for mechanical rigidity.

Electrochemically intercalated samples for EMF measurements were prepared by intercalating thin single crystals of the dichalcogenides in the standard 0.1N AgNO_3 /glycerol electrolyte, and x was determined via weighing and coulometry. The problem now often arising is that the intercalate is likely to be more concentrated at the crystal edges, as compared to the bulk, unless the sample is allowed to equilibrate properly, but this could at times take weeks at room temperature. Therefore, since the EMF of a crystal is determined by the silver ion concentration at the crystal edges, the correlation established between the total mole fraction of silver intercalated and the corresponding EMF may at times be misleading. On the other hand, a long equilibration time can cause other problems such as the corrosion/intercalation reactions initiated by water contamination. Since equilib-

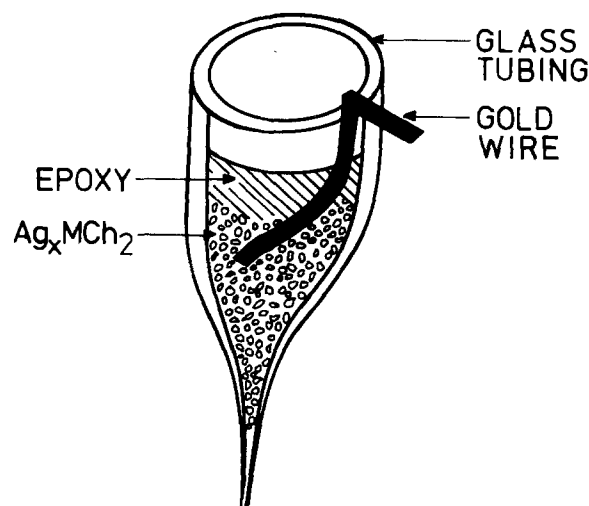


Fig. 1. Cathode construction for measuring the open-circuit potential of thermally prepared Ag_xTaS_2 or Ag_xTiS_2 powders.

rium is achieved much more quickly in thin samples, we also measured the EMF of optically transparent (<2000Å thick) single-crystals which, because they could not be handled, had to be intercalated or deintercalated *in situ*. The drawback now was that the degree of intercalation was known only relatively poorly because the amount of the host dichalcogenide present could not be directly determined. In this case, the intercalated mole fraction had to be estimated via coulometry by knowing the number of coulombs passed when intercalation appeared complete, that is, x could then be assumed to be $2/3$ mole fraction [see also Ref. (6)]. For optically transparent electrodes, equilibration times at room temperature, after partial intercalation or deintercalation, was reduced from days or even weeks to a few hours. All samples were judged to be essentially in equilibrium if the EMF drift was less than about $1 \text{ mV} \cdot \text{h}^{-1}$.

Results

Ag_xTaS₂/Ag EMF.—The experimental results for the open-circuit voltage of the Ag_xTaS₂/0.1N Ag⁺(glycerol)/Ag cell as a function of x is given in Fig. 2. The voltages are measured directly against the silver anode and each data point corresponds to an individually prepared sample. Even though there is some scatter in the data, the line drawn through the data points is thought to be the best fit. Some samples had radically different EMF's, but when they were checked for uniformity of intercalation (*e.g.*, using x-ray diffraction and x-ray fluorescence) they inevitably proved to be of poor quality, or had elemental silver deposits on their surfaces. The large scatter in the data was of particular concern in region C ($1/3 \leq x \leq 1/2$) so that a series of five samples were very carefully prepared within this concentration range, and their open-circuit potentials monitored over a period of a few months. The open-circuit potentials were all initially near 40 mV, but then gradually rose to those indicated in Fig. 2 (*i.e.*, 80-120 mV) and remained constant there.

To determine the reversibility of this electrochemical cell, an optically transparent single crystal, which allows relatively rapid measurements to be made, was used as the electrode. The open-circuit voltage was measured, after resting the cell, following partial intercalation or deintercalation, and it became quickly apparent that the cell would cycle reversibly since the open-circuit voltage could be returned to above about 190 mV following complete intercalation. Considering all the structural changes involved when a Ag_xTaS₂ electrode is cycled (1), it was very surprising to discover this reversible behavior. Therefore, to verify this reversibility more completely, x-ray powder patterns were taken of part of an Ag_xTaS₂ electrode after it was completely discharged and then recharged to $x = 1/3$, $1/6$, and zero mole fractions. The resulting powder diffraction patterns confirmed the complete reversibility in the structural changes.

Ag_xTiS₂/Ag EMF.—In Fig. 3, the EMF dependence of the Ag_xTiS₂/0.1N Ag⁺(glycerol)/Ag electrochemical cell is shown as a function of x , and the voltages are again measured directly against the silver anode. The data points were all obtained using *in situ* intercalation of a series of 1T-TiS₂ single crystals which were typically about 500Å thick. There is very little random scatter in the data points compared to the Ag_xTaS₂ results and is undoubtedly a consequence of the corrosion/intercalation side reactions being only minimally present, as previously mentioned. For $0.08 \leq x \leq 0.18$ mole fractions, the line drawn in Fig. 3 to indicate the EMF dependence on x does not follow the data points closely, but is nevertheless thought to be closer to the ideal relation. The reason for this belief is that the data indicated by the squares were taken after waiting in excess of 8h for the cell to come to equilibrium, and clearly indicates that the Ag_xTiS₂ electrodes are slow in equilibrating in this concentration range. One possible explanation will be presented later.

Attempting to deintercalate the Ag_xTiS₂ electrodes immediately showed that they were only partially reversible at room temperature since it was impossible to recover an

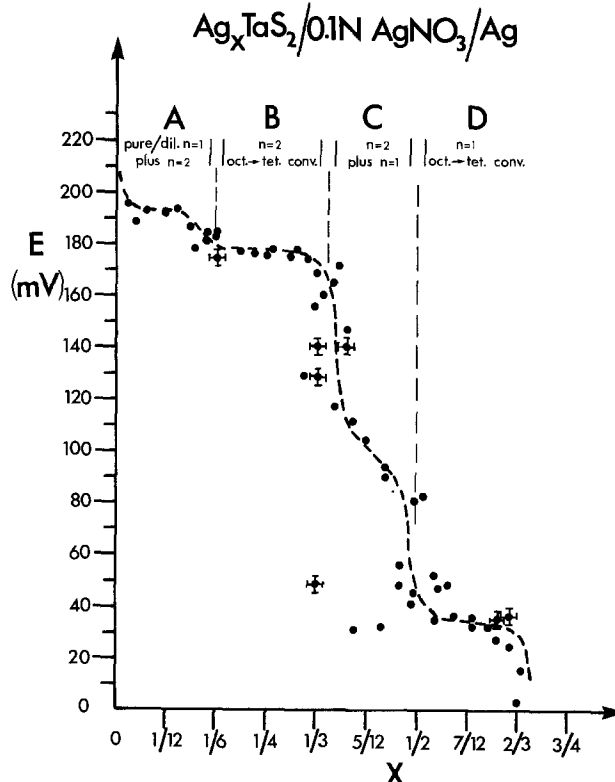


Fig. 2. The EMF of a Ag_xTaS₂/0.1N AgNO₃, glycerol/Ag electrochemical cell as a function of x . Above the data points, the phases observed in x-ray and electron diffraction studies (1, 3) are indicated. The error bars are typical of all data points and are specifically drawn on all thermally intercalated samples.

open-circuit voltage above about 50 mV. Therefore, in contrast to the Ag_xTaS₂ electrodes, the Ag_xTiS₂ electrodes will only cycle reversibly for mole fractions above about $x = 1/5$, that is, stage 1. When the electrochemical cell was heated above about 450 K, the Ag_xTiS₂ electrode did become somewhat more reversible, and open-circuit voltages near 70 mV could be observed. However, cycling the cell at elevated temperatures enhanced the deterioration of the electrolyte, in particular silver precipitated more readily, and the cell's behavior at elevated temperatures was therefore not further pursued other than by simply noting that the cell's reversibility will improve with increasing temperature.

Discussion

Plateaus in the open-circuit voltage separated by relatively sudden decreases in the EMF are observed in both the Ag_xTaS₂ and Ag_xTiS₂ intercalation systems. These features can be attributed to the dichalcogenide cathode since the free energy of the silver anode does not change. Similar features, although less pronounced, have also been observed in other intercalation systems (9, 10). As already pointed out by Berlinsky *et al.* (11), the plateaus should signal the coexistence of two or more phases, and the relatively sudden drops in the EMF, signaling corresponding increases in the free energy of the dichalcogenide electrodes, are the free energy costs to initiate a new phase. These considerations appear to apply to the Ag_xTaS₂ and Ag_xTiS₂ intercalation systems, and there is an excellent correlation between the features in the cell EMF's and the structural changes in the host as established in our previously published x-ray and electron diffraction work (1, 3, 4). Coulomb interactions of the silver ions, viewed as a lattice gas, as discussed in Ref. (11) are probably not of any significance here because, judging by the Li_xTiS₂ system (10), their influence on the cell EMF is on a much smaller scale.

Ag_xTaS₂.—In region A of Fig. 2 the initial voltage drop signals the formation of a stage 2 Ag_{1/6}TaS₂ phase [Fig. 9

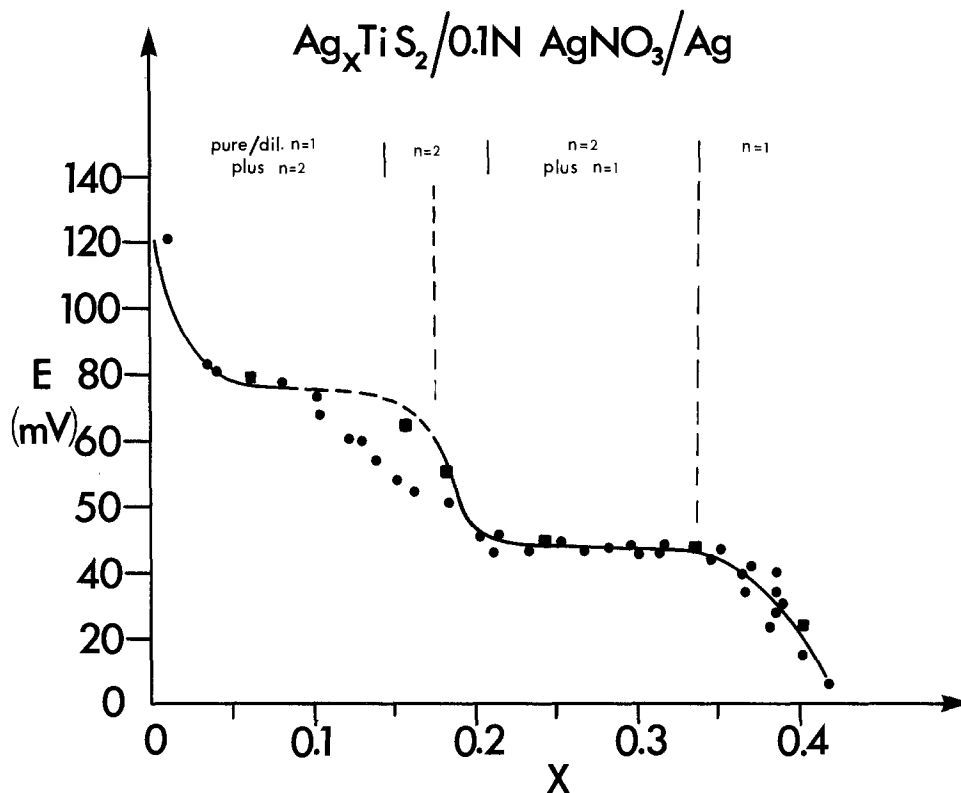


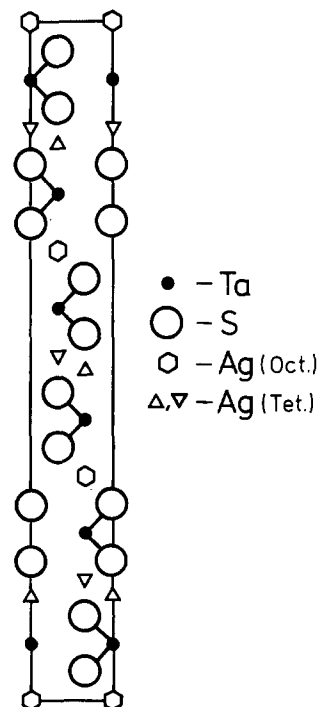
Fig. 3. The EMF of a $\text{Ag}_x\text{TiS}_2/0.1\text{N AgNO}_3$, glycerol/Ag electrochemical cell as a function of x . Above the data points are the phases determined from x-ray diffraction studies (1). The squares corresponds to data points obtained after equilibrating the electrode in excess of 8h.

in Ref. (4)] where the silver ions reside in octahedral sites with a local concentration of $x' \approx 1/3$ ($x' \approx nx$; n = stage number). It should be pointed out that so far the stacking sequence of the host layers has not changed. This stage 2 phase will grow at the expense of pure 2H-TaS₂, with increasing x , until it ideally comes to completion for $x = 1/6$. The dilute stage 1 phase (1), observed in thermally intercalated samples, is not observed and may only exist for very small concentrations, if at all, for electrochemically prepared samples as already previously observed (4). The small voltage step in the beginning of region B coincides with the appearance of $2a_0$, in addition to the $\sqrt{3}a_0$, superlattice satellites (4) and therefore suggests that some of the host layers are beginning to shift with respect to one another to form the stage 2 $\text{Ag}_{1/3}\text{TaS}_2$ phase [Fig. 4 in Ref. (1)]. This stacking rearrangement, which allows a larger local silver ion concentration ($x' \approx 2/3$) comes to completion near $x = 1/3$. As x continues to increase, stage 1 develops (1) and this is signaled by a large drop in the open-circuit voltage above $x \approx 1/3$. The large decrease indicates that a significant increase in the electrodes free energy is associated with the formation of stage 1, as might be expected. In region C, as was initially the case for stage 2, the silver ions above $x = 1/3$ are expected to reside in the octahedral sites of the empty stage 2 regions so that for $x = 1/2$ mole fraction, the idealized stage 1 structure shown in Fig. 4 may be expected, although it has not yet been confirmed. In short, the structure would be based on the $\text{Ag}_{1/3}\text{TaS}_2$ structure with, however, the octahedral sites in the empty regions now also intercalated to $x' = 1/3$ as in $\text{Ag}_{1/6}\text{TaS}_2$. There is some evidence that this structure is correct because the electron diffraction patterns in this concentration range show weak $\sqrt{3}a_0$, superlattice satellites (3) which may originate in those crystal layers similarly intercalated to those in $\text{Ag}_{1/6}\text{TaS}_2$. The especially large scatter in the data within region C, prompting the extra careful preparation of the five samples already mentioned, may in part be due to the co-existence of $\text{Ag}_{1/3}\text{TaS}_2$ and $\text{Ag}_{2/3}\text{TaS}_2$ in addition to $\text{Ag}_{1/2}\text{TaS}_2$ regions. If this is correct, it would naturally explain the tendency of the EMF's in region C to be near the $\text{Ag}_{2/3}\text{TaS}_2$ voltage plateau because this structure would be expected at the crystal edges where the sample's EMF is established. Finally, in region D the $\text{Ag}_{2/3}\text{TaS}_2$ structure

[Fig. 3 in Ref. (1)] is established and the voltage drop near $x = 1/2$ signals when the final shifting of the layers occurs (those having not yet shifted with respect to one another) in order to produce the so-called 2H-MoS₂ structure that $\text{Ag}_{2/3}\text{TaS}_2$ possesses (1).

Ag_xTiS_2 .—As can be seen in Fig. 3 for the $\text{Ag}_x\text{TiS}_2/\text{Ag}$ electrochemical cell, the variation in the open-circuit potential as a function of x is much simpler than that observed in the $\text{Ag}_x\text{TaS}_2/\text{Ag}$ cell. This is in agreement with the simpler structural changes that are observed for the Ag_xTiS_2 intercalation system (1). There are two drops in the open-circuit voltage signaling the formation of two phases, first stage 2 and then stage 1, in agreement with x-ray diffraction results (1). As was also the case for the

Fig. 4. Anticipated $\text{Ag}_{1/2}\text{TaS}_2$ stage 1 structure having $x = 1/3$ of the silver ions in the tetrahedral sites of alternative layers, and $x = 1/6$ of the silver ions in the octahedral sites of the remaining layers.



Ag_xTaS₂ system, the dilute stage 1 phase, found when the Ag_xTiS₂ samples are thermally prepared (1), is not observed in the EMF measurements of the electrochemically intercalated samples, and it appears that stage 2 coexists immediately with pure 1T-TiS₂. Then, with increasing x , the relative amount of stage 2 increases until, judging from Fig. 3, stage 2 is complete for $x \approx 0.18$. A limit of $x \approx 0.18$ for stage 2 would agree with the $x \approx 1/6$ ($x' \approx 1/3$) concentration suggested by the presence of the $\sqrt{3}a_0$ silver superlattice (12). However, it would be contrary to the x-ray work (1) which did not indicate the presence of any stage 1 material until $x \approx 1/4$ for the thermally prepared samples. This apparent discrepancy is likely associated with the different temperatures at which the samples were prepared, and, as predicted by Safran (13), formation of stage 1 is observed to be delayed to higher x for samples prepared at higher temperatures.

The irreversible intercalation of silver into 1T-TiS₂ below $x \approx 0.18$ is surprising because no structural changes, which might have large activation energies, other than a simple expansion of the host are observed up to the maximum mole fraction of $x \approx 0.42$ that we could intercalate (1). Therefore, although the cause is not clear, it would appear that this irreversible behavior may be chemical in nature.

This irreversible behavior may also explain why it is difficult to achieve equilibrium open-circuit potentials when $0.08 \leq x \leq 0.18$ (Fig. 3). Once the silver ions enter a crystal edge, thereby forming stage 2 regions (very stable), their further diffusion into the unintercalated interior crystal regions will be slow and, instead, intercalation will continue at the edges to higher concentrations including stage 1. The higher silver ion concentration at the edges, up to the creation of stage 1, will of course result in measuring a spuriously low open-circuit potential.

When increasing x above about 0.20 mole fraction, the EMF plateau results from the growth of stage 1 at the expense of stage 2 regions. Stage 1, as suggested by the $\sqrt{3}a_0$ silver superlattice (12), should ideally be complete for $x = 1/3$ ($x = 2/3$ appears unlikely). Therefore, since intercalation proceeds to 0.42 mole fraction, it will become necessary for the "excess" ions to occupy energetically less favorable sites which should decrease the cell EMF above $x = 1/3$, as can in fact be observed in Fig. 3.

Conclusions

When preparing Ag_xTaS₂ or Ag_xTiS₂ samples electrolytically using an aqueous AgNO₃ electrolyte, a spontaneous corrosion/intercalation reaction appears to occur. Even though this corrosion/intercalation process can be minimized by keeping the AgNO₃ concentration low (for 1T-TiS₂ it appears to be essentially eliminated at $\sim 0.1N$), one should not use weighing or coulometry as methods for determining the intercalated silver concentration. If an organic solvent such as glycerol or acetonitrile is used for the electrolyte, no problems should be encountered when preparing Ag_xTiS₂ samples. However, when preparing Ag_xTaS₂ samples, great care should still be ex-

ercised if x is to be determined via weighing or coulometry because, unless a dry box is used, the organic electrolyte will inevitably absorb some water.

There is good agreement in the Ag_xTaS₂ and Ag_xTiS₂ intercalation systems between changes in their structure and features in their open-circuit voltage. In the Ag_xTaS₂ system, additional phase changes, caused by stacking rearrangements, occur and are clearly evidenced by features in the cell EMF.

It is not clear why in Ag_xTiS₂ the silver ions will not deintercalate completely at room temperature, especially considering that this is the case in Ag_xTaS₂, where a series of structural changes occur. One might argue that the greater structural damage that Ag_xTaS₂ undoubtedly suffers may enhance its deintercalation process. However, this reasoning can be discounted because previous optical work (6) on thin ($\approx 1000\text{\AA}$) single crystals of Ag_xTaS₂ and Ag_xTiS₂, which do not suffer structural damage on intercalation, has also indicated that whereas the former intercalates reversibly the latter does not.

Acknowledgments

We would like to thank D. Kaluarachchi for electron microprobe x-ray fluorescence measurements, and the support of the Natural Sciences and Engineering Research Council of Canada. One of us (G.A.S.) is grateful for the support of a NSERC postdoctoral fellowship.

Manuscript submitted Nov. 28, 1983; revised manuscript received March 15, 1984.

Simon Fraser University assisted in meeting the publication costs of this article.

REFERENCES

1. G. A. Scholz and R. F. Frindt, *Mater. Res. Bull.*, **15**, 1703 (1980).
2. G. A. Scholz, P. Joensen, J. Reyes, and R. F. Frindt, *Physica*, **105B**, 214 (1981).
3. G. A. Scholz, R. F. Frindt, and A. E. Curzon, *Phys. Status Solidi A*, **71**, 531 (1982).
4. G. A. Scholz, R. F. Frindt, and A. E. Curzon, *ibid.*, **72**, 375 (1982).
5. G. A. Scholz, O. Singh, R. F. Frindt, and A. E. Curzon, *Solid State Commun.*, **44**, 1455 (1982).
6. G. A. Scholz and R. F. Frindt, *Can. J. Phys.*, **61**, 965 (1983).
7. G. A. Scholz and R. F. Frindt, *Phys. Status Solidi A*, **79**, 483 (1983).
8. H. Schäfer, "Chemical Transport Reactions," Academic Press Inc., New York (1964).
9. J. O. Besenhard, H. Meyer, R. Schöllhorn, *Z. Naturforsch., Teil B*, **31**, 907 (1976).
10. D. W. Murphy and F. A. Trumbore, *J. Cryst. Growth*, **39**, 185 (1977).
11. A. J. Berlinsky, W. G. Unruh, W. R. McKinnon, and R. R. Haering, *Solid State Commun.*, **31**, 139 (1979).
12. G. A. Scholz, Ph.D. Thesis, Simon Fraser University, Burnaby, B.C. (1982).
13. S. A. Safran, *Phys. Rev. Lett.*, **44**, 937 (1980).
14. T. Butz, A. Lerf, H. Hübler, H. Gierisch, S. Saibene, and J. O. Besenhard, *Hyperfine Interact.*, **15/16**, 925 (1983).

New Electrolyte Salts for Li/SOCl₂ Cells

W. L. Bowden,* J. S. Miller, D. Cubbison, and A. N. Dey*

Duracell, Incorporated, Duracell Laboratory for Physical Science, Burlington, Massachusetts 01803

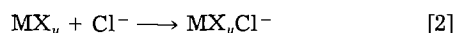
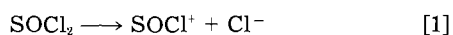
ABSTRACT

The high energy density electrochemical system Li/SOCl₂ has inherently good volumetric energy density and current capability. The currently used electrolytes of LiAlCl₄ and Li₂B₁₀Cl₁₀ possess objectionable features, and therefore new electrolyte salts were evaluated. Two promising electrolytes were discovered, LiGaCl₄ and Li₂O · 2GaCl₃. In SOCl₂, both salts had solubilities and conductivities similar to LiAlCl₄ at temperatures down to -30°C. Both electrolytes were evaluated in spirally wound D cells. At currents of 1A (approximately C/12) or below, the voltages and capacities were closely comparable to those recorded for LiAlCl₄. At higher currents of 3 or 4A, the gallium-based electrolytes delivered capacities as much as 60% greater than LiAlCl₄. This dramatic increase in high current capacity probably is due to reduced cathode passivation. Suggestions are made as to the cause of the increase in capacity.

The lithium/thionyl chloride cell is a high voltage, high energy density power source which has been shown to deliver energy densities around 300 Wh/lb and 1.2 Wh/cm³ (1-3). This cell consists of a lithium metal anode, a catalytic cathode (usually carbon), and an electrolyte composed of SOCl₂ with a salt to provide electrolytic conductivity. The salt provides an important function in SOCl₂ cells since it appears to affect growth of the passivating film on the anode which slows self-discharge and can introduce a start up problem "voltage delay" on extended storage (4-6). Electrolyte variables have also been found to effect cathode passivation and hence the cell capacity.

A number of salts have been used with SOCl₂ to form battery electrolytes, such as LiAlCl₄ (3) and Li₂B₁₀Cl₁₀ (7), as well as other lithium salts, such as LiBCL₄. LiAlCl₄ is both inexpensive and highly conductive, but is prone to developing a substantial voltage delay. The extremely expensive salts Li₂B₁₀Cl₁₀ and Li₂B₁₂Cl₁₂ are not so soluble and are partly oxidized in SOCl₂ solutions, although they give very good start-up performance (7).

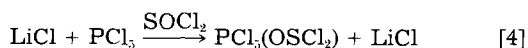
We decided to examine other lithium salts to see if any electrolyte with attractive properties of improved performance and/or reduced voltage delay could be found. Our hypothesis was that a good electrolyte could be obtained by reacting a chloride source with a chloride acceptor. Thionyl chloride itself is weak chloride donor solvent (8). In such a solvent, an acid is a chloride acceptor, while a base is a chloride donor. With SOCl₂, we are then forming an electrolyte by reacting a strong acid with the conjugate base, Cl⁻



Thionyl chloride can also form oxygen-bound complexes with acids such as AlCl₃ (Eq. [3]) to give a product which can be isolated by distillation (9)



For reaction of Lewis acids with SOCl₂, we might then expect a variety of products, ranging from a halometallate anion to a solvent complex. Reaction of halide with LiCl would then be competitive with formation of the oxygen-bound solvent complex. This competition suggests that a stronger chloride acceptor would give the simpler solution chemistry of reaction [2] rather than a mixture of reactions [2] and [3]. For example, the weak Cl⁻ acceptor PCl₅ would be expected to react as in reaction [4], while the strong Cl⁻ acceptor SbCl₅ would be expected to react as in reaction [5]



*Electrochemical Society Active Member.

To test this hypothesis that good chloride acceptors should form useful electrolyte anions, we reacted a series of chloride acceptors with lithium bases in SOCl₂. These salts were tested in SOCl₂ cells.

The reactions above say comparatively little about the kinetic stability of the electrolyte to lithium metal, although one would expect the anion in reaction [2] to be less easily reduced than an oxo complex (reaction [3]).

Experimental

Generally, halides were used as received. GaCl₃, FeCl₃, InCl₃, PCl₅, TiCl₄, SnCl₄, and LiCl were purchased from Alfa Chemicals. Li₂O was purchased from Cerac. Lithium chloride was vacuum dried at 160°C before use. In some cases the extremely hygroscopic GaCl₃ was sublimed under vacuum before use. Sublimation appeared to have little or no effect on electrolyte appearance. Thionyl chloride (M & B) was refluxed over lithium strips under Ar and then slowly distilled through a three-foot column packed with saddles. The resulting SOCl₂ was colorless or extremely light yellow in color. Electrolyte solutions were routinely refluxed over lithium strips under Ar and filtered before use. The lithium strips were replaced if the lithium became discolored, and the reflux continued until the lithium strips stayed shiny.

Electrolyte salts were generally prepared by adding 0.5 mol of the halide to 0.5 liters of distilled thionyl chloride. To this was added (0.52 or 1.04 mol for dilithio salts) freshly dried LiCl. The solution was stirred overnight under Ar. If a substantial amount of undissolved material was present, the solution was refluxed overnight. Solutions with a substantial amount of precipitate remaining were discarded. The salt LiGaCl₄ was also prepared by a fusion technique, which gave an electrolyte with somewhat less yellow color.

LiGaCl₄.—Gallium chloride (88g), finely divided, was weighed into a clean, dry 1 liter round-bottom flask in an argon-filled glove box. To this was added freshly dried LiCl (22g) (4% excess). The flask was loosely stoppered and shaken to give a reasonably intimate mixture. The flask was then carefully warmed with a heating mantle. At about 70°C, a liquid began to form. At 97°C, the entire mixture melted to form a dark liquid. The liquid was shaken to give a homogeneous mixture and quickly cooled to give dirty gray solid. The gray color appears to be due to extremely small droplets of elemental Ga present in the GaCl₃. The resulting solid was then carefully dissolved in SOCl₂ and refluxed under Ar over Li strips to remove residual water.

Li₂O · 2GaCl₃.—Gallium chloride (88g) was dissolved in 500 ml SOCl₂. To this was added Li₂O (7.5g). The Li₂O remained solid. The mixture was refluxed under Ar for several days, with the Li₂O slowly dissolving. When solution was complete, lithium strips were added and the solution refluxed under Ar.

Conductivity measurements were taken with Genrad 1657 and 1658 Digibridge conductivity bridges with the

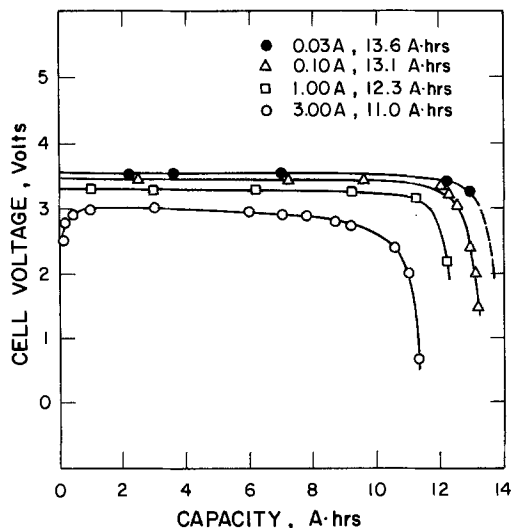


Fig. 1. Discharge curves of Li/SOCl₂ cells with 1.0M LiGaCl₄-SOCl₂ after 2 months storage at 25°C.

samples thermostated in Frigomix 1495 and 1496 constant temperature baths.

Test electrolytes were evaluated in spirally wound cells with hermetic glass to metal seals of conventional design. The nickel cans and tops were TIG welded. The tops had low pressure vents (9). The D cells were cathode limited by the carbon present and were of a variety of designs. The flat cells were of familiar design (12). Test cells were discharged through Kepco power supplies with data collection by strip-chart recorders.

Results

The donor and acceptor materials were mixed in SOCl₂ and stirred for several days in a closed container. A small excess of the appropriate base was used (LiCl or Li₂O). The Li₂O/GaCl₃ solution had to be refluxed before the Li₂O would dissolve. Results of these experiments are shown in Table I. Mixtures which gave a solution in SOCl₂ were first stirred and then refluxed over Li strips to remove the unreacted Lewis acid and hydrolysis products present. After these procedures were complete, the electrolytes which were obviously not compatible with lithium were eliminated. This left three electrolytes

Table I. Lewis acid-base combinations in SOCl₂

Acid	Base	Salt	Result	After Li reflux
GaCl ₃	LiCl	LiGaCl ₄	Light yellow solid	Light yellow solid
GaCl ₃	Li ₂ O	Li ₂ O · 2GaCl ₃	Light yellow solid	Light yellow solid
FeCl ₃	LiCl	LiFeCl ₄	Orange-red solid	Fe deposits on Li
InCl ₃	LiCl	LiInCl ₄	Insoluble	—
PCl ₅	LiCl	LiPCl ₆	Insoluble	—
SbCl ₅	LiCl	LiSbCl ₆	Light yellow solid	Light yellow solid
TiCl ₄	LiCl	Li ₂ TiCl ₆	Insoluble	—
SnCl ₄	LiCl	Li ₂ SnCl ₆	Light yellow solid	Corrodes Li

which were considered for further evaluation: LiGaCl₄, LiSbCl₆, and Li₂O · 2GaCl₃.

Spirally wound, hermetically sealed D cells were filled with 1M LiSbCl₆, 1M LiGaCl₄, and Li₂O · 2GaCl₃ electrolytes. The cells were discharged fresh and after 2 months of storage at room temperature. Discharge curves of typical cells with 1M LiGaCl₄ in SOCl₂ two months after filling are shown in Fig. 1, while discharge of typical fresh Li₂O · 2GaCl₃ cells is shown in Fig. 2. The Li₂O · 2GaCl₃ electrolyte proved extremely reactive and difficult to handle due to its extremely hygroscopic character, so testing was concentrated on cells containing LiGaCl₄. Capacities realized at lower rates were typical of those for identical LiAlCl₄/SOCl₂ cells of similar design. At the 3A (7.5 mA/cm²) rate, this was no longer true, since the LiGaCl₄ cells were substantially higher in capacity. Capacities of 11 Ah or more were realized to a 2V cutoff, where the equivalent LiAlCl₄ cell gave only 8 Ah. A capacity-rate plot for the LiGaCl₄ and LiAlCl₄ cells with 1M electrolytes is shown in Fig. 3. Figure 3 graphically shows the advantage of LiGaCl₄. Our finding of the high current capability of the LiGaCl₄ electrolyte was a bit surprising, so we built some more D cells, filled them with 1.8M electrolytes, and tested them at 4A (10 mA/cm²). On this high current, the LiAlCl₄ cell gave only 6.7 Ah, while LiGaCl₄ gave 11.0 Ah and Li₂O · 2GaCl₃ gave 10.6 Ah, a 60% improvement with the Ga electrolytes. In contrast, D cells filled with 1M LiSbCl₆ electrolyte gave very disappointing performance, with a capacity of only 1.4 Ah at 0.1A.

The LiGaCl₄ electrolyte was also tested in an extremely high rate flat cell described elsewhere (12). The cell was

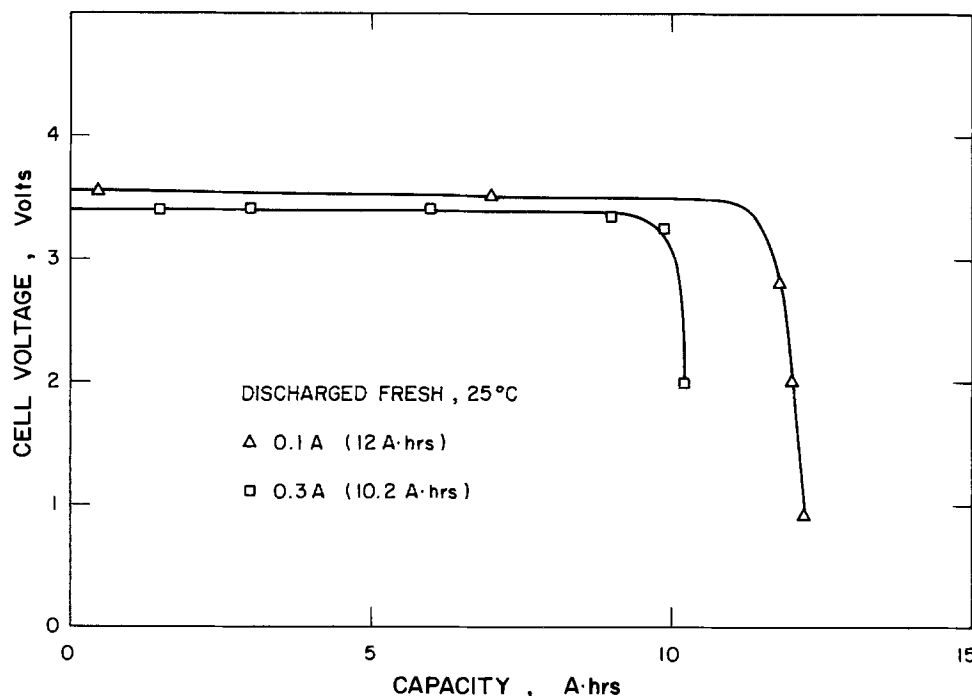


Fig. 2. Performance of D cells with Li₂O · 2GaCl₃ electrolyte.

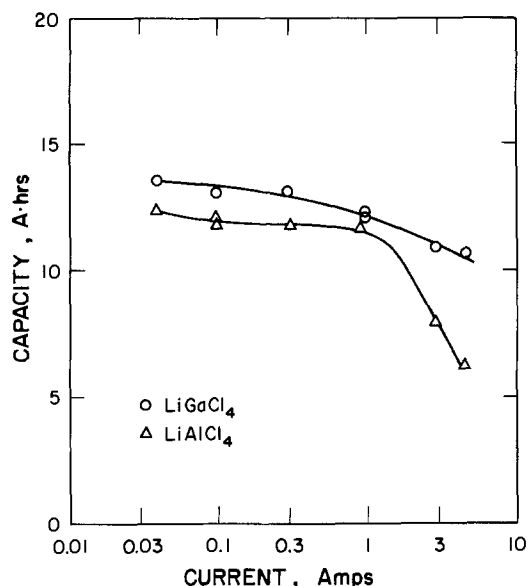


Fig. 3. Capacity-rate curve of 1M LiAlCl₄ and 1M LiGaCl₄-SOCl₂ in D cells.

tested on a pulse regime of 20 and 3.2A pulses (12), with the results shown in Fig. 4. Both the wall temperature and internal pressure were also monitored. As shown in the figure, the internal pressure rises smoothly during the discharge, in contrast to the work of Marincic *et al.* (14), where SO₂ was found to evolve only near the end of discharge in cells with SOCl₂/LiAlCl₄ electrolytes.

Even at 30 mA/cm², the 1M LiGaCl₄ electrolyte will support reasonable capacities. For a cell approximately 2/3 AA size with approximately 50 cm² electrode, discharge on a 2Ω load (approximately 30 mA/cm²) gives over 0.6h service with steady voltage, as shown in Fig. 5.

Capacity increases due to substitution of LiGaCl₄ for LiAlCl₄ can be appreciable at lower current densities as well. Comparative performances of wound AA cells with 1M LiAlCl₄ and 1M LiGaCl₄ are shown in Fig. 6. Cells with LiAlCl₄ averaged 1.31 Ah on 12.5Ω load (approximately 3.5 mA/cm²), while the cells with LiGaCl₄ delivered 1.62 Ah on identical load, a 23% improvement. Even on 3.9Ω, the wound AA cells gave 1.5 Ah. As shown in Fig. 6, the cell voltages are essentially equal for both electrolytes, while the start-up voltages are slightly lower for LiGaCl₄.

Samples of Li were stored at 72°C with 1M LiGaCl₄ in SOCl₂ and 1M LiSbCl₆ in SOCl₂. The samples stored with

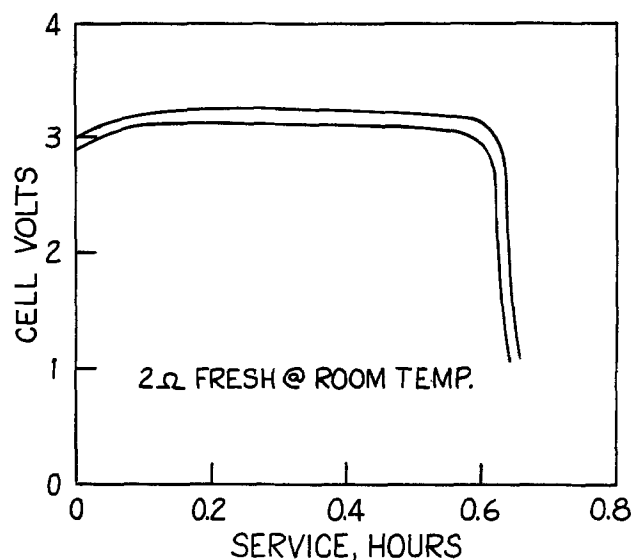


Fig. 5. Discharge of 2/3AA cell with 1M LiGaCl₄ in SOCl₂ at 30 mA/cm².

LiSbCl₆ had extremely large, regular crystals covering the lithium which showed the presence of antimony on EDAX analysis. Possibly the poor performance of cells with SbCl₆⁻/SOCl₂ electrolyte is due to deposition of Sb on the Li, passivating it. Similar samples with the Ga electrolytes gave indistinct pictures with a "smudged" appearance, which allowed no careful examination of the character of the lithium film. The gallium electrolytes were extremely hygroscopic, as expected from GaCl₃ and GaOCl (15-17). Voltage delay measurements gave extraordinarily variable results, ranging from 2 min to 3V at 1A after 5 months storage at room temperatures to 45 min at 50 mA to 2V after 2 months. It is therefore clear that voltage delay in LiGaCl₄ electrolytes is irregular and may be sensitive to relatively minor details of the cell filling operation. We suspect that momentary air exposure of the cell before filling or during the filling operation may be the root of this substantial variation in anode passivation.

Conductivities of LiGaCl₄ and Li₂O · 2GaCl₃ in SOCl₂ were measured at a variety of temperatures and concentrations. Plots of conductivity *vs.* concentration at various temperatures are shown in Fig. 7 and 8. Concentration and conductance at 25°C are listed for LiGaCl₄, Li₂O · 2GaCl₃, Li₂B₁₀Cl₁₀, and LiAlCl₄ in Table II for comparison. From the data in the table it is clear that both of the GaCl₃-based electrolytes are highly conducting in SOCl₂

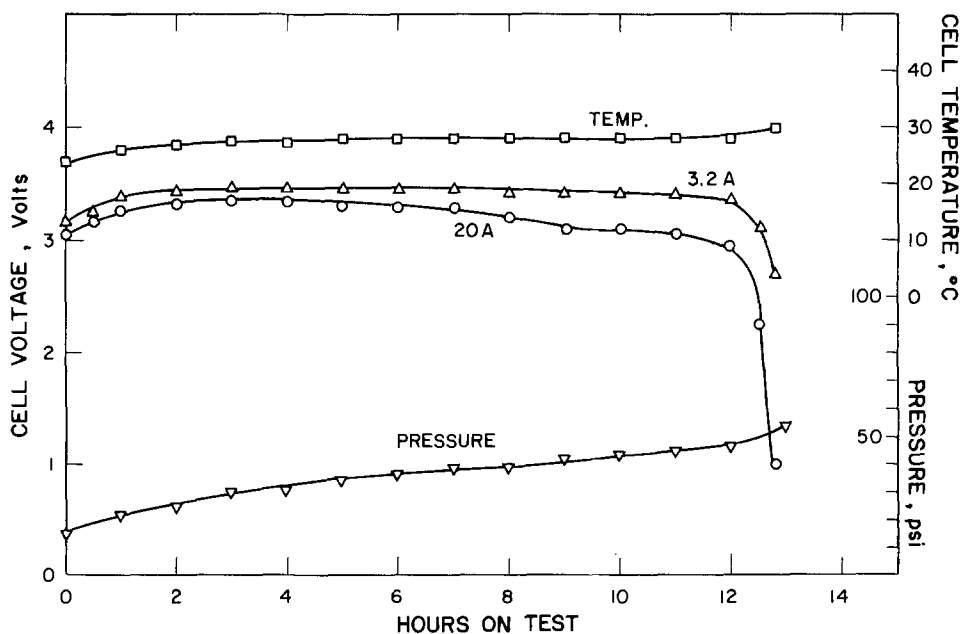


Fig. 4. Flat cell with 1.8M LiGaCl₄ on 20 and 3.2A pulses.

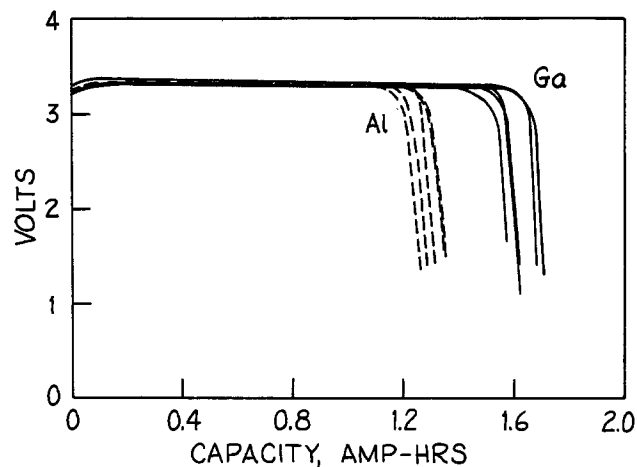


Fig. 6. Voltage vs. capacity for wound AA cells on 12.5Ω load. Al: 1M LiAlCl₄, Ga: 1M LiGaCl₄.

and show promise for evaluation in cells. Comparative conductivities at 25°C for these electrolytes are shown in Fig. 9. It should be noted that the conductivity of the Li₂O · 2GaCl₃ electrolyte is very similar to LiAlCl₄ and LiGaCl₄, while Li₂B₁₀Cl₁₀ shows rather lower limiting conductivities.

Discussion

Our original hypothesis, that extremely good chloride acceptors would give good electrolytes in the weak chloride donor SOCl₂, is clearly untenable. Of our three strong Cl⁻ acceptors, GaCl₃, FeCl₃, and SbCl₃, only GaCl₃ gave a usable electrolyte with LiCl or Li₂O. While LiGaCl₄ appears to be an excellent electrolyte for SOCl₂, cells with substantial increases (up to 60%) in delivered energy from unoptimized cell designs, the reasons for this improvement are not self-evident.

The relatively minor differences in conductivity between LiAlCl₄ and the LiGaCl₄ and Li₂Ga₂Cl₆O electrolytes are clearly inadequate to account for this increase in capacity. The D cells used in this study were "carbon limited." That is, both lithium anode and SOCl₂ catholyte were present substantially in excess of the cell capacity and the cell capacity is established by passivation of the porous carbon catalytic cathode. The low current capacities of cells with LiAlCl₄ and LiGaCl₄ are similar, so, at these relatively high rates (2.5-125h rates), self-discharge processes exert a minimal effect on cell capacity. The increase in capacity at high currents with the GaCl₃ electrolytes is therefore due to decreased cathode passivation.

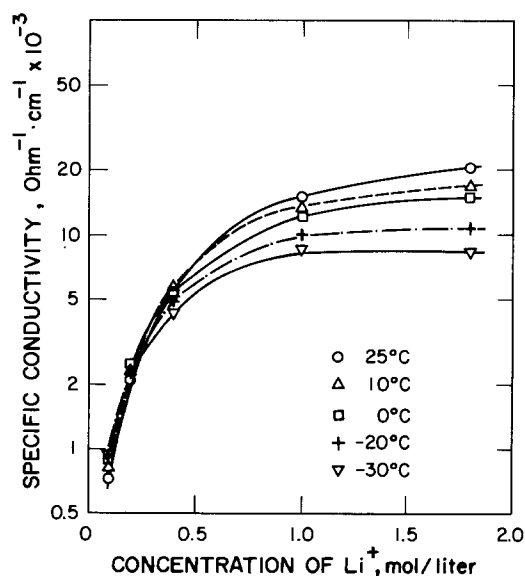


Fig. 7. Conductivity of LiGaCl₄ in SOCl₂.

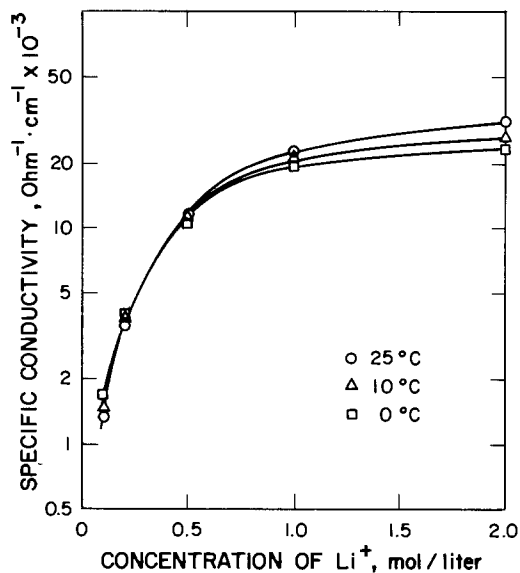
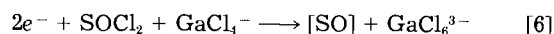


Fig. 8. Conductivity of Li₂O · 2GaCl₃ in SOCl₂.

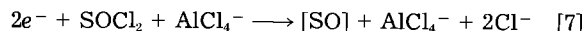
This cathode passivation has been attributed to blocking pores in the porous carbon electrode by S and LiCl.

In earlier work using cyclic voltammetry, we found that an intermediate species with delayed formation of S and SO₂ was formed when SOCl₂ was reduced at platinum in a ClO₄⁻ electrolyte (19, 20). Other workers have also concluded that these sulfur oxygen intermediates are present (21, 22). Very limited data from the flat cell suggests that this intermediate(s) is not so stable in LiGaCl₄ electrolytes. We suggest that the lowered stability of these intermediates may modify sulfur generation and thus change the morphology of both S and LiCl deposition in the cathode to reduce pore blockage. This may perhaps be due to the lessened affinity of Ga(III) for O compared to Al(III) and the greater stability of GaCl₄⁻ and GaCl₃ to oxygen species compared to AlCl₄⁻ and AlCl₃.

An alternative hypothesis for the change in pattern of LiCl deposition in the cathode is the formation of a higher octahedral chloride of Ga in the reduction process [6], while the AlCl₄⁻



cannot act as a halide acceptor (reaction [7])



Even transitory existence of the species GaCl₆³⁻ would result in some Cl⁻ transport from the site of reduction. There seems little reason to suspect the reduction of Ga(III)Cl₄ to Ga₂Cl₄(Ga(I), Ga(III)Cl₄), since the greater capacity occurs at over 3V vs. Li, well above the Ga(III) reduction potential of 2.27V.

The very similar conductivity and cell performance of the electrolyte Li₂O · 2GaCl₃ to LiGaCl₄ is worth some comment. The analogous Al electrolytes LiAlCl₄ and Li₂O · 2AlCl₃ show (13, 14) differences in cell performance. The specific conductivity of Li₂O · 2AlCl₃ is reported (11, 12) at 6 × 10⁻³ Ω⁻¹ cm⁻¹. At 1A, LiAlCl₄ cells gave 8 Ah, while Li₂O · 2AlCl₃ cells of similar Li⁺ content gave only 6 Ah.

Table II. Conductivities of electrolyte salts in SOCl₂ at 25°C

Conc. (M/l)	Salt conductivity × 10 ³ Ω ⁻¹ cm ⁻¹			
	LiGaCl ₄	Li ₂ O · 2GaCl ₃	LiAlCl ₄	Li ₂ B ₁₀ Cl ₁₀
0.1	0.72	0.79	0.80	0.7
0.2	2.2	2.1		
0.25			3.0	1.8
0.40	5.5			
0.50		6.8	7.3	3
1.0	15.3	13.7	14.6	4.8
1.8	21.0		20.0	
2.0		18.9	20.0	6.7

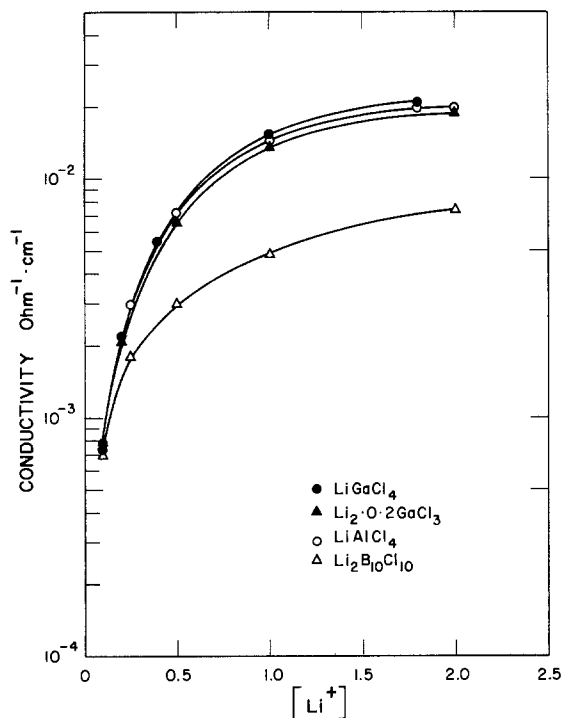
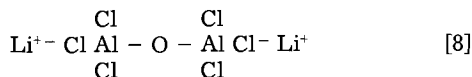


Fig. 9. Conductivities of various Li salts in SOCl_2 at 25°C

The conductivity vs. concentration of Gabano's electrolyte is very similar to the dilithium salts $\text{Li}_2\text{B}_{10}\text{Cl}_{10}$ and $\text{Li}_2\text{B}_{12}\text{Cl}_{12}$. This lends support to the hypothesis that the $\text{Li}_2\text{O} \cdot 2\text{AlCl}_3$ species should be formulated as in reaction [8]



However, the electrolyte $\text{Li}_2\text{O} \cdot 2\text{GaCl}_3$ shows conductivity nearly superimposable on LiAlCl_4 and LiGaCl_4 , as well as performance in cells similar to LiGaCl_4 . This suggests that the dimeric formulation of the salt $\text{Li}_2\text{O} \cdot 2\text{GaCl}_3$ is incorrect.

Perhaps the Li_2O reacts with SOCl_2 to form SO_2 and LiCl (23), as has been suggested, although other possible structures can be envisioned.

Gallium oxyhalides have been reported previously, although description of their properties are contradictory (17, 18). Like GaCl_3 and LiGaCl_4 , the mixture $\text{Li}_2\text{O} \cdot 2\text{GaCl}_3$ is extremely hygroscopic. Evaporation of SOCl_2 solution of this electrolyte gave extremely hygroscopic white crystals, which reacted with atmospheric moisture too quickly for satisfactory elemental analysis.

Conclusion

Both LiGaCl_4 and the oxide salt $\text{Li}_2\text{O} \cdot 2\text{GaCl}_3$ have been shown to form high conducting electrolyte solutions in SOCl_2 . In practical cell performance tests, the Ga elec-

trolytes displayed capacities similar to other electrolytes at low rates and substantially superior capacities on high rate discharges.

Manuscript submitted Oct. 27, 1983; revised manuscript received Feb. 7, 1984. This was Paper 37 presented at the Washington, DC, Meeting of the Society, Oct. 9-14, 1983.

Duracell, Incorporated assisted in meeting the publication costs of this article.

REFERENCES

- W. K. Behl, J. A. Christopoulos, M. Ramirez, and S. Gilman, *This Journal*, **120**, 1619 (1973).
- J. J. Auburn, K. W. French, S. I. Lieberman, V. K. Shah, and A. Heller, *ibid.*, **120**, 1613 (1973).
- A. N. Dey, *ibid.*, **123**, 1262 (1976).
- A. N. Dey and C. R. Schlaikjer, in "Proceedings of the 26th Power Sources Conference," Atlantic City, NJ, April 29-30, May 1-2, 1974, p. 47.
- A. N. Dey, *Electrochim. Acta*, **21**, 377 (1976).
- D. L. Chua, W. C. Merz, and W. S. Bishop, in "Proceedings of the 27th Power Sources Conference," Atlantic City, NJ, June 21-24, 1976, p. 33.
- C. R. Schlaikjer, U. S. Pat. 4,202,240; "Proceedings of the 28th Power Sources Conference," Atlantic City, NJ, June 12-15, 1978, The Electrochemical Society, Inc., p. 241 (1979).
- R. C. Paul and G. Singh, in "The Chemistry of Non Aqueous Solvents VB," J. J. Lagowski, Editor, Academic Press, New York (1978).
- D. A. Long and R. T. Bailey, *Trans. Faraday Soc.*, **59**, 594 (1963).
- V. Gutman, "Coordination Chemistry in Nonaqueous Solvents," Springer Verlag, Berlin (1968).
- A. N. Dey and P. Bro, in "Power Sources 6, Proceedings of the 10th International Power Sources Conference," D. H. Collins, Editor, p. 493, Academic Press, New York (1978).
- A. N. Dey, W. Bowden, and H. Hamilton, in "Proceedings of the 29th Power Sources Conference," Atlantic City, NJ, June 9-12, 1980, The Electrochemical Society, Inc., p. 164 (1981).
- J. P. Gabano and P. Lenfant, in "Battery Design and Optimization," S. Gross, Editor, p. 348, The Electrochemical Society Softbound Proceedings Series, Princeton, NJ (1979).
- C. R. Schlaikjer, F. Goebel, and N. Marincic, *This Journal*, **126**, 513 (1979).
- J. P. Gabano and G. Gelin, in "Proceedings of the 12th International Power Sources Symposium," p. 3, Academic Press, New York (1980).
- G. H. Wagner and W. H. Gitzen, *J. Chem. Educ.*, **29**, 162 (1952).
- F. M. Brewer, P. L. Goggin, and G. S. Reddy, *J. Inorg. Nucl. Chem.*, **28**, 361 (1966).
- A. Hardy and A. M. Hardy, *C. R. Acad. Sci. Paris*, **25**, 3477 (1963).
- W. L. Bowden and A. N. Dey, *This Journal*, **126**, 2035 (1979).
- W. L. Bowden and A. N. Dey, *ibid.*, **127**, 1419 (1980).
- G. E. Blomgren, V. Z. Leger, T. Kalnoki-Kis, M. L. Kronenberg, and R. J. Brodd, *Power Sources*, **7**, 583 (1979).
- C. R. Schlaikjer, in "Lithium Batteries," J. P. Gabano, Editor, p. 304, Academic Press, New York (1983).
- J. P. Gabano, in "Lithium Nonaqueous Battery Electrochemistry," E. B. Yeager, Editor, p. 98, The Electrochemical Society Softbound Proceedings Series, Pennington, NJ (1980).

Quantitative Measurements of Passive Dissolution of Chromium, Iron, and Molybdenum from a Stainless Steel

G. Hultquist

Department of Physical Chemistry, The Royal Institute of Technology, S-100 44 Stockholm, Sweden

C. Leygraf*

Swedish Corrosion Institute, S-114 86 Stockholm, Sweden

D. Brune

NIOM, Scandinavian Institute of Dental Materials, Oslo 3, Norway

ABSTRACT

Selective dissolution behavior and concomitant changes in surface composition have been elucidated by combined γ -spectrometry and ESCA studies of a passive stainless steel immersed in an artificial saliva solution. Quantitative γ -spectrometry data show that there is a selective dissolution of iron during all times of exposure. Quantitative ESCA data suggest that all expected surface accumulation of chromium occurs in the passive film formed. Under present conditions, the chromium content of the film increases with time of immersion, having its highest values at the outermost surface region and exhibiting a decrease when approaching the film/alloy interface.

The existing knowledge of passive film behavior on stainless steels is with almost no exclusion based on the use of experimental techniques which are capable of directly observing various properties of the passive film such as its thickness, structure, chemical composition, or semiconducting properties. See, for instance, Ref. (1), which is a recent review of the stainless steel surface. From these studies, it has become evident that the origin of the protective ability can be associated with an enrichment of chromium in the passive film (2, 3), the passivation presumably taking place by the formation of hydrated chromium oxy-hydroxide (4). It has been suggested that the buildup of the passive film on iron-based alloys and the possible surface accumulation of various alloying elements, such as chromium and molybdenum, is primarily due to a selective dissolution of iron during passive-state conditions (5, 6). However, in view of the importance of the concept of selective dissolution of iron, there exist only a small amount of quantitative data on dissolution rates of iron and its main alloying constituents as based on measurements of the chemical composition of the solution.

This work presents quantitative results of both passive film composition (as obtained by ESCA) and of dissolution rates of iron, chromium, and molybdenum (as obtained by γ -spectrometry) of a commercial ferritic stainless steel studied under passive-state conditions in an artificial saliva solution. The elemental release from biomaterials, such as stainless steels, in biological environments is an important property when evaluating these materials from a clinical point of view. By combining results obtained by ESCA as well as by γ -spectrometry, it has been possible to gain insight into the actual accumulation and in-depth distribution of, primarily, chromium in the investigated surface-alloy region.

Experimental

Material, sample configuration, and solution.—A ferritic stainless steel with chemical composition shown in Table I was mechanically polished to 1000 mesh on paper of silicon carbide and with distilled water as coolant. The sample configurations used in the radiochemical analysis are presented in Table II, and the composition of the artificial saliva solution used is found in Table III.

Radioactivation, exposure to solution, and γ -spectrometry measurements.—After mechanical polishing but prior

to exposure to solution, the samples were irradiated together with standards of chromium, iron, and molybdenum consisting of $\text{CrNO}_3 \times 9\text{H}_2\text{O}$, $\text{FeCl}_3 \times 6\text{H}_2\text{O}$, and MoO_2Br_2 in milligram quantities. The irradiation was accomplished at a thermal neutron flux of $5 \times 10^{12} \text{ n} \cdot \text{cm}^{-2} \cdot \text{s}^{-1}$ for 1 day.

Each set of two samples (Table II) was exposed in 200 ml of the solution (Table III) for subsequent periods of 24.5, 48, and 24h, respectively. Thus the total period of exposure was 96.5h. In the beginning of each exposure period, fresh solutions were introduced into the vials. The solution was kept at 37°C in limited air contact resulting in a pH 5-6. The samples were under conditions of free corrosion, *i.e.*, without any external potentiostatic control.

The radiochemical analysis was accomplished by means of the following nuclides: ^{51}Cr ($t_{1/2} = 28\text{d}$), ^{59}Fe ($t_{1/2} = 46\text{d}$), and ^{99}Mo ($t_{1/2} = 67\text{h}$). The γ -ray spectrometric measurements were conducted by a multichannel analyzer, Canberra, connected to a Ge(Li) detector. The 200 ml solutions were measured for periods up to ~ 15h.

Surface analysis.—Electron spectroscopy for chemical analysis (ESCA) in a spectrometer, LH 2000, was con-

Table I. Analysis (w/o) of stainless steel used

C	Si	Mn	P	S	Cr	Ni	Mo	Ti	Cu	Fe
0.03	0.34	0.48	0.019	0.007	18.4	0.27	2.27	0.6	0.04	77.54

Table II. Sample configurations

No. samples	Area/sample (cm ²)	Sharp edge length/sample (cm)
2	18.6	24.0
2	17.8	85.6

Table III. Composition of solution used

Compound	Amount (g/l)
NaCl	0.40
KCl	0.40
$\text{CaCl}_2 \cdot 2\text{H}_2\text{O}$	0.80
$\text{NaH}_2\text{PO}_4 \cdot 2\text{H}_2\text{O}$	0.78
$\text{Na}_2\text{S} \cdot 9\text{H}_2\text{O}$	0.005
Urea	1.0

* Electrochemical Society Active Member.

Key words: surfaces, passivity, ESCA, radioactivity.

ducted for surface analysis. Immersion of the (nonactivated) ESCA samples in the artificial saliva solution was made under identical conditions as for the (activated) γ -spectrometry samples to evaluate the influence of the immersion on the chemical composition in the steel surface. Samples with dimensions $10 \times 10 \times 1$ mm for ESCA measurements were exposed together with additional steel samples in order to reach a ratio of solution-to-sample area $\approx 5 \text{ ml} \cdot \text{cm}^{-2}$ as being the ratio in the γ -spectrometry measurements. After exposure to the solution, the samples were rinsed in distilled water for a few seconds, dried in hot air, and transferred within 2 min into the vacuum chamber for ESCA measurements.

AlK α radiation was used for excitation of the photoelectrons. Cr2p $_{3/2}$, Fe2p $_{3/2}$, and Mo3d $_{5/2}$ photoelectron lines were studied. Pure iron-sputtered foils of these elements, together with naturally formed passive films on the same foils, as well as thicker (~ 20 nm) thermally grown oxides, were analyzed as standards. A quantitative evaluation of ESCA spectra was performed by measuring the signal amplitudes of photoelectron peaks and comparing them with corresponding oxide and metal peaks of the standard samples. When taking all possible sources of errors into consideration, the accuracy of the quantitative ESCA evaluation is estimated to approximately $\pm 15\%$ (6). A free mean path of 1.4 nm is assumed for both the chromium and iron photoelectrons analyzed (7). In order to somewhat alter the surface sensitivity of the ESCA method, the take-off angle of the detected photoelectrons was varied between 90° and 20° in a plane where the angle of acceptance by the electron analyzer was $\sim 10^\circ$.

Results

γ -spectrometry.—When the alloy is immersed in the electrolyte without potentiostatic control, the total dissolution rate decreases with time in a way which is representative of stainless steel in a passive state (2). Table IV gives the accumulated amount of dissolved chromium, iron, and molybdenum (in $\mu\text{g}/\text{cm}^2$) after various times of exposure in the solution. From Table IV, it is concluded that the most intensive dissolution for all investigated elements occurs during the first 24h and decreases during further exposure, suggesting that the protective ability of the steel increases as a result of changes in surface composition. In order to possibly distinguish the dissolution behavior of flat surfaces from that of sharp sample edges, the whole samples, including sharp edges, were immersed in the saliva solution during γ -spectroscopy measurements. By varying the sample geometry and hence the ratio of the total length of sharp edges to the total area of flat surfaces, it was possible to separate both contributions from each other. Although not further discussed in this work, Table IV shows the estimated accumulated amount of chromium, iron, and molybdenum (in $\mu\text{g}/\text{cm}$ sample edge) which has dissolved from sharp sample edges. The results suggest that selective dissolution also occurs from these parts of the sample but are less pronounced than from flat sample surfaces.

The selective dissolution behavior is illustrated by introducing selectivity coefficients, Z_{Cr} and Z_{Mo} , which show by how many times the ratios of chromium or molybdenum concentration to iron concentration in dissolving species differ from the same ratios in the bulk steel (6). Hence

Table IV. Total amounts of dissolved chromium [$m(\text{Cr})$], iron [$m(\text{Fe})$], and molybdenum [$m(\text{Mo})$] after various times of immersion. Data are given for dissolution from sample surfaces ($\mu\text{g}/\text{cm}^2$) as well as from sharp sample edges ($\mu\text{g}/\text{cm}$)

Time (h)	$m(\text{Cr})$	$m(\text{Fe})$	$m(\text{Mo})$	Dissolution from
24.5	0.0168	0.474	0.0021	surface
72.5	0.0198	0.578	0.0023	surface
96.5	0.0208	0.631	0.0027	surface
96.5	0.0029	0.037	0.0002	sharp edges

Table V. Variation in time of selectivity coefficients Z_{Cr} and Z_{Mo} according to γ -spectrometry

Time (h)	Z_{Cr}	Z_{Mo}
(0)	(1.0)	(1.0)
24.5	0.149	0.151
72.5	0.144	0.136
96.5	0.139	0.146

$$Z_{\text{Cr}} = \frac{\left[\frac{m(\text{Cr})}{m(\text{Fe})} \right]_{\text{solution}}}{\left[\frac{m(\text{Cr})}{m(\text{Fe})} \right]_{\text{alloy}}} \quad [1]$$

and

$$Z_{\text{Mo}} = \frac{\left[\frac{m(\text{Mo})}{m(\text{Fe})} \right]_{\text{solution}}}{\left[\frac{m(\text{Mo})}{m(\text{Fe})} \right]_{\text{alloy}}} \quad [2]$$

with $m(\text{Cr})$, $m(\text{Fe})$, and $m(\text{Mo})$ in the solution being amounts of dissolved chromium, iron, and molybdenum in micrograms per square centimeter of exposed area and with measured values according to Table IV. The corresponding values in the alloy represent the weight content of the elements according to Table I.

Table V shows the variation in time of the selectivity coefficients both of chromium and of molybdenum and clearly indicates values significantly below 1 at all times of immersion. From the observed depletion of chromium and molybdenum detected in the solution follows an expected accumulation of the same elements in the alloy surface.

ESCA.—Figure 1 shows the observed surface content of both chromium and molybdenum after various times of immersion of the stainless steel in the solution. In accordance with γ -spectrometry results (Table V), there is observed a surface enrichment of both chromium and molybdenum which increases with time of immersion. The results in Fig. 1 for Cr/Cr + Fe and Mo/Mo + Fe atomic ratios are based on studies of the main peaks of chromium (2p $_{3/2}$), iron (2p $_{3/2}$), and molybdenum (3d $_{5/2}$) as obtained in survey ESCA spectra in which no deconvolution of metal and oxide peaks of the investigated elements could be made. Hence, atomic ratios given in Fig. 1 represent values of total surface accumulation of chromium and molybdenum, with no distinction being made of the elements in their metallic or oxidized state.

Figure 2 contains spectra of chromium (2p $_{3/2}$) and iron (2p $_{3/2}$) peaks before immersion and after 96.5h of immersion. It is possible to deconvolute these peaks into their metallic and oxidized states, as has been shown elsewhere (8). Because of too-low amplitudes, this was not possible for the Mo (3d $_{5/2}$) photoelectron peak. Quantitative evaluation of the metal and oxide peaks, respectively, yields the variation in exposure time of Cr/Cr + Fe ratios for the metallic as well as the oxidized state (Fig. 3). It can be concluded that a majority of chromium surface accu-

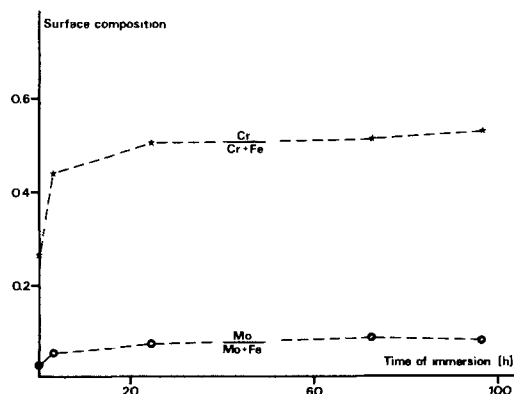


Fig. 1. Variation in time of overall chromium surface content,

$\frac{\text{Cr}}{\text{Cr} + \text{Fe}}$ and molybdenum surface content, $\frac{\text{Mo}}{\text{Fe} + \text{Mo}}$, respectively.

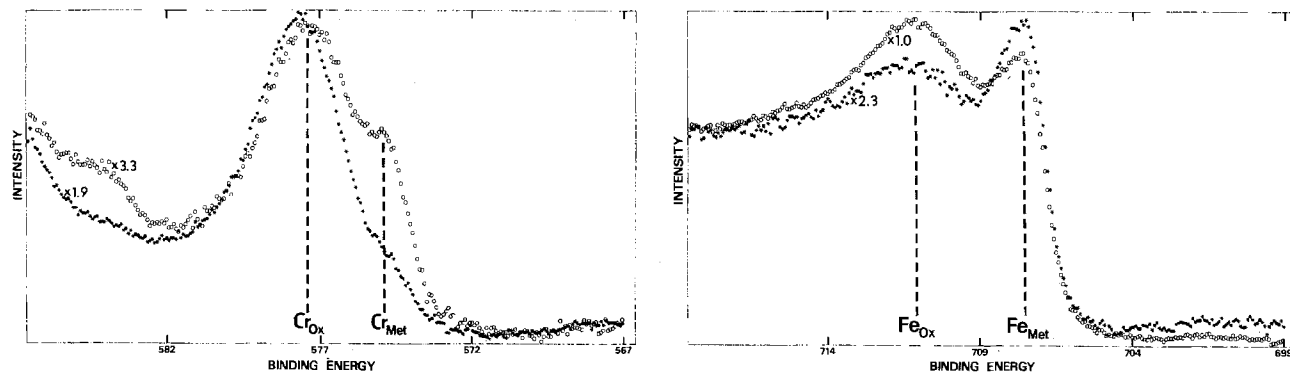


Fig. 2. Chromium (2p_{3/2}) (left) and iron (2p_{3/2}) (right) photoelectron peaks before (circles) and after 96.5h of immersion (stars) in saliva solution.

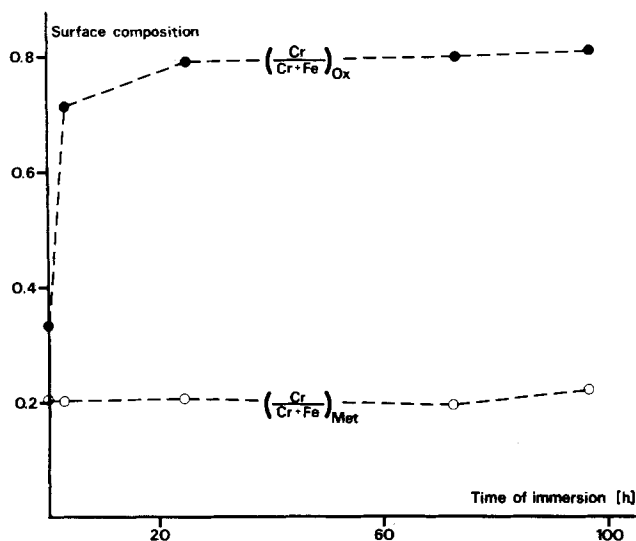


Fig. 3. Variation in time of chromium surface content, $\frac{Cr}{Cr + Fe}$, when considering the elements in their oxidized and metallic states, respectively.

accumulation occurs with chromium being in the oxidized state, whereas no significant accumulation occurs with chromium being in the metal state.

Comparison of γ -spectrometry and ESCA.—In what follows, a comparison is made between the quantitative results as obtained by γ -spectrometry and by ESCA. This is done by estimating the expected number of chromium ions accumulated in the surface region according to both methods (6).

From γ -spectrometry data of accumulated amounts of dissolved chromium and iron, $m(Cr)$ and $m(Fe)$, (see Table IV for numerical values), the excess amounts of chromium $[\Delta m(Cr)]$ after various times of exposure are presented in Table VI after calculations using the formula

$$\Delta m(Cr) = \frac{0.184}{0.775} m(Fe) - m(Cr) \quad [3]$$

Here, $\Delta m(Cr)$, $m(Fe)$, and $m(Cr)$ are expressed in micrograms per centimeter, and 0.184 and 0.775 are the weight percents (w/o) of Cr and Fe in the stainless steel studied. From ESCA data, the accumulated amount of chromium

Table VI. Accumulated amounts of chromium and of molybdenum in the surface region according to γ -spectrometry

Time (h)	$\Delta m(Cr)$ ($\mu g/cm^2$)	$\Delta N(Cr)$ ($10^{15}/cm^2$)	$\Delta m(Mo)$ ($\mu g/cm^2$)	$\Delta N(Mo)$ ($10^{15}/cm^2$)
24.5	0.096	1.11	0.012	0.07
72.5	0.117	1.36	0.015	0.09
96.5	0.129	1.49	0.016	0.10

ions $[\Delta N(Cr)]$ in the alloy surface has been estimated using the formula

$$\Delta N(Cr) = (X_{Cr} - 0.20) \cdot \frac{t}{v} \quad [4]$$

Here $(X_{Cr} - 0.20)$ represents the increase in chromium surface content ($Cr/Cr + Fe$ values taken in Fig. 3) at different times of immersion relative to a $Cr/Cr + Fe$ ratio equal to 0.20, which represents the bulk value of the steel. t is the thickness of the surface layer in which accumulation of chromium occurs. v is the assumed value of the cation volume in the passive film which, according to electron diffraction data (9), has been estimated to be equal to 28 ± 3 ($nm \pm 0.1$)³; see Ref. (6) for further details. The thickness t can be estimated by a procedure outlined elsewhere (10), which uses the fact that the intensity of photoelectrons decays exponentially with depth from where they originate. Hence, Table VII presents estimated values of thicknesses and the accumulated amount of chromium after various times of exposure using the ESCA data of Fig. 1 and 3.

A comparison of the estimated accumulated number of chromium ions according to data obtained by γ -spectrometry (Table VI) and by ESCA (Table VII) shows that the estimates are close, the numbers as obtained by γ -spectrometry being slightly smaller.

Discussion

The coincidence between estimated excess surface chromium according to γ -spectrometry and ESCA is very close when considering various sources of errors which all may have an influence on the reliability of the results. Of such sources should be mentioned the procedure for quantitative evaluation of ESCA data, the separation of dissolution from sample edges and sample surfaces, respectively, and the procedure for estimating the thickness of the region with excess chromium.

The coincidence in results based on γ -spectrometry and ESCA measurements suggests that selective dissolution of iron results in changes in chemical composition of a surface layer which is thinner than the information depth of ESCA. Table VII reveals that after 3-96h of immersion the thickness of the surface layer with excess chromium is around 1.0 nm and with an average chromium content ($Cr/Cr + Fe$) slowly increasing with time of exposure from

Table VII. Thickness (t) of surface layer in which accumulation of chromium occurs, average chromium content (X_{Cr}), and amount of accumulated chromium $[N'(Cr), N(Cr)]$ in the surface layer according to ESCA. $\Delta N(Cr) = N'(Cr) - N'(Cr)_{t=0}$ is accumulation due to immersion

Time (h)	t (nm)	X_{Cr}	$\Delta N'(Cr)$ ($10^{15}/cm^2$)	$\Delta N(Cr)$ ($10^{15}/cm^2$)
0	0.9	0.33	0.5	0.0
3	0.9	0.71	1.6	1.2
24.5	1.0	0.79	2.2	1.7
72.5	1.0	0.80	2.2	1.8
96.5	1.1	0.82	2.5	2.0

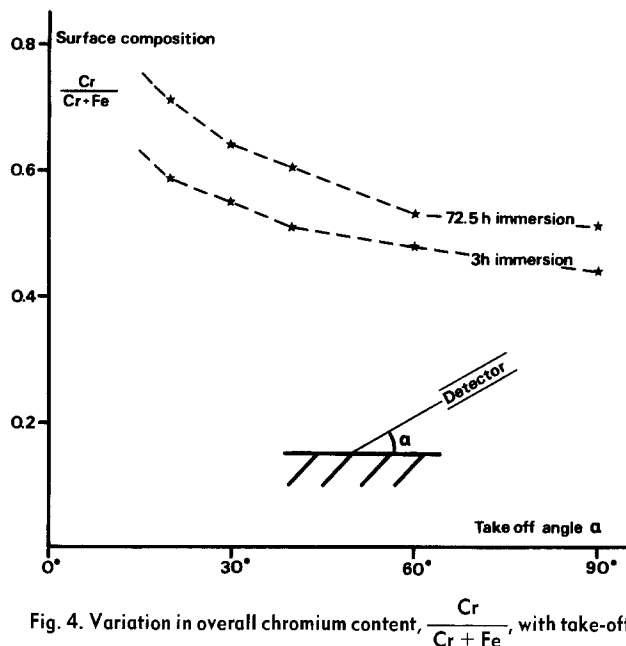


Fig. 4. Variation in overall chromium content, $\frac{\text{Cr}}{\text{Cr} + \text{Fe}}$, with take-off angle of photoelectrons detected.

0.7 to 0.8. Since all excess chromium is in an oxidized state (Fig. 3), it can be assumed that a majority of excess chromium is in the passive film of the stainless steel rather than in the alloy region adjacent to the film. A previous combined γ -spectrometry and ESCA study of passivated Fe18Cr and Fe18Cr3Mo alloys under potentiostatic control revealed much larger estimates of accumulated amounts of chromium according to γ -spectrometry measurements than according to ESCA measurements (6). This was interpreted as being due to an enrichment of chromium in a surface region thicker than the passive film itself. This suggests that selective dissolution of iron under potentiostatic polarization may result in a surface layer enriched in chromium which is significantly thicker than when selective dissolution of iron occurs under nonpotentiostatic conditions.

Although the results presented until now only have given the average chromium content of the passive film, it is of interest also to discuss the possible in-depth distribution of chromium within the film. For this purpose, the take-off angle of photoelectrons detected was varied by changing the orientation of the sample with respect to the entrance slit of the ESCA analyzer. With this procedure, it is possible to alter the surface sensitivity allowing the chemical composition to be studied at various depths in a nondestructive way (11).

Figure 4 illustrates the variation in overall chromium content, $\text{Cr}/\text{Cr} + \text{Fe}$, from lower surface sensitivity (high take-off angle) to higher surface sensitivity (low take-off angle). Because of too low ESCA amplitudes at take-off angles lower than 20° , the $\text{Cr}/\text{Cr} + \text{Fe}$ ratio in the outermost surface region cannot be measured; it can only be estimated from extrapolation of ratio values at higher

take-off angles. The results after 72.5h of immersion in Fig. 4 indicate that the $\text{Cr}/\text{Cr} + \text{Fe}$ ratio may approach 1.0 in the outermost surface region and decreases with depth. Similarly, the results after 3h of immersion indicate the highest $\text{Cr}/\text{Cr} + \text{Fe}$ ratio at the outermost surface region and a decrease in $\text{Cr}/\text{Cr} + \text{Fe}$ ratio towards increasing information depth (higher angles in Fig. 4).

The beneficial effect of enrichment of chromium in the passive film can be illustrated by inspecting the actual dissolution rates at various times of immersion. During the first 24h of immersion—characterized by lower chromium film contents—the total release of dissolving species was $\sim 0.49 \mu\text{g}/\text{cm}^2$ (Table VI), corresponding to an average current density of $\sim 0.03 \mu\text{A}/\text{cm}^2$, whereas during the final 24h of immersion—characterized by higher chromium film contents—the total release of dissolving species was approximately 10 times smaller (Table VI) corresponding to an average current density of $\sim 0.003 \mu\text{A}/\text{cm}^2$.

γ -spectrometry as well as ESCA data have furthermore shown that molybdenum is accumulated in the surface region of the stainless steel. However, because of too low intensities, it was not possible to deconvolute the Mo ($3d_{5/2}$) photoelectron peaks into their metallic and oxidized parts. For this reason, estimates of surface accumulation of molybdenum could only be made by γ -spectrometry; they are shown in Table VI.

Conclusions

Combined γ -spectrometry and ESCA studies of a ferritic stainless steel immersed in an artificial saliva solution under nonpotentiostatic conditions show that the observed selective dissolution of iron results in a surface enrichment of both chromium and molybdenum. After immersion times up to 96h the quantitative treatment of γ -spectrometry and ESCA data show that all accumulation of chromium occurs in the naturally formed passive film. During the same time interval, the average chromium content $\text{Cr}/\text{Cr} + \text{Fe}$ of the surface layer in which an accumulation of chromium is observed increases from around 0.3 to 0.8. The chromium content can be as high as 1.0 at the outermost surface region and decreases rapidly towards the film/alloy interface after immersion of the steel surface for a few hours in the solution.

REFERENCES

1. R. O. Adams, *J. Vac. Sci. Technol. A*, **1**, 12 (1983).
2. G. Hultquist and C. Leygraf, *Mater. Sci. Eng.*, **42**, 199 (1980).
3. M. Seo and N. Sato, in "10th World Congress on Metal Finishing, Kyoto," p. 427 (1980).
4. K. Asami and K. Hashimoto, *Corros. Sci.*, **19**, 251 (1979).
5. Ya. M. Kolotyrykin, in "Proceedings of the 6th International Congress on Metallic Corrosion," p. 209, Sydney, Australia (1975).
6. C. Leygraf, G. Hultquist, I. Olefjord, B-O. Elfström, V. M. Knyazheva, A. V. Plaskeyev, and Ya. M. Kolotyrykin, *Corros. Sci.*, **19**, 343 (1979).
7. C. J. Powell, *Surf. Sci.*, **44**, 29 (1974).
8. I. Olefjord, *Corros. Sci.*, **15**, 687 (1975).
9. C. L. McBee and J. Kruger, *Electrochim. Acta*, **17**, 1337 (1972).
10. C. R. Brundle, *J. Vac. Sci. Technol.*, **11**, 212 (1974).
11. M. F. Ebel, *Surf. Interfac. Anal.*, **3**, 173 (1981).

The Characterization of Doped Iron Oxide Electrodes for the Photodissociation of Water

Stability, Optical, and Electronic Properties

J. E. Turner, M. Hendewerk,* J. Parmeter, D. Neiman, and G. A. Somorjai

Materials and Molecular Research Division, Lawrence Berkeley Laboratory, and Department of Chemistry, University of California, Berkeley, California 94720

ABSTRACT

A characterization of optical and electronic properties is presented for p-type (Mg-doped) and n-type (Si-doped) iron oxides used in the photoelectrolysis of water. Photocurrent *vs.* wavelength spectra for these electrodes indicate that α -Fe₂O₃ is the active optical component for both p-type and n-type materials. Band-edge locations for p-type and n-type iron oxides in sodium hydroxide aqueous solution are determined from differential capacitance measurements. The thermodynamic feasibility of the catalytic photodissociation of water without external potential is demonstrated for a short-circuited p/n diode assembly on an energy level diagram of the electrode/electrolyte interfaces. The open-circuit voltage (V_{oc}) and short-circuit current (I_{sc}) generated by the p/n assembly as a function of the intensity of laser irradiation indicate that these doped iron oxides are low mobility, high carrier density semiconductors. Photo-oxidation of water at the n-type anode is verified through oxygen detection. Gas evolution is monitored from an operating diode assembly using mass spectrometry and isotopically labeled water (H₂¹⁸O). Photocurrents from these p/n assemblies show excellent long-term stability in aqueous solution and Auger analysis of the semiconductor surfaces indicates no evidence of electrode dissolution.

The photoelectrolysis of water over semiconductors has received considerable attention as an alternative means of harnessing solar energy. Since the first report by Fujishima and Honda (1) of the photodissociation of water over TiO₂ electrodes, much of the theoretical basis for semiconductor photoelectrolysis has been developed by Gerischer (2).

To date, the photoelectrochemical generation of hydrogen and oxygen from water has been achieved in two different cell configurations. In the first, an illuminated (n-type) photoanode or (p-type) photocathode semiconductor is immersed in solution against a metal counter-electrode (3-8). In most cases, an external bias is applied between the electrodes. The second configuration, first investigated by Nozik (8), uses two illuminated semiconductors, a p-type photocathode and n-type photoanode. Such p/n assemblies have been used for water photoelectrolysis usually without an applied potential.

The majority of systems studied have required expensive single-crystal semiconducting electrodes to achieve high efficiency for solar conversion. However, several recent reports have found that transition metal oxide semiconductors may be a less costly alternative (11-15). The Mg-doped (p-type) iron oxide/Si-doped (n-type) iron oxide photochemical diode as described by recent reports from our laboratory (16) is an interesting and economical possibility.

Iron oxide satisfies most of the requirements for an excellent solar energy conversion material. It has a bandgap of 2.3 eV (17) which allows utilization of 40% of the incident solar radiation. It also exhibits excellent stability in both acidic and alkaline electrolyte solutions. Most attractively, it has been shown that in a short-circuited configuration, a Mg-doped p-type iron oxide cathode against a Si-doped n-type anode can photodissociate water with no applied external bias (16).

In this work, an electronic and optical characterization of the Mg-doped and Si-doped iron oxide electrodes is described. The photocurrent response was obtained as a function of wavelength. Depletion layer capacitance measurements were carried out to determine band-edge locations, carrier types and concentrations. The open-circuit voltage and short-circuit current were measured as a function of light intensity. The catalytic production of oxygen was detected using labeled water (H₂¹⁸O). In addition, we present advances in the operation and stability of the p/n diode assembly.

Experimental

Preparation of doped iron oxide electrodes.—The procedure for preparing p-type and n-type doped iron oxide electrodes has been presented in detail previously (16). Powders of MgO or SiO₂ are mixed with a α -Fe₂O₃ to produce p-type or n-type doped iron oxide semiconductors, respectively. These mixed powders are pressed into pellets, sintered, and rapidly cooled in water. Finally, the doped iron oxide disks are mounted on a conductive backing of silver epoxy.

Characterization of both Mg- and Si-doped electrodes with scanning electron microscopy (SEM) and scanning auger microprobe (SAM) showed the surfaces to be heterogeneous with several phases (16). Silicon-doped samples showed some diffusion of the silicon into the Fe₂O₃ matrix, and also the presence of silicon-rich precipitates. Magnesium-doped samples showed Mg in an iron oxide matrix, as well as MgO. It is evident from these results, as well as measurements of carrier density presented later, that only a small proportion of either dopant atom actually enters the iron oxide lattice substitutionally.

Photocurrent spectra.—Quantum efficiencies of these doped polycrystalline iron oxides were measured individually as a function of wavelength over the range 300 < λ < 700 nm. Photocurrent spectra were determined at several different electrode biases using a 500W tungsten halogen source, Heath monochromator, and a Pine RDE potentiostat. Correcting for the spectral output of the lamp/monochromator assembly, absolute quantum efficiencies were obtained using a Gamma Scientific 2000 Telephotometer and calibrated thermopile detector. Tests were performed in 0.01N NaOH on undoped samples as well as those doped with Mg or Si.

Depletion layer capacitance measurements.—To determine band-edge locations, capacitances of the space charge layer (C_{sc}) of each semiconductor electrode were determined as a function of applied voltage for both the p-type and n-type electrodes. The electrode configuration consisted of a standard three-electrode electrochemical cell containing a mercury oxide reference electrode, a platinum counterelectrode, and a doped iron oxide anode or cathode immersed in 0.01N NaOH solution. An ac voltage (amplitude 10 mV) with frequency 300 Hz < f < 3 kHz was superposed on the dc voltage applied to the working electrode from a Pine RDE potentiostat. Tests were performed both in the dark and under illumination of 35 mW/cm² intensity focused from a tungsten-halogen

*Electrochemical Society Student Member.

lamp. Depletion layer capacitances were extracted from the phase shift of the ac current out relative to the ac voltage in by use of a PAR Model 124A lock-in amplifier. Corrections were included to eliminate phase shifts introduced by the potentiostat and line impedances.

Open-circuit voltage (V_{oc}) and short-circuit current (I_{sc}).—Two important parameters of the operating p-type/n-type iron oxide assembly are the open-circuit voltage generated by the diode (V_{oc}) and the short-circuit current (I_{sc}). To investigate electron/hole production in these materials, V_{oc} and I_{sc} were measured as a function of the illumination intensity from a CW Kr⁺ laser (Spectra Physics). Iron oxide electrodes containing 10 atomic percent (a/o) Si and 5 a/o Mg were immersed in 0.01N NaOH and either separated by a high impedance voltmeter or connected through an ammeter. The laser supplied several discrete wavelengths centered at approximately 411 nm (violet) and 544 nm (green). Using a lens assembly and beam splitter, the single 1.5 mm diam beam was defocused to illuminate the entire surface of both electrodes with uniform intensity. The total intensity of illumination could be varied from 20 mW to 4W covering two electrodes of ~0.6 cm² area each.

Oxygen detection from the unbiased p/n diode assembly.—To detect the production of oxygen from the unbiased p-type/n-type iron oxide assembly, a stainless steel cell (Fig. 1) was used with two quartz windows for the simultaneous illumination of both iron oxide electrodes. Tungsten-halogen illumination of approximately 5 mW/cm² intensity was focused with quartz optics and passed through a 5 cm water filter to absorb IR radiation before entering the cell. A 0.01N NaOH/H₂O solution containing 6% isotopically enriched H₂¹⁸O (Alpha Ventron Distributors) was used as the electrolyte solution. Gases produced from the water dissociation process were circulated with a small mechanical pump in a closed stainless steel loop containing Ar carrier gas which passed over the electrolyte solution. Gas samples were extracted from the loop at 24h intervals and injected into a UHV chamber for mass spectral analysis. Photoproduced oxygen was detected as ³⁴O₂.

Results and Discussion

Photocurrent spectra.—Ferric oxide (α -Fe₂O₃) is known to be an intrinsic n-type semiconductor (17) with an indirect bandgap of approximately 2.3 eV. Since the electrodes as fabricated were shown to be multiphase, it was important to establish that the active optical component is in fact α -Fe₂O₃.

The quantum efficiency, η , defined as the number of chemically active electron/hole pairs produced per incident photon, was measured as a function of wavelength over the visible range. Figure 2 shows these results for

undoped Fe₂O₃ (Fig. 2a), silicon-doped (Fig. 2b), and magnesium-doped (Fig. 2c) electrodes.

Quantum efficiencies for undoped α -Fe₂O₃ were measured as photoanodic currents at a bias of 1250 mV RHE, yielding a maximum of $\eta = 0.03$ at 3800Å. A decrease in this efficiency at higher wavelengths occurs near the Fe₂O₃ bandgap of approximately 5500Å. Since the absorption coefficient for Fe₂O₃ increases with decreasing wavelength over the visible range, shorter wavelengths produce electron/hole pairs near the surface of the semiconductor. We believe that surface defects in this near surface region increase electron/hole recombination and result in the low quantum efficiencies observed at the lowest wavelengths.

The addition of Si is believed to enhance the n-type behavior of Fe₂O₃ by improving the electron mobility in this semiconductor (18). As seen in Fig. 2b, the addition of 10% Si in Fe₂O₃ resulted in a ten-fold increase in quantum efficiency over undoped samples for the same electrode bias (1250 mV, RHE). In separate measurements, the operating potential of an unbiased p/n assembly was found to be 750 mV, RHE. To determine the characteristics of the individual electrodes in this configuration, photocurrent spectra were measured at this bias. As seen from Fig. 2b, the n-type spectral features remain essentially the same at 750 mV, RHE as at 1250 mV, RHE, while quantum efficiencies at a given wavelength are reduced by greater than an order of magnitude. This behavior is expected since the 750 mV bias results in a lesser degree of band bending and increased electron/hole recombination.

Similar measurements on the Mg-doped samples (Fig. 2c) showed photocathodic currents (indicative of p-type behavior). Despite the change in sign of the photocurrent, the spectral features of the Mg-doped Fe₂O₃ were similar to the Si-doped and undoped Fe₂O₃ electrodes. For a bias of 750 mV, RHE (the operating potential of the assembly) the p-type iron oxide yielded a maximum quantum efficiency of $\eta = 5 \times 10^{-3}$ at 3800Å. By changing the bias to 250 mV, RHE, band bending near the electrode surface was increased by 500 mV, and quantum efficiencies were enhanced by a factor of five.

From the near bandgap region of these plots, one can determine the nature of electron/hole production in these materials (19). For a direct gap semiconductor

$$I_{ph} \propto (A/h\nu) (h\nu - E_g)^{1/2} \quad [1]$$

while for an indirect gap semiconductor

$$I_{ph} \propto (A/h\nu) (h\nu - E_g)^2 \quad [2]$$

where I_{ph} is the photocurrent, $h\nu$ is the energy of illumination, E_g is the bandgap, and A is a constant dependent upon applied bias.

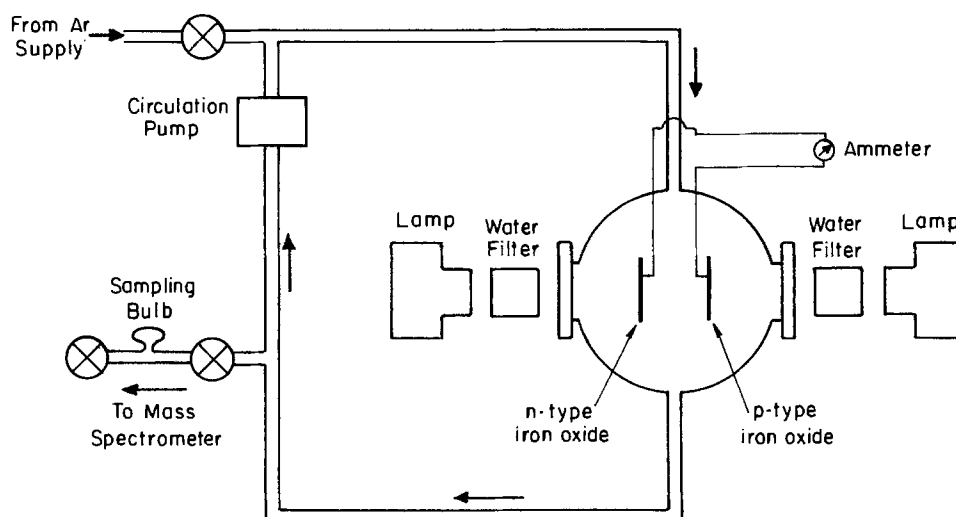


Fig. 1. Schematic diagram of the apparatus for oxygen detection from the operating p/n diode assembly.

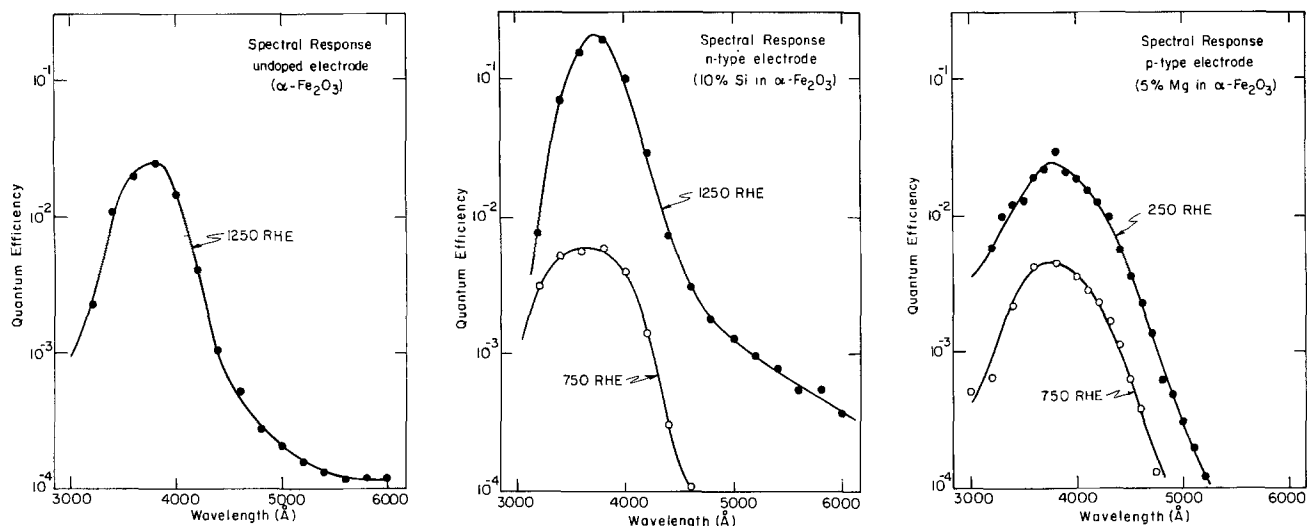


Fig. 2. Quantum efficiency vs. wavelength plots for (a, left) undoped Fe_2O_3 , (b, middle) 10% Si in Fe_2O_3 , and (c, right) 5% Mg in Fe_2O_3

Following these arguments, the data of Fig. 2b and 2c at 1250 mV bias are replotted in Fig. 3 as $(I_{ph}h\nu)^{1/2}$ vs. $h\nu$. The linear fit near the band edge confirms that both Mg- and Si-doped Fe_2O_3 are indirect bandgap semiconductors. In addition, the intercepts with the photon energy axis yield bandgaps of approximately 2.3 eV for both p-type and n-type materials. These values agree well with published values for the bandgap of undoped Fe_2O_3 (17), indicating that $\alpha\text{-Fe}_2\text{O}_3$ is most likely the photoelectrochemically active phase in these multiphase materials.

Differential capacitance measurements.—Previously, we reported the photodissociation of water in an unbiased p-type/n-type iron oxide assembly (16). In this assembly, the Mg-doped (p-type) electrode acted as a photo-

cathode and the Si-doped electrode acted as a photoanode for the generation of H_2 and O_2 from water. The spontaneous occurrence of both processes under illumination is thermodynamically feasible only with the proper positioning of the conduction and valence band-edges with respect to the redox couples in the electrolyte solution. To establish band-edge locations for the doped iron oxides, space charge capacitances of these electrodes were determined.

Differential capacitances of the semiconductor space charge layer (C_{sc}) with applied potential (V_a) were measured independently for both the p-type and n-type electrodes. Following the Mott-Schottky relation (20, 21)

$$1/C_{sc}^2 = 2(q\epsilon\epsilon_0 A^2 N)^{-1}(V_a - V_{FB}) \quad [3]$$

flatband potentials (V_{FB}) were extracted from the intercept on a plot of the reciprocal capacitance squared ($1/C_{sc}^2$) against applied voltage (V_a). Typical Mott-Schottky plots are shown in Fig. 4. These measurements were performed at 1500 Hz on a 10 a/o Si-doped and 5 a/o Mg-doped iron oxide electrode. All potentials are given relative to the reversible hydrogen electrode (RHE) which shifts 59 mV/pH unit, so that the hydrogen redox couple remains at 0.0V, RHE and the oxygen redox couple at 1.23V, RHE, independent of the pH of the electrolyte solution.

From these plots, the flatband potentials for the n-type and p-type electrodes are 200 and 2300 mV, RHE, respectively. Similar capacitance measurements performed over the frequency range 300 Hz $< f <$ 3000 Hz showed no shift in flatband potential. In addition, measurements made in the darkness and under illumination showed no appreciable variation within the accuracy of the measurement (± 200 mV).

In addition to values of the flatband potential, donor or acceptor concentrations, N , can be obtained from the Mott-Schottky plots of Fig. 4. The slope of the linear region in which relation [3] is obeyed is given by $S = 2(q\epsilon\epsilon_0 A^2 N)^{-1}$ where q is the charge on an electron, ϵ_0 is the permittivity of free space, ϵ is the dielectric constant for the sample, A is the electrode surface area, and N is the donor or acceptor concentration. Surfaces of the doped iron oxide electrodes have a roughness factor of approximately ten as measured in a krypton-helium BET apparatus (22) (Quantasorb Surface Area Analyzer, Quantachrome Corporation). From the value of $A = 6 \text{ cm}^2$ and the dielectric constant for pure $\alpha\text{-Fe}_2\text{O}_3$ ($\epsilon = 100$) (23), the acceptor or donor concentrations are calculated to be $N_A = 5 \times 10^{16} \text{ cm}^{-3}$ for the Mg-doped samples and $N_D = 2 \times 10^{18} \text{ cm}^{-3}$ for the Si-doped electrodes. Due to uncertainties in the dielectric constants for the doped iron oxides and in surface area determinations, carrier densities are correct only to within an order of magnitude.

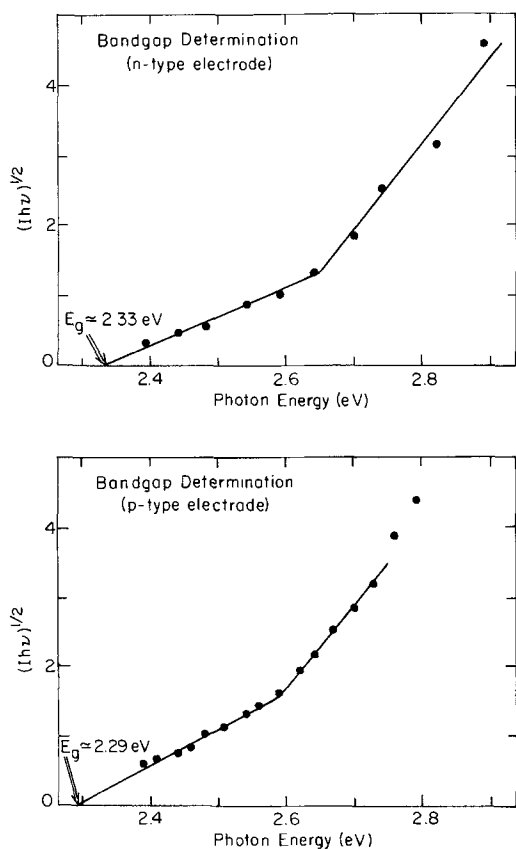


Fig. 3. Plots of $(I_{ph}h\nu)^{1/2}$ vs. $h\nu$ over the near bandgap region for (a, top) 10% Si in Fe_2O_3 , and (b, bottom) 5% Mg in Fe_2O_3 . The linear fit of this function suggests that both Si- and Mg-doped Fe_2O_3 are indirect bandgap semiconductors, with bandgaps of approximately 2.3 eV.

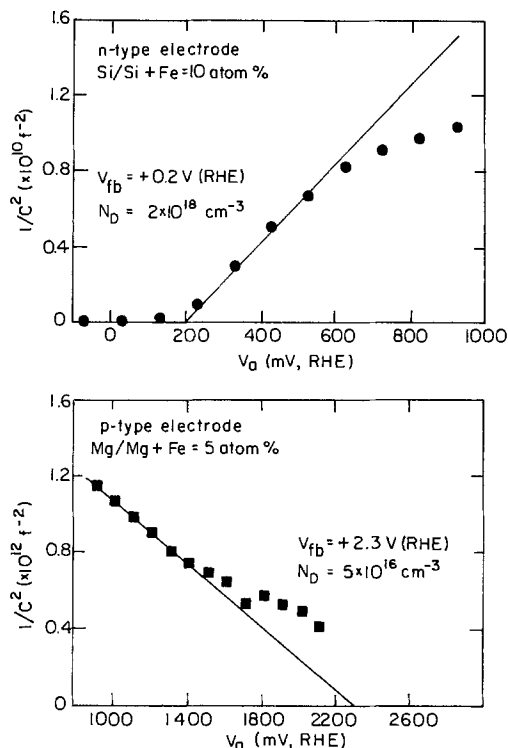


Fig. 4. Mott-Schottky plots of the inverse square of space charge capacitance $(1/C_{sc})^2$ vs. applied potential (V_a) for (a, top) 10% Si in Fe_2O_3 and (b, bottom) 5% Mg in Fe_2O_3 electrodes. Performed at 1500 Hz frequency in 0.01N NaOH against a Pt counterelectrode.

Homogeneous acceptor and donor distributions in both the p-type and n-type semiconductors may produce samples with more consistent photocurrents in a p/n diode assembly. Observed curvatures in the Mott-Schottky plots may be due to inhomogeneous doping concentration (24), particularly for the p-type electrodes. Another difficulty in sample preparation is diffusion of dopant atoms into the Fe_2O_3 matrix. A comparison of carrier densities from Mott-Schottky plots with the proportion of Mg or Si in our electrodes shows that only a small amount of either dopant enters the lattice. For the p-type electrodes with 5 a/o Mg, only about 0.002% of the Mg atoms enter the iron oxide lattice substitutionally. The vast majority of the Mg probably remains in its original oxide form (MgO). Similar calculations for the n-type electrodes show that only 0.05% of the Si contributes to donor levels. As mentioned earlier, SAM has shown that much of the Si aggregates in silicon rich precipitates, particularly at the surface (2). Thus, it might be beneficial to explore

alternative methods of incorporating ions into the iron oxide lattice rather than sintering at high temperatures.

Energy level diagram.—To understand the energetics of a short-circuited p/n assembly, information on the flat-band potentials and bandgaps may be incorporated into an energy level diagram. Such a diagram will demonstrate both the operating principles and thermodynamic feasibility of water photodissociation by the p/n assembly.

From the Mott-Schottky plots of Fig. 4, the flatband potentials for n-type and p-type electrodes were 200 and 2300 mV, RHE, respectively. For heavily doped semiconductors, the Fermi level is nearly coincident with the band containing the majority charge carriers. Thus, in the n-type iron oxide, the flatband potential designates the location of the conduction bandedge ($E_{cb}^n \cong V_{FB}^n = 200$ mV, RHE). A measured bandgap of 2.3 eV places the valence bandedge of the n-type electrode at $E_{vb}^n = 2500$ mV, RHE. Similar arguments may be made for the p-type electrode. Equating the valence bandedge to the flatband potential of the p-type ($E_{vb}^p \cong V_{FB}^p = 2300$ mV, RHE) and subsequently subtracting the bandgap energy (2.3 eV) places the conduction band at $E_{cb}^p = 0$ mV, RHE.

To derive a complete description of the unbiased p/n assembly energetics, the Fermi level of the short-circuited assembly is also needed. This was obtained by placing a connected p-type/n-type assembly in 0.01N NaOH solution and measuring the operating potential against a mercury oxide reference electrode with a high impedance voltmeter. The Fermi level of the connected assembly was thus found to be 750 mV, RHE.

Figure 5 is a representation of the electrode/electrolyte interfaces for the connected p-type/n-type iron oxide assembly in solution. In addition to the Fermi level and bandedges, we include the energy of redox potentials for hydrogen and oxygen evolution. From this diagram, the means by which water photoelectrolysis occurs in the iron oxide p/n diode is apparent. Upon illumination of both electrodes in solution, electron/hole pairs are produced near the surface of the semiconductors. Depletion layer band bending drives minority carriers to the solution interface while majority carriers diffuse away from the surface in both p-type and n-type electrodes. Electrons at the surface of the p-type photocathode mediate the conversion of hydronium ions to hydrogen gas, while electron vacancies oxidize hydroxyl species to oxygen at the n-type photoanode.

The alignment of semiconductor bandedges relative to gas evolution redox potentials is critical. Electrons must arrive at the p-type/electrolyte interface at a potential equal to or cathodic of the H^+/H_2 redox couple. Figure 5 shows that within the accuracy of our measurements, electrons reach the solution with exactly enough energy to drive this half-reaction. Conversely, holes at the n-type

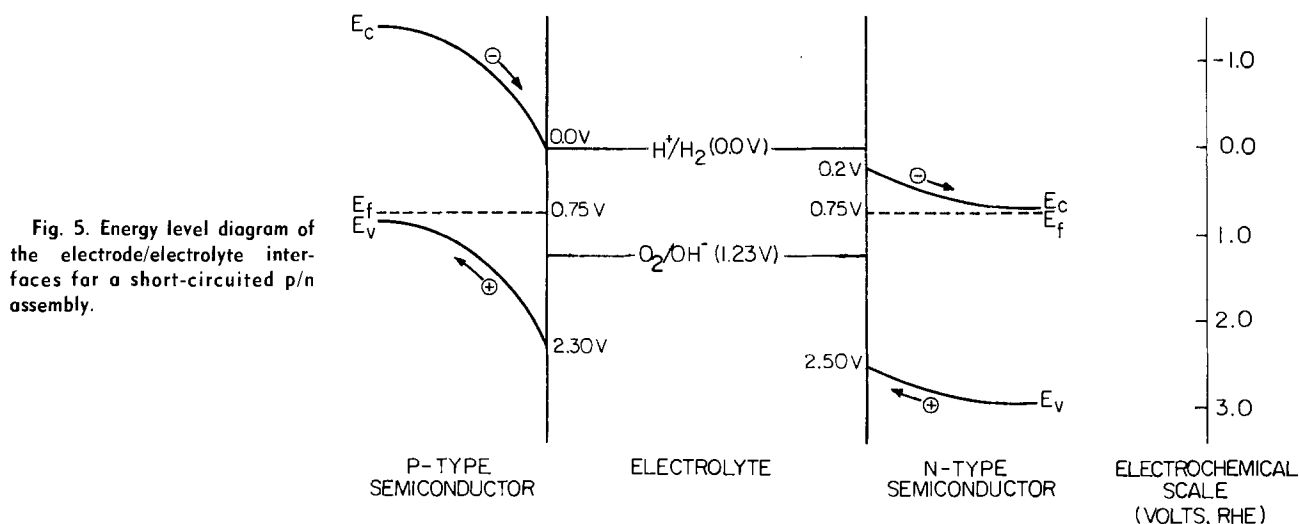


Fig. 5. Energy level diagram of the electrode/electrolyte interfaces for a short-circuited p/n assembly.

interface must arrive at a potential anodic of the O_2/OH^- half-reaction. As seen from the figure, this energy requirement is satisfied with more than 1.2 eV to spare. By meeting these basic thermodynamic criteria, it is evident that an illuminated and short-circuited p/n iron oxide assembly can photodissociate water without an external bias.

Figure 5 also shows that band-edge locations of the electrodes shift according to the dopant. The 200 mV cathodic shift of the conduction and valence bandedges of the p-type iron oxide relative to the n-type electrode may be due to the effect of introducing Mg into the iron oxide lattice. Butler and Ginley (25) have proposed a model in which the electron affinity of a composite system can be calculated using the geometric mean of the electron affinities of the constituent atoms. Thus, substitution of Mg dopant atoms ($EA = 1.2$ eV) with an electron affinity less than that of the iron atoms ($EA = 1.7$ eV) in the iron oxide lattice would lower the effective electron affinity of the semiconductor and shift the bandedges toward more cathodic potentials. Doping with Si, on the other hand, should not shift the bandedges of Fe_2O_3 since the electron affinities of silicon ($EA = 1.8$ eV) and iron are very similar.

With charge carrier concentrations from the Mott Schottky plots and band bending values (V_{bb}) from Fig. 5, depletion layer widths can also be calculated. With $W_D = (2\epsilon\epsilon_0 V_{bb}/qN)^{1/2}$, the depletion layer widths in an operating p/n assembly for the p-type and n-type electrodes are approximately 500 and 5000 Å, respectively. These results are tabulated in Table I along with a summary of flatband potentials, charge carrier concentrations, and band-edge locations for our Mg-doped and Si-doped iron oxide electrodes.

Open-circuit voltage (V_{oc}) and short-circuit current (I_{sc}) measurements.—In normal operation, the p-type/n-type iron oxide photodiode would be operated without external bias in a short-circuit configuration. As shown in the previous section (Fig. 5), pinning the Fermi levels at the same energy for p-type and n-type materials results in substantial band bending at both electrodes. Important information on electronic transport and production may be obtained, however, by allowing these Fermi levels to vary independently. The difference in the p-type and n-type electrode Fermi levels under illumination is measured as the open-circuit voltage

$$V_{oc} = E_{Fp} - E_{Fn} \quad [4]$$

In general, a positive V_{oc} under illumination indicates a spontaneous photoinduced process at one or both of the electrode/electrolyte interfaces.

Illumination of the p-type/n-type assembly in 0.01N NaOH was supplied by a CW Kr^+ laser as described earlier. Measurements of V_{oc} generated by the assembly were performed at two different wavelengths as a function of illumination intensity (I). Two important features are apparent in Fig. 6, in which the open-circuit voltage is plotted vs. $\log(I)$.

First, at a given intensity, illumination of 411 nm results in a larger open-circuit voltage than illumination by 544 nm. For example, at 100 mW intensity $V_{oc} = 290$ mV at 411 nm, while $V_{oc} = 120$ mV at 544 nm. Qualitatively, this difference may be understood in terms of the higher quan-

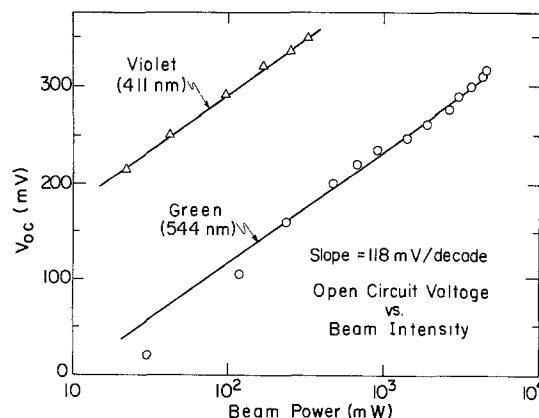


Fig. 6. Open-circuit voltage (V_{oc}) generated by the p/n assembly vs. illumination intensity. Performed under illumination from a CW Kr^+ laser in an electrolyte of 0.01N NaOH.

tum efficiency of photoconversion at 411 nm. Photo-induced carriers shift the Fermi levels in the p-type and n-type iron oxide apart towards their respective flatband conditions. The larger number of carriers generated at 411 nm shifts the Fermi levels to a greater degree and results in larger observed open-circuit voltages.

A second feature of interest in Fig. 6 is the linearity of the V_{oc} vs. $\log(I)$ plots. For both 411 and 544 nm illumination, the open-circuit voltage increases 118 mV per decade increase in light intensity. This behavior may be explained in terms of simple semiconductor theory. For an ideal photovoltaic device (26)

$$V_{oc} = \frac{kT}{q} \log \left(\frac{I}{I_0} + 1 \right) \quad [5]$$

where k , T , and q have their usual meanings, and I_0 is characteristic of the semiconductor material. This relation predicts that the open-circuit voltage will increase 59 mV for every decade increase in I as the semiconductor is driven toward flatband conditions. If the bandedges at a semiconductor/electrolyte interface remain fixed, this result may be generalized to a photoelectrochemical cell as well (27). Since a shift of $2 \times 59 = 118$ mV/decade is observed for the p/n assembly, the Fermi levels of the p-type and n-type iron oxide electrodes are shifting equally in opposite directions. This result confirms that Schottky barriers are present at both electrode/electrolyte interfaces, and the assembly is operating as a true p/n diode. The constant 118 mV/decade increase in V_{oc} up to very high intensities (>4 W/cm²) suggests that carrier production does not saturate for either the p-type or n-type iron oxides.

Unfortunately, the efficiency of the p/n diode is not determined only by the open-circuit voltage and the production of carriers. Instead, the actual photoconversion efficiency depends on the short-circuit current (I_{sc}), which reflects recombination losses of carriers before photoelectrolysis can take place. Figure 7 shows the current flow between the p-type and n-type electrodes as a function of laser illumination intensity. Due to a higher quantum efficiency for the violet beam (Fig. 2), larger currents are observed for 411 nm illumination than for 544 nm. Further, while the photogenerated currents are linear in photon flux for the 544 nm illumination, some saturation occurs at the higher current densities generated by the 411 nm beam.

The combined results of the open-circuit voltage and short-circuit current measurements suggest that these materials have high carrier densities and also high recombination rates. Experiments are currently underway to determine whether this recombination occurs in the bulk, at grain boundaries, or at the surface of these electrodes.

Detection of gases from the p/n assembly.—We have presented data on relevant optical and electronic properties

Table I. Values obtained from the Mott-Schottky plots and the energy level diagram

	p-Type iron oxide	n-Type iron oxide
Conduction band-edge	~0 mV	~200 mV
Valence bandedge	~2300 mV	~2500 mV
Band bending	~1550 mV	~550 mV
Majority carrier concentration	$\sim 5 \times 10^{16}$ cm ⁻³	$\sim 2 \times 10^{18}$ cm ⁻³
Depletion layer width	~5000 Å	~500 Å

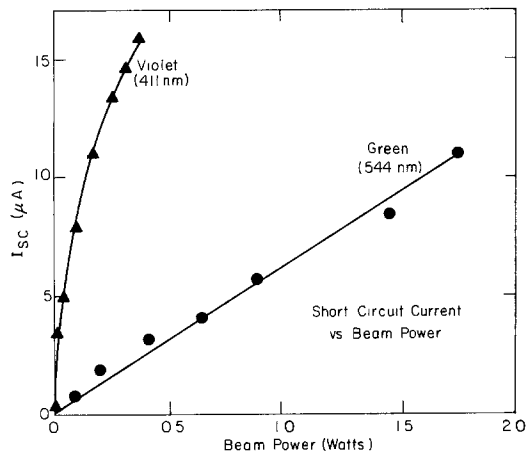


Fig. 7. Short-circuit current (I_{sc}) generated by the p/n assembly vs. illumination intensity. Performed under illumination from a CW Kr^+ laser in 0.01N NaOH.

of the Mg- and Si-doped iron oxide electrodes. In addition, we have shown that upon connecting these electrodes in an unbiased short-circuit configuration, the photodissociation of water is thermodynamically feasible. In this section, evidence is presented to show that observed photocurrents correspond to gas evolution from the cell.

In previous work, hydrogen was detected by gas chromatography from an illuminated unbiased iron oxide p/n diode assembly (16). Predicted hydrogen production from integrated photocurrents correlated with detected amounts of hydrogen gas. Unfortunately, detection of oxygen by the same method was not possible due to the presence of additional sources of oxygen, both dissolved in the electrolyte solution and entering the closed loop system through small leaks. However, as described earlier, the use of isotopically labeled water ($H_2^{18}O$) and mass spectrometry has permitted the detection of photo-produced oxygen as $^{34}O_2$.

Initial analysis of the gases in the closed loop system (Fig. 1) showed no measurable traces of $^{34}O_2$. Constant illumination was provided to the cell to prevent variations in solution temperature and spurious gas production from outgassing. Instead, oxygen production was initiated by closing the circuit between the two electrodes and stopped by opening the circuit. Figure 8 shows the $^{34}O_2$ partial pressure as a function of time for a p/n assembly giving an average photocurrent of $2 \mu A$. As seen in this figure, the $^{34}O_2$ partial pressure increased during those periods in which the circuit was closed and the current was flowing. During the open-circuit intervals, the concentration of $^{34}O_2$ decreased slightly and then remained constant.

Due to leaks from the system, a direct comparison of oxygen production and integrated photocurrents was not possible. Instead, correspondence between oxygen yield and photocurrent was determined by the ratio $^{34}O_2/^{32}O_2$. Calculation of the relative oxygen ($^{34}O_2$ and $^{32}O_2$) yields involved two assumptions. First, no spontaneous water dissociation occurred, so that the oxygen initially dissolved in solution consisted only of $^{32}O_2$ and no $^{34}O_2$. Secondly, under equilibrium conditions, the ratio of $^{34}O_2/^{32}O_2$ in the gas phase above the electrolyte solution was equal to that in solution. This equilibrium was assumed to be established rapidly as compared to sampling frequency (once every 24h). The relative amounts of $^{34}O_2$ and $^{32}O_2$ produced depended on the relative probabilities of $^{18}OH^-$ and $^{16}OH^-$ oxidation at the anode. From a solution containing 6% isotopically labeled $H_2^{18}O$, the detectable concentrations of oxygen isotopes present at any time (t) were

$$[^{32}O_2] = C_0 + 0.88rt \quad [^{34}O_2] = 0.12rt$$

where r is the rate of oxygen production for all isotopes. The concentration of $^{32}O_2$ initially saturating the solution,

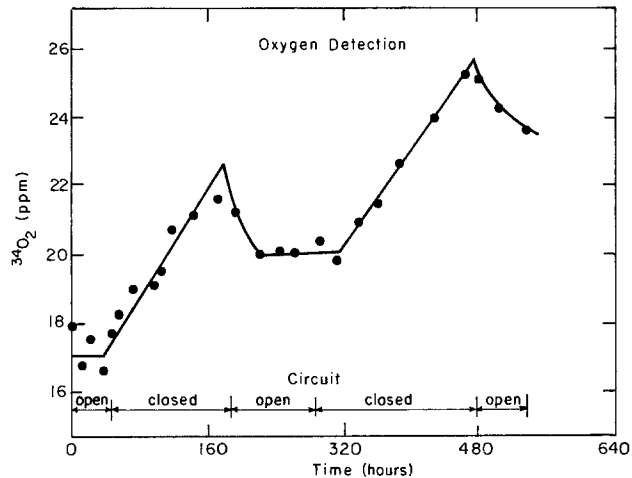


Fig. 8. Oxygen production from an operating p/n assembly. Mass spectrometry was used to monitor $^{34}O_2$ production from water enriched with isotopically labeled $H_2^{18}O$.

C_0 , was calculated from Henry's law to be 4×10^{18} molecules in 15 ml H_2O .

With these calculations, the observed total oxygen production showed good correspondence (within 20%) with the predicted value. After 340h of intermittent gas production, the predicted value for the ratio of $^{34}O_2/^{32}O_2$ was 0.059. The measured value was $^{34}O_2/^{32}O_2 = 0.047$.

Stability of the p/n assembly.—Other important factors governing the viability of the iron oxide p/n diode assembly for solar energy conversion are the long-term stability of the system and the catalytic nature of the photo-dissociation process. In the past, we found that the photocurrents from our iron oxide-based assemblies gradually declined over an 8h period until finally reaching zero. The iron oxide electrodes could be regenerated by purging the electrolyte solution with pure oxygen gas. Auger analysis of the poisoned electrode surfaces revealed large amounts of carbon, possibly originating from organic contaminants in the electrochemical cell or other parts of the system.

To determine if poisoning could be avoided, an active p/n diode assembly was illuminated in solution while the photocurrent from the production of H_2 and O_2 gases was monitored as a function of time. While an all-glass cell was used as in previous experiments, the use of stopcock grease was eliminated. As in all experiments reported here, conductive leads were isolated by silicon rubber sealant from the electrolyte solution prepared with doubly distilled water ($\rho > 2 \times 10^6 \Omega cm^{-1}$). In this stability test, shown in Fig. 9, no electrode poisoning was observed.

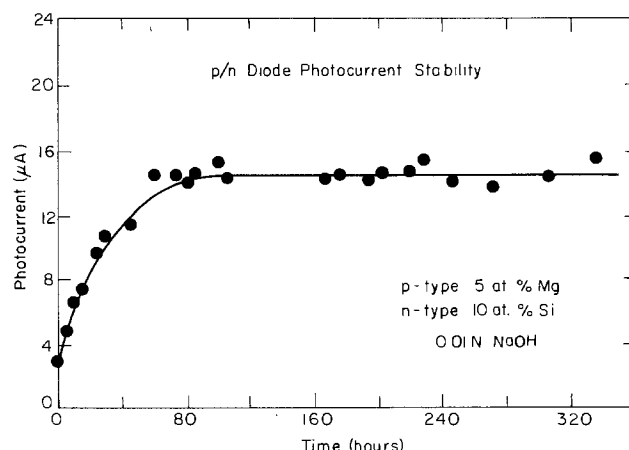


Fig. 9. Photocurrent stability for the unbiased p/n assembly. Measured at 35 mW/cm^2 illumination for two electrodes of 0.6 cm^2 area each.

At first exposure to the solution, a photocurrent of 3 μA was measured. During the succeeding 80h, the photocurrent steadily increased until it reached 15 μA . Dark currents throughout the test were $\leq 0.01 \mu\text{A}$. The p/n assembly was continuously illuminated for another 240h during which time a steady photocurrent of 15 μA persisted. Even after extended operation, no visible corrosion of the electrodes occurred. If the doped iron oxide electrodes were being reduced, operation of the p/n diode assembly for 320h at the photocurrents found here would result in the dissolution of approximately one-tenth of the electrode. However, comparison of the surface compositions of the electrodes with Auger electron spectroscopy (AES) before and after extended operation showed no change. These results support our contention that photocurrents are not a result of electrode degradation.

The 80h induction period described above is perhaps a result of a gradual modification of surface states on the electrodes. ESCA studies are underway to probe the possibility of the formation of hydroxylated intermediates or the reduction of iron in near surface layers as possible explanations.

Summary/Conclusions

The major results of this study may be summarized as follows:

1. Iron oxide powder mixed with MgO or SiO₂ and sintered at high temperatures produced semiconductors with p-type or n-type behavior, respectively.

2. Magnesium-doped electrodes show photocathodic currents at 250 mV, RHE bias with a maximum quantum efficiency of $\eta = 0.03$ for illumination at 3800Å. Silicon-doped Fe₂O₃ yields photoanodic currents with $\eta = 0.2$ at 3800Å and 1250 mV, RHE bias. Both electrodes show behavior characteristic of indirect bandgap materials with $E_g \approx 2.3 \text{ eV}$.

3. Mott-Schottky measurements were used to determine conduction and valence bandedges separately for the p-type and n-type iron oxide electrodes in 0.01N NaOH. The thermodynamic feasibility of water photodissociation is verified for the unbiased short-circuited p/n assembly.

4. Open-circuit voltage and short-circuit current generated by a p/n assembly is monitored as a function of laser illumination intensity. Results indicated that the assembly operates as a true p/n diode, and that, as fabricated, these doped iron oxides are high carrier density low mobility semiconductors.

5. Oxygen evolution is detected from an unbiased p/n assembly using a mass spectrometer and isotopically labeled water (H₂¹⁸O).

6. The assembly demonstrates excellent long-term stability and shows no decrease in photocurrents after 320h of continuous operation. Integration of the total current flux through the assembly in this test indicates that water photodissociation in this system is clearly catalytic.

The sintered and doped iron oxide photoelectrochemical diode assembly at present has a low conversion efficiency ($\eta = 0.05\%$) for solar energy to H₂ and O₂ gas. Uniformity of doping, control of the surface composition and surface states, the use of catalysts to accelerate atom recombination, and more desirable electrode configurations can all improve the degree of power conversion. Calculations using idealized models (2) indicate that power conversion efficiencies up to 7% may be attained for assemblies of this type. If the physical-chemical param-

eters currently limiting this efficiency can be understood and controlled, the doped iron oxide assembly may supply hydrogen economically in a simple passive electrochemical cell.

Acknowledgments

We would like to thank Dr. Tim Ling and Dr. Andy Kung of the San Francisco Laser Center for their technical assistance on the use of their CW Kr⁺ laser. This work was supported by the Director, Office of Energy Research, Office of Basic Energy Sciences, Chemical Sciences Division of the U.S. Department of Energy, under Contract no. DE-AC03-76SF00098. One of the authors, David Neiman, would like to acknowledge the support of the IBM Corporation.

Manuscript submitted Aug. 22, 1983; revised manuscript received Feb. 23, 1984.

REFERENCES

1. A. Fujishima and K. Honda, *Bull. Chem. Soc. Jpn.*, **44**, 1148 (1971); *Nature (London)*, **238**, 37 (1972).
2. H. Gerischer, in "Solar Energy Conversion, Topics in Applied Physics," Vol. 31, B. O. Seraphin, Editor, Springer-Verlag, Berlin (1979).
3. J. G. Mavroides, J. A. Kafalas, and D. F. Kolesar, *Appl. Phys. Lett.*, **28**, 241 (1976).
4. M. S. Wrighton, D. L. Morse, A. B. Ellis, D. S. Ginley, and H. B. Abrahamson, *J. Am. Chem. Soc.*, **98**, 44 (1976).
5. K. L. Hardee and A. J. Bard, *This Journal*, **122**, 739 (1975).
6. J. Keeney, D. H. Weinstein, and G. M. Hass, *Nature*, **253**, 719 (1975).
7. W. Gissler, P. L. Lensi, and S. Pizzini, *J. Appl. Electrochem.*, **6**, 9 (1976).
8. A. J. Nozik, in "Proceedings of the 1st World Hydrogen Energy Conference," Vol. 2, Miami Beach, FL (1976).
9. H. S. Jarrett, A. W. Sleight, H. H. Kung, and J. L. Gillson, *J. Appl. Phys.*, **51**, 3916 (1980).
10. A. J. Nozik, *Appl. Phys. Lett.*, **29**, 150 (1976).
11. F. A. Benko, C. L. MacLaurin, and F. P. Koffyberg, *Mater. Res. Bull.*, **17**, 133 (1982).
12. H. L. Sanchez, H. Steinfink, and H. S. White, *J. Solid State Chem.*, **41**, 90 (1982).
13. F. P. Koffyberg and F. A. Benko, *J. Appl. Phys.*, **53**, 1173 (1982).
14. P. Merchant, R. Collins, R. Kershaw, K. Dwight, and A. Wold, *J. Solid State Chem.*, **27**, 307 (1979).
15. D. S. Ginley and M. A. Butler, *J. Appl. Phys.*, **48**, 2019 (1977).
16. C. Leygraf, M. Hendewerk, and G. A. Somorjai, *J. Catal.*, **78**, 341 (1982).
17. C. Kittel, in "Introduction to Solid State Physics," p. 276, John Wiley and Sons, New York (1953).
18. J. H. Kennedy, R. Shinar, and J. P. Ziegler, *This Journal*, **127**, 2307 (1980).
19. M. A. Butler, D. S. Ginley, and M. Eibschutz, *J. Appl. Phys.*, **48**, 3070 (1977).
20. N. F. Mott, *Proc. R. Soc. London, Ser. A*, **171**, 27 (1939).
21. W. Schottky, *Z. Phys.*, **113**, 367 (1939); *ibid.*, **118**, 539 (1942).
22. S. Lowell, *Anal. Chem.*, **45**, 1576 (1973).
23. S. M. Wilhelm, K. S. Yun, L. W. Ballenger, and N. Hackerman, *This Journal*, **126**, 419 (1979).
24. R. DeGryse, W. P. Gomes, F. Cardon, and J. Vennik, *ibid.*, **122**, 711 (1975).
25. M. A. Butler and D. S. Ginley, *Chem. Phys. Lett.*, **47**, 319 (1977).
26. J. I. Pankove, "Optical Processes in Semiconductors," Prentice-Hall, Inc., Englewood Cliffs, NJ (1971).
27. A. Fornarini, A. J. Nozik, and B. A. Parkinson, To be published.

Film Thickness and Distribution of Electrolyte in Porous Fuel Cell Components

Joshua Mitteldorf and Gerald Wilemski*

Physical Sciences, Inc., Andover, Massachusetts 01810

ABSTRACT

The DLVO theory of liquid film stability is used to estimate the thickness of electrolyte films that may be present in molten carbonate fuel cell cathodes. Our result is $\approx 30\text{\AA}$, which is 2 orders of magnitude thinner than the values postulated in thin film models of cathode performance. We also examine carefully the thermodynamic basis of an equation governing the equilibrium of electrolyte among the different porous components of the fuel cell. We show that the validity of this equation is more general than previously recognized in that its derivation does not depend on the assumption of cylindrical or spherical pore geometry.

A molten carbonate fuel cell can be pictured as a sandwich of three distinct porous media, two electrodes and an electrolyte structure. Liquid electrolyte forms an ionic pathway between the two electrodes, but its volume is insufficient to fill the pores of all three components. How then does the electrolyte distribute itself among and within the components? Which pores are flooded; which are empty? Which pore walls are covered with liquid films, and what is the film thickness?

These questions are of interest because the electrolyte distribution affects cell performance. There are two principal effects. First, electrochemical reactions take place only where gaseous reactants have access to solid electrode and liquid electrolyte. Second, ions produced in one electrode must flow via connected liquid paths through the electrolyte structure into the opposite electrode. This conduction process may be enhanced by increasing the fraction of pore volume filled by electrolyte in each component. But in view of the first requirement, it is essential to have gas-filled volume thoroughly permeating each electrode. In practice, a compromise is reached by appropriately tailoring the pore-size distributions of the three components and by restricting the electrolyte volume to lie below the total pore volume. Electrolyte then partially fills each electrode while leaving the electrolyte structure full (or nearly so).

Based on prior work (1-3) and our own results, the following picture of the wetting physics may be constructed:

1. If the contact angle in a given component is less than 90° (as it must be for unpressurized fluid to enter the component at all), then the fluid fills all pores in that component whose diameter is smaller than a certain value D_i . Pores with larger diameters are left empty.

2. If the contact angle in any component is 0° , then all of the internal area of the component that is not flooded will be covered with thin liquid films. The film thickness δ can be estimated by equating the capillary pressure of the largest flooded pore to the disjoining pressure $\pi(\delta)$, which for given materials is a specific function of δ . The resulting equation is then solved for δ .

3. At thermodynamic equilibrium, the diameters of the largest flooded pores in the components are related (for constant ambient pressure) by

$$\gamma_1 \cos \theta_1 / D_1 = \gamma_2 \cos \theta_2 / D_2 = \dots = \gamma_i \cos \theta_i / D_i$$

where γ_i and θ_i are, respectively, the gas-liquid surface tension and contact angle of the electrolyte in the i th component, appropriate to the local gas environment.

A reasonable estimate of the volume distribution of electrolyte among the cell components can be obtained (1) using measured pore volume distribution curves and the above relationship for the D_i . This equation has been derived previously from both mechanical (2) and thermodynamic (3) considerations, but in each case idealized

cylindrical (2, 3) or spherical (3) pore geometries were assumed to simplify the analysis.

In this paper, we present a general thermodynamic derivation of this result, avoiding assumptions about pore shape, and we find a general definition for D that allows us to relate it to the pore diameter inferred from Hg-intrusion porosimetry. Our conclusion is that the diameter of the largest pores filled by electrolyte (*i.e.*, D) can be equated to the pore diameter found by porosimetry provided three conditions are met: (i) the contact angles of the wetting fluid (the electrolyte) and the nonwetting fluid (*e.g.*, Hg) are supplements, (ii) the pores of the component are sufficiently interconnected to allow both fluids to have access to all pores of each range during filling, and (iii) if (wetting) fluid films are present, they occupy negligible volume.

Besides bearing on the distribution of electrolyte, the question of film thickness also has direct implications for the electrochemical performance of a porous electrode. Therefore, we briefly consider in the next section the equilibrium thickness of molten carbonate films on a NiO substrate (the material currently used for cathodes). A more detailed presentation will be given in another article (4). Our theoretical estimate of the film thickness is $\approx 30\text{\AA}$. This is too thin for films to occupy a significant volume given typical internal electrode areas.

Following our discussion of film thickness, we develop the thermodynamics of electrolyte distribution and establish the above-noted connection with porosimetry measurements. Practical implications of our results for fuel cell design and operation will be only briefly mentioned, as many of these points have been nicely treated by Arendt (3). Also, in an earlier report (5) we used these results to analyze a limited number of fuel cell electrolyte inventory data obtained at Energy Research Corporation (6).

Estimate of Film Thickness

In this section, we estimate the maximum equilibrium thickness of molten carbonate films on NiO using the Derjaguin-Landau-Verwey-Overbeek (DLVO) theory of liquid film stability. The DLVO theory has been presented and reviewed extensively [for example, in Ref. (4, 7, 8, 9)], so we will only briefly sketch the considerations involved.

A thin liquid film can be stable on a solid surface when, relative to the bulk liquid, its chemical potential receives an additional negative contribution $\Delta\mu$. The magnitude of $\Delta\mu$ is determined by the interactions between film molecules and substrate molecules and is a function of the film thickness δ . Discussions of film stability are often made in terms of another quantity, the disjoining pressure π . The disjoining pressure can be thought of as an excess normal pressure in the film stabilizing the film from thinning. For an incompressible liquid with number density ρ , π , and $\Delta\mu$ are related by $\pi = -\rho\Delta\mu$. (The chemical potential is the derivative of the free energy with respect to number of particles N ; pressure is the negative

* Electrochemical Society Active Member

Key words: surfaces, cathode, thermodynamics, porosimetry.

derivative of the free energy with respect to volume V . Since $N = \rho V$, it follows that $\rho \Delta \mu = -\pi$.) In the DLVO theory, two contributions to π are identified: one from attractive van der Waals forces, the other from electrical double layer interactions. The two contributions are assumed to be additive.

Neglecting retardation effects, the van der Waals-London potential for a pair of atoms is $-\lambda/r^6$, where r is the distance between the atoms. It is found that the constant λ ($\approx 10^{-59}$ erg cm⁶) ranges over less than an order of magnitude for a broad range of materials. The interaction energy for the film is obtained by summing the contributions from all pairs of atoms in the film-solid system and subtracting the corresponding result for a thin liquid layer lying atop bulk liquid. For a flat film of thickness δ in contact with a semi-infinite slab, we find

$$\pi_{\text{vdw}} = A/(6\pi\delta^3) \quad [1]$$

With the atomic number densities for NiO and a 62/38 mole percent (m/o) Li/K carbonate melt and the above value of λ , the Hamaker constant A can be estimated (7, 8) to be about 1.1×10^{-12} ergs or, in more convenient units, about 7×10^6 atm (\AA)³.

Electrical double layer interactions arise when the film is thin enough to permit overlap of the ion distributions associated with the double layer at each film "surface." In a dense ionic melt, only a short-ranged, compact double layer is present. So, unless the film thickness is on the order of a few angstroms (which is not the case here), double layer interactions will not be important in an ionic melt.

A film in equilibrium with bulk liquid has adjusted its thickness until its disjoining pressure π just compensates for the mechanical pressure difference between the film and the bulk (7). For a partially-flooded porous solid, this mechanical pressure difference is due to the Laplace pressure drop across the curved meniscus of the flooded pore. Thus we have

$$\pi \approx \frac{\gamma}{R} \quad [2]$$

where γ is the liquid surface tension and R may be equated to the radius of the largest flooded pore (see next section). Typically, this radius is approximately $1 \mu\text{m}$. The surface tension of the carbonate melt is about 200 dyn/cm, hence $\pi = 2$ atm. From Eq. [1] we see that $\pi = 2$ atm corresponds to a film thickness of approximately 30\AA .

This thickness is substantially less than the values (1000-5000 \AA) used in earlier "thin film" models (10-12) of molten carbonate electrodes and assumed without physical justification. Our value of 30\AA is not very sensitive to the parameter values used to estimate it. The van der Waals contribution relies on atom densities and London potential force constants. The former are easy to evaluate and uncontroversial. The latter are also straightforward to estimate and do not vary in order of magnitude from material to material. By comparison with experiment and more accurate theory, the Hamaker approach for calculating π_{vdw} is known to be accurate to within a factor of 5. Thus, we might err, at most, by a factor of $5^{1/3}$ in estimating δ . Of greater uncertainty is what effect the ionic nature of the melt has on the van der Waals interactions. The work done to date (9) on this problem relies in part on the linearized Poisson-Boltzmann equation, and therefore would not be expected, *a priori*, to be relevant to a concentrated ionic melt. We also do not include the effects of so-called structural forces (13) that may arise from, roughly put, differences in the packing of ions in the film compared to the bulk fluid. However, because of their short range, the structural forces, if present, cannot alter the order of magnitude of our estimate.

The small estimated film thickness has two consequences for the analysis presented in the rest of this paper. First, by comparing δ with the radius of the largest flooded pore ($\approx 1 \mu\text{m}$), it is clear that films account for a negligible fraction of the pore volume occupied by elec-

trolyte. Second, the contribution of the disjoining pressure to the film surface tension is seen to be small: $\pi\delta/\gamma \approx 3 \times 10^{-3}$. Thus the film surface tension may safely be set equal to the sum of the bulk gas-liquid and solid-liquid surface tensions (14).

Equilibrium Thermodynamics of Electrolyte Distribution

The three porous components of a fuel cell are made of different materials that usually vary in their wettability by the electrolyte. They are also characterized by different pore size distributions. These two factors, the pore structure and the wettability, will determine the equilibrium electrolyte distribution among the three cell components. Electrolyte sufficient to fill some but not all of the total pore volume is infused in the cell as it is manufactured. When the cell is brought to operating temperature, the electrolyte melts and redistributes itself among and within the three components. Some pores may remain empty, some may be flooded, and others may be empty save for a thin film which coats the walls. We assume that the final electrolyte distribution will be at equilibrium, *i.e.*, that its free energy is a minimum. We then derive an equation for the equilibrium distribution by requiring that an infinitesimal volume transfer of electrolyte from any region of the cell to any other region where electrolyte is present incurs no first-order change in free energy.

Our derivation and results apply to a system with any number of porous media in contact. Although the fuel cell has three principal porous components, there are circumstances for which it may be necessary to consider more than three. For example, corrosion of originally non-porous hardware, such as a current collector, can result in a new porous component whose presence may affect the electrolyte distribution. There are also conditions, as discussed below, under which the electrolyte structure should be regarded as two components.

We treat a closed isothermal system consisting of a pure liquid phase at pressure P_i^l in each porous cell component i ($i = 1, \dots, N$) and a gas phase at pressure P_i^g in contact with the liquid in each component. The gases in contact with the two electrodes have intrinsically different compositions, and gas transport through the electrolyte structure is assumed to be negligible. In principle, the two gas streams may also be at different pressures, but this condition occurs normally only when testing for gas crossover. During routine operation, pressure differences are limited to small fluctuations in the gas supply system, but accidental upsets can lead to large imbalances.

If the electrolyte structure is partially empty, the anode and cathode sides of the structure will see different gas environments. If the variation of surface tension and contact angle with gas composition is significant, the electrolyte structure should then be treated as two components divided by a boundary surface lying wholly within the remaining flooded portion of the structure. We assume there are no connected paths of empty pores traversing the electrolyte structure.

A pressure difference exists between the gas and liquid phases because of the curvature of the gas-liquid interface in the pores. This consideration points to the Helmholtz free energy (denoted here as F) as a natural choice for describing the thermodynamics (15). The basic thermodynamics of interfacial phenomena has been developed many times [*e.g.*, by Adamson (16), Sanfeld (17), and Morrow (18)], so we proceed directly to write an expression for the free energy change dF occurring when an infinitesimal volume of liquid is redistributed among the porous components

$$dF = \sum_{i=1}^N dF_i \quad [3]$$

where, in the absence of films

$$dF_i = -P_i^g dV_i^g - P_i^l dV_i^l + \gamma_i^{lg} dA_i^{lg} + \gamma_i^{sg} dA_i^{sg} + \gamma_i^{sl} dA_i^{sl} + \mu_i^l dn_i^l \quad [4]$$

and, in the presence of films

$$dF_i = -P_i^g dV_i^g - P_i^l dV_i^l + (\gamma_i^{lg} + \gamma_i^{sl}) dA_i^{film} + \gamma_i^{sl} dA_i^{sl} + \gamma_i^{lg} dA_i^{lg} + \mu_i^l dn_i^l \quad [5]$$

Here, superscripts s, g, and l refer to the solid, gas, and liquid phases, respectively, present in each porous component. Curvature terms are absent in Eq. [4] and [5] because the Gibbs dividing surface between each pair of phases is taken to lie at the appropriate surface of tension (17). Although the entire system is closed, the number of moles of liquid n_i^l in a component may change. Thus, we include in Eq. [4] and [5] the term $\mu_i^l dn_i^l$ where μ_i is the chemical potential of the liquid. As noted above, each component is assumed to be closed to gas transfer, so terms accounting for this are absent in Eq. [4] and [5]. The PdV terms constitute the mechanical work of displacing gas and liquid volumes at their respective pressures. The γdA terms represent the work accompanying the formation of new interfacial area between the indicated phases. The γ 's are surface free energies per unit area of interface between the pair of indicated phases evaluated at the surface of tension. For fluid phases, they are commonly referred to as surface tensions. They should not be confused with specific (17) or superficial (18) surface free energies per unit area, from which they differ in (chemically) multicomponent systems. Thus, $\gamma^{lg} dA^{lg}$ is the free energy change resulting from variations in the total meniscus area within a porous component; $\gamma^{sl} dA^{sl} + \gamma^{sg} dA^{sg}$ represents the free energy change accompanying the replacement of bare solid area by wet area in flooded pores: and $(\gamma_i^{lg} + \gamma_i^{sl}) dA_i^{film} + \gamma_i^{sl} dA_i^{sl}$ denotes the free energy of forming new gas-liquid film area by withdrawing liquid from a previously filled pore. (Films, if they are present at all, are presumed to cover all surfaces in a given component that are not associated with flooded pores.) We have also assumed that the film surface tension is equal to the sum $\gamma_i^{lg} + \gamma_i^{sl}$. As discussed in the previous section, this is a good approximation.

Equations [4] and [5] can be simplified and unified by noting the following points. First, total pore volume is conserved, so that $-dV_i^g = dV_i^l = dV_i$. Next, in unfilled components new solid-liquid interface is created from an equal amount of solid-gas area, so that $dA_i^{sl} = -dA_i^{sg}$. Third, because the film thickness is much smaller than a typical radius of curvature for a pore wall, we may put $dA_i^{film} = -dA_i^{sl}$. Finally, we replace $\gamma^{sl} - \gamma^{sg}$ by means of Young's equation [14], which relates the equilibrium contact angle θ to the three γ 's.

$$\gamma^{sg} - \gamma^{sl} = \gamma^{lg} \cos \theta \quad [6]$$

If $\gamma^{lg} = \gamma^{sg} - \gamma^{sl}$, then the contact angle becomes 0° , and the formation of a film becomes energetically favorable. Upon making the indicated substitutions, we find for Eq. [4] (i.e., in the absence of films) the result

$$dF_i = (P_i^g - P_i^l) dV_i - \gamma_i^{lg} (\cos \theta_i dA_i^{sl} - dA_i^{lg}) + \mu_i^l dn_i^l \quad [7]$$

and for Eq. [5] (i.e., in the presence of films) the form

$$dF_i = (P_i^g - P_i^l) dV_i - \gamma_i^{lg} (dA_i^{sl} - dA_i^{lg}) + \mu_i^l dn_i^l \quad [8]$$

It is apparent that Eq. [8] is a special case of Eq. [7] for $\theta = 0^\circ$, which, we have remarked, is a necessary criterion for films to exist. It follows that Eq. [7] can be taken as a general result for filmed and unfilmed components.

Restricting consideration to variations such that $A_i = A_i(V_i)$, we take the incremental changes dV_i as the independent variables and rewrite Eq. [3] as

$$dF = \sum_i f_i dV_i \quad [9]$$

where

$$f_i = P_i^g - P_i^l - \gamma_i^{lg} (dA_i/dV_i) + \mu_i^l/v^l \quad [10]$$

$$dA_i/dV_i = \cos \theta_i (dA_i^{sl}/dV_i) - dA_i^{lg}/dV_i \quad [11]$$

and v^l is the molar volume of the liquid. The condition for capillary equilibrium among the porous components, filmed or unfilmed, can now be obtained by setting dF equal to zero, subject to the related constraints of constant electrolyte volume and mole number

$$0 = \sum_i dV_i = v^l \sum_i dn_i^l$$

From Eq. [9] and [10], we find

$$0 = \sum_i \mu_i^l dn_i^l - \sum_i P_i^l dV_i + \sum_i [P_i^g - \gamma_i^{lg} (dA_i/dV_i)] dV_i \quad [12]$$

At equilibrium, the chemical potential and the liquid phase pressure will be the same in each component, so, because of the volume-mole number constraint, the first two terms on the right-hand side of Eq. [12] will be zero. (Hydrostatic pressure differences are unimportant in fuel cells because of the small dimensions involved. When hydrostatic effects are big, the term $\rho^l g h_i$ must be added to the term in square brackets in Eq. [12], and the results below must be correspondingly modified; ρ^l is the liquid density, g the gravitational acceleration, and h_i the vertical distance from the level at which the pressures P_i^l are measured.)

After applying the volume constraint to the remainder of Eq. [12], we find

$$0 = \sum_{i \neq 1} \{ [P_i^g - \gamma_i^{lg} (dA_i/dV_i)] - [P_1^g - \gamma_1^{lg} (dA_1/dV_1)] \} dV_i$$

Because the remaining $N-1$ volume transfers are independent, this equation can be satisfied only when the following equality holds

$$P_1^g - \gamma_1^{lg} (dA_1/dV_1) = P_2^g - \gamma_2^{lg} (dA_2/dV_2) = \dots \quad [13]$$

Furthermore, each dF_i must separately be zero at equilibrium since an infinitesimal volume transfer wholly within a component cannot produce a change in the free energy. Thus, from Eq. [7] for a single closed component ($dn_i^l = 0$), we also have

$$P_i^g - P_i^l = \gamma_i^{lg} (dA_i/dV_i) \quad [14]$$

which is a disguised version of the Laplace equation (16) for the pressure drop across a curved interface. The quantity dA/dV defined in Eq. [11] was, in fact, shown by Gauss (19, 20) in 1830 to be equal to the curvature C^{lg} of the gas-liquid interface.

Equation [13] governs the electrolyte distribution among the porous components. Its significance can be appreciated by imagining what happens as liquid fills a porous medium. Different microscopic regions of the medium are characterized by different geometries, so that adding an infinitesimal volume of electrolyte at different points will result in different area changes, dA^{sl} and dA^{lg} . However, the liquid distributes itself in the partially filled medium, so that at equilibrium the boundary between filled and unfilled volume is a surface for which the derivative (Eq. [11]) is a constant; that is, it is a surface of constant curvature. All regions where this derivative has a value larger than that specified by Eq. [13] are full, and all regions where it has a smaller value are empty. Thus, dA/dV is a well-defined quantity (barring hysteresis effects) that characterizes the filling level of the porous medium. One may think of dA/dV as inversely proportional to an effective pore diameter; in which case small pores are flooded and large pores are empty. For example, for a solid whose pores consist of (connected) cylindrical pores of varying diameter D , we find $dA/dV = 4 \cos \theta/D$ exactly. This type of correspondence can be found for other idealized pore geometries, although the proportionality constant varies with the model.

Relation to Porosimetry: a Complementarity Theorem

Using, for example, mercury porosimetry, it is possible to measure the quantity (dA/dV) as a function of partial filling volume. In fact, under the right conditions, there

is an exact correspondence between the pore diameter D measured by porosimetry and the quantity dA/dV defined by Eq. [11]

$$\sec \theta_w (dA_w/dV_w) = dA_n^{sl}/dV_n - \sec \theta_n (dA_n^{ls}/dV_n) \equiv 4/D_1 \quad [15]$$

Furthermore, when this relationship holds, it is independent of assumptions about pore geometry. The conditions for which Eq. [15] holds are (i) that the contact angle of the wetting fluid be the supplement of the contact angle of the fluid used to measure the porosimetry curve (and hence D), (ii) that the porous material be sufficiently interconnected to allow both fluids to have access to all the pores of each size range during the filling, and (iii) that if the wetting fluid forms thin films, the films must occupy a negligible fraction of the pore volume. After using these conditions to establish the validity of Eq. [15], we will briefly discuss their applicability to molten carbonate fuel cell components.

To prove Eq. [15], consider two identical porous bodies, one partly filled with a wetting fluid (w) that has contact angle θ_w , and the other with a nonwetting fluid (n) with a contact angle $\theta_n = 180^\circ - \theta_w$. The wetting fluid will be at a pressure less than the ambient gas pressure, while the pressure in the nonwetting fluid will be greater than the gas pressure in its environs. Adjusting the pressure difference adjusts the filling level of each according to Eq. [14]. During filling, the wetting fluid will start in the small pores and work its way into the large pores, while the nonwetting fluid will first enter the large pores and eventually be forced into the small ones. For each partly filled body, there will be some pressure difference for which the fillings will be exactly complementary. That is, the wetted surface of the first sample will correspond to unwetted surface in the second, and vice versa (see Fig. 1). Furthermore, the free menisci will also be identical in shape. This is because (i) both free surfaces satisfy the "constant curvature" equation

$$|C^{lg}| = \left| \frac{1}{R_1} + \frac{1}{R_2} \right| = \text{const.}$$

where R_1 and R_2 are the principle radii of curvature at any point on the surfaces and (ii) both obey the same boundary conditions, since by assumption they meet the solid surfaces at the same angle (strictly, at supplementary angles).

For the case of 0° and 180° respective contact angles, the wetting fluid also forms films along the walls of the pores that would be filled by the nonwetting fluid—an exception to complementary filling. However, except for the case of very dilute ionic solutions, it is expected that films are only a few tens of angstroms thick (see the second section above), which makes their volume negligible for many applications, including the present one.

From the above considerations, we then have

$$dA_w^{ls}/dV_w = dA_n^{ls}/dV_n$$

and

$$dA_w^{lg}/dV_w = -dA_n^{lg}/dV_n$$

from which it follows that the equation

$$\frac{dA_w^{lg}}{dV_w} - \sec \theta_w \frac{dA_w^{ls}}{dV_w} = \frac{dA_n^{ls}}{dV_n} - \sec \theta_n \frac{dA_n^{lg}}{dV_n} \quad [16]$$

is also true, given our interconnectivity assumption.

Porosimetry curves are measured by forcing the nonwetting fluid into the sample at high pressures. The equation governing this process is Eq. [14]

$$P^g - P_n^l = \gamma_n^{lg} \cos \theta_n [dA_n^{sl}/dV_n - \sec \theta_n dA_n^{ls}/dV_n]$$

The bracketed quantity is measured by varying the pressure, but data are conventionally reported in terms of a cylindrical pore diameter D using the defining equation.

$$P^g - P_n^l = 4\gamma_n^{lg} \cos \theta_n / D \quad [17]$$

The point is that the geometric quantity (dA/dV) being

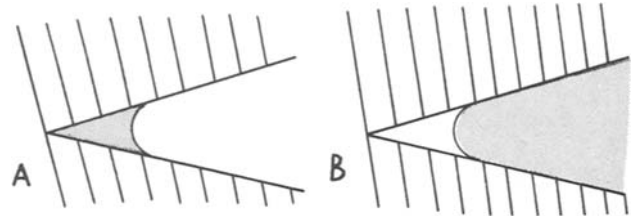


Fig. 1. Complementary filling of a pore by a wetting and a nonwetting fluid. A: Small pore filled with wetting fluid to a given level. B: Same small pore filled to complementary level with nonwetting fluid.

measured is actually the quantity that we need to solve electrolyte inventory problems. The fact that it has been reported in terms of cylindrical pore diameters via Eq. [15] and [17] has really introduced no geometric assumption, since we undo the assumption to use the data.

Thus, provided the measured pore diameters D_1 are properly interpreted, we may simplify the writing of Eq. [13] and still have an exact result

$$P_1^g - 4\gamma_1^{lg} \cos \theta_1 / D_1 = P_2^g - 4\gamma_2^{lg} \cos \theta_2 / D_2 = \dots \quad [18]$$

This equation has been obtained previously under more restrictive assumptions by Maru and Marianowski (2) and by Arendt (3), who also used constant pressure conditions.

A few comments on how well fuel cell components satisfy the three conditions governing Eq. [15] are now provided. Mercury, the most commonly used fluid in porosimetry, has a nominal contact angle of 140° on many materials. Thus, condition (i) requires that the contact angle of the wetting fluid be 40° . This is quite close to the 33° contact angle of Na/K/Li/CO₃ eutectic melt on Ni (21), a common anode material. Other fuel cell materials such as lithiated NiO (cathode) or LiAlO₂ (electrolyte structure) appear to be well wetted by molten alkali carbonates (contact angle of 0°), and, for these, condition (i) is violated. However, this mismatch in contact angles is probably not important because in the pore-size range of importance for the wetting of fuel cell components ($D < 2 \mu\text{m}$), the dA^{sl} terms of Eq. [15] should predominate.

Condition (ii) is probably the most important of the three. Judging from SEM's of cell components, large pores ($D > 2 \mu\text{m}$) are well connected, so mercury should have no trouble gaining access to all the pore volume in a monotonic fashion. However, the wetting fluid fills the smallest pores first. In a component with a broad pore-size spectrum, there should be sufficient overlap or contact between regions containing small pores to permit filling to proceed monotonically. In a component with a narrow spectrum, small pores, *i.e.*, regions in which the liquid would have a small radius of curvature, are much less likely to form a connected network. In this type of component, a liquid that cannot form a film can fill all the small pores only via the indirect and slow route of evaporation/condensation unless larger, better connected pores are also filled. So for low fill levels, condition (ii) would be violated in this component. In general, the applicability of condition (ii) will have to be decided separately for each component, taking into account specific features of its pore structure. It is likely that much more theoretical work and model construction will be necessary in order to ascertain the applicability of condition (ii) in all cases of interest.

As noted above, based on the results of the second section (above), condition (iii) appears to be satisfied for all highly concentrated electrolytes used in practice.

Summary

The equilibrium thickness of molten carbonate films in a porous NiO cathode has been estimated, and the equilibrium thermodynamics of electrolyte distribution among several porous media in contact has been developed.

In terms of the DLVO theory of liquid film stability, van der Waals forces are responsible for film formation

and double layer interactions (which are important for less concentrated electrolyte solutions) play a negligible role. Films of molten carbonate in NiO cathodes are estimated to be only $\approx 30\text{\AA}$ thick. This figure is 2 orders of magnitude too thin to contribute substantially to ionic conduction, and casts doubt on the physical basis for previous thin film models (10-12) of electrode performance that have postulated $\approx 1/2\ \mu\text{m}$ films.

The thermodynamic basis of the equilibrium distribution of bulk liquid electrolyte has been developed, and a connection has been made with porosimetry measurements. Within each porous component, small pores are flooded, and large pores are either empty or empty with filmed walls. The effective diameters of the largest filled pores in each component of a cell are mutually related as given by Eq. [18]. The analysis shows that the validity of this result is not dependent on the assumption of cylindrical (or other idealized) pore geometry. Equation [18] can be used with the porosimetry curves of the cell components to determine the equilibrium distribution of a given total electrolyte volume (1).

Acknowledgments

We thank one of the referees for valuable criticism. This work was supported by the U. S. Department of Energy under Contract no. DE-AC05-79ET-15403.

Manuscript submitted May 6, 1983; revised manuscript received Feb. 27, 1984. This was Paper 33 presented at the Hollywood, Florida, Meeting of the Society, Oct. 5-10, 1980.

Physical Sciences, Inc., assisted in meeting the publication costs of this article.

REFERENCES

- H. C. Maru, D. Patel, and L. Paetsch, Abstract No. 9, p. 27, The Electrochemical Society Extended Abstracts, Vol. 81-1, Minneapolis, MN, May 10-15, 1981.
- H. C. Maru and L. G. Marianowski, Abstract No. 31, p. 82, The Electrochemical Society Extended Abstracts, Vol. 76-2, Las Vegas, NV, Oct. 17-22, 1976.
- R. H. Arendt, *This Journal*, **129**, 942 (1982).
- G. Wilemski and J. Mitteldorf, Abstract No. 8, p. 25, The Electrochemical Society Extended Abstracts, Vol. 81-1, Minneapolis, MN, May 10-15, 1981.
- G. Wilemski, J. Mitteldorf, and G. Simons, "Diagnostic Fuel Cell Model," Physical Sciences Inc., TR-317, Andover, MA (1982).
- Energy Research Corporation, "Development of Molten Carbonate Fuel Cell Technology," SAN/11304-13 (1979), and CHI/11304-19, Danbury, CT (1980).
- R. Buscall and R. H. Ottewill, in "Colloid Science," Vol. 2, (Specialist Periodical Reports), D. H. Everett, Editor, p. 191, The Chemical Society, London (1975).
- H. Sonntag and K. Strenge, "Coagulation and Stability of Disperse Systems," R. Kondo, Translator, Israel Program for Scientific Translations, Halsted Press, New York (1972).
- J. Mahanty and B. W. Ninham, "Dispersion Forces," Academic Press, London, New York (1976).
- E. S. Argano, T. Schmidt, and D. T. Wasan, *Chem. Eng. Prog. Symp. Series*, **63**, 26 (1966).
- J. R. Selman, H. C. Maru, V. Sampath, and L. G. Marianowski, in "Electrode Materials and Processes for Energy Conservation and Storage," J. D. E. McIntyre, S. Srinivasan, and F. G. Will, Editors, p. 656, The Electrochemical Society Softbound Proceedings Series, Princeton, NJ (1977).
- G. Wilemski, *This Journal*, **130**, 117 (1983).
- R. G. Horn and J. N. Israelachvili, *J. Chem. Phys.*, **75**, 1400 (1981).
- I. E. Dzyaloshinskii, E. M. Lifshitz, and L. P. Pitaevskii, *Adv. Phys.*, **10**, 165 (1961).
- P. J. McElroy, *J. Coll. Interface Sci.*, **72**, 147 (1979).
- A. W. Adamson, "Physical Chemistry of Surfaces," 3rd ed. Wiley-Interscience, New York (1971).
- A. Sanfeld, in "Physical Chemistry, An Advanced Treatise," Vol. 1, "Thermodynamics," W. Jost, Editor, p. 245, Academic Press, New York (1971).
- N. R. Morrow, in "Flow Through Porous Media," R. J. Nunge, Editor, p. 103, American Chemical Society, Washington, DC (1970).
- K. F. Gauss, *Comment. Soc. Reg. Scient. Göttingen Re-cent.*, **7** (1830).
- D. H. Everett, *Pure Appl. Chem.*, **52**, 1279 (1980).
- G. K. Moiseev and G. K. Stepanov, in "Electrochemistry of Molten and Solid Electrolytes," Vol. 5, A. N. Baraboshkin, Editor, pp. 101-109, Consultants Bureau, New York (1967).

Properties of the Interface Between Two Immiscible Electrolytes in the Presence of Proteins

Petr Vanýsek,¹ Jonathan D. Reid, Mark A. Craven, and Richard P. Buck*

Department of Chemistry, The University of North Carolina, Chapel Hill, North Carolina, 27514

ABSTRACT

The influence of adsorbed proteins on electrochemical properties of the nitrobenzene-aqueous interface has been investigated using cyclic voltammetric and impedance techniques. Upon addition of $4\ \mu\text{g/ml}$ ovalbumin cyclic voltammetric ΔE_p values for Cs^+ transfer shifted from nearly temperature independent reversible values to more temperature-dependent irreversible values. These effects were especially pronounced at lower temperatures and suggested formation of a surface film. The cyclic voltammetry of a wide range of concentrations of bovine serum albumin (BSA) in base L/L electrolytes was also studied. Interfacial ac impedance measurements indicated an increase in diffuse layer capacitance accompanied initial BSA adsorption. At high protein concentrations, an adsorbed phase was formed which facilitates faradaic transfer of ions across an otherwise blocked interface.

The interface of two immiscible electrolytes [for reviews see Ref. (1, 2)] can be treated and experimentally investigated in ways similar to an electrode/electrolyte interface. Among many properties of the interface recently studied, the adsorption of species on the interface is of fundamental interest. Recent findings (3), showing a general effect of adsorption on irreversibility of ion transfers,

call for a more thorough investigation of adsorption properties.

Koryta *et al.* (4) studied transfer of a few ions across the interface in the presence of lecithin. Lecithin is known to form adsorbed interfacial layers. These authors carried out experiments at different temperatures and found that transfer of metallic ions across the interface was highly temperature dependent. At higher temperatures, up to 65°C , no influence of lecithin was observed. As the temperature decreased, the transfer of ions became more difficult; the interface became blocked. The change of in-

¹ On leave from J. Heyrovský Institute of Physical Chemistry and Electrochemistry, Czechoslovak Academy of Sciences, Prague, Czechoslovakia.

* Electrochemical Society Active Member.

terfacial properties, which was quite sudden at 42°C, can be related to the crystalline transition temperature of this particular lecithin.

The blocking or decreasing permeability of the interface for ion transfer results in irreversible cyclic voltammograms. These are normally characterized by an increase of the peak voltage difference (ΔE_p) from the ideal reversible value of 58 mV.

In addition, interfacial ac measurements are well-suited for revealing irreversibility and adsorption effects over a wide applied interfacial potential range (5). Cyclic voltammetry [based on Ref. (6)] and impedance measurements were used to study the influence of ovalbumin, colicine E_3 , and BSA on the nitrobenzene/aqueous interface.

Ovalbumin is a water soluble protein with molecular weight of about 45,000. The molecule consists of a simple polypeptide chain of about 400 residues, of which about half are hydrophobic (7). BSA is a water soluble protein with molecular weight of about 69,000 (7). Colicines are water soluble antibiotic proteins or polypeptides produced by a strain of *Enterobacteriaceae* (8). Colicine E_3 , used in these experiments, has a molecular weight of about 60,000.

Experimental

A custom-made four electrode potentiostat (6), based on principles described earlier (9, 10), was used for the cyclic voltammetry experiments. The experimental cell is shown in Fig. 1. Both counterelectrodes were platinum spiral wires. The aqueous phase reference electrode was Ag/AgCl wire in the aqueous base electrolyte (LiCl) solution. The reference electrode for the nitrobenzene phase was Ag/AgCl wire dipped in aqueous solution of tetrabutylammonium chloride (TBACl). This solution was in contact with a tetrabutylammonium tetraphenylborate (TBATPB) solution in nitrobenzene. This interface maintains a constant potential difference.

All routinely used chemicals were of analytical purity and were used as received. Base electrolytes for the nonaqueous phase were obtained by precipitation of suit-

able salts. TBATPB was obtained by mixing aqueous solutions of tetrabutylammonium iodide and sodium tetraphenylborate according to Ref. (11). Tetrabutylammonium dicarbollycobaltate was obtained from the Institute of Nuclear Research, Řež near Prague, Czechoslovakia. Colicines were a gift of Dr. J. Šmarda, J. E. Purkyně University, Brno, Czechoslovakia. The base electrolytes of aqueous and nonaqueous phase were brought into contact prior to measurement to bring the two phases into partition equilibrium.

Real and imaginary impedances of the L/L system were measured as previously described (5) using a Solartron 1250A frequency response analyzer interfaced with a Princeton Applied Research 173 potentiostat and a HP85A computer. Potentials were applied across the interface using the 1250A bias control. The cell, though of a somewhat different design, was principally the same as in Fig. 1. The aqueous/nitrobenzene interface of 0.18 cm² area lay in between 2 cm² Ag/AgCl electrodes connected by Pt wire to the impedance measurement system.

Results

Cyclic voltammetry.—The influence of ovalbumin on the transfer of probe Cs^+ ion was investigated using LiCl base electrolytes in water and TBATPB in nitrobenzene. CsCl was dissolved in the aqueous phase. Cyclic voltammograms were recorded at temperatures of 6° (Fig. 2), 10°, and 20°C. In the absence of ovalbumin, the transfer of Cs^+ was reversible at all temperatures according to the cyclic voltammetry, with the positive to negative peak difference being 59–62 mV.

A solution with a typical ovalbumin concentration of 4 $\mu\text{g/ml}$ in base electrolyte was used as a blank experiment to observe the influence of protein on the blocked interface. The transfer of ions of base electrolytes in the presence of ovalbumin occurred at smaller applied potentials, and narrowed the potential window of interfacial blockage by approximately 20 mV.

Upon addition of ovalbumin to the Cs^+ -containing solution (Fig. 2), the positive and negative peaks were both shifted to more extreme potentials by about 35 and 30 mV, respectively. At the same time, the peak current values decreased. The most pronounced effect on the peak-peak shift was observed at low temperatures (Fig. 3). In the course of the experiment it was possible to observe the formation of a white layer on the interface. The same effect (in absence of current) was experimentally produced on interfaces between aqueous ovalbumin solutions and other solvents (benzene, ether, chloroform,

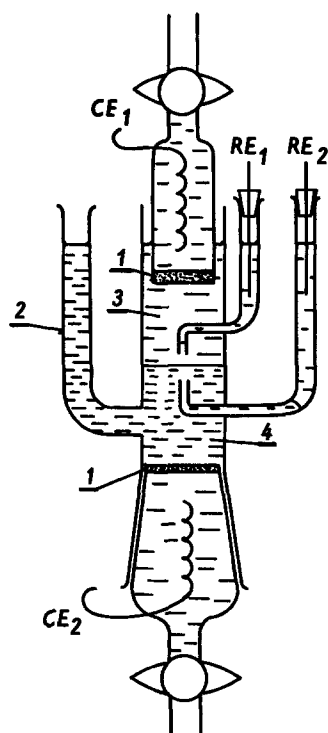


Fig. 1. Cell for L/L measurements. 1, glass frit; 2, balancing tube; 3, aqueous phase; 4, nitrobenzene phase; RE₁ and RE₂, reference electrodes; CE₁ and CE₂, counterelectrodes.

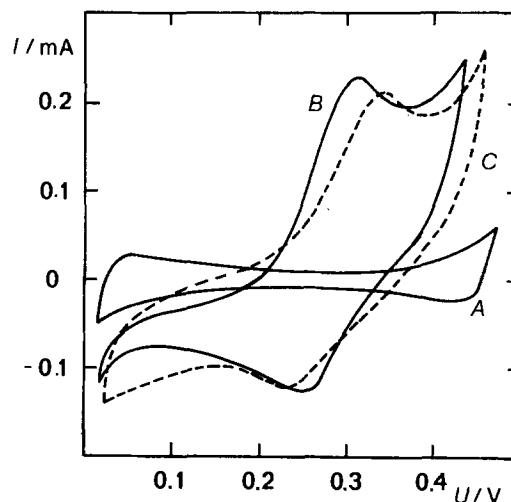


Fig. 2. Influence of ovalbumin on the transfer of Cs^+ . A, cyclic voltammogram of base electrolytes 10^{-2} mol liter⁻¹ LiCl in water, 0.025 mol liter⁻¹ TBATPB in nitrobenzene; B, transfer of Cs^+ [$c(CsCl) = 9.2 \times 10^{-4}$ mol liter⁻¹]; and C, the same case as in B in the presence of $4 \mu\text{g ml}^{-1}$ ovalbumin in the aqueous phase. The rate of polarization was 26.3 mV s⁻¹, at temperature 6°C.

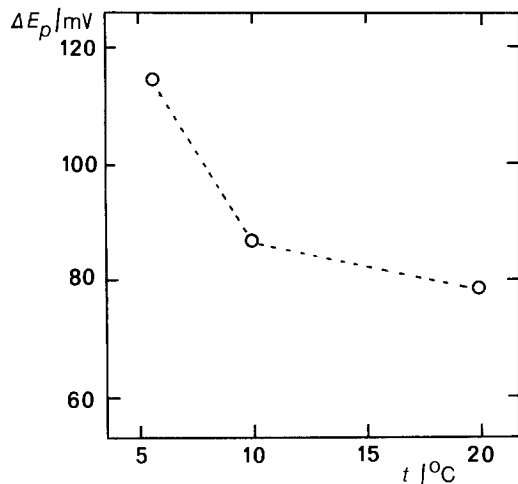


Fig. 3. The potential difference of the positive and negative peak of Cs^+ in the presence of ovalbumin as a function of temperature.

tetrachloromethane, and dichloroethane). This type of denaturation is typical for proteins and is known as a contact denaturation.

Similar experiments were done with colicine E_3 in base electrolytes of $0.01 \text{ mol liter}^{-1}$ LiCl in water and $0.017 \text{ mol liter}^{-1}$ tetrabutylammonium dicarbollycobaltate. Again, the protein in the base electrolyte alone narrowed the potential window. Addition of colicine E_3 to the systems with Cs^+ also resulted in the separation of positive and negative peaks from a reversible value of 60 mV toward 120 mV, and indicated irreversible Cs^+ transfer (Fig. 4). The degree of the shift depends on the temperature, being highest at low temperatures.

The greatest effect of both ovalbumin and colicine on the transfer of Cs^+ across the interface was observed at 6°C , the lowest usable temperature (the freezing point of the nitrobenzene solution is about 5.7°C). The character of transfer at this temperature was irreversible. The hindrance of Cs^+ transport can be explained by formation of a packed layer of insoluble peptide on the interface. Proteins are known to undergo contact denaturation when brought into contact with nitrobenzene. The denaturated protein is less soluble in water and precipitates on the interface. It is also possible that at low temperatures the denaturated protein undergoes structural rearrangements. With increasing temperature, the solubility of the deposited protein increases and diminishes the structural arrangement of the layer.

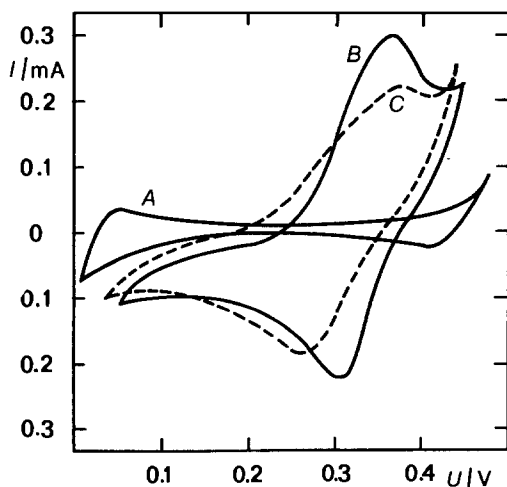


Fig. 4. Influence of colicine E_3 on the transfer of Cs^+ . A, cyclic voltammogram of the base electrolytes $0.01 \text{ mol liter}^{-1}$ LiCl in water and $0.017 \text{ mol liter}^{-1}$ tetrabutylammonium dicarbollycobaltate in nitrobenzene; B, curve of Cs^+ transfer [$c(\text{CsCl}) = 1.1 \times 10^{-3} \text{ mol liter}^{-1}$]; and C, the same case as in B, in the presence of $75 \mu\text{g ml}^{-1}$ colicine E_3 in water. The temperature was 6°C , at polarization rate 26.3 mV s^{-1} .

As described above, the precipitated protein can, due to its thickness, hinder the transfer of ions across the interface. At the same time, one can expect that the layer can be so thick that it can act as another phase with properties between those of water and nitrobenzene. An intermediate phase will thus change the ionic partition coefficients, generally narrowing the potential window of base electrolytes. At high concentrations of protein in the aqueous phase the base electrolytes lose their potential window controlling properties and the voltammetric curve becomes ohmic: a straight line indicating the current is governed by film resistance.

A set of cyclic voltammetry measurements of the base electrolytes in the presence of various BSA concentrations were obtained. The BSA concentration in aqueous phase ranged from 1 to 10,000 ppm. Figure 5 shows typical cyclic voltammograms obtained from the measurement. The width of the base electrolyte potential window decreased upon addition of the low (~ 1 ppm) amount of BSA. Upon further BSA concentration increase, the width of the base electrolyte potential window again increased. A decrease of the width was then observed upon further addition of BSA. The dependence of the potential window width on the BSA concentration is shown in Fig. 6. The width was determined as the difference between the potentials at which the base electrolyte current exceeded $90 \mu\text{A}$.

The pattern of potential width behavior strongly resembles that of the impedance measurement (5) described below.

Impedance characteristics.—Impedance characteristics of blocked and unblocked nitrobenzene/aqueous interfaces have been investigated as a function of BSA concentration and applied dc potential. Figure 7 shows the dependence of 1.0 Hz total interfacial impedance and

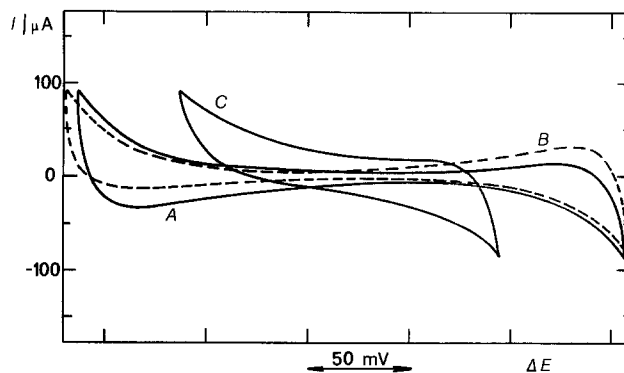


Fig. 5. Typical voltammetric curves in the presence of BSA. A, base electrolytes $0.1 \text{ mol liter}^{-1}$ TBATPB in nitrobenzene, $0.1 \text{ mol liter}^{-1}$ LiCl in water; B, addition of 3 ppm of BSA into the aqueous phase; and C, addition of 1% of BSA into the aqueous phase. The scan rate was 5 mV/s .

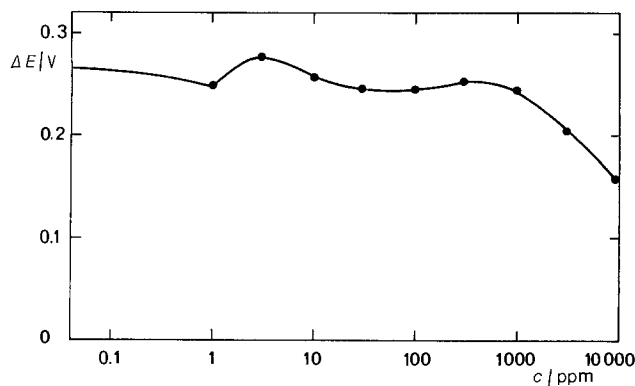


Fig. 6. The dependence of the potential window width on the BSA concentration. Base electrolytes: $0.1 \text{ mol liter}^{-1}$ LiCl in water and $0.1 \text{ mol liter}^{-1}$ TBATPB in nitrobenzene. The scan rate of the voltammogram was 5 mV/s .

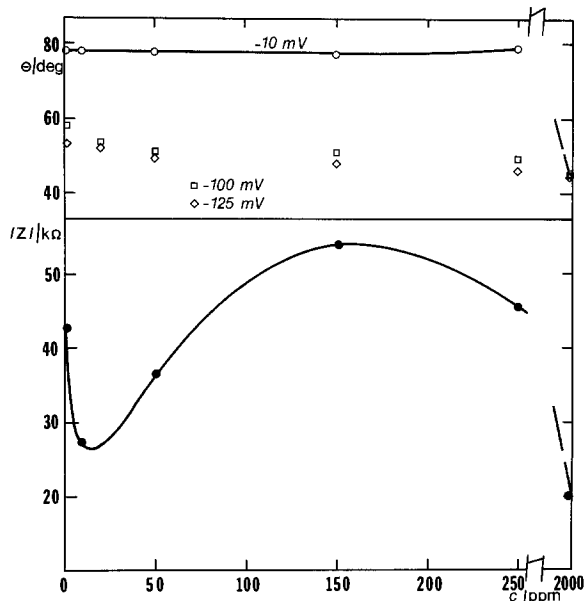


Fig. 7. Dependence of 1.0 Hz total interfacial impedance (●) and phase angle (○) upon aqueous BSA concentration at applied potential of -10 mV. Phase angles at (□) -100 mV and (◇) -125 mV.

phase angle upon aqueous BSA concentration at an applied interfacial potential of -10 mV. Phase angles at -100 and -125 mV are also indicated.

The general behavior shown for -10 mV was observed between applied interfacial potentials of -70 and $+85$ mV. Note that the phase angle remains constant and near 90° up to 250 ppm BSA. This reflects nearly ideal capacitive behavior within this potential region. A constant phase angle requires that changes in total impedance correspond to proportional changes in the imaginary impedance which is inversely proportional to capacitance ($Z_i = 1/\omega C$) for a blocked interface. The decrease in total impedance up to about 10 ppm BSA therefore corresponds to an increase of the total system capacitance. As the concentration of BSA is increased beyond 10 ppm, impedances begin to increase, indicating a decrease in total capacitance.

The initial increase of capacitance is attributed to the initial adsorption of BSA (5-10 ppm) and an associated increase in interfacial charge density or dielectric constant. This effect is modeled by a capacitor in parallel with the initial double layer capacitance. Further adsorption increases the physical thickness of the interface region. The

adsorbed film may be considered as a capacitor in series with the capacitor representing increased interfacial charge density. The total interfacial capacitance of this array decreases until film thickness reaches a saturation value.

The decreasing total impedance at even higher BSA concentrations reflects facile film-solution ion transfer which was already described for the case of ovalbumin in the voltammetry section. Phase angles at -100 and -125 mV approached 45° as BSA concentrations were increased. At these potentials, where the interface is not ideally blocked, ion transfer is increasingly facilitated by further BSA additions.

Acknowledgment

This work was in part supported by the National Science Foundation Grant CHE 8103334.

Manuscript submitted Jan. 17, 1984; revised manuscript received March 3, 1984. This was Paper 361 presented at the Cincinnati, Ohio, Meeting of the Society, May 6-11, 1984.

The University of North Carolina assisted in meeting the publication costs of this article.

REFERENCES

1. J. Koryta and P. Vanýsek, in "Advances in Electroanalytical Chemistry and Electrochemical Engineering," Vol. 12, H. Gerisher and C. W. Tobias, Editors, p. 113, Wiley, New York (1981).
2. P. Vanýsek and R. P. Buck, *J. Electroanal. Chem. Interfacial Electrochem.*, **163**, 1 (1984).
3. O. R. Melroy, W. E. Bronner, and R. P. Buck, *This Journal*, **130**, 373 (1983).
4. J. Koryta, L. Q. Hung, and A. Hofmanová, *Stud. Biophys.*, **90**, 25 (1982).
5. J. D. Reid, P. Vanýsek, and R. P. Buck, *J. Electroanal. Chem. Interfacial Electrochem.*, Submitted for publication.
6. P. Vanýsek, Dissertation, J. Heyrovský Institute of Physical Chemistry and Electrochemistry, Czechoslovak Academy of Sciences, Prague, Czechoslovakia (1982).
7. Merck Index, Vol. 10, Merck Co., Rahway, NY (1983).
8. J. Šmarda, "The Effects of Colicins," Medical Faculty of the J. E. Purkyně University, Brno, Czechoslovakia (1978).
9. Z. Samec, V. Mareček, J. Koryta, and M. W. Khalil, *J. Electroanal. Chem. Interfacial Electrochem.*, **83**, 393 (1977).
10. Z. Samec, V. Mareček, and J. Weber, *ibid.*, **100**, 841 (1979).
11. B. P. Artamonov, M. S. Grilikhes, B. K. Filanovskii, and B. E. Goltsin, *Zh. Prikl. Khim. (Leningrad)*, **47**, 588 (1974).

Properties of the Interface of Two Immiscible Electrolytes Mediated by Molecules of Biological Importance

A Literature Review

Petr Vanýsek¹ and Richard P. Buck*

Department of Chemistry, The University of North Carolina, Chapel Hill, North Carolina, 27514

ABSTRACT

It has been shown in the past few years that the interface formed between two immiscible solutions of electrolytes can be treated, from an electrochemical point of view, in the same manner as the solution/electrode interface, and essentially the same techniques of electrochemical investigation can be used. A review of the methods pertaining to biologically important materials is given. Specifically, the following groups of experiments are treated: direct transport measurement of certain ionic species (choline, acetylcholine, and dodecylsulfate), transport of probe ions across the adsorbed material (lecithin and several proteins), impedance measurements in the presence of adsorbed bovine serum albumin, and transport across the interface facilitated by antibiotics (valinomycin and monensin).

Investigations of the electrochemical properties of interfaces between two immiscible solutions containing dissolved electrolytes have attracted an increasing number of scientists in the past years. Although the first paper dealing with this matter appeared in 1902 (1), the subject was dormant until about ten years ago when the properties of this interface were recognized to parallel those of metal/solution interfaces (2). The electrochemical phenomena of the L/L interface were reviewed quite deeply by Koryta and Vanýsek (3) in 1981. An updated version (4) and a literature review (5) have been published recently. For thorough theoretical treatments and experimental setups, the reader is referred to these works.

The purpose of this paper is to emphasize the possible advantages of the L/L electrical phenomena study for biologically important systems. The general aspect of the liquid/liquid interface is that it can serve, within certain limits, as a model for half of a biological membrane. However distant this model may be, it might prove useful. The present state-of-the-art of L/L electrochemistry of biologically important molecules is of more analytical interest.

The Basic Principle of L/L Electrochemistry

Assume the contact of two immiscible liquid phases α and β containing one common ion, i , in thermodynamic equilibrium. An interfacial potential will be established across this interface; its value is given by the Nernst-Donnan equation

$$\Delta\phi^{\alpha\rightarrow\beta} = \Delta\phi^{\circ,\alpha\rightarrow\beta} + \frac{RT}{nF} \ln \frac{a_i(\alpha)}{a_i(\beta)} \quad [1]$$

The fraction in the logarithmic function represents the partition equilibrium for ion i between the two phases. When the interfacial potential is changed from outside the system by applying a voltage from some source, the standard value $\Delta\phi^{\circ,\alpha\rightarrow\beta}$ remains constant, and, therefore, the ratio $a_i(\alpha)/a_i(\beta)$ will have to change. A portion of the equilibrated ions will be transferred to the other side of the interface, and is manifested by the passage of electric current through the interface.

The choice of nonaqueous solvents is determined by the requirement that the mutual solubility with water be limited, and the dielectric constant be quite high such that dissolved salt can be dissociated. The most commonly used solvent is nitrobenzene and, in some cases, dichloroethane is useful.

By using salts of very hydrophobic ions as a base electrolyte for nonaqueous phase and very hydrophilic ions as a base electrolyte for water, one can obtain a fairly broad potential window in which practically no faradaic

current passes through the interface. Under these conditions, the interface behaves as an ideally polarizable electrode. The typical electrolyte for water is LiCl and, for nitrobenzene, tetrabutylammonium tetraphenylborate (TBATPB) or tetraphenylarsonium tetraphenylborate (TPATPB). The potential window limits are determined by the transfer of base electrolytes. Measurements within the limits enable observation of ion transfer whose hydrophobic properties are between those of the base electrolytes. The potential at which this transfer is observed can be correlated with the standard energy and standard potential of transfer for the given ion

$$\Delta G^\circ = -RT \ln K_{w\rightarrow o}^\circ = -nF\Delta\phi_{w\rightarrow o}^\circ \quad [2]$$

Experimental Methods

L/L interfaces may be treated and investigated in manners similar to the solid electrode. Two different voltammetric methods of electrode kinetics were used for

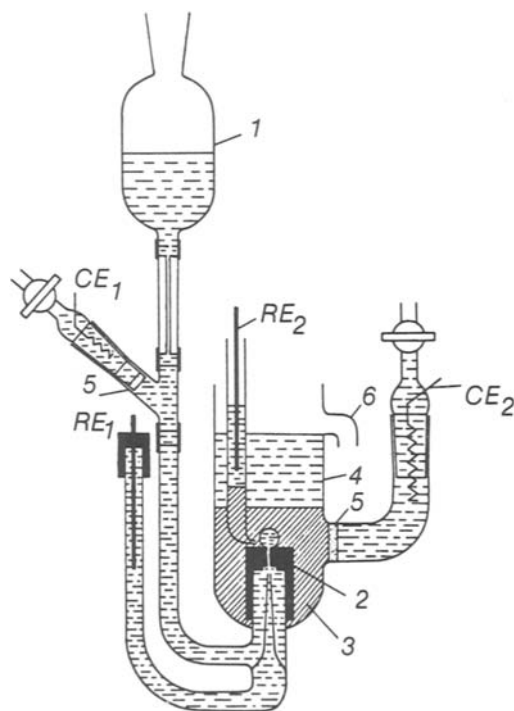


Fig. 1. Electrolyte dropping electrode assembly. 1, aqueous electrolyte reservoir; 2, Teflon orifice attachment; 3, nitrobenzene electrolyte; 4, waste aqueous electrolyte; 5, glass frit; 6, overflow; RE₁ and RE₂, reference electrodes; and CE₁ and CE₂, counter-electrodes.

* Electrochemical Society Active Member.

¹ On leave from J. Heyrovský Institute of Physical Chemistry and Electrochemistry, Czechoslovak Academy of Sciences, Prague, Czechoslovakia.

this investigation: cyclic voltammetry and polarography with a dropping electrode. The practical problem of eliminating the resistances of both phases, causing IR drops, was solved by using a four electrode potentiostat (6), preferably with a positive feedback elimination of the residual ohmic drop between the two reference electrodes (7). The potential difference across the interface was sensed by the reference electrodes, one in each phase. The electrode in the aqueous phase is an ordinary electrode of the second kind, usually Ag/AgCl. The reference electrode in the organic phase is essentially an ion selective electrode responding to the ion of the base electrolyte nonaqueous solution. It consists of an electrode of the second kind immersed in aqueous solution containing the same ion as the base electrolyte of the organic phase. Under these conditions, a reproducible (though not necessarily known) Nernst potential is established at the junction.

For polarographic studies an electrolyte dropping electrode was developed. The type with a Teflon capillary designed by Samec *et al.* (8) is shown in Fig. 1. The aqueous solution drops upward into the heavy organic phase. An improvement of the sensitivity for analytical purposes was achieved by using differential pulse stripping voltammetry in which the analytical ion is accumulated in the electrolyte hanging drop electrode (Fig. 2) (9, 10).

Chronopotentiometry, voltammetry, or impedance measurements used a cell of the type shown in Fig 3.

Impedance properties of the L/L interface are measured using an impedance bridge (11). The bridge is essentially a cross correlator which determines in-phase and 90° out-of-phase components of the response with respect to the perturbing sine wave signal.

Results

A direct study of selected ionic species of biological importance can be performed in liquid/liquid systems. Examples include choline and acetylcholine (10, 12, 13) and dodecylsulfate (14). Vanýsek and Behrendt (12) used multisweep cyclic voltammetry for the determination of standard potentials of transfer. A typical curve from this experiment is shown in Fig. 4. Mareček and Samec (10) used the hanging electrolyte dropping electrode and differential pulse stripping voltammetry (Fig. 2). The method for acetylcholine determination proved to be very sensitive. Figure 5 shows a set of differential pulse stripping voltammograms for different acetylcholine concentrations. It has also been shown that a good linear response can be obtained down to 0.5 ppm (2.75×10^{-6} mol/liter) acetylcholine. Samec *et al.* (13) used the method of convolution potential sweep voltammetry for determination of kinetic and thermodynamic parameters of cho-

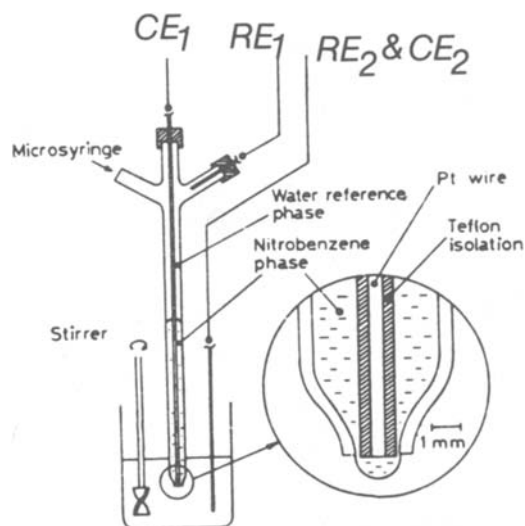


Fig. 2. Electrolyte hanging drop electrode

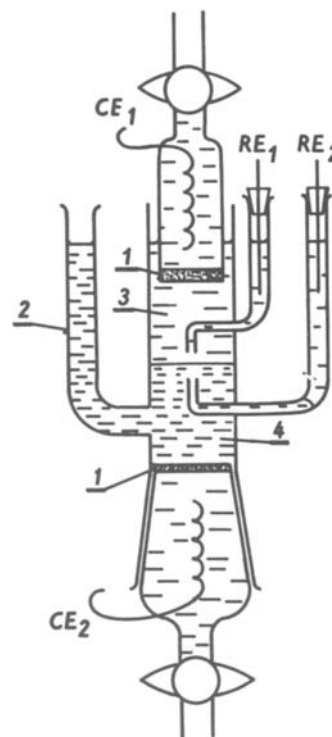


Fig. 3. Typical cell for L/L measurements. 1, glass frit; 2, balancing tube; 3, aqueous phase; 4, nitrobenzene phase; RE₁ and RE₂, reference electrodes; and CE₁ and CE₂, counter-electrodes.

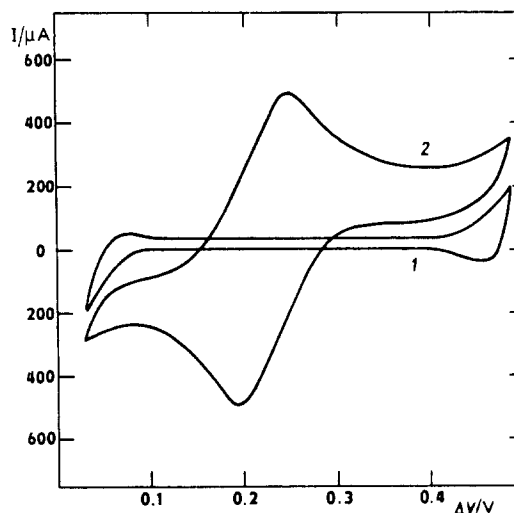


Fig. 4. Voltammogram of acetylcholine transfer. 1, base electrolytes 1 mol liter⁻¹ LiCl in water and 0.025 mol liter⁻¹ TBATPB in nitrobenzene; and 2, addition of acetylcholine (1.1×10^{-2} mol liter⁻¹). The scan rate was 12.5 mV s⁻¹.

line and acetylcholine. The standard values for the dodecylsulfate were determined by the means of electrolyte dropping electrode (14). The standard values for the above ions are given in Table I.

Another group of results deals with the electrical properties of the interface in the presence of adsorbed material. The basic approach was to study the transfer of a well-characterized probe ion in the presence and absence of adsorbed species. Koryta *et al.* (15) studied voltammetric transfer of semihydrophobic ions and ionophore-facilitated alkali metal ion transfer across the water/nitrobenzene interface covered with a lecithin monolayer. The transfer processes were slowed down particularly at low (6°C) temperatures. Figure 6 shows the effect of addition of lecithin on the transfer of the Cs⁺ probe ion.

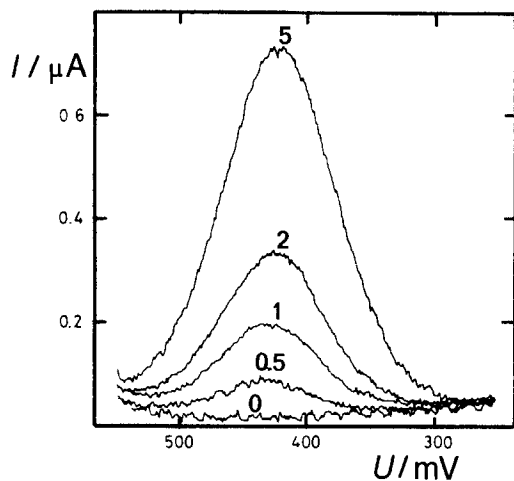


Fig. 5. Differential pulse stripping voltammetry of acetylcholine at hanging electrolyte drop electrode. The bold numbers show ppm concentrations of acetylcholine chloride in water.

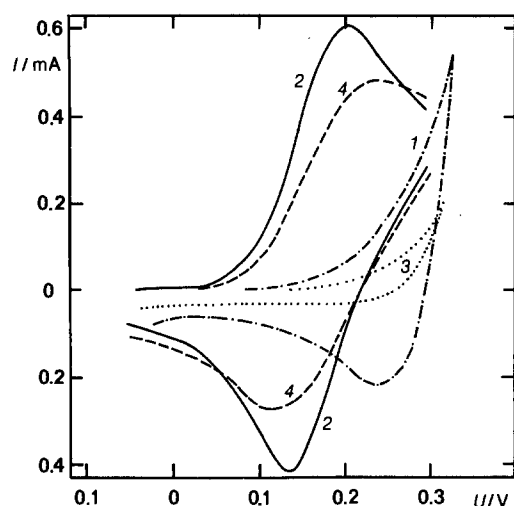


Fig. 6. Cyclic voltammogram of the transfer of 5×10^{-4} mol liter $^{-1}$ Cs $^{+}$ (as CsCl) from water to nitrobenzene and back at 6°C. Base electrolytes 0.01 mol liter $^{-1}$ LiCl in water, 0.017 mol liter $^{-1}$ TBA dicarbollyl cobaltate in nitrobenzene. 1, base electrolytes only; 2, after addition of CsCl to the aqueous phase; 3, base electrolyte with the lecithin monolayer; and 4, 3 after addition of CsCl to the aqueous phase.

The alkali metal ion transfer in the presence of an ionophore, such as a crown polyether, is considerably easier than in its absence. Figure 7 shows a dependence of the difference of cyclic voltammetry peak potentials (for positive and negative currents), ΔE_p , of sodium ion in the presence of 0.5 mol liter $^{-1}$ dibenzo-18-crown-6 on temperature with a lecithin monolayer. Similar experiments were carried out with ovalbumin and other proteins dissolved in the aqueous phase (16-18). The formation of films on the interface was observed. The transfer of alkali metal ions was retarded by the presence of protein on the aqueous side of the interface.

Another method for investigation of the properties of an interface with adsorbed material is an impedance technique. Reid *et al.* (18, 19) measured impedance characteristics of water/nitrobenzene interface in the presence of

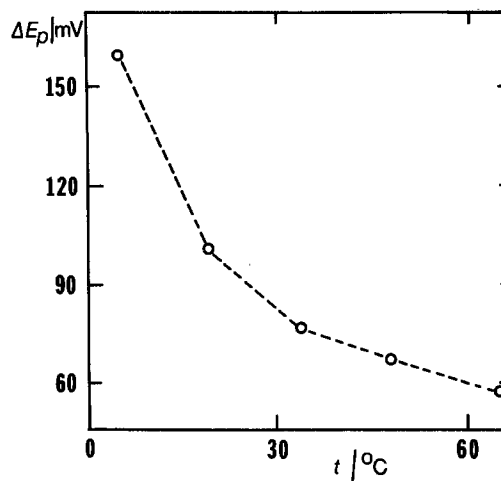


Fig. 7. Dependence of ΔE_p of Na $^{+}$ in the presence of dibenzo-18-crown-6 and lecithin monolayer on temperature.

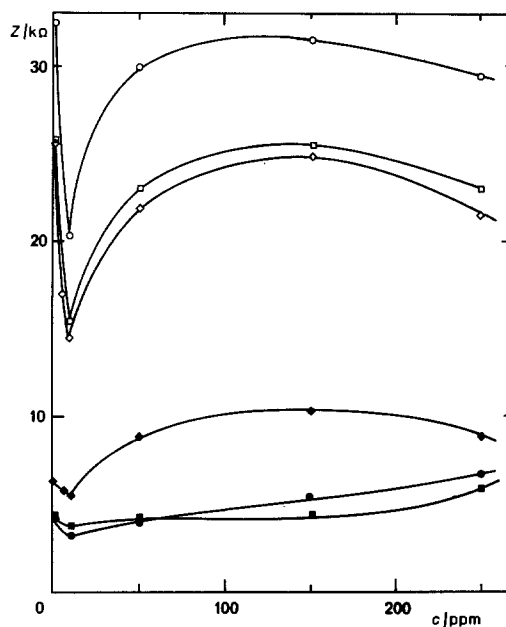


Fig. 8. 1.5 Hz real (solid symbols) and imaginary (unfilled symbols) impedances as a function of aqueous BSA concentration. Applied interfacial potentials: +35 (■ and □), -15 (● and ○), and -65 mV (◆ and ◇).

bovine serum albumin (BSA). Figure 8 (19) shows one of the impedance plots. The results indicated three phenomena occurring at the interface: an increased interfacial charge density upon initial BSA adsorption, formation of an adsorbed dielectric film, and an enhancement of faradaic base electrolyte ion leakage at high BSA concentrations.

As mentioned in the case of lecithin monolayer studies (15), the transfer of ions across the interface can be influenced by the presence of suitable ionophores. This phenomena can be used for investigation of certain biologically important molecules which have the ionophoric (translocator) properties. This is the case of valinomycin (20-22), nonactin (21, 23), and monensin (24-26) (Fig. 9). Vanýsek *et al.* (22) studied the valinomycin mediated transfer of K $^{+}$ ions across water/nitrobenzene interface by potential-sweep voltammetry. A curve for this transfer is given in Fig. 10.

Monensin, which has a practical application in veterinary pharmacology, can be determined by voltammetry at L/L interface in the concentration range between 0.05 mmol/liter and 3 mmol/liter (25). The principle which allows this determination is the facilitated transfer of sodium and hydrogen ions across the nitrobenzene/water

Table I. Standard values for selected ionic species of biological importance

	$\Delta\phi^{\circ}_{w \rightarrow nb}$ (mV)	ΔG° (kJ/mol)	Ref.
Acetylcholine	0.049	- 4.8	(12)
Acetylcholine	0.05	- 4.8	(10)
Choline	0.117	-11.3	(12)
Dodecylsulfate	-0.043	- 4.1	(14)

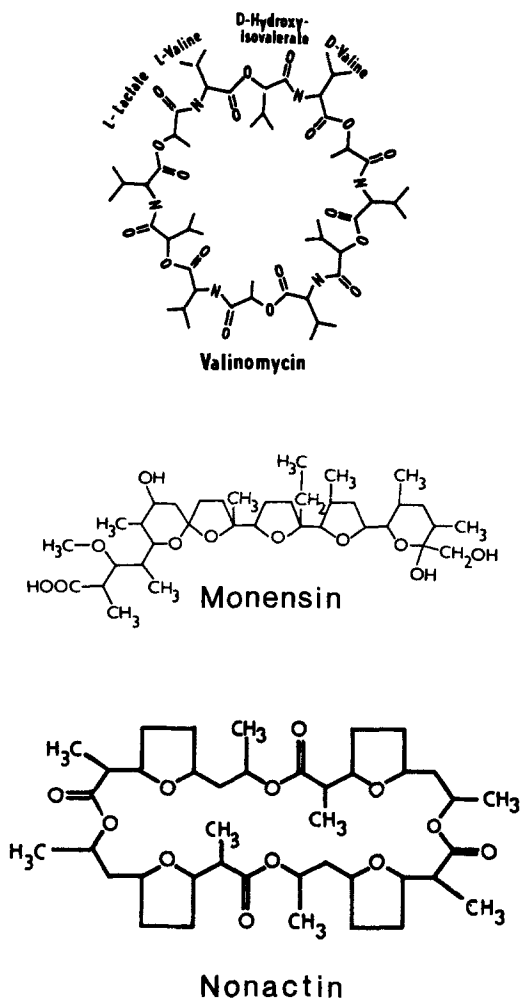
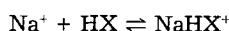


Fig. 9. Ionophores

interface. A sodium monensin molecular functional group (Fig. 9) can serve both as a sodium carrier (NaX) and a proton carrier (NaHX^+). The particle being transferred is, in both cases, NaHX^+ . This species is formed in nitrobenzene by either the reaction



with equilibrium constant $\log K_1 = 5.63$, or by the reaction

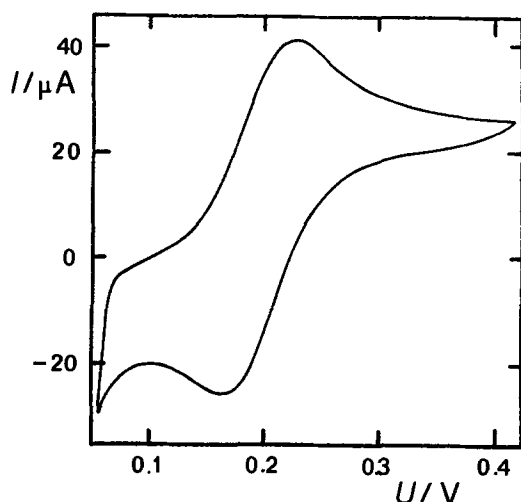
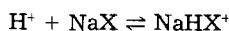


Fig. 10. Cyclic voltammogram of K^+ ($c = 5 \times 10^{-5}$ mol liter $^{-1}$) transfer facilitated by valinomycin ($c = 5 \times 10^{-4}$ mol liter $^{-1}$). Base electrolytes 10^{-3} mol liter $^{-1}$ LiCl in water, 10^{-3} mol liter $^{-1}$ TPATPB in nitrobenzene. The scan rate was 16.3 mV s $^{-1}$.

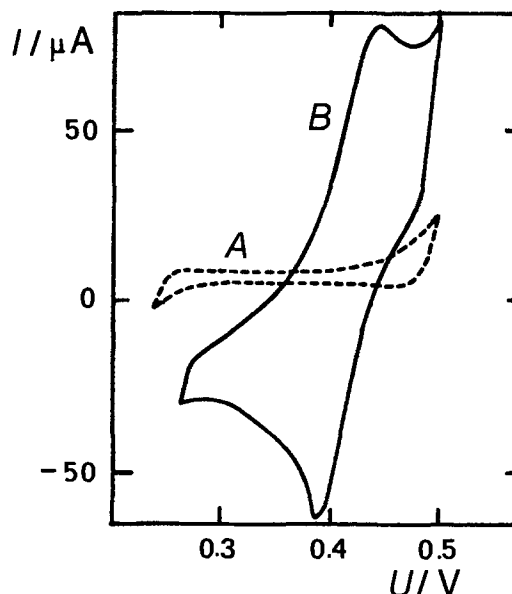
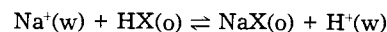


Fig. 11. Cyclic voltammogram of monensin. A, base electrolytes 0.5 mol liter $^{-1}$ sodium acetate, 0.5 mol liter $^{-1}$ acetic acid, and 10^{-3} mol liter $^{-1}$ NaCl. B, 1.12×10^{-3} mol liter $^{-1}$ monensin dissolved in nitrobenzene.

with equilibrium constant $\log K_2 = 9.88$. The principal electrochemical process is the exchange reaction



(w—water, o—nitrobenzene) with the exchange equilibrium constant $\log K_{\text{exchng}} = -3.96$. A cyclic voltammogram for this example is shown in Fig. 11.

Summary

Transport of ions across a single L/L interface can be observed without recourse to whole membrane transport studies. This new technology has begun to be applied to species of biological importance: species that adsorb and modify (usually inhibit) transport of small probe ions, and finally ionophore species that aid in transport of simple inorganic ions. Results include principally kinetic effects that are difficult to measure by other techniques.

Acknowledgments

This work was in part supported by the National Science Foundation Grant CHE 8103334.

Manuscript submitted Jan. 25, 1984; revised manuscript received March 29, 1984. This was Paper 362 presented at the Cincinnati, Ohio, Meeting of the Society, May 6-11, 1984.

The University of North Carolina assisted in meeting the publication costs of this article.

REFERENCES

1. W. Nernst and E. H. Riesenfeld, *Ann. Phys.*, **8**, 600 (1902).
2. J. Koryta, P. Vanýsek, and M. Brezina, *J. Electroanal. Chem. Interfacial Electrochem.*, **75**, 211 (1977).
3. J. Koryta and P. Vanýsek, in "Advances in Electrochemistry and Electrochemical Engineering," Vol. 12, H. Gerischer and C. W. Tobias, Editors, p. 113, Wiley, New York (1981).
4. J. Koryta, *Ion-Sel. Electrode Rev.*, **5**, 131 (1983).
5. P. Vanýsek and R. P. Buck, *J. Electroanal. Chem. Interfacial Electrochem.*, **163**, 1 (1984).
6. Z. Samec, V. Mareček, J. Koryta, and M. W. Khalil, *ibid.*, **83**, 393 (1977).
7. Z. Samec, V. Mareček, and J. Weber, *ibid.*, **100**, 841 (1979).
8. Z. Samec, V. Mareček, J. Weber, and D. Homolka, *ibid.*, **99**, 385 (1979).
9. V. Mareček, and Z. Samec, *Anal. Lett.*, **14**, 1241 (1981).
10. V. Mareček and Z. Samec, *Anal. Chim. Acta*, **141**, 65 (1982).
11. J. D. Reid, P. Vanýsek, and R. P. Buck, *J. Electroanal.*

- Chem. Interfacial Electrochem.*, **161**, 1 (1984).
12. P. Vanýsek and M. Behrendt, *ibid.*, **130**, 287 (1981).
 13. Z. Samec, V. Mareček, and D. Homolka, *ibid.*, **158**, 25 (1983).
 14. P. Vanýsek, *ibid.*, **121**, 149 (1981).
 15. J. Koryta, L. Q. Hung, and A. Hofmanová, *Stud. Biophys.*, **90**, 25 (1982).
 16. M. Behrendt, Thesis, Charles University, Faculty of Natural Sciences, Prague, Czechoslovakia (1981).
 17. P. Vanýsek, Dissertation, Czechoslovak Academy of Sciences, J. Heyrovský Institute of Physical Chemistry and Electrochemistry, Prague, Czechoslovakia (1982).
 18. P. Vanýsek, J. D. Reid, M. A. Craven, and R. P. Buck, *This Journal*, **131**, 1788 (1984).
 19. J. D. Reid, P. Vanýsek, and R. P. Buck, *J. Electroanal. Chem. Interfacial Electrochem.*, Submitted for publication.
 20. J. Koryta, *Electrochim. Acta*, **24**, 293 (1979).
 21. D. Homolka, L. Q. Hung, A. Hofmanová, M. W. Khalil, J. Koryta, V. Mareček, Z. Samec, S. K. Sen, P. Vanýsek, J. Weber, M. Brezina, M. Janda, and I. Štibor, *Anal. Chem.*, **52**, 1606 (1980).
 22. P. Vanýsek, W. Ruth, and J. Koryta, *J. Electroanal. Chem. Interfacial Electrochem.*, **148**, 117 (1983).
 23. A. Hofmanová, L. Q. Hung, and W. Khalil, *ibid.*, **135**, 257 (1982).
 24. D. Guo, J. Koryta, W. Ruth, and P. Vanýsek, *ibid.*, **159**, 413 (1983).
 25. J. Koryta, W. Ruth, P. Vanýsek, and A. Hofmanová, *Anal. Lett.*, **15**, 1685 (1982).
 26. J. Koryta, Yu. N. Kozlov, A. Hofmanová, W. Khalil, P. Vanýsek, W. Ruth, and D. Guo, *Antibiotiki (Moscow)*, **28**, 810 (1983).

Electrochemical Reduction of Benzoyl Chloride and Benzoyl Fluoride

Graham T. Cheek* and Pamela A. Horine

Department of Chemistry, U.S. Naval Academy, Annapolis, Maryland 21402

ABSTRACT

Voltammetric studies of the cathodic reduction of benzoyl chloride and benzoyl fluoride at vitreous carbon and platinum in AN/TEAP have shown that reduction occurs at potentials (E_p) of -1.82 and $-2.29V$, respectively, vs. Ag/AgNO₃ (0.1M). Reduction of benzoyl chloride involves one electron per molecule, forming a 2:1 mixture of *trans*- and *cis*-stilbenediol dibenzoate. Electrochemical reductions of both product isomers produce good yields of diphenylacetylene. Evidence for the formation of the benzoyl radical, as opposed to the benzoyl anion, was obtained from experiments in which benzoyl chloride was reduced in the presence of another, less easily reducible acyl chloride (*p*-anisoyl chloride). The involvement of benzil as an intermediate in benzoyl chloride reduction is supported by voltammetric data for benzil reduction. An n value of 1.1-1.2 was observed for benzoyl fluoride reduction, which led to the formation of benzyl benzoate, diphenylacetylene, and stilbenol benzoate (total yield: approximately 35%) as identifiable products, the remainder of the product being material of higher molecular weight. The greater stability of the anion radical produced from reduction of benzoyl fluoride (compared to that of benzoyl chloride) is evidenced by observation of a reversible system at cyclic voltammetric sweep rates above 50 V/s, and is thought to reflect the fact that fluoride is generally not as good a leaving group as is chloride.

As a general pathway in the electrochemical reduction of organic compounds, cathodic dehalogenation has been found to be particularly interesting because the radicals formed upon elimination of halide in this process are usually fairly reactive and can couple to produce compounds with rather remarkable structures (1-5). Continued interest in this area has involved investigations of the effect of temperature upon the polarographic reduction of alkyl halides, as well as the general mechanism of organohalogen compound reduction (7-10).

In a literature survey of cathodic dehalogenation, it is apparent that the cathodic reduction pathways of acyl halides have not been thoroughly studied. An early study (11) revealed a diffusion-controlled polarographic response for the reduction of benzoyl chloride in acetone/LiClO₄, the slope of the wave indicating a one-electron process, although no preparative studies were carried out. Similar results were obtained in later work at mercury in DMSO/TEAP (12). The reduction in buffered 50% dioxane/water mixtures at pH 9.3, in which the hydrolysis of benzoyl chloride is rather slow, was found to involve four electrons, leading to the formation of benzaldehyde (13). Recently, a preparative electrolysis of benzoyl chloride at mercury in acetone/LiClO₄ has been carried out, and, although little voltammetric information was given, the products were found to be *cis*- and *trans*-stilbenediol dibenzoate (14).

The present work, carried out in acetonitrile/TEAP at both glassy carbon and platinum electrodes, was undertaken to determine the reduction mechanism for benzoyl chloride as well as benzoyl fluoride in a com-

monly employed medium. The results have allowed an assessment of the generality of the reduction mechanism for benzoyl chloride in various systems, as well as an interesting insight into the effect of the halogen atom upon the reduction pathway.

Experimental

Chemicals, preparation, and purification.—Acetonitrile (Fisher Scientific Company, ACS reagent grade) was stored for several days over CaH₂ prior to fractional distillation from P₂O₅ through a double-pass column, the middle 70% being retained for use as solvent. This solvent, freshly distilled, was transferred under nitrogen to a flask containing CaH₂ for introduction into the electrochemical cell (see below). Tetraethylammonium perchlorate (Southwestern Analytical Chemical Company, electrochromic grade) was dried *in vacuo* at 70°C for approximately 1 day before use. Nitrogen (Linde purified grade) was passed through an oxygen removal tower (BTS Catalyst) and through a desiccant (Drierite) for removal of traces of oxygen and moisture present.

Benzoyl chloride (99%) and benzoyl fluoride (95%, Aldrich Chemical Company) were purified by reduced-pressure distillation, producing clear liquids. Infrared spectra of these compounds confirmed their identity, and liquid chromatographic analyses showed the presence of only one peak in each case. These compounds were stored under nitrogen in tightly stoppered round-bottom flasks, kept inside a nitrogen-flushed desiccator over calcium sulfate. *Cis*- and *trans*-stilbenediol dibenzoate were synthesized and purified according to the procedure of Trisler and Frye (15), except that further

* Electrochemical Society Active Member.

purification of the *cis* isomer by two-fold recrystallization from 75:25 hexane:benzene was required for complete removal of the *trans* isomer. Identity and purity of these compounds were established by melting point (uncorrected) [*cis* isomer, 158°-159°C; literature 159°C (15); *trans* isomer, 188°-189°C; literature 188.5°-189°C (15)], infrared spectra, and liquid chromatographic analysis. Stilbenol benzoate was prepared according to the method of Beringer *et al.* (16). Benzyl benzoate (99+%) was used as received from Aldrich Chemical Company.

Electrochemical apparatus and techniques.—Voltammetric experiments were carried out using vacuum line/inert gas line techniques. A PAR Model K60/K66 electrochemical cell, fitted with $\frac{3}{8}$ 14/20 O-ring seal joints (Ace Glass Company), was used in these studies, with the electrode connections made by means of O-ring seals (Ace-Threds, Ace Glass Company) for the working electrodes and reference electrode, and sealed-through tungsten wires for the auxiliary electrode. The cell, together with electrodes and supporting electrolyte, was placed under vacuum ($\sim 5 \mu\text{m}$) for several hours in order to ensure anhydrous conditions. Acetonitrile, previously purified as described above, was distilled by means of a current of dry nitrogen into a volumetric receiver, connected to the cell by means of an O-ring connection and vacuum stopcock, immediately before backfilling of the cell with nitrogen. After introduction of the solvent, this receiver was left in place throughout the experiments, thereby serving as a source of nitrogen for bubbling through or sweeping over the solution in the cell, these functions being selected by means of a stopcock in a pressure equalizing tube on the receiver. Working electrode materials used in this work were vitreous carbon (3 mm diam vitreous carbon rod, Atomergic, sealed in Pyrex tubing) and platinum (5 mm diam disk). The auxiliary electrode was a platinum spiral, enclosed in a fritted glass tube (porosity E, 5-8 μm , Ace Glass Company). Potentials were referenced to a Ag/0.1M AgNO₃ [in acetonitrile; 0.336V *vs.* aqueous SCE in 0.1M AN/TEAP (17)] reference electrode, separated from the solution by a double fritted junction, the outer part of which was filled with solvent/supporting electrolyte. Transfers of benzoyl chloride from the storage vessel to the electrochemical cell were made under a stream of dry nitrogen by means of a 10 μl syringe.

Preparative electrolyses were carried out in a cell larger than that described above, the usual solution volume being 150 ml. The cell was constructed from 75 mm diam O-ring Pyrex tubing, the top section being fitted with O-ring seal ports for electrodes, vacuum line connection, and solvent delivery tube of the distillation reservoir described above. Working electrodes for these preparative electrolyses were a platinum gauze electrode (50 mm diam \times 55 mm height) and a vitreous carbon crucible (35 mm diam \times 35 mm height) placed in the electrolysis cell. The auxiliary electrode was concentrically located in the cell, and consisted of a carbon rod placed inside a porous clay cup, which in turn was placed in a fine porosity fritted glass tube. Solvent introduction procedure was the same as described for the smaller cell. Electrolyses typically involved 200-300 μl of benzoyl chloride or benzoyl fluoride.

Electrochemical experiments were carried out using a PAR Model 170 Electrochemistry System, with some cyclic voltammetric experiments utilizing a function generator based on the design of Bruckenstein (18). A digital coulometer (Model 640, The Electrosynthesis Company) was employed for current integration. A Biomation Model 1010 transient recorder was used to obtain chronoamperometric data on a short (10-200 ms) time scale.

Product isolation and analytical techniques.—Electrolysis mixtures were flushed from the cell by nitrogen pressure into receiving flasks and the solvent removed either on the vacuum line or by a nitrogen stream. The residues were then extracted with hexane, benzene, or hexane/THF mixtures (anhydrous conditions) or parti-

tioned between water and benzene, these conditions usually giving equivalent results. Electrolysis products were identified by comparison of spectroscopic, voltammetric, and chromatographic characteristics for components of electrolysis mixtures with those of authentic samples.

Liquid chromatographic analyses were carried out with a Varian 8500 Liquid Chromatograph using a UV absorption detector (254 nm), a CN bonded column, and 85% hexane: 15% methylene chloride mobile phase at a flow rate of 2.00 ml/min.

A Hewlett-Packard Model 5992 gas chromatograph/mass spectrometer, using a column of 2% OV 101/20% Carbowax 20M on Chromosorb WHP, was employed in this work. Typical conditions for analysis of products from benzoyl chloride electrolyses were a column temperature of 200°C and a flow rate of 30 ml/min, whereas those for analysis of benzoyl fluoride electrolysis products involved a temperature program of 110°C (5.0 min), 110°-175°C (in 6.5 min), and 170°C (13.5 min). An LKB 9000 GC/MS instrument was also used to characterize the electrolysis product isolated from benzene extraction of the benzoyl fluoride electrolysis mixture (after evaporation of acetonitrile), this compound having the following mass spectrum: *m/z* 554 (2.6%), 478 (9.6%), 390 (22%), 298 (26%), 283 (13%), 195 (25%), and 105 (100%).

Results and Discussion

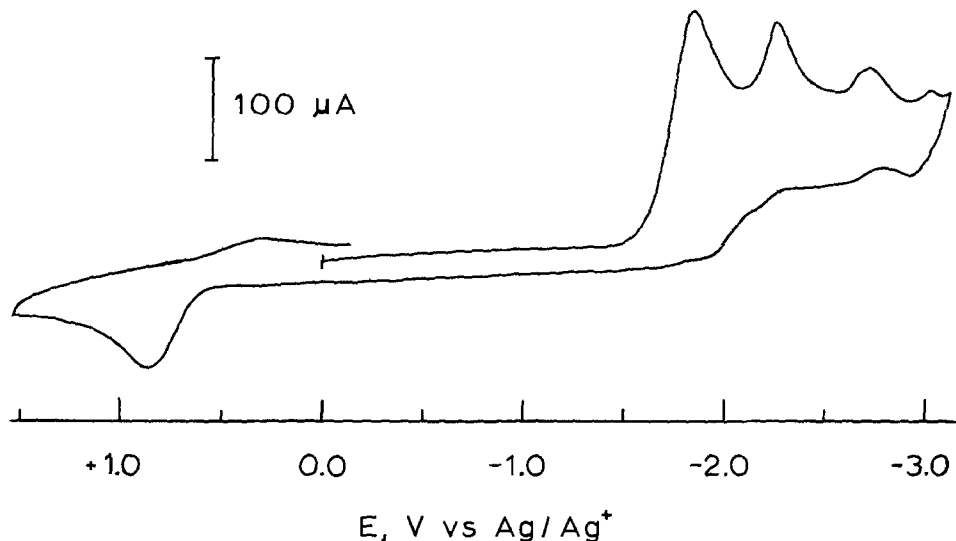
Voltammetric studies of benzoyl chloride.—As shown in Fig. 1, the reduction of benzoyl chloride in acetonitrile/TEAP at vitreous carbon occurs at -1.82V (E_p , *vs.* Ag/0.10M AgNO₃ reference electrode), with the peaks at more negative potentials corresponding to reduction of products formed in the initial benzoyl chloride reduction (see below). On the return sweep, a rather large peak at $+0.8\text{V}$ indicates oxidation of chloride released upon benzoyl chloride reduction, as confirmed by addition of tetramethylammonium chloride to an acetonitrile/TEAP solution (19). A study of peak current (i_p) for the main reduction process over the concentration range 2-10 mM revealed a linear relationship between i_p and concentration, showing that benzoyl chloride reduction proceeds rather cleanly at vitreous carbon (that is, without serious filming effects). Variation of scan rate (v) from 5 to 200 mV/s produced a linear i_p *vs.* $v^{1/2}$ plot, indicating diffusion-controlled behavior.

Cyclic voltammetric characteristics for benzoyl chloride reduction at platinum appeared qualitatively similar to those at vitreous carbon. The main reduction process occurred at -2.00V with the same further reduction processes being observed, although the cathodic background process at platinum appeared at a somewhat more positive potential (-2.8V) than at vitreous carbon.

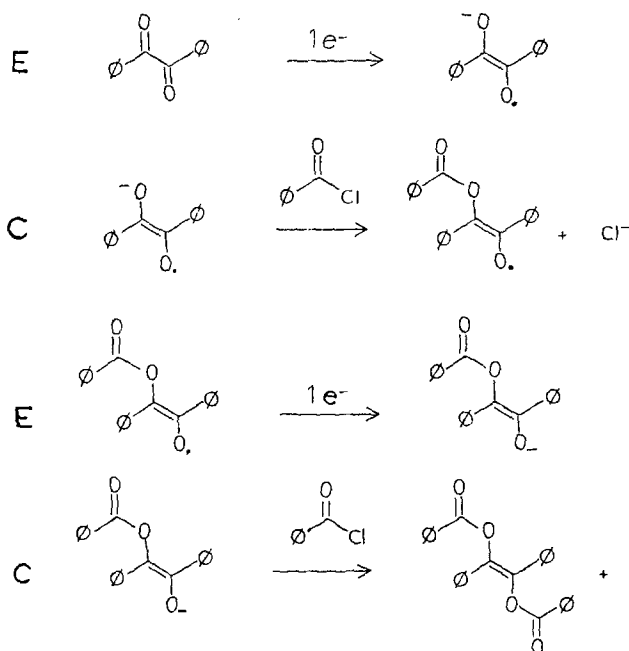
Preparative electrolyses and reaction mechanism.—Integration of current passed during preparative electrolyses and coulometric experiments produced an n value of 1.0 for benzoyl chloride reduction at platinum and vitreous carbon. The infrared spectra of isolated electrolysis products contained very strong bands at 1740 and 1600 cm^{-1} , characteristic of an ester carbonyl group and aromatic rings, respectively. Liquid chromatographic analysis of the electrolysis products showed that only two major products were formed in the electrolysis, with other products observed at shorter retention times. By comparison of chromatographic (LC and GC/MS) and voltammetric characteristics, the major products were identified as *cis*- and *trans*-stilbenediol dibenzoate (SDDDB), the *cis:trans* ratio being 1.0:2.0 with a combined yield of 85%-90%. The voltammetric responses for these products, shown in Fig. 2b and 2c, clearly indicate their formation upon reduction of benzoyl chloride (Fig. 2a).

It is interesting to note that the reduction of benzoyl chloride in acetone at mercury (14) produces similar results, indicating that, in this case, the electrochemical reaction pathway is apparently largely independent of solvent and electrode material. In this regard, the initial reduction of benzoyl chloride is pictured as a one-electron

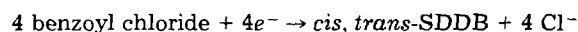
Fig. 1. Cyclic voltammogram of 8.3 mM benzoyl chloride. $v = 100$ mV/s, at vitreous carbon.



process which produces an acyl radical, two of which quickly couple to produce benzil. Cyclic voltammetry of benzil (Fig. 3) indicates that reduction of benzil to its anion radical can occur at the potential employed in the benzoyl chloride electrolysis (-1.80 V). This reduction is envisioned as the first step in an ECEC mechanism involving benzil reduction, as given by the following sequence



Coupling of the intermediate anions with benzoyl chloride produces the observed product mixture, although only the *trans* isomer formation is shown for clarity. This scheme differs from that given for the reduction at mercury in involving an initial one-electron rather than a two-electron reduction of benzil following its formation. Both mechanisms, however, account for the coulometric n value of 1.0 observed for benzoyl chloride reduction according to the overall mechanism



Another possible mechanism for benzoyl chloride reduction involves the initial formation of the benzoyl anion by two-electron reduction of benzoyl chloride, followed by chloride displacement from benzoyl chloride by this anion to form benzil. In order to determine the extent to which this benzoyl anion is involved in benzoyl chloride reduction, a cross-coupling experiment in which benzoyl chloride ($E_p = -1.82$ V) is electrolyzed in the presence of an equal concentration of *p*-anisoyl chloride (*p*-meth-

oxybenzoyl chloride, $E_p = -1.92$ V) was carried out. Electrolysis at -1.82 V (at which potential *p*-anisoyl chloride is not reducible) consumed 1.2 electrons per molecule of benzoyl chloride, at which point the concentration of *p*-anisoyl chloride was approximately 80% of its initial value. Liquid chromatographic analysis of the product mixture revealed peaks due to *cis*- and *trans*-SDDDB ($k = \{t_R - t_M\}/t_M = 2.84$ and 3.06 , respectively; combined yield 45%) as well as others having $k = 5.25$, 5.62 , and 9.40 . These same products, with an additional peak at $k = 6.52$, were obtained in an electrolysis of an equimolar mixture of benzil, benzoyl chloride, and *p*-anisoyl chloride at the first reduction potential of benzil, the peaks at longer retention times being relatively more abundant than those produced in the benzoyl chloride/*p*-anisoyl chloride electrolysis. The latter two peaks ($k = 6.52$ and 9.40) were also produced in a similar electrolysis of a 1:2 mixture of benzil:*p*-anisoyl chloride. From these results, it appears that benzoyl chloride reduction in the presence of *p*-anisoyl chloride involves the initial formation of benzil, the reduction of which leads to coupling between the benzil anion radical and the acyl chlorides present in the solution. In addition to *cis*- and *trans*-SDDDB, four more

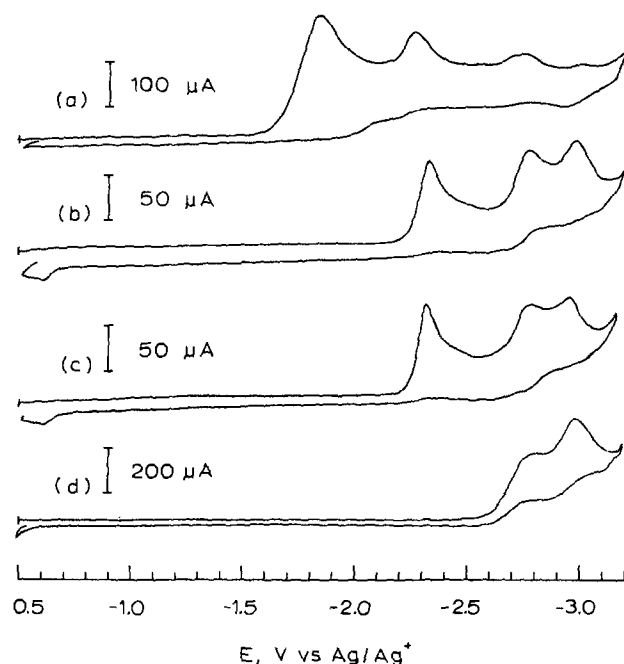


Fig. 2. Cyclic voltammograms of (curve a) benzoyl chloride, 8.2 mM, (curve b) *trans*-stilbenediol dibenzoate, 2.5 mM, (curve c) *cis*-stilbenediol dibenzoate, 2.2 mM, and (curve d) diphenylacetylene, 5.2 mM. All scans recorded at 100 mV/s.

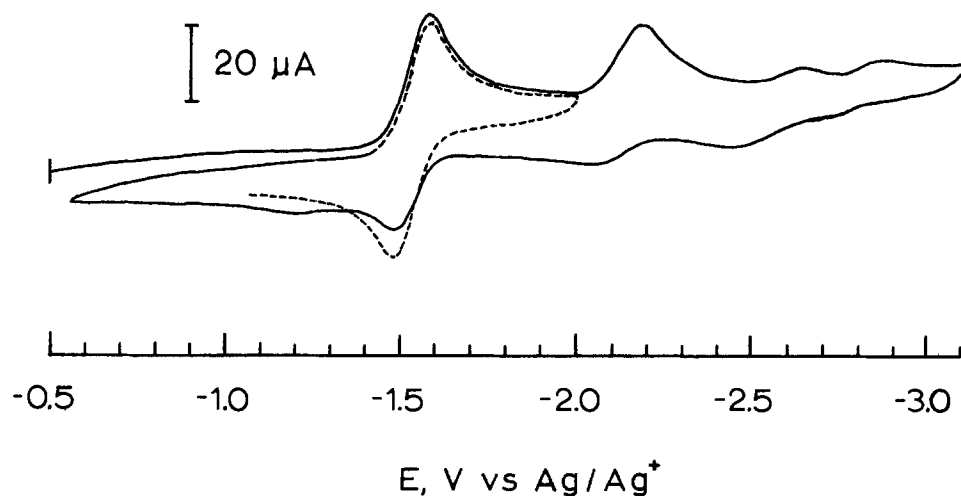


Fig. 3. Cyclic voltammogram of benzil, 1.2 mM. $\nu = 100$ mV/s. Dashed line indicates scan reversal after first reduction process.

stilbenediol diesters (*cis* and *trans* isomers of stilbenediol anisoate benzoate and stilbenediol dianisoate) are apparently formed in this process and give rise to the liquid chromatographic peaks having longer retention times than those for the SDDB isomers. The similarity of the products formed in the benzoyl chloride/*p*-anisoyl chloride and the benzil/benzoyl chloride/*p*-anisoyl chloride electrolyses supports the initial formation of benzil in the benzoyl chloride electrolysis, indicating that benzoyl radicals are involved in the initial coupling reaction to form benzil. (It is expected that attack of the benzoyl anion upon *p*-anisoyl chloride in the cross-coupling experiment would lead to the initial formation of *p*-methoxy benzil and, hence, to different ultimate products than those observed above.)

Recognizing the importance of benzil as an intermediate in the above mechanism, a brief investigation of the electrochemical properties of this molecule in the presence of benzoyl chloride was carried out. At a potential of -1.70 V, reduction of benzil to its anion radical occurs, whereas benzoyl chloride is not reduced, thereby allowing the ECEC sequence mentioned earlier to be studied. As seen in Fig. 4, the cyclic voltammetric peak height parameter $i_p/\nu^{1/2}$ for reduction of benzil at -1.70 V under these conditions increases considerably at lower scan rates, indicating the importance of the chemical reactions in the sequence (20). In this regard, the intermediate produced in the first EC step is evidently more easily reducible than is benzil itself, and its reduction contributes increasingly to the total reduction process as the scan rate decreases and its extent of formation increases. The effect of benzoyl chloride concentration on

this process is clearly shown in Fig. 4, which shows voltammetric data for benzil:benzoyl chloride ratios of 1.0:0.5, 1.0:1.0, and 1.0:2.0. In this sequence, the rate of the chemical step increases with increasing benzoyl chloride concentration, producing a noticeable effect at 200 mV/s at higher benzoyl chloride concentrations. A pseudo-first-order rate constant for this chemical step of 6.9 ± 0.5 s $^{-1}$ was obtained by treatment of chronoamperometric data for reduction of benzil (3 mM) in the presence of a large excess (60 mM) of benzoyl chloride according to the method of Alberts and Shain (21). A preparative electrolysis of a 1:2 benzil:benzoyl chloride mixture at -1.70 V produced essentially the same results as those found for benzoyl chloride reduction (2:1 *trans:cis* SDDB). At mercury (14), this electrolysis produces a 1:2 *trans:cis* SDDB ratio, and apparently involves the adsorption of benzil at the mercury electrode (14).

As can be seen in Fig. 2, the reduction of the esters formed in the reduction of benzoyl chloride leads to further products. Preparative electrolyses of *cis*- and *trans*-SDDB at vitreous carbon and platinum were found to produce diphenylacetylene in 75%-80% yield, as measured voltammetrically after positive identification by GC/MS and liquid chromatography. The n values observed (2.0-2.1) are consistent with a two-electron reduction, evidently involving the elimination of benzoate anions with the consequent formation of diphenylacetylene. The cyclic voltammogram of diphenylacetylene (Fig. 2d) illustrates its terminal position in the sequence benzoyl chloride \rightarrow *cis/trans*-SDDB \rightarrow diphenylacetylene.

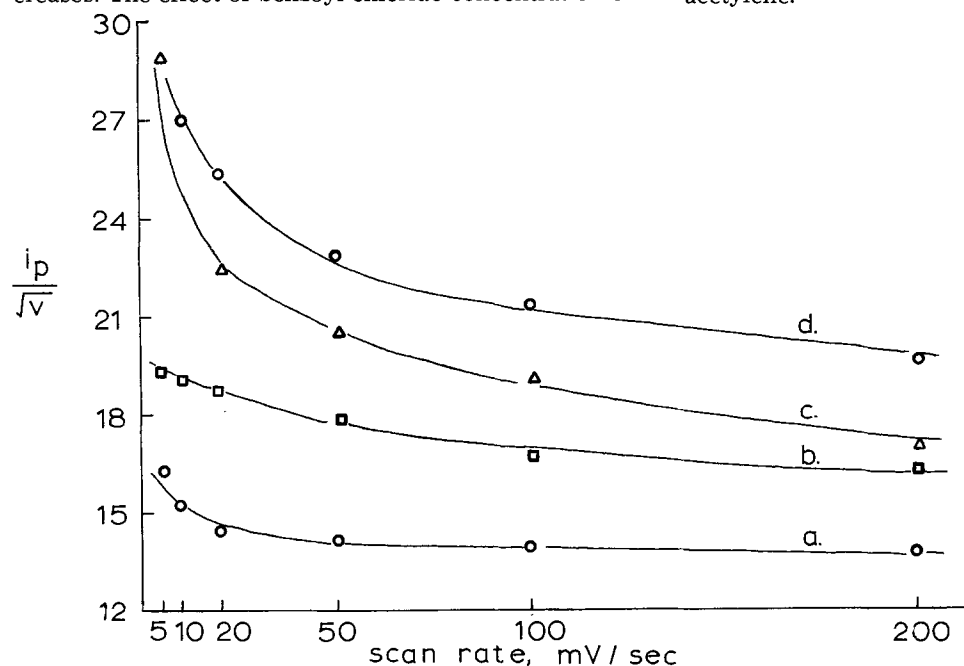


Fig. 4. Plot of peak current function $i_p/\nu^{1/2}$ for first reduction process of 4.8 mM benzil, showing effect of benzoyl chloride additions. Curve a: no benzoyl chloride added. Curve b: 1.0:0.5 benzil:benzoyl chloride molar ratio. Curve c: 1.0:1.0 benzil:benzoyl chloride molar ratio. Curve d: 1.0:2.0 benzil:benzoyl chloride molar ratio.

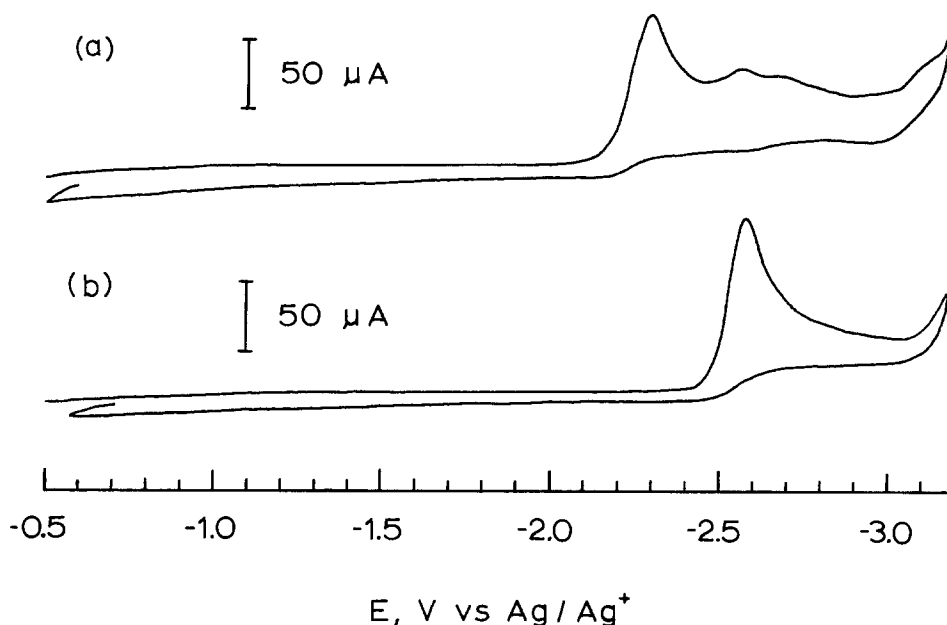


Fig. 5. Cyclic voltammograms of (curve a) benzoyl fluoride, 2.8 mM and (curve b) benzyl benzoate, 2.8 mM. Both scans recorded at 100 mV/s.

Voltammetric studies of benzoyl fluoride.—The cyclic voltammogram of benzoyl fluoride in acetonitrile at vitreous carbon (Fig. 5a) shows that it is considerably more difficult to reduce than is benzoyl chloride, in accord with the usually observed order of ease of organohalogen reduction (1, 2). A product peak is evident at -2.55V in addition to smaller processes in the voltammogram. These results indicate that the electrochemical reduction pathway of benzoyl fluoride is quite different from that of benzoyl chloride.

The benzoyl fluoride reduction process, when observed by cyclic voltammetry at a scan rate of 50 V/s, was found to be reversible, in contrast to behavior observed for benzoyl chloride reduction. AC voltammetric measurements confirmed these observations, showing that elimination of fluoride upon reduction occurs much more slowly than the elimination of chloride in the corresponding benzoyl chloride reduction. The fact that chloride is generally a better leaving group than fluoride (22) seems to account for the greater stability of the benzoyl fluoride anion radical.

Coulometric investigations of benzoyl fluoride reduction produced an n value of 1.1-1.2, indicating that the process is not so well defined as that of benzoyl chloride reduction. Analysis of products from a preparative electrolysis carried out at -2.30V showed that the major products formed in the electrolysis are benzyl benzoate and diphenylacetylene (15% and 10%-15%, respectively, based upon voltammetric measurements in the electrolysis mixture) with variable yields of stilbenol benzoate (5%-15%) also being obtained. These products were found in a hexane extract (3-75 ml portions) of the evaporated electrolysis mixture. A similar extraction with benzene produced an orange oil which, upon dissolution in 50:50 methylene chloride:hexane and passage through an alumina column, led to the isolation of a light-yellow compound (10% yield) having the mass spectral characteristics given in the Experimental section. It is evident that this product involves rather extensive coupling of intermediates formed upon benzoyl fluoride reduction, since its molecular weight (554) is much higher than that of the other products isolated. The base peak (m/z 105) indicates the presence of the benzoyl group in the product, and the peak at m/z 298 suggests that the product may be the result of further reduction and coupling of stilbenol benzoate. Further extraction with refluxing benzene gave more of the orange oil noted above (total yield, 60%) which produced no well-defined peaks in liquid chromatographic analysis and is presumably polymeric material formed in the electrolysis. The infrared spectrum of this oil contains

bands at 1740 and 1600 cm^{-1} , indicating that ester carbonyl bonds, as well as phenyl groups, are present, and that the material has some structural similarity to the lower molecular weight products formed in the benzoyl fluoride electrolysis.

The product analysis of the benzoyl fluoride electrolysis mixture indicates that the reaction pathway is very fragmented. One of the directions taken apparently involves initial stilbenediol dibenzoate formation, as in benzoyl chloride reduction, followed by reduction to diphenylacetylene and stilbenol benzoate. Benzyl benzoate may arise from reductive cleavage of the stilbenediol dibenzoate double bond, although the results on stilbenediol dibenzoate reduction seem to indicate otherwise. A more likely route for benzyl benzoate formation involves a displacement of fluoride from benzoyl fluoride by the benzoyl fluoride anion radical following benzoyl fluoride reduction. Although the concentration of benzoyl fluoride at the electrode is very low under these conditions, the lifetime of the anion radical should be long enough to permit diffusion into solution where unelectrolyzed benzoyl fluoride would be encountered. Following the displacement reaction, the pathway is not as clear, but evidently involves further reduction, corresponding to loss of fluoride, and hydrogen abstraction from solvent and/or supporting electrolyte. The remainder of the product mixture consists of the compound of molecular weight 554 and polymeric materials, evidently involving extensive coupling of benzoyl radicals formed by decay of the benzoyl fluoride anion radical, the extent of the coupling being sufficient to produce the large yield of polymeric (high molecular weight) product observed.

In an attempt to measure the rate of decay of the benzoyl fluoride anion radical, double potential-step chronoamperometric experiments (23) involving the main benzoyl fluoride reduction process were carried out at vitreous carbon on a 3 mM benzoyl fluoride solution. A rate constant of $60 \pm 15\text{ s}^{-1}$ for the first-order decay process [as specified in this treatment (23)] was obtained. Although this value is in fairly good agreement with the cyclic voltammetric results observed at higher scan rates, it must be regarded with some caution because of the multitude of products formed in subsequent radical reactions. The proposed pathway for benzyl benzoate formation (coupling of benzoyl fluoride anion radical with benzoyl fluoride), if followed, would affect the above rate constant since it does not correspond to the assumed reaction (initial decay followed by subsequent reactions); however, the amount of benzyl benzoate formed is relatively small and therefore may

not greatly alter the above finding. Further work on the mode of benzyl benzoate formation, as well as on the benzoyl fluoride reduction process in general, is in progress and is expected to clarify the role of the benzoyl fluoride anion radical in the reduction pathway.

Conclusions

It would appear, from the results of this study and that of Guirado *et al.* (14), that the mechanism of benzoyl chloride reduction is essentially the same in these two media. This similarity evidently reflects the fact that the coupling of acyl radicals is much more favorable than reactions of these radicals with the various components in either of the systems employed. Chemical reductions of benzoyl chloride by hexaphenylditin (24) and in the presence of pentacarbonyliron (25) have also been found to produce a mixture of *cis*- and *trans*-stilbenediol dibenzoate, indicating that the reaction pathway is rather general.

As studied in the present work, the effect of the halogen atom on the reduction pathway can be seen in the difference of reduction potentials for benzoyl chloride and benzoyl fluoride, as well as in the nature of the products obtained. The difference in reduction mechanisms can be attributed to the greater stability of the benzoyl fluoride anion radical formed initially in the reduction process, as well as to the more negative potential required for its reduction.

Acknowledgments

Grateful acknowledgment is made by the authors to the Naval Academy Research Council for its support of this work. Acknowledgment is also made to Dr. T. H. Jones for aid in interpreting several mass spectra.

Manuscript submitted April 18, 1983; revised manuscript received March 1, 1984.

REFERENCES

1. M. R. Rifi, in "Technique of Electroorganic Synthesis," Part II, N. L. Weinberg, Editor, p. 170, John Wiley and Sons, New York (1975).
2. J. Chang, R. F. Large, and G. Popp, in "Techniques of Chemistry," Vol. I; "Physical Methods of Chemistry," Part IIB, A. Weissberger and B. W. Rossiter, Editors, p. 34, Wiley-Interscience, New York (1971).
3. L. G. Feoktistov, in "Organic Electrochemistry," M. Baizer and H. Lund, Editors, p. 259, M. Dekker, New York (1983).
4. A. P. Tomilov *et al.*, "The Electrochemistry of Organic Compounds," p. 281, Halsted Press, New York (1972).
5. C. K. Mann and K. K. Barnes, "Electrochemical Reactions in Nonaqueous Systems," p. 201, Marcel Dekker, New York (1970).
6. W. F. Carroll, Jr. and D. G. Peters, *This Journal*, **127**, 2594 (1980).
7. D. M. LaPerriere, W. F. Carroll, Jr., B. C. Willett, E. C. Torp, and D. G. Peters, *J. Am. Chem. Soc.*, **101**, 7561 (1979).
8. A. J. Bard and A. Merz, *ibid.*, **101**, 2959 (1979).
9. F. M. Triebe, K. J. Borhani, and M. D. Hawley, *ibid.*, **101**, 4637 (1979).
10. A. Inesi, L. Rampazzo, and A. Zeppa, *J. Electroanal. Chem. Interfacial Electrochem.*, **122**, 233 (1981).
11. P. Arthur and H. Lyons, *Anal. Chem.*, **24**, 1422 (1952).
12. H. Dehn, V. Gutmann, H. Kirch, and G. Schober, *Monats. Chem.*, **93**, 1348 (1962).
13. L. Boulaers-Poinsignon and M. P. Federlin, *C. R. Acad. Sci. Paris, Ser. C*, **268**, 1664 (1969).
14. A. Guirado, F. Barba, C. Manzanera, and M. D. Velasco, *J. Org. Chem.*, **47**, 142 (1982).
15. J. C. Trisler and J. L. Frye, *ibid.*, **30**, 306 (1965).
16. F. M. Beringer, P. S. Forgione, and M. D. Yudis, *Tetrahedron*, **8**, 49 (1960).
17. R. C. Larson, R. T. Iwamoto, and R. N. Adams, *Anal. Chim. Acta*, **25**, 371 (1961).
18. D. F. Untereker, W. G. Sherwood, G. A. Martinchek, T. M. Reidhammer, and S. Bruckenstein, *Chem. Instrum.*, **6**, 259 (1975).
19. J. R. Peterson and J. Q. Chambers, *This Journal*, **129**, 529 (1982).
20. E. R. Brown and R. F. Large, in "Techniques of Chemistry," Vol. I, "Physical Methods of Chemistry," Part IIA, A. Weissberger and B. W. Rossiter, Editors, pp. 495-502, Wiley-Interscience, New York (1971).
21. G. S. Alberts and I. Shain, *Anal. Chem.*, **35**, 1859 (1963).
22. J. March, "Advanced Organic Chemistry," Second ed., p. 331, McGraw-Hill, New York (1977).
23. W. M. Schwarz and I. Shain, *J. Phys. Chem.*, **69**, 30 (1965).
24. H. Shirai, Y. Sato, and M. Niwa, *Yakugaku Zasshi*, **90**, 59 (1970).
25. T. Y. Luh, K. S. Lee, and S. W. Tam, *J. Organomet. Chem.*, **248**, 221 (1983).

Substituent Effect on *Para*-Substituted *n*-phenylpyrrole Monomers and Their Polyheterocyclic Conductors

Manuel Salmón,* Ma. Eugenia Carbajal, and Juan Carlos Juárez

Instituto de Química, Universidad Nacional Autónoma de México, Ciudad Universitaria, Circuito Exterior, Coyoacán 04510, México, D. F.

A. Díaz

IBM Research Laboratory, San Jose, California 95193

M. C. Rock

Facultad de Química, División de Estudios Profesionales, U. N. A. M., Ciudad Universitaria, Coyoacán 04510, México, D. F.

ABSTRACT

The electrochemical behaviour of a variety of *para*-substituted *n*-phenylpyrrole monomers and their corresponding polymers was analyzed. The electron-attractive or electron-repulsive nature of each *para* group substituent was perceived in the pyrrole unit through the phenyl ring and manifested in their E_{pa} values. Good linear correlations with Hammett σ^+ constants were obtained for both the monomer E_{pa} values and the electroactive polymer E_o values.

In our continuous search for new polypyrrole conducting polymers (1), it was found that functional group substitution on the phenyl ring on *n*-phenylpyrrole provides an excellent way to obtain a wide selection of chemically modified polymer films. In addition, some of these functional groups, such as $-\text{NO}_2$, $-\text{OH}$, $-\text{COOH}$, and $-\text{COCH}_3$, are able to be modified chemically before or after the electropolymerization, affording an alternative route to modify the polymer.

The chemical synthesis and anodic oxidation of 15 *para*-substituted *n*-phenylpyrrole monomers and the electrosynthesis of their polymers offers the opportunity to study the substituent electromeric effect upon their electrochemical properties.

Earlier (2) results reveal that a wide variety of *n*-phenylpyrrole polymers are potentially usable as electrodes which contain a particular chemical composition, or physical or electrochemical properties.

Materials and Procedure

The *para*-substituted *n*-phenylpyrrole monomers were synthesized from 2,5-dimethoxytetrahydrofuran and the appropriate amine refluxed in acetic acid. The pyrrole derivatives were purified by column chromatography silica gel using as eluent ethylacetate/hexane. After crystallization or vacuum distillation, the pure pyrrole monomers were identified by $^1\text{H-NMR}$, IR, and MS and compared with reported data (3).

Electrochemical experiments were performed with a PAR 173 Potentiostat with a PAR 175 Universal Programmer. The working electrode was a button of Pt (0.5 cm^2) or a thin layer of Pt (0.5 cm^2) deposited on a glass plate. A gold wire was used as counterelectrode. All potentials were measured with respect to a calomel reference electrode saturated with KCl in H_2O . Acetonitrile (J. T. Baker) distilled from phosphorous pentoxide was used as solvent in all the experiments. The redox potentials and E_o values for monomers and polymers were obtained directly from the cyclic voltammograms. The anodic, cathodic, and E_o potentials listed were measured at 100 mV/s .

Results and Discussion

A comparative overview of the *n*-substituted pyrrole monomers and their electrosynthesized polymers showed that the oxidation potentials increase gradually to anodic

* Electrochemical Society Active Member.

Key words: voltammetry, monomers, organic conducting polymers.

Table I. Cyclic voltammetric data of *n*-phenylpyrrole monomers and thin film polymers

<i>para</i> -Substituents	Monomer E_{pa}/V	E_{pa}/V	Polymer E_{pc}/V	E_o/V
$-\text{N}-(\text{CH}_3)_2$	1.26	—	—	—
$-\text{OH}$	1.28	—	—	—
$-\text{OCH}_3$	1.31	0.66	0.50	0.58
$-\text{OET}$	1.31	0.66	0.55	0.61
$-\text{H}$	1.47	0.69	0.59	0.64
$-\text{CH}_3$	1.48	0.67	0.54	0.61
$-\text{Br}$	1.51	0.82	0.62	0.72
$-\text{F}$	1.52	0.76	0.62	0.69
$-\text{CO}-\text{CH}_3$	1.52	0.86	0.70	0.78
$-\text{I}$	1.52	0.72	0.70	0.71
$-\text{Cl}$	1.53	0.85	0.69	0.77
$-\text{OAc}$	1.56	—	—	—
$-\text{COOH}$	1.56	—	—	—
$-\text{C}(\text{F})_3$	1.59	—	—	—
$-\text{NO}_2$	1.60	0.90	0.78	0.84*

* Value obtained from Ref. (3).

values in the order pyrrole < *n*-alkylpyrrole < *n*-phenylpyrrole. The chemical modification of the pyrrole unit by introduction of alkyl substituent in the nitrogen permits one to obtain a series of *n*-alkyl-substituted pyrrole polymers with different chemical and physical properties (4). However, the electropolymerization reaction of *n*-alkylpyrroles substituted with bulky groups (tert-butyl, cyclohexyl) is inhibited by steric interactions. In the series, the anodic oxidation potential of monomers and polymers is shifted as the substituent size, and steric hindrance increases. Therefore, the oxidation of the pyrrole nucleus is affected very little by the electron donating effects of the *N*-alkyl groups.

Table II. E_{pa} and E_o values of monomers and polymers

Pyrrole substituent	Monomer E_{pa}/V	Polymer E_o/V	σ^+
p-N(Me) ₂	1.26	—	-1.70
p-OH	1.28	—	-0.92
p-OMe	1.31	0.58	-0.78
p-Me	1.48	0.61	-0.31
H	1.47	0.64	0.0
p-Br	1.51	0.72	0.15
p-F	1.52	0.69	-0.07
p-I	1.52	0.71	0.14
p-Cl	1.53	0.77	0.11
p-COOH	1.56	—	0.42
p-CF ₃	1.59	—	0.61
p-NO ₂	1.60	0.84	0.79

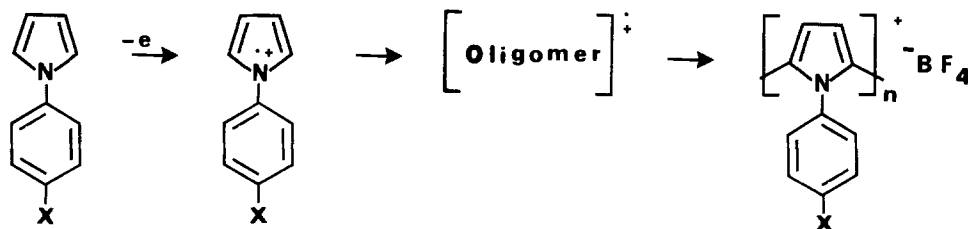


Fig. 1. Pyrrole electropolymerization mechanism.

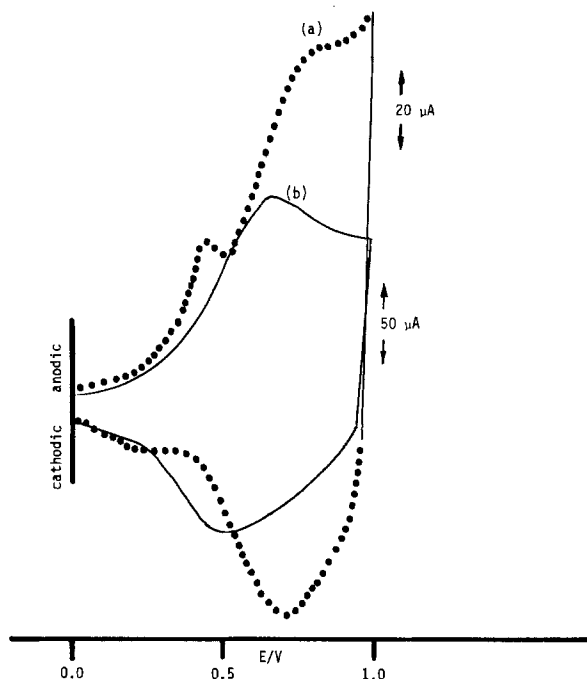


Fig. 2. Cyclic voltammograms of 20 mC/cm² thin films of poly-n-phenylpyrroles substituted with *p*-COCH₃ (curve a) and *p*-OCH₃ (curve b) at 100 mV/s in CH₃CN containing 0.1M Et₄NBF₄.

In the N-phenylpyrrole series, *ortho*-electroactive substituents showed electronic and steric effects (5), whereas in *para*-substituted n-phenylpyrroles, which will be discussed here, only electromeric effects were observed.

Therefore, the electron-attractive or electron-repulsive nature of groups was transmitted through the n-phenyl ring into the pyrrole moiety (6). According to this, the group effects were reflected in the anodic oxidation E_{pa}

values of monomers as well as in the E_{pa} , E_{pc} , and E_o values of polymers, as shown in Table I.

The first electrochemical oxidation step of n-phenyl-substituted pyrrole monomers (Fig. 1) produces a very reactive radical-cation at the anode, which initiates the chain propagation, forming oligomers (7). The polymerization process continues by reaction of the oligomer radical-cation with others or with the radical-cation of the monomer present in high concentration in the anode region.

The poly n-phenylpyrrole formed on the electrode surface as a smooth film contains the phenyl substituent, which modifies the cyclic voltammogram shape and the redox values. Also in the cyclic voltammograms of *p*-NO₂(3), *p*-COCH₃, *p*-Br, and *p*-Cl, an additional small peak appears before the pyrrole oxidation loop between 0.5-0.6V (Fig. 2). These peaks of unknown origin were not assigned.

In order to measure the substituent effect in a quantitative way and to explain some electrochemical properties of the studied pyrroles, the E_{pa} and E_o values of monomers and polymers were related with the available Hammett-Brown (8) substituent constants σ^+ listed in Table II.

When least squares regression techniques were used and these values plotted against one another, a satisfactory linear relationship was obtained.

The correlation coefficient for the pyrrole monomer series in Fig. 3, is: $r = 0.960$ and $r = 0.927$ for the polymer set Fig. 4. These values are good enough to satisfy the Jaffe's standard (9) and exemplifies for the first time a parallel substituent effect on both the monomer and their polymers on the positive charged reaction center.

Also, monomers and polymers are in accordance with a linear relationship given by Eq. [1] and [2]

$$E_{pa} = 0.16\sigma^+ + 1.49 \text{ (monomer)} \quad [1]$$

$$E_o = 0.18\sigma^+ + 0.695 \text{ (polymer)} \quad [2]$$

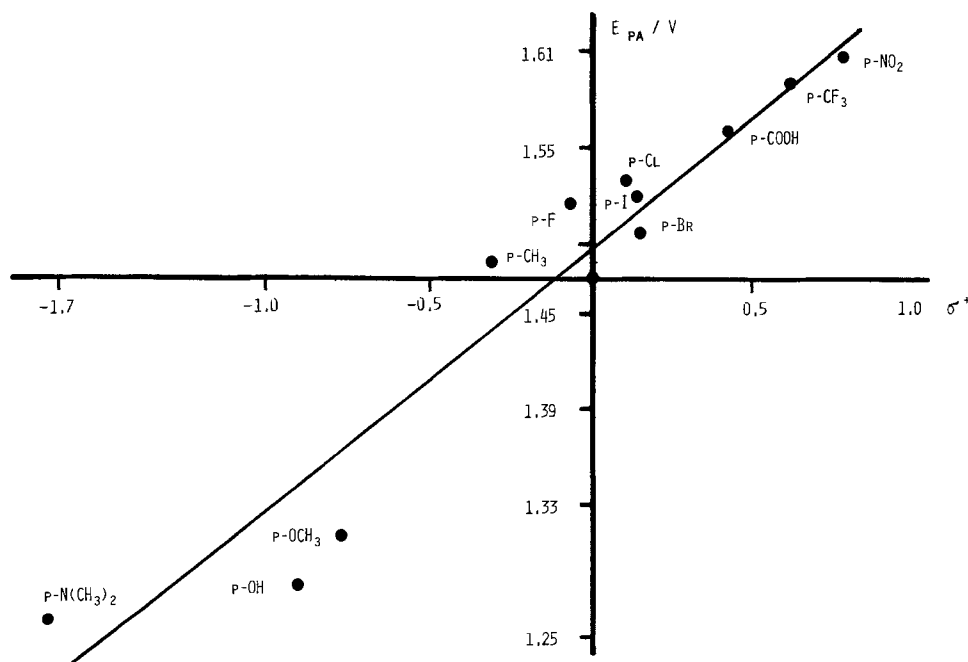
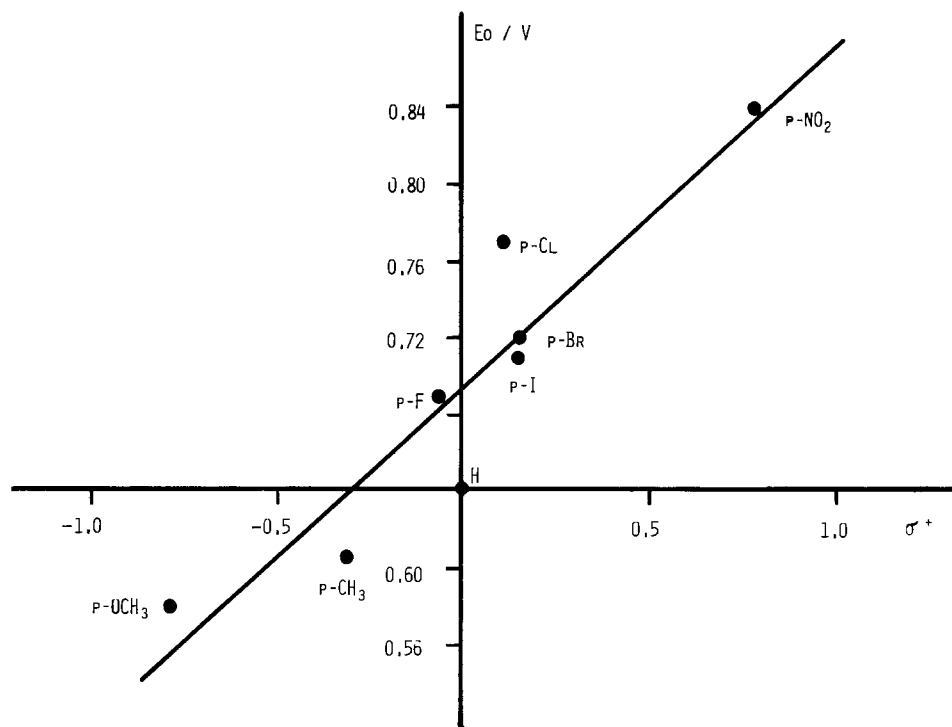


Fig. 3. Relationship of oxidation (E_{pa}) of *p*-N-phenylpyrrole monomers vs. σ^+ values of substituents.

Fig. 4. Hammett-Brown plot of the E_0 values of *p*-N-phenylpyrrole polymers.



According to the slope values, the lines are almost parallel lines, and consequently we can infer that the substituent supports the same environment in monomer and polymer and the influence is transmitted through the phenyl ring into the pyrrole reaction center, producing the same effect. Therefore, torsional angle or conformation between the two aromatic rings of *n*-phenylpyrroles before and after polymerization should be very similar.

The preliminary studies to evaluate some of the formed polymers as electrodes, showed the substituent influence on the quality of the films (5) and on the changes in the film electron-transport rate (10).

Finally, polymerization was totally inhibited when the phenyl substituents were groups such as $-\text{N}(\text{CH}_3)_2$ and $-\text{OH}$, which are easier to oxidize than the pyrrole group. When NO_2 was the substituent, only thin films and oligomers were produced (11), whereas $-\text{C}(\text{F})_3$ yielded a powdery black deposit on the electrode. Thus, it appears that *N-p*-phenylpyrroles with strongly attracting or electron inductor substituents which have large positive or negative σ^+ values will present difficulties for polymerization.

Acknowledgments

This work was performed at Instituto de Quimica, and was supported by the University of Mexico. The authors would like to thank M. Rosales Hoz and M. Saloma for critically reviewing the manuscript.

Manuscript submitted Dec. 22, 1983; revised manu-

script received March 6, 1984. This was Paper 617 presented at the Montreal, Quebec, Canada, Meeting of the Society, May 9-14, 1982.

The Instituto de Quimica assisted in meeting the publication costs of this article.

REFERENCES

1. M. Salmón, A. F. Díaz, A. J. Logan, M. Krounbi, and J. Bargon, *Mol. Cryst. Liq. Cryst.*, **83**, 265 (1982).
2. M. Salmón, A. Díaz, and J. Goitia, in "Chemically Modified Surfaces in Catalysis and Electrocatalysis," J. S. Miller, Editor, p. 65, American Chemical Society, Washington, DC (1982).
3. N. Clauson-Kaas and Z. Tyle, *Acta Chim. Scand.*, **6**, 67 (1952); M. Elming and N. Clauson-Kaas, *ibid.*, **6**, 867 (1952); H. Gross, *Chem. Ber.*, **95**, 2270 (1962).
4. A. F. Díaz, J. Castillo, K. K. Kanazawa, J. A. Logan, M. Salmón, and O. Fajardo, *J. Electroanal. Chem.*, **133**, 233 (1982).
5. M. Salmón, Ma. E. Carbajal, M. Aguilar, M. Saloma, and J. C. Juárez, *J. Chem. Soc. Chem. Commun.*, 1532 (1983).
6. G. Cauquis and M. Genies, *Bull. Soc. Chim. Fr.*, 3220 (1967).
7. E. M. Genies, G. Bidan, and A. F. Díaz, *J. Electroanal. Chem.*, **149**, 101 (1983).
8. H. C. Brown and Y. Okamoto, *J. Am. Chem. Soc.*, **79**, 1913 (1957).
9. H. H. Jaffe, *Chem. Rev.*, **53**, 191 (1953).
10. M. Salmón, M. Aguilar, and M. Saloma, *J. Chem. Soc. Chem. Commun.*, 570 (1983).
11. M. V. Rosenthal, T. A. Skotheim, A. Melo, G. Senum, and M. Salmón, Submitted to *J. Electroanal. Chem.*

Impedance Measurements in Nonaqueous Media: Measurements of an Electron-Transfer Rate Constant in the Presence of Adsorption

Xiang-Qin Lin,* Tadeusz Malinski,*¹ and Karl M. Kadish*

Department of Chemistry, University of Houston, Houston, Texas 77004

ABSTRACT

Equations are derived for the calculation of heterogeneous electron-transfer rate constants in nonaqueous media using the ac impedance method. These equations are modifications of equations in the literature and are specifically applicable for direct semiautomatic ac impedance measurements using a four-electrode system and a small ac perturbation signal. An example of combined faradaic and adsorption processes is given by the reduction of bis(N-R-2,6-pyridinedicarboxaldimine)Co(II). This compound shows adsorption at a Pt electrode in acetone, 0.1M TBAP which is not detected by cyclic voltammetry. Applications of modified ac impedance methods allowed the calculation of a $k^0 = 8.0 \times 10^{-2}$ cm/s and an $\alpha = 0.4$ in the presence of adsorption.

A well-established application of impedance measurements is in the study of adsorption and electrode kinetics. When accurate impedance measurements are required, ac bridges (1-3) have long been considered superior to direct measuring, phase-sensitive devices (4-10). However, the manual operation of an ac bridge is tedious and time consuming. It is therefore understandable that much effort has recently been devoted to designing more or less automatically operating, direct measuring devices (11-13). A great improvement in this direction was suggested by Smith *et al.* (14-17), who used a computer to control measurements and to acquire data with aid of a Fast Fourier transform algorithm. The only alternative to this Fast Fourier approach is still the direct measuring, phase-sensitive detector (11). However, nonbridge instruments are complicated and often expensive.

Recently, the design of an instrument which could be used for direct measurements of ac impedance and which could be constructed from relatively low cost commercially available components was reported (18, 19). With this device, we were able to decrease the ac perturbation signal below 0.5 μ A. In addition, by using a four-electrode system (the standard three-electrode system plus an ac counterelectrode), the frequency could be changed automatically and a complex plane spectrum could be obtained in the time that is usually needed for the obtaining of a single ac sinusoidal polarogram.

We now present an experimental and theoretical treatment of impedance data obtained from this device in order to calculate a heterogeneous electron-transfer rate constant for a redox process which occurs in nonaqueous media in the presence of adsorption. We have chosen for our investigation the six-coordinate bis(N-R-2, 6-pyridinedicarboxaldimine)Co(II) complex with substituent R = CH₂Ph. This complex was shown to exhibit an ²E(1s) \rightleftharpoons ⁴T(1s) spin-equilibrium process in both the solid and solution states (20). In nonaqueous media, the cobalt(II) complex can be reduced to a cobalt(I) species and has a rate constant of 3.7×10^{-2} cm/s when measured by cyclic voltammetry. No trend between spin state and k^0 was observed in this study (21). However, a number of other effects besides spin transition can influence the measured rate constant. One such effect is adsorption. The weak adsorption of bis(N-R-2,6-pyridinedicarboxaldimine)Co(II) on a platinum electrode could not be detected by cyclic voltammetry, but is quite evident from the impedance measurements. Thus, with this latter electrochemical technique, the characteristic of the "surface" reaction can be investigated.

Experimental

Bis(N-R-2,6-pyridinedicarboxaldimine)Co(II) where R = CH₂Ph was used for determining the heterogeneous rate

* Electrochemical Society Active Member

¹ Present address: Department of Chemistry, Oakland University, Rochester, Michigan 48063.

Key words: heterogeneous kinetics, bis(N-R-2,6-pyridinedicarboxaldimine) Co(II), four-electrode system.

constant for the Co(II)/Co(I) reaction. This compound, which we will abbreviate as LCo(II), was synthesized by the method of Simmons and Wilson (20) and was generously provided by Dr. L. J. Wilson. Impedance measurements were made with a home-built instrument whose design has been described previously (18, 19). A four-electrode system was used. This consisted of a platinum button (area = 0.08 cm²) working electrode and a Pt wire dc counterelectrode. The utilized Pt button electrode was well constructed by a competent glass-blower: a 1 mm diam commercial Pt wire was sealed into "cobalt-glass," which was sealed into Pyrex tubing to form a vacuum-tight Pt electrode. The electrode surface was polished by fine sandpaper and then a polishing agent to form a flat shiny surface. This electrode was investigated by cyclic voltammetric measurements and shows an excellent behavior without edge effects (The solution does not creep between the glass and the platinum). A 2 cm² platinum mesh served as an independent ac counterelectrode, and a saturated calomel electrode was used as the reference electrode. The latter was separated from the organic solvent by a glass frit. A constant 0.5 μ A testing alternating current flow through the cell (between the working electrode and ac counterelectrode) produced a signal measured from the in-phase output and quadrature output lock-in analyzer. A signal from the in-phase output corresponded to the sum of \dot{R}_{sol} and \dot{Z}_{Rs} and the signal from the quadrature output corresponded to the \dot{Z}_{Cs} (see Fig. 2a). The potential scan rate was 2 mV/s, and 200 and 50 kHz frequencies were applied for low and high frequency measurements, respectively.

Results and Discussion

The measurable parameters obtained from our ac impedance device can be represented by the in-series equivalent circuit shown in Fig. 1a. In this circuit \dot{Z}_{Rs} and \dot{Z}_{Cs} are the resistive and capacitive components of impedance, and R_{sol} is the resistance of the solution. The term c_1 indicates a concentration of i redox species.

The interface between a working electrode and solution where no redox species are present in solution can be represented by the parallel equivalent circuit shown in Fig. 1b, where R_L and C_L are the leaking resistance and leaking capacitance, respectively. In aqueous media at $c_1 = 0$, only the adsorption process influences C_L . In this case, R_L is assumed to be quite large and may be omitted, so the C_L represents the double layer capacitance C_{dl} . This is not the case in nonaqueous media, where C_L and R_L may be of comparable magnitude. For example, in freshly distilled acetone containing 0.1M TBAP, the values of R_L and $1/\omega C_L$ were calculated as 8 and 3 k Ω at 200 Hz frequency (both R_L and C_L were frequency dependent), and R_{sol} was measured as 450 Ω (19). This corresponds with a phase angle of the interfacial impedance of about 70°. In polar organic solvents, the phase angle should not be expected to be 90° due to the existence of adsorption and the relaxation time effect of the organic solvent molecules.

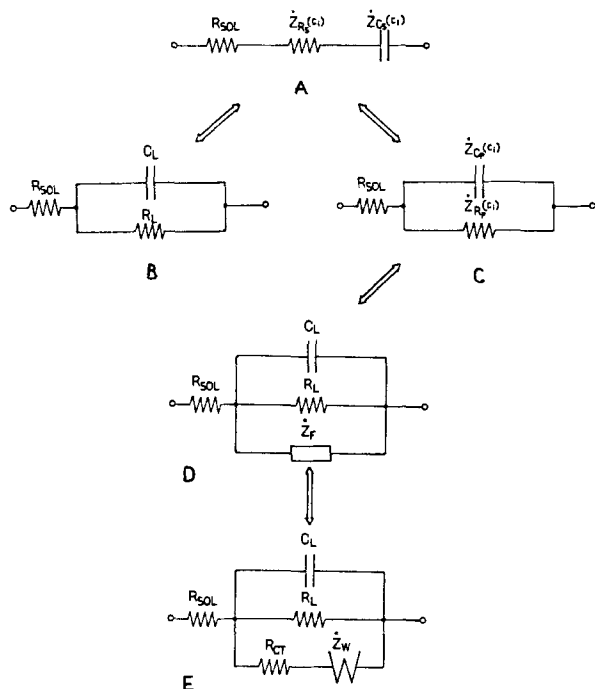


Fig. 1. A: in-series equivalent circuit of an electrochemical cell where Z_{Rs} is the resistive component of impedance, Z_{Cs} the capacitive component of impedance, and R_{sol} the solution resistance. B: parallel equivalent circuit of an electrochemical cell with solvent and supporting electrolyte (no faradaic process occurs). C_L is the leaking capacitance and R_L the leaking resistance. C, D, and E: interconversion of parallel equivalent circuit of the electrochemical cell in the case of pure faradaic process: Z_{Cp} = capacitive component of impedance, Z_{Rp} = resistive component of impedance, Z_F = faradaic impedance, R_{ct} = charge transfer resistance, Z_W = Warburg impedance. The sub "s" and "p" represent the in-series and parallel circuit, and C_i (concentration of a redox sample).

Plots of the resistive and capacitive components of impedance vs. potential for different concentrations of LCo(II) in acetone are shown in Fig. 2. The capacitive component of the impedance, Z_C , decreased with increasing concentration of LCo(II) (Fig. 2a). The resistive component, Z_R , also decreased with increasing concentration of the sample, but below a concentration of $6.5 \times 10^{-4}M$, Z_R was higher than that observed for the blank solution (Fig. 2b). In order to analyze these data, we will consider two limiting cases. These are pure faradaic processes and faradaic processes combined with adsorption.

Faradaic processes.—The half-cell equivalent circuit for a pure faradaic process is shown in Fig. 1d. In the absence of coupled reactions, the faradaic component of the first-order electrode process can be represented as a sum of the charge transfer resistance, R_{ct} , and the Warburg impedance, Z_W (22, 23) (see Fig. 1e)

$$\dot{Z}_F = R_{ct} + \dot{Z}_W \quad [1]$$

The Warburg impedance has been described as

$$\dot{Z}_W = \zeta R_{ct} (1 - j) \quad [2]$$

where ζ is the dimensionless rate parameter, which is given by the following equation (22, 23)

$$\zeta = \frac{k_R}{(2\omega D_R)^{1/2}} + \frac{k_O}{(2\omega D_O)^{1/2}} \quad [3]$$

k_R and k_O are the heterogeneous electron transfer rate constants and D_R and D_O are the diffusion coefficients for the reduced and oxidized species, respectively. The charge transfer resistance R_{ct} is dependent on the rate constants and can be described by Eq. [4]

$$\frac{1}{R_{ct}} = nFA \left(c_R \frac{\partial k_R}{\partial E} - c_O \frac{\partial k_O}{\partial E} \right) \quad [4]$$

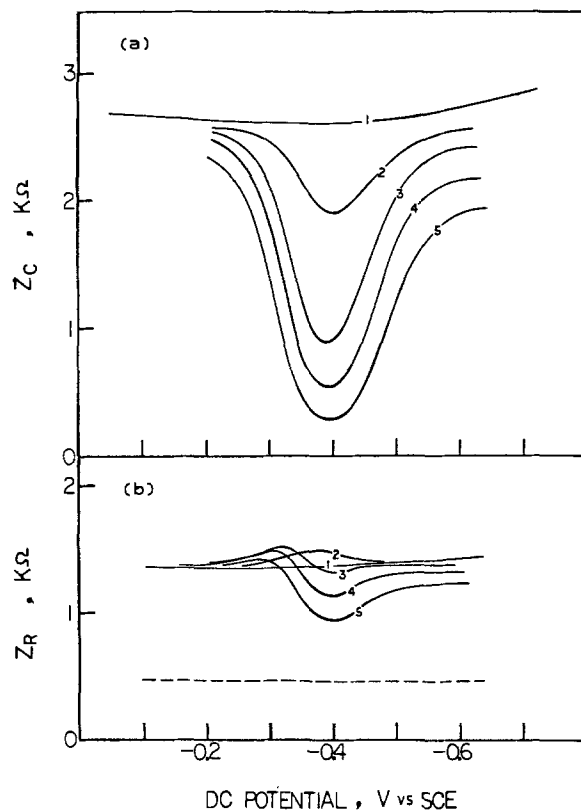


Fig. 2. (a): Capacitive (Z_C). (b): Resistive (Z_R) component of impedance-potential dependence for the reduction bis(N-R-2,6 pyridinedicarboxaldimine)Co(II) in 0.1M TBAP, acetone. Concentrations of bis(N-R-2,6 pyridinedicarboxaldimine)Co(II) were: (1) 0.0; (2) $1.4 \times 10^{-4}M$; (3) $6.5 \times 10^{-4}M$; (4) $1.3 \times 10^{-3}M$; and (5) $2.5 \times 10^{-3}M$. The dotted line indicates R_{sol} .

where c_R and c_O are the concentrations of the reduced and oxidized forms on the electrode surface, A. The other symbols have their usual meanings.

The resistance of the solution R_{sol} can be measured for a blank solution and subtracted from the value of the total impedance. The in-series circuit shown in Fig. 1a can be transformed to the parallel circuit illustrated in Fig. 1b or 1c. Equations [5] and [6] describe the impedance for the in-series (\dot{Z}_s) and parallel (\dot{Z}_p) circuit, respectively (24), and Eq. [7] and [8] describe the transformation of the in-series circuit to the parallel circuit (24)

$$\dot{Z}_s = R_s + \frac{1}{\omega C_s j} \quad [5]$$

$$\dot{Z}_p = \frac{R_p}{1 + \omega C_p R_p j} \quad [6]$$

$$Z_{Rp} = Z_{Rs} \left[1 + \left(\frac{Z_{Cs}}{Z_{Rs}} \right)^2 \right] \quad [7]$$

$$Z_{Cp} = Z_{Cs} \left[1 + \left(\frac{Z_{Rs}}{Z_{Cs}} \right)^2 \right] \quad [8]$$

Combining Eq. [1] and [2] gives

$$\dot{Z}_F = R_{ct} (1 + \zeta) - \zeta R_{ct} j \quad [9]$$

and a further transformation from the in-series circuit represented by Eq. [9] to the parallel circuit represented by Eq. [7] and [8] yields the resistive impedance, $(Z_{Rp})_F$, and the capacitive impedance, $(Z_{Cp})_F$, for the faradaic contribution

$$(Z_{Rp})_F = \frac{R_{ct}}{1 + \zeta} (1 + 2\zeta + 2\zeta^2) \quad [10]$$

$$(Z_{Cp})_F = \frac{R_{ct}}{\zeta} (1 + 2\zeta + 2\zeta^2) \quad [11]$$

Finally, the ratio $(Z_{Cp})_F / (Z_{Rp})_F$ is only a function of ζ

$$\frac{(Z_{CD})_F}{(Z_{Rp})_F} = 1 + \frac{1}{\zeta} \quad [12]$$

Thus, the impedance of a blank solution provides $Z_{Rs}(c_0)$ and $Z_{Cs}(c_0)$, from which the C_L and R_L can be calculated (see Fig. 1b). The impedance is then measured for a solution containing an electroactive species, and values of $Z_{Rs}(c_1)$ and $Z_{Cs}(c_1)$ obtained from which the $Z_{Cp}(c_1)$ and $Z_{Rp}(c_1)$ can be calculated (see Fig. 1c). R_L and C_L can then be subtracted from the total impedance (see Fig. 1d). This pure faradaic contribution can be treated using Eq. [12] to get the ζ value.

The rate parameter ζ can be calculated as shown in Eq. [13]

$$\zeta = \left[\frac{Z_{Rs}(c_1) - Z_{Rs}(c_0) \cdot \eta}{Z_{Cs}(c_1) - Z_{Cs}(c_0) \cdot \eta} - 1 \right]^{-1} \quad [13]$$

where η is a conversion factor

$$\eta = \frac{[Z_{Cs}(c_1)]^2 + [Z_{Rs}(c_1)]^2}{[Z_{Cs}(c_0)]^2 + [Z_{Rs}(c_0)]^2} \quad [14]$$

If we assume that $D_R = D_O = D$ and $k_r + k_o = k$, then Eq. [3] can be written more compactly as

$$k = \zeta(2\omega D)^{1/2} \quad [15]$$

The standard heterogeneous rate constant k^0 can be obtained from the plot of $\log k$ vs. potential (25).

Calculated k values for LCo(II) in the potential range of -0.3 to -0.45 V are presented in Fig. 3. These values were calculated using a measured diffusion coefficient of 1.3×10^{-5} cm²/s. As seen in this figure, the shape of the $\log k$ potential plot for the lowest concentration of sample (1.4×10^{-4} M) is distorted. The maximum of the plot increases with higher sample concentration, and the potential of the maximum is shifted in a negative direction. This indicates that the measured impedance is due to a faradaic process which is influenced by adsorption (25).

Combined faradaic and adsorption processes.—AC admittance measurements for combined faradaic and adsorption processes have been described by several authors (23, 25-28). Theoretical representations of the cell admittance or impedance are quite complicated and cannot be simply solved without some limiting assumptions. A general form of the half-cell equivalent circuit for the case of adsorption of the reactant and the product can be

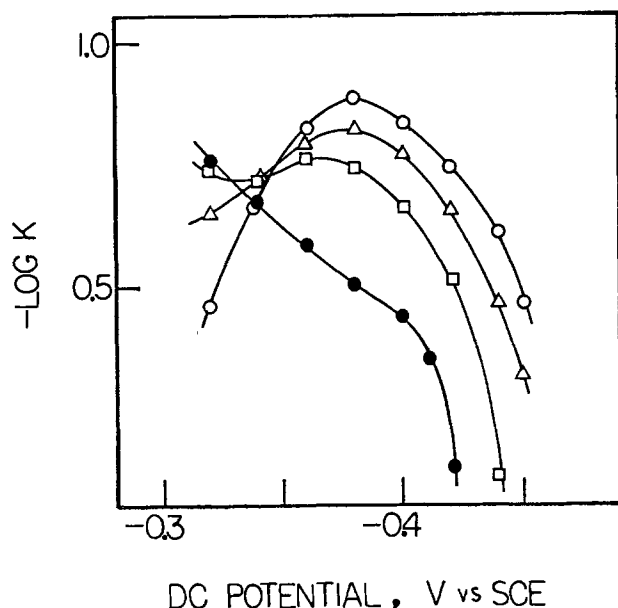


Fig. 3. Heterogeneous electron-transfer rate constant k potential dependence for the reduction of bis(N-R-2,6-pyridinedicarboxaldimine)Co(II) complex in 0.1M TBAP, acetone solution. Concentrations: 1.4×10^{-4} M (●), 6.5×10^{-4} M (□), 1.3×10^{-3} M (△), 2.5×10^{-3} M (○). Reference solution: 0.1M TBAP, acetone.

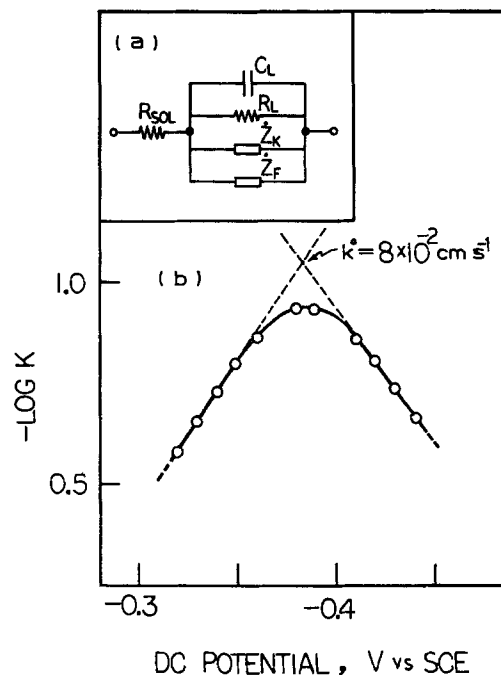


Fig. 4. (a): The equivalent circuit of an electrochemical cell for a combined adsorption and faradaic process. R_{sol} = solution resistance, C_L = leaking capacitance, R_L = leaking resistance, Z_K = kinetic impedance, Z_F = faradaic impedance. (b): Heterogeneous electron-transfer rate constant k potential dependence for the reduction of 1.3×10^{-3} M bis(N-R-2,6-pyridinedicarboxaldimine)Co(II) in 0.1M TBAP, acetone. Reference solution: 6.5×10^{-4} M bis(N-R-2,6-pyridinedicarboxaldimine)Co(II) in 0.1M TBAP, acetone.

represented as shown in Fig. 4a, where Z_K and Z_F are the desorption-adsorption impedance (a kinetic impedance) and faradaic impedance, respectively.

The representation of faradaic and adsorption processes as shown in Fig. 4a is possible only with the assumption that there is no coupling between the faradaic and the adsorption process. The coupling would be a consequence of competition by different mechanisms (redox and adsorption-desorption) for the same species, but is negligible under conditions where the ac impedance measurement is performed at a surface completely covered by electroactive species (*i. e.*, at the plateau of the isotherm where the surface concentration Γ is close to unity). In this case, the contribution of the impedance due to adsorption will be constant and can be considered as the background.

The charge transfer resistance and Warburg impedance are proportional to the bulk concentration of the electroactive species (Eq. [1], [2], and [4]). Therefore, further increasing of the concentration will only effect the faradaic component of the impedance Z_F . In this special case, we can use Eq. [13] - [15] for calculation of the heterogeneous electron-transfer rate constant on an electrode surface which is completely covered by adsorbed species. The presented treatment eliminates measurements of double layer capacity. Using as a background the value of impedance measured for 6.5×10^{-4} M LCo(II) enabled calculation of the rate constant and the $\log k$ potential plot shown in Fig. 4b. A graphical extrapolation gave $k^0 = 8 \times 10^{-2}$ cm/s and α coefficients 0.4 and 0.6. No differences were observed for the $\log k$ potential plot if the impedance of the solution with the concentration of LCo(II) larger than 6.5×10^{-4} M was assumed to be the background.

Acknowledgment

We are grateful for financial support of this work from the National Science Foundation (Grant CHE 7921536), the National Institutes of Health (Grant GM 25172), and the Robert A. Welch Foundation (Grant E-680).

Manuscript submitted July 25, 1983; revised manuscript received March 2, 1984.

The University of Houston assisted in meeting the publication costs of this article.

REFERENCES

1. D. C. Grahame, *J. Am. Chem. Soc.*, **71**, 2975 (1949).
2. R. Parsons, *Trans. Faraday Soc.*, **56**, 1340 (1960).
3. M. Sluyters-Rehbach and J. H. Sluyters, *Rec. Trav. Chim.*, **82**, 535 (1963).
4. J. H. Sluyters and J. C. C. Domen, *ibid.*, **79**, 1011 (1960).
5. J. Schon, W. Mehl, and H. Gerischer, *Z. Electrochem.*, **59**, 144 (1955).
6. N. W. Breiter, *J. Electroanal. Chem.*, **7**, 38 (1964).
7. S. Shibata, *Bull. Chem. Soc. Jpn.*, **39**, 779 (1966).
8. T. Takahashi and E. Niki, *Talanta*, **1**, 245 (1958).
9. R. de Levie and A. A. Husovsky, *J. Electroanal. Chem.*, **20**, 181 (1969).
10. I. Epelboin and M. Keddam, *This Journal*, **117**, 1052 (1970).
11. R. D. Armstrong, M. F. Bell, and A. A. Metcalfe, *J. Electroanal. Chem.*, **77**, 287 (1977).
12. C. P. M. Bongenaar, M. Sluyters-Rehbach, and J. H. Sluyters, *ibid.*, **109**, 23 (1980).
13. C. Gabrielli, "Identification of Electrochemical Processes by Frequency Response Analysis," pp. 25-45, Solartron, Paris (1980).
14. S. C. Creason and D. E. Smith, *J. Electroanal. Chem.*, **36**, 91 (1972).
15. S. C. Creason and D. E. Smith, *ibid.*, **47**, 9 (1973).
16. S. C. Creason and D. E. Smith, *Anal. Chem.*, **45**, 2401 (1973).
17. R. J. Schwall, A. M. Bond, and D. E. Smith, *ibid.*, **49**, 1805 (1977).
18. S. M. Cai, C. Y. Liu, S. M. Wilhelm, and N. Hackerman, Abstract 697, p. 1115, The Electrochemical Society Extended Abstracts, Vol. 82-1, Montreal, Quebec, Canada, May 9-14, 1982.
19. S. M. Cai, T. Malinski, X. Lin, J. A. Ding, and K. M. Kadish, *Anal. Chem.*, **55**, 161 (1983).
20. M. G. Simmons and L. J. Wilson, *Inorg. Chem.*, **16**, 126 (1977).
21. J. Zhu, C. H. Su, B. K. Lemke, L. J. Wilson, and K. M. Kadish, *ibid.*, **22**, 2527 (1983).
22. R. de Levie and A. A. Husovsky, *J. Electroanal. Chem.*, **22**, 29 (1969).
23. R. de Levie and L. Pospisil, *ibid.*, **22**, 277 (1969).
24. A. J. Bard and L. R. Faulkner, "Electrochemical Methods," pp. 322-324, John Wiley and Sons, New York (1980).
25. L. Pospisil, M. L. Mittal, J. Kuta, and J. Koryta, *J. Electroanal. Chem.*, **46**, 203 (1973).
26. H. Moreira and R. de Levie, *ibid.*, **35**, 103 (1972).
27. P. Delahay, *ibid.*, **19**, 61 (1968).
28. M. Sluyters-Rehbach and J. H. Sluyters, *J. Electrochem.*, **136**, 39 (1982).

A Cyclic Voltammetric Study of the Gold-Oxygen System

James P. Hoare*

General Motors Research Laboratories, Electrochemistry Department, Warren, Michigan 48090-9055

ABSTRACT

Cyclic voltammograms were obtained on gold bead microelectrodes in N_2 -stirred 1M H_2SO_4 and 1M HF solutions as a function of the sweep rate and the potential range scanned. It is found that H_2 and O_2 are very slightly absorbed on Au and that neither is dissolved in the bulk metal. As a result, Au makes a more stable indicator electrode than Pt, which does dissolve oxygen. It is the formation of this Pt-O alloy that necessitates a prepolarization of Pt before a steady-state cyclic voltammogram is obtained. It is noted that all contamination of Au with noble metals must be rigorously avoided.

In the literature, there is a growing body of evidence to support the conclusion that oxygen may be dissolved in Pt during anodic polarization (1-14) and with passivation in concentrated HNO_3 (15-17). To obtain a steady-state cyclic voltammogram on Pt in acid solutions, up to 20 cycles of polarization (18-22) are required, and it has been proposed that this preparation is required to free the Pt surface from absorbable, electroactive impurities even in highly purified solutions (20). From a cyclic voltammetric study of Pt in H_2SO_4 and HF solutions, it was concluded (23) that in purified solutions the predominant cause for the necessary 20 cycle prepolarization is the charging of Pt with dissolved oxygen. As oxygen is dissolved in the Pt metal, the catalytic activity of the Pt surface is modified for various electrochemical processes, and, until the surface or dermasorption layers of the metal are saturated with dissolved oxygen, a constant catalytic surface cannot be realized. Thus, a steady-state cyclic voltammogram cannot be obtained.

If such a study were carried out on gold, which does not dissolve gases (24, 25), the steady state would be expected to be established relatively quickly in purified systems. This report describes a cyclic voltammetric study of gold microelectrodes in purified H_2SO_4 and HF electrolytes.

Experimental

Test electrodes were in the form of small beads (about 0.13 cm diam) melted at the end of pure (99.9+%) gold wires (0.038 cm diam) in an oxygen torch. These gold beads were cleaned in hot concentrated HNO_3 and in a burning H_2 -jet, as described elsewhere (23), and were pot-

ted in molten polyethylene. As before (23), three test electrodes were mounted in the dual-compartmented Teflon cell, which had been leached in triply distilled water from an all-quartz still, for at least 2 weeks after having been soaked in concentrated HNO_3 for 48h. All counter- and auxiliary electrodes were made from electroformed gold gauze.

After the cell had been filled with 1M H_2SO_4 made from triply distilled water and analytical grade H_2SO_4 , the system was pre-electrolyzed with all-gold test and auxiliary electrodes connected together against gold wire pre-electrolysis electrodes. A pre-electrolysis current of 3 mA was allowed to flow for 48h before breaking the circuit by removing the gold wires.

At no point in the experimental procedure was the system permitted to come in contact with Pt. It has been shown (26-28) that the presence of only a very few Pt sites on the Au surface drastically modifies the electrochemistry of Au.

Once the pre-electrolysis electrodes were removed, the solution was stirred with purified hydrogen gas until all gold electrodes registered 0V between one another. This procedure removed the oxides and peroxides generated during pre-electrolysis, but it required a longer time to reduce the Au oxides on Au than the Pt oxides on Pt (23).

In a separate clean, Teflon cell, the α Pd-H reference electrode (29) was made. A small palladium bead was melted at the end of a Pd wire and potted in molten polyethylene. This bead was anodized in 1M H_2SO_4 against Pt for 48h, after which H_2 was bubbled around the Pd until its potential came to 50 mV vs. Pt/ H_2 gauze electrodes in the same solution. After continuing the H_2 bubbling for an additional 2h, the Pd bead was removed from the sec-

* Electrochemical Society Active Member.

Key words: oxygen absorption, sulfate adsorption, noble metal poisoning.

ond cell, rinsed in triply distilled water, and sealed in the reference compartment of the first cell in the H_2 -saturated acid solution. In this way, contamination of the Au test electrodes with adsorbed or deposited Pd was minimized, if not prevented entirely.

The procedure for obtaining the cyclic voltammetric data in purified N_2 -saturated electrolyte was virtually the same as presented earlier (23).

For those experiments using 1M HF, the electrolyte was prepared in Teflon labware and the glass frit connecting the reference and test compartments was removed.

Unless otherwise noted, all potentials are recorded vs. $\alpha Pd-H$ (50 mV vs. NHE at pH = 0) at ambient temperatures, $25^\circ \pm 1^\circ C$.

Results and Discussion

On gold in N_2 -stirred 1M H_2SO_4 , it required about ten cycles of polarization to reach a steady-state voltammogram, as shown in Fig. 1. On Pt in N_2 -stirred 1M H_2SO_4 , as shown in Fig. 2, it required many more cycles of polarization than on Au to reach a steady state, and the changes from the initial trace to the steady state are much greater on Pt than on Au. The family of cyclic voltammograms presented in Fig. 3 was obtained on Au by varying the sweep rate from 100 to 17 mV/s. The major peaks are

identified with Roman numerals. For the hydrogen region, a subscript H, is used, and in the oxygen region, O is used. The peaks on the cathodic going sweep are distinguished from those on the anodic going sweep by a prime. Since the peak heights are linearly dependent on the sweep rate, it is concluded (30) that the electrode processes responsible for the peaks are surface processes and not diffusion of some electroactive species from the solution. The shape of the traces in Fig. 3 is similar to that reported on Au in the literature (31-36).

To relate peaks appearing on the anodic going trace with those on the cathodic going trace, one may vary the range of potentials over which the electrode is scanned. In Fig. 4, a family of voltammograms is obtained by initiating the anodic sweep at successively more anodic potentials. As the beginning of the anodic sweep is shifted from -200 to 500 mV, a small reduction in the II_o , III_o , and IV_o peak heights is observed. If the anodic sweep is begun at 1000 mV, II_o is reduced, but III_o and IV_o are maintained; if at 1100 mV, II_o disappears; and if at 1200 mV, III_o and IV_o disappear.

When the cathodic sweep is begun at successively more cathodic potentials, the family of voltammograms in Fig. 5 is obtained. As one progresses from 1700 to 1400 mV, I'_o diminishes until after about 1350 mV, and both I'_o and II'_o

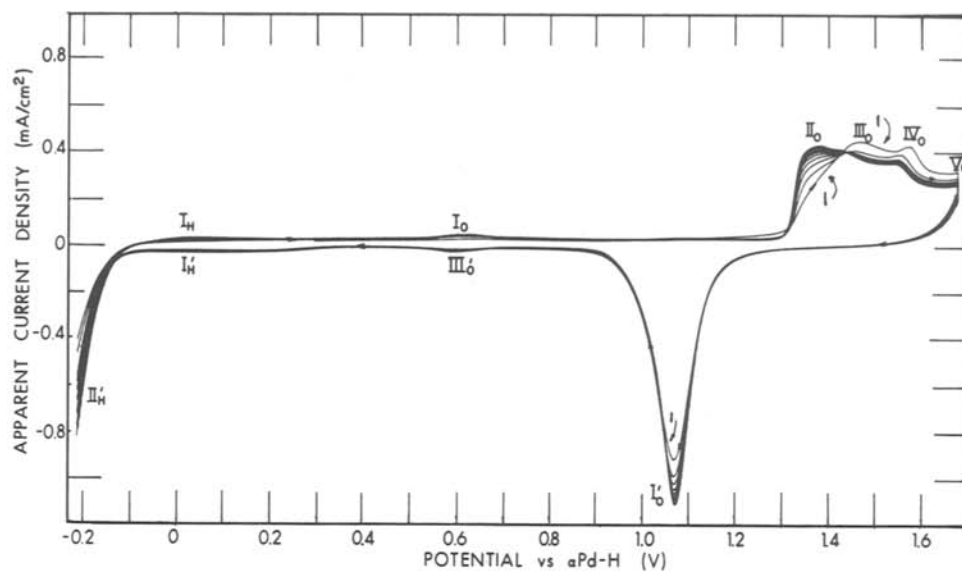


Fig. 1. Cyclic voltammograms obtained on Au in N_2 -stirred 1M H_2SO_4 showing change in pattern from initial trace to the steady-state trace. Sweep rate: 100 mV. Sweep range: -200 to 1700 mV. Initial trace indicated by arabic numeral one.

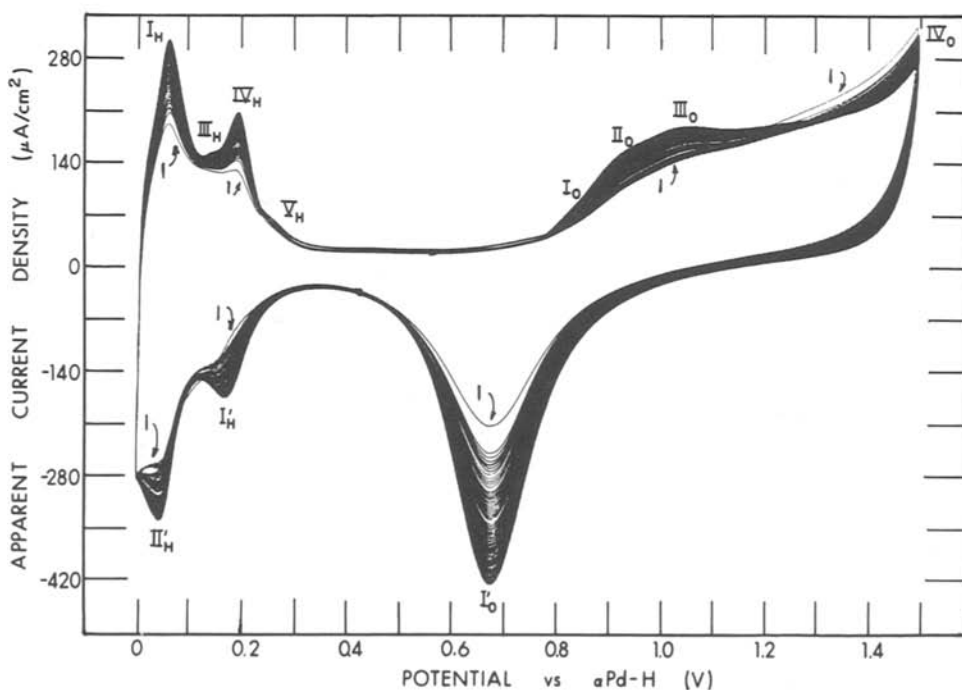


Fig. 2. Cyclic voltammograms obtained on Pt in N_2 -stirred 1M H_2SO_4 showing change in pattern from initial to the steady-state trace. Sweep rate: 100 mV/s. Sweep range: 0-1500 mV. Initial trace indicated by arabic numeral one.

Fig. 3. Family of cyclic voltammograms obtained on Au in N_2 -stirred 1M H_2SO_4 at sweep rates of 100, 83, 67, 50, 33, and 17 mV/s from -200 to 1700 mV. 100 mV/s sweep is outside trace. Roman numerals identify major peaks.

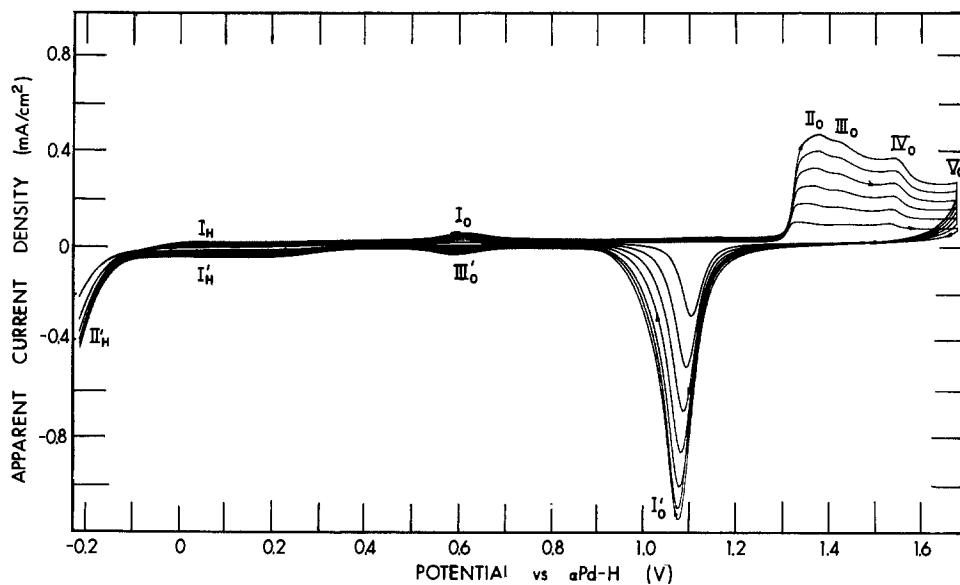
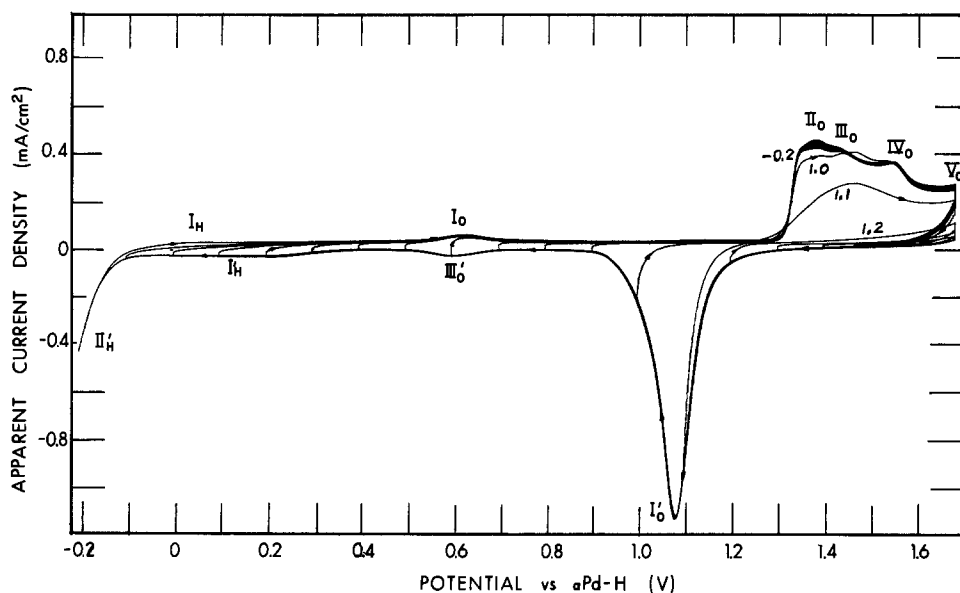


Fig. 4. Family of cyclic voltammograms obtained on Au in N_2 -stirred 1M H_2SO_4 swept at 100 mV/s by reducing the range of potentials scanned from the cathodic end in 100 mV steps. Potential at start of trace is indicated by potential value.



disappear. On the 1400 mV trace, a shoulder on I'_o appears and is designated as II'_o . Changes in II'_H as the potential range is reduced, the largest changes occurring between 1300 and 600 mV.

From these data, one associates II_o , III_o , and IV_o with I'_o , but, apparently, II_o also contains the species reduced in II'_o . In addition, I_o is related to III'_o and I_H to I'_H .

In N_2 -stirred 1M HF, the steady-state voltammogram on Au is reached relatively quickly (in about five cycles of polarization), as demonstrated in Fig. 6. The linear dependence on sweep rate shown in Fig. 7 indicates that the electrode processes involved are surface reactions. The overall shape of the traces in Fig. 7 are very similar to those on Au in 2N H_2SO_4 (Fig. 3) except that I_o and III'_o are not present and I_H and I'_H have also vanished. At about 1100 mV, an additional peak, designated VI_o , appears. Traces similar to these have been reported by Hamelin *et al.* (36) for Au in NaF solutions.

As one reduces the potential range by initiating the anodic sweep at increasingly positive potentials (Fig. 8), little or no changes occur until the sweep is begun at 900 mV, where II_o is reduced. At 1000 mV, the structure in the oxygen region is reduced to a single broad peak, which disappears at potentials above 1100 mV. Figure 9 contains the data for reduction of the potential range by initiating the cathodic sweep at increasingly greater cathodic values. Between 1700 and 1300 mV, I'_o is reduced; the shoulder II'_o appears at potentials below 1300 mV. As be-

fore, we associate II_o , III_o , and IV_o with I'_o , noting that II_o is also associated with II'_o .

It is now possible to assign electrode processes to the peaks observed on the cyclic voltammograms. As discussed in the literature (28, 35, 37), the oxide layers on Au are formed by the discharge of adsorbed water molecules to form precursor species, such as hydrated Au_2O or hydrated adsorbed oxygen (Au-O). Such species are oxidized with continued polarization to hydrated Au_2O_3 or $AuOOH$. This oxide may be formed through a place-change mechanism (38) as discussed by Schultze and Vetter (37). However, oxygen atoms remain only in the first surface layer of gold atoms and do not penetrate into the bulk metal.

In Fig. 1 and 6, the first anodic sweep on gold exhibits peaks III_o and IV_o but not II_o . With each succeeding cycle of polarization, II_o becomes more prominent at the expense of III_o and IV_o until the steady-state pattern is formed (Fig. 3 and 7). This behavior is viewed as the oxidation of the hydrated oxide precursors to a steady-state layer of hydrated Au_2O_3 . According to the literature, the oxide film on Au is a porous, poorly adherent layer of hydrated Au_2O_3 (39) that grows continuously with polarization (40-42) by the place-change mechanism at the metal-oxide interface (37). The increase in area of the reduction peak I'_o in Fig. 3 and 6 reflects the growth of the Au_2O_3 layer during the anodic going sweep until the oxide formed during anodization is just reduced during cathodization at steady state.

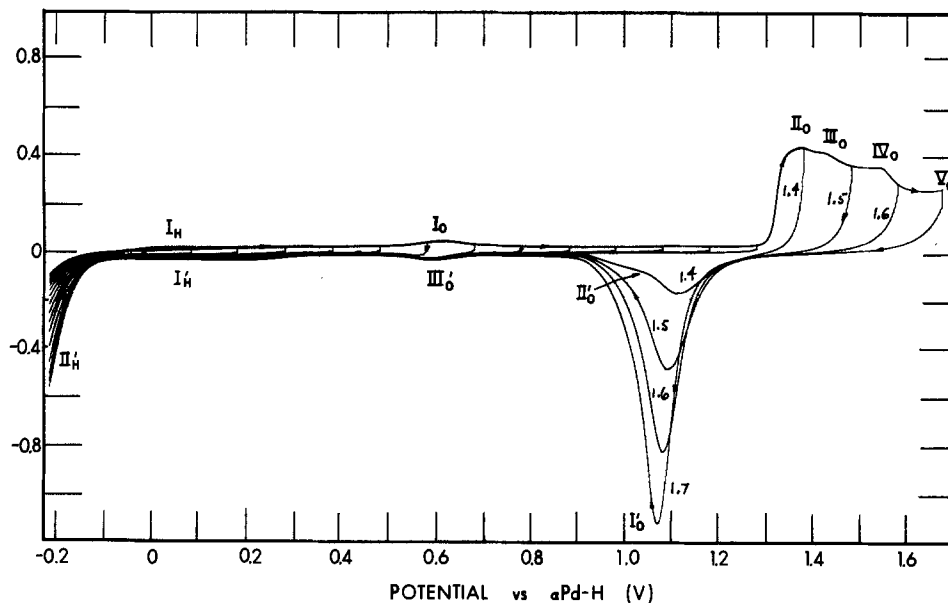


Fig. 5. Family of cyclic voltammograms obtained on Au in N_2 -stirred 1M H_2SO_4 swept at 100 mV/s by reducing the potential range scanned from the anodic end in 100 mV steps. Potential at start of trace is indicated by potential value.

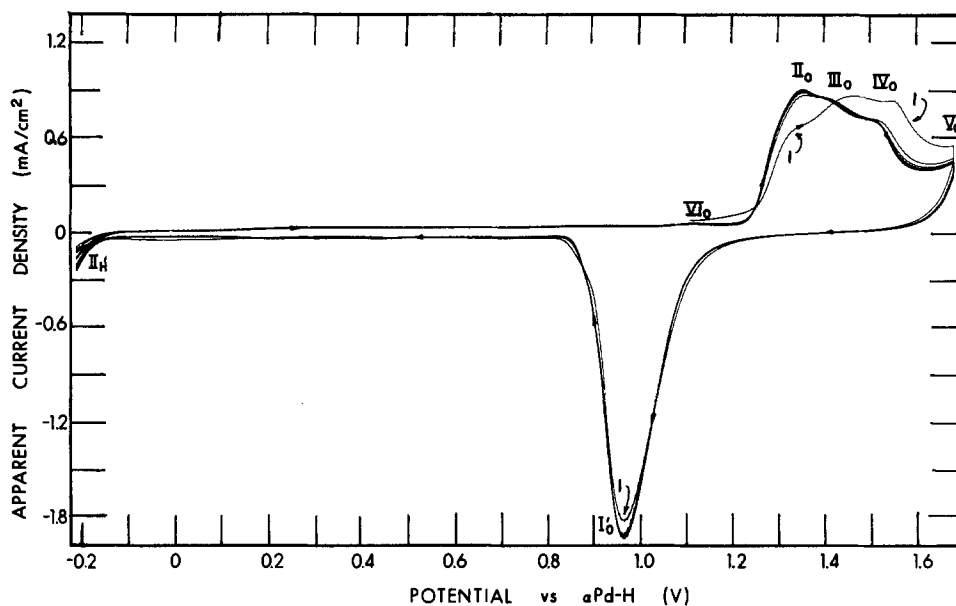


Fig. 6. Cyclic voltammograms obtained on Au in N_2 -stirred 1M HF swept at 100 mV/s from -200 to 1700 mV showing the change in pattern from the initial to the steady-state trace. Initial trace indicated by arabic numeral one.

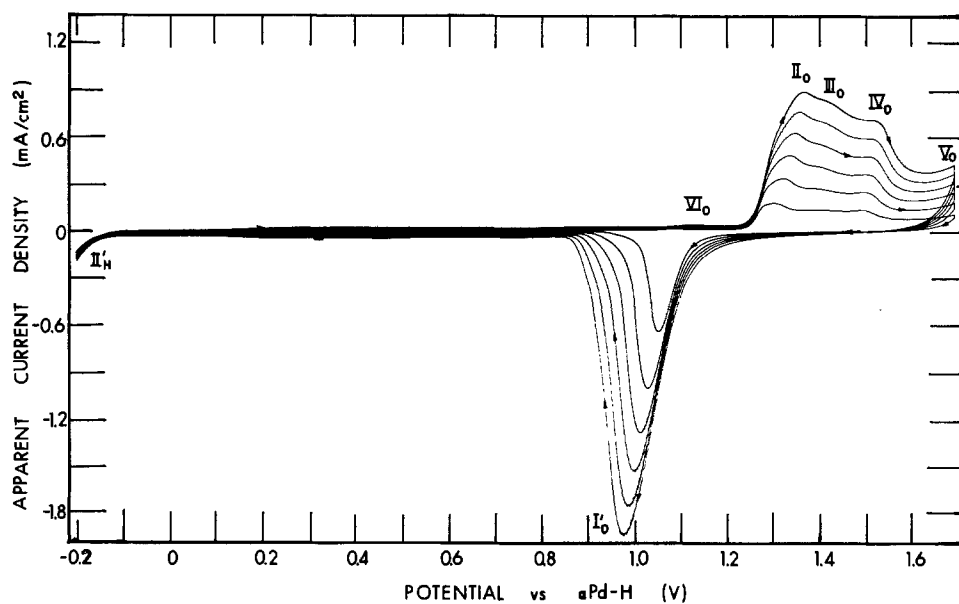


Fig. 7. Family of cyclic voltammograms obtained on Au in N_2 -stirred 1M HF swept from -200 to 1700 mV as a function of the sweep rate (100, 83, 67, 50, 33, 17 mV/s). 100 mV/s trace is the outside curve.

From the data in Fig. 5 and 9, there appears to be two kinds of oxide, a strongly bound and weakly bound form. Most of the oxide is present as relatively thick patches of

weakly bound hydrated Au_2O_3 . Under these patches or clusters of hydrated Au_2O_3 at the metal-oxide interface is a strongly bound (probably monolayer) film of Au_2O_3 in-

Fig. 8. Family of cyclic voltammograms obtained on Au in N_2 -stirred 1M HF swept at 100 mV/s by reducing the potential range scanned from the cathodic end in 100 mV steps. Potential at start of trace is indicated by potential value.

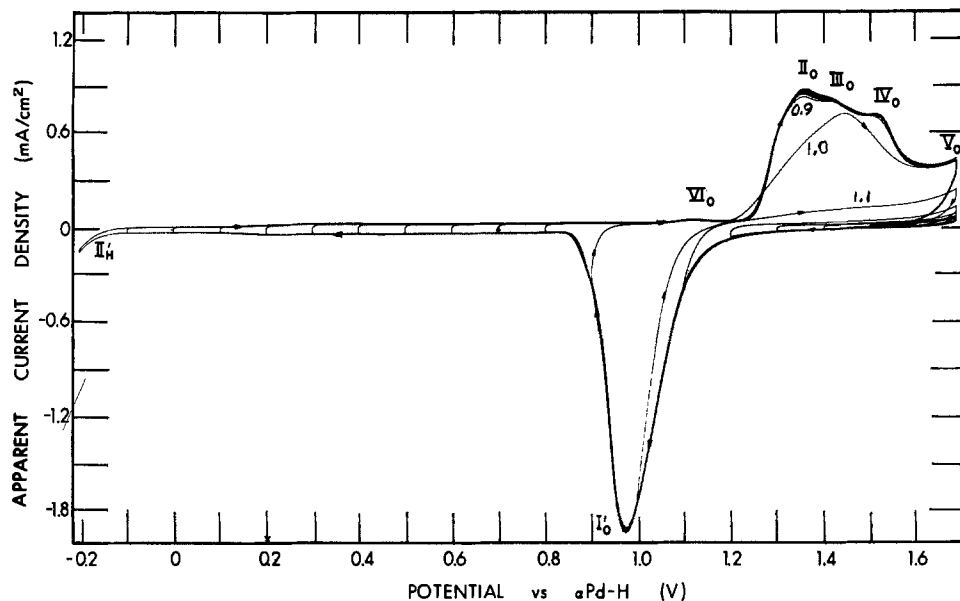
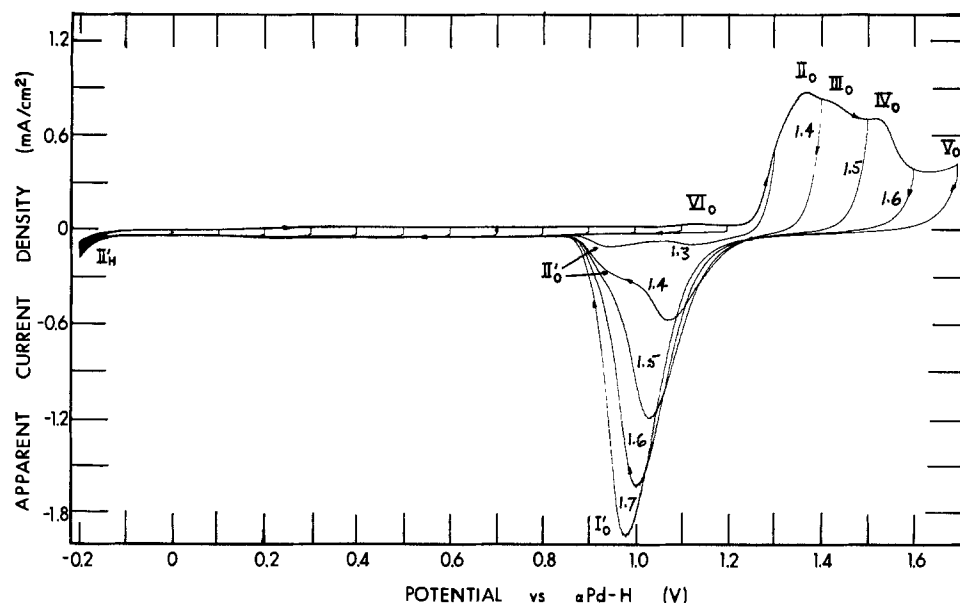


Fig. 9. Family of cyclic voltammograms obtained on Au in N_2 -stirred 1M HF swept at 100 mV/s by reducing the potential range scanned from the anodic end in 100 mV steps. Potential at start of trace is indicated by potential value.



timately tied to the surface layers of the gold metal (similar to dermasorbed Au_2O_3). The reduction of this tightly bound Au_2O_3 appears in II'_0 . In the steady-state scan (Fig. 3 and 6), II_0 , III_0 , and IV_0 may represent the formation of Au_2O_3 with different degrees of hydration.

Since peaks I_0 and III'_0 appear on voltammograms obtained on Au in H_2SO_4 solutions but not on those in HF solution, it is concluded that the adsorption of HSO_4^- ions on Au produce I_0 , and their desorption III'_0 . It is noted that VI_0 appears on scans in HF but not on those in H_2SO_4 . If it is assumed that oxygen begins to adsorb on Au at VI_0 , then the absence of VI_0 in H_2SO_4 may be traced to the interference of adsorbed HSO_4^- ions which delay the adsorption of oxygen to higher potentials. Such behavior was noted (23) on cyclic voltammograms obtained on Pt electrodes in 1M H_2SO_4 and in 1M HF solutions. This interference of adsorbed HSO_4^- ion on Au may also account for the larger number of cycles of polarization required to reach steady state in H_2SO_4 (Fig. 1) than in HF (Fig. 6).

Evolution of oxygen leads to V_0 , and evolution of hydrogen to II'_H . In HF solutions, hydrogen is virtually not adsorbed. However Fig. 8 and 9 indicate that there is some relationship between the surface reaction at low values of the polarization and that at high values of the polarization. This behavior may be accounted for by area changes during oxide formation and reduction. In H_2SO_4 solutions, this effect is exaggerated to the point that I_H

and I'_H were assigned to this region. It may be possible that HSO_4^- ion adsorption may contribute to the enhancement of the area effects in H_2SO_4 solution.

Once a steady-state cyclic voltammogram is obtained on gold in 1N HF (SS in Fig. 10), the electrode was cycled for about 20 cycles between -200 and 500 mV. When the potential range scanned was increased to 1700 mV, the steady-state curve was virtually recovered with the first cycle of polarization. For the sake of comparison, this same procedure was repeated on Pt in 1M H_2SO_4 cycled between 0 and 1500 mV. The steady-state trace is indicated by SS in Fig. 11. When the potential range was narrowed to $0-500$ mV and cycled for about 20 cycles, large changes took place in the hydrogen peaks I_H , I'_H , IV_H , and II'_H , and III_H disappeared. Upon returning the sweep range to $0-1500$ mV, one observes that it required at least five (numbered in Fig. 11) cycles of polarization to recover the steady state.

Such behavior in the case of Pt has been accounted for (23) by the dissolution of oxygen in bulk Pt at potentials above $1V$ to form a Pt-O alloy. The alloy is a better catalyst for the O_2 and H_2 reactions than is oxygen-free Pt. As shown in Fig. 2, it requires many cycles of polarization to charge up the Pt so that a steady-state Pt-O alloy surface with a stable catalytic activity can be obtained. When the system was cycled between 0 and 500 mV (Fig. 11), oxygen was removed from the Pt surface by reaction with adsorbed hydrogen, and although this hydrogen is replaced

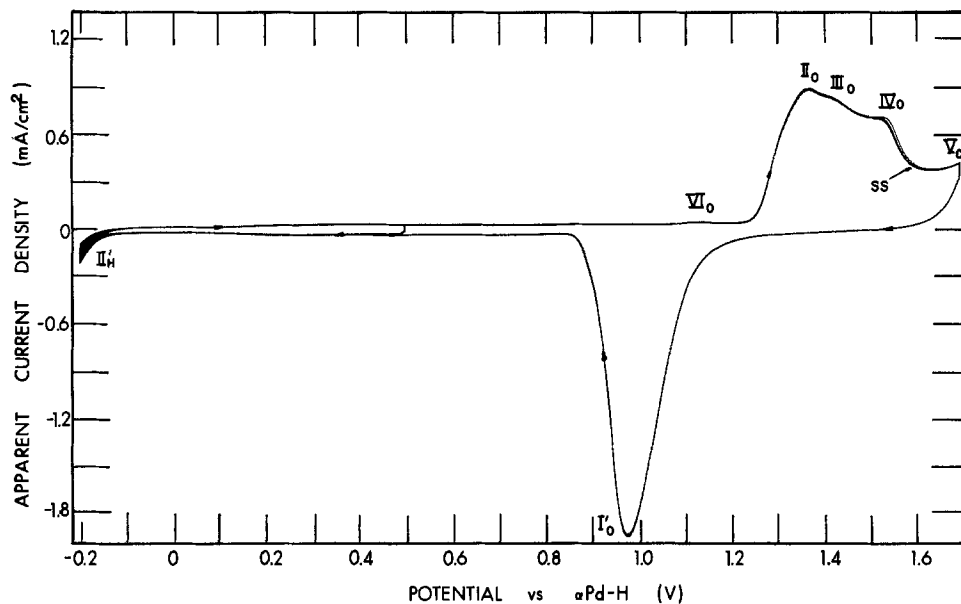


Fig. 10. Once the steady-state cyclic voltammogram had been obtained from -200 to 1700 mV at 100 mV/s on Au in $1M$ HF, the electrode was cycled between -200 and 500 mV for about 20 cycles. When the electrode was cycled again between -200 and 1700 mV, the steady-state scan (ss) was retraced on the first cycle.

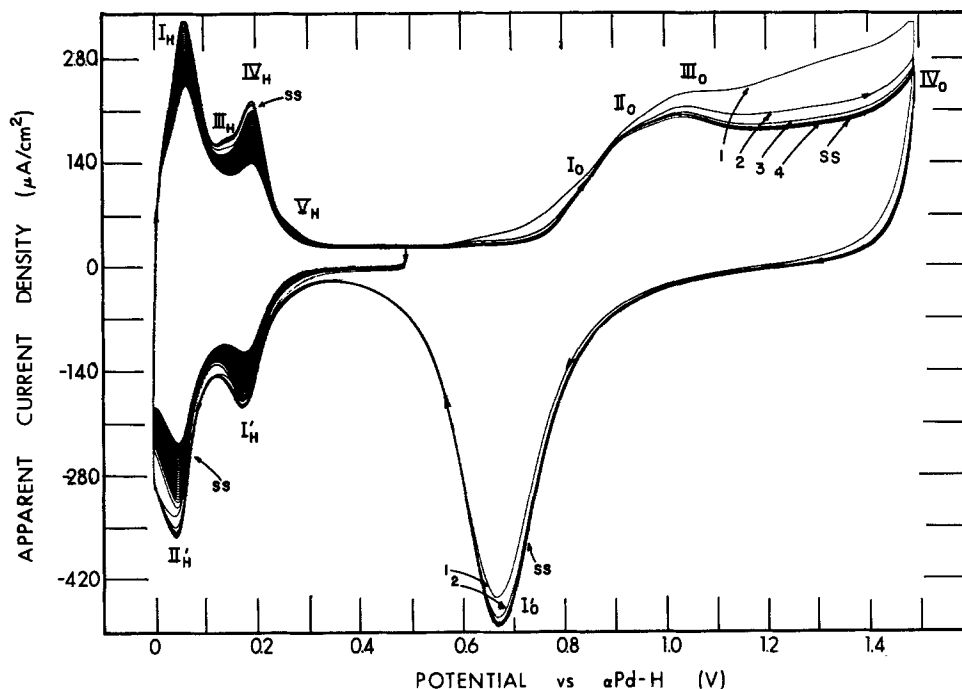


Fig. 11. Once the steady-state cyclic voltammogram was obtained on Pt in $1M$ H_2SO_4 from 0 to 1500 mV at 100 mV/s, the electrode was cycled from 0 to 500 mV for about 20 cycles. When the electrode was cycled again between -200 and 1700 mV, it required at least 5 cycles (numbered on figure) to retrace the steady-state scan (ss).

by dissolved oxygen in the metal diffusing to the surface, the catalytic activity of the Pt surface changes with each cycle because the concentration of dissolved oxygen in Pt is being continually reduced. When the anodic end of the sweep is returned to 1500 mV, the steady-state Pt-O alloy surface can be regenerated with the replacement of the lost dissolved oxygen with five cycles of polarization.

In the case of Au, only a few cycles of polarization are required to reach to steady state (Fig. 1 and 6). When cycled to 500 mV (Fig. 10), relatively little change is observed, and the steady state is reached rapidly once the sweep is returned to 1500 mV. Since Au does not dissolve oxygen, anodization or cathodization does not modify the catalytic activity of the Au surface for H_2 or O_2 reactions (Fig. 10) and a steady-state voltammogram is obtained quickly.¹

To demonstrate the effect of noble metal poisoning of the Au surface, the α -Pd-H reference electrode was pre-

pared (preanodized and charged with hydrogen) in the same solution with the Au electrodes. The family of cyclic voltammograms obtained on the poisoned Au in $1M$ HF solution scanned between -200 and 1700 mV as a function of sweep speed is presented in Fig. 12. A prominent hydrogen desorption peak, I_H , is evident and the potential at which oxygen is first adsorbed VI_0 is shifted far to the left. Here, VI_0 appears at a potential coincident with the value for the beginning of oxygen adsorption on Pt (Fig. 13). Not only is II_0 much sharper in Fig. 12 than in Fig. 3 and 7, but it is also shifted to the left by at least 100 mV. Peaks III_0 and IV_0 (evident in Fig. 7) become indistinct in Fig. 12. The oxygen reduction peak I'_0 becomes much sharper and narrower in Fig. 12 than in Fig. 7. From the data in Fig. 12, it is evident that noble metal contamination of a Au surface can severely modify the electrochemistry of the noble metal-free Au surface. Since Pt or Pd sites are much more active than Au sites, only a very few noble metal sites present on an Au surface can give it a strong noble metal character.

From these studies, it is concluded that hydrogen is only slightly adsorbed (if at all) on Au, and much less than a monolayer of oxygen ($\theta < 0.01$) is adsorbed below 1350 mV. Above 1350 mV, hydrated Au_2O_3 is formed by the place-change mechanism between Au surface atoms

¹ One of the reviewers suggested that these data could be interpreted in terms of gold's not adsorbing impurities as easily as Pt, which could account for the shorter times required to reach the steady state on Au than on Pt. Another possibility is the suggestion that the deposition of oxygen rearranges the surface Au atoms more rapidly than on Pt. Both of these mechanisms have been rejected in favor of the one proposed in the body of this report.

Fig. 12. Family of cyclic voltammograms obtained on Pd-contaminated Au in N_2 -stirred 1M HF from -200 to 1700 mV/s as a function of the sweep rate (100, 83, 67, 50, 33, 17 mV/s). 100 mV/s sweep is outside trace.

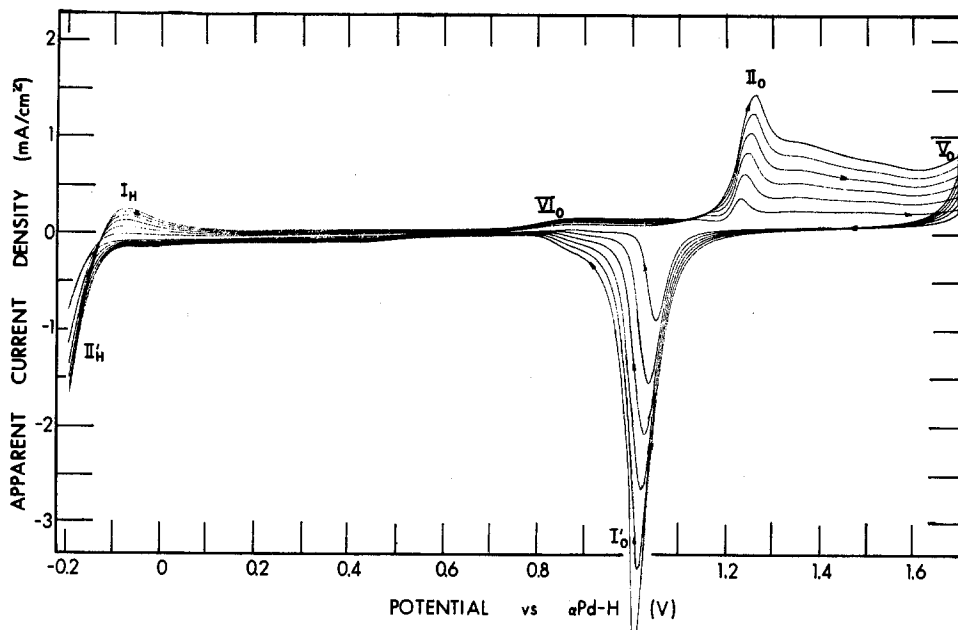
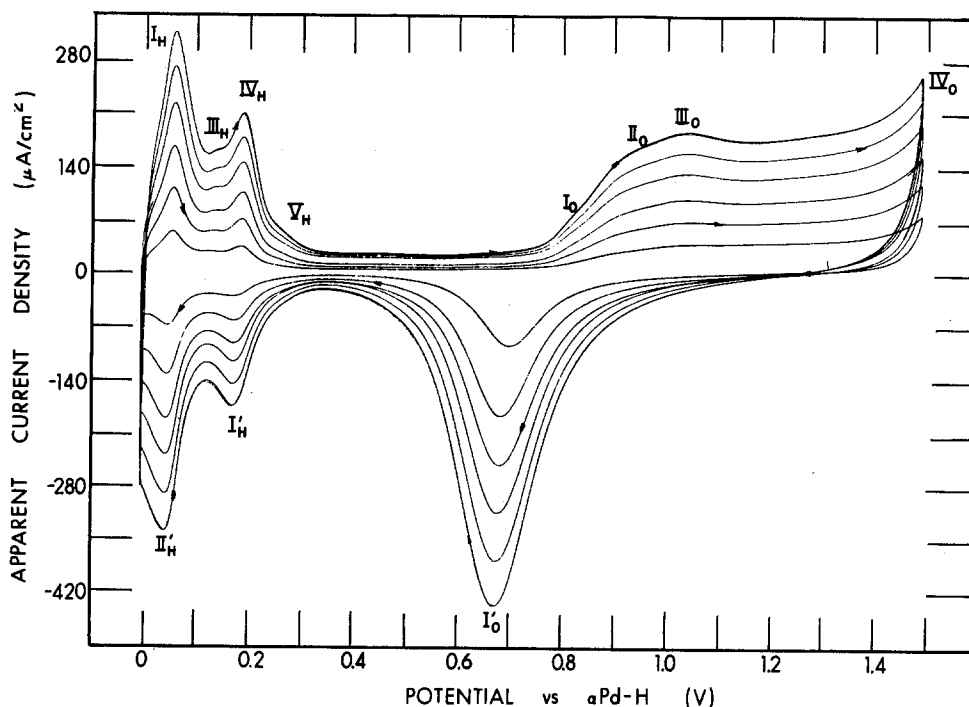


Fig. 13. Family of cyclic voltammograms obtained on Pt in N_2 -stirred 1M H_2SO_4 from 0 to 1500 mV as a function of the sweep rate (100, 83, 67, 50, 33, 17 mV/s). 100 mV/s sweep is outside trace.



and adsorbed oxygen atoms generated by the discharge of water. There are two kinds of adsorbed Au_2O_3 on the Au surface, a strongly bound, thin layer at the Au surface lying beneath a relatively thick, weakly bound layer. Oxygen does not dissolve in the bulk gold metal, nor do other gases. Consequently, Au presents a stable catalytic surface in many electrochemical systems and can make an excellent indicator electrode. Bisulfate ions can adsorb on Au and interfere somewhat with hydrogen and oxygen reactions taking place at the Au surface. For investigations of the electrochemistry of Au, one must rigorously exclude contact with noble metals.

These data also support the conclusion (23) that prepolarization of Pt is required to produce a stable catalytic surface by forming a Pt-O alloy. In this way, a reproducible and stable indicator electrode may be obtained. Although desorption of impurities (21, 22, 30) and possible dissolution of Pt (43, 44) may contribute to the need for prepolarizing Pt, the major contribution to this treatment is the formation of a Pt-O alloy with a stable catalytic surface. This work on Au supports this viewpoint because pure clean Au, which does not dissolve oxygen, does not

need this intense prepolarization to achieve a stable catalytic surface in the same purified electrolytes.

Manuscript submitted Nov. 4, 1983; revised manuscript received Jan. 23, 1984. This was Paper 408 presented at the Cincinnati, OH, Meeting of the Society, May 6-11, 1984.

General Motors Research Laboratories assisted in meeting the publication costs of this article.

REFERENCES

1. A. Hickling, *Trans. Faraday Soc.*, **41**, 333 (1945).
2. T. V. Kalish and R. Kh. Burshtein, *Dokl. Akad. Nauk SSSR*, **81**, 1093 (1951); *ibid.*, **88**, 863 (1953).
3. A. D. Obrucheva, *Zh. Fiz. Khim.*, **26**, 1448 (1952).
4. V. I. Luk'yanycheva and V. S. Bogotsky, *Dokl. Akad. Nauk SSSR*, **155**, 160 (1964).
5. S. Schuldiner, T. B. Warner, and B. J. Piersma, *This Journal*, **112**, 212, 853 (1965); *ibid.*, **113**, 573 (1966); *ibid.*, **114**, 343 (1967).
6. J. P. Hoare, *ibid.*, **116**, 612, 1390 (1969).
7. H. Shimizu, *Electrochim. Acta*, **14**, 55 (1969).
8. R. Thacker and J. P. Hoare, *J. Electroanal. Chem.*, **30**, 1, (1971); *ibid.*, **12**, 260 (1964).
9. P. R. Nedebaum and T. L. Fahidy, *Electrochim. Acta*,

- 17, 1659 (1972).
10. J. Balej and O. Spalek, *Czech. Chem. Comm.*, **37**, 499 (1972); *ibid.*, **38**, 29 (1973).
 11. R. Parsons and W. H. M. Visscher, *J. Electroanal. Chem.*, **36**, 329 (1972).
 12. J. P. Hoare, *This Journal*, **121**, 872 (1974); *ibid.*, **123**, 1823 (1976); *ibid.*, **127**, 1758 (1980).
 13. J. P. Hoare, *J. Phys. Chem.*, **79**, 2175 (1975).
 14. J. P. Hoare, *Electrochim. Acta*, **26**, 225 (1981); *ibid.*, **20**, 267 (1975).
 15. J. P. Hoare, *Nature*, **204**, 71 (1964).
 16. J. P. Hoare, *This Journal*, **113**, 1078 (1966); *ibid.*, **125**, 1768 (1978); *ibid.*, **126**, 1502 (1979).
 17. J. P. Hoare, *J. Electroanal. Chem.*, **30**, 15 (1971).
 18. M. W. Breiter, *Electrochim. Acta*, **11**, 905 (1966).
 19. S. Gilman, *J. Phys. Chem.*, **67**, 78 (1963).
 20. B. E. Conway, H. Angerstein-Kozłowska, W. B. A. Sharp, and E. E. Cridle, *Anal. Chem.*, **45**, 1331 (1973).
 21. F. G. Will and C. A. Knorr, *Z. Electrochem.*, **64**, 258 (1960).
 22. M. Breiter and B. Kennel, *ibid.*, **64**, 1180 (1960).
 23. J. P. Hoare, *Electrochim. Acta*, **27**, 1751 (1982).
 24. D. P. Smith, "Hydrogen in Metals," p. 282, University of Chicago Press, Chicago (1948).
 25. R. M. Barrer, "Diffusion in and Through Solids," p. 146, Cambridge University Press, Cambridge, England (1951).
 26. R. W. Zurilla, R. K. Sen, and E. Yeager, *This Journal*, **125**, 1103 (1978).
 27. R. A. Bonowitz and G. M. Schmid, *ibid.*, **117**, 1367 (1970).
 28. G. M. Schmidt and M. E. Curley-Fiorino, *Encycl. Electrochem. Elements*, **4**, 87 (1975).
 29. D. J. G. Ives and G. J. Janz, "Reference Electrodes," p. 712, Academic Press, New York (1961); J. P. Hoare, *G.M. Eng. J.*, **9**, 14 (1962).
 30. H. Angerstein-Kozłowska, W. B. A. Sharp, and B. E. Conway, in "Electrocatalysis," M. Breiter, Editor, p. 94, The Electrochemical Society Softbound Proceedings Series, Princeton, NJ (1974).
 31. F. G. Will and C. A. Knorr, *Z. Elektrochem.*, **64**, 270 (1960).
 32. M. W. Breiter, *Electrochim. Acta*, **10**, 543 (1965).
 33. R. Woods, *ibid.*, **14**, 533, 632 (1969).
 34. T. Takamura, K. Takamura, W. Nippe, and E. Yeager, *This Journal*, **117**, 626 (1970).
 35. G. Grueneberg, *Electrochim. Acta*, **10**, 339 (1965).
 36. A. Hamelin, T. Vitanov, E. Sevastynov, and A. Popov, *J. Electroanal. Chem.*, **145**, 225 (1983).
 37. J. W. Schultze and K. J. Vetter, *Ber. Bunsenges. Phys. Chem.*, **75**, 470 (1971).
 38. N. Sato and M. Cohen, *This Journal*, **111**, 512 (1964); B. E. Conway and S. Gottesfeld, *J. Chem. Soc. Faraday Trans. 1*, **69**, 1090 (1973).
 39. S. Barnartt, *This Journal*, **106**, 722, 991 (1959).
 40. H. A. Laitinen and M. S. Chao, *ibid.*, **108**, 726 (1961).
 41. S. B. Brummer and A. C. Makrides, *ibid.*, **111**, 1122 (1964).
 42. K. Ogura, S. Harayama, and K. Nagasaki, *ibid.*, **118**, 531 (1971).
 43. D. A. J. Rand and R. Woods, *J. Electroanal. Chem.*, **35**, 209 (1972).
 44. K. Kinoshita, J. T. Lundquist, and P. Stonehart, *J. Electroanal. Chem.*, **48**, 157 (1973).

Membrane-Covered Oxygen Sensors: An Exact Treatment of the Switch-on Transient

Janice C. Myland and Keith B. Oldham*

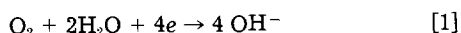
Department of Chemistry, Trent University, Peterborough, Ontario, Canada K9J 7B8

ABSTRACT

Equations are derived that exactly describe the current-time behavior of a membrane-covered oxygen sensor, following the imposition of a polarizing potential to the previously equilibrated cell. The role of the various geometric, transport, and solubility factors is evaluated without any restriction being placed upon the magnitudes of these factors. The equations are analyzed to predict the duration of Cottrellian behavior, and the interval before the onset of the steady state, for sensors of practical importance.

The membrane-covered electrochemical oxygen sensor was invented by Clark (1); its principles are comprehensively described in the monograph by Hitchman (2). The geometry of the device is as shown in Fig. 1. The medium being analyzed, which may be a gas, a water body, or an aqueous solution, contains oxygen at a uniform partial pressure p_w . An inlaid disk electrode is separated from this medium by a layer of aqueous electrolyte and a layer of a plastic membrane. The diameter $(4A/\pi)^{1/2}$ of the electrode is very large compared with the thicknesses a and b of the two layers so that oxygen effectively reaches the electrode solely by diffusion along the dimension marked y in Fig. 1.

In operation, the electrode is polarized sufficiently negative that the reaction



proceeds under diffusion controlled conditions. When the polarizing potential is applied to a previously equilibrated cell, a transient current flows that declines towards an ultimate steady-state value. Both the initial transient current and the final steady-state current are proportional to p_w , and both currents have been used analytically. The form of the current vs. time relationship depends in a complicated fashion on the geometric, transport, and solubility properties of the two layers. Previous derivations (2-4) of this relationship have imposed restrictions on

these properties. The object of the present discussion is to remove these restrictions.

Solubility and Transport Properties

The concentration of oxygen at any plane y in the electrolyte is related to the oxygen partial pressure there by Henry's law

$$c = H_e p \quad 0 \leq y \leq a \quad [2]$$

Here, H_e is the Henry's law constant for oxygen in the electrolyte solution. It is a few percent smaller than H_w , the Henry's law constant for pure water, because of the "salting out" of oxygen by the electrolyte. A similar relationship

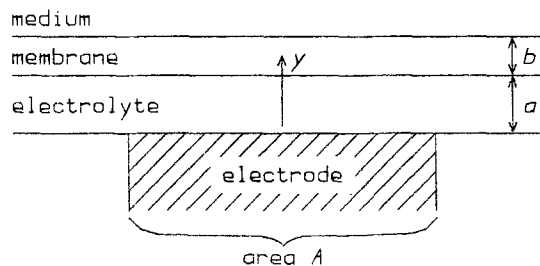


Fig. 1. The geometry of the membrane-covered oxygen sensor. The thicknesses a and b are small in comparison with the electrode radius $(4A/\pi)^{1/2}$.

*Electrochemical Society Active Member.

$$c = H_m p \quad a \leq y \leq a + b \quad [3]$$

holds in the membrane, but with a different Henry's law constant H_m .

Equilibrium may be assumed to exist at the outer and inner faces of the membrane, so that

$$p(y = a + b -) = p(y = a + b +) = p_w \quad [4]$$

and

$$p(y = a +) = p(y = a -) \quad [5]$$

Moreover, the fluxes of oxygen on each side of the membrane/electrolyte interface must be identical, *i.e.*

$$J(y = a +) = J(y = a -) \quad [6]$$

Because we assume oxygen transport to be wholly diffusive, Fick's first law

$$J = -D_e \frac{\partial c}{\partial y} = -D_e H_e \frac{\partial p}{\partial y} \quad 0 \leq y \leq a \quad [7]$$

applies, where D_e is the diffusion coefficient of oxygen in the electrolyte solution. A similar relationship

$$J = -D_m H_m \frac{\partial p}{\partial y} \quad a \leq y \leq a + b \quad [8]$$

holds within the membrane. As with his first law, Fick's second law may also be written in terms of oxygen partial pressures

$$\frac{\partial p}{\partial t} = D_e \frac{\partial^2 p}{\partial y^2} \quad 0 \leq y \leq a \quad [9]$$

and

$$\frac{\partial p}{\partial t} = D_m \frac{\partial^2 p}{\partial y^2} \quad a \leq y \leq a + b \quad [10]$$

The diffusion coefficient of oxygen in aqueous electrolyte solution is a mild function of temperature and of the nature and concentration of the electrolyte. We shall use the value (5)

$$D_e = 2.1 \times 10^{-9} \text{ m}^2 \text{ s}^{-1} \quad [11]$$

throughout this article. There is a paucity of information on the diffusion coefficients of oxygen in membrane materials but Hitchman (2) reports

$$D_m = 1.14 \times 10^{-11} \text{ m}^2 \text{ s}^{-1} \quad [12]$$

for polytetrafluoroethene (Teflon), which is commonly used for sensor membranes. Experiments in these laboratories (6) suggest that D_m approximates $3 \times 10^{-10} \text{ m}^2 \text{ s}^{-1}$ for polydimethylsiloxane (silastic rubber).

Whereas there are few diffusion coefficient data, some compilations exist of the product $D_m H_m$, which is known as the "permeability" of the membrane material. However, as Table I shows, there is poor agreement among the reported values. The related quantity

$$P_m = D_m H_m / H_w \quad [13]$$

Table I. Permeabilities of two polymers to oxygen

Polymer	$D_m H_m$ mol m ⁻¹ s ⁻¹ atm ⁻¹	Method	Ref.
Polytetra- fluoroethene	8.0×10^{-10}	Volumetric using gas/	(7)
	1.4×10^{-13}	membrane/gas system	(8)
	3.1×10^{-9}	Volumetric using water/	(7)
	1.1×10^{-10}	membrane/water system	(7)
		Electrochemical via Eq.	(2)
		[13]-[15]	
Polydimethyl- siloxane	2.3×10^{-8}	Volumetric using gas/	(7)
	1.7×10^{-8}	membrane/gas system	(8)
	1.4×10^{-7}	Volumetric using water/	(7)
		membrane/water system	(7)

is known as the "permeability coefficient" of the membrane. Hitchman (2) reports the experimental value

$$P_m = 8.2 \times 10^{-11} \text{ m}^2 \text{ s}^{-1} \quad [14]$$

for polytetrafluoroethene.

The Henry's law constant for pure water may be calculated from oxygen solubility data [Ref. (2), Appendix B] as about

$$H_w = 1.33 \text{ mol m}^{-3} \text{ atm}^{-1} \quad [15]$$

at room temperature. For aqueous 1:1 electrolytes at tenth-molar concentration

$$H_e \approx 1.28 \text{ mol m}^{-3} \text{ atm}^{-1} \quad [16]$$

for solutions typically used to fill membrane-covered sensors. The Henry's law constant for polytetrafluoroethene can be obtained as

$$H_m = 9.6 \text{ mol m}^{-3} \text{ atm}^{-1} \quad [17]$$

from Eq. [12]-[15]. Notice that oxygen is significantly more soluble in this polymer than in water or aqueous solutions.

A dimensionless grouping of terms that repeatedly occurs in the following theory is

$$\Lambda = \frac{D_e^{1/2} H_e - D_m^{1/2} H_m}{D_e^{1/2} H_e + D_m^{1/2} H_m} \quad [18]$$

This definition of Λ ensures that its value lies between -1 and +1. The constants in Eq. [11], [12], [16], and [17] lead to the representative value

$$\Lambda = 0.29 \quad [19]$$

when the sensor membrane is polytetrafluoroethene. This value will be used in numerical examples below.

There is a characteristic time associated with transport through each of the layers, namely

$$T_e = a^2 / D_e \quad [20]$$

and

$$T_m = b^2 / D_m \quad [21]$$

Probably the single most common membrane in present day use is a 0.001 in. thick film of polytetrafluoroethene. For such a membrane, one calculates, using Eq. [12]

$$T_m = 57 \text{ s} \quad [22]$$

The characteristic electrolyte time T_e may be either shorter or longer than this, according to the sensor design. Thus, a classical Clark cell has an electrolyte film of about 20 μm thickness, which gives

$$T_e = 0.19 \text{ s} \ll T_m \quad \text{Clark conditions} \quad [23]$$

when combined with the value in Eq. [11]. On the other hand, Fowler and Oldham (5) used an electrolyte solution layer of 2 mm thickness, which translates to

$$T_e = 1900 \text{ s} \gg T_m \quad \text{Fowler conditions} \quad [24]$$

Mancy and co-workers (4) considered a cell in which the two characteristic times are equal, *i.e.*

$$T_e = 57 \text{ s} = T_m \quad \text{Mancy conditions} \quad [25]$$

For brevity, we will find the definitions of a sum and difference

$$T_s^{1/2} = T_e^{1/2} + T_m^{1/2} = (a/D_e^{1/2}) + (b/D_m^{1/2}) \quad [26]$$

and

$$T_d^{1/2} = T_e^{1/2} - T_m^{1/2} = (a/D_e^{1/2}) - (b/D_m^{1/2}) \quad [27]$$

useful. The ratio $T_d^{1/2}/T_s^{1/2}$ is close to ± 1 respectively for the Fowler and Clark cells, while it is zero for the cell treated by Mancy.

General Expression for the Sensor Current Transform

We consider equilibrium to exist prior to the instant, $t = 0$, at which the electrode is polarized; therefore

$$p = p_w \quad y > 0 \quad t < 0 \quad [28]$$

Thereafter, polarization is complete at the electrode surface

$$p = 0 \quad y = 0 \quad t > 0 \quad [29]$$

and the current is given by Faraday's law applied to reaction [1]

$$i = -4AFJ \quad y = 0 \quad t > 0 \quad [30]$$

where J is the time-dependent oxygen flux along the Y-axis (Fig. 1). Combining this with Eq. [7], one obtains

$$i = 4AFH_e D_e (\partial p / \partial y) \quad y = 0 \quad t > 0 \quad [31]$$

We need to solve Eq. [9], Fick's second law for the electrolyte layer, subject to initial condition [28] and boundary condition [29]. The solution is aided by the Laplace transformation of Eq. [9] into

$$\frac{\partial^2 \bar{p}}{\partial y^2} - \frac{s\bar{p}}{D_e} = -\frac{p_w}{D_e} \quad 0 \leq y \leq a \quad [32]$$

which incorporates condition [28] and in which \bar{p} is the transform of the local oxygen partial pressure and s is the dummy variable of Laplace transformation with respect to time. Standard methods (9) permit a general solution to Eq. [32] to be written as

$$\bar{p} = \frac{p_w}{s} + G_e \cosh\left(\frac{ys^{1/2}}{D_e^{1/2}}\right) + g_e \sinh\left(\frac{ys^{1/2}}{D_e^{1/2}}\right) \quad 0 \leq y \leq a \quad [33]$$

where G_e and g_e are y -independent terms that depend on the boundary conditions. Condition [29] shows \bar{p} to be zero at $y = 0$, which requires G_e to equal $-p_w/s$ and leads to

$$\bar{p} = \frac{p_w}{s} \left[1 - \cosh\left(\frac{ys^{1/2}}{D_e^{1/2}}\right) \right] + g_e \sinh\left(\frac{ys^{1/2}}{D_e^{1/2}}\right) \quad 0 \leq y \leq a \quad [34]$$

On differentiation with respect to distance, one obtains

$$\frac{\partial \bar{p}}{\partial y} = \frac{-p_w}{s^{1/2} D_e^{1/2}} \sinh\left(\frac{ys^{1/2}}{D_e^{1/2}}\right) + \frac{g_e s^{1/2}}{D_e^{1/2}} \cosh\left(\frac{ys^{1/2}}{D_e^{1/2}}\right) \quad 0 \leq y \leq a \quad [35]$$

The membrane phase may be treated similarly, but it is more convenient to write the analog of Eq. [33] as

$$\bar{p} = \frac{p_w}{s} + G_m \cosh\left(\frac{(a+b-y)s^{1/2}}{D_m^{1/2}}\right) + g_m \sinh\left(\frac{(a+b-y)s^{1/2}}{D_m^{1/2}}\right) \quad a \leq y \leq a+b \quad [36]$$

The transform of boundary condition [4] shows \bar{p} to equal p_w/s at $y = a+b$, which requires G_m to be zero and leads to

$$\bar{p} = \frac{p_w}{s} + g_m \sinh\left(\frac{(a+b-y)s^{1/2}}{D_m^{1/2}}\right) \quad a \leq y \leq a+b \quad [37]$$

directly and

$$\frac{\partial \bar{p}}{\partial y} = \frac{-g_m s^{1/2}}{D_m^{1/2}} \cosh\left(\frac{(a+b-y)s^{1/2}}{D_m^{1/2}}\right) \quad a \leq y \leq a+b \quad [38]$$

on differentiation with respect to distance.

The remaining unknown functions of s , g_e , and g_m may be determined by using Eq. [5]-[8] to solve the $y = a$ specializations of Eq. [34], [35], [37], and [38] simultaneously. Omitting the detailed algebra, one finds

$$g_m = \frac{-p_w[1-\Lambda]}{s[\sinh(sT_s)^{1/2} - \Lambda \sinh(sT_d)^{1/2}]} \quad [39]$$

and

$$g_e = \frac{p_w[\cosh(sT_s)^{1/2} - \Lambda \cosh(sT_d)^{1/2}]}{s[\sinh(sT_s)^{1/2} - \Lambda \sinh(sT_d)^{1/2}]} \quad [40]$$

where abbreviations [18], [26], and [27] have been utilized.

To obtain the final expression

$$\bar{i} = \frac{4AFp_w H_e D_e^{1/2}}{s^{1/2}} \left[\frac{\cosh(sT_s)^{1/2} - \Lambda \cosh(sT_d)^{1/2}}{\sinh(sT_s)^{1/2} - \Lambda \sinh(sT_d)^{1/2}} \right] \quad [41]$$

for the transform of the current, one specializes Eq. [35] to $y = 0$ and combines it with Eq. [40] and the transform of Eq. [31]. The Laplace inversion of Eq. [41] is by no means trivial, and we shall consider limiting and simplifying circumstances before tackling the general case. It may bear emphasis that no assumptions about the sizes or materials of construction of the membrane or electrolyte are incorporated into transform [41] nor, therefore, into the equations of the "General Solution: First Inversion" and "General Solution: Second Inversion" sections below that result from its general Laplace inversion.

Initial Response

As $t \rightarrow 0$ only large values of s become important and the arguments of the hyperbolic terms in Eq. [41] tend towards infinity. The hyperbolic sines and cosines of infinitely large arguments are indistinguishable and, therefore, Eq. [41] collapses to

$$\bar{i} = 4AFp_w H_e D_e^{1/2} / s^{1/2} \quad s \rightarrow \infty \quad [42]$$

which inverts to

$$i = 4AFp_w H_e D_e^{1/2} / \pi^{1/2} t^{1/2} \quad t \rightarrow 0 \quad [43]$$

Equation [43], which is essentially the Cottrell equation (10), shows that the $it^{1/2}$ product is initially a constant [that we shall subsequently denote $(it^{1/2})_0$], proportional to p_w but independent of any membrane parameters. It is this independence from the membrane that provides the attraction for the pulse-after-equilibration mode of operation of the membrane-covered oxygen sensor (5).

Steady-State Current

Only small values of s are important as $t \rightarrow \infty$. In this circumstance, the hyperbolic cosine terms in Eq. [41] may be replaced by unities, and the hyperbolic sine terms by their arguments. Simplification to

$$\bar{i} = \frac{4AFp_w H_e D_e^{1/2} (1-\Lambda)}{s(T_s^{1/2} - \Lambda T_d^{1/2})} \quad s \rightarrow 0 \quad [44]$$

follows. Inversion is now straightforward and leads to

$$i = 4AFp_w / [(a/D_e H_e) + (b/D_m H_m)] \equiv i_\infty \quad t \rightarrow \infty \quad [45]$$

after some algebra.

Equation [45] for the steady-state current i_∞ has been known, in a less symmetrical form, for some time [Ref. (2), Appendix H]. Not surprisingly, this equation has the form of a current flowing through two resistors in series, one arising from the membrane and the other from the electrolyte. Depending on the details, either one of these resistors may be dominant.

It is useful to relate i_∞ to the Cottrell constant $(it^{1/2})_0$ given by Eq. [43]. The ratio of these quantities turns out to be

$$\frac{(it^{1/2})_0}{i_\infty} = \frac{T_s^{1/2} - \Lambda T_d^{1/2}}{\pi^{1/2}(1-\Lambda)} = \frac{T_e^{1/2}}{\pi^{1/2}} + \frac{1 + \Lambda T_m^{1/2}}{1 - \Lambda \pi^{1/2}} \quad [46]$$

in terms of the parameters defined previously.

Clark Simplification

Inequality [23], valid for classical Clark cells, implies that $T_s^{1/2}$ closely approximates $T_m^{1/2}$ and that $T_d^{1/2} \approx -T_m^{1/2}$. In these circumstances, Eq. [41] reduces to

$$\bar{i} = \frac{4AFp_w H_e D_e^{1/2} (1-\Lambda)}{s^{1/2} (1+\Lambda)} \coth(sT_m) \quad T_e \ll T_m \quad [47]$$

which may be inverted to either of the equivalent forms¹

$$i = \frac{4AFp_w H_m D_m^{1/2}}{\pi^{1/2} t^{1/2}} \sum_{j=-\infty}^{+\infty} \exp\left(\frac{j^2 b^2}{D_m t}\right) \quad \frac{a^2}{D_e} \ll \frac{b^2}{D_m} \quad [48]$$

or

$$i = \frac{4AFp_w H_m D_m}{b} \sum_{j=-\infty}^{+\infty} \exp\left(\frac{-j^2 \pi^2 D_m t}{b^2}\right) \quad \frac{a^2}{D_e} \ll \frac{b^2}{D_m} \quad [49]$$

via theta function identities (11).

Since all the parameters relating to the electrolyte disappeared during our Clark approximation, Eq. [48] does not correctly reduce, as $t \rightarrow 0$, to the Cottrell Eq. [43]. Likewise, the $a/D_e H_e$ term is missing from the $t \rightarrow \infty$ limit of Eq. [49]. Apart from these aberrations, the second of which will usually be very minor, Eq. [48] and [49] correctly describe the behavior of the Clark cell.

Provided that t is not too small in comparison with T_m , only the $j = 0, \pm 1$ terms in expansion [49] are of significance. In this event, the expansion can be simplified to

$$i - i_\infty \approx 2i_\infty \exp(-\pi^2 t/T_m) \quad 3\pi^2 t > T_m \ln(1/\epsilon) \quad [50]$$

where ϵ is the fractional error permissible in the approximation. (For example, when $\epsilon = 0.02$, [50] is obeyed to better than 98%.) This may be usefully recast as

$$\ln \frac{2i_\infty}{i - i_\infty} = \frac{\pi^2 t}{T_m} \quad i_\infty < i < (2\epsilon^{1/3} + 1) i_\infty \quad [51]$$

which shows that a plot of the logarithm of $2i_\infty/(i - i_\infty)$ should give a straight line through the origin when plotted against time; its gradient is $\pi^2 D_m/b^2$. Hale and Hitchman (3) essentially used this method to determine D_m for polytetrafluoroethene, and Myland (6) used it to measure D_m for polydimethylsiloxane.

Fowler Simplification

Inequality [24], appropriate to the conditions used by Fowler and Oldham (5), implies that both T_s and T_d closely approximate to T_e . Equation [41] then reduces to

$$\bar{i} = \frac{4AFp_w H_e D_e^{1/2}}{s^{1/2}} \coth(sT_e)^{1/2} \quad T_e \gg T_m \quad [52]$$

which inverts, by a similar theta function technique as before, to either

$$i = \frac{4AFp_w H_e D_e^{1/2}}{\pi^{1/2} t^{1/2}} \sum_{j=-\infty}^{+\infty} \exp\left(\frac{-j^2 a^2}{D_e t}\right) \quad \frac{a^2}{D_e} \gg \frac{b^2}{D_m} \quad [53]$$

or

$$i = \frac{4AFp_w H_e D_e}{a} \sum_{j=-\infty}^{+\infty} \exp\left(\frac{-j^2 \pi^2 D_e t}{a^2}\right) \quad \frac{a^2}{D_e} \gg \frac{b^2}{D_m} \quad [54]$$

In this case, all membrane parameters have disappeared, but no serious error is thereby likely to be introduced, even as $t \rightarrow \infty$ for cells constructed to meet the objectives of Fowler and Oldham.

At short enough times, only the $j = 0, \pm 1$ terms are important in expansion [53]. A development paralleling that in the final paragraph of the previous section can be carried out, leading to the result

¹The summations of form $\sum_{j=-\infty}^{\infty} \exp(j^2 x)$ in Eq. [48], [49], [53],

and [54] may be replaced by terms $1 + 2 \sum_{j=1}^{\infty} \exp(j^2 x)$.

$$\ln \frac{2(it^{1/2})_0}{(it^{1/2})_0 - it^{1/2}} = \frac{T_e}{t} \quad (it^{1/2})_0 \leq it^{1/2} \leq (2\epsilon^{1/3} + 1)(it^{1/2})_0 \quad [55]$$

This shows that a plot of the left member of [55] vs. $1/t$ will give a straight line of gradient T_e passing through the origin.

Mancy Simplification

If T_e and T_m are equal as Mancy and co-workers (4) assumed, T_d is zero and Eq. [41] simplified to

$$\bar{i} = \frac{4AFp_w H_e D_e^{1/2}}{s^{1/2}} [\coth(sT_s)^{1/2} - \Lambda \operatorname{csch}(sT_s)^{1/2}] \quad T_e = T_m \quad [56]$$

which inverts to

$$i = \frac{2AFp_w H_e D_e^{1/2}}{\pi^{1/2} t^{1/2}} \sum_{j=-\infty}^{+\infty} [1 - \Lambda + (-)^j (1 + \Lambda)] \exp\left(\frac{-j^2 T}{t}\right) \quad \frac{a^2}{D_e} = \frac{b^2}{D_m} \quad [57]$$

where T is the common value of a^2/D_e and b^2/D_m . An alternative inversion of Eq. [56] leads to the equation

$$i = \frac{2AFp_w H_e D_e^{1/2}}{T^{1/2}} \sum_{j=-\infty}^{+\infty} [1 - (-)^j \Lambda] \exp\left(\frac{-j^2 \pi^2 t}{4T}\right) \quad \frac{a^2}{D_e} = \frac{b^2}{D_m} = T \quad [58]$$

which is more useful than Eq. [57] at longer times.

The Mancy assumption is valuable in leading to a massive simplification of the current-time relationship. However, it seems unlikely that accidental equality of T_e and T_m would often occur in practice. Nevertheless, when rewritten as

$$it^{1/2} = (it^{1/2})_0 \left[1 + 2 \sum_{j=1}^{\infty} \exp\left(\frac{-4j^2 T}{t}\right) - \Lambda \exp\left(\frac{-(2j-1)^2 T}{t}\right) \right] \quad [59]$$

and

$$i = i_\infty \left[1 + 2 \sum_{j=1}^{\infty} \exp\left(\frac{-j^2 \pi^2 t}{T}\right) + \frac{1 + \Lambda}{1 - \Lambda} \exp\left(\frac{-(2j-1)^2 \pi^2 t}{4T}\right) \right] \quad [60]$$

Eq. [57] and [58] provide useful benchmarks against which to compare the more elaborate solutions that hold when T_m and T_e are unequal.

General Solution: First Inversion

In many designs of membrane-covered oxygen sensors, the characteristic times T_e and T_m are of comparable, but unequal, magnitudes so that none of the equations of the last three sections apply. Unless one's interest is solely in the $t \rightarrow 0$ or $t \rightarrow \infty$ limit, the task of predicting the current vs. time relationship is formidable. Nevertheless, a solution is possible in two alternative forms, as will be demonstrated in this section and in the "General Solution: Second Inversion" section.

If the abbreviations

$$M = \Lambda \exp(-2T_m^{1/2} s^{1/2}) = \Lambda \exp(-2bs^{1/2}/D_m^{1/2}) \quad [61]$$

$$E = \Lambda \exp(-2T_e^{1/2} s^{1/2}) = \Lambda \exp(-2as^{1/2}/D_e^{1/2}) \quad [62]$$

and

$$S = (1 - \Lambda^2)^{1/2} \exp(-T_s^{1/2} s^{1/2}) = (1 - \Lambda^2)^{1/2}$$

$$\exp\left[-s^{1/2} \left(\frac{a}{D_e^{1/2}} + \frac{b}{D_m^{1/2}}\right)\right] = \frac{(1 - \Lambda^2)^{1/2} M^{1/2} E^{1/2}}{\Lambda} \quad [63]$$

are adopted, Eq. [41] may be expressed as

$$\bar{i} = \frac{8AFp_w H_e D_e^{1/2}}{s^{1/2}} \left[\left(1 + E - \frac{S^2}{1-M} \right)^{-1} - \frac{1}{2} \right] \quad [64]$$

The terms $E - (S^2/1 - M)$ and M are less than unity and therefore, first $[1 + E - (S^2/1 - M)]^{-1}$ and then $1/(1 - M)$ may be expanded binomially. This leads to the series

$$\bar{i} = 8AFp_w H_e D_e^{1/2} s^{-1/2} [1/2 - E + (S^2 + E^2) + (MS^2 - 2ES^2 - E^3) + (S^4 + M^2S^2 - 2MES^2 + 3E^2S^2 + E^4) + \dots] \quad [65]$$

for which it is not possible to write a simple general term. Equation [65] involves only terms of the form $M^\mu E^\eta S^\sigma / s^{1/2}$ where μ , η , and σ are positive integers or zero. The Laplace invert of such a term is

$$\left(\begin{matrix} \mu \\ \eta \\ \sigma \end{matrix} \right) / \pi^{1/2} t^{1/2}$$

where we use the special symbol

$$\left(\begin{matrix} \mu \\ \eta \\ \sigma \end{matrix} \right) = \Lambda^{\mu+\eta} (1 - \Lambda^2)^{\sigma/2} \exp \left\{ \frac{-1}{4t} [2\mu T_m^{1/2} + 2\eta T_e^{1/2} + \sigma T_s^{1/2}]^2 \right\} = \Lambda^{\mu+\eta} (1 - \Lambda^2)^{\sigma/2} \exp \left\{ \frac{-1}{t} \left[\frac{(\mu + \sigma/2)b}{D_m^{1/2}} + \frac{(\eta + \sigma/2)\alpha}{D_e^{1/2}} \right]^2 \right\} \quad [66]$$

In terms of this symbol, Eq. [65] may be inverted to

$$i = \frac{8AFp_w H_e D_e^{1/2}}{\pi^{1/2} t^{1/2}} \left[\frac{1}{2} - \binom{0}{1} + \binom{0}{2} + \binom{0}{2} + \binom{1}{0} - 2 \binom{0}{1} - \binom{0}{3} + \binom{0}{4} + \binom{2}{0} - 2 \binom{1}{2} + \dots \right] \quad [67]$$

At short times, the terms in expansion [67] converge very rapidly and in practice few will be needed. With the first four terms written out explicitly, the full solution is

$$i = \frac{4AFp_w H_e D_e^{1/2}}{\pi^{1/2} t^{1/2}} \left[1 - 2\Lambda \exp \left\{ \frac{-a^2}{D_e t} \right\} + 2(1 - \Lambda^2) \exp \left\{ \frac{-1}{t} \left(\frac{a}{D_e^{1/2}} + \frac{b}{D_m^{1/2}} \right)^2 \right\} + 2\Lambda^2 \exp \left\{ \frac{-4a^2}{D_e t} \right\} + \dots \right] \quad [68]$$

Comparison of this result with Eq. [53] shows some striking differences. Perhaps the most interesting is that the departure from cottrellian behavior may well be in the negative direction, whereas it is invariably positive for a Fowler cell.

As an example of the convergence of Eq. [68], let us consider the case when $T_e = 4T_m$. Then we find

$$i = \frac{(it^{1/2})_0}{t^{1/2}} \left[1 - 2\Lambda \exp \left(\frac{-4T_m}{t} \right) + 2(1 - \Lambda^2) \exp \left(\frac{-9T_m}{t} \right) + 2\Lambda(1 + \Lambda - \Lambda^2) \exp \left(\frac{-16T_m}{t} \right) - 2\Lambda(2 - \Lambda - 2\Lambda^2 + \Lambda^3) \exp \left(\frac{-25T_m}{t} \right) + \dots \right] \quad T_e = 4T_m \quad [69]$$

Figure 2 was derived, in part, from this equation, the points being based on only the first four terms. Evidently, even with so few terms, accuracy is maintained to better than 98% for times as long as $10 T_m$.

Returning to the general solution, note that Eq. [68] can be rewritten as

$$it^{1/2} = (it^{1/2})_0 \left[1 + 2 \left\{ \exp \left(\frac{-(T_e^{1/2} + T_m^{1/2})^2}{t} \right) - \Lambda \exp \left(\frac{-T_e}{t} \right) + \Lambda^2 \exp \left(\frac{-4T_e}{t} \right) - \Lambda^2 \exp \left(\frac{-(T_e^{1/2} + T_m^{1/2})^2}{t} \right) + \dots \right\} \right] \quad [70]$$

and that, when $T_e = T_m = T$, the explicit terms in Eq. [70] exactly match the Mancy Eq. [59] as far as the $j = 1$ terms.

Duration of Cottrellian Behavior

At short enough times, Eq. [68] may be well approximated by

$$it^{1/2} = (it^{1/2})_0 [1 - 2\Lambda \exp(-a^2/D_e t)] \quad [71]$$

which shows that $2\Lambda \exp(-a^2/D_e t)$ is the fractional departure from cottrellian behavior after polarization for a length of time t . It therefore follows that, if a fractional er-

ror not exceeding ϵ is permissible, then during the interval

$$0 < t < \frac{a^2}{D_e \ln(2\Lambda/\epsilon)} = \frac{T_e}{\ln(2\Lambda/\epsilon)} \quad [72]$$

the Cottrell equation is effectively obeyed. Thus, for example, if $\epsilon = 0.02$ (98% obedience is acceptable) then cottrellian behavior is observed up to $0.30 T_e$, for the Λ value given in Eq. [19].

The fact that the third term in expansion [68] is of opposite sign to, and will normally have a pre-exponential

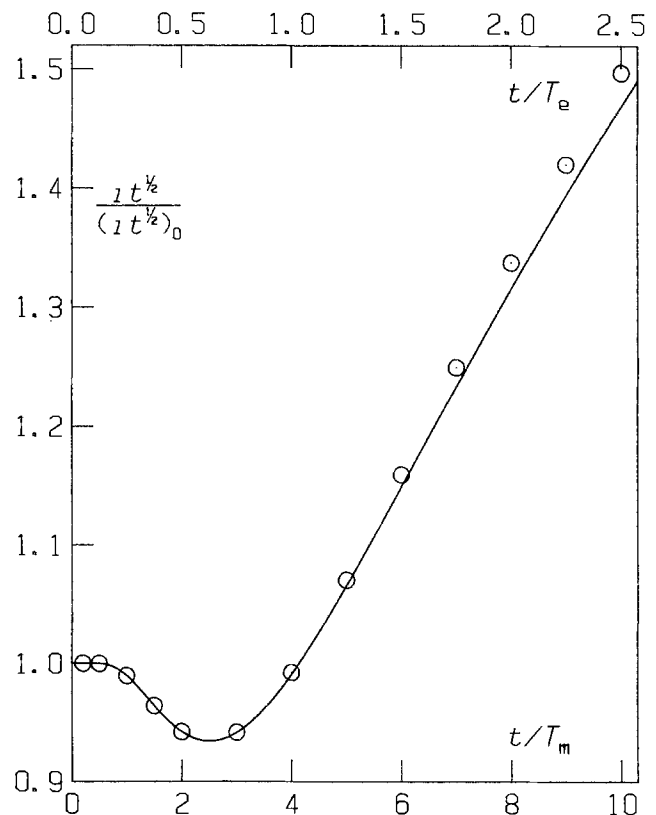


Fig. 2. Short-time response of a sensor for which $\Lambda = 0.29$ and $T_e = 4 T_m$. The line is exact, being based on Eq. [69] for $t < 2.5 T_m$ and on [86] for $t > 2.5 T_m$. The points are calculated from Eq. [69] retaining only terms up to $2\Lambda(1 + \Lambda - \Lambda^2) \exp(-16T_m/t)$.

coefficient of greater magnitude than, the second term, offers the possibility of utilizing the competition between these terms to prolong effective cottrellian behavior. This is brought out in Fig. 3 which shows a graph of $i t^{1/2}$ vs. t for four values of the T_m/T_e ratio. Note that with the judicious choice $T_m/T_e = 0.087$ cottrellian behavior (to within $\pm 2\%$) is prolonged until about $t = 0.67T_e$.

The results of the last paragraph can be generalized as follows. Cottrellian behavior to within a fractional error of $\pm \epsilon$ is observed over the time interval $0 \leq t \leq T_c$, where

$$\frac{2\Lambda(T_s - T_e)}{T_s} \left[\frac{(1 - \Lambda^2)T_s}{\Lambda T_e} \right]^{-T_e/(T_s - T_e)} = \epsilon \quad [73]$$

and T_c satisfies the equation

$$(1 - \Lambda^2) \exp\left(\frac{-T_s}{T_c}\right) - \Lambda \exp\left(\frac{-T_e}{T_c}\right) = \frac{\epsilon}{2} \quad [74]$$

General Solution: Second Inversion

Though Eq. [67] is valid at all times, its utility is greater for smaller values of t , for then few terms are needed. In this section, we will derive the complementary expression: one that is of greater utility for longer times.

The transform Eq. [41] can be written $i = U(s)/L(s)$ where $U(s)$ and $L(s)$ are the following functions of the dummy variable

$$U(s) = 4AFp_w H_e D_e^{1/2} [\cosh(sT_s)^{1/2} - \Lambda \cosh(sT_d)^{1/2}] \quad [75]$$

and

$$L(s) = s^{1/2} [\sinh(sT_s)^{1/2} - \Lambda \sinh(sT_d)^{1/2}] \quad [76]$$

Both these functions are analytic functions of s [i.e., each can be written in the form $k_0 + k_1s + k_2s^2 + \dots$ where the k 's are independent of s] and $L(s)$ is of higher order than $U(s)$ [in the sense that the ratio $U(s)/L(s) \rightarrow 0$ as $s \rightarrow \infty$]. Heaviside's expansion theorem (12) permits the inversion of such a ratio to

$$i = \sum_j U(s_j) \exp(s_j t) / \frac{dL}{ds}(s_j) \quad [77]$$

where each s_j is a root of the equation $L(s) = 0$, that is

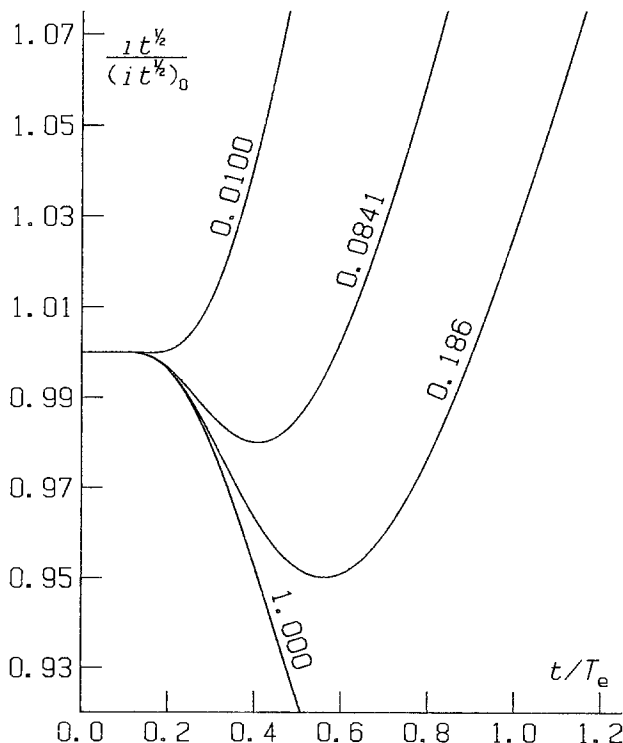


Fig. 3. Departures from cottrellian behavior for a sensor for which $\Lambda = 0.29$ and the T_m/T_e ratio has the values associated with each of the four curves.

$$s^{1/2} [\sinh(sT_s)^{1/2} - \Lambda \sinh(sT_d)^{1/2}] = 0$$

$$s = s_0, s_1, s_2, \dots \quad [78]$$

Differentiation of Eq. [76] shows that

$$\frac{dL}{ds} = \frac{L(s)}{2s} + \frac{T_s^{1/2}}{2} \cosh(sT_s)^{1/2} - \frac{\Lambda T_d^{1/2}}{2} \cosh(sT_d)^{1/2} \quad [79]$$

and therefore

$$i = 8AFp_w H_e D_e^{1/2} \sum_{j=0,1}^{\infty} \frac{[\cosh(s_j T_s)^{1/2} - \Lambda \cosh(s_j T_d)^{1/2}] \exp(s_j t)}{\frac{L(s_j)}{s_j} + T_s^{1/2} \cosh(s_j T_s)^{1/2} - \Lambda T_d^{1/2} \cosh(s_j T_d)^{1/2}} \quad [80]$$

It remains to determine the roots s_j .

One root of Eq. [78], say s_0 , is clearly zero. The others turn out to be negative; so let us replace s_j by $-\tau_j^2$ where τ_j is restricted to be positive. Using the identity $\sinh(-z^2)^{1/2} = (-z^2)^{1/2} \sin z$ then reduces Eq. [78] to

$$\sin(\tau T_s^{1/2}) = \Lambda \sin(\tau T_d^{1/2}) \quad \tau = \tau_1, \tau_2, \tau_3, \dots \quad [81]$$

or equivalently

$$\tan\left(\frac{\tau b}{D_m^{1/2}}\right) = \frac{1 - \Lambda}{1 + \Lambda} \tan\left(\frac{\tau a}{D_e^{1/2}}\right) \quad \tau = \tau_1, \tau_2, \tau_3, \dots \quad [82]$$

where τ is the continuum along which the values τ_j are located. Figure 4 clarifies the first of these relationships.

If the s_0 root is detached from the summation in Eq. [80], this equation may be rearranged, with the help of Eq. [45], to

$$i = i_\infty \left[1 + \frac{2(T_s^{1/2} - \Lambda T_d^{1/2})}{1 - \Lambda} \sum_{j=1}^{\infty} \frac{[\cos(\tau_j T_s^{1/2}) - \Lambda \cos(\tau_j T_d^{1/2})] \exp(-\tau_j^2 t)}{T_s^{1/2} \cos(\tau_j T_s^{1/2}) - \Lambda T_d^{1/2} \cos(\tau_j T_d^{1/2})} \right] \quad [83]$$

Use of Eq. [81] to replace Λ from within the summation leads to the simpler

$$i = i_\infty + 2i_\infty \left[\frac{a D_m^{1/2}}{b D_e^{1/2}} + \frac{1 + \Lambda}{1 - \Lambda} \right] \sum_{j=1}^{\infty} \frac{\exp(-\tau_j^2 t)}{a D_m^{1/2} / (b D_e^{1/2}) - \sin(2\tau_j a / D_e^{1/2}) \csc(2\tau_j b / D_m^{1/2})} \quad [84]$$

after considerable algebra.

In general, numerical methods will be needed to solve Eq. [81] and so find values for τ_1, τ_2 , etc. However, analytic solutions may be possible when the T_s/T_d ratio is an integer. For example, when this ratio is 9, [i.e., when $T_e = 4T_m$ or $a^2 D_m = 4b^2 D_e$], Eq. [82] can be solved to

$$\tau_j = \left[(j-1)\pi - (-)^j \arctan\left(\frac{3 - \Lambda}{1 + \Lambda}\right)^{1/2} \right] D_m^{1/2} / b \quad j = 1, 2, 3, \dots \quad [85]$$

and Eq. [84] then gives

$$i = i_\infty \left[1 + \frac{2}{1 - \Lambda} \sum_{j=1}^{\infty} \exp\left\{ \frac{-t D_m}{b} \left((j-1)\pi - (-)^j \arcsin\left(\frac{3 - \Lambda}{2}\right)^{1/2} \right)^2 \right\} \right] \quad T_e = 4T_m \quad [86]$$

Figure 5 is a test of Eq. [86], the points being calculated using terms to $j = 2$. It shows that, apart from minor discrepancies at short times, this number of terms is perfectly adequate. The full line in Fig. 5 was constructed for

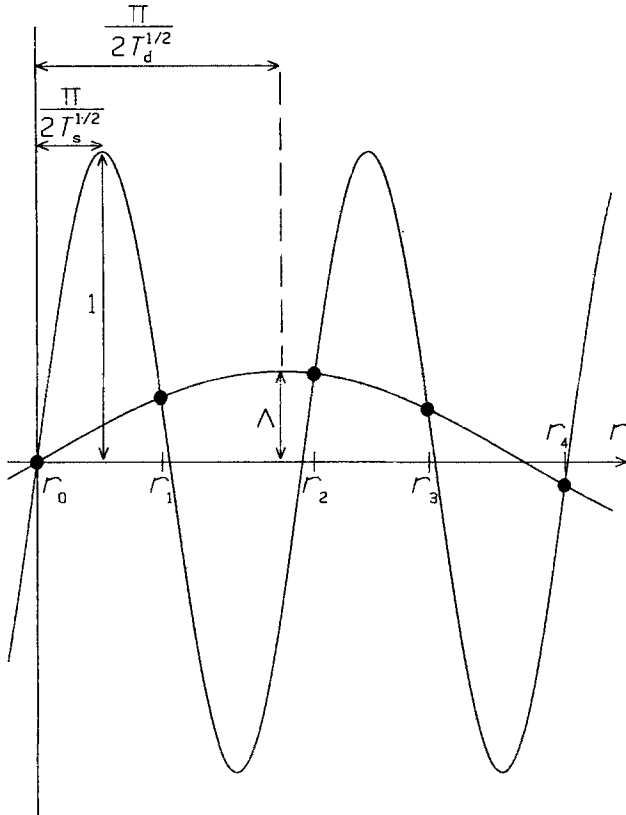


Fig. 4. Graphs vs. r of the two functions $\sin(rT_s^{1/2})$ and $\Lambda \sin(rT_d^{1/2})$. The values r_0, r_1, r_2, \dots lie at the points of intersection of the two sinusoidal curves.

$t \leq 2.5T_m$ from Eq. [69] and for $t \geq 2.5T_m$ from Eq. [86]. The perfect concordance of the two segments is evidence

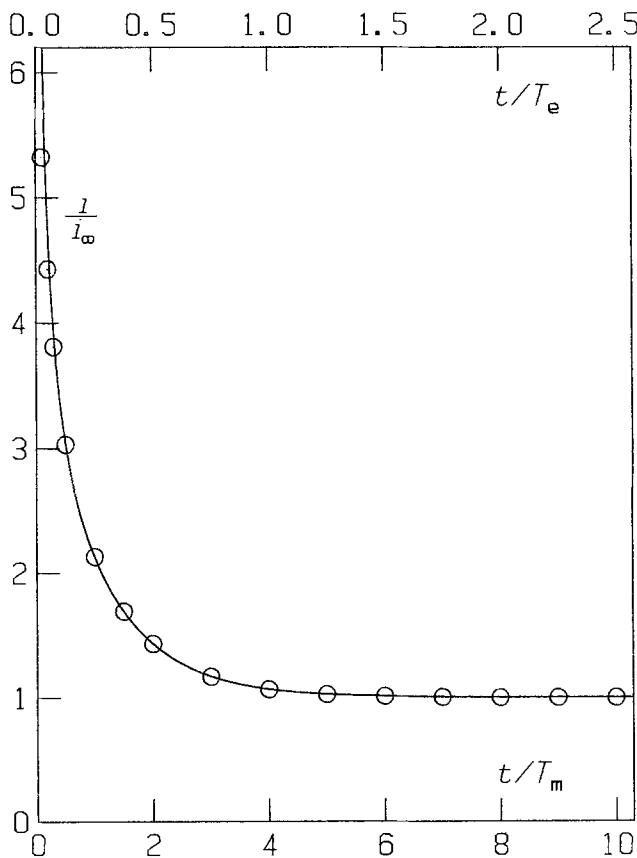


Fig. 5. The approach to a steady state for a membrane-covered oxygen sensor for which $\Lambda = 0.29$ and $T_e = 4T_m$. This line is exact, being based on Eq. [69] for $t < 2.5T_m$ and on Eq. [86] for $t > 2.5T_m$. The points are from Eq. [86] truncated after $j = 2$.

that both equations are correct and speaks to the validity of the general results, Eq. [70] and [84].

Another check is provided by inserting the Mancy condition $T_e = T_m = T$. This renders Eq. [84] indeterminate, but the equivalent relationship Eq. [83] can be shown to reduce, under these conditions, to Eq. [60].

If we return to the general case in which there is no simple relation between T_e and T_m , we are forced to determine r_1, r_2, \dots by iterative methods. From Fig. 4, which illustrates Eq. [81], it is apparent that $j\pi/T_s^{1/2}$ provides an approximate value for r_j . The algorithm shown in Fig. 6 can then be used to determine the value of a root, usually r_j .

Duration of the Transient Phase

As $t \rightarrow \infty$, the summed terms in Eq. [83] approach zero as $i \rightarrow i_\infty$. For sufficiently large t , only the first term in the summation is important and Eq. [82] reduces to

$$\frac{i}{i_\infty} = 1 + 2 \frac{(T_s^{1/2} - \Lambda T_d^{1/2}) [\cos(r_1 T_s^{1/2}) - \Lambda \cos(r_1 T_d^{1/2})]}{(1 - \Lambda)[T_s^{1/2} \cos(r_1 T_s^{1/2}) - \Lambda T_d^{1/2} \cos(r_1 T_d^{1/2})]} \exp(-r_1^2 t) \tag{87}$$

Within a fractional error of ϵ , this equation shows that i has reached i_∞ after an interval T_t given by

$$T_t = \frac{1}{r_1^2} \ln \frac{2[1 - (\Lambda T_d^{1/2}/T_s^{1/2})] [\cos(r_1 T_s^{1/2}) - \Lambda \cos(r_1 T_d^{1/2})]}{\epsilon[1 - \Lambda] [\cos(r_1 T_s^{1/2}) - (\Lambda T_d^{1/2}/T_s^{1/2}) \cos(r_1 T_d^{1/2})]} \tag{88}$$

$$T_t = \frac{1}{r_1^2} \left[\ln \left(\frac{aD_m^{1/2}}{bD_e^{1/2}} + \frac{1 + \Lambda}{1 - \Lambda} \right) - \ln \left(\frac{aD_m^{1/2}}{bD_e^{1/2}} - \frac{\sin(2r_1 a/D_e^{1/2})}{\sin(2r_1 b/D_m^{1/2})} \right) + \ln \left(\frac{2}{\epsilon} \right) \right] \tag{89}$$

Detailed calculations show that, under conditions of practical importance, Eq. [88] or [89] is more than adequate to predict the duration of the transient phase.

Application to Practical Sensors

As we stated in the "Solubility and Transport Properties" section, the most commonly adopted membrane for oxygen sensors is polytetrafluoroethene, and the most common membrane thickness is 0.001 in. or 2.54×10^{-5} m. Hence, using the diffusion coefficient data of Hitchman, Eq. [12], one calculates that the characteristic time for the membrane has a square root given by

$$T_m^{1/2} = \frac{b}{D_e^{1/2}} = 7.52s^{1/2} \tag{90}$$

As reported previously, the values of $\Lambda = 0.29$ and $D_e^{1/2} = 45.8 \mu\text{m s}^{-1/2}$ are appropriate for the most frequently used filling solutions, aqueous solutions of close to decimolar concentration.

Few analysts would claim a precision for membrane-covered oxygen sensors in excess of 2%. Hence, we can use $\epsilon = 0.02$ as a conservative estimate for the fractional error that can be tolerated in a sensor measurement.

With these values of T_m, D_e, Λ , and ϵ prescribed, a is the only adjustable parameter. We are thus in a position to determine, for any arbitrary value of the electrolyte thickness a , how long cottrellian behavior will last and how soon the steady state will be achieved. The results of calculations, using Eq. [68] and [89], are presented in Fig. 7. This diagram shows, for example, that a cell with an electrolyte thickness of 0.5 mm will obey the Cottrell equation

$$\frac{it^{1/2}}{Ap_w} \approx \frac{4FH_e D_e^{1/2}}{\pi^{1/2}} = 12.8 \text{ A s}^{1/2} \text{ m}^{-2} \text{ atm}^{-1} \tag{91}$$

$$t \leq 70s, a = 0.5 \text{ mm}$$

Fig. 6. Illustration of the iterative procedure used to solve Eq. [81].

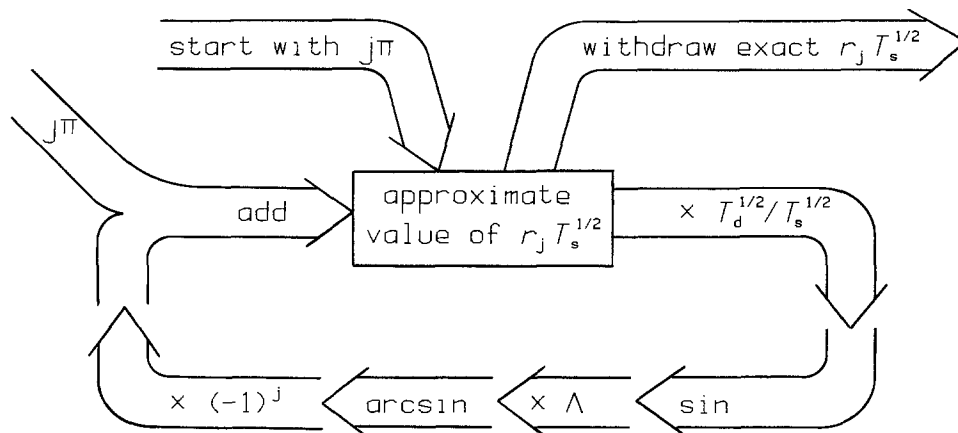
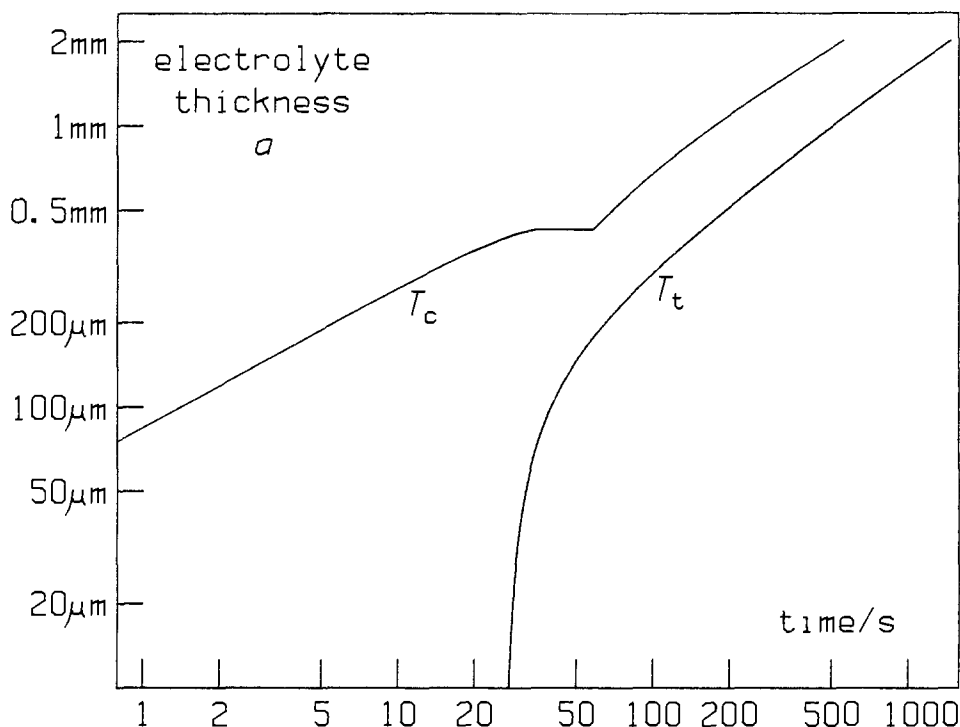


Fig. 7. The durations of cottrellian and transient behaviors for membrane-covered oxygen sensors of usual design, as a function of electrolyte thickness. When conditions fall in the top left-hand corner of this diagram, the Cottrell equation is obeyed to within 2%. In the bottom right-hand corner, the departure from a steady state is less than 2%.



for 70s. There will then be a transitional interval, until about 3 min after switch-on, before the cell assumes its steady state. In this steady state, the current has the constant value

$$\frac{i}{Ap_w} \approx \frac{4F}{\frac{a}{D_e H_e} + \frac{b}{D_m H_m}} = 0.92 \text{ A m}^{-2} \text{ atm}^{-1} \quad t \geq 190\text{s}, a = 0.5 \text{ mm} \quad [92]$$

Note that the cottrellian constant Eq. [91], is independent of the electrolyte thickness a , though the duration of obedience to the Cottrell equation is strongly dependent on a . On the other hand, the steady-state constant Eq. [92] does depend on a , unless a is less than $12 \mu\text{m}$, whereupon (to within our 2% precision specification) the steady-state constant becomes

$$\frac{i}{Ap_w} \approx \frac{4FD_m H_m}{b} = 1.66 \text{ A m}^{-2} \text{ atm}^{-1} \quad t \geq 27\text{s}, a \leq 12 \mu\text{m} \quad [93]$$

and independent of the electrolyte thickness.

The discontinuity in the T_c curve of Fig. 7 reflects the feature noted in the "Cottrellian Behavior" section: the competition between the signs of the second and third terms in the expansion of $it^{1/2}$. It shows that a decided advantage may be reaped, for a cottrellian-based sensor, in making the electrolyte thickness larger than about $400 \mu\text{m}$.

Acknowledgment

The authors thank Lisle-Matrix Limited of Toronto for financial support. This work formed part of a project aimed at upgrading the performance of oxygen sensors and was carried out in cooperation with Lisle-Matrix Limited and the National Water Research Institute, Canada Center for Inland Waters.

Manuscript submitted Oct. 14, 1983; revised manuscript received Jan. 12, 1984.

REFERENCES

1. L. C. Clark, U.S. Pat. 2,913,386 (1959).
2. M. L. Hitchman, "Measurement of Dissolved Oxygen," Wiley-Interscience, New York (1978).
3. J. M. Hale and M. L. Hitchman, *J. Electroanal. Chem.*, **107**, 281 (1980).
4. K. H. Mancy, D. A. Okun, and C. N. Reilley, *ibid.*, **4**, 65 (1962).
5. J. K. Fowler and K. B. Oldham, in "Chemistry and Physics of Aqueous Gas Solutions," W. A. Adams, G. Greer, J. E. Desnoyers, G. Atkinson, G. S. Kell, K. B. Oldham, and J. Walkley, Editors, p. 290, The Electrochemical Society Softbound Proceedings Series, Princeton, NJ (1975).
6. J. C. Myland, Unpublished (1981).
7. M. Yasuda and W. Stone, *J. Polymer Sci.*, **4**, 1314 (1966).
8. G. E. Spangler, Report 2083, U.S. Army Mobility Equipment R&D Center, Fort Belvoir, VA (1973).
9. G. M. Murphy, "Ordinary Differential Equations and

- Their Solutions," van Nostrand, Princeton, NJ (1960).
 10. D. D. Macdonald, "Transient Techniques in Electrochemistry," Plenum Press, New York (1977).
 11. G. E. Roberts and H. Kaufman, "Table of Laplace

- Transforms," Saunders, Philadelphia and London (1966).
 12. R. V. Churchill, "Operational Mathematics," McGraw-Hill, New York (1972).

Thermodynamics of Lithium Intercalation from High Resolution Electrochemical Measurements

J. R. Dahn and W. R. McKinnon

National Research Council of Canada, Division of Solid State Chemistry, Ottawa, Ontario, Canada K1A 0R9

ABSTRACT

We discuss the importance of high resolution measurements of dx/dV , the inverse derivative of the voltage (V) vs. intercalant concentration (x) relation for intercalation-based electrochemical cells. The results of experiments on $\text{Li}/2\text{H-Li}_x\text{TaS}_2$ cells demonstrate the use of high resolution measurements of dx/dV to determine a partial phase diagram for the lithium order-disorder transition near $x = 2/3$. We stress the reproducibility of our results, which were obtained using derivative constant current chronopotentiometry.

The voltage of a lithium intercalation battery varies with its state of discharge. Early experimental studies of this variation (1) were often made to determine the suitability of a particular intercalation compound as a cathode in a reversible lithium battery. These studies were intended to show the overall variation of the cell voltage (V) with intercalant composition (x). Subsequently, more careful experiments have shown fine structure in $V(x)$ for many intercalation systems (2-8). This structure, seen clearly in plots of dx/dV vs. x or V , can be caused by a variety of physical mechanisms, such as the interactions between intercalated atoms within the host or intercalation-induced structural phase transitions in the host. Therefore, careful measurements of dx/dV can be used to study the physics and chemistry of the intercalation process. Attempts have been made to explain theoretically (9-13) the features in dx/dV , especially for Li_xTiS_2 . To be convincing, any such calculation must reproduce the fine structure in dx/dV . The overall variation of $V(x)$ can often be approximated by very simple mean-field solutions to lattice gas models (9); however, these simple solutions often give results for dx/dV much different from experiment. The theories should also be able to predict other thermodynamic quantities, for example $(\partial V/\partial T)_x$, the change in cell voltage with temperature at constant intercalant concentration (14, 15).

To test the theories at a quantitative level, high resolution measurements of $V(x)$ and $-dx/dV$ of intercalation batteries are needed. In this paper, we present high resolution electrochemical measurements on $2\text{H-Li}_x\text{TaS}_2$ [the 2H and 1T polytypes of TaS_2 are described in Ref. (1)], which allow a detailed comparison between experiment and theory. Our results illustrate the wealth of information contained in dx/dV , as well as the resolution required in the measurements. Our data were obtained using derivative constant current chronopotentiometry, in which the cell voltage is measured as a function of time at constant charge or discharge current and then differentiated numerically. We present results obtained with different cells, to show the reproducibility of the method, and at different currents to illustrate the reversibility of the intercalation process and the effects of kinetics on our measurements. We also present a partial phase diagram of the order-disorder transition in $2\text{H-Li}_x\text{TaS}_2$ (16), which is in good agreement with theoretical calculations.

Basic Considerations

Many of the transition metal dichalcogenides (MX_2) can be intercalated electrochemically with alkali metals (A) to

Key words: battery, electrode, phase transformation.

form intercalation compounds A_xMX_2 (1). An electrochemical cell based on intercalation is constructed in the following general way

A/Organic electrolyte containing A^+ ions/ A_xMX_2

The voltage, V , of such a cell varies with x in A_xMX_2 except when the intercalation electrode exists as a mixture of two phases (17). In a two-phase region V is constant and $-dx/dV$ is infinite. Two phase mixtures for large coexistence ranges are easily seen in $V(x)$ (18, 19), but to observe smaller coexistence ranges it may be necessary to look at $(\partial x/\partial V)_T$. Continuous or higher order phase transitions, where derivatives of the Gibb's free energy exhibit singularities (20), should also be observable in $(\partial x/\partial V)_T$. Theoretical predictions of $-dx/dV$ at an intercalant order-disorder transition which is continuous, show a sharp peak at the voltage and composition of the transition (9, 12). Even when there are no phase transitions, measurements of $-dx/dV$ serve to characterize the intercalation system more precisely than $V(x)$. This suggestion was advanced by Balewski and Brenet (22) for electrochemical cells in general.

Measurements of $(-dx/dV)_T$ have been used to study phase transitions in Li_xVS_2 (5), Na_xTiS_2 (7), $1\text{T-Li}_x\text{TaS}_2$ (4), and Li_xNbSe_2 (6). These measurements have been made using linear sweep voltammetry (5, 7), electrochemical potential spectroscopy (4), and a constant current method (6) similar to the one we will describe below. Discussions of the interpretation of $-dx/dV$ from linear sweep voltammetry data can be found in Ref. (5) and (8). Experimental details of electrochemical potential spectroscopy are given in Ref. (3) and (23).

When a cell based on intercalation is charged or discharged at constant current, the rate of change of cell voltage with time is

$$\frac{dV}{dt} = \frac{dV}{dQ} \frac{dQ}{dt} = \frac{I}{Q_0} \frac{dV}{dx} \quad [1]$$

In Eq. [1], V is the cell voltage, I the constant current, Q_0 the charge corresponding to a change, $\Delta x = 1$, in the intercalation electrode, and t the time. By monitoring the cell voltage as a function of time, one can obtain dx/dV since

$$dx/dV = \frac{I}{Q_0} \frac{dt}{dV} \quad [2]$$

To measure dx/dV with high resolution in V and x , we monitor the voltage of the cell as a function of time with a computer-controlled voltmeter. In the standard terminology, this method of measuring dx/dV is called derivative

constant current chronopotentiometry. Equations [1] and [2] assume that the integral of the current can be directly related to the stoichiometric changes occurring within the intercalation electrode. The validity of this assumption has been best demonstrated in the case of Li_xTiS_2 where *in situ* x-ray diffraction studies (24) (using electrochemical cells with x-ray windows) have monitored the changes in crystal lattice parameters as a function of transferred charge. The lattice parameter data obtained in this way agree to within experimental error with the data obtained from chemically prepared samples (25). Equations [1] and [2] are exact only in the absence of internal impedances and overvoltages of all kinds, and are only approximate at nonzero current. For reversible electrode materials, the effect of the deviation from equilibrium can be determined from the difference between dx/dV measured on charge and discharge (8, 23). For example, an internal resistance, R , will cause a deviation of $\pm IR$ in the measured voltages from the equilibrium voltages on charge and discharge. The solid-state diffusion of the intercalant within the cathode particles in a constant current experiment also produces an overvoltage that is proportional to the magnitude of the applied current (17, 26). By examining dx/dV measured at different currents, one can usually determine the effects of the finite rate and obtain the equilibrium dx/dV . Similar studies as a function of voltage sweep rate using linear sweep voltammetry to obtain the equilibrium dx/dV for $\text{Li}/\text{Li}_x\text{Ti}_{1.05}\text{S}_2$ cells have been made (8).

Experimental Methods

2H-TaS₂ was prepared by reacting stoichiometric mixtures at Ta and S powders at 900°C for 48h, followed by cooling to room temperature at 100°C per day to ensure production of the 2H polytype. The resulting crystallites were hexagonal with $a = 3.315\text{\AA}$ and $c = 12.077\text{\AA}$, in good agreement with published values (27). X-ray diffraction profiles showed no evidence of other polytypes of TaS₂, although our material showed a high density of stacking faults like that prepared elsewhere (28).

Intercalation cathodes were prepared by spreading a slurry of 2H-TaS₂ and propylene glycol in a thin layer (=

10 mg/cm²) on a 2.5 × 2.5 cm nickel substrate, which was then baked under flowing argon until dry. Cathodes were then flattened between a set of rollers, which promotes good mechanical adhesion of the powder to the nickel substrate and results in cathode utilizations near 100%. The cathode mass was determined to ±0.1 mg. Cells with two electrodes were constructed using these cathodes and lithium metal foil, as described elsewhere (6).

The computer-controlled system used to perform constant current chronopotentiometry is based on a HP85 microcomputer, which controls a HP3478A voltmeter switched alternately between up to 20 cells by an HP3495A scanner. The computer monitors the voltage of each cell once every 100s. During each monitoring period, the cell voltage and the time are measured N times ($N = 5$ typically) and averaged to produce an average voltage, \bar{V} , and average time \bar{T} . \bar{V} is then compared to the last stored voltage, V_n , for the same cell. If $|\bar{V} - V_n| > \Delta V$ ($\Delta V = 2.5$ mV typically), \bar{V} and \bar{T} are stored as V_{n+1} and T_{n+1} ; otherwise, \bar{V} and \bar{T} are ignored. ΔV sets the resolution of the measurement and helps to limit the number of data points collected. Increasing N can sometimes help to reduce the noise in data taken with $\Delta V < 1$ mV. Constant current battery cyclers with presettable high and low voltage trip points are used to provide the currents. The current is stable to one part in 10⁴ for currents greater than 100 μA and to ±30 nA for currents less than 100 μA . Cells under test are placed in temperature-controlled environments with a stability of ±0.01 K. Experiments on intercalation electrodes usually involve cycle times ranging from 5 to 1000h; hence, examining each cell every 100s is sufficient. The scheme allows for the testing of many cells at relatively low cost.

Results and Discussion

Figure 1 shows $V(x)$ and $-dx/dV$ vs. x for $\text{Li}/1\text{M LiAsF}_6$, PC/2H-Li_xTaS₂ cell JD-19 above 1.60V. These data were measured for the second charge and third discharge of the cell at a 100h rate. (We specify the rate of charge or discharge by the time required to change the composition x by $\Delta x = 1$, based on the current and the cathode mass. For this particular cell, the cathode mass was 42.9 mg, so a 100h rate corresponds to 47.2 μA .) As there are about 300 individual data points measured for charge and discharge ($\Delta V = 2.5$ mV), we have not plotted the individual points but have joined them with a continuous curve. The value of x does not return to $x = 0$ at 2.80V, indicating that some lithium remains in the host at these rates of deintercalation. This is a real effect, as has been confirmed by *in situ* x-ray diffraction results using the techniques described in Ref. (24), and is not an artifact caused by impurities in the cell reacting with lithium on the first discharge. The *in situ* x-ray experiments at an 800h rate of charge show $x = 0.04$ at 2.80V. Except in the region of slow kinetics near $x = 0$, the data on charging and discharging in Fig. 1 are nearly identical, indicating near-equilibrium conditions for $x > 0.3$.

The first discharge of this cell (JD-19) was made at a 1h rate to a voltage cutoff of 1.6V resulting in a transfer of $\Delta x = 0.71$. Then the cell was allowed to stand at open circuit for about 0.5h while the voltage recovered to near 2.0V. The cell was given a further discharge at a 25h rate to a cutoff of 1.60V, with the total charge transfer for the two discharges corresponding to $\Delta x = 0.920$. The cell was cycled once at a 25h rate (the first charge is shown in Fig. 2) and then the data of Fig. 1 were collected. The data in Fig. 1 have not been adjusted in any way; in particular, the values of x represent those inferred from the charge transfer and the cathode mass. The rapid initial discharge was made to avoid solvent intercalation, which can occur on the first discharge of $\text{Li}/2\text{H-Li}_x\text{TaS}_2$ cells using propylene carbonate (PC), when the intercalation rate is slow. Similar effects have been observed in $\text{Li}/\text{Li}_x\text{TiS}_2$ cells (8, 24, 29) with PC. PC cointercalation, which increases the distance between adjacent host layers from ≈6 to ≈18 \AA , is probably kinetically slower than lithium

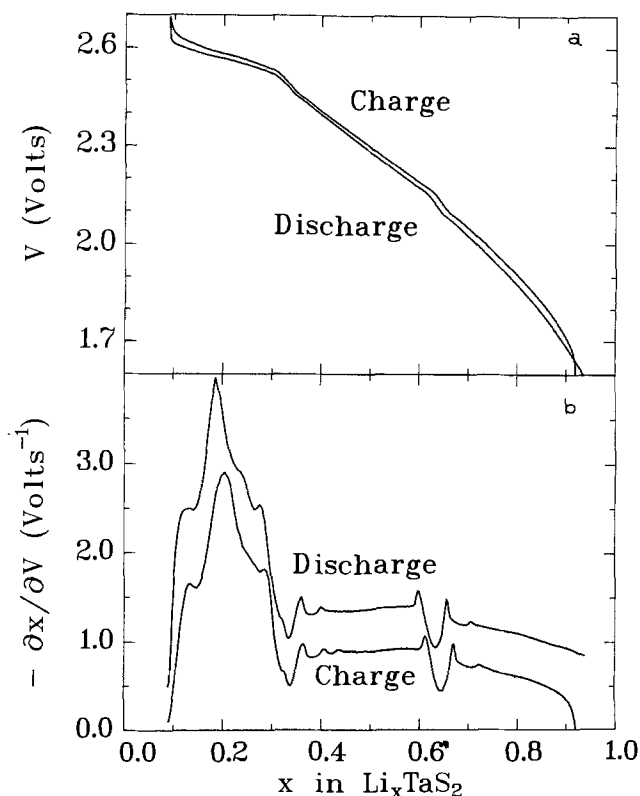


Fig. 1. (a) Cell voltage $V(x)$ and (b) inverse derivative dx/dV for the second charge and third discharge of $\text{Li}/2\text{H-Li}_x\text{TaS}_2$ cell JD-19. The discharge curve in (b) has been offset by 0.5 V^{-1} for clarity.

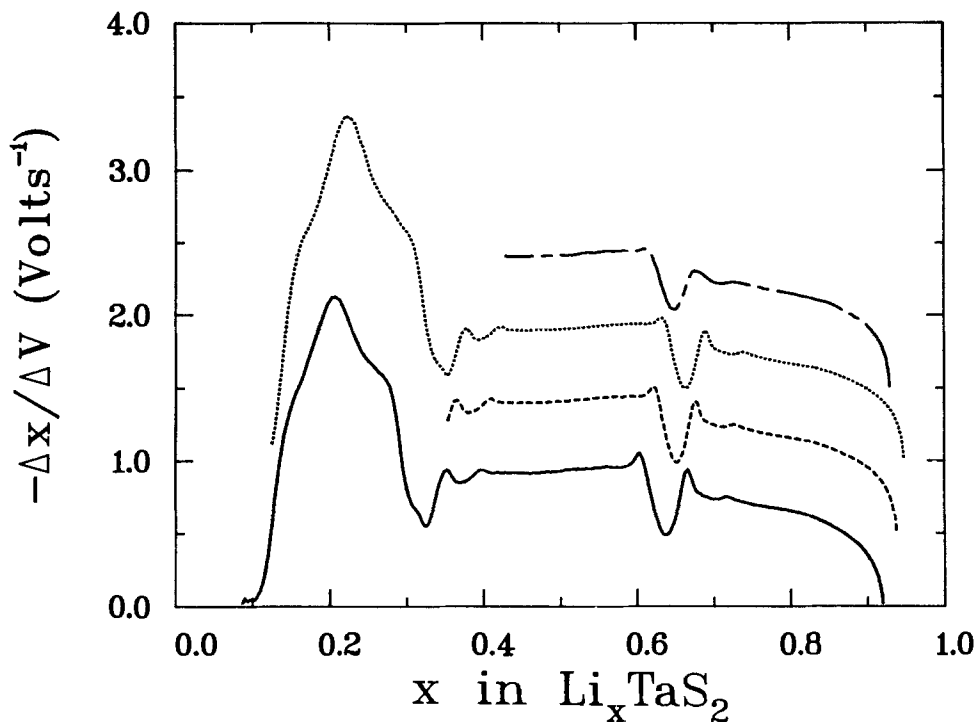


Fig. 2. $-\partial x/\partial V$ vs. x for the first charge (c1) of Li/2H-Li_xTaS₂ cells JD-17, JD-19, and JD-21 and the second charge (c2) of cell JD-17. The data has been offset successively by 0.5 V⁻¹ for clarity. —: JD-19 (c1), - - -: JD-17 (c1), . . . : JD-17 (c2), — — —: JD-21 (c1).

intercalation. By discharging rapidly, the interlayer sites are filled with lithium first, and electrolyte cointercalation is inhibited because lithium increases the bonding between adjacent layers. This prevents the large lattice expansion needed to accommodate the PC molecules. *In situ* x-ray examinations of the cathodes of cells initially discharged at 1h rates show no evidence for solvent cointercalation. In addition, if all the lithium is not removed on subsequent cycling, very little cointercalation occurs. A more detailed discussion of solvent cointercalation will appear elsewhere.

Basu *et al.* (30) measured the voltage of Li/2H-Li_xTaS₂ cells at ten values of x ($x = 0.0, 0.1, 0.2, \dots, 0.9$) and hence did not observe the structure evident in our $V(x)$ and $-\partial x/\partial V$ data. Thompson (4) studied lithium intercalation in 2H-TaS₂ and also found that $x \approx 0.92$ in Li/Li_xTaS₂ cells with a voltage of 1.600V. Thompson's $-\partial x/\partial V$ data were measured with a resolution of 20 mV and showed a single large peak for $0 < x < 1/3$, which is resolved into several peaks in our higher resolution data. Thompson's data also showed structure for $x > 1/3$ which he suggested might be due to ordering effects (4). However, no effort was made to analyze the data or to demonstrate the reproducibility of the results.

In the small x region in Fig. 1b where $-\partial x/\partial V$ is large, the crystal lattice expands rapidly with x (1), which is known to lead to peaks in $-\partial x/\partial V$ (10, 11). The behavior at low x may be associated with staging as in Li_xNbSe₂ (6) and Na_xTiS₂ (7). Also evident in Fig. 1b are minima in $-\partial x/\partial V$ near $x = 1/3$ and $x = 2/3$ with peaks on either side. Such features have been predicted (9, 12, 16, 21) to occur near an order-disorder transition involving the intercalated lithium. The peaks correspond to the phase transitions between the ordered and disordered states as x varies, and the minima occur at the compositions of the ordered structures. The values $x = 1/3$ and $x = 2/3$ suggest that the ordered state is a preferred occupation by lithium

Table I. Measured position of the minimum in $-\partial x/\partial V$ near $x = 2/3$ for several Li/2H-Li_xTaS₂ cells made in the same way

Cell	Cycle	Minimum position
JD-17	Charge 1	$x = 0.654$
JD-17	Charge 2	$x = 0.670$
JD-19	Charge 1	$x = 0.637$
JD-21	Charge 1	$x = 0.652$
RM-22	Discharge 2	$x = 0.676$

of one or two of the three interpenetrating $\sqrt{3}a \times \sqrt{3}a$ triangular superlattices of octahedral sites in the van der Waals gap. In what follows, we will concentrate on the feature near $x = 2/3$. The features at $x = 1/3$ exhibit similar behavior, but are distorted by the large peaks near $x = 0.2$.

In Fig. 2 we show $-\partial x/\partial V$ vs. x for cells JD-19, JD-17, and JD-21 to demonstrate the reproducibility of the minima in $-\partial x/\partial V$ near $x = 1/3$ and $x = 2/3$. These data were collected in a manner similar to the data in Fig. 1 except at a 25h rate. The data shown were obtained from the first charge of all three cells and the second charge of JD-17. Each of these cells reached $x = 0.93 \pm 0.01$ at 1.6V. In Table I, the position of the minimum near $x = 2/3$ is tabulated for several cells made in the same way. In Fig. 3, we show $-\partial x/\partial V$ measured from the second and third charge of cell JD-17 at a 25h rate plotted as a function of voltage to demonstrate the reproducibility of the results on different charge-discharge cycles for the same cell.

Figure 4 shows $-\partial x/\partial V$ vs. V measured from a 100h rate charge and discharge of cell RM-21 between 2.00 and 2.30V limits. Small differences in the charge and discharge data are due to the resistive and diffusive overvoltages caused by the constant current (the shift, 5 mV, is

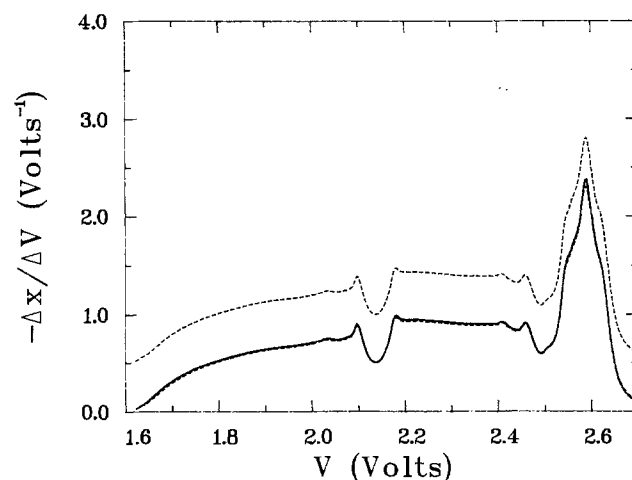


Fig. 3. $-\partial x/\partial V$ vs. V for the second (solid curve) and third (dashed curve) charge of Li/2H-Li_xTaS₂ cell JD-17. The third charge has been plotted twice, once shifted by 0.5 V⁻¹ for clarity.

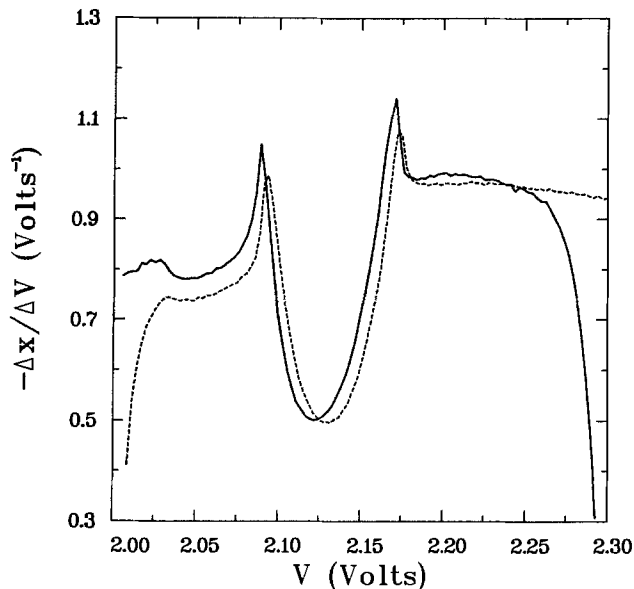


Fig. 4. $-\partial x/\partial V$ vs. V measured on discharge (solid) and charge (dashed) for Li/2H- Li_xTaS_2 cell RM-21 between 2.00 and 2.30V.

consistent with a resistance of 100 Ω). It takes several hours after the change in current direction to establish the steady-state diffusion overpotential (17, 26). This is why $-\text{d}x/\text{d}V$ appears smaller when measured on discharge near the 2.30V trip point than when measured on charge and conversely near 2.00V. These data demonstrate how cycles over a limited range of V and x can be used to study a particular feature in $-\text{d}x/\text{d}V$, provided the voltage trip points are set far enough from the feature. The sharp peaks in Fig. 4 have a width of about 10 mV and therefore were not observed clearly in Thompson's measurements (4) with 20 mV resolution.

Figure 5 compares the individual data points of Fig. 4 between 2.13 and 2.20V with $-\text{d}x/\text{d}V$ measurements on the same cell at 200 and 400h rates to show the effects of changes in intercalation rate on one of the peaks in $-\text{d}x/\text{d}V$ due to the order-disorder transition. As the current is lowered the IR losses and diffusion overvoltages decrease, and the peak becomes sharper. A cycle at an 870h rate was indistinguishable from the 400h rate data,

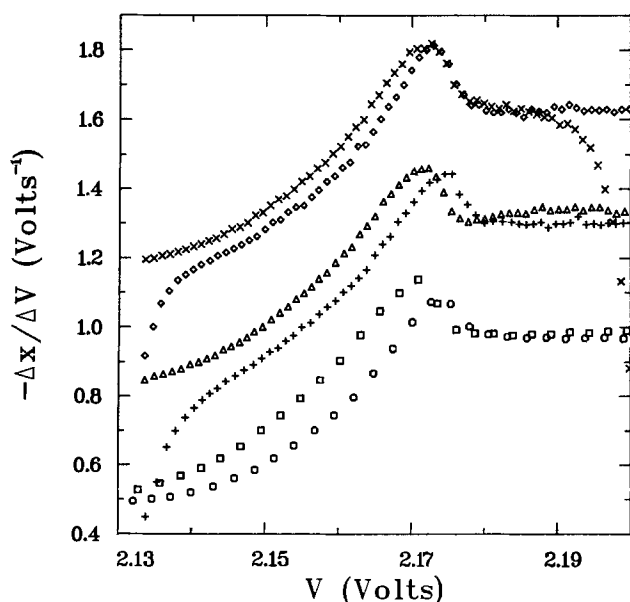


Fig. 5. $-\partial x/\partial V$ vs. V for cell RM-21 measured on charge and discharge at 100, 200, and 400h rates. 100h rate, \circ -charge, \square -discharge; 200h rate $+$ -charge, Δ -discharge; 400h rate, \diamond -charge, \times -discharge. The 200 and 400h rate data have been offset by 0.35 V^{-1} and 0.70 V^{-1} , respectively, for clarity.

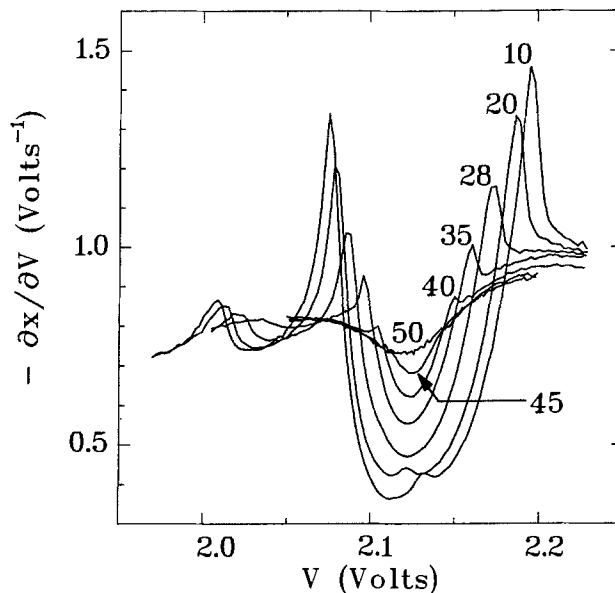


Fig. 6. Inverse derivative $-\partial x/\partial V$ vs. V for a series of discharges near $x = 2/3$. Temperatures in degrees centigrade are indicated. The currents used correspond to a change $\Delta x = 1$ in the following times: 10°C, 400h; 20°C, 200h; 28°-45°C, 100h; 50°C, 50h.

which indicates near equilibrium conditions at these slow rates. The 870h rate experiment took 90h for the cycle over the limited voltage range of Fig. 5.

Theoretical calculations of $-\text{d}x/\text{d}V$ near the order-disorder transition (9, 16, 21) predict that the phase transition occurs at the peak in $-\text{d}x/\text{d}V$; hence, by examining the peak positions as a function of x and V at different temperatures, it is possible to determine the phase diagram. Figure 6 shows $-\text{d}x/\text{d}V$ vs. V near $x = 2/3$ for a series of discharges at temperatures between 10° and 50°C. The features in $-\text{d}x/\text{d}V$ are highly temperature dependent, as expected (16) near an order-disorder transition. As the temperature is lowered, the minimum in $-\text{d}x/\text{d}V$ is enhanced and the peaks at either side move apart and grow. At higher T , the peaks disappear completely, leaving only a shallow minimum in $-\text{d}x/\text{d}V$. The feature near $x = 1/3$ shows a similar temperature dependence. The data of Fig. 6 are in good agreement with Monte Carlo calculations of $-\text{d}x/\text{d}V$ based on a two-dimensional

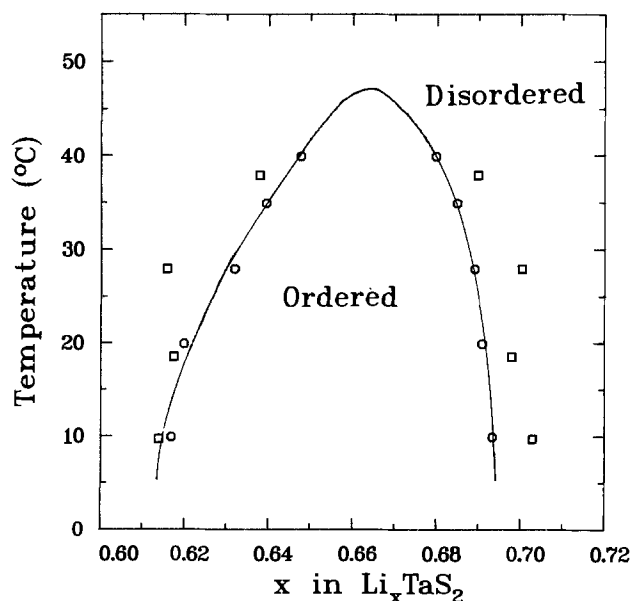


Fig. 7. Phase diagram (T vs. x) for the lithium order-disorder transition in 2H- Li_xTaS_2 . The solid curve through the data (\circ) is a guide to the eye. The Monte Carlo results of Ref. (16) (\square) are also shown.

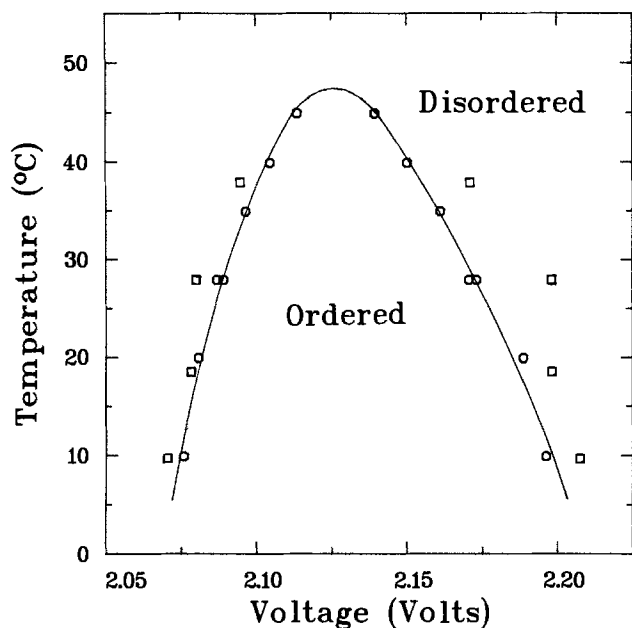


Fig. 8. Phase diagram (T vs. V) for the lithium order-disorder transition in $2H-Li_xTaS_2$. The transition occurs at the voltages and temperatures indicated in $Li/2H-Li_xTaS_2$ cells. The solid curve through the data (○) is a guide to the eye. The Monte Carlo results of Ref. (16) (□) are also shown.

triangular lattice gas model of lithium intercalation (16). Figures 7 and 8 demonstrate the agreement between the phase diagram determined from the peak positions of the data of Fig. 6 and the predictions of the Monte Carlo calculations. Possible reasons for the small discrepancies between the data and the theory are discussed in Ref. (16). Finally, Fig. 9 shows $V(x)$ for the data of Fig. 6. Figures 6 and 9 demonstrate that quantitative analysis of this phase transition is far easier when $V(x)$ is differentiated and $-dx/dV$ examined.

As has been noted before (9), ordered lithium states produce minima in $-dx/dV$ as shown by our data near $x = 1/3$ and $x = 2/3$ (Fig. 1, 2, 4, 6). This suggests that the structure in $-dx/dV$ for Li/Li_xTiS_2 cells (2, 3, 8) does not arise from lithium ordering, due to the absence of features of the type observed in Li/Li_xTaS_2 cells near the order-disorder

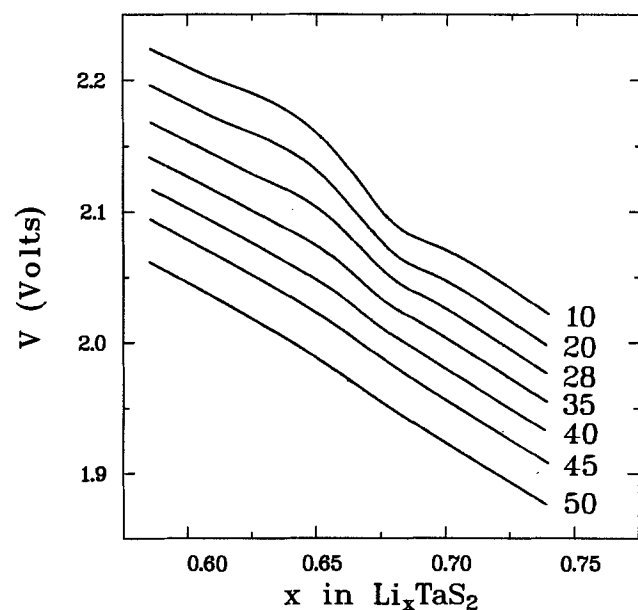


Fig. 9. Voltage as a function of x for the series of discharges shown in Fig. 6. The temperatures in degrees centigrade are indicated. Data for $20^\circ C$ and above are shifted successively by -25 mV.

transition. The $-dx/dV$ data for Li/Li_xTiS_2 cells have been qualitatively explained using a lattice gas model which includes the effects of elastic strains produced upon intercalation (10). This model indicates that the peaks in $-dx/dV$ for $x < 0.3$ in Li/Li_xTiS_2 cells arise from the formation of a disordered stage-two structure near $x = 0.14$. Other data (14, 29, 31) support this interpretation.

Conclusions

We have demonstrated how measurements of dx/dV using high resolution constant current techniques are highly reproducible and can allow quantitative analysis of phase transitions in intercalation electrodes. Our measurements on $2H-Li_xTaS_2$ determined the phase diagram of the lithium order-disorder transition near $x = 2/3$, which was shown to be in good agreement with theoretical predictions (16) based on a two-dimensional triangular-lattice-gas model of intercalation. The quality of the data obtained permit comparison with the theory at a high level of accuracy. We suggest that similar studies on other lithium intercalation systems may reveal structure in $-dx/dV$ which was not observed in earlier, lower resolution studies.

Manuscript submitted Sept. 8, 1983; revised manuscript received March 12, 1984.

The National Research Council of Canada assisted in meeting the publication costs of this article.

REFERENCES

1. M. S. Whittingham, *Prog. Solid State Chem.*, **12**, 41 (1978).
2. A. H. Thompson, *Phys. Rev. Lett.*, **40**, 1511 (1978).
3. A. H. Thompson, *This Journal*, **126**, 608 (1979).
4. A. H. Thompson, *Physica*, **99B**, 100 (1980).
5. J. R. Dahn and R. R. Haering, *Solid State Ionics*, **2**, 19 (1981).
6. D. C. Dahn and R. R. Haering, *Solid State Commun.*, **44**, 29 (1982).
7. M. Zanini, J. L. Shaw, and G. J. Tennenhouse, *This Journal*, **128**, 1647 (1981).
8. K. West, T. Jacobsen, B. Zachau-Christiansen, and S. Atlung, *Electrochim. Acta*, **28**, 97 (1983).
9. A. J. Berlinsky, W. G. Unruh, W. R. McKinnon, and R. R. Haering, *Solid State Commun.*, **31**, 175 (1979).
10. J. R. Dahn, D. C. Dahn, and R. R. Haering, *Solid State Commun.*, **42**, 179 (1982).
11. A. S. Nagelberg and W. Worell, *J. Solid State Chem.*, **38**, 32 (1981).
12. R. Osorio and L. M. Falicov, *J. Phys. Chem. Solids*, **43**, 73 (1982).
13. R. Osorio and L. M. Falicov, *J. Chem. Phys.*, **77**, 6218 (1982).
14. J. R. Dahn and R. R. Haering, *Can. J. Phys.*, **61**, 1093 (1983).
15. G. J. Dudley, K. J. Cheung, and B. C. H. Steele, *J. Solid State Chem.*, **32**, 269 (1980).
16. W. R. McKinnon and J. R. Dahn, *Solid State Commun.*, **48**, 43 (1983).
17. W. R. McKinnon and R. R. Haering, in "Modern Aspects of Electrochemistry," no. 15, R. E. White, J. O'M. Bockris, and B. E. Conway, Editors, p. 235, Plenum Press, New York (1983).
18. W. Weppner and R. A. Huggins, *This Journal*, **125**, 7 (1978).
19. D. W. Murphy, F. J. DiSalvo, J. N. Carides, and J. V. Waszczak, *Mater. Res. Bull.*, **13**, 1395 (1978).
20. H. E. Stanley, "Introduction to Phase Transitions and Critical Phenomena," Oxford University Press, Oxford, England (1971).
21. W. R. McKinnon, *Solid State Commun.*, **40**, 343 (1981).
22. L. Balewski and J. P. Brenet, *This Journal*, **115**, 527 (1967).
23. A. H. Thompson, *Rev. Sci. Instrum.*, **54**, 229 (1983).
24. J. R. Dahn, M. A. Py, and R. R. Haering, *Can. J. Phys.*, **60**, 307 (1982).
25. A. H. Thompson and C. R. Symon, *Solid State Ionics*, **3**, 175 (1981).
26. S. Atlung, K. West, and T. Jacobsen, *This Journal*, **126**, 1311 (1979).
27. A. A. Balchin, in "Crystallography and Crystal Chemistry of Materials with Layered Structures," F. Levy and D. Riedel, Editors, D. Riedel, New York (1976).
28. F. Jellinek, *J. Less-Common. Met.*, **4**, 9 (1962).
29. J. R. Dahn, Ph.D. Thesis, The University of British Co-

lumbia, Vancouver, B.C., Canada (1982).
 30. S. Basu and W. L. Worrell in "Electrode Materials and Process for Energy Conversion and Storage," J. D. E. McIntyre, S. Srinivasan, and F. G. Will, Editors, p.

861, The Electrochemical Society Softbound Proceedings Series, Princeton, NJ (1977).
 31. J. R. Dahn and R. R. Haering, *Solid State Commun.*, **40**, 245 (1981).

Hydrodynamics and Mass Transfer in a Porous-Wall Channel

Philip Lessner* and John Newman**

Applied Science Division, Lawrence Berkeley Laboratory and Department of Chemical Engineering, University of California, Berkeley, California 94720

ABSTRACT

The hydrodynamics and mass-transfer equations for a porous-wall flow channel have been solved over a large range of Re and Sc. Jorne has analyzed the low Re, high Sc case. For the high Re, high Sc case we find that $\tau_{xy}h^2/\mu xv_w = 2.43 \text{Re}^{0.5}$ and $\text{Nu} = 0.8277 \text{Re}^{0.5}\text{Sc}^{1/3}$ at the solid wall. The intermediate range is treated by numerical methods.

A flow channel with flow entering through a porous wall may find use in practical electrochemical cells (1). When the end of the channel is closed off, the mass-transfer boundary layer that forms on the solid electrode opposite the porous wall is of constant thickness. Only a few other electrodes (e.g., the rotating disk and the impinging jet) show a uniformly accessible surface. Therefore, this arrangement is of theoretical as well as practical interest.

Other authors have considered this specific problem and related problems. Berman (2) presented the first complete analysis of the porous wall channel. His channel had two porous walls. He derived the proper form of the equations of motion and stream function for a viscous, incompressible fluid and constant wall velocity. He presented a regular perturbation solution of these equations.

Sellars (3) and Yuan (4) considered the high Reynolds number solution for a channel with two porous walls. Both presented some form of a perturbation solution. White (5) obtained a series solution for this problem that was uniformly valid at all Reynolds numbers. He also obtained limiting solutions for high and low Reynolds numbers for both suction and injection. Terrill (6) presented a singular perturbation solution for the high Reynolds number case. He obtained the first three terms in the outer solution and an approximate form for some of the terms in the inner solution.

White (7) obtained an exact series solution for developed inlet flow for a channel with one solid and one porous wall. He ran into numerical convergence problems using his series solution to solve for injection Reynolds numbers greater than ten. Jorne (8) recently reworked this problem along the lines that Berman (2) had used: a low Reynolds number perturbation approach. In that work, Jorne pointed out that, if the end of the channel was closed off, a mass transfer boundary layer of constant thickness would form. Jorne solved for the low Reynolds number, high Schmidt number mass-transfer case in that work.

In this work, we consider the high Reynolds number case of a channel with one porous and one solid wall with the end closed off. Our method of attack is to develop a high Reynolds number singular perturbation expansion. This method complements White's series solution, making it easier to obtain solutions for high injection Reynolds numbers. We also obtain a numerical solution to show the limits of validity of our solution and Jorne's low Reynolds number perturbation expansion. By combining these results, we are able to picture the flow over the entire range of Reynolds number.

A similar analysis is done for mass transfer. However, we have confined our theoretical work to high Sc, which

is the region of most interest in liquid phase mass transfer. Our numerical results show where the high Sc asymptote is valid.

Hydrodynamics

We take the origin of the coordinates to be at the solid wall, at the end of a flow channel which is closed off (Fig. 1). The flow is two dimensional and is described by the Navier-Stokes equations

$$v_x \frac{\partial v_x}{\partial x} + v_y \frac{\partial v_x}{\partial y} = \frac{-1}{\rho} \frac{\partial P}{\partial x} + \nu \left(\frac{\partial^2 v_x}{\partial x^2} + \frac{\partial^2 v_x}{\partial y^2} \right) \quad [1]$$

$$v_x \frac{\partial v_y}{\partial x} + v_y \frac{\partial v_y}{\partial y} = \frac{-1}{\rho} \frac{\partial P}{\partial y} + \nu \left(\frac{\partial^2 v_y}{\partial x^2} + \frac{\partial^2 v_y}{\partial y^2} \right) \quad [2]$$

and the equation of continuity

$$\frac{\partial v_x}{\partial x} + \frac{\partial v_y}{\partial y} = 0 \quad [3]$$

The boundary conditions are

$$\text{at } y = 0, v_x = 0 \text{ and } v_y = 0 \quad [4a]$$

$$\text{at } y = h, v_x = 0 \text{ and } v_y = -v_w \quad [4b]$$

$$\text{at } x = 0, v_x = 0 \quad [4c]$$

The boundary conditions and the equation of continuity suggest the following form for the velocity components

$$v_y = Q(y) \quad [5a]$$

$$v_x = -xQ'(y) \quad [5b]$$

After substituting Eq. [5a] and [5b] into Eq. [1] and [2] and taking the curl to eliminate pressure, Berman (2) obtained the following equation for Q

$$Q'Q'' - QQ''' = -\nu Q^{iv} \quad [6]$$

with the boundary conditions

$$\text{at } y = 0, Q' = 0 \text{ and } Q = 0 \quad [7a]$$

$$\text{at } y = h, Q' = 0 \text{ and } Q = -v_w \quad [7b]$$

It is convenient to put Eq. [6] and [7] into dimensionless form by introducing the following dimensionless quantities

$$R = \frac{Q}{v_w} \quad [8]$$

$$\text{Re} = \frac{v_w h}{\nu} \quad [9]$$

$$\gamma = \frac{y}{h} \quad [10]$$

*Electrochemical Society Student Member.

**Electrochemical Society Active Member.

Key words: electrode, kinetics, battery, electrodeposition.

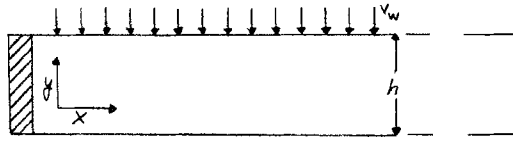


Fig. 1. Schematic of channel and coordinate axes

Then we obtain

$$R'R'' - RR''' = \frac{-1}{Re} R^{1\nu} \quad [11]$$

with boundary conditions

$$\text{at } \gamma = 0, R' = 0 \text{ and } R = 0 \quad [12a]$$

$$\text{at } \gamma = 1, R' = 0 \text{ and } R = -1 \quad [12b]$$

At low Re, Berman (2) showed that there is a regular perturbation problem. The first few terms in the expansion for the single porous wall channel have been obtained by Jorne (8). In the limit as Re becomes infinite, we lose the fourth derivative, and the problem becomes singular. Perturbation expansions need to be developed for both inner and outer regions. In the region of intermediate Re, neither the low nor high Re expansions is adequate, and we need to obtain a numerical solution of the complete equation.

The full equation is a nonlinear, two-point boundary value problem. It has been solved by reducing it to two second-order equations and linearizing them about a trial solution. The linearized equations were solved by BAND, a subroutine developed by Newman (9, 10). Figure 2a shows the velocity profile at a high Re.

Terrill (6) has considered the related singular perturbation problem in the two porous wall channel. The outer solution for the two porous wall channel is the same as for our problem. In this region our variable is denoted by

$$\bar{y} = y \quad [13]$$

The outer solution can be written as an expansion in 1/Re

$$\tilde{R} = \tilde{R}_0 + \frac{1}{Re} \tilde{R}_1 + \frac{1}{Re^2} \tilde{R}_2 + \dots \quad [14]$$

The differential equation for the first term in the outer region is

$$\tilde{R}'_0 \tilde{R}''_0 = \tilde{R}_0 \tilde{R}'''_0 \quad [15]$$

with the boundary conditions

$$\text{at } \gamma = 0, \tilde{R}_0 = 0 \quad [16a]$$

$$\text{at } \gamma = 1, \tilde{R}'_0 = 0 \text{ and } \tilde{R}_0 = -1 \quad [16b]$$

The solution to this nonlinear problem, first given by White (5), turns out to be

$$\tilde{R}_0 = -\sin\left(\frac{\pi\gamma}{2}\right) \quad [17]$$

The interested reader is referred to Terrill's work (6) for the rather more complicated solutions for the next two terms in the outer expansion.

At high Re, order of magnitude analysis shows that the proper form of the stretched distance in the inner region is

$$\bar{y} = \frac{y\sqrt{Re}}{h} \quad [18]$$

The inner flow variable is

$$\bar{R} = \frac{Q\sqrt{Re}}{v_w} \quad [19]$$

Terrill (6) suggested that the inner expansion should take the form

$$\bar{R} = Re^{1/2} \bar{R}_0 + Re^{3/2} \bar{R}_1 + Re^{5/2} (\log Re) \bar{R}_2 + Re^{5/2} \bar{R}_3 + \dots \quad [20]$$

This leads to the following differential equation for the first term in the inner solution

$$-\bar{R}'_0 \bar{R}''_0 + \bar{R}_0 \bar{R}'''_0 = -\bar{R}_0^{1\nu} \quad [21]$$

with the boundary conditions

$$\text{at } \bar{y} = 0, \bar{R}_0 = 0 \text{ and } \bar{R}'_0 = 0 \quad [22]$$

By requiring that

$$\lim_{\bar{y} \rightarrow \infty} \bar{R} = \lim_{\bar{y} \rightarrow 0} \tilde{R} \quad [23]$$

we can determine the matching conditions as \bar{y} tends toward infinity

$$\bar{y} \rightarrow \infty, \bar{R}'_0 \rightarrow -\frac{\pi}{2}, \bar{R}_0 \rightarrow 0 \quad [24]$$

The method of solution of Eq. [21] subject to boundary conditions [22] and matching condition [24] is similar to

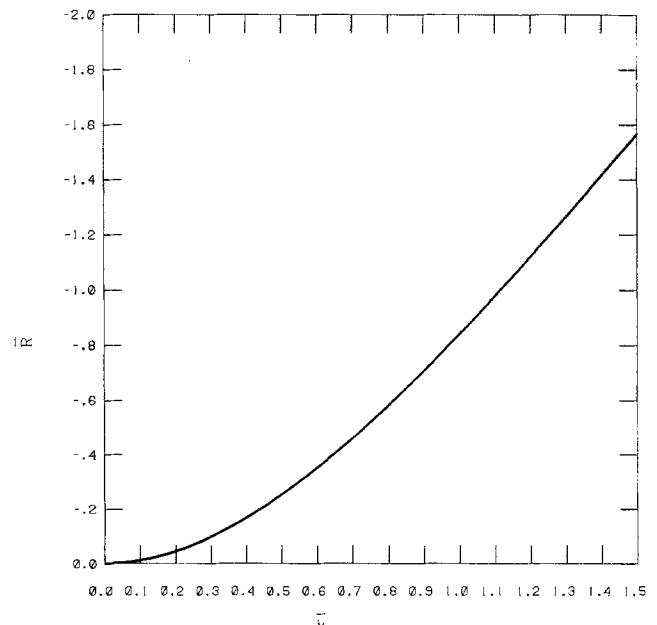
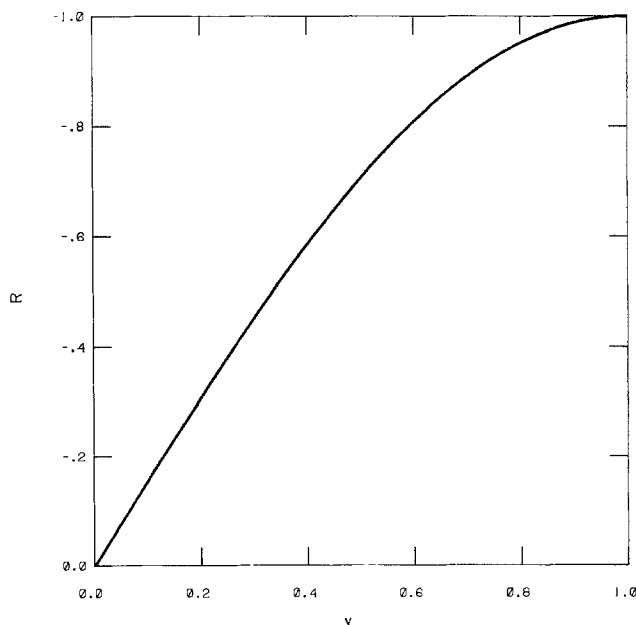


Fig. 2. a(left): Shape of y velocity profile at Re = 50,000. b(right): Detail of boundary layer region at Re = 50,000.

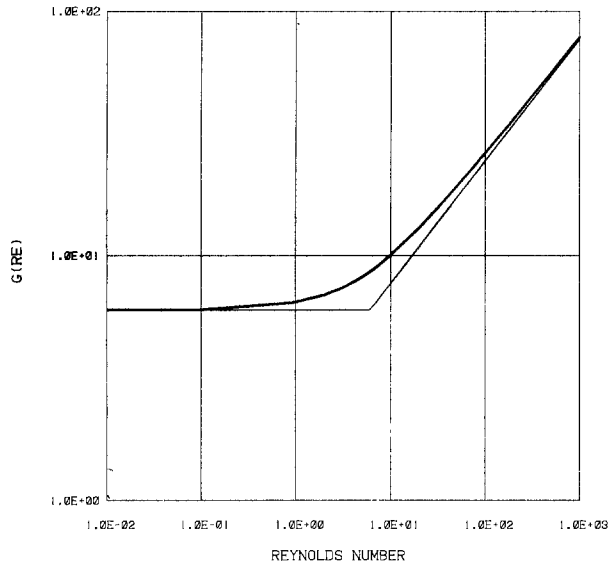


Fig. 3. Function $G(Re)$ defined by Eq. [25]

that of the full equation. Figure 2b shows the boundary layer in more detail.

The shear stress at the solid wall can be written as a function of Re

$$\frac{\tau_{xy}h^2}{\mu x v_w} = G(Re) \tag{25}$$

Our boundary layer solution yields

$$G(Re) = 2.43Re^{0.5} \tag{26}$$

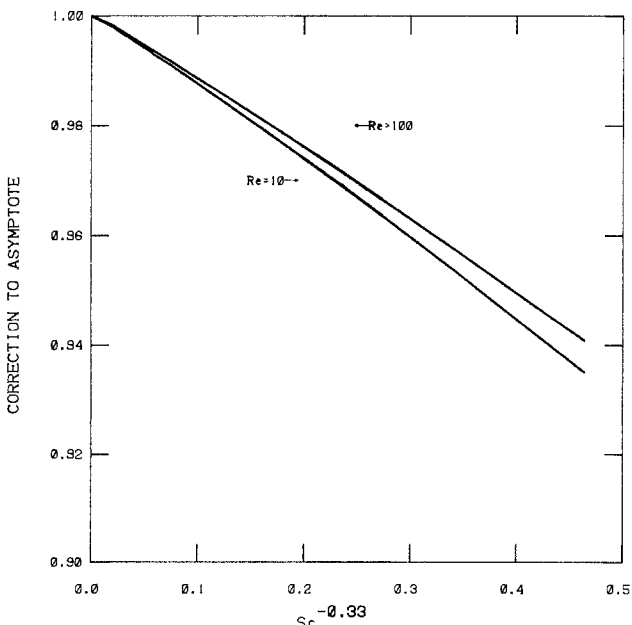
Jorne's low Re perturbation solution yields the following

$$G(Re) = 6 + \frac{16Re}{35} \tag{27}$$

Figure 3 shows a plot of $G(Re)$ vs. Re as determined by the full numerical solution. The low and high Re asymptotes are also plotted. For $Re < 1$, the low Re asymptote is a good approximation to the shear stress, while for $Re > 500$ the high Re line fits the data well. Reynolds numbers between 1 and 500 are in the intermediate region.

Mass Transfer

Since v_y is a function of y only, the equation of convective diffusion can be written as



$$v_y \frac{dc_1}{dy} = D_1 \frac{d^2c_1}{dy^2} \tag{28}$$

For our problem, the boundary conditions take the form

$$\text{at } y = 0, c_1 = c_0 \tag{29a}$$

$$\text{at } y = h, c_1 = c_b \tag{29b}$$

Equations [28] and [29] can be put in dimensionless form by introducing a dimensionless concentration

$$\Theta = \frac{c_1 - c_0}{c_b - c_0} \tag{30}$$

Then

$$\frac{d^2\Theta}{d\gamma^2} - PeR(\gamma) \frac{d\Theta}{d\gamma} = 0 \tag{31}$$

with boundary conditions

$$\text{at } \gamma = 0, \Theta = 0 \tag{32a}$$

$$\text{at } \gamma = 1, \Theta = 1 \tag{32b}$$

The solution to this equation can be represented as an integral

$$\Theta = \frac{\int_0^\gamma e^{Pe \int_0^\alpha R(\alpha) d\alpha} d\beta}{\int_0^1 e^{Pe \int_0^\alpha R(\alpha) d\alpha} d\beta} \tag{33}$$

The Nusselt number is simply

$$Nu = \left. \frac{d\Theta}{d\gamma} \right|_{\gamma=0} = \frac{1}{\int_0^1 e^{Pe \int_0^\alpha R(\alpha) d\alpha} d\gamma} \tag{34}$$

The number of points in the integration is dependent on the number of intervals used in the hydrodynamic solution. A finer mesh would be appropriate for the mass-transfer problem at high Pe , but this is limited by computer memory size. At high Pe , the exponential in the integral of Eq. [34] will change rapidly. We need to interpolate between grid points.

To do this interpolation we first stretch the distance with Sc

$$\xi = \gamma Sc^{1/3} \tag{35}$$

Then Eq. [33] takes the form

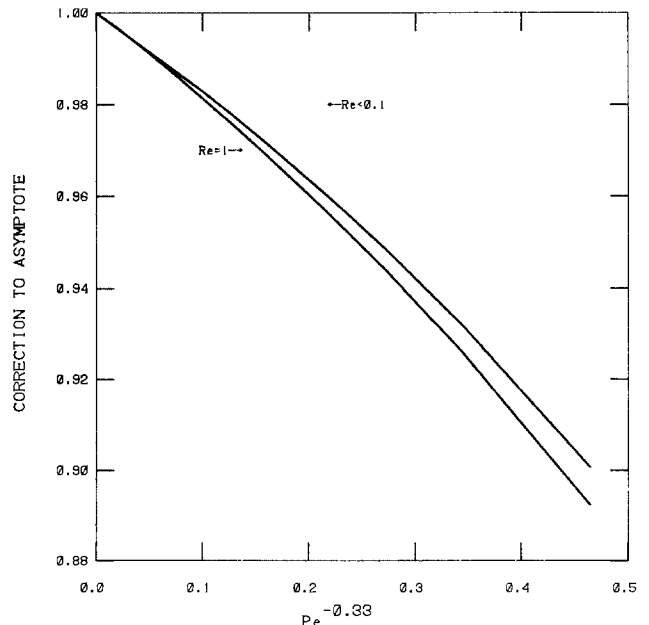


Fig. 4. Correction to high Schmidt number asymptote for (a, left) moderate and large Reynolds number and (b, right) moderate and small Reynolds number.

$$\text{Nu} = \frac{\text{Sc}^{1/3}}{\int_0^{\text{Sc}^{1/3}} e^{\text{ReSc}^{2/3} \gamma} R(\xi) d\xi} d\gamma' \quad [36]$$

At distances close to the solid wall we can write v_x in the form of a truncated Taylor series

$$v_x = \beta(x)y \quad [37]$$

$$\beta(x) = -\frac{\tau_{xy}}{\mu} \Big|_{y=0} \quad [38]$$

From Eq. [3] v_y becomes

$$v_y = -1/2 \beta'(x)y^2 \quad [39]$$

This form for the y velocity suggests that we interpolate quadratically between grid points.

At high Sc a mass-transfer boundary layer forms. Then the concentration can be represented as

$$\Theta = \int_0^\eta e^{-x^3} dx \quad [40]$$

where

$$\eta = y \frac{\sqrt{\beta}}{(9D_1 \int_0^x \sqrt{\beta} dx)^{1/3}} \quad [41]$$

Due to the functional form of $\beta(x)$, η is a function of y only. The high Schmidt number asymptote can be constructed with a knowledge of $G(\text{Re})$ from Fig. 3. Thus

$$\text{Nu}_{\text{Sc} \rightarrow \infty} = 0.6160(G(\text{Re}))^{1/3} \text{Pe}^{1/3} \quad [42]$$

Using this representation, Jorne (8) obtained for low Re, high Sc cases

$$\text{Nu} = 1.12 \left(1 + \frac{8}{108} \text{Re} \right)^{1/3} \text{Pe}^{1/3} \quad [43]$$

In the limit as $\text{Re} \rightarrow 0$, this yields

$$\text{Nu} = 1.12 \text{Re}^{1/3} \text{Sc}^{1/3} \quad [44]$$

Using our results for the hydrodynamics at high Re we obtain for the high Re, high Sc asymptote

$$\text{Nu} = 0.8277 \sqrt{\text{ReSc}^{1/3}} \quad [45]$$

The high Sc asymptote over the whole range of Re can be constructed from Eq. [42] and Fig. 3. At finite Sc, the actual value of Nu will deviate from this asymptote. Figure 4 shows the correction to be applied to the asymptote at finite Sc.

Acknowledgment

This work was supported by the Assistant Secretary for Conservation and Renewable Energy, Office of Energy Systems Research, Energy Storage Division of the U.S. Department of Energy under Contract no. DE-AC03-76SF00098.

Manuscript submitted Aug. 22, 1983; revised manuscript received March 16, 1984.

The University of California assisted in meeting the publication costs of this article.

LIST OF SYMBOLS

c	concentration (mol m ⁻³)
D	diffusion coefficient, (m ² s ⁻¹)
$G(\text{Re})$	Eq. [25] and Fig. 3
h	spacing between porous and solid wall (m)
N	molar flux (mol m ⁻² s ⁻¹)
Nu	Nusselt number ($N_1 h / D_1 \Delta c$)
P	dynamic pressure (Pa)
Pe	Peclet number, $v_w h / D$
Q	defined by Eq. [5] (m s ⁻¹)
R	dimensionless velocity
Re	Reynolds number ($v_w h / \nu$)
Sc	Schmidt number (ν / D)
v	velocity (m s ⁻¹)
x	coordinate along wall (m)
y	coordinate perpendicular to wall (m)

Greek Letters

$\beta(x)$	defined by Eq. [38] (s ⁻¹)
γ	dimensionless distance
η	defined by Eq. [41]
Θ	dimensionless concentration
μ	dynamic viscosity (kg m ⁻¹ s ⁻¹)
ν	kinematic viscosity (m ² s ⁻¹)
ξ	stretched distance
π	3.14
ρ	density (kg m ⁻³)
τ	shear stress (N m ⁻²)

Diacritical Marks

$-$	inner variable
\sim	outer variable

Superscripts

'	first derivative
''	second derivative
'''	third derivative
iv	fourth derivative

Subscripts

i	species
o	first term
w	wall
x	x direction
y	y direction

REFERENCES

1. J. Jorne, *This Journal*, **129**, 2251 (1982).
2. A. Berman, *J. Appl. Phys.*, **24**, 1232 (1953).
3. J. Sellars, *ibid.*, **26**, 489 (1955).
4. S. W. Yuan, *ibid.*, **27**, 267 (1956).
5. F. M. White, Jr., B. F. Barfield, and M. J. Goglia, *J. Appl. Mech.*, **25**, 613 (1958).
6. R. M. Terrill, *Aeronaut. Quart.*, p. 323, November 1965.
7. F. M. White, Jr., Ph.D. Thesis, Georgia Institute of Technology, Atlanta, GA (1959).
8. J. Jorne, *This Journal*, **129**, 1727 (1982).
9. John Newman, "Electrochemical Systems," Appendix C, pp. 414-425, Prentice-Hall, Inc., Englewood Cliffs, NJ (1973).
10. J. Newman, *Ind. Eng. Chem. Fundam.*, **7**, 514 (1968).

Rearrangement Energy for Electron Transfer at Semiconductor/Electrolyte Interface

Kenkichiro Kobayashi, Masasuke Takata, and Shoichi Okamoto

Faculty of Engineering, Technological University of Nagaoka, Nagaoka, Niigata, 949-54 Japan

Mitsunori Sukigara

Institute of Industrial Science, University of Tokyo, Roppongi, Minato-ku, Tokyo 106 Japan

ABSTRACT

General formulas of the rearrangement energy for the electron transfer at a semiconductor/electrolyte interface are derived by using the dielectric continuum theory. The rearrangement energy of orientational and intramolecular vibrations of solvent and lattice vibration of the semiconductor depends not only on the distance between the electrode surface and redox ions, but also on dielectric constant of the semiconductor. Theoretical values of the rearrangement energy are compared with experimental values.

Nonradiative electron transfer in a polar solvent occurs accompanying the thermal excitation and emission of many phonons and is called a multiphonon process (1). The electron transfer rate in the multiphonon process is governed by the electronic matrix element coupling the initial and the final states of the electron transfer, and by phonon-state density, which is the Franck-Condon factor statistically averaged over the initial state of phonons. The phonon-state density is responsible for the temperature dependence of the electron transfer rate, and it increases with the decrease in the rearrangement energy of various vibrations participating in the electron transfer. The rearrangement energy of orientational vibration of a solvent, $E_s(o_s)$, is one of the important factors determining the phonon-state density for the electron transfer in a polar solvent. The $E_s(o_s)$ values have been estimated from the electron transfer rate constants by assuming the transmission coefficient to be unity (2). This assumption is plausible for an adiabatic electron transfer in which the electronic matrix element is very large. On the contrary, nonadiabatic electron transfer was experimentally found in the electrochemical reductions of Fe^{3+} at the organic crystal electrode (3) and in homogeneous electron transfer reactions including europium ions (4). In the case of the nonadiabatic electron transfer, information about the transmission coefficient or the electronic matrix element is necessary to determine the accurate $E_s(o_s)$ value from the electron transfer rate. The formal application of the adiabatic electron transfer may lead to the overestimation of the $E_s(o_s)$ value by a term of the transmission coefficient. On the other hand, it was reported (5-8) that the $E_s(o_s)$ values can be determined directly from current-voltage characteristics at a semiconductor/electrolyte interface. The advantage of the above method is that, since the phonon-state density can be obtained separately from the electronic matrix element, the estimated $E_s(o_s)$ values do not involve the uncertainty of the transmission coefficient. Such experimentally obtained $E_s(o_s)$ values have been compared with the theoretical $E_s(o_s)$ values for the electron transfer at a metal electrode. The $E_s(o_s)$ values in electrochemical reactions, however, depend on the mirror image force between an electrode and an electron transferred into the oxidant ion (9). This mirror image force is related to the difference in the dielectric constants of the electrode and the solvent. Since the dielectric constant of a metal is infinite, the electric field is everywhere zero in a metal electrode, while there is a nonzero electric field inside a semiconductor. Thus, an $E_s(o_s)$ value obtained at a semiconductor electrode with a small dielectric constant may deviate from that at a metal electrode. The semiconductor is polarized by the electron transferred into the oxidant ion, and thus the

rearrangement energy of lattice vibrations of the semiconductor electrode should be taken into account. In the present paper, we derived formulas for the rearrangement energy of several vibrations governing the electron transfer rate at the semiconductor/electrolyte interface.

Theory

Model of electron transfer at semiconductor/electrolyte interface.—We are concerned with one-electron transfer from the occupied conduction band of a semiconductor to an oxidant ion, or from a reductant ion to the empty conduction band: $Ox + e \rightleftharpoons Re$, where Ox denotes an oxidant ion with the charge $m+$, Re denotes a reductant ion with the charge $(m - 1)+$, and e is an electron in the conduction band. The spatial arrangement at the interface of the semiconductor and electrolyte is schematically shown in Fig. 1. The shape of the oxidant and reductant ions is approximated as a sphere, and the center of the reductant and oxidant ions is located apart from the semiconductor surface by $R/2$. No solvent penetrates inside of the ion sphere r_b . The ion possesses intramolecular vibration of frequency $\omega \approx 10^{13} \text{ s}^{-1}$. A polar solvent such as water possesses not only orientational vibration of a permanent dipole moment but also stretching or deformation vibrations (10). The energy of the orientational vibration of the solvent is about 10^{-4} eV ($\omega \approx 10^{11} \text{ s}^{-1}$), while the energy of the deformation or stretching vibration of the solvent ranges from 0.01 to 0.1 eV ($\omega \approx 10^{13} \sim 10^{14} \text{ s}^{-1}$). For simplicity, we assume that one mode among the intramolecular vibrations of the solvent contributes to electron transfer. Self-trapping of an electron observed in ionic semiconductors is the result of the strong interaction of an electron with the lattice vibration. The electron in the reductant ion located near the ionic semiconductor surface can also interact with the lattice vibration. Since for covalent semiconductors the electron-phonon interaction is weak in comparison with that in ionic semiconductors (11), hereafter we consider only ionic semiconductors. Accordingly, the vibrations taking part in the electron transfer at the semiconductor/electrolyte interface consist of the orientational vibration of the solvent, the intramolecular vibrations of the oxidant ion and of the solvent, and the optical phonons of the lattice vibration in the ionic semiconductor. In the cathodic process, at the final state an electron has been transferred into the oxidant ion and interacts strongly with the orientational vibration of the solvent, the intramolecular vibrations of the ion and of the solvent, and the optical phonons in the ionic semiconductor. At the initial state, an electron in the conduction band is delocalized over the semiconductor, so that its interaction with the said vibrations is negligible. The difference in this electron-phonon interaction results in the shift of the equilibrium coordinate of the interaction

Key words: rearrangement energy, electron transfer, semiconductor electrode.

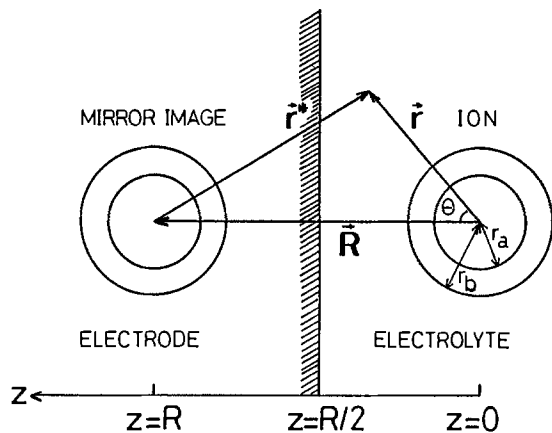


Fig. 1. Geometry in determining the dielectric displacement by an electron transferred into the oxidant ion and the mirror image charge in a semiconductor electrode.

modes of various vibrations, *e. g.*, the ion radius is varied from r_a (oxidant) to r_b (reductant) after electron transfer from the semiconductor to the oxidant ion. The orientational vibration of the solvent with the slow relaxation time cannot respond to the fast change of the ionic radius after the electron transfer and cannot follow the thermal fluctuation of the ionic radius. However, the intramolecular vibration of the solvent can follow the thermal fluctuation of the ionic radius. This indicates that the interaction energy of the electron with the intramolecular vibration of the solvent depends on the coordinate of the intramolecular vibration of the ion (12). For simplicity, in the calculation of the rearrangement energy due to the intramolecular vibration of the solvent, the ionic radius is assumed to be frozen at r_b of the reductant ion.

Electric potential inside semiconductor, solvent, and reductant ion.—A solvent and a semiconductor are treated as dielectrics, which are uniform, isotropic, and unsaturated. The electrostatic potential at any point (r, ϑ, φ) inside the sphere r_b is given by (13)

$$V_1(r, \vartheta, \varphi) = \int_{r'=0}^{\infty} \frac{e |\Psi(r', \vartheta', \varphi')|^2}{\epsilon_1 |\mathbf{r} - \mathbf{r}'|} d v' + \sum_{n=0}^{\infty} \sum_{m=-n}^n B_{nm} r^n P_n^m(\cos \vartheta) e^{im\varphi} \quad [1]$$

where e is the charge of an electron, $\Psi(r', \vartheta', \varphi')$ is the electronic wavefunction in the reductant ion at point $(r', \vartheta', \varphi')$, the $P_n^m(\cos \vartheta)$ are the associated Legendre functions, and ϵ_1 is the dielectric constant inside the sphere r_b . The second term in Eq. [1] is the result of the charge distribution outside the sphere r_b . For simplicity, we assume that $|\Psi|^2$ has the spherical symmetry and no probability outside sphere r_b . Under this condition, Eq. [1] reduces to

$$V_1(r, \vartheta, \varphi) = \frac{e}{\epsilon_1 r} \int_{r'=0}^{r=r} |\Psi(r', \vartheta', \varphi')|^2 4\pi r'^2 dr' + \sum_{n=0}^{\infty} \sum_{m=-n}^n B_{nm} r^n P_n^m(\cos \vartheta) e^{im\varphi} \quad [2]$$

The electrostatic potential inside the semiconductor having the dielectric constant ϵ_3 satisfies Laplace's equation and is taken to be zero at $r \rightarrow \infty$. Thus, we have

$$V_3 = \sum_{n=0}^{\infty} \sum_{m=-n}^n \frac{D_{nm}}{r^{n+1}} P_n^m(\cos \vartheta) e^{im\varphi} \quad [3]$$

The electrostatic potential inside the solvent having the dielectric constant ϵ_2 is written as

$$V_2 = \sum_{n=0}^{\infty} \sum_{m=-n}^n \frac{G_{nm}}{r^{n+1}} P_n^m(\cos \varphi) e^{im\varphi} + \sum_{n=0}^{\infty} \sum_{m=-n}^n \frac{C_{nm}}{(r^*)^{n+1}} P_n^m(\cos \vartheta^*) e^{im\varphi^*} \quad [4]$$

where the coordinate $(r^*, \vartheta^*, \varphi^*)$ is related to the coordinate (r, ϑ, φ) as follows

$$r^* = (x^2 + y^2 + (z - R)^2)^{1/2} = (r^2 + R^2 - 2rR \cos \vartheta)^{1/2} \\ \cos \vartheta^* = (R - r \cos \vartheta) / (r^2 + R^2 - 2rR \cos \vartheta)^{1/2} \\ \varphi^* = \varphi \quad [5]$$

At the interface of semiconductor/electrolyte ($z = R/2$), V_2 and V_3 , and the normal component of the dielectric displacement, $-\epsilon_2 dV_2/dz$ and $-\epsilon_3 dV_3/dz$, shall be equal to each other. Thus, for the component of $n = m = 0$, one gets

$$\frac{G_{00}}{[x^2 + y^2 + (R/2)^2]^{1/2}} + \frac{C_{00}}{[x^2 + y^2 + (R/2 - R)^2]^{1/2}} = \frac{D_{00}}{[x^2 + y^2 + (R/2)^2]^{1/2}} \quad [6]$$

and

$$-\epsilon_2 \left\{ \frac{R/2 G_{00}}{[x^2 + y^2 + (R/2)^2]^{3/2}} + \frac{(R/2 - R) C_{00}}{[x^2 + y^2 + (R/2 - R)^2]^{3/2}} \right\} = \frac{-\epsilon_3 R/2 D_{00}}{[x^2 + y^2 + (R/2)^2]^{3/2}} \quad [7]$$

Then, it follows that

$$G_{00} = \frac{\epsilon_2 + \epsilon_3}{2\epsilon_2} D_{00}, \text{ and } C_{00} = \frac{\epsilon_2 - \epsilon_3}{2\epsilon_2} D_{00} \quad [8]$$

In order to get the boundary condition on the surface of sphere r_b , we expand V_2 in powers of $\cos \vartheta$ in the following form

$$V_2 = \sum_{n=0}^{\infty} \sum_{m=-n}^n \frac{G_{nm}}{r^{n+1}} P_n^m(\cos \vartheta) e^{im\varphi} + \sum_{n=0}^{\infty} \sum_{m=-n}^n \frac{C_{nm} P_n^m(\cos \vartheta^*)}{(r^2 + R^2)^{(n+1)/2}} e^{im\varphi} \left[1 + \sum_{k=1}^{\infty} (-1)^k \frac{(n+1)(n+3) \cdots (n+2k-1)}{2^k} \frac{1}{k!} \left(\frac{2Rr \cos \vartheta}{r^2 + R^2} \right)^k \right] \quad [9]$$

where

$$\cos \vartheta^* = (R - r \cos \vartheta) (r^2 + R^2)^{-1/2} \left\{ 1 + \sum_j (-1)^j \frac{1}{2} \frac{3}{2} \cdots \frac{(2j-1)}{2} \frac{1}{j!} \left(\frac{2Rr \cos \vartheta}{r^2 + R^2} \right)^j \right\}$$

From the boundary condition of $V_1 = V_2$ and $-\epsilon_1 dV_1/dr = -\epsilon_2 dV_2/dr$ at $r = r_b$, we have

$$\frac{e}{\epsilon_1 r_b} + B_{00} = \frac{C_{00}}{(r_b^2 + R^2)^{1/2}} + \frac{G_{00}}{r_b} + \frac{C_{10} R}{(r_b^2 + R^2)^{3/2}} + O(h) \quad [10]$$

and

$$e^2/r_b^2 = \frac{r_b \epsilon_2^2 C_{00}}{(r_b^2 + R^2)^{3/2}} + \frac{\epsilon_2 G_{00}}{r_b^2} + \frac{3 \epsilon_2 C_{10} R r_b}{(r_b^2 + R^2)^{5/2}} + Q(h) \quad [11]$$

where $O(h)$ and $Q(h)$ are the high order terms arising from C_{n0} ($n \geq 2$). We neglect the multipole potential arising from the terms of $n \geq 1$ in V_1 , V_2 and V_3 . Under this approximation, the work for charging the sphere r_b is given by

$$\frac{eB_{00}}{2} = -\frac{e^2}{2\epsilon_1 r_b} + \frac{eC_{00}}{2(r_b^2 + R^2)^{1/2}} + \frac{eG_{00}}{2r_b} \quad [12]$$

From Eq. [10] and [11], we have

$$D_{00} = e \left\{ \frac{\epsilon_2 + \epsilon_3}{2} + \frac{\epsilon_2 - \epsilon_3}{2} \frac{r_b^3}{(r_b^2 + R^2)^{3/2}} \right\}^{-1} \quad [13]$$

We take into account only the term of $n = m = 0$, so that the subscript, 00, in G , C , D , are omitted hereafter for simplifying the description. As seen in Eq. [2], the multipole potential is not the result of the charge distribution inside the sphere r_b , but of the mirror image effect (14): the electron in the reductant ion induces the charge at the semiconductor/electrolyte interface if there is the difference in the dielectric constants between the semiconductor and the solvent. The charge induced at the semiconductor/electrolyte interface polarizes the sphere, and, in consequence, the induced dipole moment appears at the surface of the sphere r_b . The multipole potential is generated in the same manner.

Interaction of an electron with dielectrics.—The polarization of the solvent \mathbf{P}_2 consists of the electronic polarization \mathbf{P}_{2e} , the ionic polarization due to the intramolecular vibration \mathbf{P}_{2i} , and the orientational polarization of the permanent dipole moment of the solvent \mathbf{P}_{2d} . When the distribution of the electron is changed slowly, the polarization induced inside the solvent is written as

$$\mathbf{P}_2 = \mathbf{P}_{2e} + \mathbf{P}_{2i} + \mathbf{P}_{2d} = \chi_{2s} \mathbf{E}_{2s} = \frac{\epsilon_{2s} - 1}{4\pi} \mathbf{E}_{2s} \quad [14]$$

where χ_{2s} is the dielectric susceptibility of the solvent and \mathbf{E}_{2s} is the static electric field inside the solvent. Similarly, for the slow fluctuation of the electron distribution, the polarization induced inside the semiconductor is written as

$$\mathbf{P}_3 = \mathbf{P}_{3e} + \mathbf{P}_{3i} = \chi_{3s} \mathbf{E}_{3s} = \frac{\epsilon_{3s} - 1}{4\pi} \mathbf{E}_{3s} \quad [15]$$

where χ_{3s} is the dielectric susceptibility of the semiconductor and \mathbf{E}_{3s} is the electric field inside the semiconductor. The static electric field inside the solvent \mathbf{E}_{2s} is given by

$$\mathbf{E}_{2s} = G_s \frac{\mathbf{r}}{|\mathbf{r}|^3} + C_s \frac{\mathbf{r}^*}{|\mathbf{r}^*|^3} \quad [16]$$

Similarly, the static electric field inside the semiconductor is

$$\mathbf{E}_{3s} = D_s \frac{\mathbf{r}}{|\mathbf{r}|^3} \quad [17]$$

where the coefficients, G_s , C_s , and D_s , are obtained by substituting the static dielectric constant of the solvent ϵ_{2s} and that of the semiconductor ϵ_{3s} into Eq. [8] and [13], instead of ϵ_2 and ϵ_3 , respectively. When the change in the distribution of the electron is so fast that the orientational vibration of the solvent cannot follow but both the lattice vibration of the semiconductor and the intramolecular vibration of the solvent can follow, the polarization induced inside the solvent is

$$\mathbf{P}_2 = \mathbf{P}_{2i} + \mathbf{P}_{2e} = \chi_{2r} \mathbf{E}_{2r} = \frac{\epsilon_{2r} - 1}{4\pi} \mathbf{E}_{2r} \quad [18]$$

and that inside the semiconductor is

$$\mathbf{P}_3 = \mathbf{P}_{3i} + \mathbf{P}_{3e} = \chi_{3r} \mathbf{E}_{3r} = \frac{\epsilon_{3r} - 1}{4\pi} \mathbf{E}_{3r} \quad [19]$$

where ϵ_{2r} and ϵ_{3r} are the dielectric constants of the solvent and the semiconductor in the infrared region, respectively. The electric field \mathbf{E}_{2r} or \mathbf{E}_{3r} is given by replacing G_s , C_s , and D_s by G_r , C_r , and D_r , in which the dielectric constants in the infrared region are used instead of the static dielectric constants. For the very fast change in the distribution of the electron, the electronic polarization of the solvent

$$\mathbf{P}_{2e} = \chi_{20} \mathbf{E}_{20} = \frac{\epsilon_{20} - 1}{4\pi} \mathbf{E}_{20} \quad [20]$$

and the electronic polarization of the semiconductor

$$\mathbf{P}_{3e} = \chi_{30} \mathbf{E}_{30} = \frac{\epsilon_{30} - 1}{4\pi} \mathbf{E}_{30} \quad [21]$$

can follow the change. In Eq. [20] and [21], ϵ_{20} and ϵ_{30} denote the optical dielectric constants of the solvent and the semiconductor, and in the expression of \mathbf{E}_{20} and \mathbf{E}_{30} the coefficient, G_o , C_o , and D_o , are written with the optical dielectric constants.

The total Hamiltonian for the electron and the polarization of dielectrics is written as (15)

$$\mathbf{H} = \mathbf{H}_e + \mathbf{H}_p \quad [22]$$

The Hamiltonian for the electron, \mathbf{H}_e , is the sum of the interaction of the electron with the polarization, \mathbf{H}_{ep} , and another term independent of the polarization \mathbf{H}_e'

$$\mathbf{H} = \mathbf{H}_{ep} + \mathbf{H}_e' \quad [23]$$

The Hamiltonian for the polarization inside the dielectrics, \mathbf{H}_p , is written as (15)

$$\mathbf{H}_p = \sum_{n=2}^3 \int \frac{\gamma_{ni}}{2} \dot{\mathbf{P}}_{ni}^2(\mathbf{r}') d^3\mathbf{r}' + \sum_{n=2}^3 \int \frac{\gamma_{ni}}{2} \omega_{ni}^2 \mathbf{P}_{ni}^2(\mathbf{r}') d^3\mathbf{r}' + \int \frac{\gamma_{2d}}{2} \dot{\mathbf{P}}_{2d}^2(\mathbf{r}') d^3\mathbf{r}' + \int \frac{\gamma_{2d}}{2} \omega_{2d}^2 \mathbf{P}_{2d}^2(\mathbf{r}') d^3\mathbf{r}' \quad [24]$$

where the coefficient γ has been determined from Lagrange's equation of the polarization (12). In Eq. [24], the first and second terms denoted by the subscript, $n = 2$ and $n = 3$, are the kinetic and potential energy of the ionic polarization of the solvent, and those of the semiconductor, respectively. The third and fourth terms in Eq. [24] are the kinetic and potential energy of the orientational vibration of the solvent. The interaction of an electron with the polarization is given by

$$\mathbf{H}_{ep} = \int \int \Psi(\mathbf{r}^*) \Psi(\mathbf{r}) \frac{e(\mathbf{r} - \mathbf{r}')}{|\mathbf{r} - \mathbf{r}'|^3} \cdot \mathbf{P}(\mathbf{r}') d^3\mathbf{r} d^3\mathbf{r}' \quad [25]$$

In the previous section, we assumed that the distribution of an electron has the spherical symmetry with respect to the center of the reductant ion, and that the probability of the electron outside the sphere r_b is zero. Under these conditions, Eq. [25] reduces to

$$\begin{aligned} \mathbf{H}_{ep} &= - \int \frac{e \mathbf{r}'}{|\mathbf{r}'|^3} \cdot \mathbf{P}(\mathbf{r}') d^3\mathbf{r}' \\ &= - \int \mathbf{E}_v(\mathbf{r}') \cdot \mathbf{P}(\mathbf{r}') d^3\mathbf{r}' \quad [26] \end{aligned}$$

where \mathbf{E}_v is the electric field originating from the electron in the reductant ion in the vacuum.

The electric field at \mathbf{r} induces the polarization $\mathbf{P}(\mathbf{r})$ inside the dielectrics, and thus the dielectric is attracted by the force

$$\mathbf{F} = (\mathbf{P} \cdot \nabla) \mathbf{E}_v \quad [27]$$

The work done against this electrical force in carrying the dielectrics from $|\mathbf{r}'| = \infty$ to $|\mathbf{r}'|$ is $-\int_{r=\infty}^{r'} \mathbf{F}(\mathbf{r}') \cdot d\mathbf{r}'$. Thus, the total energy provided from external system is (13)

$$W = - \int d^3\mathbf{r}' \int_{r=\infty}^{r'} \mathbf{F}(\mathbf{r}') \cdot d\mathbf{r}' = - \int d^3\mathbf{r}' \int \mathbf{P} \cdot d\mathbf{E}_v \quad [28]$$

This energy W is also obtained by calculating the difference between the field energy inside the dielectrics and

that in the vacuum (16)

$$W = \frac{1}{4\pi} \int d^3\mathbf{r}' \int \mathbf{E} \cdot d\mathbf{E}_v - \frac{1}{8\pi} \int \mathbf{E}_v^2 d^3\mathbf{r}' \quad [29]$$

The field energy is the work for charging the sphere r_b . Consequently, the subtraction of $eB/2$ in the vacuum from $eB/2$ in the dielectrics

$$eG/2r_b + \frac{eC}{2(r_b^2 + R^2)^{1/2}} - e^2/2r_b \quad [30]$$

must accord with W in Eq. [29]. But in the zero order approximation, $n = m = 0$, there is a small deviation between the work W in Eq. [29] and W in Eq. [30], because the electric field in Eq. [16] includes the high order terms of $\cos \vartheta$, while those terms are neglected in $eB/2$ in Eq. [12]. The work given by Eq. [28] or [29] is converted to both the interaction energy of the electron with the dielectrics, H_{ep} , and the work to polarize the dielectrics, W_p . From Eq. [26] and [28], W_p is written as

$$W_p = - \int d^3\mathbf{r}' \int \mathbf{P} \cdot d\mathbf{E}_v + \int \mathbf{P} \cdot \mathbf{E}_v d^3\mathbf{r}' = \int d^3\mathbf{r}' \int \mathbf{E}_v \cdot d\mathbf{P} \quad [31]$$

Substituting \mathbf{E}_v and \mathbf{P} into Eq. [31], we have

$$W_p = -W = -\frac{1}{2} H_{ep} \quad [32]$$

The relation of $W_p = -W$ leads to

$$W_p = e^2/2r_b - \frac{1}{8\pi} \int \mathbf{E}_{2s} \cdot \mathbf{E}_v dv_2 - \frac{1}{8\pi} \int \mathbf{E}_{3s} \cdot \mathbf{E}_v dv_3 \quad [33]$$

and the relation of $W_p = -1/2 H_{ep}$ yields to

$$W_p = \frac{1}{2} \int \mathbf{P}_{2s} \cdot \mathbf{E}_v dv_2 + \frac{1}{2} \int \mathbf{P}_{3s} \cdot \mathbf{E}_v dv_3 \quad [34]$$

where the volume elements dv_2 and dv_3 indicate that the volume integral must be taken over the space where the solvent is present, and over the space where the semiconductor is present, respectively. Substituting the relations of Eq. [16] and [17] into Eq. [33] or [34], we have

$$W_p = e^2/2r_b - \frac{1}{8\pi} \int (G_s \frac{\mathbf{r}}{|\mathbf{r}|^3} + C_s \frac{\mathbf{r}^*}{|\mathbf{r}^*|^3}) \cdot \frac{e\mathbf{r}}{|\mathbf{r}|^3} dv_2 - \frac{1}{8\pi} \int D_s \frac{\mathbf{r}}{|\mathbf{r}|^3} \cdot \frac{e\mathbf{r}}{|\mathbf{r}|^3} dv_3 \quad [35]$$

$$W_p = \frac{\epsilon_{2s} - 1}{8\pi} \int (G_s \frac{\mathbf{r}}{|\mathbf{r}|^3} + C_s \frac{\mathbf{r}^*}{|\mathbf{r}^*|^3}) \cdot \frac{e\mathbf{r}}{|\mathbf{r}|^3} dv_2 + \frac{\epsilon_{3s} - 1}{8\pi} \int D_s \frac{\mathbf{r}}{|\mathbf{r}|^3} \cdot \frac{e\mathbf{r}}{|\mathbf{r}|^3} dv_3 \quad [36]$$

The volume integrals in Eq. [35] and [36] are carried out by the variable change as follows (see Fig. 2 and 3)

$$\int \frac{\mathbf{r}}{|\mathbf{r}|^3} \cdot \frac{\mathbf{r}}{|\mathbf{r}|^3} dv_2 = \int_{r>r_b} \frac{4\pi r^2}{r^4} dr - \int_{z=R/2}^{\infty} \int_{y=0}^{\infty} \frac{2\pi y dy dz}{(z^2 + y^2)^2} = 4\pi/r_b - 2\pi/R \quad [37]$$

$$\int \frac{\mathbf{r}}{|\mathbf{r}|^3} \cdot \frac{\mathbf{r}^*}{|\mathbf{r}^*|^3} dv_2 = \int_{r=r_b}^{\infty} \int_{\vartheta=0}^{\pi} \frac{(r^2 - Rr \cos \vartheta) 2\pi r^2 \sin \vartheta d\vartheta dr}{2r^3 (r^2 + R^2 - 2Rr \cos \vartheta)^{3/2}} - \int_{r=r_b}^{\infty} \int_{\vartheta=0}^{\pi} \frac{(r^2 - Rr \cos \vartheta) 2\pi r^2 \sin \vartheta d\vartheta dr}{2r^3 (r^2 + R^2 - 2Rr \cos \vartheta)^{3/2}} = 2\pi/R \quad [38]$$

$$\int \frac{\mathbf{r}}{|\mathbf{r}|^3} \cdot \frac{\mathbf{r}}{|\mathbf{r}|^3} dv_3 = \int_{z=R/2}^{\infty} \int_{y=0}^{\infty} \frac{2\pi y dy dz}{(z^2 + y^2)^2} = 2\pi/R \quad [39]$$

Accordingly, the work W_p is written as

$$W_p = e^2/2r_b - eG_s/2r_b - eC_s/2R \quad [40]$$

or

$$W_p = e \epsilon_{2s} G_s/2r_b - eG_s/2r_b - eC_s/2R \quad [41]$$

But W_p in Eq. [41] deviates from W_p in Eq. [40] by the small term of $2^{-1}e^2b^2 (b^2 + R^2)^{-3/2} (\epsilon_{2s} - \epsilon_{3s}) (\epsilon_{2s} + \epsilon_{3s})^{-1}$, which disappears when the distance R is larger than r_b . This deviation is ascribed to the inaccuracy of the zero order approximation of the coefficient G , C , and D . The rearrangement energy for one vibrational mode is defined as the energy required to attain the new equilibrium of the interaction mode after electron transfer. Except for the electronic polarization, the ionic and orientational polarization can be related to the characteristic vibrations. The rearrangement energy due to one vibrational mode can be defined as the work required to induce the polarization arising from such vibrational mode. The polarization of the solvent, \mathbf{P}_{2e} , \mathbf{P}_{2i} , and \mathbf{P}_{2d} is independently determined by using the response time to the fluctuation of the electron distribution. The energy W_p in Eq. [40] is the total work to induce the electronic, ionic, and orientational polarization inside the dielectrics. Since the semiconductor has no low energy vibration such as the orientational vibration of the solvent, the rearrangement energy due to the orientational vibration of the solvent

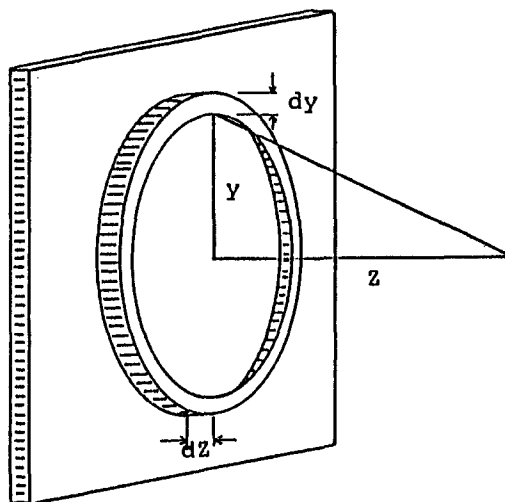


Fig. 2. Volume element considered for determining the volume integral in Eq. [37].

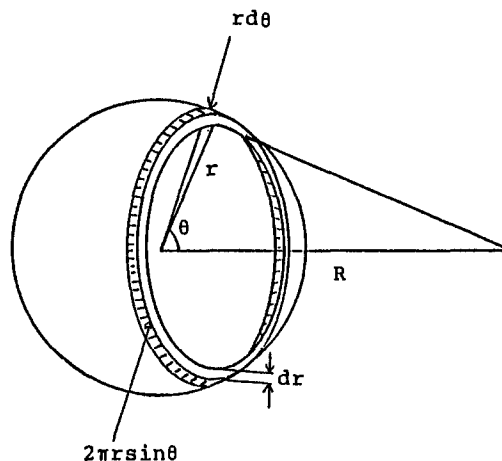


Fig. 3. Volume element considered for determining the volume integral in Eq. [38].

can be obtained by subtracting the work required to induce the polarization in the infrared region, $W_p(\text{IR})$ from the total work W_p

$$E_s(\text{os}) = \frac{e}{2r_b} (G_r - G_s) + \frac{e}{2R} (C_r - C_s) \quad [42]$$

The rearrangement energy for the high energy vibration $E_s(\text{IR})$ is

$$E_s(\text{IR}) = \frac{e}{2r_b} (G_o - G_r) + \frac{e}{2R} (C_o - G_r) \quad [43]$$

The response time of the lattice vibration is similar to that of the intramolecular vibration of the solvent, so that the rearrangement energy due to the lattice vibration cannot be separated from that for the intramolecular vibrations of the solvent. The residual term due to the electronic polarization modifying the electronic energy has been usually included in H_e' (15).

For comparison, we show the formulas of $E_s(\text{os})$ and $E_s(\text{IR})$ for the electron transfer at the metal/electrolyte interface. Dielectric constant of a metal is infinite, because the electric field inside a metal is screened by free electrons. By introducing the relation of $\epsilon_{3s} = \epsilon_{3r} = \epsilon_{3o} = \infty$ into Eq. [42] and [43], we have

$$E_s(\text{os}) = e^2 (1/\epsilon_{2r} - 1/\epsilon_{2s}) (1/2 r_b - 1/2 R) (1 - r_b^3 (r_b^2 + R^2)^{-3/2})^{-1} \quad [44]$$

$$E_s(\text{IR}) = e^2 (1/\epsilon_{3o} - 1/\epsilon_{2r}) (1/2 r_b - 1/2 R) (1 - r_b^3 (r_b^2 + R^2)^{-3/2})^{-1} \quad [45]$$

When the distance R is large enough compared with r_b , Eq. [44] and [45] coincide with Marcus formulas for $E_s(\text{os})$ and $E_s(\text{IR})$ at a metal electrode. That is, Marcus formulas for $E_s(\text{os})$ for heterogeneous electron transfer reactions are valid for the limiting case of $R \geq r_b$ (17). In the practical case that the distance R is at least larger than $2r_b$, the correction due to the term $1/[1 - b^3 (b^2 + R^2)^{-3/2}]^{-1}$ is less than 8%.

The rearrangement energy due to the interaction between an electron and the intramolecular vibration in an ion, $E_s(\text{intra})$, is written as (2, 9)

$$E_s(\text{intra}) = \sum_j \frac{f_j \times f_j^*}{f_j + f_j^*} (\Delta q_j)^2 \quad [46]$$

where f_j and f_j^* are the force constants of the j th interaction mode in the oxidant and reductant ions, respectively, and Δq_j is the change in the equilibrium coordinate of the interaction mode before and after electron transfer.

Results and Discussion

The experimental $E_s(\text{os})$ values have been estimated from the electron transfer rate constants by using Marcus formula (9), or from the I-V characteristics (5-8). In order to compare theoretical $E_s(\text{os})$ and $E_s(\text{IR})$ values with experimental values, we consider the role of the rearrangement energy on the electron transfer rate. When the non-adiabatic electron transfer occurs from the occupied conduction band to the oxidant ion, the cathodic current density is given by (19)

$$i = \frac{4 \pi e}{\hbar} \int C_o(x) dx \int | \langle \Psi_i(E) | U(x, E) | \Psi_f(x, E) \rangle |^2 \rho_D(x, E) \rho_{sc}(E) dE \quad [47]$$

where C_o is the concentration of the oxidant ion, Ψ_i is the wavefunction of the electron in the conduction band, Ψ_f is the wavefunction of the electron in the reductant ion, ρ_D represents the state density of phonons, ρ_{sc} represents the state density of the conduction band, U is the perturbation causing the electron transfer, x is the distance between the semiconductor surface and the center of the reductant ion, and E is the energy of the transferring electron. The phonon-state density depends on the dis-

tance between the electrode surface and the center of the ion, because the phonon-state density is dependent on the rearrangement energy, which is a function of the distance x . Since the square of the matrix element in Eq. [47] decreases quickly with the increase in the distance, Eq. [47] can be approximated as follows (20)

$$i = \frac{4 \pi e}{\hbar} C_o d \int | \langle \Psi_i(E) | U(d, E) | \Psi_f(d, E) \rangle |^2 \rho_D(d, E) \rho_{sc}(E) dE \quad [48]$$

where d is nearly the sum of the ion radius r_b and the thickness of the Helmholtz layer d_H . The current density, which is observed experimentally at a metal or a semiconductor/electrolyte interface, may provide information about $E_s(\text{os})$ and $E_s(\text{IR})$ values at $R/2 = r_b + d_H$. For the comparison of theoretical $E_s(\text{os})$ and $E_s(\text{IR})$ values with experimental values we calculated the theoretical $E_s(\text{os})$ and $E_s(\text{IR})$ values at $R/2 = b + d_H$. The calculated $E_s(\text{os})$ and $E_s(\text{IR})$ values for some redox species are listed in Table I.

As is seen in Table I, the theoretical $E_s(\text{os})$ values at two semiconductor electrodes are larger than that at metal electrodes. The variation of the theoretical $E_s(\text{os})$ values among electrodes arises from the difference in the magnitude of the induced mirror image charge. Besides theoretical $E_s(\text{os})$ values, the large theoretical $E_s(\text{IR})$ values due to the intramolecular vibration of the solvent and the lattice vibrations in ionic semiconductors were evaluated for $\text{Fe}^{2+/3+}$, $\text{Ce}^{3+/4+}$, and $\text{Fe}(\text{bpy})_3^{2+/3+}$ at the SnO_2 and TiO_2 electrodes. Further, the appreciable $E_s(\text{intra})$ values due to the symmetric breathing mode of metal-ligand stretching vibration in the first coordinational sphere (M-L vibration) have been obtained experimentally for $\text{Fe}^{2+/3+}$ and $\text{Ce}^{3+/4+}$. This result implies that the electron transfer at an ionic semiconductor/electrolyte interface occurs with accompanying the excitation and emission of multiphonons in these high energy vibrations. The role of M-L vibration on the electron transfer in polar solvents was first considered classically by Hush and Marcus (2, 21). Subsequently, quantum treatment of M-L vibration was carried out by Kestner *et al.* (18), who gave the phonon-state density as

$$\rho_D(d, E) = \left(\frac{1}{4 \pi K T E_s(\text{os})} \right)^{1/2} \sum_{m=-\infty}^{\infty} \exp [- (E - E^\circ - E_s(\text{os}) - m \hbar \omega_c)^2 / 4 K T E_s(\text{os})] \times \exp [- Z_c \cosh(\hbar \omega_c / 2 K T) + m \hbar \omega_c / 2 K T] I_m(Z_c) \quad [49]$$

where $Z_c = E_s(\text{intra})/\hbar \omega_c \times \text{cosech}(\hbar \omega_c / 2 K T)$, and $I_m(Z_c) =$

$(Z_c/2)^m \sum_{k=0}^{\infty} (Z_c/2)^{2k} / [k!(m+k)!]$. In Eq. [49], E° is the electronic

energy corresponding to the standard redox potential, $\hbar \omega_c$ is the energy of the M-L vibration. High energy vibrations in the initial state are not sufficiently excited at room temperature. For endothermic or small exothermic reactions, the phonon state density arising from these high energy vibrations accords approximately with the Franck-Condon factor between the ground vibrational state at the initial state and that at the final state, and is independent of the free energy difference. In such case, only $E_s(\text{os})$ values can be determined from the free energy relationship of the electron transfer rate (17). For large exothermic reactions, since electron transfer can occur via excited vibrational states in the final state and the phonon-state density is influenced by high energy vibrations, the electron transfer rate is prompted. In order to evaluate quantitatively the effect of the high energy vibrations on the phonon-state density, we quote experimental values of the rearrangement energy estimated from the electrochemical rate constants at the zero overvoltage, or values from the isotropic exchange rate. If the exponential term of the phonon-state density at zero-free energy difference, $\Delta E = E - E^\circ = 0$, is formally written as $\exp(-E_s/4kT)$, the total rearrangement energy E_s at room temperature is approximately given by (18, 19, 22)

Table I. Theoretical and experimental rearrangement energy for several redox species

Electrode	Solvent	Redox species		Helmholtz layer thickness (Å)	$E_s(o_s)$ (eV)	$E_s(IR)$ (eV)	$E_s(intra)$ (eV)	E_s (eV)
SnO ₂ $\epsilon_{30} = 4^a$ $\epsilon_{3r} = 10^b$ $\epsilon_{3s} = 10^a$	H ₂ O $\epsilon_{20} = 1.78$	Fe ^{2+/3+}	(A)	3.0	0.39	0.58	(0.46)	1.00
			(B)	1.0	0.37	0.55	(0.46)	0.97
			(B)	—	(0.5) ^d	—	0.46 ^e	1.20 ^f
	Ce ^{3+/4+}	(A)	3.0	0.36	0.53	(0.10)	0.62	
		(B)	1.0	0.34	0.52	(0.10)	0.60	
		(B)	—	0.65 ^g	—	0.10 ^e	1.75 ^f	
Fe(bpy) ₃ ^{2+/3+}	ε _{2s} = 78	(A)	3.0	0.20	0.29	(0.0)	0.30	
		(B)	1.0	0.19	0.29	(0.0)	0.29	
		(B)	—	0.15 ^h	—	0.0 ⁱ	—	
TiO ₂ $\epsilon_{30} = 7.6^c$ $\epsilon_{3r} = 89^c$ $\epsilon_{3s} = 89^c$	H ₂ O $\epsilon_{20} = 1.78$	Fe ^{2+/3+}	(A)	3.0	0.33	0.57	(0.46)	0.93
			(B)	1.0	0.29	0.54	(0.46)	0.88
			(B)	—	(0.5) ^d	—	0.46 ^e	—
	Ce ^{3+/4+}	(A)	3.0	0.31	0.53	(0.10)	0.57	
		(B)	1.0	0.27	0.51	(0.10)	0.53	
		(B)	—	—	—	0.10 ^e	—	
Fe(bpy) ₃ ^{2+/3+}	ε _{2s} = 78	(A)	3.0	0.16	0.29	(0.0)	0.26	
		(B)	1.0	0.14	0.28	(0.0)	0.23	
		(B)	—	—	—	0.0 ⁱ	—	
Metal	H ₂ O $\epsilon_{20} = 1.78$	Fe ^{2+/3+}	(A)	3.0	0.32	0.46	(0.46)	0.89
			(B)	1.0	0.27	0.38	(0.46)	0.81
			(B)	—	—	—	0.46 ^e	1.2 ^j , 1.5 ^k
	Ce ^{3+/4+}	(A)	3.0	0.3	0.42	(0.10)	0.53	
		(B)	1.0	0.25	0.36	(0.10)	0.46	
		(B)	—	—	—	0.10 ^j	1.3 ^j , 2.1 ^m	
Fe(bpy) ₃ ^{2+/3+}	ε _{2s} = 78	(A)	3.0	0.15	0.21	(0.0)	0.22	
		(B)	1.0	0.13	0.19	(0.0)	0.19	
(B)	—	—	—	0.0 ⁱ	0.35 ⁿ			

(A): Theoretical values of rearrangement energy.

(B): Experimental values of rearrangement energy.

^a From Ref. (27). ^b From Ref. (28). ^c From Ref. (29). ^d From Ref. (3). ^e From Ref. (30). ^f From Ref. (5). ^g From Ref. (7). ^h From Ref. (23). ⁱ From Ref. (31). ^j From Ref. (32). ^k From Ref. (33). ^l From Ref. (34). ^m From Ref. (35). ⁿ From Ref. (36).

$$E_s = E_s(o_s) + \frac{4KTE_s(IR)}{\hbar\omega_r} [\coth(\hbar\omega_r/2kT) - \operatorname{cosech}(\hbar\omega_r/2kT)] + \frac{4KT E_s(intra)}{\hbar\omega_c} [\coth(\hbar\omega_c/2kT) - \operatorname{cosech}(\hbar\omega_c/2kT)] \quad [50]$$

where $\hbar\omega_c$ is the M-L vibrational energy and $\hbar\omega_r$ is the energy of the lattice vibration or the intramolecular vibration of the solvent. In the calculation of the E_s values in Table I, the vibrational energy $\hbar\omega_r$ was assumed to be about 0.01 eV, which is the intramolecular vibrational energy of H₂O (10). The experimental E_s values at metal electrodes in Table I were estimated not only from the electrochemical reaction rate constants at metal electrodes, but also from the isotropic exchange rate constants, by using Marcus' formulas (9).

For Fe(bpy)₃^{2+/3+}, the theoretical $E_s(o_s)$ value at the SnO₂ electrode is consistent with the experimental value of 0.15 eV (23). Furthermore, theoretical E_s value is also close to the experimental E_s values. The good agreement between theory and experiment for the E_s values is attributable to the validity of the application of the adiabatic electron transfer to Fe(bpy)₃^{2+/3+}. In the reductant ion, Fe(bpy)₃²⁺, appreciable 3d electron density is found in the ligand π^* orbitals by virtue of the back-donation interaction. Similarly, in the oxidant ion, Fe(bpy)₃³⁺, the acceptor d orbital extends to the ligands. Thus, for the isotropic reaction of Fe(bpy)₃²⁺ - Fe(bpy)₃³⁺ and the electrochemical reaction of Fe(bpy)₃^{2+/3+} at a metal electrode, the electronic matrix element coupling the initial and final states of the electron transfer is expected to be large, leading to the adiabatic electron transfer (24).

The rearrangement energy for Fe^{2+/3+} and Ce^{3+/4+} reported by Memming and Möller (5) may be close to E_s

values rather than $E_s(o_s)$ values, because I-V curves at the SnO₂ electrode were measured at the high overvoltage region. Though the experimental $E_s(o_s)$ values for Fe^{2+/3+} were not obtained for two semiconductor electrodes listed in Table I, the $E_s(o_s) = 0.5$ eV was estimated at the organic crystal electrodes (3). The variation of the theoretical $E_s(o_s)$ values at the two semiconductor electrodes in Table I is not so large that the experimental $E_s(o_s)$ value for Fe^{2+/3+} at a semiconductor electrode may not be different significantly from 0.5 eV. The theoretical $E_s(o_s)$ values for Fe^{3+/4+} and Ce^{3+/4+} are smaller than the experimental values. Concerning the E_s values of Fe^{2+/3+} and Ce^{3+/4+}, the agreement between theory and experiment is very poor. This discrepancy was ascribed to the nonadiabaticity of the electron transfer (24). In fact, the transmission coefficient smaller than unity ($\kappa = 0.012$) was obtained for the reduction of Fe³⁺ by Willig *et al.* (3). For cerium ions, the accurate transmission coefficient has not been determined. Balzani *et al.* (4) reported that, from the consideration of the intensity of spectroscopic transition, the transmission coefficient is about 10⁻⁵ for the electron transfer reactions between Eu²⁺ or Eu³⁺ and an adiabatic-type partner, and that $\kappa = 10^{-10}$ for Eu²⁺-Eu³⁺ exchange reaction. Such a nonadiabatic behavior observed for lanthanide ions such as cerium or europium was interpreted in terms of the strong shield of the 4f orbitals by the 5s and 5p orbitals (4, 25). Consequently, a small transmission coefficient may be expected for the electron transfer including Ce³⁺ or Ce⁴⁺.

Kestner *et al.* (17) derived first the formula of $E_s(o_s)$ for homogeneous electron transfer, in which the ionic radius is changed after electron transfer. In their paper, the electric displacement was expressed by the charge of the oxidant or reductant ions, and the obtained formula of $E_s(o_s)$ gave the same representation of $E_s(o_s)$ as Marcus' formula if no variation of the ionic radius occurs after electron

transfer. If the ionic radius is changed, the formula of $E_s(o_s)$ derived by Kestner *et al.* increases with the increase in the charge of the oxidant ion. In principle, the formula of $E_s(o_s)$, which reflects the interaction of the electron in the reductant ion with the solvent, is independent of the charge of the oxidant ion (26). The conflicting result can be explained as follows: the ionic radius of the reductant ion, r_b , is larger than that of the oxidant ion r_a . Thus, the vacant space with the shell structure is generated by the contraction of the ionic radius after the electron transfer from the reductant ion to the electrode. The generated vacant space is filled with the solvent surrounding the ion. The solvent in the vacant space is not polarized by the transferring electron, but is polarized by the charge of the oxidant ion. According to the description of the electric displacement by Kestner *et al.*, this polarization energy of the solvent by the charge of the oxidant ion was necessarily included in the formula of $E_s(o_s)$. This polarization energy should be taken into the total adiabatic potential energy (the total free energy) rather than the rearrangement energy of the orientational vibration of the solvent, $E_s(o_s)$.

Acknowledgment

The support of this research by Grant-in-Aid for Scientific Research, is gratefully acknowledged.

Manuscript submitted July 5, 1983; revised manuscript received March 5, 1984.

The Technological University of Nagaoka assisted in meeting the publication costs of this article.

REFERENCES

1. R. Kubo and Y. Toyozawa, *Prog. Theor. Phys.*, **13**, 160 (1955); K. Freed and J. Jortner, *J. Chem. Phys.*, **52**, 6272 (1970); C. H. Henry and D. V. Lang, *Phys. Rev. B*, **15**, 989 (1977).
2. R. A. Marcus, *Electrochim. Acta*, **13**, 995 (1968); K. W. Frese, Jr., *J. Phys. Chem.*, **85**, 3911 (1981).
3. F. Willig, G. Scherer, and W. Röthamel, *Ber. Bunsenges. Phys. Chem.*, **77**, 921 (1973).
4. V. Balzani, F. Scandola, G. Orlandi, N. Sabbatini, and M. T. Indelli, *J. Am. Chem. Soc.*, **103**, 3370 (1981).
5. R. Memming and R. Moller, *Ber. Bunsenges. Phys. Chem.*, **76**, 475 (1972).
6. K. E. Heusler and K. S. Yun, *Electrochim. Acta*, **22**, 977 (1977).
7. K. Kobayashi, Y. Aikawa, and M. Sukigara, *Bull. Chem. Soc. Jpn.*, **55**, 2820 (1982).
8. K. W. Frese, Jr., M. J. Madou, and S. R. Morrison, *This Journal*, **128**, 1527 (1981); S. R. Morrison, M. J. Madou, and K. W. Frese, Jr. in "Photoeffect at Semiconductor-Electrolyte Interfaces," A. J. Nozik, Editor, ACS Symposium Series 146, American Chemical Society (1981).
9. R. A. Marcus, *J. Chem. Phys.*, **43**, 679 (1965).
10. J. B. Hasted, "Aqueous Dielectrics," Chapman and Hall, London (1973).
11. W. A. Harrison, "Solid State Theory," McGraw-Hill, New York (1970).
12. H. Fröhlich, *Adv. Phys.*, **3**, 325 (1954).
13. K. W. H. Panosky and M. Philips, "Classical Electricity and Magnetism," Addison-Wesley, London (1969).
14. J. G. Kirkwood, *J. Chem. Phys.*, **2**, 351 (1934).
15. H. Haken, "Quantenfeldtheorie des Festkörpers," B. G. Teubner, Stuttgart, Germany (1973).
16. R. A. Marcus, *J. Chem. Phys.*, **24**, 979 (1956).
17. R. D. Cannon, *Chem. Phys. Lett.*, **49**, 299 (1977).
18. N. R. Kestner, J. Logan, and J. Jortner, *J. Phys. Chem.*, **78**, 2148 (1974).
19. K. Kobayashi, Y. Aikawa, and M. Sukigara, *J. Electroanal. Chem.*, **134**, 11 (1982).
20. V. G. Levich, in "Physical Chemistry, an Advanced Treaty," Vol. 9B, H. Eyring, D. Henderson, and W. Jost, Editors, p. 985, Academic Press, New York (1970).
21. N. S. Hush, *Trans. Faraday Soc.*, **57**, 557 (1961).
22. R. R. Dogonadze, A. M. Kuznetsov, and M. A. Vorotyntsev, *Z. Phys. Chem.*, **100**, 1 (1976).
23. K. Kobayashi, M. Takata, S. Okamoto, Y. Sekine, Y. Aikawa, and M. Sukigara, *Chem. Phys. Lett.*, **104**, 253 (1984).
24. M. Chou, C. Creutz, and N. Sutin, *J. Am. Chem. Soc.*, **99**, 5615 (1977).
25. H. Taube, *Adv. Chem. Ser.*, **162**, 127 (1977).
26. J. O'M. Bockris and S. U. M. Khan, "Quantum Electrochemistry," Plenum Press, New York (1979).
27. R. Summitt, *J. Appl. Phys.*, **39**, 3762 (1968).
28. P. Siders and R. A. Marcus, *J. Am. Chem. Soc.*, **103**, 741 (1981); J. B. Hasted, "Aqueous Dielectrics," Chapman and Hall, London (1973).
29. F. A. Grant, *Rev. Mod. Phys.*, **31**, 646 (1959); W. D. Kingery, H. K. Bowden, and D. R. Uhlmann, "Introduction to Ceramics," John Wiley and Sons, New York (1976).
30. J. M. Hale, in "Reactions of Molecules at Electrodes," N. S. Hush, Editor, John Wiley and Sons, London (1971).
31. C. Creutz, M. Chou, T. L. Netzel, M. Okumura, and N. Sutin, *J. Am. Chem. Soc.*, **102**, 1309 (1980).
32. J. Silverman and R. W. Dodson, *J. Phys. Chem.*, **56**, 846 (1952); K. W. Frese, Jr., *ibid.*, **85**, 3911 (1981).
33. D. Jahn and W. Vielstich, *This Journal*, **109**, 849 (1962).
34. B. Siegler and B. Masters, *J. Am. Chem. Soc.*, **79**, 6353 (1957); K. W. Frese, Jr., *J. Phys. Chem.*, **85**, 3911 (1981).
35. R. Greef and H. Aulich, *J. Electroanal. Chem.*, **18**, 295 (1968).
36. I. Ruff and M. Zimonyi, *Electrochim. Acta*, **18**, 515 (1973).



A New Miniature Lithium-Iron Sulfide Battery

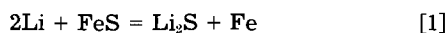
W. E. Aker,^{*1} N. Margalit,^{*2} D. P. Johnson,^{*3} R. J. Ekern,^{*} N. A. Fleischer,^{*} and R. J. Brodd,^{*4}

RAYOVAC Corporation, Madison, Wisconsin 53703

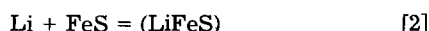
The present market for button cells which power low drain microelectronic devices is served mainly by aqueous silver-zinc and mercury-zinc cells. The mercury cell seems to be of declining interest because of the potential environmental hazards associated with mercury as evidenced by their ban or control in Sweden and Japan. Silver-zinc cells, while totally acceptable for performance, are susceptible to the market price for silver. Lithium cells, as an alternative to both systems, can deliver essentially the same hours of service as silver cells, have less costly components, and are less prone to leakage. Present lithium organic electrolyte cells, however, are for low drain applications only, such as analog watches or LCD watches without backlight or alarm.

Lithium-metal sulfide couples have been explored extensively for high temperature molten salt battery systems (1). Extensive work has been carried out on the Li-TiS₂ system at room temperature (2). Kegelman (3), Kronenberg (4), and Uetani *et al.* (5) have suggested the lithium-iron sulfide system for room temperature operation, but present limited data to substantiate cell performance.

A lithium-iron sulfide cell system is described below which gives performance essentially equivalent to commercial silver cells. Based on the cell reaction



the system has a theoretical voltage of about 1.78V and a theoretical energy density of about 2.14 Wh/cm³ based on the above reaction and the volume of reactants. The reaction product may involve the formation of a compound of the type LiFeS



If this is the case, the theoretical cell voltage could fall in the range 1.55-1.65V.

Experimental

In order to make meaningful comparisons of performance with the existing silver system, all experiments were carried out in a commercial cell construction (IEC designation SR-55). The cell casing material is 316 stainless steel and the sealing insulating grommet is polypropylene. Figure 1 shows the construction of the test cells. All cells were constructed in a dry room with <2% relative humidity. Exposure of lithium and electrolyte to the atmosphere was minimized to prevent contamination. Also, since one of the solvents in the electrolyte mixture, dimethoxyethane (DME), has a high vapor pressure, it evaporates rapidly, and the solvent ratio can change significantly if left exposed for even a short period of time.

The electrolyte solvent, a mixture of propylene carbonate (PC) and DME, was examined at various ratios with

* Electrochemical Society Active Member.

¹ Present address: Rexnord Electronics Company, Malvern, Pennsylvania 19355.

² Present address: Combustion Engineering Incorporated, South Windsor, Connecticut 06074.

³ Present address: BRK Electronics, Aurora, Illinois 60504.

⁴ Present address: Amoco Research Center, Naperville, Illinois 60566.

three solutes, lithium perchlorate (LiClO₄), lithium hexafluoroarsenate (LiAsF₆), and lithium trifluoromethyl sulfonate (LiCF₃SO₃). The PC, obtained from Burdick & Johnson, was dried over Linde 3A molecular sieves. The DME was obtained from Ansul Chemical and redistilled

using a spinning band column. The LiClO₄, from Foote Mineral Company, was specially dried to 25-50 ppm of water. The LiCF₃SO₃ from Minnesota Mining and Manufacturing Company, called Fluorad 124, was dried overnight at 110°C under 10⁻² torr. The LiAsF₆ from USS Agrichemicals was used as received.

A Karl Fisher analysis of the electrolyte prior to cell assembly gave total water concentrations of less than 200 ppm for electrolytes used in cell assembly. A gas chromatographic analysis on the electrolyte extracted from cells after assembly was used to establish the solvent ratio (PC/DME) in the cell.

The anode was 0.014g of pure lithium (99.8% min.) ribbon obtained from Foote Mineral Company. At anode assembly, the lithium is cut to fit inside the cell top and the mating surface was prepared by scraping or buffing. The cell top interior was also scratched just before applying the prepared lithium surface to ensure a good cold weld connection. Lithium alloy anodes were constructed by placing a clean aluminum foil (0.008 cm) in contact with the lithium surface adjacent to the electrolyte. This relates to an alloy composition of approximately 40% aluminum overall. Alloying occurs spontaneously on contact with the electrolyte. This process is very similar to that described by Rao (6). Alloying occurred in this instance after cell closure, *i.e.*, an *in situ* process.

Various iron sulfide (FeS) cathode materials were evaluated in experimental cells. The analytical grade FeS materials obtained from J. T. Baker Chemical Company, Fisher Scientific Company, and Cerac, Incorporated were heated to 910°C. The treated powder was pressed into cathode pellets, reheated to 250°C, and stored at <2% RH for assembly into cells. A particularly active FeS material was prepared by mixing and heating iron powder (Cerac, 100 mesh, 99.6% pure) and sulfur powder (Mallinckrodt, precipitated, UPS) in 1:1.1 weight ratio. The powders were ground in a mortar until a light green homogeneous color developed. This mixture was heated in a mullite tube furnace for 5h at 910° ± 5°C in an argon atmosphere in porcelain boats. This material is referred to as synthesis 4 iron sulfide. An examination of the iron-sulfur phase diagram shows that after heating to 910°C, all materials should be in the iron-rich position of the phase diagram. An x-ray diffraction pattern of the material also indicated some spinel formation. Margalit *et al.* (7) suggested the use of iron-rich sulfide in primary cells.

In cathode assembly, the 0.125g FeS pellets are vacuum-filled with electrolyte and placed in the cathode cup on top of a nickel mesh spacer and current collector. A lithium strip under the nickel mesh served as the voltage reducer. This reduces about 1% of the FeS in the cathode. A Reeve Angel glass matte separator was then placed on the pellet and wetted with a drop (0.02 cm³) of

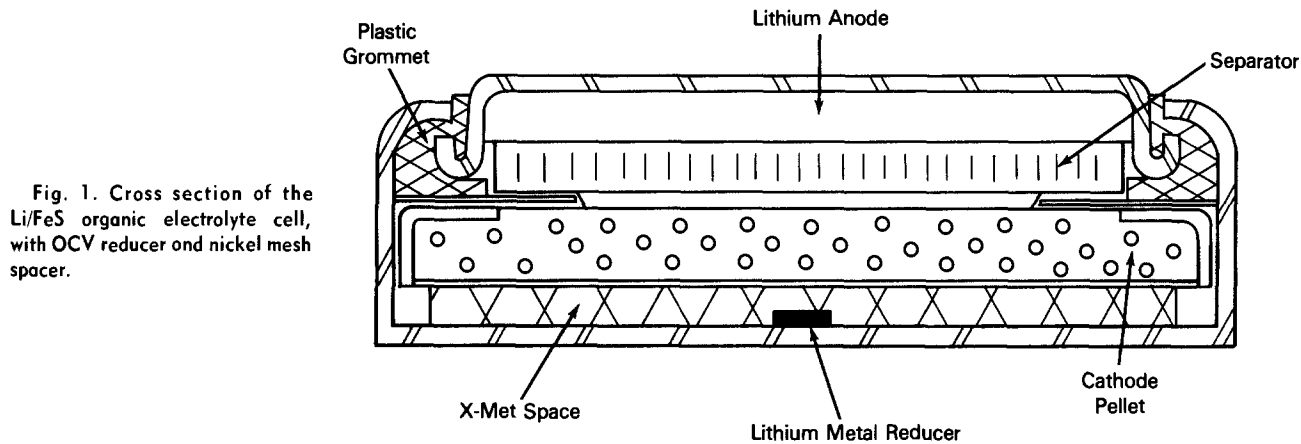


Fig. 1. Cross section of the Li/FeS organic electrolyte cell, with OCV reducer and nickel mesh spacer.

electrolyte. The completed cathode assembly had a 316 stainless steel load bearing ring placed between pellet and separator.

Cell assembly was completed by crimp closing the anode and cathode assemblies in a cell closing die. This operation forms the plastic compression seal common to button cell construction. The cells were stored for a minimum of 72h prior to discharge and exhibited a stable open-circuit voltage (OCV) of about 1.7-1.8V at that time.

The cells were discharged on various regimes of load, time, and temperature, as described below. Low temperature discharges were conducted using a Neslab Endocal RTE-8 refrigerated circulating bath. Measurements of the ohmic drop for the complete cell were made at various stages of discharge. Specific test regimes used to determine cell performance were:

1. Continuous discharge at room temperature on various loads to 1.2V end point (EP) to ascertain cell capacity, rate capability, and voltage level on discharge.

2. Continuous discharge at low temperature (-10°C) to 1.1V EP.

3. Pulse measurements at -10°C on 1 M Ω quiescent load (QL) and 2000 Ω pulse load (PL) for 8 ms/s at selected progressive depths of discharge (DOD). This accelerated test is designed to simulate performance requirements of the electronics for an analog watch.

4. Pulse measurements at room temperature on 300 k Ω QL, 200 Ω PL for 5s duration at 20s intervals, three pulses at selected progressive DOD. This accelerated test is designed to simulate the requirements of the electronics and backlight for a digital liquid crystal watch.

5. Accelerated storage at 60°C for 40 days followed by cell discharge on selected loads to determine capacity retention. A constant temperature laboratory oven was used for 60°C storage. The cells were weighed periodically to determine leakage. This storage condition is thought to correspond to 2 years storage at ambient temperature.

Results and Discussion

Most lithium organic electrolyte cells have a spurious high OCV just after cell assembly. The cells in this study were no exception. This voltage is thought to be associated with absorbed water or active oxygen species on the surface of the cathode powders and, in this case, free sulfur species as well. Several approaches were used to eliminate or reduce this high OCV effect (6-9). These included: (i) pulse discharge after cell assembly, (ii) reducing with an active metal (e.g., Li, Zn) attached to the cathode, (iii) reducing the cathode pellet in butyl lithium, and (iv) improving cathode conductivity using conductive materials, such as lithium nitride and iron powders and by using an iron-rich FeS cathode material.

A lithium nitride addition improved cathode conductivity and low temperature discharge but it did not produce the desired OCV reduction. Cathode reduction using electrolyte-soluble butyl lithium lowered the OCV, but uniformity and extent of reduction were difficult to control.

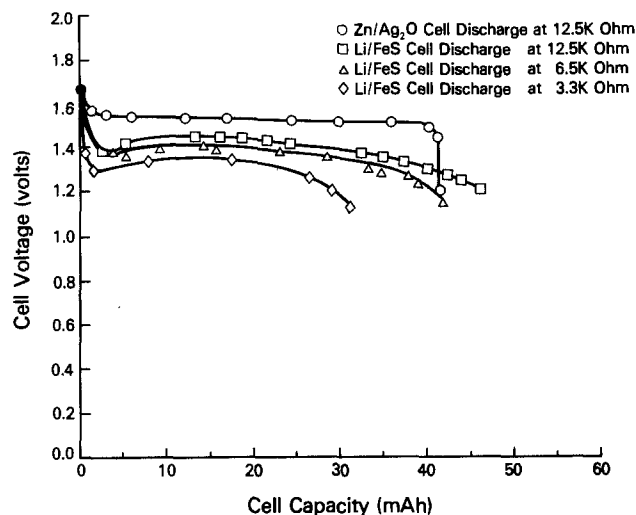


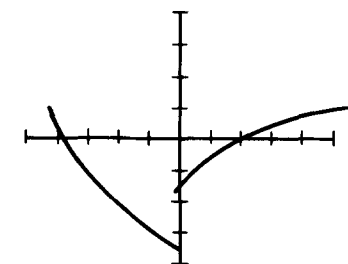
Fig. 2. Continuous discharge performance of Li/FeS on three loads at room temperature. The continuous discharge performance of Zn/Ag₂O on 12.5 k Ω is included for purposes of comparison.

A small strip of lithium attached to the nickel grid cathode collector just before cell assembly proved to be the most practical and reproducible method overall. This technique uniformly reduced about 1% of the active material in the cathode along with extraneous impurities and produced stable OCV's at or near the reversible cell voltage. It also improved cathode performance and led to better high rate cell performance. The final cell design used the lithium strip reducer and an iron-rich iron-sulfide cathode material.

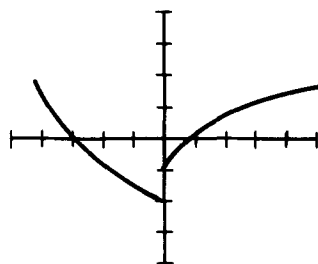
Typical cell discharge behavior is shown in Fig. 2. The cells deliver over 40 mAh on 10 k Ω and lower drain rates. The best cells gave over 45 mAh at similar drains. In comparison with a Zn-Ag₂O cell, the silver cell has about 100 mV higher discharge voltage and can deliver over 43 mAh capacity. The efficiency of utilization of the FeS cathode is about 60% at the lower current drains. Table I gives the results of accelerated storage. The capacity retention is excellent. The cells showed negligible loss of capacity at 12.5 k Ω load after 40 days at 60°C . None of the cells gained or lost weight during accelerated storage. The plastic compression seal proved to be reliable for this applica-

Table I. Capacity retention for Li/FeS cells after storage at 60°C for 40 days

Discharge load (k Ω)	Capacity		Capacity retention (%)
	Initial (mAh)	After storage (mAh)	
6.5	43.3	41.9	96.8
12.5	46.0	45.9	99.8

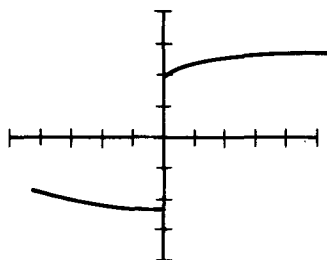


Horizontal Axis: 20 ms/Div
 Vertical Axis: 20 mV/Div
 Depth of Discharge: 11.1 mAh
 Cell Impedance: 44 Ω



Horizontal Axis: 2 ms/Div
 Vertical Axis: 20 mV/Div
 Depth of Discharge: 20.8 mAh
 Cell Impedance: 21 Ω

Fig. 3. Li/FeS cell voltage during analog pulse test at -10°C .



Horizontal Axis: 2 ms/Div
 Vertical Axis: 50 mV/Div
 Depth of Discharge: 45.8 mAh
 Cell Impedance: 270 Ω

tion. This period of 60°C storage corresponds to approximately 2 yr storage at room temperature.

Cells which performed well on continuous discharge at -10°C generally gave good overall performance. The LiClO_4 electrolyte gave the best performance followed by LiCF_3SO_3 and then LiAsF_6 . Cyclohexane addition to the electrolyte to lower viscosity and improve conductivity had little effect on overall performance. Cells with lower solute content and lower DME content gave better performance. Best performance on continuous discharge was obtained from cells having about 1.2M LiClO_4 in a 62 weight percent (w/o) PC/38 w/o DME solvent mixture with less than 60 ppm H_2O content. At -10°C , the best cells discharged on a 3.3 k Ω load for 6 min to 1.2V and over 280 min to the 1.1V cutoff. These results satisfied a minimum performance requirement for low temperature operation of electronic devices.

Of the cathode materials, only the synthesis 4 FeS could sustain the analog pulse beyond 40 mAh and also meet the room temperature backlight pulse regime at about 40 mAh (87% DOD). In both the analog and digital pulse tests, the best cell construction was an Li/Al alloy anode, synthesis 4 cathode, and 45 w/o PC/55 w/o DME/1.4M LiClO_4 electrolyte. Typical cell polarization and recovery curves for this system during analog pulse tests are shown in Fig. 3. The IR component of the cell polarization decreases slightly as the discharge proceeds through about 50% DOD. At this point, the total polarization and its ohmic component are at their lowest levels and so the pulse voltage is at its highest level. The lower polarization could result from an increase in surface area available for reaction as a result of the breaking up of FeS particles to produce smaller particles with higher total reaction area. The decrease in pulse polarization at mid-DOD is also associated with a slight increase in the quiescent load operating voltage (Fig. 2). This slight increase may be due to the formation of iron, a low resistance reaction product, in the cathode. The IR component then increases gradually until about 95% DOD where it begins to increase rapidly and becomes the dominant factor in cell failure on this test. Activation and concentration polarization are relatively small fractions of the total cell polarization towards the end of discharge.

At the end of discharge, the microporosity developed in the cathode during discharge is thought to cause the cathode to absorb electrolyte from the relative open-structure separator. This drying out of the separator likely accounts for the increased internal resistance and resultant cell fail-

ure before complete utilization of the active materials. The precipitation of the nonconductive Li_2S reaction product at the cathode would also block off the electrode and increase internal resistance.

An examination of the cells after discharge showed incidence of swelling. The amount of swelling generally increased with cell discharge. A full discharge resulted in about a 15% increase in cell height. Cell swelling has been isolated to at least a cathode phenomenon and is a complex event, affected by original pellet porosity and the discharge products, Fe and Li_2S . Lithium sulfide aggravates the problem because it is insoluble in the electrolyte and has a high molar volume (27.7 cm^3/mol).

Conclusions

A lithium-iron sulfide, propylene carbonate-dimethoxyethane, lithium perchlorate cell system has been identified which shows promise of equaling the performance of silver cells in selected applications. The use of alloy anodes improves pulse capability of lithium anodes in organic electrolytes. The cathode composition controls the overall efficiency of utilization and the energy density. Iron-rich FeS cathode compositions were shown to have excellent performance for various cell applications.

Acknowledgment

This work was performed at Inco Sterling Forest with the financial support of RAYOVAC Corporation. The authors thank RAYOVAC for permission to publish the information contained herein.

Manuscript submitted Dec. 7, 1983; revised manuscript received Jan. 3, 1984.

REFERENCES

1. R. U. Glazebrook and M. J. Willars, *J. Power Sources*, **8**, 327, 341 (1982).
2. M. S. Whittingham, *Prog. Solid State Chem.*, **12**, 41 (1978); G. C. Farrington and J. L. Briant, *Science*, **204**, 1371 (1979); D. W. Murphy and P. A. Christian, *ibid.*, **205**, 651 (1979).
3. M. R. Kegelman, U.S. Pat. 4,084,045 (1978).
4. M. L. Kronenberg, U.S. Pat. 3,951,685 (1978).
5. Y. Uetani, K. Yokoyama, and T. Kawai, in "Proceedings of the 28th Power Sources Conference," Atlantic City, NJ, June 12-15, 1978, The Electrochemical Society, Inc., p. 217 (1979).
6. B. M. L. Rao, U.S. Pat. 4,056,885 (1977).
7. N. Margalit, A. Joshi, D. Johnson, and W. E. Aker, U.S. Pat. 4,322,869 (1982).
8. A. Joshi, U.S. Pat. 4,307,764 (1981).
9. M. B. Dines, *Mater. Res. Bull.*, **10**, 287 (1975).

Calculation of the Free Energy of Formation of Ferrous Chloride Tetrahydrate

E. McCafferty*

Naval Research Laboratory, Washington, DC 20375

Under certain conditions, ferrous chloride tetrahydrate, $\text{FeCl}_2 \cdot 4\text{H}_2\text{O}$ is a corrosion product on iron or steel in chloride environments. $\text{FeCl}_2 \cdot 4\text{H}_2\text{O}$ has been identified as a corrosion product on plain carbon steel in hydrochloric acid solutions (1) and in hydrochloric acid vapors (2, 3). Although not a major corrosion product in the atmospheric corrosion or marine corrosion of iron, ferrous chloride salts can be found in localized regions within natural rust layers (4-7).

In the localized corrosion of iron or steel, Pourbaix has developed a generalized model of the thermodynamic conditions within pits, crevices, or stress corrosion cracks (8). According to Pourbaix's model, the internal electrolyte within such "occluded corrosion cells" (9) is a saturated ferrous chloride solution, in equilibrium with the solid corrosion products Fe_3O_4 and $\text{FeCl}_2 \cdot 4\text{H}_2\text{O}$. A number of experimental studies, mostly with stainless steels, have confirmed that occluded cell electrolytes become concentrated in metallic cations and in chloride ions (10-15). Recent thermodynamic calculations taking activity coefficients into account (16) have verified that at equilibrium, the internal electrolyte in the case of pure iron is saturated solution of ferrous chloride. The stable solid phase in equilibrium with saturated ferrous chloride solutions is the tetrahydrate $\text{FeCl}_2 \cdot 4\text{H}_2\text{O}$ (17, 18); and its presence in scaled-up models of localized corrosion cells on iron has been confirmed experimentally (19, 20).

Despite the importance of $\text{FeCl}_2 \cdot 4\text{H}_2\text{O}$ in both the localized and general corrosion of iron and steel, thermodynamic data for the tetrahydrate are somewhat lacking. Standard compilations (21) list the enthalpy of formation ΔH_f° , but not the free energy of formation ΔG_f° of $\text{FeCl}_2 \cdot 4\text{H}_2\text{O}$. The only published value for the free energy of formation of $\text{FeCl}_2 \cdot 4\text{H}_2\text{O}$ appears to be the value calculated by Susarev *et al.* (22).

The free energy of formation of $\text{FeCl}_2 \cdot 4\text{H}_2\text{O}$ has been calculated here in three ways: (i) from the equilibrium between the hydrate and its saturated solution, (ii) by estimation of the entropy of formation ΔS_f° , and (iii) by comparison of free energies of formation of a series of hydrates with values for their anhydrous salts. The average result of these calculations is $\Delta G_f^\circ [\text{FeCl}_2 \cdot 4\text{H}_2\text{O}_{(s)}] = -306.0$ kcal/mol. The value given previously by Susarev *et al.* is -304.3 kcal/mol (22).

Equilibrium Between $\text{FeCl}_2 \cdot 4\text{H}_2\text{O}$ and Its Saturated Solutions

This method has been used by Susarev *et al.* (22), but we repeat their calculations using slightly different values for the properties of the saturated solution. Figure 1 illustrates a thermodynamic cycle for the formation of crystalline $\text{FeCl}_2 \cdot 4\text{H}_2\text{O}$ through a saturated solution of ferrous chloride. In the reaction

* Electrochemical Society Active Member.

Fig. 1. Thermodynamic cycle for the formation of ferrous chloride tetrahydrate.

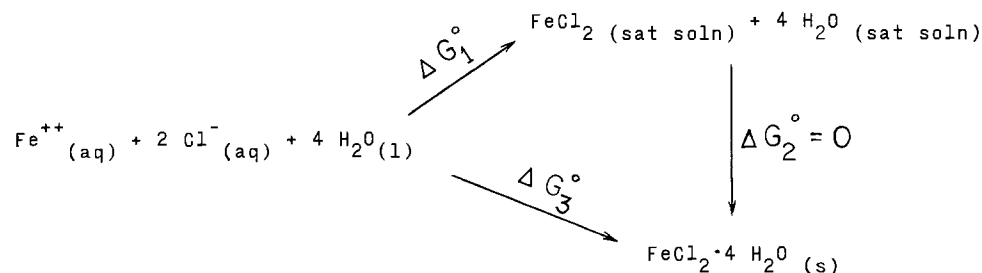
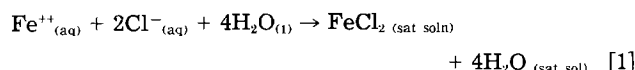


Table I. Properties of saturated ferrous chloride solutions

Quantity	Value	Source
Molality, m	5.09	Ref. (18)
γ_{\pm}	2.5	Extrapolated from
a_w	0.59	Ref. (22), (23)
$\Delta G_f^\circ (\text{Fe}^{++}_{(aq)})$	-18,850 cal/mol	NBS (21)
$\Delta G_f^\circ (\text{Cl}^{-}_{(aq)})$	-31,372 cal/mol	NBS (21)
$\Delta G_f^\circ (\text{H}_2\text{O}_{(l)})$	-56,687 cal/mol	NBS (21)

Table II. Calculated free energy of formation of $\text{FeCl}_2 \cdot 4\text{H}_2\text{O}$

Method	ΔG_f° (kcal/mol)
Equilibrium between the crystalline hydrate and its saturated solution	-305.7
Estimation of the entropy term $T\Delta S_f^\circ$	-305.9
Comparisons between anhydrous salts and their hydrates	-306.3
	Avg: -306.0

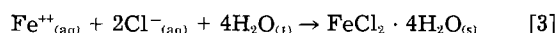


if the reactants are each in their standard states (unit activity) at 298.15 K, then

$$\Delta G_1^\circ = 2.303 RT \log a_{\text{FeCl}_2} a_w^4 \quad [2]$$

where a_{FeCl_2} and a_w are the activities of FeCl_2 and water, respectively, in the saturated solution. For the 2-1 electrolyte FeCl_2 , $a_{\text{FeCl}_2} = 4(m\gamma_{\pm})^3$. Use of the values of m , γ_{\pm} , and a_w listed in Table I for saturated FeCl_2 solutions gives: $\Delta G_1^\circ = 4088$ cal/mol.

For the reaction



$$\Delta G_3^\circ = \Delta G_f^\circ [\text{FeCl}_2 \cdot 4\text{H}_2\text{O}_{(s)}] - \Delta G_f^\circ [\text{Fe}^{++}_{(aq)}] - 2\Delta G_f^\circ [\text{Cl}^{-}_{(aq)}] - 4\Delta G_f^\circ [\text{H}_2\text{O}_{(l)}] \quad [4]$$

Taking the standard free energies of formation for $\text{Fe}^{++}_{(aq)}$, $\text{Cl}^{-}_{(aq)}$, and $\text{H}_2\text{O}_{(l)}$ from the NBS tabulations (21) and using the relation $\Delta G_3^\circ = \Delta G_1^\circ + \Delta G_2^\circ$ gives the result: $\Delta G_f^\circ [\text{FeCl}_2 \cdot 4\text{H}_2\text{O}_{(s)}] = -305.7$ kcal/mol.

Estimation of the Entropy of Formation

The enthalpy of formation ΔH_f° of $\text{FeCl}_2 \cdot 4\text{H}_2\text{O}$ has been reported to be -370.3 kcal/mol (21). A second way of calculating ΔG_f° is by estimating the term $T\Delta S_f^\circ$ and then using the relation $\Delta G_f^\circ = \Delta H_f^\circ - T\Delta S_f^\circ$.

Both the free energy and enthalpy of formation have been tabulated for the hydrates of many divalent metal chlorides (21). For a given series of hydrates $\text{MCl}_2 \cdot n\text{H}_2\text{O}$, the term $T\Delta S_f^\circ/n$ decreases (in negative value) with increasing degree of hydration. That is, successive water

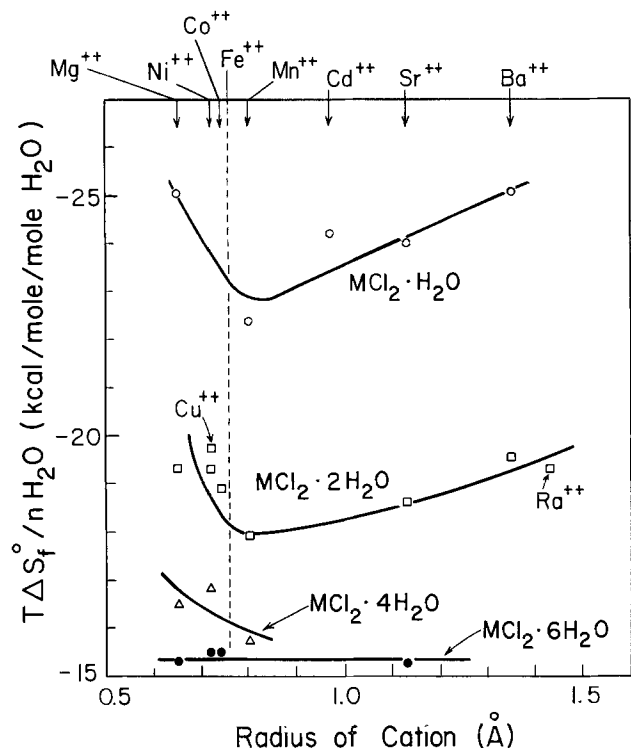


Fig. 2. Relationship between $T\Delta S_f^\circ/nH_2O$ and the radius of the metal cation for various series of hydrated divalent metal chlorides.

molecules produce progressively smaller contributions to the entropy change of hydrate formation. As noted by Ladd and Lee (24), the hydrate is stabilized by the interactions between the water dipole and metal cation. These interactions depend on the ion-dipole distance, which in turn is related to the radius of the metal cation. Figure 2 shows values for $T\Delta S_f^\circ/n$ as a function of the radius of the metal cation. The ionic radii are taken from Pauling (25)

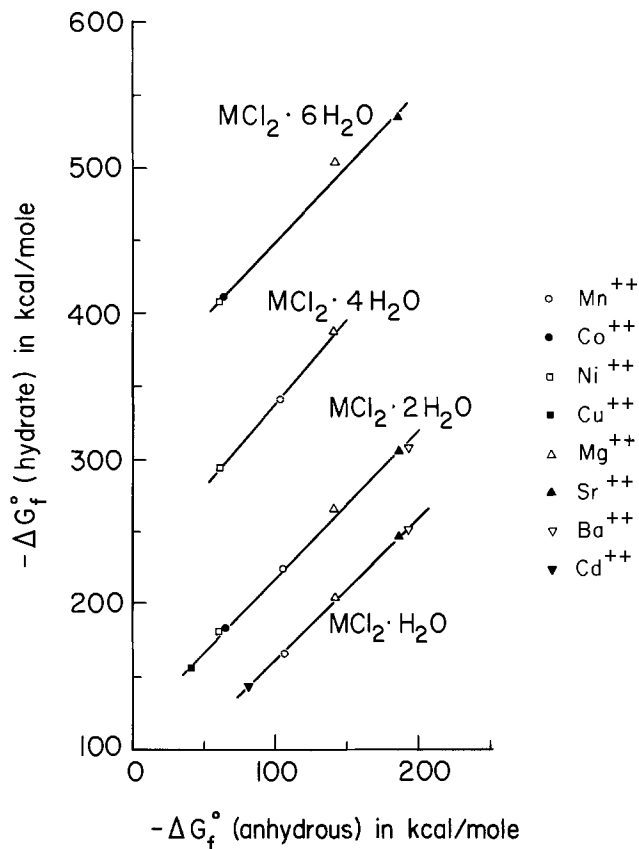


Fig. 3. Relationship between free energies of formation of hydrated and anhydrous divalent metal chlorides.

or from the compilation of Parsons (26). Interpolating in Fig. 2 gives $T\Delta S_f^\circ/n$ for $FeCl_2 \cdot 4H_2O$ as -16.1 kcal/mol/mol H_2O , so that $\Delta G_f^\circ = -305.9$ kcal/mol. This value is in good agreement with the result calculated in the previous section (see Table II).

Comparisons Between Hydrated and Anhydrous Chlorides

A third method of estimating ΔG_f° for $FeCl_2 \cdot 4H_2O$ is by comparison of the free energies of formation of various anhydrous chlorides with the free energy values for their hydrates. Figure 3 shows the correlation for the divalent metal halides and their various hydrates. A similar correlation has been noted between the enthalpies of formation of various metal chlorides and their dihydrates (27). For the hydration reaction



the standard free energy change is given by

$$\Delta G_{\text{hydration}}^\circ = \Delta G_f^\circ [\text{hydrate}] - \Delta G_f^\circ [\text{anhydrous}] - n(-56.687) \quad [6]$$

Using ΔG_f° values from the NBS compilations (21), it can be shown that $\Delta G_{\text{hydration}}^\circ$ is approximately -1 to -4 kcal/mol H_2O for all the metal dichloride hydrates shown in Fig. 3, except for the hydrates of $MgCl_2$, which have higher $\Delta G_{\text{hydration}}^\circ$ values of -4 to -8 kcal/mol H_2O . By setting $\Delta G_{\text{hydration}}^\circ \cong n \cdot A$, Eq. [6] takes the form

$$\Delta G_f^\circ [\text{hydrate}] = \Delta G_f^\circ [\text{anhydrous}] - n(56.687 - A) \quad [7]$$

For all the metal cations shown in Fig. 3 (except for Mg^{2+} , which does not quite obey Eq. [7]), the three curves can be combined into a single curve having the form of Eq. [7] and given by the least squares fit

$$\Delta G_f^\circ [\text{hydrate}] = 1.009 \Delta G_f^\circ [\text{anhydrous}] - n(56.687 + 1.656) \quad [8]$$

Using the tabulated value (21) of $\Delta G_f^\circ (FeCl_2) = -72.26$ kcal/mol in Eq. [8] gives the result: $\Delta G_f^\circ [FeCl_2 \cdot 4H_2O_{(s)}] = -306.3$ kcal/mol.

Summary

The values of $\Delta G_f^\circ [FeCl_2 \cdot 4H_2O_{(s)}]$ calculated by the three different approaches are listed in Table II. The average value is -306.0 kcal/mol.

Manuscript submitted Feb. 24, 1984; revised manuscript received March 23, 1984.

The Naval Research Laboratory assisted in meeting the publication costs of this article.

REFERENCES

- V. M. Chistyakov, P. V. Kupreev, F. A. Kondrar, and I. A. Smirnova, *J. Appl. Chem. USSR*, **40**, 1098 (1965). [Translated from *Zh. Prikl. Khim.*, **40**, 1141 (1965)].
- V. Ramshesh, K. Ravichandran, and K. S. Venkateswarlu, *Indian J. Chem.*, **20A**, 867 (1981).
- P. Keller, *Werkstoff. Korros.*, **20**, 102 (1969).
- M. R. Gilberg and N. J. Seeley, *Stud. Conserv.*, **26**, 50 (1981).
- N. A. North, *ibid.*, **27**, 75 (1982).
- S. Rao Addanki and A. K. Dey, *NMR Tech. J.*, **13**, 27 (1971).
- K. Barton, "Protection Against Atmospheric Corrosion," p. 33, John Wiley and Sons, New York (1976).
- M. Pourbaix, in "Localized Corrosion," R. W. Staehle, B. F. Brown, J. Kruger, and A. Agrawal, Editors, p. 12, NACE, Houston (1974).
- B. F. Brown, *Corrosion*, **26**, 249 (1970).
- M. H. Peterson, T. J. Lennox, Jr., and R. E. Groover, *Material. Protect. Perf.*, **9**, 23 (1970).
- G. Sandoz, C. T. Fujii, and B. F. Brown, *Corros. Sci.*, **10**, 839 (1970).
- T. Suzuki, M. Yamabe, and Y. Kitamura, *Corrosion*, **29**, 18 (1973).
- F. D. Bogar and C. T. Fujii, "Solution Chemistry in Crevices on Fe-Cr Binary Alloys," NRL Report 7690, Naval Research Laboratory, Washington, DC (1974).
- J. Mankowski and Z. Sklarska-Smialowska, *Corros.*

- Sci.*, **15**, 493 (1975).
15. E. D. Verink, Jr., K. K. Starr, and J. M. Bowers, *Corrosion*, **32**, 60 (1976).
 16. E. McCafferty, *This Journal*, **128**, 40 (1981).
 17. W. F. Linke and A. Seidell, "Solubilities of Inorganic and Metal-Organic Compounds," Vol. I, p. 1013, D. Van Nostrand, Princeton, NJ (1958).
 18. M. V. Ionen and A. A. Kozhakova, *J. Appl. Chem. USSR*, **46**, 865 (1973). [Translated from *Zh. Prikl. Khim.*, **46**, 816 (1973)].
 19. C. T. Fujii, Rapp. Tech. CEBELCOR, RT 213, Jan. 1974.
 20. B. E. Wilde, Paper presented at NACE Corrosion Research Conference, Anaheim, CA, March 1973; see *Corros. Abstr.*, **12**, 68, March 1973.
 21. "Selected Values of Chemical Thermodynamic Properties," NBS Technical Notes 270-3 (1968), 270-4 (1969), 270-6 (1971), National Bureau of Standards, Washington, DC.
 22. M. P. Susarev, L. I. Gorelik, A. M. Toikka, R. V. Lyzlova, and Yu. L. Ponomarev, *J. Appl. Chem. USSR*, **49**, 1086 (1976). [Translated from *Zh. Prikl. Khim.*, **49**, 1045 (1976)].
 23. W. Kangro and A. Groeneveld, *Z. Phys. Chem. N.F.*, **32**, 110 (1962).
 24. M. F. C. Ladd and W. H. Lee, *J. Phys. Chem.*, **69**, 1840 (1965).
 25. L. Pauling, "Nature of the Chemical Bond," p. 346, Cornell University Press, Ithaca, NY (1949).
 26. R. Parsons, "Handbook of Electrochemical Constants," p. 2, Butterworths, London (1959).
 27. M. Le Van My, *C. R. Acad. Sci. Paris, Ser. C*, **272**, 125 (1971).

Inhibition of Localized Corrosion as Determined by a Galvanodynamic Method

Alfred Viehbeck* and David W. DeBerry*

SumX Corporation, Austin, Texas 78758

Most of the fundamental studies of organic adsorption inhibitors have been concerned with the effects of these compounds on the uniform corrosion of metals in the active state (1). There is only limited information on the effects of such compounds on the localized corrosion of passive metals. This communication describes the inhibition of pitting on Type 304L stainless steel by a surface active chelating agent (N-lauroylsarcosine or NLS) in aqueous solutions containing chloride ions (2). A galvanodynamic method was developed for study of this system and appears to have attractive features for the study of pitting corrosion in general.

Type 304L stainless-steel electrodes were formed from 0.15 cm thick sheet into a "flag" shape. The electrode "pole," which extended above the solution level, was insulated with Glyptal varnish to eliminate the metal/solution/gas interface. The 6.0 cm² exposed flag was polished to a mirror finish using 0.3 μm alumina and degreased with methanol. The primary test solution contained 0.1M NaCl and 0.2M sodium acetate adjusted to pH 5.1. Test solutions using water purified by a Milli-Q reagent water system or distilled from permanganate gave similar experimental results. Inhibited solutions were prepared from this stock solution by addition of 3.0 mM NLS.

Electrochemical experiments were performed at 23° ± 1°C in a three-compartment Pyrex cell fitted with a Pt counterelectrode and SCE reference electrode. All potentials are reported with respect to the SCE. Prior to each electrochemical run, the electrode was degreased, rinsed thoroughly with water, and placed in the deoxygenated test solution for 1h. Solutions were magnetically stirred and blanketed with purified nitrogen throughout the experiment. After the open-circuit stand, the electrode was polarized for 3 min to either -0.60V or -8 μA before initiating the potential or current scan, respectively.

A typical linear potential scan (LPS or "potentiodynamic" scan) for a Type 304L stainless-steel electrode in the uninhibited solution at a scan rate of 0.20 mV/s is shown by the dashed curve in Fig. 1. The breakdown potential (E_b) associated with the onset of pitting is signaled by the rapid increase in current occurring at +0.20V on the forward scan to more positive potentials. On the return scan (after reversal at 0.1 mA/cm²), the current hysteresis trace intersects the passive current trace at the so-called protection potential (E_{prot}) at -0.08V. Below this

potential any active pits are repassivated (3). This is shown by the observation that a second positive going scan following the return to potentials negative of E_{prot} results in a current response which closely follows the original scan. The LPS measurement method has received much study but is complicated by induction time and other effects which can cause the results to vary with scan rate and incidental experimental parameters.

The effect of NLS in solution on the LPS is shown by the solid curve in Fig. 1. The initial response on the forward scan is quite similar to that for the uninhibited case, suggesting that the surface passivation process is not affected by NLS. However, there is a substantial effect of NLS on the current response at higher potentials. The breakdown processes are suppressed, and small current spikes and plateaus appear which are probably due to the nucleation and subsequent repassivation of pits. Above +1.20V, the transpassive region begins, and finally a

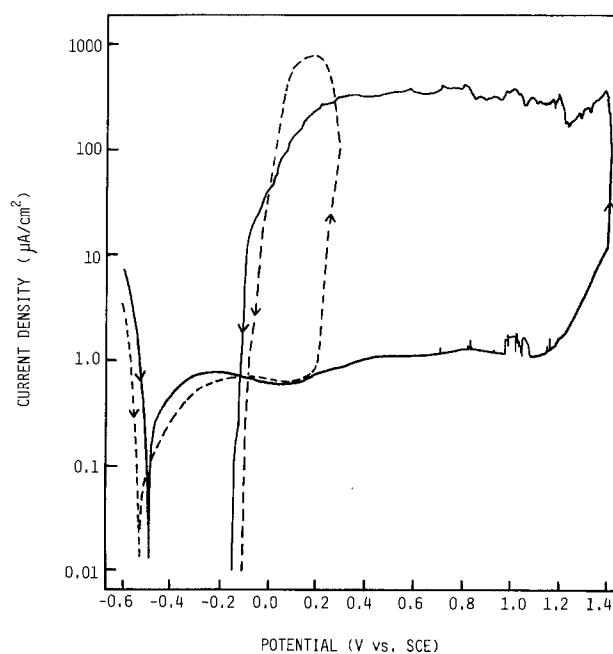


Fig. 1. LPS curves for Type 304L SS electrode in 0.1M NaCl with 0.2M Na acetate solution (pH 5.1) and scan rate of 0.2 mV/s. Dashed curve is for uninhibited solution, and solid curve is for solution with 3.0 mM NLS.

* Electrochemical Society Active Member.

Key words: corrosion inhibition, linear current scan, N-lauroylsarcosine, pitting, 304 stainless steel.

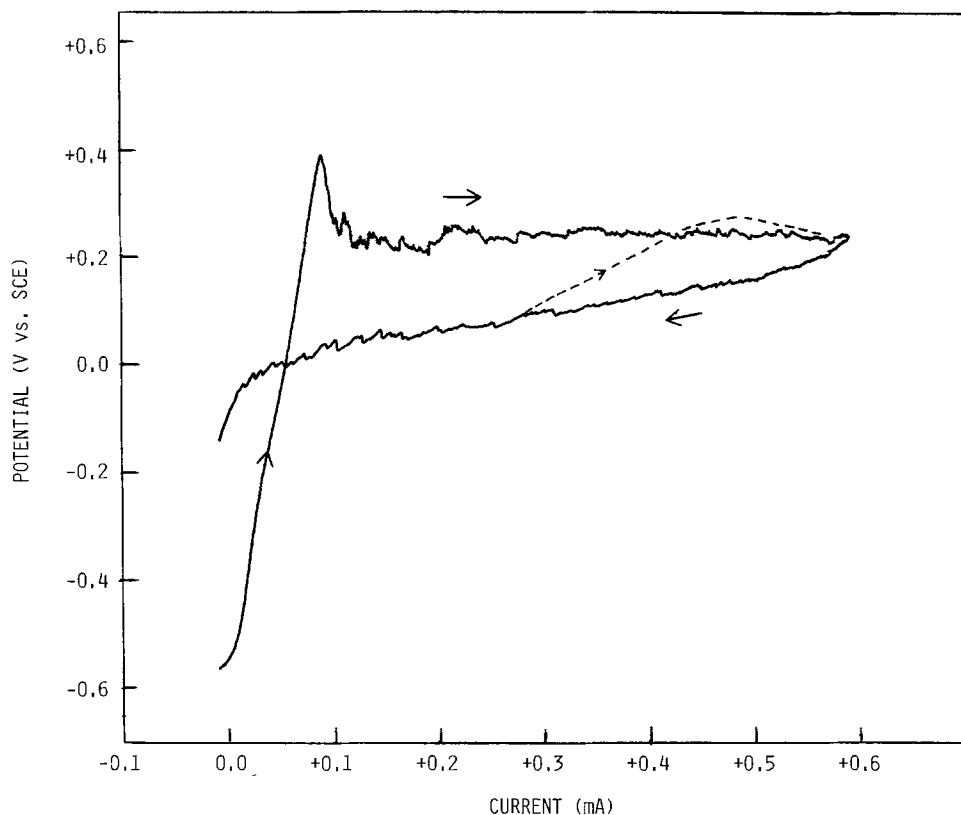


Fig. 2. LCS curve for Type 304L SS electrode in test solution not containing NLS. Current scan rate: $0.5 \mu\text{A/s}$. Dashed line shows response on scan reversal.

sharp current rise is seen at $E_b = +1.39\text{V}$. The return scan gives an $E_{\text{prot}} = -0.12\text{V}$, which is slightly more active than the value observed in the absence of NLS. In general, these results indicate that NLS inhibits the breakdown of passivity and perhaps aids repassivation of incipient pits. However, once breakdown has occurred to a certain stage, pits can continue to propagate in the presence of NLS. Visual examination of the metal surfaces showed that electrodes polarized in inhibited solution had a few large pits ($0.1\text{-}1 \text{ mm}^2$), while those tested in the absence of NLS had many (>100) small pits ($<0.001 \text{ mm}^2$) uniformly distributed over the surface.

Although the linear current scan (LCS) method has not previously been used to study localized corrosion and its inhibition, we have found that it provides a rapid and accurate means of measuring important corrosion parameters. In the LCS method, a triangular current ramp is imposed on the electrode and the resulting potential is recorded. This approach provides direct control of the total charge passed and extent of pit propagation occurring in a given experiment. As pointed out by Hirozawa for other current-controlled methods, the LCS is "active" in nature and is not influenced by the induction-time effects introduced in potential-controlled measurements (4).

An LCS curve obtained for a Type 304L SS electrode subjected to a current scan rate of $0.5 \mu\text{A/s}$ in the uninhibited solution is shown in Fig. 2. On the forward (increasing positive current) scan, there is an initial rapid rise in the potential. The charge in this region is consumed by any active metal dissolution, adsorption, or passive film formation processes as well as the maintenance of the quasistationary film condition. The potential peak which follows is believed to be due to pit nucleation involving the most favorable surface sites. The peak potential and current density are a function of the kinetics of the passivity breakdown process. Further work on extracting kinetic information from LCS results is in progress.

The nearly constant potential obtained after the initial peak now represents E_b defined as the minimum potential for which pits will continue to nucleate and propagate with increasing current. The value of $+0.21\text{V}$ measured for E_b in this manner is in good agreement with that measured using the LPS method. When the current sweep di-

rection is reversed, a potential hysteresis curve is obtained. During this return scan (decreasing current), the current is used for continued pit propagation. If the current scan direction is again switched to increasing values, the potential response moves positive to reach the forward scan potential as illustrated by the dashed line in Fig. 2. This behavior is not an induction effect but is attributed to the additional driving force needed to nucleate new or repassivated pits as compared to that for propagation alone. This also indicates that the hysteresis observed on the decreasing current scan is due to the lower driving force requirements for pit propagation alone.

The effects of varying current scan rate (β) on the LCS response are shown in Fig. 3. As β is increased, several characteristics change, including the slope of the potential response in the passive region, the peak potential, and the current at which the peak potential occurs. However, the charge density at the peak maximum is not affected by β , even though the initial response appears to show β -dependent charging effects. Therefore, under any β , the charge density for passivity breakdown (Q_b) can be readily obtained; for the present system, $Q_b = 1.4 \text{ mC/cm}^2$. Note that E_b and the following portions of the potential curve are also independent of scan rate.

Extrapolating the potential response on the return scan to zero current yields a value for the LCS analog of the protection potential ($E_{\text{prot}} = -0.03\text{V}$) that is also independent of β . In addition, the effect of increasing the current limit is an increase in the slope of the return response. However, the value of E_{prot} is still unchanged for different scan limits, *i.e.*, different total charge passed. The LCS value for E_{prot} is somewhat more noble than the value found using the LPS method. The LCS method thus allows the rapid measurement of E_b , E_{prot} , and Q_b with minimal interference by induction time effects.

The response obtained for a LCS ($\beta = 1.0 \mu\text{A/s}$) on Type 304L SS in the presence of 3.0 mM NLS is shown in Fig. 4. Although the overall features of the trace are similar to those obtained in the absence of NLS, there are certain distinct differences. For instance, the initial peak maximum occurs at higher current density and more positive potential. These results indicate that the organic compound influences the interfacial processes in such a way that the electrode can sustain a higher charge density (Q_b)

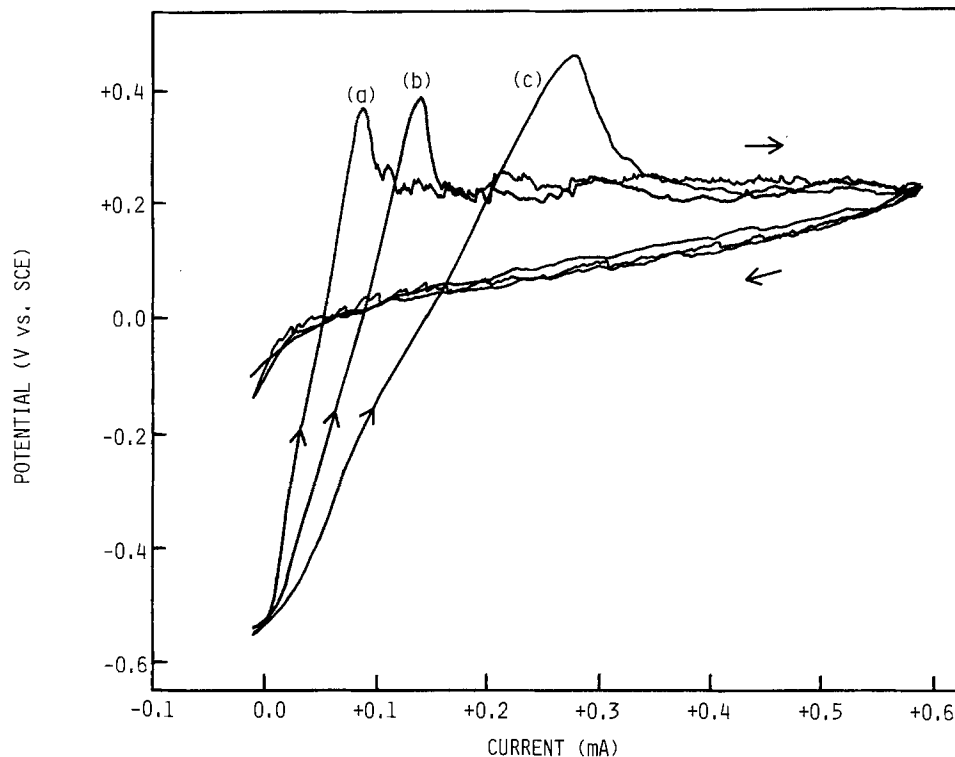


Fig. 3. LCS curves for Type 304L SS electrode in test solution without NLS. $\beta = 0.5$ (a), 1.0 (b), and 5.0 (c) $\mu\text{A/s}$, respectively.

before localized breakdown of passivity takes place. The Q_b in this case is 2.6 mC/cm^2 .

A pronounced effect of NLS on the sustained pit nucleation and propagation potential is again observed. Although still substantially positive of the uninhibited value, the LCS measured E_b ($\sim +0.50\text{V}$) is not as positive as that measured by the slow LPS. This may be due to the pronounced effect of the inhibitor on the pit induction time. The LCS value is practically independent of scan rate. The return potential response has a lower slope with more "noise" but gives essentially the same value of E_{prot} as in the NLS-free solution. The presence of NLS appears to significantly increase the noise associated with the E_b plateau, perhaps indicating that it continues to interfere with pit nucleation and propagation even after the initial breakdown.

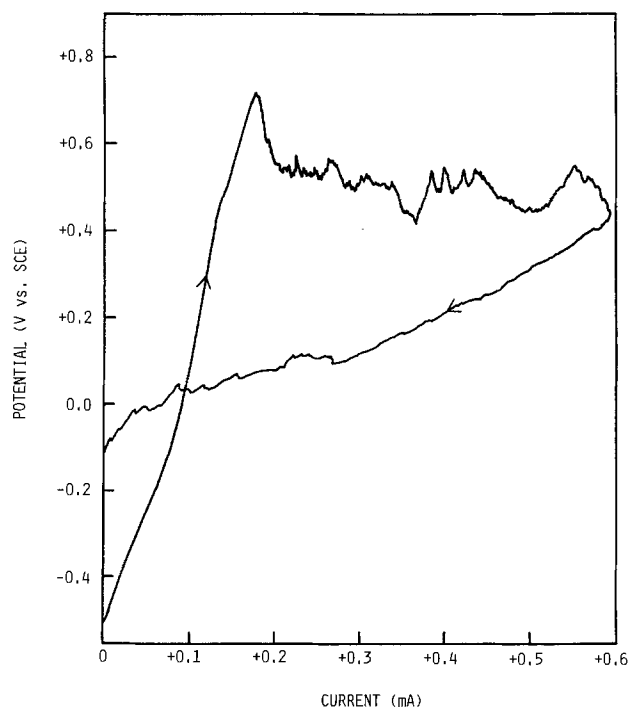


Fig. 4. Results of LCS for Type 304L SS electrode in test solution containing 3.0 mM NLS at $\beta = 1.0 \mu\text{A/s}$.

A mechanism for inhibition of uniform corrosion by N-lauroylsarcosine involves the formation of multiple "chelating" bonds to the bare metal surface (5). The present results suggest that the molecule may also be attached to the surface cations of the passive film through the amide nitrogen and carboxyl oxygen, forming an insoluble, passive film stabilizing surface compound. Preliminary capacitance (C_d) measurements (using the fast galvanostatic pulse method) show that the average C_d from -0.60 to 0.60V decreases from $18 \mu\text{F/cm}^2$ in the uninhibited solution to $1.5 \mu\text{F/cm}^2$ with 3.0 mM NLS in solution. The higher Q_b and more positive potentials required for maintaining localized attack may result from a strong tendency for surface complex formation at those sites on the surface which are most susceptible to pit formation. Work is continuing on the possibilities associated with using compounds such as NLS as probes of localized corrosion mechanisms.

Acknowledgment

The support of the Army Research Office, Dr. Robert R. Reeber, Project Manager, is gratefully acknowledged.

Manuscript submitted Nov. 22, 1983; revised manuscript received Feb. 13, 1984.

SumX Corporation assisted in meeting the publication costs of this article.

REFERENCES

1. R. H. Hausler in "Corrosion Chemistry," G. R. Brubaker and B. P. Phipps, Editors, pp. 262-320, ACS Symposium Series 89, The American Chemical Society, Washington, DC (1979).
2. D. W. DeBerry, G. R. Peyton, and W. S. Clark, *Corrosion*, **40**, 250 (1984); A. Betti, L. Cavallaro, G. Trabanelli, and F. Zucchi, *ibid.*, **18**, 351 (1962).
3. M. Pourbaix, L. Klimzack-Mathieiu, Ch. Mertens, J. Meunier, Ch. Vanlengenhaghe, L. de Munck, J. Laureys, L. Neelmans, and M. Warzee, *Corros. Sci.*, **3**, 239 (1963); B. C. Syrett, *Corrosion*, **33**, 221 (1977).
4. S. T. Hirozawa, *This Journal*, **130**, 1718 (1983); See also S. Smialowska and M. Czachor, in "Localized Corrosion," R. W. Staehle, B. F. Brown, J. Kruger, and A. Agrawal, Editors, pp. 353-360, NACE-3, Houston (1974).
5. A. Weisstuch, D. A. Carter, and C. C. Nathan, *Mater. Prot. Perf.*, **10**, 11 (1971); D. C. Zecher, *ibid.*, **15**, 33 (1976); R. H. Hausler, Paper 252, NACE Corrosion/81, Toronto, April 6-10, 1981.

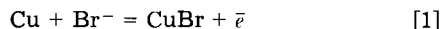
Potentiodynamic Investigation of Copper in the Presence of Bromide Ions

Louis Brossard*

Institut de recherche d'Hydro-Québec, Varennes, Québec, Canada J0L 2P0

The anodic dissolution of copper in the presence of bromide ions has received little attention (1-3). It has been established that the valence of dissolution of copper is one (1), while the dissolution rate of bare metal is controlled by diffusion of ions in the solution as CuBr_2^- and CuBr_3^- (2).

At potential values larger than the reversible potential for the reaction



the formation of CuBr is observed on copper surface (2, 3). Two peaks of oxidation are present on the E-i curves, and the current of dissolution mainly results in the accumulation of copper bromide.

The aim of the present work is to establish the rate-determining step of the dissolution reaction in the region of the peaks in solutions having 0.05-1.2M NaBr. The influence of temperature (22°-64°C) is also investigated.

Experimental

The electrochemical cell, its accessories, and the test procedures have been described in previous papers (4, 5). In the present investigation, a copper wire electrode with a diameter of 0.06 cm and a total surface area of 0.4 cm^2 was used. The solution contained 0.05-1.2M NaBr, and the temperature was raised from 22° to 64°C. A potassium phthalate-based buffer was used to stabilize the pH at 4. The solution was carefully deaerated by nitrogen bubbling, which was discontinued just prior to the experiments.

The working electrodes were polarized from -450 to +400 mV_{SCE} by the linear potential sweep method. The scan rate, dE/dt was varied from 5 to 70 $\text{mV} \cdot \text{s}^{-1}$ in order to determine the influence of the scan rate on the peak currents.

All electrodes potential values are given in relation to the saturated calomel electrode except when otherwise specified.

Results

Figure 1 shows the potentiodynamic traces of copper at 0.2 and 0.9M NaBr. The scan rate is 12 $\text{mV} \cdot \text{s}^{-1}$, and the solution is quiescent. Two waves of oxidation are observed. The difference between the applied potential and the reversible potential, $E_{\text{Cu/CuBr}}$, of reaction [1] is given on the potential scale. The reversible potential of reaction [1] is given by (6, 7)

$$E_{\text{Cu/CuBr}} = -0.239 - 0.059 \log_{10}(\text{Br}^-) \quad [2]$$

where $E_{\text{Cu/CuBr}}$ is expressed in volts with respect to the saturated calomel electrode.

The difference between the peak potentials, E_{p1} and E_{p2} , and $E_{\text{Cu/CuBr}}$ is

$$E_{p1} - E_{\text{Cu/CuBr}} = 160 \pm 5 \text{ mV} \quad [3]$$

$$E_{p2} - E_{\text{Cu/CuBr}} = 385 \pm 5 \text{ mV} \quad [4]$$

Expressions [3] and [4] are practically unaffected by a change of Br^- ion concentration from 0.05 to 1.2M.

The main characteristics of the behavior of the copper anode in the region of the peaks are as follows. (i) The peak current of the first, i_{p1} , and the second wave, i_{p2} , depends on the intensity of the solution agitation (Fig. 2). (ii)

*Electrochemical Society Active Member.

Key words: bromide ions influence, copper dissolution kinetics, anodic dissolution.

The plot of i_{p1} and i_{p2} against the square root of the scan rate, on a stationary electrode in a quiescent solution, is a straight line (Fig. 3 and 4), with an ordinate at its origin equal to zero. The experimental relationships for solution of 0.2M NaBr are

$$i_{p1} = 0.23 \left(\frac{dE}{dt} \right)^{1/2} \quad [5]$$

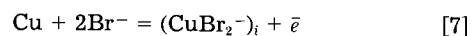
$$i_{p2} = 0.28 \left(\frac{dE}{dt} \right)^{1/2} \quad [6]$$

where i_{p1} and i_{p2} are expressed in amperes per square centimeter and dE/dt in volts per second. (iii) The order of the reaction in relation to Br^- ion concentration, ξ , is close to one in the first peak region between 0.05 and 0.2M NaBr (Fig. 5). ξ is 0.5 in the first peak region, and found to be -0.6 in the second peak region above 0.2M. (iv) The anodic charge (Q_{ox}) obtained by the integration of the E-i curve in the peak region, e.g., from $E = E_{\text{Cu/CuBr}}$ to $E = E_{\text{Cu/CuBr}} + 500 \text{ mV}$, is practically unaffected by a change of Br^- ion concentration. For example, Q_{ox} is 490 mC cm^{-2} in 0.2M NaBr in comparison with 450 mC cm^{-2} in 0.9M NaBr (Fig. 1); the sweep rate is 12 mV s^{-1} . (v) The general shape of the E-i curve and its peak potentials remained unaffected by a change of the solution temperature (Fig. 6). However, the peak currents are higher as the solution temperature is increased. For example, i_{p1} is 16 mA cm^{-2} at 22°C and 32 mA cm^{-2} at 60°C.

Discussion

Below the equilibrium potential $E_{\text{Cu/CuBr}}$ a two-step reaction was considered (2) from which the dissolution process of the copper anode may be entirely explained.

The reaction is



and

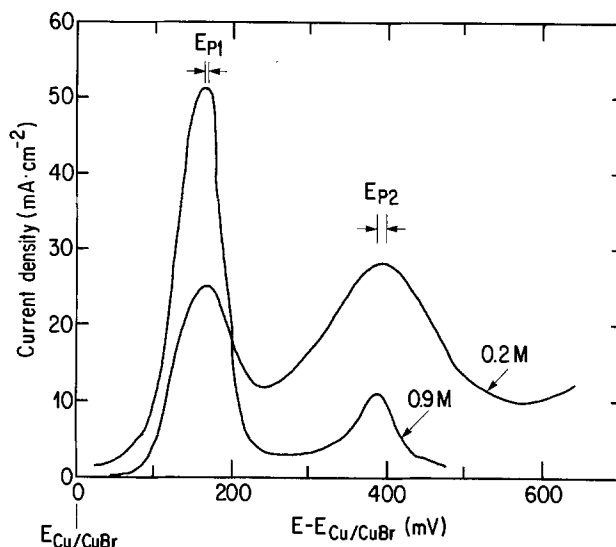
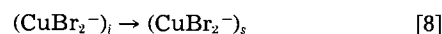


Fig. 1. Potentiodynamic traces on a copper wire electrode in a quiescent solution of 0.2 and 0.9M NaBr. The electrode potential is given in relation to the reversible potential of $\text{Cu} + \text{Br}^- = \text{CuBr} + e$ (Eq. [2]). $dE/dt = 12 \text{ mV} \cdot \text{s}^{-1}$, $T = 22^\circ\text{C}$, $\text{pH} = 4$.

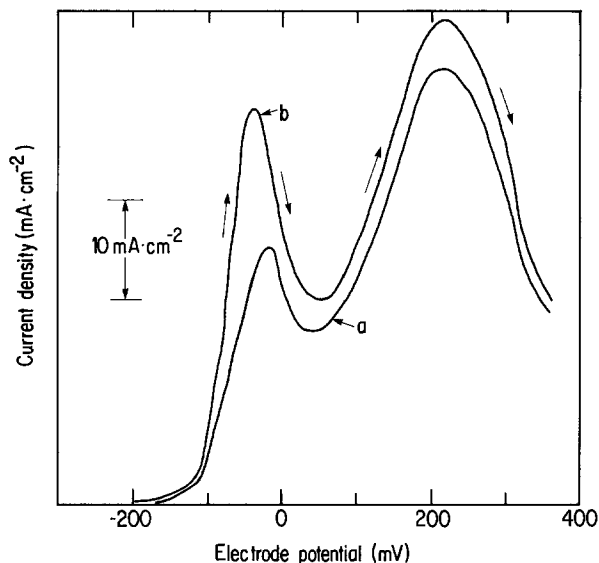


Fig. 2. Influence of the solution agitation on the potentiodynamic traces. The electrode potential is given in relation to the saturated calomel electrode in a quiescent solution (curve a) and with argon bubbling, 240 ml min^{-1} , in the solution (curve b). $\text{NaBr} = 0.2\text{M}$, $dE/dt = 12 \text{ mV} \cdot \text{s}^{-1}$. $T = 22^\circ\text{C}$, $\text{pH} = 4$.

where the subscripts i and s refer to concentrations at the copper-solution interface and the bulk solution, respectively.

The rate-determining step [8] is the diffusion transport of CuBr_2^- from the interface to the bulk solution. Step [7], the oxidation of copper to CuBr_2^- , is assumed to be in equilibrium.

The order of the reaction in relation to Br^- ion concentration is two, and the current of dissolution increases as the applied potential becomes larger.

This model is valid as long as the Br^- ion concentration at the copper-electrode interface, $(\text{Br}^-)_i$, and in the bulk solution, $(\text{Br}^-)_s$, is close together while the surface is free of corrosion products.

In the region of the peaks, the current results almost entirely in the accumulation of copper bromide on copper

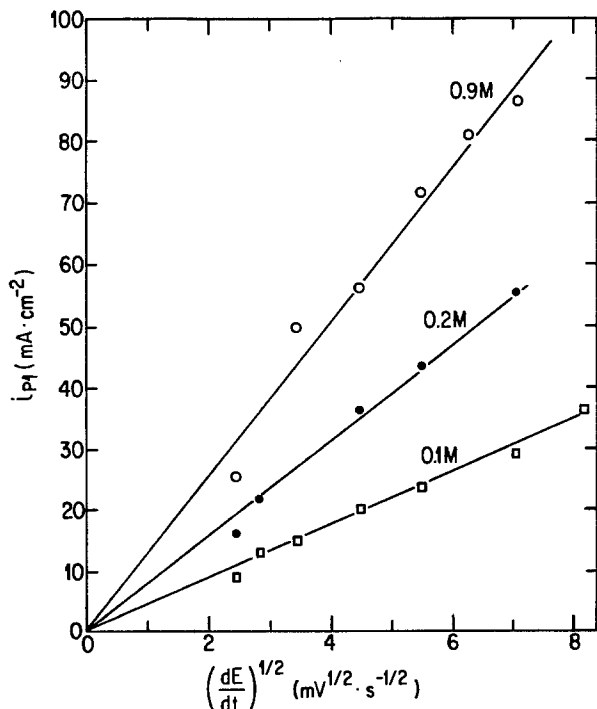


Fig. 3. The anodic peak current of the first wave vs. the square root of the scan rate at three different NaBr concentrations. The solution is quiescent.

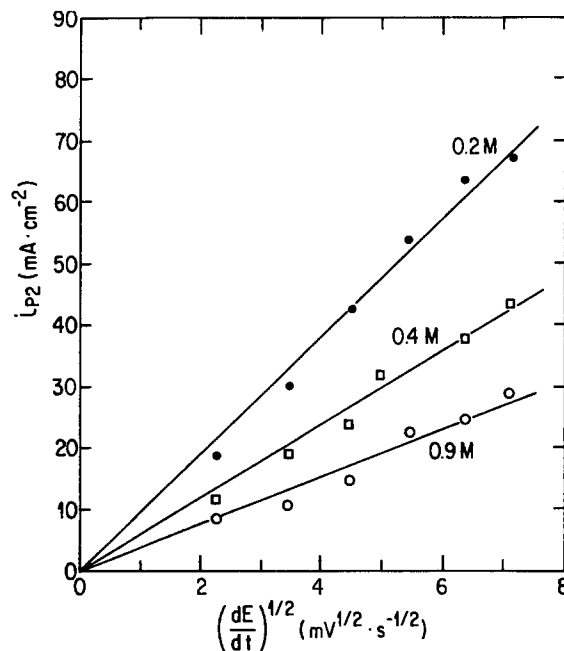


Fig. 4. The anodic peak current of the second wave vs. the square root of the scan rate. The solution is quiescent.

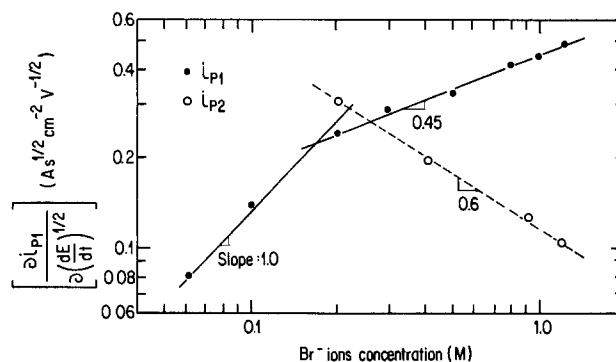


Fig. 5. Influence of Br^- ion concentration on the slope value of $i_{p1} - (dE/dt)^{1/2}$ and $i_{p2} - (dE/dt)^{1/2}$ relationships. The solution is quiescent.

surface at sweep rate values close to or larger than $5 \text{ mV} \cdot \text{s}^{-1}$ (3). It is in agreement with the fact that the rate of dissolution of CuBr is $\sim 0.073 \times 10^{-8} \text{ mol cm}^{-2} \text{ s}^{-1}$ in a quiescent solution of 0.2M NaBr at 22°C , e.g., 0.071 mA cm^{-2} in comparison with an oxidation current having an average value of 7 mA cm^{-2} (Fig. 6).

Considering the formation of CuBr from reaction [1] and the large value of the peak currents (Fig. 3 and 4), the depletion of Br^- ions at the electrode surface, $(\text{Br})_s \ll (\text{Br})_i$, may be eventually considered. The diffusion-

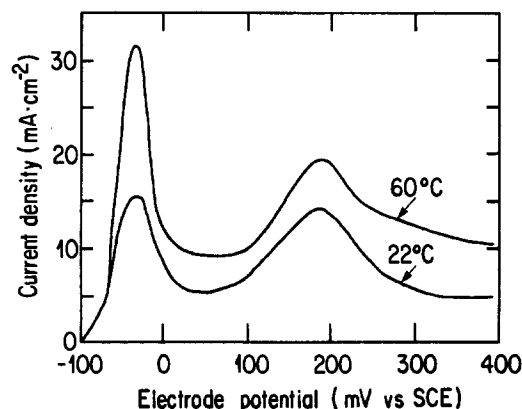


Fig. 6. Influence of solution temperature on the potentiodynamic trace at 0.2M NaBr . The solution is quiescent, and $dE/dt = 5 \text{ mV} \cdot \text{s}^{-1}$.

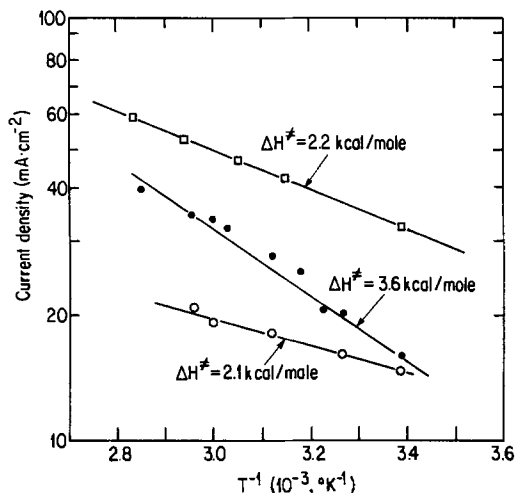


Fig. 7. Dependence of the peak currents on the temperature in 0.2M NaBr solution. $dE/dt = 5 \text{ mV} \cdot \text{s}^{-1}$. ●: Experimental values of i_{p1} . ○: Experimental values of i_{p2} . □: Relative values calculated from Eq. [10].

controlled transport of Br^- ions from the bulk solution to the copper electrode is the rate-determining step in the oxidation reaction. Consequently, the current should reach a maximum in the E-i curves (8), i_p , and the plot of i_p against $(dE/dt)^{1/2}$ should be a straight line with an ordinate at its origin equal to zero. In addition, an order of reaction of one concerning i_p in relation to Br^- ion concentration may be predicted.

The characteristics marked (i), (ii), and (iii) deduced from Fig. 2, 3, and 5 suggest that the dissolution process in the region of the first peak is under the diffusion control of Br^- ions between 0.05 and 0.2M NaBr.

For a diffusion-controlled process, the peak current is related to the scan rate by the equation (8)

$$i_{p1} = 2.69 \times 10^5 n^{3/2} D^{1/2} \left(\frac{dE}{dt} \right)^{1/2} C_i \quad [9]$$

where i_{p1} is the peak current (in A cm^{-2}), D the diffusion coefficient ($\text{cm}^2 \text{ s}^{-1}$), (dE/dt) the scan rate ($\text{V} \cdot \text{s}^{-1}$), C_i the concentration of the electro-active species (mol cm^{-3}), and n the number of exchanged electrons. Considering Br^- ions as the diffusing species, its diffusion coefficient may be determined from the experimental relationship $i_{p1} - (dE/dt)^{1/2}$ and the values of n and C_{Br^-} . For 0.2M NaBr, n is 1 in the first peak region (1), $C_{\text{Br}^-} = 0.2 \times 10^{-3} \text{ mol cm}^{-3}$, and the slope of the $i_{p1} - (dE/dt)^{1/2}$ curve is $0.23 \text{ A cm}^{-2} \text{ V}^{-1/2} \text{ s}^{1/2}$ (Fig. 3). The substitution of these values in relation [9] gives $1.8 \times 10^{-5} \text{ cm}^2 \text{ s}^{-1}$ for D_{Br^-} , which is in agreement with those given in the literature for D_{Cl^-} and D_{I^-} (9).

The relative values of the peak current, corresponding to the curve for which ΔH^\ddagger is equal to $2.2 \text{ kcal mol}^{-1}$ in Fig. 7, were calculated considering that the change of the diffusion coefficient of Br^- ions in the solution with the temperature. From Eq. [9], the relative values of i_{p1} is given by

$$i_{p1} \propto D_{\text{Br}^-}^{1/2} \quad [10]$$

The values of D_{Br^-} at different solution temperature were calculated from the equation (10)

$$\frac{D\mu}{T} = \text{constant} \quad [11]$$

where μ is the viscosity of the solution given in Ref. (11). The relative values of i_{p1} are plotted against T^{-1} in Fig. 7. The slope of this curve gives a ΔH^\ddagger value equal to $2.2 \text{ cal} \cdot \text{mol}^{-1}$. The experimental value of ΔH^\ddagger is $3.6 \text{ kcal} \cdot \text{mol}^{-1}$ for the first peak and $2.1 \text{ kcal mol}^{-1}$ for the second peak. Therefore, the change of the peak current with temperature is attributed to the variation of D_{Br^-} .

Above 0.2M NaBr, the fractional value of ξ in the first peak region, characteristic (iii), suggests that the limitation of the current is not only due to the diffusion of ions in the solution. From the work of Kozin and co-workers (12, 13), it may tentatively be attributed to the presence of a corrosion product on the electrode surface, since the surface is partly covered by copper bromide at E_{p1} (2).

Concerning the second peak, it is strongly dependent on the first one, since the sum of Q_{ox} for the two waves is practically unaffected by a change of Br^- ion concentration (Fig. 1). This behavior is consistent with the fact that ξ is 0.5 in the first peak region and found to be -0.6 in the second peak region above 0.2M NaBr. In addition, n for the second peak may be higher than 1 (12). Therefore, the theoretical determination of i_{p2} from relation [9] is questionable. However, the experimental relationship $i_{p2} - (dE/dt)^{1/2}$, characteristic (ii), with an ordinate at its origin equal to zero, the dependence of i_{p2} on the intensity of the solution agitation (Fig. 2) and the value of ΔH^\ddagger for the second peak (Fig. 7) promote the idea that the rate-determining step of the dissolution in the second peak region is the diffusion of ions in the solution.

In summary, the two waves of oxidation observed on the potentiodynamic traces have their peak potential independent of Br^- ion concentration. The second peak is dependent on the first one since the sum of Q_{ox} for the two waves is practically unaffected by a change of Br^- ion concentration. The limitation of the dissolution current in the peak region is ascribed to the diffusion of ions in the solution. It is suggested that the species are Br^- ions in the first peak region between 0.5 and 0.2M NaBr.

Manuscript submitted Oct. 21, 1983; revised manuscript received Jan. 3, 1984.

Institut de recherche d'Hydro-Québec assisted in meeting the publication costs of this article.

REFERENCES

1. L. F. Kozin, E. E. Kobrand, and K. K. Lipesov, *Izv. Akad. Nauk. Kaz. SSR Ser. Khim.*, **74**, 31 (1974).
2. L. Brossard, *Can. J. Chem.*, **62**, 36 (1984).
3. L. Brossard, *Can. J. Chem.*, To be published.
4. L. Brossard, *ibid.*, **61**, 2022 (1983).
5. L. Brossard, *ibid.*, **60**, 616 (1982).
6. M. Pourbaix, "Atlas d'Equilibre Electrochimique," p. 605, Gauthier-Villars, Paris (1963).
7. C. E. Wicks and F. E. Block, *Bulletin* 605, p. 43, U.S. Bureau of Mines, Washington (1963).
8. A. J. Bard and L. R. Faulkner, "Electrochemical Methods," p. 218, John Wiley and Sons, New York (1980).
9. R. Parsons, "Handbook of Electrochemical Constants," p. 77, Butterworths, London (1959).
10. I. A. Semenov, V. F. Lazarev, and A. I. Levin, *Sov. Electrochem.*, **11**, 1013 (1975).
11. R. B. Bird, W. E. Stewart, and E. N. Lightfoot, "Transport Phenomena," p. 8, John Wiley and Sons, New York (1960).
12. L. F. Kozin, K. K. Lipesov, and S. N. Naguibin, *Izv. Akad. Nauk. Kaz. SSR. Ser. Khim.*, **6**, 28 (1980).
13. L. F. Kozin, K. K. Lipesov, and S. N. Naguibin, *ibid.*, **4**, 11 (1980).

NiO Solubility in Molten Li/K Carbonate under Molten Carbonate Fuel Cell Cathode Environments

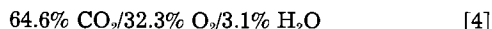
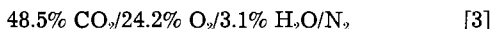
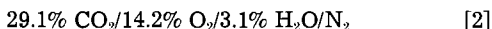
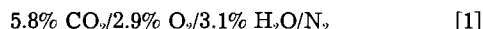
Charles E. Baumgartner*

General Electric Company, Corporate Research and Development, Schenectady, New York 12301

The corrosion of molten carbonate fuel cell (MCFC) NiO cathodes during cell operation has been brought to attention recently (1-5) and is considered one of the major technical difficulties facing MCFC development at the present time. NiO, solubilized in the molten Li/K carbonate (62/38 mole ratio) at the cathode/carbonate interface, is diffusively transported through the carbonate reservoir towards the anode. At some location intermediate between the two electrodes, the local cell environment's oxygen partial pressure decreases below the level where NiO is stable and metallic nickel precipitates. Recent evidence obtained from cell tests has shown the extent of cathode degradation to be accelerated by increasing either the P_{CO_2} or the total $P(CO_2 + O_2)$ supplied to the cathode. This is important since commercial fuel cells are expected to operate with oxidant gases such as humidified 30% CO_2 /bal air at elevated pressures of between 6 and 10 atm. Estimations of the extent of cathode degradation occurring under these elevated pressures requires an understanding of how the NiO/carbonate equilibrium changes as a function of changing cathode gas environment. This note documents the measured equilibrium NiO solubility in Li/K carbonate melts under various humidified $CO_2/O_2/N_2$ gases containing a constant P_{CO_2}/P_{O_2} ratio of 2/1.

Experimental

Pellets of NiO, approximately 1.2 cm in diam, were pressed at 20,000 psi and air sintered for 24h at 1123 K. Equilibrium solubility measurements were made by placing one pellet in the bottom of a clean 7.5 cm tall \times 1.6 cm diam gold crucible along with 20 ± 1 g of premelted and ground high purity binary Li/K carbonate of eutectic composition 62 mole percent (m/o) $Li_2CO_3/38$ m/o K_2CO_3 (Apache Chemical Company, Seward, Illinois). The crucibles were placed in an $\alpha-Al_2O_3$ -lined box furnace whose cover was adapted for two thermocouples, a gas inlet, and a sampling tube. The cover gases utilized for this study, possessing P_{CO_2}/P_{O_2} ratios of 2/1 with a N_2 balance, were water saturated at 298 ± 1 K to give the following gas compositions



The samples were allowed to equilibrate at temperature for at least 150h. Beginning at that time, approximately 1g aliquots of molten carbonate were removed at 24h intervals by inserting an $\alpha-Al_2O_3$ pipette just below the melt's upper surface. These aliquots were transferred to clean gold crucibles where they cooled for subsequent nickel analysis by atomic absorption spectroscopy. The quoted solubilities represent a nickel analysis which did not vary more than $\pm 10\%$ relative to a mean over a 3 day period. The limit of $\pm 10\%$ represents the reproducibility obtained on identical samples and constitutes the cumulative deviation in the solubility and analytical techniques. In addition, a carbonate blank consisting of an identically prepared crucible containing carbonate only was occasionally carried through the procedure adjacent to the sample crucible to confirm that samples were not contaminated from the furnace environment.

*Electrochemical Society Active Member.
Key words: electrolyte, fuel cell, solubility.

Results and Discussion

The measured NiO solubility under the four gas environments is shown in Fig. 1. In each case, the solubility increased as a function of temperature once the equilibrium solubility level exceeded the background nickel concentration present in the nascent carbonates. Under experimental conditions where the equilibrium solubility remained below this level, the anolyte concentration did not decrease with time. It is suggested that this was due either to NiO supersaturation in the melt or to the homogeneous precipitation of a fine NiO suspension which was subsequently sampled along with the solubilized form. Samples were not left on test for times exceeding 500h to determine if the lower equilibrium values are slowly approached. In any event, the linear \ln solubility vs. inverse temperature relationship is clearly visible from the remaining data. As anticipated from the previously mentioned cell test experience, the highest solubility was recorded under the gas possessing the highest total $P(CO_2 + O_2)$. Measurements at temperatures exceeding 1143 K under the 5.8% $CO_2/2.9\% O_2$ containing gas were further complicated by carbonate dissociation shown previously to occur under similar conditions by Spedding and Mills (6). A significant increase in NiO dissolution occurred under these conditions; these data are not shown in Fig. 1.

Figure 2 shows a rearrangement of the data to illustrate the analyzed NiO concentration's dependency on the total gas ($CO_2 + O_2$) partial pressure at four different temperatures. (Some of the 923 K data were obtained by extrapolation due to the background nickel interference.) Each temperature's solubility is linear as a function of total $P(CO_2 + O_2)$ with the 923 K data, the operating tempera-

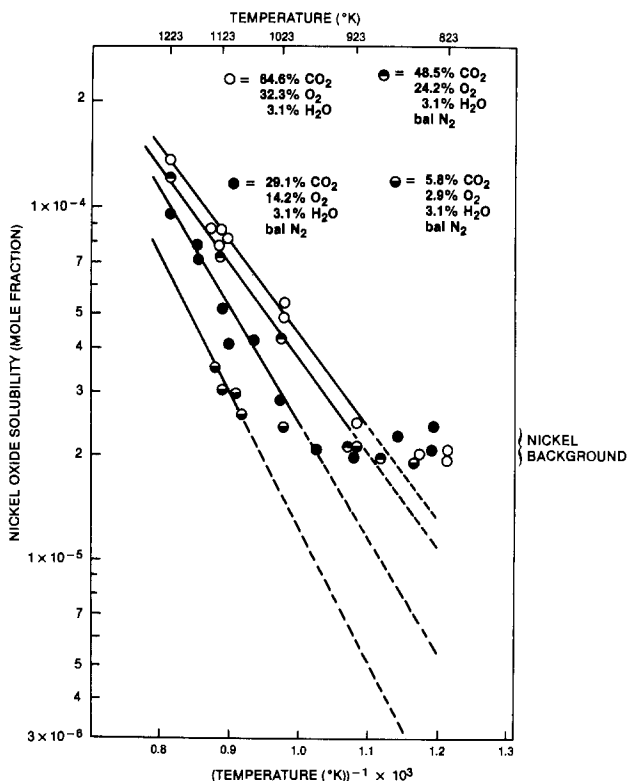


Fig. 1. Nickel oxide equilibrium solubility in Li/K carbonate as a function of temperature under various gases.

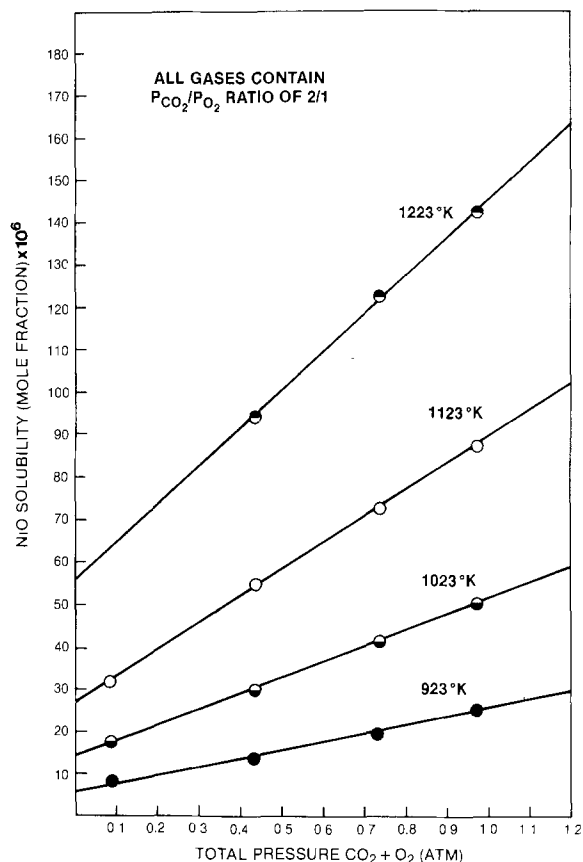


Fig. 2. Nickel oxide equilibrium solubility in Li/K carbonate at various temperatures as a function of CO₂ + O₂ pressure for gases with a P_{CO₂}/P_{O₂} ratio of 2/1.

ture of a MCFC, possessing a slope of 20.3×10^{-6} mole fraction NiO/atm (CO₂ + O₂) and a Y-intercept of 5.5×10^{-6} mole fraction NiO. From this linear relationship, the impact of MCFC system changes on NiO cathode solubility, and hence on the cathode corrosion rate, can be esti-

mated. For example, the calculated NiO equilibrium solubility under a rich oxidant (64.6% CO₂/32.3% O₂/3.1% H₂O) at 1 atm pressure with 25% oxidant electrochemical utilization is 20.3×10^{-6} mole fraction, and is equivalent to that calculated under a leaner gas (20% CO₂/10% O₂/3.1% H₂O/bal N₂) operated at 10 atm pressure and 75% oxidant utilization. Therefore, ignoring any electropotential influence on the cathode's solubility and assuming that the relevant transport properties are independent of gas pressure, cathodes operated under these two fuel cell conditions should exhibit similar corrosion rates.

The data presented in Fig. 2 also suggests that the NiO/carbonate equilibrium is not established simply by the CO₂ partial pressure as suggested previously (5, 7) since increasing the P_{CO₂} by a factor of 10 at constant temperature never resulted in more than a factor of 3.5 increase in solubilized nickel. This indicates that the solubilization mechanism is indeed complex and in need of further exploration.

Acknowledgment

This work was funded through Oak Ridge National Laboratory under Contract no. 11X-43123C.

Manuscript submitted Nov. 7, 1983; revised manuscript received March 9, 1984.

REFERENCES

1. C. E. Baumgartner, Paper 379 presented at The Electrochemical Society Meeting, Montreal, Que., Canada, May 9-14, 1982.
2. W. M. Vogel, L. J. Bregoli, S. W. Smith, and H. R. Kunz, Paper 386 presented at The Electrochemical Society Meeting, Montreal, Que., Canada, May 9-14, 1982.
3. C. E. Baumgartner, R. H. Arendt, C. D. Iacovangelo, and B. R. Karas, Abstract, p. 113, 1982 National Fuel Cell Seminar, Newport Beach, CA, Nov. 14-18, 1982.
4. J. W. Sim, G. H. Kucera, J. L. Smith, A. M. Breindel, and R. D. Pierce, Abstract, p. 108, 1982 National Fuel Cell Seminar, Newport Beach, CA, Nov. 14-18, 1982.
5. H. R. Kunz, Abstract, p. 116, 1982 National Fuel Cell Seminar, Newport Beach, CA, Nov. 14-18, 1982.
6. P. L. Spedding and R. Mills, *This Journal*, **112**, 594 (1965).
7. M. D. Ingram and G. J. Janz, *Electrochim. Acta*, **10**, 783 (1965).

Large Nickel Particle Powder Formed by Electrodeposition on a Metal Surface Partially Covered with a Polytetrafluoroethylene Layer

O. Teschke*

Instituto de Fisica, UNICAMP, 13.100 Campinas SP, Brazil

F. Galembek

Instituto de Quimica, UNICAMP, 13.100 Campinas SP, Brazil

Powdery metal deposits were obtained using electrolysis by Priestley (1) as early as 1803. Extensive studies on a large number of metals (Cu, Ni, Fe, Pb, Sn, Mn, Zn, Cd, Pd, W, Co) have been carried out since then. A detailed survey of this work was made by Ibl (2).

Kudra (3) first observed that the product of current density and the square root of the radius of electrodeposited particles is a constant. Theoretical work performed by this author leads to results compatible with this experimental observation. However, the poor adherence be-

*Electrochemical Society Active Member.

Key words: electrodeposition, coating, metal, film.

tween electrodeposited particles and the substrate was not explained. Atanasui and Calusaru (4) have also treated this problem on theoretical grounds. They proposed that the energy barrier for quantum mechanical tunneling is widened with decreasing concentration of the discharging species. However, the reason for the appearance of loosely connected outgrowths on a substrate has not been elucidated. Their loose connections are sufficiently strong to allow free flow of electrons and weak enough for the particles to fall off at the slightest disturbance. Powder particles are formed by nucleation and not by the extended growth of already existing irregularities. A

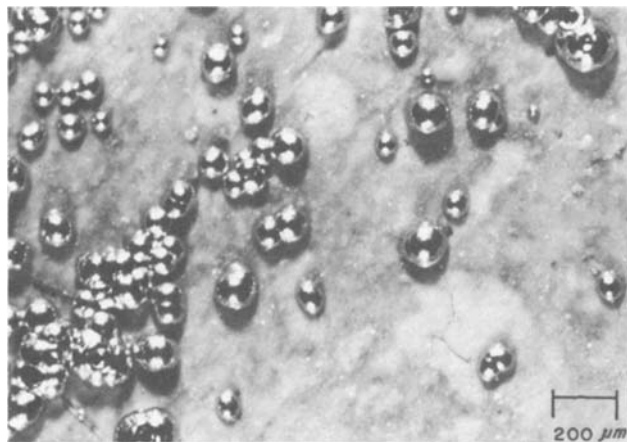


Fig. 1. Optical micrograph showing nickel particles formed by electrodeposition over a PTFE-covered nickel surface.

model of the mechanism of powder formation is not yet available, as far as we know.

This work describes a technique which was developed to form large particle powder. The technique consists of electrodeposition of nickel onto a metallic substrate covered by a thin polytetrafluoroethylene (PTFE) layer. Optical microscopy and scanning electron microscopy (SEM) observations were then performed to study the shape of the particles, which are loosely connected to the substrate.

Experimental

Stainless steel plates (5 cm × 2 cm × 1 mm) were initially nickel plated in a Watts solution at 30°C. The sample was rotated about its longer axis at a constant speed (20 rpm) in order to smooth out local electric field differences. All samples were prepared from the same stainless steel plate. The plate was initially washed in a detergent solution, mechanically scrubbed, and then cleaned in the usual sequence. A detailed description of the experimental condition is presented in Ref. (5).

The nickel plating solution consisted of the following compounds dissolved in distilled water: NiSO₄ · 6H₂O, 300 g/l, NiCl₂ · 6H₂O, 45 g/l, and H₃BO₃, 30 g/l. The resulting solution was stirred at 30°C in a Pyrex beaker. The counterelectrode was a nickel sheet.

A first nickel plating was given to the sheet for a total time of 12 min. The apparent current density was approx-

imately 10 mA/cm². After plating, the plates were washed with distilled water and dried.

PTFE T30 Teflon¹ dispersion was dialyzed against water to remove the stabilizing surfactant, and diluted to ca. 1% in distilled water. The dispersion was then allowed to settle within a long (ca. 60 cm) glass cylinder for 15 min, after which time the lower 10% of the cylinder contents was discarded. The dispersion was allowed to settle again, and after 1h the upper half of the cylinder contents was also discarded. To prevent excessive coagulation, 1% sodium laurylsulfate was added to the remaining dispersion, for storage. Prior to use, it was drained from a stock, the dispersed solid allowed to settle, and the liquid replaced by distilled water.

The previously plated metal sample was dipped into the Teflon dispersion, allowed to dry under air, and heated to 370°C. The electrode surface was then washed in an acidic solution (5% H₂SO₄ for 1 min) to remove the oxides formed, and another layer of nickel was electrolytically deposited on the electrode. The apparent current density was approximately 10 mA/cm², resulting in a much larger actual current density since only a few protrusions and pinholes are effective sites for the charge transfer reaction. During this second deposition, powder particles are formed over the PTFE layer. A photograph of the resulting surface is shown in Fig. 1. A cathode potential of 2V against a saturated calomel reference electrode was observed during the nickel deposition.

After the nickel electrodeposition, a thin nickel layer of about 150Å was evaporated over the samples for observation under a scanning electron microscope. SEM photographs giving more microscopic details are shown in Fig. 2. Pinholes at the surface of the PTFE film are shown in Fig. 2b. Typical pinhole diameters at the PTFE film are about 5 μm. Pinholes in the PTFE layer as well as cracks and protrusions in it are paths for electrons during the deposition, and metal is deposited around them. A SEM micrograph of a PTFE covered nickel surface before the particle formation shows a structure similar to that shown in the top portion of Fig. 2b. The PTFE shows a very irregular and spongy structure. The conductive metallic overlayer will not be deposited in most of the cavities. It is difficult then to determine which sites will effectively transfer electrons and result in particle growth.

Figures 1 and 2 show that the nickel deposit is made of round particles. Cross sections of the plates were obtained by cutting and polishing. Some of these are pre-

¹Teflon is a trademark of E. I. du Pont de Nemours and Company, Wilmington, Delaware.

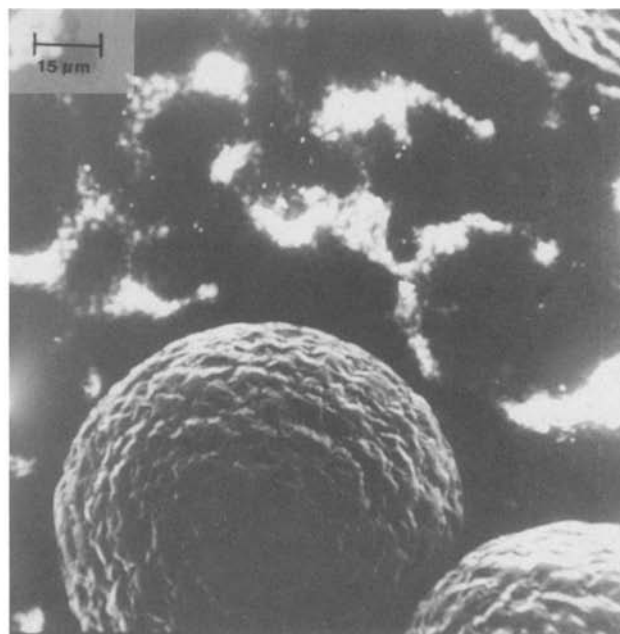
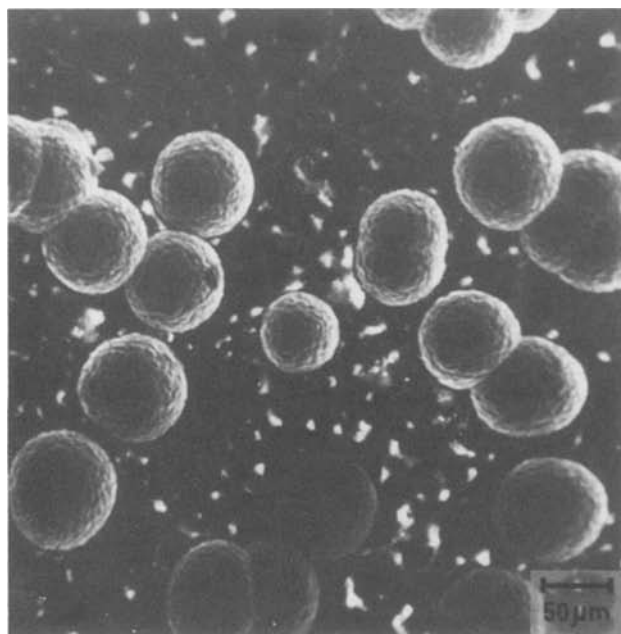


Fig. 2. Scanning electron micrographs of nickel particles formed by electrodeposition over a PTFE-covered nickel surface.

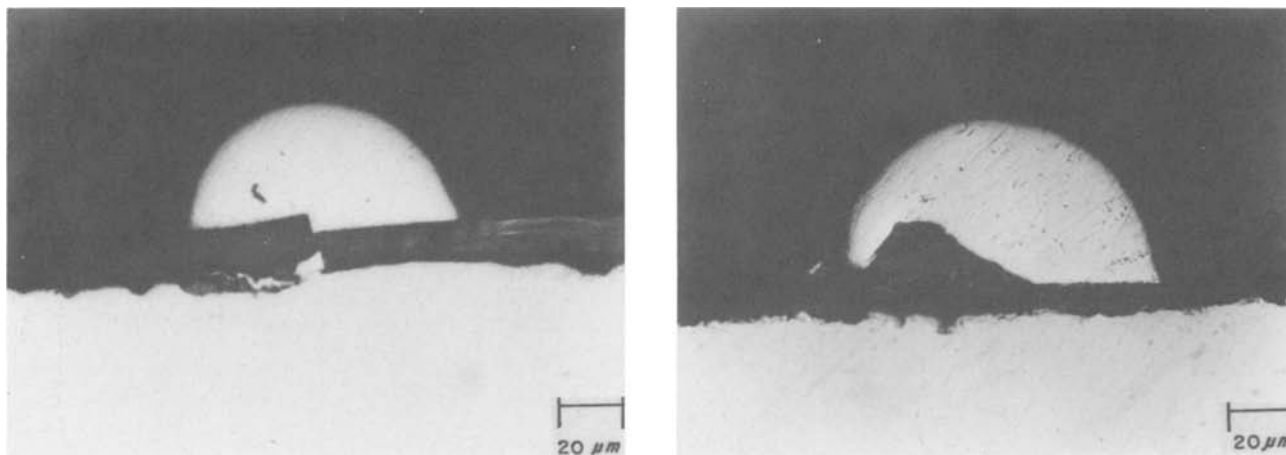


Fig. 3. Polished cross-sectional view of the nickel particles, PTFE layer, and nickel substrate.

sented in Fig. 3 and show common features: (i) nickel particles are obtained which have very little direct contact with the substrate metal, (ii) these particles take the approximate shape of half-spheres, (iii) their bases juxtapose to the PTFE layer, and (iv) metal tips connecting the substrate to the particles are not discernible, due either to small size or to damage during polishing.

Discussion and Conclusions

The shape of the particles reflects the influence of the PTFE layer. Protrusions and pinholes in the PTFE layer as well as cracks in it are paths for electrons during the deposition, and metal is deposited around them. After an initial growth, the layer is well away from the interface, and the deposition gives spherical particles. Since the PTFE layer imposes a fixed boundary to the particle growth, the deposits are half-spheres, as shown in Fig. 3. The particles have a diameter of 10-100 μm , but have a weak binding to the substrate since only tips of diameters around a few microns connect them to the substrate.

Figure 1 also shows that in some regions there is appreciable coalescence of the grown particles. The coales-

cence process following contact is characterized by the growth of the neck formed between the contacting powder particles (6).

In conclusion a technique was developed to form large particle powder. Nickel was deposited onto a metallic substrate covered by a thin PTFE layer. The deposit tends to form half-spherical particles with a weak binding to the substrate. The shape of the particles reflects the influence of the PTFE layer.

REFERENCES

1. J. Priestley, *Gilbert's Anal.*, **12**, 466 (1803).
2. N. Ibl, in "Advances in Electrochemistry and Electrochemical Engineering," Vol. 2, C. W. Tobias, Editor, Interscience, New York (1962).
3. O. Kudra and M. E. Lerner, *Ukr. Khim. Zh.*, **17**, 890 (1951).
4. J. Atanasiu and A. Calusaru, *Stud. Cercet. Metal.*, **2**, 337 (1957).
5. O. Teschke and D. M. Soares, *This Journal*, **130**, 306 (1983).
6. L. E. Murr, "Interfacial Phenomena in Metals and Alloys," Addison-Wesley, London (1975).

Comparison of the Activity of PdSn Colloidal Catalysts with the Activity of Pure Metals for HCHO Oxidation: Enhancement of the Activity by Ionic Tin

Jean Horkans

IBM, Thomas J. Watson Research Center, Yorktown Heights, New York 10598

The formation of a metallic conductor on an insulating substrate can often be accomplished most conveniently through the use of electroless deposition processes, which are initiated by a catalyst deposited on the insulator surface. The catalyst frequently is a PdSn mixed colloid, consisting of a metallic core of an alloy of Pd and Sn surrounded by a stabilizing layer of Sn(II) with the necessary counterions (mostly Cl^-) (1). It is assumed that the metallic Pd acts as the catalyst, whereas the ionic tin serves only to stabilize the colloid in solution. Indeed, excess ionic tin on the surface can be detrimental and is usually removed by following the activation step (the deposition of the colloid) by an acceleration step (2-5) (immersion in a solution that selectively dissolves ionic tin).

Earlier methods (6, 7) used to evaluate the activity of PdSn catalysts are not directly related to the role of the

Key words: electroless plating, organic voltammetry.

colloid in initiating electroless deposition. The work reported here examines PdSn colloids as catalysts for formaldehyde electro-oxidation. Of the two major partial electrode reactions occurring in electroless Cu plating, formaldehyde oxidation is the reaction that is kinetically limited and strongly influenced by the catalyst. The ionic tin in the colloid was found to be important to its function as a catalyst for the formaldehyde reaction.

The results suggest analogies to the changes in the catalytic activity of metal electrodes for the oxidation of organic molecules caused by the underpotential deposition (UPD) of less-noble adatoms (8-12). The first step in the oxidation of molecules like HCHO is thought (12) to be dissociative adsorption. During the oxidation of the carbon containing fragment, strongly bound intermediates (perhaps requiring several surface metal atoms) can form and can poison the reaction.

Motoo and Shibata (9) interpret their results in terms of this model. The enhancing UPD adatoms fall into two groups. In one group, the enhancement depends on the number of surface sites occupied by the adatom on the Pt electrode. The formation of the poison is blocked, since the required number of adjacent Pt sites is unavailable in the presence of the adatom. The second group of adatoms has a much larger effect on activity than the first. The activity is increased through a mechanism in which these adatoms adsorb oxygen containing species that participate in the oxidation reaction.

Other methods of depositing ionic species on metal electrodes also can result in increased activity of fuel cell catalysts (13, 14). The tin-covered surfaces of the present study were prepared by yet another method: deposition of a colloid. These catalysts show interesting parallels to the other adatom-covered metallic electrocatalysts.

Experimental

Formaldehyde oxidation was studied under conditions like those used during electroless Cu plating. The electrolyte was 0.4M Na₂SO₄, 0.03M HCHO, the pH adjusted to 11.7 with NaOH. A more detailed description of the experimental conditions is given elsewhere (15). The formaldehyde was used without further purification. No interference from the CH₃OH stabilizer was found (15). The temperature of the solution was maintained at 75°C. The reference was a mercury sulfate electrode (MSE), Hg/Hg₂SO₄, sat. K₂SO₄, in a separate compartment at room temperature.

The electrodes were evaporated metal films on glass substrates. An adhesion layer of 200Å of Nb was first deposited, followed by 2000Å of the desired metal. Some of the electrodes examined were prepared by depositing a colloid on the surface of the evaporated metal. The PdSn colloid was made by diluting with NaCl solution, a concentrate similar to that described in the patents of Zeblicky (16). Gold was chosen as the support material. It is known from electron microprobe analyses (7) that a 5 min immersion of a Au surface in the PdSn colloid typically results in coverages of ~ 1 µg/cm² of Pd and ~ 2-5 µg/cm² of tin. The SnCl₂ colloid was prepared according to the method suggested by Cohen and West (17) and consisted of 30 g/l SnCl₂ · 2H₂O with 10 ml/l of conc. HCl. It was aged for 2 days before use. Immersion of a metal surface in the SnCl₂ colloid deposits ~ 0.6 µg/cm² of tin (18).

Electrodes were maintained at the open-circuit potential while the solution was being deaerated with N₂. Tin salts have significant solubilities at pH 11.7 (19), and repeated cycling of the electrode potential results in changes in the curves as the colloid, or a component of the colloid, is removed from the surface. The first sweep is fairly reproducible, however, and only the first anodic sweep is reported here.

Results and Discussion

Representative curves for formaldehyde oxidation on Au, Pd, and PdSn-covered Au are shown in Fig. 1. The reaction occurs at a much less positive potential on the PdSn-covered surface than on either Au or Pd. The increased catalytic activity is due to one of the following: (i) an interaction between the Au electrode and the tin in the colloid, (ii) an interaction between the Au electrode and the Pd in the colloid, or (iii) an interaction between the Pd in the colloid and the surrounding tin. These possibilities can be narrowed by further experiments.

The interaction between Au and ionic tin is explored in Fig. 2. The interaction between Pd and ionic tin has also been investigated. Formaldehyde oxidation on Au and Pd surfaces covered by a SnCl₂ colloid (Fig. 2) occurs at less positive potentials than HCHO oxidation on Au and Pd (Fig. 1). In both cases, however, a more positive potential is required than on PdSn-covered Au. Thus, the interaction of Au with the tin salts cannot entirely account for the observations of Fig. 1.

In order to investigate the Au-Pd interaction, a 20Å thick film of Pd metal was evaporated on a Au electrode.

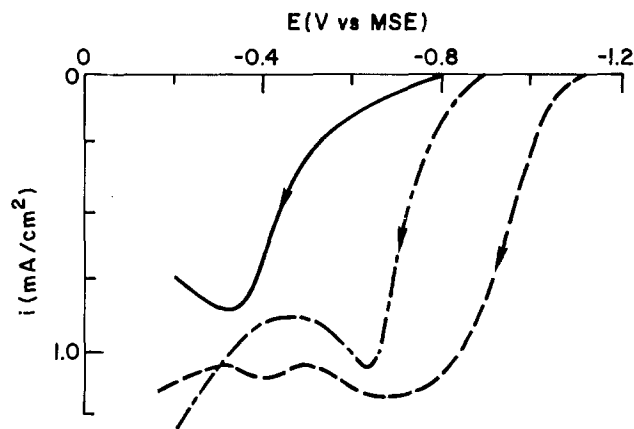


Fig. 1. Formaldehyde oxidation on clean Au (—), clean Pd (— · —), and Au covered with PdSn colloid (— —) in a pH 11.7 solution of 0.4M Na₂SO₄ and 0.03M HCHO. The temperature was 75°C. The sweep speed was 20 mV/s.

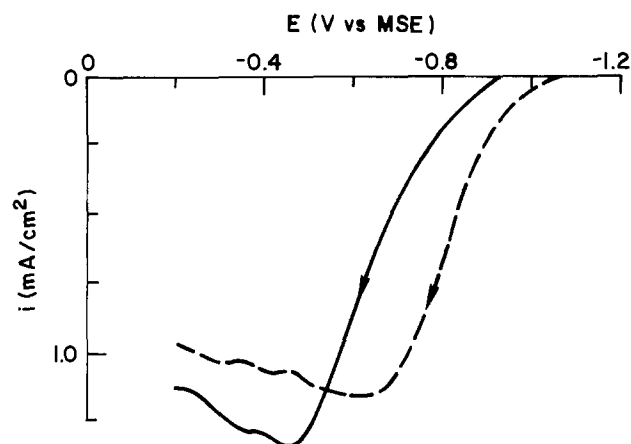


Fig. 2. Same as Fig. 1 for Au covered with a SnCl₂ colloid (—) and Pd covered with a SnCl₂ colloid (— —).

So thin a Pd film may not be continuous, but an island film would be an even better model than a continuous film for comparison with the PdSn-covered Au electrode. The results are given in Fig. 3, which shows that a thin Pd film does not shift HCHO oxidation on Au to less positive potentials. The interaction of the Pd in the colloid with the Au electrode therefore cannot explain the results of Fig. 1. It is thus evident that the ionic tin in the colloid plays a role in the high activity of the PdSn-covered Au electrode.

The effect of an accelerating step is shown in Fig. 4. The dashed curve was obtained on the PdSn-covered Au. The solid line was obtained on a Au surface that, after deposition of the PdSn colloid and rinsing, was immersed

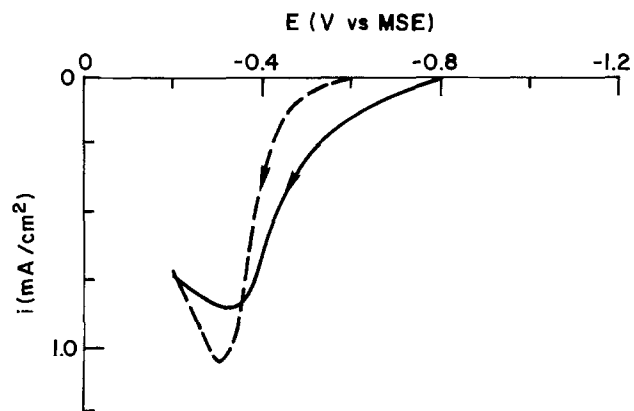


Fig. 3. Same as Fig. 1 for a Au electrode (—) and for a Au electrode with 20Å of evaporated Pd (— —).

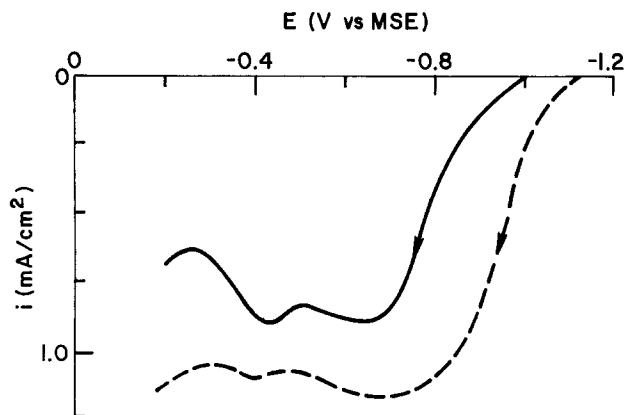


Fig. 4. Same as Fig. 1 for a PdSn-covered Au electrode before (—) and after (---) immersion in 1M NH_4HF_2 .

for 1 min in 1M NH_4HF_2 , a common accelerator, and then rinsed. This acceleration process is known (20) to remove from the surface approximately half of the tin but very little of the Pd. Removing tin shifts the curve to considerably more positive potentials.

Conclusions

The immersion of a metal in a SnCl_2 colloidal suspension will deposit the same order of magnitude of tin species as UPD, but the environment of the tin is very different. There is no orderly association of the tin atoms with the substrate atoms; the deposited material will exist in three-dimensional clumps; a variety of anions (mainly Cl^-) will be associated with the tin. The extent of charge transfer to the tin probably also differs between the colloid and UPD adatoms. Nonetheless, colloidal tin was found to be able greatly to enhance the catalytic activity of Pd and Au electrodes for HCHO oxidation.

The enhancement of the activity of Au and Pd by colloidal tin is probably by a mechanism similar to that discussed by Motoo and Shibata (9). The tin on the surface provides a site on which oxygen containing species can adsorb. These species can then participate in the oxidation of the adsorbed formaldehyde fragment.

Formaldehyde oxidation occurs at a much less positive potential on the PdSn-covered Au surface than on any of the other surfaces examined, including pure Pd and tin-covered Pd. The interaction causing the enhancement in activity seems to be between the Pd in the colloid and the tin in the colloid. One could ask, however, why the enhancement caused by the Pd-tin interaction in the colloid should be any greater than that caused by tin on a bulk Pd electrode. The answer probably lies in the small size of the Pd nuclei in the colloid, which is in the range of 10-50Å (21). The difference in surface energy between small particles and bulk metals may change the interaction with the tin. In addition, the Pd in the colloid is alloyed with a small amount of metallic Sn (1), and the environment of Pd at the center of the colloid is different

from that of Pd metal covered by a SnCl_2 colloid. Acceleration, by removing ionic tin from the PdSn colloid, shifts the formaldehyde-oxidation reaction to more positive potentials.

Acknowledgments

The author greatly appreciates the help of H. C. McGrath, who provided experimental assistance, and that of V. Markovich and B. Stoeber, who furnished the catalysts used in this investigation.

Manuscript submitted Sept. 12, 1983; revised manuscript received March 23, 1984.

IBM Corporation assisted in meeting the publication costs of this article.

REFERENCES

1. R. L. Cohen and K. W. West, *This Journal*, **120**, 502 (1973).
2. R. L. Cohen, R. L. Meek, and K. W. West, *Plating*, **63**, 52 (1976).
3. R. L. Meek, *This Journal*, **122**, 1177 (1975).
4. T. Osaka, H. Nagasaka, and F. Goto, *ibid.*, **128**, 1687 (1981).
5. J. J. Grunwald, S. Gottesfeld, and D. Laser, *Plating*, **68**, 71 (1981).
6. T. Osaka, H. Takamatsu, and K. Nihei, *This Journal*, **127**, 1021 (1980).
7. J. Horkans, *ibid.*, **130**, 311 (1983).
8. M. Watanabe and S. Motoo, *J. Electroanal. Chem.*, **60**, 259 (1975); *ibid.*, **60**, 267 (1975).
9. S. Motoo and M. Shibata, *ibid.*, **139**, 119 (1982).
10. R. R. Adzic, D. N. Simic, A. R. Despic, and D. M. Drazic, *ibid.*, **65**, 587 (1975); R. R. Adzic, *Isr. J. Chem.*, **18**, 166 (1979); M. D. Spasojevic, R. R. Adzic, and A. R. Despic, *J. Electroanal. Chem.*, **109**, 261, (1980); R. R. Adzic and M. L. Avramov-Ivic, *ibid.*, **134**, 177 (1982); R. R. Adzic, A. V. Tripkovic, and N. M. Markovic, *ibid.*, **150**, 79 (1983).
11. H. Angerstein-Kozlowska, B. MacDougall, and B. E. Conway, *This Journal*, **120**, 757 (1973).
12. B. E. Conway, in "Electrodes of Conductive Metallic Oxides," Vol. B. S. Trasatti, Editor, Elsevier, New York (1980).
13. Yu. B. Vassiliev, V. S. Bagotzky, N. V. Osetrova, and A. A. Mikhailova, *J. Electroanal. Chem.*, **97**, 63 (1979).
14. M. R. Andrew, J. S. Drury, B. D. McNicol, C. Pinnington, and R. T. Short, *J. Appl. Electrochem.*, **6**, 99 (1976); M. M. P. Janssen and J. Moolhuysen, *Electrochim. Acta*, **21**, 861 (1976); B. D. McNicol, R. T. Short, and A. G. Chapman, *J. Chem. Soc. Faraday 1*, **72**, 2735 (1976).
15. J. Horkans, *This Journal*, **131**, 1615 (1984).
16. R. J. Zablisky, U.S. Pat. 3,672,938 (1972); U.S. Pat. 3,672,671 (1972).
17. R. L. Cohen and K. W. West, *This Journal*, **119**, 433 (1972).
18. J. Horkans and J. Kuptsis, Unpublished work.
19. J. Kragten, "Atlas of Metal-Ligand Equilibria in Aqueous Solution," pp. 613, 623, Halsted, New York (1981).
20. J. Horkans, R. Abber, and A. Boulding, Unpublished work.
21. S. Herd, J. Horkans, and H. C. McGrath, Unpublished work.



Distribution of Anions and Protons in Oxide Films Formed Anodically on Aluminum in a Phosphate Solution

H. Takahashi,* K. Fujimoto, H. Konno,* and M. Nagayama*

Analytical Chemistry Laboratory, Faculty of Engineering, Hokkaido University, Sapporo 060, Japan

ABSTRACT

Pure Al foil specimens were galvanostatically anodized in a neutral phosphate solution (pH = 7.0, 20°C), and the thickness and composition profile of the formed oxide films were examined as functions of the anode potential and current density (c.d.). Analysis of the films was made by chemical sectioning with a H₂SO₄ solution, combined with (i) electron microscopy, (ii) x-ray photoelectron spectroscopy, (iii) capacitance measurements, (iv) dc polarization measurements, and (v) solution analysis. The films were found to consist of two parts, an outer part containing PO₄³⁻ and OH⁻ ions, and an inner part consisting of pure alumina. The outer part dissolved in the H₂SO₄ solution at a rate faster than that of the inner part, and thus the two parts were clearly distinguished by following the time variations in the reciprocal of capacitance during the chemical sectioning. For films formed with a constant c.d., the thickness ratio of the two parts, $\delta_{\text{out}}/\delta_{\text{in}}$, and the phosphate concentration in the outer part do not change with the anode potential or the total film thickness. With increasing c.d., the two values tend to increase. The mechanism controlling the anion and proton distribution in the oxide film is discussed.

Anodic oxide films formed on aluminum contain an appreciable amount of anions brought from the anodizing solution. When anodizing in phosphate solutions, the incorporated anions locate in the outer part of the film, while an inner part next to the metal consists of stoichiometric oxide. This was first reported by Randall and Bernard (1), who used a radiotracer method combined with a film sectioning technique. Using SIMS, Wood and co-workers (2) obtained phosphorus profiles qualitatively similar to those reported by Randall. More recently, we applied XPS combined with chemical sectioning of the film and ascertained that phosphorus in the outer part exists in the form of PO₄³⁻ and that some protons are also incorporated in the outermost part of the oxide (3). Lanford *et al.* (4) measured hydrogen profiles for a variety of anodic oxide films using a nuclear reaction technique, and reported that protons exist only in the outermost part, at concentrations equivalent to about 1 mole percent (m/o) water in alumina.

The purpose of the present investigation was to obtain quantitative measurements of the phosphate and proton profiles of oxide films formed galvanostatically in a phosphate solution and also to examine the effects of the anode potential and current density (c.d.) for films formed in phosphate solution at conditions similar to those used here.

Experimental

Anodizing procedure.—Pure, 99.99% Al foil coupons (2 × 3 cm, tag shaped) were electropolished in a 4:1 mixture of glacial acetic acid and 60% perchloric acid at 10°–15°C by applying an anodic current of 100 mA/cm². The polished coupons were then immersed in a 20 g/l CrO₃–35 ml/l H₃PO₄ solution (90°C) for 20 min to remove oxide film formed during the electropolishing, washed with methanol, and dried. Anodizing was carried out in a 0.033M NH₄H₂PO₄–0.067M (NH₄)₂HPO₄ solution (pH = 7.0, 20°C, stirred), by applying a constant current, i_a , of 1 mA/cm² until the potential, E_a , reached desired values, mainly 50V

(vs. SCE). To examine the effect of c.d., i_a was changed in the range 0.05–10 mA/cm².

After anodizing, the amount of Al³⁺ in the formed oxide, W_o , was determined by subtracting the dissolved amount of Al³⁺, W_d , from the total amount of oxidized aluminum, W_T , estimated with Faraday's law. Here, the charge consumed by oxygen evolution was so small that it could be neglected (5).

Chemical sectioning of the films.—The anodized specimens were immersed for different times in a 2M H₂SO₄ solution stirred at 60°C to dissolve and section the films from the outside. During the sectioning, the following measurements were carried out.

Amount of dissolved Al³⁺ ions, W_d .—Solution samples taken at intervals were analyzed by the oxinate extraction method in which Al³⁺ oxinate were extracted into chloroform at a pH around 9.3 to avoid the interference from the phosphate (6).

Amount of dissolved PO₄³⁻ ions, W_p .—Solution samples were analyzed by the molybdenum blue method (7).

Capacitance of the remaining oxide, C_p .—Specimens were transferred to a 0.5M H₃BO₃–0.05M Na₂B₄O₇ solution (pH = 7.4, 20°C), and the measurements were conducted at 120 Hz using a Yokokawa-Hewlett Packard Model 4284A Capacitance Meter.

Voltage sustained by the remaining oxide, ΔE .—Measurements were made in the same borate solution as for C_p measurements, by applying a small anodic current, i_a , of 10 μ A/cm².

Remaining film thickness, δ .—This was measured from electron micrographs of the sections of films. Sliced samples were prepared by an ultrathin sectioning technique using a Porter-I ultramicrotome with a diamond knife (8). The samples were examined by a transmission electron microscope (Hitachi Model HU-12A); the acceleration voltage was 125 kV, and the magnification was checked with standard polyethylene latex particles.

* Electrochemical Society Active Member.

Key words: aluminum, anodic oxide film, anion distribution, surface analysis

XPS spectra for the exposed film surfaces.—The instrument used was a Vacuum Generators ESCA 3 electron spectrometer. Specimens were irradiated by $MgK\alpha$ x-ray ($h\nu = 1253.6$ eV) in a vacuum of 10^{-7} Pa (10^{-10} torr range). The analyzer was set to give a resolution of 1.18 eV for FWHM of the Au 4f 7/2 peak. The spectrometer was calibrated with pure copper relative to the photoelectron peaks of Au 4f 7/2 (84.0 eV) and Cu 2p 3/2 (932.70 eV). The intensities of Al 2s, O 1s, and P 2p were obtained from the corresponding peak areas. For a given specimen, the measurements were made after removing a surface layer of about 0.5 nm by ion sputter etching. S 2p and C 1s spectra showed that all contaminating species brought from the chemical sectioning solution were completely removed by this procedure. Preferential sputtering was insignificant for all the elements in the oxide, and derivation of the film composition was made as in Ref. (9).

Results

Determination of the composition of 50V films formed at 1.0 mA/cm².—Figure 1 shows the time variations in the anode potential, E_a , and the amount of Al ions in the oxide, W_o , during anodizing at $i_a = 1.0$ mA/cm². The current efficiency for the oxide formation was 98%, and the 50V film had a W_o value of 9.9 $\mu\text{g}/\text{cm}^2$.

Dissolution behavior of oxide.—Figure 2 shows the time variations in the amount of dissolved Al^{3+} and PO_4^{3-} ions, W and W_p (as phosphorus), followed during the chemical sectioning. As can be seen from the W - t_d curve, the dissolution rate of the film up to 40 min is faster than that after 40 min, and the film is fully dissolved at 60 min; the exposed substrate metal dissolves faster than the oxide. The amount of dissolved Al^{3+} ions at 60 min agrees well with the value of W_o . The W_p - t_d curve shows that the dissolution of phosphate is complete at 40 min, where the amount of dissolved phosphate reaches a steady value, 0.32 $\mu\text{g}/\text{cm}^2$, as phosphorus. Thus, Fig. 2 implies that the film consists of two parts: an outer part containing phosphate and dissolving faster and an inner part without any phosphate and dissolving slower. The phosphate profile obtained from Fig. 2 will be discussed below with reference to Fig. 7. The average concentration of phosphate in the whole oxide was calculated to be 5.1 weight percent (w/o), assuming the chemical composition as $\text{Al}_x\text{O}_y(\text{PO}_4)_z$.

In Fig. 3, the reciprocal of the film capacitance, $1/C_p$, is plotted against the dissolution time, t_d ; $1/C_{p,0}$ is the value at $t_d = 0$. Assuming the dielectric constant of the oxide to be constant, $\epsilon = 9.8$,¹ the remaining film thickness, δ , corresponding to $1/C_p$, was calculated and is indicated on the

¹ The dielectric constant, $\epsilon = 9.8$, is higher than the generally accepted value (~ 8.4). Our value was obtained by substituting 66 nm and 0.131 $\mu\text{F}/\text{cm}^2$ for δ_0 and $C_{p,0}$ into $\epsilon = (\delta_0 \cdot C_{p,0}) / (8.86 \times 10^{-5})$. The $C_{p,0}$ value is influenced by the roughness of the surface. Assuming the roughness factor to be 1.2, the value for ϵ becomes 8.2.

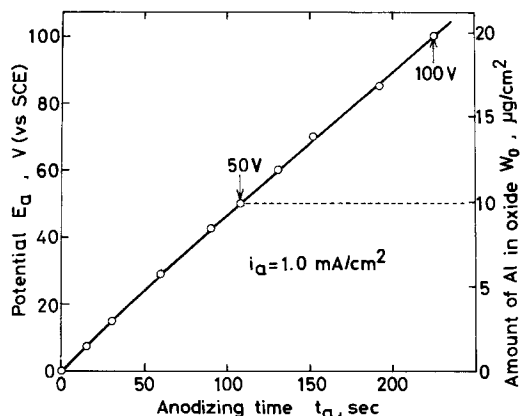


Fig. 1. Changes in the anode potential, E_a , and the amount of Al^{3+} ions in the oxide, W_o , with anodizing time, t_a . Anodizing was carried out by applying a constant c.d. of 1.0 mA/cm² in 0.067M $\text{NH}_4\text{H}_2\text{PO}_4/0.033\text{M}$ $(\text{NH}_4)_2\text{HPO}_4$ solution ($\text{pH} = 7.0$; 20°C).

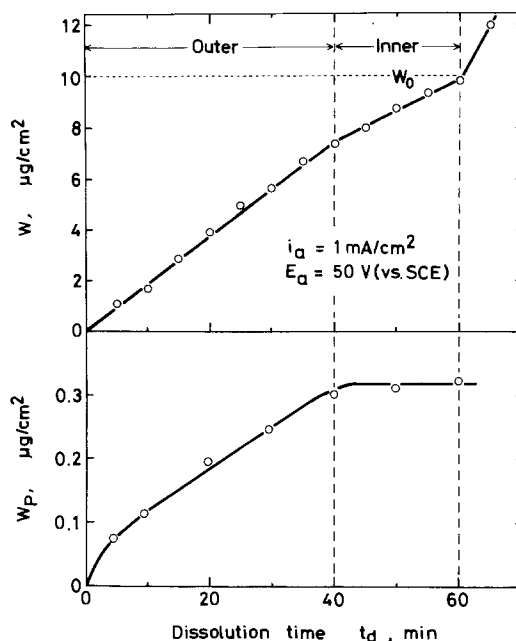


Fig. 2. Time variations in the amounts of dissolved Al^{3+} ions, W , and PO_4^{3-} ions, W_p (as phosphorus), during film sectioning in 2M H_2SO_4 solution at 60°C . The oxide film was formed by anodizing with $i_a = 1.0$ mA/cm² up to 50V (vs. SCE) in 0.067M $\text{NH}_4\text{H}_2\text{PO}_4/0.033\text{M}$ $(\text{NH}_4)_2\text{HPO}_4$ solution ($\text{pH} = 7.0$, 20°C).

right ordinate. The thinning rate slows down at 40 min and the film dissolution is complete at 60 min, in agreement with the result in Fig. 2. Here, the thickness of the outer part is proportional to $1/C_{p,0}$ minus $1/C_p^*$, and that of the inner part is proportional to $1/C_p^*$, the value at $t_d = 40$ min.

Electron micrographs of sections of films taken at different t_d 's (Fig. 4) clearly show the progress of the chemical sectioning. Figure 4 shows the metal substrate (M), and the oxide layer (O), and a thin layer of resin used to embed the sample. The micrographs show that the original film thickness, δ_0 , is about 66 nm, and the film thins almost uniformly until it is all dissolved at $t_d = 60$ min. This again coincides with the W - t_d and $1/C_p$ - t_d behavior.

Figure 5 shows how the dc polarization sustained by the remaining oxide, ΔE , decreases with t_d ; ΔE was measured by applying a small i_a , 10 $\mu\text{A}/\text{cm}^2$, in the borate solution. For every t_d , steady ΔE was attained within 10s, consuming only about 1×10^{-4} C. This very small charge again suggests the uniform dissolution of the oxide during the chemical sectioning. It should be noted here that for $t_d = 0$, the steady value of ΔE is 44V , smaller than the anodizing voltage of 50V because of the smaller value of i_a ($= 10$ $\mu\text{A}/\text{cm}^2$) compared to 1 mA/cm².

The time variations in the film thickness, δ , were estimated from the measured values of W , C_p , and ΔE using

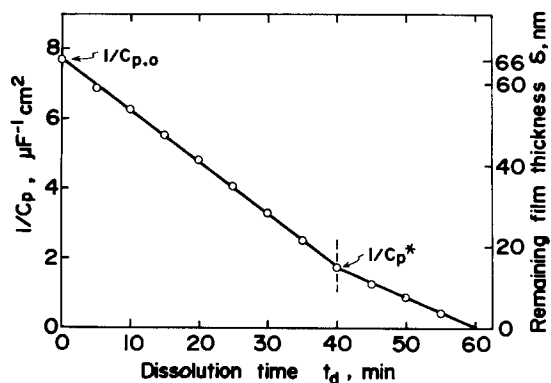


Fig. 3. Time variations in the reciprocal capacitance, $1/C_p$, of film, and the remaining film thickness, δ , during film sectioning in 2M H_2SO_4 solution at 60°C . Anodizing conditions are the same as in Fig. 2.

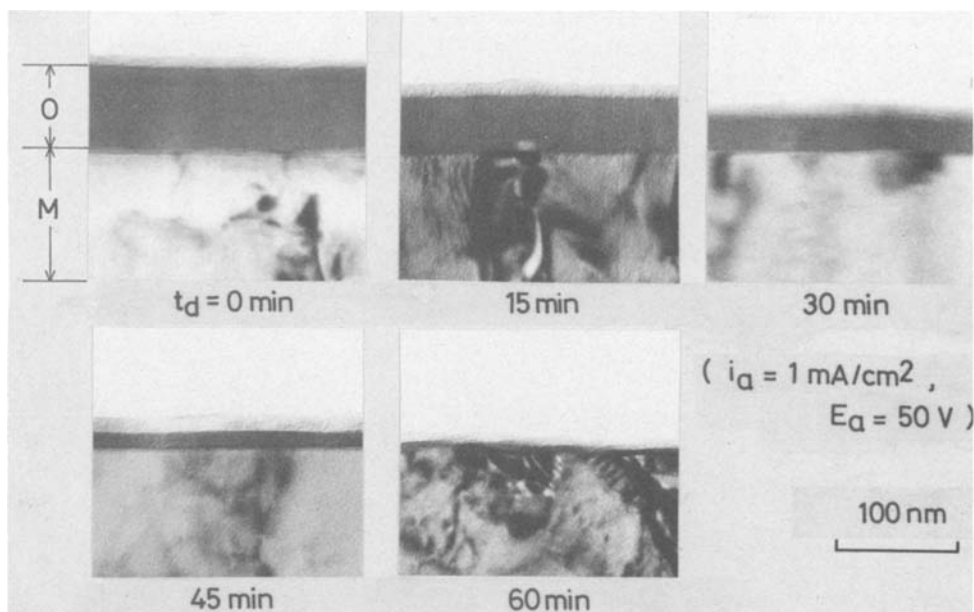


Fig. 4. Electron micrographs showing the progress of film thinning in 2M H_2SO_4 at 60°C. Anodizing conditions as in Fig. 2.

the following equation, and the results were compared with those from electron microscopy (Fig. 6)

$$\delta = 8.86 \times 10^{-8} \epsilon / C_p, \delta = (W_o - W) / \rho k, \text{ and } \delta = KE \quad [1]$$

In Fig. 6 the open circles are the data obtained from the C_p measurements with the dielectric constant of the oxide, $\epsilon = 9.8$. The small solid circles are from the amounts of dissolved Al^{3+} ions, W , assuming that the oxide density, ρ , is 2.95 and the weight fraction of Al^{3+} in the oxide, k , is 0.51. Error bars indicate the range of the data from electron microscopy. The open triangles indicate the data obtained from the ΔE measurements by assuming the thickness/voltage ratio, K , to be 1.5 nm/V. The ϵ , ρ , k , and K values used here are based on reported values, and the film thickness data estimated by the different methods are in good agreement. Thus, the total thickness of the 50V film is $\delta_o = 66$ nm, and the boundary between the outer and inner parts is around $\delta^* = 51$ nm inward from the surface of the oxide.

Phosphate profile from measurements of W and W_p .—From Fig. 6, it is possible to determine the depth position of the film, $x = (\delta_o - \delta)$, which will be exposed at a given dissolution time, t_d . By comparing the slopes of the W_p - t_d and W - t_d curves in Fig. 2 at various depths (or dissolution times), we obtained the P/Al mole ratio profile. The result is shown as the broken curve in Fig. 7. The P/Al mole ratio is almost 0.1 at the top of the film, it decreases steeply to about 0.03, and then stays constant down to a depth of nearly 50 nm. Beyond this depth phosphorus is not detected.

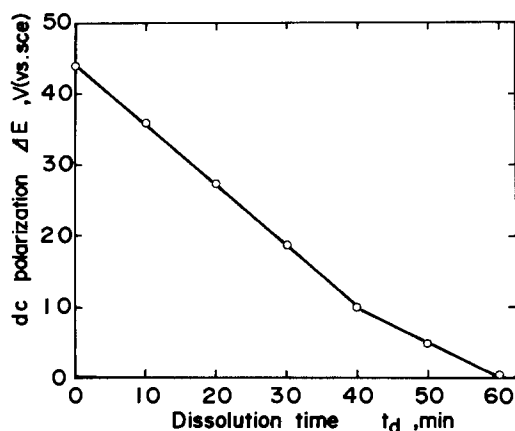


Fig. 5. Time variation in the steady value of dc polarization, ΔE , during film sectioning in 2M H_2SO_4 solution at 60°C. Anodizing condition as in Fig. 2.

Film composition estimated from XPS.—Typical XPS spectra taken for the outer and inner parts of the film are shown in Fig. 8. Phosphorus is detected in the outer part but not in the inner part. The peak positions of the spectra compared with those of standard samples suggest that Al and P exist in the form of Al^{3+} and PO_4^{3-} (or possibly HPO_4^{2-}). The composition profile of the film is shown by the solid curve in Fig. 7. The O/Al mole ratio is about 2 at the outer surface of the oxide, but it decreases with

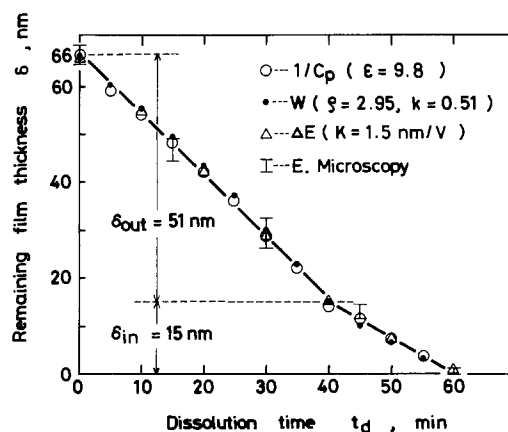


Fig. 6. Time variation in the film thickness, δ , estimated by the measurements of C_p , W , ΔE and electron microscopy during film sectioning. Anodizing condition as in Fig. 2.

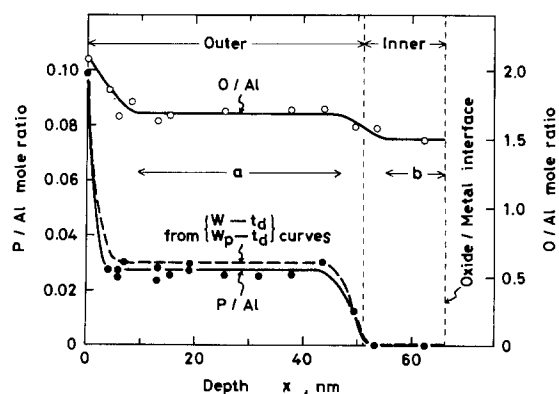


Fig. 7. Depth profiles of O/Al and P/Al mole ratio across oxide films formed by anodizing with 1 mA/cm² up to 50V (vs. SCE). Solid curves were obtained from XPS, and the dotted curve was obtained from the measurements of W and W_p .

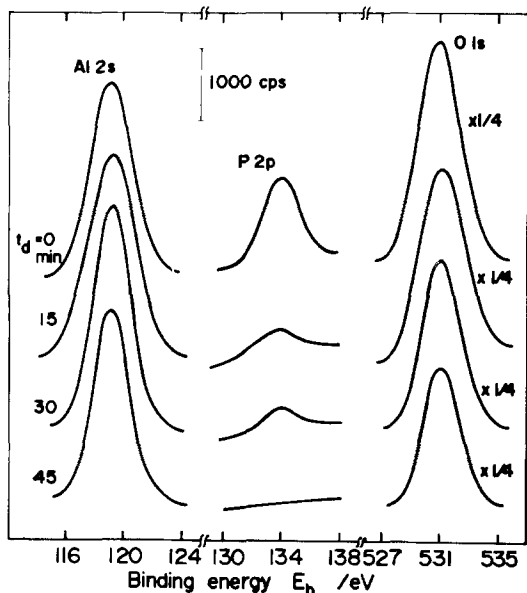


Fig. 8. XPS spectra of Al 2s, P 2p, and O 1s orbitals for oxide films immersed in 2M H_2SO_4 solution at 60°C for different durations. Anodizing condition as in Fig. 2.

depth to reach about 1.7 within the first 10 nm, stays constant at this value until about $x = 50$ nm, and then decreases to 1.5, corresponding to the composition of a stoichiometric oxide. The 1.5 value appears to be maintained throughout the inner layer. The P/Al profile agrees quite well with that obtained by the W and W_p measurements, though the value of 0.028 for the outer part is slightly lower than the value estimated from the W and W_p measurements.

Effect of E_a and c.d. on the film composition.—The chemical sectioning behavior was observed for films formed by anodizing to various potentials, E_a , with $i_a = 1.0$ mA/cm² (see Fig. 1). Figure 9 shows W_p - t_d curves obtained for films with different anodizing potentials. All the W_p - t_d curves for films of different anodizing potentials coincide until W_p reaches steady values. The steady value of W_p indicates the total amount of phosphate incorporated in the films, and it increases with increasing anodizing potential. The time needed for complete dissolution of phosphate (broken vertical bars) also increases with E_a . The time required for the total dissolution of the film, obtained from the $1/C_p$ - t_d curves (Fig. 10), is shown by solid vertical bars. Except for the 14.9V film, the time required for complete dissolution of phosphate is considerably shorter than that required for whole film. For 14.9V film, the two bars nearly coincide, implying that there is no inner part free from phosphate. The coincidence of the inclined line segments, irrespective of E_a , suggests that for all the films the outer part, containing

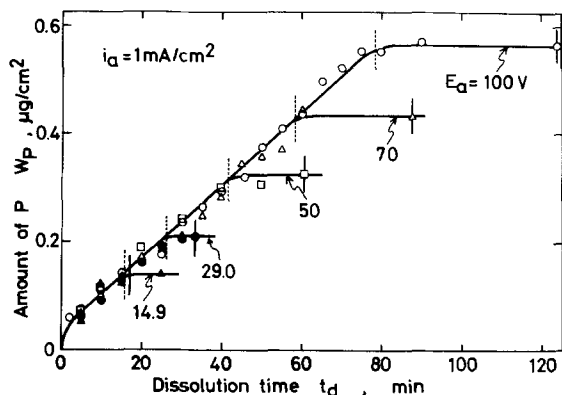


Fig. 9. Time variation in the amount of dissolved phosphate, W_p (as phosphorus) during the sectioning of oxide films formed by anodizing with 1.0 mA/cm² up to different anode potentials.

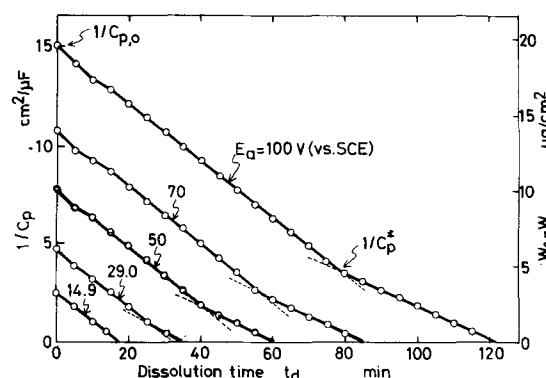


Fig. 10. Time variation in the reciprocal capacitance, $1/C_p$, during the sectioning of oxide films formed by anodizing with 1.0 mA/cm² to different anode potentials.

phosphate, dissolves at one rate, and also that they have the same phosphate concentration in this part.

The $1/C_p$ - t_d curves obtained for films with different anodizing potentials are shown in Fig. 10. Break points distinguishing the outer and inner parts are seen in all the curves except in the 14.9V curve, in agreement with Fig. 9. Here again, $1/C_{p,0}$ is proportional to the total film thickness and $1/C_p^*$ is proportional to the thickness of the inner part. The amounts of Al^{3+} remaining in the oxide, $W_o - W$, are calculated by using the values of ϵ , ρ , and k described above and indicated on the right ordinate in Fig. 10.

In Fig. 11, the values of $1/C_{p,0}$ and $1/C_p^*$ are plotted as functions of E_a . The film thickness δ calculated as before is indicated on the right ordinate. The films formed below 20V consist of only a single phase similar to the outer part, and the films formed above 20V show almost constant δ_{out}/δ_{in} ratio (the ratio is 3.5 at 20V and 3.3 at 100V). Using the W_p - t_d curves (Fig. 9) and the corresponding W - t_d and δ - t_d relationships (Fig. 10), the P/Al profiles can be calculated as in Fig. 12. It is seen that, except for the 14.9V film, the outer part containing phosphate is clearly distinguishable from the inner part without phosphate incorporation. Here, the total film thickness is indicated by vertical bars on the abscissa, and the boundary between the two parts by broken, vertical lines. There is a high concentration of P at the top, and the P/Al ratio of about 0.03 is constant, irrespective of the thickness of the outer part for an $i_a = 1$ mA/cm².

The effect of c.d. on the phosphate profile was examined for 50V films formed at i_a of 0.1, 1, and 10 mA/cm², and is shown in Fig. 13. The phosphate concentration in the outer part increases with i_a . An increase in i_a causes a decrease in the thickness of the inner part. The thickness of the outer part is little affected by i_a . This is seen more clearly in Fig. 14, which shows the effect of i_a on $1/C_{p,0}$ and $1/C_p^*$. It is also recognized from Fig. 14 that the thinning rate of the outer part increases with increasing i_a , but that of the inner part is independent of i_a .

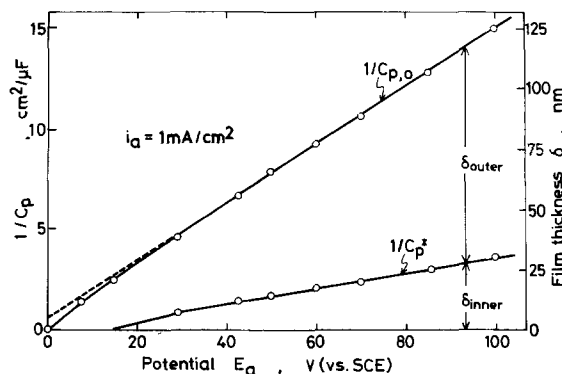


Fig. 11. Effect of anode potential, E_a , on $1/C_{p,0}$ (total film thickness, $\delta_{out} + \delta_{in}$) and $1/C_p^*$ (inner part thickness, δ_{in}) of oxide films formed by anodizing with 1.0 mA/cm².

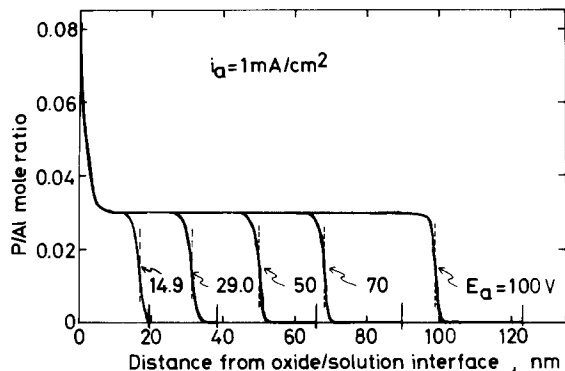


Fig. 12. Effect of anode potential, E_a , on the depth profile of the P/Al mole ratio across oxide films formed by anodizing with 1.0 mA/cm^2 .

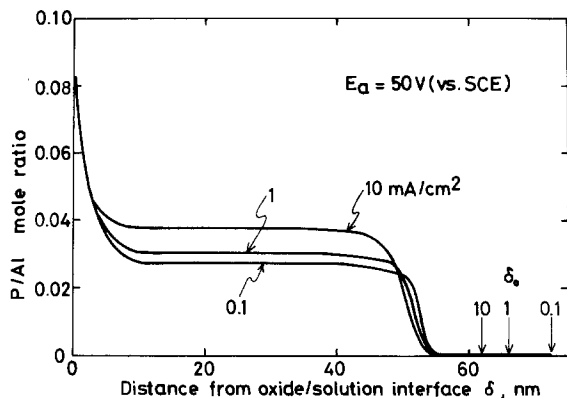


Fig. 13. Effect of c.d. on the depth profile of P/Al mole ratio across oxide films formed by anodizing to 50 V (vs. SCE) .

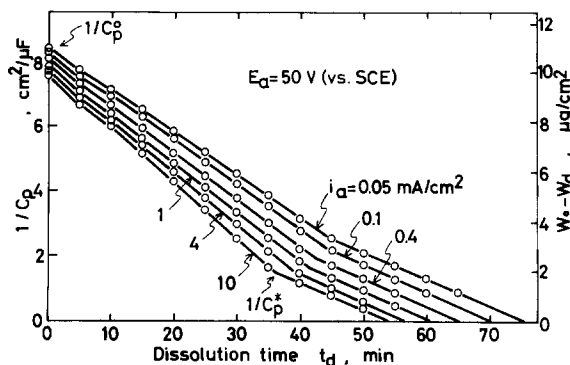


Fig. 14. Time variation in the reciprocal capacitance, $1/C_p$, during the sectioning of oxide films formed by anodizing with different c.d. to 50 V (vs. SCE) .

Discussion

Mechanism controlling the composition profile.—It was shown above that phosphate is included only in the outer part of the oxide and its concentration increases as the anodizing c.d. is increased. This may be explained by the model for film growth shown in Fig. 15. When anodizing, oxide forms both at the metal/oxide and oxide/solution interfaces corresponding to the field-assisted transport of O^{2-} and Al^{3+} ions through the oxide. Here, Al^{3+} ions reaching the oxide/solution interface react with PO_4^{3-} as well as O^{2-} ions to form the outer phosphate incorporating part of the oxide, whereas O^{2-} ions arriving at the oxide/metal interface react with Al^{3+} ions to form the inner part consisting of pure alumina. The reason why phosphate is not included in the inner part is explained on the assumption that phosphate is almost immobile in the oxide because of its larger size. This assumption agrees with the fact that the phosphate concentration is almost constant throughout the outer part of the oxide except for the outermost part, where the concentration is considerably

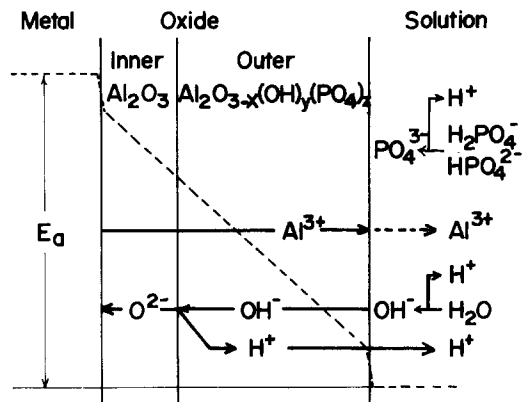


Fig. 15. Schematic model showing the transport of ions across the oxide film during anodizing in a neutral phosphate solution.

higher. Thus phosphate can be used as a marker to estimate the transport number of Al^{3+} , $T_{\text{Al}^{3+}}$. Provided there is no dissolution of oxide during anodizing, $T_{\text{Al}^{3+}}$ would be equal to the thickness of the outer part divided by the total thickness of the oxide. As some dissolution is unavoidable, the exact determination of $T_{\text{Al}^{3+}}$ will be described later.

Using the XPS data shown in Fig. 7, the chemical composition of the outer part of the 50 V film can be determined. Assuming $\text{Al}_2\text{O}_x(\text{OH})_y(\text{PO}_4)_z$, the composition is $\text{Al}_2\text{O}_{2.92}(\text{OH})_{0.48}(\text{PO}_4)_{0.056}$. Alternatively, assuming $\text{Al}_2\text{O}_x(\text{PO}_4)_y \cdot z\text{H}_2\text{O}$, the composition becomes $\text{Al}_2\text{O}_{2.92}(\text{PO}_4)_{0.056} \cdot 0.26\text{H}_2\text{O}$. The XPS spectra for O 1s cannot predict which formula applies, because of the similarity in the binding energy of O 1s for OH^- and H_2O species (Fig. 8). It is, however, notable that both formulas allow a 0.4%–0.5% proton content in the outer part. This implies that OH^- ions rather than O^{2-} ions move in the outer part, but protons may move back from the boundary between the inner and outer parts, as suggested by Hoar and Mott (10).

Lanford *et al.* (4) have measured the proton profiles in barrier type oxide films with a nuclear reaction technique and reported only 0.17 w/o as H_2O (0.02 w/o as proton) in the outer surface. The cause of the discrepancy between this proton content and the one obtained in the present study is not clear, but the difference seems to depend upon the difference in anodizing conditions. Konno *et al.* (3) reported that the proton concentration in the outer part is almost zero after keeping the specimen at a constant anode potential after anodizing galvanostatically.

The high concentration of phosphate at the outermost part is considered to be either due to adsorption of phosphate during anodizing (1) or due to a thin film formed by the immersion of the specimen in the $\text{H}_3\text{PO}_4/\text{CrO}_3$ solution prior to the anodizing. In an XPS study to be published, we found a 5 nm hydrous oxide layer, which contains a high concentration of phosphate, is formed by the immersion of electropolished specimens in the $\text{H}_3\text{PO}_4/\text{CrO}_3$ solution (11). The hydrous oxide layer appears to play an important role in the formation of the oxide layer during the subsequent anodizing; the $\delta_{\text{out}}/\delta_{\text{in}}$ value is different between anodic oxide films on electropolished specimens and films on specimens electropolished and then immersed in the $\text{H}_3\text{PO}_4/\text{CrO}_3$ solution (11). The lack of inner layer for oxide films formed at less than 20 V may be related with the action of the pre-existing layer.

The effect of c.d. on the phosphate concentration in the outer part may be explained in the following manner. It is certain that any increase in the anodic c.d. is associated with the increase in the electric field at the oxide/solution and oxide/metal interfaces as well as that across the bulk oxide. The increase in the electric field in turn enhances the deprotonation of H_2PO_4^- and HPO_4^{2-} ions to form the more negatively charged species PO_4^{3-} , which has a higher coordinating ability toward Al^{3+} ions. Deprotonation of H_2O to form OH^- and O^{2-} is also facilitated,

and these ions will provide some competition with PO_4^{3-} ions in coordinating with Al^{3+} ions, but this does not alter the above interpretation. The increase in the phosphate concentration with increasing c.d. may be qualitatively explained in this manner.

Determination of the transport number of Al^{3+} ions.—As described above, $T_{\text{Al}^{3+}}$ is equal to the ratio of $\delta_{\text{out}}/(\delta_{\text{out}} + \delta_{\text{in}})$, if there is no dissolution during anodizing. However, some dissolution is unavoidable, and we used the following equation to estimate exact values of $T_{\text{Al}^{3+}}$

$$T_{\text{Al}^{3+}} = \frac{\delta_{\text{out}} + (\delta_{\text{out}} + \delta_{\text{in}})(1/\eta - 1)}{(\delta_{\text{out}} + \delta_{\text{in}})/\eta} = 1 - T_{\text{O}^{2-}}$$

where η is the current efficiency for the formation of oxide and $T_{\text{O}^{2-}}$ is the transport number of O^{2-} ions. Figure 16 shows the changes in $T_{\text{Al}^{3+}}$ (calculated) and η (experimental) with i_a . As is seen, $T_{\text{Al}^{3+}}$ gradually increases with increasing i_a from 0.73 at 0.05 mA/cm² to 0.81 at 10 mA/cm². As described above, an increase in i_a is always associated with an increase in electric field across the oxide, and hence it is reasonable that the transport of Al^{3+} ions, having smaller size and higher valency, is facilitated in preference to O^{2-} ions.

The method applied here is the same in principle as that reported by Randall and Bernard (1). They examined the effect of temperature and electrolyte concentration on $T_{\text{Al}^{3+}}$ and obtained the figures ranging from 0.72 to 0.84. The transport number of Al^{3+} obtained above is based on the immobility of the phosphate ions in the oxide. The possibility that the phosphate ions may be mobile has been pointed out by Davies *et al.* (12) and Pringle (13). They showed that smaller values for $T_{\text{Al}^{3+}}$ are obtained by using a xenon marker method, and the values do not change with the kind of inert gas markers. Thus, it is possible to explain the large value of $T_{\text{Al}^{3+}}$ obtained in the present study by the movement of phosphate inwards according to the electric field. However, it is notable that the transport number obtained by the marker method is dependent on the pre-existing films (14) and the acceleration voltage at the ion implantation of the marker (15).

Dissolution characteristics of the oxide.—As can be seen from Fig. 6 and 14, oxide films dissolve uniformly in the sulfuric acid solution, and the thinning rate of the outer part increases with i_a , while the thinning rate of the inner part does not change. It is likely that the dissolution rate is controlled by the amount of incorporated phosphate; the higher the concentration of phosphate, the faster the dissolution rate. Because the inner part does not contain any phosphate, this part dissolves at a slower rate, and it

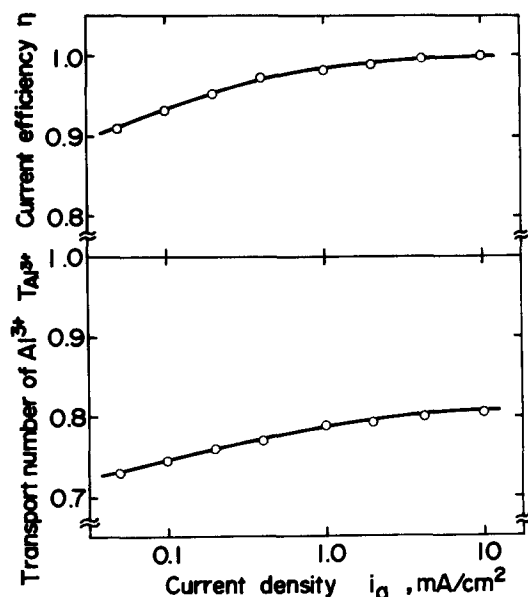


Fig. 16. Changes in the current efficiency for oxide formation, η , and transport number of Al^{3+} , $T_{\text{Al}^{3+}}$, with c.d.

is not affected by the anodizing condition. A detailed description of the effect of phosphate incorporation on the dissolution behavior of oxide in acid solutions will be published separately. It could be that protons included in the outer part of the oxide play an important role in the dissolution, but this is not the case because plenty of protons are present in the film sectioning solution.

Conclusion

In the present study, the composition of barrier oxide films on aluminum anodically formed in a neutral phosphate solution was examined as a function of the anodizing condition. Techniques used were film sectioning in a H_2SO_4 solution combined with XPS, solution analysis, polarization measurements, and electron microscopy. The results are as follows.

1. During the sectioning in the H_2SO_4 solution, oxide films dissolve uniformly from the outside. The dissolution rate of the outer part is faster than that of the inner part.

2. The outer part of the oxide contains several percent of phosphate. Its concentration does not change throughout the outer part, except for the outermost part, where the concentration is quite high. A small amount of protons is included in the outer part. The inner part consists of pure alumina without any phosphate and protons.

3. For films formed by applying a constant current (i_a) up to different potentials (E_a), both the thickness of the outer part, δ_{out} , and that of the inner part, δ_{in} , increase in proportion to E_a , but there is no inner part at $E < 15\text{V}$. The phosphate concentration in the outer part is independent of E_a .

4. For 50V films formed with different i_a , δ_{in} decreases with i_a , but δ_{out} scarcely changes, and the phosphate concentration in the outer part increases with i_a . These findings are explained in terms of the enhancements of (i) Al^{3+} transport through the oxide and (ii) dissociation of protonated phosphate ions at the oxide/solution interface, due to the increase in the electric field.

Acknowledgments

The authors are indebted to the Ministry of Education, Science and Culture, and the Light Metal Education Foundation of Japan for financial support.

Manuscript submitted Aug. 31, 1983; revised manuscript received March 20, 1984. This was Paper 29 presented at the Minneapolis, Minnesota, Meeting of the Society, May 10-15, 1981.

Hokkaido University assisted in meeting the publication costs of this article.

REFERENCES

- J. J. Randall, Jr. and W. J. Bernard, *Electrochim Acta*, **20**, 653 (1975).
- M. F. Abd Rabbo, J. A. Richardson, and G. C. Wood, *ibid.*, **22**, 1375 (1977).
- H. Konno, S. Kobayashi, K. Fujimoto, H. Takahashi, and M. Nagayama, "Interfinish 80," p. 281, Kyoto (1980).
- W. A. Lanford, R. S. Alwitt, and C. K. Dyer, *This Journal*, **127**, 405 (1980).
- H. Takahashi and M. Nagayama, *Electrochim. Acta*, **23**, 279 (1978).
- H. Takahashi, K. Yamada, and M. Nagayama, *J. Metal. Finish. Soc. Jpn.*, **28**, 286 (1977).
- H. Takahashi and M. Nagayama, *J. Chem. Soc. Jpn.*, **1974**, 453 (1974).
- H. Takahashi, M. Nagayama, H. Akahori, and A. Kitahara, *J. Electron Microsc.*, **22**, 149 (1973).
- H. Konno, S. Kobayashi, H. Takahashi, and M. Nagayama, *Electrochim. Acta*, **25**, 1667 (1980).
- T. P. Hoar and N. F. Mott, *J. Phys. Chem. Solids*, **9**, 97 (1959).
- H. Takahashi and M. Nagayama, Submitted to *J. Metal. Finish. Soc. Jpn.*
- J. A. Davies, B. Domeij, J. P. S. Pringle, and F. Brown, *This Journal*, **112**, 675 (1965).
- J. P. S. Pringle, *ibid.*, **120**, 398 (1973).
- F. Brown and W. D. Mackintosh, *ibid.*, **120**, 1096 (1973).
- J. P. Thomas, M. Fallavier, Spender, and E. Francois, *ibid.*, **127**, 585 (1980).

Properties of ZnO-B₂O₃-SiO₂ Glasses for Surface Passivation

Yutaka Misawa

Hitachi Limited, Hitachi Research Laboratory, Hitachi, Ibaraki, Japan

ABSTRACT

Two ZnO-B₂O₃-SiO₂ glasses, glass A (ZnO: 65.4, B₂O₃: 24.5, SiO₂: 10.1 weight percent [w/o]) and glass B (ZnO: 63, B₂O₃: 29, SiO₂: 8 w/o), were prepared for the purpose of passivating high voltage silicon devices. Their physical and electrical properties were compared using DTA characteristics, SEM observations, x-ray diffraction patterns, thermal expansion coefficients, and surface charge densities, as a function of firing temperature. Reverse characteristics of semiconductor devices passivated with these glasses were also investigated. Differences in the variation of properties with firing temperature between the two glasses were found to originate mainly from differences in the variation of crystal morphology in the glasses as a function of firing temperature.

Surface passivation using glass powders with ZnO-B₂O₃-SiO₂ as the principal component results in good reliability for high voltage silicon power devices like thyristors, transistors, and diodes. Recently, higher breakdown voltage has been required for silicon power devices. One of the methods for obtaining higher breakdown voltages for glass passivated devices, without changing other electrical properties, is to control the surface charge density of the glass on the silicon so as to lower the surface electric fields of the devices. For instance, the negative surface charges deplete n-type silicon surface and lower the surface fields of the p⁺-n junction. However, the positive surface charges accumulate n-type silicon surface and are higher than the surface fields of the p⁺-n junction. We have already reported that surface charge density of ZnO-B₂O₃-SiO₂ glass/Si system could be controlled by changing glass composition (1). However, it is desirable that glasses for surface passivation have the following properties, except for surface charge density: (i) a thermal expansion coefficient nearly equal to that of silicon, (ii) low glass firing temperature, and (iii) no harmful effects on the p-n junction. The thermal expansion coefficient of ZnO-B₂O₃-SiO₂ glasses changes with glass composition (2). Furthermore, the surface charge density of the ZnO-B₂O₃-SiO₂ glass also changes with glass firing temperature (2, 3). Therefore, glasses for surface passivation of high voltage devices must be considered after considering both thermal and mechanical properties, except surface charge density.

In this paper, we describe various properties of two typical ZnO-B₂O₃-SiO₂ glasses with different negative surface charges which were selected as passivants for high voltage silicon devices from our previous work (1): glass A (ZnO: 65.4, B₂O₃: 24.5, SiO₂: 10.1 weight percent [w/o]) and glass B (ZnO: 63, B₂O₃: 29, SiO₂: 8 w/o), both as a function of firing temperature.

Experimental

Glass preparation.—The zinc oxide, boron oxide, and silicon oxide components were weighed and mixed in a revolving mixer. The purities of these materials were over 99.99%. The powder was fused at 1300°C in air and then poured into cold water. The glass frits that were produced were ground in a ball mill to give mean particle sizes of about 4 μm.

Measurements.—Thermal properties of the glasses were measured by differential thermal analysis (DTA) using 1g samples and a heating rate of 5°C/min. Characterization points such as softening point (*T_s*), crystallization starting point (*T_{cs}*), first crystallization point (*T_{c1}*) and second crystallization point (*T_{c2}*) were determined from the DTA curve, as mentioned later.

Cylindrical glass blocks (10 mm diam × 50 mm) were used for thermal expansion coefficient measurements which were made by a Type-8003SH dilatometer from RIGAKU DENKI. The samples were prepared by cutting and polishing the blocks after firing in platinum boats.

Key words: interfaces semiconductor, crystallization, charge.

Thermal expansion coefficients were computed from the expansion of samples between 50° and 350°C for a heating rate of 10°C/min.

The crystallized phase was observed by scanning electron microscopy (SEM) and x-ray diffraction techniques. Glasses, fired on silicon substrates, were used for these samples.

Surface charge density (*N_{FB}*) in the glass/silicon system was measured with metal-glass-silicon (MGS) capacitors. The MGS capacitors were prepared as follows. An electrophoretic method was used to deposit the glass powder on a phosphorus-doped (111) plane-oriented silicon substrate with a resistivity of 10 Ωcm. In this method, the colloidal suspension used consisted of isopropyl alcohol as a suspension medium, with a small amount of additive electrolyte, and glass powder whose size was controlled by decantation. Before glass deposition, about 2 μm of the silicon wafer surface was etched off. The deposited glass powder was then fired in oxygen. The glass film thickness was controlled to about 20 μm. Metal electrodes (2 mm diam) were formed on the glass film by evaporating aluminum. Deviation of the glass film thickness under the electrode for each sample was less than 3 μm. The capacitance of the MGS capacitors was measured with an MIS capacitance meter at a frequency of 1 MHz. Voltage was applied to the sample 0 – ±500V using a dc voltage source connected to the capacitance meter. Voltage shift, with hysteresis, of the C-V curve was several volts. This voltage corresponded to a surface charge density of 10¹⁰ cm⁻², which was very small and hence neglected.

The reverse characteristics of the p-n junction, passivated with glass, were investigated using samples like that shown in Fig. 1. Using a diffusion process, the samples were prepared on the (111)-plane-oriented n-type silicon substrates with a resistivity of 70-90 Ωcm. A deep moat was formed by chemical etching. The glass powder was deposited into the moat by the electrophoretic method and fired in oxygen. The electrodes were prepared by a vacuum evaporation of aluminum.

Results and Discussion

Thermal properties.—Figure 2 shows the DTA curves for glasses A and B. Table I lists thermal properties for glasses A and B. Their characteristic points as deter-

Table I. Thermal properties for glasses A and B

Glass		A	B
DTA	<i>T_s</i> (°C)	636	638
	<i>T_{cs}</i> (°C)	690	692
	<i>T_{c1}</i> (°C)	724	807
	<i>T_{c2}</i> (°C)	755	870
Size of crystal		Small	Large
	Firing temp (°C)	αZnO · B ₂ O ₃ 680(A), 720(B)	3ZnO · B ₂ O ₃
Crystalline state	Firing temp (°C)	αZnO · B ₂ O ₃ 740(A, B)	3ZnO · B ₂ O ₃ β5ZnO · B ₂ O ₃
		αZnO · B ₂ O ₃ 3ZnO · B ₂ O ₃	
		α5ZnO · B ₂ O ₃	

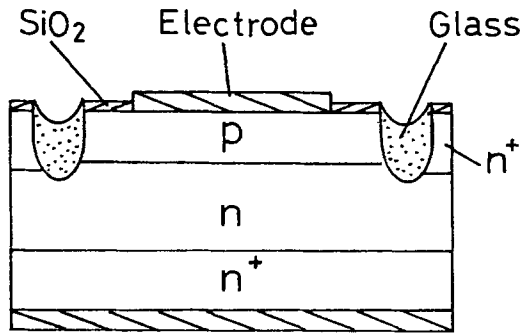


Fig. 1. Schematic of the glass-passivated devices

mined from DTA curve, as shown in Fig. 2. These glasses had two crystallization points. The first and second crystallization points for glass B were considerably higher than those for glass A, although their softening points and crystallization starting points were nearly equal. Furthermore, the peak height of the first crystallization point for glass A was smaller than that of the second, and vice versa for glass B.

Next, the phases of crystallization, which were expected to differ, were observed by SEM. Figure 3 shows several photomicrographs for glasses fired on silicon at different temperatures. Lumps of fine needle-like crystals, appearing like chestnut burrs, were observed in glass A. However, large needle-like crystals were observed in glass B. The crystals occurred on the surface only when the glass B firing temperature was 680°C. Crystallization was inside when the temperature was 700°C, and more crystals were observed for the sample fired at 720°C. That is, crystallization started from the surfaces such as condensation phase. In glass A, crystallization was observed

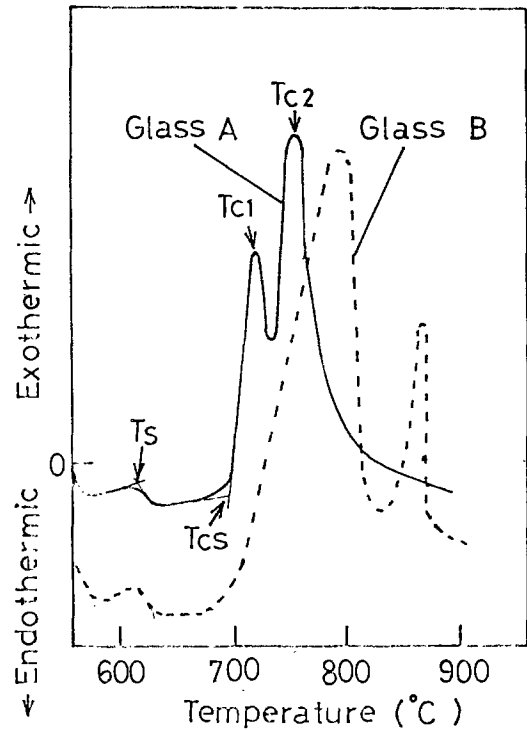


Fig. 2. Comparison of DTA curves for glasses A and B

all over, even when the firing temperature was 700°C as determined from SEM observations.

X-ray diffraction studies were used to identify the difference in crystallization between glasses A and B. The typical crystalline states are shown in Table I for glasses

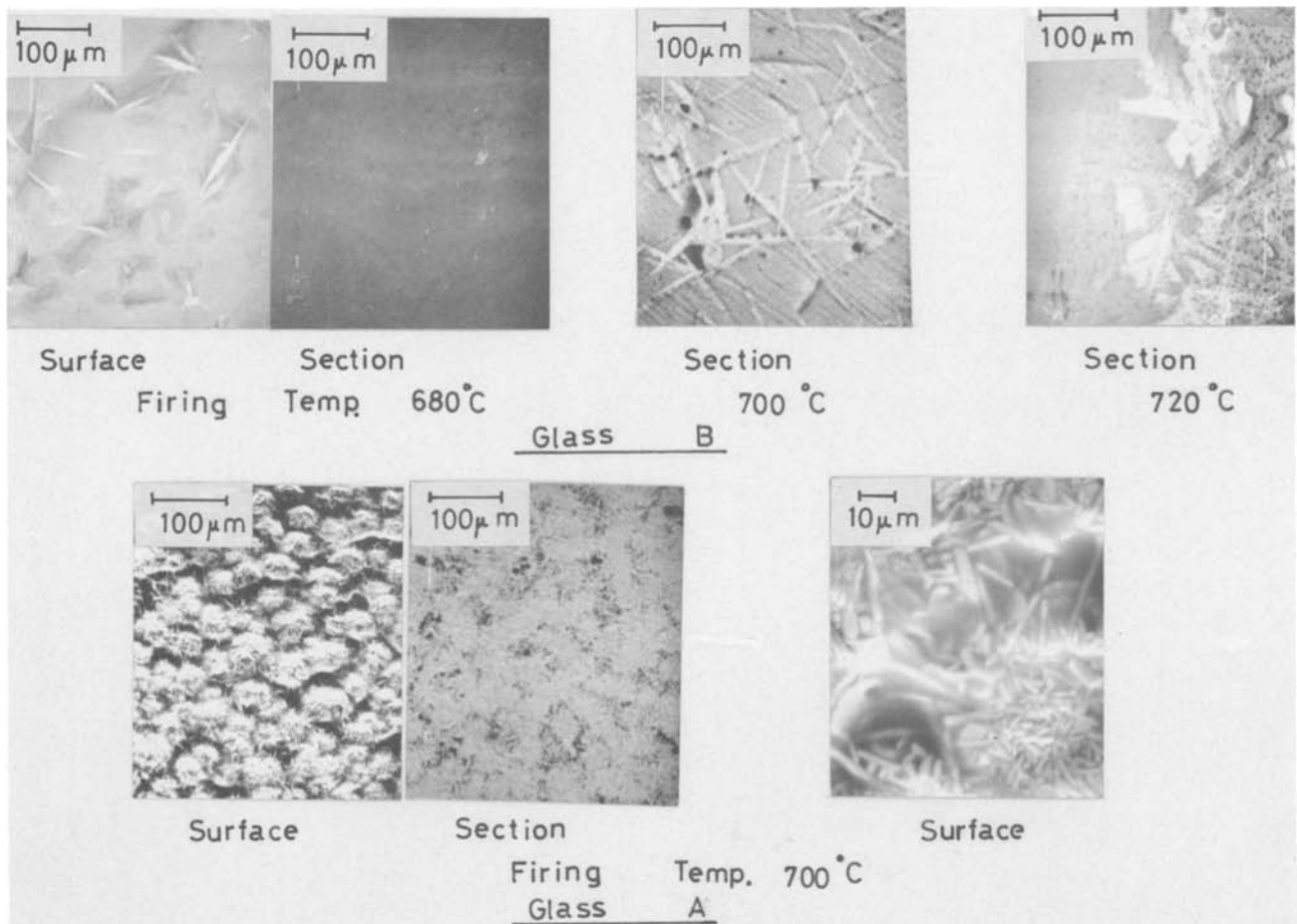


Fig. 3. Scanning electron micrographs of glasses fired on silicon at different temperatures

fired at different temperatures. Patterns were observed for samples fired above 680°C for glass A and above 720°C for glass B. The extent of crystallization for glass B was less than for glass A under the same firing conditions. For the latter, crystals were mainly $\alpha\text{ZnO} \cdot \text{B}_2\text{O}_3$ and $3\text{ZnO} \cdot \text{B}_2\text{O}_3$ when the firing temperature was 680°C. Above 700°C, the amount of $3\text{ZnO} \cdot \text{B}_2\text{O}_3$ crystals increased and $\alpha 5\text{ZnO} \cdot \text{B}_2\text{O}_3$ crystals appeared. However, for glass B when the firing temperature was low (720°C), only $3\text{ZnO} \cdot \text{B}_2\text{O}_3$ crystals were observed. At 740°C, $\beta 5\text{ZnO} \cdot \text{B}_2\text{O}_3$ crystals appeared. These results differ from other published work, in which $2\text{ZnO} \cdot \text{SiO}_2$ crystals appeared at low temperatures and $\alpha\text{ZnO} \cdot \text{B}_2\text{O}_3$ crystals at high temperatures (2).

Thermal expansion.—Figure 4 shows the relationship between the thermal expansion coefficient and glass firing temperature. The thermal expansion coefficient of glass A decreased rapidly between 680° and 700°C. However, that of glass B decreased gradually between 680° and 740°C. The thermal expansion coefficient of glasses in which crystallization was extensive, *i.e.*, firing temperature was more than 740°C, was nearly the same for glasses A and B. Changes in thermal expansion coefficient with firing temperature originated from the degree of crystallization. Consequently, these changes could be interpreted using the DTA results. The difference between crystallization starting point and first crystallization point was small in glass A, but large for glass B. Therefore, crystallization proceeded rapidly in the former and gradually in the latter. Furthermore, the extent of crystallization in the glasses could be attributed to the difference in crystallization rate, as mentioned above. However, the origin in the difference of crystal morphology between glasses A and B was not clear.

Surface charge density.—The relationships between glass composition, firing conditions, and surface charge density of glass/Si systems have been investigated previously (2, 3) and are considered only briefly here. Figure 5 shows the surface charge densities for glasses A and B fired on n-type silicon at various temperatures. Surface charges in both glasses were negative, indicating the direction of inversion on the n-type silicon, and became even more negative with increasing firing temperature. This tendency was the same as that for $\text{ZnO-B}_2\text{O}_3\text{-SiO}_2$ glasses with added PbO , SnO , and Sb_2O_3 (3). The surface charge density of glass B was larger in the negative direc-

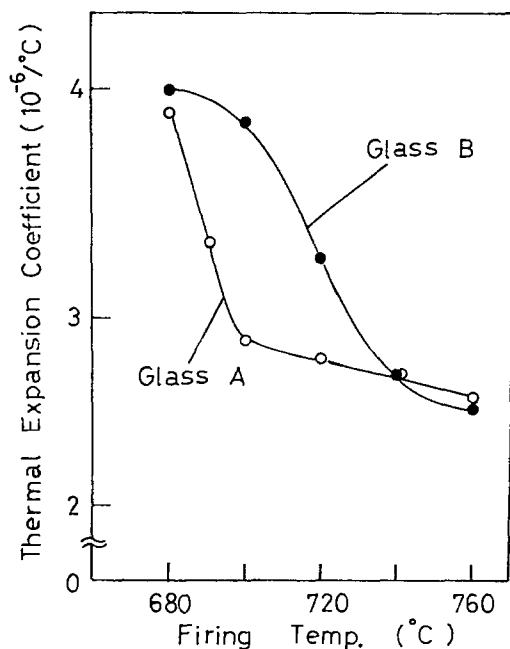


Fig. 4. Thermal expansion coefficient of glasses A and B fired at various temperatures.

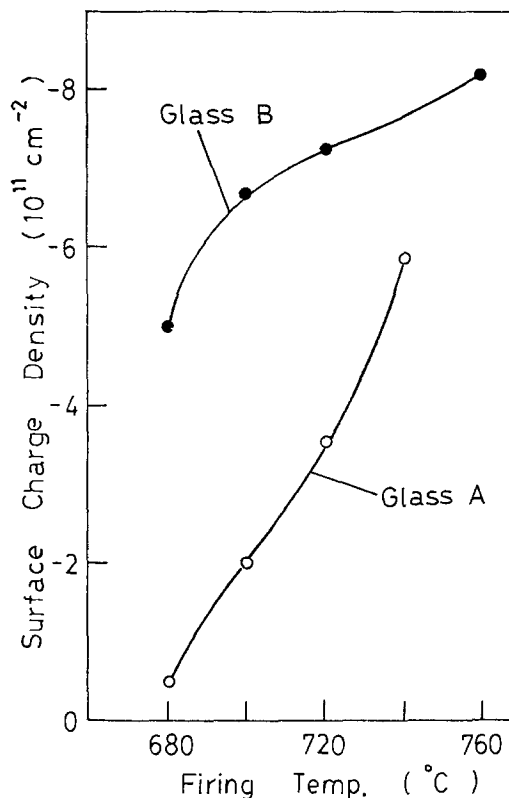


Fig. 5. Surface charge density of the samples made with glasses fired on n-type silicon at various temperatures.

tion than that of glass A, for which the B_2O_3 content was smaller. This result is in agreement with previous work (1).

Reverse characteristics of glass-passivated devices.—Figure 6 shows the relationship between breakdown voltage of glass-passivated devices and glass firing temperature. The glass film thickness was 20-40 μm . Breakdown voltage was defined as the voltage having a leak-

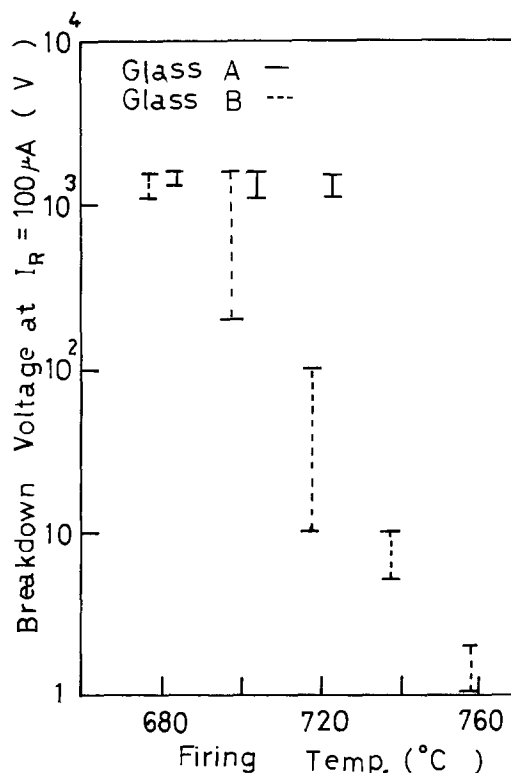


Fig. 6. Breakdown voltage of glass-passivated devices for glasses fired at various temperatures.

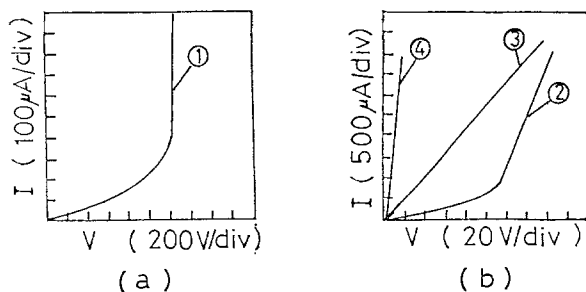


Fig. 7. Typical V-I characteristics of glass-passivated devices made with the glass B fired at various temperatures. Curves are shown for firing temperature equal to 700°C (curve 1), 720°C (curve 2), 740°C (curve 3), and 760°C (curve 4).

age current of 100 μ A. Breakdown voltage for glass B decreased remarkably with increasing firing temperature above 700°C. That is, high breakdown voltage could not be obtained at firing temperatures for which that thermal expansion coefficient was low. The breakdown voltage for glass A, however, scarcely varied between 680° and 720°C. The maximum breakdown voltage for glass A was equal to that for glass B. Thus, glass A was determined to be a suitable passivant of high voltage devices.

Figure 7 shows typical voltage-leakage current (V-I) characteristics for glass passivated devices made with glass B fired at various temperatures. V-I characteristics of devices with low breakdown voltages showed V-I characteristics of resistor above a critical voltage. However, the resistivity of the glass film measured using MGS capacitors made with glass fired on n-type silicon under the same conditions was by far lower than that of the glass-passivated devices. Consequently, it was believed that this low resistivity originated in the interface between the glass and silicon. Furthermore, the breakdown

voltage for glass B decreased when crystallization occurred at the glass-silicon interface. For glass A, the breakdown voltage did not decrease in spite of crystallization at the interface. The large crystallization seen in glass B caused poorer reverse characteristics of the semiconductor devices.

Conclusions

Two ZnO-B₂O₃-SiO₂ glasses, glass A (ZnO: 65.4, B₂O₃: 24.5, SiO₂: 10.1 w/o) and glass B (ZnO: 63, B₂O₃: 29, SiO₂: 8 w/o), were studied as a function of firing temperature. For glass A, crystallization proceeded rapidly with increasing firing temperature, and the crystals formed were fine needles. For glass B, the crystallization proceeded gradually, and the crystals formed were large. The leakage current of semiconductor devices passivated with the glasses having large crystals was large. Glass A was suitable as a passivant for high voltage devices. Crystal morphology in glass seemed to play the most important part in properties of ZnO-B₂O₃-SiO₂ glasses.

Acknowledgments

The authors wish to thank Mr. H. Yagi, Mr. T. Suzuki, and Mr. M. Takahashi and Dr. M. Okamura, Dr. H. Hachino, and Dr. M. Monma for their helpful suggestions and encouragement during this study.

Manuscript submitted Oct. 5, 1983; revised manuscript received March 27, 1984.

Hitachi, Limited assisted in meeting the publication costs of this article.

REFERENCES

1. Y. Misawa, H. Hachino, S. Hara, and M. Hanazono, *This Journal*, **131**, 359 (1984).
2. K. Miwa, *Nihon Denki Gihō*, **108**, 193 (1973).
3. Y. Misawa, H. Hachino, S. Hara, T. Ogawa, and H. Yagi, *This Journal*, **128**, 614 (1981).

Plasma-Activated Deposition and Properties of Phosphosilicate Glass Film

Akira Takamatsu, Miyoko Shibata, Hideo Sakai, and Takeo Yoshimi

Hitachi, Limited, Musashi Works of Hitachi Limited, Kodaira-shi, Tokyo 187, Japan

ABSTRACT

Phosphosilicate glass film deposited by a plasma-activated reaction system (P-PSG) was studied. Fundamental characteristics of the P-PSG were investigated by systematically varying deposition parameters. In this plasma deposition method, the P-PSG having a high deposition rate (130 nm/min) and a high doped phosphorus concentration [about 10 weight percent (w/o) P] was deposited using the reaction gases SiH₄, PH₃, and N₂O. The P-PSG deposited by this method showed properties such as a strong film crack resistance during heat-treatments, a conformal step coverage, and a controllable compressive stress, compared with those of conventional PSG film deposited under atmospheric pressure (AP-PSG).

A plasma-activated silicon oxide film (P-SiO) (1-4) has been widely studied as an insulator for multilayer interconnects in semiconductor devices. The P-SiO gives good step coverage and a low dielectric constant. The P-SiO, however, has no gettering effect against contamination by alkali ions. In other words, it shows MOS instability after contamination. It is known that a phosphosilicate glass layer acts as a getter for Na⁺ ions and as a barrier to their entrance from the environment. Phosphosilicate glass layers deposited by chemical vapor deposition of silane plus phosphine under atmospheric pressure have been conventionally used as passivation films. However, the conventional PSG film deposited under atmospheric

pressure (AP-PSG) has undesirable step coverage and insufficient mechanical strength. The P-PSG was tried in order to improve step coverage, mechanical strength, and electrical properties. The deposition of the phosphosilicate glass film deposited by a plasma-activated reaction system (P-PSG) has been studied, without a detailed investigation of the film properties³.

In this report, the P-PSG was deposited using the reaction gases SiH₄, PH₃, and N₂O (5, 6). The reactor has parallel electrodes. The deposition parameters (substrate temperature, RF power, and reaction gas composition) were varied systematically. In this paper, fundamental characteristics of the P-PSG were investigated in detail. These properties were evaluated and compared to those of the AP-PSG. The purpose of our work was to determine the

Key words: insulation film, multilayer interconnects, step coverage.

optimum deposition conditions and to present the minute properties of the P-PSG.

Experimental

A basic reactor system for P-PSG deposition is shown in Fig. 1. The reaction chamber consisted of a quartz reaction tube 350 mm high and of 220 mm diam. A silicon wafer was placed on a susceptor, which was made of aluminum and heated by a resistance heater located under the susceptor. 4% SiH₄ and 1% PH₃, both in Ar gas, were introduced through the upper shower-type electrode, which was designed to improve the uniformity of gas flow at the surface of the wafer. Nitrous oxide (N₂O) was introduced through the top of the reaction chamber and then activated by the plasma discharge from an induction coil. The system was evacuated by a rotary pump. An RF power supply (13.56 MHz) was divided into two paths. One path went through the upper shower-type electrode, and the other path went to the induction coil wound around the reaction chamber. The distance between the shower-type electrode and the grounded susceptor was 25 mm.

Deposition parameters of the P-PSG were varied, as follows: deposition temperature was 200°-380°C; ratio of N₂O to SiH₄ + PH₃ from 5 to 80; mole percent (m/o) PH₃ in SiH₄ + PH₃ was from 0 to 25 m/o; pressure 0.8-2.0 torr; RF power 50-250W; total gas flow 50-900 ml/min. Each parameter was individually changed while all other variables were kept constant. The usual deposition condition was: deposition temperature = 380°C, RF power = 250W, pressure = 1 torr (133 Pa), PH₃ in SiH₄ + PH₃ = 8 m/o, ratio of N₂O to SiH₄ + PH₃ = 23, total gas flow = 190 ml/min.

Film thickness was measured mechanically with a Taylor-Hobson Talystep. Chemical etch rates were measured using the etchant BHF (buffered hydrofluoric acid), at 25°C. The refractive index was measured using an ellipsometer, at a wavelength of 632.8 nm. The phosphorus concentration was determined by fluorescent x-ray analysis (FXA). Infrared absorption spectra were taken with a Hitach EPI-G2 type spectrophotometer on wafers with 0.5 μm film thickness. The step coverage was evaluated by using a scanning electron microscope (SEM). The mechanical strength of the P-PSG was measured with a Vickers hardness tester. The defect density of the P-PSG was checked by a chemical etching method after heat-treatment. The breakdown voltage was measured by applying the P-PSG as a MOS structure. To determine Na⁺ contamination, ΔN_{FB} was calculated from the difference between flatband voltage, V_{FB}, before and after bias and temperature (BT) treatments. Dielectric constant was measured by using a capacitance meter at 1 MHz frequency.

Results and Discussion

Fundamental properties of the P-PSG were tracked as the following four deposition parameters which were systematically varied: (i) RF power, (ii) deposition tem-

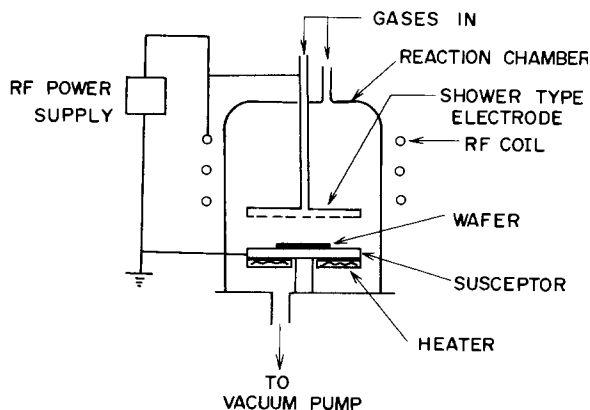


Fig. 1. Schematic diagram of P-PSG deposition apparatus

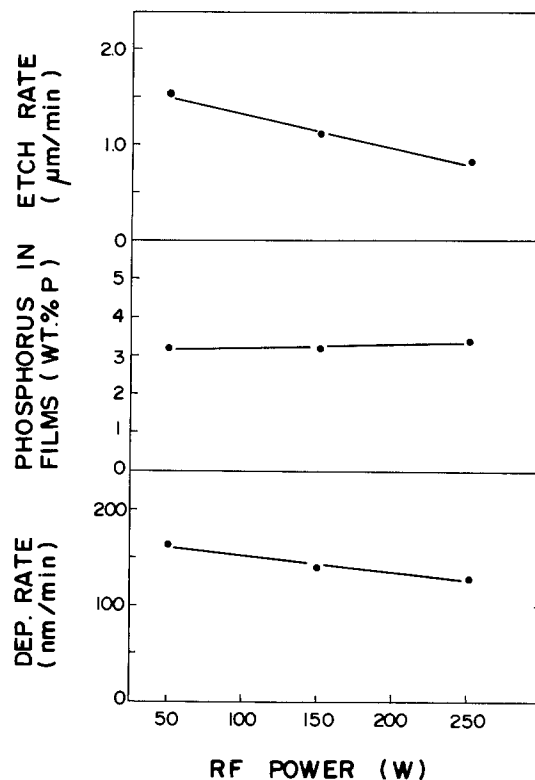


Fig. 2. Properties of P-PSG as a function of RF power

perature, (iii) ratio of N₂O to SiH₄ + PH₃, and (iv) mole percent of PH₃ in SiH₄ + PH₃. The effects on deposition rate, phosphorus concentration, and etch rate are shown in Fig. 2-5.

RF power.—As shown in Fig. 2, RF power in the range 50-250W was selected. The deposition rate of the P-PSG gradually decreased with increasing RF power. The deposition rate was 130 nm/min under the usual condition (RF power = 250W). The phosphorus concentration was independent of RF power. The etch rate decreased lineally as RF power was increased.

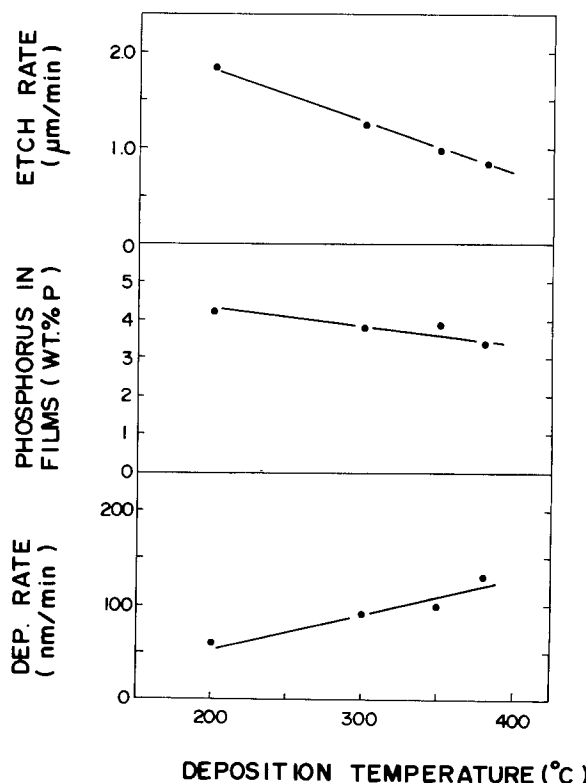


Fig. 3. Properties of P-PSG as a function of deposition temperature

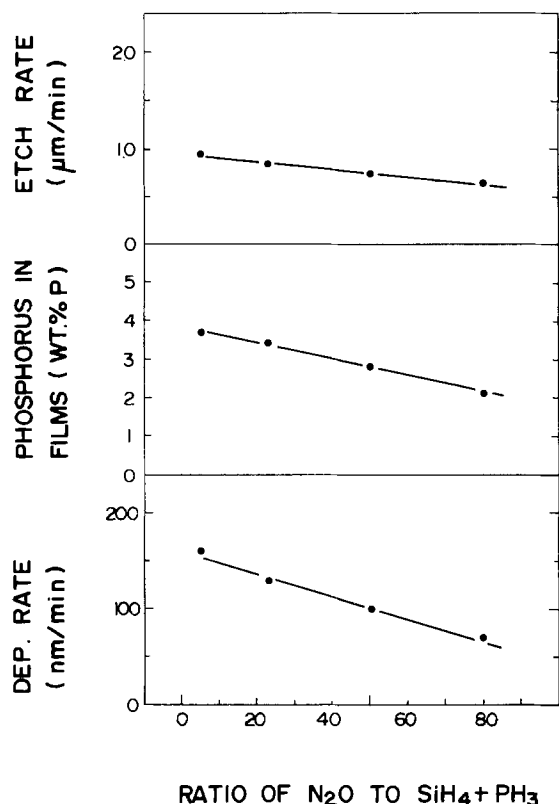


Fig. 4. Properties of P-PSG as a function of ratio of N_2O to $SiH_4 + PH_3$.

Deposition temperature.—The range of deposition temperatures studied was 200°–380°C (Fig. 3). With increasing deposition temperature, the deposition rate of the P-PSG increased slightly, while the phosphorus concentration decreased slightly. The etch rate decreased rapidly as the deposition temperature was increased.

Ratio of N_2O to $SiH_4 + PH_3$.—The ratio of N_2O to $SiH_4 + PH_3$ was varied in the range of 5–80, as shown in Fig. 4. The deposition rate and the phosphorus concentration decreased as the ratio of N_2O to $SiH_4 + PH_3$ was increased. The etch rate decreased only slightly as the ratio of N_2O to $SiH_4 + PH_3$ was increased. The decrease of etch rate

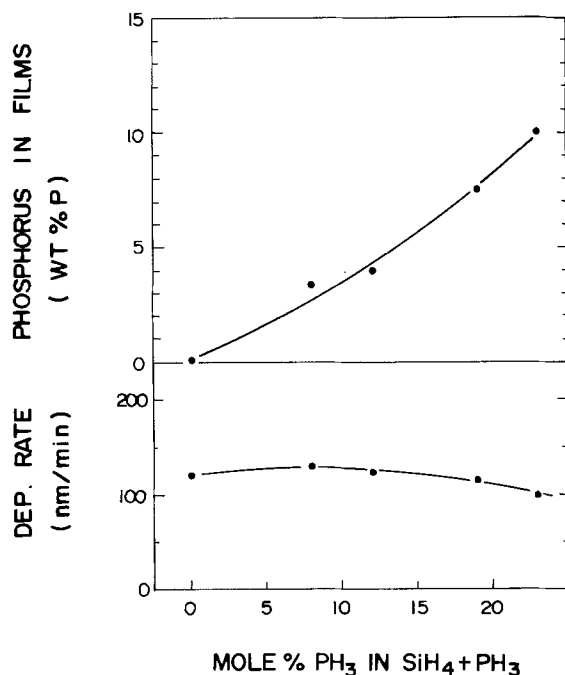


Fig. 5. Phosphorus concentration and deposition rate as a function of m/o PH_3 in $SiH_4 + PH_3$.

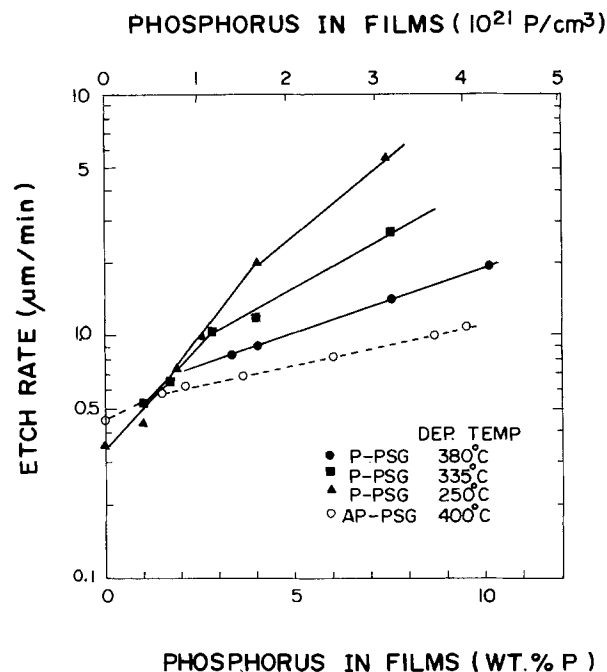


Fig. 6. Etch rate as a function of phosphorus concentration at various deposition temperatures.

corresponds to the decrease in phosphorus concentration (7).

Mole percent of PH_3 in $SiH_4 + PH_3$.—The mole percent of PH_3 in $SiH_4 + PH_3$ was varied in the range of 0–25 m/o, as shown in Fig. 5. The deposition rate of P-PSG appeared to decrease gradually as the mole percent of PH_3 in $SiH_4 + PH_3$ was increased. The phosphorus concentration of the P-PSG showed lower phosphorus concentration than that of the AP-PSG deposited using the same gas composition [PH_3 and $SiH_4 + PH_3$ (8, 9)]. However, the P-PSG having a high doped phosphorus concentration (more than 10 w/o) was also obtained when the ratio of the mole percent of PH_3 in $SiH_4 + PH_3$ was over 20 m/o.

Figure 6 shows how the chemical etch rates of P-PSG changed as a function of phosphorus concentration at various deposition temperatures. In general, the etch rate of the P-PSG increased with increasing phosphorus concentration, and, as the deposition temperature of the P-PSG was increased, the etch rate decreased. The etch rate of the P-PSG, which was deposited at 380°C, came close to that of the AP-PSG. It is considered that etch rates of the P-PSG are affected by some characteristics of the film such as bond strain in Si–O or P=O.

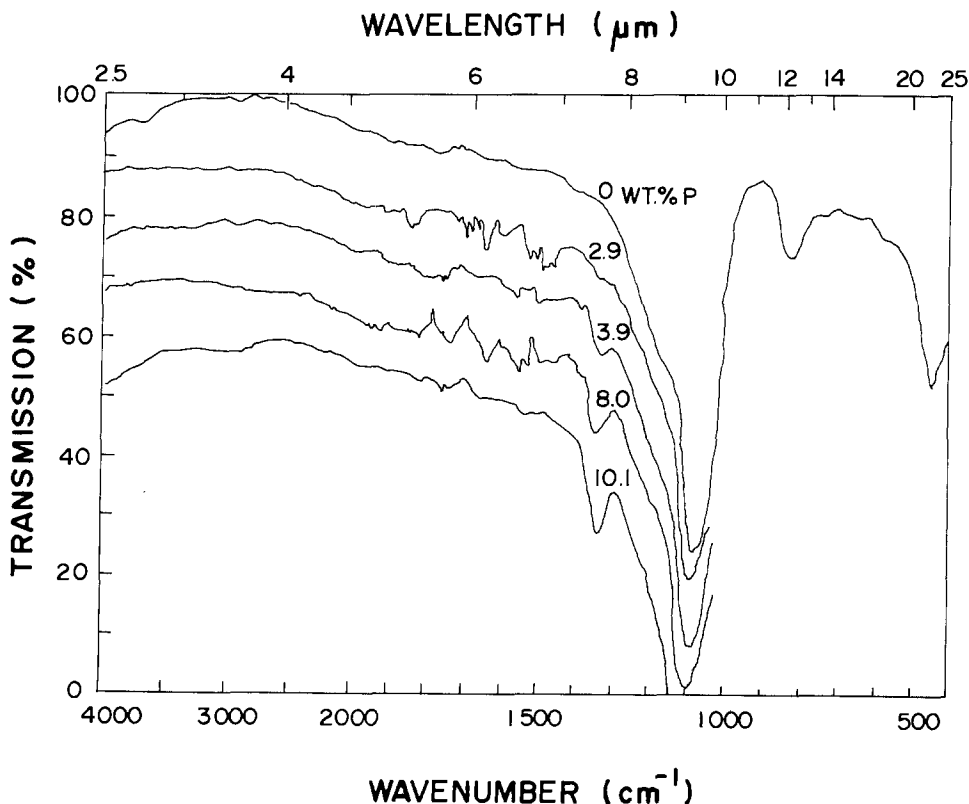
Pressure.—The total pressure during deposition was varied from 0.8 to 2 torr. The deposition rate of the P-PSG was independent of the pressure. The phosphorus concentration and the etch rate did not change appreciably with changes in pressure.

The refractive index of the P-SiO was 1.47. This value increased to 1.49 when the phosphorus concentration was over 10 w/o.

Infrared analysis.—The infrared absorption spectra of the P-PSG having various phosphorus concentrations are shown in Fig. 7. In the P-PSG, bands with wave numbers of 1330, 1090, 810, and 450 cm^{-1} were observed. These infrared spectra of the P-PSG are similar to those of the AP-PSG (10). As shown in detail in Fig. 8, absorption due to the P=O stretching at 1330 cm^{-1} increased as the phosphorus concentration in the P-PSG increased. The absorption due to Si–O stretching in the P-PSG was at a slightly higher wave number (1090 cm^{-1}) than that in the P-SiO (1070 cm^{-1}). These shifts were consistent with those of the AP-PSG (10, 11).

Other absorption bands of the P-PSG due to SiOH stretching (3650 cm^{-1}), H_2O (3350 cm^{-1}), and SiOH bending (950 cm^{-1}) (4, 11–13) were detected. These peaks

Fig. 7. Infrared absorption spectra of P-PSG. Film thickness: 0.5 μm .



were reduced with increasing deposition temperature and RF power.

Figure 8 shows absorbance for the P = O bond as a function of phosphorus concentration. The P-PSG which was deposited under low power or low deposition temperature showed low values in the P = O absorbance compared with those of the AP-PSG. The absorbance of the P-PSG deposited at 380°C and 250W RF power showed the same value as that of the AP-PSG at most phosphorus concentrations. This result shows that the

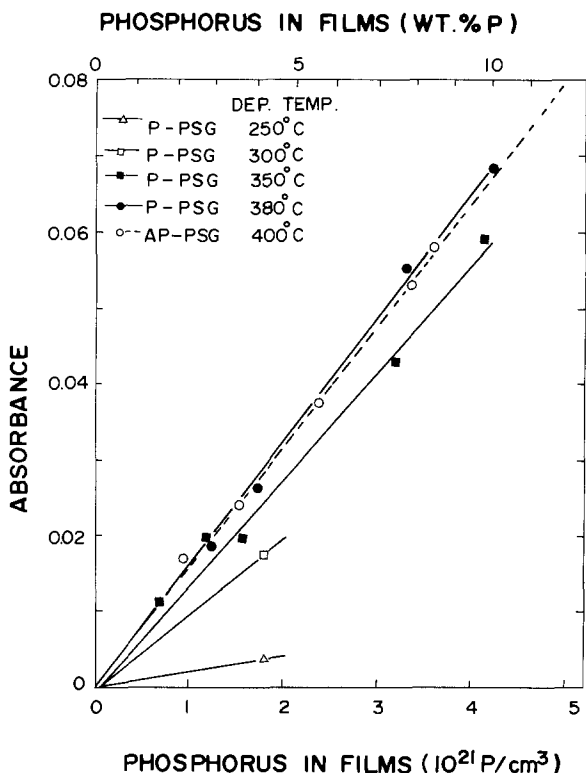
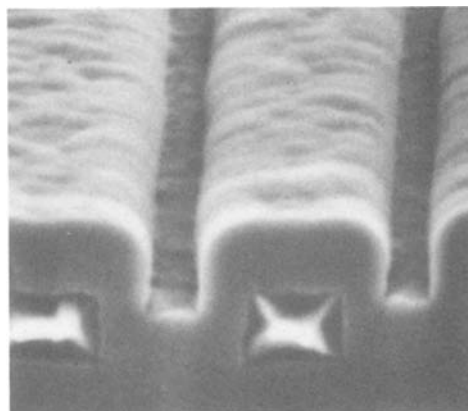
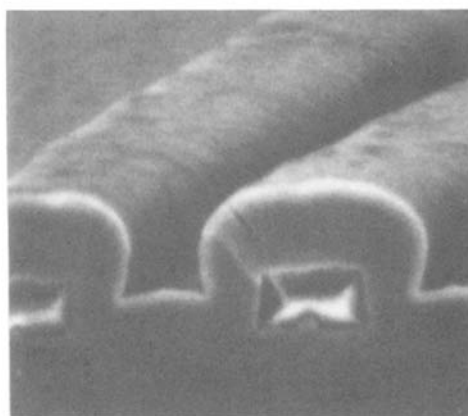


Fig. 8. Absorbance of P=O bond (1330 cm⁻¹) as a function of phosphorus concentration at various deposition temperatures.



P-PSG



AP-PSG

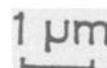


Fig. 9. Comparison of step coverage in P-PSG and AP-PSG

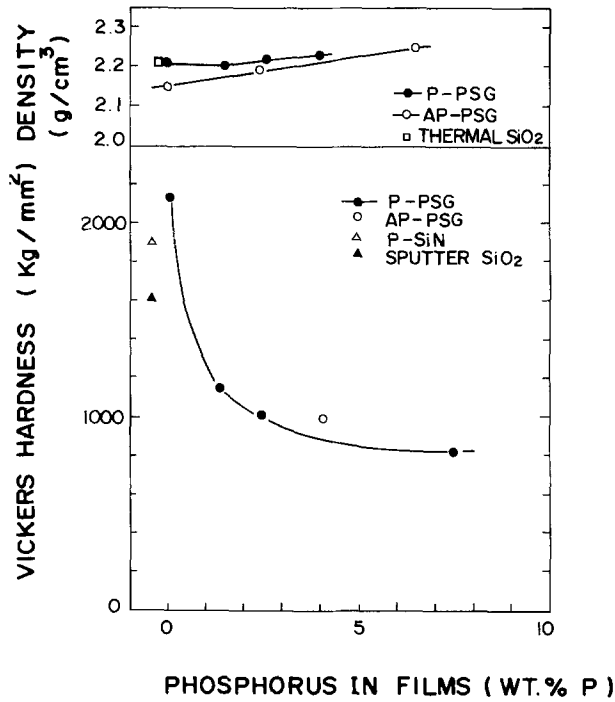


Fig. 10. Vickers hardness and density as a function of phosphorus concentration.

P-PSG deposited under low RF power or low deposition temperature includes phosphorus of lower states in the film which cannot be detected by infrared absorption.

Step coverage.—Cross-section views of the step coverage in the P-PSG and the AP-PSG are shown in Fig. 9. The step coverage over the steps of patterned aluminum was observed by SEM. The P-PSG produced a more conformal profile than that of the AP-PSG. This is one advantage of this plasma CVD process.

Mechanical strength.—The relationship of phosphorus concentration and Vickers hardness is shown in Fig. 10. Vickers hardness decreased rapidly with increasing phosphorus concentration. For example, in undoped film, the Vickers hardness is about 2000 kg/mm². However, in the P-PSG at 4 w/o P, it is about 1000 kg/mm². The density of

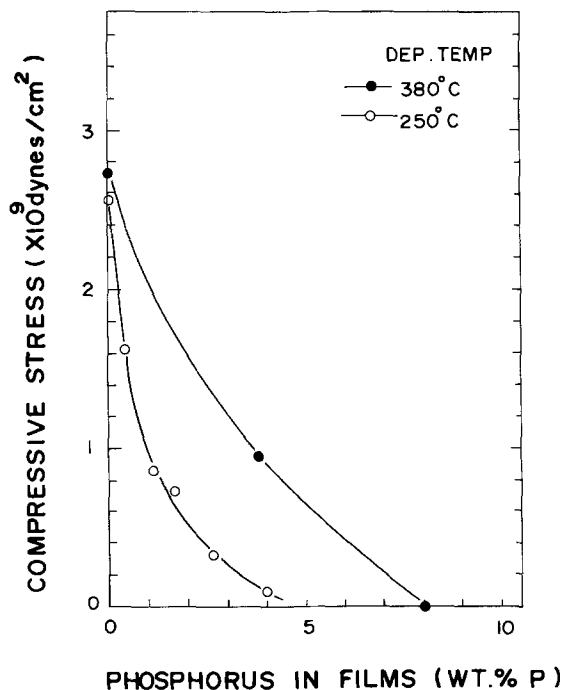


Fig. 11. Absolute value of the film stress in P-PSG as a function of phosphorus concentration.

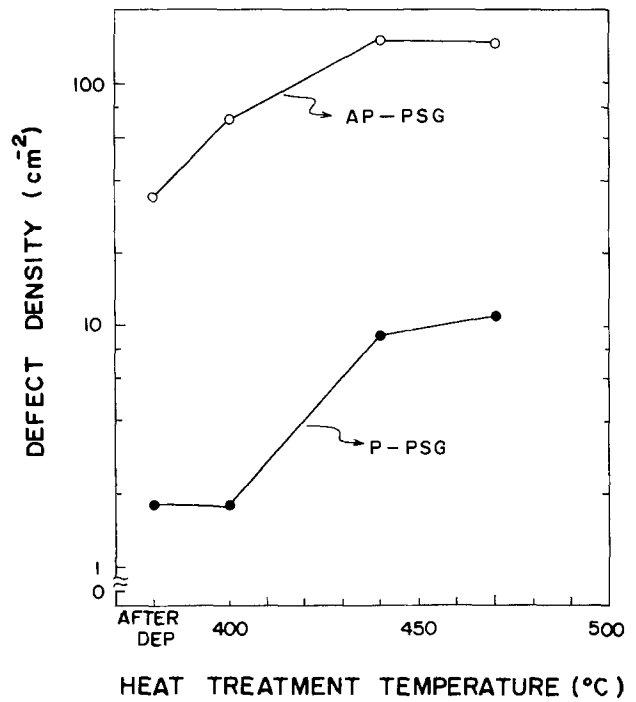


Fig. 12. Defect density as a function of temperature during heat treatments.

the P-PSG is also shown in the Fig. 10. The density of the P-PSG increased slowly as phosphorus concentration increased. The density of the P-PSG was 2.23 g/cm³ at 4 w/o P.

The relationship between phosphorus concentration and film stress is shown in Fig. 11. The stress in the P-PSG was compressive, but that of the AP-PSG was tensile (14). The compressive stress in the P-PSG decreased as phosphorus concentration increased. The tensile stress in the AP-PSG decreased in a similar way.

The film crack resistance for heat-treatment of the P-PSG is shown in Fig. 12. The P-PSG deposited on aluminum was annealed in N₂ ambient, at temperatures from 400° to 470°C. The thickness of film was 0.8 μm. Defect densities of the P-PSG were approximately ten times less than those of the AP-PSG.

Electrical properties.—The electrical stability of the P-PSG is shown in Fig. 13. The value of ΔN_{FB} represents

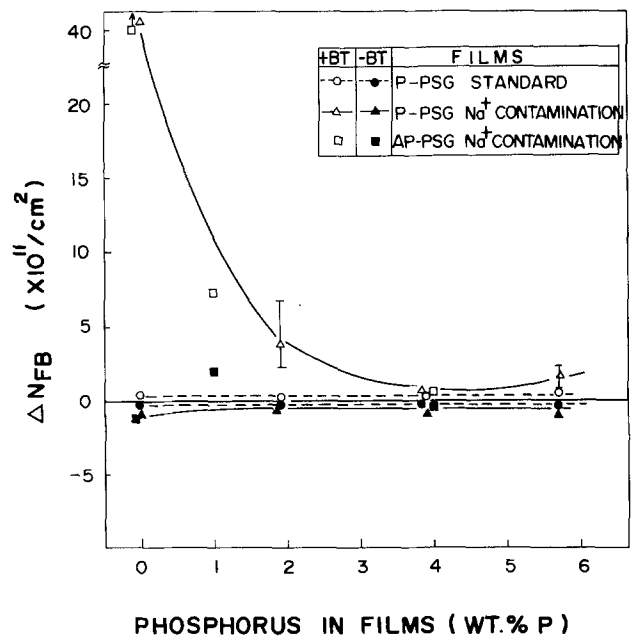


Fig. 13. ΔN_{FB} as a function of phosphorus concentration at positive and negative bias stressing.

Table I. Characteristics of the P-PSG standard and the AP-PSG standard

Measurement	Film	P - PSG (4WT.% P)	AP - PSG (4WT.% P)
Reactor System		Plasma CVD	Atmos. CVD
Reaction Gases		SiH ₄ -PH ₃ -N ₂ O	SiH ₄ -PH ₃ -O ₂
Temperature (°C)		380	400
Pressure (Torr)		1.0	760
Uniformity (%)		± 5	± 7
Dep. Rate (nm/min)		130	100
Ech Rate (nm/min)		900 (BHF)	600 (BHF)
Refractive Index		1.48	1.46
Density (g/cm ³)		2.23	2.21
Stress (dynes/cm ²)		Compressive -1.0 x 10 ⁹	Tensile 1.0 x 10 ⁹
Step Coverage		Good	Overhang
Crack Resistance		Strong	Weak
Vickers Hardness (kg/mm ²)		900	1000
Infrared Absorption (cm ⁻¹)		P=0: 1330	P=0: 1330
ΔN _{FB} (cm ⁻²)		5 x 10 ¹⁰	5 x 10 ¹⁰
Dielectric Constant		4.0 - 4.3	4.0
Breakdown Voltage (V/cm)		3 - 8 x 10 ⁶	6 x 10 ⁶

the number of mobile ions such as Na⁺ contained within the film. In the P-PSG standard which did not undergo Na⁺ contamination treatment, ΔN_{FB} was approximately 5 × 10¹⁰/cm², and was constant with increasing phosphorus concentrations. However, after Na⁺ contamination treatment, ΔN_{FB} of the undoped film (P-SiO) was 5 × 10¹²/cm², which was two orders of magnitude greater than that of the P-PSG. This result implies that the P-PSG has a gettering effect for alkali ions, as does the AP-PSG, while undoped film does not have a barrier effect against them. The breakdown voltage of the P-PSG was about 300-800V at 1.0 μm film thickness. The dielectric constant of the P-PSG at 1 MHz was 4.0-4.3.

Conclusion

In this process, the P-PSG was deposited by using a plasma-activated reaction. Fundamental properties of the P-PSG were investigated by systematically varying deposition parameters and then comparing them to those of AP-PSG. In this deposition method, the P-PSG having

good uniformity, a high doped phosphorus concentration and a high deposition rate were achieved.

Some characteristics of the P-PSG are as follows.

1. The P-PSG had good step coverage.
2. The P-PSG showed the remarkable gettering effect for Na⁺ contaminations, while the P-SiO did not have this gettering effect.

3. The film crack resistance of the P-PSG during heat-treatments was improved, as compared to AP-PSG.

Other characteristics of the P-PSG are tabulated in Table I.

The optimum deposition condition for the P-PSG included high RF power and high deposition temperature. In order to obtain better insulation characteristics, features of the reaction system, such as the choice of reaction gases (SiH₄-PH₃-CO₂), and RF frequency (10-500 kHz), are being investigated.

As density of devices increases, an increasingly fine technology is necessary. At this point, it is expected that the P-PSG deposited by this plasma process will meet the challenge of the future VLSI technology.

Manuscript submitted July 18, 1983; revised manuscript received Oct. 18, 1983.

Hitachi, Limited, assisted in meeting the publication costs of this article.

REFERENCES

1. E. P. G. D. Van de Ven and J. A. M. Sanders, Abstract 196, p. 525, The Electrochemical Society Extended Abstracts, Vol. 78-2, Pittsburgh, PA, Oct. 15-20, 1975.
2. M. Vandenberg, Abstract 99, p. 262, The Electrochemical Society Extended Abstracts, Vol. 79-1, Boston, MA, May 6-11, 1979.
3. J. R. Hollahan, *This Journal*, **126**, 930 (1981).
4. A. C. Adams, F. B. Alexander, C. D. Capio, and T. E. Smith, *ibid.*, **123**, 1545 (1981).
5. T. Yoshimi, M. Shibata, A. Takamatsu, and H. Sakai, Abstract 88, p. 236, The Electrochemical Society Extended Abstracts, Vol. 80-1, St. Louis, MO, May 11-16, 1980.
6. A. Takamatsu, M. Shibata, H. Sakai, and T. Yoshimi, Abstract 305, p. 762, The Electrochemical Society Extended Abstracts, Vol. 81-1, Minneapolis, MN, May 10-15, 1981.
7. W. Kern, *RCA Rev.*, **37**, 78 (1976).
8. M. Shibata and K. Sugawara, *This Journal*, **122**, 155 (1975).
9. M. Shibata, T. Yoshimi, and K. Sugawara, *ibid.*, **122**, 157 (1975).
10. W. Kern and R. C. Heim, *ibid.*, **117**, 568 (1970).
11. W. A. Pliskin, *J. Vac. Sci. Technol.*, **14**, 1064 (1977).
12. K. H. Beckmann and N. J. Harrick, *This Journal*, **118**, 614 (1971).
13. E. A. Taft, *ibid.*, **126**, 1728 (1979).
14. W. Kern, G. L. Schnable, and A. W. Fisher, *RCA Rev.*, **37**, 3 (1976).

Radial Etch Rate Nonuniformity in Reactive Ion Etching

A. G. Nagy

Motorola, Incorporated, SPS, Process Technology Laboratory, SRDL, Phoenix, Arizona 85008

ABSTRACT

A study was performed to determine some of the causes of the edge-to-center "bullseye" clearing pattern, in which the etch rate decreases monotonically from the wafer periphery to its center, observed when certain films are etched in a parallel-plate reactive ion etching system. It was found that gradients in local reactant concentrations, with a higher number density present near the edge of the substrate than over the center, are largely responsible for the observed nonuniformity. The concentration gradients appear to come about as a consequence of two reactant generation phenomena and one loss mechanism. The reactant generation phenomena are: (i) the "hot spot," which the edge of the wafer may represent to the plasma, causing enhanced reactant generation there, and (ii) differences in capacitive coupling from the RF generator to the plasma between the wafer's location on the cathode and the rest of the cathode. Stronger coupling surrounding the wafer leads to increased production of reactant around the wafer compared to the area directly above it. The reactant loss mechanism is controlled by the relative etch rates of the wafer *vs.* the cathode material, the using cathodes which etch at an appreciable rate in the plasma was found to promote improved uniformity. Ion bombardment was found to be uniform across the surface of the wafer, and, consequently, etch processes which are strongly bombardment dependent were found to be uniform.

Nonuniform clearing of films etched in plasma and reactive ion etching systems is a major problem in current integrated circuit patterning technology. In particular, when polysilicon, aluminum, or silicon nitride, as well as many other films, are etched in a parallel-plate system, they often display an edge-to-center "bullseye" clearing pattern in which the etch rate decreases monotonically from the periphery of the wafer to its center. This clearing pattern causes problems in selectivity and dimensional control. The present work was done to determine the relative importance of several possible causes of the bullseye effect.

Five possible causes were investigated: (i) local reactant concentration gradients near the wafer, (ii) temperature effects (possible thermal gradients across the wafer and their effect on etch rate), (iii) a possible gradient in the degree of ion bombardment across the wafer, (iv) the effects of the abrupt step represented by the edge of the wafer on the local discharge intensity and chemistry, and (v) the effect of the series capacitance represented by the wafer on the coupling of the RF to the plasma.

Apparatus

A plasma reactor, modified to give field-assisted etching in a pseudo-parallel-plate configuration (Fig. 1), was used in all of the experiments. The modifications are as follows: an aluminum plate ("dark shield" in Fig. 1), whose length (28.1 cm) is equal to the length of the cylindrical reactor, was welded to the inner wall of the chamber, effectively bisecting it. The discharge is confined to the upper half of the reactor. The chamber diameter (and dark shield width) is 34.2 cm. The reactor wall is grounded and serves as the anode. The 13.56 MHz signal is fed to another slightly smaller aluminum plate ($l = 24.2$ cm, $w = 26.1$ cm, $T = 3.18$ mm) which is separated from the dark shield by a 3.18 mm thick glass plate. This second aluminum plate serves as the cathode, giving an anode:cathode area ratio of 3.1:1.

Etch Conditions

The baseline process used in these experiments for etching undoped (615°C, 100 Pa SiH_4 ambient) polysilicon and silicon dioxide (grown in 1100°C steam ambient, atmospheric pressure) is as follows: the source gas is CF_4 , flow = 7 sccm, pressure = 13.3 Pa (0.10 torr), and RF power = 400W (0.62 W/cm²). This results in a nominal etch rate of 300 Å/min for both Si and SiO_2 . The 7.6 cm wafer was placed in the center position on the cathode in all etch runs. Where appropriate, these conditions were varied to determine their relative importance on the degree of nonuniformity.

Key words: plasma, etching, discharge, semiconductor.

Analytical Techniques

The etch rates of the samples were measured at nine equally spaced points across a diameter of the wafer using an IBM 7840 Film Thickness Analyzer. The etch rate at each point was obtained by dividing the etch depth by the etch time. The degree of etch nonuniformity was expressed as the ratio of average etch rate of the two outermost points to the etch rate of the slowest etching point on the wafer, usually the center. The average etch rate of the two next-to-outermost points was also divided by the slowest etching point to give an indication of the radial extent of the nonuniformity. For example, a typical value of nonuniformity is (1.16, 1.04), indicating a 16% and 4% faster etch rate compared to the central etch rate at the outermost and next-to-outermost radii, respectively.

Emission spectra were recorded to identify and monitor reactant species in the plasma. A Heath EV-700 monochromator was used to select the wavelength of interest, which was then detected by an RCA-IP28 photomultiplier.

Results and Discussion

Using the standard operating conditions, nonuniformity of undoped polysilicon films was found to be (1.16, 1.04) in the reactor described above when a quartz cover was placed over the aluminum cathode. The five possible causes of nonuniformity mentioned above were then investigated.

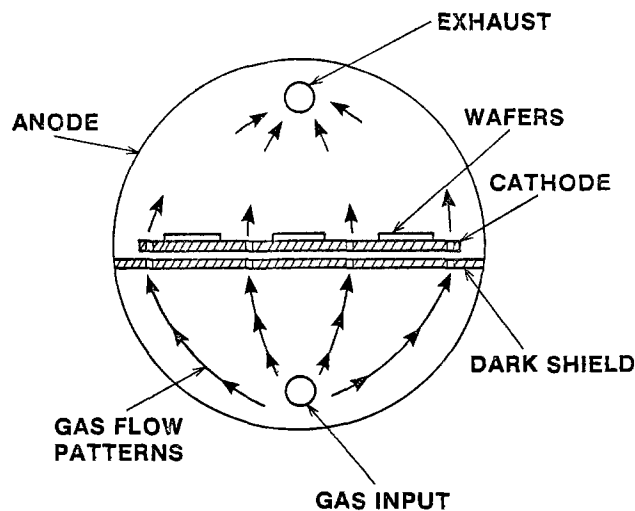


Fig. 1. Modification of the reactor for field assist etching showing the wafer platen, dark shield, and the gas flow pattern employed.

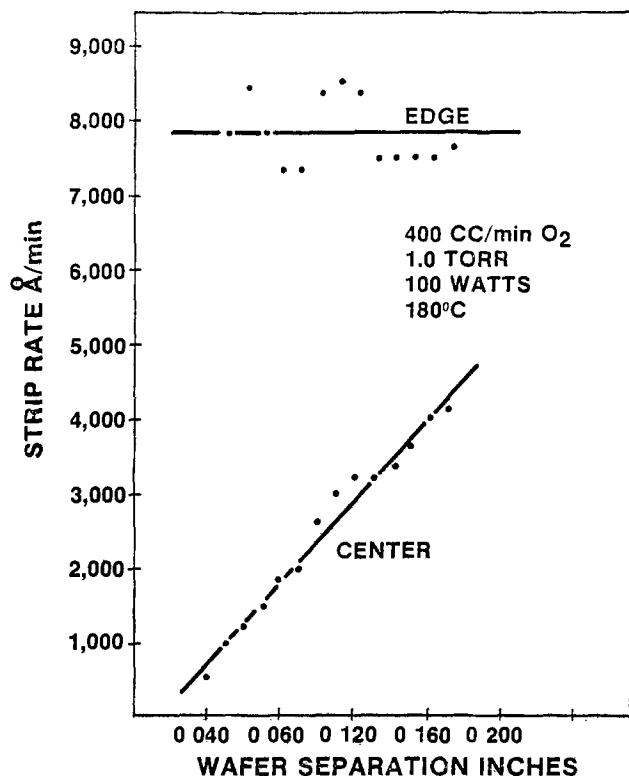


Fig. 2. Strip rate at the wafer edge and center as a function of wafer separation under conditions of constant molecular oxygen flow rate, pressure, and power. The edge strip rate is independent of separation; the center strip rate is linear in separation (1).

Local reactant concentration gradients.—Battey (1) found that reactant diffusion effects due to system geometry are the dominant cause of nonuniformity in photoresist stripping in a barrel-type system. The etch rate at the center of the wafers was found to be proportional to the spacing between the wafers on the boat, while that at the edges is independent of wafer spacing (Fig. 2). The ability of reactant species to diffuse to the center of the wafers is impaired when the separation between them is small, resulting in a larger concentration of reactant at the periphery of the wafers than at their centers, which brings about unequal etch rates.

A single wafer resting on the center of the cathode in the present system is analogous to etching in a barrel reactor at infinitely large wafer spacing, implying that local reactant diffusion effects in the vicinity of the wafer are minimal. This simple analogy predicts uniform etching in a parallel-plate system, for the lines in Fig. 2 meet when extrapolated to large wafer separations.

Experimentally, this is not the case. Table I shows results obtained when comparing etching of polysilicon with the wafer resting directly on the aluminum cathode (the unloaded case, as aluminum does not form a volatile fluoride) to that with various reactive covers placed over the cathode (loaded case). The results in Table I are plotted in Fig. 3.

The fact that polysilicon etches more nonuniformly in a parallel-plate system with a nonreactive cathode than with a reactive one implies that reactant concentration

Table I. Loaded case vs. unloaded case

Configuration	Etch rate at center (Å/min)	Nonuniformity
Aluminum cathode	315	1.34, 1.13
Quartz cathode cover (3.18 mm thick)	325	1.16, 1.04
Graphite cathode cover (3.18 mm thick)	168	1.17, 1.06
Silicon cathode cover (0.33 mm thick)	135	1.16, 1.04

CATHODE MATERIAL DEPENDENCE

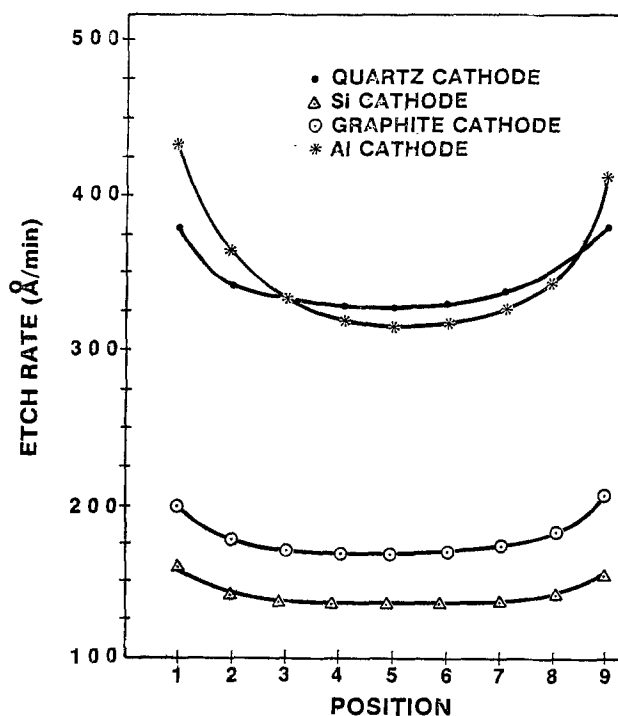


Fig. 3. Etch rate vs. position for polysilicon etched on different cathode materials.

gradients are present in this configuration as well. This is not surprising; when a reactive cathode is used, atomic fluorine [the etchant species in CF_4 -plasma silicon etching (2-7)] is consumed at comparable rates over the entire cathode. When a nonreactive cathode is used, the only sink for fluorine atoms is the wafer itself; therefore, the concentration of reactant will be higher at the perimeter than at the center of the wafer. Gas phase diffusion is apparently not rapid enough to overcome reactant concentration gradients across the substrate surface, and the larger these gradients are, the more nonuniform the etch process becomes.

An attempt was made to measure the spatial variation of atomic fluorine concentration using optical spectroscopy while etching a rectangular silicon slab in the reactor. The experiment was done as follows: a strip of silicon 0.51 mm thick, 5.08 cm wide \times 24.2 cm long (the length of the cathode) was placed lengthwise on top of an aluminum plate the same size as the cathode. The assembly was placed on top of the cathode and pushed forward against the plexiglass reactor door to minimize any effect the front edge of the aluminum plate may have on the discharge. The detector for the spectrophotometer was positioned so that the fluorine concentration was monitored in five regions: over the plate about 7.5 cm on either side of the strip, over each of the two edges of the strip, and over the center of the strip. The regions were labeled 1 through 5 from the point to the left of the strip to the point to the right. The detector was about 1 cm above the surface of the plate in all cases. An edge-on view of the experimental configuration is shown in Fig. 4.

A small quantity of argon was added to the CF_4 , and the 7504Å argon line and the 7037Å fluorine line were monitored in accordance with the method described by Coburn and Chen (8).

Table II shows the relative fluorine concentrations observed, normalized to the point of lowest concentration. The fluorine concentration shows a clear dip over the silicon strip, consistent with the observed clearing pattern.

Thermal effects.—If the etch rate of polysilicon in CF_4 is temperature dependent, the existence of a positive thermal gradient from the center of the wafer outward could cause increasing etch rates toward the periphery.

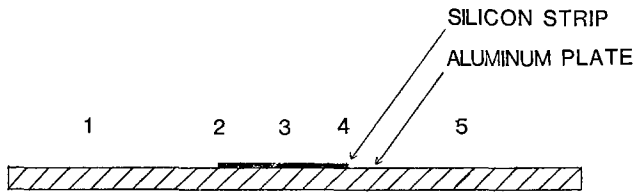


Fig. 4. Experimental configuration to spectroscopically determine the spatial variation of fluorine concentration.

To investigate the possibility of such a temperature dependence, a 7.6 cm polysilicon wafer was first etched under standard conditions with the reactor cold, and then the etch rate was compared to that seen after running the reactor for a period of time sufficient to bring the cathode temperature up to approximately 100°C. No significant increase was seen, implying that, even if a severe thermal gradient exists across a wafer, this alone is not enough to cause significantly nonuniform etching. This conclusion is consistent with that drawn in a previous study (9).

Ion bombardment effects.—It is believed that while atomic fluorine is the principal etchant species in CF_4 plasma silicon etching, bombardment of the substrate by heavy ions (mainly CF_3^+) may result in the enhancement of the reaction rate of fluorine atoms with the silicon (2). Consequently, it was hypothesized that nonuniform ion bombardment across the surface of the wafer may result in nonuniform clearing patterns.

To explore this possibility, the following experiment was performed: a 10.2 cm wafer with 10,000Å of aluminum deposited upon 9000Å of silicon dioxide was patterned so that two concentric aluminum rings, each 1.27 cm wide, with 1.27 cm separating the two rings, remained on the wafer. The surface area of the outer ring was 35.2 cm², and the inner ring area was 11.8 cm². A fine wire was bonded to each of the rings with silver paint, and this wire was run out of the reactor through a feed through and connected through an RF choke to an external circuit (shown in Fig. 5) which allowed a dc bias to be applied to the ring.

It is known (10) that if an increasingly negative bias is applied to a probe in a glow discharge, a condition will be reached where only a steady flow of positive ions reaches the probe. This ion current is relatively independent of bias voltage. The rings were biased to this potential, and the ion current was measured. A difference in measured current density in the two rings would imply unequal positive ion flux across the wafer.

An average positive ion current density of 7.48×10^{-2} mA/cm² was measured at the inner ring under standard CF_4 plasma conditions vs. 7.53×10^{-2} mA/cm² for the outer ring, a difference of less than 1%.

As another test of ion bombardment uniformity, SiO_2 was etched in the present system under standard conditions. SiO_2 etching in fluorine chemistry is known to be an ion bombardment dominated process, that is, fluorine atoms will not etch SiO_2 at a significant rate unless the surface is simultaneously bombarded with ions or electrons (6). The etch rate of SiO_2 at the given conditions in a downstream tunnel-type reactor (in which no ion bombardment is possible) described in a previous paper (11) would be approximately 14 Å/min, calculated using the correlation presented in that paper.

Table II. Observed fluorine concentrations

Region	Experimental relative fluorine concentration
1	1.19
2	1.13
3	1.00
4	1.06
5	1.19

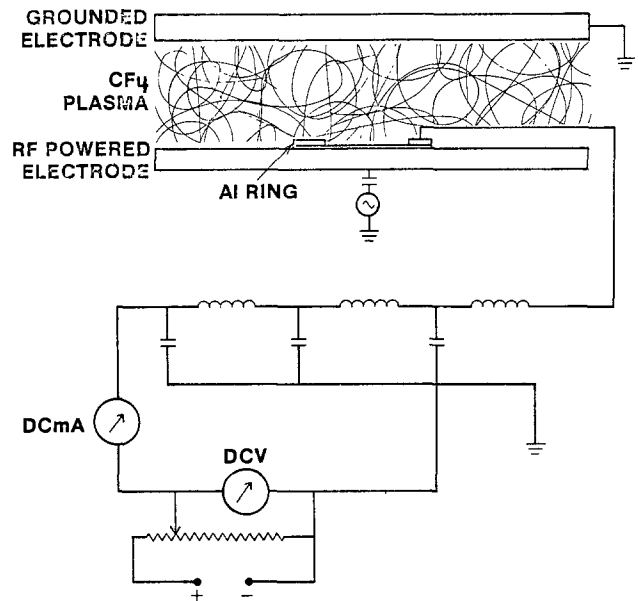


Fig. 5. DC bias circuit for measurement of ion bombardment to the wafer

Figure 6 shows that SiO_2 etching in the present system is indeed quite uniform. Since ion bombardment dominates SiO_2 etching in CF_4 , the uniform clearing pattern seen here supports the results obtained on ion bombardment uniformity described above. Uniform etching was also seen for undoped polysilicon in chlorine-rich chemistry [also known to be a bombardment-dominated process (12)] under standard conditions in the present system.

Based on these experimental results, it is concluded that ion bombardment is uniform in both CF_4 and CF_4/Cl_2 plasmas and thus cannot contribute to nonuniform etching.

Wafer edge effects.—The presence of any sharp edge or surface in a plasma environment will produce an intensified discharge at the region of discontinuity. The

SiO_2 ETCHING

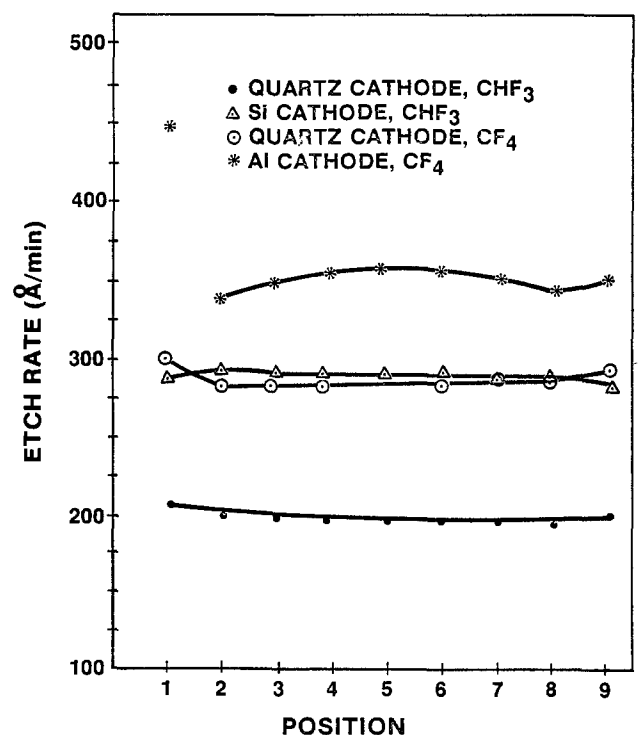


Fig. 6. Etch rate vs. position for SiO_2 etched in CF_4 and CHF_3 on different cathode materials.

edge of the wafer may represent such a region, though proving this experimentally is difficult.

Elevating the wafer on a conductive disk will make the edge of the wafer appear as a larger step, without affecting the wafer's capacitive coupling to the generator. Etching a 7.6 cm polysilicon wafer placed on top of a 3.18 mm thick, 7.6 cm diam copper disk (quartz platen) resulted in a nonuniformity of (1.29, 1.08) compared to the (1.16, 1.04) nonuniformity obtained with the wafer resting directly on the quartz platen. This implies that edge effects apparently play a role in etch nonuniformity.

Effects of the series capacitance represented by the wafer on the local discharge intensity.—When a wafer rests on the cathode, it represents an additional series capacitance term in the circuit connecting the RF generator to the glow space (Fig. 7). Thus, the impedance of this "leg" of the circuit is greater than that of paths not including the wafer (the surrounding cathode). Consequently, the intensity of the discharge may be expected to be greater where the wafer does not rest (9), which would result in a concentration gradient leading to etch nonuniformity.

Two approaches were tried to test this effect. In one case, the wafer was decoupled from the generator, and in the other case (the inverse situation) the environment surrounding the wafer was decoupled. For the first case, the capacitive coupling of the generator through the wafer was made weaker by placing the etching wafer on top of a series of 7.6 cm diam, 3.18 mm thick glass disks. The wafer/disk assembly was surrounded by one or more 3.18 mm thick cathode-sized aluminum plates with 7.6 cm holes cut in their centers, the number of plates being equal to the number of disks. The purpose of the plates was to keep the surface level to hold edge effects to a minimum. For the inverse situation, copper disks were used in place of the glass disks, and the plates were made of glass instead of aluminum. The surface of the top glass plate was covered with aluminum foil to provide identical reactant loss mechanisms for the two configurations.

Decoupling the wafer was expected to increase the reactant concentration gradient between the wafer area and the surrounding cathode, leading to more nonuniform etching. Conversely, decoupling the surrounding cathode was expected to reduce the gradient, resulting in improved uniformity.

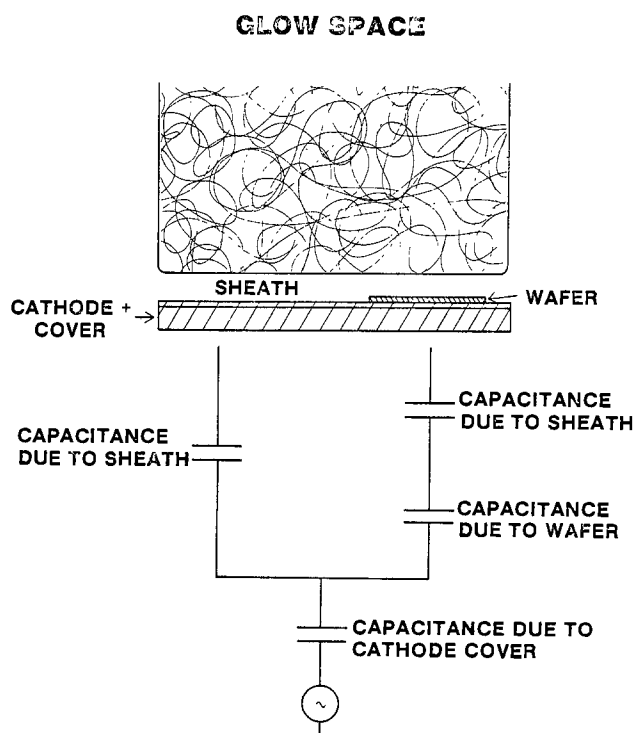


Fig. 7. Schematic representation of the capacitance coupling of the RF generator to the glow space.

While the increased concentration gradient produced by decoupling the wafer was expected to increase nonuniformity, this decoupling should not greatly alter the quantity of reactant available for the etch reaction. Therefore, the etch rate was not expected to change significantly during the wafer decoupling experiments. The effective "focusing" of the discharge obtained when surrounding the wafer with dielectric might be expected to slightly increase the etch rate, however. The results of the two experiments are given in Table III.

The results are in basic agreement with the expectations. It is difficult to determine if the observed changes in etch rate are significant, or if they are largely the result of experimental error. The trends are in the expected direction, however.

The capacitive impedance at 13.56 MHz of a wafer with 5000Å of undoped polysilicon deposited over 1000Å of silicon dioxide is approximately 3.2 Ω/cm², while that of 3.18 mm thick glass is about 8400 Ω/cm². The impedance rises by factors of about 2 with each successive elevation. Thus, it is not surprising that the nonuniformity changed dramatically after the first elevation in both experiments, and then remained relatively constant.

These results are not consistent with those of Mundt *et al.* (9), who were studying the bullseye effect while etching aluminum with CCl₄. They used a configuration similar to the second one described above, except that Teflon spacers were used instead of glass, and the wafer was allowed to rest directly on the lower electrode. The degree of nonuniformity decreased proportionately with the thickness of the Teflon spacer, and the clearing pattern even switched to one where etching proceeded from the center of the wafer outward to an increasing degree as the spacer thickness was increased above 0.86 mm.

The above results may, however, be partly explained by the fact that Teflon is known to release fluorine, a passivant to aluminum etching, under plasma conditions. As the Teflon thickness was increased, the quantity of fluorine released near the edge of the wafer rose because of the increase in available surface area. This should automatically slow down the rate of aluminum etching near the wafer periphery. Also, no attempt was made to keep the etching surface level, which may contribute to the differences between their results and those presented here.

Summary

The following conclusions may be drawn from the present study.

1. Ion bombardment across a wafer is uniform in the situation studied here. This suggests that ion-assisted processes, such as the etching of polysilicon in chlorine-containing plasmas, are preferred over more chemistry-dominated processes from the standpoint of uniformity.

2. The concentration of reactant is lower over the etching wafer than over the rest of the cathode. This concentration gradient comes about as a result of nonuniform local reactant production due to (i) the possibility that the edge of the wafer may represent a "hot spot" to the plasma, which would result in an intensified production of reactant species there, and (ii) differences between

Table III. Effects of series capacitance on local discharge intensity

Condition	Elevation (mm)	Etch rate at center (Å/min)	Nonuniformity
Polysilicon on bare Al cathode	0.00	315	1.34, 1.13
Wafer elevated on glass disks	3.18	326	1.51, 1.20
	6.35	330	1.54, 1.19
	9.53	331	1.52, 1.19
	12.70	297	1.59, 1.21
Wafer elevated on copper disks	3.18	346	1.12, 1.05
	8.73	414	1.14, 1.02
	14.29	364	1.13, 1.05

where the wafer lies on the cathode and the rest of the cathode, in capacitive coupling from the RF generator to the plasma. Uniformity may be improved or made worse by varying this capacitive coupling through the use of dielectric spacers either under or surrounding the wafer. It is apparently not possible to eliminate nonuniformity merely by decreasing the degree of capacitive coupling around the wafer without altering the discharge chemistry, flow patterns, system geometry, etc.

3. Reactant loss processes due to loading contribute to nonuniform etching. The local concentration gradient of reactant may be controlled by the choice of cathode material. Cathodes which do not form volatile species with the reactant promote increased etch rate nonuniformity.

Acknowledgments

The author would like to thank C. J. Tracy for many clarifying discussions, and R. Sitek for his assistance with the experimental work.

Manuscript submitted ca. Sept. 19, 1982; revised manuscript received Jan. 31, 1984.

REFERENCES

1. J. F. Battey, *This Journal*, **124**, 437 (1977).
2. J. W. Coburn, H. F. Winters, and T. J. Chuang, *J. Appl. Phys.*, **48**, 3532 (1977).
3. J. W. Coburn and H. F. Winters, *J. Vac. Sci. Technol.*, **16**, 391 (1979).
4. J. W. Coburn and E. Kay, *Solid State Technol.*, **21**, 117 (1979).
5. J. W. Coburn, *J. Appl. Phys.*, **50**, 5210 (1979).
6. D. L. Flamm, *Solid State Technol.*, **21**, 109 (1979).
7. C. J. Mogab, *This Journal*, **124**, 1262 (1977).
8. J. W. Coburn and M. Chen, *J. Vac. Sci. Technol.*, **18**, 3134 (1981).
9. R. Mundt, R. C. Patel, and K. Cowen, in "Proceedings of the 1980 IEEE Symposium, Washington, DC," p. 409 (1980).
10. J. D. Cobine, "Gaseous Conductors, Theory and Engineering Applications," pp. 134-142, Dover Publications, New York (1941).
11. D. L. Flamm, C. J. Mogab, and E. R. Sklaver, *J. Appl. Phys.*, **50**, 6211 (1979).
12. V. M. Donnelly and D. L. Flamm, *Solid State Technol.*, **24**, 161 (1981).

Antimony Diffusion in Silicon: Effects of Ambient Gas and Time

F. Pintchovski,* P. J. Tobin,* M. Kottke, and J. B. Price*†

Motorola, Incorporated, Advanced Product Research and Development Laboratory, MOS Group, Mesa, Arizona 85202

ABSTRACT

A study of the effect of the furnace ambient composition (O_2 -Ar vs. O_2 - N_2) on the diffusion of antimony into silicon from a doped-glass source deposited by low pressure CVD was conducted. Two minima in sheet resistance were observed as a function of O_2 content for O_2 -Ar diffusions. Only one minimum was observed for O_2 - N_2 diffusions. Auger electron spectroscopy, Rutherford backscattering spectroscopy, secondary ion mass spectroscopy, and spreading resistance probe techniques were used to investigate the changes that occur at the doped-glass/silicon interface and in the doping profiles as a function of the diffusion ambient. The formation of a $Sb_xSi_yO_z$ thin film phase was observed and characterized. A model is proposed to account for the presence of two minima in sheet resistance (maxima in surface concentration) as a function of O_2 content in the diffusion ambient.

Doped silicate glasses are widely used in the semiconductor industry as diffusion sources. A large body of literature has been published on the mechanisms of dopant diffusion from the glass into silicon substrates. Barry and Olofsen (1-3) published a series of papers on the diffusion of phosphorus and boron from doped glasses. Wong and Ghezzi (4) and Ghezzi and Brown (5) reported on the diffusion of arsenic from doped glasses. A significant result of the recent work is that two spatially separated processes control the doping of silicon by the glass. The first of these is the flux of dopant through the glass/silicon interface. The second is the atomic motion of dopant through the silicon and the effect of crystal point defects upon this motion. These two processes will be discussed briefly in turn.

The role of the doped-glass/silicon interface in the diffusion has been studied in detail for the cases of boron, phosphorus, and arsenic. In all these cases, the authors found that for some diffusion ambients, a chemical reaction occurs at the doped-glass/silicon interface, resulting in the formation of a thin film phase which dramatically affects the motion of dopant into the substrate. Metallic arsenic was found at the interface for inert atmosphere diffusion from arsenic-doped glasses (6). A phase tentatively identified as SiB_6 was detected for the case of boron-doped glasses (7, 8), and a P_2O_5 -rich silicate phase was observed for phosphorus-doped glasses (9).

As an off-shoot of work on oxidation-induced stacking faults (OSIF), the phenomena of oxidation-enhanced diffusion (OED) and oxidation-retarded diffusion (ORD) have been reported in the literature. OED is well docu-

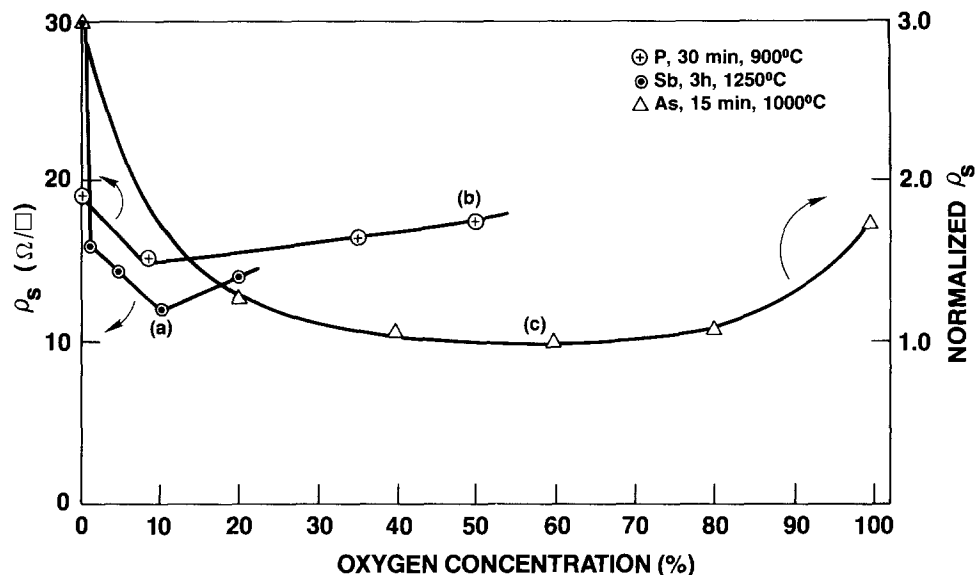
mented for phosphorus and boron (10-12). It has been proposed (11) that since boron and phosphorus diffuse via a partial interstitialcy mechanism, the enhanced diffusion in an oxidizing ambient is due to an increase in the concentration of Si self-interstitials. ORD has been observed for antimony diffusion by Mizuo and Higuchi (13). These authors propose that the concentration of vacancies decreases and the concentration of interstitials increases during oxidation. Antimony is proposed to diffuse via vacancies, and therefore its diffusion is retarded in an oxidizing atmosphere.

Both interface and substrate effects are directly related to the composition of the diffusion ambient. Diffusions are generally done in either nonoxidizing (N_2 or Ar) or oxidizing (N_2 - O_2 or Ar- O_2 mixtures) ambients. All of the previously reported work concerning diffusion of n-type dopants [P (14), As (15), Sb (16a)] from doped-glass sources is consistent in the following sense: a similar dependence of sheet resistance ρ_s upon O_2 concentration in the diffusion ambient is observed. High ρ_s is measured at both low and high O_2 contents in the diffusion ambient, with a ρ_s minimum at intermediate O_2 contents. As noted in Fig. 1, this behavior is independent of dopant, temperature, or diffusion time. An explanation for this common behavior based on interface effects has been advanced by Beyer (17) for the case of As-doped glasses. According to Beyer, under inert atmosphere conditions, a diffusion barrier is formed at the interface (in this case, metallic As) resulting in high sheet resistance. With the introduction of oxygen into the ambient, the barrier phase is oxidized, allowing the dopant to diffuse into the substrate and therefore lowering the sheet resistance. At high oxygen concentration, a competition results between oxidation and diffusion, creating an oxide at the interface which, in

* Electrochemical Society Active Member.

† Present address: Motorola New Enterprises, Mesa, Arizona.

Fig. 1. Sheet resistance vs. oxygen concentration for Sb, P, and As diffusion. (a): Ref. (14). (b): Ref. (16a). (c): Ref. (15).



turn, delays the arrival of the dopant to the substrate, *i. e.*, the sheet resistance increases.

Most of the work reported on diffusion from doped glasses concentrates on B, P, and As, while only recently some attention has been devoted to Sb-doped glasses (16a, 16b, 18). In this work, the effect of ambient composition and diffusion time on the doping of silicon with a stibino silicate glass is described. Experiments have been performed in both nonoxidizing (N_2 , Ar, or He) and oxidizing (Ar- O_2) ambients. The results demonstrate a dependence of sheet resistance on ambient composition which is different from those reported previously (Fig. 1). It will be shown that this behavior is a result of using Ar- O_2 mixtures for oxidizing ambients as opposed to the N_2 - O_2 mixtures used in most previous investigations. In order to understand the dependence of the Sb diffusion on the ambient, electrical measurements and standard analytical techniques including Rutherford backscattering spectroscopy (RBS), Auger electron spectroscopy (AES) and secondary ion mass spectroscopy (SIMS) were used to characterize both the Sb-doped glass and the Si substrate. A model is proposed to explain the experimental results.

Experimental Procedures

The diffusions were performed using antimony-doped glasses as sources. The glasses were deposited by low pressure chemical vapor deposition (LPCVD) at 360°C and 0.6 torr (19). Silane, oxygen, and trimethylantimony (a high vapor pressure liquid) were used as gas sources. The structure consisted of a p-type (100), 6-8.5 Ω -cm, 75 mm diam substrate, upon which a 700Å thick stibinosilicate glass was deposited with an antimony concentration of 20 weight percent (w/o) Sb (6.1 mole percent [m/o] Sb). A 700Å undoped SiO_2 layer was deposited on top of the doped glass to minimize dopant evaporation during diffusion. Anneals were carried out at 1250°C in Ar- O_2 mixtures. For each gas mixture, diffusion times of 0.5, 1, 2, 4, and 8h were used (Table I). Some diffusions were carried out in He or N_2 atmospheres.

The experimental apparatus consisted of a 30 in. hot-zone furnace equipped with a quartz diffusion tube. A mineral oil bubbler was adapted to the end cap to avoid atmospheric backstreaming during high temperature processing. Wafers were loaded in a quartz diffusion boat with 3/16 in. spacing and a 75-wafer capacity. Each run

Table I. Experimental conditions

Diffusion temperature	1250°C
Diffusion times	0.5, 1, 2, 4, 8h
Ar- O_2 gas composition	0%, 0.10%, 0.25%, 0.5%, 1%, 5%, 10%, 25%, 100% O_2
He- O_2 gas composition	0%, 1% O_2
N_2 - O_2 gas composition	0%, 1%, 5%, 10%, 25%, 100% O_2

consisted of three doped-glass-coated wafers placed at the center of the boat with the remainder of the boat filled with dummies. Bare silicon wafers were placed at both ends and at the center of the boat, such that the temperature uniformity and gas composition could be monitored through measurements of thickness of the oxide grown on these wafers during diffusion. For high oxygen concentrations, facility supplied oxygen and argon were used. For oxygen contents equal to or lower than 1% by volume, a 1% O_2 in Ar certified standard bottle¹ was used as a source and diluted as necessary.

Rotameters² were used for gas flow metering. After diffusion, the wafers were stripped in 48% HF, and the sheet resistance was measured in five places on the wafer with a four-point probe. Junctions were obtained by the bevel and stain technique. Sb concentration profiles within the Si substrate were derived from spreading resistance probe (SRP) measurements,³ using Irvin's curves (20).

AES was performed in a PEI⁴ thin film analyzer system which employs a stationary large-diameter primary electron beam. The concentration of the Sb in the doped glass is sufficiently high that AES depth profiles could be measured. However, in making those measurements, we have found that the shape of the Sb profiles could be affected by what is believed to be electric field-induced migration of the Sb, which occurs during the analysis. We have been able to minimize but not yet solve this problem and therefore have omitted AES Sb profiles in this paper. Some of the RBS and SIMS analyses were performed at commercial analytical facilities.⁵ SIMS profiles of the Sb in the glass were also found to be affected by the analytical measurement procedure and so they also are omitted.

Results and Discussion

Characterization of as-deposited SbSG.—Figure 2 is a random mode RBS spectrum of the as-deposited samples used in this study. From this spectrum, atomic densities can be calculated: antimony = 2.2×10^{21} cm^{-3} , oxygen = 3.7×10^{22} cm^{-3} , silicon in the cap = 1.8×10^{22} cm^{-3} , and silicon in the SbSG = 1.6×10^{22} cm^{-3} . This results in a stoichiometry of $SiO_{2.1}$ for the cap layer and $SiO_{2.3}Sb_{0.14}$ for the SbSG. From these results, it is calculated that the Sb makes up 20.8% by weight of the SbSG layer, in excellent agreement with the previously quoted value of 20% which was calculated from x-ray fluorescence data.⁶

¹ Matheson Corporation, East Rutherford, New Jersey.

² Emerson Electric Company, Brooks Instruments Division, Hatfield, Pennsylvania.

³ Solid State Measurements, Monroeville, Pennsylvania.

⁴ Physical Electronics Industries, Eden Prairie, Minnesota.

⁵ C. Evans and Associates, San Mateo, California.

⁶ The x-ray spectrometer was calibrated using wet chemical methods.

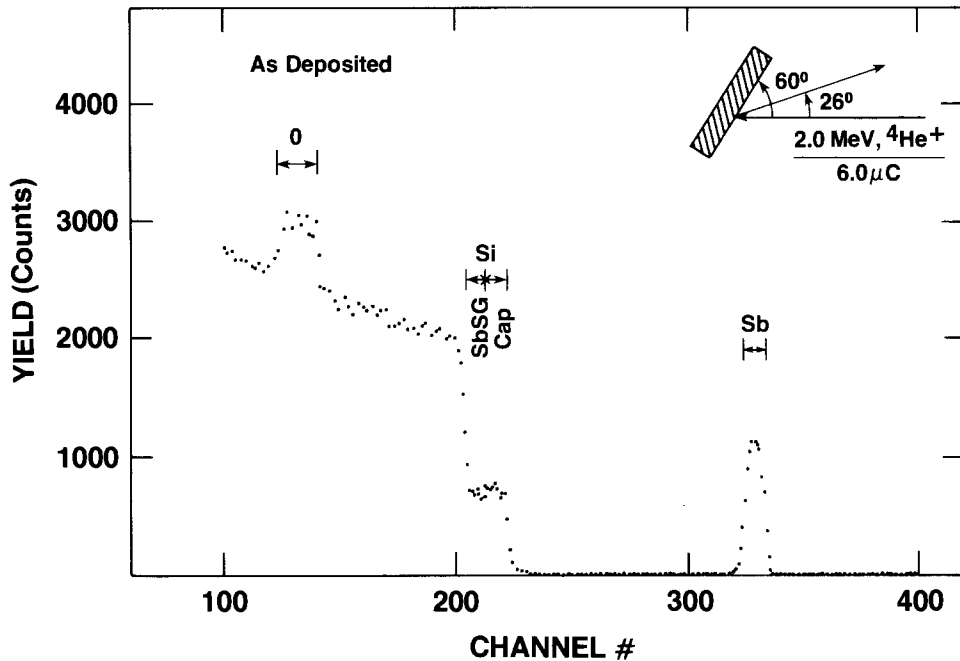


Fig. 2. Random mode RBS spectrum of as-deposited structure.

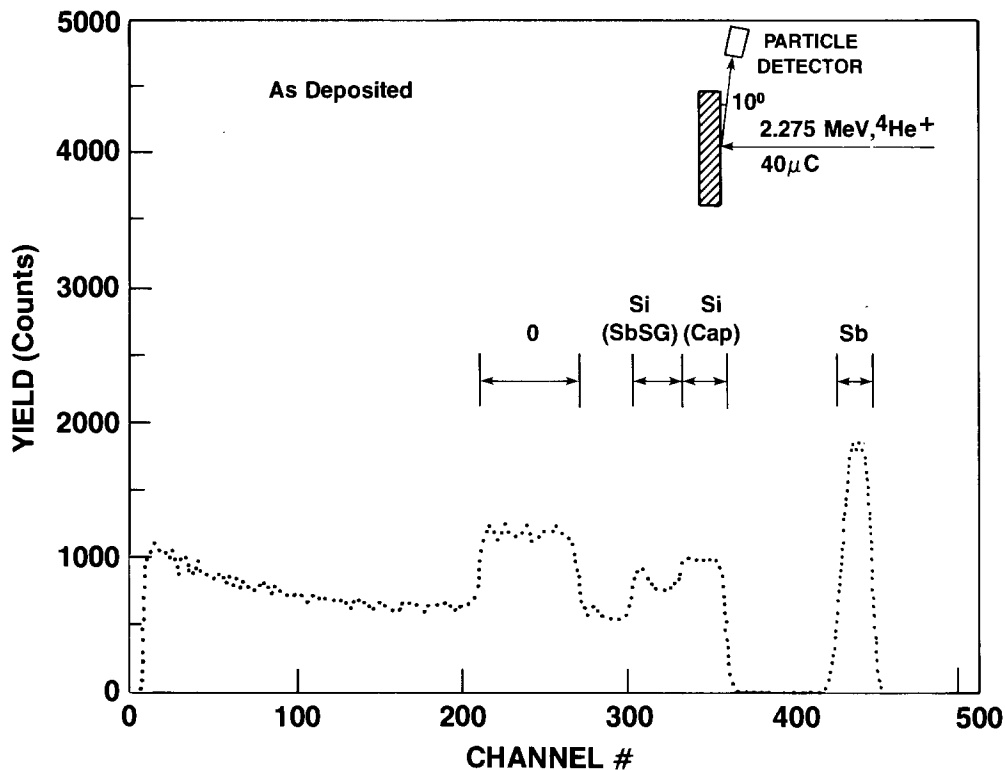


Fig. 3. Channelled mode RBS spectrum of as-deposited structure.

The spectrum shown in Fig. 2 suggests slightly lower Si concentration in the SbSG layer (compared to the cap layer), but the two layers are not well resolved in this spectrum. Figure 3 is recorded with the incident beam channelled down the (100) axis of the substrate. The particle detector is located at an angle of 80° with respect to the surface normal in order to enhance depth resolution (21). Note that the SbSG and SiO_2 cap layers are well resolved in this spectrum, and the Sb concentration appears uniform with depth. With the better depth resolution of this spectrum, the difference in Si concentration between the SbSG and cap layers is more apparent.

Sheet resistance measurements.—In Fig. 4, ρ_s is plotted against percent O_2 by volume and as a function of diffusion time. While previously reported work (14-16) showed only one minimum in ρ_s as a function of O_2 content in the ambient, two minima are reported in this work. One minimum, which occurs at 0% O_2 (100% Ar) is always the lower

minimum and is independent of time. The second minimum is time dependent and shifts to lower O_2 concentrations for longer diffusion times. A replot of this data using an expanded scale shows the low O_2 portion in greater detail (Fig. 5).

To ascertain whether the appearance of two minima is an idiosyncrasy of Ar diffusions, a number of diffusions were performed in He-O_2 and $\text{N}_2\text{-O}_2$ mixtures. The minimum observed for inert Ar atmospheres was reproduced in 100% He atmospheres, while no minimum was observed for 100% N_2 diffusions. Figure 6 displays a comparison of the sheet resistance for wafers diffused in N_2 , Ar, and He atmospheres. It is apparent that the diffusions in N_2 give unique results. We discuss this further below.

Diffusion in N_2 ambient.—Data shown in Fig. 6 demonstrate that diffusions performed in N_2 give very different results from diffusions performed in Ar or He. While both Ar and He are inert gases, work by Raider *et al.* (22) on

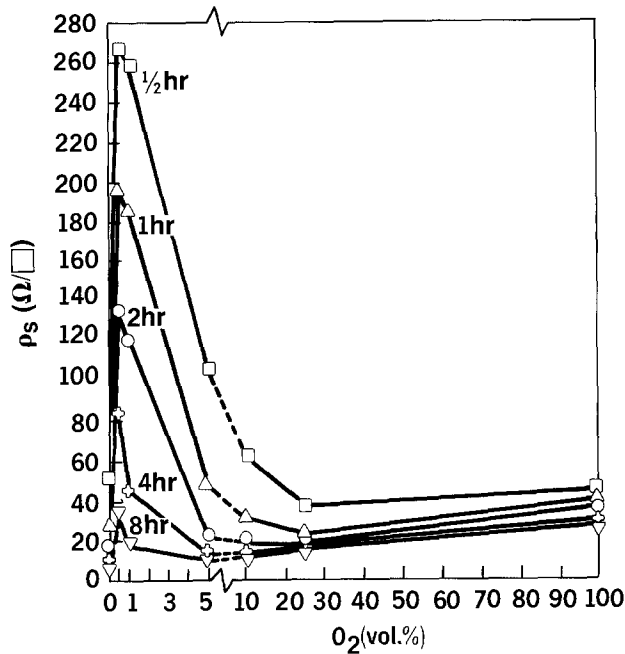


Fig. 4. Sheet resistance as a function of oxygen content in the diffusion atmosphere and time.

the N_2 reaction at the Si-SiO₂ interface suggests that N_2 gas diffuses to the interface where it reacts to form an oxynitride. This suggests that in the case of diffusions performed in Ar or He, the phase formed at the interface is solely due to interaction between the doped glass and the substrate, while, in N_2 diffusion, interface interactions are modified by the presence of N_2 as a reactant.

AES was used to further investigate this possibility. Figure 7b is an AES survey spectrum representing the surface of a wafer which was diffused for 1h at 1250°C in 100% N_2 . The spectrum shows that the N_2 has reacted with the outer surface of the SiO₂ cap to form an oxynitride. Figure 8 is an AES depth profile of the same sample. It shows that the oxynitride formed at the surface of the SiO₂ cap is very thin. Further, N was also found distributed within the SbSG layer, reaching a maximum in concentration at the SbSG/substrate interface. This N peak near the interface is consistent with Raider's (22) observation from ESCA and etch-rate data of an oxynitride or mixed oxide and nitride at the oxide/substrate inter-

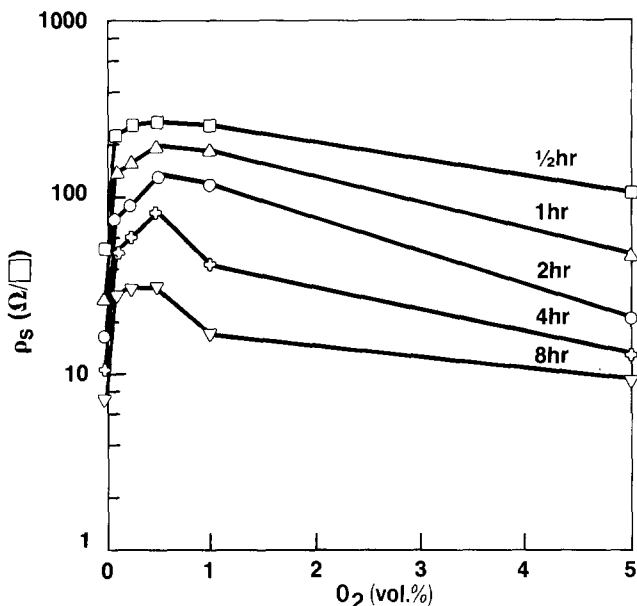


Fig. 5. Replot of the data in Fig. 4 emphasizing low oxygen concentrations.

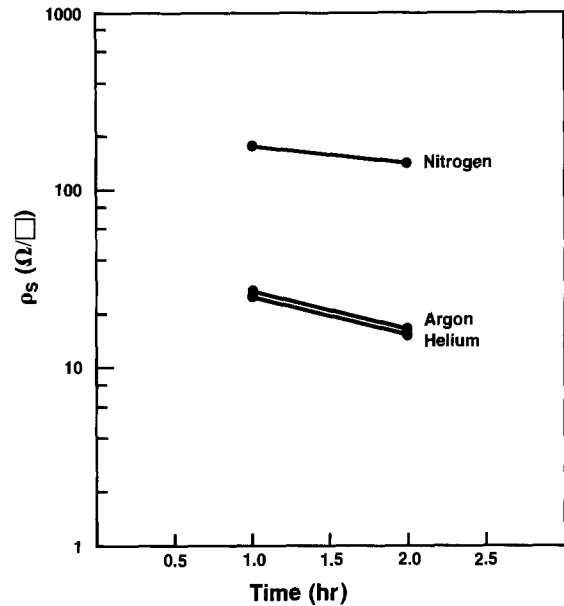


Fig. 6. Sheet resistance for wafers diffused in Ar, He, and N_2 vs. time.

face. Although the concentration of N at the SbSG/substrate interface is small (note the expanded scale for the N_2 profile), it apparently affects the interface reactions. No HF insoluble interfacial films were observed for diffusions performed in N_2 . It is evident that N_2 should not be considered an inert ambient in the presence of SiO₂ at high temperatures.

Substrate dopant profiles.—Figure 9 displays concentration profiles obtained from SRP measurements for diffusions performed for 4h in 0%, 1%, 10%, and 100% oxygen ambients. These traces show the changes in dopant surface concentration (C_s) as a function of ambient composition. In Fig. 10a and 10b, C_s as obtained from SRP measurements is plotted against diffusion times for various ambient compositions. Figure 10a concentrates on oxygen-rich atmospheres with 0% O_2 plotted as a reference. No change in C_s with time is observed for 0% O_2 , indicating infinite-source-type behavior. This time independence is also found at 5% O_2 . Between 10% and 100% O_2 , a decrease in C_s is noted for increasing diffusion times. This is similar to Beyer's (17) observation for the case of arsenic-doped glasses diffused in a high O_2 ambient. Under these conditions, thermal oxide which grows at the doped-glass substrate interface slows down the arrival of dopant to the substrate and therefore decreases C_s . The shift of the second minimum in ρ_s to shorter times with

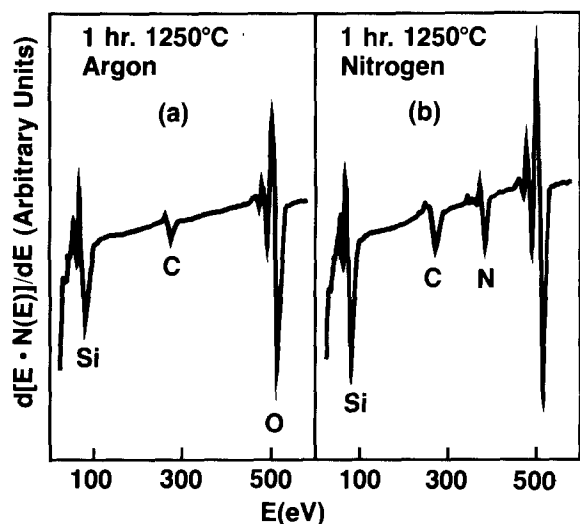


Fig. 7. AES survey spectra of glass surface for wafers diffused in (a) argon and (b) nitrogen. Primary beam conditions: $E_p = 1.5$ keV, $J_p = 10$ mA/cm².

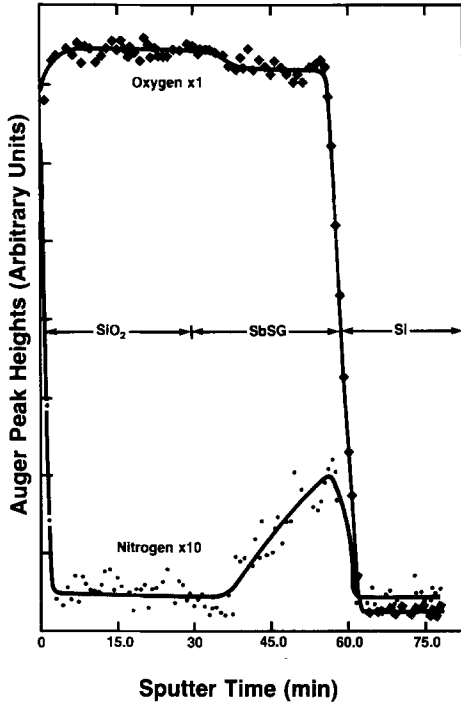


Fig. 8. AES depth profile of wafer diffused in nitrogen for 1h at 1250°C.

increasing O_2 concentration (Fig. 4) is also indicative of a thermal oxide barrier growing at the doped-glass/silicon interface. This can be inferred as follows: the thermal oxide thickness can be approximated by

$$d_{ox} = [X_0 B(t + \tau)]^{1/2}$$

where X_0 is the molar fraction of O_2 in the ambient, B is the parabolic rate constant (dependent on the O_2 concentration), t is the time, and τ is the time constant which corrects for the presence of an initial oxide (23). As X_0 in-

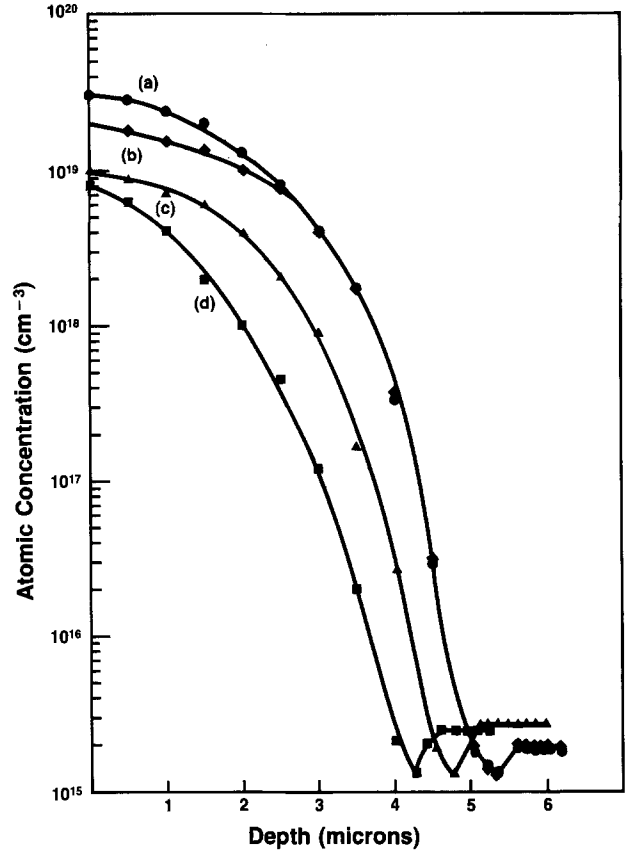


Fig. 9. Antimony concentration profiles from SRP measurements for 4h diffusions in (a) 100% Ar, (b) 10% O_2 , (c) 100% O_2 , and (d) 1% O_2 .

creases, the time required to form an oxide thick enough to significantly retard the diffusion must decrease.

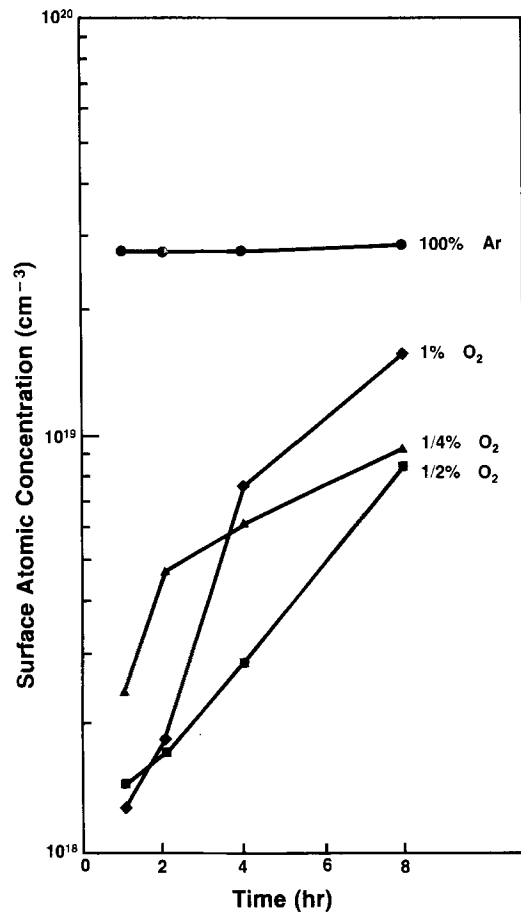
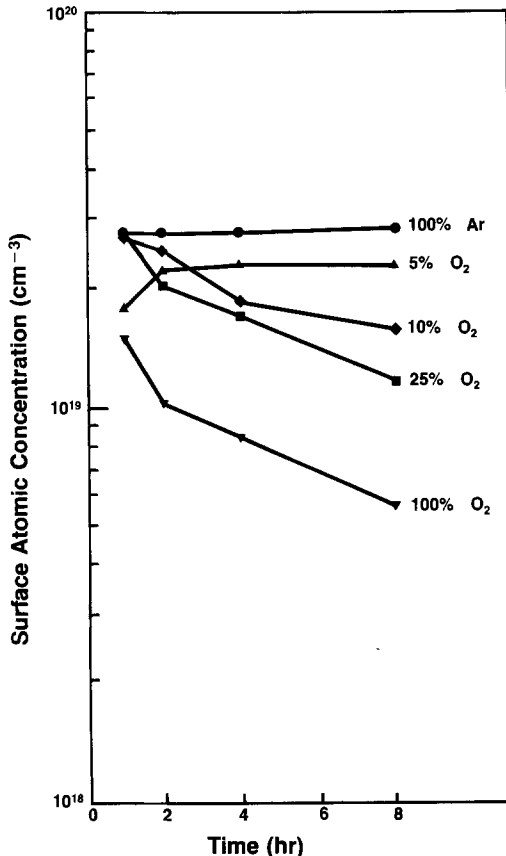


Fig. 10. A(left): Surface concentrations (obtained from SRP measurements) vs. diffusion time and as a function of ambient composition ($O_2 \geq 5\%$). B(right): Same as Fig. 10A, but $O_2 \leq 1\%$.

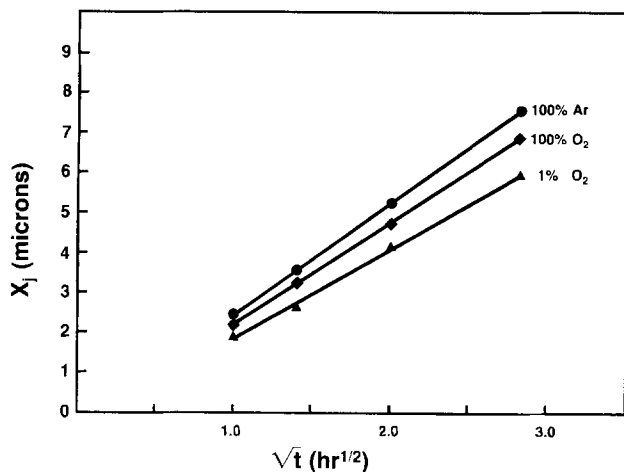


Fig. 11. Junction depth vs. $t^{1/2}$ as a function of O_2 content in the diffusion ambient.

Figure 10b displays a plot of C_s vs. diffusion time for oxygen-poor ambients. Again, 0% O_2 is plotted as a reference. In Fig. 10b, the behavior is opposite to that in Fig. 10a in that C_s now increases as a function of diffusion time. This behavior is consistent with the formation and subsequent oxidation of a diffusion barrier at low O_2 contents. For longer diffusion time, *i.e.*, increased arrival of O_2 at the doped-glass/Si interface, the barrier is oxidized allowing for diffusion of dopant to the Si substrate and therefore increasing C_s . The above statements are supported by the behavior of x_j as a function of ambient and diffusion time, as plotted in Fig. 11. The shallower junctions obtained at low oxygen concentration are ascribed here to a barrier at the interface. Intermediate junction values at high O_2 /Ar ratios are consistent with a reduction of the dopant flux at the substrate surface due to thermal oxide formation.

Although the shallower junctions at high O_2 content (as compared to x_j in an inert atmosphere) could be attributed to ORD effects as reported by Tan and Gosele (24), the decrease in C_s with increasing oxidation time can by itself account for the decrease in junction depth. Take 8h

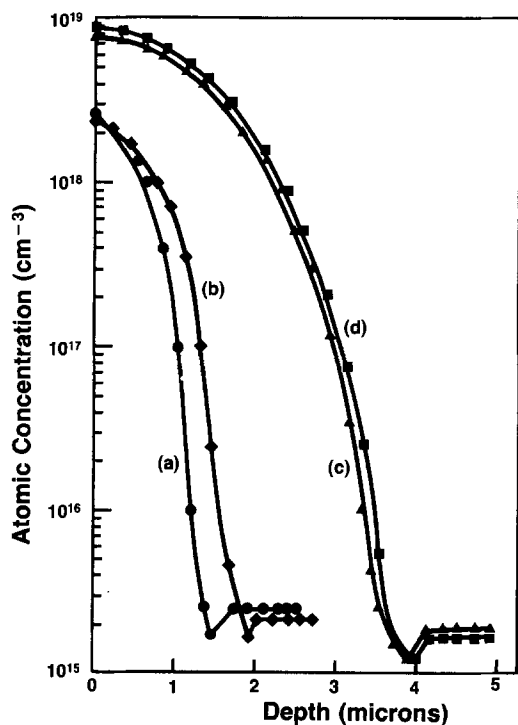


Fig. 12. Dopant concentration profiles for: (a) 1100°C, oxide side, (b) 1100°C, Si_3N_4 masked, (c) 1250°C, oxide side, and (d) 1250°C Si_3N_4 masked.

diffusions for 100% O_2 and inert atmosphere (100% Ar) as an example

	100% O_2	100% Ar	
x_j (μm)	7.0	7.5	(from Fig. 11)
C_s (cm^{-3})	6×10^{18}	3×10^{19}	(from Fig. 10a)

For simplicity, a ratio between junction depths as a function of C_s is obtained assuming infinite source behavior (erfc) and using Barry and Olofsen's formula (2). A similar ratio can be obtained for a finite source behavior (Gaussian) assumption.

$$x_j = 2 \sqrt{Dt} \operatorname{erfc}^{-1} \left(\frac{C_b}{C_s} \right)$$

and the ratio between x_j can be calculated from the ratio between erfc's

$$\left. \frac{x_j(O_2)}{x_j(Ar)} \right]_{\text{calc}} = 0.90 \quad \text{and} \quad \left. \frac{x_j(O_2)}{x_j(Ar)} \right]_{\text{exp}} = 0.93$$

Thus, the measured x_j difference between high oxygen and inert atmosphere diffusions could be attributed to the decrease in C_s .

Oxidation retarded diffusion.—Diffusions were conducted at 1100° and 1250°C to ascertain the presence of ORD in Sb diffusions into Si. The experimental procedure was similar to that reported by Mizuo and Higuchi (13), where Si substrates were predeposited with Sb, from a doped-glass source, and coated with Si_3N_4 , which was subsequently etched off from half of the wafer. The wafers were diffused in an O_2 atmosphere, and the junction depths in the Si_3N_4 covered and exposed areas were compared. Results plotted as concentration profiles are shown in Fig. 12. They indicate that, while ORD can be seen clearly for diffusions at 1100°C, it is not a significant effect for 1250°C diffusions.

HF insoluble film.—For O_2 concentrations less than 1% in Ar, a hydrophobic, HF insoluble film was present after diffusion. The film was more evident with decreasing oxygen content, and it became less apparent with increasing diffusion times. No film was observed after 8h diffusions.

Several analytical techniques were used to characterize this HF insoluble film. Figure 13 shows SIMS depth profiles of two samples. Both samples were diffused for 1h at 1250°C. One sample was diffused in a 100% Ar ambient, and the other in an Ar-1% O_2 ambient. Following the diffusions, both samples were etched in an HF solution. After etching, the sample diffused in 100% Ar exhibited a residual unetchable film, whereas the sample diffused in Ar-1% O_2 had the appearance of a clean Si surface.

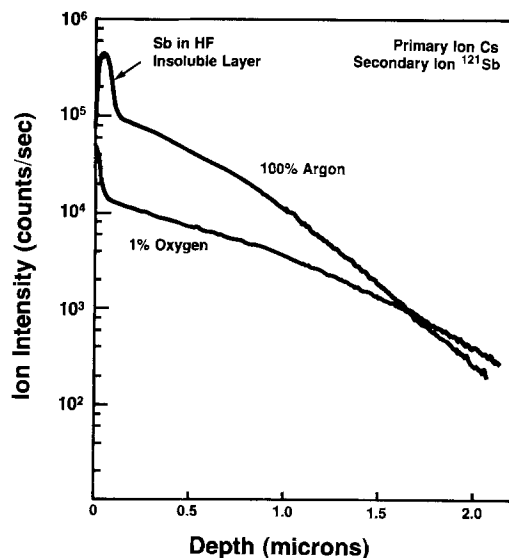


Fig. 13. SIMS depth profile of substrates diffused in 100% Ar and 1% O_2 atmospheres (glass stripped in 48% HF).

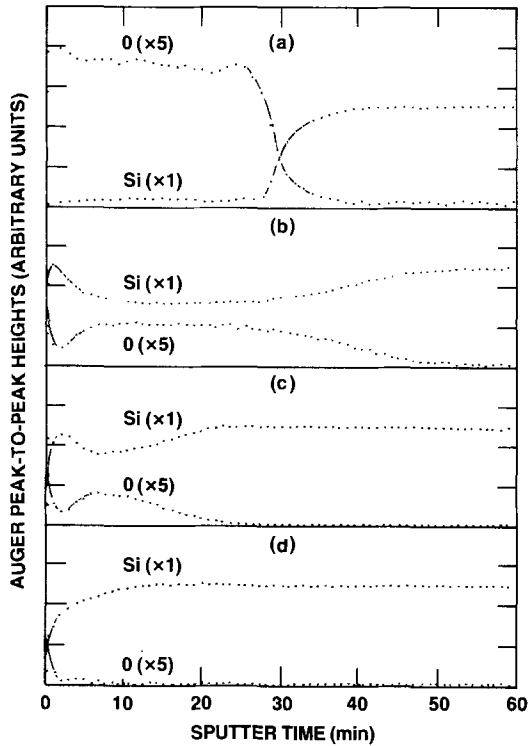


Fig. 14. AES depth profiles of the HF insoluble films: (a) as deposited SbSG, (b) 100% He, 1h, 1250°C, HF stripped, (c) 1/4% O₂, 1h, 1250°C, HF stripped, and (d) 1/2% O₂, 1h, 1250°C, HF stripped.

The SIMS Sb profile of the sample diffused in 100% Ar shows a surface layer characterized by high Sb counts. Assuming a constant sputter rate, over the depth of the sputter crater, this layer has roughly the same thickness as the original SbSG layer. The profile of the sample diffused in Ar-1% O₂ does not show evidence of this layer. Finally, we note that these SIMS Sb profiles show that there is about a ten times greater surface concentration of Sb in the substrate of the sample diffused in 100% Ar, in agreement with SRP measurements described previously.

Figures 14b-14d show AES depth profiles of the HF insoluble films on samples diffused in 100% He, Ar-1/4% O₂, and Ar-1/2% O₂, respectively. For reference, Fig. 14a shows an AES depth profile of a 700Å SbSG layer which was not diffused. The Si LMM peak (92 eV) characteristic

Table II. Composition of HF insoluble film as determined from RBS measurements

	Cap	As Deposited SbSG	HF insoluble film
Si (cm ⁻³)	1.8×10^{22}	1.6×10^{22}	3.4×10^{22}
O (cm ⁻³)	3.7×10^{22}	3.7×10^{22}	8.2×10^{21}
Sb (cm ⁻³)	—	2.2×10^{21}	3.0×10^{20}
Stoichiometry	SiO _{2,1}	SiO ₂ Sb _{0,14}	SiO _{0,24} Sb _{0,0089}

of elemental Si is being monitored in these profiles, thus accounting for the low Si signal in Fig. 14a.

The AES depth profiles show that the HF insoluble film can be characterized basically as a silicon-oxygen compound which is very oxygen deficient compared to the original SbSG. Sb was not detectable in those residual films with AES, although it was detectable with SIMS. We shall show below that it is detectable with RBS also. The thickness of the HF insoluble film can be seen in Fig. 14b-14d to be inversely related to the concentration of O₂ in the diffusion ambient. Only very small partial pressures of O₂ are needed to prevent the appearance of the HF insoluble film. The AES profiles also show that the outer surface of the film is nearly pure Si, which may account for the failure of the film to etch in HF. The film/substrate interface is very broad compared to the SbSG/substrate interface (Fig. 14a). This suggests that the HF insoluble film is nonuniform in thickness and/or composition over the wafer surface.

Figure 15 shows an RBS spectrum of the HF insoluble film on the sample diffused in 100% He. This spectrum was recorded under conditions identical to those used to record the spectrum of the as-deposited sample (Fig. 2). From this spectrum, we can calculate the composition of the HF insoluble film. The results are summarized in Table II along with the previously calculated composition of the as-deposited sample. Once again, it can be seen that the HF insoluble film is both Sb and O deficient with respect to the as-deposited SbSG, while the Si concentration has more than doubled.

To summarize, the SIMS, AES, and RBS data have shown that the HF insoluble film can be characterized as being oxygen and antimony deficient with respect to the as-deposited SbSG. The AES data suggest that the surface of the film is rich in Si. The film is roughly the same thickness as the original SbSG layer for a 1h 1250°C diffusion in pure inert atmosphere, but it rapidly becomes thinner for small partial pressures of O₂ in the diffusion

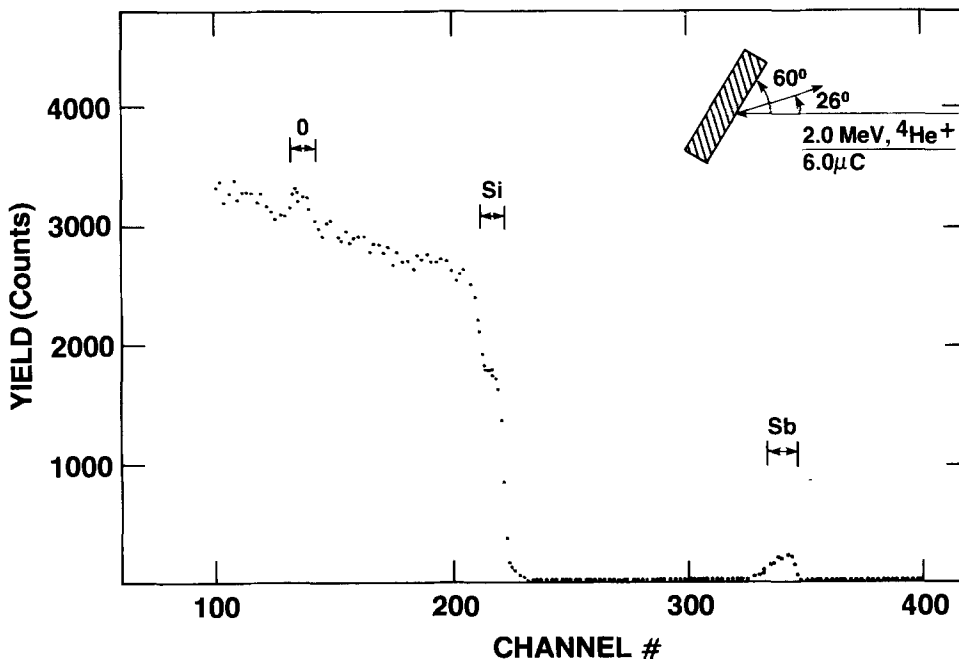


Fig. 15. RBS spectrum of HF insoluble film for wafer diffused in 100% He atmosphere.

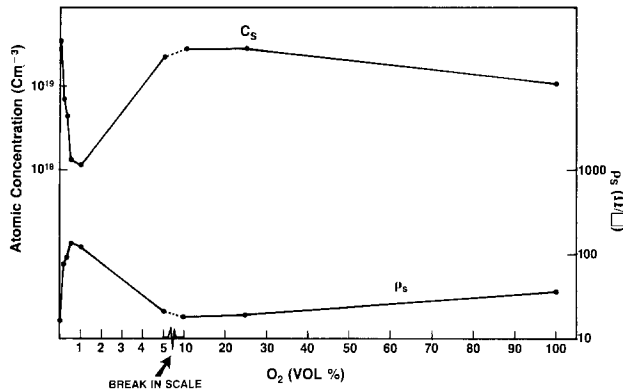


Fig. 16. Sheet resistance and surface concentration (C_s) as a function of O_2 concentration in the diffusion atmosphere.

ambient. For a 1h 1250°C diffusion in Ar-1% O_2 , no residual film could be detected.

Model

Both ρ_s and C_s are plotted against O_2 concentration in Fig. 16, where their inverse relationship becomes apparent.

In Fig. 17, a model is proposed to account for the presence of two maxima in C_s as a function of diffusion ambient composition (see Fig. 16). The C_s vs. percentage of O_2 curve can be separated into four parts: (i) inert atmosphere, (ii) low O_2 , (iii) medium O_2 , and (iv) high O_2 regions. The as-deposited structure consists of an undoped SiO_2 cap, a Sb-doped glass (2×10^{21} cm^{-3}), and a Si substrate with a background boron concentration of 2×10^{15} cm^{-3} . In the first segment (i), in inert atmosphere, a hydrophobic HF-insoluble film forms at the doped-glass/Si interface. Through various microchemical and electrical measurements we have shown that this film composition has the form $Sb_xSi_yO_z$ and acts as a high concentration source of Sb atoms. The idea of an infinite source is reinforced by the observation that C_s is independent of time for diffusions in inert atmospheres (see Fig. 10).

In the second segment of the curve (ii), at low O_2 concentrations the source film is thinner, making it a limited source, accounting for lower C_s values. The AES depth profiles (Fig. 14) demonstrate the progressively thinner layer for increasing concentrations of O_2 between 0% and about 1%. The interface film is postulated to act both as a source and a barrier to Sb diffusion from the stibinosilicate glass. For inert or low O_2 concentrations, the film forms rapidly at the interface and isolates the doped glass from the substrate (barrier action) so that the Sb diffusion into the substrate comes exclusively from the film (source action). For thick films (inert atmosphere diffusion), the source is infinite (Fig. 10a), while for thin films, the supply of Sb is limited and is not readily replenished by the glass.

In the third part of the curve (iii) an increase in C_s is observed for $1\% < \%O_2 \leq 25\%$. In this range, $Sb_xSi_yO_z$ is initially formed and supplies Sb to the substrate such that an initial rise in C_s occurs, analogous to a predeposition step. As opposed to the O_2 -poor part (ii), in the medium O_2 range this phase is rapidly oxidized. The initial dopant concentration at the substrate is now enhanced by both the Sb flux from the doped glass and also, as oxidation develops, by the pile-up effect. This effect which is caused by dopant redistribution between the growing oxide and silicon was first reported by Grove *et al.* (25) on his work on the oxidation of doped substrates.

As long as the diffusivity of Sb in SiO_2 (D) is greater than the parabolic oxidation rate constant (B), an increase in C_s with the oxygen concentration in the ambient will be observed. From Ghezzi and Brown (26) and at 1250°C, D (Sb in SiO_2) = $0.09 \mu/h^{1/2}$. From an extrapolation of Irene's data (26) to 1250°C, $B = 0.196 \mu/h^{1/2}$ for atmospheric pressure. Since Deal and Grove (23), report that B is proportional to the O_2 partial pressure in the ambient, the

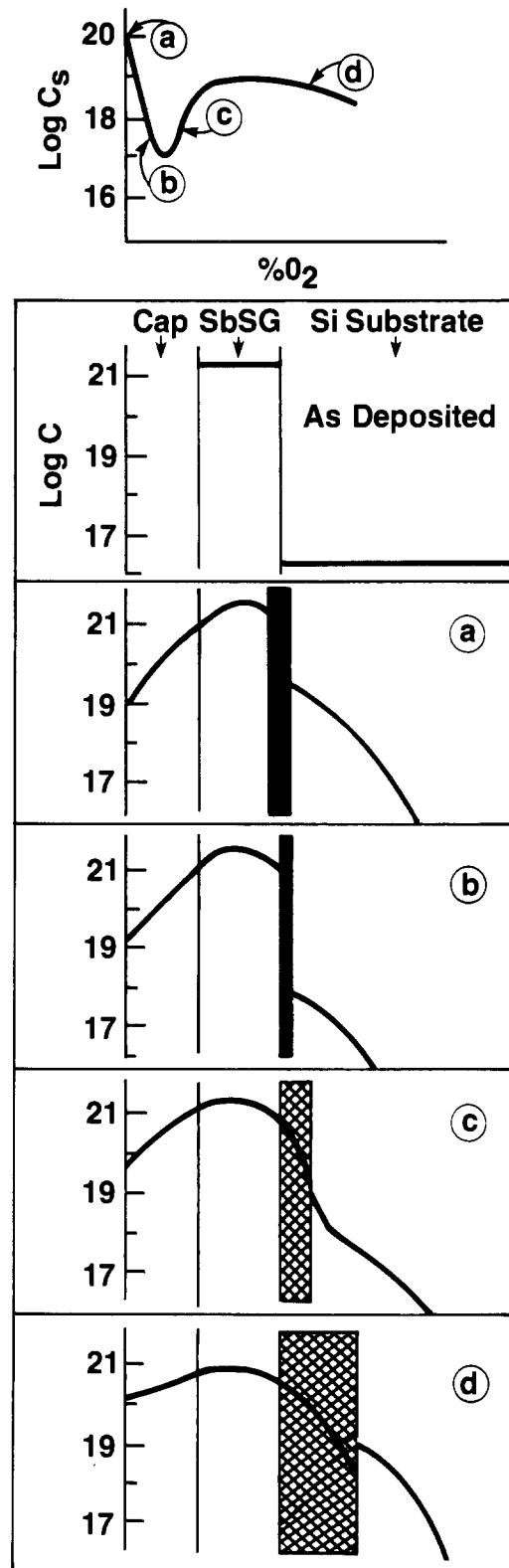


Fig. 17. Schematic of proposed model

value of B can be calculated for any O_2 concentration. At 25% O_2 , $D = B$ such that up to 25% O_2 , the $D > B$ condition holds.

With increasing O_2 concentration in the diffusion ambient, as in part (iv), a competition between diffusion and oxidation becomes evident. As the O_2 concentration increases over 25%, D (Sb in SiO_2) $< B$, so that the thermal oxide growing at the doped oxide/substrate interfaces is now thick enough to slow down the arrival of Sb to that interface. This causes a decrease in C_s relative to C_s at intermediate O_2 concentrations. A similar argument for low C_s at high O_2 concentration has been proposed by Beyer (17) for the diffusion of As from doped-glass sources.

Summary

The effects of ambient and time on the diffusion of Sb into Si from a doped-glass source were studied. Two minima in C_s were found as a function of O_2 concentration in the diffusion ambient, when Ar- O_2 mixtures were used. From similar experiments using N_2 - O_2 mixtures it was determined that at high temperatures N_2 interacts with the doped-glass/silicon interface. This interaction affects the diffusion of Sb into silicon.

The formation of an interface film, $Sb_xSi_yO_z$, at low oxygen concentrations, for Ar- O_2 diffusion was identified. This film was characterized through AES, SIMS, and RBS analyses. A diffusion mechanism is proposed to account for the presence of two surface-concentration maxima as a function of O_2 content in the diffusion ambient. This mechanism is based on the formation of $Sb_xSi_yO_z$ at the doped-glass/silicon interface at low O_2 concentration and on pile-up effects at higher O_2 concentrations.

At present, we are performing additional RBS analyses on samples covering the entire range of oxygen concentrations in the ambient. These results and their implications with regard to the above model will be discussed in a subsequent paper.

Acknowledgments

The authors would like to thank Dr. Syd Wilson for his help in acquiring and interpreting the RBS data. Thanks are also due to Doris Travers and Karen Kobold for their contribution in running the LPCVD tubes and in the electrical characterization of the buried layers.

Manuscript submitted Nov. 17, 1983; revised manuscript received March 30, 1984. This was Paper 391 presented at the Denver, Colorado, Meeting of the Society, Oct. 11-16, 1981.

Motorola, Incorporated assisted in meeting the publication costs of this article.

APPENDIX

Diffusion Coefficient

Assuming an erfc dopant-distribution profile (for oxygen concentrations of 0% and 5%), and from C_s and junction depth values obtained from SRP data, a diffusion coefficient for antimony in silicon at 1250°C was calculated. As can be seen in Table A-I the diffusion coefficient obtained in this work agrees fairly well with the reported literature values.

Table A-I

D (μ^2/h) (1250°C)	Ref.
0.243 ± 0.026	This work
0.277	(18)
0.242 ± 0.011	(16)
0.306	(28)

REFERENCES

1. M. L. Barry and P. Olofsen, *Solid State Technol.*, **11**, 39 (1969).
2. M. L. Barry and P. Olofsen, *This Journal*, **116**, 854 (1969).
3. M. L. Barry, *ibid.*, **117**, 1405 (1970).
4. J. Wong and M. Ghezze, *ibid.*, **119**, 1413 (1972).
5. M. Ghezze and D. M. Brown, *ibid.*, **120**, 110 (1973).
6. T. Sakurai, H. Nishi, T. Furryya, H. Hashimoto, and H. Shibayama, *Appl. Phys. Lett.*, **22**, 219 (1973).
7. E. Dominguez, E. Lora-Tamayo, and B. Blanchard, *This Journal*, **125**, 1521 (1978).
8. K. M. Busen, W. A. Fitzgibbons, and W. K. Tsang, *ibid.*, **115**, 291 (1968).
9. E. Kooi, *ibid.*, **111**, 1383 (1964).
10. K. Taniguchi, K. Kurosawa, and M. Kashiwagi, *ibid.*, **127**, 2243 (1980).
11. S. M. Hu, *J. Appl. Phys.*, **45**, 1567 (1974); D. A. Antoniadis and I. Moskowitz, *ibid.*, **53**, 6788 (1982).
12. G. Masseti, S. Solmi, and G. Soncini, *Philos. Mag.*, **11**, 613 (1976).
13. S. Mizuo and H. Higuchi, *Jpn. J. Appl. Phys.*, **20**, 739 (1981).
14. D. L. Flowers, K. Ridgeway, and C. E. Wu, Paper RNP 16 presented at The Electrochemical Society Meeting, Seattle, WA, May 21-26, 1978.
15. K. Reindl, *Solid State Electron.*, **16**, 181 (1973).
16. (a) C. E. Wu, *This Journal*, **128**, 1805 (1981); (b) F. Pintchovski, P. J. Tobin, M. Kottke, and J. B. Price, Abstract 391, p. 949, The Electrochemical Society Extended Abstracts, Vol. 81-2, Denver, CO, Oct. 11-16, 1981.
17. K. D. Beyer, *This Journal*, **124**, 630 (1977).
18. S. H. Song, S. Matsumoto, and T. Niimi, *Jpn. J. Appl. Phys.*, **18**, 2181 (1979).
19. F. Pintchovski, P. J. Tobin, and J. B. Price, Abstract 418, p. 654, The Electrochemical Society Extended Abstracts, Vol. 83-1, San Francisco, CA, May 8-13, 1983.
20. J. C. Irvin, *Bell Syst. Tech. J.*, **41**, 387 (1962).
21. C. W. Young, P. P. Pronko, S. R. Wilson, B. R. Appleton, J. Narayan, and R. T. Young, *J. Appl. Phys.*, **50**, 3261 (1979).
22. S. I. Raider, R. A. Gdula, and J. R. Petrak, *Appl. Phys. Lett.*, **27**, 150 (1975).
23. B. E. Deal and A. S. Grove, *J. Appl. Phys.*, **36**, 3770 (1965).
24. T. Y. Tan and U. Gosele, *Appl. Phys. Lett.*, **40**, 616 (1982).
25. A. S. Grove, O. Leistiko, Jr., and C. T. Sah, *J. Appl. Phys.*, **33**, 2695 (1964).
26. M. Ghezze and D. M. Brown, *This Journal*, **120**, 146 (1973).
27. E. A. Irene and Y. J. Van der Meulen, *ibid.*, **123**, 1380 (1976).
28. C. S. Fuller and J. A. Ditzenberger, *J. Appl. Phys.*, **27**, 544 (1956).

Process-Induced Defects in Borosilicate Glass-Diffused Silicon

O. Aina¹

General Electric Company, Corporate Research and Development Center, Schenectady, New York 12345

R. Kennedy

General Electric Company, Discrete Semiconductor Device Center, Syracuse, New York 13201

ABSTRACT

The defects caused by high temperature diffusion from a borosilicate glass source have been detected using deep level transient spectroscopy (DLTS). Energy levels at $E_c - 0.12$ eV, $E_c - 0.26$ eV, $E_c - 0.36$ eV, $E_c - 0.55$ eV, and $E_v + 0.23$ eV have been measured. It is shown that these levels are annealed out by subsequent processing steps such as phosphorus predeposition, thermal oxidations, and drive-in diffusion. An increase in carrier lifetime from 10 to 36 μ s was found to be associated with the decrease in the defect concentration.

The conventional diffusion processing steps have been known (1, 2) to cause process-induced defects in silicon. The energy levels within the silicon bandgap associated with these defects have been measured by Yau (1) and Sah (2). For the high temperature diffusion of boron and phosphorus at high surface concentrations obtained from BN and P₂O₅ sources, respectively, the energy levels were found to be $E_c - 0.08$, $E_c - 0.22$, $E_c - 0.264$, $E_c - 0.298$, and $E_c - 0.542$ eV. They showed that, unlike impurities, these defects could not be gettered either by surface oxide glasses or by a high concentration degenerate diffused layer but only by slow (0.42°C/min) cooling followed by a quench from the diffusion temperature to room temperature. In addition to the process-induced defects, the defects associated with radiation-induced damage (3-5) have been identified and some have been found to have the same energy levels as those indicated above.

Borosilicate glasses have been shown (6) to be preferable to boron nitride as a p-type planar diffusion source because the usual periodic reactivation cycles are not required (as it is for BN) due to the presence of boron in its activated state. No defect studies, however, have been done for a diffusion process for which borosilicate glasses have been used as a diffusion source. Neither have the effects of the subsequent processing steps that eventually lead to device fabrication been studied.

We report here, the results of a study of process-induced defects caused by diffusion from a borosilicate glass source and from subsequent processing steps using deep level transient spectroscopy (DLTS). Specifically, after boron predeposition diffusion from a borosilicate glass source, energy levels at $E_c - 0.12$, $E_c - 0.26$, $E_c - 0.36$, $E_c - 0.55$, and $E_v + 0.23$ eV were found within the Si bandgap. After the drive-in diffusion, however, deep levels are still present but their concentrations have been considerably reduced. Similar reductions in concentration were also found for subsequent processing steps such as POCl₃ predeposition diffusion and the final thermal oxidation. An increase in the carrier lifetime (as determined by the open-circuit voltage decay technique) from 10 μ s following the boron predeposition step to 36 μ s after the thermal oxidation step was also found, which correlates quite well with the decrease in defect concentration indicated above. The following describes our experimental techniques, results, and the conclusions that can be drawn from them.

Experimental Techniques

The starting material used was n-type silicon with a resistivity of 40 Ω -cm. Before any processing, it was chemically etched to 12 mil. Seven sets of samples (group 1-group 7) were obtained after each of the seven processing steps used for device fabrication. Group 1 samples were obtained after the boron predeposition step which consisted of diffusion from a borosilicate glass source at

1040°C for 60 min in a flowing nitrogen ambient. Since the diffusion was double-sided, the resulting structure was P⁺NP⁺. Group 2 samples went through a boron drive-in diffusion step at 1250°C for 25h in an oxygen and nitrogen ambient. The resulting structure was still P⁺NP⁺ and the junction depth was 1.56 mil (measured by angle lapping), while the surface boron concentration was 3.4×10^{18} cm⁻³. Next, phosphorus predeposition was done on one side (by masking the other side) from a POCl₃ source at 1100°C for 60 min. The result was a P⁺NP⁺N⁺ structure from which group 3 samples were obtained. This was followed by a drive-in diffusion at 1250°C for 7h in nitrogen ambient. The resulting structure was again P⁺NP⁺N⁺, and the junction depth of the P⁺N⁺ side was 0.9 mil. Group 4 samples were obtained from this lot. Group 5 samples were obtained after a gettering step at 1200°C for 60 min with borofilm on the P⁺ side (commercially available from Emulsitone). Group 6 samples, however, were obtained after a POCl₃ gettering heat-treatment at 1100°C for 60 min (on the N⁺ side). These samples did not go through a borofilm gettering step so that group 5 and group 6 samples could be compared with respect to the effectiveness of the two gettering processes. The final step resulting in group 7 samples was a wet thermal oxidation of both groups 5 and 6 samples at 1100°C for 9h. The structure for groups 4-7 samples was P⁺NP⁺N⁺. After processing, the samples from each group were back-side (N⁺ side) lapped to 9 mil. This removed the P⁺ region (in the case of groups 1 and 2 samples) or the P⁺N⁺ region (in the case of groups 3, 4, 5, 6, and 7 samples). A 10,000Å layer of Al was next deposited on the P⁺ side, while 10,000Å of Au-As alloy was deposited on the N-side. The samples were then sintered at 475°C for 10 min in nitrogen ambient to form ohmic contacts.

After packaging into a gold-plated T05 header, DLTS measurements were made using a system consisting of a 50 MHz capacitance bridge, PAR boxcar averager, and associated amplifiers (3, 7). The details of the DLTS measurement can be found elsewhere (7, 8). Briefly, the method consists of reverse biasing a p-n junction in such a way that the reverse bias can be momentarily reduced by a pulse. This results in a reduction in the width of the depletion layer during the pulse. Traps within the region where there is now no longer a depletion region capture charge carriers. After the pulse and as the depletion layer returns to equilibrium, the traps emit the captured charges by thermal stimulation giving rise to a decaying capacitance transient. The decay rate of the transient is related to the emission rate of the traps, which for electrons is given by

$$e_n = \sigma_n < V_n > N_D / g_1 \exp(-E_t / KT) \quad [1]$$

where σ_n is the capture cross section, $< V_n >$ the thermal velocity, N_D the carrier concentration, g_1 the degeneracy of the trap, and E_t the trap energy level with respect to the conduction band. By varying the temperature of the

¹Present address: Bendix Advanced Technology Center, Columbia, MD 21045.

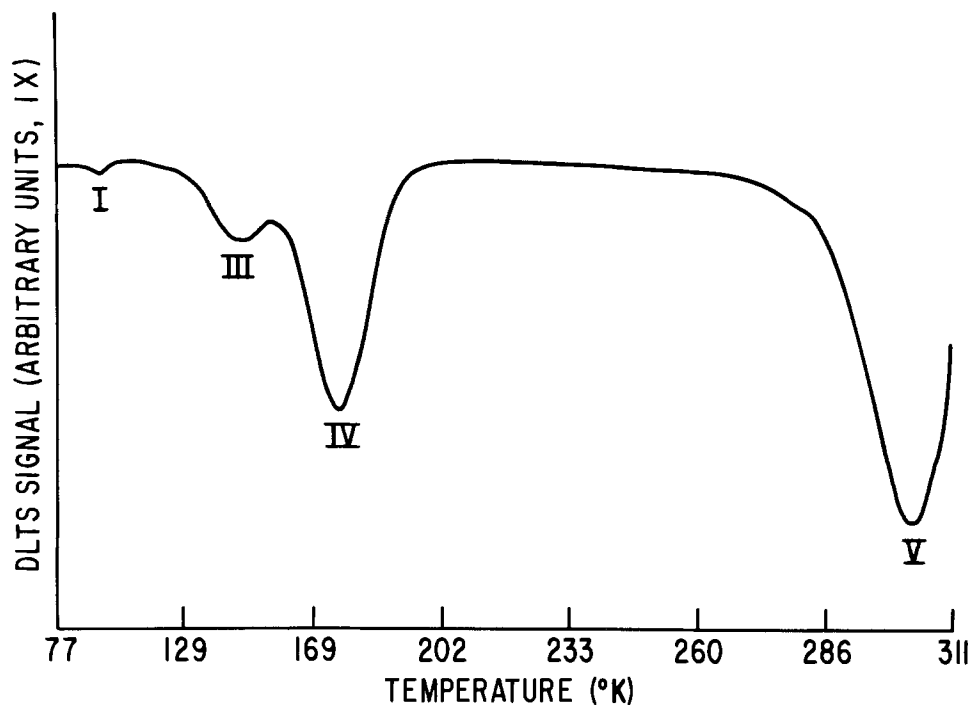


Fig. 1. DLTS spectrum after boron predeposition, group 1, showing deep levels at $E_c - 0.12$, $E_c - 0.26$, $E_c - 0.35$, and $E_c - 0.55$ eV.

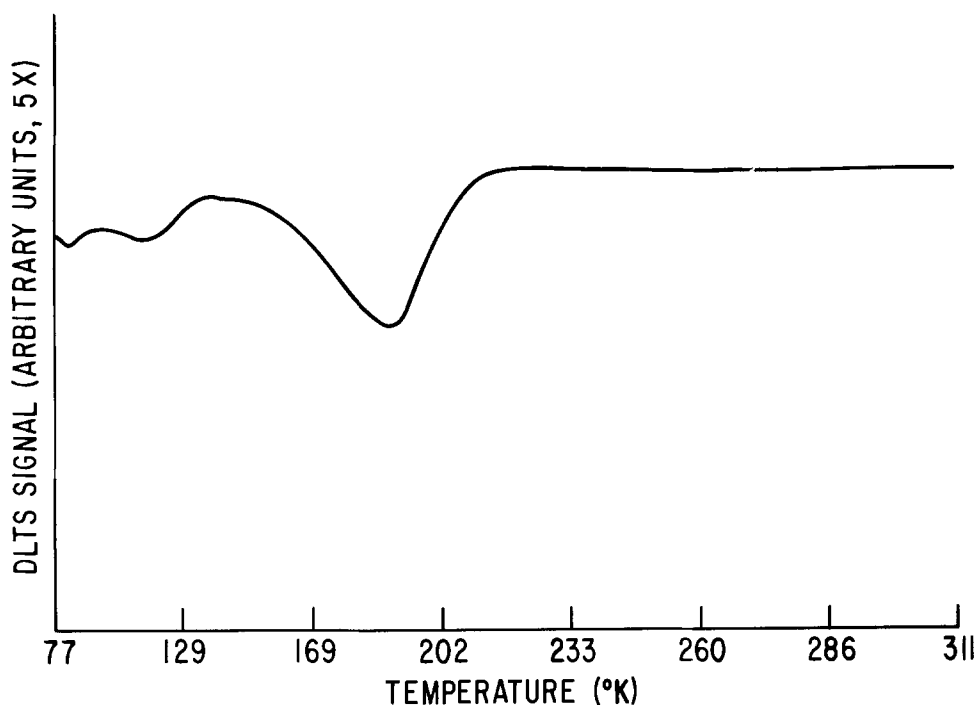


Fig. 2. DLTS spectrum for a group 2 sample (after boron drive-in) showing reduced concentrations of deep levels.

sample from 77 to 300 K, for example, the trap emission rates are also varied. The trap emission rates can be measured by the DLTS apparatus in such a way that the output is maximum when a rate window set on the apparatus is equal to the capture rate of the trap. This gives rise to a DLTS spectrum, the peaks of which correspond to trap energy levels. The energy level of the trap, E_t , can be obtained from the experimental data using Eq. [1]. The trap concentration can be obtained from the magnitude of the DLTS peak and calibration of the measurement system, while the capture cross section can be obtained by a method already described by Lang (7).

Results

Figure 1 shows a complete DLTS run for a group 1 sample (after boron predeposition from a borosilicate glass source). Four majority carrier deep levels are present as the peaks show. By injecting holes into the N-region using a forward biasing pulse, a minority carrier trap was also detected. The energy levels, capture cross

sections, and trap concentrations were accurately obtained for peaks II, III, IV. The data for all the traps are shown in Table I. After the boron drive-in diffusion, the deep levels are still present, but have been severely reduced in concentration as Fig. 2 shows for group 2 samples. Similarly, after the POCl_3 predeposition (group 3), all the levels remain (Fig. 2) except for the level at $E_c - 0.55$ eV. The level at $E_c - 0.12$ eV appeared to have in-

Table I. Deep levels in a group 1 sample (boron predeposition)

DEEP LEVEL	I	III	IV	V	II
Activation Energies E_T (eV) ± 0.03	$E_c - 0.12$	$E_c - 0.26$	$E_c - 0.36$	$E_c - 0.55$	$E_v + 0.23$
Defect Density N_{TT} (cm^{-3})		1.88×10^{12}	6.06×10^{12}	9.05×10^{12}	
Capture Cross-section σ_n (cm^2)		1.67×10^{-16}	2.2×10^{-16}	1.85×10^{-16}	

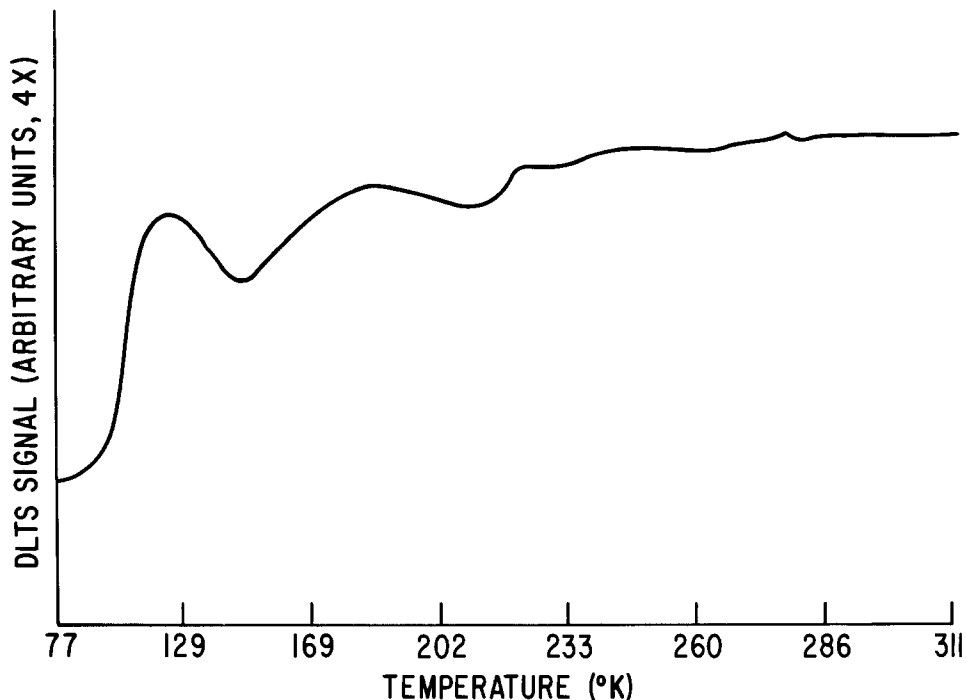


Fig. 3. DLTS spectrum for a group 3 sample (after POCl_3 predeposition) showing reduced concentration of deep levels.

creased at this point and is now the most dominant level. The same seems to be true after the final thermal oxidation step (group 7), as the DLTS spectrum in Fig. 4 shows.

Minority carrier lifetime values were obtained for samples from all groups using the open-circuit voltage decay technique (9). The effect of basewidth limitation of the lifetime was taken into consideration using the expression (9, 10)

$$\frac{1}{\tau_{\text{eff}}} = \frac{1}{\tau} + \frac{1/(W^2)}{2D} \quad [2]$$

where τ_{eff} is the measured lifetime, τ is the actual carrier lifetime, and $(W^2/2D)$ is the charge carrier transit time within the N region of the diode. W is the width of the N region, and D is the carrier diffusion coefficient. The resulting lifetime values are shown in Table II. An increase in lifetime with successive processing steps can be seen. This is in agreement with the reduction in deep level defect concentrations described above.

Discussion

The deep levels found after predeposition from the borosilicate glass source is due to the damage done by stresses caused by the high concentration of boron atoms at the surface ($2.5 \times 10^{20} \text{ cm}^{-3}$). These stresses result in the formation of defects other than those normally formed at these temperatures (such as simple vacancies). Other defects that may form at high boron concentrations are, for example, boron-vacancy pairs and divacancies. In fact, the results of ion bombardment and electron irradiation (3-5, 11, 12) show that some of the deep levels detected are identical to the energy levels for process-induced defects. For example, the level at $E_c - 0.26 \text{ eV}$ (this work) has been associated with the doubly negatively charged state of a divacancy (5). Another level usually found in electron-irradiated silicon is the level at $E_c - 0.17 \text{ eV}$ (close to our observed level at $E_c - 0.12 \text{ eV}$), which has been associated with oxygen-vacancy pairs (O-V). Other levels have been associated with hydrogenic dopant-vacancy pairs, such as Sb vacancy pair ($E_c - 0.39$

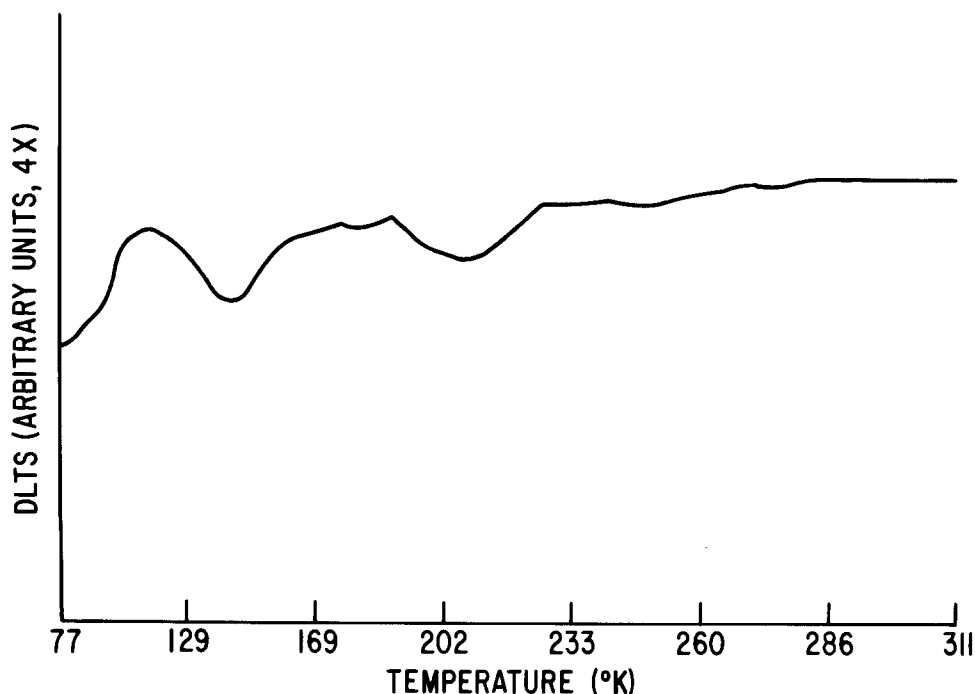


Fig. 4. DLTS spectrum for a group 7 sample (after thermal oxidation) showing reduced concentration of deep levels.

Table II. Carrier lifetime as a function of processing step

GROUP	1	2	3	4	5	6	7
Prior Processing Steps	Boron Predep	Boron Predep Boron Drive	Boron Predep Boron Drive POCL ₃ Predep	Boron Predep Boron Drive POCL ₃ Predep Phos. Drive	Boron Predep Boron Drive POCL ₃ Predep Phos. Drive Borofilm Getter	Boron Predep Boron Drive POCL ₃ Predep Phos. Drive POCL ₃ Getter	Boron Predep Boron Drive POCL ₃ Predep Phos. Drive POCL ₃ Getter Therm. Oxidation
Lifetime (μs)	5.96-14.8	12.82-18.46	36	36	36	36	36

eV), arsenic-vacancy pair ($E_c - 0.42$ eV). Our measured level at $E_c - 0.36$ may be due to a defect of this type, possibly a boron-vacancy complex. A level at $E_c + 0.23$ eV has also been found in electron-irradiated silicon and has been suggested to be created by annealing above 225°C (12). Finally, the level at $E_c - 0.55$ eV is also found in electron-irradiated silicon and has been associated with a divacancy (12). Sah *et al.* has also shown that this level can be found in silicon whose surface has been mechanically lapped.

The fact that these defect levels are severely reduced by the subsequent processing steps is in conformity with the annealing properties of the defects discussed above. All of these defects (5) have been found to anneal out at temperatures of 700°C or higher. All the processing steps subsequent to the predeposition are at these high temperatures (~1000°C) which annealed out the defects created by the predeposition. The increase in the carrier lifetime with the processing steps is also in agreement with an annealing out of these defects.

Sah (2) indicated that a very slow cooling rate of about 0.42°C/min, from the diffusion temperature, is required for annealing out the defects. The cooling rate in our furnace was 1°C/min. The defects created by the predeposition were not annealed out by the predeposition cooling however, possibly due to a higher concentration of boron in our experiments. This, nonetheless, indicates that a much lower cooling rate is necessary to anneal out defects created by diffusion processes. Even if the defects are not annealed out during the cooldown from the boron predeposition, our results show that the subsequent processing steps will anneal them out.

Summary

It has been shown that high temperature diffusion from a borosilicate glass source results in high concentrations of deep levels. These levels, at $E_c - 0.12$, $E_c - 0.26$, $E_c - 0.55$, and $E_v + 0.23$, were found to be annealed out by the subse-

quent processing steps that lead to device fabrication. A corresponding increase in carrier lifetime with successive processing steps was observed. These defect levels were shown to be similar to those measured in ion- or electron-bombarded silicon, indicating that they may be due to stresses caused by the high boron concentration, resulting in the formation of complex defects.

Acknowledgment

We would like to acknowledge the help of Dr. E. Sun, with whom part of this work was initially started, and also the assistance of Mr. S. Bevacqua, who supervised some of the high temperature operations.

Manuscript submitted Sept. 7, 1983; revised manuscript received Jan. 15, 1984.

General Electric Company assisted in meeting the publication costs of this article.

REFERENCES

1. L. D. Yau and C. T. Sah, *Solid State Electron.*, **17**, 193 (1974).
2. C. T. Sah and C. T. Wang, *J. Appl. Phys.*, **46**, 1767 (1975).
3. A. O. Evwaraye and E. Sun, *ibid.*, **47**, 3776 (1976).
4. K. L. Wang, Y. H. Lee, and J. W. Corbett, *Appl. Phys. Lett.*, **33**, 547 (1978).
5. J. Garrido, E. Calleja, and J. Piquera, *Solid State Electron.*, **24**, 1121 (1981).
6. J. J. Steslow, J. E. Rapp, and P. L. White, *Solid State Technol.*, **18**, 31 (1975).
7. D. V. Lang, *J. Appl. Phys.*, **45**, 3023 (1974).
8. G. L. Miller, D. V. Lang, and L. C. Kimerling, *Ann. Rev. Mater. Sci.*, **7**, 377 (1977).
9. S. K. Ghandhi, "Semiconductor Power Devices," John Wiley and Sons, New York (1977).
10. S. K. Ghandhi, "Theory and Practice of Microelectronics," John Wiley and Sons, New York (1968).
11. J. E. Walker and C. T. Sah, *Phys. Rev. B*, **7**, 17, 4587 (1973).
12. E. Sun, unpublished results.

Boron and Phosphorus Determination in Low Resistivity Solar-Grade Silicon

L. P. Hunt,* R. W. Francis,* and J. P. Dismukes*

Exxon Research and Engineering Company, Clinton, New Jersey 08801

ABSTRACT

A technique is developed to analyze boron and phosphorus concentrations in silicon by determining net carrier concentrations from Hall-effect measurements. The goal of the technique is to measure these impurities in purified metallurgical silicon (PMS) which is to be ultimately used for fabricating solar cells. Net carrier concentrations are measured on two wafers cut from a second-generation Czochralski ingot pulled from PMS. Boron and phosphorus concentrations in the PMS and the ingots are calculated from the net carrier concentrations by applying the segregation equations of the impurities. The accuracy of the boron measurements between 1 and 30 ppma is equivalent to that obtained on similar samples analyzed by multiple-pass float zoning. Phosphorus levels can be measured down to about 20% of that of the boron concentrations. Excellent precision of the Hall-effect technique is demonstrated. Sensitivity calculations show that net carrier concentration is the most critical parameter affecting the accuracy of the method. Overall, the technique is considered to be sufficient for making quality-control decisions with respect to boron and phosphorus levels in PMS and ingots grown from it.

The analytical technique described herein was developed to measure the concentrations of boron and phosphorus in a special grade of silicon for use in photovoltaic applications. This particular grade of silicon is, or has been, the focus of research and development programs (1, 9) with the common goal of increasing the purity of silicon that is metallurgically produced by the carbothermic reduction of silica in an arc furnace. The specific research and development programs involve some combination of the following procedures: (i) silicon of greater than 99% purity, produced from high purity raw materials and high purity arc-furnace operations, is upgraded by (ii) recrystallization from solution, (iii) slagging, (iv) acid leaching, and/or (v) gas blowing (10). This grade of silicon undergoes further purification via impurity segregation during certain forms of crystal growth which ultimately yield a material suitable for fabrication into solar cells.

A survey of Ref. (1-9) shows that PMS, before crystal growth, has the following general composition expressed in parts per million atomic (ppma): $1 < \text{Al} < 100$, $1 < \text{B} < 10$, $1 < \text{Fe} < 100$, $0.3 < \text{P} < 5$, and $\text{M} < 5$, where M stands for other transitional-series metals. Alkali and alkaline earth impurities are not considered to be significant since they vaporize from the silicon melt during crystal growth. The concentrations of Al, Fe, and transition metals can be measured by several analytical techniques such as atomic absorption or emission, x-ray fluorescence, and spark-source mass spectroscopy. However, none of the above techniques were found to provide reliable analyses for boron of about 1 ± 0.2 ppma or for phosphorus at somewhat lower concentrations.

The technique described below for determining boron and phosphorus is somewhat analogous to that used in the semiconductor industry for analyzing polysilicon produced by the Siemens process. The concentrations of boron and phosphorus in semiconductor polysilicon are calculated from resistivity measurements made on the one-pass and seven-pass sections of a multiple float-zone silicon rod (11). In the simplest float-zone case, one-pass resistivity is related to net carrier concentration [B]-[P], whereas the seven-pass resistivity is a measure of the boron concentration, [B], only. The concentration of the two impurities in polysilicon can be calculated by appropriately using (12) their segregation coefficients in the solution of two simultaneous equations involving net carrier concentration.

Purified metallurgical silicon is also subjected to crystal growth. Therefore, subsequent electrical measurements will allow calculation of the boron and phosphorus concentrations. A Czochralski (CZ) ingot that is grown from PMS is polycrystalline and can contain aluminum in

addition to boron and phosphorus. Therefore, a second-generation CZ ingot is grown from the first ingot. Since the second-generation ingot contains no measurable concentration of aluminum, Hall-effect measurement of the net carrier concentration is made on wafers cut from both the seed and tang ends of this second-generation ingot. Actual boron and phosphorus concentrations in both ingots and in the PMS can then be calculated from the net carrier concentrations. The calculations involve the positions along the ingot at which the net carrier concentrations were measured and the segregation coefficients of the two impurities.

The next section demonstrates the computational method for relating net carrier concentrations to those of boron and phosphorus. The theory and reason for Hall-effect measurements are also discussed.

Experimental

Hall-effect measurements.—Hall-effect measurements provide two valuable pieces of information for characterizing semiconductors that are not available from electrical resistivity measurements alone: majority carrier mobility and concentration. The latter equals the difference in the acceptor and donor concentrations and is relevant to this work provided the donors and acceptors are electrically active, *i.e.*, exist neither as neutral ion pairs nor as precipitated phases.

The principle of the technique (13) is to apply a magnetic field at right angles to a current flowing through a triple H-shaped sample of p- or n-type silicon. The generated electric field, E_H , is orthogonal and proportional to both the current density and the magnetic field. The Hall voltage associated with E_H is

$$V_H = \frac{RIB}{W} \quad [1]$$

where R is the Hall coefficient, I the current, B the magnetic field, and W the sample thickness. Calculation of the Hall coefficient from V_H and W permits the net majority carrier concentration to be calculated from

$$[\text{P}] = \frac{r_p}{Rq} \text{ or } [\text{n}] = -\frac{r_n}{Rq} \quad [2]$$

for p- or n-type samples, respectively. In the above equations, q is the electronic charge, and r is the Hall factor which depends on the band structure and the mechanism of carrier transport and scattering in a particular semiconductor. For silicon at room temperature, the p-type Hall factor is 0.71, while the n-type factor is 1.18, *i.e.*, $3\pi/8$ (14).

Under the assumption that all impurities are electrically active, the net carrier concentration determined from Eq.

*Electrochemical Society Active Member.

Key words: impurity, photovoltaic, solidification.

[1] and [2] equals the net ionized impurity concentration |B-P|. Sensitivity analysis indicates an experimental precision of within 5% in obtaining R in Eq. [1] and an accuracy in the determination of |B-P| from Eq. [2] of $\pm 10\%$. The latter stems primarily from a variation in the Hall factor with dopant density (15).

Computational procedure.—The translation of Hall-effect measurements into boron and phosphorus concentrations is more easily understood by first considering the mass flow of impurities from the PMS, through crystal growth, to the measured wafers. The mass flow of an impurity during crystal growth is determined by the segregation equation (16)

$$C = C_0 k_{\text{eff}} (1 - g)^{(k_{\text{eff}}-1)} \quad [3]$$

where g is the fraction of the melt solidified, C and C_0 are the impurity concentrations at points g and $g = 0$, respectively, and k_{eff} is the effective distribution coefficient of the impurity (17). It is convenient to rearrange Eq. [3] into a more general form involving relative concentrations

$$C/C_0 = k_{\text{eff}} (1 - g)^{(k_{\text{eff}}-1)} \quad [4]$$

The variation of C/C_0 for boron as a function of g is shown in Fig. 1 for $k_{\text{eff}} = 0.80$ (18).

The computational procedure being developed here also involves use of the average relative impurity concentration between two points, g_1 and g_2 , in an ingot. This is obtained by integrating Eq. [4]

$$\overline{C/C_0} = \frac{1}{g_2 - g_1} \int_{g_1}^{g_2} k_{\text{eff}} (1 - g)^{(k_{\text{eff}}-1)} dg \quad [5]$$

$$\overline{C/C_0} = \frac{1}{g_2 - g_1} [(1 - g_1)^{k_{\text{eff}}} - (1 - g_2)^{k_{\text{eff}}}] \quad [6]$$

The variation of $\overline{C/C_0}$ with g is also shown in Fig. 1 for boron.

The mass flow of impurities can be visualized with the aid of the mass flow diagram in Fig. 2. Purified metallurgical silicon is loaded into a Czochralski puller and polycrystalline ingot CZ1 is grown.¹ The seed and tang ends of the ingot are cropped at positions g_1 and g_2 , respectively. The cropped ingot becomes the melt for a second CZ growth in which ingot CZ2 is produced. Ingot CZ2 is cropped at positions g_3 and g_4 and then wafers are cut from the seed and tang ends. Wafers cut at positions g_{w1} and g_{w2} are used in the Hall-effect measurements. The growth and processing of the nominally 11 cm diam ingots used in this work were performed at Solar Power Corporation.

The following equations are developed considering the flow of boron from the initial PMS to the final wafers

¹Impurity segregation is no longer described by these equations when crystallite sizes are less than about 1 mm.

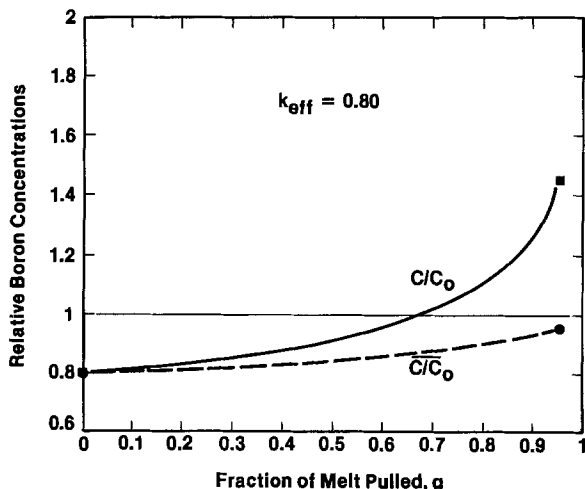


Fig. 1. Variation of boron concentration with fraction of the melt solidified.

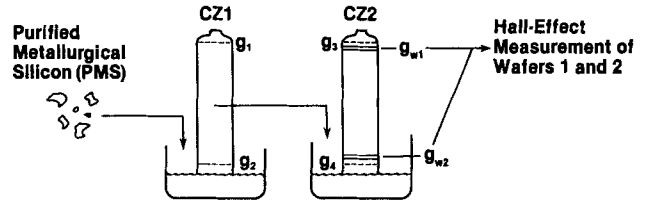


Fig. 2. Mass flow diagram for impurities from PMS through wafers for Hall-effect analysis.

used for analysis. Similar equations apply to phosphorus, or to any other impurity.

The average boron concentration in PMS is the initial boron concentration in the melt for CZ1

$$\overline{B}_{\text{PMS}} = B^0_{\text{CZ1}} \quad [7]$$

The average boron concentration in CZ1, between points g_1 and g_2 , can be calculated from the initial melt concentration by using Eq. [6]

$$\overline{B}_{\text{CZ1}} = B^0_{\text{CZ1}} \cdot (\overline{B/B_0})_{\text{CZ1}} \quad [8]$$

Since cropped ingot CZ1 is used to charge the crucible for the second crystal growth step, then

$$B^0_{\text{CZ2}} = \overline{B}_{\text{CZ1}} \quad [9]$$

The average boron concentration in ingot CZ2, between points g_3 and g_4 , is calculated in the same way as was done for ingot CZ1

$$\overline{B}_{\text{CZ2}} = B^0_{\text{CZ2}} \cdot (\overline{B/B_0})_{\text{CZ2}} \quad [10]$$

Equations [7], [8], and [10] provide the average boron concentrations in PMS, CZ1, and CZ2. These are now related to the Hall-effect measurements on wafers w_1 and w_2 through the initial CZ2 melt concentration, B^0_{CZ2} . The boron concentration of a wafer, w , at point g_w is

$$B_w = B^0_{\text{CZ2}} \cdot (B/B_0)_w \quad [11]$$

It is now possible to set up two simultaneous equations in order to determine the concentrations of both boron and phosphorus. Since the Hall-effect technique measures net carrier concentration, n , then

$$B_{w1} - P_{w1} = n_{w1} \quad [12]$$

$$B_{w2} - P_{w2} = n_{w2} \quad [13]$$

By substituting Eq. [11] and its phosphorus equivalent into Eq. [12] and [13], one can calculate the concentration of both impurities in the initial CZ2 melt

$$B^0_{\text{CZ2}} \cdot (B/B_0)_{w1} - P^0_{\text{CZ2}} \cdot (P/P_0)_{w1} = n_{w1} \quad [14]$$

$$B^0_{\text{CZ2}} \cdot (B/B_0)_{w2} - P^0_{\text{CZ2}} \cdot (P/P_0)_{w2} = n_{w2} \quad [15]$$

In summary, the Hall-effect technique for determining the concentrations of boron and phosphorus consists of (i) measuring net carrier concentration of wafers from the seed and tang ends of a second-generation CZ ingot, (ii) solving Eq. [14] and [15] for the initial impurity concentrations in this ingot, and (iii) calculating the average impurity concentrations in the polysilicon, first-, and second-generation ingots from Eq. [7], [8], and [10].

The complete analysis for boron and phosphorus requires eight pieces of data: g_1 , g_2 , g_3 , g_4 , g_{w1} , g_{w2} , n_{w1} , and n_{w2} .

All the following calculations use $k_{\text{eff}} = 0.80$ for boron and $k_{\text{eff}} = 0.35$ for phosphorus (18).

Results

Accuracy.—Various grades of PMS were used for analysis. Their purity varied over a considerable range depending upon the quality of the raw materials used in their preparation, the conditions under which the arc furnace was operated, and the additional refining steps that were employed. Some of the materials were obtained from commercial vendors. One of the samples differed

substantially from the others: p-type semiconductor silicon was boron doped by adding a weighed amount of boron to the silicon in an attempt to provide a "standard."

Hall-effect measurements were compared to float-zone analyses performed at Hemlock Semiconductor Corporation. A third sequential CZ-growth step provided a 25 mm diam rod for float zoning. Resistivity data supplied by Hemlock Semiconductor were used to calculate average concentrations in a manner similar to that already outlined above. The resistivity values were converted to concentrations using the recently reported correlations by Thurber *et al.* (19). Their data show a maximum deviation of 68% at 0.07 Ω -cm from Irvin's curves (20). Deviations exceed 10% for resistivities between 0.004 and 0.7 Ω -cm.

Eight measurements must be made per Hall-effect analysis, as described earlier. The range of each measurement is presented in Table I.

A comparison of Hall-effect analyses with those from multiple-pass float zoning appear in Table II. The data are arranged according to increasing boron concentration. In the case of boron, Hall-determined concentrations generally agree well with those from float zoning when the errors of the analyses are considered. This agreement covers a range from about 1 to 30 ppma. It is important that the Hall technique provides accurate boron concentrations at the 1 ppma level since solar cell efficiency decreases significantly at concentrations exceeding this value. The actual weighed amount of boron added to the semiconductor silicon in sample 32 amounted to an average concentration in the ingot of 1.3 ppma. This value falls between the two analytically measured concentrations of 1.0 and 1.5 ppma.

Reasonable correspondence is found between the phosphorus concentrations using both analytical techniques. Lower concentrations, however, have a larger uncertainty associated with them. This is due to solving the simultaneous equations first for boron and then for phosphorus. In this procedure, errors propagate. "Less than" concentrations for the two methods result when calculations give a phosphorus that is slightly negative but close to zero when the error is considered. The data in Table II show that phosphorus can be determined down to about 10% to 30% of the boron concentration. Therefore, the

Table I. Range of measurements for Hall-effect analyses of boron and phosphorus

Measurement	Range
g_1, g_3	0*
g_2	0.70-0.88
g_4	0.62-0.80
g_{w1}	0.02-0.06
g_{w2}	0.37-0.74
n_{w1}, n_{w2}	1.3-24 ppma
ρ_{w2}, ρ_{w1}	~0.3-0.04 Ω -cm

* Assumes seed end not cropped.

Table II. Comparison of boron and phosphorus concentrations (ppma) from Hall-effect and float-zone techniques

Ingot number	Boron		Phosphorus	
	Hall-effect	Float-zone	Hall-effect	Float-zone
32*	1.5 \pm 0.2	1.0 \pm 0.2	0.1 \pm 0.2	0.3 \pm 0.1
59	2.1 \pm 0.8	3.0 \pm 0.6	<0.4	<0.6
65	2.9 \pm 0.6	3.4 \pm 0.7	<0.6	<0.7
44	7.2 \pm 0.6	7.6 \pm 1.1	1.8 \pm 0.7	1.9 \pm 0.5
46	9.8 \pm 1.8	9.7 \pm 1.3	2.7 \pm 2.2	3.0 \pm 0.8
19	13 \pm 3	11 \pm 2	4 \pm 4	<2
26	18 \pm 1	23 \pm 2	20 \pm 1	39 \pm 5
41	23 \pm 2	26 \pm 3	5 \pm 3	5 \pm 1
40	32 \pm 5	30 \pm 3	6 \pm 7	<6

* \bar{B}_{CZ2} = 1.3 ppma from actual weighed amounts of B and Si.

phosphorus concentration was set equal to 20% of the boron concentration when negative values were incurred.

Precision.—An indication of the precision of the Hall-effect technique was determined by growing three CZ1 ingots from the same batch of PMS. One additional CZ2 ingot was grown from each CZ1 ingot. Table III gives the results of the three Hall-effect analyses in terms of the average boron and phosphorus concentrations in PMS, CZ1, and CZ2. Precision is considered to be excellent.

Sensitivity.—Sensitivity calculations were carried out to determine the influence of the eight measured parameters on the derived boron and phosphorus concentrations. The effect on the calculated concentrations of making percentage changes in the parameters is indicated in Table IV. A 2% change in g values, which is considered to be the experimental error, results in \leq 1% change in boron and \leq 3% change in phosphorus. Therefore, errors in g values were not considered when calculating the errors given in Tables II and III.

The errors in Table III were determined by incorporating the estimated errors of the net carrier concentrations into the equations developed in the Experimental section. By adjusting the error in the net carrier concentrations, a value of $\pm 4\%$ was obtained that caused the boron concentration errors in Table III to agree with the spread in the absolute boron concentrations. Reported errors, then, are indicative of precision rather than accuracy.

Different values for the effective segregation coefficients of boron and phosphorus have been reported (18, 21-23). The sensitivity calculations in Table IV demonstrate that only a minor change in boron and phosphorus concentrations occur over the range of values of the segregation coefficient indicated.

Sensitivity calculations were performed for a given set of impurity conditions. Different errors are expected to occur in other circumstances.

Conclusions

Hall-effect analyses, performed on wafers cut from a second-generation CZ ingot pulled from PMS, provide an accurate measurement of boron and phosphorus concentrations, compared with those obtained from the multiple-pass float-zone method of analysis. Boron levels be-

Table III. Analyses (ppma) of second-generation CZ ingots grown from the same batch of PMS

	Silicon	Boron	Phosphorus
PMS-20		1.9 \pm 0.1	2.2 \pm 0.6
CZ1-74		1.7 \pm 0.1	1.1 \pm 0.3
CZ2-76		1.5 \pm 0.1	0.6 \pm 0.1
PMS-20		1.6 \pm 0.1	2.0 \pm 0.6
CZ1-75		1.5 \pm 0.1	1.2 \pm 0.2
CZ2-77		1.4 \pm 0.1	0.6 \pm 0.1
PMS-20		1.9 \pm 0.1	2.2 \pm 0.6
CZ1-82		1.7 \pm 0.1	1.2 \pm 0.3
CZ2-83		1.5 \pm 0.1	0.6 \pm 0.2

Table IV. Effect of parameter variations on the concentrations of boron and phosphorus (ppma) in second-generation CZ ingots

Parameter	% Change	(B)	(P)
Base case	—	1.48	0.58
g_1 or g_2	+2	1.49	0.59
g_3 or g_4	+2	1.48	0.58
g_{w1}	+2	1.48	0.58
g_{w2}	+2	1.47	0.56
n_{w1}	+4	1.58	0.65
n_{w2}	+4	1.45	0.54
$k_{eff}(B)^*$	+2.5	1.42	0.52
$k_{eff}(P)^{**}$	+14	1.56	0.66

* 0.80 \rightarrow 0.82.

** 0.35 \rightarrow 0.40.

tween about 1 and 30 ppma were determined with an average error of approximately $\pm 20\%$. The lower limit of phosphorus measurement is about 20% of that for boron.

The precision of the Hall-effect technique, as determined by analyzing multiple samples prepared from the same batch of silicon, was excellent at the low-ppma level for both impurities.

Sensitivity calculations demonstrate that measurement of net carrier concentration is the most critical parameter affecting the analyses.

The Hall-effect method of analyzing boron and phosphorus in PMS via CZ ingots produced from it, is sufficient at a pilot-plant scale of production for characterizing the quality of these materials with respect to their suitability for fabricating solar cells. This presumes knowledge of concentrations of other impurities from different analytical techniques.

Acknowledgments

Appreciation is extended to E. Shipp for performing Hall-effect measurements, to R. Sylvain of Solar Power Corporation for overseeing growth and processing of ingots, and L. Tarhay of Hemlock Semiconductor Corporation for coordinating float-zone analyses.

Manuscript submitted July 15, 1983; revised manuscript received Jan. 3, 1984. This was Paper 209 presented at the San Francisco, California, Meeting of the Society, May 8-13, 1983.

Exxon Research and Engineering Company assisted in meeting the publication costs of this article.

REFERENCES

1. F. N. Smith and R. K. Dawless, Abstract 477, p. 1147, The Electrochemical Society Extended Abstracts, Vol. 81-1, Denver, CO, Oct. 11-16, 1981.
2. L. P. Hunt and V. D. Dosaj, in "Second E. C. Photovoltaic Solar Energy Conference," R. Van Overstraeten and W. Palz, Editors, p. 98, D. Riedel Publishing Company, Boston (1979).
3. L. Pelosini, A. Parisi, and S. Pizzini, U.K. Pat. Appl. GB 2,036,708A (1979).
4. D. Helmreich and G. Ast., in "Electronic and Optical Properties of Polycrystalline or Impure Semiconductors and Novel Silicon Growth Methods," K. Ravi and B. O'Mara, Editors, p. 233, The Electrochemical Society Softbound Proceedings Series, Pennington, NJ (1980).
5. H. A. Aulich, K.-H. Eisenrith, H.-P. Urbach, and J. C. Grabmaier, Abstract 53, p. 88, The Electrochemical Society Extended Abstracts, Vol. 82-1, Montreal, Ont., Canada, May 9-14, 1982.
6. P. S. Kotval and H. B. Strock, U.S. Pat. 4,124,410 (1978).
7. J. Linnmayer and Z. Putney, in "Record of the 15th IEEE Photovoltaics Specialists Conference," p. 572, Institute of Electrical and Electronic Engineers, New York (1981).
8. Poly Solar, Inc., Final Report, Department of Energy Report DOE/ET/23048-T1 (1980).
9. F. Secco D'Aragona, H. M. Liaw, and D. M. Heminger, in "Materials and New Processing Techniques for Photovoltaics," J. A. Amick, E. Sirtl, P. Rai-Choudhury, and J. P. Dismukes, Editors, p. 119, The Electrochemical Society Softbound Proceedings Series, Pennington, NJ (1981).
10. D. Helmreich, E. Sirtl, and J. Dietl, in "Crystals, Growth, Properties, and Applications," Vol. 5, J. Grabmaier, Editor, p. 43, Springer-Verlag, Berlin (1981).
11. M. C. Arst, Final Report, Air Force Materials Laboratory Report AFML-TR-76-125 (1978).
12. L. D. Crossman, Personal communication.
13. W. R. Runyan, "Semiconductor Measurements and Instrumentation," p. 133, McGraw-Hill, New York (1975).
14. F. J. Morin and J. P. Maita, *Phys. Rev.*, **96**, 28 (1954).
15. J. F. Lin, S. S. Li, L. C. Linares, and K. W. Teng, *Solid-State Electron.*, **24**, 827 (1981).
16. W. G. Pfann, "Zone Melting," John Wiley & Sons, Inc., New York (1966).
17. J. A. Burton, R. C. Prim, and W. P. Slichter, *J. Chem. Phys.*, **21**, 1987 (1953).
18. F. A. Trumbore, *Bell Syst. Tech. J.*, **39**, 205 (1960).
19. W. R. Thurber, R. L. Mattis, Y. M. Liu, and J. J. Filliben, *This Journal*, **127**, 2291 (1980).
20. J. C. Irvin, *Bell Syst. Tech. J.*, **41**, 387 (1962).
21. H. F. Wolf, "Semiconductors," Wiley-Interscience, New York (1971).
22. H. R. Huff, T. G. Diggs, Jr., and O. B. Cecil, *J. Appl. Phys.*, **42**, 1235 (1971).
23. A. Murgai, in "Silicon Processing," D. C. Gupta, Editor, p. 39, Vol. STP 804, American Society for Testing and Materials, Philadelphia, PA (1983).

Compositional Analysis of Silicon for Solar Cells

Lee P. Hunt*

Exxon Research and Engineering Company, Clinton, New Jersey 08801

ABSTRACT

A potential route to silicon for solar cells involves using an improved version of the carbothermic process to give an intermediate product capable of being upgraded by chemical and physical means to an acceptable end product. The compositional analysis of these intermediate and end products is discussed from the viewpoint of someone who must make research and development or business decisions based on information supplied by analysts. Methods are discussed for analyzing dopants (B and P), metals (Al, Fe, and others), and nonmetals (C, O, and SiC). Adequate methods are available, except when trying to measure the sub-ppm concentrations of metals present in the final silicon product. A plan is suggested for developing a quality assurance method for the time when the industry grows to the extent of requiring its own source of silicon rather than by-products from the semiconductor industry.

This paper deals with the compositional analysis of silicon from a user's point of view. The user is one who must make decisions based on analytical data concerning the purity of silicon. Such decisions must be made at various stages in a product's life. At the research and development stage, rapid analytical results from established techniques are needed so that decisions can be made to guide the research and development program. These techniques are hopefully available from outside analytical houses which have low cost and fast turnaround services. However, these two attributes usually do not go hand-in-

hand with the accurate and low level analyses needed for high purity silicon.

Since this review is concerned with silicon for solar cells, a product very young in its evolutionary cycle, most of the analytical techniques described are those readily available. Limitations of present capabilities are noted and suggestions are made for further development of techniques.

Silicon solar cells are typically fabricated from wafers cut from single or polycrystalline ingots. These ingots may be grown from semiconductor-grade silicon (SeG-Si) manufactured using the Siemens C process, which in-

*Electrochemical Society Active Member.

volves the high temperature hydrogen reduction of very pure trichlorosilane. This silicon compound, in turn, is prepared by the hydrochlorination of 98% pure metallurgical-grade silicon (MG-Si). Since the cost of solar cells must be considerably reduced in order to penetrate large-scale markets, much attention has been focused on upgrading MG-Si using lower cost metallurgical procedures (1-4) compared to higher cost chemical methods, such as the chlorosilane routes. This paper more particularly discusses the use of various analytical techniques for analyzing the composition of metallurgically processed silicon.

The compositional analysis of two grades of silicon are considered. Purified metallurgical silicon (PMS) is defined as the product of the carbothermic reduction of silica in an arc furnace under purer-than-normal conditions. This silicon can be upgraded by various chemical and physical techniques, e.g., acid leaching, slagging, directional solidification, etc., to produce a material of sufficient quality to be directionally solidified under conditions which provide for the effective segregation of impurities. The final ingot, called solar-grade silicon (SoG-Si), can be cut into wafers for solar cell fabrication. Table I shows typical impurity concentrations in PMS and SoG-Si based upon data reported in the literature.

The most important impurities in PMS and SoG-Si have been categorized for ease of discussion. Boron and phosphorus are the most common dopants, as well as the most difficult impurities to remove from silicon. This is because their segregation coefficients between liquid and solid silicon are very close to unity.

Of the metal impurities, aluminum and iron are treated separately because of their typically higher concentrations in PMS. This results from their common occurrence in raw materials as well as the construction materials used in metallurgical processing. Although aluminum is a dopant, its concentration in SoG-Si is lower than that of boron and phosphorus because it is easily removed both chemically and physically. In addition, only about 10% of the aluminum in silicon is electrically active. Even though the chemical methods of removing iron from silicon are not as numerous as those for aluminum, the concentration of iron can be reduced significantly during directional solidification because of iron's favorable segregation coefficient.

Other metal impurity concentrations in PMS can also be reduced to a great extent during directional solidification since their segregation coefficients are in the general range of 10^{-5} to 10^{-8} . The most important of these impurities are the lifetime killers such as Mo, Ti, V, and Zr. Fortunately, the most severe lifetime killers are the ones with the smallest segregation coefficients.

The remaining category of impurities is that of the non-metals. Included in this group is interstitial oxygen, and its various forms of precipitates, substitutional carbon, and silicon carbide as a second-phase material. Oxygen and carbon are important with respect to their influence on structural defects in crystalline SoG-Si. Silicon carbide particles can cause formation of twin planes during crystal growth and also can act as nucleation sites for impurities that lead to shunting of solar cells.

Boron and Phosphorus

Hall effect and float zone.—There are only two methods that appear to be reliable enough to provide accurate, precise analyses for boron and phosphorus at concentrations covering the range from sub-ppma to about 100 ppma. These are the float-zone, resistivity method that is traditionally used for evaluating semiconductor-grade polycrystalline silicon, and the Hall-effect technique (5).

The correlation between boron concentrations measured by these two methods is shown in Fig. 1. A least squares fit to the logarithm of the concentrations shows a slope of 0.94 and a Y-intercept of 0.04 for boron data covering a range of about 1 to 30 ppma. The square of the correlation coefficient indicates that 96% of the variation in the Hall boron concentration is explained by the re-

Table I. Concentrations of impurities reported in purified metallurgical silicon and SoG-Si

Impurity	Impurity concentration (ppmw)	
	PMS	SoG-Si
Al	50-500	0.005-0.05
B	0.1-10	0.1-10
C	50-100	0.5-1
Fe	50-100	<<1
Other metals	1-10	<<1
O	5-20	10-20
P	0.1-10	0.02-2
SiC	100-300	<1

gression equation. Although the Hall-effect method has not been tested in the sub-ppma range, it is projected to be an even more accurate method than the established float-zone technique (5).

Phosphorus is determined simultaneously with boron since the Hall effect measures the difference in net impurity concentration. Phosphorus was determined in the same silicon samples, as indicated above for boron, to ascertain the correlation between the Hall-effect and float-zone methods. Data are presented in Fig. 2 for fewer samples than for boron since phosphorus cannot be measured by either method to concentrations less than 20% of the boron concentration. The slope of the log-log plot is 1.08 with a Y-intercept of -0.21 . The square of the correlation coefficient is 0.94 for only five data points covering a phosphorus concentration range of about 0.1 to 20 ppma. As with boron, further work is required to establish that the method can be applied to even lower concentrations; prospects seem favorable.

Spark-source mass spectroscopy (SSMS).—SSMS provides a multielement analysis. However, its success strongly depends on the capability and skill of the analyst. Expertise developed within semiconductor companies for sparking directly to a solid silicon sample provides the greatest sensitivity (~ 0.01 ppma), provided that the equipment is dedicated to high-purity silicon. Even then, the difficulty in establishing accurate sensitivity factors to relate line intensities to concentrations results in analyses of boron and phosphorus that are lower than concentrations obtained by electrical resistivity measurements. A special method using silicon powder mixed with gallium has been reported (6). Another variation of this method, as performed by most commercial analytical laboratories, involves sparking dry graphite that contains the silicon sample previously dissolved in acid. This method has a sensitivity of about 0.01–0.5 ppma, depending upon the analyst, and also requires ultrapure acids and graphite.

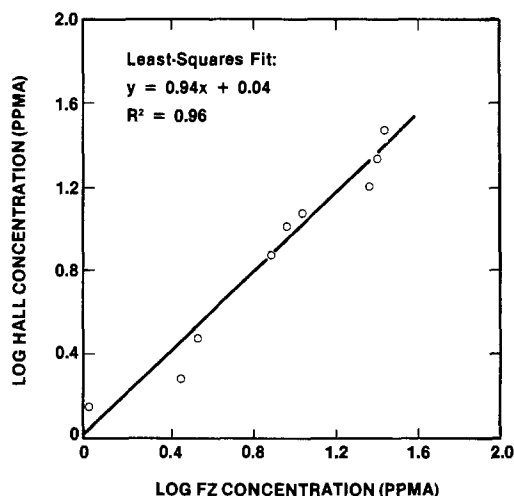


Fig. 1. Correlation of boron analyses by Hall-effect and float-zone methods.

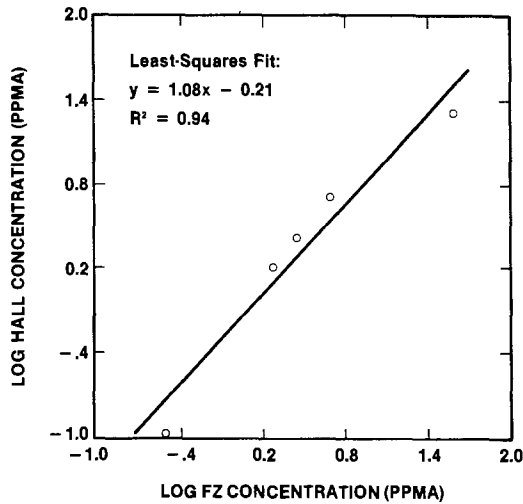


Fig. 2. Correlation of phosphorus analysis by Hall-effect and float-zone methods.

A comparison of the analysis of equivalent Czochralski wafers by the Hall-effect method and SSMS is shown in Fig. 3 for boron concentrations between 0.01 and 17 ppma. The SSMS concentrations are on the average about six times lower than equivalent Hall-effect concentrations. A comparison between two labs of equivalent silicon samples analyzed by SSMS for boron is provided in Fig. 4. The ratio of the concentrations reported by the two labs ranges from 0.07 to 3 for boron concentrations in the range of 0.4 to 8 ppma, as determined from resistivity measurements on single-crystal samples.

Similar comparisons are made for phosphorus analyses. The ratio of concentrations determined by the Hall-effect and SSMS methods are given in Fig. 5 for a relatively small range of phosphorus concentrations (1-6 ppma). The SSMS values are on the average three times lower than the Hall-effect concentrations, which agree with resistivity measurements. A comparison of determinations made by different labs on seven equivalent, phosphorus-doped samples gave a ratio of their concentrations that ranged from 0.5 to 20. These samples covered phosphorus levels from 1 to 30 ppma (Fig. 6).

SSMS has adequate sensitivity for measuring boron and phosphorus concentrations in silicon for solar cell applications. However, the method appears to have neither sufficient accuracy nor precision.

Emission spectroscopy (ES).—In the early stages of many research and development programs, emission spectroscopy has been used to analyze silicon because it is a widely available service that provides a fast multielement scan at reasonable cost. The method is capable of providing reliable data concerning order-of-magnitude changes in concentrations; it can be misleading for determination of smaller changes in impurity levels. ES data have been reported on the repeated analy-

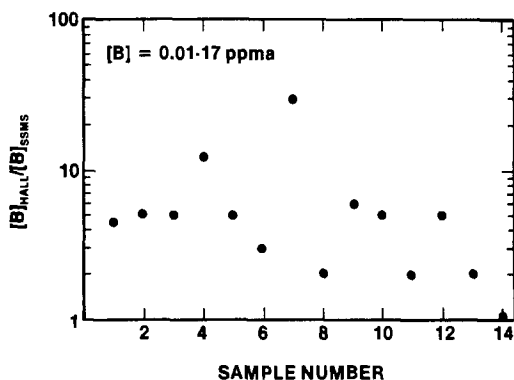


Fig. 3. Ratio of boron concentrations measured by Hall-effect and SSMS.

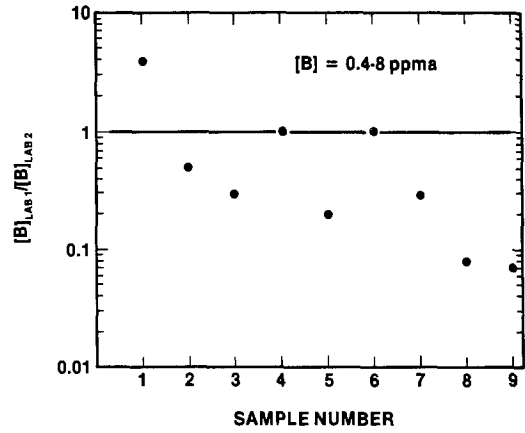


Fig. 4. Ratio of boron concentrations measured at two laboratories using SSMS.

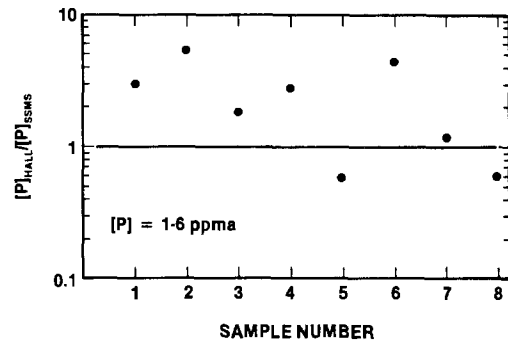


Fig. 5. Ratio of phosphorus concentrations determined by Hall effect and SSMS.

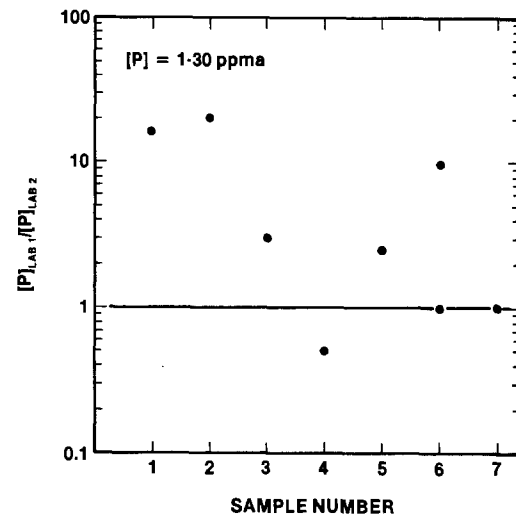


Fig. 6. Ratio of phosphorus concentrations measured at two laboratories using SSMS.

sis of a powdered MG-Si sample that was used as a standard by which to compare other ES analyses of purified MG-Si (7). The data, summarized in Fig. 7 for 37 analyses, show the concentration of boron to range from 23 to 240 ppma. The mean concentration of 96 ppma has a standard deviation of ± 61 ppma. This one-sigma value statistically implies that any given analysis has a 68% chance of falling within the range of 96 ± 61 ppma. For more exact work, the two-sigma standard deviation (95% probability) puts the mean boron concentration at 96 ± 121 ppma, indicating that any measured boron concentration has a greater than 100% error associated with it. For an impurity as important as boron, this error size is unacceptable. In addition, the lower limit of detection of about 3-30 ppma boron in silicon is not low enough for the 0.1-1 ppma upper concentration levels allowable for SoG-Si.

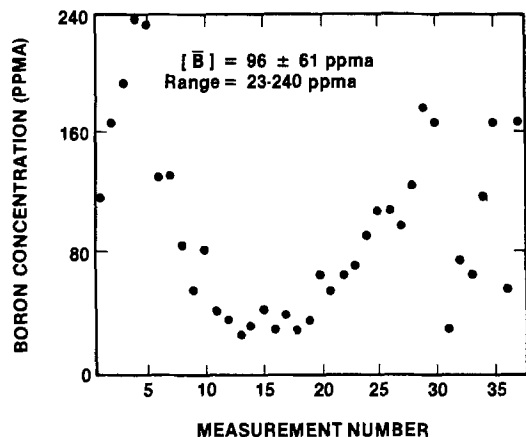


Fig. 7. Multiple ES analyses of boron in a standard MG-Si sample

Phosphorus cannot be determined by ES at concentrations less than about 1000 ppma. The values reported by most analytical labs involve use of a separate spectrophotometric measurement of the blue phosphomolybdate complex. Multiple analyses of the powdered MG-Si standard (7) using this method are summarized in Fig. 8. The mean is 42 ± 26 ppma for values that ranged from 2 to 140 ppma. This spectrophotometric method is neither sensitive nor accurate enough to be used for phosphorus determination in silicon intended for photovoltaic applications.

Other methods.—Boron determination in silicon down to 0.1 ppma has been reported using inductively coupled plasma emission spectroscopy (ICP-ES) (8). In order to reach this low level, silicon must be volatilized from the dissolved sample. This requires special chemical treatment to prevent boron loss from the sample along with the silicon. X-ray fluorescence spectrometry (XRFS) cannot be used to determine boron because of its low atomic number.

Preliminary analyses of silicon for phosphorus using ICP-ES showed a detection limit of about 0.1 ppma. However, sufficient data were not available to draw firm conclusions. Further work on this technique is warranted. XRFS, which can measure phosphorus concentrations down to about 10 ppma, is insufficient for solar silicon needs.

Aluminum, Iron, and Other Metals

As mentioned earlier, Al and Fe differ from the other metal impurities because of their much higher concentrations in PMS. Titanium is used below as a representative of the other lower concentration metal impurities.

The overall analytical picture for metal impurities is similar to that for B and P. Emission spectroscopy has a detection limit of about 10 ppmw and also has a large er-

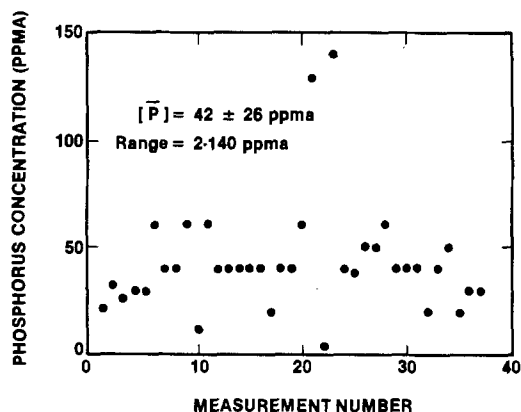


Fig. 8. Multiple ES analyses of phosphorus in a standard MG-Si sample.

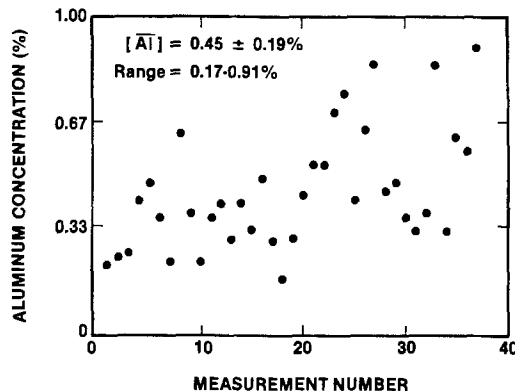


Fig. 9. Multiple ES analyses of aluminum in a standard MG-Si sample

ror associated with each analysis. Analyses of the MG-Si standard, described in the previous section, are shown in Fig. 9 for aluminum (7). Measured concentrations ranged from 1700 to 9100 ppmw with a mean and one standard deviation of 4300 ± 1900 ppmw. Equivalent data for iron were 8100 ± 2500 over a range of 5,000 to 15,000 ppmw (0.5%-1.5%); and for titanium, 440 ± 210 ppmw over a range of 40 to 1300 ppmw.

XRFS has not been investigated in as much detail, but the method is expected to give detection limits similar to that of ES.

Metal concentrations in various grades of silicon were analyzed using SSMS by two service laboratories. The results are summarized in Table II. The ratio of a concentration reported by Lab 1 to that reported by Lab 2 varied by as much as a factor of ten. In the case of titanium, Lab 1 provided a detection limit in the sub-ppmw range. However, it is pointed out that this sensitivity level was achieved under research and development-type conditions, as opposed to commercial-laboratory conditions, as indicated by equivalent Lab 2 data. In any case, titanium and other metal impurities were below the detection limit of SSMS performed at both laboratories. In summary, SSMS is adequate for indicating the general level of metal concentrations in PMS. It can also be used to check for possible metal contamination in SoG-Si, but cannot absolutely measure the very low level of metal concentrations that can affect solar cell efficiency (9).

The analyses in Table II show Al and Fe concentrations of 1-10 ppmw in wafers cut from ingots grown from MG-Si under different crystal-growth conditions. These concentrations are, at first glance, much higher than would be expected since segregation of Al and Fe is very effective during crystal growth. These concentrations have been confirmed using ICP-ES. Ward has reported up to almost 1 ppmw Fe as FeSi_2 precipitates in Czochralski wafers used in device production (10). The source of such iron is uncertain, as is also the case for aluminum. Since iron at the 1 ppmw level would severely degrade solar cell efficiency, the absence of degradation suggests that iron must be effectively removed in get-

Table II. Comparison of SSMS analyses from two laboratories

Silicon grade	SSMS impurity concentration (ppmw)					
	Al		Fe		Ti	
	Lab 1	Lab 2	Lab 1	Lab 2	Lab 1	Lab 2
MG-Si	7000	>1000	1000	1000	700	200
	3000	>1000	500	1000	700	1000
	200	>1000	1500	1000	30	20
	150	>1000	1000	> 1000	30	100
	4000	>1000	300	> 1000	7	5
MG-Si, 1 Cz	15	10	7	1	< 2	< 1
MG-Si, 2 Cz,	1	5	10	2	< 0.07	< 1
1 Fz	2	5	3	1	< 0.07	< 1
	1	5	3	2	< 0.07	< 1
SeG-Si	0.3	—	3	—	< 0.07	—

tering steps during solar cell processing. Further work is required to elucidate this problem.

ICP-ES has been used to determine metal concentrations at levels around the 0.1 ppmw level. The real capabilities of the technique remain to be established.

Nonmetals

Carbon and oxygen.—The same infrared technique used to measure C and O concentrations in SeG-Si can also be used for analyzing various grades of recrystallized PMS. A limitation exists for solar grades of silicon since silicon becomes opaque to infrared radiation when the boron concentration in it exceeds about 3–4 ppma.

Fourier transform infrared (FTIR) spectroscopy was used at room temperature to compare the C and O levels in PMS and SeG-Si recrystallized using Czochralski, Bridgman, and float zoning methods (11). Most of the data compared in Table III are averages from between 10 to 30 analyses of wafers cut from ingots; only limited data were available from Bridgman samples. When SeG-Si was the starting material, carbon levels were < 1 ppma. Oxygen concentrations were about 10 ppma in samples grown from crucibles, and < 1 ppma for float-zoned material. When PMS was the starting material, oxygen concentrations were again about 10 ppma because of the crucible, which contained the silicon during crystal growth. The complex topic of precipitated oxygen is purposely not dealt with in this paper. Carbon levels were about 15 ppma in once-crystallized ingots, and about 2 ppma in twice-crystallized Czochralski material, as would be predicted from carbon's segregation coefficient of 0.07. Carbon concentrations are higher in ingots from PMS than SeG-Si since PMS comes directly from a carbothermic reduction process.

Carbon cannot be determined in pure silicon using combustion techniques in the manner that they are usually practiced for other materials. These methods involve burning of a sample to form CO₂, which is measured in various ways in different equipment. Although the techniques are used to determine carbon in silicon alloys of lower silicon content, some unidentified problem, e.g., incomplete combustion, results in erratic results for high silicon alloys. Table IV summarizes data for carbon determinations carried out by five different laboratories using the Leco and Richard Steeps combustion methods (12). Analyses were performed on polycrystalline SeG-Si that had a supplier specification of < 0.3 ppma via FTIR. The combustion analyses indicated concentrations in excess of 100 ppma.

As a rule of thumb, the saturation solubility of carbon in silicon is about 10 ppma, and approximately an additional 10 ppma can be present under conditions of super-

saturation. Carbon concentrations in excess of about 20 ppma will precipitate as silicon carbide.

Silicon carbide.—Microscopic observation appears to be the only means to measure the content of SiC in silicon. Three methods have been used: counting of particles (i) on a filter paper through which a dissolved silicon sample has been passed, (ii) on a polished silicon surface, and (iii) within the volume of a silicon slab. Particle size and number are used to calculate SiC concentration.

1g samples of MG-Si and PMS were dissolved in boiling 3N NaOH and filtered through 0.6 μm paper (13). Silicon that had been fast cooled, after being tapped from an arc furnace, contained about 350 particles which showed a sharp size distribution centered around an average "diameter" of 4 μm. Nearly all particles were < 10 μm in size.

Polished samples of PMS and MG-Si, and of their directionally solidified ingots, were analyzed for SiC by microscopically counting the particles intersecting the surface (14). The method has a resolution of 0.5 μm and a sensitivity of 400 particles per 100 cm². Analyses of PMS and various sources of MG-Si showed SiC concentrations between 110 and 270 ppmw.

Infrared microscopy has a lower resolution (10 μm) than the optical method because of the limited depth of focus at higher magnification. However, the IR method allows the volume of samples to be surveyed, thereby eliminating the uncertainty that particles might not intersect a surface. This volume probe increases the sensitivity to five particles in a 500 μm thick, 100 cm² wafer. Twice-crystallized ingots grown by the Czochralski method contain no detectable SiC particles. Since SiC particles grow in size when silicon is molten, the 10 μm resolution of the IR microscope does not appear to be a limitation. As the size of any particles decrease, their number has to increase enormously to represent a significant weight fraction. Therefore, the concentration of SiC in once- or twice-crystallized Si is estimated to be << 1 ppmw. However, their effect on solar cell performance still needs to be explored.

Conclusions

The doping impurities boron and phosphorus can be simultaneously measured either by the float-zone/resistivity or the Czochralski/Hall-effect methods. Both methods give concentrations with adequate accuracy and precision. Other analytical methods have proved inadequate for determining either of these impurities. An exception is ICP-ES, which is sensitive enough for boron but which must be further investigated for phosphorus.

Metal impurities can be measured in PMS using either ES, XRFs, SSMS, or ICP-ES. All of the methods are semiquantitative in that they yield concentrations reliable within about a factor of two. This degree of reliability is good enough, however, to make adequate decisions concerning PMS quality for either research and development or production purposes.

Only SSMS, and perhaps ICP-ES, has adequate sensitivity to determine whether SoG-Si is pure enough with respect to metal impurities for use in manufacture of solar cells having acceptable efficiencies. If the SoG-Si is pure enough, neither method is sensitive enough to monitor such concentrations. However, the techniques can provide a means to test SoG-Si for inadvertent contamination.

The nonmetals, O, C, and SiC, can be measured by conventional methods. FTIR is adequate for determining both O and C. Laborious methods involving microscopic counting are sufficient for measuring the concentration of SiC, if necessary.

As the solar silicon industry grows, quality assurance of silicon could probably be met to a large extent by developing a strong capability of ICP-ES. With reasonable success, this method might be adequate for determining B and P concentrations in addition to metal concentrations, thereby simplifying the variety of techniques and associated equipment required. The Czochralski/Hall-effect

Table III. Carbon and oxygen analysis via FTIR as a function of silicon source and growth method

Starting material	Growth method	[C] (ppma)	[O] (ppma)
SeG-Si	None	< 0.3*	< 0.05*
	1 Fz	< 1	< 1
	1 Cz	< 1	13 ± 1
	1 Br	< 1	7 ± 5
PMS	1 Cz	14 ± 3	9 ± 2
	2 Cz	2 ± 1	13 ± 2
	1 Br	15 ± 5	~ 5

* Supplier specification.

Table IV. Analysis (ppma) of polycrystalline SeG-Si with a carbon specification of < 0.3 ppma by two combustion methods

Lab A	LECO			R. Steeps
	Lab B	Lab C	Lab D	Lab E
230	1950	220 ± 100	120 ± 10	160 ± 20

method appears to be the simplest and most reliable way to measure B and P concentrations in the mean time. Both C and O can be easily measured using FTIR. Various microscopic techniques would allow the determination of SiC, as well as the general defect structures that are always a problem in silicon.

Acknowledgments

Development of the background knowledge for this paper has been assisted by many of my co-workers over the years at Exxon Research and Engineering Company, Elkem a/s, and Dow Corning Corporation. I also thank P. Schumacher of Battelle Columbus Laboratories and J. Cline of Interlake's Globe Metallurgical Division for their efforts.

Manuscript submitted Aug. 29, 1983; revised manuscript received Jan. 3, 1984. This was Paper 214 presented at the San Francisco, California, Meeting of the Society, May 8-13, 1983.

Exxon Research and Engineering Company assisted in meeting the publication costs of this article.

REFERENCES

1. L. P. Hunt and V. D. Dosaj, Final Report, Department of Energy Report DOE/JPL/954559-78/7 (1979).
2. S. Pizzini, in "Materials and New Processing Techniques for Photovoltaics," J. P. Dismukes, P. Rai-Choudhury, E. Sirtl, and L. P. Hunt, Editors, p. 26, The Electrochemical Society Softbound Proceedings Series, Pennington, NJ (1982).
3. H. A. Aulich, K.-H. Eisenrith, H.-P. Urbach, and J. C. Grabmaier, *ibid.*, p. 177.
4. J. A. Amick, J. P. Dismukes, R. W. Francis, L. P. Hunt, P. S. Ravishankar, M. Schneider, K. Matthei, R. Sylvain, K. Larsen, and A. Schei, in "Materials and New Processing Techniques for Photovoltaics," J. A. Amick, V. K. Kapur, and J. Diel, Editors, p. 67, The Electrochemical Society Softbound Proceedings Series, Pennington, NJ (1983).
5. L. P. Hunt, R. W. Francis, and J. P. Dismukes, *This Journal*, **131**, 1888 (1984).
6. A. Hurrle and J. Diel, "Electronic and Optical Properties of Polycrystalline or Impure Semiconductors and Novel Silicon Growth Methods," K. V. Ravi and B. O'Mara, Editors, p. 106, The Electrochemical Society Softbound Proceedings Series, Pennington, NJ (1980).
7. L. P. Hunt, V. D. Dosaj, and J. R. McCormick, Quarterly Report no. 3, Department of Energy Report ERDA/JPL-954559-77/1 (1977).
8. E. Grallath, P. Tschoepel, G. Koelblin, U. Stix, and G. Toelg, *Fresenius Z. Anal. Chem.*, **302**, 40 (1980).
9. R. H. Hopkins, J. R. Davis, A. Rohatgi, M. H. Hanes, P. Rai-Choudhury, and H. C. Mollenkopf, Final Report, Department of Energy Report DOE/JPL-954331-81/4 (1982).
10. P. J. Ward, *This Journal*, **129**, 2573 (1982).
11. P. K. Dutta, D. J. Eustace, and J. A. Amick, Internal report, Exxon Research and Engineering Company (1983).
12. Internal Exxon Research and Engineering Company and Elkem a/s reports (1982).
13. Internal report Elkem a/s (1982).
14. P. S. Ravishankar and L. Younghouse, Internal report, Exxon Research and Engineering Company.

The Nitridation of Thick Germanium Oxide Films on Single-Crystal Germanium

E. E. Crisman

Division of Engineering, Brown University, Providence, Rhode Island 02912

O. J. Gregory

Department of Chemical Engineering, University of Rhode Island, Kingston, Rhode Island 02881

P. J. Stiles

Department of Physics, Brown University, Providence, Rhode Island 02912

ABSTRACT

The far-infrared (FIR) transmission properties and index of refraction of thick ($\sim 2000 \text{ \AA}$) vitreous germanium oxide films on single-crystal germanium have been measured before and after high temperature reaction with flowing ammonia gas. Significant shifts in the transmission spectra were observed as a function of both time at temperature and NH_3 flow rate. Correlation was observed with transmission minima reported in the literature for fine powders of germanium nitride and for thin ($<1000 \text{ \AA}$) layers of ion-implanted and annealed germanium/oxygen and germanium/nitrogen complexes. In addition, when the nitrided films were reoxidized at high pressure, structure was observed which corresponded to FIR transmission of hexagonal-phase GeO_2 powder specimens.

Insulating layers on semiconductor surfaces are an essential part of the current technology in planar devices and particularly in the metal-insulator-semiconductor structure often used to construct the basic unit (FET) of VLSI circuits. Oxides and nitrides of silicon can be formed directly on silicon single-crystal surfaces by thermal reaction with gases. However, other semiconductors of interest do not react as readily to form uniform layers of "native" insulators. Other means of formation, such as sputtering, evaporation, wet chemistry, etc., have been used, but these techniques generally lead to undesirable electrical properties at the interface between the in-

Key words: germanium, germanium insulator, germanium oxides, germanium nitrides, far-infrared transmission.

ulator and the substrate, even on silicon. Compared to silicon, electron and hole mobilities are more nearly the same, and higher in absolute value in germanium. Because of this, germanium has been suggested as an attractive candidate for low temperature CMOS elements (1). Recently, Hua *et al.* (2) have explored the possibility of forming nitrides on germanium by thermal reaction with ammonia/nitrogen mixtures. They observed that very thin films of oxynitride were formed with a 2.5:1 nitrogen-to-oxygen ratio. Further studies by Rosenberg (3) have indicated that an initial partial pressure of oxygen in the reaction chamber was a necessary condition for the reaction to occur between germanium and ammonia in a uniform manner over the surface. In those two stud-

ies, it was concluded that this procedure limited film thickness to the order of 100Å because of the barrier to oxygen and nitrogen diffusion presented by the uniform nitride (or oxynitride) layer that subsequently formed. In the studies reported here, a relatively thick (~2000Å) oxide layer on germanium was used as the starting point for high temperature reaction with ammonia gas. Displacement of the oxygen by nitrogen during the thermal reaction was monitored by means of infrared transmission in the 8-40 μm range. The extinguishing and developing of well-defined absorption maxima were compared to published data and to FIR transmission of pressed powder specimens of Ge₃N₄ and GeO/GeO₂.

Experimental

Specimens were prepared from a single wafer of (111) p-type germanium of 0.1 Ω-cm resistivity. The wafer was first given an organic contamination cleaning in hot trichloroethylene, hot acetone, hot methanol, hot deionized H₂O, 48% HF acid dip (30s), and final deionized H₂O rinse with zero-grade nitrogen blow dry. This was followed by a 30s etch in CP-4, another DI H₂O rinse, and nitrogen blow dry. Approximately 30% of the wafer was removed during the CP-4 etch leaving a surface that had a slight "orange peel" look and a final wafer thickness of 8.8 mil. Infrared transmission was then measured on the wafer in the 8-40 μm wavelength range via a Perkin Elmer Model 580 infrared spectrometer. At 8 μm, transmission was found to be on the order of 47%, which is approximately the value for germanium infrared optical components prepared commercially. The wafer was then scribed into several pieces and placed in a high pressure chamber used for oxide formation (4). An oxidation treatment of the specimens was performed in which the chamber was brought to 650°C at a pressure of 340 atm for 10 min with hydrocarbon-free, zero-grade oxygen. Upon removal from the pressure vessel, ellipsometry measurements (Rudolph Research Auto EL-II ellipsometer) disclosed, in general, that the layer formed had an index of refraction of 1.55-1.85 and a thickness on the order of 2200Å, with variations depending on the position of the particular piece in the pressure chamber. Previous studies of high pressure oxidation of germanium typically resulted in index of refraction values that were greater than the 1.6 usually reported in the literature (4). Individual pieces of the original specimen were then subjected to various schedules of temperature and time in flowing electronic grade H₂(5%)/N₂ and NH₃ gases in a silica-lined, 1 cm diam tube furnace. For those processings, the specimen was loaded into the center of the tube furnace on an alumina pallet. The system was then flushed for 0.5h at room temperature with zero-grade H₂/N₂ mixture supplied through clean fluorocarbon tubing. The outlet end of the furnace tube was sealed against ambient atmosphere backstreaming by connection, via fluorocarbon tubing, to a bubbler containing Dow 704 diffusion pump oil. For runs in which ammonia was used, an additional flush of NH₃ for 0.5h at about 250 sccm was used before commencing furnace heating. The volume of the furnace tube was approximately 50 cm³. The furnace was heated to the operating temperature at a rate of about 50C°/min, and cooled somewhat faster - about 100C°/min, by opening the halves of the split-tube furnace. Long-term cooling with the furnace closed (~3h) gave films that appeared identical to those that were rapidly cooled. In all cases, gas flow was maintained until the furnace tube temperature was <200°C.

After each run, the transmission and the index of refraction of the specimen were remeasured. Optical inspection of the surface was also performed with a Lietz Orthoplane metallurgical microscope equipped with a Nomarski interference contrast attachment.

Analyzed powders of GeO, GeO₂, and Ge₃N₄ were obtained from CERAC/PURE, Incorporated, and pressed with KBr into standard transmission disks in a metallurgical mounting press (at 20,000 psi) in a ratio of about 5 mg of specimen powder per gram of KBr. X-ray diffrac-

tion pattern measurements confirmed that the GeO₂ powder was predominately hexagonal crystalline in nature, and the Ge₃N₄ specimen was approximately a 20/80 ratio of the α/β-nitride. Infrared transmissions of the pressed powder specimens were normalized with a KBr blank disk in the reference beam. FIR transmission traces were made on the pressed powder specimens for comparison with the single-crystal germanium oxide and oxynitride films of this report.

Results

The transmissions of the cleaned and etched germanium wafer, and a piece of that same wafer after high pressure oxidation, are presented as traces 1 and 2 in Fig. 1. The structure between 25 and 40 μm is due to the Ge-Ge stretching vibrations. The spike at 15 μm is artificial and is caused by a filter change in the spectrometer. The relatively thin (~225 μm) specimen results in some surface to surface interference fringe resonances which are enhanced by the presence of the native oxide on the two specimen surfaces as shown in trace 2 of the figure. That trace is typical of the transmission measured on thick oxides formed by high pressure on (111) germanium. The index of refraction of this particular specimen was 1.70-1.81, as measured at various points on the surface. A broad shoulder from 9 to 11 μm (1100-950 cm⁻¹) and two minima at 11.5 μm (860 cm⁻¹) and 18 μm (570 cm⁻¹) are coincident with the structure reported in the literature for germania. The general shape of trace 2 corresponds well to that observed by Boal *et al.* (5) for thermally grown thick (~3800Å) silica films on single-crystal (111) silicon wafers, and the location of the two minima are coincident with those reported by Stein (6) for ion-implanted oxygen in single-crystal germanium (orientation unspecified) and by Murphy and Kirby for vitreous germania powder (7). This suggests that the GeO_x grown by high pressure oxidation are more nearly amorphous than crystalline at least on (111) surfaces.

When, as in Fig. 1, trace 3, the germanium oxide is exposed to flowing (180 sccm) NH₃ at 650°C, a finite broadening is observed to occur in the 860 cm⁻¹ minimum. The change in shape was observed after 0.5h and remained unchanged thereafter. Trace 3 of Fig. 1 shows the typical

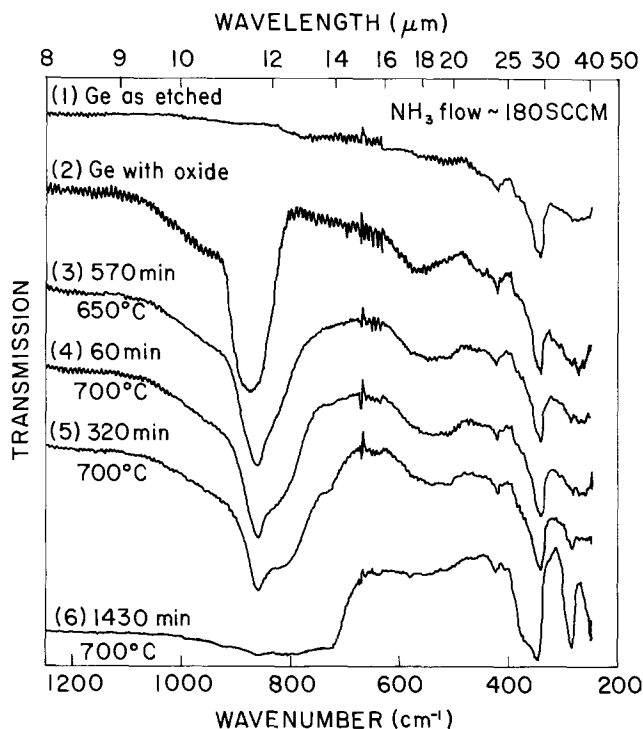


Fig. 1. Nitridation of germanium oxide film. Traces (3), (4), (5), and (6): under condition of "high" ammonia flow. Reference traces: (1) bare germanium crystal after etching and, (2) same specimen as (1) after high pressure oxidation at 340 atm at 550°C for 10 min. Specimen no. GEN-30707c.

transmission waveform after 9.5h at 650°C. Essentially the same shape was obtained after 1h at 600°C with no further change for longer times at temperature. Upon increasing the temperature to 700°C, further change in the shape of the original oxide minimum centered at 860 cm^{-1} was observed, as shown in successive traces 4, 5, and 6 of Fig. 1. There, remnants of the broad, short wavelength shoulder and minimum of the characteristic oxide absorption band are still evident, but a definite shift is observed toward longer wavelength, with a new minimum evident in the vicinity of 720 cm^{-1} . It should be noted that the curves here have been offset along the ordinate axis for clarity. The actual transmissions at 8 μm (left-hand margin) of traces 1 through 4 were $\sim 46\%$, for trace 5, 39.5%, and for trace 6, 5.5%.

Noticeably different results were obtained when the experiment was repeated at a much lower ammonia flow rate of 3.5 sccm (about one chamber volume change every 14 min vs. about 4 changes per min in the first series). As shown in Fig. 2, a minimum of 730 cm^{-1} developed within the first hour and continued to increase with time at temperature. By 12h total time, a second well-defined minimum could be observed at 775 cm^{-1} , and, finally, by 20h, yet another minimum was observed at 910 cm^{-1} . Remnants of the 860 cm^{-1} oxide peak could still be detected after 29.5h at 700°C. In addition, no significant change was observed in the rather broad minimum at 570 cm^{-1} , which has been reported by others as being related to the germanium oxide absorption (7, 8). In comparison, treatment by $\text{H}_2(5\%)/\text{N}_2$ had no effect on the germania layers other than to enhance the rate of reduction/decomposition at temperatures above about 550°C. For example, at 600°C, repeated thermal treatments in H_2/N_2 at flows on the order of 100 sccm resulted only in a reduced depth of the transmission minimum at 860 cm^{-1} . Six hours in the H_2/N_2 mixture at 600°C was sufficient to completely remove the transmission minima at 860 and 570 cm^{-1} .

Trace 1 of Fig. 3 shows the specimen of Fig. 2 after a final (29.5h total) $\text{NH}_3/700^\circ\text{C}$ treatment in the low flow condition. Note that all of the minima mentioned above are still apparent in that trace as well. In trace 2 of Fig. 3, the results of a 15 min rinse in 25°C deionized H_2O is shown. The major change from the trace above is the further reduction of the oxide associated minimum at 860 cm^{-1} . When the same specimen was subsequently re-

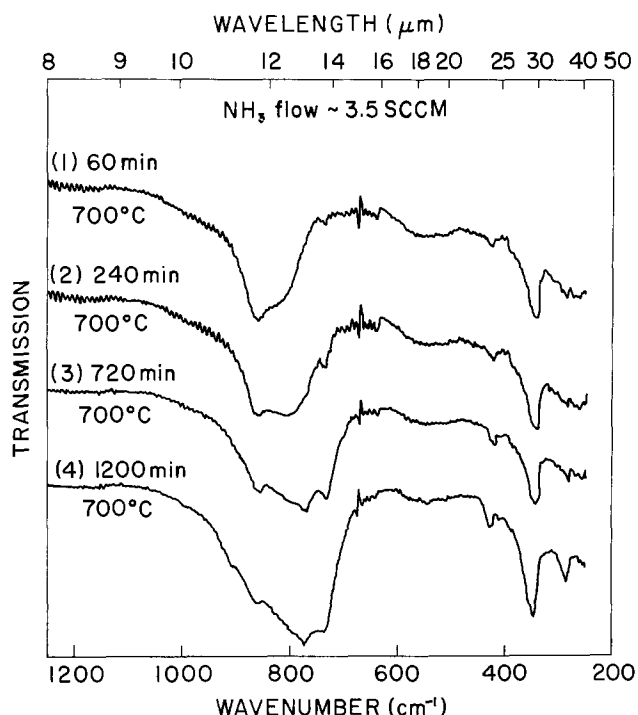


Fig. 2. Nitridation of germanium oxide film under condition of "low" ammonia flow. Specimen no. GEN-30707e.

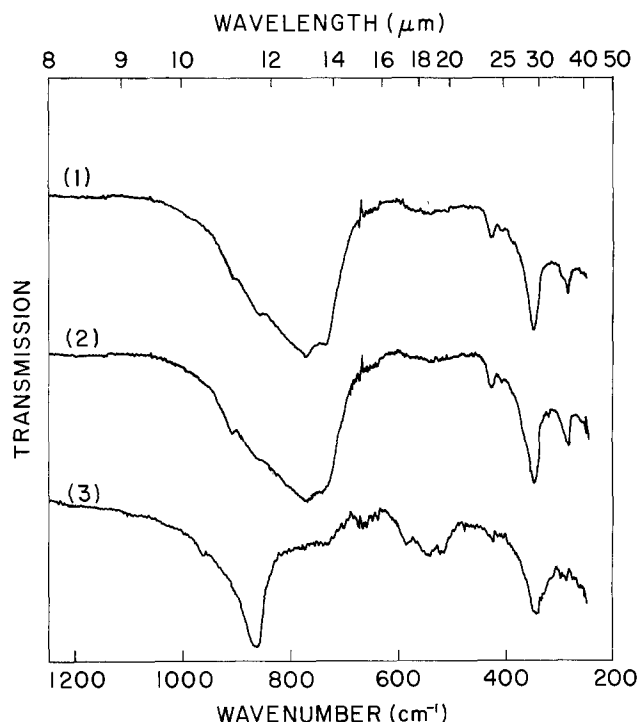


Fig. 3. Effect of high pressure reoxidation of ammonia-treated film. (1): After 1770 min in NH_3 at 700°C and 180 sccm flow. (2): Specimen as in trace (1), plus 15 min in 25°C deionized H_2O . (3): Specimen as in trace (2) plus 10 min of 650°C in oxygen, 340 atm. Specimen no. GEN-30707e.

exposed to oxygen at high pressure, the transmission measurements (trace 3, Fig. 3) disclosed that the oxide layer had regrown at the expense, at least in part, of the nitride or oxynitride. In addition, the dominant 860 cm^{-1} absorption is narrower, the subsidiary oxide associated minimum near 570 cm^{-1} had developed noticeable structure, and a new shorter wavelength minimum near 960 cm^{-1} can also be seen. Some of this structure has been subsequently observed in (100) specimens reacted with oxygen at high pressure for a longer time and is quite similar to hexagonal crystalline GeO_2 powders reported in the literature (7, 8).

Discussion

The nitrides of germanium appear to be polymorphic compositions of Ge_3N_4 . Ruddleston and Popper (9), in detailed powder x-ray diffraction studies, have essentially established that germanium nitrides are isomorphous with silicon nitrides. As with $\beta\text{-Si}_3\text{N}_4$, $\beta\text{-Ge}_3\text{N}_4$ is more readily formed from the reaction of the oxide with ammonia rather than by direct chemical combination of nitrogen with elemental germanium (9-12). Also, the α -phase of Ge_3N_4 appears, as with $\alpha\text{-Si}_3\text{N}_4$ (13), to form by condensation from the gaseous state whereas the β -phase develops within the condensed germanium oxide surface. This conclusion is supported in these studies as well. Microscopic examination of the surfaces after various temperature/time/flow treatments show the development of two distinctly different solids: one of hair-like fibers extending out of the plane of the surface, and the other a petal-like structure which develops and spreads in the plane of the oxide. In general, the fibrous material emanates from thermal etch pits; these are usually characteristic of preferential volatilization (14). Also, the number and length of the fibers are noticeably greater in the low NH_3 flow experiments, which is consistent with the concept that they grow by vapor deposition and are swept away at high flow conditions. Rosenberg (3) has also observed that a uniform film grows rapidly on the surface of germanium in an ammonia atmosphere followed by anisotropic vapor etching initiated at points on the surface where there were film discontinuities.

The initial reaction at 600°-650°C between NH_3 and the oxide is attributed to free or incompletely bonded germanium within the oxide layer. This conclusion would also explain the large variations in index observed on the oxidized layer before nitridation. Similar broadening was not observed when a N_2/H_2 mixture was used instead of NH_3 , indicating the necessity of having some atomic nitrogen present to promote the reaction. The inactivity of molecular nitrogen with germanium has been documented by others for conditions where relatively low temperatures are maintained - usually <700°C (12, 15). The 775 cm^{-1} minimum that develops in the sequence of Fig. 1 we attribute to the predominance of $\beta\text{-Ge}_3\text{N}_4$. Further evidence of this relationship was obtained by comparison with a transmission trace of commercially prepared $\beta\text{-Ge}_3\text{N}_4$ powder (trace 3 of Fig. 4) that was verified by x-ray diffraction to contain ~20% α -nitride. The minimum of the pressed powder specimen was also observed to be at 775 cm^{-1} . The reduction and shift of transmission observed in trace 6 of Fig. 1 corresponded to an extremely disturbed surface on the side of the specimen that was in contact with the alumina pallet on which the wafer was resting. We believe that buildup of α -phase nitride occurred in the stagnant space between the specimen and the pallet, resulting in the domination of 730 cm^{-1} α -nitride absorption, and that vaporization and redeposition of that phase contributed to increased surface scattering, thereby reducing the total transmission substantially over the span of the trace. The index of refraction for this specimen increased from 1.7-1.8 to 2.0-2.3 after the first 700°C treatment, and thereafter remained, on average, at 2.1. Index values could not be obtained on the "bottom" side due to decreased reflection. The final thickness of the layers were estimated by ellipsometry to be 1800 \AA , which is somewhat thinner than the original 2200 \AA oxide layer. This also supports the conclusion that

at high flow the α -phase is swept away by the gas. The specimen used to generate Fig. 2 was from the same wafer as that for Fig. 1 and had essentially the same transmission curve for the bare surface, high pressure-oxidized surface and the 650°C nitrided surface as given in Fig. 1. The Fig. 2 specimen was propped away from the pallet with a silica spacer so that NH_3 flow could proceed equally on both sides. After 4h (trace 2), distinct minima could be observed at 730 and 775 cm^{-1} , and they remained established throughout the subsequent treatment. In addition to these two and the remnant of the oxide (860 cm^{-1}) minimum, another is also observed at 910 cm^{-1} . The 910 cm^{-1} minimum was also observed in the transmission measurement of the $\beta\text{-Ge}_3\text{N}_4$ pressed powder (trace 3 of Fig. 4). Microscopic examination of both surfaces disclosed significantly more of the fibrous material on the surface of this specimen than on the specimen of Fig. 1. Reaction of germanium dioxide powder with flowing ammonia at 800°C shows only one minimum near 800 cm^{-1} , as reported by Elliott and Thompson (16). We conclude then that the 730 cm^{-1} minimum is associated with the α -phase nitride, and the 775 cm^{-1} minimum is associated with the β -phase. Similar two-phase growth (17) and transmission structure (16) has been observed for silicon nitride. Fine structure of this order of resolution has been observed for silicon nitride thin films (18), which had the same general form that we report here. More recently, high resolution transmission spectroscopy has demonstrated that still further substructure can be resolved (19). The index of refraction of the specimen of Fig. 2 was 1.65 after oxidation and 2.35 after 20h of NH_3 treatment. During the interim steps of nitridation, the ellipsometry values would not converge consistently to an index value, indicating possibly multiple layer or oxide/nitride phase mixing during the transition. The final thickness after 20h of nitridation was on the order of 2600 \AA .

When the specimens of Fig. 1 and 2 were reoxidized at the same conditions as in the original process (650°C/340 atm), decidedly different characteristics were observed in the subsequent transmission curves: compare Fig. 3, trace 3, with Fig. 1, trace 2. While the oxide had redeveloped at the expense of the nitride, the minimum at 860 cm^{-1} is noticeably narrower. In addition, structure is observed in the 570 cm^{-1} oxide minimum, and a new peak is observed at about 960 cm^{-1} . These general features are also observed in the pressed powder transmission of GeO_2 shown as trace 1 of Fig. 4 and in Ref. (7) for hexagonal GeO_2 . Oxidation of the nitrided layer appears to have a crystalline character rather than an amorphous one, as was observed for the bare surface germanium oxidation.

Conclusions

Thick films, with FIR structures characteristic of germanium nitride, have been produced on germanium crystal surfaces by reacting ammonia with thick germanium oxide layers. The development of specific and nonshifting FIR transmission structure suggests that definite changes in amounts of the phases occur rather than a continuous variation of solid solution Ge-O-N components. The relative amounts of α -like and β -like material remaining on the surface can be controlled to some extent by varying the flow of the ambient gas. Infrared transmission measurements can identify the presence of either (or both) phase on the crystal surface where the minimum at 775 cm^{-1} correlates with the β -phase and the 730 cm^{-1} minimum correlates with the α -phase.

When the nitrided layers are reoxidized at high pressure, the oxide formed at the expense of the nitrogen bearing layer has narrower transmission and fine structure, indicating that a crystalline oxide develops following the pattern established by the nitrided structure.

Acknowledgments

This research was sponsored primarily by the Materials Research Laboratory at Brown University, funded by the National Science Foundation. Additional support was

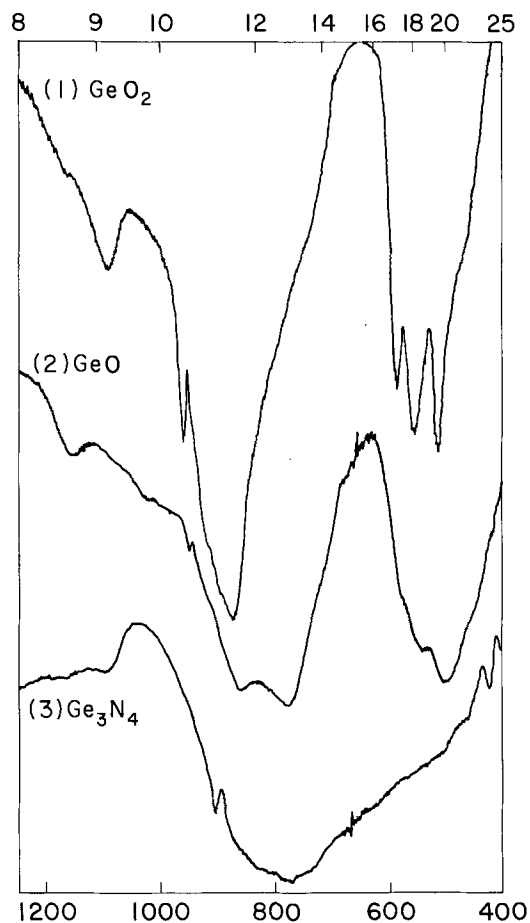


Fig. 4. Transmission of powder specimen disks pressed with KBr and normalized with KBr disk in reference beam. (1): Hexagonal GeO_2 . (2): Amorphous GeO . (3): Ge_3N_4 approximately 20%/80% α , β phases.

provided by the Office of Naval Research under ONR Grant no. N00014-82-K-2046.

Manuscript submitted Oct. 20, 1983; revised manuscript received March 20, 1984.

Brown University assisted in meeting the publication costs of this article.

REFERENCES

1. J. Rosenberg, Paper presented at the Device Research Conference, Burlington, Vermont, June 1983, To be published in *IEEE Trans. Electron. Dev.*
2. Q. Hua, J. Rosenberg, J. Ye, and E. S. Yang, *J. Appl. Phys.*, **53**, 8969 (1982).
3. J. J. Rosenberg, Ph.D. Thesis, Columbia University, New York (1983).
4. E. E. Crisman, Y. M. Ercil, J. J. Loferski, and P. J. Stiles, *This Journal*, **129**, 1845 (1982).
5. J. V. Boal, J. T. Edmond, and B. Lawrenson, *Solid-State Electron.*, **25**, 698 (1982).
6. H. J. Stein, *This Journal*, **121**, 968 (1974).
7. M. K. Murthy and E. M. Kirby, *Phys. Chem. Glasses*, **5**, 144 (1964).
8. E. R. Lippincott, A. Van Valhenburg, E. E. Weir, and E. N. Nunting, *J. Res. Nat. Bur. Stand.*, **61**, 61 (1958).
9. S. N. Ruddlesden and P. Popper, *Acta Cryst.*, **11**, 465 (1958).
10. P. Popper and S. N. Ruddlesden, *Nature*, **179**, 1129 (1957).
11. J. A. Nemetz and R. E. Tressler, *Solid State Technol.*, **25**, 79 (1983).
12. G. H. Morey and W. C. Johnson, *J. Phys. Chem. Soc.*, **54**, 3603 (1932).
13. A. Atkinson, A. J. Moulson, and E. W. Roberts, *J. Am. Ceram. Soc.*, **59**, 285 (1976).
14. B. J. Dalgleish, H. M. Jennings, and P. L. Pratt, in "Special Ceramics 7," P. Popper, Editor, p. 85, British Ceramic Research Association, Stoke-on-Trent, England (1981).
15. W. C. Johnson and G. H. Ridgely, *J. Am. Chem. Soc.*, **156**, 2395 (1934).
16. S. Wild, H. Elliott, and D. P. Thompson, *J. Mater. Sci.*, **13**, 1769 (1978).
17. B. J. Dalgleish, H. M. Jennings, and P. L. Pratt, *Sci. Ceram.*, **10**, 369 (1980).
18. T. Ito, S. Hijiya, T. Nozaki, H. Arakawa, M. Shinoda, and Y. Fukukawa, *This Journal*, **125**, 448 (1978).
19. J. P. Luongo, *ibid.*, **130**, 1560 (1983).

The Incorporation of Boron in Silicon Epitaxial Layer Growth in the Presence of Small Amounts of Water

H. T. J. M. Hintzen,¹ J. Bloem,* and L. J. Giling

Faculty of Science, R. I. M., Department of Solid State III, Catholic University of Nijmegen, Toernooiveld, 6525 ED Nijmegen, The Netherlands

ABSTRACT

The amount of electrically active boron which is incorporated during the CVD of silicon using SiH₄ in H₂ at atmospheric pressure and B₂H₆ as dopant appears to be very sensitive to the input pressure of HCl and the presence of small amounts of water. Equilibrium gas-phase compositions have been calculated for this system using an iterative procedure. Assuming thermodynamic equilibrium between gas phase and solid phase, the experimentally observed dependences can be satisfactorily described. Based on these calculations also, an explanation can be given for the unexpected experimental results on boron autodoping.

Some years ago, a number of investigations were done on the kinetics (1-4) and thermodynamics (4-11) of the incorporation of dopant elements during growth of silicon from the vapor phase. Later on, Kühne (12) gave a theoretical consideration about the incorporation process. Recent papers of Reif (13) treat the respective role of kinetics and thermodynamics in doping processes with emphasis on transient effects.

Consideration of the equilibrium composition of the gas phase above the growing silicon layer turned out (10) to be useful in the interpretation of the observed dependence of the concentration of built-in phosphorus on the input partial pressure of the dopant compound. The implicit assumption made is that the growth rate is so low that the dopant compounds in the gas phase just above the growing layer are in thermodynamic equilibrium with the solid, such that the incorporation process is dominated by thermodynamics.

In this paper, an effort will be made to describe semi-quantitatively the incorporation of boron during the chemical vapor deposition (CVD) of silicon in the presence of hydrogen chloride and small amounts of water by considering the composition of the gas phase. Experimentally, a rather strong dependence has been observed by Bloem (14) in a region where the amount of boron which is incorporated does not depend on the silicon growth rate.

*Electrochemical Society Active Member.

¹Present address: Philips Research Laboratories, Eindhoven, The Netherlands.

Key words: silicon, boron dope, CVD, gas-phase equilibrium, autodoping.

Calculation of the Equilibrium Composition

Use has been made of the computer program ECCVD-MAL (15), which calculates the equilibrium partial pressures of the various components by means of an iterative procedure. The B-H-Si, B-H-Si-Cl, B-H-Si-O, and B-H-Si-Cl-O systems contain 15, 30, 36, and 57 components, respectively. The thermodynamic data have been collected from Ref. (16). In each calculation, solid Si(s) has been assumed to be in equilibrium with the gas mixture, whereas always the presence of solid B(s) as a condensed phase has been taken as a possibility. Although boron silicides are known to exist (8, 17), unfortunately no reliable thermodynamic data concerning these compounds could be found. When oxygen is present SiO₂(s) has also been taken as a possible condensed phase, although it is known (18) that SiO₂(s) formation at 1400 K will only occur above 40 ppm of water, while at 1500 K more than 200 ppm is needed to precipitate solid SiO₂. Also, some of the B₂H₆O₂ compounds can be responsible for the formation of a condensed phase. The saturation

Table I. Saturation pressures at T = 1500 K for various B and O containing compounds

Compound	MP (K)	BP (K)	log P _{sat}	Ref.
B ₂ O ₃ (l)	723	2316	-4.633	(16)
BH ₃ O ₂ (s)	509	—	0.802	(16)
BH ₃ O ₃ (s)	444	573	5.906	(16)
B ₂ H ₄ O ₄ (s)	Unknown	—	6.117	(16)
B ₃ H ₃ O ₃ (s)	Unknown	—	3.958	(16)

pressures for these compounds, as far as they are known, are collected in Table I. From this table it can be seen that only $B_2O_3(l)$ can be envisaged as a likely additional condensed compound. Because of program limitations, only the condensed phases $Si(s)$, $B(s)$, and $SiO_2(s)$ were taken into account in the computer program. However, afterwards, a check was always done to see if one of the critical saturation values for the $B_xH_yO_z$ compounds had been surpassed.

Results and Discussion

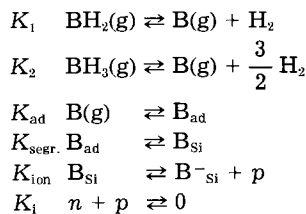
For the sake of completeness and simplicity, first the equilibrium composition of the B-H-Si system and the B-H-Si-Cl system will be treated. Then the influence of H_2O will be investigated in the B-H-Si-O system and B-H-Si-Cl-O system, respectively.

B-H-Si system.—Figure 1 gives the calculated partial pressures of the various components in the equilibrium mixture consisting of the elements silicon, hydrogen, and boron (e.g., for an input gas which is a mixture of SiH_4 , H_2 , and B_2H_6) as a function of the input pressure of diborane ($P_{B_2H_6}^0$) at a temperature of 1500 K and for a total pressure of 1 atm. It can be seen from Fig. 1 that the slope of $\log P_{B_xH_y}$ vs. $\log P_{B_2H_6}^0$ equals p . It can also be seen from Fig. 1 that above $P_{B_2H_6}^0 = 10^{-5}$ atm the partial pressure of $B(g)$ attains the saturation pressure of $B(s)$, whereupon solid B is formed. This fixes the partial pressures of all B containing compounds.

Further, it is clear that BH_2 and BH_3 are the most abundant B containing compounds, also at high diborane input partial pressures. This is in contrast to the case of phosphorus dope, where at increasing phosphine input partial pressures the most abundant P containing compounds change from PH_2 and PH_3 to P_2 (10).

The simplest model of boron incorporation in the growing layer considers the incorporation of monatomic boron from the gas phase. According to this model, the B containing compounds with the highest partial pressures are thought to dissociate at high temperature into monatomic boron, which will adsorb at the Si surface and finally will be incorporated at a substitutional silicon site in the crystal. Thereupon B_{Si} dissociates into B_{-Si}^- and p (hole).

The foregoing can be summarized in the following equations



This, together with the condition

$$2P_{B_2H_6}^0 = \sum_{x,y} x P_{B_xH_y}$$

or, approximately (see Fig. 1)

$$2P_{B_2H_6}^0 = P_{BH_2} + P_{BH_3}$$

(and the assumption that the doped-silicon layer at the growth temperature behaves as an intrinsic semiconductor, i.e., $n = p = K_1^{1/2}$) leads to

$$[B_{-Si}^-] = \frac{K_{ad}K_{segr.}K_{ion}}{K_1^{1/2}} \cdot \frac{2P_{B_2H_6}^0}{\frac{P_{H_2}}{K_1} + \frac{P_{H_2}^{3/2}}{K_2}} \quad [1]$$

$[B_{-Si}^-]$ can be determined by means of resistivity measurements at room temperature, which essentially gives a hole concentration equal to $[B_{-Si}^-]_{high\ temp.}$ According to this equation, a plot of $\log [B_{-Si}^-]$ vs. $\log P_{B_2H_6}^0$ for $P_{B_2H_6}^0$ lower than 10^{-5} atm would yield a straight line with slope 1.

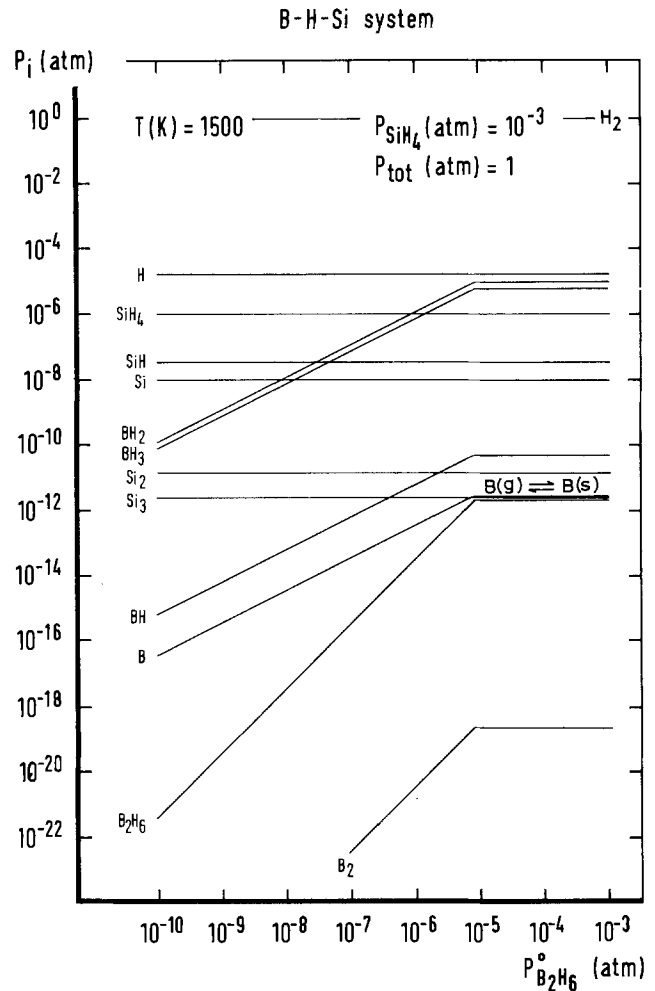
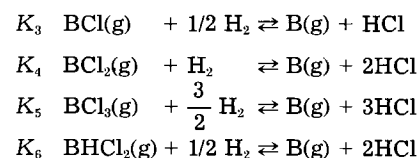


Fig. 1. Calculated equilibrium composition of the B-H-Si system as a function of the input partial pressure of diborane $P_{B_2H_6}^0$ ($P_{SiH_4}^0 = 10^{-3}$ atm, $P_{tot} = 1$ atm, $T = 1500$ K).

Above $P_{B_2H_6}^0 \approx 10^{-5}$ atm, the amount of B-containing compounds in the gas phase remains constant, and a constant amount of incorporated boron can be expected above this value.

B-H-Si-Cl system.—The calculated gas-phase composition of the B-H-Si-Cl system (e.g., for an input gas which is a mixture of $SiCl_4$, H_2 , and B_2H_6) is given in Fig. 2 as a function of the input pressure of diborane ($P_{B_2H_6}^0$) at a temperature of 1500 K and a total pressure of 1 atm. Here too, for low input partial pressures of diborane, a plot of $\log P_{B_xH_yCl_z}$ vs. $\log P_{B_2H_6}^0$ yields a straight line with slope p . The higher value of $P_{B_2H_6}^0$ ($\approx 10^{-4}$ atm), which is needed to condense $B(s)$ as compared with the B-H-Si system, can be ascribed to the fact that boron now also forms gaseous compounds with chlorine.

In a similar way as for the B-H-Si system, the incorporation of boron in the silicon matrix can be described by decomposition reactions for the most abundant B containing species which are present in the gas phase. (With respect to the B-H-Si system, only the new reactions are given)



Together with the condition

$$2P_{B_2H_6}^0 = P_{BH_2} + P_{BH_3} + P_{BCl} + P_{BCl_2} + P_{BCl_3} + P_{BHCl_2}$$

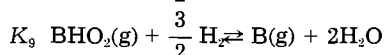
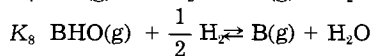
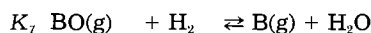
and the assumption that at the growth temperature $n = p = K_1^{1/2}$, it follows

$$[B^-_{Si}] = \frac{K_{ad}K_{segr}K_{ion}}{K_1^{1/2}} \times \frac{2P^{\circ}_{B_2H_6}}{\left(\frac{P_{H_2}}{K_1} + \frac{P_{H_2}^{3/2}}{K_2} + \frac{P_{HCl}}{K_3 P_{H_2}^{1/2}} + \frac{P_{HCl}^2}{K_4 \cdot P_{H_2}} + \frac{P_{HCl}^3}{K_5 \cdot P_{H_2}^{3/2}} + \frac{P_{HCl}^2}{K_6 \cdot P_{H_2}^{1/2}} \right)} \quad [2]$$

According to Eq. [2], a plot of $\log [B^-_{Si}]$ vs. $\log P^{\circ}_{B_2H_6}$ yields a straight line with slope 1 for low input pressures of diborane, as has been experimentally found by Rai-Choudhury [(8) and Fig. 3 thereafter]. It is obvious that at the input pressure of diborane where according to the calculations in Fig. 2 B(s) is present as a condensed phase, and in the experimental curve of Fig. 3, a deviation from linearity appears. On account of electron diffraction measurements, Rai-Choudhury argues (8) that this is due to the formation of $SiB_4(s)$. Although, however, this cannot be predicted from the calculations because of a lack of thermodynamic data for $SiB_4(s)$, this compound could be formed from a reaction between Si(s) and B(s), which gives a simple explanation for the fixed partial pressures of the boron compounds. The observed decrease of boron content in the silicon layer for diborane input pressures exceeding 10^{-4} atm (see Fig. 3) can be explained by assuming gas phase nucleation of B(s), which decreases the amount of B(g) for doping.

B-H-Si-O system.—From the calculation of the equilibrium composition of the B-H-Si-O system (e.g., the input gas is a mixture of SiH_4 , H_2 , B_2H_6 , and H_2O), it follows that BH_2 , BH_3 , BO , BHO , and BHO_2 are the most abundant B containing species. Again, a plot of $\log P_{B_2H_6}$ vs. $\log P^{\circ}_{B_2H_6}$ yields a straight line with slope p (Fig. 4).

The decomposition reactions, taking place at the growing silicon layer, are then (omitting the already cited reactions)



Together with the condition

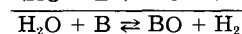
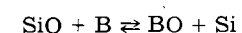
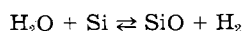
$$2P^{\circ}_{B_2H_6} = P_{BH_2} + P_{BH_3} + P_{BO} + P_{BHO} + P_{BHO_2}$$

and the assumption that at the growth temperature $n = p = K_1^{1/2}$, it follows

$$[B^-_{Si}] = \frac{K_{ad}K_{segr}K_{ion}}{K_1^{1/2}} \times \frac{2P^{\circ}_{B_2H_6}}{\frac{P_{H_2}}{K_1} + \frac{P_{H_2}^{3/2}}{K_2} + \left(\frac{1}{K_7 \cdot P_{H_2}} + \frac{1}{K_8 \cdot P_{H_2}^{1/2}} \right) P_{H_2O} + \frac{1}{K_9 \cdot P_{H_2}^{3/2}} \cdot P_{H_2O}^2} \quad [3]$$

From Eq. [3], it follows that a plot of $\log [B^-_{Si}]$ vs. $\log P^{\circ}_{B_2H_6}$ gives a linear relationship with slope 1, as has been found experimentally for different values of $P^{\circ}_{H_2O}$ [(14) and Fig. 5 thereafter]. When the input pressure of H_2O is increased also, the partial pressures of the boron and oxygen containing compounds become larger, if solid SiO_2 is not present as a condensed phase (see Fig. 6). The effect of increasing water concentration is that the decomposition reactions (K_7 , K_8 , K_9) are hampered, so that the amount of incorporated boron decreases.

The experimentally determined dependency of $[B^-_{Si}]$ on $P^{\circ}_{H_2O}$ (14) (see Fig. 7) also in this case nicely follows the calculated partial pressure of monatomic boron and certainly not those of the B-O or B-O-H compounds, demonstrating that it is B - and not the B-O or B-O-H compounds - which is directly responsible for the amount of $[B^-]$ incorporated in the silicon matrix. Besides the direct visual relation between $[B^-]$ and P_B , a more indirect proof can be given by using Eq. [3], assuming that $P_{H_2O} = P^{\circ}_{H_2O}$, which is allowed because in all cases $P^{\circ}_{H_2O}$ is far in excess with respect to $P^{\circ}_{B_2H_6}$. (The use of $P^{\circ}_{H_2O}$ remains correct even if the reaction of water with silicon to SiO is taken into account, because the reactions are coupled via



After insertion of $P_{H_2} = 1$ atm and the appropriate thermodynamic data for $T = 1400$ K (16), Eq. [3] reads

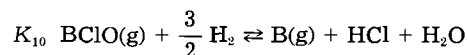
$$[B^-_{Si}] = \frac{K_{ad}K_{segr}K_{ion}}{K_1^{1/2}} \times \frac{2P^{\circ}_{B_2H_6}}{(6.11 \times 10^7 + 1.77 \times 10^{15} \cdot P^{\circ}_{H_2O} + 6.32 \times 10^{18} \cdot (P^{\circ}_{H_2O})^2)} \quad [4]$$

For a fixed input pressure of diborane, a plot of $\log [B^-_{Si}]$ vs. $\log [6.11 \times 10^7 + 1.77 \times 10^{15} \cdot P^{\circ}_{H_2O} + 6.32 \times 10^{18} \cdot (P^{\circ}_{H_2O})^2]$ should give a linear relationship. The data from Fig. 7 can be taken to check this relationship, taking $P^{\circ}_{B_2H_6} = 10^{-9}$ atm. This has been done in Fig. 8, and, indeed, a good correspondence is obtained. The slope, 1.2, deviates somewhat from the expected value, 1.0. However, it is clear that the slope could be closer to unity than calculated with the least squares method if we look at the error in the experimental data (Fig. 7) and consider the uncertainty in the thermodynamic data for gaseous BHO (16) which K_p value according to the most recent data (16) is a factor 10^4 higher with respect to the earliest data (16). This could also be the reason for the discrepancy of the calculated ($P^{\circ}_{H_2O} \approx 3 \times 10^{-4}$ atm, see Eq. [4]) and experimental ($P^{\circ}_{H_2O} \approx 4 \times 10^{-5}$ atm, see Fig. 7) input pressure of H_2O for which BO and BHO , on the one hand, and BHO_2 , on the other, are equally important for the incorporation of elementary boron. As seen from Eq. [4], an increasing water-input pressure influences the position of the equilibria in such a way that the decomposition of B and O containing compounds at the surface is more difficult and $[B^-_{Si}]$ decreases. For low water-input pressures (where BO and BHO are the compounds which yield at decomposition the greatest part of monatomic gaseous boron), $[B^-_{Si}]$ is proportional to the reciprocal of $P^{\circ}_{H_2O}$ (see Fig. 7). For high water-input pressures (where BHO_2 is the compound which yields the greatest part of monatomic

gaseous boron), $[B^-_{Si}]$ is proportional to the reciprocal of the square of $P^{\circ}_{H_2O}$.

Finally, the incorporation of B and O containing species in solid silicon during growth cannot be excluded. However, as yet no experimental evidence is present to substantiate this point.

B-H-Si-Cl-O system.—Figure 9 shows the result of the calculation of the equilibrium composition of the gas phase, containing the elements silicon, hydrogen, boron, chlorine, and oxygen (e.g., the input gas is a mixture of SiH_4 , H_2 , B_2H_6 , HCl , and H_2O). Also in this case, a plot of $\log P_{B_2H_6}$ vs. $\log P^{\circ}_{B_2H_6}$, $\log P^{\circ}_{HCl}$, and $\log P^{\circ}_{H_2O}$ yields a straight line with slopes p , τ , and s , respectively. The most abundant B containing species are: BH_2 , BH_3 , BCl , BCl_2 , BCl_3 , $BHCl$, BO , BHO , BHO_2 , and $BClO$. With respect to the B-H-Si-Cl and B-H-Si-O systems, only one additional decomposition reaction has to be given



Together with the condition

$$2P^{\circ}_{B_2H_6} = P_{BH_2} + P_{BH_3} + P_{BCl} + P_{BCl_2} + P_{BCl_3} + P_{BHCl} + P_{BO} + P_{BHO} + P_{BHO_2} + P_{BClO}$$

and the assumption that $n = p = K_1^{1/2}$ this leads to

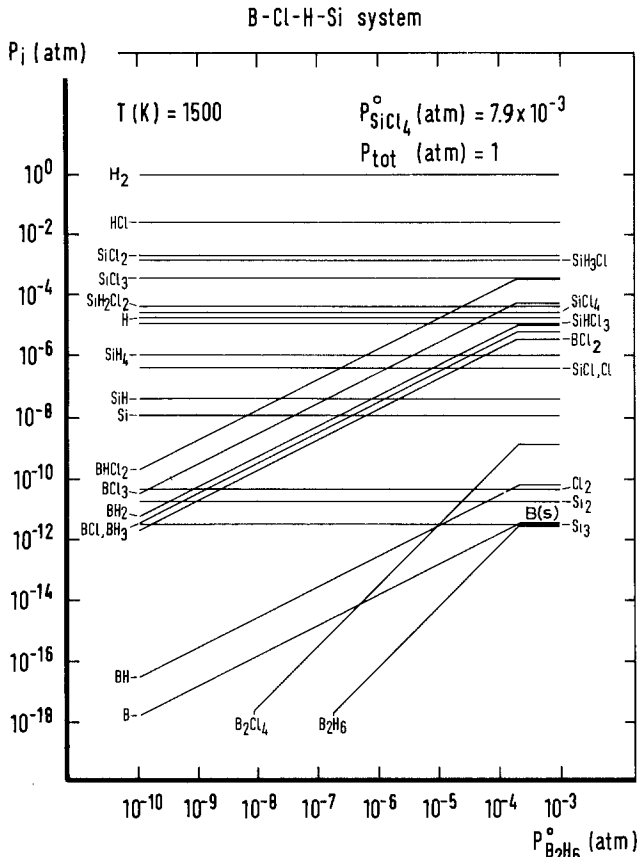


Fig. 2. Calculated equilibrium composition of the B-H-Si-Cl system as a function of $P_{B_2H_6}^0$ ($P_{SiCl_4}^0 = 7.9 \times 10^{-3}$ atm, $P_{tot} = 1$ atm, $T = 1500$ K).

$$[B^-_{Si}] = \frac{K_{ad}K_{segr}K_{ion}}{K_1^{1/2}} \times$$

$$2P_{B_2H_6}^0$$

$$\frac{P_{H_2}}{K_1} + \frac{P_{H_2}^{3/2}}{K_2} + \frac{P_{HCl}}{K_3 \cdot P_{H_2}^{1/2}} + \frac{P_{HCl}^2}{K_4 \cdot P_{H_2}} + \frac{P_{HCl}^3}{K_5 \cdot P_{H_2}^{3/2}} + \frac{P_{HCl}^2}{K_6 \cdot P_{H_2}^{1/2}} + \frac{P_{H_2O}}{K_7 \cdot P_{H_2}} + \frac{P_{H_2O}}{K_8 \cdot P_{H_2}^{1/2}} + \frac{P_{H_2O}^2}{K_9 \cdot P_{H_2}^{3/2}} + \frac{P_{H_2O} \cdot P_{HCl}}{K_{10} \cdot P_{H_2}^{3/2}} \quad [5]$$

Insertion of $P_{H_2} = 1$ atm and the needed thermodynamic data for $T = 1400$ K (16) in Eq. [5] gives

$$[B^-_{Si}] = \frac{K_{ad}K_{segr}K_{ion}}{K_1^{1/2}} \times$$

$$2P_{B_2H_6}^0$$

$$(6.11 \times 10^7 + 1.77 \times 10^{15} \cdot P_{H_2O} + 6.32 \times 10^{18} \cdot P_{H_2O}^2 + 5.40 \times 10^{18} \cdot P_{HCl} + 7.02 \times 10^{12} \cdot P_{HCl}^2 + 6.00 \times 10^{13} \cdot P_{HCl}^3 + 2.62 \times 10^{15} \cdot P_{H_2O} \cdot P_{HCl}) \quad [6]$$

Inspection of Fig. 10, which shows the calculated $[B^-_{Si}]$ curves as a function of the HCl input pressure for three different H_2O input pressures and a fixed B_2H_6 input pressure, shows that the influence of P_{HCl}^0 on $[B^-_{Si}]$ decreases if $P_{H_2O}^0$ increases, as has been experimentally observed by Bloem (14) (see Fig. 11). Because of the multiparameter problem in this case, and the large uncertainty of the actual concentrations, no real quantitative comparison is permitted. However, when both curves [the calculated (Fig. 10) and the experimental one (Fig. 11)] are compared, one again has to come to the conclusion that thermodynamics can describe the incorporation process rather well.

Enhanced growth rate of (heavily) doped polysilicon layers.—The above-given thermodynamic calculation can be extended to lower temperatures, which regime is normally used to grow polycrystalline silicon layers. It is known that when high partial pressures of diborane are used the growth rate is enhanced (19, 20) and the grain size increases (21). From the above-given thermodynamic analysis, it will follow that for these temperatures and concentrations of diborane, the saturation pressure of liquid B_2O_3 ($P_{sat}[B_2O_3(l)] = 10^{-11.5}$ atm at $800^\circ C$) is exceeded,

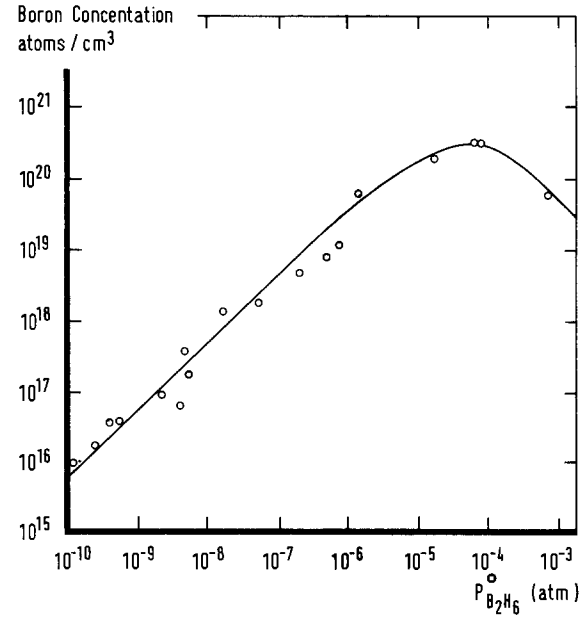


Fig. 3. Experimentally determined boron concentration as a function of $P_{B_2H_6}^0$ (8) for the B-H-Si-Cl system ($P_{SiCl_4}^0 = 7.9 \times 10^{-3}$ atm, $P_{tot} = 1$ atm, $T = 1500$ K). Experimental data from Ref. (8).

so it can be expected that a liquid layer of B_2O_3 (or droplets of liquid B_2O_3) is present on the growing silicon layer. If one assumes that in the carrier gas always enough residual O_2 (and/or H_2O) is present for the formation of B_2O_3 , then this liquid layer could be responsible for the enhanced growth rate with boron doping (19, 20) via a VLS mechanism, as well as for the reported enhanced grain size (21). The role of boron dope can also be the getting of oxygen, thus preventing the formation of solid SiO_2 .

Autodoping.—The calculations given above constitute another example to show that doping with n-type as well

as p-type impurities can be explained via the value of the free monatomic dopant vapor pressure in the gas phase (p_p, p_{As}, p_{Sb}, p_B) (22), and that equilibrium calculations give good predictions on the doping behavior.

Apart from the equilibrium considerations, there are also kinetic arguments to be fulfilled. One of these shows up as a function of growth rate as observed for phosphorus doping (3, 7). Another example is given by the effect of autodoping (23-25). Autodoping can be defined as the undesired dopant contribution from substrate wafers to the growing epitaxial layer (26). Apart from the direct solid-state diffusion of impurities, there is a considerable contribution to the autodoping via the gas phase.

It has been found that autodoping can be reduced considerably by a prebake and growth at reduced total pressures (26). The explanation given points to an easier desorption of impurities accompanied by an enhanced diffusion away from the surface at reduced pressures, leading to a smaller dopant partial pressure near the growing surface and thus to a lower effective segregation coefficient (23-25).

At higher temperatures, the direct solid-state diffusion of impurities from substrate to growing layer is increased.

B-H-Si-O system

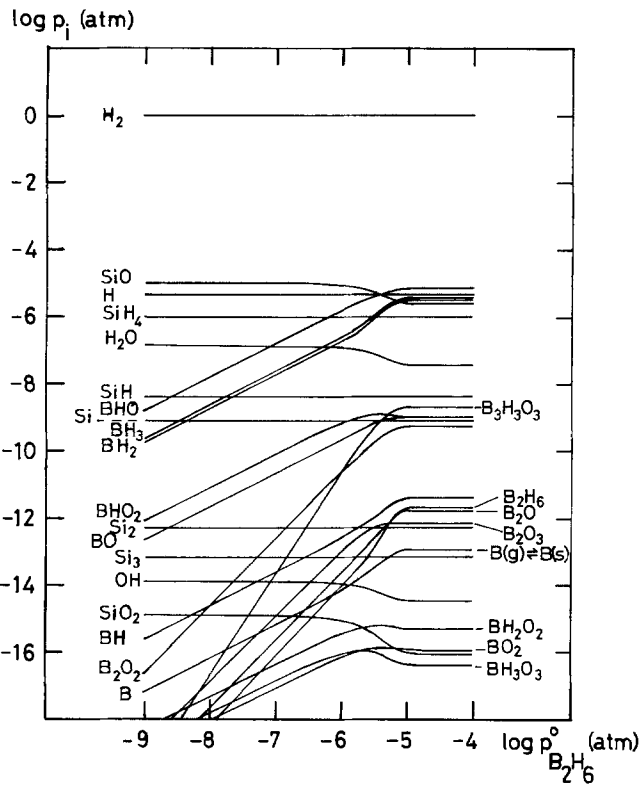


Fig. 4. Calculated equilibrium composition of the B-H-Si-O system as a function of $P_{B_2H_6}^0$ ($P_{SiH_4}^0 = 10^{-3}$ atm, $P_{H_2O}^0 = 10^{-5}$ atm, $P_{tot} = 1$ atm, $T = 1400$ K).

The transport via the gas phase is reduced as the segregation coefficient decreases with increasing temperature for the n-type impurities. Desorption is also made easier at higher temperatures.

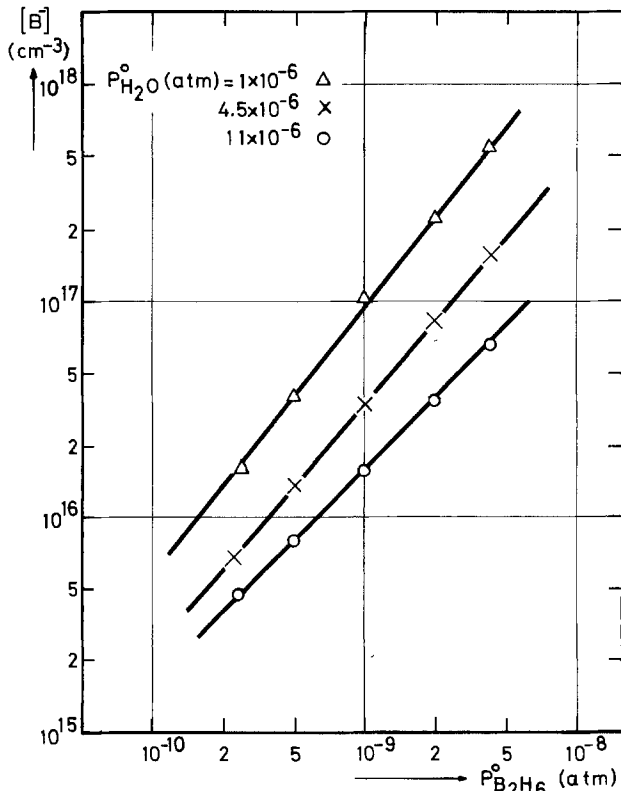


Fig. 5. Experimentally determined boron concentration as a function of $P_{B_2H_6}^0$ (14) for the B-H-Si-O system with $P_{H_2O}^0$ as a parameter ($P_{SiH_4}^0 = 10^{-3}$ atm, $P_{tot} = 1$ atm, $T = 1150^\circ\text{C}$). Experimental data from Ref. (14).

B-H-Si-O system

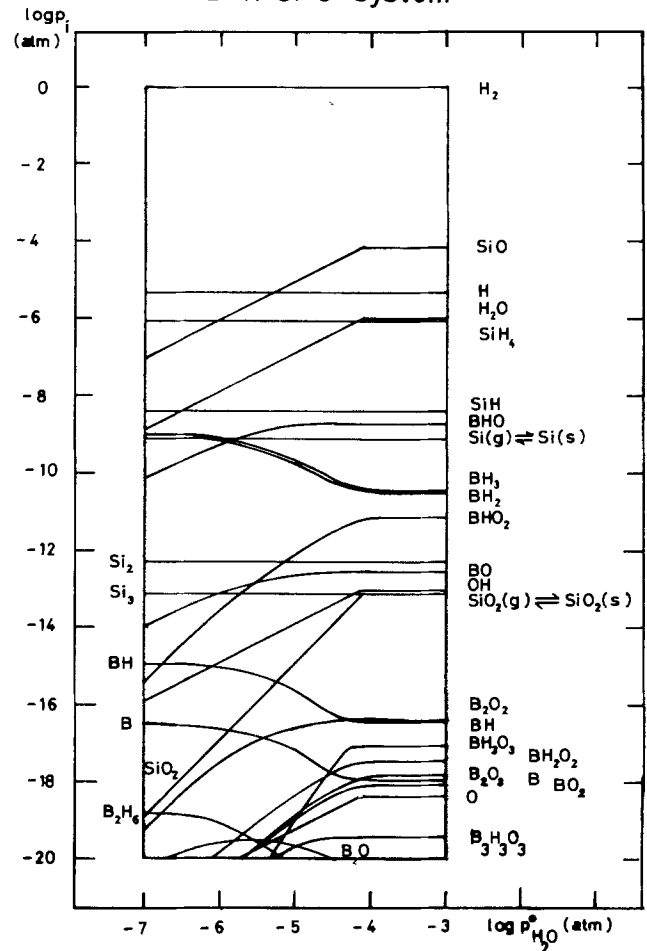


Fig. 6. Calculated equilibrium composition of the B-H-Si-O system as a function of $P_{H_2O}^0$ ($P_{SiH_4}^0 = 10^{-3}$ atm, $P_{B_2H_6}^0 = 10^{-9}$ atm, $P_{tot} = 1$ atm, $T = 1400$ K).

The beneficial effects on autodoping at reduced pressures only applies to n-type impurities (P, As, Sb). For boron doping, unexpectedly, an increase in autodoping is observed at reduced total pressures, whereas a change in temperature is hardly of influence (27).

The physical effects described above of desorption and ease of diffusion away from the substrate surface will equally apply to n-type and p-type dopants. For boron doping, however, the high reactivity of boron towards oxygen, i.e., the chemical influence of trace amounts of impurities such as water vapor, have to be considered additionally. In Fig. 6, it can be seen that small amounts of water which are normally present in reactors at atmospheric pressure (> 1 ppm) are already sufficient to take away a part or even most of the input concentration of B_2H_6 . This amount is converted into the inactive chemical species BHO, and thus the partial pressure of monatomic boron is effectively reduced. By reducing the total pressure in a clean system, the water vapor pressure will be reduced also. A reduction in water content shifts the gas-phase equilibria such that more free boron is available, leading to an increase in doping capabilities and increased autodoping as well.

As a function of temperature in the boron case there are two competing mechanisms (1) higher temperatures lead to easier desorption hence to a lower segregation coefficient (2). The influence of water vapor on the equilibria is reduced at higher temperatures, which increases the effective segregation coefficient. The balance thus depends on the impurity content of the system.

In this way, the differences in autodoping between n-type and p-type impurities can be explained qualitatively. A quantitative explanation needs a better knowledge of the impurity levels in the reactor.

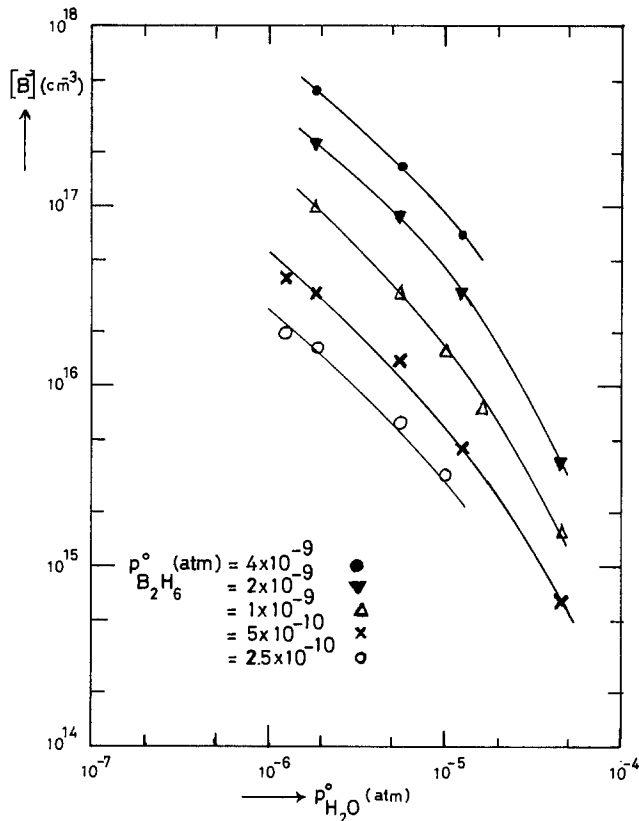


Fig. 7. Experimentally determined boron concentration as a function of $P_{H_2O}^0$ (14) for the B-H-Si-O system. The diborane input concentration has been taken as a parameter. ($P_{SiH_4}^0 = 10^{-3}$ atm, $P_{tot} = 1$ atm, $T = 1150^\circ\text{C}$). The value $P_{H_2O}^0 = 1 \times 10^{-6}$ atm from Ref. (14) has been taken as 2×10^{-6} atm because in the carrier gas already 1 ppm H_2O is present (29). Experimental data from Ref. (14).

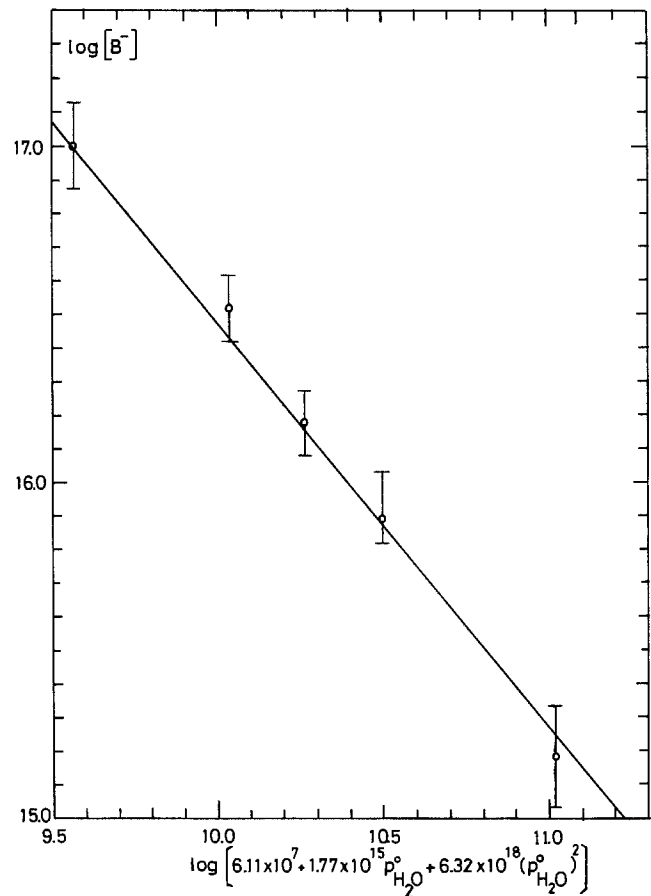


Fig. 8. Experimentally determined boron concentration for $P_{B_2H_6}^0 = 10^{-9}$ atm (see Fig. 7) as a function of the theoretical parameter $[6.11 \times 10^7 + 1.77 \times 10^{15} \cdot P_{H_2O}^0 + 6.32 \times 10^{18} \cdot (P_{H_2O}^0)^2]$ (see Eq. [4]). The data points are calculated from Ref. (14).

Water vapor thus appears to be undesirable when good quality epi is desired; however, it reduces the autodoping in the boron system. The same is true for the presence of HCl; autodoping therefore could be less a problem in growth via chlorosilanes compared to growth via silane (SiH_4). Undoubtedly, the surface coverage with foreign atoms will also influence the growth rate as a function of orientation of the substrate. In this respect, the pattern shift and pattern recognition will depend on small differences in surface contamination. Indications in this direction are available (28), but much study in this direction is still needed.

Conclusion

With the assumption that at the growing silicon surface equilibrium exists between the dopant compounds in the gas phase near the surface, calculation of the gas-phase composition yields valuable results that can be used for studying the equilibrium between the gas phase and the solid. This has been done for the interpretation of the quantity of boron which can be incorporated in silicon in the presence of small amounts of water during the growth of silicon by CVD from SiH_4 in H_2 at atmospheric pressure. The one-to-one correspondence which is obtained between equilibrium calculations and experimental results once more gives a firm indication that equilibrium calculations are quite valuable to obtain insight in the chemistry and physics of CVD processes. In addition, now an explanation can be given for the unusual behavior of boron autodoping at lower pressures.

Manuscript submitted Nov. 28, 1983; revised manuscript received March 23, 1984.

Katholieke Universiteit assisted in meeting the publication costs of this article.

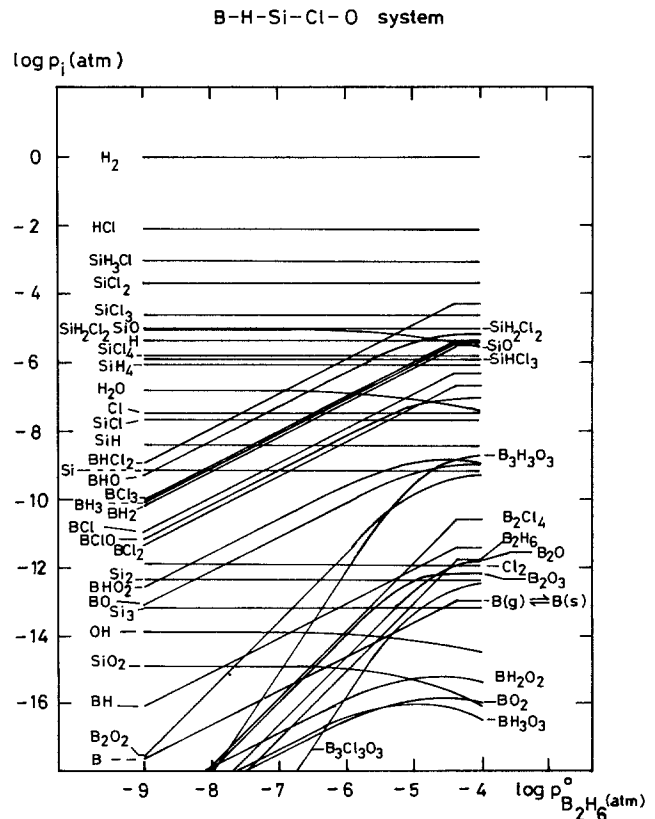


Fig. 9. Calculated equilibrium composition of the B-H-Si-Cl-O system as a function of $P_{B_2H_6}^0$ ($P_{SiH_4}^0 = 10^{-3}$ atm, $P_{HCl}^0 = 10^{-2}$ atm, $P_{H_2O}^0 = 10^{-5}$ atm, $P_{tot} = 1$ atm, $T = 1400$ K).

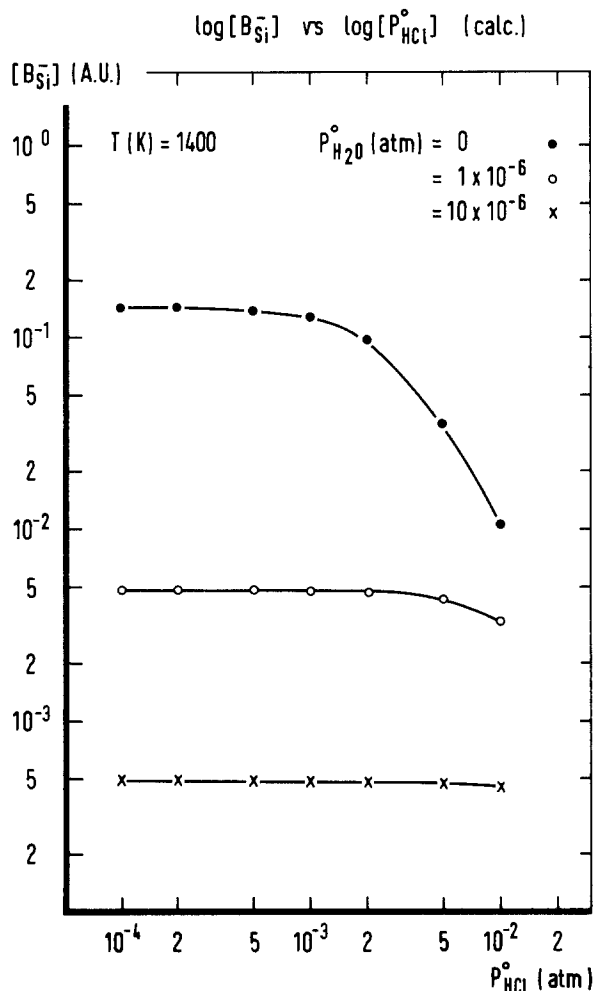


Fig. 10. Calculated boron concentration as a function of P_{HCl}° for the B-H-Si-Cl-O system with $P_{\text{H}_2\text{O}}^{\circ}$ as a parameter ($P_{\text{SiH}_4}^{\circ} = 10^{-3}$ atm, $P_{\text{tot}} = 1$ atm, $T = 1400$ K).

REFERENCES

- W. H. Shepherd, *This Journal*, **115**, 541 (1968).
- J. Bloem, *J. Cryst. Growth*, **13/14**, 302 (1972).
- J. Bloem, in "Semiconductor Silicon 1973," H. R. Huff and R. R. Burgess, Editors, pp. 213-226, The Electrochemical Society Softbound Proceedings Series, Princeton, NJ (1973).
- J. Bloem, *J. Cryst. Growth*, **31**, 256 (1975).
- T. B. Swanson and R. N. Tucker, *This Journal*, **116**, 1271 (1969).
- P. Rai-Choudhury, *J. Phys. Chem. Solids*, **30**, 1811 (1969).
- P. Rai-Choudhury and E. Salkovitz, *J. Cryst. Growth*, **7**, 353 (1970).
- P. Rai-Choudhury and E. Salkovitz, *ibid.*, **7**, 361 (1970).
- D. T. J. Hurle, R. M. Logan, and R. F. C. Farrow, *ibid.*, **12**, 73 (1972).
- J. Bloem, L. J. Giling, and M. W. M. Graef, *This Journal*, **121**, 1354 (1974).
- L. J. Giling and J. Bloem, *J. Cryst. Growth*, **31**, 317 (1975).
- H. Kühne, *Krist. Tech.*, **13**, 841 (1978); *ibid.*, **13**, 939 (1978); *ibid.*, **13**, 1059 (1978); *ibid.*, **14**, 333 (1979); *ibid.*, **14**, 413 (1979); H. Kühne and R. Sperling, *ibid.*, **15**, 403 (1980); H. Kühne, R. Sperling, and Th. Morgenstern, *ibid.*, **15**, 1051 (1980); H. Kühne, *Cryst. Res. Technol.*, **17**, 181 (1982); *ibid.*, **17**, 1097 (1982); *ibid.*, **17**, 1217 (1982); *ibid.*, **17**, 1379 (1982).
- R. Reif, T. I. Kamins, and K. C. Saraswat, *This Journal*, **125**, 1860 (1978); *ibid.*, **126**, 644, 653 (1979); R. Reif and

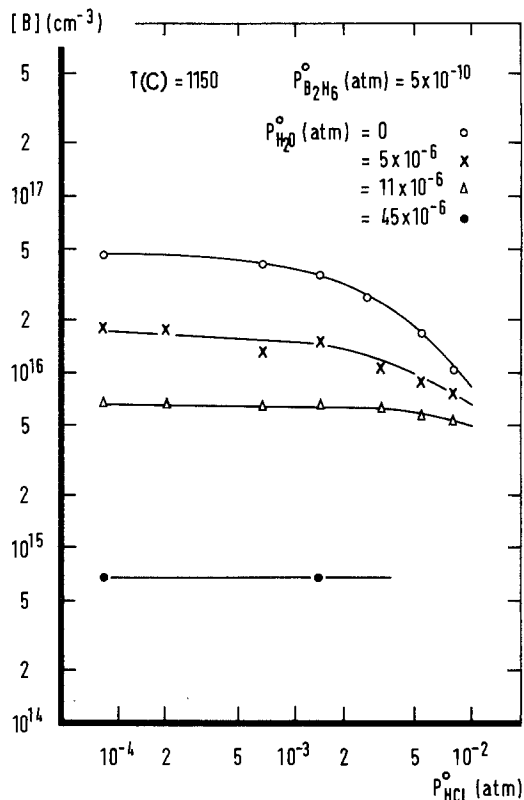


Fig. 11. Experimentally determined boron concentration as a function of P_{HCl}° (14) for the B-H-Si-Cl-O system for various input partial pressures of water ($P_{\text{SiH}_4}^{\circ} = 10^{-3}$ atm, $P_{\text{B}_2\text{H}_6}^{\circ} = 5 \times 10^{-10}$ atm, $P_{\text{tot}} = 1$ atm, $T = 1150^{\circ}\text{C}$). Experimental data from Ref. (14).

R. W. Dutton, *ibid.*, **128**, 909 (1981); R. Reif and M. Vanzi, *ibid.*, **128**, 218 (1981); R. Reif, *ibid.*, **129**, 1122 (1982).

- J. Bloem, *ibid.*, **118**, 1839 (1971).
- G. W. M. Staarink and F. Jakma, Equilibrium Computations in the Chemical Vapour Deposition Systems using the Mass Action Law for describing the system (ECCVD-MAL), (Computer program), Catholic University Nijmegen, Nijmegen, March 1979.
- Janaf Thermochemical Tables, 2nd ed., (NSRDS-NBS 37), U.S. Department of Commerce, (1971) and Supplements (1974, 1975, 1978).
- E. Dominguez, E. Lora-Tamayo, B. Blanchard, and J. Bellanto, *This Journal*, **125**, 1521 (1978).
- H. J. Rijks, J. Bloem, and L. J. Giling, *J. Cryst. Growth*, **47**, 397 (1979).
- F. C. Eversteijn and B. H. Put, *This Journal*, **120**, 106 (1973).
- P. Rai-Choudhury and P. L. Hower, *ibid.*, **120**, 1761 (1973).
- J. Bloem and L. J. Giling, in "Current Topics in Materials Science," Vol. 1, E. Kaldis, Editor, Chap. 4, p. 309, North Holland, Amsterdam (1978).
- J. Bloem, L. J. Giling, and M. W. M. Graef, *This Journal*, **122**, 840 (1975).
- P. H. Langer and J. I. Goldstein, *ibid.*, **121**, 563 (1974).
- P. H. Langer and J. I. Goldstein, *ibid.*, **124**, 591 (1977).
- G. R. Srinivasan, *ibid.*, **127**, 1334 (1980).
- M. L. Hammond, *Solid State Technol.*, **20**, 68 (1978).
- D. H. Tang, T. K. Ning, R. D. Issac, G. C. Feth, S. K. Wiedemann, and H. N. Yu, *IEEE Trans. Electron. Devices*, **ed-27**, 1379 (1980).
- J. F. Corboy, C. W. Cullen, and R. Pagliaco, Jr., Paper 202 presented at Semicon Europe, Zürich, March 1983.
- J. Bloem, Private communication.

Thermal Oxidation of Sputtered Silicon Carbide Thin Films

W.-J. Lu and A. J. Steckl*

Center for Integrated Electronics, Rensselaer Polytechnic Institute, Troy, New York 12181

T. P. Chow* and W. Katz

General Electric Corporate Research and Development, Schenectady, New York 12345

ABSTRACT

The physical properties and oxidation behavior of silicon carbide thin films are reported. These films were RF sputtered from a composite target of stoichiometric proportion onto thermally oxidized silicon substrates. The refractive index of the carbide films, after annealing at 1100°C in hydrogen, was very close to the bulk value of 2.65. Structural and compositional properties were studied by Rutherford backscattering spectrometry, secondary ion mass spectrometry, and x-ray diffraction techniques. Thermal oxidation was carried out in wet and dry oxygen at 900°-1100°C for a period of up to 16h. Depending on the temperature and time period, the oxidation rate of silicon carbide was about 2-11 times slower than that of single-crystal (100) Si. The oxide layer grown out of the carbide films was determined to be silicon oxide. The average activation energy for wet and dry oxidation was calculated to be 50 and 43.5 kcal/mol, respectively. The patterning of the SiC films was investigated using CF_4/O_2 and NF_3 plasmas. "Bird's beak" profiles, obtained upon field oxidation of SiC/SiO₂/Si structures, were studied.

Silicon carbide has been used for various industrial applications. Among these are (i) for making electron devices (1, 2) because of its semiconducting properties and chemical inertness and stability at very high temperatures, and (ii) for surface coatings (3) due to its high wear resistance.

In this paper, however, thin films of silicon carbide are being investigated as an alternative or addition to silicon nitride in local oxidation technology (LOCOS) for Si VLSI fabrication. Like silicon nitride, silicon carbide is refractory and fairly resistant to oxidation in bulk form. In Table I, some of the appropriate physical properties of SiC, Si₃N₄, SiO₂, and Si are shown from Ref. (4-9).

As can be seen from Table I, a range of values has been published for the Young modulus of SiC, Si₃N₄, and Si. At best, the Young modulus for SiC is a factor of 5 higher than that of Si₃N₄. In that case, a more rigid SiC layer would result in reduced "bird's beak" formation.

A variety of methods for depositing SiC films have been reported, including RF sputtering (3, 10-12), chemical vapor deposition (1, 13-15), and reactive evaporation (16). In this work, RF sputtering from a composite SiC target was used for film deposition.

Ellipsometry, secondary ion mass spectrometry (SIMS), x-ray diffraction, and Rutherford backscattering spectrometry (RBS) were used to investigate the structural and physical properties of these thin films.

In order to apply SiC in the LOCOS technology, the oxidation behavior of carbide films needs to be studied in detail. Thermal oxidation properties of SiC films were investigated in both wet and dry oxygen. "Bird's beak" profiles were obtained from plasma-etched and oxidized SiC/SiO₂/Si structures and examined with cross-sectional scanning electron microscopy.

Experimental Procedure

A Veeco sputtering system was used for the carbide film deposition. A hot-pressed stoichiometric SiC composite target (99.7%) was used as cathode. The SiC films were RF sputtered onto thermally oxidized or unoxidized (100) silicon substrates in an argon pressure of 6×10^{-3} torr. The RF power ranged from 75 to 200W, and the substrate temperature was maintained at either 25° or 300°C. The background pressure before sputtering was usually less than 2.0×10^{-6} torr. Unless otherwise specified, after deposition, the SiC films were annealed at 1100°C in H₂ ambient for 30 min.

The SiC film deposition rate as a function of RF power is shown in Fig. 1. Film thickness was calculated from

*Electrochemical Society Active Member.

Key words: oxidation kinetics, activation energy, plasma etching, bird's beak.

SIMS and RBS profiles. Typical depositions were performed with an RF power of 200W (~ 5 W/cm²), resulting in a deposition rate of $\sim 125\text{\AA}/\text{min}$. The substrate temperature appears to have little effect on the deposition rate.

Thin Film Deposition

In order to study the refractive indexes of deposited SiC thin films for various annealing temperatures, the SiC films were first deposited on silicon substrates, and then annealed in a H₂ ambient for 30 min over the temperature range of 800°-1100°C. An automated ellipsometer (Rudolph Research) was used to determine the refractive index at a wavelength of 6328Å. The silicon substrate is assumed to have a refractive index of 3.86 and an absorption index of 0.018. Figure 2 illustrates the dependence of the refractive index of SiC films on the annealing temperature. The refractive index of as-sputtered SiC films is between 3.1 and 3.35. The refractive index of annealed films decreases as the annealing temperature increases.

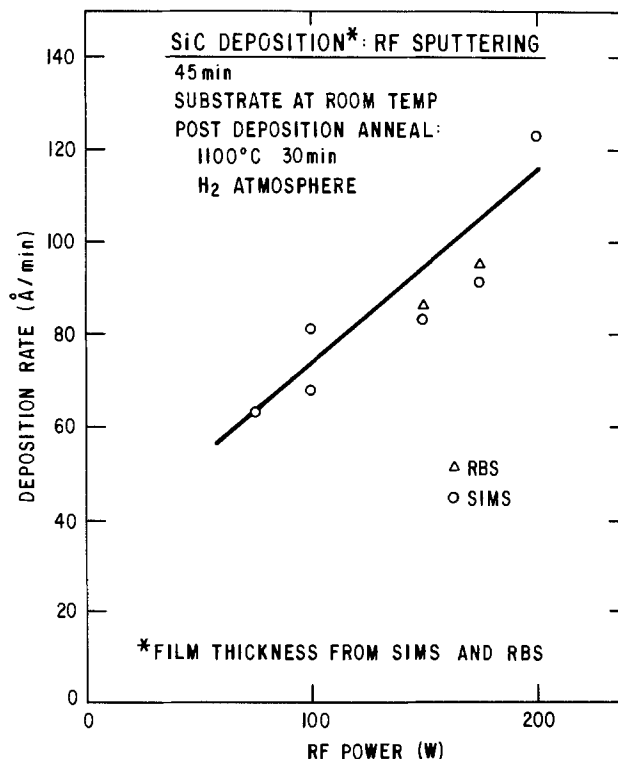


Fig. 1. SiC deposition rate as a function of RF power

Table I. Physical properties of SiC, Si₃N₄, SiO₂, and Si

	Melting point (°C)	Refractive index	Heat of formation (kcal/g-mol)	Dielectric constant	Coefficient of thermal expansion ($\times 10^{-6}$ °C ⁻¹)	Young's modulus ($\times 10^6$ psi)
SiC	2700 (6)	2.65 (6)	-27 (6)	10.0 (4)	4.2 (4)	70 (6) 50 (9)
Si ₃ N ₄	1900 (6)	2.05 (5)	-179 (6)	7.5 (5)	2.8 (7)	55 (6) 13 (9)
SiO ₂	1600 (5)	1.46 (5)	-205 (6)	3.9 (5)	0.55 (6)	10.4 (6) 26 (6)
Si	1410 (6)	3.86 (8)	0 (6)	11.9 (5)	2.6 (5)	16 (9)

For an annealing temperature of 1100°C, the index reaches an average value close to the SiC bulk value of 2.65. The decrease in refractive index with increasing anneal temperature is believed to be related to the concomitant increase in the crystallinity of the SiC films (17).

RBS was performed to determine the Si/C ratio and contaminants present in the films. A 2 MeV ⁴He⁺ beam from a linear accelerator was used. The Si/C ratio computed from the data shown in Fig. 3 is very close to unity. Argon, which was used for film deposition, has been incorporated into the SiC layer and is estimated to be at ~ 2.2 atom percent.

SIMS analysis was performed with a Cameca IMS3-f ion microscope in order to study the major contaminants

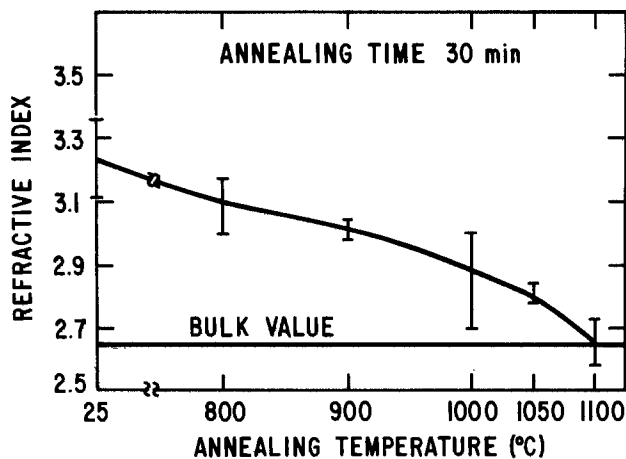


Fig. 2. Refractive index as a function of annealing temperature

Fig. 3. RBS spectrum of annealed silicon carbide film.

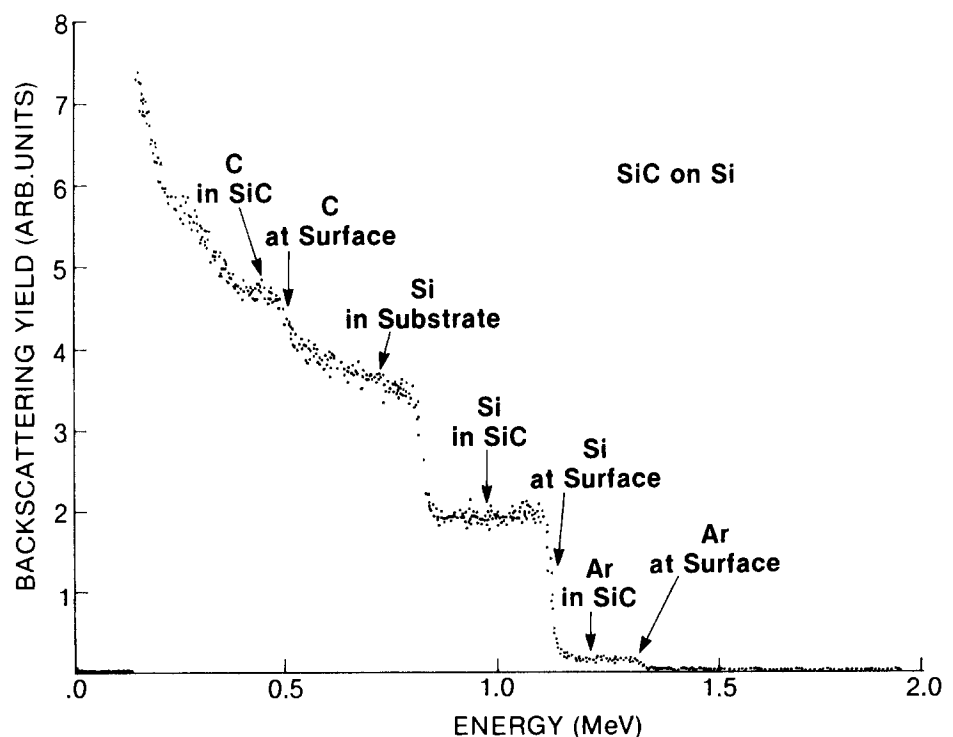


Table II. Deposition conditions and related thin film properties

Sample	Background pressure (torr)	O/C ratio (from SIMS)	X-ray peaks	Oxidation resistance
MA-1-1	8.3×10^{-6}	0.6	SiO ₂	Lowest
MS-16	$< 2 \times 10^{-6}$	0.054	SiC	Highest
MA-4-1	3×10^{-6}	0.1	SiO ₂ , SiC	High

in annealed SiC films. Under the bombardment of a cesium primary beam with an impact energy of 17 eV, the relative intensities of various negative ion species—silicon (³⁰Si⁻), carbon (¹²C⁻), argon (⁴⁰Ar⁻), and oxygen (¹⁶O⁻)—were sampled as a function of depth. Figures 4a-4c show the SIMS data for three samples deposited under different conditions (see Table II), but annealed under essentially the same condition.

The SIMS data indicate a constant Si/C ratio with depth for all three samples. Oxygen was present in considerable amounts in the film of Fig. 4a, and to a lesser degree in the films of Fig. 4b and 4c. We found that minimizing the oxygen content in the carbide films results in increasing resistance to thermal oxidation. Under the same oxidation conditions (1000°C, wet O₂, 60 min), sample MA-1-1 (Fig. 4a) exhibited a 3400Å thick oxide, while samples MS-16 (Fig. 4b) and MA-4-1 (Fig. 4c) had oxides of 375 and 700Å, respectively.

X-ray diffraction was performed to investigate the crystallinity of the carbide films using a D-500 Siemens automated diffractometer. The x-ray spectra of Fig. 5a, 5b, and 5c are for the same samples as the SIMS profiles of Fig. 4a, 4b, and 4c. The peaks at 2θ angles of 35° and 70° correspond to SiC and Si, respectively. Since only one sil-

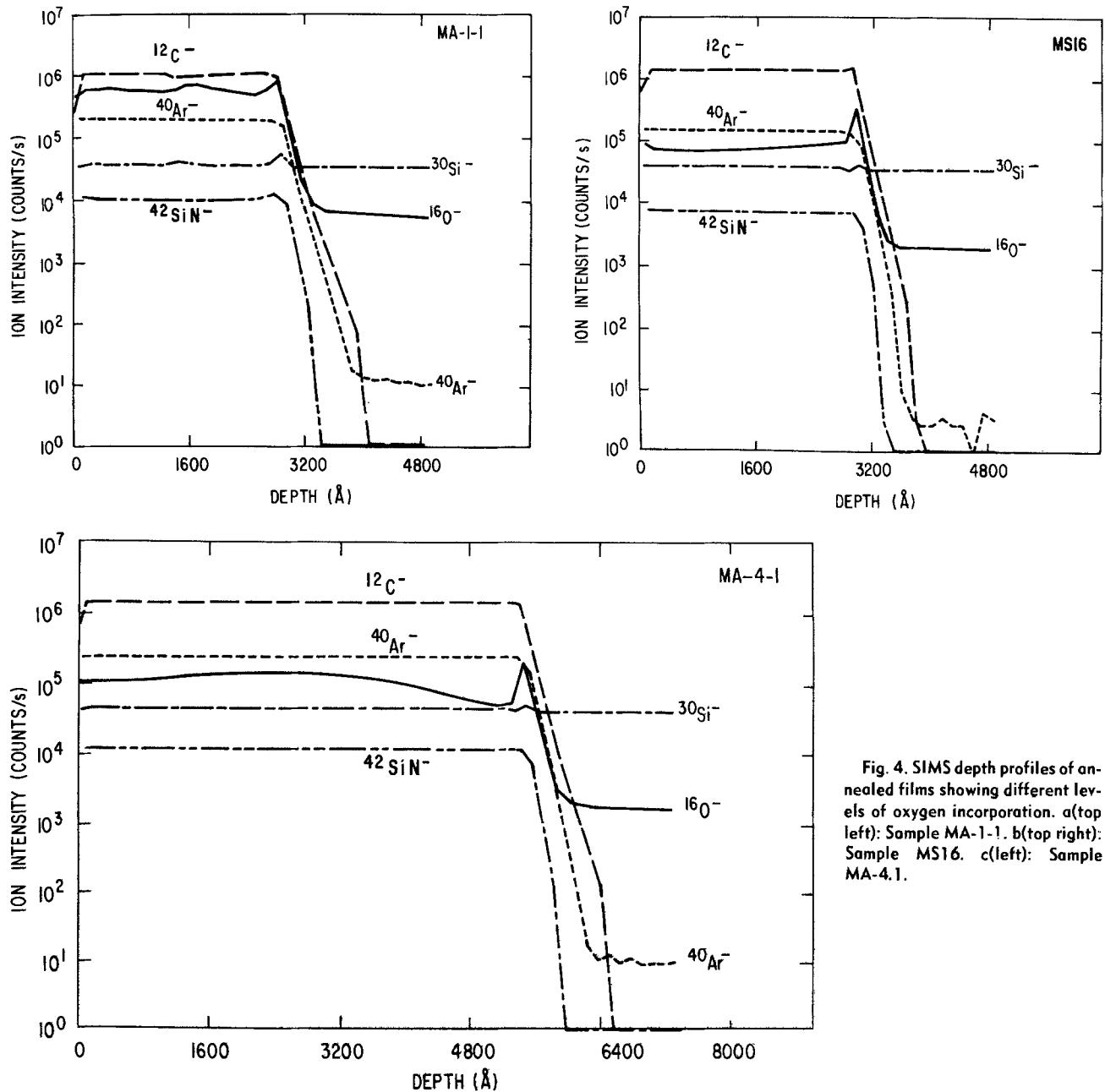


Fig. 4. SIMS depth profiles of annealed films showing different levels of oxygen incorporation. a(top left): Sample MA-1-1. b(top right): Sample MS16. c(left): Sample MA-4.1.

icon carbide peak was detected (corresponding to 2.51\AA), we could not determine the phase of our SiC films. The peak at 1.36\AA corresponds to the (400) peak of the Si substrate (18). The peaks at 2θ angles ranging from 15° to 25° are attributed to SiO_2 (19). For sample MA-1-1, shown in Fig. 4a as having the highest oxygen concentration, no SiC peak is observed in Fig. 5a. For sample MS-16, which exhibited the minimum O_2 contamination (as shown in Fig. 4b), the SiC peak is very strong and not accompanied by the SiO_2 lines (Fig. 5b). These data clearly show the strong effect of oxygen on the crystallinity of the silicon carbide films.

The relationship between deposition conditions (*i.e.*, background pressure) and thin film properties is summarized in Table II.

Oxidation Properties

It is known that the presence of water vapor in O_2 greatly accelerates the oxidation rate of Si and also enhances the oxidation rate of hot-pressed SiC (20). There have been many reports on the oxidation of SiC powder or crystal (20-23). However, to the best of our knowledge, no SiC thin film oxidation has been previously reported.

To study the oxidation resistance of SiC thin films, wet and dry thermal oxidation was conducted from 900° to

1100°C for periods of time of 15 min to 16h. Wet oxygen was prepared by bubbling the oxygen through deionized water at 95°C . The flow rate of oxygen was 1.9 l/min. The SiC thin films used for oxidation were prepared by RF sputtering for 45 min ($\sim 5500\text{\AA}$ thick) onto oxidized Si (100) wafers, followed by an anneal in H_2 at 1100°C for 30 min.

The oxide layer grown out of unannealed silicon carbide consisted only of silicon and oxygen, as shown by the SIMS depth profile in Fig. 6. Similar results were obtained in the case of films annealed prior to oxidation. The absence of carbon in oxide films grown out of bulk, single-crystal SiC was also reported by Suzuki *et al.* (21).

It has been found that the oxidation rate of as-sputtered SiC films is generally higher than that of annealed films (24). Figure 7 shows the effect of preoxidation annealing on wet oxidation of SiC films. The annealing temperature ranged from 800° to 1100°C and took place in H_2 for 30 min. As can be seen from the data in Fig. 7, the oxidation rate at lower temperatures ($T_{\text{ox}} = 950^\circ\text{C}$) is strongly influenced by preoxidation annealing. When the annealing temperature is increased by 100°C from 900° to 1000°C , a decrease in oxidation rate of a factor of 15 is achieved at $T_{\text{ox}} = 950^\circ\text{C}$. However, at higher oxidation temperatures (1050°C), the annealing process appar-

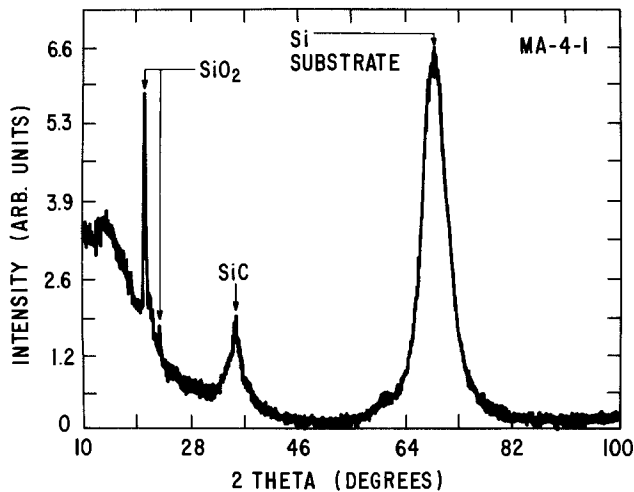
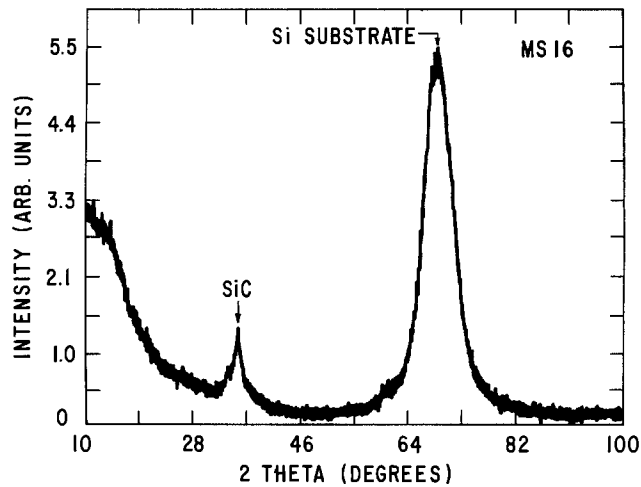
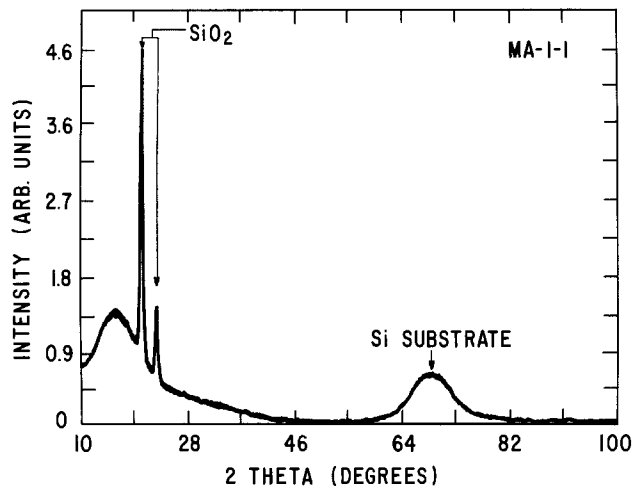


Fig. 5. X-ray diffraction spectra for the films shown in Fig. 4. a(top left): Sample MA-1-1. b(top right): Sample MS16. c(left): Sample MA-4-1.

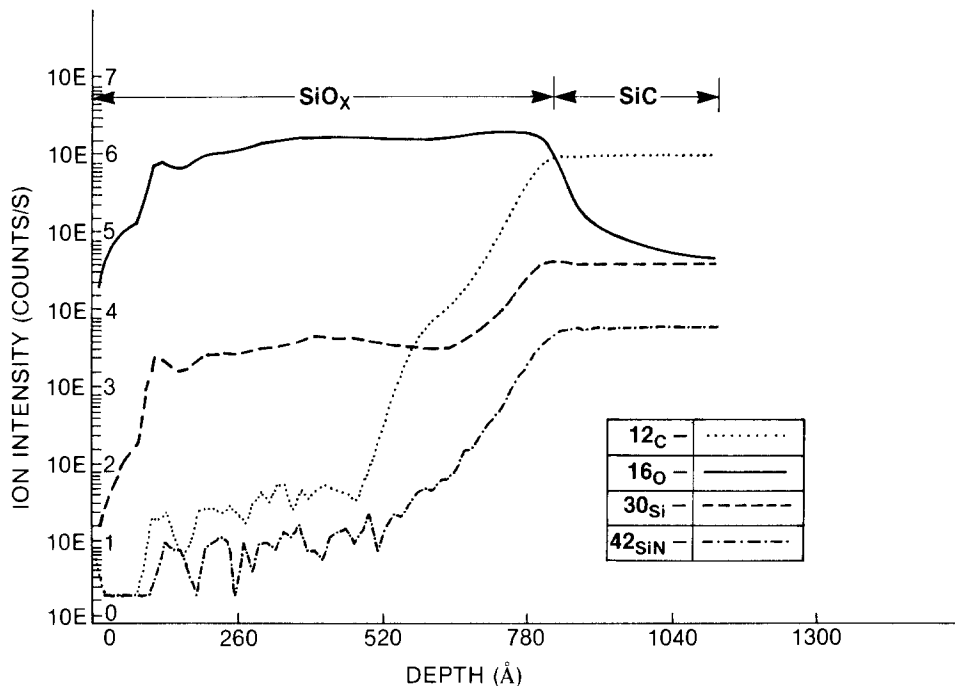
ently takes place concurrently with the oxidation, resulting in a drastically reduced difference in oxidation rate. Figure 8 shows that a similar effect of preoxidation annealing on dry oxidation takes place.

The wet oxide thickness grown from annealed (1100°C) films as a function of time and temperature is shown in Fig. 9. The average oxidation rate of SiC crystal reported by Suzuki *et al.* (21) for $T_{ox} = 1000^{\circ}\text{C}$ is also shown for comparison. In general, the oxidation of our films agrees

well with the reported single-crystal oxidation data, except at long periods of time where our films do not follow the parabolic oxidation law.

Figure 10 shows the oxide thickness on silicon carbide as a function of dry oxidation time and temperature. The preoxidation annealing conditions were the same as in the case of wet oxidation. The dry oxidation also does not appear to obey the parabolic law for periods as long as 16h.

Fig. 6. SIMS depth profiles of oxidized silicon carbide films.



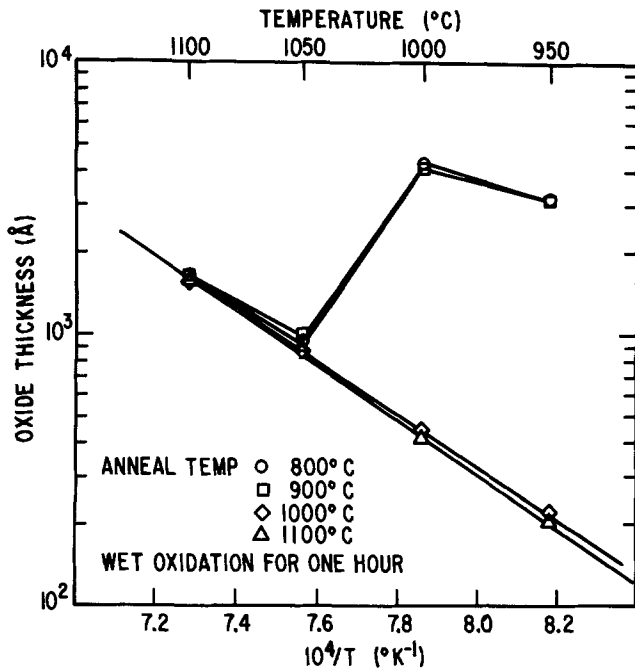


Fig. 7. Effect of pre-oxidation annealing on wet oxidation

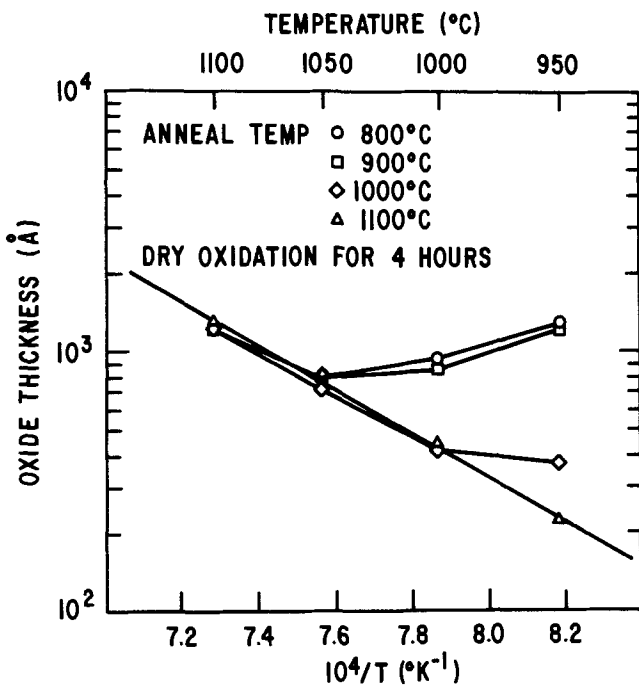


Fig. 8. Effect of pre-oxidation annealing on dry oxidation

The Si (100)/SiC wet and dry oxidation rate ratio is shown in Fig. 11 and 12 as a function of oxidation time and temperature. For the same conditions, the ratio is higher for wet oxidation than for dry oxidation. It can also be seen that the ratio is highest at lower oxidation temperatures and decreases as time or temperature increases. It is expected that by continuing to decrease the temperature ($T_{ox} < 900^\circ\text{C}$), one can obtain further increases in oxidation rate ratio.

The wet and dry oxide thickness obtained at different temperatures are shown in Arrhenius plots in Fig. 13 and 14, respectively. Using the equation

$$X^n = Cte^{-E_a/kT}$$

for thermal oxidation kinetics, where X is the oxide thickness, C is a constant, and t and T are the oxidation time and temperature, respectively, one can calculate the value

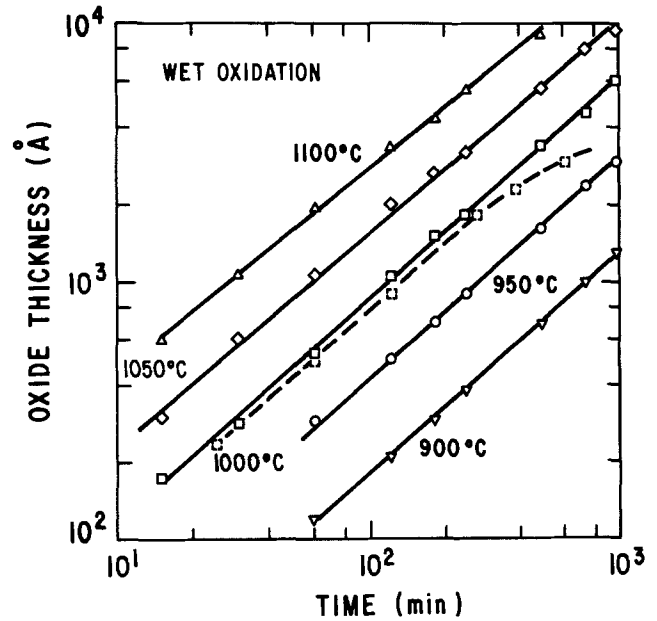


Fig. 9. Silicon carbide wet oxidation thickness as a function of time and temperature. Dashed line is data of Suzuki *et al.* (21), showing average of Si- and C-face wet oxidation of SiC single crystal at 1000°C .

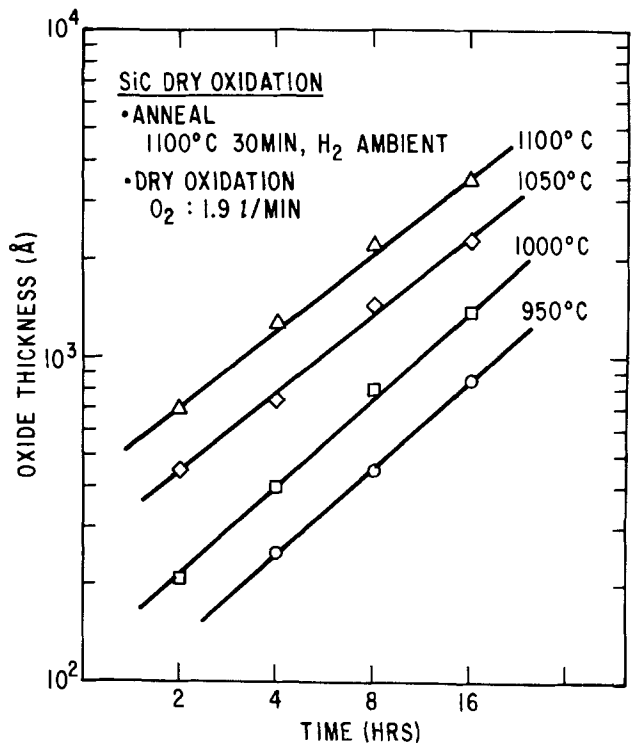


Fig. 10. Silicon carbide dry oxidation thickness as a function of time and temperature.

of the activation energy, E_a . For wet oxidation we obtained values of n of 1.15-1.34 and activation energies ranging from 49-52 kcal/mol. For the case of dry oxidation, the respective values were $n = 1.13-1.31$ and $E_a = 37-48$ kcal/mol. It is interesting to note that for both wet and dry oxidation similar values of n were obtained. The activation energies are also comparable in these cases. As shown in Table III, it is difficult to compare our results with those published in the literature on the oxidation of SiC crystals. The crystalline form and phase of the SiC have a strong effect on its oxidation properties. Comparing the data of Suzuki *et al.* (21), and Harris and Call (25), one can note that in the parabolic region ($n = 2$) they obtain the same activation energy (47-48 kcal/mol) for the C-face under wet and dry oxidation. This activation en-

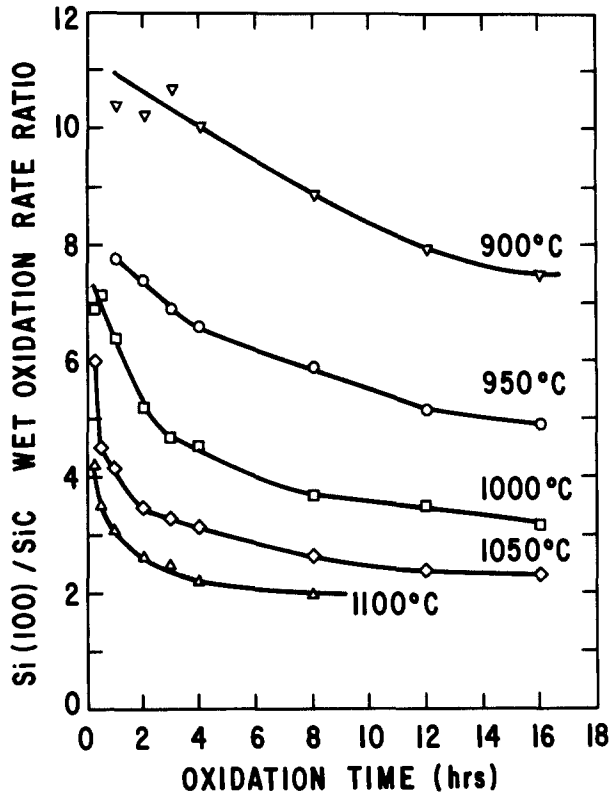


Fig. 11. Silicon-silicon carbide wet oxidation rate ratio

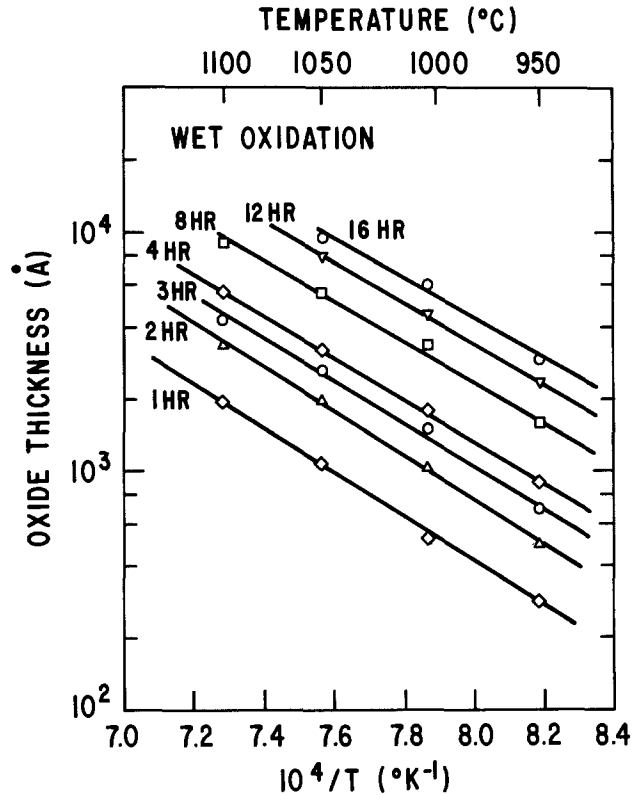


Fig. 13. Activation energy for silicon carbide wet oxidation

ergy also roughly agrees with our results under both wet and dry conditions. However, for our thin film oxidation, we are essentially in the linear region with values of *n* closer to 1. This suggests that in our case the oxidation is limited more by the reaction rate than by the diffusion of various species.

Application to IC Processing

The use of SiC as an oxidation mask in the LOCOS process is being studied. The patterning of the SiC films was investigated using CF₄/O₂ and NF₃ plasmas. The etch rate

of unannealed films was generally higher than that of annealed films. For the latter, in a planar reactive ion etching system (Plasma Therm PK 1241) using NF₃, the etch rate was 320 Å/min at a pressure of 100 mtorr and a power of 200W. In a planar plasma system (Technics P.E. II), using CF₄/4% O₂, the etch rate was ~ 500 Å/min at a pressure of 300 mtorr and power of 300W. "Bird's beak" profiles were obtained upon field oxidation of the SiC/SiO₂/Si structures. A positive photoresist (Shipley AZ-1350J) was used for masking the SiC film during patterning. For example, Fig. 15 shows bird's beak profiles

Fig. 12. Silicon-silicon carbide dry oxidation rate ratio.

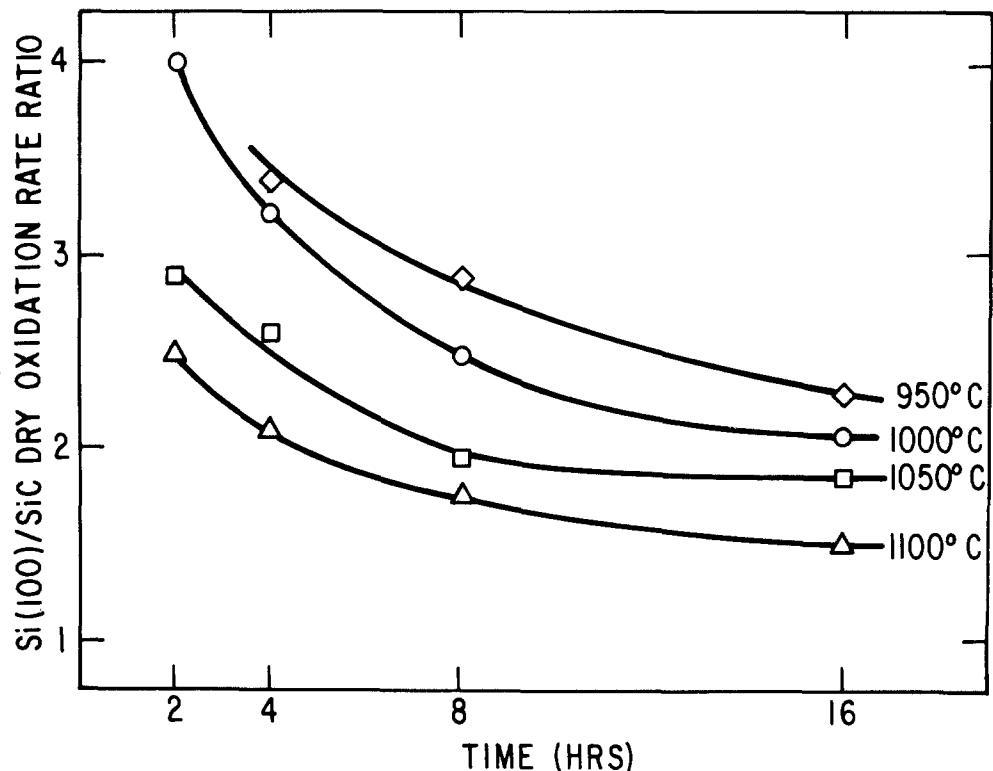


Table III. Comparison of oxidation kinetics for SiC bulk crystals and thin films

SiC form	Ambient	n^*	E_a (kcal/mol)	Temp. range	Ref.
6H crystal	Wet O ₂	1	26	850°-1100°C	(21)
C-face		2	48		
6H α -SiC	Dry O ₂	2	47	970°-1245°C	(25)
C-face		1	85		
RF-sputtered thin films	Dry O ₂	1.13-1.31	37-48	950°-1100°C	This work
	Wet O ₂	1.15-1.34	49-52		

$$* X^n = C t \exp(-E_a/kT).$$

resulting from a wet oxidation at 1000°C for 150 min for a structure consisting of a SiC layer of $\sim 4000\text{\AA}$ and a pad oxide of 280\AA . The resulting field oxide was $\sim 5000\text{\AA}$

while the SiC oxidized layer had a thickness of $800\text{-}900\text{\AA}$. The bird's beak figure of merit was measured to be $M = t_{\text{BB}}(10\%-90\%)/t_{\text{FOX}} \approx 0.5$. The bird's beak effect was observed to increase with pad oxide and field oxide thickness.

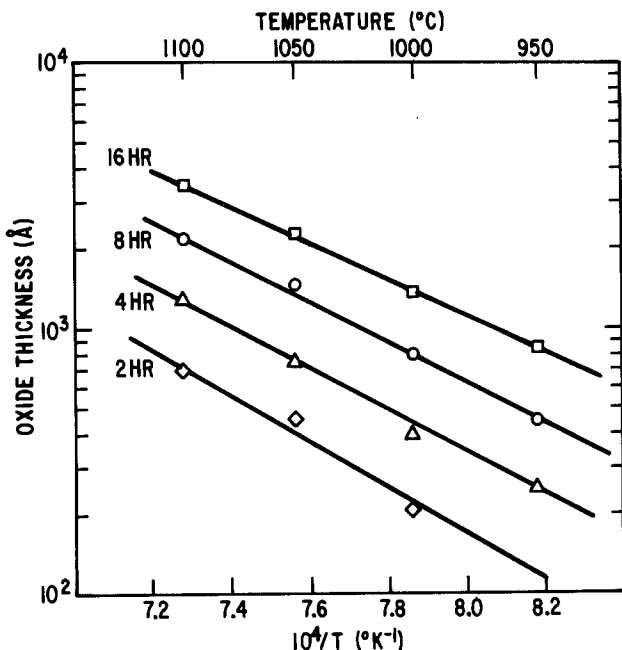


Fig. 14. Activation energy for silicon carbide dry oxidation

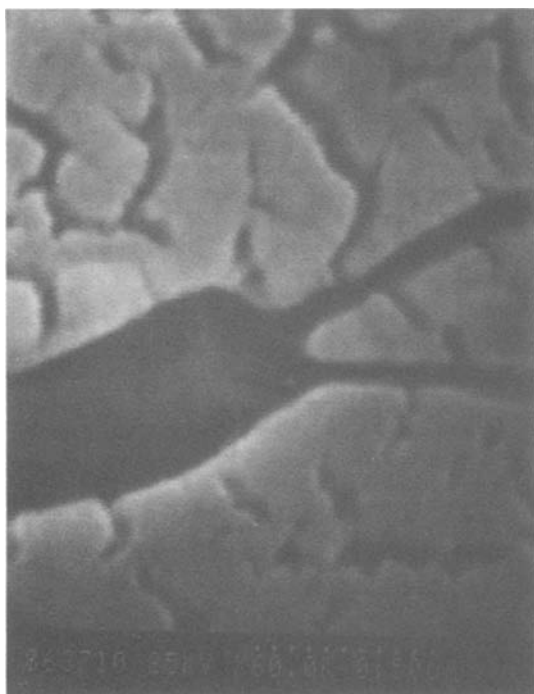


Fig. 15. "Bird's beak" profile obtained with the following parameters: $t_{\text{SiC}} = 4000\text{\AA}$, $t_{\text{SiO}_2(\text{pad})} = 280\text{\AA}$, and $t_{\text{SiO}_2(\text{field})} = 5000\text{\AA}$ (150 min, 1000°C).

Summary

The thermal oxidation of silicon carbide thin films has been shown to result in the growth of silicon oxide overlayer. The growth rate is sufficiently slow, such that LOCOS-type structures using SiC are feasible.

Acknowledgments

Two of the authors (W. J. L. and A. J. S.) would like to acknowledge partial support from the Office of Naval Research. The authors would like to thank R. Goehner for x-ray diffraction data and G. Smith for RBS measurements.

Manuscript submitted Nov. 16, 1983; revised manuscript received March 23, 1984.

REFERENCES

1. S. Nishino, A. Ibaraki, H. Matsunami, and T. Tanaka, *Jpn. J. Appl. Phys.*, **19**, L353 (1980).
2. W. V. Muench and P. Hoeck, *Solid State Electron.*, **21**, 479 (1978).
3. Y. Hirohata, M. Kobayashi, S. Maeda, K. Nakamura, M. Mohri, K. Watanobe, and T. Yamashina, *Thin Solid Films*, **63**, 237 (1979).
4. R. C. Marshall, J. W. Faust, Jr., and C. E. Ryan, "Silicon Carbide 1973," pp. 668-673, University of South Carolina Press, Columbia, SC (1974).
5. S. M. Sze, "Physics of Semiconductor Devices," pp. 850-852, 2nd ed., John Wiley and Sons, New York (1981).
6. "Handbook of Chemistry and Physics," R. C. Weast, Editor, 62nd ed., CRC Press, Cleveland, OH (1981-1982).
7. H. F. Wolf, "Semiconductors," Wiley Interscience, New York (1971).
8. AutoEL^R—II Automatic Ellipsometer Instruction Manual. Rudolph Research.
9. P. T. B. Shaffer, "No. 1 Materials Index, Handbook of High Temperature Materials," pp. 50, 235, 284, Plenum Press, New York (1964).
10. K. Wasa, T. Nagai, and S. Hayakawa, *Thin Solid Films*, **31**, 235 (1976).
11. S. Nishino, H. Matsunami, M. Odaka, and T. Tanaka, *ibid.*, **40**, L27 (1977).
12. T. Tohda, K. Wasa, and S. Hayakawa, *This Journal*, **127**, 44 (1980).
13. S. Nishino, Y. Hazuki, H. Matsunami, and T. Tanaka, *ibid.*, **127**, 2674 (1980).
14. J. Chin, P. K. Gantzel, and R. G. Hudson, *Thin Solid Films*, **40**, 57 (1977).
15. W. V. Muench and I. Pfaffeneder, *ibid.*, **31**, 39 (1976).
16. Y. Murayama and T. Taka, *ibid.*, **40**, 309 (1977).
17. W.-J. Lu, T. P. Chow, and A. J. Steckl, To be published.
18. Standard Powder Diffraction Pattern 5-0560.
19. Standard Powder Diffraction Pattern 14-260.
20. S. C. Singhal, *J. Am. Ceram. Soc.*, **59**, 81 (1976).
21. A. Suzuki, H. Ashida, N. Furui, K. Mameno, and H. Matsunami, *Jpn. J. Appl. Phys.*, **21**, 579 (1982).
22. M. V. Muench and I. Pfaffeneder, *This Journal*, **122**, 642 (1975).

23. G. Ervin, Jr., *J. Am. Ceram. Soc.*, **41**, 347 (1958).
 24. W.-J. Lu, T. P. Chow, A. J. Steckl, and W. Katz, Abstract 86, p. 133, The Electrochemical Society Extended Abstracts, Vol. 83-1, San Francisco, CA, May 8-13, 1983.

25. R. C. A. Harris and R. L. Call, in "Silicon Carbide — 1973," R. C. Marshall, J. W. Faust, Jr., and C. E. Ryan, Editor, p. 329, University of South Carolina Press, Columbia, SC (1974).

A Defect Etchant for $\langle 100 \rangle$ InGaAsP

J. A. Lourenco

AT&T Bell Laboratories, Murray Hill, New Jersey 07974

ABSTRACT

A defect revealing etching technique for n-InGaAsP grown on $\langle 100 \rangle$ InP by LPE is reported. A chemical solution used with illumination produces protrusions in thin quaternary layers, which correlate well with dislocation pits in underlying and overlying InP layers. Using the new etchant, an increase in defect density in the active layer over the defect density in the buffer layer has been detected in lattice matched ($\approx 0.04\%$) InGaAsP/InP LED structures.

The importance of the InGaAsP/InP material system, for its applications in fiber optics, is well established. In particular, heterostructures grown on InP by liquid phase epitaxy (LPE) are becoming increasingly important for fabrication of lasers, light emitting diodes, and photodiodes.

During LPE, defects from the substrate propagate through the various epitaxial layers when growth takes place. High quality single-crystal InP substrates are therefore used in order to minimize defects in the heterostructure. Nevertheless, the dislocation density in the epitaxial layers can be greater than in the substrate (1). Misfit dislocations can also arise at the interface between two layers, if interfacial stress is present (2).

It is well known that degradation of GaAlAs/GaAs devices is in large part due to defects in the heterostructure, particularly in the active layer (3, 4). In addition, it has been shown that dislocations cause deleterious effects in InGaAsP and InP photodiodes (5, 6). Study of lattice defects is therefore important in order to improve material and device quality.

Chemical etching is the simplest method for revealing dislocations and other defects in crystals. A number of papers have been published recently dealing with chemical, electrochemical, and photochemical etching of InP (7-11), InGaAs (12, 13), and InGaAsP grown on $\langle 111 \rangle$ B InP (14, 15). However, the $\langle 100 \rangle$ orientation is widely utilized for LED's, lasers, and other devices, but no chemical etchant that selectively reveals dislocations in $\langle 100 \rangle$ InGaAsP layers has yet been reported. The difficulty in finding a suitable chemical etchant for quaternary layers lies in their thickness, which rarely exceeds $2.0 \mu\text{m}$. A defect etchant for such layers will have to be extremely preferential and have a slow etching rate in order to reveal the defects with minimal material removal.

In this paper, a technique is presented which can reveal dislocations in $\langle 100 \rangle$ n-InGaAsP layers. A chemical etchant with a very low etch rate is used, which becomes very preferential when coupled with illumination. This allows for the formation of small protrusions in quaternary layers that exactly match dislocation pits in neighboring InP layers. Etching studies of n-type quaternary layers grown on Sn-doped InP are reported. Dislocation propagation through the epitaxial layers in InGaAsP/InP double heterostructures is also described.

Experimental

The material for etch investigations was InP and InGaAsP grown by liquid phase epitaxy from two-phase melts, using a conventional multiwell graphite boat (16). The substrate was $\langle 100 \rangle$ oriented S-doped (to $\sim 5 \times 10^{18} \text{cm}^{-3}$) InP, polished with a 1.0% bromine-methanol solution. On the substrate, a $\sim 4.0 \mu\text{m}$ thick Sn-doped InP

layer was grown, followed by an undoped or lightly Sn-doped InGaAsP layer ($\lambda = 1.3 \mu\text{m}$), approximately $1.2 \mu\text{m}$ thick. To prevent any thermal dissolution of the quaternary layer, due to disproportionate loss of phosphorus from the InGaAsP surface during the cooling period after epitaxy, an additional undoped InP layer was grown on the n-InGaAsP. This is an important step, because any thermal damage to the quaternary surface will be selectively attacked by the etchant and interfere with the results.

The different etching solutions used in this study are listed in Table I. After epitaxy, the protective InP layer was removed using a 1:1 HCl:H₃PO₄ solution (17) (solution A), exposing a quaternary surface which is free of any thermal or chemical damage. A sample was then cut from the LPE wafer and etched for 10 min using a solution of 100 ml of H₂O, 8g KOH, and 0.5g K₃Fe(CN)₆ (18) (solution B). The etching took place under illumination from a microscope lamp with a 15W tungsten filament bulb, placed directly over the sample. Under these conditions, the etch rate was approximately $1.5 \mu\text{m/h}$. Illumination was required to reveal etch features since solution B was not preferential without the light, even though there was no significant difference in the etch rate. After photoetching, the specimen was examined by optical interference microscopy and etch features could be observed. SEM analysis showed them as protrusions on the sample surface. Figure 1a is an optical micrograph of the etched surface, showing these protrusions. Using a solution of 100 ml of H₂O, 8g KOH, and 12g K₃Fe(CN)₆ (solution C), the rest of the quaternary layer was then removed, exposing the Sn-doped InP epitaxial layer surface.

For etching of InP, the Huber etch (19) (solution D) is usually taken as the most reliable in revealing material defects (20). However, preliminary experiments had shown that a 1:3 HNO₃:HBr solution (9) (solution E) was superior to it with respect to reproducibility and surface quality after etching. This was particularly true when etching p-InP. Therefore, solution E was the InP defect etchant of choice in this experiment. Thus, the Sn-doped InP surface was etched using this solution for approximately 10s, revealing etch pits. Figure 1b shows an optical micrograph of the etched sample, with every etch pit matching a protrusion on Fig. 1a, confirming that most of

Table I. Etching solutions used in this study

Solution	Composition
A	1 part HCl, 1 part H ₃ PO ₄
B	100 ml H ₂ O, 8g KOH, 0.5g K ₃ Fe(CN) ₆
C	100 ml H ₂ O, 8g KOH, 12g K ₃ Fe(CN) ₆
D	2 parts H ₃ PO ₄ , 1 part HBr
E	1 part HNO ₃ , 3 parts HBr

Key words: photoetching, dislocations, defect propagation.

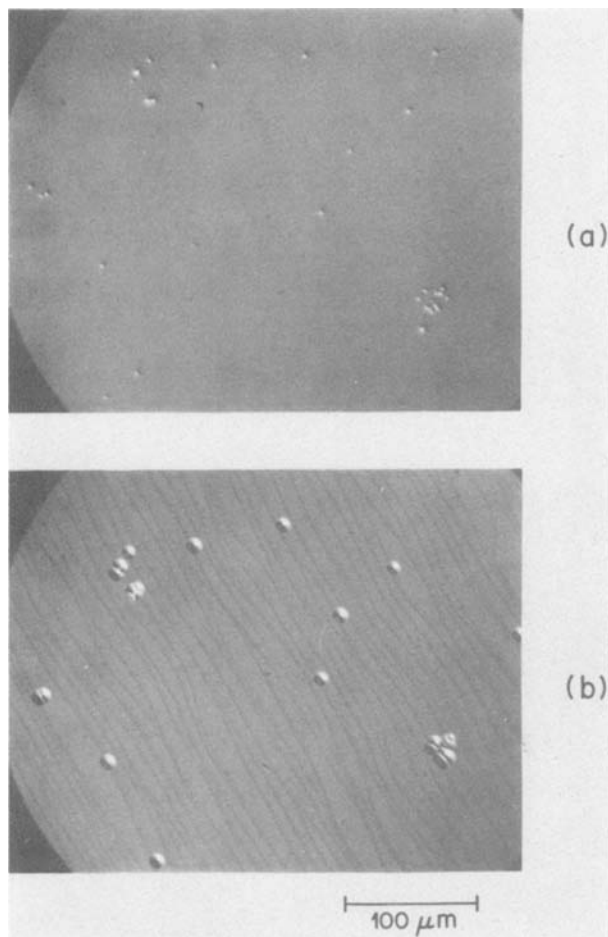


Fig. 1. Interference contrast micrograph showing etch features: (a) n-type quaternary layer etched with solution B under illumination; and (b) underlying Sn-doped InP layer etched with solution E.

the features on the quaternary layer are dislocations propagating through the epitaxial layers.

Although in many samples the etch features on the quaternary layer matched closely the ones on the InP layer, quite often there was an increase in the defect density of the InGaAsP over the dislocation density of the InP. To determine if these extra features on the etched surface of the quaternary layer were real defects and not etching artifacts, several four-layer InGaAsP/InP LED structures (21), grown by LPE, were examined. They consisted of a Sn-doped InP buffer layer ($\sim 4 \mu\text{m}$ thick) on a S-doped <100> oriented InP substrate, followed by a $1.2 \mu\text{m}$ thick quaternary layer ($\lambda = 1.3 \mu\text{m}$ and lattice matched to InP to better than $\pm 0.06\%$), a $1.5 \mu\text{m}$ thick Zn-doped InP confining layer, and a Zn-doped quaternary cap layer. First, the quaternary cap was removed with solution C. This exposed the p-InP confining layer, which was etched for 10s using solution E. Figure 2a is an optical interference micrograph of the etched surface, showing the defects in the confining layer. This layer was then completely removed with solution A, exposing the smooth and damage-free top surface of the quaternary active layer.

When trying to defect etch this surface using the new photoetchant, as described above, a major problem arose: the illuminated solution reacted with the surface, changing its morphology and in effect destroying it. The same phenomenon was observed when trying to defect etch p-InGaAsP single layers. In the LED heterostructures studied, only the top ($\sim 0.2 \mu\text{m}$) of the active layer was p-type, as a result of acceptor diffusion from the confining layer. Most of the $\sim 1.2 \mu\text{m}$ thick active layer remained n-type quaternary material. Using solution C for approximately 20s, the top of the active layer was removed, and the remaining quaternary was all n-type.

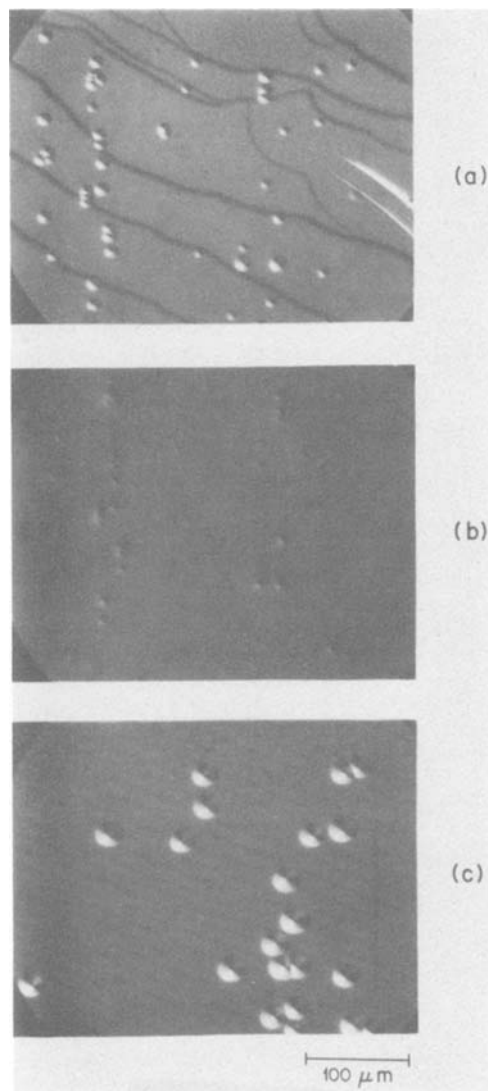


Fig. 2. Interference contrast micrograph of defect etched layers of a InGaAsP/InP double heterostructure: (a) Zn-doped InP confining layer etched with solution E; (b) quaternary active layer etched with solution B under illumination; and (c) Sn-doped InP buffer layer etched with solution E.

When examined under an optical microscope, the new surface showed no signs of damage or preferential etching. Using solution B under illumination for 10 min, no deleterious surface reaction was observed. Figure 2b is an interference contrast micrograph of the etched n-portion of the active layer, showing etch features that exactly match the defects revealed on the confining layer.

When the active layer is totally removed and the underlying n-InP buffer layer is etched using solution E, dislocation pits are observed, most of which correspond exactly to the defects revealed in the upper layers. However, once again many of the defects present in the quaternary and confining layers are absent from the buffer. Figure 2c shows the surface of the n-InP layer after defect etching: all the etch pits in this micrograph have matching features in Fig. 2a and 2b, but many of the defects in Fig. 2a and 2b are missing in Fig. 2c.

The difference in defect density between the buffer and the quaternary layers becomes striking when dislocation-free material is used as the substrate. A few heterostructures grown on substrates with defect density of $<100 \text{ cm}^{-2}$ were investigated. No significant difference in defect density between the buffer layer and the substrate was detected, but a large increase in the number of defects in the quaternary layer was observed. These defects then propagated into the confining layer without significant change in number. The increase in defect density in

the heterostructures was observed throughout the whole wafer in every wafer studied, although it was different in different parts of the wafers and also from wafer to wafer. The additional defects ranged in value from 3×10^3 to 8×10^4 cm⁻², and it was usually lower in the center portion of the wafers.

Results and Discussion

A 100 ml solution of 8.0g potassium hydroxide and 0.5g potassium ferricyanide, coupled with illumination, etches <100> n-InGaAsP slowly and preferentially, allowing for the formation of protrusions on the quaternary surface. Because of deleterious reaction between the photoetchant and the Zn-doped surface, no results were obtained for p-type quaternary layers. The pattern of defects on the n-InGaAsP surface exactly matches the pattern of etch pits in InP layers grown on the quaternary layer. It also correlates well with the defect pattern of the InP layer on which the InGaAsP layer was grown.

A one-to-one correlation between the dislocations in epitaxial InP layers and in the substrate has been shown by other workers (1), and the present results agree with it. In this study, a one-to-one correlation between the defects in the quaternary active layer and in the InP confining layer has also been observed, but a substantial increase in defect density in the active layer over the defect density in the buffer layer has been detected in most samples. This increase in defect number, ranging from 3×10^3 to 8×10^4 cm⁻² in the samples studied, is not very important in heterostructures grown on substrates with high dislocation densities (greater than 10^4 cm⁻²). However, when the dislocation density of the substrates is low (less than 10^3 cm⁻²), lattice defects generated during crystal growth become very significant. With dislocation density in many substrates presently approaching zero, these additional defects will preclude achieving zero dislocation epitaxial material.

Generation of these lattice defects in the InGaAsP layer may be due to several factors, such as interfacial stress, less than perfect wipe-off of the epitaxial surface, or poor wetting by the quaternary melt. It may also be due to thermal dissociation of the InP surface during the time it takes to move the substrate from well to well in the graphite boat. However, the exact source of these additional defects has not yet been determined, and more work is needed to track it down and, if possible, eliminate it.

Acknowledgments

The author is indebted to B. H. Chin for helpful comments and critical reading of this manuscript, A. K. Chin

for valuable suggestions, F. Ermanis for the SEM analysis, and R. H. Saul for his support.

Manuscript submitted Sept. 28, 1983; revised manuscript received March 16, 1984.

AT&T Bell Laboratories assisted in meeting the publication costs of this article.

REFERENCES

1. S. Mahajan, V. G. Keramidas, A. K. Chin, W. A. Bonner, and A. A. Ballman, *Appl. Phys. Lett.*, **38**, 255 (1981).
2. S. Yamazaki, Y. Kishi, K. Nakajima, A. Yamaguchi, and K. Akita, *J. Appl. Phys.*, **53**, 4761 (1982).
3. P. M. Petroff and L. C. Kimerling, *Appl. Phys. Lett.*, **29** 461 (1976).
4. O. Ueda, S. Isozumi, T. Kotani, and T. Yamaoka, *J. Appl. Phys.*, **48**, 3950 (1977).
5. T. P. Lee, C. A. Burrus, and A. G. Dentai, *IEEE J. Quant. Elect.*, **QE-15**, 30 (1979).
6. T. P. Lee and C. A. Burrus, *Appl. Phys. Lett.*, **36**, 587 (1980).
7. C. R. Elliott and J. C. Regnault, *This Journal*, **128**, 113 (1981).
8. S. N. G. Chu, S. Mahajan, K. E. Sturge, W. D. Johnston, and A. A. Ballman, *Appl. Phys. Lett.*, **38**, 766 (1981).
9. S. N. G. Chu, C. M. Jodlauk, and A. A. Ballman, *This Journal*, **129**, 352 (1982).
10. P. D. Augustus and D. J. Stirland, *ibid.*, **129**, 614 (1982).
11. A. Yamamoto, S. Tohno, and C. Vemura, *ibid.*, **128**, 1095 (1981).
12. V. Gottschalch, R. Srnanek, and G. Wagner, *J. Mater. Sci. Lett.*, **1**, 358 (1982).
13. K. Ishida, Y. Matsumoto, and K. Tagushi, *Phys. Status Solidi*, **70**, 277 (1982).
14. T. Kotani, S. Komiya, S. Nakai, and Y. Yamaoka, *This Journal*, **127**, 2273 (1980).
15. S. Komiya and K. Nakajima, *J. Cryst. Growth*, **48**, 403 (1980).
16. M. A. Pollack, R. E. Nahory, J. C. DeWinter, and A. A. Ballman, *Appl. Phys. Lett.*, **33**, 314 (1978).
17. S. B. Phatak and G. Kelner, *This Journal*, **126**, 287 (1979).
18. J. J. Hsieh, J. A. Rossi, and J. P. Donnelly, *Appl. Phys. Lett.*, **28**, 709 (1976).
19. A. Huber and N. T. Linh, *J. Cryst. Growth*, **29**, 80 (1975).
20. S. Mahajan and A. K. Chin, *ibid.*, **54**, 138 (1981).
21. M. A. DiGiuseppe, H. Temkin, and W. A. Bonner, *ibid.*, **58**, 279 (1982).

Characterization of Near-Surface Line Defects Formed during High-Temperature Annealing of Gold-Metallized III-V Compound Semiconductors (InP and GaAs)

S. Nakahara,* E. C. Felder, and H. Temkin*

AT&T Bell Laboratories, Murray Hill, New Jersey 07974

ABSTRACT

We report a transmission electron microscope study on the new type of line defects which appeared near the {001} surface of Au-metallized InP and GaAs compound semiconductors as a result of high temperature annealing. The line direction of these defects was along the [110], and the nature of the strain field was similar to that of an edge dislocation having the Burgers vector of $a/2$ [110] type. Because the magnitude of the strain contrast was found to vary sensitively with the length of the defects, the possibility of these line defects being a dislocation has been ruled out. In addition, they lie at the bottom of rectangular pits created by a direct interfacial reaction with a Au overlayer, and the strain field was determined to originate from the elastic coherency present between the semiconductor and Au containing surface film.

There is an increasing interest in III-V compound semiconductor materials for a number of electronic applications. Various metallization schemes have been proposed for these semiconductors and used to obtain suitable electronic characteristics of a Schottky barrier or an ohmic contact. Gold, in combination with various dopants, is one of the elements which has been used extensively as a contact metal for this application. Heat-treatment of such a contact, necessary for obtaining low resistivity and strong mechanical bond, results in not only a lattice diffusion of Au into the semiconductor, but also a direct interaction with Au at the interface (1). Since such a metallization is often composed of more than one kind of metal, understanding of its interaction mechanism with the semiconductor may be difficult. Even a room-temperature interdiffusion within metallization layers alone was found to present quite a complex problem and involved an interfacial cracking accompanied by void formation, as recently observed in Au/Sn layers on GaAlAs LED's (2).

During the course of studying interactions between a Au metallization and III-V compound semiconductors (InP and GaAs), we have discovered a number of line defects lying along the [110] direction (but not along the $[1\bar{1}0]$) at the interface between a Au-metallization and the {001} surface of III-V compound semiconductors. We will show that the appearance of these line defects is connected with the early stages of reaction pit formation as a result of the preferential interaction of Au with the In or Ga component of InP or GaAs substrate. It will also be shown that these defects are not dislocations, but are rather lines of a strain center which is believed to have originated from an interaction of Au with the semiconductor. The contrast therefore arises from a coherency strain generated locally between the semiconductor substrate and a Au containing thin surface film.

Experimental

Metallizations (1000Å thick Au) were deposited on the chemically polished {001} face of InP or GaAs substrate by electron-beam deposition technique in a vacuum of better than 1×10^{-6} torr. The substrate was not intentionally cooled or heated during film deposition, but is believed to be close to room temperature. The metallized semiconductors were subsequently heat-treated at 420°C for 6 min in an atmosphere of forming gas (14% of H_2 in N_2). For a transmission electron microscope (TEM) observation, the heat-treated samples were cut into 3 mm square pieces, which were then mounted on a polished steel block while masking the metallized side with black wax. Some specimens were rinsed quickly in a KI solution (400g KI, 100g I_2 , and 400 ml H_2O) to remove an

*Electrochemical Society Active Member.

unreacted Au film prior to masking the metallized face with black wax. The 3 mm square pieces were polished mechanically down to about 200 μm with 600-grit slurry paste (Al_2O_3). After the mechanical thinning, the polished pieces were given an additional black wax around the circumferences, allowing only the center region to be exposed for the final chemical polishing in 5% Br-methanol solution. After the center region is perforated, the specimen was mounted on a holder for the subsequent TEM observation.

TEM micrographs were obtained with a JEM 200 electron microscope operated at 200 kV.

Results and Discussion

The interfacial region of Au-metallized (1000Å thick) and subsequently heat-treated {001} InP or GaAs substrates contained two characteristic features: rectangular surface pits elongated along the $\langle 110 \rangle$ direction and line defects lying parallel to the longer side of the pits. Since these features appear on both the Au-metallized InP and GaAs, we will illustrate only the InP case in the following discussion.

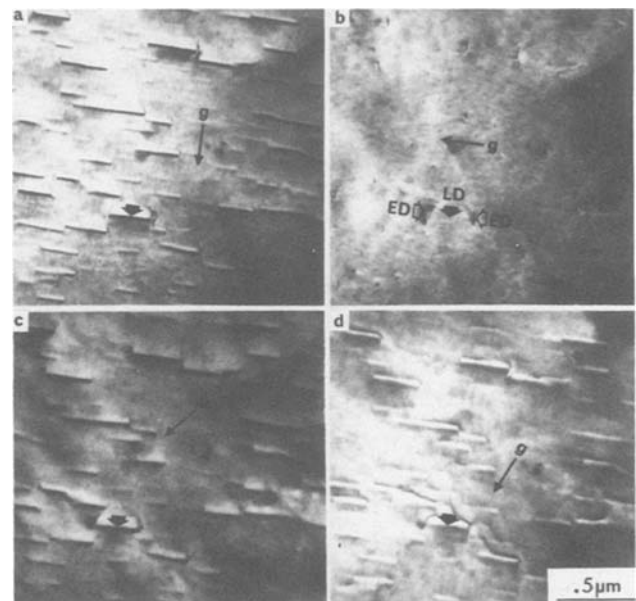


Fig. 1. Images of line defects taken with various two-beam conditions. a(top left): Reflection $g = (220)$, zone axis $Z = [001]$. b(top right): $g = (220)$, $Z = [001]$. c(bottom left): $g = (040)$, $Z = [001]$. d(bottom right): $g = (131)$, $Z = [114]$. Symbols LD and ED in b denote the line defect and its associated edge defect, respectively.

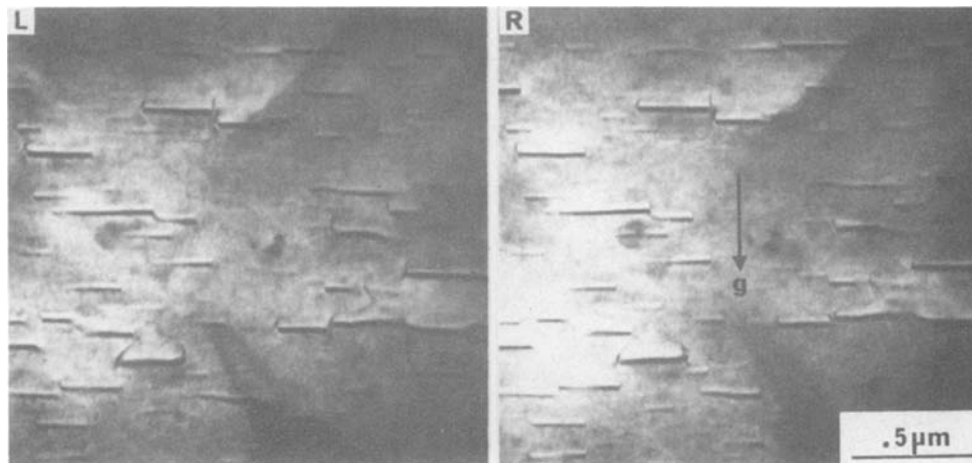


Fig. 2. A stereo-pair showing the images of line defects lying near the Au-metallized surface of InP $g = (2\bar{2}0)$.

The line defects were imaged using various two-beam conditions. Available reflections around the $\{001\}$ zone within the specimen tilt angle of $\pm 30^\circ$ were $\{220\}$, $\{400\}$, and $\{311\}$ type. Results of this contrast experiment are shown in Fig. 1. It is seen that the line defect (LD) images disappear for $\bar{g} = (2\bar{2}0)$, but their associated two edge (ED) images (see Fig. 1b) remain in-contrast for all reflections. To further understand these two image features, *i.e.*, those of line and edge parts, we took the stereomicrograph in the dynamical two-beam condition (see Fig. 2). The LD parts of the defects are seen to lie parallel to the Au-metallized surface but slightly below it. The associated edge defects ED are steeply extended from the two ends of LD toward the surface. To understand the nature of the ED parts, we imaged these defects in both the dynamical and kinematical conditions, while keeping the reflection that makes the LD part out of contrast. Figures 3a and 3b are taken in the dynamical [$g = (220)$] and kinematical conditions, respectively. One black arrow indicates the exact location of a line defect, and two white arrows the sites of the associated edge defects. As seen in Fig. 3b, the defect is actually located inside a reaction pit commonly observed at the interface of heat-treated Au/III-V semiconductors. The two edges are quite steep as compared with the long face of the elongated pit. Because of this steep angle of the edges, the thickness fringes associated with dynamical reflections always appear at these edge-face regions (see two white arrows in Fig. 1b), regardless of the type of reflections used.

From this contrast experiment, it can be inferred that these line defects, LD, have a strain field similar to a pure edge dislocation having the $[110]$ -type Burgers vector and lie at the bottom of reaction pits. As noted in Fig. 1, however, the size varies from one defect to another, and, therefore, these defects cannot be assigned to be dislocations, because dislocations should have a constant image width as long as they lie on the same depth of the crystal. It is also noted that in addition to the variable line widths these defects have variable lengths.

An interesting observation in TEM was that heating has caused the gradual disappearance of the LD images. Figure 4 illustrates these image features before and after beam heating inside a microscope. The beam heating was achieved by simply removing the second condenser aperture, thus exposing the specimen to an intense electron beam at the crossover for about 5 min. This exposure caused the black-white (BW) LD images to disappear slowly, leaving only the images of the two edges, and, in addition, to form the mottled background behind. A careful examination of this mottled background at high resolution revealed it to correspond to a continuous distribution of small islands which were formed on the surface by the local agglomeration of an unidentified surface film. When a specimen is not irradiated, the BW line defects have never disappeared. This observation indicates that the BW line defects are connected with surface straining at the bottom of the elongated pits, probably by an un-

known surface film. An intense electron irradiation breaks up this film into small islands, resulting in a relaxation of such a strained state. This leads to the formation of the mottled background, accompanied by the disappearance of the strong BW images. It can be therefore concluded that the relatively unstable strain region is present between a surface film and the substrate.

The nature of strain fields associated with these line defects can be determined using $\pm g$ reflections in combi-

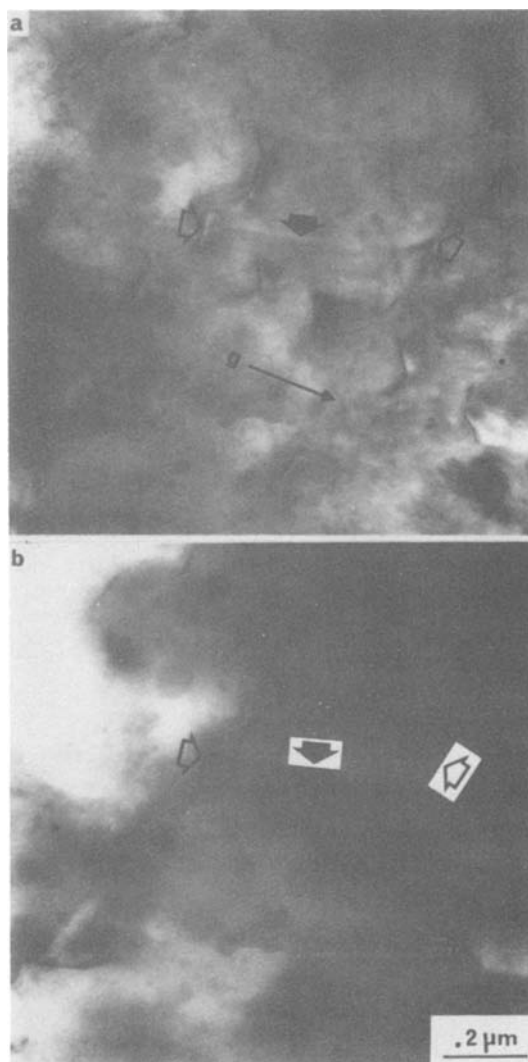


Fig. 3. The images of line defects taken in the (a, top) dynamical [$g = (220)$] and (b, bottom) kinematical conditions. A black arrow marks the position of a line defect which is out of contrast and white arrows indicate the associated edge defects.

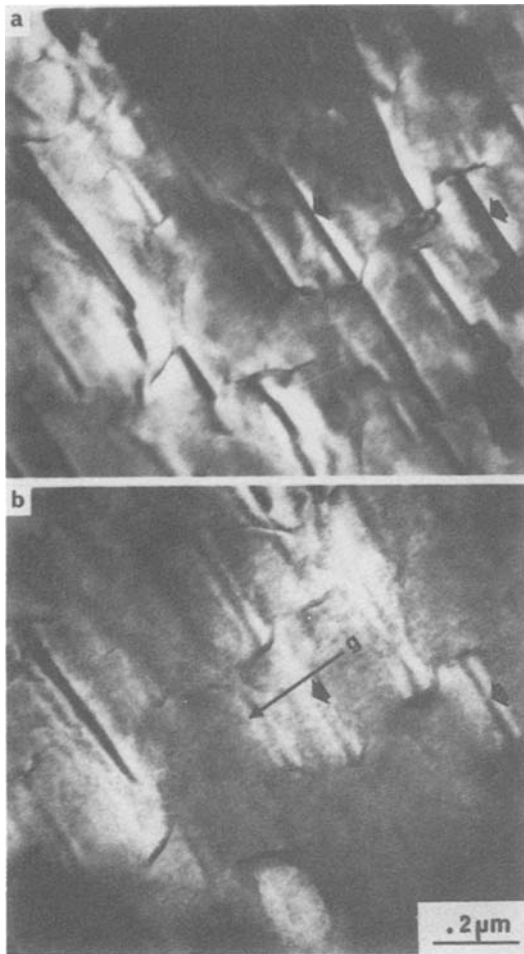


Fig. 4. The images of line defects (black arrows) taken (a, top) before and (b, bottom) after electron beam irradiation inside a microscope. $g = (220)$.

nation with bright- and dark-field images. This technique was previously demonstrated (3) to be useful in establishing the nature of strain fields for three-dimensional epitaxial islands of Ni grown on $\{001\}$ Cu. The bright-field images of the line defects taken with $\pm g$ reflections are shown in Fig. 5. Here, we found that the line defects exert a compressive stress on the surface of the semiconductor. This is schematically shown in Fig. 6. This strain state can be achieved equivalently by a local removal of rows of atoms from the surface of the semiconductor. It is conceivable that the preferential interaction of Au atoms with the In or Ga component can cause a similar stress state. This assumption is consistent with our observation (4) that interactions of Au with GaAs or InP result in the evolution of As or P gas. Gold presumably reacts preferentially with In or Ga (1), and rejects P or As, leading to the lattice collapse state (compressive state), as indicated by the strain fields associated with LD's.

The fact that the observed line defects are arranged along the $\langle 110 \rangle$ direction can be rationalized by the presence of atomic anisotropy in the $\{100\}$ plane. A close examination of stacking sequence along the $\{100\}$ plane indicates that the planes of P and In alternate along the $\langle 100 \rangle$ direction. In other words, similar to the $\{111\}$ planes, the $\{100\}$ planes are polar surfaces. This anisotropy results in the formation of elongated reaction pits previously observed (5) on Au-metallized GaAlAs surface. Chang *et al.* (5) discussed the formation of the reaction pits in terms of this anisotropy in the atomic arrangement in the $\{100\}$ faces. It appears, therefore, that the observed line defects are responsible for the early stages of pit formation and its subsequent growth. Although reactions of InP and GaAs with Au-metallization lead to the formation of pits, Pd metallization did not produce such pits. This

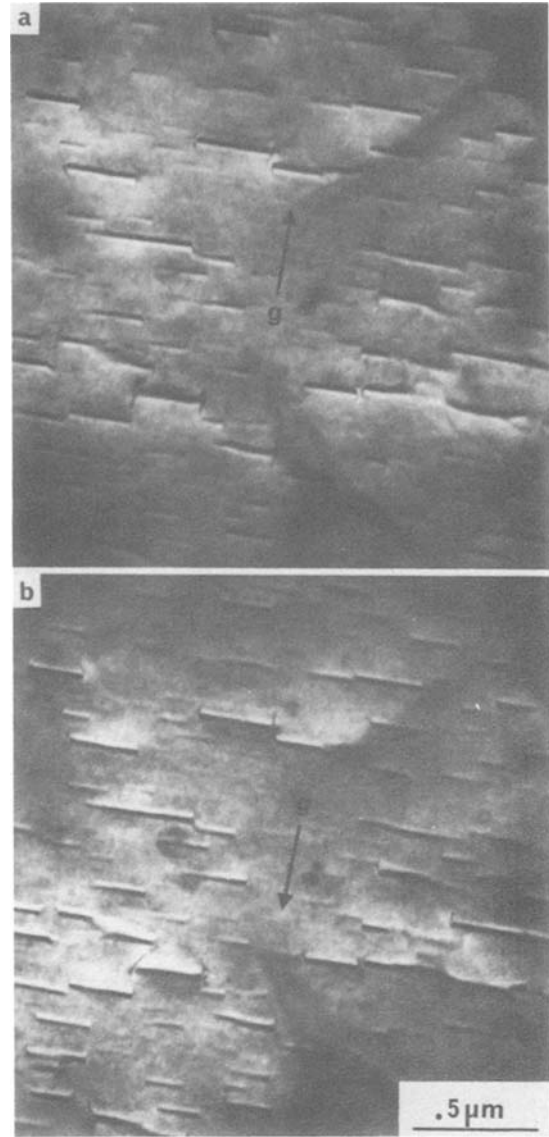


Fig. 5. The images of line defects taken with $\pm g$ reflections. a(top): $g = (220)$. b(bottom): $g = (220)$.

trend is found to be similar for the line defects; the line defects were not observed on Pd-metallized InP or GaAs. This structural difference can be rationalized (3) in terms of Pd's being capable of interacting equally with both the metal and metalloid components of the compound semiconductors, whereas Au can react strongly only with the metal component. For Au, this results in an ejection of P during heat-treatment, which leads to the lattice collapse state. Therefore, the presence of crystalline anisotropy

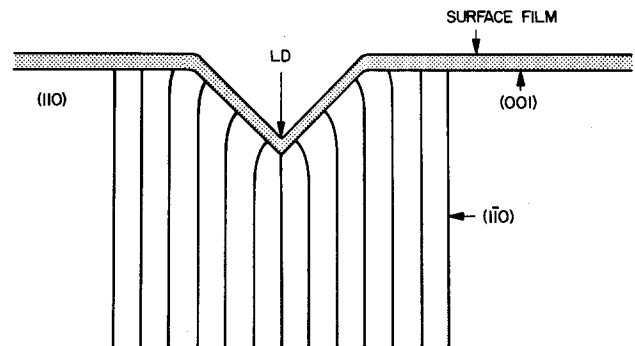


Fig. 6. A schematic illustration showing the stress state of a (001) InP substrate as a result of an interaction with Au. The vertical lines indicate the bending of the $(1\bar{1}0)$ lattice planes of InP.

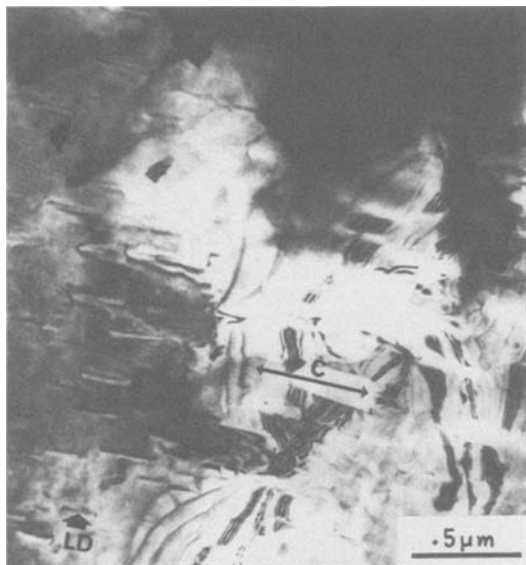


Fig. 7. TEM micrograph showing the line defects (LD's) lying along the channels of thinned Au-metallization on InP.

will manifest itself in the unique morphology of pit structures, which is also followed by the LD structure.

It has been shown that the exact location of the LD's is at the bottom of pits. Although there is undoubtedly some surface film associated with such defects, the exact chemical composition could not be easily determined. But, we believe that the surface film is an alloy containing Au and In. In fact, we found regions where the part of unreacted Au still remains on the surface (see Fig. 7). A careful examination of such regions indicated that the unreacted part of Au film is actually split by channels in which the film is effectively thinner or almost absent. Furthermore, we found that the line defects lie inside these channels. A direct reaction of the semiconductor surface with Au is presumably responsible for the formation of the LD's.

In a device structure, the observed defects may play an important role in the spreading (6) of a Au-contact layer outside of a defined mask after heat-treatment, because

the surface diffusion of Au on the compound semiconductors can be quite high. In fact, it was recently shown (7) that the use of a passivation layer could minimize such a spreading. To determine the property of the unknown surface film, we have tested the effect of In film on the defect structure of InP, and found that under the same experimental condition In alone does not produce such a line defect. It is therefore most likely that the surface film associated with the line defects must have contained Au. In addition, the reaction pits should be present to stabilize such defects. It is concluded that Au primarily interacts with the In or Ga component via a surface (or interfacial) diffusion mechanism and forms the line defects. A continuous line defect formation leads to the creation of macroscopic reaction pits, where their intermetallic binary alloys (Au-In or Au-Ga) are accommodated.

We are currently conducting an experiment to provide an answer as to which plane the Au-metallized side is. An identification of In or P plane in the case of InP substrates should determine unambiguously the direction of line defects on the {001} plane, *i.e.*, [110] or [$\bar{1}\bar{1}0$]. This result will be reported shortly.

Acknowledgment

The authors would like to thank Dr. S. Mahajan for fruitful discussions and continuing interest in pursuing this project.

Manuscript submitted Sept. 15, 1983; revised manuscript received April 9, 1984.

AT&T Bell Laboratories assisted in meeting the publication costs of this article.

REFERENCES

1. J. M. Vandenberg, H. Temkin, R. Hamm, and M. A. DiGiuseppe, *J. Appl. Phys.*, **53**, 7385 (1982).
2. S. Nakahara and R. J. McCoy, *This Journal*, **128**, 1781 (1981).
3. S. Nakahara, *Thin Solid Films*, **69**, 241 (1980).
4. S. Nakahara, P. K. Gallagher, H. Temkin, and E. C. Felder, Unpublished results (1982).
5. C. C. Chang, T. T. Sheng, R. J. McCoy, S. Nakahara, V. G. Keramidas, and F. Ermanis, *J. Appl. Phys.*, **50**, 7030 (1979).
6. V. G. Keramidas, H. Temkin, and S. Mahajan, in "GaAs and Related Compounds," p. 293, Institute of Physics Series 56, Institute of Physics, London (1980).
7. A. K. Chin, Personal communication (1982).

Determination of Oxygen in Silicon by Photon Activation Analysis for Calibration of the Infrared Absorption

H. J. Rath, P. Stallhofer, and D. Huber

Wacker Chemitronic, Gesellschaft für Elektronik-Grundstoffe GmbH, D-8263 Burghausen, Germany

B. F. Schmitt

Bundesanstalt für Materialprüfung, D-1000 Berlin 45, Germany

ABSTRACT

The oxygen content of silicon wafers has been determined by infrared absorption and photon activation analysis (PAA). We find a linear relationship between the absorption coefficient α_{ox} and the oxygen content (PAA). The conversion factor γ_{ox} is $3.0 \times 10^{17} \text{ cm}^{-2}$, in remarkable agreement with various recent investigations employing independent analytical methods.

The interstitial oxygen content of silicon crystals plays an important role in modern device technology due to its electrical behavior and its dominant influence on precipitation for internal gettering kinetics (1). Its amount is commonly determined spectroscopically by measuring Key words: interstitial oxygen in silicon, infrared absorption, photon activation analysis.

the well-known $9 \mu\text{m}$ band of the Si-O-Si vibration (2) (Fig. 1). The absorption coefficient α_{ox} derived from this IR transmittance curve is multiplied by a calibration factor γ_{ox} in order to get a concentration value.

Today, several calibration factors are used in the silicon industry. The first calibration factor employed, $\gamma_{ox} = 2.83 \times 10^{17} \text{ cm}^{-2}$, was found by Kaiser and Keck (3, 4). Other

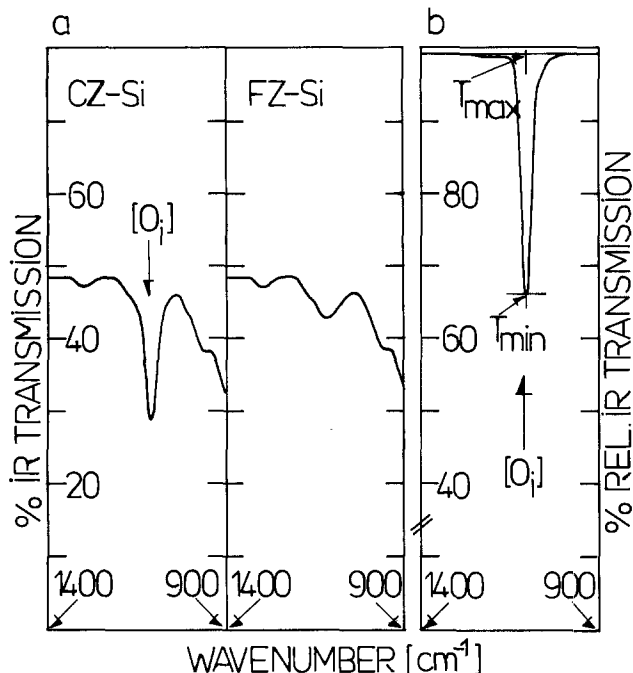


Fig. 1. IR spectra of a 2 mm thick silicon slice polished on both sides taken in the range between 1400 and 900 cm^{-1} . a(left): CZ-Si containing interstitial oxygen and FZ-Si without detectable oxygen showing the pure lattice absorption of silicon. b(right): Interstitial oxygen band of the CZ-Si slice after subtracting the background absorption of the Si-lattice; the transmission minimum and maximum of the O_i band are marked.

calibration factors were determined by Baker (5, 6) and Graff (7) to be $\gamma_{\text{ox}} = 4.81 \times 10^{17} \text{ cm}^{-2}$ and $2.45 \times 10^{17} \text{ cm}^{-2}$, respectively.

The latter was used by measurement standard 50438 issued by DIN (Deutsches Institut für Normung) (8), and was taken over by ASTM (9) in 1981. Recently, a Japanese group (10) re-evaluated the calibration curve again and determined it to be

$$\gamma_{\text{ox}} = 3.05 \times 10^{17} \text{ cm}^{-2}$$

This value was already found in 1973 by Yatsurugi *et al.* (11). However, Yatsurugi's value got only little attention. A further confirmation for this new value has been published by a Chinese research group (12).

Although three consistent values are published for the calibration factor, some open questions still exist regarding the validity of its determination, such as for the precipitated oxygen which does not contribute to the 9 μm band.

Experimental

The samples were taken from silicon crystals produced with today's state-of-the-art oxygen-controlled CZ-growth technique. The crystals were boron doped with a specific resistivity greater than 15 $\Omega \text{ cm}$, (100) oriented with a diameter of 100 mm. Samples were taken from eight crystals with different oxygen content ranging from 4 to $11 \times 10^{17} \text{ cm}^{-3}$ (DIN calibration). From each ingot, three adjacent pieces were cut with 10 and 2 mm thickness. The 2 mm slices were used for IR measurement, the 10 mm slug for photon activation analysis. The IR samples were polished on both sides with diamond slurry. Cylindrically shaped samples were drilled from the center and regions far enough from the edge for the PAA; the PAA samples were bright-etched and chemically cleaned.

Redissolution experiments carried out between 1250° and 1300°C (13) showed that the material investigated did not contain any measurable precipitated oxygen already introduced during the pulling process. However, for high oxygen samples (O_i greater than $10 \times 10^{17} \text{ atom/cm}^3$, DIN calibration), we know from diffusion length measurements (14) that small amounts of oxygen can be precipi-

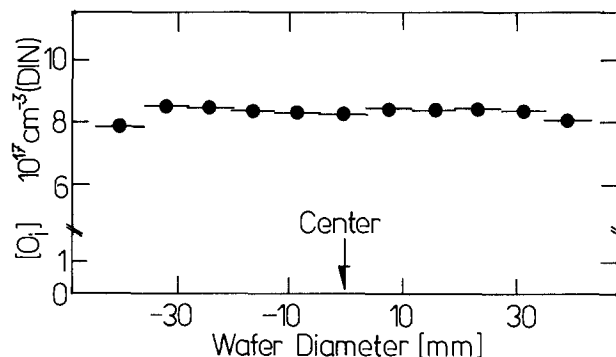


Fig. 2. Typical radial oxygen distribution of the silicon slices used in the experiment.

tated if the diffusion length is smaller than 400 μm . The material we used had always diffusion lengths greater than 400 μm , indicating that only negligible amounts of oxygen may not be built-in on interstitial sites (14, 15). The homogeneity of the radial oxygen distribution was checked by scanning an IR spot over the diameter. Figure 2 shows a typical result.

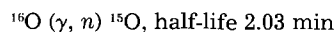
IR analysis.—The IR analyses were carried out using two different pieces of equipment: a Fourier transform spectrometer (FTS 14 Digilab), and a dispersive spectrometer (PE 580 B).

For determining the interstitial oxygen content, the IR transmittance between 1400 and 900 cm^{-1} was recorded (Fig. 1). Due to the superposed multiple phonon excitations of the silicon host lattice, all sample spectra have been subtracted from an oxygen-free reference spectrum. For calculating the oxygen absorption coefficient α_{ox} , Eq. [1] has been applied, taking into account multiple reflection contributions (6, 16)

$$\alpha_{\text{ox}} = -\frac{1}{d} \ln \left[\frac{-B + \sqrt{B^2 + 4AT}}{2A} \right] \quad [1]$$

The abbreviations A , B , T , and d are explained in the Appendix. The diameter of the IR spot employed was 8 mm. Thus, the IR signal averages the oxygen data in a sample volume which is comparable to that used in PAA.

Photon activation analysis combined with inert gas fusion.—The absolute oxygen content in silicon is analyzed by activation with high energy photons (17, 18) generated by bombardment of a tungsten target with 30 MeV electrons. This means that the maximum of intensity of the Bremsstrahlung is in the range of about 20 MeV. This energy range delivers a giant resonance for the nuclear reaction



which the analysis is based on. During the irradiation, the sample rotates to get a homogeneously activated sample. The entire homogeneously activated sample volume is then used in the analysis. After irradiation, the samples are etched with nitric acid/hydrofluoric acid (1:1) in order to remove activated surface oxide and to eliminate blank value problems. The inert gas fusion is performed in a graphite crucible with iron as metallic bath. The sample is completely dissolved at 2000°C, under helium gas flux. The sample collection efficiency is about 100%. The molten silicon reacts preferentially with graphite, whereas oxygen reacts with carbon to yield carbon monoxide. The oxidation of the generated CO to CO_2 is caused by Schütze reagent I_2O_5 . Carbon dioxide is absorbed on ascarite.

The determination of the activated oxygen is based on the annihilation radiation, generated by β^+ -radiation of ^{15}O , which reacts with an electron under emission of two gamma rays of 511 keV

Table I. List of values of oxygen contents (PAA) and IR absorption coefficients

Series	Oxygen content (10^{17} at. cm^{-3}) (PAA)	IR absorption coefficient (cm^{-1})	
		PE 580 B	FTS 14
A: A_1	6.37 ± 0.76	1.90	1.93
A_r		2.11	2.04
A_m		1.99	
B: B_1	7.61 ± 0.56	2.49	2.44
B_r		2.49	2.40
B_m		2.45	
C: C_1	8.16 ± 0.32	2.86	2.82
C_r		2.90	2.84
C_m		2.86	
D: D_1	9.68 ± 1.25	3.06	3.01
D_r		3.00	2.98
D_m		3.02	
E: E_1	11.15 ± 1.29	3.41	3.46
E_r		3.48	3.49
E_m		3.47	
F: F_1	13.19 ± 1.31	4.21	4.17
F_r		4.16	4.17
F_m		4.18	
G: G_1	14.22 ± 1.74	4.48	4.50
G_r		4.51	4.49
G_m		4.50	
H: H_1	12.53 ± 2.52	4.67	4.68
H_r		4.57	4.59
H_m		4.63	

$$\beta^+ + e^- = 2\gamma$$

$$E_\gamma = 511 \text{ keV}$$

For measuring the 511 keV line, it is necessary to take the gas fusion process, in order to avoid an interference of the 511 keV line by the Compton effect of ^{28}Al , which comes from the following nuclear reaction

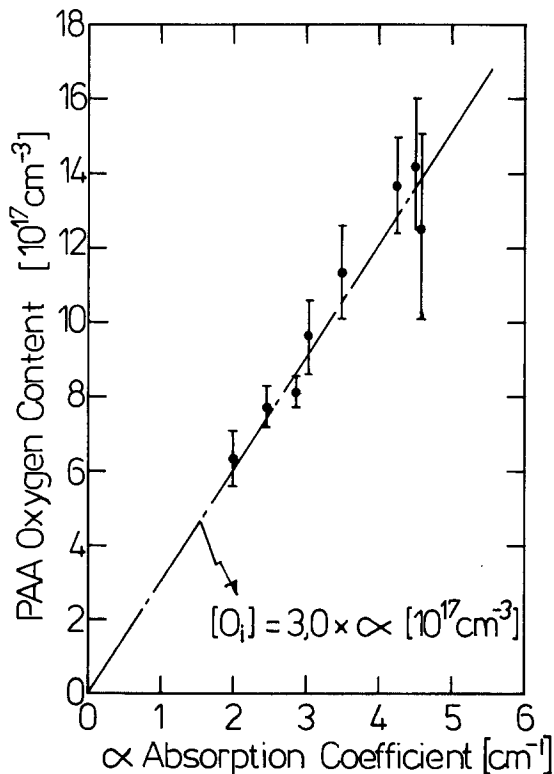
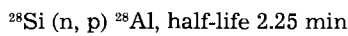


Fig. 3. Plot of the oxygen concentrations determined by the photon activation analysis (PAA) vs. the absorption coefficient of the IR active oxygen band at 1106 cm^{-1} . A least mean squares fit yields a conversion factor $\gamma_{\text{ox}} = 3.0 \times 10^{17} \text{ cm}^{-2}$.

The 511 keV γ -line is measured with two NaI (TI) detectors in coincidence in order to determine oxygen decay curve and content. The calibration of the analysis method described above is done by a standard; in case of oxygen Al_2O_3 is taken. Al_2O_3 is measured without chemical separation on a second detector design.

Results

Table I compares the oxygen concentrations obtained by photon activation analysis (PAA) with the absorption coefficients determined by IR spectroscopy. For each class of oxygen concentration, eight individual photon activation analyses were carried out.

The accuracy of the oxygen determination by PAA is typically better than $\pm 15\%$. The detection limit of this method is $5 \times 10^{15} \text{ cm}^{-3}$. However, the accuracy of the IR data is better than $\pm 2\%$.

In Fig. 3, the data listed in Table I are plotted. A least mean squares fit yields a straight line with a slope of $3.0 \times 10^{17} \text{ cm}^{-2}$. The standard deviation amounts to $\pm 0.2 \times 10^{17} \text{ cm}^{-2}$. This gives the following calibration factor for the IR absorption method

$$\gamma_{\text{ox}} = [3.0 \pm 0.2] \times 10^{17} \text{ cm}^{-2}$$

Discussion

The calibration factor of $3.0 \times 10^{17} \text{ cm}^{-2}$ is close to the values recently published by Li *et al.* (12), Iizuka *et al.* (10), and Yatsurugi *et al.* (11). Also, our calibration factor is close to the value of $2.83 \times 10^{17} \text{ cm}^{-2}$, which was the first to be published by Kaiser *et al.* (3). All these factors

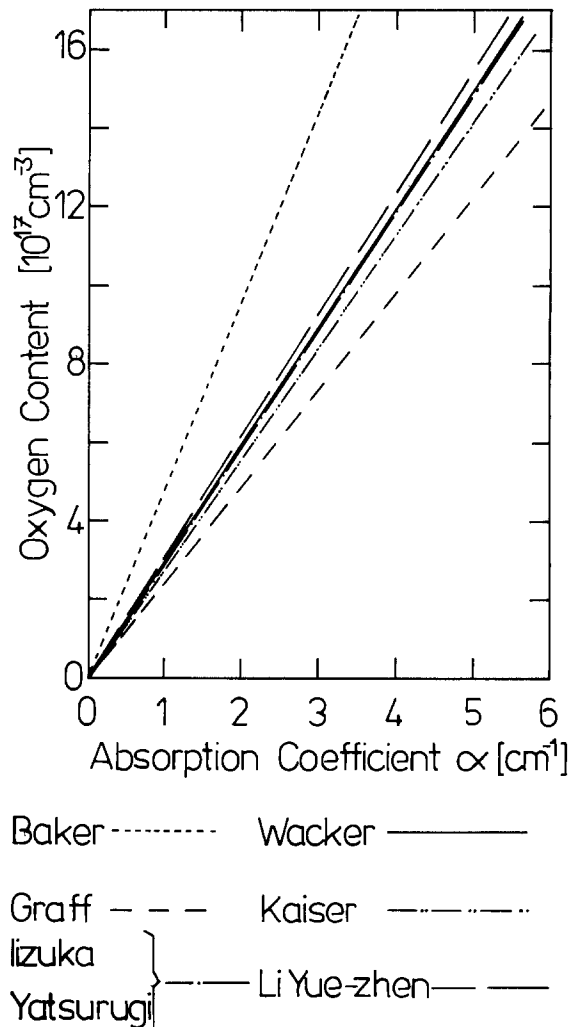


Fig. 4. Calibration curves for the oxygen concentration published by different authors.

quoted were obtained by different analytical methods. Li *et al.* used charged particle activation and helium carrier gas fusion-gas chromatography (12). Yatsurugi *et al.* used charged particle activation (11). Kaiser *et al.* used vacuum fusion gas analysis (3). T. Iizuka *et al.* used charged particle activation (10). In this work, we used photon activation combined with inert gas fusion.

When compared with the calibration factors employed in ASTM and DIN standards (Fig. 4), a calibration factor of $3 \times 10^{17} \text{ cm}^{-2}$ appears to be reasonable. It gains additional importance and credibility in that a variety of recent investigations yields practically the same value. Therefore, a new discussion about the calibration factors used in the actual standards is deemed necessary.

Acknowledgment

We thank Mr. Bittersberger for his assistance in the IR measurements.

Manuscript submitted Dec. 2, 1983; revised manuscript received April 6, 1984.

Wacker Chemitronic assisted in meeting the publication costs of this article.

APPENDIX

The abbreviations used in Eq. [1] stand for the following expressions

d sample thickness (cm); α_L (1106 cm^{-1}) = 1 cm^{-1} (19)

R 0.3 reflection index

T (T_{\min}/T_{\max}) where T_{\min} and T_{\max} are transmission minimum and maximum, respectively, of the absorption band at 1106 cm^{-1} (see Fig. 1) (16)

$A = TR^2 e^{-2\alpha_L d}$; $B = -R^2 e^{-2\alpha_L d}$

REFERENCES

1. J. E. Lawrence and H. R. Huff, in "VLSI Electronics-Microstructure Science," Vol. 5, N. G. Einspruch, Editor, Academic Press, New York (1982).
2. W. Kaiser, P. H. Keck, and C. F. Lang, *Phys. Rev.*, **101**, 1264 (1956).
3. W. Kaiser and P. H. Keck, *J. Appl. Phys.*, **28**, 882 (1957).
4. *ASTM Data Ser.*, F 45.
5. J. A. Baker, *Solid-State Electron.*, **13**, 1431 (1970).
6. *ASTM Data Ser.*, F 120 (1975); *ibid.*, F 121 (1979).
7. K. Graff, E. Grallath, S. Ades, G. Goldbach, and G. Tölg, *Solid State Electron.*, **16**, 887 (1973).
8. Deutsches Institut für Normung, 50 438/1.
9. *ASTM Data Ser.*, F 120 (1981).
10. T. Iizuka, S. Takasu, M. Tajima, T. Arai, M. Nozaki, N. Inoue, and M. Watanabe, in "Defects in Silicon," W. M. Bullis and L. C. Kimerling, Editors, p. 265, The Electrochemical Society Softbound Proceedings Series, Pennington, New Jersey (1983).
11. Y. Yatsurugi, N. Akiyama, Y. Endo, and T. Nozaki, *This Journal*, **120**, 975 (1973).
12. Y. Li, H. He, G. Zaho, R. You, Q. Lu, and M. Qi, *Mater. Lett.*, **101** (1983).
13. L. Jastrebski, P. Zanzucchi, D. Thebault, and J. Lagowski, *This Journal*, **129**, 1638 (1982).
14. D. Huber, R. Wahlich, and A. Bachmeier, in "Proceedings of the 16th IEEE Photovoltaic Specialists Conference," p. 480, San Diego, CA, Sept. 27-30, 1982.
15. D. Huber, J. Reffle, P. Stallhofer, and C. Weigel, in "Aggregation Phenomena of Point Defects in Silicon," E. Sirtl and J. Goorissen, Editors, p. 111, The Electrochemical Society Softbound Proceedings Series, Pennington, NJ (1983).
16. P. Stallhofer and D. Huber, *Solid State Technol.*, **26**, 233 (1983).
17. B. F. Schmitt and H. U. Fusban, *Metall (Berlin)*, **33**, 1265 (1979).
18. B. F. Schmitt and H. U. Fusban, in "Analysis of Non-Metals in Metals," G. Kraft, Editor, p. 1265, W. de Gruyter and Co., Berlin (1981).
19. B. Pajot, *Analisis*, **5**, 7, 293 (1977).

The Growth and Characterization of HgTe Epitaxial Layers Made by Organometallic Epitaxy

I. Bhat* and S. K. Ghandhi**

Department of Electrical, Computer, and Systems Engineering, Rensselaer Polytechnic Institute, Troy, New York 12181

ABSTRACT

Mercury telluride layers have been grown on cadmium telluride substrates, by the reaction of diethyltelluride and mercury. Typical growth rates, at 415°C, are 3.3 $\mu\text{m/h}$. Resulting films had an apparent Hall mobility of $1 \times 10^5 \text{ cm}^2/\text{V}\cdot\text{s}$ at liquid nitrogen temperature, and an effective electron concentration of $2 \times 10^{19}/\text{cm}^3$. The growth and electrical characteristics of these films are described in this paper.

Mercury telluride is a semimetallic compound which has been investigated because of its unique material properties and also because it is the major component of the mixed II-VI compounds, $\text{Hg}_{1-x}\text{Cd}_x\text{Te}$. Conventionally, these compounds are grown in closed systems. Vapor transport systems, with elemental sources, have also been used (1), but require multiple zone furnaces and are relatively complex in their operation. The growth of HgTe by organometallic chemical vapor deposition (OMCVD),

using elemental mercury and diethyltelluride, offers the alternative of a relatively simple open-flow system. Here, high growth rates at low temperatures can be achieved with comparable crystal morphology.

Kuech *et al.* (2) used a hotwall system to grow HgTe on CdTe substrates, by using elemental mercury and dimethyltelluride. However, the growth rate reported was very low (0.3-0.6 $\mu\text{m/h}$) and no electrical characteristics of the layer were given. Irvine *et al.* (3) used diethyltelluride and elemental mercury to grow HgTe at 410°C. Again, no details of the technique were provided, and no detailed study of the growth characteristics was attempted.

*Electrochemical Society Student Member.

**Electrochemical Society Active Member.

Key words: MOCVD, OMVPE, HgTe, epitaxy, organometallic.

In this work, we report on the growth of HgTe on (100)-oriented CdTe substrates, and over a wide range of deposition temperatures and reactant partial pressures. It is shown that the 77 K mobility of these layers is higher than that presented in earlier work.

Experimental

Epitaxial growth of HgTe was carried out at atmospheric pressure in a quartz horizontal reactor tube, using palladium-purified hydrogen over heated mercury.¹ Diethyltelluride (DETe)² vapor was introduced by bubbling hydrogen through DETe bubbler, which was held at 15°C.

The main reactor tube was 51 mm diam, and used a RF-heated graphite susceptor, located 6 cm from the inlet. The mercury vapor source was provided by passing hydrogen over a heated chamber containing mercury. In addition, the tube wall in front of the susceptor was heated to prevent mercury condensation.

Substrates used for epitaxial deposition were (100)-oriented undoped CdTe wafers.³ Several wafers of (100) 3° → (110) orientation have also been used for our work. Substrates were purchased in polished form. These were first cleaned in organic solvents, after which 20 μm of the surface was etched off in a 2% Br-methanol solution to result in a highly polished, shiny surface.

After loading the substrates, the system was thoroughly purged with nitrogen followed by hydrogen. The hydrogen flow through the Hg line was set at 8-10 cm³/min, and the flow through all other flowmeters adjusted to their appropriate values. The RF was turned on followed by the tube heater. The Hg heater was turned on when the susceptor temperature reached about 250°C. This sequence of steps was necessary to prevent any condensation of Hg on the substrates prior to growth. At all times during the growth run, the susceptor temperature was kept higher than Hg temperature. This prevents mercury droplets, which are not saturated with tellurium, from etching the substrate and causing etch pits in the grown layer. Once the substrate temperature reached the growth temperature, hydrogen through the Hg line was increased to the desired value, the DETe bubbler was turned on. The total gas flow used was 0.67 l/min in all these experiments.

The RF heater was shut down at the end of the deposition run, which lasted 1-2h. Next, the hydrogen flow through DETe bubbler was turned off, followed by the tube heater and the Hg heater. The total flow through the system was increased to 4 l/min to allow a faster cool-down of the system. Once the susceptor reached 150°C, the hydrogen flow through the mercury was turned off, and the system was purged with nitrogen prior to removing the substrates from the reactor.

The thickness of the deposited layer was measured gravimetrically. In some cases, this was verified by scribing the substrates, and then observing with the aid of a scanning electron microscope. No separate etching was found necessary to delineate the interface. Good correlation was obtained between these techniques.

Electrical measurements were made by the van der Pauw technique, after deposits from the edge and the back side were etched off. Ohmic contacts were made to the substrate using silver epoxy. No thermal alloying cycle was found necessary to ensure a good ohmic contact to these samples.

Results and Discussion

Initial HgTe growth attempts were made over a wide range of reactor conditions in order to establish the conditions for growing good epitaxial layers. Next, a few growth runs were carried out under the following conditions. (i) for a fixed partial pressure of Hg, DETe, and total flow, the susceptor temperature was varied from 395° to 440°C. (ii) The hydrogen flow through the DETe bubbler was varied from 64 to 190 ml/min, (corresponding to

the DETe partial pressure of 0.7×10^{-3} to 2×10^{-3} atm). Other parameters, such as a mercury partial pressure, total flow through the system, and substrate temperature, were fixed during these experiments. (iii) The susceptor temperature, total flow through the system, and DETe partial pressure were kept fixed, while the Hg partial pressure was varied from 0.03 to 0.1 atm.

In all the above experiments, the Hg reservoir temperature was held at 300°C, and the tube in front of the susceptor was heated to 250°C.

Layer morphology.—The surface of all the grown HgTe layers shows a series of steps, all running parallel to one of the (011) directions. The direction of this pattern was independent of the position or the orientation of the sample in the reactor. The step features were more prominent on the layers grown on (100) 3° → (110)-oriented substrates, than on (100) substrates. Other workers (3) have also reported similar types of surface features for HgTe layers grown on (100) 2° → (110) CdTe substrates. Figure 1 shows the surface morphology for a typical layer grown during the course of this work.

In all our work, we observed that the layer morphology was strongly dependent on the substrate quality, with samples cut from some substrates providing consistently better morphology than those cut from other substrates. This is indicative of the immature state-of-the-art of bulk CdTe substrate technology.

Effect of temperature.—The substrate temperature is the main parameter affecting the growth rate, and control of this temperature to within $\pm 1^\circ\text{C}$ is very important for obtaining reproducible results. The growth rate of the HgTe layer was measured as a function of the substrate temperature over the range 395°-440°C, while maintaining all the other parameters constant. The gas flows chosen for these experiments were a total hydrogen flow of 0.67 l/min, a DETe flow of 1.3 ml/min, and a Hg flow of 38 ml/min, corresponding to partial pressures of 2×10^{-3} and 5.7×10^{-2} atm, respectively (flow rate of the pure reactants are given here). Figure 2 shows the variation of the growth rate with temperature, and exhibits an activation energy for the deposition process of 30 kcal/mol over the entire range. Little or no growth was observed below about 400°C. In a pyrolysis study (3) of DETe, it was noted that the partial dissociation enthalpy of the C-M bond is about 25 kcal/mol, which agrees reasonably well with the activation energy obtained by direct measurement of the deposition process. Hence, the growth of HgTe is probably limited by the stability of the DETe molecule.

Effect of mercury partial pressure.—The growth rate at any specific temperature was found to be independent of

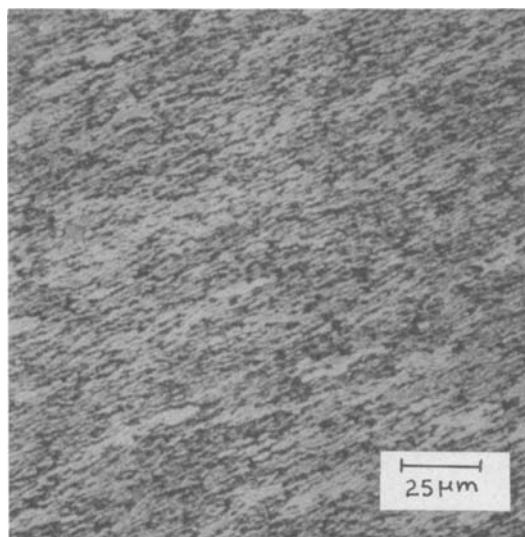


Fig. 1. Surface morphology for a HgTe layer. $T: 415^\circ\text{C}$. Growth rate: 3.3 μm/h. $p_{\text{Hg}}: 0.055 \text{ atm}$. $P_{\text{DETe}}: 2 \times 10^{-3} \text{ atm}$.

¹Bethlehem Apparatus Company, Incorporated, Hellertown, Pennsylvania 16056

²Alfa-Ventron, Danvers, Massachusetts 01923

³Two-Six Incorporated, Saxonburg, Pennsylvania 16056

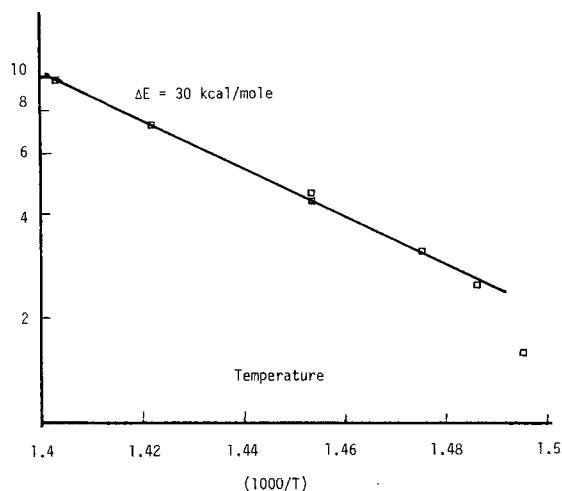
Growth Rate
($\mu\text{m/hr}$)

Fig. 2. Growth rate of HgTe layers vs. $10^3/T$. $p_{\text{DETe}}: 2 \times 10^{-3}$ atm. $p_{\text{Hg}} = 0.05$ atm. Total flow: 0.67 l/min.

the mercury partial pressure, within experimental error. This is expected because p_{Hg} is 20 to 40 times higher than p_{DETe} , so that the DETe flow will be the rate limiter in the transport process. The minimum Hg pressure is determined by the equilibrium partial pressure of Hg at the growth temperature and is approximately 0.01 atm at 415°C (4, 5). A somewhat higher mercury pressure (by a factor of 2-4) was used to prevent decomposition of the growing layers.

Effect of DETe flow.—Experiments were conducted to determine the effect of DETe flow rate on the growth rate of HgTe. These were carried out with a hydrogen flow rate of 64-190 ml/min through DETe bubbler, with 78 ml/min of hydrogen over the mercury reservoir. This corresponds to 0.4-1.3 ml/min of pure DETe and 38 ml/min of pure mercury flow. The total hydrogen flow was 0.67 l/min. For these experiments, the susceptor temperature was kept at 415°C, the reactor tube at 250°C, and the mercury reservoir at 300°C.

Figure 3 shows a sublinear behavior in the growth rate with DETe flow. A Langmuir-Hinshelwood model (6) can be invoked to explain this behavior. We note that the deposition process is kinetically controlled for the following reasons: first, the growth rate of HgTe varies with the growth temperature (with an activation energy of 30 kcal/mol); second, the growth rate observed at 415°C is

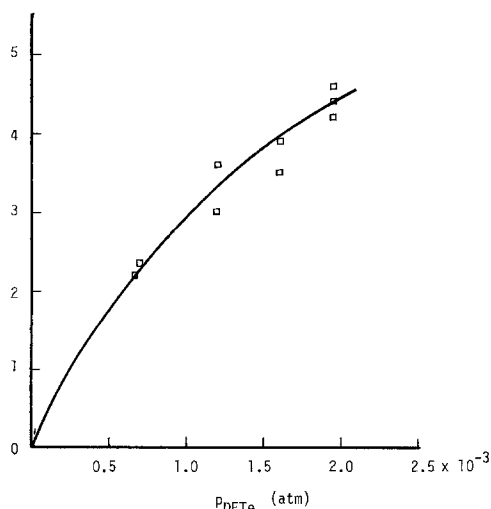
growth rate
($\mu\text{m/hr}$)

Fig. 3. Growth rate vs. p_{DETe} . $T: 415^\circ\text{C}$. $p_{\text{Hg}}: 0.05$ atm. Total flow: 0.67 l/min.

approximately one tenth of what would be expected if the process were mass-transport limited; finally, the growth rate depends on the substrate orientation.

We propose that the growth of HgTe occurs by the simultaneous noncompetitive adsorption of $(\text{C}_2\text{H}_5)_2\text{Te}$ or $(\text{C}_2\text{H}_5)_2\text{Te}$ and Hg atoms, followed by a surface catalyzed reaction. The growth rate R for this model is given by

$$R = K_1 \theta_{\text{DETe}} \theta_{\text{Hg}}$$

where K_1 is a rate constant, and θ_{DETe} and θ_{Hg} are the surface coverages of DETe and Hg, respectively. The surface coverage can be related to the respective gas phase partial pressure by

$$\theta_{\text{DETe}} = \frac{\beta_{\text{DETe}} p_{\text{DETe}}}{(1 + \beta_{\text{DETe}} p_{\text{DETe}})}$$

Here, p_{DETe} is the DETe gas phase partial pressure and β_{DETe} is the ratio of the rate constant for adsorption of DETe to the rate constant for desorption. In addition

$$\theta_{\text{Hg}} = \frac{\beta_{\text{Hg}} p_{\text{Hg}}}{(1 + \beta_{\text{Hg}} p_{\text{Hg}})}$$

where all the terms have their usual meanings. Hence

$$R = \frac{K_1 \beta_{\text{DETe}} p_{\text{DETe}} \beta_{\text{Hg}} p_{\text{Hg}}}{(1 + \beta_{\text{DETe}} p_{\text{DETe}})(1 + \beta_{\text{Hg}} p_{\text{Hg}})}$$

Since elemental mercury is used, at vapor pressures in excess of the equilibrium value, it is reasonable to assume that $\beta_{\text{Hg}} p_{\text{Hg}} \gg 1$. Then

$$R = \frac{K_1 \beta_{\text{DETe}} p_{\text{DETe}}}{(1 + \beta_{\text{DETe}} p_{\text{DETe}})}$$

so that the predicted growth rate is sublinear in p_{DETe} and independent of p_{Hg} .

The actual reaction mechanisms are, in all probability, more complex than those proposed here. However, in the absence of detailed experimental data, it serves no useful purpose to present them now.

Electrical characteristics.—Hall and resistivity measurements were made at 77 and 300 K by means of the van der Pauw method, with a magnetic field strength of 2.3 kG. All the layers were n-type at liquid nitrogen temperature with an apparent carrier concentration in the range of $1-4 \times 10^{16} \text{ cm}^{-3}$. No significant changes in the carrier concentration or resistivity at room temperature were observed on different HgTe layers grown under various growth conditions. This is expected of a semi-metal like HgTe, in which the intrinsic carrier concentra-

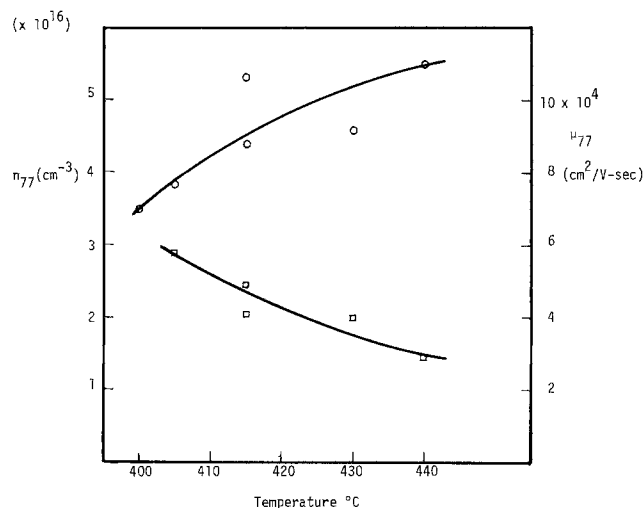


Fig. 4. Apparent mobility and carrier concentration at 77 K vs. T . $p_{\text{DETe}}: 2 \times 10^{-3}$ atm. $p_{\text{Hg}}: 0.05$ atm. Total flow: 0.67 l/min. \circ : Mobility. \square : Carrier concentration.

tion at room temperature is approximately $4 \times 10^{17} \text{ cm}^{-3}$ (7). Hence, the external impurities or the defects do not play a dominant role in controlling its electrical properties at room temperature.

Even though single-carrier analysis of Hall mobility data cannot be applied to find the net carrier concentration in HgTe, this measurement gives a qualitative measure of the relative values of holes and electrons. Figure 4 shows the apparent mobility and carrier concentration (8) at 77 K as a function of the growth temperature. We note that the carrier concentration decreases as the growth temperature is increased. This can be explained as follows: for a constant Hg pressure, we can expect a higher Hg vacancy concentration in the layers as the growth temperature is increased. Since Hg vacancies are believed to behave like acceptors (9), the material becomes more p-type, thus indicating a lower net electron concentration. Measurements made on samples grown at 415°C over a range of Hg pressures (3×10^{-2} to 8×10^{-2} atm) show an increase in electron concentration from 2.2×10^{16} to $3 \times 10^{16} \text{ cm}^{-3}$ and lend support to this argument.

The outdiffusion of impurities from the substrate also plays a role in determining the electrical characteristics of the layers. In fact, it is possible that their diffusion rate in HgTe at the growth temperature can even be higher than the growth rate (10). Residual impurities on the substrate surface after chemical etching can also alter the electrical characteristics of the layer.

Conclusion

HgTe layers have been grown onto CdTe substrates by OMCVD using elemental mercury and diethyltelluride. The growth characteristics have been studied at different growth temperatures and at various reactant partial pressures. The activation energy for the deposition process has been found to be 30 kcal/mol, which is in fair agreement with the partial dissociation enthalpy of the M-C

bond of diethyltelluride. The electrical characteristics of the layers are comparable to those of the best bulk HgTe. In conclusion, this work establishes the feasibility of obtaining device-quality HgTe layers by OMCVD techniques. It is planned to extend this work to the growth of the ternary alloy $\text{Hg}_{1-x}\text{Cd}_x\text{Te}$.

Acknowledgments

The authors would like to thank A. Hayner for manuscript preparation. This program was initiated by a research grant from the General Electric Company, Research and Development Center, Niskayuna, New York. This support is gratefully acknowledged.

Manuscript submitted Aug. 29, 1983; revised manuscript received March 2, 1984.

REFERENCES

1. P. Vohl and C. M. Wolfe, *J. Electron. Mater.*, **7**, 659 (1978).
2. T. F. Kuech and J. O. McCaldin, *This Journal*, **128**, 1142 (1981).
3. J. C. Irvine, J. B. Mullin, and A. Royle, *J. Cryst. Growth*, **57**, 15 (1982).
4. R. F. Brebrick and A. J. Strauss, *J. Phys. Chem. Solids*, **26**, 989 (1965).
5. R. A. Farrar, C. J. Gillham, and B. Bartlett, *J. Mater. Sci.*, **12**, 836 (1977).
6. D. W. Shaw, in "Mechanisms in Vapor Epitaxy of Semiconductors, Crystal Growth, Theory and Techniques," Vol. 1, C. H. L. Goodman, Editor, Plenum Press, New York (1974).
7. R. R. Galazka, *Phys. Lett. A*, **32**, 101 (1970).
8. D. J. Howarth, R. H. Jones, and E. H. Putley, *Proc. Phys. Soc. B*, **70**, 124 (1957).
9. T. C. Harman, in "Physics and Chemistry of II-VI Compounds," M. Aven and J. S. Prener, Editors, North Holland Publishing Company, Amsterdam (1967).
10. M. Brown and A. F. W. Willoughby, *J. Cryst. Growth*, **59**, 27 (1982).

Controlled Film Formation during CCl_4 Plasma Etching

S. E. Bernacki*¹ and B. B. Kosicki²

Sperry Research Center, Sudbury, Massachusetts 01776

ABSTRACT

Carbon tetrachloride plasma etching can be performed in a regime in which a film-like product is simultaneously formed on vertical surfaces but inhibited from forming on horizontal surfaces. If the photoresist profile is properly tailored, this process is capable of etching polysilicon or layered refractory metal (tantalum, molybdenum) silicided polysilicon films with virtually no change in linewidth from the developed photoresist image. We discuss the influence of the masking profile on the etched film profile and present conditions necessary for controlled film formation.

Dry etching is replacing wet chemical etching in selected semiconductor device fabrication steps because of its ability to accurately etch images into underlying films with either vertical or controllably sloped sidewalls. Vertical sidewalls are essential to achieve the degree of linewidth control necessary for the successful operation of MOS transistors on the micron scale. Regardless of which technology is used (plasma etching, reactive ion etching) the origin of the anisotropic etching behavior ultimately lies in directional ion bombardment normal to the substrate surface arising from applied electric fields. Even though this is the root cause of anisotropy, however, other chemical effects can heavily influence the degree of anisotropy actually realized.

In this paper we will investigate one of these chemical effects: that of polymerization or spontaneous deposition of material onto surfaces exposed to the plasma. Gener-

ally, polymerization is regarded as something to be avoided in as much as it may coat chamber and work surfaces and lead to cross contamination or erratic etching behavior. In some instances, however, this phenomenon has been exploited by intentionally coating chamber walls with material that forms volatile products upon ion bombardment, thereby eliminating the redeposition of nonvolatile sputtered material from the chamber walls. Another use of polymerization can be seen in the reactive ion etching of silicon dioxide down to a silicon surface, reducing its etch rate and thereby enhancing the silicon dioxide to silicon etch rate ratio.

We will describe a third use of intentional polymerization, where the operating point is chosen such that the determining factor in the competitive balance between etching and deposition is the local angle between the substrate surface and the ion bombardment direction.

Experimental Procedure

The samples used in this study consisted of LPCVD polysilicon layers 0.3 to 0.5 μm thick, deposited at 615°C onto oxidized, 3 in. diam <100> 20-50 $\Omega\text{-cm}$, p-type silicon

* Electrochemical Society Active Member.

¹ Present address: Raytheon Equipment Development Laboratory, Sudbury, Massachusetts 01776

² Present address: Massachusetts Institute of Technology, Lincoln Laboratory, Lexington, Massachusetts 02173

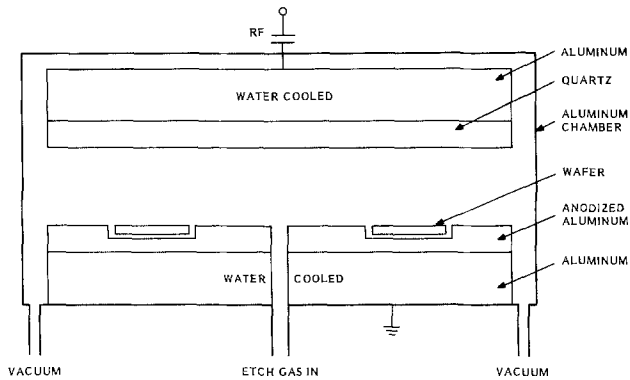


Fig. 1. Cross-sectional diagram of plasma etching chamber

wafers. The polysilicon was doped either by arsenic ion implantation or POCl₃ sourced phosphorus diffusion to resistivities of 10⁻³ to 10⁻² Ω-cm. Within this range, etch rate decreased very slightly with increasing resistivity. The underlying oxide thickness varied between 25 and 500 nm and had no effect on the results. Shipley 3000 positive photoresist of initial thickness 1.2 μm was used throughout, with exposures performed with a Canon PLA 521. Intentional sloping of the photoresist sidewall was obtained by simply postbaking vertical sidewalled resist patterns at temperatures between 110° and 140°C for various lengths of time.

The etching apparatus consisted of the rectangular parallel plate etching chamber diagrammed in Fig. 1. The etching samples rest on the lower grounded electrode with the top electrode excited by a 13.56 MHz RF generator through an appropriate matching network. Both electrodes are rectangular with dimensions of 35 × 53 cm with a 1 cm spacing, giving an enclosed volume of 1.85 liters. The gas feed is via a series of holes spaced 1 in apart along the entire centerline of the long axis of the lower electrode, and the pumping ports are below the outer edge of the lower electrode, as shown. The top electrode is covered by a 1 cm thick quartz plate, and the bottom electrode is anodized aluminum. All other chamber surfaces are aluminum. The entire chamber volume of 12.4 liters is pumped by a 100 cfm Roots blower. The rotary piston roughing pump is charged with Halovac® fluid which is continuously filtered during use. The etching gas was carbon tetrachloride, controlled by a mass flowmeter from a liquid source heated to 36°-40°C. All experiments were carried out at 23°C, with no temperature rise noted throughout the short etching times used (typically a few minutes). Temperatures were measured by means of a thermocouple imbedded in the lower electrode.

Results and Discussion

Table I lists vertical etching rates of common semiconductor materials under chamber conditions of 13 Pa pressure, 35 sccm CCl₄ throughput, and 1000W RF power applied to the top electrode. Estimation of exact power density or volume is difficult because of unknown dissipation in the tuning network and other leakage paths, but the dark space between the plasma and the grounded substrate electrode was approximately 1 mm. With this etch rate ratio of 20 to 1 for doped polysilicon to silicon dioxide, we have been able to routinely define 0.5 μm thick polysilicon gates over 25 nm thermal silicon dioxide without difficulty on 3 in. wafers.

When doped-polysilicon samples masked by photoresist with vertical sidewalls are etched under these con-

Table I. Vertical etch rates of semiconductor materials in a CCl₄ plasma in Å/min

Phosphorous-doped polysilicon	2000
Thermal silicon dioxide	100
Silicon nitride	1000
Hunt, Shipley positive resist	1000
Molybdenum disilicide	1000
Tantalum disilicide	3000

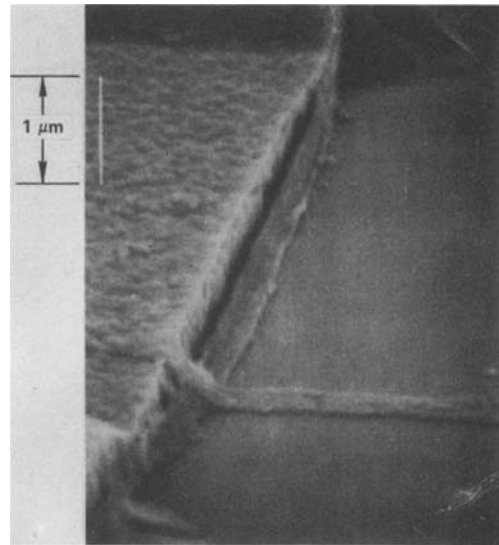


Fig. 2. SEM of polymer film partially dislodged from the sidewall of a doped polysilicon pattern. The horizontal film was completely lifted from the sample and redeposited at right angles to the polysilicon edge.

ditions, vertical walled polysilicon profiles are easily produced (1). The reason for this behavior can be seen in Fig. 2, which shows that a sidewall film has been formed along the polysilicon edge during etch. The film in this photograph has been partially dislodged by a 1 min dip in a 130°C sulfuric acid solution. The observation of this sidewall film is direct evidence of the surface inhibitor mechanism, which has been cited as the predominant cause of vertical walled behavior at comparatively high chamber pressures and low ion bombardment energies (2). This phenomenon is also more likely to occur in chlorinated gas systems rather than fluorinated because of the increased susceptibility of chlorine containing plasmas to form polymerized films (3).

The etching system lends itself to several interesting and difficult etching applications. One of these is the patterning of layered films of metal silicides on doped polysilicon to produce low resistivity MOS gate electrodes. Most attempts to etch these films have resulted in either poor etching results or complicated multistep etching procedures because of the generally different vertical and horizontal etching rates of the composite layers. Even

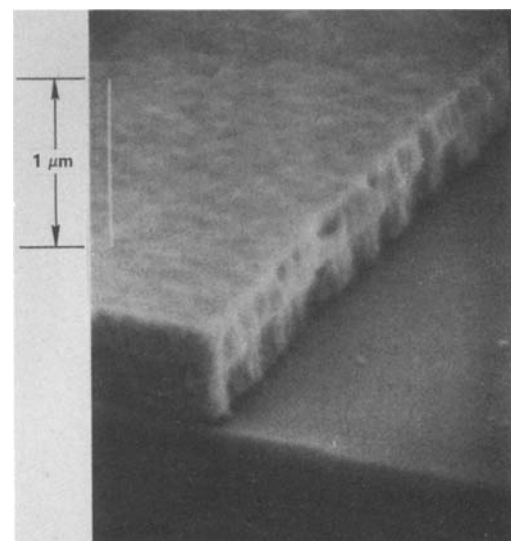


Fig. 3. SEM of the edge of an etched film consisting of 1500Å molybdenum silicide on top of 2000Å phosphorus-doped polysilicon. Both the masking photoresist and the sidewall film have been removed in this photograph.

though the vertical etching rates are different here also (see Table I), the presence of this sidewall film results in zero horizontal etching of all layers, allowing smooth, continuous vertical walled profiles to be produced, as can be seen in Fig. 3, which shows an etched film of molybdenum silicide on doped polysilicon.

Another property of this etching system is the ability to severely overetch samples with no observable undercut or sidewall attack, due to the masking nature of this film after it has been formed. A small overetch is generally needed to allow for nonuniformity in most dry etching schemes, but in some cases substantial overetch becomes necessary, for example, to clear filamentary residues where the polysilicon film conformally crosses over steps in the substrate. Such a situation is depicted in Fig. 4, showing etched polysilicon lines crossing over $0.5\ \mu\text{m}$ oxide steps in the substrate with the resist still in place. In Fig. 4a, the sample has been etched just to completion, that is, just to clearing on horizontal surfaces. Note the silicon residues along both sides of the oxide step, which is merely a consequence of the strictly anisotropic etching behavior of this system and the large vertical thickness of poly at this step. The top surface exhibits the characteristic roughness of partially etched polysilicon. Figure 4b has been subjected to a 100% overetch, which was just sufficient to clear the poly filaments. The etched polysilicon sidewall, being coated by polymer, faithfully replicates the photoresist image with no discernible undercut in spite of the necessary overetch. Further study of this etching system has produced evidence revealing the presence of a similar sidewall film upon the photoresist mask itself, in addition to the etched layer. Such a film is shown in Fig. 5, where it has been partially mechanically peeled away from the resist mask. Other photographs show that this film is, in fact, continuous across the resist-polysilicon boundary, and indicates that this is just an extension of the sidewall film previously detected on the polysilicon alone (Fig. 2).

In order to systematically study the properties of these films, a better method of sample preparation was needed rather than the chemical soaking or mechanical displacement shown in the previous samples, which are time consuming and disturb the film. An encapsulation technique devised for this purpose is illustrated in Fig. 6.



Fig. 5. SEM of a polymer film mechanically peeled away from a photoresist sidewall masking a doped polysilicon layer after etching.

After an original resist pattern is used to mask a polysilicon plasma etching operation, the entire sample is coated with an additional layer of thick resist, referred to as encapsulating resist in the figure. The sample is then cleaved, exposing a cross-sectional face of the entire structure. We then make use of the differential etch rate in an oxygen plasma to recess the resist face with respect to all other materials, including the sidewall film, which is held in place by both resists. A key feature is that the film is rigidly constrained in its original configuration, in contrast to earlier preparation methods which relied on mechanical or chemical methods to dislodge the film for

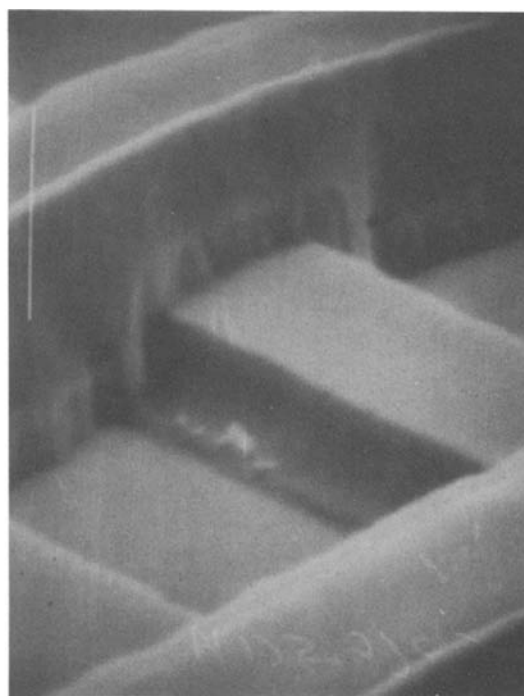
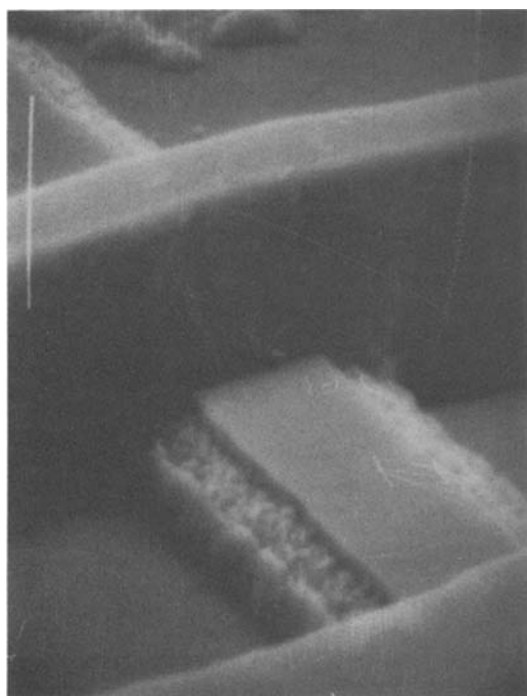


Fig. 4. Etched polysilicon patterns crossing over $0.5\ \mu\text{m}$ substrate steps. A(left): etched just to completion. B(right): etched to completion plus 100% overetch.

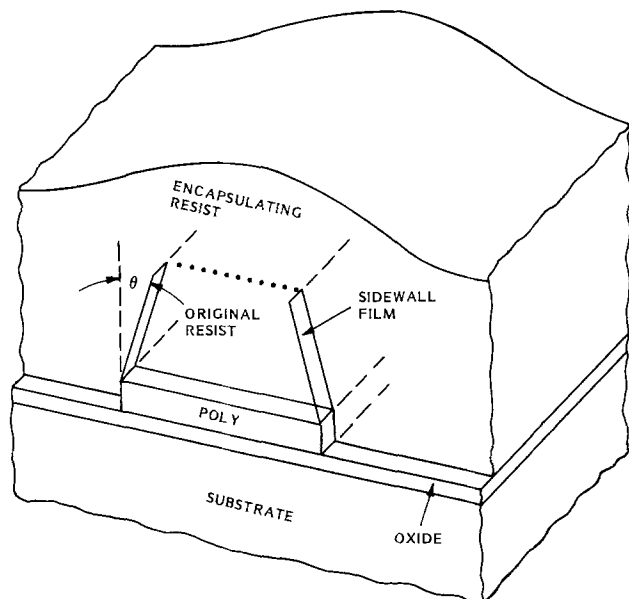


Fig. 6. Diagram of encapsulation technique developed to study sidewall film formation.

observation, losing the information conveyed by its original position. From the above description, it is clear that this technique will reveal the sidewall film only on the photoresist and not on the underlying polysilicon line, as the poly will not be recessed by the oxygen plasma. However, as already noted, the film is continuous across the resist-polysilicon boundary, and in every sample which exhibited a polymer film on the resist we have been able to observe the film on the polysilicon. That is, our observations are that the existence of the film on the resist implies existence on the poly.

Figure 7 shows an SEM of a sample prepared as above clearly showing the film along the resist sidewalls. The film does not form on the top surface; presumably, it is prevented from doing so by normal ion bombardment. Also, the film does not cover the entire sidewall, but disappears near the top of the resist as soon as the vertical wall starts rounding off to the top surface. The film is uniform and appears to be 300Å thick on vertical walled samples such as these. Auger analysis of the film reveals mostly carbon and chlorine, suggesting that it is a decomposition product of the CCl₄ feed gas similar to "glow polymer" depositions reported elsewhere in similar RF discharge environments (4).

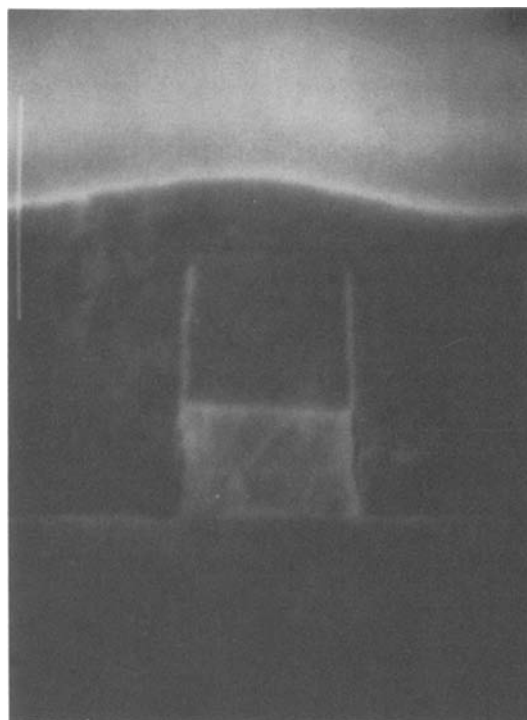


Fig. 7. SEM of a 0.8 μm wide line etched into a 0.5 μm doped-polysilicon layer prepared by the encapsulation technique in Fig. 6.

There are instances, however, where under these same plasma etching conditions samples exhibit sloped polysilicon walls and a reduction in linewidth dependent on overetch time, implying that the sidewalls were in fact being etched and that the protective film was not forming. Sloping photoresist sidewalls such as those obtained by negative E-beam exposure or resulting from poor mask sample contact during optical contact printing are always associated with such behavior, although the reverse is not always true. That is, vertical polysilicon sidewalls may be associated with either sloping or vertical photoresist sidewalls. This observation, coupled with the disappearance of the film as soon as the sidewall starts to round off at the top surface of the encapsulated samples, as noted above, suggests that this parameter, *i. e.*, "degree to which sidewall is perpendicular to wafer," plays an important role in polymer formation.

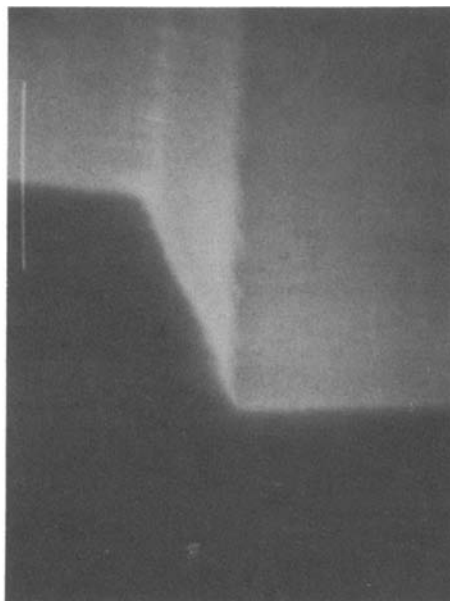
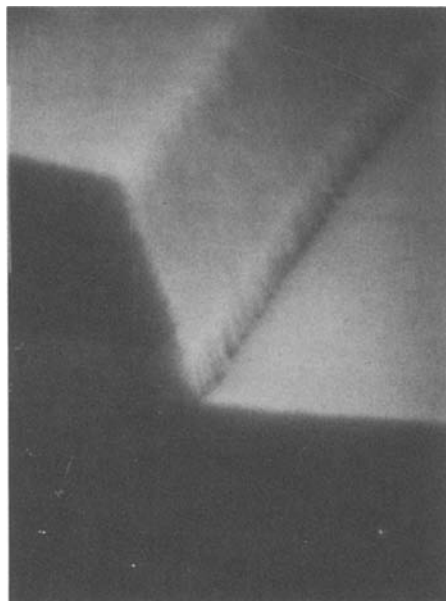


Fig. 8. SEM cross sections of resist-polysilicon profiles where no sidewall film and lateral etching are observed.

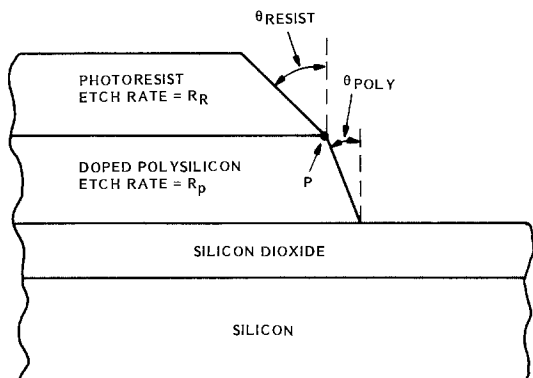


Fig. 9. Anisotropic etching model used to describe profiles such as seen in Fig. 8.

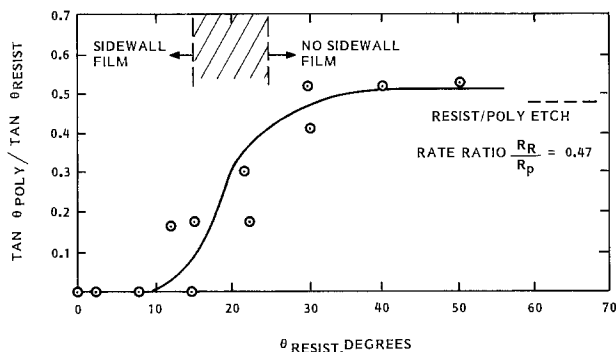


Fig. 10. Measured sidewall angle tangent ratios plotted against initial photoresist angle. Also indicated are the resist-poly etch rate ratio and the region of sidewall film formation.

To study the relationship between photoresist sidewall slope, polymer film formation, and polysilicon sidewall slope, a series of measurements were made of etching profiles resulting from controlled slope resist patterns created by overbaking vertical-walled patterns. Profile angles were taken from SEM cross sections such as shown in Fig. 8, and sidewall film presence was detected by the encapsulation technique described earlier.

When the masking photoresist has sidewalls possessing large angles, as defined in Fig. 6, the resulting etch profiles closely fit those predicted by a simple, purely anisotropic etching model, which assumes that all points of an exposed surface are etched at constant etch rate R in the vertical direction. Figure 9 applies the model to the current situation of a photoresist mask with sidewall angle θ_{resist} . As a consequence of the resists being etched vertically with rate R_R , the point P in the figure moves to the left at rate $R_R \tan \theta_R$. The movement of point P , the effective mask edge, combines with the etch rate of the polysilicon R_P to produce a sidewall angle θ_{poly} satisfying the relation $R_R \tan \theta_R = R_P \tan \theta_P$. Therefore, $\tan \theta_{\text{poly}} / \tan \theta_{\text{resist}} = R_R / R_P$, independent of θ . Incidentally, this is mathematically equivalent to previous anisotropic models (5), where the normal etch rate of a surface depends on the cosine of the angle between the surface and the vertical. This formulation, however, emphasizes the simplifying assumption of constant vertical etch rate of all surfaces.

When we apply our encapsulation technique to samples in which the photoresist exhibits a large slope, we find

no evidence of sidewall film formation on the masking resist. Conversely, when samples with small or zero angles are etched, we observe vertical polysilicon sidewalls, no change in poly linewidth even upon overetching as much as 300%, and the clear presence of sidewall film as revealed by the encapsulation method.

Figure 10 presents the data from a set of samples as a plot of the sidewall angle tangent ratio vs. θ_R , the original resist angle. Also indicated in the figure is the unpatterned etch rate ratio of the two films, 0.47, obtained from independent runs. For initial $\theta_R > 30^\circ$, the tangent ratio is constant and agrees quite well with the etch rate ratio, as predicted above. As the resist angle decreases below 30° , however, the polysilicon angle no longer decreases in accordance with the model, but rather drops abruptly to zero at about 10° resist angle.

Also shown in the figure are the results of SEM observations of the encapsulated wafer indicating either the presence of the film for $\theta_{\text{resist}} < 15^\circ$ or the absence of the film for $\theta_{\text{resist}} > 25^\circ$. The indeterminate region between 15° and 25° signifies that the film was present in some instances and absent in others, reflecting the sensitivity of this operating region to minor fluctuations in etching parameters.

The results shown in Fig. 10 suggest a relationship between the formation of a polymer film and a deviation from the simple anisotropic etching model, namely, that the film, once formed, can act as an etching mask to prevent any lateral etching. Note that the terms "anisotropic" and "vertical walled" are not the same and cannot be used interchangeably. This can be seen in the discussion involving Fig. 9, where, even though strict anisotropy is assumed, sloping polysilicon sidewalls will occur and are expected if the photoresist is sloped. In the absence of polymer film formation, vertical polysilicon sidewalls will result only with vertical resist sidewalls, whereas in the presence of film formation, vertical polysilicon walls can result even with a finite resist sidewall slope. That is, we can say this film enhances the ability to produce vertical-walled structures by interfering with the sideways etching mechanisms under certain conditions without affecting the intrinsic anisotropy of the etching system.

The question of whether the polymerization phenomenon is related to the intrinsic anisotropy of the system, although an interesting one, will not be addressed in this paper.

The reason for the angular dependence of film formation lies in the flux of positive ion bombardment normal to the substrate surface. For small sidewall angles, the flux onto the sidewall is either zero for $\theta = 0$ or very small, proportional to $\sin \theta$ allowing the polymer film to form under proper conditions. As θ increases, the surface is increasingly exposed to the clearing effect of the ion bombardment, until θ_{crit} , when a rough balance exists between protective film removal and formation. This is not a simple, sharp boundary, however; rather, there exists a blurred transition where both competing effects can occur simultaneously, as is evident from the data. For $\theta > \theta_{\text{crit}}$, the polymer film is completely prevented from forming and etching of the substrate material proceeds. In summary, Fig. 11 illustrates the three distinct etching profiles determined solely by photoresist sidewall angle which may result under identical plasma etching conditions. Clearly, for maximum polysilicon linewidth control the sidewall angle θ should be less than θ_{crit} and prefera-

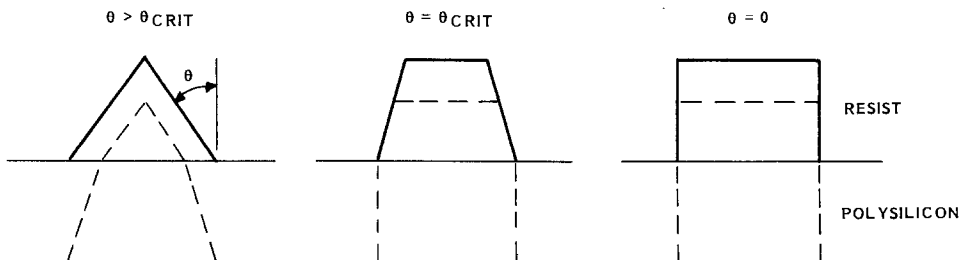


Fig. 11. Illustration of the three different results which can occur under identical plasma etching conditions as a result of photoresist sidewall angle.

bly zero to assure polymer formation and vertical-walled polysilicon patterns. This is hard, if not impossible, to achieve with projection aligners, which makes this of great potential importance.

The quantity θ_{crit} , therefore, is an observable or a measurable quantity which can provide information about the internal state of the plasma environment and the degree of balance between deposition and etching. Since the degree of deposition is dependent upon (among other parameters) concentration of polymerizing species and the tendency of film removal (and hence etching) is dependent upon ion bombardment flux and energy, one can actually manipulate the θ_{crit} of a system by varying these parameters. For example, the θ_{crit} of our system can be driven towards 90° by increasing the gas flow to 84 sccm, the pressure to 17 Pa, and reducing the power to 800W. Figure 12 shows a sample etched under these conditions resulting in vertical polysilicon sidewalls even for extremely sloping resist sidewalls. However, the figure also shows a disadvantage of pushing the critical angle too high: a high probability of residue in the etched areas. This is to be expected, of course, since by the above parameter variations we have altered the balance point of the system towards spontaneous deposition everywhere.

Conclusions

This paper demonstrates that during plasma etching the original photoresist profile can exert a dominating influence on the lateral etching mechanism through the intermediary phenomenon of selective polymerization on photoresist and etched polysilicon sidewalls. When such is the case, the condition of near vertical photoresist sidewall results in reliable film formation, no observable pattern erosion, and greatest linewidth control. The concept of θ_{crit} is introduced as a measure of the balance point of the competing reactions of etching and film deposition which exists in the plasma environment, and indicates the latitude of photoresist sidewall slope which can be tolerated before any lateral etching takes place.

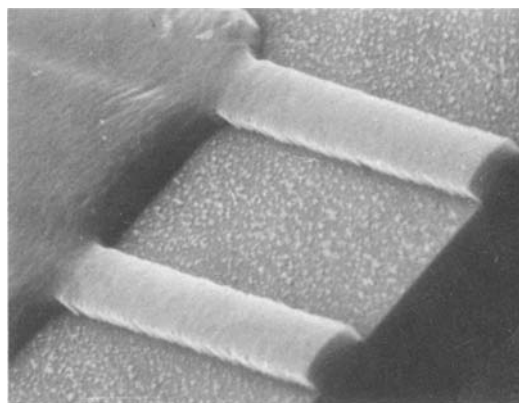


Fig. 12. Etching residue resulting from forcing θ_{crit} close to 90°

Manuscript submitted Aug. 4, 1983; revised manuscript received April 10, 1984. This was Paper 167 presented at the San Francisco, California, Meeting of the Society, May 8-13, 1983.

Sperry Corporation assisted in meeting the publication costs of this article.

REFERENCES

1. S. E. Bernacki, Paper 214 presented at the Electrochemical Society Meeting, Montreal, Que., Canada, May 9-14, 1982.
2. D. L. Flamm, V. M. Donnelly, and D. E. Ibbotson, *J. Vac. Sci. Technol. B*, **1**, 23 (1983).
3. A. G. Nagy and D. W. Hess, *This Journal*, **129**, 2530 (1982).
4. H. J. Tiller, D. Berg, and R. Mohr, *Plasma Chem. Plasma Proc.*, **1**, 247 (1981).
5. W. G. Oldham, A. R. Neureuther, C. Sung, J. L. Reynolds, and S. N. Nandgaonkar, *IEEE Trans. Electron. Devices*, **ed-27**, 1455 (1980).

Porosity-Controlled Nickel Electrode Film by Vacuum Deposition

M. Bica de Moraes, D. M. Soares, and O. Teschke*

Grupo de Hidrogênio, Instituto de Física, UNICAMP, Campinas, 13.100 São Paulo, Brazil

ABSTRACT

We report, for the hydrogen evolution reaction, the electrochemical properties of porous nickel films prepared by vacuum deposition in argon atmosphere. The argon pressure in the deposition chamber determines the film structure. A correlation between electrolytic activity and film structure was observed.

Porous electrodes have been extensively used in electrochemical reactions (1, 2). The advantage of a porous surface structure is a many-fold increase per unit of cross-sectional area of the active surface area. Even though the apparent current density increases considerably, the actual current density is lower than that encountered in conventional plane electrodes, thus leading to a lesser overvoltage. The high specific electrode surface area makes the module more compact both in volume and weight. The catalytic properties of these electrodes can be understood in terms of their macroporosity and microporosity. The macroporosity is the space between crystallite agglomerates and it is a function of their arrangement. It can be observed under an optical microscope and it can be considered as having a definite cross-sectional and geometric perimeter. Microporosity is the very fine porosity existing within or on the surface of the crystallites. It

is characterized by different crystallite diameters which determines the number of adsorbed atoms located in different positions. Recently, nickel deposits with different structural characteristics were obtained by vacuum deposition under different condensation and annealing conditions (3). Electrocatalytic characteristics of nickel electrodes are altered by changes in their crystalline structure (4, 5).

One method of preparation of high porosity nickel films is by evaporation in an atmosphere of inactive gases at low pressures. This technique has been used for the preparation of black metal surfaces for infrared absorption (6) and for the preparation of fine metal particles (7, 8).

This paper describes a method developed for making porous nickel electrodes with controlled porosity by vacuum evaporation. The macroporosity and microporosity were modified by changing the argon pressure during deposition. A correlation between electrocatalytic activity and the electrode surface structure is observed.

*Electrochemical Society Active Member.

Key words: thin films, vacuum deposition, nickel electrode.

Table I. Argon pressures during each deposition

Electrode	First deposition pressure (torr)	Second deposition pressure (torr)
1	0.1	—
2	0.1	0.37
3	0.1	0.75
4	0.1	1.1

Experimental

The electrodes were prepared in an ordinary high vacuum evaporation unit by deposition of nickel films onto metal screens in argon gas at low pressures. Nickel was evaporated inside the vacuum chamber by means of a tungsten wire basket heater. When evaporation was carried out in an argon pressure not lower than ≈ 0.05 torr, a film of porous structure (black nickel) was formed onto the metal screen. Argon gas (purity better than 99.99%) was admitted to the chamber by means of a variable leak valve. Evaporations were made with high purity nickel (99.96%), while the wire basket heating current was provided by an ac power supply. In order to attain, for a given argon pressure in the chamber, good reproducibility on the thickness and porosity of the nickel films, the

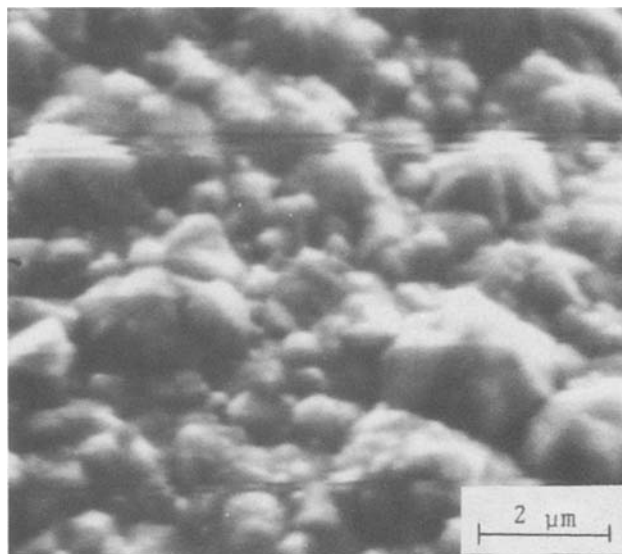


Fig. 1. Micrograph of a nickel electroplated electrode surface

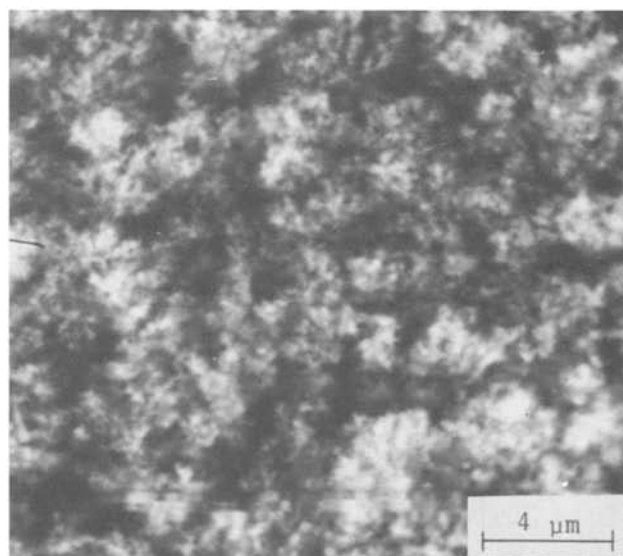
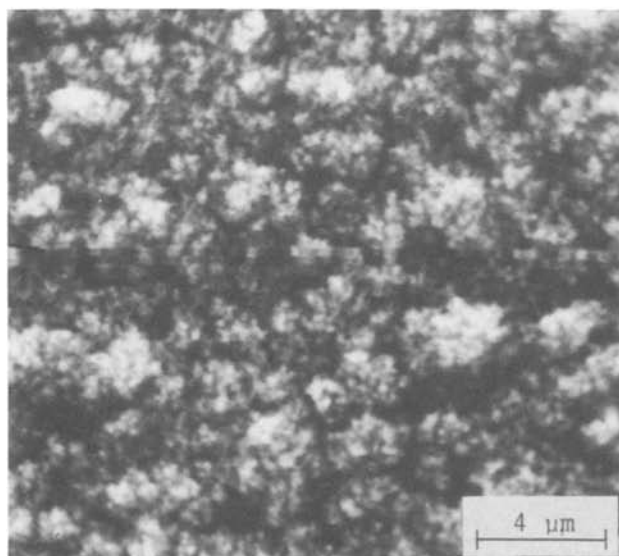
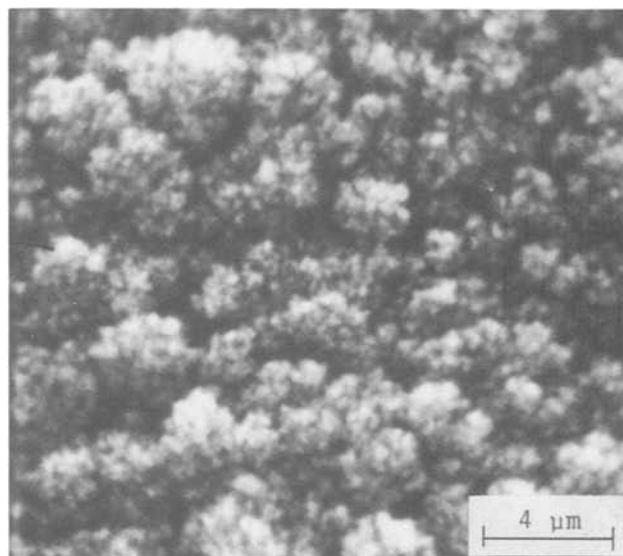
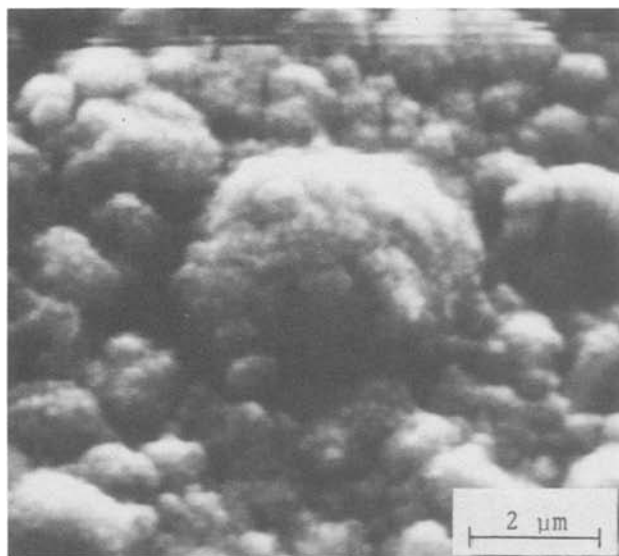


Fig. 2. Morphologies of black nickel catalyst films deposited at various argon pressures P . a(top left): single-layer film, $P = 0.1$ torr. b(top right): two-layer film, $P = 0.1$ torr (first layer) and $P = 0.37$ torr (second layer). c(bottom left): two-layer film, $P = 0.1$ torr (first layer) and $P = 0.75$ torr (second layer). d(bottom right): two-layer film, $P = 0.1$ torr (first layer) and $P = 1.1$ torr (second layer).

same weight of nickel (0.1g) was evaporated in each deposition. The low residual background pressure in the chamber ($\sim 2 \times 10^{-6}$ torr) before evaporation assured a very small degree of contamination of the films.

The metal screens that supported the nickel electrocatalysts were 25 cm² squares cut from the same stainless steel 40 mesh screens. The screens were cleaned, degreased, and nickel electroplated prior to the electrocatalyst vacuum deposition. One of screens was deposited with a single black nickel layer, while all the others were deposited with two successive layers at two different argon pressures, as shown in Table I.

One of the inherent difficulties with black nickel films is their poor adhesion to the substrate (3). However, we found that treatment of the samples by a hot KOH solution improves adhesion to a large extent. After vacuum deposition, the screens were immersed in a 10% KOH solution at room temperature. The temperature of the solution was then slowly raised. The screens remained in the solution for about 20 min, when the temperature reached 70°C. Black nickel films treated in this way showed not only improved mechanical adhesion, but also withstood corrosion by the alkaline electrolyte in a very satisfactory way. All the screens listed in Table I underwent the KOH fixing treatment described above. When two layers were deposited on the same screen, the fixing treatment was repeated after each deposition.

Results and Discussions

The morphologies of the film surfaces were studied by means of scanning electron microscopy (SEM). SEM micrographs of regions of several electrode surfaces are shown in Fig. 1 and Fig. 2a to 2d. Figure 1 shows the surface of an electrode before receiving the vacuum-deposited nickel overlayer. Its crystallite structure is characteristic of electrolytic nickel depositions made with a Watts solution at 80°C and a current density of 10 mA/cm². We may also observe that there is no significant microporosity in this sample. The surface of an electrode with a vacuum-deposited black nickel film at an argon pressure of 0.1 torr (electrode no. 1) is shown in Fig. 2a. The photograph shows that the macrostructure of the electrode film was enhanced by the formation of larger crystallite conglomerates, resulting in a larger macroporosity. We may also observe that the crystallites' microstructure is now substantial. The surface structure of the electrode no. 2 is shown in Fig. 2b. The first deposition essentially increased the macrostructure area, while the second one gave a finer structure to the crystallites, increasing substantially their microareas. The micrograph of Fig. 2c exhibits the surface of electrode no. 3. Void electrode spaces are estimated by comparing the light color region in the photograph with the gray and the black ones, which correspond, respectively, to the upper, intermediate, and bottom levels of the deposited structure. The surface structure of electrode no. 4 is shown in Fig. 2d. The second deposition produces a fusion of a few crystallite conglomerates resulting in a decrease in the macroporosity.

In order to relate the film structure to its catalytic activity, the films were tested for the hydrogen evolution reaction (HER). Electrochemical studies of the catalysts were performed in an electrolysis test cell by measuring the voltage drop between the working electrode and the reference electrode. The working electrodes consisted of 10 cm² disks cut from each one of the prepared square screens. The reference electrode was Hg/HgO, and Luggin capillary tubing was used to make the electrical connections between the reference electrode and the electrolysis cell components. The counterelectrode was a 10 cm² platinum disk. In all electrochemical measurements, KOH 30% at 80°C was used as an electrolyte. The temperature was thermostatically controlled. The electrochemical activity of the electrodes was measured by a current interrupter technique, which is described elsewhere (9).

A satisfactory reproducibility of the electrochemical measurements was obtained after pretreatment of the electrodes at 1 A/cm² during 30 min. The set of Tafel plots

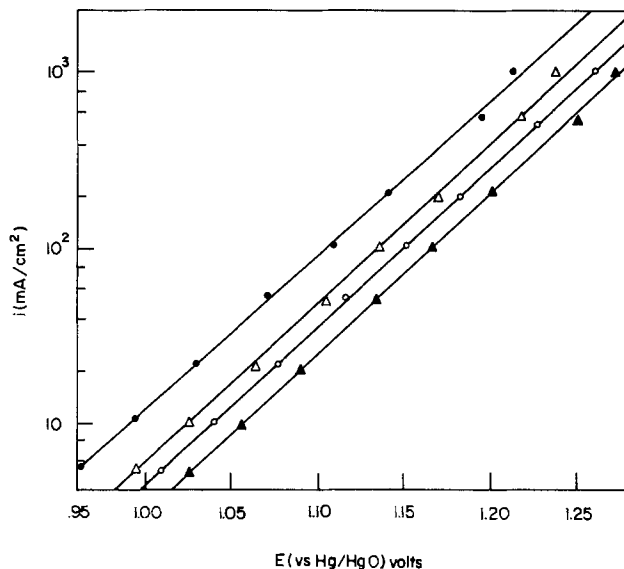


Fig. 3. Tafel diagrams for the hydrogen evolution reaction for various nickel-deposited electrodes. \blacktriangle , \triangle , \bullet , and \circ correspond to electrode films whose surface morphologies are shown in the micrographs of Fig. 2a, 2b, 2c, and 2d, respectively.

for the hydrogen evolution reaction is plotted in Fig. 3. Each plot corresponds to one of the electrodes whose surfaces are shown in Fig. 2a through 2d.

A correlation between electrolytic activity and film structure is observed by means of the plots of the electrode voltage against the reference electrode as a function of the argon pressure at which the uppermost nickel film layer is deposited. These plots are given in Fig. 4. They were obtained from the plots of Fig. 3 by taking the electrode current density as a parameter. The plots show that there is a minimum of the electrovoltage for an argon deposition pressure of the uppermost layer of approximately 0.7 torr. The different overvoltage presented by each electrode is related to their different structural characteristics.

The hydrogen in the interior surface is produced, and a steady current will be supported only if an efficient gas

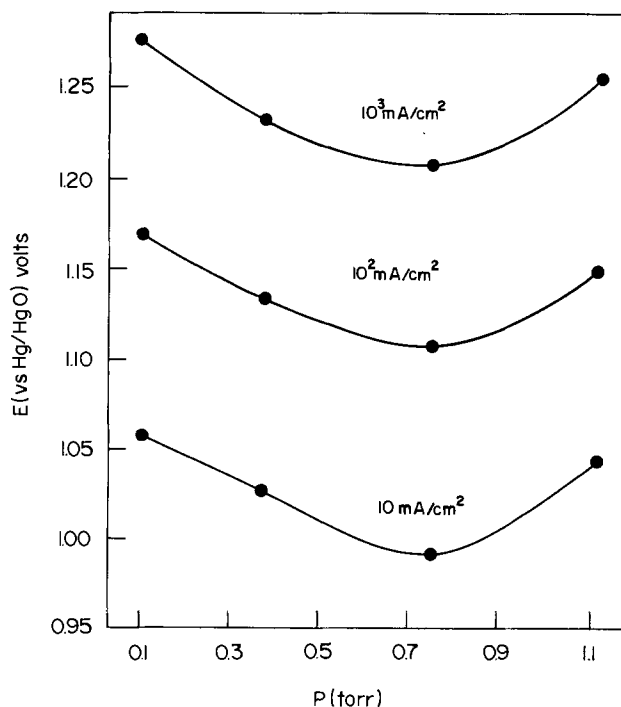


Fig. 4. Electrode polarization voltage E as function of the argon deposition pressure for the uppermost nickel film layer for various current densities.

and ion transport from the surface to the bulk electrolyte through the pore structure takes place. The minimum overvoltage for the various electrodes was obtained by the maximum macroporosity film showing that mass transport plays an important role in electrode overvoltage. From Fig. 3, we observe that for the maximum measured current density the transport-limited current density plateau was not yet reached.

Conclusions

We have shown that vacuum-deposited black nickel films can be successfully used as electrocatalysts for the hydrogen evolution reactions with high current densities. The deposition of the catalytic film on the nickel-electroplated electrodes was found to cause a reduction on their overvoltage, and to depend on the argon pressure at which the uppermost film layer was deposited. An optimum nickel film structure for which the overvoltage reduction is a maximum was found to exist.

Acknowledgment

This work was supported by CESP-Companhia Energética de São Paulo.

Manuscript submitted Dec. 21, 1982; revised manuscript received April 10, 1984.

The Instituto de Física, UNICAMP assisted in meeting the publication costs of this article.

REFERENCES

1. "Handbook of Fuel Cell Technology," C. Berger, Editor, Prentice Hall, Englewood Cliffs, NJ (1968).
2. P. Ragunathan, S. K. Mitra, and M. G. Naylor, *J. Hydrogen Energy*, **6**, 487 (1981).
3. L. Angely, G. Bronoel, and G. Peslerbe, *J. Electroanal. Chem. Interfacial Electrochem.*, **96**, 183 (1978).
4. L. Angely, G. Bronoel, and G. Peslerbe, *ibid.*, **96**, 191, 203 (1978).
5. J. P. Candy, P. Fouillox, C. Grabrielly, M. Keddan, and H. Takenoutti, *C. R. Acad. Sci.*, **285**, 463 (1977).
6. A. H. Pfund, *J. Opt. Soc. Am.*, **23**, 375 (1983).
7. O. Beek, A. E. Smith, and A. Wheeler, *Proc. R. Soc. London, Ser. A*, **177**, 62 (1940).
8. K. Kimoto, Y. Kamiya, N. Nonoyama, and R. Uyeda, *Jpn. J. Appl. Phys.*, **2**, 702 (1963).
9. O. Teschke, D. M. Soares, and C. A. P. D. Evora, *J. Appl. Electrochem.*, **13**, 371 (1983).

Characterization of Implanted Nitride for VLSI Applications

M. J. Kim* and M. Ghezzi*

General Electric Company, Corporate Research and Development, Schenectady, New York 12301

ABSTRACT

A silicon nitride layer formed by nitrogen implantation was characterized for VLSI application. Molecular nitrogen was implanted in an energy range of 5 to 60 keV for forming various nitride layers during subsequent annealing at 1000°C in nitrogen. The nitride layers formed were characterized before and after furnace annealing with differential IR, SIMS, and ellipsometry to find a useful implantation condition for a local oxidation mask. The initial IR peak of the implanted nitrogen was 815 cm⁻¹ for the entire implantation energy range. While the position shifted to a higher wave number for the high energy implants after annealing, the low energy implants peak remained very close to 830 cm⁻¹, which is comparable to the LPCVD nitride peak. This finding suggests that the composition of the low energy nitrides is nearly stoichiometric. Annealing shifted the concentration profile toward the surface and increased the peak nitrogen concentration. The nitride profile peaked at the surface or disappeared below 10 keV. The masking properties of these nitrides were tested by growing 5300Å oxide in steam at 1000°C. The nitrides with dosages of 5×10^{16} N₂⁺/cm² ions formed an effective oxidation mask for implantation energy below 40 keV. Under the experimented conditions, the nitride formed with 10 keV appeared to be an effective oxidation masking with adequate etching selectivity to SiO₂, reducing the "bird's beak" size to one fourth of the conventional LOCOS.

LPCVD nitride has been used extensively for local oxidation (LOCOS) (1) for VLSI processes. The nitride is generally used in combination with a thin buffer oxide between the silicon and the nitride to prevent the silicon from cracking due to thermal stresses. The buffer oxide acts as a conduct for the oxidants, extending the field oxidation beyond the edges of the active areas. In order to improve the LOCOS and isolation processes, many studies (2-6) have been made. The adjustment of the relative thicknesses of nitride and buffer oxide was attempted, to reduce the lateral oxide extension (3). Stress analysis (7, 8) was done, to suppress the edge lifting of the nitride that enhances the lateral penetration of the oxidant. More recently, the sidewall mask isolation (SWAMI) (9-11) process was developed in which a nitride layer made of nitride, oxide, and silicon is conformally deposited on active areas with nearly vertical sidewalls. Unmasked RIE etching of the nitride layer leaves nitride sidewall protection along the mesa perimeter, which blocks the penetration of the oxidant into the buffer oxide (12). A relatively sharp oxide edge was obtained by means of a progressive nitride edge lifting on the sidewall and planar surfaces during oxidation. This process was done by controlling the silicon etch depth, with added cost and process complexity.

Another method used to prevent channeling of the oxidant through the buffer oxide is sealed interface localized oxidation (SILO) (13, 14) where a thin silicon nitride layer is formed directly on silicon to seal the interface. One type of SILO nitride is formed by a direct thermal reaction of silicon under ammonia plasma (15). The most important factor is preservation of the original silicon from contamination and defect generation. In this regard, nitrogen implantation appears to be the better method because it is cleaner and generates a more gradual transition between silicon and silicon nitride. Etch pitting along the nitride mask was not observed for the implanted nitride (12). Oxidation inhibition in nitrogen-implanted silicon has been studied for the N₂⁺ energies between 40 and 200 keV and doses between 10¹⁵ and 4×10^{16} N₂⁺/cm² (16). The characterization of the implanted film has also been performed for a high energy range, from 48 to 150 keV (17-20).

The purpose of this study was to characterize an implanted-nitrogen layer formed at low energy and to optimize the implant conditions for application to LOCOS. For film characterization differential Fourier transform infrared (FTIR) and secondary ion mass spectroscopy (SIMS) analyses were extensively used before and after the nitridization annealing. The FTIR spectrum produces useful information about the structural changes in the nitride layers. The concentration profiles made by SIMS help us to understand the real nitrogen distribution after

*Electrochemical Society Active Member.

Key words: semiconductor, dielectric isolation, ion implantation, LOCOS, annealing.

each process step. We observed that nitrides formed by implantation at an energy below 40 keV effectively mask 5300Å steam oxidation. The low energy nitride is also selectively etchable for exposing the active area for subsequent device processing. Among the low energy nitrides, both optimum and practical process conditions could be found through extensive analysis and property characterization.

Experimental Procedure

The substrates used for the experiment were <100> n-type silicon wafers with an average resistivity of 5 Ω -cm. The interstitial oxygen content of the Czochralski-grown wafer was analyzed by infrared (IR) spectroscopy, according to the ASTM F121-80 method. The oxygen content was determined to be about 1.7×10^{18} atom/cm³.

To form a nitrogen-implantation mask, the wafers were oxidized in steam at 1000°C to grow 0.3 μ m of SiO₂. The oxide was patterned to form three different regions: test structures, uniform oxide cover, and bare silicon. Instead of 0.3 μ m SiO₂, a resist pattern was also used as an implantation mask for some of the wafers. The test structure contained a variety of 1-9 μ m² windows, which made it possible to test whether such small patterns can be resolved during oxidation. By virtue of the masking properties of oxide and resist, only the openings in the test patterns and the exposed silicon were nitrogen doped; the nitrogen implant was blocked elsewhere. Molecular nitrogen ions (N₂⁺) at an energy range of between 5 and 60 keV were implanted with doses between 1×10^{16} and 5×10^{16} N₂⁺ ion/cm². The temperature of the wafers was kept near room temperature (20° ± 2°C) during implantation. The nitrogen concentration profile was measured with a Cameca IMS 3-ion microscope using Se⁺ primary ions. In order to maximize the detection sensitivity, the ⁴²SiN⁺ species was profiled. Differential FTIR was used for IR spectroscopy in the energy range of 400-4000 cm⁻¹. After the initial nitrogen profile was made and IR spectroscopic analysis completed, the wafers were annealed in dry nitrogen at 1000°C for 1h. Postannealing analyses using SIMS and IR were also performed to compare the property changes.

Field oxidation was then carried out under conditions similar to those for conventional LOCOS. Thus, nitrogen-implanted LOCOS was performed in steam at 1000°C for selective growth of 5380Å oxide. Wafers with different

doses and ion energies were examined with a scanning electron microscope (SEM). The thicknesses of nitrides and field oxides were also measured with an ellipsometer at a wavelength of 0.6328 μ m. The step height between the nitride and local oxide was measured with a mechanical surface profilometer (Dektak). The masking nitride was etched away in hot phosphoric acid at 180°C to check the etch selectivity of the Si₃N₄ vs. the SiO₂.

Results and Discussion

FTIR analysis.—Figure 1 shows the IR spectra of areas implanted with a dose of 5×10^{16} N₂⁺/cm². The implantation energies were 5, 10, 20, 30, 40, 50, and 60 keV, as specified.

In order to obtain an accurate measurement of the Si-N bonds, a differential intensity spectrum was plotted for each sample. That is, the IR absorptions from the nitrogen-implanted and unimplanted areas were first obtained; then the latter was subtracted from the former to find the contribution of nitrogen. The large peaks, near 815 cm⁻¹, are associated with Si-N bond vibration caused by nitrogen interstitials. The small peaks at 1115 and 620 cm⁻¹ for the oxidized specimens were contributed by the uncompensated oxygen and silicon of the reference area. Assuming that 0.18 μ m of silicon was consumed for the oxidation and that the original wafer thickness was 343 μ m, a fraction of each element, equivalent to 0.18/343, is responsible for the uncompensated peaks. The resist-masked wafers (NC2-1, 2, and 3) do not have these minor peaks, but only a broad low-energy peak near 490 cm⁻¹, which can be linked with the inherent nitride bonds in a pure nitride spectrum.

The measured absorbances are effective absorbances; we assume that the reflective loss variations to implant energy are small. The peak absorption intensities in Fig. 1 are different from each other. The peak absorbance increases with ion implantation energy, although the dose is fixed. The intensity decrease at low energy may be caused by a larger loss of nitrogen near the surface for low energy implants and by a larger fraction of inactive nitrogen atoms in the high concentration region. The native oxide of the implanted wafer was measured to be about 20Å. Since the projected range is lower for lower energy, the number of nitrogen ions captured by the native oxide is correspondingly higher. In our case, the doped native oxide had been etched away together with

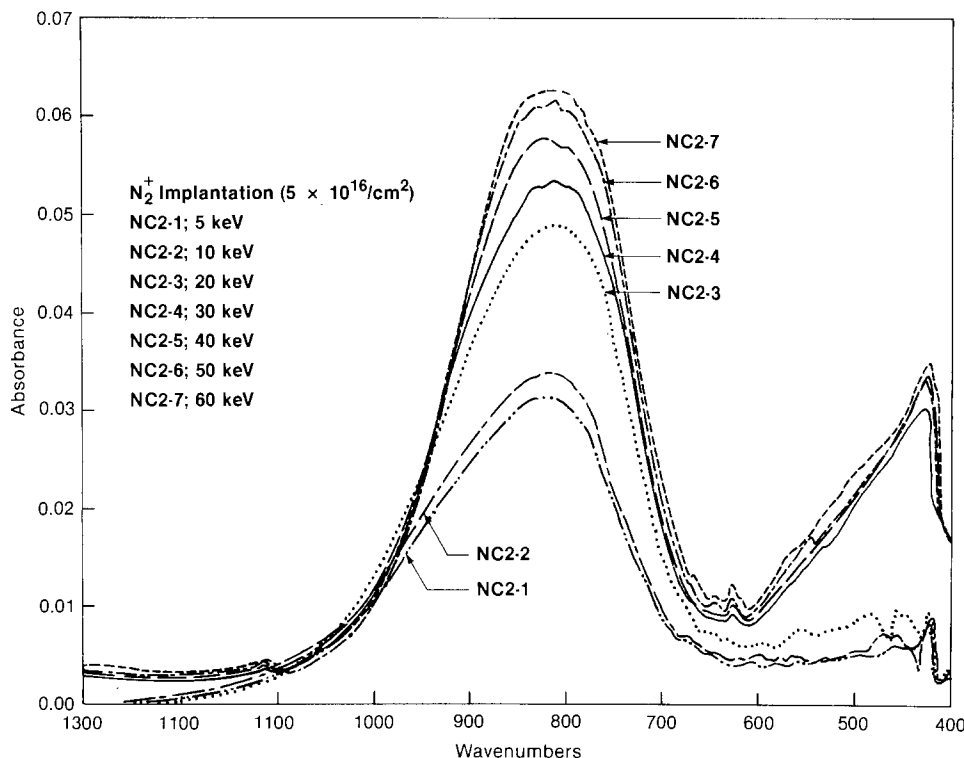


Fig. 1. IR absorbance spectrums of implanted nitrogen at specified energies. The major peak is centered at 820 cm⁻¹. The resist-masked NC2-1, 2, and 3 have better nitride spectra, with absence of the false peak near 420 cm⁻¹.

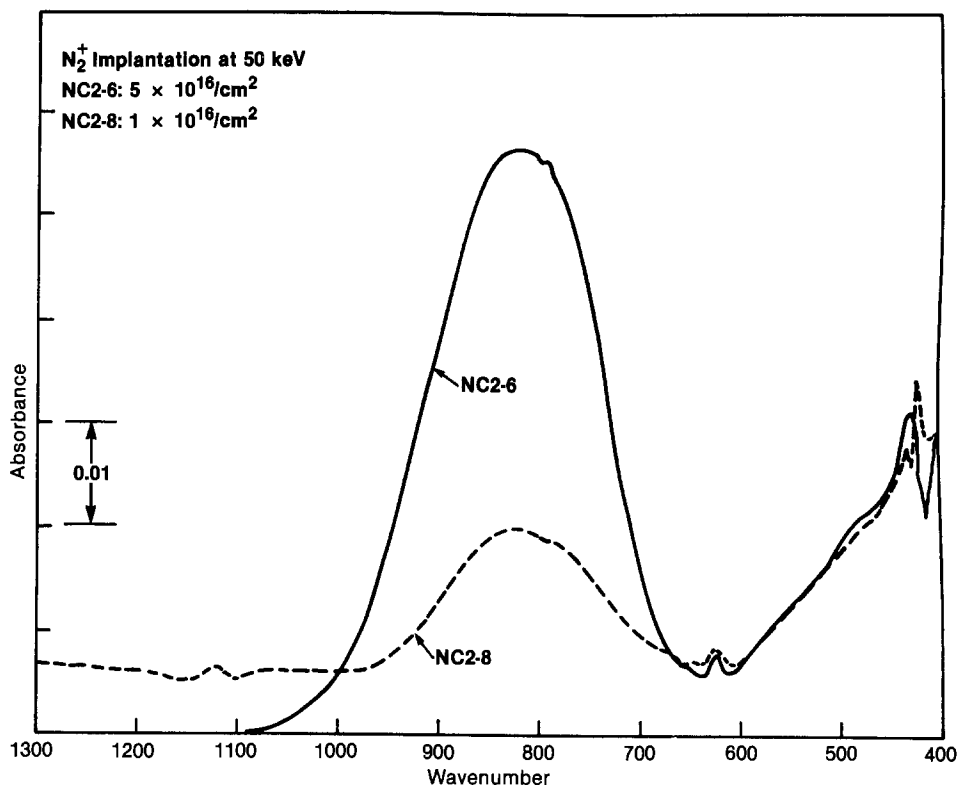


Fig. 2. Effect of N_2^+ fluence on the IR intensity for 50 keV implantation. The intensity is proportional to the fluence.

the masking oxide on the reference area, carrying away its share of N_2 atoms. However, the major cause of the peak intensity reduction may be linked to inactive excess nitrogen atoms, such as nitrogen bubbles, in the high concentration layer implanted at low energy, which cannot contribute to the IR absorption. According to a TEM analysis of a nitrogen-implanted silicon layer (21), nitrogen bubbles actually were observed. The measured absorbances for 5, 10, 15, 30, 40, 50, and 60 keV wafers are 0.026, 0.030, 0.044, 0.048, 0.051, 0.055, and 0.056, respectively. All the peaks are consistently positioned at 815 cm^{-1} .

Figure 2 shows the change of the nitrogen peak intensity with the ion dose. With the energy fixed at 50 keV, NC2-8 with a dose of $1 \times 10^{16} \text{ N}_2^+/\text{cm}^2$ is compared to NC2-6 with a dose of $5 \times 10^{16} \text{ N}_2^+/\text{cm}^2$. The NC2-8 peak intensity is 0.012, approximately one-fifth of the NC2-6

peak intensity, which indicates that the inactive nitrogen loss is very small at 50 keV. This finding agrees with the results shown in Fig. 1: while the intensity losses decrease from 15% to 30 keV to 7% at 40 keV, there is little change from 50 to 60 keV. Because the implantation energy must be minimized without a significant loss of nitrogen ions, it was concluded that there is no need to increase the implantation energy above 50 keV.

Figure 3 shows an IR spectrum of the nitride layers after annealing in nitrogen at 1000°C for 1 h. There is little loss of nitrogen intensity, except for the 5 keV specimen having an extremely shallow layer. However, there are two significant changes in peak position and peak width. While the high energy peaks are broadening, the low energy peaks are being sharpened. The most significant phenomenon is that the peak position is dependent on

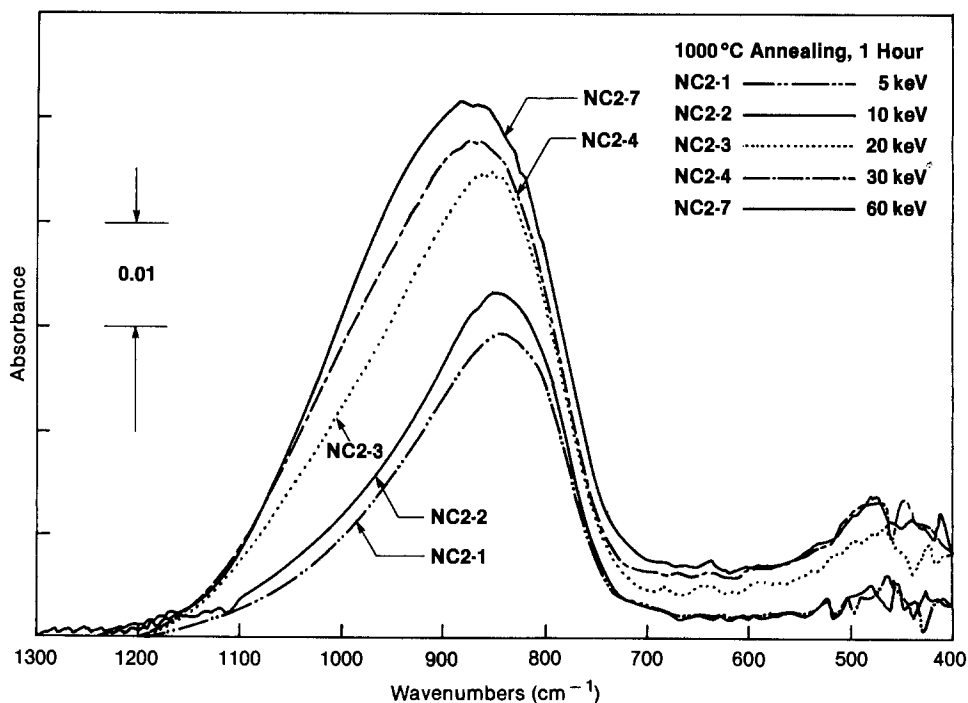


Fig. 3. IR spectrum after nitridation annealing for 1h at 1000°C . The amount of peak shift increases with energy.

the implantation energy. The peak positions of 5, 10, 20, 30, and 60 keV specimens are 840, 845, 855, 865, and 875, respectively. While the peak for the 5 keV wafer was shifted by 25 cm^{-1} from the original 815 cm^{-1} , the peak for the 60 keV wafer was shifted by 50 cm^{-1} .

In order to compare the properties of the implanted nitride with those of a pure nitride, an IR spectrum of a deposited nitride was made. An LPCVD furnace was used for the nitride deposition at 825°C from SiH_2Cl_2 and NH_3 . The measured thickness was 877\AA . The peak position of the Si-N absorbance of the LPCVD nitride was 833 cm^{-1} . The low-energy peak, near 490 , was attributed to single-phonon absorption (19) in regions of damaged or strained silicon adjacent to and in the nitride layer. Since the peak position was closely related to the stoichiometric ratio of the compound (6), the nitride layers made with an implantation energy lower than 10 keV approached a N/Si ratio of $4/3$.

Nitrogen redistribution.—The absolute nitrogen density was measured by SIMS profile, as implanted and after annealing at 1000°C . The initial distribution of the implanted nitrogen was close to the standard Gaussian distribution, except for the appearance of a shoulder at a concentration level of about $10^{19}/\text{cm}^3$. This shoulder is associated with the deeper penetration of monatomic nitrogen generated from the dissociation of molecular nitrogen ions. The profile was calibrated by using the as-implanted sample (6). By comparing the intensity counts of the sample with the intensity counts of the known peak concentration, the actual nitrogen concentration profile could be obtained.

Figure 4 shows the nitrogen concentration profile for six different implantation energies of molecular nitrogen ions. The total dose of these profiles is fixed at $5 \times 10^{16} \text{ N}_2^+/\text{cm}^2$. A progressive reduction of penetration depth with lower implantation energy was observed, as expected. However, this result does not necessarily mean that all of the atoms are incorporated in the silicon layer. The appearance of the shoulder at the $10^{19}/\text{cm}^3$ level is particularly significant for the higher energy profile. Under these conditions, the collision impact is expected to

be higher, with a larger proportion of monatomic nitrogen atoms being generated. The larger the number of dissociated N_2^+ molecules, the more pronounced is the shoulder.

The projected range, R_p , for 50 keV implantation is about 696\AA . Thus, the nitrogen fluence required to make stoichiometric Si_3N_4 is approximately $2.1 \times 10^{17} \text{ N}_2^+/\text{cm}^2$ from a relation of $F = C \cdot R_p \cdot d$, where F is the dose (N_2^+/cm^2) of molecular nitrogen, C is number of nitrogen ions per molecule, and d is molecular density. Compared to the atomic oxygen fluence required for buried oxide isolation (6), the theoretical fluence for implanted nitride is lower by a factor of 6. Moreover, the experimental dose is even smaller, as will be seen in the annealed profiles.

After annealing, the concentration profile moves to the left of the initial curve. (Indeed, each of the annealed curves shown in Fig. 8 and 9 moved toward the surface.) This is opposite to a normal thermal redistribution, where the profile widens and moves to the right. We explain this singularity as follows. The peak of energy deposition in the crystal, because of the atomic collisions associated with ion implantation, takes place to the left of the concentration peak (6). Hence, the profile of vacancies and defects created by implantation damage also lies to the left of the nitrogen concentration peak (6). These defects attract nitrogen to the left, to form silicon nitride during the high temperature annealing process.

The nitrogen migration not only shifts the peak position, but also increases the nitrogen concentration at the peak. This is a natural consequence of the accumulation of nitrogen in a narrower layer while preserving the area density. The nitrogen migration toward the vacancy peak creates an effective oxidation mask, even with a nitrogen fluence of $5 \times 10^{16} \text{ N}_2^+/\text{cm}^2$ and with low implantation energy. Several unique features can be noted in the curves of Fig. 5 and 6. In addition to the concentration profile shift to the left after annealing, the shape of the profile changes. The increase in peak nitrogen concentration after annealing was linked with the implantation-induced defects, as explained above. The shoulder associated with the monatomic nitrogen tends to disappear during annealing. This is particularly significant for the 60 keV case. Since the diffusivity of the nitrogen atoms is much

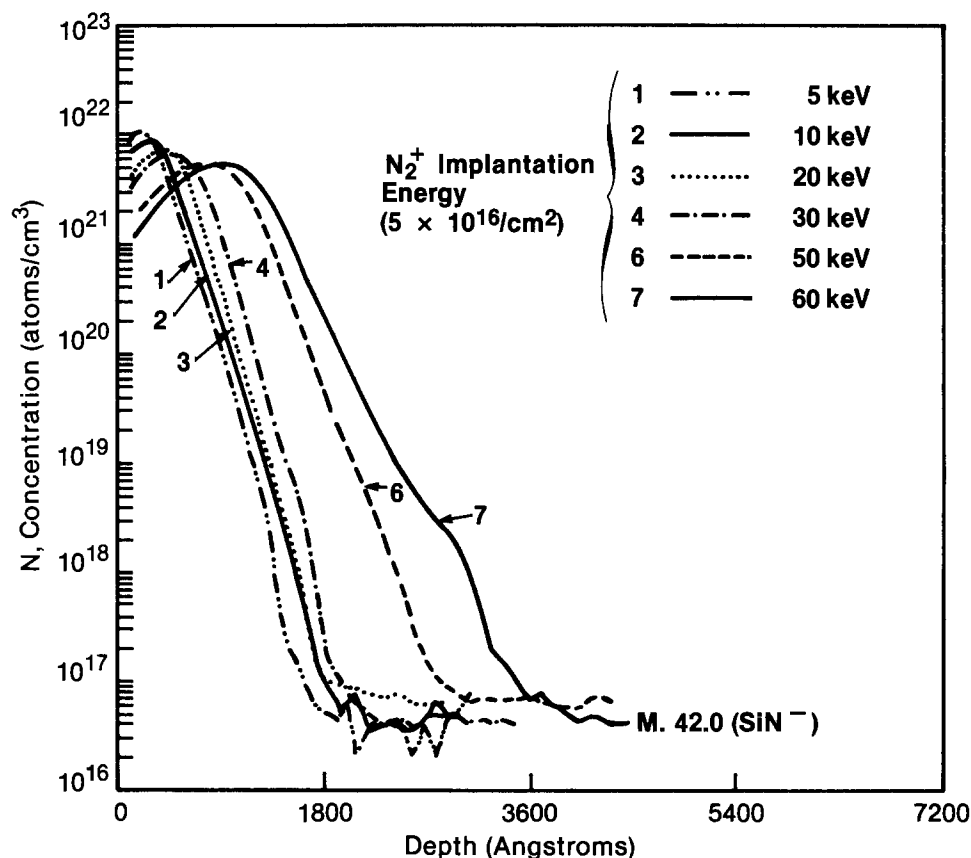


Fig. 4. SIMS profile of nitrogen implanted at specified energies for $5 \times 10^{16} \text{ N}_2^+/\text{cm}^2$.

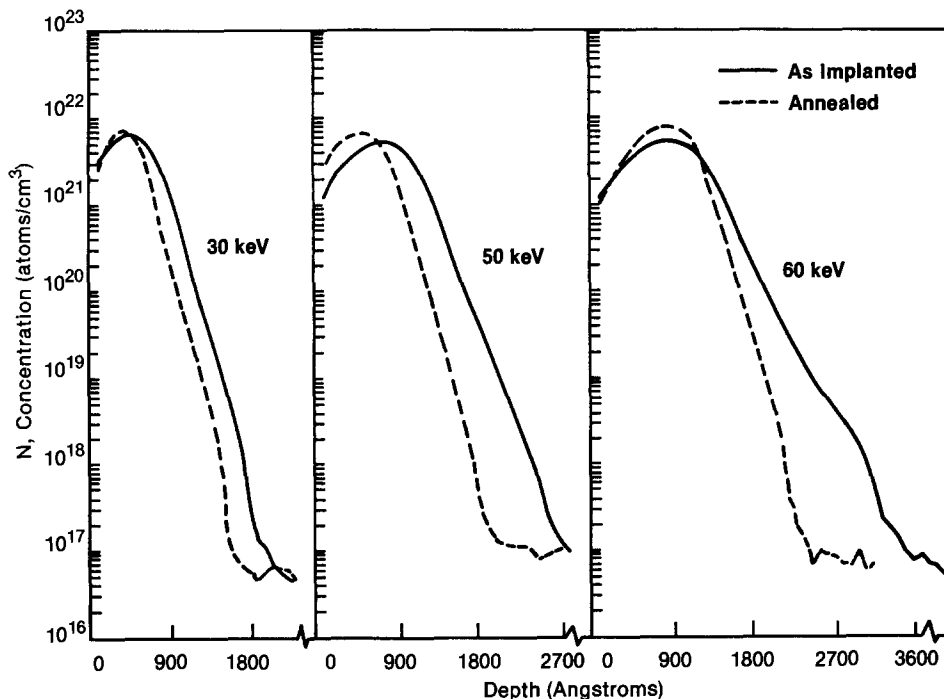


Fig. 5. Concentration profile shift toward the surface by annealing. The monatomic nitrogen "shoulder" disappears with annealing.

higher than that of molecular nitrogen ions, the nitrogen atoms can migrate to the peak at a much faster rate. This assumption is supported by the fact that all of the lower parts of the annealed curves are shifted much more than the upper parts. All the annealed curves with energy above 20 keV show that the concentration peak is located well below the surface, which means that a complete extension of nitride to the surface is lacking. The remaining silicon layer on the surface will interfere with the selective etching of nitride on the active area. The annealed samples implanted at 5 and 10 keV, which do not have the concentration peak below the surface, are more useful for the practical applications of nitrogen-implanted LOCOS. All of the annealed curves are plotted together in Fig. 7. As the implantation energy decreases, the peak concentration increases in a way similar to the as-implanted. The peak plateau of the 10 keV curve exactly matches the surface of the wafer. The 5 keV profile shows neither peak nor plateau, which indicates that a large amount of nitro-

gen is lost by outdiffusion during annealing. This loss is apparent for curve 1 in Fig. 7, where the 5 keV profile after annealing did not reach the concentration peak of the as-implanted. This loss is also confirmed by the IR intensity reduction shown in Fig. 3. However, for 10 keV, the plateau of curve 2 is perpendicular to the surface and the IR intensity loss is negligible. Therefore, the 10 keV implantation appears to be superior for forming the densest nitride at the surface, for only the annealing conditions described.

Practice of nitrogen-implanted LOCOS.—The nitrogen-implanted nitrides were tested for the effectiveness of oxidation masking during a field oxidation in steam. All the wafers were selectively implanted with molecular nitrogen ions in the 5-60 keV energy range. They were then annealed in N_2 for 1h at 1000°C to form nitride patterns. Annealing in another inert ambient such as argon or helium would be as effective. These nitride patterns were used as an oxidation mask during a steam oxidation at 1000°C for

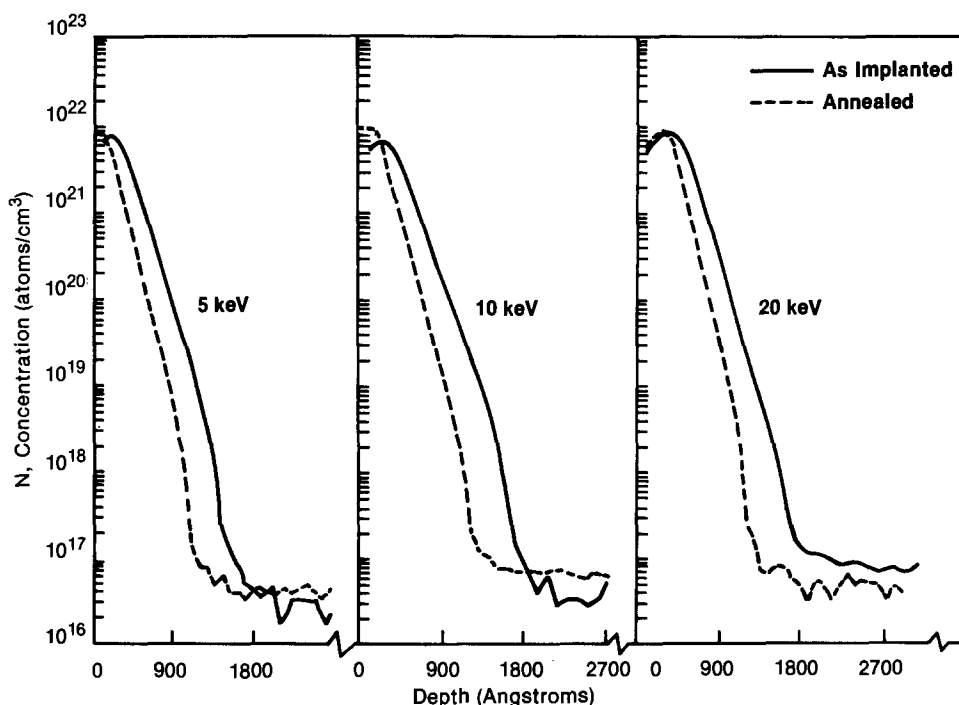


Fig. 6. Concentration profile changes of the 5, 10, and 20 keV nitrogen-implanted samples after annealing. The peak of the 20 keV sample remains under the surface, that of 10 keV coincides with the surface, and that of 5 keV disappears.

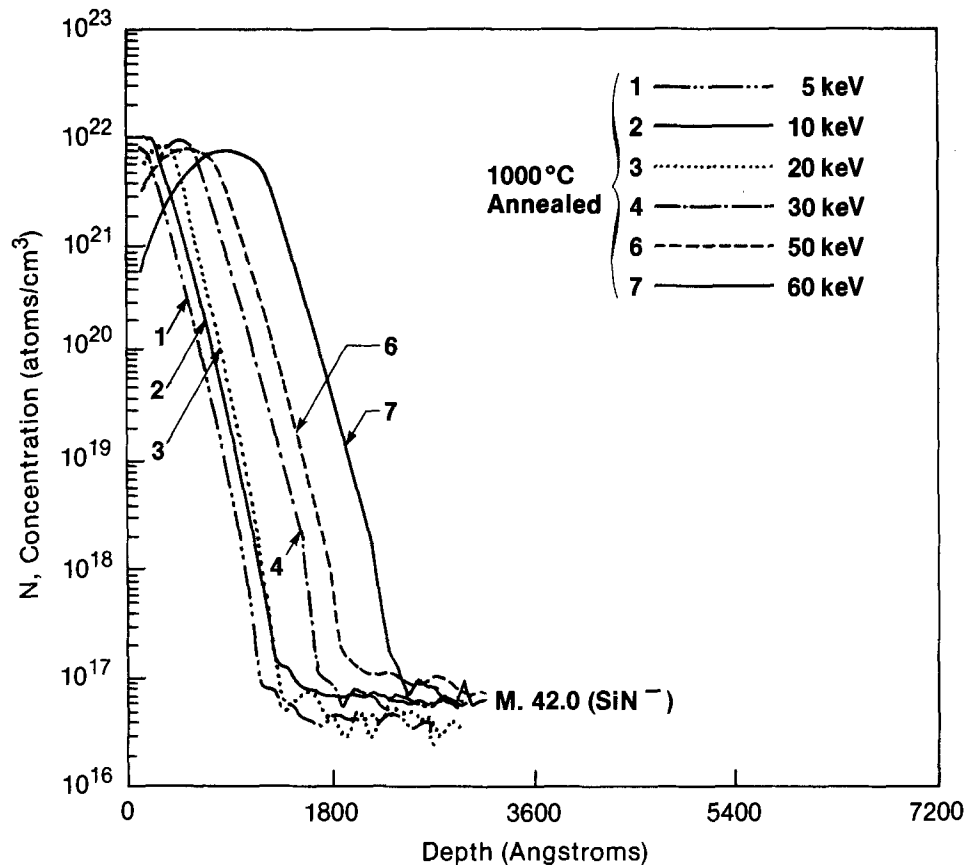


Fig. 7. Nitride profile after annealing. All the peak concentrations increase except the nitride made from implantation at 5 keV.

2h, which produced an oxide 5380Å thick over bare silicon.

The most effective method of evaluating the masking capability of the nitrides was found to be the step height measurement. Figure 8 shows the step heights measured between the nitrides and field oxides. A large step of about 3030Å was generated up to 40 keV, but the step height rapidly declined above 40 keV. The observed step

height for the 50 keV wafer was 2800Å, and that for the 60 keV wafer was only 1600Å. In order to show the effect of nitrogen fluence, the step height produced by 1×10^{16} N₂⁺/cm² at 50 keV is also presented in Fig. 8. In this case, the step was only 620Å, indicating no masking capability. The measured layer thicknesses in the regions implanted at 50 keV nitride with 5×10^{16} N₂⁺/cm² dosage, 60 keV nitride with 5×10^{16} N₂⁺/cm² dosage, and 50 keV nitride with

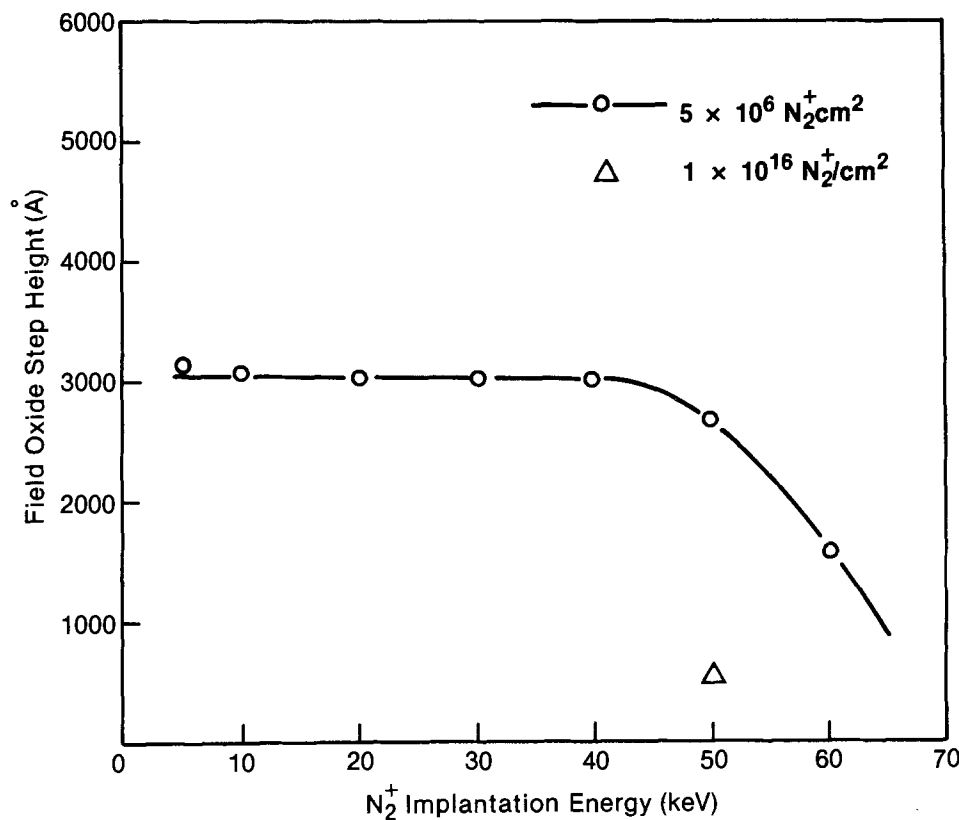


Fig. 8. Field oxide step height as a function of nitrogen implantation energy, measured from the masking nitrides. The nitrides with implantation higher than 50 keV are not capable of masking 5300Å steam oxidation at 1000°C.

1×10^{16} N_2^+ /cm² dosage were, respectively, 1290, 2100, and 4950 Å after the local oxidation. The thick nitrides after annealing are not true nitrides, but are matrices of silicon and nitride. During LOCOS, the silicon crystals are apparently oxidized, and the oxidizing agents are channeled through the partial oxides. Thus, the low concentrated, thick nitrides do not have masking capability against the oxidation. The lower the energy is, the higher the nitrogen concentration and the more effective the mask, as shown in Fig. 8. However, a 5×10^{16} N_2^+ /cm² dose implantation at 5 keV required 9h, with a medium-current implanter (Extrion Model 200 CF4), and a low energy one is not economical. The slight deviation from the horizontal level of the step height for 5 and 10 keV in Fig. 8 comes from the thinner nitrides produced at these energies.

Figure 9 shows SIMS profiles of nitride (SiN^+) and silicon (Si^{++}) of the regions with 5×10^{16} N_2^+ /cm² dosage at 40 keV and 1×10^{16} N_2^+ /cm² dosage at 60 keV after the field oxidation. The dense nitride is retained after the field oxidation with a formation of oxide on its top. Since the step height shown in Fig. 8 does not change much up to 40 keV, it seems that the surface oxidation apparently pushes the nitride inward, leaving some trace of nitride at the surface. The 60 keV profile also supports the result shown in Fig. 8. The oxynitride profile step approximately coincides with the measured dielectric thickness.

A selective nitride etching experiment was performed after utilizing the masking properties. All of the locally oxidized wafers were submerged in hot phosphoric acid at 180°C, after the hydrofluoric acid (HF) dip, to remove the surface oxide. While the thin nitrides could be selectively etched away, the thicker nitrides were not completely etched away and left hazy surfaces. The thicker nitrides could easily be etched away with 10% buffered HF. This fact indicates that they are oxide and nitride mixtures with compositions closer to oxide when the implantation energy is high. This experiment also suggests that the thinner nitride is superior for etching selectivity and desirable for the nitrogen-implanted LOCOS (NILO) process.

Figure 10 shows a comparison of a conventional LOCOS cross section with one made by this method. In the case of Fig. 10a, there is a 300 Å buffer SiO_2 layer between the 800 Å LPCVD nitride and the silicon substrate. The buffer oxide is thermally grown to protect the silicon surface from cracking due to thermal stresses caused by the nitride. The buffer oxide layer becomes a route for the

oxidant to diffuse underneath the nitride, thus extending the oxidation within the perimeter of the active area. The extended oxidation can exert enough force to lift the nitride edges, resulting in an accelerated oxidant channeling. The parasitic lateral oxidation channel, known as a "bird's beak," in this case is 0.75 μ m long. Since it is nearly constant, as shown in Fig. 10b, it limits scaling to 1 or <1 μ m VLSI circuits. Conversely, in the case of nitrogen implantation, no native oxide exists. Since the nitride is formed by a direct reaction with silicon, the interface is completely sealed. Initially, the oxidation takes place only vertically. As the oxidation proceeds isotropically at the nitride edges, the silicon is oxidized laterally, but at a much slower rate. In Fig. 10c, the lateral extension of oxide is about 0.2 μ m, which is about a four-fold reduction from the conventional LOCOS result, previously reported.

Conclusions

The relevant features of the NILO process are summarized as follows. For a fixed fluence, the intensity of Si-N bond absorption significantly increases with the nitrogen-implanted energy up to 50 keV. The Si-N absorption peak is centered at 815 cm^{-1} for all the implanted layers in the energy range between 5 and 60 keV. At higher implantation energy (~ 50 keV), the absorption intensity is proportional to the fluence of nitrogen implantation. The peak position of the IR spectrum after annealing shifts to a higher wave number as the nitrogen implantation energy increases. The IR peaks for the low energy implanted wafers are close to those for LPCVD-deposited nitrides. The annealing always shifts the nitrogen profile toward the surface, and the annealed peak concentration is higher than the as-implanted, except at 5 keV implantation. The nitride profile peaks are located below the surface for all the implantation energies above 20 keV. The peak plateau for 10 keV coincides with the surface, whereas the 5 keV peak disappears after the 1000°C annealing. The nitrides made with an implantation dose of 5×10^{16} N_2^+ /cm² and energy less than 40 keV effectively mask 5380 Å steam oxidation at 1000°C. The nitrides with energy higher than 40 keV and lower dosage are converted to oxynitrides during the NILO process. The low energy nitrides can be selectively etched in hot phosphoric acid, whereas the high energy oxynitride is more readily etched in hydrofluoric acid. Experimentally, the nitride formed with 10 keV implantation appears to be the most practical and effective NILO mask. The lateral

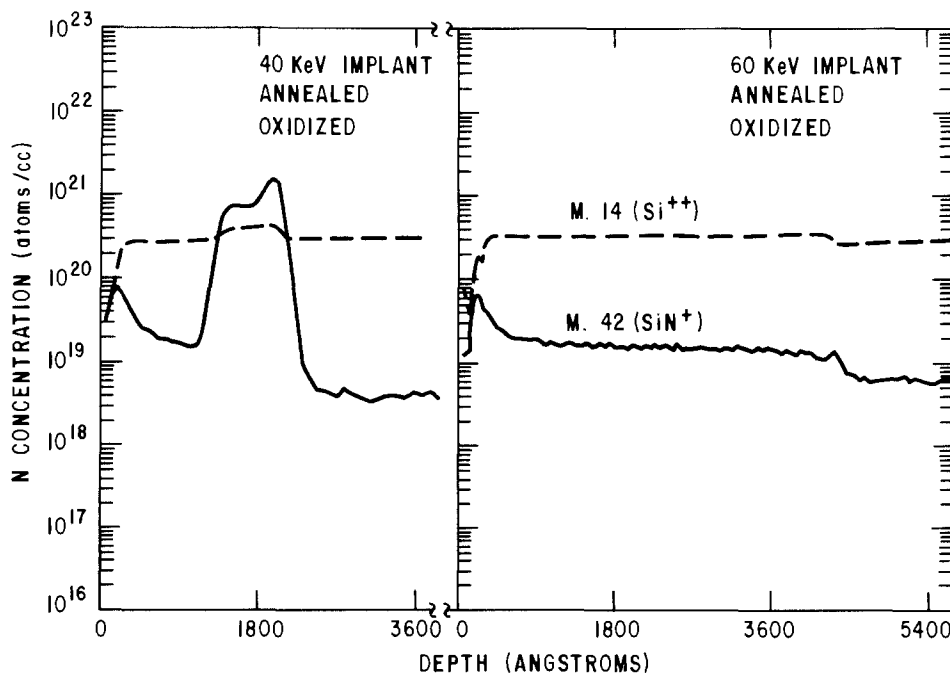


Fig. 9. SIMS profiles of the nitride and silicon in the implanted regions after the field oxidation. The dense nitride with 5×10^{16} N_2^+ /cm² dosage at 40 keV survives, whereas the nitride with 1×10^{16} N_2^+ /cm² dosage at 40 keV is completely converted to oxynitride.

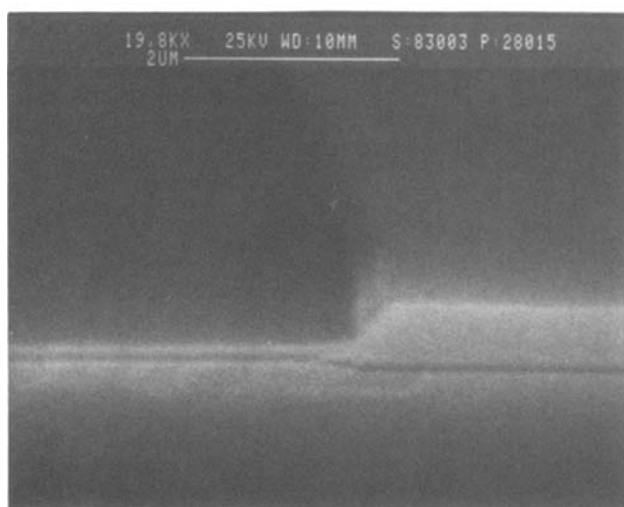
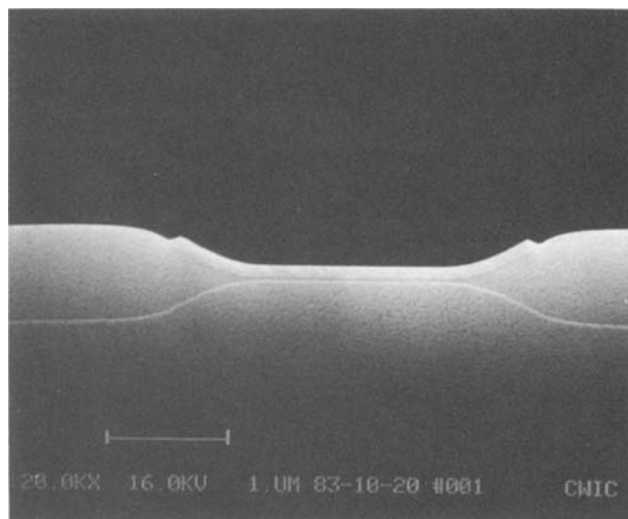
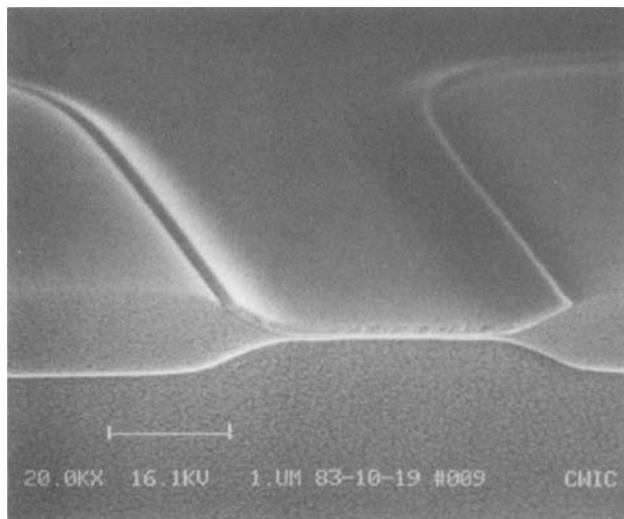


Fig. 10. Cross-section SEM photomicrographs of the conventional LOCOS process (a, top left and b, top right) and the NILO process (c, left). The lateral oxidation of NILO is reduced four-fold from that of the LOCOS process.

oxidation of NILO is reduced four-fold from that of the conventional LOCOS.

Acknowledgments

The authors wish to acknowledge the constructive advice and encouragement given by K. G. Vosburgh and D. M. Brown. The authors also wish to acknowledge help in processing from T. J. Soltys, C. E. Logan, P. A. Piacente, and R. F. Reihl. Special thanks are extended to J. F. Norton for SEM photomicrographs, and to W. Katz and G. A. Smith for SIMS analysis.

Manuscript submitted Aug. 9, 1983; revised manuscript received April 10, 1984.

General Electric Company assisted in meeting the publication costs of this article.

REFERENCES

- J. A. Appels, E. Kooi, M. M. Paffen, J. J. H. Schatorje, and W. H. C. G. Verkuylen, *Philips Res. Rept.*, **25**, 118 (1970).
- S. P. Murarka, C. C. Chang, and A. C. Adams, *This Journal*, **126**, 996 (1979).
- E. Bassous, M. N. Yu, and V. Maniscalco, *ibid.*, **123**, 1729 (1976).
- T. Ito, T. Nazaki, and H. Ishikawa, *ibid.*, **127**, 2053 (1980).
- T. Ito, T. Kato, T. Nozaki, T. Nakamura, and H. Ishikawa, *Appl. Phys. Lett.*, **38**, 370 (1981).
- M. J. Kim, D. M. Brown, and M. Garfinkel, *J. Appl. Phys.*, **54**, 1991 (1983).
- D. Chin, R. W. Dutton, S. Y. Oh, and J. L. Moll, *Ext. Abstr. IEDM*, 228 (1982).
- E. P. Eernisse, *J. Appl. Phys.*, **48**, 3337 (1977).
- K. Y. Chiu, J. J. Moll, and J. Manolin, *IEEE Trans. Electron. Devices*, **ed-29**, 536 (1982).
- K. Y. Chiu, R. Fang, J. Lin, J. L. Moll, C. Lage, S. Angelos, and R. Tillman, *Ext. Abstr. IEDM*, 224 (1982).
- T. P. Chow and M. Ghezzeo, U.S. Pat. 4,333,965 (1982).
- P. J. Tsang, S. Ogura, W. W. Walker, J. F. Shepard, and D. L. Critchlow, *IEEE Trans. Electron. Devices*, **ed-29**, 590 (1982).
- J. Hui, T. Y. Chiu, S. Wong, and W. G. Oldham, *IEEE Trans. Electron. Devices Lett.*, **ed1-2**, 244 (1981).
- M. Ghezzeo, U.S. Pat. 4,333,964 (1982).
- J. Hui, T. Y. Chiu, S. Wong, and W. G. Oldham, *Ext. Abstr. IEDM*, 220 (1982).
- W. J. M. J. Josquin and Y. Tamminga, *This Journal*, **129**, 1803 (1982).
- W. J. M. J. Josquin, *Radiat. Eff.*, **47**, 221 (1980).
- J. B. Mitchell, P. P. Pronko, J. Shewchun, and D. A. Thompson, *J. Appl. Phys.*, **46**, 332 (1975).
- J. Stephen, B. J. Smith, G. W. Hinder, D. C. Marshall, and E. M. Wittam, in "Proceedings of the International Conference on Ion Implantation in Semiconductors, VIII," p. 487 (1971).
- R. J. Dexter and S. B. Watelski, *Appl. Phys. Lett.*, **23**, 455 (1973).
- C. D. Fung, J. L. Liao, K. R. Elsayed, and J. J. Kopanski, Abstract 132, p. 210, The Electrochemical Society Extended Abstracts, Vol. 83-1, San Francisco, CA, May 8-13, 1983.

The Phase-Transition Phenomenon in a Sodium Sulfate Crystal

M. Sakaguchi,* M. Ohta,* and S. Miyazaki

Department of Applied Chemistry, Faculty of Engineering, Niigata University, Niigata, Japan

ABSTRACT

The V \rightleftharpoons I phase-transition reactions of a Na₂SO₄ crystal in the pure Li⁺-, K⁺- or Cs⁺-blended Na₂SO₄ samples were investigated in various atmospheres (N₂, dry air, or wet air). In all samples, both the V \rightarrow I and the I \rightarrow III phase-transition reactions proceeded rapidly, but the III \rightarrow V phase-transition reaction hardly proceeded at all after several hours in N₂ or dry air. In wet air, however, the reaction proceeded rapidly. This fact suggested that the migration of the constituent ion was accelerated as soon as the ions on the crystal surface were hydrated. All phase-transition reactions were suppressed by the existence of the foreign materials which were isostructural with the host crystal before the reaction.

Many studies have been carried out for the phase transition of a Na₂SO₄ crystal which is known to exist in three metastable modifications (phases IV, III, II) between phase V (low temperature orthorhombic structure) and phase I (high temperature hexagonal structure) (1-7). Most of the studies were limited to the V \rightarrow I phase transition and/or the I \rightarrow III phase transition. However, although no detailed study for the III \rightarrow V phase transition has been carried out, Eysel (2) pointed out the sluggishness of the reaction.

Sakaguchi *et al.* have found recently that the kinetics of phase-transition reactions of a ZnS crystal (8, 9) and a metal phthalocyanine crystal (10) were characteristically affected by the heating atmosphere or impurities contained in the crystal.

We were interested, therefore, in investigating how the III \rightarrow V phase-transition reaction is affected by the adsorption of water vapor on the hygroscopic surface of a Na₂SO₄ crystal.

The present work was carried out to study the role of water vapor contained in a reacting atmosphere on the phase-transition reaction in pure and foreign-cation containing Na₂SO₄ crystals.

Experimental

Materials.—The starting material used was prepared by evaporation to dryness of an aqueous solution of Na₂SO₄ (Junsei Chemical Company, Limited; guaranteed reagent grade) or of Na₂SO₄ to which Li₂SO₄ (Koso Chemical Company, Limited; guaranteed reagent grade), K₂SO₄ (Junsei Chemical Company, Limited; guaranteed reagent grade), or Cs₂SO₄ (Mitsuwa Chemical Company, Limited; purity: 99.9%) was added to the amount of 10 mole percent (m/o). This was followed by vacuum drying for 2h at 130°C, and then grinding (325 ~ 400 mesh). The composition of the starting materials is determined by a x-ray powder diffraction method: the Li⁺-blended Na₂SO₄ sample contains 80 m/o phase V (orthorhombic Na₂SO₄ crystal) and 20 m/o trigonal LiNaSO₄ compound. The K⁺-blended Na₂SO₄ sample contains 90 m/o phase V and 10 m/o hexagonal (K,Na)₂SO₄ solid solution. The Cs⁺-blended Na₂SO₄ sample contains 90 m/o phase V and 10 m/o orthorhombic Cs₂SO₄ crystal.

The pure and blended Na₂SO₄ samples used for the III \rightarrow V phase-transition reaction at 25°C were prepared by removing the bound water (11) contained in the starting material. That is, the bound water was removed by heating the starting material at 750°C in N₂, then the sample was ground (325 ~ 400 mesh) in dry air of about 10% relative humidity (RH) at 25°C in order to prevent the read-sorption of water vapor.

The gases used were prepared as follows: N₂ was prepared by evaporation of pure liquid N₂. The dry air (10% RH) or the wet air (100% RH) was prepared by leaving it in contact with CaCl₂ or distilled water for more than 12h at 25°C in desiccator.

*Electrochemical Society Active Member.

Key words: phase transition, sodium sulfate, adsorption, atmosphere.

Procedure.—The phase-transition phenomena in the pure and blended Na₂SO₄ samples during heating or cooling in N₂ flow (100 ml/min) were investigated by using an apparatus which enabled a simultaneous measurement of high temperature x-ray diffraction and differential thermal analysis (DTA) (Rigaku Denki Company, Limited).

The III \rightarrow V phase-transition phenomena in the pure and blended Na₂SO₄ samples at 25°C in the dry air or wet air were investigated by measuring the peak height of the x-ray powder diffraction trace. The fraction of the reaction (*F*) was calculated by following equation

$$F = \frac{(V_{28.0} + V_{29.0})}{1.2(III_{22.6} + III_{23.6}) + (V_{28.0} + V_{29.0})} \times 100 (\%)$$

where III_{22.6}, III_{23.6}, V_{28.0}, and V_{29.0} represent the peak heights at 2 θ = 22.6°, 23.6°, 28.0°, and 29.0° on the x-ray powder diffraction trace, respectively.

Results and Discussion

The phase-transition reaction of the pure Na₂SO₄ sample in N₂ flow was continuously examined by using simultaneous high temperature x-ray diffraction and DTA, as shown in Fig. 1. During the heating process, the diffraction peak of the phase V disappeared, while that of the phase I appeared at 251°C with a simultaneous endothermic effect on the DTA curve. In the cooling process, the diffraction peak of the phase I disappeared at 233°C, while that of the phase III appeared with an exothermic effect on the DTA curve. However, the diffraction peak of the phase V did not emerge even if the sample was cooled to 25°C. These results were similar to that obtained by Eysel (2).

Analogous experiments were carried out on the Li⁺-, K⁺- and Cs⁺-blended Na₂SO₄ samples in N₂ flow. The results obtained are shown in Table I. On heating, the V \rightarrow I phase-transition reaction proceeded at 252°C in both the Li⁺- and K⁺-blended Na₂SO₄ samples similar to that in the pure Na₂SO₄ sample, but occurred about 10°C higher

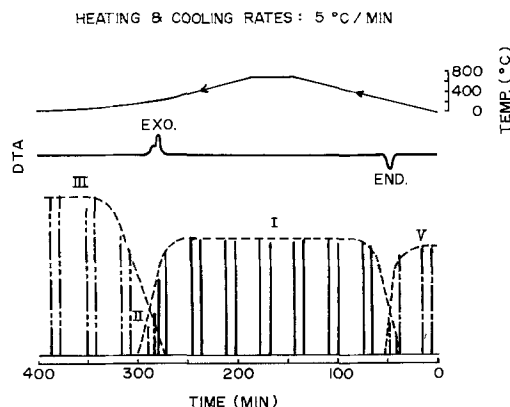


Fig. 1. High temperature x-ray diffraction trace and DTA trace on an undoped Na₂SO₄ crystal in N₂ flow.

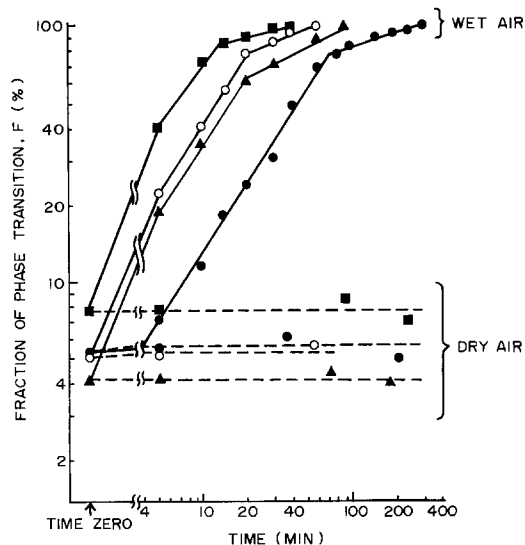


Fig. 2. III \rightarrow V phase transition in undoped and Li⁺-, K⁺-, or Cs⁺-doped Na₂SO₄ samples in wet and dry air at 25°C. These samples were pre-treated at 750°C for 1 h in N₂. ○: Undoped. ●: Li⁺-doped. ▲: K⁺-doped. ■: Cs⁺-doped.

(262°C) in the Cs⁺-blended Na₂SO₄ sample. On cooling, the I \rightarrow III phase-transition reaction proceeded at 229°C in the Cs⁺-blended Na₂SO₄ sample similar to that in the pure Na₂SO₄ sample, but occurred about 10° and 35°C lower (221°, 186°C) in the Li⁺- and K⁺-blended Na₂SO₄ samples, respectively. The composition of the (K,Na)₂SO₄ solid solution in the K⁺-blended Na₂SO₄ sample became rich in Na near 650°C during heating, while a phase III Na₂SO₄ crystal was separated from the Na-rich solid solution at 186°C with an exothermic effect on the DTA curve on cooling. As with the pure sample, the diffraction peak of the phase V in any blended Na₂SO₄ sample did not emerge even when these were cooled to 25°C.

Figure 2 is a log-log plot for the results on the III \rightarrow V phase-transition reaction in the pure and Li⁺-, K⁺- or Cs⁺-blended Na₂SO₄ samples at 25°C in both the dry and the wet airs. The reaction in any Na₂SO₄ sample did not proceed in the dry air within 400 min, but rather accelerated considerably in the wet air. The rate of the reaction in the wet air decreased in the order Cs⁺-blended > pure > K⁺-blended > Li⁺-blended. While the reaction in the dry air proceeded gradually for 3 months.

On the basis of these results, the effect of a foreign cation on the phase-transition reaction of a Na₂SO₄ crystal can be considered to be as follows: it is known that the phases V, III, and I of a Na₂SO₄ crystal are orthorhombic, orthorhombic (quasi hexagonal), and hexagonal, respectively. Then, the V \rightarrow I phase-transition reaction in the Cs⁺-blended Na₂SO₄ sample might be considerably suppressed as a result of the stabilizing ("epitaxialcy") (12) of the phase V due to the existence of a Cs₂SO₄ crystal, which is isostructural with a phase V Na₂SO₄ crystal. However, the promotive effect for the V \rightarrow I phase-transition reaction in the Li⁺- or K⁺-blended Na₂SO₄ sample could not be detected, in spite of the existence of a LiNaSO₄ compound or a (K,Na)₂SO₄ solid solution which is isostructural with a phase I Na₂SO₄ crystal. That is, it is likely that the phase transition of a Na₂SO₄ crystal is considerably suppressed by the existence of foreign material, which is isostructural with the host crystal before the re-

Table I. Phase transition of undoped and Li⁺-, K⁺-, or Cs⁺-doped Na₂SO₄ samples in N₂ flow

Sample	Phase-transition point (°C)	
	Heating process V \rightarrow I	Cooling process I \rightarrow III*
Undoped	251	233
Li ⁺ -doped	252	221
K ⁺ -doped	251	186
Cs ⁺ -doped	262	229

* The form II appeared transiently during the I \rightarrow III phase-transition reaction.

action. Consequently, both the I \rightarrow III and III \rightarrow V phase-transition reactions in the K⁺- or Li⁺-blended Na₂SO₄ sample were also considerably suppressed as a result of the epitaxialcy of phases I and III with the hexagonal (K,Na)₂SO₄ and the trigonal LiNaSO₄ phases, respectively.

The promotive effect of the water sorbed on the crystal surface in the III \rightarrow V phase-transition reaction must be caused by accelerating the migration of the constituent ion because the crystal lattice was relaxed by the hydrate formed on the crystal surface layer (13).

Furthermore, the accelerative effect on the III \rightarrow V phase-transition reaction in the Cs⁺-blended sample (which is a mixture of Na₂SO₄ and Cs₂SO₄) resulted from promoting the sorption of water vapor on a Na₂SO₄ crystal in the neighborhood of a Cs₂SO₄ crystal because a Cs₂SO₄ crystal is more hygroscopic than other crystals.

Acknowledgments

The authors are grateful to Mr. K. Uematsu and Mr. T. Sasaya for their assistance with the experimental work. The authors are grateful to Nagaoka Sanso Company, Limited for the offer of liquid N₂. The present work was partially financed by Grant-in-Aid for Scientific Research of the Ministry of Education, Science and Culture of the Japanese Government.

Manuscript submitted March 18, 1983; revised manuscript received April 22, 1984.

Niigata University assisted in meeting the publication costs of this article.

REFERENCES

1. F. C. Kracek and R. E. Gibson, *J. Phys. Chem.*, **34**, 188 (1930).
2. W. Eysel, *Am. Mineral.*, **58**, 736 (1973).
3. H. F. Fischmeister, *Monatsh. Chem.*, **93**, 420 (1962).
4. M. Miyake, I. Minato, and S. Iwai, in "Fifth International Conference on Thermal Annealing," p. 174 (1977).
5. V. Amirthalingham, M. D. Karkhanavala, and U. R. K. Rao, *Z. Kristallogr.*, **148**, S.83 (1978).
6. R. M. Murry and E. A. Secco, *Can. J. Chem.*, **56**, 2616 (1978).
7. Y. Saito, K. Kobayashi, and T. Maruyama, *Solid State Ionics*, **3/4**, 393 (1981).
8. M. Sakaguchi and T. Hirabayashi, *J. Appl. Phys.*, **44**, 2530 (1973).
9. M. Sakaguchi, M. Ohta, M. Satoh, and T. Hirabayashi, *This Journal*, **124**, 550 (1977).
10. M. Sakaguchi, M. Ohta, T. Nozawa, and M. Takada, *ibid.*, **127**, 1832 (1980).
11. M. Sakaguchi, M. Ohta, K. Nakazato, and T. Kondoh, *ibid.*, **124**, 1272 (1977).
12. I. Bonev, *Acta Crystallogr., Sect. A*, **28**, 508 (1972).
13. A. Weyl, *Ceram. Age*, **60**, 28 (1952).

Isotope Labeling Studies of the Oxidation of Silicon at 1000° and 1300°C

J. A. Costello*¹ and R. E. Tressler

Department of Materials Science and Engineering, The Pennsylvania State University, University Park, Pennsylvania 16802

ABSTRACT

Oxygen-18 profiles in thermal oxides grown on silicon at 1000° and 1300°C in sequential oxidation steps in the parabolic oxidation regime indicate a change in the dominant oxygen transport process. At 1000°C, oxygen-18 pile-up at the surface and at the oxide/silicon interface is consistent with a large flux of oxygen via molecular oxygen permeation and very slow diffusion of lattice oxygen ions ($D_o = \sim 4 \times 10^{-15}$ cm²/s). At 1300°C, the oxygen-18 concentration is uniformly high across the oxide, which suggests a much larger lattice oxygen diffusivity and a total flux due to lattice oxygen diffusion which contributes significantly to the supply of oxygen to the growth interface.

Owing to its importance in the semiconductor industry, the oxidation of silicon has been extensively studied. It is generally accepted that the oxidation process in the parabolic growth regime is controlled by the permeation of oxygen molecules through the oxide film (1-3). Indirect evidence supporting this conclusion includes platinum marker experiments (4), the linear oxygen partial pressure dependence of the parabolic oxidation rate (1), and the correspondence with oxygen permeation studies of fused silica (5). The most direct evidence comes from isotope labeling studies. The technique involves the sequential oxidation of the silicon in oxygen-16- and oxygen-18-rich environments. Following the oxidation treatments, an appropriate measurement technique which can discriminate between the two oxygen isotopes is used to profile each across the oxide film. The most common include nuclear reaction resonance and secondary ion mass spectrometry (SIMS). The location of each isotope in the oxide profiles provides information about the migrating species which control the oxidation reaction.

The nuclear reaction resonance technique was used by Rosencher *et al.* (6) to investigate silicon oxidation in dry oxygen at 930°C. The oxygen isotope profiles resulting from the double oxidation sequence revealed that the majority of oxygen-18 isotope accumulates near the oxide-silicon interface. This result and the correspondingly low oxygen-18 concentration in the bulk oxide indicated that the permeation of the oxidant to the interface is responsible for the parabolic oxidation of silicon, as proposed by Deal and Grove (1). A thin oxygen-18-rich layer (7-12Å) was observed near the oxide surface, which was explained as isotope exchange between the oxidant and the lattice bound oxygen at the oxide surface. It has been reported that the exchange mechanism is enhanced by trace amounts of water in the oxidation environment (7). Rosencher *et al.* assumed that the water content in their system was in the ppm range in light of the shallowness of the exchanged layer.

A superior detection sensitivity is obtained using the SIMS technique. The analysis provides a direct measure of the isotope concentration profile and eliminates the laborious deconvolution procedures required by the nuclear reaction resonance technique. However, profile broadening due to ion beam mixing must be accounted for when considering the measured profile. Cristì and Condon (8) reported ion microprobe mass analyzer results for silicon doubly oxidized at 700°C. Similar to Rosencher *et al.*, an interstitial diffusion (permeation) of oxygen molecules was suggested as the mechanism controlling oxidation. Isotope exchange with the lattice oxygen was observed at the oxide surface, and a diffusion coefficient corresponding to oxygen diffusion via the oxygen sublattice was calculated to be $\sim 10^{-19}$ cm²/s at 700°C. It was

calculated that a diffusion coefficient of this low magnitude was insufficient to support the observed oxidation rate. Recent work by Rouse *et al.* (9) demonstrates the sensitivity of the SIMS technique when applied to the double oxidation experiment. Using a purified oxygen gas having a reduced oxygen-18 background, a slightly decreasing isotope profile was measured through the bulk oxide in addition to the isotope build up in the new oxide and at the oxide surface as previously described. The profile indicated that permeation mechanisms control the oxidation and that exchange of the diffusing oxidant occurs throughout the oxide. The exchange rate is much higher at the oxide surface. Special treatment of the gases minimized the water content in the system, suggesting that these artifacts were not water related.

In the present study, double oxidation of silicon was investigated at 1000° and 1300°C. Differences in the isotope profiles obtained by SIMS are discussed in terms of the competing transport processes.

Experimental Procedure

Boron-doped silicon (100) having a 3-5 Ω-cm resistivity was used in this investigation. Samples were prepared from a full wafer by dicing into 1/4 × 1/4 in. squares, the sample size required by the SIMS holder. The first oxidation was performed in dry oxygen at 1000°C for 2h. The oxide thickness as measured by ellipsometry was 103 nm. The background oxygen-18 concentration in the gas was 0.2%. The second oxidation was performed in an isotope exchange furnace where following the evacuation of the oxidation chamber, an oxygen-18 enriched gas is introduced (10).¹ The percentage of oxygen-18 in the gas was adjusted to approximately 40% each time. In the enriched gas, samples were oxidized at 1000° and 1300°C for 10 and 35 min, respectively.

Isotope profiling of the samples was accomplished using the SIMS mode of the Gatan scanning ion microprobe.² The ion beam consisted of positive argon ions accelerated to 7 keV and focused to a diameter of approximately 100 μm. Adjustable beam rastering and signal gating were set for optimum depth resolution. A focused electron gun provided charge neutralization of the sputtering surface during profiling. Three mass settings were continuously monitored during profiling, including oxygen-16, oxygen-18, and silicon-30.

Results and Discussion

The SIMS profile shown in Fig. 1 corresponds to the silicon sample oxidized in the oxygen-18 enriched gas at 1000°C for 10 min. The silicon-30 mass is monitored to indicate that proper charge neutralization is provided with the electron gun. This process is characterized by a uniform silicon signal across the oxide, as shown in Fig. 1.

*Electrochemical Society Active Member.

¹Present address: U.S. Army Electronics Technology and Devices Laboratory, Fort Monmouth, New Jersey 07703.

¹J. Cauley, Case Western Reserve University, 1982.

²Gatan, Incorporated, Pittsburgh, Pennsylvania.

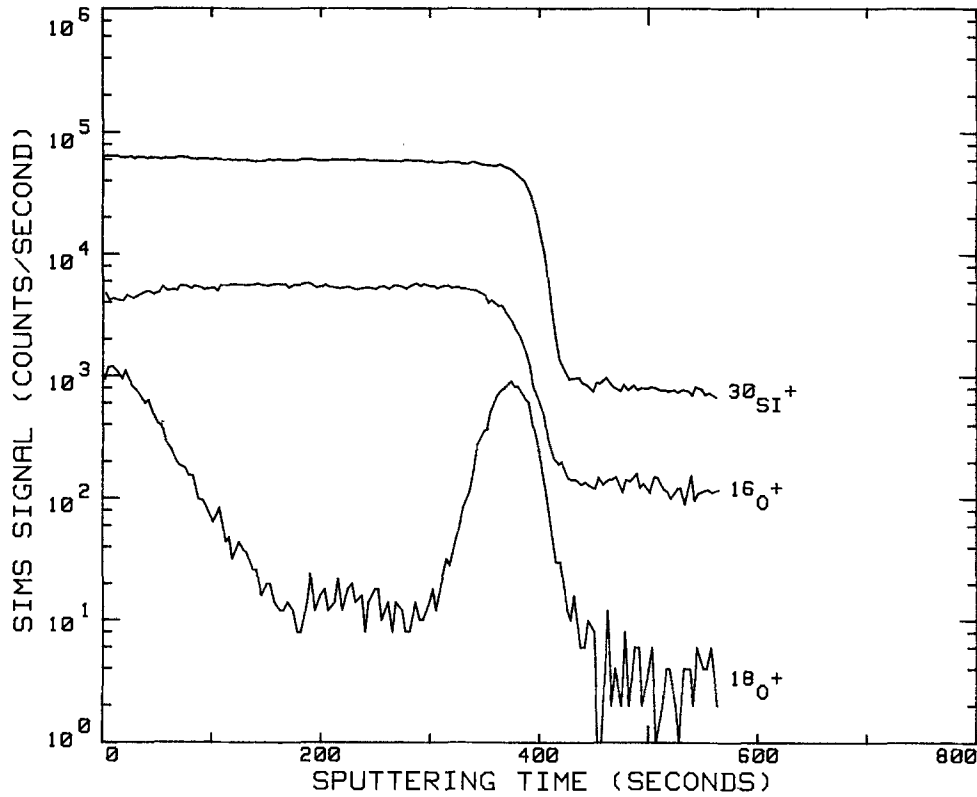


Fig. 1. SIMS data for silicon sample oxidized at 1000°C for 2h in dry oxygen-16 followed by 10 min in oxygen-18-enriched gas.

Signal instability at the oxide surface was typically less than 30s in duration. The changing oxygen signals, however, correspond to actual concentration variations of each isotope across the oxide film. Upon reaching the oxide silicon interface, a sharp drop in signal of up to 3 orders of magnitude occurs in each case. In the silicon, the oxygen counts approach system background levels. The relatively high background signal for oxygen-16 in the silicon is caused by electron stimulated desorption (ESD) from the electron beam interacting with the sample surface. This signal does not significantly contribute to the overall oxygen-16 signal when profiling through the oxide.

The isotope profiles can be better analyzed by converting the data into the oxygen-18 fraction as a function of depth. The oxygen-18 fraction is obtained by dividing the oxygen-18 signal by the sum of the two oxygen signals. An experimentally measured sputtering rate of 17 nm/min in the oxide was used to convert to units of depth. Figures 2 and 3 are profiles for samples oxidized 10 and 35 min, respectively, at 1000°C in the oxygen-18-rich environment. As found by other investigations, the isotope is concentrated at the oxide-silicon interface as well as at the surface. The maximum isotope concentration corresponds to the amount of oxygen-18 enrichment of the oxidizing gas (~ 40%). The minimum concentration

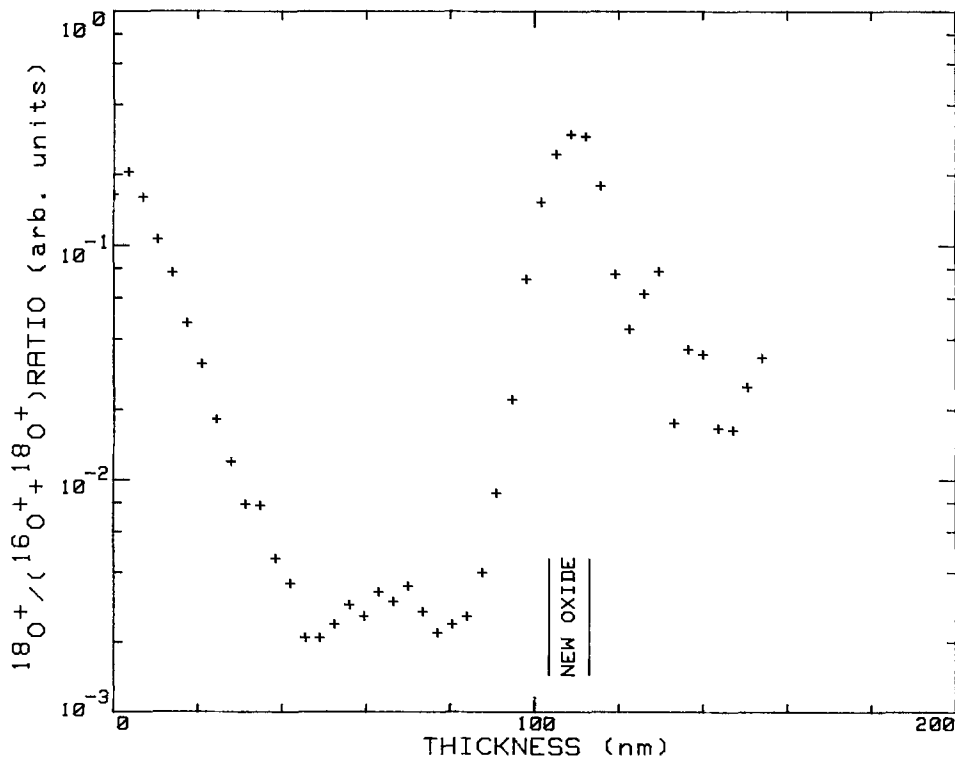
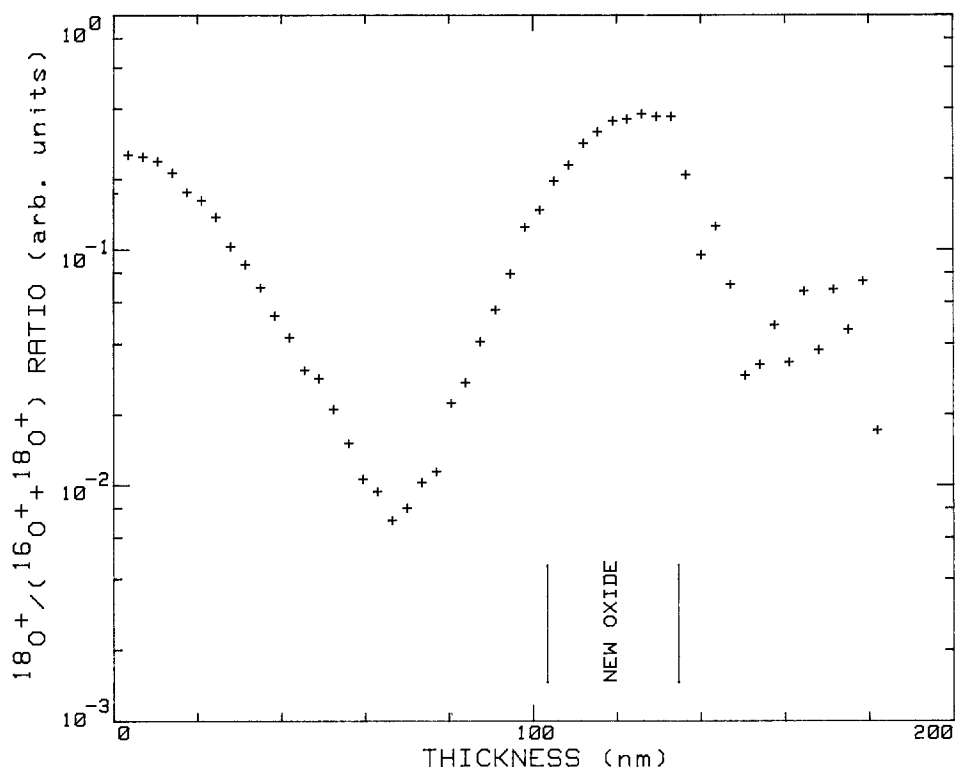


Fig. 2. Oxygen-18 profile for 10 min reoxidation sample at 1000°C.

Fig. 3. Oxygen-18 profile for 35 min reoxidation sample at 1000°C.



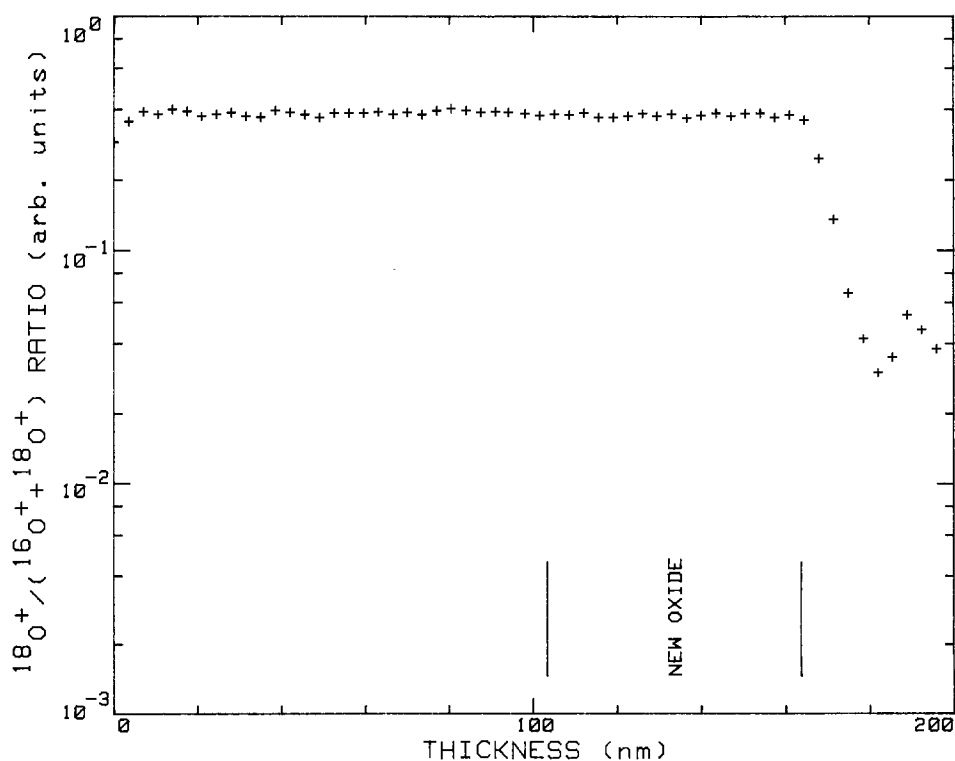
which is found in the bulk oxide (Fig. 2) is equal to the background concentration of oxygen-18 in the original oxidizing gas (0.2%).

The observed profiles are explained in terms of the transport mechanisms present, as well as by the exchange of the oxidant with the lattice oxygen. The accumulation of oxygen-18 isotope near the oxide-silicon interface results from the permeation of oxygen molecules through the oxide and formation of new oxide at the oxide/silicon interface. The decreasing profile near the oxide surface into the bulk oxide is explained by the diffusion of the oxygen isotope through the oxygen sublattice following exchange at the oxide surface. A diffusion coefficient for the isotope of 4×10^{-15} cm²/s was calculated from the initial profile using the complementary error function. This

value is in good agreement with literature values for oxygen diffusion in fused silica (11, 12). As indicated in previous investigations, a diffusion coefficient of this magnitude could not by itself provide sufficient flux of oxygen to cause the observed oxidation rate. In addition to the isotope diffusion into the bulk from the oxide surface, the isotope can diffuse into the bulk from the newly formed oxide. This is apparent from the sloped isotope profiles near the original oxide-silicon interface.

The isotope profiles for samples oxidized at 1300°C were quite different. As shown in Fig. 4 for the 10 min oxidation, the oxygen-18 isotope profiles were uniform across the oxide. This result implies that lattice diffusion of oxygen is significant at this temperature and contributes to the supply of oxidant to the growth interface; a

Fig. 4. Oxygen-18 profile for 10 min reoxidation sample at 1300°C.



calculated profile using oxygen diffusivity values in fused silica from the literature approximates the observed flat profile. The single activation energy reported for the parabolic oxidation of silicon (27 kcal/mol) holds up to near the melting point, however, and is much lower than the value reported for lattice diffusion (70 kcal/mol) by Sucov (11). This would imply that the oxidant supply at 1300°C is dominated by the permeation mechanism. The activation energy value reported by Sucov has been questioned by other investigators (12, 13), who suggest that the lattice diffusion of oxygen is characterized by a much lower activation energy. The temperature dependence of the lattice diffusion mechanism is currently being investigated by the authors using the present technique. It is interesting to note that other silicon-base materials such as SiC, TiSi₂, and MoSi₂ exhibit an increase in the activation energy for the parabolic oxidation at temperatures above 1400°C (14, 15). This change in activation energy may correspond to control of oxidation by the lattice diffusion mechanism.

This discussion has not addressed the possibility that the oxygen-18 profiles are the result of an exchange reaction between the permeating isotope species and point defects (presumably oxygen vacancies) in the oxide. The isotope profile would then be flatter at 1300° than at 1000°C if the vacancies were created at the gas/SiO₂ interface and diffused much more rapidly at 1300° than at 1000°C. Future experiments will discriminate between these two possibilities.

Summary

Silicon oxidation in the parabolic growth regime at 1000° and 1300°C was investigated using isotope labeling experiments with SIMS for profiling. At the lower temperature, the measured profiles indicate that the oxidation process is controlled by the permeation of oxygen molecules through the oxide film to the oxide-silicon growth interface. Isotope exchange and subsequent diffusion via the oxygen sublattice apparently occurs near the oxide surface. A calculated value for the lattice diffusivity of oxygen is significantly below the value necessary to sustain the observed oxidation rate; this corroborates the domination of the oxidation process by permeation. At the higher temperature, the lattice diffusion of oxygen is significantly increased, which may lead to domination of

the oxidation rate by lattice diffusion at higher temperatures. An alternative interpretation of the observed oxygen-18 profiles may be that the exchange reaction between permeating O₂ and vacant lattice sites causes the observed profiles if the vacancies are created at the gas/SiO₂ interface and diffuse much faster at 1300° than at 1000°C.

Acknowledgments

This work was supported by the U. S. Army Research Office, Division of Materials Science. The authors are grateful to Dr. J. Cauley and Dr. J. Halloran, Case Western Reserve University, Cleveland, Ohio who performed the oxygen-18 treatments.

Manuscript submitted Dec. 16, 1983; revised manuscript received March 30, 1984.

The Pennsylvania State University assisted in meeting the publication costs of this article.

REFERENCES

1. B. E. Deal and A. S. Grove, *J. Appl. Phys.*, **36**, 3770 (1965).
2. J. R. Ligenza and W. G. Spitzer, *J. Phys. Chem. Solids*, **14**, 131 (1960).
3. R. H. Doremus, *J. Phys. Chem.*, **80**, 1773 (1976).
4. P. J. Jorgensen, *J. Chem. Phys.*, **37**, 874 (1962).
5. R. J. Norton, *Nature*, **171**, 701 (1961).
6. E. Rosencher, A. Straboni, S. Rigo, and G. Amsel, *Appl. Phys. Lett.*, **34**, 255 (1979).
7. R. Pfeffer and M. Ohring, *J. Appl. Phys.*, **52**, 777 (1981).
8. S. S. Cristi and J. B. Condon, *This Journal*, **128**, 2170 (1981).
9. J. W. Rouse, C. R. Helms, and C. J. Han, in "Computer-Aided Design of Integrated Circuit Fabrication Processes for VLSI Devices," Final Report, p. 261, Stanford University, Stanford, CA (1982).
10. A. R. Cooper, A. H. Heuer, and L. D. Majors, Jr., "Use of Nuclear-microanalysis, Part 1 — Proton Activation Studies of the Thermal Oxidation of Silicon," Tech. Report AFML-TR-78-119; Part 1, Air Force Materials Laboratory (1978).
11. E. W. Sucov, *J. Am. Ceram. Soc.*, **46**, 14 (1963).
12. E. L. Williams, *ibid.*, **48**, 190 (1965).
13. A. G. Revesz and H. A. Schaeffer, *This Journal*, **129**, 357 (1982).
14. J. Costello, Ph.D. Thesis, The Pennsylvania State University, University Park, PA (1983).
15. J. Schlichting, *Ceram. Int.*, **4**, 162 (1978).

Denuded Zones in Czochralski Silicon Wafers

Ping Wang, L. Chang, and L. J. Demer

Department of Metallurgical Engineering, College of Mines, University of Arizona, Tucson, Arizona 85721

C. J. Varker*

Motorola, Incorporated, Semiconductor Research and Development Laboratory, Semiconductor Group, Phoenix, Arizona 85258

ABSTRACT

Denuded zones in the near-surface regions of Czochralski silicon wafers were investigated by means of both optical microscopy (OPM) and transmission electron microscopy (TEM). The results of this investigation show that the (nearly defect-free) denuded zones formed near the wafer surface depend strongly on the initial oxygen concentration and the thermal history of the wafers, *e. g.*, wafer annealing-temperature sequence, gas ambient, and annealing duration. Clear denuded zones were observed in wafers annealed under conditions in which the oxygen out-diffusion process is enhanced, *e. g.*, in a high-low, two-step anneal (1050°C for 16h and 800°C for 16h), in a nonoxidizing ambient. A high initial oxygen concentration ($1.5 \times 10^{18} < [O]_i < 2.0 \times 10^{18} \text{ cm}^{-3}$), using the old ASTM calibration factor (ASTM F121-79), is required for the detection of a denuded zone, since defect generation in the bulk resulting from oxygen precipitation provides the demarcation layer.

It has been found that microdefects existing in the active region of Czochralski (CZ) silicon wafers have many detrimental effects on the performance of semiconductor devices, such as minority carrier lifetime degradation, junction leakage enhancement, etc. (1-4). Therefore, it is desirable to eliminate these detrimental effects by providing a nearly microdefect-free zone, which is commonly referred to as a "denuded zone," in the active region of silicon wafers.

It has been previously reported (5-19) that denuded zones can form in the near-surface region if wafers are subjected to a proper preannealing treatment before normal device fabrication processes. The depth of the denuded zones depends strongly on the wafer preannealing conditions, *e. g.*, annealing temperature sequence, gas ambient, and time. However, the reported effects of these conditions are not conclusive.

Two major mechanisms of denuded zone formation have been suggested. One is the oxygen out-diffusion mechanism (9, 10, 15, 17). It is proposed that interstitial oxygen atoms which enter silicon wafers during crystal growth can diffuse out of the wafer surface when subjected to high temperature annealing. This causes a zone of oxygen interstitial undersaturation near the wafer surface, resulting in a nearly microdefect-free (denuded) zone, since oxygen precipitation does not occur there. The other mechanism is one involving the retardation of oxygen precipitation at the wafer surface by excess silicon interstitials. Craven and Korb (19) believe that excess silicon interstitials generated in the near-surface region of wafers during oxidation will annihilate some vacancies, which are supposed to act as the nucleation sites of oxygen precipitates, resulting in a retardation of oxygen precipitation in the near-surface region. From this, a clear denuded zone will then be formed. On the other hand, they believe that excess vacancies generated in the near-surface region during preannealing in HCl containing ambient will enhance the oxygen precipitation, and under this condition, no clear denuded zone can be formed near the surface. They offer experimental results confirming their proposed mechanism.

In this paper, the effects of initial concentrations of oxygen and carbon in the wafers, and the effects of wafer annealing variables, such as temperature sequence, gas ambient, and time, on the formation and width of the denuded zone are reported, having been investigated by optical microscopy (OPM) and transmission electron microscopy (TEM). The active mechanism of denuded zone

formation, as supported by the experimental results obtained, is discussed.

Experimental Procedures

The wafers were n- and p-type, with a diameter of 3 in., a thickness of 500 μm , a (100) orientation, and an interstitial oxygen concentration $[O]_i$ in the range of $1.30 \times 10^{18} \leq [O]_i \leq 1.89 \times 10^{18} \text{ cm}^{-3}$, as measured by infrared absorption (ASTM F 121-79). These oxygen concentration values are approximately a factor of 2 larger than the values calculated using the new ASTM document, F 121-80. The wafers were subjected to specific annealing temperatures with different annealing sequence, gas ambient, and time.

Several seed-end wafers were subjected to a high-low, two-step annealing. They were first annealed at 1050°C for 16h in Ar, followed by an anneal at 800°C in dry O_2 for 0, 4, or 16h. The OPM results showed a denuded zone depth of about 20 μm on all of these wafers, with a similar high density of microdefect etch pits (about $2.9\text{-}3.0 \times 10^9 \text{ cm}^{-2}$) confined to the bulk.

The annealing ambient also plays a very important role in denuded zones in silicon wafers. In this investigation, only the effect of the annealing ambient at the high temperature step was studied, since oxygen out-diffusion at low temperatures (*e. g.*, 800°C) is very slow and can be neglected. Three seed-end wafers were subjected to high-low, two-step annealing in three different ambients (1050°C for 16h in Ar, dry O_2 , or $\text{N}_2 + 3\% \text{ HCl}$, respectively), followed by 800°C for 16h in dry O_2 .

Annealing duration at the first step, 1050°C, of high-low, two-step annealing is very important, since it affects the amount of oxygen diffusing out of the wafer surface. We annealed several seed-end wafers at 1050°C in Ar for 1, 4, or 16h, respectively, followed by annealing at 800°C for 16h in dry O_2 .

Subsequently, the wafers were sawn and broken into small, 2 \times 3 mm rectangular pieces with edges in $\langle 110 \rangle$ directions. For OPM samples, six small pieces were arbitrarily chosen from the central region of a wafer. These were stacked face-to-face (mirror surfaces) and bonded with epoxy glue and were mounted with a black Bakelite mounting powder with the $\{110\}$ surfaces facing the bottom of the mount. In this way, the wafer surfaces were protected by the epoxy glue from etching, only cross-sectional surfaces were subjected to the etchant, and accurate measurements of denuded zones were achieved. The cross section was prepared on the $\{110\}$ surfaces which were polished and Wright etched (20) to delineate the defects.

The distributions of defect etch pits on the $\{110\}$ wafer cross sections were examined by optical microscopy. The depth of the denuded zones was measured from the wafer

* Electrochemical Society Active Member.

Key words: denuded zones, silicon microdefects, sequential annealing.

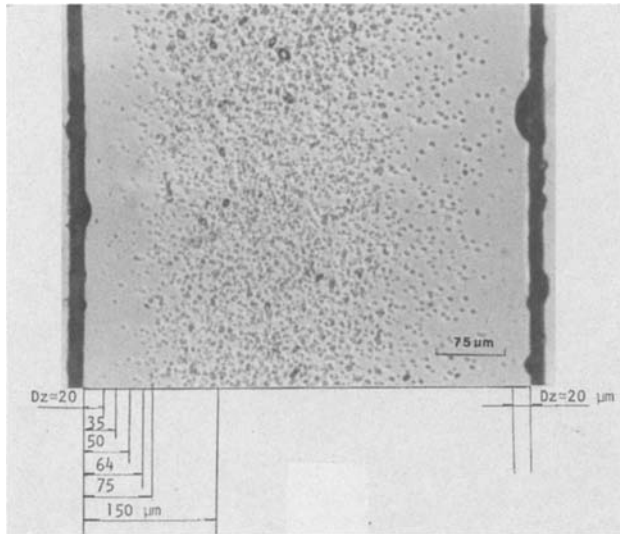


Fig. 1. An OPM photomicrograph of the cross-sectional, $\{110\}$ surface, of a seed-end wafer annealed at 1050°C for 16h in Ar and at 800°C for 4h in dry O_2 , after 8 min in Wright etch, showing clear denuded zones of $\sim 20\ \mu\text{m}$ at the subsurface regions with a high density of etch pits in the bulk.

surface to the "boundary," where the defect etch pits appeared in significant numbers. The defect depth distribution below the wafer surface was further obtained by TEM. Rectangular wafer pieces with a $\{110\}$ surface, measuring $2 \times 3\ \text{mm}$, were step-thinned to increasing depths from the front surface (see Fig. 1) and subsequently jet-thinned from the back side. TEM specimens of $\{110\}$ cross section were also prepared, by grinding and polishing a composite of six small pieces to a thickness of 8 mil and then thinning to transparency by chemical etching in a $\text{HF}:\text{HNO}_3$, 1:4 solution (18).

Results and Discussion

Temperature effects.—The results of this study show that the thermal history of a wafer can affect the denuded zone formation. The effects of annealing conditions are now considered. Figure 1 shows the microdefect distribution for $\{110\}$ cross section of a seed-end wafer after a high-low, two-step anneal. The density of etch pits is high in the bulk region and decreases gradually toward the wafer surface. This corresponds to the decrease of interstitial oxygen concentration toward the surface due to oxygen out-diffusion during annealing (9). The depth of denuded zones formed on all these wafers was about $20\ \mu\text{m}$, regardless of the annealing time for the low temperature (800°C) anneal. This suggests that the denuded zones were mainly formed during the first-step, high

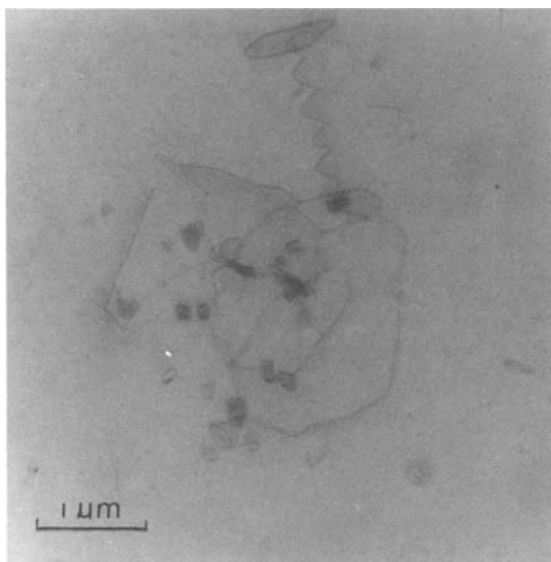
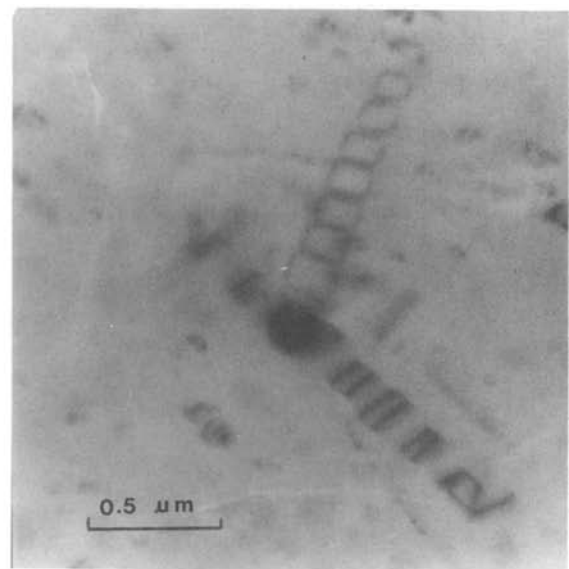
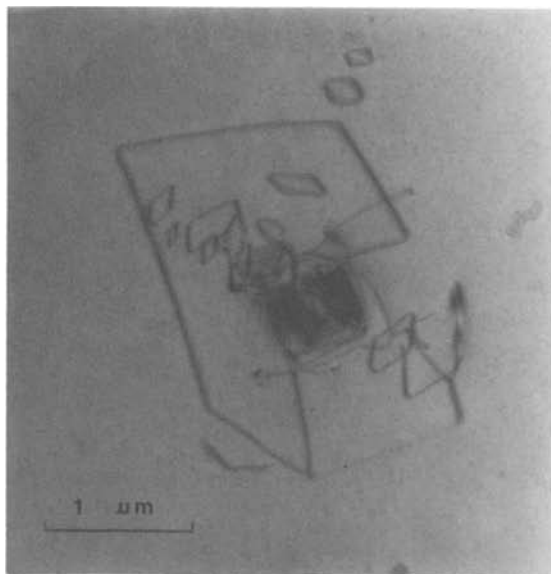


Fig. 2. TEM micrographs of a seed-end wafer, annealed at 1050°C for 16h in Ar and at 800°C for 4h in dry O_2 (multiple-beam condition). a(top left): Two flat oxygen precipitates at different levels in the bulk of the wafer, with punched-out dislocation loops in various oblique $\langle 100 \rangle$ directions, in a region $\sim 75\ \mu\text{m}$ below the $\{100\}$ front surface. b(top right): An oxygen precipitate with punched-out dislocation loops in three $\langle 110 \rangle$ directions. This foil surface is a $\{110\}$, cross-sectional surface, thinned by the immersed chemical thinning method. c(left): A cluster of oxygen precipitates and dislocations with a dislocation helix in the bulk of the wafer, $\sim 150\ \mu\text{m}$ below the $\{100\}$ front surface.

temperature (1050°C) anneal. This result is reasonably consistent with Andrews (21) regarding the denuded zone depth for a dry oxidation anneal at 1100°C for 4h, when allowance is made for the temperature and time via the Dt product. Oxygen out-diffusion at 800°C is much slower than at 1050°C, since the diffusivity of oxygen in silicon, calculated according to Takano and Maki (22), is about 6.5×10^{-11} cm²/s at 1050°C, while only 4.8×10^{-13} cm²/s at 800°C. These values are in good agreement with Stavola *et al.* (23). Therefore, oxygen out-diffusion at the low temperature step is negligible. At 1050°C in Ar, the dissolved interstitial oxygen atoms will out-diffuse from the wafer surface to the ambient. The interstitial oxygen concentration below the surface is lowered wherever oxygen concentration is not supersaturated, and oxygen precipitation is negligible in this region. However, the interstitial oxygen concentration in the bulk of the wafer remains high and is supersaturated. Oxygen atoms will tend to precipitate in the form of amorphous SiO₂ in the bulk during the anneal, forming the denuded zone at the subsurface region of the wafer during the first-step, high temperature anneal. The denuded zone remains relatively stable during the subsequent low temperature anneal if the interstitial oxygen concentration remains low inside the zone.

The TEM results show that the microdefects appear only in the region about 50 μm below the front surface. In the region less than 50 μm, the microdefect density was too low to be detected by TEM. The microdefects in nondenuded regions of the wafers after high-low, two-step annealing observed by TEM were mostly oxygen precipitates with punched-out dislocation loops (see Fig. 2a and 2b). A few stacking faults (not shown) and dislocation helices (see Fig. 2c) were observed. It is also noticeable that the shapes of the punched-out dislocation loops, when viewed from <100> and <110> directions, are different (compare Fig. 2a and 2b). The basic geometry of the loops is that they are rhombus-shaped with sides aligned in <112> directions on {111} planes. They are punched out in <110> directions (24). The loops appear rhombus-shaped for the oblique <110> directions from a {100} surface plane (24) (see Fig. 2a). However, when viewed along the <110> directions, the appearance of the punched-out dislocation loops may vary from near-square to near-rectangular shapes (see Fig. 2b), depending on the specific <110> direction in which dislocations were punched out and the specific {110} plane.

Many authors have reported that the denuded zones could form at the wafer surfaces after a low-high, two-step annealing (8, 12, 13). In our experiments we annealed several seed-end wafers in a low-high, two-step condition

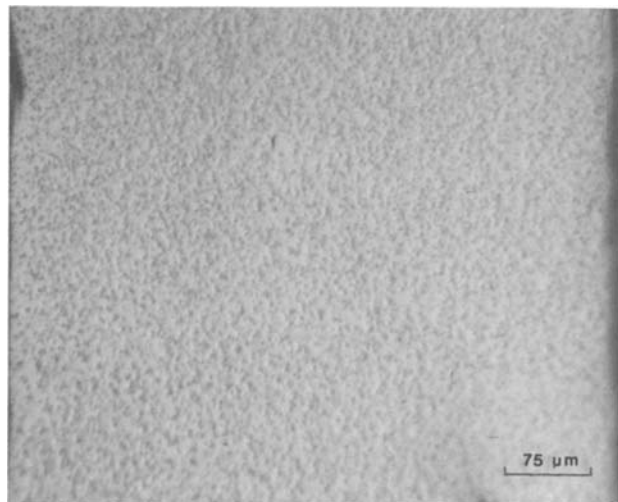


Fig. 3. An OPM photomicrograph of the cross-sectional, {110} surface of a seed-end wafer, annealed at 800°C for 16h in dry O₂, and at 1050°C for 16h in Ar, after 60s in Wright etch, showing high density microdefect etch pits uniformly with no clear denuded zone formed.

(800°C for 16h, in dry O₂, followed by 1050°C for 1, 4, or 16h in Ar, respectively). However, the results showed that no denuded zones formed at the surfaces of any of these wafers. The microdefect etch-pit density of about 3.2×10^{10} cm⁻³ was uniformly distributed over the entire cross-sectional surfaces of the wafers (see Fig. 3). Since oxygen out-diffusion at 800°C is small, and the driving force for oxygen precipitation in silicon wafers is large at this temperature, the interstitial oxygen atoms precipitate rapidly both in the bulk and at the surface of the wafer. During the subsequent high temperature annealing, some of the precipitates formed at the low temperature step, whose size is greater than the critical radius, r^* , for oxygen precipitation at 1050°C, will continue to grow, and some of the precipitates, whose size is smaller than r^* , will shrink both at the wafer surface and in the bulk (7, 15). The critical radius increases with increasing annealing temperature and, in this investigation, it is about 10 Å at 1050°C (7). After 16h annealing at 800°C, the size of the oxygen precipitates may grow to about 350 Å-square (25), which is much greater than the critical radius, r^* , for oxygen precipitates at subsequent 1050°C annealing. Thus, shrinkage of the precipitates will not occur at subsequent 1050°C annealing. Therefore, denuded zone formation is unlikely after a low-high, two-step annealing.

It may be noted that the density of etch pits on the cross section of the wafer annealed at 800°C for 16h in dry O₂ without subsequent high temperature anneal is much lower than for wafers annealed by a low-high or a high-low, two-step treatment (compare Fig. 4a and 3). Since the maximum nucleation rate reported was generally near 750°C for oxygen precipitation in silicon (7, 15), it was expected that a high density of microdefects would form in the wafer after an anneal at 800°C for 16h. TEM observations show a high density of microdefects have indeed formed in the wafer (see Fig. 4b). The microdefects were too small to be completely delineated by the Wright-etch technique. The etch pits in Fig. 4a may only be the result of large microdefects with dislocation loops around them. When this low temperature anneal was followed by a high temperature anneal (1050°C for 1, 4, or 16h in Ar), only stacking faults were observed with TEM.

Annealing ambient effects.—Figure 1 shows that denuded zones of about 20 μm in depth formed in a seed-end wafer after being annealed in an Ar ambient. The microdefect etch-pit distribution on the {110} cross-section surface of a seed-end wafer after being annealed in an oxidizing ambient (dry O₂) is shown in Fig. 5. Only very narrow denuded zones (≈ 5 μm) are present near the wafer surfaces, since the oxygen out-diffusion process is slower in the oxidation ambient than in an inert ambient. Another seed-end wafer was annealed in N₂ + 3% HCl ambient. Wide and clear denuded zones (about 25-30 μm) were formed in the subsurface region of the wafer (see Fig. 6) after being annealed. However, Hu (26) stated that the addition of 1% HCl to the oxygen ambient was not distinguishable from a pure-oxygen ambient for oxygen precipitation in silicon wafers. The experimental results of Craven and Korb (19) also showed that no apparent denuded zones were formed in HCl containing ambients, whereas clear denuded zones were formed in the oxygen ambients. They explained that the excess vacancies generated in HCl ambient enhanced the oxygen precipitation, since, they believed, these vacancies could act as the nucleation centers of oxygen precipitates, while excess silicon interstitials generated during oxidation annihilated some vacancies, resulting in a retardation of oxygen precipitation in the near-surface region. However, de Kock and van de Wijgert (27) indicated that silicon self-interstitials could act as nucleation centers of oxygen precipitates, and, thus, enhance the oxygen precipitation process in silicon.

The results of our investigation disagree with the results of Hu and of Craven and Korb mentioned above. Wide and clear denuded zones were formed in HCl containing ambients. During annealing in an HCl containing

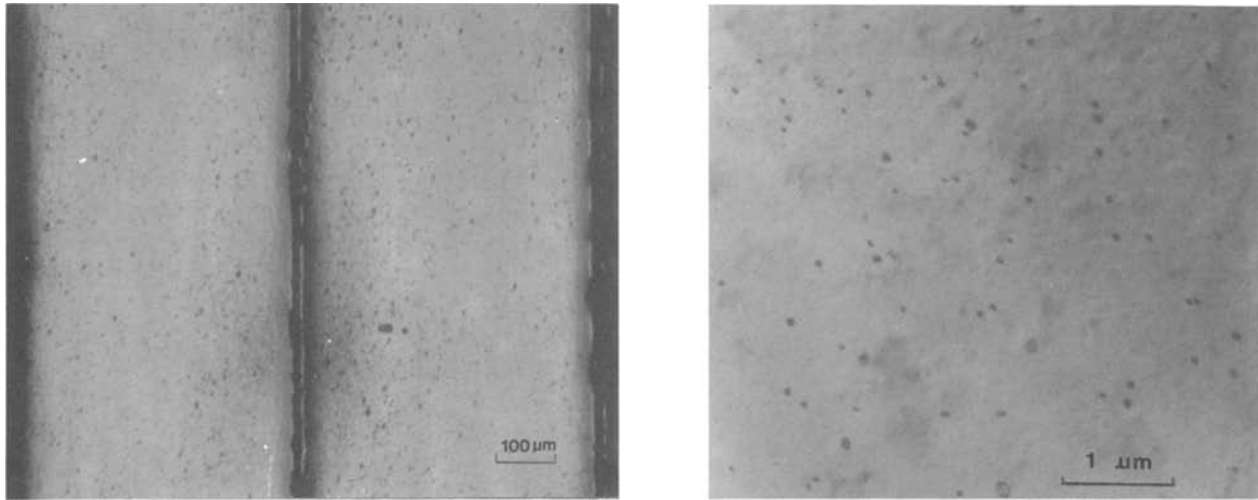


Fig. 4. An OPM photomicrograph (a), and a TEM micrograph (b) of a seed-end wafer, annealed at 800°C for 16h in dry oxygen. a(left): The low density etch pits are randomly distributed throughout the cross sections of the wafer after 8 min in Wright etch. No obvious denuded zones formed at the subsurface region. b(right): Very high density of tiny microdefects in the wafer, $\sim 135 \mu\text{m}$ below the $\{100\}$ front surface. (Multiple-beam condition.)

ambient, excess vacancies were generated in the subsurface region of the wafer (19, 28, 29). We believe that these vacancies enhanced the oxygen out-diffusion process, and resulted in a wider denuded zone at the wafer surface than those formed in a non-HCl containing ambient. Therefore, oxygen out-diffusion appears to be the dominant mechanism for denuded zone formation, according to this investigation.

Annealing-time effects.—OPM results show that for annealing duration at the first step, of 0 to 4h at 1050°C, the wafers did not have a clear denuded zone at the surfaces. When this duration was increased to 16h, denuded zones of about $20 \mu\text{m}$ wide were formed (see Fig. 1). This result agrees favorably with the optimum anneal time of 16h calculated by Andrews (21) for oxygen-out diffusion during a dry oxidation anneal at 1050°C.

Initial oxygen concentration.—In addition to seed-end wafers, several tang-end wafers with $[\text{O}]_i = 1.30 \times 10^{18} \text{ cm}^{-3}$ (ASTM F121-79) were examined after a high-low, two-step anneal. OPM observation showed that there were only a few etch pits existing over the entire cross-sectional surface of these tang-end wafers. No meaningful measurements of denuded zones are possible for these tang-end wafers, as Series *et al.* (10) also pointed out. However, for these tang-end wafers, oxygen precipitation

is minimal in the bulk because of their low initial oxygen concentration levels.

Initial carbon concentration.—To examine the effect of carbon concentration, several seed-end wafers sliced from two CZ crystals with different initial carbon concentrations were annealed, employing the same high-low, two-step conditions (1050°C for 16h in Ar, followed by 800°C for 16h in dry O_2). One of these two CZ crystals had a carbon concentration ($7.0 \times 10^{16} \text{ cm}^{-3}$), or 1.4 ppma, seven times as high as the other one (0.28 ppma). The OPM observations show that denuded zones were formed at the subsurface region in all of these wafers, regardless of the carbon concentrations. It has been shown that carbon-oxygen complexes can act as nucleation centers for the precipitation of oxygen (30). However, during the first step, 1050°C annealing, the interstitial oxygen atoms diffuse out of the wafer surface and lower the oxygen concentration in the subsurface region to an undersaturated level, and oxygen precipitation at the subsurface region will not occur, despite the high concentration of carbon atoms existing in this region. Further, since both the diffusivity and the concentration of carbon atoms in silicon are quite small compared to oxygen, it is also unlikely for carbon atoms to precipitate out as carbide particles (31). Hence, the effect of the initial carbon concentration on the formation of precipitate nuclei may be

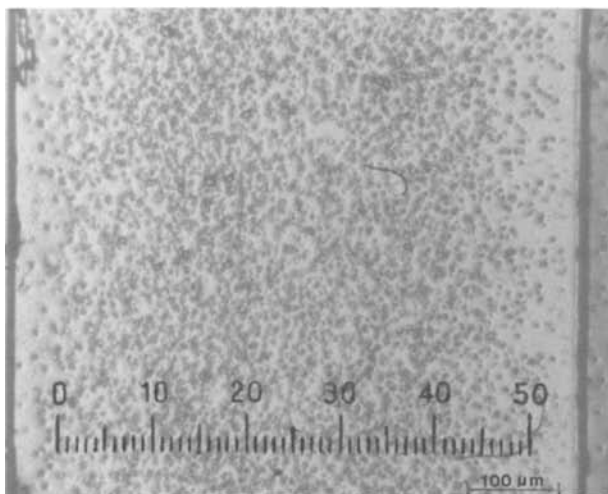


Fig. 5. An OPM photomicrograph of the cross-sectional $\{110\}$ surface of a seed-end wafer, annealed for 16h in dry O_2 at both 1050°C and 800°C. Very narrow denuded zones ($<5 \mu\text{m}$) were formed in the subsurface region.

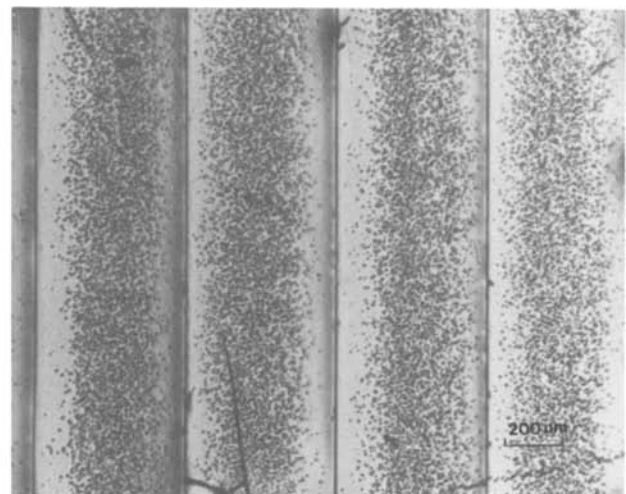


Fig. 6. An OPM photomicrograph of the cross-sectional, $\{110\}$ surfaces of a seed-end wafer, annealed at 1050°C for 16h in $\text{N}_2 + 3\% \text{HCl}$ and at 800°C for 16h in dry O_2 . Wide and clear denuded zones of 25-30 μm were formed in the subsurface regions.

insignificant in the region where oxygen undersaturation exists, *i. e.*, in the near-surface region.

Summary and Conclusions

In this study, almost-defect-free denuded zones, formed in CZ silicon wafers heat-treated under different thermal histories, have been investigated. The principal results are as follows.

1. A high-low, two-step annealing (first, at 1050°C, then at 800°C) results in a clear denuded zone at the wafer surface, while the reverse sequence, *i. e.*, a low-high, two-step annealing (first, at 800°C, then at 1050°C) does not.

2. Annealing in an inert or an HCl containing inert ambient results in a much wider denuded zone (20-30 μm) than in an oxidation ambient ($\approx 5 \mu\text{m}$).

3. An annealing time of 16h at 1050°C is sufficient to form a denuded zone $\approx 20 \mu\text{m}$ wide.

4. A high initial oxygen concentration ($1.5 \times 10^{18} < [\text{O}]_i < 2.0 \times 10^{18} \text{ cm}^{-3}$), [old ASTM method (ASTM F121-79)] sufficient to induce bulk precipitates in the wafer, is required to delineate the oxygen out-diffused layer.

5. The highest carbon concentration present in the silicon wafers ($7.0 \times 10^{16} \text{ cm}^{-3}$) exerted no significant effect on the denuded zone formation.

6. The above results support the view that oxygen out-diffusion is the dominant mechanism for the formation of denuded zones in Czochralski silicon crystal wafers. These results do not agree with the excess-silicon-interstitial mechanism proposed by Craven and Korb (19).

Acknowledgments

The authors would like to thank Dr. Seshan, of the University of Arizona, Department of Metallurgical Engineering, for his valuable discussions during the course of this work, and Pat Huegle, of Motorola, Incorporated, for the wafer processing.

Manuscript submitted Nov. 28, 1983; revised manuscript received April 6, 1984.

The University of Arizona assisted in meeting the publication costs of this article.

REFERENCES

1. J. R. Monkowski, *Solid State Technol.*, **24**, 44 (1981).
2. C. J. Varker, J. D. Whitfield, and P. L. Fejes, in "Proceedings of Symposium on Silicon Processing, San Jose, CA, Jan. 1982," H. Huff, R. Kriegler, and Y. Takaishi, Editors, p. 369, ASTM Special Tech. Pub. 804, ASTM, Philadelphia (1983).
3. C. J. Varker, J. D. Whitfield, and P. L. Fejes, in "Symposia Proceedings of Materials Research Society," Vol. 14, p. 187, Boston (1983).
4. C. J. Varker, *IEEE Trans. Electron. Devices*, **ed-27**, 2205 (1980).
5. G. A. Rozgonyi and C. W. Pearce, *Appl. Phys. Lett.*, **31**, 343 (1977).
6. S. Kishino, Y. Matsushita, and M. Kanamori, *ibid.*, **35**, 213 (1979).
7. R. A. Craven, in "Semiconductor Silicon 1981," H. Huff, R. Kriegler, and Y. Takaishi, Editors, p. 254, The Electrochemical Society Softbound Proceedings Series, Pennington, NJ (1981).
8. T. J. Magee, C. Leung, H. Kawayoshi, B. K. Furman and G. A. Evans, Jr., *Appl. Phys. Lett.*, **39**, 631 (1981).
9. K. Kugimiya, S. Akiyama, and S. Nakamura, in "Semiconductor Silicon 1981," H. Huff, R. Kriegler, and Y. Takaishi, Editors, p. 294, The Electrochemical Society Softbound Proceedings Series, Pennington, NJ (1981).
10. R. W. Series, K. G. Barraclough, and W. Bardsley, in "Semiconductor Silicon 1981," H. Huff, R. Kriegler, and Y. Takaishi, Editors, p. 304, The Electrochemical Society Softbound Proceedings Series, Pennington, NJ (1981).
11. F. Shimura, H. Tsuya, and T. Kawamura, *J. Appl. Phys.*, **51**, 269 (1980).
12. K. Yamamoto, S. Kishino, Y. Matsushita, and T. Iisuka, *Appl. Phys. Lett.*, **36**, 195 (1980).
13. H. Tsuya, K. Tanno, and F. Shimura, *ibid.*, **36**, 658 (1980).
14. J. M. Andrews, S. Muller, G. A. Rozgonyi, and C. A. Clark, in "VLSI Science and Technology," C. J. Dell'Oca and W. M. Bullis, Editors, p. 43, The Electrochemical Society Softbound Proceedings Series, Pennington, NJ (1982).
15. N. Inoue, K. Wada, and J. Oosaka, in "Semiconductor Silicon 1981," H. Huff, R. Kriegler, and Y. Takaishi, Editors, p. 282, The Electrochemical Society Softbound Proceedings Series, Pennington, NJ (1981).
16. S. Kishino, S. Isomai, M. Tamura, and M. Maki, *Appl. Phys. Lett.*, **32**, 1 (1978).
17. S. Kishino, K. Nagasawa, and T. Iizuka, *Jpn. J. Appl. Phys.*, **19**, L466 (1980).
18. P. Wang, M.S. Thesis, The University of Arizona, Tucson, AZ (1983).
19. R. A. Craven and H. W. Korb, *Solid State Technol.*, **24**, 55 (1981).
20. M. W. Jenkins, *This Journal*, **124**, 757 (1977).
21. J. Andrews, in "Defects in Silicon," W. M. Bullis and L. C. Kimerling, Editors, p. 133, The Electrochemical Society Softbound Proceedings Series, Pennington, NJ (1983).
22. Y. Takano and M. Maki in "Semiconductor Silicon 1973," H. R. Huff and R. R. Burgess, Editors, p. 469, The Electrochemical Society Softbound Proceedings Series, Princeton, NJ (1973).
23. M. Stavola, J. R. Patel, L. E. Kimberling, and P. E. Freeland, *Appl. Phys. Lett.*, **42**, 73 (1983).
24. L. H. Chang, L. J. Demer, and C. J. Varker, *This Journal*, To be published.
25. K. Wada, J. Inoue, and K. Kohra, *J. Cryst. Growth*, **49**, 749 (1980).
26. S. M. Hu, *Appl. Phys. Lett.*, **36**, 561 (1980).
27. A. J. R. de Kock and W. M. van de Wijert, *ibid.*, **38**, 11 (1981).
28. H. Shiraki, *Jpn. J. Appl. Phys.*, **15**, 1 (1976).
29. T. Hattori, *Solid State Technol.*, **25**, 83 (1982).
30. G. S. Oehrlein, J. L. Lindstrom, and J. W. Corbett, *Appl. Phys. Lett.*, **40**, 241 (1982).
31. J. Wang and M. Kulkarni, Abstract 532, p. 1330, The Electrochemical Society Extended Abstracts, Vol. 80-2, Hollywood, FL, Oct. 5-10, 1980.

Cathodoluminescence of $\text{Ca}_{1-x}\text{Mg}_x\text{S:A}$ ($A = \text{Eu}$ or Ce)

Hiroyuki Kasano, Kouichi Megumi, and Hajime Yamamoto*

Hitachi Limited, Central Research Laboratory, Kokubunji, Tokyo 185, Japan

ABSTRACT

Cathodoluminescent properties of Eu^{2+} - or Ce^{3+} -activated MgS and $\text{Ca}_{1-x}\text{Mg}_x\text{S}$ phosphors are investigated at 300 K. It is found that MgS:Eu (0.01 mole percent [m/o]) exhibits a high energy efficiency ($\sim 16\%$) and an improved water-resistance if residual oxide content is less than 1 m/o. Under these highly sulfurizing conditions, MgS is confirmed to be completely miscible with CaS in any compositional ratio. The composition $\text{Ca}_{0.1}\text{Mg}_{0.9}\text{S:Eu}$ (0.05 m/o), Ba (0.1 m/o), whose color coordinates are comparable to the red phosphor $(\text{Y}_{0.964}\text{Eu}_{0.036})_2\text{O}_2\text{S}$, exceeds the latter in brightness by 15% at 18 kV excitation. Additionally, Eu^{2+} -activated alkaline-earth binary sulfides are examined. A complete miscibility is ascertained in the pseudobinary system where the difference in cation radius is less than 0.035 nm. Stress-induced peak shifts are observed in MgS:Eu and $\text{A}_{1-y}\text{B}_y\text{S}$ (A or $B \equiv \text{Mg}, \text{Ca}, \text{Sr}$ or Ba , $A \neq B$). Some mechanisms for these shifts are proposed.

It has been pointed out (1) that alkaline earth sulfides can be excellent cathodoluminophors when doped with proper activators. Among rare earth-activated phosphors, very high energy efficiencies were reported in green CaS:Ce ($\sim 22\%$) and red $\text{CaS:Eu}, \text{Ce}$ ($\sim 16\%$) (2) both of which utilize f-d transitions of the rare earth ions. However, energy efficiency has seldom been reported on for alkaline earth sulfides other than CaS . This is because poor chemical stability (3) prevents them from being used for practical applications. Therefore, it is preferable from the standpoints of both chemical stability and chromaticity control to form solid solutions with CaS . Some properties of these pseudobinary sulfide phosphors have been reported in the CaS-SrS system (completely miscible (4)), CaS-MgS system (partially miscible) (5), and CaS-BaS system (partially miscible) (6). However, cathodoluminescence in rare earth-doped phosphors has been investigated only in the CaS-SrS system (7).

This paper deals with the preparation and cathodoluminescent properties of MgS -based phosphors (MgS and $\text{Ca}_{1-x}\text{Mg}_x\text{S}$) activated with Eu and/or Ce . It is emphasized that the CaS-MgS system is completely miscible when fired in a highly sulfurizing atmosphere, and that $\text{Ca}_{1-x}\text{Mg}_x\text{S:Eu}$ exhibits promising luminescent properties. Peak shifts of an Eu^{2+} emission band observed in alkaline earth sulfides are also discussed.

Experimental

Magnesium sulfide-based phosphors are prepared by the method illustrated in Fig. 1: on firing MgS , MgSO_4 (optical grade, Hakushin Kagaku Laboratory Company, Limited) mixed with Eu and/or Ce compounds (4N, Rare Metallic Company, Limited) were used as a starting material. Carbonate was used for CaS . The mixtures charged in a quartz boat were first heated at 1100°C in a H_2S stream (4N, Seitetsu Kagaku Company, Limited) for 3 or 4 h. Then, the product was lightly ground and refired at 1200°C for 3 h in a sulfurizing atmosphere. This process was repeated once again. During the last firing, PCl_3 was introduced into a reaction tube for 30 min. The compound PCl_3 (5N, E. Merk Company), was reserved in a quartz bubbler at 25°C and carried with argon at partial pressures of $4 \sim 8 \times 10^3$ Pa. Calcium sulfide was obtained in a similar manner. Compound $\text{Ca}_{1-x}\text{Mg}_x\text{S:A}$ was prepared by firing a mixture of $(1-x)$ mole fraction of CaS:A and x mole fraction of MgS:A at 1200°C in H_2S for 1 or 2 h. In some cases, $\text{Ca}_{1-x}\text{Mg}_x\text{S:Eu}$ was directly synthesized from CaCO_3 , MgSO_4 , Eu_2O_3 , and H_2S . A similar firing process was also used with PCl_3 doping.

The sulfide percentage of the fired products was estimated by weighing before and after firing. This is because an x-ray diffraction analysis showed that the products were simply composed of the sulfide and the oxide, and because the transport loss during the run could be ignored. Grain size, lattice constant, impurity concentration, and chlorine content were measured by SEM, x-ray

diffraction, spectrophotometric, and chemical analyses, respectively. Cathodoluminescence was measured at 300 K with a demountable cathodray apparatus. An electron-beam current was typically 100 nA, and the accelerating voltage was 18 or 27 kV. Raster size was 2×1 cm^2 . Emission was observed through a glass window with a grating monochromator (Nikon P-25) and a photomultiplier (RCA 7265). All spectra were corrected for monochromator transmission and photomultiplier response, and given in terms of emission intensity per unit wavelength interval as a function of wavelength. The spectral resolution limit was 0.02 eV. Brightness and energy efficiency were measured with a photometer radiometer (United Detector Technology II A) and given as relative values to the standard sample, i. e., $(\text{Y}_{0.964}\text{Eu}_{0.036})_2\text{O}_2\text{S}$ for a red phosphor and $\text{ZnS:Cu}, \text{Al}$ (P-22) for a green phosphor. The sample screen was formed by sedimentation of the stirred phosphor powder in ethyl alcohol onto a steel substrate. Screen weight was kept to be 9-11 mg/cm^2 .

Waterproof testing of MgS:Eu was carried out at 300 K. First, 50 mg of MgS:Eu powder was stirred in 1000 ml of deionized water for a desired time. Then, the phosphor was rinsed in ethyl alcohol and formed into the screen, as mentioned above.

Results

Influence of sulfurized ratio on characteristics of MgS:Eu .—There has been little reported on the emission efficiency of MgS:Eu , although the emission spectrum

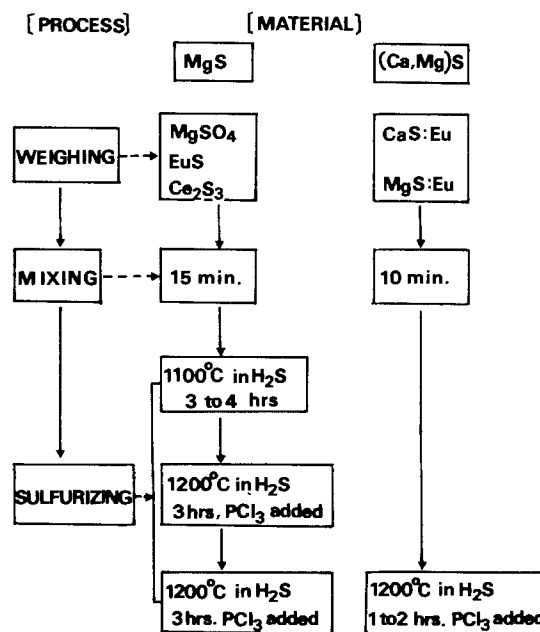
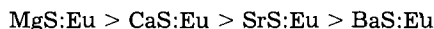


Fig. 1. Firing process of MgS -based phosphors

* Electrochemical Society Active Member

peaked at 591 nm (300 K) was shown to be narrower than those of CaS:Eu and SrS:Eu (8). In this study, it was found that the energy efficiency as well as chemical stability of MgS:Eu are strongly dependent on the sulfurized ratio of the host material, as was typically shown in Fig. 2, where the Eu concentration involved was kept to 0.04 mole percent (m/o). The fact that phosphor properties are noticeably improved with increasing sulfurized ratio is indicated in Fig. 2. This is especially so in a highly sulfurized region, where the grain size rapidly increases and the lattice constant approximates to 5.2015 Å for a sulfurized ratio above 85%. The slightly large value of the ultimate lattice constant compared with that of undoped MgS ($a = 5.200$ Å) is thought to be caused by Eu doping. Energy efficiency exceeds 120% relative to $(Y_{0.964}Eu_{0.036})_2O_2S$, the red phosphor used for color TV, when the sulfurized ratio exceeds 99%. This means that the absolute efficiency exceeds 15.5% in this sulfurized range, where the full width at half maximum (FWHM) of the Eu^{2+} band approaches 1130 cm^{-1} . For simplicity, the term "half-width" is used in the figures of this paper instead of the term "FWHM." These high efficiencies have not yet been reported in any other phosphor activated only with Eu. It is noteworthy that such an efficient phosphor was obtained with Eu concentrations less than 1/100 of that in Y_2O_2S , 1/5 of that in SrS, and 1/2 of that in CaS. Efficiencies of the alkaline earth sulfides were found to be in the order



The MgO is very hard to completely sulfurize in H_2S , in contrast to CaO, SrO, or BaO. The fact that the firing products were sulfurized above 98% in the present work is mainly due to the effect of PCl_3 flux. Similarly, both grain growth and Eu diffusion are markedly promoted by PCl_3 doping.

To examine chemical stability, a waterproof test of MgS:Eu was carried out. The data are shown in Fig. 3.

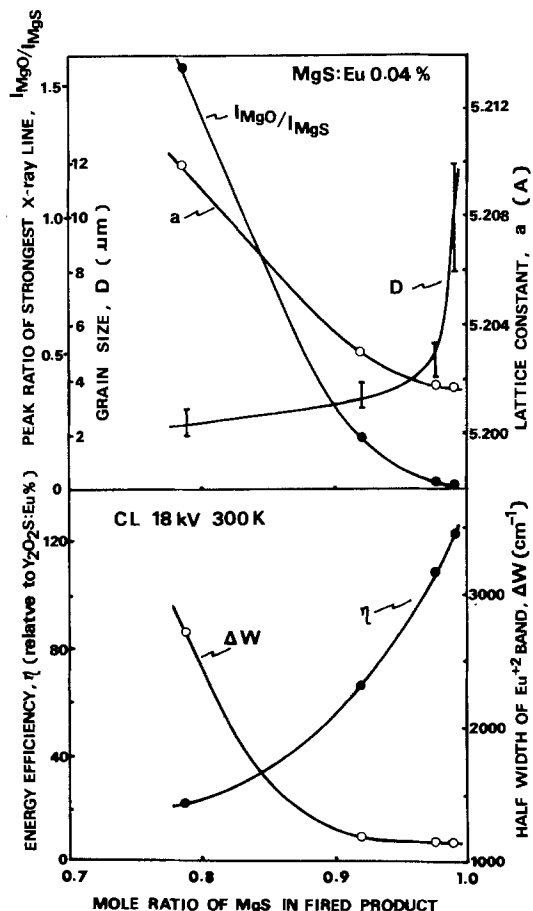


Fig. 2. Characteristics of MgS:Eu(0.04 m/o) dependent on sulfurized ratio of host material.

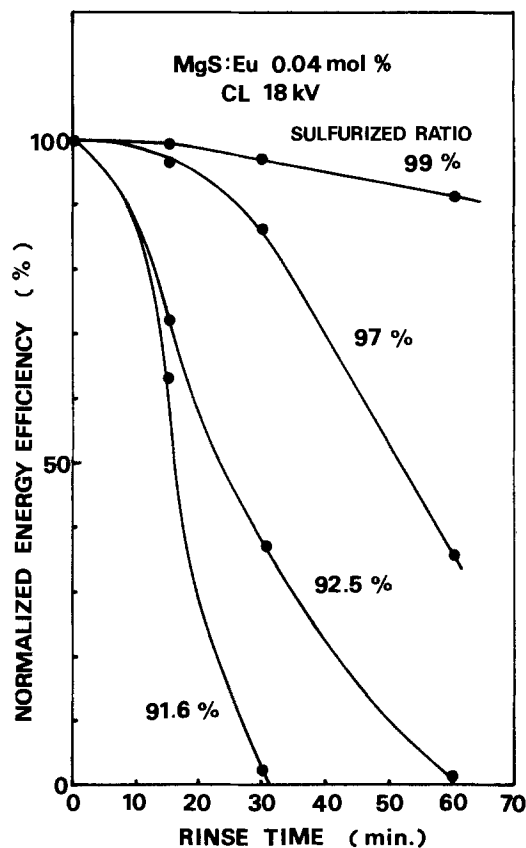


Fig. 3. Degradation of MgS:Eu(0.04 m/o) due to chemical reaction with water. Sulfurized ratio is used as a parameter.

The CL efficiencies of four samples whose sulfurized ratio differ are normalized by those obtained prior to rinsing. It is found that increased sulfurized ratios make the phosphor more resistive to water; in a 99% sulfurized case, the efficiency remains 96% of the initial value even after the phosphor was rinsed for 1h. Degradation may be caused by surface layer reoxidation, because MgO was clearly detected in the degraded sample by x-ray diffraction analysis. Extrapolatedly speaking, the degradation may be ignored if the sulfurized ratio reaches 100%.

Influence of activator concentration on energy efficiency of MgS:A.—Solubility of Eu or Ce in MgS is supposed to be less than that in CaS since the ionic radius of Mg^{2+} (0.65 Å) is rather small compared with that of Ca^{2+} (0.99 Å). Concentration dependence of efficiency η is illustrated in Fig. 4. Maximum value of η in MgS:Eu would be obtained at about 0.01 m/o of Eu. This value is 1/5 that of the CaS:Eu case (2). However, optimum Ce concentration in MgS:Ce is about 0.04 m/o, which is comparable to the CaS:Ce case (2). However, η in MgS:Ce is lower by about 30% than in CaS:Ce ($\eta \approx 110\%$ relative to P-22). When using $MgCO_3$ as a starting material, η remains at still lower levels because the sulfurized ratio is somewhat lower (about 97%). Moreover, the coactivator Ce in MgS:Eu, which was expected to improve η drastically (2), brought no fruitful result. Although one example MgS:Eu (x m/o), Ce (0.28x m/o) is shown in Fig. 4, a similar conclusion was obtained in any mole ratio of Ce to Eu. The relatively low η levels observed in MgS:Eu, Ce may be due to some kinds of lattice defects introduced by Ce codoping. This is because the shape of the η curve resembles that of MgS:Ce and also because the optimum Eu concentration shifts toward the higher side compared with the MgS:Eu case.

Composition dependence of CL in $Ca_{1-x}Mg_xS:A$.—To observe the properties of the pseudobinary phosphor, $Ca_{1-x}Mg_xS:A$ ($A = Eu$ or Ce) was synthesized from $CaS:A_1$ ($A_1 = 0.1$ m/o Eu or 0.04 m/o Ce) and $MgS:A_2$ ($A_2 = 0.04$ m/o Eu or 0.04 m/o Ce) by heating the sulfide mixture with a desired ratio at $1200^\circ C$ in H_2S . As was de-

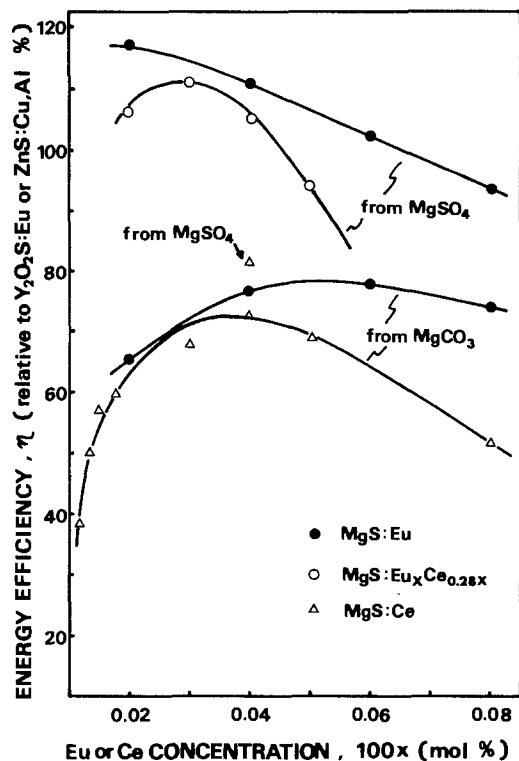


Fig. 4. Variation in CL efficiency of Eu- or Ce-activated MgS as a function of activator concentrations.

scribed above highly sulfurized (99%) MgS grows to 10 μm in size with an excellent crystalline quality. Using this type of MgS, we succeeded in obtaining Ca_{1-x}Mg_xS:A with an optical composition ratio, *i.e.*, the CaS-MgS system was found to be completely miscible by x-ray diffraction analysis, although partial miscibility (14% MgS in CaS and 12% CaS in MgS) (5) was reported previously. The miscibility gap was probably due to the low-sulfurized ratio of MgS. Mutual solubility of CaO and MgO are limited to within 5% from the end components (9). Variation in lattice constant is shown as a function of compositional ratio x in Fig. 5. Vegard's law was found to hold in the CaS-MgS system.

Cathodoluminescent properties of Ca_{1-x}Mg_xS:Eu are also included in Fig. 5. Both peak wavelength λ_0 , and full width at half maximum, *i.e.*, half-width ΔW of the Eu²⁺ band vary with x . Peak wavelength reaches the longest one, 658 nm, at $x \approx 0.35$. In a composition range of $x < 0.6$, ΔW increases with increasing x , but becomes constant in $x \geq 0.6$ except around 0.95 (anomaly point) where ΔW rapidly increases. The other anomaly point exists at about 0.05, where a slight broadening of ΔW was observed. The CL band becomes more asymmetrical at these anomaly points. The lattice constant also deviates slightly from Vegard's law near these points, as is shown in Fig. 5. Judging from these results, crystalline quality is disturbed at compositions near these points where alloying is somewhat difficult. This is confirmed by x-ray diffraction analysis. The composition dependence of a splitting index b/a in a high-angle ($\sim 85^\circ$) diffracted x-ray line is shown in Fig. 6, *i.e.*, a ratio of the dip height "b" between the CuK _{α 1} line and the CuK _{α 2} line to the peak height "a" of the CuK _{α 1} line in comparison with the variation in η . A larger b/a value corresponds to a lower crystalline quality. The figure indicates that b/a rapidly increases at compositions near 5% from the end members of the alloy, where η locally drops. A decrease in η is additionally observed in the broad ranges of compositions, $0.3 \leq x \leq 0.5$ and $0.7 \leq x \leq 0.8$. The decrease in the former range implies an inferior crystalline quality as suggested from b/a , while that in the latter range does not. It is believed that the η drop in the former range is due to an insufficient firing, but the latter case may be essential, since further firing at

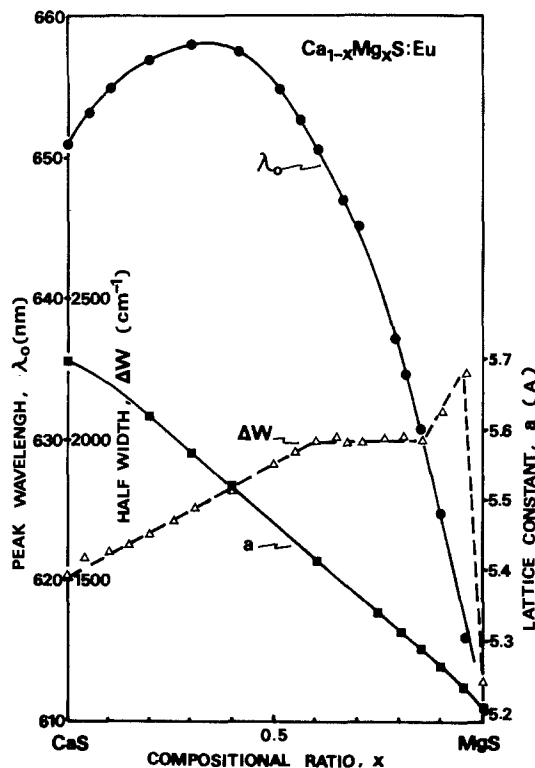


Fig. 5. Characteristics of Ca_{1-x}Mg_xS:Eu dependent upon compositional ratio x . Half-width ΔW means full width at half maximum.

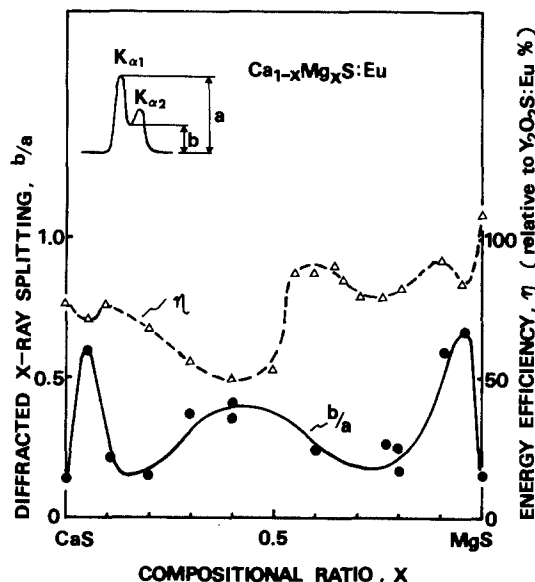


Fig. 6. Comparison of CL efficiency with crystalline quality in Ca_{1-x}Mg_xS:Eu as a function of compositional ratio x .

1200°C in H₂S easily improved both η and b/a in the former but not in the latter.

Similar anomalies were observed in the Ce-activated case. The λ_0 and ΔW in the Ce³⁺ band of Ca_{1-x}Mg_xS:Ce(0.04 m/o) are illustrated in Fig. 7. As is well known in MgS (1), CaS (2), and SrS (10), the Ce³⁺ band has a second peak on the lower energy side of the main peak, corresponding to the spin-orbit splitting of the Ce³⁺ ground state. Here, ΔW includes the contribution of the both emission bands. It is found that ΔW expands linearly with the increase of x , though anomalously at $x \approx 0.05$ and 0.95. Around 0.65 of x , λ_0 and η take the longest and minimum values, respectively. This is different from the case of Eu²⁺ activation. However, it is noteworthy that η in Ca_{1-x}Mg_xS phosphors becomes lowest at $x \approx 0.7$ both in Eu²⁺ and Ce³⁺ activated cases. In Ca_{1-x}Mg_xS:Ce, the η observed is far lower in comparison with the value expected from that of

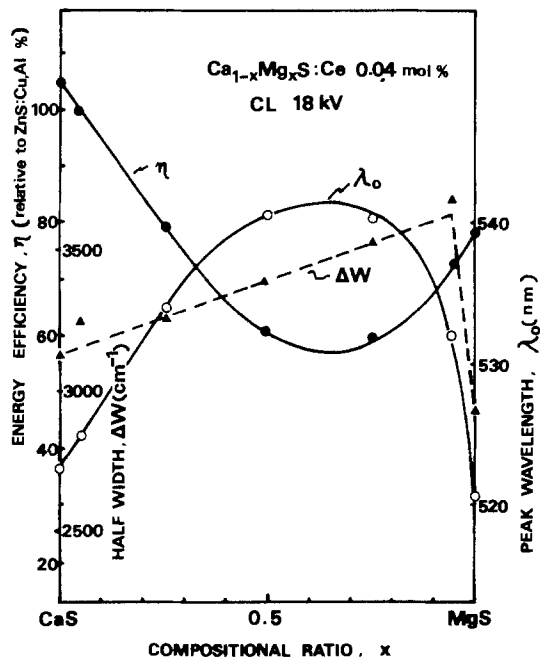


Fig. 7. CL properties of $\text{Ca}_{1-x}\text{Mg}_x\text{S}:\text{Ce}(0.04 \text{ m/o})$ as a function of x . Full width at half maximum ΔW is represented as half-width in the figure.

$\text{Ca}_{1-x}\text{Mg}_x\text{S}:\text{Eu}$. Therefore, η in $\text{Ca}_{1-x}\text{Mg}_x\text{S}:\text{Eu}$, Ce is at a level similar to that in $\text{Ca}_{1-x}\text{Mg}_x\text{S}:\text{Eu}$.

Highly bright red phosphor $\text{Ca}_{0.1}\text{Mg}_{0.9}\text{S}:\text{Eu}$.—Chromatic shift in $\text{Ca}_{1-x}\text{Mg}_x\text{S}:\text{Eu}$ (0.05 m/o) dependent upon x is shown on the CIE x - y color coordinates in Fig. 8. By varying x , chromaticity changes from deep red ($x = 0.695, y = 0.303$) to orange ($x = 0.575, y = 0.425$), along with the high (x, y) locus of the pure spectral radiation. Red phosphors suitable to a color TV system are obtained in composition range $x = 0.85 \sim 0.92$, where the y value can be adjusted to $(\text{Y}_{0.964}\text{Eu}_{0.036})_2\text{O}_2\text{S}$ ($x = 0.648, y = 0.344$) by means of the Eu concentration. The x values of these alloy phosphors are somewhat larger than $(\text{Y}_{0.964}\text{Eu}_{0.036})_2\text{O}_2\text{S}$. This is preferable from the viewpoint of color coordination, since the freedom of color display design becomes broader. Fur-

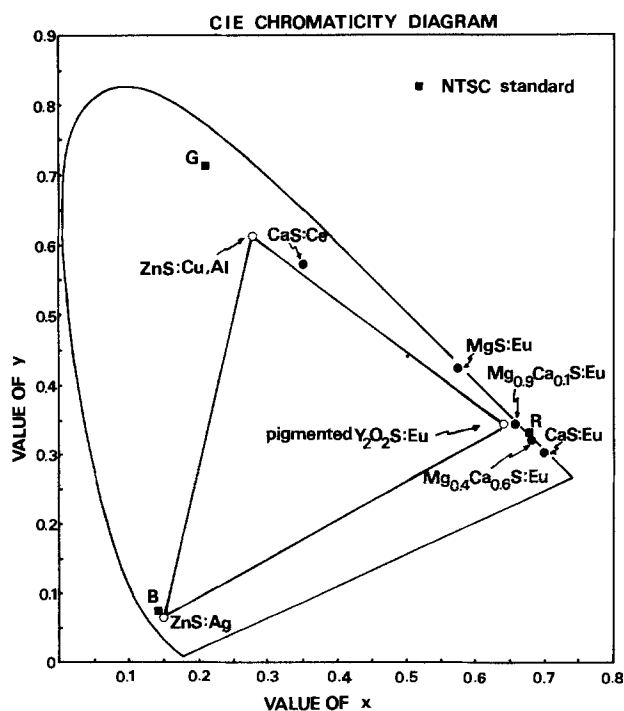


Fig. 8. CIE chromaticity diagram showing color coordinates of $\text{Ca}_{1-x}\text{Mg}_x\text{S}:\text{Eu}$. Some other phosphors are also included for comparison.

thermore, $\text{Ca}_{1-x}\text{Mg}_x\text{S}:\text{Eu}$ has a red body color and, thus, does not need to be pigmented.

The data in Fig. 5, 6, and 8 are for samples prepared simply by heating the mixture of Eu-activated CaS and MgS at 1200°C in a H_2S atmosphere. This is conventional, but is not the best method to improve η . The phosphors with high brightness were prepared first by firing the undoped 1:9 mixture of CaS and MgS at 1200°C for 3h and then refring the mixture of Eu_2O_3 and $\text{Ca}_{0.1}\text{Mg}_{0.9}\text{S}$ at 1200°C for 2.5h both in the H_2S atmosphere. Brightness B and η of $\text{Ca}_{0.1}\text{Mg}_{0.9}\text{S}:\text{Eu}$ are shown in Fig. 9a as a function of Eu concentration. Maximum brightness was given at 0.05 m/o of Eu. The y value of the color coordinate was 0.345 at Eu concentrations of 0.045 m/o or less, and decreased above 0.05 m/o. To improve η, y m/o of BaS was further added to $\text{Ca}_{0.1}\text{Mg}_{0.9}\text{S}:\text{Eu}$ (0.04 m/o) during the firing process. This is because BaS has been found in our experiment to be effective for Eu diffusion in CaS (11). By varying y, B , and λ_0 of $\text{Ca}_{0.1}\text{Mg}_{0.9}\text{S}:\text{Eu}$, Ba moved as shown in Fig. 9b. An enhanced brightness was observed in the y range below 1 m/o, whereas λ_0 monotonically increased with increasing y . The η and B reach maximum at $y \approx 0.1$ m/o. The decrease in η with the increase of y was partially caused by mechanical damage introduced while crushing the products. This is because the products cohered severely with increasing y . Cathodoluminescence of highly sulfurized $\text{Ca}_{0.1}\text{Mg}_{0.9}\text{S}:\text{Eu}$ (0.05 m/o), Ba (0.1 m/o) exceeds $(\text{Y}_{0.964}\text{Eu}_{0.036})_2\text{O}_2\text{S}$ in brightness by about 15% when excited at 18 kV, as indicated in Fig. 9. This implies that the absolute efficiency exceeds 14%. There have been few reports of red cathodoluminophors with such high brightness in such a low Eu doping range. Exciting current dependence of efficiency in $\text{Ca}_{0.1}\text{Mg}_{0.9}\text{S}:\text{Eu}$, Ba (0.1 m/o) is shown in Fig. 10. For 0.04 m/o Eu, η is nearly independent of the current in this experimental range, although a slight increase was observed in a low current region. On the contrary, a clear current dependence was found in the case of 0.01 m/o Eu. Excitation-voltage dependence of η was inverse in these two Eu concentrations. The excitation current density corresponding to a typical color TV set is about 100 nA (Fig. 10).

Discussion

Energy efficiency in $\text{MgS}:\text{Ce}$.—Maximum energy efficiencies observed in the experiment for Ce- or Eu-

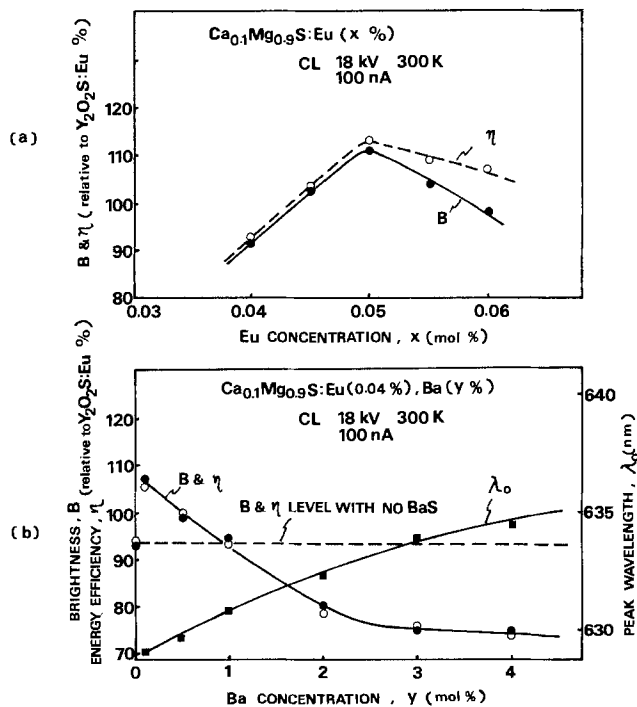


Fig. 9. CL properties of highly bright $\text{Ca}_{0.1}\text{Mg}_{0.9}\text{S}:\text{Eu}$ (x m/o), Ba (y m/o). From (9a) and (9b), optimum concentrations for brightness are found to be $x = 0.05$ and $y = 0.1$.

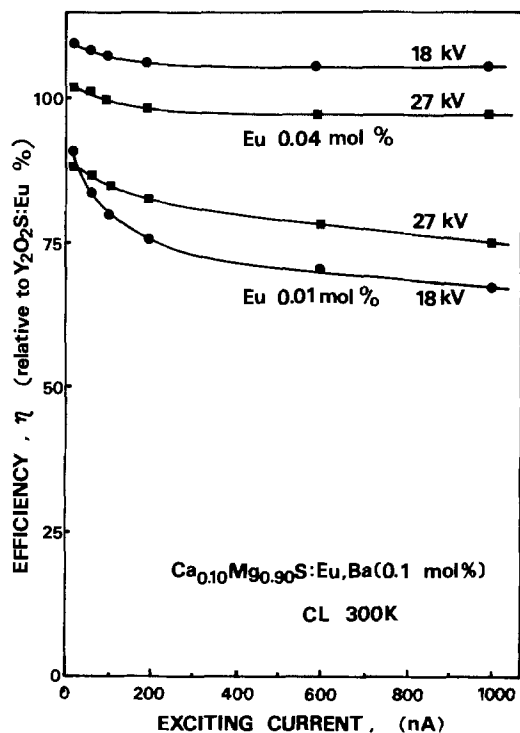


Fig. 10. Exciting current dependence of efficiency in Ca_{0.1}Mg_{0.9}S:Eu (x m/o), Ba(0.1 m/o). The cases $x = 0.01$ and 0.04 m/o are illustrated.

activated alkaline earth sulfides are shown in Fig. 11 as a function of an ionic radius of cation. As was indicated above, η_{\max} in MgS:Ce stayed at an unreasonable level. This is lower, by about 50%, than the value expected from the extrapolated curve in Fig. 11. This gap may be caused by (i) the difference in the ionic radius between Ce³⁺ and Mg²⁺, (ii) the difference in valency between Ce³⁺ and Mg²⁺, or (iii) the influence of residual oxygen in MgS. As is well known, the ionic radius of Ce³⁺ (1.01Å) is about 50% larger than that of Mg²⁺ (0.65Å). In such simple rock salt structures as alkaline earth sulfides, it is certain that impurities larger than a host ion in size are difficult to incorporate compared with the case of a host with lower crystal symmetry, because lattice flexibility is lower in the former. The differences in optimum Eu concentration

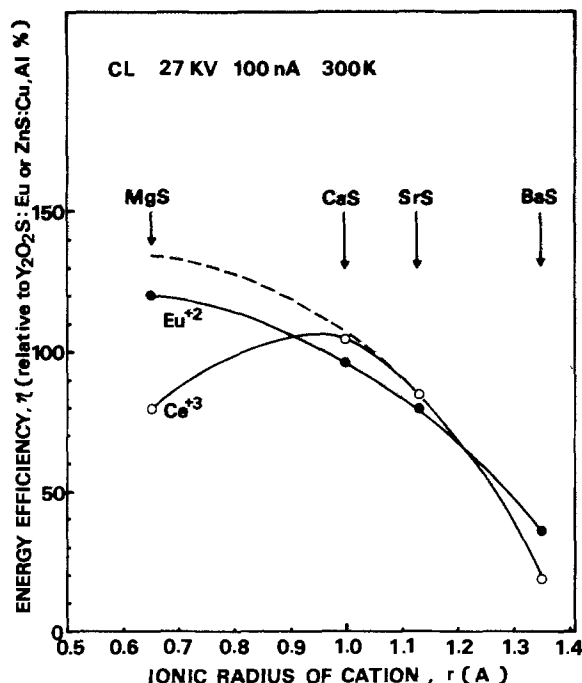


Fig. 11. Maximum CL efficiencies observed in this experiment for Eu- and Ce-activated alkaline earth sulfides.

among alkaline earth sulfides mentioned above is thought to be related to solubility in the sulfides. However, this anomaly is not simply due to stress caused by the difference in size between Ce³⁺ and Mg²⁺, because η is sufficiently high in MgS:Eu, where the ionic radius difference between Eu²⁺ (1.15Å) (12) and Mg²⁺ is larger than the former. This brings to mind the Mg-S phase diagram where no compound other than MgS has yet been found, although AS_{1-x} (A = Ca, Sr, and Ba) was reported (12). This implies that cation vacancies are easily generated in CaS, SrS, and BaS when excess sulfurization takes place, whereas the situation is different in MgS. That is, in the former sulfides an excess charge of a Ce³⁺ ion can be compensated in such a way as to generate a Ce₂S₃ structure locally in the matrices. As is well known (13), Ce₂S₃ is easily formed from CeO₂ by heating at 900° ~ 1400°C in a H₂S atmosphere. This Ce₂S₃ is considered to be γ -type in the former sulfides, because Ce₂S₃ powder shows a red body color (13) in the CaS matrix when it is not sufficiently diffused. The γ -Ce₂S₃ crystallizes with a defect cubic structure (14), the electronic requirements for tetrahedral bonding being fulfilled by the incorporation of a lattice vacancy on one-third of the cation sites. In other words, γ -Ce₂S₃ is stable in the excess-sulfurized CaS matrix. Actually CL efficiency in CaS:Ce containing no coactivators exceeds 80% that of CaS:Ce doped with PCl₃, if fired under excess-sulfurized conditions.

However, MgO could not be sulfurized perfectly in this experiment. As a result, it is likely that (i) Ce³⁺ ion charge compensation due to introduction of the cation vacancies is not completely performed, or (ii) residual oxygen atoms in MgS prevent the f-d transition of a Ce³⁺ ion. Therefore, the smallest alkaline metal Li was diffused into MgS:Ce as a charge compensator in an additional experiment. In this experiment, the mixture of MgS:Ce(0.05 m/o) and Li(1 m/o to MgS:Ce) was fired at 1200°C for 1h in a vacuum-sealed quartz ampule or in a H₂S stream. Phosphors thus obtained were tested, and the results are summarized in Table I. The detected Li concentration in fired phosphors is two orders of magnitude lower than the charged one. This is probably due to active reaction of Li with the quartz boat. It is plausible, based on the data in Table I, that Li metal is rather harmful in MgS:Ce for the f-d transition of a Ce³⁺ ion. We confirmed experimentally that radiation from a Ce³⁺ ion in MgS was not enhanced by codoping of other alkaline metals Na, K, Rb, and Cs. This result agrees with that described above: radiation enhancement by PCl₃ doping was not observed for MgS:Ce. At this stage, it seems that the low CL efficiency in MgS:Ce results from the existence of oxygen atoms in quantities a few tens times as much as cerium in mole fraction. A killer mechanism by the residual oxygen is still unclear. One possibility is a Ce₂O₂S formation. The Ce₂O₂S is nonluminescent.

Peak shifts of Eu-band in alkaline earth sulfides.—As was typically shown in Fig. 5, peak wavelength of the Eu²⁺ band varies according to the composition of the alkaline earth sulfide host. Generally, these peak shifts are explained in connection with the crystal field strength, such as 10 Dq, which is governed by both a lattice constant and an ionicity of the cation (8). However, the profile shown in Fig. 5 cannot be reasonably explained by this model. It is indicated that the stress fields imposed on an Eu²⁺ ion also cause peak shift in addition to the native crystal field. Both green and red shifts were observed as follows.

Green shifts.—Peak wavelength of MgS:Eu is shorter than that in CaS:Eu, which is the shift inverse to that expected from the periodic table. To clarify this phenomenon, peak positions of Eu²⁺ and Ce³⁺ bands in various alkaline earth sulfides were measured at 300 K (summarized in Table II) with 10 Dq and the ionic radius ratio of an activator to a host cation. For reference, the peak wavelength of the Mn²⁺ band is also included. As is well known, radiative emissions from Eu²⁺ or Ce³⁺ ions are due to f-d transitions. Energy splitting of the d state by the native crystal field

Table I. Effect of Li codoping in MgS:Ce. Prefired sample was MgS:Ce (0.05 m/o) mixed with 1 m/o of Li. Firing conditions were at 1200°C for 1 h in a vacuum-sealed (closed) tube or in H₂S

Li in pre-fired sample	Firing method	CL at 27 kV		Analyzed value in phosphor	
		$\eta\%$ (relative to ZnS:Cu, Al)	Peak (nm)	Ce (ppm)	Li (ppm)
None	in closed tube	80	522.2	100 ~ 500	—
Yes	in H ₂ S	68	520.7	100 ~ 500	50 ~ 100
Yes	in closed tube	<1	—	50 ~ 100	50 ~ 100

Table II. Peak positions of Eu²⁺, Ce³⁺, and Mn²⁺ bands in alkaline earth sulfides, comparing with 10 Dq and ionic radius ratios of activator to host cation

Host	10 Dq (cm ⁻¹)*	Peak wavelength (nm)			Ionic radius ratio**		
		Eu (0.1%)	Ce (0.04%)	Mn (0.2%)	r_{Eu}/r_{AE}	r_{Ce}/r_{AE}	r_{Mn}/r_{AE}
MgS	19,500	591	521	~700	1.77	1.55	1.23
CaS	18,750	651	520	585	1.16	1.02	0.81
SrS	17,400	616	503	~550	1.02	0.89	0.71
BaS	16,100	572	~480	541	0.85	0.75	0.59

* Calculated based on Ref. (8) and (18).

** Pauling ion radii.

10 Dq increases monotonically from BaS to MgS. Since radiation occurs corresponding to an electron transition from the lower d level to the ground state, a larger value of 10 Dq generally gives a longer peak wavelength. For Mn²⁺ activators where radiation is due to d-d transitions, the peak position must be influenced more by the crystal field strength, as was reported in (Zn, Cd)S:Mn (15). The data in Table II are roughly subject to this rule except for MgS:Ce and MgS:Eu. In the latter, the largest green shift is observed, even though it was confirmed by ESR data that an Eu²⁺ ion substituted a Mg site, forming no "off-center" (8). A comparison of the spectrum data with the ionic radius ratio leads to the conclusion that local stress imposed on activator ions from the neighboring lattice (denoted as type I stress) is an important factor in green shift. According to the configurational coordinate model, distance R_0 between the lowest energy points of two adiabatic potential curves, which represent the excited state and the ground state, is governed by electron-phonon coupling. It is supposed that in the cases of MgS:Ce and MgS:Eu, R_0 shrinks because the lattice constant of MgS differentially expands around Ce or Eu atoms incorporated in the lattice sites. If this is so, a red shift of the excitation spectrum must be simultaneously observed in addition to the green shift of the emission spectrum. Nakao (8) reported 80 K excitation spectra where the transition from the ground state to the $^8\Gamma_4(t_{2g})$ band in MgS:Eu was slightly on the lower energy side of that in CaS:Eu; namely, the red shift was shown in the excitation spectrum.

Red shift.—A distinctive peak shift was observed in the pseudobinary host crystals, as was typically shown in Fig. 5 (Ca_{1-y}Mg_yS:Eu) and 7 (Ca_{1-y}Mg_yS:Ce). Emission spectra shift toward the lower energy side in the alloyed composition range. These "red" shifts were common at least in Eu-activated binary sulfides A_{1-y}B_yS except for Ca_{1-y}Sr_yS. Peak wavelength λ_0 in A_{1-y}B_yS:Eu is shown in Fig. 12 as a function of composition parameter y , which is not necessarily equal to the alloy composition. Here, y is taken as the composition of a sulfide having a larger chemical potential, i. e., A_{1-y}B_yS where $\mu_{AS}^i < \mu_{BS}^i$. In the CaS-MgS system, $y = 1 - x$ because $\mu_{MgS}^i < \mu_{CaS}^i$. Although 10 Dq simply varies with y , the change in λ_0 with y significantly deviates from the proportional rule. Longest peak wavelength λ_m in each pseudobinary was plotted as a function of the difference in ionic radius $|r_A - r_B|$ in Fig. 13, where the kink wavelength at $y \approx 0.4$ was taken only in the Ca_{1-y}Sr_yS:Eu case. A certain regularity is present for the red shift as indicated in Fig. 12 and 13: (i) the composition corresponding to λ_m is nearly constant in each pseudobinary ($y \approx 0.35$ or 0.65) and (ii) λ_m is sensitive to

$|r_A - r_B|$; λ_m increases with $|r_A - r_B|$ in a completely miscible region but is vice versa in a partially miscible region. It is suggested from (ii) that the red shift is caused by lattice stress due to the difference in the ionic radius of the divalent host cations. This stress is denoted here as type II stress. With the increase of $|r_A - r_B|$, elastic strain increases. Therefore, red shift is emphasized until plastic deformations happen due to the cluster or grain-boundary formations. Here, the red shift decreases as a result of the partial release in stress. Red shift is believed due to a structural change in energy bands as was reported by Cardona (16) for silver and cuprous halide pseudobinaries.

As to the mechanism of resulting type II stress, a periodic composition model is proposed on the basis of the following, 1-3, predictions coupled with the metallurgical rule described in 4.

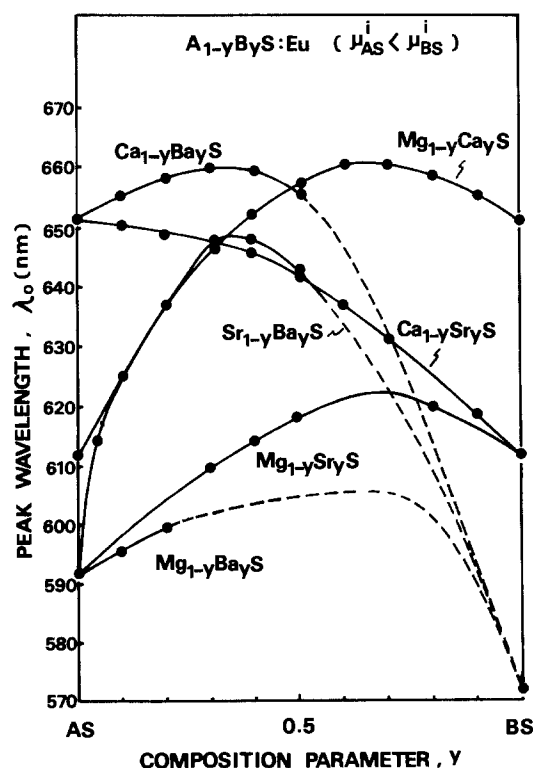


Fig. 12. Peak shifts observed in alkaline earth binary sulfide A_{1-y}B_yS:Eu, where $\mu_{AS}^i < \mu_{BS}^i$, as a function of composition parameter y .

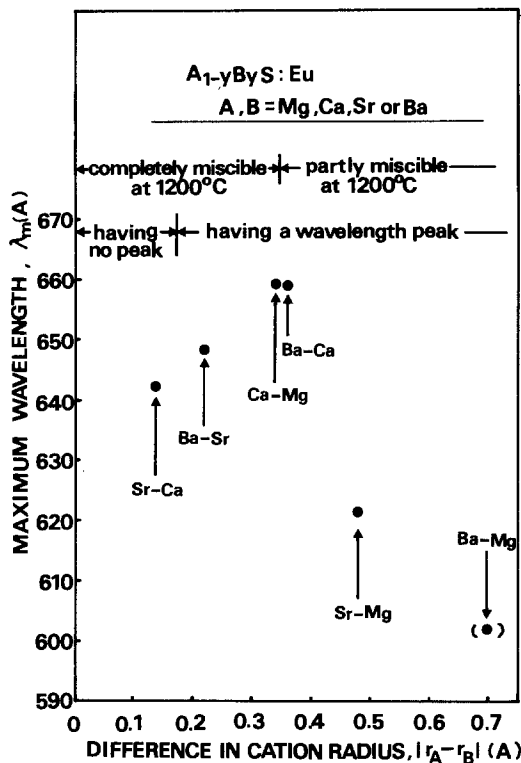


Fig. 13. Longest peak wavelengths in alkaline earth binary sulfide as a function of difference in cation radius.

1. Judging from Fig 7 and 12, internal stress reaches a maximum at $y \approx 0.35$ in pseudobinary sulfides.

2. For Eu- or Ce-activated Ca_yMg_{1-y}S, η hits a minimum around $y = 0.35$.

3. Nevertheless, crystalline quality of Ca_{0.35}Mg_{0.65}S is rather good according to x-ray diffraction data shown in Fig. 6, which means $y = 0.35$ is a stable alloy composition.

4. In a pseudobinary alloy system where a crystal structure is cubic with $r_A \neq r_B$, a generated elastic strain energy hits a minimum along a $\langle 100 \rangle$ direction and a maximum along a $\langle 111 \rangle$ direction (17). In this case, the different kinds of cations are generally inclined to take a split arrangement with each other along the $\langle 100 \rangle$ direction. The horizontal stripes along a $\langle 100 \rangle$ axis in a TiO₂-SnO₂ system are a typical example of this splitting. These stripes are caused by a periodic change in composition due to the spinodal dissolution (18). Also, in an alkaline earth sulfide pseudobinary, an alloying BS into AS may be accompanied with such a periodic microstructure as BS preferably occupying one of $\{100\}$ planes of a unit cell.

According to this model, structural alteration along the $\langle 100 \rangle$ axis results in uniaxial stress. This stress must reach maximum when one $\{100\}$ plane of an AS unit cell is completely replaced by BS: namely, $y \approx 0.35$ (5/14 of A atoms is replaced in the NaCl-type crystal structure). Since $\mu_{AS}^I < \mu_{BS}^I$ is provided in this section, composition $y \approx 0.35$ is thought to be most stable in the AS-BS pseudobinary system, and that of $y = 0.65$, i. e., an alloy composition where one $\{100\}$ plane of a BS unit cell is completely replaced by AS, is the next most stable. This is indicated based on a free energy vs. alloy composition curve generally given for the binary system. Even in the partially miscible system shown in Fig. 12 and 13, this structural alteration is thought to occur in each alloyed region. In these partially miscible pseudobinaries, emission from the BS-rich alloy was found to be very weak compared to the AS-rich alloy. Consequently, an emission spectrum of the binary was still apparently single-peaked, although intensity was decreased corresponding to increasing BS.

Finally, the compositional difference for λ_m shown in Fig. 12, i. e., $y = 0.35$ and $y = 0.65$, is discussed. As is con-

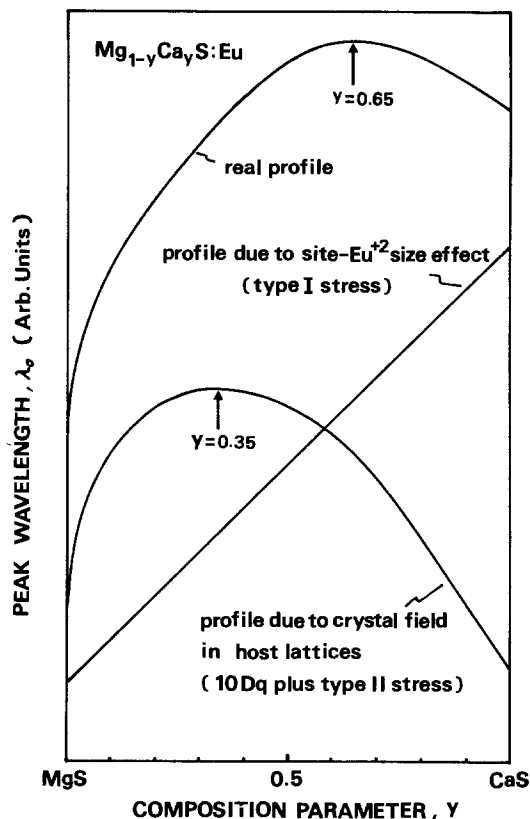


Fig. 14. Stress effects on peak shift of Mg_{1-y}Ca_yS:Eu as a function of y . If type I stress were ignored, λ_p profile must have a peak at $y = 0.35$, similar to Eu-activated binary sulfides without MgS.

sidered above, peak shift is principally subject to the modified crystal field potential, that is, the sum of 10 Dq, the homopolar local stress causing the green shift (type I stress) and the uniaxial stress causing the red shift (type II stress). For pseudobinaries containing MgS:Eu, type I stress plays an important role, as was shown in Table II. Then, λ_m shifts from $y \approx 0.35$ (determined from 10 Dq plus type II stress) to $y \approx 0.65$, as schematically illustrated in Fig. 14. If the influence of type I stress were ignored, the λ_p profile must be very similar to that of Mg_{1-y}Ca_yS:Ce.

Conclusion

It is confirmed that a highly sulfurized (up to 99%) condition is essential for MgS phosphors, although MgO is difficult to completely convert to MgS. As the sulfurized ratio increases, the important characteristic of the phosphor, such as crystalline quality, radiative efficiency, and resistivity to water, were remarkably improved. Under these highly sulfurized conditions, MgS was found to form a solid solution with CaS in any compositional ratio. The compound Ca_{1-x}Mg_xS:Eu having a reddish body color is promising for the red cathodoluminophor since η is sufficiently high ($\sim 15\%$) under europium concentrations as low as 0.01 \sim 0.05 m/o.

The f-d transitions of rare earth ions such as Eu²⁺ and Ce³⁺ are strongly influenced in the alkaline earth-sulfide hosts by some kinds of lattice stresses, in addition to the crystal field potential ordinarily subject to both the lattice constant and ionicity (19). Emission wavelength exhibits green shift due to homopolar stress localized around activator ions when the ionic radius is greater than site radius. However, red shift is observed in binary sulfides where the difference in cation radius exceeds 0.02 nm. As to the origin of this red shift, uniaxial stress due to periodic microalteration in composition along the $\langle 100 \rangle$ axis is proposed because the certain regularities are present between the composition and the maximum peak wavelength in the binary. This model must be hereafter verified experimentally.

Acknowledgments

The authors wish to thank Y. Kawamata and T. Suzuki for measuring CL. Thanks are also due to T. Ishiba for x-ray diffraction analysis and S. Nakagawa for spectrophotometric analysis.

Manuscript submitted June 10, 1983; revised manuscript received Nov. 22, 1983.

Hitachi, Limited assisted in meeting the publication costs of this article.

REFERENCES

1. J. W. Gilliland, *J. Appl. Phys.*, **38**, 2427 (1967).
2. W. Lehmann and F. M. Ryan, *This Journal*, **118**, 477 (1971).
3. W. Lehmann, *ibid.*, **117**, 1389 (1970).
4. O. Sorge, Thesis, Technologic Universität, Berlin (1959).
5. R. Ward, "Preparation and Characteristics of Solid Luminescent Materials," p. 36, American Physical Society, John Wiley and Sons, Inc., New York (1948).
6. U. K. Mishra and S. L. Mor, *Indian J. Pure Appl. Phys.*,

- 18**, 6 (1980).
7. F. Okamoto and K. Kato, *This Journal*, **130**, 432 (1983).
8. Y. Nakao, *J. Phys. Soc. Jpn.*, **48**, 534 (1980).
9. E. M. Levin and H. F. McMurdie, "The Phase Diagrams for Ceramists," p. 102, American Ceramic Society, Incorporated (1964).
10. E. Banks and R. Ward, *Trans. Electrochem. Soc.*, **96**, 297 (1949).
11. H. Kasano, K. Megumi, and H. Yamamoto, U.S. Pat. Appl. 215,876 (1980).
12. G. V. Samsonov and S. V. Drozdova, "Sulfides," Chap. III, Metallurgy Publication, Moscow (1972).
13. E. D. Eastman, L. Brewer, L. A. Bromley, P. W. Gilles, and N. L. Lofgren, *J. Am. Chem. Soc.*, **72**, 2248 (1950).
14. H. Hohn and W. Klenger, *Z. Anorg. Chem.*, **259**, 135 (1948).
15. S. Shinoya, "Luminescence of Inorganic Solids," p. 269, Academic Press, New York (1966).
16. M. Cardona, *Phys. Rev.*, **129**, 69 (1963).
17. J. W. Cahn, *Acta Metall.*, **9**, 795 (1961); *Trans. AIME*, **242**, 166 (1968).
18. A. H. Schltz and V. S. Stubican, *Philos. Mag.*, **18**, 929 (1968).
19. J. A. Van Vechten, *Phys. Rev.*, **182**, 891 (1969).

Resolution of Fast and Slow Charging Processes in Ruthenium Oxide Films: An AC Impedance and Optical Investigation

J. Rishpon and S. Gottesfeld*

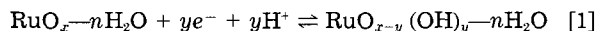
Department of Chemistry, Tel Aviv University, Ramat Aviv 69978, Israel

ABSTRACT

Ellipsometry and ac impedance measurements were employed for *in situ* investigation of anodic oxide films on Ru and of oxide films formed by thermal decomposition of Ru chloride. An instrumental setup for experiment control, data acquisition, and data analysis in automated measurements of the ellipsometric parameters and of the ac impedance is described. The effects of the applied bias and of proton concentration in solution on the rate of the double injection process of protons and electrons were studied. The charging process in the oxide film could be resolved into a faster mode, attributed to the charging of grain surfaces, and a slower bias dependent mode, which apparently involves incorporation of aqueous protons into oxide grains. The slower mode of charging is associated in hydrous oxide films with an effective diffusion coefficient of 10^{-11} - 10^{-12} cm²s⁻¹. The overall impedance due to the faster mode of charging in hydrous films in 0.1-1M acid solutions is smaller than 0.1 Ω cm², and this fast mode becomes diffusion controlled in solutions 10⁻³M in acid. However, in relatively dry films, e.g., "as-immersed" thermal oxide films, slower bias dependent rates are found for the fast mode of proton injection, probably due to a bias-dependent diffusion of protons along oxide grain surfaces.

The kinetics of "double injection" in oxide films, which involves the reversible uptake of ions and electrons, resulting in the net incorporation of a hydrogen or metal atom into an oxide structure, is of interest in several fields of electrochemistry: (i) it is the basis of the electrochromic characteristics of oxides such as WO₃ and MoO₃ (1), as well as anodic (2, 3) and sputtered (4, 5) iridium oxide and anodic rhodium oxide films (6), (ii) it seems to be the key for the electrocatalytic properties of such oxides, some of which exhibit activity in cathodic processes, e.g., H₂ evolution at WO₃, and some in anodic processes, e.g., oxygen evolution at iridium oxide or ruthenium oxide films, and (iii) it has been shown (7, 8) that even in simple Faradaic processes the electrochemical reactivity of hydrous oxides varies strongly depending on the extent of coupling between the internal redox system of the oxide and the redox system in solution. The activity of this internal redox system seems to depend, in turn, on the rate of the double injection process (8).

The process of double injection can be written in the following way for the case of electron-proton injection into a hydrous oxide, e.g., of Ru



i.e., a H atom is incorporated into a hydrous oxide by injection of an electron from the ohmic contact and a proton from solution, thus lowering the formal oxidation state of Ru by one unit. The reverse electro-oxidative process involves the double ejection of an electron and a proton. It can be seen that in the investigation of the kinetics of this reaction the elementary processes of interfacial transfer and of bulk transport of both an electron and a proton have to be considered. In previous investigations of hydrous oxides belonging to this family (9), it has been demonstrated that the effective conductivity of the oxide film with respect to the double injection process may change by several orders of magnitude as a function of applied bias. This happens particularly for these oxides which change from a "bleached" to a "colored" form as a function of applied bias, with the bleached form exhibiting the lowered effective conductivity. In such cases, the bleached form of the oxide may exhibit also blocking or nonblocking behavior in faradaic reactions as a function of the potential of the redox couple in solution (7, 8).

Optical measurements were applied in the past to the study of hydrous oxide films and provided information on hydrous oxide growth on metal substrates regarding the film thickness and its porous and hydrous nature (8),

* Electrochemical Society Active Member.

Key words: ellipsometry, proton diffusion, double injection.

as well as the detailed variations in the films optical properties with applied potential (10, 11). The ac technique has been applied previously to the study of charging processes in hydrous films in aqueous as well as nonaqueous media (9, 12). In the last contribution (12), a theoretical detailed analysis of the form of the impedance plot (Z plot) for the double injection process has been described, where control by charge transfer and by one-dimensional diffusion normal to the film surface have both been considered. The result is a Z plot which may include a semicircular branch at higher frequencies due to the interfacial resistor (in parallel combination with the double layer capacitor), followed at lower frequencies by a branch due to diffusion through the film. This last branch, which is due to one-dimensional diffusion through a layer of finite thickness, is equivalent from an electrical point of view to the impedance of a finite transmission line (with capacitive termination), and is given by the following expression (13)

$$Z_D = Z_{D0} \text{ctnh}(i\omega L^2/D)/(i\omega L^2/D)^{1/2}; Z_{D0} = L^2/DC_T \quad [2]$$

where L is the film thickness, D the effective diffusion coefficient, L^2/D the characteristic diffusion time in the film, and C_T represents the total charge capacity of the film associated with the diffusion-controlled process, measured at a low frequency such that $\omega \ll D/L^2$. A similar description, in terms of a finite transmission line, for the charging of iridium oxide films by hydrogen has been given in Ref. (9).

In the work presented here, we investigated the optical characteristics and the ac impedance of ruthenium oxide films. The investigation included ellipsometric and ac impedance measurements performed on anodic Ru oxide films, formed by constant potential anodization or by potential multicycling of Ru metal in acid solutions. Measurements of the ac impedance were performed also on thermal Ru oxide films, produced by thermal decomposition of $\text{RuCl}_3 \cdot 3\text{H}_2\text{O}$ on gold substrates. The interest in Ru oxide was due to the following two reasons: (i) investigation of the features controlling the exceptional electrocatalytic properties of anodes based on Ru oxide point to the nature and the activity of the internal redox process in the film as a key factor (14) and (ii) contrary to Ir or Rh, which have one extra electron per ion in the +3 state as compared with Ru, the $d-\pi^*$ band in Ru oxide is not expected to be filled by bringing the oxidation state down to Ru^{+3} (15). As a result, Ru oxide films do not tend to "bleach," and it is not expected that the transport rate of electrons in Ru oxide would be strongly affected by applied bias, other than, perhaps, following extreme cathodization (16). Thus, effects of bias on the rate of double injection in Ru oxide films may depend more strongly on the variations of the proton transport rate with applied potential. Compared with previous ac impedance investigations of oxide films in aqueous solutions (9, 17, 18), we extended the measurements in this work to lower frequencies, down to the millihertz range. This extension allowed the resolution of slower bias-dependent charging processes in Ru oxide films.

Experimental

Electrode preparation.—Ru rod (Johnson & Matthey 99.9%) was inserted in a Teflon or epoxy housing so as to expose a single surface of a disk to the solution and mechanically polished to a mirror finish.

Ruthenized gold electrodes were prepared by electroplating Ru on a gold foil from a RuCl_3 , 0.1N HCl solution, as described by Vukovic *et al.* (19). The solution was prepared from ruthenium III chloride trihydrate (Aldrich).

Thermal ruthenium oxide electrodes were prepared by repetitive immersion of a gold plate in a 5 mg/ml RuCl_3 solution, drying over a hot plate, and then heating in air at 350°C (20). Pt wire or gauze were used as a counterelectrode, and a SCE as a reference electrode. All potentials are reported *vs.* SCE, unless otherwise specified.

The experimental set up.—Figure 1 shows a schematic diagram of the system for automated ellipsometry and ac impedance measurements employed in this work. An S-100 microcomputer is used for experiment control and data acquisition and analysis in both the ellipsometric and the impedance measurements. In the ellipsometric measurement, the microcomputer controls the rate of revolution of a rotating analyzer with an accuracy of 1:5000 ($\omega = 250 \pm 0.05$ Hz). This level of stability is achieved by on-off control of a simple dc motor, applied according to the cycle time continuously clocked by the computer. This stability of revolution allows one to obtain a precision of 10^{-2} deg in phase angle reading, after averaging for less than a second. The sinusoidal output of the photomultiplier is digitized by an A/D converter and analyzed by the microcomputer, using a fast algorithm which yields the three Fourier coefficients for the signal after each single cycle. The values of Δ and ψ for the reflecting surface are then calculated by the computer from these coefficients, and further numerical analysis gives film thickness and refractive index.

In the impedance measurement mode, the microcomputer scans the frequency of an oscillator between 5×10^{-3} – 4×10^3 Hz by a voltage ramp applied from a D/A unit. (The high frequency limit is set by the response of the existing A/D.) Exactly the same algorithm employed for the analysis of the optical sinusoidal waveform is employed also to evaluate the amplitude and phase of the periodic current signal resulting from the ac potential perturbation. Presentation of the experimental ac impedance results as either a complex z plot or a complex C plot ($C = 1/j\omega Z$) could be chosen. The last form of presentation turned out to be advantageous when the overall charge capacity and the resolution of several charging processes are of interest, as is the case for the system investigated here. [In all the figures containing complex capacitance plots, the capacitance units are in millifarads (mF), and the frequencies in hertz are designated on the curves.]

Results

Ellipsometric-reflectometric measurements.—Figure 2 depicts results reported previously (8) for the growth of an oxide film on ruthenium metal by constant potential anodization or by cyclic potential multipulsing. Figure 3 shows results obtained for the cyclic multipulsing mode of growth on our home-built automatic ellipsometer, and the similarity of the results obtained for the optical properties of the Ru oxide film can be verified. While some variation in n_{film} is found in a set of growth experiments, the following features were reproducible: (i) the uniform isotropic film growth model appeared to be a reasonable, if not a perfect model for both modes of film growth. (ii) The optical properties of the films grown at constant anodic potential are close to those reported for the film formed by oxygen adsorption from the gas phase on Ru metal (21),¹ and the absorption coefficient in the visible is exceptionally high compared to any other reported value for anodic oxides in a wet environment. Goel *et al.* have evaluated the complex refractive index spectrum for single-crystal RuO_2 in the visible and the UV (22). They obtained for, $\lambda = 546$ nm, $n_{\text{RuO}_2} = 1.9-0.9i$, which may be considered in good agreement with the result of our ellipsometric analysis for the anodic Ru oxide film, bearing in mind the microcrystalline structure of the latter. (iii) The film grown by cyclic potential multipulsing is seen to be of a more open structure and a larger water content, as judged from the smaller values of both n_{film} and k_{film} . Furthermore, as pointed out before (8), the "multipulsed film" can be grown up to a thickness exceeding 1000Å, while the film grown on Ru by constant potential anodization reaches a limited thickness of ca. 300Å.

One of the solutions for the ellipsometric results obtained for oxygen adsorption on ruthenium, which, for some reason, was regarded unreasonable, yielded for the surface layer formed a value of $n_{\text{film}} = 3 - i$ (18).

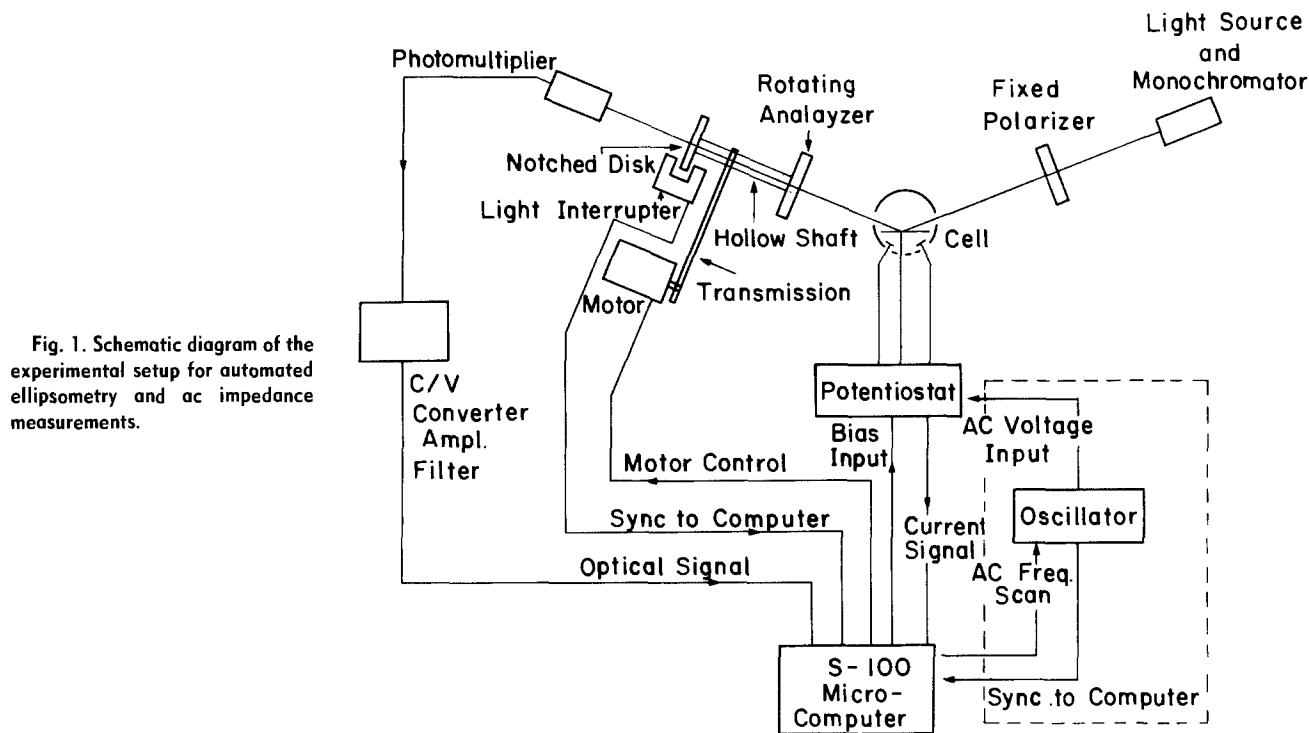
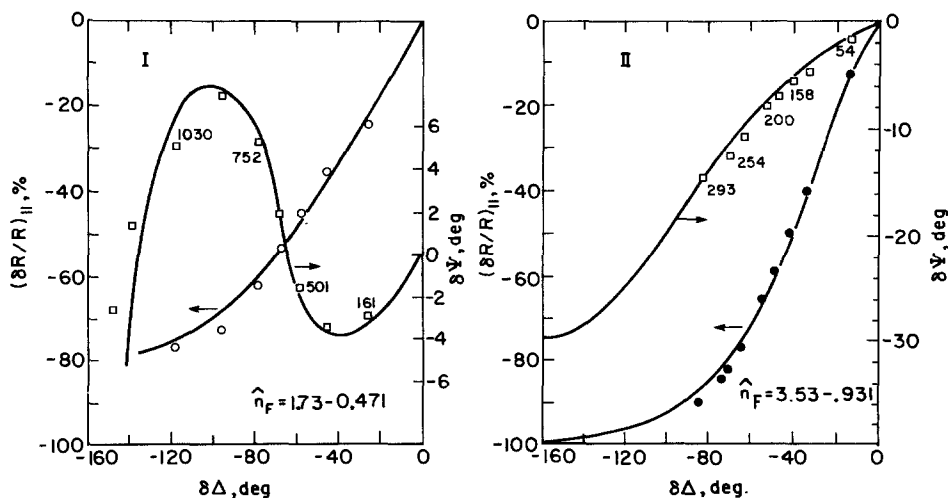


Fig. 1. Schematic diagram of the experimental setup for automated ellipsometry and ac impedance measurements.

Figure 4 shows the measured variations in Δ , ψ , and the reflectance as a function of applied bias for a Ru electrode covered by an oxide film grown under constant applied anodic potential in $0.5M H_2SO_4$. It can be seen that cathodization brings about a lowering of several degrees in Δ , combined with an increase of several degrees in ψ . It can be seen that the cathodic process is relatively slow, and develops further with holding under a constant cathodic applied potential. It can also be seen that the optical effect can be reversed by the reapplication of anodic potentials. Such variations in Δ , ψ , and the reflectance could be quantitatively accounted for in the framework of a single-film model by a combination of an increase in film thickness and a lowering in n_{film} (both the real and imaginary components) under cathodic applied potentials. For example, a Ru oxide film 280\AA thick with $n_{film} = 3.5-0.8i$, as found following growth under constant anodic potential, would bring about a change of: $\delta\Delta = -3^\circ$; $\delta\psi = +2^\circ$, and $\delta R/R = -10\%$ if its thickness would grow to 310\AA and its complex refractive index be at the same time lowered to $3.45-0.7i$. This optical evidence for a slow process of film swelling under cathodic applied potentials was helpful in the clarification of the ac impedance results obtained at low modulation frequencies, as discussed below.

AC impedance measurements—Teflon-mounted Ru rod electrode.—Figure 5 shows the complex capacitance plot ($C = 1/j\omega Z$) obtained for oxide films grown on the Ru rod electrode, which served also in the optical investigation. (The ohmic drop in solution is not subtracted.) It can be seen that the plots contain a semicircular feature, which reflects the fast charging process in the hydrous film, followed by an additional feature at lower frequencies. The plot of the diameter of the semicircular branch vs. the optically evaluated film thickness is shown in Fig. 6. The plot is reasonably close to a straight line with zero intercept. This dependence of film capacitance on thickness seem to be evenly distributed along its width. This result implies film uniformity, and supports, therefore, the assumption made in the evaluation of the optical properties. In the measurements in $0.5M H_2SO_4$, the apparent electrical behavior in the frequency domain corresponding to the semicircle is very simple, since the impedance associated with any transfer or transport process in the film is small compared with the ohmic resistance in solution. The semicircle is thus simply due to the charging of the anodic film through the solution resistor alone ($1.2-1.6\Omega$). On the basis of these results, it can only be concluded that the total resistance due to both proton and electron

Fig. 2. Experimental points and computer-fitted curves for a uniform film growth model, for the growth of anodic Ru oxide films on Ru in $0.5M H_2SO_4$, as reported previously (8). I(left): by cyclic multipulsing at 0.5 Hz between 1.225 and $-0.3V$. II(right): at constant potential of 1.225V. Thickness in angstroms designated. The ellipsometric measurements were taken at 546 nm.



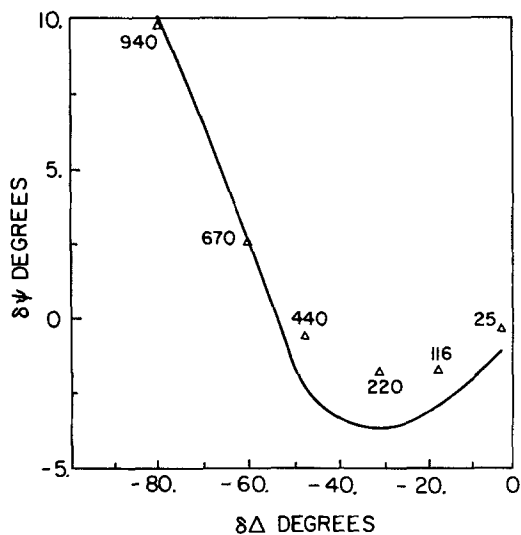


Fig. 3. Experimental points and the computer-fitted curve for a uniform film growth model, for oxide growth on Ru in 0.5M H_2SO_4 by cyclic multipulsing. These results were obtained with the new computer-operated ellipsometric setup (Fig. 1). The solution for the complex refractive index of the film was: $n_f = 1.65 - 0.39i$. ($\lambda = 546$ nm.)

transfer and transport is less than $0.1 \Omega \text{ cm}^2$ in this fast mode of charging of anodic Ru oxide films. Work with Ru electrodes of a much smaller area may yield more quantitative information on the kinetics of this fast charging mode in hydrous Ru oxide in acid solutions.

Figure 7 shows the effect of the lowering of the acidity in solution on the complex capacitance plot. Bringing the

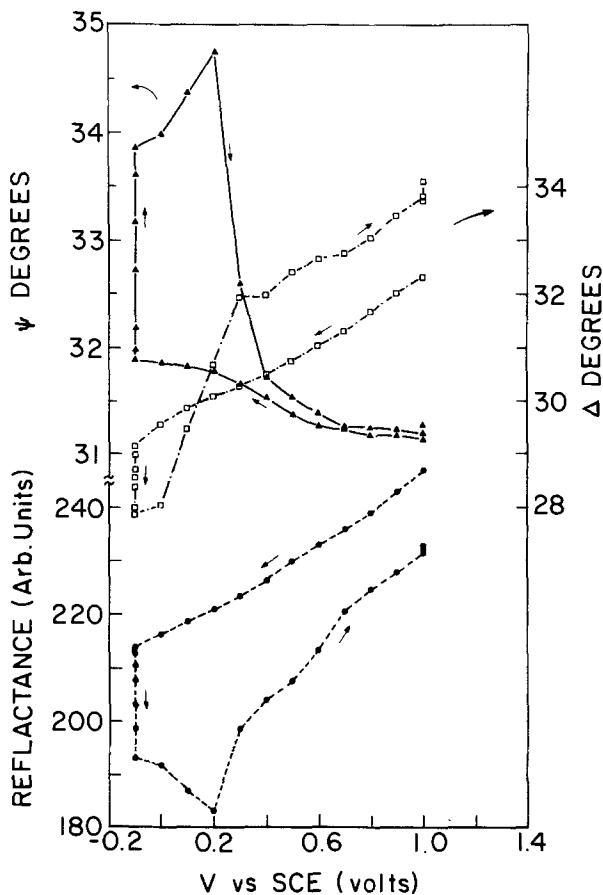


Fig. 4. Variations of $\Delta\psi$, $\Delta\Delta$, and the reflectance (for light linearly polarized at 45°) during a cathodic and subsequent anodic applied potential scan. The potential was held for 2 min at each potential, and for 40 min at $-0.1V$.

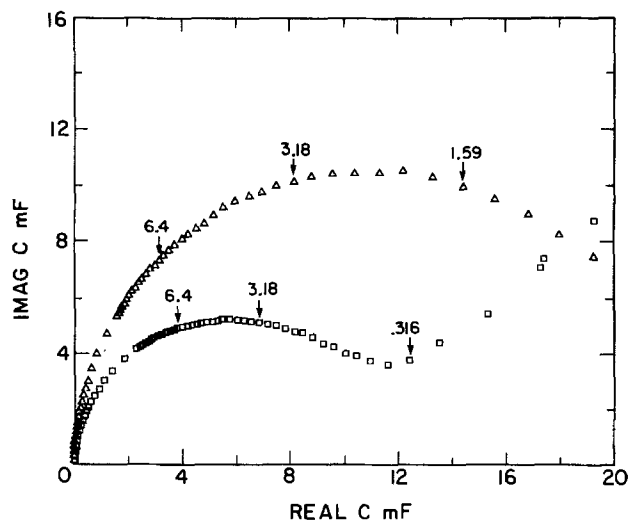


Fig. 5. Complex capacitance plots, measured at 0.5 (upper curve) and at 0.0V (lower curve) in 0.5M H_2SO_4 , following oxide film growth on Ru at 1.225V for 10 min. Solution resistance not corrected. Disk area: 0.52 cm^2 .

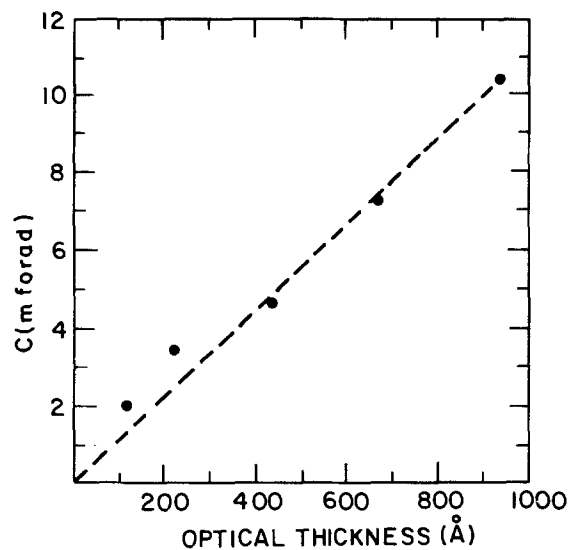


Fig. 6. Oxide capacitance (due to the fast charging mode) at 0.5V in 0.5M H_2SO_4 as found from the diameter of the semicircle in the complex C plot, plotted vs. the optically evaluated thickness for film growth by multipulsing for 2, 4, 8, 12, and 16 min. Disk area: 0.22 cm^2 .

acidity down to 5 mM H_2SO_4 , but maintaining the total electrolyte concentration at a high level (0.5M Na_2SO_4) results in the replacement of the semicircular main branch by a circular arc, very close in shape to a quarter-circle. This is the shape expected for a capacitor charged via a Warburg impedance, due to semi-infinite diffusion of the charging species (9). This result, therefore, confirms the selective consumption of protons in the charging process in hydrous Ru oxide, according to Eq. [1]. The diffusion coefficient can be calculated from Fig. 6 according to the frequency corresponding to the maximum of Imag C in the complex C plot: $\omega_{\max} = 1/\sigma^2 C^2$, where $\sigma\omega^{-1/2}(1-j)$ is the Warburg impedance, and $\sigma = RT/(F^2[C]D^{1/2})$, ($[C]$ being the concentration of the diffusing species). The result for D of the diffusing species in this case is $1 \times 10^{-5} \text{ cm}^2/\text{s}$, in accordance with HSO_4^- ions being involved in the process of diffusion from solution towards the electrode surface.

The other plot in Fig. 7 was obtained in a Na_2SO_4 solution containing no added acid. Following subtraction of the solution resistance, a fast feature is revealed, followed

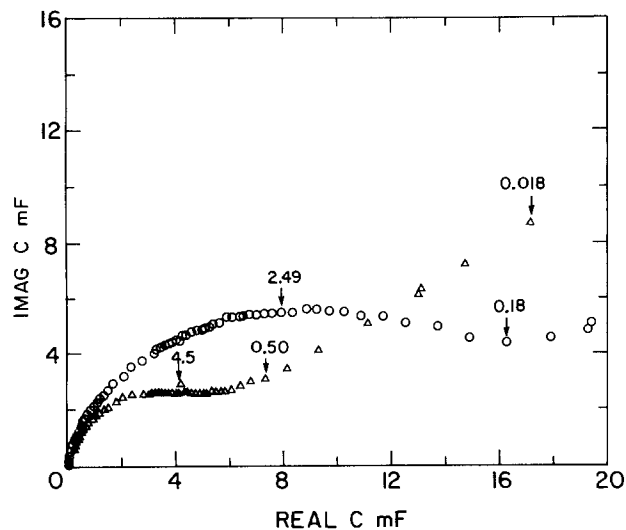


Fig. 7. Complex capacitance plots for the Ru/RuO_x electrode. Oxide was grown in 0.5M H₂SO₄ for 10 min at 1.225V, and the electrode then transferred to a 5 mM H₂SO₄ + 0.5M Na₂SO₄ solution (upper plot), or to a 0.5M Na₂SO₄ solution (lower plot). Measurements taken at 0.72V RHE in each solution. (Equivalent to a potential of 0.5V SCE in 0.5M H₂SO₄.) Disk area: 0.52 cm². Solution resistance corrected.

by much slower charging processes. The fast charging process involves ca. 25% of the total number of fast charging sites in the same oxide film in strong acid solution. It seems that ca. 25% of the fast charging sites are available for simple "double layer charging" in which Na⁺ (and, perhaps, SO₄⁻) ions may participate in the reversible oxide charging process. This is, probably, the percentage of sites located at the outer surface of the film or in contact with larger solution-filled pores.

As mentioned above, the complex capacitance plot in Fig. 5 contains, in addition to the semicircular branch which reflects a fast process of double injection, an additional feature at very low frequencies. However, it turned out to be quite difficult to obtain reliable information on the low frequency branch from measurements with Teflon- or epoxy-mounted Ru rod electrodes. Minute penetration of the electrolyte solution between the rod and the insulating Teflon housing caused considerable irreproducibility of the very small currents measured at such low frequencies. Furthermore, such currents tended to increase with time of immersion and of anodic polarization for a particular electrode used. This problem brought us initially to a conclusion that these low frequency currents were primarily due to this leakage artifact (18). However, by using a different electrode configuration, of Ru deposited on a gold foil, the leakage problem was removed, and it could be demonstrated that the very low frequency feature is indeed associated with a charging process in Ru oxide, as discussed below.

Ruthenized gold foil electrode.— This electrode gave very reproducible results of ac currents in the very low frequency (VLF) domain and, furthermore, showed a very clear and reproducible dependence of the VLF branch on the applied bias. Figure 8 shows the two well-resolved charging branches for the ruthenized gold electrode in 0.5M H₂SO₄ at 0.5V, following potential multicycling to induce oxide growth. The same figure contains also simulation of this electrical behavior by an equivalent circuit, which appears in the insert. The following features are noticeable: (i) the higher frequency branch is again due to a simple RC series combination — R_{soln} in series with the capacitance of fast charging sites in the oxide. (ii) The low frequency branch could not be simulated by a single RC series combination. It could be well fitted, however, by a finite transmission line model, the total capacitance of which at $\omega \ll D/L^2$ is about twice that of the fast

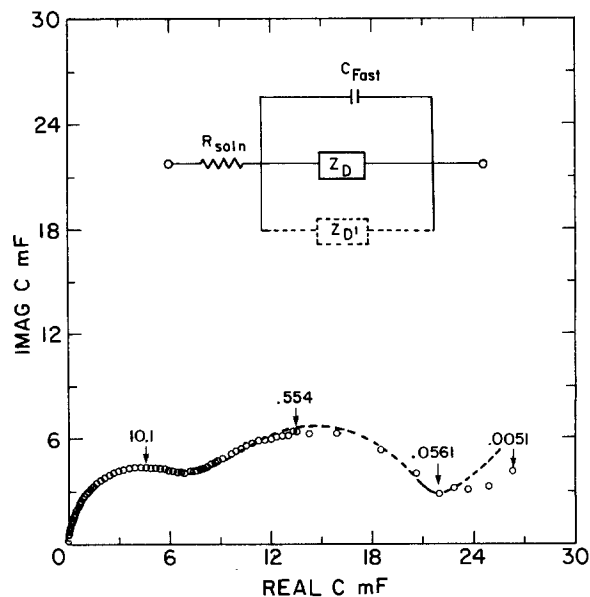


Fig. 8. Complex capacitance plot for a Au/Ru/RuO_x electrode in 0.5M H₂SO₄ at 0.5V. Oxide was formed by 50 triangular potential multicycles between 1.22 and -0.3V. Points: experimental. Smooth curve: simulation by the equivalent circuit depicted, with the following parameters: $C_{\text{fast}} = 7.0$ mF; $R_{\text{soln}} = 1.6\Omega$; $C_{\text{slow}} = 13$ mF; $L^2/D = 1.0$ s; $\sigma' = 600\Omega$ s^{1/2}. (C_{slow} is equivalent to C_T in Eq. [2].)

charging sites, with a typical time constant $\tau = L^2/D$ of 1.0s. (With further oxide film growth, both capacitors, C_{fast} and C_{slow} , grew together.)

Figure 9a shows that the slower charging process is associated with an even larger capacitance at 0.0V. Furthermore, at this potential, the slow charging process could be best simulated by a series combination of an interfacial resistor and a finite transmission line. The need here of the additional resistor in the slow charging branch is particularly clear from observation of the Z plot given in Fig. 9b: the semicircular feature which appears in the Z plot at the higher frequencies is due to an R-C parallel combination, and is typical for the case where a charge transfer resistance, which precedes the diffusional transport, becomes significant (12). (This is a good example where a specific feature is immediately apparent from examination of the Z plot. In contrast to this case, the basic resolution of the slow and fast charging processes is not easily apparent from a Z plot, but shows very clearly in the C plot, as in Fig. 8.) The insert in Fig. 9 shows the equivalent circuit which simulates the complex plane plot obtained for the Ru/RuOx system at 0.0V.

Figure 10 exhibits the behavior recorded under a higher positive applied potential of 1.0V, together with the plot obtained at 0.5V, which is repeated in this figure for direct comparison. At 1.0V, the slow charging process practically disappears. Only the fast charging sites in the oxide are seen to be active at the higher applied bias.

It can be seen from Fig. 8-10 that yet another additional parallel branch, probably of a transmission line character, has to be used in the equivalent circuit to account for deviations from pure capacitive behavior at "ultra low" frequencies (ULF), i.e., at $\omega \ll D/L^2$, where D is the typical diffusion time in the slow charging process discussed above. This ULF region, for which only the high frequency end is covered in these measurements, was simulated by assuming an additional parallel transmission line for which the Warburg factor σ' was estimated. This last branch is designated by Z_D' in the equivalent circuits and the (very rough) estimate of σ' is given in the captions. Such an ultra-slow charging process may perhaps reflect film growth (24), and may thus be associated with the much slower transfer and transport of Ru ions in the film.

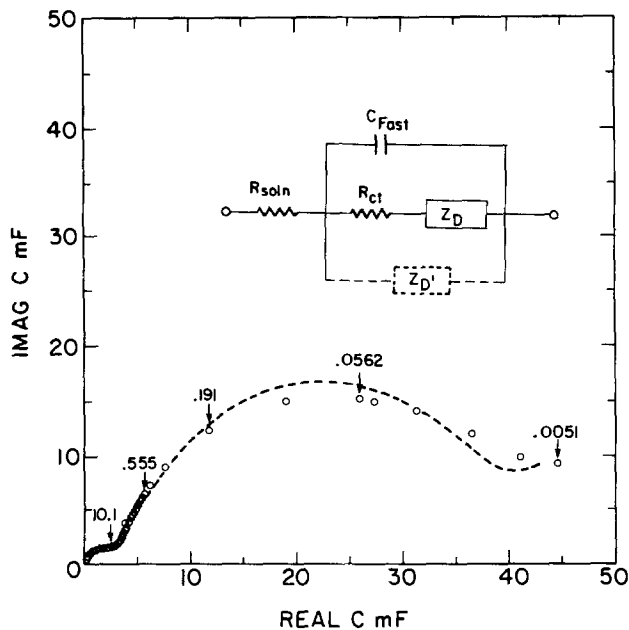


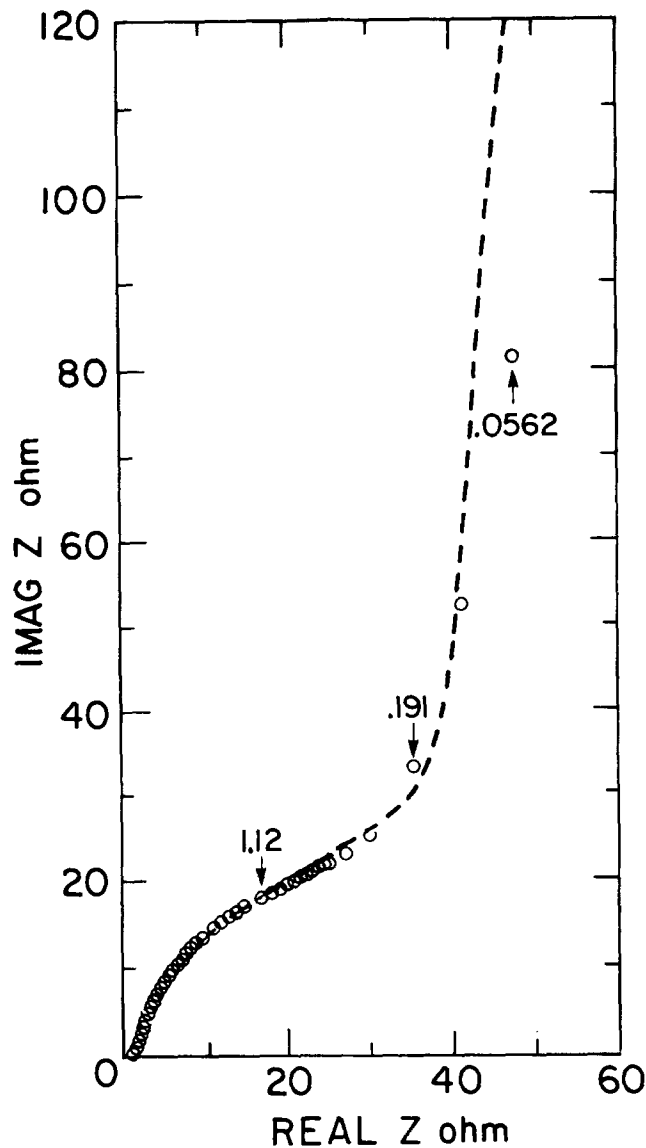
Fig. 9. a(above): Same as Fig. 8, but for a bias of 0.0V vs. SCE. The parameters in the simulation are: $R_{\text{soln}} = 1.6\Omega$; $C_{\text{fast}} = 3 \text{ mF}$; $C_{\text{slow}} = 32 \text{ mF}$; $L^2/D = 3\text{s}$; $R_{\text{ct}} = 20\Omega$; $\sigma' = 400\Omega \text{ s}^{1/2}$. (C_{slow} is equivalent to C_T in Eq. [2].) b(right): The same results for 0.0V SCE, presented in the form of a complex impedance plot (Z plot). The smooth curve is based on the same circuit with the same parameters as described for Fig. 9a.

Thermal Ru oxide films.—Figure 11 shows the complex capacitance plots obtained for thermal ruthenium oxide under three applied potentials in the “as-immersed” state, and Fig. 12 shows the same plots after 30 cycles of potential multipulsing have been applied to the thermal oxide. The following features are apparent: (i) following multicycling (Fig. 12), the fast charging sites in the thermal oxide behave in much the same way as in the anodic oxide, yielding at 1.0 and at 0.5V similar semicircular branches, corresponding to charging via the solution resistance alone. However, prior to multicycling (Fig. 11), the branch corresponding to fast charging is in the form of a depressed circular arc, with a significantly lower capacitance at 0.5 than at 1.0V. (ii) The VLF charging process seems to be much slower in the case of the thermal oxide as compared with the anodic oxide. This is reflected by the absence of a second well-resolved arc in the complex capacitance plot at 0.5V (Fig. 12), which can be clearly seen in the VLF region in the case of the anodic Ru oxide film (Fig. 8). (iii) Although the VLF charging process is slower, its amplitude at 0V seems to be larger in the thermal oxide than in the anodic Ru oxide. (Compare Fig. 12 and 9a.)

Discussion

The nature of the faster and slower charging modes in the oxide.—The following picture is suggested for the charging process in the Ru oxide films investigated in this work: the process can be seen to be well resolved into faster and slower charging modes. The faster mode is associated with proton uptake, but about 25% of the fast charging sites in the film can be apparently charged by ions other than H^+ if the concentration of proton donors is lowered well below 10^{-3}M . At a concentration level of 10^{-3}M of proton donors in solution (HSO_4^- ions in our case) the charging is found to be controlled by the diffusion of proton donors from solution towards the oxide surface (Fig. 7). The rate of the fast charging process in acid solutions is high, and, at this point, it can be claimed only that the impedance associated with it is significantly smaller than the resistance of the solution, i.e., $\ll 1 \Omega \text{ cm}^2$.

A slower charging mode, which is well resolved in the plots for the oxide film on ruthenized gold, results in an



electrical behavior of a finite transmission line, shown before to be typical for a process of diffusion through oxide films of finite thicknesses undergoing the double-injection process (12). The typical diffusion time associated with this slower mode is of the order of 0.1-s. For a diffusion length of 100-1000Å, which corresponds to the film thicknesses measured optically in this work, such diffusion times mean an effective diffusion coefficient in the film of $D = 10^{-11}\text{-}10^{-12} \text{ cm}^2/\text{s}$. This is three to four orders of magnitude smaller than the effective diffusion coefficient found for the fast charging mode in hydrous electrochromic films of e.g., anodic iridium oxide or anodic rhodium oxide (2, 7). As pointed out above, this slower process is clearly apparent in the thermal oxide at 0.0V, at which potential it is associated with a relatively large capacitance.

A model which seems to account for all these results involves the charging of grain surfaces in a hydrous microcrystalline structure as the fast charging mode, while charging of the bulk of the grain accounts for the slower charging mode. The slower mode is apparently associated with incorporation of aqueous protons during the cathodic half-cycle, and thus with a partial hydration and swelling of the oxide grains. The nature of the well-resolved slower mode of charging is substantiated by three aspects of the experimental results: (i) the dependence of its amplitude and rate in the anodic oxide on applied bias, demonstrated in Fig. 8-10, (ii) the results presented in Fig. 4 of slow variations in the optical properties of the oxide film under cathodic applied potentials, and

Fig. 10. Complex capacitance plots for the Au/Ru/RuOx electrode measured (I) at 0.5, and (II) at 1.0V. (The plot obtained at 0.5V includes the well-defined arc due to the slower charging mode, while the plot obtained at 1.0V includes the semicircle due to fast charging alone.)

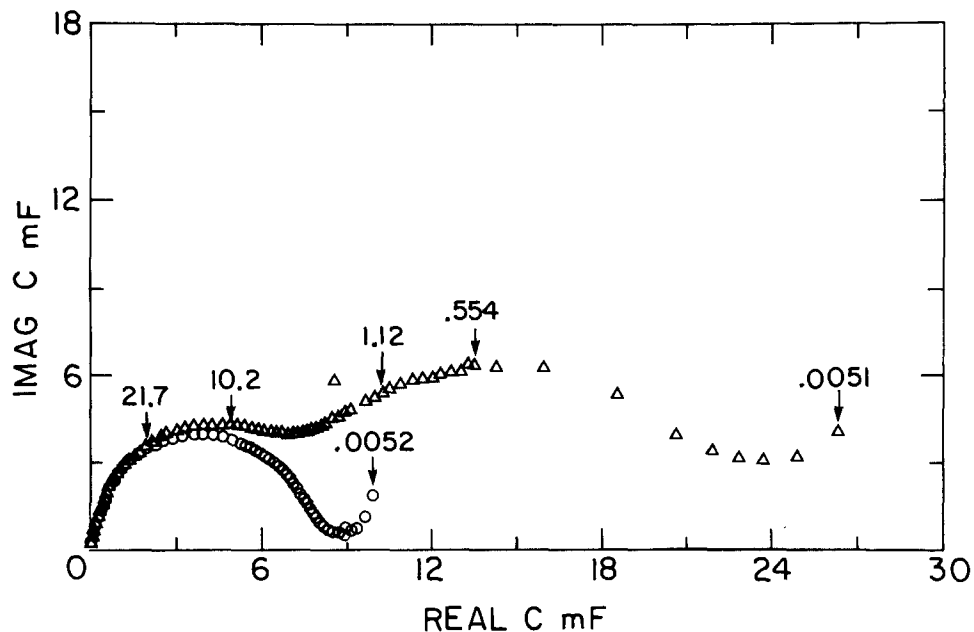
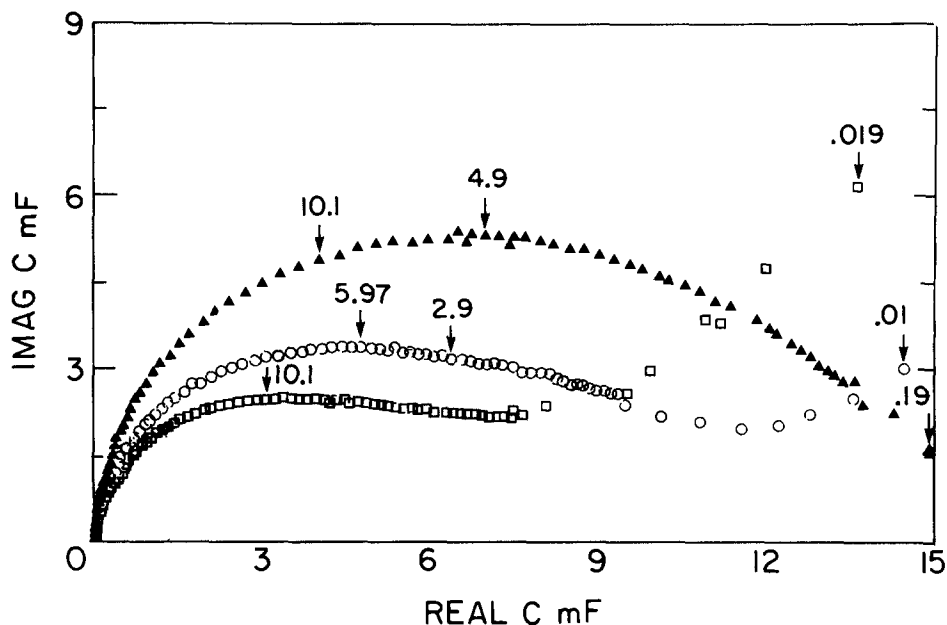


Fig. 11. Complex capacitance plots for an "as-immersed" thermal Ru oxide electrode (on gold substrate) in 0.5M H₂SO₄. ▲ ▲ ▲ : 1.0V. ○ ○ ○ : 0.5V. □ □ □ : 0.0V.



(iii) the large amplitude and slow kinetics of the VLF charging mode found at 0V for the thermal Ru oxide on a gold substrate (Fig. 11 and 12). The dependence of the VLF branch on bias as found for the anodic oxide films means that the slow charging mode is enhanced under cathodic applied potentials, and is thus associated with a slower and more radical form of oxide reduction. The optical results (Fig. 4) supplement the results of the impedance measurements by showing that a slow process in the oxide, which occurs under cathodic applied potentials, is associated with the generation of a more hydrous and slightly thicker ruthenium oxide film, most probably due to the incorporation of aqueous protons into oxide grains. The optical measurements also demonstrate that anodization is capable of reversing this process, apparently by the ejection of the excess aqueous protons. The charging of the bulk of oxide grains, especially if accompanied by significant hydration, as suggested, may be associated with the relatively smaller diffusion coefficient of 10^{-11} - 10^{-12} cm²/s as evaluated from the simulations shown in Fig. 8 and 9. The charging of grain surfaces, which requires only the transport of protons along aqueous pores or along inner surface trapping sites (see below), may be associated, however, with a much higher effective diffusion coefficient. Finally, the results for the slower charg-

ing mode obtained for the thermal oxide support the model suggested in two ways: they show, by the presence of the slow charging branch at 0.0V, that it is associated with a process within the Ru oxide phase, rather than with any process at the Ru/RuOx interface, since such interface does not exist at all in the Au/RuOx (thermal) electrode. Furthermore, the absence of the slower charging mode at 0.5V in the thermal oxide and its sluggish appearance at 0.0V are explained by the larger barrier required for H₂O incorporation into the less hydrated structure of the thermal oxide. It thus seems that under a relatively thin outer hydrous layer (ca. 100-1000Å) the underlying thermal oxide is water free, and further water incorporation is slow and requires a significant cathodic overvoltage.

Slow effects in hydrous oxide films, which occur on a time scale much longer than that of the fast reversible charging mode, were described before. Thus, the electrochromic response in Ir, and particularly in Rh oxide, was shown to become sluggish following prolonged excessive cathodization (6-8). This phenomenon was explained by a slow excessive incorporation of water which lowers the electronic conductivity in the oxide film. Glarum and Marshall recently reported complex capacitance plots for nickel oxide films containing a VLF branch (17), which is

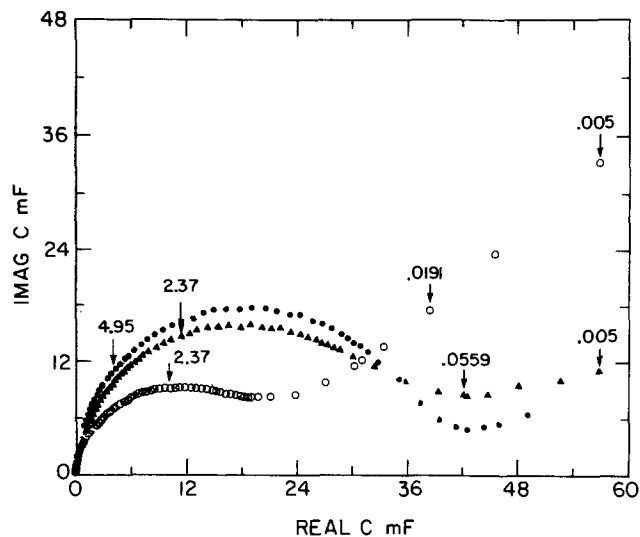
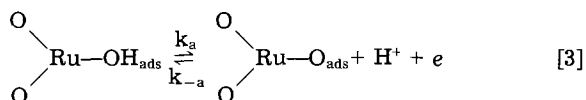


Fig. 12. Same as Fig. 11, but following 30 cycles of potential multipulsing between 1.22 and $-0.3V$. \cdots : $1.0V$. \blacktriangle : $0.5V$. \circ : $0.0V$.

probably due to a similar slow process in nickel oxide. It should be stressed again that only by the use of the ruthenized gold foil electrode, which has no structural features that can bring about solution penetration problems, could the very low frequency branch be recorded reproducibly, and the process ascribed to bulk grain charging quantitatively analyzed.

The rate of grain boundary charging in "semi-dry" oxide films.—The results in Fig. 11 and 12 contain some interesting information on the mode of charging in the "as-immersed" thermal oxide. After multicycling, the charging process is represented by the regular semicircular branch due to fast charging of (surface) sites in a hydrous layer, which is rate limited only by ohmic solution resistance (Fig. 12). In the "as-immersed" thermal oxide, however, the depressed circular arcs (Fig. 11) mean that the charging process is relatively slower, and behaves electrically as a combination of a large number of parallel RC branches with a continuous spectrum of charging times. Interestingly, under such circumstances, *i.e.*, when the structure has not been properly hydrated, the response is faster and the completeness of charging is better at more positive potentials: while there is no difference between the extents and the rates of charging at 0.5 and at 1.0V in the hydrated oxide layer (Fig. 12), the rate and extent of charging seem to be significantly higher at 1.0 than at 0.5V prior to hydration (Fig. 11). Dry Ru oxide is expected to exhibit very satisfactory electronic conductivity at both 0.5 and 1.0V. The reason for the difference in the rates of charging at 0.5 and 1.0V must be, therefore, traced to differences in the rate of protonic diffusion in the relatively dry oxide, induced by the applied bias. A bias-dependent diffusion coefficient for the diffusion of hydrogen in a hydrous oxide was described in Ref. (9): expressing the diffusion coefficient as a product of a frequency K_a and a jump distance d , *i.e.*, $D = Kad^2/2$, it was argued that K_a could be the electrochemical rate constant of a surface deprotonation reaction. Written here for Ru oxide, this surface deprotonation process may be described as follows



where each event of deprotonation may be followed by a proton jump (coupled, possibly, with an e jump) to a neighbor surface site. The frequency of surface deprotonation events may thus dictate the frequency of the individual diffusional jumps, while the distance of an individual jump may be identical to the distance between

adjacent proton trapping sites, located at the surface of the oxide grain (9). It can be realized from Eq. [3] that the residence time of protons at an oxide surface site may be shorter the higher the positive applied potential. This is true as long as the potential difference falls essentially across the oxide-electrolyte interface, as is expected for the electronically conducting Ru oxide.

A bias-dependent surface protonic diffusion process seems to explain the results of Fig. 11: in a relatively dry Ru oxide structure, the electronic component of transport should not pose a significant barrier for charging, but the small water content forces the proton to diffuse along oxide grain surfaces. Under such conditions of surface diffusion control, the double injection process is seen to be significantly faster at more positive applied potentials. It thus seems that these oxides exhibit enhanced activities under more positive potentials not only thanks to ejection of excess water (6-8). The enhanced activity may be also due to an increase in the rate of protonic transport, the proton diffusion along grain surfaces being assisted by the positive applied potentials (Eq. 3). In any case, interpretation of a measured apparent conductivity for the double proton-electron injection process in this type of oxides in terms of electronic conductivity alone (5) is questionable, as these results for thermal Ru oxide seem to suggest.

Acknowledgment

This research was supported in part by a grant from the United States-Israel Binational Science Foundation (BSF), Jerusalem, Israel, and in part by the Fund for Applied Industrial Research in Israeli Universities, Jerusalem. The authors wish to acknowledge the important contributions of Mr. I. Reshef to the development of the experimental setup.

Manuscript submitted Aug. 9, 1983; revised manuscript received ca. Jan. 23, 1984.

REFERENCES

1. B. W. Faughnan, R. S. Crandall, and M. A. Lampert, *Appl. Phys. Lett.*, **27**, 275 (1975).
2. S. Gottesfeld, J. D. E. McIntyre, G. Beni, and J. L. Shay, *ibid.*, **33**, 208 (1978).
3. S. Gottesfeld and J. D. E. McIntyre, *This Journal*, **126**, 742 (1979).
4. J. L. Shay, G. Beni, and L. Schiavone, *Appl. Phys. Lett.*, **33**, 942 (1978).
5. K. S. Kang and J. L. Shay, *This Journal*, **130**, 766 (1983).
6. S. Gottesfeld, *ibid.*, **127**, 272 (1980).
7. S. Gottesfeld, *ibid.*, **127**, 1922 (1980).
8. S. Gottesfeld, J. Rishpon, and S. Srinivasan, in "Electrocatalysis," W. E. O'Grady, P. N. Ross, and F. G. Will, Editors, p. 155, The Electrochemical Society Softbound Proceedings Series, Pennington, NJ (1982).
9. S. H. Glarum and J. H. Marshall, *This Journal*, **127**, 1467 (1980).
10. S. Gottesfeld and S. Srinivasan, *J. Electroanal. Chem.*, **86**, 89 (1978).
11. J. L. Ord, *This Journal*, **129**, 335 (1982).
12. C. Ho, I. D. Raistrick, and R. A. Huggins, *ibid.*, **127**, 343 (1980).
13. D. R. Franceschetti and J. R. Macdonald, *ibid.*, **129**, 1754 (1982).
14. S. Trasatti and W. O'Grady, in "Advances in Electrochemistry and Electrochemical Engineering," Vol. 12, H. Gerischer and C. W. Tobias, Editors, p. 177, John Wiley and Sons, New York (1981).
15. D. B. Rogers, R. D. Shanon, A. W. Slight, and J. L. Gillson, *Inorg. Chem.*, **8**, 841 (1968).
16. S. Hadzi-Jordanov, H. Angerstein-Kozłowska, M. Vukovic, and B. E. Conway, *This Journal*, **125**, 1471 (1978).
17. S. H. Glarum and J. H. Marshall, *ibid.*, **129**, 535 (1982).
18. J. Rishpon, I. Reshef, and S. Gottesfeld, in "Passivity of Metals and Semiconductors," M. Froment, Editor, p.205. Elsevier, New York (1983).
19. M. Vukovic, H. Angerstein-Kozłowska, and B. E. Conway, *J. Appl. Electrochem.*, **12**, 193 (1982).
20. R. S. Yeo, J. Orehotsky, W. Visscher, and S. Srinivasan,

This Journal, 128, 1900 (1981).

21. J. J. Carroll, T. E. Madey, A. J. Melmed, and D. R. Sandstorm, *Surf. Sci.*, 96, 508 (1980).

22. A. K. Goel, G. Skorinko, and F. H. Pollak, *Phys. Rev. B*, 24, 7342 (1981).

23. W. D. Ryden, A. W. Lawson, and C. C. Saratin, *Phys. Lett.*, 26A, 209 (1968).

24. M. Kedam, J. F. Lizée, C. Pallotta, and H. Takenouti, in "Passivity of Metals and Semiconductors," M. Fromont, Editor, p. 51, Elsevier, New York (1983).

Technical Note



The Mechanism of Plasma Oxidation on Floating Silicon Substrates

K. K. Ng and J. R. Ligenza

AT & T Bell Laboratories, Murray Hill, New Jersey 07974

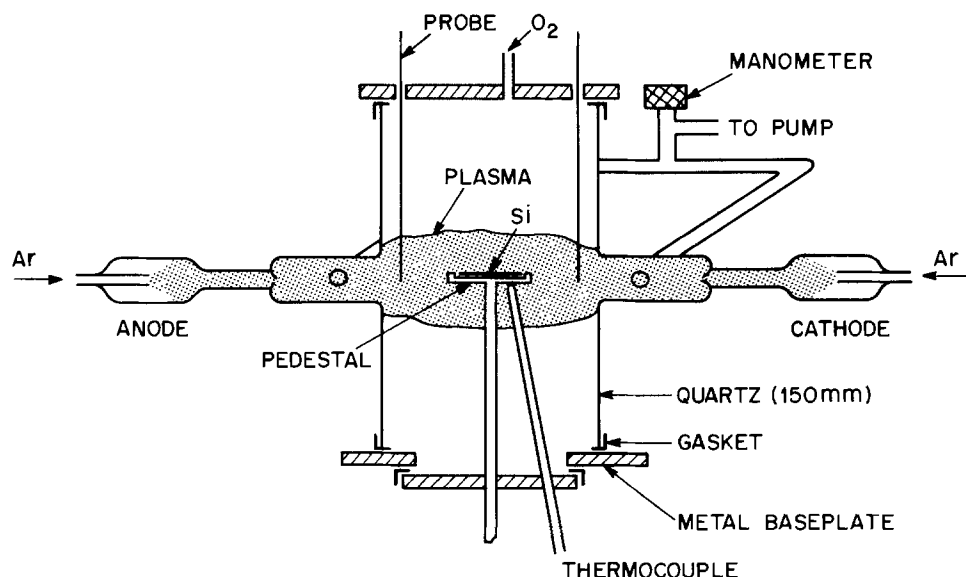
Oxidation in plasma environment offers the opportunities of fast oxidation rates and low temperature processing. An oxygen plasma can be formed in a microwave, RF, or dc discharge. Oxidation on externally biased substrates is referred to as plasma anodization while on unbiased substrates it is referred to as plasma oxidation (1-3). The origin of plasma anodization is believed to be due to negative oxygen ions, but the exact mechanism has been a subject of discussion, and no model has been generally accepted. The growth rate for constant voltage anodization was observed to be parabolic. The mechanism of plasma oxidation is seldom explained in literature and its data are more limited. The growth rate in this case was also found to be parabolic (4). Nonparabolic behavior was observed (5) but it was interpreted as being due to the coexistence of sputtering. In this experiment, plasma oxidations were performed at a variety of substrate positions and the thickness distributions of oxide across the wafers were recorded and analyzed in order to understand the oxidation process.

The plasma apparatus used is shown in Fig. 1 and its features are similar to that described in Ref. (6). Tantalum hot hollow electrodes with rolled foil structure (7) were used, and the pumping arms were designed to minimize oxygen partial pressure around the electrodes to avoid their oxidation. Different pedestals were also made in order to support the silicon wafers in different schemes in

the positive column of the plasma. A dc plasma is advantageous in this experiment since the plasma potential monotonically decreases along its column. All the experiments were performed with an argon pressure of 0.30 torr, oxygen pressure of 0.10 torr, plasma current of 3.0A, for a period of 1.0h. The substrate temperature was measured by the thermocouple to be $\approx 250^{\circ}\text{C}$. Silicon wafers of 75 mm diam were used unless otherwise specified, and the oxide thickness was measured by ellipsometry. The oxide distributions for a bisected wafer placed parallel to the axis of the plasma column is shown in Fig. 2. The oxide thickness is widely nonuniform along one direction but reasonably uniform along the other. This is clearly an electric field effect exerted by the plasma. The fact that the two halves display similar peaks indicates that the oxide was not deposited from sputtering the quartz wall. Since for a dc plasma, the plasma potential changes monotonically along its column, there must exist a current in the silicon substrate. In fact, if the wafer sits on a quartz pedestal, the current must enter the wafer from the end close to the anode and leave from the other. From this argument, and further experimental evidence that follows, plasma oxidation is in fact local plasma anodization, biased not externally but by the plasma potential itself.

To relate this plasma oxidation to anodization, typical Langmuir probe characteristics are shown in Fig. 3. The horizontal axis represents voltage on the substrate (V_{sub})

Fig. 1. Schematic diagram for the dc plasma oxidation system.



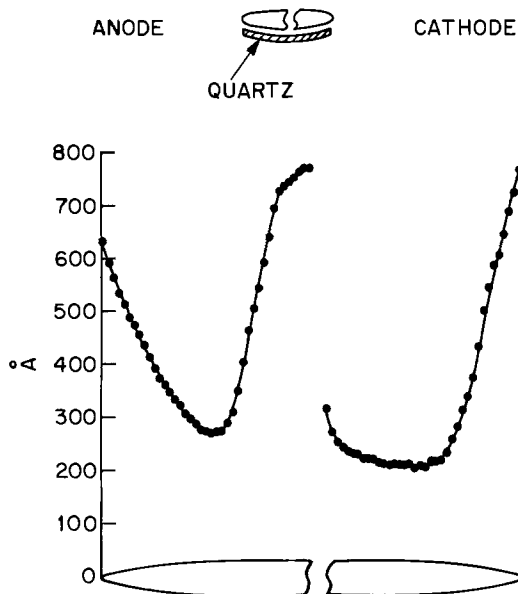


Fig. 2. Thickness distribution of oxide while the bisected wafer was placed parallel to the plasma column.

and the vertical axis represents current density flowing away normally from the surface to the plasma. The wall potential V_w is defined as the substrate voltage for zero current. Above this V_w , current flows away from the silicon surface to the plasma, and the reverse happens for substrate voltage below V_w . As mentioned before, since the plasma potential changes monotonically along its column, the wall potential also varies accordingly. The two curves shown in Fig. 3 represent the characteristics at two different locations, with the left curve (lower V_w) corresponding to the surface near the cathode. These characteristics show the extremes at the wafer ends and they vary continuously with position. The voltage difference between V_{w1} and V_{w2} was measured to be $\approx 25V$. For the sake of argument, the substrate potential is taken to be the same at different locations by assuming that the internal current, and thus the resistive voltage drop, is small.

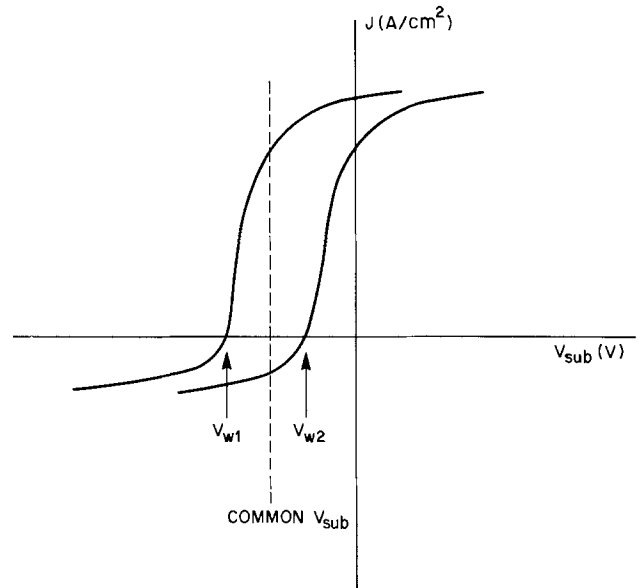


Fig. 3. Langmuir probe characteristics for different parts of the silicon surface. The parallel shift is caused by the difference in wall potentials. The curve with a lower V_w corresponds to the surface close to the cathode.

By drawing a vertical line between the extremes of the two wall potentials for some arbitrary common substrate voltage, one can see that current enters the wafer from the anode side (negative J) and leaves the wafer from the cathode side (positive J). By comparing the oxide thickness distribution in Fig. 2, it can be seen that oxide grows faster with a positive current than with a negative current.

The data for silicon substrates placed perpendicular to the plasma column are shown in Fig. 4. In Fig. 4(a) and 4(b), the current enters the side facing the anode and leaves from the other. Again the data show that oxidation is more efficient with a positive current (surface facing cathode), a condition in which all the plasma anodizations are carried out. In Fig. 4(c), the silicon was backed by a

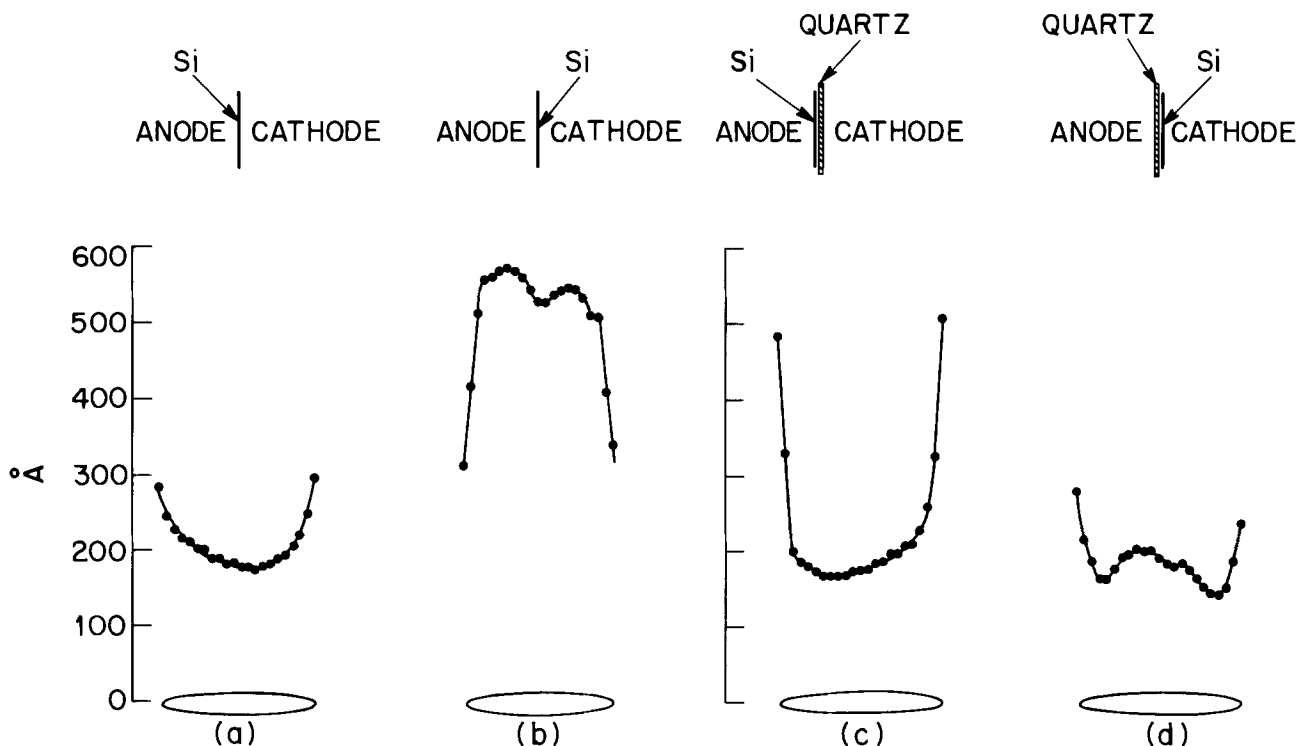


Fig. 4. Thickness distribution of oxide while the silicon wafer was placed perpendicular to the plasma with (a) surface facing anode, (b) surface facing cathode, (c) surface facing anode and backed by quartz plate, (d) surface facing cathode and backed by quartz plate.

quartz plate and current enters the center of the wafer and leaves around the edge, where the oxide film is observed to be thicker. In Fig. 4(d), current enters around the edge and leaves at the center. All the above observations are consistent with the model proposed. It has to be mentioned that when samples were placed perpendicular to the plasma column, a slightly stronger glow was observed around the edge, and the higher ion density may account for some of the oxide formation around the edge of the wafer. Ligenza (1), and Ray and Reisman (8) reported nonuniform oxides on floating substrates, but little explanations were given. The model also explains the parabolic growth in plasma oxidation seen by Ligenza (4), since this process is equivalent to anodization with a constant low anodization voltage, biased by the plasma internally.

Additional experiments were performed with other parameters varied one at a time. When 38 mm wafers were used instead of 75 mm, they showed very similar oxide distributions. When the substrate doping was increased, the overall oxide thickness was increased due to a larger internal current, but the oxide distributions were again similar. Oxide was also grown on wafers having a platinum coating at the back surface, and results indicated reduced oxide thickness with only a slight improvement on the distribution.

These experiments can only point out the first order effects. They cannot, however, resolve the details in oxidation kinetics. One of the questions remaining to be answered is whether oxidation takes place on the silicon surface when its substrate potential is exactly equal to the local wall potential. Due to the fact that the plasma has a flickery appearance, this cannot be resolved experimentally. Compounding this, there also exists a radial field from the center of the plasma to the chamber wall. An-

other factor is that the disk geometry of the wafers played some role in balancing the internal current density. All these factors make it difficult to account for all the details of oxide distributions observed, such as the dips at the centers of the two halves shown in Fig. 2. Nevertheless, the conclusion that oxidation is related to the passage of current through the silicon surface is apparent.

In summary, it is found that the mechanism of dc plasma oxidation on floating silicon substrates is actually due to local anodization caused by currents which are induced by the spatial variations of plasma potentials in an inhomogeneous plasma. Because of this nature, to obtain uniform oxide on an unbiased substrate is difficult, with the portion of the wafer close to the cathode being oxidized at a higher rate.

Acknowledgments

The authors would like to thank G. E. Smith and S. M. Sze for support of this work and careful review of the manuscript.

Manuscript submitted Dec. 27, 1983; revised manuscript received March 5, 1984.

AT & T Bell Laboratories assisted in meeting the publication costs of this article.

REFERENCES

1. J. R. Ligenza, *J. Appl. Phys.*, **36**, 2703 (1965).
2. A. K. Ray, *Thin Solid Films*, **84**, 389 (1981).
3. J. F. O'Hanlon, *J. Vac. Sci. Technol.*, **7**, 330 (1970).
4. J. R. Ligenza, Unpublished data.
5. J. Kraitchmann, *J. Appl. Phys.*, **38**, 4323 (1967).
6. J. R. Ligenza and M. Kuhn, *Solid State Technol.*, **13**, 33 (1970).
7. J. R. Ligenza and E. I. Povilonis, U.S. Pat. 3,476,971 (1969).
8. A. K. Ray and A. Reisman, *This Journal*, **128**, 2466 (1981).



Electrochemical Properties of B_2S_3 - Li_2S - LiI Vitreous Electrolytes

M. Menetrier, A. Levasseur, and P. Hagemuller

Laboratoire de Chimie du Solide du CNRS, Université de Bordeaux I, 33405 Talence Cedex, France

ABSTRACT

The electrochemical properties of new Li^+ ion conducting glasses belonging to the B_2S_3 - Li_2S - LiI system have been investigated. The electronic conductivity is at least 10^6 times lower than the ionic one ($\sigma_e < 10^{-9} \Omega^{-1} \text{cm}^{-1}$ and $\sigma_i \approx 10^{-3} \Omega^{-1} \text{cm}^{-1}$ at 25°C for the best ionic conductors); the electrochemical stability range determined by cyclic voltammetry is about 4.5V from lithium metal.

The energy crisis has focused large interest on energy saving problems, which involves energy storage for later use. Direct electrochemical storage of electricity is actually an attractive way because of the large use of electricity which is the most convenient energy vector, and of its adaptability to vehicle traction as well as to stationary applications. In that way, an efficient electricity storage is essential for the development of new alternative energies like photovoltaic conversion or transformation of the wind energy.

One of the most advanced electricity storage systems could be a lithium // intercalation compound secondary battery, although, so far, the reactivity problems of liquid organic electrolytes do not allow a good cycling behavior.

Recently, new vitreous materials with a rather attractive lithium ionic conductivity have been developed (1-5).

Synthesis and ionic conductivity of glasses belonging to the B_2S_3 - Li_2S and B_2S_3 - Li_2S - LiI systems performed in our laboratory have been described previously (4, 5).

This paper shows that their electrochemical characteristics (electronic conductivity and electrochemical stability range) should allow their use as electrolytes in lithium "all-solid-state" batteries working at room temperature.

All experiments have been carried out with a $0.28B_2S_3$, $0.33Li_2S$, $0.39LiI$ glass, which is among the best glasses obtained in the ternary system [$\sigma \approx 10^{-3} \Omega^{-1} \text{cm}^{-1}$ at 25°C for a bulky material and $4 \cdot 10^{-4} \Omega^{-1} \text{cm}^{-1}$ for pressed powder pellets (5)].

Electronic Conductivity

The first feature of an electrolyte must be a very low electronic conductivity. It was determined from the dc polarization technique proposed by Yokota (6).

Experimental.—Bulky glass samples or pressed powder pellets (10 t/cm^2 , 1 cm diam, 1 mm thick) were used with blocking electrodes consisting of sputtered gold or platinum on both sides. A fixed potential was applied between those electrodes, and the current measured with a Keithley 616 electrometer was recorded *vs.* time.

The cell was placed in an airtight glass container (under argon atmosphere) which was in a grounded Faraday box.

Results and discussion.—The application of a voltage is followed by a first current response, which decreases quickly with time; it corresponds to the motion of Li^+ ions within the material. Once a steady-state situation is attained, these ions, blocked along the gold or platinum electrodes, do not move any longer. The measured current is, therefore, of electronic origin.

The variation of current *vs.* time is shown in Fig. 1 for a given value of the applied voltage. A steady state is usu-

ally obtained within 24h (or even less when the sample is not depolarized by a short circuit between two experiments).

Figure 2 shows the variation of the steady-state current *I* *vs.* applied voltage *V*. These values correspond to Ohm's law when the voltage *V* is lower than 60 mV, so that *I* is small. As *V* increases, overvoltages at the gold (or platinum)/glass interfaces become significant and the real voltage applied to the sample is $v < V$ (Fig. 3). Therefore, Ohm's law cannot be used to calculate the resistance from the values of *V* and *I* when *V* exceeds 60 mV.

Decomposition of the sample was observed for an applied voltage of 7.5V.

The values of σ_e (determined from the slope of the linear part of the former diagram) (Fig. 2) for pressed pellets

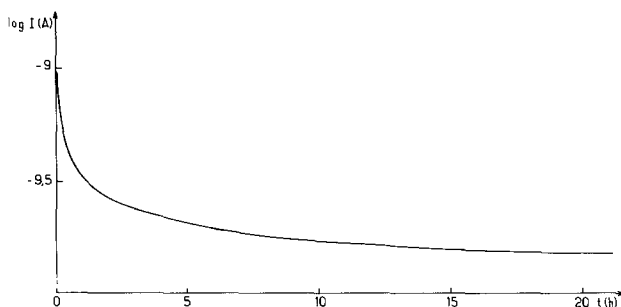


Fig. 1. Variation of $\log I$ *vs.* time for a gold/glass pellet/gold cell. Applied voltage: 50 mV.

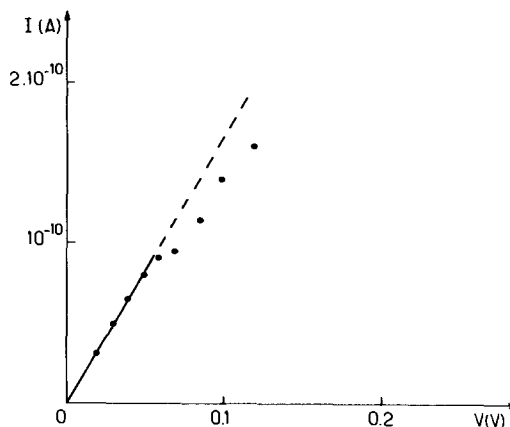


Fig. 2. Variation of the steady-state current *I* *vs.* applied voltage *V* for a gold/glass/gold cell.

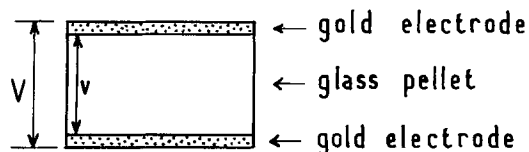


Fig. 3. Applied (V) and real voltage (v) in a gold/glass/gold cell

or bulk glass are smaller than $10^{-9}\Omega^{-1}\text{cm}^{-1}$ at 25°C , which is really negligible compared to $10^{-3}\Omega^{-1}\text{cm}^{-1}$ for total (*i.e.*, ionic) conductivity determined by ac measurements.

Estimation of self-discharge in a battery.—The self-discharge current of a $\text{Li} //$ intercalation compound (such as TiS_2) battery with a sulfur glass as electrolyte can be estimated from the value of σ_e . For example, it would correspond to the use of less than $20\ \mu\text{g}$ of TiS_2 per year in a $1\ \text{cm}^2$ area battery; in other words, its influence would be practically negligible. This result is confirmed by the constant open-circuit voltage given by a $\text{Li}/\text{glass}/\text{TiS}_2$ battery for over 8 months.

Electrochemical Stability Range

The electrochemical stability range has been determined using the cyclic voltammetry method which was first applied to solid materials by Rigaud (7, 8).

Experimental.—The electric circuit and electrode configuration on the sample are shown in Fig. 4. The sample is a pressed powder pellet of glass. The three electrodes are constituted as follows: (i) the working (WE) and counterelectrodes (CE) were sputtered gold or platinum, and (ii) the reference electrode (RE) was an Ag/Ag^+ couple realized with a mixture of Ag_3SI (in which Ag^+ ions are mobile and which is also a good electronic conductor), with powdered metallic silver. The potential of the redox couple is situated in a zone where no electrochemical reaction occurs in the vitreous sample. As sample and reference materials are not conductors of the same type of ion, there is a junction potential at the glass/RE interface. Ag/Ag^+ is therefore not really a reference electrode, but is, rather, a comparison electrode. Its potential *vs.* lithium metal, measured with a sulfur glass as electrolyte, is 2.14V .

Cycling started with anodic polarization and the speed of voltage sweeping was $1\ \text{V}/\text{mn}$.

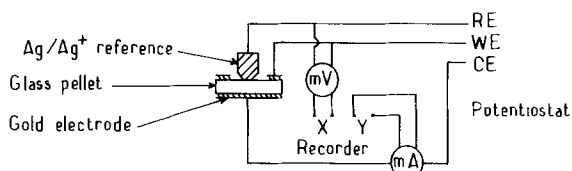


Fig. 4. Electric circuit and cell configuration for voltammetry studies.

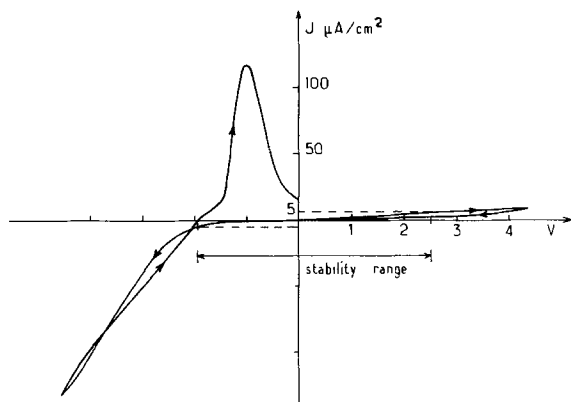


Fig. 5. Cyclic voltammogram of a ternary $\text{B}_2\text{S}_3\text{-Li}_2\text{S-LiI}$ glass. Reference electrode: Ag/Ag^+ couple.

As before for the electronic conductivity studies, the sample was placed in a special airtight container under argon atmosphere, and cycles were realized at 25°C .

Results and discussion.—Figure 5 shows the voltammogram obtained for a $0.28\text{B}_2\text{S}_3, 0.33\text{Li}_2\text{S}, 0.39\text{LiI}$ glass.

The cathodic reaction which limits the existence region is the reduction of Li^+ ions occurring at a 2.1V potential, which is close to the thermodynamic potential because of the quick migration speed of the Li^+ ions to the electrode. During the return process, an oxidation peak is observed, which corresponds to the reoxidation of one part of the lithium formed. As no reaction was detected between glass and lithium (even for long-time contact at 50°C), the other part of the lithium formed is supposed to constitute an alloy with the gold electrode. A similar phenomenon was reported by Rigaud (7).

The anodic part of the diagram has been assigned to the oxidation of sulfide ions for the following reasons: (i) the anodic process of a binary glass ($\text{B}_2\text{S}_3\text{-Li}_2\text{S}$) is similar to that of ternary glasses ($\text{B}_2\text{S}_3\text{-Li}_2\text{S-LiI}$), and (ii) the addition of lithium iodide to a powdered binary or ternary glass causes the appearance of the oxidation peak of I^- ions at a very low potential (Fig. 6a), which also occurs with pure LiI at 100°C (Fig. 6b).

The aspect of the oxidation curve and the decrease of the current with the number of anodic sweep (Fig. 7) show that the oxidation process is limited by the diffusion of the S^{2-} ions to the electrode, which indicates that these ions are poorly mobile in the glass compared to the Li^+ ions. Furthermore, the fact that I^- ions in ternary glasses are not oxidized shows that they really belong to the matrix and are too large to move.

As the anodic process is limited by diffusion, it is not possible to extrapolate the oxidation peak to determine the anodic limit of the stability range. That limit was therefore arbitrarily fixed as a $5\ \mu\text{A}/\text{cm}^2$ current density, considering that a lower current does not show any electrochemical reaction, but is due to an ionic motion as

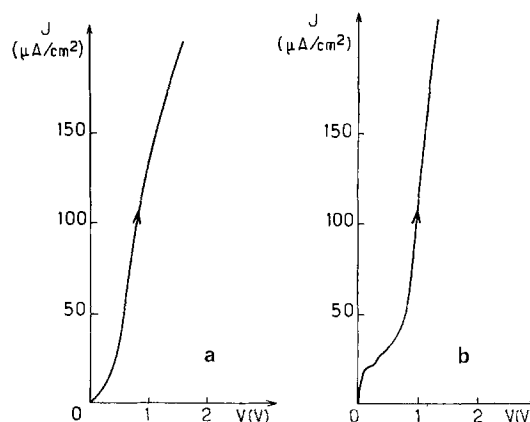


Fig. 6. Anodic part of voltammogram with: (a, left) glass + LiI mixture, and (b, right) pure LiI (100°C).

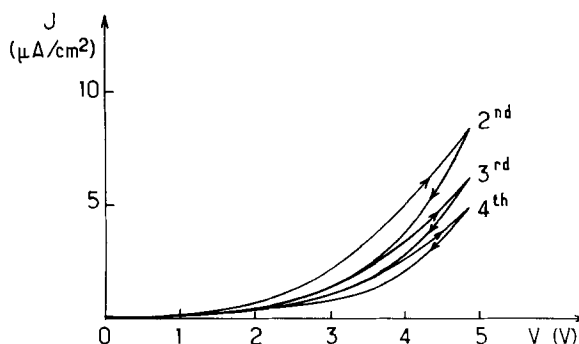


Fig. 7. Evolution of anodic voltammograms for a ternary $\text{B}_2\text{S}_3\text{-Li}_2\text{S-LiI}$ glass with the number of anodic sweeps. Only three sweeps are shown.

mentioned in the second part of the present paper. The reason is that the sweeping speed does not allow reaching steady-state conditions.

The electrochemical stability range of the ternary glass is thus about 4.5V from lithium metal.

Conclusions

The electrochemical characteristics of new vitreous sulfide electrolytes have been determined.

Their electronic conductivity is negligible and does not create a significant self-discharge in batteries.

The voltammetry study suggests that the stability range of the ternary glass allows using lithium metal as a negative electrode (and of course of a LiAl alloy, whose potential is + 0.3V vs. lithium metal), and intercalation compounds with high potential vs. lithium as positive electrodes, without decomposition of the electrolyte.

These properties and the good ionic conductivity [exceeding $10^{-3}\Omega^{-1}\text{cm}^{-1}$ at 25°C (5)] allow their use as an electrolyte in experimental "all-solid-state" batteries working at room temperature according to the scheme: Li (or LiAl alloy)/glass/lithium intercalation compound.

The study of such cells is in progress and will be described elsewhere.

Acknowledgment

Authors wish to acknowledge the financial support by the Energy Conservation program of the EEC.

Manuscript submitted Oct. 20, 1983; revised manuscript received April 24, 1984.

REFERENCES

1. R. Mercier, J. P. Malugani, B. Fahys, and G. Robert, *Solid State Ionics*, **5**, 663 (1981).
2. B. Barraud, J. L. Souquet, and M. Ribes, *C. R. Acad. Sci.*, **190**, 353 (1980).
3. B. Carette, thèse Docteur-Ingénieur, Montpellier, France (1982).
4. A. Lavasseur, R. Olazcuaga, M. Kbalá, M. Zahir, and P. Hagenmüller, *C. R. Acad. Sci.*, **293**, 563 (1981).
5. H. Wada, M. Ménétrier, A. Levasseur, and P. Hagenmüller, *Mater. Res. Bull.*, **18**, 189 (1983).
6. I. Yokota, *J. Phys. Soc. Jpn.*, **16**, 11, 2213 (1961).
7. Ph. Rigaud, thèse Docteur-Ingénieur, I.N.P. Grenoble, France (1980).
8. M. B. Armand, M. J. Duclot, and Ph. Rigaud, *Solid State Ionics*, **3/4**, 429 (1981).

Lifetime Studies in H₂/Br₂ Fuel Cells

G. G. Barna,* S. N. Frank,* T. H. Teherani,* and L. D. Weedon

Texas Instruments, Incorporated, Dallas, Texas 75265

ABSTRACT

A fully computerized system has been set up for the life testing of H₂ electrodes in 48% HBr, and of H₂/Br₂ fuel cells. Given a fuel cell design with dry H₂ and no anolyte loop, the prime parameters influencing the operating lifetime are the hydrophobicity of the anode and the electrolyte transport property of the membrane. A systematic optimization of all the parameters has generated fuel cells that have operated for 10,000h at 2 A/in.², with no significant degradation.

During the development of Texas Instruments Solar Energy System (TISES), a major emphasis in the fuel cell portion of the program was the optimization of the initial performance of the gas diffusion, Pt-black-catalyzed, H₂ electrode. Having developed the fabrication process to the level where these electrodes reproducibly performed at the kinetically controlled limit (1), attention was focused on the lifetime performance of these electrodes and fuel cells. Life testing was initiated with a datalogger and a manual plotting of the data. During the next 4 yr, this system was continuously upgraded to the level where all aspects of the life testing, *i.e.*, current cycling, continuous monitoring of the voltages, data acquisition and reduction, were all under full computer control.

There were many reasons for establishing such a life testing system. First, lifetime data had to be generated on both anodes and fuel cells. Second, these life tests provided a vehicle for the development and refinement of analytical techniques for the diagnosis of failure modes. Third, it also allowed for the evolution of peripheral hardware necessary to run these long-term experiments. This paper will describe the life test data generated on the H₂ electrode in HBr, and on the H₂/Br₂ fuel cells, the degradation modes, and some of the other principal parameters affecting the lifetime of these fuel cells.

Experimental

The Teflon-bonded Pt-black-catalyzed gas diffusion electrodes were prepared as previously described. Life testing was performed in two parallel systems: in a half-cell mode with the described electrode, or in a fuel cell mode, with a SiC-covered electrode. Since the setup and analysis was quite distinct in these two modes, they will be described separately.

Half-cell studies.—The electrode was placed in a Teflon cell, with the necessary gas and electrolyte ports for diffusing H₂, purified through Pd, behind the electrode and the electrolyte (8.9M HBr) in front of the electrode (Fig. 1). A Pt-foil served as a counterelectrode; a 6.9M HBr/1M Br₂ reference electrode, connected through a narrow capillary tube in the cell body, sensed the electrode potential at ~ 1 mm away from the edge of the H₂ electrode. After the initial evaluation of some necessary electrochemical parameters, the test cell was connected to the computer. It was then load cycled at 4, 3, and 2 A/in.² (620, 465, and 310 mA/cm², respectively) for 4h at each current density, with ~ 2 min on open circuit between the successive current steps. Voltages were recorded both at the beginning and end of each current step, and in the open-circuit condition. The computer continuously monitored the potential of the anode; if it went more positive than a certain prescribed limit, the current was automatically decreased to the next lower level, or ultimately to zero. At the conclusion of the testing, the cell was disconnected from the computer, and the pertinent electrochemical parameters were again measured.

Fuel cell studies.—The electrode, coated with a thin layer of SiC powder, was assembled into a fuel cell with an appropriate membrane and a porous carbon (or graphite) Br₂ electrode (Fig. 2). The SiC layer served as an electrolyte matrix, as these fuel cells were run with dry H₂ and no free flowing anolyte. Electrolyte management on the anode side was maintained solely by the judicious choice of the membrane. The design criteria were that the membrane possess a high enough electrolyte diffusion so that the SiC matrix, on the anode, would remain adequately wetted. The fuel cell was then connected to an electrolyzer which maintained the fuel concentration at the desired level, usually 1M Br₂/6.9M HBr, throughout

* Electrochemical Society Active Member.

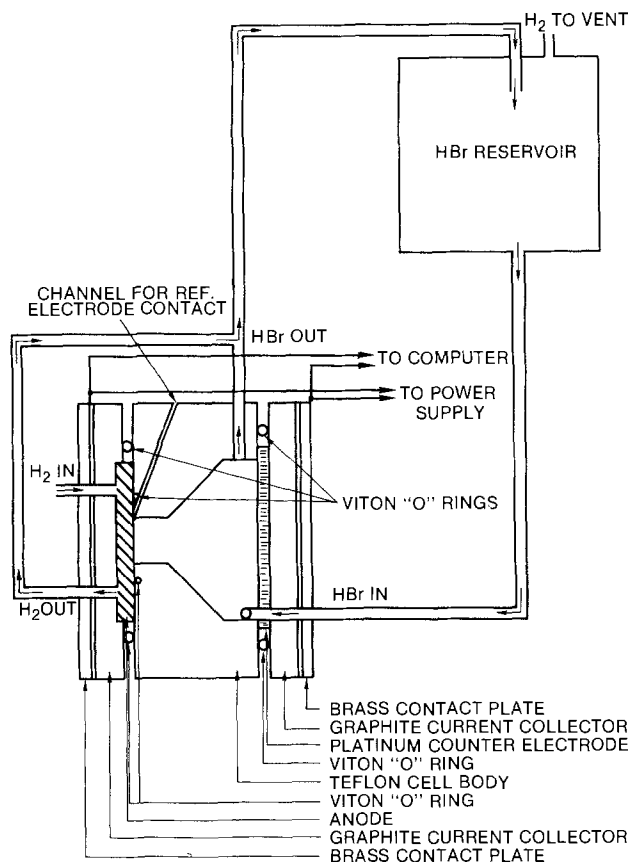


Fig. 1. Schematic of the anode life test cell

the duration of the test. Purified hydrogen was allowed to diffuse behind the anode. The fuel cell was connected to the computer, which adjusted the load to a steady 2 A/in.² (310 mA/cm²), or sometimes higher. Cell potential was monitored constantly and recorded once every 4h along with an OCV value. Again, if the cell voltage dropped below a prescribed limit, the computer placed the cell on open circuit.

Computer system.—Data acquisition, storage, and analysis were all performed on a dedicated Fluke 1720 Instrument Controller connected to the life test cells through a Fluke 2400A Measurement and Control Link. A block dia-

gram of the system is shown in Fig. 3. Both units were remote from the laboratory in clean, air-conditioned space. The 2400A was programmed by uploading programs from the 1720A and was then independent of the 1720A. Data were down-loaded from the 2400A into the 1720A for permanent storage on 5.25 in floppy disks. The controlling and monitoring software was developed in-house, and is all in BASIC.

In addition to the current/voltage/time data files for each life tested anode/fuel cell, a completely separate set of data files were also generated. These files contained two significant portions. First, using a standard format as in Table 1, all the material parameters and the definable processing steps were recorded. For each of the 63 parameters, there could be typically 3-10 specific attributes, evolved throughout the process development phase. The second portion of this data file contained both quantitative and qualitative operating parameters that were obtained throughout the life test cycle (e.g., peak power and limiting currents at various time intervals, operating voltages, etc.). Using this data base from all the life tested anodes/fuel cells, correlations could be made between the materials/processing parameters and the resulting operating characteristics. The results of some of these correlations will be described.

Results

The total extent of the life testing effort is described in Table II. A total of 235,896h of life testing has been performed, with the pertinent data on the longest sustained anode (12,072h) and 1 and 10 in.² fuel cells (10,056 and 2,832h, respectively) lifetests shown in Fig. 4-8.

Half-cell studies.—The two major parameters used in the diagnosis of anode performance and degradation mode were the low polarization slope (LPS) and the limiting current. The LPS is a measure of the dV/dI , with a H_2 partial pressure of 1, in the range of $\eta = 0-3$ mV. This is an iR -free value, generated by subtracting the internal resistance obtained by standard current interrupt techniques, using an in-house-built current interrupter. It can be shown (2) that $(LPS)^{-1}$ is a function of i_0 , a purely kinetic value free of any diffusional effects. Hence, a change in $(LPS)^{-1}$ with time is solely a function of a change in the active catalyst area or of the kinetic rate. In contrast, a change in the limiting current, obtained with 5% H_2/N_2 , which is kinetically limited at $t = 0$ only, can be due to either kinetic or diffusional losses. Therefore, by following the change in $(LPS)^{-1}$ and I_{lim} (5% H_2/N_2) with time, the

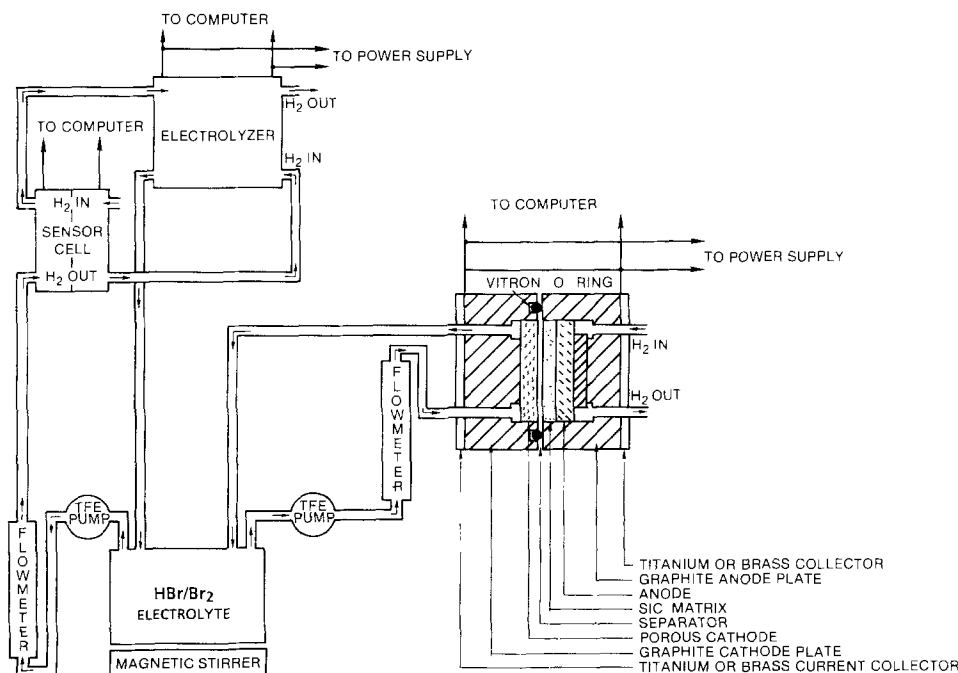


Fig. 2. Schematic of the fuel cell life test cell.

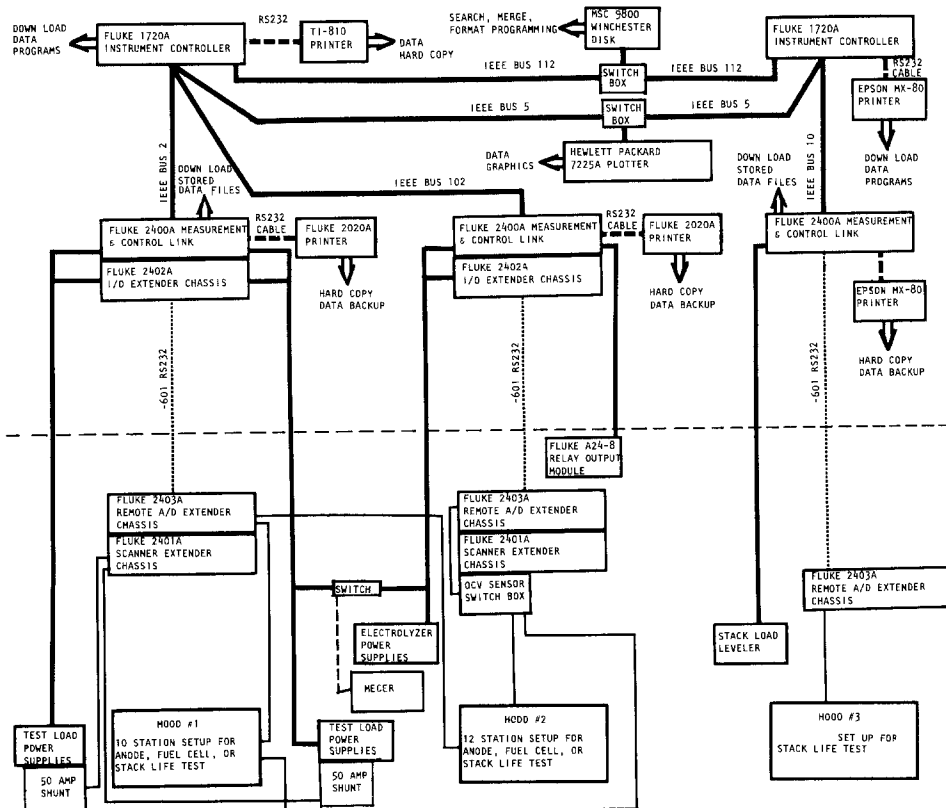


Fig. 3. Block diagram of life test computer system.

degradation mode of an electrode can be determined from the relative changes, as shown in Table III.

These parameters were generated at the beginning and the end of each life test, and at various random intervals in between. The data were reduced by the appropriate software to graphical representation, as in Fig. 9. Other quantitative descriptions of the life testing were the time

increments to a 25% and 50% decay in I_{lim} , and the % (LPS)⁻¹ at these times, determined from the plot in Fig. 9. Another useful quantitative description of the anode performance is the scaling factor, defined as

$$\text{Scaling Factor} = \frac{I_{lim}(100\% H_2)}{I_{lim}(5\% H_2/N_2) \times 20}$$

Since any gas diffusional limitations are eliminated when going from 5% to 100% H₂ (3), this parameter is a measure of ionic diffusion losses in the anode. This factor was therefore determined at the beginning and at the end of the life testing. Finally, the time for which the anode sustained 4 A/in.² (620 mA/cm²) was also recorded, as this value has been empirically found to be a good descriptor of the quality of the anode. These quantitative operating parameters, along with a description of the degradation anode, were then employed in the processing *vs.* performance correlations.

Fuel cell studies.—A large number of life tests were initiated. Some were left undisturbed such that a degradation rate could be established. Other tests, such as those involving the effect of membrane properties, were terminated when the useful information has been collected. In addition to the periodically recorded polarization values, the life testing was interrupted at random intervals and computer-controlled current/voltage data were generated and recorded. These data were reduced to plots of peak power *vs.* time and peak current *vs.* time (Fig. 6 and 8). At the end of each test, all these data were further reduced to quantitative parameters to be used in the fabrication *vs.* performance correlations. This data generated included: (i) the operating voltage at the applied current density and the times when this voltage has decreased by 5%, 10%, and 15%, (ii) similar data in terms of overvoltage, (iii) peak power at $t = 0$, and the times when the peak power has reached 90%, 80%, 65%, and 50% of the original value, (iv) the I_{max} value at the specific decay times found in (iii), and (v) total running time and reason for termination of the life test. The failure mode determination was made from all the available data after the autopsy of the dismantled cell. A summary of the reasons for the termination of all the 1 in.² fuel cell life tests are shown in Table IV.

As mentioned previously, the structure of the data files allowed for data analysis in terms of performance *vs.* fabrication parameters. In effect, this permitted sorting of

Table I. Database for life tested fuel cell components

*** CATALYST PARAMETERS ***	*** MEMBRANE PARAMETERS ***
0 ANODE NO.:	35 MEMBRANE:
1 CATALYST:	36 MEMBRANE THICKNESS:
2 SPECIFIC AREA:	37 TREATED:
3 Pt LOADING: mg/cm ²	*** MEMBRANE ACTIVITY ***
4 ANODE BATCH:	38 MEMBRANE RESISTANCE: mohm-in. ²
5 TFE IN CATALYST:	39 Br ₂ DIFFUSION: mA/in ²
6 WEIGHT OF TFE IN CATALYST:	*** CATHODE PARAMETERS ***
7 CATALYST APPLIED BY:	40 MATERIAL:
8 SUSPENDING AGENT:	41 THICKNESS:
9 SiC ON ANODE:	42 SPUTTERED Ir:
10 SiC SUSP. WITH:	43 Ir ON:
11 SiC TFE:	44 CATHODE CAVITY:
12 CATALYST SINTERED FOR:	*** FUEL CELL PARAMETERS ***
13 CATALYST SINTERED AT:	46 CELL TYPE:
14 CATALYST PRESSED:	47 NO. CELLS:
15 CATALYST PRESSED AT:	48 ANOXYTE WICKING:
16 PRESS. TEMP.:	49 BODY:
17 PRESSING TIME:	50 ANODE MATRIX:
18 BAKING TIME:	51 MATRIX THICKNESS:
19 BAKING TEMP.:	52 CONDUCTIVE MATRIX:
*** SUBSTRATE PARAMETERS ***	53 MEMBRANE STRETCHING:
20 SUBSTRATE:	54 PLATE SPACER:
21 WETPROOFING:	55 ANODE PREMETTED:
22 REPLICATION:	56 ACTIVATION:
23 BAKED AT:	57 PRETEST SOL. CHANGE:
24 BAKED FOR:	58 EVALUATED WITH 2M Br ₂ :
25 SINTERED AT:	59 LIFE TESTED AT:
26 SINTERED FOR:	60 LIFE TESTING CH ₂ Cl ₂ M:
27 SUBSTRATE PRESSED:	61 ANODE PLATE ID:
28 SUBSTRATE PRESSED AT:	62 CATH. PLATE ID:
29 PRESSED FOR:	63 A/C PLATE BR:
30 PRESSED AT:	
31 BATCH PENETRATION: in. H ₂ O	
32 BATCH RESISTIVITY: mohm-cm	
*** ANODE BATCH ACTIVITY @ (mg/cm ²) ***	
33 I(11a) WITH 5% H ₂ /N ₂ : A/cm ²	
34 I(11a) WITH 100% H ₂ : A/cm ²	

Table II. Life test summary

System	Area (in. ²)	No. of tests	Total run time (h)
Anodes	1	32	55,416
Fuel cells	1	87	124,368
	10	25	14,664
Electrolyzers	1	14	31,464
	10	12	9,984
		Total	235,896

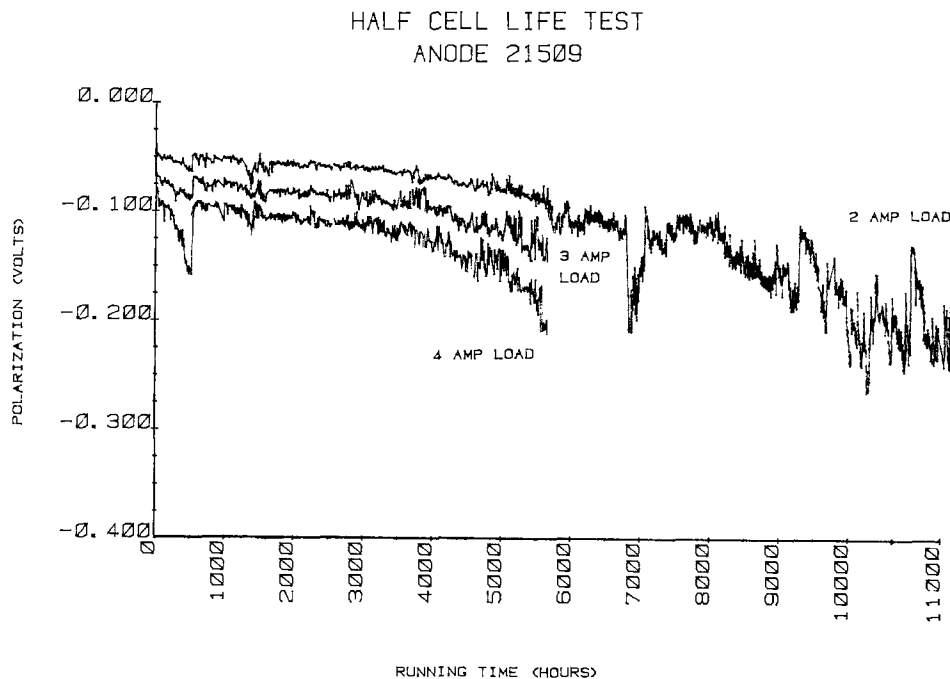


Fig. 4. Hydrogen electrode polarization vs. running time at 2, 3, and 4 A/in.².

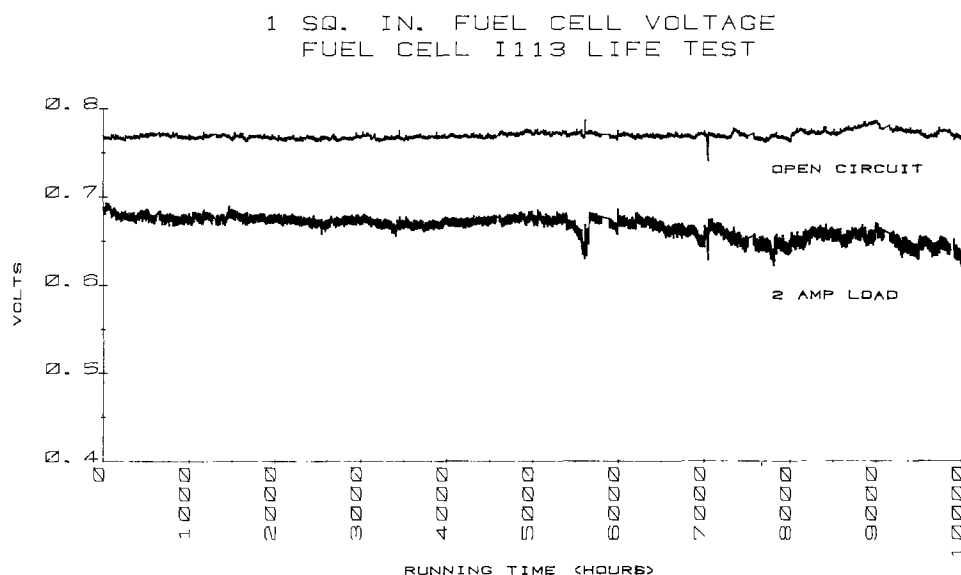


Fig. 5. 1 in.² fuel cell polarization vs. running time on a 2 A/in.² load.

data according to variations in any of the processing parameters. The results of this kind of analysis for fuel cells are shown in Fig. 10 and 11. It has to be emphasized that these data are an average of all the available data on fuel cells that met a certain set of specifications, e.g., 25% TFE in the anode catalyst layer, sintered at 327°C, with all the other parameters not necessarily the same.

Discussion

Analysis of the half-cell data such as that in Fig. 9, suggests that the anodes typically decay by a flooding mechanism, sometimes aided by the effects of poisoning. This is supported by the correlations that were run on the data. The trends indicate that a higher sintering temperature, which would be expected to cause the TFE in the catalyst layer to flow more and hence make the catalyst more hydrophobic, does decrease the rate of decay and extends the operating life time of these electrodes. Similarly, increasing the TFE content of the catalyst increases the running and decreases the degradation rates. These are the anticipated results if the decay mode is due to a flooding mechanism.

As seen from Table IV, the biggest challenge in life testing is keeping the peripherals and the external sources of poisons from degrading the test. Of the 87 fuel

cells life tested, only 21 reached the state where they were terminated for actual degradation or failure.

Analysis of the fuel cell lifetime data shows that anode hydrophobicity and membrane properties are the two key parameters. While not providing the highest activity (i.e., limiting current), the more hydrophobic anodes give fuel cells with longer operating life. The relative decay rates of fuel cells with anodes of different TFE content and sintering temperatures are shown in Fig. 10. This correlation is quite predictable.

As stated before, the choice of membranes was dictated primarily by the requirement that it possess high enough electrolyte transport properties to keep the anode fully wetted, since the system constraints resulted in a fuel cell design with an absence of an anolyte loop, and the use of dry H₂. As a result of this design, a "worst case" situation is shown in Fig. 12. This fuel cell was assembled with a du Pont membrane with essentially zero electrolyte transport properties. While it still provides a stable operation at current densities of up to 450 mA/cm², at higher current densities the anode gradually dries up, which shows up as a voltage loss. However, if the current density is decreased at this time, the anode rewets and the polarization returns to the original value. Hence, for a fuel cell of this design, the optimum membrane is one with larger electro-

MAX POWER RATIO/*I*_{max} (A) VS TIME
FUEL CELL I113 LIFE TEST

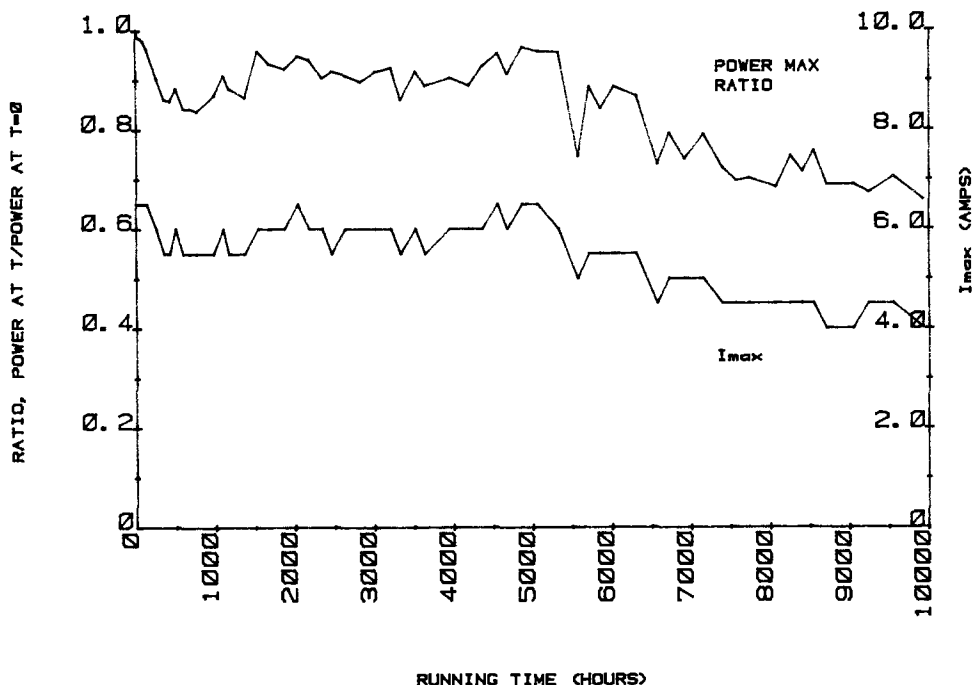


Fig. 6. Decay in the peak power (386 W/ft² at *t* = 0) and limiting current (6.5 A/in.² at *t* = 0) for the longest running 1 in.² fuel cell test.

10 SQ. IN. FUEL CELL VOLTAGE
FUEL CELL FTCA04 LIFE TEST

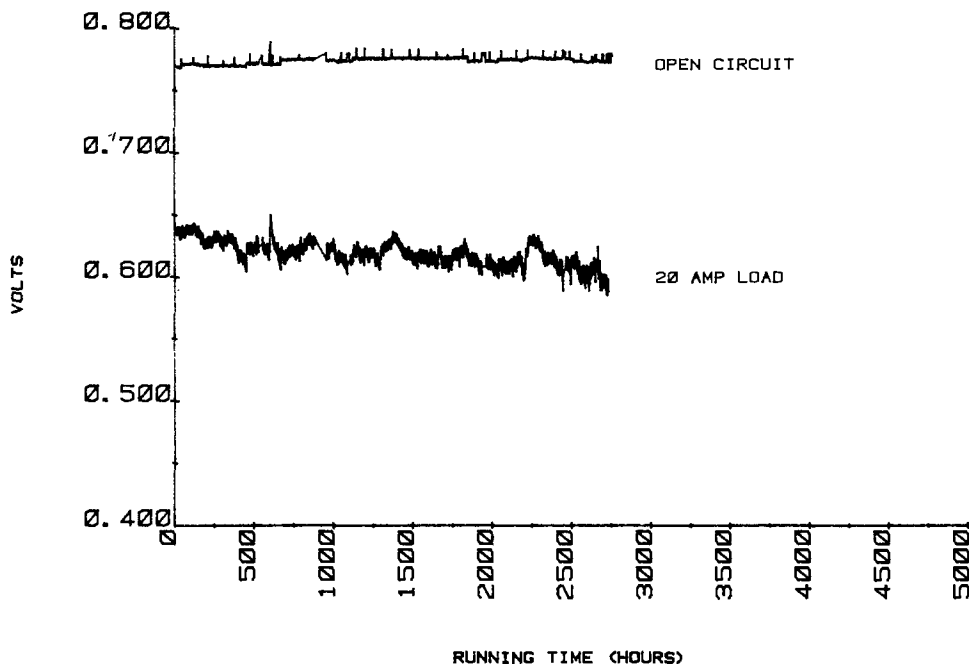


Fig. 7. 10 in.² fuel cell polarization vs. running time on a 2 A/in.² load.

lyte transport values, such as the RAI P1010 membrane (a styrene-based sulfonic acid polymer) with an electrolyte "leakage" of ~ 0.3 cm³/in.²/h, from a 1M Br₂/6.8M HBr catholyte.

One problem that became apparent as a result of our database management system was that these membranes were not identical from lot to lot. Using two lots of these RAI membranes, P1010 and R1010, the average lifetimes of fuel cells, with the major anode parameters being the same, were significantly different (Fig. 11). Since the Br₂ diffusion and resistance values for these membranes are very similar, the difference is attributed to some undefined contaminant in the R1010 membranes.

In terms of scale-up, going from a 1 to a 10 in.² fuel cell, there is a typical degradation of 30% or less in both the normalized peak powers and current densities, slightly less than that shown in Fig. 6 and 8. The decrease in performance is probably less than these values, since the pumping constraints allowed for a 7 cm³/in.²/min catholyte flow in the 1 in.² cell, but only 3 cm³/in.²/min in the 10 in.² cell. However, the operating parameters of this 10 in.² fuel cell, 244 W/ft² and 4 A/in.² at *t* = 0 and the reasonable degradation shown in Fig. 8 are still significantly superior to most other devices currently being developed.

Long-term life testing has shown some effect on the active Pt catalyst. The major effect, a net loss of Pt, is typi-

MAX POWER RATIO/ I_{max} (A) VS TIME
FUEL CELL FTCA04 LIFE TEST

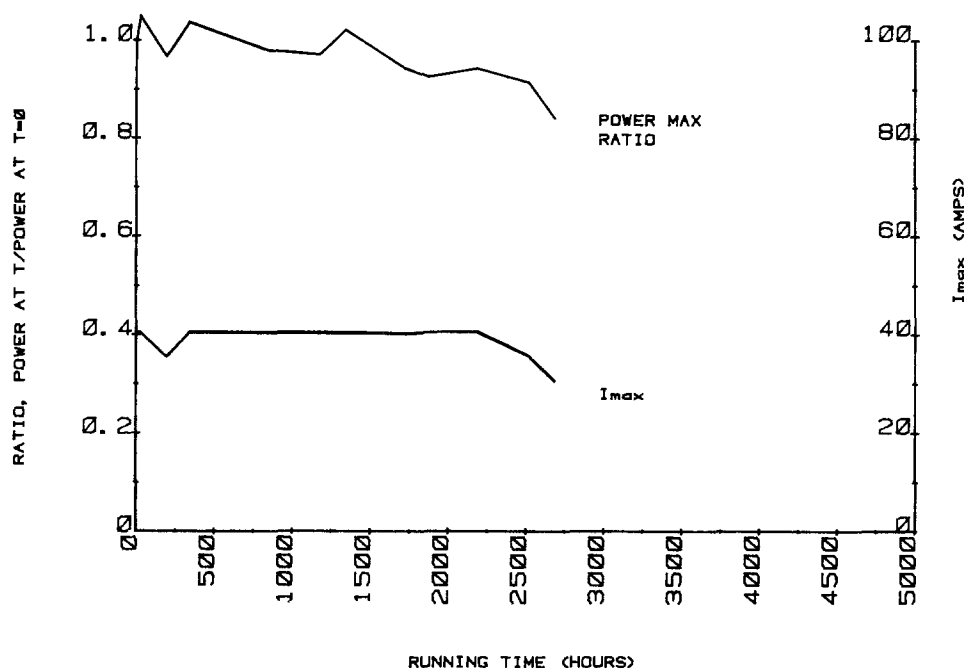


Fig. 8. Decay in the peak power (244 W/ft² at $t = 0$) and limiting current (4.0 A/in.² at $t = 0$) for the longest running 10 in.² fuel cell test.

INVERSE LPS RATIO & LC RATIO
ANODE A29418 LIFE TEST

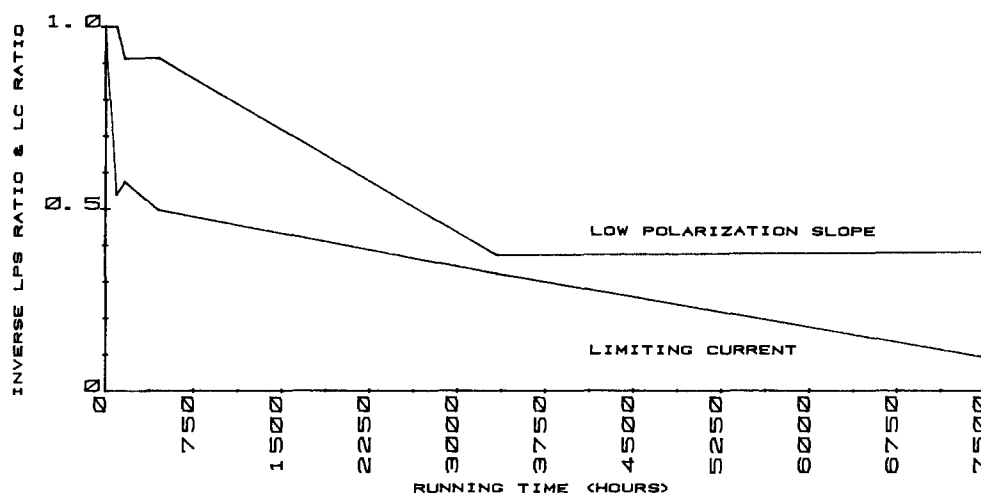


Fig. 9. Decay in LPS⁻¹ and limiting current, used for diagnosis of anode degradation mechanisms.

cally associated with an inadvertent brief pulsing of the anode to a high positive potential, where Br₂ is generated within the catalyst layer. In the normal operating mode, since the anode is posed at the reversible hydrogen potential, any Br₂ diffusing to the anode will be immediately reduced. As long as the H₂ supply is not interrupted, there should be no loss of Pt. We have also seen Pt recrystallization in one particular case of an 8700h anode life test, which also showed a 37% loss in total Pt loading. Pt agglomeration is not expected to occur at the low operating temperature (~ 30°C). It is assumed that this electrode

may have suffered a brief positive pulse, during the numerous necessary interruptions to the life testing. This would cause Pt to dissolve and subsequently to recrystallize upon reduction. We do not, as yet, have sufficient data to suggest that there is some fundamental mechanism responsible for the gradual degradation of the catalyst.

Table III. Determination of the degradation modes of anodes in a 8.9M HBr

LPS ⁻¹	I_{lim} (5% H ₂ /N ₂)	Degradation
Constant	Decreasing	Flooding
Decreasing by X%	Decreasing by X%	Poisoning
Decreasing by X%	Decreasing by Y% (Y > X)	Poisoning and flooding

Table IV. Reason for the termination of the 1 in.² fuel cell life tests

Reasons	Definition	No. of cells	Percentage of total
Needed space, no more useful data	Nothing	22	25.3
Leaks, hardware problems, human error	Peripherals	33	37.9
Copper on membranes, anodes (brass current collector)	Poisoning	11	12.6
> 20% increase in η , > 30% decrease in peak power	Degradation	15	17.2
Cannot support 3 A/in. ²	Failure	6	6.9

LIFETESTED FUEL CELLS
EFFECT OF ANODE HYDROPHOBICITY

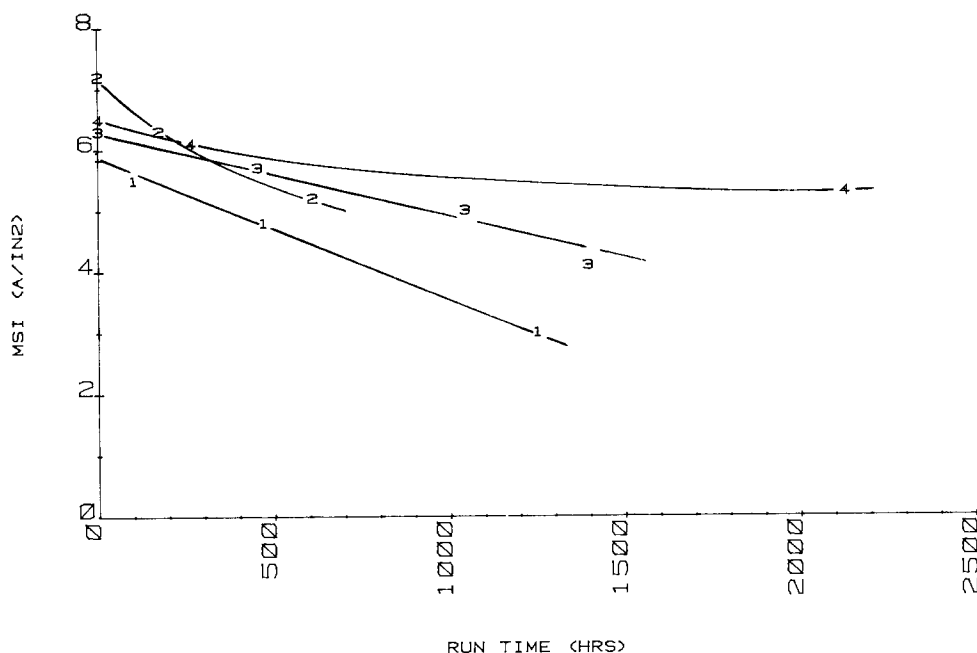


Fig. 10. Maximum sustained current (MSI) vs. running time for all 1 in.² fuel cells, with Pt-black-catalyzed anodes processed with: (curve 1) 25% TE-3170, sintered at 327°C/10 min, (curve 2) 25% TE-3170, sintered at 350°C/10 min, (curve 3) 30% TE-3170, sintered at 327°C/10 min, and (curve 4) 30% TE-3170, sintered at 350°C/10 min.

LIFETESTED FUEL CELLS
EFFECT OF MEMBRANE

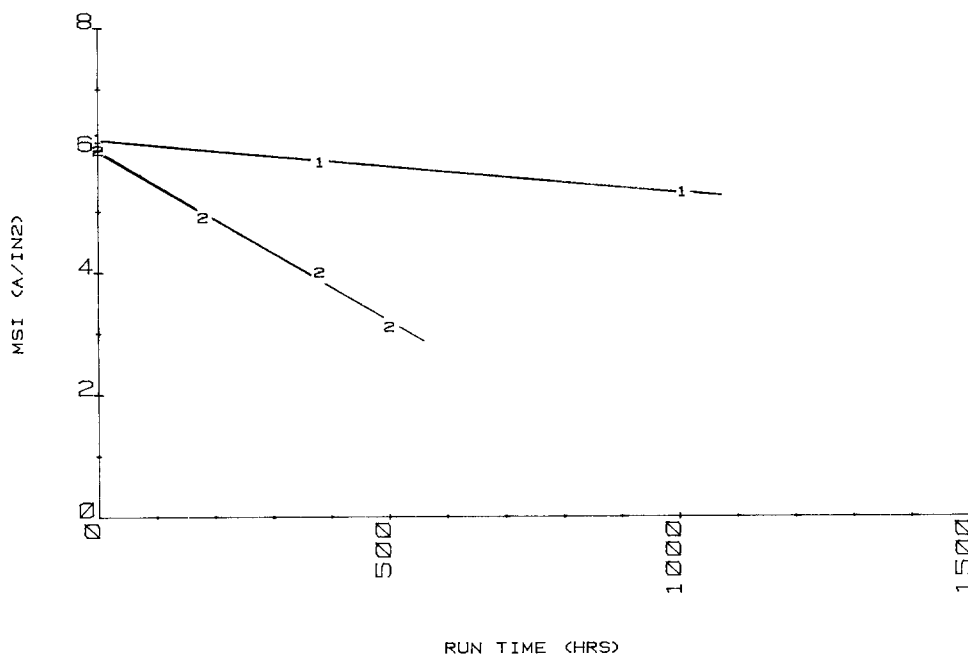


Fig. 11. Maximum sustained current (MSI) vs. running time for all 1 in.² fuel cells with Pt-black-catalyzed anodes processed with 30% TE-3170 and sintered at 327°C/10 min, and using membrane-type: (curve 1) RAI P-1010 (lot no. 2), and (curve 2) RAI R-1010 (lot no. 1).

Conclusion

After a total of 235,896h of anode/fuel cell life testing, the main parameters determining fuel cell operating lifetime have been found to be the hydrophobic nature of the anodes and the properties of the membrane. It has been shown that anode development cannot be solely guided by the obtaining of the largest current possible at $t = 0$. Such an anode is too hydrophilic to last extensively. There is a trade-off in making anodes more hydrophobic, where the initial performance is lower, but the operating endurance is better. The control of anode flooding is of primary concern, as these anodes (operating at 25°-50°C) have shown no catalyst sintering after 12,000h. Mem-

branes can be selected on the basis of their electrolyte transport properties, but certain intangibles, such as impurities, can have a marked effect. But, optimizing all these parameters independently and then in conjunction with all other factors such as electrolyte purity, cell design, etc., H₂/Br₂ fuel cells have been run for > 10,000h without significant degradation. The actual lifetime of these fuel cells is thus well in excess of 10,000h, limited in practice by the failure of the peripherals.

Acknowledgments

The authors wish to thank Dr. P. N. Ross for useful discussions and Ms. B. J. Griffith for the management of the computer data. This work was partially performed under

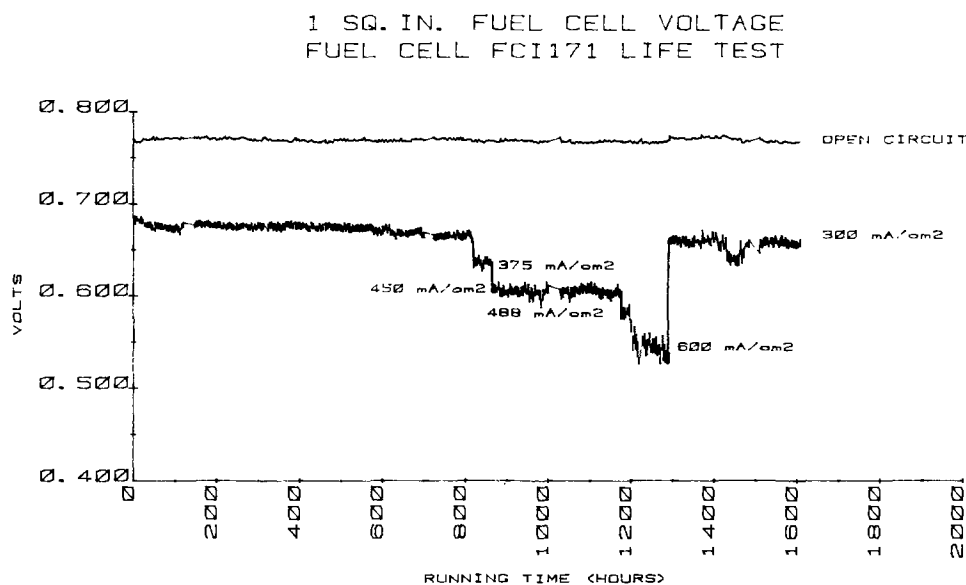


Fig. 12. Polarization of a 1 in.² fuel cell, with the du Pont membrane of virtually zero electrolyte transport, as a function of current density and time.

the Texas Instruments/DOE Cooperative Agreement DE-AC-1-79ER10000.

Manuscript submitted Dec. 17, 1983; revised manuscript received March 22, 1984.

Texas Instruments, Incorporated assisted in meeting the publication costs of this article.

REFERENCES

1. G. G. Barna, S. N. Frank, and T. H. Teherani, *This Journal*, **129**, 2464 (1982).
2. J. Winnick and P. N. Ross, *ibid.*, **128**, 991 (1981).
3. R. P. Iczkowski and M. B. Cutlip, *ibid.*, **127**, 1433 (1980).

On the Relation Between the Overpotentials and Structures of Graphite Fluoride Electrode in Nonaqueous Lithium Cell

N. Watanabe,* R. Hagiwara, and T. Nakajima

Department of Industrial Chemistry, Faculty of Engineering, Kyoto University, Kyoto-shi, Sakyo-ku, 606, Japan

ABSTRACT

A study was made of the relation between the cathode overpotentials and structures of two kinds of graphite fluorides, $(CF)_n$ and $(C_2F)_n$ in nonaqueous lithium battery. The overpotential of $(CF)_n$ electrode decreased with increasing interlayer spacing and decreasing thickness of the crystallite along the C axis. However, it was found that the overpotential of $(C_2F)_n$ electrode primarily depended on the amount of the defects which would be present in the form of polynuclear aromatic carbon rings in $(C_2F)_n$. The defects in $(C_2F)_n$ would give the short circuiting paths for the transfer of a lithium ion in diffusion layer. The higher discharge potential of $(C_2F)_n$ than that of $(CF)_n$ was mainly attributed to the effect of the defects contained in $(C_2F)_n$.

Poly(carbon monofluoride), $(CF)_n$, has many excellent characteristics as a cathode material for lithium battery in nonaqueous electrolyte systems (1-4). Besides this well-known graphite fluoride, poly(dicarbon monofluoride), $(C_2F)_n$, which was recently found in our laboratory, has also high possibilities as a new active mass owing to the higher discharge potential than that of $(CF)_n$ in 1M lithium perchlorate-propylene carbonate solution (5-7). Graphite fluorides are obtained in the form of a paracrystallite by the direct fluorination of carbon materials at high temperatures. For example, when natural graphite is used as a starting material, $(CF)_n$ is formed around 600°C, while $(C_2F)_n$ is prepared at a lower temperature of 350°-400°C. With increasing fluorination temperature, the composition changes from $(C_2F)_n$ to $(CF)_n$ via their mixture, in which $(CF)_n$ content increases with increasing temperature. It is noted that $(C_2F)_n$ is prepared only from a highly crystallized graphite, such as natural graphite or graphitized petroleum coke, at a relatively low temperature (8). The carbon layers of graphite fluoride consist of an infinite array of trans-linked cyclohexane chairs without

aromatic nature. Both in $(CF)_n$ and $(C_2F)_n$, carbon atom with sp^3 -hybridized orbital is covalently bonded to fluorine. $(CF)_n$ is regarded as a first stage compound, whereas $(C_2F)_n$ is of the second stage, the structure of which has been recently investigated in detail (9).

The electromotive force of $(CF)_n$ -Li cell was calculated to be 4.57V by Margrave *et al.* (10) on the assumption that the discharge reaction produces carbon and lithium fluoride. However, the open-circuit voltage (OCV) of a real cell composed of lithium and graphite fluoride prepared from natural graphite is around 3.2-3.3V at 25% discharge in 1M $LiClO_4$ -propylene carbonate solution. It is lower by more than 1V than the calculated value. For this fact, Whittingham (11) and Watanabe *et al.* (5, 6) have proposed that the cell reaction is the formation of a graphite intercalation compound of lithium fluoride. The analysis of discharge products (12) and OCV's in different solvents (13) have indicated that the cell reaction includes the formation of a graphite intercalation compound of lithium fluoride solvated by solvent molecules. The flat discharge potential of graphite fluoride-Li cell suggests that the discharge reaction proceeds heterogeneously, namely by the formation of a ternary intercalation compound of

* Electrochemical Society Active Member.

graphite, followed by the decomposition to carbon, lithium fluoride, and solvent molecule. This would maintain the constant thickness of a so-called diffusion layer through which a solvated lithium ion is transferred to the electrode surface. It has been proposed that a fairly large overpotential of graphite fluoride cathode is due to the delay of lithium ion transfer in the diffusion layer consisting of the ternary intercalation compound of graphite (6), which is consistent with the fact that the cathode overpotential increases with increasing size of solvated lithium ions (13).

This paper is concerned with the relation between the cathode overpotentials and structures of $(CF)_n$ and $(C_2F)_n$. The overpotentials are discussed on the basis of the results obtained by x-ray diffraction, ^{19}F -NMR, and ESR measurements.

Experimental

$(CF)_n$ and $(C_2F)_n$ -type graphite fluorides were prepared by fluorination of Madagascar natural graphite, petroleum coke (original and heat-treated at 2800°C), vapor-grown carbon fiber (heat-treated at 3000°C) and exfoliated graphite in fluorine gas of 1 atm at temperatures between 290°-600°C. Some of $(C_2F)_n$ -type graphite fluorides were prepared via graphite intercalation compound of MgF_2 and F_2 (GIC) (14). Synthetic conditions are listed in Table I.

Sample L was heat-treated in fluorine gas of 1 atm at 400°, 500°, 550°, and 600°C for 24h to investigate the heat-treatment effect on $(C_2F)_n$. In addition to the heat-treatment in fluorine atmosphere, treatment *in vacuo* at 400°C was also performed for comparison.

The prepared samples were analyzed by means of elemental analysis, x-ray diffractometry, ^{19}F -NMR and ESR spectroscopies. NMR measurements were made using a Crossed Coil NMR Spectrometer (Varian WL 109) with scanning of the magnetic field at a fixed radio frequency of 15 MHz. ESR measurements were carried out by the aid of Nihon Denshi, JES-3BX with scanning of the magnetic field at a fixed radio frequency of 9.4 GHz (X-band).

Discharge of graphite fluorides was performed at a fixed current density of 0.5 mA/cm² in 1M LiClO₄-propylene carbonate solution at 25°C. The polarization curves were also obtained in the range of 10⁻⁷-10⁻³ A/cm². Preparation of electrodes and cell assembly were the same as those reported previously (13).

Results and Discussion

The relation between crystallinity and cathode overpotential of graphite fluorides.—Figure 1 shows the plots of the cathode overpotentials of $(CF)_n$ at 25% discharge against the interlayer spacing, $d_{(001)}$ and half-width, $\beta_{(001)}$ of (001) diffraction line. The overpotential decreased with increasing $d_{(001)}$ and $\beta_{(001)}$. Since the thickness of

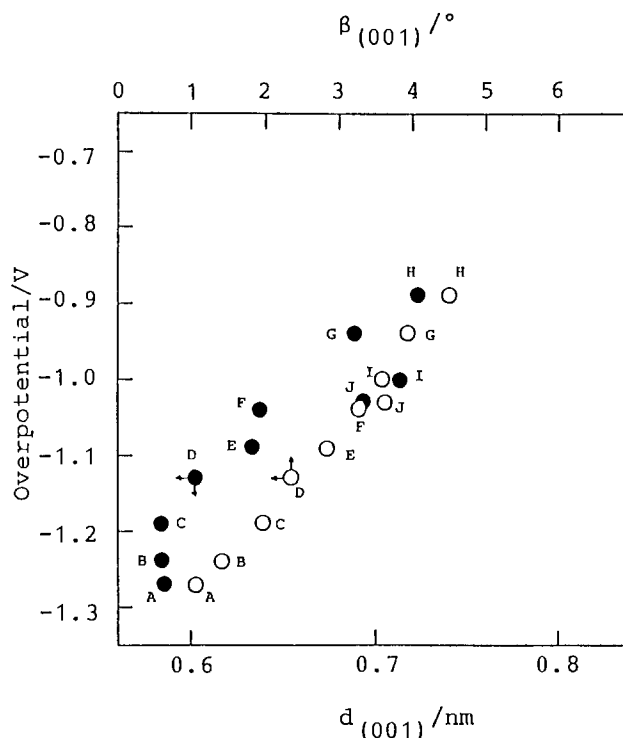


Fig. 1. The cathode overpotentials of $(CF)_n$ -type graphite fluorides in lithium cells (0.5 mA/cm², at 25% discharge) as a function of $d_{(001)}$ and $\beta_{(001)}$.

monolayer of graphite fluoride is the same among all the samples, the space between monolayers increases with increasing $d_{(001)}$. The half-width, $\beta_{(001)}$ is inversely proportional to the thickness of the graphite fluoride crystallite along C axis. As the crystallite size and $d_{(001)}$ spacing of graphite fluoride strongly depend on the crystallinity of a starting carbon material, these factors can be controlled by choosing the starting carbon material as well as reaction temperature. It has been already pointed out that the overpotential of graphite fluoride electrode depends on the rate of transfer of solvated lithium ion in the diffusion layer (13). The increase in the space between monolayers of graphite fluoride with increasing $d_{(001)}$, and the decrease in thickness of the crystallite along C axis would facilitate the transfer of lithium ion in the diffusion layer on the discharge process (Fig. 2). It was confirmed prior to this experiment that the overpotential was independent of the particle size of graphite fluoride. It means that the rate of discharge reaction is not determined by the transfer of lithium ion among the particles but by that inside the particles of graphite fluoride.

Table I. Synthetic conditions of graphite fluorides

Sample	Starting carbon	Reaction temp (°C)	Reaction time (h)	F/C	Notes
A	Madagascar natural graphite	590	28	1.01	$(CF)_n$ -type
B	Petroleum coke heat-treated at 2800°C	600	11	1.10	$(CF)_n$ -type
C	Petroleum coke heat-treated at 2800°C	510	11	0.99	$(CF)_n$ -type
D	Exfoliated graphite	590	11	1.00	$(CF)_n$ -type
E	Non-heat-treated petroleum coke	420	7	1.11	$(CF)_n$ -type
F	Non-heat-treated petroleum coke	360	7	1.13	$(CF)_n$ -type
G	Non-heat-treated petroleum coke	340	9	1.10	$(CF)_n$ -type
H	Non-heat-treated petroleum coke	290	21	1.14	$(CF)_n$ -type
I	—	—	—	1.05	$(CF)_n$ -type
J	—	—	—	1.06	$(CF)_n$ -type
K	Madagascar natural graphite	390	168	0.61	$(C_2F)_n$ -type
L	Madagascar natural graphite	350	504	0.66	$(C_2F)_n$ -type
M	Madagascar natural graphite	340	97	0.58	$(C_2F)_n$ -type
N	Madagascar natural graphite	390	23	0.63	$(C_2F)_n$ -type
O	Petroleum coke heat-treated at 2800°C	340	50	0.59	$(C_2F)_n$ -type
P	Vapor-grown carbon fiber heat-treated at 3000°C	370	50	0.59	$(C_2F)_n$ -type

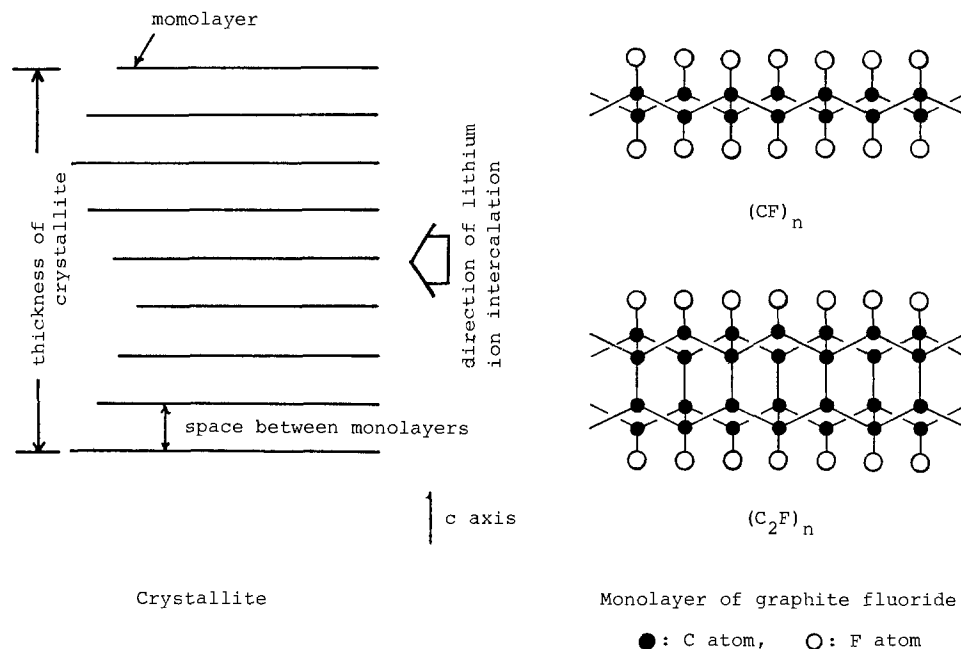


Fig. 2. Schematic illustrations of graphite fluorides.

However, it is difficult to prepare $(C_2F)_n$ -type graphite fluorides with large differences in crystallinity, $d_{(001)}$, and $\beta_{(001)}$, because starting carbon materials and reaction temperature are limited in this case. $(C_2F)_n$ can be prepared only from a highly graphitized carbon material such as natural graphite at 350–400°C (8). Ungraphitized petroleum coke with low crystallinity gives only $(CF)_n$ at any temperature. For every $(C_2F)_n$ prepared, the overpotential at a current density of 0.5 mA/cm² was about 0.9V, which corresponded to the minimum value for that of $(CF)_n$.

Figure 3 shows the typical discharge curves of $(CF)_n$ and $(C_2F)_n$. The flatness of discharge potential for $(CF)_n$ was improved with increasing crystallinity of the sample while the discharge potential decreased. In other words, the height and flatness of discharge potential are compensative with each other. Even for $(CF)_n$, the overpotential was decreased approaching to that of $(C_2F)_n$ by choosing a carbon with low crystallinity as a starting material and by fluorinating at a low temperature; however, the flatness of discharge potential was inferior.

The effects of the heat-treatment of $(C_2F)_n$ on the discharge characteristics and structure.—Figure 4 and Table II show the discharge characteristics of heat-treated $(C_2F)_n$ in lithium battery. With increase of the heat-treatment temperature, the discharge potential decreased and the flatness of discharge potential was improved at the beginning of discharge. The effects of the heat-treatment at 400°C on discharge characteristics were scarcely observed. As can be seen in Table II, the decrease of discharge potential is caused by the increase of

overpotential rather than the decrease of open-circuit voltage. In the present work, as described below, the improvement of crystallinity of $(C_2F)_n$ by the heat-treatment was not found as far as the analysis by x-ray diffractometry was concerned. Nevertheless, the overpotential was fairly changed by the heat-treatment.

With increasing temperature of the heat-treatment in fluorine gas, the color of $(C_2F)_n$ gradually changed from black to white, while the weight of the sample scarcely changed, except for that heat-treated at 600°C, whose weight decreased by 1%–2%. The $d_{(001)}$ and $\beta_{(001)}$ were also unchanged by the heat-treatment for every sample, which indicates that the improvement of crystallinity was not achieved by this treatment. The F/C ratio, $d_{(001)}$, and $\beta_{(001)}$ were 0.66 ± 0.02 , 0.81 ± 0.01 nm and $3.2^\circ \pm 0.2^\circ$, respectively.

Figure 5 shows ¹⁹F-NMR spectra of $(C_2F)_n$, where two kinds of resonance absorptions were observed. One was very broad with peak-to-peak width, $\Delta H'$ of 9.0 ± 0.1 G, and the other was sharp one with $\Delta H'$ of 1.5 ± 0.1 G. No change of linewidth was observed by the heat-treatment. Differential gradient method showed that the narrow absorption line was Lorentzian, which is related to homogeneous system where the energy absorbed from oscillating magnetic field is distributed so that the spin system may maintain the thermal equilibrium through the resonance process. The narrow linewidth would correspond to motional narrowing, which means that fluorine atoms make weak chemical bonds with carbon atoms, therefore having higher activity than those covalently bonded. This

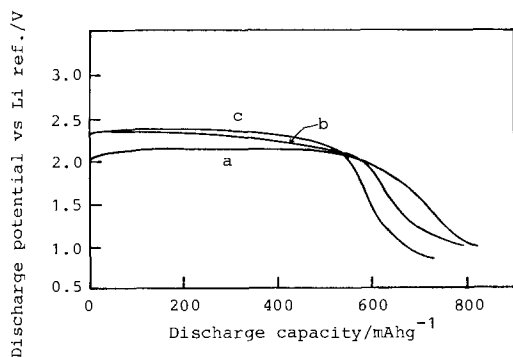


Fig. 3. Discharge curves of graphite fluorides (0.5 mA/cm²). Curve a: $(CF)_n$ (sample A). Curve b: $(CF)_n$ (sample E). Curve c: $(C_2F)_n$ (sample K).

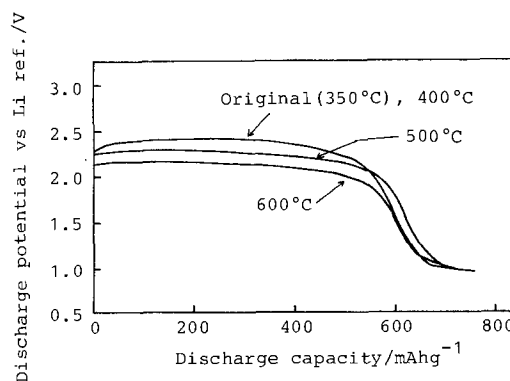


Fig. 4. Effects of heat-treatment on discharge characteristics of $CF_{0.66}$ (0.5 mA/cm², sample L).

Table II. Discharge characteristics of heat-treated $\text{CF}_{0.66}$ prepared from natural graphite (sample L)

Temp ($^{\circ}\text{C}$)	OCV at 25% discharge (V)	Discharge potential (V)	Overpotential (V)	Discharge capacity (mAh/g)
350	3.30	2.41	0.89	690
400	3.28	2.38	0.90	730
500	3.26	2.28	0.98	720
600	3.24	2.14	1.10	710

absorption line decreased as the heat-treatment temperature increased and almost disappeared at 600°C . A slight decrease of the open-circuit voltage, shown in Table II, might be caused by the decrease of these fluorines weakly bonded with carbon atoms. The decrease of absorption intensity by the heat-treatment was slightly larger *in vacuo* at 400°C than in fluorine gas at the same temperature. The broad absorption line was approximately gaussian, where each spin is situated in different local fields, which causes the line broadening. By taking the linewidth and peak intensity into consideration, this spin component is attributable to the major part of fluorine atoms in graphite fluoride, namely, fluorine atoms covalently bonded to carbon atoms. Consequently, there are two kinds of fluorine species in $(\text{C}_2\text{F})_n$. For $(\text{CF})_n$

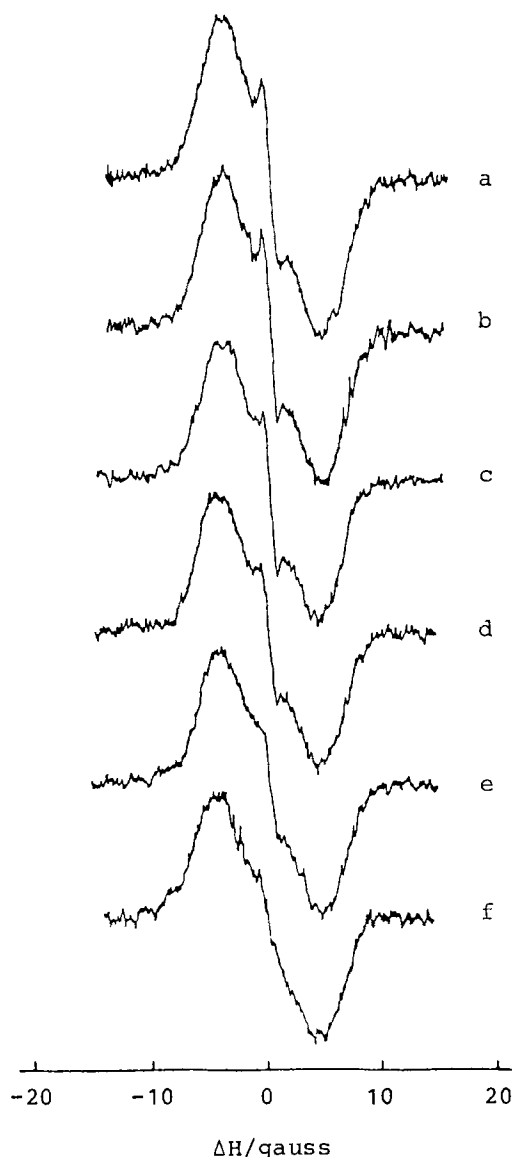


Fig. 5. ^{19}F -NMR spectra of heat-treated $\text{CF}_{0.66}$ (sample L). Curve a: original (prepared at 350°C). Curve b: 400°C in F_2 . Curve c: 400°C *in vacuo*. Curve d: 500°C in F_2 . Curve e: 550°C in F_2 . Curve f: 600°C in F_2 . $\nu = 15 \text{ MHz}$. $H_0 = 3750\text{G}$. $MA = 0.5\text{G}$.

prepared from highly graphitized carbon at around 600°C , only one broad absorption line was observed with the same $\Delta H'$ as that of $(\text{C}_2\text{F})_n$, which means that $(\text{CF})_n$ has only a covalent bond between fluorine and carbon atoms.

Figure 6 shows the results of ESR measurements. ESR spectra of $(\text{C}_2\text{F})_n$ gave a single peak with a constant g value of 2.004 having no dependence on the heat-treatment temperature. From the g value, the radicals observed are reasonably ascribed to carbon. As the g value was also 2.004 in case of $(\text{CF})_n$, the radicals are the same kind, even though the intensity of the signal was much smaller than that of $(\text{C}_2\text{F})_n$. As shown in Fig. 6, the peak-to-peak width, $\Delta H'$, increased rapidly with increasing heat-treatment temperature, however, gradually increasing above 500°C . Furthermore, the differential gradient method showed that the type of the absorption line was changed from lorentzian to gaussian with increasing heat-treatment temperature. The P value (the product of the peak-to-peak height with the square of the linewidth of a differential absorption line) approximately corresponding to radical concentration decreased monotonously with increasing heat-treatment temperature.

From the above results, the following discussion is derived. The ESR measurement indicates that $(\text{C}_2\text{F})_n$ contains a small amount of unreacted carbon which is so randomly distributed as being unable to be detected by x-ray diffractometry and elemental analysis. The presence of unreacted carbon was recently confirmed by a high resolution electron microscope (15). It is regarded as a kind of defect which would be present in the form of polynuclear aromatic carbon rings in $(\text{C}_2\text{F})_n$. This carbon produces carbon radicals by making covalent bonds partially with fluorine atoms or the cleavage of double bond. The black color of $(\text{C}_2\text{F})_n$ is therefore caused by these defects. Namely, the defects in the $(\text{C}_2\text{F})_n$ heat-treated at low temperatures have fairly long conjugated π systems, so the π - π^* transition energy is in the range of visible lights. The n - π^* transition by the delocalized radicals is also in this range. The fluorine species giving a narrow absorption line detected in ^{19}F -NMR measurements have weak chemical bonds with the unreacted carbon. With increasing heat-treatment temperature, the double bonds are cleaved to make covalent bonds with mobile fluorine species, which causes the decrease and localization of radicals. Consequently, the broadening of the line width and the transformation from lorentzian to gaussian are observed in ESR spectra. At the same time, the intensity of the narrow-width line is lowered in NMR spectra. In this way, the defect concentration decreases with increasing heat-treatment temperature. By the destruction of the conjugated π systems, the light absorption shifts out of the visi-

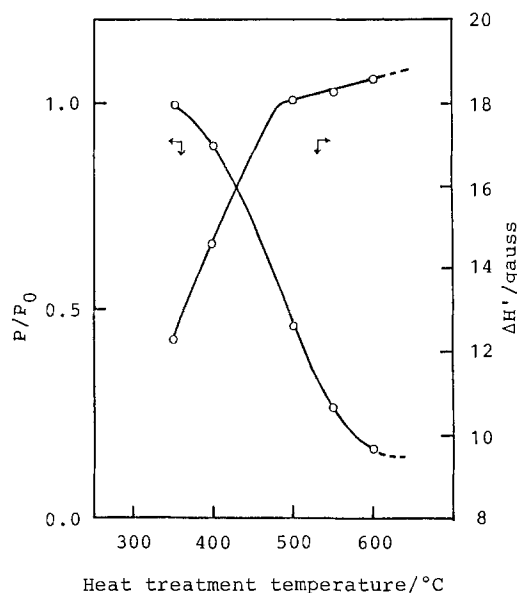


Fig. 6. ESR measurement of $\text{CF}_{0.66}$ (sample L). $\Delta H'$: peak-to-peak width. P : absorption intensity, $x(\Delta H')^2$. P_0 : P of original one.

ble light range and the color of $(C_2F)_n$ is changed to white. The difference between the heat-treatments in fluorine gas and *in vacuo* was not so remarkable at 400°C. The interaction between fluorine gas and the carbon radicals inside the graphite fluoride (16) would not be so strong at such a temperature. It is interesting to estimate the absolute radical concentration in graphite fluoride. The comparison was made using carbonized dextrose as a standard sample whose spin density has been already known (17). According to this method, the order of radical concentration in $(C_2F)_n$ was 10^{20} - 10^{21} spins/g, which means that it has one radical per several tens to several hundreds of carbon atoms. The radical concentration in $(CF)_n$ was less than tenth part of that in $(C_2F)_n$ heat-treated at 600°C.

The effects of the defects in $(C_2F)_n$ on the discharge characteristics can be described as follows. The defects are in the form of polynuclear aromatic carbon rings in $(C_2F)_n$. Around these defects, the chemical bond between carbon and fluorine atoms would be so weak that the ternary compounds, $C_2 \cdot F^{\delta-} \cdot Li^{\delta+} \cdot zS$, produced by the discharge reaction (13) might be more easily decomposed to carbon, lithium fluoride, and solvent molecules, which would make the transfer of lithium ion easier. Such defects in $(C_2F)_n$ are considered to be a kind of short circuiting path that decreases the overpotential. This factor would be dominant in case of $(C_2F)_n$. For $(CF)_n$, this kind of effect is much smaller than in $(C_2F)_n$ because the defect concentration is much lower. The heat-treatment of $(C_2F)_n$ is just the elimination of the defect which lowers the overpotential. The improvement of the flatness of discharge potential would arise from the decrease of the defect concentration inside the graphite fluoride crystallite by heat-treatment.

The difference in the discharge performance between $(CF)_n$ and $(C_2F)_n$.—Figure 7 shows typical cathodic polarization curves of $(CF)_n$ (sample A), $(C_2F)_n$, and that heat-treated at 600°C (sample K) at 25% discharge. All the samples were prepared from Madagascar natural graphite. Their open-circuit voltages were almost the same, $3.27 \pm 0.02V$ at 25% discharge. In every case, the plots of cathode potentials against the logarithms of current densities gave a straight line in the range of less than $10^{-4} A/cm^2$ with a bending point at the current density of 10^{-6} - $10^{-5} A/cm^2$. However, the current-interrupter method revealed that no activation overpotential was present in this region. It can be said that the rate-determining step of the discharge reaction is the transfer of lithium ion into graphite fluoride layers in the whole region in Fig. 7.

Two factors must be taken into consideration to evaluate the difference in discharge potentials between $(CF)_n$ (sample A) and $(C_2F)_n$ (sample K). One is the thickness of graphite fluoride crystallite along the C axis, discussed above, and the other is the short circuiting paths which

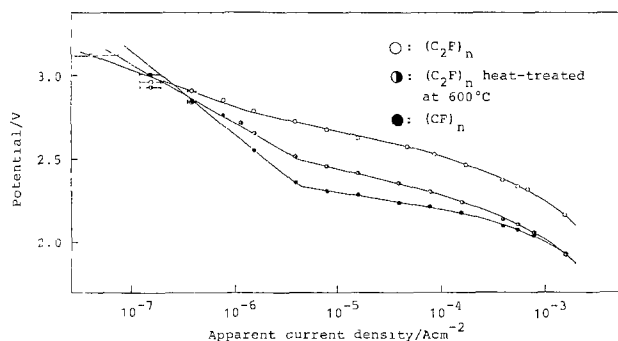


Fig. 7. Galvanostatic polarization curves of graphite fluorides (at 25% discharge). $(CF)_n$: sample A. $(C_2F)_n$: sample K.

arise from the defects in graphite fluoride, also discussed above. The space between monolayers of graphite fluoride was found to be almost the same for both $(CF)_n$ and $(C_2F)_n$ when they were prepared from a highly graphitized carbon material (9). The discharge potential of $(C_2F)_n$ (sample K) was higher by 0.3-0.4V than that of $(CF)_n$ (sample A) in the range of 5×10^{-6} - $5 \times 10^{-4} A/cm^2$, being, however, decreased by 0.2V with heat-treatment at 600°C in fluorine gas. This difference in the discharge potentials between the original and heat-treated $(C_2F)_n$'s is attributed to the decrease in the defect concentration. $(C_2F)_n$ with more short circuiting paths gives the higher discharge potential than the heat-treated one. Consequently, the difference in the discharge potentials between $(CF)_n$ (sample A) and heat-treated $(C_2F)_n$ ($\leq 0.1V$) would be mainly due to the difference in the thickness of the crystallite of graphite fluoride along C axis, which was 3 nm for heat-treated $(C_2F)_n$ and 6 nm for $(CF)_n$ (sample A) by the approximate calculation from the half-width of (001) diffraction line, $\beta_{(001)}$. The transfer of lithium ion between graphite fluoride layers would be faster in heat-treated $(C_2F)_n$ with the thinner crystallite than in $(CF)_n$ on the discharge process.

Acknowledgments

The authors wish to thank Dr. Fujinobu Nakamura of Kyoto University for his assistance in ^{19}F -NMR measurement, and Professor Yukio Kanaji and Mr. Shigehito Deki of Kobe University for their assistance in ESR measurement. Fluorine gas used in this study was supplied by courtesy of Daikin Kogyo Company Limited, which is also gratefully acknowledged.

Manuscript submitted Oct. 24, 1983; revised manuscript received April 9, 1984.

Kyoto University assisted in meeting the publication costs of this article.

REFERENCES

1. N. Watanabe and M. Fukuda, U.S. Pat. 3,536,532 (1970); 3,700,502 (1972).
2. M. Fukuda and T. Iijima, *Prog. Batt. Solar Cells*, **1**, 26 (1978).
3. J. Watanabe, H. Ogawa, and R. Okazaki, *ibid.*, **1**, 39 (1978).
4. J. Watanabe, E. Kawakubo, T. Shinagawa, and Y. Kajikawa, *ibid.*, **3**, 74 (1980).
5. N. Watanabe, *Solid State Ionics*, **1**, 87 (1980).
6. N. Watanabe and K. Morigaki, *Denki Kagaku*, **47**, 169, 174 (1979).
7. N. Watanabe, R. Hagiwara, N. Kumagai, T. Sakai, and T. Nakajima, *ibid.*, **51**, 183 (1983).
8. Y. Kita, N. Watanabe, and Y. Fujii, *J. Am. Chem. Soc.*, **101**, 3832 (1979).
9. H. Touhara, K. Kadono, and N. Watanabe, *Tanso*, **117**, 98 (1984).
10. A. J. Valerga, R. B. Badachhape, G. D. Parks, P. Kamarchick, J. L. Wood, and J. L. Margrave, Final Report, Contract DAAB 07-73-C-0056 (ECOM), Rice University, Austin, TX (1974).
11. M. S. Whittingham, *This Journal*, **122**, 526 (1975).
12. H. Touhara, H. Fujimoto, A. Tressaud, and N. Watanabe, To be submitted to *Solid State Ionics*.
13. N. Watanabe, R. Hagiwara, T. Nakajima, H. Touhara, and K. Ueno, *Electrochim. Acta*, **27**, 1615 (1982).
14. T. Nakajima, M. Kawaguchi, and N. Watanabe, *Carbon*, **20**, 287 (1982).
15. H. Touhara, K. Kadono, M. Endo, and N. Watanabe, in "The 10th Annual Meeting of the Carbon Society of Japan," p. 136, Tokyo (1983).
16. S. Koyama, Ph.D. Thesis, Kyoto University, Kyoto, Japan (1980).
17. R. H. Hoskins and R. C. Pastor, *J. Appl. Phys.*, **31**, 1506 (1960).

Low Temperature Performance Characterization of Lithium Sulfuryl Chloride Cells

Michael Binder,* Sol Gilman,* William Wade, Jr., and Charles Walker, Jr.

U.S. Army Electronics Technology and Devices Laboratory, ERADCOM, Power Sources Division, Fort Monmouth, New Jersey 07703

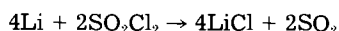
ABSTRACT

Lithium sulfuryl chloride cells containing various concentrations of LiAlCl_4 were constructed and discharged at 2.5 mA/cm^2 constant current at 25° and -32°C . The solid discharge product in the cathode was analyzed and found to contain only LiCl . No sulfur or other lithium salt was found. An explanation of the reduced capacity and decreased operational voltage of these cells discharged at -32°C is offered. At electrolyte concentrations $\geq 0.75M$ cathode capacity is primarily limited by conductivity, while for electrolyte concentrations $\leq 0.75M$, diffusion appears to be the limiting factor. The decreased operational voltage for cells discharged at -32°C is due to a decrease in the amount of catalytically produced Cl_2 .

The $\text{Li/SO}_2\text{Cl}_2$ primary cell has received widespread research and development interest ever since initial reports on its discovery appeared (1-3). The cell consists of a lithium anode, inert porous carbon cathode on expanded nickel screen (which serves as both a structural support and current collector), and a SO_2Cl_2 solution serving a dual role as both ionizing solvent for dissolving the conducting LiAlCl_4 electrolyte salt and as an active cathode depolarizer.

In these cells (known as soluble or liquid cathode cells), the liquid SO_2Cl_2 cathode remains in physical contact with the lithium anode and has the obvious advantage of minimizing mass-transfer effects associated with supplying oxidant to electrode-electrolyte layers. Spontaneous chemical reaction of anode and cathode is prevented by formation of a passivating insoluble film of LiCl on the anode surface as soon as lithium and the oxyhalide solvent come in contact. The LiCl film has relatively low electronic conduction and forms an electronically insulating interphase between metal and solution (4). This protective film slows internal self-discharge and is responsible for providing potentially long shelf life.

The $\text{Li/SO}_2\text{Cl}_2$ cell has higher open-circuit voltages than analogous Li/SOCl_2 cells, which eventually should translate into higher load voltages and higher energy densities for fully engineered cells. Although both types of cells have high boiling and low freezing points, and thus broad temperature windows for battery applications, $\text{Li/SO}_2\text{Cl}_2$ should be safer because at room temperature and medium current drains ($\leq 2.5 \text{ mA/cm}^2$) only LiCl and SO_2 are formed and no sulfur (1).



Elemental sulfur (or other insoluble sulfur species) are undesirable products in lithium cells since differential thermal analysis studies have identified exothermic reactions occurring between lithium and elemental sulfur at 150°C (5). This temperature may easily be reached under cell abuse conditions such as cell shorting or forced overdischarge. Lack of sulfur in discharged $\text{Li/SO}_2\text{Cl}_2$ cells implies that SO_2Cl_2 would be more abuse resistant for lithium-based cells than SOCl_2 .

In addition, SO_2 formed is soluble up to $\sim 1.0M$ in SO_2Cl_2 (1, 6), precluding internal pressure buildup during or after discharge. The $\text{Li/SO}_2\text{Cl}_2$ cell has an observed open-circuit voltage of $3.91V$ at room temperature. At low-to-medium discharge rates, the load voltage remains constant until close to end of discharge, when a rapid voltage drop occurs (1). Although system performance characteristics and electrochemical reactions taking place in ambient temperature cells have been fairly well described (1-3), low temperature performance characterizations have been generally neglected. Better understanding of

overall reaction mechanisms and reaction products formed during discharge is necessary in order to improve low temperature cell performance in $\text{Li/SO}_2\text{Cl}_2$ cells, as for Li/SOCl_2 cells (7, 8), decreased cell performance at low temperatures or at increased discharge rates is primarily attributable to cathode polarization. Electrochemical reduction of SO_2Cl_2 at porous carbon cathodes is limited by the capacity of the cathode for retaining the LiCl discharge product as it precipitates within pore structures. Therefore, cell performance is limited by accumulation of LiCl in the pores of the cathode.

Because basic information is needed to further improve the cathode, this paper explores limitations introduced at low temperatures and medium current drains and attempts to explain these results and offer possible solutions to relieve poor low temperature performance. We also present results of analytical studies aimed at characterizing chemical and electrochemical reactions occurring during cell discharge.

Experimental

Detailed description of laboratory electrochemical cells, experimental procedures, cell component fabrication, as well as discharge experiments, have been described earlier (1). Briefly, our experimental arrangement consisted of a porous carbon cathode sandwiched between two lithium anodes in an all-Teflon cell housing. Both the cathode and two anodes had nickel-screen current collectors. The porous cathode was constructed using United XC-6310 a high area carbon that had previously been shown to yield highest overall performance among the carbons tested for $\text{Li/SO}_2\text{Cl}_2$ cells (1). The cathodes had an area of 5 cm^2 on one side. We should point out that, in this paper, we are following the generally accepted convention and measure total cathode area by taking twice the geometric area ($l \times w$) of our cathodes. This is because our cells are constructed with both sides of the cathode facing lithium anodes.

In order to identify and characterize insoluble products formed in the cathode during discharge, spent cathodes from cells discharged to $1.5V$ at constant current were removed, rinsed with distilled SO_2Cl_2 to dissolve any adhering LiAlCl_4 electrolyte, heated under vacuum to drive off the sulfuryl chloride rinse solution, and the discharge products within the dried cathode extracted with distilled water. These water solutions were then analyzed for Li^+ , Cl^- , SO_4^{2-} , and Al^{+++} ions. Lithium ion concentrations were determined by atomic absorption, while the Cl^- concentration was determined using potentiometric titration with $0.1M \text{ AgNO}_3$. Despite rigorous washings with sulfuryl chloride, we could not exclude the possibility of having occluded or adhered LiAlCl_4 electrolyte remaining in the cathode. Thus, true Cl^- concentration, due to only LiCl discharge product, was calculated by measuring the Al^{+++} concentration colorimetrically and subtracting the

* Electrochemical Society Active Member.

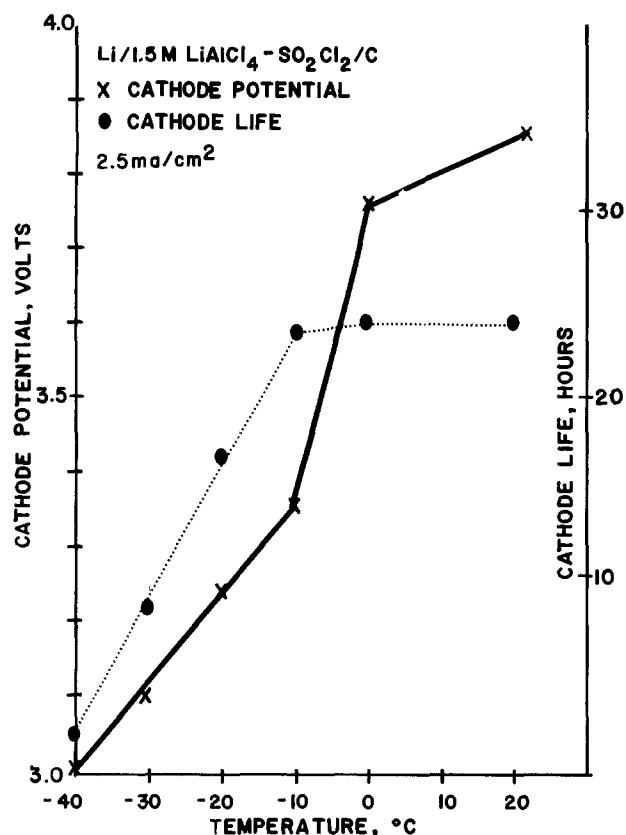


Fig. 1. Cathode load potential vs. a lithium reference and total cathode life as a function of temperature for Li/1.5M LiAlCl₄-SO₂Cl₂/C cells discharged at constant current of 2.5 mA/cm².

stoichiometric Cl⁻ concentration (*i.e.*, four Cl⁻ for every Al⁺⁺⁺) attributable to occluded LiAlCl₄ from total chloride concentrations measured potentiometrically. In all cases, this chloride correction was less than 5% of the total measured Cl⁻ concentration. As a check, we also analyzed the aqueous wash solutions using a Dionex 2120i Ion Chromatograph, and the results agreed well with results of the wet chemical analysis.

Results and Discussion

Figure 1 plots both cathode voltage and cathode capacity as a function of operating temperatures during constant current discharge. Loss of cell performance at reduced temperatures is quite pronounced. Both cathode voltage and capacity remain fairly constant down to temperatures ~0° and -10°C, respectively, where both decline sharply. The discharge curves for these cells are fairly flat, even at low temperatures, and show fairly well-defined transition times in the discharge curves (where cell voltage declines sharply). We will discuss and attempt to explain capacity losses and load voltage reduction at reduced temperatures in that order.

Cell capacity reduction at lower temperatures.—The following factors which may contribute to diminished cell capacity at reduced temperatures are considered individually along with their relevant analytical data: (i) precipitation of electrolyte salt, (ii) alternate cell products formed, and (iii) ohmic and concentration polarization.

Precipitation of electrolyte salt.—If precipitation of the LiAlCl₄ electrolyte salt in the cathode pores occurs at reduced temperatures, we would expect considerable reduction in cathode life due to the blocking of the cathode pores by LiAlCl₄ and the resulting ion transport limitations. However, the linearity of the conductivity curves shown in Fig. 2 as well as simultaneous visual observations in conductivity cells of LiAlCl₄-SO₂Cl₂ electrolyte solutions as their temperatures were slowly reduced to -60°C, clearly ruled out precipitation of any solid material. It is unlikely that supersaturated solutions of LiAlCl₄-

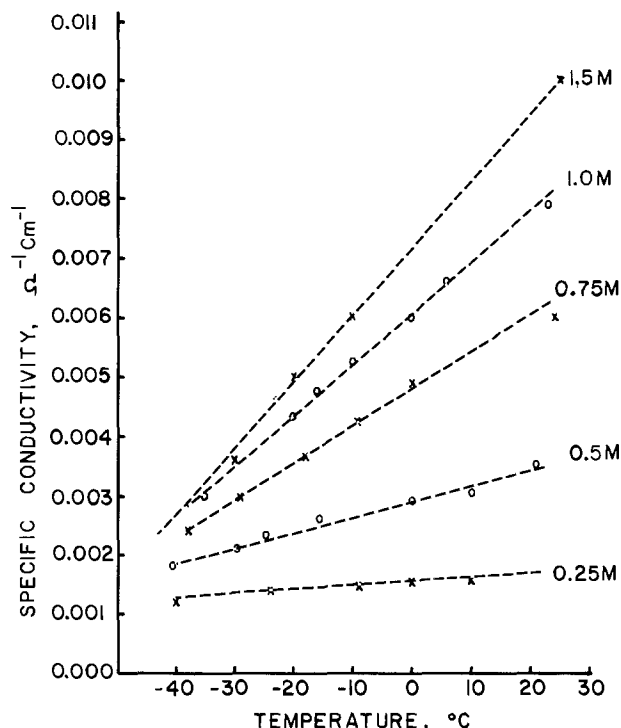


Fig. 2. Specific conductivity as a function of temperature for various LiAlCl₄-SO₂Cl₂ concentrations.

SO₂Cl₂ electrolyte could be formed at low temperatures in our conductivity cells since the platinized electrodes would have surely provided adequate nucleation sites for precipitation to occur. The fact that no precipitate is formed implies that we can safely rule out electrolyte precipitation as the cause of decreased cathode life during low temperature operation.

Alternate cell products.—It is possible that different cell-discharge mechanisms are operational at reduced temperatures and cause additional insoluble discharge products, such as Li₂SO₄ or Li₂S₂O₄, to form. These materials may more effectively clog active cathode pores than LiCl, thus causing premature cathode failure. In order to test this possibility, spent cathodes from Li/SO₂Cl₂ cells discharged at 2.5 mA/cm² at -32°C were removed from their cells and the insoluble product quantitatively analyzed for Li⁺, Cl⁻, and SO₄⁼ ions. Table I summarizes results found for four cathodes discharged at -32°C.

The Li⁺/Cl⁻ ratio was 1.07 ± 0.12. The fact that this ratio was unity within experimental error already implies that only LiCl is formed. No other insoluble (in SO₂Cl₂) lithium salt is deposited in the cathode. However, the low and variable collection efficiency for solid product in the cathode based on the coulombs transferred still leaves open the possibility that another soluble lithium salt was formed. Such a salt, if formed, would not appear at the cathode, but could, nevertheless, allow a ratio of unity for the Li⁺/Cl⁻ found in the cathode. Such salts cannot be Li₂SO₄ or Li₂S₂O₄, as has been proposed for thionyl chloride cell products (9), since their solubilities in sulfuryl chloride were measured to be less than 5 × 10⁻⁴M at room temperature.

Table I. Chemical analysis of discharged cathodes taken from Li/1.5M LiAlCl₄-SO₂Cl₂ cells discharged at -32°C and 2.5 mA/cm² constant current to 1.5V

	Cathode Li ⁺ /Cl ⁻	Electrolyte SO ₄ ⁼ /Cl ⁻	Cathode collection efficiency
Run 1	0.97	0.066	67%
Run 2	0.89	0.0032	63%
Run 3	1.26	0.13	110%
Run 4	1.06	0.09	79%
	1.04 ± 0.11		80 ± 15%

It is unlikely that solubility Li_2SO_4 or $\text{Li}_2\text{S}_2\text{O}_4$ increases as temperature is lowered; therefore, we can safely rule out these two salts as products since, had they been present, our measured Li^+/Cl^- ratio for the solid cathode discharge product would have been much larger than unity.

Presence of SO_4^- was also of interest in our product analysis study. One proposed chemical precursor of SO_4^- in these cells is SO_3Cl^- which could form according to mechanisms outlined by Blomgren (9).

If LiSO_3Cl was indeed formed, then after dissolving our cathode precipitate in water, the Li^+/Cl^- as well as the $\text{SO}_4^-/\text{Cl}^-$ ratio should be close to unity. The fact that our measured $\text{SO}_4^-/\text{Cl}^-$ ratio was about one order of magnitude less than unity convinces us that we can safely rule out SO_3Cl^- as a predominant product of sulfur chloride cathode reduction at low temperatures. Thus, the only discharge product is LiCl . No major parallel discharge mechanism exists. The traces of SO_4^- observed were probably due to contamination by water, which yields the well-known hydrolysis product chlorosulfonic acid, which forms SO_4^- in water solutions.

For cathodes discharged at room temperature, the collected Li^+ and Cl^- agreed well with the number of coulombs transferred (collection yield averaged greater than 92%). The collection yield, however, for cathodes discharged at -32°C represented only approximately 85% of the theoretical yield. This discrepancy may be due to: (i) LiCl precipitated in locations other than the cathode, (ii) formation of uncollected soluble lithium salts, (iii) poor product collection efficiency due to crumbling of low temperature discharge cathodes, (iv) or not all of the carbon cathode material's being collected.

Since elemental sulfur is a known product of cell discharge reactions in the Li/SOCl_2 system (9), we wanted to determine whether it was produced in $\text{Li}/\text{SO}_2\text{Cl}_2$ cells during discharge at -32°C .

Separators, cathode, and remaining electrolyte taken from $\text{Li}/\text{SO}_2\text{Cl}_2$ cells discharged at $2.5 \text{ mA}/\text{cm}^2$ at -32°C , were rinsed with SO_2Cl_2 and dried. Extraction with CS_2 yielded $\sim 75 \text{ mg}$ of a yellow waxy material whose ultraviolet spectrum in tetrahydrofuran was unlike that of stock sulfur solutions (10). If we assume that absorption at 2850\AA for our known solution corresponds entirely to sulfur, the calculated maximum concentration of sulfur present in the extract was only $\sim 1 \text{ mg}$. Since control experiments on undischarged cathodes also yielded this same waxy material, probably a reaction product of Triton X-100 (a surfactant present in TFE-30 emulsions) with SO_2Cl_2 , sulfur is ruled out as a major discharge product.

To summarize, analytical results show that LiCl is the only major insoluble cathode discharge product of $\text{Li}/\text{SO}_2\text{Cl}_2$ cells at -32°C . No sulfur is produced.

Ohmic and concentration polarization.—The specific conductivity of various concentrations of $\text{LiAlCl}_4\text{-SO}_2\text{Cl}_2$ solutions as a function of temperature is shown in Fig. 2. In going from 25° to -32°C , specific conductivities of 1.5M solutions decrease linearly by approximately a factor of three, while specific conductivities of 0.25M solutions change only slightly. Other researchers have also noticed that changes in specific conductance of $\text{LiAlCl}_4\text{-SO}_2\text{Cl}_2$ solutions with temperature (slope of the lines in Fig. 2) in the range of 22° to 60°C are larger for higher electrolyte concentrations (11). We did not correct our electrolyte concentrations for density; our estimate of temperature dependence of electrolyte density indicates changes less than 10% over the range of 25° to -30°C . The question arises as to whether increased electrolyte resistance encountered at low temperature could in itself be a significant contribution to decreased cell operating voltage or whether it is simply causing other effects indirectly. During cell discharge, even in regions of steepest voltage dropoff at 25° and -32°C , galvanostatic pulse experiments indicate that the pure resistive component of the cathode does not exceed 40% of the total cathode voltage polarization. We cannot attribute the sudden voltage drop at end of life to loss of active cathode surface area

since effective surface area would have to be diminished by several orders of magnitude in order to show polarization of several tenths of a volt. This would require all but small fractions of the carbon cathode be electrically isolated from conduction paths by insulating coatings of LiCl . If cathode surface area were mostly insulated, it would be unlikely that the resistive portion of total voltage polarization would remain low.

We can therefore conclude that although increased ohmic polarization in the cathode pores contributes somewhat to decreased cathode capacity, it apparently does not make the most significant contribution.

We next examine the dependence of cathode capacity on electrolyte concentration. Cell capacities (which are primarily determined by cathode performance) as a function of electrolyte concentration at both 25° and -32°C and $2.5 \text{ mA}/\text{cm}^2$ constant current discharge are shown in Fig. 3. For electrolyte concentrations $\leq 0.75\text{M}$, both 25° and -35°C cell capacity data nearly coincide and increase approximately linearly with concentration.

For electrolyte concentrations $> 1.0\text{M}$, the cell capacity curve at -32°C levels off with increasing electrolyte concentrations and lies well below the extrapolated linear relationship found for lower electrolyte concentrations. Although cells discharged at 25°C also show a leveling off in capacity vs. electrolyte concentration curve (not shown here), this leveling-off point occurs at concentrations $\geq 2.5\text{M}$ and results in only slightly higher cell capacities. The fact that the -32°C capacity vs. temperature curve remains relatively unchanged for electrolyte concentrations $\geq 1.0\text{M}$ implies that from a practical view, in $\text{Li}/\text{SO}_2\text{Cl}_2$ cells, one may reduce electrolyte concentrations from 1.5 to 1.0M while maintaining identical overall cell capacities for -32°C cell discharge.

In order to understand the capacity vs. electrolyte concentration curves of Fig. 3, it is helpful to first study morphological differences between LiCl deposited during -32° and 25°C discharge for various electrolyte concentrations. Postdischarge SEM of cathode surfaces taken from cells following constant current discharge at -32°C for various electrolyte concentrations are shown in Fig. 4. The LiCl deposits on the discharge cathode surfaces taken from the 1.5M electrolyte cell was distinctly glassy. As electrolyte concentrations were decreased, the resulting postdischarge LiCl deposits on their respective

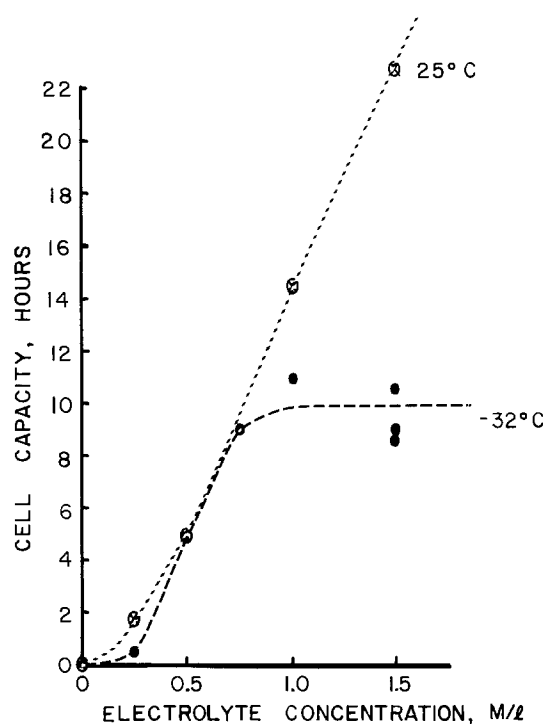


Fig. 3. Cell capacity plotted against electrolyte concentration for both room temperature and -32°C discharge at $2.5 \text{ mA}/\text{cm}^2$.

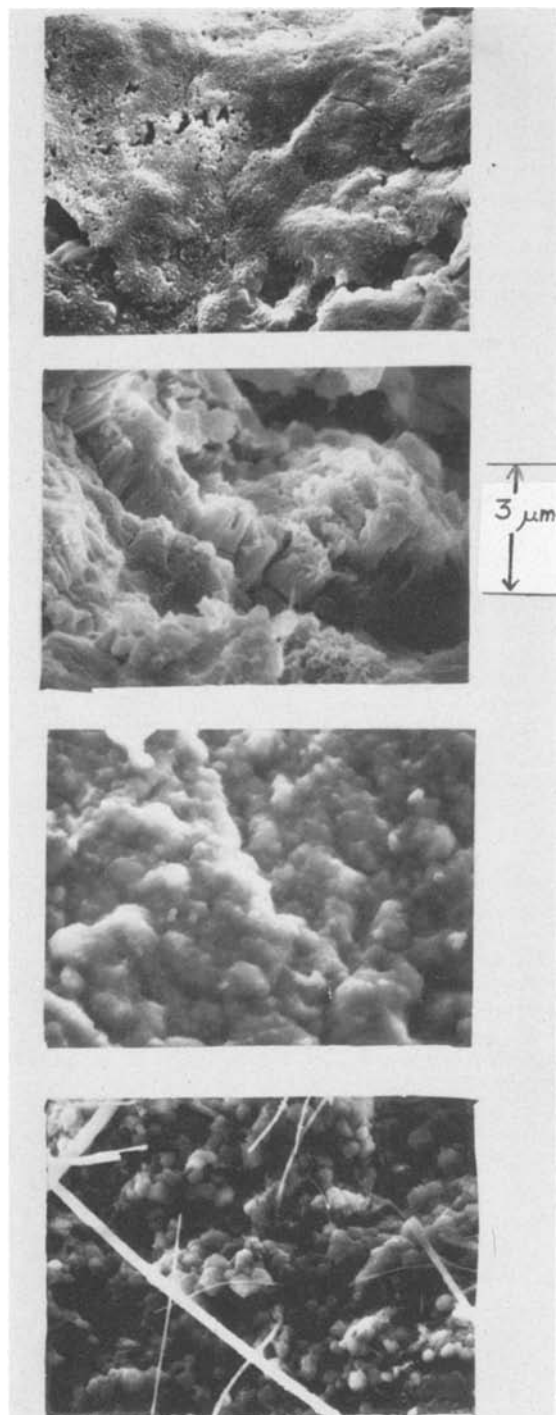


Fig. 4. Postdischarge SEM of surfaces of cathodes taken from cells of Fig. 3. These cathodes had all been discharged at 2.5 mA/cm^2 to a 1.5 V cutoff at -32°C , but differed in the cell electrolyte concentration. A (top): $\text{Li}/1.5\text{M LiAlCl}_4\text{-SO}_2\text{Cl}_2/\text{U.C.}$ B (second from top): $\text{Li}/1.0\text{M LiAlCl}_4/\text{SO}_2\text{Cl}_2/\text{U.C.}$ C (third from top): $\text{Li}/0.75\text{M LiAlCl}_4\text{-SO}_2\text{Cl}_2/\text{U.C.}$ D (bottom): $\text{Li}/0.5\text{M LiAlCl}_4\text{-SO}_2\text{Cl}_2/\text{U.C.}$

cathode surfaces appeared less glassy and seemed more crystalline in nature. These results should be contrasted to SEM data on 25°C discharged cathodes (not shown here), where even for the 1.5M electrolyte concentration, the discharge product definitely appeared crystalline.

We will first present what we feel is a reasonable explanation of these morphological observations and then present a rationalization for the shapes of the capacity *vs.* concentration curves in Fig. 3.

Crystallinity or glassiness of precipitating deposits may be related to electrolyte concentration and temperature through the well-known Von Wiemann ratio, W , which re-

lated precipitate size to solubility, S , and supersaturation, Q

$$W = \frac{Q - S}{S}$$

Small values of W correspond to large-sized crystals, while large values of W correspond to granular or glassy deposits. Since supersaturation Q is independent of temperature and concentration for a particular current drain, the ratio W should vary with solubility. The solubility is temperature sensitive through its dependence on the mean activity coefficient, which is a function of the dielectric constant, temperature, and ionic strength. Qualitatively, as the temperature is lowered, the dielectric constant, mean activity coefficient, and thus LiCl solubility all decrease. The net result is smaller sized crystals or even a glassy deposit of LiCl . Reducing electrolyte concentration at a given temperature increases the ionic strength and the mean activity coefficient, decreasing W and increasing the crystal size of the precipitate. This is what has been observed.

For electrolyte concentrations $\leq 0.75\text{M}$, final accumulations of LiCl deposits in the cathode pores are small and fairly crystalline at all discharge temperatures; electrolyte conductivities are not seriously changed at either 25° or -32°C .

For electrolyte concentrations $\leq 0.75\text{M}$, temperature alone does not appear to play a very important role in influencing cell capacity since both capacity *vs.* concentration curves almost coincide. This is understandable since, for electrolyte concentrations $\leq 0.75\text{M}$, electrolyte specific conductivity is not very strongly temperature dependent, as shown in Fig. 2.

The concentration regions where discharged cathodes have similar morphological appearances seem to indicate that a common factor is dominant.

The approximate linear relationship shown between cathode capacity and electrolyte concentrations $\leq 0.75\text{M}$ for both 25° and -32°C discharge is suggestive of a diffusion-related dependence. Our basic hypothesis is that cathode capacity is a strong function of two separate current density terms. The first term, i_{app} , is the constant current load applied to the cathode. The second term is an intrinsic limiting current, i_L , which depends on the physical state and extent of discharge of the porous cathode.

This limiting current, defined in the same manner as the limiting current in the Nernst diffusion equation

$$i_L = \frac{nFDC}{\delta}$$

represents the maximum transport rate of Li^+ through cathode pores to reach available cathode reaction sites and is proportional to the Li^+ ion diffusion coefficient and concentration.

As long as $i_{\text{app}} \ll i_L$, which would be the case for either fresh cathodes that contain little LiCl deposits or for low values of i_{app} , the cathode can easily maintain the constant current load by allowing adequate Li^+ ion flow to cathode reaction sites without any severe concentration polarization.

However, as the cell discharge reaction proceeds and the cathode pores become filled with solid insulating LiCl discharge product, Li^+ ion diffusion through the deposit becomes increasingly difficult and i_L therefore decreases.

At this point, $i_{\text{app}} \sim i_L$, and severe cathode concentration polarization occurs. This concept of concentration polarization in the porous cathode appears to explain the rather long times (several minutes) required to reach open-circuit potentials when almost fully discharged cells are removed from load. Since at this point the carbon cathode is blocked with LiCl product, it takes a long time for ionic equilibrium to be reestablished within the cathode matrix.

We will show that i_L , which ultimately determines useful cathode life, is proportional to both Li^+ concentration

and extent of cathode discharge. This should explain the linear relationship between cathode capacity and electrolyte concentration.

Let us assume that δ , which normally represents the diffusion-layer thickness, represents an increasing volume of LiCl products formed in the cathode pores. This is not unreasonable since the solid LiCl acts as a concentration gradient and hinders flow of Li^+ and SO_2Cl_2 to the cathode interior. If we further assume that δ can be represented as a linear function of discharge time, t , in the form $\delta = A + Bt$, where A and B are constants, then it is clear that i_l is a function of t . Specifically, the limiting current increases linearly with concentration and is inversely proportional to discharge time.

The concept of equating the diffusion layer thickness, δ , with a solid buildup of LiCl in the porous cathode is not unreasonable. Figure 5 shows voltage sweeps of porous cathodes obtained during 25°C constant current discharge. The decrease of the apparent limiting currents as a function of discharge time are indicative of the cathode being blocked by LiCl deposits.

To summarize: decreased cathode capacity at electrolyte concentrations $\leq 0.75\text{M}$ during 25° and -32°C discharge reflects the reaching of diffusion limits for mass transport of SO_2Cl_2 and/or Li^+ ions in the cathode pores due to choking of pores by precipitation of solid LiCl reaction product. Concentration limits from depletion of Li^+ transport species are strongly suggested by sensitivity of cell capacity to LiAlCl_4 electrolyte concentration.

For electrolyte concentrations $\geq 0.75\text{M}$, the capacity vs. concentration plot of Fig. 3 at -32°C parallels electrolyte conductivity vs. concentration plot shown in Fig. 6, which also shows leveling off at higher electrolyte concentrations. This implies that, although transport limitations are no doubt important, conductivity is the limiting factor.

The leveling off in the -32°C capacity vs. concentration curve of Fig. 3 may be simply due to the inelastic nature of the Teflon binder at low temperatures. Cathode capacity depends on cathode elasticity since the porous cathode must expand sufficiently to accommodate the LiCl

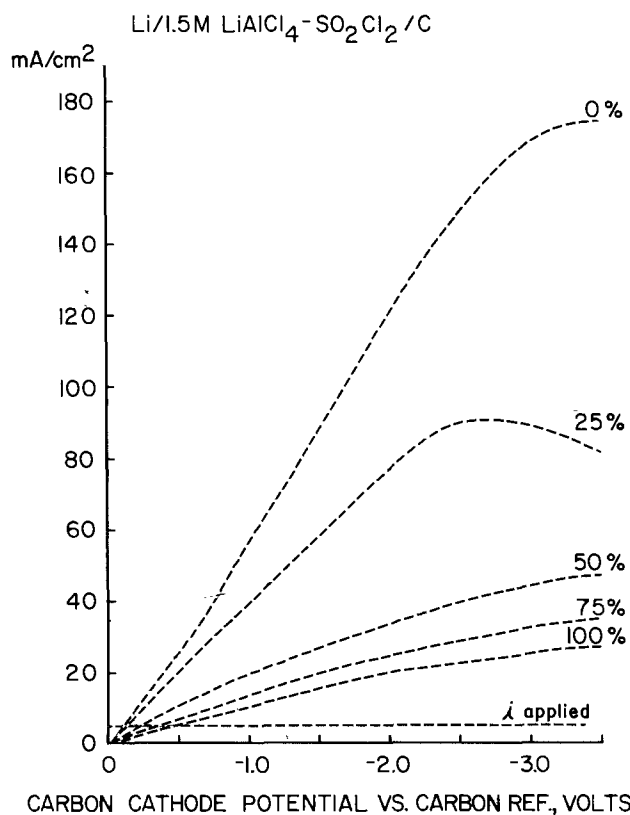


Fig. 5. Potentiometric polarization sweeps of a cathode (0.5 cm^2) in a $\text{Li}/\text{SO}_2\text{Cl}_2$ half-cell at various times during constant current discharge. The constant current level of $5\text{ mA}/\text{cm}^2$ is shown by the dashed line as i_{appl} .

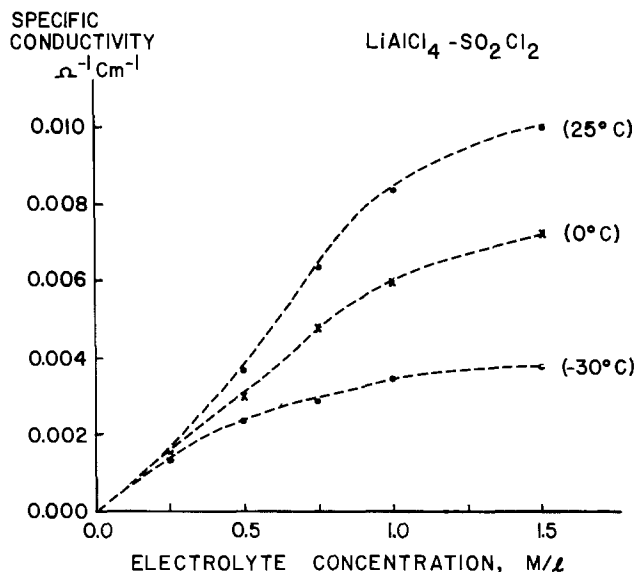
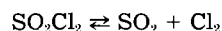


Fig. 6. Replotted data of Fig. 2 showing specific conductivity of $\text{LiAlCl}_4\text{-SO}_2\text{Cl}_2$ solutions as a function of concentration for 25°, 0°, and -30°C.

deposits. If the Teflon binder does not stretch adequately, the cathode will tend to crack rather than swell. Decreased elasticity of the Teflon binder at reduced temperature is evident from the fact that discharged cathodes were stiff and rigid even after warming to room temperature; carbon particles did not adhere well to the screen and tended to flake off rather easily. This breaking of carbon-to-carbon and carbon-to-screen contact was not observed with cathodes discharged at room temperature. This disruption of original cathode structure results in capacity losses.

The above is in agreement with observations that cathodes discharged to a 1.0V cutoff at -32°C, then warmed to 25°C, and further discharged at 25°C exhibited the same total ampere-hours expected for normal uncycled 25°C discharged cathodes. This was not due to a time dependent self-healing of the cathode since cells discharged at low temperatures, allowed to warm to room temperatures, then brought down to -32°C for additional constant current discharge showed no considerable capacity increase.

Voltage reduction at reduced temperatures.—The plot of cell operating voltage vs. temperature shown in Fig. 1 appears discontinuous at temperatures $\leq 0^\circ\text{C}$. From a simplified Tafel equation for irreversible reduction reactions, closed-circuit cathode voltages would be expected to be linear with temperature. The discontinuity in operating voltages vs. temperature plot of Fig. 1 suggests that changes in cell reaction mechanism are occurring at temperatures $\leq 0^\circ\text{C}$. This can be explained as follows: normally, high operating potentials for $\text{Li}/\text{SO}_2\text{Cl}_2$ cells discharged at temperatures $\geq 0^\circ\text{C}$ correspond to reduction of molecular Cl_2 produced by thermal decomposition of SO_2Cl_2 . The decomposition is catalyzed by highly active carbon cathodes or added catalysts (12, 13) as suggested previously (1) for room temperature discharge



At reduced temperatures, where thermally activated catalytic dissociation of SO_2Cl_2 at carbon cathodes is incapable of maintaining adequate Cl_2 production for current drains applied, lower cell potentials are a result of direct reduction of SO_2Cl_2 . Since the $\text{Li}/\text{SO}_2\text{Cl}_2$ couple has a lower potential than does the Li/Cl_2 couple, the cathode operates at lower potentials. This is also true during later stages of discharge, when catalytic activity of the carbon cathode has been reduced and Cl_2 production is limited.

Addition of Cl_2 to cells where catalysis is slow (as would be the case when low surface area Shawinigan acetylene carbon black is used to make cathodes), has already been shown by Liang *et al.* (6) to substantially improve cell

operating voltages over wide temperature ranges in Li/SO₂Cl₂ cells. This is a result of accelerated Cl₂ utilization. Our argument that formation and subsequent utilization of Cl₂ increases operating cell voltages is further substantiated by experiments performed at various temperatures with 1.5M LiAlCl₄-SO₂Cl₂ electrolyte saturated with Cl₂ both in the electrolyte and void space above the cell prior to cell discharge.

Maximum solubility of Cl₂ in SO₂Cl₂ at room temperature is less than ~1.0M (1, 6). Typical constant current cell discharge curves and Cl₂-saturated cells shown in Fig. 7 illustrate two important differences when compared with unsaturated base lines. First, operating voltages for Cl₂-saturated electrolytes were indeed higher than for unsaturated base lines, and voltage enhancement became more pronounced as cell discharge temperatures decreased. At 25°C, addition of Cl₂ does not increase operating voltages significantly, since for high area carbon used in this study, the cathode itself is fully capable of producing adequate amounts of Cl₂ from heterogeneous dissociation of SO₂Cl₂. At reduced temperatures, however, thermally activated dissociation is essentially frozen out, and the cathode is incapable of supplying adequate Cl₂ for the particular current drain. Addition of Cl₂ from an external source results in increased cell plateau voltages of up to ~0.5V.

Cell operating voltages at early points in cell discharge for Cl₂-saturated electrolyte cells are inserted as open circles in Fig. 8. It is clear that the voltage vs. temperature line at temperatures below 0°C extends toward the Cl₂ data points down to -30°C and implies that if the cathode were capable of maintaining adequate amounts of Cl₂ on its own, operating voltages would be higher.

Measured specific conductivities of Cl₂-saturated 1.5M LiAlCl₄-SO₂Cl₂ electrolytes do not differ significantly from that of unsaturated electrolytes over the temperature range of -30° to 25°C. Thus, higher operating voltages observed with Cl₂-saturated solutions are not simply due to decreased IR losses but rather are due to the mechanisms outlined above.

Both experimental and theoretical work in our laboratory is currently underway to elucidate the detailed nature of SO₂Cl₂ dissociation processes at porous carbon cathodes and the physical and chemical factors in porous carbon cathodes operating voltages and capacities. Preliminary results have already been reported (14).

A second difference between Cl₂-saturated cells and base-line cells is that cells with Cl₂-saturated electrolytes showed substantially decreased capacities when compared to base-line cells. A few possible explanations are offered.

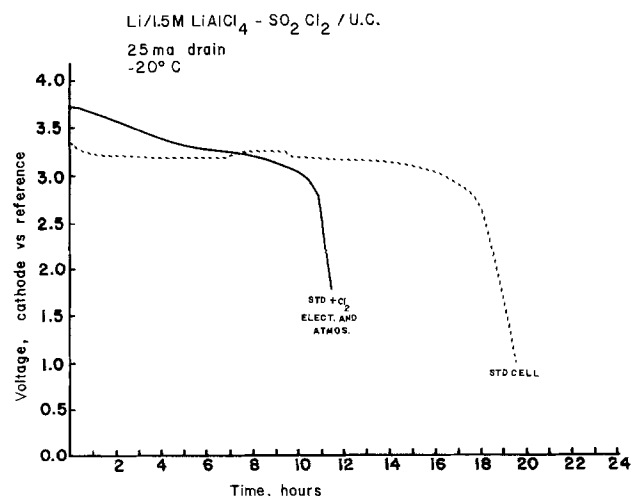


Fig. 7. Cathode potential vs. lithium as a function of time for constant current discharge for two Li/SO₂Cl₂ cells. The solid line refers to a cell whose electrolyte and void space above the electrolyte solution was saturated with Cl₂. The dashed line refers to a control cell.

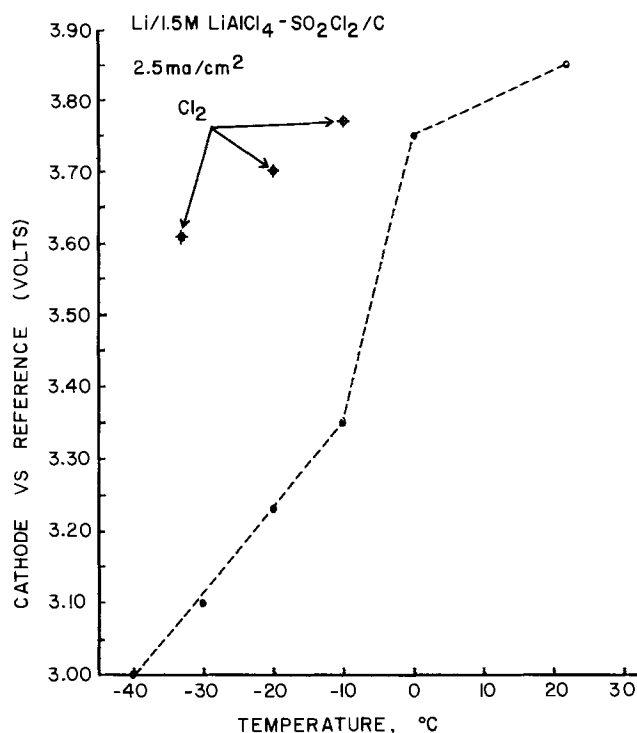
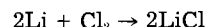


Fig. 8. Cathode load potential vs. lithium reference (copied from Fig. 1). The added points represent plateau voltages for Cl₂-saturated cells.

Initially, Cl₂ dissolved in electrolyte within the cathode volume is rapidly utilized and LiCl reaction product is homogeneously deposited within the pores. However, as cell discharge proceeds, the cell first utilizes all dissolved Cl₂ contained within the cathode pore interior. Diffusion of Cl₂ from electrolyte bulk occurs preferentially at the interface of the cathode surface with the bulk electrolyte solution. These deposits formed at cathode surfaces have greater tendencies to clog surface entrances to pores and limit transport, thus resulting in premature cell failure.

When electrolyte solutions are saturated with Cl₂, equilibrium SO₂Cl₂ dissociation into SO₂ and Cl₂ shifts to the left, and less dissolved SO₂ exists in solution. Since SO₂ strongly coordinates Cl⁻ ions due to pi bonding between low lying 3d orbitals of sulfur and 3p orbitals of Cl⁻ (15), reduced SO₂ concentrations imply diminished complexation and more free Cl⁻ remaining in solution. Higher Cl⁻ concentration provides greater likelihood of LiCl formation and premature cell failure.

When Cl₂ is present, lithium can react directly with Cl₂ dissolved in the solution to form LiCl



Since no volatile products are formed in this reaction, the LiCl film may be more compact and block the cathode more efficiently than LiCl formed simultaneously with SO₂.

Decreased capacity with Cl₂-saturated electrolytes disagrees with results of Liang *et al.* (6), who found increased cell capacity in similar cases. The difference may result from physical properties of the carbon blacks used. Liang *et al.* used Shawinigan acetylene black (surface area: 65 m²/g), while we used United XC-6310 (surface area: 1000 m²/g). Differences in surface areas may effect Cl₂ utilization rate. Another reason may be the lower electrolyte concentrations used by Liang *et al.*

Acknowledgments

We wish to thank Dr. Wishvender K. Behl for assistance in preparing electrolyte salts and for stimulating discussions. We also wish to acknowledge the able technical as-

sistance of Edward Collins in assembling cells and performing various low temperature discharge experiments. Don Eckert assisted greatly in obtaining the SEM. The assistance of Paul Bramhall during initial stages of this work is also acknowledged.

Manuscript submitted Nov. 4, 1983; revised manuscript received March 23, 1984.

The U.S. Army Electronics Technology and Devices Laboratory assisted in meeting the publication costs of this article.

REFERENCES

1. S. Gilman and W. Wade, Jr., *This Journal*, **127**, 1427 (1980).
2. G. Razzini, S. Rovellini, F. Alessandrini, B. D. Pietro, and B. Scrosati, *J. Power Sources*, **5**, 263 (1980).
3. J. J. Auburn and N. Marincic, in "Power Sources 5," D. H. Collins, Editor, p. 683, Academic Press, London (1975).
4. E. Peled, *This Journal*, **126**, 2047 (1979).
5. A. N. Dey, *Thin Solid Films*, **43**, 131 (1977).
6. C. C. Liang, M. E. Bolster, and R. M. Murphy, *This Journal*, **128**, 1634 (1981).
7. A. N. Dey and P. Bro, *ibid.*, **125**, 1574 (1978).
8. K. A. Klinedinst and M. J. Domeniconi, *ibid.*, **127**, 539 (1980).
9. G. E. Blomgren, V. F. Leger, T. Kalnoki-Kis, M. L. Kronenberg, and R. J. Brodd, in "Power Sources," J. Thompson, Editor, p. 583, Academic Press (1979).
10. J. R. Driscoll, S. B. Brummer, P. Gudrais, G. L. Holleck, D. E. Toland, and M. J. Turchan, Final Report, ECOM-74-0030-F, Contract no. DAAB07-74-C-0030, EIC Corp., Newton, MA, March 1978.
11. F. Marikar, First Quarterly Report, DELET-TR-81-0421-1, Contract no. DAAK20-81-C-0421 Gould Laboratories, Rolling Meadows, IL, March 1982.
12. K. A. Klinedinst, Abstract 76, p. 190, The Electrochemical Society Extended Abstracts, Vol. 81-2, Denver, CO, Oct. 11-16, 1981.
13. N. Doddapaneni, Abstract 583, p. 1398, The Electrochemical Society Extended Abstracts, Vol. 81-2, Denver, CO, Oct. 11-16, 1981.
14. W. Wade, Jr., C. Walker, Jr., M. Binder, and S. Gilman, Paper 26 presented at the Workshop on Electrochemistry of Carbon, Cleveland, Ohio, Aug. 17-19, 1983.
15. S. B. Salama and S. Wasif, *J. Chem. Soc. Dalton Trans.*, 151 (1975).

Solvent Mixing Effects on the Electrode Characteristics of Secondary Li/TiS₂ Cells

Yoshiharu Matsuda,* Masayuki Morita, and Ken-ichi Takata

Department of Industrial Chemistry, Faculty of Engineering, Yamaguchi University, Tokiwa-dai, Ube, Yamaguchi, Japan

ABSTRACT

Charge-discharge characteristics of Li negative and TiS₂ positive electrodes have been studied in LiBF₄ solutions of tetrahydrofuran (THF), 1,3-dioxolane (DOL), and their mixture. Solvent mixing effects on the charge-discharge characteristics were investigated. Charge-discharge potentials at the Li electrode in THF-DOL/LiBF₄ were more stable than those in THF/LiBF₄ and DOL/LiBF₄, and they showed the least variation with the cycles. Ionic behavior in the solutions is discussed through the data of current-potential curves of the electrodes and electrolytic conductivity of the solutions. With respect to the TiS₂ electrode, charging efficiency in THF was seemingly the best, but the efficiency variation with the cycle in DOL-THF was very small. It was concluded that advantages of solvent mixing should be evaluated totally in Li/TiS₂ cells.

A variety of ambient temperature Li secondary cells with positive electrodes of layered compounds has been proposed during past several years (1, 2). In the course of the development of the cells, it has been noted that the choice of an electrolyte system is of special importance in the rechargeability of the Li electrode (3, 4). Koch and his co-workers found that 2-methyltetrahydrofuran/lithium hexafluoroarsenate (2Me-THF/LiAsF₆) is an excellent electrolyte system for secondary Li electrodes (5-7). The Li cycling efficiency was further improved by the addition of alcohols to 2Me-THF/LiAsF₆ (8). Foos and McVeigh proposed polymethoxymethanes as a stable and efficient solvent for Li electrodes (9). However, it has been also pointed out that the charge-discharge characteristics of positive electrodes such as TiS₂ are influenced by electrolytic solutions (10-12). It is important to know which of the electrodes governs the cell performance in a

practical secondary Li cell. Therefore, the effects of electrolytic solution on both negative electrode and positive electrode should be examined concurrently.

Up to the present, solutions consisting of ether solvents are most promising as an organic electrolyte solution of the secondary Li cell. In this work, tetrahydrofuran (THF), 1,3-dioxolane (DOL), and their blends were mainly used as a solvent, and the solvent mixing effects on both TiS₂ positive electrode and Li negative electrode were demonstrated. THF tends to decompose on the Li electrode as well as to cause Li dendrite deposition (4, 13). DOL/LiClO₄ solution is susceptible to detonation (14), and DOL tends to polymerize in its LiAsF₆ solution (8). However, it may be possible to reduce these faults by blending the solvents and by using other electrolytic salts. For instance, Johnson *et al.* obtained good cell performance by using DOL-1,2-dimethoxyethane/Li closoborane (15). The Li cycling characteristics in THF-diethylether/LiAsF₆ blend electrolytes were also investigated (7, 16). In the

* Electrochemical Society Active Member.

present paper, the charge-discharge characteristics of the Li electrode and the TiS_2 electrode were studied in lithium tetrafluoroborate (LiBF_4) solutions of THF-DOL blends. The results were compared with those in the solutions consisting of the pure solvents.

Experimental

Materials.—The solvents were purified and dehydrated by distillation. THF (Toyo Soda Manufacturing) was first distilled in presence of CuCl at 66°C . Then it was fractionally distilled after the addition of CaH_2 (17). DOL (Tokyo Kasei Kogyo) was refluxed over CaH_2 for 48h followed by distillation at 75°C . Then metallic Na chips were added and the solution was stirred for 48h or longer. Finally, it was distilled at 75°C again. The electrolytic salt was anhydrous LiBF_4 (Morita Chemical Industries, > 98%). It was further dried under reduced pressure at 80°C for 24h or longer. The desiccated LiBF_4 was dissolved in the solvents (1.0M [mol dm^{-3}]) under a dry Ar atmosphere.

Lithium foil was obtained from Kyokuto Metal Industries, sealed under Ar. TiS_2 powder (Mitsuwa Chemical, > 99.8%) was used as received.

Test cells.—A cylindrical Teflon cell (volume: $1.33\text{ cm}^2 \times 1.5\text{ cm}$) was used for cycling tests of the electrodes. In the Li electrode experiments, both test electrode and counterelectrode were Li foil disks ($1.33\text{ cm}^2 \times 0.02\text{ cm}$, 0.014g). Polypropylene nonwoven cloth impregnated with the electrolytic solution was sandwiched between two electrodes. A Ni mesh was used as a current collector. A Li fragment on the tip of Ni wire was placed close to the test electrode as a reference electrode. For cycling tests of the TiS_2 electrode, one of the Li electrodes was replaced with the TiS_2 electrode in the cylindrical cell. The TiS_2 positive electrode was prepared by mixing the TiS_2 powder (0.029g) with scaly graphite (Nakarai Chemicals, C-325, 0.088g) and Teflon powder (Mitsui Fluorochemical, Teflon-6J, 0.012g). Thus, the cell performances would be cathode limited. The graphite used here was well crystallized. It was preliminarily established that this kind of graphite was virtually inactive itself and did not accelerate the decomposition of the electrolytes. The mixture was molded into tablet with a pressure of $4.4 \times 10^3\text{ kg cm}^{-2}$. However, the preparative conditions have not been optimized yet, and the electrochemical characteristics of the TiS_2 positive electrode as presented here would not be the best possible. It was merely as a standard procedure in order to investigate the solvent mixing effects.

A beaker-type glass cell was also used for measuring current-potential relationships at Li and TiS_2 electrodes. The volume of the cell was 100 cm^3 . A Li chip and a Li sheet with large surface area were used as the reference electrode and the counterelectrode, respectively.

Measurements.—The charge-discharge tests of the Li electrode were mainly carried out by a cycling procedure in which Li was discharged at 1 mA ($= 0.75\text{ mA/cm}^2$) for 10 min followed by charging at the same current density for 10 min. The variation of the electrode potential was measured during the first 30 cycles. Li cycle efficiency was determined by Koch's method (18), in which a Ni sheet was used as the substrate. The plating and stripping current densities (i_p , i_s) were 2 mA/cm^2 , and the plated charge (Q_p) was 0.2 C/cm^2 . The cycling test of the TiS_2 electrode was conducted by galvanostatic discharge and charge ($0.5\text{ mA} = 0.38\text{ mA/cm}^2$). The voltage limits were 1.75V for discharge and 3.5V (or 3.0V) for charge. Current-potential curves of the electrodes were potentiostatically measured, where the electrode potential was stepwise changed at first from the rest potential to discharging ones and then changed to charging potentials. All experiments were carried out in a dry Ar atmosphere at room temperature ($18^\circ\text{--}20^\circ\text{C}$), except for conductivity measurements, which were carried out by a usual bridge method at 30°C .

Results and Discussion

Li electrode.—Figure 1 shows the charge-discharge curves of Li electrodes in THF/LiBF_4 and DOL/LiBF_4 . The potential variation with cycling in THF/LiBF_4 was

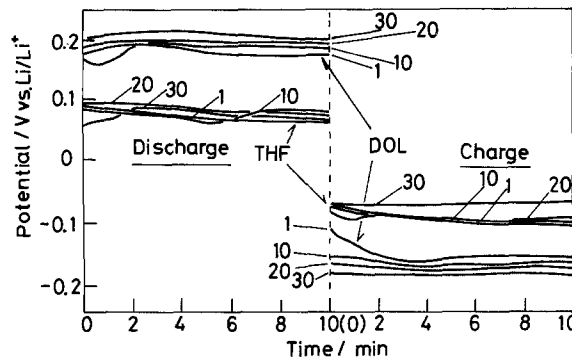


Fig. 1. Charge-discharge curves of the Li electrodes in 1M LiBF_4 solutions of THF and DOL. Current density: 0.75 mA/cm^2 .

relatively small, but the potentials varied by a few tens of millivolts during 10 min in each cycle. However, in the DOL solution, the potential difference between charge and discharge gradually increased with cycling, even though the potential variation in each cycle was small. The charge-discharge curves in the mixed electrolyte, DOL-THF/LiBF_4 , are shown in Fig. 2, where the mixing ratio is 1:1 volume (54 mole percent [m/o] DOL). There are two attractive characteristics in the mixed solution, compared with those in the solutions consisting of the pure solvents. The one is that charging and discharging potentials remain almost constant during 10 min in each cycle. The other is that the potential variation with cycling is extremely small. In addition, dendritic deposition of Li which was liable to occur in THF/LiBF_4 took place scarcely in the DOL-THF/LiBF_4 solution. It seemed that the mixed DOL-THF holds concurrently the good points which DOL and THF have individually.

Anodic and cathodic current-potential relations at Li electrodes were measured in a beaker-type cell. The current-potential curves in THF, DOL, and DOL-THF (1:1 volume) are shown in Fig. 3. The curves were first measured in the anodic direction and then measured in the cathodic one. The solid curves in Fig. 3 indicate that the measurements were carried out without stirring the solutions and the broken curves correspond to the measurements with solution stirring. Current densities without stirring in DOL-THF/LiBF_4 were higher than those in THF/LiBF_4 or DOL/LiBF_4 at given potentials. That is, polarization of the Li electrode for both anodic (discharge) and cathodic (charge) reactions in the mixed solution was smaller than that in THF or DOL. This is compatible with the results shown in Fig. 1 and 2, where lower overvoltages were observed during charge and discharge in the mixed solution than in THF or DOL. In these electrolytic solutions the Li electrode reactions



are mostly controlled by mass-transfer process, if the potential is somewhat far from the reversible potential. In the present case, two mass-transfer processes would be possible: one is Li^+ ion diffusion in the electrolytic solu-

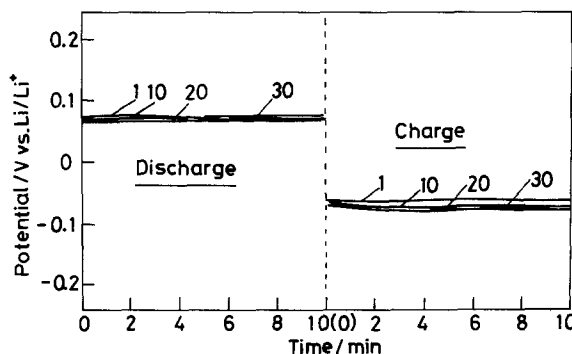


Fig. 2. Charge-discharge curves of the Li electrode in 1M LiBF_4 solution of DOL-THF (1:1 volume). Current density: 0.75 mA/cm^2 .

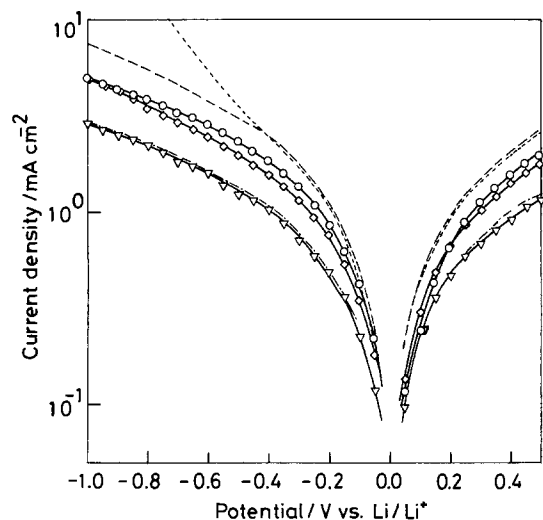


Fig. 3. Current-potential curves of the Li electrodes in 1M LiBF₄ solutions. (○, —): DOL-THF (1:1 volume). (◇, - - -): THF. (▽, —): DOL. (○, ◇, ▽): solution not stirred. (—, - - -, - - -): solution stirred.

tion and the other is Li⁺ ion diffusion across the Li passivating film (4). As shown in Fig. 3, the current densities, especially in THF and DOL-THF, were dependent on solution stirring. Therefore, the processes were mainly controlled by Li⁺ ion diffusion in the solution, and not by Li⁺ ion diffusion across the Li passivating film. The current increase with solution stirring at more negative potentials (~ -1.0V) in THF was probably due to increase in true surface area of the electrode by dendritic deposition of Li. In DOL, however, the current increase with solution stirring was rather small. The results shown in Fig. 3 suggest that the diffusion rate in the mixed solution is higher than those in the solutions consisting of neat solvents.

Solvent mixing effects were also observed in electrolytic conductivity of the solution. Figure 4 shows the conductivity of LiBF₄ in THF, DOL, and DOL-THF (1:1 volume) as a function of LiBF₄ concentration. The conductivity of the mixed solution was higher than that of THF/LiBF₄ or DOL/LiBF₄. This means that the ionic mobility, or the diffusion rate, of Li⁺ ion in the mixed solution is higher than that in THF or DOL, and then it is

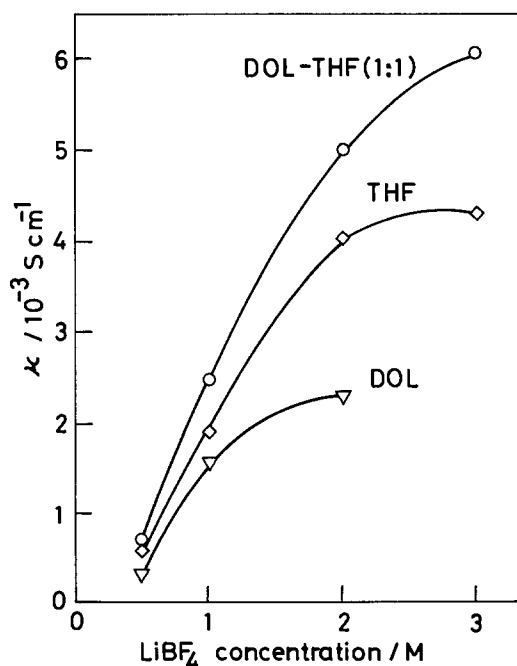


Fig. 4. Conductivity of LiBF₄ in THF (◇), DOL (▽), and DOL-THF (1:1 volume) (○) at 30°C.

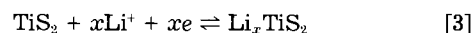
consistent with the results shown in Fig. 3. Ionic mobility is virtually determined by size of solvated ion and viscosity of solution (19, 20), as shown in Stokes' equation

$$u = \frac{|z|e}{6\pi\eta_0 r_s} \quad [2]$$

where u is ionic mobility, η_0 is solvent viscosity, r_s is Stokes' radius of the ion, and other symbols have their usual meanings. It was presumed that a suitable solvation state of Li⁺ ion in DOL-THF and/or lowering of viscosity by blending THF and DOL mainly contribute to higher diffusion rate of Li⁺ ion (21). The suitable ion solvation might also be responsible for the stable potential change during the cycle in mixed DOL-THF. Consequently, solvent mixing effects on the conductivity would highly relate to those on the Li electrode characteristics. However, further details of Li⁺ ion behavior will be discussed elsewhere (21).

Li cycle efficiency determined by Koch's method (18) is shown in Fig. 5. In spite of low plating and stripping current densities (2 mA/cm²) and low plated charge (0.2 C/cm²), the efficiency in DOL/LiBF₄ was much less than those in others. The efficiency variation in THF/LiBF₄ was quite similar to those obtained by Koch and Young (22). There was no great effect on the efficiency in initial cycles by mixing THF with DOL, but it seemed that the efficiency variation with cycle number in DOL-THF was less than that in THF. However, quantitative values of the efficiency were not presented here because of their lesser reproducibility. Further investigations of the solvent mixing effects on the cycle efficiency are now in progress under various experimental conditions.

TiS₂ electrode.—Figure 6 shows the current-potential curves of the TiS₂ electrode in THF/LiBF₄, DOL/LiBF₄, and DOL-THF (1:1)/LiBF₄. The measurements were carried out in the direction of arrows on the curves. A hysteresis observed on each cathodic curve seems to originate from partial reduction during the measurement. Some difference in zero-current potential was detected between three electrolytic solutions. This is probably due to variations in the state of charge and in the degree of relaxation of the electrode during the measurement and not to the change in the electrolyte itself. The order of current density at given potential was DOL-THF > THF > DOL, which was similar to the case of the Li electrode. However, the TiS₂ electrode reaction



is not limited only by mass-transfer process, in contrast to the Li electrode reaction. The detail of reaction [3] is complicated. The reaction involves not only charge-transfer process and Li⁺ ion diffusion in the solution but also ion transfer in pores of the electrode mixture and the transfer

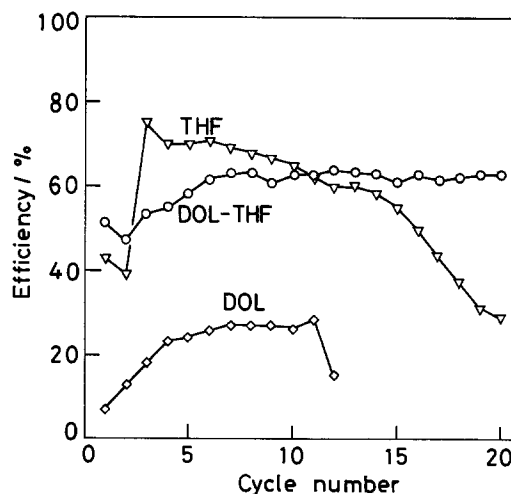


Fig. 5. Cycle efficiency of the Li electrodes in THF (▽), DOL (◇), and DOL-THF (1:1 volume) (○). Substrate: Ni sheet. $Q_p = 0.2 \text{ C/cm}^2$, $i_p = i_s = 2 \text{ mA/cm}^2$.

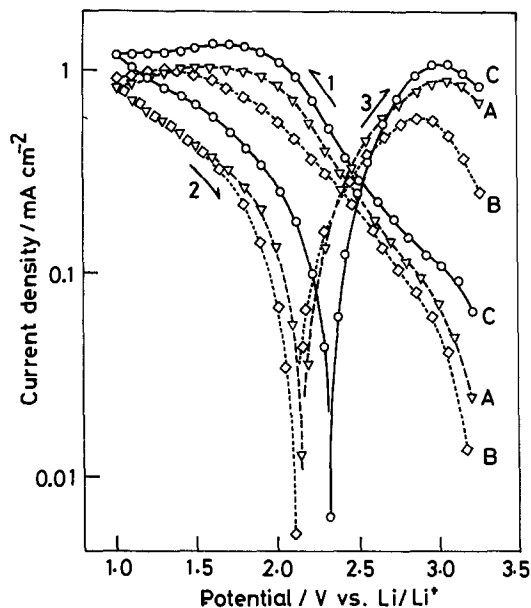


Fig. 6. Current-potential curves of the TiS_2 electrodes in 1M LiBF_4 solutions of THF (A), DOL (B), and DOL-THF (1:1 volume) (C).

in the layered structure of TiS_2 crystal (11). Although it is not clear which step is rate determining in the TiS_2 electrode reaction, one might expect from the current-potential curves that blending THF and DOL has a good effect on the charge-discharge reaction of the TiS_2 electrode.

The charge-discharge curves of the TiS_2 electrode in THF/LiBF_4 , DOL/LiBF_4 , and $\text{DOL-THF(1:1)/LiBF}_4$ are shown in Fig. 7, 8, and 9, respectively. As open-circuit voltages became almost constant within 1h, the measurements were carried out after standing the cells for 1h. Further standing before the cycle did not show any change in the first cycle capacity. Discharge (or charge) time of 10h corresponds to $x = 0.72$ in Eq. [3] from the calculation based on the TiS_2 weight. Equivalence of Li used

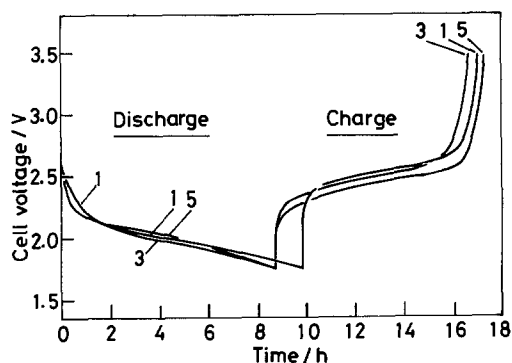


Fig. 7. Charge-discharge curves of the Li/TiS_2 cell. Electrolyte: THF/LiBF_4 (1M). Current density: 0.38 mA/cm^2 .

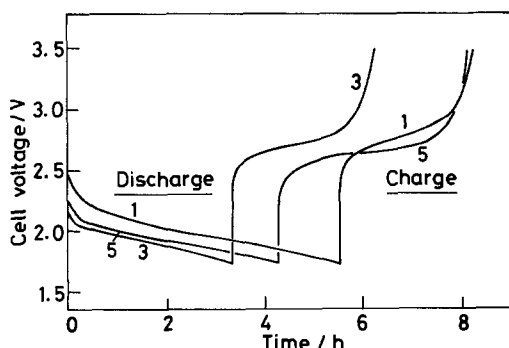


Fig. 8. Charge-discharge curves of the Li/TiS_2 cell. Electrolyte: DOL/LiBF_4 (1M). Current density: 0.38 mA/cm^2 .

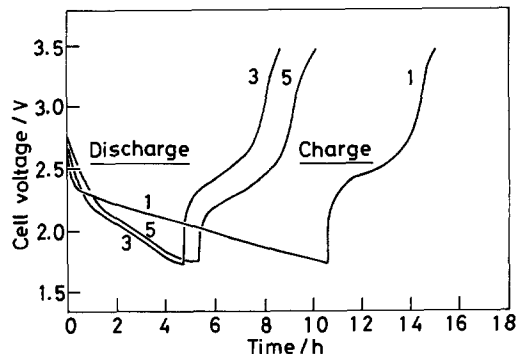


Fig. 9. Charge-discharge curves of the Li/TiS_2 cell. Electrolyte: $\text{DOL-THF (1:1 volume)/LiBF}_4$ (1M). Current density: 0.38 mA/cm^2 .

in this study as the counterelectrode was about 7.8 times of that of TiS_2 (see Experimental). Accordingly, variation of cell voltage is mainly attributable to the potential change at the TiS_2 electrode. Charge-discharge efficiencies in THF were seemingly better than those in DOL and DOL-THF, during the first five cycles. In DOL-THF/LiBF_4 , discharge capacity at the first cycle was comparable to that in THF, but efficiency of the first charge was ca. 50% of the first discharge. However, the subsequent charging efficiencies no longer decreased and were more than 80% of corresponding discharge. Thus, if any side reactions are not involved, it is considered that charge and discharge of TiS_2 in DOL-THF/LiBF_4 reversibly cycle in the range of about $0.4 \leq x \leq 0.7$. Similar cycling behavior was observed in the DOL solution, except for relatively low capacities of the first discharge and the subsequent charge.

Extended cycling efficiencies of the Li/TiS_2 cells were also examined with the same test cell. Charge-discharge curves in THF and DOL-THF(1:1) are shown in Fig. 10 and 11, respectively. Viscosity of the DOL/LiBF_4 solution tended to increase with cycles extended over a long time. This would be due to polymerization of DOL initiated by small amount of acids (23), which were either contained as impurity in the original LiBF_4 or evolved electrochemically during charge-discharge cycles. Thus, cycling efficiencies in DOL steeply decreased after five cycles. Charge-discharge efficiency in THF/LiBF_4 decreased

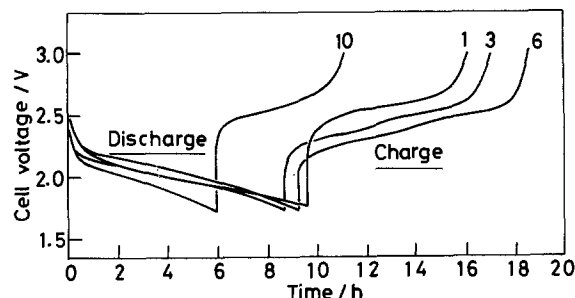


Fig. 10. Charge-discharge curves of the Li/TiS_2 cell. Electrolyte: THF/LiBF_4 (1M). Current density: 0.38 mA/cm^2 .

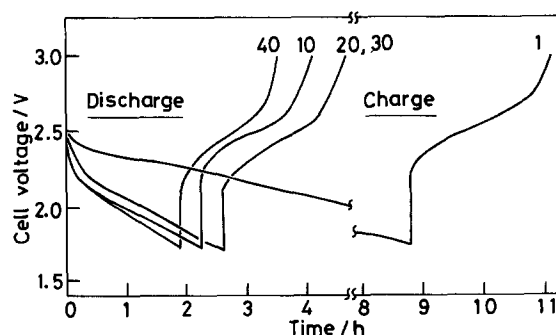


Fig. 11. Charge-discharge curves of the Li/TiS_2 cell. Electrolyte: $\text{DOL-THF (1:1 volume)/LiBF}_4$ (1M). Current density: 0.38 mA/cm^2 .

gradually after the sixth charge, and the cycle became impossible after the thirteenth charge. At the end of this cycling, Li dendrite deposition was observed even in the porous polypropylene separator. It was thought that short circuits were formed between the positive and negative electrodes through the dendrite. Charge-discharge capacities (Ah) in DOL-THF kept almost constant, except for the first discharge. After 40 cycles, however, charge-discharge efficiencies decreased slowly, and the capacities were exhausted practically after 45 cycles. A rise in the viscosity was not observed in DOL-THF/LiBF₄, in contrast to the DOL solution. Since the cells were initially cathode (TiS₂) limited, total accumulated cell capacity might be evaluated for theoretical capacity of TiS₂ used (so-called FOM_{TiS₂}). Resulted FOM_{TiS₂}'s were about 7 in THF, 1.5 in DOL, and 9 in DOL-THF. However, increasing in the cycle number in DOL-THF would be owing primarily to the improved cycling characteristics at the Li electrode in that solution.

X-ray diffraction of the TiS₂ electrodes was examined after the cycles. Diffraction intensities of TiS₂ were decreased with cycling in every solution. This suggested that the layered structure of TiS₂ crystal diminished with cycling. From the fact that the efficiency of the first charge in DOL-THF was much different from that in THF, it was supposed that the solvent took part in the charging reaction of TiS₂. However, no marked difference was detected in x-ray diffraction data between two solutions. Further detailed investigations should be required to clarify the relation between the electrolyte composition and cycling characteristics of the TiS₂ electrode. Cycling efficiency of the Li/TiS₂ cell with the DOL-THF(1:1) solvent was not very high, so far as the present work, but it will be improved by changing experimental conditions such as preparation of the TiS₂ electrode and the test cell construction.

Conclusions

Solvent mixing effects on the electrode characteristics of Li/TiS₂ cells have been investigated in the DOL-THF system, and the results are summarized as follows.

1. Charge-discharge potentials at the Li negative electrode in a DOL-THF blend were more stable than those in neat THF or DOL. The Li electrode in DOL-THF/LiBF₄ showed the least polarization. These seemed to relate that the electrolytic conductivity of LiBF₄ was improved by mixing the solvents.

2. Current-potential relations at the TiS₂ positive electrode suggested higher cyclability of TiS₂ in DOL-THF than in THF or DOL. Initial charging efficiency in DOL-THF was rather low, but its variation with the cycle was very small.

3. The total cycle performance of the cell was initially the best in THF/LiBF₄, because the cells used in this work

were cathode (TiS₂) limited. With increasing the cycle number, however, the cell performance became anode (Li) limited, and then the cycle life of the cell with DOL-THF/LiBF₄ was the best.

Acknowledgments

We wish to thank J. Harada for some experimental work. We are grateful to the Japan Securities Scholarship Foundation (No. 249) for partial support of this research.

Manuscript submitted Oct. 25, 1983; revised manuscript received March 26, 1984.

Yamaguchi University assisted in meeting the publication costs of this article.

REFERENCES

1. M. S. Whittingham, *J. Chem. Soc. Chem. Commun.*, 329 (1974); *Science*, **192**, 1126 (1976); *Prog. Solid State Chem.*, **12**, 41 (1978).
2. K. M. Abraham, *J. Power Sources*, **7**, 1 (1982).
3. J. O. Besenhard and G. Eichinger, *J. Electroanal. Chem.*, **68**, 1 (1976).
4. V. R. Koch, *J. Power Sources*, **6**, 357 (1981).
5. V. R. Koch and J. H. Young, *Science*, **204**, 499 (1979).
6. J. L. Goldman, R. M. Mank, J. H. Young, and V. R. Koch, *This Journal*, **127**, 1461 (1980).
7. K. M. Abraham, J. L. Goldman, and D. L. Natwig, *ibid.*, **129**, 2404 (1982).
8. P. G. Glugla, *ibid.*, **130**, 113 (1983).
9. J. S. Foos and J. McVeigh, *ibid.*, **130**, 628 (1983).
10. G. L. Holleck and J. R. Driscoll, *Electrochim. Acta*, **22**, 647 (1977).
11. A. J. Vaccaro, T. Palanisamy, R. L. Kerr, and J. T. Maloy, *This Journal*, **129**, 677, 682 (1982).
12. Y. Matsuda, M. Morita, and K. Ohta, *Denki Kagaku*, **51**, 291 (1983).
13. V. R. Koch, *This Journal*, **126**, 181 (1979).
14. G. H. Newman, R. W. Francis, L. H. Gaines, and B. M. L. Rao, *ibid.*, **127**, 2025 (1980).
15. J. W. Johnson and M. S. Whittingham, *ibid.*, **127**, 1653 (1980); J. W. Johnson and A. H. Thompson, *ibid.*, **128**, 932 (1981).
16. V. R. Koch, J. L. Goldman, C. J. Mattos, and M. Mulvaney, *ibid.*, **129**, 1 (1982).
17. Y. Matsuda, Y. Yamamoto, and M. Morita, *Denki Kagaku*, **49**, 653 (1981).
18. V. R. Koch and S. B. Brummer, *Electrochim. Acta*, **23**, 55 (1978).
19. R. A. Robinson and R. H. Stokes, "Electrolyte Solutions," p. 124, Butterworths, London (1959).
20. Y. Matsuda, H. Nakashima, M. Morita, and Y. Takasu, *This Journal*, **128**, 2552 (1981).
21. Y. Matsuda, M. Morita, and T. Yamashita, Submitted to *This Journal*.
22. V. R. Koch and J. H. Young, *ibid.*, **125**, 1371 (1978).
23. Y. Yamashita, M. Okada, and M. Hirota, *Angew. Makromol. Chem.*, **9**, 136 (1969).

Li/SOCl₂ Battery Intercell Currents

S. Szpak* and C. J. Gabriel

Naval Ocean Systems Center, San Diego, California 92152

J. R. Driscoll*

Altus Corporation, San Jose, California 95112

ABSTRACT

A general method for computing parasitic intercell currents in series connected electrochemical cells with common electrolytic path is described. This method covers systems operating with constant as well as variable parameters such as usually are encountered in practice. The Li/SOCl₂ battery is selected to illustrate the evolution of parasitic intercell currents in the course of battery discharge.

Often, it is necessary to construct a battery having a high energy density that must be able to operate at high power outputs. One way that this goal can be accomplished is by selecting a lithium battery and using bipolar electrodes, which provide a compact series connection of the individual cells. Such a design is very attractive. However, because of the reactivity of metallic Li when in contact with an electrolyte, only a reserve configuration is practical, which means that a continuous electrolytic path through all of the cells must be provided for either filling the battery or flowing the electrolyte.

Our purpose in this communication is to discuss the effects of current flowing in the common electrolytic path on the operational characteristics of batteries and other electrochemical devices. Although most of the treatment is general, the results are illustrated using a Li/SOCl₂ battery employing thin disk-shaped cells of bipolar construction.

Theoretical

Qualitatively, intercell current is an ionic current that originates in one cell and terminates in another cell. This current does not perform any useful work; on the contrary, it is considered a parasitic current resulting not only in the loss of power but also in the loss of capacity, and it may contribute to the premature failure of individual cells by the formation of passive films or by the corrosion of structural parts.

The operation of a battery is a dynamic event consisting of a series of consecutive elementary processes wherein the slowest determines the overall rate. To illustrate, let us consider the Li/SOCl₂ system (Fig. 1). Two processes occur at the negative; they are the charge transfer reaction (oxidation) and the transport of Li⁺ ions through the protective LiCl film whose thickness depends on the electrolyte composition and the rate of battery discharge (1). The situation at the positive is far more complex because, first, the reaction takes place within the confines of a porous structure, and, second, the physicochemical properties of the electrolyte change in the course of battery discharge. In spite of this complexity, each elementary process obeys, at least approximately, a generalized Ohm's law, *i.e.*, it can be described by an equation of the type, $j = kX$, relating the flux j to the driving force X through a phenomenological rate constant k . Such a description suggests that an electric circuit analog can be used to represent the overall process occurring in the interior of the cell.

Equivalent circuit analog.—An electric circuit analog of a reserve battery during discharge is shown in Fig. 2. This representation greatly simplifies the real situation and yet permits the treatment of the intercell currents in a more general way than similar models that have appeared in the literature (2-7). Here, the phenomenological coefficients associated with ionic current in the segments of the

electrolyte in the fill path and the feed line into the entrance port of the cell are replaced by equivalent resistances, $R_{t,i}$ and $R_{f,i}$, respectively. This replacement requires that the current distribution on the cross section of the

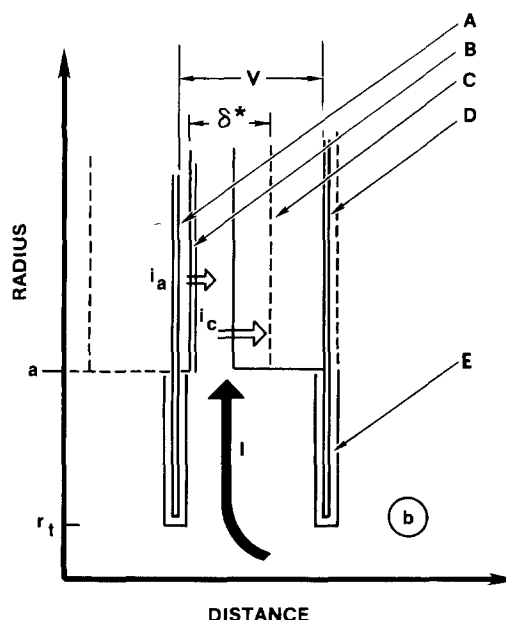


Fig. 1. Li/SOCl₂ cell. A: Li foil. B: protective film. C: porous carbon electrode. D: bipolar Ni plate. E: insulators. δ^* : distance (equivalent) between charge transfer planes. Intercell current indicated by heavy arrow.

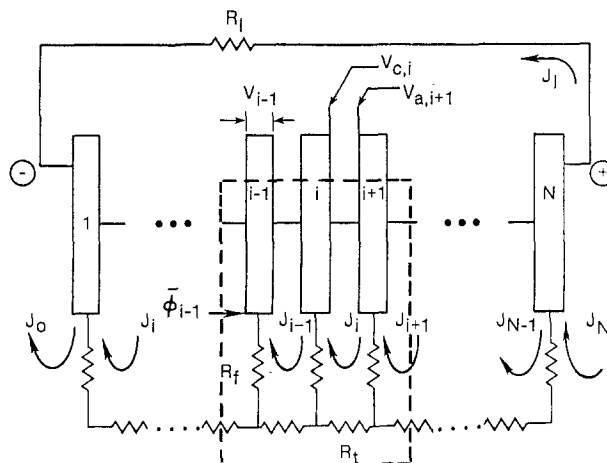


Fig. 2. Battery representation by equivalent electric circuit. V_{i-1} : cell voltage. Φ_{i-1} : potential at manifold inlet to ($i-1$)th cell. J_i : circulating current. J_j : loop current in an external resistor R_f . R_f : manifold feed-line resistor. R_t : equivalent fill-tube resistor. Control volume element indicated by heavy dashed line.

* Electrochemical Society Active Member.

electrolytic path be uniform, which, in practice, is only approximately correct. Further, if we assume that the potentials in the electrolyte at the entrance port to the cells, $\bar{\phi}_i$, are uniform and equal to a longitudinal average between the cell electrodes and that the electrodes are equipotential with the potential difference of $V_i = V_{c,i} - V_{a,i}$ between them, then the loop equations for the current, J_i , in the external load, R_i , and for the circulating currents in the fill path, J_i , are given, respectively, by

$$J_1 R_1 = \sum_{i=1}^N V_i \quad [1]$$

and

$$-J_{i-1} R_{t,i} + J_i (R_{t,i} + R_{t,i+1} + R_{t,i}) - J_{i+1} R_{t,i+1} = \bar{\phi}_{i+1} - \bar{\phi}_i, \quad (i = 1, 2, \dots, N-1) \quad [2]$$

where we neglect the potential drop across the separator.

Since the circulating current, J_i , flows in the reverse direction in the i th segment of the fill path, then

$$J_0 = J_N = 0 \quad [3]$$

Furthermore, the intercell current into a cell, I_i , is given by

$$I_i = J_i - J_{i-1}, \quad (i = 1, 2, \dots, N) \quad [4]$$

while the total electrode current into a cell, *i.e.*, the anodic current, $I_{a,i}$, is

$$I_{a,i} = J_1 + J_{i-1}, \quad (i = 1, 2, \dots, N) \quad [5]$$

Finally, we have the requirement that the bipolar plate be equipotential, *i.e.*

$$V_{a,i+1} = V_{c,i}, \quad (i = 1, 2, \dots, N-1) \quad [6]$$

where again the potential drop across the separator is ignored.

Reformulation of applicable equations.—The N Eq. [1] and [2] can be solved for J_1 and J_i if $\bar{\phi}_i$ and V_i can be expressed in terms of the $I_{a,i}$ and I_i . To obtain the needed information, it is necessary to consider in some detail the current and potential distributions within a cell that is operating in the presence of intercell current. Results for a cell having cylindrical symmetry have been given elsewhere (2); however, a treatment is given in Appendix A in order to provide the results relevant to the further discussion. Thus, suppressing the cell index when all quantities in an equation refer to the same cell, the potentials at the entrance ports of the cells and the potential differences across the cells are, respectively

$$\bar{\phi} = \bar{\phi}_0 + I R_p \quad [7]$$

and

$$V = U_c - U_a - (I_a + I\sigma_c) R_z \quad [8]$$

Here, the potential to the entrance port in the absence of the intercell current is

$$\bar{\phi}_0 = (V_a - U_a) \sigma / \sigma_c + (V_c - U_c) \sigma / \sigma_a \quad [9]$$

and the impedance to the intercell current at the entrance port and the internal cell impedance are, respectively

$$R_p = \frac{r_c}{\pi a \delta^* (\kappa_a + \kappa_c)} \left[\frac{I_1(b/r_c) K_0(a/r_c) + K_1(b/r_c) I_0(a/r_c)}{I_1(b/r_c) K_1(a/r_c) - K_1(b/r_c) I_1(a/r_c)} \right] \quad [10]$$

and

$$R_z = \frac{1}{\pi (b^2 - a^2) \sigma} \quad [11]$$

The functions I_ν and K_ν , ($\nu = 0, 1$), are the modified Bessel functions of the order ν , which arise because of the symmetry of the cell. Other quantities are defined as follows: the characteristic depth of penetration, the effective electrode resistivities, and the effective cell resistivity are given respectively, by

$$r_c^2 = \frac{1}{2} \delta^* \left[\frac{2\kappa_a \kappa_c (\kappa_a + \kappa_c) + \delta^* (\kappa_a^2 \kappa_c + \kappa_c^2 \kappa_a)}{2\kappa_a \kappa_c (\kappa_a + \kappa_c) + \delta^* (\kappa_a + \kappa_c) \kappa_a \kappa_c} \right] \quad [12]$$

$$1/\sigma_\nu = 1/\kappa_\nu + \frac{1}{2} \delta^* / \kappa_\nu, \quad (\nu = a, c) \quad [13a]$$

$$1/\sigma = 1/\sigma_a + 1/\sigma_c \quad [13b]$$

Having the information developed in Appendix A and summarized in Eq. [7]-[13], we are in a position to complete the description of the battery model, *i.e.*, to express Eq. [1] and [2] in terms of the circulating currents. This is a relatively simple matter for Eq. [1]. Starting with Eq. [8] and combining it with Eq. [4] and [5], we get the potential depression across a cell

$$U_i - V_i = (J_1/\sigma_i + J_{i-1}/\sigma_{a,i} + J_i/\sigma_{c,i}) R_{z,i} \sigma_i \quad [14]$$

Summation of both sides of Eq. [14], taking into account Eq. [3], and substitution of the result into Eq. [1] yields

$$J_1 \left[R_1 + \sum_{i=1}^N R_{z,i} \right] = \sum_{i=1}^N U_i - \sum_{i=1}^{N-1} J_i R_{z,i}^* \quad [15]$$

where

$$R_{z,i}^* = R_{z,i+1} \sigma_{i+1} / \sigma_{a,i+1} + R_{z,i} \sigma_i / \sigma_{c,i} \quad [16]$$

A more complex procedure is required to express Eq. [2] in terms of J_i and J_i . Following the development presented in Appendix B, we use Eq. [6], [7], [9], and [14] to rewrite the right side of Eq. [2] and obtain

$$-J_{i-1} R_{t,i}^* + J_i (R_{t,i}^* + R_{t,i+1}^* + R_{z,i}^* + R_{b,i}) - J_{i+1} R_{t,i+1}^* = U_i^* - J_1 R_{z,i}^*, \quad (i = 1, 2, \dots, N-1) \quad [17]$$

where the equivalent feed line resistance is

$$R_t^* = R_t + R_p - R_z \sigma^2 / (\sigma_a \sigma_c) \quad [18]$$

and the equivalent open-circuit potential of a cell is

$$U_i^* = U_{c,i} - U_{a,i+1} \quad [19]$$

Equations [15] and [17] with Eq. [3] constitute the set of N equations that must be solved to obtain the circulating currents, J_1 and J_i ($i = 1, 2, \dots, N-1$).

Intercell current and potential distributions.—Using the relations developed in Appendix A, we have for the local anodic and cathodic current densities

$$i_a = \sigma(U-V) - \frac{\sigma \delta^* (\kappa_a + \kappa_c)}{2 r_c^2 \sigma_c} (\bar{\phi} - \bar{\phi}_0) \quad [20]$$

and

$$i_c = \sigma(U-V) + \frac{\sigma \delta^* (\kappa_a + \kappa_c)}{2 r_c^2 \sigma_a} (\bar{\phi} - \bar{\phi}_0) \quad [21]$$

respectively, where the radial potential distribution is

$$\bar{\phi} - \bar{\phi}_0 = \frac{I r_c}{\pi a \delta^* (\kappa_a + \kappa_c)} \left[\frac{I_1(b/r_c) K_0(\tau/r_c) + K_1(b/r_c) I_0(\tau/r_c)}{I_1(b/r_c) K_1(a/r_c) - K_1(b/r_c) I_1(a/r_c)} \right] \quad [22]$$

and $U = U_c - U_a$ is the open-circuit potential.

Equations [20] and [21] show clearly the effect of the intercell current, I , and the potential depression, $U-V$, on the local charge transfer current density. Their radial dependence is contained in the term determined by Eq. [22], where, from the properties of the modified Bessel functions, we find that for positive I , $\bar{\phi} - \bar{\phi}_0$ is a positive, monotonically decreasing function of the radius, r . Inspection of Eq. [20] and [21] reveals that if the intercell current, I , is of the same sign as the potential depression, $U-V$, then current reversal is possible only on the anode, while if these quantities are of the opposite sign, then current reversal can take place only on the cathode. Since $U-V$ is positive for a discharging cell, for positive I , *i.e.*, for intercell current into the cell, reversed current can occur on the inner portion of the anode, proceeding from $r = a$ outward to $r = r_0$, *i.e.*, that is to where $i_a = 0$, while for negative intercell current, reversed current is possible on the inner portion of the cathode. Such a current reversal would force the cell to act as an electrolyzer over the affected electrode area.

The total amount of reversed current is calculated by integrating the local current density, either Eq. [20] or [21], over the affected electrode area, $\pi(r_0^2 - a^2)$. The result is either

$$I_a(r_o) = \pi(r_o^2 - a^2) \sigma (U-V) - I\gamma\sigma/\sigma_c \quad [23]$$

or

$$I_c(r_o) = \pi(r_o^2 - a^2) \sigma (U-V) + I\gamma\sigma/\sigma_a \quad [24]$$

where

$$\gamma = 1 - \frac{r_o}{a} \left[\frac{I_1(b/r_o) K_1(r_o/r_o) - K_1(b/r_o) I_1(r_o/r_o)}{I_1(b/r_o) K_1(a/r_o) - K_1(b/r_o) I_1(a/r_o)} \right] \quad [25]$$

and where r_o is either the radius for zero c.d. on the anode or the cathode, respectively.

Computational results.—Equations [15] and [17] describe a battery model in which the cell parameters can vary from cell to cell. Indeed, this will be the case, since in a discharging battery the intercell currents vary from cell to cell. Thus, in general, the N in Eq. [15] and [17] can be solved only numerically.

A simpler case is that with constant coefficients that are uniform from cell to cell, where the solution can be obtained in closed form. Equations [15] and [17], with constant and uniform parameters, reduce to

$$J_i(R_1 + NR_z) = NU - R_z \sum_{i=1}^{N-1} J_i \quad [26]$$

and

$$-J_{i-1}R_t^* + J_i(2R_t^* + R_z + R_1) - J_{i+1}R_t^* = U - J_iR_z, \quad i = (1, 2, \dots, N-1) \quad [27]$$

respectively, with the only reference to a particular cell occurring on the circulating currents.

This set of N equations can be solved using the method of undetermined coefficients (see Appendix C). The results are as follows

$$J_1 = \frac{N(1-\xi)U}{R_1 + N(1-\xi)R_z} \quad [28]$$

$$J_i = J_p \left(1 - \frac{\lambda^{N-i} + \lambda^i}{\lambda^N + 1} \right), \quad (i = 0, 1, \dots, N) \quad [29]$$

and from Eq. [4]

$$I_i = J_p \frac{\lambda - 1}{\lambda^N + 1} \left(\lambda^{N-i} - \lambda^{i-1} \right), \quad (i = 1, 2, \dots, N) \quad [30]$$

where

$$J_p = \frac{R_1 U}{R_1 + N(1-\xi)R_z} \left(\frac{1}{R_1 + R_z} \right) \quad [31]$$

$$\lambda = 1 + \frac{R_1 + R_z}{2R_t^*} + \sqrt{\frac{R_1 + R_z}{2R_t^*} \left(2 + \frac{R_1 + R_z}{2R_t^*} \right)} \quad [32]$$

and

$$\xi = \frac{R_z}{R_1 + R_z} \left[1 - \frac{(\lambda^N - 1)(\lambda + 1)}{N(\lambda^N + 1)(\lambda - 1)} \right] \quad [33]$$

Application to Li/SOCl₂ Battery

The principal disadvantage of a common electrolytic path is the continuous discharge of the cells which results in an underutilization of the reactants as well as in a loss of power. In marginal designs, circulating currents may contribute to thermal management problems. Additionally, the post-test examination of a number of discharged Li/SOCl₂ batteries of the reserve type has revealed the dendritic growth of metallic Li in cells at the negative end and evidence of an oxidation reaction in cells at the positive end.

In what follows, we will begin by examining the characteristics of the intercell and circulating currents in batteries with uniform and constant parameters; next, we will illustrate the effect of changing parameters upon the distribution of these currents; and, finally, we will briefly consider implications involving current reversal.

Constant parameters.—The uniformity of battery parameters can be approximately realized only in battery designs employing flowing electrolyte and operating at constant power output. In other designs, such assump-

Table I. Data for modeling of intercell currents

Electrode inner radius	a	1.8 cm
Electrode outer radius	b	5.7 cm
Electrode separation	δ^*	0.01 cm
Fill tube radius	r_t	0.2 cm
Fill tube segment length	l_t	0.04 cm
Thickness of feed path	d	0.03 cm
Electrolyte conductivity	κ	0.01 S cm ⁻¹
Separator porosity in cell	ϵ_z	0.5
Separator porosity feed path	ϵ_f	0.8
Electrode polarization: anode	k_a	5.0 S cm ⁻²
Electrode polarization: cathode	k_c	1.0 S cm ⁻²
Open circuit potential	U	3.6V
Discharge time	T	600s
Discharge CD	$j_a j_c$	≈ 80 mA cm ⁻²

tions have only limited validity; nevertheless, they serve the useful purpose of illustrating how the electrochemical and design parameters interact, and thus can provide guidance on an approach to minimize the intercell currents.

Figures 3a-3c show the change in the computed distributions of the intercell and circulating currents as a function of the number of cells. The parameters used in these and the following calculations are assembled in Table I. In each case, the load resistance was chosen to be 0.5Ω per cell so as to make the load current approximately the same for all of the batteries and the fill-tube and feed-line resistances were approximated by the expressions, respectively

$$R_t = \frac{l_t}{\pi r_t^2 \kappa_t} \quad [34]$$

and

$$R_f = \frac{1}{2\pi d \kappa_f} \ln \left(\frac{a}{r_t} \right) \quad [35]$$

where l_t and r_t are, respectively, the length and radius of the segment of the fill tube that connects two cells, d is the thickness of the annular feed line into each cell, and κ_t and κ_f are the effective conductivities of the electrolyte in the fill tube and feed line, respectively. In addition, we assumed $\kappa_a = \kappa_c = \kappa \epsilon_z$, $\kappa_f = \kappa \epsilon_f$, and $\kappa_t = \kappa$, where ϵ_z and ϵ_f indicate the respective porosities.

Qualitatively, all of the batteries exhibit a maximum in the circulating currents at the central cells; whereas, the intercell currents are largest at the end cells and change their sign from positive to negative, *i.e.*, from entering a cell to exiting a cell at the negative and positive ends of the battery, respectively. Interestingly, for batteries having a small number of cells (Fig. 3a), all cells generate intercell currents. However, with an increase in the number of cells, *e.g.*, for $N = 40$ (Fig. 3b), the centrally located cells contribute significantly less, and for $N = 80$ (Fig. 3c), the majority of the cells do not contribute to the intercell current at all, *i.e.*, a large section of the battery does not suffer underutilization of its reactants.

The rapid decrease in the intercell current for the centrally located cells, particularly when N is large (Fig. 3c), implies that a battery can be viewed as consisting of segments near each end, OB and CE, where a substantial underutilization of reactants occurs, and a central segment, BC, where cells operate with equal anodic and cathodic currents. Furthermore, if the intercell current exceeds a critical value, which depends on the potential depression and thus on the cell load, additional segments may be identified, OA and DE: namely, those where the electrode current is reversed over part of an electrode. The effect of reversed current is illustrated in Fig. 4a-4c, wherein photographs of the feed-line region of a series stack show clear evidence of electrochemical activity at the positive (Fig. 4a), and negative (Fig. 4b) ends, and no measurable amounts at the center (Fig. 4c).

The λ parameter.—For a given number of cells, the relative distributions of both the circulating and intercell currents depend on the value of the parameter λ . This parameter is given by Eq. [32] and is a function of the ratio: $(R_1 + R_z)/(R_1 + R_p - R_z \sigma^2 / \sigma_a \sigma_c)$, *i.e.*, it depends on the battery de-

Fig. 3. Distributions of circulating (thin line) and intercell currents (heavy lines) as functions of the number of cells. a: small number of cells ($N = 10$). b: moderate number of cells ($N = 40$). c: large number of cells ($N = 80$).

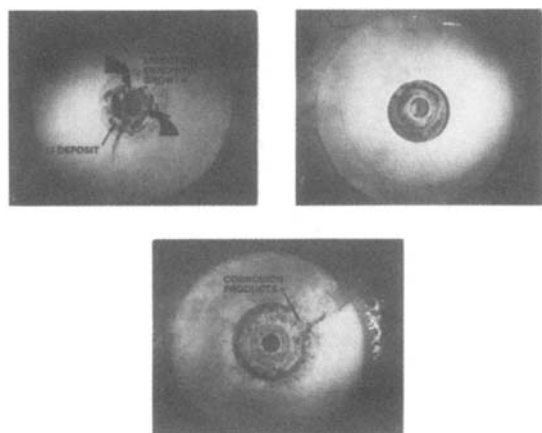
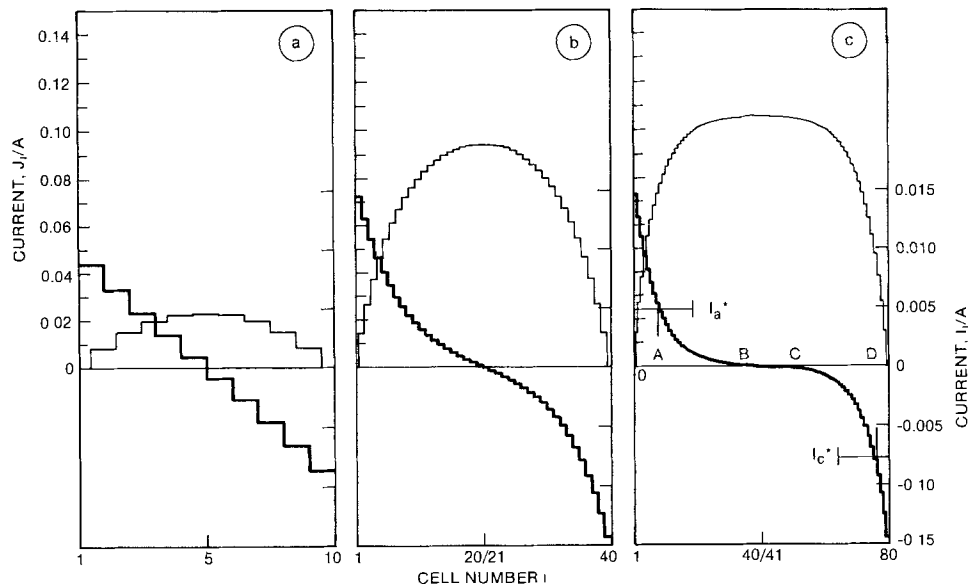


Fig. 4. Effect of intercell current at the cell entrance and within the annular feed line. a (top left): Cell located at negative end. $I > I_a^*$; metallic Li and direction of its growth are indicated by arrows. b (top right): Cell located in the central region of an 80-cell assembly. c (bottom): Cell located at the positive end. $I > I_c^*$; corrosion products indicated by arrow.

sign (dimensions) as well as on the properties of the electrolyte and the kinetics of charge transfer reaction. For large values of R_i , λ will be large, while for large values of R_e , λ will be near unity.

For large numbers of cells, λ gives the ratio of intercell currents for adjacent cells in the segments near the ends of the battery, i.e., Eq. [30] yields either

$$I_{i+1}/I_i \approx 1/\lambda, \quad i \approx 1 \quad [36]$$

or

$$I_{i+1}/I_i \approx \lambda, \quad i \approx N \quad [37]$$

since, according to Eq. [32], $\lambda > 1$.

In general, the effect of λ on J_i and I_i is more complicated. In particular, Fig. 5 shows plots of J_i/J_p and I_i/J_p vs. λ in a 40-cell battery. It is seen that for $i = 1$, curves J_i/J_p and I_i/J_p coincide, in agreement with Eq. [4]; moreover, they increase monotonically with an increase in λ . For $i > 1$, the I_i/J_p ratios decrease with increasing i and, furthermore, each exhibits a maximum, which shifts towards $\lambda = 1$ as i approaches $N/2$. The J_i/J_p ratios increase with i as i approaches $N/2$ for all values of λ . It is noteworthy that for all values of i , J_i/J_p approaches unity for large λ .

Due to the symmetry, for $i > N/2$ the I_i/J_p change sign and increase in magnitude as i approaches N . Similarly, the J_i/J_p decrease with an increase in i , when $i > N/2$.

Figure 6 illustrates the effect of the number of cells in a battery on the circulating and the intercell currents, again

expressed as J_i/J_p and I_i/J_p ratios. Evidently, the dependence on N is substantial only for $\lambda < 2$ and $N < 40$.

The current distributions can be summarized as follows: for λ near unity, the tails of the current distributions extend into the battery, and for $N < 40$ the shape of the tails depends on N ; while for large λ , the terminal cells carry most of the intercell currents independent of the value of N . However, large values of λ generally result from large values of R_i rather than from small values of R_e , so that, according to Eq. [31], J_p becomes small so that generally the intercell currents even in the end cells are small for large λ .

In practice, volumetric energy density constraints and conditions imposed either on the time required for activating a battery employing static electrolyte or on the pressure drop for flowing electrolyte designs result in values of λ near unity and produce intercell current distributions that tail slowly off into the battery. However, after the cells are nearly discharged, intercell current distributions corresponding to large values of λ can occur.

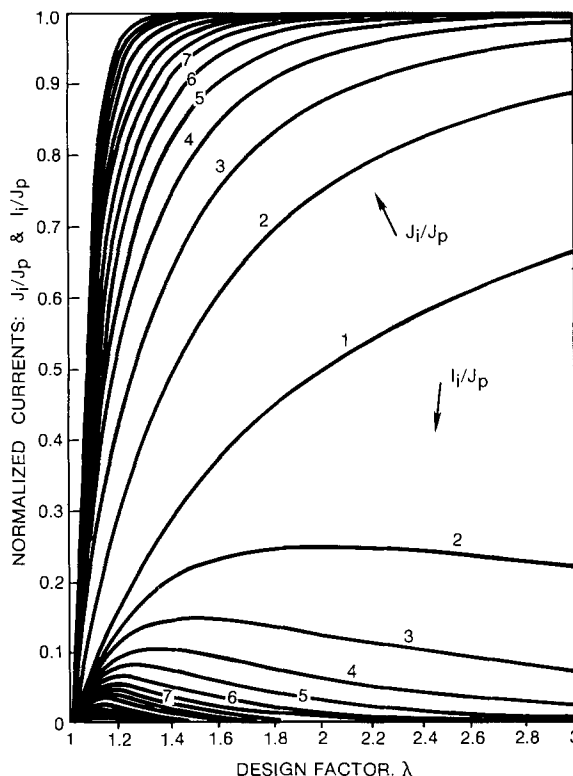


Fig. 5. Plot of normalized circulating, J_i/J_p , and intercell currents, I_i/J_p , as functions of the design factor, λ . The numbers indicate the value of i .

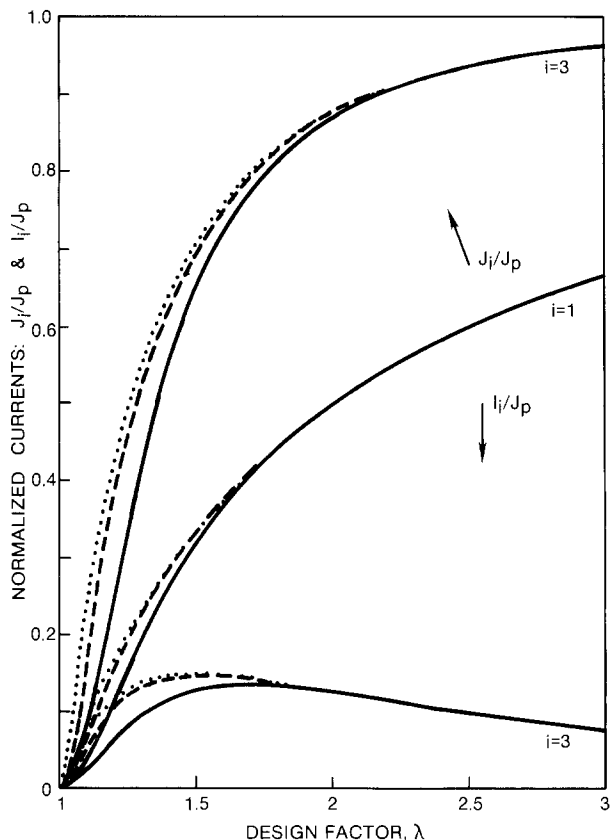
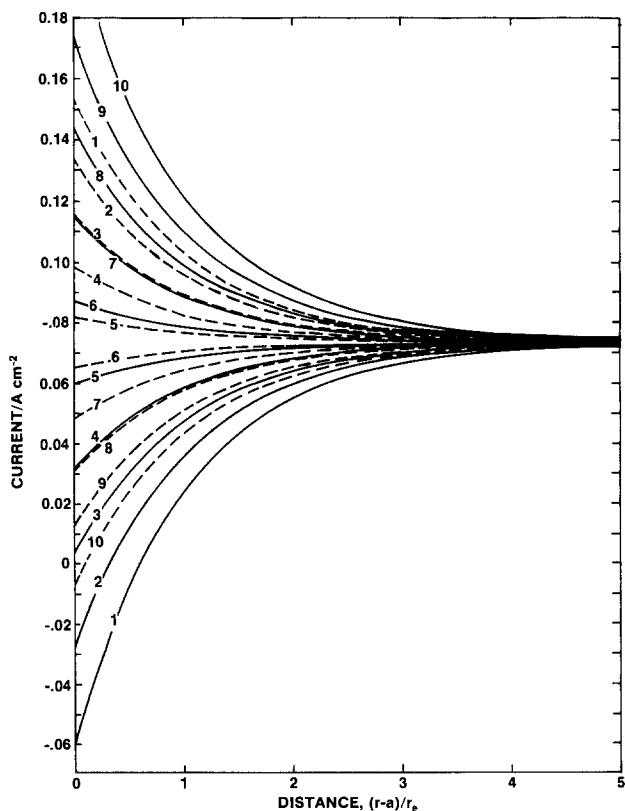


Fig. 6. Plot of the normalized circulating currents J_1/J_p and J_3/J_p and the intercell currents I_1/J_p and I_3/J_p as functions of design for $N = 10$ (—), $N = 40$ (- - -), and $N = 80$ (· · · ·).

Reversal of electrode currents.—The effect of the intercell current, I , on the radial distribution of the anodic and cathodic currents is shown in Fig. 7a and 7b for a 10-cell and an 80-cell battery, respectively.



Results that are presented in Fig. 3a and 3c and those in Fig. 7a and 7b indicate that the intercell current into the first two cells of the 10-cell battery stack and into the first eight cells of the 80-cell assembly exceed their critical values, I_a^* , and experience current reversal at their negative. Only one of the cells located at the positive end of the 10-cell battery and five of the cells of the 80-cell assembly suffer current reversal at their positive. This is illustrated in Fig. 8 for the 80-cell battery, where the dimensionless depth of penetration of the reversed current, $(r_o - a)/r_e$, is plotted as a function of the cell number. Evidently, the depth of reversed current penetration is a linear function of the cell number and has the same slope, except for sign, at either end of the battery. This linearity follows from Eq. [20] and [21] and by the asymptotic behavior of the modified Bessel functions for large arguments, since in all practical cases, a/r_e is a large number.

Specifically, under the conditions that $a \gg r_e$, $\tau \approx a$, and $J_1 \gg J_p$, Eq. [20] and [21] can be approximated by

$$i_a \approx \frac{\sigma}{2\pi \tau_e a \sigma_c} [I_a^* - Ie^{-(r-a)/r_e}] \quad [38]$$

and

$$i_c \approx \frac{\sigma}{2\pi \tau_e a \sigma_a} [I_c^* + Ie^{-(r-a)/r_e}] \quad [39]$$

where the critical intercell currents are

$$I_a^* = 2\pi a \tau_e \sigma_c J_1 R_z \quad [40]$$

and

$$I_c^* = 2\pi a \tau_e \sigma_a J_1 R_z \quad [41]$$

If the intercell current exceeds I_a^* , then current reversal takes place on the anode; whereas, if the intercell current is more negative than $-I_c^*$, then current reversal takes place on the cathode.

Furthermore, if the number of cells is large, then the intercell current for cells near the negative end of the battery can be approximated by

$$I_i \approx J_p (\lambda - 1) / \lambda^i, \quad i \approx 1 \quad [42]$$

and near the positive end by

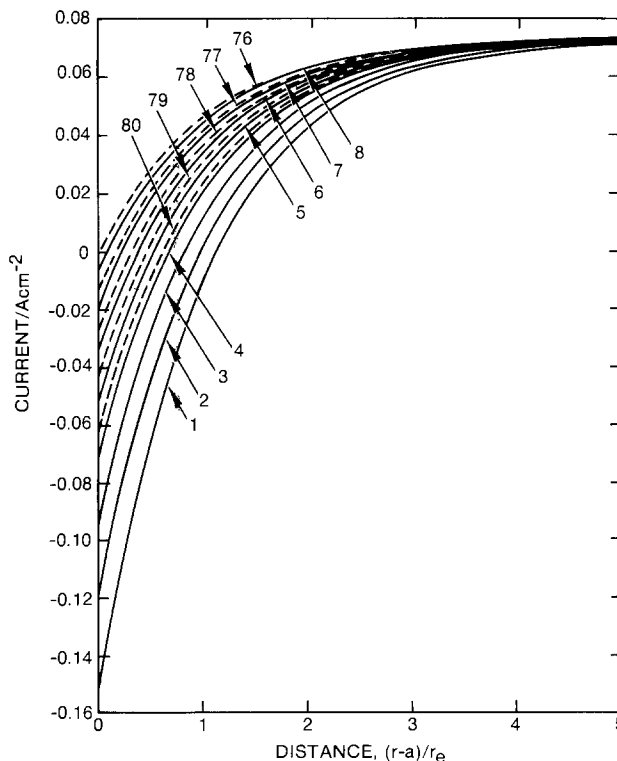


Fig. 7. Plot of the electrode currents as a function of $(r - a)/r_e$. Solid lines indicate anode, and dashed lines indicate the cathode for the cell numbers that are shown. a(left): For 10-cell battery. b(right): For 80-cell battery.

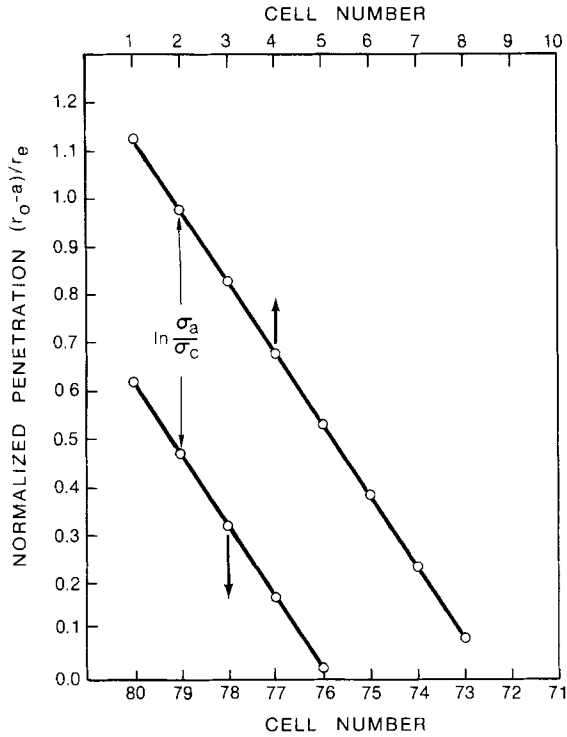


Fig. 8. Plot of normalized penetration depth of reversed current (r_{o-a}/r_e) vs. cell number for an 80-cell battery.

$$I_i = -J_p (\lambda - 1) / \lambda^{N+1-i}, i \approx N \quad [43]$$

Upon substitution of Eq. [42] and [43] into Eq. [38] and [39] with i_a and i_c set to zero, respectively, and r taken to be r_o , we obtain

$$\frac{r_{o,i} - a}{r_e} = -i \ln \lambda + \ln \left[\frac{J_p (\lambda - 1)}{I_a^*} \right], i \approx 1 \quad [44]$$

and

$$\frac{r_{o,i} - a}{r_e} = -(N + 1 - i) \ln \lambda + \ln \left[\frac{J_p (\lambda - 1)}{I_c^*} \right], i \approx N \quad [45]$$

which are straight lines with slopes $-\ln \lambda$ and $\ln \lambda$, respectively, and whose intercepts for $i = 1$ and $i = N$ differ by $\ln (\sigma_a/\sigma_c)$ (Fig. 8).

The total reversed current on an electrode, given by either Eq. [23] or [24], becomes, in this approximation, either

$$I_a(r_o) \approx I_a^* \frac{\sigma}{\sigma_c} \left[1 - \frac{I}{I_a^*} + \ln \left(\frac{I}{I_a^*} \right) \right], I \geq I_a^* \quad [46]$$

or

$$I_c(r_c) \approx I_c^* \frac{\sigma}{\sigma_a} \left[1 + \frac{I}{I_c^*} + \ln \left(\frac{-I}{I_c^*} \right) \right], I \leq -I_c^* \quad [47]$$

where for large N , Eq. [42] and [43] can be used to obtain I .

Variable parameters.—The assumption that the dimensional and physicochemical parameters remain uniform from cell to cell in the course of the Li/SOCl₂ battery discharge is not realistic. For example, the uniformity of the electrode spacing, δ^* , cannot be maintained because (i) for a fixed position of the bipolar plates the surface of the dissolving Li recedes and (ii) the reaction front penetrates into the expanding structure of the positive electrode (8). These processes proceed at rates that depend on the electrode currents in the cell; consequently, δ^* will vary from cell to cell as the battery discharges.

Of the various parameters, only R_i can be taken as remaining reasonably constant in the course of battery dis-

charge. Other parameters, such as R_z and R_f^* , certainly will change with time during the discharge depending on the amount of charge transferred; therefore, to solve Eq. [15] and [17] during discharge, we must assign to them a functional dependence on time. This assignment requires consideration of the elementary processes summarized in Fig. 1. Here, we shall consider changes in the conductivity of the electrolyte in the cell in the region near the cathode, κ_c , and in the conductivity of the electrolyte in the feed line, κ_f , and neglect changes in other parameters such as δ^* and U^* . The change in κ_c represents the precipitation of LiCl within the porous structure of the cathode, which occurs during the discharge of the cell and increases R_z , while the change in κ_f arises from the presence of undesired deposits in the feed line, e.g., due to electrode processes taking place at or near the entrance port due to reversed current, and can either increase or decrease R_f . In the Li/SOCl₂ battery, these deposits appear in the form of dendritic growth of metallic Li in the direction toward the fill tube at the negative end (Fig. 4a) and in the form of insoluble corrosion products at the positive end (Fig. 4c). In our calculations, we limit changes to those due to current reversal at the anode.

Linear functions of transferred charge will be assumed (see Appendix D). Specifically, for a small change in time, dt

$$d\kappa_c = - \frac{\kappa_c I_c}{T J_1(0)} dt \quad [48]$$

where $J_1(0)$ is the initial load current, T is the expected lifetime of the cell, and I_c is the cathode current at the time t , which is obtained from Eq. [5] by observing that $I_{a,i+1} = I_{c,i}$. Initially, $\kappa_c = w \kappa_{c0}$, where w is a computational factor introduced to account for cell deficiency arising from component variations. After an amount of charge $wT J_1(0)$ has been transferred, $\kappa_c = 0$ and a cell is considered to be fully discharged. Similarly

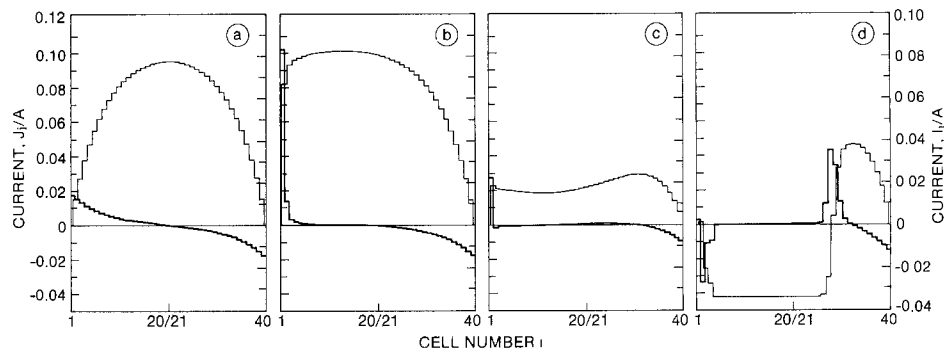
$$d\kappa_f = - (\kappa_d - \kappa) \frac{V_d I_a(r_o)}{F V_f} dt \quad [49]$$

where κ_d is the conductivity of the undesired deposit, V_d is the volume occupied by an equivalent weight of the deposit, $V_f = \pi(a^2 - r_f^2)d$ is the volume of the feed line, F is the Faraday constant, and $I_a(r_o) < 0$, is the total reversed current on the anode, Eq. [23]. Initially, $\kappa_f = \kappa_{f0}$; however, after an amount of charge $\epsilon_f V_f F / V_d$ has been transferred, the feed line is filled by the deposit and $\kappa_f = \kappa_d \epsilon_f$. Subsequent transferred charge was ignored.

Figures 9 and 10 show the computed time evolution of the circulating and intercell currents for a 40-cell battery. Specifically, Fig. 9 illustrates the time dependence when κ_d is large, i.e., when growing Li dendrites fill the feed path, while Fig. 10 examines their behavior for small κ_d , which is usually associated with the precipitation of corrosion products.

The time evolution of circulating and intercell currents for large κ_d is shown in Fig. 9a-9d. Because the cells are uniform initially, at the moment of activation of the battery, i.e., at $\tau = 0$, where $\tau \equiv t/T$, the current distributions are symmetric (Fig. 9a). However, with the passage of time, the symmetry is destroyed, giving rise to a rapid increase in the intercell current generated at the negative end of a battery at the expense of adjacent cells (Fig. 9b). At the same time, the circulating currents increase slightly at the negative end. It is noteworthy that the distribution at the positive end remains essentially unaffected. Toward the end of discharge, at $\tau = 1.0$, some of the cells in the central region become fully discharged. Under those conditions, the circulating currents become small and a reversal of the intercell current at the negative end of a battery occurs (Fig. 9c). Such a behavior is a result of the load current that is being supplied by the cells that are not fully discharged, bypassing the discharged cells of the central region through the fill tube. With further passage of time, at $\tau = 1.2$ (Fig. 9d), this situa-

Fig. 9. Time evolution of the circulating (left scale, light lines) and intercell (right scale, heavy lines) currents for a 40-cell battery that is uniform initially. $\kappa_d = 100$ S/cm. a: $\tau = 0$, $J_1 = 6.73$ A. b: $\tau = 0.15$, $J_1 = 6.70$ A. c: $\tau = 1.05$, $J_1 = 2.06$ A. d: $\tau = 1.2$, $J_1 = 0.042$ A.



tion develops fully and shows reversal of the intercell current in cells other than the end cells.

For small κ_d , as illustrated in Fig. 10a-10c, the effect is quite different. The symmetry in the distributions of the circulating and intercell currents is maintained throughout the period of the discharge, but with their values diminishing with time. Toward the end of discharge (Fig. 10b), the distributions of these currents change radically yet maintain their symmetry. The intercell current changes its direction at two additional points, A and B in Fig. 10b. With further increase in time, *i.e.*, at $\tau = 1.2$, the resulting intercell currents increase and substantially exceed their initial values (Fig. 10c).

Figures 11a-11c illustrate the computed time-dependent distribution of intercell and circulating currents when a few cells, namely, cells 29, 30, and 31, are assumed to be deficient with $w = 0.2$. It is seen that in the early period, *i.e.*, for $\tau = 0.15$, the distribution of the circulating current exhibits a depression (point A in Fig. 11b), as well as the asymmetry in the distribution of intercell and circulating currents caused by increasing κ_t . With further progress in time, we note a rapid change in the distributions of both currents. In particular, for $\tau = 0.35$ (Fig. 11c), the intercell current changes sign in the third cell, then becomes more negative with increasing cell number until,

at the 29th cell, it undergoes an abrupt change in sign and increases in magnitude in the 32nd cell, where it is equal to the magnitude of circulating current in the previous two segments of the fill tube. Calculations for other deficiency factors indicate similar evolution except for the time scale. Thus, for $w = 0.9$ the same development is not achieved until $\tau = 1.05$.

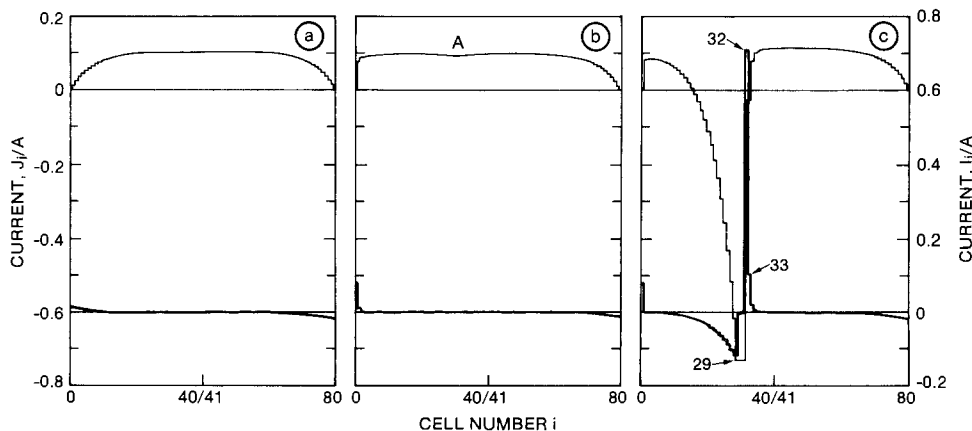
This large intercell current occurs in cells that are not yet fully discharged, so that according to Eq. [40], I_a^* can still be small. This situation can result in large reversed currents at the anodes of these cells. The hazard is compounded by large, heat producing circulating currents in the fill tube connecting nearby cells.

Implications of reversed electrode currents.—As indicated in Fig. 4a, in the case of current reversal the growth of dendritic lithium is observed at the negative end of the stack. Since the intercell currents are usually rather small, no serious problems are expected. However, on occasions when quality control is not maintained during production, there is a finite probability for the occurrence of large reversed currents and the subsequent development of internal shorts during the activation or the operation of a battery. Specific designs for reduction or elimination of such currents are generally considered proprietary information. One method of reducing intercell

Fig. 10. Time evolution of the circulating (left scale, light lines) and intercell (right scale, heavy lines) currents for a 40-cell battery that is uniform initially $\kappa_d = 10^{-6}$ S/cm. a: $\tau = 0$, $J_1 = 6.73$ A. b: $\tau = 1.05$, $J_1 = 2.15$ A. c: $\tau = 1.2$, $J_1 = 0.056$ A.



Fig. 11. Time evolution of the circulating (left scale, light lines) and intercell (right scale, heavy lines) currents for an 80-cell battery that initially has cells 29-31 deficient with $w = 0.2$. Other cells have $w = 1$. $\kappa_d = 100$ S/cm. a: $\tau = 0$, $J_1 = 6.70$ A. b: $\tau = 0.15$, $J_1 = 6.60$ A. c: $\tau = 0.3$, $J_1 = 0.73$ A.



currents is through the introduction of auxiliary electrodes (9). This method, however, might not be a general solution to the problems caused by internal currents in batteries employing static electrolyte since their magnitude and distribution vary with the operation of a battery especially toward the end of discharge and during over-discharge.

The methods for achieving control of intercell currents must rely on increasing the values of R_i and R_r for the system. In general, in order to eliminate the undesirable effects of intercell currents, R_i and R_r should be maximized.

Concluding Remarks

Intercell currents will always be generated in series connected electrochemical devices with a common electrolytic path. Generally, the major areas of concern are the effects of these currents on the power output and capacity of these devices. However, in Li power sources, the electrochemical processes that generate the intercell currents must be considered as well, because these processes result in the formation of undesirable byproducts if the intercell currents exceed their critical values. In particular, the undesirable reaction product is the dendritic growth of lithium. Beyond this, the electrochemical device can be inactivated by the production of passive films or excessive corrosion of component parts.

The calculations of the time evolution of the intercell and circulating current distributions, while based on a model of wide applicability, were limited in scope to two effects only. Here, we examined the effect of the increase in cell resistance due to the decrease in electrolyte conductivity near the cathode, and the effect of the change in feed-line resistance due to deposits near the cell inlet port. This method can be extended to cover in a realistic manner more complex situations by including additional discharge effects. One obvious limitation of this approach is that the cell parameters cannot be given a radial dependence.

Acknowledgments

This work was funded by Naval Sea Systems Command (NAVSEA 63R-32) and constitutes a fraction of a program to establish a technology base for high discharge rate Li/SOCl₂ batteries. We thank Mr. F. Romano (NAVSEA 63R-32) for his interest and support.

Manuscript submitted Oct. 21, 1983; revised manuscript received April 27, 1984.

The Naval Ocean Systems Center assisted in meeting the publication costs of this article.

APPENDIX A

Cell Discharge Characteristics with Intercell Current

Within a cell outside of the electric double layer, we assume that the potential, ϕ , and the c.d., j , obey Laplace's equation and Ohm's law. Selecting cylindrical coordinates, with the Z axis on the axis of circular symmetry, we can write these as, respectively

$$\frac{1}{r} \frac{\partial}{\partial r} \left[r\kappa(z) \frac{\partial \phi(r,z)}{\partial r} \right] + \frac{\partial}{\partial z} \left[\kappa(z) \frac{\partial \phi(r,z)}{\partial z} \right] = 0 \quad [A-1]$$

and

$$j_z = -\kappa(z) \frac{\partial \phi(r,z)}{\partial z} \quad [A-2]$$

$$j_r = -\kappa(z) \frac{\partial \phi(r,z)}{\partial r} \quad [A-3]$$

where, for simplicity, the conductivity, κ , is taken to have no radial dependence.

The problem can be made one dimensional by introducing the longitudinal averages

$$\overline{\kappa\phi(r)} = \frac{1}{\delta^*} \int_0^{\delta^*} \kappa(z)\phi(r,z) dz \quad [A-4]$$

and

$$\bar{j}_r = \frac{1}{\delta^*} \int_0^{\delta^*} j_r(r,z) dz \quad [A-5]$$

i.e., $\kappa\bar{\phi}$ and \bar{j}_r are functions of r only. Here, δ^* is an effective cell thickness, i.e., the distance between the electrode surfaces, not including the thicknesses of the electric double layers, which we shall assume to be negligibly thin. Upon integration with respect to z using Eq. [A-2] to replace the partial derivatives of ϕ with respect to z by the z component of the c.d. at the electrode-electrolyte interface, and introduction of Eq. [A-4], Eq. [A-1] becomes

$$\frac{1}{r} \frac{\partial}{\partial r} \left(r \frac{\partial \kappa\bar{\phi}}{\partial r} \right) - \frac{1}{\delta^*} [i_c(r) - i_a(r)] = 0 \quad [A-6]$$

where $i_c(r) = j_z(r, \delta^*)$ and $i_a(r) = j_z(r, 0)$, are the cathodic and anodic c.d.'s, respectively, just outside of the double layer (dl).

To construct a solution to Eq. [A-6], it is necessary to express $i_c(r)$ and $i_a(r)$ in terms of $\kappa\bar{\phi}(r)$. This can be done only approximately with the aid of an idealized plot of the longitudinal distribution of $\phi(r,z)$, as illustrated in Fig. A-1. The potential difference between electrodes, $V = V_c - V_a$, can be expressed as

$$V = U - \eta_a(r) - \eta_c(r) - \int_0^{\delta^*} \frac{j_z(r,z)}{\kappa(z)} dz \quad [A-7]$$

in which $U = U_c - U_a$, where U_a and U_c are, respectively, the anode and cathode potentials in the absence of current flow, and $\eta_a(r)$ and $\eta_c(r)$ are their respective overpotentials.

Using Fig. A-1 and the trapezoidal rule to evaluate approximately the integrals in Eq. [A-4] and [A-7], we have

$$\overline{\kappa\phi(r)} = \frac{1}{2} \{ \kappa_c [V_c - U_c + \eta_c(r)] + \kappa_a [V_a - U_a - \eta_a(r)] \} \quad [A-8]$$

and

$$V = U - \eta_a(r) - \eta_c(r) - \frac{1}{2} \delta^* [i_c(r)/\kappa_c + i_a(r)/\kappa_a] \quad [A-9]$$

where κ_a and κ_c are conductances at $z = 0$ and $z = \delta^*$, i.e., at the anode and cathode surfaces just outside of the electric double layer, respectively.

Assuming linear current-potential relationships, $i_a = k_a \eta_a$ and $i_c = k_c \eta_c$, and using them to eliminate the overpotentials from Eq. [A-8] and [A-9], we get

$$\kappa_c i_c / k_c - \kappa_a i_a / k_a = 2(\overline{\kappa\phi} - C) \quad [A-10]$$

and

$$i_c / \sigma_c + i_a / \sigma_a = U - V \quad [A-11]$$

where the σ_ν ($\nu = a, c$) are given by Eq. [13a], and

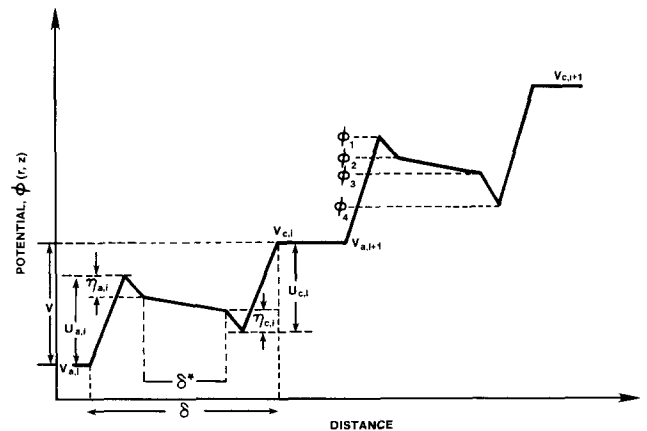


Fig. A-1 Idealized plot of the distribution of the potential $\phi(r,z)$ for a particular value of r . Sign convention:

$$U_a = V_a - \phi_1, U_c = V_c - \phi_4; \\ \eta_a = \phi_1 - \phi_2, \eta_c = \phi_3 - \phi_4;$$

$$\int_0^{\delta^*} \frac{j_z}{\kappa} dz = \phi_2 - \phi_3.$$

$$C = \frac{1}{2} [\kappa_c(V_c - U_c) + \kappa_a(V_a - U_a)] \quad [\text{A-12}]$$

Equations [A-10] and [A-11] can be solved simultaneously for i_a and i_c , and their difference then used to reformulate Eq. [A-1]. Thus

$$i_a = \chi [\kappa_c(U - V)/k_c - 2(\overline{\kappa\phi} - C)/\sigma_c] \quad [\text{A-13a}]$$

and

$$i_c = \chi [\kappa_a(U - V)/k_a + 2(\overline{\kappa\phi} - C)/\sigma_a] \quad [\text{A-13b}]$$

where

$$1/\chi = \kappa_a/(k_a\sigma_c) + \kappa_c/(k_c\sigma_a) \quad [\text{A-14}]$$

After some algebraic manipulations, we obtain

$$(i_c - i_a)/\delta^* = (\overline{\kappa\phi} - \kappa\phi_0)/r_e^2 \quad [\text{A-15}]$$

where r_e is given by Eq. [12] and

$$\overline{\kappa\phi_0} = \frac{1}{2} (\kappa_a + \kappa_c) \overline{\phi_0} \quad [\text{A-16}]$$

in which $\overline{\phi_0}$ is given by Eq. [9]. Substitution of Eq. [A-15] into [A-6] yields

$$\frac{1}{r} \frac{\partial}{\partial r} \left(r \frac{\partial \overline{\kappa\phi}}{\partial r} \right) - \frac{(\overline{\kappa\phi} - \kappa\phi_0)}{r_e^2} = 0 \quad [\text{A-17}]$$

Boundary conditions are obtained from the requirements that the radial current at the entrance port, where $r = a$, will be the intercell current, I , and at the outer radius, where $r = b$, it will be zero. Using Eq. [A-3] and [A-5], we find

$$\left. \frac{\partial \overline{\kappa\phi}}{\partial r} \right|_{r=a} = - \frac{I}{2\pi a \delta^*} \quad [\text{A-18a}]$$

and

$$\left. \frac{\partial \overline{\kappa\phi}}{\partial r} \right|_{r=b} = 0 \quad [\text{A-18b}]$$

Here, we have neglected the intercell current entering the cell within the electric double layer.

The solution to Eq. [A-17] is of the form

$$\overline{\kappa\phi} - \kappa\phi_0 = A K_0(r/r_e) + B I_0(r/r_e) \quad [\text{A-19}]$$

where A and B are coefficients to be determined from the boundary conditions, Eq. [A-18]. After some manipulations, we obtain Eq. [22], where the definitions

$$\overline{\kappa\phi} = \frac{1}{2} (\kappa_a + \kappa_c) \overline{\phi_0} \quad [\text{A-20}]$$

and Eq. [A-16] have been applied.

By using Eq. [A-15], Eq. [A-13] can be rewritten as Eq. [20] and [21], respectively. By integrating Eq. [20] over the area of the anode, the total anodic current can be found. The result, from which Eq. [8] is derived by rearrangement, is obtained by setting $r_o = b$ in Eq. [23].

APPENDIX B

Evaluation of the Term $\overline{\phi_{i+1}} - \overline{\phi_i}$ in Eq. [2]

Let $U = U_c - U_a$ be the cell potential in the absence of current flow, then from the definition: $V = V_c - V_a$

$$U - V = U_c - V_c - U_a + V_a \quad [\text{B-1}]$$

Using Eq. [B-1], either of the terms $V_c - U_c$ or $V_a - U_a$ can be eliminated from Eq. [9]. Thus, either

$$\overline{\phi_0} = V_a - U_a - (U - V)\sigma/\sigma_a \quad [\text{B-2}]$$

or

$$\overline{\phi_0} = V_c - U_c + (U - V)\sigma/\sigma_c \quad [\text{B-3}]$$

Expressing $\overline{\phi_{o,i+1}}$ and $\overline{\phi_{o,i}}$ by means of Eq. [B-2] and [B-3], respectively, and using Eq. [6], we get

$$\begin{aligned} \overline{\phi_{o,i+1}} - \overline{\phi_{o,i}} &= U_{c,i} - U_{a,i+1} - (U_{i+1} - V_{i+1}) \sigma_{i+1}/\sigma_{a,i+1} \\ &\quad - (U_i - V_i) \sigma_i/\sigma_{c,i} \end{aligned} \quad [\text{B-4}]$$

The term: $\overline{\phi_{i+1}} - \overline{\phi_i}$ in Eq. [2] can be evaluated with the aid of Eq. [7]; thus

$$\overline{\phi_{i+1}} - \overline{\phi_i} = \overline{\phi_{o,i+1}} - \overline{\phi_{o,i}} + I_{i+1}R_{p,i+1} - I_iR_{p,i} \quad [\text{B-5}]$$

Using relationships, Eq. [4], [B-4], and [14], Eq. [B-5] can be expressed in terms of circulating currents, J_i and J_i . The result is

$$\begin{aligned} \overline{\phi_{i+1}} - \overline{\phi_i} &= U_i^* - J_i R_{z,i}^* + J_{i-1} R_{p,i}^* \\ &\quad - J_i (R_{p,i}^* + R_{p,i+1}^* + R_{z,i}^*) + J_{i+1} R_{p,i+1}^* \end{aligned} \quad [\text{B-6}]$$

where

$$R_{p,i}^* = R_p - R_z \sigma^2 / (\sigma_a \sigma_c) \quad [\text{B-7}]$$

and R_z^* and U_i^* are defined in Eq. [16] and [19], respectively. Substitution of Eq. [B-6] into Eq. [2] yields Eq. [17].

APPENDIX C

Solution of Eq. [26] and [27]

by the Method of Undetermined Coefficients

Equation [27] has a solution, in terms of J_i , that can be written as a sum of a particular solution of the non-homogeneous equation, $J_{p,i}$, and a general solution of the homogeneous equation, $J_{h,i}$

$$J_i = J_{p,i} + J_{h,i} \quad [\text{C-1}]$$

A suitable particular solution to Eq. [27] is the constant

$$J_p = (U - R_z J_i) / (R_z + R_i) \quad [\text{C-2}]$$

For the homogeneous equation, we seek a solution in the form

$$J_{h,i} = A \lambda^i + B \lambda^{-i} \quad [\text{C-3}]$$

where A and B are coefficients satisfying Eq. [3] and λ is either root of the characteristic equation

$$\lambda^2 - [2 + (R_i + R_z)/R_i^*] \lambda + 1 = 0 \quad [\text{C-4}]$$

one of which is given by Eq. [32].

Applying Eq. [3], we have

$$J_p + A + B = 0 \quad [\text{C-5a}]$$

$$J_p + A \lambda^N + B \lambda^{-N} = 0 \quad [\text{C-5b}]$$

Solving Eq. [C-5] for A and B and substituting into Eq. [C-3], we get Eq. [29], where J_p is given by Eq. [C-2].

To obtain J_i , we return to Eq. [26] and evaluate the sum appearing there by the use of Eq. [29] and the results for the sum of a geometric series. Thus, with

$$\sum_{i=0}^N J_i = J_p N \xi (R_z + R_i) / R_z \quad [\text{C-6}]$$

where ξ is given by Eq. [33], we find Eq. [28], which, in turn, produces Eq. [31] upon substitution into Eq. [C-2].

APPENDIX D

Derivation of Eq. [48] and [49]

A number of the parameters we use depend on the depth of discharge. For simplicity, we have chosen to let only two of them vary with time. These two were chosen because their variation introduces many of the effects observed in Li/SOC₂ batteries upon discharge.

We assume that the electrolyte conductivity near the cathode decreases linearly with charge transferred to the cathode and that after charge Q_c has been transferred κ_c will be essentially zero and the useful life of the cell expended. Initially, the conductivity near the cathode is given by

$$\kappa_c(0) = w \kappa_{\epsilon_z} \quad [\text{D-1}]$$

where w is a factor that is introduced to account for the possibility that a particular cell might not have the designed lifetime. The expected lifetime, T , is defined by the relationship

$$Q_c = w T J_i(0) \quad [\text{D-2}]$$

where $J_i(0)$ is the initial load current. Therefore

$$\frac{d\kappa_c}{dQ_c} = - \frac{\kappa_c(0)}{Q_c} = - \frac{\kappa_{\epsilon_z}}{T J_i(0)} \quad [\text{D-3}]$$

Setting $dQ_c = I_c dt$, where I_c is the total cathode current, we have Eq. [48].

Similarly, we assume that the electrolyte conductivity in the feed line, κ_f , changes linearly between the initial value

$$\kappa_f(0) = \kappa \epsilon_f \quad [D-4]$$

and the final value

$$\kappa_f = \kappa_d \epsilon_f \quad [D-5]$$

with the charge, Q_f , transferred to the anode under reversed current conditions. The total charge that can be transferred before the feed-line volume, V_f , is fully occupied by deposit is

$$Q_f = \epsilon_f V_f F / V_d \quad [D-6]$$

where V_d is the volume occupied by an equivalent weight of the deposit and F is the Faraday constant. Therefore

$$\frac{d\kappa_f}{dQ_f} = - \frac{(\kappa_d - \kappa) \epsilon_f}{Q_f} = - \frac{(\kappa_d - \kappa) V_d}{V_f F} \quad [D-7]$$

Setting $dQ_f = I_a(r_o) dt$, where $I_a(r_o)$ is the total reversed anode current, we have Eq. [49].

LIST OF SYMBOLS

<i>a</i>	inner electrode radius (cm)
<i>A</i>	a constant
<i>b</i>	outer electrode radius (cm)
<i>C</i>	a constant defined by Eq. [A-12]
<i>d</i>	thickness of annular fill path (cm)
F	Faraday constant
<i>i</i>	local c.d. (A cm ⁻²)
<i>I</i>	intercell current (A)
<i>I</i>	Bessel function
<i>j</i>	current density (A cm ⁻²)
<i>j</i>	flux, phenomenological
<i>J</i>	current (A)
<i>k</i>	rate constant, phenomenological
<i>k</i>	electrode rate constant (linearized) (S cm ⁻²)
<i>K</i>	Bessel function
<i>l</i>	length (cm)
<i>N</i>	number of cells
<i>r</i>	radius (cm)
<i>r_e</i>	radius, defined by Eq. [12]
<i>R</i>	resistance (Ω)
<i>t</i>	time (s)
<i>T</i>	cell lifetime (s)
<i>U</i>	cell voltage at zero current (V)
<i>U</i>	(with subscripts) electrode potential at zero current (V)
<i>V</i>	volume (cm ³)
<i>V</i>	cell voltage (V)
<i>V</i>	(with subscripts) electrode potential (V)
<i>w</i>	deficiency factor

X driving force, phenomenological
z coordinate

Greek Letters

γ	defined by Eq. [25]
δ^*	effective cell thickness, cm
ϵ	porosity
η	overpotential (V)
κ	electrolyte conductivity (S cm ⁻¹)
λ	deposit conductivity, (S cm ⁻¹)
λ	defined by Eq. [32]
ξ	defined by Eq. [33]
σ	cell conductivity (S cm ⁻²)
τ	(=t/T), dimensionless
ϕ	potential (V)
$\bar{\phi}$	potential at $r = a$, averaged over z
χ	defined by Eq. [A-14]

Subscripts

<i>a</i>	anode
<i>c</i>	cathode
<i>d</i>	deposit in feed line
<i>f</i>	feed line
<i>h</i>	defined by Eq. [C-1]
<i>i</i>	running index
<i>l</i>	load
<i>o</i>	initial conditions
<i>o</i>	r_o radius of current reversal, (cm); Eq. [23] and [24]
<i>o</i>	$\bar{\phi}_o$ defined by Eq. [9]
<i>o</i>	J_o defined by Eq. [3]
<i>p</i>	cell entrance port
<i>t</i>	fill tube
<i>z</i>	cell, internal
ν	running index (order of Bessel function)

Superscript

*	equivalent
*	critical, defined in text

REFERENCES

1. J. R. Driscoll, Unpublished results (1982).
2. O. S. Ksenzhek and N. D. Koshel, *Electrokhimiya*, **6**, 1587 (1970); *ibid.*, **7**, 353 (1971).
3. N. D. Koshel and O. S. Ksenzhek, *ibid.*, **7**, 850 (1971).
4. B. P. Nesterov, T. A. Razevig, and N. V. Korovin, *ibid.*, **10**, 1088 (1974).
5. V. A. Onishchuk, *ibid.*, **8**, 698 (1972).
6. W. Thiele, M. Schleiff, and H. Matschiner, *Electrochim. Acta*, **26**, 1005 (1983).
7. E. A. Kaminski and R. F. Savinell, *This Journal*, **130**, 1103 (1983).
8. S. Szpak and J. R. Driscoll, *J. Power Sources*, **10**, 343 (1983).
9. R. J. Bellows and P. G. Grimes, U.S. Pat. 4,279,732 (1981).

Rechargeable Lithium/Chromium Oxide Cells

Y. Takeda, R. Kanno, Y. Tsuji, and O. Yamamoto*

Department of Chemistry, Faculty of Engineering, Mie University, Tsu, 514, Japan

ABSTRACT

The charge and discharge behaviors of organic electrolyte lithium cells with chromium oxides, Cr_2O_5 , Cr_3O_8 , and amorphous chromium oxide ($\alpha\text{-Cr}_3\text{O}_8$) as the cathodes have been examined, where $\alpha\text{-Cr}_3\text{O}_8$ was obtained by heat-treating the mixture of Cr_3O_8 and water. The lithium cells with these chromium oxides gave satisfactory discharge performances in term of energy density. The cycling characteristics of the cells have been examined for various ranges of charge transferred in the chromium oxide electrode, such as 0.1-0.3, 0.4-0.6, and 0.7-0.9 e^-/Cr . The $\text{Li}/\text{Cr}_3\text{O}_8$ cells showed a poor cycling performance for the whole range of charge transferred. The rechargeability of the $\text{Li}/\text{Cr}_3\text{O}_8$ cells was good, in the range 0.4-0.6 and 0.7-0.9 e^-/Cr , but poor in the range 0.1-0.3 e^-/Cr . The $\text{Li}/\alpha\text{-Cr}_3\text{O}_8$ cells worked well as a rechargeable cell for the whole range of charge transferred.

A wide variety of metal oxides and chalcogenides with two-dimensional layer structures or three-dimensional framework tunnel structures has been studied as the cathode material for secondary organic electrolyte lithium batteries (1-2). Most previous works have focused on two-dimensional metal chalcogenides such as TiS_2 , although metal oxides with framework structure such as V_6O_{13} (3), Cr_3O_8 (4), and a number of MO_2 oxides with the rutile structure (3) have demonstrated reversible lithium incorporation. Of these cathode materials, Cr_3O_8 has been reported to have the highest energy density and the highest cell voltage. The calculated theoretical energy density of the couple $\text{Li}/\text{Cr}_3\text{O}_8$ is 1210 Wh/kg based on experimental utilizations of Cr_3O_8 , a value which is about two times higher than that of the Li/TiS_2 couple (5). The open-circuit voltage and the averaged discharge voltage at a current drain of 0.5 mA/cm² for the $\text{Li}/\text{Cr}_3\text{O}_8$ couple were 3.8V and approximately 3.0V, respectively. The cell voltage is comparable to that of commercially available primary lithium batteries with manganese dioxide or carbon fluoride cathodes. However, it has been reported that the energy density of Cr_3O_8 drops to around 500 Wh/kg at 1 mA/cm² after 20 cycles (1). In this study, the cyclic behaviors of lithium cells with Cr_2O_5 and Cr_3O_8 chromium oxides were examined in detail. In addition, an amorphous phase of chromium oxide, obtained by the heat-treatment of Cr_3O_8 and water, was examined as a cathode material for secondary lithium batteries.

Experimental

The chromium oxides were prepared from CrO_3 according to the phase diagrams of Kubota (7) and Wilhelmi (8). Cr_2O_5 and Cr_3O_8 were obtained by heating CrO_3 for 24h at 340° and 270°C, respectively, in an autoclave. The x-ray diffraction patterns of the reaction products were in good agreement with those reported previously (8, 9). Amorphous chromium oxides were prepared by heating a mixture of Cr_3O_8 and water. The mixture of 0.7g Cr_3O_8 and 30 ml water was well mixed and heated for 24h at a temperature of 110°-300°C. The chromium-oxygen stoichiometry was determined by reducing the sample to Cr_2O_3 using TGA (Rigaku Denki TG4) in open air.

The cells used for electrochemical tests were constructed in a cylindrical configuration. The anode was a disk of lithium foil of 15 mm diam. The separator was a microporous polypropylene sheet. The cathode consisted of a mixture of 0.1g chromium oxide, 0.15g graphite, and 0.04g Teflon powder, which was pressed into a tablet of 13 mm diam under a pressure of about 9 MPa. The cathode thickness was around 0.6 mm. In order to see the characteristics of the rechargeable miniature cells, coin-type cells were also made, which had an external diameter of 12.5 mm and an external thickness of 2.5 mm. The cathode was a mixture of 0.085g chromium oxides, 0.01g acetylene black, and 0.01g Teflon powder, which was pressed into a tablet of 7.5 mm diam. The current density was based on the cross section of the cathode tablet. The

electrolyte was 1M LiClO_4 in 1:1 propylene carbonate-1,2 dimethoxy ethane by weight. The organic solvents were dried (10, 11). Lithium perchlorate (Nakarai Chemicals extra-pure reagent) was dried for 2h at 120°C and then for 5h at 200°C *in vacuo*.

All the electrochemical measurements were carried out after at least one overnight stand under zero current flow. The x-ray patterns were obtained using a Rigaku Denki diffractometer with $\text{CuK}\alpha$ radiation. X-ray photoelectron spectroscopy (XPS) spectra were measured ($\text{Cr } 2\text{P}_{3/2}$) with a Shimadzu ESCA 750 spectrometer. Spectra of Au were used as a standard for the chemical shift.

Results and Discussion

Table I shows the chromium-oxygen stoichiometry and the results of x-ray diffraction analysis for samples of CrO_x , which were obtained by heat-treating mixtures of Cr_3O_8 and water at various temperatures. The oxygen content in the samples decreases with increasing the heat-treatment temperature. The samples heated at 200°C were very hygroscopic and had about 3% free water, the exact amount of which depended on the period of exposure to atmosphere. Samples heated over 250°C had no free water and were not hygroscopic. The x-ray diffraction data indicate that Cr_3O_8 -water mixtures transfer to an amorphous phase ($\alpha\text{-Cr}_3\text{O}_8$) by heating. It could be that Cr_3O_8 particles absorbed water and are crashed to very small particles when water is driven out by heating. The mixture of Cr_2O_5 and water showed no remarkable change in the chromium-oxygen stoichiometry or x-ray diffraction patterns by heat-treating below 270°C.

The XPS spectra of $\alpha\text{-Cr}_3\text{O}_8$ obtained by heating at 250°C are shown along with those of various chromium oxides in Fig. 1. Cr_5O_{12} and CrO_2 were prepared by the method reported previously (6). By a computer fitting method, the spectra of the higher oxidation state chromium oxides, $\alpha\text{-Cr}_3\text{O}_8$, Cr_3O_8 , Cr_2O_5 , and Cr_5O_{12} can be resolved into two peaks, near 576.4 and 579.0 eV, which correspond to the values of chemical shifts of $\text{Cr}^{3+}2\text{P}_{3/2}$ in Cr_2O_3 (576.5 eV) and $\text{Cr}^{6+}2\text{P}_{3/2}$ in CaCrO_4 (578.8 eV), respectively. The intensity ratio of the Cr^{3+} to Cr^{6+} spectra was fitted to the calculated value from the ratio of Cr/O obtained by TGA. The $\text{Cr}^{3+}/\text{Cr}^{6+}$ ratio in Cr_3O_8 , 1:2.7, is also in agreement with that obtained from magnetic measurements, 1:3 (12). That is, Cr_3O_8 , $\alpha\text{-Cr}_3\text{O}_8$, Cr_2O_5 , and Cr_5O_{12}

Table I. Characteristics of Cr_3O_8 with water heat-treated at various temperatures

Heating temp (°C)	x in CrO_x	Observed phase	Energy density* (Wh/kg)
Crude Cr_3O_8	2.64	Cr_3O_8	1020
200	2.63	amorphous	760
250	2.55	amorphous	1130
270	2.55	amorphous	1170
300	2.41	amorphous	500

* Electrochemical Society Active Member.

* Based on a 2.0V cutoff at 500 $\mu\text{A}/\text{cm}^2$.

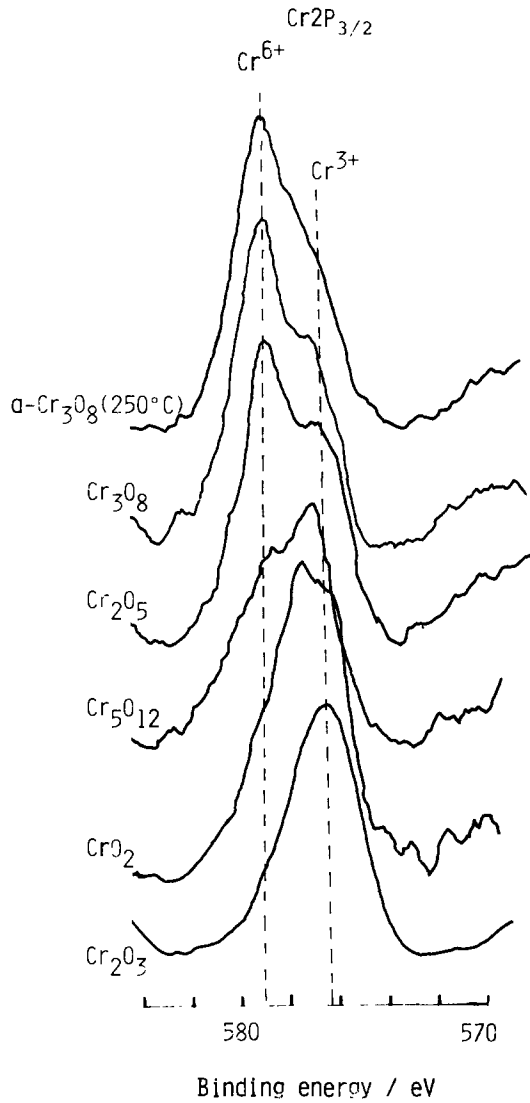


Fig. 1. XPS spectra of Cr $2P_{3/2}$ region for various chromium oxides

are presented as the mixture of Cr^{6+} and Cr^{3+} oxidation state. White and Roy also reported that chromium in Cr_3O_8 , Cr_2O_5 , and Cr_5O_{12} exhibits two valences of III and VI (13).

Figure 2 shows the open-circuit voltage (OCV) as a function of charge transferred in Cr_3O_8 , $a-Cr_3O_8$, and Cr_2O_5 at room temperature, where $a-Cr_3O_8$ was prepared by heating at $250^\circ C$. A constant current of 0.5 mA/cm^2 was passed through the cell for some period, and the cell voltages on open circuit were considered as the quasi-OCV when the deviations at the measured cell voltage was within 10 mV for 1h. The OCV curve for the cell $Li/a-Cr_3O_8$ is similar to that for the cell Li/Cr_3O_8 . The OCV's of

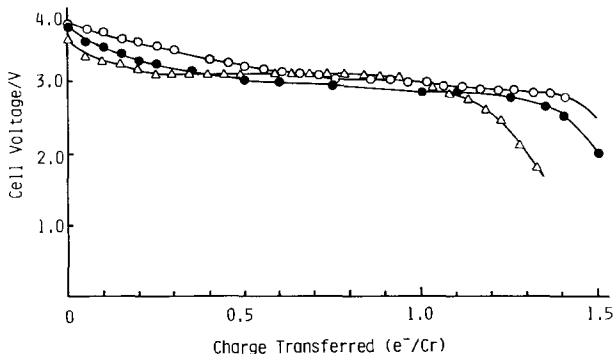


Fig. 2. OCV vs. charge transferred (e^-/Cr) curves for the cells with Cr_3O_8 (\circ), $a-Cr_3O_8$ (\bullet), and Cr_2O_5 (Δ).

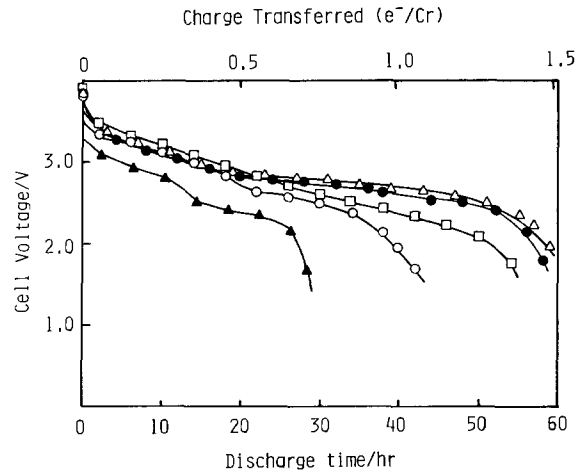


Fig. 3. Constant current ($500\ \mu A/cm^2$) discharge curves for the cells with Cr_3O_8 (\square), $a-Cr_3O_8$ heated at $200^\circ C$ (\circ), $250^\circ C$ (\bullet), $270^\circ C$ (Δ), and $300^\circ C$ (\blacktriangle).

both the cells decrease gradually with increasing x at least up to $x = 1.4$. In the case of the Li/Cr_2O_5 couple, the OCV curve shows a voltage plateau at 3.1V from $x =$

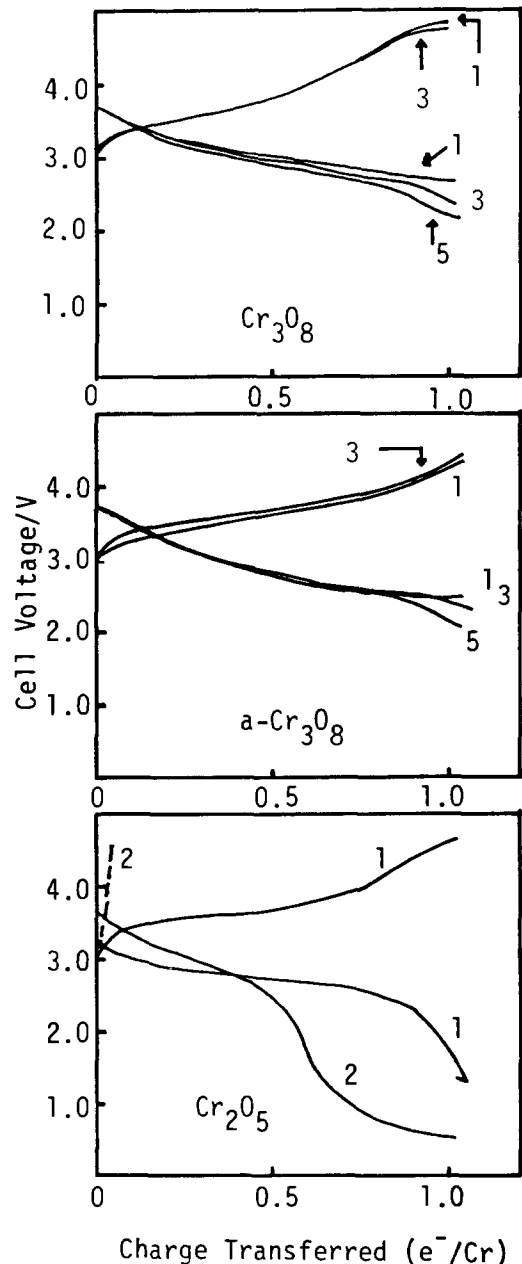


Fig. 4. Cycling behavior of the cells with Cr_3O_8 , $a-Cr_3O_8$, and Cr_2O_5

0.2-0.9. The x-ray diffraction patterns of the electrochemical reaction products $\text{Li}_{3-x}\text{Cr}_3\text{O}_8$, $\text{Li}_{2-x}\text{Cr}_2\text{O}_5$, and $\text{a-Li}_{3-x}\text{Cr}_3\text{O}_8$ have been examined. $\text{Li}_{3-x}\text{Cr}_3\text{O}_8$ ($0 \leq x \leq 1.0$) and $\text{Li}_{2-x}\text{Cr}_2\text{O}_5$ ($0 \leq x \leq 1.0$) showed only broad diffraction lines, and no change of the d values was observed. No diffraction lines due to lower oxidation chromium oxides and no ternary compound such as LiCr_3O_8 (14) was observed. In the case of $\text{a-Li}_{3-x}\text{Cr}_3\text{O}_8$, no diffraction line was observed in the range of 2θ of 10° - 80° . These results suggest that the crystals of chromium oxides become too small of particles during Li^+ insertion and reaction products appear amorphous. The cracking of the crystal lattice during electrochemical Li^+ insertion has been observed in the $\text{Li}/\text{single-crystal MoO}_3$ cell (15). The different shape of the OCV vs. e^-/Cr curves indicates there is a difference in the electrode reactions between the $\text{Li}/\text{Cr}_3\text{O}_8$ or $\text{Li}/\text{a-Cr}_3\text{O}_8$ couple and the $\text{Li}/\text{Cr}_2\text{O}_5$ couple.

Constant current (0.5 mA/cm²) discharge curves obtained at room temperature for cells with $\text{a-Cr}_3\text{O}_8$ prepared at various temperatures are shown in Fig. 3. The discharge performance of $\text{a-Cr}_3\text{O}_8$ is affected by the preparation temperature. The energy density, calculated from the discharge curves, based on the weight of the chromium oxides and to a 2.0V cutoff are shown also in Table I. The highest energy density, 1170 Wh/kg, was obtained for the cell with $\text{a-Cr}_3\text{O}_8$ treated at 270°C . This value is

slightly higher than that for the cell with the nontreated Cr_3O_8 . The dynamic discharge curve for the cell with $\text{a-Cr}_3\text{O}_8$ treated at 250°C is similar to the OCV curve shown in Fig. 1. The significantly lower energy density for the cell with $\text{a-Cr}_3\text{O}_8$ treated at 300°C may be due to the low oxidation state of Cr, 4.8, in the $\text{a-Cr}_3\text{O}_8$. In our previous paper, we reported that the energy density of cells with lower oxidation state chromium oxides such as Cr_3O_{12} , CrO_2 , and Cr_2O_3 , the average oxidation number of which is less than five, are considerably lower than those of cells with Cr_3O_8 and Cr_2O_5 .

In Fig. 4, the charge-discharge curves for the cells with Cr_3O_8 , Cr_2O_5 , and $\text{a-Cr}_3\text{O}_8$ heat-treated at 250°C are shown. The discharge and charge current densities are 0.5 and 0.25 mA/cm², respectively. For the cells with Cr_3O_8 and $\text{a-Cr}_3\text{O}_8$, the first cycle discharge and charge curves closely resemble the fifth cycle in overall shape. The charge curve for the cell with Cr_3O_8 shows a flat region in the final stage of the charging, where the decomposition of electrolyte may be occurring.

In the case of Cr_2O_5 , the second cycle discharge capacity reduces to about 65% of the initial cycle. During the second charge cycle, the cell voltage increases extremely rapidly with charging time.

In order to help understand the detail of the charge-discharge process for the chromium oxide cathode cells,

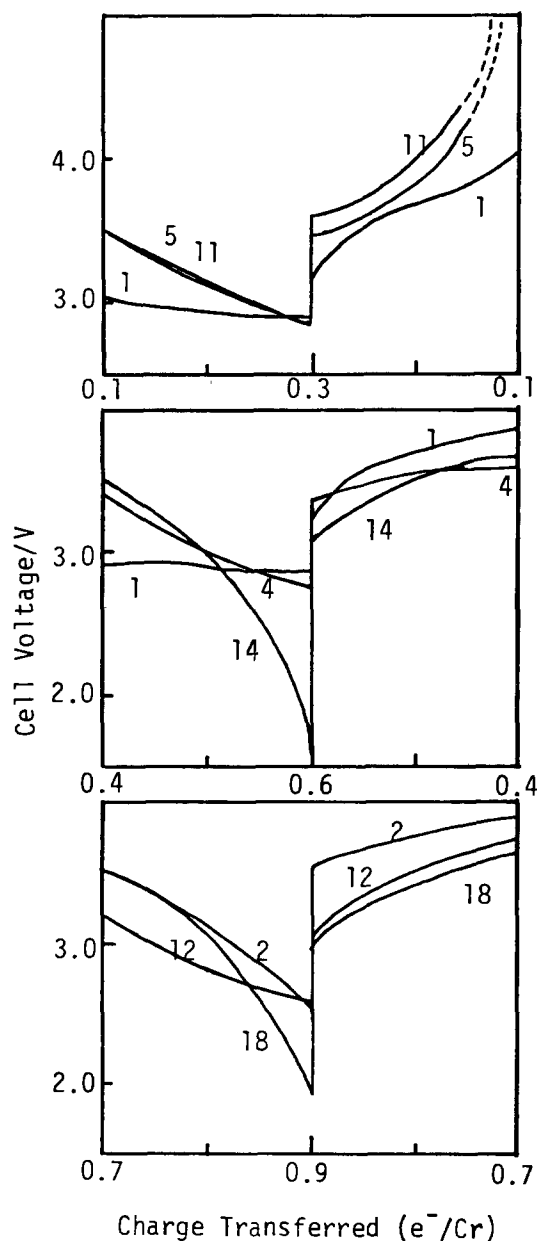


Fig. 5. Cycling behavior of the $\text{Li}/\text{Cr}_2\text{O}_5$ cells

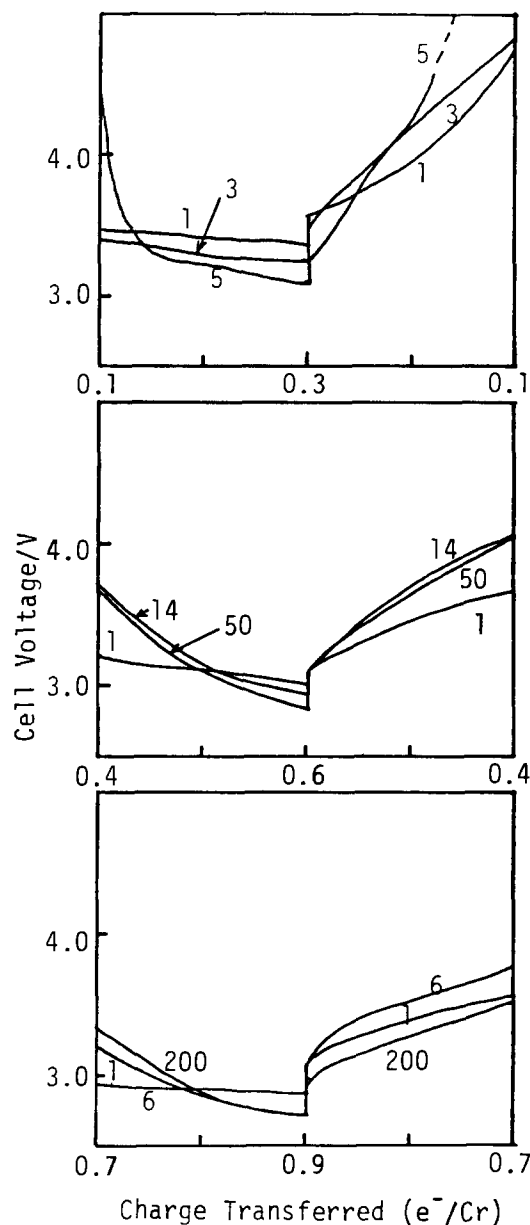


Fig. 6. Cycling behavior of the $\text{Li}/\text{Cr}_3\text{O}_8$ cells

cycling curves were examined for various charge transferred ranges in the chromium oxide electrode, such as 0.1-0.3, 0.4-0.6 and 0.7-0.9 e^-/Cr ratio. Charge and discharge current densities were $0.5 \text{ mA}/\text{cm}^2$. Figure 5 shows the cycle data for cells with Cr_2O_3 . In the charge transferred range of 0.1-0.3 e^-/Cr , the charging efficiency falls to 80% after five cycles, where charging efficiency was calculated to 4.5V cutoff. However, the discharging efficiency decreases in the ranges of 0.4-0.6 and 0.7-0.9 e^-/Cr ratio after several more than ten cycles.

The cells with Cr_3O_8 show good rechargeability in the deep charge transferred region as shown in Fig. 6. In the e^-/Cr range of 0.7-0.9, the 200th charge and discharge profiles show no significant degradation compared to the first ones, whereas, in the range of 0.1-0.3 e^-/Cr , the charging efficiency rapidly falls with cycling. In Fig. 7, the charge-discharge behavior of cells with $\alpha\text{-Cr}_3\text{O}_8$ are shown. These cells have good cycling performance. Even in the e^-/Cr range of 0.1-0.3, no remarkable change is found after 50 cycles. Charging voltages are less than 4.0V, except for the first few cycles. The good rechargeability of cells with $\alpha\text{-Cr}_3\text{O}_8$ may be due to the large effective surface area of $\alpha\text{-Cr}_3\text{O}_8$ because the charge and discharge profiles depended on the current density. The cells with Cr_3O_8 predischarged to 1.0 e^-/Cr ratio showed good rechargeability in the range of 0.1-0.3 e^-/Cr . Their good performance may be due to the transformation of Cr_3O_8 to the amorphous phase by predischARGE, which was

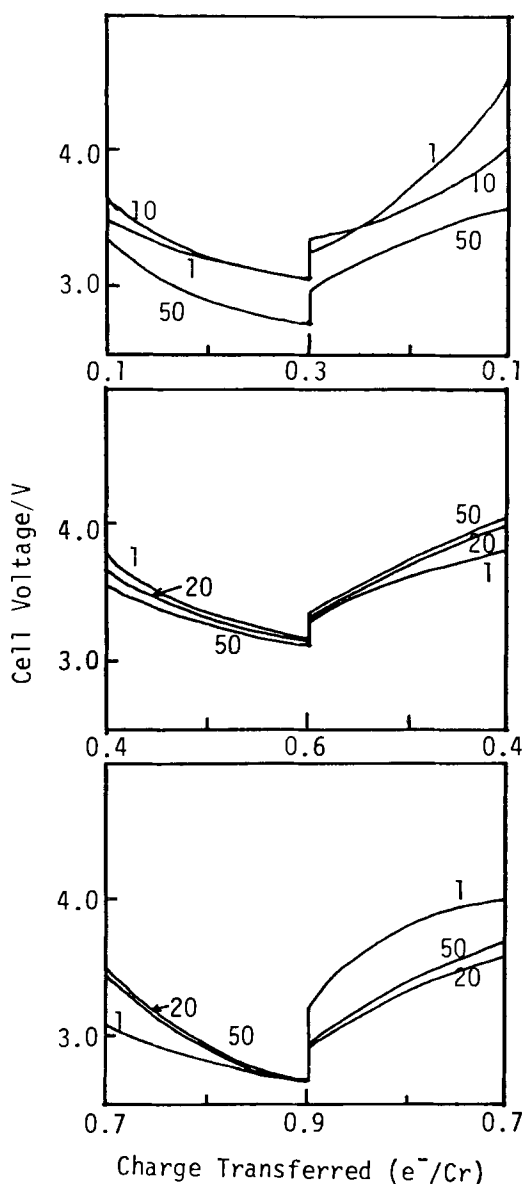


Fig. 7. Cycling behavior of the $\text{Li}/\alpha\text{-Cr}_3\text{O}_8$ cells

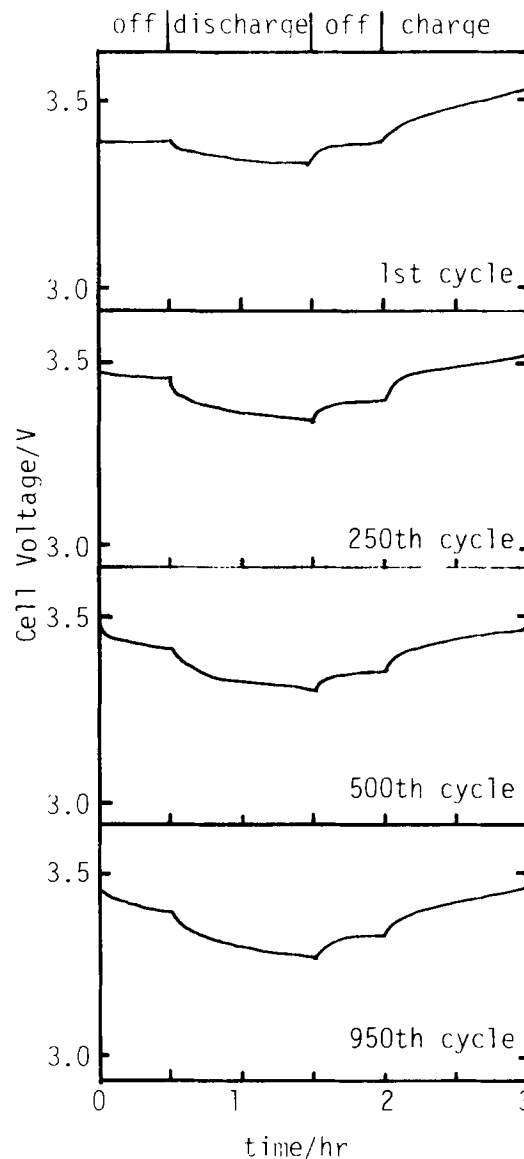


Fig. 8. Cycling behavior of the coin-type $\text{Li}/\alpha\text{-Cr}_3\text{O}_8$ cell

confirmed by x-ray analysis. Although Cr_2O_3 also becomes amorphous on discharge, cells with Cr_2O_3 predischarged to a 1.0 e^-/Cr showed poor rechargeability. The difference in rechargeability between Cr_2O_3 and Cr_3O_8 may be explained by the structural difference in the two amorphous phases " Li_xCrO_y " formed by the discharging process of the two oxides.

Figure 8 shows the discharge curves of the coin-type cells with $\alpha\text{-Cr}_3\text{O}_8$ heat-treated at 250°C . The charge and discharge currents were $220 \mu\text{A}$, and the depth of discharge was 0.8%. As can be seen, no significant change in the charge-discharge curves is observed during 950 cycles. This type of rechargeable miniature cell could be used in electronic devices, such as an electronic wrist watch, in combination with a solar cell. Since the current consumption of the latest standard watch is $2\text{-}3 \mu\text{A}$, the $200 \mu\text{Ah}$ discharge will be equivalent to 3-4 days of discharge.

From the above experimental results, the high oxidation chromium oxides, especially amorphous chromium oxide formed from Cr_3O_8 , is considered to be a promising cathode materials for organic electrolyte lithium cells with high energy density and good rechargeability.

Manuscript submitted Nov. 30, 1983; revised manuscript received April 4, 1984.

Mie University assisted in meeting the publication costs of this article.

REFERENCES

1. M. S. Wittingham, *Prog. Solid State Chem.*, **12**, 41 (1978).
2. B. Scrosati, *Electrochim. Acta*, **26**, 1559 (1981).
3. D. W. Murphy, P. A. Christian, F. J. Disalvo, and J. N. Carides, *This Journal*, **126**, 497 (1979).
4. J. O. Besenhard and R. Schöllhorn, *ibid.*, **124**, 968 (1977).
5. D. W. Murphy, F. A. Disalvo, J. N. Carides, and J. V. Waszczak, *Mater. Res. Bull.*, **13**, 1935 (1978).
6. Y. Takeda, R. Kanno, Y. Tsuji, and O. Yamamoto, *J. Power Sources*, **9**, 325 (1983).
7. B. Kubota, *J. Am. Ceram. Soc.*, **44**, 239 (1961).
8. K. A. Wilhelmi, *Acta Chem. Scand.*, **22**, 2565 (1968).
9. R. S. Schwartz, I. Fankuchen, and R. Ward, *J. Am. Chem. Soc.*, **72**, 1676 (1952).
10. T. Saito, H. Ikeda, Y. Matsuda, and H. Tamura, *J. Appl. Electrochem.*, **6**, 85 (1976).
11. Y. Matsuda, Y. Ouchi, and H. Tamura, *ibid.*, **4**, 53 (1974).
12. G. Lorthioir and A. Michel, *Bull. Soc. Chim. Fr.*, 1165 (1965).
13. R. B. White and R. Roy, *Geochim. Cosmochim. Acta*, **39**, 803 (1975).
14. K. A. Wilhelmi, *J. Chem. Soc. Chem. Commun.*, **13**, 437 (1966).
15. J. O. Besenhard, J. Heydecke, and H. P. Fritz, *Solid State Ionics*, **6**, 215 (1982).

Corrosion Monitoring of Iron, Protected by an Organic Coating, with the Aid of Impedance Measurements

J. Hubrecht and J. Vereecken

Department of Metallurgy and Electrochemistry, Faculteit Toegepaste Wetenschappen, Vrije Universiteit Brussel, 1050 Brussel, Belgium

M. Piens*

Coatings Research Institute, Limelette, Belgium

ABSTRACT

The ac impedance measurement has proved to be a useful electrochemical technique for mainly qualitative studies of electrochemical and corrosion systems. Even for complicated systems such as coated metals in corrosive environments this technique has been used with success. The system chosen for the present study is an ARMCO iron plate, coated with a SrCrO₄-pigmented styrene acrylic polymer, and immersed for several weeks in an aqueous NaCl solution. Impedance measurements analyze a system under test into its constituting phenomena. The dependence of system parameters on coating layer thickness, NaCl concentration, and pigmentation of the coating during the immersion time provides insight into the corrosion and protection mechanisms at the coating/metal interface, besides the behavior of the coating itself.

In the last years, the study of corrosion prevention by organic coatings has shown a remarkable development. For the manufacturer as well as for the user, it is indeed of great interest to know the protection mechanism and the anticorrosive properties of the coating.

Therefore, it is not sufficient to gather information about the physical properties of the coating, *e.g.*, its thickness, its porosity, its dielectric constant, etc.; one must also consider the electrochemical interaction between the corrosive medium and the metal, whether affected by the coating or not.

The impedance measurement is a well-known electrochemical technique used to monitor the corrosion of metals and to investigate its mechanisms (1-7).

Coated metals have also been investigated with the impedance technique (2, 8-31). The purpose of this work is to show that the behavior of the sample is reflected quite well by the ac impedance characteristic, when some system parameters are varied.

Experimental

The metal used in this investigation is Armco iron; before coating application, the iron plate is polished with 600 grit paper, cleaned ultrasonically, and degreased with ethanol.

A water-base emulsion coating is chosen, which consists of Ercusol AS250 (a styrene acrylic polymer) and red iron oxide and strontium chromate pigments. The coated samples are mounted in a three-electrode cell, depicted elsewhere (15, 18).

The coated metal is covered with Scotchrap corrosion protection tape to delimit a circular surface with an apparent area of 28.3 cm². A glass cylinder is then cemented

to the protection tape with silicone sealant to form a cell and is filled with an aqueous sodium chloride solution.

The cell is open to the air. The counterelectrode is a platinum grid, and the reference electrode is an SCE.

Coating layer thickness, NaCl concentration, presence of chromate pigment in the coating, and immersion time are the investigated parameters of which samples 1 to 4 are representative (see Table I).

The impedance is always measured at the corrosion potential, using a Schlumberger Solartron 1170 frequency response analyzer, connected to a Tacussel Pit 20-2X potentiostat. The analyzer is controlled by a Tektronix 4051 desktop computer to perform automatic measurements and data transmission. The frequency ranges between 10 kHz and 10 mHz.

The amplitude of the superimposed sinusoidal voltage is 20 mV. The results are plotted in the complex plane. The corrosion potential of the samples is also measured as a function of time.

Results

Figure 1 gives the variation of the impedance curve of sample 1 as a function of immersion time; Fig. 2 is a detail.

A few hours after immersion, only two arcs are observed in the complex plane presentation of the imped-

Table I. Investigated parameters for samples 1-4

Sample no.	Coating layer thickness (μm)	NaCl concentration (M)	Addition of chromate pigment
1	80	0.5	yes
2	190	0.5	yes
3	80	0.05	yes
4	80	0.5	no

* Electrochemical Society Active Member.

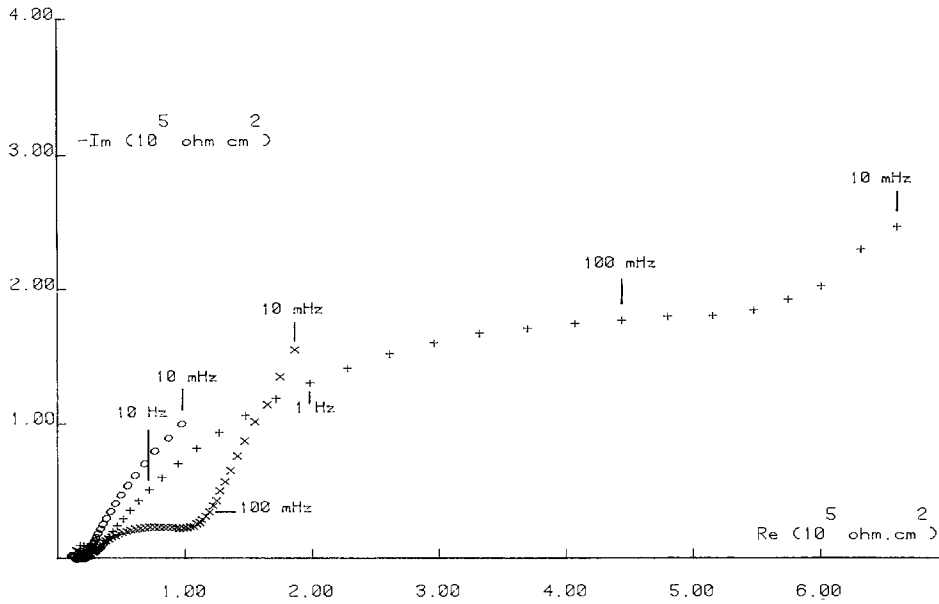


Fig. 1. Complex impedance diagram of sample 1 after 10 (+), 16 (x), and 28 days (o); complete plot. Parameter: frequency.

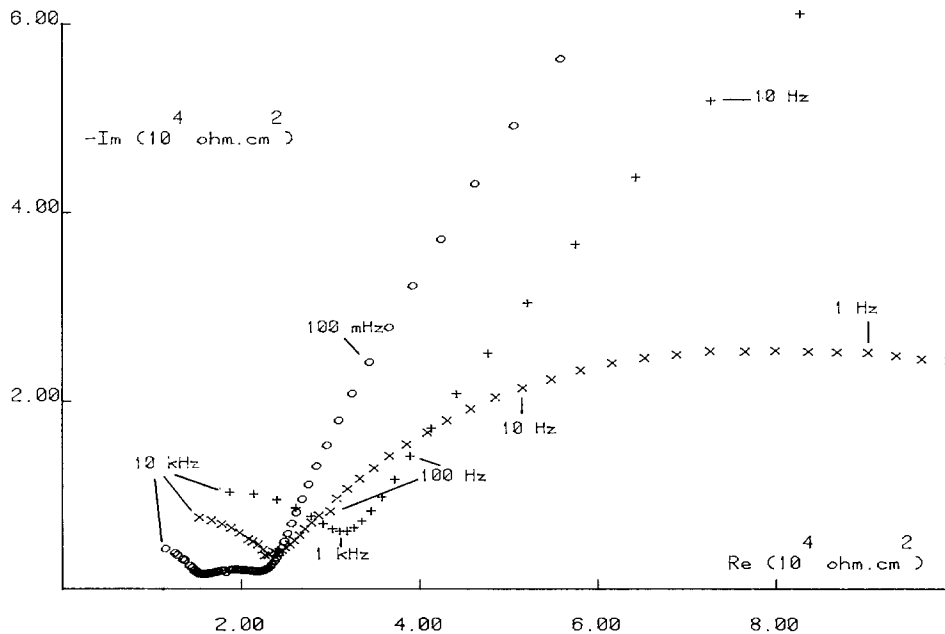


Fig. 2. Expanded plot of Fig. 1

ance data; for longer immersion times (days), the curve is completed with a third one. For instance, the impedance characteristics of sample 1 after 10, 16, and 28 days, respectively, are shown in Fig. 1 (complete plot) and 2 (expanded plot). After 10 days, a first arc is found at frequencies higher than 1 kHz (high frequencies or HF), a second one between 1 kHz and 50 mHz (intermediate frequencies or IF), and a third one under 50 mHz (low frequencies or LF). Table II sites the different arcs in the chosen frequency range for all the curves and samples, and mentions the corresponding field of the real impedance part (R). The area of the HF arc of sample 1 decreases gradually as a function of time. The area of the IF arc however increases during the first three days, then decreases continuously and finally disappears completely; it is this arc which in the beginning takes the biggest portion of the total impedance curve. Afterward, the LF arc becomes relatively more important.

The results for sample 2 lead to similar observations. However, the impedance values, especially those of the HF arc, are much higher than in the former case, and the general decrease occurs slower than for sample 1 (see Fig. 3 and 4). The successive increase and decrease of the IF arc is also much more pronounced (see also Table II).

In the case of sample 3 (Fig. 5 and 6), a linear shape of the IF part is noticed. It is quite clear that here the HF impedances are much higher than for sample 1. The LF arc also gains relative to the IF arc during immersion.

Sample 4 exhibits completely modified impedance curves (Fig. 7). After 28 days' immersion, the real impedance value at 10 mHz still reaches more than $6 \cdot 10^7 \Omega \text{ cm}^2$, indicating a far greater impedance scale than for the other samples. The figure shows also the usual decrease of the impedance values during immersion.

Figure 8 illustrates the corrosion potential dependence on immersion time for three samples. The open-circuit potential of sample 1 falls relatively fast at the beginning of the immersion, then moves to a first and a second plateau.

Sample 2 shows a much slower potential decay. The potential of sample 3 remains constant, at about -120 mV/SCE . The potential/time dependence of sample 4 is not represented in Fig. 8, because it is rather unstable.

For samples 1 and 2, after some 10 days' immersion, blistering of the coating surface is observed, with no visible perforation onto the metal surface. The growth of the blisters must have progressed gradually, only gradual no sudden changes in the other observations, such as the im-

Table II. *f* and *R* ranges of the different arcs in the impedance curves of Fig. 1-6.*f* = frequency and *R* = real impedance value ($\Omega \cdot \text{cm}^2$)

	10 days (+)	Sample 1 (Fig. 1 and 2) 16 days (x)	28 days (o)
arc 1 HF	$f > 1 \text{ kHz}$ $R < 3.1 \times 10^4$	$f > 1.5 \text{ kHz}$ $R < 2.3 \times 10^4$	$f > 600 \text{ Hz}$ $R < 1.6 \times 10^4$
arc 2 IF	$1 \text{ kHz} > f > 50 \text{ mHz}$ $3.1 \times 10^4 < R < 5.2 \times 10^5$	$1.5 \text{ kHz} > f > 500 \text{ mHz}$ $2.3 \times 10^4 < R < 1 \times 10^6$	$600 \text{ Hz} > f > 10 \text{ Hz}$ $1.6 \times 10^4 < R < 2.2 \times 10^4$
arc 3 LF	$f < 50 \text{ mHz}$ $R > 5.2 \times 10^5$	$f < 500 \text{ mHz}$ $R > 1 \times 10^6$	$f < 10 \text{ Hz}$ $R > 2.2 \times 10^4$
	23 hours (+)	Sample 2 (Fig. 3 and 4) 5 days (x)	49 days (o)
arc 1 HF	$f > 20 \text{ Hz}$ $R < 5.9 \times 10^5$	$f > 60 \text{ Hz}$ $R < 2.6 \times 10^5$	$f > 300 \text{ Hz}$ $R < 6.6 \times 10^4$
arc 2 IF	$20 \text{ Hz} > f > 200 \text{ mHz}$ $5.9 \times 10^5 < R < 8.7 \times 10^5$	$60 \text{ Hz} > f > 25 \text{ mHz}$ $2.6 \times 10^5 < R < 1.4 \times 10^6$	$300 \text{ Hz} > f > 200 \text{ mHz}$ $6.6 \times 10^4 < R < 1.9 \times 10^5$
arc 3 LF	$f < 200 \text{ mHz}$ $R > 8.7 \times 10^5$	$f < 25 \text{ mHz}$ $R > 1.4 \times 10^6$	$f < 200 \text{ mHz}$ $R > 1.9 \times 10^5$
	3 days (+)	Sample 3 (Fig. 5 and 6) 70 days (x)	
arc 1 HF	$f > 50 \text{ Hz}$ $R < 3.8 \times 10^5$	$f > 150 \text{ Hz}$ $R < 8 \times 10^4$	
arc 2 IF	$f < 50 \text{ Hz}$ $R > 3.8 \times 10^5$	$150 \text{ Hz} > f > 30 \text{ mHz}$ $8 \times 10^4 < R < 5.3 \times 10^5$	
arc 3 LF	—	$f < 30 \text{ mHz}$ $R > 5.3 \times 10^5$	

pedance, were noticed; the solution of the cell gets yellow colored by diffusion of chromates from the coating.

Sample 3 shows neither of the two phenomena, and sample 4 shows blistering, but there is no yellow coloring of the solution because there are no chromates in the coating.

Discussion

Compared to what can be found in the case of uncoated iron, the coated samples presented here exhibit extremely high impedances, *e.g.*, sample 4 shows a real impedance part of almost $2.5 \times 10^8 \Omega \text{ cm}^2$ at 10 mHz after 1 day immersion, most likely because only a very small fraction of the apparent surface area is active. As time goes on, the impedances are reduced, mainly because the density of pores perforating the coating is growing and consequently raising the active fraction of the total electrode area. The reduction of the impedances in the case of sample 2 is slower than for sample 1 because the perforation of a thicker coating takes more time.

Our measurements confirm the generally accepted matter (9, 13, 14) that the HF arc in the impedance curve corresponds with the impedance of the coating layer itself, and that at lower frequencies the latter impedance is augmented with the impedance resulting from the faradaic processes, connected with the metallic corrosion.

Thus, increasing the thickness of the coating should cause a wider HF arc, as the ionic resistance of the coating is increased. This is indeed what could be found by comparing the results of sample 1 and sample 2.

For samples 1, 2, and 3, the impedance part, reflecting the faradaic processes, appears to increase in the beginning of the immersion, and to decrease subsequently, suggesting that after immersion some active sites are passivated by a particular process, and that they are depassivated again by another process after longer immersion.

The growing importance of the LF arc relative to the HF arc can be explained by an expansion of the active sites under the coating, as indeed this accelerates the overall corrosion and makes the mass transport of active components through the coating increasingly rate controlling.

As to the impedance of the coating, obviously the NaCl concentration in the bulk solution has a marked effect on the coating behavior: a lower NaCl concentration in the cell of sample 3 causes a higher ionic resistance of the coating, and a larger HF arc. The lack of yellow coloring of the solution of sample 3 should also be remembered, pointing out that there must be a smaller exchange of substances between the solution and the coating, and a lesser degree of coating penetration by the solution.

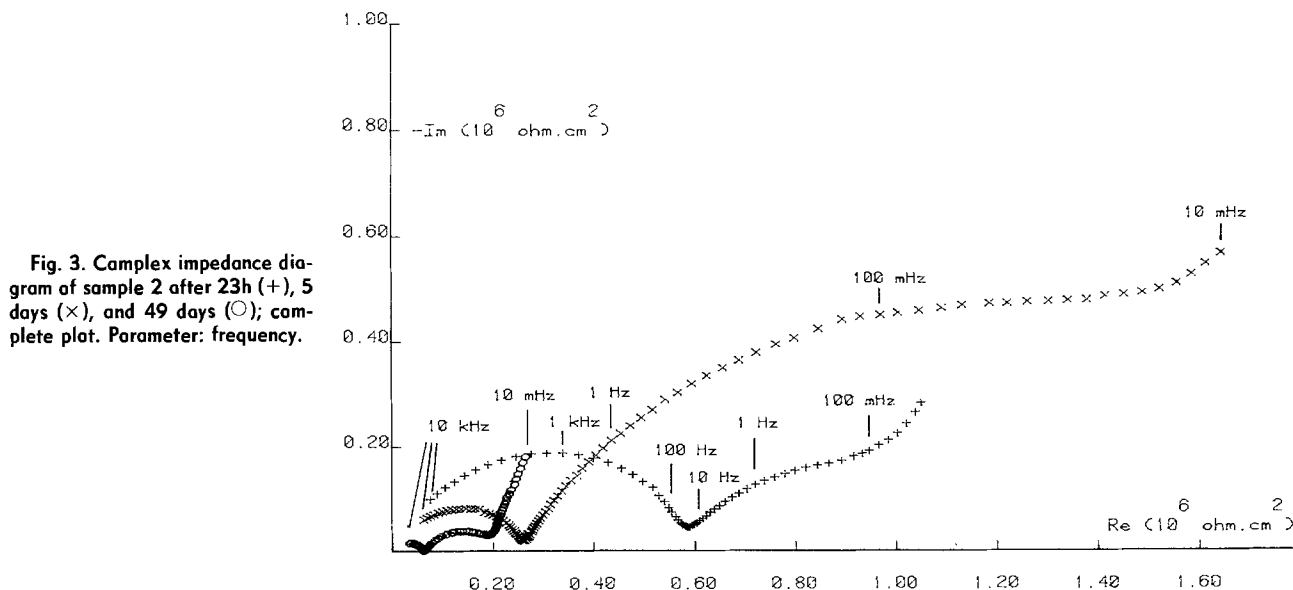


Fig. 3. Complex impedance diagram of sample 2 after 23h (+), 5 days (x), and 49 days (o); complete plot. Parameter: frequency.

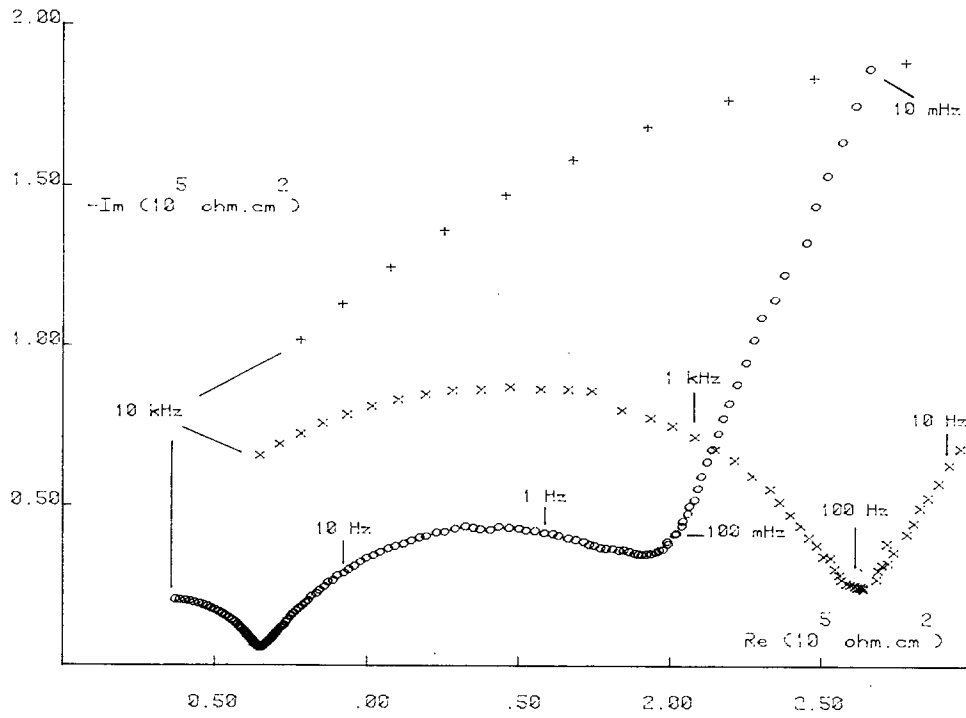


Fig. 4. Expanded plot of Fig. 3

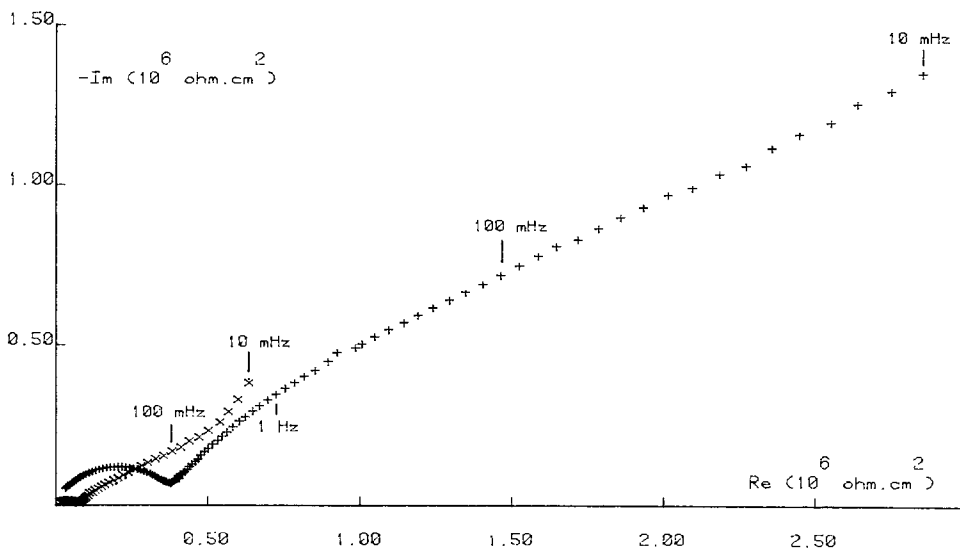


Fig. 5. Complex impedance diagram of sample 3 after 3 (+) and 70 days (x); complete plot. Parameter: frequency.

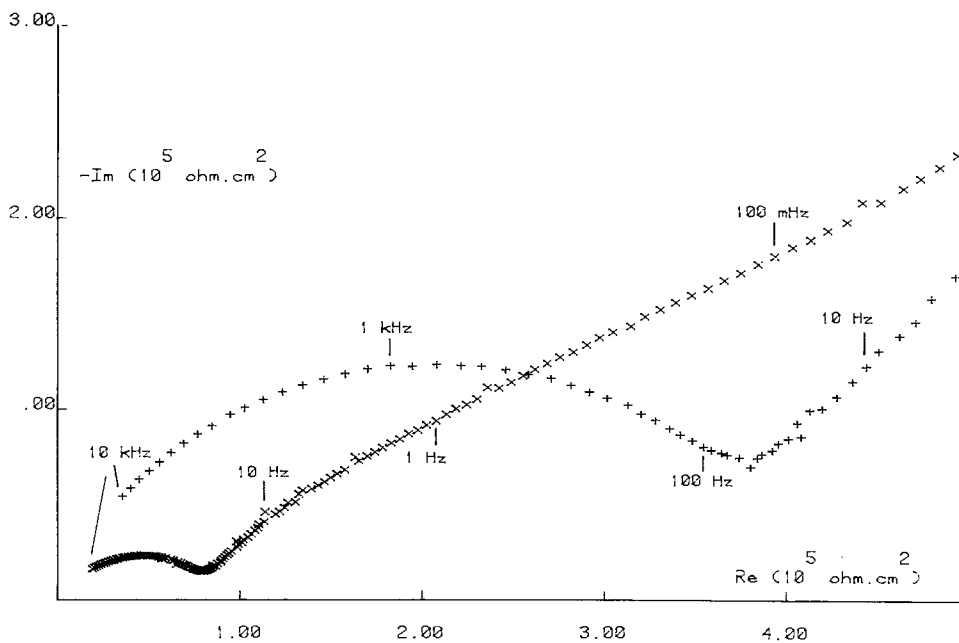
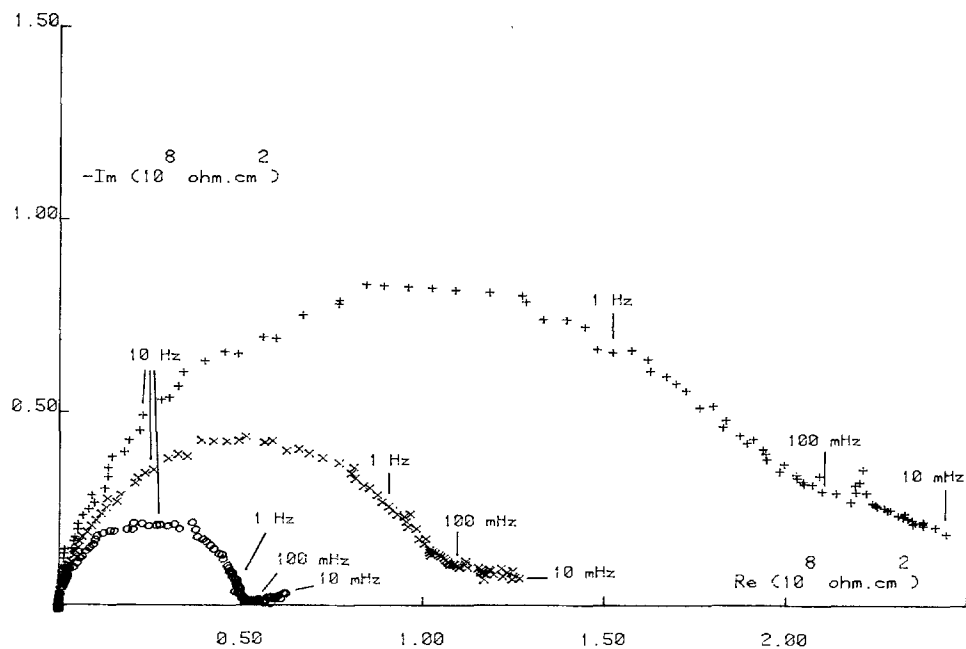


Fig. 6. Expanded plot of Fig. 5.

Fig. 7. Complex impedance diagram of sample 4 after 25h (+), 4 days (x) and 28 days (o); complete plot. Parameter: frequency.



Moreover, the NaCl concentration seems to affect not only the coating, but also the faradaic process, as the IF arc of sample 3 shows a different shape from the impedance characteristic of samples 1 and 2.

Of the four samples, number 4 shows the biggest impedance range, which must be due to the important ionic resistance of the coating. So the absence of chromates in the coating produces a prominent enlargement of its ionic resistance, or otherwise stated, the chromate pigment increases in a radical way the conductivity of the coating. The chromate pigment is a water-soluble substance—sparingly however, to ensure a sufficiently long inhibitive action—which is not completely bound by the present latex coating (32).

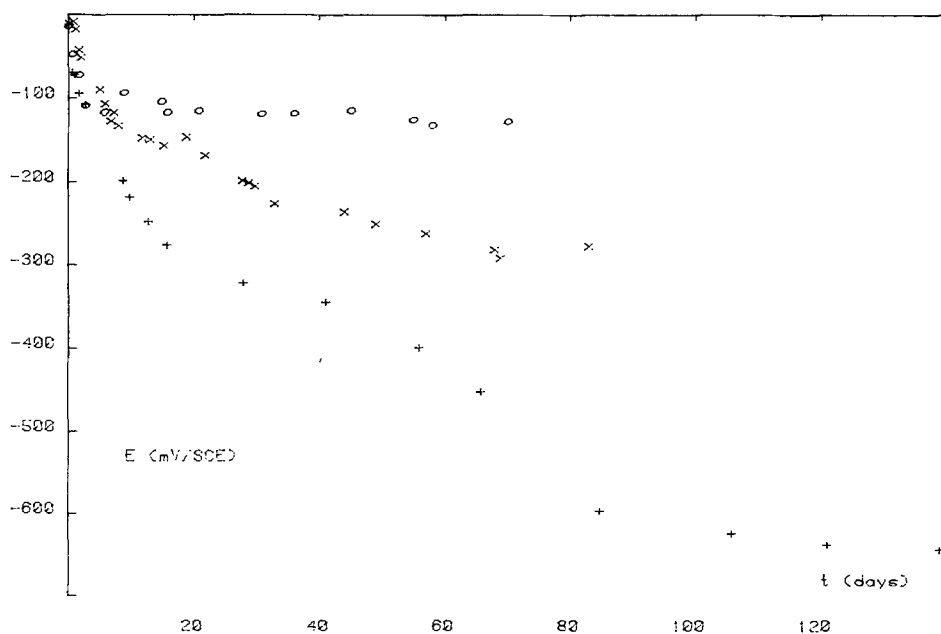
The first plateau in the open-circuit potential of sample 1 is presumably determined by the $\text{Cr}^{6+}/\text{Cr}^{3+}$ equilibrium; the chromate pigment supplied by the coating can indeed be reduced by the iron. After a longer immersion time (more than 100 days), the potential moves towards the corrosion potential of uncoated iron in the same environment. An additional observation in the corrosion process is the blistering of the coating surface.

The slower decay of the potential and the slower variation of the impedance curve for sample 2 point out that a thicker coating can only retard this corrosion process.

The constant potential behavior and the apparently intact surface condition of sample 3 suggest that the iron is passivated by the chromates present in the coating, whereas this could not happen to the former samples due to the higher Cl^- concentration in the bulk solution.

Thus far, replying on the foregoing results and observations, it is possible to give the following description of the investigated system. On immersing the coated iron sample, water is taken up by the coating and penetrates through existing pores and via the boundaries of latex particles onto the metal, in this way dissolving chromates from the pigment reservoir in the coating. During the immersion, other substances such as O_2 and Cl^- , diffuse from the bulk solution into the coating. Only when a pore reaches the iron surface does an electrochemical interaction occur. It is a fact that chromate pigment in a coating not only plays a definite part in the conductivity of the coating, *i.e.*, that the presence of chromate pigment reduces the ionic resistance of the coating, but is also able to affect an anticorrosive action on iron (20, 33-36). It is a foregone conclusion, however, that a high ohmic resistance or a slow diffusion of passivating substances can maintain or accelerate the active state, even if there is a sufficient amount of pigment in the coating. This makes it difficult to find out whether there is passivation or not

Fig. 8. Variation of corrosion potential E with immersion time t . +: sample 1. x: sample 2. o: sample 3.



(20, 33). Besides, chloride anions are known to breakdown the passivation layer; they raise the minimum required pigment concentration to obtain a passive layer (20, 36, 37).

So, it is thought that when the chloride concentration at the metal/solution interface is below a certain limit, *i.e.*, in the beginning of the immersion or when the bulk concentration is low, the chromates are able to protect the iron, producing the Cr^{3+} component, which is reflected by the behavior of the open-circuit potential. However, the passivation reduces the electroactive area, thus increases the IF part in the impedance curve. Nothing happens to the protection as long as the Cl^- limit is not exceeded, which is only the case for sample 3.

For samples 1 and 2, the Cl^- limit is exceeded after a certain immersion time and passivity breaks down, causing the known consequences on the potential, the impedance, and the surface aspect.

So, the Cl^- concentration in the bulk solution is obviously another important factor controlling the system. It affects also the coating: there seems to exist another critical Cl^- concentration above which a marked diffusion of chromate from the coating can occur, together with an important reduction of the ionic resistance of the coating.

An increasing thickness logically enlarges the ionic resistance of the coating and delays the mentioned deterioration.

In any case, the pore density increases with time, as well as the contact area at the pore basis, and this is reflected by the decrease in the HF impedances, and the relatively growing importance of the mass transfer (LF) part.

Conclusions

An immersed coated metal was subjected to impedance measurements. Varying some system parameters such as coating layer thickness, concentration of NaCl in the solution, and pigmentation of the coating has a marked influence on the characteristic impedance curve. The dependence on immersion time also supplies much information about the physical and electrochemical system behavior.

Manuscript submitted July 26, 1982; revised manuscript received April 23, 1984.

Vrije Universiteit Brussel assisted in meeting the publication costs of this article.

REFERENCES

1. I. Epelboin, M. Keddam, and H. Takenouti, *J. Appl. Electrochem.*, **2**, 71 (1972).
2. F. Mansfeld, Abstract 233, p. 611, The Electrochemical Society Extended Abstracts, Vol. 80-2, Hollywood, FL, Oct. 5-10, 1980.
3. I. Epelboin, M. Keddam, and H. Takenouti, Abstract 108, Proceedings of the 17th CITCE meeting, Tokyo, 1966.
4. I. Epelboin, M. Keddam, O. R. Mattos, and H. Takenouti, Abstract 108, p. 429, Extended Abstracts 7th ICMC, Rio de Janeiro, 1978.
5. I. Epelboin, C. Gabrielli, and M. Keddam, *Corros. Sci.*, **5**, 155 (1975).
6. I. Epelboin, P. Morel, and H. Takenouti, *This Journal*, **118**, 1282 (1971).
7. H. Schweikert, W. J. Lorenz, and H. Friedburg, *ibid.*, **127**, 1693 (1980).
8. L. M. Callow and J. D. Scantlebury, *J. Oil Col. Chem. Assoc.*, **64**, 83 (1981).
9. L. M. Callow and J. D. Scantlebury, *ibid.*, **64**, 119 (1981).
10. L. M. Callow and J. D. Scantlebury, *ibid.*, **64**, 140 (1981).
11. G. W. Walter, Abstract 70, p. 380, Extended Abstracts 7th ICMC, Rio de Janeiro, 1978.
12. Y. Sato, *Prog. Org. Coatings*, **9**, 85 (1981).
13. "Rapport d'activité du Laboratoire I.V.P., biennale 1979-1981," p. 22, Internal Report of I.V.P., Belgium.
14. G. W. Walter, *J. Electroanal. Chem.*, **118**, 259 (1981).
15. M. Piens and R. Verbist, in "Proceedings of the XVth FATIPEC Congress," Vol. III, p. 273, Amsterdam, June 1980.
16. J. D. Scantlebury and K. N. Ho, *J. Oil Col. Chem. Assoc.*, **62**, 89 (1979).
17. J. D. Scantlebury and G. A. M. Sussex, in "Proceedings of the NACE Meeting on Corrosion Control by Organic Coatings," p. 235, Lehigh University, Bethlehem, PA (1980).
18. M. Piens and R. Verbist, in "Proceedings of the NACE Meeting on Corrosion Control by Organic Coatings," p. 163, Lehigh University, Bethlehem, PA (1980).
19. M. W. Kendig and H. Leidheiser, Jr., *This Journal*, **123**, 982 (1976).
20. "Rapports d'activité du Laboratoire I.V.P. biennale 1975-1977," p. 20, Internal Report of I.V.P., Belgium.
21. F. Mansfeld, M. Kendig, and S. Tsai, in "Proceedings of the 8th ICMC," p. 1014, Mainz, Sept. 1981.
22. A. Bonnel, M. Duprat, F. Dabosi, L. Cot, J. J. Robin, and J. Durand, in "Proceedings of the 8th ICMC," p. 1979, Mainz, Sept. 1981.
23. J. C. Rowlands and D. J. Chuter, in "Proceedings of the 8th ICMC," p. 1068, Mainz, Sept. 1981.
24. G. A. M. Sussex and J. D. Scantlebury, in "Proceedings of the 8th ICMC," p. 1074, Mainz, Sept. 1981.
25. M. Piens, J. Hubrecht, and J. Vereecken, in "Proceedings of the 8th ICMC," p. 1021, Mainz, Sept. 1981.
26. F. Mansfeld, M. Kendig, and S. Tsai, VI 44, p. 1065, Extended Abstracts 32nd Meeting of the International Society of Electrochemistry, Vol. II, Dubrovnik, Sept. 1981.
27. J. Hubrecht, M. Piens, and J. Vereecken, Abstract 146, p. 369, The Electrochemical Society Extended Abstracts, Vol. 81-1, Denver, CO, Oct. 11-16, 1981.
28. J. M. Parks, M. C. Hughes, and H. Leidheiser, Jr., Abstract 147, p. 371, The Electrochemical Society Extended Abstracts, Vol. 81-1, Denver, CO, Oct. 11-16, 1981.
29. F. Mansfeld, M. Kendig, and S. Tsai, Abstract 148, p. 373, The Electrochemical Society Extended Abstracts, Vol. 81-1, Denver, CO, Oct. 11-16, 1981.
30. M. Kendig, F. Mansfeld, and S. Tsai, Abstract 149, p. 376, The Electrochemical Society Extended Abstracts, Denver, CO, Oct. 11-16, 1981.
31. J. P. Lomas, L. M. Callow, J. D. Scantlebury, and G. A. M. Sussex, Abstract 150, p. 379, The Electrochemical Society Extended Abstracts, Denver, CO, Oct. 11-16, 1981.
32. C. H. Hare, *J. Paint Technol.*, **47**, 69 (1975).
33. M. Piens, *J. Coatings Technol.*, **51**, 66 (1979).
34. T. C. Patton, Editor, "Pigment Handbook," Vol. 1, pp. 848-857, John Wiley and Sons, New York (1973).
35. "Rapports d'activité du Laboratoire I.V.P., biennale 1977-1979," p. 16, Internal Report of I.V.P., Belgium.
36. Z. Szklarska-Smialowska, in "Passivity of Metals," R. P. Frankenthal and J. Kruger, Editors, pp. 443-462, The Electrochemical Society, Corrosion Monographs Series, Princeton, NJ (1978).
37. K. J. Vetter, "Electrochemical Kinetics," pp. 754-759, Academic Press, New York (1967).

Electrochemical Behavior of Passive Iron in Acid Medium

I. Impedance Approach

M. Keddam, J.-F. Lizée, C. Pallotta,¹ and H. Takenouti

Groupe de Recherche no. 4 du CNRS, "Physique des Liquides et Electrochimie," associé à l'Université Pierre et Marie Curie, 75230 Paris Cedex 05, France

ABSTRACT

Wide frequency range impedance measurements are applied to a kinetic investigation of passive iron in various acidic media. Special care was taken in the electrode preparation to reach stable current densities ($7 \mu\text{A} \cdot \text{cm}^{-2}$ in $\text{Fe}/1\text{M H}_2\text{SO}_4$, 25°C). Impedance data were obtained as a function of potential and temperature in the steady state. An original approach to the nonsteady-state behavior is introduced by combining transient response to the time dependence of the impedance. Contributions from transport in the film and interfacial impedance are separated. The classical view of high field conduction mechanism is refined with respect to the generality of the description and also to the film properties in various environments leading to the concept of chemically dependent high field ion migration. Low frequency behavior in the millihertz range supported this conclusion by ruling out the idea of diffusion-controlled passive current. The capacitance observed is attributed to the film-growth kinetics.

In the last ten years, passivity was mainly investigated by means of *in situ* optical techniques and non-*in situ* surface spectroscopies (1-8). These studies resulted in a certain amount of information on the chemistry of passive layers, but their use is often confined to weakly or mildly aggressive media (*e.g.*, boric-borate-buffered solutions). In these media, however, kinetics studies are difficult because the passive current is very low, often at the level of the background current of oxygen reduction or of the feedback current of most regulating devices. However, during the same period, the electrochemical behavior of passive metals in acid media was disregarded. Therefore, in spite of marked progress in nonsteady-state electrochemical methods such as impedance measurements at very low frequencies by FFT or by correlation techniques, the most elaborate concepts on passivity formulated from classic experiments were not thoroughly worked out (9-18).

Vetter assumed that the major part of applied overvoltage is located in the passive film following a high field conduction process (17). The film growth is also supposed to be governed by this field, whereas the passive current is determined by a chemical process taking place at the film/solution interface and closely related to the stoichiometry of the film material (18). Difficulties in analyzing the kinetics of passive electrodes are in major part due to the overlapping of several elementary processes such as charge transfer at interfaces, transport properties across the film, and film growth. The problem can also be formulated in terms of the potential profile between the metal and electrolyte or of the rate-determining step involved in the passive current. The separation of these contributions may be improved by measuring the electrode impedance over a wide frequency range or by recording current or potential transients performed over a wide range of time. In the case of small perturbations, these two techniques are related through the Fourier transform. It is then possible to distinguish between the steady state and transient phenomenon and to obtain relevant information on the potential distribution and concentration distribution across the interface.

The existence of a passive film may lead one to describe the system by an equivalent circuit. Although it seems fruitful as a guiding representation, this approach is only a way to translate experimental data or theoretical predictions and does not in any way provide new information on the physico-chemical system itself. In many cases, several designs of equivalent circuits may be found, which show the difficulty of attributing unambiguously a given element to a definite elementary process. Along the same lines, the arrangement of the

electrical elements should not be construed to be identical with the postulated steps in the real system. In highly intricate systems, it often turns out that circuit elements are frequency dependent and the representation tends to lose its advantage.

Early impedance measurements used for studying passivity of metals were usually aimed at capacitance determination in order to estimate film thickness or dielectric properties of the film material. Furthermore, the potential dependence of the high frequency capacitance was tentatively related to the semiconducting character of the film through the Mott-Schottky relation (19-21).

One of the most controversial points is the electrical resistance of the passive film. There is an apparent contradiction between good electronic conductivity and a high electrical field assisting ionic currents across the film. If a major part of the applied overvoltage is located across the film, a nearly linear dependence of the resistance with respect to potential is expected, regardless of whether the conduction process is ohmic or high field. Surprisingly enough, no investigations were made to check this basic point. Current transients generated by potential perturbations were interpreted by Vetter in terms of an electrochemical potential driven from its equilibrium, at the solution/film interface, as responsible for film growth (9). More recently, ion diffusion across the film was considered as a limiting step by Sukhotin *et al.* (22, 23), but this model was not clearly supported by experimental data. Macdonald *et al.* (24, 25) developed a "point defect" description of film growth. According to these authors, the steady-state passive current is determined by the diffusion of ions or ions vacancies in the film.

Many impedance measurements on the passivity of iron were performed at frequencies greater than 1 Hz. This frequency domain is too high to give access to the relaxation of film thickness and even to the transport properties of the film. Haruyama *et al.* (26) performed impedance measurements in the millihertz range on passive iron, mostly in a boric-borate buffer solution. Impedance of metals in the active, active-to-passive, and passive ranges were extensively studied by Epelboin *et al.* (27-29) and Armstrong *et al.* (30, 31). However, treatment of their results on the passive film was restricted to bidimensional layer models and, therefore, ignored film growth and potential distribution in the layer depth.

This brief literature review leads to the conclusion that Vetter's views on passive iron are the most complete ones. They have largely stimulated the present work, which is devoted to a detailed analysis of electrode impedance.

Impedance of Passive Electrodes: A General Framework

Complex impedance techniques are widely used to examine electrochemical processes. On a very general basis,

¹ Postdoctoral fellow of the Consejo Nacional de Investigaciones Científicas y Técnicas de la República Argentina.

the electrode impedance can be formally represented as a potential-dependent resistance $R(E)$. The change of this resistance with potential is noninstantaneous since it involves finite rate processes such as transport phenomena and/or physico-chemical transformation at the interface, which gives rise to the overall nonlinear behavior of the system.

The simplest way to describe this feature in the frequency domain is through a single (nondistributed) relaxation. Then the impedance Z can be expressed as

$$\frac{1}{Z(\omega)} = \frac{1}{R(E)} \left(1 - \frac{A(E)}{1 + j\omega\tau} \right) \quad [1]$$

where ω is the angular frequency ($\omega = 2\pi f$, f in Hz), τ a relaxation time constant, $j = \sqrt{-1}$, and $A(E)$ a nondimensional parameter.

According to this equation, the impedance $Z(\omega)$ is identical to $R(E)$ at very high frequencies compared to $1/\tau$, since under those conditions $R(E)$ can be regarded as frozen. At zero frequency, the impedance tends to the polarization resistance R_p , given by

$$\frac{1}{R_p} = \frac{1}{Z(0)} = \frac{1}{R(E)} [1 - A(E)] \quad [2]$$

Schematic Nyquist representations of Eq. [1] are given in Fig. 1 according to the value of $A(E)$. In most systems, this low frequency limit can be approached only by extending the measurement towards the millihertz range. In the case of passive systems, the polarization curve is extremely flat, and the polarization resistance is practically infinite within the experimental accuracy.

Early studies on the impedance of passive electrodes were carried out only in the range of medium frequencies, e.g., 50 Hz, and concluded at the capacitive behavior of the passive film. In this context, no attempt was made to establish a connection with the dc properties of the passive electrode. Further analysis of impedance data in the intervening low frequency domain is needed, since it may reflect three-dimensional processes in the film such as ion transport and growth mechanism.

The so-called resistance of the film is sometimes discussed with reference to the ratio of the dc potential to the dc current. The electrochemical systems being essentially nonlinear, this consideration is completely irrele-

vant except under very particular conditions described below. A restricted class of nonlinear systems can be described by a generalized Ohm's law relating the dc current flowing through the system to the dc voltage according to

$$R(E) = \frac{E}{I} \quad [3]$$

where $R(E)$ is identical to the high frequency limit of the resistance governed by the general Eq. [1] according to

$$\frac{1}{Z} = \frac{1}{R(E)} \left[1 - \frac{E}{R(E)(1 + j\omega\tau)} \frac{dR(E)}{dE} \right] \quad [4]$$

This property provides an easy criterion for discriminating this class of systems and is perfectly verified by nonisothermal metallic or semiconducting resistors exhibiting respectively impedances of the types a and b in Fig. 1. In these systems the potential dependence of $R(E)$ arises from its temperature dependence through Joule's law. In the case of electrochemical systems, no absolute potential scale can be defined. Consequently, Eq. [3] cannot be checked against impedance data. The derivative of Eq. [3] could be applied to constant current systems (passive electrodes)

$$\frac{dR(E)}{dE} = \frac{1}{I} \quad [5]$$

Equation [5] clearly means that any change of voltage induces a proportional change in the resistance value according to the generalized Ohm's law. It should be emphasized that activated charge transfer or conduction processes do not obey this law, as will be shown in the next section.

Experimental Procedure

An accurate measurement of electrode impedance at low frequencies for passive iron in a strongly acid medium is extremely difficult. This is due to an underlying attack taking place between metal and embedding material (9, 12). In this work, this problem is overcome as explained below, and steady-state passive currents as low as $7 \mu\text{A} \cdot \text{cm}^{-2}$ were observed during a week for Fe/1M

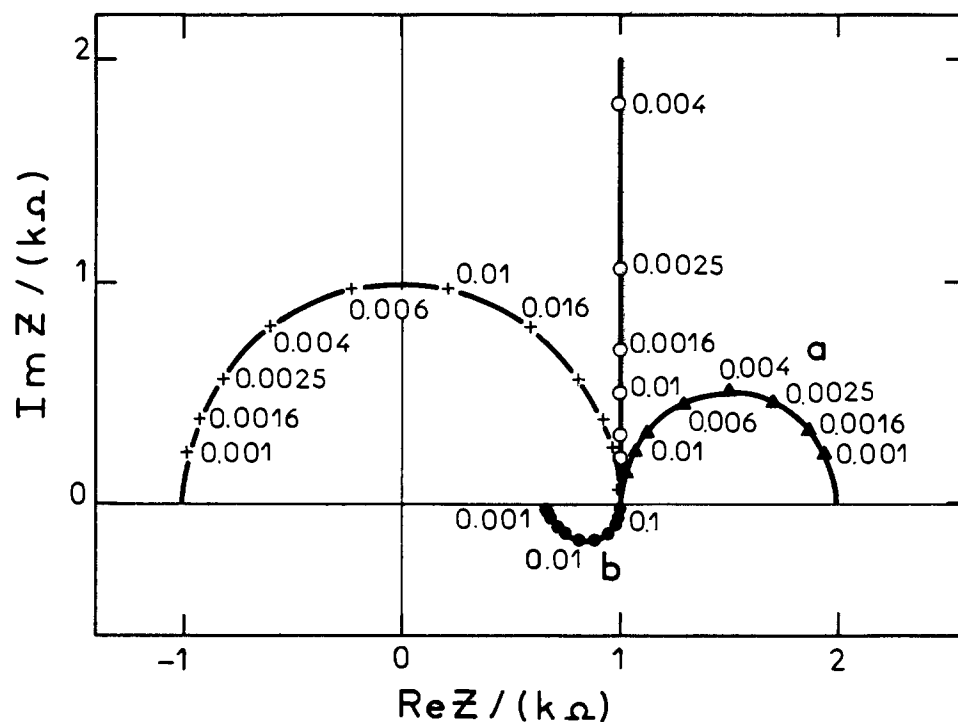


Fig. 1. Calculated Nyquist representations according to Eq. [1] for different values of $A(E)$. +: $A(E) > 1$. ○: $A(E) = 1$. ●: $A(E) < 1$. ▲: $0 < A(E) < 1$. $\tau = 20\text{s}$. (a) metallic and (b) semiconducting resistors.

H₂SO₄ at 25°C. This enables one to obtain reproducible data at very low frequencies.

Electrodes.—The working electrode was prepared from iron rod of 5 mm diam (Johnson-Matthey) as received without any heat-treatment. The cross section of rod was allowed to contact with electrolyte, thereby forming a disk electrode, the surface of which was 0.2 cm². The remaining surface of rod was first covered with an epoxy-phenolic varnish cured at 200°C, then embedded in a thermosetting phenol resin at 200°C under pressure (3.5 bar). The electrode thus prepared was polished by emery paper of up to 1200-grade under running water, rinsed with ion-exchanged water, and immediately set in a cylindrical electrolytic cell. A Pt-gauze of large surface area (200 cm²) surrounding the cell wall is used as a counterelectrode. Potential was measured and referred against a mercurous sulfate electrode in saturated K₂SO₄ (SSE) located in the solution bulk.

Solutions.—Various acid solutions were prepared of p.a. reagents (Merck "proanalysis" quality) and ion-exchanged water. These solutions are H₃PO₄, H₂SO₄, HNO₃, and HClO₄, 1M concentration.

Phosphate and sulfate media of different pH's were prepared by the mixture of molar acid and 1M KH₂PO₄ or 1M Na₂SO₄ in varied proportions. The electrolytic cell of ca 0.3 liter of solution was deaerated by Ar bubbling and maintained at constant temperature.

Devices.—The polarization of electrode interface and impedance measurements were carried out with a Solartron-Schlumberger equipment, electrochemical interface 1186, and Frequency Response Analyzer 1250. Very low frequency data ($f < 0.01$ Hz) were obtained also by FFT processing (Fourier Analyzer: Hewlett-Packard 5451C) of the current response to a stepwise potential perturbation.

Procedures.—Prior to impedance measurements, the electrode was prepolarized at a passive potential, 0.85V in most cases, for 24h. It was found in preliminary experiments that the electrode impedance continued to change for a long period after the passive current reached its steady-state value.

To investigate the potential dependence of the impedance, the potential was then switched to the selected value. Approximately an additional 1h was needed after that to reach the steady-state current and to perform the measurements. No significant dependence of the results on the initial polarization potential was observed.

Results and Discussion

Steady-state measurements.—The passive range extends between the Flade potential and oxygen evolution in general (transpassive dissolution in perchlorate media). From the Flade potential ca. -0.2V, the current decreases with potential. Beyond 0.2V, the current is independent of potential, except in phosphate medium, in which a slight current change can be observed. This so-called full passive range is mainly dealt with in this paper and allows one to define a constant passive current density I_p . The I_p values obtained for various experimental conditions are summarized in Table I. As can be seen, at a given temperature and pH, the passive current increases proportionally as the charge-to-size ratio of anions: PO₄³⁻ > SO₄²⁻ > NO₃⁻ > ClO₄⁻.

In solutions of a given anion, the concentration of which is kept constant, the passive current decreases at increasing solution pH. Regardless of anions, the following relation was observed at 25°C

$$\frac{d \log I_p}{dpH} = -0.78 \quad [6]$$

It was also found that the passive current depends on temperature. Arrhenius plots obtained in 1M H₃PO₄ are shown in Fig. 2. An apparent activation energy of ca. 12 kcal · mol⁻¹ was calculated. In sulfate solutions at pH = 1, the same value for the activation energy was recorded,

Table I. Influence of the electrolyte composition and temperature on the steady-state passive current and the diameter R_{HF} of HF loop

Solution	pH	T (°C)	I_p ($\mu A \cdot cm^{-2}$)	R_{HF} (k Ω)	$R_{HF} \cdot I_p$ (mV)
H ₃ PO ₄ 1M	1.0	25	58.0	10.7	124
		37	130.0	4.9	127
H ₃ PO ₄ + KH ₂ PO ₄ 1M	2.2	25	27.6	23.1	128
H ₃ PO ₄ + KH ₂ PO ₄ 1M	2.8	25	12.2	53.6	131
H ₃ PO ₄ + KH ₂ PO ₄ 1M	3.4	25	3.4	205.4	140
H ₂ SO ₄ 1M	0.03	25	8.2	74.0	122
		50	55.0	10.5	116
H ₂ SO ₄ + Na ₂ SO ₄ 1M	1.0	25	3.0	193.4	116
H ₂ SO ₄ + Na ₂ SO ₄ 1M	1.8	25	0.3		
H ₂ SO ₄ 0.5M	0.4	25	4.8	121.0	117
HNO ₃ 1M	0.0	25	3.9	117.0	91
		37	8.65	55.0	95
HClO ₄ 1M	0.0	25	0.22	2260.0	97
		45	2.0	251.0	100

All values were obtained at $E = 0.65V$.

whereas in 1M HClO₄, the value was found to be ca. 15 kcal · mol⁻¹.

Electrode impedance.—Figure 3 shows an example of the impedance diagrams obtained for two different solution compositions, in the full passive range. In this figure, three frequency domains can be separated: (i) a capacitive loop at relatively high frequencies (HF capacitive loop), (ii) an inductive loop at medium frequencies (MF domain), and (iii) another capacitive domain for low frequencies (LF capacitive loop).

These diagram features were obtained regardless of potential, solution anion, pH value (0-3.4), and temperature, provided that the electrode was polarized in the full passive range. The only difference observed between these impedance diagrams was the diameter of each loop and its frequency domain.

HF capacitive loop.—This loop is close to a semicircle centered below the real axis (depressed semicircle) as also generally observed on solid electrodes including noble metals (33). The capacitance values determined at the maximum of the imaginary part lie between 10 and 50 $\mu F \cdot cm^{-2}$ depending on the experimental conditions. If analyzed in terms of a parallel R-C circuit at each frequency,

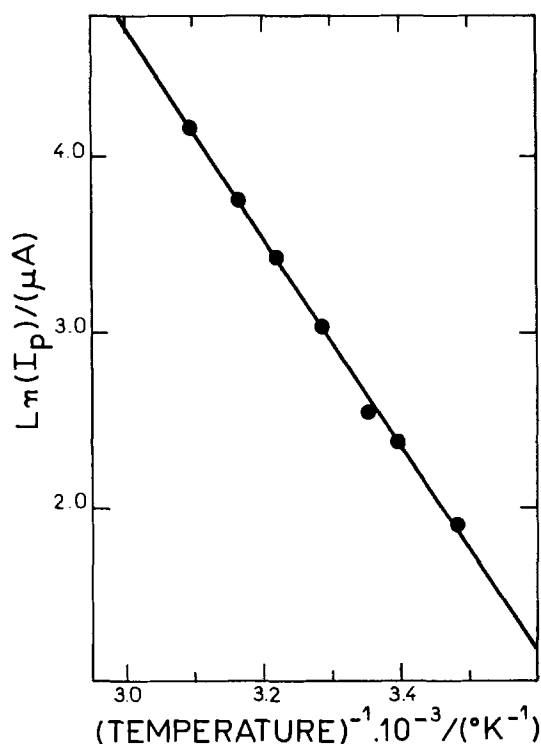


Fig. 2. Arrhenius plot for Fe/1M H₃PO₄, $E = 0.60V$

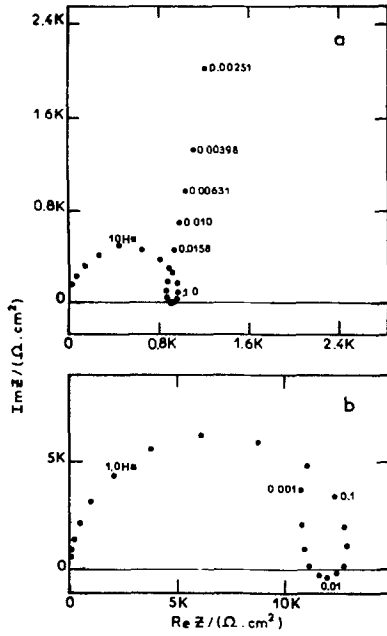


Fig. 3. Complex impedance diagrams: (a) Fe/1M H₃PO₄, 37°C, E = 0.65V; (b) Fe/1M H₂SO₄, 25°C, E = 0.35V.

it is noteworthy that the frequency dependence is reflected particularly on the resistive component (34, 35). Aspects related to this frequency dependence were not investigated in greater detail in this paper. The interest is focused on the real axis intercept R_{HF} , which must be regarded as a property of the electrode at a sufficiently high frequency to freeze the modulation of the film thickness. Charge transport and/or interfacial charge transfer at the metal/film and film/electrolyte interfaces may be involved at the same time, which is hardly distinguishable.

Separation of the interfacial and film contributions to R_{HF} can be performed on the basis of its potential dependence. As illustrated in Fig. 4, R_{HF} increases linearly with potential in the full passive range. It can hence be written as

$$R_{HF} = R_{HF}^{Flade} + K(E - E^{Flade}) \quad [7]$$

where E^{Flade} is the Flade potential, R_{HF}^{Flade} indicates R_{HF} value extrapolated back to E^{Flade} , and K is a constant. The values of R_{HF}^{Flade} and K are dependent on solution composition and are shown in Table II.

Equation [7] actually suggests that R_{HF} can be split into a contribution located in the film bulk (R_{film}), which is proportional to film thickness, and another contribution linked with charge transfer processes at the film boundaries (R_i).

Consideration of the product $R_{HF}I$ provides deeper insight into the nature of the resistive component of the impedance. A constant value of this quantity is related to an

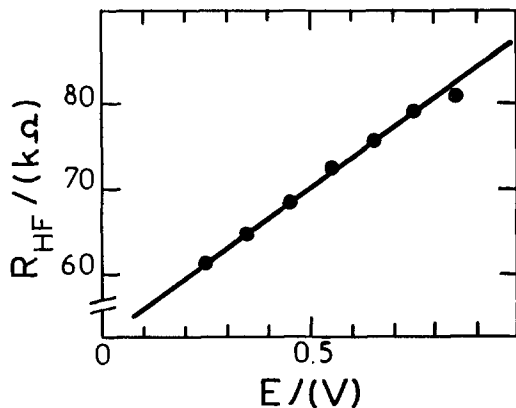


Fig. 4. Potential dependence of R_{HF} . Fe/1M H₂SO₄, 25°C

Table II. R_{HF}^{Flade} and K values related to Eq. [7] for different solutions at 25°C

Solution	K (kΩ · V ⁻¹ · cm ²)	R_{HF}^{Flade} (kΩ · cm ²)
H ₂ SO ₄ 1M	7.0	9.5
H ₃ PO ₄ 1M, pH = 1.0	0.93	1.1
H ₃ PO ₄ + KH ₂ PO ₄ 1M, pH = 2.8	5.6	5.3
H ₃ PO ₄ + KH ₂ PO ₄ 1M, pH = 2.2	2.5	2.3

irreversible charge transfer obeying a Tafel law, whereas, according to the foregoing introduction, $R_{HF}I$ can be also used as a characterization of the conduction mechanism in the film.

The product $R_{HF}I$, where I is the measured current density at a given applied potential, is compared for various solutions in Fig. 5.

First, variations at potentials less anodic than the full passive range were investigated. In Fig. 6, the polarization curve near the active-passive transition potential obtained in 1M H₂SO₄ is shown. In the same figure, three impedance diagrams (A to C) obtained at the corresponding points on the steady-state polarization curve are also shown. In these diagrams, the features of impedance diagram change drastically as the polarization point approaches active-passive transition. The zero frequency limit of the impedance for point A is negative, in agreement with the negative slope of the polarization curve. The product $R_{HF}I$ is independent of potential in the low anodic potential range. The value of this product is close to 70 mV at potentials close to the active-passive transition potential, then increases and reaches a value equal to 100 mV at 0.3V for solutions of pH > 1 (Fig. 5). Beyond this potential, the electrode is polarized in the full passive range where I becomes the passive current density independent of potential. $(I_p) \cdot R_{HF} \cdot I_p$ increases linearly with potential showing a similar variation for all solutions investigated as shown in Fig. 5. However, the position of the straight lines is dependent on solution pH following 60 mV/pH law for a given anion. The linear relationship between $R_{HF} \cdot I_p$ and the potential is qualitatively in agreement with Eq. [5]. However, the experimental slope of 0.06 is in disagreement with the unit slope expected from Eq. [5]. If an ohmic drop was actually involved in a passive film of potential dependent thickness, it would concern only a small fraction of the overpotential located within the film. In other words, a rough model as that described by Eq. [5] is able to account only qualitatively for the resistive component of the impedance of passive iron [Fig. 1, A(E) = 1].

It is noteworthy that in spite of large differences between passive currents observed in various solutions (cf. Table I), the slope of $R_{HF} \cdot I_p/E$ is essentially the same for

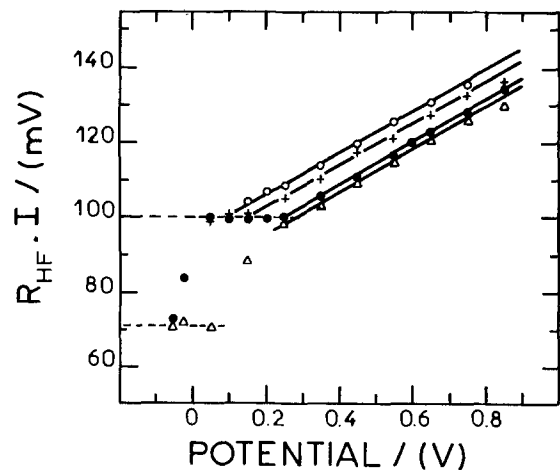


Fig. 5. Potential dependence of $R_{HF} \cdot I$ for iron in different solutions at 25°C. Δ : 1M H₂SO₄. \bullet : 1M H₃PO₄. $+$: 1M (H₃PO₄ + KH₂PO₄), pH = 2.2. \circ : 1M (H₃PO₄ + KH₂PO₄), pH = 2.8.

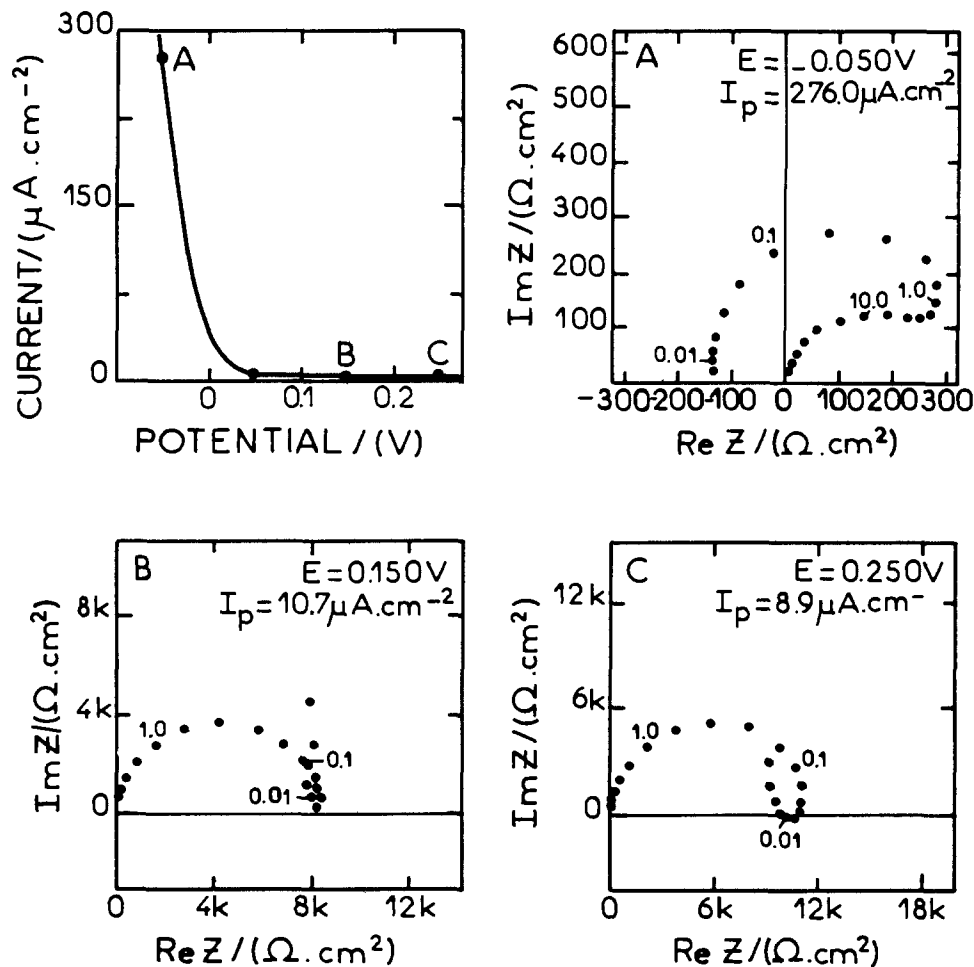


Fig. 6. Steady-state polarization curve in the passive region. Complex impedance diagrams measured at different points labeled A to C. Fe/1M H₂SO₄ at 25°C. Frequencies in hertz.

all solutions. This establishes some kind of similarity in the electrochemical properties of the passive film in all solutions investigated. This result will be of importance for the modeling of the passive electrode. Surprisingly, this behavior seems to occur even more generally, taking into account similar experiments performed by Crevecoeur *et al* (34) on aluminum in ammonium pentaborate/ethylene glycol solutions. From Fig. 1 of Ref. (34), one can calculate a slope equivalent to $d(R_{HF} \cdot I_p)/dE$ of about 0.07. If, as suggested by Vetter (17) for iron and commonly assumed for valve metals, the movement of ions through the film obeys a high field migration, the $R_{HF} \cdot I_p/E$ dependence is easily understood. The current I flowing through this film is expressed by

$$I = I^0 \exp\left(\frac{BE}{l}\right) \quad [8]$$

where $B = \frac{z\alpha F}{RT}$, a = half-jump distance, z = electric charge of the mobile species, T = temperature, and l = film thickness. According to Eq. [8]

$$\frac{d(RI)}{dE} = \frac{l}{BE} \quad [9]$$

the slope corresponds to the argument of the exponential Eq. [8]. From the experimental data, $d(R_{HF} \cdot I)/dE = 0.06$ and assuming $a = 5\text{\AA}$, a reasonable value for an oxide lattice parameter, the calculated electric field is ca. $3 \cdot 10^6 \text{ V} \cdot \text{cm}^{-1}$ at 25°C or a change in thickness of the order of $35\text{\AA} \cdot \text{V}^{-1}$, in agreement with the literature of valve metals.

The conclusions regarding the properties of the passive film partially support Vetter's view of the dominating role of the electric field. More precisely, regardless of the experimental conditions, the steady-state seems only

compatible with a particular value of this field. It is established that the film thickness remains practically the same at a given potential. Changes in the ionic dissolution current across the film must be entirely accounted for by the pre-exponential factor of the high field equation. However, it is to be remarked that these conclusions are based on a whole set of impedance data for the same value of the mean steady-state electric field in the film. No direct evidence is provided in favor of Eq. [8] in terms of current-electric field plot. Deviation from the stationary field can only be obtained under nonsteady-state conditions that give rise to either growth or dissolution of the film.

In an attempt to estimate the value of R_{HF} during the transient response to a stepwise change of potential, the impedance-time profile was sampled using the data storage facilities of the 1250 analyzer. Because of the deviation of the HF arc from a perfect semicircle, two frequencies were selected: one close to the top of the loop and the other one two or three times smaller. It was checked that errors arising from the contribution of the transient current response to the correlation remain negligible.

In Fig. 7 and 8 the transient current response (curve a) and R_{HF} profile (curve b) in 1M H₃PO₄ solution after potential steps of 0.4V in anodic and cathodic directions are shown. The amplitude of this potential step was such that the system was perturbed far beyond the linearity domain.

Figure 9 shows the change of $R_{HF}I$ as a function of time. A steadily decreasing transient is found. This result is obviously incompatible with an irreversible charge transfer at interfaces and a high field conduction mechanism in the film bulk. Under these assumptions, Eq. [8] predicts that $R_{HF}I$ would simply reproduce the smooth increase of "I" from its initial to its final value following the potential step. The origin of this behavior can be clarified in some extent. If a Tafel law is postulated for the interfacial

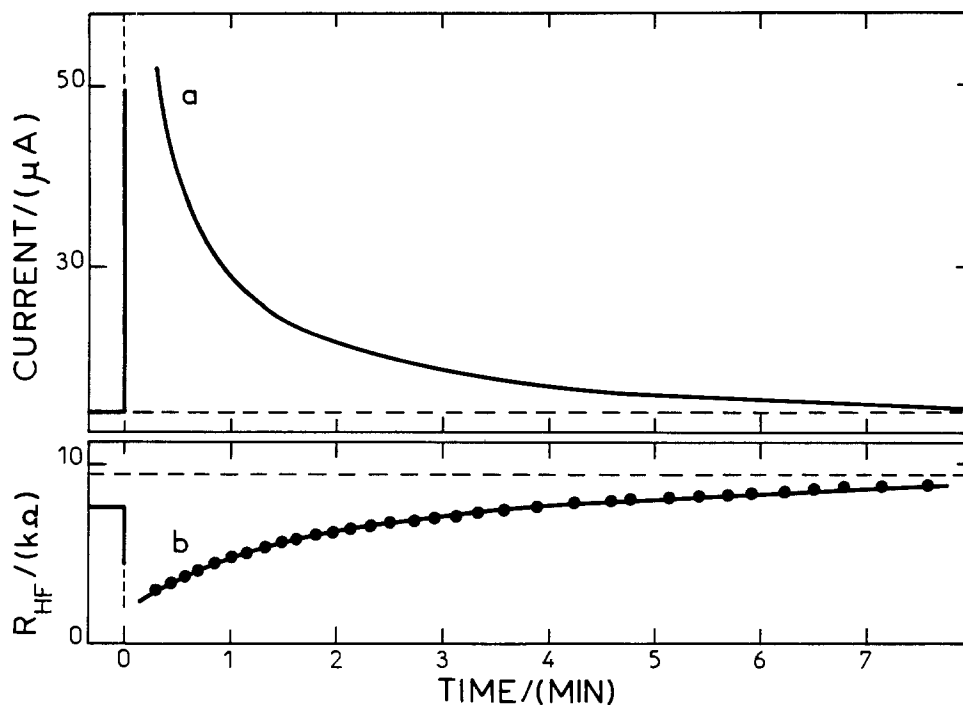


Fig. 7. a: Current/time response resulting from a potential anodic step from 0.4 to 0.8V. b: R_{HF} /time relationship measured during the anodic transient. R_{HF} calculated from impedance at 4 and 1.6 Hz. Fe/1M H_3PO_4 , 25°C.

charge transfer, the constant value of $R_t I$ can be deduced from Fig. 5 by extrapolating back to the zero-thickness region and thereby, the change of R_{film} during the transient estimated. Applying this procedure, it is found that the variations of R_{film} between initial and final states of the passive film cannot be restituted correctly with a constant value of $R_t I$. Instead, a value of $R_t I$ decreasing with the current during the transient must be used. This strongly suggests an explanation based on a partially reversible interfacial charge transfer rather than a deviation of the conduction mechanism from the exponential law at high field strength. This explanation is even more convincingly supported by the time response of $R_{\text{HF}} I$ during a backward cathodic potential step. $R_{\text{HF}} I$ steadily increases from an initial value as low as 0.04V (Fig. 9). In this case,

the evaluation of the film resistance by assuming the constant value 0.1V of $R_t I$ would lead to a negative value of R_{film} . However, a partially reversible interfacial transfer (i.e., smaller values of $R_t I$ associated with small anodic currents) during the cathodic transient consistent with this experiment occurs. On the whole range of currents covered by anodic and cathodic transients, i.e., between 1.38 and 52 μA , the charge transfer parameter $R_t I$ has to vary from 0.055 to 0.129V. The steady-state value 0.1V lies in the midrange. The dependence of $R_{\text{HF}} \cdot I_p$ with passive current through anions at constant pH (Table I) also supports this view. However, additional contributions to the impedance measured during the transient arising from side reactions related to the growth or dissolution of the film may also be considered.

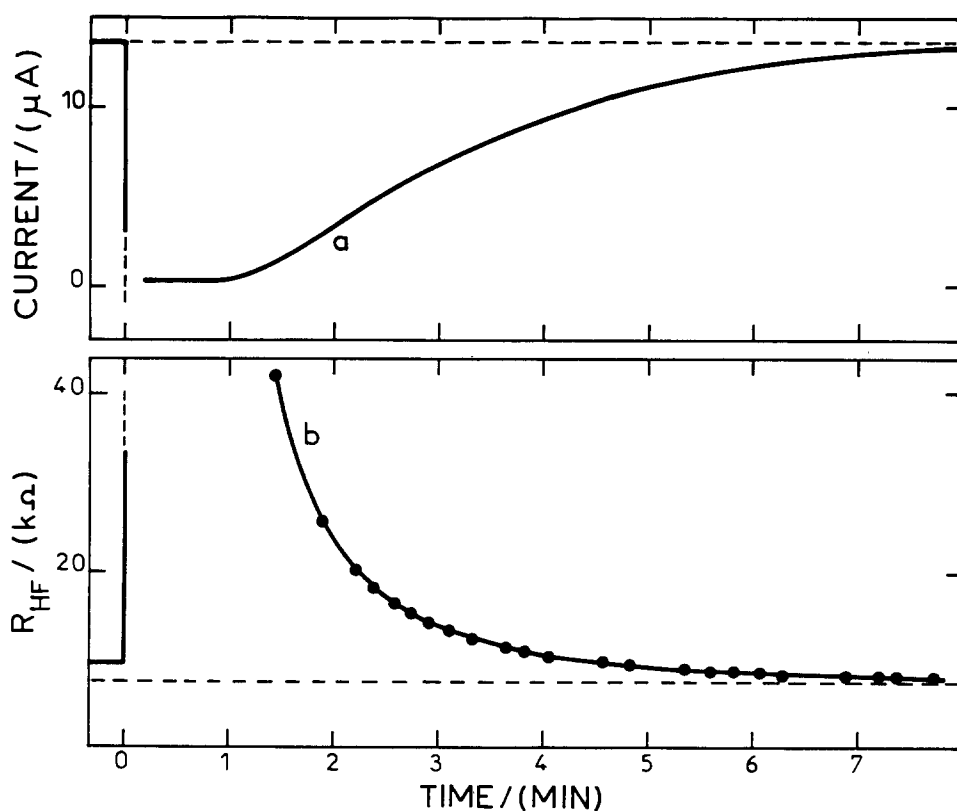


Fig. 8. Same as Fig. 7, but in cathodic direction from $E = 0.8\text{-}0.4\text{V}$.

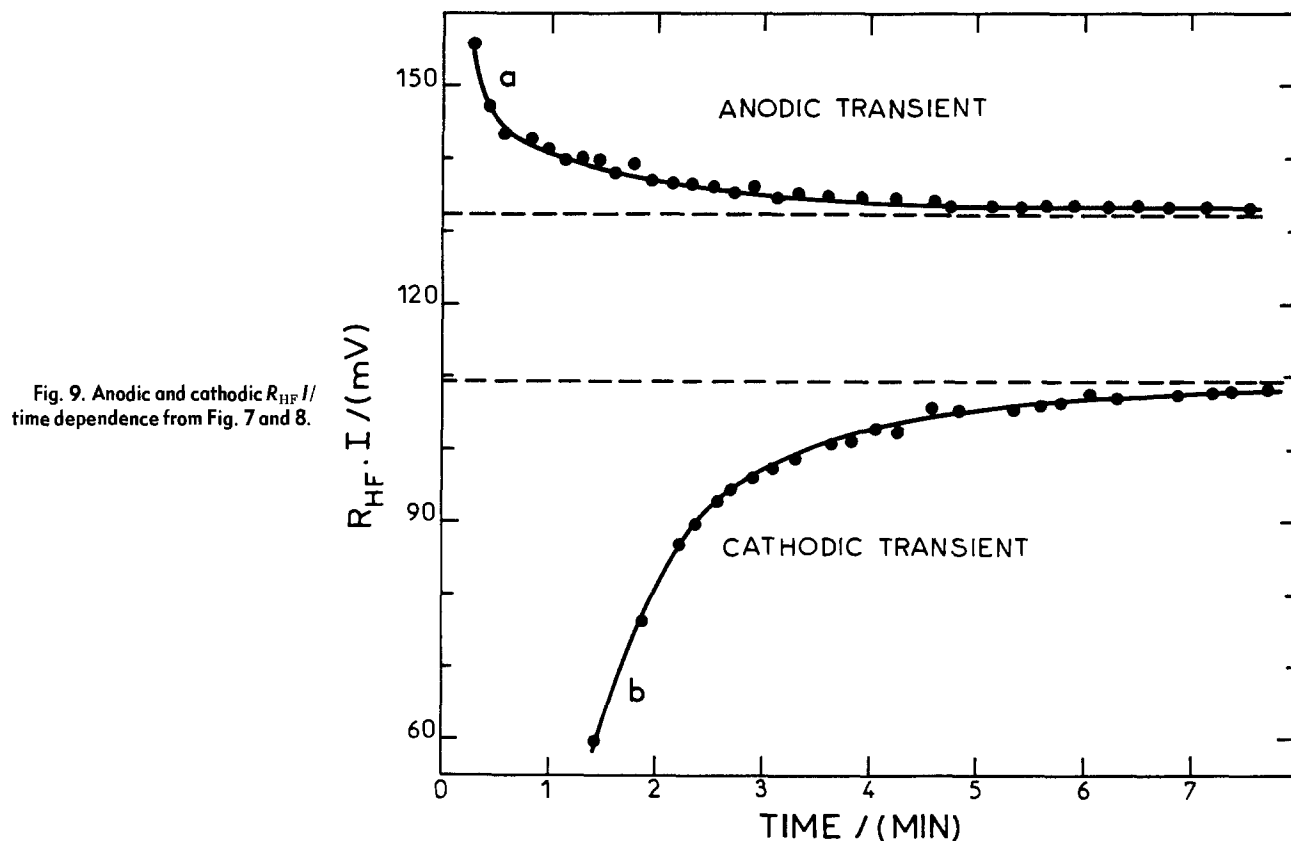


Fig. 9. Anodic and cathodic R_{HF}/I time dependence from Fig. 7 and 8.

Medium frequency domain.—The iron/acid interface polarized in the fully passive range exhibits an inductive loop in the medium frequency range. This behavior is observed only if the electrode is carefully protected against undermining attack between metal and insulating material (37).

The associated characteristic time constant τ can be defined by the frequency at the bottom of the inductive loop. The product $I_p\tau$ is potential dependent and goes through a minimum by $E = 0.6V$ for $1M H_3PO_4$. This minimum value is of the order of $70 \mu C \cdot cm^{-2}$ and was found to remain between 70 and $180 \mu C \cdot cm^{-2}$ for each composition and temperature investigated. This explains why the inductive behavior was not observed in $HClO_4$ solutions. In these solutions, the passive current is as low as $0.1 \mu A \cdot cm^{-2}$ and the characteristic frequency might fall at a fraction of millihertz. This inductive behavior was also observed on aluminum in an ammonium pentaborate-ethylen glycol solution (36) and is obviously equivalent to the overshoot mentioned in early studies of the transient response of Al and other valve metals. Its origin was thoroughly discussed in terms of bulk or surface relaxation. On the basis of impedance data, it was recently attributed to the buildup of a surface charge (36). It can be noticed that the inductive effect is not observed with Ni and thus might be related to an intermediate oxidation step in the film (37).

Low frequencies domain.—As shown in Fig. 3, the electrode impedance exhibits a capacitive branch in the low frequency domain. Similar to the behavior observed in the high and medium frequency ranges, this branch appears at higher frequencies for a higher passive current. Consequently, accurate measurements in this region are easier in phosphate media and at temperature greater than $25^\circ C$. The capacitance Γ calculated in H_2SO_4 and H_3PO_4 exhibits a slight frequency dependence. If $1/\Gamma^2$ is plotted as a function of frequency, a roughly linear relationships is found as shown in Fig. 10. The limiting capacitance at zero frequency does not depend much on experimental conditions. For instance, Γ changes only from 40 to $55 mF \cdot cm^{-2}$ when a temperature rise increases the current from 63 to $370 \mu A \cdot cm^{-2}$ in $1M H_3PO_4$ (Fig. 10).

FFT signal processing as applied to the transient response allowed one to investigate with better accuracy the frequency range below 1 mHz. Current responses to anodic and cathodic steps, shown in Fig. 11, are clearly

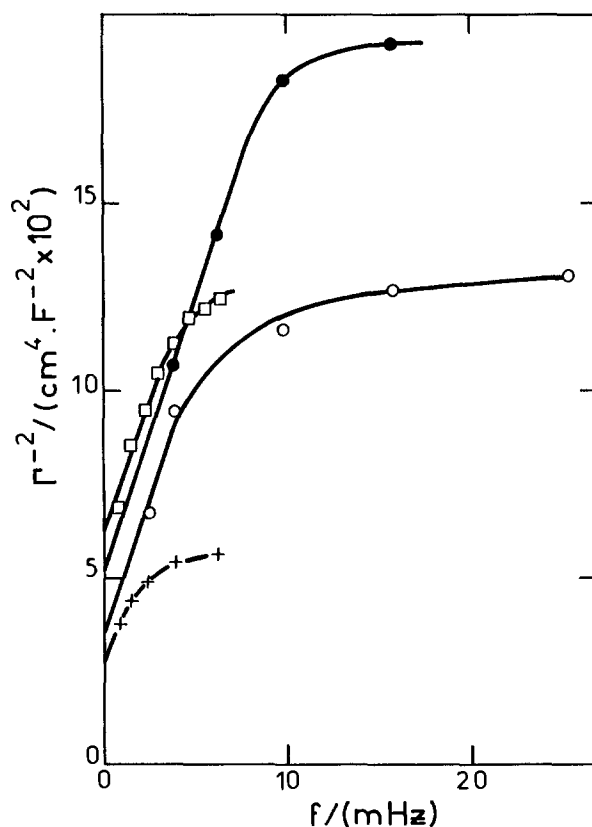


Fig. 10. Γ^{-2} /frequency dependence for various experimental conditions. $Fe/1M H_3PO_4$, $E = 0.65V$. \square , $25^\circ C$, $I_p = 63 \mu A \cdot cm^{-2}$. \bullet : $37^\circ C$, $I_p = 130 \mu A \cdot cm^{-2}$. \circ : $54^\circ C$, $I_p = 370 \mu A \cdot cm^{-2}$. $+$: $Fe/1M H_2SO_4$, $E = 0.4V$, $50^\circ C$, $I_p = 55 \mu A \cdot cm^{-2}$. Limiting zero frequency Γ values in $mF \cdot cm^{-2}$: 40.5, 44.3, 55.1, and 61, respectively.

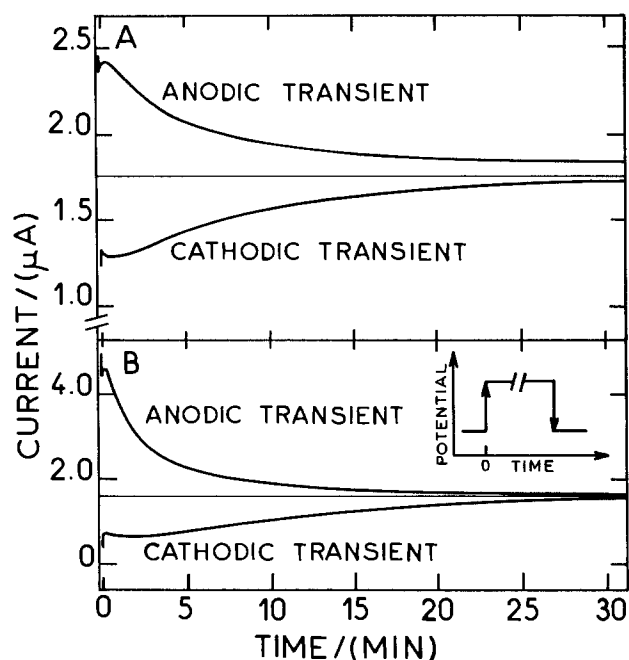


Fig. 11. Anodic and cathodic current/time transients resulting from potential steps. Fe/1M H₂SO₄, 25°C. $E = 0.6V$. A: $\Delta E = 0.03V$. B: $\Delta E = 0.10V$.

asymmetrical, even for amplitude as low as 0.03V. Even if linearity requirements are not completely fulfilled, it was verified that the mean value of the anodic and cathodic Nyquist loci reproduces accurately the complex impedance measured by ac signal at the same potential as proved by a comparison of Fig. 12 and 3a. The capacitance deduced from the cathodic Nyquist locus is practically independent of the frequency and close to 25 mF · cm⁻² in 1M H₃PO₄ at 25°C. In contrast, the anodic response yields a capacitance exhibiting a frequency dependence.

The physical origin of this low frequency branch is easily understood by emphasizing its strict connection with the existence of an infinite polarization resistance or, in other words, with the process ensuring a constant passive current in the steady state. Owing to the particular accuracy of FFT techniques in this frequency range (32), it can be concluded from the shape of the diagram in the low frequency range that diffusion is not the controlling process. According to the data obtained at high frequencies,

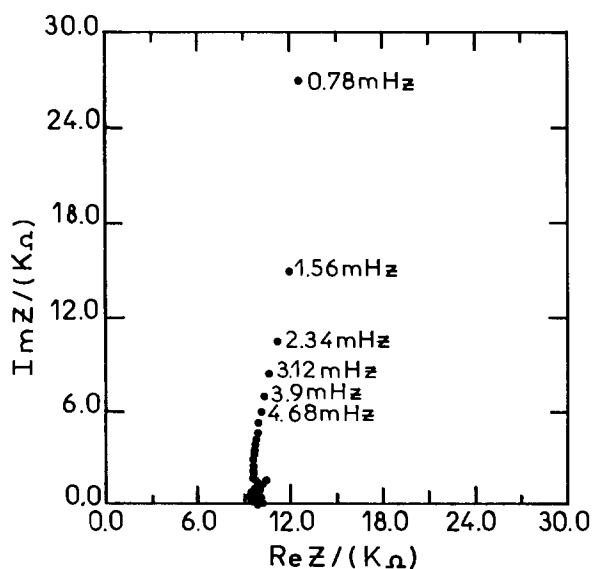


Fig. 12. Nyquist representation calculated by FFT processing of potentiostatic step experiments. The impedance is the mean value from a cathodic (0.7-0.6V) and an anodic (0.6-0.7V) response.

the electrode process can be described as a chemically dependent high field conduction mechanism. Consequently, the low frequency capacitance arises from the potential dependence of the film thickness, and it is worth discussing the value of Γ with respect to the amount of electricity stored in the film. Assuming a film composed of a trivalent iron oxide (specific gravity 5g · cm⁻³) and with a thickness of 35Å V⁻¹; this leads to a capacitance of ca. 3 mF · cm⁻², whereas Γ is approximately ten times greater. In other words, only one tenth of the alternating current is stored in the film, while the remaining component corresponds to a modulation of the dissolution current across the film. However, it is doubtful whether this ratio between dissolution and growth components remains independent of the frequency. Different responses in frequency dependence of Γ and possibly to the inductive behavior. This variation in frequency response is suggested by the fact that the diameter of the inductive loop is also approximately one-tenth of R_{HF} over the whole experimental conditions investigated.

Conclusion

Impedance analysis of passive iron permitted the separation of the transport properties in the film from the charge transfer at interfaces, on one hand, and the film growth, on the other hand.

A resistance obeying a linear dependence on the potential is found as expected from the existent theories. The charge transfer contribution is partially reversible as established from nonsteady-state experiments. A high field-assisted ion migration with an electric field of the order of 3 · 10⁶ V · cm⁻¹ or a thickness of ca. 35Å · V⁻¹ is corroborated.

The capacitive behavior observed in the low frequency range is related to film growth and allowed to estimate the ratio of the film forming current to the dissolution current under nonsteady states.

The passivation current depends on electrolyte composition through the charge carrier concentration in the film (pre-exponential term in the high field equation), whereas the film thickness seems to remain independent of the electrolyte investigated. On the whole, the electrode process can be described as a chemically dependent high field assisted ion migration. It is significant that the value of the passive current determines unambiguously the most important parameters involved in the characterization of the system.

Manuscript submitted Nov. 30, 1983; revised manuscript received April 24, 1984.

CNRS assisted in meeting the publication costs of this article.

REFERENCES

1. J. L. Ord, in "Fifth International Symposium on Passivity," p. 95, Société de Chimie Physique, Bombannes, France (1983).
2. Z. Sklarska-Smialowska and W. Kozłowski, in "Fifth International Symposium on Passivity," p. 89, Société de Chimie Physique, Bombannes, France (1983).
3. R. Dupeyrat, M. Froelicher, A. Hugot-le Goff, M. Masson, and C. Pallotta, in "Fifth International Symposium on Passivity," p. 101, Société de Chimie Physique, Bombannes, France (1983).
4. C.-T. Chen and B. D. Cahan, *This Journal*, **129**, 17 (1982).
5. H. Leidheiser, Jr., in "Passivity of Metal," R. P. Frankenthal and J. Kruger, Editors, p. 223, The Electrochemical Society Corrosion Monographs Series, Princeton, NJ (1978).
6. J. L. Ord, in "Passivity of Metal," R. P. Frankenthal and J. Kruger, Editors, p. 273, The Electrochemical Society Corrosion Monographs Series, Princeton, NJ (1978).
7. N. Sato, K. Kudo, and T. Noda, *Z. Phys. Chem. N.F.*, **98**, 217 (1975).
8. J. L. Ord and P. J. Desmet, *This Journal*, **113**, 1258 (1966).
9. K. J. Vetter and F. Gorn, *Electrochim. Acta.*, **18**, 321 (1973).

10. C. Wagner, *Ber. Bunsenges. Phys. Chem.*, **77**, 1090 (1973).
11. K. J. Vetter, *Electrochim. Acta*, **16**, 1923 (1971).
12. K. J. Vetter and F. Gorn, *Werkst. Korros.*, **21**, 703 (1970).
13. J. L. Ord and J. H. Bartlett, *This Journal*, **112**, 160 (1965).
14. K. J. Vetter, *ibid.*, **110**, 597 (1963).
15. K. J. Vetter, *Z. Elektrochem.*, **62**, 642 (1958).
16. K. G. Weil, *ibid.*, **59**, 711 (1955).
17. K. J. Vetter, *ibid.*, **58**, 230 (1954).
18. K. J. Vetter, *Z. Phys. Chem.*, **202**, 1 (1953).
19. U. Stimming and J. W. Schultzze, *Ber. Bunsenges. Phys. Chem.*, **80**, 1297 (1976).
20. D. Wheeler, B. D. Cahan, C. T. Chen, and E. B. Yeager, in "Passivity of Metals," R. P. Frankenthal and J. Kruger, Editors, p. 546, The Electrochemical Society Corrosion Monographs Series, Princeton, NJ (1978).
21. B. D. Cahan and C.-T. Chen, *This Journal*, **129**, 474 (1982).
22. M. D. Reingeverts, O. S. Andreeva, and A. M. Sukhotin, *Elektrokhimiya*, **15**, 972 (1979).
23. A. M. Sukhotin and O. S. Andreeva, *ibid.*, **14**, 208 (1978).
24. C. Y. Chao, L. F. Lin, and D. D. Macdonald, *This Journal*, **128**, 1187 (1981).
25. C. Y. Chao, L. F. Lin, and D. D. Macdonald, *ibid.*, **129**, 1874 (1982).
26. S. Haruyama and T. Tsuru, in "Passivity of Metals," R. P. Frankenthal and J. Kruger, Editors, p. 564, The Electrochemical Society Corrosion Monographs Series, Princeton, NJ (1978).
27. M. Baddi, C. Gabrielli, M. Keddum, and H. Takenouti, "Passivity in Metals," R. P. Frankenthal and J. Kruger, Editors, p. 625, The Electrochemical Society Corrosion Monographs Series, Princeton, NJ (1978).
28. I. Epelboin, C. Gabrielli, M. Keddum, and H. Takenouti, *C. R. Acad. Sci.*, **276**, 146 (1973).
29. I. Epelboin, M. Keddum, and Ph. Morel, in "Proceedings of the Third International Congress on Metallic Corrosion," Vol. 1, p. 110, Moscow (1969).
30. R. D. Armstrong, *J. Electroanal. Chem.*, **34**, 387 (1971).
31. R. D. Armstrong and K. Edmondson, *Electrochim. Acta*, **18**, 937 (1973).
32. C. Gabrielli, F. Huet, M. Keddum, and J. F. Lizee, *J. Electroanal. Chem.*, **138**, 201 (1982).
33. S. H. Glarum and J. H. Marshall, *This Journal*, **126**, 424 (1979).
34. C. Gabrielli, M. Keddum, H. Takenouti, V. Q. Kinh, and F. Bourelier, *Electrochim. Acta*, **24**, 61 (1979).
35. M. Keddum, R. Oltra, J. C. Colson, and A. Desestret, *Corros. Sci.*, **23**, 441 (1983).
36. H. J. De Wit, C. Wijenberg, and C. Crevecoeur, *This Journal*, **126**, 779 (1979).
37. M. Keddum, J. F. Lizee, C. Pallotta, and H. Takenouti, in "Fifth International Symposium on Passivity," p. 51, Société de Chimie Physique, Bombannes, France (1983).

Cyclic Voltammetric Studies and Caustic Cracking of Steel at Various Temperatures

Andrzej Wieckowski,¹ Edward Ghali,* and Huy Ha Le

Department of Mining and Metallurgy, Laval University, Laval, Quebec, Canada G1K 7P4

ABSTRACT

Cyclic voltammetric studies were carried out for an iron electrode and for pressure vessel quality steel A516 in 1 and 7.73M sodium hydroxide solutions as a function of temperature. Cyclic voltammograms for strained electrodes of steel were also made. The stress corrosion cracking susceptibility was measured by the slow strain rate method. The examined temperature range was between 25° and 105°C. A correlation was found between the electrochemical behavior of unstrained electrodes (cyclic voltammograms) and the susceptibility to caustic cracking. A critical zone of temperatures, above which cyclic voltammograms are sensibly different and stress corrosion cracking occurs, was obtained.

The resistance of steel to corrosion and stress corrosion cracking (SCC) in caustic soda solutions is an important issue in various industrial applications, including the electrolysis and dissolution of minerals performed in steel containers. The need for corrosion prevention, as well as the commercial interest in iron alkaline batteries, stimulated numerous investigations of the electrochemical behavior of iron in alkaline media. Surveys of the pertinent papers are available (1, 2). Most of the studies, especially those under single-scan or cyclic voltammetry conditions, have been carried out at normal temperatures, but some high temperature investigations reported up-to-date indicate that the i-E profiles obtained at low and high temperatures are different (3-5). No systematic study of the effect of temperature on the cyclic voltammetry of iron electrode has been made.

It is worthwhile to add that the practical examples of failures in sodium hydroxide solution have occurred largely above room temperature. A statistical analysis of industrial failures done by Schmidt *et al.* (6) showed that 5% NaOH solution caused stress corrosion cracking above 95°C and a 50% NaOH solution above 40°C. A collective survey on the caustic cracking of mild steel, which deals with more recent data (7), indicates that no cracks below ca. 50°C were reported by industrial sources. The examination of other results (8, 9) for the caustic cracking of steel as a function of temperature and concentration of

the sodium hydroxide solution shows that the limits of the caustic danger zone may be varied by a number of other factors, especially environmental and metallurgical ones.

In this study, the effect of temperature on the cyclic voltammograms of an iron and a steel in the range of 25°-105°C were studied, the upper limit depending on the concentration of the NaOH solution. Also, stress corrosion cracking susceptibility of the steel was studied employing the slow strain rate method at different temperatures. Since temperature is dominant factor in SCC susceptibility, it is important to examine its effect on the electrochemical behavior and the relation of this to cracking.

Experimental

The experiments were carried out in a two-compartment, all-Teflon cell, equipped with circulating system (all-Teflon, Cole-Palmer pump, C-7149-20). The reference electrode compartment (saturated calomel electrode) and the main cell were connected by a thin bridge filled with the supporting electrolyte and terminated with a Teflon Luggin capillary. The tip of the capillary was situated less than 1 mm from the center of the working electrode. The counterelectrode was a rolled platinum wire, 0.5m long, installed in the main cell. The working electrode (0.28 cm²) was made of Teflon-embedded pure iron (ferrovac) of the following composition (in percentage); C(0.007), Mn(0.001), Si(0.006), S(0.007), P(0.002), Ni(0.04), N(0.003), Cr(0.01), Mo(0.01), and Cu(0.014).

The electrode was polished with emery paper of various grades (from 100 to 600), followed by rinsing in distilled

* Electrochemical Society Active Member.

¹ On leave from Department of Chemistry, University of Warsaw, Warsaw, Poland. Present address: Department of Chemistry, University of California, Santa Barbara, California, 93106.

water. After mounting in the electrochemical cell filled with the deaerated test electrolyte at a constant temperature, the electrode was cathodically activated at -1.1V for 5 min. The electrolyte was deaerated in the thermostated container (2 liter capacity) of the circulating system by prepurified argon. The temperature of the solution in the cell was maintained with an accuracy of $\pm 0.2^\circ\text{C}$. All potentials are given with respect to the normal hydrogen electrode.

The slow strain-rate tests were conducted with an MTS machine. The test cell was similar to that used for cyclic voltammetry experiments, with the exception that it was possible to incorporate the working steel electrode tension specimens, machined according to ASTM standards. The steel A516 (pressure vessel quality) of the following composition (in percentage) was used in these experiments

C	Mn	P	S	Si
0.24	1.15	0.008	0.007	0.25
Cu	Ni	Cr	Mo	Sn
0.044	0.025	0.033	0.004	0.002

The caustic solutions employed were 1 and 7.73M. Preliminary results showed that the more susceptible strain rate for SCC was $2.6 \times 10^{-6} \text{ s}^{-1}$. 10^{-5} s^{-1} gave less SCC, but these two strain rates were employed to examine the effect of temperature. The elongation of the specimens was measured by the use of Gage marks on the reduced section of the specimen. Also, the reduction in area was determined for every sample by measuring the diameter of the reduced section before and after testing. The surface of the specimen was well cleaned with acetone and rinsed with distilled water. After inserting in the test cell, the electrode was cathodically polarized at -1.1V for 5 min. The temperature of the electrolyte in the cell was controlled by a Chromel-Alumel thermocouple to an accuracy of $\pm 2^\circ\text{C}$. Working electrodes (0.28 cm^2) from A516 steel were also machined for cyclovoltammetric studies.

Results and Discussion

Cyclic voltammetry studies.—The cyclic voltammetry studies were made for different scan rates from 5 to 500 mV s^{-1} . Six scan rates were examined in this region, since the voltammograms have almost showed the same shape, only a noble shift of the peak potential and an increase in the peak current as a function of the increase in the scan rate was observed, the results presented here are limited to the rate of 50 mV s^{-1} , which is considered as an average speed. Figure 1 shows the evolution of the voltammograms recorded at 25°C : approximately 30 cycles were needed to obtain a stable profile. The evolution of the curves (indicated by the directions of arrows) as well as the initial (broken line) and the final shape of the potentiodynamic plots are in agreement with the results of other authors (1, 3, 10). Similar evolution of the i - E profiles was observed at 35°C , but the current density of peak III (Fig. 1) was ca. 30% lower. It was also noted that in the case of peaks III and V, a certain resemblance is present especially in the formation of a shoulder as a sequence of successive cyclation (shoulders B and B', Fig. 1).

Figure 2 shows the voltammetric behavior of iron at higher temperatures. At 45°C , the evolution of the voltammograms was still observed, but the upward shift of peak III and V and the downward shift of peak VI were very slow. It should be noted that peak III which prevailed at the lower temperatures is reduced substantially. At 55°C , peaks III and V practically disappear. Moreover, only a few cycles were needed to obtain stable conditions (at $t > 55^\circ\text{C}$, no significant difference was found between the first and the stable profiles). Peak II systematically increases with temperature (5) and at $t > 55^\circ\text{C}$ predominates over the other anodic peaks. At 95°C , the potentiodynamic plots are similar to that obtained by Macdonald and Owen in 1.0M LiOH at 200°C (3).

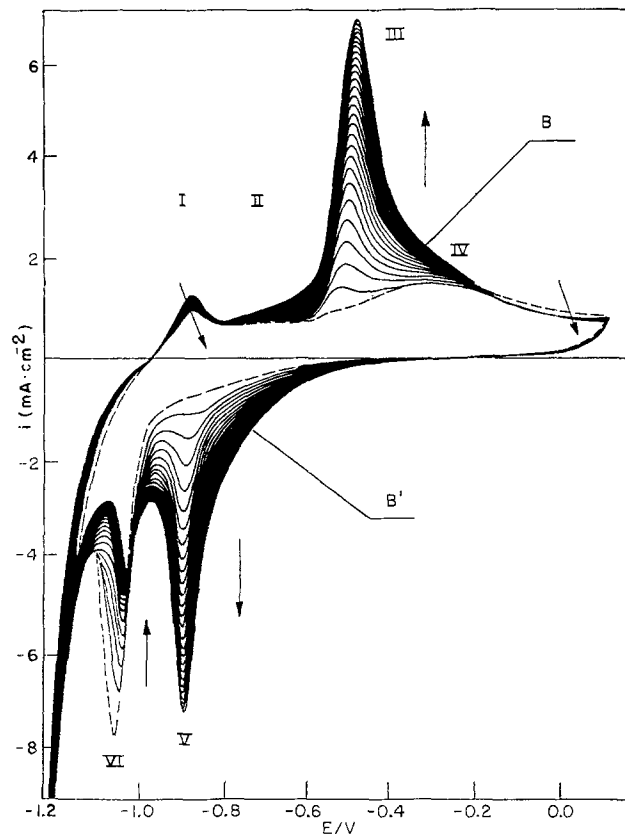


Fig. 1. The cyclic voltammetry of iron electrode at 25°C in 1M NaOH : the first scan (broken line) and subsequent profiles are shown. The shift of particular peaks (denoted by Roman figures) is indicated by arrows. The attention on anodic shoulders of peak III and peak V is drawn by letters B and B', respectively. Scan rate: 50 mV s^{-1} . Electrode area: 0.28 cm^2 .

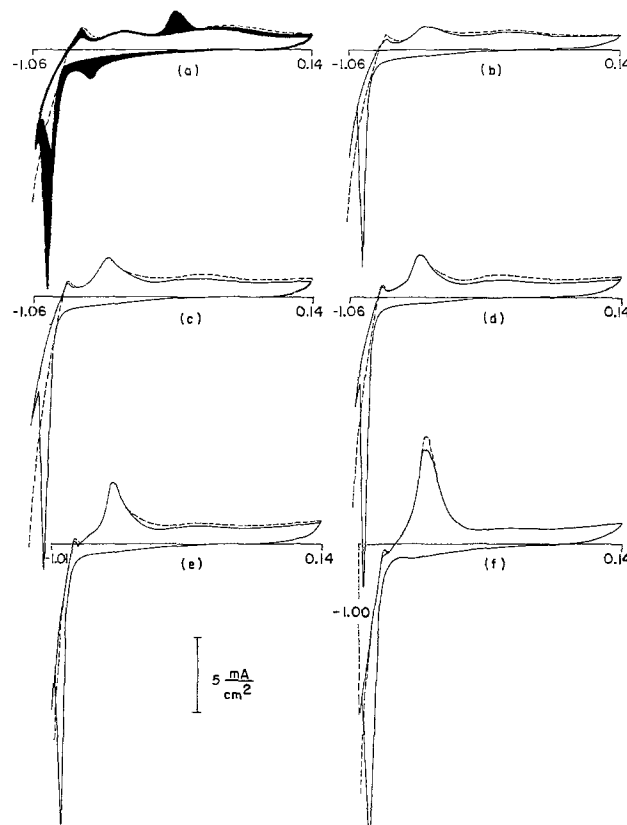


Fig. 2. The cyclic voltammograms of iron electrode in 1M NaOH at various temperatures: (a) 45° , (b) 55° , (c) 65° , (d) 75° , (e) 85° , and (f) 95°C . First scans are indicated by broken lines, stable profiles by solid lines. Scan rate: 50 mV s^{-1} . Electrode area: 0.28 cm^2 .

Comparison of the voltammograms obtained at low ($t < 45^\circ\text{C}$) and high temperatures shows that the dissolution-precipitation mechanism (11-12) which most probably accounts for the formation and evolution of peaks III and V, is no longer operating above 55°C . It is also clearly seen that peak II should be attributed to the active-passive behavior of iron, the inference being in agreement with that of Armstrong and Baurhoo (5). As shown by Parkins (13), the potential region of caustic cracking of mild steel coincides with that of the active-passive transition of the steel, so that cracking susceptibility should be by consideration of peak II, obtained at low and high scan rates, rather than that of peak III, as it has incorrectly been suggested earlier (14).

Similar voltammetric experiments carried out with A516 steel, showed the same tendency as in Fig. 2, but peaks III and V practically disappeared at 65°C rather than at 55°C with iron.

The observation concerning the temperature-dependent iron oxide (hydroxide) redox couple represented by peaks III and V, with the equilibrium potential situated exactly in the region of the maximum susceptibility of SCC (13) (Fig. 1), is concluded to be relevant to the discussion of a critical temperature for SCC phenomena (13). The critical temperature of 50°C , below which no stress corrosion cracking occurs under industrial conditions, coincides with a dramatic decrease in the tendency for the formation of peaks III and V on iron and with a substantial decrease on A516 steel. Therefore, it seems that the formation of a passive layer by the dissolution-precipitation mechanism below a critical temperature is responsible for a reparation mechanism in the initial stages of crack formation.

One of the proposed mechanisms of SCC can be: crack growth arises from an enhanced anodic dissolution reaction on oxide-free surfaces which have been created by the rupture of the passivating oxide films as a result of the localized plastic strain at the tip of a SCC. The crack advances by a rapid anodic dissolution and subsequent passivating film formation. This film is then ruptured by further plastic strain and the process repeats. This suggested that the mechanism should show transgranular propagation of the fracture. Fractographic studies confirmed this aspect; however, initiation and early stages of propagation showed clearly intergranular features which can be interpreted in terms of the pre-existing path theory for initiation and early stages of propagation.

Effect of temperature and concentration.—It is interesting to compare here the voltammograms of unstrained and strained electrodes as a function of temperature and concentration.

In 1M NaOH, for temperatures below 65°C , strained specimens in the elastic range of A516 steel gave almost the same pattern of voltammograms as that obtained with stable electrodes: the dominating peak was peak III. In presence of plastic deformation, peak II was well identified and the peak current is enormously increased, while peak III was increased by a factor of 3 and remained the most important. For temperatures above 65°C , no major difference was observed between the evolution of cyclic voltammograms for unstrained and elastic deformed electrodes; as in the case of stable electrodes, we noted the disappearance of peak III in spite of the increase of peak II, and this latter was not sensibly changed because of an elastic deformation. In the plastic deformation region, the peak current II was even doubled. This means that plastic deformation, like temperature, has an important influence on the active-passive behavior of steel, which is believed to be closely related to SCC phenomena.

For more concentrated solutions of NaOH (7.73M, for example), the observations made above for stable and deformed (elastic or plastic) electrodes were verified. Below 65°C , in this concentrated solution peak III current was decreased by a factor of 2; meanwhile, peak II current was double or even tripled with respect to that obtained in 1M; however, the peak III remained higher than peak

II. It can be stated that the difference in height between the peaks current II and III was reduced as a function of the increase in concentration of NaOH. This was true for stable or strained (elastic and plastic) specimens. At temperatures above 65°C , the tendency in 7.73M NaOH was the same as that in 1M NaOH: peak II increased while peak III disappeared. The evolution of peak II was very important with a plastic deformation (doubled) like that found in dilute solution of NaOH (1M).

The combined effect of concentration and temperature have, as it is expected, an influence on the peaks current, i.e., on the mechanisms of caustic embrittlement. An increase in concentration from 1 to 7.73M and an increase in temperature from 80° to 105°C led to an increase of peak II by a factor of 1.5. This was appreciable, since peak II was already important at 80°C . This was observed for stable or strained electrodes.

Slow strain-rate SCC studies.—Correlation between the voltammetric behavior of iron at different temperatures (Fig. 2) and temperature dependent caustic cracking susceptibility of A516 steel (Fig. 3 and 4), which validates the above hypothesis, will be shown below by using slow strain-rate technique.

The potential of maximum susceptibility of A516 steel to stress corrosion cracking (13) in 7.73M NaOH was found to be -733 mV. This potential was imposed during slow strain-rate ($2.6 \times 10^{-6} \text{ s}^{-1}$ and 10^{-5} s^{-1}) experiments at different temperatures. The results obtained in 7.73M NaOH are shown in Fig. 3. For both strain rates, the reduction of the surface area (ROA) of the specimen decreased (the susceptibility of A516 steel to SCC increased) with temperature. The first monotonic drop in ROA is followed by a distinctive downward curvature which leads to a new ROA vs. T line. In effect, the overall plot may be approximated by two straight lines with different slopes, the second (high temperature one) being more negative than the first. Similar results were obtained in 1.0M NaOH, but the SCC effects were less pronounced and the curvature of the ROA vs. temperature plot was less marked.

It should be noted that the intersection of the ROA vs. T straight lines (the change of the slope) occurs in the temperature region where the peaks III and V practically dis-

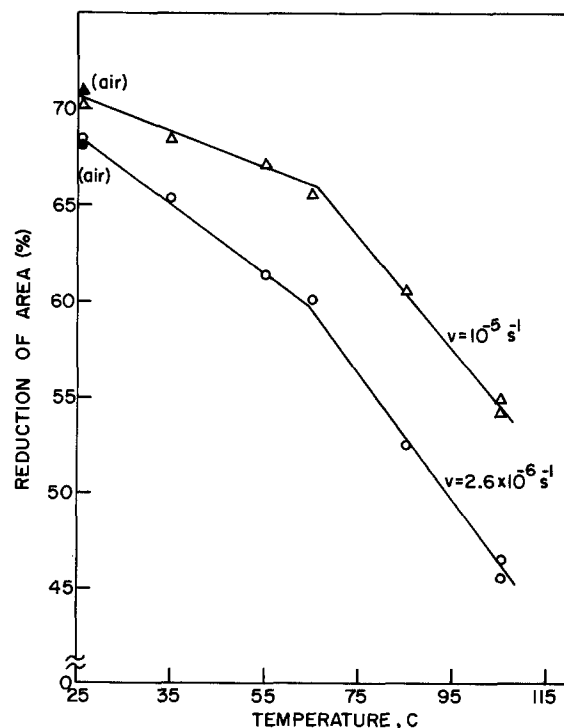


Fig. 3. Effect of temperature on the reduction of area of steel A516 (PVQ) in 7.73M NaOH. Potential imposed $E = -733$ mV. v means the rate of deformation.

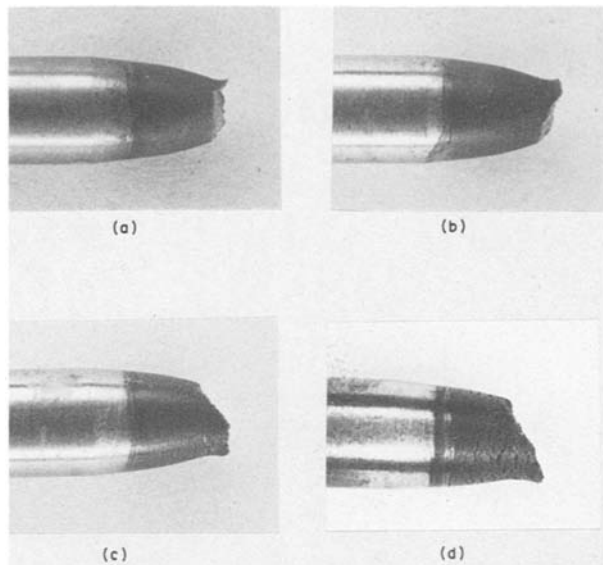


Fig. 4. Portion of Gage length of steel A516 (PVQ) at fracture location in 7.73M NaOH. Potential-imposed E : -733 mV. Rate of deformation: $2.6 \times 10^{-6} \text{ s}^{-1}$. (a): $T = 35^\circ\text{C}$. (b): $T = 55^\circ\text{C}$. (c): $T = 85^\circ\text{C}$. (d): $T = 105^\circ\text{C}$.

appeared from the voltammograms of the nonstrained electrodes (Fig. 2 and test). Therefore, the inference made above that the mechanism of the electrochemical contribution to SCC is different below and above a critical temperature ($50^\circ\text{--}65^\circ\text{C}$) is substantiated not only by the correlation of the industrial vs. voltammetric data [Ref. (6) and (7) and Fig. 2], but also by the interdependence of the SCC laboratory test results and the voltammetric behavior of iron (Fig. 3 vs. Fig. 2).

The reduction of the surface area of specimens investigated in NaOH solutions below 65°C , and especially at 25°C , was close to that observed in air, which indicates the virtual absence of SCC.

Figure 4 shows different types of fractures of A516 steel in 7.73M NaOH solution. For temperatures below 65°C , the ductile tensile fracture was the classic "cup and cone" failure, with considerable necking characteristic of plastic deformation prior to the failure. Similar fractures were observed during tests carried out in air. As the temperature increased ($t > 65^\circ\text{C}$), numerous secondary cracks in the reduced section were seen (Fig. 4). At 105°C , those cracks, which are indicative of severe SCC failure, became deeper and wider. Decrease of the strain rate from 10^{-5} to $2.6 \times 10^{-6} \text{ s}^{-1}$ caused a measurable increase in the number of the secondary cracks as well as contributed to the larger reduction of the surface area and of the elongation of the specimens.

Conclusions

1. No major differences were observed in the voltammograms of unstrained and elastic-strained electrodes. With plastic deformation the shape of the voltammograms remained the same, but peak II is wider for strained electrodes, especially at high temperatures and concentrated solutions.

2. The temperature has an influence on the evolution of the cyclovoltammograms of iron in caustic solutions. With an increase in temperature, the peak II increased while peak III decreased, but this latter stayed the most important peak for temperatures below a critical one (55°C for iron and 65°C for A516 steel). Above this critical zone of temperatures, peak III disappeared and that is accompanied by a marked evolution of peak II.

3. The increase in concentration of caustic solutions gave the same influence on the peaks II and III as the elevation of temperature. The combined influence of temperature and concentration showed that peak II was quite important at concentrated solutions of NaOH at 105°C .

4. There is a certain correlation between the cyclic voltammogram of steel (strained or not) and its resistance to caustic cracking. A critical region of temperatures is observed for the examined steel where the cyclic voltammograms showed disappearance of the peaks III and V and broadening of the anodic peak II in the same time of the appearance of fragile cracking accompanied by surface reduction, elongation decrease, and secondary cracks. The absence of peak III and V and the increase of peak II above a critical region of temperatures marked the susceptibility of the metal to SCC.

Acknowledgments

The facilities and assistance provided by the Industrial Materials Research Institute of the National Research Council of Canada, Montreal, and financial support from Supply Services Canada are gratefully acknowledged.

Manuscript submitted Sept. 8, 1983; revised manuscript received March 16, 1984.

Université Laval assisted in meeting the publication costs of this article.

REFERENCES

1. R. S. Schrebler Guzman, J. R. Vilche, and A. J. Arvia, *Electrochim. Acta*, **24**, 395 (1979).
2. R. S. Schrebler Guzman, J. R. Vilche, and A. J. Arvia, *J. Appl. Electrochem.*, **11**, 551 (1981).
3. D. D. Macdonald and D. Owen, *This Journal*, **120**, 317 (1973).
4. G. J. Bignold, *Corros. Sci.*, **12**, 145 (1972).
5. R. D. Armstrong and I. Baurhoo, *J. Electroanal. Chem. Interfacial Electrochem.*, **34**, 41 (1972); *ibid.*, **40**, 325 (1972).
6. H. W. Schmidt, P. J. Gegner, C. Heinemann, C. F. Pogacar, and E. H. Wyche, *Corrosion*, **7**, 295 (1951).
7. G. Fulford, "Review of Data on Caustic Cracking of Mild Steel," Alcan Research Laboratories, Kingston, Ontario, Canada (1982).
8. A. A. Berk and W. F. Waldeck, *Chem. Eng.*, **57**, 235 (1950).
9. C. D. Weir, *Cent. Belge Étude Doc. Eaux*, **20**, 87 (1953).
10. D. Geana, A. A. Miligy, and W. J. Lorenz, *J. Appl. Electrochem.*, **4**, 337 (1974).
11. L. Ojefors, *This Journal*, **123**, 1691 (1976).
12. T. G. Stepina, A. Z. Iofa, E. V. Kosatkin, V. A. Shepelin, and V. A. Safonov, *Elektrokhimiya*, **16**, 1884 (1980).
13. R. N. Parkins, in "SCC and Hydrogen Embrittlement of Iron Base Alloys," NACE, France, 1973, National Association of Corrosion Engineers, Houston, TX (1976).
14. G. Bruni, S. Casadio, and G. D'Alessandro, *Electrochim. Acta*, **22**, 673 (1977).

Anomalous Electrochemical Oxidations at an Electrodeposited Polycarbazole Electrode

R. N. O'Brien

Department of Chemistry, University of Victoria, Victoria, British Columbia, Canada V8W 2Y2

N. S. Sundaresan and K. S. V. Santhanam

Tata Institute of Fundamental Research, Bombay 400 005, India

ABSTRACT

The electrodeposition of polycarbazole by passing a constant current through a solution of carbazole in *N,N*-dimethylformamide containing 0.1M tetra-*n*-butyl ammonia perchlorate has been followed using multiple beam laser interferometry. The deposited film was used as an electrode in the electrochemical oxidations of Fe^{2+} , $\text{Fe}(\text{CN})_6^{4-}$, and hydroquinone (H_2Q). While the oxidation of H_2Q proceeds in a diffusion-controlled manner, the others show interesting differences.

In previous papers, we reported (1, 2) following the deposition of a relatively thick polypyrrole layer on gold by laser interferometry. The fringe patterns yielded refractive index gradients which were easily converted to concentration-time/distance profiles. The Nernstian boundary layer thickness becomes obvious and measurable, as does, from its growth, the progress and path of electrolysis.

In continuation of this type of approach to polymer-coated electrodes, we have investigated the electrodeposition of polycarbazole (another of the depositable conducting polymers) using multiple beam laser interferometry to study the behavior of the electrodeposited film as an electrode material. For this purpose, the electrochemical oxidations of Fe^{2+} , $\text{Fe}(\text{CN})_6^{4-}$, and hydroquinone (H_2Q) were carried out at a bare platinum surface and also on a polycarbazole film deposited on the platinum. The choice of electroactive materials was based on consideration of the charge on the ions or molecule. At the film-covered electrode, the oxidation of charged ions produces concentration-distance or concentration-time profiles showing significant deviation from those of the bare electrode. The above profiles for H_2Q show very little deviation at the two electrodes. These deviations have been analyzed in terms of permeability of the electronically conducting film.

Experimental

The experiments were carried out in a Fabry-Perot Interferometer giving Fizeau-type multiple-beam-wedge fringes, which is similar in design to cells previously reported (3, 4). The cell was 1.39 mm thick, and the electrodes, which were made of platinum, were separated by 6 mm. The electrodes were made by sputtering platinum on semicircular glass disks (3 cm long and 1.3 cm radius). The disks were soaked in chromic acid for about 4h to remove grease, etc. They were then washed with water and alcohol. The curved regions and the flat portions of the plates were covered with cellophane tapes, leaving only the long side of the disk to receive the sputtered platinum. To make electrical contact to the platinum, a small quantity of silver epoxy was painted at one of the edges of the sputtered disks. The thickness of the platinum layer on the glass disk was 100Å.

The experimental arrangement consisted of a Spectra-Physics Model 122 He-Ne single-mode laser as light source, a Sony Model AVC-3210 video camera, a Sony AV-3650 half-inch video recorder, and a 26 in. monitor. The interferometer was mounted on a brass support between the pole pieces of the electromagnet.

Electrodeposition of polymers was carried out galvanostatically at several c.d.'s: 0.10 mA cm⁻², 0.55 mA cm⁻², 1.10 mA cm⁻², 1.52 mA cm⁻², 3.20 mA cm⁻², and 7.6 mA cm⁻². The fringe system was recorded and analyzed at 30,

60, 120, 180, 240, 360, and 900s of electrolysis, and the complete experiment was video taped for replay and examination.

N,N-dimethylformamide (DMF) was obtained from MCB (ACS reagent-grade) and was used as received. Tetra-*n*-butyl ammonium perchlorate (South Western Analytical Chemicals) was dried under vacuum for 24h before use. The hydroquinone (J. T. Baker) sample was recrystallized from hot water before use. FeSO_4 and $\text{K}_4\text{Fe}(\text{CN})_6$ were of analar-grade chemicals. Double distilled water was used in all the experiments.

The refractive index of the solutions was measured using a Bausch and Lomb precision Abbe refractometer thermostated at 25°C.

The electrodeposition (5) of polycarbazole was carried out by passing a constant current through 60 mM carbazole solution in DMF containing 0.1M tetra-*n*-butyl ammonium perchlorate with the anode and cathode positioned in a vertical (V-position) configuration. The deposit was washed with acetone and air dried before use. For interferometric studies, the cell is filled with about 2 ml of the solution after mounting the electrodes in the desired configuration.

All the experiments reported here were carried out in a deep-vertical (V) or cathode over anode (C/A) configuration.

Results and Discussion

Electrodeposition of polycarbazole.—The electrochemical oxidation of carbazole at a platinum anode produces a golden yellow polymeric film of polycarbazole on the electrode at c.d.'s of about 0.50 mA cm⁻². Figure 1 shows the impressed voltage vs. current density plot, and it reveals a plateau from 0.50 to 2.50 mA cm⁻². The deposition of the polymer was also carried out by raising the c.d. beyond 2.50 mA cm⁻², but it produces deleterious effects on the film—it easily peels off the electrode. The deposit obtained at these higher c.d.'s has purple streaks on the upper middle portions of the electrode. This can be prevented by applying a magnetic field during the deposition process. The film thickness has been varied by controlling the duration for which the electrolysis was carried out. All the electrochemical experiments reported here were carried out by controlling the surface excess at 7.24 μmol cm⁻² giving a nominal thickness of 0.25 mm.

The deposition of the polymer was followed by multiple beam laser interferometry. Figure 2 shows the interferogram obtained during an electrolysis at 0.58 mA cm⁻². A smooth downturn of the fringes was observed at the anode indicating a decrease in refractive index of the medium in that region. At this electrode the oxidation of carbazole occurs to produce a cation ($n = 1$), which upon polymerization produces the film (6) and a decrease in concentration and refractive index. The complementary

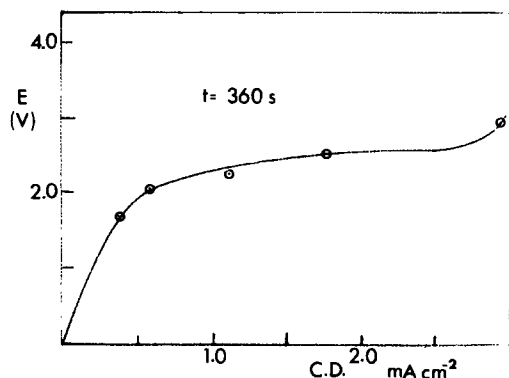


Fig. 1. Potential-current plot for the electrodeposition of polycarbazole at a platinum electrode. The voltage was measured at 360s of electrolysis upon passing a constant current.

reaction at the cathode (during the above electrolysis) was the reduction of carbazole to its anion radical ($n = 1$) (7). Since the anion radical is known to react rapidly with the medium to regenerate carbazole, the refractive index of the medium in this region was not significantly altered during the electrolysis except at the highest c.d.'s.

Since the deposition of the polymer occurred at the anode, the fringes at this electrode have been analyzed in detail. The fringe shift (F) during this deposition varied linearly at the electrochemically active surface with the square root of electrolysis time suggesting a diffusion-controlled oxidation as expected from "Sand's behavior" (8) (see subsequent discussion). This linearity in F vs. \sqrt{t} breaks down at c.d.'s $> 2.5 \text{ mA cm}^{-2}$ because of the onset of convection in the electrochemical cell. A plot of fringe

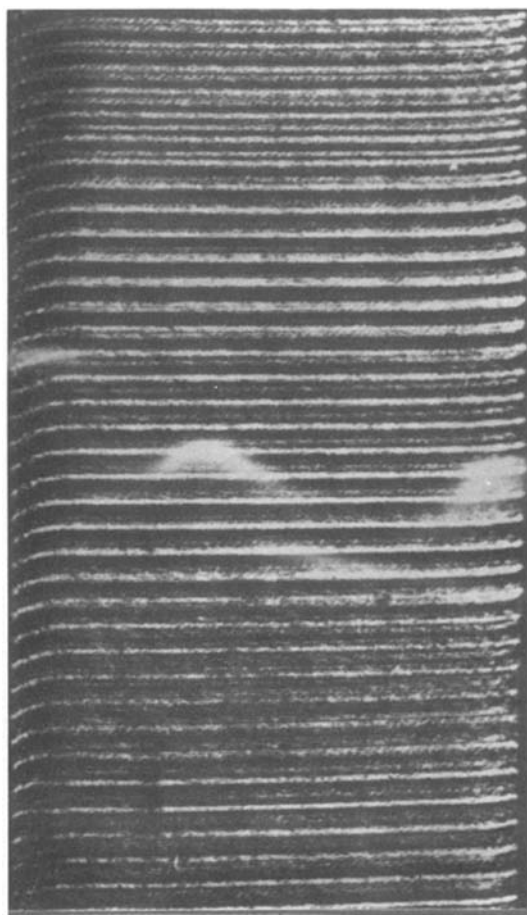


Fig. 2. The interference patterns observed at the anode during the electrolysis of 60 mM carbazole in N,N -dimethylformamide containing 0.1M tetra- n -butyl ammonium perchlorate. The fringe pattern was recorded at 420s. Left side is the cathode and right side is the anode.

shift as a function of c.d. at two selected periods of electrolysis shows the pattern in Fig. 3. In the higher c.d. region, the fringes are not well defined beyond 30s of electrolysis. At these c.d.'s, the deposits on the electrode were brittle. The convective flow which occurs during the deposition was also followed using holographic interferometry (9). This flow resulted in violet streaks appearing on the yellow deposits. The origin of the color is not clear, but it may be due to the free radical's getting trapped on/in the yellow polymer.

The deposition of the polymer was also conducted in magnetic fields of 1.0, 3.0, and 6.0 kG with a view to obtaining smooth deposits (10). The interferometric fringes were smoother in the presence of a magnetic field, and the deposition of the polymer was free from violet streaks. Scanning electron micrographs (SEM's) were taken of the samples obtained in the magnetic field. Figure 4 shows the SEM picture obtained in a 6.0 kG magnetic field.

The interferometric fringes in the magnetic field were compared with the zero field patterns. The concentration-distance profiles during electrolysis are shown in Fig. 5. The negative ΔC values at zero field indicates the existence of strong convection in the cell.

Behavior of polycarbazole electrode towards electrolytic oxidations.—The Pt/polycarbazole electrode response towards the oxidation of H_2Q was examined in aqueous sulfuric acid (1M) and in phosphate buffers of pH 6.0. Galvanostatic electrolysis produces interferometric patterns of the conventional types (11, 12), with the fringes at the anode showing a downturn due to decrease in refractive index in that region. The growth of the Nernst diffu-

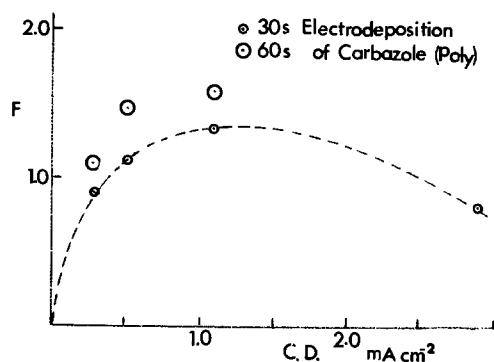


Fig. 3. The maximum fringe shift vs. current density plot during the electrodeposition of polycarbazole. The durations of the electrolysis are 30 and 60s.

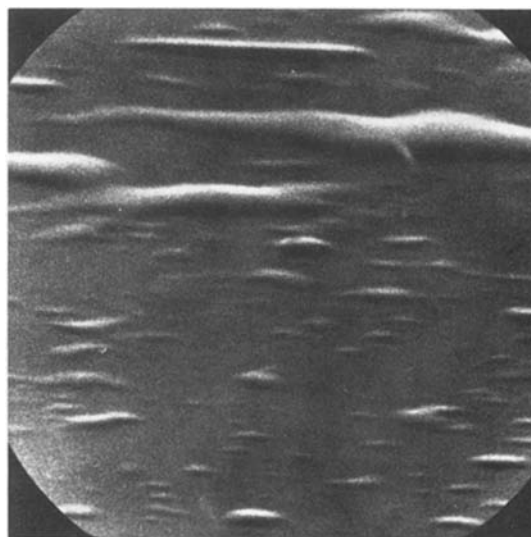


Fig. 4. A scanning electron micrograph recording of an electrodeposited polycarbazole. $i_0 = 0.55 \text{ mA cm}^{-2}$. Duration of electrolysis: 1260s. Magnetic field strength = 6.0 kG. Magnification: 2000 \times .

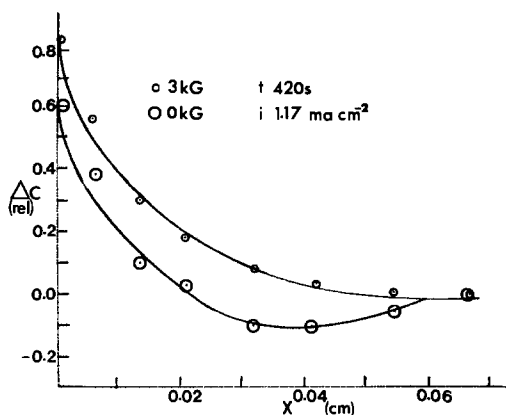


Fig. 5. The relative concentration changes during electrolysis of 60 mM carbazole in DMF containing 0.1M tetra-n-butyl ammonium perchlorate at the anode. The top curve is obtained in a magnetic field of 3 kG. The lower curve was obtained at zero field. $i_0 = 1.17 \text{ mA cm}^{-2}$. The profile refers to an elapsed time of electrolysis of 420s.

sion layer during this electrolysis proceeds steadily until the electrolysis of the supporting electrolyte begins. The fringe shift (F) in a galvanostatic electrolysis is given by

$$F_{(0,t)} = \frac{2I}{nF} \cdot k \sqrt{\frac{t}{11D}} \quad (0.546) \quad [1]$$

where n is the number of electrons consumed at the electrode, F is the Faraday, and D is the diffusion coefficient of the molecule. k is defined as

$$k = \frac{2ta}{\lambda} \quad [2]$$

where t is the thickness of the cell, a is the correlation constant between refractive index and concentration of H_2Q , and λ is the wavelength of laser light (6328Å). A plot of F vs. \sqrt{t} for the electrolysis of H_2Q is shown in Fig. 6. With a view to comparing its behavior at an uncoated electrode, the electrolysis of H_2Q solutions were also carried out at a platinum electrode. The data obtained in these experiments are also shown in Fig. 6. The results obtained at the two electrodes are comparable to one another but have different slopes consistent with the c.d.'s used.

The growth of the Nernst diffusion layer proceeds smoothly during electrolysis of H_2Q , and the relative changes in concentrations from the electrode surface to the bulk were followed by recording the fringes at different times. Figure 7 shows the plot of relative concentrations as a function of the distance from the electrode surface at Pt/polycarbazole and Pt. The concentration changes are very similar at the two surfaces, suggesting that H_2Q is oxidized at our near the polymer surface.

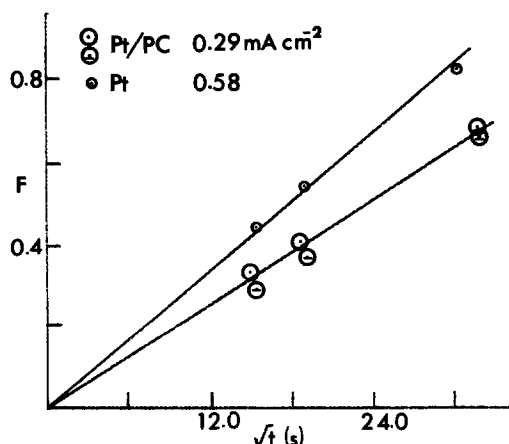


Fig. 6. The plot of maximum fringe shift vs. \sqrt{t} during electrochemical oxidation of 60 mM hydroquinone in 1.0M H_2SO_4 .

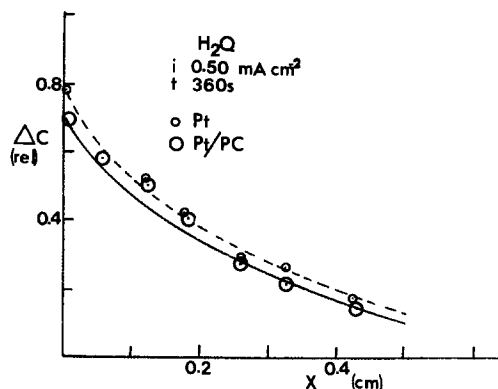


Fig. 7. The relative changes in concentration of H_2Q as a function of distance from the electrode at 360s of electrolysis of 60 mM H_2Q in 1M H_2SO_4 at Pt and platinum covered with polycarbazole film (Pt/PC).

The impressed voltage changes with time during an electrolysis of H_2Q at a Pt/polycarbazole electrode are shown in Fig. 8 for two selected c.d.'s of 0.294 or 0.588 mA cm^{-2} . These plots for the electrolysis of H_2Q at a Pt anode are very close to identical. The similarities observed at the two electrodes suggest the mechanisms of oxidation of H_2Q are following identical pathways at the two types of electrodes.

The electrochemical oxidations of inorganic ions such as aquo Fe^{2+} and $\text{Fe}(\text{CN})_6^{4-}$ at Pt/polycarbazole follow different pathways from bare Pt. The oxidation of Fe^{2+} in 1M H_2SO_4 in the interferometric cell produces an upturn of the fringes at the anode, indicating an increase in the refractive index of the medium. The counterelectrode process during the electrolysis was the reduction of hydrogen ion. At low c.d.'s ($< 0.55 \text{ mA cm}^{-2}$), the production of

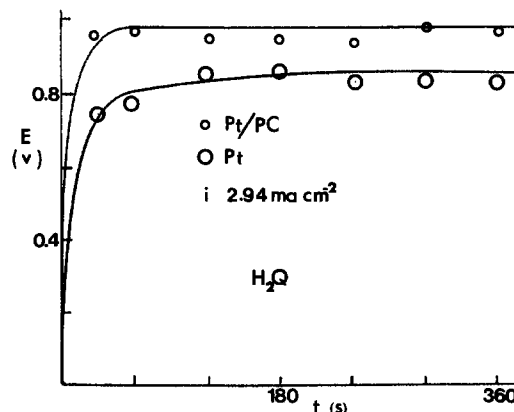


Fig. 8. The impressed voltage vs. time plot during an electrolysis of 60 mM H_2Q in 1M H_2SO_4 at platinum and Pt/PC electrodes. The impressed current density was kept constant at 2.94 or 5.88 mA cm^{-2} .

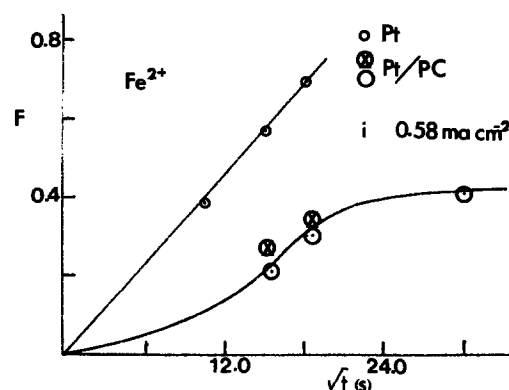


Fig. 9. A plot of maximum fringe shift vs. square root of time of electrolysis of 0.50M FeSO_4 in 1M H_2SO_4 at a Pt or Pt/PC anode. The current density was kept constant at 0.58 mA cm^{-2} .

hydrogen was slow, and hence no significant convection (13) was noticed in the central part of the cell. The fringe shift at the Pt anode varies linearly with the square root of the time of electrolysis, as shown in Fig. 9, suggesting a diffusion-controlled behavior. The electrolysis carried out with higher c.d.'s showed deviations from linearity due to the onset of hydrodynamic flows produced in the cell. The results obtained at the Pt/polycarbazole anode showed two significant deviations: (i) the fringe shift at this electrode was not linear with $t^{1/2}$ during the progress of electrolysis and (ii) the fringe shift at longer times (>240s) was almost constant during extended periods of electrolysis.

Figure 10 shows the concentration-distance plots during the electrolysis of FeSO_4 at Pt and Pt/polycarbazole anodes. The extent to which the region around the electrode is depleted differs in the two situations. While at a Pt surface the depletion region increases with continuation of the electrolysis, this growth was not significant with Pt/polycarbazole. This difference is attributed to the flux differences at the two electrodes: the flux of Fe^{2+} at the polymer surface and the flux within the polymer.

The electrolysis of $\text{K}_4\text{Fe}(\text{CN})_6$ in aqueous KCl medium between two Pt electrodes is well documented (14). The oxidation of $\text{Fe}(\text{CN})_6^{4-}$ occurs at $E_{\text{pa}} = 0.36\text{V vs. SCE}$ and consumes 1e in this electrolysis. The galvanostatic electrolysis of $\text{K}_4\text{Fe}(\text{CN})_6$ in the Fabry-Perot interferometer produces fringe patterns like those shown in Fig. 10. The

analysis of the fringes at the anode shows the fringe shifts are proportional to the square root of time (see Fig. 11). However, with Pt/polycarbazole as the anode in the experiments, the above plots show deviations from those for Pt. At higher c.d.'s (>1.10 mA cm^{-2}), the fringe shift was constant beyond 120s of electrolysis in a way similar to that observed with Fe^{2+} . This constancy was not observed at Pt in either case.

The diffusion gradients for H_2Q are established from the beginning of the electrolysis and progress throughout the electrolysis, indicating oxidation at or near the polymer surface, the porous conducting polymer appearing to have an areal resistance of about $40 \Omega \text{ cm}^{-2}$. A contrasting situation develops when the ions [Fe^{2+} or $\text{Fe}(\text{CN})_6^{4-}$] pass into the polymer film. Part of the diffusion layer appears to be inside the polymer layer in contrast to the neutral H_2Q results. The film thus behaves like a polyelectrolyte where the presence of negative and positive charges in the film brings out the above type of behavior. It should also be remembered that these films were produced under low c.d. or high magnetic field, i.e., low concentration polarization, and should have reasonable electronic conductivity. Hence, simple ions could be discharged at various depths in the polymer, including at the electrode itself. The concept of just part of the concentration gradient's being inside the polymer layer does not totally explain the $\text{Fe}^{2+}/\text{Fe}(\text{CN})_6^{4-}$ results, although in Fig. 10, adding the thickness of the polymer layer (0.25 mm) to the observed diffusion layer (0.15 mm) gives 0.4 mm, a value very comparable to the bare electrode diffusion layer thickness. It seems more likely that the polymer is also behaving to some extent as a polyelectrolyte.

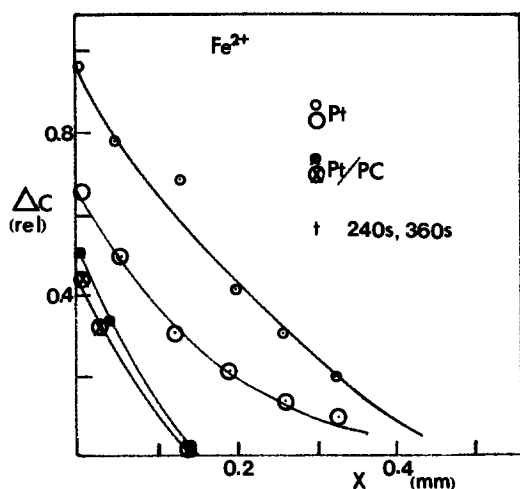


Fig. 10. The relative concentration changes during electrolysis of 0.50M FeSO_4 in $1\text{M H}_2\text{SO}_4$ at Pt anode or Pt/PC anode plotted as a function of distance from the electrode.

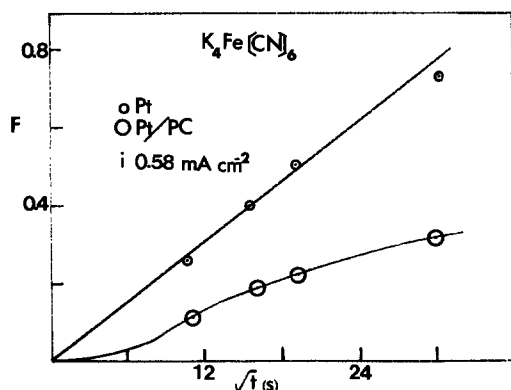


Fig. 11. A plot of maximum fringe shift vs. square root of time of electrolysis of $0.05\text{M K}_4\text{Fe}(\text{CN})_6$ in 1M KCl at an impressed constant current of 0.58 mA cm^{-2} .

Acknowledgment

The authors wish to acknowledge the support for this work by Natural Sciences and Engineering Research Council of Canada and the help of Teddy Gathwright of Triumph and Bu-Dong Zhao.

Manuscript submitted Sept. 16, 1983; revised manuscript received April 9, 1984.

The University of Victoria assisted in meeting the publication costs of this article.

REFERENCES

- R. N. O'Brien and K. S. V. Santhanam, *This Journal*, **130**, 1114 (1983).
- K. S. V. Santhanam and R. N. O'Brien, Paper presented at Surface Canada, 1983, Vancouver, B.C., Canada.
- R. N. O'Brien, W. Michalik, B. B. Kulkarni, and K. S. V. Santhanam, *Can. J. Chem.*, **59**, 1933 (1981).
- R. N. O'Brien and K. S. V. Santhanam, *This Journal*, **129**, 1266 (1982).
- S. Fletcher and R. G. Barradas, *ibid.*, **125**, 1960 (1978).
- N. S. Sundaresan and K. S. V. Santhanam, *Trans SAEST*, To be published.
- K. S. V. Santhanam, R. N. O'Brien, and A. D. Kirk, *Can. J. Chem.*, **47**, 1355 (1969).
- C. R. Wilke, H. Eisenberg, and C. W. Tobias, *This Journal*, **100**, 513 (1953).
- R. N. O'Brien and K. S. V. Santhanam, Work in progress.
- B. B. Kulkarni and K. S. V. Santhanam, *Trans. SAEST*, **11**, 89 (1976).
- R. N. O'Brien, in "Techniques of Chemistry, Physical Methods," Vol. 1, A. Weissberger and B. Rossiter, Editors, Part IIIA, Chap. I, Wiley-Interscience, New York (1972).
- R. N. O'Brien, *This Journal*, **113**, 389 (1966).
- S. Mohanta and T. Z. Fahidy, *Can. J. Chem. Eng.*, **150**, 248 (1972).
- R. N. Adams, "Electrochemistry at Solid Electrodes," Dekker, New York (1968).

Electrodeposition of CdTe Thin Films

R. N. Bhattacharya and K. Rajeshwar*

Department of Chemistry, The University of Texas at Arlington, Arlington, Texas 76019-0065

ABSTRACT

Cadmium telluride thin films were fabricated on Ti and Nesatron® substrates by electrodeposition and characterized by x-ray diffraction, scanning electron microscopy, energy dispersive x-ray analyses (EDAX), optical transmission measurements, and photoelectrochemical (PEC) studies. The deposition-bath preparation procedure was slightly modified from the literature method to permit initial speciation of TeO₂ and thereby increase the loading level of Te in the film. New data are presented on the electrochemistry of the deposition process and on the cyclic voltammetric behavior of TeO₂ containing electrolytes in the pH range from ~0.7 to 11.0. The films after suitable annealing in an Ar atmosphere show x-ray diffraction behavior consistent with a hexagonal structure. Data from EDAX show that the Cd/Te ratio in the film is sensitive to the annealing process. Concomitantly, the conductivity also changes from p-type to n-type, as shown by PEC measurements on the films containing a protective α -PbO₂ coating in contact with alkaline polysulfide electrolytes. Finally, some preliminary data are presented on PEC cells based on these CdTe thin films in a nonaqueous electrolyte system comprising the ferrocene/ferrocenium ion redox couple.

Of the emerging materials for solar cell applications, CdTe is one candidate which has received much attention in recent years (1). Two features in the optical characteristics of this material are particularly attractive for photovoltaic conversion of sunlight: (i) its energy bandgap of 1.5 eV, which provides an optimal match with the solar spectrum and thus facilitates its efficient utilization and (ii) the direct mode of the main optical transition which results in a large absorption coefficient and in turn permits the use of thin layers (1-2 μ m) of active material.

Electrodeposition methods have been successfully employed for the fabrication of cadmium chalcogenide thin films in general (2) and CdTe in particular (3). In principle, both anodic and cathodic deposition are possible, although more precise control of film stoichiometry is obtained with the latter approach. The conditions to be met to achieve cathodic deposition of compounds have been analyzed by a previous author (4). The key factor here is the extent to which the deposition potential of the less noble component (*i.e.*, Cd in this case) is shifted relative to that of the noble species (*i.e.*, Te in this case) by the free energy gained from compound formation. For CdTe, the difference in standard potentials (0.954V) is greater than ($G_{\text{CdTe}}/298/2F$) (G_{CdTe} = free energy of formation of CdTe) such that Cd remains the potential-determining species throughout the stability range of the compound (3a, 4). Parametric variables for controlling film stoichiometry have been established by previous authors, and both n- and p-type layers have been electrodeposited (3a, 3b).

Information on the characteristics (structural, morphological, compositional, and electronic) of electrodeposited CdTe thin films, effect of thermal treatment, and electrochemistry involved in the deposition process, however, is limited in the literature (3a, 3b); therefore, we have undertaken a systematic study of these aspects in our laboratory. Our findings to date are presented in this paper along with some preliminary results bearing on photoelectrochemical (PEC) applications.

Experimental

Substrates.—Substrates for CdTe electrodeposition were either Ti or Nesatron® glass from commercial sources. These substrates were carefully degreased and rinsed with acetone followed by air-drying. In the case of Ti, the substrates were then polished by garnet finishing paper and etched with 10% HF. They were then preheated in an Ar stream (containing ~0.5% O₂) at ~650°C till a change in color to sky-blue was noted. This procedure was found to be essential for good adherence of the films.

Chemicals.—All chemicals were of Analar® or Pura-tronic® grade purity and were used as received. Deionized water was used in all cases.

* Electrochemical Society Active Member

Electrodeposition bath and procedure.—The deposition bath was slightly modified from the one originally used by Panicker *et al.* (3a), which consisted of CdSO₄ (1M) and TeO₂ (10⁻⁵-10⁻³M), the pH being adjusted to 2.5-3.0 with H₂SO₄. We speciated the TeO₂ initially with NaOH (~pH 9-10) and then brought the solution into the acidic pH range (1-3) by slow addition of H₂SO₄. The initial solution in NaOH permits introduction of a higher TeO₂ conc. in the bath for the growth of p-type films.

Nominal deposition potentials ranging from -0.65 to -0.85V (*vs.* SCE)¹ and current densities in the range ~0.3-0.5 mA/cm² were employed. A conventional three-electrode cell was employed, the counterelectrode being either a Pt spiral or a glassy C electrode. In some cases, a twin-anode deposition system [comprising an active Te anode, *cf.* Ref. (3a)] was also used. All depositions were carried out at temperatures above ambient (40°-60°C) since microscopic examination of room-temperature films showed them to have poor physical characteristics (grain size and morphology) (see below). This observation is consistent with previous findings (3b). No significant differences were observed for various films grown within the above temperature window such that further differentiation is not made for the results described below.

Photoelectrochemical (PEC) characterization.—In view of the fact that CdTe is not photoelectrochemically stable in aqueous solutions, two methods were adopted for their PEC characterization. In the first one, a coating of α -PbO₂ (~1000Å thick) was deposited on the CdTe film surface by electroless deposition from a bath containing 1 × 10⁻²M PbOAc, 1.2M NH₄OAc, and 6 × 10⁻²M K₂S₂O₈ according to procedures described elsewhere (5). These coated films were tested in alkaline polysulfide electrolyte. In the second approach, a nonaqueous electrolyte comprising methanol, tetrabutyl ammonium perchlorate as the supporting electrolyte and ferrocene/ferrocenium ion as the redox species was employed. In either case, an ELH tungsten-halogen lamp was used for illuminating the CdTe film. Three-electrode geometry comprising a Pt pseudoreference electrode was used for these measurements.

Instrumentation.—A Princeton Applied Research (PAR) electrochemistry system consisting of a Model 173 potentiostat/galvanostat, a Model 175 Universal Programmer, and a Model 179 digital coulometer was employed for electrochemical deposition and PEC analyses. X-ray diffraction data were obtained on a Rigaku Rotaflex Model RU 200 powder diffractometer using CuK α radiation. Energy dispersive analysis of x-ray fluorescence (EDAX) and scanning electron microscopy (SEM) were carried out on a Philips Model P505 unit.

Optical measurements on CdTe thin films were performed on a Cary Model 219 spectrophotometer. These

¹ All potentials herein are quoted w.r.t. SCE unless otherwise specified.

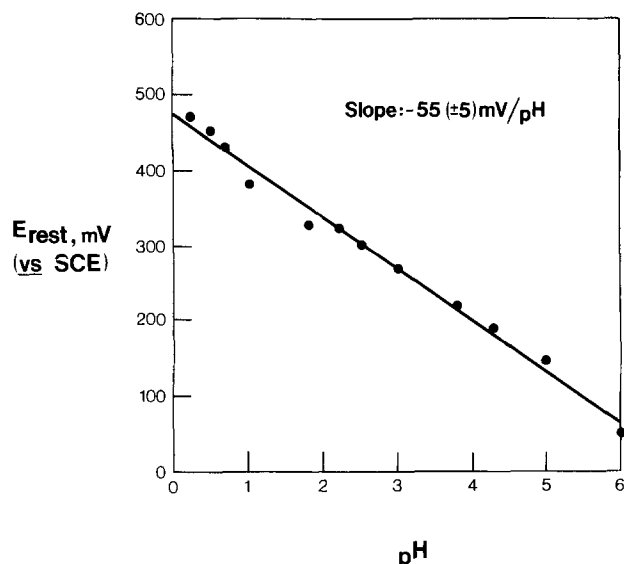
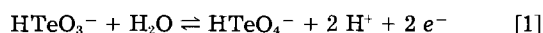


Fig. 1. Variation of rest potential with pH for a Pt wire in contact with the CdTe plating bath at 25°C.

measurements were performed in the conventional transmission mode utilizing Nesatron substrates. Film thicknesses were measured on a Sloan Dektrak instrument (Sloan Technology Corporation, Santa Barbara, California).

Results and Discussion

Deposition bath electrochemistry.—Figure 1 illustrates the variation in rest potential with pH for a Pt wire in contact with 1M CdOAc and $1.0 \times 10^{-2}M$ TeO₂ at 25°C. Protonation of the TeO₂ species is believed to be the major potential-determining equilibrium and the measured slope of 55 ± 5 mV would be consistent with the following equilibrium (6)



Existence of species of the type HTeO₃⁻ and TeO₃²⁻ (see below) is predicated by the amenability of TeO₂ to speciation with NaOH.

Figure 2a contains cyclic voltammograms for a $5.0 \times 10^{-4}M$ solution of TeO₂ at pH 2.4 at varying scan rates in the range 100-500 mV/s. A set of quasireversible anodic and cathodic waves is observed. The peak separation is a sensitive function of scan rate (see inset). The species responsible for this behavior do not seem to undergo

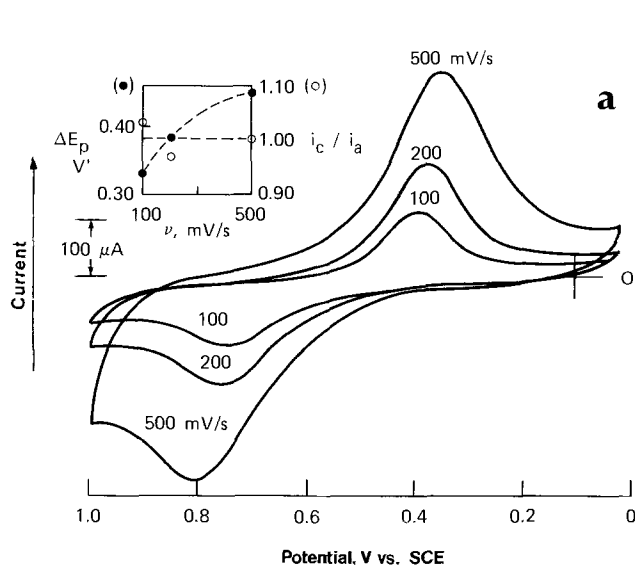


Fig. 2. a(left): Cyclic voltammograms for Pt microelectrode in a $5.0 \times 10^{-4}M$ soln of TeO₂ at pH 2.4. The inset shows the variation of peak separation, ΔE_p , and peak current ratio, i_c/i_a with scan rate, ν . b(right): Plots of peak current, i_p for the anodic and cathodic waves in Fig. 2a vs. $\nu^{1/2}$.

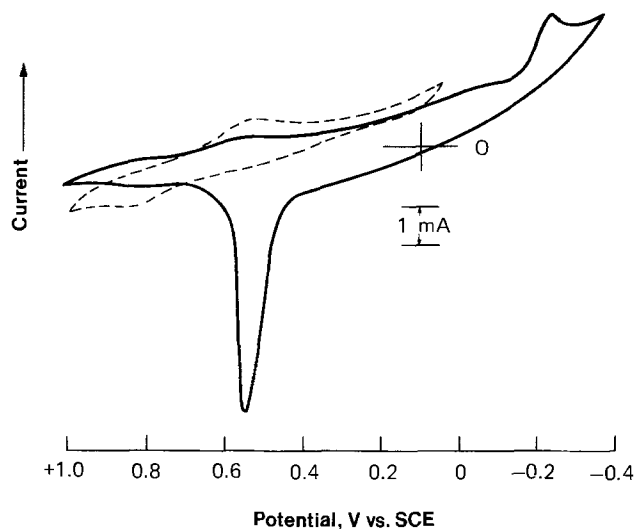
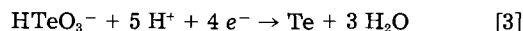
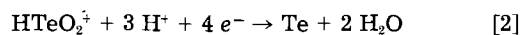
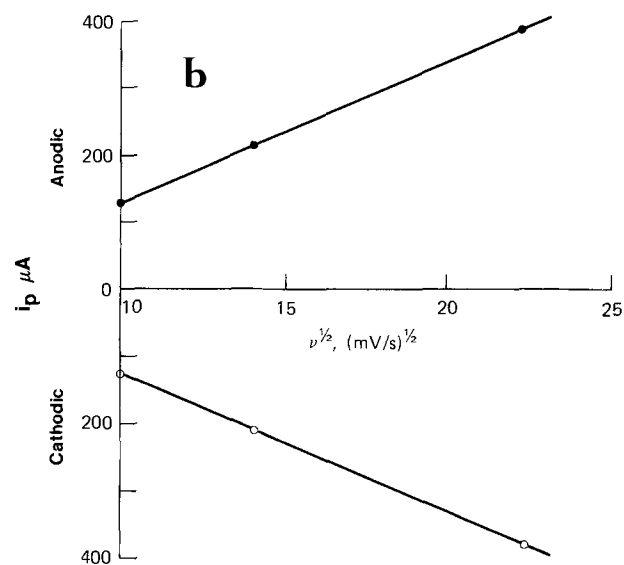


Fig. 3. Cyclic voltammogram (scan rate: 100 mV/s) for a Pt microelectrode in a $2.0 \times 10^{-2}M$ solution of TeO₂ at pH ≈ 0.7 . The dashed line corresponds to data similar to those in Fig. 2a (see text).

complicating chemical reactions either preceding or following charge transfer since the peak current ratio remains sensibly close to unity at all scan rates investigated (cf. inset). Additionally, adherence to the classical linear i_p vs. $\nu^{1/2}$ behavior (i_p = peak current, ν = potential scan rate) is observed for this electrochemical reaction (cf. Fig. 2b) confirming the diffusion-limited characteristic of the charge-transfer process. Based on these data, it seems reasonable to attribute the observed voltammetric behavior to sluggish redox reactions (at least on the Pt surface) involving dissolved HTeO₃⁻/HTeO₄⁻ species in the bulk electrolyte. If instead of terminating the scan at 0V, the potential is swept to $\sim -0.4V$, a reduction peak becomes clearly evident with concomitant development of a black deposit on the electrode surface (cf. Fig. 3). This deposit is stripped from the electrode on the positive-going scan. This behavior is clearly due to the deposition of Te as described by either of the following reactions.



Note that the pH dependencies of the reduction potential for these two reactions are different (-0.04 and $-0.07V$ per unit change in pH, respectively). The two species

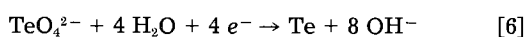
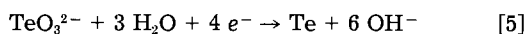


HTeO_3^+ and HTeO_3^- presumably coexist in equilibrium via a reaction of the type (6)



Complications in the redox behavior of HTeO_3^- species (Eq. [1]) from this equilibrium could explain the features in the cyclic voltammograms shown in Fig. 2a.

In basic electrolytes, an overall shift in redox behavior to negative potentials is observed (cf. Fig. 4). The predominant Te species in the basic pH range are probably TeO_3^{2-} and TeO_4^{2-} (cf. Eq. [1]). Reduction of either of these species, possibly via reactions of the type represented by Eq. [5] and [6]



is sluggish on Pt as evidenced by the fact that voltammograms analogous to that in Fig. 3 could not be observed down to very low scan rates.

Film characterization.—Optical properties.—Figure 5 presents the optical absorption characteristics of representative CdTe thin films on Nesatron substrate for varying film thicknesses in the range 1000–3500 Å. Data are shown in terms of both absorbance vs. wavelength (Fig. 5a) and transmittance vs. wavelength plots (Fig. 5b). These measurements enable computation of the absorption coefficient, α , via the relationship $\alpha = (d_2 - d_1)^{-1} \ln T_1/T_2$ where d and T are the film thickness and percentage of transmittance, respectively (7). Plots of α^2 vs. $h\nu$ will then yield the energy bandgap, E_g . Two such plots are shown in Fig. 6 using α values computed from 1000 and 3300 Å (Fig. 6a) and from 1000 and 3600 Å (Fig. 6b), respectively. The value extrapolated from the plots for E_g is 1.41 ± 0.01 eV; this value is somewhat lower than that quoted for single-crystal CdTe [1.5 eV, cf. Ref. (1)]. Two reasons can be put forth for the occurrence of nontrivial absorption at energies below E_g ; namely, the presence of (i) free Te in the deposit and/or (ii) states in the bandgap arising from significant disorder in the thin film relative to the single-crystal case. The observation of pronounced “tailing” in optical absorption curves for CdTe thin-films prepared in our laboratory by the electrodeless method seems significant in this regard (8). The presence of free Te in these films was established by x-ray diffraction (8), although free Te does not manifest to the same extent in similar data on our electrodeposited CdTe films (see below). It is, therefore, possible that both factors are important here.

X-ray diffraction—As-deposited films both on Ti and Nesatron substrates were amorphous as shown by x-ray diffraction. Annealing of these films at temperatures in the range 600°–650°C in an Ar atmosphere enabled development of a hexagonal crystal structure ($a = 4.58$ Å and $c = 7.50$ Å). Typical x-ray diffractograms are shown in Fig. 7a and 7b for CdTe thin-films electrodeposited on Nesatron and Ti, respectively. Relevant analyses based on these data are exemplified in Table I for the Ti substrate. Low temperature (< 350°C) annealing of these films produced the cubic modification in essential agreement with the findings of previous authors (3a, 3b).

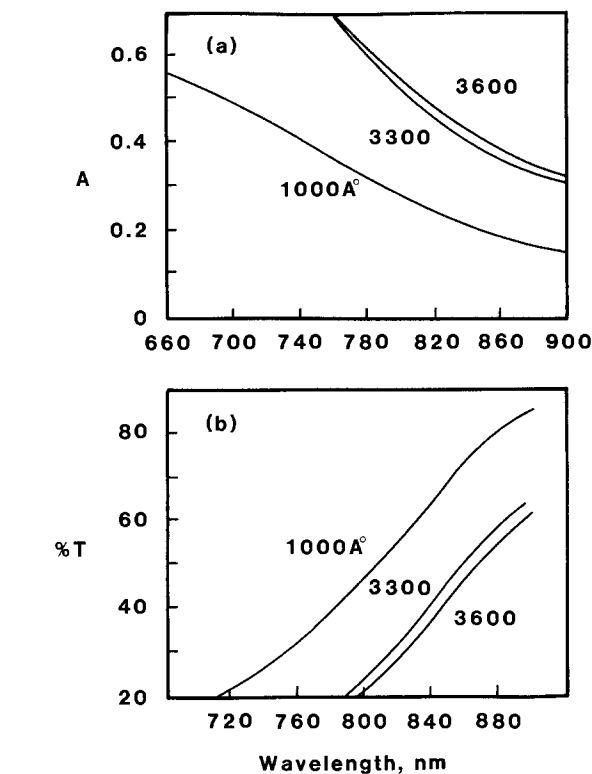


Fig. 5. a(top): Plots of absorbance vs. wavelength for electrodeposited CdTe thin films on Nesatron substrate. Parameter is film thickness. b(bottom): Plots of percentage of transmittance vs. wavelength for electrodeposited CdTe films on Nesatron substrate. Parameter is film thickness.

EDAX/SEM.—Figures 8a and 8b show typical EDAX data on a CdTe thin film on Nesatron and Ti substrates, respectively. Both the observed peak patterns and the computer fit to these data based on the peak assignments to individual elements are shown in the figure. The “background” signals from the Nesatron substrate interfere with semiquantitative estimates of the relative Cd:Te ratio in the film (cf. Fig. 8a). Such estimates for the Ti case, however, yield an average ratio of ~45:55.

Figure 9 shows the SEM photographs of a representative CdTe thin film on Nesatron at two different magnifications. The film morphology is fairly typical of these

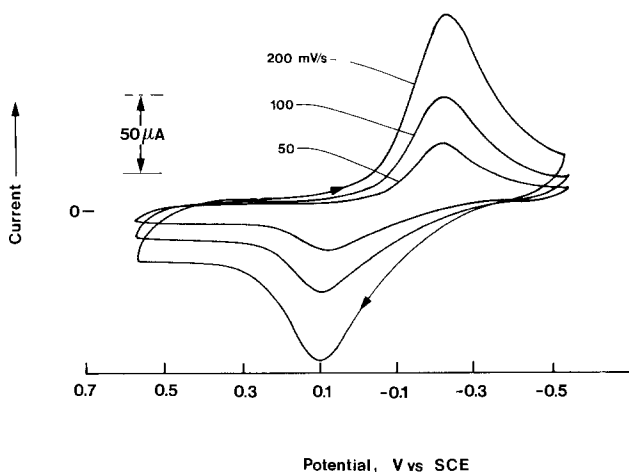


Fig. 4. Cyclic voltammogram (scan rate: 200 mV/s) for a Pt microelectrode in a 5.00×10^{-4} M soln of TeO_2 at $\text{pH} \approx 11$.

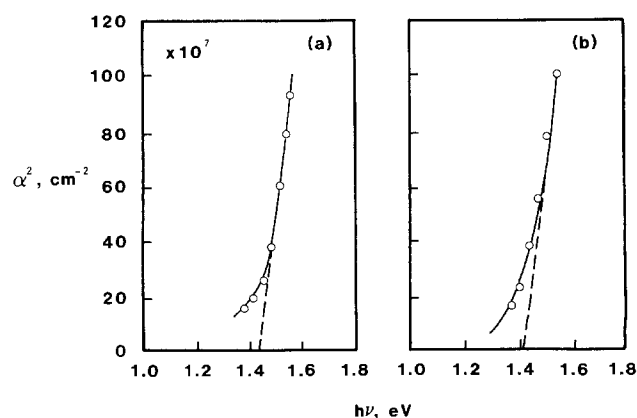


Fig. 6. Plots of α^2 (α = absorption coefficient) vs. $h\nu$ for electrodeposited CdTe films using data from 1000 and 3300 Å films (Fig. 6a) and from 1000 and 3600 Å films (Fig. 6b).

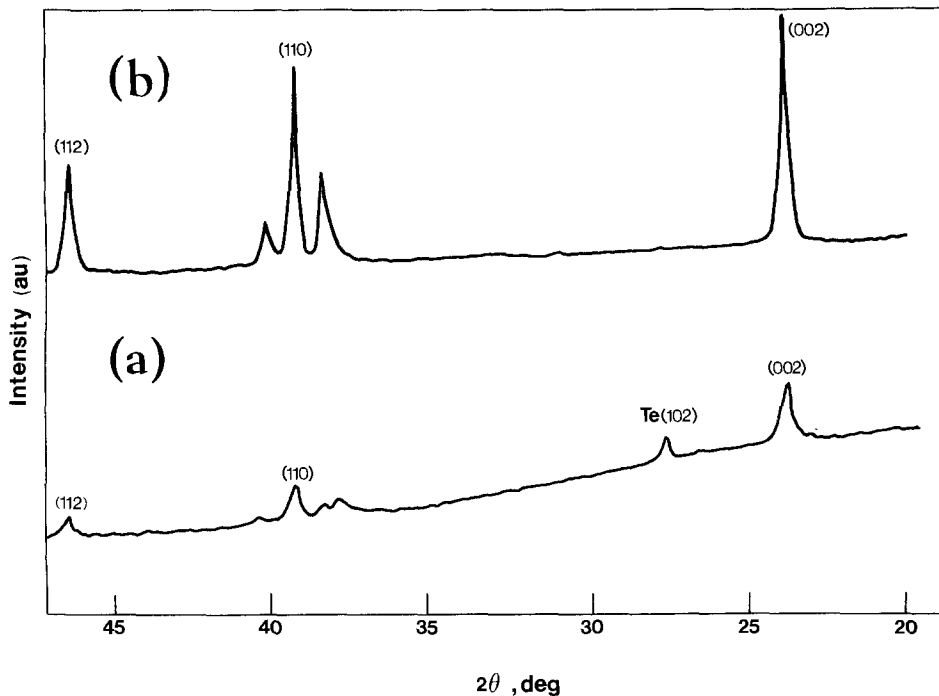


Fig. 7. Partial x-ray diffractograms for electrodeposited CdTe thin films on (curve a) Nesatron and (curve b) Ti. The films were thermally annealed prior to measurement.

materials (3a, 3b), although its sensitivity to substrate material is quite striking (cf. Fig. 9 and 10).

Photoelectrochemistry.—Liquid contacts offer a convenient means of assessing changes in film stoichiometry and corresponding variations in electronic conductivity brought about by prior treatment. The utility of PEC methods for monitoring such changes is illustrated by typical data in Fig. 11. The data in Fig. 11a are for an as-deposited CdTe thin film (i.e., no thermal treatment) on Ti substrate, whereas the curves in Fig. 11b pertain to another film subjected to prior thermal treatment (~600°C in Ar atmosphere for ~50 min). In both cases, the CdTe film surface had a protective coating of α -PbO₂ to prevent it from undergoing PEC corrosion (see above). Alkaline polysulfide was used as the redox electrolyte. The dark current flow shown in Fig. 11a and 11b arises from the conducting α -PbO₂ overlayer. Electronic carriers in the underlying CdTe substrate serve only to “bias” the conductivity of this overlayer (9). Consider Fig. 11a. Bandgap illumination of the CdTe layer creates electron-hole pairs. A large fraction of these pairs recombine. Some of the photogenerated carriers, however, traverse the field at the CdTe/PbO₂ junction and augment the charge transfer processes occurring at the PbO₂/electrolyte interface. The enhancement of cathodic current flow at this interface on illumination of CdTe, minimal changes in the anodic regime, and the positive shift in the

rest potential of the CdTe/PbO₂ electrode on illumination (cf. Fig. 11a) are all consistent with the presence of a p-type CdTe film underneath the PbO₂ overlayer. On thermal treatment, the Cd/Te ratio is increased (a result borne out by EDAX measurements) and the nonstoichiometry in the resultant film renders it n-type (cf. Fig. 11b). Note the negative shift in the rest potential for this film

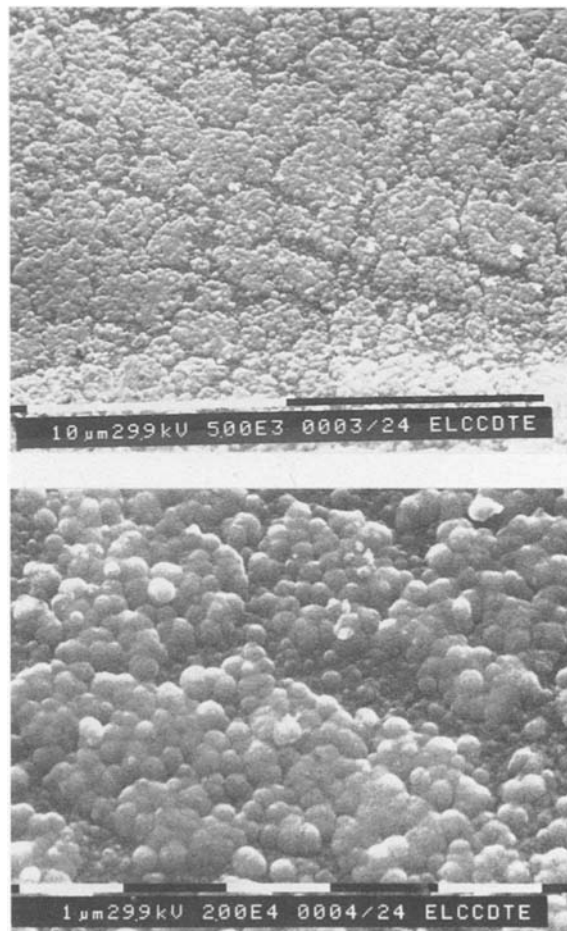


Fig. 9. SEM photographs of an electrodeposited CdTe thin film on Nesatron at two magnifications.

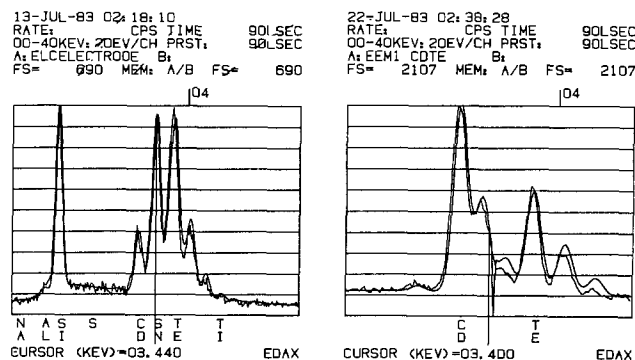


Fig. 8. EDAX data on electrodeposited CdTe thin films on (a, left) Nesatron and (b, right) Ti. The electron beam energy in the two cases were 15 and 20 keV, respectively. The actual spectra are superimposed on the computer fit to these spectra based on the peak assignments as shown.

Table I. X-ray diffractogram analysis of an annealed CdTe thin film on Ti substrate

2θ	Observed d	I/I_1	2θ	Reported* $d(\text{\AA})$	I/I_1	hkl
23.90	3.72	100	23.70	3.75	100	002
39.40	2.29	84	39.30	2.30	100	110
40.27	2.24	16	42.71	2.12	80	103
46.52	1.95	46	45.42	2.00	75	112
53.08	1.72	10	52.06	1.76	16	202
62.50	1.48	11	62.02	1.50	25	210
71.30	1.32	9	71.20	1.32	30	300
76.30	1.25	8	76.14	1.25	20	302

* ASTM Powder Diffraction File 19-193 for hexagonal CdTe.

on illumination—a behavior consistent with n-type conductivity in the underlying semiconductor layer (9). The lack of asymmetry in the current voltage characteristics on illumination (compare Fig. 11a and 11b) is best explained by the presence of a “leaky” n-CdTe/PbO₂ interface.

The PEC method of ascertaining carrier type in semiconductor thin films as described above would be partic-

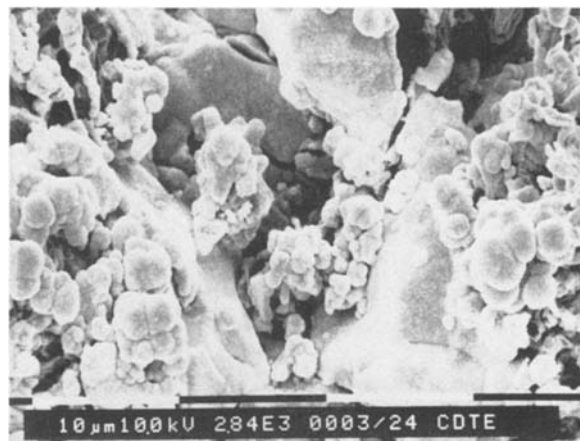


Fig. 10. SEM photograph of an electrodeposited CdTe thin film on Ti. Magnification same as in Fig. 9b.

ularly useful in cases wherein more conventional Hall or hot-probe measurements would be precluded by the high conductivity of the substrate [cf. Ref. (3b)].

Fig. 11. Steady-state current-voltage scans for electrodeposited CdTe thin films on Ti in polysulfide redox electrolyte (Na₂S/NaOH/S, 3M each before (a, left) and after (b, right) thermal treatment of the films. Data are compared in each case in the dark and under illumination with white light from a tungsten-halogen lamp (uncorrected light intensity $\approx 60 \text{ mW/cm}^2$). The electrolyte was quiescent and the potential scan rate was 100 mV/s. The films had a protective coating of $\alpha\text{-PbO}_2$ (see text).

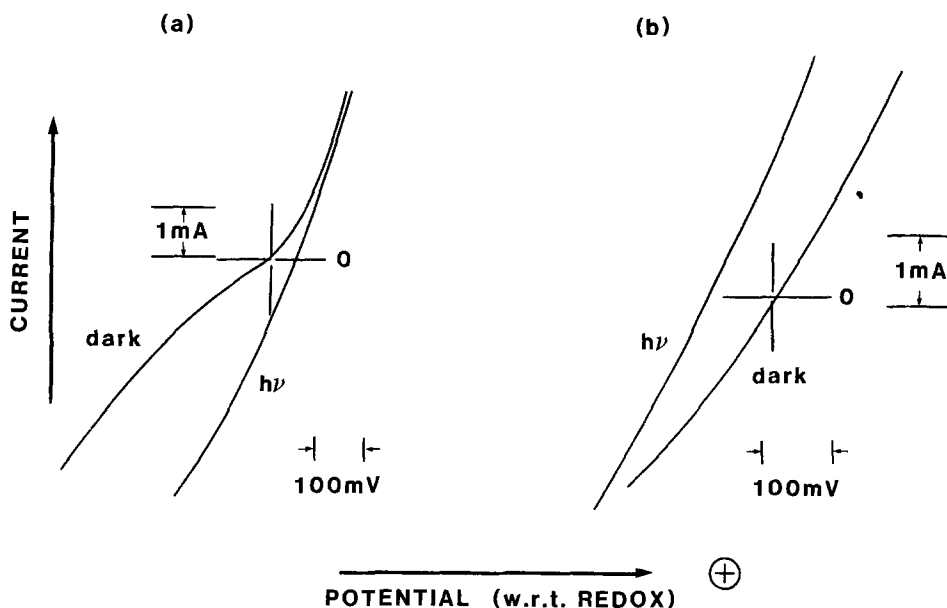
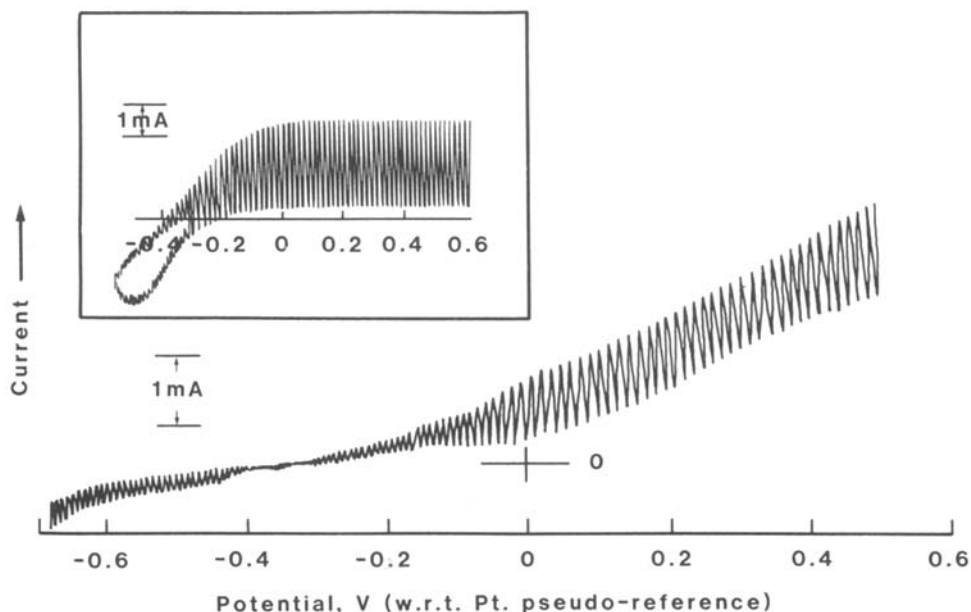


Fig. 12. Photoelectrochemical behavior in chopped white light (80 mW/cm^2) of an electrodeposited CdTe thin film (Ti substrate) in methanol/TBAP (0.5M) electrolyte containing ferrocene/ferricenium ion redox couple (0.2M/0.5 mM). The film area (uncorrected for surface roughness) was 1 cm^2 . The film was subjected to prior thermal treatment. The inset shows for comparison the corresponding behavior of an n-CdTe single crystal (0.2 cm^2) at 60 mW/cm^2 . In both cases, a Pt pseudoreference electrode was employed, and the potential scan rate was 100 mV/s.



Photoelectrochemical cells.—CdTe is characterized by its extreme susceptibility to PEC corrosion in aqueous electrolytes (see above), and the problem is even worse in thin films relative to the single-crystal case (10). In our search for alternative redox electrolytes, we have found the methanol/tetrabutyl ammonium perchlorate/ferrocene/ferricenium ion system (11) to be effective in suppressing PEC corrosion. Typical measurements on three-electrode PEC cells based on this electrolyte are shown in Fig. 12; both for an electrodeposited CdTe thin film and an n-CdTe single crystal for comparison (*cf.* inset). Note that the PEC behavior is consistent with n-type behavior of the film after thermal treatment (*cf.* Fig. 11b). The solar cell parameters for this nonoptimized cell geometry are short-circuit current density (1.5 mA/cm^2) and open-circuit potential ($\sim 300 \text{ mV}$). The fill factor is much inferior to the single-crystal case, indicating substantial degradation in cell efficiency through carrier recombination. Thus the performance characteristics of these films in terms of solar cell applications are admittedly modest at present, although the facile reduction observed for the photogenerated ferricenium ion in the negative going scan for single-crystal CdTe (*cf.* inset, Fig. 12) underlines the problem with nonoptimum location of the ferrocene/ferricenium ion couple with respect to the CdTe band-edges and offers the encouraging prospect of better performance with a redox couple having a more positive standard potential. The results of further optimization of PEC cells based on electrodeposited CdTe thin-films will be reported at a later date.

Acknowledgments

This research was made possible by a sub-contract (No. XL-3-03048-01) from the U.S. Department of Energy and the Solar Energy Research Institute (SERI). The authors also thank R. N. Noufi of SERI for many valuable discussions and for the x-ray diffraction data. Thanks also to J. M. Owens and D. K. De of the Department of Electrical Engineering for generous donation of their time and the facility for film thickness measurements.

Manuscript received Jan. 4, 1984.

The University of Texas assisted in meeting the publication costs of this article.

REFERENCES

- a: K. Zanio, "Cadmium Telluride," Vol. 13 of "Semiconductors and Semimetals," R. K. Willardson and A. C. Beer, Series Editors, Academic Press, New York (1978); b: *Rev. Appl. Phys.*, **12** (1977).
- a: J. F. McCann and M. Skyllas-Kazacos, *J. Electroanal. Chem.*, **119**, 409 (1981) and references therein; b: L. S. R. Yeh, P. G. Hudson, and A. Damjanovic, *J. Appl. Electrochem.*, **12**, 153, 343 (1982); c: D. J. Miller and D. Haneman, *Solar Energy Mater.*, **4**, 223 (1981); d: R. A. Boudreau and R. D. Rauh, *ibid.*, **7**, 385 (1982); e: M. Tomkiewicz, I. Ling, and W. S. Parsons, *This Journal*, **129**, 2016 (1982); f: G. J. Houston, J. F. McCann, and D. Haneman, *J. Electroanal. Chem.*, **134**, 37 (1982); g: A. S. Baranski, W. R. Fawcett, K. Garner, A. C. McDonald, J. R. MacDonald, and M. Selen, *This Journal*, **130**, 579 (1983); h: R. N. Bhattacharya, *Solar Energy Mater.*, To be published.
- a: M. P. R. Panicker, M. Knaster, and F. A. Kroger, *This Journal*, **125**, 566 (1978); b: R. L. Rod, R. Banshah, O. Stafsudd, B. M. Basol, and P. Nath, U.S. DOE Final Report DOE/ET/23008-T1, Monosolar, Inc., Santa Monica, CA (1980); c: Z. Shkedi and R. L. Rod, in "Proceedings of the 14th IEEE Photovoltaics Specialists' Conference," p. 472 (1980); d: G. Fulap, M. Doty, P. Meyers, J. Betz, and C. H. Liu, *Appl. Phys. Lett.*, **40**, 327 (1982); e: B. M. Basol, E. S. Tseng, and R. L. Rod, in "Proceedings of the 16th IEEE Photovoltaics Specialists' Conference, San Diego, CA 1982," p. 805, IEEE, New York (1982).
- F. A. Kroger, *This Journal*, **125**, 2028 (1978).
- R. N. Bhattacharya and P. Pramanik, *Bull. Mater. Sci.*, **2**, 287 (1980).
- E. Deltombe, N. de Zoubov, and M. Pourbaix, Rapport technique R7.33 du Cebelcor (1956).
- J. N. Gan, T. Tauc, V. G. Lambrecht, Jr., and M. Robbins, *Phys. Rev. B*, **12**, 5797 (1975).
- R. N. Bhattacharya, K. Rajeshwar, and R. N. Noufi, Submitted to *This Journal*.
- G. Hodes, L. Thompson, J. DuBow, and K. Rajeshwar, *J. Am. Chem. Soc.*, **105**, 324 (1983).
- R. N. Bhattacharya and K. Rajeshwar, Unpublished results (1983).
- K. D. Legg, A. B. Ellis, J. M. Bolts, and J. S. Wrighton, *Proc. Natl. Acad. Sci.*, **74**, 4116 (1977).

A Photoelectrochemical Storage Cell with n-CdSe and p-CdTe Electrodes

H. J. Gerritsen,¹ W. Ruppel, and P. Würfel

Institut für angewandte Physik der Universität, Universität Karlsruhe, D-7500 Karlsruhe, Germany

ABSTRACT

Charge and energy storage is presented for a photoelectrochemical cell, in which in a CdSO₄ electrolyte one electrode, n-CdSe, is photodecomposed under illumination, and the other electrode, p-CdTe, is photoelectroplated by Cd. These processes lead to a galvanic cell with Se on CdSe as one electrode, and Cd on CdTe as the other electrode. The discharge products, when the cell is discharged in the dark, are the original photosensitive semiconductors. Each of these photosensitive electrodes, as well as their combined performance, is discussed, together with the source of irreversibilities for this method of photoelectrochemical energy conversion.

Known photoelectrochemical cells or photoelectrochemical storage cells convert light energy into chemical energy in a redox system like S/S²⁻ in the liquid, or use bulk storage in a third electrode (1-3). More recently, n-MoSe₂ has been used in various bromine redox electrolytes (4). In these studies corrosion of the semiconductor has been avoided at all costs. In contrast, the work reported here is based on such corrosion, because the chemical energy storage comes from light-induced decomposition of the surface of the semiconductors. Be-

sides photoelectrochemical cells, storage of energy in the electrolyte has been investigated (5-8). These devices are, however, based on quite different physical principles than are involved in the present paper. Closer to our work, is the work by Skotheim (9), who used a combination of p-CdTe and n-CdS, but with a polysulfide redox couple as photovoltaic cell.

Photocorrosion, namely, decomposition of ionic electrodes by light, with subsequent ion migration in the cell is a thermodynamically irreversible process. Nevertheless, it may at least be partly reversed, as any irreversible process, when an increase in entropy in the surroundings

¹ Permanent address: Department of Physics, Brown University, Providence, Rhode Island 02912.

is taken into account. Solar radiation constitutes an energy current at high temperature, being accompanied by a low entropy current. Solar radiation may, therefore, be used to restore a discharged battery at the expense of increasing the entropy outside the battery. Charging a discharged lead accumulator by an illuminated p-n junction solar cell would be an example of this concept.

In this paper, we will describe an accumulator into which a type of solar cell is incorporated. It consists of two photosensitive semiconductor electrodes of the composition A^+B^- in an electrolyte. Irradiation of the electrodes raises the free energy of the system A^+B^- by converting it into $A + B$



In the dark, the process is reversed, and, conducted properly, may deliver electrical energy to an external load.

As photosensitive electrodes, we will use n-CdSe and p-CdTe. Their principles of performance as photosensitive electrodes in an electrolyte will be described below. A photoelectrochemical storage cell using both of these electrodes will also be presented below. The chosen electrodes have no particular merits for application but serve to demonstrate this concept and the problems of photoelectrochemical charge and energy storage. The photocorrosion is not completely reversed upon illumination.

Electrodes

CdSe.—Polycrystalline disks of n-CdSe were used with a thickness of 1 mm and an area of 0.5 cm². They were cut from low resistivity (0.5 Ω cm n-type) rods grown according to the Piper-Polich method. They were subsequently polished, washed in acetone, and etched for 30s in aqua regia, HCl:HNO₃ (4:1 by volume), washed in distilled water, rinsed in a 10% (by weight) KCN solution in water for 2 min, and washed in distilled water. The dry crystal was then attached to a plexiglass holder with some molten phenolphthalein on a hot plate and further secured with epoxy, which at the same time prevented any electrolyte to shorten out the crystal by getting at the back of it. Electric contact was established by bringing a drop of an alloy of gallium-indium, which is liquid at room temperature, at the back side of the crystal and inserting a copper rod in it. This liquid metal wets the semiconductor well and makes a good ohmic contact.

The CdSe disks were then placed in a 0.1M CdSO₄ solution with, as counterelectrode, a strip of Cd metal. A variable voltage could be applied between the CdSe disk and the Cd, and the resulting current measured with a Keithley electrometer. Figure 1, taken from earlier work (10), shows the result. The sign convention chosen for the bias voltage is that it represents the voltage of the semiconductor, taking the Cd as at zero voltage. The current is chosen as positive when in the electrolyte the current, and thus the Cd²⁺, flows from the Cd metal to the semiconductor. The measurements were done in a N₂ atmosphere, though not much difference results when they are done in air.

It is by now a well-established fact [see, for example, Ref. (11-13)] that photocorrosion of cadmium chalcogenides proceeds in two different ways, depending on whether the semiconductor is n- or p-type. In n-type CdSe, immersed in an aqueous electrolyte, a potential barrier is formed, similar to the Schottky barrier at a semiconductor-metal interface (12). This surface barrier, when illuminated, will drive the light-generated majority carriers into the bulk of the semiconductor, while the minority carriers, in this case the holes, will assemble at the interface with the electrolyte. There they may either oxidize some ion in the solution, for example oxidize the reduced state of a redox couple, or they may proceed to oxidize the surface of the semiconductor (2). In our case this would occur via

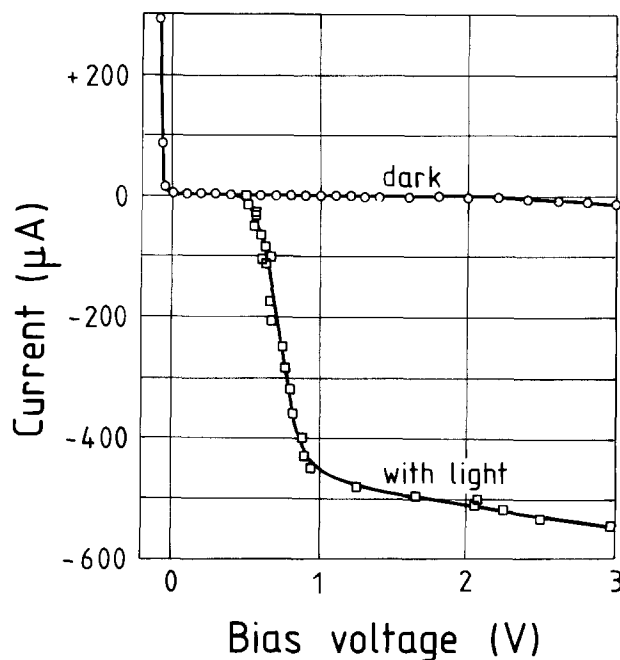
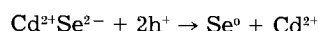


Fig. 1. Current voltage curve of n-CdSe in the dark and with 5 mW 6328 Å illumination. The electrode is immersed in a 1M CdSO₄ solution with Cd metal as a counterelectrode. The positive direction of current flow is that of positive charge flowing toward the CdSe electrode. Taken from Ref. (10).

where the Se⁰ would stay back on the surface as a brown film and Cd²⁺ would diffuse out into the electrolyte.

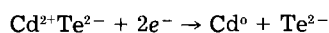
Figure 1 shows the rectifier characteristics of the n-CdSe semiconductor in the dark. Bandbending in a semiconductor in contact with an electrolyte, leading to efficient separation of the light generated electron-hole pair, has been observed in many systems, as summarized in Ref. (12). Thus in the forward direction, the n-CdSe is negatively biased with respect to the Cd counterelectrode. Absorption of a photon in the depletion layer results in a subsequent separation of the photogenerated hole and electron such that the minority carrier moves to the semiconductor-electrolyte interface where it oxidizes CdSe to Se⁰ and Cd²⁺. As can be seen in Fig. 1, this process requires a bias voltage above about +0.5V for the Cd²⁺ to leave the CdSe.

Next, the semiconductor was given a bias voltage in the back direction, at which little dark current flows. Subsequently, the light was turned on for several minutes and the total charge flow measured, indicative of the amount of photocorrosion. The CdSe was then externally short-circuited with the Cd electrode. A dark current was observed in the opposite direction of the previous photocurrent, indicating partial restoration of the photocorrosion of the CdSe. On a fresh crystal and for a photogenerated charge of 35 mC/cm², the return charge after 1/2h was 25 mC/cm² or 70%, while for the larger photogenerated charge of 200 mC/cm² only 25% had returned in 1/2h. After repeated recycling, at which in the dark the bias with respect to the Cd electrode was reduced to zero but in the light was raised to +0.5V, some reduction in photosensitivity was observed, while the return charge in the first half-hour was typically between 20% and 50%.

CdTe.—The CdTe disks were cut from rods grown from the melt by a modified Bridgman method. They were p-type and of rather large resistivity, about 8000 Ω cm. Cleaning was done by washing in acetone followed by brief etching in a 2% brominated methanol solution, followed by 20 min etching in 0.5% brominated methanol and washing in methanol. Ohmic contact was made to the disk by putting a drop of an aqueous solution of H₂AuCl₄ on the surface of the p-CdTe, which results in formation

of a gold electrode. The holder was similar to the one described for CdSe, except that a small brass spring was used instead of the GaIn alloy, to serve as contact between the gold electrode and the copper finger.

The current-voltage characteristic of p-CdTe in a 0.1M CdSO₄ solution with Cd metal as counterelectrode, as described for CdSe, is shown in Fig. 2, taken from Ref. (10). The sign convention is the same as in the former case. Positive current flow in p-CdTe under illumination consists of photogenerated electrons forced to the surface by the field inside the semiconductor. The reaction at the surface can now be represented by



What happens subsequently depends on the composition of the electrolyte. In our case, where Cd²⁺ ions were present in large quantity in the electrolyte, free Te²⁻ ions cannot exist in the solution and CdTe will be reformed immediately. This amounts to a plating of the illuminated CdTe with cadmium metal.

In order to examine the reversibility of the photocorrosion of the CdTe electrode, we exposed it to light at zero voltage bias. With light, even at zero voltage bias, the electrode covered itself with a Cd layer, easily visible to the eye. These Cd films were removed when the Cd-covered CdTe was connected externally to a bar of Te in the solution. Quantitatively, a 2 min exposure of CdTe to a low power HeNe laser transported 11 mC of Cd onto the CdTe surface. After 6 min in the dark, the restoring current had dropped to 1/10 of its initial value and the Te had accepted back 5 mC of the Cd. When the CdTe was exposed to the laser for 5 min, 33 mC of Cd was deposited on it. By connecting it subsequently in the dark to the Te electrode, a reverse charge flow of 12 mC was measured in 20 min, again in the time for the current to drop to 1/10 of its initial value. Thus, in relatively short times, the Te electrode had received back 46% and 37%, respectively, of the Cd photodeposited on the CdTe. If one repeats the experiment many times, a further gradual reduction in photoefficiency is observed. Probably, some Cd is buried and trapped in the CdTe, and also conversion from large crystallite size (about 1 × 1 mm) to a smaller size may take place.

Storage Cell with n-CdSe and p-CdTe Electrodes

A storage cell, which includes the storage capacities of both photosensitive semiconductors discussed so far, is obtained when the n-CdSe and p-CdTe serve as electrodes and the Cd counterelectrode is omitted. It is shown in Fig. 3. A silicon p-n photocell, though not absolutely necessary, helps considerably to increase the current during the illumination part of the cycle.

Under illumination, both photodecomposition and photoplatin, as discussed above, occur (Fig. 4). Se forms as photocorrosion product on n-CdSe, and Cd on p-CdTe. When the two semiconductors are connected, light forces Cd²⁺ ions out of the CdSe onto the CdTe, where it will form Cd. The electrons needed for this flow through the external connection from the CdSe to the CdTe.

In the dark, one can expect the chemical cell, consisting of a layer of Cd on the CdTe and of Se on the CdSe, to discharge, whereby Cd will go into solution as Cd²⁺ from the CdTe electrode and onto the Se-covered CdSe, where it will reform CdSe. The electrons for the discharge of the Cd²⁺ will have flown through the external conductor from the CdTe to the CdSe. This flow is opposite to the electron flow in the light. This concept is that of a reversible battery, activated with light, in which the different kinds of photocorrosion reactions at both semiconductor electrodes are taken advantage of.

The CdSe and CdTe crystals in the 0.1M CdSO₄ electrolyte connected with each other were irradiated with a 75W incandescent lamp. A small (0.1V) potential developed, and a current of 1 μA flowed from the CdSe to the CdTe. Larger currents were obtained when the cell was biased, as noted before. A photocurrent of 60 μA was measured for a bias of 0.5V, conveniently obtained from an illuminated silicon p-n junction. It increased to 300 μA when two such junctions were connected in series to give the n-CdSe a potential of +0.9V with respect to the p-CdTe. The data given below apply to the case of two junctions in series.

The storage effect was mainly due to the semiconductor electrode reactions and not to electrolysis driven by the bias voltage, as follows from the observation that light only on the Si n-p junctions caused a photocurrent of 24 μA, on both the Si n-p junctions and on the CdSe of 190 μA, and on Si, CdSe, and CdTe of 260 μA.

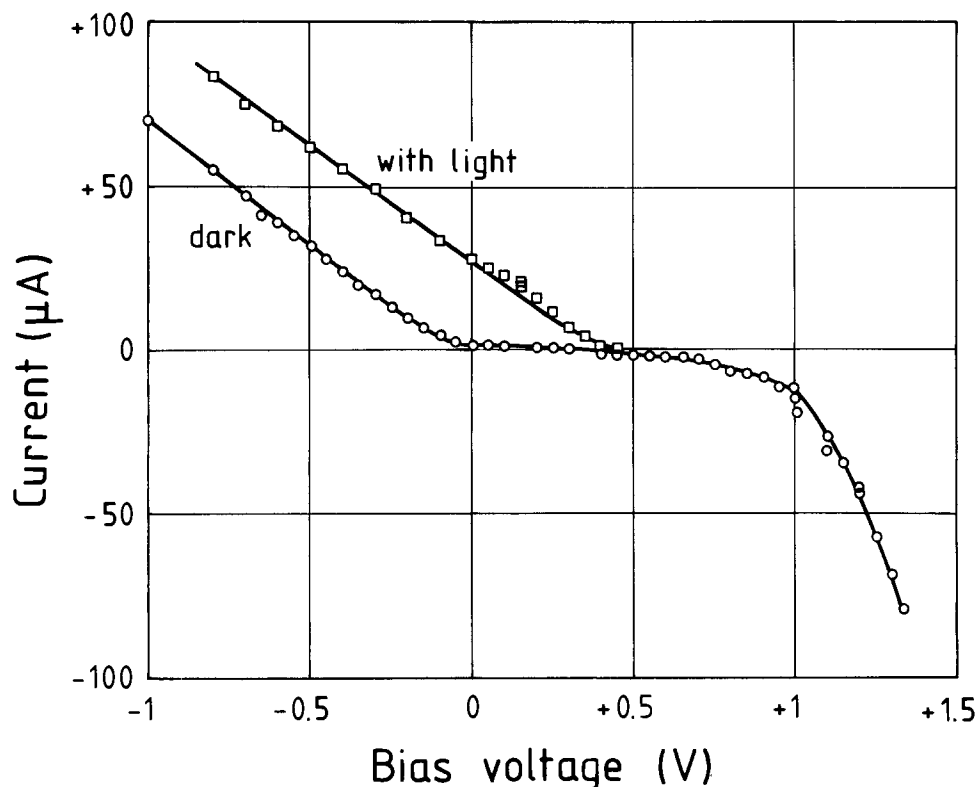


Fig. 2. Current-voltage curve of p-CdTe in the dark and with 5 mW 6328Å illumination for conditions as in Fig. 1. The positive direction of current flow is, as in Fig. 1, that of positive charge flowing toward the CdTe electrode. Taken from Ref. (10).

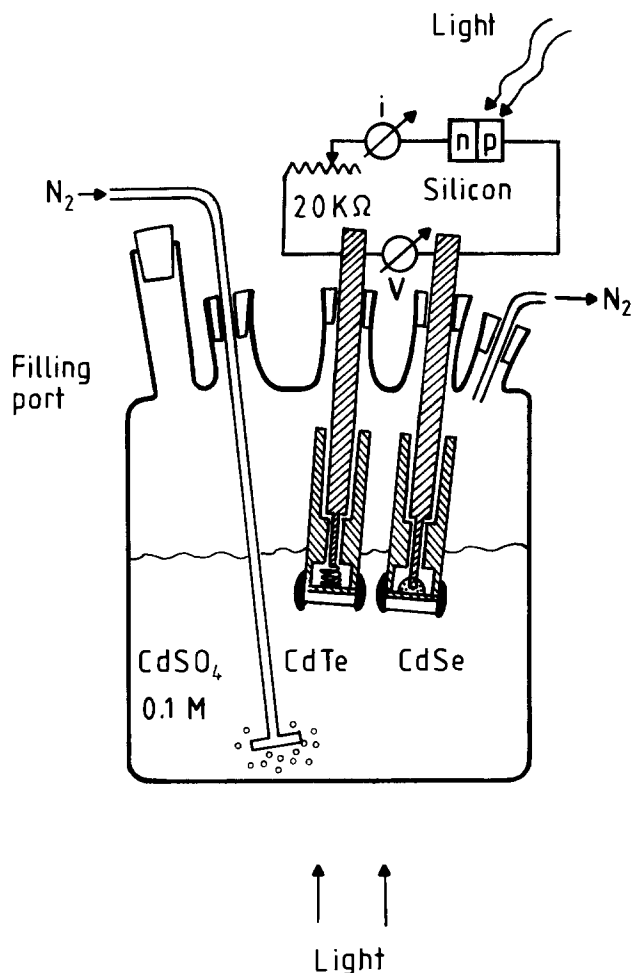


Fig. 3. Photoelectrochemical cell with n-CdSe and p-CdTe as electrodes in an aqueous 1M CdSO_4 electrolyte. An auxiliary bias voltage is provided under illumination by a Si p-n photocell.

Considerable amounts of charge could be stored. By illuminating for 50 min, during which the photocurrent dropped from 260 to 190 μA , a charge of 1.3C on 1 cm^2 was stored, of which 0.36C returned in the dark during 10h. The reverse reaction in the dark drops off relatively fast, towards the end always accompanied by somewhat unstable behavior (Fig. 5). The smaller the photogenerated charge, the shorter the time during which large reverse dark currents flow. Figure 5 shows further the slight decrease in photoresponse during three cycles, at a somewhat constant initial reversed current, corresponding to a dark voltage of about -0.12V . While the photogenerated charges in the three subsequent cycles were 0.20, 0.18, and 0.175 C/cm^2 , the return charges were about 15% of the former after 1h in the dark.

Equally important as the recuperation of the charge is the property of the battery to make good use of the ab-

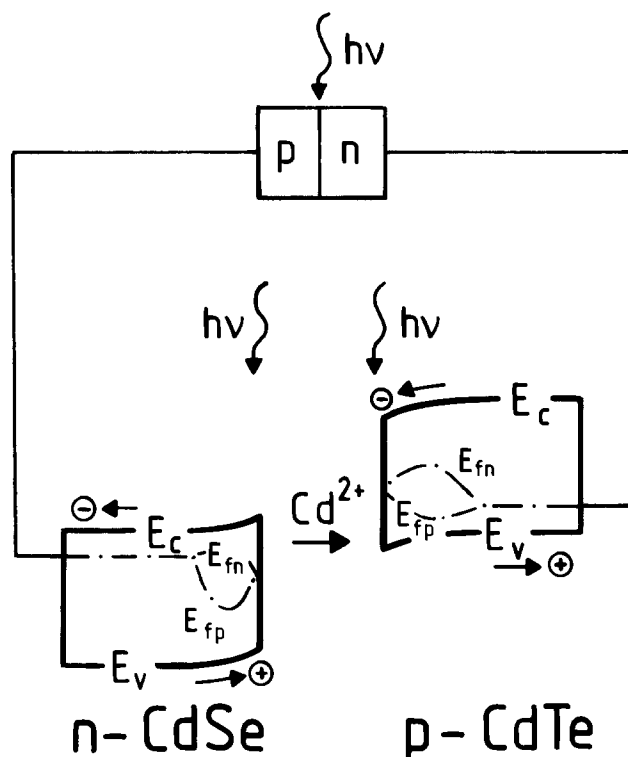


Fig. 4. Charge flow in the n-CdSe and p-CdTe electrodes and in the electrolyte under illumination, as it leads to the photodecomposition and plating reactions discussed in the "Electrodes" section. For the illuminated semiconductor electrodes, the spatial distribution of the bandedges E_c and E_v , and of the quasi-Fermi-levels E_{fn} and E_{fp} , whose gradients act as the driving forces for the charge flow, are roughly sketched.

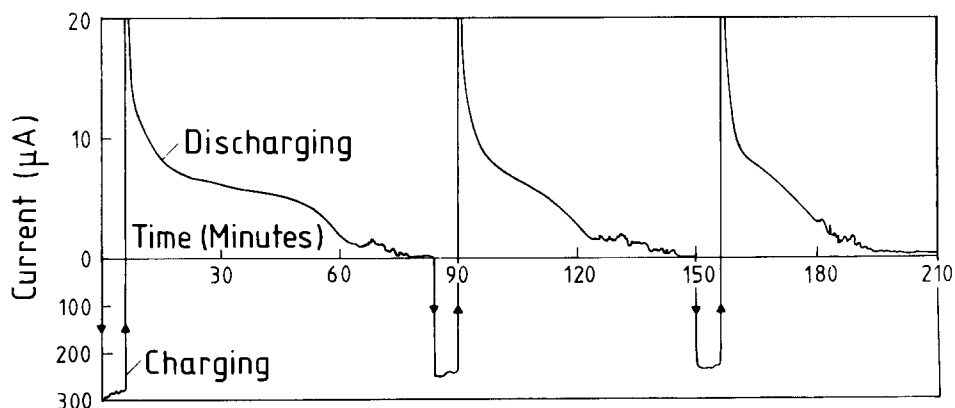
sorbed photons in transferring Cd^{2+} ions from CdSe to CdTe under illumination. In this respect, the cadmium chalcogenides are well qualified. For instance, p-type CdTe in an alkaline electrolyte has been reported to have very high quantum efficiencies of up to 0.97 elementary charges transferred per absorbed photon (14). Measurements on the CdTe used in our experiments gave a quantum efficiency of 0.16 (0.18 when corrected for reflection) at a wavelength of 6328Å of the HeNe laser.

While we have monitored the discharging of the battery in the dark under short-circuit conditions, discharging close to open-circuit conditions would be required in order to get out most of the energy stored in the battery during illumination. The open-circuit voltage between the Se on CdSe and the Cd on CdTe electrodes which transforms the transferred charge to stored energy was 0.65V and did only little depend on the amount of transferred charge.

Conclusions

Light-induced charge storage in an electrochemical cell was demonstrated for single photosensitive n- and p-type semiconductor electrodes. The combined action of both

Fig. 5. Three subsequent charging and discharging cycles of the photoelectrochemical cell in Fig. 3. Note the different scales for the negative charging current under illumination and the positive discharging current in the dark.



photosensitive electrodes was presented. While the reported observations demonstrate the feasibility of this principle of photoelectrochemical energy conversion, the actual charge recuperation is far from being complete. The charge recuperating in the dark is only approximately one-quarter of the photogenerated charge. This incomplete charge return is caused by various irreversibilities.

A parameter that determines to a large extent the main source of irreversibilities is the length of the time intervals of the charging period of the battery in the light and of the subsequent discharging in the dark. An extended illumination period causes the n-CdSe to photodecompose into a large depth. The CdSe is then shielded from the illumination. Furthermore, the Se-layer is not entirely restored to CdSe in the dark, or may even fall off from the electrode when becoming too heavy. Similarly, the p-CdTe, when electroplated by too thick a Cd-layer, is buried and isolated from both the radiation field and the electrolyte.

A further parameter that has not been optimized in the observations presented above is the fraction of light incident on either photosensitive electrode, and on the auxiliary Si n-p junction. Optimally, the two electrodes must be illuminated such that the photoinduced minority carrier currents be equal, providing for an equal photodecomposition rate of the n-CdSe and photoplate rate of the p-CdTe. Insufficient illumination of one electrode leads to different rates of formation of Se on CdSe and of Cd on CdTe. This difference inevitably involves electrolysis of the aqueous electrolyte, and the corresponding charge cannot be regained in the dark. Unbalanced illumination would in addition convert the less illuminated electrode to a back-biased rectifier series resistance as is obvious by inspection of Fig. 4. This strongly limits the current flow and thereby the photochemical reaction rates in the cell.

The mentioned irreversibilities occur in conjunction with others, such as the degradation of the crystal structure of the electrode approaching an amorphous state upon repeated cycling. Furthermore, the excess Se on the n-CdSe electrode may convert this electrode in the direction to p-type, as has been observed with Te on n-CdTe (15). Only the detailed investigation of all irreversibilities can show whether they may be suppressed to an extent that the photoelectrochemical energy conversion based on the principles presented in this paper may eventually find practical application.

Further study of the degree of reversibility of the n- and p-type photocorrosion under a variety of conditions, combined with a study of the surface morphology, is being considered.

Acknowledgments

One of us (H.J.G.) wants to thank the Deutsche Forschungsgemeinschaft for financial support of a sabbatical stay at the University of Karlsruhe. We gratefully acknowledge the receipt of the CdSe crystals from the Crystal Growth Laboratory of our Physics Department, and that of the CdTe crystals from the University of Freiburg.

Manuscript submitted Sept. 15, 1983; revised manuscript received March 2, 1984.

Universität Karlsruhe assisted in meeting the publication costs of this article.

REFERENCES

1. G. Hodes, J. Manassen, and D. Cahen, *Nature*, **261**, 403 (1976).
2. J. Manassen, G. Hodes, and D. Cahen, *This Journal*, **124**, 532 (1977).
3. J. Manassen, G. Hodes, and D. Cahen, *Chemtech*, 112 (Feb. 1981).
4. P. G. P. Ang and A. F. Sammells, *This Journal*, **129**, 233 (1982).
5. E. Rabinowitch, *J. Phys. Chem.*, **8**, 551 (1940).
6. K. G. Mathai and E. Rabinowitch, *ibid.*, **66**, 663 (1962).
7. T. I. Quickenden and G. K. Yim, *Solar Energy*, **19**, 281 (1977).
8. M. Sharon, S. G. Sharan, B. M. Prasad, A. P. Bholagir, and R. R. Pradhananga, *Solar Energy Int. Prog.*, 1257 (1978).
9. T. Skotheim, *Appl. Phys. Lett.*, **38**, 712 (1981).
10. H. J. Gerritsen, *This Journal*, **133**, 136 (1984).
11. H. Gerischer, in "Topics in Applied Physics," Vol. 31, B. O. Seraphin, Editor, p. 133, Springer-Verlag, Berlin (1979).
12. H. Gerischer, *J. Electroanal. Chem. Interfacial Electrochem.*, **58**, 263 (1975).
13. S. R. Morrison, "Electrochemistry at Semiconductor and Oxidized Metal Electrodes," pp. 331-347, Plenum Press, New York (1980).
14. Y. Nashimoto, S. Fuyuki, T. Akutagawa, and S. Hayakawa, *Jpn. J. Appl. Phys.*, **20**, 565 (1981).
15. C. Vazquez-Lopez, F. Sanchez-Sinacio, J. S. Helman, J. L. Pena, A. Lastras-Martinez, P. M. Raccach, and R. Triboulet, *J. Appl. Phys.*, **50**, 5391 (1979).

Comparison of Behavior of Single-Crystal and Polycrystalline CdS in Photoelectrochemical Cells

James H. Reeves and Michael Cocivera*

The Guelph-Waterloo Center for Graduate Work in Chemistry, Department of Chemistry, University of Guelph, Guelph, Ontario, Canada N1G 2W1

ABSTRACT

Capacitance in the dark and photoresponse were determined from single-crystal CdS $\langle 001 \rangle$ and polycrystalline CdS (deposited cathodically from dimethylsulfoxide). Three different solvents employed (water, triethyleneglycol dimethyl ether and acetonitrile) gave results that lead to essentially the same conclusion. Thus, single-crystal CdS having a "clean" surface gives identical onset and shut-off potentials that are the same as the flatband potential determined from Mott-Schottky (MS) plots of capacitance data. These MS data are independent of the scan direction for the potential. Surface sulfur that results from photooxidation causes the onset to shift negative of the shutoff. Also, the MS intercept becomes dependent upon the scan direction of the potential. These results can be explained by the effect of the oxidation level of the surface sulfur on the flatband potential. In contrast, for fresh polycrystalline CdS that has not been subjected to photo-oxidation, the onset potential is negative of the shut-off potential. These and other results can be used as evidence that the growing process incorporates one or more sulfur containing impurities that are uniformly distributed throughout the film.

Recently, there has been some interest in the use of cathodically deposited, polycrystalline CdS films (1) as a component in photovoltaic cells (PVC) (2). In addition, this film has been used in photoelectrochemical cells (PEC) as an uncoated (3a) and a coated photoanode (4). While some structural and compositional characterization has been reported (3), more information concerning the properties of the film could be helpful in understanding its response in a PVC and the effects of protective coatings in a PEC. Consequently, additional studies of the behavior of this film and single-crystal CdS in PEC's are reported in this paper. In particular, the value of the flatband potential (V_{FB}) determined from Mott-Schottky plots is compared with onset potentials determined from chopped light studies in water and in triethyleneglycol dimethyl ether, which appears to be a convenient solvent for electrochemical studies. For both single-crystal and the polycrystalline film, these parameters depend upon the history of the surface. In addition, the response of the polycrystalline film is consistent with the presence of one or more electrochemically reducible impurities.

Experimental

Materials.—Doubly distilled deionized water was used in all experiments involving aqueous systems.

Triethyleneglycol dimethylether (TGDE), obtained from Aldrich Chemical Company, was refluxed over lithium aluminum hydride (LAH) at 70°-80°C (at 1-2 mm Hg) for 3-5h. The activity of the LAH in the ether was verified by pipeting a small amount of the solution into methanol, after which the ether was distilled directly into the electrochemical cell (distillation temperature 70°-80°C). The cell was brought to atmospheric pressure using dry nitrogen (Canox) and connected to a nitrogen-filled glass rack where TGDE saturated nitrogen was passed continuously into it. Although the age of the solvent appeared to have no direct effect on the experimental results, the ether was replaced every 3-5 days.

Acetonitrile (spectroscopic-grade, Burdick Jackson Laboratories, Incorporated) was passed over an activated alumina column directly into the electrochemical cell, which was purged continuously with acetonitrile-saturated dry nitrogen.

Sodium sulfate, potassium ferrocyanide, and potassium ferricyanide were reagent grade and used as received. Tetraethylammonium perchlorate (TEAP), obtained from Kodak, was recrystallized from deionized water and dried at 100°C under vacuum in a drying pistol for at least 4h. Sodium trifluoromethanesulfonate was synthesized from freshly distilled trifluoromethanesulfonic acid by the addition of sodium hydroxide to a ca. 10% solution of the

acid in water to attain pH 7. The soluble salt was recovered by removing the water, first at reduced pressure on a rotary evaporator and then in a drying pistol at 100°C. Both TEAP and sodium trifluoromethanesulfonate were stored under vacuum in a desiccator.

Semiconductor electrodes.—Two ca. 10g single crystals of CdS (6 Ω -cm resistivity) were donated by Eagle Picher Corporation. Electrodes were cut from the crystals by means of a wire saw using diamond grit paste. An ohmic contact was made by electrodepositing nickel metal onto the surface of the semiconductor at a constant current density of 1 mA/cm² from an aqueous solution of 0.8M NiCl₂, 30 g/l boric acid, and 0.39 g/l sodium laurylsulfate at 44°-55°C. The nickel coated surface was attached to copper with indium, and the liquid junction occurred at the $\langle 001 \rangle$ face. The crystal orientation was determined using a Hilger & Watts Y290 four-circle x-ray diffractometer. The surface of the electrode was then covered with an insulating compound so that only 0.02-0.04 cm² of the semiconductor was exposed. In order to insure that the photoeffects observed were due to properties of the semiconductor rather than to its interaction with impurities present in the insulator, five different materials [parafin, 5 min epoxy (Devcon), Epoxy-patch (Dexter Corporation), and Bostik polymer, and RTV silicon rubber adhesive sealant (GE)] were tried. The most durable insulation proved to be 5 min epoxy coated with the silicon adhesive. Before each experiment, the semiconductor was etched for 10-20s with concentrated hydrochloric acid, rinsed thoroughly with deionized water, and dried with warm air from a heat gun. When extensive oxidation of the crystal had occurred, the surface was lightly sanded with 3/0 Carborundum polishing paper before the HCl etch. Finally, the semiconductor electrode was immersed in the photoelectrochemical cell and cycled over the potential range +1 to -1V in the dark for 15-30 min prior to data collection.

Polycrystalline CdS was cathodically deposited at 110° from reagent-grade dimethyl sulfoxide (DMSO) containing 0.055M CdCl₂ and 0.19M sulfur (1). A current density of 2.5 mA/cm² resulted in films ranging in thickness from 1600 to 9600Å (3a) for 50-300s. The substrate for the deposition in most photoresponse experiments was Mo foil, which was cut by means of a punch to provide flags with 1 cm² area. The flags were etched for 5 min in 5 ml of concentrated HCl containing five to ten drops of hydrogen peroxide, then rinsed thoroughly with deionized water, and dried with acetone. They were then mounted in a Teflon holder, which permitted electrical contact to a copper wire lead by means of a nylon set screw. For capacitance measurements in the dark, platinum wire (0.1

* Electrochemical Society Active Member.

cm diam, 1 cm long) sealed in glass and rounded at the end served as the CdS substrate. In some cases, the CdS electrodes were etched for 10s in 0.1M hydrochloric acid. Some electrodes were annealed under vacuum in a drying pistol at 100° or 250°C in an argon atmosphere. Electrodes that were not used the same day in which they were grown were stored in a vacuum desiccator.

Cell design.—Two cell designs were used. For experiments involving capacitance measurements, a three-neck round-bottom flask was fitted with a large surface area Pt-foil auxiliary electrode, a semiconductor working electrode, and a reference electrode separated from the test solution by either a medium porosity glass frit inside a Luggin capillary or a solvent-soaked filter paper inserted into a capillary tip. Flatband potentials were within 40 mV for the two reference designs. The reference electrodes used were aqueous Ag/AgCl/sat KCl for water, Ag/Ag⁺ (0.1M) for acetonitrile, and a Cd/Cd²⁺ (0.1M) for TGDE. The nonaqueous reference electrodes were calibrated by means of cyclic voltammetry (CV) of 0.002M benzoquinone (Fisher, sublimed) in the appropriate solvent (5). All potentials are reported relative to SCE. The cell was purged continuously with nitrogen introduced with stainless steel syringe needle.

Photoresponse was measured either in this cell or a cylindrical glass cell with a Pyrex window. In the latter the semiconductor electrode is located 0.5-1 cm from the optical flat, and a coiled Pt-wire auxiliary electrode and the reference electrode bridge are positioned immediately behind the working electrode. Dry N₂ was introduced either directly into the solution or passed over it through a glass tube. Stirring was accomplished by means of a small magnetic stirring bar.

Electrochemical experiments were carried out using either a PAR Model 173 potentiostat/galvanostat equipped with a Model 176 current follower or a Bioanalytical Systems (BAS) Model CV-1B cyclic voltammetry unit. The potential sweep generator of a BAS Model CV-1A was used as the programmer for the PAR 173. Results were recorded on a Heath Model SR-207 X-Y recorder.

For capacitance measurements, a Hewlett-Packard Model 4204A oscillator was used to superimpose 2.5 mV ac signal of the appropriate frequency (100 Hz-10 kHz) on the dc voltage ramp (2-3 mV/s) applied to the electrochemical cell. Using a PAR Model 5204 lock-in amplifier, the 0° and 90° components of the resulting current were resolved and recorded on a Nicolet Model IIIA Digital Explorer Oscilloscope equipped with a Model 201 plug-in unit.

Data were analyzed by assuming an equivalent circuit containing a resistance in series with the space charge capacity (C_{sc}). Thus, C_{sc} was calculated by means of the equation $1/C_{sc} = \omega A_{out}/(A_{in}^2 + A_{out}^2)$, in which A_{in} and A_{out} are the 0° and 90° components of admittance calculated from the equivalent current, respectively. For single-crystal electrodes in water and acetonitrile solutions, this equation reduced to $1/C_{sc} = \omega/A_{out}$ because $A_{in} \ll A_{out}$, i.e., $\omega^2 \tau^2 C_{sc} \ll 1$. For the less conductive TGDE solution, the A_{in} is a significant fraction of A_{out} (between 0.1 and 0.4) and could not be ignored in the calculations.

In-phase and out-of-phase currents as a function of potential were analyzed using a Rockwell Aim 65 computer programmed to calculate the slope, the x-intercept (V_{FB}), their respective uncertainties, and the correlation coefficient. In all experiments, dc dark currents were less than 1 μ A over the entire potential range investigated (typically +1 to -0.7V for single-crystal CdS and +1 to -0.4V for the polycrystalline materials, indicating no faradaic component to the impedance). The absence of significant frequency dispersion for single-crystal samples over the frequency range 1-10 kHz suggests that the surface-state capacity (C_{ss}) does not make a significant contribution to the equivalent circuit at these frequencies.

Irradiation of the semiconductor was accomplished using either a 100W mercury lamp, a 150W mercury-xenon lamp (Oriol Corporation), or a 300W ELH quartz-

iodine projector lamp (GE). In each case, the beam was passed through a 5 cm water filter and a series of lenses so that a uniform beam of 40-100 mW/cm² was focused on the semiconductor. The power output of the lamp was determined with an Eppley thermopile. A rotary sector was used to provide periodic illumination of the electrode in chopped light experiments for which potential sweep rates of 10-20 mV/s were generally used. Power curve determinations were carried out under N₂ in a cylindrical Pyrex cell using a 12 cm² indium-doped tin oxide counterelectrode connected to the SCE across a variable load (EICO resistance decade box). The electrodes were immersed in a solution containing 0.4M KCl, 0.2M K₄Fe(CN)₆·3H₂O, and 0.01M K₃Fe(CN)₆. No attempt to optimize cell conditions for maximum power was made, and results were not corrected for the absorption of light by the solution.

Results and Discussion

Power measurements.—Efficiencies for conversion of light to electrical power were determined to insure that the single-crystal CdS was properly mounted and that the surface treatment did not have a deleterious effect. Power measurements for the polycrystalline film have been reported (4).

The photocurrent/photovoltage characteristics of three single-crystal CdS electrodes in H₂O using a Fe(CN)₆⁴⁻³⁻ couple gave efficiencies between 5.7% and 7.4% based on 40 mW cm⁻² incident light from the full spectrum of a 150W Xe arc lamp. The short-circuit current, open-circuit

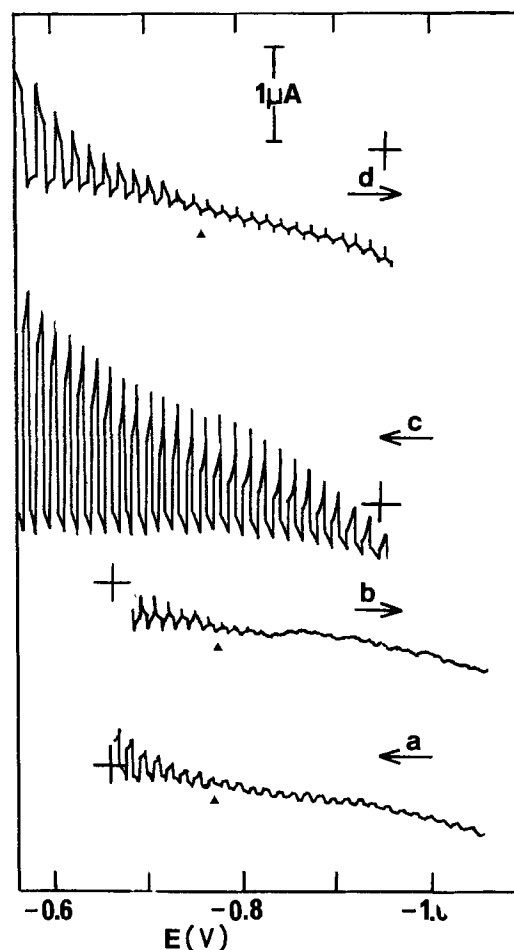


Fig. 1. Chopped light linear potential sweep experiments (cyclic voltammograms) in aqueous 0.05M Na₂SO₄ solutions: (a) anodic and (b) cathodic voltammograms of freshly etched (conc. HCl, 10s) single-crystal CdS; (c) anodic and (d) cathodic voltammograms of CdS single crystal after surface oxidation caused by sweeping the potential to 0V under illumination. Scan rate 10 mV/s; potential reported vs. SCE; exposed surface area 0.08-0.10 cm². The solid triangle marker indicates the onset or shut-off potential. The cross designates zero for the Y-direction (current) for each trace.

voltage, and fill factor were, on the average, 4.5 mA/cm², 1.1V, and 0.65, respectively. No correction was made for light intensity decrease due to solution absorption, and photoetching (6) was not employed to improve performance. For comparison, the maximum efficiency, open-circuit voltage and short-circuit current under very similar conditions are reported to be 9.5%, 1V, and 6 mA/cm², respectively (7a). Thus, it appears that single-crystal CdS electrodes, which are used in the studies described below, are of reasonably good quality. The polycrystalline film provides a substantially lower efficiency of 0.1%-0.2% based on 100 mW cm⁻² incident light from a 150W Xe lamp (4).

Chopped light and capacitance in water.—When the surface of single-crystal CdS is carefully prepared, both the capacitance data and the chopped light experiments give the same flatband potential in water and triglyme. Thus, for the chopped light experiment when the surface is fresh, a positive potential sweep (-1.0 to -0.5V SCE) gives an onset potential of -0.76V vs. SCE (Fig. 1a), which is identical to the potential at which the photoanodic current stops (shut-off potential) for the negative potential sweep (-0.5 to -1.0 or -1.2V vs. SCE) (Fig. 1b). Mott-Schottky (MS) plots of the capacitance data (Fig. 2) (1-10 kHz) give a flatband potential of -0.73V, which is identical to the value reported previously (8, 9) and agrees well with the value obtained from the chopped illumination studies above. These results are obtained when the electrode is freshly prepared, *i.e.*, HCl etched prior to use. Under these conditions the capacitance data (and V_{FB}) are independent of the direction of potential scan. Furthermore, the lack of any substantial frequency dispersion in the MS plots verifies that surface-state capacitance does not make appreciable contribution in the frequency range employed. From the slope of the MS plots the donor density, n_D is calculated (10) to be $8.7 \times 10^{15}/\text{cm}^3$ and the bulk conductivity of $0.3 \Omega^{-1} \text{cm}^{-1}$ is calculated using $n\mu$ in which the carrier density $n = n_D$, e is the electronic charge, and μ ($\sim 200 \text{cm}^2/\text{Vs}$) is the carrier mobility.

When the surface is purposely oxidized by extending the positive sweep to 0.0V (SCE) to increase the duration and extent of the photoanodic current, the flatband potential (from MS and from chopped light) depends on the ramp direction. In fact, the MS results are identical with the chopped light results, *i.e.*, starting at a negative potential causes a negative shift in the flatband relative to the

clean surface, whereas there is no shift when the ramp is started at a positive potential. Thus, for chopped light, the shut-off potential remains unchanged at about -0.70V; however, the onset shifts progressively in the negative direction so that at the third cycle the onset occurs at -1.0V (Fig. 1c). After extensive oxidation the photoresponse for the cathodic scan resulted in a resurgence photo-oxidation negative of the -0.6 to 0.7V region (Fig. 3b).

AC impedance measurements after the electrode has been oxidized slightly (chopped illumination while the potential is cycled once between -1.2 and -0.5V) give capacitance data that are now dependent upon the potential scan direction (Fig. 2). Under these conditions, the MS plots are still linear with the same slope; however, the intercepts are -0.76V (1.0 to -0.5V scan) and -0.90 (-0.7 to +1.0V scan). For the latter, the potential was held at -1.0V prior to the scan. In this regard, the capacitance data seem more sensitive than the onset potential measurement, *i.e.*, the amount of sulfur resulting from one cycle between -1.2 and -0.5V during chopped illumination is not sufficient to cause a measurable shift in the onset potential. After extensive chopped light oxidation of single-crystal CdS in H₂O, the MS plots are no longer linear, and the capacitance values are larger than those for a fresh electrode.

We have purposely chosen conditions (Na₂SO₄ in H₂O) that other workers (7, 8) have employed to produce surface sulfur by photo-oxidation. Consequently, we propose the following description to account for the chopped light and MS results. With a fresh sample having no appreciable sulfur on the surface, the onset and shut-off potentials are identical, indicating that V_{FB} may be determined by potential sweep in either direction during chopped illumination. However, once sulfur is adsorbed on the surface in appreciable amounts, it can shift V_{FB} when it is reduced to form S_n^{2-} in which $n > 1$. In other words, surface sulfur in a reduced form can act in the same manner as S^{2-} in solution, which is known to chemisorb to single-crystal CdS (8b) and cause a shift in V_{FB} to values as negative as -1.45V (SCE) depending on concentration (9). This reduced form would be generated for the negative to positive potential scan used for the ac impedance and chopped light experiments. However, surface sulfur is not reduced during the cathodic scan until the potential is negative of V_{FB} . Sulfur in the unreduced form does not shift V_{FB} and, therefore, the shut-off potential is not

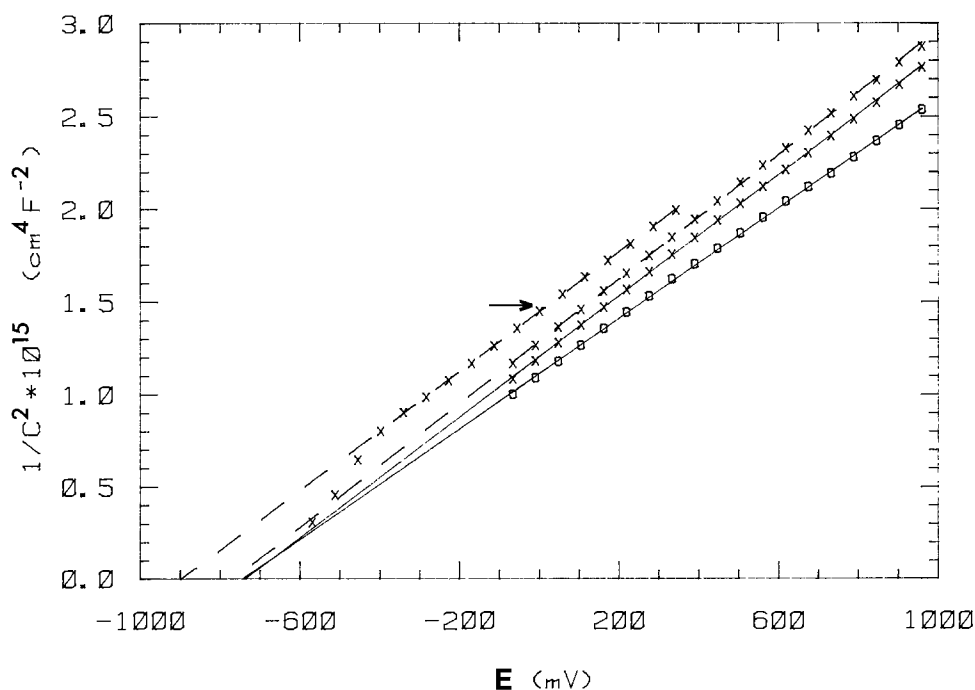


Fig. 2. (—): Mott-Schottky plots of freshly etched single-crystal CdS in aqueous 0.50M Na₂SO₄ at 1 kHz (○) and 10 kHz (×). (---): Mott-Schottky plots at 10 kHz for single-crystal CdS after the potential was swept to -0.60V under chopped illumination. The arrow indicates the data obtained for the anodic sweep direction.

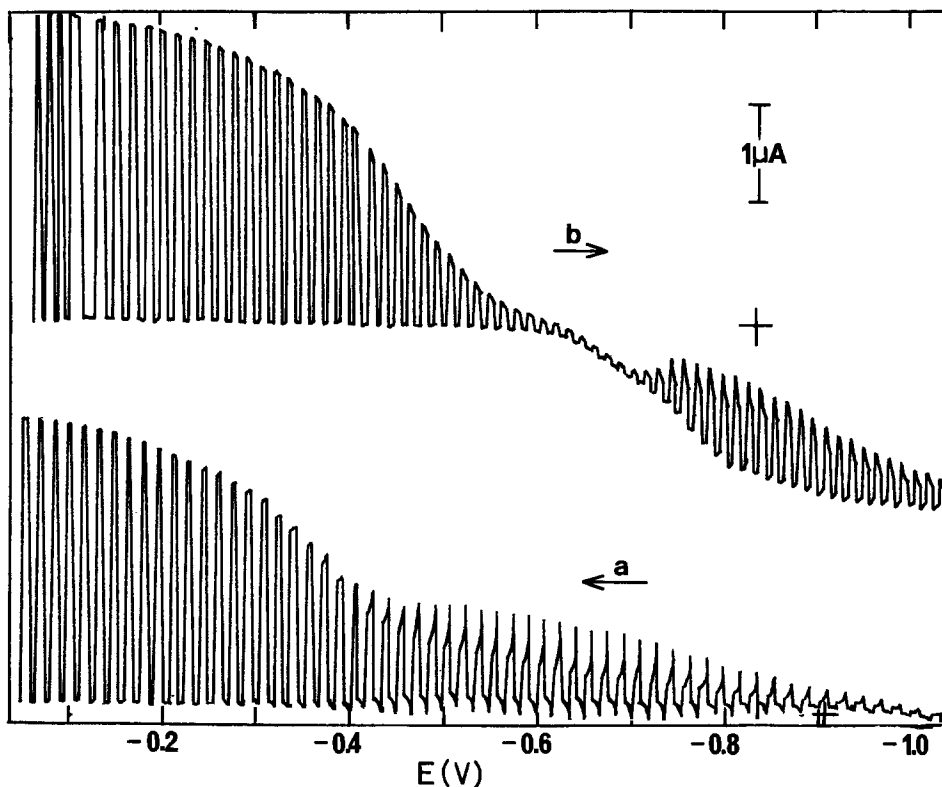


Fig. 3. Chopped light (a) anodic and (b) cathodic linear potential sweep voltammograms for single-crystal CdS in water after illumination at 0V for 1 min. Scan rate 10 mV/s, potential vs. SCE; exposed surface area 0.05 cm².

shifted in the negative direction. Consequently, the cathodic scan for ac impedance and chopped light gives a realistic measure of V_{FB} for moderately oxidized surface. In Fig. 3b, the photoresponse of CdS that has been oxidized more extensively exhibits a resumption of photoanodic current negative of the shut-off potential. This behavior is consistent with our description since the dark cathodic current at potentials negative of the shutoff can be attributed to the reduction of sulfur which is oxidized during the light-on phase.

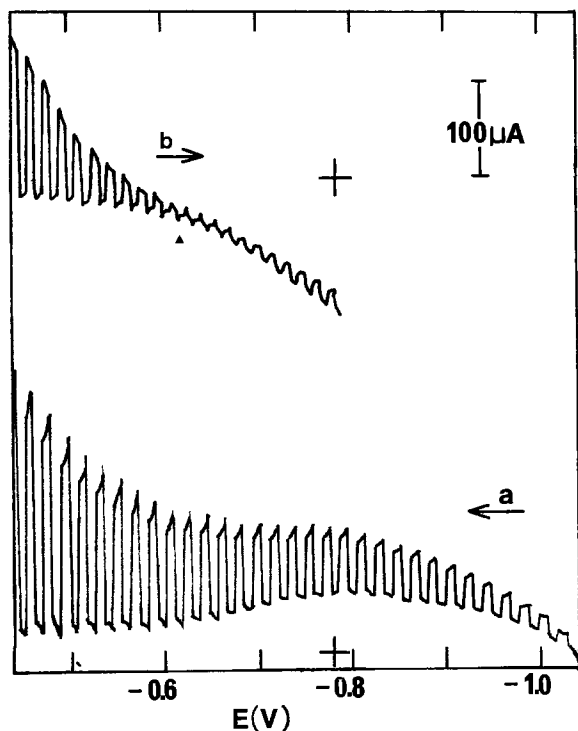


Fig. 4. Chopped light (a) anodic and (b) cathodic linear potential sweep voltammograms of freshly etched (0.1M HCl, 10s) and dried (100°C, vacuum) polycrystalline CdS in aqueous 0.50M Na₂SO₄. Sweep rate, 10 mV/s; potential vs. SCE; exposed surface area, 0.5 cm².

For polycrystalline CdS films in aqueous Na₂SO₄, a variable onset potential also occurs. In this case, however, even the fresh film has an onset potential that differs from the shut-off potential (Fig. 4). Thus, for fresh films starting with an initial potential of -1.1V and sweeping in the positive direction to various potentials (-0.5 to 0.0V), the onset occurs immediately at about -1.1V vs. SCE. However, the return sweep in the negative direction gives a shut-off potential ranging from -0.60 to -0.65V. These results are essentially the same for a variety of treatments of the film, *i.e.*, unetched films that were freshly grown and dried prior to use or samples that were prepared 1-3 days before use. The age of the growing solution also did not appear to affect the onset and shut-off potentials. Various methods of drying (vacuum desiccator, vacuum pistol at 100°C, and Ar atmosphere at 250°C) gave the same difference between onset and shut-off potentials. The high temperature treatment provided films with the lowest dark currents at potentials positive of -0.8V, but these increased substantially after the first chopped light cycle, indicating surface oxidation. Etched films (0.1M HCl) gave the same results as unetched films. In all these cases, the films exhibit a substantial dark cathodic current at -1.0V.

These results may be explained in general by invoking grain boundaries and surface defects. However, a more specific description which is based on the close analogy between the effects observed for surface-oxidized single-crystal CdS and those for unoxidized polycrystalline CdS would be that the polycrystalline film contains unreduced or partly reduced sulfur.

Chopped light and capacitance in TGDE.—The study was extended to TGDE because the explanation presented above requires that the effects should be independent of solvent. Although TGDE apparently has not been employed for electrochemical studies, it seems attractive for this purpose since it is easily purified and has a rather large potential range (-1.5 to +1.0V vs. SCE). In this solution, the chopped light results are similar to those in water for single-crystal CdS (Fig. 5). Thus, for a fresh electrode, the onset and shut-off potentials are -0.85 and -0.80V, respectively, vs. SCE. After purposely oxidizing the surface by scanning to +0.1V under illumination, however, the onset shifts to *ca.* -1.0V; and at potentials

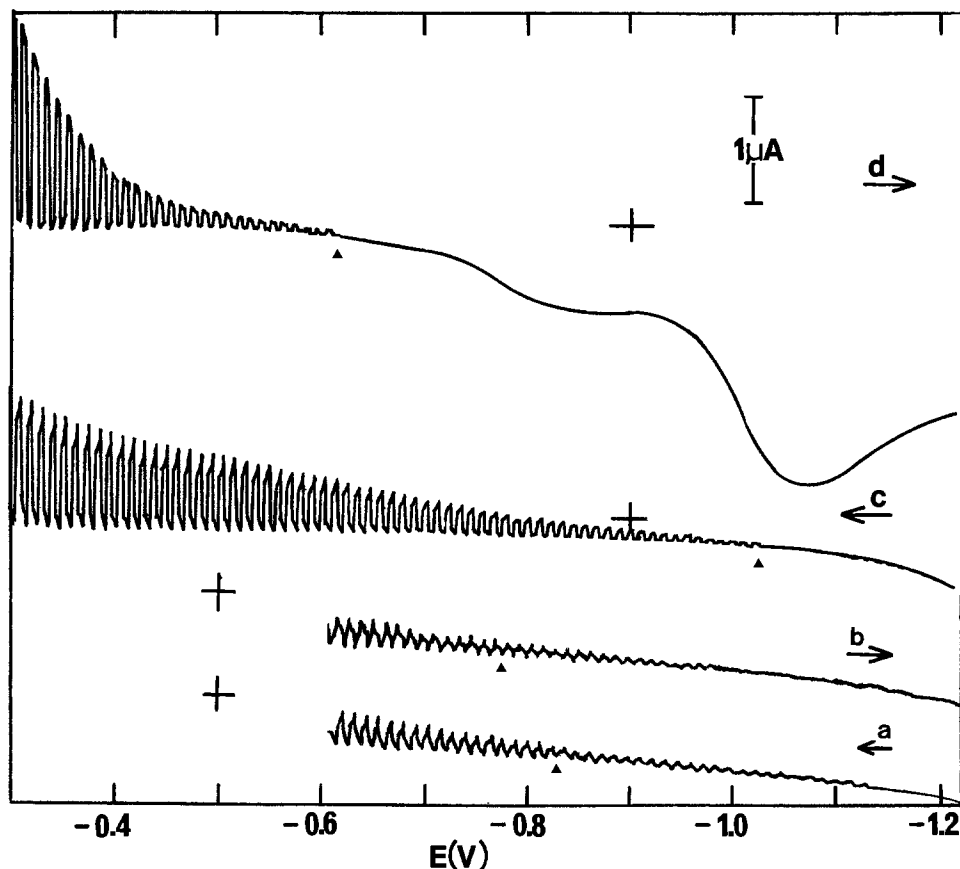


Fig. 5. Chopped light linear potential sweep experiments in TGDE solutions containing 0.20M NaCF_3SO_3 . (a) Anodic and (b) cathodic voltammograms of freshly etched single-crystal CdS, (c) anodic and (d) cathodic voltammograms of single-crystal CdS after the potential was swept to +0.1V under chopped illumination. Scan rate 10 mV/s, potential reported vs. SCE, surface area 0.02 cm^2 .

negative of the shut-off potential (-0.6V), dark cathodic current develops (shoulder at ca. -0.8 and peak at -1.08V). The dark currents are similar to those observed for single-crystal CdS in acetonitrile (5).

The MS plots for single-crystal CdS in TGDE are similar to those in H_2O with the capacitance values and carrier density about the same and a V_{FB} of -0.85V (Fig. 6). Very little frequency dispersion (1-10 kHz) is observed, and the capacitance values are not dependent upon the direction of the potential scan when the electrode is fresh. After the surface of the electrode has been oxidized by illumination for one cycle between -1.22 and +0.48V, the capacitance data are no longer independent of the direction of poten-

tial scan, although the MS plots remain linear and the slopes are the same for both scan directions (Fig. 6). Thus, the intercepts for the cathodic scan (+0.48 to -0.62V) and the anodic scan (-0.92 to +0.48V) are -0.76 and -1.18V, respectively. For the latter, the electrode was biased at -1.5V for a few minutes prior to scan. The similarity between these results and those obtained in H_2O indicates that the same description concerning surface sulfur probably applies. Consequently, for single-crystal CdS, the onset potential reflects the extent to which surface sulfur is present.

The chopped light results for polycrystalline CdS in TGDE are similar to those in H_2O in that the onset poten-

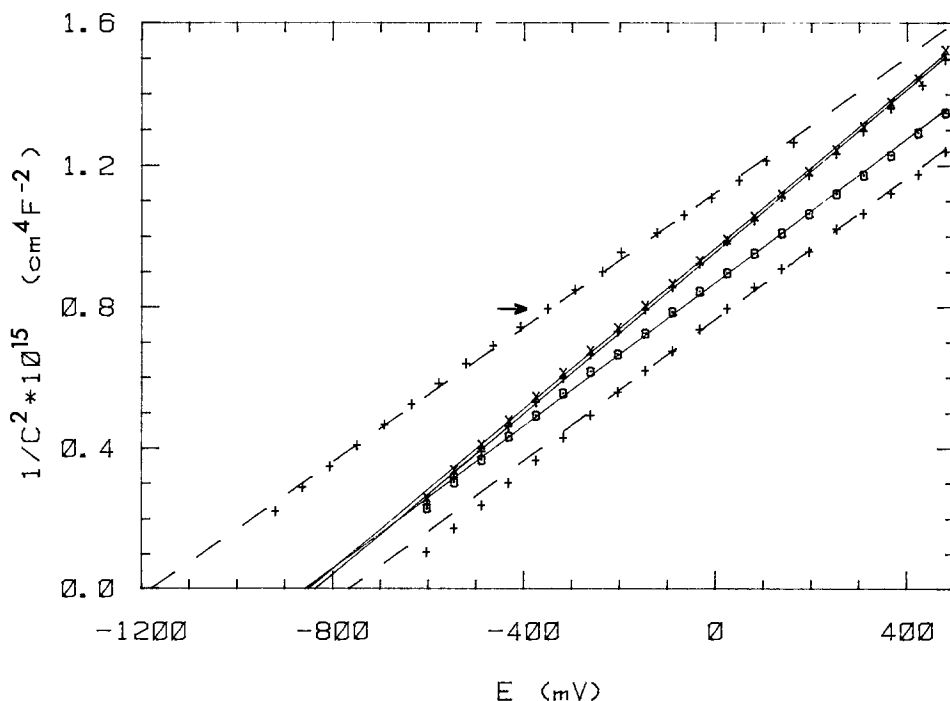


Fig. 6. (—): Mott-Schottky plots of freshly etched single-crystal CdS in TGDE containing 0.20M NaCF_3SO_3 at (○) 1, (+) 5, and 10 kHz (×). (- - -): Mott-Schottky plots of single-crystal CdS after its potential was cycled to +0.5V under chopped illumination. The arrow indicates the data obtained for the anodic sweep direction commencing at ca. -1V. Potential vs. SCE; scan rate, 2-3 mV/s.

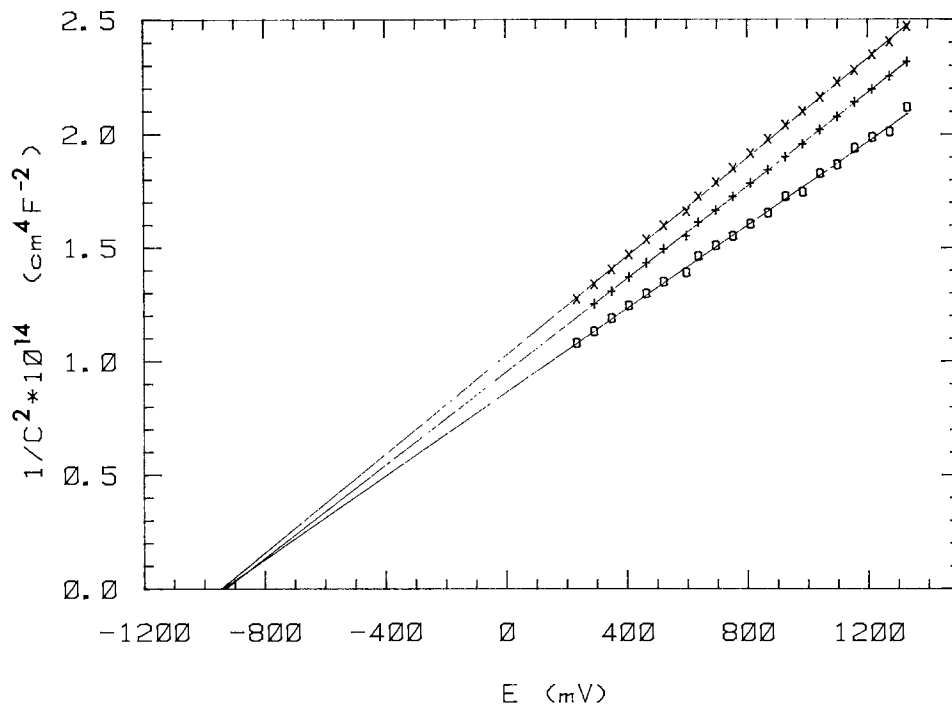


Fig. 7. Mott-Schottky plots of freshly etched (conc HCl, 10s) single-crystal CdS in acetonitrile containing 0.20M TEAP at 1 (○), 5 (+), and 10 kHz (×).

tial (-1.1V) differs from the shut-off potential (-0.72V). These results are consistent with the description that the film contains a reducible sulfur impurity and rules out the possibility that a specific interaction between water and the film surface is responsible.

Earlier work (5) indicated that capacitance data for single-crystal CdS in acetonitrile are frequency dependent and that the MS plot gave frequency-dependent intercepts. We find that freshly etched single-crystal CdS electrodes in acetonitrile give little frequency dispersion in the region 1.3-0.2V (Fig. 7) and that this method gives $V_{FB} = -0.93V$, in reasonable agreement with $-0.85V$ obtained from chopped-light experiments (5).

In summary, Mott-Schottky and chopped-light results indicate that surface sulfur causes V_{FB} to depend on the scan direction of the potential. This dependence occurs because sulfur on the surface of CdS can be reduced at sufficiently negative potentials. Since freshly etched single-crystal CdS does not exhibit this behavior, it is possible that the previously observed inconsistencies associated with the slopes and intercepts of MS plots for CdS (11) may be caused by the presence of surface sulfur. Although the behavior of polycrystalline CdS film is similar to that of the single crystal, there is one notable difference. The dependence of V_{FB} on scan direction occurs even before any photoanodic process has occurred. Consequently, one possible explanation is that one or more impurities similar to sulfur are incorporated in the film during the electrochemical deposition process.

Acknowledgments

We are pleased to acknowledge very useful discussions with Dr. A. S. Baranski, Dr. M. Bennett, Dr. A. C. McDonald and Dr. W. R. Fawcett. We thank Dr. P. Szczecinski for preparation and power measurements of the single-crystal electrodes, and Dr. G. Ferguson for determination of the crystal orientation. This work was supported in

part by a grant (to M. C.) from the Natural Sciences and Engineering Council of Canada.

Manuscript submitted March 3, 1983; revised manuscript received Oct. 31, 1984. This was Paper 521 presented at the San Francisco, California, Meeting of the Society, May 8-13, 1983.

The University of Guelph assisted in meeting the publication costs of this article.

REFERENCES

1. A. S. Baranski and W. R. Fawcett, *This Journal*, **127**, 766 (1980).
2. H. J. Wagner and R. O. Loutfy, *J. Vac. Sci. Technol.*, **20**, 300 (1982).
3. (a) A. S. Baranski, W. R. Fawcett, K. Gatner, A. C. McDonald, J. R. MacDonald, and M. Selen, *This Journal*, **130**, 579 (1983); (b) A. S. Baranski, W. R. Fawcett, A. C. McDonald, and R. M. de Nobrega, *ibid.*, **128**, 963 (1981).
4. J. H. Reeves and M. Cocivera, *J. Chem. Soc. Chem. Commun.*, 1003 (1982).
5. (a) P. A. Kohl and A. J. Bard, *J. Am. Chem. Soc.*, **99**, 7531 (1977); (b) F. Quarto and A. J. Bard, *J. Electroanal. Chem.*, **127**, 43 (1981).
6. R. Tenne, *Appl. Phys.*, **25**, 13 (1981).
7. (a) H. Gerischer and J. Gobrecht, *Ber. Bunsenges. Phys. Chem.*, **80**, 327 (1976); (b) *ibid.*, **82**, 520 (1978).
8. (a) T. Inoue, T. Watanabe, A. Fryishima, K. Honda, and K. Kohayakawa, *This Journal*, **124**, 719 (1977); (b) H. Minoura and M. Tsuiki, *Electrochim. Acta*, **23**, 1377 (1978); (c) R. Williams, *J. Chem. Phys.*, **32**, 1505 (1960).
9. (a) H. Minoura, M. Tsuiki, and T. Oki, *Ber. Bunsenges. Phys. Chem.*, **81**, 588 (1977); (b) T. Inoue, T. Watanabe, A. Frjishima, and K. Honda, *Bull. Chem. Soc. Jpn.*, **52**, 1243 (1979).
10. S. R. Morrison, "Electrochemistry at Semiconductor and Oxidized Metal Electrodes," Chap. 4, Plenum Press, New York (1980).
11. E. C. Dutoit, R. L. Van Meirhaeghe, F. Cardon, and W. P. Gomes, *Ber. Bunsenges. Phys. Chem.*, **79**, 1206 (1975).

Photoelectrochemical Properties of α - and β -ZnP₂ Electrodes and Powders

D. H. M. W. Thewissen, A. H. A. Tinnemans, E. A. van der Zouwen-Assink, and A. Mackor

Institute of Applied Chemistry TNO, 3502 JA Utrecht, The Netherlands

H. von Känel, R. Hauger, and P. Wachter

Laboratorium für Festkörperphysik, ETH-Hönggerberg, CH-8093 Zürich, Switzerland

ABSTRACT

The basic photoelectrochemical behavior of tetragonal p-type α -ZnP₂ has been investigated for the first time. The photoinduced current as a function of applied voltage and the spectral distribution of the photoresponse were measured in alkaline solutions (pH 13). Photosensitivity up to 580 nm in the visible range of the spectrum has been observed. From a linear Mott-Schottky relation, an approximate value of the flatband potential ($V_{FB} = -0.7 \pm 0.05 V_{SCE}$) at pH 13 for monoclinic β -ZnP₂ has been determined. As a function of pH, V_{FB} shows Nernstian behavior. For tetragonal α -ZnP₂, V_{FB} could not be determined. The onset of the cathodic photocurrent ($\approx -0.4 V_{SCE}$ at pH 13) indicates, however, a somewhat more positive V_{FB} for α -ZnP₂. Upon illumination with visible light, hydrogen evolution from alkaline EDTA solutions containing ZnP₂ powders loaded with a catalyst is very efficient. For α -ZnP₂ loaded with 0.5 weight percent of RuO₂, a formal quantum efficiency of 12% is found at 470 nm.

Much effort has been devoted in the last few years to the search for new materials or material combinations for the photoelectrolysis of water with visible light. One class of compounds to which little attention has been paid so far, at least with respect to the conversion of solar energy, is the series of monoclinic transition metal phosphides and arsenides MX₂ with, e.g., M = Cu, Ni, Zn and X = P, As. In a previous publication (1), we have reported a first photoelectrochemical investigation of one of these, i.e., p-type monoclinic β -ZnP₂, which should be ideally suited for solar cell applications both because of the abundance of its constituents and due to its direct bandgap of ≈ 1.5 eV. While the flatband potential V_{FB} could only be estimated before (1), we report in this paper new capacity measurements from which V_{FB} can be determined unambiguously.

Much before the discovery of β -ZnP₂ (2), another modification of this compound had been reported in the literature (3). In contrast to β -ZnP₂, this tetragonal α -ZnP₂ modification was found to have an indirect bandgap around 2.1 eV (2, 4).

In the following, we shall describe first photoelectrochemical measurements on single-crystal α -ZnP₂ electrodes. For both modifications, a first account of the hydrogen evolution on catalyst covered semiconductor particles shall be given.

Experimental

Crystal growth and electrode fabrication.— α - and β -ZnP₂ are synthesized in a two-step process. First, Zn metal and red electronic-grade phosphorus are sublimed in a quartz ampul, yielding Zn₃P₂. After purification of Zn₃P₂ by a further sublimation, this compound is phosphidized to ZnP₂ in an atmosphere of excess phosphorus. The pressure in the ampuls depends on the temperature and the amount of excess phosphorus. At temperatures of 800°-850°C and at pressures around 10 bar, the black β modification results, from which single crystals are obtained in a phosphorus atmosphere by sublimation. The red α modification is obtained by sublimation under stoichiometric conditions or low phosphorus pressures in the same temperature regime. Large single crystals require a very good stabilization of temperature and pressure.

The as-grown crystals of the β modification had resistivities around 1000 Ω cm. These could be lowered down to ≈ 10 Ω cm by annealing the crystals in a phosphorus pressure of 10 bar and at temperatures up to 500°C.

For α -ZnP₂, however, resistivities in the range of $\approx 10^5$ Ω cm could not be significantly reduced, even by annealing

the crystals at temperatures up to 700°C at 10 bars. Thus, a different doping procedure will have to be found.

For all experiments on β -ZnP₂ single crystals described below, the as-grown (100) face (without polishing) was exposed to the electrolyte. Electrical contacts were made by first sputtering gold on both sides of the crystals. After a brief heat-treatment (30s at 400°C in air) the current-potential curves generally showed excellent linearity up to the highest voltages which could be applied without overheating the samples. Thus the contacts were found to be perfectly ohmic.

Platelets of α -ZnP₂ were obtained by cleaving large single crystals perpendicular to the tetragonal C-axis. They were contacted in the same way as described above. In this case, however, the contacts were not strictly ohmic.

The electrodes were prepared in the usual way (1) after the Au contact on the face to be exposed to the electrolyte had been removed. All electrodes were etched in H₂O:HCl:HNO₃ = 1:2:2.

Experiments with single-crystal electrodes.—The solutions used for these measurements were made from deionized water and reagent-grade chemicals. The Mott-Schottky plots were obtained from admittance measurements as a function of electrode potential in the frequency range from 150 Hz up to 20 kHz. The real and imaginary part of the admittance were measured simultaneously by modulating the electrode potential with a 10 mV_{pp} sine wave and by recording the potential drop induced by the cell current across a small resistor with an Ithaco Dynatrac 393 lock-in amplifier. All signals were calibrated with a Hewlett-Packard 4440 B decade capacitor.

For a resistor and a capacitor C_p in parallel, the imaginary part of the admittance is proportional to the capacitance while for a series circuit the series capacitance C_s has to be calculated using both the real and the imaginary part of the admittance. In all of the data reported below, the real part of the admittance was small enough such that within the experimental errors $C_p = C_s$.

The photocurrent spectra and the photocurrent-potential curves were recorded using standard lock-in techniques. Illumination was provided by a 450W xenon lamp filtered through a ZEISS PMQII double-prism monochromator. Intensities were measured with a Moletron PR 200 pyroelectric radiometer.

Preparation and modification of powdered ZnP₂.—Both α - and β -ZnP₂ powders were made by crushing small crystals in an agate mortar.

α -ZnP₂/0.5 weight percent (w/o) Rh and β -ZnP₂/0.5 w/o Rh.—500 mg of the appropriate ZnP₂ were added to a red solution of 4.54 mg Rh₄(CO)₁₂ (Strem Chemicals) in 4 ml of CH₂Cl₂. The mixture was stirred and then sonicated for 0.5h. The solvent was evaporated. The powder was dried and heated at 160°C for about 2h. In the IR spectra of these compounds, no CO absorptions were observed.

α -ZnP₂/0.5 w/o RuO₂ and β -ZnP₂/0.5 w/o RuO₂ (RuCl₃ method).—A suspension of 1g of the appropriate ZnP₂ and 0.76 ml of a 0.05M RuCl₃ · 3H₂O (Drijfhout) solution in 1N HCl was stirred and then sonicated for 0.5h. The solvent was evaporated. The powder was dried and subsequently heated in an oven at 400°C for 6h under a stream of air.

β -ZnP₂/0.5 w/o RuO₂ (RuO₄ method).—2.4 ml of a solution, containing 130 mg of RuO₄ (Alfa Chemicals) in 50 ml of distilled water (ca. 6.24 mg of RuO₄) were added dropwise to a sonicated suspension of 1g of β -ZnP₂. No visible reaction took place. The mixture was stirred for 26h. The black powder was filtered, stirred with 100 ml of distilled water, and centrifugated. After removal of the water, the powder was dried above KOH.

Illumination experiments with ZnP₂ powders.—Illuminations were carried out with an Oriel XBO 450W xenon lamp, using a Schott KV-418 cutoff filter. The flat reaction vessel, thermostated at 40°C, containing 75 mg of the ZnP₂ powder in 75 ml of solution, adjusted to pH 13, was equipped with a gas burette, connected with a paraffin filled expansion flask. The produced hydrogen was measured volumetrically at atmospheric pressure.

Monochromatic measurements were performed using a Bausch and Lomb high intensity monochromator. A cutoff filter (KV-370) was used to prevent second-order radiation effects. Light intensity at 470 nm was determined by ferrioxalate actinometry (5). The reaction vessel was fitted with a septum and a valve. 50 μ l gas samples were taken at intervals with a syringe through the septum. The formed hydrogen was monitored on a Varian 3700 gas chromatograph with TC detection using a 1.3m \times 44 mm (id) glass column, packed with mol sieve 5 Å at 40°C. Argon was used as the carrier gas; the flow was 20 ml/min.

Results and Discussion

Single-crystal electrodes.— β -ZnP₂ Figure 1 shows the Mott-Schottky plots obtained from the imaginary part of

the measured admittance for several frequencies between 150 Hz and 20 kHz. The electrolyte used was 1M Na₂SO₄, adjusted to pH 13 by the addition of NaOH. For all frequencies, the plots are reasonably linear, but below \approx 1.5 kHz a significant shift of the intercepts with the potential axis in the negative direction is seen to occur. The concomitant increase of the capacity might be due to the increasing contribution of surface states towards low frequencies (6). Since the curves deviate only slightly from one another at frequencies above 1.5 kHz we can deduce the flatband potential with reasonable accuracy. From Fig. 1, we get $V_{FB} = -0.7 \pm 0.05 V_{SCE}$. In the absence of a knowledge of the surface roughness, we can at best give a rough estimate of the doping concentration N_A . Assuming a roughness factor of 2 and a dielectric constant $\epsilon = 10$ (7), we obtain N_A of $\approx 7 \times 10^{17} \text{ cm}^{-3}$ from the slope of the Mott-Schottky plots.

Due to the highly negative position of the flatband potential $V_{FB} = -0.7 V_{SCE} = -0.46 V_{NHE}$, the hydrogen evolution reaction on the illuminated β -ZnP₂ electrode is strongly exothermic. This explains the steep rise of the photocurrent-potential curves on the bare semiconductor surface, which has been found before (1). The small photovoltage achieved at pH 14 with redox couples such as Fe³⁺/Fe²⁺ triethanolamine (TEA) with a reversible potential of $-1 V_{SCE}$ (1) is also consistent with the negative V_{FB} . Furthermore, as expected in our previous paper (1), the flatband potential does indeed shift by approximately 60 mV per pH unit. This can be seen in Fig. 2, which shows the Mott-Schottky plots at a frequency of 4.7 kHz for several pH values. The electrolyte used in this case was 0.5M K₂SO₄. The electrode had a somewhat smaller doping level than the one described above.

In the next section we examine photoelectrochemical hydrogen evolution from sulfide solutions over β -ZnP₂ powders. As anions such as S²⁻ may cause a cathodic shift of V_{FB} , we have also examined the influence of sulfide on V_{FB} at the β -ZnP₂/electrolyte interface. In contrast to the large shift as a function of pH, the addition of sulfide at pH 13 results only in a small negative shift of V_{FB} . This is displayed in Fig. 3, in which the Mott-Schottky plots for a frequency of 10 kHz are shown before (*) and after (+) the addition of $\approx 7 \cdot 10^{-2} \text{ MS}^{2-}$.

α -ZnP₂.—Since we have not yet performed any doping experiments on the tetragonal α -ZnP₂ crystals (other than annealing them in a phosphorus atmosphere), the photo-

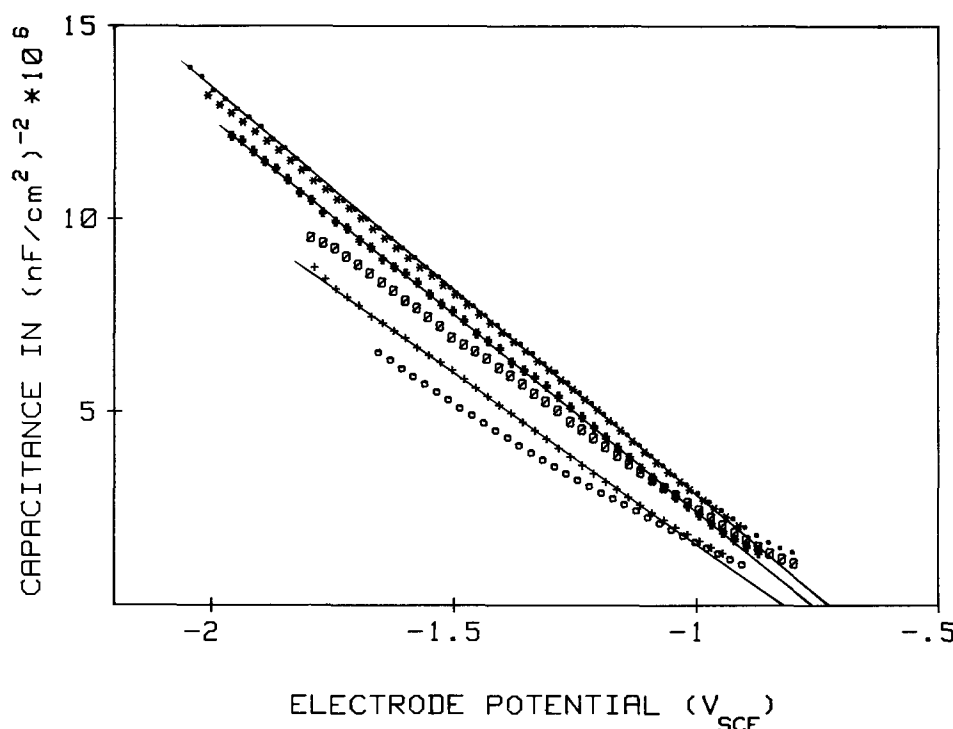


Fig. 1. Mott-Schottky plots for a β -ZnP₂ electrode in 1M Na₂SO₄ at pH 13 for different frequencies: (○) 150 Hz, (+) 1 kHz, (⊘) 1.5 kHz, (≠) 10 kHz, (•) 15 kHz, and (★) 20 kHz.

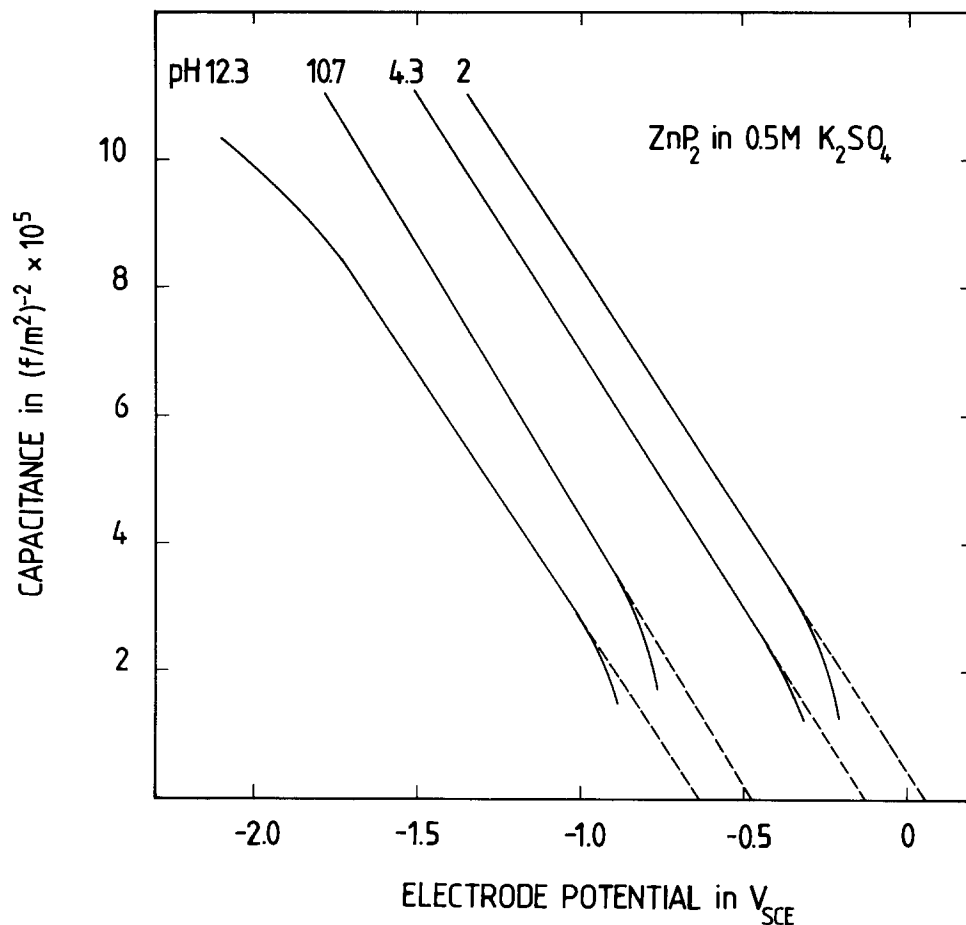


Fig. 2. pH dependence of the space charge capacity of β -ZnP₂ in 0.5M K₂SO₄. $\nu = 4.7$ kHz.

electrochemical results on the highly resistive electrodes are of a somewhat preliminary nature. In particular, we have not yet been able to measure the flatband potential because of an excessive frequency dependence of the Mott-Schottky plots. For the powder experiments, however, we do not expect any major changes for a more highly doped material.

Despite the low doping level, we have only measured a cathodic photocurrent characteristic of a p-type semicon-

ductor. The photocurrent-potential curves show a step rise near the onset potential $V_{on} \approx -0.4 V_{SCE}$ at pH 13, and saturation is attained very rapidly for low light intensities. This is shown in Fig. 4, in which the photocurrent-potential curves are displayed for four different light intensities covering a range of 3 decades. All the curves are normalized to unit intensity. The latter was varied by introducing neutral density filters, the transmission of which differed by a factor of 10 each, in front of the monochro-

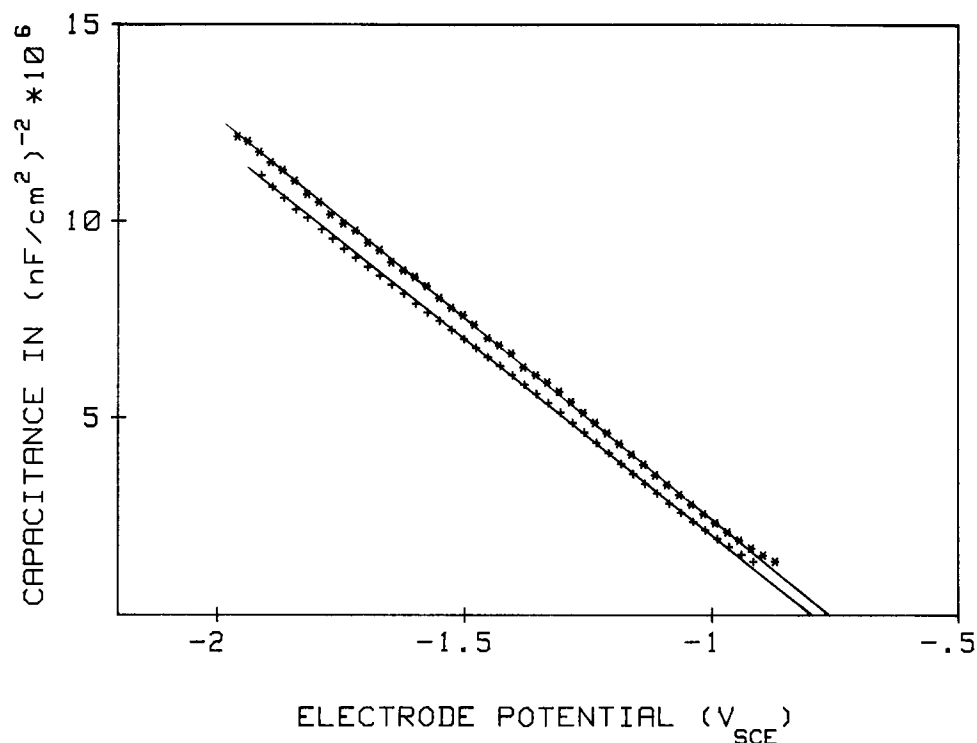


Fig. 3. Space charge capacity of β -ZnP₂ in 1M Na₂SO₄, pH 13 before (*) and after (+) the addition of $7 \times 10^{-2} M S^{2-}$. ($\nu = 10$ kHz).

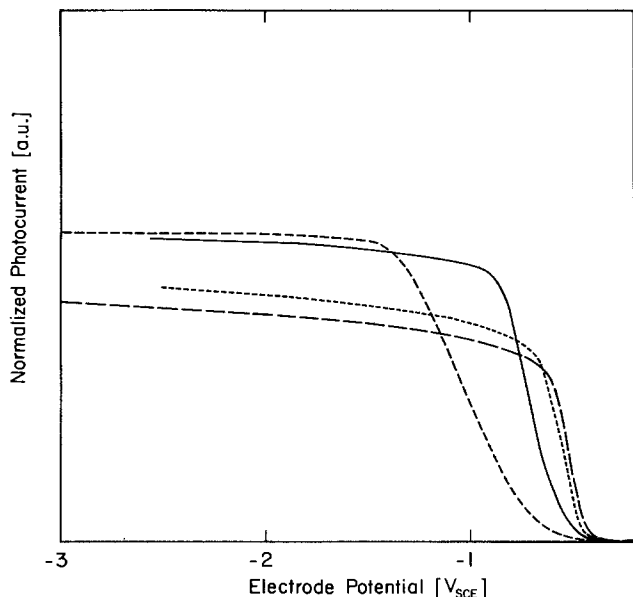


Fig. 4. Normalized photocurrent-potential curves for an α -ZnP₂ photocathode in 1M Na₂SO₄ at pH 13 for different illumination intensities, $\lambda = 470$ nm. The respective intensities are, in arbitrary units: (---) 1, (—) 0.1, (····) 0.01, and (- - -) 0.001.

mator ($\lambda = 470$ nm). There is a much slower rise to the saturation value at the higher light intensities, signifying increased recombination near the electrode surface. For (more intense) white light illumination, this effect is even more drastic. In this case, saturation is no more achieved at high intensities even up to potentials of $-5 V_{SCE}$. Provided that the electrodes can be suitably doped, it should be possible to eliminate this drawback in the future.

The measured cathodic-dark current was negligible in the potential range displayed in Fig. 4 (below $0.1 \mu A$). The addition of sulfide to the electrolyte did not affect the photocurrent-potential curves appreciably. Hence a significant shift of the flatband potential due to the adsorption of S^{2-} can probably be ruled out for α -ZnP₂ as well.

In Fig. 5, is depicted the quantum yield (uncorrected for reflection) as a function of wavelength for an electrode potential of $-3 V_{SCE}$ and at an intensity for which saturation is reached (see also Fig. 4). We have encountered an appreciable variation of the quantum yield of different electrodes. Figure 5 can be regarded to represent the behavior of a typical electrode. The values are comparable to those found in β -ZnP₂ (8), but of course the rise as a function of decreasing wavelength (or rather increasing

photon energy) is much slower due to the indirect nature of the energy gap.

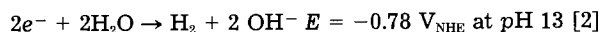
Powders: characterization of the materials.— α -ZnP₂.—The x-ray powder diffractogram of the untreated red α -ZnP₂ reveals the presence of a few percent of β -ZnP₂. Upon application of a catalyst, *viz.* Rh or RuO₂, and the accessory heat-treatment, no reflections disappear, nor can new lines be observed. Likewise, the diffractogram remains unchanged after prolonged illumination. Apparently, α -ZnP₂ is not susceptible to temperatures up to 400°C or visible irradiation.

β -ZnP₂.—The untreated black β -ZnP₂ contains a small amount of another compound, the diffraction lines of which can be most probably assigned to Zn₃P₂. After illumination, the diffractogram also reveals the presence of traces of α -Zn₃(PO₄)₂. Deposition of Rh onto the particles and further heating to 160°C gives no noteworthy changes in the x-ray pattern. However, application of RuO₂, either from RuCl₃ and subsequent calcination at 400°C, or from RuO₄, leads to significant changes. Apart from the Zn₃P₂ lines, also reflections, attributable to α -Zn₃(PO₄)₂ occur in the diffractogram in both cases. The diffractograms of β -ZnP₂ loaded with Rh or with RuO₂, measured after illumination, also show new reflections of low intensity, which we have not been able to assign.

Powders: photochemical production of hydrogen.—Upon bandgap excitation of particles of the p-type semiconductors, α -ZnP₂ ($E_g \approx 2.1$ eV) and β -ZnP₂ ($E_g \approx 1.5$ eV) electron-hole pairs are generated



From the position of the flatband potential (*vide supra*), electrons in the conduction band will have sufficient energy to reduce water to give hydrogen



The holes can be used for oxidation. In this work, we have sacrificed EDTA, cysteine, and sulfide as donors in the anodic processes. Following loss of an electron, EDTA and cysteine are known to undergo kinetically irreversible reactions, which prevent the thermodynamically favorable backreaction (9). Depending on thermodynamic and kinetic considerations, both oxidation of the substrate and of the semiconductor material may occur. In competition with the oxidation of the organic substrate, anodic dissolution of ZnP₂ can take place, which can be described according to the equation

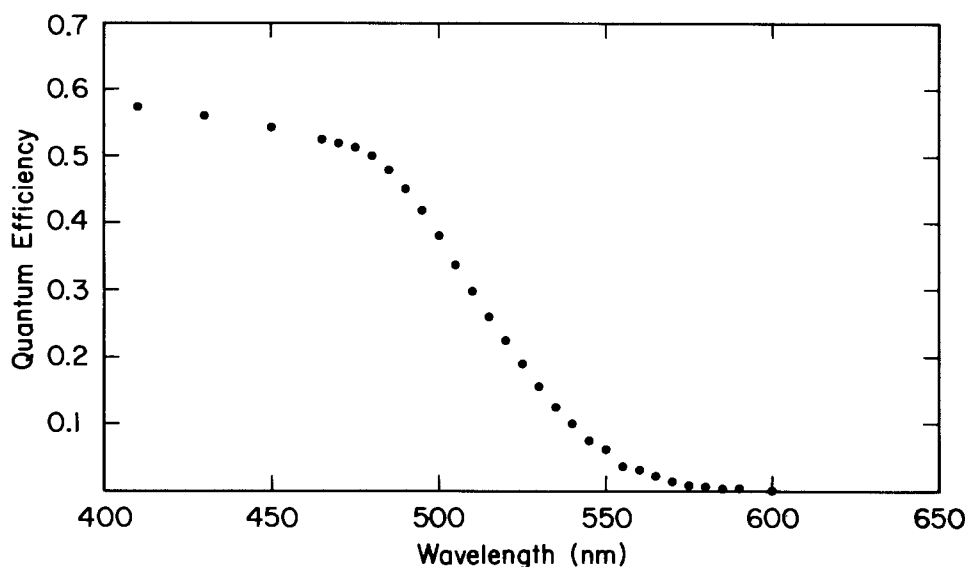
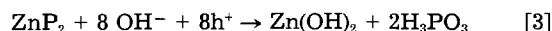
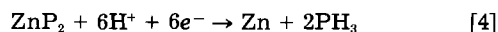


Fig. 5. Quantum yield spectrum of an α -ZnP₂ electrode in 1M Na₂SO₄ at pH 2. Electrode potential $-3 V_{SCE}$.

Free energy values of $\text{Zn}(\text{OH})_2$ and H_3PO_3 are to be found in Ref. (10). Jordan has calculated a standard enthalpy of formation for $\alpha\text{-ZnP}_2$ $\Delta H_f^{298} = -24.3 \text{ kcal mol}^{-1}$ as well as the standard entropy of $\alpha\text{-ZnP}_2$ $S_0 = 14.4 \text{ e } \mu\text{mol}^{-1}$ (11). This ΔH_f^{298} value is in fairly good agreement with the experimental value of $-20.4 \text{ kcal mol}^{-1}$, determined by Alikhanyan *et al.* (12). Using these thermodynamic data, calculated by Jordan, we have computed the potential corresponding to Eq. [3] to be $E = -0.95 \text{ V}_{\text{NHE}}$ at pH 13. This value is fairly well comparable with that calculated for GaP [$-1.07 \text{ V}_{\text{NHE}}$ at pH 13 (13)]. So on thermodynamic grounds photocorrosion of ZnP_2 is a more favorable anodic reaction than water oxidation ($E_{\text{OH}^-/\text{O}_2} = +0.45 \text{ V}_{\text{NHE}}$ at pH 13) and is even easier than the oxidation of the used donors, but kinetic factors favor the latter processes. Nevertheless, photocorrosion of ZnP_2 has to be taken into account, as previously both α - and $\beta\text{-ZnP}_2$ have been found to be unstable under certain conditions (1).

Apart from anodic dissolution, cathodic decomposition of ZnP_2 according to

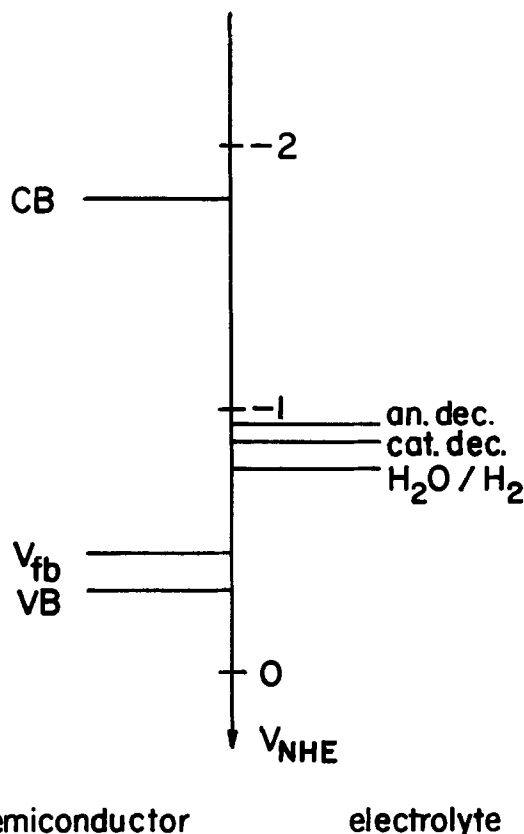


has to be considered as well. From the values given in Ref. (10, 11), we have calculated $E = -0.89 \text{ V}_{\text{NHE}}$ at pH 13.

Relative energy levels at the ZnP_2 -electrolyte interface are given below.

EDTA substrates.—Figure 6 shows the hydrogen production as a function of the illumination time from a 0.1M EDTA solution at pH 13 and 40°C for various α - and $\beta\text{-ZnP}_2$ powders. Apart from the first hour, the untreated powders hardly show hydrogen formation. Deposition of Rh onto $\alpha\text{-ZnP}_2$ gives no perceptible improvement. However, application of RuO_2 evidently enhances the activity, and sustained hydrogen evolution is observed.

For $\beta\text{-ZnP}_2$, the best results are obtained with Rh. In this case, RuO_2 , formed from either RuCl_3 or RuO_4 , also improves the rate of hydrogen formation. Yet, in compari-



Scheme 1. Energy levels at the $\beta\text{-ZnP}_2$ /electrolyte interface at pH 13. For $\alpha\text{-ZnP}_2$, V_{FB} is somewhat more positive according to the photocurrent onset ($\approx -0.4 \text{ V}_{\text{SCE}}$). The position of the bandedges is also different due to the different bandgaps.

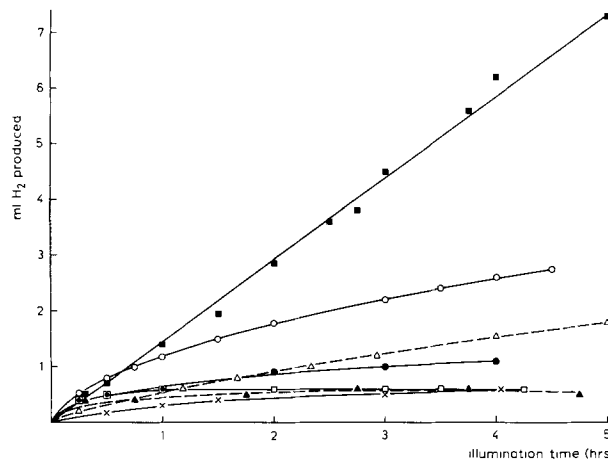


Fig. 6. Hydrogen production as a function of the illumination time [EDTA] = 0.1M, pH = 13, $T = 40^\circ\text{C}$, and $\lambda > 418 \text{ nm}$. \square : $\alpha\text{-ZnP}_2$. \circ : $\beta\text{-ZnP}_2$. \blacktriangle : $\alpha\text{-ZnP}_2/0.5 \text{ w/o Rh}$. \circ : $\beta\text{-ZnP}_2/0.5 \text{ w/o Rh}$. \blacksquare : $\alpha\text{-ZnP}_2/0.5 \text{ w/o RuO}_2$. \bullet : $\beta\text{-ZnP}_2/0.5 \text{ w/o RuO}_2$. \triangle : $\beta\text{-ZnP}_2/0.5 \text{ w/o RuO}_2$ (RuO_4 method).

son with $\alpha\text{-ZnP}_2/0.5 \text{ w/o RuO}_2$, the less pronounced effect may be due to the fact that $\beta\text{-ZnP}_2$ is not stable under oxidative and/or heating conditions, as could be deduced from the x-ray diffractograms. As the $\alpha\text{-ZnP}_2/0.5 \text{ w/o RuO}_2$ powder clearly displays the highest activity, we have carried out further experiments using this system.

Figure 7 shows the rate of hydrogen evolution from a 0.1M EDTA solution over $\alpha\text{-ZnP}_2/0.5 \text{ w/o RuO}_2$ particles vs. the wavelength of the light employed (O). The spectral dependence has three important features. A steep increase around 530 nm is observed, which corresponds to the bandedge of approximately 2.1 eV. A decrease in efficiency occurs towards lower wavelengths, where the light penetrates less deeply into the material and surface recombination becomes more important. Moreover, an appreciable subbandgap response is found. So far, we have no satisfactory interpretation of this phenomenon. It cannot be caused by reactions in the dark, because, as shown in Fig. 7, the rate of hydrogen production in the absence of light is relatively unimportant and amounts to only a few percent of the values measured under illumination. Photodissolution of $\alpha\text{-ZnP}_2$ can only account for a minor part of the hydrogen production at these longer wavelengths, as appears from an independent experiment in the absence of EDTA (\cdot). The hydrogen production at $\lambda = 650 \text{ nm}$ and $\lambda = 520 \text{ nm}$ amounts to ca. 3% and 15% of the values obtained in the presence of EDTA, respectively. In the absence of EDTA the anodic

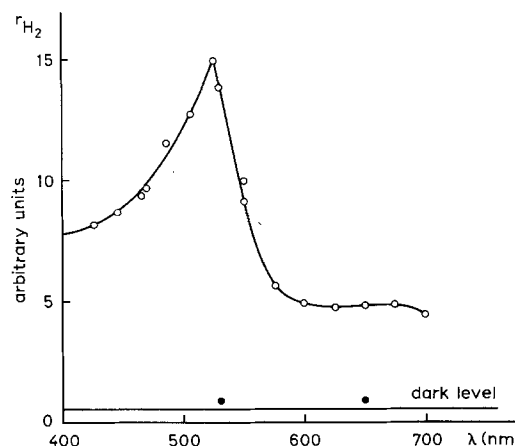


Fig. 7. Rate of hydrogen production over $\alpha\text{-ZnP}_2/0.5 \text{ w/o RuO}_2$ particles in aqueous suspension upon illumination at pH 13 and 40°C as a function of wavelength (corrected to constant energy). \bullet : [EDTA] = 0. \circ : [EDTA] = 0.1M. Under dark conditions, the rate of hydrogen production is as indicated by the full line (dark level).

counter-reaction must be dissolution of α -ZnP₂ into Zn²⁺ and PO₃³⁻ ions, according to Eq. [3]. Consequently, in the presence of EDTA, the figures can be regarded as upper limits for photocorrosion, since EDTA is expected to stabilize the ZnP₂ material. Presumably, the subbandgap effect can be understood by the presence of intermediate levels, likely arising from the occurrence of other photoactive defects or surface states. These levels may act as efficient recombination centers. On the contrary, if the recombination process is relatively slow, accumulation of charge onto the surface will be possible, where this charge will then react with adsorbed species. A similar subbandgap effect has been previously reported to occur in SiC (14).

For one wavelength, viz, $\lambda = 470$ nm, where the rate of hydrogen production reaches about two thirds of its maximum value (at $\lambda \approx 530$ nm), and at room temperature, we have determined the formal quantum efficiency, defined as

$$\Phi = \frac{\text{number of atoms of H}}{\text{number of incident photons}} \times 100\%$$

For a suspension containing 1 mg/ml α -ZnP₂/0.5 w/o RuO₂ and 0.1M EDTA at pH 13, we find a value for Φ of 12%. This will correspond to the lower limit for the true quantum yield. For the photochemical to chemical energy conversion (combustion energy of H₂), we calculate a value of ca. 6%.

In the case of β -ZnP₂ powders, we have encountered difficulties in measuring the rate of hydrogen evolution as a function of the wavelength. The dark reaction for the system β -ZnP₂/0.5 w/o RuO₂/EDTA gives approximately the same values as the α -ZnP₂/0.5 w/o RuO₂/EDTA system. Under light conditions, the rate of hydrogen formation increases by a factor 2-4, depending on the wavelength. Cathodic decomposition according to Eq. [4] cannot *a priori* be ruled out in view of the comparable values of $E_{\text{H}_2\text{O}/\text{H}_2} = -0.78$ V_{NHE} and $E_{\text{cat.dec.}} = -0.89$ V_{NHE} at pH 13. The hydrogen production with concomitant photocorrosion of β -ZnP₂/0.5 w/o RuO₂, measured in the absence of a donor, is about the same as the hydrogen formation in the dark with EDTA. The x-ray diffraction pattern of β -ZnP₂, recorded after the illumination experiment, shows the presence of oxidation products. From its anodic instability and its inactivity under these conditions, we conclude that β -ZnP₂ is unattractive with respect to PEC applications in aqueous powder suspension systems.

Other substrates.—Apart from EDTA, which is a valuable compound, we have also sacrificed sulfide as an electron donor. H₂S is an abundant waste product, and therefore the cleavage of H₂S into H₂ and S or polysulfide is a process of potential industrial significance.

Figure 8 shows the hydrogen formation from a 0.1M sulfide solution at pH 13 over β -ZnP₂ particles as a function of the illumination time.

A substantial decline in the hydrogen production is shown, after which a plateau is reached and no further hydrogen is released. Although on thermodynamic

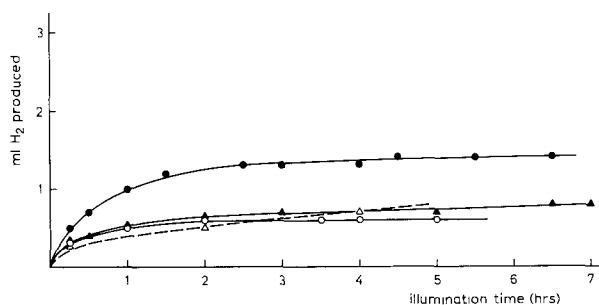


Fig. 8. Hydrogen production from a 0.1M S²⁻ solution as a function of the illumination time at pH 13 and 40°C. ●: β -ZnP₂/0.5 w/o Rh, [SO₃²⁻] = 0. ○: β -ZnP₂/0.5 w/o Rh, [SO₃²⁻] = 0.1M. ▲: β -ZnP₂/0.5 w/o RuO₂, [SO₃²⁻] = 0. △: β -ZnP₂/0.5 w/o RuO₂, [SO₃²⁻] = 0.1M.

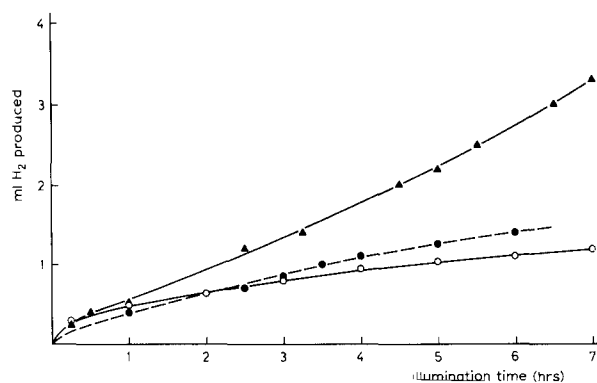


Fig. 9. Hydrogen production from a 0.1M cysteine solution as a function of the illumination time at pH 13 and 40°C. ▲: α -ZnP₂/0.5 w/o RuO₂. ●: β -ZnP₂/0.5 w/o Rh. ○: β -ZnP₂/0.5 w/o RuO₂.

grounds ($E = -0.45$ V vs. NHE at pH 13) sulfide is expected to be a good substrate for hydrogen production, parameters such as adsorption may provide an explanation for the ceasing of the process.

Adsorption of sulfide may cause poisoning of the catalytically active sites at the surface, or may even lead to chemical reactions with the material. In a previous paper on hydrogen formation from alkaline sulfide substrates over CdS powders, we have reported that addition of sulfite makes the process more efficient because in the anodic reaction thiosulfate is formed (15). In the present case, addition of sulfite has clearly a negative influence on the hydrogen evolution.

We have also used cysteine as a donor, as its behavior will be interjacent to that of an organic donor such as EDTA and sulfide, because of the presence of a sulfidic group. The results, given in Fig. 9, are in agreement with these expectations. It is true that the hydrogen productions do not reach a plateau, but they remain behind the values observed with EDTA. Again, the α -ZnP₂/0.5 w/o RuO₂ displays the highest activity.

Conclusion

So, in conclusion, we can state that α -ZnP₂ is an attractive material in view of its good optical properties. A large fraction of the solar spectrum is absorbed. Loaded with 0.5 w/o RuO₂, the formal quantum yield for hydrogen formation from EDTA (0.06 mol H₂ einstein⁻¹ at $\lambda = 470$ nm) compares favorably with the value of 0.04 at $\lambda = 436$ nm reported recently for a system consisting of platinized CdS, a semiconductor with similar optical properties, and of 0.1M EDTA (16).

However, before this material can be applied on a large scale, the contribution of photocorrosion under various conditions should be studied in detail. Possible problems with respect to dissolution of α -ZnP₂ have then to be solved.

On the other hand, β -ZnP₂ seems much less useful – at least in aqueous powder suspension systems – due to its instability and its disappointingly low activity for the production of hydrogen.

Acknowledgments

Technical assistance by Mr. K. Timmer and by Mr. L. Gantert is gratefully acknowledged. This research was supported by grants from the Netherlands' Ministry of Economic Affairs and from the EC-Solar Energy R&D-Programme, Project D as well as by the NEFF (National Energy Research Fund of Switzerland). We appreciate the donation of semiconductor-grade red phosphorus by Aluisse Corporation, Switzerland. One of us (H.v.K.) would like to express special gratitude to Ms. M. Lübke from the Fritz-Haber-Institut der Max-Planck-Gesellschaft, Berlin, Germany, for her help in some of the capacity measurements.

Manuscript submitted Oct. 11, 1983; revised manuscript received March 4, 1984.

REFERENCES

- H. von Känel, R. Hauger, and P. Wachter, *Solid State Commun.*, **43**, 619 (1982).
- J. Hegyi, E. E. Loebner, E. W. Poor, Jr., and J. G. White, *J. Phys. Chem. Solids*, **24**, 333 (1963).
- M. U. Stackelberg and R. Paulus, *J. Phys. Chem.*, **28**, 427 (1935).
- M. Rubenstein and P. J. Dean, *J. Appl. Phys.*, **41**, 1777 (1970).
- C. G. Hatchard and C. A. Parker, *Proc. R. Soc. A*, **235**, 518 (1956).
- R. Memming, *Philips Res. Rpt.* **19**, 323 (1964).
- K. Ito, Y. Matsuura, T. Nakazawa, and H. Takenouchi, *Jpn. J. Appl. Phys.*, **20**, Suppl. 20-2, 109 (1981).
- H. von Känel, L. Gantert, R. Hauger, and P. Wachter, To be published in "Proceedings of the 5th World Hydrogen Energy Conference," Toronto, 1984.
- M. Graetzel, *Ber. Bunsenges, Phys. Chem.*, **84**, 981 (1980); K. Kalyanasundaram, J. Kiwi, and M. Graetzel, *Helv. Chim. Acta*, **61**, 2720 (1978); K. Kalyanasundaram and M. Graetzel, *Angew. Chem. Int. Ed. Engl.*, **18**, 701 (1979); P. Keller, A. Moradpour, E. Amouyal, and H. B. Kagan, *Nouv. J. Chim.*, **4**, 377 (1980).
- W. M. Latimer, "Oxidation Potentials," 2nd Ed., pp. 169, 106, Prentice-Hall Inc., Englewood Cliffs, NJ (1964).
- A. S. Jordan, *This Journal*, **118**, 1362 (1971).
- A. S. Alikhanyan, A. V. Steblevskii, Ya. Kh. Grinberg, S. F. Marenkin, G. G. Magomedgadzhiev, and V. I. Gorgoraki, *Izv. Akad. Nauk. SSSR Neorg. Mater.*, **14**, 1966 (1978).
- R. Memming and G. Schwandt, *Electrochim. Acta*, **13**, 1299 (1968); R. Memming, *This Journal*, **125**, 117 (1978).
- D. H. M. W. Thewissen, A. H. A. Tinnemans, M. Eeuwhorst-Reinten, K. Timmer, and A. Mackor, *Nouv. J. Chim.*, **7**, 73 (1983).
- D. H. M. W. Thewissen, A. H. A. Tinnemans, M. Eeuwhorst-Reinten, K. Timmer, and A. Mackor, *ibid.*, **7**, 191 (1983).
- J. R. Darwent, *J. Chem. Soc. Faraday Trans. 2*, **77**, 1703 (1981).

Effective Medium Theory for Perfluorinated Ionomers and Blends

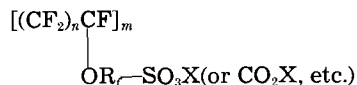
William Y. Hsu

E. I. du Pont de Nemours and Company, Central Research and Development Department, Experimental Station, Wilmington, Delaware 19898

ABSTRACT

The effective medium theory is applied to delineate transport and elastic properties of perfluorinated ionomers and their blends. The predicted critical dependence of current efficiency on blend morphology is verified experimentally in sulfonate/carboxylate and sulfonamide/carboxylate blends.

Perfluorinated ionomers are composed of carbon-fluorine backbone chains with perfluoro side chains containing sulfonate, carboxylate, or sulfonamide groups. The general chemical formula is



These ionomers possess exceptional transport, thermal, chemical, and mechanical properties and have been employed as membrane separators, acid catalysts, and polymer electrodes.

In this paper, we shall discuss the composite (1) and percolation (2, 3) nature of wet perfluorinated ionomers, outline an effective medium theory (4) to model their elastic moduli (5), and generalize the theory to track the morphological dependence (6) of ion transport and selectivity in perfluorinated ionomer blends.

Composite and Percolation Nature of Wet Ionomers

The unique transport properties of perfluorinated ionomers can be traced to a spontaneous phase separation occurring in wet polymers: the conductive aqueous-phase forms domains that are randomly distributed in the insulative fluorocarbon phase (1). This clustering phenomenon is very general and has been observed in other ionomers (7). Ion transport in wet ionomers is, therefore, dominated by the connectivity of ion clusters and percolation among them (2).

The essence of percolation can be qualitatively understood as follows (3). At low aqueous content, conductive clusters are scarce and isolated so that macroscopic ion transfer would be difficult. As the water content is increased, the clusters begin to associate until a threshold concentration, f_0 , is reached. At this stage, a macroscopic association of clusters pervading the whole polymer is formed and the system becomes conductive. Above f_0 , the macroscopic association of clusters becomes denser and the conductivity, σ , increases according to the power law

$$\sigma = \sigma_0(f - f_0)^t \quad [1]$$

where f is the volume fraction of the aqueous phase, t is a universal constant that normally depends on the spatial dimensionality only and is typically $1 \cdot 7$ in 3D, and σ_0 is a prefactor that depends on the type of ionomers and caustic concentration. For perfluorinated ionomers, f_0 is typically 8 ~ 10 volume percent (v/o). Figure 1 summarizes our transport data, which were obtained using published methods (2, 8). The universal character of (σ/σ_0) is clearly exhibited. Experimentally, t is 1.53 ± 0.10 , which agrees quite well with theoretical expectation.

The range of validity of Eq. [1] may appear unexpectedly wide at first sight from Fig. 1. However, Stinchcombe (9) had found theoretically on Bethe lattices that the critical regime for percolation theory is $0 \leq (p - p_c) \leq z^{-1}$, where p is the fraction of occupied bonds in a Bethe lattice of coordination number z and p_c is the critical value of p . For $z = 4$ and $p_c = 0.5$, the critical regime would extend to $(p - p_c)/p_c = 0.5$, which is much larger than the corresponding values from other phase transition problems (10). Our data are certainly consistent with Stinchcombe's theory. In addition, a wide critical range for Eq. [1] has also been observed in thick film resistors based on conductive pyrochlores (11) and carbon/polyvinylchloride composites (12), and for the dielectric analogue of Eq. [1] in Ag/KCl composites (13).

Effective Medium Theory

Physical properties of composite systems can also be modeled by the effective medium theory (4) under proper conditions (6, 14). In this approach, we imagine replacing the composite system by a homogeneous medium that has the same macroscopic properties and physical constants as the composite system. Changes in relevant fields are then evaluated when a small portion of the effective medium is replaced by one of the component materials that made up the composite. To ensure self-consistency, we require the average change in these

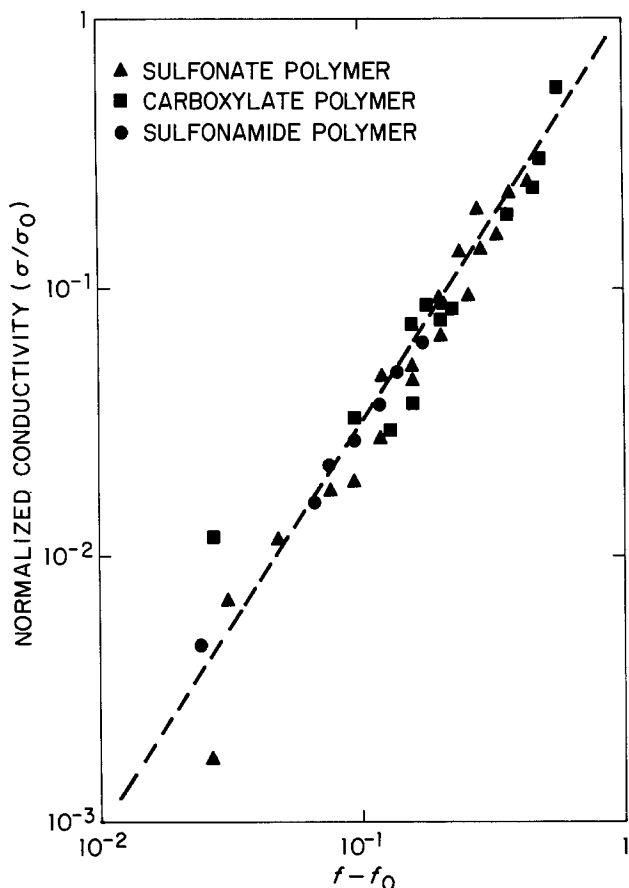


Fig. 1. Log-log plot of normalized conductivity (σ/σ_0) vs. the excess volume fraction of aqueous phase ($f - f_0$). The straight line is a fit of theory (Eq. [1]) to data. The slope t is 1.53 ± 0.10 .

fields to be zero when the components are dispersed randomly. When applied to the bulk and shear moduli, K and G , of wet perfluorosulfonate ionomers, a pair of equations (5, 15) that relate K and G to the elastic moduli [K_w , $G_w (= 0)$, K_p , and G_p] of water and dry fluoropolymer emerge. Eliminating K , we obtain a cubic equation for G , the effective shear modulus of the composite (5)

$$32G^3 + \alpha G^2 + \beta G + \lambda = 0 \quad [2]$$

where

$$\alpha = 24(K_w + K_p) + 12[fK_w + (1-f)K_p] + 16G_p(5f - 2) \quad [3a]$$

$$\beta = 27K_wK_p + 12(K_w + K_p)G_p(5f - 2) - 12G_p[fK_w + (1-f)K_p] \quad [3b]$$

$$\lambda = 9K_wK_pG_p(5f - 3) \quad [3c]$$

Using this method, we have computed the tensile modulus E of a 1200 EW perfluorosulfonate ionomer at room temperature and for $f \leq 0.4$. The theoretical result is compared to data (16) in Fig. 2 and has also been fitted to the following empirical form (16)

$$E = E_0 \exp[-A/f2(1-f)] \quad [4]$$

where $E_0 = 4.01 \times 10^4$ psi, and where A is 3.31 which is within 15% of the experimental value 2.94. In the above comparison, the only inputs to the theory were the water content and the known moduli of water and dry ionomer: $K_w = 2.55 \times 10^{10}$ dyn-cm² at 20°C and atmospheric pressure, $K_p = 3.47 \times 10^{10}$ dyn-cm⁻², and $G_p = 9.22 \times 10^8$ dyn-cm².

The advantages of effective medium theory are its conceptual and mathematical simplicity and its versatility. It will now be generalized to include morphological effects (6).

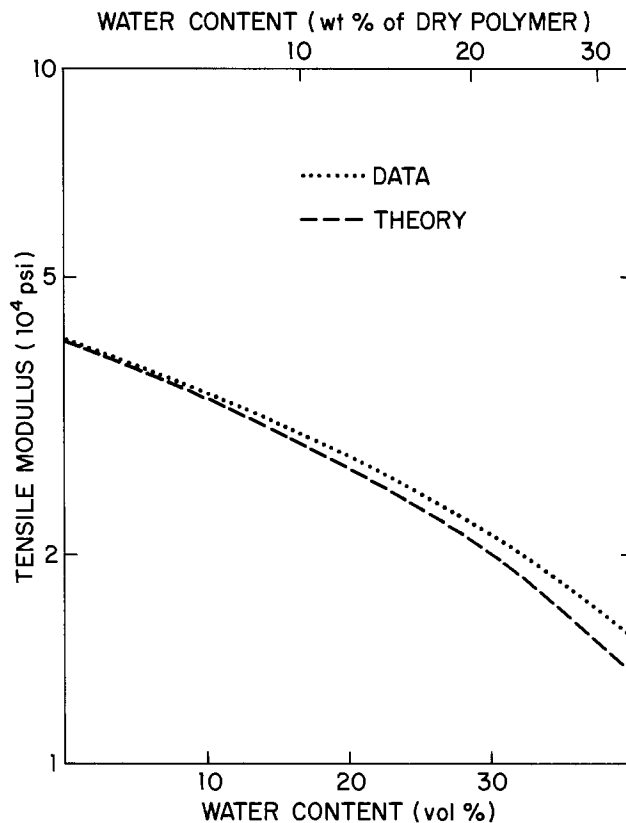


Fig. 2. Comparison of theoretical and experimental values of the tensile modulus for a 1200 EW perfluorosulfonate ionomer. Data are from Ref. (16).

Morphological Effects

Consider a collection of oriented spheroids. They can be either prolate $a \geq b = c$ or oblate $a = b \geq c$, where a, b, c are the semi-principal axes of an ellipsoid. The geometry and orientation are depicted in Fig. 3. For both cases, the eccentricity e of the spheroids is $[1 - (c/a)^2]^{0.5}$, where $0 \leq (c/a) \leq 1$ is the aspect ratio. The remaining space is now completely filled with spheroids of a different material but of the same eccentricity and orientation. Let σ_1 and σ_2 represent the diagonal component of the conductivity tensor along the field direction for the two media, respectively. Following the spirit of the previous section, we obtain a quadratic equation for the effective conductivity, σ , of the composite medium

$$[1 - F(e)]\sigma^2 + \{\sigma_1[F(e) - f_1] + \sigma_2[F(e) - f_2]\}\sigma - \sigma_1\sigma_2F(e) = 0 \quad [5]$$

where f_1 and f_2 are the volume concentrations of the two media, and where the function F depends on the shape of the spheroid (cf. Fig. 4)

$$F(e) = \frac{(1 - e^2)}{2e^3} \left\{ \ln \left(\frac{1 + e}{1 - e} \right) - 2e \right\} \quad [6a]$$

for the prolate case, and

$$F(e) = \frac{1}{e^2} \left\{ 1 - \left(\frac{\sqrt{1 - e^2}}{e} \right) \arctan \left(\frac{e}{\sqrt{1 - e^2}} \right) \right\} \quad [6b]$$

for the oblate case. Equation [5] is generally applicable when

$$10^{-2} \leq (\sigma_1/\sigma_2) \leq 10^2 \quad [7]$$

A unique feature of this model is that the shape of the inclusions can be continuously altered between lamellar ($e = 1$) and spherical ($e = 0$) for the oblate geometry, and between fibrillar ($e = 1$) and spherical ($e = 0$) for the prolate case. For the spherical limit ($e = 0$, $F = 1/3$), Eq. [5] reduces to the standard form given in the literature (4).

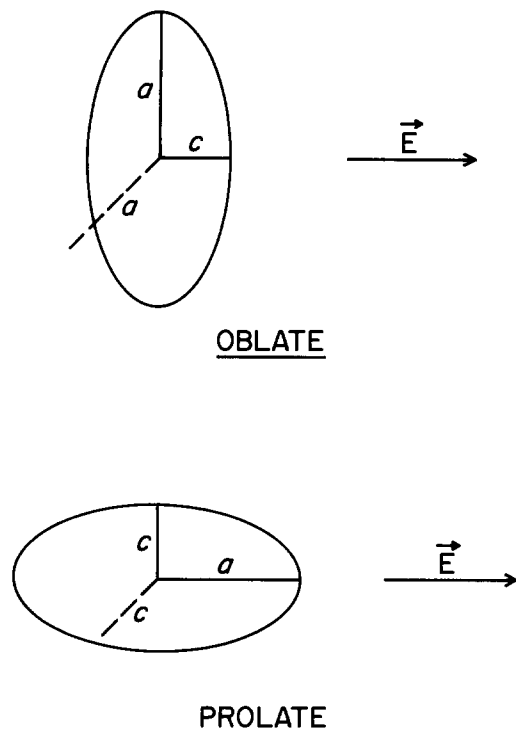


Fig. 3. Geometry and orientation of spheroids. The ellipse is a projection of the spheroid under consideration onto the a - c plane and E is the applied field.

Ion Selectivity in Ionomer Blends

The morphological information contained in Eq. [5] is most conveniently illustrated with blends of perfluorinated ionomers since the various ionomers have very different properties, and since the domain morphology in blends can be altered and controlled by rheology. We define the current efficiency as the fractional contribution to the total current by the Na^+ ions. For the ionomers

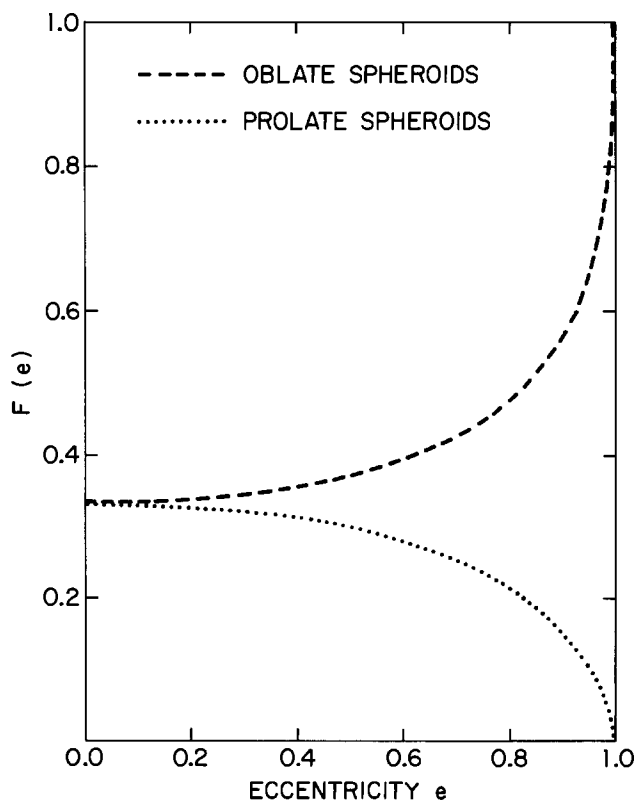


Fig. 4. Eccentricity dependence of the F function (Eq. [6])

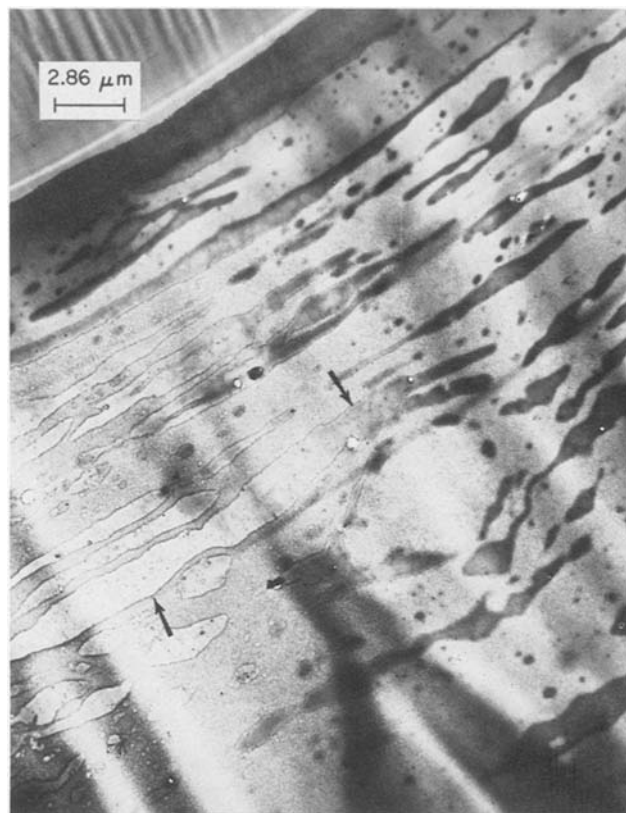


Fig. 5. Cross-sectional micrograph of a pressed film of 25% carboxylate and 75% sulfonate blend of perfluorinated ionomers. The elongated regions (arrows) are the carboxylate phase.

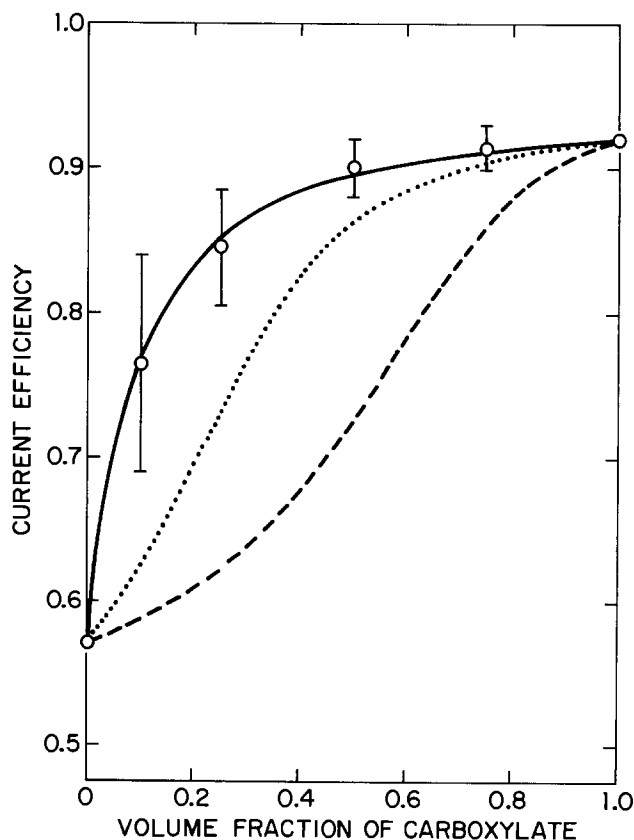


Fig. 6. Current efficiency of perfluorinated carboxylate/sulfonate blends. Open circles and vertical bars are average data and experimental uncertainty, respectively. The three continuous curves are predicted behavior of oriented oblate spheroids with lamellar (top curve) to almost spherical (bottom curve) morphologies; the aspect ratios c/a are, from top to bottom, 0.01, 0.25, and 0.995, respectively.

Table I. Ionic conductivities and current efficiency of 1100 EW perfluorinated ionomers

Ionomer	σ_{Na}^+ ($10^{-3}\Omega^{-1}\text{cm}^{-1}$)	σ_{OH^-} ($10^{-3}\Omega^{-1}\text{cm}^{-1}$)	c.e. (%)
Sulfonate	18.0	13.6	57
Carboxylate	6.99	0.61	92
Sulfonamide	1.44	0.25	85

under consideration, the c.e.'s and ionic conductivities are listed in Table I. Appropriate ratios of the conductivities obviously satisfy the validity conditions Eq. [7]. Assuming independent Na^+ and OH^- channels, the composite conductivity and c.e. can be evaluated.

Typical pressed films of the blends have a pronounced lamellar morphology, as shown in Fig. 5. For perfluoro-sulfonate/carboxylate blends, the computed c.e. for oriented oblate spheroids at three eccentricities are plotted as function of blend composition and compared to experimental data in Fig. 6. Obviously, the computed c.e. for the lamellar morphology agrees very well with the data. Notice the dramatic difference between spherical and lamellar morphologies. For the spherical case, the c.e. increases slowly and turns over gradually as the carboxylate content is increased. In contrast, the c.e. rises steeply and turns over rapidly with the lamellar morphology. To verify this pronounced morphological dependence, the rheology of a 25% carboxylate/75% sulfonate blend is altered to produce the abnormal spherical morphology (Fig. 7). In contrast to its lamellar counterpart and in agreement with the theoretical prediction, this film has an unusually low c.e., as shown in Table II.

The lamellar morphology, however, may not always be desirable. It is beneficial in the above example because it has prevented OH^- ions from flowing through the conductive but poorly selective sulfonate phase. By the same token, the lamellar morphology would also hinder OH^- ions from reaching the selective and relatively conductive carboxylate phase in perfluorosulfonamide/carboxylate blends. The resultant c.e. is distinctly concave (Fig. 8), in marked contrast to the convex curvature of sulfonate/carboxylate blends. Consequently, despite sulfonamide ionomers are more selective than sulfonate, the c.e. of sulfonate/carboxylate blends could surpass comparable

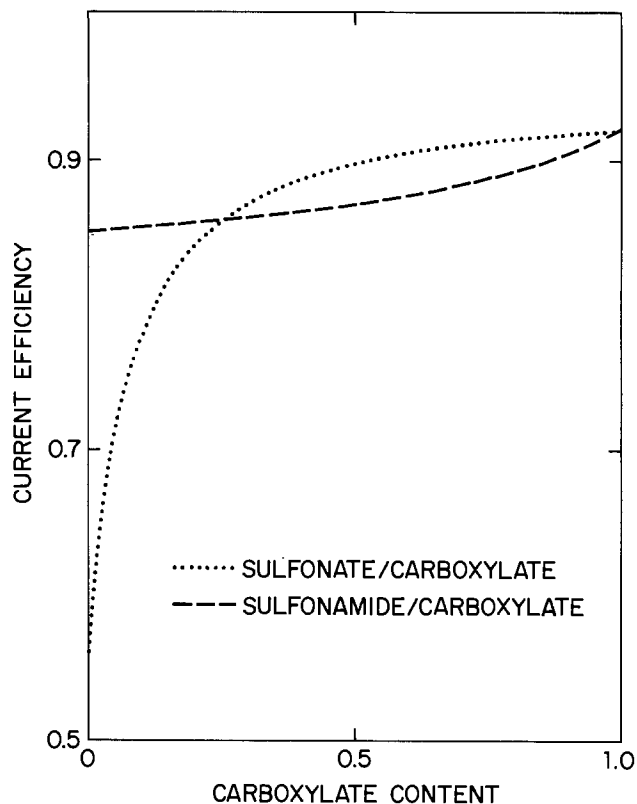


Fig. 8. Computed ion selectivity (c.e.) of lamellar perfluorinated ionomer blends.

sulfonamide/carboxylate blends with a lamellar morphology. This predicted anomaly was confirmed in perfluorinated ionomer blends containing 50% carboxylate (Table II). In this case, due to the low conductance of sulfonamide, spherical or tubular morphology can better promote ion flow through the selective carboxylate phase.

Conclusion

In summary, we have applied the effective medium theory to delineate the elastic properties of perfluorinated ionomers and their blends. The theory has also been

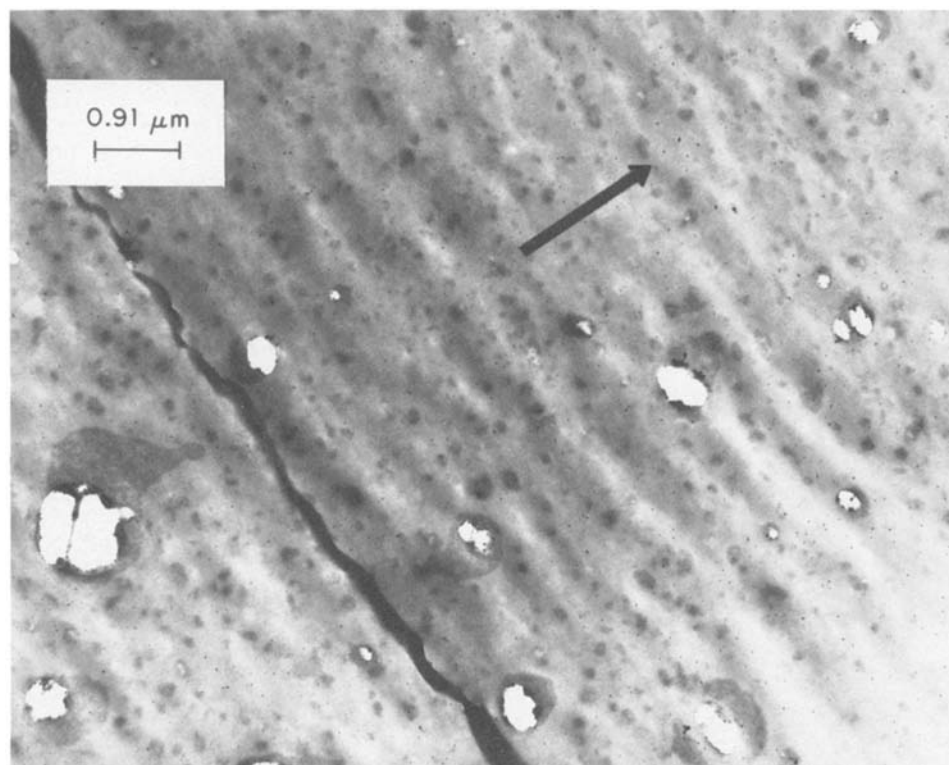


Fig. 7. Cross-sectional micrograph of a pressed film of similar composition as Fig. 5. The rheology, however, has been adjusted to produce spherical carboxylate domains (arrow). The dark line from upper left-hand corner to central bottom is due to fold over the microtomed sample film.

Table II. Morphological dependence of c.e. for 25% carboxylate and 75% sulfonate blends of perfluorinated ionomers

Morphology	Predicted c.e. (%)	Observed c.e. (%)
Spherical (Fig. 7)	62	56
Lamellar (Fig. 5)	86	89

Table III. c.e. of perfluorinated ionomer blends containing 50% carboxylate. The EW is approximately 1100, and the blend morphology is predominantly lamellar

Blend	Predicted c.e. (%)	Observed c.e. (%)
Sulfonate/carboxylate	90	91
Sulfonamide/carboxylate	87	86

extended to include morphological dependence. The principal predictions were verified with perfluorosulfonate/carboxylate blends and perfluorosulfonamide/carboxylate blends. We demonstrated that a universally preferred morphology beneficial to all ionomer blends does not exist. The ideal morphology must be individually determined based on component properties.

Acknowledgment

I thank Dr. T. Berzin, Dr. T. D. Gierke, and Dr. C. J. Molnar for supplying some of the data.

Manuscript submitted Dec. 16, 1983; revised manuscript received March 30, 1984. This was Paper 225 presented at the Cincinnati, Ohio, Meeting of the Society, May 6-11, 1984.

E. I. du Pont de Nemours and Company assisted in meeting the publication costs of this article.

REFERENCES

- W. Y. Hsu and T. D. Gierke, *J. Membr. Sci.*, **13**, 307 (1983).
- W. Y. Hsu, J. R. Barkley, and P. Meakin, *Macromolecules*, **13**, 198 (1980).
- For a general review of percolation theory, see R. Zallen, in "Proceedings of the 13th IUPAP Conference on Statistical Physics," Vol. 1, D. Cabib, C. G. Kuper, and I. Riess, Editors, pp. 310-321, Israel Physical Society (1977).
- D. M. Wood and N. W. Ashcroft, *Philos. Mag.*, **35**, 269 (1977) and references therein.
- W. Y. Hsu, M. Giri, and R. M. Ikeda, *Macromolecules*, **15**, 1210 (1982).
- W. Y. Hsu, T. D. Gierke, and C. J. Molnar, *ibid.*, **16**, 1945 (1983).
- See, for example, K. A. Mauritz and A. J. Hopfinger, in "Modern Aspects of Electrochemistry," Vol. 14, J. O'M. Bockris, B. E. Conway, and R. E. White, Editors, Chap. 6, pp. 467-474, Plenum, New York (1982).
- T. Berzins, Paper 437 presented at the Electrochemical Society Meeting, Atlanta, Georgia, Oct. 10-14, 1977: *This Journal*, **124**, 318C (1977).
- R. B. Stinchcombe, *J. Phys. C*, **7**, 179 (1974).
- E. H. Stanley, "Introduction to Phase Transitions and Critical Phenomena," Clarendon, Oxford, England (1971).
- P. F. Carcia, A. Ferretti, and A. Suna, *J. Appl. Phys.*, **53**, 5282 (1982).
- J. Balberg and S. Bozowski, *Solid-State Commun.*, **44**, 551 (1982).
- D. M. Grannan, J. C. Garland, and D. B. Tanner, *Phys. Rev. Lett.*, **46**, 375 (1981).
- M. H. Cohen, J. Jortner, and I. Webman, *Phys. Rev. B*, **17**, 4555 (1978).
- Similar equations were first obtained by R. H. Hill, *J. Mech. Phys. Solids*, **13**, 213 (1965) and independently by B. Budiansky, *ibid.*, **13**, 233 (1965).
- W. G. F. Grot, G. E. Munn, and P. N. Walmsley, *This Journal*, **119**, 108C (1972).

Cyclic Voltammetry in Solutions of Aluminum Bromide and KBr in Aromatic Hydrocarbons

III. The Behavior of Ag and Cu

M. Elam, E. Peled,* and E. Gileadi*

Department of Chemistry, Tel Aviv University, Ramat Aviv 69978, Israel

ABSTRACT

The electrochemical behavior of AgBr and CuBr has been studied in a solution consisting of 0.80M KBr and 1.0M Al₂Br₆ in ethylbenzene. A significant crystallization overpotential is observed for Cu on Pt, while silver exhibits only a marginally small crystallization overpotential. Measurements of the diffusion coefficients by different methods and comparison with earlier results yield values in the range of $(1.1-2.9) \times 10^{-6}$ cm²/s (corresponding to Stokes radii of 9-4Å), except for Cu, which yields a value of $(10-21) \times 10^{-6}$ cm²/s. These high apparent values are probably due to catalytic decomposition of the solvent caused by the presence of cuprous ions. The relatively high value for the diffusion coefficient of mercuric ions in toluene reported in an earlier publication is probably due to the same effect.

In a previous publication (1) the electrochemical behavior of dilute solutions of SnBr₂ and PbBr₂ in solutions of 1.0M Al₂Br₆ and 0.80M KBr in ethylbenzene was studied. Only the divalent state of Pb and Sn were observed in the available potential region, between aluminum deposition on the cathodic side and bromine evolution (or bromination of the solvent) on the anodic side. A nucleation overpotential of ca. 30-40 mV was observed for the deposition of both metals on Pt. The electrodeposition of aluminum was inhibited by low concentrations of PbBr₂, while SnBr₂ exhibited no such effect. The diffusion coefficients were estimated as 1.1×10^{-6} cm²/s for lead and 2.7×10^{-6} cm²/s for tin. Formation of a thermodynamically unstable Al/Pb alloy at sufficiently cathodic potentials was indicated.

*Electrochemical Society Active Member.

The relevant literature was surveyed briefly in our previous paper (1) and in greater detail in an earlier publication (2).

In the present paper, the electrochemical properties of dilute solutions of AgBr and CuBr in the same solvent system were studied. The diffusion coefficients were determined by three independent methods, and cyclic voltammograms were measured with the aid of a microcomputer used both to control the experiments and to analyze and plot the results.

Experimental

All measurements were performed in rigorously dried solutions of 1.0M Al₂Br₆ and 0.80M KBr in ethylbenzene, inside a glove box containing purified argon. The methods of purification of the electrolyte and the solvent were

described previously (3-5). Silver bromide (ROC/RIC, anhydrous 99.9%) and cuprous bromide (ROC/RIC, anhydrous 99%) were used without further purification.

The cell and the electrodes employed for the measurements of cyclic voltammograms were described in the first paper in this series (3). A microcomputer (Delta Products) based on an IEE 696, bus S-100, and Zilog Z80 microprocessor with 64K RAM was used to control the experiments. The triangular waveform was generated through a 12 bit D/A converter (Tecmar). The software developed allows determination of the voltage limits, the sweep rate, and the number of repetitions. Before each run, the solution was stirred for 20s and left quiescent for 30s. Each voltammogram shown represents the average of at least three runs. The voltammograms were displayed on a 24 in. graphic video monitor (Leedex Model 100) and recorded on 8 in. floppy disks for further analysis, including replotting and analyzing the results, such as the peak potential and peak current *vs.* the concentration and the sweep rate in the usual manner. In some cases, the value of the potential $E_{p/2}$ at half the peak current was used instead of E_p , since it could be determined with a higher degree of accuracy.

The potentiostatic transients were performed as described elsewhere (1). All potentials reported were measured against a reversible aluminum electrode in the same solution (RA1E).

Determination of the diffusion coefficients with a rotating disk system (Pine Instruments, Model ASR-2) were also performed inside the glove box. The solutions of $PbBr_2$ and $SnBr_2$ used in these measurements were prepared as described earlier (1).

Results and Discussions

Cyclic voltammograms for AgBr.—Two voltammograms taken in solution containing AgBr are shown in Fig. 1. The cathodic peak current, $i_p(c)$, is proportional to the concentration of AgBr at all sweep rates tested ($d \log i_p(c)/d \log C = 1.00 \pm 0.01$). The dependence of peak current on sweep rate is given by $d \log i_p(c)/d \log v = 0.48 \pm 0.01$, close to the value of 0.50 expected for a simple charge transfer process (6).

The potential at half-peak current ($E_{p/2}$) varies significantly with sweep rate and with peak current, as expected for an irreversible charge transfer process (6-8). The semilogarithmic plots shown in Fig. 2 are not linear but tend, at higher sweep rates, to the limiting values of $dE_{p/2}/d \log v = 29 \pm 3$ mV/decade and $dE_{p/2}/d \log i_p = 60 \pm 5$ mV/decade. However, $E_{p/2}$ depends on the concentration of AgBr ($dE_{p/2}/d \log C = 63 \pm 4$ mV/decade), as would be

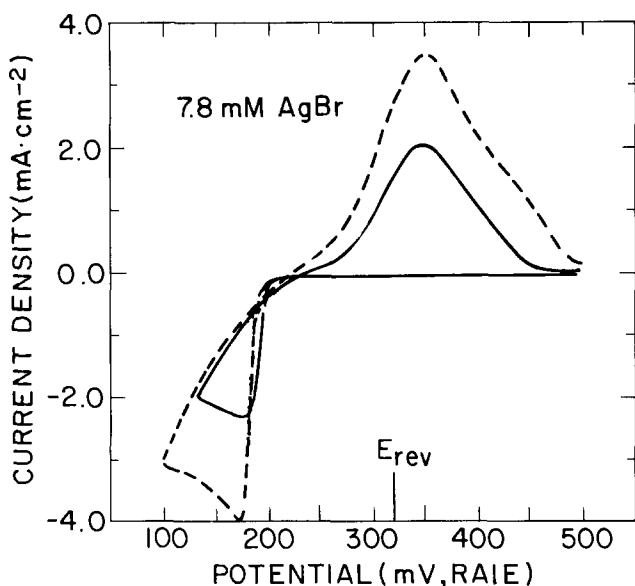


Fig. 1. Cyclic voltammograms for AgBr. Sweep rates (in V/s): solid line - 0.396; broken line - 1.174.

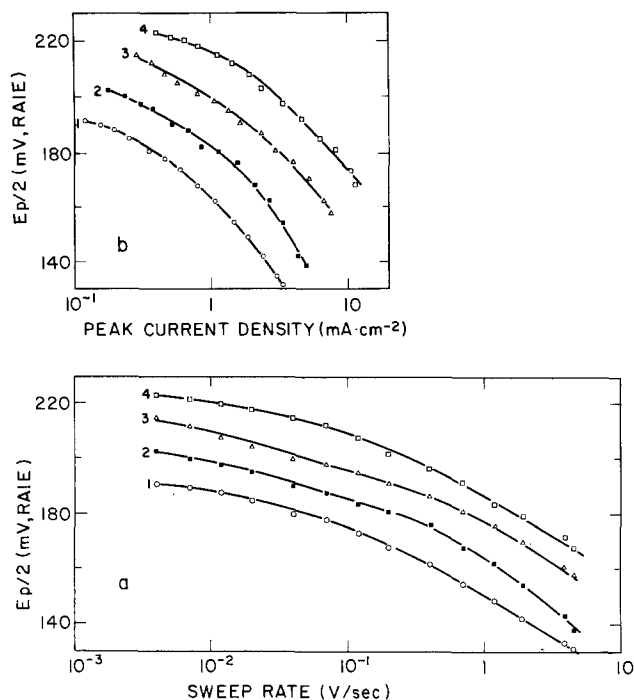


Fig. 2. Cathodic half-peak potentials for AgBr as a function of (a) $\log i_p$ and (b) $\log v$. Concentration of AgBr: (curve 1) 3.3, (curve 2) 5.2, (curve 3) 7.8, and (curve 4) 11.4 mM.

expected for a one-electron reversible metal deposition process. Measurements of the reversible potential as a function of concentration yielded a Nernst slope of 57 mV/decade (9).

A further anomaly is found when the difference between the cathodic peak potential [$E_p(c)$] and the cathodic half-peak potential [$E_{p/2}(c)$] is considered. The difference $\Delta E = E_p - E_{p/2}$ should be $-0.77RT/nF = 0.020/n$ V at 25°C for the reversible deposition of an insoluble substance (10), and should increase with increasing sweep rate in the irreversible region. The values of ΔE found experimentally range from 10-20 mV only and they decrease with increasing concentration of AgBr.

Although the nucleation overpotential for silver deposition on clean platinum is relatively small (11), as indicated by the narrow overpotential range where a current maximum occurs in the pulse potentiostatic curves, it could be the cause of the discrepancies noted above. It should also be noted that different electroactive species may occur in this system (9, 12) giving rise to various reaction mechanisms occurring simultaneously, leading to unusual values of the observed diagnostic parameters.

Cyclic voltammetry for CuBr.—Typical cyclic voltammograms for solutions containing CuBr are shown in Fig. 3

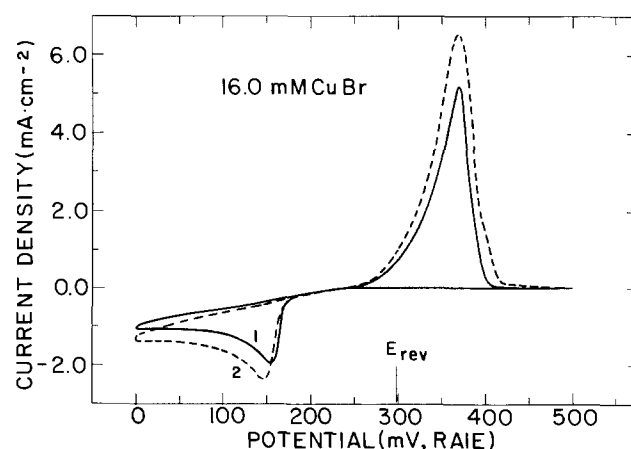


Fig. 3. Cyclic voltammograms for CuBr. Sweep rates (mV/s) (curve 1) 12 and (curve 2) 21.

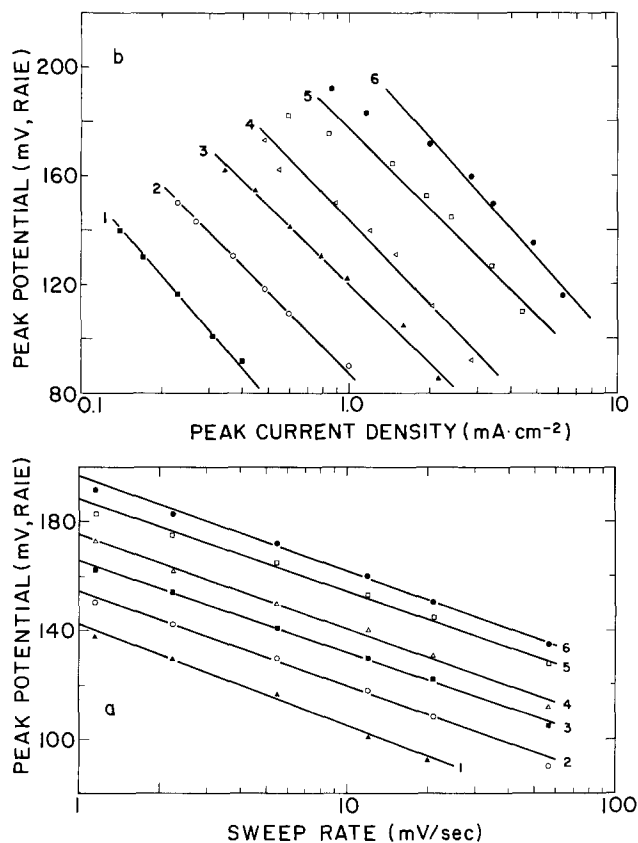


Fig. 4. Cathodic peak potentials for CuBr as a function of: (a) $\log v$ and (b) $\log i_p$. Concentrations of CuBr: (curve 1) 2.6, (curve 2) 3.9, (curve 3) 6.5, (curve 4) 10.2, (curve 5), 16, and (curve 6) 23 mM.

for two sweep rates. The anodic peak has the characteristic shape (1, 13) corresponding to the oxidation of metallic Cu to Cu^+ . A second anodic peak, which would correspond to the oxidation of monovalent to divalent copper, could not be detected in the whole potential region up to bromine evolution. This confirms our earlier findings (9) that the reversible potential for the $\text{Cu}^+/\text{Cu}^{2+}$ couple is more positive than the bromine-evolution potential and that monovalent copper is much more stable than divalent copper in this solvent system. Note the relatively large difference between the anodic and the cathodic peak potentials in Fig. 3, which is caused by nucleation overpotential, as will be discussed below.

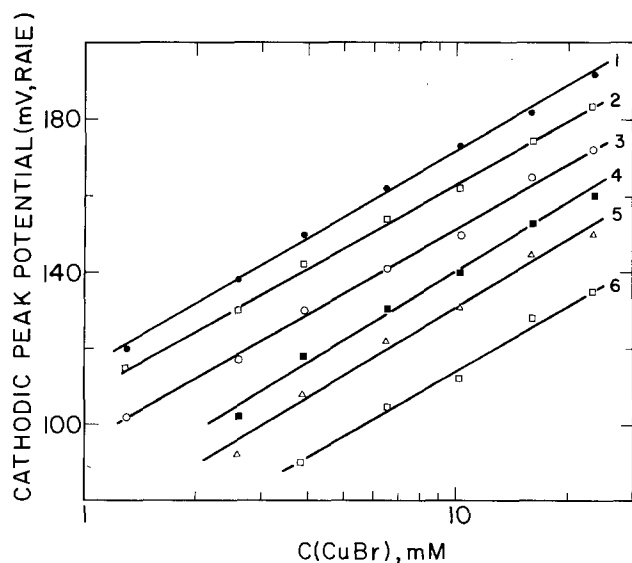


Fig. 5. Cathodic peak potentials as a function of $\log C$ (CuBr). Sweep rates (mV/s): (curve 1) 1.1, (curve 2) 2.2, (curve 3) 5.5, (curve 4) 12, (curve 5) 21, and (curve 6) 55.

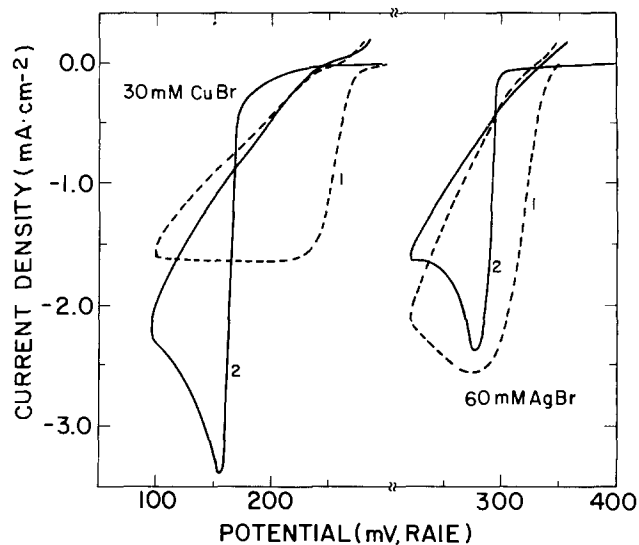


Fig. 6. Comparison of the initial potentials for deposition of Ag or Cu on Pt and on the respective metal. Sweep rate: 12 mV/s. Curve 1: Ag deposited on Ag (or Cu on Cu). Curve 2: Ag (or Cu) deposited on Pt.

The cathodic peak potential changes with sweep rate and with peak current, as expected for an irreversible process. The slopes observed in Fig. 4 are $dE_p/d \log V = 33 \pm 1$ mV/decade and $dE_p/d \log i_p = 104 \pm 7$ mV/decade. Accordingly, the variation of peak current with sweep rate should be $d \log i_p/d \log v = 0.32$, while a somewhat higher value of 0.39 is found experimentally. The deviation of this last parameter from the expected value of 0.50 is most likely due to the high crystallization overpotential observed for copper on platinum (cf. Fig. 3). This also accounts for the fact that the peak potential is a function of the concentration of CuBr, as would be expected for a reversible process. The average slope $dE_p/d \log C$ shown in Fig. 5 is 58 ± 2 mV/decade, to be compared with a value of 49 ± 1 mV/decade reported in our earlier publication (9). The potential difference $\Delta E = E_p - E_{p/2}$, which should be equal to 20 mV for a reversible, one-electron process, exhibits a behavior similar to that shown above for AgBr, increasing slightly with sweep rate from 10 to 20 mV and decreasing with concentration of CuBr.

Nucleation.—Formation of metal deposits controlled by the rate of nucleation has been studied for some time

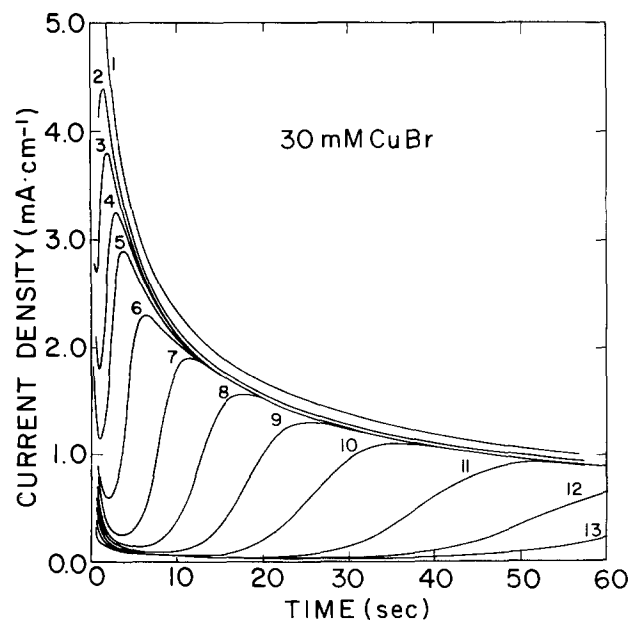


Fig. 7. Potentiostatic transients for deposition of Cu on Pt. Overpotential (mV): curve 1, 212; curve 2, 182; curve 3, 172; curve 4, 162; curve 5, 152; curve 6, 142; curve 7, 132; curve 8, 127; curve 9, 122; curve 10, 116; curve 11, 112; curve 12, 110; curve 13, 108.

Table I. Diffusion coefficients measured by different methods (cm²/s) × 10⁶

Method	PbBr ₂	SnBr ₂	AgBr	CuBr	HgBr ₂	TiBr ₄
Cyclic voltammetry	1.1 ± 0.2(1)	2.9 ± 0.6(1)	2.5 ± 0.4(2)	—	—	1.8 ± 0.1(3)
Potential pulse	—	2.7 ± 0.2(1)	2.5 ± 0.3(2)	21 ± 1(2)	—	1.8 ± 0.1(3)
Rotating disk	1.3 ± 0.3(2)	2.1 ± 0.2(2)	2.1 ± 0.4(2)	10 ± 1(2)	—	—
Polarography	—	—	0.8(M)(4)	—	4.0(T)(5) 0.8(M)(5)	—

All measurements in ethylbenzene, except where marked M (for mesitylene) or T (for toluene).
(1): Ref. (1). (2): present work. (3): Ref. (21). (4): Ref. (2). (5): Ref. (22).

(14-18), and was described for different metals deposited from aqueous solutions (14) as well as from molten salt systems (19, 20).

Figure 6 shows the occurrence of nucleation overpotential. Curve 1 is taken in both cases on a platinum electrode freshly coated with the respective metal, while curve 2 is taken on a bare Pt electrode. Deposition of copper on platinum does not start until an overpotential of more than 120 mV is reached, at which point nucleation occurs and the deposition can proceed. Because of this overpotential, the surface concentration, as determined by the Nernst relation, is considerably higher than that in the vicinity of the reversible potential. This leads to a higher concentration gradient of copper ions when the surface concentration is suddenly depleted and hence to a sharp and high peak current. In the experiment shown in Fig. 6, it is more than twice that obtained on a copper electrode where a nucleation overpotential does not exist. Very similar results were obtained in a molten alkali nitrate system (14). Nucleation overpotential of silver on a clean platinum electrode is relatively small, as pointed out elsewhere (11), but still a sharp rise of current is observed.

A different experiment describing the same type of phenomenon is shown in Fig. 7, where current/time transients following a potential step from the open-circuit potential to the value marked, are plotted: At the most cathodic overpotential (-212 mV), the current decays in a regular manner with time ^{-1/2}. At less cathodic overpotentials, the current on the bare platinum electrode first decreases, but as soon as a layer of Cu is formed, nucleation overpotential diminishes and the current rises to the value it would have on a freshly prepared Cu electrode.

The coordinates of the maxima in Fig. 7 can serve as a diagnostic criterion for the type of nucleation process taking place. Thus, it was shown (11) that the relationship

$$i_{\max}^2 \cdot t_{\max} = k(nFC)^2 D \quad [1]$$

holds. The numerical constant k should be equal to 0.260 for progressive nucleation and to 0.163 for instantaneous nucleation. In order to evaluate experimentally the constant k , one has to determine the diffusion coefficient by an independent experiment. This was calculated from the slope of a plot of i vs. $t^{-1/2}$ taken at an overpotential of -212 mV (uppermost curve in Fig. 7). Using the value of $(2.1 \pm 0.1) \times 10^{-5}$ cm²/s obtained in this manner the constant k was found to be 0.25 ± 0.01 at low overpotentials and 0.18 ± 0.01 at high overpotentials. A plot of i_{\max} vs. $t_{\max}^{-1/2}$ is shown in Fig. 8. The transition of the slope between small and large values of t_{\max} is clearly seen. Thus instantaneous nucleation appears to be predominant at high overpotentials and slow progressive nucleation occurs at low overpotentials, in agreement with results reported for aqueous solutions (11).

The diffusion coefficients.—The diffusion coefficients of copper and silver were measured by three independent methods: from the peak current in cyclic voltammetry, from current decay following a potential step at high overpotentials (where nucleation is essentially instantaneous on the time scale used, say, in Fig. 7), and by determining the limiting current on a rotating disk electrode. The last method was also used to determine the diffusion coefficients of lead and tin in order to compare to results reported earlier (1) for these two elements.

A summary of these results is shown in Table I. The data obtained from cyclic voltammetry should be consid-

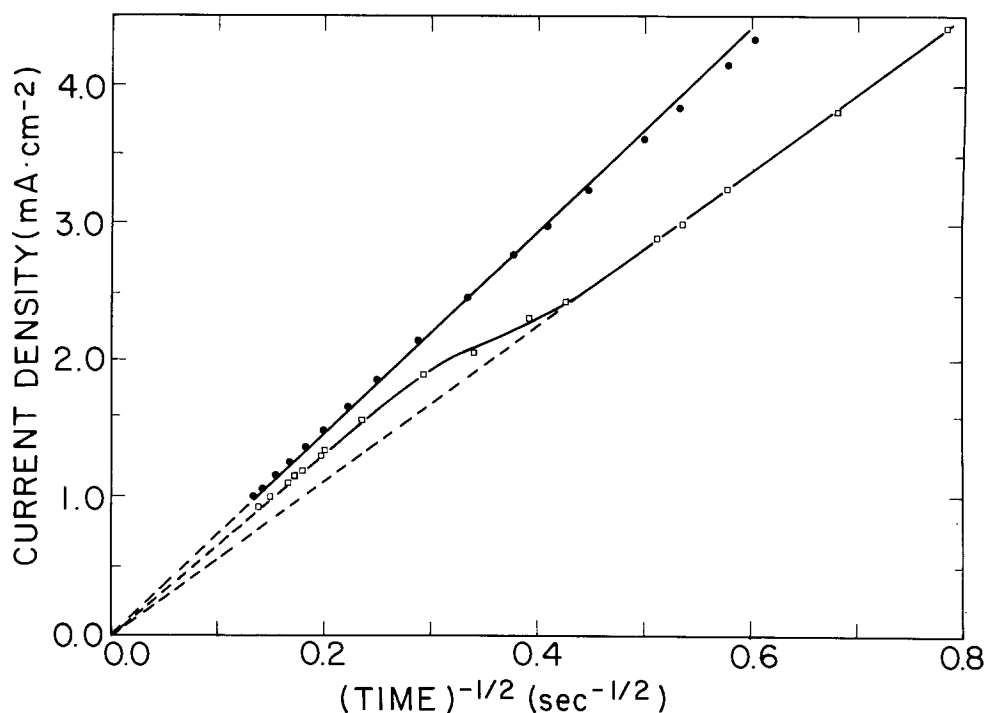


Fig. 8. Plots of current density as a function of (time)^{-1/2} for potentiostatic transients of CuBr on Pt. (xxx): i_{\max} vs. $t_{\max}^{-1/2}$. (ooo): i vs. $t^{-1/2}$ of the uppermost curve in Fig. 7.

ered the least reliable, since some degree of nucleation overpotential, causing a rise of i_p above that calculated for simple diffusion and deposition, occurs in all cases. Values of the diffusion coefficient of tetravalent titanium obtained in this laboratory (21) are also included in Table I.

Outstanding among the results shown in Table I is the exceptionally high value observed for copper. A value of $(10 \pm 1) \times 10^{-6}$ cm²/s obtained from rotating disk measurements would lead to a Stokes radius of ca. 1Å, about equal to the crystallographic radius of copper. It was assumed that cuprous ions act as catalysts for the electrochemical reduction of the solvent. This was confirmed by the low faradaic efficiency observed for electrodeposition of copper (ca. 65%), compared to 100% efficiency for lead and tin.

Manuscript submitted Dec. 28, 1983; revised manuscript received March 28, 1984.

REFERENCES

1. M. Elam, E. Peled, and E. Gileadi, *This Journal*, **130**, 585 (1983).
2. E. Peled, A. Mitavski, A. Reger, and E. Gileadi, *J. Electroanal. Chem.*, **75**, 677 (1977).
3. M. Elam and E. Gileadi, *This Journal*, **126**, 1474 (1979).
4. A. Reger, E. Peled, and E. Gileadi, *ibid.*, **123**, 638 (1976).
5. S. Ziegel, E. Peled, and E. Gileadi, *Electrochim. Acta*, **23**, 361 (1978).
6. R. S. Nicholson and I. Shain, *Anal. Chem.*, **36**, 706 (1964).
7. E. Gileadi, E. Kirowa-Eisner, and J. Penciner, in "Interfacial Electrochemistry—An Experimental Approach," pp. 109-111, Addison-Wesley, Reading, MA (1975).
8. P. Delahay, in "New Instrumental Methods in Electrochemistry," pp. 115-129, Interscience, New York (1954).
9. M. Elam, I. Bahatt, E. Peled, and E. Gileadi, *J. Phys. Chem.*, To be published.
10. G. Mamantov, D. L. Manning, and D. M. Dale, *J. Electroanal. Chem.*, **9**, 253 (1965).
11. G. Gunawardena, G. Hills, I. Montenegro, and B. Scharifker, *ibid.*, **138**, 225 (1982).
12. A. Reger, E. Peled, and E. Gileadi, *J. Phys. Chem.*, **83**, 869 (1979).
13. N. White and P. Lawson, *J. Electroanal. Chem.*, **26**, 113 (1970).
14. G. J. Hills, D. J. Schiffrin, and J. Thompson, *Electrochim. Acta*, **19**, 657 (1974).
15. M. Fleischmann and H. R. Thirsk, in "Advances in Electrochemistry and Electrochemical Engineering," Vol. 3, P. Delahay and C. W. Tobias, Editors, Chap. 3, Interscience, New York (1963).
16. J. A. Harrison and H. R. Thirsk, in "Electroanalytical Chemistry," Vol. 5, A. J. Bard, Editor, pp. 68-148, Marcel Dekker, New York (1971).
17. R. Kaishev and B. Mutaftschiw, *Electrochim. Acta*, **10**, 643 (1965).
18. D. J. Astley, J. A. Harrison, and H. R. Thirsk, *J. Electroanal. Chem.*, **19**, 325 (1968).
19. P. Rolland and G. Mamantov, *This Journal*, **123**, 1299 (1976).
20. C. L. Hussey, L. A. King, and R. A. Carpio, *ibid.*, **126**, 1029 (1979).
21. M. Elam, Ph.D. Thesis, Tel-Aviv University, Tel-Aviv, Israel (1984).
22. E. Peled, A. Mitavski, and E. Gileadi, *Z. Phys. Chem.*, **98**, 111 (1975).

Polarization of the Molten Carbonate Fuel Cell Anode and Cathode

C. Y. Yuh* and J. R. Selman**

Department of Chemical Engineering, Illinois Institute of Technology, Chicago, Illinois 60616

ABSTRACT

A dual-porosity, agglomerate-type model for the porous anode and cathode of the molten carbonate fuel cell is developed and used to predict electrode performance in a small, differential-conversion, cell. The model is based on a phenomenological treatment of mass transport, electrode kinetics, and ionic conduction, combined with structural assumptions. The model predicts the steady-state performance, given a minimum number of structural parameters. Comparison with experimental data for a 3 cm² anode and cathode shows good agreement for plausible values of these parameters.

Both the anode and the cathode of the molten carbonate fuel cell are porous gas-diffusion electrodes. Porous electrodes have numerous industrial applications, primarily because they promote intimate contact of the electrode material with the electrolyte solution or melt, and with both solution and gaseous phase when a porous gas-diffusion electrode is used. Simulation of porous electrode performance is important for design purposes. It is necessary to establish a model which accounts for the essential features of an actual electrode without going into exact geometric detail. Ideally, the model should make use of parameters which can be established by measurements at solid electrodes and in bulk electrolyte. The theoretical analysis of porous electrodes is complicated because the contact of electrode and electrolyte in porous electrodes makes the ohmic conduction and mass-transfer processes occur both in series and in parallel with the electrode reaction, with no easy way to separate them. This work aims to make a contribution to improved simulation of porous gas-diffusion electrodes by an extension of the agglomerate model.

*Electrochemical Society Student Member.

**Electrochemical Society Active Member.

Review of Previous Work

In the past 20 years, several models have been developed to simulate the behavior of a porous gas-diffusion electrode. The simplest model is the "simple" (or flooded) pore model (1). This model, however, is too primitive, and in most cases predicts too low a value for the mass-transport-limited current. The thin film (2, 3) and finite-contact-angle meniscus models (4) are extensions of the simple pore model and account for variations in the wetting tendency of the electrolyte. In a pore with finite-angle meniscus (Fig. 1b), as in a flooded (Fig. 1a), most of the current is concentrated in a small part of the pore wall. In a film-covered pore (Fig. 1c), the electrode reaction, although less restricted, still tends to be concentrated in that part of the film which is close to the bulk electrolyte. Migration of reactants on the surface of the electrode has also been included (5). In real porous electrodes, there is a spectrum of pore sizes; to account for this, several types of dual-porosity models (6-8) have been developed. A relatively simple model is that developed by Giner and Hunter (9) for the Teflon-bounded oxygen electrode of low temperature alkaline fuel cells. They assumed that this electrode can be represented by parallel

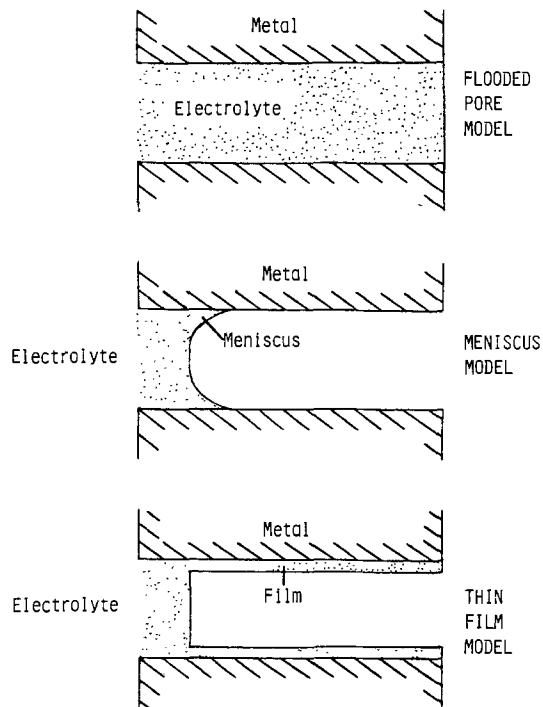


Fig. 1. Schematic diagrams of flooded pore, meniscus, and thin film models.

cylindrical columns of microporous, flooded catalyst (agglomerates) held together by capillary forces and surrounded by gas phase. In their model, there is no film on the external surface of the agglomerate.

Most of the models cited above were restricted in their application to a particular system. The applicability of a certain model depends on the electrode structure and wetting characteristics of the electrolyte; these are obviously not the same in different kinds of fuel cells. Some simple models (thin film and flooded pore model) have been applied to the molten carbonate fuel cell (10-12) and fitted to a limited range of performance data. From postoperation micrographs of porous nickel anodes and nickel oxide cathodes, there is some reason to believe that the agglomerate model may represent electrode structure more adequately than the thin film model. However, the anode and cathode have different wetting characteristics, and it is necessary to account for this. Thus, the nickel anode is not well wetted under reducing conditions, which would correspond reasonably well with the absence of an extended film (dry agglomerate model). However, the cathode is very well wetted (contact angle 0°), and the agglomerates are probably covered by a film. Thus one needs, as also suggested by Giner and Hunter (9), to develop an extension of their agglomerate model. This is termed here the "filmed agglomerate model." An extension of the original agglomerate model is necessary also in a second respect. Giner and Hunter's model contains only one reactant species (dissolved oxygen) and neglects product activity variation (strong KOH electrolyte). The kinetics of both the molten carbonate anode and cathode involve several species dissolved in the melt. It is necessary to develop separate mass balances for these species, and couple them with the electrode-kinetic rate expression. This entails greater mathematical complexity.

Analysis

As shown in Fig. 2, the electrode structure can be pictured as one in which catalyst particles form agglomerates which, under working conditions, are flooded with electrolyte. When current is drawn from the electrode, reactant gas diffuses through the macropores, and dissolves in the electrolyte contained in the agglomerate. After diffusing a certain distance, it reacts at available sites on the catalyst particles.

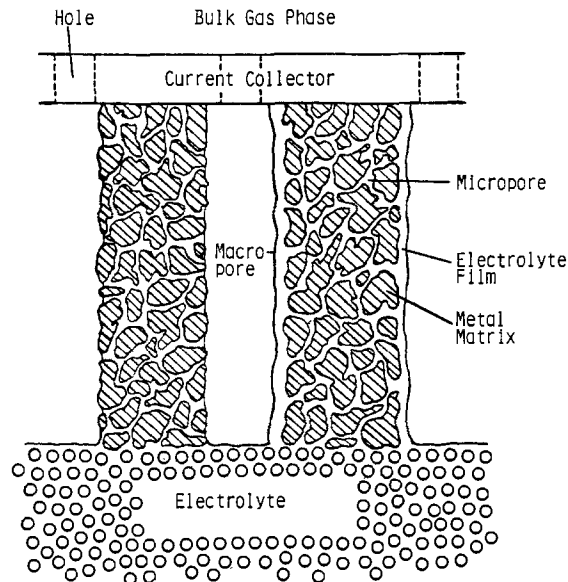


Fig. 2. Schematic of porous structure

We make the following assumptions in order to simplify the mathematical analysis without detailing the actual geometry within the agglomerates.

1. The electrode is made up of a number of cylinders of catalyst with radius R and length L as shown in Fig. 3a and 3b. The agglomerate is flooded with electrolyte. If there is a film on the external surface, the film thickness δ is uniform.

2. The electrolyte and catalyst in the agglomerate cylinders are homogeneously mixed and form a quasicontinuum.

3. The Butler-Volmer equation is a suitable representation of the electrode kinetics. The transfer coefficients, α_a and α_c , are constant.

4. The transport of current through the electrolyte follows Ohm's law. The IR drop in the metal phase is negligible.

5. The gas-phase mass-transfer resistance is negligible.

6. The current flows in the cylinder only in the axial direction, *i.e.*, potential gradients in the radial direction are

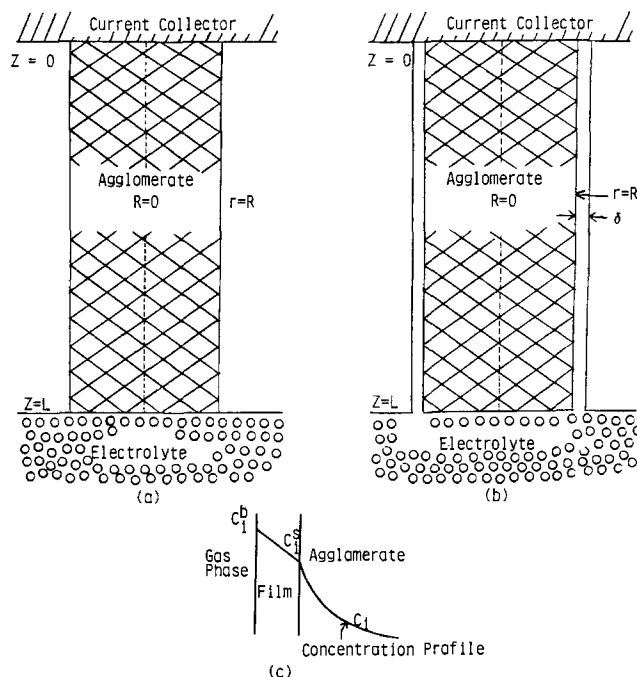


Fig. 3. Schematic of porous electrode structure in two agglomerate models. (a): Dry agglomerate model. (b): Film agglomerate model. (c): Detail of film agglomerate model.

negligible, and concentration gradients in the axial direction are negligible.

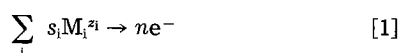
7. The concentration of dissolved gases at the gas-electrolyte interface follows Henry's law. In the case of oxygen, this appears to be justified by the proportionality of observed limiting current at the cathode with oxygen partial pressure. However, there is uncertainty as to the form in which dissolved oxygen is present (superoxide, peroxide); this should affect the solubility behavior (13, 14).

8. The system is isothermal, isobaric, and at steady state.

9. The activity of CO_3^{2-} ions is everywhere equal to unity.

10. All physical parameters are constant.

The following generalized reaction takes place at the electrode surface



The species balance which incorporates diffusion and reaction is

$$\bar{D}_i \nabla^2 C_i = \frac{s_i A i_n}{n F} \quad [2]$$

Here i_n is the transfer current density at the electrode-electrolyte interface and can be expressed by the Butler-Volmer equation

$$i_n = i_0^b \prod_i (C_i/C_i^b)^{\gamma_i} \{ \exp(\alpha_a F \eta_s / RT) - \exp(-\alpha_c F \eta_s / RT) \} \quad [3]$$

The following dimensionless quantities are defined

$$\bar{C}_i = C_i/C_i^b, \quad \xi = r/R, \quad \zeta = z/L$$

Neglecting the diffusion term in the axial direction, we have

$$\frac{1}{\xi} \frac{\partial}{\partial \xi} \left(\xi \frac{\partial \bar{C}_i}{\partial \xi} \right) = s_i N_i i_n \quad [4]$$

for species i , where

$$N_i = \frac{R^2 A}{\bar{D}_i C_i^b n F}$$

We need one more equation, *i.e.*, the current balance. In the molten carbonate fuel cell, the anode and cathode have different current balance equations because only the cathode is covered by a film, whereas the anode may be treated as a "dry agglomerate."

Dry agglomerate model (anode).—Here the current balance is, for example, for hydrogen

$$\frac{d^2 \Phi_L}{dz^2} = - \frac{2n \bar{D}_1 F}{s_1 R} \left(\frac{dC_1}{dr} \right) \Big|_{r=R} \quad [5]$$

Equation [5] states that the diffusion flux of species 1 into the differential volume is related to the current generation inside the differential volume. For each species, the relationship depends on the stoichiometric ratio n/s_i in Eq. [1]. Here, the subscripts denote: 1 hydrogen, 2 CO_2 , and 3 H_2O . In dimensionless form

$$\frac{d^2 \psi_L}{d\zeta^2} = P_1 \left(\frac{d\bar{C}_1}{d\xi} \right) \Big|_{\xi=1} \quad [6]$$

where $P_1 = -2n \bar{D}_1 F C_1^b \phi L^2 / \kappa R^2 S_1$, $\psi_L = \phi \Phi_L$, and $\phi = F/RT$. The boundary conditions are

$$\zeta = 0, \quad \frac{d\psi_L}{d\zeta} = 0 \quad [7a]$$

$$\zeta = 1, \quad \psi_L = \psi_0 \quad [7b]$$

$$\xi = 0, \quad \frac{d\bar{C}_i}{d\xi} = 0 \quad [7c]$$

$$\xi = 1, \quad \bar{C}_i = 1 \quad [7d]$$

Filmed agglomerate model (cathode).—In the case of the cathode, the film exerts additional diffusion resistance. This will change boundary condition [7d] and also current balance Eq. [6].

For species 1, the diffusion flux in the film toward the electrode surface must be equal to the depletion rate caused by reaction at the external surface, plus the diffusion flux toward the interior of the agglomerate. In mathematical terms

$$\bar{D}_i \left(\frac{dC_i}{dr} \right) \Big|_{r=R} = D_i \frac{C_i^b (1 - \bar{C}_i^s)}{R \Delta} - s_i (1 - \epsilon) i_n / n F \quad [8]$$

In dimensionless form

$$\frac{d\bar{C}_i}{d\xi} - F' (1 - \bar{C}_i) + P_1'' i_n = 0 \text{ at } \xi = 1 \quad [9]$$

where

$$F' = 1/\epsilon \Delta, \quad P_1'' = \frac{s_i (1 - \epsilon) R}{n F C_i^b \bar{D}_i}$$

and $\Delta = \ln [(R + \delta)/R]$.

Equation [9] is substituted for the boundary condition [7d] in the case of a filmed agglomerate.

The current balance Eq. [6] has to be changed because both the film and the agglomerate conduct current. By a similar derivation at the cathode, except that the diffusion flux of species into the differential volume is represented by the flux in the film, (Fig. 3c)

$$\frac{d^2 \psi_L}{d\zeta^2} = P P_1 (1 - \bar{C}_i^s) \quad [10]$$

where

$$P P_1 = \frac{-2n F D_1 C_1^b \phi L^2}{\kappa R_1 (R + \delta)^2 \Delta S_1}$$

and

$$R_1 = \frac{\left\{ R + \frac{(R + \delta)^2 - R^2}{\epsilon} \right\}}{(R + \delta)^2}$$

Here, the subscript 1 stands for O_2 , and 2 for CO_2 . Finally, we have four partial differential equations for the anode and three for the cathode. The relationship between Φ_L and η_s can easily be expressed by the Nernst equation. The final unknowns are \bar{C}_i and ψ_L .

Input Parameters

The input parameters needed to apply the agglomerate model are the kinetic, transport, and thermodynamic properties of the electrode/electrolyte combination, as well as structural parameters of the porous electrode. In the case of the anode, we adopt the reaction mechanism proposed by Ang and Sammells (15). This mechanism predicts dependence of i_0^b and C_1 as follows

$$i_0^b = i_0^0 (\text{H}_2)^{0.25} (\text{CO}_2)^{0.25} (\text{H}_2\text{O})^{0.25} \quad [11]$$

It also predicts $\alpha_a = 0.5$ and $\alpha_c = 1.5$. For fuel oxidation at nickel in Li/K melt at 923 K, they obtained the standard exchange current density, $i_0^0 = 105 \text{ mA/cm}^2$. For fuel oxidation at Cu in Li/K melt, Lu (16) obtained a slightly lower i_0^0 , 72.4 mA/cm^2 .

Adequate investigations of the oxygen reaction kinetics are available only on gold electrodes. Appleby and Nicholson (17, 18) proposed two mechanisms for this reaction: (i) the "peroxide mechanism," leading to the kinetic expression

$$i_0^b = i_0^0 (\text{O}_2)^{0.375} (\text{CO}_2)^{-1.25} \quad [12]$$

$$\alpha_a = 1.5, \quad \alpha_c = 0.5$$

and (ii) the "superoxide mechanism," leading to

$$i_0^b = i_0^a(O_2)^{0.625}(CO_2)^{-0.75} \quad [13]$$

$$\alpha_a = 2.5, \alpha_c = 0.5$$

At 650°C and at a gold surface, in Li-K melt (62-38 mole percent [m/o]), i_0^a is 0.012 mA/cm² for the peroxide mechanism and 0.003 mA/cm² for the superoxide mechanism (17, 18, 19b).

There are no i_0^b values available for the less expensive metals used in practice. In particular, thus far, no i_0^b value has been determined at a smooth nickel oxide electrode because of the unstable character and unknown surface area of the nickel oxide matrix. However, using the above two mechanisms and applying them to porous electrodes, one can expect to obtain some insight concerning the value of i_0^b and the concentration dependence of i_0^b .

The ionic conductivity and viscosity of the electrolyte, as well as the diffusivity and solubility of the various dissolved gaseous species, are essential parameters in modeling the fuel cell electrodes. Values can be estimated or taken from surveys of these properties, as available in the literature (19a, 19b). Wilemski *et al.* (11), using the values listed in the IGT report (19b), have correlated the diffusivities, solubilities, and conductivities. These correlations are used in the present work.

Structural parameters are based on measured porosities and BET surface areas. The method of calculating the agglomerate radius, R , and the external surface area are described in Ref. (20).

Method of Solution

The solution of the model equations was carried out on a Harris-120 digital computer using a finite difference numerical procedure (21). Since the species balance Eq. [4] and current balance Eq. [6] and [10] are coupled only through the nonlinear reaction kinetics, we can solve them separately by the following algorithm: (i) linearize Eq. [4], (ii) solve the linearized Eq. [4] using Newman's subroutines (18) for solving a set of ordinary differential equations at some selected input value of ψ_L , (iii) the flux at the surface is expressed as a polynomial in ψ_L by simple interpolation. A fifth-order polynomial gives sufficient accuracy, and (iv) substitute the polynomial expression into Eq. [6] and [10] and solve again by linearization, using Newman's technique. Solutions of the nonlinear equations were obtained by iteration on the approximate linear solutions; convergence was usually achieved with ten iterations.

Results and Discussion

Tables I and II gave the transport and kinetic properties used as input to the agglomerate models. Geometric data for the nickel and nickel oxide cathode are taken from the IGT cell EPRI-56, and those for the copper anode from IGT cell RD-1 (22). In the dry agglomerate model, not all surface area measured by the BET method is wetted by the electrolyte. The surface on the "outside" of the agglomerate cylinder is dry and not available for

Table I. Input parameters for nickel and copper anode

	Copper	Nickel
Agglomerate length	0.0737 cm	0.0762 cm
Agglomerate radius	9.98 μ m	3.87 μ m
Porosity	0.625	0.65
Microporosity	0.143	0.157
Agglomerate specific surface area	1500 cm ² /cm ³	6080 cm ² /cm ³
Exchange current density i_0^a	72 mA/cm ²	110 mA/cm ²
Temperature	923 K (650°C)	
Ionic conductivity	1.386 Ω^{-1} cm ⁻¹	
Diffusivity	H ₂ 1.57 $\times 10^{-5}$ cm ² /s CO ₂ 1.00 $\times 10^{-5}$ H ₂ O 1.33 $\times 10^{-5}$	
Solubility	H ₂ 5.8 $\times 10^{-6}$ mol/cm ³ -atm CO ₂ 1.2 $\times 10^{-5}$ H ₂ O 5.8 $\times 10^{-6}$	
Reaction mechanism	After Ang and Sammells (15)	

Table II. Input parameters for nickel oxide cathode

Agglomerate length	0.0406 cm
Agglomerate radius	3.36 μ m
Porosity	0.76
Microporosity	0.24
Agglomerate specific surface area	9230 cm ² /cm ³
Temperature	923 K (650°C)
Ionic conductivity	1.42 Ω^{-1} cm ⁻¹
Diffusivity O ₂	1.20 $\times 10^{-5}$ cm ² /s
Diffusivity CO ₂	1.00 $\times 10^{-5}$ cm ² /s
Solubility O ₂	2.73 $\times 10^{-7}$ mol/cm ³ -atm*
Solubility CO ₂	1.20 $\times 10^{-5}$ mol/cm ³ -atm*

* Value at 1 atm. Proportionality with partial pressure assumed between 0.01 and 1 atm.

the electrochemical reaction. The pores inside the agglomerate are flooded due to the very strong capillary forces. The external area was calculated assuming that 90% of the measured porosity is macroporosity, *i.e.*, space between the agglomerates. This gave good results for both nickel and copper anodes. Figures 4 and 5 show how the concentration and overpotential distributions vary with respect to the polarization (terminal potential) of the electrode. Higher polarization causes a more nonuniform reaction distribution, which "squeezes" the reaction zone toward the bottom of the agglomerates. High exchange current densities and low electrolyte conductivities also have this effect. As expected, best overall electrode performance results from high exchange current density and ionic conductivity. Using kinetic parameters measured by Ang and Sammells (15) for a nickel anode and by Lu (16) for a copper anode, we can predict the performance. Figures 6 and 7 show that the predictions are in very good agreement with the experimental results. The fuel gas used in both cases is high Btu fuel humidified at 58°C, having equilibrium composition H₂ 54%, CO₂ 10.2%, CO 10.8%, and H₂O 25% at 650°C (cell temperature). It should be noted that this prediction still involves an adjustable parameter: namely, the ratio of macroporosity to microporosity. This ratio is the same for both nickel and copper anodes.

The application of this model to the cathode is more complicated. In the filmed agglomerate model, we need to estimate the film thickness (δ), which is not directly measurable. Tang *et al.* (23) have performed a systematic study of the effect of oxygen concentration on cathodic performance. For very low oxygen concentration (less than 3% oxygen) and high CO₂ concentrations, polarization curves show a clear limiting current; this allows us to

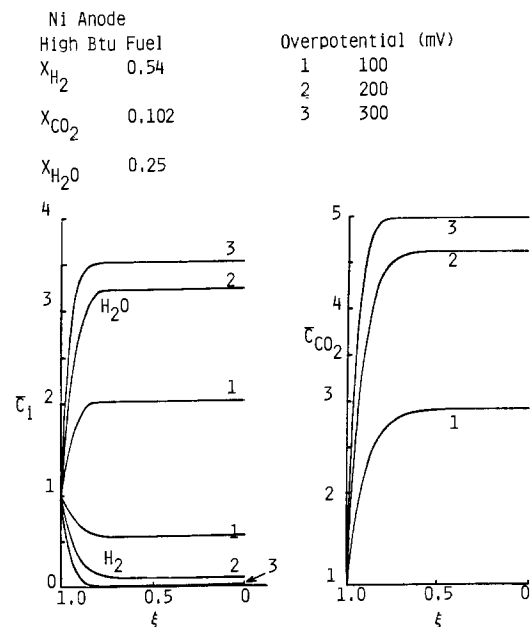


Fig. 4. Effect of overpotential on concentration profiles

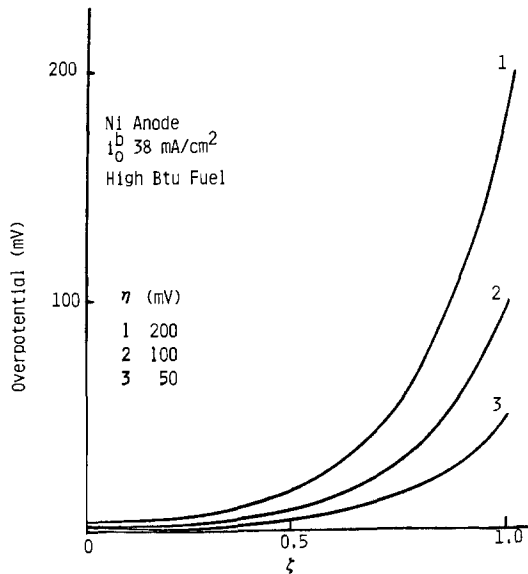


Fig. 5. Effect of polarization on overpotential profiles

estimate δ , assuming limiting oxygen diffusion through a film. However, by adjusting the exchange current density, we can fit the rising portion of the polarization curve for these very low oxygen concentrations.

Using the exchange current density and the film thickness thus obtained, we can predict the polarization curves at other compositions characterized by high oxygen concentrations. As mentioned earlier, it is difficult to prepare an electrode of nickel oxide having a well-defined smooth surface and adequate stability in the carbonate melt. Therefore, fitting porous electrode data to the filmed agglomerate model is an attractive engineering approach to determining the kinetic parameters of oxygen reduction at a nickel oxide cathode.

In this work, it is assumed that the film thickness determined by fitting low oxygen polarization curves is independent of gas compositions and overpotential. This may not be true in practice, but it is a convenient assumption, since operating molten carbonate fuel cells are practically inaccessible to optical measurement *in situ*.

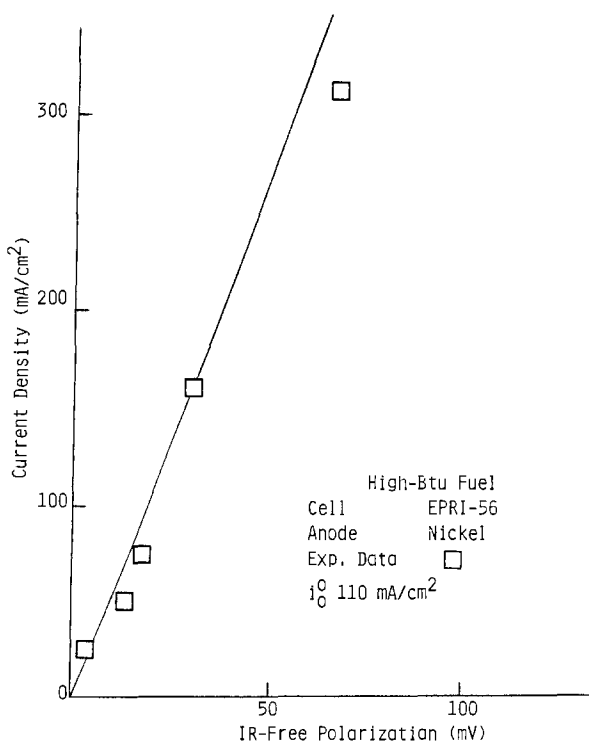


Fig. 6. Prediction of polarization curve at nickel anode

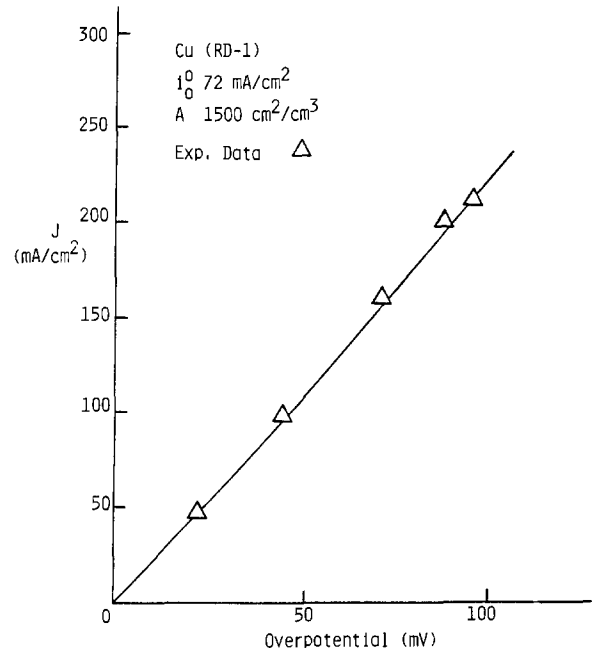


Fig. 7. Predicted polarization curve at copper anode

Figure 8 shows the effect of the local overpotential on the concentration profiles. Because the film is highly conductive, it can be expected that the axial overpotential distribution is very uniform. The analysis confirms this. Higher polarization tends to make the overpotential less uniform, but the effect is negligibly small. Parametric studies show that a very thin film and a high exchange current density yield the best electrode performance, in agreement with qualitative predictions (20).

To demonstrate the utility of the filmed agglomerate model for analyzing the cathodic rate process, selected experimental results are compared with predictions according to the peroxide or superoxide model. (Fig. 9 and 10). The peroxide mechanism appears to give a better fit than the superoxide mechanism. Note, however, that the peroxide mechanism would predict that the limiting current depends on the square root of oxygen partial pressure, whereas the experimental data strongly suggest a linear dependence (as reflected in our use of a Henry's coefficient for oxygen). The superoxide mechanism would predict an 0.75 power dependence on oxygen partial pressure, which is closer to the experimental evidence, although still too small. However, the superoxide mechanism predicts in any case much too high current density overall. Neither mechanism appears to predict correctly over the whole range; other mechanisms, or combinations of mechanisms, should be considered. Ob-

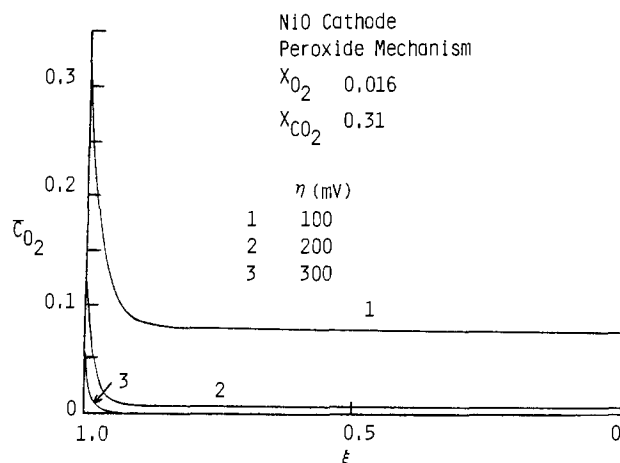


Fig. 8. Effect of local overpotential on concentration profiles

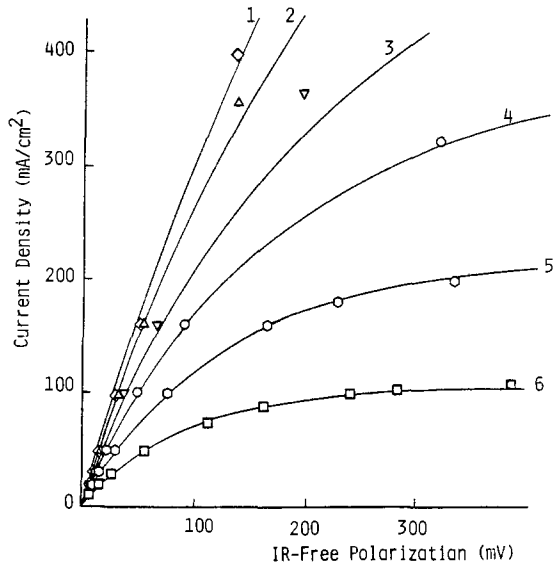


Fig. 9. Fitting of cathodic data by peroxide mechanism, Gas compositions 1-6 (Table III). Best fit: i_o^b (mA/cm²) = 1.91 (X_{O₂})^{0.375} (X_{CO₂})^{-1.25}.

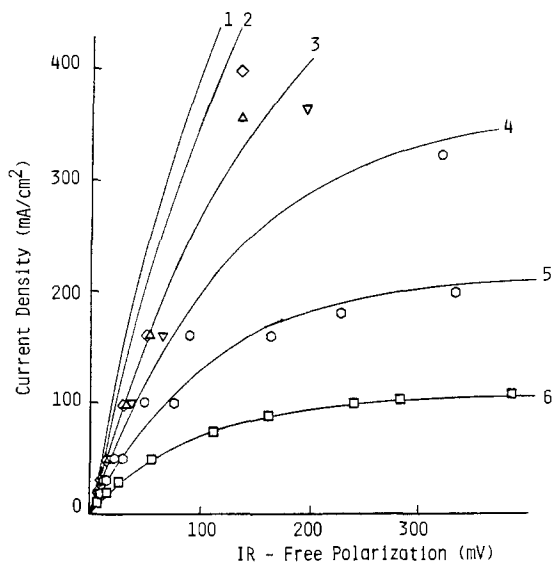


Fig. 10. Fitting of cathodic data by superoxide mechanism. Gas compositions 1-6 (Table III). Best fit: i_o^b (mA/cm²) = 19.3 (X_{O₂})^{0.625} (X_{CO₂})^{-0.75}.

viously, more extensive data are also required for a definite identification of the oxygen reduction mechanism.

Effects of Electrode Geometry

We can also adjust the geometric parameters, such as the electrode thickness, to see how they affect the electrode performance. This is very important for design purposes where the objective is the optimizing the structure of an electrode. Too thin an electrode may not provide enough catalytic surface. Too thick an electrode may have too large an ohmic resistance. Figures 11 and 12 show typical examples of performance variation with varying electrode thickness. They clearly show a plateau-

Table III. Oxidant compositions used in Fig. 8 and 9 (partial pressures in atm)

O ₂	CO ₂	N ₂	Exp	Fit
0.15	0.30	0.55	◇	1
0.12	0.30	0.58	△	2
0.08	0.30	0.62	▽	3
0.054	0.30	0.646	○	4
0.032	0.31	0.668	○	5
0.016	0.31	0.674	□	6

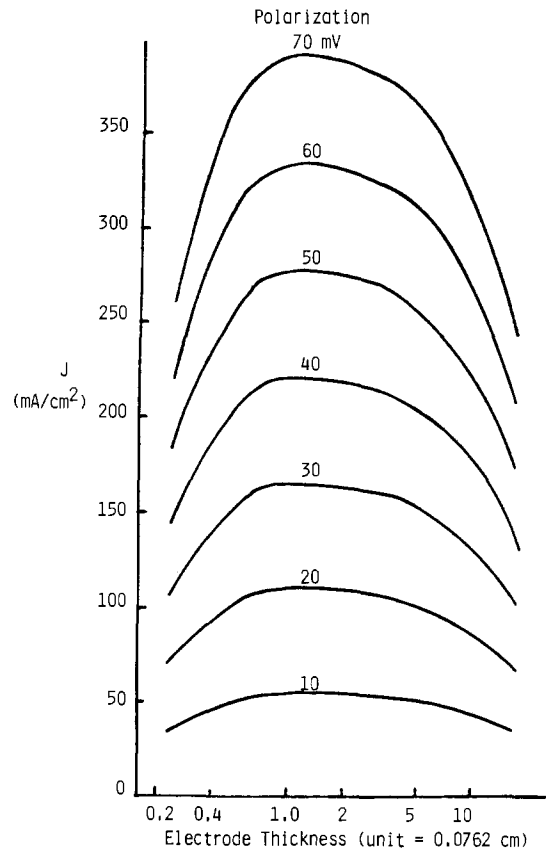


Fig. 11. Optimization of nickel anode thickness with respect to performance. Gas composition: 80% H₂, 20% CO₂. Area factor (A) = 6080 cm²/cm³. Standard exchange current density = 110 mA/cm².

type optimum performance and indicate a range of electrode thicknesses for which overall electrode performance does not vary much.

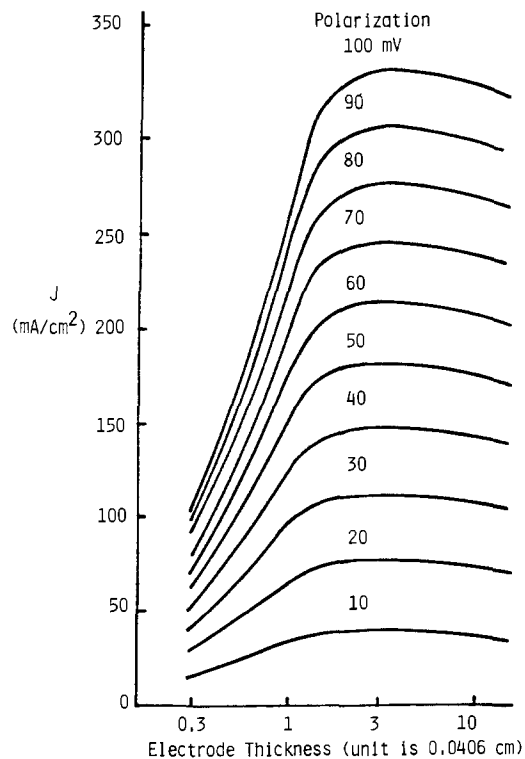


Fig. 12. Optimization of nickel oxide cathode thickness with respect to performance. Gas composition: 15% O₂, 30% CO₂, 55% N₂. Area factor (A) = 5000 cm²/cm³. Standard exchange current density = 4.3 mA/cm²; peroxide mechanism assumed.

In the case of the anode, this may form the basis for fabricating a thicker electrode serving as an electrolyte reservoir, without sacrificing too much of the electrolyte performance. The existence of an optimum may be explained in terms of a compromise between the kinetic and ohmic resistances. The performance eventually drops if the electrode becomes too thick because of too much ohmic resistance, in spite of the larger surface area.

In the case of the cathode, a highly conductive film exists and the performance drops more slowly than in the case of the anode. Too thin an electrode causes a performance drop because the available surface area decreases in spite of the smaller ohmic resistance. In the case of the cathode, the external surface area covered by film produces most of the current, and decreasing it would cause a much faster performance drop than in the case of the anode. Since changing the electrode thickness is equivalent to "filling up" the macropore as shown in Fig. 13, the performance variation can also be interpreted in terms of anodic wetting. The reason is that the portion of the electrode below the electrolyte level in a macropore is essentially unutilized because of very high mass-transfer resistance. This result is consistent with experimental data, which show that in the case of the anode the degree of electrolyte filling has little effect on electrode performance under the usual operating conditions, i.e., 160 mA/cm² (24).

Conclusions

Two types of agglomerate models, discussed and quantitatively analyzed in this work, enable us to predict the distribution of potential and reaction rate in the molten carbonate fuel cell anode and cathode, and allow us to estimate the electrode utilization in each case.

The models described in this work are based on assumptions which naturally affect their applicability. In order to make the models more generally applicable, a number of assumptions may be removed or substantially altered. Ohm's law may be replaced by a more complicated expression to include ionic migration in the melt (25). Agglomerate flooding, film thickness variation, and coverage all can be varied with respect to temperature, gas composition, polarization, and melt composition if adequate empirical information is available. A nonisothermal model may be derived. The model can also be expanded to account for nonuniform porosity distribution. Finally, more efficient computation methods, e.g., orthogonal collocation, may be substituted for the conventional finite-difference method.

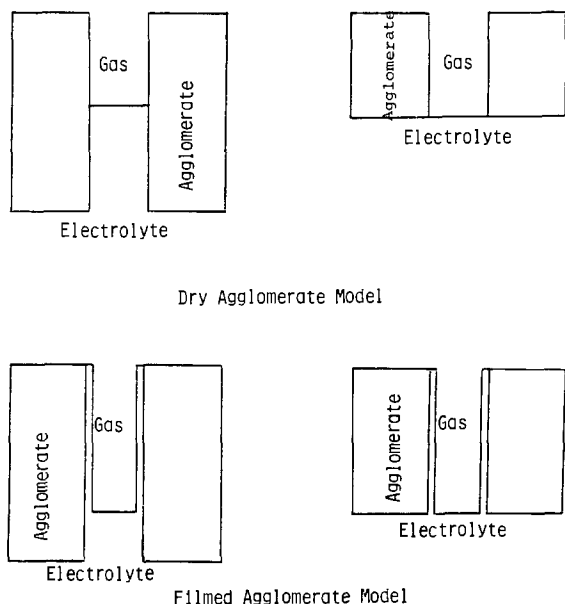


Fig. 13. Equivalence of macropore flooding to variation in electrode thickness.

Acknowledgments

This work was supported by the Division of Materials Sciences, Office of Basic Energy Sciences, U.S. Department of Energy. The experimental data were taken from measurements made at the Institute of Gas Technology, Chicago, Illinois, under sponsorship of the Electric Power Research Institute, Palo Alto, California. The interest and cooperation of Mr. E. H. Camara and others of the Institute of Gas Technology staff are gratefully acknowledged.

Manuscript submitted Aug. 9, 1983; revised manuscript received Jan. 9, 1984. This was Paper 382 presented at the Montreal, Quebec, Canada, Meeting of the Society, May 9-14, 1982.

The Institute of Gas Technology assisted in meeting the publication costs of this article.

LIST OF SYMBOLS

A	specific surface area (cm ² /cm ³)
C	species concentration (mol/cm ³)
\bar{C}	dimensionless concentration (C/C^b)
D	diffusivity (cm ² /s)
\bar{D}	effective diffusivity (cm ² /s)
F	Faraday constant (C/g-eq)
F'	$\frac{1}{\epsilon\Delta}$
i_n	transfer current density (A/cm ²)
i_0^b	exchange current density (A/cm ²)
L	electrode thickness (cm)
N_1	$\frac{R^2 A}{\bar{D}_1 C_1^b n F}$
n	number of electrons transferred
P_1	$\frac{-2nF\bar{D}_1 C_1^b \phi L^2}{\kappa R^2 S_1}$
PP_1	$\frac{-2nF\bar{D}_1 C_1^b \phi L^2}{\kappa R_1 (R + \delta)^2 \Delta S_1}$
P_1''	$\frac{s_i (1 - \epsilon) R}{n F C_1^b \bar{D}_1}$
r	radial distance from the axis of the agglomerate (cm)
R	agglomerate radius (cm)
R_1	$\left\{ R^2 + \frac{(R + \delta)^2 - R^2}{\epsilon} \right\}$
s_i	stoichiometric coefficient
T	temperature (K)
z	longitudinal distance from the current collector

Greek Characters

ϕ	F/RT
α_a, α_c	transfer coefficient
η	overall electrode polarization (V)
η_s	surface overpotential (V)
ζ	z/L
ξ	r/R
ϵ	agglomerate porosity
ψ_0	$\phi\Phi_0$
ψ_L	$\phi\Phi_L$
Φ_0	electrolyte potential at tile-electrode contact
Φ_L	electrolyte potential (V)
κ	electrolyte effective conductivity (1/Ω-cm)
Δ	$\ln \left(\frac{R + \delta}{R} \right)$

Subscript

i species

Superscript

b bulk electrolyte
 s external surface of electrolyte
 $-$ dimensionless (concentration) or effective (diffusivity)

REFERENCES

- L. G. Austin, M. Ariet, R. D. Walker, G. B. Wood, and R. H. Comyn, *IEC Fundam.*, **4**, 321, (1965).
- F. G. Will and D. J. Ben Daniel, *This Journal*, **116**, 933 (1969).
- D. N. Bennion and C. W. Tobias, *ibid.*, **113**, 589 (1966).
- J. T. Cobb, Jr. and L. F. Albright, *ibid.*, **115**, 2 (1968).

5. R. P. Iczkowski, *ibid.*, **111**, 1078 (1964).
6. R. C. Burshtein, V. X. Markin, A. G. Pshenionnikov, V. A. Chismadgev, and Y. G. Chirkov, *Electrochim. Acta*, **9**, 773 (1964).
7. E. A. Grens, II, *IEC Fundam.*, **5**, 542 (1966).
8. R. Brown and L. A. Horve, Abstract 203, p. 109, The Electrochemical Society Extended Abstracts, Vol. I-7, Dallas, TX, May 5-12, 1967.
9. J. Giner and C. Hunter, *This Journal*, **116**, 1124 (1969).
10. D. T. Wasan, T. Schmidt, B. S. Baker, and E. S. Argano, Chemical Engineering Progress Symposium, Fundamental Research on Heat and Mass Transfer, **63**, (77), 16-31 (1966).
11. G. Wilemski, D. Bloomfield, M. L. Finson, E. R. Pugh, and V. L. Wray, Physical Science, Inc., "Performance Model for Molten Carbonate Fuel Cells," Final Report, July 5, 1978-July 5, 1979.
12. W. L. Lo, M.S. Thesis, Illinois Institute of Technology, Chicago, IL (1980).
13. A. J. Appleby and C. Van Drunen, *This Journal*, **127**, 1655 (1980).
14. S. W. Smith, W. M. Vogel, and S. Kapelner, *ibid.*, **129**, 1668 (1982).
15. P. G. P. Ang and A. F. Sammells, *ibid.*, **127**, 1287 (1980).
16. S. H. Lu and J. R. Selman, Submitted to *This Journal*.
17. A. J. Appleby and S. B. Nicholson, *J. Electroanal. Chem.*, **112**, 71 (1980).
18. A. J. Appleby and S. B. Nicholson, *ibid.*, **83**, 309 (1977).
19. a. "Fuel Cell Research on Second-Generation Molten-Carbonate Systems, Vol. II. Characteristics of Carbonate Melts," Project 8894 Quarterly Status Report, July 1-Sept. 30, 1976, Institute of Gas Technology, Chicago, IL (1976); b. J. R. Selman and H. C. Maru, in "Advances in Molten Salt Chemistry," Vol. 4, G. Mamantov and J. Braunstein, Editors, p. 159 (1981).
20. C.-Y. Yuh, M.S. Thesis, Illinois Institute of Technology, Chicago, IL (1981).
21. J. Newman, "Electrochemical Systems," Appendix C, Prentice-Hall, Englewood Cliffs, NJ (1973).
22. T. D. Claar, Private communication (1982).
23. J. R. Selman, W. L. Lo, T. E. Tang, and T. D. Claar, Abstract 128, p. 349, The Electrochemical Society Extended Abstracts, Vol. 80-2, Hollywood, FL, Oct. 5-10, 1980.
24. H. C. Maru, D. Patel, and L. Paetsch, Abstract 9, p. 27, The Electrochemical Society Extended Abstracts, Vol. 81-1, Minneapolis, MN, May 10-15, 1981.
25. R. Pollard and J. Newman, *This Journal*, **126**, 1713 (1979).

Activities and Other Partial Molar Properties of the Quarternary Molten Salt System MnCl₂-NaCl-KCl-CsCl

C. A. Pickles

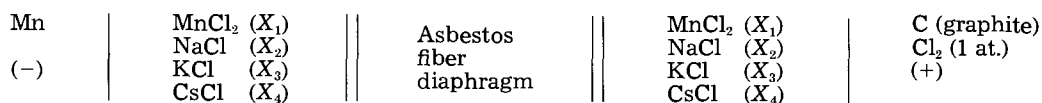
Department of Metallurgical Engineering, Queen's University, Kingston, Ontario, Canada

S. N. Flengas

Department of Metallurgy and Materials Science, University of Toronto, Toronto, Ontario, Canada, M5S 1A4

ABSTRACT

The thermodynamic properties of the quarternary molten salt system MnCl₂-NaCl-KCl-CsCl have been investigated by EMF measurements using a formation cell of the type



It was found that the partial molar free energies of mixing of MnCl₂ in the quarternary solutions are well represented by a previously developed expression given as

$$\overline{\Delta G}_{\text{MnCl}_2}^{\text{(in quarternary)}} = (1 - S)[(1 - t) \overline{\Delta G}_{\text{MnCl}_2}^{\text{(in MnCl}_2\text{-CsCl)}} + t \overline{\Delta G}_{\text{MnCl}_2}^{\text{(in MnCl}_2\text{-KCl)}}] + S \overline{\Delta G}_{\text{MnCl}_2}^{\text{(in MnCl}_2\text{-NaCl)}}$$

which is valid at constant X_{MnCl_2} . In this expression, $\overline{\Delta G}_{\text{MnCl}_2}^{\text{(in MnCl}_2\text{-CsCl)}}$ etc. refer to the corresponding partial molar free energy of MnCl₂ in the designated binary system having the same MnCl₂ content as the quarternary. The composition parameters S and t are defined as

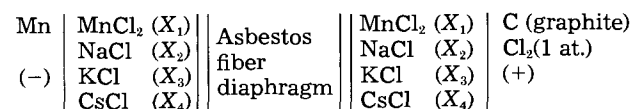
$$t = \frac{X_{\text{KCl}}}{X_{\text{KCl}} + X_{\text{CsCl}}}, \quad S = \frac{X_{\text{NaCl}}}{X_{\text{NaCl}} + X_{\text{KCl}} + X_{\text{CsCl}}}$$

In previous publications from this laboratory (1, 2), theoretical equations have been developed from which the molar and partial molar properties of ternary and quarternary molten salt solutions may be calculated from available data on the component binary systems.

The thermodynamic properties of binary fused-salt solutions have been the object of several systematic investigations, and extensive compilations of thermodynamic data are available. However, similar information on ternary fused-salt solutions is limited to only a few selected systems, and for quarternary solutions there is hardly any information at all. Yet, systems of metallurgical importance are usually multicomponent, and the application of the thermodynamic approach to high temperature equilibria is restricted by the lack of experimental data. Thus, it is evident that expressions from which the ther-

modynamic properties of ternary and quarternary systems may be predicted from available information on the related binary systems should be of considerable theoretical and practical importance.

In the present investigation, the thermodynamic properties of MnCl₂ in the quarternary molten salt system MnCl₂-NaCl-KCl-CsCl have been obtained from EMF measurements using a formation cell of the type



For this system, the thermodynamic and structural properties of the binary solution MnCl₂-NaCl, MnCl₂-KCl, MnCl₂-CsCl, as well as of the ternary MnCl₂-NaCl-CsCl,

have been investigated in this laboratory and elsewhere (3-6).

It is of interest that the MnCl_2 -NaCl system is characterized by relatively low exothermic enthalpies of mixing which reach the maximum value of -1900 cal/mol at a composition of about 35 mole percent (m/o) MnCl_2 . Also, the change of volume on mixing indicates only slight positive deviations from additivity (6, 7). On the contrary, in the MnCl_2 -KCl and the MnCl_2 -CsCl systems, the enthalpies of mixing are strongly exothermic and the changes of volume on mixing show pronounced positive deviations from additivity, which is indicative of compound formation. For example, at 33 m/o CsCl the integral enthalpy of mixing in the MnCl_2 -CsCl system has a value of -5400 cal/mol at 700°C . Because of such pronounced differences in the properties of the binary systems, the quaternary system MnCl_2 -NaCl-KCl-CsCl should be considered as a test system for establishing the validity of the proposed theoretical expressions (1, 2).

Experimental

The alkali chlorides employed in the present work were reagent-grade materials, and the anhydrous MnCl_2 was 99.5 weight percent (w/o) pure. These salts were further dehydrated by heating under vacuum for several days at 200°C . The materials were handled and weighed in a dry box filled with anhydrous argon gas.

The cell design was similar to that used in the previous work (7). It consisted of a Mn indicator electrode immersed in the MnCl_2 -NaCl-KCl-CsCl molten solution of known composition, and a graphite-chlorine electrode which also dipped into a molten salt solution of the same composition. The two cell compartments were separated by an asbestos fiber diaphragm fused into silica glass (8).

The chlorine electrode was continuously flushed with anhydrous research-grade chlorine gas. The Mn electrode was made by placing a tungsten rod, 1/8 in. diam, and crushed electrolytic manganese metal in a stabilized zirconia ceramic tube closed at one end, which was heated to about 1400°C under an argon atmosphere. The molten Mn was allowed to solidify very slowly to avoid cracking as it passed through its crystallographic transformation (9). This electrode was about 10 mm diam by 4 cm long and was acid polished prior to use. During a run, the Mn electrode was operated under an atmosphere of deoxygenated argon gas.

The asbestos diaphragm had a resistance in the range 1000-2000 Ω . Its construction has been described elsewhere (8).

During a run, EMF readings were taken at intervals of about 25°C , up to approximately 850°C . Potentials were fully reproducible to within 2 mV during a temperature cycle, and cell reversibility was also established through polarization tests at currents of about 1 mA.

Volatility of MnCl_2 for the salt compositions used in this work was insignificant and did not affect the reproducibility of the EMF measurements during a temperature cycle.

Data Treatment and Results

Compositions in a quaternary system are represented (10) by points within the volume of an equilateral tetrahedron, as shown in Fig. 1, in which the four apexes correspond to the pure components MnCl_2 , NaCl, KCl, and CsCl, and the edges represent the six binary systems MnCl_2 -NaCl, MnCl_2 -KCl, MnCl_2 -CsCl, KCl-NaCl, KCl-CsCl, and NaCl-CsCl.

The triangular faces represent the four ternary systems MnCl_2 -NaCl-KCl, MnCl_2 -NaCl-CsCl, MnCl_2 -KCl-CsCl, and NaCl-KCl-CsCl.

It is a property of all equilateral tetrahedra that lines originating from any internal point P , drawn parallel to the four different faces, have a total length equal to one edge, and each of these segments may be taken to define the mole fraction of a particular component occupying an apex.

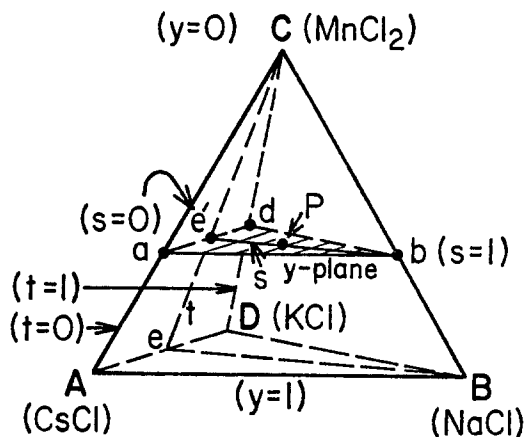


Fig. 1. Representation of compositions in a quaternary system in terms of the parameters y , t , and S , where

$$y = 1 - X_{\text{MnCl}_2}$$

$$t = \frac{X_{\text{KCl}}}{X_{\text{KCl}} + X_{\text{CsCl}}}$$

$$S = \frac{X_{\text{NaCl}}}{X_{\text{NaCl}} + X_{\text{KCl}} + X_{\text{CsCl}}}$$

Any composition P lies on a S plane which represents the intersection of y and t planes.

In view of the complexity of such three-dimensional plots, useful composition paths have been defined mathematically (2), and the composition parameters, y , t , and S have been defined by the following expressions

$$y = 1 - X_{\text{MnCl}_2} \quad [1]$$

where $1.0 \geq y \geq 0$

$$t = \frac{X_{\text{KCl}}}{X_{\text{KCl}} + X_{\text{CsCl}}} \quad [2]$$

where $1.0 \geq t \geq 0$, $t = 1$ along the MnCl_2 -KCl binary, and $t = 0$ along the MnCl_2 -CsCl binary

$$S = \frac{X_{\text{NaCl}}}{X_{\text{NaCl}} + X_{\text{KCl}} + X_{\text{CsCl}}} \quad [3]$$

where X is mole fraction.

Considering Fig. 1, in which MnCl_2 is placed at the apex of the tetrahedron, constant " t " represents the pseudoternary composition surface BeC . All compositions along that surface have in common the constant ratio of $X_{\text{KCl}}/X_{\text{KCl}} + X_{\text{CsCl}}$.

Also, constant " y " represents compositions along a pseudoternary surface parallel to the base of the equilateral tetrahedron having a constant X_{MnCl_2} content.

The intersection of the planes, t and y , defines the line " S " which has the following limiting values: within the binary MnCl_2 -NaCl at point " b ", $S = 1$, and at point e' within the ternary MnCl_2 -KCl-CsCl, $S = 0$.

The relationship between primary mole fractions and the composition parameters y , t , and S , is readily found as

$$X_{\text{CsCl}} = y(1-t)(1-S) \quad [4]$$

$$X_{\text{NaCl}} = yS \quad [5]$$

$$X_{\text{KCl}} = ty(1-S) \quad [6]$$

$$X_{\text{MnCl}_2} = 1 - y \quad [7]$$

Considering the S path be' , within the quaternary tetrahedron shown in Fig. 1, which is defined by the intersection of the y - and t -planes, all compositions along be' have the same X_{MnCl_2} content and the same ratio of KCl to CsCl. However, as S changes from 0 (point e') to 1 (point b), the amount of NaCl in the quaternary changes in proportion to S (Eq. [5]), and the value of any thermodynamic property measured along such an S composition path

$$\overline{\Delta G}_{\text{MnCl}_2} = -ZF(E - E^\circ) \quad [11]$$

$$\overline{\Delta H}_{\text{MnCl}_2} = -ZF B \quad [12]$$

$$\overline{\Delta S}_{\text{MnCl}_2} = ZFA \quad [13]$$

where A and B and the constants given in Table I, $E - E^\circ$ is given in millivolts, Z is the valence of the metal cation, and F is the Faraday constant expressed as 23.060 cal/mV eq.

The activities of MnCl_2 are calculated from the measured cell EMF's using the well-known Nernst equation written as

$$E_{\text{cell}} = E^\circ_{\text{MnCl}_2} - \frac{RT}{ZF} \ln a_{\text{MnCl}_2} \quad [14]$$

where E_{cell} and $E^\circ_{\text{MnCl}_2}$ are expressed in millivolts, and the ideal gas constant $R = 1.987$ cal/mol K.

Activities of the MnCl_2 calculated for Eq. [4] refer to pure molten MnCl_2 as the standard state of reference.

Partial molar heats of mixing, entropies of mixing, and activities of MnCl_2 calculated from the data, are also included in Table I. Plots of $E - E^\circ$ vs. temperature, for various X_{MnCl_2} , S , and t values are given in Fig. 2 and 3.

Discussion

The previously derived expression (2) for the calculation of the partial molar free energies of mixing in the quaternary system is

$$\overline{\Delta G}_{\text{MnCl}_2} = (1-S)[(1-t) \overline{\Delta G}_{\text{MnCl}_2}^{\text{in MnCl}_2\text{-KCl}} + t \overline{\Delta G}_{\text{MnCl}_2}^{\text{in MnCl}_2\text{-KCl}}] + S \overline{\Delta G}_{\text{MnCl}_2}^{\text{in MnCl}_2\text{-NaCl}} \quad [15]$$

The quantities $\overline{\Delta G}_{\text{MnCl}_2}^{\text{in MnCl}_2\text{-CsCl}}$, $\overline{\Delta G}_{\text{MnCl}_2}^{\text{in MnCl}_2\text{-KCl}}$, and $\overline{\Delta G}_{\text{MnCl}_2}^{\text{in MnCl}_2\text{-NaCl}}$ are the partial molar free energies of mixing of MnCl_2 in the designated binary systems having the same MnCl_2 content and temperature as the quaternary.

From Eq. [11] and [15], $E - E^\circ$ values were calculated and are given as dotted lines in Fig. 2.

The quantities $\overline{\Delta G}_{\text{MnCl}_2}$, for the three binary systems, plotted as $E - E^\circ$ vs. X_{MnCl_2} , were available from previous measurements (3) and are given in Fig. 4.

From Fig. 2 and 3, it is evident that the agreement between the experimental and calculated partial molar free energies of mixing expressed by the $E - E^\circ$ quantities is better than 3% over the investigated composition range of the quaternary system.

From Eq. [15], the expression for the activity of MnCl_2 in the quaternary system is readily derived as

$$a_{\text{MnCl}_2}^{\text{(in quaternary)}} = a_{\text{MnCl}_2}^{\text{(in MnCl}_2\text{-CsCl})} (1-S)^{(1-t)} \cdot a_{\text{MnCl}_2}^{\text{(in MnCl}_2\text{-KCl})} (1-S)^t \cdot a_{\text{MnCl}_2}^{\text{(in MnCl}_2\text{-NaCl})} S \quad [16]$$

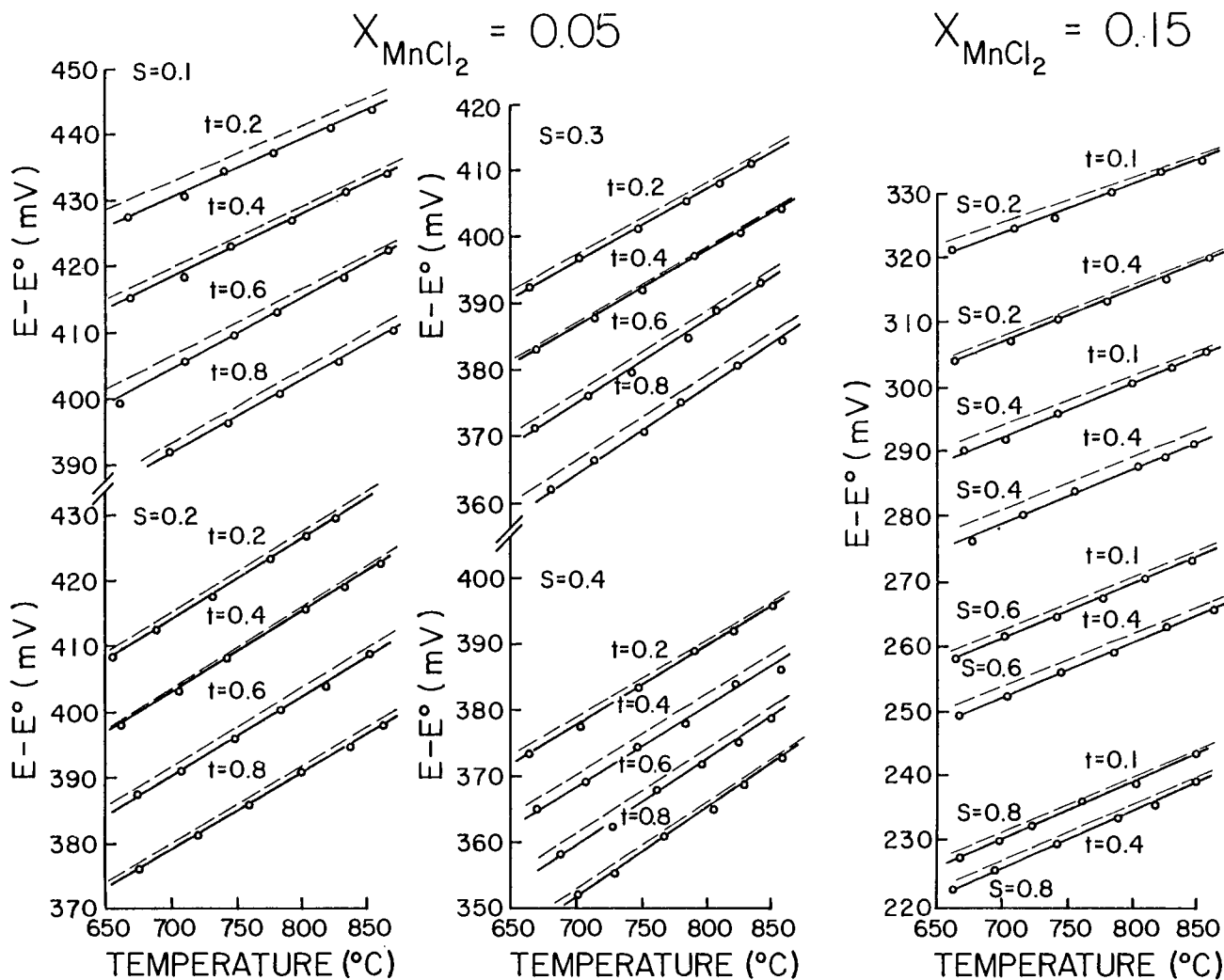


Fig. 2. EMF's of the cell

Mn	MnCl ₂	(X ₁)	Asbestos	MnCl ₂	(X ₁)	C (+)
(-)	NaCl	(X ₂)	fiber	NaCl	(X ₂)	(graphite)
	KCl	(X ₃)	diaphragm	KCl	(X ₃)	Cl ₂
	CsCl	(X ₄)		CsCl	(X ₄)	(g, 1 at.)

plotted as $E - E^\circ$ vs. temp. for various values of X_{MnCl_2} , S , and t in the quaternary system $\text{MnCl}_2\text{-NaCl-KCl-CsCl}$. E° represents $X_{\text{MnCl}_2} = 1$. Solid circles: experimental. Dashed lines: calculated from Eq. [11] and [15].

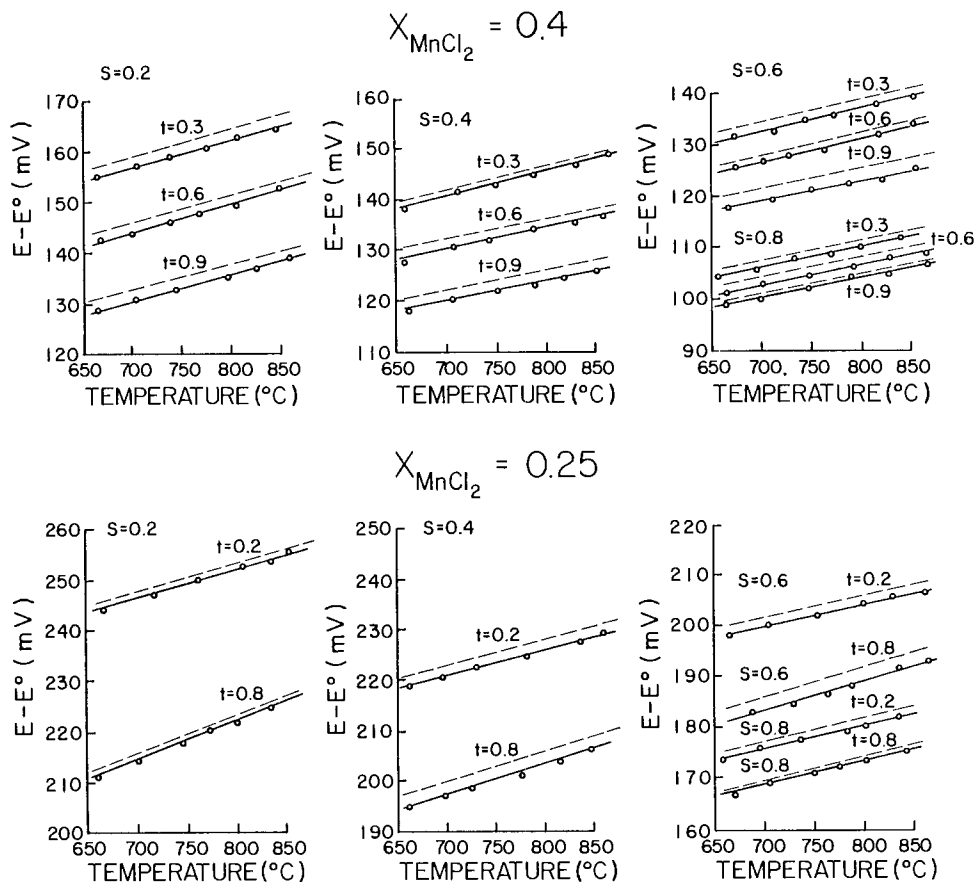


Fig. 3. Same as in Fig. 2, but with $X_{MnCl_2} = 0.4$ and 0.25 .

In terms of activity coefficients, Eq. [16] may be written as

$$\gamma_{MnCl_2}^{(in\ quaternary)} = \frac{(\gamma_{MnCl_2}^{in\ (MnCl_2-CsCl)})^{1-S}(1-t) \cdot (\gamma_{MnCl_2}^{in\ (MnCl_2-KCl)})^{1-St} \cdot (\gamma_{MnCl_2}^{in\ (MnCl_2-NaCl)})^S}{[17]}$$

where the quantities in parentheses represent activity coefficients in binary systems at compositions having the same X_{MnCl_2} values as in the quaternary.

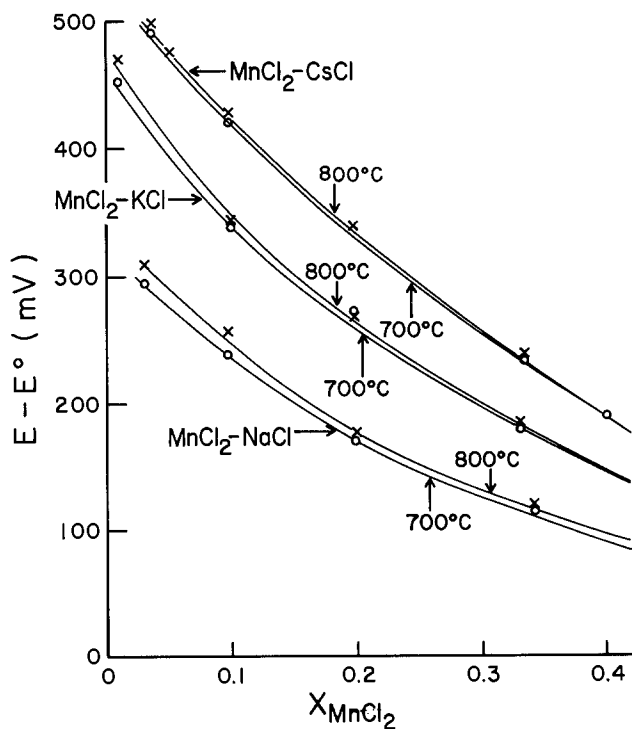


Fig. 4. Plots of $E - E^\circ$ for the three binary systems (3) MnCl₂-NaCl, MnCl₂-KCl, and MnCl₂-CsCl and 700° and 800°C.

Plots of the partial molar free energies of mixing of MnCl₂ as functions of the parameters S at constant y and t values are given in Fig. 5 to 8.

Activities of MnCl₂ in the quaternary system, calculated from Eq. [16], are plotted as a function of X_{MnCl_2} at constant temperature and constant S and t values. The various curves correspond to different t values, and the composition path followed in this case starts from solutions very dilute in MnCl₂ and moves upwards through the quaternary to $X_{MnCl_2} = 0.4$.

These plots are given in Fig. 9 and include the few experimental points available for such a composition path. Again, agreement is indicated between Eq. [16] and the experimental values.

The partial molar enthalpies of mixing, $\Delta \bar{H}_{MnCl_2}$ shown in Table I, become more exothermic as t decreases, i.e.,

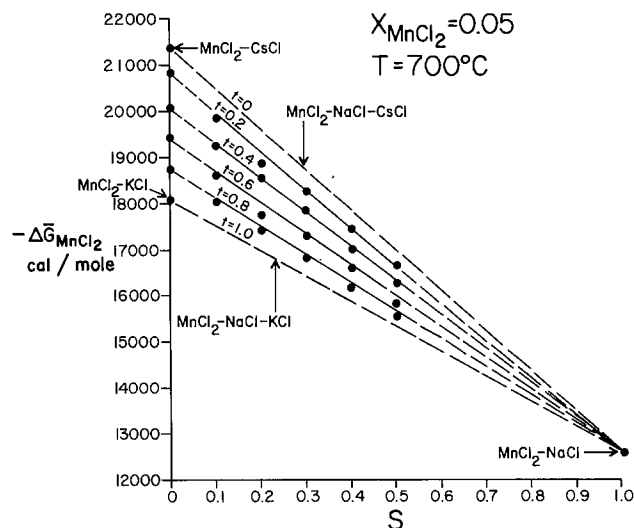
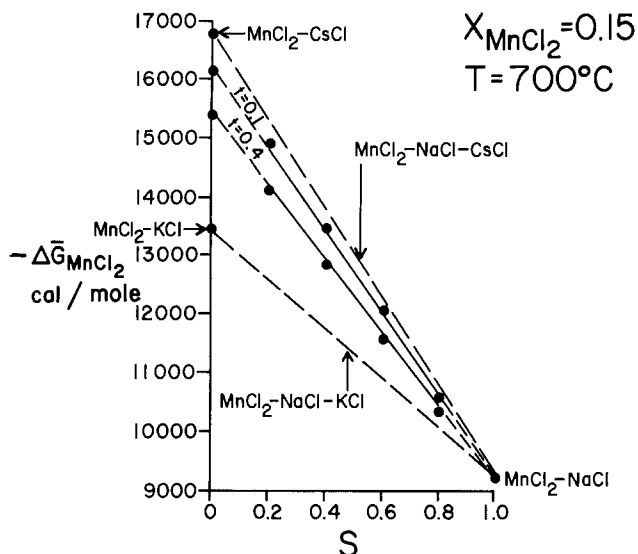
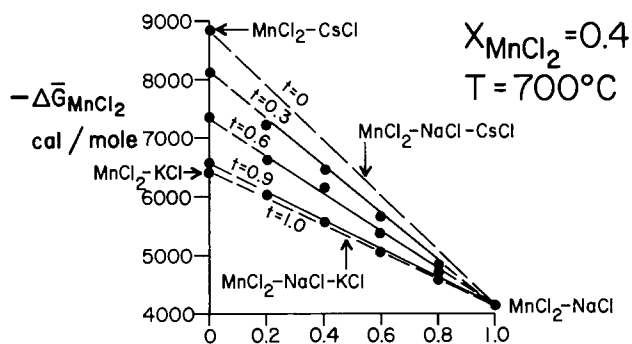
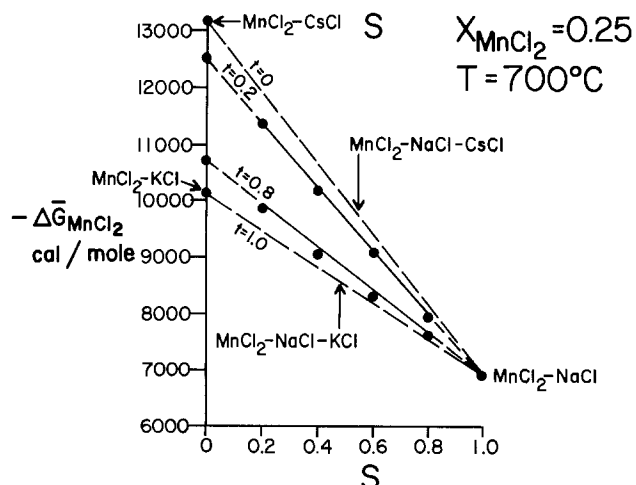
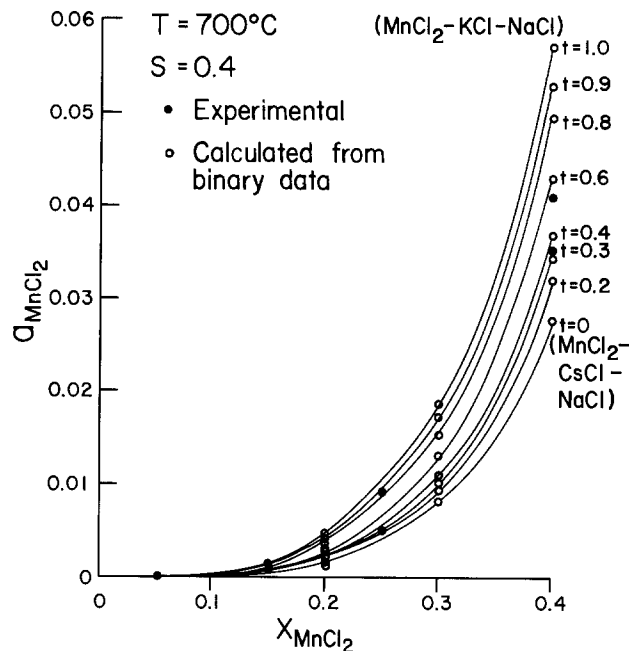


Fig. 5. Plot of the partial molar free energy of mixing of MnCl₂ as function of S , with y and t constant. Group of curves covers the entire composition surface of a Y-plane. Points: experimental. Straight lines: calculated from theory.

Fig. 6. Same as Fig. 5, but with $X_{\text{MnCl}_2} = 0.15$ Fig. 7. Same as Fig. 5, but with $X_{\text{MnCl}_2} = 0.4$

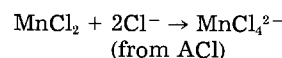
when the CsCl content of the melt increases. $\overline{\Delta H}_{\text{MnCl}_2}$ becomes less exothermic as S increases, i.e., when the NaCl content of these melts increases. As expected, the activities of MnCl_2 indicate pronounced negative deviations from ideality, particularly for the CsCl-rich melts.

Equations [15], [16], and [17] should be strictly valid for charge asymmetric molten salt solutions (2) like the system $\text{MnCl}_2\text{-NaCl-KCl-CsCl}$, in which the charge asymmetric component MnCl_2 is known to react with the alkali metal chlorides. Although as exact knowledge of the structure of such complexes is not necessary for a thermodynamic treatment, there are certain indirect indications regarding their probable configuration. For example, recent structural evidence (11) as well as mea-

Fig. 8. Same as Fig. 5, but with $X_{\text{MnCl}_2} = 0.25$ Fig. 9. Activity isotherms of MnCl_2 at 700°C , calculated at constant $S = 0.4$. Solid circles: experimental. Open circles and lines: calculated from theory.

surements of electrical conductivities and molar volumes (6, 12) suggest that solutions of MnCl_2 in alkali chloride melts appear to contain tetrahedrally coordinated complexes of the type MnCl_4^{2-} .

For a tetrahedral configuration, the following reaction is expected to occur upon mixing



and the enthalpies of mixing in binary melts containing alkali metal chlorides, should reach maximum values at a MnCl_2 content of 33 m/o. Deviations from ideality may be attributed to the relative stability, or strength, of such complexes. Experimental evidence (3) indicates that the observed negative deviation in the activities of MnCl_2 increases with increasing size of the alkali metal cations in the order $\text{Li}^+ \rightarrow \text{Na}^+ \rightarrow \text{K}^+ \rightarrow \text{Rb}^+ \rightarrow \text{Cs}^+$.

Such trends reflect the effects of competing interactions between the Mn^{2+} and A^+ cations for the same Cl^- anions in which the alkali chloride acts as a ligand donor and the reactive metal chloride MnCl_2 is the ligand acceptor. Alkali metal cations like Na^+ , because of their small size, are strongly attracted to their chloride anions and effectively the NaCl salt is less "dissociated" than the other alkali metal chlorides containing larger cations like K^+ or Cs^+ . The difference in the strength of the complexes which are formed when the reactive metal chloride, MnCl_2 , is mixed with either of the alkali chlorides of the type AlCl or BCl is simply reflected by the difference in the bond distances in configurations of the type Mn-Cl-A or Mn-Cl-B.

The spatial arrangement of such complexes within the ionic melt structure should be compatible with the requirement of local electrical neutrality and with the concept of interlocking anionic and cationic "quasi-lattices" as proposed by Temkin (13).

Conclusions

It has been shown that the thermodynamic properties of nonideal and nonregular charge asymmetric fused-salt systems may be calculated from data on component binary systems along composition paths representing constant content of the charge asymmetric component MnCl_2 . Although the derivation of Eq. [15] was based on the formation of complex species in the binary solutions, its application depends only on the availability of experimental data on binary systems.

Regarding quaternary systems, the introduction of the composition parameters y , t , and S serves in the planning of experiments and in reducing the large number of compositions to be studied in order to characterize a quaternary system adequately.

Also, the use of these composition parameters makes it possible to plot thermodynamic data along well-defined composition paths and to identify the effects of competing interactions on a charge asymmetric cation. For example, the complexing effects of CsCl or KCl on MnCl₂ become evident as the quaternary solutions become richer in CsCl, or in KCl, respectively.

The successful application of Eq. [15], [16], and [17] to such nonideal charge asymmetric fused-salt solutions indicates that in quaternary, and possibly even in higher order systems, reactions within the binary solutions account for most of the internal reactivity which is responsible for deviations from ideality. Thus, the formation of a higher order system represents mixing of such prereacted binary systems and the properties of the multicomponent system should be predictable.

However, it should be noted that Eq. [15], [16], and [17] are only applicable to the "acid," or higher valence, component of a charge asymmetric fused-salt mixture.

Acknowledgment

The authors are grateful to the Natural Sciences and Engineering Research Council of Canada for a grant in support of this work.

Manuscript submitted Dec. 27, 1983; revised manuscript received April 2, 1984.

The University of Toronto assisted in meeting the publication costs of this article.

REFERENCES

1. D. R. Sadoway and S. N. Flengas, *This Journal*, **122**, 515 (1975).
2. S. N. Flengas and D. R. Sadoway, in "Molten Salts," G. Mamontov, M. Blander, and G. P. Smith, Editors, pp. 68-94, The Electrochemical Society Softbound Proceedings Series, Pennington, NJ (1981).
3. A. S. Kucharski and S. N. Flengas, *This Journal*, **119**, 1170 (1972).
4. S. N. Flengas and J. Skeaff, *Can. J. Chem.*, **50**, 1345 (1972).
5. G. N. Papatheodorou and O. J. Kleppa, *J. Inorg. Nucl. Chem.*, **33**, 1249 (1971).
6. N. R. Carmichael and S. N. Flengas, *This Journal*, **128**, 2098 (1979).
7. A. S. Kucharski and S. N. Flengas, *ibid.*, **121**, 1298 (1974).
8. S. N. Flengas, *High Temp. High Pres.*, **5**, 551 (1973).
9. O. Kubaschewski and C. B. Alcock, "Metallurgical Thermochemistry," 5th ed., p. 294, Pergamon Press, New York (1979).
10. A. Prince, "Alloy Phase Equilibria," Elsevier, New York (1966).
11. K. Tamemoto and T. Nakamura, *Chem. Lett.*, 351, 356 (1975).
12. N. R. Carmichael and S. N. Flengas, *This Journal*, **126**, 2104 (1979).
13. M. Temkin, *Z. Fiz. Khim.*, **20**, 105 (1946).

Reactions Involving Silver Ions and Silver Metal in Molten Nitrates

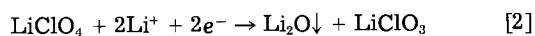
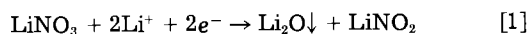
M. H. Miles,* G. E. McManis,* and A. N. Fletcher*

Chemistry Division, Naval Weapons Center, China Lake, California 93555

ABSTRACT

The electrochemical reduction of molten LiNO₃ on platinum or nickel electrodes produces insoluble Li₂O that passivates the cathode at high current densities. The presence of small amounts of silver ions prevents this passivation by undergoing reduction to silver metal in the form of dendritic deposits that increase the effective area of the electrode. The deposited silver is unstable in molten LiNO₃ and reacts with the melt to regenerate silver ions. Corrosion studies of silver coupons gave a weight loss rate of 280 μg h⁻¹cm⁻² in molten LiNO₃ at 350°C, but of only 5 μg h⁻¹cm⁻² in KNO₃ at 375°C. The presence of water in the LiNO₃ melt increases the corrosion rate of silver. Additions of Li₂O, LiNO₂, LiCl, or AgNO₃ to molten LiNO₃ significantly decreases the corrosion rate. The addition of oxide ions to a AgNO₃ containing melt produces a dark precipitate of Ag₂O in NaNO₃ or KNO₃, but not in LiNO₃. The decomposition reaction of Ag₂O into its elements is kinetically slow in molten nitrates with a rate similar to that observed in air.

The relatively low melting points of oxidizing molten salts such as nitrates and perchlorates makes them attractive for use in thermal battery cells where they can function as both the electrolyte and oxidizer (1, 2). Previous work has shown that the lithium salts of these compounds are electrochemically reduced much more readily than the sodium or potassium salts (3-5). At high current densities, however, the reduction of fused LiNO₃ or LiClO₄



produces insoluble Li₂O as a product (4-7). When Li₂O is formed at the electrode surface faster than it can be removed, thus blocking the reacting substance from reaching the electrode substrate, severe polarization occurs (2, 4, 7).

The performance of the cathode in oxidizing molten salts is greatly improved by the addition of small amounts of AgNO₃ to the electrolyte (2, 8). This work is focused mainly on the study of the reactions involving silver ions

in molten nitrate melts. Although previous reports suggest that the cathodically deposited silver is relatively stable in molten nitrates (9-13), our studies show that this stability is dependent on the electrolyte composition, the temperature of the melt, and the nature of any extraneous substances that may be present.

Experimental

The design of the electrochemical cell was similar to that of a previous study (14). The platinum and nickel working electrodes were in the form of wires sealed in glass and cut to a length to give a geometrical area of 0.10 cm² (0.45 cm length, 0.07 cm diam). The counterelectrode consisted of either a platinum wire coil at the bottom of the cell or a platinum wire spiral separated from the main cell compartment by a section of fritted glass tubing. All potentials were measured against a AgNO₃ (0.1M)/Ag reference electrode that is described elsewhere (14). Electrochemical studies were made with the cell placed in a fluidized sand bath (Tecam) where the temperature was monitored with a Chromel-Alumel thermocouple digital thermometer (Fluke, 2165 A). Temperature fluctuations observed with the cell placed in the center of the sand bath and the thermocouple positioned adjacent to the cell

* Electrochemical Society Active Member.

were generally less than $\pm 5^\circ\text{C}$. A modified cell was used in some experiments that allowed the temperature to be measured directly in the cell by means of a thermocouple inlet consisting of a section of glass tubing with an opening through the cell wall and extending into the melt. Temperatures measured in the cell were relatively constant during the experiments and, on the average, were within 2°C of the temperature measured outside the cell. In experiments requiring mass transport by diffusion, both the sand bath and the helium flow were turned off to give a quiescent solution free of vibrations. The hot sand surrounding the cell acted as a thermal insulator, thus the temperature measured in the cell remained constant within $\pm 1^\circ\text{C}$ for time periods up to 10 min.

The reagent-grade salts used in the cell were dried in a vacuum oven at 130°C for several days. The cell was always rinsed well with acetone (spectrophotometry suitable) and baked with a heat gun and then baked again in the sand bath prior to adding the salt. The bubbling of dried helium gas through the molten salt in the cell at 350°C for at least 1h was used to remove any residual water. Cyclic voltammetric studies of these melts using platinum electrodes gave no evidence of any water wave (4, 15). Generally, either 30.0g of predried LiNO_3 or 33.0g of NaNO_3 or KNO_3 were used in the cell to give a melt volume of 17.4, 17.8, or 17.7 cm^3 , respectively, at 350°C , based upon reported densities (16). For the study of mixed salts, the amount of each salt was calculated to give about this same volume of liquid.

The electrochemical measurements used a potentiostat/galvanostat (PAR 173) equipped with either a current follower plug-in (PAR 176) or a digital coulometer plug-in (PAR 179). Results were monitored with an X-Y recorder (Hewlett-Packard 7047 A) or a digital oscilloscope (Nicolet Model 206). In experiments involving potential scans, a PAR 175 programmer was used. The reproducibility of the potential scan experiments was improved by a standard conditioning of the working electrode between successive potential sweeps that involved an anodic treatment evolving NO_2 and O_2 , followed by a waiting time of 30s at the initial potential before beginning another sweep. For experiments involving exhaustive galvanostatic or potentiostatic electrolysis, a large platinum or nickel electrode ($A = 10 \text{ cm}^2$) was used in the molten nitrate solution that was rapidly stirred by the flow of helium gas to maximize mass transport.

Corrosion studies were conducted by placing a polished silver coupon ($2 \times 2 \text{ cm}$) into 20-23g of the molten nitrate solution and determining the weight loss of the silver after 2h. These experiments were conducted in a quartz tube with a cap that provided for helium stirring throughout the experiment to minimize any effects due to water. All experiments used helium gas (99.995%, oil and water-vapor free) that was passed through indicating Drierite and two tubes of phosphorus pentoxide (Aquasorb, Mallinckrodt) and a tube filled with fiberglass before being admitted into the nitrate melt. The helium was then exhausted through another P_2O_5 -filled tube to prevent any backflow of atmospheric water vapor. The glassware was always rinsed well with spectro-grade acetone and prebaked both with a heat gun and in the sand bath before the nitrate salt was added.

Results and Discussion

Voltammetric studies in molten LiNO_3 on both platinum and nickel electrodes reveal a large reduction peak similar to that shown in Fig. 1 (4, 17). The electrode reaction is the reduction of molten LiNO_3 to Li_2O and LiNO_2 (Eq. [1]); the peak is due to the blocking of the electrode surface by insoluble Li_2O rather than the usual depletion of the reactant in the diffusion layer. Due to resistive effects of the precipitated Li_2O on the electrode surface, the peak potential depends on the magnitude of the current and varies with both the potential sweep rate and the area of the electrode. Voltammograms for the reduction of molten nitrates vary when different electrode metals are used (18).

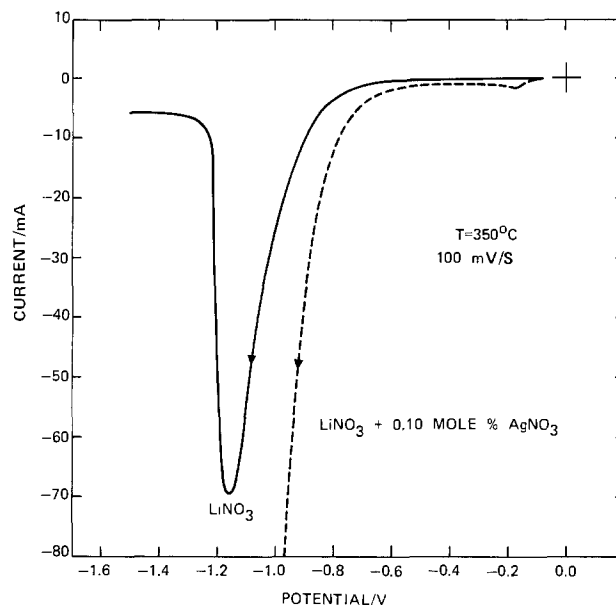
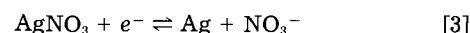


Fig. 1. Effect of AgNO_3 on the cathodic reaction in molten LiNO_3 at 350°C . Measurements were made in a helium atmosphere using a platinum wire electrode ($A = 0.10 \text{ cm}^2$) and a potential scan rate of 100 mV/s. Solid line: pure LiNO_3 . Dashed line: $\text{LiNO}_3 + 0.10 \text{ m/o AgNO}_3$.

As illustrated in Fig. 1, the addition of 0.10 mole percent (m/o) AgNO_3 permits the current to continue to increase, and thus no peak is observed. The reversible electrode reduction of silver nitrate



accounts for the relatively small peak observed at -0.18 V . The increased background current following this small peak, as well as the larger currents observed for the LiNO_3 reduction wave, indicates an increase in the effective surface area of the platinum electrode due to the deposited silver.

High current densities are required for many thermal battery applications. Therefore, constant current studies at 100 mA/cm^2 were made for the cathodic reactions. The results in Fig. 2 show that the reduction of LiNO_3 at 350°C in gently stirred solutions sustains 100 mA/cm^2 for only 105s before it severely polarizes. The addition of 0.10 m/o AgNO_3 completely prevents the onset of this passivation; in fact, the potential slowly increases during the cathodic reaction. Similar results were obtained with nickel electrodes. It is likely that Ag^+ and NO_3^- ions are being simultaneously reduced, thus the depositing silver gives a gradually increasing surface area, resulting in a decreasing

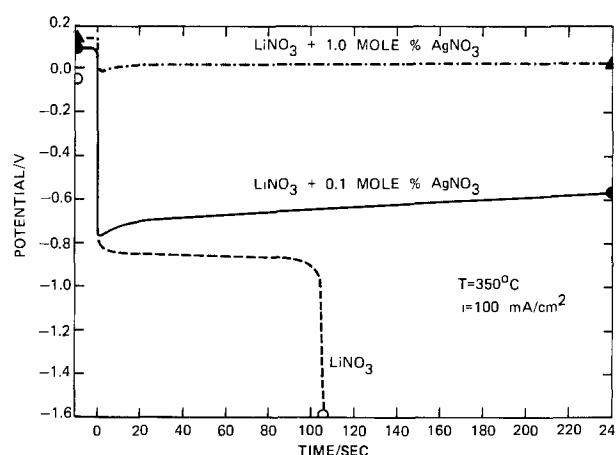


Fig. 2. Constant current cathodic studies at 100 mA/cm^2 in gently stirred solutions consisting of pure LiNO_3 (dashed line), $\text{LiNO}_3 + 0.10 \text{ m/o AgNO}_3$ (solid line), and $\text{LiNO}_3 + 1.0 \text{ m/o AgNO}_3$ (dash-dot line). Studies were made at 350°C using a platinum wire electrode ($A = 0.10 \text{ cm}^2$).

overtoltage for LiNO_3 reduction. In molten LiNO_3 containing 1.0 m/o AgNO_3 , the reduction of Ag^+ is apparently capable of sustaining 100 mA/cm^2 (Fig. 2). The potential remains very stable and close to that of the Ag^+/Ag reference electrode used. Other investigators have noted that AgNO_3 additions affect the cathodic reactions in molten nitrates (18, 19).

Exhaustive electrolysis experiments supplying large platinum or nickel electrodes ($A = 10 \text{ cm}^2$) with a constant current (10 mA) in vigorously stirred solutions gave inflections in potential that indicated depletion of the added silver ions. As illustrated in Fig. 3, the experimental inflections are close to $1.0 e^-/\text{Ag}^+$ for studies in molten NaNO_3 and KNO_3 , but no inflection could be detected in molten LiNO_3 . In fact, continuation of the experiments for time periods corresponding to more than $3 e^-/\text{Ag}^+$ failed to reveal any significant change in the potential in molten LiNO_3 . Experiments in equimolar $\text{LiNO}_3\text{-LiClO}_4$ at 350°C also failed to show any inflection in the potential. These results suggest that the deposited silver is not stable in molten LiNO_3 or $\text{LiNO}_3\text{-LiClO}_4$ at 350°C and undergoes corrosion reactions that, in effect, recycle the silver ions. The results shown in Fig. 3, however, were obtained at 1 mA/cm^2 . At high current densities, the rate of reaction [3] will exceed the rate of corrosion, and thus there will be a buildup of deposited silver on the electrode surface.

Constant potential coulometry offers the advantage of higher currents and shorter electrolysis times, and hence the effect of corrosion reactions on the measurement of e^-/Ag^+ can be minimized. Results for the reduction of AgNO_3 at -0.400V in molten LiNO_3 and KNO_3 at 375°C in vigorously stirred solutions are shown in Fig. 4. These curves differ from the normal exponential decrease in current with time in that a peak in the current is observed. This peak is likely related to the increase in the effective electrode surface area due to the depositing silver metal. Any reaction of the deposited silver with the melt would retard the increase in surface area and yield a smaller peak current as found in molten LiNO_3 .

Photomicrographs of platinum and nickel electrode surfaces following constant potential coulometry experiments in molten LiNO_3 at 375°C are shown in Fig. 5a and 5b. A thick bed of dendritic needles covers the platinum surface (Fig. 5a). The deposits on nickel electrodes tend to fall off easily during washing to remove the salt, hence the nickel surface can be seen at the edge of Fig. 5b. Nickel surfaces darken in molten nitrates, perhaps due to nickel oxide formation. Greater magnification reveals that the deposits on nickel are similar to those on platinum except for their much finer structure. Finer deposits were also observed on platinum in other experiments. A SEM micrograph of dendritic deposits on platinum is shown in Fig. 6a. Elemental analysis using energy dis-

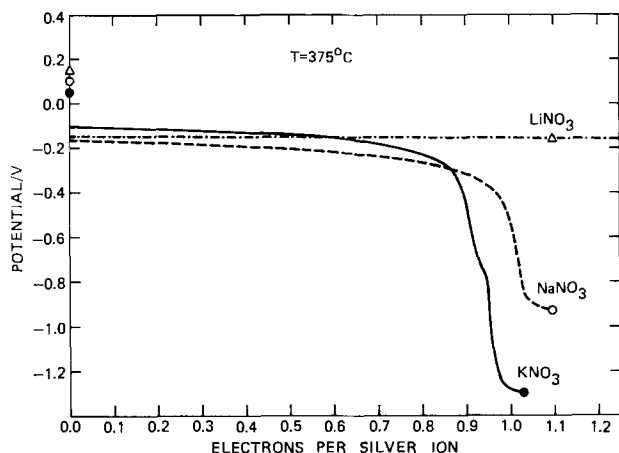


Fig. 3. Exhaustive electrolysis studies of silver ion reduction on platinum ($A = 10 \text{ cm}^2$) at 375°C using a constant current of 10 mA. The molten salt was rapidly stirred by the flow of helium gas. Concentrations of AgNO_3 were 5.89×10^{-3} , 5.78×10^{-3} , and $5.69 \times 10^{-3}\text{m}$ (0.0405, 0.0491, and 0.0574, m/o) in LiNO_3 , NaNO_3 , and KNO_3 , respectively.

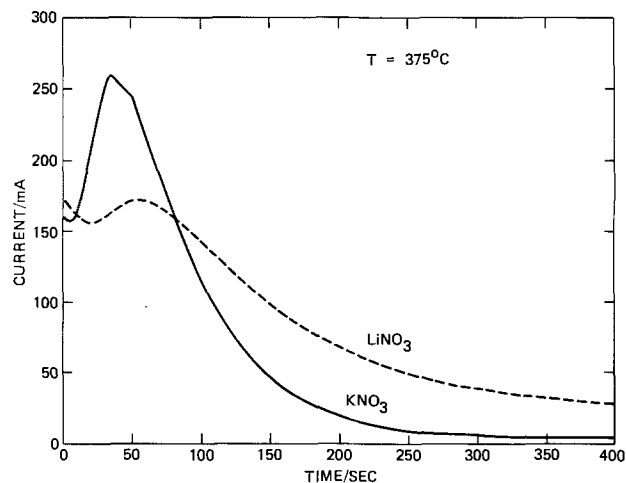


Fig. 4. Constant potential coulometry studies of the reduction of AgNO_3 on platinum ($A = 10 \text{ cm}^2$) in molten LiNO_3 and KNO_3 at 375°C . The working electrode was potentiostated at -0.400V vs. the Ag^+/Ag reference electrode. The melt was rapidly stirred by the flow of helium gas. Concentrations of AgNO_3 were 9.08×10^{-3} and $8.24 \times 10^{-3}\text{m}$ (0.0626 and 0.0832 m/o) in LiNO_3 and KNO_3 , respectively.

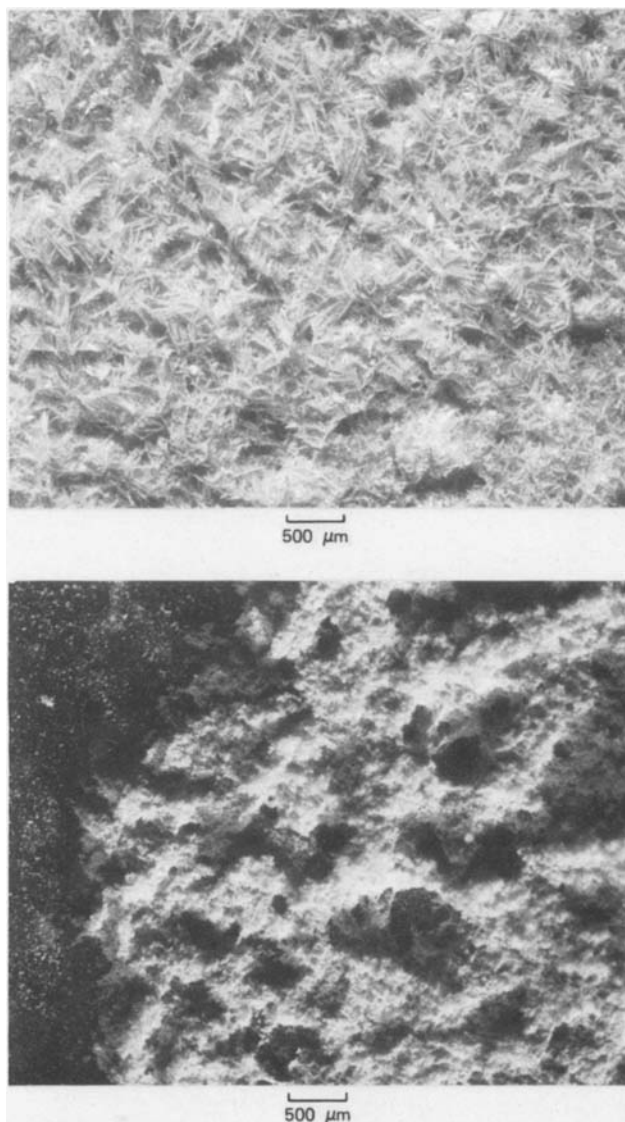


Fig. 5. Optical micrographs of electrode surfaces following constant potential coulometry studies similar to those shown in Fig. 4. a(top): Platinum electrode. b(bottom): Nickel electrode. Part of the deposit was lost from the nickel surface during the washing procedure exposing the darkened nickel surface (edge of Fig. 5b).

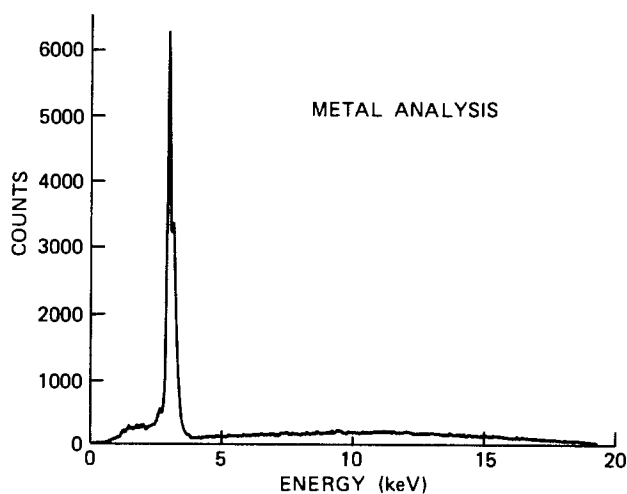
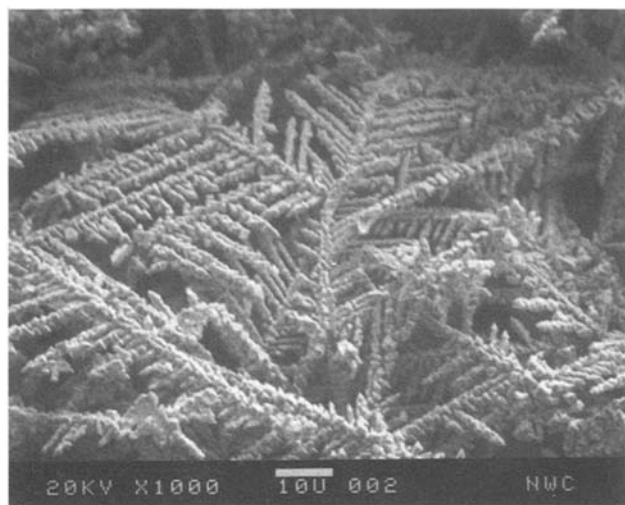


Fig. 6. a(top): Scanning electron micrograph of the silver deposits on a platinum electrode following constant potential coulometry studies similar to those shown in Fig. 4. b(bottom): EDX spectra for the same electrode showing that the deposits consist mainly of silver (Ag, $L_{\alpha 1} = 2.98$ keV, $L_{\beta 1} = 3.15$ keV). The silver deposits mask the detection of the platinum substrate (Pt, $L_{\alpha 1} = 9.44$ keV).

persive x-rays (EDX) shows that the surface deposits are essentially pure silver (Fig. 6b). The deposits of silver even mask the detection of the platinum substrate using EDX (Pt, $L_{\alpha 1} = 9.44$ keV). Results of Auger analysis were similar; the surface deposit was mostly silver metal with traces of oxygen, sulfur, and chlorine.

The increased surface area in coulometry experiments is also manifested by background currents that were considerably larger at the end of the electrolysis than those observed prior to adding AgNO_3 . Background currents were always higher in molten LiNO_3 than in KNO_3 due to the much higher energy barrier for the reduction of the latter salt (3, 4). After compensating for the background currents at -0.400V , the coulombs passed for 300s in Fig. 4 correspond to $1.0 e^-/\text{Ag}^+$ in molten KNO_3 and $1.1 e^-/\text{Ag}^+$ in molten LiNO_3 . Corrosion reactions as well as the increase in background current likely contribute to the higher coulombic value observed in molten LiNO_3 . Although there is some evidence in the literature for the existence of divalent silver ions (20), results of Fig. 3 and 4 indicate that the monovalent silver ion is primarily present in molten LiNO_3 , NaNO_3 , and KNO_3 .

Corrosion studies were made in molten nitrates using polished silver coupons and determining their weight loss over a 2h period. Results of these studies, summarized in Table I, confirm the electrochemical investigations by showing the instability of silver metal in molten LiNO_3 . The corrosion rate of silver, however, varies markedly

Table I. Weight loss studies of polished silver coupons in molten nitrates

Molten salt	Temperature (°C)	Cell atmosphere	Weight loss ($\mu\text{g h}^{-1} \text{cm}^{-2}$)
LiNO_3^a	350	air	1980
LiNO_3^b	330	N_2	896
LiNO_3^c	350	He	280
$\text{LiNO}_3 + \text{LiNO}_2$ (0.5 m) ^c	350	He	100
$\text{LiNO}_3 + \text{AgNO}_3$ (0.2 m) ^c	350	He	50
$\text{LiNO}_3 + \text{AgNO}_3$ (0.2 m) + LiCl (1.0 m) ^c	350	He	20 ^d
$\text{LiNO}_3 + \text{Li}_2\text{O}$ (0.5 m) ^{c,e}	350	He	20
$\text{LiNO}_3 + \text{LiNO}_2$ (0.5 m) + AgNO_3 (0.3 m) ^c	350	He	0 ^f
NaNO_3^c	350	He	16
KNO_3^c	375	He	5
$\text{NaNO}_3\text{-KNO}_3^b$	324	N_2	0.04

^a Undried salt (Baker, analyzed reagent).

^b Results reported by Conte and Ingram (21).

^c Salt vacuum dried, cell prebaked, helium passed through P_2O_5 .

^d Yellow precipitate forms (AgCl).

^e Solubility limit exceeded, saturated solution.

^f Silver metal forms in melt.

with the nitrate salt used as shown by the weight loss of $280 \mu\text{g h}^{-1}\text{cm}^{-2}$ in carefully dried molten LiNO_3 at 350°C , but only $5 \mu\text{g h}^{-1}\text{cm}^{-2}$ in KNO_3 at 375°C . The presence of other substances greatly affects the corrosion rate in molten LiNO_3 . The use of undried LiNO_3 (Baker, reagent grade) without any helium flow and with the cell opened directly to the air increased the corrosion rate to $1980 \mu\text{g h}^{-1}\text{cm}^{-2}$. Additions of LiNO_2 , Li_2O , AgNO_3 , or LiCl to molten LiNO_3 significantly decreased the corrosion rate. The presence of both LiNO_2 and AgNO_3 gave no measurable corrosion; in fact, a reaction occurs that forms silver metal in the melt. The corrosion rate diminished noticeably after several hours, as would be expected from the buildup of reaction products such as AgNO_3 , LiNO_2 , and Li_2O . Our values in Table I are in reasonable agreement with corrosion studies by Conte and Ingram (21). A much smaller corrosion rate for silver in molten LiNO_3 suggested by EMF measurements of activity coefficients by Boxall and Johnson (22) may be explained by their addition of AgNO_3 to the melts. The rate of silver weight loss measured in carefully dried molten LiNO_3 at 350°C is equivalent to a corrosion current density of 0.070 mA/cm^2 , that for a surface roughness factor of 15 attributable to silver deposits, could sustain the cathodic reaction indefinitely at 1 mA/cm^2 , as seen in Fig. 3.

These corrosion studies show that the potential of Ag^+/Ag reference electrodes in molten nitrates may change with time, especially if the silver metal in the reference electrode is in contact with molten LiNO_3 . Problems encountered in cell EMF measurements have suggested the corrosion of silver electrodes in fused nitrates (23, 24). Diffusion studies in molten $\text{Ca}(\text{NO}_3)_2\text{-KNO}_3$ also show evidence for the corrosion of silver electrodes and silver deposits (25, 26). Thermodynamic calculations of potential vs. pO^{2-} diagrams for silver in fused nitrates predict that silver is less stable in molten LiNO_3 than in the $\text{NaNO}_3\text{-KNO}_3$ eutectic melt (21). The small size of the Li^+ ion makes it a good oxide ion acceptor (Lux-Flood acid) that should enhance the corrosion of silver in LiNO_3 melts.

The corrosion of silver in molten salts can be conveniently studied by galvanostatically depositing silver onto a platinum electrode for a fixed time period and then reversing the current in anodic stripping experiments. Any corrosion of the deposited silver shortens the anodic time period. Table II presents results of such studies in several equimolar salt mixtures at 250° and 400°C . Corrosion is almost undetectable for experiments in $\text{NaNO}_3\text{-KNO}_3$ at 400°C , yet it can be quite significant in melts containing Li^+ ions. At 400°C , very little of the deposited silver can be detected electrochemically in molten $\text{LiNO}_3\text{-LiClO}_4$ due to the high corrosion rate. The calculation of corrosion

Table II. Percent of cathodically deposited silver that is recovered during anodic stripping experiments

Molten salt ^a	250°C	400°C
NaNO ₃ -KNO ₃	95%	95%
LiNO ₃ -KNO ₃	95%	90%
LiNO ₃ -NaNO ₃	85%	60%
LiNO ₃ -LiClO ₄	85%	5%

The silver was deposited onto a platinum electrode ($A = 10 \text{ cm}^2$) for 120s at 10 mA and then stripped off at the same current.

^a Equimolar mixture.

rates based on these galvanostatic studies is complicated by the unknown surface area of the deposited silver.

Potential scan studies of AgNO₃ reduction in molten LiNO₃ at 350°C are shown in Fig. 7. Distortions of the waveform occur at slow sweep rates that produce a flattened peak. At scan rates of 10 mV/s or less, a broad wave with no precise peak is observed. These distortions of the waveform are likely caused by the corrosion reaction of the deposited silver with molten LiNO₃ that alters the concentration gradient of silver ions at the electrode surface. A further complication is the increase in the effective electrode area during the potential scan due to the deposits of silver. At fast potential scan rates, both distortions are minimized, and the experimental peak currents obey the theoretical equation

$$i_p = 2.54 \times 10^5 n^3 A C^0 D^{1/2} \nu^{1/2} \quad [4]$$

for the reversible deposition of an insoluble substance at 350°C (27, 28). The condition of linear diffusion is applicable to the Pt wire electrode for scan rates greater than 0.1 V/s (27). A diffusion coefficient of $2 \times 10^{-5} \text{ cm}^2/\text{s}$ for the Ag⁺ ion in molten LiNO₃ at 350°C is obtained from this equation using scan rates varying 1000-fold (0.1-100 V/s) and correcting for the background currents to obtain $di_p/d\nu^{1/2} = 2.92 \times 10^{-2} \text{ A cm}^{-2} (\text{V/s})^{-1/2}$ (correlation coefficient = 0.9996, $n = 10$) for a melt containing $C^0_{\text{AgNO}_3} = 2.61 \times 10^{-5} \text{ mol cm}^{-3}$. The background currents were determined by similar measurements in the absence of AgNO₃. Extrapolations based on other studies yield a value of $2.7 \times 10^{-5} \text{ cm}^2/\text{s}$ for the diffusion coefficient of the Ag⁺ ion in LiNO₃ at 350°C (16, 29).

Cyclic voltammograms are shown in Fig. 8 for the reversible electrode reaction of AgNO₃ (Eq. [3]) in molten

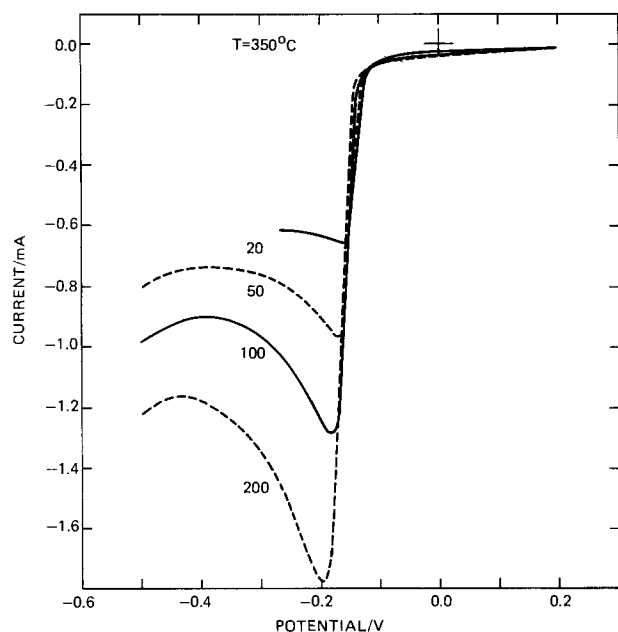


Fig. 7. Potential scan studies of silver ion reduction on a platinum wire electrode ($A = 0.10 \text{ cm}^2$) in molten LiNO₃ at 350°C containing 0.10 m/o AgNO₃ ($1.46 \times 10^{-2} \text{ m}$ or $2.52 \times 10^{-5} \text{ mol/cm}^3$). Potential scan rates shown are 20, 50, 100, and 200 mV/s.

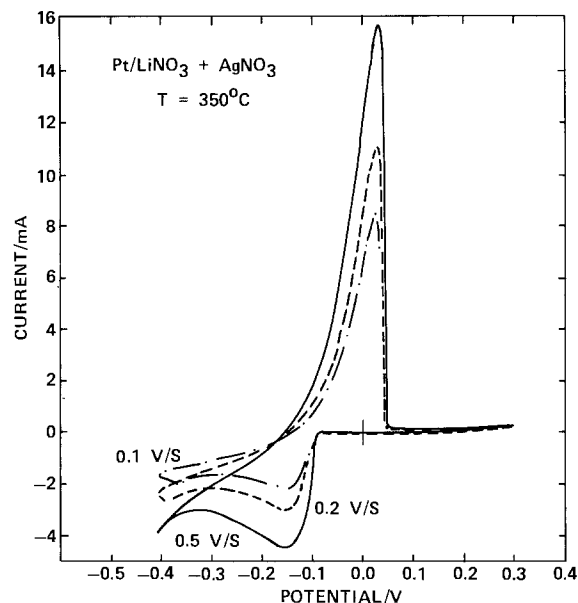
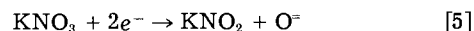


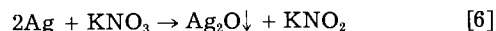
Fig. 8. Cyclic voltammograms for the electrode reactions of AgNO₃ (0.10 m/o) in molten LiNO₃ at 350°C using a platinum wire electrode ($A = 0.10 \text{ cm}^2$). Potential scan rates shown are 0.1, 0.2, and 0.5 V/s.

LiNO₃ at 350°C. The sharp drop in current following the anodic peak is characteristic for the depletion of a deposited metal (12, 13, 30, 31). At scan rates where the corrosion is negligible, the area under the anodic peak is equal to that under the cathodic peak. The cathodic peak current is considerably smaller than the anodic peak current, but the cathodic peak is broader and reduction continues after the cathodic sweep reversal up to about -0.15V.

A significant loss of reducible silver ions occurs with repeated cathodic and anodic studies in fused NaNO₃ or KNO₃ when a one-compartment cell is used. For example, constant potential coulometry studies of AgNO₃ in molten KNO₃ at 375°C yield the same amount of charge for both the cathodic and the following anodic reaction ($1.0 e^-/\text{Ag}^+$). The solution, however, darkens in color during the anodic reaction suggesting that oxide ions formed at the counterelectrode

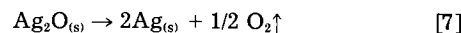


combine with silver ions generated at the working electrode to yield the net cell reaction



that produces insoluble Ag₂O in the bulk solution. Studies in molten NaNO₃ gave similar results, showing loss of silver ions with repeated cathodic and anodic studies when a one-compartment cell is used. Equilibria reactions involving peroxide and superoxide ions may also occur in both melts (4, 7). The loss of reducible silver ions in such experiments could be significantly decreased by using a two-compartment cell that confines the oxide ions formed to the counterelectrode compartment, thereby hindering their reaction with the silver ions in solution. Results in molten LiNO₃ using a one-compartment cell were again quite different; there was no evidence for the formation of insoluble Ag₂O during the anodic reaction, and very little loss of silver ion activity occurs. The oxide ions produced at the counterelectrode during silver oxidation in molten LiNO₃ precipitate as insoluble Li₂O (4). These results suggest a solubility order of $\text{Li}_2\text{O} < \text{Ag}_2\text{O} < \text{K}_2\text{O}$; hence, insoluble Li₂O rather than Ag₂O forms in molten LiNO₃.

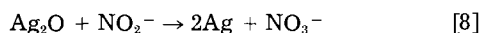
Thermodynamic calculations for the decomposition of Ag₂O



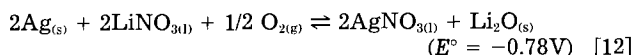
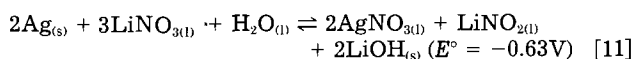
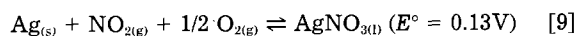
suggest that Ag₂O decomposition becomes possible at 140°C at a partial oxygen pressure of 0.21 atm. Although

perceptible decomposition of Ag_2O into its elements occurs above 160°C (20), the kinetics of this reaction are rather slow, as found in classical studies many years ago by Lewis and others (32-34).

The addition of Na_2O to a NaNO_3 - KNO_3 melt containing AgNO_3 produces an instantaneous dark precipitate and the loss of the electrochemical activity of the silver ions. This precipitate remains unchanged at temperatures up to 350°C , suggesting that the rate of decomposition of Ag_2O is quite slow in molten nitrates. At 400°C , the dark color of the precipitate gradually lightens over a time period of several hours and slight gas evolution can be detected. A comparison study of pure Ag_2O in a glass tube at the same temperatures revealed no significant difference in the rate of decomposition of Ag_2O in air over the rate in molten nitrates. It should be noted that many of our experiments with Ag^+ ions in molten nitrates produced specks of silvery film on the surface of the molten nitrates. These films could result from the free silver formed in Eq. [7] or from the reaction of Ag_2O with nitrite ions (21)



Possible corrosion reactions of silver and their estimated E° values at 350°C in molten LiNO_3 include



The latter three reactions are possible only when the reaction products are present at low activities. Under a helium atmosphere in a dry melt, reaction [10] would be the most likely corrosion reaction. The Ag_2O formed would be converted by the displacement reaction



into AgNO_3 and Li_2O . In agreement with the experimental studies (Table I), the presence of sufficient amounts of the end products (LiNO_2 , AgNO_3 , and Li_2O) in the melt can slow the corrosion rate or even reverse the reaction direction. Since the displacement reaction with Ag_2O does not occur in molten NaNO_3 and KNO_3 , the lower corrosion rates in these melts may be due to the formation of a passivating film of Ag_2O on the silver surface. Corrosion rates may also be related to the observation that the reduction of molten NaNO_3 and KNO_3 is kinetically slower than the reduction of molten LiNO_3 (4).

The addition of chloride ions to nitrate melts containing AgNO_3 produces a cloudy solution due to the formation of insoluble AgCl (35). Studies of the silver ion cathode in several molten nitrate mixtures before and after chloride addition show that AgCl is readily reduced; albeit, the experimental potentials are generally 0.3-0.4V more negative than those observed for the reduction of silver ions. In molten LiNO_3 - LiClO_4 mixtures, the addition of AgNO_3 produces a cloudy solution that suggests the presence of Cl^- ions either as an impurity or as a product of the self-decomposition reaction of LiClO_4 (5). No significant electrochemical activity was observed for Ag_2O in molten nitrates. This could be due to its observed tendency to coalesce and precipitate from the nitrate melt, whereas, AgCl is present as a fine suspension. Discussions of thermal battery cells utilizing AgNO_3 are presented elsewhere (36, 37).

Summary

The addition of AgNO_3 to molten nitrates permits the cathode to sustain current densities of 100 mA/cm^2 or larger. The electrochemical reduction of silver ions produces dendritic deposits of silver metal and yields values close to $1.0 e^-/\text{Ag}^+$. The corrosion rate for silver metal is

higher in molten LiNO_3 than in either molten NaNO_3 or KNO_3 . In fused NaNO_3 and KNO_3 containing silver ions, insoluble Ag_2O forms when oxide ions are present. In molten LiNO_3 , insoluble Li_2O forms rather than Ag_2O . The decomposition of Ag_2O in molten nitrates is slow at temperatures up to 400°C . Insoluble AgCl is electrochemically reducible in molten nitrates.

Acknowledgments

The authors thank Dr. Marian E. Hills for obtaining micrographs of the silver deposits. The authors also thank Mr. Robert W. Woolever for SEM micrographs and the EDX analysis, and Mr. Arold K. Green for the Auger analysis.

Manuscript submitted May 24, 1983; revised manuscript received April 9, 1984. Portions of this work were presented as Paper 586 at the Denver, Colorado, Meeting of the Society, Oct. 11-16, 1981, and as Paper 341 at the Detroit, Michigan, Meeting of the Society, Oct. 17-21 1982.

The Naval Weapons Center assisted in meeting the publication costs of this article.

REFERENCES

1. M. H. Miles and A. N. Fletcher, *J. Appl. Electrochem.*, **10**, 251 (1980).
2. M. H. Miles and A. N. Fletcher, *This Journal*, **128**, 1489 (1981).
3. A. N. Fletcher, M. H. Miles, and M. L. Chan, *ibid.*, **126**, 1496 (1979).
4. M. H. Miles and A. N. Fletcher, *ibid.*, **127**, 1761 (1980).
5. M. H. Miles and A. N. Fletcher, *ibid.*, **128**, 821 (1981).
6. M. G. Sustersic, W. E. Triaca, and A. J. Arvia, *An. Asoc. Quim. Argent.*, **66**, 299 (1978).
7. S. Sternberg and T. Visan, *Rev. Roum. Chim.*, **27**, 345 (1982).
8. M. H. Miles, G. E. McManis, and A. N. Fletcher, Paper 586 presented at the Electrochemical Society Meeting, Denver, Colorado, Oct. 11-16, 1981.
9. D. L. Manning, *Talanta*, **10**, 255 (1963).
10. G. Mamantov, J. M. Strong, and F. R. Clayton, *Anal. Chem.*, **40**, 488 (1968).
11. W. K. Behl and H. C. Gaur, *J. Electroanal. Chem.*, **32**, 293 (1971).
12. G. J. Hills, D. J. Schiffrin, and J. Thompson, *Electrochim. Acta*, **19**, 657 (1974).
13. T. Visan, D. P. Geana, and S. Sternberg, *Rev. Roum. Chim.*, **21**, 1153 (1976).
14. M. H. Miles, D. A. Fine, and A. N. Fletcher, *This Journal*, **125**, 1209 (1978).
15. D. G. Lovering and R. M. Oblath, in "Ionic Liquids," D. Inman and D. G. Lovering, Editors, pp. 165-183, Plenum Press, New York (1981).
16. G. J. Janz, C. B. Allen, N. P. Bansal, R. M. Murphy, and R. P. T. Tomkins, "Physical Properties Data Compilations Relevant to Energy Storage. II. Molten Salts: Data on Single and Multicomponent Salt Systems," pp. 132-166, NSRDS-NBS 61, Part II, U.S. Government Printing Office, Washington, DC (1979).
17. S. Shibata and M. P. Sumino, *Electrochim. Acta*, **20**, 871 (1975).
18. G. J. Hills and K. E. Johnson, in "Advances in Polarography," Vol. 3, I. S. Longmuir, Editor, pp. 974-981, Pergamon Press, New York (1960).
19. T. Yoshimori, H. Kawahara, T. Hara, and A. Ikeda, *Anal. Chim. Acta*, **98**, 171 (1978).
20. F. A. Cotton and G. Wilkinson, "Advanced Inorganic Chemistry," pp. 968-975, Wiley-Interscience, New York (1980).
21. A. Conte and M. D. Ingram, *Electrochim. Acta*, **13**, 1551 (1968).
22. L. G. Boxall and K. E. Johnson, *Trans. Faraday Soc.*, **67**, 1433 (1971).
23. J. Lesourd, C. Vallet, and Y. Doucet, *J. Electroanal. Chem.*, **48**, 99 (1973).
24. B. Holmberg, *Acta Chem. Scand.*, **A28**, 284 (1974).
25. B. J. Welch and G. A. Angell, *Aust. J. Chem.*, **25**, 1613 (1972).
26. M. D. Ingram and G. G. Lewis, *J. Chem. Soc. Faraday Trans. 1*, **70**, 490 (1974).
27. P. Delahay, "New Instrumental Methods in Electrochemistry," pp. 120-125, Interscience, New York (1954).

28. G. Mamantov, D. L. Manning, and J. M. Dale, *J. Electroanal. Chem.*, **9**, 253 (1965).
29. S. Sternberg and C. Herdlicka, *Rev. Roum. Chim.*, **14**, 991 (1969).
30. W. K. Behl, *This Journal*, **120**, 1692 (1973).
31. H. D. Burk and F. Umland, *Ber. Bunsenges. Phys. Chem.*, **80**, 1293 (1976).
32. G. N. Lewis, *Z. Phys. Chem.*, **52**, 310 (1905).
33. G. N. Lewis, *J. Am. Chem. Soc.*, **28**, 139 (1906).
34. F. G. Keyes and H. Hara, *ibid.*, **44**, 479 (1922).
35. D. Inman and J. O'M. Bockris, *J. Electroanal. Chem.*, **3**, 126 (1962).
36. G. E. McManis, M. H. Miles, and A. N. Fletcher, *This Journal*, **131**, 283 (1984).
37. G. E. McManis, M. H. Miles, and A. N. Fletcher, *ibid.*, **131**, 286 (1984).

Photoelectrochemical Properties of Single-Crystalline n-SiC in Aqueous Electrolytes

H. Morisaki, H. Ono, and K. Yazawa

The University of Electro-Communications, Chofu-shi, Tokyo 182, Japan

ABSTRACT

The photoelectrochemical properties of n-SiC were studied in aqueous electrolytes. The onset potential of the anodic photocurrent in steady state was found to be about 1V more anodic than that of the photocurrent measured by the lock-in method ($-2V$ vs. SCE). This discrepancy was ascribed to the presence of transient photocurrent observed in the potential range between -1.9 and $+0.6V$ vs. SCE. Possible mechanisms of the transient photoresponse were examined. The flatband potential deduced from the Mott-Schottky plot of the C-V characteristics was found to shift into the cathodic direction of potential in the course of the photoelectrochemical measurements. The shift was explained by a hypothesis that thin oxide layer grows on the SiC surface during anodic polarization under strong illumination.

Silicon carbide (SiC) is a stable high temperature semiconductor material with 2.2 – 3.0 eV bandgap energy depending on the crystallographic structures: ~ 3 eV for various polytypes (α -SiC (2H, 4H, 6H, ...) and 2.2 eV for β -SiC (3C). Electronic properties of this material have been widely investigated, and several electronic devices such as blue light emitting diodes have already been fabricated (1).

In contrast to this, very few studies have been reported on electrochemical properties of SiC: the first systematic study on the photoelectrochemical behavior of this material has been reported by Gleria and Memming (2). They investigated charge transfer processes between SiC and various redox systems and observed that the flatband potential of this material in aqueous electrolytes is exceptionally cathodic ($\sim -1.6V$ vs. SCE at pH 1). We are attracted to this material from this point of view because, if this is true, the material would be a very good coating material for unstable small-bandgap semiconductors to make heterostructure photoanodes for photoelectrochemical energy conversion (3). At present, studies on the photoelectrolysis of water have been hampered by the lack of electrode materials with better performances (4-11).

In the present study, we have reexamined the photoelectrochemical properties of n-SiC in aqueous electrolytes and found that the onset potential of the photocurrent changed remarkably depending on the experimental conditions. We have also studied the stability of SiC electrodes in aqueous electrolytes under illumination.

Experimental

SiC electrodes used in the present experiments were made of single-crystalline n-type material (mostly 6H modification) grown at National Institute for Research in Inorganic Materials, Ibaraki, Japan. The ohmic contacts on the crystal were made by co-evaporation of Au and Ta. Copper wires were connected on the evaporated surfaces with Ag paste. The whole surface except the front plane of each sample was molded with epoxy resin. The front surfaces of the electrodes were etched in hydrofluoric acid (HF:46%) for 1 min before each measurement.

The photoelectrochemical measurements were made by using a Pt electrode as a counterelectrode, a saturated calomel electrode (SCE) as a reference electrode, a potentiostat, and a 500W Xe lamp combined with ND

filters and monochromator as a light source. When the photocurrents were measured by a lock-in amplifier, the light was chopped at a frequency in the range between 10 and 200 Hz.

The space charge capacitance of the electrodes was determined from measurements of impedance of the cell: a 1 μ A 1 kHz ac current was superimposed in the circuit, and both the ac potential difference between the semiconductor electrode and the counterelectrode as well as the phase difference between the ac current and the potential were measured by using a dual-phase lock-in amplifier.

Results

Steady-state photoelectrochemical properties of n-SiC.—Typical current-potential characteristics of n-SiC observed in 0.1N NaOH under illumination of 500W Xe lamp are shown in Fig. 1. Here, the potential was first swept from cathodic to anodic direction and the sweep direction was inverted at 2V vs. SCE. The sweep rate was 4 mV/s. The dark current (broken lines) is very low in the anodic polarization above $-0.5V$ vs. SCE. Note that the onset potential of the photocurrent (~ -1.0 vs. SCE) is not so cathodic as the previously reported value (2). This subject will be discussed later. We take hereafter the onset potential of the photocurrent as the potential where the current under illumination starts to deviate from the dark current. It is noted in the curve that a hysteresis loop is traced when the sweep direction is inverted. Apparently this is related to some corrosion of the electrode surface, because the photocurrent shows gradual decrease if the potential sweep is stopped at a certain potential more anodic than 0 V vs. SEC. The decrease in the photocurrent during the photoelectrochemical measurements recovers to the original value after dipping the electrode in HF for about 1 min, indicating that the corrosion is related to the formation of SiO₂ layer.

Current-potential characteristics of the n-SiC electrode measured in electrolytes with different pH values are shown in Fig. 2. It is noticed that the shift of the curve to the anodic direction occurs at a pH value between 11 and 12. The shift in the onset potential of the photocurrent is about 0.7V. As a possible explanation of this potential shift, we can venture that the dominant oxidizing species for the photo-oxidation change from OH⁻ ions to water molecules at some pH value between 11 and 12. The simi-

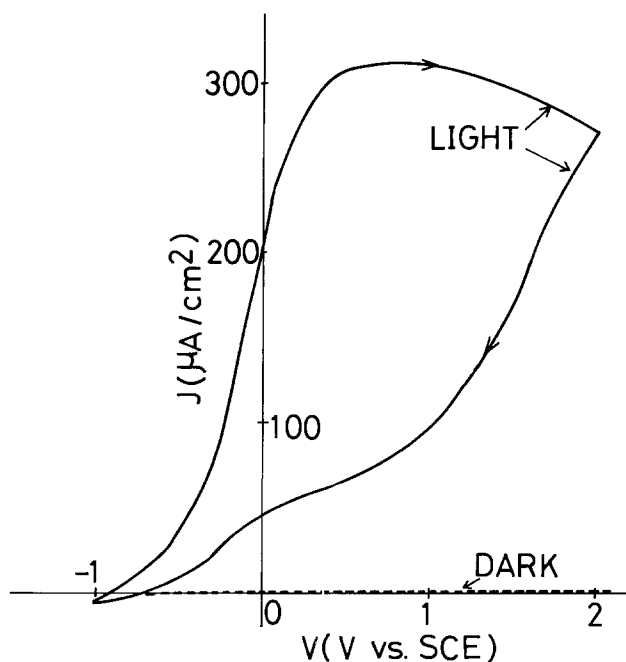


Fig. 1. Current-potential characteristics of an n-SiC electrode in 0.1N NaOH. The potential was first swept from cathodic to anodic direction and was inverted at 2V vs. SCE. The sweep rate was 4 mV/s. The light source was 500W Xe lamp (440 mW cm^{-2}).

lar effect has been observed in a TiO_2 photoanode (12). Alternatively, the results may be explained by some change in corrosion kinetics at the particular pH value.

Spectral distribution of photocurrent in n-SiC at 0 V vs. SCE is shown in Fig. 3. The main photoresponse starts to increase at about 410 nm, which corresponds to the band-gap energy of SiC (3.0 eV), although a weak tail is noted in the longer wavelength range. Similar long wavelength response has been observed by Gleria *et al.* (2). It is also noted in the curve that there is a small shoulder at about 320 nm, indicating that an optical transition to a higher subband becomes dominant for photons with larger energy. The maximum quantum yield in n-SiC is found to be about 4.5% at 1V vs. SCE, which is considerably lower than the values in oxide semiconductors such as n- TiO_2 , etc. (8).

Figure 4 is the time dependences of the photocurrent at a constant anodic potential (2V vs. SCE) observed in elec-

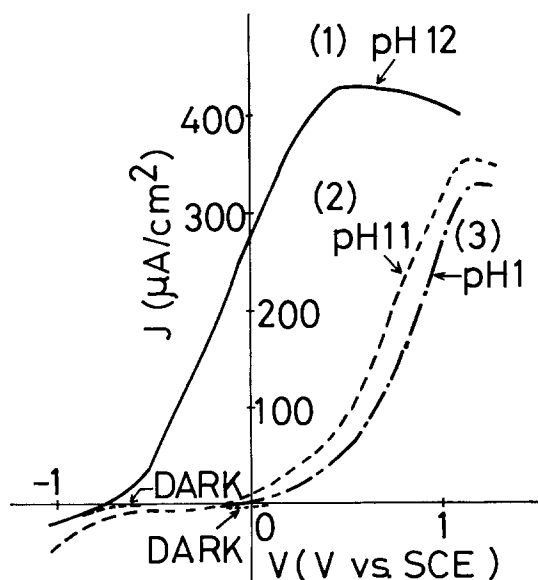


Fig. 2. Current-potential characteristics of the n-SiC electrodes at several pH values. The electrolytes used are (1) 0.01N NaOH (pH 12); (2) 0.1M $\text{Na}_2\text{SO}_4 + \text{NaOH}$ (pH 11); (3) 0.1N H_2SO_4 (pH 1). The light source was 500W Xe lamp.

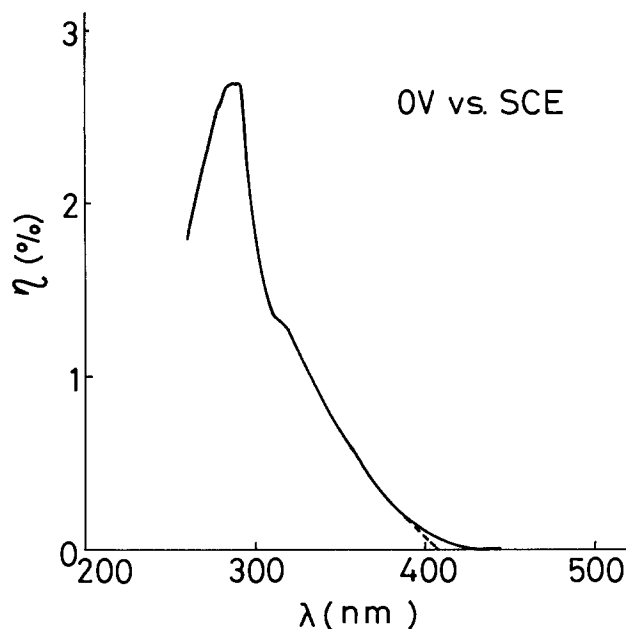


Fig. 3. Spectral distribution of photocurrent in n-SiC at 0 V vs. SCE. The electrolyte used was 0.1N NaOH (pH 13).

trolytes with various pH values. At pH 14 (not shown), the reduction of photocurrent was very small. The reduction rates of the photocurrent for pH 11 and 12 at the initial stage (≤ 3 min) are about the same, whereas the rate for pH 13 is considerably slower than the former two cases. We notice that the initial photocurrent at pH 13 is somewhat lower than it is at pH 11 or 12. This type of uncertainty in the initial photocurrent was always observed in SiC electrodes after etching. Presumably, the rate of surface recombination will be changed by the surface treatment to some extent. It will be shown later that the photocurrent of SiC electrodes is strongly influenced by the surface recombination.

Transient photoresponse of n-SiC.—Figure 5 shows photocurrent-potential characteristics of n-SiC measured with a lock-in amplifier illuminating the electrode by chopped light of a Xe lamp. Here, the electrolyte used in the experiment was 0.1N NaOH. It should be emphasized that the potential for photoresponse (-1.9V vs. SCE) is well negative in this case (*cf.* Fig. 1). Similar results were obtained in 0.1N H_2SO_4 , the onset potential being about -1.2V vs. SCE . These values are in good agreement with

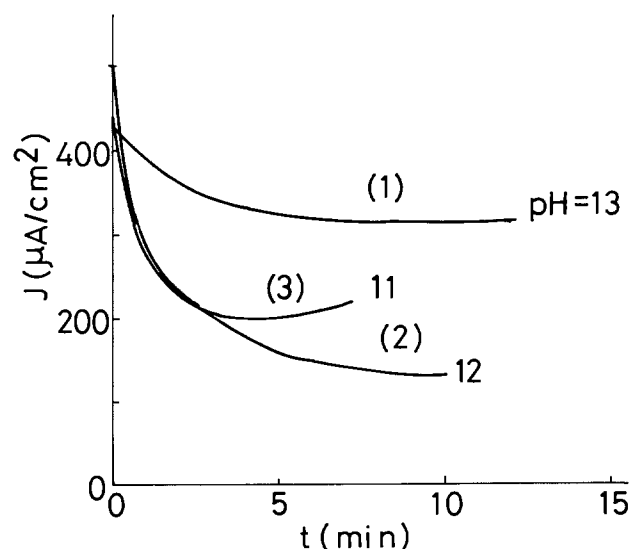


Fig. 4. Time dependence of the photocurrent at 2V vs. SCE. The electrolytes used are: (1) 0.1N NaOH (pH 13); (2) 0.01N NaOH (pH 12); (3) 0.1M $\text{Na}_2\text{SO}_4 + \text{NaOH}$ (pH 11). The light source was 500W Xe lamp.

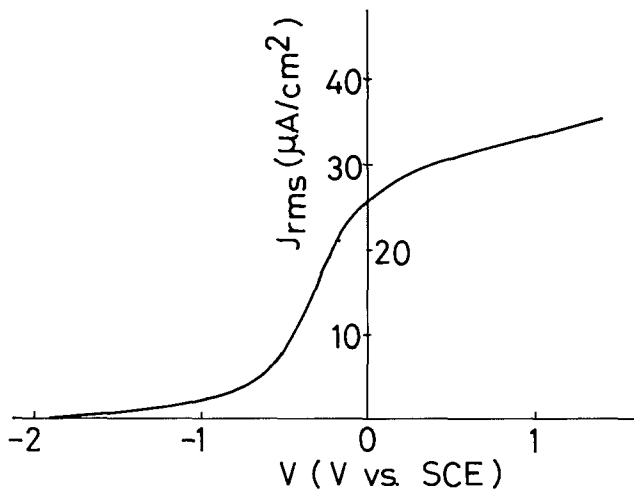


Fig. 5. Photocurrent-potential characteristics of the n-SiC electrode in 0.1N NaOH measured with a lock-in amplifier. The chopper frequency was 150 Hz. The light source was 500W Xe lamp combined with a 30% (transmission) ND filter. This means that the light intensity is about 130 mW/cm².

the onset potential reported previously (2). Note that the photocurrent-potential characteristics appeared in the literature (2) have been measured by the lock-in technique.

Another point which we should like to emphasize is that the apparent photocurrent measured by this method is a function of the chopper frequency, especially in the potential range more cathodic than 0 V vs. SCE, the signal increasing with lowering frequency. Since the intrinsic (steady-state) photocurrent should be independent of the chopper frequency, the photoresponse measured by the lock-in method is supposed to include some transient component. Incidentally, it is usual with a transient response that the signal increases with increasing frequency due to the transient's being a greater fraction of the length of the pulse. The reason for the signal increase with lowering frequency in the present case is that the initial rise-rate of the transient photocurrent has not been as fast as the chopper frequency used in our present experiment.

In order to investigate further the relation between the steady-state and transient photoresponses, we measured the current-potential characteristics of n-SiC electrodes by illuminating the electrode surface intermittently while sweeping the electrode potential from cathodic to anodic direction. The results are illustrated in Fig. 6. We note that there are current spikes corresponding to some transient phenomena: the positive transient current (anodic transient) flows in the wide range of potentials from -1.9 to +0.6V vs. SCE, whereas the negative transient current (cathodic transient) flows at potentials more cathodic than -0.5V vs. SCE. The transient response was most enhanced at potentials around -1V in both directions.

The transient photoresponse was investigated also in the time dependence of the photocurrent at several different potentials, as shown in Fig. 7. It is noted in the figure that the time constant of the transient photoresponse lengthens with increasing anodic potential, being about 0.6s at -0.8V vs. SCE and about 1.8s at -0.2V vs. SCE.

In contrast to the transient responses, the steady-state photocurrent in the anodic direction starts to flow at about -1V vs. SCE and increases with increasing the anodic potential as already seen in Fig. 1. It is clear from the above experimental results that the current-potential characteristics measured by the lock-in technique include both the transient and steady-state photoresponses.

Capacitance-potential relationship of n-SiC.—In order to estimate the flatband potential as well as the donor density of n-SiC, we measured the differential capacitance as a function of potential. Figure 8 is the Mott-Schottky plot (C^{-2} vs. V) of the capacitance-potential relationship measured in 0.1N NaOH. The curves show

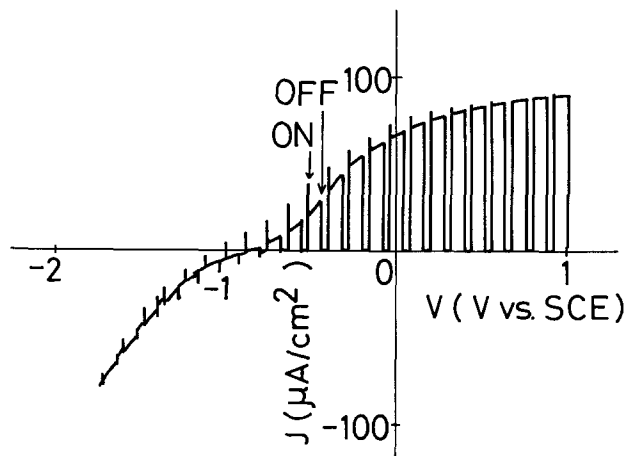


Fig. 6. Current-potential characteristics of the n-SiC electrode in 0.1N NaOH measured by illuminating intermittently. The potential sweep is from cathodic to anodic direction. The sweep rate is 4 mV/s.

straight lines in parallel at potentials more anodic than -0.7V vs. SCE. At more cathodic potentials below -0.7V vs. SCE, however, the curves deviate from the straight lines, the extrapolation of the curves intersecting with the potential axis at -1.15V vs. SCE. It was also noticed that the deviation from the straight portion is accompanied by the increase in the cathodic dark current, which is particularly notable at potentials more cathodic than about -1V.

Applying the well-known Mott-Schottky relation

$$C^{-2} = \frac{2}{q \epsilon \epsilon_0 N_D} \left[V - V_{FB} - \frac{kT}{q} \right] \quad [1]$$

to the straight portion of the curves in Fig. 8, we can estimate both the donor density N_D and the flatband potential V_{FB} (the other symbols have their usual meanings) from the curves in Fig. 8. Here, it should be emphasized that the flatband potential thus deduced is only an apparent value for electrodes with heterogeneous structure as in the present case (see the Discussion section).

The apparent flatband potential of n-SiC obtained from the Mott-Schottky plot strongly depends on the sequence

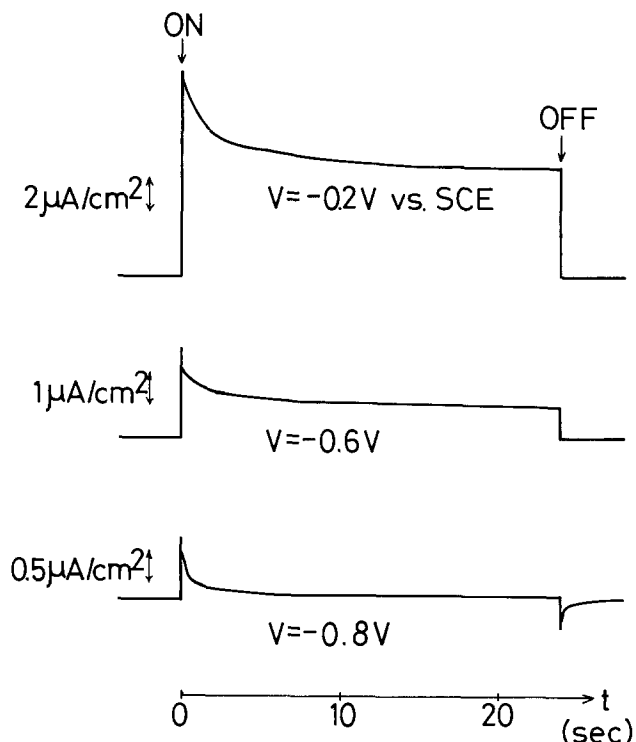


Fig. 7. Transient photoresponse of n-SiC in 0.1N NaOH. The light source was 500W Xe lamp.

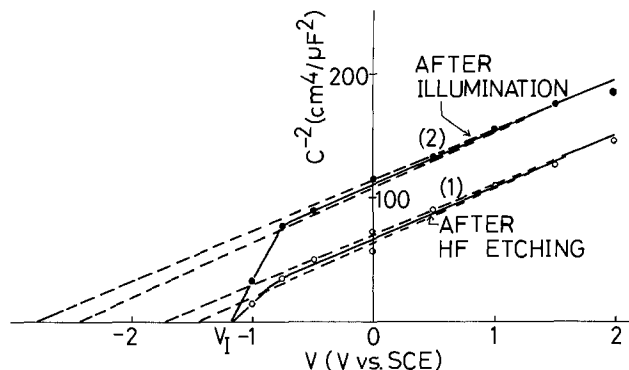


Fig. 8. The Mott-Schottky plot of capacitance-potential relationship of n-SiC measured in 0.1N NaOH. The frequency of the measurement was 1 kHz. Curve 1 is the results immediately after etching the surface in HF (46%) for 1 min. Curve 2 is the results measured after the surface has been illuminated by a 500W Xe lamp for 10 min under anodic bias condition at 2V vs. SCE.

of photoelectrochemical measurements. Curve 1 in the figure is the results obtained immediately after etching the electrode surface in hydrofluoric acid for 1 min. The apparent flatband potential V_{FB} determined from the straight portion of the curve is within the range between -1.45 and -1.65 V vs. SCE. Curve 2, however, is the results obtained after the surface has been illuminated for 10 min by a 500W Xe lamp under anodic bias condition at 2V vs. SCE. Obviously, the apparent flatband potential shifts to the cathodic direction by about 1V, being in the range between -2.4 and -2.8 V vs. SCE.

The donor density of n-SiC used in the present experiment deduced from the slope of the curves is

$$N_D = 3.2 \sim 3.5 \times 10^{17} \text{ cm}^{-3} \quad [2]$$

being consistent with the values estimated from the conductivity measurement ($\sim 10^{17} \text{ cm}^{-3}$). Here, we have assumed that the relative dielectric constant ϵ of SiC is 10 (13).

Discussion

According to the surface characterization with ESCA, the surface of SiC is always covered with thin layer of SiO_x . Our experimental results indicate that the oxide layer on the SiC surface grows further during photoelectrochemical measurements, the growth rate being enhanced by illumination under anodic polarization, as noted in Fig. 1.

The low quantum yield of the photoresponse observed in Fig. 3 is apparently the consequence of the oxide formation on the electrode surface, the photocurrent being restricted by strong recombination of photogenerated carriers at the SiC/surface layer interface. The hole flux Φ'_h charge transferred to the electrolyte for the anodic photocurrent is given by

$$\Phi'_h = \frac{F_T}{F_T + F_R} \Phi_h \propto I_{\text{photo}} \quad [3]$$

where Φ_h is the flux of photogenerated holes supplied to the SiC-SiO_x interface, and F_T and F_R are the transfer rate through the surface layer and the recombination rate at the interface, respectively. The low quantum yield observed in SiC means that $F_T \ll F_R$ at the SiC-SiO_x interface.

The experimental results in Fig. 4 indicate that the growth rate of the surface layer is enhanced in less alkaline electrolytes, the rate of current reduction being more significant in electrolytes with lower pH values. Since the actual growth rate of the surface layer is expected to be determined by balance of the formation rate and dissolution rate of the film, the slower decay in the photocurrent at pH 13 would be explained by considering that the SiO_x layer is more soluble at the more alkaline electrolytes. We are now investigating the photoelectro-

chemical properties of SiC in a HF containing electrolyte (e.g., 0.1N NaOH:0.46%HF = 3:2) to appreciate the effect of SiO_x layer: preliminary results show that the photocurrent is about ten times larger than the results in Fig. 1 without showing any current reduction with time.

Next, consider the flatband potential of SiC and the related onset potentials for the photocurrent. Several characteristic potentials observed in the present experiments are tabulated in Table I. It is noted that the values are distributed in relatively wide range of potentials from -1.0 to -2.8 V vs. SCE.

The onset potential of the photoresponse measured by the lock-in method (-1.9 V vs. SCE) should be essentially equal to the value for the transient photocurrent, as stated before. This transient photoresponse will be discussed later.

The apparent flatband potential of n-SiC electrodes at pH 13 determined from the straight portion of the Mott-Schottky plot of our experimental results is about -1.5 V vs. SCE before the photocurrent measurement and about -2.5 V after the measurement. Memming *et al.* (2) have reported that the flatband potential of n-SiC in alkaline medium is about -2.1 V vs. SCE, this being an intermediate of the two values of the present study.

It should be noted that the interpretation of the Mott-Schottky plot is rather complicated when a surface layer is present on a semiconductor as in the present case. The flatband potential of a semiconductor electrode with heterogeneous structure can be determined from the intersection point of the C^{-2} vs. V line to the potential axis only if the heterogeneous structure of the semiconductor surface is such that the surface layer is the same as the bulk material with different donor density. In fact, the present situation is much more complicated because the surface layer is most probably SiO_x. This fact means that the flatband potential cannot be estimated from the Mott-Schottky plot in this case.

In spite of this, we believe that the actual flatband potential of SiC electrodes is not far from the intersection potential V_1 (-1.15 V vs. SCE) of the C^{-2} vs. V curves because of the following reasons: (i) the apparent flatband potentials deduced from the straight portion of the C^{-2} vs. V curves (~ -2.5 V after illumination) are not realistic because the values are far more cathodic from the onset of the cathodic current, (ii) the onset potential of cathodic dark current (-0.7 V) is reasonably close to V_1 , (iii) as stated before, the steep increase in differential capacitance corresponding to the kink in the C^{-2} vs. V curves is closely related to the increased dark current: in particular, the capacitance measured by the lock-in method was found to be difficult at potentials more cathodic than V_1 because of the increased real component of the ac current (the dark current), (iv) the onset potential of the steady-state photocurrent (-1.0 V) is very close to V_1 , and (v) the transient photoresponse is most enhanced in this potential range.

The discrepancy between the actual flatband potential and the apparent flatband potentials deduced from the straight portion of the C^{-2} vs. V lines is explained by the effect of the insulating layer (SiO_x) grown on the SiC surface. The effect of an insulating layer on the capacitance of semiconductor electrodes has been examined by De

Table I. Several characteristic potentials related to the flatband potential of n-SiC. The electrolyte used was 0.1N NaOH.

Description	Potential (V vs. SCE)
1. Onset potential of steady-state photoresponse	-1.0
2. Onset potential of transient photoresponse	-1.9
3. Onset potential of cathodic dark current	-0.8
4. Onset potential of photoresponse by lock-in method	-1.9
5. Extrapolation of straight portion of C^{-2} vs. V line (after HF etching)	-1.45
(after illumination)	-1.65
6. Intersection potential (V_1) of C^{-2} vs. V curve	-2.4
	-2.8
	-1.15

Gryse *et al.* (14). Assuming that there is no extra charge on the semiconductor surface, they have shown that the intersection potential of the Mott-Schottky plot should shift by

$$\Delta V = - \frac{2 \epsilon \epsilon_0 q}{C_1^2} N_D \quad [4]$$

from the real flatband potential, where C_1 is the extra capacitance stacked on the electrode surface. Applying the above relation to the present case, we can estimate the capacitance C_1 from the potential shift. Assuming that the actual flatband potential is about $-1.15V$ vs. SCE, the thickness of the surface layer deduced from this capacitance was 7.3 nm after HF etching and 19 nm after illumination. Here, the surface layer was assumed to be SiO_2 ($\epsilon = 4.0$) and other parameters used were $\epsilon(\text{SiC}) = 10$ and $N_D = 3.3 \times 10^{17} \text{ cm}^{-3}$.

It should be pointed out that the above estimation of the surface-layer thickness is only of first approximation, because details on the surface layer are unknown: various kinds of electronic charge introduced into the SiC-SiO_x interface (and/or within SiO_x) will also shift the flatband potential to some extent. In the metal-oxide-semiconductor (MOS) structure of Si devices, for example, similar potential shift is known to be induced by ion migration such as Na⁺ ions into the surface layer (15).

Finally, consider the transient photoresponse observed at potentials anodic than $-1.9V$ vs. SCE. At present, we are not certain whether the transient current is the faradaic one or it is due to the charging effect. The model, in either case, should explain consistently the fact that the transient anodic photocurrent is observed in a fairly wide range of the potential from cathodic to anodic polarization. For example, a simple model based on the charging effect of the surface layer capacitance due to photogenerated carriers should be excluded because, if this were the case, the anodic charging current would be observed only in the anodic polarization.

As a probable mechanism of the transient response based on the faradaic current, we have considered the possibility of photo-oxidation reaction which occurs transiently. Here, we tentatively assume that only the dominant reaction at the SiC-electrolyte interface is the photo-oxidation of water. Just after turning on the illumination, part of photogenerated holes in the vicinity of the SiC-SiO_x interface will charge transfer, probably by tunneling across the surface layer resulting in anodic current. The decrease in the photocurrent in the next step is then the back reaction which will become dominant only after the accumulation of oxidized species (O₂ molecules in the present model) at the surface. However, with this model it is hard to explain the transient response under cathodic polarization because the O₂ reduction is expected to proceed quite effectively under cathodic polarization.

It is also plausible that the transient photocurrent is related to the photocorrosion of SiC: the photodissolution of SiO_x may be enhanced only just after turning on the illumination. Similarly, the cathodic transient current is explained by some back reaction of the corrosion or adsorption of the chemical products, although we have not considered this possibility further.

As the other explanation to the transient photoresponse, we have considered the effect of localized states at the SiC-SiO_x interface. A schematic representation of the interface states is illustrated in Fig. 9. Here, the localized states are assumed to act as efficient hole traps, that is, the capture cross section for holes σ_h is much larger than that for electrons σ_e . Just turning on the illumination, some of the photogenerated holes will be captured in the hole traps charging the surface layer capacitance. This can occur even under weakly cathodic polarization because most of the potential is applied to the insulating surface layer, the band bending within SiC being small enough over a relatively wide range of the polarization.

Figure 10a is a possible equivalent circuit of the photoelectrochemical cell composed of the SiC electrode and the counterelectrode. Here, the current source means the

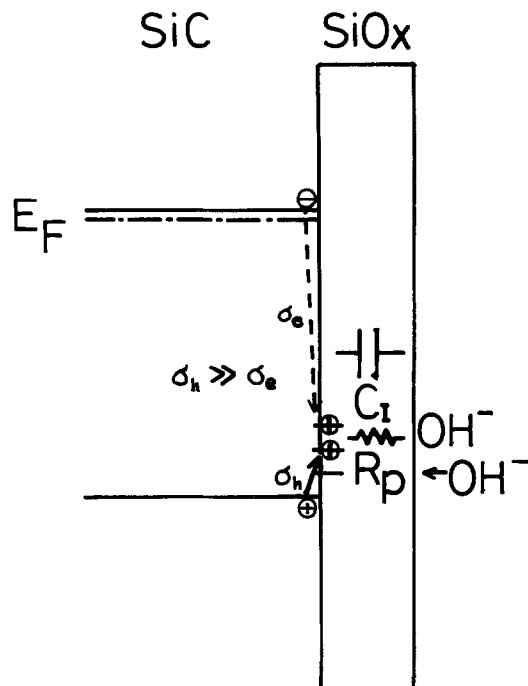


Fig. 9. A schematic representation of interface states which act as efficient hole traps. σ_h and σ_e are the capture cross sections for holes and electrons, respectively.

effect of photogenerated carriers, C_s is the depletion-layer capacitance, C_1 and R_p the capacitance and the parallel resistance of the surface layer on the SiC, respectively, C_H the Helmholtz layer capacitance, R_f means the effect of faradaic current, and R_l is the series resistance of the photoelectrochemical cell.

Assuming that $C_H \gg C_s$, C_1 and $R_p \gg R_l$, we have modified the equivalent circuit to the more simplified one as shown in Fig. 10b. Here, we have neglected the effect of faradaic current ($R_f = \infty$), assuming that the current is purely capacitive. The time constant of the transient response is then given by

$$\tau = R_p (C_1 + C_s) \quad [5]$$

Substituting $\tau = 1s$ and $C_1 = C_s = 0.1 \mu\text{F}$ as typical values, we get $R_p \approx 5 \text{ M}\Omega$ as the resistance of the surface layer.

So far, we have not discussed the photoelectrolysis product. Since O₂ evolution has not been observed directly, it is not possible to exclude the possibility that the entire photocurrent is associated with corrosion with formation of SiO_x (and perhaps CO₃²⁻). A steady corrosion

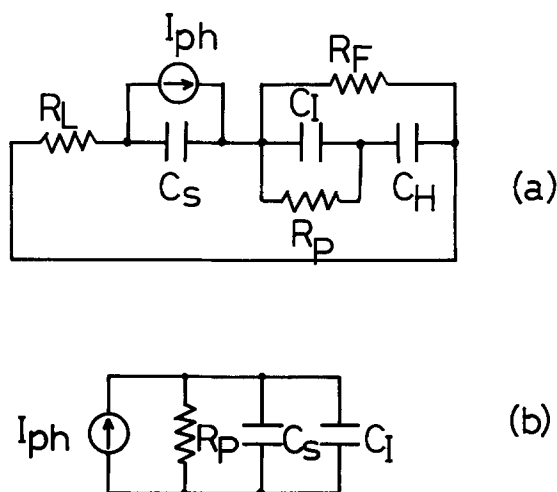


Fig. 10. A possible equivalent circuit of the photoelectrochemical cell composed of the SiC electrode and the counterelectrode (a) and the simplified model (b).

current of $200 \mu\text{A}/\text{cm}^2$ (Fig. 4) means the formation rate of SiO_2 and thus the dissolution rate of about $100 \text{ nm}/\text{min}$. Taking into account that the substantial increase in the oxide layer thickness estimated from the capacitance measurements is about 120 nm by 10 min illumination, it would be more natural to suppose that practically both the corrosion and photo-oxidation of water occurs simultaneously at the SiC-electrolyte interface.

Conclusion

We reexamined the photoelectrochemical properties of n-SiC in aqueous electrolytes and found that an insulating layer on the SiC surface (probably SiO_2) grows further during the photoelectrochemical measurement. The surface layer thickness was estimated from the capacitance measurements. It was found that the surface layer thus formed controls the rate of charge transfer as well as the flatband potential of the n-SiC electrodes. The onset potential of the anodic photocurrent in steady state was found to be about 1V more anodic than that of the photocurrent measured by the lock-in method (-2V vs. SCE). This discrepancy was due to the presence of transient photocurrent observed in the potential range between -1.9 and $+0.6\text{V}$ vs. SCE. We have concluded from a series of experimental studies that the flatband potential of n-SiC at pH 13 is about -1V vs. SCE, which is about 1V more anodic than the previously reported value. We have also investigated the transient photoresponse observed in the potential range near the flatband condition and proposed possible mechanisms for this phenomenon on the basis of the presence of the surface layer.

Acknowledgments

We thank Dr. Y. Inomata for providing single crystals of n-SiC. T. Okada, M. Sato, and S. Uemura helped in the ex-

periment. This work was supported in part by a Grant-in-Aid for Scientific Research, Ministry of Education of Japan.

Manuscript submitted Oct. 12, 1983; revised manuscript received March 18, 1984.

The University of Electro-Communications assisted in meeting the publication costs of this article.

REFERENCES

1. R. C. Marshall, J. W. Faust, Jr., and C. E. Ryan, Editors, "Silicon Carbide 1973," University of South Carolina Press (1974).
2. M. Gleria and R. Memming, *J. Electroanal. Chem.*, **65**, 163 (1975).
3. H. Morisaki, H. Ono, H. Dohkoshi, and K. Yazawa, *Jpn. J. Appl. Phys.*, **19**, L148 (1980).
4. A. Fujishima and K. Honda, *Nature (London)*, **238**, 37 (1972).
5. K. L. Hardee and A. J. Bard, *This Journal*, **124**, 215 (1977).
6. H. H. Kung, H. S. Jarrett, A. W. Sleight, and A. Ferretti, *J. Appl. Phys.*, **48**, 2463 (1977).
7. M. A. Butler and D. S. Ginley, *This Journal*, **125**, 228 (1978).
8. J. G. Mavroides, *Mater. Res. Bull.*, **13**, 1379 (1978).
9. V. Guruswamy and J. O'M. Bockris, *Solar Energy Mater.*, **1**, 141 (1979).
10. H. P. Maruska and A. K. Ghosh, *ibid.*, **1**, 411 (1979).
11. D. E. Scaife, *Solar Energy*, **25**, 41 (1980).
12. J.-L. Desplat, *J. Appl. Phys.*, **47**, 5102 (1976).
13. W. G. Spitzer, D. A. Kleinman, C. J. Frosch, and D. J. Walsh, in "Silicon Carbide," J. R. O'Connor and J. Smitlens, Editors, Sec. III-3, Pergamon Press, New York (1960).
14. R. De Gryse, W. P. Gomes, F. Cardon, and J. Vennik, *This Journal*, **122**, 711 (1975).
15. S. M. Sze, "Physics of Semiconductor Devices," Chap. 9, John Wiley & Sons, New York (1969).

Photoelectrochemical Studies of Prussian Blue on n-Type Semiconductor (n-TiO₂)

Kingo Itaya*

Department of Chemical Engineering, Tohoku University, Sendai 980, Japan

Isamu Uchida* and Shinobu Toshima

Department of Applied Chemistry, Faculty of Engineering, Tohoku University, Sendai 980, Japan

Richard M. De La Rue

Department of Electronics and Electrical Engineering, The University, Glasgow, G. 12, Scotland

ABSTRACT

Electron transfer reactions in the open-spaced crystal of Prussian blue (PB) by photo-oxidation at a n-type semiconductor (n-TiO₂) are discussed. The reduction of PB at n-TiO₂ electrodes occurs, but the corresponding oxidation is not possible in the dark. The photo-oxidation of Prussian white (the reduced form of PB) does occur at n-TiO₂ electrodes in aqueous solutions at potentials about 600 mV less positive than that observed at metallic electrodes. The photo-oxidation of PB itself also occurs at n-TiO₂ electrodes at about 1100 mV less positive potentials. The fully oxidized form (Prussian brown) of PB, which can be prepared by photo-oxidation, is stepwise reduced to PB at -0.16V and to Prussian white at -0.35V vs. SCE. The energy level is represented.

We have very recently disclosed a versatile new method of preparation for Prussian blue film and its analogues on inert electrodes such as platinum (Pt), glassy carbon (GC), and SnO_2 (2-7). The spectroelectrochemistry (5) and its application for a stable electrochromic device (2) have been discussed. Recently reports by Neff *et al.* have shown a chemical method of preparation for a thin film

*Electrochemical Society Active Member.

of PB on Pt and gold (Au) electrodes and demonstrated the redox behavior of PB (8-10). Although mechanistic studies of chemical synthesis of the PB films demonstrated by Neff have not yet been reported, we have found that well-cleaned SnO_2 electrodes could not acquire the PB deposit by a simple dipping method (5). However, the electrochemical method employed by us can give quantitative formation concerning the PB de-

posit on various electrode surfaces (2, 3, 5). The spectroelectrochemistry of PB-modified SnO_2 electrodes has clearly revealed that the fully oxidized form of PB is a definite compound and shows only an absorption band at 420 nm in the visible region (5). The formula of PB is water-insoluble one, i.e., $\text{Fe}_4^{3+}[\text{Fe}^{\text{II}}(\text{CN})_6]_3$, which was previously determined by a coulometric study with a PB-modified SnO_2 electrode in 1M KCl (5). However, in 1M KCl, a fairly large background prevented a precise determination of the charge consumed at the oxidation wave of PB. In this paper, a refined result for a coulometric study is reported.

Electron transfer reactions in the open-spaced crystal of PB by photo-oxidation at a n-type semiconductor allow us to obtain the further understanding of PB. Recently, DeBerry and Viehbeck reported an electron transfer reaction at TiO_2 electrodes (1). However, they have described only the photo-oxidation of Prussian white (reduced form of PB) on both single-crystal and polycrystalline TiO_2 electrodes. In this paper, it will be shown that photo-oxidation of Prussian white (PW) and of PB do occur at n- TiO_2 electrodes in aqueous solutions at potentials less positive than that observed at metallic electrodes such as Pt, GC, and SnO_2 . These results also lead to consideration of the application of electron transfer reactions in the film on n- TiO_2 electrodes for an erasable optical signal recording system.

Experimental

A single-crystal TiO_2 sample was heated to 650°C in vacuum at 10^{-4} torr for 2-3h; this will be referred to as "the moderately doped sample" having a donor density of about $2 \times 10^{18}/\text{cm}^3$, as determined from a Mott-Schottky plot. The crystal sample (1 mm thick) was provided with an ohmic contact (11, 12) and mounted in a glass tube. The back and sides of the crystal were insulated from the solution with an ethylene-propylene copolymer, dissolved in toluene. This material was relatively impervious to attack from the solution of ferric-ferricyanide, which is a strong oxidant (5). The electrode was polished with alumina slurry and etched in $\text{HNO}_3/\text{HF}/\text{CH}_3\text{COOH}$ (5:3:3) for 15s prior to use (11, 12).

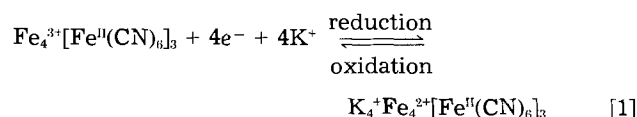
The SnO_2 electrodes used were thin films deposited on glass substrates (Corning, 10 Ω/\square films) and were used with an ohmic contact wrapped with a platinum wire (5). The PB films on TiO_2 electrodes were prepared in an aqueous ferric-ferricyanide solution of an equal-volume mixture of 20 mM $\text{K}_3\text{Fe}(\text{CN})_6$ in 0.01M HCl and 20 mM

FeCl_3 (pH = 2.0), as previously described (2-6). The electrodes were cathodically polarized in the above ferric-ferricyanide solution in the dark under a galvanostatic condition with a current density of 10 $\mu\text{A}/\text{cm}^2$. An electrode potential of about 0.15V vs. a saturated calomel electrode (SCE) was observed at the TiO_2 electrode during the formation of PB.

The light source used was a 150W xenon lamp. Electrochemical measurements were carried out with a PAR Model 173 instrument equipped with a Model 179 digital coulometer. 0.5M K_2SO_4 was used throughout as supporting electrolyte. The pH was adjusted to 4.0 by using dilute sulfuric acid. The cell used consisted of a SCE reference electrode and a Pt wire as the counterelectrode. Nitrogen gas was passed through the solution before the experiments and above the solution during the experiments, since the reduced form of PB, Prussian white, is oxidized to PB by oxygen (29).

Results and Discussion

Electrochemistry of PB on a SnO_2 electrode.—Figure 1 shows a cyclic voltammogram and a coulometric curve of a PB-modified SnO_2 electrode in 0.5M K_2SO_4 (pH = 4.0). The reductive and oxidative waves observed at 0.2V vs. SCE have been formulated as follows as the result of an *in situ* Mössbauer effect measurement, as previously discussed (6)



where Fe^{3+} , Fe^{II} , and K^+ are the high spin iron ions, the low spin iron ions, and the potassium ions, respectively. Only the high spin iron ions, Fe^{3+} and Fe^{2+} , are involved in the electron transfer reaction in the film (5, 6). The above mechanism was written under the assumption that the formula of PB is the "water insoluble one," $\text{Fe}_4^{3+}[\text{Fe}^{\text{II}}(\text{CN})_6]_3$. Ellis *et al.* assumed that the deposit obtained by a chemical method was "water soluble PB," $\text{KFe}^{3+}\text{Fe}^{\text{II}}(\text{CN})_6$ (9).

The electrochemical oxidation of PB occurred at the electrode potentials more positive than 0.8V. Interestingly, the second oxidation wave is clearly seen at about 1.2V vs. SCE, and the corresponding reduction peak does appear on the cathodic scan. The coulometric curves in Fig. 1 were simultaneously recorded on the cyclic

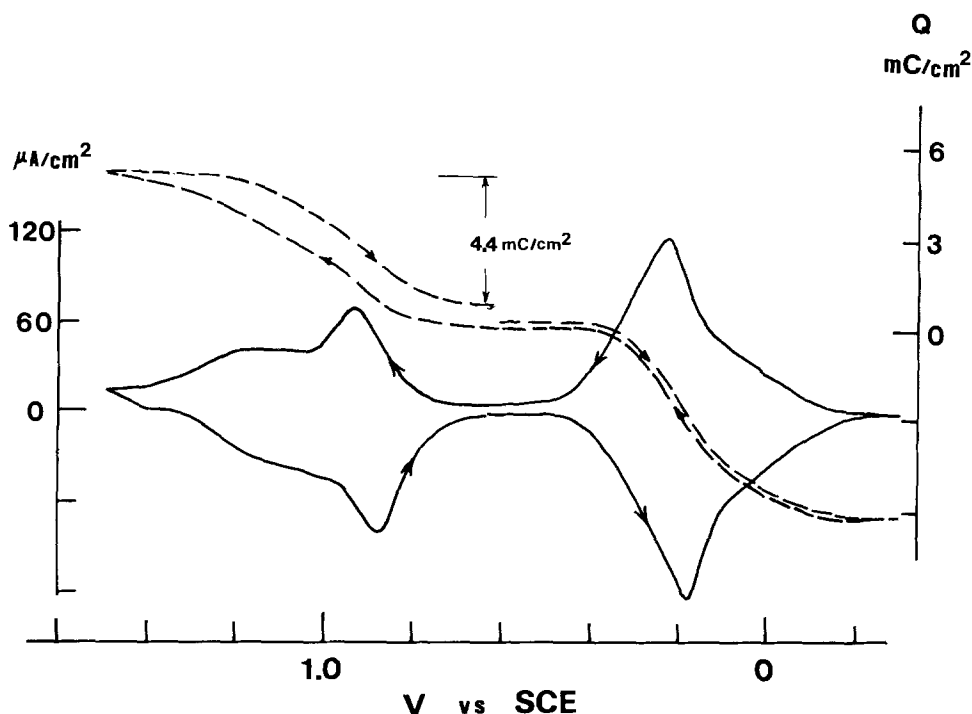


Fig. 1. Cyclic voltammograms of a PB-modified SnO_2 electrode with 6.2 mC/cm^2 as a total charge consumed at the reduction of PB. The film of PB was prepared at a current density of 10 $\mu\text{A}/\text{cm}^2$. The scan rate was 5 mV/s. The solution was 0.5M K_2SO_4 (pH = 4.0). The dashed lines show the integrated current-potential curves for the reduction and oxidation waves of PB.

voltammogram. On the scan from 0.6 to -0.2V , the integrated current of 6.2 mC/cm^2 was obtained. The coulometric curve came back to almost zero, indicating that no side reaction was involved in the waves at 0.2V . In the coulometric curve obtained on the scan from 0.6 to 1.5V and on the reverse scan, a small asymmetric behavior is observed, as shown in Fig. 1. On the scan from 0.6 to 1.4V in 1.0M KCl , a fairly large background prevented a precise determination of the charge consumed at the oxidation wave of PB [see Fig. 4 in Ref. (5)]. Such a large background seems to be due to the oxidation of chloride ions. However, the background level was very decreased in $0.5\text{M K}_2\text{SO}_4$. The asymmetric nature in the coulometric

curve, though, shown in Fig. 1, is obviously due to the small contribution of the background anodic current observed at potentials more positive than 1.3V even in $0.5\text{M K}_2\text{SO}_4$. Taking into account this background current, it can be fairly accurately estimated that the total charge required for the full oxidation of PB is 4.4 mC/cm^2 . The ratio of the charges obtained above is 0.71. This value shows directly that the averaged formula of PB in the film is "water insoluble PB," $\text{Fe}_4^{3+}[\text{Fe}^{\text{II}}(\text{CN})_6]_3$. Exactly the same conclusion has been drawn in our previous paper (5) from a similar coulometric measurement in 1.0M KCl , although the anodic background current was much larger than that in $0.5\text{M K}_2\text{SO}_4$.

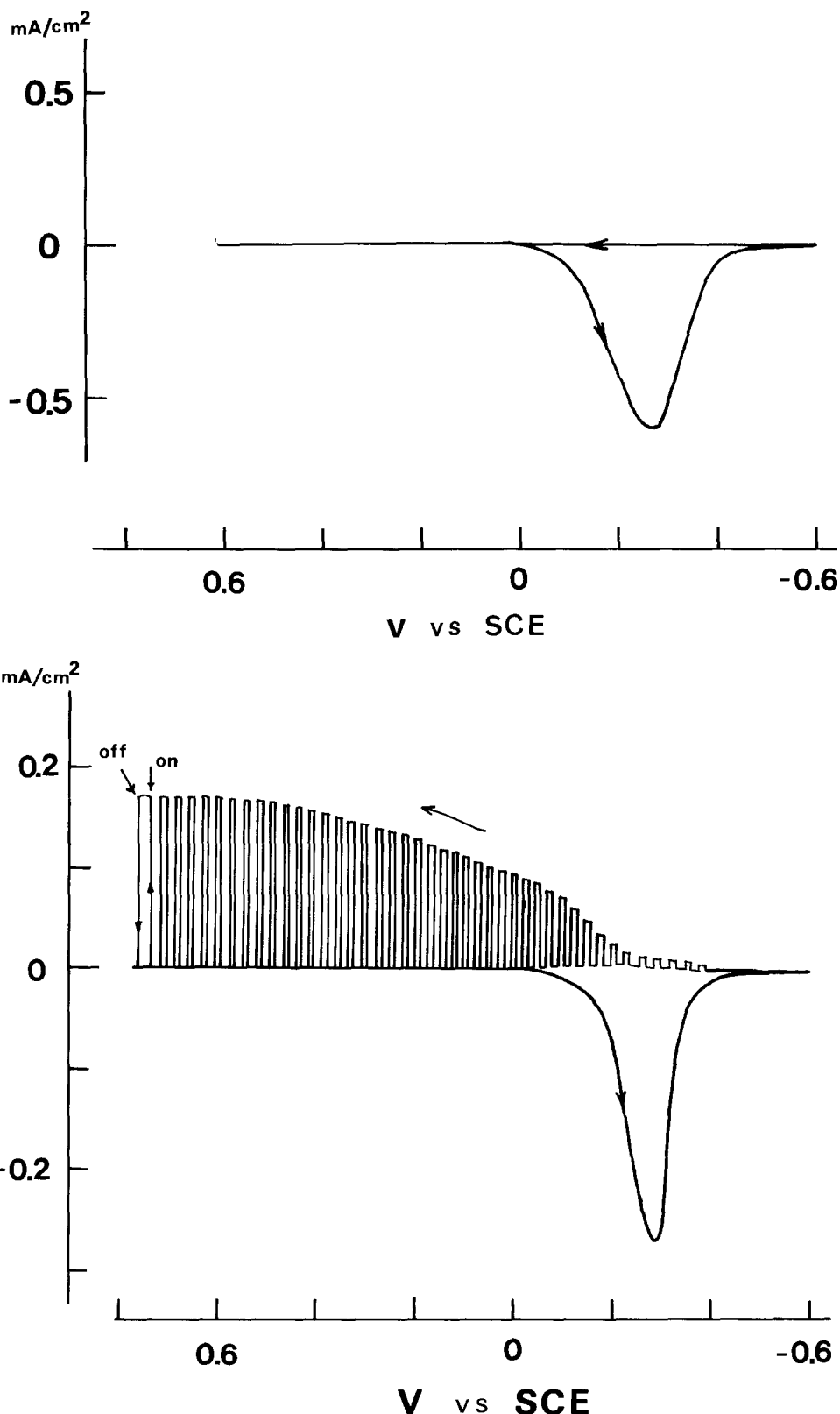


Fig. 2. a(top): A cyclic voltammogram of a PB-modified TiO_2 electrode with 5 mC/cm^2 as a total charge consumed at the reduction of PB in the dark. The scan rate was 20 mV/s . The first scan was started from 0.6V vs. SCE to -0.6V , and the potential was reversed. b(bottom): Cyclic voltammograms of a PB-modified TiO_2 electrode. The electrode potential was scanned from -0.6 to 0.8V under pulsed illumination and then scanned from 0.8 to -0.6V in the dark. The scan rate was 20 mV/s .

Photoelectrochemical studies on n-TiO₂.—Well cleaned TiO₂ electrodes did not acquire PB deposit by the chemical method (9) proposed by Neff *et al.* However it was found that the electrochemical method would acquire quantitatively desired amounts of PB on n-TiO₂ electrodes, just as on SnO₂ electrodes. Figure 2a shows a voltammogram for PB on a n-TiO₂ electrode obtained in the dark on a scan from 0.6 to -0.6V. The blue color of the surfaces of the n-TiO₂ electrode was completely bleached by this reduction current. Therefore, the current observed at -0.25V is obviously due to the electrochemical reduction of PB leading to PW on the TiO₂ electrode. On the reverse scan, no current was observed in the dark at the potential examined here. On the second scan, again, no cathodic current was observed. These results indicate that only the reduction of PB occurred but that the corresponding oxidation was not possible on n-TiO₂ electrodes in the dark. When the electrode potential was kept at 0.6V for 30 min in the dark, the color of the surface of the n-TiO₂ electrode remained essentially unchanged, *i.e.*, transparent. This shows directly that the corresponding oxidation is not possible at n-TiO₂ electrodes in the dark. Note that no dark anodic current was observed, even when the electrode potential was scanned to 1.5V. This indicates that the oxidation of PB is also impossible on n-TiO₂ electrodes in the dark. These irreversible electron transfer reactions at semiconductor solution interfaces have been well characterized by many investigators (12-14).

Figure 2b shows a voltammogram obtained under illumination with chopped white light and in the dark, respectively, when the electrode potential was scanned from -0.6 to 0.8V and from 0.8 to -0.6V. The photocurrent due to the oxidation of PW commenced at about -0.4V *vs.* SCE, which was very close to the flatband potential (V_{FB}). The photocurrent increased with increasing electrode potential and reached a plateau at a potential less negative than 0.6V. Under the experimental conditions above, the color of the surface turned out to be blue. Such a color change could be seen with good contrast because the moderately doped n-TiO₂ was almost transparent. On the scan from 0.8 to -0.6V in the dark, the cathodic current peak appears at -0.28V. This dark current is obviously due to the reduction of PB which was formed under illumination, as described above.

Figure 3 shows the dependence of the dark cathodic current appeared at about -0.3V on the degree of photo-oxidation. The photo-oxidation of PW was carried out at 0.6V *vs.* SCE for different periods of time, and then the electrode potential was scanned to -0.6V in the dark. As shown in Fig. 3, the peak currents increased with increase in the duration of the photo-oxidation. Integrations of the photocurrent and the dark current were simultaneously measured in this experiment. The direct relationship of the integrated currents for the photoanodic oxidation and for the reduction in the dark emerges, as shown in Fig. 4. A perfectly straight line with a slope of about 0.8 was found. This slope suggests that the efficiency of the photo-oxidation of PW to PB is 80% on n-TiO₂ electrode. The remaining 20% of the photocurrent seems to be consumed in the oxidation of water. The identical efficiency is obtained at any potentials more positive than 0.0 V *vs.* SCE. This result indicates straightforwardly that the photo-oxidation of PW to PB is basically potential-independent as long as the electrode potential is fairly more positive than the flatband potential.

Figure 5 shows voltammetric curves for further oxidized forms of PB. The electrode was illuminated at 0.6V by white light just as in Fig. 3. The blue color of the film was changed to green. At the end of the photo-oxidation (the curve labeled c in Fig. 5), the color was brown, not green, indicating that the oxidation of PB was completed. It has been found in our previous paper (5) that the fully oxidized form of PB can be prepared electrochemically as a definite compound and is visually brown. As shown in Fig. 5, the voltammogram obtained in the dark showed two reduction peaks at -0.16 and -0.35V *vs.* SCE.

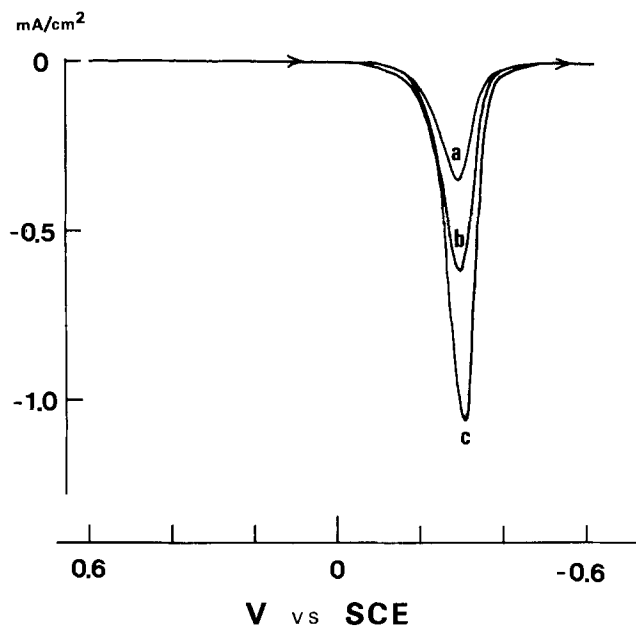


Fig. 3. Voltammograms of a PB-modified TiO₂ electrode. The electrode was illuminated at 0.6V, and, after the photo-oxidations, the dark cathodic scan was recorded. The charges consumed for the photo-oxidation of PW at 0.6V (Q_a) are 2, 3.7, and 5.2 mC/cm² for the curves labeled a, b, and c, respectively. The electrode potential was scanned at 20 mV/s.

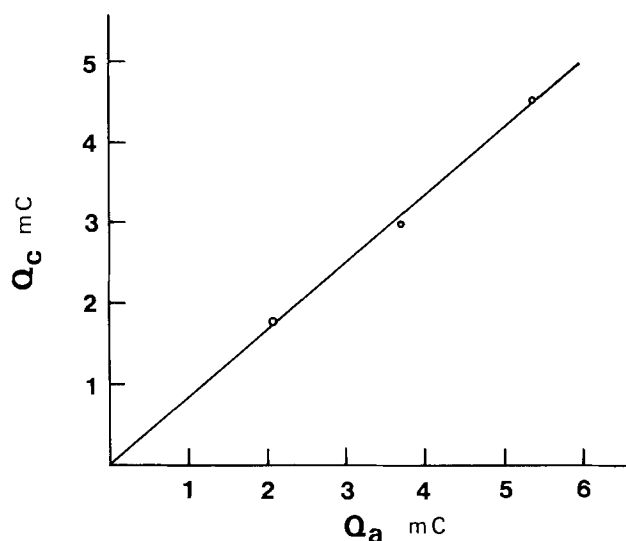


Fig. 4. Relationship of the integrated currents for the photo-oxidation (Q_a) and for the reduction in the dark (Q_c) shown in Fig. 3.

The first reduction peak seems to be due to the reduction of the low spin iron ions, Fe^{III}, in the crystal. The blue color appeared at this reduction peak. The second peak is for the reduction of PB to PW, as discussed above. The efficiency of the photo-oxidation of PB to Prussian brown is somewhat less than the value of 80% which was obtained for the photo-oxidation of PW to PB, as discussed above. From the relationship of the integrated currents for the photoanodic oxidation of PB and for the reduction (the first wave in Fig. 5), a value of about 50% was obtained. In this case, the oxidation of water seems to compete with the oxidation of PB because the potential for water oxidation (13) is now near the energy level of the low spin iron ions in the film. After all PB is photo-oxidized to Prussian brown, the oxidation of water can be a major reaction at n-TiO₂ electrodes.

The reductions of Prussian brown and of PB start at a potential near the flatband potential ($V_{FB} = -0.4V$ *vs.* SCE). However, the reduction of Prussian brown starts at a potential more positive than V_{FB} by about 0.4V. This result seems to diminish an electron transfer mechanism via tunneling from the conduction band to Prussian

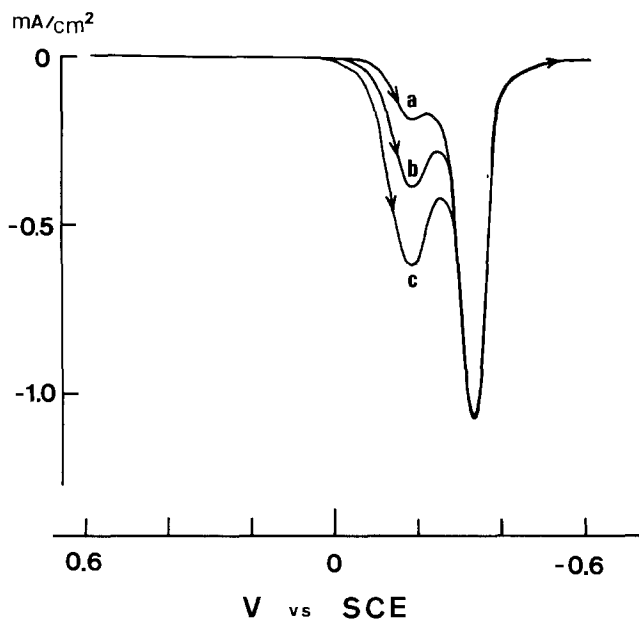


Fig. 5. Voltammograms of a PB-modified TiO_2 electrode. The charges consumed for the photo-oxidation of PW at 0.6V (Q_a) are 6.5, 10, and 15 mC/cm^2 for the curves labeled a, b, and c, respectively. Other conditions are as in Fig. 3.

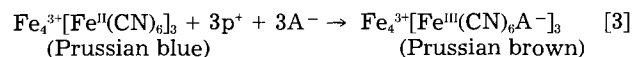
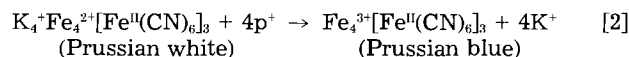
brown. The reduction of electroactive species with redox potentials well positive of V_{FB} at TiO_2 electrodes has been examined in aqueous solutions (12, 13). The reduction peaks of the redox couples of $\text{IrCl}_6^{2-/-3-}$ and $\text{Fe}(\text{CN})_6^{3-/-4-}$ have been observed at -0.24V vs. SCE and 0.02V at an n- TiO_2 electrode in $0.5\text{M H}_2\text{SO}_4$ (12). However, in acetonitrile, couples with redox potentials more than 1.5V positive of V_{FB} were all reduced at potentials about 1V below the conduction bandedge (14). This has been explained by the location of intermediate levels in the bandgap of the n- TiO_2 electrode (12). In the case of the PB-modified TiO_2 electrodes, the behavior is similar to the situation of n- TiO_2 electrodes in aqueous solutions as reported by Noufi *et al.* (12). The dark reductions observed here can be explained by the large reorganization energy of the low spin iron ions, Fe^{III} , in the crystal or by the location of surface states closer to the conduction band due

to interaction of the redox centers in the crystal with the n- TiO_2 surface.

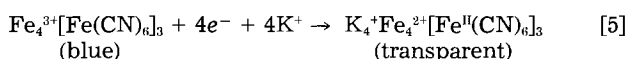
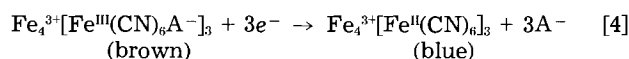
Figure 6 shows voltammetric and coulometric curves for the fully photo-oxidized form of PB. The coulometric curve shown in Fig. 6 indicates that the charges consumed are 3.5 and 5 mC/cm^2 for the reduction of Prussian brown and PB, respectively. The ratio of the charges obtained above is 0.7. The expected ratio is 0.75 if the formula of PB is the "water insoluble one," i.e., $\text{Fe}_4^{3+}[\text{Fe}^{\text{II}}(\text{CN})_6]_3$. The correspondence obtained above is a new direct proof that PB films prepared by the electrochemical method have the formula of $\text{Fe}_4^{3+}[\text{Fe}^{\text{II}}(\text{CN})_6]_3$.

The mechanisms of the photo-oxidations and reductions in the dark can be formulated as follows

Photo-oxidation



Dark reduction



where p^+ and A^- are a hole in the valence band and an anion of the supporting electrolyte, respectively. Note that the reactions of the low spin iron ions are tentatively formulated here as Eq. [3] and [4] based on the formula of $\text{Fe}_4^{3+}[\text{Fe}^{\text{II}}(\text{CN})_6]_3$. No direct proof that the anions are involved in these reactions has been obtained. The details have been under investigation.

The energy level is represented in Fig. 7. As shown in Fig. 7, the edge of the valence band is located at the potential ($\approx 2.8\text{V vs. SCE}$), fairly below the redox potentials of the iron ions in the film. Since the photogenerated hole can have an oxidizing power equal to E_v , the direct photo-oxidation of both the low and high spin iron ions would be possible

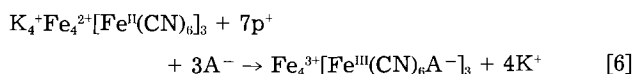
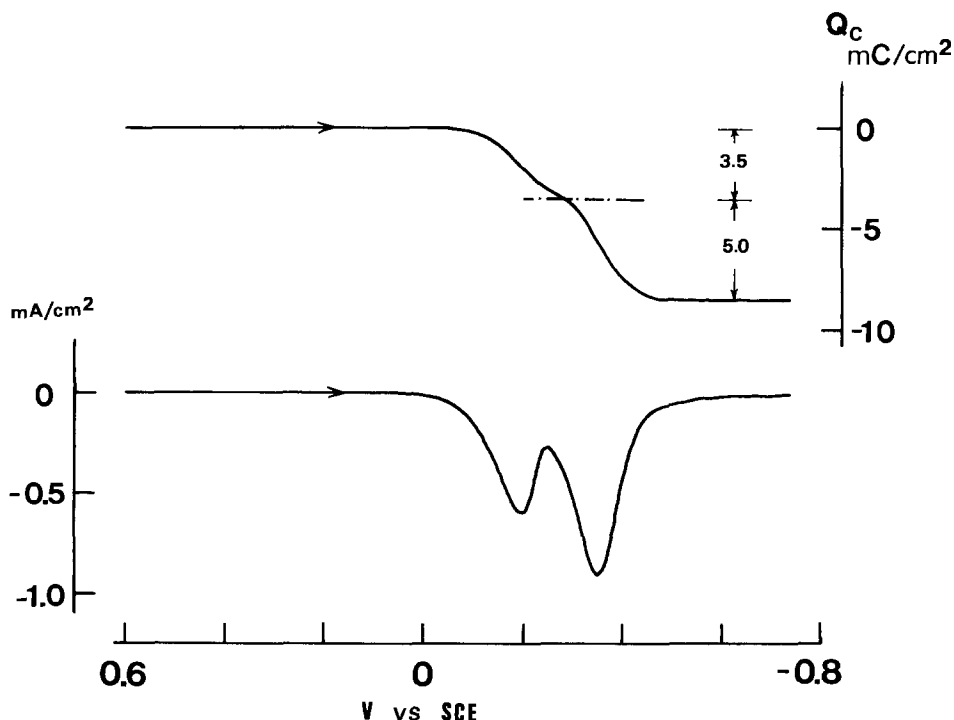


Fig. 6. Cyclic and coulometric curves of a "fully oxidized form of PB" modified TiO_2 electrode. The photo-oxidation of PW was carried out at 0.6V till the charge of about 12 mC/cm^2 was consumed. The scan rate was 20 mV/s .



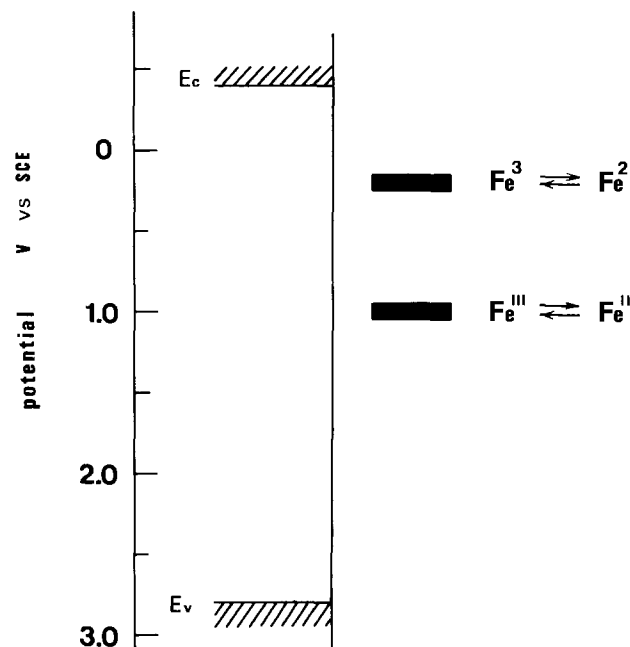


Fig. 7. Relative energy positions of n-TiO₂ and the redox couples in the PB film. Fe³⁺ ⇌ Fe²⁺ and Fe^{III} ⇌ Fe^{II} represent the reactions of high spin iron ions and low spin iron ions in the film, respectively. E_c and E_v are bottom of the conduction band and top of the valence band, respectively.

However, the rapid oxidation of PW by Prussian brown could be expected by the theory of Marcus (28) because the difference of the redox potentials of two kinds of iron ions in the film is quite large (≈ 0.6 V). This seems to be the reason that only PB was produced by the photo-oxidation of PW until all PW is converted to PB (see Fig. 2 and 3).

The stability of the films on the n-TiO₂ electrode was excellent. Only 5% decrease was observed after 1×10^5 repeated cycles of an experiment similar to that shown in Fig. 3. Such high stability is extremely important for possible application as an erasable optical signal recording system. Photoactivated displays based on metal deposition (15, 16) and precipitation of viologens (17, 18) on semiconductor electrode have been reported. A recent report by Reichman *et al.* has shown the principles of a display based on precipitation of heptylviologen at a point on a p-GaAs electrode (18). However, because the contrast ratio for viologens on GaAs is not good (18), the use of a wide bandgap semiconductor is desirable to obtain a high contrast ratio. In addition, most of the viologen radical salts have shown an "aging effect" with consequently poor erasure behavior in electrochromic displays (19, 20). Therefore, the system represented here can be useful for these applications (1).

There have been several investigations on the electrical properties of a series of compounds of the type Fe₄[M(CN)₆]₃ (M = Fe^{II}, Ru^{II}, and Os^{II}) (21, 22). If PB acts as a semiconductor, energy situation and reaction kinetics would be controlled by charge carrier densities in the conduction and/or valence bands, and by the position of the Fermi level. However, no photocurrent was observed under illumination of He-Ne laser at PB-modified Pt and GC electrodes in solutions containing various redox couples (23). This indicates that the electron transfer reaction is essentially governed by a hopping mechanism between the redox centers in the PB film. It should be noteworthy

that an observed photoaction spectrum directly demonstrated that the bandgap transition of TiO₂, not of PB, was uniquely responsible for the production of a photocurrent. No semiconductor behavior of PB has been obtained.

Finally, it is noteworthy that Wrighton *et al.* have shown that the surfaces of n-type semiconductors such as Ge, Si, and GaAs can be modified with polyferrocenes, demonstrating that modified photoelectrodes are more durable than bare electrodes with respect to deleterious photoanodic passivation (24-27). The uses of the PB films for this purpose would be of special interest.

Manuscript submitted Feb. 1, 1983; revised manuscript received ca. May 24, 1983.

Tohoku University assisted in meeting the publication costs of this article.

REFERENCES

1. D. W. DeBerry and A. Viehbeck, *This Journal*, **130**, 249 (1983).
2. K. Itaya, K. Shibayama, H. Akahoshi, and S. Toshima, *J. Appl. Phys.*, **53**, 804 (1982).
3. K. Itaya, H. Akahoshi, and S. Toshima, *This Journal*, **129**, 1498 (1982).
4. K. Itaya, T. Ataka, and S. Toshima, *J. Am. Chem. Soc.*, **104**, 3751 (1982).
5. K. Itaya, T. Ataka, and S. Toshima, *ibid.*, **104**, 4767 (1982).
6. K. Itaya, T. Ataka, S. Toshima, and T. Shinohara, *J. Phys. Chem.*, **86**, 2415 (1982).
7. K. Itaya, I. Uchida, and S. Toshima, *Denki Kagaku*, **51**, 89 (1983).
8. V. D. Neff, *This Journal*, **125**, 886 (1978).
9. D. Ellis, M. Eckhoff, and V. D. Neff, *J. Phys. Chem.*, **85**, 1225 (1981).
10. K. P. Rajan and V. D. Neff, *ibid.*, **86**, 4361 (1982).
11. R. E. Malpas, K. Itaya, and A. J. Bard, *J. Am. Chem. Soc.*, **103**, 1622 (1981).
12. R. Noufi, P. A. Kohl, S. N. Frank, and A. J. Bard, *This Journal*, **125**, 246 (1978).
13. R. Memming, in "Electroanalytical Chemistry," Vol. 11, A. J. Bard, Editor, pp. 1-84, Marcel Dekker, New York (1979), and references therein.
14. S. N. Frank and A. J. Bard, *J. Am. Chem. Soc.*, **97**, 7427 (1975).
15. T. Inoue, A. Fujishima, and K. Honda, *Chem. Lett.*, **11**, 1197 (1978).
16. T. Inoue, A. Fujishima, and K. Honda, *This Journal*, **127**, 1582 (1980).
17. M. Yamana, *Appl. Phys. Lett.*, **29**, 571 (1976).
18. B. Reichman, Fu-Ren F. Fan, and A. J. Bard, *This Journal*, **127**, 333 (1980).
19. J. Bruinink, C. G. A. Kregting, and J. J. Ponjee, *ibid.*, **124**, 1854 (1977).
20. H. Akahoshi, S. Toshima, and K. Itaya, *J. Phys. Chem.*, **85**, 818 (1981).
21. D. F. Fielding and D. P. Mellor, *ibid.*, **22**, 1155 (1954).
22. H. Inoue and S. Yanagisawa, *J. Inorg. Nucl. Chem.*, **36**, 1409 (1974).
23. K. Itaya, I. Uchida, and S. Toshima, *J. Phys. Chem.*, **87**, 105 (1983).
24. J. M. Bolts, A. B. Bocarsly, M. C. Palazzotto, E. G. Walton, N. S. Lewis, and M. S. Wrighton, *J. Am. Chem. Soc.*, **101**, 1378 (1979).
25. A. B. Bocarsly, E. G. Walton, and M. S. Wrighton, *ibid.*, **102**, 3390 (1980).
26. N. S. Lewis, A. B. Bocarsly, and M. S. Wrighton, *J. Phys. Chem.*, **84**, 2033 (1980).
27. M. S. Wrighton, *Acc. Chem. Res.*, **12**, 303 (1979), and references therein.
28. R. A. Marcus, *Ann. Rev. Phys. Chem.*, **15**, 155 (1964).
29. K. Itaya, N. Shoji, and I. Uchida, *J. Am. Chem. Soc.*, **106**, 3423 (1984).



Poly(Thiophene): A Stable Polymer Cathode Material

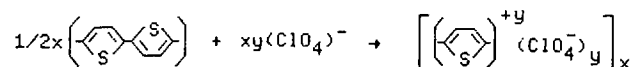
J. H. Kaufman, T.-C. Chung, A. J. Heeger, and F. Wudl

Institute for Polymers and Organic Solids, University of California, Santa Barbara, Santa Barbara, California 93106

The development of electroactive materials made from conducting organic polymers has stimulated interest in their application in lightweight storage batteries (1-8). Primary research employing polyacetylene, $(\text{CH})_x$, has shown promise for this new technology. However, while $(\text{CH})_x$ behaves excellently as an n-doped (anode-active) electrode, instability of the p-doped (cathode-active) material at higher voltages (above 3.5V vs. Li) has been somewhat discouraging. In this communication, we report the use of electrochemically synthesized polythiophene (PT) as an electrode in an electrochemical cell. Without resorting to extraordinary techniques to insure purity, coulombic efficiencies of better than 95% have been obtained at voltages above 3.8V corresponding to doping levels of ~4%-5% per carbon. Such excellent stability at high voltage, coupled with high peak power and energy densities, suggest the use of polythiophene as the cathode material in an electrochemical storage battery, possibly employing polyacetylene as a counterelectrode.

Sample Preparation and Cell Construction

Polythiophene (Fig. 1) was polymerized electrochemically under dry box conditions. Films were grown either on platinum foil substrates or on conducting glass, using an aluminum counterelectrode with 0.1M monomer (either thiophene or dithiophene) dissolved in the starting electrolyte (0.5M LiClO_4 in acetonitrile). A constant current (0.05 mA/cm²) was applied across the cell. The resulting voltage (during electrochemical polymerization) was thereby kept relatively small compared with that used previously (9-12): 3.6V vs. Li using the dithiophene monomer or 4.6V using the thiophene monomer. The reaction at the electrode involves simultaneous polymerization and doping; for example



The substrate surface quickly becomes covered by the conducting polythiophene film; polymerization times used were about 2 min to grow a semitransparent film and about 1h to grow a film suitable for electrochemical measurements (~3 cm² with a mass of 1.8 mg). As grown, the polymer is oxidized with ClO_4^- as counterion at a concentration determined by the voltage applied during polymerization. Thin films prepared on conducting glass reveal the as-grown polymer to be translucent blue. Upon reduction to neutral, the sample changes to ruby red in color. Thicker films appear black in the oxidized state and became red when undoped (reduced) back to neutral polythiophene. A detailed description of the chemistry and the optical properties (carried out *in situ* during doping and undoping) will be reported elsewhere (13).

Battery cells were constructed with Pt films grown from dithiophene (polymerized at 3.6V) on platinum foil. After washing, the polymer electrode and a Li counterelectrode (pressed in Ni mesh and spotwelded to Ni wire) were inserted into rectangular glass tubing. The electrodes were separated by glass filter paper (previously heated under vacuum to remove water). The electrolyte

used in these initial studies was 1M LiClO_4 in propylene carbonate. Prior to use, the propylene carbonate was vacuum distilled, and the LiClO_4 was melted under vacuum in order to remove impurities and residual water. The evacuated rectangular glass was then sealed twice across the electrode leads. Subsequently, the cell was moved into a controlled-atmosphere dry box, where all measurements were made.

Experimental Techniques and Results

Measurements were made using computer-controlled electrochemical voltage spectroscopy (EVS) (14-16). The experiment starts after the electrochemical cell equilibrates at some initial voltage, V_0 . The cell is then displaced from equilibrium by a small potential step dV . Current through the cell is monitored via a shunt resistor. When the current falls below a designated minimum value, the current is integrated over time yielding the charge dQ that flowed in the step dV . The process is repeated until the cell potential reaches some preset extremum, at which point the sign of dV is reversed and the voltage stepped back to V_0 . This process can be repeated for any number of cycles. At each step the charge dQ that flowed in the step $V_0 + dV$ is stored on magnetic disk. The derivative dV/dQ is later integrated, yielding the voltage vs. charge relation for the cell.

The information obtained from EVS is similar to that obtained from cyclic voltammetry. Both the derivative dQ/dV vs. V (from EVS) and i vs. V (from cyclic voltammetry) measure the number of charges transferred as a function of energy. There are, however, some important differences. The minimum current in the EVS method can be made arbitrarily small, so that the system is in diffusion equilibrium. In cyclic voltammetry, electrode reactions are considered to be in equilibrium if the kinetics of charge transfer are rapid compared to mass-transport rates. The method, therefore, probes the surface of the polymer. However, the amount of charge stored on the surface of a polymer is typically orders of magnitude less than that accommodated in the bulk. By sacrificing speed, features corresponding to parts per million of doping can routinely be resolved with EVS.

Figure 2 shows the V vs. Q data for Pt vs. Li. The results are presented as V vs. y , where y is the dopant concentration in mole percent (m/o). For a given concentration of dopant, the charge per unit volume of dopant is $Q(y) = eAy\rho/M$, where e is the electronic charge, A is Avogadro's number, ρ is the polymer density, and M is the molecular weight of thiophene. The data were taken at $I_{\min} = 2 \mu\text{A}/\text{mg}$ with voltage steps $dV = 0.02\text{V}$ over the range 2.5V < $V_{\text{ext}} < 3.8\text{V}$. The corresponding dopant level varied from zero at the neutral point ($\approx 2.5\text{V}$ vs. Li) to a maximum of about 10% per thiophene ring or about 2.5% per carbon. Throughout this range, we obtained coulombic efficiencies greater than 95%. Cycles to cell potentials

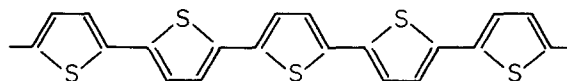


Fig. 1. Chemical structure diagram of poly(thiophene)

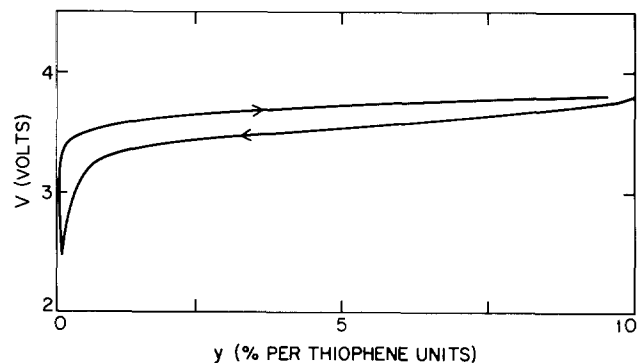


Fig. 2. V vs. y curve (vs. Li) from EVS; the concentration is given in m/(per thiophene).

above 4.0V yielded better than 85% efficiency at doping levels $> 5.0\%$ per carbon. The neutral point was determined by comparing the *in situ* optical absorption spectrum (13) with that of pure chemically synthesized pristine polythiophene (17). At 2.5V (vs. Li), the two were virtually identical, with the onset of interband absorption at $\hbar\omega = E_g \approx 2$ eV, where E_g is the energy gap.

Charge injection (oxidation) occurs above ~ 3.5 V vs. Li. Preliminary attempts at n-doping (reduction) the polymer exhibited a threshold of approximately 1.6V. The potential difference between n- and p-type charge injection (oxidation and reduction thresholds) of ~ 1.9 V is consistent with the bandgap of polythiophene as measured by optical absorption (13). A similar agreement between optical and electrochemical measurements of the energy gap has been obtained with polyacetylene (15, 18).

Hysteresis is observed in the V vs. Q cycle, reminiscent of similar effects reported earlier for polyacetylene (15, 16). An analysis of the $(CH)_x$ data has demonstrated that charge is injected near the bandedge, but stored in gap center states associated with soliton pairs generated by structural relaxation around the injected charges (15, 16, 18). In polythiophene, because the ground state is nondegenerate, the coupling of π electrons to chain distortions leads to the formation of bipolarons (stabilized dications) (13). The charge-discharge relation is explained (13) in terms of charge injection near the bandedge, and charge removal from bipolaron gap states. *In situ* opto-EVS measurements reveal two absorption peaks in the bandgap of polythiophene, consistent with the creation of bipolaron states (13).

The internal resistance of the electrochemical cell was $\sim 100\Omega$. After charging to an open-circuit voltage of 3.8V, corresponding to $\sim 4.5\%$ doping (per carbon), short-circuit currents of about 20 mA/mg were obtained. At the same concentration, the maximum power density was 2.5×10^4 W/kg, based on the weight of doped polymer and the mass of lithium consumed. EVS cycles up to 4.2V ($\sim 6\%$ per carbon) demonstrated an energy density of 140 Wh/kg normalized in the same way. Corresponding values for polyacetylene (vs. Li) cells at 6% (per carbon) doping are ~ 25 mA/mg (short-circuit current), $\sim 3 \times 10^4$ W/kg (maximum power density), and ~ 176 Wh/kg (energy density)

(1). The latter numbers are based on the weight of the doped polymer and the mass of lithium consumed. These numbers are for comparison only; corresponding values for packaged cells would be lower.

Conclusion

The high voltages and excellent stability obtained with polythiophene employed as a cathode (vs. Li) suggest the construction of an all polymer battery consisting of a PT cathode and $(CH)_x$ anode. Such a cell should have an open-circuit voltage of ~ 2.8 V. The all-polymer construction may lead to power and energy densities (packaged) competitive with (or even superior to) conventional lead-acid batteries.

Acknowledgment

This research was supported by a grant from Showa Denko K.K.

Manuscript submitted Nov. 28, 1983; revised manuscript received April 16, 1984.

The University of California assisted in meeting the publication costs of this article.

REFERENCES

1. K. Kaneto, M. Maxfield, D. P. Nairns, A. G. MacDiarmid, and A. J. Heeger, *J. Chem. Soc. Faraday Trans. 1*, **78**, 3417 (1982).
2. P. J. Nigrey, D. McInnes, Jr., D. P. Nairns, A. G. MacDiarmid, and A. J. Heeger, *This Journal*, **128**, 1651 (1981).
3. D. McInnes, Jr., M. A. Druy, P. J. Nigrey, D. P. Nairns, A. G. MacDiarmid, and A. J. Heeger, *J. Chem. Soc. Chem. Commun.*, 317 (1981).
4. P. J. Nigrey, A. G. MacDiarmid, and A. J. Heeger, *ibid.*, 594 (1979).
5. L. W. Shacklette, R. L. Elsenbaumer, R. H. Baughman, *J. Phys. C*, **3**, 559 (1983).
6. M. Armand, *ibid.*, **3**, 551 (1983).
7. P. Bernier, A. El-Khodary, F. Maurice, C. Fabre, P. Mirebeau, and A. M. Ledunois, *ibid.*, **3**, 583 (1983).
8. T. Nagatome, T. Honma, C. Yamamoto, K. Negishi, and D. Omoto, *Jpn. J. Appl. Phys.*, **22**, L275 (1983).
9. K. Kaneto, Y. Kohno, K. Yoshino, and Y. Inuishi, *J. Chem. Soc. Chem. Commun.*, 382 (1983).
10. G. Tourillon and F. Garnier, *J. Electroanal. Chem.*, **135**, 173 (1982).
11. S. Hotta, T. Hosaka, and W. Shimotsuma, *Syn. Metal*, **6**, 69 (1983).
12. R. J. Walthan, J. Bargon, and A. T. Diaz, Submitted to *J. Phys. Chem.*
13. T.-C. Chung, J. H. Kaufman, A. J. Heeger, and F. Wudl, *Phys. Rev. B*, To be published.
14. A. H. Thompson, *Physica (Utrecht)*, **99B**, 100 (1980); *Phys. Rev. Lett.*, **40**, 1511 (1978).
15. J. H. Kaufman, J. W. Kaufer, A. J. Heeger, R. Kaner, and A. G. MacDiarmid, *Phys. Rev. B., Rapid Commun.*, **26**, 2327 (1982).
16. J. H. Kaufman, T.-Chung, and A. J. Heeger, *Solid-State Commun.*, **47**, 585 (1983).
17. M. Kobayashi, J. Chen, T.-C. Chung, F. Moraes, A. J. Heeger, and F. Wudl, *Synth. Met.*, **9**, 77 (1984).
18. A. Feldblum, J. H. Kaufman, S. Etemad, A. J. Heeger, T.-C. Chung, and A. G. MacDiarmid, *Phys. Rev. B*, **26**, 815 (1982).



Effect of Crystallographic Orientation of Single-Crystal RuO₂ Electrodes on the Hydrogen Adsorption Reactions

Tadeusz Hepel* and Fred H. Pollak*

Department of Physics, Brooklyn College of CUNY, Brooklyn, New York 11210

William E. O'Grady*

Department of Energy and Environment, Brookhaven National Laboratory, Upton, New York 11973

ABSTRACT

Linear potential scan and cyclic voltammetric behavior of the single-crystal RuO₂ (110), (001), (111), (101), and (100) surfaces in 0.5 mol/dm⁻³ H₂SO₄ solution have been studied. Significant differences in electrochemical characteristics observed in the hydrogen adsorption/desorption region have been correlated with the differences in composition and structure of the ideal, model surfaces of the RuO₂ single crystals. A cathodic/anodic pair of peaks H_{2C}, H_{2A} observed at about -0.3V (SCE) for the RuO₂ faces (110), (001), (111), and (101) has been ascribed to the reversible hydrogen adsorption/desorption on ruthenium sites. Another pair of peaks H_{1C} and H_{1A} at about $E = 0$ V (SCE), which appeared only on surfaces where oxygen is present, *i.e.*, faces (110) and (001) has been attributed to the hydrogen chemisorption on oxygen sites. The adsorption Temkin coefficients g have been estimated. The correlation between the chemisorption peak currents and the surface density of the ruthenium sites is presented and discussed in detail. An interesting kinetic effect has been observed for the (100) RuO₂ surface. The peak structure for RuO₂ (100) cannot be correlated with the properties of the ideal surface, probably because of the surface restructuring effects. The best electrocatalytical properties have been found for the (101) RuO₂ surface, good ones have been found for the (111) face, and poor for (110) and (001) faces.

Ruthenium dioxide is of considerable interest as a corrosion-resistant material for electrocatalytical evolution of chlorine and became widely used in chlorine industry in the form of mixed RuO₂ + TiO₂ coatings on titanium anodes (1-7). A significant decrease in the anodic oxygen overpotential has also been found for RuO₂ electrodes in comparison with other electrodes applied in today's electrometallurgy (8-10). Catalytic photodecomposition of water on n-TiO₂ has recently been shown to proceed at a higher rate when small amounts of RuO₂ are deposited on a photoanode surface (11). The RuO₂ crystals possess a metallic conductivity due to ruthenium d electrons, and any problems with the ohmic potential drop within the electrode material do not complicate their electrochemical behavior. A few comprehensive review articles concerning electrocatalytic and structural properties of RuO₂-based electrodes have recently been published (1, 2, 12).

Previous investigations have primarily been performed on thermal RuO₂ films (3-15) or small crystal cluster (16) electrodes because of unavailability of single crystals of sufficient size. Preliminary results of work on oxygen evolution on RuO₂ single crystals with several orientations have recently been announced (17). In this paper, we present voltammetric characteristics for single crystal RuO₂ "as-grown" surfaces (110), (001), (111), (101), and (100) in 0.5 mol/dm³ H₂SO₄ solutions. The use of single crystals with various orientations offers a new degree of freedom in studying the relations between the electrocatalytic properties and surface characteristics of the electrode. We describe the general correlations between the peak structure in cyclic voltammetry (CV) characteristics in the hydrogen adsorption region and the composition and structure of these different crystallographic orientations of the material.

*Electrochemical Society Active Member.

Experimental

The RuO₂ samples were synthesized from ruthenium powder (Strem Chemicals, Incorporated), and oxygen by the method (18) of chemical vapor transport in a flowing gas system, a technique similar to that used by Reames (19) and Shafer *et al.* (20). Under high temperature conditions and in the presence of oxygen, volatile RuO₃ is formed from Ru or RuO₂ polycrystallites. The RuO₃ is transported by a gas stream to the cooler zone of a horizontal pipe furnace, where it decomposes and crystallizes in a ceramic boat in form of RuO₂ single crystals. Optimum conditions for this process were determined in previous work (18) to be: reaction temperature 1350°C, decomposition and crystallization temperature 1150°C, and the oxygen flow rate 60 cm/min at atmospheric partial pressure. The crystals obtained were of a few millimeters in size. The "as-grown" faces of single crystals were then oriented by the Laue backscattering x-ray diffraction method.

Crystals were mounted on a small copper plate by means of a conducting silver epoxy resin and insulated using epidian-5. The whole assembly was sealed to a glass tube holder. Electrodes with the following exposed faces were used for measurements: (001), (100), (101), (110), and (111). Geometrical surface areas of these electrodes were in the range from 0.005 to 0.04 cm².

No additional polishing of naturally grown surfaces was employed. Before each experiment, electrodes were rinsed with deionized water and kept in the solution, to be examined for 30 min. Electrodes were stored in dry state. This procedure seems to give the most ideal surfaces, at least in the case of RuO₂, for which good etchants are not known because of its extreme resistivity to corrosion. However, final preparation procedure as recommended for Pt single-crystal electrodes (21) has to leave

significant roughness on the surface and to expose other crystallographic faces.

Standard electrochemical two-compartment Teflon cells were used for measurement. All potentials were measured with respect to the saturated (KCl) calomel electrode, SCE. Pt foil was used as the counterelectrode.

An EG&G Model 173 Potentiostat and Model 175 Universal Programmer were employed for linear scan voltammetry (LSV) and CV experiments. In order to ensure a proper potential program, in some measurements two programmers were used allowing for automatic triggering of the desired voltage sequences.

Measurements were performed in 0.5 mol/dm³ H₂SO₄ solution prepared from the analytical-grade reagent and deionized water.

Results

Cyclic voltammograms for five "as-grown" crystals having (110), (001), (101), (111), and (100) surfaces indicate some systematic development of the peak structure, and because of this they are presented below in a preselected order. At first are shown CV and other characteristics for (110) and (001) faces which show more developed voltammograms. The current-voltage characteristics for the (100) surface are discussed at the end because this surface shows more complicated behavior than the remaining faces.

RuO₂ (110) surface.—Shown in Fig. 1 are the cyclic voltammograms for the (110) "as-grown" surface of single-crystal RuO₂ in 0.5 mol/dm³ H₂SO₄ solution. Two distinct peaks are observed in cathodic scan of CV curves. We attribute these peaks to the hydrogen adsorption reactions and label them H_{1c} and H_{2c}, respectively, in Fig. 1. Both reactions are quite reversible, and two anodic peaks corresponding to hydrogen desorption, labeled H_{2a} and H_{1a}, appear at nearly the same peak potentials as H_{2c} and H_{1c}, respectively. We note that the currents *i*_{p,a} and *i*_{p,c} for the peaks H₁ are about a factor of 2-3 smaller than those for the second pair of the reduction/oxidation peaks H₂. The dependence of the peak current upon the potential scan rate, *v*, for all four peaks observed in the hydrogen adsorption/desorption reaction region is linear indicating surface-controlled reactions. In Fig. 1 are shown CV curves for only three values of *v* for purposes of clarity. Similarly, as discussed earlier (22), for the case of voltammograms not involving hydrogen adsorption region, established CV characteristics do not differ significantly from LSV curves and well-reproducible voltammograms can be obtained after a few cycles.

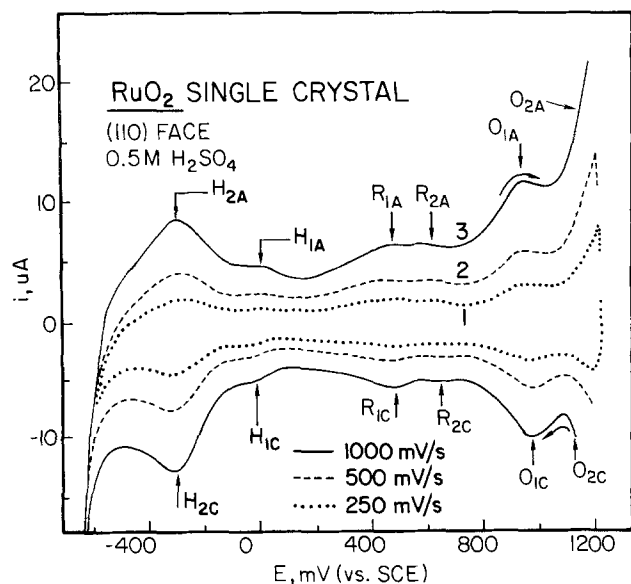


Fig. 1. CV characteristics for the surface (110) of the RuO₂ single-crystal electrode in 0.5 mol/dm⁻³ H₂SO₄ solution. Scan rates: (1) 250, (2) 500, (3) 1000 mV s⁻¹.

The next two pairs of anodic/cathodic peaks appearing in the oxide rearrangement region (200–750 mV vs. SCE) on CV curves are labeled R_{1A}, R_{2A}, R_{1C}, and R_{2C} in Fig. 1. Their interpretation has been briefly discussed in previous paper (22).

The third region of electrode potentials is mainly determined by the oxygen adsorption reactions. First, reversible process occurs at the potential 950 mV (SCE) and the respective anodic and cathodic peaks are designated O_{1A} and O_{1C} in Fig. 1. The second surface process can be deduced from the voltammograms presented in Fig. 1 as proceeding at the potential approximately 1150 mV. The symbols O_{2A} and O_{2C} are used for the anodic and cathodic reactions, respectively.

In order to prove that five pairs of peaks H₁, H₂, R₁, R₂, O₁, and also O₂ correspond to the same but reverse electrode reactions, the potentiodynamic characteristics with sequentially increasing or decreasing E_i were analyzed (a typical example of this analysis is illustrated in Fig. 5 for the oxide rearrangement region). Detailed examination of these kinds of characteristics for the entire potential range provides a proof for above designation of peaks.

RuO₂ (001) surface.—A typical cyclic voltammogram for the (001) face is presented in Fig. 2. As in the case of the surface (110), two pairs of the anodic/cathodic peaks are observed on CV curves in the potential region of the hydrogen adsorption reactions. They are situated at the same peak potentials, about 0 and -300 mV (SCE), respectively. Because of this and also following results of structural considerations presented in interpretation section, we used the same designation of these four peaks as for the (110) face. Unlike in case of the latter surface, peak currents *i*_{p,c} and *i*_{p,a} for the reaction H₁ at (001) surface are comparable with those for the reaction H₂. It is seen from Fig. 2 that peaks H₂ are much broader than peaks H₁, suggesting existence of some repulsive surface interactions. A pronounced hydrogen evolution commences at about -620 mV (SCE). The oxide rearrangement reactions R_A and R_C proceed at the RuO₂ (001) face with the formation of only one pair of the reduction/oxidation peaks at ~500 mV (SCE). The oxygen adsorption region is again similar to that observed at (110) surface. However, peak potential for the reaction O₁ is now more positive by 50 mV. The same shift in potential should probably be ascribed to the reaction O₂.

RuO₂ (111) surface.—The surface (111) of the RuO₂ single crystals shows only one-peak behavior in the hydrogen adsorption region. This situation is illustrated in Fig. 3, where CV characteristics obtained in 0.5 mol/dm³

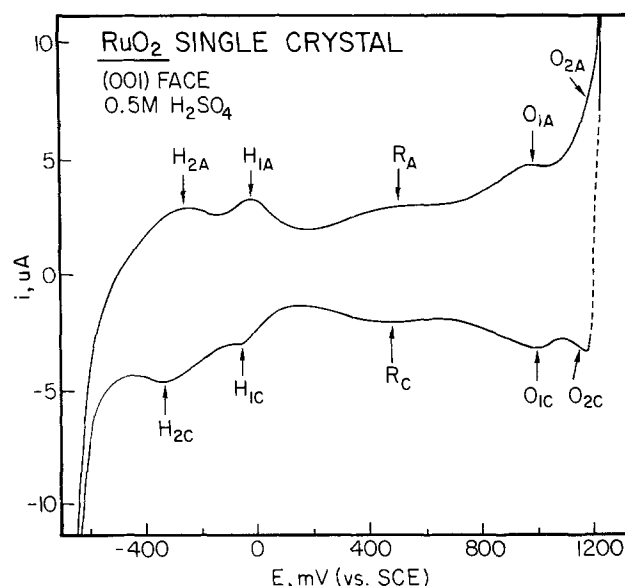


Fig. 2. Cyclic voltammogram for the RuO₂ (001) surface in 0.5 mol/dm⁻³ H₂SO₄ for *v* = 500 mV s⁻¹.

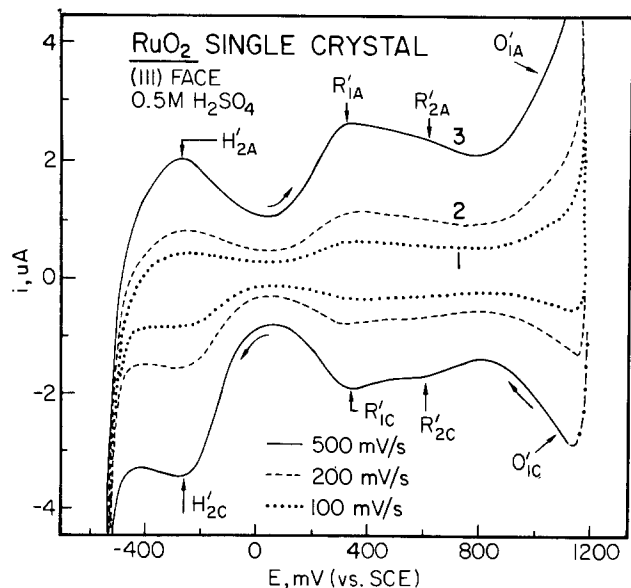


Fig. 3. Dependence of CV curves for the RuO_2 (111) surface in 0.5 mol dm^{-3} H_2SO_4 upon the potential scan rate v [mV s^{-1}]: (1) 100, (2) 200, (3) 500.

H_2SO_4 solutions are presented for three potential sweep speeds marked in the figure. Although the peak potentials $E_{p,c}$ and $E_{p,a}$ appear at -250 mV (SCE), not very different from those for the reaction H_2 at (110) and (001) surfaces, we mark differently the adsorption/desorption reactions at the face (111) for reasons discussed later in this paper. We note also that hydrogen evolution starts at lower overpotential ($E \approx -520$ mV) at the surface (111) than at surfaces described previously.

The (111) surface exhibits two-peak behavior in the oxide rearrangement reaction area, as seen in Fig. 3. Both reactions R'_{1A} (R'_{1C}) and R'_{2A} (R'_{2C}) are highly reversible. Despite the overlap of peaks R'_{1A} (R'_{1C}) and R'_{2A} (R'_{2C}) and the fact that their full appearance is not completely reversible, it can be seen from the CV curves that the peaks R'_{1A} and R'_{1C} , corresponding to the first surface reaction, are sharper and higher than those corresponding to the second reaction, R'_{2A} and R'_{2C} .

In the oxygen evolution region, no peaks are observed. However, from the shape of CV characteristics as well as from the i - V dependence, we can deduce that current is controlled by the surface reaction. We assume that this is the oxygen adsorption/desorption process which is to be denoted O'_{1A} and O'_{1C} , for the anodic and cathodic reactions, respectively.

RuO_2 (101) surface.—A cyclic voltammogram for RuO_2 (101) electrode is presented in Fig. 4 for $v = 500$ mV/s. It shows the lowest degree of development of the peak structure. In each of the three potential regions (hydrogen adsorption, oxide rearrangement, and oxygen adsorption), there is seen only one pair of the reduction/oxidation peaks. They are labeled H'_{2C} and H'_{2A} , R'_A and R'_C , O'_C , respectively, in Fig. 4. The H_2 reaction is superimposed on the following step of hydrogen evolution reaction and forms a prewave before sharp current increase due to hydrogen bubbling. It is to be noted that the latter process commences at a significant rate at a potential about -500 mV. The reversibility of reactions proceeding on (101) surfaces is illustrated in Fig. 5. For all inversion potentials, current steps are observed.

RuO_2 (100) surface.—The behavior of the RuO_2 (100) electrodes is different from that of all other RuO_2 surfaces in that it does not show the same high degree of symmetry as they do. The fast scan CV characteristics are presented in Fig. 6. All curves are sloped and the anodic-cathodic charges do not compensate in any of the three potential regions discussed for other surfaces. The situation in the hydrogen adsorption region is more clearly shown in Fig. 7, where the potential scans are limited to

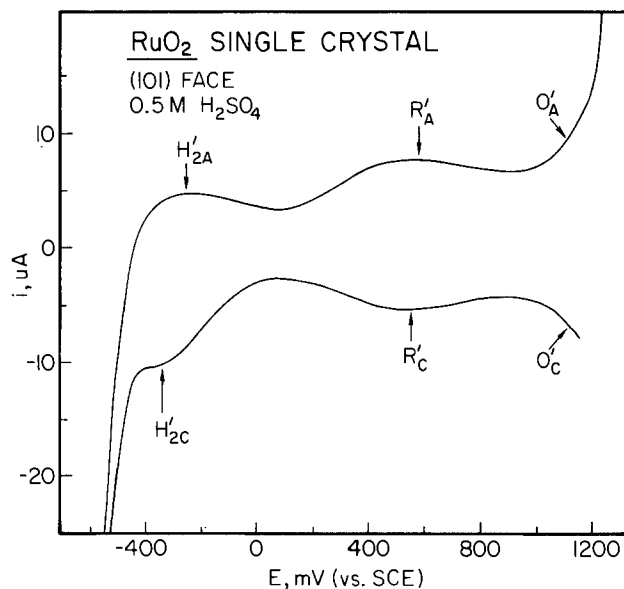


Fig. 4. CV characteristic for the face (101) of the RuO_2 single-crystal electrode in 0.5 mol/ dm^{-3} H_2SO_4 at $v = 500$ mV s^{-1} .

the range -550 to 800 mV (SCE). Two cathodic/anodic peaks at about 0 and -50 mV are initially observed at $v = 100$ mV/s. However, the cathodic peak splits into two peaks as the potential sweep speed is increased up to 1000 mV/s. These two peaks are labeled H'_{1C} and H'_{2C} in Fig. 7. At the same time, the anodic peak designated H'_{1A} remains without significant changes and the peak current follows linear dependence upon v , as also the cathodic peak currents do. The peak potentials for H'_{1A} and H'_{1C} do not change as v increases, while that for H'_{2C} shifts in cathodic direction increasing separation of the cathodic peaks. It is characteristic that asymmetry of CV curves for (100) face remains even at very slow scan rates. The voltammogram obtained at $v = 1$ mV/s is presented in Fig. 8. The cathodic and anodic peak potentials are -97 and -12 mV (SCE), respectively. Exact cathodic wave is seen at potentials lower than about 0 mV. The evolution of hydrogen bubbles at significant rate commences at $E = -700$ mV (SCE), as can be seen from Fig. 6.

The oxide rearrangement proceeds with the formation of one couple of anodic/cathodic peaks. In the oxygen adsorption region, a pair of peaks O'_{1A} and O'_{1C} can be re-

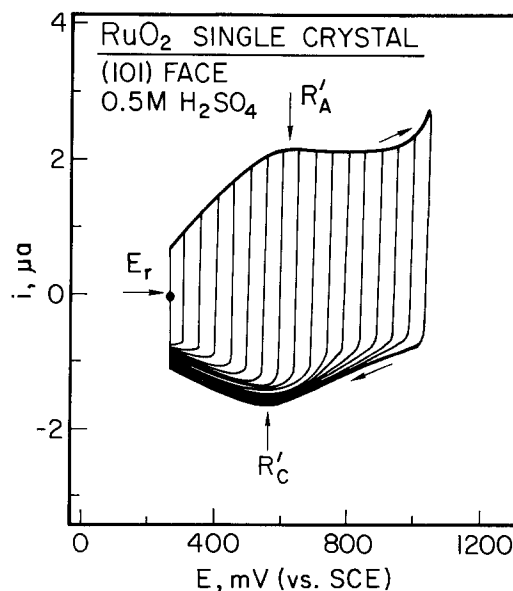


Fig. 5. Dependence of LSV characteristics for the RuO_2 (101) surface in 0.5 mol/ dm^{-3} H_2SO_4 upon the anodic inversion potential. The electrode was kept at E_r for 15 min before each run.

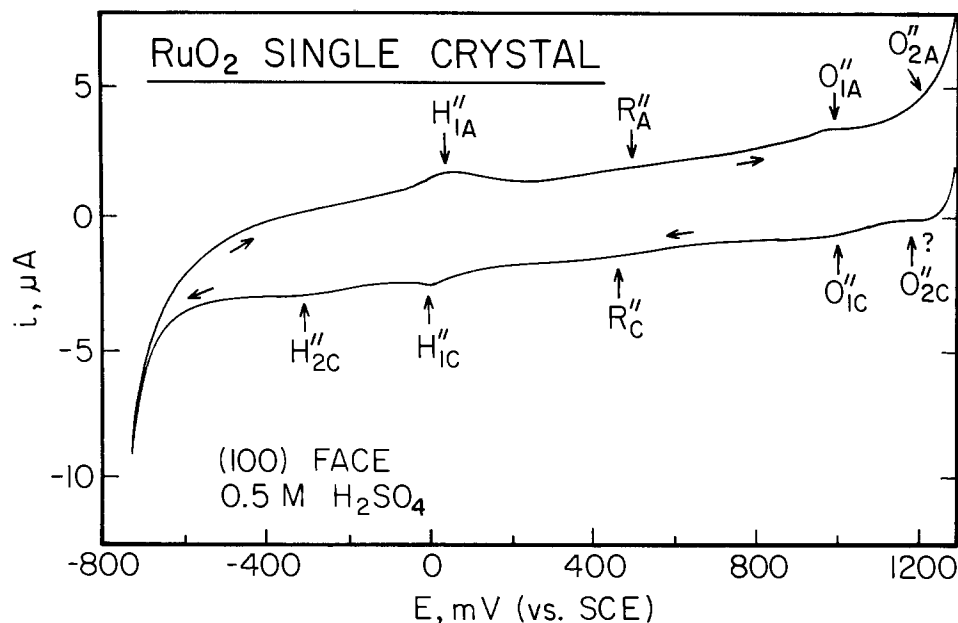


Fig. 6. CV characteristics for (100) face of RuO₂ single-crystal electrode in 0.5 mol/dm⁻³ H₂SO₄ solution for $\nu = 500 \text{ mV s}^{-1}$.

solved at 1000 mV (Fig. 6) and eventually the sloped part of CV curves can be ascribed to the reactions O''_{2A} and O''_{2C}.

Interpretation of Experimental Results

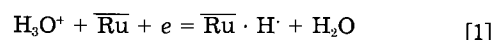
The aim of the present study of the electrochemical behavior of the RuO₂ single crystals is to find a correlation between the obtained voltammograms and the structure and composition of RuO₂ surfaces. The use of single crystals for this purpose gives the additional degree of freedom in looking for such correlations. These investigations were impossible earlier because of the unavailability of the RuO₂ single crystals.

The compositional and structural data for the ruthenium dioxide, crystallizing in the rutile-type structure, are

given in Table I. The sketch of ideal model surfaces (110), (001), (111), (101), and (100) of the RuO₂ single crystals is presented in Fig. 9. There are substantial differences in structure and composition of different crystallographic faces of the RuO₂ single crystals. While crystals with orientations (101), (111), and (100) have only ruthenium atoms present on the surface, both ruthenium and oxygen are present on the (110) and (001) faces. The plane lying below the top plane has only oxygen in the case of (110), (101), (100), and (111) orientations, while both ruthenium and oxygen are found in the (001) case. Also, the ruthenium and oxygen ions on each surface are not identical. The numbers of oxygen ions n_{ox} required by a particular kind of surface ruthenium ion to restore their octahedral coordination are given in Table I.

In further discussion, we use the term "oxygen-free surfaces" for the model, ideal surfaces (101), (111), and (100) and the term "(Ru,O)-composite surfaces" for the ideal crystallographic faces (110) and (001).

On the basis of a general consideration of the properties of the model RuO₂ crystal, we expect a great influence of the oxygen presence at the crystal surface on its electrochemical behavior. In the limiting case, adsorption of hydrogen can proceed on two different kinds of active surface sites, Ru and \bar{O} , and separate voltammetric peaks can appear. Then the following electroreduction reactions ought to be ascribed to the chemisorption of H⁺ on the \bar{Ru} sites



and on the \bar{O} sites

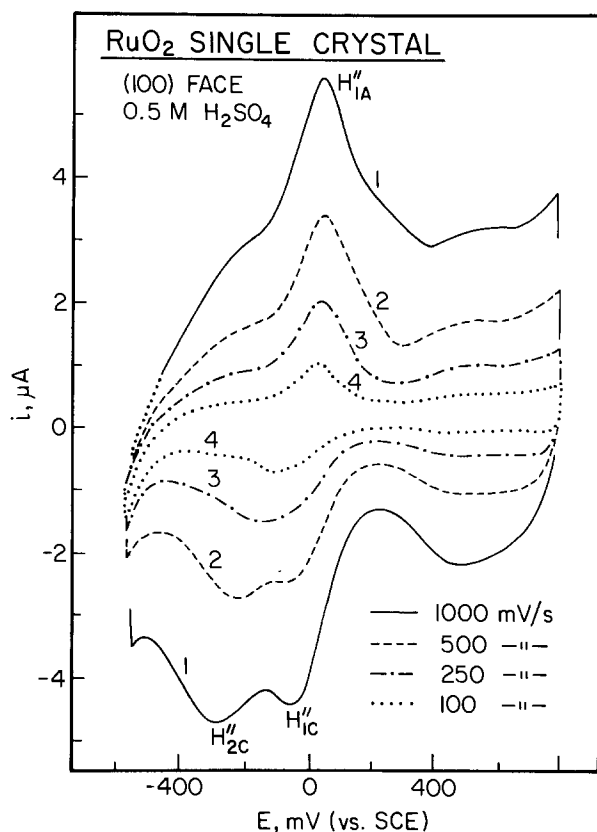


Fig. 7. CV for RuO₂ (100) surface in 0.5 mol/dm⁻³ H₂SO₄ in the hydrogen adsorption region ν [mV s⁻¹]: (1) 100, (2) 250, (3) 500, (4) 1000.

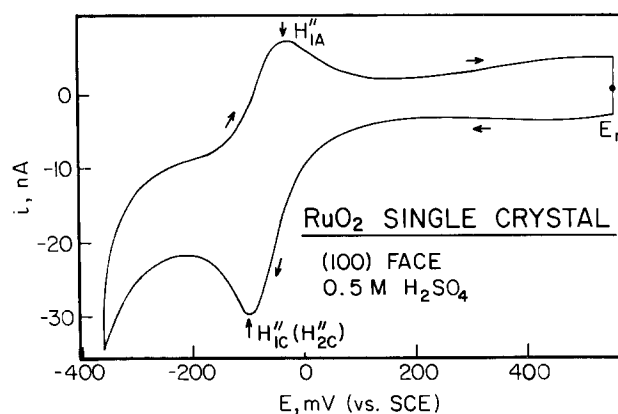


Fig. 8. Slow-scan rate ($\nu = 1 \text{ mV s}^{-1}$) LSV characteristic for the (100) face of the RuO₂ single-crystal electrode in 0.5 mol/dm⁻³ H₂SO₄ solution. First sweep: cathodic, from $E_r = +550 \text{ mV (SCE)}$.

Table I. Relevant structural and electrochemical parameters of the various surfaces of single-crystal RuO₂

Surface	Composition	ν_{Ru} (at./cm ²)	Area projection of unit cell (cm ²)	Ru-Ru distances (Å)	Ru-O distances (Å)	Number of broken Ru-O bonds	PZC* (mV vs. SCE)	$Q_{\text{Ru-H}_2}$ ($\mu\text{C}/\text{cm}^2$)
(110)	2 Ru 2 O	1.0×10^{14}	1.97×10^{-15}	3.11 3.53	1.94 1.98	2(Ru') 1(Ru'')	-90	160
(001)	1 Ru 2 O	5.0×10^{14}	2.02×10^{-15}	4.49	1.94 1.98	2	-20	80
(111)	$\frac{1}{2}$ Ru	3.5×10^{14}	1.41×10^{-15}	5.46 6.35	—	3	-110	56.8
(101)	2 Ru	8.2×10^{14}	2.45×10^{-15}	3.53 4.49	—	3	-160	131.2
(100)	1 Ru	7.1×10^{14}	1.4×10^{-15}	5.46 3.11 4.49	—	3	-50	113.6

* After Ref. (23).



From the comparison of the experimental CV characteristics in the hydrogen adsorption region, we can see that only one pair of reduction/oxidation peaks appears in case of the oxygen-free surfaces [i.e., (101) and (111); about the (100) face, see below]. These peaks are situated at approximately -0.3V (vs. SCE). For the (Ru,O)-composite faces, we observe two pairs of adsorption/desorption peaks, the first at about 0 V (SCE) and the second at -0.3V. Hence, the peak at -0.3V, present on CV characteristics for all four faces (101), (111), (110), and (001), can be ascribed to the chemisorption of H⁺ on the Ru sites according to the reaction Eq. [1]. The peaks at 0 V appear only for the composite faces, so we ascribe them to H⁺ adsorption on the O sites (reaction [2]).

If the above hypothesis is correct, the adsorption energy for hydrogen chemisorbed on the $\bar{\text{O}}$ sites ($E_p \cong 0$) would be much more negative than that for the electroadsorption of H⁺ on Ru sites ($E_p \cong -0.3\text{V}$). The bond strength W for Ru · H⁺ and O · H⁺ can be estimated from the Pauling equation, which for these two cases can be written in the form

$$W(\bar{\text{Ru}} \cdot \text{H}) = \frac{1}{2} W(\bar{\text{Ru}} - \text{Ru}) + W(\text{H} - \text{H}) + 23.06 (\chi_{\text{Ru}} - \chi_{\text{H}})^2 \quad [3]$$

and

$$W(\bar{\text{O}} \cdot \text{H}) = \frac{1}{2} W(\bar{\text{O}} - \text{Ru}) + W(\text{H} - \text{H}) + 23.06 (\chi_{\text{O}} - \chi_{\text{H}})^2 \quad [4]$$

where χ is the electronegativities for isolated atoms. The term $W(\bar{\text{Ru}} - \text{Ru})$ is used in former equation because the adsorbed hydrogen is supposed to replace the Ru atom that would be the nearest neighbor of Ru if the crystal would not be terminated. The same applies to Eq. [4]. The use of the term $W(\bar{\text{O}} - \text{Ru})$ seems to be more adequate to the real system than use of the term $W(\bar{\text{O}} - \text{O})$ because the adsorbed hydrogen will act rather as an individual replacing Ru cations in the coordination shell of the $\bar{\text{O}}$ site. Both Eq. [3] and [4] should now be developed to account for the multiple broken bonds. In an elementary treatment, this leads to the expressions

$$W(\bar{\text{Ru}} \cdot \text{H}) = \frac{1}{n+1} n x W(\bar{\text{Ru}} - \text{Ru}) + W(\text{H} - \text{H}) + 23.06 (\chi_{\text{Ru}} - \chi_{\text{H}})^2 \quad [5]$$

$$W(\bar{\text{O}} \cdot \text{H}) = \frac{1}{m+1} m x W(\bar{\text{O}} - \text{Ru}) + W(\text{H} - \text{H}) + 23.06 (\chi_{\text{O}} - \chi_{\text{H}})^2 \quad [6]$$

where n and m stand for the number of broken bonds Ru-Ru and O-Ru, respectively. Despite the simplified treatment (not clear is especially the role of other broken bonds), Eq. [5] and [6] take into account different situations on different crystallographic planes of a single-crystal electrode. Although a detailed analysis of the bond energies is beyond the scope of this paper, we can state qualitatively that the bond strength $W(\bar{\text{O}} - \text{Ru})$ is certainly greater than $W(\bar{\text{Ru}} - \text{Ru})$. Similarly, the electronegativity differences between oxygen and hydrogen are greater than between ruthenium and hydrogen. Therefore, the binding energy for hydrogen adsorbed on the $\bar{\text{O}}$ site should be much greater than that for the surface dipole $\bar{\text{Ru}} \cdot \text{H}$. On the basis of Eq. [5], we can also expect that the differences in the bond strength $W(\bar{\text{Ru}} \cdot \text{H})$ for different crystallographic planes should influence the voltammetric behavior of the RuO₂ single crystals to much smaller extent than the difference between $W(\bar{\text{Ru}} \cdot \text{H})$ and $W(\bar{\text{O}} \cdot \text{H})$ does. All the above considerations justify our preference in assigning well-separated peaks H₁ and H₂ to the adsorption of hydrogen at "chemically" different kinds of active surface sites.

In support of our assumption that the energy interaction between H⁺ and $\bar{\text{Ru}}$ centers is not very different

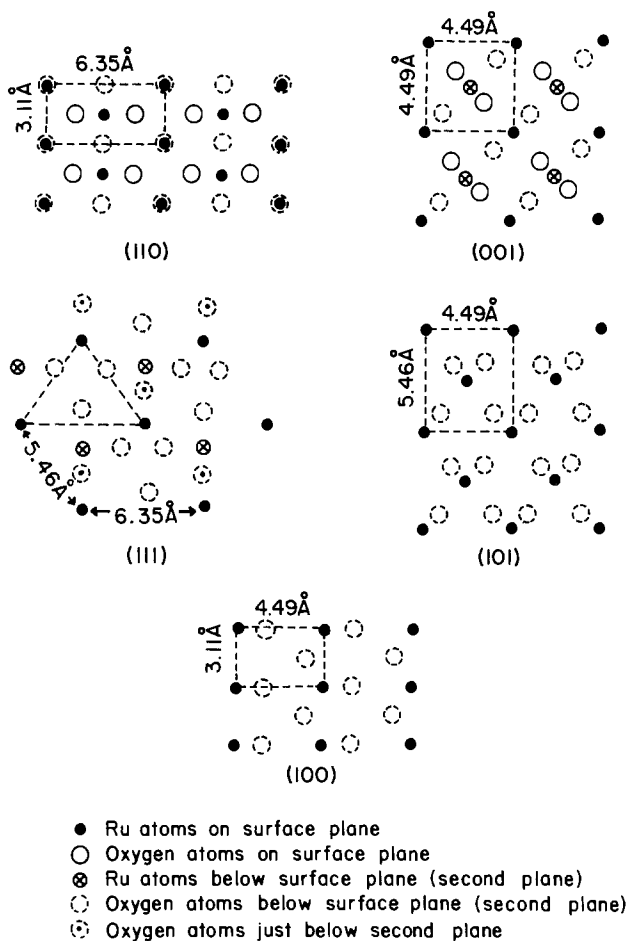


Fig. 9. Scheme of the atomic compositions of the ideal RuO₂ (110), (001), (111), (101), and (100) single-crystal surfaces. Broken lines denote unit cells.

among the four surfaces (110), (001), (101), and (111) causing only secondary effects in the peak structure of RuO₂ electrode in hydrogen adsorption region, come recent measurements of the PZC (23) for the oriented RuO₂ single crystals. It appears that within the experimental error the PZC, Φ , equals $-0.09 \pm 0.1V$ (SCE) for all surfaces (23). Following arguments of Kolb *et al.* (24) and Trasatti (25), who derived an expression for the underpotential deposition of metals, we can write for the hydrogen adsorption on Ru sites

$$\Delta E_{i_j}^{\text{UPD}} - \Delta E_{i_j}^{\text{UPD}} = e(\Phi_i - \Phi_j) \quad [7]$$

where ΔE^{UPD} is the potential shift for UPD and the indexes i, j stand for two different crystallographic faces. As the right-hand side of Eq. [7] approximates to zero, there should not be significant differences in peak potentials for H_{2C} reaction at various surfaces. The same should apply to the peak H_{1C}, and this is what we see experimentally.

Further proof for ascribing reaction [2] to peaks H_{1C} and H_{1A} comes from the consideration of the relative densities of different sites on the RuO₂ faces (110) and (001). On the former face, one oxygen atom falls per one ruthenium atom, while on the latter face, two oxygens are present on the surface per one ruthenium atom. Comparison of the CV curves for the faces (110) and (001) (Fig. 1 and 2) shows clearly relative increase of the peaks H_{1C} and H_{1A} with respect to H_{2C} and H_{2A} when going from (110) to (001). However, there is one apparent inconsistency. The surface densities of oxygen sites are the same on both surfaces (110) and (001) while that of Ru sites are 10×10^{14} and $5 \times 10^{14} \text{ cm}^{-2}$ for (110) and (001) surfaces, respectively. One could expect then that the peaks H_{2A} and H_{2C} ought to be higher for the (110) face than for the (001) face (if lateral interactions are the same, see below). But it is not the case. The peak current densities do not depend linearly upon the surface concentration of the Ru sites. And it applies not only to the above two surfaces. In Fig. 10, we present a correlation between the peak current densities and the surface density of ruthenium sites for all four faces (110), (001), (101), and (111).

The peak currents are not corrected for currents due to other than hydrogen adsorption reactions. It is seen from Fig. 10 that the whole effect of n_{Ru} on the peak currents for the reactions H₂ is removed far to lower values of n_{Ru} , below $3 \times 10^{14} \text{ cm}^{-2}$. Above this value, rather surprisingly, n_{Ru} has almost no influence on $i_{p,2}$. (Slightly higher values

of i_p for the reaction H_{2A} at surfaces (001) and (110) may be due to the shoulders of the peaks H_{1A}). However, the peaks H₁ appear only when the oxygen sites are available on the electrode surface, and there is no correlation between $i_{p,1}$ and n_{Ru} . The shape of the curves for $i_{p,1}$ has then no physical meaning. These curves were drawn to emphasize clearly our model of hydrogen adsorption based on reaction Eq. [1] and [2].

At the present stage of our knowledge, we cannot analyze fully all of the surface interactions associated with the hydrogen adsorption reactions. However, some temporary conclusions can be drawn. Despite the peaks H_{1C} and H_{2C} observed at (110) and (001) surfaces overlap (as also their anodic counterparts do), we can figure out that they differ significantly in the half-peak width $\Delta E_{1/2}$. In case of the Langmuirian adsorption isotherm

$$\frac{\theta}{1-\theta} = C \exp \{-(E - E_f^0)e/kT\} \quad [8]$$

(where θ is the surface coverage, C is the concentration of H₃O⁺ in solution, E_f^0 is the formal standard electrode potential for the reaction of hydrogen discharge, and other symbols have their usual meanings), the half-peak width is $\Delta E_{1/2} = 90.6 \text{ mV}$. This corresponds (26) to the absence of the lateral interactions (or the lack of induced heterogeneity). Both the peaks H₁ and H₂ have greater values of $\Delta E_{1/2}$. On the basis of the Frumkin electroadsorption isotherm

$$\frac{\theta}{1-\theta} = C \exp \{-g\theta\} \exp \{-(E - E_f^0)e/kT\} \quad [9]$$

greater values of $\Delta E_{1/2}$ than 90.6 mV can be attributed to the repulsion surface interactions associated with the coverage dependent heat of chemisorption $g\theta RT$. In order to estimate the interaction coefficient g , the following relation can be used

$$\Delta E_{1/2} = \frac{2RT}{F} \left[ga + \ln \frac{(0.5 + a)}{(0.5 - a)} \right] \quad [10]$$

where

$$a = 0.5 \sqrt{\frac{g+4}{g+8}} \quad [11]$$

It should be noted that $\Delta E_{1/2}$ is independent of the monolayer charge Q_0 , and the scan rate v . For the reactions pro-

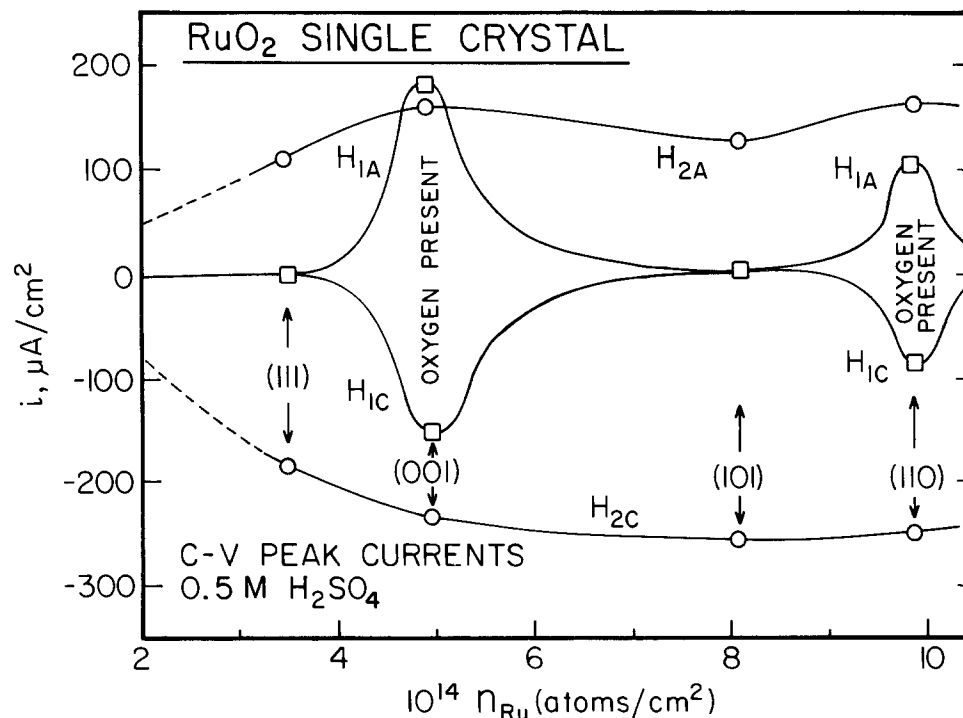


Fig. 10. The correlation between the peak current densities i_p for the processes H_{2C}, H_{2A}, H_{1C}, and H_{1A} and the atomic surface density of the ruthenium sites at different crystallographic faces of the RuO₂ single-crystal electrode. The peaks H_{1C} and H_{1A} appear only when oxygen sites are present on a model, ideal surface. The shape of the curves H_{1C} and H_{1A} is thus arbitrary.

ceedings in the region of peaks H_{2C} and H_{2A} , we have estimated $g = 8.5 \pm 0.5$ for both (110) and (001) surfaces. It corresponds to the maximum (at $\theta = 1$), coverage-dependent heat of chemisorption ΔH_0^{\max} about 5 kcal/mol. The surface interaction coefficient is smaller for the reactions H_{1C} and H_{1A} (at the same surfaces) and is estimated to be $g = 5 \pm 1$, which gives $\Delta H_0^{\max} = 3$ kcal/mol. In conclusion, we can then state that the lateral repulsions between hydrogens adsorbed on oxygen sites are smaller than those between hydrogen atoms adsorbed on ruthenium sites. For the RuO_2 (111) surface which does not contain \bar{O} sites, the value of g is approximately 8, i.e., very close to g for the $\text{Ru} \cdot \text{H}$ surface dipoles at (110) and (001) faces. Probably a little smaller value of g can be ascribed for hydrogens adsorbed on the (101) surface, but here the H chemisorption peaks are not well separated from the gaseous hydrogen evolution wave and the correct value of g cannot be determined.

The voltammetric behavior of the RuO_2 (100) surface cannot be simply correlated with the properties of the ideal model (100) surface of the rutile structure. From the presence of only ruthenium atoms on the model surface (see Fig. 8), one might expect the occurrence of one pair of hydrogen adsorption/desorption peaks at a potential near -0.3V (SCE). However, the peak structure in the voltammograms (Fig. 6-8) for real (100) surfaces show rather complicated electrochemical behavior. It is evident from Fig. 7 that a pronounced kinetic effect is involved. The separation of cathodic peaks H'_{1C} and H'_{2C} with increasing potential scan rates is only possible when there is significant difference between the rate constants of these two processes. The reaction H'_{1C} is thus reversible (approximately no change of the peak potential with v), and the reaction H'_{2C} is irreversible, showing significant shift of E_p with v . The position of the first cathodic peak (H'_{1C}) might be ascribed to the hydrogen chemisorption on the oxygen sites rather than on the ruthenium sites if the adsorption energies would not change very much in comparison to those for the faces (110), (001), (111), and (101). However, the origin of the second peak H'_{2C} is not clear since the peak potential at slow potential scans is close to that for H'_{1C} . Besides, there is no desorption peak H'_{2A} corresponding to H'_{2C} (if it is assumed to be the adsorption process). In this situation, an attempt has been made to consider the possible effect of reconstruction of the model surface (100). In LEED experiments, it has been found that the RuO_2 (100) surface undergoes restructuring. Similar observations have been made for the rutile TiO_2 (100) surface (27). It has also been found that the RuO_2 (110) surface is unreconstructed (28), similar to the TiO_2 (110) surface (29, 30). The complex electrochemical behavior of the RuO_2 (100) surface may then be a natural consequence of the reconstruction effects. On the basis of data (29) obtained for TiO_2 we may also expect that the (001) surface of RuO_2 is unstable and faces to planes with higher coordination of Ru by oxygen. In case of (001) TiO_2 , the facets {011} and {114} have been observed (29). However, further discussion of the correlations between the reconstruction and faceting effects and the voltammetric behavior should await some more experimental data for RuO_2 , especially by LEED and XPS.

Conclusion

We have observed significant differences of the electrochemical behavior in the hydrogen adsorption region for single-crystal surfaces (110), (001), (111), (101), and (100) in 0.5M H_2SO_4 solution. For the former four faces, there is a strong correlation between the cyclic voltammograms and the composition and structure of the ideal, model surfaces of the RuO_2 rutile material. The cathodic/anodic pair of peaks appearing at approximately the same potential -0.3V (vs. SCE) for these planes can be ascribed to the adsorption of hydrogen on ruthenium sites, while the additional pair of peaks at 0V (vs. SCE) observed for the RuO_2 (110) and (001) surfaces can be attributed to the chemi-

sorption of hydrogen on the oxygen sites which are present only on these two model surfaces.

The cyclic voltammograms obtained for the RuO_2 (100) face are not readily correlated to the properties of the ideal (100) surface. We suggest that this may be due to the surface reconstruction effects observed by LEED for this face. The effect of slow electrochemical kinetics leading to the splitting of the cathodic peak at higher potential scan rates has been found. Further investigations are necessary to correlate the electrochemical and physical properties of the reconstructed (100) surface.

Acknowledgment

This work was supported by the U.S. Department of Energy under Contract no. DE-AC02-80ER10654.

Manuscript submitted Sept. 12, 1983; revised manuscript received April 30, 1984.

Brooklyn College of the City University of New York assisted in meeting the publication costs of this article.

REFERENCES

1. S. Trasatti and W. E. O'Grady, in "Advances in Electrochemistry and Electrochemical Engineering," H. Gerischer and C. W. Tobias, Editors, Vol. 12, pp. 177-261, John Wiley & Sons, New York (1981).
2. D. M. Novak, B. V. Tilak, and B. E. Conway, in "Modern Aspects of Electrochemistry," J. O'M. Bockris and B. E. Conway, Editors, Vol. 14, pp. 195-318, Plenum Press, New York (1982).
3. A. T. Kuhn and C. J. Mortimer, *This Journal*, **120**, 231 (1973).
4. B. V. Tilak, *ibid.*, **126**, 1343 (1979).
5. G. Bianchi, *J. Appl. Electrochem.*, **1**, 231 (1971).
6. S. Trasatti and G. Buzzanca, *J. Electroanal. Chem.*, **29**, App. 1 (1979).
7. S. Ardizzone, A. Carugati, G. Lodi, and S. Trasatti, *This Journal*, **129**, 1689 (1982).
8. G. Lodi, E. Sirieri, A. deBattisti, and S. Trasatti, *J. Appl. Electrochem.*, **8**, 135 (1978).
9. C. Iwakura, K. Jirao, and H. Tamura, *Electrochim. Acta*, **22**, 329 (1977).
10. I. E. Veselovskaya, S. D. Khodkevich, R. I. Malkina, and L. M. Yakimenko, *Elektrokhimiya*, **10**, 74 (1974).
11. T. Kawai and T. Sakata, *Chem. Phys. Lett.*, **72**, 1 (1980).
12. S. Trasatti and G. Lodi, in "Electrodes of Conductive Metallic Oxides," S. Trasatti, Editor, Part A, Chap. 7, pp. 301-358, Elsevier, Amsterdam (1980).
13. R. G. Erenburg, L. I. Kirshthalik, and I. P. Yaroshevskaya, *Elektrokhimiya*, **11**, 1068, 1072, 1236 (1975).
14. R. G. Erenburg, L. I. Kirshthalik, and V. I. Bystrov, *ibid.*, **8**, 1740 (1972).
15. L. I. Kirshthalik, *Electrochim. Acta*, **26**, 329 (1981).
16. J. Horkans and M. W. Shafer, *This Journal*, **124**, 1202 (1977).
17. M. W. Shafer, R. A. Figat, R. Johnson, and R. A. Pollak, in "Proceedings of the International Conference on Electrochemistry," p. 83, Trohnheim, Norway (1980).
18. Y. S. Huang, H. L. Park, and F. H. Pollak, *Mater. Res. Bull.*, **17**, 1305 (1982).
19. F. M. Reames, *ibid.*, **11**, 1019 (1976).
20. M. W. Shafer, R. A. Figat, B. Olsen, S. J. LaPlaca, and J. Angilello, *This Journal*, **126**, 1625 (1979).
21. C. L. Scortichini, F. E. Woodward, and C. N. Reilley, *J. Electroanal. Chem.*, **139**, 233, 247, 265 (1982).
22. W. E. O'Grady, A. Goel, F. H. Pollak, H. L. Park, and Y. S. Huang, *ibid.*, To be published.
23. M. Tomkiewicz, Y. S. Huang, and F. H. Pollak, *This Journal*, **130**, 1514 (1983).
24. D. M. Kolb, M. Przasnyski, and H. Gerischer, *J. Electroanal. Chem.*, **54**, 25 (1974); *Surf. Sci.*, **43**, 662 (1974).
25. S. Trasatti, *J. Electroanal. Chem.*, **123**, 121 (1981).
26. B. E. Conway, E. Gileadi, and M. Dzieciuch, *Electrochim. Acta*, **8**, 143 (1963).
27. Y. W. Chung, W. J. Lo, and G. A. Somorjai, *Surf. Sci.*, **64**, 588 (1977).
28. W. E. O'Grady, Lj. Atanasoska, F. H. Pollak, and Y. S. Huang, *J. Electroanal. Chem.*, To be published.
29. L. E. Firmit, *Surf. Sci.*, **116**, 205 (1982).
30. R. H. Tait and R. V. Kasowski, *Phys. Rev. B*, **20**, 5178 (1979).

Thermoelectricity

VII. The Seebeck Quality Factor, Q_s , a Semiconductor Characterization Tool

Donald Tuomi*¹

Borg-Warner Corporation, Roy C. Ingersoll Research Center, Des Plaines, Illinois 60018

ABSTRACT

Through the electron mobility-effective mass product, $\mu_0 (m^*/m_0)^{3/2}$, used as a parameter in single-band theory description of electron transport in a degenerated semiconductor, a new variable Q_s , the Seebeck quality factor is proposed for characterizing the quality of electronic transport within doped semiconductor alloys. This empirically defined variable, based upon acoustic vibrational mode and alloy scattering of electrons, provides a useful route for correlating the electron transport variables of Seebeck coefficient and electrical conductivity to structural-chemical and process variables in bulk materials. The fundamental parameter of $\mu_0(m^*/m_0)^{3/2}$ is reserved to characterize only the highest quality materials.

Publication of A. F. Ioffe's "Energetic Principles of Semiconductor Thermoelectric Batteries," in 1949 (1), followed by "Semiconductor Thermoelements," in 1957 (2), touched off worldwide research programs on semiconductor alloys. The revolutionary goal was replacing conventional steam power generators and Freon refrigerators with solid-state thermoelectric systems (3, 4).

The key to progress was finding n- and p-type semiconductors with high figures of merit, Z , a measure of system efficiency. This is $Z = S^2\sigma/K$, where S is the Seebeck coefficient ($\mu V/K$), σ the electrical conductivity (mho/cm), and K the thermal conductivity (mW/cm K). Attainment of Z between 8 and $10 \times 10^{-3}/K$ promised revolutionary changes, while $4.5 \times 10^{-3}/K$ would create significant new business opportunities.

As work progressed, thousands of alloys were prepared and tested, but none were capable of contributing to the revolutionary changes. In fact, many became disillusioned, and hope for progress vanished. Few strove to build specialty businesses from the better material with figures of merit ranging from 1×10^{-3} to 2.5×10^{-3} , with $3 \times 10^{-3}/K$ being exceptional (5, 6).

The semiconductor materials screening work focused upon discovering high figure of merit alloys (7). Rigorous guiding frameworks for organizing information did not emerge (8). Elementary theories called for optimizing the Seebeck coefficient near 200 $\mu V/K$ while optimizing the σ/K ratio. The Price loop correlation of Seebeck coefficient and electrical conductivity (9) led to assuming that the key to progress resided in the K term of Z . The thermal conductivity consisted of (i) an electronic component, K_e , related to the electrical conductivity through the Wiedeman-Franz law, and (ii) a lattice component of thermal conductivity, K_L , related to structural-chemical details of the alloy. The challenge was thought to be the optimization of Z by reducing the lattice thermal conductivity component (10).

As silicon supplanted germanium as the key to electronics technology advances, and the III-V compounds proved recalcitrant to the development of production technology giving high quality materials, the interest in thermoelectric materials vanished in the western nations, with only a few exceptions.

The voluminous data on thermoelectric properties remained as bits in the literature relating to low figure of merit samples. The data has continued to be augmented by Russian investigators following the earlier practices of using Seebeck coefficient and electrical conductivity data as alloy-characterization tools. The exceptionally large value for $S^2\sigma$, the power coefficient, remains elusive, as does the exceptionally small lattice thermal conductivity necessary for large Z .

Theoretical Descriptions of Alloys

Early in the research and development effort, attention was given to technologies for measuring the parameters used to calculate figures of merit (1). Until Ioffe's studies, no one had simultaneously determined all three parameters S , σ , and K on a single semiconductor sample.

The evolution of the Harman Z meter (11, 12) provided a source for S , σ , and K data, as well as the engineering parameter Z . Frequently, the power coefficient, $S^2\sigma$, was optimized while reserving actual thermal conductivity measurements for the select samples having large values. The slowness of electrical and thermal data generation led to stringent *a priori* judgments on samples for complete characterization of Z .

From the beginning, solid-state band theory was viewed as a tool to provide guidance to the experimental work (1, 2). The earliest studies brought attention to the importance of the electron mobility-effective mass product, $\mu_0(m^*/m_0)^{3/2}$, to the thermoelectric properties. Difficulties in measuring the electron effective mass led to focusing upon the electron mobility as a critical variable.

The availability of Harman Z meter data, as well as the derived individual parameters, quickly identified how complex the experimentalist's routes were to optimize Z in any specific alloy. This created a need for estimating the probable performance of optimally doped alloy from limited data.

In 1959, Chasmar and Stratton (14) utilized a spherical energy band model for an extrinsic semiconductor to extend Ioffe's earlier descriptors (1, 2). The figure of merit \times temperature product, ZT , a measure of thermoelectric efficiency, was derived using the basic Fermi integral description for electronic transport in a semiconductor. The analysis identified a "materials factor," B , as a critical parameter

$$B = 0.8952 \times 10^{-5} \mu_0(m^*/m_0)^{3/2}(T/300)^{5/2}(1/K_L)$$

where μ_0 is the classical limiting electronic mobility, m^*/m_0 the electronic effective mass ratio, T the absolute temperature, and K_L the lattice thermal conductivity.

The maximum for the ZT product could be calculated using selected values of B in combination with values for ν , the electronic energy relaxation time exponential parameter. The Fermi level, η , was systematically varied to estimate simultaneously the optimum doping level and the maximum value of ZT with the relaxation time parameter varying from $-3/2$ to $+3/2$.

Practical applications required identifying for a particular alloy sample the applicable scattering parameter, ν ; the temperature, the $\mu_0(m^*/m_0)^{3/2}$ product, and the lattice thermal conductivity. Unfortunately, the fundamental parameters are not readily accessible, so a clear basis did not exist for extrapolating optimum properties.

The parameter, $\mu_0(m^*/m_0)^{3/2}$, directly related the Seebeck coefficient to the electrical conductivity along a characteristic theoretical curve for a given alloy. Thus an alloy

*Electrochemical Society Active Member.

¹Permanent address: Donald Tuomi, Ph.D. and Associates, Limited, 221 South Illinois Drive, Arlington Heights, Illinois 60005.

having, for example, a 200 ($\mu\text{V/K}$) Seebeck coefficient and a 1000 (mho/cm) electrical conductivity would be characterized by a mobility-effective mass product varying from 25 to 1050 $\text{cm}^2/\text{V-s}$, as shown in Fig. 1 for the assumed variations in scattering modes (13)

Scattering mode	Scattering parameter
(curve a) ionized impurity	3/2
(curve b) high temperature polar optical	1/2
(curve c) alloy and/or acoustic vibration	-1/2
(curve d) lead salt according to Ioffe (1)	-3/2

The illustration based upon an S, σ point set for a good alloy emphasizes the difficulties encountered in the interpolation or extrapolation of values far from optimum utilizing theoretical approaches in combination with points far from optimum.

Chasmar and Stratton stimulated a long series of studies (12-23) directed towards (i) identifying the variables interacting to limit the maximum attainable ZT , (ii) identifying optimum doping levels at the maximized figures of merit for experimental materials using the S, σ , and K data on one, two, or, at most, three specimens, and (iii) estimating reasonable limits to the attainable figures of merit using varied ranges of assumptions.

The analytical approaches did not give guidance on discovering or optimizing experimental alloys in a direct way. A feeling emerged that the dependence of the effective mass for electrons upon the reciprocal of the electron mobility removed the figure of merit dependence upon $\mu_0(m^*/m_0)^{3/2}$ so the only route to high Z lay in further decreasing the thermal conductivity of the lattice by alloying (10).

The Seebeck Quality Factor

Early in our materials work, we recognized the general inadequacy of figures of merit or power coefficients to characterize experimental samples. They were device-engineering variables rather than ones directly related to material characteristics. The question kept arising as to how to judge two different alloy samples as to excellence. An excellence ratio needed to be defined.

A likely candidate appeared to be the $\mu_0(m^*/m_0)^{3/2}$ parameter, but what relaxation time parameter for electron energies should be used? A series of figures were drawn of S vs. σ , using the $\mu_0(m^*/m_0)^{3/2}$ product as the variable parameter for $-3/2, -1/2, 1/2$, and $3/2$ values of the scattering parameter, ν . Experimental S, σ data from varied sources for different alloys were plotted on different copies of the master figures with the goal being to identify the best option for use in defining alloy excellence.

The fit of data for n-type doped $\text{Bi}_2\text{Te}_{2.1}\text{Se}_{0.9}$ compositions is shown in Fig. 2 for quenched and Bridgman grown rods with $\text{I}_2, \text{Cu}_2\text{Br}_2$, and BiI_3 dopants. The mobility effective mass product classifies the samples as 65, to 180, to 260 $\text{cm}^2/\text{V-s}$ class materials.

The $\mu_0(m^*/m_0)^{3/2}$ description of S, σ crystal anisotropy for the Bi_2Te_3 -class alloys is illustrated in Fig. 3 for direc-

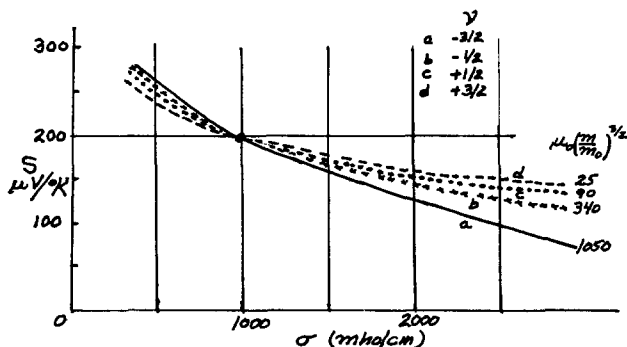


Fig. 1. The characteristic mobility-effective mass parameter curves passing through the point 200 $\mu\text{V/K}$ and 1000 mho/cm for scattering parameter, ν . Variations: (curve a) $-3/2$ lead salt scattering, (curve b) $-1/2$, alloy and/or acoustic vibrational, (curve c) $+1/2$, high temperature polar optical, and (curve d) $+3/2$, ionized impurity mode.

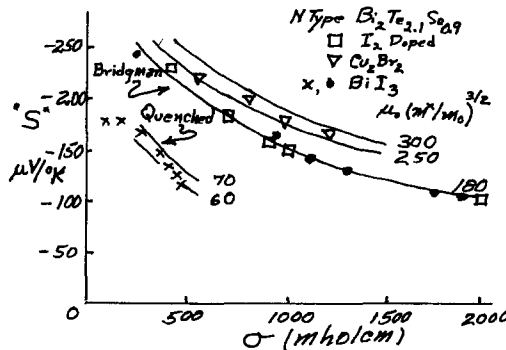


Fig. 2. The experimental data fit of n-type $\text{Bi}_2\text{Te}_{2.1}\text{Se}_{0.9}$ quenched and Bridgman-grown rod alloys acoustic mode-alloy scattering, $\mu_0(m^*/m_0)^{3/2}$ parameter curves relating Seebeck coefficient to electrical conductivity by single-band theory.

tions perpendicular and parallel to cleavage plane of the layer lattice structure. The temperature-dependent data of Dennis (36) for p-type is characterized as 75 perpendicular to cleavage plane and 350 $\text{cm}^2/\text{V-s}$ parallel, while the n-type is 50 and 350 $\text{cm}^2/\text{V-s}$, respectively. The variability shown by the other specimens suggests variations in sample quality.

Similar categories of fits were encountered for extrinsic samples of $\text{Bi}_2\text{Te}_3\text{-Sb}_2\text{Te}_3$ and $\text{Bi}_2\text{Te}_3\text{-Bi}_2\text{-Se}_3$ alloys incorporating varying levels of doping, as well as in the temperature-dependent parameter studies when the S, σ experimental points were directly plotted as in Fig. 3.

The surprising feature emerging from the exercise was the variabilities encountered in $\mu_0(m^*/m_0)^{3/2}$ for different sample series (24). This fundamental parameter was proving to be a variable parameter of both chemical composition and processing condition. The acoustic mode-alloy scattering relaxation time, $\nu = -1/2$, curves for a S - σ correlation were providing simple $\mu_0(m^*/m_0)^{3/2}$ numbers which measured the alloy quality. This was an experimental variable of the alloys!

The Seebeck Quality Factor Curves

The work of Donohue *et al.* (25) suggested a general definition for the quality factor, as well as a presentation framework.

For Bi_2Te_3 alloys, they found that the electronic transport could be described using the single-band extrinsic semiconductor model with spherical constant energy surfaces and an acoustic vibrational mode relaxation time for the energy dependence of electron scattering. The electron transport equations became

$$S = (\pm) k/e (2F_{1(\eta)})/F_{0(\eta)} - \eta$$

$$\sigma = neu$$

$$\mu = [\pi^{1/2}/2] [F_{0(\eta)}/F_{1/2(\eta)}] \mu_0$$

$$n = (4/\pi^{1/2}) (2\pi m^* kT/h^2)^{3/2} F_{1/2(\eta)}$$

where the symbols are as follows

- S = Seebeck coefficient
- σ = electrical conductivity
- μ = carrier mobility
- μ_0 = nondegenerate carrier mobility
- m^* = density of states effective mass of charge carrier
- k = Boltzmann's constant
- n = number of charge carriers
- e = electronic charge
- F_n = Fermi integral of index N
- η = Fermi level
- T = absolute temperature
- h = Planck's constant

utilizing these equations, the Seebeck quality factor curves of constant $\mu_0(m^*/m_0)^{3/2}$ in $\text{cm}^2/\text{V-s}$ were constructed using a logarithmic electrical conductivity scale, as in Fig. 4, and a linear scale, as in Fig. 5.

The discovery of reasonably good fits for extrinsic samples of the Bi_2Te_3 - and PbTe -class alloys for either variable doping or for varying temperature dependence

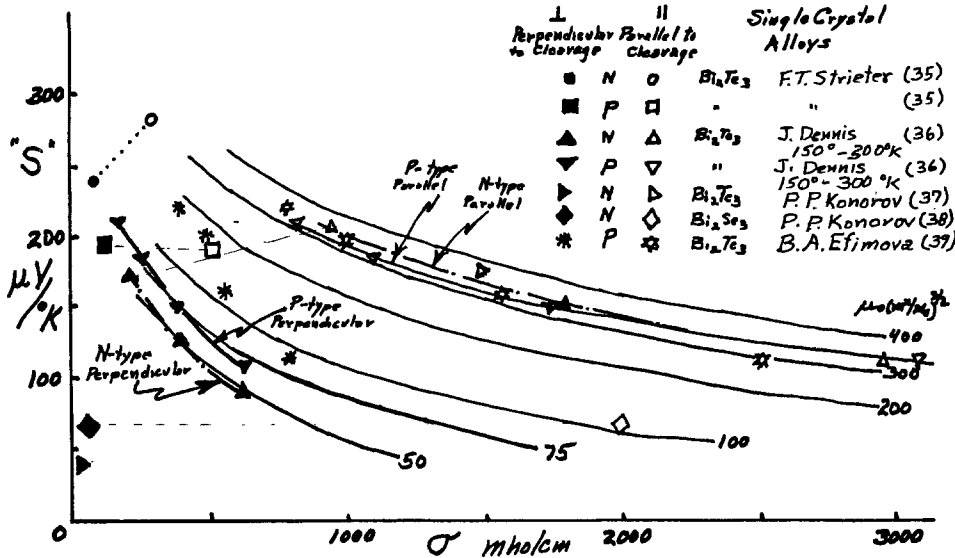


Fig. 3. The experimental data fits for the perpendicular and parallel to cleavage plane measurements of the Seebeck coefficients and electrical conductivity on single-crystal alloys of Bi₂Te₃ compared to the $\mu_0(m^*/m_0)^{3/2}$ parametric curves using acoustic mode-alloy scattering relaxation times in single-band theory.

led to ignoring the existence of a temperature-dependent effect on the mobility and effective mass of the carriers. Through the strategy of defining the curves as having characteristic values of

$$Q_s = \text{Seebeck quality factor}$$

an empirically useful tool for the materials scientist was created. The Q_s could be used to identify and to describe composition and process variable effects on a material parameter, which could be related to the device parameter in the later stage of material optimization through controlled doping at constant Q_s .

In Fig. 4, a set of reference curves for the S - σ relationship are shown with ν varying from $-3/2$ to $+3/2$. These were anticipated as a useful adjunct for identifying the critical scattering variables in different alloys as systematic changes in doping were undertaken. This has proven to be of limited value as increasingly sophisticated experiments identified the conditions giving the largest outlier Q_s for a particular composition using particular combinations of processing variables.

Applications of Q_s

Over the intervening years since the initial 1963 conceptualization, diverse applications of Q_s to data analysis, materials characterization, and materials optimization have all emphasized the utility of such zero or first-order quality characterizations of electronic transport processes in experimental materials.

A first illustration in Fig. 6 shows the surprisingly large Seebeck quality variation for p- and n-type bismuth telluride alloys, which were considered in the early 1960's to

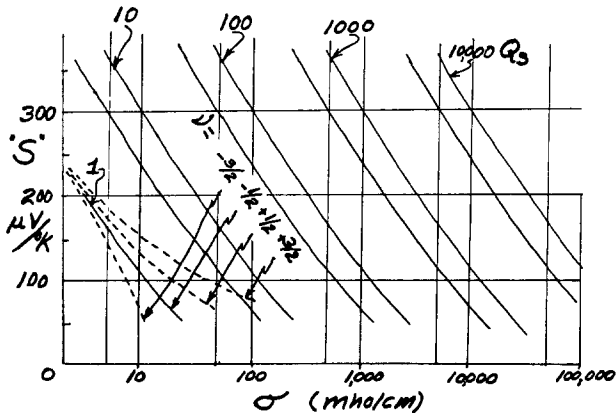


Fig. 4. The semilogarithmic Seebeck quality factor curves relating Seebeck coefficients to electrical conductivities in extrinsic semiconductor alloys. Reference curves for ν , the scattering parameter of $-3/2$, $-1/2$, $1/2$, and $3/2$.

be superior or commercial-class materials. The large Q_s variations of nominally similar class figure of merit alloys suggests that either serious measurements errors confounded the results or the alloys had not been fully optimized. The implication continues to be true - best outlier figure of merit alloys of p- and n-type have not been made reproducibly for device use.

Subtle doping-variable-related effects have been noted in Fig. 2. Further evidence is provided in Beckman and Bergvall's studies on the n-type doping of Bi₂Te_{2.7}Se_{0.3} composition Bridgman-grown rods (26). The highest quality was found for copper doping (a 360 Q_s), lowest for BiI₃ (a 320 Q_s), and with Cu₂Br₂ or CuBr₂, an intermediate quality (340 Q_s).

Another illustration is the dramatic degradation of p-type Bi₂Te₃ by addition of no more than 0.5% Sn. The initially 350 Q_s p-type alloy precipitously decreased in Seebeck coefficient with only a slight increase in electrical conductivity, as shown in Fig. 7. The phenomena are related to polyphase, circulating current effects.

The bismuth telluride alloy data of Fig. 2 show the n-type-doped, quenched samples are in the 65 Q_s class, while the Bridgman-grown rods are 180-300 Q_s . All quenched alloys of the (Bi, Sb)₂(Te, Se)₃ system show below 100 Q_s alloy quality. Broad surveys of published S , σ data on varied alloys show this to be the rule for heavily doped semiconductors. Associated defects form during this processing which prove to be difficult to remove by annealing bulk alloy samples.

Telkes' early exploratory studies on power generator alloys (28) provides a further illustration of Q_s classification. The characteristics were as follows

Alloy	Q_s	Alloy	Q_s
n-PbS	80-190	p-Te	190
p-PbS	0.8-1.8	p-ZnSb	90-210
n-SnO ₂	2.1	p-Bi ₂ Te ₃	60-225
p-Cu ₂ S	17-27	n-Bi ₂ Te ₃	225

The existence of n and p lead sulfide near 200 Q_s (29) and Bi₂Te₃ alloys at 400 and higher Q_s (30) emphasizes the challenge present in alloy performance optimization (6).

Finally, a survey of the Si/Ge alloys utilized in power generators brings attention to a temperature-dependent behavior in Q_s . In Fig. 8, limited data for extrinsic behaving 80/20 Si/Ge alloys (30-32) show that Q_s increases with increasing temperature. At the high temperatures of the power generator environment (1200 K), the Seebeck qualities are in the 300 Q_s range, with n-type being superior to p-type. This behavior is crucial to the improvement in the figure of merit with increased temperature. By contrast, the Q_s of Gd₂Se₃, PbTe, and (Bi, Sb)₂(Te, Se)₃ extrinsic alloys are independent of temperature and, respectively, in the 100, 300, and above-400 Q_s classes.

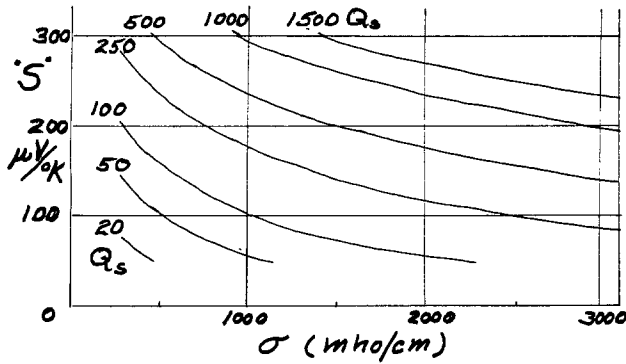


Fig. 5. The Seebeck quality factor relationships of Seebeck coefficients and electrical conductivities for ranges relevant to thermoelectric alloy optimization.

Summary

Heavily doped semiconductors (33, 34) are the basis from which thermoelectric power generation and refrigeration will evolve into an increasingly sophisticated device technology. Theory and experiment will need to proceed hand in hand as the imperfection structures of nearly perfect crystals are brought under full structural-chemical control in an economically viable technology.

The phenomena degrading alloy performance need to be progressively minimized on the macro-, micro-, submicro-, and atomic-dimensional scales. A true materials science integration of chemists, physicists, and metallurgists' perspectives is necessary for systematic progress to take place.

A key factor in reaching the goals lies in being able and willing to make value judgments on the quality of alloys. The electronic transport phenomena related to the power coefficient numerator of the figure of merit are conveniently described by the Seebeck quality factor, Q_s , as an empirical materials-classification variable.

Though originally related to a simple single-band model of a semiconductor dominated by acoustic mode-

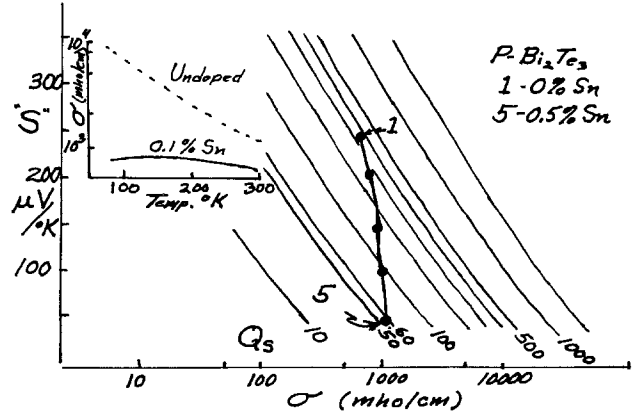


Fig. 7. The Q_s degradation of p-type Bi_2Te_3 through tin doping at 0% to 0.5% levels (27).

alloy scattering of electrons, the Q_s characteristics have proven experimentally to have rather universal utility to alloy-optimization research. With passage of time, the distinction between Q_s and $\mu_0(m^*/m_0)^{3/2}$ has become conceptually sharpened.

The defect structures modifying electron scattering in three-dimensional complex crystal lattices will also perturb the thermal conductivity. The electronic structures of the molecular orbital or band structure system create the three-dimensional structures of the x-ray crystallographer's electronic density maps. Within this electronic framework, the massive atomic nuclei oscillate in a quantum mechanically defined electric field space. This reality poses a "Catch-22" for modeling the ways to alter lattice and electronic components of thermal conductivity to optimize alloy performance.

Thus, a further conceptual evolution is needed, the defining of a thermal conductivity quality factor, Q_k , which facilitates alloy optimization as the $Q_s/Q_k = M$, materials parameter (40). The final stage of evolution is selecting the optimally doped alloy combinations of n- and p-type which provides the optimized performance in engineered devices.

The recommendation that Johann Seebeck be honored by adoption of Q_s , the Seebeck quality factor, as an experimentalist's approach to optimizing the electronic performance of semiconducting alloys is presented. Johann Seebeck was our first semiconducting alloy materials scientist working pragmatically on a significant exploratory research program.

Acknowledgments

This paper reflects over two decades of work in the heavily doped semiconductor area. Special acknowledgments need to be made to Stanley Cook and John Horwath at the Roy C. Ingersoll Research Center of Borg-

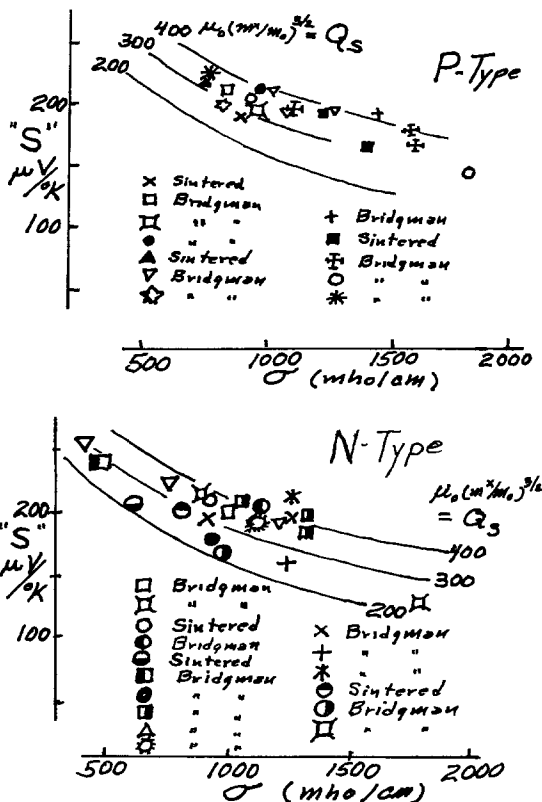


Fig. 6. The Q_s variations of higher figure of merit and commercial alloys, circa 1961, of the p- and n-type $(Bi, Sb)_2 (Te, Se)_3$ class.

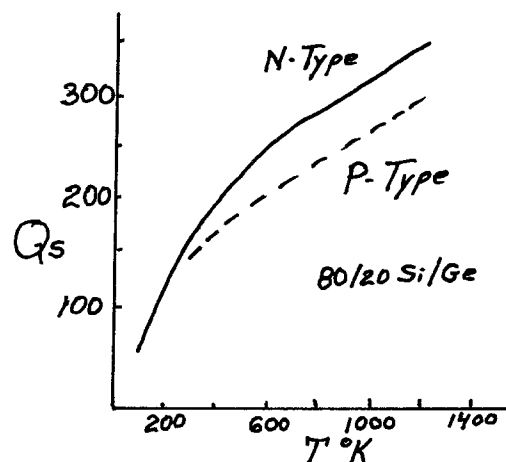


Fig. 8. The temperature dependence of the Seebeck quality factor for the 80/20 silicon/germanium power generator alloys.

Warner Corporation for their invaluable contributions experimentally, and to Dr. Jack Madigan (deceased) for his willingness to teach physics to a chemist. The support of Dr. Donald W. Collier and Dr. Leonard V. Sloma through the early conceptual struggles to the present time has given the author heart to continue to meet the challenges present within a positive framework.

Special thanks and gratitude is presented to the staffs of Borg-Warner Corporation, as well as to the Research Center for continued support and encouragement. The continued support of colleagues near and far is deeply appreciated.

Manuscript received Nov. 15, 1983. Parts of this article were presented as Paper 573 RNP at the St. Louis, Missouri, Meeting of the Society, May 11-16, 1980, and as Paper 377 presented at the Minneapolis, Minnesota, Meeting of the Society, May 10-15, 1981.

Donald Tuomi, Ph.D., and Associates, Limited assisted in meeting the publication costs of this article.

REFERENCES

1. A. F. Ioffe, "Energetic Principles of Semiconductor Thermoelectric Batteries," Academy of Sciences of USSR (1949).
2. A. F. Ioffe, "Semiconductor Thermoelements and Thermoelectric Cooling," Infosearch, Ltd., London (1957).
3. C. Zener, Industrial Laboratories, (1958) Nov. 30-40.
4. D. Tuomi, Paper 799396 presented at the 14th Intersociety Energy Conversion Engineering Conference, American Chemical Society, Boston, MA, Aug. 5-10, 1979.
5. D. Tuomi, Paper 809314 presented at the 15th Intersociety Energy Conversion Engineering Conference, American Institute of Aeronautics and Astronautics, Seattle, WA, Aug. 18-22 (1980).
6. D. Tuomi, in "Proceedings of the 4th International Conference on Thermoelectric Energy Conversion," 130-2 (1982).
7. J. W. Davisson and J. Pasternak, with B. B. Rosenbaum, NRL Memoranda Reports 901, 940, 969, 1037, 1089, 1127, 1177, 1241, 1361, and 1404, U.S. Naval Res. Lab, Naval Res. Lab Problems G4P03-03 (1959-1963).
8. F. A. Kroger, "Chemistry of Imperfect Crystals," Vol. 1-3, North Holland - American Elsevier, New York (1974).
9. P. J. Price, *Phys. Rev.*, **104**, 1223 (1956).
10. H. Weiss, *Festerkorperprobleme*, **14**, 43 (1974).
11. T. C. Harman, *J. Appl. Phys.*, **29**, 1373 (1958).
12. T. C. Harman, J. H. Cahn, and M. J. Logan, *ibid.*, **30**, 1351 (1959).
13. R. P. Chasmar and R. Stratton, *J. Electron. Control.*, **7**, 52 (1959).
14. A. H. Wilson, "The Theory of Metals," 2nd ed., Cambridge University Press, Cambridge, England (1953).
15. F. J. Donahue, *Elect. Eng.*, **79**, 702 (1960).
16. H. Littman, *J. Appl. Phys.*, **33**, 2655 (1962).
17. R. Simon, *ibid.*, **33**, 1830 (1962).
18. R. Simon, *Adv. Energy Convers.*, **3**, 515 (1936).
19. E. S. Rittner and G. F. Newmark, *J. Appl. Phys.* **34**, 2971 (1963).
20. J. D. Wasscher, W. Albers, and C. Haas, *Solid State Electron.*, **6**, 261 (1963).
21. R. Simon, *Appl. Phys. Lett.*, **3**, 58 (1963).
22. J. F. Goff and J. R. Lowney, in "Proceedings of the Inst. Conference Thermoelectric Energy Conversion," University of Texas at Arlington, Sept. 1-3, 1976, p. 47.
23. T. C. Harman and J. M. Honig, "Thermoelectric and Thermomagnetic Effects and Applications," McGraw-Hill Book Company, New York (1967).
24. D. Tuomi, "Thermoelectric Material Quality—The Seebeck Coefficient—Electrical Conductivity Relationship," Internal Report B-W-R, 3259-01, (Nov. 1962).
25. L. M. Testardi, J. H. Bierly, and F. J. Donohue, *J. Phys. Chem. Solids*, **23**, 1209 (1962).
26. O. Beckman and P. Bergvall, *Arkiv. Fysik.*, **24**, 113 (1963).
27. V. Birkholz, *Z. Naturforsch.*, **13a**, 780 (1958).
28. M. Telkes, *J. Appl. Phys.*, **18**, 116 (1947).
29. A. A. Averkin, *Fiz. Tver. Tela.*, **4**, 3667 (1962).
30. D. Tuomi, Abstract 377, p. 941, The Electrochemical Society Extended Abstracts, Vol. 81-1, Minneapolis, MN, May 10-15, 1981.
31. M. W. Heller, R. D. Nashby, and R. T. Johnson, Jr., *J. Appl. Phys.*, **47**, 4113 (1976).
32. V. Raag, Paper presented at the 2nd International Conference on Thermoelectric Energy Conversion, University of Texas at Arlington, March 1978.
33. V. I. Fistul', "Heavily Doped Semiconductors," Plenum Press, New York (1969).
34. V. L. Bonch-Bruyevich, "The Electronic Theory of Heavily Doped Semiconductors," American Elsevier Publishing Co., New York (1946).
35. F. T. Streiter, *Adv. Energy Convers.*, **1**, 99 (1961).
36. J. Dennis, *ibid.*, **1**, 99 (1961).
37. P. P. Konorov, *Sov. Phys. Solid State*, **1**, 1371 (1957).
38. P. P. Konorov, *ibid.*, **1**, 1365 (1957).
39. B. A. Efimova, I. Korenblit, V. I. Novihov, and A. G. Ostroumov, *ibid.*, **3**, 2004 (1961).
40. D. Tuomi, Work in progress.

Magnetron-Sputtered SiO₂ Films in Hydrogen-Argon Mixtures

T. Serikawa and T. Yachi

Nippon Telegraph and Telephone Public Corporation, Musashino Electrical Communication Laboratory, Midoricho, Musashino-shi, Tokyo 180, Japan

ABSTRACT

SiO₂ films are deposited from SiO₂ targets by RF planar magnetron sputtering in hydrogen-argon mixtures. Properties of the SiO₂ films are measured and compared with SiO₂ films deposited in only an argon mixture and thermally grown SiO₂ films. The following points are clarified by our experiments. The addition of hydrogen to the sputtering gas prevents the formation of film structures having microvoids, which appear when only argon is used. This results in film densification and a smooth surface texture. The addition of hydrogen greatly improves film property uniformities over the substrate. Infrared absorption spectra and Auger electron spectra show that the SiO₂ films sputtered in hydrogen-argon mixtures are indistinguishable in composition from the films by other methods.

SiO₂ films have played a major role in the development of silicon semiconductor devices (1, 2). The chemical vapor deposition method and the thermal oxidization of silicon in an oxygen ambient have been most widely used to deposit SiO₂ films in semiconductor device fabrication (1, 3). These methods, however, have a problem, in that they result in a high substrate temperature. Certain de-

vices or processing schemes require that the SiO₂ films be deposited at low temperatures.

Recently, a magnetron sputtering technique has been developed, which is a potentially attractive method for overcoming the above problem (4). Lower temperatures are obtained using this technique, even when the deposition rates are significantly high. Therefore, magnetron-

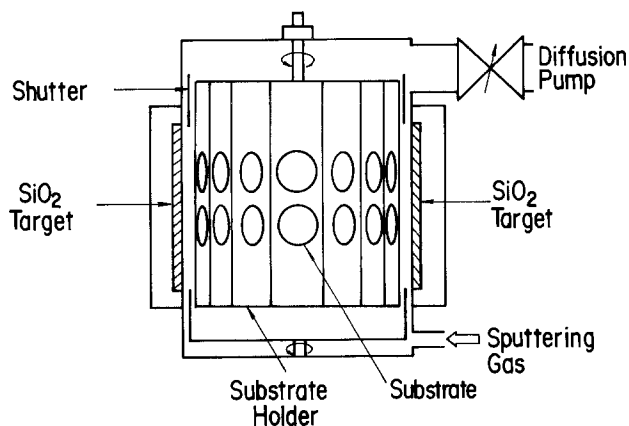


Fig. 1. The RF planar magnetron-sputtering apparatus

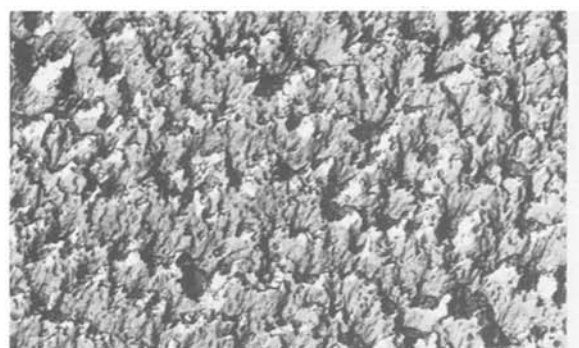
sputtered SiO_2 films are potentially useful, especially as an insulating material for aluminum multilevel interconnections in semiconductor devices (5-7).

The sputtered SiO_2 films are deposited as a result of the glow discharge of argon gas. However, films deposited in only argon suffer from the problem of a porous film structure (8). To overcome this problem, several sputterings, such as oxygen mixing and substrate biasing, have been studied (9, 10).

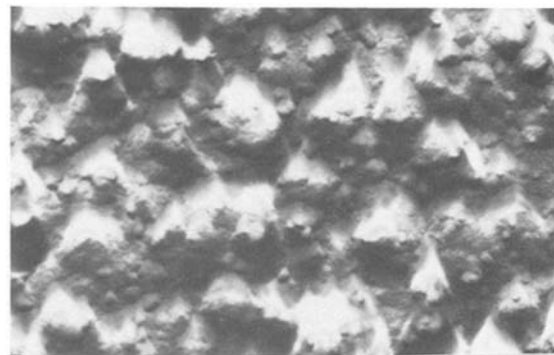
We have previously reported that the addition of hydrogen to the sputtering gas has the effect of improving SiO_2 film properties (11). The present study has been undertaken to further clarify the properties of SiO_2 films deposited by magnetron sputtering in hydrogen-argon mixtures.

Experimental

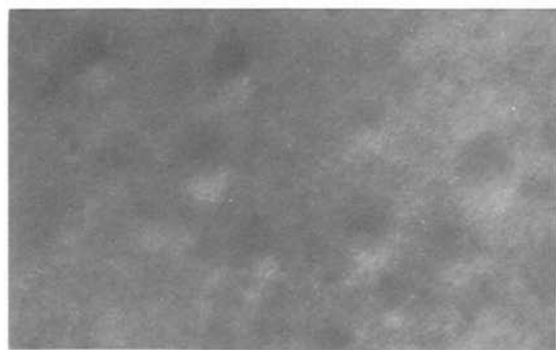
In our experiment, the SiO_2 films were deposited on a silicon substrate by the RF planar magnetron sputtering



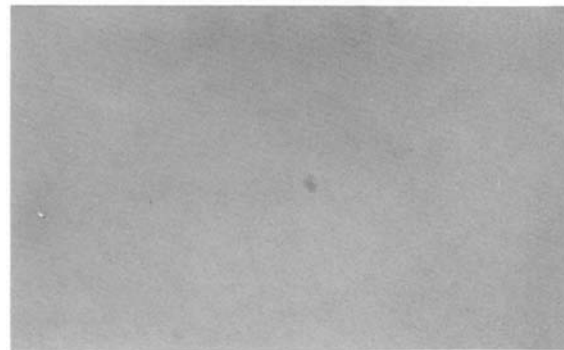
1 μm



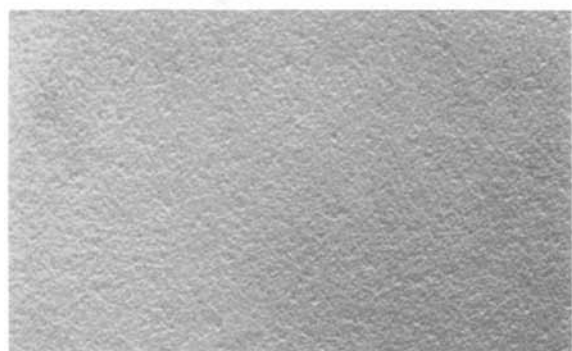
0.2 μm



0.2 μm



0.1 μm



0.1 μm

Fig. 2. Transmission electron micrographs of carbon replicas of slightly etched SiO_2 films. Micrographs a (top left), b (top right), c (middle left), and d (middle right) correspond to hydrogen partial pressure of 0, 0.016, 0.1, and 0.6 Pa, respectively, where sputter depositions were carried out at 2.0 Pa pressure and at a 200°C substrate temperature. Micrograph e (left) corresponds to 1 μm thick thermally grown SiO_2 film.

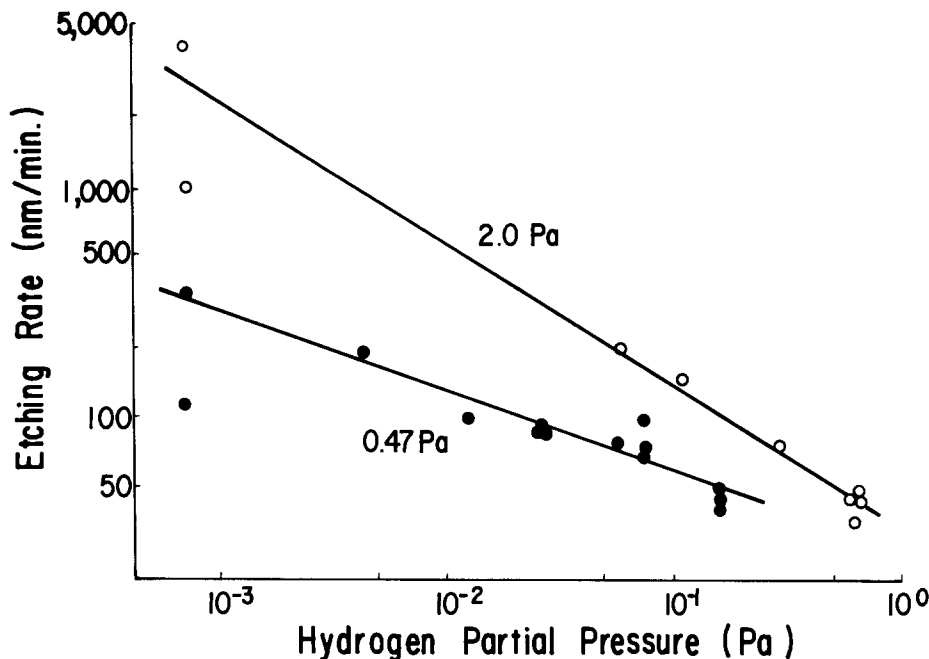


Fig. 3. Effect of hydrogen partial pressure on etching rates for SiO₂ films deposited at 2.0 and 0.47 Pa. Substrate temperature was 200°C.

apparatus with two SiO₂ targets which is shown in Fig. 1 (11). The SiO₂ targets (99.99% pure) having an area of 5 × 15 in. and a thickness of 0.25 in. were mechanically clamped to water-cooled RF electrodes. The targets were covered with an adjustable shutter mounted approximately 25 mm in front of the targets. The substrates were put on a barrel-type rotatable substrate holder having a diameter of 500 mm and a height of 530 mm, which was electrically floated. Both the holder and shutter were made of titanium.

Before admitting the sputtering gas, the system was pumped to less than 4×10^{-4} Pa with a diffusion pump. The argon or hydrogen-argon mixtures were admitted to the sputtering system at a flow rate of 100 sccm. The sputtering power and rotation of the substrate holder were fixed at 2 kW per target and 10 rpm, respectively. Films having thickness of 0.1–2.5 μm were deposited on (100)-oriented, p-type, 10 Ω cm resistivity silicon substrate of 3 in. diam at various sputtering gas pressures and hydrogen partial pressures.

Properties of the SiO₂ films were evaluated by examining the etching rate, surface texture, film density, infrared absorption spectra, and Auger electron spectra.

Etching rates were calculated from the etched depth in a 30°C buffered hydrofluoric acid BHF [100 ml (50% HF) + 860 ml (40% NH₄F)] and from the etching time. The etched depths were measured by a roughness tester (Taly-Step™).

The surface textures of as-deposited films and slightly etched films in a 30°C BHF for 5s were observed using a transmission electron microscope of carbon replica.

Film densities were measured by a gravimetric technique.

Thermally grown SiO₂ films, on which most studies have been conducted, were also measured and used as a standard for comparison. These thermally grown SiO₂ films 1 μm thick were formed on (100)-oriented, p-type, silicon substrates in a 1000°C oxidization atmosphere.

Results and Discussion

Figures 2a to 2e show surface textures of SiO₂ films prepared at various hydrogen partial pressures, as well as the surface texture for thermally grown SiO₂ films. The SiO₂ films were etched for 5s in BHF at 30°C before looking at them. In the SiO₂ film deposited in only argon, shown in Fig. 2a, many microvoids of a few tens of nanometers in diameter are observed. As shown in Fig. 2b and 2c, at low hydrogen pressures, although microvoids formation is significantly decreased, microvoid marks still remain. However, as can be seen from Fig. 2d, high

hydrogen partial pressure completely removes microvoids. The SiO₂ film prepared at 0.6 Pa hydrogen partial pressure shown in Fig. 2d has a smooth surface texture, which is superior to that of the thermally grown film shown in Fig. 2e.

As a result of this decrease in microvoid formation achieved by introducing hydrogen into the sputtering gas mixture, the SiO₂ film is densified. This fact was experimentally demonstrated by the fact that the densities of the films sputtered at 2.0 Pa in only argon alone and in 0.6 Pa hydrogen partial pressure mixed gas, are 2.10 (g/cm³) and 2.33 (g/cm³), respectively. Moreover, the density of hydrogen partial pressure-sputtered SiO₂ film is slightly greater than the 2.30 (g/cm³) density of thermally grown SiO₂ films. This is inferred from the surface textures shown in Fig. 2d and 2e.

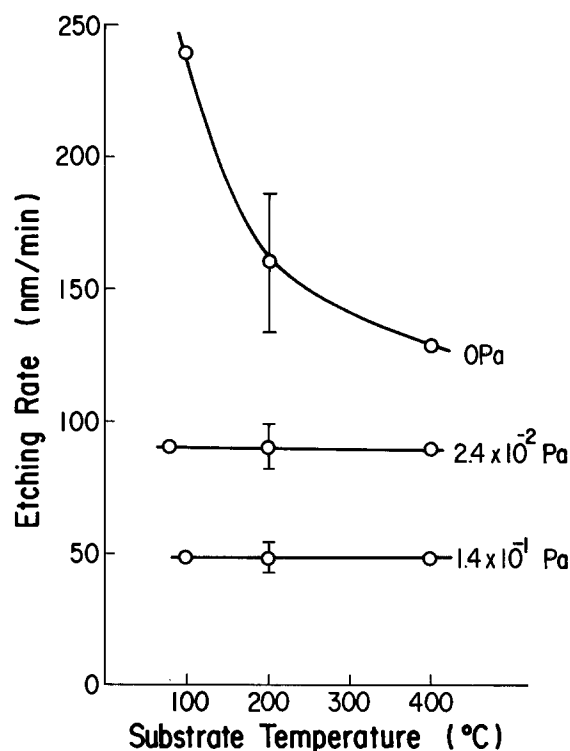


Fig. 4. Dependencies of etching rates in SiO₂ films deposited at various hydrogen partial pressures on substrate temperature. Sputtering gas pressure was 0.47 Pa.

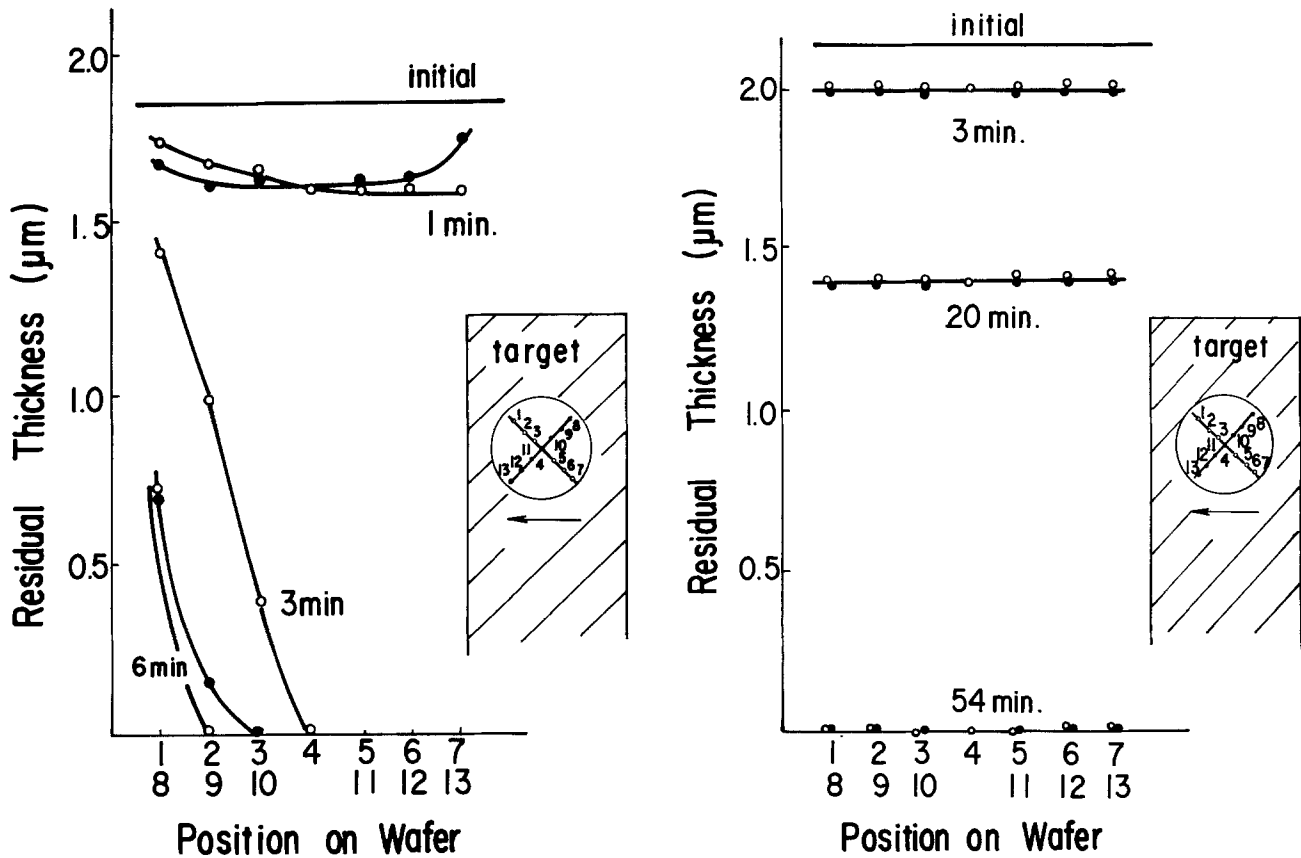


Fig. 5. Changes in residual thickness distributions of SiO_2 films over substrates as a function of etching time. The films were deposited in only argon (a, left), and 0.14 Pa hydrogen partial pressure mixture (b, right), where sputtering gas pressure and substrate temperature were 0.47 Pa and 200°C , respectively.

Changes in the etching rate as a function of hydrogen partial pressure at different sputtering gas pressures are shown in Fig. 3. Etching rates decrease proportionally with an increase in partial pressure. The films deposited at higher sputtering gas pressures have a higher rate, because of the formation of more microvoids (12, 13). Comparing Fig. 2a, 2b, 2c, and 2d, one sees that the etching rate decreases as the surface texture becomes smoother. That is, the removal of microvoids by intro-

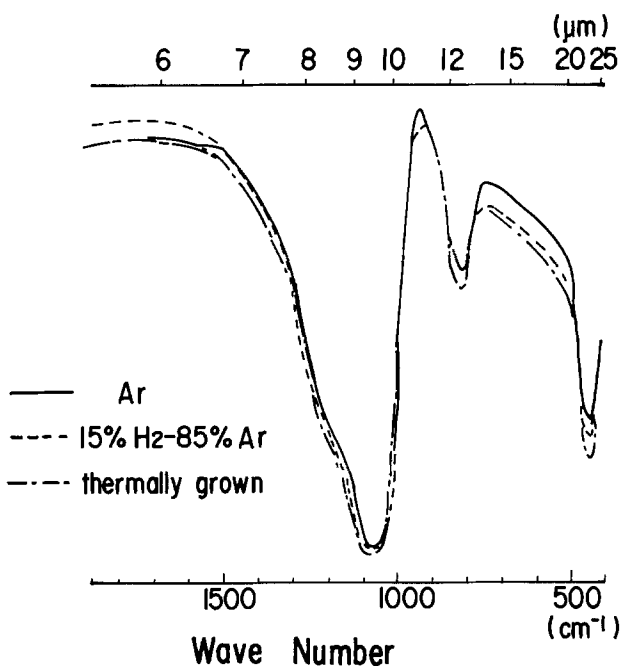


Fig. 6. Infrared absorption spectra of SiO_2 films deposited by various methods. Sputtered films were deposited at 0.47 Pa and 200°C .

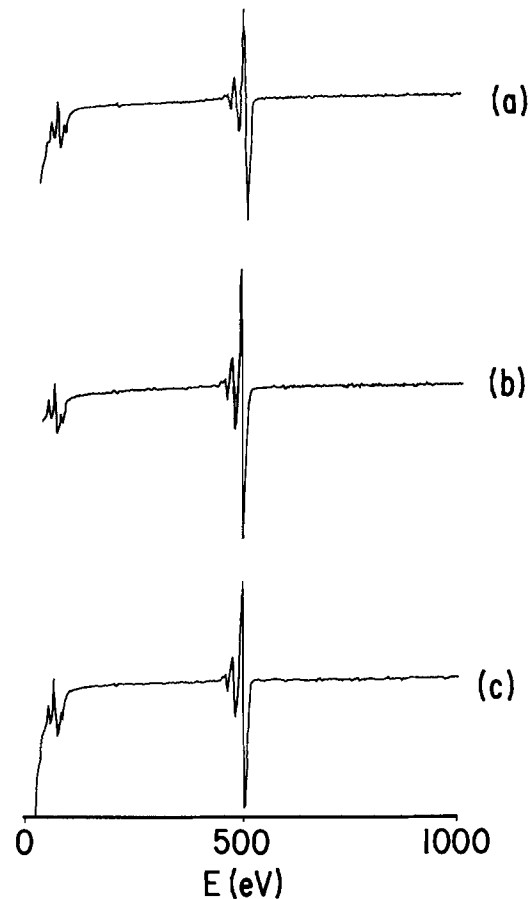


Fig. 7. Auger electron spectra of SiO_2 films deposited by sputtering in only argon (curve a), 0.14 Pa hydrogen partial pressure mixture (curve b), and thermal oxidation (curve c). Sputter conditions were the same as in Fig. 6.

ducing hydrogen lowers the etching rate. Moreover, under optimum hydrogen partial pressure, etching rates lower than the 70 nm/min are obtained. These etching rates are lower than thermally grown SiO₂ films.

In the case where only argon is used, the etching rate drops sharply with a rise in the substrate temperature, as shown in Fig. 4. By introducing a hydrogen partial pressure of higher than 2.4×10^{-2} Pa, this phenomenon disappears. Moreover, even at a low substrate temperature, low etching rate films can be deposited. Therefore, hydrogen mixing in sputtering gases is more effective in preventing microvoid formation than raising the substrate temperature.

In Fig. 5, distributions of residual thickness of SiO₂ films as a parameter of etching time are shown. The residual thickness was defined as SiO₂ film thickness after etching in a 30°C BHF. The insets in Fig. 5a and 5b indicate the relative configuration between the target and substrate, as well as the measurement positions on the substrate. The substrates move against the targets in the direction indicated by the arrows. In the case where only argon is used (Fig. 2a), the residual thickness distribution is nonuniform, especially over the upper part of the substrate. However, simply by introducing hydrogen, distribution uniformity is improved, as shown in Fig. 5b.

The properties of sputtered films are influenced by many factors, such as the energies and incident angle distributions of sputtered particles, substrate potential in relation to plasma, as well as the geometrical configuration of the system (4, 12, 13). These many factors are difficult to uniformly apply over the substrate. Therefore, film properties, such as the etching rate, become nonuniform despite a uniform deposition rate as shown in Fig. 5a. Hydrogen mixing in sputtering gas has the effect of decreasing microvoid formation, as shown in Fig. 2a to 2d. SiO₂ films are densified over the whole of the substrate, resulting in the uniform etching rate shown in Fig. 5b.

Figures 6 and 7 show the infrared absorption spectra and Auger electron spectra of sputtered SiO₂ films, compared with thermally grown SiO₂ films. Absorptions at 1100, 800, and 450 cm⁻¹, which are peculiar to silicon dioxide, are present in all the films shown in Fig. 6. No additional peaks were observed. In the Auger electron spectra, the peaks for silicon and oxygen appear at 78 and 500 eV, respectively. Therefore, it is concluded from Fig. 6 and 7 that the SiO₂ films in hydrogen-argon mixtures are similar in composition to the films sputtered in only argon or thermally grown SiO₂ films.

By increasing hydrogen partial pressure, the deposition rate decreases, as shown in Fig. 8. This figure also shows the deposition rate for sputtering in a 5% oxygen-95% argon mixture, which has been commonly used to improve SiO₂ film property. The decrease in the deposition rate due to the addition of hydrogen is the result of the large sputtering yield difference between argon and hydrogen (14, 15). The decrease for the hydrogen mixture is much smaller than that for the oxygen mixture.

As has been shown in Fig. 2 and 5, when only argon is used, the SiO₂ films exhibit film structures with many microvoids and the nonuniformity of film properties. The microvoids as well as this nonuniformity affect production yield and the long-term reliability of devices. However, the addition of hydrogen to the sputtering gas has the effect of preventing the formation of SiO₂ film with microvoids. Consequently, high density SiO₂ films can be uniformly deposited over the substrate even at low substrate temperatures. Moreover, this sputtering method is very simple and effective. Therefore, magnetron-sputtered SiO₂ films prepared in hydrogen-argon mixtures are very important in the fabrication of advanced devices.

Conclusion

It was experimentally demonstrated that magnetron sputtering in a hydrogen-argon mixture remarkably im-

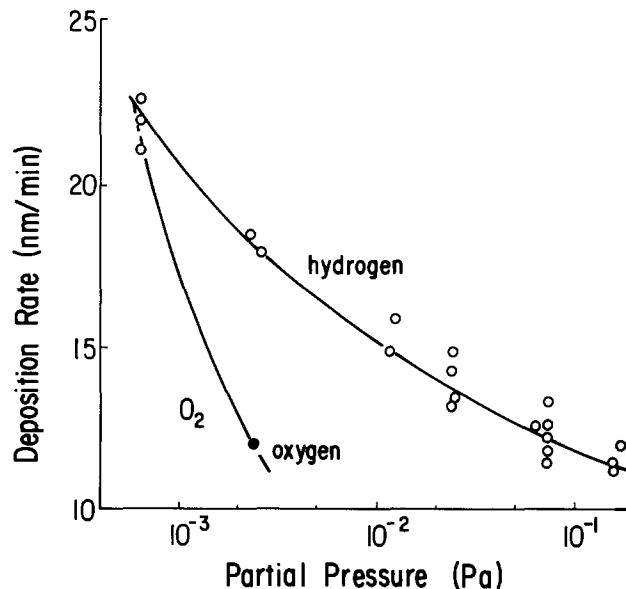


Fig. 8. Changes in deposition rates as a function of partial pressure of hydrogen and oxygen. Sputter depositions were done at 0.47 Pa and 200°C.

proves SiO₂ film properties. Under proper hydrogen partial pressures, the SiO₂ films were found to be superior in film density and film surface texture to thermally grown SiO₂ films. Moreover, sputtering in a hydrogen-argon mixture eliminates property nonuniformity, which appears when only argon is used.

This sputtering in a hydrogen-argon mixture results in high density SiO₂ films even at low substrate temperatures. Moreover, this sputtering technique is simple. Therefore, it is very useful in the preparation of SiO₂ films for advanced devices.

Acknowledgment

The authors would like to thank Dr. A. Ishimoto for his encouragement and many helpful suggestions.

Manuscript submitted Nov. 3, 1983; revised manuscript received May 3, 1984.

Nippon Telegraph and Telephone Public Corporation assisted in meeting the publication costs of this article.

REFERENCES

1. J. A. Amick, G. L. Schnable, and J. L. Vossen, *J. Vac. Sci. Technol.*, **14**, 1053 (1977).
2. W. A. Pliskin, *ibid.*, **14**, 1064 (1977).
3. A. S. Grove, "Physics and Technology of Semiconductor Devices," John Wiley and Sons, New York (1967).
4. J. L. Vossen and W. Kern, "Thin Film Processes," Academic Press, New York (1978).
5. K. Urbanek, *Solid State Technol.*, **20**, 87 (1977).
6. S. F. Meyer and E. J. Esieh, *Thin Solid Films*, **64**, 383 (1979).
7. R. A. Larsen, *IBM J. Res. Dev.*, **24**, 268 (1980).
8. K. Hara, Y. Suzuki, and Y. Taga, *Jpn. J. Appl. Phys.*, **18**, 2027 (1979).
9. R. E. Jones, H. F. Winter, and L. I. Maissel, *J. Vac. Sci. Technol.*, **5**, 84 (1968).
10. H. R. Koenig and L. I. Maissel, *IBM J. Res. Develop.*, **14**, 168 (1970).
11. T. Serikawa and T. Yachi, *Jpn. J. Appl. Phys.*, **20**, L111 (1981).
12. J. A. Thornton, *J. Vac. Sci. Technol.*, **11**, 666 (1974).
13. C. M. Mogab, P. M. Petroff, and T. T. Sheng, *This Journal*, **122**, 815 (1975).
14. E. Stern and H. L. Caswell, *J. Vac. Sci. Technol.*, **17**, 128 (1967).
15. J. B. Webb, *J. Appl. Phys.*, **53**, 9043 (1982).

The Material Properties of Silicon Nitride Formed by Low Energy Ion Implantation

T. Y. Chiu^{*,1} and W. G. Oldham^{**}

Department of Electrical Engineering and Computer Sciences, and the Electronics Research Laboratory, University of California, Berkeley, California 94720

C. Hovland

Perkin-Elmer, Physical Electronics Division, Eden Prairie, Minnesota 55344

ABSTRACT

This paper reports on silicon nitride formation by low energy implantation of nitrogen or ammonia into silicon. Extensive material investigation on nitrogen-implanted films using various analytical methods, including ellipsometry, chemical etching, transmission electron microscopy (TEM), x-ray photoelectron microscopy (XPS), infrared transmission spectroscopy (IR), and Rutherford backscattering spectroscopy (RBS) is discussed. A new technique to derive the film thickness, density, refractive index, and dielectric constant is developed. This method employs a combination of ellipsometry, capacitance measurement, and nitrogen areal density obtained by RBS. A major finding indicates that the implanted nitride films have a low density compared to CVD nitride. Other material properties are also summarized.

Thermal nitridation and nitridation of oxide have been shown to have certain advantages over thermal oxidation (1-3). The thin dielectric obtained is very uniform and exhibits high breakdown strength. In addition, the nitrided layer has a higher dielectric constant than oxide and is impervious to impurity diffusion. The film is also less susceptible to process-induced gate failures (3). With the scaling of the gate dielectric in VLSI, thin nitride is a potential candidate to be investigated.

We have shown that thin nitride can be formed by using low energy implantation of N_2 in an ion milling machine (4). Since the ion milling machine can deliver a high current density over a large area, the through-put of this process is comparable with single-wafer processing. The implantation of N_2 is accompanied by surface sputtering. The sputter-implantation process produces a very uniform layer. Rutherford backscattering spectroscopy (RBS) indicates that the total nitrogen incorporated into the Si surface is about $3.2 \sim 3.5 \times 10^{18} \text{ cm}^{-2}$ at 1.7 keV. The as-implanted layer has a N/Si ratio of 1. A damaged layer about 3 ~ 4 nm thick at the interface extending into the Si substrate is also present. After thermal treatment, the ratio approaches the stoichiometric nitride value of 1.3. The damage to the Si substrate is reduced but not totally removed after annealing at 900°C for 1/2h. A damaged layer about 0.8 nm thick remains. Transmission infrared spectroscopy shows the existence of N-Si bonding in both the as-implanted and the annealed samples. However, the transmission minimum shifts from about 850 to 800 cm^{-1} after heat-treatment.

Experiments

The substrates used in the studies were (100)-oriented silicon wafers. The native oxide is removed before loading into an ion milling machine (Veeco Microetch System). The system is first pumped down to below 2×10^{-6} torr and then the implantation is carried out with nitrogen or ammonia at a pressure of 8×10^{-5} torr. The total dose of the implant is always greater than 0.3 C/cm^2 . The samples are then annealed in dry nitrogen or oxidized in wet oxygen.

Results

Ellipsometry measurements.—Ellipsometry is often used to obtain the thickness and the refractive index of a dielectric layer independently. The calculation is based on the following assumptions: (i) the dielectric film is

lossless, (ii) the dielectric film is homogeneous, (iii) the dielectric-substrate interface is abrupt, and (iv) the substrate refractive index is known. For the study of very thin films, the ellipsometric parameter Δ is of special interest. In Fig. 1, we plot $\Delta_{\text{SI}}-\Delta$ vs. the product nd , where n is the refractive index and d is the dielectric thickness, for n between 1.4 and 1.7. A very good linear relationship is observed. This means that Δ can be used to determine the product of n and d .

All the above assumptions are questionable when the nitride in the as-implanted form is considered. However, the parameter still is a qualitative measurement of the film thickness, assuming the same refractive index. Information about the dependence of layer thickness on implant energy and the effects of annealing can be deduced using this method.

The data were taken using a He-Ne laser source (632.8 nm). The angle of incidence was 70°. Figure 2 shows the ellipsometric parameter Δ vs. the implantation energy. The results indicate that film thickness increases with higher implant voltages. Figure 3 shows Δ as a function of annealing time at a temperature of 950°C. The data indicate that the film reaches a steady-state condition in 5 min of heat-treatment. A difference in annealing transient between the N_2 implanted and the NH_3 implanted is observed. No nitridation due to the nitrogen annealing ambient is detected.

If the annealed film satisfies the condition for ellipsometric analysis, it is theoretically possible to derive the film thickness and the refractive index independently. In practice, the uncertainty in the data yields a thickness of 10 ± 3 nm and a refractive index between 1.4 and 1.6. However, the product of refractive index and dielectric thickness, nd , can be determined by Δ . For a 1.7 keV implant, n times d equals 14 nm.

Chemical etching.—Figure 4 shows the etching characteristics of the unannealed films. The etch rate is much higher for the ammonia-implanted layer than the nitrogen-implanted film. Figures 5 and 6 show the etching data for the annealed and oxidized films, respectively. The etching behavior becomes almost similar after heat-treatment, and the etch rate is retarded. For N_2 -annealed films, the nitride near the substrate-dielectric interface is more resistant to the HF etching than that in the middle of the film. In addition, the film appears to have a three-layer structure. The XPS result, which will be discussed later, shows that the top surface of the nitrogen annealed films is partially oxidized.

The etching study indicates that, prior to the heat-treatment, the films produced by the N_2 implant and NH_3

* Electrochemical Society Student Member.

** Electrochemical Society Active Member.

¹Present address: AT&T Bell Laboratories, Holmdel, New Jersey 07733.

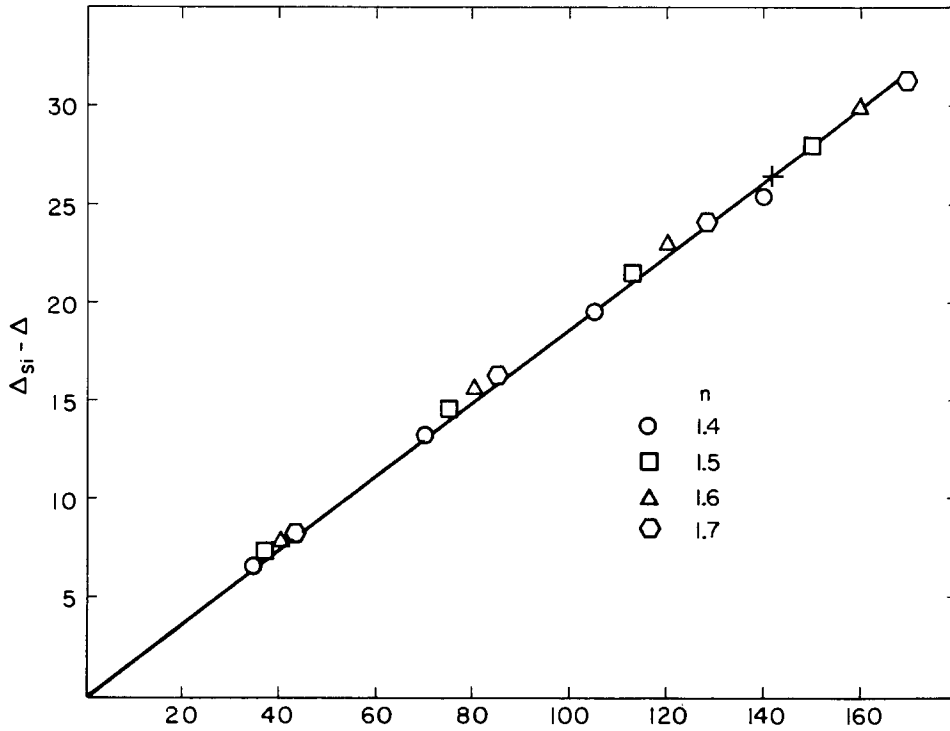


Fig. 1. The ellipsometric parameter, Δ vs. the product of n times d . The data show that for a thin film with low dielectric constant, Δ is almost linearly proportional to n times d . The cross indicated in the plot is the experimentally determined Δ for a 1.7 keV N_2 -implanted film after nitrogen annealing.

implant have very different chemical properties. However, the chemical properties become similar after annealing and are stabilized. Since one sample is prepared for each data point, the results indicate that the etching characteristics are very controllable.

X-ray photoelectron spectroscopy (XPS).—The XPS technique has been used for compositional analysis as well as chemical-state identification. Since chemical etching is well controlled, one can utilize this method to probe the film at the region of interest. To establish refer-

ences, measurement on three CVD nitride samples after a brief 20:1 HF etch were made. The average nitrogen to silicon atomic ratio (N/Si) is 1.39.

XPS analysis was also done on the N_2 -implanted samples. The nitrogen annealed film is found to be partially oxidized on the surface. During the compositional analysis, care is taken to etch through this oxynitride layer. Overetching to the point that the Si substrate contribution could significantly distort the N/Si ratio is also avoided. Therefore the measurement is confined between $171 > \Delta > 159$.

Four measurements on nitrogen-implanted layers were carried out on both unannealed and annealed film types. The data show that the N/Si ratio is 1.18 for the as-implanted layer and 1.26 for the annealed film. It should be noted that both ratios are lower than the CVD nitride standard. This result is consistent qualitatively with our RBS measurements (4). The as-implanted film is highly Si rich. After nitrogen annealing, the layer changes to a more stoichiometric ratio.

X-ray-induced Auger analysis.—The Si KLL Auger emission spectrum can offer further clues to the film

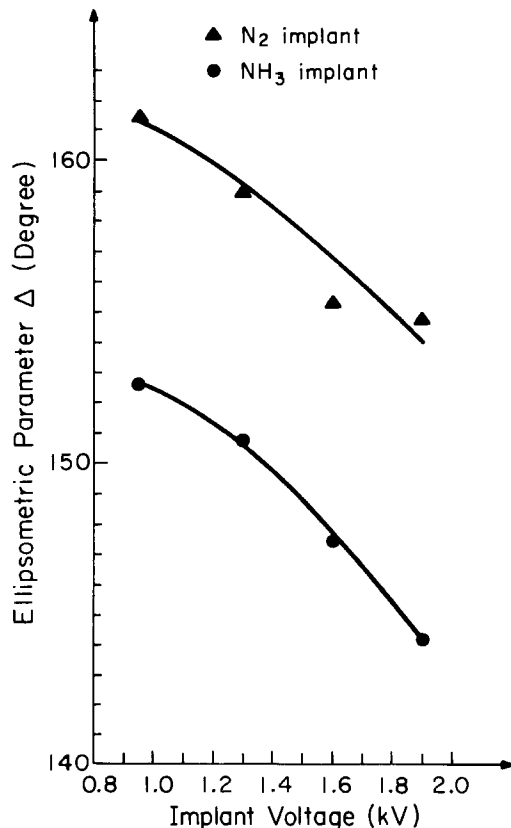


Fig. 2. The ellipsometer parameter, Δ , vs. the implantation energy. The data are taken on the as-implanted samples.

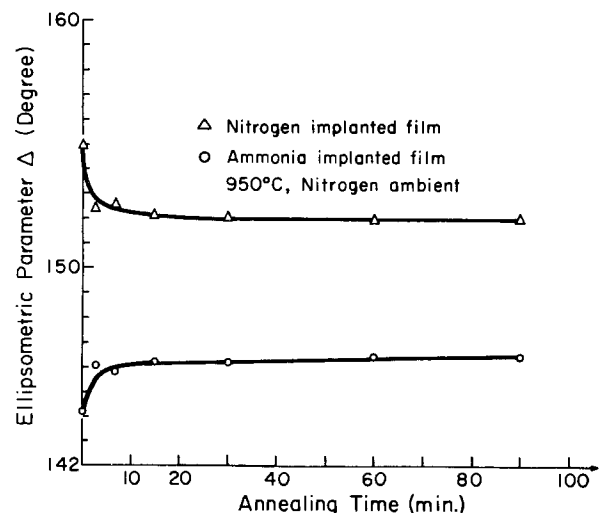


Fig. 3. The ellipsometric parameter, Δ , vs. the annealing time. Note that Δ reaches a steady state within 5 min.

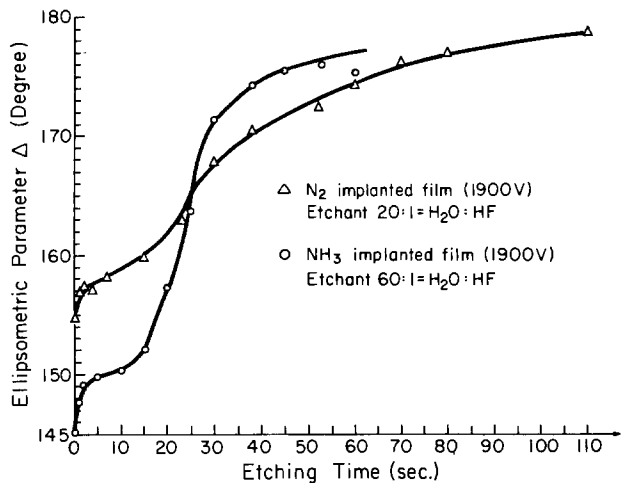


Fig. 4. The ellipsometer parameter, Δ , of the as-implanted sample vs. the etching time. Note that the etching solutions had different hydrofluoric acid concentration.

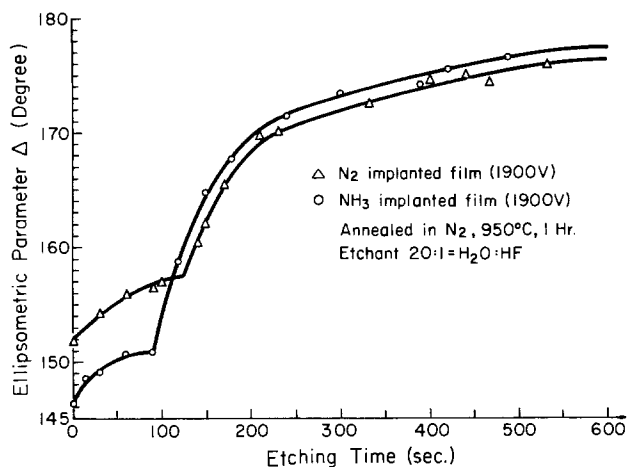


Fig. 5. The ellipsometer parameter, Δ , of the nitrogen annealed samples vs. the etching time. The surface appears to have a different etching characteristic in comparison to the bulk. XPS analysis reveals that the surface has a high oxygen content and is probably partially oxidized by the residual oxidant in the nitrogen ambient.

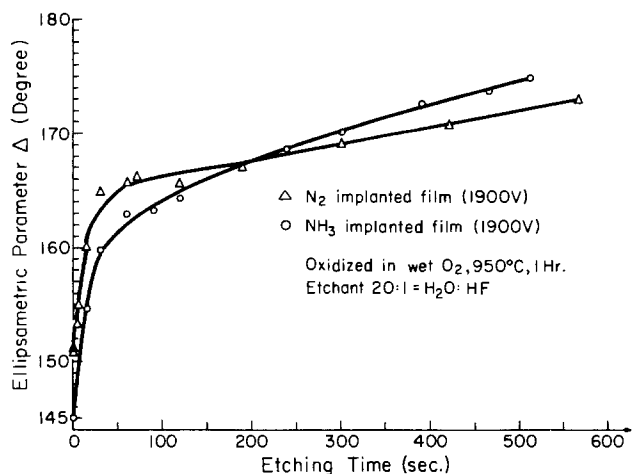


Fig. 6. The ellipsometer parameter, Δ , of the oxidized sample vs. the etching time. The two films showed very similar etching behavior.

composition. The Si KLL peak is excited by the Bremsstrahlung portion of the incident x-ray.

It is possible that, during the annealing, excess Si precipitates. The elemental peak of the Si KLL Auger line is the sum of emission from the substrate and the precipitate. In Fig. 7, the Si KLL signal can be deconvolved and the contributions from the elemental Si and nitrogen

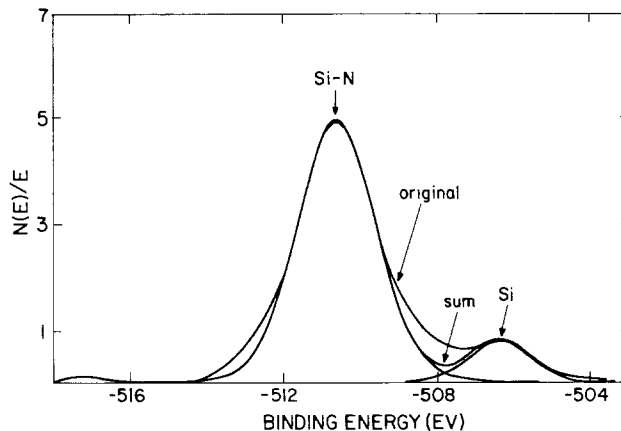


Fig. 7. The deconvolution of Si KLL Auger signal. We have indicated the deconvoluted signal for nitrogen-bonded Si and elemental Si. The original signal is larger than the sum of the two deconvoluted signals. This suggests that some of the Si atoms are in an incompletely bonded form.

bonded Si may be extracted. The ratios of nitrogen-bonded Si peak area to the elemental Si peak area, $I_{Si_3N_4}/I_{Si}$, are obtained. After the XPS analysis, the Δ of the samples are again measured.

Figure 8 is a theoretical calculation of $I_{Si_3N_4}/I_{Si}$ vs. the normalized film thickness, d/λ , where λ is the electron mean free path. The parameter R is the percentage ratio of precipitated Si to that of Si bonded to nitrogen. In the absence of experimental data, the mean free path in the implanted nitride and bulk Si is calculated based on Penn's model (5). They are 2.55 and 2.86 nm, respectively. In the calculation, we have also incorporated the appropriate implanted nitride density. The experimental data in Fig. 8 indicate that excess Si in the form of precipitation is less than 5%. However, excess Si may still exist in an incompletely bonded form.

Chemical state identification.—Table I lists the binding energy of N1s, Si2p peaks and the kinetic energy of N KLL and Si KLL peaks. Because of charging of the thick CVD nitride standard, modified Auger parameters, α^*_{N} and α^*_{Si} , are calculated for comparison (6). The modified Auger parameter is a sensitive measurement of the atomic chemical environment and is independent of charging. It is clear from Table I that the chemical state of

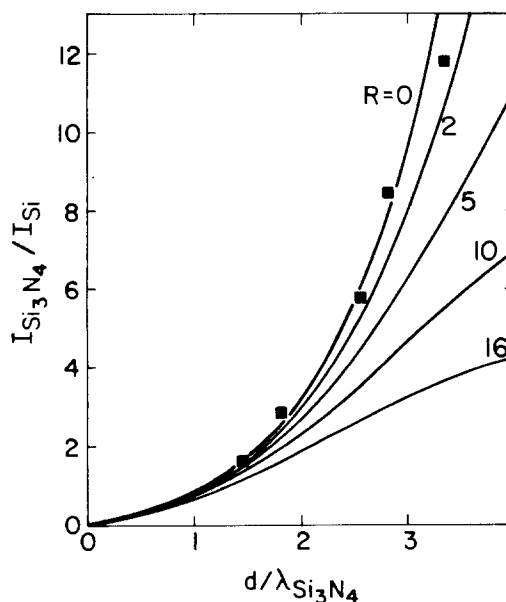


Fig. 8. The ratio of Si bonded to nitrogen to elemental Si, $I_{Si_3N_4}/I_{Si}$, vs. d/λ , the film thickness normalized by the electron mean free path. The parameter R is percent Si in the precipitated form. The filled squares are the measured data. The electron mean free path is calculated using Penn's model.

Table I. Binding energy, Auger electron energy, and Auger parameter (eV)

	N1s	N KLL	α^*_N	Si2p	Si KLL	α^*_{Si}
Standard	399.1	378.2	777.3	103.3	1610.9	1714.2
As-implanted	397.5	380.0	777.5	101.7	1612.6	1714.3
Annealed	397.5	379.6	777.1	101.7	1612.3	1714.0

the as-implanted and the annealed films are very close to that of standard CVD nitride. However, a difference of 0.3-0.4 eV in the Auger parameter between the as-implanted and the annealed samples is observed. The annealed film has a lower modified Auger parameter than the unannealed layer. The modified Auger parameter, α^* , is a measure of the extra-atomic relaxation energy, or, in other words, the polarization energy of the solid (7). A smaller α^* means that the compound is less polarizable.

To examine the sputter-implant process (4), a bare Si wafer was implanted in the XPS analysis chamber. In this experiment, we used a combined x-ray source of Au and Mg. Before the implant, the chamber was pumped down to below 10^{-9} torr. The high vacuum kept the contamination level to a minimum. Figure 9 shows the evolution of the Si KLL peak in various stages of the implant. Before the implant, the two peaks associated with the Si substrate; the native oxide are clearly resolvable and are indicated by arrows. Figure 10 shows the respective N_{1s} photoelectron lines.

Figure 9 indicates that as N_2 is implanted into the Si a new peak appears next to the elemental Si position and gradually shifts to the position expected of the nitride. The oxide peak decreases steadily and eventually disappears. However, the N_{1s} line remains fairly steady. The evolution of the Si KLL peaks suggests that the Si atoms are gradually being surrounded by nitrogen atoms. The nitrogen atoms react fully once they enter the substrate. This observation indicates that the film is likely to be Si rich. The disappearance of oxide is just due to the surface sputtering. These data are in agreement with our implant-sputter model (4) as well as the IR measurement.

Thickness, refractive index, dielectric constant, and density.—It is possible to determine the thickness, d , the dielectric constant, ϵ , the refractive index, n , and the density, ρ , based on the following assumptions: (i) the film is stoichiometric and homogeneous in composition, (ii) the chemical nature and the polarizability of the Si-N bond are the same as for CVD nitride, and (iii) the dielectric-bulk interface is abrupt.

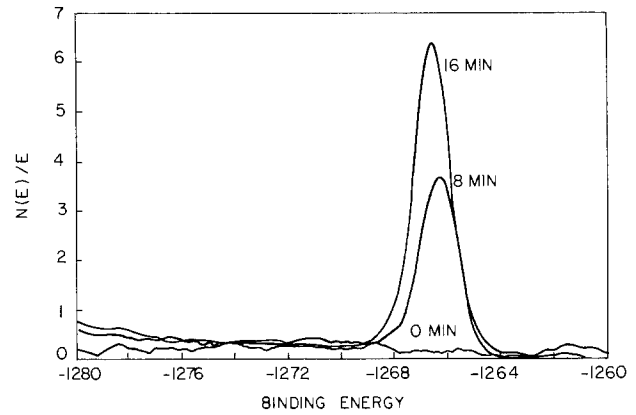


Fig. 10. Evolution of N_{1s} photoelectron line. No apparent shift in energy peak is observed.

As shown in Fig. 1, Δ is related to nd

$$nd = \alpha(\Delta_{Si} - \Delta). \quad [1]$$

The accumulation capacitance relates the thickness and the dielectric constant, which is a function of refractive index

$$C = \frac{\epsilon}{d} \quad [2a]$$

$$\frac{n}{n_{CVD}} \approx \left(\frac{\epsilon}{\epsilon_{CVD}} \right)^{1/2} \quad [2b]$$

The total nitrogen content can be equated to the product of density and film thickness. The density is related to refractive index through the Lorenz-Lorentz relation

$$D_n = 4A\rho \frac{d}{M} \quad [3a]$$

$$k\rho = \frac{(n^2 + 1)}{(n^2 - 1)} \quad [3b]$$

The parameters, D_n , A , ρ , and M are the nitrogen areal density, Avogadro's number, the film density, and the molecular weight, respectively. The nitrogen areal density is obtained by RBS measurements. The k in the Lorenz-Lorentz relationship can be determined by the known data for CVD nitride. In the calculations above, the CVD nitride is assumed to have the following parameters, $n = 2.05$; $\rho = 3.1$, $\epsilon_{CVD} = 7.5$ (8).

The parameters, Δ , C , and D_n are directly measurable by ellipsometry, capacitance, and RBS, respectively. A refractive index-thickness curve can be obtained from each of the equation sets above and are plotted in Fig. 11. The

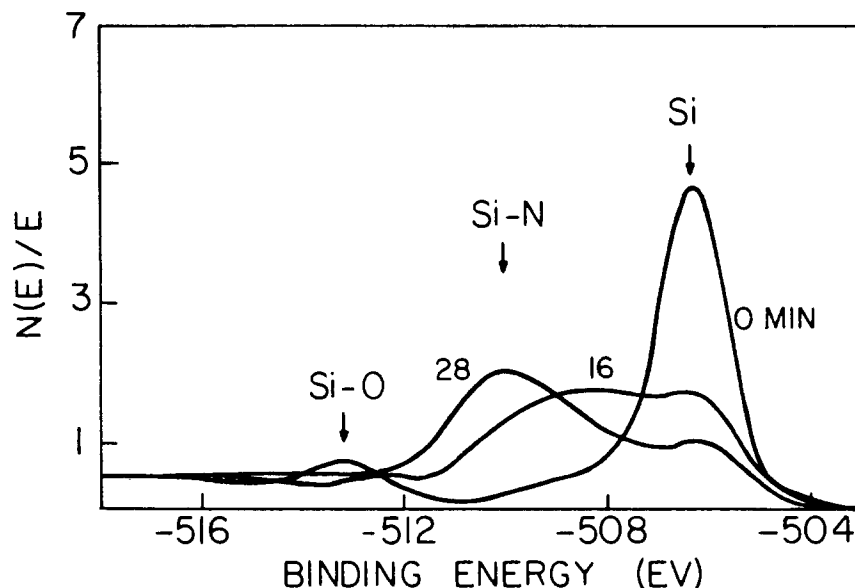


Fig. 9. Evolution of Si KLL Auger peaks as a function of implantation time. The implantation is done in the XPS analysis chamber. The long time span is due to the low beam current. Peak positions for oxide, nitride, and elemental Si are labeled.

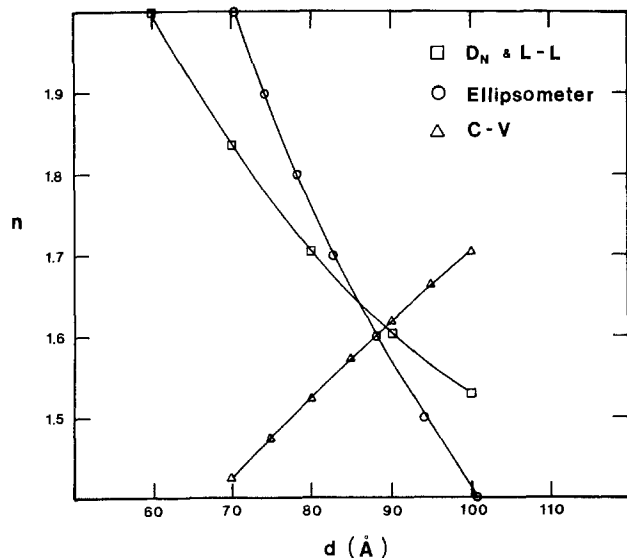


Fig. 11. Determination of the refractive index and film thickness. The three curves are deduced from the measured quantities of total nitrogen areal density, the ellipsometry, and capacitance. The refractive index and the film thickness are obtained by the intersection of the three curves.

intersection of any two of the three curves determines the film thickness and refractive index. From these intersections, the physical parameters of the annealed film are fixed within the following ranges: d : 8.5-9 nm, ρ : 2.1- 2.2 g/cm³, n : 1.6-1.65, and ϵ : 4.6-4.9. The most surprising finding of the analysis is the film's exceptionally low density. This causes the other parameters to deviate from the accepted CVD nitride values. One can imagine that the violent implantation process produces a low density nitride film.

Transmission electron microscopy.—A direct measurement of the film thickness was done using TEM. Figure 12 is a cross-sectional picture of a 1.9 keV N₂-implanted film. A 9 ± 1 nm thick amorphous layer is formed. The film is apparently divided into two parts by a layer of features about 2 ~ 3 nm in size. The nature of these features is unknown at the present. It may be due to artifacts in sample preparation. However, one can firmly conclude that a 9 ± 1 nm layer has been formed, and it appears to be amorphous. The data agree with the thickness derived in the last section.

Summary and Discussion

Hezel *et al.* (9) and Thomas *et al.* (10) have also investigated low energy N₂ implantation into Si. They have employed sputter AES profiling as the composition analysis technique. Instead of detecting excess Si, they conclude

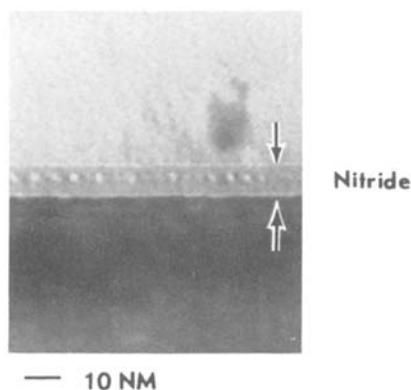


Fig. 12. The cross sectional TEM picture of the nitrogen implanted layer. The amorphous layer is found to be 9 ± 1 nm thick. (Courtesy of Dr. Ken Ritz, Signetic Company, and Dr. William Stacy of Philips Research Laboratories.)

that the as-implanted nitride has stoichiometric or near-stoichiometric composition. However, our measurements indicate that the film in the as-implanted form is Si rich. We feel that this is not a significant discrepancy due to the low resolution of AES composition analysis. The nitrogen atomic ratio in a stoichiometric nitride is 57%. It is too close to the atomic ratio of 50% in a film with N/Si = 1. As the resolution limit of AES improves, this discrepancy may be resolved.

The uniformity of the film composition in the as-implanted stage is indicated by all of our work. A layer of damaged Si, extending about 4 nm into the Si, is located at the film-substrate interface (4). The amount of damage observed here is less than reported by Thomas *et al.* After N₂ annealing, the composition approaches stoichiometric Si₃N₄. The damage is also reduced to a layer about 0.8 nm thick.

The chemical nature of the film has also been examined. It is investigated with wet etching, transmission infrared spectroscopy, and XPS. These studies indicate that a stabilization of chemical bonding occurs as result of N₂ heat-treatment. The stabilization exhibits itself in the compositional change, the reduction of etch rate, the shifting of transmission minimum in IR, and the decrease in the Si-N polarizability detected by XPS. It should be stressed that both IR and XPS investigations indicate that the chemical nature and the polarizability of the annealed film are very similar to CVD nitride films.

Another indication of the compositional change is the resistivity of the implanted layer. The as-implanted layer is highly conductive. After heat-treatment, the film is insulating. The lowering of conductivity is probably due to a reduction of excess Si. The resistivity increase also causes a decrease in the polarizability of the layer as measured by XPS. The XPS studies also reveal that, under N₂ bombardment, the Si substrate is gradually enriched with nitrogen until a steady state is reached. The nitrogen reacts fully once it enters the substrate. Si-N bonds exist in the as-implanted state.

To determine d , n , ϵ and ρ , we made three assumptions. First, the film is stoichiometric and homogeneous in composition. RBS, which is better for composition measurement, and AES profiling, which is the preferred profiling technique, indicate so. Second, the chemical nature and the polarizability of the Si-N bonds are the same as CVD nitride. This is indeed confirmed by our IR and XPS measurements. Third the dielectric-bulk interface is abrupt. TEM examination shows that this is a good assumption. The determination of d , n , ϵ , and ρ shows that the implanted film has very different physical parameters compared to CVD nitride. The low density is the cause of the low refractive index and dielectric constant. The low density is probably due to the sputter-implant process. The dielectric thickness of 8.5 ~ 9 nm is confirmed by direct TEM measurement. The data are also consistent with our ellipsometric measurements. It indicates that the annealed film has $d = 10 \pm 3$ nm and $1.4 \leq n \leq 1.6$.

Electrical studies have shown that, after annealing, the implanted nitride films contain a high density of positive fixed charge and trapping states. A full account of the electrical properties of the implanted nitride film will be

Table II. Material characteristics measured

	As-implanted	Annealed	Si ₃ N ₄ (CVD)
Stoichiometry	SiN	Si ₃ N ₄	Si ₃ N ₄
Damage	very high	reduced	—
Bonding	Si-N	Si-N	Si-N
Etch rate	high	reduced	—
Thickness (nm)	9	8.5 ~ 9	—
Density (g/cm ³)	—	2.1 ~ 2.2	3.1
n	—	1.6 ~ 1.65	2.05
ϵ	—	4.6 ~ 4.9	7.5
I-V	ohmic	insulator	insulator
C-V	—	positive fixed charge < 1 × 10 ¹⁹ /cm ²	—

-

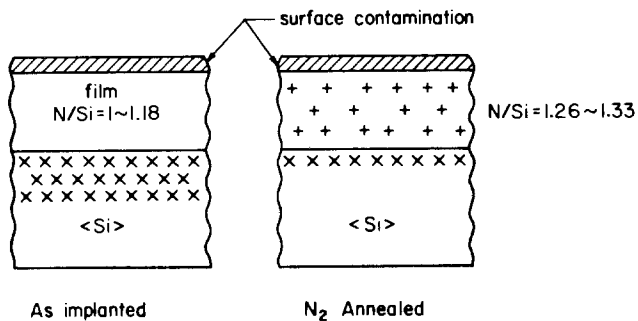


Fig. 13. The present understanding of the implanted nitride. The as-implanted nitride has a N/Si ratio of 1 and a layer of substrate damage is observed. After heat-treatment, the damage is partially removed, and the N/Si ratio approaches 1.3. Positive charge is detected.

presented elsewhere. The various material characteristics which have been measured are summarized in Table II.

The present understanding of the material properties of the implanted film is presented in pictorial form in Fig. 13. In the as-implanted state, the film is in a highly non-equilibrium, conducting, binding solid solution of nitrogen and silicon. After the annealing, the film relaxes to a

more stable, stoichiometric and insulating form. A high density of fixed charge and trapping states are also observed.

Acknowledgments

We would like to express our sincere thanks to Dr. L. Gilbransen for her assistance in XPS measurements. This research was sponsored by the Philips Research Laboratory and DARPA.

Manuscript submitted Nov. 28, 1983; revised manuscript received March 20, 1984. This was Paper 129 presented at the San Francisco, California, Meeting of the Society, May 8-13, 1983.

REFERENCES

1. T. Ito, T. Nozaki, H. Arakawa, M. Shinoda, and Y. Fukukawa, *This Journal*, **125**, 448 (1978).
2. M. L. Naiman, F. L. Terry, J. A. Burns, J. I. Raffel, and R. Aucoin, *I.E.D.M.*, 562 (1980).
3. T. Ito, T. Nakamura, and H. Ishikawa, *IEEE J. Solid-State Circuit*, **ssc-17**, 128 (1982).
4. T. Y. Chiu, H. Bernt, and I. Ruge, *This Journal*, **129**, 488 (1982).
5. D. R. Penn, *J. Electron Spectrosc. Relat. Phenom.*, **9**, 29 (1976).
6. J. A. Taylor, *Appl. Surf. Sci.*, **7**, 168 (1980).
7. C. D. Wagner, *J. Chem. Soc. Faraday Discuss.*, **60**, 291 (1975).
8. S. M. Sze, "Physics of Semiconductor Devices," 2nd Ed., Wiley, New York, (1981).
9. R. Hezel, and N. Lieske, *This Journal*, **129**, 379 (1982).
10. G. E. Thomas, L. J. Beckers, F. H. P. M. Habraken, and A. E. T. Kuiper, *Appl. Phys. Lett.*, **41**, 56 (1982).

Thermal Cleaning of InSb Surfaces in an Ultrahigh Vacuum

F. D. Auret

Department of Physics, University of Port Elizabeth, Port Elizabeth, Republic of South Africa

ABSTRACT

In and Sb surfaces of (111) InSb crystals were analyzed by Auger electron spectroscopy (AES) before, during, and after heating them in an ultrahigh vacuum system. Heating the samples to 450°C resulted in stoichiometric and oxygen-free surfaces. Sulfur due to chemical precleaning is removed at 470°C. Further, if the initial carbon concentration is low enough (< 10% surface coverage), then it can be almost totally removed by thermal cleaning at 450°C.

The degree of cleanliness of semiconductor surfaces is of the utmost importance during semiconductor device fabrication and has a pronounced influence on the characteristics and performance of these devices (1, 2). For GaAs, it was reported that the composition of the surface and the contaminants thereon could be related to the properties of Schottky barrier and ohmic contact devices formed on it (3, 4). Also, poor device characteristics in the case of InSb have been ascribed to nonstoichiometric surfaces caused by certain cleaning procedures prior to the metallization step (5). Auger electron spectroscopy (AES) studies of GaAs (3, 4, 6) and InSb (7) led to the optimization of cleaning procedures which yielded surfaces with a high degree of stoichiometry and with only small amounts of oxygen and carbon on them.

In order to further reduce the surface contaminants, several types of methods may be used. First, low energy sputter etching (8), plasma etching (9), or reactive ion etching (10) may be used to strip the surface of unwanted oxides and impurities. These techniques, however, cause a damage layer at the surface, consisting of, among others, positively charged donor states in the bandgap of the semiconductor (11-13). These defects change the effective barrier height of a Schottky barrier device, and can lead to very leaky devices on n-type substrates (8, 11, 12, 14). Second, *in situ* substrate heating may be used to clean the surface. The surfaces of GaAs substrates that were

heated to 550°C were completely stoichiometric and oxygen free, and contained only a small amount of carbon (6). The high degree of cleanliness, stoichiometry, and crystallographic order of these surfaces allowed gold films deposited on them to grow epitaxially (6).

It is the purpose of this paper to report on the results obtained when thermally cleaning InSb crystal surfaces by heating them in an ultrahigh vacuum (UHV). These results were obtained by using AES to monitor the surface stoichiometry and cleanliness as a function of substrate temperature.

Experimental Procedure

Three sets of samples, prepared from (111)-orientated n-type Te-doped ($4 \times 10^{15}/\text{cm}^3$) InSb crystals were studied. Each set consisted of two samples, of which the In and Sb surfaces were, respectively, investigated. Before inserting them into the Auger system, each set's samples were cleaned by different chemical procedure, as outlined in Table I. These three methods were selected because they yielded, respectively, high carbon, high oxygen, and high sulfur concentrations on the surface (7).

In the Auger system, samples were mounted on a heater block with their surface normals at an angle of 30° with respect to the incident electron beam and the analyzer axis. Auger measurements were obtained with a

Table I. Chemical cleaning methods for InSb before heat-treatment*

Cleaning step	Method I	Method II	Method III
Degrease and H ₂ O rinse	Yes	Yes	Yes
Etch in 1:10 HNO ₃ : lactic acid (2 min)	No	Yes	Yes
H ₂ O rinse	Yes	Yes	Yes
CP4A etch (5s)	No	Yes	Yes
Na ₂ S (10 ⁻³ M) rinse	No	No	Yes
H ₂ O rinse	Yes	Yes	Yes
N ₂ blow dry	Yes	Yes	Yes

* For a detailed description of the cleaning procedures, see Ref. (7).

Varian cylindrical mirror analyzer using a 3 keV electron beam. Analysis commenced after reaching a pressure of lower than 1×10^{-8} torr. This relatively high pressure was used because it is believed that the results thus obtained would still be valid in commercial metal deposition systems, where thermal substrate cleaning could be implemented.

After Auger analyzing the sample's surface at room temperature, its temperature was increased to 480°C at a rate of 0.1°C/s. At this rate, the sample, thermocouple, and heater block were always in thermal equilibrium. During heating, the Auger signals of the substrate as well as the contaminants were continuously monitored and recorded. Upon reaching the final temperature (480°C in most cases), the sample was kept at this temperature for about 5 min in order to ensure that its surface remains stoichiometric. Thereafter, the sample was cooled down to room temperature, at which stage a final Auger analysis was made.

The percentage surface coverage of each element is calculated from the simplified semiquantitative formalism, which requires only the Auger peak-to-peak heights and inverse sensitivity factors α_i of the surface elements (15). The α_i 's for In and Sb were experimentally determined for InSb (16), while those for carbon, oxygen, and sulfur were assumed equal to those for the GaAs matrix (17). This assumption is not completely valid for oxygen because most of it is present in the form of a surface oxide. However, it enables one to qualitatively compare the amounts of impurities obtained with different cleaning techniques.

Results and Discussion

Both the In and Sb surfaces exhibited the same thermal behavior; hence, only results of In sides are presented. Figure 1 is a typical temperature profile of a sample cleaned by method II (Table I). This profile may be divided into two regions. In region I, which extends from room temperature to 290°C, the concentrations of the substrate components and contaminants remain constant upon heating. The In/Sb ratio here is about 1.2. Region II, which extends from 290°C upwards, is characterized by a change in the In/Sb ratio and a decrease in the carbon and oxygen concentrations at the surface. The In/Sb ratio first increases to a maximum of 1.5 and then decreases to unity at 430°C. At about 400°C, the oxygen concentration starts to decrease sharply, and at 450°C it is completely absent from the surface. From 250°C upward, the carbon concentration also decreased from 8% surface coverage to 2% at 450°C. Upon further heating the sample to 480°C, the In/Sb ratio remains constant with 2% carbon as the only surface contaminant. In Fig. 2, the Auger surface scans of a sample cleaned by method II is shown. These scans were recorded before (Fig. 2a) and after heating (Fig. 2b).

The temperature profiles of samples cleaned by method I were similar to that described above for method II except for one difference. The initially high carbon concentration of 45% could not be reduced to below 35% even upon heating the substrate to 530°C.

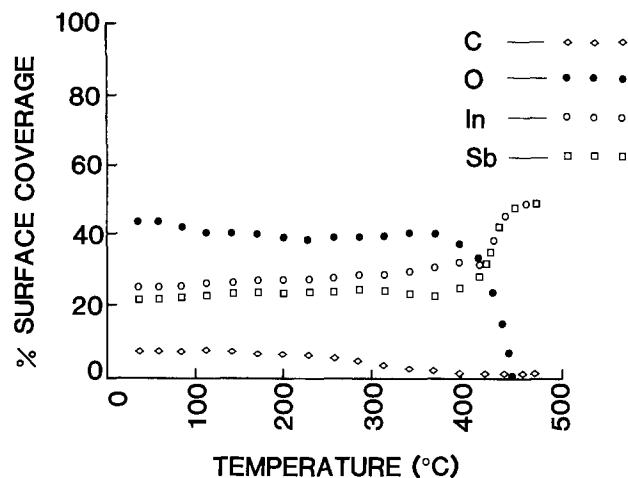


Fig. 1. Temperature profile of a CP4A-etched InSb sample

Figure 3 displays the temperature profile of a sample cleaned by method III. The main difference between this method and method II is that, in this case, most of the usual surface oxide was replaced with sulfur during the Na₂S rinse. As before, the profile may be divided into two regions. In the first region (< 250°C), the concentrations of oxygen and sulfur are approximately constant, and the carbon concentration increases slightly; the In/Sb ratio is less than one and increases gradually to reach unity at 250°C. In region II above 250°C, this ratio increases further to a maximum at 360°C and then gradually decreases to unity at 430°C, where it remains constant upon further heating. At 350°C, the sulfur concentration starts increasing, reaches a maximum at 410°C, and then decreases to zero at 470°C. The oxygen disappeared from

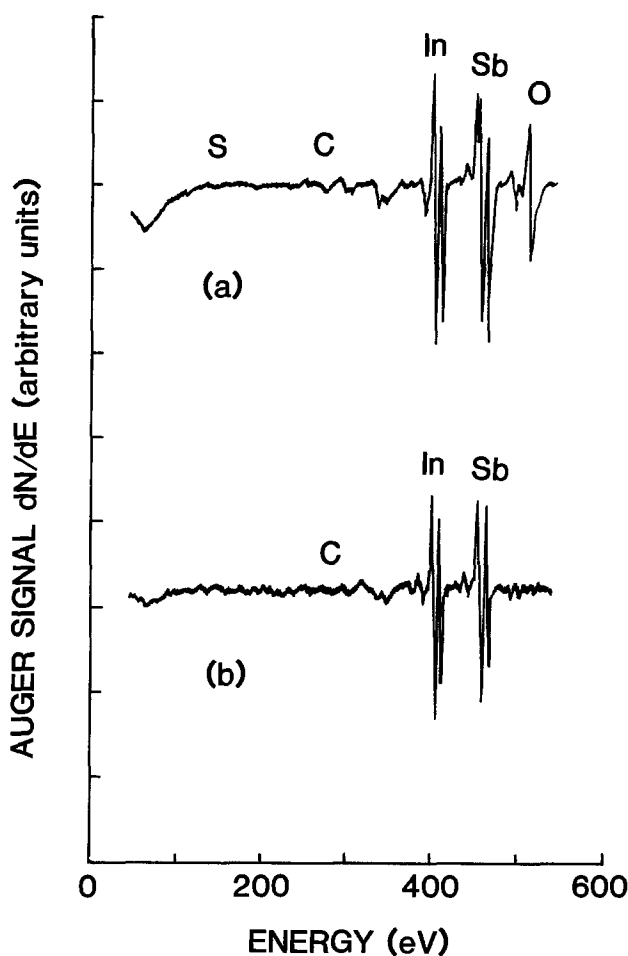


Fig. 2. Auger surface scans obtained (a) before and (b) after heating a CP4A-etched InSb sample to 480°C.

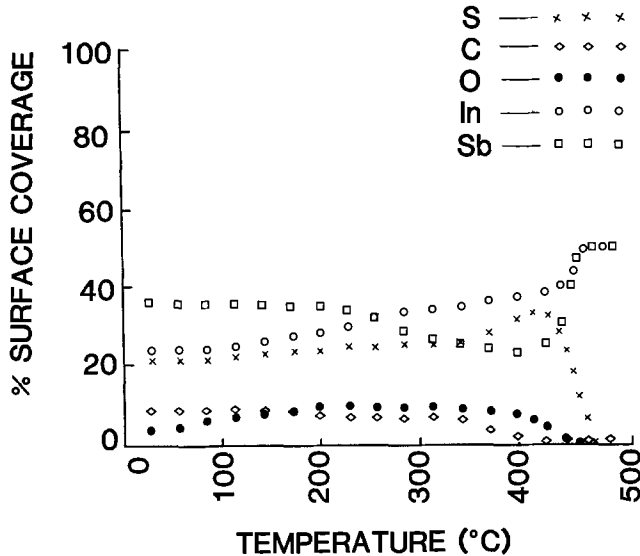


Fig. 3. Temperature profile of an InSb sample that were CP4A etched followed by a $\text{Na}_2\text{S}(10^{-5}\text{M})$ rinse.

the surface at 450°C as before. For this cleaning method, the carbon was reduced to below 1% surface coverage at 450°C.

The results of surface analyses obtained before and after heat-treatment of the crystals are depicted in Table II for methods I-III. They show that for all three cleaning methods, an oxygen- and sulfur-free surface with a unity In/Sb ratio can be obtained by heating the samples to above 400°C. A further point of interest is that if the initial carbon concentration is low enough ($< 10\%$) (methods II and III), then it can be reduced to acceptably low levels ($< 2\%$) by heat-treatment. However, if the initial carbon concentration is too high (method I), then heat-treatment is not efficient in removing it.

Recently, Chang (18) has shown that residual carbon left on GaAs substrates after chemical cleaning could be removed by heating the substrates to temperatures of between 350° and 400°C. It was further observed that if these substrates are exposed to an Auger electron beam during heating, then subsequent removal of carbon above 350°C becomes very difficult because of a strengthening of the bonds between the surface carbon and the substrate. In contrast, we observed that, although surfaces with an initially low carbon concentration (methods II and III) were continuously exposed to the Auger electron beam during heating, all carbon except 1%-2% could be removed by heating to above 400°C. This small amount of residual carbon may be ascribed to electron beam stimulated carbon buildup (19) caused by the Auger electron beam. It thus seems that almost all the carbon observed on the InSb surface after cleaning by methods II and III is present as weakly bonded or "physisorp-like" bonded (18) carbon, and that its bonding to the surface does not become stronger when exposing the surface to the Auger electron beam during heating. However, we found that where carbon was initially present in large concentrations (method I), the thermal removal of only a fraction thereof was possible. We speculate that, after cleaning the substrates by method I, most of the carbon present was strongly bonded to the InSb surface and could thus not be removed thermally. This is likely because method I only removes carbon by "degreasing," whereas in methods II

Table II. Surface contamination and stoichiometry of InSb before and after heating to 480°C*

Contaminant/stoichiometry	Percentage surface coverage Chemical cleaning method number					
	I		II		III	
Carbon	(45)	35	(7)	2	(8)	1
Oxygen	(25)	0	(40)	0	(3)	0
Sulfur	(0)	0	(0)	0	(23)	0
In/Sb	(1.5)	1	(1.2)	1	(0.7)	1

* The figures in parentheses were obtained after chemical cleaning but before heat-treatment; the unbracketed figures are for heat-treated samples.

and III carbon together with In and Sb is removed from the surface by etching.

Conclusions

We have demonstrated that it is possible to obtain oxygen- and sulfur-free surfaces with an In/Sb ratio of unity on InSb crystals by heating them to 470°C in a vacuum of less than 1×10^{-8} torr. The only contaminant present on the surface after heat-treatment is carbon, and its percentage surface coverage can be limited to below 2% by applying an appropriate chemical pre-cleaning before heat-treatment. This method should prove very valuable during device fabrication where an atomically clean and stoichiometric surface is of great importance.

Acknowledgments

The author wishes to thank M. E. Lee for experimental assistance and G. Over for many helpful discussions.

Manuscript submitted Dec. 3, 1983; revised manuscript received May 16, 1984.

The University of Port Elizabeth assisted in meeting the publication costs of this article.

REFERENCES

1. D. J. Fitzgerald and A. S. Grove, *Surf. Sci.*, **9**, 347 (1968).
2. M. M. Atalla, E. Tannenbaum, and E. J. Schneibner, *Bell Syst. Tech. J.*, **38**, 749 (1959).
3. I. Schiota, K. Motoya, T. Omi, N. Mijamoto, and J. Nishizawa, *This Journal*, **124**, 155 (1977).
4. A. W. R. Leitch, M. Sc. Thesis, University of Port Elizabeth, Port Elizabeth, Republic of South Africa, (1980).
5. H. L. Henneke, *J. Appl. Phys.*, **36**, 2967 (1965).
6. J. S. Vermaak, L. W. Snyman, and F. D. Auret, *J. Cryst. Growth*, **42**, 132 (1977).
7. F. D. Auret, *This Journal*, **129**, 2752 (1982).
8. N. Suzuki, H. Kataoka, T. Hariu, and Y. Shibata, *Jpn. J. Appl. Phys.*, **18**, 1879 (1979).
9. R. H. Burton and G. Smolinsky, Abstract 265, p. 645, The Electrochemical Society Extended Abstracts, Vol. 81-2, Denver, CO, Oct. 11-16, 1981.
10. R. A. Powell, *Jpn. J. Appl. Phys.*, **21**, L170 (1982).
11. S. K. Ghandhi, P. Kwan, K. N. Bhat, and J. M. Borrego, *IEEE Electron Device Lett.*, **ed1-3**, 48 (1982).
12. S. J. Fonash, S. Ashok, and R. Singh, *Appl. Phys. Lett.*, **39**, 423 (1981).
13. H. Matsumoto and T. Sugano, *This Journal*, **129**, 2823 (1982).
14. P. Kwan, K. N. Bhat, J. M. Borrego, and S. K. Ghandhi, *Solid State Electron.*, **26**, 125 (1983).
15. C. C. Chang, *Surf. Sci.*, **48**, 9 (1975).
16. F. D. Auret, *ibid.*, **140**, L225 (1984).
17. C. C. Chang, P. H. Citrin, and B. Schwartz, *J. Vac. Sci. Technol.*, **14**, 943 (1977).
18. C. A. Chang, *ibid.*, **21**, 663 (1982).
19. R. E. Kirbey and D. Lichtman, *Surf. Sci.*, **41**, 447 (1974).

Heating Effects in Reactive Etching of Nb and Nb₂O₅

Mao-Min Chen^{*,1} and Young H. Lee^{*}

IBM Thomas J. Watson Research Center, Yorktown Heights, New York 10598

ABSTRACT

The reactive etching mechanism of Nb and Nb₂O₅ in CF₄/O₂ RF plasma has been studied in a flexible diode reactor, with special emphasis on a thin film heating effect. Etch rates of both materials during reactive ion etching are determined by a combination of the ion bombardment enhanced etching mechanism and the chemical etching mechanism. In niobium, the chemical etching always dominates over the ion enhanced etching. Etch rates in the plasma etching mode are primarily due to the chemical etching mechanism. The activation energy in the chemical etching is estimated to be 0.22 and 0.11 eV for Nb and Nb₂O₅, respectively. The Nb chemical reactivity (etch rate divided by a number density of the fluorine atoms) shows a substantial increase proportional to RF power and, surprisingly, to Nb film thickness. The thicker the film, the higher the etching rate observed during plasma etching. We argue that this is due to a temperature rise in a Nb film caused by the eddy current generated by the RF magnetic field (*i.e.*, the RF inductive heating).

The substrate temperature plays a very important role during plasma etching, because etching rates due to the chemical etching mechanism normally exhibit the Arrhenius-type dependence on wafer temperature (1-6). Reproducibility of the etching process not only depends on how tightly one can control plasma parameters such as gas pressure, flow rate, and RF power, but also how precisely one can control the wafer temperature during etching. Also, etching uniformity across a wafer or from wafer to wafer within a batch may be influenced by a nonuniform distribution of wafer temperature, if contribution from the chemical etching mechanism is large. In a RF parallel-plate reactive etching system, it is difficult to measure the wafer temperature accurately and routinely because of the RF interference as well as a poor thermal contact between a temperature probe and wafer surface. Several proposals have been suggested to solve this problem (7-9). In addition to this, it is also troublesome to implement a reliable heat-transferring technique, which can effectively and reproducibly remove the heat from the wafer surface to a temperature-controlled substrate table without causing any detrimental contamination problem to the wafer surface and to the plasma. Thus, it is important to know a temperature dependence of etching rate for a particular reactive etching process. Temperature dependence of the Si and SiO₂ etching rates has been studied in great detail for a fluorocarbon gas plasma (6). Temperature dependence of etching rate in various materials has been reviewed and summarized by Vossen and Kern (10). As usual, the activation energy of reactive plasma etching was measured from a slope of the Arrhenius plot of etching rate *vs.* temperature. We note that, even in silicon which has been studied extensively, the activation energy reported in the literature shows a wide variation depending on the etching conditions (1-6). In this paper, we will clarify the temperature effect of etching rates in Nb and Nb₂O₅ films by measuring the fluorine atom density and etching rates at various plasma etching conditions. Also, our result sheds a light on the reason why the activation energy for silicon etching, having been reported in the literature, appeared to vary with experimental conditions.

Niobium, a superconductor, is a very important material widely used for fabricating Josephson tunnel junctions for application to high speed digital circuits. Niobium can be used as an electrode of the tunnel junction and a wiring material of Josephson IC circuits. Therefore, reactive plasma etching of niobium and Nb₂O₅ becomes a crucial technique in fabrication of a potential VLSI-type Josephson device. Although the plasma etching process has been successfully utilized for Josephson device fabrication (11-15), much more effort is needed to fully understand the reactive etching mechanisms of Nb in various gas plasma and also to evaluate the impact of the etching process on the device characteristics.

In this paper, we present a temperature dependence of the etching rate for Nb and Nb₂O₅ and demonstrate the importance of an effective heat transferring technique between the wafer back-surface and the substrate table. We also show that the total etching rate of Nb and Nb₂O₅ in CF₄/O₂ plasma consists of contributions from the chemical etching mechanism and from the ion-bombardment-enhanced etching mechanism, as in the case of silicon etching. Such physical quantities as wafer temperature, activation energy, ion-bombardment energy, and fluorine density play a key role in determining etch rates and are invoked in explaining the RF power dependence and the loading effect (alteration of a cathode surface material from Al to Si) of etching rate observed for both Nb and Nb₂O₅. Results will be directly compared with undoped polysilicon results obtained under the identical plasma condition. Also, we will show the experimental evidence that good conductors, like niobium, receive additional heat from the RF inductive heating due to the eddy current generated within the film, which is absent in poor conducting films like Nb₂O₅ and undoped polysilicon.

Experimental

The plasma reactor used was a flexible diode system similar to the one described elsewhere (16), in which both the perforated aluminum top electrode (30.5 cm diam) and the water-cooled aluminum bottom electrode (30.5 cm diam) were separately powered by two Plasma-Therm RF generators (13.56 MHz) through automatic matching networks. The bottom electrode served as the substrate electrode. A temperature of the bottom electrode is maintained by a temperature controlled water circulation bath (Neslab RTB-8). It can regulate the electrode temperature between 8° and 90°C. The reactor chamber (50 cm diam) was pumped by a Balzer turbomolecular pump (500 liter/s) and backed by a Roots blower system. A multigas pressure/flow controller (MKS-245) was used to control a gas pressure (± 0.01 Pa) at a downstream position with an automatic throttle valve (15 cm diam) and also to regulate a gas flow rate (± 0.5 sccm) at an upstream position. Good etching uniformity is obtained by feeding the gas from the top of the chamber with a symmetric inlet configuration.

Reactive etching experiments were carried out with one of the electrodes powered by a RF generator, while the opposite electrode was always dc grounded. The plasma etching mode (PE) is defined as the situation where wafers lie on the bottom, grounded electrode and the RF power is fed to the top electrode. The reactive ion etching mode (RIE) is the case where wafers sit on the RF-powered bottom electrode while the top electrode is dc grounded. Niobium films are E-beam deposited onto thermally oxidized silicon wafers to a thickness of 230 to 1000 nm with a minimum residual resistance ratio of 5, which represents a high purity of Nb films. Niobium penta-oxide is a 220 nm thick film grown by partially anodizing 230 nm thick Nb film in a chemical solution of ammonium penta-borate and ethylene glycol. Etching

^{*}Electrochemical Society Active Member.

¹Present Address: IBM Research Laboratory, San Jose, California 95193.

rates are determined by using either a Talystep, when samples are patterned by photoresist, or a He-Ne laser interference detector, when samples are blanket Nb₂O₅ and Nb films. Nominal sample size was about 3 cm². Samples are usually loaded on the aluminum bottom electrode without any further means of thermal bonding. To investigate the RF heating effect, a series of experiments were carried out with the sample thermally bonded to the bottom electrode by vacuum grease (Apiezon H). No obvious chemical effects due to the presence of the vacuum grease in the system was observed. This was checked out by loading two samples on the substrate electrode, in which one sample was bonded by vacuum grease and another free of it. The etching rate of Nb on the substrate without thermal bonding was the same as that obtained at the identical etching condition immediately before this control experiment. The companion sample which was thermally bonded to the water-cooled bottom electrode gave a Nb etching rate much lower than that without thermal bonding, presumably because of an effective cooling by vacuum grease. For cathode loading experiments, we loaded blanket silicon wafers (57 mm diam) so that 42% of the aluminum cathode surface area was covered by silicon wafers.

A PAR-1450 optical multichannel analyzer was installed so that the spectrometer entrance slit lies at a level of 1 cm above the substrate electrode. This monitors the emission spectra from a glow discharge through a quartz window mounted on the side wall. The spectra with wavelength range from 365 to 850 nm were acquired during etching. Argon actinometry (17) was employed to estimate the ground-state fluorine atom concentration.

Results and Discussion

Temperature effect.—The temperature sensitivity of Nb and Nb₂O₅ etching rates during plasma etching was measured by varying the temperature of the substrate electrode while holding other plasma etching conditions constant. The reason for using the plasma etching mode was to evaluate the temperature sensitivity of the chemical etching rate and to minimize any contribution arising from ion bombardment in a parallel-plate reactor. RF power was chosen to be 70W (0.1 W/cm²) in an effort to reduce any possible RF heating at a high power density. As we will show below, RF heating of Nb films was observed even at this power density. Figure 1 shows the temperature dependence of etching rate (ER) during plasma etching for both Nb and Nb₂O₅. Samples were loaded on the electrode without any means of thermal bonding between a sample and the temperature-controlled electrode. The activation energy estimated from the slope of log (ER) vs. 1/T plot are 0.22 eV for Nb and 0.11 eV for Nb₂O₅. The fluorine atom density, estimated by argon actinometry, remained the same as substrate temperature was increased.

Hence, the etching rate of Nb film is more sensitive to temperature variations than that of Nb₂O₅. For comparison, the activation energy of undoped poly-Si is also estimated to be 0.07 eV under identical experimental conditions in the same reactor, in reasonable agreement with some of the results reported in the literature (1, 4, 6). Note that a wide variation of the activation energy has been reported for Si etching in the fluorocarbon gas plasma. We will discuss the reason for this wide variation in activation energy below. The result in Fig. 1 also suggests that an etching rate (ER_{PE}) during plasma etching can be expressed by the equation

$$ER_{PE} = Kc \cdot N_f \cdot \exp(-\Delta E/kT) \quad [1]$$

where Kc is a rate constant which depends on the gas temperature, N_f the fluorine concentration, k the Boltzmann constant, T a wafer temperature, and ΔE the activation energy. From the process development point of view, it will be very helpful if one knows the activation energy of materials to be etched under the same plasma etching condition, because ΔE and Kc determine the etching rate selectivity of the materials involved.

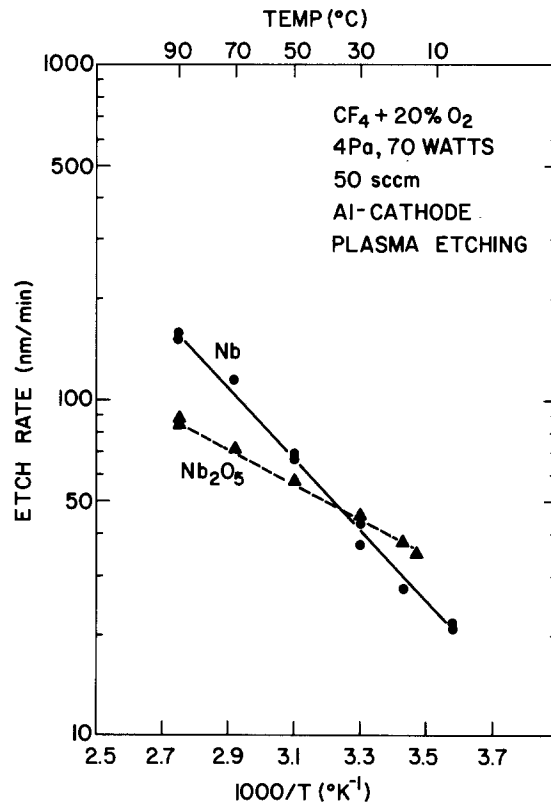


Fig. 1. Temperature dependence of etch rates of Nb (●) and Nb₂O₅ (▲) measured during plasma etching. The activation energy which was calculated from the slope is 0.22 and 0.11 eV for Nb and Nb₂O₅, respectively. Temperature was measured at the water circulation bath, so that it may not be a "true" temperature of the sample surface.

There has been some experimental evidence (7) that wafer temperature increases rapidly with RF power during etching, if the wafer is not thermally bonded to the temperature controlled electrode. Figure 2 shows the effect of thermal bonding on the etching rate of Nb at various temperatures. Thermal bonding was achieved by applying vacuum grease (Apiezon H) to the back side of a sample. The solid line represents temperature dependence measured without thermal backing, and the dotted line is with thermal backing. Since solid and dotted lines in Fig. 2 are roughly parallel to each other, our estimate of the Nb activation energy in Fig. 1 should be correct, as long as the relative temperature was measured accurately. Also, we can estimate from Fig. 2 that the actual temperature of wafer without thermal bonding should be about 20° to 30°C higher than that with thermal bonding. Similar experiments were carried out also for Nb₂O₅ films and the results are shown in Fig. 3. The difference in the etching rates between bonded and nonbonded samples can hardly be observed. The temperature difference could be, at the worst, about 10°C or less. Since the heat removal rate should be about the same because a similar vertical structure was used for both samples, the amount of heat generated at the Nb surface may be larger than the heat generated on the Nb₂O₅ surface during RF plasma etching.

Power dependence.—The RF power dependence of etching rates was measured for Nb and Nb₂O₅ during both plasma etching and reactive ion etching, and the results are shown in Fig. 4. The fluorine population (a relative intensity of the FI emission line against the ArI line, I_F/I_{Ar}) was measured at the same time as a function of power and is illustrated in Fig. 4, also. At a fixed RF power, the fluorine density in the CF₄/O₂ plasma is more or less the same between plasma etching and reactive ion etching within our experimental error as long as the Al electrodes are not loaded with a fluorine consuming material (18). The power dependence of Nb₂O₅ etching rate is very similar to that of undoped polysilicon we reported

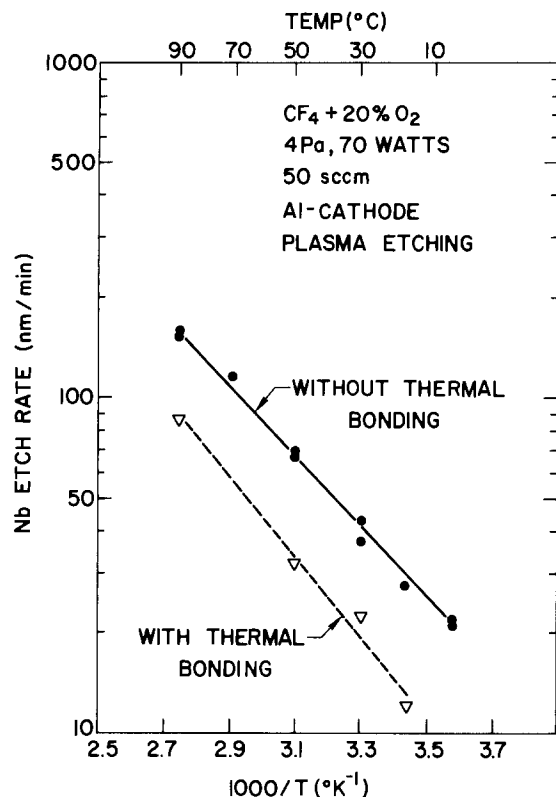


Fig. 2. Temperature dependence of the Nb etching rates in the plasma etching mode with (dotted line, ∇) and without (solid line, \bullet) thermal bonding between the substrate electrode and the back surface of a sample. A temperature at the Nb surface without thermal bonding is about 30°C higher than a temperature at the substrate electrode. The activation energy of Nb is 0.22 eV in both cases.

previously (18), but Nb etching rate appears to behave quite differently from undoped polysilicon.

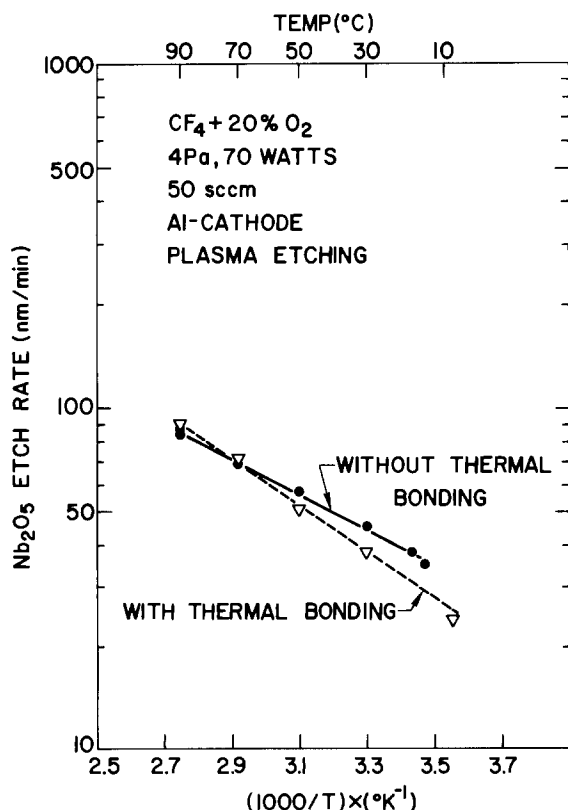


Fig. 3. Temperature dependence of the Nb_2O_5 etching rates in the plasma etching mode with (dotted line, ∇) and without (solid line, \bullet) thermal bonding between the substrate electrode and a sample.

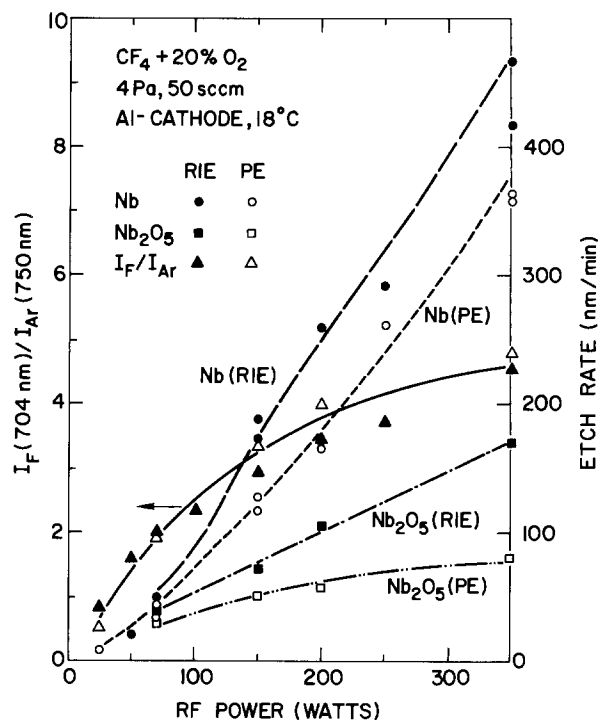


Fig. 4. Etch rate vs. RF power for Nb and Nb_2O_5 measured in the plasma etching mode (PE) and the reactive ion etching mode (RIE). The substrate electrode is made of Al, and etch rates were measured under no loaded condition. I_F/I_{Ar} , which represents a number density of the neutral fluorine atoms in the plasma, is almost equal between plasma etching and reactive ion etching.

In Fig. 5, we plot the chemical reactivity (etching rate divided by a F concentration or I_F/I_{Ar}) of Nb and Nb_2O_5 as a function of RF power during plasma etching. The chemical reactivity of Nb_2O_5 increases slightly as the power is increased, as in the case of polysilicon. However, niobium

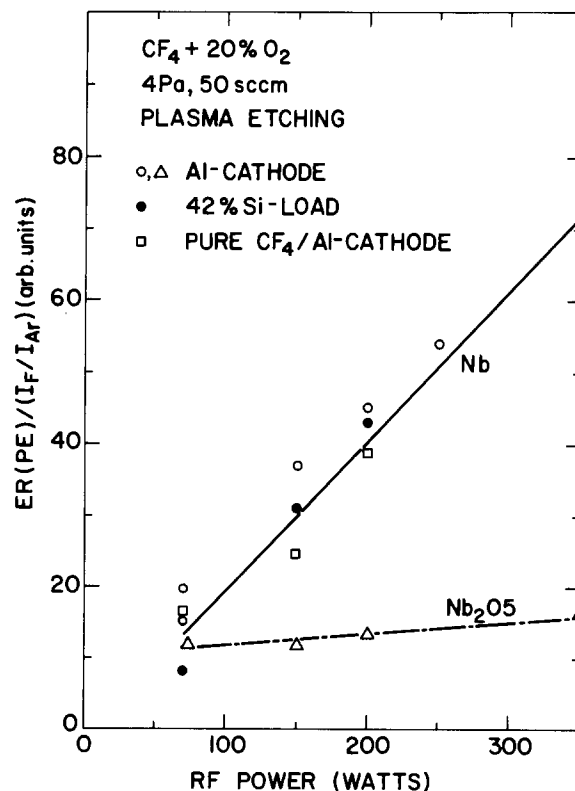


Fig. 5. RF power dependence of the chemical reactivity of Nb and Nb_2O_5 measured in the plasma etching mode. The chemical reactivity, etch rate divided by a fluorine density, is the same, independent of a cathode loading.

exhibits a drastic increase in the chemical reactivity, proportional to RF power. The apparent chemical reactivity of Nb at a given power is relatively constant, regardless of a large change in the fluorine population, which may be achieved by varying a cathode loading condition or O₂% in CF₄/O₂ without changing the gas pressure, flow rate, and RF power. Therefore, we argue that a strong power dependence of the Nb chemical reactivity could be caused by any variation in wafer temperature due to RF power (see Eq. [1]). Also, the Nb activation energy, which is larger than that of both Nb₂O₅ and Si, should be to some extent responsible for a high sensitivity of the Nb etching rate contributed by the chemical etching mechanism. However, as we will describe later, there is some indication that the Nb wafer temperature increases with increasing the power density at a rate much faster than that of Nb₂O₅ and Si. A difference in wafer temperature between Nb and Nb₂O₅ becomes larger as the power density is increased. Because of higher temperature and activation energy, the Nb chemical reactivity (ER/N_r) increases with RF power much faster than those of Nb₂O₅ and Si, as shown in Fig. 5. Since the etching rate of Nb is more sensitive to the wafer temperature than that of Nb₂O₅ and Si, controlling the temperature during etching is critical, especially at high power density for Nb films. This may explain why Nb etching rates sometimes exhibit wide variations, particularly at high power, if heat transfer is poor.

We have shown previously (18) that the total etching rate in undoped Si during reactive ion etching contains contributions from the chemical etching mechanism as well as from the ion-bombardment-enhanced etching mechanism. Hence, etching rate due to the ion-enhanced etching mechanism alone can be estimated by subtracting the chemical etching component from the total etch rate. Under our unloaded condition where the fluorine population is the same between plasma etching and reactive ion etching (see Fig. 4), the chemical etching contribution should be almost equal in the two etching modes (RIE and PE). Thus, we subtract the etch rate in plasma etching from the total etch rate during reactive ion etching to obtain the ion-enhanced etching contribution. We find that, in the case of Nb, the etching rate contribution from the ion-enhanced etching mechanism is much smaller than that from chemical etching mechanism, especially at high power density, as shown in Fig. 4. Etch rates due to the ion enhanced etching mechanism follow the similar power law of the dc self-bias voltages (V) as we found in undoped polysilicon; that is

$$ER_i = K_1 V^n \quad [2]$$

We estimated $n = 3.1 (\pm 0.3)$ for Nb and $n = 2.2 (\pm 0.3)$ for Nb₂O₅ from the slope of a $\log (ER_i)$ vs. $\log (V)$ plot. K_1 is a constant. Thus, during the reactive ion etching mode, the total etching rate for both Nb and Nb₂O₅ can be expressed by

$$ER_T = K_c N_F \exp(-\Delta E/kT) + K_1 V^n \quad [3]$$

We note that the chemical etching component (the first term in Eq. [3]) results in the isotropic etching profile, and the ion-enhanced etching component (the second term in Eq. [3]) yields the directional etching profile parallel to the direction of impinging ions. If one uses the same plasma parameters as those specified in Fig. 4 and a nonerodible mask such as aluminum film, one would expect less undercutting in Si than in Nb. In other words, it is easier to produce vertical edge profiles for undoped poly-Si than for Nb in CF₄/O₂ plasma because the chemical etching component of Nb is substantially larger than the ion-enhanced etching contribution, but the relative magnitude of those two components is reversed in Si. Therefore, in order to achieve a vertical sidewall, the important consideration is to suppress the chemical etching by reducing a wafer temperature as well as fluorine population in plasma and to maximize the ion enhanced etching by increasing the self-bias voltage. This general rule has been verified in both Nb and undoped polysilicon

(20) and would apply to any material which can be etched by fluorine, unless polymerization comes into play.

Loading effect.—The cathode loading effect has been reported in reactive plasma etching for many materials, including Nb (15) and Si (3). Figure 6 presents the Nb etching rates during both reactive ion etching and plasma etching with 42% of the cathode area loaded with Si wafers. Using optical emission and argon actinometry, we have shown that the fluorine atom density decreases upon loading Si wafers due to a consumption of fluorines at the wafers (18). This reduction in a number density of the neutral fluorine atoms is primarily responsible for the decrease in etching rates due to silicon loading. The extent to which the Nb etching rate decreases upon Si loading is much larger during reactive ion etching than that during plasma etching. We observed that etch rates during reactive ion etching are always lower than those during plasma etching, independent of RF powers we studied. It is to be noted that, in the unloaded case, the reactive ion etching mode gives a higher etch rate than the plasma etching mode, as shown in Fig. 4. The reason for reversing the relative magnitude between the two etching modes (RIE vs. PE) upon silicon loading is simply due to the fact that the chemical etching predominates over the ion-enhanced etching in Nb. Since the fluorine atom density is about the same between the RIE and PE modes under the unloaded condition, the chemical etching component without Si loading should be almost equal between the RIE and PE modes, independent of RF power. Also, we know that the plasma potential was estimated to be relatively low and Nb is mostly etched through chemical reaction between Nb and F (19).

When silicon wafers are loaded onto the Al cathode, a fluorine density decreases in both RIE and PE modes but the amount of decrease is much higher during reactive ion etching (a factor of 2 to 5) than during plasma etching (30%). Because of a large difference in F depletion between the two etching modes, the chemical etching component decreases during RIE more than during PE. Hence, the total Nb etch rate during reactive ion etching becomes lower than that during plasma etching, even though a contribution from the ion-bombardment-enhanced etching mechanism certainly exists during reactive ion etching. Niobium is a typical example of the fact that ion-bombardment-enhanced etching does not necessarily dominate over chemical etching.

We note that the loading effect could introduce an error into the activation energy for the plasma etching process. The activation energy was normally estimated from the Arrhenius plot of etching rates against wafer temperatures. Although silicon etching by fluorine radicals has

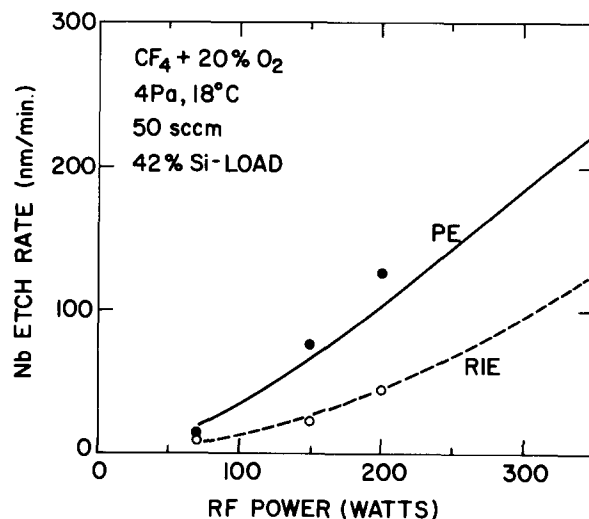


Fig. 6. Niobium etch rate vs. RF power measured under a Si loaded condition. Etch rates in plasma etching (PE) is faster than etch rates in reactive ion etching (RIE).

been studied very extensively, the reported activation energy varies from 0.02 to 0.14 eV, depending on experimental conditions. A lower activation energy was obtained upon loading silicon wafers in the etching system. One would expect the activation energy to be a constant for a given set of radicals and materials, unless the loading effect alters chemistry of the etching process. When the cathode is loaded with a F consuming material, the fluorine density inside the reactor chamber could vary with the substrate temperature. This is expected because higher substrate temperature means higher etching rate, resulting in a smaller number of fluorines available in the plasma. Since the activation energy originates from the chemical etching mechanism which prevails during plasma etching, the activation energy must be derived from the plot of $\log(ER/N_F)$ vs. $1/T$, instead of $\log(ER)$ vs. $1/T$. Figure 7 illustrates the difference between these two methods of estimating the activation energy. When the Al electrode is not loaded, the fluorine population is constant, independent of the substrate temperature, and, consequently, there is no difference whether ER or ER/N_F is used. When the cathode is loaded with Si wafers, ER/N_F must be used to estimate the activation energy. In Fig. 7, the activation energy of Nb derived from ER/N_F is constant (0.22 eV), independent of whether the system is either unloaded or loaded with Si. However, if ER is used, it becomes 0.10 eV, a factor of 2 smaller than the true value. Therefore, the activation energy should be estimated under no cathode loading and requires not only etching rates and wafer temperatures, but also accurate measurement of the fluorine population.

Film thickness dependence.—We have mentioned above that Nb is heated more than Nb_2O_5 by the CF_4/O_2 RF plasma. Furthermore, the chemical reactivity of Nb appears to have a strong dependence on RF power (see Fig. 5), which differs from the results we observed in undoped silicon (18). Since the chemical reactivities of Nb, Nb_2O_5 , and Si were measured under the same plasma condition in the same reactor, the power dependence should be caused by the inherent characteristics of Nb rather than the chemical and physical properties of the CF_4/O_2 plasma. Also, Nb etching rates in the plasma etching

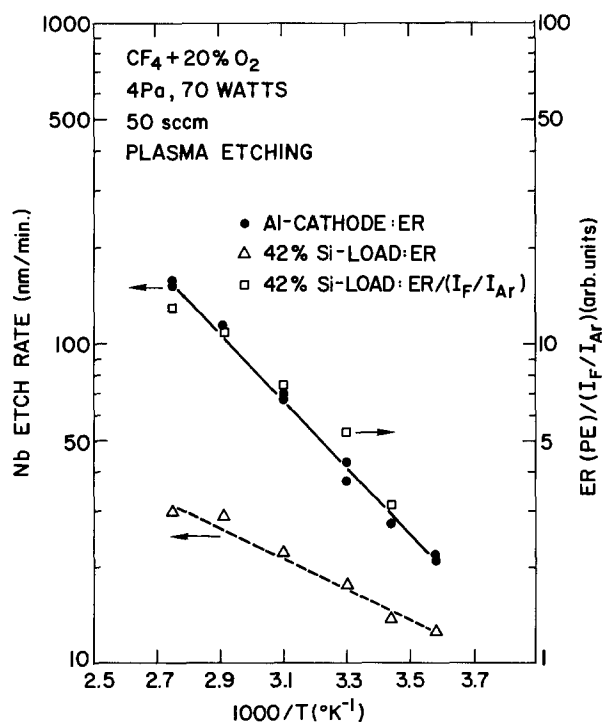


Fig. 7. Niobium etch rate vs. temperature, measured in the plasma etching mode with loading Si wafers which covers 42% of the Al electrode surface. The chemical reactivity (\square), measured under a Si-loaded condition, gives the same slope as Nb etch rate measured without loading Si wafers.

mode are predominantly due to the chemical etching mechanism, which does not require energetic ion bombardments (20).

The surface of a wafer could be heated by many different forms of energy present in RF plasma. The ambient temperature of RF glow discharge is proportional to power, and heat always flows from a volume of the intense glow to the surrounding walls, including the sample surface, by means of radiative conduction and, more effectively, through convection current of gas particles. In a parallel-plate reactor, an energetic particle such as ions and electrons impinges on a substrate surface and dissipates the kinetic energy to a substrate, consequently heating a wafer. Also, chemical reaction at a sample surface may accompany a heat release, if the reaction is exothermic or if excited species of radicals are involved. All the heat sources described above should affect both Nb and Nb_2O_5 equally. Another source of heat is the RF inductive heating (21) due to the eddy current which is normally generated in a highly conductive material by the ac magnetic field. Although the eddy current in a material such as insulator and semiconductor is negligible, the RF dielectric heating (21) due to the displacement current might become significant in plasma etching Si and Nb_2O_5 , if RF voltages were very large. Therefore, the RF inductive heating would play very important roles in the reactive etching process in RF plasma reactors, particularly in etching metal films and degenerate semiconductors (22) at a high RF power.

We measured Nb etch rates in the plasma etching mode for three different film thicknesses. The results are shown in Fig. 8 as a function of RF power. At a fixed power, the etch rate of a thicker Nb film is always higher than that of a thinner film. Moreover, etch rates of a thicker film increases with increasing RF power much faster than those of a thinner film. Thus, the difference in etch rate among different thickness films becomes more substantial at a higher RF power. N_F is fixed at a given power. The activation energy and the rate constant in Eq. [1] must be independent of the film thickness. Also, our Nb samples were prepared at a high 10^{-8} torr by E-beam evaporation, and exhibit the tensile stress of 0.8% ~ 0.9% and a fiber texture highly aligned along $\langle 110 \rangle$ direction, independent of a thickness within the range used in the present etching study (23). The residual resistance (a ratio of the sheet resistance at 300 K against that at 9.2 K, the superconductor critical temperature of Nb) is always higher than 5, which warrants the purity of our Nb films. Hence, neither film structure nor purity plays any role in the thickness dependence of Nb etch rates we have observed. We argue that the thickness dependence of Nb etch rates must arise from a difference in the temperature; that is, the thicker the film, the higher the substrate temperature is gained during RF plasma etching. Note that heating by radiation, gas convection, or

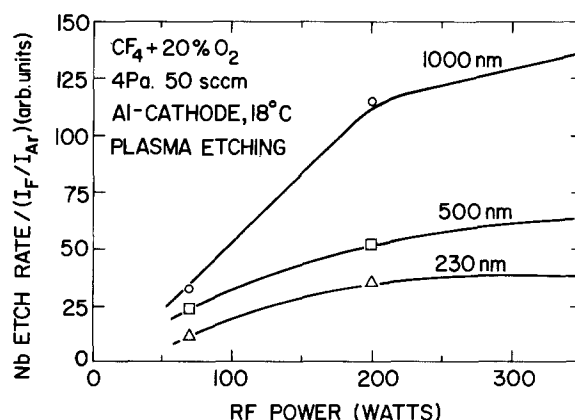


Fig. 8. RF power dependence of etch rate for three different thickness of Nb film. A thicker film yields a higher etching rate at a fixed RF power. Etch rates were measured in the plasma etching mode with the Al electrode (unloaded condition).

chemisorption should be independent of a film thickness; inductive heating is not. The eddy current flows below the surface to the effective skin depth, which depends on the electrical conductivity and electrical properties of the material to be etched. The depth of current penetration should be less than the depth of the heating zone, because thermal conduction pulls the heat in from the surface. The effective skin depth of Nb is roughly 50 μm at 13.56 MHz, much larger than Nb film thickness ($\leq 1 \mu\text{m}$) we studied. Thus, only a small portion of the input power can be dissipated at the Nb film, and the rest would be either reflected back or penetrate through. In any event, a RF power dissipation per unit area is approximately constant throughout the film, because Nb film thickness is less than 2% of the skin depth. We argue that the total heat quantity generated by RF dissipation per unit area would be directly proportional to a film thickness, resulting in a higher film temperature in a thicker film. At a fixed film thickness, substrate temperature increases with power. Therefore, we regard this thickness dependence of Nb etch rates as a strong experimental evidence that the RF inductive heating exists in metal films during RF plasma etching and this local heating effect enhances the contribution due to the chemical etching mechanism. We have observed a similar behavior in the heavily doped n-type silicon, suggesting that the doping effect in reactive etching would be caused by the RF inductive heating (22).

Summary

An efficient thermal contact between a substrate and the substrate electrode is essential to achieve good etching uniformity and reproducibility, especially in etching metal films like niobium. Reactive plasma etching of both Nb and Nb₂O₅ is contributed by chemical etching as well as ion-bombardment-enhanced etching, as in the case of silicon etching. The chemical etching mechanism predominates in plasma etching, but both chemical etching and ion-enhanced etching mechanisms are present in reactive ion etching. Competition between these two etching mechanisms determines the sidewall etch profile. The chemical reactivity of Nb exhibits a substantial increase proportional to RF power. This is attributed to the RF inductive heating due to the eddy current, which should be only effective in a highly conducting material such as metals, silicides, and heavily doped degenerate semiconductors. The RF inductive heating in Nb is so significant that Nb etching rates during plasma etching varies with a film thickness. The thicker the Nb film, the higher film temperature results from the inductive heating, leading to a higher etch rate.

Acknowledgments

We would like to thank J. Cataldo, M. Chow, and D. Favreau for technical help, Dr. J. Coburn and Dr. H.

Winters for technical discussions at the initial stage of this work, Dr. T. Yogi for providing us with niobium samples, and Dr. R. H. Wang and Dr. B. van der Hoeven for critical reading of the manuscript and managerial support throughout this work.

Manuscript submitted Nov. 23, 1983; revised manuscript received March 7, 1984.

IBM Corporation assisted in meeting the publication costs of this article.

REFERENCES

1. Y. Horiike and M. Shibagaki, *Jpn. J. Appl. Phys.*, **15**, (Suppl.), 13 (1976).
2. R. G. Poulsen, *J. Vac. Sci. Technol.*, **14**, 266 (1977).
3. C. J. Mogab, *This Journal*, **124**, 1262 (1977).
4. T. Enomoto, M. Dena, A. Yasuoka, and H. Nakata, *Jpn. J. Appl. Phys.*, **18**, 155 (1979).
5. A. R. Reinberg, in "Etching for Pattern Definition," H. Hughes and M. Rand, Editors, p. 91, The Electrochemical Society Softbound Proceedings Series, Princeton, NJ (1976).
6. D. L. Flamm, V. M. Donnelly, and J. A. Mucha, *J. Appl. Phys.*, **52**, 3633 (1981).
7. G. C. Schwartz and P. M. Schaible, in "Plasma Processing," R. Frieser and C. Mogab, Editors, p. 133, The Electrochemical Society Softbound Proceedings Series, Pennington, NJ (1981).
8. E. J. Egerton, A. Nef, W. Millikin, W. Cook, and D. Baril, *Solid State Technol.*, **25**, 84 (1982).
9. P. Kolodner, A. Katzir, and N. Hartsough, *Appl. Phys. Lett. B*, **42**, 749 (1983).
10. J. L. Vossen and W. Kern, "Thin Film Processes," p. 535 Academic Press, New York (1978).
11. S. A. Reible, *IEEE Trans. Magn.*, **mag-27**, 303 (1981).
12. T. T. Foxe, B. D. Hunt, C. Rogers, A. W. Kleinsasser, and A. Buhrman, *J. Vac. Sci. Technol.*, **19**, 1394 (1981).
13. T. Harada, K. Gamo, and S. Namba, *Jpn. J. Appl. Phys.*, **20**, 259 (1981).
14. R. F. Broom, A. Oosenbrug, and W. Walter, *Appl. Phys. Lett.*, **37**, 237 (1980).
15. M. M. Chen and R. H. Wang, *J. Vac. Sci. Technol.*, **A1**, 708 (1983).
16. L. M. Ephrath, *IEEE Trans. Electron Devices*, **ed-28**, 1315 (1981).
17. J. W. Coburn and M. Chen, *J. Appl. Phys.*, **51**, 3134 (1980).
18. Y. H. Lee and M. M. Chen, *ibid.*, **54**, 5966 (1983).
19. H. F. Winters, Personal communication.
20. D. Favreau, M.-M. Chen, and Y. H. Lee, Unpublished data.
21. J. W. Cable, "Induction and Dielectric Heating," Chap. 2, Reinhold, New York (1954); also see "American Institute of Physics Handbook," 2nd ed., D. E. Gray, Editor, Sect. 5, McGraw Hill, New York (1972).
22. Y. H. Lee and M.-M. Chen, Unpublished data.
23. M. Murakami and T. Yogi, *J. Appl. Phys.*, To be published.

High Frequency Capacitance Characteristics of the Thin-Based MOS Electrode

A. G. Anastopoulos, P. Nikitas, and D. A. Jannakoudakis

Laboratory of Physical Chemistry, University of Thessaloniki, Thessaloniki, Greece

ABSTRACT

The differential capacity characteristics of the MOS electrode with very thin ($< 0.4 \mu\text{m}$) semiconductor substrate are studied under high measurement frequencies. Model equations for the electric field, the differential space-charge capacitance, and the gate voltage are derived and numerically solved. The capacitance-voltage characteristics show that the formation of the depletion layer is limited by the thickness of the substrate. The absence of the contribution of minority carriers reveals the potential region corresponding to the formation of the depletion layer. The inversion and the depletion layers are found to coexist for a range of gate voltage values. Conclusions are drawn relative to the doping level, the oxide, and the substrate thickness for practical applications of the MOS electrode in electrochemical systems.

The study of the thin film metal-insulator-semiconductor (MIS) arrangements is currently dealing with the fabrication of the corresponding systems and the recording of their I-V characteristics (1-6). Special attention is paid to the nature of the dielectric layer which is deposited with various techniques on the semiconductor base (5-6).

The research work on the MIS structures has mainly advanced to the direction of the use of thin film metal-oxide-semiconductor (MOS) capacitors as variable reactors, but it has not dealt with the possibility of using such systems with a very thin semiconductor base ($< 0.4 \mu\text{m}$) in the form of electrodes in electrochemical cells. In our opinion, the use of such electrodes has a considerable interest in electrochemical applications, and this is supported by the findings of recent works on similar systems as oxide-electrolyte and metal-oxide-electrolyte systems (7-8).

A part of the research performed in our laboratory is directed towards the theoretical study of the thin-based ($< 0.4 \mu\text{m}$) MOS-electrolyte system under various conditions regarding the polarization, the semiconductor characteristics, and the chemical composition of the solution, etc.

In a preceding publication (9), we studied the C-V characteristics of a MOS system with a p-type thin ($< 0.4 \mu\text{m}$) base, under low measurement frequencies. However, due to the fact that a situation quite frequently encountered in practice in electrochemical applications of semiconductors is that of medium and high frequencies, we have attempted in this work to obtain model equations for the space-charge density, the differential capacitance, and the gate voltage of a thin-based MOS structure under these conditions. The equations derived are numerically solved for a series of base thicknesses ranging from 0.1 to 0.3 μm and for a set of physical simulation parameters. On the basis of the results obtained, we come to a series of practical conclusions which are outlined at the end of this work.

Derivation of a Model Equation for the Electric Field of the Very Thin-Based MOS Electrode under High Measurement Frequencies

The boundary conditions for a MOS structure (Fig. 1) with a very thin base ($x = d$) regardless of whether equilibrium conditions are established or not are the following (i) the potential is a function of distance $x: \Psi = f(x)$, (ii) at $x = 0$, $\Psi = \Psi_s$ (surface potential), (iii) at $x = d$, $\Psi = \Psi_0 \neq 0$ (back-side potential).

For reasons of convenience, a series of physical boundary conditions are also assumed. Thus, we do not account for the eventual existence of work function differences and surface states at either the front or the back surface.

Under high frequencies of measurement signals, we can assume that the minority carriers cannot follow the varia-

tions of the electric field, and thus they can be considered as being practically immobile.

We, therefore, expect that at potentials corresponding to depletion and accumulation, the majority carriers, which have very short equilibration times and are predominantly defining the capacitance characteristics of the MOS structure, will lead to capacitance values not differing from the low frequency case.

At potentials corresponding to inversion, the contribution of minority carriers practically vanishes under high frequencies. We assume that the dc gate bias at which measurements are carried out is varied slowly enough so that even at high measurement frequencies the charge distribution in the semiconductor can be adequately described by the equilibrium analysis. Therefore, at high frequencies and at thermodynamic equilibrium the expression for the charge density of a p-type nondegenerate substrate takes the following form

$$\rho = -qp_b(1 - e^{-\beta\psi'}) \quad [1]$$

where $\psi' = \Psi - \Psi_b$ and Ψ_b, p_b are the bulk values of Ψ and p . So, Poisson's equation take the following form

$$\frac{d^2\psi'}{dx^2} = -\frac{\rho}{\epsilon_s\epsilon_0} = \frac{q}{\epsilon_s\epsilon_0} [p_b(1 - e^{-\beta\psi'})] \quad [2]$$

where ϵ_s and ϵ_0 are the permittivities of the semiconductor and the free space, respectively.

On the basis of these assumptions, the integration of this equation from Ψ_0 to Ψ_s and from $x = 0$ to $x = d$ leads to the following expression for the electric field within the semiconductor crystal

$$E = \frac{1}{\beta L} \{[(\gamma + 1)(\beta\Psi_s + e^{-\beta\psi_s}) - \gamma] - [(\gamma + 1)(\beta\Psi_0 + e^{-\beta\psi_0})]^{1/2}\} \quad [3]$$

where

$$\gamma = \frac{M}{(M^2 + 4n_i^2)^{1/2}}$$

and $M = N_A - N_D$, the difference between the acceptor and donor concentrations, n_i is the concentration of the intrinsic carriers. In Eq. [3] we also have set

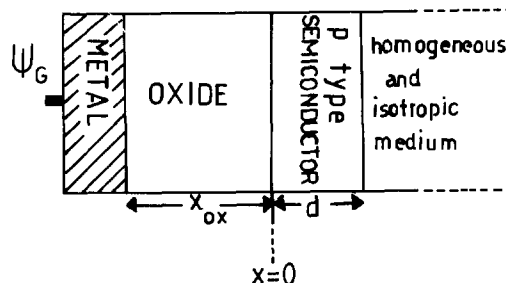


Fig. 1. The thin-based MOS structure

$$L = \frac{\epsilon_s \epsilon_0 kT}{q^2 (M^2 + 4n_i^2)^{1/2}} \quad \text{and} \quad \beta = q/kT$$

The ideal physical conditions assumed at either the front or the back surface (the back surface is assumed to be in contact with a homogeneous and isotropic medium, *i.e.*, an electrolyte solution) make Eq. [3] separable in two terms.

The first term results from the contribution of the surface potential, Ψ_s , while the second one comes out from the contribution of the potential at the back side, Ψ_0 .

The above contributions are provided in reduced form in Eq. [4] and [5], respectively

$$F_{HF}^2(\Psi_s) = [(\gamma + 1)(\beta\Psi_s + e^{-\beta\Psi_s}) - \gamma] \quad [4]$$

$$F_0^2 = F_{HF}^2(\Psi_0) = [(\gamma + 1)(\beta\Psi_0 + e^{-\beta\Psi_0}) - \gamma] \quad [5]$$

where

$$F(\Psi) = \beta LE \quad [5a]$$

is the reduced electric field.

Thus, from Eq. [3] with simple algebra, we can obtain an analytical expression for the space-charge differential capacitance of the MOS structure.

However, this equation cannot be used for calculation of the capacitance-voltage characteristics before an equation describing the dependence of the back-side potential Ψ_0 and the gate voltage is obtained.

This can be achieved by appropriately modifying Poisson's equation. Thus, since $E = d\Psi/dx$ by combination of Eq. [3] and [5], we obtain

$$\frac{dX}{[F_0^2 + (\gamma + 1)(X + e^{-X}) - \gamma]^{1/2}} = \frac{dx}{L} \quad [6]$$

where $X = \beta\Psi_s$ is the reduced surface potential.

If Eq. [6] is set in integral form, it can be solved numerically since analytical solution is impossible.

The limits of the integration are 0 and d for the substrate thickness x and accumulation to inversion voltage values for the reduced potential X .

High Frequency Space-Charge Differential Capacitance

Using the relation $Q_{sc} = \epsilon_s \epsilon_0 E_s$, we can obtain an expression for the charge of the thin-based device at high frequencies

$$Q_{sc} = \frac{\epsilon_s \epsilon_0}{\beta L} [F_0^2 + (\gamma + 1)(X + e^{-X}) - \gamma]^{1/2} \quad [7]$$

Therefore, since $C_{sc} = dQ_{sc}/dX$, we come to a model equation for the space-charge differential capacitance of the thin based MOS electrode under the above conditions

$$C_{sc} = \frac{\epsilon_s \epsilon_0}{\beta L} \cdot \frac{F_0 (dF_0/dX) + (\gamma + 1)(1 - e^{-X})}{[F_0^2 + (\gamma + 1)(X + e^{-X}) - \gamma]^{1/2}} \quad [8]$$

Finally, for the derivation of a model equation for the gate voltage we work as follows: the gate voltage Ψ_G divides between the oxide layer and the semiconductor base, *i.e.*

$$\Psi_G = \Psi_{ox} + \Psi_{base} \quad [9]$$

The potential drop Ψ_{base} across the semiconductor consists of two terms, one corresponding to the surface potential Ψ_s , and the other to the back-side potential Ψ_0 , arising from the charge distribution at the oxide-semiconductor and the semiconductor contacting homogeneous and isotropic medium interfaces, respectively. Thus

$$\Psi_G = \Psi_{ox} + \Psi_s + \Psi_0 \quad [10]$$

where $\Psi_s = X/\beta$ is the incremental surface potential relative to the back side and

$$\Psi_0 = xE_0 = \frac{x}{\beta L} F_0$$

For Ψ_{ox} it can be, similarly to a previous publication (9), shown that since $C_{ox} = \epsilon_{ox} \epsilon_0 / x_{ox}$, then $\Psi_{ox} \approx Q_{sc} / C_{ox} = Q_{sc} x_{ox} / \epsilon_{ox} \epsilon_0$ and therefore

$$\Psi_{ox} = \frac{\epsilon_s x_{ox}}{\beta L \epsilon_{ox}} [F_0^2 + (\gamma + 1)(X + e^{-X}) - \gamma]^{1/2}$$

where ϵ_{ox} and x_{ox} are the permittivity and the thickness of the oxide layer, respectively.

Thus, the expression for the gate voltage takes the following form

$$\Psi_G = \frac{1}{\beta} \left\{ X + \frac{X}{L} F_0 + \frac{\epsilon_s x_{ox}}{\beta L \epsilon_{ox}} [F_0^2 + (\gamma + 1)(X + e^{-X}) - \gamma]^{1/2} \right\} \quad [11]$$

Results and Discussion

The simultaneous computer solution of Eq. [6], [8], and [11] for a p-type substrate with doping levels equal to 1.50×10^{14} , 1.50×10^{16} , and $1.50 \times 10^{18} \text{ cm}^{-3}$, respectively, results in the curves of space charge capacitance *vs.* the gate voltage given in Fig. 2, 3, and 4. Calculations for Fig. 2, 3, and 4 use $x_{ox} = 0.2 \text{ } \mu\text{m}$, $T = 300 \text{ K}$, $n_i = 1.45 \times 10^{10} \text{ cm}^{-3}$, $C_{ox} = 1.73 \times 10^{-2} \text{ } \mu\text{F/cm}^2$, the Debye length $L = 3.34 \times 10^{-6} \text{ cm}$. The numerical solution of Eq. [6], after it was set in integral form, was performed by Romberg's integration method (IBM programming Handbook, 1974) and Gaussian quadrature integration method (ICL Technical Publications, 1974).

Both methods gave exactly the same set of x *vs.* F_0 data for each value of the base thickness. Those data sets were, in turn, fed into the computer programs used for the solution of Eq. [8] and [11], thus yielding C_{sc} against Ψ_G data, provided in Fig. 2, 3, and 4.

It is seen that for substrate thicknesses greater than $0.30 \text{ } \mu\text{m}$, the MOS structure falls into a thick-base device (infinite substrate thickness), and therefore for the typical thicknesses suggested in the literature (10), no thin-base behavior can be detected as it was also found under low measurement frequencies (9).

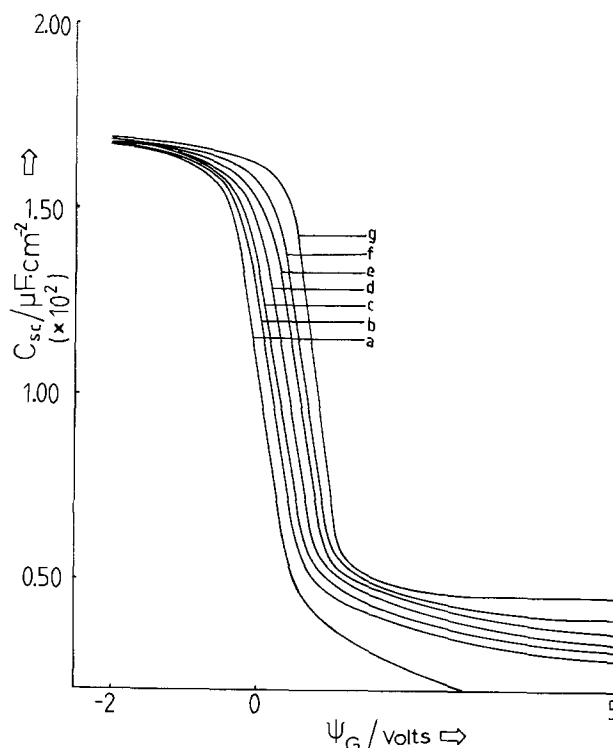


Fig. 2. Capacitance-voltage characteristics of a MOS structure with p-type substrate under high measurement frequencies. Doping level $M = 1.5 \times 10^{14} \text{ cm}^{-3}$. Base thickness (μm): (a) infinite, (b) 0.30, (c) 0.25, (d) 0.20, (e) 0.15, (f) 0.125, and (g) 0.10.

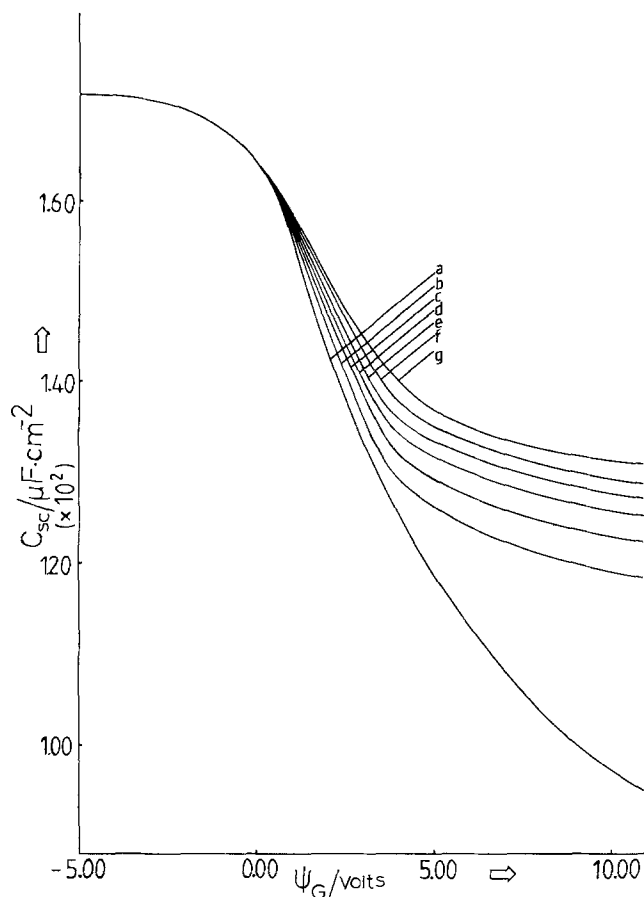


Fig. 3. Capacitance-voltage characteristics of a MOS structure with p-type substrate under high measurement frequencies. Doping level $M = 1.5 \times 10^{16} \text{ cm}^{-3}$. Base thickness (μm): (a) infinite, (b) 0.30, (c) 0.25, (d) 0.20, (e) 0.15, (f) 0.125, and (g) 0.10.

The C_{sc} vs. Ψ_G curves corresponding to infinite base thickness in Fig. 2-4 show that the behavior of the device when the contribution of the minority carriers is eliminated is not typically a high frequency one.

For the high frequency mode, it is known (11-12) that at voltages corresponding to inversion, the depletion region reaches to a limit, and therefore the capacitance becomes practically constant.

Instead of that, it is seen from Fig. 2-4 that with increasing bias beyond depletion, the capacitance of the infinite substrate (curves labeled a) keeps decreasing. This behavior of our model device denotes that, under increasing bias, the width of the depletion layer is continuously increasing. Phenomenologically, this is the case of rapidly changing bias voltage, *i.e.*, of transient conditions (13-14), which is not our case. This behavior of our model device is a result of completely ignoring the contribution of minority carriers. However, for substrate thicknesses equal to or less than $0.3 \mu\text{m}$, the device seems like switching from transient to high frequency response.

In this case, the acceptor ions in the crystal are totally exposed, *i.e.*, the substrate is completely depleted and thus the depletion layer does not increase any longer because it is limited by the width of the substrate itself.

A comparison between the corresponding low (9) and high frequency capacitance-voltage curves (Fig. 2-4) reveals some differences which go further than the expected ones. These differences include deviations between the low and high frequency curves at the potential range from accumulation to depletion. At this potential range, the C_{sc} high frequency values are somewhat lower than the low frequency ones, which were expected to practically coincide. Deviations are also observed at the potentials where the low frequency curves reach to a minimum. At this point, the high frequency curves keep decreasing down to a minimum value attained at large posi-

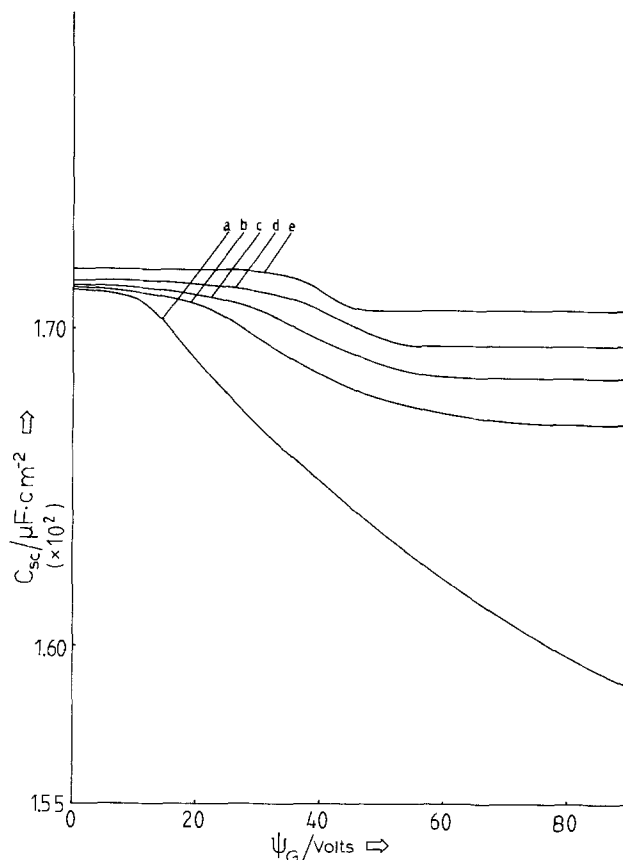


Fig. 4. Capacitance-voltage characteristics of a MOS structure with p-type substrate under high measurement frequencies. Doping level $M = 1.5 \times 10^{18} \text{ cm}^{-3}$. Base thickness (μm): (a) infinite, (b) 0.30, (c) 0.25, (d) 0.20, (e) 0.15.

tive potentials. The above deviations are made more clear through the plot of Fig. 5. In this figure, we provide the relative variation of the reduced quantities F_0 and X . The corresponding curves of Fig. 5 follow the same variation pattern. However, differences appear in what concerns the limiting values attained at inversion potentials and also the setting on potential of these limiting values.

Although, generally it is not quite reasonable to attach a physical interpretation to the behavior of a system when it is studied by means of model equations, the deviations observed call for such an interpretation.

Our opinion is that the deviations from the expected behavior pattern can be generally ascribed to the conditions assumed which imply the immobility of the minority carriers (17-18). However, under low measurement frequencies, the mobile minority carriers produce a series of screening effects.

For a p-type material at the potential region where the depletion layer is formed (small positive potentials), small amounts of electrons may be attracted to the surface. The electrons start to build up the inversion layer although the depletion layer is still developing. At these potentials when the contribution of electrons is ignored, deviations are produced between the low and high frequency curves.

For the interpretation of the continuous decrease of the nonequilibrium C_{sc} values beyond the minimum of the equilibrium curves—which formally is considered as the marking point (15-16) of the integration of the depletion layer—we have to recourse again to the role played by the minority carriers.

The continuous decrease of the C_{sc} values reveals that the depletion layer continues its development even at potentials corresponding to inversion.

This development for the very thin-based MOS electrode is limited by the physical dimensions of the substrate.

The above situation is also displayed in Fig. 5, where it is seen that $(F_0)_{LF} < (F_0)_{HF}$ and that the potentials at which

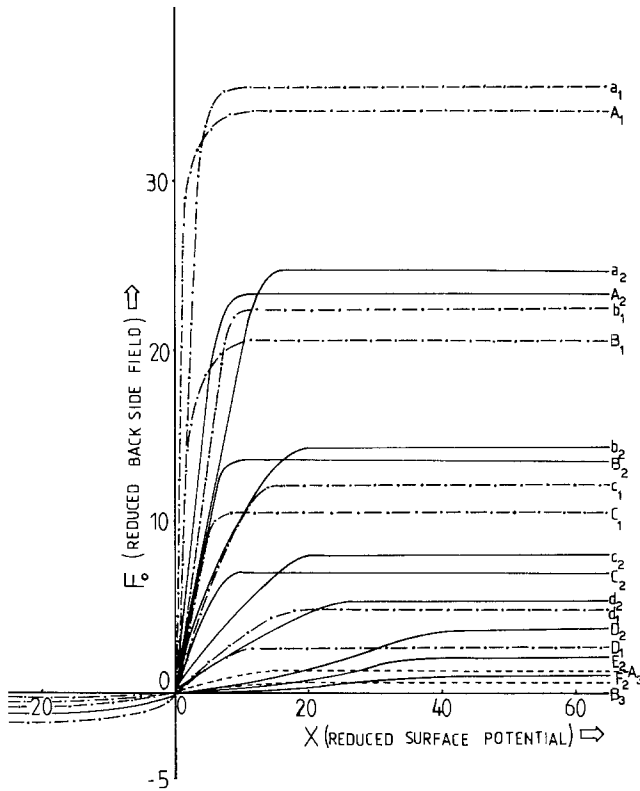


Fig. 5. Variation of the reduced back-side field against the reduced surface potential for a thin-based MOS structure. Doping levels: (—) 1.5×10^{14} , (—) 1.5×10^{16} , (---) $1.5 \times 10^{18} \text{ cm}^{-3}$. Capital letters represent low measurement frequencies. Base thicknesses (μm) for I: (a_1, A_1) 0.15, (b_1, B_1) 0.20, (c_1, C_1) 0.25, and (d_1, D_1) 0.30. Base thicknesses (μm) for II: (a_2, A_2) 0.10, (b_2, B_2) 0.125, (c_2, C_2) 0.15, (d_2, D_2) 0.20, (E_2) 0.25, and (F_2) 0.3. Base thicknesses (μm) for III: (A_3) 0.15, (B_3) 0.20.

the limiting value is reached, are always higher for high frequency than for low frequency curves.

The differences of the back-side field can be also seen from the point of view of the charge distribution under the inversion conditions given in Fig. 6.

Thus, the relation $(F_0)_{LF} < (F_0)_{HF}$ can be attributed to the assumption that the inversion layer is not formed under high frequencies. Under these conditions in the expression for the total charge within the MOS structure

$$Q_s = Q_n - qN_A d + Q_p$$

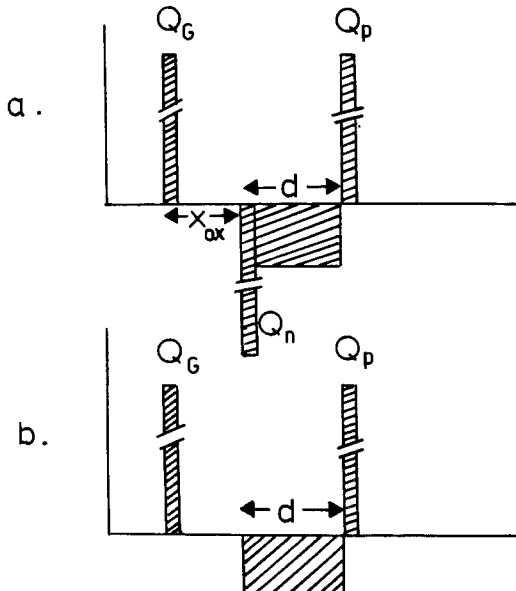


Fig. 6. Schematic representation of the charge distribution within the MOS structure under low (a) and high measurement (b) frequencies.

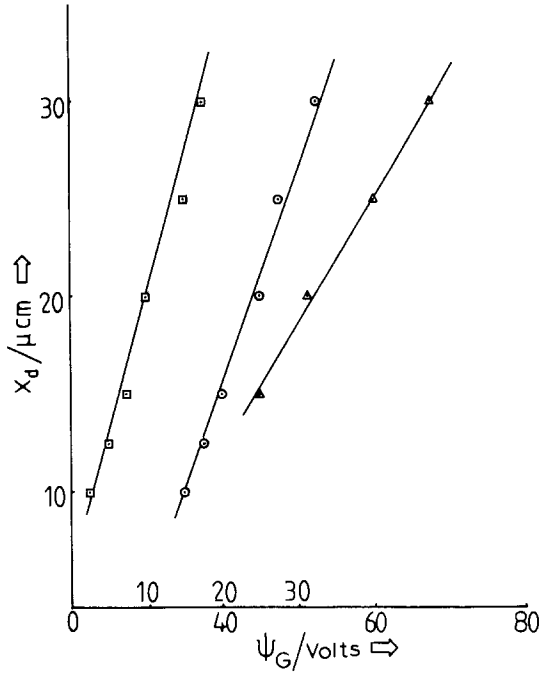


Fig. 7. The width of the depletion layer against the gate voltage. Doping levels: (\square) 1.5×10^{14} , (\odot) 1.5×10^{16} , (\triangle) $1.5 \times 10^{18} \text{ cm}^{-3}$. Points (\square) and (\odot) correspond to the upper division and points (\triangle) to the lower division of Ψ_G axis.

the term Q_n , which represents the charge of the inversion layer, vanishes.

Therefore, since Q_p (the positive charge accumulated at the back side under positive gate voltage) has a sign different than Q_n , Q_s increases under high measurement frequencies, thus leading to greater values of reduced back-side field.

The turning points of the curves of Fig. 5 denote the completion of the formation of the depletion layer. Therefore, the potentials corresponding to these points are the potentials at which the substrate is totally depleted. In Fig. 7, we provide the variation of these potentials against the corresponding base thickness. It is seen that the pattern of this variation is linear, which is typical (11) for the variation of the depletion layer width against the electrical variables of the system. It can be, therefore, concluded that the formation of the depletion and inversion layers seem to be to some extent a simultaneous process.

The immobility of the minority carriers reveals the limits of the development of the depletion layer. However, those limits must be applicable only in the transient case. Under equilibrium or quasi-equilibrium conditions, the formation of a strong inversion layer acts as a shield, preventing the further development of the depletion layer.

Summary

The work made up to this point has revealed the following practical conclusions relative to the use of the MOS electrode in electrochemical works (20-21).

1. The doping levels must be kept low or intermediate levels because otherwise the potential variation will override the limits of interfacial impedance studies.
2. The oxide thickness must be of the order of $0.2 \mu\text{m}$, because such a thickness insures good insulating properties and also prevents the contribution of C_{ox} to the total capacity to become excessive.
3. The substrate thickness used must lie between 0.2 and $0.3 \mu\text{m}$ because thinner substrates will produce back-side potentials inappropriate for interfacial impedance studies, while for base thicknesses greater than $0.3 \mu\text{m}$, a typical thick-base behavior is obtained.

Manuscript submitted Dec. 14, 1983; revised manuscript received May 5, 1984.

The University of Thessaloniki assisted in meeting the publication costs of this article.

REFERENCES

1. J. E. Foster and J. M. Swartz, *This Journal*, **117**, 1410 (1970).
2. L. G. Meiners, R. P. Pan, and J. R. Sites, *J. Vac. Sci. Technol.*, **14**, 961 (1977).
3. L. G. Meiners, *ibid.*, **15**, 1402 (1978).
4. D. H. Phillips, W. W. Grannemann, L. E. Coerver, and G. J. Kuhlmann, *This Journal*, **120**, 1087 (1973).
5. W. D. Brown and W. W. Grannemann, *Thin Solid Films*, **51**, 119 (1978).
6. C.-S. Su and W. W. Grannemann, *This Journal*, **130**, 125 (1983).
7. E. A. Nechaev and V. A. Volgina, *Elektrokhimiya*, **13**, 146 (1977).
8. L. L. Odyne, *ibid.*, **13**, 274 (1977).
9. A. G. Anastopoulos and D. A. Jannakoudakis, *This Journal*, **129**, 2547 (1982).
10. T. W. Collins and J. N. Churchill, *IEEE Trans. Electron Devices*, **ed-22**, 90 (1975).
11. A. S. Grove, B. E. Deal, *et al.*, *Solid State Electron.*, **8**, 145 (1965).
12. A. S. Grove, E. H. Snow, *et al.*, *J. Appl. Phys.*, **35**, 2458 (1964).
13. F. P. Heiman, *IEEE Trans. Electron Devices*, **ed-14**, 781 (1967).
14. S. R. Hofstein, *ibid.*, **ed-14**, 785 (1967).
15. S. M. Sze, "Physics of Semiconductor Devices," John Wiley and Sons, New York (1969).
16. A. S. Grove, "Physics and Technology of Semiconductor Devices," John Wiley and Sons, New York (1967).
17. J. Muller and B. S. Scheik, *Solid State Electron.*, **13**, 1319 (1970).
18. C. T. Sah and H. S. Fu, *Phys. Status Solidi*, **11**, 297 (1972).
19. C. T. Sah and H. S. Fu, *ibid.*, **14**, 59 (1972).
20. V. A. Myamlin and Y. V. Pleskow, "Electrochemistry of Semiconductors," Plenum Press, New York (1967).
21. B. J. Boddy, *J. Electroanal. Chem.*, **10**, 199 (1965).

On the Effect of Impurities on the Photovoltaic Behavior of Solar-Grade Silicon

I. The Role of Boron and Phosphorous Primary Impurities in p-type Single-Crystal Silicon

S. Pizzini*

Department of Physical Chemistry and Electrochemistry, University of Milan, Milano, Italy

C. Calligaris

HELIOSIL S.p.A., Milano, Italy

ABSTRACT

The electrical and photovoltaic properties of partially compensated p-type silicon samples have been investigated in order to understand the influence of the contemporaneous presence of donors and acceptors on the behavior of majority and minority carriers. It has been shown that the majority carrier properties are only slightly influenced by the presence of donors in p-type samples and that the minority carrier properties depend on the excess acceptor concentration up to an excess donor concentration close to 5×10^{16} at./cm³. A theoretical explanation of these features has been proposed, on the base of the Shockley-Read-Hall model of recombination at shallow traps and donor-acceptor pairs formation.

The need for a material considerably cheaper than the conventional electronic-grade silicon for terrestrial photovoltaic cells fabrication is still a mandatory issue, in spite of the substantial improvements recently achieved with the advanced Siemens processes (1). As it is consistently demonstrated that the balance of systems costs is heavily leveraged by cell efficiency, it appears, however, that a compromise between material cost and conversion efficiency must be pursued. This is particularly important in the case of MG silicon feedstocks, where the cascade process for impurity removal introduce additional costs in the material preparation route, which increase in a nonlinear fashion with the degree of upgrading required.

A considerable amount of knowledge on the effect of deep level impurities on the structural, electrical, and photovoltaic behavior of single-crystal silicon has been already obtained in the course of extensive investigation carried out at Dow Corning, Westinghouse, and Monsanto (2-3).

Less attention has been paid, however, to the behavior of electrically active impurities, such as boron and phosphorus, although the knowledge of their threshold concentration as single impurities or on the amount of tolerable compensation is of primary importance for the development of solar silicon as they represent, together with carbon, the least easily removable impurities from a MG silicon feedstock (1, 4, 5).

To the scope of providing the necessary information on this regard, systematic work has been carried out on p-type, n-type and p-type compensated samples, which concerned the preparation and the complete electrical characterization of the samples.

The results of this investigation are reported and discussed in this paper.

Experimental

Crystal growth, structural, and chemical characterization.—B-doped, p-doped, and partially compensated p-type <111> silicon ingots were grown using a Czochralski furnace. The charge consisted of 700g of EG polycrystalline silicon having a boron content less than 0.14 ppba and a donors content less than 0.35 ppba.

Boron doping was carried out using standard boron silicon alloys for samples which should contain less than 10^{16} at./cm³ or metallic boron for heavier doped samples. Phosphorous doping was carried out using standard phosphorous silicon alloys.

All the materials employed were furnished by Dynamit Nobel Silicon.

After completion of the growth (70% of the charge weight), the ingots were slowly cooled directly in the furnace chamber, and no further heat-treatment was thereafter applied.

The silicon ingots, after being sliced, were submitted to a complete chemical, structural, and electrical characterization.

* Electrochemical Society Active Member.

Table I. Oxygen and carbon content as determined by IR spectroscopy in different reference samples

Sample no.	Oxygen (at./cm ³)		Carbon (at./cm ³)	
	Seed end slices	Seed end slices	Seed end slices	Seed end slices
8	1.6 × 10 ¹⁸	1.0 × 10 ¹⁸	0.7 × 10 ¹⁷	1.9 × 10 ¹⁷
9	—	0.6 × 10 ¹⁸	—	1.4 × 10 ¹⁷
10	1.6 × 10 ¹⁸	0.9 × 10 ¹⁸	0.8 × 10 ¹⁷	2.6 × 10 ¹⁷
11	1.4 × 10 ¹⁸	1.0 × 10 ¹⁸	0.7 × 10 ¹⁷	—
12	1.7 × 10 ¹⁸	0.7 × 10 ¹⁸	1.3 × 10 ¹⁷	3.8 × 10 ¹⁷
13	1.7 × 10 ¹⁸	0.8 × 10 ¹⁸	0.8 × 10 ¹⁷	1.9 × 10 ¹⁷
15	1.2 × 10 ¹⁸	0.9 × 10 ¹⁸	0.5 × 10 ¹⁷	1.3 × 10 ¹⁷

FTIR spectroscopy was used for determining the interstitial oxygen and substitutional carbon content.

Spark source mass spectrometry has been used for the determination of P content, and neutron activation analysis was used for measuring the content of impurities not intentionally added but resulting from process contamination.

Results of chemical characterization are reported in Tables I and II, which show that the as-grown crystals present oxygen and carbon levels largely comparable with those of commercially available CZ silicon, while those of some deep level impurities, notably iron and nickel, are larger by about one order of magnitude than the corresponding quantities of commercially available EG CZ-grown silicon.

Dislocation density was systematically checked using standard etching procedures, while other structural imperfections were spot-wise determined by TEM and x-ray topography.

Samples were generally dislocation free; only on the most heavily compensated samples dislocation loops and locally stressed lattice regions were occasionally observed on the tag-end slices.

The radial distribution of the dopants was investigated using a collinear four-point probe.

The dopants were found to be homogeneously distributed within each single slice, being the resistivity fluctuation of the order of ± 20%, at the most, for the more heavily compensated samples.

Electrical characterization.—Hall effect measurements at 9 kG magnetic field strength were carried out on all the samples in order to determine the Hall mobility μ_H and the actual donors, acceptors, or excess acceptors concentration N_D , N_A , or $(N_A - N_D)$.

For p-type compensated samples, we applied the expression of the Hall coefficient for semiconductors having multiple energy minima in the conduction band (6) which could be written

$$R_H = - \frac{1}{e} \frac{r_e b^2 n - r_h p}{(bn + p)^2} \quad [1]$$

Table III. Summary of Hall measurements on p-type samples

Sample no.	Boron conc. (added) at./cm ³	Boron conc. (target) at./cm ³	N_A (Hall) at./cm ³	ρ_{Hall} Ω cm	μ_{Hall} cm ² V ⁻¹ s ⁻¹
41	2.4 × 10 ¹⁶	2.16 × 10 ¹⁶	2.4 × 10 ¹⁶	0.74	344
46	3.2 × 10 ¹⁶	4.30 × 10 ¹⁶	4.8 × 10 ¹⁶	0.42	312
47	7 × 10 ¹⁶	6.30 × 10 ¹⁶	1.3 × 10 ¹⁷	0.19	261
48	1.7 × 10 ¹⁷	1.50 × 10 ¹⁶	2.1 × 10 ¹⁷	0.12	238
49	3.8 × 10 ¹⁷	3.40 × 10 ¹⁶	3.1 × 10 ¹⁷	0.09	217

Table IV. Summary of Hall measurements on n-type samples

Sample no.	Phosphorous conc. (added) at./cm ³	Phosphorous conc. (target) at./cm ³	N_A (Hall) at./cm ³	ρ_{Hall} Ω cm	μ_{Hall} cm ² V ⁻¹ s ⁻¹
34	7.3 × 10 ¹⁵	3.40 × 10 ¹⁵	3.4 × 10 ¹⁵	1.04	1745
22	9.2 × 10 ¹⁵	4.20 × 10 ¹⁵	4 × 10 ¹⁵	0.80	1670
32	6.9 × 10 ¹⁶	3.10 × 10 ¹⁶	3.3 × 10 ¹⁶	0.16	1210
31	1 × 10 ¹⁸	4.60 × 10 ¹⁷	2.3 × 10 ¹⁷	0.04	655
24	2 × 10 ¹⁸	1.38 × 10 ¹⁸	8 × 10 ¹⁷	0.02	370

Table II. Residual impurity in reference ingots

Element	Atomic fraction	at./cm ³
Ag	2.6 × 10 ⁻¹¹	1.3 × 10 ¹²
Au	1 × 10 ⁻¹²	5 × 10 ¹⁰
Co	6.7 × 10 ⁻¹²	3.3 × 10 ¹¹
Cr	2.3 × 10 ⁻¹¹	1.1 × 10 ¹²
Fe	2 × 10 ⁻⁹	1 × 10 ¹⁴
Hf	1 × 10 ⁻¹²	5 × 10 ¹⁰
La	2 × 10 ⁻¹²	1 × 10 ¹¹
Mo	6 × 10 ⁻¹²	3 × 10 ¹¹
Ni	2 × 10 ⁻⁹	1 × 10 ¹⁴
Pt	2 × 10 ⁻¹¹	1 × 10 ¹²
Sb	4 × 10 ⁻⁹	2 × 10 ¹⁴
V	3 × 10 ⁻¹²	1.5 × 10 ¹¹
Zn	9 × 10 ⁻¹¹	4.5 × 10 ¹²
Zr	1 × 10 ⁻⁹	5 × 10 ¹³

where

$$r_e = \frac{\mu_{H,e}}{\mu_{d,e}}, \quad r_h = \frac{\mu_{H,p}}{\mu_{d,p}}$$

$\mu_{H,e}$ and $\mu_{d,e}$ are the Hall and drift mobility for electrons, $\mu_{H,p}$ and $\mu_{d,p}$ the Hall and drift mobilities for holes, and

$b = \frac{\mu_{d,e}}{\mu_{d,p}}$ the drift mobility ratio and which reduces to

$$R_H = \frac{1}{e} \frac{1}{p - n} \quad [2]$$

at high magnetic field strength, thus permitting the determination of the excess acceptor concentration $(N_A - N_D)$ and, then, the Hall mobility $\mu_H = R_H \sigma$, where σ is the measured electrical conductivity.

Tables III and IV report the most relevant electrical parameters of the reference boron doped and phosphorous doped samples, while Table V reports the corresponding data for p-type compensated samples.

Instead of the Hall coefficient R_H , the Hall resistivity

$$\rho_H = \frac{R_H}{u_H}$$

is reported throughout.

From Tables III and IV, one can remark that the acceptor and donor concentrations, as determined by Hall-effect measurements, closely correspond to those calculated from the known B and P additions to the melt and effective segregation coefficients taken equal to 0.9 and 0.46, respectively.

From Fig. 1, one could remark that the Hall mobilities for electrons and holes in n-type and p-type samples significantly compare with the values of the corresponding drift mobilities calculated according the Caughly and Thomas relation (7)

$$\mu = \frac{\mu_{max} - \mu_{min}}{1 + (N/No)^a} + \mu_{min} \quad [3]$$

Table V. Summary of Hall and diffusion length measurements on compensated, p-type samples

Sample no.	Boron conc. (added) at/cm ³	Phosphorous conc. (added) at/cm ³	Phosphorous conc. (SSMS) at/cm ³	$N_A - N_D$ (Hall) at/cm ³	ρ_{Hall} Ω cm	μ_{Hall} cm ² V ⁻¹ s ⁻¹	L_D μ m	τ^* μ s
41	2.1×10^{16}	—	—	2.40×10^{16}	0.74	344	78	2.4
43	4.5×10^{16}	1.9×10^{16}	3.5×10^{16}	3.10×10^{16}	0.69	288	71	2.1
38	7×10^{16}	6.9×10^{16}	2.6×10^{16}	1.03×10^{16}	2.4	251	77	2.08
44	1.7×10^{17}	3×10^{17}	3.5×10^{16}	6.7×10^{16}	0.49	190	35	0.6
45	3.8×10^{17}	10.5×10^{17}	8×10^{16}	4.8×10^{16}	1.25	105	31	0.45
50	8×10^{16}	8×10^{16}	4.5×10^{16}	3.5×10^{16}	1.02	240	55	1.2

* From calculated values of D and experimental values of L_D .

using the following figures for the constants

	μ_{max} (cm ² V ⁻¹ s ⁻¹)	μ_{min}	α	No at./cm ³
holes	495	47.7	0.76	6.3×10^{16}
electron	1330	65	0.72	8.5×10^{16}

being, however, the Hall mobilities for electrons systematically slightly in excess over their drift mobilities. This discrepancy could be explained, as remarked earlier by Mousty *et al.* (8), by considering that the Irvin curves (9) displaying the resistivity *vs.* dopant concentration relationships for n-type silicon (from which also the Caughly and Thomas relation is obtained) are interpolation of data referring to different donors, and that, at a given impurity concentration, the mobility is somewhat higher in the case of phosphorous doping.

As for the Hall mobilities of compensated samples, they fit instead quite well the Caughly and Thomas ones, when plotted as a function of the sole acceptors content up to about $2 \cdot 10^{17}$ at./cm³ thus indicating that the majority carriers' mobility does not depend very much on the compensation.

Diffusion length (L_D) measurements of the minority carriers were also systematically carried out on p-type compensated samples (see Table V), using the surface photovoltage method, in order to study the relationships between the diffusion length of electrons and the degree of compensation.

It is observed in Fig. 2 that the experimental L_D values reasonably fit the calculated values, if one calculates the L_D value as $\sqrt{\tau_n D_n}$, by assuming that L_D is function of the excess acceptors concentration ($N_A - N_D$), that the minority carrier diffusion constant

$$D_n = \frac{k}{e} \mu_n \quad [4]$$

could be calculated via the Caughly-Thomas equation (1) for the mobility of electrons which was already shown to

give a good fit of the experimental data for both p- and n-type samples, by using the excess acceptor concentration as a measure of the number of scattering centers and determining the lifetime τ_n of the electrons via the Fossum (10) equation

$$\tau_n = \frac{\tau_{no}}{1 + \frac{(N_A - N_D)}{6N_A}} \quad [5]$$

when using for the values of the constants the same value of $N_A = 7.7 \times 10^{15}$ at./cm³ used in Ref. (8) and a value of $\tau_{no} = 0.85 \times 10^{-5}$ s, which is a factor of two lower than that used by Fossum.

A slightly worse, although still satisfactory, fitting with the Fossum equation is observed when instead of the L_D values one displays in Fig. 3, directly the minority carriers lifetime τ , determined from the experimental values of L_D and the calculated values of D_n according to Eq. [4].

Solar cell fabrication and characterization.— 1×1 cm² diffuse junction solar cells were fabricated by conventional open-tube phosphorous diffusion at 900°C for 7 min using POCl₃ as the phosphorous source. The ohmic front grid collector was formed using photolithographically etched vacuum-deposited Ti/Ag contact, while Al was used for the back ohmic contact.

An 8000 nm thick, single SiO layer was used as the AR coating.

Reference cells for base-line determination were prepared using slices cut from a 2.4×10^{16} at./cm³ B-doped ingot, having an L_D value major than 150 μ m, which resulted to be 15% efficient using a water filtered 100 mW/cm² tungsten-halogen lamp.

The photovoltaic characteristics of the p-type compensated samples, measured under the same illumination conditions, as well as the base-minority carrier diffusion lengths and lifetime measured on the completed cells, are reported in Table VI.

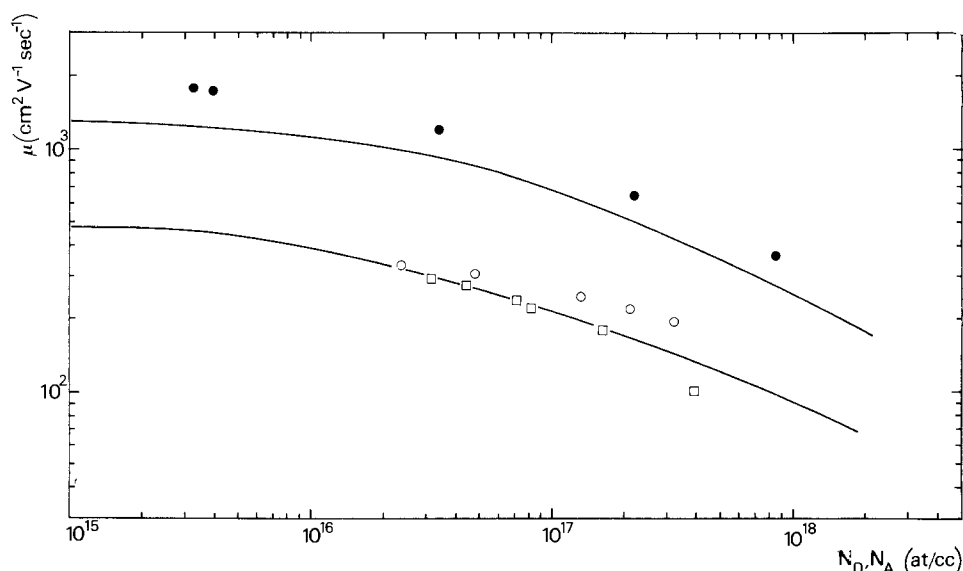


Fig. 1. Hall mobility of the majority carriers in n- and p-type samples. ●: n-type samples. ○: p-type samples. □: compensated, p-type samples. Solid lines display the calculated dependence of the drift mobility.

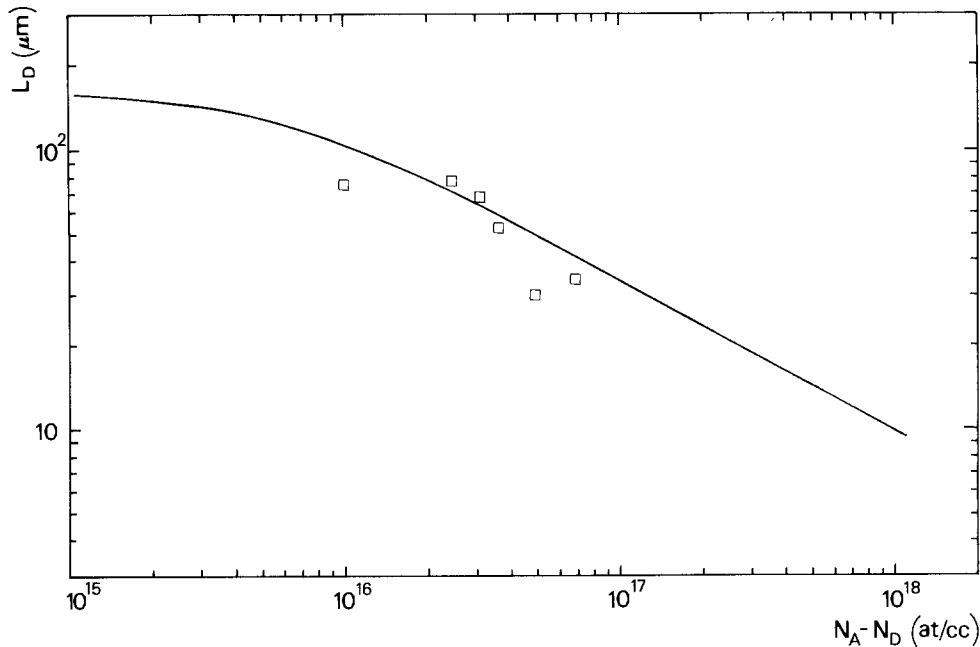


Fig. 2. Experimental and calculated (solid line) dependence of the diffusion length on the excess acceptor concentration in p-type compensated samples.

One could remark that, apparently, only the samples 44 and 45 containing boron and phosphorous in excess of 10^{17} at./cm³ show a significant decrease of the normalized efficiency η/η_0 , which is accompanied by a small, but significant decrease of the diffusion length and lifetime values of the minority carriers, with respect to those of the unprocessed slices (see Table V).

Figure 4, which displays the excess acceptors concentration dependence of the normalized efficiency, shows that a threshold exists around $(N_A - N_D)$ values close to 5.5×10^{16} at./cm³.

Discussion

It is well known from the literature (11) that the minority carrier lifetimes in p-type and in n-type samples is supposed to be limited by a Shockley-Read-Hall-type mechanism (12) at dopant concentration lower than 2×10^{18} at./cm³, while Auger recombination dominates their behavior at higher concentrations. From the calculated capture sections of traps constituted by shallow donors or acceptors is also known that the dominant mechanism of carrier trapping into shallow impurity states is by phonon emission (12-14). It is, eventually, also known that on p-type base cells the efficiency is practically independent of the acceptor concentration up to $\approx 5 \times 10^{16}$ at./cm³ (1 ppm) (15) in good agreement with earlier findings (16).

From the results of this present investigation, it appears that the recombination mechanism and the photovoltaic properties thereafter are not significantly affected by the contemporaneous presence of acceptors and donors, provided the excess acceptor concentration is lower than $\approx 5 \times 10^{16}$ at./cm³ which is a figure very close to the threshold boron concentration tolerated in p-type samples.

Furthermore, it has been demonstrated that the minority carrier properties do depend only on the excess ac-

ceptor concentrations $N = N_A - N_D$ (see Fig. 2 and 3) and that their lifetime dependence on the traps concentration is well described by the Fossum equation, using as the traps concentration that of the excess acceptors.

These experimental results could be well understood when considering the following.

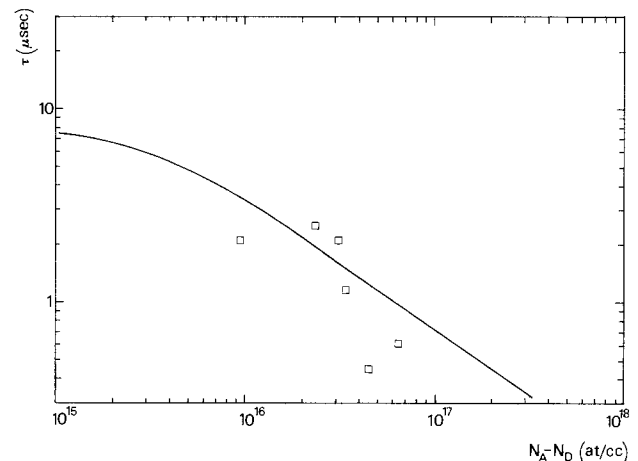


Fig. 3. Experimental and calculated (solid line) dependence of the lifetime on the excess acceptor concentration in p-type compensated samples.

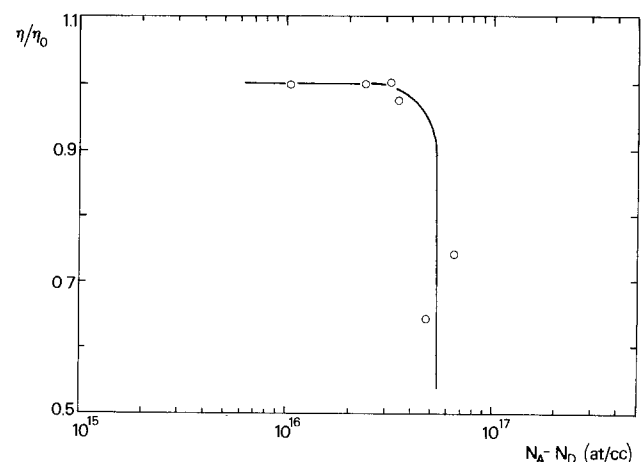


Fig. 4. Experimental dependence of the normalized efficiency on the excess acceptor concentration in p-type compensated samples.

Table VI. Summary of photovoltaic parameters of solar cells prepared with compensated, p-type samples

Sample	L_D (μm)	τ^* (μs)	J_{sc} (mA/cm^2)	V_{oc} (mV)	FF	η (%)	η/η_0
41	83	2.7	33.9	590	0.75	15	1
43	94	3.6	34.6	595	0.75	15.5	1.03
38	77	2.1	33.9	585	0.75	14.9	99.3
44	22	0.25	26.6	585	0.71	11.1	74
45	13	0.21	22.9	511	0.74	9.7	64
56	60	1.3	32.1	585	0.75	14.6	97

* From experimental values of L_D and calculated D .

First, that in a compensated semiconductor for which $N_A > N_D$, $kT > \epsilon_D$, ϵ_A , and $kT \ll Eq$ (where ϵ_D and ϵ_A are the energy levels of the donor and acceptor states), a concentration N_D of acceptors is associated in (A^-D^+) pairs (17) as N_D acceptor levels are occupied by electrons from the N_D donor levels, so that the number of available holes in the valence band is

$$N = N_A - N_D$$

which is sufficiently large to recombine with electron trapped at the D^+ species in the (A^-D^+) pairs before being reemitted, which then behave like traps for minority carriers. The lifetime should then be given by Eq. 4, written as

$$\tau_n = \frac{\tau_{no}}{1 + \frac{N_D}{N_A^0}}$$

if we neglect the influence of the traps consisting of empty acceptor sites and recognize that a τ_{no} value different from that of pure p-type semiconductors should be used to account for the different trap nature.

Second, that in a sample close to being fully compensated ($N_A \geq N_D$), the concentration of holes in the valence band is not sufficiently large to recombine with electrons into the empty traps, within the donor-acceptor pairs. Only free acceptors whose concentration is $(N_A - N_D)$ should act as traps and

$$\tau_n = \frac{\tau_{no}}{1 + \frac{N_A - N_D}{N_A^0}}$$

We can therefore conclude that in p-type compensated samples and in the 10^{16} – 10^{17} at./cm³ range of both acceptors and donors it is the excess acceptor concentration which dominates the recombination mechanism while ionized donors in the pair behave like electrically inactive species.

A threshold for photovoltaic efficiency close to 5×10^{16} at./cm³ of excess acceptors like in pure p-type samples could be therefore justified in compensated p-type samples, as recombination at ionized donors in donor-acceptor pairs seem to play a negligible role.

Acknowledgments

The authors are indebted to Dr. M. Finetti and Dr. P. Negrini of LAMEL (Bologna, Italy) for having carried out the photovoltaic characterization. The neutron activation analysis of impurities has been carried out by the CNRS

(Centre National de la Recherche Scientifique), Group de Chimie du Laboratoire Pierre S ue, Saclay, France. Part of the material of this work has already been published (18).

Manuscript submitted Sept. 16, 1983; revised manuscript received March 2, 1984.

The University of Milan assisted in meeting the publication costs of this article.

REFERENCES

1. S. Pizzini, *Solar Energy Mater.*, **6**, 253 (1982).
2. R. H. Hopkins *et al.*, Final Report DOE/JPL Contract no. 954331 (1980).
3. H. W. Gutsche and D. E. Hill, Final Report ERDA/JPL Contract no. 954338-76 (1976).
4. J. Dietl, in "Materials and New Processing Techniques for Photovoltaics," J. A. Amick, V. K. Kapur, and J. Dietl, Editors, p. 52, The Electrochemical Society Softbound Proceedings Series, Pennington, NJ (1983).
5. S. Pizzini, in "Materials and New Processing Techniques for Photovoltaics," J. P. Dismukes, E. Sirtl, P. Choudhury, and L. P. Hunt, Editors, p. 26, The Electrochemical Society Softbound Proceedings Series, Pennington, NJ (1982).
6. R. A. Smith, "Semiconductors," p. 125, Cambridge University Press, Cambridge, England (1978).
7. D. M. Caughly and R. E. Thomas, *Proc. IEEE Lett.*, **55**, 2129 (1967).
8. F. Mousty, P. Ostojica, and L. Passari, *J. Appl. Phys.*, **45**, 4576 (1974).
9. J. C. Irvin, *Bell Syst. Tech. J.*, **41**, 387 (1962).
10. J. G. Fossum, *Solid State Electron.*, **19** (1976).
11. J. Dzierziour and W. Schmid, *Appl. Phys. Lett.*, **31**, 346 (1977).
12. W. Shockley and W. T. Read, *Phys. Rev.*, **87**, 835 (1952).
13. W. W. Anderson, *Solid State Electron.*, **18**, 235 (1975).
14. J. Melngailis, G. E. Stillman, J. O. Dommick, and C. M. Wolfe, *Phys. Rev. Lett.*, **23**, 1111 (1969).
15. J. A. Amick, J. P. Dismukes, R. W. Frances, L. P. Hunt, P. S. Ravishankar, M. Schneider, K. Matthei, R. Sylvain, K. Larsen, and A. Schei, in "Materials and New Processing Techniques for Photovoltaics," J. A. Amick, V. K. Kapur, and J. Dietl, Editors, p. 67, The Electrochemical Softbound Proceedings Series, Pennington, NJ (1983).
16. P. A. Iles and S. I. Soclof, in "Proceedings of the 11th IEEE Photovoltaics Specialists' Conference," p. 19 (1975).
17. J. S. Prener and F. E. Williams, *J. Phys. Chem. Solids*, **8**, 565 (1959).
18. S. Pizzini, L. Giarda, A. Parisi, M. Finetti, and P. Negrini, in "Proceedings of the Second European Photovoltaic Solar Energy Conference," p. 726, D. Reidel, New York (1979).

Applications of Optical Properties of Sputtered-Chromium Thin Films in Photomask Making

L. C. Hsia*

IBM Corporation, General Technology Division, Hopewell Junction, New York 12533

ABSTRACT

Optical properties of thin $\text{Cr/Cr}_x\text{O}_y$ films sputtered on glass for photomask making are investigated using Auger spectroscopy, ellipsometry, and reflectometry techniques. The films selected for the study vary from very rich to very poor in oxygen. The complex indexes of refraction are derived from the ellipsometry data using metal film calculation. The reflectance is then calculated to compare with that directly measured. These comparisons are important in understanding the film properties and their application in microlithography. The optical properties are found to be closely related to the oxygen concentration and its profile in the film. Optical intensity profiles in the photoresist are calculated for various photoresist/ $\text{Cr/Cr}_x\text{O}_y$ systems, yielding optimal conditions for minimizing resist line-width variations. An experiment is also carried out to illustrate the main points predicted by the theory.

With integrated circuit complexity and the number of circuits per chip increasing continuously, it has become necessary to fabricate devices with very small geometries. These advances in device design have imposed stringent requirements on photomasks used for device fabrication. The chromium photomasks have been used in semiconductor industry for many years, and great progress has been made in photomask processing (1). However, the improved reliability, defect reduction, and image-size control depend heavily on a better understanding of the properties of $\text{Cr/Cr}_x\text{O}_y$ thin films on glass. In the chromium thin-film preparation, oxygen is often introduced to alter the film complex index of refraction (thus reducing the reflectivity), which is one of the key parameters in image-size control. The sputtered-Cr films grown under different conditions present a rather complex system for characterization and analysis; the atomic ratio of Cr to O can vary drastically in the films. However, the surface layer has the most important implication in photolithography.

Auger Analysis

In this study, three types of $\text{Cr/Cr}_x\text{O}_y$ thin films with oxygen content poor, medium, and rich are chosen (which will be referred to as type A, B, and C, respectively). These films were prepared by sputtering chromium onto borosilicate glass. Auger electron spectroscopy analysis was performed, and the results are reported in Fig. 1-3. In each figure, the peak-to-peak intensity, which is proportional to the atomic concentration of the elements under investigations is shown. In all Auger profiles, this is limited to carbon, chromium, and oxygen, listed along the ordinate. Type A was prepared by sputtering pure chromium onto the glass substrate in a helium gas environment. The film has a thickness 700\AA , which roughly corresponds to 30 min of sputtering time in Fig. 1. Beyond 30 min, a film/glass interface region is reached, and the tail of the profile is due to the glass material (SiO_2). It can be observed that this is quite a homogeneous film with an atomic ratio of Cr to O 4:1 across the film. The carbon component may be due to contamination.

In the preparation of type B film, oxygen was purposely introduced into the sputtering chamber such that, while the film was grown, oxidation took place and a Cr_2O_3 film was formed. The film thickness is about 1250\AA , which roughly corresponds to 37 min of sputtering time in Fig. 2. Apart from the surface layer (about 30\AA), the film is relatively homogeneous with an atomic ratio of Cr to O 3:2. Some carbon contamination was also detected.

In order to further increase the oxygen concentration while maintaining high optical density, type C film was prepared by first sputtering chromium in an environ-

ment similar to that of type A. Then, the oxygen content was increased in the chamber. As a result, a film with complicated profile was grown, as shown in Fig. 3. The film has a thickness of 1900\AA , which roughly corresponds to 50 min of sputtering time in Fig. 3. The atomic ratio varies tremendously across the film. The oxygen-rich surface layer, which itself has a complex profile, has a thickness of about 500\AA .

Optical Properties

The optical properties of a homogeneous, isotropic medium are completely describable in terms of index of refraction of $N = n - ik$, where the imaginary part, k , is the extinction coefficient. The k is due to the intensity attenuation of an electromagnetic wave traversing the medium, and thus closely related to the optical density. The n and k are wavelength dependent. The reflectance is determined by the complex index of refraction. The reflectance R is given by

$$R = [(1 - n)^2 + k^2] / [1 + n^2 + k^2] \quad [1]$$

At present, most 10:1 optical projection mask-making systems employ the near-UV region; while for wafer fab-

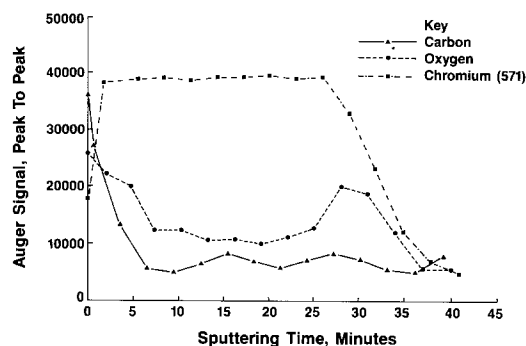


Fig. 1. Auger profiles of type A chromium film. Thickness = 700\AA

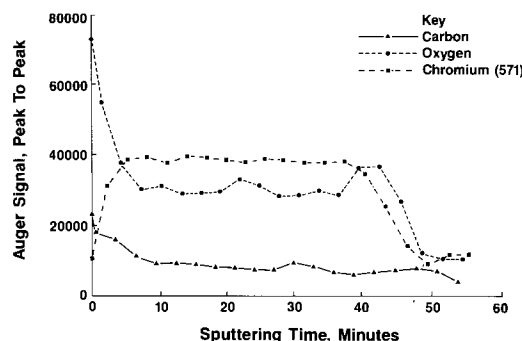


Fig. 2. Auger profiles of type B chromium film. Thickness = 1250\AA

* Electrochemical Society Active Member.

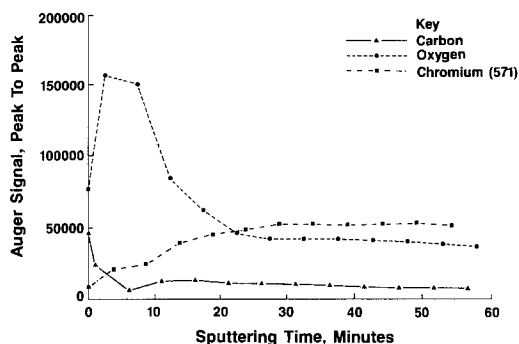


Fig. 3. Auger profiles of type C chromium film. Thickness = 1900 Å

rication, medium UV or deep UV light is utilized. Thus, properties of photomask materials have to be investigated from the near-UV to the deep-UV region.

Figure 4 shows the reflectance for the three types of Cr/Cr₂O₃ films as a function of the wavelength. A reflectometer with variable wavelength feature was used for the measurement. It can be observed that although the reflectance varies from 60% for the oxygen poor to 10% for the oxygen rich, it remains relatively flat within the region of interest for all three types of films.

The complex indexes of refraction were calculated from ellipsometry measurements. The ψ and Δ were derived from intensity signals at prescribed conditions using a rotating element ellipsometer at $\lambda = 4880 \text{ \AA}$ (2). The index of refraction was calculated using a computer program developed for metal films. Table I contains the measured ω and Δ for each film. The reflectance can be calculated from Eq. [1]. A comparison between the directly measured and calculated values of these parameters offers a better understanding of the dependence of film properties on the oxygen concentration. Table II is a comparison of the calculated reflectance with that of the direct measurement. In general, good agreement between the calculated and the measured is observed. However, as the oxygen concentration increases, the difference between the two becomes larger. This may be caused by the fact that as the film resistivity increases, the condition deviates further away from the assumption of a conducting metal film. In particular, for type C, which is extremely inhomogeneous, the surface oxygen-rich layer plays a dominant role in determining the surface optical properties such as reflectance and polarization.

Calculation of Intensity Profile in Photoresists

For an optical projection mask making system, two of the major lithography-related parameters are the achievable image-size control and the practical resolution limit. Linewidth variations are principally caused by the standing wave effects (3) in mask fabrication, since the slope or bulk effect (4), which is important in wafer fabrication, is virtually nonexistent in mask making. The standing wave effects are determined by the optical properties of the

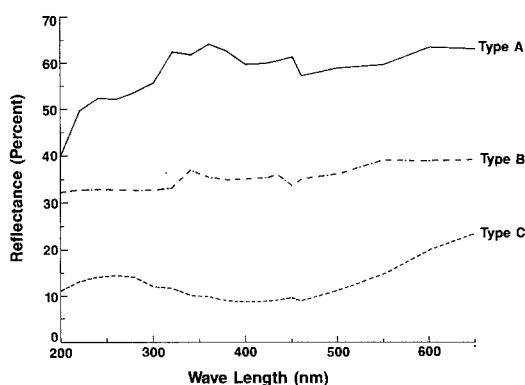


Fig. 4. Reflectance as a function of wavelength

Table I. Indexes of refraction calculated from ellipsometry data ψ and Δ . Thickness measured independently ($\lambda = 4800 \text{ \AA}$).

Type	ψ	Δ	n	k	Thickness (Å)
A	29.12	135.18	3.47	3.83	700
B	19.42	109.96	2.67	1.86	1250
C	24.23	52.03	1.39	0.88	1900

Table II. Comparison of reflectance between the direct measurement and calculation (%)

Type	Measured	Calculated
A	58.1	57.1
B	34.6	40.0
C	8.6	13.4

Cr/Cr₂O₃ thin film and photoresist absorption and thickness. Like other metal thin films encountered in wafer fabrication, lithography-related properties of Cr films are characterized by the complex indexes of refraction. This means a significant phase change of light occurring upon reflection and partial reflection has to be the standing wave effects, along with some simplifying assumptions, is used to illustrate the major points. The approximation of a weakly absorbing resist film on a partially reflecting substrate with monochromatic illumination is made. Although this is a special case, it does approximate optical mask making situations. In this work the wavelength of illumination is $\lambda = 4350 \text{ \AA}$.

The standing wave intensity in the resist film can be calculated using the concept of the complex amplitude and multiple reflection (5). The situation is illustrated in Fig. 5. The incident light is imaged normally into a weakly absorbing film of thickness d , coating a Cr/Cr₂O₃ film with the index of refraction $N_2 = n_2 - ik_2$. The intensity of each reflection, either from the Cr/resist or resist/air interface, can be expressed as

$$E_i = A_i E_0 e^{i(\omega t \pm r_i k)} \quad [2]$$

where

$$k = 2\pi N/\lambda$$

The total standing wave amplitude is given by summing up all the E_i 's.

$$E_s = \sum_{i=1}^{\infty} E_i = E_0 t_{ole} e^{i\omega t} (1 + f_{12} e^{2ik_1(x-d)}) \frac{e^{-ik_1 x}}{1 - f_{12} f_{10} e^{2idk_1}} \quad [3]$$

where

$$f_{12} = (N_1 - N_2)/(N_1 + N_2) \quad [4]$$

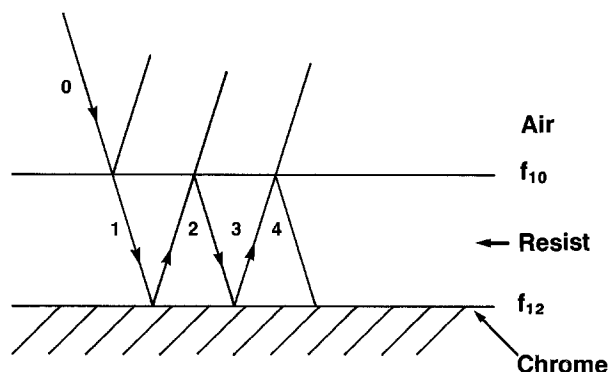


Fig. 5. Light incident on an air/resist/Cr substrate system, producing multiple reflections.

Table III. Resist thickness corresponding to maximum or minimum standing wave envelope (in units of wavelength)

A		B		C	
Max	Min	Max	Min	Max	Min
0.4315	0.5830	0.4232	0.5748	0.5300	0.6815
0.7345	0.8860	0.7269	0.8778	0.8331	0.9846
1.0375	1.1891	1.0293	1.1808	1.1361	1.2876
1.3406	1.4921	1.3324	1.4839	1.4391	1.5906
1.6436	1.7951	1.6354	1.7869	1.7421	1.8937
1.9466	2.0981	1.9384	2.0899	2.0452	2.1967

$$f_{10} = (N_1 - 1)/(N_1 + 1) \tag{5}$$

$$t_{01} = 2/(1 + N_1) \tag{6}$$

$$N_1 = n_1 - ik_1, \text{ resist index} \tag{7}$$

$$N_2 = n_2 - ik_2 \text{ Cr/Cr}_2\text{O}_3 \text{ index} \tag{8}$$

Only the relative intensity is meaningful, which is given by

$$RI = \frac{E_s^2}{E_0} \tag{9}$$

It is obvious from Eq. [3] that the amplitude of the standing wave $E(x, d)$ is dependent on thickness d . It can be readily shown that the maximum and minimum intensity envelopes are given, respectively, by

$$d_{\text{max}} = (\phi + 2m\pi) \lambda / 4n_1\pi \tag{10}$$

$$d_{\text{min}} = (\phi + (2m + 1)\pi) \lambda / 4n_1\pi \tag{11}$$

where ϕ is the phase change during the reflection and $m = 0, 1, 2, \dots$. The condition $k_1 \ll n_1$ has been used.

Table III contains the first few maxima and minima calculated for types A, B, and C films cannot determine these extrema. In fact, a commercially available mask blank has almost the same reflectance as type B (about 34%), but has very different index of refraction (1.78 - i 2.36). For wavelength = 4350Å, the correspondent minimum intensity envelope occurs at a thickness 5080Å instead of at 5598Å as for type B. This shows that the reflectance alone cannot determine the optimal thickness for minimizing the standing wave effects, which are crucial for the image-size control.

The standing wave intensities at thicknesses $d = 1.037\lambda$ and $d = 1.189\lambda$ are plotted for type A in Fig. 6. These two thicknesses correspond to Eq. [10] and [11] for a maximum and minimum, respectively. It is seen that for a highly reflecting surface such as type A, coated with a weakly absorbing film of resist, the film thickness d is a powerful variable in determining the intensity of the standing wave in the resist film. By choosing a resist film thickness corresponding to a minimum, better linewidth control can be achieved. Thus, for metal surfaces, such as Al, Pt, and Cr, resist film thicknesses must be carefully chosen. However, as shown in Fig. 7, the case

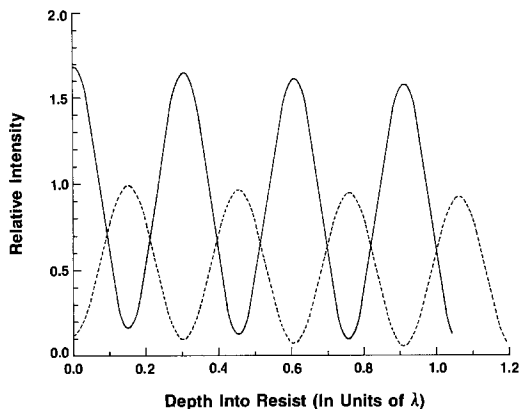


Fig. 6. Effect of thickness to produce maximum ($d = 1.037\lambda$) and minimum ($d = 1.188\lambda$) standing wave intensity envelopes for type A. (—): Max. (---): Min.

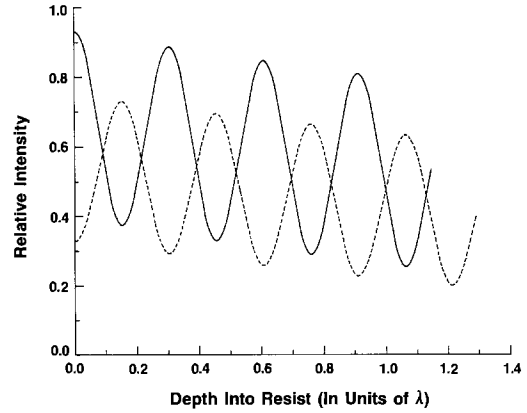


Fig. 7. Effect of thickness to produce maximum ($d = 1.36\lambda$) and minimum ($d = 1.188\lambda$) standing wave intensity envelopes for type C. (—): Max. (---): Min.

for type C, which has much smaller reflectance, this effect is much less conspicuous. It is, therefore, much more important to reduce film thickness variation for highly reflecting surfaces.

The standing wave intensities at $d = 5800\text{Å}$ for types A, B, and C are plotted in Fig. 8. This gives a ratio $d/\lambda = 1.33$. This thickness does not correspond to any extrema determined by Eq. [10] and [11]. However, this thickness is chosen for the experiment later. It is seen that there always exist underexposed layers which correspond to the nodes in Fig. 8, and the higher the reflectance, the more unexposed the nodal layers. However, by using an active developer, there is little difficulty in breaking through the underexposed layers and clearing resist from the resist-substrate interface for geometries layer than $1\ \mu\text{m}$; it will be shown later that for submicron geometries this is more difficult to achieve. In Fig. 9, the standing wave intensities at the photoresist/Cr-Cr₂O₃ interface as a function of film thickness are plotted. Since none of the substrates are perfectly reflecting, the phase change upon reflection is much less than π . These cause the first intensity minimum to be shifted from the interface as illustrated in Fig. 8, and a finite light intensity appears. It is also clear that the substrate with the highest index of refraction (type A) receives the smallest dose at the interface.

Finally, Fig. 10 shows the standing wave intensities at the thickness corresponding to the minimum ($d = 1.189$ for A, $d = 1.181$ for B, $d = 1.287$ for C).

The results of this section should serve as a guide for searching optimal conditions for minimizing standing wave intensities for metal surfaces.

Experimental Results and Discussion

The purpose of this experiment is to demonstrate a few important points shown in the last section. While the min-

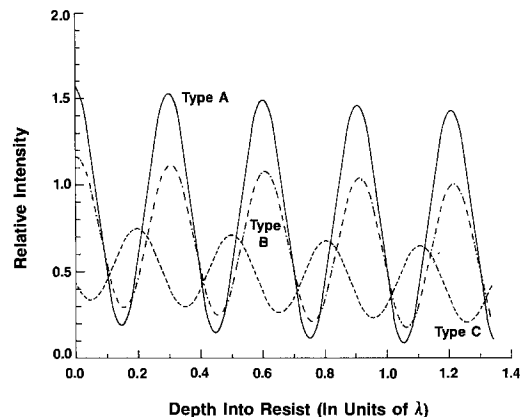


Fig. 8. Comparison of standing wave intensity for thickness $d = 5800\text{Å}$

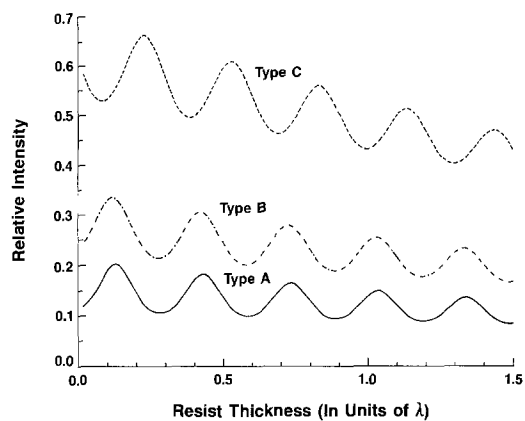


Fig. 9. Comparison of intensity at resist/substrate interface as a function of resist thickness.

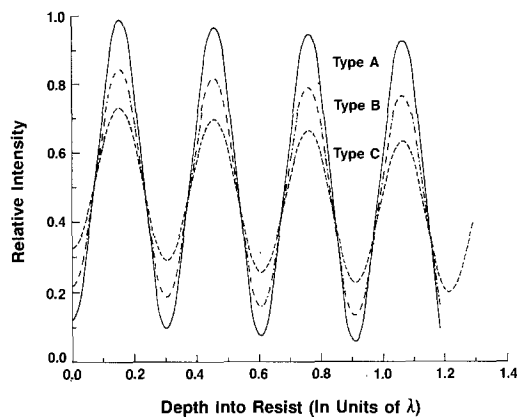


Fig. 10. Minimum intensity envelopes for types A, B, and C

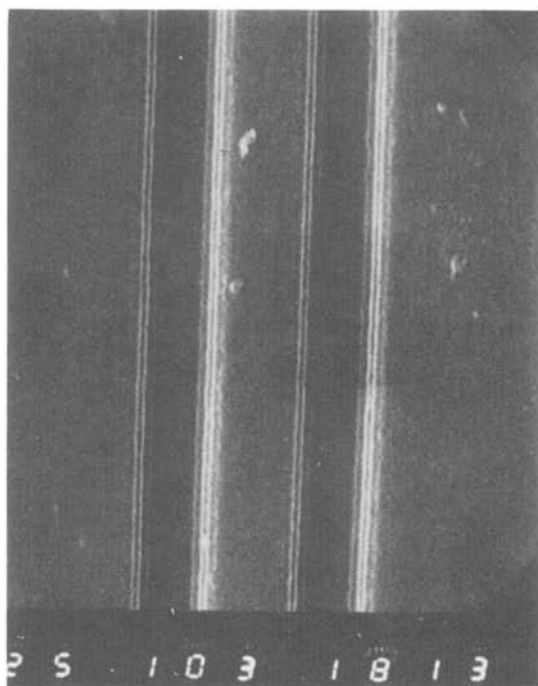
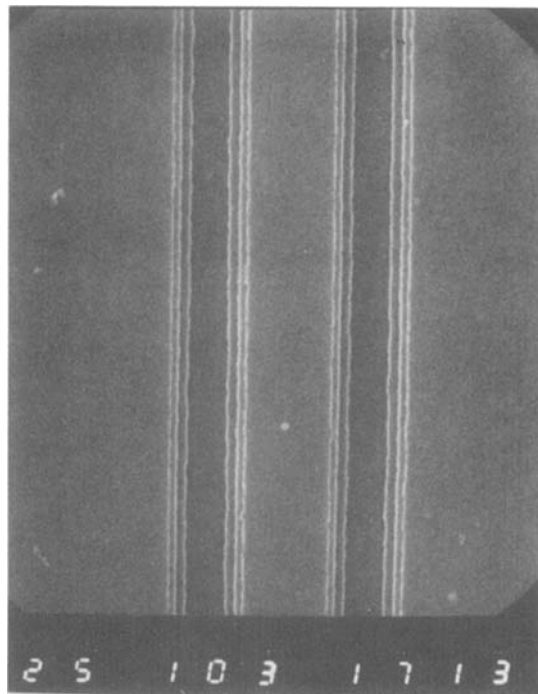
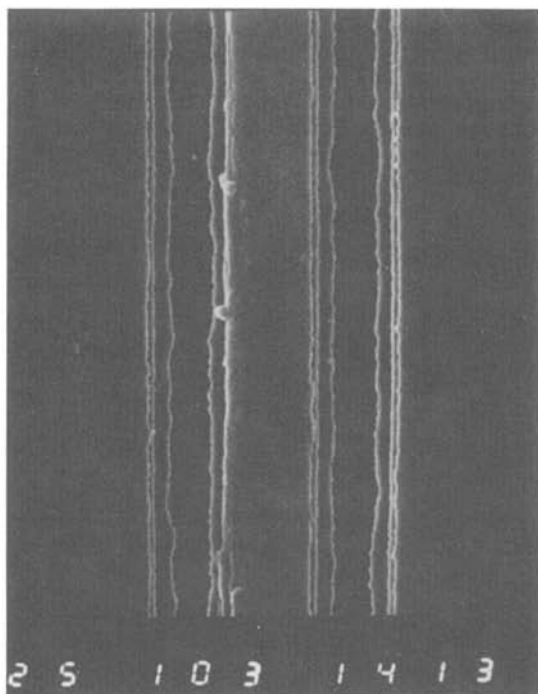


Fig. 11. Scanning electron micrographs of photoresist images with nominal $0.8 \mu\text{m}$. (a): Type A, (b): type B, (c): type C.

Table IV. Resist image size (thickness = 5800Å)
in units of micrometers

Nominal	A			B		C		
	mean	std	Ratio	mean	std	mean	std	Ratio
1.5	1.40	0.08	0.73	1.02	0.05	0.72	0.07	0.71
1.75	1.61	0.07	0.76	1.22	0.05	0.92	0.04	0.75
2.00	1.91	0.07	0.77	1.47	0.05	1.15	0.03	0.78

imum standing wave intensity lengthens the exposure time, it is preferred for better image-size control. In particular, the exposure variations caused by small photoresist thickness variations can be minimized.

The 10:1 projection system used in this experiment has an exposure wavelength = 4350Å. Other wavelengths are all filtered out and can be totally ignored. The photoresist used is AZ1350J, which, when unexposed, has an index of refraction $N = 1.65 - i0.02$.

After the exposure, the inhibitor concentration is greatly reduced, and, therefore, for most of the exposure, the resist is quite transparent. The three types of substrates A, B, and C are first spin coated with resist having a thickness of 5800Å. The resist thickness is measured using an IBM thin film measurement system. After exposure, the patterns are then developed using an AZ developer. In order to have a truthful comparison, the process variation must be minimized. For this purpose, the three types of substrates are exposed one after the other, giving the same exposure time. A test pattern with various linewidths is used for patterning. The patterned masks are then developed together. The resist images are then measured. Table IV contains the results of the measurements. The 1.5 μm nominal lines or above are all well developed. It is seen that as the reflectance increases, so do the standing wave intensities in the films, the image size variations increase also. The large variation for 1.5 μm nominal lines for type C is mainly due to the limitations of the measurement tools. What is interesting in this experiment is that the image sizes for different substrates are found to be roughly proportional to their maximum standing wave intensities in the films. The maximum intensity ratios calculated from standing wave theory are: $E_B^2/E_A^2 = 0.71$ and $E_C^2/E_B^2 = 0.70$ for the three types of substrates under investigation. Good agreement is found when comparing these ratios with those in rows 4 and 9 calculated from the image sizes. These results are repeatable.

The lines with nominal under less than 1 μm were not developed out for type A. As shown in the micrographs in Fig. 11, resist is not completely cleared from the film substrate interface, while under the same conditions it is cleared for both types B and C, which have much lower reflection.

This observation is consistent with Fig. 9, where the intensities at the resist/substrate have been plotted. This indicates that for submicron geometries either longer exposure time or longer development time is required for type A, which is often not desirable. The standing wave effects can be clearly observed in Fig. 11. Figure 11a, which corresponds to type A, shows much more conspicuous standing wave effects than do Fig. 11b or 11c, as predicted by the theory.

Conclusion

For future photomask manufacturing using photolithography, it is necessary to control image sizes much closer than is done now. Optical properties of the chromium substrates must be made to suit the need for deep-UV lithography used in wafer fabrication. This work offers some understanding from both theoretical and experimental point of view, and the lithography-related parameters such as reflectance have been investigated. The index of refraction has been shown to be an extremely important parameter in metal film lithography because it determines the standing wave effects, which place a limitation on the resolution capability of conventional resists. The relationship between the resist absorption, film thickness, and index of refraction of Cr/Cr_xO_y system has been derived and discussed. An experiment has also been carried out to illustrate some features of standing wave effects and minimization.

Acknowledgments

The author is grateful to L. Bureau, D. Miller, M. Rock, and J. Overmeyer for their valuable technical assistance. The technical and managerial support by R. West throughout this work is sincerely appreciated.

Manuscript submitted Feb. 15, 1984; revised manuscript received April 30, 1984.

IBM Corporation assisted in meeting the publication costs of this article.

REFERENCES

1. B. Curtis, H. Brunner, and M. Ebnoether, *This Journal*, **130**, 2242 (1983).
2. R. Azzam and N. Bashara, "Ellipsometry and Polarized Light," pp. 77-96, North-Holland, New York (1977).
3. F. Dill, A. Neurenther, J. Tuttle, and E. Walker, *IEEE Trans. Electron Devices*, **ed-22**, 465, (1975).
4. A. Arden, "Submicron Photolithography with 10:1 Projection Printing," Siemens Forsch. Entw.-Ber Bd., 11 (1982) no. 4, pp. 169-173, Springer-Verlag, Berlin (1982).
5. M. Born and E. Wolf, "Principles of Optics," pp. 274-301, Pergamon Press, New York (1975); L. Levi, "Applied Optics," Chap. 4, John Wiley and Sons, Inc., New York (1968).

Corner Undercutting in Anisotropically Etched Isolation Contours

M. M. Abu-Zeid*

Eindhoven University of Technology, 5600 MB Eindhoven, The Netherlands

ABSTRACT

Corner undercutting of mesa structures anisotropically etched in (100) silicon using ethylene diamine-water solution at 85°C is shown to be gradual with the prominent beveling facets on the {212} planes and ending with small ledges on {323} planes. Considering the undercutting to be a beveling on the {212} planes, relations are derived to calculate corner compensation masks of different shapes. It is further shown that when the mask edge is tilted with respect to the wafer flat, the etched mesa sidewall is formed by a striated sidewall plane running parallel to the mask edge and intersecting the corner beveling planes unsymmetrically. The conditions to obtain straight sidewall traces on the (100) surface at a certain etching height are given.

Convex corner cutting under the oxide mask of mesa structures anisotropically etched in (100) single-crystal silicon arises in the fabrication process of three-dimensional microstructures (1, 2). It is significant in dielectric isolation techniques of integrated circuits (3, 4), where it presents limitation to the useful surface area when deep etching is used. In this case, two methods are usually used to correct for corner undercutting (3): (i) the addition of compensation patterns to the mask corners and (ii) the tilting of the mask side with respect to the wafer flat by a small angle. However, controlled corner undercutting can be used as a micromachining process in rounding sharp corners in high voltage termination contours and channel structures (5).

In this paper, a detailed investigation is presented of the convex corner facets of anisotropically etched mesa structures using ethylene diamine-water etch solution at 85°C, complementing previously reported studies using KOH (3, 4) and hydrazine (8, 9) etch solutions. The corner profile was constructed from the measured etching parameters and then modeled by a single beveling plane. The simplified beveling model is used in calculating the dimensions of different compensation patterns. It is also used in investigating the shapes and textures of the etched mesa sidewalls and their traces on the (100) surface with different mask tilt angles and etching heights.

Experimental

The etch solution is a mixture of 55 volume percent (v/o) ethylene diamine in deionized water at 85°C (6, 7). Mesa structures were etched in (100) silicon using $100 \times 100 \mu\text{m}^2$ SiO₂ masks making successive angles with the (011) wafer flat ranging from 0° to 45° in steps of 5°. For each structure, corner and sidewall facets were examined at various etching heights using SEM and high resolution optical microscopes. The measured etch rates of the (100) and (111) planes are 0.5 and 0.018 $\mu\text{m}/\text{min}$, respectively.

When the mask edge is aligned with the wafer, flat corner undercutting starts from the (111) plane and increases gradually on various orientation planes as shown in Fig. 1 and Fig. 5. It is best represented by a {212} beveling plane intersecting the (100) surface at 48.2° and its trace making an angle $\alpha = 18.4^\circ$ with the (111) trace. The {212} beveling planes differ from the reported {331} planes using KOH-water-propanol etch solution (3, 4) and the {112} planes using hydrazine-water-isopropyl alcohol (8, 9). The top part of the undercut corner is in the form of a ledge that increases in width gradually from the (111) plane. The most prominent plane forming the lower side of the ledge was identified as (323), intersecting the (100) surface at 50.24°.

Figure 2 illustrates the case when the mask is rotated so that its edge is tilted with respect to the wafer flat by a small angle θ and the mesa is etched to a height H much smaller than the mask length L . The mesa corners continue to be bounded by the {212} beveling planes. A sidewall plane is formed whose trace on the (100) surface is parallel with the mask edge at a distance d_s and intersects

the traces of the beveling planes unsymmetrically. This plane coincides with the corresponding crystallographic plane. Its surface is striated and terminates on the (100) surface plane by a small ledge not shown in Fig. 2. The measured sidewall edge undercutting given by the normalized value $U_s = d_s/H$, and the sidewall plane slope ϕ varies with θ , as shown in Fig. 3 for $H/L = 0.24$. The effect of varying H/L and θ on the shapes of the etched mesa structures is given later.

Mesa Corners

A two-dimensional profile of the convex mesa corner undercuts on the (100) surface was constructed using a modified Wulff-type construction (10). For this procedure the lateral etch rate vectors on the (100) surface are represented by the experimentally determined values of U_s , and their polar diagram as a function of the crystallographic direction around the mask corner as origin is shown in Fig. 4. The corner undercutting profile is given by the envelope of the normals to the rate vectors. The diagram of one side of the constructed profile shown is bounded by many planes starting with the slowest etch rate (111) plane and ending with the medium-fast etch rate (313) plane, which touches the tip of the mesa corner and makes 26.57° with the mask edge. A large facet of the undercut corner within a radius making 30° from the mask diagonal is contributed by the (212) plane.

The constructed corner profile with the (323) top ledge is illustrated in Fig. 5. In section a-a, the relative thickness of the ledge at the mesa corner is $h/H = 0.052$. For the sake of clarity, the top ledge will not be considered in the following analysis, and the (212) beveling planes will be extrapolated to intersect the (100) surface. The extrapolated profile is shown with long dashed lines. The corner undercutting is measured by the conventional normalized factor $U_c = d_c/H$, where d_c is the perpendicular from the mask tip on to the trace of the (212) beveling plane on the

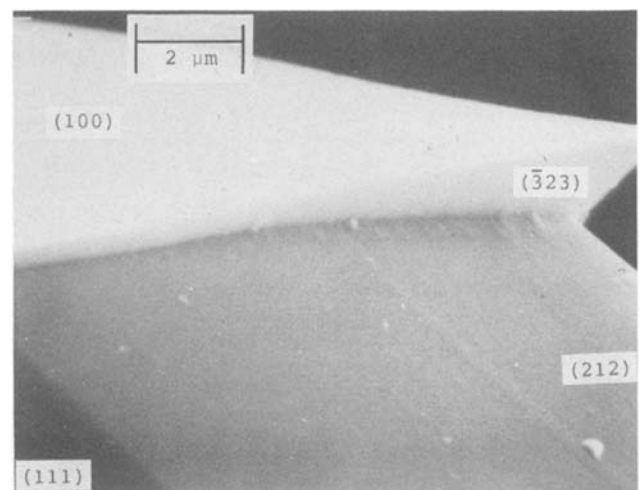


Fig. 1. Photomicrograph of undercut mesa corner with a top ledge

*Electrochemical Society Active Member.

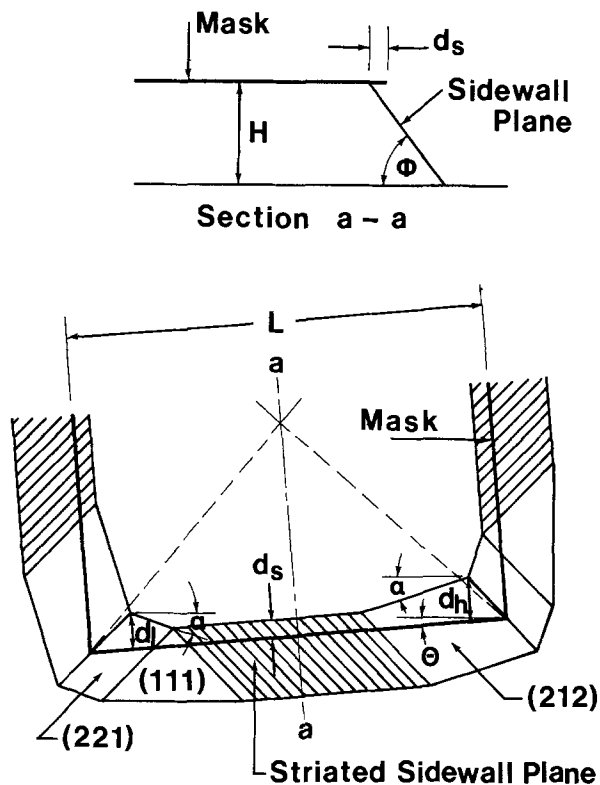


Fig. 2. Facets of a mesa sidewall etched using a mask edge tilted by $\theta = 5^\circ$ and $H/L = 0.24$. d_h and d_l are the perpendiculars from the beveled corner tips on to the mask edge.

(100) surface (8). With our etch solution $U_c = 0.5$ and is independent of the etch height, since d_c is proportional to H , in agreement with the reported results using KOH etch solution (1).

Mask Corner Compensation

Square patterns are usually added to the mask corners in order to correct for corner undercutting (1, 3). However, other geometrical patterns can be used when spac-

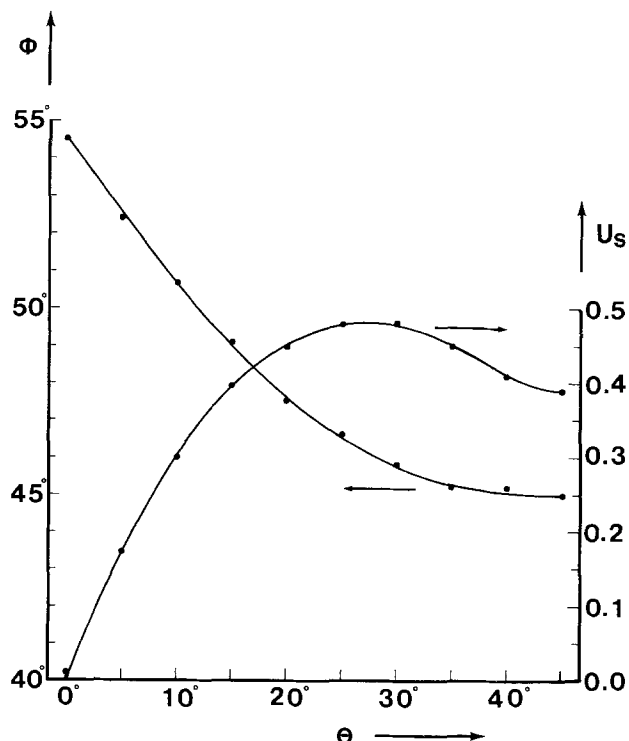


Fig. 3. Variation of the normalized edge undercutting $U_s = d_s/H$ and the sidewall plane slope Φ with the mask tilt angle θ for $H/L = 0.24$.

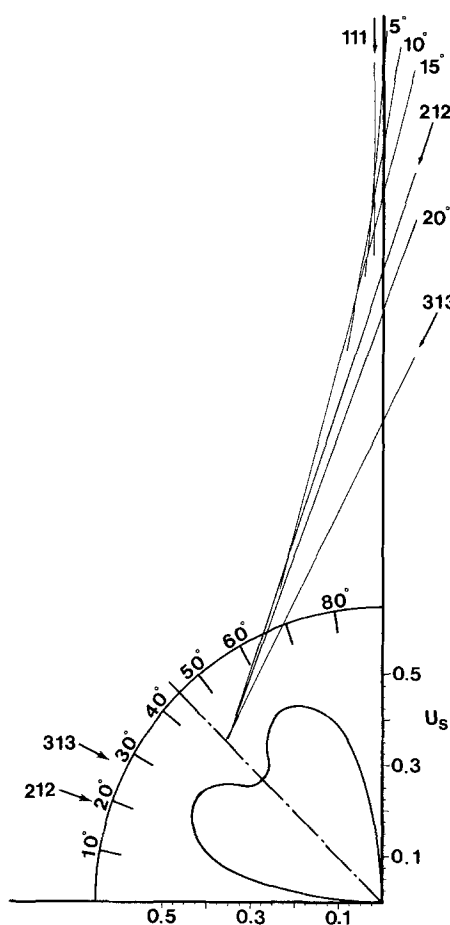


Fig. 4. Profile of a constructed undercut corner from the U_s vs. θ polar diagram.

ings between masks are limited. These are formed by superimposed rectangular stripes and square geometries. The criterion in calculating their dimensions is that the receding peaks of the convex corners under the compensating pattern have to reach the main mesa tip simultaneously when the specified etched height is reached. However, if etching continues, corner undercutting starts again.

Neglecting the sidewall undercutting of the {111} planes and assuming the receding convex corners to be bounded by the {212} planes only, a part of a compensating mask in the form of a long stripe having a small width W gives the successive etched shapes shown in Fig. 6a. After the two adjacent beveled planes meet at the mask edge, the tip recedes along the plane of symmetry as etching continues. At P , the two outer beveled planes meet, and at R , all the mesa surface disappears. The mesa height when its tip recedes from the mask edge by a distance d is given by

$$H = (0.5 W \sin \alpha + d \cos \alpha) / U_c \quad \text{for } d \leq 0.5W$$

and

$$H = (0.5 W \cos \alpha + d \sin \alpha) / U_c \quad \text{for } d \geq 0.5W$$

Etching follows the same pattern when a long rectangle having width of $0.5W$ is bounded by two orthogonal {111} planes, as shown in Fig. 6b.

These relations were used to calculate four patterns shown in Fig. 7 that give the same compensating results for a mesa height of $25.25 \mu\text{m}$. Even though the intersections of the mesa sidewalls on the (100) surface formed perfect squares when the specified etched height was reached, the sidewall intersections around the corners were surrounded by cones whose facets depend upon the geometrical shape of the compensating mask. Figure 8 shows a mesa corner etched out to the specified height using the mask with square compensating patterns. Even though there is no corner undercutting, the cones

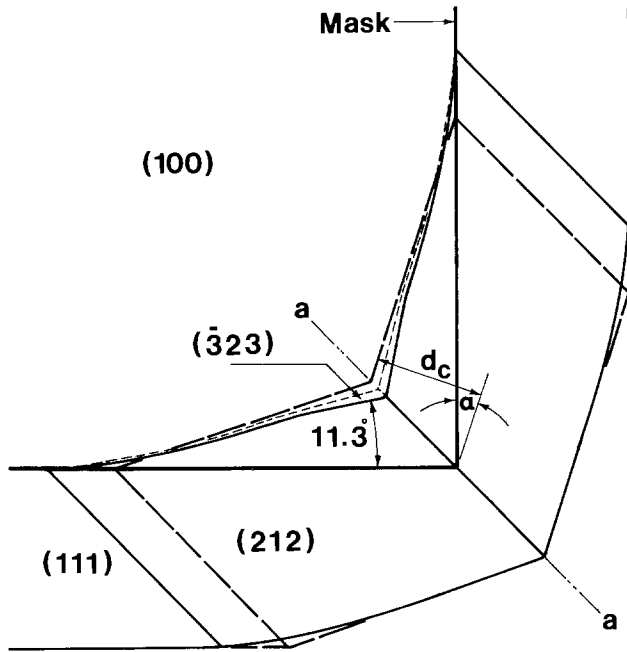
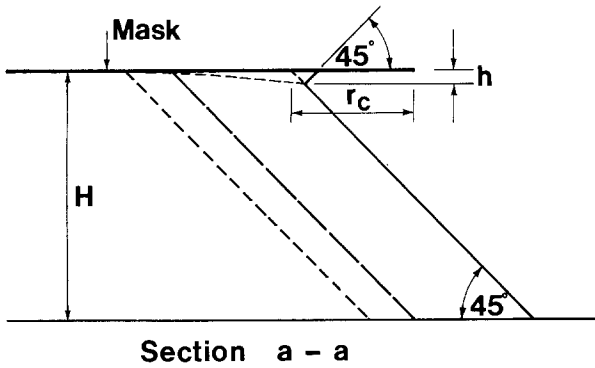


Fig. 5. Facets of a beveled corner

surrounding the corner intersections give the mesa the shape of a tablecloth. This is due to the difference in the inclinations of the {111} and {212} planes, as illustrated in the plan view shown in Fig. 9. The facet planes forming the corner cone meet at the mesa tip O, and the projections of their lines of intersections equal the mesa height. The corner cones disappear and the {111} sidewall planes meet when the etching height is increased by 0.185 times the calculated value. Corner undercutting resumed when the etching height was further increased.

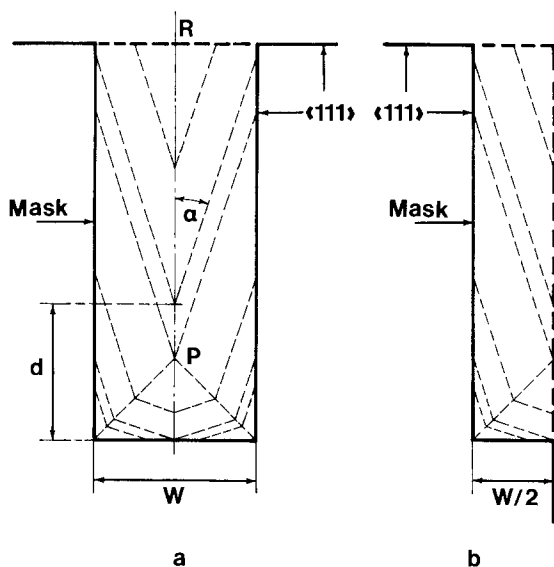


Fig. 6. Successive etching shapes with a long rectangular mask.

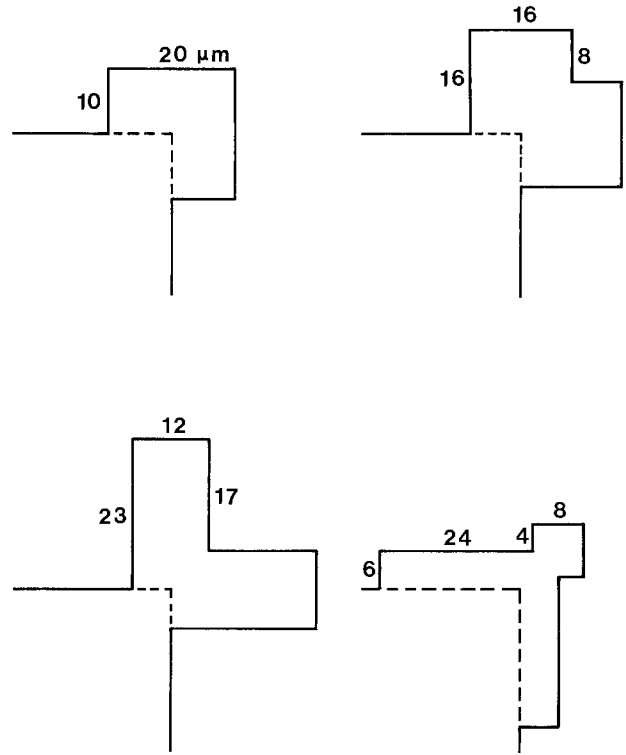


Fig. 7. Mask compensating patterns for a mesa height of 25.25 μm

Mesa Sidewalls with Tilted Masks

The etching shapes of the mesa sidewalls when the masks are tilted through successive angles depend on both the tilt angle θ and the ratio H/L . The H/L vs. θ plane shown in Fig. 10 is divided into five regions by curves A and B and line C, giving the boundary $\theta = \alpha$. In region 1, the sidewall plane intersects the two adjacent beveling planes unsymmetrically, as illustrated in Fig. 2. From the photomicrograph of this sidewall shown in Fig. 11, it is clear that the surface of the sidewall plane is striated, indicating that it is formed by more than one plane, in accordance with the ledge etching model proposed by Kendall (10). We also noticed that it is usually terminated at the (100) surface by a small top ledge, similar to that associated with an undercut corner. However, the following analysis does not take the top ledges into consideration. Detailed investigation using the ledge etching model to explain the variation of Φ and U_s with θ as shown in Fig. 3, together with the sidewall surface textures and etching mechanism, will be reported later. Region 1 is bounded

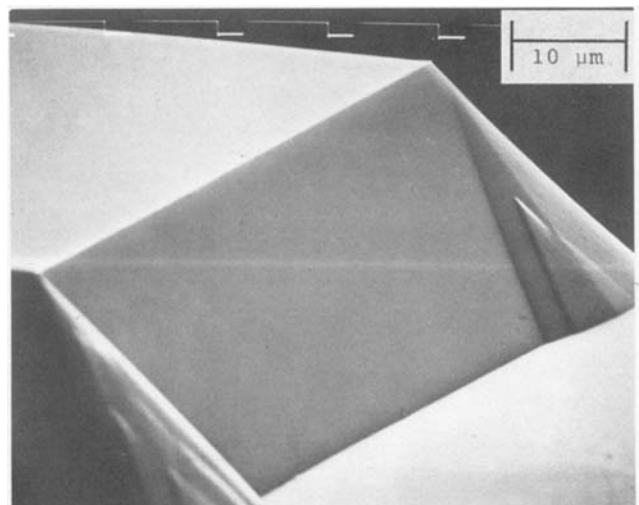


Fig. 8. Photomicrograph of a mesa sidewall etched with a mask having square compensating patterns.

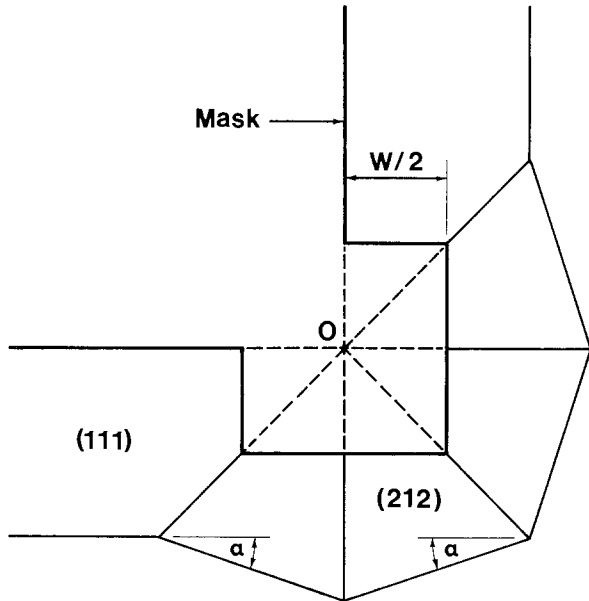


Fig. 9. Plan view of a mesa corner etched with a mask having square compensating patterns.

by curves A and B. Curve A gives the boundaries where one of the beveling planes passes through the two adjacent mesa corners and is given by

$$H/L = [(1 + \cot \alpha) \sin(\alpha - \theta)]/2 U_c$$

Curve B gives the values of H/L vs. θ , where the undercutting produced by the beveling planes of two adjacent corners just exceeds the sidewall plane undercutting d_s . Referring to Fig. 2 and 5, this situation exists when

$$L = \sqrt{2} r_c \cos \theta + (d_h - d_s) \cot(\alpha - \theta) + (d_1 - d_s) \cot(\alpha + \theta)$$

giving

$$L/H = [2 \sin \alpha / (\sin^2 \alpha - \sin^2 \theta)] (U_c \cos \theta - U_s \cos \alpha) \text{ for } 0 < \theta < \theta_t$$

where θ_t is the transition angle when curves A and B intersect. it satisfies the relation

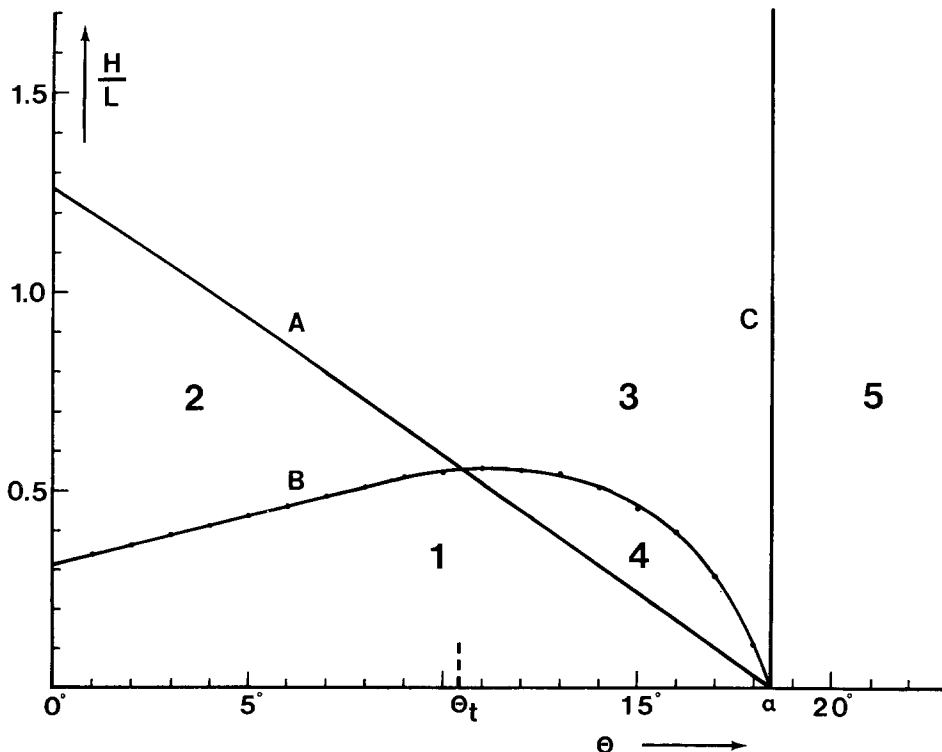


Fig. 10. H/L vs. mask tilt angle θ at the threshold of one beveling plane joining the two adjacent mesa tips (A) and sidewall planes disappear (B). $\theta_t = 10.4^\circ$.

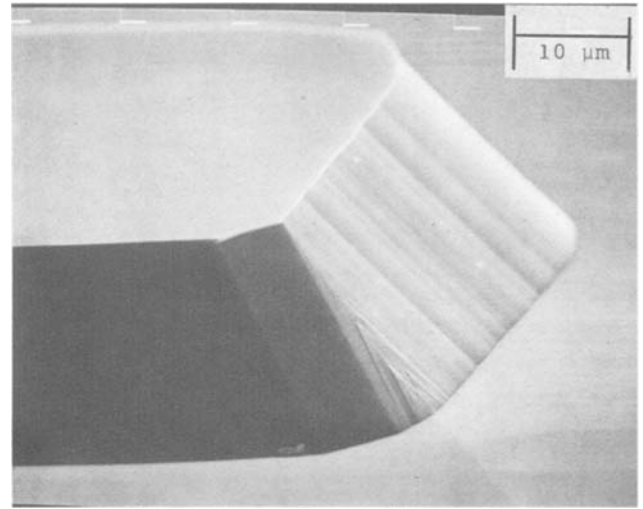


Fig. 11. Photomicrograph of a mesa sidewall etched with a mask tilted 5° and $H/L = 0.2$.

$$U_s/U_c = \sin(45 - \theta) / \sin(45 + \alpha)$$

With $\theta > \theta_t$, one beveling plane extends along the whole sidewall and intersects those of the adjacent sidewalls at right angles. In this case

$$L = \sqrt{2} r_c \cos \theta + (d_h - d_s) \cot(\alpha - \theta) + (d_1 - d_s) \tan(\alpha - \theta)$$

giving

$$L/H = \frac{2}{\sin 2(\alpha - \theta)} \left[\frac{\cos \theta + \sin(2\alpha - \theta)}{\sin \alpha + \cos \alpha} U_c - U_s \right] \text{ for } \theta_t < \theta < \alpha$$

The mesa sidewall in region 2 is formed by two beveling planes making $180^\circ - 2\alpha$ with each other, and the sidewall plane disappears, as illustrated in Fig. 12a. In region 3, it is formed by one beveling plane making $\alpha - \theta$ with the mask edge and 90° with the beveling planes forming the adjacent sidewalls, as illustrated in Fig. 12b, and recedes parallel to itself when etching continues. In region 4, it consists of a sidewall plane and one beveling plane, as

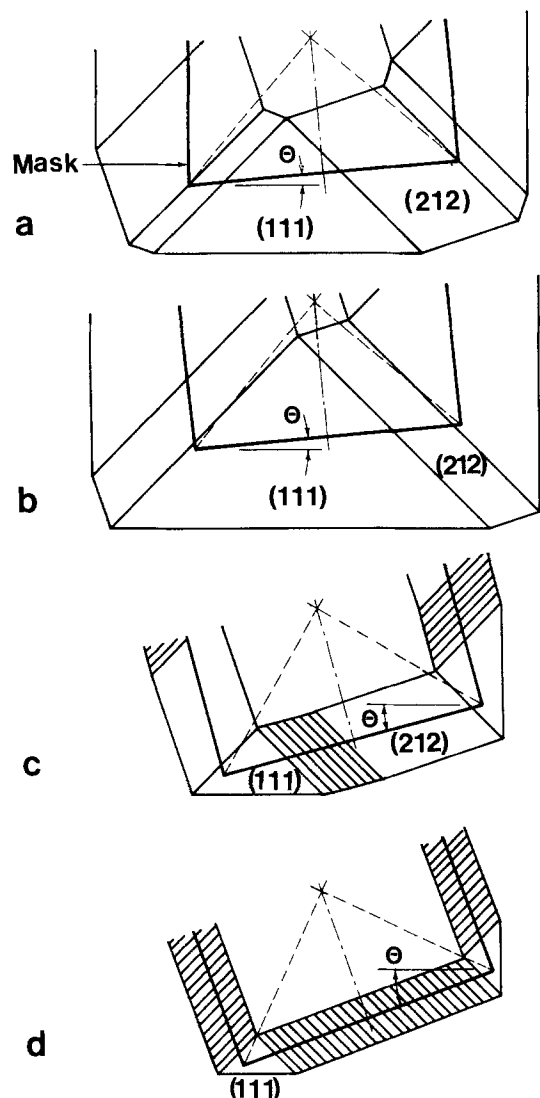


Fig. 12. Etched shapes of mesa sidewalls that correspond to the regions shown in Fig. 10. a: $\theta = 5^\circ$, $H/L = 0.7$, region 2. b: $\theta = 5^\circ$, $H/L = 1.0$, region 3. c: $\theta = 15^\circ$, $H/L = 0.35$, region 4. d: $\theta = 20^\circ$, $H/L = 0.2$, region 5.

shown in Fig. 12c. In region 5, the sidewall plane is parallel with the mask edge and extends between the mesa tips without corner undercutting, as illustrated in Fig. 12d. However, corner undercutting starts when θ exceeds 35° .

The trace of the sidewall plane on the (100) surface becomes straight, without corner undercutting, in regions 3 and 5. However, in both regions, sidewall undercuttings occur. For equal mesa heights, the trace of the sidewall plane at the boundary of region 3 given by curve A, with a small tilt angle θ , is slightly longer than that at the boundary of region 5 with tilt angle α . The increase related to

the mask length L is given by

$$\Delta d / L = \sqrt{2} \sin (45 + \alpha - \theta) - 1$$

Conclusions

When ethylene diamine-water etch solution at 85°C is used to etch mesa structures, convex corner undercuttings start from the {111} planes and increase gradually on various orientation planes with the top parts covered with small ledges. The prominent facets contributing to the undercuttings coincide with the {212} planes. Various pattern geometries can be designed for mask corner compensation at a specified etched height. At that height, the corner intersections are surrounded by cones that disappear when the etched height is further increased by a small specified amount. Undercutting starts again when etching is further resumed.

When the mask edge is tilted with respect to the wafer flat, the sidewall consists of different facets depending on the tilt angle θ and the etched height H . There are two regions in the H/L vs. θ plane where the sidewall trace on the (100) surface is straight. In both regions the sidewall makes smaller angles than the (111) plane with the (100) surface and the compensation is independent of the etched height. However, the sidewall surfaces are usually striated with large edge undercuttings.

Acknowledgment

The author would like to thank A. A. B. Thepass for his active assistance in installing and testing the etch apparatus. He is grateful to L. C. A. Sintnicolaas, J. H. Bijsterbosch, and L. H. Verstappen for helping in the measurements.

Manuscript submitted Sept. 19, 1983; revised manuscript received April 9, 1984. This was Paper 133 presented at the Montreal, Quebec, Canada, Meeting of the Society, May 9-14, 1982.

Eindhoven University of Technology assisted in meeting the publication costs of this article.

REFERENCES

1. K. E. Bean, *IEEE Trans. Electron. Devices*, **ed-25**, 1185 (1978).
2. K. E. Peterson, *Proc. IEEE*, **70**, 420 (1982).
3. K. E. Bean and W. R. Runyan, *This Journal*, **124**, 5C (1977).
4. K. E. Bean, R. L. Yearley, and T. K. Powell, Abstract 23, p. 58, The Electrochemical Society Extended Abstracts, Vol. 74-1, San Francisco, CA, May 12-18, 1974.
5. M. M. Abu-Zeid, to be published.
6. M. M. Abu-Zeid and H. Groendijk, in "4th Symposium on Solid State Device Technology," Abstract A5-4, p. 89, Munich, Germany, Sept. 10-14, 1979.
7. M. M. Abu-Zeid, in "Proceedings of the Second Czechoslovak Conference on Microelectronics," Section B, p. 56, Bratislava, Sept. 9-11, 1980.
8. M. J. Declercq, L. Gerzberg, and J. D. Meindl, *This Journal*, **122**, 545 (1975).
9. D. B. Lee, *J. Appl. Phys.*, **40**, 4569 (1969).
10. D. W. Shaw, *J. Cryst. Growth*, **47**, 509 (1979).
11. D. L. Kendall, *Appl. Phys. Lett.* **26**, 195 (1975).

Grain Growth Studies in Polysilicon by Ar⁴⁰ Ion Implantation and Thermal Annealing

Anjan Bhattacharyya* and Kenneth N. Ritz*

Philips Research Laboratories Sunnyvale, Signetics Corporation, Sunnyvale, California 94086

ABSTRACT

We have used the technique of multiple ion implantations of Ar⁴⁰ in polycrystalline silicon films for amorphization and subsequent thermal annealing for recrystallization. We observe dendritic grain growth with grain sizes ($\approx 0.75 \mu\text{m}$) about ten times larger than in original polycrystalline silicon films. This ion implantation technique can be used to form a device quality polysilicon film with large grains on an amorphous substrate.

In recent years, there has been much interest to form a device-quality silicon film on an amorphous substrate (e.g., SiO₂). The most commonly used techniques are recrystallization by laser or strip-heater (1, 2). However, the main drawbacks of these techniques are the high temperature needed for melting the polysilicon layer and lack of good reproducibility. Also, the melting cannot be always limited to the polysilicon layer and disturbs the material underlying the oxide.

It would be better to induce grain growth in polysilicon at comparatively lower temperatures ($<900^\circ\text{C}$) by a reproducible alternative process. Such a technique then could be used for the fabrication of stacked CMOS or multi-layered SOI devices and circuits (3).

In this investigation, we have determined a well-controlled processing condition, i.e., ion implantation, with a species (Ar⁴⁰) of dose compatible with current implanter capabilities which does amorphize the polysilicon and leads to grain growth after thermal annealing. The technique of ion implantation is a reproducible and controlled way to amorphize polysilicon or single-crystal silicon. The strain energy stored in the polysilicon due to the implanted ions could lead to a strain-induced recrystallization mechanism.

Also, the electrical properties of polysilicon such as the electrical conductivity (4) and excess carrier lifetime (5) depend on the grain size. The present technique of grain size growth can also have potential for solar cell applications.

Ion Implantation Conditions

We have to choose the implant conditions (energy, dose) for a particular ion (e.g., Ar⁴⁰) in polysilicon film which would produce amorphization. Such a process would totally destroy the grain boundary structure and could promote recrystallization of the amorphous state to a new structure, different from the original one. If the implant conditions do not produce amorphization, then there will be no major change in grain size and the grain structure will be morphologically similar to the original film.

To produce "uniform amorphization" of the polysilicon film, we have used three successive implants each with a dose of $2 \times 10^{15}/\text{cm}^2$ with projected ranges such that the superposition of three Gaussian implant profiles would give us a square profile. We have used the following implantation energies in sequence, with the projected ranges as shown

Energy (keV)	Projected Range (Å)
50	500
110	1092
180	1816

The energies are chosen in such a fashion that we would "uniformly amorphize" the polysilicon film of thickness 2500Å.

Sample Preparation

We have prepared samples with implantation doses less than and greater than the critical dose of $2 \times 10^{15}/\text{cm}^2$. All the samples were implanted sequentially at three different implantation energies, as described before.

The polysilicon films of thickness 2500Å were prepared by LPCVD ($\approx 620^\circ\text{C}$) onto a 650Å thick layer of SiO₂ grown at 950°C by oxidation of p-type $<100>$ Si wafers of resistivity 5-20 Ω-cm.

We used four different implantation doses (Ar⁴⁰) ($1 \times 10^{14}/\text{cm}^2$, $1 \times 10^{15}/\text{cm}^2$, $2 \times 10^{15}/\text{cm}^2$, and $4 \times 10^{15}/\text{cm}^2$) to study the dependence of grain growth on implantation dose. In each case, the samples were implanted three times with a particular dose at energies as shown above. After implantation the samples were annealed for 30 min in dry N₂. For comparison purposes, as-deposited polysilicon samples were also annealed in dry N₂.

Samples with all the various doses were annealed at 900°C. We have studied in detail the samples implanted with a dose of $2 \times 10^{15}/\text{cm}^2$ by annealing at 700°, 800°, 900°, 1000°, and 1100°C.

The samples were then prepared for planar TEM section studies to study the polysilicon grain size. Electron

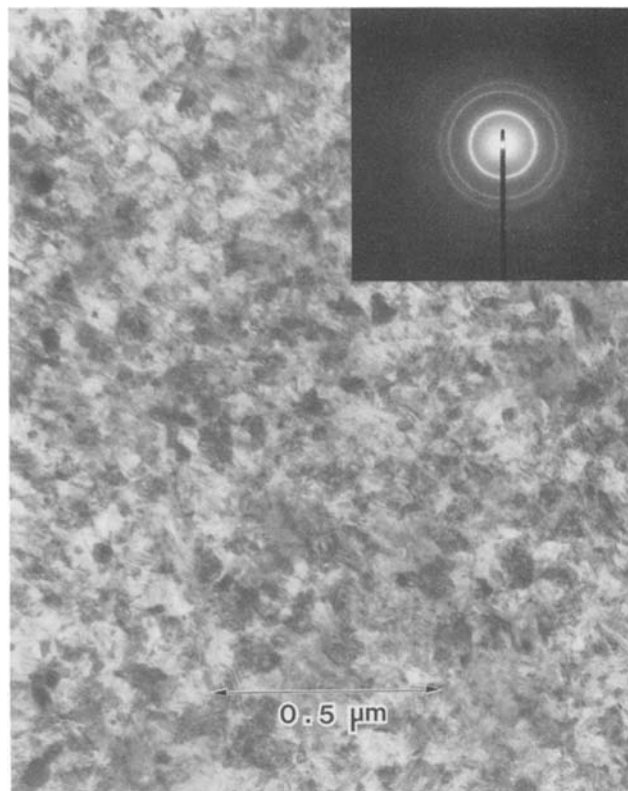


Fig. 1. As-received polycrystalline silicon sample, selected area diffraction pattern.

* Electrochemical Society Active Member.

diffraction patterns were also obtained to study the "amorphous" to "crystalline" phase change.

Large area electron transparent TEM samples were prepared using a thinning technique similar to that used by Kolbesen *et al.* (6), wherein the samples are etched from the back surface with a 5:1:1 mixture of nitric, hydrofluoric, and acetic acids.

Results and Discussion

Figure 1 shows a TEM micrograph and a selected area electron diffraction pattern for the as-deposited polysilicon film. We note that the grain size is in the range 0.04-0.1 μm . The grain size of the polysilicon after annealing at 900°C for 30 min in N_2 increases to 0.05-0.15 μm .

Now, let us consider a sample which was implanted with a dose of $2 \times 10^{14}/\text{cm}^2$, which is less than the critical dose for amorphization. We found from TEM micrographs that there are some grains with size 0.25 μm , but no evidence of any dendritic grain growth or grains with large diameters. The recrystallization produced a structure which was morphologically similar to the original polycrystalline film.

We now consider samples implanted with a dose of $1 \times 10^{15}/\text{cm}^2$, which is comparable to the dose of ($2 \times 10^{15}/\text{cm}^2$) required for amorphization. From the TEM micrograph as shown in Fig. 2, we see that the original polysilicon grain structure has been completely destroyed and the polysilicon film has been transformed to an amorphous structure. The detailed features in the TEM micrograph is possibly due to contamination by organic solvents during TEM sample preparation. Figure 2 also shows the typical diffuse diffraction ring images which are characteristic of amorphous silicon.

We have examined closely the grain in samples implanted with the dose of $2 \times 10^{15}/\text{cm}^2$ by annealing them in dry N_2 for 30 min at different temperatures to determine the minimum processing temperature at which the grain growth is almost complete.

Figure 3 shows a TEM micrograph and an electron diffraction pattern of samples implanted with a dose of $2 \times 10^{15}/\text{cm}^2$ and annealed at 900°C.

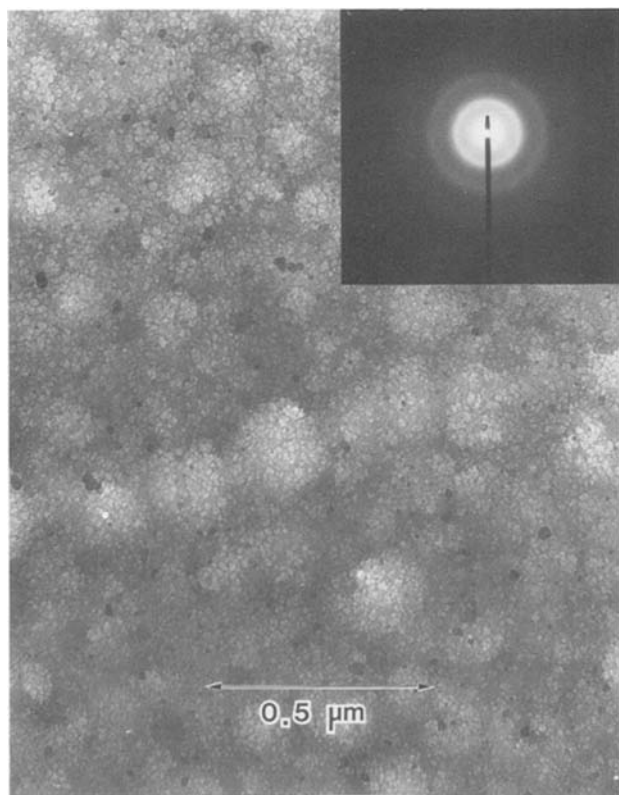


Fig. 2. Polysilicon sample implanted with a dose of $1 \times 10^{15}/\text{cm}^2$, selected area diffraction showing diffuse rings only.

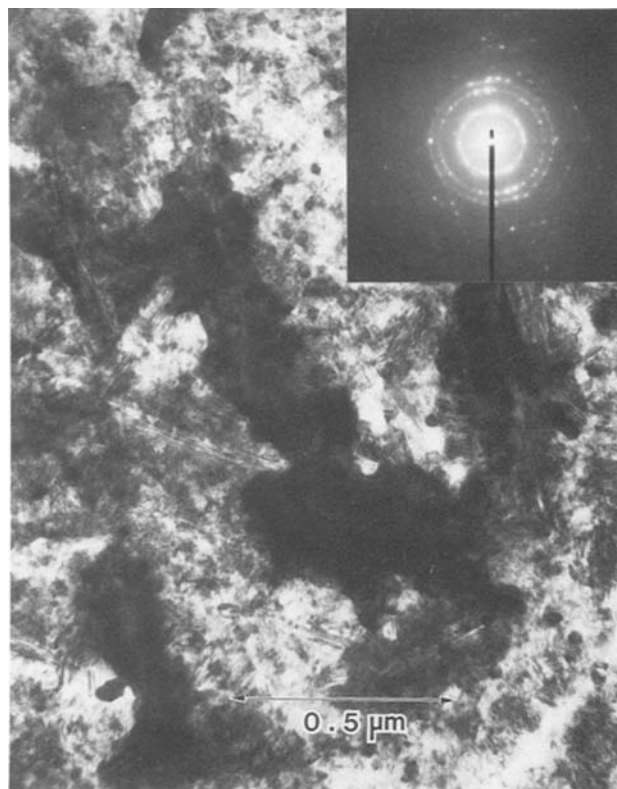


Fig. 3. Polysilicon sample implanted with a dose of $2 \times 10^{15}/\text{cm}^2$ and annealed at 900°C for 30 min in dry N_2 , selected area diffraction pattern showing growth of large dendritic grains.

If we examine the TEM micrograph the sample annealed at 900°C, we note that the recrystallized polysilicon has a structure totally different from the original polycrystalline form. We observe appearance of a dendritic structure. The average size of the dendritic grain is $\approx 0.75 \mu\text{m}$, which is remarkably larger than the grain size (0.04-0.1 μm) of as-deposited polysilicon. The electron diffraction pattern is clearly more discrete than obtained from the original polycrystalline film.

The TEM micrographs of the samples annealed at 700°, 800°, and 1100°C also show similar dendritic grains. Any increase in annealing temperature beyond 900°C does not substantially increase the grain size.

For the samples implanted with a higher dose of $4 \times 10^{15}/\text{cm}^2$ and annealed at 900°C for 30 min, we did not observe any further increase in grain size.

Figure 4 shows a plot of the average dendritic grain size in micrometers *vs.* annealing temperature. The samples implanted with $2 \times 10^{15}/\text{cm}^2$ showed dendritic grains after annealing at 700°C. We note that with increase in the annealing temperature, the average dendritic grain size increases to 0.75 μm at 900°C. Beyond 900°C, we did not observe any further increase in grain size. Also shown in the graph are average grain sizes for samples implanted with a dose of 1×10^{14} , 1×10^{15} , and $4 \times 10^{15}/\text{cm}^2$ and annealed at 900°C in dry N_2 for 30 min.

Polysilicon films deposited in a Tempress (Unicorp) LPCVD reactor over the temperature range 580°-640°C have been studied by Kamins *et al.* (7). In particular, the films deposited at 580°C were amorphous and showed marked change in structure after thermal annealing at 800°-1200°C. However, the particular condition of deposition of amorphous films, *e.g.*, by evaporation (8) or by atmospheric pressure CVD in a nitrogen ambient (9) determines the structure of the films after thermal annealing. The amorphous films deposited (7) at 580°C and annealed at 800°C showed a definite structure, but films with better defined larger grains did not appear until the anneal temperature was increased to 1200°C.

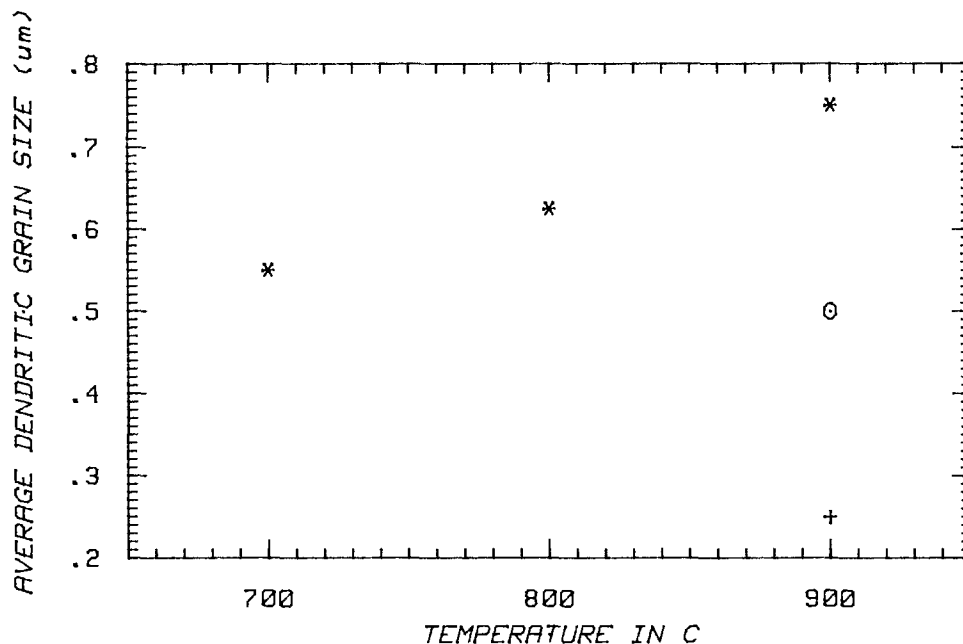


Fig. 4. Average dendritic grain size in micrometers vs. annealing temperature. *: Dose of $2 \times 10^{15}/\text{cm}^2$, various anneal temperatures. O: $1 \times 10^{15}/\text{cm}^2$, 900°C anneal. +: $1 \times 10^{14}/\text{cm}^2$, 900°C anneal.

The present technique of amorphization of polysilicon films by ion implantation is a reproducible and controlled mechanism and is not strongly dependent on processing conditions as in the different alternatives in depositing amorphous films (7-9). The grain growth for the samples implanted with a dose of $2 \times 10^{15}/\text{cm}^2$ was complete after annealing at 900°C with no significant increase in grain size when the annealing temperature was increased to 1100°C . Such a process has the potential of application in processing sequences where the maximum temperature is limited to 1000°C or less.

Conclusions

The present unique technique produces a significant grain growth in polysilicon film. The implantation dose of $2 \times 10^{15}/\text{cm}^2$ and annealing temperature of 900°C produces the optimum conditions for dendritic grain growth. The implantation conditions have to be such that the polycrystalline film is amorphized, and such that it loses its past history of grain size and grain boundaries. This technique could have significant application to produce large grain polysilicon film on amorphous substrates as required in silicon-on-insulator technology.

Acknowledgments

It is a pleasure to acknowledge Gerard de Groot, Albert Schmitz, and Earl Dobelbower for processing the wafers and Bill Stacy for helpful discussions and suggestions.

Manuscript submitted Oct. 3, 1983; revised manuscript received ca. Feb. 15, 1984.

Philips Research Laboratories assisted in meeting the publication costs of this article.

REFERENCES

1. A. Gat, L. Gerzberg, J. F. Gibbons, T. J. Magee, J. Peng, and J. D. Hong, *Appl. Phys. Lett.*, **33**, 775 (1978).
2. B. Y. Tsaur, J. C. C. Fan, R. L. Chapman, M. W. Geis, D. J. Silversmith, and R. W. Mountain, *IEEE Electron Dev. Lett.*, **ed1-3**, 398 (1982).
3. T. I. Kamins, *ibid.*, **ed1-3**, 341 (1982).
4. K. Board and M. Darwish, *J. Appl. Phys.*, **51**, 446 (1980).
5. A. K. Ghosh, C. Fishman, and T. Feng, *ibid.*, **51**, 446 (1980).
6. B. O. Kolbesen, K. R. Mayer, and G. E. Schuh, *J. Phys. E.*, **8**, 197 (1975).
7. T. I. Kamins, M. M. Mandurah, and K. C. Saraswat, *This Journal*, **125**, 927 (1978).
8. R. M. Anderson, *ibid.*, **120**, 1540 (1973).
9. N. Nagasima and N. Kubota, *J. Vac. Sci. Technol.*, **14**, 54 (1977).

Photo-CVD for VLSI Isolation

John Yuan-tai Chen^{*,1} and Richard C. Henderson*

Hughes Research Laboratories, Malibu, California 90265

James T. Hall and John W. Peters

Hughes Aircraft Company, El Segundo, California 90245

ABSTRACT

This paper reviews the technique of photochemical-assisted vapor deposition (photo-CVD), and its applications in silicon IC processing. The photo-CVD process deposits SiO₂ films (PHOTOX™) at temperatures as low as 50°C. The deposition process, the resulting film properties, and the use of PHOTOX SiO₂ for lateral isolation among transistors and vertical isolation between two-level interconnects are discussed. A novel process employing PHOTOX deposition in conjunction with a photoresist liftoff can be used to achieve totally isoplanar isolation. Photo-CVD can also be extended to produce other dielectrics such as silicon nitride and aluminum oxide.

In fabricating VLSI circuits, low temperature processing may be one of the most important techniques for achieving the precise control required for device structures, isolation, and interconnection (1). Specific effects that may be minimized include wafer warpage, defect generation, Al hillock formation, Al/Si interface degradation, and dopant diffusion. However, the needs of the IC industry for high quality, uniform, pinhole-free dielectrics have always resulted in some high temperature steps in the process: thermal oxides obtained at > 900°C in the most demanding situations, or CVD films at > 300°C. Consequently, the need exists for a low temperature insulator deposition process that results in high quality oxide or nitride films.

Consider the electrical isolation between active devices on an IC chip. The degree of isolation required is extreme in order to obtain several thousand integrated devices without cross-talk between them (2). For MOS IC's, this isolation is generally achieved with a thick oxide (field oxide) between transistor areas. One well-known technique for defining the field oxide patterns is known as LOCOS (3), in which a nitride film is masked and etched to form the desired pattern followed by a high temperature oxidation. The nitride pattern prevents oxide growth within the area that becomes the transistor region. The long high-temperature process in the LOCOS process can generate defects in the silicon substrate. Moreover, the periphery of the transistor area is overtaken by oxide encroachment beneath the nitride edges, resulting in a bird's beak structure which can reduce the yield of gate-lines crossing it. Encroachment also results in a narrower MOSFET channel, thereby reducing the current driving capacity, and hence the ultimate speed of the IC's. Several approaches have been developed to reduce the bird's beak phenomena (4, 5), at the expense of complicating the processing, and without solving the problem of thermally induced defects. Moreover, non-LOCOS techniques have similar problems. For example, etching the desired field pattern in a uniform oxide (6-9) leaves sharp steps at the window edges.

Vertical isolation between two levels of metalization is another area of IC processing that could effectively employ insulators formed in low temperatures. The insulator separating the Al or Al alloy interconnection structures must have low pinhole density, low stress, a smooth surface morphology, high breakdown voltage, low dielectric constant, and high resistivity. With the conventional method of depositing SiO₂ by low pressure CVD (LPCVD), Al and Si interdiffuse at the deposition temperature (≤ 400°C), which can cause leakage (10, 11). Moreover, at 400°C, hillocks form on the Al surfaces which result in reduced breakdown voltages or electrical shorts (12) in the insulators that cover them. It is therefore desirable to deposit an insulator at temperatures much lower than 400°C.

*Electrochemical Society Active Member.

¹Present address: Xerox Palo Alto Research Center, Palo Alto, California 94303.

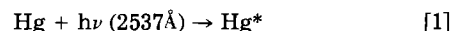
A unique new approach to obtaining insulator films at low temperature is to use UV irradiation to form vapor-phase reactants that enhance the desired reaction (12-15). Silicon oxides and nitrides, as well as alumina, have been deposited by these techniques. This photochemical-assisted CVD process (photo-CVD) has already been employed successfully to deposit the insulator between two levels of Al metalization (12, 13). It has also been used for isolation (16) by masking the transistor areas with photoresist, etching the field region, and then refilling the etching region with a photo-CVD oxide. Excess oxide is later lifted off to form an isoplanar structure. With this lift-off technique, one avoids the defects and the bird's beak formation. The low temperature photo-CVD process (~100°C) permits lift-off with a photoresist medium which would degrade at higher temperatures. The resulting isolation structure is fully recessed, isoplanar, and much simpler to implement than earlier attempts using Al (17) or Mo (18) to lift off SiO₂ deposited at ~300°C by plasma-CVD.

The remainder of this paper describes methods of photo-CVD, characterization of the resulting SiO₂ films, applications to Si device technology, and extensions to other semiconductor technologies.

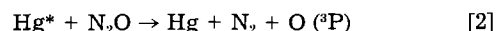
Methods of Photo-CVD

There are two basic photo-CVD mechanisms: Hg-sensitized photolysis and direct photolysis (14, 15). A new technique of laser photolysis is a promising extension of direct photolysis.

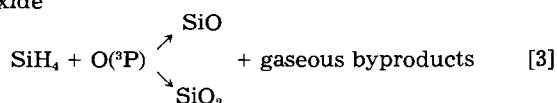
The reactor system for the Hg-sensitized photo-CVD is similar to other low pressure CVD systems. The difference is the source of excitation. The reaction chamber employs a UV-grade quartz window above a heated substrate platform, and low pressure Hg lamps provide UV illumination on the substrate. Figure 1 is a schematic of such a reactor system. Note that the Hg reservoir in the gas inlet manifold provides minute quantities of Hg vapor to the reactant stream. During photo-CVD, Hg vapor resonantly absorbs UV radiation at a wavelength of 2537Å and catalytically transfers energy to the reactant gases via the reaction



In Hg-sensitized photo-CVD, N₂O is typically the oxygen source because it readily reacts with excited Hg atoms and yields neutral atomic oxygen in the ground state



The ground-state oxygen atom can convert many reactant gases to their respective oxides. For example, SiH₄ reacts spontaneously with atomic oxygen to form the monoxide or dioxide



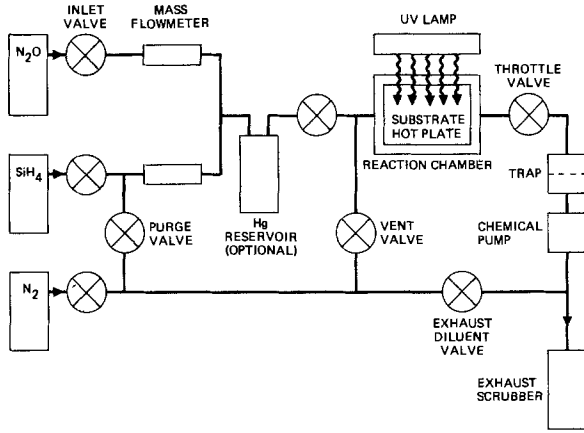
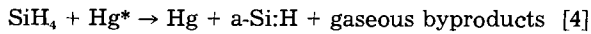


Fig. 1. Schematic of PHOTOX reactor system

SiH_4 can also react with excited Hg atoms to form an amorphous silicon (19)

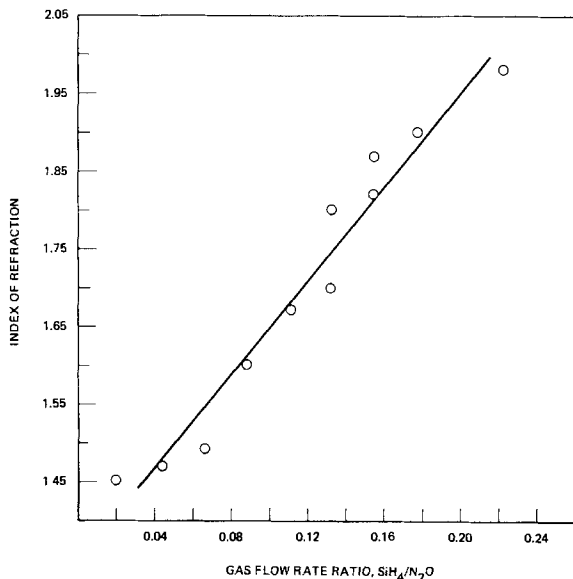


It is possible to deposit films of the desired O to Si stoichiometry (SiO_x , $0 \leq x \leq 2$) by varying the SiH_4 -to- N_2O flow ratio. At one extreme (low $\text{SiH}_4/\text{N}_2\text{O}$), SiO_2 forms; at the other extreme (pure SiH_4), a-Si:H forms; and at intermediate ratios, SiO_x forms. SiO and SiO_2 have indexes near 2.0 and 1.45, respectively, and different mixtures have different indexes between these limits. Figure 2 shows a linear relation of film refractive index to the $\text{SiH}_4/\text{N}_2\text{O}$ flow ratio.

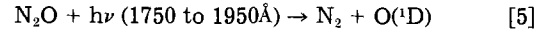
The deposition rate depends primarily on UV intensity and weakly on substrate temperature (temperature affects film density and etch rate). The deposition rate, along with stoichiometry and uniformity, also depends on the reaction chamber geometry, chamber pressure, and pumping speed. A rate of $\sim 150 \text{ \AA}/\text{min}$, spread uniformly over an area of $\sim 150 \text{ cm}^2$, is routinely achieved in a square reaction chamber with a window area of $\sim 650 \text{ cm}^2$.

Photo-CVD is not limited to silicon oxides and amorphous silicon. Photo-CVD of P-doped SiO_2 and SiO_xN_y films can be accomplished with the addition of the reactant gases PH_3 and NH_3 , respectively (14, 20). Photo-CVD of alumina can also be accomplished by replacing SiH_4 with $\text{Al}(\text{CH}_3)_3$ (21).

An alternative to the Hg-sensitized method is direct photolysis employing UV excitation of reactant gases. The reactor system is the same as shown in Fig. 1, but without the Hg reservoir. UV radiation at a high enough

Fig. 2. PHOTOX- SiO_x (100°C) refractive index vs. reactant gas ratio

energy splits N_2O directly and produces oxygen in an excited state



Upon collisional relaxation of the $\text{O}(^1\text{D})$ to the ground state, deposition proceeds according to Eq. [3]. A good choice of wavelength is 1849 \AA because it is readily obtainable from low pressure Hg lamps, and because SiH_4 is nearly transparent in this region of the spectrum.

The deposition rate of direct photolysis, however, is lower than with the Hg-sensitized process by about an order of magnitude. This is thought to be primarily a result of lower intensity at the required wavelength and inefficiency in Eq. [3]. Where no Hg contamination can be tolerated, there may be an advantage to using the direct photolytic method over the Hg-sensitized method. However, no detrimental effects with MOS devices have yet been ascribed to Hg contamination. Trace analyses for Hg content will be discussed in the next section.

A new direct photolytic method using an ArF laser with a wavelength of 1930 \AA , was recently described (22, 23). In this method, the laser beam (a much more powerful UV source) passes about $\sim 1 \text{ mm}$ parallel to the substrate surface, and deposition proceeds at rates up to $\sim 3000 \text{ \AA}/\text{min}$. Uniform deposition has occurred over a rectangular area $\sim 1 \text{ cm}$ wide, the width of the beam. This laser-CVD is very promising for many applications which require a very high deposition rate.

Properties of PHOTOX SiO_2

Table I lists a number of optical, electrical, physical, and chemical properties of PHOTOX- SiO_2 films and those of thermal- SiO_2 films (24). PHOTOX SiO_2 deposited at 200°C is quite similar to thermal SiO_2 grown at $>900^\circ\text{C}$. Upon annealing for short periods, the etch rates of PHOTOX SiO_2 approach those of thermal SiO_2 .

Excellent adhesion has been observed for PHOTOX SiO_2 on Si substrate. As shown in Table I, adhesive strength as high as $69 \times 10^6 \text{ Pa}$ was obtained from PHOTOX SiO_2 film. Film adhesion was measured by pulling tensile specimens, which were formed by cementing metal studs to a film on Si substrate. The adhesive strength for PHOTOX SiO_2 on Si substrate, however, is less than the PHOTOX SiO_2 adhesion by about an order of magnitude (25).

Figure 3 compares the infrared spectrum of a 4600 \AA thick film of PHOTOX SiO_2 produced at 200°C with the spectrum of a 4000 \AA thick film of thermal SiO_2 produced at 925°C . These spectra were obtained using Fourier transform techniques and subtracting the absorption of bare substrates (wafers of intrinsic Si, resistivity $> 10^4$

¹PHOTOX is a trademark process of Hughes Aircraft Company.

Table I. PHOTOX- SiO_2 and thermal SiO_2 material properties

PROPERTY	PHOTOX SiO_2 (200°C)	THERMAL SiO_2 (DRY)
REFRACTIVE INDEX	1.45 - 1.47	1.46 - 1.47
DIELECTRIC CONSTANT	3.9 - 4.0	3.9
RESISTIVITY ($\times 10^{15} \Omega\text{-cm}$ AT 300 K)	~ 1	3 - 20
DIELECTRIC STRENGTH (MV/cm)	3 - 6	8
DENSITY (gm/cm^3)	2.0 - 2.2	2.24 - 2.27
TENSILE STRENGTH (-ADHESIVE STRENGTH TO Si, MPa)	$\sim 56 - 69$	-
ETCH RATE (BUFFERED HF AT 25°C, $\text{ \AA}/\text{min}$)	UNDENSIFIED	~ 140
	ANNEALED, 15 min N_2 AT 450°C	~ 90
	ANNEALED, 15 min $\text{O}_2 + \text{H}_2$ AT 925°C	~ 17

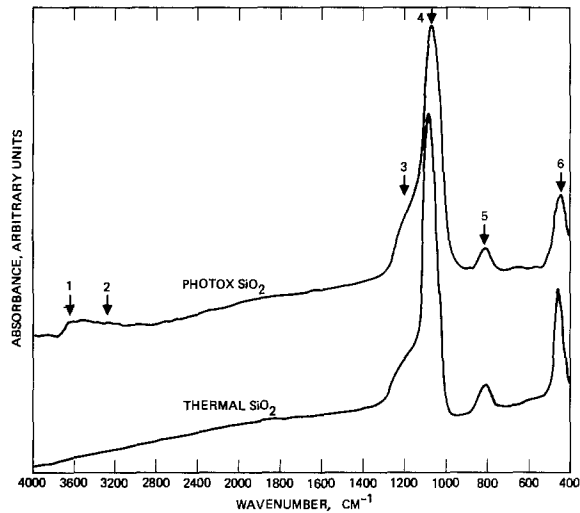


Fig. 3. IR spectra of 4600Å thick PHOTOX-SiO₂ (200°C) and 4000Å thick thermal SiO₂.

Ω-cm). The absorbance levels for both spectra were identical. The PHOTOX spectra was offset for clarity. The spectra are quite similar in all the absorption peaks (peak 3-6), except for small OH stretch mode (shown as peak 1 and 2) in PHOTOX SiO₂. Using calibrated formulas, analysis of this spectral structure gives a water content of ~2% by weight in the PHOTOX SiO₂.

Hydroxyl ions and water molecules are common in SiO₂ films deposited at low temperatures, and the water content may be as much as 5% by weight if they are not annealed above 800°C (26).

Auger electron spectroscopy (AES), electron spectroscopy for chemical analysis (ESCA), and Rutherford backscattering spectroscopy (RBS) have all been used to characterize PHOTOX SiO₂ deposited on Si. Figure 4 shows the peak-to-peak AES signals for O, Si, P, and C vs. etch time for a 1000Å PHOTOX film. On the same sample, ESCA data were obtained after removing 200Å. The elemental percentages determined are shown in Table II. For comparison, Table II also lists the elemental percentages of control samples of thermal SiO₂, P-doped PHOTOX SiO₂, and a PHOTOX SiO_xN_y sample. Within background experimental errors (~5%), PHOTOX SiO₂ has the 2:1 O:Si ratio expected for SiO₂. RBS experiments were unable to detect Hg in Hg-sensitized photolysis (limit ~100 ppm).

Figure 5 displays capacitance-voltage (C-V) behavior at 1 MHz of a MOS device before and after bias-temperature stressing (10V on gate for 5 min at 200°C). The metal is Al, the dielectric is 1000Å of PHOTOX SiO₂ produced at 200°C, and the semiconductor is ~5 Ω-cm n-type. These C-V curves show well-behaved MOS characteristics with

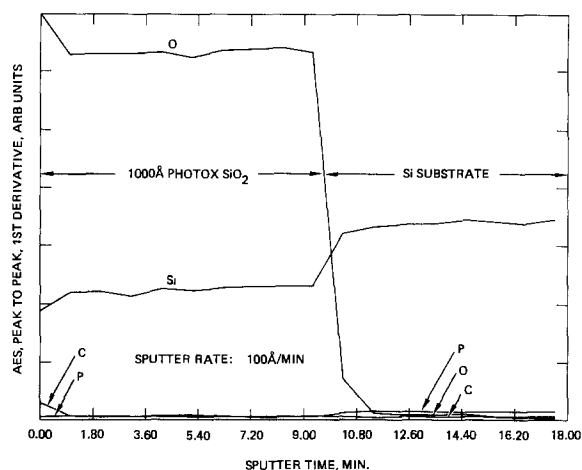


Fig. 4. Sputter AES profile of 1000Å thick PHOTOX-SiO₂ on Si

Table II. Elemental analyses in percentage of field insulator film

	PHOTOX -SiO ₂	P-DOPED PHOTOX -SiO ₂	PHOTOX SiO _x N _y	THERMAL OXIDE
Si	34	31	33	35
O	61	67	24	58
N	—	—	43	—
P	—	2	—	—
C	5	—	1	7

NOTES: THE CARBON CONTENT MAY JUST BE AN ARTIFACT OF THE MEASUREMENT; A CONTROL BACKGROUND SUBTRACTION WOULD ELIMINATE CARBON WITHIN EXPERIMENTAL ERROR, WHICH IS ABOUT ±5%. THE MEASUREMENTS GIVEN ARE AT A DEPTH OF OVER 200Å INTO THE BULK

a flatband voltage shift (ΔV_{FB}) of $-0.3V$, yielding a mobile-ion surface density of $8 \times 10^{10} \text{ cm}^{-2}$. This quantity is not excessive, but it is higher than the $\sim 1 \times 10^{10} \text{ cm}^{-2}$ produced by well-established thermal oxidation processes.

To summarize, PHOTOX SiO₂ has properties and characteristics that are comparable with thermal SiO₂ produced at much higher temperatures. This suggests the compatibility of PHOTOX SiO₂ for insertion into Si device technology.

Applications to Si Technology

Low temperature photo-CVD may be useful in many processing steps of MOS IC fabrication where high temperature thermal oxidation and conventional CVD may induce problems. Table III lists the sequence of a basic MOS fabrication process and the steps where photo-CVD technology may be considered to replace the conventional technique. Figure 6 shows a cross section of the corresponding MOSFET device. Of the five different insulating films that might be provided by photo-CVD, different requirements lead to separate evaluations of each case. This section primarily discusses application to lateral isolation and interlevel isolation, and briefly summarizes other applications.

Lateral isolation.— In standard IC's, a relatively thick ($\geq 0.4 \mu\text{m}$) field insulator provides a high field inversion voltage for electrical isolation between transistors. The pinhole density of the material used for the field insulator must be low, and the residual charge density must be minimal in order to avoid leakage and field inversion. It must also be compatible with standard MOS IC processing steps such as etching and various anneals.

NMOS transistors have been made with a $0.4 \mu\text{m}$ thick PHOTOX SiO₂ as the field insulator in a process using conventional window isolation. The standard process takes several hours at 925°C to grow a $0.4 \mu\text{m}$ thick thermal oxide, but with photo-CVD at 100°–200°C, it takes less than 30 min. It is difficult to transfer a precise IC pattern into the as-deposited PHOTOX SiO₂ because of its high etch rate. However, PHOTOX SiO₂ densified at 925°C for 15 min etches at nearly the same rate as that of a

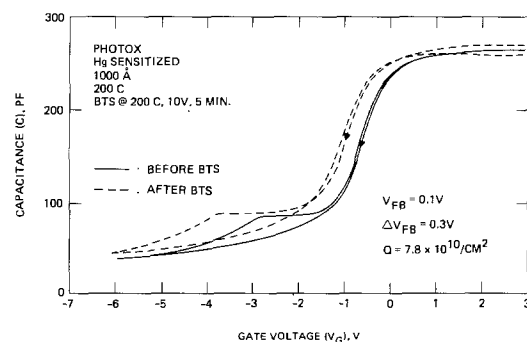


Fig. 5. BTS-CV measurement of Al/PHOTOX-SiO₂/Si MOS device

Table III. Fabrication sequence for a basic MOS process

PROCESS SEQUENCE	CONVENTIONAL TECHNIQUES	PHOTO-CVD TECHNIQUES
FIELD INSULATOR	THERMAL SiO ₂	PHOTOX SiO ₂
ACTIVE AREA DEFINITION, ION IMPLANTATION		
GATE OXIDE	THERMAL SiO ₂	PHOTOX SiO ₂
GATE DEFINITION, SOURCE/DRAIN IMPLANT		
INSULATOR ON POLY-SI	PHOSPHO-SILICATE-GLASS (PSG)	P-DOPED PHOTOX SiO ₂
REFLOW AT ~900° C, CONTACT DEFINITION, FIRST LEVEL Al		
INTERLEVEL DIELECTRIC	CVD SiO ₂	PHOTOX SiO ₂
SECOND LEVEL Al		
FINAL PASSIVATION	CVD SiO ₂ OR PLASMA CVD - NITRIDE	PHOTOX NITRIDE
PAD DEFINITION		

thermal-SiO₂ film (Table I). Figure 7 compares an IC test pattern etched into various 0.4 μm thick SiO₂ films using a buffered HF etchant. Notice that the pattern is well defined in densified PHOTOX SiO₂. In addition, PHOTOX-SiO₂ films do not exhibit stress or adhesion problems after the thermal cycling. Films subjected to the entire IC process show no degradation in integrity.

The most important requirement of PHOTOX SiO₂ in this isolation application is low leakage current (< 1 pA) between transistors with a common gate. Figure 8 shows the leakage current for a PHOTOX SiO₂ isolation oxide with a spacing of 1.6 μm between two transistors. Leakage is < 1 pA for a gate voltage of ~14V, and the corresponding field inversion voltage (typically defined as the gate voltage at a leakage of 1 μA) is ~20V. These characteristics provide a sufficient margin of isolation among MOS transistors operated with a standard 5V power supply.

Because of the unique capability of depositing high quality SiO₂ at a low temperature, PHOTOX can be used to achieve a novel isoplanar isolation (16). In this technique, a photoresist pattern is used to mask the transistor areas on a bare Si wafer while the field region is etched to a depth of 0.4 μm. PHOTOX SiO₂ is then deposited uniformly to a thickness of 0.4 μm. Finally, the photoresist is lifted off with an ultrasonic solvent bath to remove the excess PHOTOX SiO₂ and expose the active areas for subsequent processing. Although more work is needed to establish a reproducible lift-off technique that is suitable

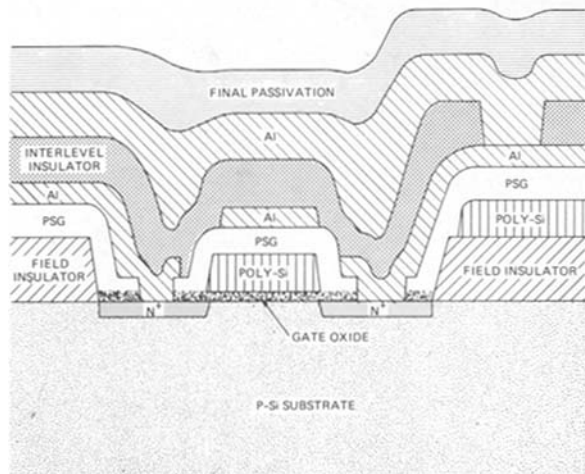


Fig. 6. Schematic cross section of an N-channel MOSFET device

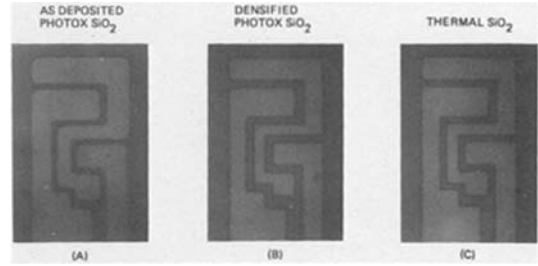


Fig. 7. IC patterns etched through 0.4 μm thick SiO₂ on Si

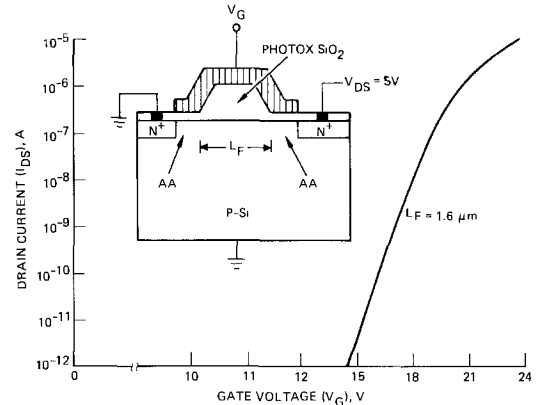


Fig. 8. Subthreshold leakage current under the field insulator formed by PHOTOX-SiO₂.

for high yield IC processing, this simple technique provides a fully recessed, isoplanar structure, as shown in Fig. 9.

With this isoplanar isolation structure, field oxide encroachment (the "bird's beak") is completely eliminated, and thermally induced defects are avoided. MOSFET's with excellent device characteristics have been fabricated, and narrow channel effects have been virtually eliminated, as shown in Fig. 10. Here, identical MOSFET threshold voltages were found with varying channel widths down to 1.6 μm, the narrowest width attempted. Figure 11 shows the gain of these MOSFET's improves dramatically over MOSFET's fabricated with the nonplanar window isolation method. The result of modeling studies of these two structures, have shown that with the isoplanar structure, field pinching in the channel is minimal, resulting in the absence of narrow channel effects (16).

Interlevel isolation.—The use of PHOTOX SiO₂ between two levels of Al metalization has been studied as a replacement for conventional CVD processes (12). A test chip was fabricated containing a large area capacitor, several via chains with 100 vias/chain, and a serpentine capacitor with a total of 1200 perpendicular crossovers. Figure 12 shows the serpentine capacitor with two perpendicularly crossing levels of Al metalization isolated by PHOTOX-SiO₂. Several wafer lots were prepared using 1 μm thick PHOTOX-SiO₂ films deposited at 200°C. Excellent mechanical properties, such as conformal coating, smooth surface morphology, low defect density, and

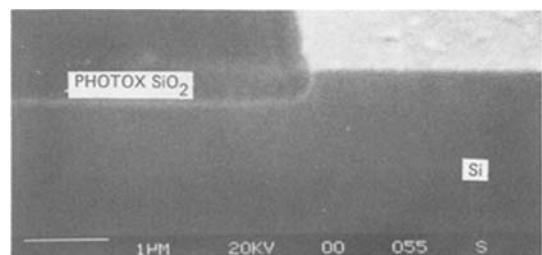


Fig. 9. SEM micrograph of an isoplanar structure produced by photoresist lift-off of PHOTOX-SiO₂.

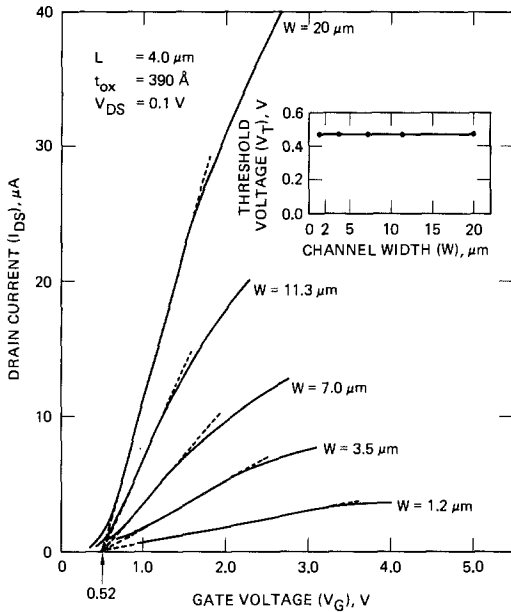


Fig. 10. I-V measurements for N-MOSFET threshold voltage (plotted in insert) as a function of channel width.

good adhesion, were obtained with the PHOTOX-SiO₂ films. The 1 μm thick films deposited on Al substrates showed pinhole densities of < 3-7 cm⁻² and dielectric strengths of > 3 × 10⁶ V/cm. Electrically active defect densities were estimated by the Poisson relation ($Y = e^{-DA}$), where Y is the capacitor yield, D is the defect density, and A is the capacitor area. Table IV shows the experimental yield obtained from three different wafer lots. The absence of Al hillock formation in PHOTOX-SiO₂ is believed to be a major reason for the high yields shown.

Other applications.—As a gate insulator, PHOTOX-SiO₂ must demonstrate low leakage, high dielectric strength,

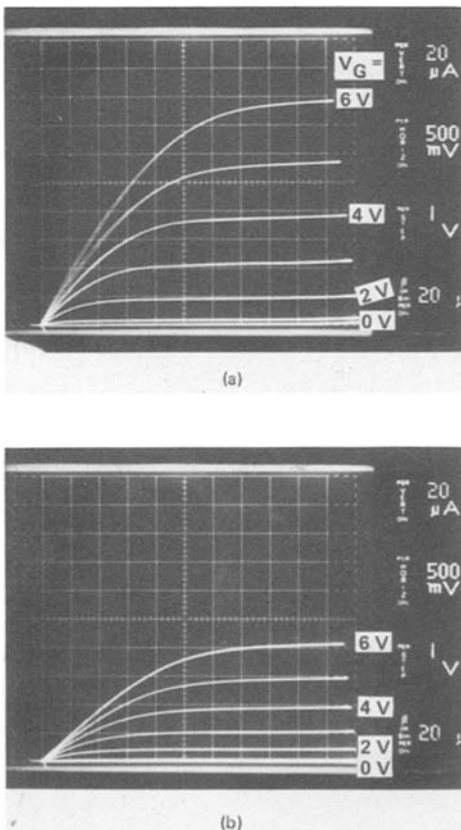


Fig. 11. I-V curves of narrow-channel MOSFET's fabricated by (a) isoplanar PHOTOX and (b) nonplanar technique. Channel widths are 1.5 μm for both cases.

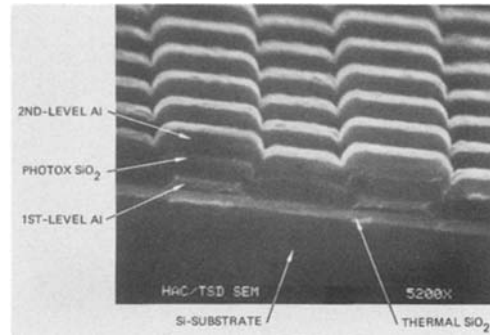


Fig. 12. SEM micrographs of double-level Al isolated by PHOTOX-SiO₂.

low mobile-ion density, and a low interface density of states. For insertion into Si technology, it should be better than standard thermal oxides, which are usually produced in a short period (<30 min) at temperatures of 800°–1000°C. Although the mobile ion density in PHOTOX-SiO₂ is not excessive (see the “Properties” section, above) it cannot compete with the excellent interface properties of thermal SiO₂. PHOTOX-SiO₂ may be employed, however, with semiconductors that do not have a good native oxide or that are temperature sensitive. For example, SiO₂ deposited by photo-CVD at 100°C has demonstrated good passivation characteristics of HgCdTe (27) operated at 77 K. PHOTOX-SiO₂ has also been used to passivate InP devices operated at room temperature (14). Another promising gate insulator material is PHOTOX-Al₂O₃ (21).

Another application of PHOTOX-SiO₂ is P-doped SiO₂, which reflows at a temperature low enough (~950°C) to avoid significant amount of dopant diffusion in the silicon substrate. Such a reflow provides sloped and smooth oxide contours over relatively sharp poly-Si corners. P-doped SiO₂ may also be useful as a barrier against mobile ions. P-doped PHOTOX-SiO₂ has been demonstrated, but significant characterization data are not yet available.

PHOTOX-SiO_xN_y has been employed as a final passivation to coat fully wire bonded lead-frame assemblies (20). It was found that this material was compatible with the assemblies and could protect devices from metallic particles. It was also found that the PHOTOX-SiO_xN_y was comparable to the nitride produced by plasma-CVD (28). (Nitride films are preferred for their barrier resistance to moisture and mobile ions.) Another promising material with high barrier resistance is PHOTOX-Al₂O₃, which has also been deposited with photo-CVD.

Summary

Isolation is critical for achieving high density circuits in VLSI. Furthermore, avoiding high temperatures during fabrication of small device structures is desirable because it reduces dopant redistribution, defect generation, and Al/Si degradation. Low temperature processes could be employed in VLSI fabrication for lateral isolation among

Table IV. Evaluation of PHOTOX-SiO₂ (200°C) for interlevel insulator

LOT	YIELD, %	DEFECT DENSITY, cm ⁻²
1	98	5
2	97	7
3	99	3

active devices, and vertical isolation among multilevel metalizations.

The low temperature (50°–200°C) process of photochemical-assisted chemical vapor deposition (photo-CVD) meets these demands. Photo-CVD involves the discrete absorption of energy from UV radiation to initiate deposition. This process depends primarily on UV intensity and only weakly on substrate temperature, and it thus avoids the high temperatures and energies of thermal-CVD and plasma-CVD.

Photo-CVD SiO₂ (PHOTOX) has demonstrated excellent mechanical and electrical properties for isolation between two levels of Al metalization. This interlevel insulator provides low pinhole density ($\leq 3\text{--}7\text{ cm}^{-2}$), high breakdown strength ($\geq 3\text{ MV/cm}$), and good uniformity ($> 3\%$ across a 4 in. wafer). Furthermore, the low temperature processing minimizes Al/Si interdiffusion and Al hillock formation, which occur at higher temperatures.

Photo-CVD at temperatures ($\sim 100^\circ\text{C}$) permits a simple lift-off technique for achieving a fully recessed, isoplanar field isolation. Narrow channel MOSFET's fabricated with this technique escape the "bird's beak" formation that accompanies high temperature oxidation, achieve much larger gain, and do not have narrow channel effects.

One major concern in applying Hg-sensitized PHOTOX films in Si processing is Hg contamination. Although RBS measurements did not detect Hg in these films, the detection sensitivity ($\sim 100\text{ ppm}$) is not high enough. Hg contamination as high as 10^{18} cm^{-3} could be present in these films. The Hg impurities which may not have deleterious effect in MOS devices can be detrimental to minority-carrier devices such as bipolar transistors. More analyses are needed to determine the actual concentration of Hg atoms in the Hg-sensitized PHOTOX films. Although one can apply PHOTOX films by direct photolysis, the deposition process is very slow ($15\text{--}30\text{ \AA}/\text{min}$). Even with Hg-sensitized process, we can only obtain a rate of $150\text{ \AA}/\text{min}$, whereas laser-CVD can provide deposition rate up to $\sim 3000\text{ \AA}/\text{min}$. The low PHOTOX deposition rate has been a limitation in the application of PHOTOX to Si production process. Furthermore, the uniformity of film thickness can also limit wafer production. Although the uniformity over a 4 in. wafer is better than 3%, the uniformity across the entire substrate heater (which holds five 4 in. wafers) is $\sim \pm 10\%$ (25). At present, wafer throughput is limited due to the low deposition rate and nonuniformity among wafers.

Applications of photo-CVD extend beyond isolation in Si technology. The benign nature of photo-CVD permits processing on sensitive substrates such as InP and other temperature-sensitive compound semiconductors. Finally, photo-CVD is not limited to SiO₂; PHOTOX-SiO_xN_y and PHOTOX-Al₂O₃ have been demonstrated for high quality dielectrics.

Acknowledgments

The authors are grateful for the assistance provided by L. Bailey and E. M. Yee.

Manuscript submitted Dec. 27, 1983; revised manuscript received April 27, 1984. This was Paper 167 pre-

sented at the Cincinnati, Ohio, Meeting of the Society, May 6-11, 1984.

Hughes Research Laboratories assisted in meeting the publication costs of this article.

REFERENCES

1. S. C. Su, *Solid State Technol.* 72 (1981).
2. W. G. Oldham, *IEDM Digest*, **82**, 216 (1982).
3. E. Kooi, J. G. VanLierop, and J. A. Appels, *This Journal*, **123**, 1117 (1976).
4. J. Hui, T. Y. Chiu, S-W S. Wong, and W. G. Oldham, *IEEE Trans. Electron. Devices*, **ed-29**, 554 (1982).
5. K. Y. Chiu, J. L. Moll, and J. Manoliu, *ibid.*, **ed-29**, 536 (1982).
6. R. A. Monline and G. W. Reutlinger, *ibid.*, **ed-20**, 1129 (1973).
7. J. Y. Chen and R. C. Henderson, *IEEE Electron Device Lett.*, **edl-3**, 13 (1982).
8. K. L. Wang, S. A. Sadler, W. R. Hunter, P. K. Chatterjee, and P. Yang, *IEEE Trans. Electron Devices*, **ed-29**, 541 (1982).
9. J. Y. Chen, R. C. Henderson, and D. E. Snyder, *ibid.*, **ed-30**, 1521 (1983).
10. H. M. Naquib and L. H. Hobbs, *This Journal*, **124**, 573 (1977).
11. J. M. Aitken and C. Y. Ting, *IEDM Tech. Digest*, **81**, 50 (1981).
12. E. M. Yee and J. W. Peters, *SPIE Proc.*, **319**, 22 (1982).
13. R. F. Sarkozy, "CVD Silicon Oxide Below 100°C Utilizing Photochemical Combustion of SiH₄ and O₂," 1981 Symposium on VLSI Technology, Maui, HI, p. 68, IEEE, New York (1981).
14. J. W. Peters, *IEDM Tech. Digest*, 240 (1981).
15. J. W. Peters, H. N. Rogers, J. T. Hall, and E. M. Yee, Abstract 202, p. 324, The Electrochemical Society Extended Abstracts, Vol. 82-1, Montreal, Que., Canada, May 9-14, 1982.
16. J. Y. Chen, R. C. Henderson, J. T. Hall, and E. M. Yee, *IEDM Digest*, **82**, 233 (1982).
17. K. Kurosawa, T. Shibata, and H. Isuka, *ibid.*, 384 (1981).
18. K. Ehara, T. Morimoto, S. Muramoto, T. Hosoya, and S. Matsuo, in "VLSI Science and Technology/1982," C. J. Dell'Oca and W. M. Bullis, Editors, p. 30, The Electrochemical Society Softbound Proceedings Series, Pennington, NJ (1982).
19. T. Saito, S. Muramatsu, T. Shimada, and M. Migitaha, *Appl. Phys. Lett.*, **42**, 678 (1983).
20. J. W. Peters, F. L. Gebhart, and T. C. Hall, *Solid State Technol.* **23**, 121 (1980).
21. J. W. Peters, H. N. Rogers, and E. M. Yee, Paper presented at American Vacuum Society Annual Symposium on Microfabrication Technology, Boston, June 1983.
22. P. K. Boyer, G. A. Roche, W. H. Ritchie, and G. J. Collins, *Appl. Phys. Lett.*, **40**, 716 (1982).
23. R. Solenski, W. H. Ritchie, and G. J. Collins, *ibid.*, **43**, 454 (1983).
24. E. H. Nicollian and J. R. Brews, "MOS Physics and Technology," John Wiley and Sons, New York (1982).
25. Tylan Corporation, "Photochemical Vapor Deposition Reactor," *Solid State Technol.*, **29** (1982).
26. W. A. Pliskin, *J. Vac. Sci. Technol.*, **14**, 1064 (1977).
27. J. A. Wilson, V. A. Cotton, and P. Morgan, *J. Vac. Sci. Technol. A*, **1**, 1719 (1983).
28. A. K. Sinha, H. J. Levenstein, T. E. Smith, G. Quintana, and S. E. Haszko, *This Journal*, **125** 601 (1978).

Ion Beam Exposure of Polymer Resist PMMA

N. Chan Tung

Centre National d'Etudes des Télécommunications, B. P. 98, 38243 Meylan, France

ABSTRACT

Ion beam exposure characteristics of a positive polymer resist, polymethylmetacrylate (PMMA) have been investigated. The samples were irradiated with B^+ ions in the energy range of 20–160 keV, the ion dose varying between 8×10^{11} and $5 \times 10^{13} \text{ cm}^{-2}$. In the energy range considered, beam sensitivity and resist contrast were found to be between $4.5 \times 10^{12} \text{ cm}^{-2}$ and 2.3–2.5, respectively. An empirical formula is proposed to approximate the characteristic dissolution curves (thickness removed *vs.* dissolution time). The empirical values agree with the experimental results within an accuracy better than 12%. A procedure is described whereby the total number of scission chain fragments as a function of resist depth may be extracted from the experimental curves.

Ion beam lithography is a novel technique which bypasses some of the drawbacks of electron beam lithography. In general, resists are more sensitive to ions than to electrons. This is due to a greater energy deposition per unit volume. Another advantage in ion beam lithography is its feeble lateral spread (100Å) for heavy ions. Ion beams, as compared to electron beams, produce low energy electrons and negligible amount of high energy backscattered electrons. In the case of direct writing using an ion beam, pattern dimensions are limited only by the beam size. Indeed, pattern dimensions inferior to 1000Å (1, 2) have been obtained with a liquid-metal gallium ion source.

Ion lithography can be carried out in two different ways: through direct writing and through the ion projection exposure technique as developed by Sacher Technik Wien (3). A liquid metal ion source (4–8) can be used for direct writing, as in electron beam lithography, but with reduced computing time owing to the absence of proximity effects and enhanced ion sensitivity. Another method of transferring patterns to resists is through direct contact masking of the resist; channeling (9) may also be used; typical mask to resist distances are 20 μm .

Komuro *et al.* (10) have investigated the ion beam sensitivity of positive PMMA and negative PDMS (polydimethylsiloxane) using He^+ ions (60 and 200 keV) and Ar^+ ions (150 and 250 keV). According to their measurements, the calculated Gel and Gn values are 1.7 and 0.9, respectively, for PMMA whose average molecular weight is 1.85×10^5 . Gel and Gn are the radiation yields per 100 eV absorbed for main chain scission brought about by electronic and nuclear collisions, respectively. Hall *et al.* (11) have studied the behavior of positive and negative resists using high energy ions: hydrogen, helium, and oxygen at 1.5 MeV. They proposed a model to account for the variation of the energy distribution around the particle track in terms of the number of sites required for exposure. Ryssel *et al.* (12) presented the dissolution characteristics of both positive and negative resists exposed to argon, gallium, hydrogen, and helium ions.

Karapiperis *et al.* (13) have used Monte Carlo computer simulations to calculate the electronic and nuclear energy losses of 60 keV H^+ ions in PMMA. For these ions, electronic energy losses per unit length predominate. The electronic energy loss *vs.* resist depth is initially a slowly decreasing curve, which then falls rapidly.

At the resist surface the energy loss value is 1.14×10^9 eV/cm/particle. Gel permeation chromatography (GPC) measurements reveal that Gel = 0.7 for 100 keV H^+ ions (14). Dissolution characteristics were carried out for 50 keV H^+ ions for an ion dose varying between 9×10^{12} and $2 \times 10^{13} \text{ cm}^{-2}$. Maximum removed thickness measurements were also carried out by Adesida (14) for H^+ ions (40–300 keV) and for B^+ ions (50–300 keV). To our knowledge, no dissolution characteristics (developed depth *vs.* time curves) for these H^+ ions, with the exception of those for 50 keV, nor for B^+ ions have been published by Adesida; only maximum removed thickness measurements have been presented.

In this work, the dissolution characteristics of PMMA. (Elvacite 2041) are presented. The resist was irradiated with B^+ ions whose energy varies between 20 and 120 keV. An empirical formula is proposed to approximate the dissolution curves. Using these data, and applying Greeneich's model (15) modified by Komuro to 160 keV ions, the total number of scission fragments *vs.* resist depth is extracted for 20, 40, and 80 keV B^+ ions.

Experimental Procedure

The PMMA used for our experiments has an average number molecular weight of 1.93×10^5 (value given by du Pont). The resist was dissolved in trichloroethylene, the concentration of the solution depending upon the desired thickness. Different resist thicknesses ranging from 0.2 to 0.9 μm were spin-coated onto clean silicon wafers; the thickness chosen depended upon the energy of the impinging ions.

The coated wafers were prebaked for 30 min at 160°C. After exposure to the ion beam, the wafer was cleaved into samples, and its thickness measured by a commercially available Rudolf ellipsometer ($\lambda = 632.8 \text{ nm}$). For each cleaved piece, the thickness was measured at five different points in a cross-like manner near the center. The mean value of the measurements was considered as the initial resist thickness. In all our measurements, the refractive index of the resist was fixed to 1.488.

Each sample was then developed in a solution of methyl isobutyl ketone (MIBK) and iso-propyl alcohol (IPA) in the proportion of 1:2. The development varied from 6s to 20 min; the temperature of the developer was between 18° and 21°C. The sample was rinsed in an IPA bath stirred by a magnetic agitator and blown dry with nitrogen.

The resist was then postbaked for 30 min at 160°C. Final thickness measurements were then carried out as described above, by ellipsometry. Repetitive ellipsometric thickness measurements made at the same point (without moving the sample), differed only by a few angstroms from run to run. The difference between the initial and final values gave the removed resist thickness. The removed thickness measurements as performed by ellipsometry were compared to those done using a Talystep (before and after development). For B^+ 40 keV ions (doses = 3×10^{12} and $7 \times 10^{12} \text{ cm}^{-2}$), the removed thickness (as measured by the two different methods) differ from one another by about 80Å.

Results and Discussion

Dissolution characteristics.—The dissolution characteristics of PMMA exposed with B^+ ions of 20, 40, and 80 keV are shown in Fig. 1, 2, and 3, respectively, the irradiation dose ranging between 8×10^{11} and $5 \times 10^{13} \text{ cm}^{-2}$. Based on these curves, the following remarks can be made: first, for a given ion energy, the saturation value of the removed thickness rises slowly with increasing ion dose. For 40 keV ions, the saturation thickness increases from 2340 to 2700Å when the dose is increased from 7×10^{12} to $5 \times 10^{13} \text{ cm}^{-2}$. This slow saturation thickness increase

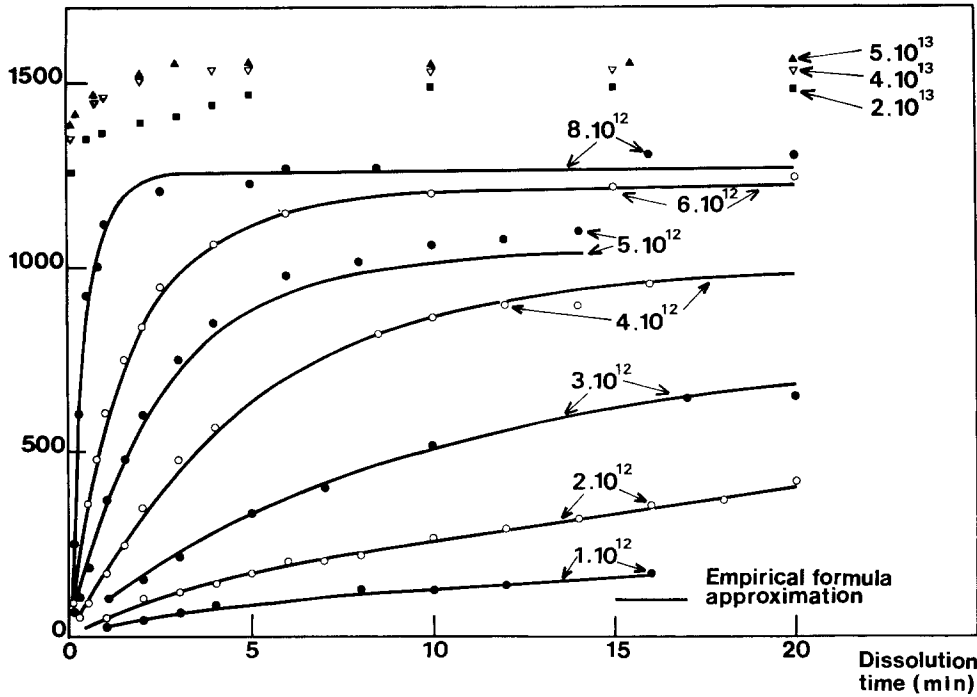


Fig. 1. Characteristic dissolution curves of 20 keV B⁺ ions.

may be due to the fact that towards the end of the ion range, an increase in the ion dose does not bring about any substantial increase in the number of chain scission fragments per unit volume. This can be interpreted in terms of absorbed energy density threshold. Saturated removed resist thickness have also been observed by Ryssel (12) for other ions. Second, for the removal of a given nonsaturated resist thickness, the necessary dissolution time decreases for increasing ion doses. An ion dose increase means an augmentation of the energy deposited per unit volume. This in turn leads to an increase in the number of chain scissions per unit volume and, thus, an increase of the dissolution speed. Finally, the saturated removed thickness increases with ion energy. This is attributed to a greater ion range within the resist for increasing energy. As has been explained elsewhere (14), the saturated developed depth can be taken as the mean path length in PMMA for light ions.

For the highest dose used (i.e., $5 \times 10^{13} \text{ cm}^{-2}$), the maximum removed thicknesses are, respectively: 1550, 2700,

and 4500 Å for 20, 40, and 80 keV ions. The experimental values of the dissolution curves are shown Fig. 1-3.

Proposed empirical formula.—The experimental data can be approximated by means of an empirical formula of the form

$$z(t) = a(1 - \exp^{-bt}) + c \cdot t^d$$

where: z is the removed thickness, t the dissolution time, and a , b , c , and d adjustable parameters. The overall calculated values (solid lines, Fig. 1-3) agree with the experimental results within 12%. For a development time greater than 3 min, the agreement falls within 6%. The parameters are adjusted in order to minimize the difference between observed and calculated curves over the dissolution time range. Table I shows the values of the constants a , b , c , and d used for 40 keV B⁺ ions and the maximum percentage difference between the calculated and the experimental data over the considered dissolution time. The empirical formula allows calculation of the dissolution speed (dz/dt) of the resist for a given depth.

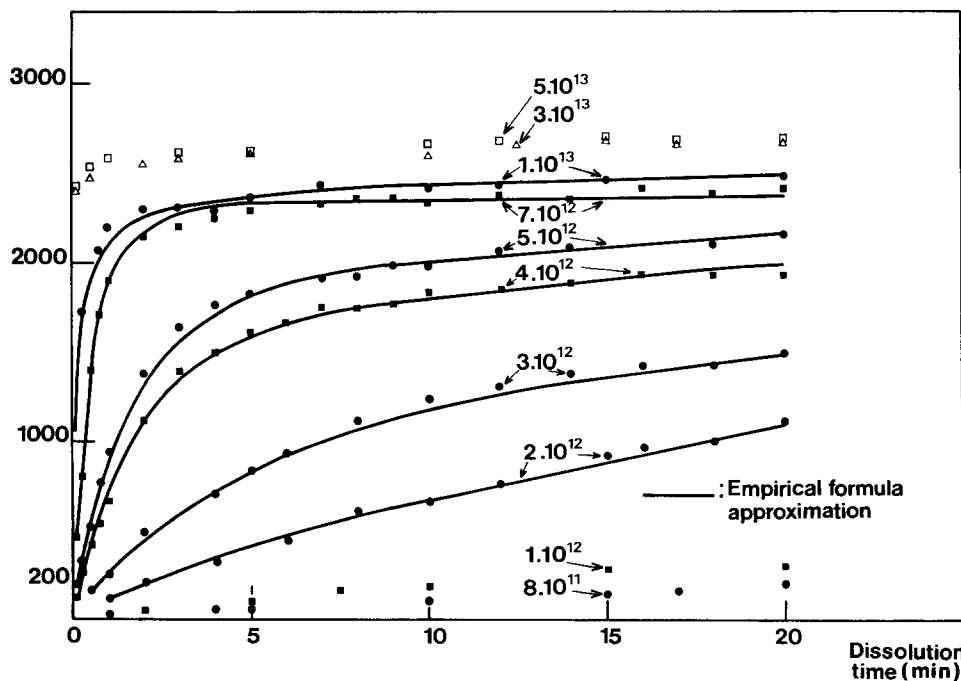


Fig. 2. Characteristic dissolution curves of 40 keV B⁺ ions.

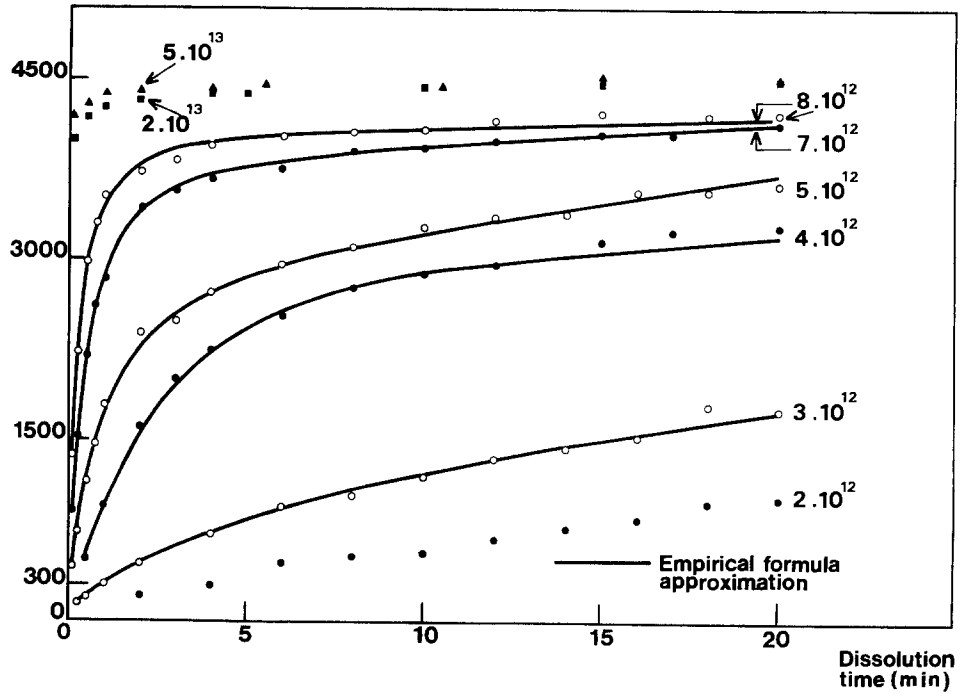


Fig. 3. Characteristic dissolution curves of 80 keV B⁺ ions.

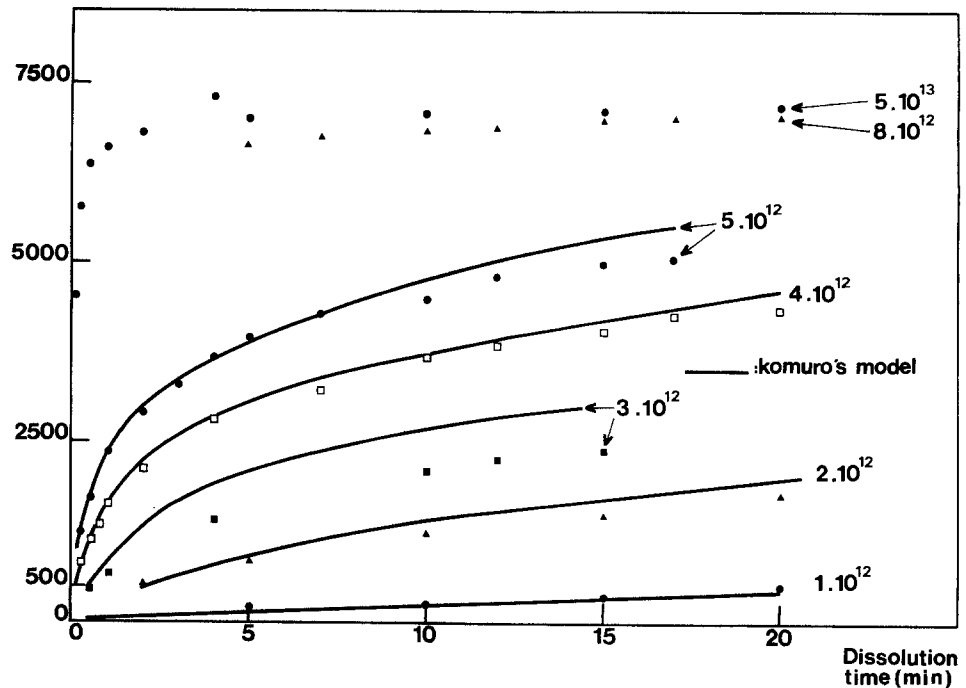


Fig. 4. Characteristic dissolution curves of 160 keV B⁺ ions and comparison with Komuro's model.

The value of *a* (except for $1 \times 10^{13} \text{ cm}^{-2}$), *b* (except for $3 \times 10^{12} \text{ cm}^{-2}$), and *c* increase with the ion dose since an increase in the dose brings about an increase in the removed thickness for a given time *t*. For the 40 keV ions, the maximum percentage difference between calculated and experimental results is 11.7%.

Table I. Values of adjusted parameters *a*, *b*, *c*, and *d* used for B⁺ 40 keV ions and maximum percentage difference between empirical and experimental results

Ion dose (cm ⁻²)	Values of the adjusted constants for B ⁺ 40 keV ions				Maximum percentage difference between empirical and calculated values
	<i>a</i>	<i>b</i>	<i>c</i>	<i>d</i>	
2×10^{12}	200	0.3	60	0.9	7.5
3×10^{12}	900	0.2	100	0.6	9.3
4×10^{12}	1400	0.6	100	0.6	11.7
5×10^{12}	1500	0.6	200	0.4	10.7
7×10^{12}	2100	1.6	200	0.1	8.9
1×10^{13}	1300	3.1	900	0.1	11.7

The dissolution characteristics for B⁺ 160 keV ions are shown in Fig. 4. No dissolution time lag has been observed in these curves (Fig. 1-4). The same observation has been made by Hoffmann *et al.* (16). It must, however, be noted that time-lag phenomena have been observed by Komuro. Owing to lack of experimental data, this point is still not clear.

Total number of chain scission vs. resist depth.—The calculations performed to extract the total number of chain scissions vs. resist depth are as follows.

Table II. Comparison of ion sensitivity and contrast of B⁺ ions (20-160 keV) to 20 keV electrons

Type	Ion energy (keV)				Electron energy (keV)
	20	40	80	160	
Sensitivity (cm ⁻²)	5×10^{12}	4.1×10^{12}	4.4×10^{12}	5×10^{12}	$2.5-5 \times 10^{14}$
Contrast	2.3	2.4	2.5	2.5	2-3

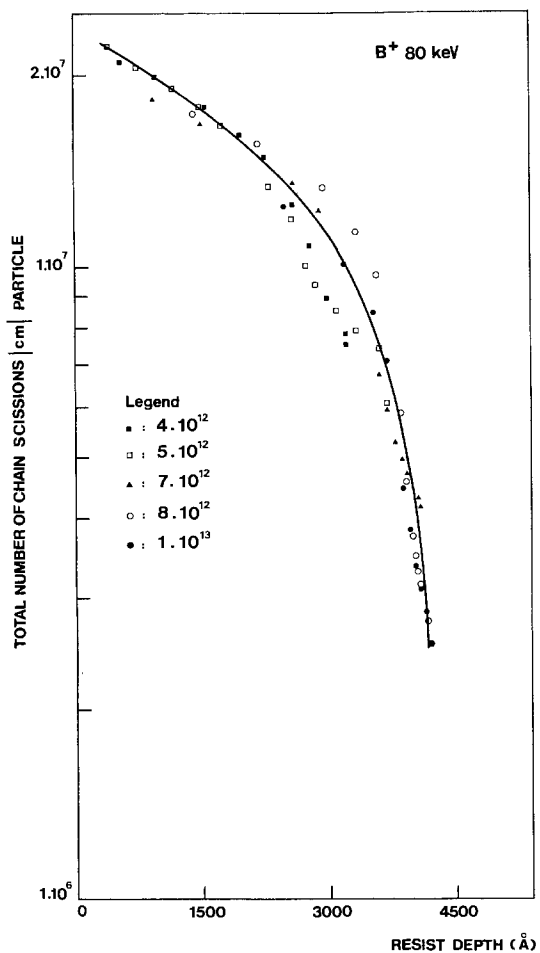
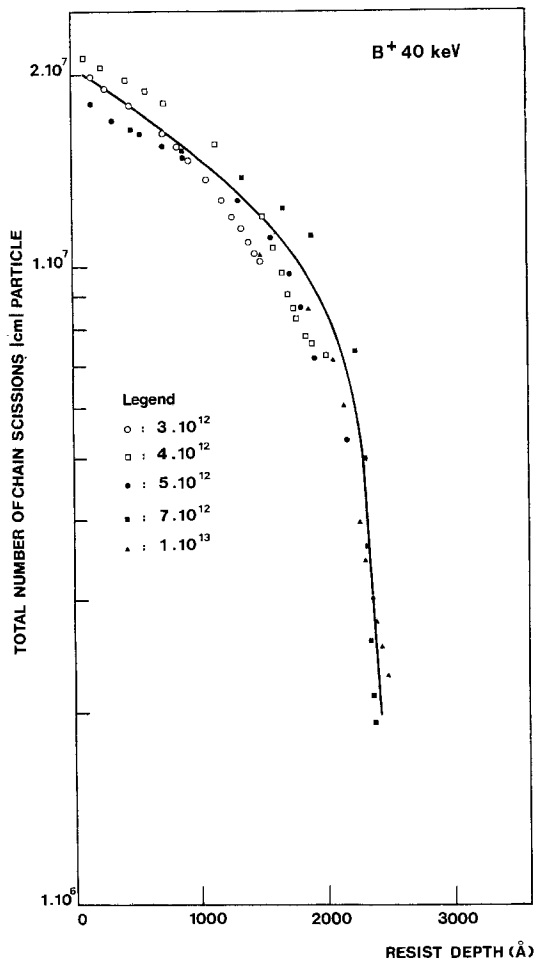
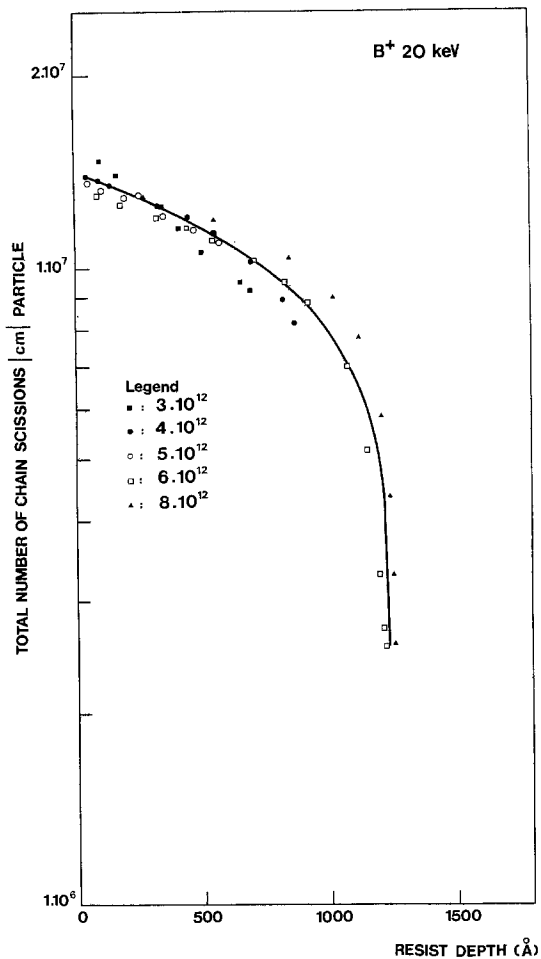


Fig. 5. Total number of chain scissions vs. resist depth for 20 keV B⁺ ions (a), for 40 keV B⁺ ions (b), and for 80 keV B⁺ ions (c).

For a given depth z , the development speed is given by the Greenich (15) formula

$$\frac{dz}{dt} = R_0 + \frac{\beta}{M_f^\alpha} \quad [1]$$

where R_0 , β , and α are fitted constants, and M_f is the fragmented average molecular weight after energy exposure. M_f is related to M_n (initial number average molecular weight) by

$$\frac{1}{M_f} = \frac{1}{M_n} + \text{Dose} \left\{ \frac{\text{Gel Sel}(z) + \text{Gn Sn}(z)}{\rho N_a 100} \right\} \quad [2]$$

where ρ is the resist density, N_a Avogadro's number, Gel, Gn the radiation yields for main chain scission caused by electronic and nuclear collisions respectively (events/100 eV) and Sel(z) and Sn(z) the energy deposition rates of the ion beam resulting from electronic and nuclear collisions (eV/cm). ρ is taken to be 1.2. The parameter [Gel Sel(z) + Gn Sn(z)]/100 denoted by $G S(z)/100$ represents the total number of chain scissions (nuclear + electronic)/unit length/particle brought about by ion exposure. Combining Eq. [1] and [2], the development speed (from Greenich's model modified by Komuro) is given by

$$\frac{dz}{dt} = R_0 + \beta \left[\frac{1}{M_n} + \frac{\text{Dose} \{ \text{Gel Sel}(z) + \text{Gn Sn}(z) \}}{N_a \rho 100} \right] \quad [3]$$

The left-hand side of Eq. [3] is calculated from the empirical formula approximation described above. The values of M_n , dose, ρ , and N_a are known.

For 160 keV B^+ ions, the values of R_0 , β , and α are chosen such that for the various ion doses $1 \times 10^{12} - 5 \times 10^{12} \text{ cm}^{-2}$, the $G.S(z)/100$ values vs. resist depth form a quasi-unique curve, similar in shape to Fig. 5a, 5b, and 5c. For a given ion energy, the $G.S(z)/100$ curve is independent of the ion dose since we are comparing chain scission numbers for one particle.

The values of the constants are: $R_0 = 0 \text{ \AA}/\text{min}$, $\beta = 4 \times 10^{18} \text{ \AA}/\text{min}$, and $\alpha = 4$. In order to test the validity of the values of R_0 , β , and α , the removed thickness d is calculated by

$$T = \int_0^d \frac{dz}{R_0 + \beta \left\{ \frac{1}{M_n} + \frac{\text{Dose} G.S(z)}{\rho N_a 100} \right\}^\alpha} \quad [4]$$

where T is the dissolution time.

The calculated curves (solid lines in Fig. 4) agree with the experimental measurements. Using the procedure described above, the total number of chain scissions for 20, 40, and 80 keV ions are shown in Fig. 5a, 5b, and 5c, respectively, the ion doses varying between 3×10^{12} and $1 \times 10^{13} \text{ cm}^{-2}$. The values of R_0 , β , and α are those reported above. These curves give rise to the following remarks.

1. The shape of the extracted curves (chain scission numbers vs. resist depth) is similar to that calculated directly by both Karapiperis (H^+ 60 keV) and Komuro (electronic energy loss vs. resist depth calculations). That is, the typical curve is initially a slowly decreasing curve which decreases rapidly. Our extracted curves can be compared to those calculated by these authors as only a proportionality factor separates them.

2. For a given ion energy, the $G.S(z)/100$ curve is independent of the ion dose. This is as expected since we are comparing chain scission numbers for one particle; otherwise, the parameters R_0 , β , and α would be incorrect.

3. At the origin ($z = 0$), $G.S(z)/100 \sim 10^7/\text{cm}/\text{particle}$. This result is compatible with that calculated by Karapiperis (13), who obtained $\sim 8 \times 10^6/\text{cm}/\text{particle}$ for H^+ 60 keV (Sel $\sim 1.4 \times 10^9 \text{ eV}/\text{cm}$; Gel = 0.7) (13).

4. The number of chain scissions $G.S(z)/100$ increases with ion energy; this is due to an increase in the deposited energy.

Resist sensitivity and contrast.—Irradiated resists are commonly characterized by their sensitivity and contrast.

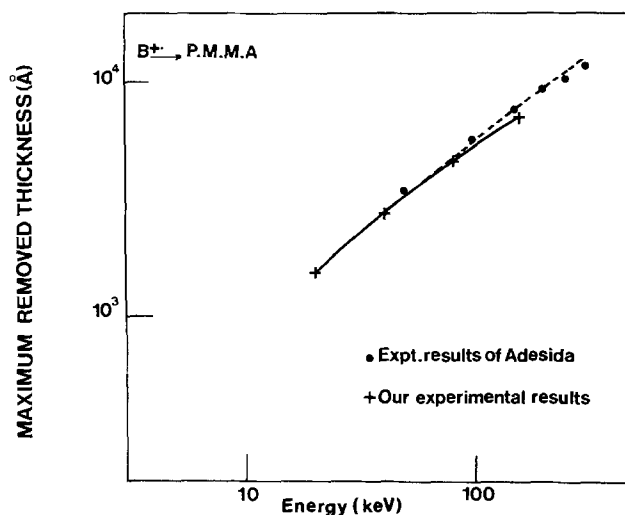


Fig. 6. Comparison of our maximum removed thickness measurements with Adesida's.

Sensitivity is defined as the fluence required to remove 50% of the resist thickness. Table II compares our results for B^+ ions (20-160 keV) to those published by Ryssel (12) for 20 keV electrons. In our case, the development time was fixed to 3 min. The resist is 60-100 times more sensitive to B^+ ions than to 20 keV electrons. From the point of view of contrast, ions are comparable to electrons. A resist sensitivity of $5 \times 10^{12} \text{ cm}^{-2}$ is amply sufficient for technological applications. To our knowledge, no PMMA Elvacite 2041 resist sensitivity and contrast results have been published in the literature for B^+ ions.

Figure 6 compares our maximum removed thickness for B^+ ions (20-160 keV) to those measured by Adesida for the same ions at an energy of 50-300 keV. Our experimental results are in good agreement.

Conclusion

An empirical formula has been proposed to approximate the characteristic dissolution curves of B^+ ions in the energy range of 20-160 keV. The calculated values agree with the experimental results within an accuracy of, or better than, 12%. This formula may be extended to the dissolution curves of other charged particles. Our maximum removed thickness measurements are in good agreement with the results of Adesida for the same ions. A resist sensitivity of $4.5 \times 10^{12} \text{ cm}^{-2}$ is obtained for B^+ ions (20-160 keV); this is sufficient from the point of view of technological applications. Comparison of B^+ ion sensitivity to that of 20 keV electrons shows an enhancement factor of 60 to 100 for the ion beam with respect to the electron beam (in terms of particle fluence).

A procedure is described wherein the total number of chain scission fragments as a function of resist depth may be extracted from experimental dissolution curves. These extracted curves are comparable to those calculated directly by means of computer simulations by others. This procedure has the advantage of saving time, since it is relatively easy to put into practice.

Acknowledgments

The author wishes to thank the Polymer Group for their help in resist-coating, J. P. Dœuvre and A. Brun for the ion implantation, and A. Golanski and J. L. Buevoz for discussions and interest shown in this work. Our thanks are also extended to L. Karapiperis for the review of this paper and to J. Dargent for the linguistic corrections.

Manuscript submitted Jan. 24, 1984; revised manuscript received April 10, 1984.

Centre National d'Etudes des Telecommunications assisted in meeting the publication costs of this article.

REFERENCES

1. R. L. Seliger, R. L. Kubena, R. O. Olney, J. W. Ward, and V. Wang, *J. Vac. Sci. Technol.*, **17**, 1610 (1980).
2. R. L. Seliger, J. W. Ward, W. Wang, and R. L. Kubena, *Appl. Phys. Lett.*, **34**, 310 (1979).
3. G. Stengl, R. Kaitna, H. Loschner, R. Rieder, P. Wolf, and R. Sacher, *J. Vac. Sci. Technol.*, **19**, 1164 (1981).
4. L. W. Swanson, G. A. Schwind, A. E. Bell, and J. E. Brady, *ibid.*, **16**, 1864 (1979).
5. V. E. Krohn and G. R. Ringo, *Appl. Phys. Lett.*, **27**, 479 (1979).
6. A. Wagner and T. M. Hall, *J. Vac. Sci. Technol.*, **16**, 1871 (1979).
7. K. Gamo, T. Ukagawa, Y. Inomoto, Y. Ochiai, and S. Namba, *ibid.*, **19**, 1182 (1981).
8. A. Wagner, T. Venkatesan, P. M. Petroff, and D. Barr, *ibid.*, **19**, 1186 (1981).
9. L. Csepregi, P. Eichinger, and A. Heuberger, *Microcircuit Engineering*, Grenoble, France, Oct. 1982.
10. M. Komuro, N. Atoda, and H. Kawakatsu, *This Journal*, **126**, 483 (1979).
11. T. M. Hall, A. Wagner, and L. F. Thompson, *J. Vac. Sci. Technol.*, **16**, 1889 (1979).
12. H. Ryssel, K. Habberger, and H. Kranz, *ibid.*, **19**, 1358 (1981).
13. L. Karapiperis, I. Adesida, C. A. Lee, and E. D. Wolf, *ibid.*, **19**, 1259 (1981).
14. I. Adesida, *Nucl. Inst. Meth.*, **209-210**, 79 (1983).
15. J. S. Greeneich, *This Journal*, **122**, 970 (1975).
16. K. Hoffmann, K. Habberger, M. Forster, and H. Ryssel, *Microcircuit Engineering*, Grenoble, France, Oct. 1982.

Thermodynamics and Phase Diagram of Pseudobinary ZnTe-CdTe System

L. A. Zabdyr

Institute for Metal Research, Polish Academy of Sciences, 30-059 Kraków, Poland

ABSTRACT

The thermodynamic properties of solid ZnTe and CdTe as well as of pseudobinary ZnTe-CdTe solid solutions have been determined by means of EMF technique. Results for ZnTe-CdTe solid solutions have been interpreted by regular solution model with the parameter $\alpha^s = -80$ cal. Based on the solidus and liquidus data of Steininger, Strauss, and Brebrick and assuming liquid solution to be regular, the solution parameter $\alpha^l = +50$ cal has been calculated. Finally, phase diagram calculations have been performed using the parameters mentioned above. The results seem to fit experimental solidus and liquidus data excellently.

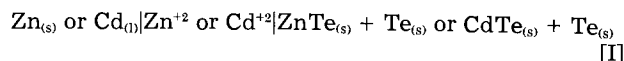
The development of crystal-growth technique from the melt has created a need for accurate thermodynamic data and a knowledge of the phase equilibria in semiconductor alloy systems. A strong interest exists, especially in systems forming pseudobinary solid solutions. The ability for variation of electron properties with composition makes them very useful in semiconductor industry.

The pseudobinary ZnTe-CdTe system forms a complete series of solid solutions with lattice parameter following Vegard's rule. This has been first confirmed by Goryunova and Fedorova (1). Gromakov *et al.* (2) have performed thermal analysis study to determine ZnTe-CdTe phase diagram, but their results were more than 40 K lower than the most recent data, even for pure compounds. Steininger *et al.* (3) have carried out extensive studies on ternary Zn-Cd-Te and pseudobinary ZnTe-CdTe systems by means of thermal analysis. Their liquidus data combined with ideal solution model for both solid and liquid phases resulted in pseudobinary phase diagram. Laugier (4) obtained solid solution parameter $\alpha^s = 1340$ cal assuming ideal liquid and regular solid solution by fitting experimental data of Steininger *et al.* (3). His phase diagram differed slightly from that of Steininger *et al.*, but in both cases agreement with experimental data was satisfactory. A regular solution model for both solid and liquid phases and the experimental data of Steininger have been combined by Ilegems and Pearson (5) to adjust solid and liquid solution parameters, $\alpha^s = 100$ cal and $\alpha^l = -1300$ cal, respectively. The phase diagram calculated under those conditions was close to those given by Steininger and Laugier. Different best fit values of α parameters obtained from the same set of experimental data demonstrate that results for α^l depend on choice of α^s and vice versa.

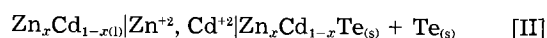
In this situation, it seemed desirable to find the experimental value of at least one of solution parameters, and this was the main aim of this study. Having a well-developed EMF technique, it was decided to apply it for determination of thermodynamic properties of solid ZnTe-CdTe solutions.

Experimental

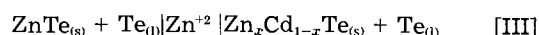
Two kinds of galvanic cells were used: cells of formation and concentration cells, both with liquid salt electrolyte. Formation cells of the type



were applied for redetermination of the formation properties for solid compounds ZnTe and CdTe. Formation cells of the type



were used to get free energy of formation of solid $\text{Zn}_x\text{Cd}_{1-x}\text{Te}$ compounds for a few x values. Finally, concentration cells



were employed for determination of activity of ZnTe in ZnTe-CdTe solid solution.

Electrode materials.—Zinc and cadmium of 5N purity were supplied by Zakład Doświadczalny at Skawina, Poland, and tellurium 99.99% was obtained from ASARCO, USA.

Alloy electrodes were prepared as follows: appropriate amounts of constituents were melted together in evacuated silica capsules, equilibrated at least 24h at about 50 K above liquidus and then rapidly cooled to the room temperature. Next, they were annealed for a long period at about 50 K below solidus. Samples prepared in this way were checked metallographically and x-ray analysis gave lattice parameters in accord with literature data.

Electrolyte constituents were obtained from several sources: KCl from POCH, Poland; LiCl from CHEMAPOL, Czechoslovakia; anhydrous ZnCl_2 and CdCl_2 from FLUKA AG, Germany and UCB, Belgium, respectively. Electrolyte compositions were as follows: 70 weight percent (w/o) ZnCl_2 , 18 w/o KCl, 12 w/o NaCl for the ZnTe version of cell [I]; 65 w/o ZnCl_2 , 8 w/o CdCl_2 , 18 w/o

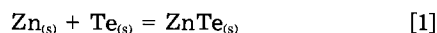
KCl, 9 w/o NaCl for both the CdTe version of cell [I] and cell [II], and 43 w/o LiCl, 52 w/o KCl, and 5 w/o ZnCl₂ for cell [III]. Molybdenum wires sheathed by high melting glass tubes served as current leads. Cell assembly and experimental procedure were similar to those applied in one of previous works (6). Temperature was controlled by Pt-PtRh10 thermocouple and EMF readings were taken by a V 534 ELWRO, Poland, high resistance digital voltmeter from both heating and cooling cycles. Since solid-state reactions were involved, it took a long time to reach equilibrium at a certain temperature. In case of cell [III], it was at least 12h for a single measurement.

Results

Zinc-tellurium.—Alloys of eight compositions ranging from 90 to 98 atom percent (a/o) of Te were investigated at temperatures between 503 and 692 K, and linear dependence of EMF on temperature was found from 150 experimental points as follows

$$E(\pm 1.5) = 609.5(\pm 1.3) - 0.057(\pm 0.002)T \text{ (mV)}$$

Using the well-known relation: $\Delta G = -nFE$, the free energy of formation was calculated due to reaction



and

$$\Delta G_1(\pm 69) = -28117(\pm 137) + 2.63(\pm 0.21)T \text{ cal/mol} \quad [2]$$

Heat capacity data taken for ZnTe from Mills (7) enabled the calculation of the standard heat of formation, ΔH_{298}° and standard entropy S_{298}° for the solid zinc telluride. Numerical data are presented below.

Cadmium-tellurium.—Alloys of five compositions ranging from 80 to 97 a/o Te were investigated at temperatures between 619 and 719 K. Linear dependence of EMF on temperature was found as well from 84 experimental points

$$E(\pm 1.02) = 559.1(\pm 2.6) - 0.089(\pm 0.0039)T \text{ (mV)}$$

and free energy of formation of cadmium telluride was calculated as above due to reaction



and

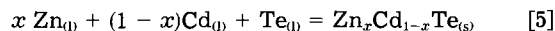
$$\Delta G_3(\pm 47) = -25,792(\pm 120) + 4.11(\pm 0.18)T \text{ cal/mol} \quad [4]$$

Standard thermodynamic functions were calculated and presented as those for ZnTe compound.

Zinc-cadmium-tellurium.—Formation cells [II] were not as convenient in operation as cells [I] and gave considerable experimental errors. Results of only two out of eight compositions, *i.e.*, $x = 0.6$ and 0.3 , proved to be of the satisfactory accuracy. Reasons for that will be discussed later. An EMF *vs.* temperature plot for $x = 0.6$ is shown in Fig. 1 as an example. The overall cell [II] reaction



combined with fusion data for tellurium (8) and with mixing data for Zn-Cd liquid alloys (9) gave the free energy of formation of solid $\text{Zn}_x\text{Cd}_{1-x}\text{Te}$ compound from liquid constituents due to the reaction



and

$$\Delta G_5(x = 0.6) = -33,600 + 9.7T \text{ cal/mol} \quad [6]$$

$$\Delta G_5(x = 0.3) = -35,800 + 14.3T \text{ cal/mol} \quad [7]$$

Combining reactions [5], [1], and [3] with fusion data from zinc and tellurium (8), one may obtain the following reaction

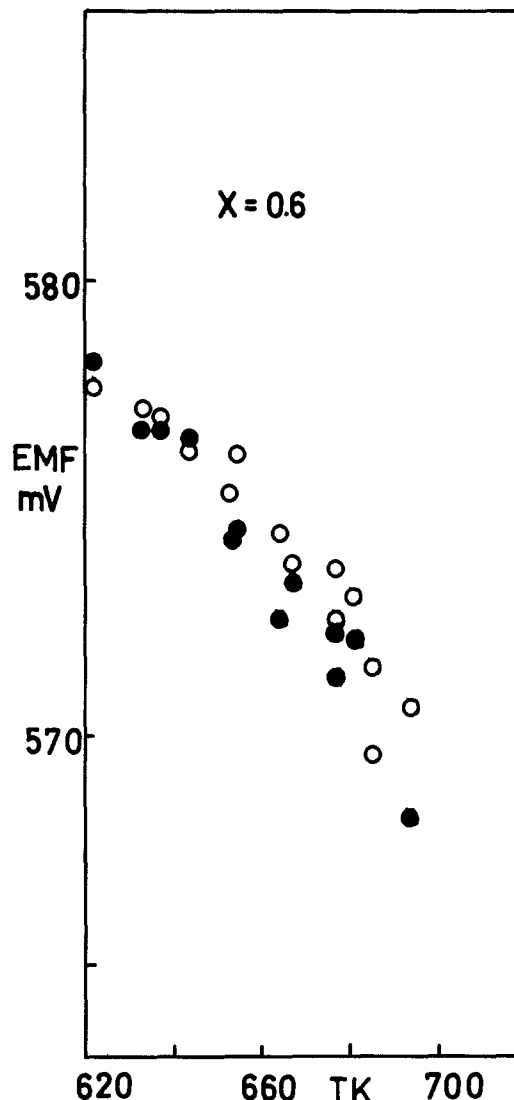
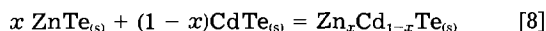


Fig. 1. Plot of experimental EMF values on temperature for cell [II] at $x = 0.6$. Open and closed points represent results of different runs.

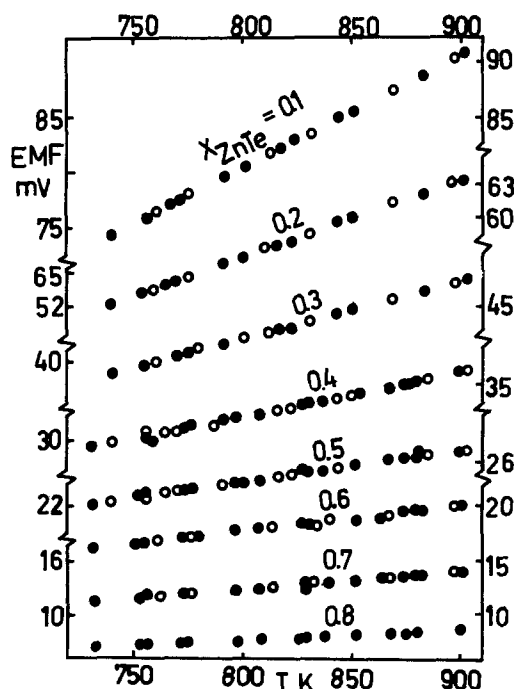


Fig. 2. Plot of experimental EMF values on temperature for cells [III] at x ranging from 0.1 to 0.8. Open and closed points represent results of different runs.

Table I. Experimental data obtained from cells [III]

X_{ZnTe}	E (mV)		$dE/dT \times 10^3$ (mV/K)	$-\Delta\bar{G}_{\text{ZnTe}}$ (cal/mol)		$-\Delta G^E_{\text{ZnTe}}$ (cal/mol)	
	750 K	900 K		750 K	900 K	750 K	900 K
0.8	7.30	8.72	9.49	337	402	4.2	(± 2.3)
0.7	11.70	14.01	15.38	540	646	8.2	(± 2.3)
0.6	16.75	20.10	22.30	773	927	11.5	(± 3.2)
0.5	22.76	27.22	29.72	1050	1256	17.0	(± 3.2)
0.4	30.17	36.11	39.58	1392	1666	26.3	(± 3.7)
0.3	39.63	47.43	51.96	1828	2188	34.0	(± 4.6)
0.2	53.11	63.48	69.14	2450	2927	51.6	(± 4.6)
0.1	75.67	90.69	100.16	3491	4184	59.4	(± 4.2)

and its free energy change ΔG_s is equal to free energy of mixing ΔG^M of a pseudobinary solid solution of an appropriate composition. Unfortunately, the error in ΔG_s was too large for further calculation of ΔG^E and α^s . Nevertheless, qualitative analysis showed that solid solution under investigation should exhibit slightly negative deviation

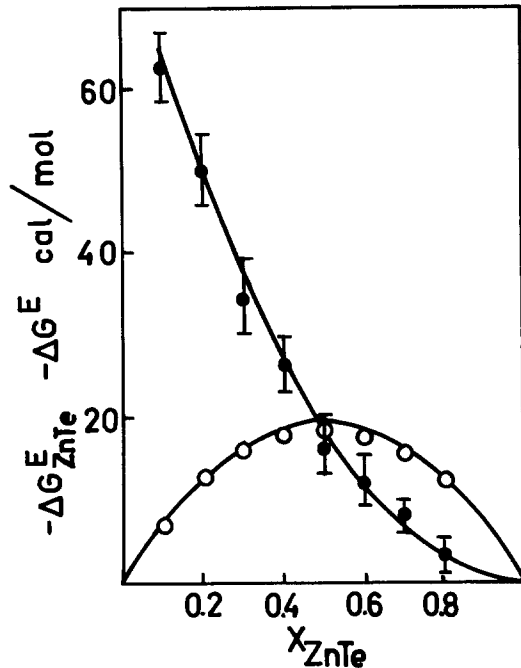


Fig. 3. Plots of ΔG^E_{ZnTe} and ΔG^E vs. composition, calculated from [9] and [11], solid line. Dots represent ΔG^E_{ZnTe} taken as an average of last two columns in Table I, and circles show ΔG^E values calculated through Gibbs-Duhem integration.

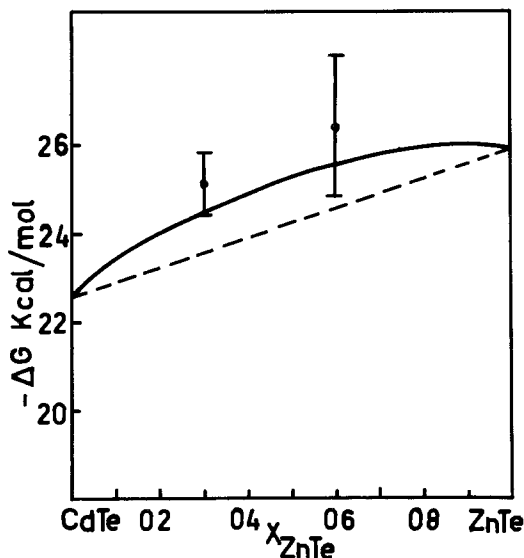


Fig. 4. Free energy of formation of solid $\text{Zn}_x\text{Cd}_{1-x}\text{Te}$ compound from pure liquid elements, calculated from ΔG^M , ΔG_1 , and ΔG_3 at 750 K (solid line), as a function of composition X_{ZnTe} . Points represent experimental values obtained from cells [II].

Table II. Results of phase diagram calculations based on regular solution model and experimentally determined α^s value. Melting data of compounds used: $H^F_{\text{ZnTe}} = 15.6$ kcal/mol, $T^F_{\text{ZnTe}} = 1563$ K, $H^F_{\text{CdTe}} = 12.0$ kcal/mol, $T^F_{\text{CdTe}} = 1365$ K

T	$X_{\text{ZnTe}(s)}$	$X_{\text{ZnTe}(l)}$
1540	0.940	0.897
1520	0.885	0.809
1500	0.825	0.718
1480	0.765	0.634
1460	0.690	0.538
1440	0.610	0.446
1420	0.510	0.346
1400	0.375	0.231
1380	0.190	0.104

from ideality. To have more accurate values of ΔG^M , concentration cells [III] have been employed to realize reaction [8].

Preliminary experiments showed that high accuracy of EMF measurements is required, especially for high x values, to obtain reliable ΔG^E data.

Careful electrode and electrolyte preparation and many times repeated measurements resulted in EMF accuracy of order of 0.05 – 0.10 mV.

Twenty-four alloy compositions have been investigated with X_{ZnTe} ranging from 0.1 to 0.8 and with excess of tellurium of 60, 70, and 80 a/o, respectively, for each X_{ZnTe} value. EMF readings were taken at temperatures between 732 and 901 K, and a linear dependence on temperature was observed in all cases (Fig. 2). Partial free energy of mixing of ZnTe was calculated from experimental data using well-known relationship

$$\Delta\bar{G}_{\text{ZnTe}} = -nF E_{\text{III}}$$

with $n = 2$ and $F = 23.066$ cal/mV · mol.

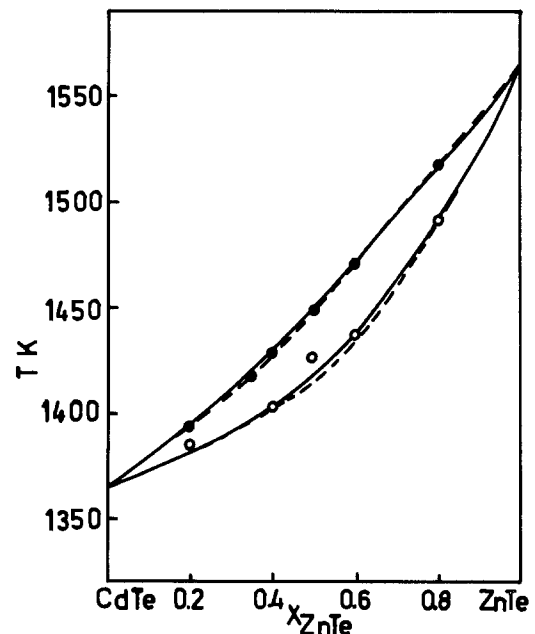


Fig. 5. Pseudobinary ZnTe-CdTe phase diagram calculated for $\alpha^s = -80$ cal and $\alpha^l = +50$ cal (solid line). Dashed lines represent phase diagram after Steininger et al. (3), with their DTA data shown as points.

Table III. Comparison of thermodynamic properties of ZnTe and CdTe obtained in this work with respective data selected by Mills (7)

Thermodynamic function	Zinc telluride This work	Mills	Cadmium telluride This work	Mills
$-\Delta H_{298}^{\circ}$ (cal/mol)	27.87 ± 0.14	28.5 ± 0.1	24.09 ± 0.12	24.1 ± 0.2
S_{298}° (cal/mol · K)	19.68 ± 0.31	18.6 ± 0.5	23.04 ± 0.28	22.8 ± 0.5

Experimental data and calculated $\Delta\bar{G}_{\text{ZnTe}}^{\circ}$ and $\Delta G_{\text{ZnTe}}^{\text{E}}$ are listed in Table I. Analysis of last two columns of Table I leads to the conclusion that, within estimated error limits ranging from ± 2.3 to ± 4.6 cal, $\Delta G_{\text{ZnTe}}^{\text{E}}$ may be assumed to be independent of temperature and may be described by the regular solution model

$$\Delta G_{\text{ZnTe}}^{\text{E}} = \alpha^{\text{s}}(1 - X_{\text{ZnTe}})^2 \quad [9]$$

with solution parameter $\alpha^{\text{s}} = -80$ cal. Thus, other thermodynamic functions for pseudobinary solid solutions ZnTe-CdTe are as follows

$$\Delta G_{\text{CdTe}}^{\text{E}} = \alpha^{\text{s}}X_{\text{ZnTe}}^2 \quad [10]$$

and

$$\Delta G^{\text{E}} = \Delta H^{\text{M}} = \alpha^{\text{s}}(1 - X_{\text{ZnTe}})X_{\text{ZnTe}} \quad [11]$$

Plots of $\Delta G_{\text{ZnTe}}^{\text{E}}$ and ΔG^{E} vs. composition, calculated from [9] and [11], are presented in Fig. 3. As can be seen, relations [9] and [11] describe satisfactorily experimental data.

The free energy change for reaction [5], ΔG_{s} , may be calculated again from ΔG^{E} using Eq. [11] and a combination of ΔG_{s} and ΔG_{s} with the fusion data for zinc and tellurium. Results of such a calculation at 750 K are shown in Fig. 4. Finally, calculations were carried out to match regular solution model for the liquid phase with solidus-liquidus data of Steininger *et al.* (3) and experimentally determined parameter $\alpha^{\text{l}} = -80$ cal for the regular solid solution. The best fit value for the liquid solution parameter is $\alpha^{\text{l}} = +50$ cal.

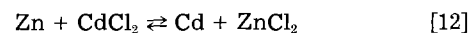
Using fusion data for both compounds taken from Kulwicki (10) and the parameters derived above, phase diagram calculation has been performed, and the results are shown in Fig. 5 and listed in Table II.

Discussion

The values of standard thermodynamic functions for ZnTe and CdTe obtained in this work are compared with respective data selected by Mills (7) in Table III.

As can be seen, agreement is excellent, especially for cadmium compound.

In the case of cells [II], low melting electrolyte has been used containing ZnCl_2 and CdCl_2 . Since both zinc and cadmium ions present in the melt were in contact with liquid Zn-Cd electrode, a side reaction might occur



If reaction [12] goes to the right, it should decrease zinc content in liquid ZnCd electrode and move the points shown in Fig. 4 to the left.

On the other hand, a high concentration of ZnCl_2 in electrolyte might shift equilibrium of reaction [12] to the left.

To solve this problem exactly, thermodynamic data are needed for four-component system ZnCl_2 - CdCl_2 - KCl - LiCl and the knowledge of kinetics of possible reactions with metallic phase involved. Thus, free energy values calculated from [6] and [7] are of the qualitative character.

High accuracy EMF measurements from cells [III] enabled confirmation of slightly negative deviation of pseudobinary solid solution from ideality and description of its thermodynamic properties by regular solution model.

Moreover, one can calculate free energy of formation of ternary $\text{Zn}_x\text{Cd}_{1-x}\text{Te}$ compounds from their constituents along pseudobinary line.

Finally, calculated phase diagram seems to fit excellently both solidus and liquidus experimental data.

All mentioned error limits were calculated for 90% confidence level.

Manuscript submitted Oct. 31, 1983; revised manuscript received March 23, 1984.

REFERENCES

1. N. A. Goryunova and N. A. Fedorkova, *Dokl. Akad. Nauk SSSR*, **6**, 1039 (1953).
2. S. D. Gromakov, I. W. Zoroatskaya, Z. M. Latypov, M. A. Tsvala, E. A. Edelman, L. I. Badygina, and L. G. Zarypova, *Zhur. Neorg. Khim.*, **9**, 2485 (1964).
3. J. Steininger, A. J. Strauss, and R. F. Brebrick, *This Journal*, **117**, 1305 (1970).
4. A. Laugier, *Rev. Phys. Appl.*, **8**, 259 (1973).
5. M. Ilegems and G. L. Pearson, *Ann. Rev. Mater. Sci.*, **5**, 366 (1975).
6. L. A. Zabdyr, *Can. Metal. Quart.*, **19**, 359 (1981).
7. K. C. Mills, "Thermodynamic Data for Inorganic Sulphides, Selenides and Tellurides," Butterworths, London (1974).
8. O. Kubaschewski and C. B. Alcock, "Metallurgical Thermochemistry," Pergamon Press, London (1979).
9. W. Ptak, *Arch. Hutn.*, **2**, 71 (1954).
10. B. M. Kulwicki, Ph.D. Thesis, University of Michigan, Ann Arbor, MI (1963).

Heat Effects in Zircaloy Oxidation by Steam

Donald R. Olander

Materials and Molecular Research Division, Lawrence Berkeley Laboratory and Department of Nuclear Engineering, University of California, Berkeley, California 94720

ABSTRACT

Partitioning of the heat of combustion during Zircaloy oxidation between the gas-oxide and oxide-metal interfaces was determined. The spatial distribution of the heat release is very sensitive to the poorly known partial molar enthalpy of oxygen dissolution in ZrO_2 . This uncertainty is of minor consequence in the thermal analysis, however, because temperature gradients in the specimen due to the heat released by oxidation are very small. The temperature is mainly a function only of time. A simple lumped-capacity thermal analysis suffices to describe the temperature transient initiated by the corrosion process. A method of coupling the temperature rise due to the heat release to the corrosion kinetics was developed.

Although oxidation of a metal is accompanied by considerable release of heat, most analyses of this process assume that the temperature of the reacting solid is specified by the external environment. However, when external heat removal rates are low, the heat of combustion can be a significant heat source, as was dramatically illustrated by the accident at the Three Mile Island nuclear reactor. In this case, the energy released by oxidation of the Zircaloy cladding exceeded that provided by decay of the fission products in the fuel contained by the cladding tubes. In laboratory experiments in which a specimen is held in a furnace or heated by induction or by resistance, rapid oxidation can provide a heat source comparable in magnitude to that supplied by the applied heating method. The localized nature of the heat release by oxidation can cause temperature nonuniformities in the reacting metal which must be understood quantitatively if the corrosion process is to be properly modeled.

In this work, oxidation of zirconium¹ is analyzed with reaction heating considered. Zirconium oxidizes by formation of a coherent oxide scale through which oxygen is transported by ionic diffusion from the gas to the metal. At the oxide-metal boundary, the incoming oxygen either converts some of the metal to oxide or dissolves into the metal and continues to penetrate by interstitial diffusion. At high temperature, the metal phase consists of a α -zirconium and β -zirconium components, but, for the present study, the distinction between the two is not important.

In the following section, the heat of combustion of zirconium is broken down into three parts. First, addition of oxygen to the initially pure metal produces α -Zr saturated with oxygen. Second, sufficient additional oxygen is supplied to convert the saturated metal to zirconia at the lower phase boundary. Finally, the hypostoichiometric oxide is saturated with oxygen to achieve ZrO_2 .

In a slab of metal exposed to steam, these steps occur simultaneously but at different locations in the specimen, rather than sequentially in time but uniformly throughout the solid. In addition, water vapor must be decomposed to produce the oxygen which enters the solid and the reaction product hydrogen which returns to the gas phase. Application of the three-step oxidation process to this case permits determination of the heat releases at various positions in the corroding specimen, particularly at the gas-oxide and the oxide-metal interfaces. This analysis is presented in the "Heat Release" section.

In the succeeding sections, the effect of the heat released during the corrosion process on the temperature distribution within the specimen and on the kinetics of scaling are considered. To this end, a simplified problem is analyzed. The system considered closely resembles the method by which corrosion kinetics are studied in laboratory tests, but the general features of the analysis are also applicable to nuclear fuel elements, wherein oxidation of

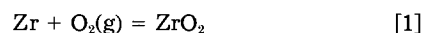
¹Nuclear reactor fuel cladding is fabricated from the zirconium-based alloy Zircaloy, which contains 1.5% tin and smaller amounts of iron and chromium. This alloy is superior to pure zirconium for normal reactor use, but the high-temperature oxidation characteristics of the two are very similar.

the cladding proceeds from the surface exposed to the coolant toward the inner surface adjacent to the fuel. The system consists of a slab specimen initially placed in an inert environment at temperature T_0 . In the absence of chemical reaction, the specimen acquires the temperature of its surroundings, which is maintained constant at T_0 at all times. Steam at temperature T_0 is admitted at time zero and proceeds to oxidize the slab from both sides. Thus, the midplane of the specimen is adiabatic for heat-transfer purposes. The half-thickness of the specimen is assumed to be sufficiently large so that the oxygen diffusion process occurs as in an infinite medium. Heat-transfer between the enclosure and the specimen, whether by radiation to the walls or by convection to the steam, is characterized by a heat-transfer coefficient h .

In the "Temperature Distribution" section, the problem described above is analyzed without considering coupling of the heat release and oxidation kinetics. In the following section, a commonly used approximate coupling scheme is analyzed. Finally, rigorous linkage of the heat- and mass-transfer processes is developed.

Components of the Heat of Combustion of Zirconium

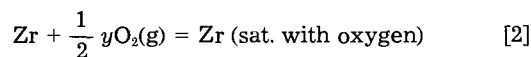
The heat of formation of ZrO_2 , $\Delta H_{ZrO_2}^0$, is the enthalpy change of the reaction



where the zirconium reactant is initially free of oxygen and the oxide product is stoichiometric (*i.e.*, with O/Zr ratio of 2). The heat of formation of zirconium dioxide at 298 K is given in Ref. (1). Extrapolating to temperatures of interest here (1200°-1600°C) and taking into account the difference in heat capacities of products and reactants [also given in Ref. (1)] gives $\Delta H_{ZrO_2}^0 = -1088$ kJ/mol.

With reference to the isotherm on the phase diagram of Fig. 1, the heat of formation of ZrO_2 corresponds to the difference in enthalpy between points a and d. This difference can be divided into three parts.

a-b.—Addition of $\frac{1}{2} y$ mol of gaseous oxygen to 1 g atom of pure zirconium to produce the saturated metal (O/Zr = y) can be written as



and the heat release is

$$Q_{a-b} = -\frac{1}{2} \int_0^y \overline{\Delta H}_M dy' \approx -\frac{1}{2} \overline{\Delta H}_M y \quad [3]$$

where $\overline{\Delta H}_M$ is the partial molar enthalpy of oxygen in the metal. Komarek and Silver (2) measured the oxygen pressures in equilibrium with solutions of oxygen in α -Zr. Their data yield a heat of solution $\overline{\Delta H}_M = -1138$ kJ/mol at 10-15 atom percent (a/o) oxygen and a variation of ~ 54 kJ/mol between infinite dilution and saturation. The latter variation is neglected, and the heat of solution is as-

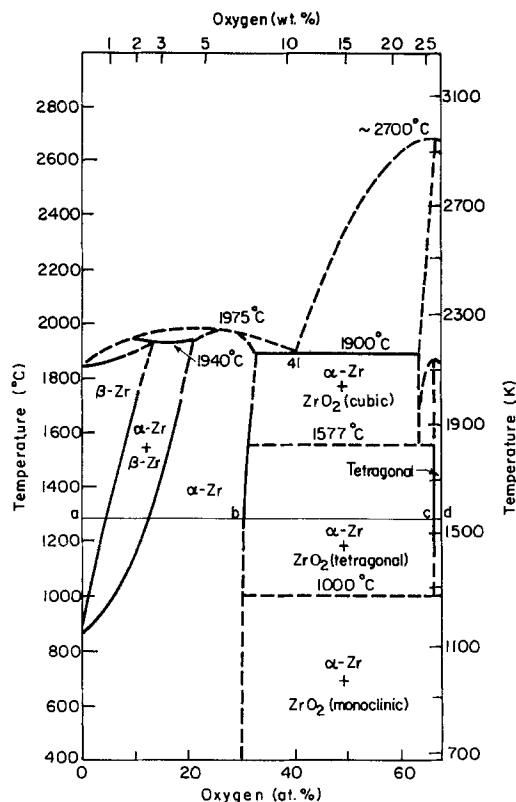
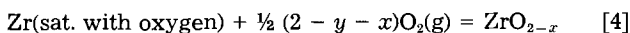


Fig. 1. Zr-O equilibrium phase diagram from Ref. (18) with isotherm at 1300°C.

sumed to be independent of composition. In addition, as explained earlier, it is assumed to be the same for the α and β modifications of zirconium.

b-c.—Addition of oxygen to the oxygen-saturated metal to produce 1 mol of the oxide at the lower phase boundary ($O/Zr = 2 - x$). This reaction can be written as

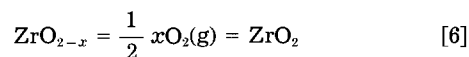


The heat released by this equilibrium reaction is

$$Q_{b-c} = -\Delta H_R \quad [5]$$

where ΔH_R is the standard enthalpy change of reaction [4].

c-d.—Dissolution of oxygen in the hypostoichiometric oxide to produce perfect stoichiometry corresponds to the reaction



and the heat release for this step is given by

$$Q_{c-d} = -\frac{1}{2} \int_0^x \overline{\Delta H}_{\text{ox}} dx' \quad [7]$$

where $\overline{\Delta H}_{\text{ox}}$ is the partial molar enthalpy of oxygen in ZrO_{2-x} , which is a function of the O/Zr ratio.² The only work that provides some information on the partial molar enthalpy of solution of oxygen in ZrO_2 is that of Aronson [3]. Unfortunately, the oxygen potential he obtained changes temperature dependence across the ZrO_{2-x} phase field in a manner which implies changes in the signs of $\overline{\Delta H}_{\text{ox}}$ and the partial molar entropy of solution, $\overline{\Delta S}_{\text{ox}}$. This unusual behavior may be due to the fact that the temperature range of his experiments (900°-1100°C) spanned the monoclinic-tetragonal transition temperature of zirconia (1000°C). Rather than accept the odd variation of $\overline{\Delta H}_{\text{ox}}$

²The oxygen solution reaction given by Eq. [6] need not imply that this element enters the oxide lattice as interstitial neutral atoms, as it does in the metal. Rather, the final state of oxygen entering the oxide is the substitutional ion O^{2-} , achieved by addition of two oxygen atoms to vacant anion lattice sites and acquisition of two electrons from the solid. The experimental enthalpy of solution, $\overline{\Delta H}_{\text{ox}}$, reflects this charge-exchange step.

with O/Zr implied by these data, we use only the measured oxygen potentials at 1100°C, which apply to tetragonal zirconia. These data, in conjunction with a theoretical estimate of $\overline{\Delta S}_{\text{ox}}$, determine $\overline{\Delta H}_{\text{ox}}$ by

$$\overline{\Delta H}_{\text{ox}} = \overline{\Delta G}_{\text{ox}} + T\overline{\Delta S}_{\text{ox}} \quad [8]$$

The partial molar entropy of solution is given by

$$\overline{\Delta S}_{\text{ox}} = 2\overline{S}_0 - S^{\circ}_{\text{O}_2} \quad [9]$$

where $S^{\circ}_{\text{O}_2}$ is the entropy of molecular oxygen and \overline{S}_0 is the partial molar entropy of oxygen ions in ZrO_{2-x} . The former consists primarily of a translational entropy contribution with a smaller contribution from rotation. At temperatures above 1200°C, the methods described in Ref. (4) give the value $S^{\circ}_{\text{O}_2} \approx 210 \text{ J/mol}\cdot\text{K}$.

The tetragonal structure of zirconia is simply a distorted fluorite lattice (5), and the dominant point defects in the nonstoichiometric compound are oxygen vacancies. Consequently, $\overline{\Delta S}_{\text{ox}}$ of ZrO_{2-x} should behave in a manner similar to other oxygen-deficient oxides with the fluorite structure, such as $(\text{U},\text{M})\text{O}_{2-x}$ where M is another cation. Wadier (6) has shown that \overline{S}_0 for the hypostoichiometric mixed uranium-neodymium oxide can be satisfactorily represented by a simple model which assumes a perfect cation sublattice and isolated vacancies on the anion sublattice. His result, which is applicable to zirconia as well, is

$$\overline{S}_0 = -R \ln \left(\frac{2-x}{x} \right) \quad [10]$$

Using this estimate of $\overline{\Delta S}_{\text{ox}}$ and Aronson's values of $\overline{\Delta G}_{\text{ox}}$ at 1100°C in Eq. [8] yields the partial molar enthalpy of solution shown in Fig. 2. Although there is no way of accurately estimating $\overline{\Delta H}_{\text{ox}}$ at exact stoichiometry (because of the mathematical form of Eq. [10]), the shape and magnitude of the curve in Fig. 2 are consistent with those observed for $(\text{U},\text{Pu})\text{O}_{2-x}$ (7).

The sum of the heat releases in the three steps is equal to the negative of the heat of combustion of pure zirconium

$$\Delta H^{\circ}_{\text{ZrO}_2} = \frac{1}{2} \overline{\Delta H}_{\text{M}y} + \Delta H_R + \frac{1}{2} \int_0^x \overline{\Delta H}_{\text{ox}} dx' \quad [11]$$

Estimates of the oxide-metal interface compositions x and y can be obtained from the Zr-O phase diagram. The solubility limit of oxygen in α -Zr is nearly temperature independent, but the lower phase boundary of ZrO_{2-x} is slightly temperature sensitive (8).

Heat Release during Zircaloy Oxidation

Corrosion kinetics are customarily expressed as the rate of weight gain and the rate of growth of the oxide scale. In the case of zirconium oxidation, a layer of oxygen-

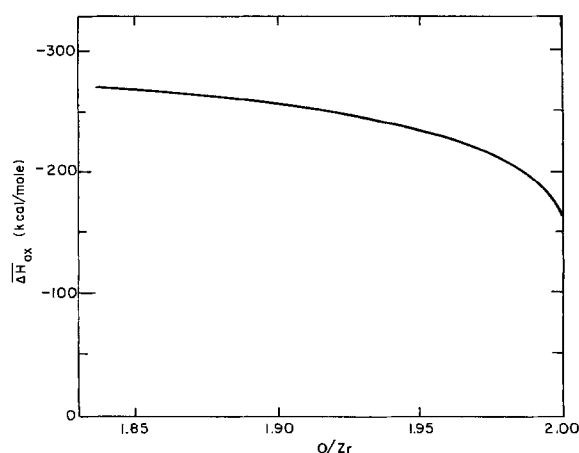


Fig. 2. Composition dependence of the partial molar enthalpy of solution of oxygen in zirconia.

stabilized α -Zr forms between the oxide scale and the substrate. In the present analysis, the α -Zr layer is not distinguished from the remaining β -Zr because the two phases are assumed to have similar thermal properties. Figure 3 shows typical scale formation on zirconium. The points labeled a, b, c, and d correspond to those in Fig. 1. Because the change in O/Zr ratio across the oxide phase is small, the segment d-c of the oxygen distribution is assumed to be a straight line. If the initial thickness of the oxygen-free zirconium slab is L_{M0} , and L_M and L_{ox} denote the thickness of metal ($\alpha + \beta$) and oxide at time t , conservation of zirconium leads to

$$\rho_M(L_{M0} - L_M) = \rho_{ox}L_{ox} \quad [12]$$

where ρ_M and ρ_{ox} are numbers of gram atoms of zirconium per unit volume of metal and oxide, respectively.

In a time interval Δt the result of oxidation is $\Delta N_T =$ total uptake of oxygen (g atoms/cm²) and $\Delta L_{ox} =$ increase in oxide layer thickness.

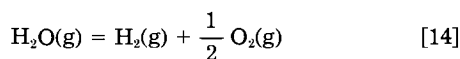
The number of gram atoms of zirconium contained in a unit area of oxide scale is $\rho_{ox}L_{ox}$, and the average O/Zr ratio of the scale is at all times equal to $2 - \frac{1}{2}x$. Therefore, the change in the amount of oxygen bound in the oxide scale as a result of the increase of ΔL_{ox} in thickness is $(2 - \frac{1}{2}x)\rho_{ox}\Delta L_{ox}$. However, the oxide scale grows by converting $\rho_{ox}\Delta L_{ox}$ g atoms per cm² of adjacent zirconium metal which is saturated with oxygen. Thus, of the change in the amount of oxygen in the scale, an amount $y\rho_{ox}\Delta L_{ox}$ is supplied by the converted metal, with the remainder being supplied from the total uptake from the oxidizing gas. The difference

$$\Delta N_M = \Delta N_T - (2 - \frac{1}{2}x - y)\rho_{ox}\Delta L_{ox} \quad [13]$$

is the quantity of oxygen which enters the metal phase.

As a first approximation determining the heat release, the partial molar heats of solution of oxygen in the metal and in the oxide are considered to be independent of composition. The consequence of this assumed behavior is the absence of heat release in the bulk oxide and metal phases due to oxygen diffusion down concentration gradients. The heat effects of corrosion are localized at the interfaces between the gas and the oxide and between the oxide and the metal.

For oxidation in steam, the heat released at the gas-oxide interface consists of two components. The oxygen entering the specimen must first be produced by decomposing water



for which the heat release is the standard heat of formation of water, $\Delta H^0_{fH_2O}$. The oxygen gas is dissolved in the surface of the oxide according to Eq. [6]. The heat release per gram atom of oxygen absorbed at the gas-oxide surface is

$$Q_{g-ox} = -\frac{1}{2} \overline{\Delta H}_{ox} + \Delta H^0_{fH_2O} \quad [15]$$

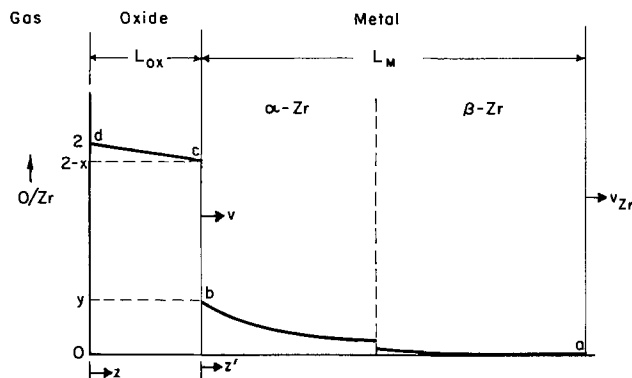
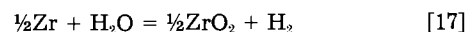


Fig. 3. Oxide scale growth and oxygen concentration distribution during steam oxidation of Zircaloy.

The ΔN_T g atoms of oxygen entering the surface ultimately appear in one of three locations. An amount ΔN_M enters the metal at the oxide-metal interface where the heat released is $(\frac{1}{2}\overline{\Delta H}_{ox} - \frac{1}{2}\overline{\Delta H}_M)\Delta N_M$. A portion $(2 - x - y)\rho_{ox} \Delta L_{ox}$ reacts with the metal at the oxide-metal interface to produce ZrO_{2-x} . The heat released at this interface by this process is $(2 - x - y)\rho_{ox} \Delta L_{ox}(\frac{1}{2}\overline{\Delta H}_{ox}) - \Delta H_R\rho_{ox}\Delta L_{ox}$. The remaining $\frac{1}{2}x\rho_{ox}\Delta L_{ox}$ g atoms of oxygen stay in the oxide but contribute nothing to the heat release because in the present approximation, $\overline{\Delta H}_{ox}$ is composition independent. Adding these contributions, eliminating ΔN_M by using Eq. [13], and ΔH_R by Eq. [11] (with $\overline{\Delta H}_{ox}$ a constant for this approximation), yields the heat release at the oxide-metal interface per gram atom of oxygen absorbed by the specimen

$$Q_{ox-M} = \frac{1}{2} \overline{\Delta H}_{ox} - \frac{1}{2} \Delta H_M - \left[\Delta H^0_{fZrO_2} - \frac{1}{4}x\overline{\Delta H}_{ox} - \left(2 - \frac{1}{2}x\right) \left(\frac{1}{2} \overline{\Delta H}_M\right) \right] \rho_{ox} \frac{\Delta L_{ox}}{\Delta N_T} \quad [16]$$

Current analyses which attempt to account for the heat effect of the metal-water reaction assume that the thermal source term is equal to the negative of the integral heat of the reaction



which is

$$\Delta H^0 = \frac{1}{2}\Delta H^0_{fZrO_2} - \Delta H^0_{fH_2O} \quad [18]$$

However, during the corrosion process, the appropriate source term is the differential heat of reaction

$$Q = Q_{g-ox} + Q_{ox-M} \quad [19]$$

This quantity is obtained from Eq. [15] and [16] as

$$Q = \Delta H^0_{fH_2O} - \frac{1}{2}\overline{\Delta H}_M - \left[\Delta H^0_{fZrO_2} - \frac{1}{4}x\overline{\Delta H}_{ox} - \frac{1}{2}(2 - \frac{1}{2}x)\overline{\Delta H}_M \right] \rho_{ox}\Delta L_{ox}/\Delta N_T \quad [20]$$

The following argument demonstrates that Eq. [18] and [20] are self-consistent. Complete oxidation by steam contacting one face of a slab which contains $\frac{1}{2}$ g-atom Zr is accomplished in two steps. In the first step, sufficient oxygen is added to convert all of the metal to an oxide which has an O/Zr ratio of 2 on the steam side and $2 - x$ on the opposite side, with a linear variation between the two faces. The average O/Zr ratio of the nearly fully oxidized slab is thus $2 - \frac{1}{2}x$. Using Eq. [12] with $L_M = 0$, $\rho_M L_{M0} = \frac{1}{2}$, the term $\rho_{ox}\Delta L_{ox}$ in Eq. [20] is seen to be $\frac{1}{2}$. The quantity of oxygen added to the slab in step 1 (ΔN_T in Eq. [20]) is $\frac{1}{2}(2 - \frac{1}{2}x)$ g atoms and the heat release for this step is

$$Q_1 = \frac{1}{2}(2 - \frac{1}{2}x)Q \quad [21]$$

where Q is given by Eq. [20] with the values of $\rho_{ox}\Delta L_{ox}$ and ΔN_T determined above. The second step is the addition of $\frac{1}{2}x$ g atoms of oxygen to bring the slab to exact stoichiometry, for which the enthalpy change is

$$Q_2 = \frac{1}{2}xQ_{g-ox} \quad [22]$$

where Q_{g-ox} is given by Eq. [15]. Adding the contributions of the two steps shows that

$$Q_1 + Q_2 = -\frac{1}{2}\Delta H^0_{fZrO_2} + \Delta H^0_{fH_2O} \quad [23]$$

which is exactly the negative of the integral enthalpy of reaction given by Eq. [18].

Thus, although the heat released by complete oxidation of zirconium is given by the overall thermochemistry of reaction [17], the heat effect during oxidation (i.e., while some metal is still present) is determined by the differential heat of reaction of Eq. [20]. This heat effect is not a purely thermodynamic quantity, because it depends upon the ratio of increments of oxide layer growth ΔL_{ox} to total oxygen absorbed, ΔN_T , which depends on the details of the corrosion process. In order to evaluate Q ,

specification of the kinetics of corrosion is required. For isothermal oxidation in an infinite-medium specimen, parabolic kinetics prevails and Q can be computed. We will perform this computation, but its restrictions to the isothermal, infinite medium case should be kept in mind. When we deal with the transient situation in the following sections or with an isothermal reaction in a finite slab, the appropriate expression for $\Delta L_{ox}/\Delta N_T$ must be used in Eq. [20].

For parabolic scaling, we may write

$$\frac{dL_{ox}}{dt} = \frac{k_{ox}}{\sqrt{t}} \quad [24]$$

$$J = \frac{dN_T}{dt} = \frac{k_T}{\sqrt{t}} \quad [25]$$

Where J is the oxygen uptake rate and k_{ox} and k_T are the scaling constants for oxide layer growth and total oxygen uptake, respectively. Using Eq. [24] and [25] in Eq. [20] yields the appropriate thermal source term during parabolic scaling of zirconium in steam

$$Q(\text{parabolic}) = \Delta H^{\circ}_{H_2O} - \frac{1}{2}\Delta H_M - [\Delta H^{\circ}_{ZrO_2} - \frac{1}{4}x\overline{\Delta H}_{ox} - \frac{1}{2}(2 - \frac{1}{2}x)\overline{\Delta H}_{ox}] \frac{\rho_{ox}k_{ox}}{k_T} \quad [26]$$

The preceding analysis was also based upon the assumption that the enthalpy of solution of oxygen in zirconia was independent of composition. A more accurate analysis allows for the composition-variation of $\overline{\Delta H}_{ox}$ given in Fig. 2. This curve can be fitted to the quadratic formula

$$\overline{\Delta H}_{ox} = (\overline{\Delta H}_{ox})_0 + ax + bx^2 \quad [27]$$

Repeating the analysis developed above for $\overline{\Delta H}_{ox} = \text{constant}$, the heat sources in the solid for the variable $\overline{\Delta H}_{ox}$ case are found to be

$$Q_{g-ox} = -\frac{1}{2}(\overline{\Delta H}_{ox})_0 + \Delta H^{\circ}_{H_2O} \quad [28]$$

$$Q_{ox-M} = \frac{1}{2}(\overline{\Delta H}_{ox})_0 - \frac{1}{2}\overline{\Delta H}_M - \left[\Delta H^{\circ}_{ZrO_2} - \frac{1}{4}x(\overline{\Delta H}_{ox})_0 - \frac{1}{4}ax^2 - \frac{1}{6}bx^3 - \frac{1}{2}(2 - \frac{1}{2}x)\overline{\Delta H}_M \right] \frac{\rho_{ox}\Delta L_{ox}}{\Delta N_T} \quad [29]$$

In addition, there is a bulk heat release in the oxide scale due to the change in $\overline{\Delta H}_{ox}$ as oxygen diffuses from the gas-oxide interface to the metal-oxide interface. This contribution can be shown to be given by

$$Q_{ox} = -\frac{1}{2}x^2 \left(\frac{1}{3}a + \frac{1}{4}bx \right) \frac{\rho_{ox}\Delta L_{ox}}{\Delta N_T} \quad [30]$$

The total heat release per gram atom of oxygen absorbed by the specimen for this case is given by

$$Q = Q_{g-ox} + Q_{ox} + Q_{ox-M} \quad [31]$$

Table I shows the contributions of the various heat sources calculated in this section. The data used in the computations are collected in the first part of Table I. Parabolic oxidation kinetics are assumed, so that the term $\Delta L_{ox}/\Delta N_T$ is the ratio of the parabolic scaling constants k_{ox}/k_T . The total heat releases according to Eq. [26] and [31] are given as functions of temperature between 1500 and 1900 K. The heat releases per gram atom of oxygen absorbed by the specimen are quite insensitive to temperature in this range and to the assumption concerning the composition dependence of $\overline{\Delta H}_{ox}$. However, the average value of $Q \approx 307$ kJ/g-atom O is $\sim 3\%$ larger than the integral heat of reaction, given by Eq. [18] and the data in Table I as $\Delta H^{\circ} = 297$ kJ/g-atom O. This slight increase in the heat release may be significant in analysis of the chemical heat effect in severe fuel damage codes for nuclear reactors.

The last part of Table I shows the way that the reaction heat is partitioned in the solid. Here the concentration effect on the heat of solution of oxygen in zirconia has a

Table I. Contributions to the zirconium oxidation heat sources during isothermal oxidation of a semi-infinite medium (parabolic kinetics)

Data (kJ/mol)		
$\Delta H^{\circ}_{ZrO_2} = -1088$	} Ref. (1)	
$\Delta H^{\circ}_{H_2O} = -247$		
$\overline{\Delta H}_M = -1138$	} Ref. (2)	
$\overline{\Delta H}_{ox} \text{ (avg)} = -1050$		
$(\overline{\Delta H}_{ox})_0 = -678$	} Fig. 2	
$a = -8370$		
$b = 35,150$		
$x = 10^{-4} T(K)$	} Ref. (8)	
$k_{ox} = 0.075 \exp(-9000/T) \text{ cm}^2/\text{s}^{1/2}$		
$k_T = 0.018 \exp(-10,000/T) \text{ g atoms O/cm}^2 \text{ -s}^{1/2}$		
$\rho_{ox} = 0.0472 \text{ g atoms Zr/cm}^3$	} Ref. (9)	
Total heat release as a function of temperature		
T(K)	Total heat release, kJ/g atom oxygen absorbed by specimen	
	Constant $\overline{\Delta H}_{ox}$	Variable $\overline{\Delta H}_{ox}$
1500	304	305
1600	305	306
1700	306	307
1800	306	307
1900	307	308
Components of the heat release at 1600 K		
Location	Heat release, kJ/g atom oxygen absorbed by specimen	
	Constant $\overline{\Delta H}_{ox}$	Variable $\overline{\Delta H}_{ox}$
Gas-oxide interface	278	92
Oxide layer	0	7
Oxide-metal interface	27	207

profound effect. If $\overline{\Delta H}_{ox}$ is taken to be a constant equal to the average value given in the top of Table I, 90% of the reaction heat appears at the gas-oxide interface. However, if the composition-dependence shown in Fig. 2 is adopted, only 30% of the reaction heat appears at the surface. However, in both cases, despite the endothermicity of reaction [14], the large energy release upon incorporation of gaseous oxygen in the oxide makes the overall surface reaction exothermic. This result is just the opposite of the conclusion recently reached by Cubicciotti (10). The bulk heating of the oxide layer is relatively minor.

Effect of the Heat of Reaction on the Temperature Distribution

All experimental studies of Zircaloy corrosion by steam assume a uniform temperature distribution within the reacting sample. However, temperature nonuniformities may result from the partitioning of the heat release between the gas-oxide and oxide-metal interfaces. The location as well as the magnitude of the heat release due to oxidation may have a significant effect on calculation of cladding temperatures in a reactor accident situation which involves oxidation of Zircaloy.

To assess the importance of the heat-source location on the temperature distribution, the idealized situation described above is analyzed. For the present, we assume that the oxidation kinetics are those for parabolic scaling at the constant base temperature T_0 ; acceleration of the corrosion rate by the heat release is neglected. Our object here is to obtain estimates of the temperature nonuniformities caused by discrete heat sources in the slab.

With this restriction, the growth rate of the oxide scale and the flux of oxygen into the specimen are given by Eq. [24] and [25], respectively, with the scaling constants k_{ox} and k_T those at the base temperature T_0 . The planar heat sources at the gas-oxide and metal-oxide interfaces are equal to $Q_{g-ox}J$ and $Q_{ox-M}J$, respectively, where Q_{g-ox} and Q_{ox-M} are given by Eq. [15] and [16], respectively.

The heat balance at the specimen surface includes the radiative-convective loss to the environment, the heat

conducted to the specimen from the interior (given by the product of the oxide thermal conductivity and the temperature gradient in the oxide), and the heat source $Q_{g-ox}J$. The balance consists of equating the difference in the first two terms to the last.

The thermal response time of the oxide layer is L_{M0}^2/α_{ox} , where α_{ox} is the thermal diffusivity of ZrO_2 . The characteristic scale growth time is equal to L_{M0}^2/k_{ox}^2 . Because the latter is very much larger than the former (by a factor of $\sim 10^5$ at 1300°C), quasisteady-state heat conduction applies to the oxide layer, or the temperature distribution in this phase is linear at all times.

In addition, because the thermal conductivity of the metal is very large compared to that of the oxide, the thermal response of the metal phase can be treated as a lumped capacity and temperature gradients neglected here. Consequently, the transient heat-conduction equation in the metal portion of the specimen can be replaced by an energy balance which equates the time rate of change of the heat content of the metal phase to the difference between the reaction heat source at the oxide-metal interface, $Q_{ox-M}J$, and the heat transferred away from this interface by conduction into the oxide.

Elaboration of this model in Ref. (11) leads to equations giving the time variations of the metal phase and oxide surface temperatures following introduction of steam into the system. Calculations were performed for a variety of external heat transfer coefficients (h) ranging from that for pure radiation from the surface to a medium at constant temperature to smaller values intended to represent convection to slowly flowing steam that might be encountered in a core-uncovery situation in a nuclear reactor accident. In all cases, the calculations showed that despite the low thermal conductivity of ZrO_2 , temperature gradients over the oxide scale were negligible at all but the very earliest times during the transient. The reason for this result is Biot number, hL_{M0}/κ_{ox} , where κ_{ox} is the thermal conductivity of ZrO_2 , is very much less than unity. This condition is encountered in other solid-fluid heat-transfer situations (12), and simply reflects the fact that in such cases external heat-transfer provides the major thermal resistance in the system. The same conclusion has been reached by use of the detailed thermal analysis modules in the nuclear reactor severe fuel damage codes SCDAP (13) and PWR HEATUP (14).

The consequences of this behavior are twofold. First, the thermal response of the oxidizing metal is independent of the manner in which the heat of the chemical reaction is partitioned between the gas-oxide and metal-oxide interfaces and depends only upon the total heat release given by Eq. [20]. Second, the entire specimen can be characterized by a spatially uniform temperature whose time dependence is given by a lumped-capacity energy balance. This balance takes on the following simple but accurate form if the change in the solid heat capacity due to oxidation is neglected

$$\rho_M C_{PM} L_{M0} \frac{d}{dt} (T - T_0) = QJ - h(T - T_0) \quad [32]$$

where ρ_M and C_{PM} are the density and heat capacity of the metal, respectively. The temperature of the environment (T_0), representing the enclosure surfaces for radiation and steam temperature for convection, can be time dependent. The heat release due to reaction (Q) is given by Eq. [20], and the oxygen uptake rate (J) is described by the appropriate corrosion kinetics (which need not be those of parabolic scaling). Although the form of Eq. [32] was obtained without considering the temperature dependence of J , the simple lumped-capacity heat balance can be employed with models that account for coupling of J to the temperature transient.

Approximate Coupling of Corrosion Kinetics and Thermal Response

The approximate coupling method adopted by Markworth (15) and used in severe fuel damage codes (13, 14)

consists of assuming that the basic parabolic scaling laws apply in a temperature transient but the scaling coefficients are thermally activated. According to this prescription, the oxygen uptake rate given by Eq. [25] is replaced by

$$J = \frac{dN_T}{dt} = \frac{k_{T_0}}{\sqrt{t}} \exp \left[-\frac{E_T}{R} \left(\frac{1}{T} - \frac{1}{T_0} \right) \right] \quad [33]$$

where k_{T_0} is the parabolic rate constant at temperature T_0 and E_T is the activation energy for the total oxygen uptake determined by isothermal corrosion experiments at various temperatures.

Similarly, Eq. [24] is generalized to

$$\frac{dL_{ox}}{dt} = \frac{k_{ox0}}{\sqrt{t}} \exp \left[-\frac{E_{ox}}{R} \left(\frac{1}{T} - \frac{1}{T_0} \right) \right] \quad [34]$$

where k_{ox0} is the parabolic rate constant for oxide scale growth at T_0 and E_{ox} is its activation energy.

The heat of reaction Q is obtained by substituting Eq. [33] and [34] into Eq. [20] in order to eliminate $\Delta L_{ox}/\Delta N_T$. The result is multiplied by Eq. [33] to obtain the heat source QJ . Using this result in Eq. [32] gives

$$C_1 \frac{d\theta}{dt} = \frac{A_1 \exp(E_1\theta)}{\sqrt{t}} - \frac{A_2 \exp(E_2\theta)}{\sqrt{t}} - C_2\theta \quad [35]$$

where

$$C_1 = \rho_M C_{PM} L_{M0} T_0$$

$$C_2 = hT_0$$

$$A_1 = (\Delta H_{H_2O}^0 - \frac{1}{2} \Delta \bar{H}_M) k_{T_0}$$

$$A_2 = [\Delta H_{ZrO_2}^0 - \frac{1}{4} x \Delta \bar{H}_{ox} - \frac{1}{2} (2 - \frac{1}{2} x) \Delta \bar{H}_M] \rho_{ox} k_{ox0}$$

$$E_1 = E_T/RT_0$$

$$E_2 = E_{ox}/RT_0$$

and

$$\theta = (T - T_0)/T_0 \quad [36]$$

is the dimensionless temperature of the specimen.

Equation [35] can be solved numerically using the initial condition $\theta(0) = 0$ to yield the temperature variation during the transient initiated by introduction of steam at time zero. Using this result in Eq. [33] and [34] permits the corrosion rate to be determined.

The above formulation assumes a constant heat of solution $\Delta \bar{H}_{ox}$. If the more accurate representation of this quantity according to Eq. [27] is employed, Eq. [31] is used for Q and different coefficients A_1 and A_2 , obtained from Eq. [28]-[30], result. Both cases apply only to oxidation of a semi-infinite solid, however.

Accurate Coupling of Heat and Mass Transport during Corrosion

The major shortcoming of the coupling method described in the previous section is the description of the corrosion process by parabolic kinetics in a temperature transient. This is, in principle, wrong, because parabolic kinetics requires time-independent parameters such as oxygen diffusion coefficients and interface concentrations. Thus, application of Eq. [33] and [34] to situations with time-dependent temperatures is open to question. This deficiency can be eliminated by analyzing the corrosion process from the same basic principles that have been applied to isothermal corrosion kinetics. The material properties are permitted to be time dependent, but the temperature is assumed to be spatially independent because the demonstration of this property in the "Temperature Distribution" section remains valid.

The kinetics of oxidation are determined by solving the oxygen diffusion equations in the oxide and metal zones of the specimen and matching fluxes and concentrations at the metal-oxide interface. This technique has been used by Paweł (16) to analyze isothermal oxidation of Zir-

caloy. We apply the same type of analysis to the present transient problem with the aid of the following simplifications: (i) the oxygen concentration profile in the oxide layer is assumed to be a linear function of distance, (ii) the distinction between α -Zr and β -Zr is neglected, and (iii) the system is semi-infinite insofar as oxygen penetration is concerned.

The system is depicted in Fig. 3. Because of the volume change upon oxidation, the metal lattice moves away from the gas-oxide interface with a velocity denoted by v_{zr} . From Fig. 3

$$v_{zr} = \frac{d}{dt} (L_{ox} + L_M)$$

This motion can be related to the velocity of the oxide-metal interface by using the zirconium balance given by Eq. [12]

$$\frac{dL_M}{dt} = -\frac{\rho_{ox}}{\rho_M} \frac{dL_{ox}}{dt} = -\frac{1}{B} \frac{dL_{ox}}{dt}$$

where B is the ratio of the zirconium atom densities in the metal and oxide phases (the Pilling-Bedworth ratio). Combining these two equations and noting that $dL_{ox}/dt = v$ yields

$$v_{zr} = \left(\frac{B-1}{B}\right) v \quad [37]$$

Because the oxygen distribution in the oxide layer has been assumed to be linear, we may write

$$\frac{C_d - C_{ox}}{C_d - C_c} = \frac{z}{L_{ox}} \quad [38]$$

where C_{ox} is the oxygen concentration at location z in the oxide layer and C_d and C_c are the boundary concentrations of oxygen at points d and c in Fig. 3, respectively. These correspond to stoichiometric zirconia and to substoichiometric zirconia at the lower phase boundary.

In the metal phase the oxygen conservation equation is

$$\frac{\partial C_M}{\partial t} = \frac{\partial J'}{\partial z'} \quad [39]$$

where C_M is the oxygen concentration in the metal and J' is the oxygen flux in the metal phase with respect to the coordinate origin of z' , which is chosen as the moving oxide-metal interface. This flux consists of two terms, a Fick's law component representing oxygen diffusion relative to the zirconium lattice and a convection term reflecting movement of the zirconium lattice with respect to the oxide-metal interface. The convective velocity is the difference between the lattice velocity with respect to the fixed gas-oxide interface and the velocity of the oxide-metal interface with respect to the same plane

$$v_M = v_{zr} - v = -v/B \quad [40]$$

The oxygen flux in the metal is

$$J' = -D_M \frac{\partial C_M}{\partial z'} + v_M C_M \quad [41]$$

where D_M is the diffusion coefficient of oxygen in the metal. Combining Eq. [39]-[41] gives the oxygen diffusion equation in the metal phase

$$\frac{\partial C_M}{\partial t} - \frac{v}{B} \frac{\partial C_M}{\partial z'} = D_M \frac{\partial^2 C_M}{\partial z'^2} \quad [42]$$

The initial and boundary conditions are

$$C_M(z', 0) = 0 \quad [43]$$

$$C_M(0, t) = C_b \quad [44]$$

$$C_M(\infty, t) = 0$$

where C_b is the saturation concentration of oxygen in α -Zr. The last condition embodies the semi-infinite medium condition and neglects the transformation from α -Zr to β -Zr.

Equality of oxygen fluxes in the oxide and metal phases at the interface is expressed by

$$-D_{ox} \left(\frac{\partial C_{ox}}{\partial z} \right)_{L_{ox}} - v C_c = -D_M \left(\frac{\partial C_M}{\partial z'} \right)_0 - \frac{v}{B} C_b \quad [45]$$

where D_{ox} is the oxygen diffusivity in ZrO_2 .

Isothermal solution.—If the diffusion coefficient and the boundary concentrations are all constant, the velocity in Eq. [42] is $v = k_{ox}/\sqrt{t}$, where k_{ox} is the parabolic scaling constant, and the solution to Eq. [42] is

$$\frac{C_M}{C_b} = \frac{\operatorname{erfc} \left(\frac{z'}{2\sqrt{D_M t}} + \frac{k_{ox}}{B\sqrt{D_M}} \right)}{\operatorname{erfc} \left(\frac{k_{ox}}{B\sqrt{D_M}} \right)} \quad [46]$$

Substituting Eq. [38] and [46] into Eq. [45] and noting that $L_{ox} = 2k_{ox}\sqrt{t}$ yields

$$\begin{aligned} & \frac{D_{ox}(C_d - C_c)}{2k_{ox}} - k_{ox}(C_c - C_b/B) \\ &= C_b \left(\frac{D_M}{\pi} \right)^{\frac{1}{2}} \frac{\exp \left[-\left(\frac{k_{ox}}{B\sqrt{D_M}} \right)^2 \right]}{\operatorname{erfc} \left(\frac{k_{ox}}{B\sqrt{D_M}} \right)} \end{aligned} \quad [47]$$

The kinetic equation for the rate of oxygen uptake is obtained from

$$\frac{dN_T}{dt} = -D_{ox} \left(\frac{\partial C_{ox}}{\partial z'} \right)_0 = \frac{k_T}{\sqrt{t}}$$

or

$$k_T = \frac{D_{ox}(C_d - C_c)}{2k_{ox}} \quad [48]$$

The isothermal rate constants k_{ox} and k_T can be determined by using the oxygen diffusion coefficients and interface concentrations in Eq. [47] and [48]. Using the following data given in Ref. (16) for 1300°C

$$C_d = 2\rho_{ox} = 0.094 \text{ g atom oxygen/cm}^3$$

$$C_c/C_d = 1.84/2 = 0.092$$

$$C_b/C_d = 0.31$$

$$D_{ox} = 2.0 \times 10^{-6} \text{ cm}^2/\text{s}$$

$$D_M = 3.2 \times 10^{-7} \text{ cm}^2/\text{s (for } \alpha\text{-Zr)}$$

$$B = \rho_M/\rho_{ox} = 1.5$$

Equation [47] gives $k_{ox} = 2.5 \times 10^{-4} \text{ cm/s}^{1/2}$ and Eq. [48] yields $k_T = 3.5 \times 10^{-5} \text{ g atom oxygen/cm}^2 \cdot \text{s}^{1/2}$. These results are in excellent agreement with the measured scaling constants (see Table I), which is not surprising since these data were used by Pawel (16) to determine D_{ox} and D_M . All that we have done is to reverse this process. However, the comparison does demonstrate that assumptions (i) and (ii) given at the beginning of this section are adequate for the corrosion analysis, and will be retained in analyzing the transient case.

Nonisothermal solution.—Analysis of diffusive transport during a transient is simplified by the spatial uniformity of the temperature. Because of this feature, the diffusion coefficients, which are functions of temperature, depend on time but not on position. As a consequence, the oxygen concentration distribution in the oxide and metal phases is still determined by Eq. [38] and [42], respectively, and the oxygen flux match at the oxide-metal interface is correctly expressed by Eq. [45]. What is inapplicable in the case of time-dependent diffusion coefficients is the assumption of parabolic scaling expressed by the relationship $v = k_{ox}/\sqrt{t}$.

The diffusivity of oxygen in zirconium metal can be considered as a function of time via the temperature

$$D_M = D_{M_0} f \quad [49]$$

where D_{M_0} is the diffusion coefficient at temperature T_0 and the factor f is given by

$$f = \exp \left[-\frac{E_{DM}}{R} \left(\frac{1}{T} - \frac{1}{T_0} \right) \right] = e^{16.3\theta} \quad [50]$$

where $E_{DM} = 213$ kJ/mol is the activation energy of oxygen diffusion in α -Zr [Ref. (16)] and θ is dimensionless temperature defined by Eq. [36].

The only other quantity with a significant temperature dependence is the product of the oxygen diffusivity in the oxide and the oxygen concentration driving force across the oxide layer. The former exhibits Arrhenius behavior, but the difference in O/Zr ratio between stoichiometric zirconia and the reduced oxide at the lower phase boundary is approximately proportional to the absolute temperature (x in Table I). However, the temperature dependence of this product can be expressed in Arrhenius form with an activation energy slightly larger than that which characterize the diffusion coefficient in the oxide. Thus

$$D_{ox}(C_d - C_c) = [D_{ox}(C_d - C_c)]_0 g \quad [51]$$

where the bracketed coefficient with the zero subscript is the diffusivity-driving force product at temperature T_0 and the factor g is

$$g = \left(\frac{T}{T_0} \right) \exp \left[-\frac{E_{Dox}}{R} \left(\frac{1}{T} - \frac{1}{T_0} \right) \right] = e^{12.1\theta} \quad [52]$$

where $E_{Dox} = 144$ kJ/mol is the activation energy of oxygen diffusion in the oxide phase (16).

Equation [49] is substituted into Eq. [42], and a new time variable is defined by

$$u = \int_0^t f dt' \quad [53]$$

The result is

$$\frac{\partial C_M}{\partial u} - \frac{v}{Bf} \frac{\partial C_M}{\partial z'} = D_{M_0} \frac{\partial^2 C_M}{\partial z'^2} \quad [54]$$

In analogous fashion, the derivative on the left-hand side of Eq. [45] is evaluated from Eq. [38] along with Eq. [51]. Using Eq. [49] for D_n transforms the oxygen flux match to

$$\frac{[D_{ox}(C_d - C_c)]_0 g}{f L_{ox}} - \frac{v}{f} \left(C_c - \frac{C_b}{B} \right) = -D_{M_0} \left(\frac{\partial C_M}{\partial z'} \right)_0 \quad [55]$$

The temperature dependence of the difference $(C_c - C_b/B)$ is small, and so this quantity is evaluated at T_0 .

There is no exact analytical solution to Eq. [54] and [55] when f and g are arbitrary functions of the time variable u . However, an approximately analytical solution can be obtained by assuming that the ratio v/f is inversely proportional to \sqrt{u}

$$\frac{v}{f} = \frac{k}{\sqrt{u}} \quad [56]$$

where k is a constant which replaces the scaling constant k_{ox} of the isothermal case.

The oxide scale thickness in the first term of Eq. [55] is determined by

$$L_{ox} = \int_0^t v dt' = k \int_0^t \frac{f(t') dt'}{\sqrt{u(t')}} = 2k\sqrt{u} \quad [57]$$

where Eq. [53] has been used.

Substituting Eq. [56] into Eq. [54] produces an equation whose form is identical to that for the isothermal situation. The solution for the transient temperature process is thus given by Eq. [46] with k_{ox} replaced by k , t by u , and D_M by D_{M_0} . This solution is used to evaluate the derivative on the right-hand side of Eq. [55]. With v and L_{ox} on the left-hand side given by Eq. [56] and [57], Eq. [55] becomes

$$\begin{aligned} & \frac{[D_{ox}(C_d - C_c)]_0 g}{2k} \frac{1}{f} - k \left(C_c - \frac{C_b}{B} \right) \\ &= \left(\frac{D_{M_0}}{\pi} \right)^{1/2} C_b \frac{\exp \left[-\left(\frac{k}{B\sqrt{D_{M_0}}} \right)^2 \right]}{\operatorname{erfc} \left(\frac{k}{B\sqrt{D_{M_0}}} \right)} \end{aligned} \quad [58]$$

Except for the ratio g/f in the first term on the left-hand side, this equation is identical to its isothermal counterpart, Eq. [47]. Although the activation energies of the factors g and f are large, the ratio g/f is only slightly temperature dependent because the activation energies of D_M and D_{ox} are comparable and the temperature dependencies of g and f approximately cancel. Consequently, the approximation $g/f = 1$ in Eq. [58] is acceptable, from which there follows

$$k = k_{ox_0}$$

where k_{ox_0} is the parabolic scaling constant at T_0 .

The temperature function $\theta(t)$ is determined by solution of Eq. [32], wherein the heat source Q is the sum of the gas-oxide and oxide-metal components given by Eq. [15] and [16], respectively. These in turn depend upon the corrosion kinetics through the quantities dN_T/dt and dL_{ox}/dt . The rate of weight gain is equal to the flux of oxygen across the oxide layer

$$\frac{dN_T}{dt} = \frac{D_{ox}(C_d - C_c)}{L_{ox}} = \frac{[D_{ox}(C_d - C_c)]_0 g}{2k_{ox_0}} \frac{1}{\sqrt{u}} = k_{T_0} \frac{g}{\sqrt{u}} \quad [59]$$

Similarly, Eq. [56] yields

$$v = \frac{dL_{ox}}{dt} = \frac{k_{ox_0} f}{\sqrt{u}} \quad [60]$$

The heat source in Eq. [32] is obtained as follows. The term Q is the sum of the components given by Eq. [15] and [16]. The ratio $\Delta L_{ox}/\Delta N_T$ in the latter is obtained from Eq. [59] and [60] as $k_{ox_0} f/k_{T_0} g$. When this value of Q is multiplied by the oxygen flux J given by Eq. [59], the result is

$$QJ = 10.1 \frac{g}{\sqrt{u}} - 0.5 \frac{f}{\sqrt{u}}, \text{ W/cm}^2 \quad [61]$$

The solution is accomplished by iteration. An initial guess of $\theta(t)$ is obtained, either from the no coupling solution described in the "Temperature Distribution" section or from the approximate coupling method of the "Coupling" section. This guess determines the first estimate of the time-dependent functions f and g from Eq. [50] and [52]. The new time variable u is computed from Eq. [53] and Eq. [61], then provides the oxidation heat source for the next iteration. The new temperature function is obtained by solving Eq. [32], with QJ given by Eq. [61], and the iteration process continues until the solution has converged. The growth of the oxide scale as a function of time is calculated from Eq. [57].

Results and Discussion

Figures 4 and 5 show the results of the thermal and corrosion kinetic analyses for a 1 mm thick slab of Zircaloy oxidized on both sides by steam at 1300°C.

Figure 4 shows the temperature transient calculated by the three methods described in previous sections: no coupling of heat and chemical reaction, approximate coupling by application of Arrhenius-type temperature dependences to the parabolic scaling constants, and the accurate coupling method, wherein temperature influences the basic thermodynamic and transport properties of the reacting solid. The results in Fig. 4 and 5 show that the approximate method of coupling produces poorer predictions than ignoring coupling entirely. The curves labeled "accurate coupling" were obtained by iteration starting either from the no coupling or approximate coupling initial guesses.

A substantial temperature perturbation occurs at the start of the oxidation process when the rates of oxygen

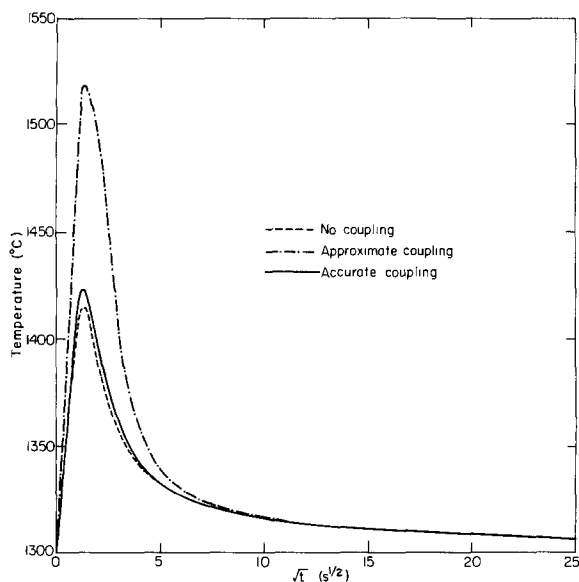


Fig. 4. Temperature perturbation due to inability to rapidly remove reaction heat during oxidation of Zircaloy at 1300°C. Heat removal parameter $C_2 = hT_0 = 100 \text{ W/cm}^2$. Specimen heat capacity parameter $C_1 = \rho_M C_{pM} L_{M_0} T_0 = 194 \text{ J/cm}^2$. Three methods of calculating the temperature transient are represented.

uptake by the solid is highest, but the temperature eventually approaches the ambient value because the thick oxide scale considerably reduces the rate of corrosion and hence the strength of the heat source inside or on the surface of the specimen. Figure 5 shows that correct simultaneous solution of the heat- and mass-transport equations in the solid predicts a scale thickness which is $\sim 7 \mu\text{m}$ larger than that given by the theory of isothermal scaling. The approximate coupling analysis overestimates the extent of oxygen absorption.

The results are sensitive to the heat removal rates from the specimen. This factor is contained in the external heat-transfer parameter hT_0 , which was chosen as 100 W/cm^2 for preparing the curves of Fig. 4 and 5. When more effective heat-transfer to the surroundings is simulated by increasing hT_0 to 150 W/cm^2 , the peak temperatures shown in Fig. 4 are reduced by 50°C and the oxide layer thicknesses are several percent less than those shown by the solid curve in Fig. 5.

Although radiation cooling provides a lower limit to the heat-transfer coefficient in the case of a single tubular specimen in a laboratory test, comparable minimum heat removal capability is not assured in a bundle of tubes as in a nuclear reactor fuel assembly. Because each cladding tube is surrounded by other tubes which are undergoing comparable oxidation, radiant interchange between one tube and its environment is drastically reduced. Only con-

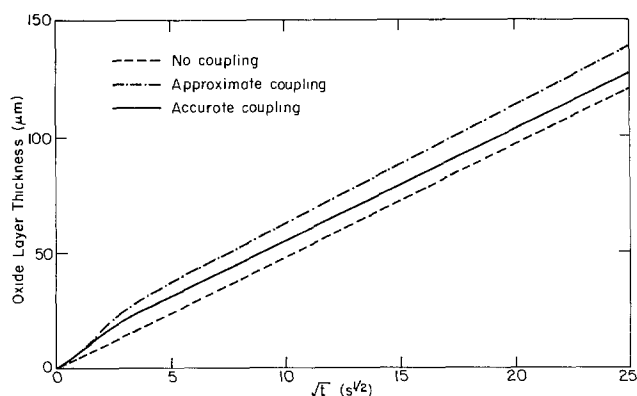


Fig. 5. Oxide scale growth during reaction in the temperature transient displayed in Fig. 4. The results of three methods of coupling the heat- and mass-transport processes are shown.

vective heat-transfer to the flowing steam remains as a mechanism of removing the heat oxidation. In this case, the heat removal parameter hT_0 could be considerably smaller than the value of 100 W/cm^2 used in the sample calculations presented here and the temperature spike larger than that shown in Fig. 4.

The temperature excursion shown in Fig. 4 is qualitatively very similar to that observed by Hagen (17) in a fuel rod simulation test. In this configuration, heat was supplied from a central tungsten rod inside an annular fuel stack clad in Zircaloy. A Zircaloy shroud was placed around the specimen to simulate the presence of surrounding fuel pins. Initially, argon flowed in the annular gap between rod and shroud. Upon adding steam to the argon flow, the Zircaloy temperatures rose from the steady pretest value of 1700° to 2200°C and returned to less than 1700°C in less than 1 min. The time scale of the transient was thus very close to that shown in Fig. 4, in which the comparable duration is $\sim 1/2$ min. However, the amplitude of the experimental transient (500°C) was much larger than the one represented in Fig. 4 (125°C). Moreover, in Hagen's experiment, the surface temperature following the transient was lower than it was prior to addition of steam.

The reason for the latter observation is the dominance of convection rather than radiation cooling in Hagen's test; radiative heat transfer was effectively reduced by the surrounding shroud, which reacted in much the same way as the cladding and thus did not provide a radiation heat sink. Addition of steam to the argon flow sufficiently increased the convective heat-transfer coefficient to give temperatures lower than prereaction values when the Zircaloy had become oxidized to an extent that heat release by residual corrosion was small.

The larger amplitude of the temperature transient reported by Hagen compared to the one analyzed in this work is probably due to the higher initial temperature in the former. Since the scaling constants are thermally activated, the magnitude of the transient should be greater at higher temperatures. Moreover, the calculations were based on rate constants appropriate to a tetragonal zirconia scale, while the experimental temperatures probably resulted in a cubic zirconia layer and, at least during part of the excursion, in liquid zirconium.

Conclusions

1. The energy released during oxidation of Zircaloy by steam appears as planar sources of heat at the gas-oxide and oxide-metal interfaces. The sum of the heat releases at these two locations is approximately 3% larger than the integral heat of reaction of water vapor with Zircaloy to produce hydrogen gas and zirconium dioxide. The portion released at the gas-oxide interface is equal to the part molar enthalpy of oxygen solution in ZrO_2 less the heat of formation of water, and is always exothermic. The principal difficulty in accurately assessing the partitioning of the heat release between the two interfaces is lack of reliable information on the partial molar enthalpy of solution of oxygen in ZrO_2 .

2. The thermal response of the oxidizing metal to the heat released by the reaction is practically independent of the details of the location of the heat sources inside the specimen. Despite the low thermal conductivity of the ZrO_2 scale, spatial variations of temperature in the oxide and the metal phases are negligible. The temperature of the specimen as a function of time is determined by a lumped-capacity heat balance, which divides the reaction enthalpy into heat removal by external cooling or increase in specimen temperature.

3. The method of coupling the heat-transfer problem with scale formation kinetics is critical to accurate modeling. The conventional technique of assuming Arrhenius temperature dependences of the parabolic scaling constants (which were determined by isothermal experiments at different temperatures) is in principle incorrect and in practice inaccurate. Linkage of heat and mass transfer must be performed by according the appropriate

temperature dependences to the basic properties which enter the conservation laws: namely, the equilibrium interface concentrations and the oxygen diffusion coefficients. An analytical solution based on the near equality of the activation energies of oxygen diffusion in the oxide and in the metal is proposed.

Acknowledgment

This work was supported by the Director, Office of Energy Research, Office of Basic Energy Sciences, Materials Sciences Division of the U.S. Department of Energy under Contract no. DE-AC03-76SF0009.

Manuscript submitted ca. Oct. 15, 1983; revised manuscript received Feb. 21, 1984.

The University of California assisted in meeting the publication costs of this article.

REFERENCES

- O. Kubaschewski and C. B. Alcock, "Metallurgical Thermochemistry," 5th ed., p. 362, Pergamon Press, New York (1979).
- K. L. Komarek and M. Silver, in "Proceedings of the Symposium on Thermodynamics of Nuclear Materials," p. 749, IAEA, Vienna (1962).
- S. Aronson, *This Journal*, **108**, 312 (1961).
- G. N. Lewis, M. Randall, K. S. Pitzer, and L. Brewer, "Thermodynamics," 2nd ed., Chap. 27, McGraw-Hill, New York (1961).
- R. C. Garvie, in "High Temperature Oxides, Part II," A. M. Alper, Editor, Academic Press (1970).
- J. F. Wadier, "Phase Diagram and Thermodynamic Properties of the Uranium-Neodymium-Oxygen System," Commissariat a l'Energie Atomique Tech. Rept. CEA-R-4507 (1973).
- D. R. Olander, "Fundamental Aspects of Nuclear Reactor Fuel Elements," p. 153, National Technical Information Service (1976).
- R. E. Pawel and J. J. Campbell, ASTM-STP 754, p. 370 (1982).
- R. E. Pawel, J. V. Cathcart, and R. A. McKee, *This Journal*, **126**, 1105 (1979).
- D. Cubiociotti, *ibid.*, **130**, 729 (1983).
- D. R. Olander, "The Distribution in Space and Time of the Heat of Reaction during Oxidation of Zircaloy and its Effect on Corrosion Kinetics," LBL-15465, University of California, Berkeley, CA (1982).
- E. R. G. Eckert and R. M. Drake, "Heat and Mass Transfer," 2nd ed., p. 48, McGraw-Hill, New York (1959).
- C. Allison, Personal communication (1983).
- V. Denny, Personal communication (1983).
- A. J. Markworth, *Metal. Trans. A*, **8**, 2014 (1977).
- R. E. Pawel, *This Journal*, **126**, 1111 (1979).
- S. Hagen, in "Proceedings of the Sixth International Conference on Zirconium in the Nuclear Industry," Vancouver, ASTM, Philadelphia (1982).
- V. F. Urbanic, in "Zirconium in the Nuclear Industry," A. L. Lowe, Jr. and G. W. Parry, Editors, pp. 168-181, ASTM STP 633, American Society for Testing and Materials, Philadelphia (1977).

Electrotransport and Diffusivity of Molybdenum, Rhenium, Tungsten, and Zirconium in β -Thorium

F. A. Schmidt, M. S. Beck, D. K. Rehbein, R. J. Conzemius, and O. N. Carlson

Ames Laboratory, USDOE, Iowa State University, Ames, Iowa 50011

ABSTRACT

The electric mobilities, diffusivities, and effective valences were determined for molybdenum, rhenium, tungsten, and zirconium in β -thorium. All four solutes migrated in the same direction as the electron flow. Rhenium and molybdenum were found to be very mobile, with tungsten somewhat slower. Zirconium was found to move at a rate near that of the self-diffusion of β -thorium, *viz.*, about 10^{-11} m²/s at 1500°C. The electromigration velocities showed a similar trend. A comparison was made between experimental data obtained by scanning laser mass spectrometry and theoretical transport equations for two purification experiments. Good agreement was obtained with both the concentration profile predicted by DeGroot and the purification ratio predicted by Verhoeven.

One of the most effective methods of purifying refractory metals of undesirable solutes is by electrotransport at high temperatures. In this process, a constant voltage is applied across the metal sample which yields an internal electric field and a constant current, which heats the sample. The solutes are stimulated by the charge carriers to move toward one of the ends of the sample, thereby leaving a major portion of the sample virtually free of impurities.

The migration of solutes in solid metals under the influence of a direct current has been known since 1928, when Coehn and Specht (1) observed hydrogen transport in palladium. Many of the earlier investigators of electrotransport of interstitial solutes interpreted the direction and velocity of migration on the basis of a charge on the solute particle. In 1953, Seith and Wever (2) showed this interpretation to be incomplete to the extent that one cannot separate the contributions to the force moving the solute which arise from the charge on the solute in an electric field and the momentum transfer from the scattering of electrons or holes. Reviews by Heuman (3), Verhoeven (4), Huntington (5), and Pratt and Sellors (6) consider both the electrostatic force and the force resulting from moving electrons being scattered by the solute. The potential for applying electrotransport to the ultrapurification of

metals has been described by Verhoeven (7) and Peterson (8).

The purpose of this investigation is to continue our study of the electrotransport behavior of metallic solutes in refractory metals. In our previous work concerning the electrotransport purification of thorium (9), we found that not only the interstitial solutes carbon, nitrogen, and oxygen migrated in thorium when under the influence of the electric field but that several nonvolatile metallic solutes also moved. In our present work, we determined the electrotransport parameters of molybdenum, rhenium, tungsten, and zirconium since these metals are common impurities in thorium and are very difficult to remove by volatilization due to their low vapor pressures. The development of the scanning laser mass spectrometric (SLMS) technique (10) as a quantitative method of determining the concentration profile of a sample containing these solutes enables us to compare our experimental data with the concentration profile predicted from equations developed by DeGroot (11) and by Verhoeven (7).

Conceptual Approach

Determination of electrotransport parameters.—A current theoretical model of the electrotransport process as developed by Verhoeven (7) considers a force to be ex-

erted on the diffusing species by the applied electric field. This force contributes to the diffusing flux J such that

$$J = -D \frac{dc}{dx} \pm UEc \quad [1]$$

where D is the diffusion coefficient, dc/dx is the gradient of the concentration c with respect to distance, x , U is the electromigration mobility, and E is the applied electric field. The product UE is a velocity imparted to the diffusing species by the field E . The divergence of the total atom flux gives rise to the time rate of change of the concentration in the form of Fick's second law of diffusion, viz.

$$\frac{\partial c}{\partial t} = -\frac{\partial J}{\partial x} = D \frac{\partial^2 c}{\partial x^2} \pm UE \frac{\partial c}{\partial x} \quad [2]$$

This relation assumes D is independent of concentration and position, i.e., allowing no thermal gradients as D is a strong function of temperature. Equation [2] also assumes U and E are independent of position.

For short-time experiments using a sample with a step in the central portion of the concentration profile, the diffusion is confined to the central portion of the sample. A simple solution of Eq. [2] for these experiments can be expressed in terms of the error function

$$c(x,t) = c_1 + \frac{c_2 - c_1}{2} \left[1 + \operatorname{erf} \left(\frac{x \pm UEt}{\sqrt{4Dt}} \right) \right] \quad [3]$$

where x is measured from the initial position of the step, c_1 and c_2 are the initial solute atom concentrations below and above the step, respectively, and

$$\operatorname{erf}(z) = \frac{2}{\sqrt{\pi}} \int_0^z e^{-s^2} ds \quad [4]$$

By rewriting Eq. [3] in the form

$$\left[2 \left(\frac{c(x,t) - c_1}{c_2 - c_1} \right) - 1 \right] = \operatorname{erf} \left(\frac{x \pm UEt}{\sqrt{4Dt}} \right) \quad [5]$$

the inverse error function can be expressed as

$$\operatorname{erf}^{-1} \left[2 \left(\frac{c(x,t) - c_1}{c_2 - c_1} \right) - 1 \right] = \frac{x \pm UEt}{\sqrt{4Dt}} \quad [6]$$

In the diffusion zone, Eq. [6] is a function linear in x with slope $1/\sqrt{4Dt}$ from which the diffusion coefficient can be obtained. If the origin is located at the initial position of the step, the point x at which $c(x) = (c_2 + c_1)/2$ may be used to determine the electromigration mobility according to $\Delta x = UEt$. This displacement is illustrated schematically in Fig. 1. Thus, by interpreting the solute atom concentration profile in terms of Eq. [3], values of the parameters D and U can readily be obtained.

An effective valence for the migrating solute may be obtained from the relation

$$Z^* = \frac{UkT}{De} = \frac{\Delta x kT}{EtDe} \quad [7]$$

where k is Boltzmann's constant, e the unit electric charge, and T the absolute temperature. Z^* is a measure of the interaction strength between the electromigrating species and the applied electric field.

The diffusion coefficient, D , is usually considered to have a temperature dependence of the form

$$D = D_0 \exp \left(-\frac{Q}{kT} \right) \quad [8]$$

where D_0 is a constant and Q is the activation energy for the diffusion process. By performing the electrotransport experiments at several different temperatures, the parameters in Eq. [8] can be determined.

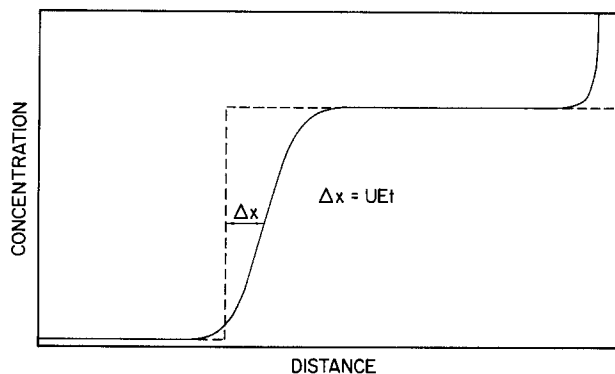


Fig. 1. Schematic illustration of the solute concentration profile before (dashed line) and after (solid line) electrotransport showing resulting displacement, Δx .

Purification of metals by electrotransport processing.—The purification of metals by electrotransport as described by Verhoeven (4), for the case of a metal having an initial impurity concentration of C_0 , requires continuing the electrotransport operation until near steady state is achieved. In terms of the above model, this requires solving Eq. [2] as a boundary-value problem; the boundary conditions being that no flux enters the sample through the ends or from the environment. Verhoeven obtained this solution and expressed it in terms of the mean concentration in the purified half of the rod, $C_m(t)$. Normalized to the original concentration of the rod C_0 , this solution is of the form

$$\frac{C_m(t)}{C_0} = 2 \left[\frac{1 - e^{-S/2}}{1 - e^{-S}} - \sum_{n=1}^{\infty} C_n e^{-S/4} \sin \left(\frac{n\pi}{2} \right) e^{-\lambda_n t} \right] \quad [9]$$

where

$$C_n = \frac{32n\pi S [1 - (-1)^n e^{S/2}]}{(S^2 + 4n^2\pi^2)^2}$$

$$\lambda_n = \left(n^2\pi^2 + \frac{S^2}{4} \right) \frac{D}{l^2}$$

$$S = -\frac{U}{D} El$$

and l is the length of the sample. This equation should hold, assuming that U , D , and the electric field, E , are independent of position along the sample and that there is no external source of contamination.

An earlier solution of Eq. [2] as derived by DeGroot (11) for the same boundary conditions and assumptions has the form

$$\frac{C(x,t)}{C_0} = \frac{Se^{-Sx}}{1 - e^{-S}} + \sum_{n=1}^{\infty} C_n e^{-Sx/2} \left(\sin n\pi X - \frac{2n\pi}{S} \cos n\pi X \right) e^{-\lambda_n t} \quad [10]$$

where

$$C_n = \frac{16\pi n S^2 [1 - (-1)^n e^{S/2}]}{(S^2 + 4n^2\pi^2)^2}$$

$$S = \frac{U}{D} El$$

$$X = x/l$$

$$\lambda_n = \left(n^2\pi^2 + \frac{S^2}{4} \right) \frac{D}{l^2}$$

DeGroot's solution expresses the ratio of the solute concentration $C(x,t)$ to the initial concentration C_0 , at any point x , where $x = 0$ at the end of the sample to be puri-

fied, and at any time t . Solution of DeGroot's equation will, therefore, allow the calculation of the entire solute concentration profile at any time up to and including steady state.

Experimental

The experimental method used in this investigation to measure the transport properties of molybdenum, rhenium, tungsten, and zirconium in β -thorium was similar to that described by Peterson *et al.* (9). In this work, rods having a sharp concentration gradient of the solute were joule heated with a dc current under vacuum for various times at various temperatures. The displacement of the center of this diffusion couple from the original weld interface was used to measure the electrotransport mobility of a solute in a metal. The net effect of the electric field is a displacement Δx of the concentration profile by an amount, $\Delta x = UEt$, where U is the mobility, E the electric field, and t the time. Times were chosen at each temperature to give a reasonable smoothing by diffusion of the step-like concentration profile and a measurable displacement of the mean concentration from the weld interface. Pressures $< 2.6 \times 10^{-5}$ Pa were generally achieved during each experiment.

The diffusion coefficient, D , was calculated from the concentration profiles by the Grube method (12), taking the midpoint at a distance Δx from the weld interface. The values were obtained using the inverse error function, and a least squares analysis was used to estimate the slope from which a value of D was obtained. The effective valence, Z^* , was calculated from the mobility and diffusion coefficient using Eq. [7].

Materials.—The high purity thorium used in this work was prepared by the magnesium intermediate alloy process developed by Peterson *et al.* (13). This material had been triple electron-beam melted and contained less than 230 weight parts per million (wt ppm) total impurity. The major impurities were carbon 50 wt ppm, nitrogen 45 wt ppm, oxygen 25 wt ppm, and less than 100 wt ppm of total metallic impurities.

The molybdenum, rhenium, tungsten, and zirconium used as alloy additions were cut from electron-beam-melted ingots of the respective metals and were obtained from commercial sources. These metals were of 99.95 weight percent (w/o) or greater purity. The tantalum metal used as adapters for the thorium samples was of 99.95 w/o purity. It was also electron-beam melted for further purification before it was fabricated into the desired parts.

Sample preparation.—The binary alloys were made by separately arc melting nominal amounts of the high purity solute material with 50g of the high purity thorium metal. The nominal alloy concentrations were typically 80-90 wt ppm, low enough to be in solid solution, yet high enough to be detected by mass spectrometric analysis. The arc-cast alloys were fabricated by rolling and subsequent swaging into rods of 0.00254m diam.

The specimens used in the electrotransport mobility measurements were rods 0.066m long and of 0.0025m diam. One third of the rod consisted of pure thorium, and the remainder consisted of the thorium containing solute additions of molybdenum, rhenium, tungsten, or zirconium. Prior to butt welding these segments together in an inert atmosphere, they were surface cleaned by electropolishing in a chilled methanol-perchloric acid bath (14). The composite sample thus contained a sharp step in the solute concentration profile at the weld interface similar to that shown in Fig. 1.

Apparatus.—The apparatus used to contain the electrotransport specimens during processing consists of a stainless steel sample chamber equipped with two electrodes, a sight glass for viewing the sample and to optically monitor its temperature, and a vacuum system capable of obtaining a pressure of $< 10^{-5}$ Pa. The composite thorium specimen was threaded onto high purity tantalum U-shaped adapters and inserted between the two elec-

trodes; the pure thorium end of the specimen being connected to the cathode of the power supply. A regulated direct current power supply with voltage and current mode control was used to joule heat the sample to the desired temperature. The temperature of the sample was measured with an optical pyrometer and the observed temperature was corrected according to the equation

$$\text{True temp} = 1.167 (\text{observed temp}) - 97.23 \quad [11]$$

This equation was obtained from data of a separate experiment in which several observed surface temperatures were compared to temperatures of adjacent black-body holes in the electropolished thorium specimen. An additional 15° - 25° C was added to compensate for loss due to absorption by the viewing window. The viewing window correction was determined after each experiment using a tungsten lamp. The temperature at any point along the specimen was constant to within 10° C during an experiment. The center of the sample was about 25° C hotter than the ends because the tantalum adapters were somewhat cooler than the specimen.

Analysis.—After the specimens were heated for a specific time and temperature, their concentration profiles were obtained using a scanning laser mass spectrometric technique (15). The rod specimens were ground flat on two sides and electropolished to provide a flat longitudinal surface along which to measure the concentration profile. The mass spectrographic technique utilizes a vacuum system in which a pulsed laser beam is rastered across the sample while making a continuous scan longitudinally along the sample. The scanning laser beam vaporizes and ionizes a small amount of the specimen, and these ions are collected and sorted by the mass spectrometer, permitting the intensity of a single ion to be monitored. These solute atom ion signals are normalized to the total ion beam signal by taking the ratio of this solute atom ion current to the ion beam current from the thorium ions ($^{232}\text{Th}^{+}$). Since the number of thorium ions remains essentially constant along the sample, the ratio gives a relative intensity of the solute atoms present. By selecting an ion of a solute atom and plotting its relative intensity while the laser longitudinally scans the sample, an intensity profile proportional to the solute atom concentration is obtained as a function of distance along the sample. The isotopes monitored during the individual mass spectroscopic concentration profile measurements were ^{99}Mo , ^{187}Re , ^{184}W , and ^{90}Zr . During the scan, the laser is extinguished periodically, leaving blank spaces on the sample and on the intensity graph. These spaces are used for a precise spatial correlation between the graph and the sample. This correlation is necessary to locate the position of the initial weld interface on the intensity profile from which the distance of electromigration, Δx , is measured. The measurement of the distance of these spaces

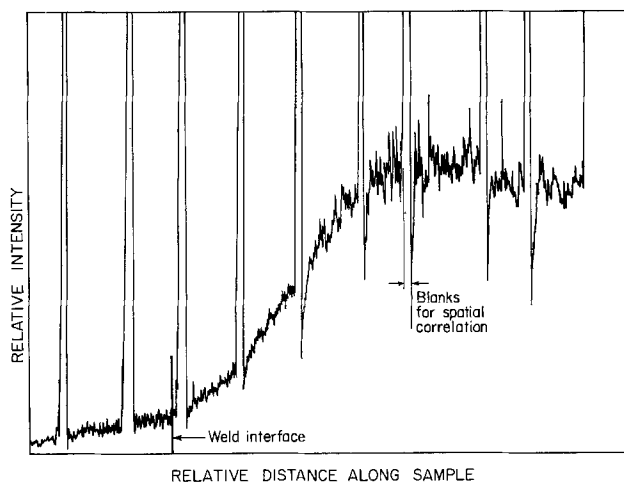


Fig. 2. A ^{99}Mo intensity graph showing the solute atom concentration profile in thorium following electrotransport for 3h at 1530°C .

Table I. Electrotransport mobilities, diffusion coefficients, and effective valences for molybdenum, rhenium, tungsten, and zirconium in β -thorium

Solute	Temp (°C)	$\Delta x \times 10^2$ (m)	t (h)	$E \times 10^2$ (V/m)	$U \times 10^9$ (m ² /V s)	$D \times 10^{10}$ (m ² /s)	Z^*
Molybdenum	1600	0.63	2	0.181	47.7	13.8	-5.6
	1530	0.70	3	0.163	39.8	9.83	-6.3
	1465	0.54	4	0.148	25.4	4.81	-7.9
	1425	1.25	15.5	0.138	16.2	3.53	-6.7
Rhenium	1670	0.78	2	0.196	55.4	20.2	-4.6
	1520	0.76	3	0.152	46.1	18.5	-3.8
	1465	0.59	3	0.150	36.6	11.3	-4.8
	1390	0.45	3	0.134	30.9	8.64	-5.1
Tungsten	1545	0.45	5.5	0.166	13.8	2.97	-7.3
	1500	0.62	11	0.153	10.2	1.73	-9.0
	1460	0.50	11	0.149	8.82	1.78	-7.4
	1410	0.41	12	0.133	7.16	1.17	-8.9
Zirconium	1600	0.30	104	0.184	0.428	0.356	-1.9
	1500	0.13	125	0.160	0.174	0.089	-3.0

from the weld interface was accomplished using a precision microscope equipped with a vernier eyepiece. Figure 2 shows a composition profile in which the relative solute intensity is plotted as a function of the relative distance for the ⁹⁹Mo³⁺ ion in a composite thorium/thorium-molybdenum sample which was run for 3h at 1530°C. The position of the weld interface is shown and the shift of the solute concentration from its initial step-shape can be seen.

Analysis of the solute atom concentration profile graphs was performed statistically, data points having been taken off the intensity graphs as functions of arbitrarily scaled abscissas. From the corresponding blanks on each sample and graph, a scale factor was determined to correlate the graph abscissa with the sample. From each graph, upper and lower concentration levels were determined for c_2 and c_1 , respectively, and the data were normalized and transformed as in Eq. [6]. A linear least squares analysis was used to calculate values of the slope and of the intercept of the straight line with the abscissa. Values of D and U were then calculated.

In order to test the purification equations, Eq. [9] and [10], composite samples were prepared consisting of a 0.025m length of the pure thorium and a 0.137m length of thorium containing 100 wt ppm molybdenum. These samples were then heated with a direct current for 30h at a pressure of about 1×10^{-6} Pa. The center of each of the samples was maintained at a temperature of about 1500°C. After several hours of heating considerable sagging in the center section was observed. A 0.015m long section on either end of the sample was too cool to creep and deform under the pull of gravity, and remained straight. The use of the pure thorium section at the cathode end eliminated any effect of a temperature gradient. After each experiment, the entire rod was cut into sections and analyzed with the mass spectrometer to obtain the complete profile of the sample.

Results and Discussion

The electrotransport parameters for thorium composite samples consisting of a dilute binary alloy of molybdenum, rhenium, tungsten, or zirconium and a segment of pure thorium were determined between 1390° and 1670°C, as shown in Table I. All four solutes move toward the anode, *i.e.*, in the direction of the electron flow during electrotransport. The electrotransport parameters follow a regular variation with temperature except for the effective valence, Z^* , which shows considerable scatter. Verhoeven (7) has stated that Eq. [7] for the calculation of Z^* should include the correlation factor, f , for movement by a substitutional solute-vacancy mechanism. Since the mechanism of diffusion for molybdenum and rhenium and possibly tungsten is uncertain, however, the correlation factor was not included in any of the calculations.

From the data in Table I, it is seen that molybdenum and rhenium exhibit considerably higher electric mobilities and diffusivities than either tungsten or zirconium at all temperatures studied. These values for molybdenum and rhenium are about two orders of magnitude greater

than those for zirconium at comparable temperatures with tungsten lying somewhere between. This can be seen from Fig. 3, which is an Arrhenius-type plot of $\ln V/j$ vs. $1/T$ for the four solutes, where V is the migration velocity in cm/s and j is the current density. Huntington and Grone (16) used a similar plot to obtain a "pseudo-activation" energy of electrotransport, Q_E . They found that this value for gold was about 20% lower than the activation energy for self-diffusion for the same metal. Values of Q_E were obtained for each of the solutes from least squares best-fit straight lines. These values are listed in Table II.

Figure 4 shows similar Arrhenius-type plots of the diffusion coefficients vs. reciprocal temperature for the four solutes. The slope of the least squares best-fit straight line in Fig. 4 is the activation energy, Q_D , in Eq. [8], and the intercept gives the pre-exponential, D_0 . These values are also given for each of the solute atoms in Table II. The activation energies for electrotransport and diffusion, Q_E and Q_D , respectively, shown in Table II exhibit differences of from 18% for rhenium to 33% for zirconium, with Q_E in every instance being smaller than Q_D . Similar differences have been reported in Q_E and Q_D for self-transport of aluminum and silver (17) and for vanadium, niobium, and tantalum solutes in β -thorium (18).

Generally, these solute atoms could be considered to be substitutional impurities in thorium. Their diffusive movement would thus be determined by a vacancy mechanism similar to self-diffusion. The variability in both the electric mobility and diffusion rates, however, indicates the possibility of some other transport mechanism as the faster moving solutes have electric mobilities and diffusivities in the range of those observed for interstitial solutes in thorium. The atom sizes, for instance, appear to have some significance. Upon considering the atomic radii of these solute atoms, rhenium is the smallest of the four, followed by molybdenum, tungsten, and zirconium. The electric mobilities and diffusivities of these atoms in β -thorium show decreasing magnitudes in the same order. Thus, one might conclude that there is a simple size dependence for solute atom migration in β -thorium. Consideration of the behavior of other solute atoms, however, shows that this is not a completely reliable indicator of the magnitude of the mobility or diffusivity.

The results obtained in this investigation compare favorably with the diffusivities obtained for vanadium, niobium, and tantalum (20) and iron, cobalt, and nickel (18) in β -thorium, as can be seen from Fig. 5. Earlier studies (18) have shown that iron, cobalt, and nickel are fast dif-

Table II. Electrotransport and diffusion parameters for molybdenum, rhenium, tungsten, and zirconium in thorium

Solute	Q_E (kJ/mol)	Q_D (kJ/mol)	D_0 (m ² /s)
Molybdenum	173	216	1.51×10^{-3}
Rhenium	66	84	4.04×10^{-7}
Tungsten	131	160	1.03×10^{-5}
Zirconium	257	384	1.73

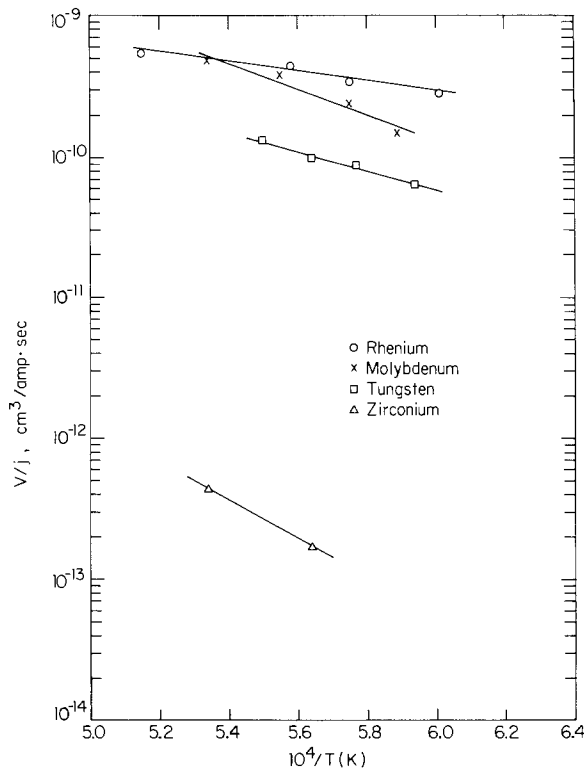


Fig. 3. Arrhenius-type plot of $\ln V/i$ vs. reciprocal temperature for rhenium, molybdenum, tungsten, and zirconium in β -thorium.

fusing solutes in α - and β -thorium. The diffusivity of cobalt is similar in magnitude to that of rhenium ($D > 10^{-9}$ m²/s, $T > 1400^\circ\text{C}$), with iron and nickel being slightly higher. Molybdenum exhibits diffusivities equal to or greater than rhenium at temperatures above about 1600°C , as is seen from Fig. 5. Its atomic radius is about the same as that of rhenium. Both rhenium and molybdenum, however, have atomic radii considerably larger than iron, cobalt, or nickel, the latter three atoms being very similar in size.

Vanadium is anomalous since it has an atomic radius smaller than molybdenum and rhenium but diffuses slower than either. Tungsten, niobium, tantalum, and zirconium all diffuse at rates slower than vanadium; their magnitudes decreasing in the order listed and their

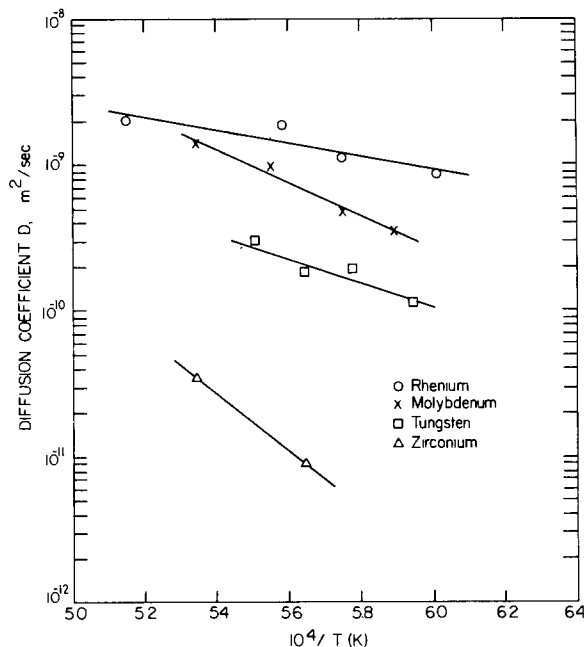


Fig. 4. Arrhenius-type plots for diffusivity of rhenium, molybdenum, tungsten, and zirconium in β -thorium.

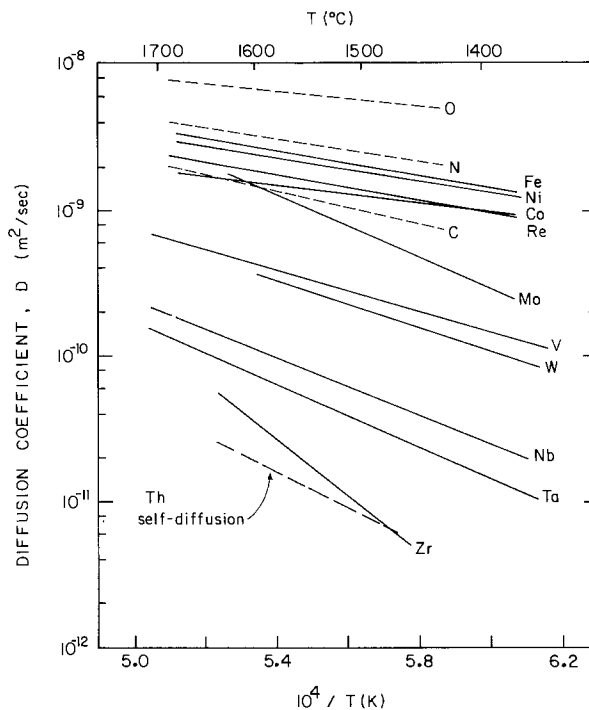


Fig. 5. Arrhenius-type plot for diffusivity of oxygen, nitrogen, carbon (20), iron, cobalt, nickel, niobium, tantalum, vanadium, rhenium, molybdenum, tungsten, and zirconium in β -thorium.

atomic radii increasing in the same order. The diffusivity of zirconium is of the same order as that for self-diffusion in β -thorium, *i.e.*, about 10^{-11} m²/s at 1500°C (21). Thus, those solutes in Fig. 5 that diffuse slower than tungsten appear to follow a size-dependent behavior. The fast diffusing solutes in β -thorium, namely, iron, cobalt, nickel, and rhenium, exhibit a more complicated diffusivity behavior.

Two purification runs were made using molybdenum as the solute. Molybdenum was chosen since it has a relatively high solubility and mobility in thorium at the temperatures of interest. It was also important that the experiments be performed in a molybdenum-free system to eliminate any possibility of external contamination. In order to obtain a valid test of the theoretical transport equations, it was necessary to perform the purification runs at a temperature and for a length of time such that the solute concentration would be above the detection limit (1 wt ppm) of the SLMS apparatus in at least 75% of the rod. A temperature of 1500°C was chosen. According to previous results at this temperature, the diffusivity, D , equals 6.8×10^{-10} m²/s, and the electromigration velocity, V , equals 0.002 m/h. By the solution of Eq. [9] using these values and a sample length, l , equal to 0.137m, a purification ratio, C_m/C_o , equal to 0.15 was calculated for a time of 30h at 1500°C . Since $C_o = 100$ wt ppm, this ratio predicts an average concentration of 15 wt ppm in the purer half of the rod.

The experimental molybdenum concentration as a function of distance after purification at 1500°C is shown in Fig. 6. Also shown for comparison are two theoretical concentration profiles calculated from Eq. [10] for 30h at 1465°C and 1500°C . As can be seen from Fig. 6, the best agreement was obtained between the experimental curve and the theoretical curve calculated at 1465°C . This difference may in part be due to uncertainties in the experimental temperature. From this plot, a C_m value of 28 wt ppm was obtained for the experiment, which is in reasonably good agreement with the predicted value of 15 wt ppm. There is a significant deviation between theory and experiment, however, in the high concentration end of the rod. A second purification experiment was made as a check on the data from the first run. The data from the two experiments agreed within a few percent throughout

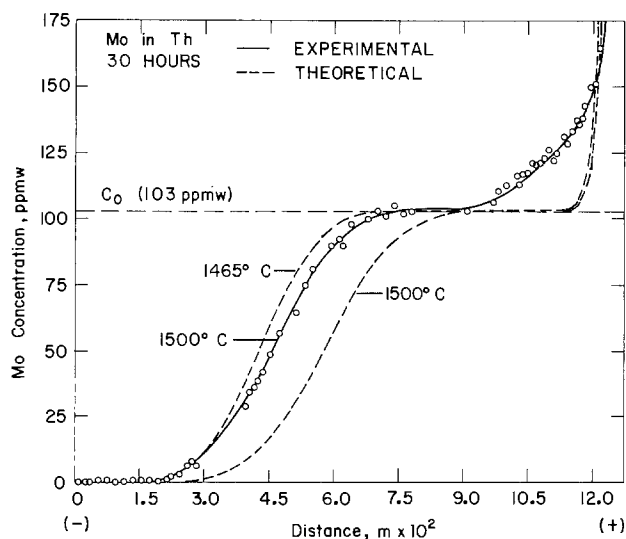


Fig. 6. Comparison of experimental and theoretical molybdenum concentration in thorium rod as a function of distance after heating for 30h.

the length of the two samples, with both experiments showing the same deviation from the theoretical prediction.

Summary

The electric mobilities, diffusivities, and effective valences of the metallic solutes, molybdenum, rhenium, tungsten, and zirconium in β -thorium were determined. All four solutes migrate in the same direction as the electron flow. Rhenium and molybdenum exhibit high electric mobilities in thorium, whereas zirconium was found to be extremely slow, with tungsten lying somewhere between. The "pseudo-activation" energy for electrotransport, Q_e , of rhenium in β -thorium is quite low at 66 kJ/mol, with molybdenum and tungsten having energies of 173 and 131 kJ/mol, respectively, and zirconium having a high activation energy of electrotransport of 257 kJ/mol.

The diffusion parameters, Q_D and D_0 , for the four solutes in β -thorium were also determined. The diffusivities range from those of fast diffusing solutes to those observed for vacancy-controlled diffusion, *i.e.*, from rhenium with $D(1500^\circ\text{C}) \sim 2 \times 10^{-9} \text{ m}^2/\text{s}$ to zirconium with $D(1500^\circ\text{C}) \sim 9 \times 10^{-12} \text{ m}^2/\text{s}$. The values obtained for Q_e are considerably lower than those observed for Q_D , with the differences ranging from only 18% for rhenium to 33% for zirconium. The magnitude of the diffusion constants, D_0 , for rhenium, molybdenum, and tungsten are reasonable for metallic solutes, but that for zirconium is excessively large. However, it is based on only two points and could have a large error. The observed electrotransport behavior of the slower diffusing solutes in β -thorium, tungsten, and zirconium, is consistent with our previous conclusion that a correlation exists between the electric mobility or diffusivity and the relative atomic sizes of the solute and host metals. For the faster diffusing solutes, this correlation is not apparent, and a more complicated relationship must exist.

Two purification-type experiments were performed to provide data for comparison with theoretical predictions. Good agreement between theory and experiment was

found for the purified portion of the rods, but a significant deviation from theory was noted in the high concentration end.

Acknowledgment

The authors gratefully acknowledge Dr. W. A. Oran of the National Aeronautics and Space Administration for his interest in and support of this work. We also appreciate the efforts of Dr. R. J. Naumann, Mr. J. R. Williams, and Mr. W. Moore of the George C. Marshall Space Flight Center for their suggestions and excellent cooperation. We acknowledge Dr. D. T. Peterson of the Ames Laboratory for his consultations and Mr. M. E. Thompson for helping with the experimental work. This work was supported by the National Aeronautics and Space Administration under Contract no. H-34328 B. This work was performed at the Ames Laboratory. Ames Laboratory is operated by Iowa State University for the U. S. Department of Energy under Contract no. W-7405-Eng-82.

Manuscript submitted June 29, 1983; revised manuscript received ca. March 15, 1984.

Iowa State University assisted in meeting the publication costs of this article.

REFERENCES

1. A. Coehn and W. Specht, *Z. Phys.*, **62**, 1 (1930).
2. W. Seith and Wever, *Z. Electrochem.*, **57**, 891 (1931).
3. Th. Heuman, in "The Physical Chemistry of Metallic Solutions and Intermetallic Compounds," Vol. 1, Paper 2C, Her Majesty's Stationery Office, London (1959).
4. J. D. Verhoeven, *Met. Rev.*, **8**, 311 (1963).
5. H. B. Huntington, in "Diffusion in Solids," A. S. Nowick and J. J. Burton, Editors, p. 303, Academic Press, New York (1975).
6. J. N. Pratt and R. G. R. Sellors in "Electrotransport in Metals and Alloys," Riechen, Editor, Trans. Tech SA, 1973.
7. J. D. Verhoeven, *J. Metals*, **18**, 26 (1966).
8. D. T. Peterson, in "Atomic Transport in Solids and Liquids," A. Lodding and T. Lagerwall, Editors, p. 104, Verlag der Zeitschrift für Naturforschung, Tübingen, Germany (1971).
9. D. T. Peterson, F. A. Schmidt, and J. D. Verhoeven, *Trans. AIME*, **236**, 1311 (1966).
10. R. J. Conzemius and H. J. Svec, *Anal. Chem.*, **50**, 1854 (1978).
11. S. R. DeGroot, *Physica*, **9**, 699 (1942).
12. G. Grube, *Z. Metallkd.*, **19**, 438 (1927).
13. D. T. Peterson, W. E. Krupp, and F. A. Schmidt, *J. Less-Common Met.*, **7**, 288 (1964).
14. E. N. Hopkins, D. T. Peterson, and H. H. Baker, Report ORNL-TM-1161, Oak Ridge National Laboratory, Oak Ridge, TN (1976).
15. R. J. Conzemius, F. A. Schmidt, and H. J. Svec, *Anal. Chem.*, **53**, 1899 (1981).
16. H. B. Huntington and A. R. Grone, *J. Phys. Chem. Solids*, **20**, 76 (1961).
17. R. E. Hummel, in "Electro- and Thermotransport in Metals and Alloys," R. E. Hummel and H. B. Huntington, Editors, p. 93, AIME, Inc., New York (1977).
18. W. N. Weins and O. N. Carlson, *J. Less-Common Met.*, **66**, 99 (1979).
19. F. A. Schmidt, R. J. Conzemius, and O. N. Carlson, *ibid.*, **59**, 53 (1978).
20. D. T. Peterson and T. Carnahan, *Trans. AIME*, **245**, 213 (1969).
21. J. F. Smith, O. N. Carlson, D. T. Peterson, and T. E. Scott, "Thorium," p. 385, Iowa State University Press, Ames, Iowa (1975).

Characterization of LPCVD Aluminum for VLSI Processing

R. A. Levy,* M. L. Green,* and P. K. Gallagher

AT&T Bell Laboratories, Murray Hill, New Jersey 07974

ABSTRACT

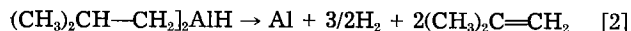
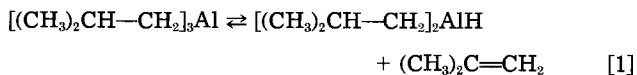
Aluminum and aluminum alloys are widely used for metallizing devices in VLSI processing. Such films can be deposited by a variety of techniques, which all presently suffer from inadequate step coverage. In this paper, we discuss the properties of aluminum films deposited by a low pressure chemical vapor deposition process using tri-isobutyl aluminum as a source. Results of this work demonstrate that this process provides conformal step coverage, introduces no surface states, and promises to yield high wafer throughput. Films deposited on oxidized silicon monitors exhibit excellent properties in terms of chemical purity, adhesion, and electrical resistivity. Films deposited on device wafers prove to be compatible with current VLSI processing in terms of patterning, dry etching, and bondability and appear to have no effect on overall device performance. However, drawbacks of LPCVD aluminum appear to be in its structure-related properties: namely, electromigration resistance and Al-Si interdiffusion. These problems and potential solutions are addressed.

Aluminum and aluminum-silicon-copper alloy films are widely used for metallizing devices in VLSI processing. Such films have normally been deposited by electron-beam (E-Gun[®]) or RF induction-source (In-Source[®]) evaporation, although more recently sputtering has become prominent. All these line-of-sight deposition techniques suffer, however, from inadequate step coverage, which often results in the formation of microcracks and discontinuities at corners of deep steps. With the expected increase in the use of multilevel metallization for vertical integration, coupled with the expected increase in packing density of devices with horizontally reduced dimensions, the development of a deposition technique which provides conformal step coverage becomes essential. In this paper, we will discuss the properties of aluminum films deposited on both oxidized silicon monitors and device wafers by a low pressure chemical vapor deposition (LPCVD) process using tri-isobutyl aluminum (TIBAL) as a source. Little has been published regarding LPCVD aluminum or its alloys because of the lack of suitable sources dissociating below the melting point of the metal (660°C) and the well-known chemical activity of aluminum with residual oxygen and water. Results of this work will establish a basic understanding of the properties of these LPCVD aluminum films, and their suitability for current VLSI processing.

Properties and Plating Chemistry of TIBAL

TIBAL (1) used in the present investigation, is a clear liquid with a density of 0.8 g/cm³. It has a melting point of -6°C and a boiling point of 40°C at 0.1 torr of Hg. It is pyrophoric, mildly toxic, and explosive in contact with water. Hence, extreme care should be exercised in the handling and disposing of the source liquid and the unreacted product of the dissociation.

The following chemical reactions occur during thermal decomposition (2)



Reaction [1] occurs from 50° to 150°C. During this step, TIBAL decomposes to di-isobutyl aluminum hydride by releasing isobutylene gas. At about 220°C, reaction [2] occurs, during which the di-isobutyl aluminum hydride thermally dissociates to pure Al by releasing both H₂ and isobutylene gas. Reaction [1] is reversible, and the formation of di-isobutyl aluminum hydride can be suppressed by adding excess isobutylene gas. Reaction [2] is not reversible and is known to proceed only over a narrow temperature range (220°-300°C) which, unfortunately, precludes in this process the simultaneous dissociation of SiH₄ (~450°C) and codeposition of Si in these films.

*Electrochemical Society Active Member.

Deposition Procedure

LPCVD Al films are becoming commercially available. The films, under present investigation, were deposited by ASM America, Incorporated, in an experimental LPCVD reactor shown in Fig. 1. Details on the design of the reactor as well as the process used by the vendor have been previously reported (3). The TIBAL liquid was evaporated at 45°C with the vapor flowing down a 1200 mm long, 150 mm diam stainless steel reactor tube. The reactor tube was loaded with as many as fifty 75 mm wafers within a three-zone furnace and pumped down with the aid of a liquid nitrogen cold trap and a Roots rotary pump combination. At the start of the operation, the LPCVD reactor was evacuated and purged with hydrogen at 450°C to reduce adsorbed air and moisture and the temperature in the center zone ramped down to ~260°C. The wafers were then exposed to TiCl₄ vapor, at a pressure of 0.5 torr, to "activate" the substrate surface prior to deposition. Without TiCl₄ acting as a nucleation catalyst, the aluminum is known to nucleate randomly on the surface, causing the growth of large individual crystallites. Following pumpdown of the TiCl₄ vapor, the dissociation reaction of TIBAL proceeded, at the previously fixed conditions of temperature and pressure, yielding a deposition rate of ~300 Å/min. At the end of the operation, the reactor went through a final pumpdown and was backfilled with nitrogen to atmospheric pressure. Table I details the process sequence used and the operating time for each step.

Physical Properties of LPCVD Aluminum

The chemical composition and adhesion, as well as the electrical, structural, and optical properties of LPCVD aluminum have been characterized by investigating films deposited on thermally oxidized monitors. Each of these properties will now be described.

Chemical composition.—One of our primary concerns in the use of TIBAL was the possible inclusion of carbon in the films. To check that possibility, Auger spectra were

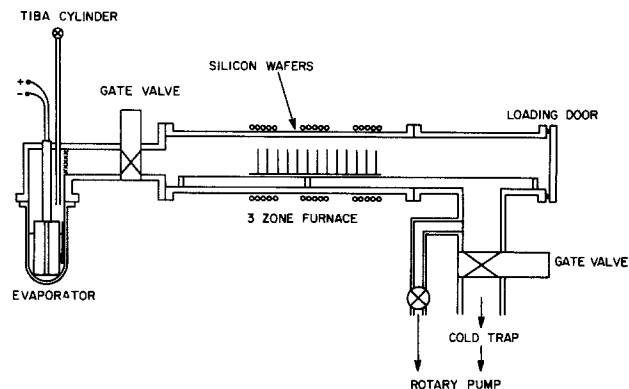


Fig. 1. Experimental LPCVD aluminum reactor

Table I. LPCVD aluminum process sequence

Event	Time (min)
Load/unload	10
Pumpdown	5
Heat to 450°C	5
backfill H ₂	
Pumpdown	5
TiCl ₄ treatment	1
Pumpdown	5
Deposition	25-50
Pumpdown	1
N ₂ backfill	1

gathered both on the surface and at a depth of 1000Å. Figure 2 shows an elemental survey of the surface which indicates the presence of aluminum, oxygen, carbon, and sulfur. The tendency of aluminum to react readily with the ambient to form a thin corrosion-resistant film of Al₂O₃ accounts for the presence of the oxygen. The carbon and sulfur are considered, here, to be normal surface contaminants. A second elemental survey, shown in Fig. 3, taken after ion milling with neon to a depth of 1000Å, exhibits the aluminum peaks but fails to reveal, at this magnification, observable contaminants beyond the expected neon signal. An expansion of the spectrum in the vicinity of the carbon signal, shown in Fig. 4, reveals an estimated carbon content in the film of $\approx 0.3\%$. Mass spectrometric gas evolution analysis performed on part of a monitor wafer over a temperature range extending from 27° to 700°C failed to reveal significant evolution of carbonous material beyond that in the background of the system. This data coupled with the Auger analysis sets the purity of these films to better than 99.7%.

Adhesion.—A segment of Scotch tape applied and peeled off the surface of the aluminum film failed, under repeated testing, to show signs of flaking. This test, however rudimentary, illustrates the degree of adherence of the LPCVD aluminum film to the underlying thermal oxide.

Electrical properties.—In order to evaluate the electrical properties of these films, the resistivity and electromigration resistance were determined. The resistivity was determined using two different methods. In one case, both the sheet resistance and thickness were measured over several areas of the film using a four point probe and Dektak® stylus. By combination of the average of these two parameters, a value for the resistivity of the LPCVD aluminum film was calculated to be $3.36 (\pm 0.24) \times 10^{-6} \Omega\text{-cm}$. In the other case, an electromigration meander tester was used, where the track was 1 cm long and had a deposited film thickness of $7774 \pm 303 \text{Å}$ and a patterned linewidth of $2.30 \pm 0.07 \mu\text{m}$. The resistance of the line was measured with a digital multimeter. From known values of resistance, length, and cross-sectional area, the resistiv-

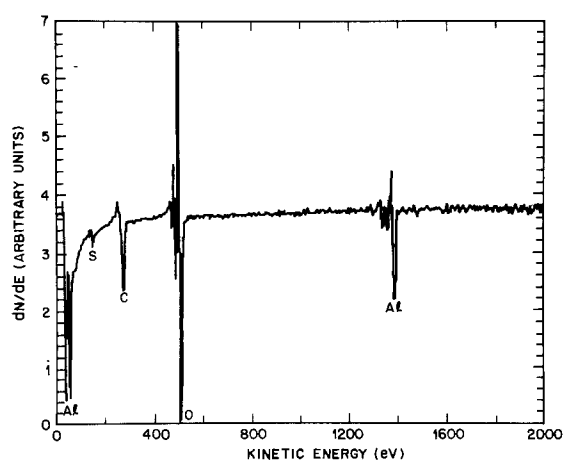


Fig. 2. Auger elemental survey of LPCVD aluminum surface

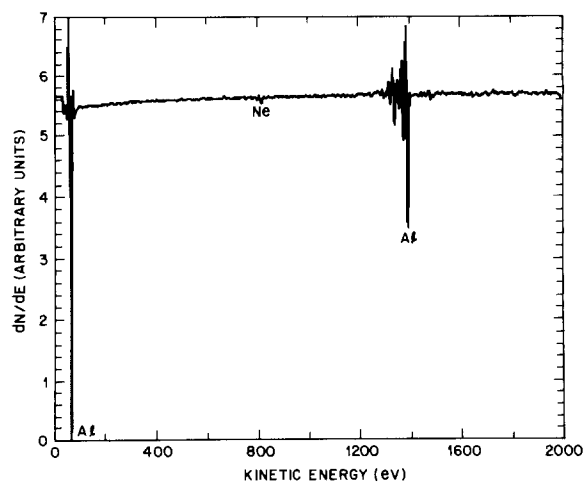


Fig. 3. Auger elemental survey of LPVCD aluminum at 1000Å depth

ity was calculated to be $3.42 (\pm 0.17) \times 10^{-6} \Omega\text{-cm}$. Both these measuring techniques yielded values of resistivity $\sim 10\%$ higher than those reported for typical aluminum films (4).

The electromigration measurements were carried out on a group of typically 12 packaged testers with $2.25 \mu\text{m}$ wide aluminum meander lines under accelerated conditions of temperature (T) set at 192°, 214°, and 270°C and current density (J) set at $1.85 \times 10^6 \text{ A/cm}^2$. All films which underwent this test were reactive ion etched and sintered at 300°C/30 min/H₂. From a plot of the measured values of the median time-to-failure, MTF, vs. $1/T$, shown in Fig. 5, an activation energy, Q , of 0.51 eV was calculated. This is in excellent agreement with values reported for fine-grained In-Source aluminum films (5). Using the present value of Q , the median time-to-failure (MTF) extrapolated to 80°C and $1 \times 10^5 \text{ A/cm}^2$, was calculated with the use of the relationship $\text{MTF} = AJ^{-2} \exp [Q/kT]$, to be equal to $9.1 \times 10^4 \text{ h}$. This value compares well with the reported value of $7.6 \times 10^4 \text{ h}$ for the $2.9 \mu\text{m}$ wide meander lines of In-Source Al-0.5%Cu similarly deposited at a rate of 300 Å/min and sintered at 300°C/30 min/H₂ (6). However, it is significantly lower than the value of $5.3 \times 10^6 \text{ h}$ observed by the authors for In-Source Al-0.5%Cu deposited at 300°C at a rate of 140 Å/s and sintered at 300°C/30 min/H₂. This difference is believed to be primarily due to the copper contribution as well as structural differences. As will be described further in this report, LPCVD aluminum films exhibit grains that are small in size; a fact that has been shown to adversely affect both Q and MTF (7). Furthermore, the nonuniform thickness observed across the film is expected to modulate the magnitude of the current density, thereby enhancing the electromigration failure in the thinner cross-sectional areas. Electromigra-

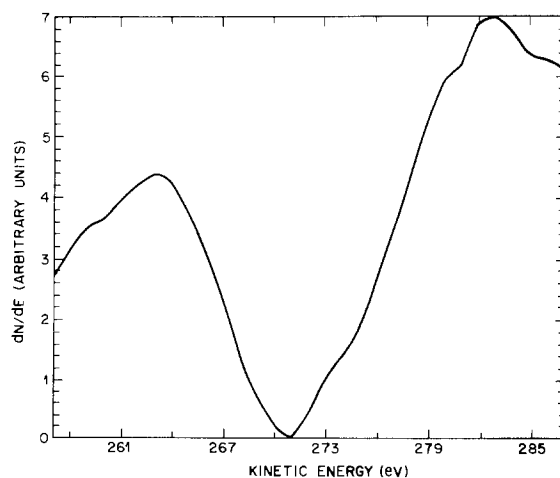


Fig. 4. Expanded Auger spectrum at vicinity of carbon signal

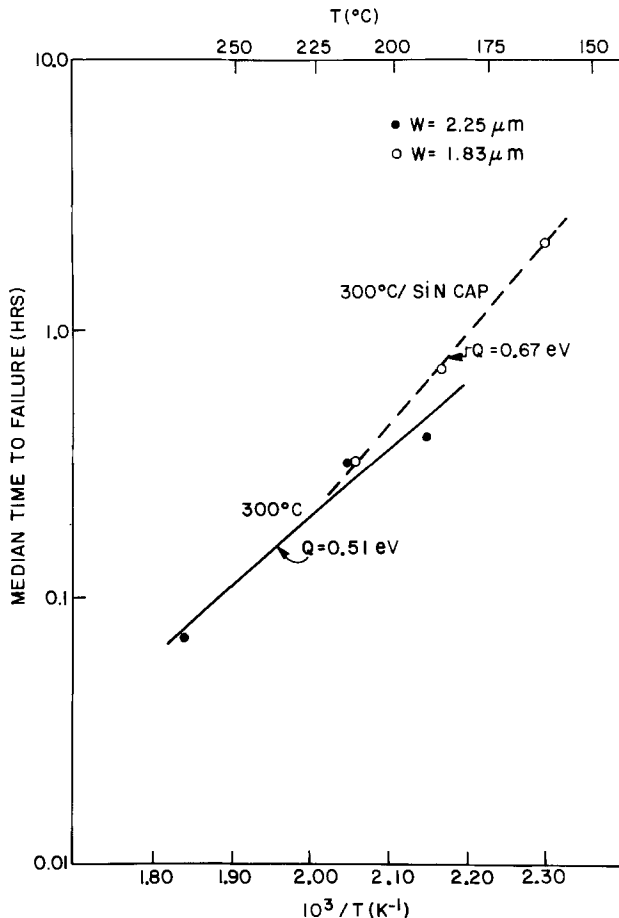


Fig. 5. Median time to failure vs. reciprocal temperature at an accelerated current density. (—): Sintered at 300°C/30 min/H₂. (---): Sintered at 300°C/30 min/H₂ with 1.4 μm plasma SiN.

tion data were also gathered on 1.34 μm wide meander lines, subjected to an accelerated temperature of 186°C and a current density of 1.85×10^6 A/cm². The extrapolated value (80°C, 1×10^5 A/cm²) for MTF, using $Q = 0.51$ eV was calculated to be 1.1×10^5 h, showing little variation, in this case, with narrower linewidths.

In order to examine the effect of capping the LPCVD aluminum with plasma SiN, groups of typically 18 meanders with 1.83 μm linewidth were tested, under accelerated conditions, at temperatures of 162°, 187°, and 212°C and at a constant current density of 1.85×10^6 A/cm². The 1.4 μm plasma SiN cap layer was deposited at ~300°C for 110 min on the entire wafer and subsequently patterned and plasma etched to expose the aluminum pads for wire bonding. A plot of MTF vs. $1/T$ yielded a value of 0.67 eV, possibly reflecting the increase in aluminum grain growth with additional heat-treatment. The extrapolated value of MTF (80°C, 1×10^5 A/cm²) was calculated to be 4.5×10^5 h with the increase, as shown in Fig. 5, resulting from the higher activation energy.

Structural properties.—One of the most prominent features of LPCVD aluminum is its surface topography. Under visual examination, the films have a distinctive non-specular, cloudy appearance. At 1100× magnification, a rough grainy structure becomes evident. At still higher magnification, with the aid of a scanning electron microscope (SEM), the steep peaks and valleys, which account for the poor reflectance of the surface, could be readily seen (Fig. 6). This surface roughness is believed to be directly related to the deposition process which governs the nucleation and growth mechanism of aluminum. In the present LPCVD process, we postulate that the aluminum atoms, after decomposition of the adsorbed alkyl molecules, stick to the substrate without significant surface diffusion. In an improperly activated substrate surface, nucleating sites are few and randomly distributed across

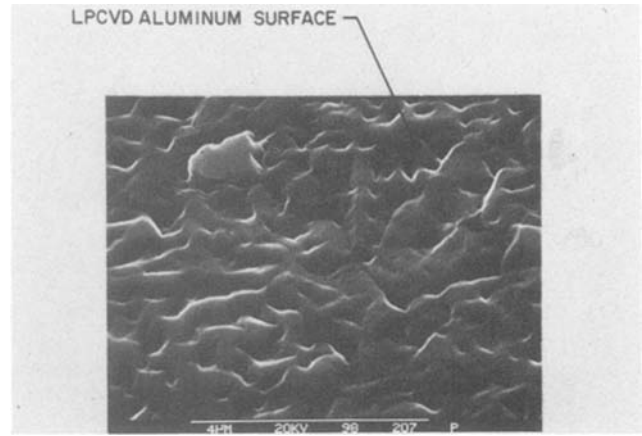


Fig. 6. SEM micrograph illustrating surface topography of LPCVD aluminum.

the surface. The growth of nuclei is believed to be three dimensional, but anisotropic with preferred growth occurring normal to the surface. During the growth process, these nuclei coalesce and form crystallographically shaped islands. As deposition continues, secondary nucleation occurs in open areas, and these nuclei in turn grow and coalesce to form new islands which eventually merge with the older ones to form a coherent film. Depending, therefore, on the time lag between primary and secondary nucleation and the growth kinetics of these nuclei, a wide range of topography may be expected. Figure 7 shows a transmission electron micrograph of a thin vertical cross section of an LPCVD aluminum film. The average film thickness, in this case, is ~6000Å with a maximum peak to valley height of ~2500Å. These variations from the average film thickness are expected to further increase with thicker films. Figure 8 shows a transmission electron micrograph of a thin horizontal cross section of an LPCVD aluminum film subjected to a 300°C/30 min/H₂ sinter. The grain-size distribution is observed to be wide, ranging from 1 to 4 μm. Using the conventional line intersection technique, a value for the average grain size was measured to be 1.4 ± 0.3 μm. Both the grain size and grain size distribution appear to be significantly different from those of In-Source Al-0.5%Cu deposited at 300°C, at a rate of 140 Å/s and sintered at 300°C/30 min/H₂. Such a film, shown in Fig. 9, has a distribution of grain sizes ranging from 1 to 6 μm with an average grain size of 1.8 ± 0.4 μm.

X-ray diffraction data taken with CuKα radiation at 45 kV and 30 mA, on both as-deposited LPCVD aluminum and In-Source Al-0.5%Cu deposited at ~220°C and at a rate of ~60 Å/s, reveal significant differences. Besides reflections parallel to the <100> Si substrate, which were common in both samples, the comparative spectra, shown in Fig. 10, exhibit, in the case of the LPCVD alu-

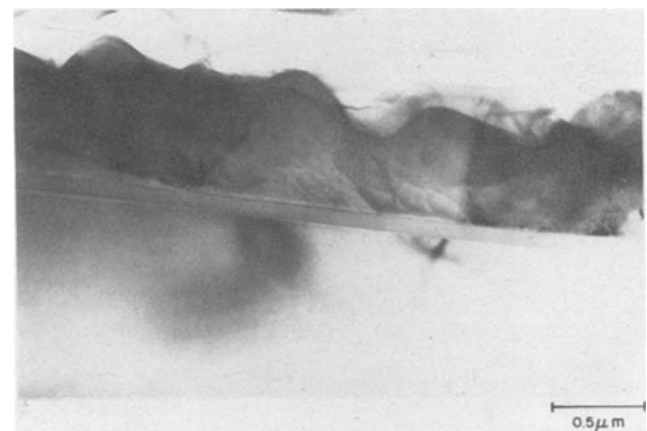


Fig. 7. TEM vertical cross-section micrograph of LPCVD aluminum



Fig. 8. TEM horizontal cross-section micrograph of LPCVD aluminum

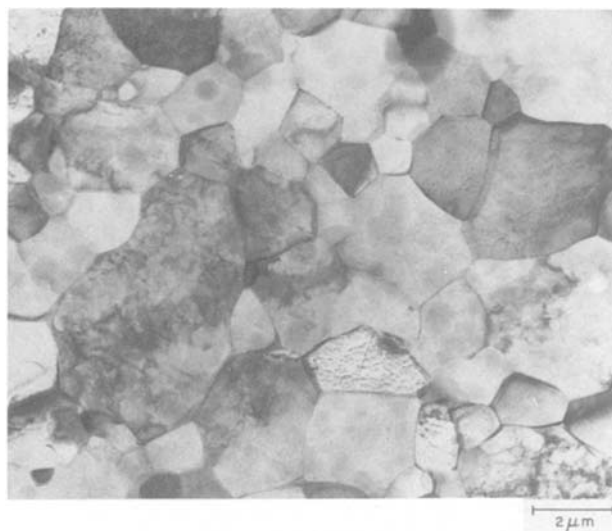


Fig. 9. TEM horizontal cross-section of In-Source Al-0.5%Cu

minum, a highly textured $\langle 111 \rangle$ structure. This is evident from the intensity ratio (I_{111}/I_{200}), which has been calculated to be (100/2) compared to the (100/47) expected of polycrystalline aluminum with random orientation. Although reflections from the $\langle 311 \rangle$ and $\langle 222 \rangle$ planes were evident, the $\langle 220 \rangle$ diffraction peak was absent from this x-ray pattern. The In-Source Al-0.5%Cu spectrum, on the other hand, reveals a lower degree of $\langle 111 \rangle$ texture as indicated by the calculated (I_{111}/I_{200}) intensity ratio of (100/6), the weaker reflections of the $\langle 222 \rangle$ planes and the emergence of the $\langle 220 \rangle$ diffraction peak.

Optical properties.—In order to investigate the optical properties of LPCVD aluminum, reflectance measurements were gathered over the optical wavelength scan of 0.20 to 0.90 μm using a Perkin-Elmer (Coleman 575) spectrophotometer. Figure 11 shows the percentage of reflectance of a 0.5 μm thick Al film relative to that of a 1 μm thick In-Source Al-0.5% Cu film in the wavelength range where photolithographic processing is prevalent. The data indicate a broad minimum with a 5% reflectance ratio centered around the 0.35 μm wavelength. Below this minimum, a 14% reflectance ratio is reached at the lowest investigated wavelength of 0.20 μm , and a 40%

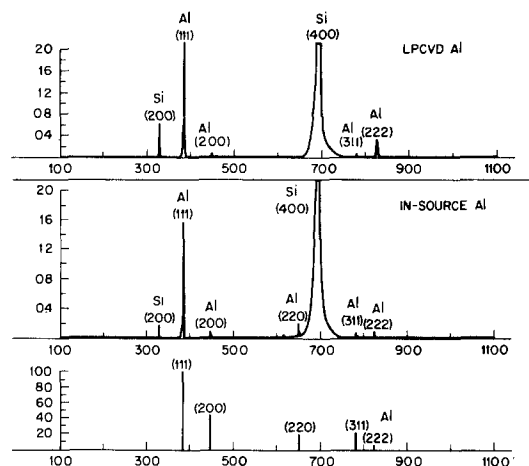


Fig. 10. Comparative x-ray spectra of LPCVD Al and In-Source Al-0.5%Cu.

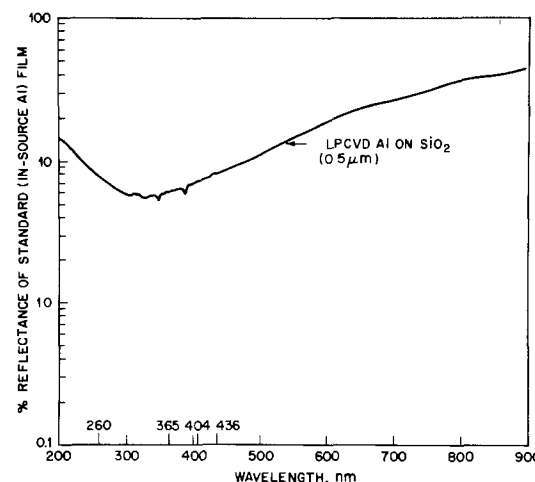


Fig. 11. Percentage of reflectance of LPCVD aluminum relative to In-Source Al-0.5% Cu vs. wavelength.

reflectance ratio at the highest investigated wavelength of 0.90 μm . The poor reflectance of LPCVD aluminum, which may prove to be beneficial in photolithographic processing, is directly related to the surface roughness of the film. A reflected beam is known to form only if the average depth of the surface irregularities of the reflector is substantially less than the wavelength of the incident light. In the present case, where our surface irregularities are of the order of $\sim 2500\text{\AA}$, enhancement of the reflectance occurs, as, indeed, observed in Fig. 11, at longer wavelengths.

Suitability of LPCVD Aluminum to VLSI Processing

The suitability of LPCVD aluminum to current VLSI processing was investigated with the use of 75 mm device wafers fabricated in accordance with the 2.5 μm Twin-Tub CMOS process (with TaSi_2) (8). The processed wafers included IGFET, contact resistance, van der Pauw, and MOS testers which were automatically probed, after aluminum patterning, at four sites across each wafer. All wafers received a preclean ($\text{H}_2\text{SO}_4/\text{H}_2\text{O}_2$) and an HF etch prior to insertion into the LPCVD reactor. For correlation purposes, device wafers metallized with sputtered Al as well as In-Source Al-0.5% Cu were processed with the experimental batch. The etching profile, step coverage, spiking, bondability, and effect on device performance of LPCVD aluminum will now be considered.

Etching profile.—Following photolithography, the aluminum was reactive sputter etched in a HEX reactor using a chlorine-based gas mixture. Figure 12 illustrates the quality of the etch in various parts of a wafer. Examination of the photographs reveals no residue between the

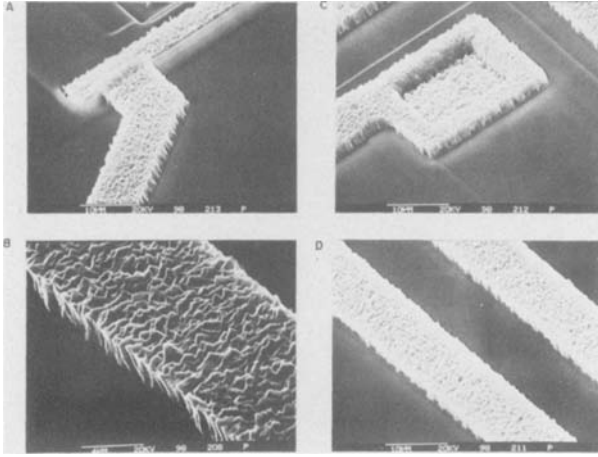


Fig. 12. Etching profile across device wafer for LPCVD aluminum

delineated patterns, no signs of undercutting, and no Al wall erosion or severe linewidth loss.

Step coverage.—The possibility of achieving conformal step coverage has been the primary objective in the development of LPCVD aluminum. Evaporation and sputtering techniques have been known to produce films that thinned down considerably along window walls and bulged upward at the bottom of the window. Although considerable effort was directed toward improvement of step coverage by adopting higher deposition temperatures to enhance surface mobility or optimizing the planetary motion to improve uniformity, fundamental limits restricted further improvements. Figure 13 shows a series of SEM cross-sectional photographs illustrating the quality of step coverage for LPCVD aluminum deposited over contact windows to silicon and polycide. Measurements of the film thickness along the window sidewalls and along the top or bottom regions of the window yield identical values everywhere, confirming the conformal step coverage of this process. An increase in the aluminum film thickness to $\sim 1.3 \mu\text{m}$ is expected, in the present $2.5 \mu\text{m}$ design pattern, to totally plug the windows and establish a markedly reduced topography. This can be seen in Fig. 14, where Al appears to have filled the cavities in the P-glass between polycide runners. The plasma SiN used for capping devices appears, as shown in Fig. 15A, to replicate the conformal CVD coverage of the underlying aluminum and P-glass structures while exhibiting, as seen in Fig. 15B, its characteristic surface morphology.

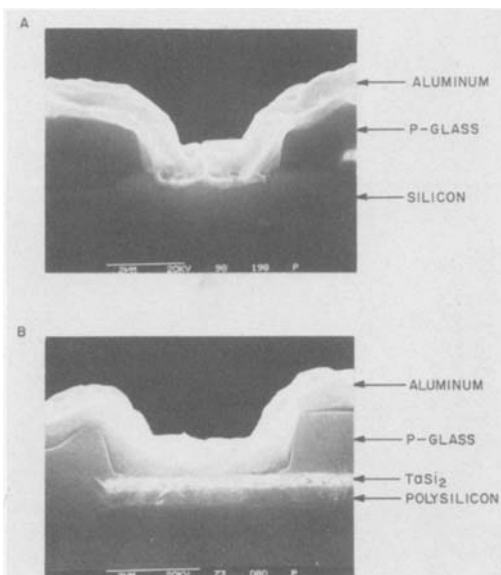


Fig. 13. Step coverage of LPCVD aluminum over contact windows to (A) silicon and (B) polycide.

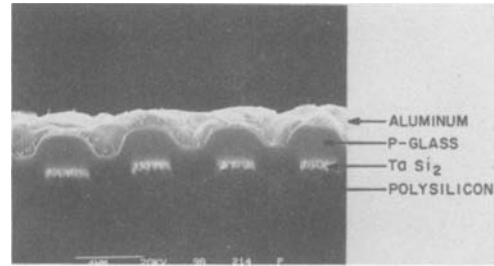


Fig. 14. Step coverage of LPCVD aluminum over P-glass. Magnification bar is $4 \mu\text{m}$.

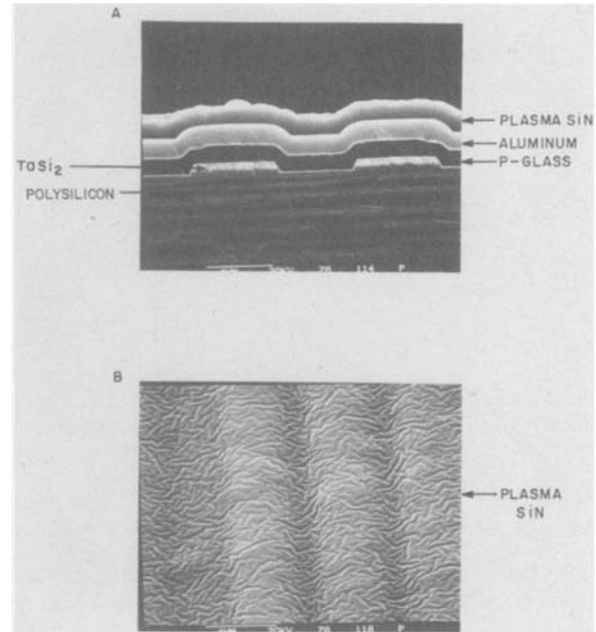


Fig. 15. (A) Overall step coverage of plasma SiN cap, LPCVD aluminum and P-glass. (B) Surface topography of plasma SiN cap. Magnification bar is $4 \mu\text{m}$.

Junction spiking.—Prior to LPCVD aluminum deposition, all wafers in the present investigation were preheated at $\sim 450^\circ\text{C}$ in H_2 to reduce air and moisture in the reactor. The temperature was then ramped down to $\sim 260^\circ\text{C}$ to activate the substrate surface with TiCl_4 and dissociate the TIBAL. Following aluminum patterning, a group of device wafers was sintered at $300^\circ\text{C}/30 \text{ min}/\text{H}_2$. Part of that group received a $1 \mu\text{m}$ thick plasma SiN cap film deposited at 300°C for 95 min, with one wafer getting an additional $450^\circ\text{C}/30 \text{ min}/\text{H}_2$ sinter. Figure 16 shows SEM cross-sectional micrographs of contact windows to silicon and polycide taken after stripping the aluminum and prior to the $300^\circ\text{C}/30 \text{ min}/\text{H}_2$ sintering step. These micrographs indicate that, although the contact window to polycide remained intact after the $\sim 260^\circ\text{C}$ aluminum deposition (Fig. 16B), the contact window to silicon has been significantly eroded. Measurements of the depth of this pit at several points below the Si surface yielded values as high as $\sim 2000\text{\AA}$. We believe that this interdiffusion occurred, at these relatively low deposition temperatures ($\sim 260^\circ\text{C}$), in a continuous fashion across the interface due to the etching of the native oxide during the pretreatment process. In the presence of an imperfect native oxide, the interdiffusion as observed for evaporated or sputtered aluminum has been reported (9) to proceed through pinholes in the oxide, causing preferential spiking along $\langle 111 \rangle$ crystallographic planes. Further evidence for this native oxide etch, to be discussed further below, is provided by the remarkably low values for aluminum contact resistance to N^+ silicon. Figure 17 is a SEM micrograph taken after stripping the aluminum from contact windows to silicon and polycide. The surface morphology of

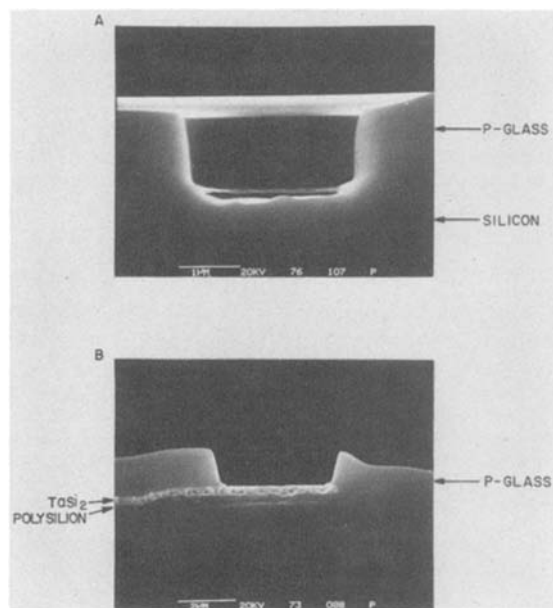


Fig. 16. SEM cross-sections of contact windows to (A) silicon and (B) polycide, after aluminum removal.

the silicon window appears quite rough. For shallow junction devices ($<0.25 \mu\text{m}$) this interdiffusion is a significant problem, which can be resolved by further reduction of the aluminum deposition temperature and that of subsequent processing, or by the use of a diffusion barrier. Ongoing efforts are addressing these possibilities. Figure 18 shows SEM cross-sectional micrographs of stripped contact windows to silicon and polycide following the $300^\circ\text{C}/30 \text{ min}/\text{H}_2$ sinter. The interdiffusion of silicon and aluminum is seen to have extended over a maximum depth of 4000\AA below the Si surface. This temperature-dependent erosion of the interface provides supporting evidence that our observations are consistent with a thermally activated interdiffusion phenomenon. Additional thermal processing caused by plasma SiN capping of the devices at 300°C for 95 min, and a supplemental $450^\circ\text{C}/30 \text{ min}/\text{H}_2$ sinter was observed to further enhance interdiffusion of silicon and aluminum down to a depth of $\sim 6000\text{\AA}$.

It is interesting to note that a series of highly oriented crystallographic precipitates of silicon, as determined by x-ray energy dispersive analysis, was observed on a few of the contact windows to polycide for samples which had received the $300^\circ\text{C}/30 \text{ min}/\text{H}_2$ sinter. The presence of these faceted crystals, shown in Fig. 19, is quite surprising in view of the fact that the TaSi_2 substrate is

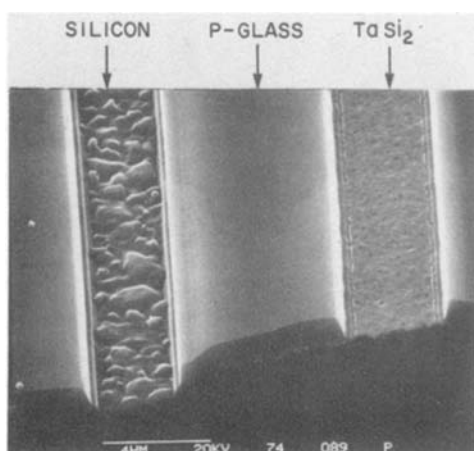


Fig. 17. Top view of an SEM micrograph of contact windows after aluminum removal.

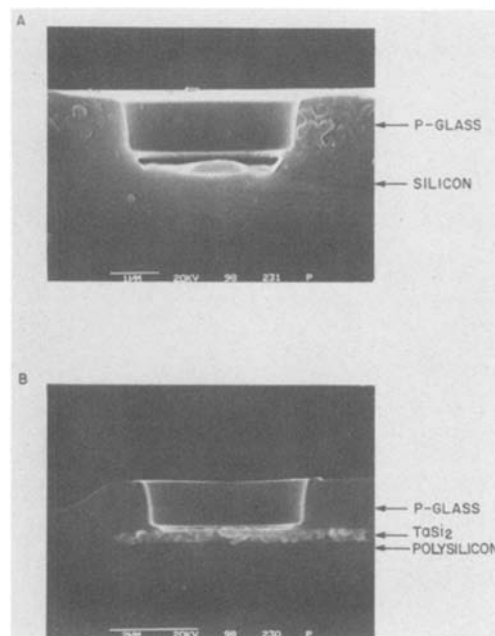


Fig. 18. SEM cross sections of contact windows to (A) silicon and (B) polycide following the $300^\circ\text{C}/30 \text{ min}/\text{H}_2$ sinter and after aluminum removal.

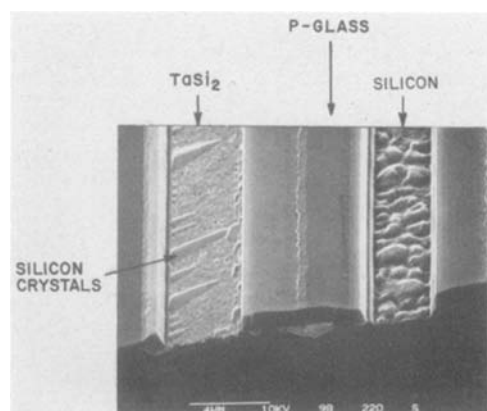


Fig. 19. SEM micrograph of contact windows after aluminum removal illustrating presence of faceted crystals on polycide contact windows.

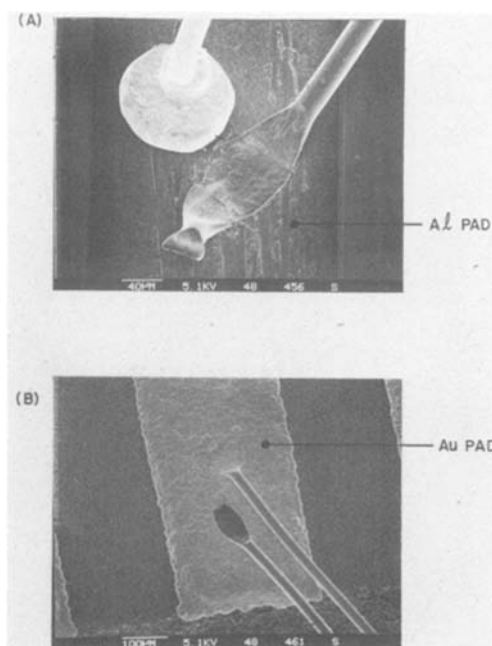


Fig. 20. SEM micrographs illustrating quality of ball-wedge and wedge-wedge wire bonds to (A) chip pad and (B) package pad.

Table II. Comparison of CMOS parametric data for as-deposited aluminum

		LPCVD Al	In-Source Al	Sputtered Al
IGFET tester	Nominal P-Chan: V_T (V)	1.04 ± 0.01	1.02 ± 0.01	1.01 ± 0.01
	β ($\mu\Omega/V$)	696.35 ± 86.53	650.13 ± 41.97	720.33 ± 107.22
	N-Chan: V_T (V)	0.66 ± 0.01	0.66 ± 0.01	0.67 ± 0.01
	β ($\mu\Omega/V$)	2218.32 ± 328.92	2081.98 ± 175.88	2305.36 ± 419.61
	Square P-Chan: V_T (V)	1.02 ± 0.01	1.01 ± 0.01	1.00 ± 0.01
	β ($\mu\Omega/V$)	19.81 ± 0.27	19.44 ± 0.14	19.53 ± 0.17
	N-Chan: V_T (V)	0.66 ± 0.01	0.65 ± 0.01	0.66 ± 0.01
van der Pauw tester Log leakage current:	β ($\mu\Omega/V$)	62.37 ± 0.46	62.04 ± 0.45	61.76 ± 0.59
	N ⁺ /PTUB (A)	-9.11 ± 0.47	-9.66 ± 0.54	-8.71 ± 0.73
	P ⁺ /NSUB (A)	-9.40 ± 0.44	-9.54 ± 0.28	-9.65 ± 0.27
Contact resistance tester Log leakage current:	PTUB/NSUB (A)	-9.42 ± 0.84	-9.12 ± 0.15	-9.23 ± 0.08
	N ⁺ /PTUB (A)	-9.91 ± 0.31	-9.70 ± 0.02	-9.70 ± 0.01
	P ⁺ /NSUB (A)	-10.11 ± 0.28	-10.12 ± 1.73	-10.76 ± 0.22
2.5 μm Contact resistance:	N ⁺ (Ω)	2.46 ± 0.43	84.36 ± 12.48	24.99 ± 8.03
	P ⁺ (Ω)	2.58 ± 0.53	7.79 ± 3.58	3.46 ± 0.42
	Polycide (Ω)	112.97 ± 156.94	74.94 ± 82.59	58.95 ± 29.50

polycrystalline, and tends to indicate that silicon diffusion from or through the TaSi₂ is possible. In such cases, the use of a barrier becomes necessary not only to prevent reaction with aluminum at silicon junctions but also diffusion at polycide gates.

Bondability.—The ability to wire bond to LPCVD aluminum films was investigated with the use of several electromigration tester chips which had been eutectically bonded to 40 pin dual-in-line packages. Both Au and Al-1%Mg wires 25 μm thick were wire bonded to aluminum pads on the chip side and gold pads on the package side. The gold wires were drawn automatically out of a spool, with the package heated at 150°C, to ultrasonically form a ball bond on the aluminum pad and a wedge bond on the gold pad. The aluminum wires were wedge-wedge bonded ultrasonically, at room temperature, to both the aluminum and gold pads. Figure 20 shows SEM micrographs illustrating the quality of these ball-wedge and wedge-wedge wire bonds. Aluminum wire bonds which subsequently underwent high temperature treatments (180°C) for ~17h during electromigration testing remained intact in all cases.

Effect on device performance.—The effect of LPCVD aluminum on device performance was evaluated by automatically probing the IGFET, van der Pauw, contact resistance, and MOS testers present at four sites across each of three device wafers fabricated in accordance with the 2.5 μm Twin-Tub CMOS process (8). Table II offers a comparison of the CMOS parametric data for the nonsintered LPCVD, In-Source, and sputtered aluminum films. An examination of those data reveals insignificant differ-

ences in the characteristics of the square transistor for all three types of aluminum as determined by values of threshold voltage and beta per square. However, slight variations in the values of beta for the nominal transistors are observed in a comparison among these three deposition processes. These variations appear to be related to corresponding changes in channel length believed to be caused by gate definition. The van der Pauw data, similarly, reveal little variation in the values of leakage current among the three types of aluminum. The most striking difference characterizing the LPCVD aluminum films is found in the values of the contact resistance to N⁺ and P⁺ source/drain regions. For the 2.5 × 2.5 μm contact windows, the value of contact resistance to N⁺ is a factor of ~30 less than that of In-Source aluminum and a factor of ~10 less than that of sputtered aluminum. The value of contact resistance to P⁺, however, is identical to that of N⁺, but is still significantly lower than the corresponding values for In-Source and sputtered aluminum. We postulate that this unusually low value of contact resistance to N⁺ is related to the effect of the TiCl₄ pretreatment, which results in the etching of the native oxide as well as part of the underlying Si surface. The fact that In-Source aluminum deposited at ~220°C exhibits a significantly higher contact resistance to N⁺ than that of sputtered aluminum deposited at ~300°C is consistent with the presence of an interfacial oxide barrier which is easier to reduce at higher deposition temperatures. The contact resistance of aluminum to TaSi₂ appears to be unusually high in all three cases. This is believed to be a result of properties related to the TaSi₂ rather than those of LPCVD aluminum.

Table III. Comparison of CMOS parametric data for LPCVD aluminum at various processing steps

		As-deposited	After sintering (300°C/ 30 min/H ₂)	After SiN capping (300°C/95 min)	After additional sintering (450°C/ 30 min/H ₂)
IGFET tester	Nominal P-Chan: V_T (V)	1.04 ± 0.01	1.03 ± 0.02	1.30 ± 0.56	1.02 ± 0.02
	β ($\mu\Omega/V$)	696.35 ± 86.53	683.50 ± 91.63	603.76 ± 196.10	700.96 ± 118.89
	N-Chan: V_T (V)	0.66 ± 0.01	0.66 ± 0.01	0.85 ± 0.36	0.66 ± 0.00
	β ($\mu\Omega/V$)	2218.32 ± 328.92	2186.69 ± 332.45	1973.04 ± 387.58	2210.26 ± 383.55
	Square P-Chan: V_T (V)	1.02 ± 0.01	1.01 ± 0.02	1.06 ± 0.10	1.00 ± 0.02
	β ($\mu\Omega/V$)	19.81 ± 0.27	19.66 ± 0.29	18.49 ± 1.47	19.31 ± 0.21
	N-Chan: V_T (V)	0.66 ± 0.01	0.65 ± 0.01	0.77 ± 0.18	0.66 ± 0.01
Van der Pauw tester Log leakage current:	β ($\mu\Omega/V$)	62.37 ± 0.46	61.97 ± 0.53	59.26 ± 4.99	63.19 ± 0.16
	N ⁺ /PTUB (A)	9.11 ± 0.47	9.13 ± 0.45	8.89 ± 0.21	9.01 ± 0.32
	P ⁺ /NSUB (A)	9.40 ± 0.44	9.35 ± 0.40	9.26 ± 0.40	8.92 ± 0.33
Contact resistance tester Log leakage current:	PTUB/NSUB (A)	9.42 ± 0.84	9.28 ± 0.60	9.36 ± 0.62	9.13 ± 0.21
	N ⁺ /PTUB (A)	9.91 ± 0.31	9.89 ± 0.20	9.99 ± 0.21	5.48 ± 3.39
	P ⁺ /NSUB (A)	10.11 ± 0.28	9.93 ± 0.05	9.96 ± 0.10	10.15 ± 0.09
2.5 μm Contact resistance:	N ⁺ (Ω)	2.46 ± 0.43	2.84 ± 0.70	2.72 ± 0.55	14.79 ± 2.16
	P ⁺ (Ω)	2.58 ± 0.53	2.98 ± 0.76	2.90 ± 0.46	2.56 ± 0.12
	Polycide (Ω)	112.97 ± 156.94	159.76 ± 252.13	109.68 ± 157.71	4.82 ± 6.18

Table III draws a comparison of the CMOS parametric data at various steps in the process following LPCVD aluminum deposition. The data reveal little change in any of the device characteristics following the 300°C/30 min/H₂ sinter. However, after SiN capping two of the device wafers at 300°C for 95 min, a significant change in the values of the threshold voltage for both N- and P-channel transistors was observed. An additional 450°C/30 min/H₂ treatment is shown in Table III to restore the threshold voltages back to their values prior to SiN capping. However, that additional heating step is also seen to generate large leakage currents in the N⁺/P Tub contact resistance tester caused by the severe junction spiking occurring at these relatively high temperatures.

Conclusion

Our results have established that LPCVD aluminum is close to being a viable VLSI technology. It provides 100% conformal step coverage, introduces no surface states, and promises to yield high wafer throughput. The LPCVD aluminum films have been shown to exhibit excellent properties in terms of chemical purity, adhesion, electrical resistivity, and contact resistance. The films have also been proven to be suitable for VLSI processing in terms of patterning, dry etching, and bondability and appear to have no effect on overall device performance. One of the drawbacks of LPCVD aluminum has been shown to be its structure-dependent properties: namely, electromigration resistance and Al-Si interdiffusion. We believe that both these problems can be resolved with a proper diffusion barrier, which would not only eliminate junction spiking but also allow for higher sintering temperatures that in turn should enhance crystal growth and electromigration resistance. The remaining concern at the present is the hazard associated with the handling of TIBAL, which can possibly be overcome by the adoption of strict safety procedures during operation or the devel-

opment of an alternatively safer LPCVD aluminum transport process. Both these options are under present investigation.

Acknowledgments

The authors wish to thank R. S. Rosler at ASM America Incorporated for depositing the aluminum, W. Y. C. Lai for providing us with the device wafers, C. C. Chang for gathering the Auger data, R. V. Knoell for the transmission electron microscopy work, T. E. McGahan for the SEM micrographs, L. J. Lecheler for assisting in various tasks of this project, and L. C. Parrillo as well as J. T. Clemens for many fruitful discussions.

Manuscript received Feb. 22, 1984.

AT&T Bell Laboratories assisted in meeting the publication costs of this article.

REFERENCES

1. T. Mole and E. A. Jeffrey, "Organoaluminum Compounds," p. 85, Elsevier Publishing Co., Amsterdam (1972).
2. G. B. Sakharovskaya, N. N. Korneev, N. N. Smirnov, and A. F. Popov, *J. Gen. Chem. USSR*, **44**, 560 (1974).
3. M. J. Cooke, R. A. Heinecke, R. C. Stern, and J. W. C. Maes, *Solid State Technol.*, p. 62, December (1982).
4. P. S. McLeod and J. L. Hughes, *J. Vac. Sci. Technol.*, **16**, 369 (1979).
5. S. Vaidya, D. B. Fraser, and W. S. Lindenburger, *J. Appl. Phys.*, **51**, 4475 (1980).
6. S. Vaidya, D. B. Fraser, and A. K. Sinha, in "Proceedings of the 18th Rel. Physics Symposium IEEE," p. 165, IEEE, New York (1980).
7. E. Kinsbron, *Appl. Phys. Lett.*, **36**, 968 (1980).
8. L. C. Parrillo, L. K. Wang, R. D. Swenumson, R. L. Field, R. C. Melin, and R. A. Levy, "Twin-Tub CMOS II—An Advanced VLSI Technology," IEEE Tech. Dig. International Electron Device Meeting, p. 706, IEEE, San Francisco (1982).
9. H. M. Naguib and L. H. Hobbs, *This Journal*, **124**, 573 (1977).

Large Grain Copper Indium Diselenide Films

T. L. Chu* and Shirley S. Chu*

Southern Methodist University, Dallas, Texas 75275

S. C. Lin and J. Yue

Poly Solar Incorporated, Garland, Texas 75041

ABSTRACT

Large grain thin films of copper indium diselenide with a preferred {112} orientation have been prepared by (i) the deposition of nearly stoichiometric films of copper and indium on suitable substrates using vacuum evaporation or electrodeposition, and (ii) the heat-treatment of Cu-In films in a hydrogen-selenium atmosphere at temperatures above 630°C. The compositional, structural, and electrical properties of the films have been evaluated. In an alternate approach, a copper film on a substrate was first converted into cuprous selenide, followed by the deposition of indium and selenization. The resulting CuInSe₂ films have the same properties as those from the selenization of Cu-In films.

Copper indium diselenide, CuInSe₂, a direct gap semiconductor with a room temperature energy gap of about 1 eV, has very large optical absorption coefficients at the bandedge and beyond (1), and the minority carrier diffusion length becomes relatively unimportant in the operation of photovoltaic devices. Thus, CuInSe₂ is particularly suited for thin film devices. Since the first report of a single-crystalline n-CdS/p-CuInSe₂ heterojunction device with a conversion efficiency of 12% (2), considerable efforts have been directed to the fabrication and characterization of thin film devices of the same configuration (3). The deposition of CuInSe₂ films on foreign substrates was carried out, in most cases, by vacuum techniques such as evaporation and sputtering, and the

* Electrochemical Society Active Member.

accurate control of the copper and indium fluxes at the substrate surface is essential for obtaining stoichiometric CuInSe₂ films. In spite of the small grain size (about 1 μm) in films deposited by vacuum techniques, short-circuit current densities similar to those reported for single crystalline devices (40 mA/cm²) have been obtained, and heterojunction solar cells with AM1 efficiencies of near 11% have been reported (4).

In this work, CuInSe₂ films have been prepared by two chemical approaches: (i) the deposition of Cu and In films on a suitable substrate by vacuum evaporation or electrodeposition followed by the treatment of Cu-In film with selenium vapor at high temperatures, and (ii) the formation of Cu₂Se film on a suitable substrate by the selenization of Cu film, followed by the deposition of In

film and selenium treatment. The use of electroplating and selenization processes has distinct cost advantages as compared with the current technology. The compositional, structural, and electrical properties of deposited films have been investigated. The experimental procedures and results are summarized in this paper.

Experimental

The important process parameters in the preparation of CuInSe_2 films by the selenization of Cu-In films are: (i) the stoichiometry of the Cu-In film, (ii) the temperature of selenium treatment, and (iii) the partial pressure of selenium and the duration of selenium treatment. The Cu-In phase diagram indicates that the 1:1 Cu-In alloy melts at about 630°C (5). Thus, the selenium treatment of Cu-In films at 630°C or above involves gas-liquid reactions, while that at lower temperatures involves gas-solid reactions. For low temperature selenium treatment, nearly any inert substrates, such as graphite, may be used. When selenium treatment is carried out at high temperatures, the uniform wetting of the substrate surface by the liquid Cu-In film is essential for obtaining uniform CuInSe_2 films. Tungsten-coated graphite, prepared by the thermal reduction of tungsten hexafluoride with hydrogen on the surface of graphite at 500°C - 600°C , was found to be suitable.

The Cu-In films were deposited on the substrate surface by vacuum evaporation or by electroplating. Evaporation was carried out in the conventional manner under a pressure of 10^{-6} torr or less using elements of 99.999 + % purity, and the substrate-source was arranged to yield large area films with thickness variations less than 3%. In the evaporation process, the order of depositing Cu and In films is not important, while Cu must be electroplated before In because of the reaction of In with the Cu plating solution. The electroplating of Cu was carried out from a sulfuric acid solution of copper sulfate at a current density of 50-75 mA/cm²; the deposition rate was determined to be 1.1 $\mu\text{m}/\text{min}$ at 50 mA/cm². The electroplating of In was carried out from a sulfuric acid solution of indium sulfamate and sodium sulfamate (pH = 1.5-2) at a current density of 10-20 mA/cm² (6); the deposition rate was determined to be 0.19 $\mu\text{m}/\text{min}$ at 20 mA/cm². The samples were thoroughly cleaned before and after the plating process. On the basis of the densities of Cu, In, and CuInSe_2 , the use of 2.21 μm of In film and 1.0 μm of Cu film should yield 5 μm of CuInSe_2 film after selenium treatment.

The selenium treatment of Cu on Cu-In films was carried out in a hydrogen atmosphere using the apparatus shown schematically in Fig. 1. Hydrogen was purified by diffusion through palladium-silver alloy. A selenium container and the samples to be selenized were placed in a fused silica reaction tube of 59 mm od, and the tube was heated in a two-temperature zone furnace with each zone separately heated and controlled. The selenium was of 99.999 + % purity, and the selenium container was maintained at 440°C (vapor pressure of $\text{Se}_2 = 10$ torr). The partial pressure of selenium in the reaction tube was controlled by adjusting the flow rates of hydrogen through the selenium container and through the reaction tube. The temperature of Cu and Cu-In films was varied over a wide range, 300°C - 750°C . The duration of selenization was determined from the selenium content of the reaction mixture and the substrate temperature, usually 2-6h.

In the second approach, a Cu film on graphite was first selenized at 600°C to yield Cu_2Se films, and indium was deposited followed by selenium treatment at 550°C - 600°C .

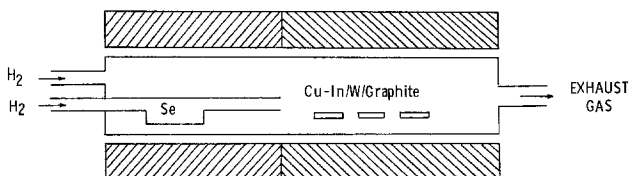


Fig. 1. Schematic diagram of the apparatus for the treatment of Cu or Cu-In films with selenium.

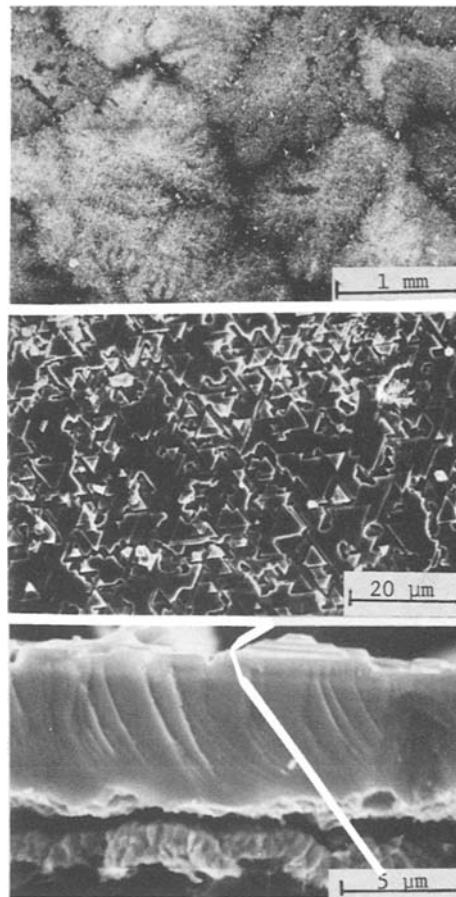


Fig. 2. Scanning electron micrographs of the surface of and vertical cross section of a CuInSe_2 film prepared by the selenium treatment of a Cu-In film on a W/graphite substrate at 650°C .

Results and Discussion

All Cu-In films used for selenium treatment consist of 2.21 μm of In and 1.0 μm of Cu. The selenization of Cu-In/W/graphite structures was carried out over the temperature range 300°C - 750°C . The use of high temperatures, such as 650°C or above, yields films with large grains, several millimeters in size. Figure 2 shows scanning electron micrographs of the surface of a typical film at two magnifications and the vertical cross section of the sample. The cross-sectional photograph indicates that the film is about 5 μm thick, as expected. The low magnification photograph of the surface shows only several grain boundaries, and the higher magnification photograph shows a large number of isosceles triangles of the same orientation, indicating that this crystallite has a two-fold symmetry. The formation of the large grain films is due apparently to the gas-liquid reaction, where the surface of liquid Cu-In film first reacted with selenium to form CuInSe_2 , and the subsequent diffusion of selenium through the surface film completes the transformation of Cu-In into CuInSe_2 . The composition of the large grain films was analyzed by the electron microprobe technique using a 10 keV, 25 nA beam on 60 spots of a specimen; the results including the standard deviations shown in Table I (sample no. 1) indicate that the large grain films are essentially stoichiometric CuInSe_2 .

The crystallographic properties of large grain CuInSe_2 films were determined by the x-ray diffraction technique. CuInSe_2 crystallizes in the chalcopyrite structure, and polycrystalline CuInSe_2 powder of random orientation is known to show three strong diffraction peaks associated with {112}, {204} and {220}, and {116} and {312} reflections with 2θ values of 26.66° , 44.36° , and 52.45° , and relative intensities of 70, 100, and 85, respectively. The diffraction spectra of large grain CuInSe_2 films were obtained by scanning 2θ in the range of 20° - 60° . An example

Table I. Composition of three copper indium selenide films by electron microprobe analysis

Sam- ple no.	a/o Cu (1σ)	a/o In (1σ)	a/o Se (1σ)
1	24.67 \pm 0.3 (0.35)	25.96 \pm 0.31 (0.40)	49.40 \pm 0.59 (0.67)
2	25.43 \pm 0.65 (1.13)	25.11 \pm 0.64 (0.76)	49.43 \pm 1.26 (1.52)
3	25.58 \pm 1.02 (0.74)	25.6 \pm 1.02 (0.67)	48.79 \pm 1.59 (0.59)

is shown in Fig. 3, where only the diffraction peak with 2θ value of about 26.70 is present, indicating that the large grain films are of {112} orientation.

The electrical resistivity of large grain CuInSe_2 films was measured by evaporating gold ohmic contacts on the surface and measuring the resistance through the thickness of the specimen. The Au- CuInSe_2 contact resistance was determined by the potential probe measurements, and the CuInSe_2 -substrate contact resistance was found to be negligible (less than $0.1 \Omega\text{-cm}^2$). The conductivity type and electrical resistivity of CuInSe_2 films were found to depend on the partial pressure of selenium, the flow rate of the reaction mixture, and the duration of selenium treatment. Qualitatively, when a less than stoichiometric amount of selenium was used, the resulting film was always n-type. On further treatment with selenium, the film became p-type, and its resistivity decreased with increasing duration of selenium treatment. No systematic work on the dependence of the resistivity of CuInSe_2 films on the selenization parameters was carried out. However, by controlling the process parameters to introduce an excess (0.1–0.6%) of selenium into the reaction tube, electrical resistivities in the range of 1 to $20 \Omega\text{-cm}$ have been obtained.

When the selenization of Cu-In films was carried out at temperatures below the melting point of Cu-In alloy, such as 500°C , the resulting films consisted of small grains, 2–3 μm in size. Figure 4 shows scanning electron micrographs of the surface and vertical cross section of a CuInSe_2 film prepared by the selenium treatment of a Cu-In film at 500°C . The film appears to be loosely packed. The thickness of the film measured from the vertical cross section is considerably larger than $5 \mu\text{m}$, indicating high porosity in the film. The porosity is apparently the result of the gas-solid reaction and is not readily controlled. However, the electron microprobe analysis (Table I, sample no. 2)

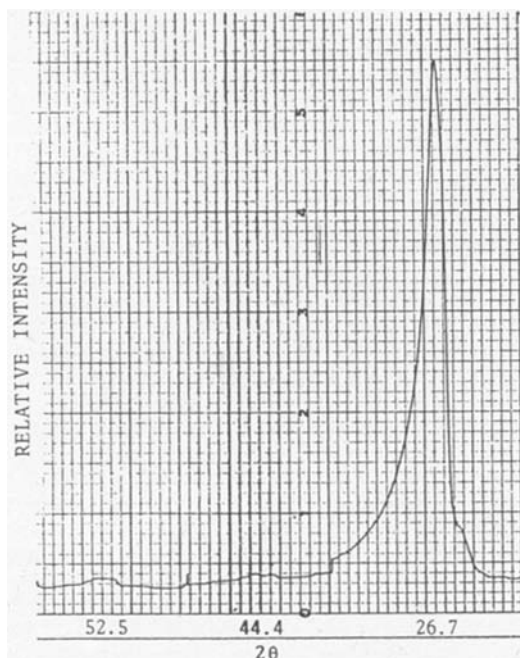


Fig. 3. X-ray diffraction spectrum of a large grain CuInSe_2 film on a W/graphite substrate.

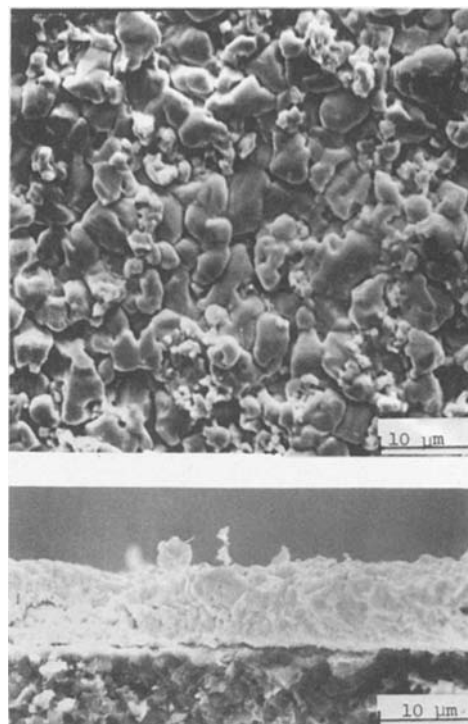


Fig. 4. Scanning electron micrographs of the surface and vertical cross section of a CuInSe_2 film prepared by the selenium treatment of a Cu-In film on a W/graphite substrate at 500°C .

indicates that the films are essentially stoichiometric in composition. X-ray diffraction spectrum showed the presence of all three diffraction peaks with 2θ values of 26.7° , 44.4° , and 52.5° . As the temperature of selenization was further reduced (to 350°C , for example), multiple-phase material was obtained; selenides of copper and indium

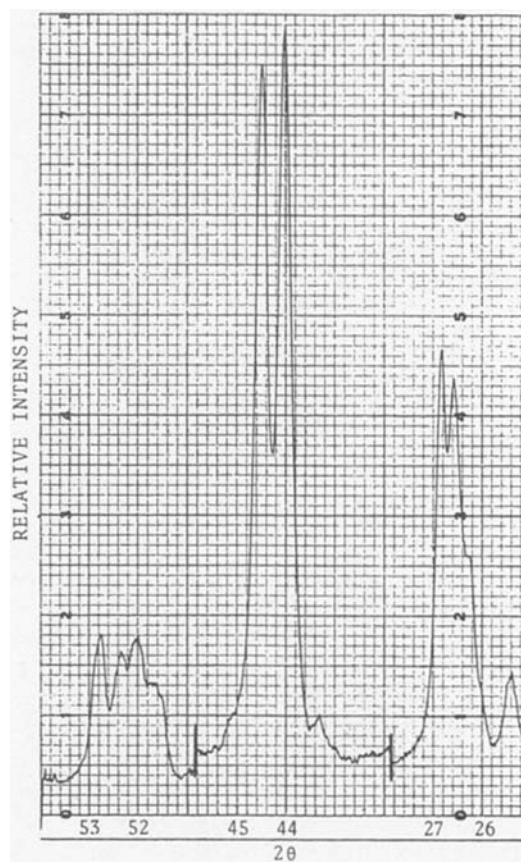


Fig. 5. X-ray diffraction spectrum of a typical cuprous selenide film on a graphite substrate.

were present in addition to CuInSe₂. While Cu forms only Cu₂Se, In forms four selenides: In₂Se, InSe, In₃Se₆, and In₇Se₃.

The conversion of Cu-films on graphite substrates to cuprous selenide takes place readily at 600°C. The selenization product was found to be Cu₂Se or a mixture of Cu₂Se and Cu_{2-x}Se, depending on the extent of selenization. The strong diffractions in polycrystalline Cu₂Se are associated with {111}, {220}, and {311} reflections with 2θ values of 26.34, 43.69, and 51.91 and relative intensities of 80, 100, and 80, respectively. The strong diffractions in polycrystalline Cu_{2-x}Se ($x \sim 0.15$) are associated with {111}, {220}, and {311} reflections with 2θ values of 26.75, 44.83, and 52.91 and relative intensities of 90, 100, and 80, respectively. Figure 5 shows a typical diffraction spectrum of a cuprous selenide film. The deposition of In followed by selenium treatment at 600°-650°C produced large grain CuInSe₂ films as identified by electron microprobe (Table I, sample no. 3) and x-ray diffraction. These films have essentially the same properties as those obtained by the high temperature selenium treatment of a Cu-In/W/graphite structure.

Summary

The heat-treatment of Cu-In films in a hydrogen-selenium atmosphere has been used for the preparation of CuInSe₂ films. The most important process parameter affecting the microstructure of CuInSe₂ is the temperature of the Cu-In film. Using liquid Cu-In films on a suitable substrate, the gas-liquid reaction yields single-phase, large grain, essentially stoichiometric CuInSe₂ films with a preferred {112} orientation, as shown by compositional analysis and x-ray diffraction. The electrical resistivity of

CuInSe₂ films can be controlled by the duration of selenization; the use of a large excess of selenium yields low resistivity p-type films. At Cu-In film temperatures below 600°C, the selenization process involves gas-solid reactions, and the resulting films consisted of loosely packed small grains and are porous in structure. Large grain CuInSe₂ films can also be prepared by the deposition and selenization of copper, followed by the deposition of indium and the selenization of cuprous selenide-indium structures.

Acknowledgment

This research was supported by the Electric Power Research Institute under Contract no. RP-1193-2.

Manuscript submitted Feb. 10, 1984; revised manuscript received April 17, 1984.

REFERENCES

1. W. Horig, H. Neumann, H. Sobotta, B. Schumann, and G. Kühn, *This Solid Films*, **48**, 67 (1978).
2. S. Wagner, J. L. Shay, and P. Migliorato, *Appl. Phys. Lett.*, **25**, 434 (1974).
3. See, for instance, L. L. Kazmerski, F. R. White, and G. K. Morgan, *ibid.*, **29**, 268 (1975); R. A. Michelsen and W. S. Chen, *ibid.*, **36**, 371 (1980); J. Peikoszewski, J. J. Loferski, R. Beaulieu, J. Beall, B. Roessler, and J. Shewchun, in "Conference Record of the 14th IEEE Photovoltaic Specialists Conference," p. 980, IEEE, New York (1980).
4. R. A. Mickelsen and W. S. Chen, in "Conference Record of the Sixteenth IEEE Photovoltaic Specialists Conference," p. 781, IEEE, New York (1982).
5. M. Hansen, "Constitution of Binary Alloys," p. 591, McGraw-Hill Book Co., New York (1958).
6. "Indium Plating," Indium Corporation of America, New York.

Photoelectrochemical Imaging

M. A. Butler*

Sandia National Laboratories, Albuquerque, New Mexico 87185

ABSTRACT

A device is described for producing video images from localized photocurrent measurements on electrode surfaces. Images generated from photoinduced electron-hole pair currents in passivating oxide layers on polycrystalline titanium and high resistance polycrystalline GaP photoelectrodes are shown as examples. The applicability of this device for producing images from other optically induced effects is also discussed. It is proposed that the localized heating from a focused laser beam can be used to image the current distribution on metal electrodes.

In a recent paper (1), localized photoelectrochemical measurements were used to study the properties of a 100Å thick oxide layer on polycrystalline titanium metal. Using a computer-controlled X-Y stage, crude line images, or maps of the photocurrent response of this sample were produced. Since that time, we have improved the equipment to the point where real video images can be made from the localized photocurrent measurements. The purpose of this paper is to describe the new apparatus, demonstrate the kind of images it can produce, and discuss possible applications to other situations.

Photocurrent generated by a focused light beam or electron beam has been used to produce images for some time in solid-state devices (2-4). The response time of such devices is rapid enough to allow generation of a whole image in a fraction of a second. Thus, the image can be displayed on a conventional cathode ray tube and periodically refreshed just as with conventional television images. For a semiconductor-electrolyte junction, however, the large interfacial capacitance limits the response time and requires that the image be built up slowly (5). This suggests outputting each piece of the picture as it is

formed, as with the line scans (5), or storing the information in a memory until the complete image is produced. The latter approach is the one we have taken with the present device.

Experimental

A schematic of the laser scanning system as it is presently configured is shown in Fig. 1. The laser is a Coherent Model CR-750k krypton laser with lines available from 800 to 351 nm. The beam is chopped at an appropriate frequency, usually 15.6 Hz, and focused onto the electrochemical cell. The cell is mounted on a computer controlled X-Y table, Klinger Model MT-160. The cell uses a quartz window with a thin (3 mm) electrolyte layer to minimize distortions of the laser beam. A conventional saturated calomel reference electrode is used. The cell is operated under potentiostatic control with lock-in detection of the photocurrents.

All measurements are made under active control of the computer which, through the Klinger controller, tells the table when to move, the direction, and step size. The individual localized photocurrent measurements are stored in the Colorado Video video expander, Model CV-275. This device contains a 256 × 256 digital memory array and

*Electrochemical Society Active Member.

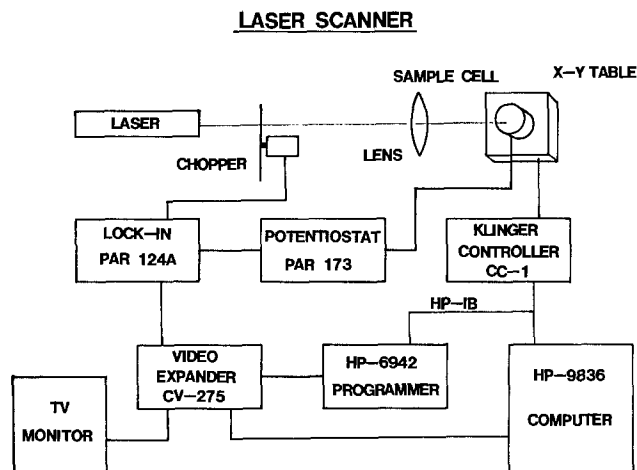


Fig. 1. Laser scanning system. Details of the operation are given in the text.

video signal generating circuitry which scans this memory 30 times a second to produce the video signal. The programmer, Model HP-6942, generates timing pulses at the command of the computer to digitize the incoming analog signal from the lock-in amplifier and to determine the memory location in which the digitized signal is stored. Thus the measurement sequence involves several steps. The computer tells the X-Y table to move to some position and wait for a given period of time. The computer then tells the video expander to digitize the analog signal from the lock-in amplifier and store it in a location corresponding to the position of the table. This process is then repeated until the complete image is produced. During this time, the contents of the memory are visible on the TV monitor so that the slow buildup of the image can be observed.

The computer also has direct access to the memory array in the video expander. This allows complete images to be entered into the computer for image processing or storage on disk files. In addition, the computer can write directly into the image memory array. This is useful for putting scale factors or additional information directly on the monitor screen and to display previously stored images.

This system with direct computer control of the measurement process provides considerable flexibility because many factors are controlled by the software. For example, the dwell time of each point is set by typing it into the computer. Since the image always consists of an array of 256×256 data points, the resolution of any image is one step. Since the step size is entered into the computer, the resolution and the magnification of the image may be easily changed at the computer keyboard. The smallest step size with these tables is $1 \mu\text{m}$. Thus the maximum magnification will be an image $256 \times 256 \mu\text{m}$.

A number of other factors are important in determining the resolution besides the minimum step size of $1 \mu\text{m}$. The focused laser spot is ultimately limited by diffraction effects to

$$\Delta \approx 2\lambda \frac{F}{d} \quad [1]$$

where λ is the wavelength of light, and F the focal length of the lens and d the laser beam diameter. One also has to worry about vibration, and a good optical table is important if one is trying to approach the diffraction limit. Another problem is damage to the sample. 1 mW of power focused onto $10 \mu\text{m}^2$ gives a power density of 10 kW/cm^2 . This can have drastic consequences for the surface, particularly at the solid-liquid interface. Finally, we must be concerned with the effects of scattered light as the whole electrode surface is photosensitive rather than just the spot on which the laser is focused. For short focal length lenses necessary to achieve small spot sizes, scattering

within the lens system and from the sample surface and back off the lens can illuminate a considerable area of the surface. Since the scattered light illuminates a much larger area, relatively weak scattered light can cause a signal comparable to that arising from the focused laser beam. All of these factors conspire to limit the resolution of the laser scanning system. The best we have observed, without a floated optical table, is $3 \mu\text{m}$.

Results

The kind of photoelectrochemical image that this system can produce is illustrated in Fig. 2. This is an image of high resistance polycrystalline GaP. The step size is $6 \mu\text{m}$ in the Y direction and $8 \mu\text{m}$ in the X direction. Different step sizes in different directions are necessary so as to not distort the image. The memory is a 256×256 square array while all video displays have a 4×3 relationship between X and Y axes. This modification was made by simply changing the program. Typical photocurrents are $0.1\text{--}1 \mu\text{A}$. At the exciting wavelength, 476 nm , the optical absorptions depth is $5\text{--}10 \mu\text{m}$.

A number of interesting features are immediately obvious. It seems that the grain boundaries are brighter (more photocurrent) than the exposed faces of the grains. This is in contrast with images of polycrystalline silicon solar cells, where grain boundaries show up dark because of enhanced recombination at the grain boundaries (6). Comparison of the photocurrent image with a photograph of the surface, shown in Fig. 3, indeed shows that the bright lines correspond to grain boundaries. However, not all grain boundaries result in significantly increased photocurrents. Apparently, some other factor is necessary for the boundaries to show up bright in the photocurrent image. One explanation might be that for these highly resistive samples the electrically active grain boundaries act as conductive regions and collect minority carriers from surrounding grains while most of the carriers recombine at defects and impurities. Thus, only the electrically active boundaries would show up bright in the photoelectrochemical image. These are the boundaries with large lattice mismatch and thus high densities of states.

Another interesting feature is the dark streaks, which are not localized to individual grains. These also appear on the photograph (Fig. 3), and they are probably scratches left over from the polishing of the sample. Apparently, mechanical polishing of GaP introduces recombination centers in the material to a considerable depth (7). There are also other dark patches, which are surface effects. Etching and Ru ion treatment of the surface produces marked changes in these features of the image.

Another interesting photocurrent image is shown in Fig. 4. The photoresponse from the $\sim 100\text{\AA}$ thick TiO_2 layer on polycrystalline titanium clearly shows evidence of the underlying metal grain structure. This may be compared with a photograph of the same region of the sample shown in Fig. 5. Apparently, the properties of the oxide depend on the underlying crystallographic face on which it grows.

The photoresponse of the passivating layer also depends on the growth conditions for the oxide and its history with respect to exposure to bandgap light. We find that the grain structure is only weakly visible for oxide grown in $0.2N \text{ Na}_2\text{SO}_4$ under potentiostatic control by slowly increasing the applied potential to $+2.0V(\text{SCE})$ while keeping the current density below $3 \mu\text{A/cm}^2$. However, flooding the surface with 30 mW/cm^2 of 351 nm light for 2 min makes the grain structure clearly visible. This is illustrated in Fig. 6 for identical measurement conditions. One possible explanation is the filling of electronic traps in the oxide by the bandgap light, which then distorts the electric field in the oxide layers and, thus, changes the photoresponse (1). The variations from grain to grain would then come from differing trap densities. Such an interpretation suggests that the contrast could be removed by emptying the traps. We tried to do this by flooding the surface with red (647 nm) light at 1 W/cm^2 for 20 min and by leaving the cell under open-circuit con-

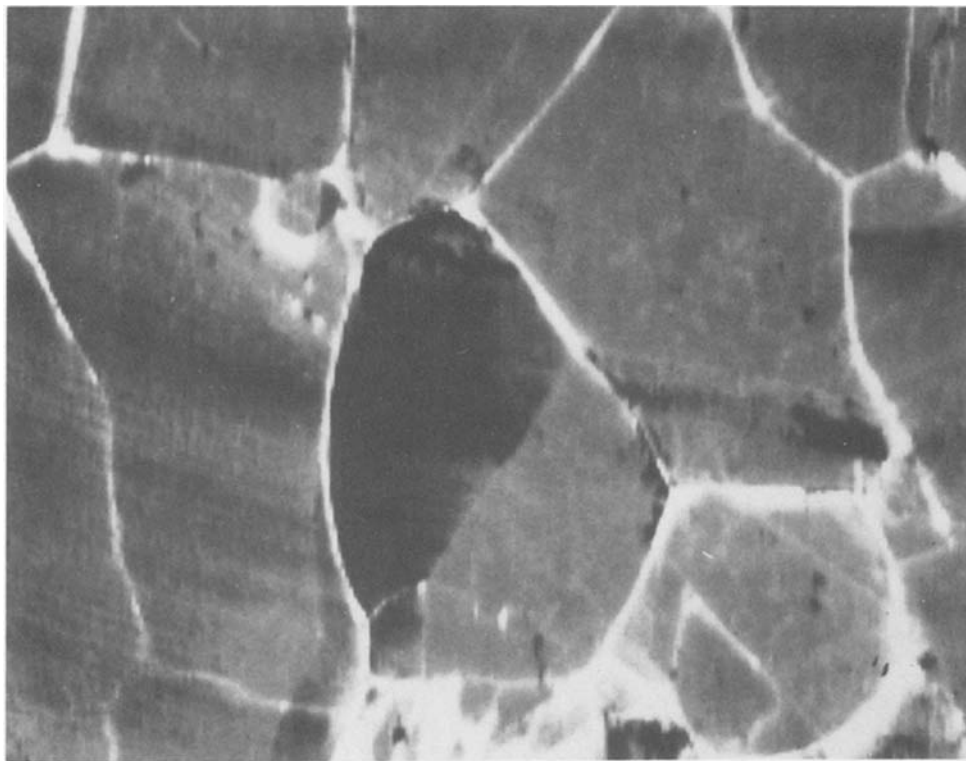


Fig. 2. Photoelectrochemical image of polycrystalline GaP photoelectrode in 0.1M HClO₄ at -1.0V (SCE). Dwell time at each point is 0.15s. Light source is 476 nm line of an argon ion laser with 1 mW incident power.

ditions overnight. Neither experiment had a significant effect on the visibility of the grain structure.

Growth of the oxide layer on the polycrystalline titanium under potentiostatic control by stepping the potential to +2V(SCE) results in a uniform photoresponse with no grain structure visible. Furthermore, flooding with bandgap light reduces the overall photoresponse but does not make the grain structure visible. Thus, the probable different morphology of the film with different growth rates modifies the photoresponse of the passive film on

a polycrystalline surface. We speculate that the optical activation necessary to see the grain structure comes from charging of trap states associated with defects. These defects then move under the influence of the large electric field in the film (10^6 V/cm) and are trapped at one of the two interfaces. This is why the effect is not easily reversible. The density of available defects depends on the underlying metal crystallographic face, and this explains the variations in photocurrent from grain to grain. In the more rapidly grown film, the growth rate is such as to

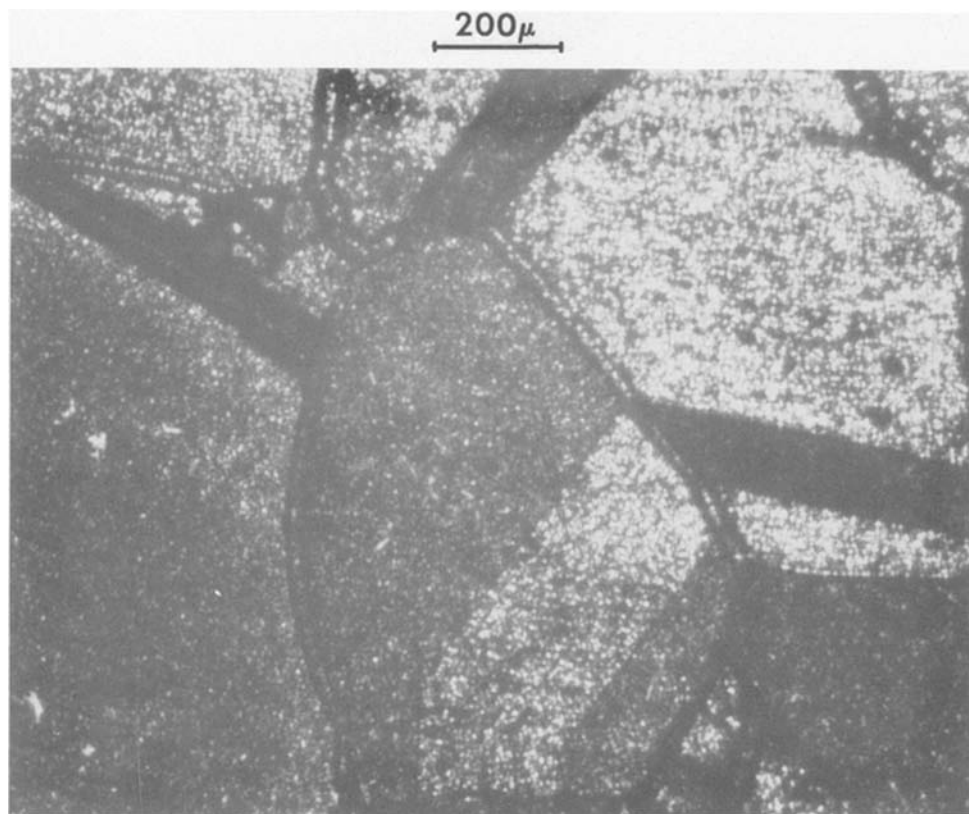
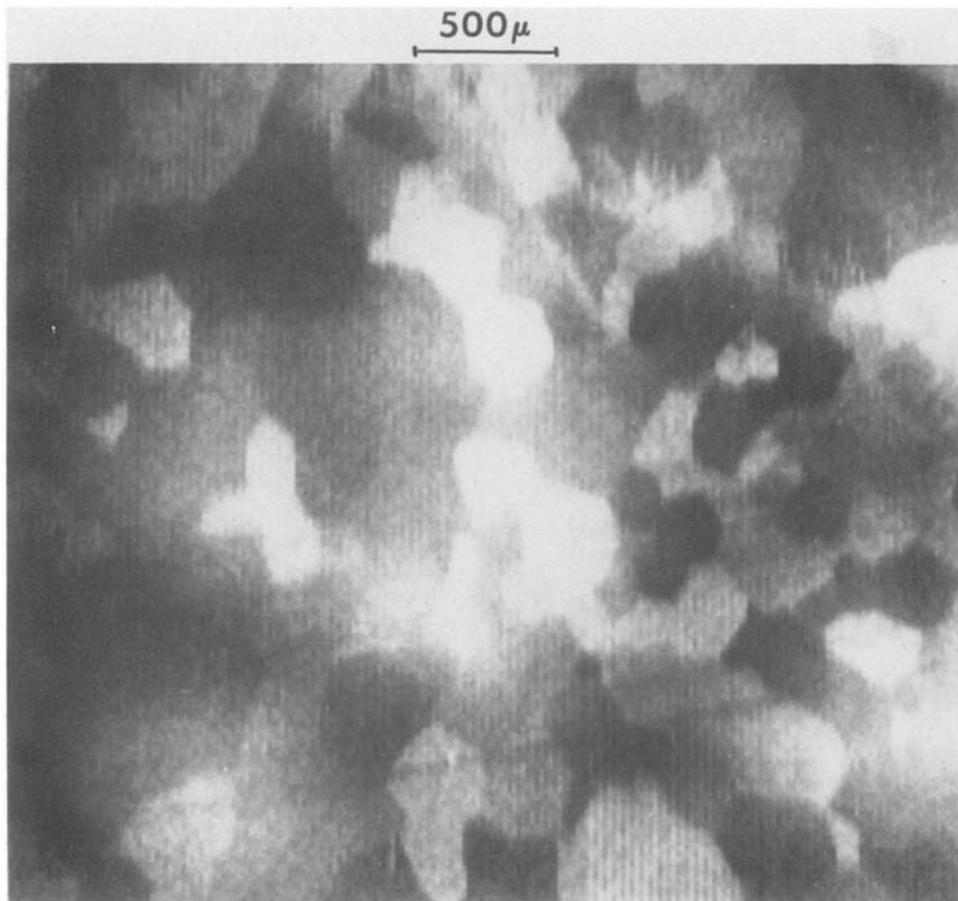


Fig. 3. Photograph of the polycrystalline GaP photoelectrode used to produce the photocurrent image.

Fig. 4. Photoelectrochemical image of 100Å thick oxide layer on polycrystalline titanium. The electrolyte is 0.2N Na₂SO₄, and the potential is +2.0V (SCE). Light source is the 351 nm line of a krypton laser with incident power of 300 μW. The dwell time at each point is 0.1s. Typical photocurrents are a few tenths of a microampere.



produce a uniform density of defects, which results in a uniform photoresponse.

Clearly, the above interpretation is very speculative, and further experiments are needed to find out what is really happening. However, these results clearly show that photoelectrochemical images of passive films on titanium can give valuable information about the detailed structure of the oxide.

Discussion

While this paper is principally concerned with photoelectrochemical imaging of solid-liquid interfaces, it is worthwhile to spend some time to point out the versatility of this imaging system. Images can be produced using any optically stimulated effect that can be quantitatively measured. Previously, we have produced line images from measured variations in optical absorption in a thin sample of polycrystalline GaP (8) and from the photoluminescence of GaAs, ZnSe, and GaAsP (9). Images could also be made with reflectivity, electroreflectance, Raman, and ellipsometric measurements.

There is one other aspect of optically stimulated effects that is worth exploring in some detail. In addition to inducing effects directly related to light absorption such as photocurrent, the absorbed light can be degraded to produce local heating of the interface. Thus, we should expect that thermally induced effects can be used to produce images. In particular, we should be able to modulate locally the current density at any electrode on which an electrochemical reaction is occurring. As we will show, this allows the mapping of the current density of a reaction on an electrode. You should be able to study, for example, the relative current densities on crystalline faces and grain boundaries in polycrystalline metal electrodes.

In order to explore this idea, let us consider a simple model. This model is undoubtedly lacking in many respects, but perhaps contains enough factors to realistically display the effect of interest. We will only consider the measurements in the Tafel region, where the current density is assumed to have the following simple form

$$j = j_0 \exp\left(\frac{\alpha\eta}{kT}\right) \quad [2]$$

where α is a parameter between 0 and 1, η is the overpotential, k Boltzmann's constant, T is the absolute temperature, and j_0 the exchange current density. Normally we think of the exchange current density as having a temperature dependence of the form (10)

$$j_0 = A \exp(+\phi/kT) \quad [3]$$

where any weak temperature dependence to A will be ignored. We also assume that current density may be position dependent. Thus the total current is given by

$$J = \sum_k j_k \quad [4]$$

The area of each element k is small compared to the total area of the electrode and for simplicity is taken as equal to the illuminated area. Similarly we assume a uniform temperature T for the electrode surface except for the illuminated element which has a temperature $T + \Delta T$. This approximation implies similar optical absorption and loss mechanisms across the whole surface. Otherwise ΔT may be position dependent. It also implies poor thermal conduction in the plane of the interface. Finally, we assume a single overpotential between electrode and electrolyte. This is appropriate in the limit of infinitely conductive electrodes and electrolytes; otherwise, nonuniform overpotentials would result in sustained charge flows parallel to the interface.

Within the limits of this simple model, we can now explore the effects of illuminating a small area of an electrode at which a simple electrochemical reaction is taking place. Since measurements may be made galvanostatically or potentiostatically, we will consider these two possibilities in this order. For the galvanostatic case with no light, the current is given by

$$J = \sum_k j_k = \sum_k A_k \exp\left(\frac{\alpha\eta + \phi}{kT}\right) \quad [5]$$

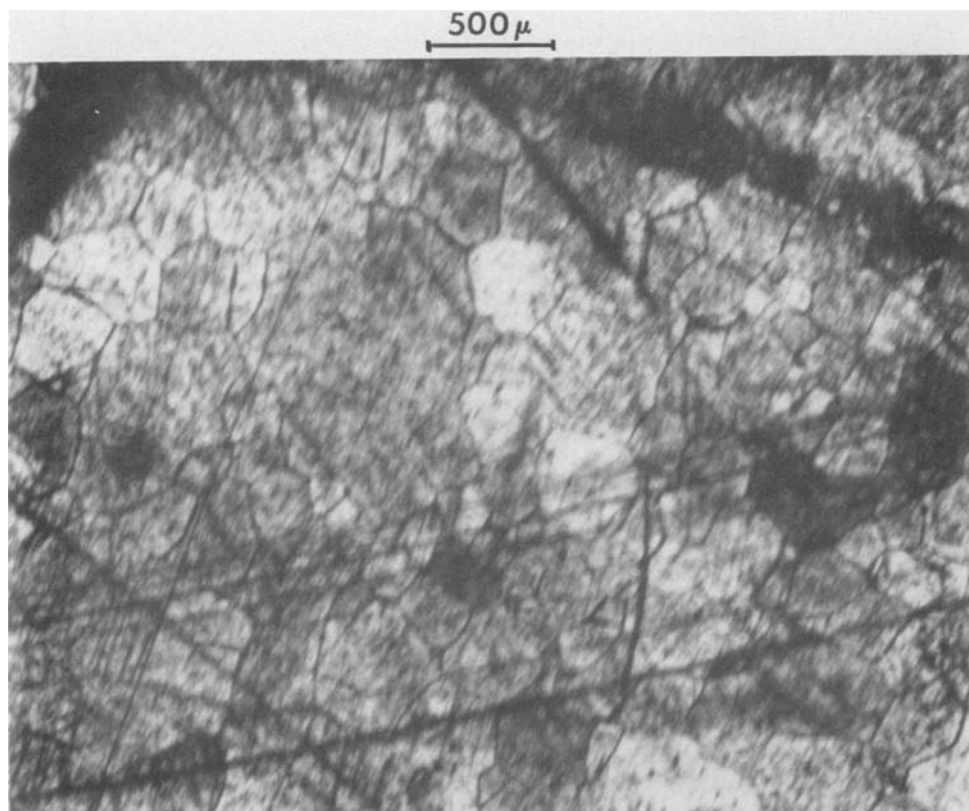


Fig. 5. Photograph of polycrystalline titanium electrode surface showing the same region as in Fig. 4.

When the area of element m of the electrode surface is illuminated, the total current is given by

$$J = \sum_k A_k \exp\left(\frac{\alpha[\eta + \Delta\eta] + \phi}{kT}\right) + A_m \exp\left(\frac{\alpha[\eta + \Delta\eta] + \phi}{k[T + \Delta T]}\right) - A_m \exp\left(\frac{\alpha[\eta + \Delta\eta] + \phi}{kT}\right) \quad [6]$$

In the limit of very small thermal modulation, we can expand the exponentials and only keep terms to first order in $\Delta\eta$ and ΔT . Then, solving for $\Delta\eta$, we find

$$\Delta\eta = \left(\frac{\Delta T}{T}\right) \left(\eta + \frac{\phi}{\alpha}\right) \frac{A_m}{\sum_k A_k} \quad [7]$$

A much simpler argument can be made for the potentiostatic case. Since η is held fixed and the temperature

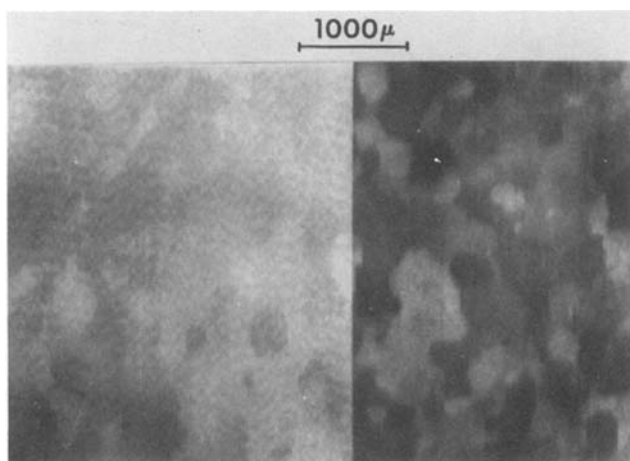


Fig. 6. Photocurrent image of passive film on polycrystalline titanium surface under the same conditions as in Fig. 4. The left side is freshly grown oxide, while the right side is after flooding the surface with 351 nm light, as discussed in the text.

only changes for the illuminated element m , the only change in current will be for element m . Taking the current expression for this element only

$$j_k = A_k \exp\left(\frac{\alpha\eta + \phi}{kT}\right) \quad [8]$$

and differentiating with respect to T , we find

$$\Delta j_m = -j_m \left(\frac{\Delta T}{T}\right) \left(\frac{\alpha\eta + \phi}{kT}\right) \quad [9]$$

Thus it appears that, within the limits of the simple model, an effect should be observed both under galvanostatic and potentiostatic control. It is of interest to explore the size of the effects expected from thermal modulation of the electrochemical reaction. Two papers (11, 12) have recently appeared which utilize thermal modulation with no spatial resolution to study the electrochemical kinetics. The importance of these papers is that they demonstrate the effect. The only extension required here is localization of the heat input to produce images. Miller (11) observes a ratio $\Delta j/j \sim 1$ with a power density of ~ 10 W/cm² incident upon a strongly absorbing surface. By focusing the light, the size of the effect decreases by the ratio of the areas. However, the incident power and thus the term $\Delta T/T$ should increase correspondingly. This all suggests that the effect will be large enough to observe if the electrochemical reaction is carefully chosen.

Preliminary experiments have been performed using the old version of the laser scanner which only produced line maps (1). Effects were observed using Cu electrodes in CuSO₄/H₂SO₄ electrolytes. The electrode was biased so as to decrease the likelihood of the existence of copper oxide. However, lack of reproducibility and concerns about a photoelectrochemical response from possible copper oxide do not allow the results to be convincing evidence of the effect. It is hoped that others will pursue this avenue of research and produce convincing evidence for thermal imaging of electrochemical reactions.

Conclusions

The device described in this paper is a useful tool for studying the solid-liquid interface. Images convey infor-

mation in a manner that humans can easily assimilate. Furthermore, the spatial resolution gives insight into the role of grain boundaries and defects. This device can also be used to examine other surfaces and to form images from photoinduced effects other than the photocurrent. It appears that using the focused laser to locally heat an electrode surface will allow imaging of electrochemical reactions by thermal modulation of the reaction kinetics. This kind of effect would be very useful for studying the role of grain boundaries on polycrystalline metal electrodes.

Acknowledgment

The author would like to thank W. H. Smyrl for many useful discussions and D. A. Bouchard for technical assistance.

Manuscript received March 12, 1984.

Sandia National Laboratories assisted in meeting the publication costs of this article.

REFERENCES

1. M. A. Butler, *This Journal*, **130**, 2358 (1983).
2. T. H. DiStefano, *J. Appl. Phys.*, **44**, 527 (1973).
3. C. H. Henry and R. A. Logan, *ibid.*, **48**, 3962 (1977).
4. D. V. Lang and C. H. Henry, *Solid State Electron.*, **21**, 1519 (1978).
5. T. E. Furtak, D. C. Canfield, and B. A. Parkinson, *J. Appl. Phys.*, **51**, 6018 (1980).
6. C. H. Seager, *ibid.*, **53**, 5968 (1982).
7. M. A. Butler and D. S. Ginley, *This Journal*, **128**, 712 (1981).
8. M. A. Butler and C. H. Seager, Unpublished data.
9. M. A. Butler and W. Hobson, Unpublished data.
10. P. Delahay, "Double Layer and Electrode Kinetics," p. 154, Interscience, New York (1965).
11. B. Miller, *This Journal*, **130**, 1639 (1983).
12. C. Gabrielli, M. Keddan, and J. F. Lizec, *J. Electroanal. Chem.*, **148**, 293 (1983).

Technical Notes

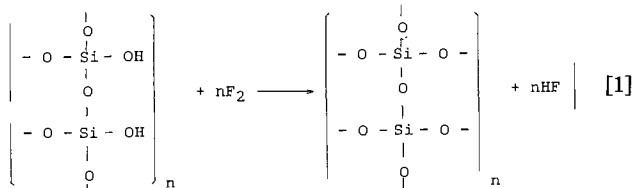


Viscosity Points and OH Absorption Removal for ZnO-B₂O₃-PbO-SiO₂ Passivation Glasses

Keiji Kobayashi

Toshiba Corporation, Toshiba Research and Development Center, Kawasaki, Japan

Low flow point (1), low polarization (2), and OH-free highly purified glasses have recently been needed for semiconductor device passivations. Additionally, high water durability, high electrical resistivity, and noncrystallizable glass properties are also indispensable to assure the reliability of the devices. Passivation glasses filled under several conditions described herein can be obtained from the compositional improvement of glasses (3, 4). Glass compositions including fluoride containing ZnO-B₂O₃-PbO-SiO₂ systems have been formulated and investigated. It is generally known that the flow point or softening point of such glasses can be lowered by increasing B³⁺ and Pb²⁺ contents, and that the durability of glasses to water can be enhanced by raising Si⁴⁺ and Zn²⁺ contents. Also, the polarizability of the glasses can be reduced by increasing the B³⁺ content in glass compositions (5). Batch compositions were melted at 1350°C for 3h in a Pt crucible using an electric furnace. After melting, molten glass was poured on a stainless steel plate and annealed. Glass was shaped into a 10 × 20 × 2 mm plate by grinding for infrared transmission measurement. Infrared absorption spectra were measured by the use of a Hitachi spectrophotometer. The OH radicals removal is represented in the following reaction



In addition, dry air bubbling technique is effective for the complete removal of OH to prevent near-infrared OH absorption. This technique involves blowing dry air

through the molten glass liquid during melting. This paper discusses variations in viscosity points, including the flow point, with chemical compositions and the removal of the near infrared OH absorption band for a typical passivation glass. Chemical compositions of ZnO-B₂O₃-PbO-SiO₂ glass systems are represented in Table I. Differential thermal analysis (DTA) curves for them, measured

Table I. Chemical composition of passivation glasses (w/o)

composition glass No	ZnO	ZnF ₂	Al ₂ O ₃	P ₂ O ₅	B ₂ O ₃	PbO	SiO ₂
(1)	18	1	5		8	25	43
(2)	55		5	5	30		5
(3)	54	1	5	5	31		4
(4)	58			5	24	3	10
(5)	15	1	3		55	10	16

Table II. Glass viscosity points measured using DTA curves

viscosity glass No point	T _g (°C)	M _g (°C)	T _s (°C)	T _{5int} (°C)	T _f (°C)
(1)	572	617	700	750	770
(2)	560	580	630	660	—
(3)	560	585	630	660	755
(4)	565	585	635	665	720
(5)	535	565	—	610	675

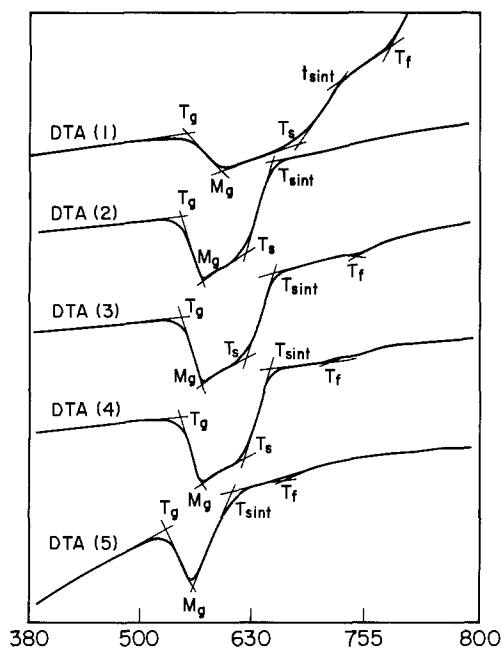


Fig. 1. DTA curves for ZnO-B₂O₃-PbO-SiO₂ passivation glasses

using the Rigaku DTA system, are given in Fig. 1, where T_g is glass transition point ($\log \eta = 13.3$), M_g is deformation point ($\log \eta = 11.0$), T_s is softening point ($\log \eta = 7.6$), T_{sint} is sintering point ($\log \eta = 6.0$), and T_f is flow point ($\log \eta = 5.0$). The heating rate for measuring DTA curves was 10°C/min. As listed in Table II, T_g , T_s , T_f , and the other points are raised with an increase in SiO₂ and a decrease in B₂O₃, regardless of the amount of ZnO and PbO. As the Al₂O₃, P₂O₅, and ZnF₂ contents are small, it seems likely that they do not affect the variations in glass viscosity points. Typical infrared absorption spectra are represented in Fig. 2, which exhibit sharp absorption bands nearly at 2.7 μ m, caused by OH stretching vibration. Compared with the spectrum for an untreated glass without fluoride, the OH absorption band removal was carried out completely by dry air bubbling treatment for a fluoride containing molten glass. Low flow point and OH-free glasses are suitable for semiconductor device passivations, because they are not harmful to the reliability and I-V curves of passivated devices.

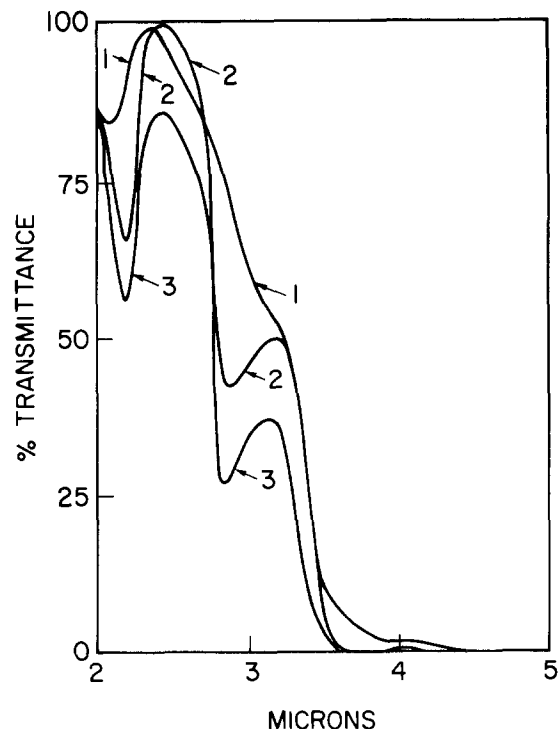


Fig. 2. Infrared transmittance for a typical ZnO-B₂O₃-PbO-SiO₂ glass (no. 5.). Curve 1: Fluoride containing glass treated for 30 min by dry air bubbling. Curve 2: Fluoride containing glass. Curve 3: Fluoride-free untreated glass.

Acknowledgment

The author is indebted to Mr. Minoura of Toshiba Glass Industry Company for passivation glass melting.

Manuscript submitted March 13, 1984; revised manuscript received May 16, 1984.

Toshiba Corporation assisted in meeting the publication costs of this article.

REFERENCES

1. A. Yamamoto, *Jpn. Analyst*, **14**, 692 (1965).
2. E. H. Snow and M. E. Dumesnil, *J. Appl. Phys.*, **37**, 2123 (1966).
3. D. L. Flowers, *This Journal*, **128**, 2179 (1981).
4. M. E. Dumesnil and H. Hewitt, *ibid.*, **117**, 100 (1970).
5. K. Kobayashi, *J. Appl. Phys.*, To be published.

Corrosion of FeCrAl, FeCrAlY, and FeCrAlHf Alloys in High Temperature H₂-H₂O-H₂S Environments

T. T. Huang,* Y. C. Lin, D. A. Shores,* and E. Pfender

Corrosion Research Center, University of Minnesota, Minneapolis, Minnesota 55455

High temperature corrosion plays an important role in the development of many combustion and coal gasification processes. In gasification processes, various grades of fuel gas are produced by the reaction of coal with steam and oxygen at high temperatures. The resulting gas contains hydrogen, steam, carbon dioxide, carbon monoxide, and some methane. It also contains low levels of hydrogen sulfide and other impurities derived from the coal. Reaction of such impurities with alloys is a common cause of corrosion. For example, sulfidation has been shown to have a devastating effect on many metallic structural components in coal gasification environments (1-3).

*Electrochemical Society Active Member.

In a typical coal gasification process, the atmosphere has a low oxygen activity, but relatively high activities of sulfur, carbon, hydrogen, and nitrogen (1). It is becoming increasingly apparent that available stainless steels and superalloys do not have adequate corrosion resistance in such environments (3, 4). To survive, an alloy must form a compact, protective scale, which acts as a barrier to the penetration of sulfur or carbon to the metal. All stainless steels and superalloys form oxide scales in these environments, but the scales offer widely differing degrees of protection. Many factors may contribute to the less-than-optimum performance of the oxide scales. Much previous work has been carried out to evaluate the performance of alloys in environments that simulate to varying degrees the expected exposure conditions in coal gasifiers.

Recently, several studies have addressed mechanistic questions concerning the protection offered by oxide scales to environments containing H_2S (5-9). Most studies found that the resulting kinetics of attack and the morphology of the scale depend upon the initial exposure conditions. If the alloys were exposed to oxidation/sulfidation conditions from the start, the scale typically would be composed of both oxides and sulfides, and the rate of attack would be fairly fast (5-9). If the alloys were preoxidized, then the environment switched to oxidation/sulfidation conditions without cooling the specimen, these oxide scales were found to be protective in some cases; however, the details differ among investigators. Rao *et al.* (5) found preoxidation of 310 stainless steel at 877°C in low oxygen potentials to be beneficial. Loudjani *et al.* (7) also found preoxidation of Fe-Cr-Al, Fe-Ni-Al, and Fe-Ni-Cr-Al at quite a high temperature (1200°C) to be beneficial, and concluded that Al_2O_3 scales were more effective barriers than Cr_2O_3 scales. However, Mari *et al.* (8) found the preoxide scale formed on Fe-Cr-Al at 1000°C to be an effective barrier to sulfur vapor, but to eventually breakdown in H_2 - H_2S environments. The time to breakdown increased as the preoxidation time, and hence the scale thickness, increased. The question of whether the sulfur penetrates the scale by solid-state diffusion or by permeation down cracks and pores is not universally resolved. Indeed, a variety of behavior may be observed, depending on the morphology of the oxide scale, which in turn depends on the alloy system, the temperature, and the environment in which it was grown.

In this work, the protection provided by an Al_2O_3 scale in a simple simulation of a coal gasification environment has been studied. Particular attention has been paid to the effect of the addition of a reactive element, Y or Hf, on sulfidation resistance. These elements are known to enhance oxidation resistance by promoting scale adherence (10, 11).

Experimental Procedure

The alloys which have been studied are Fe-18%Cr-6%Al, Fe-18%Cr-6%Al-0.3%Y, and Fe-18%Cr-6%Al-1%Hf (weight percent). Samples of these alloys were obtained from ingots that had been tungsten arc melted several times in an argon atmosphere, then drop-cast into a water-cooled copper mold. The ingots were subsequently homogenized at 1050°C for 10h in sealed quartz capsules. Small coupons from the ingots were polished through 600 grit SiC paper, followed by thorough cleaning and degreasing.

Gaseous environments containing H_2 and H_2O or H_2 - H_2O - H_2S were prepared by passing carefully metered flow rates of H_2 through a water saturation column held at a controlled temperature. In cases "C" to "E," a H_2/H_2S mixture was blended with the H_2/H_2O flow. Five different gas mixtures were prepared; their compositions and the equilibrium activities of oxygen and sulfur at 900°C are listed in Table I.

Coupons were exposed under two different conditions: some were exposed directly to gases "C," "D," or "E"; others were first preoxidized in "A" (various times at 900°C) or in "B" (10h at 1100°C), then the gas was changed to one of the sulfur bearing gases. Only FeCrAl specimens were preoxidized at 1100°C; they were slowly cooled to 900°C, then exposed to gas "E." The compositions of gases "C," "D," and "E" are indicated on the Ellingham plot of $\log(p_{S_2})$ vs. $\log(p_{O_2})$ shown in Fig. 1. After expo-

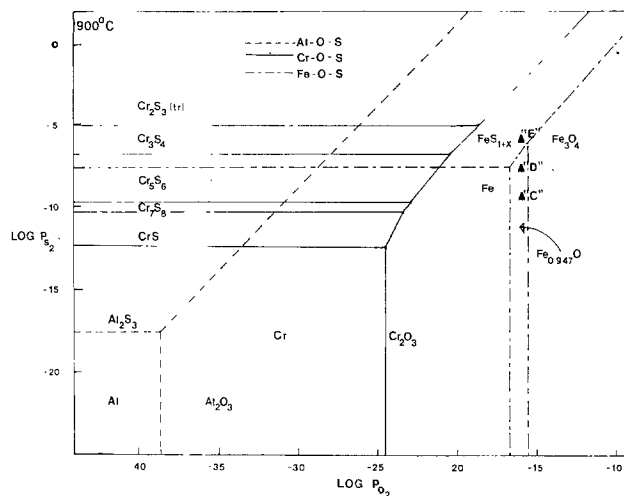


Fig. 1. Ellingham diagram for the systems Al-S-O, Cr-S-O, and Fe-S-O at 900°C. The triangles labeled "C," "D," and "E" are experimental gas compositions (see Table I).

sure, the coupons were examined metallographically and by scanning electron microscopy. Auger electron spectra (AES) were obtained from some of the specimens.

An acoustic emission technique was developed to determine whether oxide scales cracked during preoxidation. A schematic diagram of the experimental setup is shown in Fig. 2. The specimen was suspended directly on an Al_2O_3 rod in the center of a high temperature resistance furnace. The temperature of the specimen was measured with a thermocouple. The Al_2O_3 rod, which served as the waveguide, was clamped cantilever-fashion to a piezoelectric transducer outside the furnace. The specimen and transducer were inside a quartz tube, through which the gas mixtures were passed. When cracks occurred, the elastic energy released traveled to the transducer, which produced an electrical signal. The transducer was sensitive to a wide range of frequencies, but the output was filtered to a range of 150-250 kHz. The signal from the transducer was amplified, filtered, then amplified again, and passed to a digital counter. The total amplification was 97 dB. The counter summed the number of signals above a preset threshold. A practical threshold setting was determined with the sample in place and gas flowing but with the furnace cold; the gain was slowly increased until the background noise began to be counted, then the setting was backed off slightly. An analog voltage proportional to the count summation was plotted vs. time (using a ramp generator) on an X-Y plotter. It is well known from acoustic emission studies of cracking in metals that a single cracking event can produce a burst of several elastic waves, and hence the num-

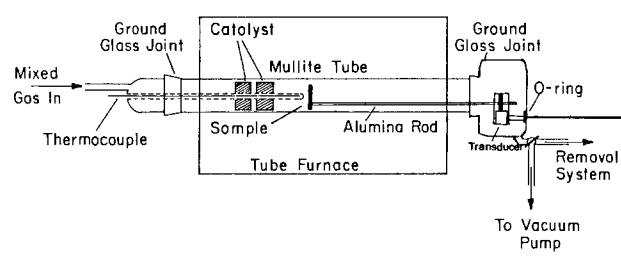


Fig. 2. Schematic diagram of the experimental setup for acoustic emission measurements during high temperature oxidation.

Table I. Compositions of gaseous environments (atm)

	$p(H_2)$	$p(H_2O)$	$p(H_2S)$	$p(Ar)$	$\log(p_{O_2})$	$\log(p_{S_2})$
"A"	0.414	0.586	—	—	-15.9	—
"B"*	0.968	0.0313	—	—	-16.0	—
"C"	0.384	0.544	0.00011	0.072	-15.9	-9.96
"D"	0.321	0.455	0.00092	0.223	-15.9	-7.96
"E"	0.135	0.191	0.0030	0.671	-15.9	-6.10

* Gas "B" was used for preoxidation at 1100°C.

ber of counts will usually far exceed the number of individual cracks. In the present work, bursts of acoustic signals were widely separated in time, usually minutes apart to even hours apart. For the present purposes, it was not necessary to determine if a burst corresponded to several closely spaced, sequential cracks or to a single crack giving multiple counts; the different alloys behaved very differently, and the conclusions are clear without a detailed analysis of the individual signals. Clearly, a detailed signal analysis would be desirable, and work along that avenue has begun.

Results

Oxidation/sulfidation experiments.—Coupons of FeCrAl, FeCrAlY, and FeCrAlHf alloys were exposed to gas mixtures "C," "D," and "E" at 900°C. The activities of sulfur and oxygen in the gas were within the phase stability regions of Al_2O_3 , Cr_2O_3 , and FeS, as shown in Fig. 1 on the Ellingham diagram for the superimposed systems Fe-S-O, Cr-S-O, and Al-S-O (13). The results on the FeCrAl alloy are illustrated in Fig. 3-6. AES from the surface of the specimens after reaction are shown in Fig. 3a-3c. These data show that only Al_2O_3 formed on the surface of this alloy after exposure to gas "C." At a higher sulfur activity, gas "D," (but at the same oxygen activity of 10^{-16} atm) a small amount of Cr_2O_3 appeared on the surface along with the predominant Al_2O_3 (Fig. 3b). At a still higher sulfur activity, gas "E," the scale was largely sulfide (predominantly FeS).

A scanning electron micrograph (SEM) of the surface of the sulfide scale is shown in Fig. 4 for FeCrAl. An enlarged view is shown in Fig. 5a, where the brighter area represents the sidewall of a sulfide block and the darker area is the top. Figure 5 also includes the corresponding AES mapping for S, Fe, O, and Cr for the same area. It is apparent that the sidewall is rich in Al and O (Al_2O_3) and the top is rich in Fe and S (FeS). Using Ar ion sputtering to remove successive layers from the surface at points "1" and "2" (as indicated on Fig. 5a), the chemical composition at different depths in the scale can be revealed. The results, shown in Fig. 6a and 6b, indicate that each block is essentially FeS containing some Cr and a small amount of Al, with a thin layer of Al_2O_3 at the surface of each block. These results suggest that Al can diffuse through FeS to the surface of the blocks, where it is oxidized. A cross section (fracture surface) of the sulfide scale is shown in Fig. 7. The outer layer is FeS; the inner scale is largely Al_2S_3 with an iron-chromium sulfide spinel intermediate layer (as determined by x-ray diffraction analysis).

Exposure of FeCrAlY and FeCrAlHf coupons to gases "C," "D," and "E" produced results very similar to those described above for FeCrAl. Since these tests were isothermal, the beneficial effect of the reactive elements on scale adherence was of little advantage. In particular, these alloys also formed sulfide scales in gas "E." It has been suggested that Hf and Y promote nucleation and formation of oxide scales and, therefore, enhance sulfidation resistance (14). However, our experience with the experimental procedure outlined above does not support a view that Hf or Y are inherently beneficial. As will be shown later, the physical integrity of the scale is critical. Under exposure conditions such as thermal cycling, where scale adherence is poor without Hf or Y, these elements could well be beneficial to sulfidation resistance.

Preoxidation followed by sulfidation.—In the previously described experiments, sulfur was available in the gas to react directly with the alloy during the transient oxidation stage. Because of their fast growth rates, sulfides formed during transient scaling might be able to persist even though in the normal evolution of scale structures a protective Al_2O_3 would be expected to develop eventually. Therefore, to avoid the effects of transient scaling structures, the alloys described above were first preoxidized for various times, then, without changing temperature, the specimens were exposed to oxidiz-

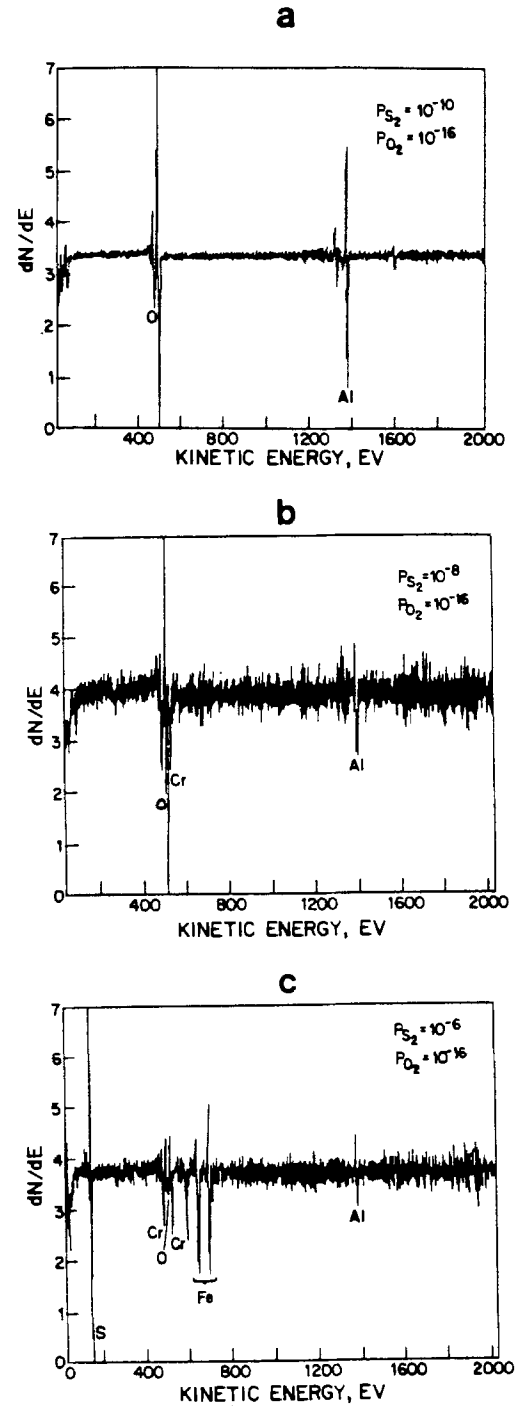


Fig. 3. Auger electron spectra from the surface of FeCrAl alloys exposed to oxidation/sulfidation at 900°C for 24h. a: gas "C." b: gas "D." c: gas "E."

ing/sulfidizing environments. Preoxidation was carried out for 1, 24, 65, and 105h in gas "A" at 900°C. Sulfur can attack the underlying alloy by either chemical diffusion through the preformed Al_2O_3 scale or by permeation through microcracks and pores.

No sulfide was found on the scale surface or at the scale/metal interface of the specimens that had been preoxidized for 1 or 24h. However, when the preoxidation time was 65h, the Al_2O_3 scale on the FeCrAl alloy became less protective against sulfur attack, as illustrated in Fig. 8. Small sulfide particles (chromium sulfides) were found on the bare metal surface beneath the oxide scale in areas where the scale had become detached. When the preoxidation time was increased to 105h, sulfur was able to pass through the scale on both FeCrAl and FeCrAlY, as illustrated in Fig. 8b and 8c. The sulfides formed on the FeCrAlY were found to be concentrated in regions overlying the boundaries of dendrites in the alloy, as shown in

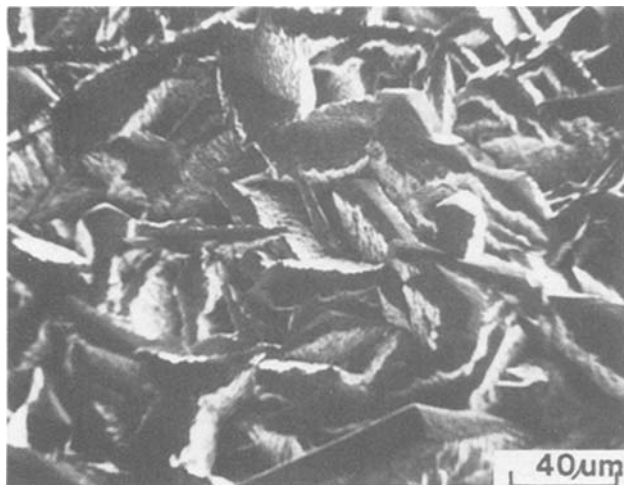


Fig. 4. SEM micrograph of the surface of FeCrAl exposed to gas "E" for 24h at 900°C. The platelets are largely iron sulfide.

Fig. 9. These boundaries contain precipitates which are rich in Y as a result of segregation during solidification. Figures 9a and 9b show sulfide particles emerging through cracks in the Al_2O_3 scale. The metal surface, where scale spalled during cooling, is shown in Fig. 9c and 9d. The particle in Fig. 9d is a Y-rich oxide in a dendrite boundary; the sulfides at the gas/scale surface (Fig. 9a and 9b) were iron- and chromium-rich. Examination of the Al_2O_3 scale on FeCrAlY formed during preoxidation of 105h showed that the scale had cracked primarily in the area of the Y-rich precipitates, as shown in Fig. 8c. In contrast to this behavior, the FeCrAlHf maintained the integrity of the scale throughout the preoxidation and the sulfidation exposures, and as a result suffered no sulfidation in these tests.

The results of the preoxidation/sulfidation tests run counter to what might be expected from the simple idea that thicker Al_2O_3 scales, formed by longer preoxidation,

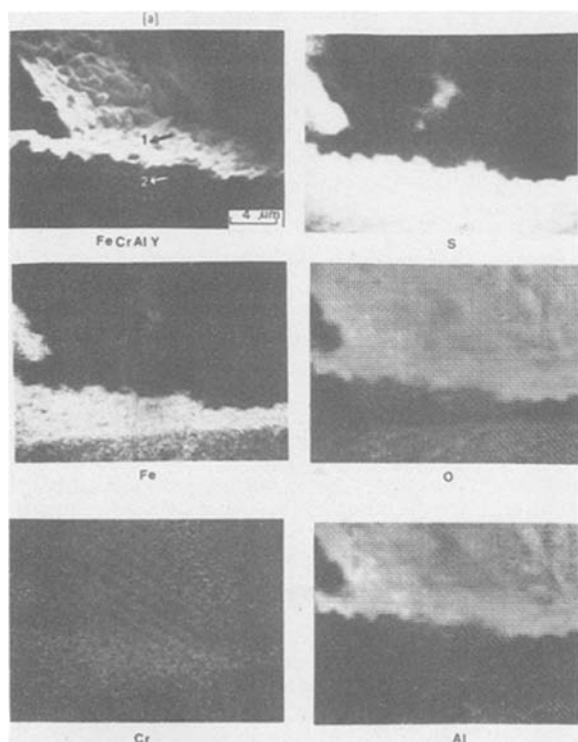


Fig. 5. Scanning Auger elemental maps of part of a single platelet on the specimen shown in Fig. 4. On the image in a (top left), the top of the platelet is labeled "2," and the side or wall is "1." The elemental maps for S, Fe, O, Cr, and Al indicate that the top of the platelet is rich in Fe and S (FeS) and the sidewall is rich in Al and O (Al_2O_3).

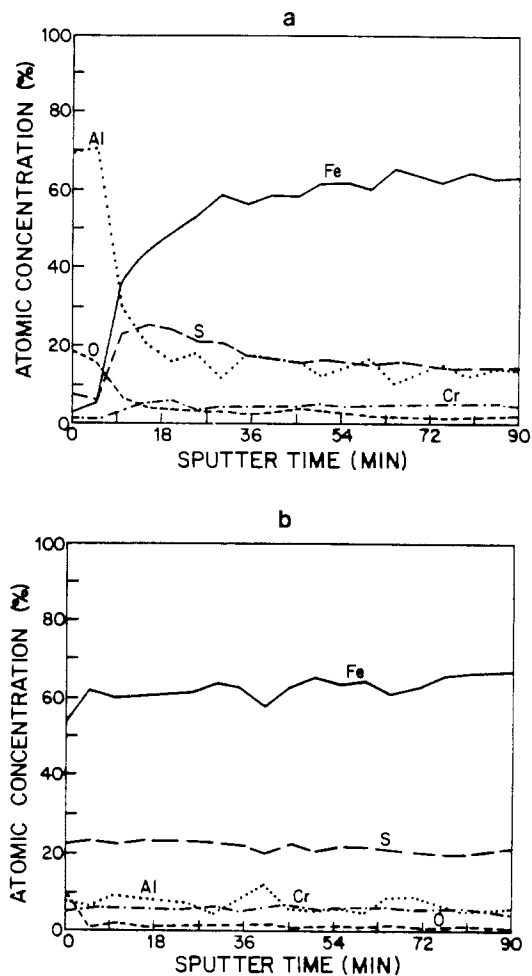


Fig. 6. Composition as a function of depth into the platelet determined by Auger analysis after argon ion sputtering. a (top): location "1" on Fig. 3a. b (bottom): location "2" on Fig. 3a.

ought to be more effective barriers to sulfur penetration. Indeed, the thicker scales were less effective on FeCrAl and FeCrAlY. This implies that lattice diffusion of sulfur through the oxide was not an important step in these experiments. The results also suggest that Al_2O_3 scales on these alloys crack as they grow isothermally, although less so on FeCrAlY than on FeCrAl. It is proposed that sulfur, as H_2S gas, permeates down the cracks to react with the underlying alloy, forming sulfides. From this perspective, Hf has an advantage over Y as an additive in that the Al_2O_3 scales on FeCrAlHf cracked far less exten-

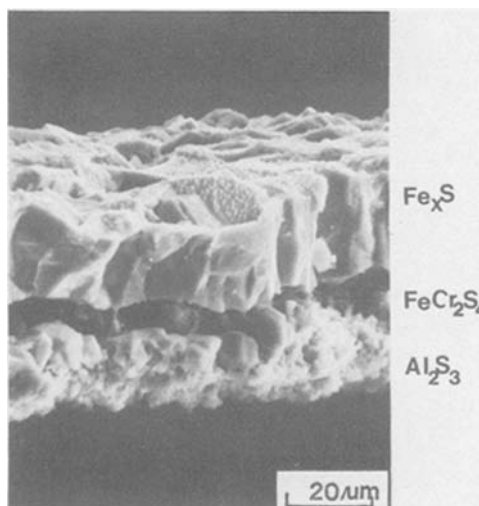


Fig. 7. SEM micrograph of a cross section (fracture surface) of the sulfide scales formed on FeCrAl after exposure to gas "E" for 24h at 900°C.

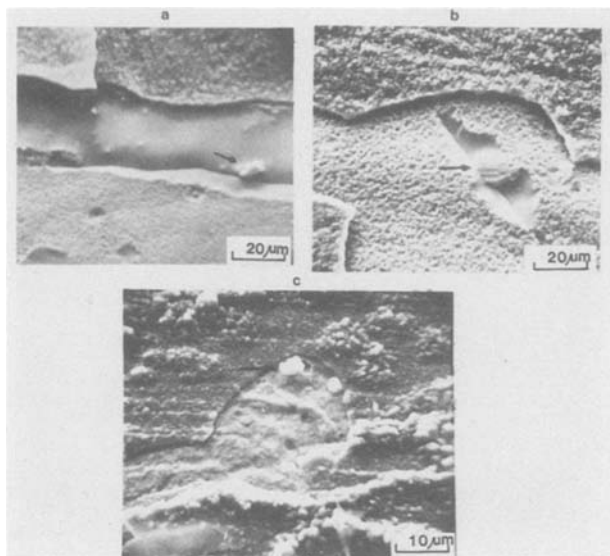


Fig. 8. SEM micrographs of Cr_2S particles (located by arrows) at the metal/scale interface on alloys preoxidized in gas "A," then sulfidized for 24h in gas "E." a (top left): FeCrAl preoxidized 64h. b (top right): FeCrAl preoxidized 105h. c (bottom): FeCrAlY preoxidized 105h.

sively. It is noted that Hf is more soluble in the alloy, and therefore more dispersed, than Y, which is present largely as precipitates.

Acoustic emission tests.—In order to help verify the proposed mechanism that sulfur attacks the metal through microcracks in the scale, an acoustic emission technique was used to monitor oxide cracking during oxidation. When the oxide cracks, a transient elastic wave is generated, which propagates through the specimen. The acoustic emission technique has been used extensively to study cracking during metal fracture, but its application to oxidation studies is relatively new (15, 16).

A summary of some preliminary results is shown in Fig. 10 as a plot of accumulated counts vs. time for three alloys during oxidation at 900°C. The FeCrAl alloy generated "counts" more or less continuously during isothermal oxidation, whereas FeCrAlY generated a few widely spaced "bursts of counts" during the same time. Even fewer counts were recorded for FeCrAlHf. All the tests were conducted at the same sensitivity threshold. We interpret these data as indicating that the Al_2O_3 scale on FeCrAl cracks continuously during isothermal exposure,

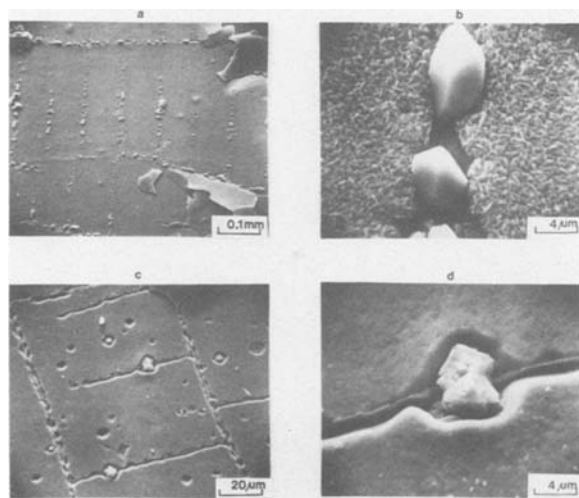


Fig. 9. SEM micrographs of preoxidized (105h) and sulfidized FeCrAlY. a (top left): surface of the oxide scale showing Cr_2S emerging through the Al_2O_3 in a pattern corresponding to metal grain boundaries. b (top right): enlarged view of Cr_2S from a. c (bottom left): metal surface beneath spalled scale showing grain boundaries delineated by Y-rich compound. d (bottom right): enlargement of a Y-rich segregate from c.

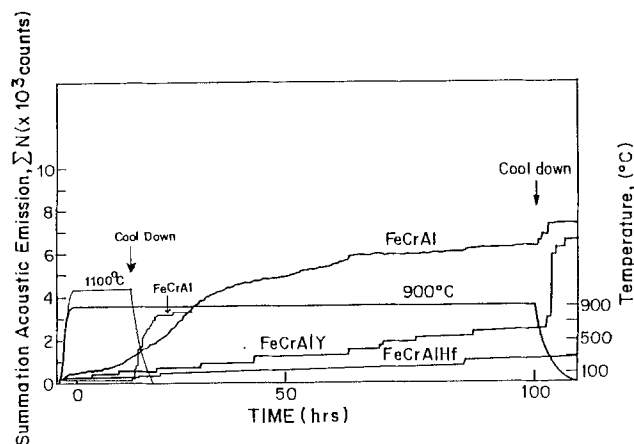


Fig. 10. A plot of the accumulated acoustic emission events as a function of time during oxidation of FeCrAl, FeCrAlY, and FeCrAlHf at 900°C and FeCrAl at 1100°C. Specimen temperatures are superimposed on the plot.

but much less so on FeCrAlY and even less so on FeCrAlHf. Although the details of the cracking mechanism are not known, it is clear even with this qualitative interpretation that the acoustic emission technique is capable of monitoring scale cracking. Upon cooling to room temperature after about 100h exposure, as indicated by the superimposed temperature plot in Fig. 10, FeCrAl and FeCrAlY (but not FeCrAlHf) suffered further cracking owing to the thermally generated stresses. A few samples of FeCrAl were preoxidized in "B" at 1100°C for a shorter time calculated to produce the same thickness of oxide as 100h at 900°C. These samples did not generate acoustic counts at 1100°C, as shown in Fig. 10, possibly because the greater plasticity of the oxide scale or of the underlying alloy kept the growth stresses below the fracture limit. When cooled to room temperature, these samples did emit counts, and cracks were evident in the scale. However, samples could be cooled slowly to 900°C without cracking, as monitored by acoustic emission. When the slowly cooled samples were exposed to H_2 - H_2O - H_2S at 900°C, they did not suffer sulfidation.

These acoustic emission data are qualitative at this time and must be interpreted cautiously since the technique is not well established for this application. Nevertheless, these results are strikingly in accord with the proposal that the superior resistance of Al_2O_3 scales on FeCrAlHf is due to their physical integrity, and that the relatively poorer performance of FeCrAl (at 900°C) and FeCrAlY results from scale cracking. This is further supported by the observation that Al_2O_3 scales on FeCrAl, grown free of cracks at 1100°C, were impervious to sulfidation under conditions that caused severe sulfidation to samples preoxidized at 900°C.

Summary and Conclusions

FeCrAl, FeCrAlY, and FeCrAlHf alloys, which form Al_2O_3 scales, have been exposed to oxidizing/sulfidizing environments at 900°C. Two different exposure sequences were used: in the first, samples were exposed directly to H_2 - H_2O - H_2S mixtures in which the activity of sulfur varied from 10^{-6} to 10^{-10} atm; in the second, samples were preoxidized for various times in H_2 - H_2O , then exposed to H_2 - H_2O - H_2S mixtures as above. In the latter sequence, the samples were not cooled between the preoxidation and the oxidation/sulfidation exposures. Auger electron spectroscopy was used extensively to analyze the corrosion products.

Upon direct exposure to an oxidizing/sulfidizing gas, the alloys formed predominately an Al_2O_3 scale at low sulfur activities, but at high activities, the scale was predominately FeS. Preoxidation to form a barrier layer of Al_2O_3 to prevent the formation of FeS was successful if the preoxidation times were short. However, thicker oxide scales, formed by longer preoxidation times, were less

effective. This suggests that sulfur penetration by lattice or grain boundary diffusion was unlikely to be important. FeCrAlHf was the most resistant to sulfide formation after preoxidation, FeCrAlY less so, and FeCrAl the least resistant. Some preliminary experiments with an acoustic emission technique indicated that the Al_2O_3 scales crack even during isothermal oxidation at 900°C. The order of resistance to cracking (FeCrAlHf >> FeCrAlY > FeCrAl) paralleled the order of resistance to sulfidation attack after preoxidation. Crack-free Al_2O_3 could be grown on FeCrAl at 1100°C, and these scales were impervious to subsequent sulfur penetration at 900°C under the test conditions used here. The evidence supports the proposal that sulfidation under these conditions was initiated by permeation of gaseous H_2S through cracks in the oxide scale. Once formed at crack sites, sulfide phases provide paths of fast mass transport and lead to rapid attack. The ability of the scale to resist cracking is crucial to corrosion resistance, since healing of the cracks apparently is prevented in sulfidizing environments.

Acknowledgment

This work was supported under Department of Energy Contract DOE/DE-AC02-79ER10450. The authors also acknowledge the assistance of Y. H. Zhang, a visiting scholar from China.

Manuscript submitted Sept. 21, 1983; revised manuscript received April 9, 1984.

The University of Minnesota assisted in meeting the publication costs of this article.

REFERENCES

1. K. Natesan and M. F. Delollane, in "Corrosion-Erosion Behavior of Materials," K. Natesan, Editor, p. 1, Metallurgical Society of AIME, Warrendale, PA (1980).
2. M. Danielewski and K. Natesan, *Oxid. Met.*, **12**, 227 (1978).
3. T. C. Tietz, Jr. and K. Natesan, *ibid.*, **17**, 1 (1982).
4. K. Natesan, To be published in "Proceedings of the Conference on Corrosion-Erosion-Wear of Materials in Emerging Fossil Energy Systems," Berkeley, CA, Jan. 27-29, 1982.
5. D. B. Rao, K. T. Jacob, and H. G. Nelson, *Metall. Trans.*, **14A**, 295 (1983).
6. D. S. Williams, R. Moller, and H. J. Grabke, *Oxid. Met.*, **16**, 253 (1981).
7. M. Loudjani, J. C. Pivin, C. Roques-Carmes, P. Lacombe, and J. H. Davidson, *Metall. Trans.*, **13A**, 1299 (1982).
8. P. A. Mari, J. M. Chaix, and J. P. Larpin, *Oxid. Met.*, **17**, 315 (1982).
9. W. F. Chu and A. Rahmel, *ibid.*, **16**, 175 (1981).
10. I. M. Allan, D. P. Whittle, and J. Stringer, *ibid.*, **12**, 35 (1978).
11. I. M. Allan, D. P. Whittle, and J. Stringer, in "Corrosion-Erosion Behavior of Materials," K. Natesan, Editor, p. 103, Metallurgical Society of AIME, Warrendale, PA (1980).
12. Annual report of the University of Minnesota Corrosion Research Center to Department of Energy under Contract DOE/DE-AC02-79ER10450, Jan. 1983.
13. E. A. Gulbransen and G. H. Meier, Report no. DOE/FE/13547-01, prepared for the U.S. Department of Energy under Contract no. DE-AC01-79ET-13547 (1980).
14. F. A. Golightly, G. C. Wood, and F. H. Stott, *Oxid. Met.*, **14**, 217 (1980).
15. C. Coddet, G. Beranger, and J. F. Chretien, in "Materials and Coatings to Resist High Temperatures Corrosion," D. R. Holmes and A. Rahmel, Editors, p. 175, Applied Science, London (1978).
16. A. Ashary, G. H. Meier, and F. S. Pettit, in "High Temperature Protective Coatings," S. C. Singhal, Editor, p. 105, Metallurgical Society of AIME (1982).



Long Cycle-Life Secondary Lithium Cells Utilizing Tetrahydrofuran

K. M. Abraham,* J. S. Foos,* and J. L. Goldman*

EIC Laboratories, Incorporated, Norwood, Massachusetts 02062

The tetrahydrofuran (THF)/LiAsF₆ electrolyte solution, except for its high reactivity with Li (1), is highly desirable for use in ambient temperature rechargeable Li cells (2). In a recent patent application (3), we have disclosed that the use of unsaturated organic additives such as 2-methyl-furan (2Me-F) enables high efficiency Li cycling in THF/LiAsF₆. A most important consequence of this discovery has turned out to be the utility of the high rate, low temperature mixed solution, 50:50 THF:2Me-THF/LiAsF₆(1.5M) (2,4,5), in 5 A-hr Li/TiS₂ cells to achieve, for the first time, more than 200 cycles of 60% depth-of-discharge (d.o.d). The Li anode cycling efficiency in these 5 A-hr cells exceeded 97%. We now believe that this mixed electrolyte is significantly better than 2Me-THF/LiAsF₆ for use in ambient temperature secondary Li cells. The relevant data are reported in this communication.

In prior publications (6-8), we have reported on the superior ability of the 2Me-THF/LiAsF₆ solution to cycle Li with high efficiencies which span the range of 96-97.5% (Figure of Merit, F.O.M._{Li} = 25-40) for Li charge densities of 7-10 mA-hr/cm². A persistent impurity in distilled 2Me-THF is 0.2-0.4 volume-percent (v/o) of 2Me-F (4,7,9), the unsaturated analog of 2Me-THF (see Table II. for structural formulas). In fact, most of the published results discussing the use of 2Me-THF/LiAsF₆ in rechargeable Li cells have dealt with an electrolyte solution containing ~0.2-0.4 v/o 2Me-F. This has come about because of the difficulty of removing the 2Me-F by fractional distillation of the solvent.

Recently we have found that this 2Me-F can be completely converted into 2Me-THF by hydrogenating the "impure solvent" over a Pt catalyst at ambient temperature and pressure (3). Li/TiS₂ laboratory cells using the 2Me-F-free-2Me-THF/LiAsF₆ solution, to our surprise, have

exhibited inferior cycle lives; typically, about half of that of cells utilizing the "regular electrolyte" with 0.2-0.4% 2Me-F. The cycle tests at 1 mA/cm² and 7 mA-hr/cm² were performed in 0.68 A-hr Li/TiS₂ laboratory test cells, identical to those we have previously described in ref. 7. Indeed, the cycle numbers for the various cells reported in Table I are directly comparable to those presented in Figures 4 and 5 of ref. 7. It should be noted that all cell capacities mentioned in this paper are based on 1e⁻/TiS₂. As discussed in ref. 7, the theoretical Li capacity in a cell is much larger than the TiS₂ capacity. Following the surprise with the 2Me-F-free-electrolyte, we deliberately prepared 2Me-F-containing solutions by adding 0.3, 0.6 or 1.2 v/o of 2Me-F into the solution in neat 2Me-THF, obtained via the hydrogenation procedure. Performance of laboratory Li/TiS₂ cells employing these solutions is summarized in Table I. It is clear that 0.3 to 0.6 v/o of 2Me-F doubles the cycle life of 2Me-THF/LiAsF₆-based cells.

Table I. Effect of 2-Methyl-furan (2Me-F) on the Cycle Life of Li/TiS₂ Laboratory Cells^(a)

Cell No.	Electrolyte	Amount of 2Me-F v/o	Number of Cycles ^(b)
98-18	2Me-THF ^(c) /LiAsF ₆ (1.4M)	0.0	96
98-07		0.3	150
98-26		0.6	177
98-29		1.2	198
140-19	THF/LiAsF ₆ (1.5M)	0.0	7
35-10		0.5	111
35-32 ^(d)		0.5	92
98-06		1.0	96
98-11		1.5	110
98-15		2.0	105
101	2Me-THF (50 v/o): THF (50 v/o)/LiAsF ₆ (1.5M)	0.5 ^(e)	145
102	2Me-THF (50 v/o): THF (50 v/o)/LiAsF ₆ (1.5M)	1.0	140

(a) Each type of cell has been cycled at least in duplicate. Temperature, 25°C.

(b) Obtained at 1 mA/cm² for 7 mA-hr/cm²; compare Fig. 5 in Ref. 7.

(c) Obtained by hydrogenating distilled 2Me-THF containing 0.2-0.4 v/o 2Me-F over Pt catalyst and subsequently preparing the LiAsF₆ solution.

(d) Stored 14 days at 50°C prior to cycling.

(e) Stored for 1 month at 50°C prior to cycling. Unstored cells gave ~10 cycles less.

*Electrochemical Society Active Member
Key Words: Li Battery, Electrolytes

An obvious question is whether 2Me-THF/LiAsF₆ is less reactive in secondary Li cells than THF/LiAsF₆, as previously claimed (8). The answer is yes, although about half of the cycles of the cell presented in Figure 5 of ref. 7 appears to be due to the effect of 2Me-F.

We have also found 2Me-F to improve substantially the cycle life of cells utilizing THF/LiAsF₆. Some relevant data are given in Table I. Cells utilizing THF/LiAsF₆ plus 0.5 v/o 2Me-F exhibit about 100 cycles as opposed to 7 in 2Me-F-free cells. Interestingly enough, a significant increase in cycles is not seen at the higher 2Me-F concentrations of 1, 1.5 and 2 v/o. It appears from the data obtained from both THF and 2Me-THF cells, that there is a stoichiometric relationship between the amount of effective 2Me-F and the Li being electrochemically cycled. Our present data indicate that about 0.4 mmoles of 2Me-F is required per 1 A-hr of Li for the manifestation of an optimum additive effect in THF/LiAsF₆. This Li-to-additive mole ratio has been satisfactorily tested in 5 A-hr prismatic Li/TiS₂ cells (vide infra). The practical significance of this discovery is very clear. For the first time, high rate, low temperature discharge and long cycle life have all been achieved in the same electrolytes, namely THF/LiAsF₆ and its blends.

We believe that 2Me-F is effective as a cycle life enhancing additive because it forms a protective film on the Li surface. The film may be of the solid electrolyte (10) or of the polymer electrolyte (11) type, enabling Li discharge and charge, while preventing or significantly slowing down direct chemical reactions at the Li surface. Further studies to fully elucidate the chemistry of the additive effect are in progress.

In laboratory test cells, the 50:50 THF:2Me-THF/LiAsF₆(1.5M) electrolyte solution with 0.5 v/o 2Me-F has given cycle lives mid-way between those given by cells containing the parent solutions plus the additive (see Table I). However, in 5 A-hr prismatic Li/TiS₂ cells this order of additive effects changes. In these larger cells, employing a practical Li-to-electrolyte ratio, the mixed THF:2Me-THF solution plus 2Me-F has produced the longest cycle life. Thus a 5 A-hr Li/TiS₂ cell (12) utilizing a solution of the composition, THF (48.3 v/o):2Me-THF(48.3 v/o):2Me-F(3.4 v/o)/LiAsF₆ (1.5M), has given more than 225 cycles when cycled at a d.o.d. of 60% (Figure 1). As indicated earlier, the amount of the additive required is determined by the total Li in the cell, and the larger additive concentration in

these cells is due to the larger Li to electrolyte ratio. Under similar cycling regimes, 2Me-THF/LiAsF₆ cells gave 125 cycles and the THF/LiAsF₆ cells 120 cycles. In all cases, cell failure occurred due to increased impedance and dendrite shorting. The blended solution, in addition, has exhibited relatively good thermal stability (see Table I) and its low temperature performance is superior to that of the parent solutions. A 5 A-hr Li/TiS₂ cell employing the blended solution has yielded ~2.5 Ahr at -20°C at 2mA/cm² (2,4,5). For the same temperature and current density, capacities were non-existent in the cells utilizing the parent solutions. The superior -20°C performance of the mixed solution over THF/LiAsF₆, despite the higher conductivity of the latter (2), may be related to the more desirable Li⁺-solvates in the blend, permitting better Li⁺ diffusivities and a consequently high rate capability. The 2Me-THF system is impractical below 0°C because of the formation of sparingly soluble Li⁺-solvates (2,7).

In exploring the field, we have discovered other additives as well suitable for improving the cycle life of THF/LiAsF₆-based secondary Li cells. Some examples are given in Table II. To date 2Me-F appears to be the most effective. Detailed studies of the various additives are in progress.

ACKNOWLEDGEMENT

This work was supported by the Office of Naval Research. We appreciate discussions with Dr. S. B. Brummer.

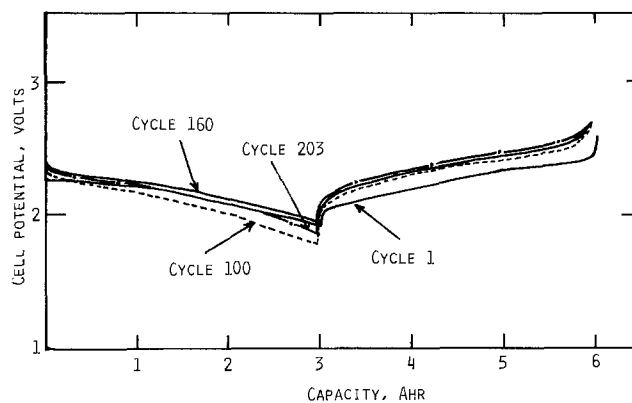

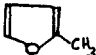
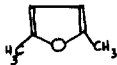
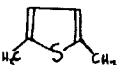


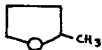


Figure 1. Typical cycles of a 5 A-hr theoretical capacity Li/TiS₂ cell utilizing THF (48.3 v/o):2Me-THF(48.3 v/o):2Me-F(3.4 v/o)/LiAsF₆(1.5M). Current: Cycles 1 and 100, $i_d = 0.5A$, $i_c = 0.25A$; Cycles 160 and 203, $i_d = i_c = 0.25A$. All cycling was performed to a depth-of-discharge of 60% (3A-hr).

REFERENCES

- (1) V. R. Koch, *J. Electrochem. Soc.*, **126**, 181 (1979).
- (2) K. M. Abraham and J. L. Goldman, *J. Power Sources*, **9**, 239 (1983).
- (3) K. M. Abraham, S. B. Brummer and J. S. Foos, U. S. Patent filed (1983).
- (4) K. M. Abraham, P. B. Harris and D. L. Natwig, *J. Electrochem. Soc.*, **130**, 2309 (1983).
- (5) K. M. Abraham, "Ambient Temperature Secondary Lithium Cells", in *Lithium Chemistry*, R. O. Bach ed., John Wiley and Sons (book to be published).
- (6) K. M. Abraham, J. L. Goldman and M. D. Dempsey, *J. Electrochem. Soc.*, **128**, 2493 (1981).
- (7) K. M. Abraham, J. L. Goldman and D. L. Natwig, *J. Electrochem. Soc.*, **129**, 2404 (1982).
- (8) J. L. Goldman, R. M. Mank, J. H. Young and V. R. Koch, *J. Electrochem. Soc.*, **127**, 1461 (1980).
- (9) S. P. S. Yen, D. Shen, R. P. Vasquez, F. J. Grunthaner and R. B. Somoano, *J. Electrochem. Soc.*, **128**, 1434 (1981).
- (10) E. Peled, *J. Electrochem. Soc.*, **126**, 2047 (1979).
- (11) M. Garreau, Fall Meeting of the Electrochemical Society, Washington, D. C. (1983). Abstract No. 58.
- (12) K. M. Abraham, J. L. Goldman, P. B. Harris, J. Avery and S. B. Brummer, Fall Meeting of the Electrochemical Society, Detroit, MI (1982), Extended Abstract No. 314.

Table II. Effect of Several Additives^(a) on the Cycle Life of Li/TiS₂ Laboratory Cells Utilizing THF/LiAsF₆(1.5M).

Additive ^(c)		Percent by Volume (v/o)	Number of Cycles ^(b)
None	—	—	7
Furan,		0.5	46
2-Methyl-furan,		0.5	110
2,5-dimethyl-furan,		0.5	37
2,5-dimethyl-thiophene,		0.5	38
4,5-dihydropyran,		0.5	32
3,4-dihydrofuran,		0.5	28
2-methyl-THF,		0.5	8

^(a)Additional additives are given in our patent (3).

^(b)Obtained at 7 mA-hr/cm² and 1 mA/cm² (7).

^(c)It appears that at least one double bond in the ring is necessary.

Manuscript submitted Jan. 9, 1984; revised manuscript received April 5, 1984.

EIC Laboratories, Incorporated assisted in meeting the publication costs of this article.

In Situ Measurement of Resist Dissolution with a Psi-Meter

Warren W. Flack,* James S. Papanu, Dennis W. Hess,* David S. Soong, and Alexis T. Bell

Department of Chemical Engineering, University of California, Berkeley, California 94720

INTRODUCTION

The dissolution of exposed resists in developer solutions is a critical step in the fabrication of microelectronic devices. A number of process parameters, e.g. developer strength, temperature, and molecular weights in the exposed and unexposed regions, significantly affect the outcome of the process. Fundamental studies of the complex dependence of resist development on these process variables will greatly facilitate process design and optimization.

Critical information needed for fundamental understanding and mathematical modeling of the resist development process entails determination of resist film thickness as a function of time in the developer solution. Traditional procedures rely on repeated development of a resist for various predetermined times, followed by quenching in a nonsolvent and baking to drive off the developer before measuring the remaining film thickness (1,2). This technique is prone to errors due to the presence of induction periods and failure to stop dissolution immediately when desired.

Recently, several in-situ thickness-monitoring techniques for photoresist development have been reported. Konnerth and Dill (3) used a computer controlled spectrophotometer to measure the relative reflectivity of the resist sample as a function of wavelength. Film optical properties and a complex method for converting relative to absolute reflectivity were necessary to determine film thickness. A laser endpoint detection system based on interferometry principles was developed by Willson (4). This device provides data to within an integer multiple of one-half a wavelength. Thus, the resolution is not sufficient for detailed kinetic studies. Oldham (5) has developed a technique for measuring the capacitance between conductive developer solutions and substrates. Here, use is made

*Electrochemical Society Active Member.

of the fact that the total thickness of dielectric is related to the capacitance.

In this communication, we report the development and successful application of a simplified ellipsometer (psi-meter) (6) for the in-situ measurement of resist film thickness in developer solutions. Preliminary data suggesting the formation of a gel layer over the remaining glassy film will be discussed.

EXPERIMENTAL

Figure 1 shows a block diagram of our experimental arrangement. The psi-meter consists of a 2 mW helium-neon polarized laser source, a quarter-wave retardation plate to generate circularly polarized light, and a synchronously rotating polarizer to convert the beam to linearly polarized light with time-dependent orientation. Light reflected from the wafer placed in the optical cell enters a photodetector. The signal from the detector is split into AC and DC components by a ratiometer. Final data acquisition and storage are achieved with a dedicated Commodore PET 2001 computer. The amplitude ratio of the AC to DC components is equal to $-\cos(2\psi)$, where ψ is related to the optical constants of the substrate, film, and ambient, the wavelength of the light, the angle of incidence and the film thickness through the Drude equation (7). Since only ψ is determined by this apparatus (Δ , characterizing the change in phase upon reflection, is not measured), the refractive index of the film must be known a priori to calculate the film thickness.

Our experimental conditions were as follows. Silicon wafers were coated with approximately 700 nm of PMMA resist and prebaked at 160°C for one hour. Film dissolution took place in the optical cell, where a developer solution at room temperature was circulated at 100 ml per minute. The optical cell has a volume of 250 ml.

The motor-driven polarizer was adjusted to a rotation frequency of 100 Hz. An incident angle of 75° was chosen to give a high sensitivity. The wavelength was 632.8 nm. Data were collected at a rate of one point per second, allowing detailed delineation of the dissolution phenomenon.

RESULTS AND DISCUSSION

Figure 2 shows plots of AC/DC amplitude ratios as a function of dissolution time for wafers immersed in developer solutions of methyl ethyl ketone (MEK) and isopropanol (IPA) with compositions of 3:2 and 1:1 volume ratios of the two components. Appreciably different time scales are used to display the amplitude ratio variation, suggesting different rates of developer penetration and film dissolution. The AC/DC curves can be related to the variation of film thickness through a program developed by McCrakin (8) based on the Drude equation. The curve for the stronger solution (3:2) indicates a linear decrease in film thickness with time, with no apparent induction period and no distinct multiple layer formation. An extra maximum emerges at short times when the strength of the solution is reduced to 1:1.

We speculate that this extra maximum is associated with the formation of a gel layer at the solution-resist interface (9). Polymer dissolution involves both solvent penetration into the glassy matrix, converting it into a rubbery gel phase, and detachment of chain molecules from the entangled gel network into the solution. Different physical phenomena govern the rates of the two processes. The former is influenced by the mobility of small solvent molecules penetrating the glassy phase, whereas the latter is affected by chain diffusion. Thermodynamic compatibility of the developer and the resist also plays an important role in the development process. A thorough analysis of the resist dissolution kinetics will further elucidate the underlying physics. Detailed modeling is underway, and a systematic experimental program is currently being pursued.

ACKNOWLEDGMENT

This project was supported by the Air Force Office of Scientific Research.

REFERENCES

1. F. Dill, IEEE Trans. Electron Dev., 22, 445 (1975).

2. A. Ouano, Polym. Eng. Sci., 18, 306 (1978).
3. K. Konnerth and F. Dill, IEEE Trans. Electron Dev., 22, 452 (1975).
4. G. Willson, IBM Corporation, San Jose, CA, private communication.
5. W. Oldham, SPIE Semiconductor Micro-lithography III, 135, 153 (1978).
6. A. Zaghloul and R. Azzam, Surface Sci., 96, 169 (1980).
7. R. Azzam and N. Bashara, "Ellipsometry and Polarized Light", North Holland Publishing Co., New York, 1977.
8. F. McCrakin, "A Fortran Program for Analysis of Ellipsometer Measurements", National Bureau of Standards, Technical Note 479 (1969).
9. K. Ueberreiter, in "Diffusion in Polymers," J. Crank, ed., Academic Press, 1968, pp. 219-257.

Manuscript received May 9, 1984.

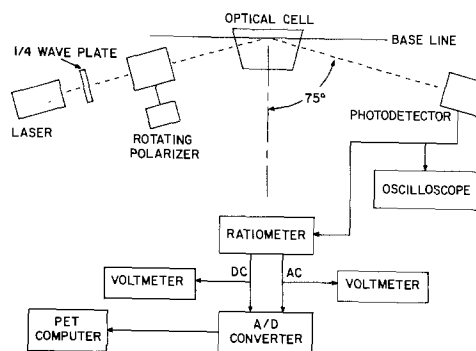


Fig. 1. Schematic block diagram of the psi meter setup with the major optical and detection components identified.

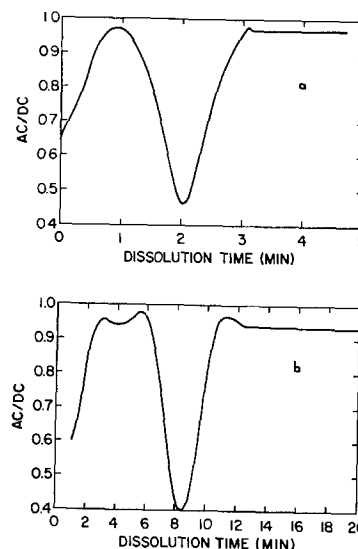


Fig. 2 Amplitude ratios of the AC to DC components as functions of time for PMMA dissolution in MEK and IPA developer solutions with the following compositions (volume ratios of MEK to IPA): a. 3:2, b. 1:1.

Process Characterization of PSG and BPSG Plasma Deposition

S. Shanfield* and S. Bay

LFE Corporation, Clinton, Massachusetts 01510

A concern in the fabrication of high density integrated circuitry is the topography of interlayer dielectric steps over which metal conductor lines will pass. These steps, occurring as a result of underlying topography or via etching, should be gradually tapered to ensure continuity in subsequently deposited metal interconnect lines. Tapered steps can be achieved by reflow of phosphosilicate (PSG) or borophosphosilicate glass (BPSG) interlayer dielectric at device-compatible temperatures. PSG and BPSG deposition has been demonstrated using atmospheric-CVD(1), low-pressure-CVD(2), and recently, using plasma enhanced CVD in tube-type systems (3-5). In this communication, we report on process characterization of plasma-enhanced deposition of PSG and BPSG. A parallel-plate cold wall plasma deposition system was used.

Description

Dilute silane (2%-5% in Ar), nitrous oxide, dilute phosphine (5% in Ar), and dilute diborane (5% in Ar) are mixed in a manifold and admitted into the deposition chamber through five in-line showerhead electrodes (6). Gases exiting the reactor pass through a pressure-controlling throttle valve into a two stage mechanical pump. The plasma discharge is maintained by RF power (13.56 MHz) applied to the showerheads. Spacing between the 14 cm diameter showerheads and track was set at 1.4 cm. Wafers are automatically placed on the heated track beneath the showerheads. In normal operation, wafers receive one-fifth of the required deposition thickness under each showerhead.

Procedure

Thin films of PSG and BPSG were deposited on bare silicon wafers and as interlayer dielectric in MOS device structures. PSG and BPSG films on bare silicon were characterized for thickness and thickness uniformity using a Nanometrics Nanospec™ AFT, and index of refraction was measured with an ellipsometer. Dopant content (in weight percent phosphorous or boron) was measured by electron microprobe, and depth profiles of phosphorous content were obtained by Auger analysis. Etch rate and etch rate uniformity of films in buffered oxide etch were also measured. The degree of film particulate contamination was determined using a Tencor Surfscan™ 200 set to detect one micron or larger particles. SEM sections were used to characterize the profile of reflowed BPSG film over MOS device topography.

All depositions were performed with a substrate temperature of 340°C. Nitrous oxide flow was fixed at 1700 cc/min. while silane flow was varied between 20 and 60 cc/min. Chamber pressure during deposition was set at 2.35 torr. The phosphine-to-silane flow ratio ranged between 0 and 0.3 while the diborane-to-silane flow ratio ranged between 0 and 0.7.

Results

Films characterized were nominally 10,000 Å thick with typical across-wafer uniformity of ±2%. The index of refraction ($\lambda = 6328 \text{ \AA}$) for films with 0-11 weight percent phosphorous and 0-6 weight percent boron fell in the range of 1.46-1.47. Dopant level uniformity was typically ±0.1 weight percent across-wafer. Depth profile measurements in PSG films indicated ±0.5 weight percent variation in phosphorous content through 90% of the film thickness. Particulate levels in deposited films were in the range of 0.06-0.12 particles per cm². No evidence of homogeneous nucleation was observed, and the particulate levels were primarily a

function of walls, load lock, and track cleanliness.

Fig. 1 shows the theoretical relationship between silane flow and the maximum obtainable deposition rate of undoped silicon dioxide (solid line). The maximum obtainable deposition rate, $(dh/dt)_{\text{max}}$, is derived under the assumption that all of the silicon in the silane flow is converted to silicon dioxide in the film. This condition corresponds to silicon material utilization, U_m , equal to one in the equation below:

$$\frac{dh}{dt} = \frac{W_{\text{SiO}_2}}{W_{\text{SiH}_4}} \cdot \frac{\rho_{\text{SiH}_4}}{\rho_{\text{SiO}_2}} \cdot \frac{F_{\text{SiH}_4}}{A_d} \cdot U_m \quad (1)$$

where

W_x = atomic weight, gm/mole

ρ_x = density, gm/cm³

F_{SiH_4} = volumetric flow rate of silane, cm³/min.

A_d = deposition area, cm²

U_m = silicon material utilization

($0 \leq U_m \leq 1$)

By adjusting the silicon material utilization (U_m) or the silane flow (F_{SiH_4}), a range of deposition rates could be obtained. Experimental silane flow rates and the corresponding deposition rates used in this study are also shown in Fig. 1. For silane flows used in the study, silicon utilization, U_m , was fixed at about 75% by adjusting the RF power. At a silane flow of 20 cc/min., 75% silicon utilization was obtained with forward RF power set at 20 watts per electrode (0.13 w/cm²). The undoped oxide deposition rate under these conditions was about 1500 Å/min. Using a silane flow of 60 cc/min, forward RF power was set at 45 watts per electrode (0.30 w/cm²) to maintain 75% utilization. In this case, the undoped oxide deposition rate was about 3800 Å/min. With silane flow and RF power established, the relation between flows of dopant gases and the level of doping in the films was investigated.

Fig. 2 compares the theoretical and experimental relationships between weight percent phosphorous in BPSG films and the phosphine-to-silane flow ratio used in depositing the film. The theoretical relationship is derived by assuming that all phosphorous in the flow is incorporated as phosphorous in the films (i.e. 100% phosphorous utilization). The experimental points correspond to films with varying phosphorous content and a range of boron content between 0 and 7 weight percent. Fig. 2 indicates that the experimental relationship between phosphorous content and the phosphine-to-silane flow is approximately linear and, that the plasma deposition process utilized a large percentage of the phosphorous available. In addition, the data in Fig. 2 suggests that the level of diborane in the flow does not affect the phosphorous utilization.

Fig. 3 shows a comparison of the theoretical and experimental relationship between boron content in BPSG films and the diborane-to-silane flow ratio used during deposition. In this figure, the theoretical relationship is derived by assuming that all of the available boron in the flow ends up as boron in the films (similar to the assumption in Fig. 2). The experimental points correspond to films with varying boron content and a range of phosphorous content between 0 and 11 weight percent. Within experimental error, the relationship between boron content and the diborane-to-silane flow ratio is linear and the

boron content is independent of the level of phosphine flow. The plasma deposition process appears to use approximately one-half of the available boron in the diborane flow.

Fig. 4 plots the ratio of weight percent phosphorous to weight percent boron in deposited films as a function of the ratio of volumetric flow of phosphine to the volumetric flow of diborane used to deposit these films. A theoretical prediction of the relationship between these ratios advanced by Ramiller and Yau (3) is shown as a broken line in Fig. 4. An alternate prediction, derived by using the ratio of the theoretical relationships in Figs. 2 and 3, is shown as a solid line. This theoretical relationship, which appears to agree with experimental points plotted in Fig. 4, is given by

$$\text{wt. \% P/wt. \% B} = 2.8 \text{ PH}_3/\text{SiH}_4 \quad (2)$$

Eqn. 2 is based on the assumption of an independent level of utilization associated with each dopant. In contrast, the relationship derived by Ramiller and Yau assumes competition in the incorporation of phosphorous and boron in the film, as occurs in a thermally activated process. The assumption of independent dopant utilization (Eqn. 2) may be applicable under the conditions where the deposition is primarily plasma-activated (i.e. not thermally activated).

Fig. 5 shows an example of plasma deposited BPSG (5 weight percent P and 3 weight percent B) reflowed over a MOS device structure. The film was first densified at 800°C in dry nitrogen for 30 minutes. The temperature was then raised to 920°C for 30 minutes to accomplish the reflow shown. Reflow of 4 weight percent P and 4 weight percent B BPSG in dry nitrogen has been observed to occur between 825°C and 850°C. No evidence of cracking or bubbling was observed in any of the reflowed PECVD BPSG samples.

Conclusion

We have reported on process characterization of PSG and

BPSG film deposition using a parallel plate PECVD system. The films obtained were uniform in both thickness and dopant content. Deposition conditions were established by maintaining a fixed level of silicon material utilization. The amount, in weight percent, of phosphorous incorporated in BPSG films was found to be proportional to the phosphine-to-silane gas flow ratio. Similarly, the level of boron incorporation was found to be proportional to the diborane-to-silane gas flow ratio. The experimental relationship between the phosphine-to-diborane gas flow ratio and the weight percent phosphorous-to-weight percent boron ratio in deposited films suggests that the deposition process was primarily plasma-activated. Independent variation of phosphine and diborane gas flow rates in a plasma-assisted reaction allows correspondingly independent phosphorous and boron incorporation rates. For this reason, plasma-assisted deposition of doped silicon dioxides is expected to be easier to characterize and provide a more repeatable process in a device fabrication environment.

Acknowledgement

The authors wish to acknowledge Brad Mattson and Denis McGreivy for many helpful suggestions.

References

1. W. Kern and G. L. Schnable, *RCA Review*, 43, 423 (1982)
2. L. W. Winkle and C. W. Nelson, *Sol. State Tech.*, 24 (1981)
3. C. Ramiller and L. Yau, *Proc. Semicon/West Technical Program*, 29-37 (1982)
4. I. Avigal, *Sol. State Tech.*, 26, 217 (1983)
5. J. E. Tong, K. Schertenleib, R. A. Carpio, *Sol. State Tech.*, 27, 161, (1984)
6. A. B. Weiss, *Semi. Int.*, 7, 88 (1983)

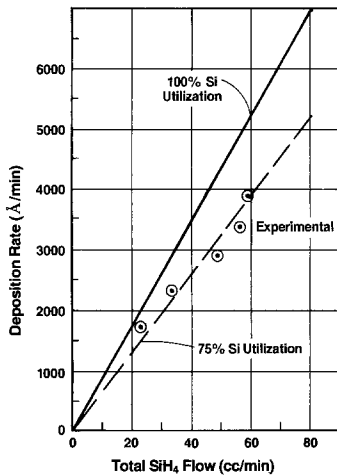


Fig. 1. Theoretical relationship between silane flow and deposition rate. Deposition rates used in study were chosen to correspond to 75% silicon utilization.

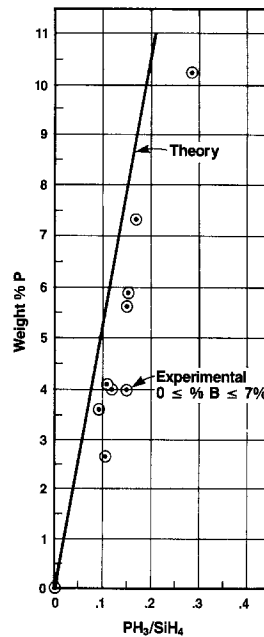


Fig. 2. Relation between measured phosphorous content in BPSG films and the phosphine to silane flow ratio used.

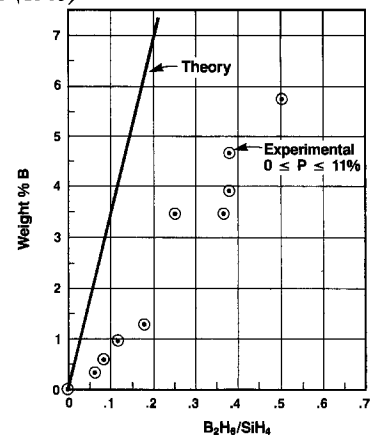


Fig. 3. Relation between measured boron content in BPSG films and the diborane to silane flow ratio used.

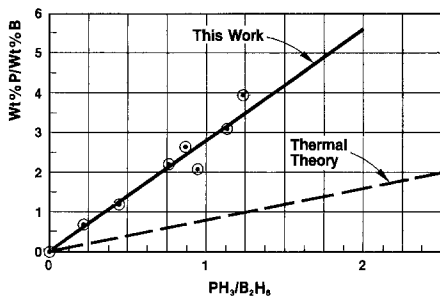


Fig. 4. The ratio of weight percent phosphorous to weight percent boron in deposited films is plotted as a function of the phosphine to diborane flow ratio.

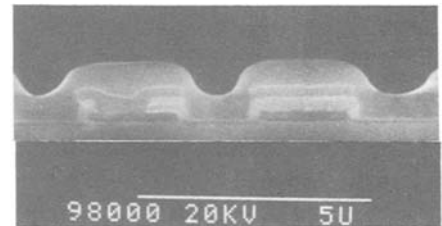


Fig. 5. Reflowed plasma BPSG (5 wt. % P and 3 wt. % B) over MOS device structure. Densified film was reflowed in dry N₂ at 920°C for 30 min.

Manuscript submitted April 10, 1984; revised manuscript received April 29, 1984.

*Electrochemical Society Active Member.

Electroluminescence of Polycrystalline CdSe Thin Film Photoelectrodes: A Sensitive Probe for Surface Recombination

N. Müller, M. Abramovich,* F. Decker,* F. Iikawa, and P. Motisuke

Instituto de Física, UNICAMP, 13.100 Campinas, SP, Brasil

Photoluminescence (PL) and Electroluminescence (EL) measurements have been used to characterize the excited state properties of Cd-chalcogenide single crystal electrodes in photoelectrochemical solar cells (PEC's) (1). Polycrystalline thin film electrodes of these materials, which are promising candidates for the efficient photoelectrochemical solar energy conversion, have been studied only very recently using PL (3). As EL originates more close to the surface of the electrodes, it is considered a probe of recombination more sensitive than PL to the surface conditions of the sample (1). We report the first EL measurements with electrodeposited thin film CdSe electrodes and the enhancement of EL efficiency upon photoetching (4).

CdSe thin film electrodes were prepared onto Ti substrates by electroplating according to literature procedures (2a). The electrodes were annealed at 600°C in N₂ and photoetched in a (0.3:9.7:90) HNO₃:HCl:H₂O solution under white light illumination shortening the photoelectrode to a carbon counterelectrode. Room temperature luminescence spectra were taken with a 0.5m SPEX monochromator and a cooled S-1 EMI photomultiplier. The 5145 Å line of a Coherent Radiation model 52 Ar⁺ ion laser was used to excite PL. The laser beam was expanded, having an intensity of about 100mW/cm² at the sample. During PL the sample was kept in air. EL measurements were performed in a N₂ purged 0.1 M Na₂S₂O₈ + 2.5 M KOH electrolyte. The electrode potential was pulsed between 0 V (SCE) (10 s) and -1.5 V (SCE) (1 s) while scanning the monochromator at 5Å/s. A specially constructed electrode holder enabled us to mount the electrodes in a reproducible way for taking the spectra.

Fig. 1 shows the PL and EL spectra of an electrodeposited CdSe thin film electrode at 295°K. In contrast to spectra measured earlier with CdSe single crystal electrodes (1), a broad subbandgap band dominates the PL spectra of our samples. Red luminescence corresponding to the bandgap peak can be observed with the dark adapted eye. The relative heights of the

bandgap and subbandgap peaks vary drastically with the electrode annealing conditions (5). The bandgap peak at 720 nm and the subbandgap peak at 1060 nm appear at the same position in PL and EL. A second subbandgap structure appears at 945 nm in EL, which has no counterpart in the PL spectrum. A similar phenomenon was reported in the literature (6). Direct hole injection from the SO₄⁻ radical ion into intermediate surface ⁴ states might be responsible for this additional peak.

Usually the subbandgap intensity in the PL spectra is an order of magnitude larger than the bandgap one. The origin of the subbandgap band is either a high density of structural defects or impurities in the electrodeposited samples. The PL of pasted CdSe thin film electrodes (7) shows a pronounced subbandgap band as well, though high purity starting material was used to prepare the samples (5). Irrespective of the kind of lattice defects responsible for this subbandgap luminescence, these defects probably decrease the solar-to-electric conversion efficiency in a PEC cell with such electrodes. Optimal results for CdSe thin film electrodes are obtained with a photoelectrochemical etching procedure, which increases the real surface area of the electrode (4). There are indications that as a simultaneous effect the photoetch also removes surface recombination centers (4b, 4c). EL being a sensitive probe of surface recombination should indicate whether a removal of surface recombination centers indeed contributes to the effect of photoetch.

Fig. 2 shows the EL spectra of an electrodeposited CdSe electrode before and after photoetching. While the height of the subbandgap peak remains almost unchanged, the bandgap peak has increased nearly 100% after the photoetch. Probably nonradiative surface recombination is reduced by the photoetch thereby increasing the radiative bandgap recombination as well as the photocurrent of the electrode in a PEC. Though the amount of the increase in EL intensity induced by photoetching varies from electrode to electrode, a large increase

*Electrochemical Society Active Member.

in the bandgap luminescence has been found with every electroplated electrode that has been tested. Since the electrode current during EL is not affected by the photoetch, the observed enhancement of EL cannot be related simply to the increase of the electrode surface areas. Therefore, we consider EL of polycrystalline thin film semiconductor electrodes as an useful probe for analyzing the effect of surface treatment which do change the density of surface recombination centers.

The effect of photoetching on the PL spectra of our samples is found to be very small, sometimes even a slight decrease in intensity of the bandgap peak is found. As EL originates more close to the surface of the electrode, it is able to monitor surface recombination properties more sensitively than PL. A more detailed study of EL and PL properties of electrodeposited and painted CdSe electrodes is under work, testing the effect of electrode annealing conditions on EL, PL and x-rays diffraction patterns as well as the electrode power output in the PEC cells (5).

Acknowledgements: N.M. thanks O.A.S. for enabling his stay at UNICAMP. The financial support from FINEP and CNPq is acknowledged.

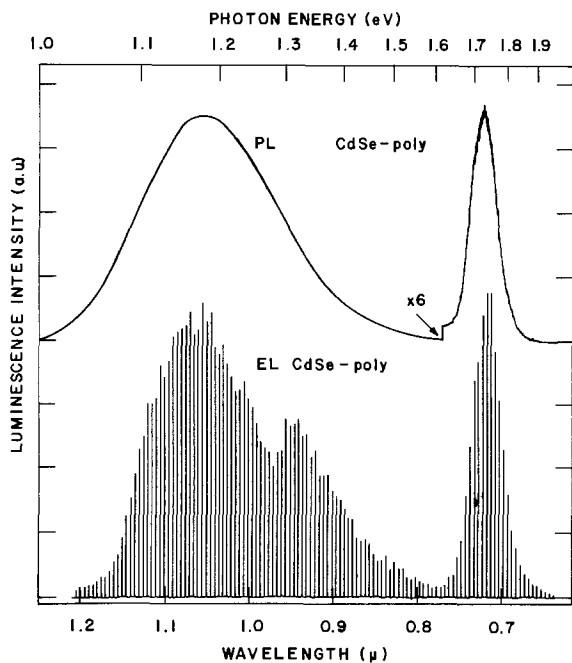


Figure 1: PL-uncorrected photoluminescence spectrum of an electrodeposited CdSe electrode in air at 2950K. The 1.5 cm² samples were excited with 100mW/cm² of 5145 Å light. EL-uncorrected electroluminescence of the sample at 2950K. The electrolyte was 0.1M S₂O₈²⁻ + 2.5M OH⁻. The electrode was continuously pulsed between 0.0 V(10 s) and -1.5 V(1 s) while the

spectrometer was scanned at 5 Å/s.

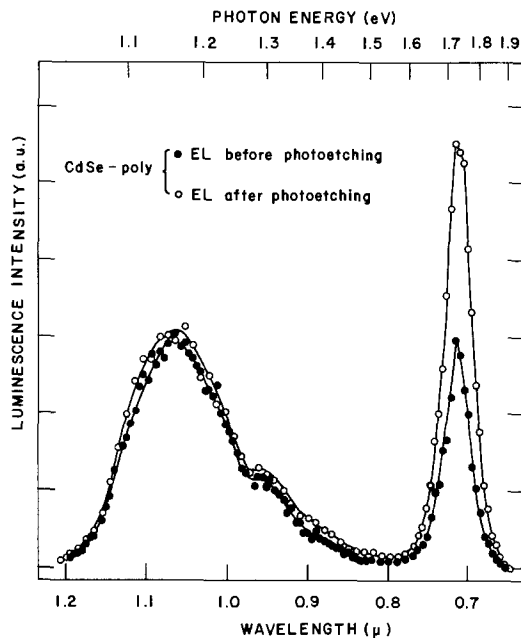


Figure 2: ● uncorrected electroluminescence spectrum of an electrodeposited CdSe electrode before photoetching. Experimental conditions as in Fig. 1. ○ same as before, but after photoetching in (0.3:9.7:90) HNO₃: HCl:H₂O.

REFERENCES

- (a) H.H. Streckert, J. Tong, M.K. Carpenter and A.B. Ellis, *This Journal* 129,772(1982)
(b) M.K. Carpenter, H.H. Streckert and A.B. Ellis, *J. Sol. State Chem.* 45, 51 (1982).
- (a) G. Hodes, J. Manassen and D. Cahen, *Nature (London)* 261, 403 (1976);
(b) A.B. Ellis, S.W. Kaiser and M.S. Wringhton, *J. A., Chem. Soc.* 98, 1635 (1976);
(c) B. Müller and A. Heller, *Nature(London)* 262, 680 (1976).
- R.P. Silberstein and M. Tomkiewicz, *J.Appl. Phys.* 54, 5428 (1983).
- (a) G. Hodes, *Nature (London)* 285,29(1980).
(b) R. Tenne and G. Hodes, *Appl. Phys.Lett.* 37, 428 (1980);
(c) N. Müller and R. Tenne, *Appl.Phys.Lett.* 39, 283 (1981).
- F. Decker, P. Motisuke, P. Salvador, M. Abramovich, M.J.P. Brasil, N. Müller Stolzenburg et al., in preparation.
- A.B. Ellis, *J. Chem. Ed.* 60, 332 (1983).
- G. Hodes, D. Cahen, J. Manassen and M. David, *This Journal*, 127, 2252 (1980).

Manuscript received Feb. 7, 1984.

Ceramic Membranes for Precise pH Measurements in High Temperature Aqueous Environments

S. Hettiarachchi* and D. D. Macdonald**

Fontana Corrosion Center, Department of Metallurgical Engineering, The Ohio State University, Columbus, Ohio 43210

Recently, Niedrach (1,2) and Macdonald and Tsuruta (3) described the use of yttria-stabilized zirconia (YSZ) membranes for the measurement of pH of aqueous solutions at temperatures as high as 300°C. In these studies, membrane electrodes with both aqueous and Cu/Cu₂O internal elements were used. This membrane electrode has been found to exhibit a nearly-Nernstian pH-response at elevated temperatures, and appears to be ideally suited for the measurement of pH of a wide variety of aqueous systems.

Although the preliminary studies demonstrated the potential use of YSZ membranes as pH sensors, its apparent lack of high precision as demanded by many research and control applications of high temperature technology, has led us to investigate the possible use of Hg/HgO as an internal reference (4). We have also attempted to eliminate the use of calculated pH values in evaluating the performance of these membrane electrodes. In order to achieve this second objective, the potential of the sensor and the potential of a hydrogen reference electrode were measured against a pressure balanced Ag/AgCl, 0.1M KCl reference electrode in systems containing known amounts of dissolved hydrogen. The excellent one-to-one correlation obtained between these measurements, as reported in this paper,

proves beyond any doubt that the Nernstian behavior expected of the hydrogen electrode with respect to the hydrogen ion is exactly followed by the zirconia (9%Y₂O₃) pH-sensors constructed by us (4).

All potentials were measured using a Keithley 614 electrometer having an input impedance of $5 \times 10^{13} \Omega$. Measured potentials were corrected for liquid junction potentials. Experiments were performed in the temperature range 175°C–275°C at 25°C intervals. Since the system was found to be sensitive to static charge, all measuring cables and electrode assemblies were placed in a Faraday cage.

Figure 1 shows the response of the pH-sensor and an internal reference hydrogen electrode (H₂, Pt/H⁺), both measured against a Ag/AgCl, 0.1M KCl reference electrode at various temperatures. The perfect one-to-one correlation obtained in these plots resulting in a regression coefficient of almost unity (Table I), proves that the pH-sensor behaves in a Nernstian manner, thus enabling us to estimate the pH of high temperature aqueous solutions to a high degree of precision. Furthermore, these findings also show that the lack of such high precision in previous studies is certainly not due to a fault of the pH-sensor, but can be traced to uncertainty in the calculated pH values of the buffer solutions used for the calibration.

The ability to measure pH to such a high degree of accuracy in aqueous systems at elevated temperatures opens up a whole new area of solution chemistry, since we are now in a position to study hydrolysis reactions and to determine activity coefficients for ions more accurately. This is an area which has only been briefly investigated by solution chemists.

The pH-sensor electrode is capable of withstanding high temperatures and

* Department of Chemistry, University of Colombo, Sri Lanka

** Electrochemical Society Active Member
Present Address: Chemical Laboratories,
SRI International, Menlo Park, CA 94025

Key Words: ceramic membranes,
pH-measurements

Manuscript received May 21, 1984.

SRI International assisted in meeting the publication costs of this article.

pressures and showed good long term stability, and is not affected by H_2 , O_2 or chloride ions in solution. These findings and the calibration procedure for precision high temperature pH measurements will be communicated shortly. (4).

ACKNOWLEDGMENTS

This work was supported by the Standard Oil company of Ohio under the contract No. 00196-4634-AB.

REFERENCES

1. L.W. Niedrach, J. Electrochem. Soc., 127, 2122 (1980).
2. L.W. Niedrach, *ibid*, 129, 1446 (1982.)
3. T. Tsuruta and D.D. Macdonald, J. Electrochem. Soc., 129, 1221 (1982).
4. P. Kedzierzawski, S. Hettiarachchi, and D.D. Macdonald, in preparation.

Table I

SLOPES OF THE PLOTS OF E_{sensor} VS Ag/AgCl, 0.1M KCl AGAINST $Pt, H_2/H_{\text{aq}}^+$ VS Ag/AgCl, 0.1M KCl AT VARIOUS TEMPERATURES.

Temperature/ $^{\circ}\text{C}$	Slope	γ^2 **
175	1.018	0.9993
200	1.012	0.9990
225	1.002	0.9999
250	1.002	0.9985
275	0.997	0.9997

** γ^2 is the regression coefficient.

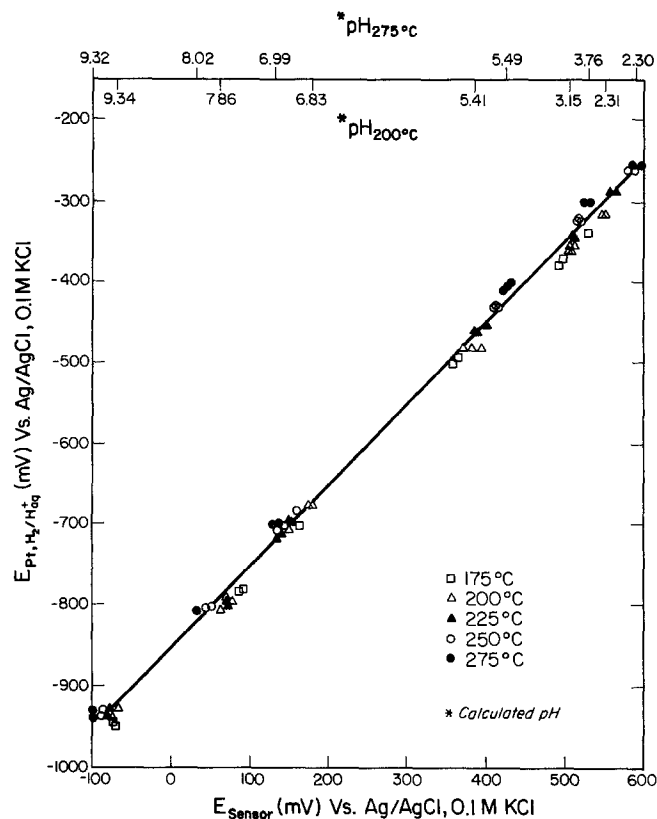


Figure 1 Response of the pH-sensor and an internal reference hydrogen electrode both measured against a Ag/AgCl, 0.1M KCl reference electrode at various temperatures.

Electrically Conducting Poly(Vinyl Acetate)

M. C. Wintersgill, J. J. Fontanella,* and J. P. Calame

Department of Physics, U. S. Naval Academy, Annapolis, Maryland 21402

S. G. Greenbaum

Department of Physics and Astronomy, Hunter College of CUNY, New York, New York 10021

C. G. Andeen

Department of Physics, Case Western Reserve University, Cleveland, Ohio 44106

Electrically conducting polymers have recently been the subject of intense interest. Polyacetylene has been widely studied as an electronic conductor. Ionic conductors include poly(ethylene oxide) (1), poly(propylene oxide) (2), polyacrylonitrile (3), poly(vinylidene fluoride) (3), poly(tetramethylene oxide) (4) and poly(ethylene succinate) (5). In the present note, the observation of electrically conducting poly(vinyl acetate) (PVAc) is reported. Ionic conduction is inferred from the data.

PVAc (MW 1.5×10^6) was obtained from Polysciences, Inc. PVAc and LiClO_4 in the ratio 8:1 were dissolved in methanol then dried in air on a teflon plate at about 55°C . The result was a brittle, clear solid at room temperature. Pure PVAc was prepared by the same method for comparison. Aluminum electrodes were then evaporated onto the faces of several samples and audio frequency complex impedance measurements were performed in a vacuum at temperatures from 5.5 K to 380 K using techniques described elsewhere (6). The results for one frequency (100 Hz) are shown in figure 1. Four other frequencies from 100 – 10^4 Hz gave similar results and are omitted for clarity. It is seen that the d.c. conductivity of the LiClO_4 complexed material at 100°C is about three orders of magnitude larger than that of the pure material and increases exponentially with an activation energy of about 2.1 eV. However, at about 50°C the a.c. conductivity of the pure material (a.c. loss due to the relaxation peak associated with the glass transition) is slightly greater than that for the complexed material at the same temperature. The glass transition in the complexed material is shifted to higher temperatures where it is probably masked by the d.c. conductivity. This temperature shift is confirmed by differential scanning calorimetry (DSC) studies. The DSC results together with further electrical relaxation studies will be presented elsewhere.

*Electrochemical Society Active Member.

Manuscript received March 14, 1984.

The U. S. Naval Academy assisted in meeting the publication costs of this article.

In order to gain further information concerning this material, ^7Li NMR linewidth and spin-lattice relaxation T_1 measurements were conducted at 155 MHz with a JEOL GX400 NMR spectrometer, after sealing the sample in an evacuated quartz tube. Over the temperature range studied, the ^7Li spectra exhibit a single absorption with no apparent quadrupolar broadening (as deduced by the appropriate $\pi/2$ pulsewidth condition). The temperature dependence of the full-width-at-half-maximum (FWHM) linewidth is shown in figure 2 (triangles). The T_1 -recovery process was found to be slightly non-exponential, which may indicate the presence of more than one relaxation time. However, no significant temperature dependence of the recovery profile was observed, which allowed the use of an "effective T_1 ," defined as the time required for the magnetization to recover 63% of its maximum value. A plot of T_1 (effective) vs. $1000/T$ also appears in Figure 2 (squares). The value of the "rigid linewidth" (4.4 kHz), which occurs below about 220K and the observed motional narrowing behavior bear a close similarity to results reported for PEO-Li⁺-based materials,^{7,8} which suggests a comparable degree of Li⁺ and/or polymer chain motion in PVAcg-LiClO₄. There are, unfortunately, no T_1 measurements above 383K at present, but it is likely that a T_1 minimum would occur at or near the melting point of the complex. T_1 does, however, exhibit Arrhenius behavior throughout the motional narrowing region (above room temperature) with an activation energy of 0.14 ± 0.03 eV. This small value presumably reflects localized motion with a correspondingly small potential energy barrier. The relation between the apparent localized process and motion resulting in long-range transport is not clear at the present time.

Finally, the following cell was constructed: $\text{Li/PVAcg-LiClO}_4/\text{MnO}_2\text{-C-PVF}_2$. The composition of the cathode was about 82% MnO_2 , 9.6% C and 8.4% PVF_2 by weight. The materials were hot-pressed at about 205°C to form a conducting disk about 2.54 cm in diameter and 1 mm thick. The polymer film was about 0.4 mm thick and 2 cm in diameter, while the lithium electrode was about 1 mm thick with a diameter of about

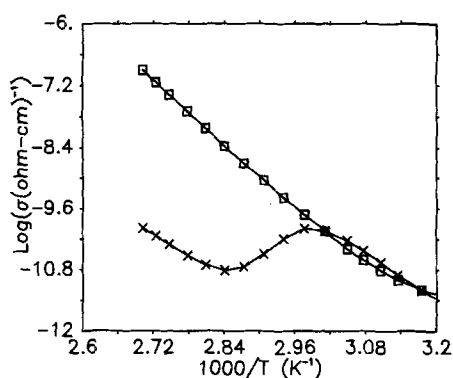


Fig. 1. $\text{Log}(\sigma(\text{A-cm})^{-1})$ vs. $1000/T$ for pure PVAc (x) and PVAc₈-LiClO₄ (□) at 100 Hz

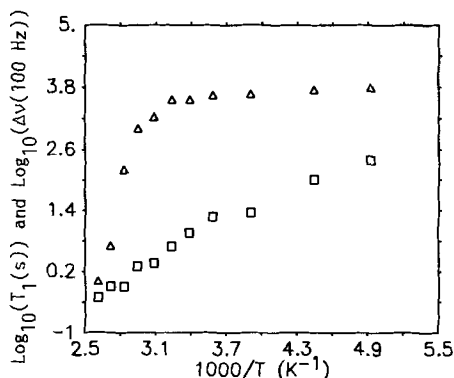


Fig. 2. Temp. dependencies of ⁷Li FWHM linewidth (Δ) and effective T₁ (□)

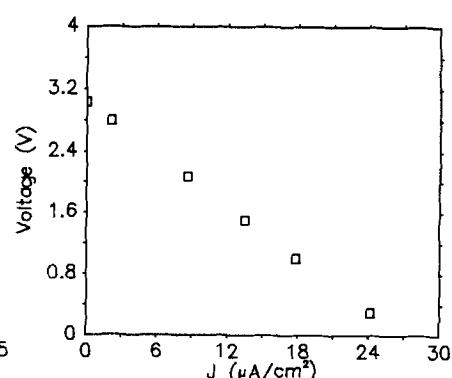


Fig. 3. Voltage (V) vs. $J(\mu\text{A}/\text{cm}^2)$ for the cell Li/PVAc₈-LiClO₄/MnO₂-C-PVF₂ at 125°C

1.2 cm. The three disks were spring loaded into a cell under an argon atmosphere. The cell was not hermetically sealed. Although the present data were obtained with the cell in air, similar results were obtained when the experiment was carried out under vacuum. The discharge characteristics are shown in figure 3. Further tests showed that with a 100kΩ load, the voltage decreased gradually from 1.8V to 0.9V over a period of 16 hours. The cell failed at that time. While the discharge characteristics of the present cell are not particularly impressive, it should be emphasized that no attempt was made to optimize the performance of the cell. The construction of the cell was rather primitive and, for example, a higher operating temperature or thinner polymer would decrease the internal resistance of the cell. The "open circuit" voltage (the resistance of the Keithley 195 DMM is about 10⁶ ohms) is about 3.04 volts, which is not unreasonable for a cell of this type. Further, the initial internal resistance of the cell, was about 93 kΩ and was about 85 times larger than the resistance predicted from the a.c. conductivity measurements described above. While there is considerable uncertainty in the latter value due to the ambiguities in the geometry of the cell, it is clear that the internal resistance of the cell is larger than the a.c. resistance of the bulk polymer material. This is not surprising since, for example, anions as well as cations may be contributing to the a.c. conductivity, thus giving rise to a lower a.c. resistance. Finally, a similar cell was constructed using a pure PVAc film in place of the PVAc₈-LiClO₄. No voltage was detected for this cell.

All results are consistent with ion transport.

ACKNOWLEDGMENTS

This work was supported in part by the Office of Naval Research. S.G.G. also acknowledges support from the Research Corporation.

REFERENCES

1. P. V. Wright, Br. Polym. J., 7, 319 (1975).
2. M. B. Armand, J. M. Chabagno and M. J. Duclot, in: Fast ion transport in solids, eds. P. Vashishta, J. N. Mundy and G. K. Shenoy (North Holland, Amsterdam, 1979) p. 131.
3. M. Watanabe, M. Kanba, H. Matsuda, K. Tsunemi, K. Mizoguchi, E. Tsuchida and I. Shinohara, Makromol. Chem. Rapid Commun., 2, 741 (1981).
4. M. Watanabe, K. Nagaoka, M. Kanba and I. Shinohara, Polym. J., 14, 877 (1982).
5. R. Dupon, B. L. Papke, M. A. Ratner and D. F. Shriver, Submitted for publication.
6. J. J. Fontanella, M. C. Wintersgill, J. P. Calame and C. G. Andeen, Solid St. Ionics, 8, 333 (1983).
7. F. L. Tanzella, W. Bailey, D. Frydrych, G. C. Farrington, H. S. Story, Solid St. Ionics, 5, 681 (1981).
8. A. Killis, J. F. LeNest, A. Gandini, H. Cheradame, J. P. Cohen-Addad, Polymer Bull., 6, 351 (1982).



Electrochemistry of Carbonaceous Materials and Coal

Su-Moon Park*

Department of Chemistry, University of New Mexico, Albuquerque, New Mexico 87131

ABSTRACT

Electrochemistry of carbonaceous material and coal is reviewed comprehensively. The subject is divided into five categories: electrochemistry of various forms of carbon, chemical oxidation and reduction of coal, electrochemical oxidation and reduction of coal, photoelectrochemistry of coal, and direct power generation from coal burning fuel cells. Oxidation of coal by air or oxygen and reduction through hydrogenation reactions are not included in this review. Only reports relevant to solution chemistry are included. Characterization and derivatization of coal and carbonaceous material employing the above electrochemical reactions are discussed in each section.

Since comprehensive reviews of electrochemistry of inorganic (1) or organic (2) derivatives of carbon compounds have been compiled in the literature, we will limit this review to the electrochemistry of carbonaceous materials relevant to coal. In reviewing the subject, we classify it into several categories: (i) electrochemistry of various forms of carbon, (ii) chemical oxidation and reduction of coal, (iii) electrochemical oxidation and reduction of coal, (iv) photoelectrochemistry of coal and carbons, and (v) direct power generation from coal burning fuel cells.

Electrochemistry of Various Forms of Carbon

The oxidation of carbonaceous materials has been studied mainly for two purposes: to characterize surfaces of various carbons and to characterize carbon as an electrode material. We will review these two subjects in this section.

Surfaces of carbon black particles were characterized electrochemically by subjecting them to a polarographic experiment as a suspension in *N,N'*-dimethylformamide (DMF) as a solvent with, *e.g.*, 0.1M tetra-*n*-butylammonium perchlorate (TBAP) as a supporting electrolyte (3). A limiting current was observed with the half-wave potential ($E_{1/2}$) in the range $-0.58 \sim -0.78V$ (*vs.* Hg pool) depending on the supporting electrolyte used. When carbon black was treated by strong reducing agents such as lithium aluminum hydride, the polarographic wave was no longer observed. This treated sample, however, gave an anodic wave at about $+1.0V$ (*vs.* Hg pool), indicating that oxidizable surface species have been produced upon treatment. This anodic wave disappeared when the sample was treated with oxidants such as hydrogen peroxide (H_2O_2). From these electrochemical results along with infrared (IR) spectroscopic results, Hallum and Drushel suggested that benzoquinone-like surface groups are responsible for the reduction current. Later, these authors (4) estimated the amount of quinone oxygen and hydroquinone hydroxyl groups on the surface of carbon blacks by controlled potential coulometric reduction or oxidation. The benzoquinone content ranged from 0.002% to $\sim 0.26\%$; the hydroquinone content was 0.016% – $\sim 0.47\%$, depending on the sample. These observations were later substantiated by Jones and Kay (5), who used polarographic methods with a stirred aqueous suspension of activated charcoal.

Mamantov *et al.* (6) have shown that electrochemical

* Electrochemical Society Active Member.

anodization or chemical oxidation with strong oxidants such as Ce(IV) results in the formation of a film on the surface of pyrolytic graphite. The anodized sample gave a broad cathodic voltammetric peak at about $+0.5V$ *vs.* SCE ($E_{p/2} = +0.48V$ *vs.* SCE), whereas a sharp reduction peak was observed at approximately $+0.5V$ *vs.* SCE, which was followed by a broad peak at $\sim 0V$. The authors suggested electrolytic lamellar compounds of graphite as a possibility. In this study and the ones described below, the carbonaceous material was used as an electrode as opposed to the previously described studies, in which a mercury electrode was used in a suspended solution of the carbon.

Kinoshita and Bett (7) employed the cyclic voltammetric method to detect surface oxides on carbon black (Vulcan XC-72) which had been subjected to heat-treatment, electrochemical and chemical oxidation, and also gas-phase oxidation. These investigators used a carbon black with a surface area of $220 \text{ m}^2/\text{g}$, which was fabricated into an electrode using small quantities of Teflon (du Pont), $\sim 10\%$ by weight. The cyclic voltammetric test was made after the carbon black was oxidized or heat-treated under various conditions. The quinone-hydroquinone redox reaction was observed in the potential range of $0.05 \sim 1.28V$ *vs.* NHE. Surface concentrations of $10^{-10} \sim 10^{-11} \text{ mol}/\text{cm}^2$ of quinone oxides were estimated. The results indicate that various oxidation procedures increase the amount of surface oxides, whereas heat-treatment at 2000° and 2700°C decreases the amount of surface oxides. This is because the oxides desorb as CO from the surface upon heat-treatment. Blurton (8) reported similar but much better defined voltammetric peaks using graphite electrodes in $1N \text{ H}_2\text{SO}_4$ solution. A maximum of three anodic and three cathodic peak currents were observed depending on the experimental conditions. Two peaks at lower potentials showed reversibility at slow scan rates up to about $10 \text{ mV}/\text{s}$, while the peak separation became larger at higher scan rates, indicating a sluggish electron transfer. This author attributed anodic currents to the oxidation of hydroquinone-like surface species and cathodic currents to the reduction of quinone-like groups in different environments.

The above observations may be summarized as follows: (i) carbon surfaces are covered with quinone-like and hydroquinone-like functional groups, which are electroactive and thus give polarographic or voltammetric currents, (ii) concentrations of these groups are estimated to be $10^{-10} \sim 10^{-11} \text{ mol}/\text{cm}^2$ or up to 0.26% benzoquinone and

0.47% hydroquinone by electrochemical methods, (iii) the surface concentrations of these groups are increased upon mild anodic, chemical, or air oxidations, and (iv) these groups desorb as carbon oxides upon heat-treatment. This information, as will be discussed below, gives an insight into the oxidation mechanism of carbons and graphites.

Probably the most comprehensive study on the anodic oxidation of various carbons, including graphitized active carbon, charcoal, soot, and graphite, was carried out by Binder *et al.* (9). They employed the current-potential curves, chronopotentiometric measurements, volumetric determination of the product CO₂, chemical analysis, x-ray analysis, and electrical resistance measurements as their techniques while the electrode was polarized. From these studies, they concluded that when the electrode potential was lower than the oxygen equilibrium potential, about 80% of the charge was used for oxidation of the carbon electrode to CO₂ and about 20% for the surface oxide formation. They ran these experiments in H₂SO₄ or H₃PO₄ medium, and the results appeared to be relatively independent of the medium and temperature.

Several other groups of investigators reported the chronopotentiometric (galvanostatic) behavior of various carbon electrodes (10-12). These investigators report that the electrode potentials level off at several values before they reach the sharply increasing potentials upon application of constant anodic currents. These results indicate that the carbon surface becomes oxidized at several different potentials to different surface species; the findings are consistent with previously reviewed reports (above) in which mainly the surface characterization has been made.

Kokhanov and Milova (13) reported the product distribution of oxidations of graphite electrodes in phosphate buffer solutions as a function of pH. These investigators employed a current density of 3.7 mA/cm² and monitored the electrode potential as well as the product gas composition. At pH lower than 6.7, a current efficiency (CE) for CO₂ production was ~91% with about 6% for CO and 3% for O₂. When the pH was increased from 6.7 to 13.0 the CO₂ content gradually decreased down to 5%; oxygen production increased to 95%. The CO product went down almost to nil. At pH higher than 13, the gas composition remained almost the same.

This observation was substantiated by another group of investigators employing polyethylene-impregnated graphite electrodes (14). These investigators performed quite comprehensive studies employing different current densities. Using log of current densities of -1.5, -2.0, -3.0, -4.0, and -5.0 (unit = mA/cm²), they classified three potential-pH domains and four regions for different types of oxide surface production.

The electrochemical oxidation of a high surface area carbon black (1000 m²/g) in 96% H₃PO₄ at 135°C was investigated by Kinoshita and Bett (15). The total anodic current, amount of CO₂ evolved, and oxygen content at the carbon surface were measured as a function of time and potential. Their results indicate that two anodic processes occur: the formation of a surface oxide, and the evolution of CO₂. The rates of both processes decrease with time but at different rates, so that the CO₂ evolution becomes the major reaction in later stages of electrolysis. The current efficiency (CE) for the CO₂ evolution can be expressed by an equation

$$CE = \frac{1}{1 + Q_{ox}/Q_{CO_2}} \quad [1]$$

where Q_{ox} is the charge used for the surface oxide formation and Q_{CO_2} is for the CO₂ evolution. The charge for the CO₂ evolution was measured by determining the amount of CO₂ assuming that CO₂ production requires a four electron process.

At all potentials the formation of surface oxides is the predominant process at the beginning of the electrolysis, whereas CO₂ formation predominates in later stages of electrolysis. Thus, the current efficiency for CO₂ produc-

tion approaches unity as the ratio Q_{ox}/Q_{CO_2} approaches zero. The current efficiency for CO₂ production approaches unity more rapidly at higher applied potentials at the anode. These investigators summarized their observations as follows.

1. Two processes occur initially: surface oxide formation and CO₂ evolution. As the rate of surface oxide formation decreases, CO₂ evolution becomes the major anodic process.

2. The two processes are independent. The surface oxide does not inhibit CO₂ formation.

3. The surface oxide coverage approaches, but is less than, a monolayer, and continues to grow even after CO₂ is the major product.

4. The dissolution rates of carbon black electrodes are independent of water concentration or CO₂ pressure.

The electrode kinetic parameters were studied by several groups of investigators by following Tafel relationship between current density and potential (14, 16-18). In general, Tafel slopes are dependent on the pH of the medium, indicating different mechanisms for the oxidation reactions. Most of these investigators used galvanostatic measurements for investigations of the oxidation reactions of the various carbon electrodes.

Not much attention has been paid to the mechanism of CO production from carbon oxidation, mainly because of its lower fraction in the product composition. It appears that the desorption of oxides occurs in the form of CO in gaseous state under vacuum (7). In aqueous solution, CO₂ appears to be a major product with a few percent of CO detected (10). When the amount of CO₂ produced becomes sizable, the Boudouard reaction in pores behind the electrode surface

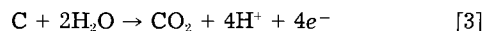


may occur producing a small amount of CO as a product (19). Thus, CO may be produced only if a large electrolysis current is passed.

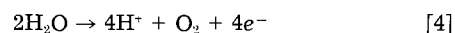
Studies reviewed thus far were concerned with the electrochemical behavior of carbonaceous material either in suspension at Hg electrodes or as an electrode in a buffered solution that is not electroactive itself. Many investigators, however, studied electrochemical corrosion of graphite anodes in aqueous chloride electrolytes (20-22) or while electrowinning aluminum (19). The basic processes occurring under these environments are similar, but reaction mechanisms are more complicated due to the generation of oxidants such as OCl⁻, ClO₃⁻, etc. The readers may consult the references cited for these studies.

Summarizing this section, we may conclude that oxidation of various carbons occurs through two pathways: formation of surface oxides and CO₂ evolution. These two reaction pathways were claimed to be independent of each other by Kinoshita and Bett (15). It appears, however, that this may not be the case. Although not proved, it is reasonable to suggest that the formation of surface oxide precedes the CO₂ evolution reaction. When all the surface is covered with oxide film, the oxide desorbs as CO under vacuum and as CO₂ as electrolysis goes on. This is evident even in Kinoshita and Bett's data; the current efficiency for CO₂ evolution increases with electrolysis time.

Although the mechanism for carbon oxidation is not well understood, one can readily conclude that the electron transfer reaction does not include the water molecule, proton, or hydroxide ion. If the stoichiometry



correctly represents the carbon oxidation, the electrode potential would be pH dependent and thus, the product distribution should remain independent of pH. Actually, the oxygen evolution



becomes predominant at higher pH, indicating that the type of electrochemical reaction is different at low and

high pH. Potentials monitored during the galvanostatic electrolysis of polyethylene-impregnated graphite decreased from about +1.6V at pH = 1.0 to about 0.70V at pH = 14.5 (13). Thus, the electrode potential is controlled by carbon oxidation at low pH where oxygen overvoltages are high; the oxygen evolution reaction determines the electrode potential in higher pH regions.

Chemical Oxidation and Reduction of Coal

In reviewing this subject, the scope will be limited to the ones pertinent to the electrochemical reactions. Hence, only wet chemical oxidations or reductions in both aqueous and nonaqueous media will be considered. Oxidations with gaseous oxygen, metal oxides, etc. in the mixed solid form will be excluded, since these reactions do not have direct relevance to the understanding of the electrochemical behavior of coals. The subject will be divided into two categories: oxidations and reductions.

Oxidation reactions.—Chemical oxidation of coals has been carried out mostly as a tool to probe the structure of coal, mainly from product analysis. Oxidations were carried out using oxidants such as HNO₃, permanganate, and hypohalite in aqueous alkali media. Generally, oxidations in alkaline media were preferred because the oxidation products are easily solubilized due to carboxylic or phenolic groups found in the products. The product acids are usually not soluble in acidic solutions. The ultimate oxidation products of coal are carbonic acid, carboxylic acids, and phenols. Early studies on this area were reviewed by Howard in 1945 (24); most recent work on oxidation of coal was reviewed comprehensively by Hayatsu *et al.* (25).

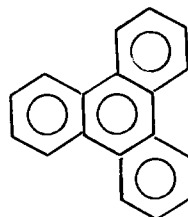
Francis (26) was the first to propose that oxidation of coal occurs in three stages. According to him, coal undergoes stepwise oxidation reactions: the formation of surface oxides, followed by the formation of humic acid, and eventually of small aromatic as well as aliphatic acids.

Surface oxides formed may be desorbed as CO₂ or CO upon raising the temperature or as oxidation is prolonged. Coal thus oxidized shows little change in its gross property, but has more acidic properties at its surface. If oxidation is continued, products called "regenerated humic acids" form. These acids are soluble in alkaline medium, but form precipitates similar to Fe(OH)₃ in acidic medium. The rate of humic acid formation in 1N HNO₃ is coal-rank dependent (27). Low rank coals rapidly oxidized to humic acids, while high-rank Pocahontas coal display an induction period. Low rank (Illinois no. 6) coal pass through a period with a maximum yield of humic acid formation, which then decreases due to further oxidation to lower molecular weight acids. Humic acids produced from Pittsburgh seam coal (28) had average molecular weights of 193-242 and average equivalent weights (carboxylic acids) of 192-244. However, these properties vary widely. Oden (29), for example, reports the estimated molecular weight of 1000 ~ 1350 with an equivalent weight of about 340 for humic acids produced from peat. In general, the molecular weight of humic acids is approximately 1000 with three or four acidic (either carboxylic or hydroxyl) groups.

If the oxidation process is continued, humic acids are eventually broken down into smaller organic acids. Oxidizing agents such as HNO₃, MnO₄⁻, H₂SO₄, or peroxides were used in aqueous acidic media at elevated temperatures. In general, oxidation in the acidic medium produces poor yields of simple, soluble organic acids and carbonic acid. Product acids detected in earlier studies included pyromellitic acid and other benzene carboxylic acids (30), oxalic acid (31), trinitro-resorcinol (31), mellitic acid (32), and acetic, succinic, and picric acids (33), depending on the type of coal, reaction conditions, and reactants.

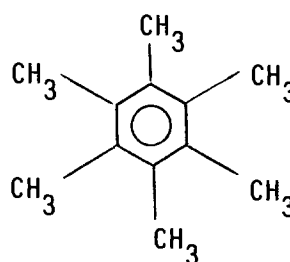
Carbonic, acetic, oxalic, and several different benzene-carboxylic acids were produced when various types of coals were oxidized by alkaline permanganate solution (34). Oxidation of a Pittsburgh seam bituminous coal with

alkaline permanganate gave a carbon distribution of 45.0% carbonate, 2.2% acetate, 15.0% oxalate, and 30.8% aromatic acids, totaling 93.0% of carbonate recovered as alkali salts (35). Usually, 50 ~ 60% of the nonvolatile acids produced by alkaline permanganate oxidation were aromatic. Typically, aromatic acids were in the form of mellitic, benzenepentacarboxylic, and terephthalic acids. Howard (24) speculates that mellitic acid can be formed only by oxidation of condensed carboxylic hydrocarbons, of which the simplest form could be



triphenylene

or of a benzene ring completely alkylated, such as



hexamethylbenzene

or mixtures of these two types. Actually, the yield of mellitic acid from triphenylene was 44.8% of the theoretically expected amount, while hexamethylbenzene produced CO₂ almost exclusively when the same oxidation procedure was used (24). Oxidation of an Australian coal by the same procedure produced about 1.1% oxalic, 0.3% succinic, 5.0% benzenedicarboxylic (o-, m-, and p-phthalic acids), 17.4% benzenetricarboxylic (both 1,2,3- and 1,2,4-), 21.7% benzenetetracarboxylic (1,2,3,4-, 1,2,3,5-, and 1,2,4,5-), 41.1% benzenepentacarboxylic, and 13.4% benzenehexacarboxylic (mellitic) acids of the soluble acid products (36). Aliphatic acids such as acetic, propionic, butyric, pentanoic, and heptanoic acids were also found in small amounts from the basic permanganate oxidation of coal (37). Acids above pentanoic were isolated only from the lower rank coals; none above propionic was isolated from the low-volatile coal.

Perhaps the most extensive studies on the oxidation of coal are those reported by Yokakawa *et al.* (38, 39). These investigators employed either boiling 1N HNO₃ or alkaline permanganate as an oxidant for the oxidation of humic acids and 30 model compounds. Results indicate that the most vulnerable structure destroyed in the first stage of humic acid oxidation was alicyclic or hydroaromatic, and that in the second stage various structures were destroyed unselectively with some differences in reaction rates. From this study, they reached the conclusion that a molecule of coal consists of two parts: alicyclic or hydroaromatic structures, which are vulnerable to oxidations, and condensed aromatic structures, which are more resistant to oxidations. They pointed out from their data that (i) the high reactivity and the lack of selectivity in oxidation reactions of low rank coal are due to the hydroxyl groups in the aromatic structure part, the basic structural unit of bituminous coal, and (ii) the degree of condensation of the aromatic structure is rather small. Phenolic hydroxyl groups were found to degrade to CO₂ and oxalic acid rather quickly upon oxidation. Later, these investigators (39) extended their work to "artificial" coals, which were prepared from cellulose and lignin, and they obtained similar results.

Concentrated nitric acid is not only a powerful oxidant, but also is a nitrating agent. This is somewhat disadvantageous for derivatization of coal, since the nitration reac-

tion introduces additional nitrogen. Recently, Hayatsu *et al.* (25) reported that aliphatic-rich macromolecules in coal are oxidized by concentrated HNO_3 without extensive degradation of aromatic rings. From the oxidation of methylated cannel-like high volatile A bituminous coal (Ohio PSOC 297) with 70% HNO_3 at 110°C for 48h, organic acids (31 weight percent [w/o] of the substrate), and regenerated humic acids (58.25%) were recovered; approximately 47% of the organic acids were found to consist of aliphatic unbranched dicarboxylic acids ranging from C_4 to C_{14} . Deno *et al.* (40) reported similar results from oxidation of various coals with 40% HNO_3 at 60°C.

The kinetics of alkaline permanganate oxidation of coal was studied by Smith and Mapstone (41) by monitoring the amount of permanganate consumed as a function of time. The rate of oxidation of several different coals was expressed by the equation

$$Q = (a - X_0) + X_0(1 - e^{-k_1 t}) + k_2 t \quad [5]$$

where Q represents the quantity of permanganate decomposed at time t (as milliliters of 1.0N), a is the amount of MnO_4^- that would have decomposed at $t = 0$ for the third stage of the reaction, X_0 is the amount of MnO_4^- decomposed for the second stage (first-order) reaction at $t = 0$, k_1 is the rate constant of the second stage (first-order) decomposition reaction, and k_2 is the slope of the linear plot for the last stage of the decomposition reaction. Thus, $(a - X_0)$ represents a rapid initial reaction, $X_0(1 - e^{-k_1 t})$ a further first-order reaction in which k_1 is possibly constant for all coals, and $k_2 t$ a 0th-order decomposition of permanganate continuing to extended reaction times. Correlation between particular terms in the above equation and various coal ranks was not satisfactory; only general trends were observed between the two. The general sequence of the coal oxidation kinetics is consistent with Francis' three-stage mechanism (26).

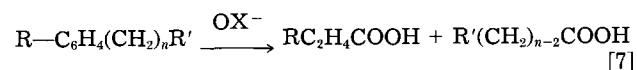
The action of oxygen at elevated temperatures and pressures on aqueous alkaline suspensions of coals has been studied (42-44). Typical reaction conditions were at 100° ~ 300°C and under up to 75 kg/cm² of pressures. One advantage of this method is that the oxidation reaction may be driven to CO_2 completely and water or to any desired stage. When "appropriately" oxidized, products included CO_2 , oxalic acid, and benzene carboxylic acids. Various U.S. (42), Japanese (43), and Chinese (44) coals were studied by this method.

In more recent studies, instrumental methods such as a nuclear magnetic resonance (NMR) (45), or infrared (IR) spectroscopies (46) were used for identification of oxidation products. Results reported from these studies are consistent with the previous findings.

A controversy started when Chakrabarty *et al.* published a series of papers (47) in which they claimed from their oxidation studies using basic hypochlorite as an oxidant that about 55%-60% of the total carbon in coal exists in the sp^3 valence state. They further stated that coal structures are made of modified bridged tricycloalkane systems or polyamantanes. This is a rather surprising statement, since the current understanding of the coal structural model is that coal has predominantly aromatic, with some hydroaromatic, structures. According to these investigators, hypochlorite (OCl^-) is a relatively mild and highly specific oxidant for coal. The specificity of this reagent can be shown by reactions such as



and



where X is a halogen, R a properly oriented activating group (e.g., acetyl or β -keto function), and R' a hydrogen, alkyl, or aryl group with or without activating influence. They showed from their experiments using

appropriate model compounds that hypochlorite oxidation will occur only when a carbanion can form at the methylene or methyl site and then stabilize itself on the substrate molecule. Thus, the oxidation can only cleave the sp^3 carbon but not the aromatic rings. Oxidation of an activated alicyclic compound containing a tertiary sp^3 carbon system may result in loss of one, two, or three carbon atoms as CO_2 or CHCl_3 via 1,3- and 1,4-halogenation steps. To obtain the reaction specificity, one has to control the pH of the medium at higher than 12.

Based on the above control experiments and other oxidation experiments on coal samples using basic hypochlorite as an oxidant, these investigators reached the conclusions listed below.

1. A minimum of 3%-5% of the total carbon in any coal exists as n-propyl groups, while n-butyl groups account for less than 1% of the total carbon in low-rank coals and about 2% in high-rank ones (47a).

2. In low-rank coals, at least 17% of the total carbon is present in the form of activated $-\text{CH}_2-$ and/or $-\text{CH}_3$. Detection of formic acid in the oxidation products indicates the presence of similarly activated $-\text{C}_2\text{H}_5$ groups.

3. Even in 500°C chars, at least 14% of the total carbon is nonaromatic ($-\text{CH}_2-$), and 3%-4% are contributed by n-propyl and/or n-butyl groups, not the corresponding alkanes.

4. It is estimated that between 55% and 60% of the total carbon in coal exists in the sp^3 valence state, which is much higher than the accepted hydroaromaticity of coals. These structures are modified bridged tricycloalkane systems or polyamantanes.

The above conclusions on coal structures were strongly disputed in the coal research community by other investigators (48-53). To argue against the oxidation mechanism of Chakrabarty *et al.*, these investigators used model compounds such as phenol (48, 51), naphthol-formaldehyde polymer (49), fluorescein (44), 2-naphthol (48, 51), 2-naphthoic acid (48, 53), 1-naphthol (51), 2,3-naphthalenedicarboxylic acid (51), 1-hydroxyanthracene (51), naphthalene (52), and 2-methylnaphthalene (52) for the hypochlorite oxidation under similar or the same experimental conditions. Results indicate that these aromatic compounds undergo oxidation reactions to end products including phthalic acid and CO_2 , invalidating some conclusions made by Chakrabarty. Aczel *et al.* (50) employed liquefaction experiments and showed that adamantane was extremely stable under the conditions in which more than 60% of Illinois no. 6 coal was converted to cyclohexane soluble liquids. Chakrabarty and Berkowitz (54) later pointed out that adamantane would be different from polyamantanes.

Mayo and Kirshen (53) ran extensive experiments using various coals and showed that the product composition depends mostly on pH during oxidation and on the state of subdivision of the coal. There appear to be two mechanisms of oxidations by aqueous NaOCl , a mechanism at $\text{pH} > 11$ and a second mechanism operative at $\text{pH} < 10$. The former mechanism is specific to enolizable compounds and some other compounds having acidic hydrogen atoms, as was shown by Chakrabarty and Kretschmer, whereas the latter may involve many more, perhaps most, organic compounds whether or not they react by the first mechanism. Thus, aqueous NaOCl would oxidize most organic, both aromatic and aliphatic, compounds indiscriminately by the second mechanism. The reaction path and the intermediate for the second mechanism are not known. For the oxidation of coal, high fractions of carbon appear in the soluble form of acids with only about 13% as CO_2 in the oxidation product at $\text{pH} = 13$, while the yields of soluble acids are lower and CO_2 higher at $\text{pH} 9-11$. These results as well as those of Landolt *et al.* (51) point to the fact that phenols are the most reactive groups in coal at high pH. Although the high pH mechanism of Mayo and Kirshen (53) agrees with that of Chakrabarty *et al.* (47), Mayo and Kirshen concluded from the (H + C)/C ratios and carbon and oxygen distributions in the oxidation products of coal that

CO₂ during high pH oxidation must arise from the aromatic compounds, probably hydroxylated rings. These results are consistent with the structure of bituminous coal in which aggregates of condensed aromatic, hydroaromatic, and bridged alicyclic rings held together by ether (or sulfide), methylene or polyethylene links, or combinations of these, are crosslinked in a three-dimensional fashion. Conventional oxidations break mostly aliphatic and ethereal bonds producing aromatic acids, but NaOCl apparently produces a different group of acids by cleaving some of the aromatic rings. Obviously, more characterizations must be done with respect to the hypochlorite oxidations.

More recently, sodium dichromate (55, 56), alkaline cupric oxide (57-59), hydrogen peroxide in acetic acid (peracetic acid; 60, 61), and pertrifluoroacetic acid (62, 63) were used to oxidize coal. Dichromate showed different degrees of oxidative power depending on pH of the medium. At lower pH, ring degradation occurred readily, but dichromate behaved as a mild oxidant. Peracetic acid (CH₃COOOH) led to the oxidative degradation of aromatic rings and the formation of dibasic acids. Pertrifluoroacetic acid (CF₃COOOH) behaved similarly, with the production of aliphatic acids as degradation products of alkyl aromatics. This acid might be a good reagent for studying the aliphatic structure in coals. Trifluoroacetic acid oxidation appeared to preserve aromatic rings containing nitrogen or sulfur heterocyclics (64, 65).

In summary, the oxidation of coal by chemical oxidants is accomplished in three stages: surface oxide formation, oxidation to humic acids, and final oxidation to end products including smaller aliphatic and aromatic acids and CO₂. Low-rank coals appear to produce higher yields of aliphatic acids compared to high-rank coal, whereas the inverse can be stated for the mellitic acid in oxidation products. This indicates that low-rank coals consist of more branched hydrocarbons, while high-rank coals approach a highly aromatic structure as in graphite. Finally, the hypochlorite oxidation apparently cleaves aromatic rings, producing different oxidation products compared to the conventional oxidants. Investigations of oxidation reactions provide the method of probing coal structures as well as of producing coal-derived chemicals, such as many organic acids.

Reduction reactions.—As already mentioned, chemical reductions of coal pertinent to electrochemical reactions will be reviewed in this section. Coal reduction by hydrogenation is reviewed elsewhere (65). Reductions of various coals can be accomplished by an electron transfer reaction from alkali metals such as Li (66-71, 73), Na (72, 73), K (73-77), LiAlH₄ (71), or Na-K alloy (77) in various organic solvents, including ethylene diamine (66-71), benzene (71), liquid NH₃ (72), tetrahydrofuran (THF) (73, 74), and a mixture of several ethers (76, 77). A variety of different ranks of coals (66-68, 70, 72-77) as well as some cokes and chars (69) and asphaltenes (71) have been studied by this method. In most cases, solvents behave as proton donors for the reduced coal, but some investigators used isopropyl alcohol as a proton donor. Many of these studies have been performed in either or both of two perspectives: to characterize coal structures and/or to prepare coal derived chemicals.

Reggel *et al.* (68) added to a vitrain of 90% carbon as many as 55 atoms of hydrogen per 100 carbon atoms using lithium as a reductant in ethylene diamine. Later Niemann and Homback (77) reported that they added up to 87 hydrogen atoms per 100 carbon atoms to a medium volatile bituminous coal by repeated reductions with potassium or sodium-potassium (1:1) alloy as reductants and isopropylalcohol as a proton donor. Brooks and Silverman (69) employed the reduction reaction to study some cokes and chars and suggested that the low reducibility and the low hydrogen content of the 900°C coke are due to the presence of carbon atoms predominantly in a divalent state. Sawatzky and Montgomery (71) studied asphaltenes using lithium in ethylenediamine and report

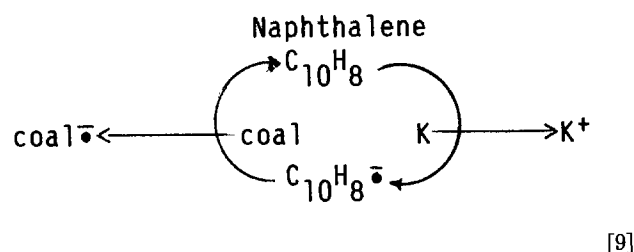
that considerable amounts of hydrogen have been added to asphaltenes and most of the sulfur has been removed. They noticed the reduction in molecular weight due to the cleavage of ethereal bonds and thioethers. Sternberg *et al.* (70) studied temperature effects on lithium reduction of coal and pointed out that reduction at higher temperature (90° ~ 100°C) is much more efficient than at lower temperature (17°C).

The nature of reduction was considered by several groups of investigators (71, 72, 77). As already mentioned, Sawatzky and Montgomery reported a decrease in molecular weight when asphaltenes are reduced and found that ethereal bonds of oxygen and sulfur are cleaved. Lazarov and Angelova (72) used sodium metal in liquid ammonia (at -33°C), since it is known to cleave oxygen and sulfur bonds according to the reaction



The reaction proceeds easily with diaryl ethers, aryl ethers of the benzyl type and aryl-alkyl ethers, but not with the aliphatic ethers. The results indicate, however, that the hydrogen uptake by the 87.6% carbon coal was more than expected by the cleavage of ethereal bonds calculated from the amount of such bonds. Thus, the excess of hydrogen consumed in the reaction was assumed to be used to reduce the aromatic part of coal. This assumption was later justified by other investigators (77) by monitoring the absorbance of bands of the IR spectra due to aromatic rings (810 cm⁻¹ and 745 cm⁻¹) of coals successively reduced by potassium.

The most interesting chemistry of coal reduction has been reported by Sternberg and co-workers (73, 74). These investigators improved methods of reducing coal by introducing naphthalene as an electron-transfer mediator in THF solution. The reaction is catalytic and may be represented by a scheme



The coal anion, containing 12 charges per 100 carbons, can then be alkylated using alkyl halides through the reaction



Using Pocahontas low volatile bituminous coal, they were able to add 8.1 methyl and 8.8 ethyl groups per 100 carbon atoms, respectively. When alkali metals were compared, lithium was least effective with the addition of 7.2 ethyl groups and potassium was most effective with the addition of 8.8 ethyl groups. Sodium had properties similar to those of lithium. The solubility increased from 0% and 3% in benzene and pyridine for untreated coal to 95% in both solvents for the ethylated coal. The same study was later extended to other coals including Colorado subbituminous (72% carbon), Bruceston (83% C), and Pocahontas (90% C), and anthracite (96% C) coals by Sternberg and Delle Donne (74). The results indicate that the Colorado subbituminous coal is most effective in adding alkyl groups (14 alkyl groups added per 100 carbon atoms) while the anthracite is least effective with addition of only 0.6 alkyl groups per 100 carbon atoms. They attributed this to the steric hindrance, since the anthracite was shown to carry as many as 11 electrons per 100 carbon atoms. Similar approaches were used by other investigators in later studies (75-77). The limitation of this method of studying coals, however, was pointed out (78).

In the course of studies described above, the IR spectroscopic method proved to be a powerful technique for

following reactions (72, 77). The increase or decrease in various absorption bands was monitored for successively treated coals.

In summary, coal can be reduced by alkali metals in a variety of solvents; as many as 88 hydrogen atoms per 100 carbon atoms were shown to be added to coal. The reduced coal anions can easily be alkylated using alkyl halides. Alkylated coals have much higher solubilities in organic solvents including benzene and pyridine making many studies on coal in such media possible. Also, many coal derived chemicals may be prepared in organic solvents.

Electrochemical Oxidation and Reduction of Coal

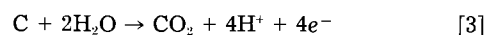
The processes of electrochemical oxidation and reduction of various coals resemble those for chemical oxidation and reduction, reviewed in the previous section. The oxidation has been studied both in basic and acidic media, but not much in nonaqueous media. The reduction of coal has been studied extensively in nonaqueous solvents including tetrahydrofuran (THF), dimethylsulfoxide (DMSO), and dimethyl formamide (DMF). Most of these studies were carried out to elucidate coal structures; some were concerned with the derivatization of coal. Although the first work on electrolytic oxidation appeared in the literature in 1932 (79), the whole area is still fairly new to electrochemists.

Electrochemical oxidation of coal.—Early investigators (79-81) used alkaline media for electrolysis of coal slurries, probably because chemical oxidations were carried out mostly in basic media. The products of oxidation, humic acids, are soluble in a high pH medium. Lynch and Collett (79) performed an extensive study on the electrolytic oxidation of Pittsburg coal in a 3N NaOH solution at copper, nickel, lead, or platinum electrodes. Of these electrodes, the copper electrode was found to perform best. The current density was maintained at 3 mA/cm², and the experiments were carried out at room temperatures. Carbon dioxide, oxygen, humic acids, and traces of carbon monoxide and hydrocarbons were detected as anodic products. Oxygen accounted for about 94% of the gaseous product excluding CO₂. The rate of humic acid formation reached a maximum value at about 70h of electrolysis, whereas the maximum rate of CO₂ formation occurred at about 130h of electrolysis, indicating that the electrolysis of coal produced humic acids first, followed by CO₂ evolution in later stages. The electrolysis reaction appeared to stop at the humic acid stage at copper electrodes but it proceeded to further products at platinum electrodes. When humic acids were subjected to anodic oxidations, they were efficiently oxidized at platinum electrodes but not at copper electrodes. Lynch and Collett (79) therefore suggested that coal may be electrolyzed stepwise to any desired products or intermediate species depending on electrolysis conditions.

Various improvements were made by Eddinger and Demorest (80) on electrolysis conditions for electrolysis of coal in basic media. They used a graphite electrode as well as catalysts such as vanadium pentoxide or cobalt chloride. Belcher (81) published a series of papers detailing anodic oxidations of bituminous coals and some anthracites. Khundkar and Kamal (82) carried out anodic oxidation of peat in an alkaline solution using a current density of 10 ~ 20 mA/cm². They found that a nickel anode at a current density of 20 mA/cm² gave the best yield of humic acids, about 48% yield (dry ash-free basis) for 12h electrolysis. These investigators also used the above-mentioned catalysts without much effect on the reaction rate. Studies on temperature dependencies (20° ~ 80°C) showed that electrolysis at ~60°C gave the highest yield for humic acids. Recently, Senftle *et al.* (83) studied the anodic oxidation of anthracite by employing it as an electrode in an alkaline medium. Results showed that humic acids were generated as products. They proposed after some control experiments that major oxidants for the anthracite oxidation were molecular and radical species

formed by the electrolytic decomposition of water.

Only recently have studies on anodic electrolysis of coal in acidic media appeared in the literature (84-94). Coughlin and Farooque published a series of papers on the anodic oxidation of coal in sulfuric acid solution (84-88). According to them, coal slurries are oxidized at the platinum anode in a sulfuric acid solution, producing carbon dioxide and carbon monoxide as anodic products and hydrogen as a cathodic product. The stoichiometric reactions proposed for the electrolytic process was



or



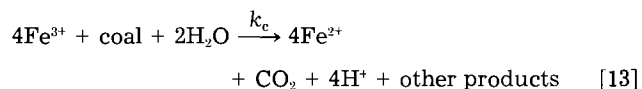
at the anode and



at the cathode. This stoichiometry offers a possibility of gasifying coal at lower temperatures by electrolysis rather than by other means (high temperature and pressure gasification, since from the above stoichiometry the standard electrode potential for the anodic reaction is calculated to be only 0.228V vs. NHE. They also pointed out that coal slurries could be used as anodic depolarizers for metal electrowinning (85). Various parameters affecting coal electrolysis including coal-particle size, concentration of coal, temperature, and the supporting electrolyte were reported (86). The ratio of H₂ to CO₂ + CO was monitored for as long as about 450h of electrolysis; it was much higher (9 ~ 4) than would be expected from the above stoichiometry, *i.e.*, 2. This indicates that the anodic charge is used not only for the evolution of CO₂ or CO but for other processes, assuming that the current efficiency for the hydrogen evolution is 100%. The electrolysis can be carried out with less than 1V of biased potentials. Of various coals tested, the North Dakota lignite showed the highest current density of about 1.4 mA/cm² at room temperature when 0.475 g/cm² of coal was present in the solution as a slurry (87).

Baldwin *et al.* (90) carried out detailed voltammetric studies on coal oxidation in acidic media and also in nonaqueous solution, and suggested from their results that the major electrolysis current in a coal slurry electrolysis resulted mostly from the oxidation of iron(II), which had been extracted from coal into the strong acidic electrolyte. They made this suggestion by comparing the voltammetric behavior of the extracted solution with that of the iron(II)/iron(III) redox pair. Iron was also shown by the atomic absorption analysis to be a major component in the filtrate. Okada *et al.* (91) reached a similar conclusion, *i.e.*, that Fe(II)/Fe(III), dissolved in the electrolytic solution, is responsible for currents observed at lower anodic overpotential in the electrolysis of coal slurries. There is an apparent disparity, however, between the argument that the anodic current was caused by the oxidation of iron(II) and the observation of Coughlin and Farooque, in which electrolysis currents were maintained for as long as 450h. Either the iron(II) would be leached out continuously or coal itself would undergo the oxidation reaction.

This disparity was resolved by Dhooge *et al.* (92, 93), who performed detailed studies on the mechanism of coal slurry oxidations using various electrochemical techniques. In their studies also, practically no anodic currents were observed with thoroughly washed coal introduced into 1M sulfuric acid solution. Coal particles were washed by stirring in 1:1 H₂SO₄ for more than 50h. When, however, iron(III) was added to the washed coal and the anodic potential was maintained such that iron(II) would be oxidized, the anodic currents were observed, indicating that iron(II) was generated by oxidizing coal. They concluded from their experiments that coal was oxidized by Fe(III) in the solution according to the reaction



followed by an electrode reaction



at the anode and



at the cathode. The catalytic nature of the reaction was also demonstrated by several other experiments, which included controlled potential oxidation of the Fe(II) with the perturbation of washed coal (92) and the direct addition of oxidants to the coal slurry and monitoring the concentration of the reductant produced by electrochemical methods (93). Also, if the stoichiometry outlined by reaction [3] or [11] were correct, the equilibrium potential should be dependent on the pH of the medium (-59 mV/pH unit). Experimental results showed that it was independent of pH, indicating that the anodic reaction does not involve water or ions derived from it, *i.e.*, H^+ or OH^- .

The rate of reaction [4] for various catalysts can be determined by controlled potential experiment methods (92), from the steady-state electrolysis current (92), or by monitoring the concentration of the reductant produced after addition of an oxidant (93). Catalytic rate constants determined with these methods agree well with each other. Some of the rate constant values are listed in Table I; these were determined by monitoring the reductant concentration (93).

A rapid increase in the reaction rate is noted in the table at redox potentials of catalysts of approximately $+0.6$ and $+0.9\text{V}$, respectively. These values seem to indicate that some specific functional groups on the coal are responding to the catalyst oxidants. These functionalities may correspond to hydroquinone- or quinone-like groups (6-9, 15). Note also that Ce(IV) and bromine are the most effective electrocatalysts. The activation energies for the process are in the range of $12 \sim 16$ kcal/mol (86, 91, 92). It is only 7.0 kcal/mol for Ce(IV) for the oxidation of coal (92).

Current efficiencies (CE) for the evolution of CO_2 were reported to be $15\% \sim 30\%$ in early studies (91, 92), but Dhooze and Park reported a 100% CE at longer electrolysis time (93). In general, it appears that the CE is very high at the very beginning of the reaction, probably because of the evolution of CO_2 from carbonates and bicarbonates present in coal. In a very short period (~ 15 min), the CE decreases to $15\% \sim 30\%$ and increases slowly up to 100% after $50 \sim 100\text{h}$ of electrolysis. This is probably because the charge is used up for the formation of surface oxides and humic acids in the first stage of the reaction, and later predominantly, for CO_2 evolution. The formation of surface oxides and humic acids was shown by the difference Fourier transform infrared (FTIR) spectra obtained from coals before and after electrolysis (94).

Dhooze and Park (94) also showed that the oxygen atom in the product, CO_2 , came from water by using 10% H_2^{16}O as a solvent. The ratio of $\text{C}^{18}\text{O}^{16}\text{O}/\text{C}^{16}\text{O}_2$ in the product monitored by the FTIR was $0.23 \sim 0.25$, in agreement with the expected value of 0.249 . This experiment also showed that CO_2 was produced from coal and water by

electrolysis rather than from the decomposition of carbonates or bicarbonates by the action of the solvent acid.

Summarizing this section, the oxidation of coal by electrolytic methods is not fundamentally in its mechanism different from the chemical oxidation. That is, surface oxides and humic acids appear to form first, and eventually smaller molecules and CO_2 are formed as oxidation proceeds. The formation of humic acids is more efficient in an alkaline medium.

One may speculate that iron ions catalyze hydroxylation reactions of methoxy aromatic rings under acidic electrolytic conditions as in oxidation reactions by Fenton's reagent [H_2O_2 and Fe(II)] or H_2O_2 catalyzed by Fe(III) and catechol (95, 96). Consider, for example, the mechanism of Senfile *et al.* (83), in which oxidation products of water such as $\cdot\text{OH}$ were postulated to be responsible for anthracite oxidation to lead to final products, *i.e.*, regenerated humic acids. The postulated species here are similar to those in H_2O_2 , peracetic, or trifluoroacetic acid oxidations. Hydroxylated coal may then undergo further oxidation to quinoids, which could open the ring to finally form dicarboxylic acids. These acids may then lose CO_2 upon further oxidation through the Kolbe electrolysis (97, 98) to produce smaller hydrocarbons. The Kolbe reaction normally requires high overvoltages; however, standard electrode potentials for most acids are quite low as one can verify from simple calculations (99) employing thermodynamic data in the literature (100). When catalyzed by a homogeneous solution species such as iron(III), the Kolbe reaction could proceed at a much lower applied potential. As pointed out already, elucidation of the mechanism of electrochemical oxidation of coal is still in its infancy; more work should be carried out in this area.

Electrochemical reduction of coal.—Electrolytic reductions were first used for the characterization of coal. The reduction process has been studied somewhat more thoroughly than the oxidation, probably because of the fact that only reductions could be carried out with polarographic methods at mercury electrodes by early investigators. Again, the chemistry involved in electrolytic reduction processes is not drastically different from that in chemical reduction. The end product following the initial electron transfer to coal from electrodes is hydrogenated coal.

Brown and Wyss (101) pointed out in their communication that coal extracts in N,N' -dimethylformamide (DMF) were reduced polarographically between -0.15 and -0.9V vs. the Hg pool, with a fairly well-defined wave at approximately -0.5 to -0.6V . They attributed this wave to the reduction of quinones. Given and Schoen (102) performed an extensive study on the polarographic reduction of coal extracts in DMF solution. Polarograms of all the solvent extracts of coals showed distinct waves in the range of -0.5 to -0.7V vs. the Hg pool. Comparison of half-wave potentials with values for known aromatic carbonyl compounds studied under the same conditions (103) showed that carbonyl groups in the solvent extracts of coals must be responsible for the reduction waves observed.

Also, analysis of the $\log(i/i_1 - i)$ vs. E curve gave an n value of approximately 1, indicating that coal accepts one electron from the electrode. Here i , i_1 , and n are the polarographic current, limiting currents, and the number of electrons transferred, respectively. The authors pointed out that the carbonyl groups must be strongly conjugated to aromatic systems, and with some other evidence reached a conclusion that quinone groups should be present in coals. They further estimated from polarographic diffusion currents that the pyridine extracts of coal contained approximately 2 g-atoms of oxygen as quinone per 3000-5000g coal. These investigators also ran an exhaustive electrolysis at -1.5V vs. SCE; the product showed a decrease in the IR peaks corresponding to carbonyl groups (~ 1600 cm^{-1}). In a study published later, Given and Peover (104) showed that several waves were

Table I. Standard electrode potentials and catalytic reaction rate constants of several solution catalysts

System	E° or $E^{o'}$	k_c , at 20°C , s^{-1}
Fe(CN)_6^{3-} in sat. K_2SO_4	0.36	3.6×10^{-6}
Fe(III) in 1M H_2PO_4	0.44	7.3×10^{-7}
Fe(III) in 1M H_2SO_4	0.68	9.6×10^{-6}
Fe(CN)_6^{3-} in 1M H_2SO_4	0.72	2.1×10^{-5}
Fe(III) in 1M HClO_4	0.75	1.9×10^{-5}
Fe(III) in 1M HCl	0.77	1.6×10^{-5}
Br_2 in 1M H_2SO_4	1.06	1.1×10^{-3}
Ce^{4+} in 1M H_2SO_4	1.45	4.1×10^{-4}

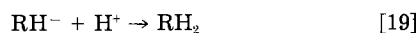
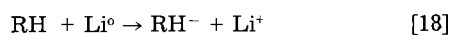
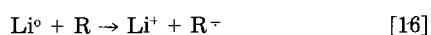
observed in a polarogram of coal if the potential is scanned down to about $-2.2V$ vs. Hg pool. Diffusion currents at both -1.0 and $-2.07V$ were increased upon addition of a proton donor, e.g., phenol. This indicates that the intermediate species generated from electrolysis reacts rapidly with protons. Actually, the exhaustive electrolysis of the coal extracts at a controlled potential of -2.1 to $-2.2V$ brought about an increase in hydrogen content corresponding to 15 ~ 38 hydrogen atoms being added per 100 carbon atoms (104-105). Prior reductive acetylation increased the uptake of hydrogen. The electron uptake determined coulometrically was in all cases greater than could be accounted for by the hydrogen introduced, oxygen removed, and carbonyl group reduced. As already pointed out in the previous section, this is probably due to the reduction of aromatic hydrocarbons. Employing reductive acetylation in DMF solution by electrolysis at controlled potentials and ^{14}C -labeled acetic anhydride (106), the carbonyl oxygen was estimated to be 1% ~ 2.5% of total oxygen in coal extracts. About 80%-90% of the oxygen in the extracts could be accounted for as carbonyl plus hydroxyl oxygens. Simple aromatic ketones such as benzophenone accounted for only a small fraction of carbonyl groups in the coal extracts, and there was no evidence that any aliphatic ketones were present (106).

A more extensive study on the electrochemical reduction of coal was reported by Markby *et al.*, using carbon electrodes in ethylene diamine with lithium chloride as supporting electrolyte (107). The current efficiency for this reaction was 46% at the beginning, dropping to about 10% after 15h of electrolysis. These investigators report that as many as 44 hydrogen atoms could be added per 100 carbon atoms for the Pocahontas vitrain. An interesting result was that the solubility of the electrolytically reduced coal in pyridine at room temperature (74%) was higher than that of the chemically reduced coal (63%). Various parameters affecting electrochemical reduction of coal were studied in detail by these investigators (108-110). In these experiments, coal slurries in ethylenediamine, not the coal extracts, were used. When an aluminum cathode was used in a solution saturated with lithium chloride, as many as 53 hydrogen atoms could be added to coal per 100 carbon atoms. Since these investigators used more rigorous reduction conditions, i.e., 0.5A with 110V, many of the polycyclic aromatic hydrocarbons along with quinones must have undergone reduction reactions. Ultimate analysis, catalytic dehydrogenation with palladium, and UV, IR, and NMR spectroscopic methods were used to identify reduced products. The mechanism of reduction is no different from that of chemical reduction using Li as a reductant reported by the same investigators (70). The reaction mechanism may be summarized as follows

At the cathode



In the solution



where R represents an aromatic hydrocarbon-like functional group on coal. This series of reactions is possible because of the high solubility of lithium metal in certain solvents such as ethylenediamine or ammonia. Any compounds, whose reduction potentials are less negative than that of lithium, would be expected to reduce according to this reaction. The proton donor was the solvent in the above case, but phenol was deliberately added by Peover and Given (104) to facilitate protonation steps.

Finally, an interesting remark was made by Sternberg *et al.* (108-111) that sulfur removal from coal might be accomplished by electrolytic reductions. The removal of sulfur from the vitrain took place after the more reactive

aromatic rings were reduced. Specifically, sulfur was removed only after about 25 hydrogen atoms per 100 carbon atoms had been added to the coal. A similarity between the removal of sulfur from coal and from dibenzothio-*phene* by electrolytic reductions has been pointed out (111).

A method of classifying genetic groups of coals using electrochemical oxidation and reduction has been reported by Russian investigators (112, 113). The method is based on the fact that coal is catalytically oxidized or reduced by Ce^{4+} or Cr^{2+} , respectively. The anodic current observed from the oxidation of Ce^{3+} and the cathodic current for the reduction of Cr^{3+} in aqueous solution containing some p-dioxane when the coal powder is present are indicative of the amount of reduced and oxidized functional groups on coal surfaces. The measurements were made at a stationary polarized smooth platinum electrode with KCl as a supporting electrolyte. The integrated areas of the anodic and cathodic currents, S_a and S_c , are used for the definition of the coefficient of the degree of reduction, K_r , according to the equation

$$K_r = \frac{S_c - S_a}{S_a} \quad [20]$$

By this definition, K_r would be 0 when the amounts of the oxidized and reduced groups are the same, while $K_r > 0$ for oxidized coals. The method was tested on some treated anthracites and shown to be sensitive to various states of coal surfaces.

In summary, the electrolytic reduction process has been studied either on organic extracts of coal or on a coal slurry employing catalytic processes in nonaqueous medium. It appears that a quinone type of functional group is reduced at less negative potentials, whereas polycyclic aromatic hydrocarbons are reduced at more negative potentials. Since the solubility of coal in most organic solvents is very low, a reagent whose reduced state can be dissolved must be used. For this purpose, lithium metal was used in the electrolytic reduction. As mentioned already, naphthalene was used as an electron-transfer mediator in chemical reductions employing alkali metals (73-74). Since anion radicals of most organic compounds accept protons rather easily, one should be careful about using organic compounds as catalysts. On the other hand, alkali metals have low solubility in many organic solvents.

As was the case in the chemical oxidation and reduction, coals can be degraded to smaller molecules—humic acids. It would be very interesting, therefore, to combine these two processes. That is, after humic acids are produced through an oxidative process, they may be subjected to the electrolytic reduction. The products are expected to be solids of low melting points or liquids. The electrolytic process has advantages over chemical methods for treating coals, since electrons are used as a reagent. Discovering proper catalysts for both oxidation and reduction would be extremely important in liquefying or derivatizing chemicals from coal.

Also, electrolytic oxidation and reduction may be very profitably used for characterizing coal. By measuring electron exchange rates of various electrocatalysts with coal and with model compounds, one may be able to identify the functional groups on coal surfaces. Oxidations in nonaqueous media and reductions in aqueous media of coal are virtually nonexistent; new structural information may result from these studies.

Photoelectrochemistry of Coal and Carbonaceous Materials

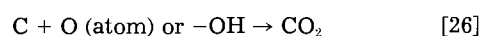
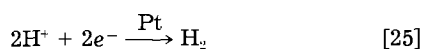
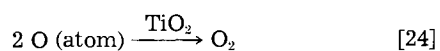
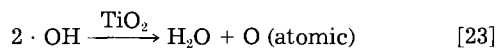
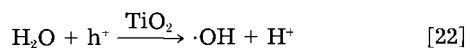
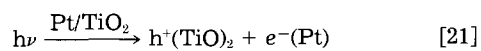
The field of photoelectrochemistry has received much attention since Fujishima and Honda (114) first reported that water could be electrolyzed to oxygen and hydrogen with the aid of light. The energy of the light source must be the same as or greater than the bandgap of the semiconductor electrode. The electron-hole pairs generated in the space-charge region of a semiconductor electrode

upon illumination should be separated effectively; electrons or holes should be captured at the semiconductor electrode surface by an oxidant or a reductant present, depending on the type of the semiconductor used. Various parameters must be considered for efficient conversion of the light energy into the electrical or chemical energy and its storage. Many reviews of this field have appeared (115-117).

Since, as reviewed in previous sections, gasification or derivatization of coal may be achieved by electrochemical techniques, the concept of photoelectrochemistry may also be applied to these reactions. In this section, we will review attempts that have been made employing solar radiation energies to apply these principles to coal conversion. Because coal does not dissolve easily in almost any solvent, no photoelectrochemical cells for coal oxidation have been built yet.

Kawai and Sakata (118, 119) reported in 1979 that carbon monoxide and hydrogen were produced from the reaction of carbon with water in the presence of catalysts (TiO_2 - RuO_2 mixture) when the reaction system was illuminated. Typically 30 mg of TiO_2 , 10 mg of RuO_2 , and 3 mg of active carbon were mixed, placed in a Pyrex glass bulb, and illuminated with a 500W high pressure Hg lamp for 5h. Appreciable quantities of H_2 and CO were formed only when TiO_2 , RuO_2 , C, and H_2O were all present; under such conditions the relative quantum efficiency of the evolution was at least 100 times greater than in a system that contained only TiO_2 and H_2O . When D_2O was used instead of H_2O , D_2 was detected.

More detailed and quantitative studies were carried out by Sato and White (120-122). These investigators used water vapor for the reaction along with carbonaceous materials, e.g., Texas lignites (120), activated charcoal (121, 122), or ethylene (121). Platinized titania was used as a catalyst. Platinized titania upon illumination also catalyzes the oxidation of acetic acid in liquid phase (123). When Texas lignite and water vapor were illuminated with ultraviolet light in the presence of platinized titania (TiO_2), hydrogen and CO_2 were produced as major products with the molar ratio (H_2/CO_2) of 2.5 ~ 2.75. Minor amounts of O_2 and CH_4 were also found. The H_2/CO_2 ratio might be greater than 2.0 (stoichiometric ratio) probably because hydrogen atoms in the lignite were partly converted to H_2 . The authors estimate a quantum yield of about 0.01 with an energy efficiency of 0.0003. Similar results were obtained between carbon (activated charcoal) (121, 122), or ethylene (121) and water vapor in the presence of platinized TiO_2 when illuminated. A study on the wavelength dependency of the reaction (122) showed that the onset of the reaction was observed when the light energy was about the same as or greater than the bandgap of TiO_2 . This indicates that the reaction occurs only if the hole-electron pairs are generated by light illumination as in the photoelectrochemical cell. These investigators thus proposed a mechanism in which the following reactions occur



Here, holes generated upon illumination are captured by water, whereas electrons migrate to platinum and reduce protons. The mechanism thus involves exactly the same concept as in the photoelectrochemical process.

Since in almost all reactions considered in previous and current sections CO_2 was a major anodic product, it

would be beneficial if CO_2 can be reduced to a useful product. The electrolytic reduction of CO_2 at various metal electrodes in both aqueous or nonaqueous media have been reported by many investigators (124-129). Direct electroreductions require applied potentials more negative than about 2V vs. SCE with the production of formic acid as a product in aqueous media. A possibility of reducing CO_2 to CO with the tetraazamacrocyclic complexes of cobalt or nickel present as catalysts has been reported by Fischer and Eisenberg (130). CO_2 was reduced catalytically to CO at potentials less negative than -1.6V vs. SCE in dimethylsulfoxide. The current efficiency, depending on the catalyst used, was in the range of 44 ~ 98%.

Photoelectrochemical (131, 132) or photochemical reductions (133) of CO_2 have also been investigated. Hemminger *et al.* (131) reported that the reaction of water and carbon dioxide in the gas phase led to the product, methane, when the reactants were adsorbed and illuminated on clean single-crystal strontium titanate surfaces of (111) orientation that were in contact with platinum foil. The reaction took place without any externally biased potential when the clean, reduced SrTiO_3 (111) crystal was illuminated with light having energy greater than the bandgap of SrTiO_3 . The reaction may be summarized as



The total amount of methane produced was 5 ~ 10 times the number of surface sites on the SrTiO_3 crystal, indicating a catalytic mechanism. Carbon dioxide in the presence of semiconductor powders suspended in water (132) was reduced photoelectrocatalytically to organic compounds such as formic acid, formaldehyde, methyl alcohol, and methane. Inoue *et al.* (132) used powders of semiconductors such as TiO_2 , ZnO , CdS , GaP , SiC , and WO_3 . When the experiments were carried out in the dark or under illumination with light of lower energy than the bandgap of the semiconductor used, no products were detected. Further, the yields of methyl alcohol increased as the conduction band of semiconductors became more negative than the redox potential of $\text{H}_2\text{CO}_3/\text{CH}_3\text{OH}$. This indicates that the photocatalytic reduction of CO_2 takes place by the action of the photogenerated electrons and holes.

Lehn and Ziesel (133) report that illumination of CO_2 with $\text{Ru}(\text{bipyridine})_3^{2+}$ and cobalt(II) chloride as sensitizers in an acetonitrile-water-triethylamine mixture lead to the production of CO and H_2 as products.

Photoassisted water-gas shift reactions over platinized TiO_2 were studied in detail (134). The activation energy was determined to be 7.5 kcal/mol, and the quantum efficiency was estimated to be approximately 0.5% at 25°C. Similar mechanisms to those described by these authors in the carbon oxidation were proposed (122). The products were CO_2 and H_2 from the reactants, CO and H_2O vapors. Many aspects of the water gas shift reaction have recently been reviewed (135).

As can be seen from the discussion and references cited in this section, work in this area began to appear only after 1979. Both oxidations and reductions were shown to occur through the electron-hole pair generation upon illumination of semiconductor powders present in the system. It has yet to be demonstrated that the same processes occur at illuminated semiconductor electrodes. In addition, the achievement of higher efficiencies for such processes should receive more attention in this area. The advantages of using heterogeneous catalyst systems have been pointed out (120).

Direct Power Generation from Coal Burning Fuel Cells

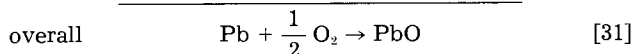
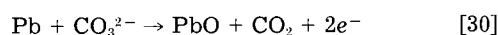
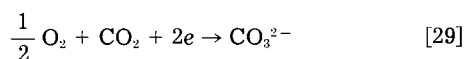
As a source of energy, coal can be burned directly to release the energy in the form of heat or electrochemically for the direct generation of electricity. Coal may also be utilized after its conversion to other forms, e.g., gas or liquid. Coal gas, for example, can be used as a fuel for fuel cells (136). Molten carbonate and phosphoric acid fuel

cells are being developed for the utilization of coal gas (136). Direct coal burning fuel cells may be more efficient than the ones using coal gas. However, only a few investigations have been carried out on the direct electrochemical oxidation of coal in fuel cells.

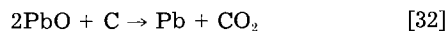
McKee and Adams (137) were the first to discuss the direct production of electricity from coal by electrochemical means. They used a cell in which a mixture of WO_3 and CeO_2 was used as an electrolyte with a graphite anode and an iron oxide or platinum cathode, operated at 1150°-1200°C. A current density of 19 mA/cm² at 0.45V or 10 mA at 0.60V was obtained, and the maximum efficiency of energy conversion calculated to be about 2% based on the energy released from the reaction



A much more detailed study on the electrochemical power generation was reported recently by Anbar *et al.* (138). These authors demonstrated the fundamental feasibility of a combined chemical-electrochemical process for generating electrical power from solid carbonaceous fuels. The system converts the free energy of oxidation of coal or coal char directly to electricity by combining electrochemical oxidation of molten lead with carbothermic reduction of the lead oxide. The study was performed in a molten carbonate medium in the temperature range 500°-800°C. The system consisted of electrochemical oxidation of molten lead to produce lead oxide and electricity, and the simultaneous regeneration of the lead metal by reduction of the lead oxide with coal or coal char. The system can be described by the following reactions



The lead oxide is then reduced by coal



Various parameters including the electrochemical kinetics of the lead-air cell, open-circuit potentials, polarization of the lead electrode, the kinetics of lead oxide reduction by carbon, and the electrochemical kinetics of lead oxidation in the presence of carbon have been studied in detail. The system has been shown not to be limited by kinetic factors, either electrochemical or chemical. An operating voltage of up to 0.760V at a current density of 108 mA/cm² was obtained at 700°C; it corresponds to approximately 75% voltage efficiency. The authors list a number of advantages of this integrated chemical-electrochemical energy conversion system for the carbonaceous material.

Although few studies have been carried out in this area, the concept is very interesting and also promising. The direct generation of power eliminates many conversion processes, thus allowing high energy conversion efficiencies. Effects of various components other than carbon such as sulfur, nitrogen, and minerals have not been studied; this process offers many advantages over other types of energy extraction methods, in view of the fact that a large fraction of the cost of the latter methods goes into the clean-up process in all coal conversion processes. Fundamental studies on various aspects in this area are essential for technological development.

Acknowledgment

Grateful acknowledgment is made to the U.S. DOE, Fossil Fuel Program (DE-AC21-81MC16377) for support of this research.

Manuscript submitted June 27, 1983; revised manuscript received Nov. 10, 1983.

REFERENCES

- J.-P. Randin, in "Encyclopedia of Electrochemistry of the Elements," Vol. VII, A. J. Bard, Editor, p. 1-249, Marcel Dekker, New York (1976).
- A. J. Bard and H. Lund, Editors, "Encyclopedia of Electrochemistry of the Elements," Vol. XI-XIII, Marcel Dekker, New York (1976).
- J. V. Hallum and H. V. Drushell, *J. Phys. Chem.*, **62**, 110 (1958).
- H. V. Drushell and J. V. Hallum, *ibid.*, **62**, 1502 (1958).
- I. F. Jones and R. C. Kay, *J. Electroanal. Chem.*, **20**, 213 (1969).
- G. Mamantov, D. B. Freeman, F. J. Miller, and H. E. Zittel, *ibid.*, **9**, 305 (1965).
- K. Kinoshita and J. A. S. Bett, *Carbon*, **11**, 403 (1973).
- K. F. Blurton, *Electrochim. Acta*, **18**, 869 (1973).
- H. Binder, A. Köhling, K. Richter, and G. Sandstede, *ibid.*, **9**, 255 (1964).
- N. G. Bardina and L. I. Brishtalik, *Elektrokhimiya*, **2**, 216 (1966).
- H. Wolf and R. Lansberg, *J. Electroanal. Chem.*, **29**, 255 (1971).
- O. Mateiovici, *Rev. Roum. Chim.*, **18**, 233 (1973).
- G. N. Kokhanov and N. V. Milova, *Elektrokhimiya*, **5**, 93 (1969).
- N. T. Piet, D. V. Kokoulina, and L. I. Krishtalik, *ibid.*, **8**, 384 (1972).
- K. Kinoshita and J. Bett, *Carbon*, **11**, 237 (1973).
- N. G. Bardina and L. I. Krishtalik, *Elektrokhimiya*, **2**, 334 (1966).
- G. N. Kokhanov and N. G. Milova, *ibid.*, **6**, 73 (1970).
- L. I. Krishtalik and Z. A. Rotenberg, *ibid.*, **2**, 351 (1966).
- R. Farr-Wharton, B. J. Welch, R. C. Hannah, R. Dorin, and H. J. Gardner, *Electrochim. Acta*, **25**, 217 (1980).
- L. J. Janssen and J. G. Hoogland, *ibid.*, **14**, 1097 (1969); *ibid.*, **15**, 339, 941, 1667 (1970).
- A. Tash, L. E. Vaaler, and J. M. Finn, *This Journal*, **117**, 219 (1970).
- J. H. Entwisle, *J. Appl. Electrochem.*, **4**, 293 (1974).
- R. Farr-Wharton, B. J. Welch, and R. C. Hannah, *Electrochim. Acta*, **25**, 217 (1980).
- H. C. Howard, in "Chemistry of Coal Utilization," H. H. Lowry, Editor, Chap. 9, John Wiley and Sons, New York (1945).
- R. Hayatsu, R. G. Scott, and R. E. Winans, in "Oxidation in Organic Chemistry," Organic Chemistry, A Series of Monographs, Vol. 5-D, W. S. Trahanovsky, Editor, Chap. IV, Academic Press, New York (1982).
- W. Francis, *Fuel*, **17**, 363 (1938).
- H. H. Lowry, *J. Inst. Fuel*, **10**, 291 (1937).
- B. S. Biggs, *J. Am. Chem. Soc.*, **58**, 1020 (1936).
- S. Oden, "Die Huninsäuren," Theodor Steinkopff, Dresden (1922).
- S. Giraud, *Bull. Soc. Chim. Fr.*, **11**, 389 (1894).
- E. Guignet, *Compt. Rend.*, **88**, 590 (1879).
- G. Dickson and T. H. Easterfield, *J. Chem. Soc. Proc.*, 163 (1898).
- W. Francis and R. V. Wheeler, *J. Chem. Soc.*, **127**, 2236 (1925).
- W. A. Bone, L. G. B. Parsons, R. H. Sapiro, and C. M. Groocock, *Proc. R. Soc. London Ser. A*, **148**, 492 (1935).
- B. Juettner, R. C. Smith, and H. C. Howard, *J. Am. Chem. Soc.*, **59**, 236 (1941).
- C. R. Kent, *Fuel*, **19**, 119 (1940).
- G. R. Yohje and J. M. Harris, *ibid.*, **40**, 339 (1961).
- C. Yokakawa, Y. Watanabe, S. Kajiyama, and Y. Takegami, *ibid.*, **41**, 209 (1962).
- C. Yokokawa, S. Kajiyama, and Y. Takegami, *ibid.*, **43**, 21 (1964).
- N. C. Deno, K. W. Curry, A. D. Jones, K. R. Keegan, W. G. Pakitsky, C. A. Richter, and R. D. Minard, *ibid.*, **60**, 210 (1981).
- J. W. Smith and G. E. Mapstone, *ibid.*, **36**, 191 (1957).
- R. C. Smith, R. C. Tomarelli, and H. C. Howard, *J. Am. Chem. Soc.*, **61**, 2398 (1939).
- Y. Kamiya, *Fuel*, **40**, 149, 457 (1961).
- J. W. Shih, *ibid.*, **42**, 395 (1963).
- S. E. Moschopedis and J. G. Speight, *ibid.*, **50**, 211 (1971).
- S. E. Moschopedis and J. G. Speight, *ibid.*, **50**, 34 (1971).
- (a) S. K. Chakrabarty and H. O. Kretschmer, *ibid.*, **51**, 160 (1972); (b) *ibid.*, **53**, 132 (1974); (c) *J. Chem. Soc. Perkin Trans. 1*, 222 (1974); (d) S. K. Chakrabarty and N. Berkowitz, *Fuel*, **53**, 240 (1974).
- F. R. Mayo, *ibid.*, **54**, 273 (1975).
- G. Ghosh, A. Banerjee, and B. K. Mazumdar, *ibid.*, **54**, 294 (1975).
- T. Aczel, M. L. Gorbaty, P. S. Maa, and R. H. Schlosberg, *ibid.*, **54**, 295 (1975).

51. R. G. Landolt, *ibid.*, **54**, 299 (1975).
52. J. L. Angert, S. L. Gattton, M. T. Reilly, and R. B. Landolt, *ibid.*, **56**, 224 (1977).
53. F. R. Mayo and N. A. Kirshen, *ibid.*, **58**, 698 (1979).
54. S. K. Chakrabarty and N. Berkowitz, *ibid.*, **55**, 362 (1976).
55. R. Hayatsu, R. L. G. Scott, L. P. Moore, and M. H. Studier, *Nature (London)*, **257**, 378 (1975).
56. A. E. Barse, J. L. Cox, and M. Hillman, "Production of Chemicals by Oxidation of Coal," Battelle Energy Program, Columbus, Ohio (1975).
57. R. Hayatsu, R. E. Winans, R. G. Scott, R. L. McBeth, L. P. Moore, and M. H. Studier, *Nature (London)*, **278**, 41 (1979).
58. H. M. Chang and G. G. Allen, in "Lignin," K. V. Sarkanen and C. H. Ludwig, Editors, Wiley Interscience, New York (1971).
59. R. Hayatsu, R. E. Winans, R. L. McBeth, R. G. Scott, L. P. Moore, and M. H. Studier, *Advances in Chemistry Series*, no. 192, American Chemical Society, Washington, D.C. (1981).
60. R. Hayatsu, R. E. Winans, R. G. Scott, L. P. Moore, and M. H. Studier, *Fuel*, **57**, 541 (1978).
61. R. Hayatsu, R. E. Winans, R. G. Scott, L. P. Moore, and M. H. Studier, in "Organic Chemistry of Coals," American Chemical Society Symposium Series, no. 71, Washington, D.C. (1978).
62. N. C. Deno, B. A. Greigger, L. A. Messer, M. D. Meyer, and S. G. Stroud, *Tetrahedron Lett.*, 1703 (1977).
63. N. C. Deno, B. A. Greigger, and S. G. Stroud, *Fuel*, **57**, 455 (1978).
64. R. Liotta and W. S. Hoff, *J. Org. Chem.*, **45**, 2287 (1980).
65. For an early review, see J. F. Weller in Ref. (25). For technology and economy of such processes, see L. Grainger and J. Gibson, "Coal Utilization: Technology, Economics and Policy," Chap. 9, 10, 16, 17, Halsted Press, London (1980).
66. L. Reggel, R. Raymond, S. Friedman, R. A. Friedel, and I. Wender, *Fuel*, **37**, 126 (1958).
67. P. H. Given, M. E. Peover, and W. F. Wyss, *ibid.*, **39**, 323 (1960).
68. L. Reggel, R. Raymond, W. A. Steiner, R. A. Friedel, and I. Wender, *ibid.*, **40**, 339 (1961).
69. J. D. Brooks and H. Silverman, *ibid.*, **41**, 67 (1962).
70. H. W. Sternberg, C. L. Delle Donne, L. Reggel, and I. Wender, *ibid.*, **43**, 143 (1964).
71. H. Sawatzky and D. S. Montgomery, *ibid.*, **43**, 453 (1964).
72. L. Lazarov and G. Angelova, *ibid.*, **47**, 333 (1968).
73. H. W. Sternberg, C. L. Delle Donne, P. Pantages, E. C. Moroni, and R. E. Markby, *ibid.*, **50**, 432 (1971).
74. H. W. Sternberg and C. L. Delle Donne, *ibid.*, **53**, 172 (1974).
75. L. Lazarov, I. Rashkov, and S. Angelov, *ibid.*, **51**, 637 (1978).
76. K. Niemann and U. B. Richter, *ibid.*, **58**, 838 (1979).
77. K. Niemann and H. P. Hombach, *ibid.*, **58**, 853 (1979).
78. J. A. Franz and W. E. Skiens, *ibid.*, **57**, 502 (1978).
79. C. S. Lynch and A. R. Collett, *ibid.*, **11**, 408 (1932).
80. R. Eddinger and D. Demorest, *ibid.*, **26**, 157 (1947).
81. R. Belcher, *J. Soc. Chem. Ind.*, **67**, 213, 217, 218, 265, 267 (1948).
82. M. H. Khundkar and M. M. Kamal, *Fuel*, **45**, 9 (1966).
83. F. E. Senftle, K. M. Patton, and I. Heard, Jr., *ibid.*, **60**, 1131 (1981).
84. R. W. Coughlin and M. Farooque, *Nature (London)*, **279**, 301 (1979).
85. M. Farooque and R. W. Coughlin, *ibid.*, **280**, 666 (1979).
86. M. Farooque and R. W. Coughlin, *Fuel*, **58**, 705 (1979).
87. R. W. Coughlin and M. Farooque, *Ind. Eng. Chem. Process Des. Dev.*, **19**, 211 (1980).
88. R. W. Coughlin and M. Farooque, *J. Appl. Electrochem.*, **10**, 729 (1980).
89. V. A. Vaseen, U.S. Pat. 4,228,683 (1980).
90. R. P. Baldwin, K. F. Jones, T. T. Joseph, and J. L. Wong, *Fuel*, **60**, 739 (1981).
91. G. Okada, V. Guruswamy, and J. O'M. Bockris, *This Journal*, **128**, 2097 (1981).
92. P. M. Dhooge, D. E. Stilwell, and S.-M. Park, *ibid.*, **129**, 1719 (1982).
93. P. M. Dhooge and S.-M. Park, *ibid.*, **130**, 1029 (1983).
94. P. M. Dhooge and S.-M. Park, *ibid.*, **130**, 1539 (1983).
95. G. A. Hamilton and J. P. Friedman, *J. Am. Chem. Soc.*, **85**, 1008 (1963).
96. G. A. Hamilton, J. P. Friedman, and P. M. Campbell, *ibid.*, **88**, 5266 (1966).
97. C. K. Mann and K. K. Barnes, "Electrochemical Reactions in Nonaqueous Systems," Chap. 4, Marcel Dekker, Inc., New York (1970).
98. S. D. Ross, M. Finkelstein, and E. F. Rudd, "Anodic Oxidation," Chap. 6-7, Organic Chemistry, A Series of Monographs, Vol. 32, Academic Press, New York (1975).
99. S.-M. Park and M. E. Barber, *J. Electroanal. Chem.*, **99**, 67 (1979).
100. See, for example, National Bureau of Standards, Technical Note 270 Series, National Bureau of Standards, Washington, D.C., 1965-present.
101. J. K. Brown and W. F. Wiss, *Chem. Ind.*, 1118 (1955).
102. P. H. Given and J. M. Schoen, *J. Chem. Soc.*, 2680 (1958).
103. P. H. Given, M. E. Peover, and J. M. Schoen, *ibid.*, 2674 (1958).
104. P. H. Given and M. E. Peover, *Fuel*, **39**, 463 (1960).
105. P. H. Given, V. Lupton, and M. E. Peover, *Nature*, **181**, 1059 (1958).
106. P. H. Given and M. E. Peover, *J. Chem. Soc.*, 394 (1960).
107. R. E. Markby, H. W. Sternberg, and I. Wender, *Nature*, **199**, 997 (1963).
108. H. W. Sternberg, C. L. Delle Donne, R. E. Markby, and I. Wender, *Fuel*, **45**, 469 (1966).
109. H. W. Sternberg, R. E. Markby, C. L. Delle Donne, and I. Wender, U.S. Department of the Interior, Bureau of Mines, Report of Investigations 7017 (1967).
110. H. W. Sternberg, Symposium on the Science and Technology of Coal, pp. 168-174, Department of Energy, Mines and Resources, Ottawa, Canada, March 29-31, 1967.
111. H. W. Sternberg, C. L. Delle Donne, and I. Wender, *Fuel*, **47**, 219 (1968).
112. A. A. Lapin, *Solid Fuel Chem.*, **11**, 30 (1977).
113. A. A. Lapin and G. A. Pereversez, *ibid.*, **11**, 46 (1977).
114. A. Fujishima and K. Honda, *Nature (London)*, **238**, 37 (1972).
115. A. J. Bard, *J. Photochem.*, **10**, 59 (1979).
116. S. R. Morrison, "Electrochemistry at Semiconductor and Oxidized Metal Electrodes," Plenum Press, New York (1980).
117. A. Heller, Editor, "Semiconductor Liquid-Junction Solar Cells," The Electrochemical Society Softbound Proceedings Series, Princeton, NJ (1977).
118. T. Kawai and T. Sakata, *J. Chem. Soc. Chem. Comm.*, 1047 (1979).
119. T. Kawai and I. Sakata, *Nature.*, **282**, 283 (1979).
120. S. Sato and J. M. White, *Ind. Eng. Chem. Prod. Res. Dev.*, **19**, 542 (1980).
121. S. Sato and J. M. White, *Chem. Phys. Lett.*, **70**, 131 (1980).
122. S. Sato and J. M. White, *J. Phys. Chem.*, **85**, 336 (1981).
123. B. Kraeutler and A. J. Bard, *J. Am. Chem. Soc.*, **100**, 2239 (1978).
124. L. V. Haynes and D. Sawyer, *Anal. Chem.*, **39**, 332 (1967).
125. D. A. Trysee, T. H. Wagegknecht, M. M. Baizer, and J. L. Chrums, *Tetrahedron Lett.*, 4809 (1972).
126. E. Lamy, L. Nadjo, and J. M. Saveant, *J. Electroanal. Chem.*, **78**, 403 (1977).
127. P. G. Russell, N. Kovac, S. Srinivasan, and M. Steinberg, *This Journal*, **124**, 1329 (1977).
128. J. C. Gressin, D. Michelet, L. Nadjo, and J. M. Saveant, *Nouv. J. Chim.*, **3**, 345 (1979).
129. Y. Hori and S. Suzuki, *Bull. Chem. Soc. Jpn.*, **55**, 660 (1982).
130. B. Fischer and R. Eisenberg, *J. Am. Chem. Soc.*, **102**, 7361 (1980).
131. J. C. Hemminger, R. Carr, and G. A. Somorjai, *Chem. Phys. Lett.*, **57**, 100 (1978).
132. T. Inoue, A. Fujishima, S. Konishi, and K. Honda, *Nature (London)*, **277**, 637 (1979).
133. J. M. Lehn and R. Ziessel, *Proc. Natl. Acad. Sci. USA*, **79**, 701 (1982).
134. S. Sato and J. M. White, *J. Am. Chem. Soc.*, **102**, 720 (1980).
135. F. C. Ford, *Acct. Chem. Res.*, **14**, 31 (1981).
136. T. Benjamin, E. H. Camara, and L. G. Marianowski, "IGT Fuel Cell Handbook," Institute of Gas Technology, Chicago, IL (1980).
137. J. H. McKee and A. M. Adams, *Fuel*, **28**, 6 (1949).
138. M. Anbar, D. F. McMiller, and R. D. Weaver, in "Record of the Tenth Intersociety Energy Conversion Engineering Conference," The Institute of Electrical and Electronics Engineers, Inc., New York (1975).

Report of the Electrolytic Industries for the Year 1983¹

Richard D. Varjian*

Dow Chemical Company, Louisiana Applied Science and Technology Laboratory, Plaquemine, Louisiana 70765

Dale E. Hall*

American Cyanamid Company, Chemical Division Laboratories, Stamford, Connecticut 06904

I. Chlorine-Caustic Soda

Production and capacity.—World.—Chlorine production capacity for major world areas is given in Table I (1).

United States.—U.S. chlorine production was about 10.2 million tons in 1983, up about 10% from 1982, according to the Chlorine Institute (2).

U.S. chlorine and caustic soda production capacities are given in Table II (3, 4).

Brine electrolysis accounts for 95% of chlorine production and essentially 100% of the caustic soda production capacity (5).

A few plant expansions were announced.

Vulcan expanded its 500 ton/day (chlorine) plant in Wichita, Kansas, by 210 ton/day (3, 4). The expansion utilizes ion exchange membrane cell technology and is the largest such installation in the United States. Eltech Systems supplied electrolyzer technology, and du Pont provided Nafion membranes (10-14).

Vulcan also started up a 200 metric ton/day ion exchange membrane plant in Birmingham, Alabama (6).

Vulcan added 75 ton/day of chlorine capacity to its 590 ton/day unit in Geismar, Louisiana (3, 4).

LCP Chemicals has announced that its Linden, New Jersey, chlorine-caustic soda facility, which has been temporarily closed (3, 4, 6, 7), will re-open in 1984 as a

chlorine-caustic potash operation (15). Phase I chlorine capacity is 36,000 ton/yr. This comes on the heels of the closure of the joint Occidental Chemical and International Minerals and Chemicals chlorine-caustic potash plant in Niagara Falls, New York. LCP was awarded all potassium product contracts formerly held by the joint venture (16, 17).

Plant closings announced during 1983 are given below.

BASF closed its 920 ton/day (chlorine) plant in Geismar, Louisiana (3, 4, 6, 7).

PPG shut down its 350 ton/day (chlorine) Barberton, Ohio, plant (3, 4, 6, 7).

Shell Oil Company shut down its 300 ton/day chlor-alkali unit at its Deer Park, Texas, manufacturing complex (8, 9).

P. J. Kienholz, Chlor-Alkali Business Manager for PPG, believes that an additional 2890 ton/day of chlorine capacity could be shuttered during the next few years (6).

Four plants have been closed temporarily or are on stand-by status.

Dow's 1000 ton/day (chlorine) unit in Midland, Michigan, was closed temporarily in June, 1982, and remains down (3, 4, 6, 7). Dow wrote off this unit in its fourth-quarter economic statement in 1983 (103, 105).

LCP temporarily closed its 450 ton/day plant at Linden, New Jersey (3, 4, 6, 7).

Olin's 350 ton/day (chlorine) McIntosh, Alabama, plant is on standby (3, 4, 6, 7).

Hooker's 230 ton/day (chlorine) Montague, Michigan, plant is on standby (3, 4, 6, 7).

PPG Industries completed a modernization of its diaphragm cell plant in Lake Charles, Louisiana. The \$100 million plus project involved conversion of outmoded cells to more efficient bipolar electrolyzer technology developed by PPG. The new cells reduce the energy requirement by 25%. PPG has undertaken a similar modernization at its Natrium, West Virginia, complex, scheduled for completion in early 1985 (19-22).

Georgia-Pacific plans to build a \$80-\$100 million cogeneration facility at its Plaquemine, Louisiana, plant.

* Electrochemical Society Active Member.

¹ This report is sponsored by the Industrial Electrolytic Division of The Electrochemical Society. It represents a summary of the published information on production, plant capacities, consumption, markets and trends, prices, raw materials, new developments, and health and environmental aspects in the electrolytic and related industries.

The material presented herein has been obtained from many sources, as noted in the list of references, and does not necessarily represent the opinions of the authors.

The Industrial Electrolytic Division is grateful for the support received from the Vittorio de Nora-Diamond Shamrock Fund, which assisted with the publication costs of this report.

Table I. World chlorine production capacity, 1983
(Thousands of metric tons/yr)

	March 1983	Projected
Western Europe	11,112	326
Common Market	9,097	171
Other Europe	2,015	155
North America	15,321	82
U.S.	13,700	—
Canada	1,205	82
Mexico	416	—
Latin America	1,379	186
Argentina	266	—
Brazil	900	183
Africa	367	186
Mid-East	196	358
Saudi Arabia	7	330
Iraq	40	—
Israel	101	28
Asia and Oceania	5,553	349
Australia	150	—
India	852	156
Japan	3,700	—
Taiwan	450	170
Communist World	6,315	770
China	N.A.	100
Eastern Europe	3,115	360
USSR	3,200	250
Total world	40,243	2,138

Table II. U.S. chlorine and caustic soda capacity (ton/day)

	Chlorine	Caustic soda
Alcoa	352	398
BASF	920	1,036
Convent	1,150	1,265
Diamond Shamrock	3,380	3,850
Dow	11,800	12,250
du Pont	1,600	1,100
Ethyl	300	—
FMC	800	832
Formosa Plastics	544	600
Georgia-Pacific	1,487	1,643
Hooker	3,200	3,400
Kaiser	590	667
LCP	1,800	1,850
Mobay	300	—
Olin	2,600	2,860
Pennwalt	950	1,050
PPG	4,300	4,730
Shell	288	315
Stauffer	1,065	1,172
Vulcan	1,335	1,468
Weyerhaeuser	385	425
Others	875	600
Total	40,021	41,511

The unit will produce 140 MW of electricity plus process steam (23).

Plant operating rates increased slightly during the year, according to Chlorine Institute figures. The overall 1982 operating rate was 62% (24), but the rate in December, 1982, was only 57.9% (25). The January, 1983, rate was 63.6% of capacity (25). It climbed above 70% for the first time in May (70.7%), fell back in June, recovered in July, and remained above 70% until November (26-29, 34, 53). The December operating rate was 67.1% (2, 104). The maximum operating rate, 74.7%, was achieved in September (30). Firmer markets accounted for most of the improvement. However, onstream capacity fell about 2.2% between 1982 and 1983 (31).

Actual operating rates were probably 80%-85% of available capacity (26, 32) since some idle capacity may be unusable (33). One observer thought plants might be running at 87% of available capacity (29).

The Chlorine Institute estimates that chlorine capacity will fall to 13.6 million tons per year by 1985, a reduction of 4.2% from 1983 levels. The industry operating rate is expected to average 79% in 1985 (24).

Consulting Resources Corporation states that the average chlor-alkali plant was unprofitable entering 1984. Plants with relatively inexpensive hydropower or cogenerated power might be able to turn a slight profit. New plant economics were decidedly negative at this time. They predict that producers who have neither developed a low-cost position nor a safe market niche will drop out of the business during the next economic downturn (54).

About 20% of industry capacity has been shut down in recent years. Dow Chemical, the world's largest chlorine producer, has kept 25% of its capacity idle and has not announced a restart date for any plants. Some producers wonder whether the industry could produce enough to meet a truly thriving demand (54).

Japan.—Caustic soda output was 2.77 million metric tons in 1982, a 3.3% decrease from 1981 levels (35).

Japanese producers have 1.23 million metric tons of mercury cell capacity (32.4%), 2.23 million metric tons of diaphragm cell capacity (58.5%), and 347,000 metric tons of membrane cell capacity (9.1%) (36). Power accounts for 55% and raw salt 10% of production costs in Japanese plants. Most salt is imported from Mexico, Australia, and China (35).

The Japanese government has given 19 companies a reprieve from the December, 1984, deadline it had imposed for halting mercury cell production. The new deadline is June, 1986. Companies must begin the changeover before the end of 1984. All 19 companies, with a capacity of 1.3 million metric tons of caustic soda, intend to switch to ion-exchange membrane cells. Sixteen companies have already complied with the government's directive, first issued in 1973 (36, 37).

Kureha Chemical will convert its mercury cell plant at Nishiki, Fukushima Prefecture, to Asahi Chemical membrane technology. Annual capacity is 96,000 metric tons per year of caustic soda at the site. Start-up is scheduled in January, 1985 (38).

Tokuyama Soda, Mitsui Toatsu, and nine other producers are switching from diaphragm to ion-exchange membrane plants. Over 33% of existing diaphragm capacity is to be converted. The driving force for the changeover is a reduction in energy costs available with the membrane technology (39).

Nikkei Kako's 36,000 ton/year plant in Kanbara, Japan, built in 1975, will be converted from Diamond-Shamrock's MDC diaphragm cells to Asahi Chemical's bipolar membrane cells. Start-up of the converted plant is scheduled for January, 1984 (40, 41).

Europe.—Akzo Zout Chemie has started up the world's largest membrane process chlor-alkali plant near Rotterdam, The Netherlands. The plant has a capacity of 280,000 metric tons of caustic soda per year and uses Asahi Chemical membrane technology (42, 43).

Mercury cells still account for more than 70% of Euro-

pean capacity, even though diaphragm and membrane cells are more energy efficient (54).

Markets and prices.—Chlorine.—U.S. chlorine consumption by end use and average annual growth for the next ten years are in Table III (6, 44, 45, 54).

Chlorine does not really move in international trade, except for overland shipments. Organic derivatives such as vinyl chloride monomer and polyvinylchloride are exported from the U.S. in large quantities (54).

Chlorine prices rose throughout the year as chlorinated derivative markets recovered from the recession (46, 47). In September, 1983, producers were able to implement their fifth consecutive quarterly price increase for chlorine. These increases totaled almost \$100/ton (46). Producers tried for another increase of \$15/ton beginning January 1, 1984, bringing list prices to \$170.00 FOB plant site (19, 29, 31, 48, 49).

Some producers are forecasting a growth of 7%-9% in chlorine demand through 1984 (46). Chlorine shortages showed up in the fourth quarter. Producers anticipate a double-digit surge in PVC sales in the spring of 1984, which should only aggravate the tight chlorine situation (19, 47).

Producers can expect marginal demand increases in the next decade, according to PPG's P.J. Kienholz. The slow growth is due to a series of adverse environmental, toxicological, and process change impacts as well as a generally slowing world economy (50). Tables III and IV contain Mr. Kienholz's predictions.

Another market analysis foresees a similar pattern. Market growth is expected to track the GNP. Vinyl chloride is expected to be a leading growth market for chlorine averaging a 5%-6% growth rate (3).

Predicasts reports that chlor-alkali markets will grow at only 3.6% per year through 1995 vs. 4.4% per year historically (51).

Substitution of other oxidizing agents in pulp and paper bleaching will hurt chlorine demand in this market (51, 52).

Caustic soda.—U.S. caustic soda consumption by end use and average annual growth rate for the next ten years are in Table IV (6, 44, 45, 54).

Table III. U.S. chlorine consumption and average annual growth rate forecast

	Percent of total market	Annual growth rate
Vinyl chloride monomer	22	4%-5%
Pulp and paper	16	1%
Chlorinated methanes	8	4%
Chlorinated ethanes	9	—
Polyurethane	8	4%
Titanium dioxide	3	2%
Water and waste treatment	6	1%
Other inorganic	9	3%
Other organic	19	2%-3%
Weighted average		2.7%

Table IV. U.S. caustic soda consumption and average annual growth rate forecast

	Percent of total market	Annual growth rate
Pulp and paper	20	2%
Aluminum		
Domestic	4	1%
Export	4	4%
Anhydrous caustic	3	2%
Other inorganic	31	3.2%
Propylene oxide	6	3%
Petroleum production and refining	4	6%
Textiles	3	2%
Other organic	21	4%
Other exports	4	0%
Weighted average		3.0%

Caustic prices fell nearly all year. List prices for 50% solution began the year at \$230/ton on the Gulf Coast, a reduction of \$40/ton from late 1982 levels (55). By October, the list prices were down to \$150/ton in Gulf Coast markets (56, 57). Discounts were available in a buyer's market. Actual prices were firming at about \$75/ton (46). However, one export deal was struck for as low as \$51/ton during the year (4).

Producers were waiting for an upturn in alumina production to spark demand for caustic (58). Though alumina production accounts for less than 10% of demand, it is more cyclical and thus has a substantial effect on demand swings (59). Aluminum makers had large alumina stockpiles early in the year (46). With alumina production moving overseas, caustic soda exports should rise substantially (46).

Pulp and paper markets were not expected to grow much during the year since the paper industry was already operating at high levels (19). U.S. pulp mill consumption should only rise by 6%, to 1.8 million tons (60).

Alkaline oil field flooding is one of the few growth markets for caustic soda (54).

Caustic's long-term outlook is slightly better than chlorine's. The growth rate is expected to range one or two percentage points over chlorine through the eighties. Caustic soda has a broad end-use base and is less sensitive to economic cycles than are many commodity chemicals. The pulp and paper industry will be using more caustic than chlorine. Demand for environmentally related uses, such as waste-water treatment, will grow at a healthy rate. Petroleum and gas exploration production and processing markets should provide moderate growth. Caustic is forecast to be in tight supply more often than not long through this decade (4).

Technological developments.—Ion-exchange membrane plants came of age during 1983 with the start-up of the two major Vulcan installations in the United States (10-14, 61) and the world-scale Akzo Zout plant in The Netherlands (42, 43). Eltech has licensed 11 membrane cell plants worldwide (62). Asahi Chemical's membrane cell technology sales amount to 520,000 metric ton/year of caustic soda capacity. Asahi Glass's sales amount to 42,000 metric ton/year, while Tokuyama Soda's are 13,600 metric ton/year (63). Membrane cell plants announced in 1983 are listed in Table V.

Olin has licensed technology to retrofit diaphragm cells with ion-exchange membranes from Kanegafuchi Chemical of Osaka, Japan. The agreement allows Olin to sub-license the technology in the United States, Canada, and Mexico. The investment cost for retrofitting is said to be lower than that for newly built membrane cells (80, 81). Kanegafuchi says the technology involves narrowing

the anode-cathode gap and expects to receive U.S. Patent protection (82).

Kanegafuchi also has developed technology to retrofit mercury cells with ion-exchange membranes. The cells are specially processed after the mercury is removed. Then the membrane is lined into the cell sections where the mercury used to run. The process cuts switchover costs by 80% (83, 84).

Olin licensed its Remote Computerized Anode Adjuster system to Vulcan. The system monitors, adjusts, and protects anodes in mercury cells in order to maintain optimum electrode spacing. Vulcan is using the system on de Nora cells at its Port Edwards, Wisconsin, plant. Olin also provides adjusters for its own and Uhde cells (85).

Japan's Mitsui Toatsu Chemicals and Chlorine Engineers process membranes into bag-like shapes and slip them over diaphragm cell electrodes in order to retrofit existing plants. Plant conversion costs can be cut by 50%-66% (86, 87).

Dow Chemical has purchased 12 U.S. patents and patent applications and associated technology concerning membranes and membrane cells from Allied. Allied sold its chlor-alkali business in 1979 (88-90).

Asahi Chemical has received U.S. Patent 4,357,218 for making perfluoro ion-exchange membranes with both carboxylic and sulfonic acid groups and the use of the membranes in chlor-alkali cells (91-93).

du Pont and Diamond Shamrock agreed to settle litigation covering membrane technology for chlor-alkali production. du Pont may license customers to use its Nafion membranes for chlor-alkali production under certain Diamond Shamrock patents (94).

Although membrane cell technology has advanced rapidly, PPG's P. J. Kienholz believes that membrane cells are not economical enough to replace large, energy-efficient diaphragm cell plants (95).

Legal, environmental, and toxicological developments.—The Chlorine Institute filed a complaint with the Interstate Commerce Commission (ICC), charging many of the nation's railroads with anticompetitive actions. The complaint says that the railroads have canceled through routes, joint rates, and reciprocal switching arrangements. The Institute has asked the ICC to order the railroads to stop the anticompetitive practices (96).

Hach Company has developed an on-line instrument for monitoring residual chlorine in treated waste-water streams. The on-line monitor eliminates the need for hourly labor-intensive analyses, while assuring adequate disinfection without over-chlorinating the effluent (97).

The EPA is proposing that makers and processors of mono-, di- and trichlorinated benzenes conduct toxicity and environmental effects tests. The proposal is being

Table V. 1983 construction announcements for commercial membrane cell plants

Company/location	Capacity (metric ton/yr)	Completion date	Technology developer	Ref.
General Co. for the Paper Industry, Egypt	3,150	Late 1984	Eltech	(62, 67, 70)
Subentra, Aceh, Indonesia	160,000	1986	ICI	(64)
The Chemical Company of Malaysia, ICI Subsidiary, Padang Jawa, Malaysia	10,000	Late 1984	ICI	(65, 73, 79)
Egyptian Petrochemical Cairo, Egypt	60,000	Early 1986	Asahi Glass	(66, 78)
Bela Chemical, Bela, Pakistan	14,000	1985	Uhde	(69, 71, 72)
Nikkei Kako Kanbara, Honshu, Japan	33,000	January 1984	Asahi Chemical	(68)
Qiqihar Electrochemical Heilong Jing Province Peoples Republic of China	10,000	April 1986	Asahi Chemical	(74, 75)
Kureha Chemical Nishiki, Fukushima, Japan	87,000	January 1985	Asahi Chemical	(77)

made under the Toxic Substances Control Act. EPA has concluded that the tests are necessary because there is insufficient data available on the consequences of exposure to these chemicals (98).

OSHA has ordered asbestos exposure limits lowered from 2 fiber/m³ to 0.5 fiber/m³ (99, 100). European countries have also adopted a similar standard (101). EPA, OSHA, and the Consumer Product Safety Commission have set up a task force on asbestos. The group is to develop a coordinated federal approach to protecting the public from the health hazards of asbestos in the workplace (102).

Other Alkaline and Chlorine Compounds

Caustic potash.—U.S. nameplate capacity for caustic potash is about 260,000 tons annually. Production through June was running at 227,000 ton/yr (106).

Early in the year, the price of liquid caustic potash (45% solution) was increased by \$1.00 to \$13.00 per hundredweight. The price of the dry flake was increased by \$2.50 to \$42.35 per hundredweight (107-111).

Occidental Chemical and International Mineral and Chemicals (IMC) have terminated their 11-year joint venture to make caustic potash, chlorine, and hydrogen in Oxy's facilities at Niagara Falls, New York. Oxy decided to put the plant on standby so that its hydropower load could be shunted to its chlorine-caustic soda plant. The joint venture's sales contracts are being transferred to Linden Chemicals and Plastics (112-114).

In a related move, Linden Chemicals and Plastics will shift its Linden, New Jersey, facility, currently on standby, from a chlorine-caustic soda plant to a chlorine-caustic potash unit. The plant is slated for restart during the second quarter of 1984. Capacity is 62,000 tons of caustic potash (115, 116).

The demise of the Oxy-IMC joint venture leaves Diamond Shamrock, Linden Chemicals and Plastics, Monsanto, and Pennwalt as the only domestic caustic potash producers. Holtrachem says it is the only importer (114).

Soda ash.—U.S. soda ash production reached 8.4 million tons in 1983 vs. 7.8 million tons in 1982 and 8.3 million tons in 1981 (117, 145).

U.S. soda ash production capacity is given in Table VI (118).

Early in the year, plants were only operating at 70-73% of rated capacity (14). Operating rates jumped over 80% during the summer, but overall yearly rates averaged 73% to 74% (131).

The only remaining synthetic soda ash production plant in the United States is Allied's Syracuse, New York, facility. It has a capacity of 635,000 ton/yr (118). Though there is considerable overcapacity in the industry, Allied has strengthened its commitment to the Syracuse plant by expanding its sodium bicarbonate capacity and signing a 10 yr multimillion dollar transport contract with Conrail (119, 120).

Natrona Resources is seeking a partner to develop a 5,000 acre natural sodium bicarbonate deposit in the Piceance Basin of Colorado and Wyoming. The company will develop a solution mining project in Yankee Gulch (121).

Texasgulf Chemicals has acquired all of PQ Corporation's sodium leases in Sweetwater County, Wyoming. The leases cover 9,273 acres adjacent to Texasgulf's existing trona mine and soda ash production facility (122, 123).

Table VI. U.S. soda ash capacity
(millions of tons per year)

Allied Chemical	2.8
FMC	2.5
Stauffer Chemical	1.7
Kerr-McGee	1.3
Texasgulf	1.0
Tenneco	0.9
Total	10.2

Cleveland-Cliffs Iron and Industrial Resources of Chicago are proceeding with their July, 1982, agreement to develop an 8,359 acre deposit of natural sodium bicarbonate. The expected production rate of the facility is one million ton/yr of soda ash (124).

U.S. soda ash production should increase 3.2% per year according to Consulting Resources Corporation (125). A world-wide production forecast for the 1980's is given in Table VII (125).

Several companies are proceeding with development of new routes to soda ash. Akzo Zout Chemie is pursuing a nonelectrolytic route to vinyl chloride monomer and soda ash using a homogeneous catalyst of trimethylamine, copper II chloride, and iodine in adiponitrile solvent (126, 127, 128). Asahi Glass claims to lower the energy to produce synthetic soda ash by 55% reacting ammonia, sodium chloride, and carbon dioxide into ammonium chloride and sodium bicarbonate, which is calcined to obtain soda ash (126, 127). FMC Corporation, among others, is pursuing a solution mining route to soda ash said to cut mining costs by 25%. FMC has invested more than \$30 million in developing the technique and has applied to the Wyoming Department of Environmental Quality for clearance to construct a one million ton/yr facility by the mid-1980's (126). The department issued a permit to FMC to begin mining in December, 1984. However, Tenneco Minerals, operator of a trona mine about 5 miles from the FMC project, objected, stating the FMC's brine might flood its mine. The Department of Environmental Quality is expected to respond to Tenneco's complaint in April, 1984 (146).

The soda ash list price remained at \$84/ton f.o.b. Green River, Wyoming. However, discounts were available. In late October and November, 1983, most producers introduced a temporary voluntary allowance of \$15/ton off the list price (131-135).

The listed prices were \$140/ton in the Northeast and \$198.65/ton in southern California (132).

Major end uses for soda ash are listed in Table VIII (129, 147).

U.S. exports of soda ash were a record 1.64 million tons, up 49% from 1982 levels, according to the Bureau of Mines. Most of the exports went to the Far East, Latin America, and Africa (148).

Container glass markets are hard pressed by plastic resins. Glass recycling is growing, reducing demand for new glass (147). Flat glass and fiber glass, which have rebounded due to increased housing construction and auto production, should offset some lost tonnage. Producers hope exports will eventually rescue them (130). However, foreign markets may be hard to penetrate due to the strength of the U.S. dollar, and due to the fact that West European capacity utilization is currently only 65% of its nominal eight million ton per year capacity (136). The Eu-

Table VII. World soda ash production capacity
(millions of metric tons per year)

	1980	1990	Change
Western Europe	7.0	7.6	8.5%
North America	8.2	10.8	32.0%
Eastern Bloc	9.3	10.8	16.0%
Asia, Oceania	3.8	4.7	24.0%
Latin America	0.6	1.1	83.0%
Africa and Mid-East	0.3	1.1	266.0%
Total	29.0	36.0	24.0%

Table VIII. Major U.S. soda ash markets
(percent of total market)

Glass	54
Chemicals	20
Soap and detergents	7
Pulp and paper	4
Water treatment	4
Other	11

ropean Common Market instituted a \$20/ton anti-dumping duty against U.S. exporters (137, 138). The Canadian Department of National Revenue, Customs, and Excise also ruled that major U.S. producers dumped soda ash on the Canadian market (139, 140). Japan may prove to be a growing market for U.S. exports. The Japanese Fair Trade Commission has told four Japanese producers to eliminate an agreement to control imports (141).

Soda ash producers hope to develop new markets to relieve the apparent long term supply-demand imbalance. Allied Chemical is trying to reverse acid rain damage to a pond with soda ash. Dry injection of trona or nahcolite into smoke stacks considerably reduces sulfur emissions. The system can only be used on low sulfur (under 1%) coals. A 500 MW utility plant might require 50,000 ton/yr of trona (142-144).

Sodium chlorate.—Annual U.S. capacity for sodium chlorate is given in Table IX (149).

Early in 1983, plants were only operating at 60% of rated capacity (177).

Changes affecting U.S. production capacity announced during 1983 follow.

Kema Nord Bleaching Chemicals purchased one of Occidental Chemical's sodium chlorate plants in Columbus, Mississippi. Kema Nord also obtained Occidental's know-how, patents, and technology for making chlorine dioxide (150, 151).

Pennwalt will close its Calvert City, Kentucky, plant during the first quarter of 1984. The plant has a rated capacity of 50,000 ton/yr, but it reportedly has been operating at a lower rate for over a year. The company cited an increase in Canadian imports over the past few years as the reason for the closing (152).

Huron Chemicals has started an expansion of its plant at Riegelwood, North Carolina. Plant capacity is now 14,800 ton/yr. The expansion project was based on an improved model of the company's 240,000A cells (153).

HO Process Company, a partnership between Olin and Huron Chemicals, is building a 14,000 ton/yr. plant at Clairborne, Alabama. The plant is scheduled for startup in March, 1984. The plant is specially designed to utilize off peak power. Cell technology was developed by Huron (154, 155).

Kerr-McGee expanded its Hamilton, Mississippi, plant capacity from 40,000 to 62,000 ton/yr by installing a second line with dimensionally stable anodes (156).

Nameplate Canadian capacity is reportedly 425,000 ton/yr (157).

PPG Industries Canada completed a 6,400 ton/yr expansion at Beauharnois, Quebec. The Stanchem complex now has a capacity of 80,000 ton/yr (158-162).

Erco Industries' 36,000 ton/yr expansion at Buckingham, Quebec, originally scheduled for completion in the second half of 1983, will now start up in the fourth quarter of 1984. The expansion was delayed by the recession. The cells will use Erco's metal electrode technology. By-product hydrogen will be burned to generate steam (163-166).

BCM Technologies delayed the start-up of its \$15 million, 25,000 ton/yr plant in Amerstburg, Ontario, due to

defective anodes. The anodes were replaced and the plant opened in August, 1983. The plant uses Pechiney-Ugine-Kuhlmann's technology. BCM may double the size of the plant if it can obtain Canadian government financial assistance (167-170).

Kema Nord is planning to double capacity to 65,000 ton/yr at Magog, Quebec. The expected cost is \$21 million (Canadian) (171).

Canadian exports to the United States have been increasing between 8% and 15% per year, and should continue to increase by more than 10% per year in the near future. Through November, the export rate was about 92,000 ton/yr; 7,000 tons above 1982 levels. The reason for the growth in exports is hydropower, which allows Canadian producers to make sodium chlorate less expensively than U.S. producers can. Power prices in Canada have remained relatively stable, while U.S. power costs have been erratic and generally increasing. Canadian sodium chlorate competes with material produced in the northern United States. High shipping costs preclude Canadian product from penetrating markets in the Southeast (152).

List prices for sodium chlorate remained \$420/ton for crystalline material, though discounts were available (172, 173, 177).

Apparent consumption of sodium chlorate in the United States should be about 354,000 tons in 1983, a 4% increase (174). Pulp and paper markets account for 84% of consumption. Other markets include other chlorates 7%, uranium processing 5%, and agriculture 4% (175).

Long-term growth in sodium chlorate demand should be about 3%-4% after 1983, paralleling that of pulp output. Hydrogen peroxide and oxygen are being used increasingly in mechanical and chemical pulping processes hurting sodium chlorate's market share. Some plants should be shut down or modernized after 1985 (176).

Metals

"There is no single cause for America's recent decline as a minerals producer, and there is no single answer to our predicament. The reasons for our growing inability to compete in the world market are many—some specific to an individual deposit, others generic and affecting the entire industry. Usually a combination of forces is at work, but the combination is not the same for any two minerals."

"So let us stop looking for villains on one side, and panaceas on the other. Those of us with a real concern for America's mineral security must understand that, just as the industry's troubles are caused by a combination of forces, so must a combination of policies be assembled to combat those forces" (178).²

Difficult times for nonferrous metals continued in 1983. As a result of high metal stocks in London Metal Exchange warehouses, there was continued downward pressure on prices (179). The anticipated economic recovery was slower and less vigorous than many had hoped, and, to some extent, seemed to pass the nonferrous metals by (180). At the beginning of 1983, there were an estimated 150,000 fewer people working in the U.S. in mining and mining-related jobs than a year earlier, and roughly one-half of the capacity of the U.S. metals mining industry was idle (181).

In Canada, too, the problem was acute. The Canadian mining industry was seen as fighting for survival. The key to survival, according to Charles Baird, chairman and CEO of Inco, Limited, is more efficient production (182). Government assistance, especially in the area of tax policy, was also recommended.

Despite the gloom in the nonferrous industry, however, 1983 produced the beginning of a recovery in the aluminum and zinc markets. The recovery of those two metals was related to improvements in the housing and automotive industries (179).

U.S. Department of Commerce economists predicted that nearly all segments of the nonferrous metal industry

² Robert Horton, Bureau of Mines Director, in a speech to the American Mining Congress.

Table IX. U.S. sodium chlorate capacity (thousands of short ton/yr)

Brunswick Chemical, Brunswick, GA	25
Erco Industries, Monroe, LA	25
Georgia-Pacific, Plaquemine, LA	27
Huron Chemicals, Riegelwood, NC	12
Kema Nord Bleach Chemicals, Columbus, MS	64
Kerr-McGee, Hamilton, MS	62
Kerr-McGee, Henderson, NV	32
Occidental Chemical, Taft, LA	65
Olin, McIntosh, AL	22
Pacific Engineering, Henderson, NV	6
Pennwalt, Calvert City, KY	50
Pennwalt, Portland, OR	24
Pennwalt, Tacoma, WA	20
Total	434

would improve in 1984 (183). However, only a modest increase in demand was predicted for titanium. Military demand for Ti mill products will be flat, and needs for commercial aircraft will be relatively low, according to the Commerce Department economic forecast.

The long-term future of the metals industries can only be viewed with some concern. Major efforts are needed to cope with the accelerating pace of technology (184). At the same time, engineering and plastics are coming of age. In applications, including business machine housings, automobile body components, as well as many others, the use of engineering thermoplastics may jump by 50% by 1987, to 1 billion lb/yr (185).

Aluminum.—Production and capacity.—World.—Table X contains the current world's primary aluminum capacity and the anticipated capacity in 1986 listed by region (186, 187).

United States.—Table XI contains information on the primary aluminum capacity in the United States listed by company (188, 189).

The U.S. aluminum industry was only operating at 58% of capacity in January (188). Capacity utilization rose during the year to 72% as the economic recovery took hold (190). By year-end capacity utilization was about 80% (265).

Primary domestic production of aluminum was 3,696,000 short tons in 1983 compared to 3,609,000 short tons in 1982 (289).

Major manufacturers made the following changes in their operating capacity in 1983.

Alcoa raised its primary aluminum production to 97% of capacity by year end. The firm restarted plants in the following locations: Rockdale, Texas; Badin, North Carolina; Alcoa, Tennessee; and Warrick, Indiana. The factories accounted for 241,240 metric tons per year additional production (191-195). Alcoa may start up two idle potlines with a 44,000 metric ton/yr capacity in Vancouver, Washington, depending on power rates issued by the Bonneville Power Administration. If the lines were reopened, Alcoa's U.S. system would be operating at 100% of rated capacity (194).

Arco Aluminum restarted a 36,000 ton/yr potline in Columbia Falls, Minnesota (196), and 60,000 ton/yr potline in Sebree, Kentucky (197).

Table X. World primary aluminum capacity—1983, 1986
(thousands of metric tons per year)

	1983	1986
Africa	623	623
North America	6,108	6,221
Latin America	1,063	1,308
East Asia	800	750
South Asia	920	1,030
Europe	3,646	3,653
Oceania	713	1,106
Total	13,873	14,691

Table XI. U.S. primary aluminum capacity — 1983
(thousands of short tons per year)

Alumax	197
Aluminum Co. of America	1,576
Arco Aluminum	360
Consolidated Aluminum	182
Eastalco (Alumax-Howmet)	176
Intalco (Alumax-Howmet)	280
Kaiser Aluminum & Chemical	724
Martin Marietta Aluminum	275
National-Southwire Aluminum	180
Noranda Aluminum	230
Ormet (Revere-Consolidated)	270
Revere Copper & Brass	117
Reynolds Metals	975
Total	5,542

Kaiser shut down two potlines in Chalmette, Louisiana, totaling 55,000 tons/yr capacity but restarted potlines in Spokane, Washington, and a 40,750 ton/yr potline in Ravenswood, West Virginia, shut down since January, 1982 (199, 200, 237).

Reynolds Metals raised its operating rate to 78% of capacity by restarting potlines in the following locations: Jones Mill, Arkansas; Troutdale, Oregon; Longview, Washington; Malvern, Arkansas; and Listerhill, Alabama: totaling 217,000 tons/yr additional operating capacity (201, 202). Some of the restarts were due to lower power rates offered by the Bonneville Power Administration (BPA) in the Northwest (201, 202) and the Tennessee Valley Authority in the Southeast (211), in addition to improving markets. BPA offered the power discount through October, 1983, to firms which restarted idle capacity when it discovered 1,000 MW of surplus power (212). As a result, Alcoa, Kaiser, and Reynolds all restarted idled capacity in the Northwest (213).

Reynolds purchased Consolidated Aluminum's Lake Charles, Louisiana, aluminum production complex, including a 36,000 ton/yr primary aluminum smelter, a 240,000 ton/yr calcine coke plant, and a 135,000 ton/yr carbon anode plant. The anode plant will supply Reynolds' expansion of its Baie Comeau, Quebec, primary smelter scheduled to come on stream in early 1985 (214-216).

Alumax has deferred its plans to build a \$600 million, 220,000 metric ton/yr aluminum plant at Umatilla, Oregon. The main reason is the rapid rise of electricity costs in the Pacific Northwest (217).

Alumax purchased Howmet Aluminum, a subsidiary of Pechiney Ugine Kuhlman. The acquisition increased the size of Alumax by 50%. Alumax is owned 50% by Amax, Incorporated, 45% by Mitsui and Company, and 5% by Nippon Steel (218).

Arco Aluminum has sold its aluminum smelter at Sebree, Kentucky, plus other processing plants in the U.S. and an alumina interest in Ireland to Alcan (249, 250). Arco also wishes to sell 40% of its aluminum plant in Columbia Falls, Montana. Total capacity at the site is 180,000 ton/yr (251).

Alcoa will invest \$120 million over the next two years to modernize its Warrick, Indiana, operations. It is also evaluating an additional \$150 million investment in the aluminum smelting and rolling plant (237).

Reynolds plans to sell its Hurricane Creek alumina plant and related bauxite mining operations in Arkansas. Production ceased on August 1, 1983. The chemical products facility continues to operate using purchased alumina (219, 220).

Toth Aluminum started the first metallic chlorides plant in the U.S. based on kaolin clay raw material rather than bauxite. The plant will produce 100 million lb/yr of silica chloride, titanium chloride, and aluminum chloride by the end of 1984. Plant cost was \$8.5 million (221, 222).

Earth Sciences has applied to the Bureau of Land Management for a lease on a 1,600 acre alunite deposit in southwest Colorado. It estimates the project could support production of 500,000 ton/yr of aluminum (264).

The industry has achieved a 21.9% reduction in the amount of energy used to make aluminum vs. the base year of 1972. The industry had set a 20% reduction for 1985. Energy savings resulted from savings in the reduction process, in holding, casting, melting, and fabrication (223, 224).

Canada.—Canadian primary aluminum capacity is listed in Table XII (188). Canadian producers started the year operating at 85.7% of capacity (188). Capacity utilization was over 98% January, 1984 (233).

Alcan restarted potlines at Arvida-Jonquiere, Quebec, and Kitimat, British Columbia amounting to 41,500 ton/yr of additional production. The company finally started the last two of three potlines delayed since 1981 due to the recession at its Grand Baie, Quebec, site (225-234). The additional production was prompted by ingot orders exceeding Canadian production, especially from Western

Europe and the Far East (231).

Alcan will proceed with plans to build a \$1 billion smelter in Laterriere, Quebec, which will ultimately replace part of the production from the Arvida, Quebec, plant. The company had previously deferred its plans due to the business downturn (235-237).

Alcan may build two aluminum smelters with a combined capacity of 375,000 metric ton/yr and 700,000 kW hydroelectric plant in British Columbia pending government approval. The entire unit could cost as much as \$3 billion (Canadian) (237).

Pechiney Ugine Kuhlman will build a 230,000 metric ton/yr aluminum smelter in Becanour, Quebec. The provincial government will provide a portion of the funding for the project. Hydro-Quebec will provide 400 MW of electricity at reduced prices for 25 yr. Total cost of the project is \$1.2 billion. Capacity could be increased to 345,000 metric tons by adding a third potline. The plant will use Pechiney's 180,000A pots, which consume 13,500 kWh/ton aluminum (238-245). Alumax has an option to participate in the project (243, 246).

Canadian Reynolds will add 125,000 metric ton/yr to its Baie Comeau, Quebec, aluminum plant. The expansion will cost \$500 million. Hydro-Quebec is offering a 50% rebate on electricity until 1990 (246-248).

Alcan completed an \$82 million 1.2 million ton/yr alumina plant in Arvida-Jonquiere, Quebec (252, 253).

Japan.—Aluminum production in 1983 was expected to be about 250,000 metric tons vs. 351,000 metric tons in 1982, reflecting higher power costs. The five Japanese aluminum smelters are running at a combined 2 billion yen/month loss operating at 35% of capacity (254-256). Japanese manufacturers reduced aluminum smelting capacity by 54% between 1979 and 1982 (257).

Japanese import demand will rise to 1.8 million metric tons by 1985 and to over 2 million metric tons by 1990. The Japanese aluminum industry has invested overseas and will be entitled to 700,000 metric tons from these sources in 1985. Another 400,000 metric tons will be supplied to Japan by long-term contract in 1985 (258). The current level of aluminum imports is 1.35 million metric tons (259).

Western Europe.—The leading West European aluminum producers, and their capacities are given in Table XIII (260).

Primary aluminum production in Western Europe for 1982 is listed by country in Table XIV (261).

Australia.—Alcan, which was operating its 90,000 metric ton/yr smelter at Kurri Kurri at 64% of capacity in 1982, reached full capacity at the site by year end (262). It

Table XII. Canadian primary aluminum capacity — 1983
(thousands of short tons per year)

Alcan Aluminum	1185.0
Arvida, Que.	476.2
Isle Maligne, Que.	80.5
Shawinigan Falls, Que.	92.6
Grande Baie, Que.	188.5
Beauharnois, Que.	51.8
Kitimat, B.C.	295.4
Canadian Reynolds Metals, Baie Comeau, Que.	175.0
Total	1360.0

Table XIII. West European aluminum capacity — 1982
(thousands of metric tons)

Pechiney Ugine Kuhlman	765
Alusuisse	473
Ardal	370
VAW	345
Endasa	320
EFIM	280
Alcan	220
Norsk Hydro	160

Table XIV. West European aluminum production — 1982
(thousands of metric tons)

Austria	93.9
France	390.8
West Germany	722.8
Greece	134.9
Iceland	77.0
Italy	232.9
Netherlands	248.2
Norway	645.1
Spain	366.5
Sweden	78.9
Switzerland	75.3
United Kingdom	240.8
Total	3307.0

plans to resume construction of a third potline at the plant, raising capacity to 145,000 metric tons. Startup is anticipated by the end of 1984 (263).

Markets and prices.—Shipments by domestic aluminum producers in 1983 jumped by 16% to 13.9 billion pounds from the depressed level of about 12 billion pounds in 1982 (265). Aluminum supplies tightened as producers rushed to restart idled capacity (266). Consequently, prices rose. Spot prices went from 44 cents/lb in October, 1982 to 76 cents in November, 1983 (266). List prices were raised 6.5% to 81.5 cents/lb in August, 1983, the first list price increase since 1980 (267, 268). Prices may jump another 20% by mid-1984 (269). Some forecasters see a global aluminum shortage developing in 1984 (269), though top industry executives do not foresee a shortage occurring until 1985 (265, 266). 1984 shipments are expected to grow another 7%-9.5% over 1983 (265, 266) with the largest growth areas in transportation (22%), electrical (13.9%), and machinery and equipment (18.9%) (265, 270). In the auto industry, aluminum is being used for intake manifolds and cylinder heads. Pore-free aluminum is being used increasingly for structural components such as wheel and chassis parts and in brake cylinders, brake rotors, and calipers (271).

C. W. Parry, new chairman and chief executive officer of Alcoa, believes that the fundamentals of the aluminum business will never be the same again because 40% of the free-world's capacity is in the hands of government-controlled companies whose policies tend to depress global aluminum prices. He believes that the long-term survival of the U.S. industry will depend on new technology, company-union cooperation, and growth strategies (272, 273).

New products and technology.—TAFE Incorporated has developed an aluminum alloy which has the characteristics of conventional metals—strength, durability, machinability, and electrical conductivity—but can be rapidly dissolved by water. The company foresees a number of uses for the product, such as encapsulation of organic compounds for marine applications, sensors for water alarms for flood control, and for various delayed-release marine or military needs (274-276).

Alcoa has developed three low density aluminum-lithium aircraft alloys formulated to maximize damage tolerance or strength. Weight reductions of 8% are possible with a cocurrent fuel saving (277).

A Japanese firm, Progressive Business Group, has developed a battery using an aluminum anode, a carbon cathode, and an aqueous nitric acid electrolyte. Many efforts have been made to incorporate aluminum into batteries because of its potential ability to supply more electrons per unit weight than most other materials. Because the battery is not rechargeable and spent acid may be hard to dispose of, uses may be limited. The group will commercialize the battery through licensing or partnership agreements with other firms (278, 279).

Arco Metals will develop technology for producing aluminum chloride from kaolin clay under an agreement with Alcoa. Alcoa has already developed a process for producing aluminum via electrolytic reduction of alumi-

num chloride. Kaolin clay is widely available in the U.S. and North America, whereas bauxite, the raw material for the existing Hall process, is not. Commercialization is not expected until the 1990's (280-283).

Alcoa has modernized technology used to make carbon anodes for aluminum cells and is offering it for sale. The new technology uses better insulating materials, eliminates refractory joints, and improves air seals. The anode is more uniformly baked and increases power efficiency of the smelter by approximately 1% (284-286).

The Department of Energy has patented a new aluminum process. Crushed aluminum ore and coke are blended, pressed into pellets, and placed in a reactor. Gaseous sulfur is forced over them converting alumina to aluminum sulfide. Aluminum sulfide is heated in an electric arc furnace, where it decomposes into aluminum monosulfide, which cools and produces molten aluminum metal. The new process consumes 33% less energy than the Bayer-Hall process (287).

Chemfix Technologies has patented a process for disposing of aluminum plant wastes. The wastes, known as red mud tailings, are processed into a substance that can be used for landfill cover (288).

Beryllium.—Domestic beryllium mineral production declined in 1983 (290). Imports for consumption also dropped, from 115 short tons in 1982 to an estimated 100 short tons in 1983.

Apparent beryllium consumption, which plummeted from 303 to 150 short tons between 1981 and 1982, climbed to about 200 short tons in 1983 (290). Consumption was broken down as follows: 40% as metal in nuclear reactors and aerospace applications; 36% as an alloy and oxide in electrical equipment; 17% as an alloy and oxide in electronic components; and 4% in other applications. Beryllium recycling is insignificant.

The price of domestic beryllium metal remained at the \$194 per pound level of 1982 (290). A summary of U.S. production and consumption figures is given in Table XV (290).

Imported beryllium is obtained from China (40%), Brazil (38%), Republic of South Africa (5%), Rwanda (4%), and other sources (13%) (290). World mine production figures are given in Table XVI (290).

In August, the General Services Administration announced that it would buy beryllium from Brush Wellman Company, the free world's only integrated producer (291). The quantity was not disclosed, but was termed "substantial."

Table XV. U.S. beryllium production and consumption

	1981	1982	1983/est.
Mine production	W*	W	W
Imports for consumption (ton)	87	115	100
Apparent consumption (ton)	303	150	200
Price, dollars			
Domestic metal, per lb.	173	194	194
Imported ore, per s.t.u. (20 lb) BEO	94	121	138

* Withheld to avoid disclosing proprietary data.

Table XVI. World mine production of beryllium

Country	Mine production (ton)	
	1982	1983/est.
United States	W	W
Argentina	1	1
Brazil	35	40
Republic of South Africa	3	3
Rwanda	4	5
Other market economy countries	3	3
China	N.A.	N.A.
Other centrally planned economics	80	80
World total (Excluding U.S. and China)	126	132

Brush Wellman began a \$3.4 million government study on expanding or modernizing the company's metallic beryllium facilities in 1982 (291). Results of the study have not yet been announced. Brush Wellman will also install additional production capacity for beryllium copper round products. Work is expected to be completed by 1985.

A new copper-based alloy was introduced by Penn Precision Products to replace beryllium copper in electronics parts applications (291). The alloy costs about \$8/lb compared with about \$10.50 for beryllium copper. Also, beryllium copper has been listed as a latent carcinogen, while the new alloy is not (292).

In the first change in beryllium copper prices since September, 1982, Brush Wellman announced in December a 5%-8% increase on certain beryllium copper products, although increased discounts on large quantities were also offered (293). Following Brush Wellman's lead, Cabot Corporation posted 5%-6% increases on certain products (294). A quantity discount schedule for annual contract purchases of beryllium strip was also expanded.

Trends (290).—Estimated 1984 beryllium concentrate production will not change markedly from the 1983 level. U.S. consumption of oxide, alloy, and metal will be about 200 tons.

OSHA regulations, issued in 1975 and still under consideration in 1983, may result in higher production costs or loss of some production capacity if accepted.

Identified domestic beryllium resources are estimated at 80,000 tons. This quantity is sufficient to supply U.S. needs for the foreseeable future.

Chromium.—South African chromium ore production was estimated at 2.4 million metric tons in 1983 (a slight increase), reflecting a modest demand increase for chromite. 1983 production in other countries was not yet available (295).

The 1983 production of chromium ferroalloys and metal was running 64% behind the 1982 level (296). Producers had a 22 month supply of chromite stockpiled during the year (297).

The price of vacuum-grade electrolytic chromium metal used primarily by the superalloy industry increased 40¢ to \$4.40 per pound on July 1, 1982 (298).

American dependence on foreign supplies of strategic chromium and cobalt would be sharply reduced with the opening of the California Nickel Corporation mine and processing facility in Crescent City. The proposed \$300 million operation would supply 50% of the nation's defense needs for chromium and 80% of the military needs for cobalt (299).

The world's first plasma recycling plant is being built for Scan Dust AB in Landskrona, Sweden. The plant will recover 35,000 ton/yr of zinc, lead, nickel, chromium, molybdenum, and other metals from 70,000 ton/yr of iron and steel works baghouse dust. Dust availability could be a limiting factor. The plant is scheduled to start operations in early 1985. The technology was developed by SKF Steel (300).

The General Services Administration sent out a request for bids for upgrading chromium ore as part of the government's ferroalloy stockpiling program. Only 125,000 tons of chrome ore will be available for upgrading during the first year of the 10 year program. The total government stockpile of chrome ore is 171,034 tons (301). The stockpile program will focus on higher grade ores first since the higher energy costs to process the lower grade material would have quadrupled the program budget (302).

The British government appointed Brandeis, the Pechiney Ugine Kuhlman trading company based in London, to coordinate its stockpiling program. Various strategic ores are to be purchased, including 40,000 tons of chrome ore, 20,000 tons of high carbon ferrochrome, and 20,000 tons of charge ferrochrome (303, 304).

A new chromate conversion coating based on trivalent instead of hexavalent chromium has been introduced by

Pavco, Incorporated. The new coating will allow users to more easily comply with the stricter January, 1984, regulations (305).

du Pont is forecasting that chromium dioxide will grow at an annual rate of 20% until 1990 and is doubling its current capacity at Newport, Delaware (306).

Concerns over the future supply of chromium have caused vigorous scientific research programs to look for replacements. The most promising materials are fine-grained rapidly solidified alloys, amorphous alloys, eutectic composites, long-range ordered alloys, intermetallic compounds, and structural ceramics (307).

Copper.—The copper industry in 1983 was plagued by low prices, as sagging demand extended the problems of 1982 (308). The general improvement in the economy, particularly in the U.S., had a positive impact on zinc, but produced little optimism among copper producers, concerned with oversupply and long-term problems such as the threatened loss of electrical markets to other technologies. According to Asarco, Incorporated, consumer markets had "responded to the general economic recovery, but the capital goods sector, which accounts for more than 50% of copper consumption, has not (309).

The domestic copper industry was also depressed by high foreign production levels, sparking criticism of international economic policy.

Domestic production.—The domestic copper industry struggled in 1983, as production continued the slide beyond already-low 1982 levels. Production and consumption statistics (310) are given in Table XVII. Imports of refined copper jumped dramatically, as consumption increased while domestic production flagged (310).

Phelps Dodge assumed smelting operations at its Douglas, Arizona, operations after a 5-month shutdown (311), and expected to reach production of 300 short ton/day of anodes. The future of the Douglas smelter, however, is uncertain, because it does not meet the air pollution limits of the U.S. Clean Air Act. To satisfy the federal requirement would require almost total rebuilding, at a cost of more than \$580 million. The plant now operates under an extension permit, which expires in 1987.

Construction of Phelps Dodge's \$35 million solvent extraction electrowinning plant in Tyrone, New Mexico, was proceeding on schedule. The plan leaches low-grade material with water, to produce a copper solution, which is pumped directly to an electrowinning cell. The resulting cathodes are pure enough to sell without further refining (311).

Phelps Dodge planned to spend \$75 million to bring its Morenci smelter within pollution limits. However, the PD smelter at Ajo, which exceeds pollution limits and has no extension permit, will remain closed for the foreseeable future (311). PD's new continuous cast copper rod mill at El Paso, Texas, commenced operating in 1983, and was running at 85% of its rated 500 million lb/yr capacity in April, 1983.

Table XVII. U.S. copper production and consumption (338,363)
(thousand metric tons copper content)

	1982	1983 (prelim.)
Production		
Mine	1,140	1,045
Refinery, Primary	1,227	1,182
Refinery, Secondary	468	431
From scrap, all sources	518	465
Imports for consumption:		
Total	513	655
Ores and Concentrates	118	91
Refined	258	460
Exports		
Total	345	218
Ores and Concentrates	195	50
Refined	31	81
Refined consumption, reported	1,658	1,783
Total consumption, apparent	1,760	2,030
Refined stocks, year end	676	693

At mid-year, Phelps Dodge was struck by union workers when the company requested an 8% reduction in total labor costs (312). However, the strike did not produce a copper market rally, as labor settlements were concluded by Asarco, Ammax, and Magma.

Kennecott closed its McGill, Nevada, custom copper smelter indefinitely, citing a lack of available concentrates (313, 314). The smelter had an annual production capacity of 50,000 short tons of blister copper. Kennecott planned to restart the facility when copper business improved (315). The squeeze in concentrate supply was linked to low domestic mine production, coupled with expanding world smelting capacity, especially in the Philippines and Brazil. Tight concentrate supplies coincided with an oversupply of blister copper, as Zaire reportedly put 50,000 tons of blister on the market (313).

Kennecott was able to cut copper production costs at its Chino, New Mexico, mine and smelter to below \$0.75/lb (316). Further cost reductions are anticipated when the new flash smelter is completed in 1985. Chino's smelting capacity will be increased from 300,000 to 500,000 short ton/yr when the smelter project is finished. The Chino modernization, costing about \$120 million, will be two-thirds paid by Kennecott and one-third by its partner, Mitsubishi Corporation.

Noranda Mines announced the closing of its copper mining and vat leaching operations at Casa Grande, Arizona, in August (317, 318). Ground conditions at the mine, situated on a fault, resulted in high costs and ore losses. However, leaching operations at an adjacent sulfide ore body were continued.

Asarco scheduled the reopening of the Silver Bell copper mine in Arizona for October 1, 1984, to coincide with start-up of Asarco's new oxygen flash furnace at the nearby Hayden, Arizona, smelter (317). Silver Bell production is normally 21,000 short ton/yr of copper as concentrate. At the same time, Asarco also announced layoffs at its Mission mine near Tucson (319), due to depressed market conditions.

Because of low-cost, rich ore bodies in Latin America, it is unlikely that any new U.S. mines will be opened in the near future (320). U.S. porphyry ores average 0.6%-0.7% copper, while Chilean ore has a copper content of about 1.5%, and Peruvian ore is about 1% copper. In addition, U.S. costs per employee are about three times higher than in Chile, while productivity is comparable, according to Leon Kovisars of Met Research, Incorporated (320). Kovisars also claimed that production costs per pound were 25-40¢/lb in Chile, and 45-50¢/lb in Peru. In contrast, North American costs are 60¢ to \$1.30/lb, mostly toward the high end of the range.

In 1983, there was growing criticism from the domestic copper industry that international monetary and banking policy was financing its demise (321). An unidentified mining company official claimed that mines in Peru, Zambia, and Zaire were selling copper at 10¢ per pound below their costs, as roughly 100,000 lb/month of foreign copper are dumped on the world market (319). The World Bank and the International Monetary Fund, largely funded by the U.S., were faulted for making loans to less-developed countries to maintain or expand their state-owned copper production (321). According to L. William Seidman, director and former Vice-President of Phelps Dodge Corporation, over 40% of free-world copper production is owned or under control by governments of less-developed countries. State-owned mines, Seidman said, operate at maximum levels "to maximize foreign exchange revenue, regardless of profitability" with losses, in effect, subsidized by the IMF (322). Seidman's remarks were made in testimony before the Senate Committee on Energy and Natural Resources.

Similar criticisms were made by Charles Barber, former chairman and chief executive of Asarco, during a panel discussion at an economics symposium sponsored by the American Institute of Mining, Metallurgical, and Petroleum Engineers (323). "While U.S. mines were shutting down, the IMF was passing out [large-scale aid] to its six

clients," Barber said, referring to \$568 million in loans to Chile, Zambia, Zaire, Peru, Papua, New Guinea, and the Philippines. Similar concerns over IMF policy have also been expressed in Canada (324).

Representatives from the American Mining Congress and several leading copper producers began an educational campaign to show that copper smelters are not contributing to acid rain (325). The campaign was in response to a White House task-force report which claimed that smelters contribute to acid rain in the eastern U.S. and Canada. The representatives told EPA head William Ruckelshaus that the emissions capture rate had risen from 10% in 1970 to about 60% today, and should rise to 70%-80% by 1988.

Foreign production.—While worldwide copper production fell by 80,000 metric tons between 1982 and 1983, foreign mine production remained approximately constant, as all of the decrease was attributable to the United States. World mine production is summarized in Table XVIII (310).

Despite soft markets, some foreign copper producers made commitments to expansion in 1983. Chile's Codelco began a major expansion and modernization program to raise its smelting and refining capacity from about 533,000 ton/yr to nearly 880,000 ton/yr by the end of the decade (311). The first step was to increase the electrolytic capacity of its El Salvador division, from 78,000 to 90,000 ton/yr during 1983.

Codelco's mining capacity was not planned to increase above the current level of about 1 million ton/yr. This was attributed in part to a 27% drop in ore grade at Chuquicamata, Codelco's largest mine, from 2.2% to 1.6% copper (326). There was also concern over the recent U.S. protectionist sentiments. The U.S. normally consumes about 14% of Codelco's copper.

In Canada, Asarco announced plans to reopen its Buchan, Newfoundland, mine (327). The mine, which yielded 500 ton/yr of copper before closure in 1981, has an ore body with an estimated three-year reserve. After a poor third quarter, largely due to its copper business, Noranda Mines decided to cut its copper output by nearly half (328). Noranda's Montreal refinery was scheduled to produce 110,000 tons in 1983, against 216,590 tons in 1982. In addition, Noranda planned to operate only copper mines with significant by-product yields. Plans for developing Noranda's underground ore body in Murdochville, Quebec, were shelved, and the smelter there, operating mainly on Chilean ores, could be in peril (329).

Falconbridge Copper announced it would sink a \$7.6 million shaft near Schreiber, Ontario, beginning in the spring of 1984 (330). The ore body is estimated to contain 17.8% zinc and 0.94% copper. Cominco began mining low grade ore south of Kamloops, but milled only 23,000 ton/day (331). To raise milling to 45,000 ton/day would require a new \$250 million concentrator, which cannot be justified at a copper price below about 90¢/lb.

Table XVIII. World copper mine production and reserve base (310)
(thousand metric tons of copper content)

	Mine production		Reserve base
	1982	1983 (est.)	
United States	1,140	1,045	90,000
Australia	247	250	16,000
Canada	606	600	32,000
Chile	1,241	1,250	97,000
Peru	369	330	32,000
Philippines	293	320	18,000
Zaire	503	490	30,000
Zambia	584	580	34,000
Other market			
economy countries	1,277	1,280	101,000
Poland	348	350	15,000
USSR	970	1,000	36,000
Other centrally			
planned economies	462	460	9,000
Total	8,040	7,955	510,000

Brenda Mines of Vancouver mothballed its Peachland, British Columbia, operation (331). Placer Development sharply curtailed production at its Gibraltar mine (331). However, low-cost producer Lornex Mining Corporation, Limited, was operating at full capacity of 86,000-88,000 ton/day (331).

Sherritt Gordon continued to operate its loss-making Ruttan mine in northern Manitoba (332). By March, 1984, the company expected to find a partner to fund the \$30 million expansion necessary for the mine's survival.

Zambian copper shipments through the Dar es Salaam port were increased from 30,000 to 40,000 ton/month after, logistics problems were solved (312). However, backlog problems again surfaced later in the year, as a rail strike halted shipments in the copper belt (328). The Konkola division of Zambia Consolidated achieved a record 1.93 million tons of ore hoisted in the year ending March 31, 1983 (316). In addition, the 48,574 tons of copper output in concentrate was the highest since 1972. However, in late 1983, Zambian president Kenneth Kaunda requested other major copper producing countries to join Zambia in curtailing refined metal output to force a world price rise (333, 334). Copper accounts for over 90% of Zambia's foreign exchange earnings. It appeared that Kaunda's proposal would meet resistance among other members of the Intergovernmental Council of Copper Exporting Countries (CIPEC). In particular, Chile, the largest and most influential copper producer, is committed to expanding copper output through the decade.

CIPEC also expressed concern over draft legislation before the U.S. Congress, which would impose a tax on copper imports (326). The "environmental equalization" tax would reduce the smelting and refining cost advantage of foreign producers over domestic companies, by raising the copper duty from 0.8 to 10¢/lb.

Zaire's copper exports, through its state-owned marketing agency, Sozacom, were expected to rise from last year's 489,535 tons to as high as 500,000 tons (316). The improvement was partly due to increased sales to China and Japan.

Japan purchased more copper from Pasar of the Philippines, as well as Zaire (335). Premiums on Zambian copper through 1983, coupled with low Japanese demand, reduced Zambian exports to Japan. There was speculation that Japanese smelters would cut back production by about 10% in 1984, from current production levels of 85,000 ton/month (336). An eight-member consortium of Japanese companies, led by Nippon Mining Company, withdrew from a copper development project in Zaire, after losing some \$220 million since the project was organized in 1976 (337).

Prices.—Throughout 1983, copper prices were low. To regain market share, three of the big four Canadian producers—Noranda, Kidd Creek, and Inco—moved to COMEX-based pricing formulas, using the COMEX price plus a 3-5¢ premium. The fourth, Hudson Bay, continued with a list price (338). Later in the year, Phelps Dodge moved to price its copper rod at the COMEX price plus about a 7¢ premium (339).

In June, swollen stocks pushed prices to two-month lows (340). Domestic producer prices were 78-79¢/lb, while the COMEX price was 73.8¢/lb. Adding to the problem were worldwide production increases and restarting of North American refineries as producers, notably Inco and Phelps Dodge, attempted to improve cash flow. As a result, prices slid even further, the producer price reaching 77.5-78¢/lb (313).

According to P. E. Shortall, Jr., manager of metals purchasing at Olin Brass, excess inventory would depress prices at least into 1984 (341). Combined warehouse stocks of COMEX and the London Metal Exchange reached 620,000 tons in July, compared with about 350,000 tons in October, 1982 (342). According to the secretary general of CIPEC, Eduardo Llosa, only a further production cutback, from the 750,000 metric tons capacity already shut, mainly in the U.S. and Canada, were neces-

sary for a real boost in prices (343). Llosa said cutbacks should take place at high cost mines, and not among generally low cost CIPEC producers.

Prices slumped even lower in October, as Asarco lowered its quote to 69¢/lb, and a host of domestic producers reacted by dropping prices to 70¢/lb (344). The COMEX price, meanwhile, was 65.95¢. The retreat was blamed on a similar decline in gold and silver prices. Despite this disappointing turn, Anthony Bird Associates predicted an average 94.2¢/lb price in 1984, arising from a 10% consumption increase, coupled with only a 1.9% increase in refined production (345). Metal Trends bulletin likewise forecasted a gradual price firming to a peak in 1985-1986 (346).

At the end of 1983, Robert Horton, Bureau of Mines head, claimed that copper producers now need to get at least \$1.10/lb for copper to turn a profit (347). Horton also said that new amendments to the Clean Air Act would add another 15¢/lb to production cost.

An adequate return for a new copper venture was put at the 15% after-tax range by David James, a Richardson Greenshields mining analyst (348). According to James, this requires a price of about \$1.20/lb.

A report by Dr. Leons Kovisars of MET Research predicted copper prices, rebounding from 1983 lows, may reach more than \$2/lb (in current dollars) after 1990 (349).

Demand.—It was estimated that, at the end of 1983, world inventories of refined copper would rise to about 1.92 million short tons, up from 1.22 million short tons at the beginning of 1982 and 1.65 million short tons at the beginning of 1983 (340). Copper's recovery remained stalled, as mid-year estimates of a consumption increase of 8% in the U.S. and 1%-2% worldwide (340) failed to materialize (350). In fact, consumption in the first half of 1983 was only marginally higher in the U.S. and Great Britain, and dropped in Japan, West Germany, and France (322).

Overly bullish expectations led copper producers, particularly in the U.S., to bring idled capacity into operation too early, according to Anthony Bird Associates (351).

One bright market for copper was in domestic wire, where consumption was running about 10%-20% ahead of 1982, when total wire mill product usage was about 2.35 billion lb (352). Additionally, a long-term copper study indicates that competitive copper producers may benefit from a turnaround in which the Western World demand for refined copper grows from 6.9 million metric tons in 1982 to an estimated 9.9 million metric tons in 1991 (349).

Better times were also predicted by Grieveson, Grant, and Company (353), who saw copper consumption increasing by 5½% in both 1984 and 1985, with demand actually outstripping supply. Particular concern with supply was expressed within the European Economic Community, where increased difficulties were anticipated over the next five years (354).

G. Frank Joklik, president of Kennecott, said that he was "reasonably optimistic" about long-term demand growth for copper (355). Joklik predicted 2% per year growth in refined copper consumption for the rest of the century. Increased demand was seen principally from electrical applications.

A cautionary note was sounded by Henry Bloy of the Mining Association of Manitoba, who pointed out that Chile alone would be capable of meeting the entire world copper demand if it went into full production (348). Similar warnings were made by Sr. Alistair Frame, chief executive of Rio Tinto Zinc (356). Frame told a Metals Society copper conference that "the expected slower rate of industrial growth, the changing requirements of the developed countries, the inroads of substitution, the reduced quantities required for any of copper's surviving applications, and the absence of any really significant new outlet lead us to the inescapable conclusion that the increase in copper consumption in the coming years will at best be only very moderate."

Markets.—Faced with loss of traditional markets to other materials, copper producers need to step up their devel-

opment efforts. That message was given by Alfred Powis, chief executive of Noranda Mines, Limited (357). Powis noted intensified threats from aluminum, magnesium, stainless steels, plastics, and, more recently, from titanium and optic fibers. Calling for more product development and market research, Powis noted that the aluminum and plastics industries spend much more in these areas than does the copper industry. Powis encouraged the Copper Development Association "to strike out and capture new ground."

One challenge to copper comes from fiber optics in the telecommunications industry. Optic cables are easier to install, and can carry 40 times as many simultaneous communications as bulkier copper cables. In addition, optic cables are cheaper than copper (358). In an effort to gain an early lead, Southern New England Telephone Company joined with CSX Corporation, a railroad, to begin laying 5,000 miles of fiber-optic cables along CSX right-of-way in 20 eastern states (358).

In one study (353), fiber-optic cables for high density communications were not seen as cutting into copper's market by more than a few percentage points, despite the great successes of fiber-optic development in recent years. However, fiber optics could displace 300,000 tons of copper by 2000 (359), reducing copper's use in U.S. communication to a modest net growth. Also at stake is a replacement market as nearly 1 billion miles of AT&T copper cable, already installed, wears out (358).

Additional threats in the electrical industry are posed by hybrid graphite fibers with enhanced electrical conduction and inherently high strength (360). Balanced against this, the recent crossover in copper and aluminum prices will aid copper in recapturing market share for not only electrical applications, but also for ship mill sheathing, offshore oil rigs, and other uses (359).

A spot survey of solar industry officials indicated that sales of flat plate collectors and absorbers were up 20%-30% from 1982 (361). According to the Copper Development Association, this emerging market used 16.8 million pounds of copper in 1982. Although small, the industry is growing rapidly. American Solar King Corporation in Waco, Texas, plans to buy about 500,000 lb of copper in 1984, up from 180,000 lb in 1983 (362).

Lithium.—U.S. lithium carbonate production totaled 34 million pounds in 1983 (364).

There are only two United States lithium producers: Lithium Corporation of America and Foote Mineral (365).

The price of metallic lithium in 1000 lb lots has ranged between \$21.70 and \$23.35/lb for more than a year (365). Foote Mineral lowered its price to \$21.70 on October 1, 1983 (366).

The price of technical-grade lithium carbonate increased by seven cents to \$1.48/lb on April 1, 1983 (365-369).

Foote Mineral restarted its Kings Mountain, North Carolina, lithium compound facility during the spring after shutting it in August, 1982. Capacity is over 17,000 ton/yr of salt cake (370).

Pechiney Ugine Kuhlman's subsidiary, Metaux Speciaux, has set up a pilot facility for the electrochemical production of lithium at its Plombieres, France, plant. A decision on a large-scale lithium plant is expected toward the end of 1984 (371).

Two lithium deposits were found in Europe. Minerex AG of Austria announced the discovery of a large lithium deposit near Carinthia, in the Austrian Alps (372). The French Bureau of Geological Research has finished a feasibility study for exploiting the mineral bed of Echasieres in the Allier (373).

The European Economic Commission has reopened an anti-dumping investigation into imports of lithium hydroxide from the United States and the Soviet Union and has started new proceedings against the People's Republic of China. The EEC first imposed a duty on lithium hydroxide from the United States and the USSR in January, 1980. Imports from the three countries have risen from

57.8% to 72.2% of the EEC market. Lithium hydroxide is a lubricant used in oil production (374, 375).

Aluminum alloys containing up to 15% lithium could reduce the weight of commercial airliners making them more fuel efficient. The alloys also have better structural properties than the currently used metals (376, 377).

The key to the future growth of the lithium market rests with the consumer batteries and aerospace (365). Lithium demand could rise to 70,000 ton/yr of contained lithium by 2000 if these new uses are successfully developed. The current oversupply situation could continue for a decade. Reserves are sufficient to raise output thereafter (377).

Chile will add 18% to world capacity with the start-up of a \$61 million, 14 million lb/yr lithium carbonate plant during 1984. The producing company, Sociedad Chilena de Lito is 55% owned by Foote and 45% by the Chilean government (377).

Another new lithium producer is Greenbushes Tin of Australia, which plans to produce 20,000 ton/yr of lithium concentrates (367).

Magnesium.—After years of low sales and restrained prices, magnesium enjoyed a rebound in 1983, and prospects for the next few years are bright. The year was characterized by production and price increases, increased demand, inventory restocking, and healthy existing and new markets.

Production and price.—The recovery of the U.S. economy had a direct effect on magnesium production in the U.S. However, slower recovery elsewhere was reflected in foreign Mg production, which was virtually the same as in 1982. Production figures are shown in Table XIX (378). More detailed domestic production and consumption figures are given in Table XX.

As a result of increased demand during the first half of 1983, Dow began a six-month plan in June to increase magnesium production by 25% at its Freeport, Texas, plant. Previously, the plant had been operating at about 50% of its estimated production capacity of 230 to 250 million lb (379). The move was intended to replenish Dow's inventories, which were purposely drawn down in the preceding two years of low consumption, and to meet the rising Mg demand. In May, Amax, Dow's primary domestic competitor, was operating its Rowley, Utah, plant at about 60% of its 32,000 ton/yr capacity. Later, it was reported that Amax planned to bring on another 10,000 ton/yr capacity in the fourth quarter (380).

During most of 1983, Norsk Hydro operated at about

60% of its production capacity of 50,000 ton/yr (381). This was due, in part, to a modernization program at the Porsgrunn smelter to cut costs and energy consumption, and to increase productivity. The new technology involves production of anhydrous $MgCl_2$ from a magnesium chloride brine mixture, rather than from the more traditional dolomite/seawater mix. Full capacity production was expected to begin at the end of the year.

In October, Alcoa announced that Mg production at its North West Alloys subsidiary had increased, with eight of nine furnaces operating (381). Previously, three furnaces had been shut down for relining (382). Upon completion of a maintenance program, all furnaces will be operated. Despite the increases in power costs announced earlier by the Bonneville Power Authority, optimism in the Mg market led to the decision to increase production. Most of North West's magnesium production is consumed by Alcoa itself in aluminum alloys, for which markets were also firm.

Japan's two magnesium producers, Furukawa Magnesium and Ube Industries, raised production to 2,956 tons in the first half, a 6.8% increase over the same period in 1982 (383).

In May, Dow increased its Mg price for the first time in two years (379). In Europe, both Dow and Norsk Hydro raised prices on July 1, 1983, following the lead of Sofrem (384). Amax did not immediately follow Dow's domestic prices increase, despite sustaining losses on magnesium operations in the first half of the year (382). Further price increases were expected as demand exceeded production levels. Earlier price restraint was attributed not only to low demand, but to conscious plans for new Mg market growth (380).

Demand.—Although demand remained weak relative to the late 1970's, there were signs of a general rise in die casting and automotive markets (379). Some of the increased demand was seen as a chain reaction response to the aluminum upturn (385). The International Magnesium Association estimated that 1983 consumption would exceed production by 44,000 tons, with the shortfall being met from already low stockpiles (381).

Magnesium demand increased by 20% between the second half of 1982 and the first half of 1983 (384). Demand in West Germany in the first half was 13% higher than a year earlier (385). French and Italian producers were operating at full capacity, and were believed to be sold out through the end of the year. Japanese imports rose 4.9% during the first half of the year, to 7,458 tons, with most of the imported material coming from the U.S. (383). At the same time, there was little free market activity, as Russia and China were inactive, and Yugoslavian output was curtailed because of power shortages (385).

Markets.—The optimism among magnesium producers arises from projected increases in new and existing markets. The automotive die casting market, relatively static at 31,000-34,000 ton/yr for the last three years, was projected to rise to 55,000 ton/yr by 1987. Significant pounds per auto increases were seen as possible in the 1985 model year, through easy substitutions of magnesium for aluminum (380). With increasing aluminum prices, the magnesium-to-aluminum price ratio approached a low value of 1:6.

Increased magnesium use has met with success at Honda, and in the clutch housing in Ford Ranger light trucks (380, 386). Chrysler began studying further applications which could result in increased Mg usage of 3-4 lb/yr (383). The current Shelby Charger was fitted with a magnesium gear lever, which was expected to be used in other Chrysler cars next year. Magnesium engine component, interior door handles, and window handles are also under consideration. GM introduced a 6 lb magnesium radiator grille on the 1984 Pontiac, and an air cleaner on the Chevrolet Corvette (387).

However, magnesium substitution requires that car makers either modify their die casting and machining facilities to switch from presently used aluminum, or pur-

Table XIX. World magnesium production (378)
(thousand short tons)

	1982	1983 (est.)
United States	99	110
Canada	9	9
France	11	11
Italy	8	9
Japan	6	7
Norway	39	40
Yugoslavia	4	4
China	8	8
USSR	89	89
Total	273	287

Table XX. Domestic Mg production and consumption (378)
(thousand short tons)

	1982	1983 (est.)
Primary production	99	110
Secondary production	43	45
Imports for consumption	5	6
Exports	40	50
Consumption, reported	75	70
Consumption, apparent	102	91
Consumer stocks, year end	35	35

chase finished components from external suppliers (383). George Ditzhazy, divisional purchasing manager of GM's Central Foundry Division, pointed out that Mg applications could be hampered by cost, processing difficulties, and a lack of variety of U.S. sources which can competitively supply magnesium ingot (388). General Motors consumes about 600,000 lb/yr of Mg. According to Ditzhazy, GM forecasts no substantial increase from current consumption levels, aside from increases attributed to forecasted car volume.

Amax began marketing a new high purity magnesium alloy, AZ91HP, which could replace zinc and plastic components now used in computers and peripheral equipment (386, 389). The alloy, while three times as expensive as zinc per pound, is only one-quarter as dense, and is thus less expensive to use. In addition, the alloy offers higher structural strength than plastic and contains fewer corrosion causing impurities than similar alloys. Amax estimated that use in computers could account for 1 million lb of new demand in the U.S. in 1984. The alloy now accounts for about 90% of Amax's total magnesium production (386). Amax is also hoping to replace zinc in telecommunications industry cooling devices.

A decline in U.S. die casting demand from 26 million lb/yr in the 1970's to the current 10 million lb/yr was due largely to the low cost of aluminum (387). As the Mg/Al price ratio shrank from over 3 to about 1.6, an increased Mg usage of 15 million lb for die casting was seen possible in 1984. However, this still represents a small share of the U.S. die casting market, which consumes 600,000 ton/yr of aluminum and 210,000-225,000 ton/yr zinc.

Additional Mg demand is predicted for the desulfurization process used in steel manufacture (380, 381). Magnesium, viewed as both cost effective and environmentally benign, has already made progress in replacing calcium carbide and soda in the U.S. and Europe (381).

Manganese.—Manganese is an efficient and cost effective deoxidizer and desulfidizer of steels. Thus, the steel industry accounts for 95% of the world's manganese consumption (390).

Manganese alloy and metal consumption tended to follow the steel industry lead. All were higher early in the year and slumped slightly later on. Imports of manganese ores were generally increasing all year (391-396).

Electrolytic manganese metal list prices were lowered to 66¢/lb on May 1, 1983 (397). Prices rebounded late in the year to 70¢/lb (398-399).

The United States has an estimated 70 million metric tons of manganese resources. However, commercial sources are contained in low-grade deposits containing 0.6%-14% manganese. Production costs to exploit these deposits are prohibitive. Adequate supplies of high-grade manganese ores (45% and higher) are available from foreign mines. Therefore, the United States imports all of its requirements (400).

Haker has developed a hydrometallurgical technique for recovering silver and manganese from silver sulfide ores. Silver Tech Mines, a joint venture of Haker and Houston Mining and Resources, plans to apply the technique in a pilot plant at a mine near Tombstone, Arizona, designed to process 1-3 ton/day of ore. Conventional silver smelters cannot tolerate much manganese. The inventor claims his proprietary leaching solution overcomes such recovery problems and recovers 90% of the silver and all the manganese (400, 401).

New mineral samples taken from United States-controlled waters in the Pacific Ocean contain 32% manganese, a higher concentration than earlier sampling had indicated (402).

A carpet of manganese nodules containing 40%-41% manganese has been discovered in the Tyrrhenian Sea between Rome and Sicily (403).

United States firms may have access to Mexican manganese that is closer to home than the South African material that now predominates. Three possibilities exist for joint ventures between United States companies and

Mexican manganese producer Cia Mineara Autlan: opening the Noapa deposit near Mexico City; expanding capacity at Autlan's refinery in Tampico; and upgrading carbonate ores found in the Molango deposit to premium-grade manganese (404).

Autlan Manganese's ferromanganese and silicomanganese plant in Mobile, Alabama, did not reopen during 1983 (405).

The Bureau of Mines has developed two chromium-free steels designed to be cost-effective substitutes for standard grades of heat-treatable construction steels. The new alloys use manganese-molybdenum and manganese-nickel-molybdenum and may reduce United States vulnerability to a potential disruption in chromium supplies from South Africa and the Soviet Union, the major exporters to the United States (406).

A maximum of 100,000 tons of manganese ore will be available for processing during the first year of the U.S. government's stockpile upgrading program. The government currently has 153,105 tons of manganese ore on hand (407).

The British stockpiling program includes the purchase of 40,000 tons of manganese ore and a similar amount of high carbon ferromanganese (408).

World demand for electrolytic manganese dioxide totaled 116,900 metric tons in 1982 and should reach 121,000 metric tons in 1983 and 126,100 metric tons in 1984. Table XXI contains 1982 consumption information by region (409).

In Japan, dry cell battery production rose 13% in 1982 vs. 1981, but electrolytic manganese dioxide consumption rose only 3%. The reason is increasing miniaturization of dry cells to make them compatible with ever-smaller electronic devices (409).

Cia. Minera Autlan SA has designed a plant to produce 6,600 ton/yr of electrolytic manganese dioxide. The plant is to be located in Mexico (410).

Nickel.—Free world nickel consumption was 1,070 million lb in 1983, a 7% increase from 1982 (411).

Worldwide 1983 nickel demand exceeded disastrous 1982 levels by healthy margins. Much of the demand included inventory replenishment (412-416). As a consequence, prices rose from year-end 1982 levels of \$1.50/lb (417). Prices were as high as \$2.37/lb (418), but then fell back to the \$2.25 range (417,419). The prices slumped when consumers' inventory building ceased and when the increased availability of scrap from higher stainless steel production impacted the market (420).

Table XXII lists the major suppliers of nickel to the United States in 1982. The 1982 import total was 263,135,000 lb (421).

Hanna Mining Company has signed a new power contract with the Bonneville Power Administration and a new labor agreement with the United Steelworkers Union and will reopen the nation's only integrated nickel mine

Table XXI. Electrolytic manganese dioxide consumption, 1982 (metric tons)

Japan	18,700
Europe	19,000
North/Central Europe	36,400
Southeast Asia	21,000
Eastern Europe	15,500
Mid and Near East	6,300

Table XXII. U.S. nickel suppliers — 1982 (percent of total imports)

Canada	41%
Australia	16%
Botswana	11%
Norway	10%
South Africa	6%
USSR	2%

and smelter at Riddle, Oregon. The facility had been closed since April, 1982, due to depressed conditions in the worldwide nickel market (422, 423).

Amax suspended operations at its refinery in Braithwaite, Louisiana, during the summer, due to low nickel prices and low demand. The plant had operated at its full capacity of 80 million lb/yr during all of 1982 and the first half of 1983 (424, 425). The plant reopened in September 1983 (426, 427).

Ni-Cal Developments is continuing to progress towards its aim of establishing an open pit nickel mine and processing plant near Crescent City, California. The company will construct a 75 ton/day pilot processing plant there in 1984. An engineering and economic feasibility study says that the plant could produce 19 million lb/yr of nickel and 2.2 million lb/yr of cobalt (428, 429). The plant could supply up to 80% of the nation's need for cobalt and 35% of its needs for nickel (430).

Inco's Sudbury, Ontario, mining and milling operation reopened in April after being closed since May, 1982 (431, 432). Inco's Sudbury nickel refinery and its Thompson, Manitoba, division both closed for a month during the summer (433). Its Port Colborne, Ontario, refinery was shut down for five weeks beginning December 26, 1983 (434).

Falconbridge resumed production at its Sudbury facility early in 1983 after its having been closed since July, 1982 (435). Falconbridge plans to continue production at Sudbury throughout all of 1984 (436).

Sherritt Gordon mines installed a new recovery system at its Fort Saskatchewan, Alberta, refinery raising capacity to 46 million lb/yr from 38.7 million pounds (437).

Inco resumed development of its new open pit mine at Thompson, Manitoba, in June. The development of the mine was halted in June, 1982, to conserve cash. The completion date has been pushed back one year to 1986. The new mine will replace the existing Thompson Pipe mine, which should be depleted in 1985 (438).

Inco may replace its nickel smelter at Sudbury, Ontario, with a new reduction smelting unit to cut sulfur dioxide emission to 50% of the proposed limit. A new plant could cost \$450-500 million. Inco is trying to utilize as much of the existing processing equipment as possible to lower the cost because of its present financial condition (439).

Falconbridge's plans to raise production at Sudbury operations to 90 million lb by 1990 have been shelved. Falconbridge management feels nickel prices must be above \$3.00/lb to justify the investment. Current capacity is 69 million lb/yr (440, 441).

Talent Metal should start a \$6 million 7,000 metric ton/yr plant on Taiwan in early 1984 (442).

Japanese nickel output in 1983 was about the same as 1982—23,000 metric tons. Demand was 38,000 metric tons vs. 38,500 tons in 1982 (443, 444).

Cuba's nickel industry was in the news often in 1983. Cuba produced 40,000 metric tons of nickel oxide in 1982; about 20% was exported to Western Europe. The Punta Gorda nickel project, although delayed, may start up in late 1984. The 107,000 ton/yr Las Camaricocas project will not start up in the next three years due to technical problems and weak market demand (445). Cuban nickel production is expected to double or triple by 1990 (446).

A United States trade ban on materials containing Cuban nickel is still effective (445). The Reagan Administration effectively banned imports of Soviet-made nickel products on the grounds that they contain Cuban nickel ore (447, 448).

The European Economic Commission imposed and then lifted a 7% antidumping duty on Soviet nickel. The Commission lifted the duty when investigations revealed that the USSR prices were undercut by other nickel producers selling in Europe (449-453).

Gipronickel Institute, Leningrad, has introduced a new method for producing nickel directly from concentrates using a new hydrometallurgical process. Nickel concentrate solution is introduced into an electrolyzer cell, from which pure nickel is extracted. Bypassing the smelting

stage saves energy and allows more complete recovery of nonferrous metals. The Soviet nickel and cobalt industry will convert to the process starting in 1987 (454).

After three successive years of decline, western world nickel consumption increased about 6% in 1983. Forecasts for 1984 indicate a further increase of 8%-10% to about 1,120 million/lb (455). Western world nickel consumption is only expected to grow by 1.1%-1.7% annually through 1996. North American nickel production will still not match peak 1979 levels (456). Some market segments are expected to grow much faster. Electroless nickel plating will grow from 10%-20% per year from its current level. The growth in the electronics industry, where electroless nickel is used on computer memory disks, aerospace connectors, and copy machine rollers is the reason for the optimistic outlook (457).

United States nickel production is expected to meet only a small part of the 380,000 ton United States market in the year 2000 unless the relatively low-grade ores in Oregon and California are developed, according to the Bureau of Mines. The report maintains that 1981 nickel reserves of 54.1 million tons and anticipated new discoveries are entirely adequate to meet the high range forecast of United States and world demand (458).

Sodium.—There are three domestic producers of sodium (459). Their estimated production capacities are given in Table XXIII.

Metallic sodium production figures are given in Table XXIV (460).

By comparison, 1981 production was estimated at 109,000 tons, and 1982 production at 103,000 tons (459).

Metallic sodium is primarily used to produce anti-knock additives for motor fuel, a market which is being phased out in the U.S. and is vulnerable elsewhere (461). This caused demand to decline by 4.1% per year between 1970 and 1980. Present sodium markets, at last estimation, are listed in Table XV (461).

Titanium.—As predicted (462), the titanium market did not recover in 1983, although long-term projections are

Table XXIII. U.S. sodium producers

Producer	Capacity (million lb)
du Pont, Niagara Falls, NY	113
Ethyl Corporation, Baton Rouge, LA	90
RMI, Ashtabula, OH	74
U.S. Total	277

Table XXIV. U.S. sodium production — 1983

Month	Production (short ton)
January	7,094
February	6,662
March	6,510
April	6,730
May	6,534
June	6,638
July	7,139
August	6,910
September	7,121
October	7,476
November	7,189
December	Unavail.
Total (Jan.-Nov.)	76,057

Table XXV. Sodium markets (percent of total)

Manufacturers of gasoline additives	58%
Metals reduction, primarily Ti	21%
Miscellaneous (catalysts, dyes, metal descaling, pharmaceuticals, perfumes, and herbicides)	21%

encouraging (463). In a weak market year, there were explorations of joint ventures between producers, acquisitions, and the formation of the country's first titanium association. Procurement of titanium for the National Defense stockpile by the General Services Administration (GSA) became a major issue in a depressed year.

Production and prices.—Since the late 1970's production capacity for Ti sponge has increased dramatically worldwide (463). In the U.S., expansions and new facilities have increased capacity to more than 72 million lb/yr. In the first quarter, U.S. production remained at about 35% of capacity (464). In Europe, the ICI plant was replaced with the Deeside Titanium Limited plant with an 11 million lb/yr capacity. Japanese production capacity has more than doubled since 1977, and now stands at 73 million lb. Total free-world capacity is thus more than 154 million lb/yr. World sponge production figures are given in Table XXVI (465).

Pechiney's French subsidiary, Cezus, has begun a pilot project to produce Ti sponge to support its manufacture of semi-finished product (465). Viking Metallurgical Corporation brought a new electron beam furnace on stream in mid-year (466). The furnace, with a 7 million lb/yr capacity, increases Viking's melting capacity to 10 million lb/yr.

Showa Titanium Company announced that its Toyama Ti sponge plant would begin test runs by October (467). Capacity was estimated at 2,000 ton/yr of A-grade sponge. Sales were intended to be divided evenly between the U.S., Europe, and the local market. Showa claims that its new technology obtained from joint venture partner Ishizuka Kenkyusho, will produce Ti at 18,000 kWh/ton of Ti. In comparison, power requirements for U.S. production are estimated at 40,000 kWh/ton.

In contrast to the Showa expansion, Japan's major producers, Toho Titanium and Osaka Titanium, reduced operating rates to 40% of capacity (467). Japanese Ti sponge shipments to Europe were depressed (468) as European users turned to much-cheaper Soviet sponge (\$5.90-\$6.00/kg vs. about \$7.90/kg). Spot shortages, however, occurred in the U.S. market, due to depleted inventories. Prices up to \$3.50-\$4.00/lb were reported.

China, with a 20,000 ton/yr capacity, dropped out of the sponge market for over a year (469), and was operating at only about 50% capacity. Threshold price estimates for Chinese re-entry varied from \$3.20 to \$4.50/lb.

A joint project between Howmet and Dow Chemical, to produce Ti sponge electrolytically, was dropped when it turned out to be uneconomical (465). A joint sponge-production venture between Westinghouse Electric Corporation and Mitsubishi Metal Corporation was also dropped (470).

RMI Company and Kobe Steel Limited announced formation of a joint venture in which semi-finished Ti would be shipped from RMI to Kobe, rolled into commercially pure mill products at Kobe, and shipped back to the U.S. (470). The venture will compete with Timet, the dominant U.S. supplier of commercially pure Ti, and ALS Metals, Incorporated. ALS, a joint venture of Allegheny-Ludlum Steel and Japan's Sumitomo group, will produce mill products in the U.S. using semi-finished Ti from Sumitomo. RMI also purchased Micron Metals, Incorporated, a Ti powder producer in Salt Lake City (471), to extend its range of Ti powder products.

Albany Titanium, Incorporated announced plans to begin Ti powder production by late 1984 and sponge production a few months later (472). Revised plans call for a 10 million lb/yr sponge capacity using a process licensed from Occidental Petroleum Company. The process will use ilmenite (\$40-\$50/ton), as its raw material.

The Federal Trade Commission began investigating a proposed acquisition of TiCl₄ and TiO₂ production facilities by SCM Corporation (473). The sale would give 80% of the market to du Pont and SCM. Titanium tetrachloride is used to produce Ti sponge.

Demand.—Despite slow markets, Ti sponge consumers (474), facing dwindling inventories, began negotiating long-term supply agreements running 3-5 yr (470). Recent contracts had been as short as six months. The move to longer contracts was viewed as a ripple effect from attempts by jet engine and airframe builders to obtain long-term contracts from their suppliers.

The Federal Panel on Assessment of Titanium Availability, Current and Future Needs reported that the U.S. supply was "triply secure" (463). This conclusion was based on large domestic resources, current use of cheaper imported ores (thus conserving domestic supplies), and ability to shift Ti supplies from less critical uses in an emergency. Even under the most optimistic assumptions, Ti demand will not reach current production capacity by 1990 (463).

Markets.—The aerospace industry is the largest present market for titanium (475). The depressed state of the aircraft market (470) has had a serious negative effect on titanium demand. Worldwide commercial jet deliveries declined from 460 units in 1980 and 426 in 1981, and again to 290 units in 1982 (463). It was estimated that deliveries would decline severely to less than 200 units in 1983, before rebounding in 1984 and 1985. In commercial aircraft, the main titanium users are the 747, 757 (at 17,000 lb each), 767 (12,400 lb each), DC-10 (20,000 lb each), and Airbus. Discontinuance of L-1011 production, requiring 34,000 lb of purchased Ti per aircraft, means that future aircraft production to meet a given number of seat miles will require less Ti than in the past. However, the increasing use of composite materials in new aircraft may bring a concurrent increase in Ti usage, because Ti is more compatible than aluminum with advanced composites.

Grumman Aerospace Corporation reported advances in superplastic forming and diffusion bonding of titanium aerospace components (476). The production equipment required costs only half as much as an equivalent commercial hydraulic press and can be installed in much less time. Using the new technology, Grumman has built glove vanes for the Navy's F-14 fighter, and has designed a titanium wing section for the next generation of fighter aircraft under Air Force funding.

Testing has begun on titanium propellant and pressurant tanks for the first five Intelsat VI communications satellites (477). The tanks, measuring 4-45 in diam, will be made from standard 6AL4V titanium alloy by the Precision Sheet Metal Division of Fansteel Corporation.

The prospects for new beta and near-beta titanium alloys, which are heat-treatable to high strengths without becoming brittle, are promising (475). Most of the Ti alloys used to date in the aerospace industry have been in the soft annealed state, but the desire for stronger Ti alloys has led to work on beta-type alloys by the Department of Defense, titanium producers, aircraft manufacturers, and forging companies.

Pechiney announced plans to set up titanium sponge plants in France, to expand into high technology uses in Europe and the United States (465). Viking Metallurgical Corporation, a major U.S. producer of titanium forgings, considered moving into the Ti mill products field, which is currently more active than the aerospace industry (466). Despite a moderate decline in industrial markets since the peak year of 1980, their Ti market share has increased (463). A return to positive growth was expected for 1983, with a mature growth rate in succeeding years.

Table XXVI. World Ti sponge production (short tons)

	1982	1983 (est.)
United States	15,600	13,000
Japan	18,600	12,000
United Kingdom	2,600	2,000
China	1,500	1,500
USSR	44,000	44,000
Total	82,300	72,500

GSA stockpiling.—In a generally depressed market year, much attention was focused on government purchases for the National Defense Stockpile. The stockpile goal for Ti sponge is 195,000 short tons, of which only 25,000 short tons were on hand at mid-year (478).

The Federal Emergency Management Agency (FEMA) requested a waiver from the Trade Agreements Act, calling for commodity purchases based on worldwide bidding, to aid domestic producers (479). The request was denied by U.S. Trade Representative, William Brock (480). However, Brock advised that the import duties on foreign sponge, as much as 17.5%, would be considered by the General Services Administration (GSA) in evaluating bids.

In August, GSA announced plans to buy 4,500 short tons of titanium, in either sponge or granule form, in lots of 500 short tons or more (481). Eight bidders, including five with domestically produced material, submitted bids ranging from \$2.92 to \$6.25 per pound (482). Shortly thereafter, low bidder Billiton Metals, offering Ti from the United Kingdom Deeside plant, filed a protest, claiming exemption from import duties because of GATT agreements (483). Oregon Metallurgical also protested, claiming that GSA should invoke the Buy American Act (484).

Contracts were let to one domestic and two foreign suppliers (485). Timet was awarded 1,000 tons at \$3.57/lb, while Philipp Brothers, acting as agent for Japanese producers, received 3,000 tons at \$3.20/lb. Billiton was awarded 500 tons at \$2.92/lb (486). However, RMI Company immediately filed a request for a temporary restraining order to block the sale, and a protest against GSA's actions based on several grounds (487, 488). In December, the injunction was denied (489). RMI's protest also accused Japanese producers of price collusion (490).

Near year end, RMI followed up its earlier protest with a dumping petition against Japanese and British producers, claiming they were selling at less than fair market value (491, 492). The action was supported by Oremet (493). It is interesting to note that, in an unrelated action, four European producers of Ti milled products pushed ahead with anti-dumping proceedings against U.S. and Japanese producers, who have captured 60% of the European market (494, 495).

Titanium Development Association.—The first official titanium association in the U.S. was established in December (496). An earlier meeting, organized by seven leading Ti companies, invited participation from 300 firms to form an organization to focus on "publicity, industry marketing, market and product development, statistics, and education" (497). The 71 active members of the TDA include producers, fabricators, extruders, distributors, and recyclers (498).

Zinc.—Production and prices.—While zinc markets were soft at the beginning of the year, a general upturn in the economy near year's end produced an upsurge in both prices and production plans.

In April, Kidd-Creek, banking on the market upturn, canceled late 1982 plans to close its zinc mine in Timmins, Ontario (499). The company announced that the plant would maintain full production throughout 1983. Cominco's Trail smelter and Kimberley mine in British Columbia were idled by a strike in June (500). On June 12, the strike ended, and resumption of the former production level of 260,000 short ton/yr of zinc was planned (501). As a reaction to continuing losses, Cominco announced that 1983 capital spending would be held to \$120 million, compared with \$230 million in 1982 and \$480 million in 1981. However, modernization of the Trail zinc plant continued.

Minera Mexico began marketing Special High Grade and Prime Western zinc in the U.S. in July (502). Full-scale shipments were expected by year's end. The Mexican electrolytic refinery, partially owned by ASARCO, has a 114,000 metric ton/yr capacity.

Inspiration Mines purchased three zinc mines in Tennessee from Gulf and Western's Natural Resources

Group in July (503). The mines had been shut down earlier by Gulf and Western. Production startup at the mines was targeted for January, 1984, following engineering feasibility studies. Gulf and Western announced that it was writing down its interest in its Natural Resources Group, including a wholly-owned mine in Friedensville, Pennsylvania, and two other Tennessee mines jointly owned with Union Miniere.

U.S. Steel's zinc mine in Jefferson City, Tennessee, reached full production in September, following a 10 month shutdown (504). The reopening of the mine, with a capacity of 36,000 ton/yr of concentrate, was based on a favorable labor contract settlement and improved market conditions. In December, St. Joe Resources Company increased the capacity and operating rate of its Monaca, Pennsylvania, zinc smelter and refinery by 15,000 ton/yr to 100,000 ton/yr (505). The capacity increase was made possible by a \$2.5 million plant modernization program.

Asarco announced a three-point program to enable it to restart the Corpus Christi zinc refinery, idled in October, 1982 (506). Sufficient zinc concentrates had been lined up from Asarco's operations in Tennessee, Mexico, and Canada. In addition, Asarco was attempting to negotiate a power rate of about 35 mill, compared to the current 60 mill rate. The last point involved negotiating a labor contract with a more economical work schedule and productivity rules. Talks were scheduled to begin in December.

At mid-year, U.S. zinc producers were all posting 40¢ prices for benchmark High-Grade zinc (507). Despite considerable uncertainty in the firmness of producer price quotes at that time, zinc prices began an upward movement for the rest of the year. Backed by strong U.S. Mint tender bid quotes and tight Special High Grade supplies, the price of zinc reached 49¢/lb in October, the highest price in two year (508).

Throughout much of the year, the European Economic Community debated a plan to move towards closing of 100,000 ton/yr of zinc capacity (499). The closure plan, submitted by six major companies, called for payments to companies which agreed to shut down plants without replacing closed capacity until 1986 (509). Under the plan, producers were allowed to modernize plants without increasing capacity. However, in November, the plan was informally abandoned as a general upturn in the economy, particularly in the U.S., increased demand and raised zinc prices by one-third over year-earlier levels (506). Because the plan was never formally approved, there is some doubt that it could be reactivated, even if producers wish to reconsider closure (510).

Domestic Zn production statistics (528) are shown in Table XXVII. Although domestic consumption of zinc increased in 1983, production declined slightly, as imports increased. The estimated world mine production and reserve base (511) is shown in Table XXVIII.

Demand.—U.S. zinc consumption showed a dramatic 12% increase in the first quarter of 1983, against a year earlier, to 188,000 tons (512). However, economic recovery was slower elsewhere, as European first-quarter consumption fell 1% to 399,000 tons and Japanese consumption rose only 1.7% to 176,000 tons. Smelter stocks of zinc began to decline markedly before mid-year, dropping from year-earlier levels by 30% in Europe and almost 25% elsewhere (513). Tight supplies of Special High Grade zinc in Japan, as North Korean zinc was diverted to China (514), led to

Table XXVII. Domestic zinc production statistics
(thousand metric tons Zn content)

	1982	1983 (est.)
Mine production	300	280
Primary slab zinc production	254	262
Zn metal exports	17	16
Zn ore and concentrate exports	77	55
Producer and consumer stocks, year end	106	90

Table XXVIII. World mine production and reserve base of zinc (thousand metric ton)

	Mine production		Reserve base
	1982	1983 (est.)	
United States	300	280	53,000
Australia	629	670	39,000
Canada	1,033	1,040	56,000
Mexico	232	245	8,000
Peru	541	575	12,000
Other market economy countries	1,878	1,950	90,000
Centrally planned economies	1,397	1,400	32,000
Total	6,010	6,160	290,000

importation from nontraditional sources, such as Spain, at premium prices (515).

By September, zinc supplies had improved, reducing the chances of "panic" buying by zinc alloyers, although premium prices were common (516). Supplies were tighter on the East and West Coasts than in the Midwest. Merchant zinc was available at producer prices, with little discounting.

Sixteen companies submitted bids for a U.S. Bureau of the Mint tender for up to 23 million lb of zinc (515). While other companies generally bid at or above the prevailing producer price of 43¢ per pound, New Jersey Zinc offered to sell 10 million lb at prices from 38.7¢ to 39.7¢/lb. There was evidence of the firming zinc market in October, as another 10 million lb BuMint tender prompted bids ranging from 46.4 to 51.4¢/lb, and some major producers, particularly in Canada, did not submit bids because of other supply commitments (517). A further 25 million lb Mint tender was made late in the year (518, 519).

Markets.—Optimism in the zinc market was fueled by growing use in coinage, construction, and other markets (520). The new U.S. penny, containing 97.4% zinc, was expected to consume 45,000 tons of zinc in 1983. Galvanizing remains the largest use of zinc, accounting for roughly one-half of total consumption (520, 521). The galvanizing market was predicted to increase 38% by 1985, to 521,000 ton/yr (521).

Two new galvanized products show promise. Galvalume, a coated steel sheet developed by Bethlehem Steel in 1978, has begun to attract interest in the construction industry (521). Galvalume contains 43.5% Zn, 55% Al, and 1.5% Si (522). Galfan, a galvanized coating with 95% zinc and 5% aluminum-mischmetal alloy, was developed by ILZRO to compete with the lower-zinc Galvalume (521, 522). Galfan has been licensed to 19 companies worldwide, including three in Japan (522). However, commercial production of Galfan has been limited, with none yet produced in North America (522). ILZRO has made getting an on-shore producer "a number one priority" (523).

Galvanized parts in automobiles also represent a fast growing market (524, 525). Auto industry usage of galvanized steel sheet and strip may increase from 1982's value of 1.25 million tons to 3 million tons by 1987 (523). members, gutters, and building parts are also being considered for galvanizing, in a drive to increase product lifetime and reduce maintenance cost (523). Other uses include highway guard rails and lights, waste-treatment plants, and utility transmission towers.

Galvanized parts in automobiles also represent a fast growing market (524, 525). Auto industry usage of galvanized steel sheet and strip may increase from 1982's value of 1.25 million tons to 3 million tons by 1987 (523). The average U.S. 1983 model car contained 273 lb of precoated steel in the form of one- or two-sided galvanized, or Zincrometal accounting for 5.34 lb/unit of zinc. Chrysler's new T-van, however, uses 1,012 lb of precoated steel per unit. Future auto industry goals, including no rust perforation for 10 yr and no cosmetic rust for 5 yr, indicate a growing trend towards precoated steel.

Further increasing the automotive market for zinc, Ford Motor Company's Lincoln-Mercury division was ex-

pected to replace plastic grilles on 1985 model Cougar cars with a full zinc diecast grille (526). The move was believed to be the first time in a decade that such a grille has been specified for any U.S. car. In recent years, considerable movement from zinc die castings to plastic had occurred in a drive to reduce automobile weight.

Of the major nonferrous metals, only zinc was expected to gain enough in consumption in 1984 to pull up its market (527). Improved prices and lower stocks were predicted if world consumption grows at the expected 5.4% rate. The total zinc supply was expected to remain in deficit or in balance for 5 yr longer (514). The major source of increased U.S. supplies will come from imports, with import market sharing reaching 70% by 1988. Brass and bronze requirements, accounting for about 14% of zinc usage, will grow at about 2%/yr, while diecasting needs will increase at 2.8%/yr, after sharp declines over the last 10 yr.

The Electric Industry

More electricity was generated in 1983 than in the preceding year, reflecting the general economic upturn which was underway by the second half of the year. At the same time, DOE Secretary Donald Hodel claimed that the U.S. was in a better energy position than in 1981 (529). The fourth National Energy Policy Plan shows that total energy efficiency has increased, U.S. resources are being developed more effectively, oil prices have declined, and U.S. dependence on foreign oil supplies has decreased.

However, the report, "The Future of Electric Power in America," based on a \$2.5 million study begun by the Reagan administration, warns of U.S. power shortages in the 1990's (530). The report cited the need to construct new power plants, to supply demand which is predicted to grow for the remainder of the century. Sources such as solar energy and cogeneration, together with conservation, were viewed as playing only a minor role in the nation's electricity future. Other forecasters were criticized for assuming that high energy prices have permanently reduced demand for electricity, which the study considered to be an increasingly popular energy form.

In contrast, the Industrial Electricity Consumers Resource Council told the Department of Energy it believes expected load growth can be met by planned generating capacity additions (530). Thus, while it is generally agreed that electricity use will increase, a consensus on the magnitude and type of effort required, and thus a comprehensive energy plan, continues to be elusive.

Power generation in the U.S. (531).—After plunging sharply in 1982, electricity generation increased in 1983. However, as Table XXIX shows, U.S. electricity generation was still below 1980 and 1981 values. Despite its unpopularity, nuclear electricity continued to increase, as did electricity from both coal and hydropower. Electricity from natural gas continued a downward trend extending over the last four years.

The fossil fuel mix used in electricity generation has changed markedly in the last decade. As shown in Table XXX, the use of coal has jumped 60% in the last decade, while oil usage has dropped by well over 50%, with most of the decrease occurring since 1979. Natural gas usage has fluctuated considerably, showing a less definite historical trend than either coal or oil.

Despite difficult times, the industry managed to add modestly to its generating capacity, as Table XXXI

Table XXIX. Electricity generated, by type of fuel (531) (billions of kWh)

Year	Nuclear	Coal	Oil	Gas	Total* (Hydro)
1979	255.2	1075.0	303.0	329.5	1967.0
1980	251.1	1162.0	245.6	346.2	2010.4
1981	272.7	1203.2	206.1	345.8	2034.1
1982	282.8	1192.0	146.8	305.3	1926.8
(revised)					309.2
1983	293.7	1259.4	144.5	274.1	1971.7
					332.1

Table XXX. Fossil fuel consumption, by type (531)

Year	Coal (millions of tons)	Oil (millions of bbl)	Gas (millions of ft ³)
1973	388.7	562.5	3660.2
1974	391.2	539.1	3443.4
1975	405.9	506.6	3157.7
1976	448.3	556.5	3080.9
1977	477.0	624.2	3191.2
1978	481.6	635.8	3188.4
1979	527.1	523.3	3490.4
1980	569.5	420.2	3681.6
1981	596.8	351.1	3640.2
1982 (rev.)	593.7	249.8	3225.5
1983	625.2	245.5	2910.8

shows. Fifty percent of this increase was from nuclear plants, begun many years ago, which continue to come on stream. The bulk of the remaining increase came from steam generation plants. Capital expenditures for generation, transmission, distribution, and other requirements are shown in Table XXXII. Total expenditures were about the same as in 1982, and a similar level is expected in 1984.

Electric utility industry forecast (532).—In September, 1983, *Electrical World* released its 34th annual forecast for the electric utility industry. As the general economy improved and the recent dislocations in industry trends showed signs of abating, a healthy recovery was forecast. The assumptions used in earlier forecasts were examined, and, in some cases, revised.

A synopsis of some important points from the *Electrical World* forecast follows.

Electricity requirements, 1984-2000.—The U.S. economy is becoming more electrified as its direct dependence on fossil fuels declines. During the past decade, according to DOE Secretary Donald P. Hodel, while "use of all nonelectric forms of energy dropped by 15%, we increased our [use of] electricity by 20%." A forecast of electric utility sales for the remainder of the century is given in Table XXXIII (532).

Industrial electric usage is predicted to rise over the next few years, after the fluctuations of the late 1970's and early 1980's. Projections are shown in Table XXXIV (532). A transition in the industrial sector, from goods to services, is not expected to change the mix of utility energy sources. Electricity's percentage of total utility sales in the industrial sector should remain at 35%-40%.

Forecasts of electricity needs by the aluminum industry have been revised downward from earlier projections. It was concluded that there is little incentive for aluminum producers to develop additional domestic capacity, due to the rate of power cost increases and the availability of lower cost power in other countries.

Industrial self-generation has declined markedly for more than a decade, from 98 billion kWh in 1972 to an estimated 49 billion kWh in 1983. Beginning in the middle of this decade, a modest increase in industrial self-generation is expected, as shown in Table XXXIV.

Projections of consumer electricity use have been revised downward from earlier values, following a drop in 1983, despite an unusually hot summer. A trend towards energy saving appliances will slow demand growth, as consumers look for ways to lower their energy costs without disrupting their lifestyles. A gradual return of the housing market is predicted. As gas deregulation and the attendant price rises occur, the competitiveness of electric space heating will improve. However, other factors, politics, will restrain the number of electrically heated

homes added in the late 1980's and 1990's. Predicted residential electricity usage is given in Table XXXV.

During the remainder of the century, multiple-family dwellings will predominate over single-family dwellings. The electric heat pump will come to dominate the electric-heat housing market.

The predicted penetration of electric vehicles into the transportation market has been drastically revised downward for the remainder of the century. The forecast was cut from about 1 million units on the road in the year 2000 to only about 200,000. This resulted in a 5 million kWh reduction in the amount of electricity required. The lack of a serious effort by major manufacturers to push an electric vehicle, coupled with the lack of improvement in EV performance needed for broad consumer acceptance, were both factors in the downward revision.

In the commercial market, conservation and energy management will reduce electricity usage. However, greater office electrification, through communication and data handling growth, are expected to produce an overall positive growth.

Electricity peak-demand requirements are seen as increasing at an annual compound rate of about 3% for the next decade, and only slightly less thereafter. Growth will taper off to about 2.6% by 2000. This trend toward lower percentage growth arises from four major factors. First, conservation will increase in all market segments. Second, energy-intensive industries, such as aluminum production, will increasingly move abroad. Third, the rate of population growth will continue to decline. Finally, societal changes such as the shift of households from single family to smaller, multifamily residences will result in lower electricity requirements.

The main barrier to strong long-term growth of electric energy is its cost, which will probably rise at a rate slightly faster than general inflation.

Generating capacity.—Recent protests over "imprudent" construction of new capacity have added to the movement, already underway because of financial pressure, to cancel capacity additions.

Planned increases in the number of large coal-fired units, today still in the planning stages, will not alleviate shortages that may develop in several parts of the country later in this decade. Licensing each plant will take about 3 yr, and construction will take an additional 5 yr. In 1982, utilities placed no orders for major units. As a result, there will be very small capacity additions during the period 1987 to 1992, as only units already under construction are brought on line.

Insufficient reserve margins will develop in some regions. These will probably be alleviated by installing substantial quantities of combustion turbines.

The forecast for generating capacity additions is given in Table XXXVI. A forecast of annual capital expenditures by the electric utility industry is given in Table XXXVII.

Conventional fossil fuels.—The electric utility industry is faced with the prospect of massive capital expenditures to replace aging generation facilities. Money could be saved, however, if the operation of existing plants could be extended safely and economically. Toward that end, EPRI announced a 4 yr program to develop and test methods for extending the life of fossil fuel power plants by as much as 50% (533). The work will be funded by EPRI and carried out by project teams that will include turbine and boiler manufacturers, an engineering firm, and a host utility. Higher costs for money and equipment, uncertain demand growth, and difficulty in siting new

Table XXXI. U.S. installed generation capacity, by plant type (531) (MW)

Year	Total	Hydro	Steam	Nuclear	Gas turbine	Internal combustion
1982 (rev.)	650,105.0	78,128.3	452,011.3	63,042.0	51,972.3	5131.1
1983	658,172.6	78,967.6	455,507.7	67,073.4	51,627.9	4996.0

Table XXXII. Total U.S. electric power system capital expenditures (3) (millions of dollars)

Year	Generation		Transmission		Distribution		Miscellaneous		Total	
	Total industry	Investor owned	Total industry	Investor owned	Total industry	Investor owned	Total industry	Investor owned	Total industry	Investor owned
1980	25,688	17,875	3,280	2,279	5,307	4,365	1,650	1,297	35,925	25,816
1981	25,823	19,217	3,168	2,326	4,950	4,169	1,882	1,543	35,823	27,254
1982	29,836	22,287	3,497	2,595	5,228	4,432	1,654	1,347	40,216	31,161
1983	29,922	23,741	3,200	2,463	5,381	4,698	1,600	1,332	40,103	32,234

Table XXXIII. Electric utility sales forecast (billions of kWh)

	Residential	Change	Industrial	Change	Commercial	Change	Other	Change	Total	Change
1972	511.4	6.7%	639.5	7.9%	361.9	8.4%	65.0	6.7%	1577.7	7.6%
1973	554.2	8.4%	687.2	7.5%	396.9	9.7%	64.9	-0.1%	1703.2	8.0%
1974	555.0	0.1%	689.4	0.3%	392.7	-1.1%	63.7	-1.9%	1700.8	-0.1%
1975	586.1	5.6%	661.6	-4.0%	418.1	6.5%	67.2	5.6%	1733.0	1.9%
1976	613.1	4.6%	725.2	9.6%	440.6	5.4%	70.8	5.2%	1849.6	6.7%
1977	652.3	6.4%	757.2	4.4%	469.2	6.5%	72.1	1.8%	1950.8	5.5%
1978	679.2	4.1%	782.1	3.3%	480.7	2.5%	75.8	5.2%	2017.8	3.4%
1979 ¹	696.0	2.5%	817.6	4.5%	494.7	2.9%	76.1	0.4%	2084.4	3.3%
1980	734.4	5.5%	793.8	-2.9%	524.1	5.9%	73.7	-3.0%	2126.1	2.0%
1981	730.5 ^r	-0.5%	819.6 ^r	3.3% ^r	521.7 ^r	-0.5% ^r	78.9	6.9%	2150.7	1.2%
1982	729.2 ^r	-0.2%	770.7	-6.0%	514.1	-1.5%	79.6	0.9%	2093.6	-2.7%
1983*	735.1	0.8%	777.0	0.8%	539.5	5.0%	78.8	-1.0%	2130.5	1.8%
Forecast										
1984	749.2	1.9%	822.6	5.9%	553.0	2.5%	80.0	1.4%	2204.7	3.5%
1985	769.8	2.8%	861.0	4.7%	573.5	3.7%	81.5	1.9%	2285.5	3.7%
1986	793.2	3.0%	894.2	3.9%	594.1	3.6%	83.0	1.9%	2364.5	3.5%
1987	820.0	3.4%	921.5	3.1%	614.9	3.5%	84.6	1.9%	2441.0	3.2%
1988	848.1	3.4%	948.5	2.9%	635.8	3.4%	86.2	1.9%	2518.6	3.2%
1989	875.6	3.3%	976.1	2.9%	656.2	3.2%	87.8	1.9%	2595.7	3.1%
1990	902.0	3.0%	1004.2	2.9%	675.9	3.0%	89.4	1.9%	2671.5	2.9%
1995	1028.2	2.5%	1147.7	3.0%	766.9	2.5%	98.2	1.9%	3041.0	2.7%
2000	1157.5	2.3%	1296.8	2.4%	863.5	2.4%	108.2	2.0%	3426.0	2.3%

* Estimated.

^r Revised.¹ Basis for determining sales data revised starting 1979.Source: Edison Electric Institute, *Electrical World*.

Table XXXIV. Industrial electric usage forecast (billions of kWh)

	Manufacturing	Primary aluminum production	DOE	Total industrial	Generation by industrial plants	Utility industrial sales	Primary aluminum production (thousand ton)
1972	637.8	74.2	25.7	737.7	98.2	639.5	4122
1973	668.1	81.5	33.4	783.0	95.8	687.2	4529
1974	660.8	88.2	35.4	784.4	95.0	689.4	4903
1975	635.8	68.5	36.6	740.9	79.3	661.6	3879
1976	692.5	73.2	41.8	807.6	82.4	725.2	4251
1977	723.8	76.0	40.9	840.7	83.5	757.2	4539
1978	740.4	79.8	34.3	854.4	72.3	782.1	4804
1979 ¹	767.9	82.4	32.7	883.0	65.3	817.6	5023
1980	746.6	82.8	24.9	854.2	60.4 ^e	793.8	5130
1981	775.9 ^r	77.2	22.6	875.7 ^r	56.0 ^e	819.6 ^r	4948
1982	743.8	54.9	22.6	821.3	50.6 ^e	770.7	3609
1983*	742.3	60.0	23.8	826.1	49.1	777.0	4000
Forecast							
1984	772.0	69.0	30.0	871.0	48.4	822.6	4600
1985	799.8	71.0	38.7	909.6	48.6	861.0	4800
1986	826.2	74.0	42.8	943.1	48.9	894.2	5000
1987	852.7	73.0	45.1	970.8	49.3	921.5	5000
1988	880.0	73.0	45.6	998.6	50.1	948.5	5000
1989	908.2	73.0	45.9	1027.2	51.1	976.1	5000
1990	938.3	72.0	46.0	1056.3	52.1	1004.2	5000
1995	1098.5	74.2	33.6	1206.3	58.7	1147.7	5300
2000	1254.9	75.9	33.6	1364.4	67.7	1296.8	5500

* Estimated.

^e Estimated by EEL.^r Revised.¹ Basis for determining sales data revised starting in 1979.Source: Edison Electric Institute; U.S. Department of Energy; The Aluminum Association; McGraw-Hill Publications; Department of Economics, *Electrical World*.

units have made extending the normal 35-40 yr plant life economically attractive.

The increased importance of coal as a fuel has led to new technical developments in coal combustion technology. Energy and Minerals Research Company in Exton,

Pennsylvania, has announced an ultrasonic coal grinder which blasts coal with sound waves, leading to stress fatigue and fracture into small, uniform particles (534). The primary motivation for developing the process was the huge amount of energy, some 29 billion kWh/yr, con-

Table XXXV. Residential electric usage forecast (1983 dollars)

	Mid-year customers (millions)	Housing starts, private ¹ (thousands)	Use per customer (kWh)	Revenue per kWh (cents)	Average annual bill (dollars)	Residential sales (billion kWh)	Heating sales (billion kWh)	Residential revenue (million dollars)
1972	66.5	2357	7691	4.96	382.06	511.4	88.0	25407
1973	68.6	2045	8079	4.88	394.20	554.2	97.2	27042
1974 ²	70.2	1338	7907	5.33	421.68	555.0	100.2 ²	29597
1975	71.7	1160	8176	5.54	452.42	586.1	103.1 ²	32437
1976	73.3	1538	8360	5.66	472.83	613.1	115.7 ²	34676
1977	75.0	1987	8693	5.85	508.81	652.3	126.0 ²	38182
1978	76.8	2020	8849	5.80	513.69	679.2	132.8 ²	39428
1979 ³	78.7	1745	8843	5.87	518.64	696.0	143.1 ²	40822
1980	81.4	1292	9025	6.22	560.63	734.4	140.4 ²	45623
1981	83.0	1084	8825	6.44	568.64	730.5	155.1	47067
1982	84.2	1062	8696	6.75	587.20	729.2	157.5	49241
1983*	85.3	1200	8623	7.00	603.86	735.1	164.4	51479
Forecast								
1984	86.9	1400	8621	7.35	633.91	749.2	170.3	55087
1985	88.5	1600	8698	7.72	671.55	769.8	177.4	59435
1986	90.1	1800	8808	8.09	712.68	793.2	185.5	64179
1987	91.6	1700	8952	8.46	756.93	820.0	193.9	69334
1988	93.2	1600	9104	8.79	800.57	848.1	201.8	74575
1989	94.7	1400	9247	9.10	841.61	875.6	208.8	79696
1990	96.3	1300	9371	9.37	878.48	902.0	214.7	84556
1995	103.3	1300	9959	10.50	1045.98	1028.2	239.4	107994
2000	110.7	1300	10461	10.99	1150.18	1157.5	258.4	127271

* Estimated.

¹ Revised.² Excluding mobile homes.³ Includes space heating usage from all rate schedules. 1974-1980 figures revised based on 1980 census data.⁴ Basis for determining sales data revised starting in 1979.Source: Edison Electric Institute; *Electrical World*.

Table XXXVI. Forecast of generating capacity additions (MW) based on date of commercial operation)

	Conventional hydro	Pumped hydro	Fossil steam ¹	Nuclear steam	Combustion turbines, I.C.	Total
1973	1594	3622	24,217	5,770	5066	40,269
1974	720	1087	18,874	9,196	6236	36,113
1975	2064	305	21,726	7,281	3523	34,900
1976	300	235	11,908	4,457	2600	19,500
1977	1438	485	16,506	6,530	1647	26,609
1978	4265	841	14,454	2,162	2213	23,935
1979	2632	1200	10,999	1,874	370	17,075
1980	1078	257	14,214	2,887	446	18,882
1981	290	250	6,505	4,286	624	11,955
1982	900	1189	9,125	3,126	600	14,940
1983*	390	254	6,530	4,040	260	11,474
Forecast						
1984	494	1250	6,335	15,538	0	23,617
1985	834	1050	8,575	14,630	10	25,099
1986	583	1350	3,985	6,650	0	12,568
1987	351	848	3,604	9,855	80	14,738
1988	157	620	4,211	3,460	50	8,498
1989	120	—	4,965	3,550	0	8,635
1990	375	—	4,006	1,250	200	5,831
1991	676	—	4,241	(840)	500	5,417
1992	—	—	4,713	0	700	5,413
1993	—	—	9,496	0	500	9,996
1994	—	—	15,830	0	200	16,030
1995	—	—	17,114	0	200	17,314
1996	—	—	24,498	0	200	24,698
1997	—	—	24,798	0	400	25,198
1998	—	—	20,850	0	500	21,350
1999	—	—	19,900	0	200	20,100
2000	—	—	20,900	0	200	21,100

* Estimated.

¹ Geothermal, wind, waste capacity is included in fossil steam, 1981-2000.

sumed in the coal comminution industry. Saving 10% of the energy cost would represent \$150 million/yr in cost reduction.

A Limestone Injection Multistage Burner (LIMB) system was claimed by the Environmental Protection Agency to be the lowest-cost retrofit alternative for controlling both NO_x and SO_x emissions from coal plants (535). EPA's objectives are to achieve 50%-60% reductions of both SO_x and NO_x, from uncontrolled levels, on retrofit installations. On new systems, EPA is seeking reductions of 70%-80% in NO_x, and 70%-90% in SO_x. For both retrofit and new systems, EPA would like to

achieve those goals for at least \$100/kW less than flue-gas desulfurization. EPA will test several coals of different composition to determine if some are less likely to produce fly ash. The largest plant to use the LIMB technology thus far has been a 100 million BTU/hr unit.

Synthetic fuels.—The U.S. synfuels effort sputtered in 1983. Few synfuel projects now remain active, and are not expected to come close to the original national goal of 2 million bbl/day of synfuels by the early 1990's (536).

The barriers to synfuel development do not seem to involve the fundamental question of whether such develop-

Table XXXVII. Utility capital expenditure forecast (millions of 1983 dollars)

	Generation	Transmission	Distribution	Miscellaneous	Total
1972	21,039	4,642	8,620	1,679	35,980
1973	22,338	5,010	9,066	1,872	38,286
1974	23,291	4,565	8,525	1,908	38,289
1975	21,624	4,043	6,917	1,667	34,251
1976	26,851	4,759	7,351	1,752	40,713
1977	29,166	4,744	6,910	1,509	42,329
1978	31,453	3,922	6,229	1,744	43,348
1979	32,671	4,444	7,000	1,751	45,866
1980	30,861	3,933	6,340	1,944	43,078
1981	32,933	3,373	7,204	1,744	45,254
1982	33,800	3,700	6,700	1,750	40,172
1983*	29,922	3,200	5,381	1,600	40,103
Forecast					
1984	26,000	3,000	7,585	1,650	38,235
1985	20,500	2,500	7,620	1,375	31,995
1986	14,800	2,250	8,100	1,130	26,280
1987	13,300	2,000	8,277	1,060	24,637
1988	10,400	1,900	8,442	935	21,677
1989	9,600	1,900	8,500	900	20,900
1990	9,600	2,100	8,600	915	21,215
1991	18,200	2,500	8,830	1,330	30,860
1992	24,900	3,200	8,975	1,665	38,740
1993	31,500	4,300	9,190	2,025	47,015
1994	37,800	5,200	9,265	2,350	54,615
1995	41,860	5,700	9,460	2,565	59,585
1996	43,700	6,000	9,560	2,665	61,925
1997	42,650	5,800	9,770	2,620	60,840
1998	42,900	5,800	9,955	2,640	61,295
1999	46,200	6,200	10,060	2,810	65,270
2000	46,200	6,200	10,260	2,820	65,480

* Estimated.

ment must ultimately occur. Nor are technology, availability of capital, or future demand projections the problems. Bernard Lee, President of the Institute of Gas Technology, cites "institutional barriers" (536). Oil price is one such barrier, as the oil exporting countries attempted to peg prices below the break-even point for competing alternatives. However, an IGT study considered imported oil's effects, such as balance of trade effects on inflation on the economy, leading Lee to peg the real cost of imported oil at about \$75/bbl, rather than the market price of \$29.00.

Martin Roberts, Vice-President of Lehman Management, cited communication problems among groups that might contribute to a synfuels industry as another barrier (536). About 80% of western oil shale lies under public lands, and no firm plan has emerged for exploiting it. Also, recent oil price drops have proven that they are more elastic than formerly believed. This, according to Roberts, has reduced the sense of urgency in future energy planning, to the detriment of alternative resources. Environmental and socioeconomic problems have also been troublesome. Satisfying them can raise project costs from 40% to 100%, thus dampening investor interest. In the West, allocating scarce water to synfuel plants is a concern (536).

In many cases, especially in the West, the federal government not only controls mineral rights in leased areas, but has regulatory powers over water rights, and contributes to project subsidies. Roberts points to this as a difficult situation for private competitors to accept. Even under the best conditions, Roberts says, the investment community sees synfuels as essentially a regulated utility with marginal economics (536).

Government and industry have relegated synfuel development to limbo for another decade, or until another energy panic occurs, according to Rex Ellington of the University of Oklahoma (536). Ellington sees recent inflation, high interest rates, and eroded worker productivity as hampering the synfuel effort.

Ellington faults the present administration for encouraging unrestrained oil well drilling as a panacea for the country's oil problems, although the approach has not kept reserves and production from declining. Congress was also criticized for deserting synfuels by shying away from price supports and tax breaks. Finally, industry was

seen as being too single-minded on one line of thought for future development (536).

As a way of restoring synfuel development, Ellington suggests a "beachhead philosophy," involving development of a small technical beachhead, which could be expanded rapidly as required (536).

"World Production of Synthetic Fuels: A Realistic Assessment," a report prepared for *The Economist*, projects a generally bleak outlook, with some bright spots, for worldwide synfuel development (537). The report, based on information gathered from 500 synfuels projects, predicted world synfuel production of about 653,000 bbl/day by 1990. The outlook for coal-based synfuels from liquefaction and gasification was pessimistic. More than 800,000 bbl/day (oil equivalent) of coal gasification projects were canceled in 1982. Abandonment of their Colony oil shale project by Exxon and Tosco last year hurt the investment climate. The report projects a worldwide shale oil production range of 75,000-392,000 bbl/day by 1990, the upper figure based on completion of all projects now under construction. Tar sand and heavy oil recovery looks promising. World production, according to the report, could reach 323,000 bbl/day by 1990.

The third solicitation for synfuels proposals by the U.S. Synthetic Fuels Corporation attracted 46 proposals for loan guarantees, price supports, and other aid (538). Seventeen of the proposals were for new projects; the remainder were resubmissions. Of the projects, 10 were for coal liquefaction plants, nine for coal gasification, 13 for oil shale, and 11 for tar sands.

In May, Senator Pete Domenici (R-NM) introduced a bill to provide significant tax benefits for synfuels projects (539). The bill would extend the qualification deadline for a 10% energy tax credit, which expired on January 1, 1983, to June, 1987.

The value of tax incentives was underscored at a Senate hearing when a Kidder, Peabody, and Company official accused the federal government of being a "fickle partner" (537). Joseph Schell told the Senate Finance Energy Subcommittee that federal tax laws were a better stimulus than Synfuels Corporation loan-and-price guarantees.

A call for increased government assistance came from the National Research Council, which proposed that the United States should initiate a national research and development test fuels program (540). NRC suggested that

the program, which would be administered by the Defense Department, should include a process development-scale refinery. The report committee noted that the past 10 yr of synfuel development have not produced any currently profitable options, and concluded, "there is an urgent need for stronger leadership and commitment by the federal government in recognition of the increasing importance of this issue to future national security."

The Environmental Policy Institute, however, criticized the federal synfuels program, concluding in a report that proposed projects will not make a significant contribution to the nation's energy security (541). Technical reliability and cost-efficiency problems were cited. EPI concluded that energy conservation, fuel switching, and increased domestic oil and gas production have been much more effective. EPI contends that the synfuel industry is not ready for commercialization and cannot exist without huge federal subsidies.

Coal gasification.—The coal gasification outlook, already clouded by earlier project cutbacks, was further dimmed in 1983. The Department of Energy, in an interim report to Congress, said that it sees "no significant U.S. market for coal gasification processes" (542). There is doubt that the BI-GAS coal gasification pilot plant in Homer, Pennsylvania, will be converted to a national gasification test facility, as Congress had suggested earlier.

The Board of Directors of the U.S. Synthetic Fuels Corporation, responding to a request from sponsors of the Great Plains coal gasification project, voted against giving additional financial aid to the project (543). The corporation's analysis found that no financial crisis of the project was likely until 1988.

Despite the pessimistic scenario, a number of efforts forged ahead. The Gas Research Institute plans to spend \$7.6 million on coal gasification research in 1984, to complement \$9.5 million in federal spending and \$4.0 million from industry (537). GRI projects that coal gasification production will reach 0.3 quadrillion BTU by 1990, and 0.6 quadrillion BTU by 2000. Over the next five years, GRI plans to spend \$61.5 million on coal gasification research and development.

The Allis-Chalmers KilnGas coal gasifier, at its Woods River Project in Illinois, was tested for a four day run in June (537). No significant problems were encountered. In further tests, the plant will reach its full 600 ton/day capacity, with the low BTU product gas used in an Illinois power company's 50 MW boiler on site. The \$155 million project is sponsored by 12 utilities, the state of Illinois, EPRI, and Allis-Chalmers. In August, Allis-Chalmers began processing Illinois no. 6 high sulfur coal at Woods River (541).

Lurgi announced that it had developed a new system to allow its commercial coal gasifier to accept coal fines (544). The Lurgi gasifier, the most successful commercial system, has been combined with a circulating fluidized bed reactor and a gas liquor evaporation system to form an integral coal gasification plant. The Lurgi system will accept up to 40% coal fines, and produces substantially less waste liquor than a conventional Lurgi SNG plant.

Exxon has operated a 1 ton/day gasifier demonstration unit at its Baytown facility since 1979. The process accomplishes gasification and methanation in a large fluid bed gasifier. Development has now reached a stage where the final step is to scale up to commercial size (545).

Coal liquefaction.—A marketing and pricing study indicated that, despite recent difficulties, the total market for coal liquids could reach 226,000 bbl/day by the late 1990's (540). The analysis projected that six to ten large plants, with capacities of 25,000-40,000 bbl/day and nine to nineteen smaller plants in the range of 1000 bbl/day capacity will be built by the end of the century. However, it was cautioned that tough air pollution standards could have a serious adverse impact on the coal liquids business.

According to Emil Parente of Fluor Engineers, coal-derived liquids can be produced at a price competitive

with crude oil, but only if a number of criteria are met (545). These include: a liquid methanol product slate; lignite as the coal feedstock; indirect liquefaction technology; coproduction of a natural gas substitute; and a plant location on the Gulf Coast.

DOE's Pittsburgh Energy Technology Center, citing a need for new ideas on liquefaction, issued a solicitation for proposals (544), anticipating receipt of proposals for bench-scale research on new approaches or innovations on existing ideas. Earlier, DOE awarded \$7 million to 27 university and three industrial laboratories to study coal behavior during combustion, liquefaction, and gasification (546). Meanwhile, using lignin, high yields of liquefied coal were obtained at lower-than-normal temperatures, at the University of Connecticut (547). In the presence of lignin and an acid catalyst, yields of 19%-43% were obtained at 300°C. Without lignin, only about 5% conversion was obtained. Liquefaction reactions are usually run at temperatures above 400°C.

The Electric Power Research Institute contracted C-E Lummus to "screen and identify promising two-step liquefaction configurations" (542). The results of the Lumus study will be compared with one-step liquefaction processes.

Despite refusal of its project financing application by the Synthetic Fuels Corporation, A-C Valley Corporation decided to continue its Scrubgrass coal-to-gasoline project in Pennsylvania (542).

Many of the important developments in coal liquefaction during 1983 involved development of coal-water fuel (548). Occidental Research Corporation announced that it would enter a joint venture to produce a coal-water fuel. COM Energy, an Occidental subsidiary in Jacksonville, Florida, with a 15 ton/hr coal-oil facility, will be converted to coal-water production, with an initial capacity of 2000 bbl/day. Occidental and others believe that coal-water mixture can be produced for about \$3.30 per million BTU in commercial quantities.

Sohio also entered the coal-water mixture (CWM) business, purchasing Advanced Fuels Technologies from Gulf and Western (549). Formed in 1980, AFT has produced more than 500 tons of CWM in a 1 ton/hr pilot plant in Bridgeport, Connecticut. Using AFT's technology, Sohio will build a 50 ton/hr demonstration plant.

Several other coal-liquid ventures have been announced recently (548). These include joint efforts by Allis-Chalmers and Fluidcarbon International AB of Sweden, Foster-Wheeler Corporation and A. B. Carbogel of Sweden, and Babcock and Wilcox, Ashland Oil Incorporated, and Slurrytech, Incorporated. Electric Fuels Corporation of St. Petersburg acquired Comco, which has been producing a coal-oil mixture for Florida Power Corporation.

Oil Shale and tar sands.—In November, the Synthetic Fuels Corporation was considering four oil shale projects for future funding (544). Geokinetics, Incorporated was requesting \$50-\$100 million in loan and price guarantees for its \$30 million, 1000 bbl/day Seep Ridge project in Utah. Also under consideration was the 14,100 bbl/day Paraho-Ute project involving Paraho, Sohio, Texas Eastern, Signal Cos., and Raymond International. Union Oil's Phase II 20,000 bbl/day expansion of Parachute Creek, Colorado, was regarded as politically volatile because of Union's prior \$400 million in DOE aid. The final entry was the 16,500 bbl/day plant in White River, Utah, sponsored by Phillips, Sunoco, and Sohio.

Oil production for 1983 by Syn-Crude, the largest oil sands plant in the world, was estimated at 35-40 million barrels (540). Syn-Crude Canada, Ltd. can now produce 109,000 bbl/day, and announced a \$1.2 billion expansion program to increase production by about 20,000 bbl/day.

A new heavy oil and tar sands recovery process was successfully tested over a 2-3 yr period by James Wade Engineering, Limited of Toronto (549). Five Canadian and two or three U.S. oil companies have expressed interest in the process. Bitech of Toronto and Wade hope to con-

struct a 1000 bbl/day test pilot plant next year to process heavy oils and then tar sands.

Nuclear generation.—The nuclear power industry has been beset by numerous problems in recent years. Rapidly escalating plant costs and the long lead time for design, approvals, licensing, and construction have made it difficult to bring new plants on line. The lack of a satisfactory solution to the waste disposal problem and recent events such as the Three Mile Island malfunction have generated adverse publicity and stiffened public resistance.

To regain public acceptance and investor confidence, the industry must sustain an unblemished safety record in the future, according to Nunzio Palladino, chairman of the Nuclear Regulatory Commission (550). According to Palladino, time is the ally of the nuclear industry, provided that there are no episodes such as what happened at Three Mile Island in the future. Acknowledging that the future of the industry ultimately will be decided by the public and its elected representatives, Palladino called for a balanced relationship among the utilities, regulators, legislators, courts, and the general public.

Early in 1983, the Nuclear Regulatory Commission proposed new nuclear plant safety goals (551). The goals will be reviewed for two years before becoming final. However, NRC's Advisory Committee on Reactor Safeguards faulted the proposed guidelines for excluding a statement that social risks ought to be "as low as is reasonably achievable," and for failing to consider long-term health effects on individuals.

NRC also approved a package of legislative changes for consideration by Congress (552). The requested changes include allowing NRC to grant advance approval to standardized reactor designs and possible sites for future plants. The number of issues that could be raised at licensing hearings for new plants would also be limited, and administrative judges presiding over the hearings would be prevented from raising their own questions on potential safety problems.

Hans Bethe of Cornell University, speaking for Scientists and Engineers for Secure Energy, criticized the NRC's adversarial approach and called for a simplification of governmental regulations (553). Procedural and legislative aspects of the nuclear regulatory process, according to Bethe, have expanded to overshadow technical matters.

In April, the Supreme Court provided both good and bad news to the nuclear industry (554). The court unanimously ruled against a citizen's group challenge to NRC's decision not to consider their concerns in deciding whether to restart the undamaged reactor at Three Mile Island. In a second case, however, the court unanimously upheld a California law imposing a moratorium on new nuclear plant construction until the federal government has developed and approved a technology for permanently disposing of nuclear wastes.

After a three-month trial, a suit involving General Public Utilities, operator of the Three Mile Island reactor damaged in 1979, and Babcock and Wilcox, the reactor manufacturer, was settled out of court (555). Under the agreement, GPU will receive \$37 million, while both parties agreed that "neither has established the other as the cause" of the accident. The settlement, in the form of rebates on Babcock and Wilcox services, will be used to clean up the reactor.

Metropolitan Edison, owner of the Three Mile Island Power Plant, was charged by a federal grand jury in Harrisburg, Pennsylvania, with manipulating and falsifying test results on radiation leaks from the plant's cooling system (556). According to the charges, the company lied about leak rate data during the period immediately before the accident in order to avoid plant closure.

As a result of the introduction of new, capital-intensive nuclear plants, residential electric rates are projected to rise sharply in the 1980's and early 1990's (557). The enormous capital cost of nuclear plants now coming into ser-

vice has not, in general, been absorbed into utility rate bases during construction. The capitalization of a large nuclear plant can equal or exceed the previous capitalization of a utility. In the case of the Long Island Lighting Company, protests have already arisen over the possibility of a 50% rate increase attributable to its Shoreham Plant.

Despite the many problems, an increasing fraction of the world's electricity is supplied by nuclear energy. The International Energy Agency, noting that 21 nuclear reactors were hooked into electricity grids during 1982, says that about 10% of the world's electricity is obtained from nuclear reactors (558).

An engineering demonstration of a wet chemistry process produced 10 kg of high purity uranium oxide from scrap nuclear fuel (559). The recycling process, first developed ten years ago by General Electric, was demonstrated by Westinghouse Hanford, in Richland, Washington.

Breeder reactor (560).—After keeping the Clinch River Breeder Reactor project alive for several years, the Senate voted to delete \$1.5 billion in funds, earmarked for the project, from the fiscal 1984 supplemental appropriations bill. The House did not even consider Clinch River funding. Cost overruns have plagued the project. Initial 1971 cost estimates of \$400 million for the reactor have now ballooned to \$4.5 billion. DOE, expressing disappointment, will begin an orderly phase-out of the project, which has cost \$1.7 billion to date.

Fusion.—In tests at the Massachusetts Institute of Technology, the fusion energy break-even point was exceeded for the first time (556). The experiment reached a temperature of about 17×10^6 °C and an energy confinement time of about 50 ms. Self-sustaining fusion reactions will require a temperature of about 2×10^8 °C. The reaction will produce large quantities of high velocity neutrons, posing materials problems that remain to be overcome.

A Center For Fusion Engineering will be established at the University of Texas at Austin (551). Two other organizations engaged in fusion research have already been established at the University. The three units will be able to address experimental, theoretical, and engineering problems of thermonuclear fusion.

Fuel cells (561).—According to Graham Hagey, DOE's fuel cell program manager, the first commercial prototype fuel cells should be available by about 1986. Commercialization is the result of more than 20 yr of work, and several hundred million dollars in expenditures by government and private industry. During the 1983 fiscal year, total U.S. spending on fuel cell development was estimated at about \$100 million.

Under a program sponsored by the Gas Research Institute, DOE, 21 U.S. gas utilities and two Japanese utilities, 49 new 40 kW fuel cell plants are planned. All will use phosphoric acid cells developed by United Technologies Corporation.

Westinghouse is developing two 7.5 MW plants with air-cooled phosphoric acid cells, incorporating work by Energy Research Corporation. Inglehard Industries has tested a 5 MW methanol-air integrated phosphoric acid system. Japan, under the direction of MITI, has a national research and development program for phosphoric acid, molten carbonate, alkaline, and solid oxide fuel cells. The initial goal is to operate a 1 MW phosphoric acid demonstration unit in 1986.

A major near-term task in phosphoric acid technology development is to lower the present cost, approximately \$4000/kW. In comparison, a coal-fired power plant costs \$1450-1700/kW. EPRI hopes to reach an installed cost of \$600-\$700/kW (1981 dollars) by the end of the decade, by increasing operating temperature and pressure, and through commercial volume manufacturing economies. A Con-Edison spokesman indicated that a commercial fuel cell cost of around \$1000/kW could open up a potential utility market of thousands of megawatts.

Three current studies sponsored by EPRI and three utilities are examining coal gasification coupled with fuel cells. The molten carbonate fuel cells are about 45% efficient for electricity production, and produce high grade heat. Commercialization, however, is several years behind acid cells, the largest test so far being a 2 kW cell stack run by United Technologies. A 10 kW demonstration unit was reported to be scheduled for 1983.

Solar energy conversion.—Using a technology developed by Stanford Ovshinsky of Energy Conversion Devices, production of amorphous solar cells has begun in Japan (562). In a continuous roll-to-roll process, amorphous silicon is deposited onto stainless steel sheets. Production is being carried out by Sharp-ECD Solar, Incorporated, which is a joint venture between Japan's Sharp, Incorporated, and Standard Oil (Ohio), which has invested in ECD. Sharp plans to use the amorphous material in solar-powered calculators while ECD will use 1000 ft rolls for field testing of large-scale devices in the U.S.

The world's largest solar electric generating station was begun at a Mojave Desert site belonging to Southern California Edison Company (563). A joint venture of Edison with Luz International Limited, the generating station will use 560 line-focus parabolic trough reflectors to heat fluid circulating through the system. The first 13 MW phase of the planned 43 MW generating plant is expected to begin producing power for Edison customers in late 1984.

At Sandi National Laboratories, the first U.S. solar central receiver to use molten salt in an electricity generator system began operation (563). The molten salt is a 60/40 mixture of sodium nitrate and potassium nitrate. It is used to transfer heat to a water supply, making steam to drive a turboelectric generator. Prototype system testing will continue through the spring of 1984. Full capacity operation will provide 750 kW of electricity, enough for 200-300 typical homes.

A new photoelectrochemical cell uses silicon electrodes, and is capable of storing the generated electricity (564). The cell, developed at the Amoco research center in Naperville, Illinois, has produced a 12% conversion efficiency and a 0.59V output. Operating lifetimes have been increased from minutes to weeks. The lifetime of the cell has been extended by coating the silicon electrodes with a few angstroms of platinum to reduce corrosion. Efficiency increases were obtained by using a doped oxide layer, containing alumina or magnesia, on the silicon surface just below the Pt coating.

Nonaqueous electrolyte photoelectrochemical cells, using gallium arsenide phosphide photanodes, have produced 13.2% efficiency (565). The cells were developed at Stanford University. Providing that water is excluded from the cell, the photoanode is apparently stable. Another Stanford-developed cell uses an n-type silicon photoanode that operates at 10.1% efficiency. The Stanford cells have the highest efficiencies reported to date for nonaqueous cells, which commonly operate at only 1%-2% efficiency.

The Texas Instruments Solar Energy System (TISES) is the only reported commercial photoelectrochemical program. The novel photoelectrodes begin with the production of 0.25-0.4 mm diam silicon microspheres. In a faster, improved production method, TI drops molten silicon onto a rapidly spinning disk, which throws off the small droplets. When illuminated, the cells produce hydrogen at the cathode and bromine at the anode. Conversion efficiencies as high as 13% have been produced. The system also provides low grade thermal heat. Overall (electrical plus thermal) system efficiency is about 7%. TI hopes to increase that efficiency to 8-10% before the system is commercialized, possibly as soon as 1990 (566).

Environmental issues.—Acid rain.—The problem of acid rain, a major environmental issue, became highly politicized in 1983. Friction developed within the U.S., as regional disputes arose over the origin, magnitude, and resolution of the problem. On a larger scale, the problem

developed international overtones, especially between the U.S. and Canada. With the approach of a presidential election year in 1984, the question of acid rain became a campaign issue.

U.S. Senator Gary Hart (D-CO), a candidate for the Democratic presidential nomination, accused the U.S. government of ducking the acid rain issue (567). "There has been much better willingness on the Canadian side to discuss the common problem, to lay out some kind of time frame . . . than we have seen from the American administration," Hart said. According to Hart, it would take a decade to achieve his goal of a 50% emission reduction. Hart quantified the acid rain problem, claiming that it currently costs the U.S. \$5 billion per year.

The National Clean Air Coalition, composed of 12 environmental and labor groups, plus the League of Women Voters, called on the Reagan administration to push a tough acid rain control program (568). The request was made in a letter to the President, after EPA head William Ruckelshaus admitted that a revised acid rain policy was being delayed by sharp differences within the administration (569).

In November, the 27-member New England congressional caucus proposed a program for comprehensive acid rain control legislation (570). The bipartisan bill proposed a 50% reduction in sulfur dioxide emissions, an estimated 12 million tons, by 1993. The proposal would spread the costs of cleanup among electric consumers in the 48 contiguous states. Consumers would pay a surcharge of \$0.75-\$1.50 per month on electricity bills. The move thrust acid rain into the New England states as a major campaign issue.

The issue was especially sharply focused in New Hampshire, where a citizen's task force got the acid rain question onto municipal ballot forms (571). Voters responded overwhelmingly in favor of cutting emissions.

The results of a Louis Harris poll, taken nationwide, showed that 90% of those surveyed felt that acid rain was a serious problem (572). More than 60% favored installing air pollution scrubbers on dirty industries, such as power plants, and 70% would pay \$100 per year in taxes for pollution control. From 63% to 68% of those polled felt that U.S. governments and industries were not doing enough to combat pollution. However, in states which figure to be hard hit by the required cleanup, a different opinion emerged. In Ohio, where pollution limits are often equated with loss of jobs, a survey commissioned by Ohio Edison Company revealed that 65% of Ohioans favored improving the economy at the expense of the environment (573). Only 19% favored the environment at the expense of jobs.

In Canada, the public response to a Gallup poll was decisive (574). Of those polled, 86% favored restrictions to reduce acid rain. Only 6% opposed such restrictions.

The U.S. and Canadian Chambers of Commerce issued a joint statement in December outlining a unified program for dealing with acid rain (575). The first step would involve charting emission reductions that could be expected from full implementation of clean air laws in both countries. If these emission reductions were insufficient, the groups recommended developing a cost-effective control plan with positive economic incentives. The incentives would include accelerated depreciation and write-off of unadaptable, old plants.

Despite intensifying pressure, the Reagan administration remained split over the acid rain issue through the year. All of the cleanup strategies pose problems (576). Putting the cleanup burden on utilities emitting the most pollution would, according to utility industry groups, raise electric bills by as much as 50% (576). Environmental groups, however, claim the actual costs are far lower, i.e., 2.5%-10%. Spreading costs nationwide is unacceptable in the West, where the problem is perceived to be less serious.

At the year end, EPA's Ruckelshaus believed that the administration had only a few weeks to decide on an approach to the acid rain problem (577). Ruckelshaus antic-

ipated the need to testify before Congress when it returned to session in January of 1984. Still, Canadian Ambassador Alan Gotlieb estimated the chances of a U.S. policy announcement before the presidential election at less than 50%, and felt that any new policy would not go as far as Canada wants (578).

In Canada, Milan Nastich, chairman of Ontario Hydro, advocated use of nuclear power, rather than scrubbed coal power, as the better solution to acid rain (579). In 1981, Ontario Hydro pledged to cut acid gas emissions to 300,000 ton/yr within a decade. According to Nastich, Ontario Hydro continues to follow through on its program. A series of mishaps, resulting in Ontario Hydro nuclear plant shutdowns during the summer, put an additional 18,000 tons of sulfur dioxide into the atmosphere (580). An additional 10,000 tons was expected if the Pickering 2 nuclear generator remained shutdown through November for repairs.

In addition to electric generation plants, many of Canada's acid rain sources are related to the mining industry. The Canadian Coalition on Acid Rain proposed that Inco Limited and Canadian taxpayers should spend up to \$525 million to reduce pollution from Inco's Sudbury smelter (581). The coalition called for an 86% reduction in Inco's allowable sulfur dioxide release, from 1997 ton/day to 274 ton/day (582). The statement was backed by the United Steelworkers of America, representing Inco workers, who advocated tax breaks or low cost loans to the financially pressed nickel producer (583).

Behind the political and economic issues, fundamental questions remain on the nature of the problem itself. In the eastern U.S., man-made SO₂ and NO_x emission are 50 to 100 times higher than natural ones (584). The 20 largest coal-fired plants are claimed to account for 20%-25% of all sulfur dioxide emissions in the region (584), yet much of the acid rain problem is not caused locally. Recent studies indicate that the Midwest is the major contributor to acid rain damage in the eastern U.S. and Canada (585). Canadian SO₂ sources, although large, appear to be less significant contributors to the problem in that region, because of prevailing air patterns. When Inco's smelter, Canada's SO₂ source, was shut down, only a slight drop in air pollution occurred (585).

While the acid rain problem is widely acknowledged, some uncertainties persist. Perhaps the best U.S. records on the subject were made in New York State from 1965 to 1975, by the U.S. Geographical Survey (586). No trend in acidification was discerned. Swedish scientists, who have studied the problem longer, likewise have found no trend (586). Richard Funkhouser, former director of the EPA's Office of International Activities, called for more scientific study to clarify the problem before enormous expenditures are made for clean-up (586).

CO₂/climate (587).—Carbon dioxide, a "greenhouse" gas, absorbs little of the shortwave insolation spectrum. It does, however, absorb infrared radiation from the Earth's surface and atmosphere. As a result, increasing atmospheric concentration of CO₂, arising primarily from fossil fuels, could lead to a warmer climate.

A two-year study by the National Research Council concluded that atmospheric CO₂ will most likely double from present levels to 600 ppm late in the next century. The average world temperature increase will be 1.5°-4.5°C, with the lower half of the range more probable. A sea level rise of about 70 cm/century, compared with the current 10-20 cm/century, could occur as a result of ice melting and thermal expansion of the oceans.

However, the study also questioned whether CO₂ should be the central issue, rather than the climate change itself. Over the timespan considered, there may be changes in climate not resulting from human activity. In addition, other greenhouse gases, such as chlorofluorocarbons and nitrous oxide, could have significant effects.

A similar report, more sharply focused, was issued by the EPA. The report addressed the issue of whether specific policies, to limit fossil fuel use, would delay tem-

perature increases over the next 120 yr. Using a "best guess" baseline scenario, atmospheric CO₂ levels of 590 ppm were predicted by 2060. Associated with the CO₂ increase was a temperature rise of 2°C by around 2040, and about 5°C by 2100.

The study applied various policy alternatives to the baseline scenario to determine their effects, finding that only one significantly postponed a 2°C warming. A ban on coal, instituted by 2000, which the study concluded was not feasible, would delay the 2°C temperature rise until 2055. Banning both coal and shale oil would delay it an additional 10 yr.

The EPA study pointed towards three areas of future work, continuing the \$80 million already spent by federal agencies on the CO₂ problem. Research on improving the ability to adapt to a warmer climate should be accelerated. Effects of greenhouse gases other than CO₂ should be determined. Also, uncertainty about the thermal sensitivity of the atmosphere needs to be reduced.

REFERENCES

1. *Information Chimie*, pp. 177-194, June, 1983.
2. *Chemical Week*, p. 25, Feb. 15, 1984.
3. *Chemical Marketing Reporter*, pp. 5, 54, April 11, 1983.
4. *Ibid.*, pp. 53, 54, April 18, 1983.
5. *Chemical Purchasing*, p. 40, July, 1983.
6. *Chemical and Engineering News*, pp. 9, 10, Sept. 12, 1983.
7. *Chemical Marketing Reporter*, pp. 3, 27, March 7, 1983.
8. *Ibid.*, p. 7, July 25, 1983.
9. *Chemical Engineering*, p. 41, Aug. 22, 1983.
10. *Chemical Marketing Reporter*, p. 56, Aug. 15, 1983.
11. *Chemical Engineering*, p. 52, Sept. 5, 1983.
12. *Paper Trade Journal*, p. 48, Jan. 15, 1984.
13. *American Metal Market*, p. 17, Aug. 19, 1983.
14. *Journal of Commerce*, p. 226, Aug. 15, 1983.
15. *Chemical Marketing Reporter*, p. 7, Nov. 7, 1983.
16. *Chemical and Engineering News*, p. 8, Oct. 17, 1983.
17. *Chemical Week*, p. 13, Oct. 19, 1983.
18. *Chemical Marketing Reporter*, p. 41, Dec. 26, 1983.
19. *Ibid.*, p. 34, Dec. 12, 1983.
20. *Chemical Week*, p. 9, Aug. 24, 1983.
21. *Chemical Engineering*, p. 29, Sept. 19, 1983.
22. *Ibid.*, p. 9, Jan. 9, 1984.
23. *Chemical Week*, p. 13, Aug. 10, 1983.
24. *Ibid.*, p. 14, March 16, 1983.
25. *Chemical Marketing Reporter*, p. 30, April 18, 1983.
26. *Ibid.*, p. 29, July 11, 1983.
27. *Chemical Week*, p. 15, Aug. 10, 1983.
28. *Ibid.*, p. 37, Sept. 14, 1983.
29. *Chemical Marketing Reporter*, pp. 3, 39, Dec. 5, 1983.
30. *Ibid.*, p. 34, Nov. 7, 1983.
31. *Chemical Week*, p. 32, May 11, 1983.
32. *Chemical Marketing Reporter*, p. 29, Dec. 19, 1983.
33. *Chemical Week*, pp. 65, 66, 68, Dec. 21, 1983.
34. *Ibid.*, p. 37, Dec. 7, 1983.
35. *Japan Chemical Week*, pp. 4, 6, June 16, 1983.
36. *Ibid.*, p. 2, Nov. 3, 1983.
37. *Chemical Week*, p. 20, Dec. 21, 1983.
38. *Chemical Marketing Reporter*, pp. 5, 43, Sept. 5, 1983.
39. *Japan Chemical Week*, p. 1, Feb. 17, 1983.
40. *Chemical Marketing Reporter*, p. 21, May 16, 1983.
41. *Chemical Week*, p. 49, May 25, 1983.
42. *Chemical Marketing Reporter*, p. 5, July 4, 1983.
43. *Chemical Week*, p. 45, July 13, 1983.
44. *Paper Trade Journal*, p. 31, Nov. 11, 1983.
45. *Chemical Purchasing*, p. 38, July, 1983.
46. *Chemical Marketing Reporter*, pp. 5, 32, Sept. 19, 1983.
47. *Ibid.*, p. 7, Jan. 16, 1984.
48. *Ibid.*, pp. 26, 27, Dec. 26, 1983.
49. *Chemical Week*, p. 29, Dec. 14, 1983.
50. *Chemical Marketing Reporter*, pp. 7, 30, May 9, 1983.
51. *Paper Trade Journal*, pp. 33-45, Aug. 30, 1983.
52. *Chemical Purchasing*, pp. 42-47, Feb., 1983.
53. *Chemical Marketing Reporter*, p. 25, Jan. 30, 1984.
54. *Chemical Week*, pp. 26-29, Feb. 1, 1984.
55. *Ibid.*, p. 50, Jan. 5, 1983.
56. *Ibid.*, p. 85, Oct. 5, 1983.
57. *Chemical Marketing Reporter*, p. 46, Sept. 26, 1983.
58. *Ibid.*, p. 35, Aug. 15, 1983.
59. *Chemical Week*, p. 39, July 27, 1983.
60. *Pulp and Paper*, p. 96, Nov., 1983.
61. *Paper Journal*, p. 48, Jan. 15, 1984.
62. *Chemical Marketing Reporter*, p. 22, Aug. 29, 1983.
63. *Japan Chemical Week*, pp. 4, 6, July 14, 1983.
64. *Chimie Actualities*, p. 4, April 18, 1983.

65. *Chemical Marketing Reporter*, pp. 7, 60, June 6, 1983.
66. *Chemical Week*, p. 19, June 29, 1983.
67. *Chemical Engineering*, p. 47, June 13, 1983.
68. *Ibid.*, p. 37, May 30, 1983.
69. *Ibid.*, p. 25, July 25, 1983.
70. *Ibid.*, p. 30, Sept. 19, 1983.
71. *Europa Chemie*, p. 366, July 28, 1983.
72. *European Chemical News*, p. 26, July 18, 1983.
73. *Chemistry and Industry*, p. 489, July 4, 1983.
74. *Chemical Engineering*, p. 74, Nov. 14, 1983.
75. *European Chemical News*, p. 21, Aug. 29, 1983.
76. *Chemical Week*, p. 20, Aug. 24, 1983.
77. *Chemical Engineering*, p. 45, Oct. 3, 1983.
78. *Ibid.*, p. 26, July 25, 1983.
79. *Ibid.*, p. 29, July 25, 1983.
80. *Chemical Marketing Reporter*, p. 7, Sept. 19, 1983.
81. *Japan Chemical Week*, p. 7, Oct. 20, 1983.
82. *Chemical Week*, p. 47, Sept. 21, 1983.
83. *Japan Economic Journal*, p. 12, Sept. 6, 1983.
84. *Japan Chemical Week*, p. 1, Sept. 22, 1983.
85. *Chemical Week*, p. 42, June 22, 1983.
86. *Japan Economic Journal*, p. 16, Aug. 16, 1983.
87. *European Chemical News*, p. 17, Aug. 29, 1983.
88. *Chemical Week*, p. 38, Jan. 18, 1984.
89. *Chemical and Engineering News*, p. 20, Jan. 16, 1984.
90. *Chemical Marketing Reporter*, pp. 5, 43, Jan. 16, 1984.
91. *Chemical Week*, p. 40, Feb. 23, 1983.
92. *Chemical Marketing Reporter*, pp. 7, 37, Feb. 21, 1983.
93. *European Chemical News*, p. 21, March 7, 1983.
94. *Chemical Engineering*, p. 37, Feb. 21, 1983.
95. P. J. Kienholz, "Restoring Chlor-Alkali Profits Through Advanced Technology," paper presented at American Chemical Society Meeting, Washington, DC, August 31, 1983.
96. *Chemical Marketing Reporter*, pp. 5, 52, March 21, 1983.
97. *Water Engineering and Management*, pp. 36-38, April, 1983.
98. *Chemical Week*, p. 80, Jan. 25, 1984.
99. *Chemical and Engineering News*, p. 23, Nov. 7, 1983.
100. *Chemical Marketing Reporter*, pp. 4, 16, Nov. 7, 1983.
101. *Chemical Week*, p. 37, June 22, 1983.
102. *Chemical and Engineering News*, p. 11, July 18, 1983.
103. *Chemical Marketing Reporter*, pp. 9, 30, Feb. 6, 1984.
104. *Ibid.*, p. 35, Feb. 13, 1984.
105. *Chemical Week*, p. 9, Feb. 22, 1984.
106. *Chemical Marketing Reporter*, p. 34, Oct. 17, 1983.
107. *Ibid.*, p. 27, Feb. 28, 1983.
108. *Ibid.*, p. 30, March 14, 1983.
109. *Ibid.*, p. 30, March 21, 1983.
110. *Ibid.*, p. 27, March 7, 1983.
111. *Chemical Week*, p. 20, March 9, 1983.
112. *Chemical Marketing Reporter*, pp. 7, 62, Oct. 10, 1983.
113. *Chemical and Engineering News*, p. 8, Oct. 17, 1983.
114. *Chemical Week*, p. 13, Oct. 19, 1983.
115. *Chemical Marketing Reporter*, p. 7, Nov. 7, 1983.
116. *Journal of Commerce*, p. 22B, Nov. 8, 1983.
117. *Chemical Marketing Reporter*, pp. 34, 35, Oct. 17, 1983.
118. *Chemistry and Industry*, pp. 130-134, Feb. 21, 1983.
119. *Chemical Week*, p. 9, Sept. 14, 1983.
120. *Chemical Marketing Reporter*, p. 61, Jan. 2, 1984.
121. *Chemical Week*, p. 16, June 15, 1983.
122. *Chemical Marketing Reporter*, p. 60, Oct. 3, 1983.
123. *Chemical Week*, p. 18, Oct. 12, 1983.
124. *Ibid.*, p. 19, Feb. 16, 1983.
125. *Financial Times (London)*, p. 4, Jan. 28, 1983.
126. *Chemical Engineering*, p. 38, Aug. 8, 1983.
127. *Ibid.*, pp. 10, 11, Feb. 21, 1983.
128. *Chemical Industry*, pp. 139-141, Feb. 21, 1983.
129. *Chemical Week*, pp. 22, 23, July 6, 1983.
130. *Chemical Marketing Reporter*, pp. 7, 34, July 18, 1983.
131. *Ibid.*, pp. 5, 28, Oct. 24, 1983.
132. *Chemical Week*, p. 64, Oct. 26, 1983.
133. *Chemical Marketing Reporter*, p. 34, Nov. 7, 1983.
134. *Chemical Week*, p. 38, Nov. 23, 1983.
135. *Chemical Marketing Reporter*, p. 31, Nov. 21, 1983.
136. *Ibid.*, pp. 7, 57, Jan. 24, 1983.
137. *Chemistry and Industry*, p. 89, Feb. 7, 1983.
138. *Chemical and Engineering News*, pp. 23, 24, Feb. 14, 1983.
139. *Chemical Marketing Reporter*, pp. 3, 32, April 18, 1983.
140. *Chemical Week*, p. 18, April 20, 1983.
141. *Ibid.*, p. 42, March 23, 1983.
142. *Chemical Marketing Reporter*, pp. 3, 27, April 4, 1983.
143. *Chemical and Engineering News*, p. 15, July 25, 1983.
144. *Wall Street Journal*, p. 16, March 8, 1983.
145. *Chemical Marketing Reporter*, p. 27, Feb. 6, 1984.
146. *Chemical Week*, p. 9, Jan. 25, 1984.
147. *Chemical and Engineering News*, p. 25, Feb. 28, 1983.
148. *Chemical Week*, p. 23, Feb. 29, 1984.
149. *Chemical Purchasing*, p. 21, Aug., 1983.
150. *Chemical Week*, p. 20, May 4, 1983.
151. *Paper Trade Journal*, p. 47, June 15, 1983.
152. *Chemical Marketing Reporter*, pp. 7, 31, Nov. 21, 1983.
153. *Ibid.*, p. 4, July 25, 1983.
154. *Chemical Week*, p. 36, June 1, 1983.
155. *Chemical and Engineering News*, p. 11, July 4, 1983.
156. *Chemical Week*, p. 13, Aug. 10, 1983.
157. *Pulp and Paper*, p. 183, Aug., 1983.
158. *Chemical Purchasing*, p. 12, Aug., 1983.
159. *Corpus Chemical Report*, p. 4, July 18, 1983.
160. *Journal of Commerce*, p. 22b, June 24, 1983.
161. *Chemical Week*, p. 17, July 6, 1983.
162. *Chemical Engineering*, pp. 44, 47, July 11, 1983.
163. *Pulp and Paper*, p. 208, June, 1983.
164. *PIMA*, p. 4, May, 1983.
165. *Paper Journal*, p. 50, May 15, 1983.
166. *Chemical Marketing Reporter*, p. 7, April 4, 1983.
167. *Corpus Chemical Report*, p. 2, April 11, 1983.
168. *Chemical Week*, p. 20, Sept. 7, 1983.
169. *Corpus Chemical Report*, pp. 2, 3, Sept. 19, 1983.
170. *Chemical Marketing Reporter*, pp. 5, 25, Sept. 19, 1983.
171. *European Chemical News*, p. 24, Jan. 10, 1983.
172. *Chemical Marketing Reporter*, p. 27, March 7, 1983.
173. *Ibid.*, p. 30, March 14, 1983.
174. *Pulp and Paper*, p. 183, Aug., 1983.
175. *Ibid.*, p. 78, Nov., 1983.
176. *Chemical Purchasing*, pp. 17-21, Aug., 1983.
177. *Chemical Week*, p. 19, March 9, 1983.
178. *American Metal Market*, Sept. 21, 1983.
179. *Ibid.*, Oct. 11, 1983.
180. *Forbes*, Jan. 2, 1984.
181. *American Metal Market*, Dec. 15, 1983.
182. *Ibid.*, Oct. 21, 1983.
183. *Ibid.*, Jan. 4, 1984.
184. *New Scientist*, July 14, 1983.
185. *Chemical and Engineering News*, p. 10, Nov. 7, 1983.
186. *Metal Bulletin*, p. 15, Aug. 26, 1983.
187. *Iron Age*, p. 49, Oct. 21, 1983.
188. *American Metal Market*, pp. 1, 8, Jan. 20, 1983.
189. *Journal of Metals*, p. 9, June, 1983.
190. *Business Week*, pp. 106, 107, Aug. 22, 1983.
191. *American Metal Market*, p. 16, June 10, 1983.
192. *Chemical Marketing Reporter*, pp. 7, 16, June 13, 1983.
193. *Wall Street Journal*, p. 25, June 9, 1983.
194. *Chemical Marketing Reporter*, pp. 4, 40, Sept. 12, 1983.
195. *Ibid.*, p. 7, July 11, 1983.
196. *American Metal Market*, p. 2, June 7, 1983.
197. *Ibid.*, p. 2, July 29, 1983.
198. *Chemical Week*, p. 23, Feb. 2, 1983.
199. *Chemical Purchasing*, pp. 11, 12, May, 1983.
200. *Chemical Engineering*, p. 27, Sept. 19, 1983.
201. Reynolds News Release, pp. 1, 2, June 2, 1983.
202. *Chemical Marketing Reporter*, pp. 4, 17, July 25, 1983.
203. *Wall Street Journal*, p. 10, June 3, 1983.
204. Reynolds News Release, pp. 1, 2, July 18, 1983.
205. *American Metal Market*, p. 2, June 3, 1983.
206. *Chemical Marketing Reporter*, p. 4, July 25, 1983.
207. *Journal of Metals*, p. 12, Aug., 1983.
208. Reynolds News Release, pp. 1, 2, Sept. 2, 1983.
209. *American Metal Market*, p. 2, Sept. 7, 1983.
210. *Mining Journal*, p. 189, Sept. 9, 1983.
211. *Chemical Marketing Reporter*, p. 4, Nov. 21, 1983.
212. *Ibid.*, pp. 5, 22, April 18, 1983.
213. *Ibid.*, pp. 7, 28, Oct. 10, 1983.
214. *American Metal Market*, p. 2, Dec. 2, 1983.
215. *Ibid.*, p. 16, June 3, 1983.
216. *Mining Journal*, p. 400, June 10, 1983.
217. *Chemical Engineering*, p. 33, Feb. 21, 1983.
218. *Chemical Marketing Reporter*, p. 5, May 23, 1983.
219. *Ibid.*, pp. 3, 15, Aug. 1, 1983.
220. *Ibid.*, pp. 28, 29, Aug. 8, 1983.
221. *American Metal Market*, p. 6, Nov. 10, 1983.
222. *Chemical Marketing Reporter*, p. 4, Feb. 6, 1984.
223. *Energy*, p. 3, July 18, 1983.
224. *Industry Week*, p. 28, Aug. 8, 1983.
225. *Chemical Marketing Reporter*, pp. 5, 22, June 6, 1983.
226. *Skilling's Mining*, p. 4, July 16, 1983.
227. *Journal of Metals*, p. 13, Aug., 1983.
228. *Financial Post*, p. 8, July 30, 1983.
229. *Corpus Chemical Report*, p. 4, Aug. 1, 1983.
230. *Chemical Purchasing*, p. 12, Sept., 1983.
231. *American Metal Market*, p. 6, Oct. 28, 1983.
232. *Corpus Chemical Report*, p. 4, Oct. 31, 1983.
233. *Chemical Marketing Reporter*, p. 4, Oct. 31, 1983.
234. *Ibid.*, p. 24, July 25, 1983.
235. *Mining Journal*, p. 207, Sept. 16, 1983.
236. *American Metal Market*, p. 16, Aug. 30, 1983.
237. *Chemical Marketing Reporter*, pp. 7, 60, Jan. 23, 1984.
238. *Economist*, pp. 61, 62, Jan. 22, 1983.
239. *Mining Journal*, p. 29, July 8, 1983.
240. *Usine Nouvelle*, p. 45, July 7, 1983.

241. *Information Chimi*, p. 25, June, 1993.
242. *Metal Bulletin*, p. 9, July 1, 1983.
243. *Chemical Marketing Reporter*, pp. 5, 48, July 4, 1983.
244. *Wall Street Journal*, p. 38, June 29, 1983.
245. *Canadian Chemical Processing*, p. 8, Sept., 1983.
246. *Chemical Week*, p. 22, July 13, 1983.
247. *Canadian Chemical Processing*, p. 14, June, 1983.
248. *Chemical Week*, p. 22, Feb. 22, 1983.
249. *Chemical Engineering*, p. 30, Feb. 6, 1984.
250. *Chemical Marketing Reporter*, pp. 4, 32, Jan. 9, 1984.
251. *Wall Street Journal*, p. 41, Feb. 10, 1983.
252. *Chemical Marketing Reporter*, pp. 3, 12, Oct. 24, 1983.
253. *Chemical Week*, p. 24, Oct. 26, 1983.
254. *Mining Journal*, p. 27, Jan. 14, 1983.
255. *Japan Economic Journal*, p. 8, May 10, 1983.
256. *American Metal Market*, p. 6, Feb. 4, 1983.
257. *Business Week*, p. 56, Feb. 14, 1983.
258. *Metal Bulletin*, p. 17, Nov. 1, 1983.
259. *Mining Journal*, p. 311, May 6, 1983.
260. *Financial Times (London)*, p. 14, Feb. 9, 1983.
261. *Alum Zeit*, p. 333, April, 1983.
262. *Chemical Week*, p. 20, June 15, 1983.
263. *Chemical Marketing Reporter*, p. 5, Aug. 29, 1983.
264. *Chemical Week*, p. 19, Feb. 16, 1983.
265. *Chemical Marketing Reporter*, pp. 5, 45, Dec. 26, 1983.
266. *Ibid.*, p. 56, Nov. 21, 1983.
267. *Wall Street Journal*, p. 5, Aug. 29, 1983.
268. *Chemical Marketing Reporter*, p. 30, Sept. 5, 1983.
269. *Wall Street Journal*, p. 6, Sept. 23, 1983.
270. *Chemical Week*, p. 20, Jan. 4, 1984.
271. *Materials Engineering*, pp. 27-44, Oct., 1983.
272. *Chemical Week*, p. 11, April 27, 1983.
273. *Chemical Marketing Reporter*, pp. 4, 19, April 25, 1983.
274. *Ibid.*, p. 23, Jan. 2, 1984.
275. TAFE News Release, pp. 1, 2, Dec., 1983.
276. *Inc.*, pp. 19, 20, April, 1983.
277. *Chemical and Engineering News*, p. 24, May 30, 1983.
278. *Ibid.*, p. 23, June 27, 1983.
279. *Chemical Engineering*, p. 106, Feb. 6, 1983.
280. *Chemical Marketing Reporter*, p. 5, Nov. 7, 1983.
281. *Chemical Week*, p. 39, Nov. 9, 1983.
282. *Chemical Engineering*, p. 31, Dec. 12, 1983.
283. *American Metal Market*, pp. 1, 8, Nov. 3, 1983.
284. *Chemical Week*, p. 43, Sept. 14, 1983.
285. *Light Metal Age*, pp. 20, 21, June, 1983.
286. *Chemical Engineering*, p. 108, Feb. 6, 1984.
287. *NTN Engineering*, p. 21, Aug., 1983.
288. *Waste Age*, p. 10, Oct., 1983.
289. Jack Burger, Engineering and Mining Journal staff, Personal communication.
290. Mineral Industry Surveys, U.S. Bureau of Mines, Dec. 30, 1983.
291. *American Metal Market*, Aug. 4, 1983.
292. *Ibid.*, June 13, 1983.
293. *Ibid.*, Dec. 15, 1983.
294. *Ibid.*, Dec. 26, 1983.
295. *Engineering and Mining Journal*, p. 53, March, 1984.
296. Mineral Industry Survey—Chromium, p. 2, Sept. 8, 1983.
297. Mineral Industry Survey—Chromium, pp. 1-3, Oct. 4, 1983.
298. *American Metal Market*, p. 2, June 16, 1983.
299. *New York Times*, p. 32, March 9, 1983.
300. *Metal Bulletin (London)*, p. 17, June 21, 1983.
301. *American Metal Market*, pp. 1, 8, June 30, 1983.
302. *Ibid.*, p. 21, May 30, 1983.
303. *Metal Bulletin (London)*, p. 15, Feb. 15, 1983.
304. *American Metal Market*, pp. 1, 20, Feb. 15, 1983.
305. *Materials Engineering (Cleveland)*, p. 30, May, 1983.
306. *Industrial Minerals (London)*, p. 57, Feb., 1983.
307. *Journal of Metals*, pp. 30-36, July, 1983.
308. M. Y. C. Woo and R. D. Varjian, *This Journal*, 130, 369C (1983).
309. *Iron Age*, Nov. 25, 1983.
310. Mineral Industry Surveys, U.S. Bureau of Mines, Dec. 30, 1983.
311. *Metal Bulletin*, April 12, 1983.
312. *Ibid.*, July 5, 1983.
313. *American Metal Market*, June 17, 1983.
314. *Metal Bulletin*, June 21, 1983.
315. *Chemical Marketing Reporter*, June 20, 1983.
316. *Metal Bulletin*, July 19, 1983.
317. *Ibid.*, Aug. 26, 1983.
318. *American Metal Market*, Aug. 31, 1983.
319. *Ibid.*, Sept. 30, 1983.
320. *Ibid.*, Nov. 28, 1983.
321. *Ibid.*, July 29, 1983.
322. *Metal Bulletin*, Aug. 9, 1983.
323. *American Metal Market*, Nov. 30, 1983.
324. *The Northern Miner*, Dec. 15, 1983.
325. *American Metal Market*, Aug. 17, 1983.
326. *Metal Bulletin*, July 29, 1983.
327. *American Metal Market*, June 17, 1983.
328. *Metal Bulletin*, Nov. 8, 1983.
329. *The Toronto Globe and Mail*, Dec. 15, 1983.
330. *The Northern Miner*, Nov. 24, 1983.
331. *The Toronto Globe and Mail*, Nov. 29, 1983.
332. *Metal Bulletin*, Dec. 16, 1983.
333. *Ibid.*, Nov. 1, 1983.
334. *The Northern Miner*, Nov. 24, 1983.
335. *Metal Bulletin*, Dec. 13, 1983.
336. *American Metal Market*, Nov. 29, 1983.
337. *Chemical Marketing Reporter*, June 6, 1983.
338. *Metal Bulletin*, April 15, 1983.
339. *Ibid.*, Nov. 11, 1983.
340. *American Metal Market*, June 8, 1983.
341. *Ibid.*, June 24, 1983.
342. *Ibid.*, July 29, 1983.
343. *Ibid.*, Aug. 3, 1983.
344. *Ibid.*, Oct. 6, 1983.
345. *Metal Bulletin*, Oct. 4, 1983.
346. *The Toronto Globe and Mail*, Oct. 25, 1983.
347. *Canada Press*, Dec. 6, 1983.
348. *Winnipeg Free Press*, Oct. 28, 1983.
349. *Engineering and Mining Journal*, Sept., 1983.
350. *New York Times*, Oct. 13, 1983.
351. *Metal Bulletin*, July 12, 1983.
352. *American Metal Market*, July 28, 1983.
353. *The Northern Miner*, Sept. 1, 1983.
354. *American Metal Market*, Oct. 19, 1983.
355. *Ibid.*, Oct. 12, 1983.
356. *Ibid.*, Nov. 8, 1983.
357. *Ibid.*, June 23, 1983.
358. *Newsweek*, Sept. 12, 1983.
359. *American Metal Market*, Oct. 12, 1983.
360. *The Toronto Star*, Nov. 21, 1983.
361. *American Metal Market*, Oct. 3, 1983.
362. *Ibid.*, Sept. 15, 1983.
363. Janis Jolly, U.S. Bureau of Mines, Personal communication.
364. *Engineering and Mining Journal*, March, 1984.
365. *American Metal Market*, pp. 1, 8, May 19, 1983.
366. *Ibid.*, p. 8, Oct. 19, 1983.
367. *Chemical Week*, p. 28, March 16, 1983.
368. *Chemical Marketing Reporter*, p. 27, March 7, 1983.
369. *Journal of Commerce*, p. 22b, March 11, 1983.
370. *Chemical Marketing Reporter*, p. 27, June 13, 1983.
371. *American Metal Market*, pp. 1, 9, Sept. 29, 1983.
372. *Europa Chemie*, p. 379, Aug. 6, 1983.
373. *Inf. Chem. Hebdo*, p. 13, April 29, 1983.
374. *Chemical Week*, p. 39, April 27, 1983.
375. *European Chemical News*, p. 9, Oct. 31, 1983.
376. *Chemical and Engineering News*, p. 24, May 30, 1983.
377. *Industrial Minerals*, pp. 25, 35, Feb., 1983.
378. Mineral Industry Surveys, U.S. Bureau of Mines, Dec. 30, 1983.
379. *American Metal Market*, June 8, 1983.
380. *Metal Bulletin*, June 17, 1983.
381. *Ibid.*, Oct. 28, 1983.
382. *Ibid.*, Sept. 6, 1983.
383. *Ibid.*, Oct. 11, 1983.
384. *Ibid.*, July 1, 1983.
385. *Ibid.*, Aug. 23, 1983.
386. *Ibid.*, Aug. 5, 1983.
387. *Ibid.*, Oct. 18, 1983.
388. *American Metal Market*, Dec. 15, 1983.
389. *Ibid.*, Aug. 1, 1983.
390. *Engineering and Mining Journal*, p. 57, March, 1984.
391. Mineral Industry Survey—Manganese, pp. 1-3, May 9, 1983.
392. Mineral Industry Survey—Manganese, pp. 1, 3-5, June 29, 1983.
393. Mineral Industry Survey—Manganese, pp. 1, 3-6, July 28, 1983.
394. Mineral Industry Survey—Manganese, pp. 1, 3-6, Sept. 8, 1983.
395. Mineral Industry Survey—Manganese, pp. 1-3, Sept. 29, 1983.
396. Mineral Industry Survey—Manganese, pp. 1, 3-5, Nov. 11, 1983.
397. *American Metal Market*, p. 2, April 26, 1983.
398. *Ibid.*, pp. 29, 33, Nov. 21, 1983.
399. *Ibid.*, p. 9, Nov. 23, 1983.
400. *Chemical Week*, pp. 30, 32, Dec. 14, 1983.
401. *World Mining*, p. 64, July, 1983.
402. *American Metal Market*, p. 7, Dec. 20, 1983.
403. *World Mining*, p. 84, Jan., 1983.
404. *American Metal Market*, p. 7, Aug. 12, 1983.
405. *Ibid.*, pp. 2, 10, May 13, 1983.
406. *Ibid.*, p. 2, Sept. 23, 1983.
407. *Ibid.*, pp. 1, 8, June 30, 1983.
408. *Metal Bulletin (London)*, p. 15, Feb. 15, 1983.

409. *Japan Chemical Week*, pp. 4-5, May 19, 1983.
410. *Industrial Minerals (London)*, p. 98, Aug., 1983.
411. *Engineering and Mining Journal*, p. 51, March, 1984.
412. *Financial Times (London)*, p. 32, April 29, 1983.
413. *Metal Bulletin*, p. 11, July 5, 1983.
414. *American Metal Market*, p. 35, May 2, 1983.
415. *Metal Bulletin*, p. 9, June 3, 1983.
416. *American Metal Market*, p. 6, June 3, 1983.
417. *Ibid.*, pp. 2, 11, June 17, 1983.
418. *Ibid.*, p. 2, May 19, 1983.
419. *Ibid.*, p. 2, July 21, 1983.
420. *Metal Bulletin (London)*, p. 11, July 19, 1983.
421. Mineral Industry Survey—Nickel, pp. 1, 5-6, March 8, 1983.
422. *Chemical Marketing Reporter*, p. 53, Nov. 28, 1983.
423. *Mining Journal*, p. 350, Nov. 11, 1983.
424. *World Mining*, p. 74, March, 1983.
425. *Chemical Marketing Reporter*, p. 48, Jan. 10, 1983.
426. *American Metal Market*, p. 2, Aug. 24, 1983.
427. *Chemical Marketing Reporter*, pp. 4, 21, Aug. 29, 1983.
428. *Financial Times (Frankfurt)*, p. 25, Sept. 30, 1983.
429. *American Metal Market*, p. 6, Dec. 29, 1983.
430. *New York Times*, p. 32, March 9, 1983.
431. *American Metal Market*, p. 9, Jan. 18, 1983.
432. *World Mining*, p. 81, Jan., 1983.
433. *Metal Bulletin (London)*, p. 7, July 8, 1983.
434. *American Metal Market*, p. 2, Nov. 11, 1983.
435. *Ibid.*, p. 1, Jan. 3, 1983.
436. *Ibid.*, p. 16, Nov. 23, 1983.
437. *Ibid.*, pp. 1, 16, April 20, 1983.
438. *Ibid.*, p. 16, May 4, 1983.
439. *Chemical Week*, p. 35, May 4, 1983.
440. *World Mining*, p. 33, June, 1983.
441. *American Metal Market*, pp. 1, 16, April 12, 1983.
442. *Metal Bulletin*, p. 9, Nov. 18, 1983.
443. *Ibid.*, p. 5, July 12, 1983.
444. *American Metal Market*, p. 2, June 22, 1983.
445. *Metal Bulletin*, p. 11, Feb. 22, 1983.
446. *American Metal Market*, pp. 1, 10, April 21, 1983.
447. *Ibid.*, pp. 2, 20, Nov. 22, 1983.
448. *New York Times*, pp. 27, 32, Nov. 22, 1983.
449. *Metal Bulletin*, p. 7, Feb. 11, 1983.
450. *Ibid.*, p. 11, Feb. 15, 1983.
451. *European Chemical Week*, p. 103, March 9, 1983.
452. *Metal Bulletin*, p. 11, July 5, 1983.
453. *Ibid.*, p. 13, Oct. 21, 1983.
454. *Ibid.*, p. 12, June 3, 1983.
455. *Metal Bulletin (London)*, p. 15, Nov. 18, 1983.
456. *American Metal Market*, p. 7, Jan. 4, 1983.
457. *Chemical Marketing Reporter—Chemical Business*, p. 8, Nov. 14, 1983.
458. *American Metal Market*, p. 21, March 23, 1983.
459. Dennis Kostick, U.S. Bureau of Mines, Personal communication.
460. Current Industrial Reports—Inorganic Chemicals, U.S. Bureau of the Census.
461. *Chemical Marketing Reporter*, May 18, 1981.
462. M. Y. C. Woo and R. D. Vajian, *This Journal*, 130, 369C (1983).
463. *American Metal Market*, June 24, 1983.
464. *Metal Bulletin*, July 19, 1983.
465. Mineral Industry Surveys, U.S. Bureau of Mines, Dec. 30, 1983.
466. *American Metal Market*, Sept. 29, 1983.
467. *Metal Bulletin*, July 29, 1983.
468. *Ibid.*, Aug. 2, 1983.
469. *Ibid.*, April 8, 1983.
470. *American Metal Market*, June 24, 1983.
471. *Ibid.*, June 10, 1983.
472. *Ibid.*, Sept. 5, 1983.
473. *Ibid.*, Oct. 21, 1983.
474. *Ibid.*, Sept. 26, 1983.
475. *Metal Bulletin*, June 24, 1983.
476. *American Metal Market*, Aug. 22, 1983.
477. *Ibid.*, Oct. 10, 1983.
478. *Ibid.*, Sept. 5, 1983.
479. *Ibid.*, June 20, 1983.
480. *Ibid.*, July 1, 1983.
481. *Metal Bulletin*, July 8, 1983.
482. *American Metal Market*, Aug. 4, 1983.
483. *Metal Bulletin*, Sept. 6, 1983.
484. *Ibid.*, Sept. 20, 1983.
485. *American Metal Market*, Sept. 21, 1983.
486. *Metal Bulletin*, Nov. 4, 1983.
487. *American Metal Market*, Nov. 1, 1983.
488. *Ibid.*, Nov. 7, 1983.
489. *Chemical Marketing Reporter*, Nov. 21, 1983.
490. *American Metal Market*, Dec. 13, 1983.
491. *Ibid.*, Nov. 11, 1983.
492. *Ibid.*, Dec. 5, 1983.
493. *Ibid.*, Dec. 7, 1983.
494. *Ibid.*, Nov. 29, 1983.
495. *Metal Bulletin*, July 26, 1983.
496. *American Metal Market*, Dec. 21, 1983.
497. *Ibid.*, Dec. 12, 1983.
498. *Ibid.*, Aug. 9, 1983.
499. *Metal Bulletin*, April 12, 1983.
500. *Ibid.*, June 17, 1983.
501. *Ibid.*, June 24, 1983.
502. *American Metal Market*, July 1, 1983.
503. *Ibid.*, Sept. 2, 1983.
504. *Ibid.*, Sept. 23, 1983.
505. *Ibid.*, Dec. 12, 1983.
506. *Metal Bulletin*, Nov. 1, 1983.
507. *American Metal Market*, June 6, 1983.
508. *Ibid.*, Oct. 26, 1983.
509. *Ibid.*, June 29, 1983.
510. *Ibid.*, Dec. 14, 1983.
511. Mineral Industry Surveys, Bureau of Mines, Dec. 30, 1983.
512. *Metal Bulletin*, June 17, 1983.
513. *Ibid.*, June 28, 1983.
514. *Ibid.*, Oct. 18, 1983.
515. *Ibid.*, Aug. 2, 1983.
516. *American Metal Market*, Sept. 18, 1983.
517. *Ibid.*, Oct. 20, 1983.
518. *Ibid.*, Oct. 25, 1983.
519. *Ibid.*, Nov. 4, 1983.
520. *Ibid.*, June 1, 1983.
521. *Ibid.*, Aug. 19, 1983.
522. *Ibid.*, Dec. 28, 1983.
523. *Ibid.*, Dec. 21, 1983.
524. *Ibid.*, July 6, 1983.
525. *Ibid.*, Oct. 13, 1983.
526. *Ibid.*, Dec. 19, 1983.
527. *Ibid.*, Nov. 15, 1983.
528. James Jolly, U.S. Bureau of Mines, Personal communication.
529. *Chemical and Engineering News*, p. 18, Oct. 10, 1983.
530. *American Metal Market*, p. 30, June 27, 1983.
531. Mary Going, *Electrical World* editorial staff, Personal communication; *Electrical World*, To be published.
532. *Ibid.*, pp. 55-62, Sept. 1983.
533. *Coal Technology Report*, p. 2, July 11, 1983.
534. *Ibid.*, p. 1, Dec. 12, 1983.
535. *Ibid.*, p. 1, Nov. 28, 1983.
536. *Chemical and Engineering News*, pp. 11-14, Oct. 10, 1983.
537. *Synfuels Week*, pp. 2-3, June 27, 1983.
538. *Chemical and Engineering News*, Jan. 17, 1983.
539. *Synfuels Week*, p. 1, May 30, 1983.
540. *Ibid.*, pp. 1-2, Nov. 21, 1983.
541. *Ibid.*, pp. 3-4, Aug. 29, 1983.
542. *Ibid.*, p. 5, June 6, 1983.
543. *Chemical and Engineering News*, p. 17, Oct. 31, 1983.
544. *Synfuels Week*, p. 1, Nov. 28, 1983.
545. *Chemical and Engineering News*, pp. 26-27, Oct. 24, 1983.
546. *Coal Technology Report*, p. 2, July 11, 1983.
547. *Ibid.*, p. 2, Aug. 22, 1983.
548. *Ibid.*, p. 1, Nov. 28, 1983.
549. *Synfuels Week*, pp. 1-2, Dec. 19, 1983.
550. *Chemical and Engineering News*, p. 5, Nov. 14, 1983.
551. *Ibid.*, p. 22, Jan. 17, 1983.
552. *Ibid.*, p. 32, Jan. 24, 1983.
553. *Ibid.*, p. 28, Dec. 5, 1983.
554. *Ibid.*, p. 35, May 2, 1983.
555. *Ibid.*, p. 13, Jan. 31, 1983.
556. *Ibid.*, pp. 8, 24, Nov. 14, 1983.
557. *Electrical World*, Sept., 1983.
558. *Chemical and Engineering News*, p. 11, Oct. 24, 1983.
559. *Ibid.*, p. 15, Oct. 17, 1983.
560. *Ibid.*, p. 5, Oct. 31, 1983.
561. *Chemical Engineering*, pp. 30, 31, 33, 35, Jan. 24, 1983.
562. *Chemical and Engineering News*, p. 32, Feb. 14, 1983.
563. *Ibid.*, p. 41, Nov. 21, 1983.
564. *Ibid.*, p. 6, May 30, 1983.
565. *Ibid.*, p. 25, March 7, 1983.
566. *Science*, pp. 151-153, Oct. 14, 1983.
567. *The Toronto Sunday Star*, Aug. 7, 1983.
568. *Journal of Commerce*, Oct. 19, 1983.
569. *Chemical and Engineering News*, p. 21, Oct. 24, 1983.
570. *The Toronto Star*, Nov. 16, 1983.
571. *Ibid.*, Dec. 17, 1983.
572. *The Toronto Globe and Mail*, Dec. 14, 1983.
573. *Wall Street Journal*, Dec. 23, 1983.
574. *The Toronto Star*, Dec. 19, 1983.
575. *Journal of Commerce*, Dec. 15, 1983.
576. *Congressional Quarterly*, Oct. 22, 1983.
577. *Newsweek*, Dec. 19, 1983.
578. *The Toronto Star*, Dec. 21, 1983.
579. *Ibid.*, Dec. 31, 1983.

580. *The Toronto Globe and Mail*, Sept. 28, 1983.

581. *Ibid.*, Dec. 21, 1983.

582. *The Toronto Sun*, Dec. 21, 1983.

583. *Sudbury Star*, Dec. 21, 1983.

584. *Chemical and Engineering News*, pp. 28-29, Oct. 10,

1983.

585. *Town and Country Magazine*, Nov., 1983.

586. *The New York Times*, Aug. 18, 1983.

587. *Chemical and Engineering News*, pp. 22-24, Oct. 31, 1983.

Binary and Ternary Diffusion Experiments in Fe_3O_4 , Mn_3O_4 , and Al_2O_3

Peggy A. Barron

Department of Metallurgical Engineering and Materials Science, Carnegie Institute of Technology, Carnegie-Mellon University, Pittsburgh, Pennsylvania 15213

(1983 F. M. Becket Memorial Award Report)

In a binary system, when two solids are placed in planar contact at a fixed temperature and pressure, the Gibbs-phase rule states that there are zero degrees of freedom and therefore the boundary must remain planar. In a ternary system, when two solids are placed in planar contact under the same conditions, there is one degree of freedom remaining, and, therefore, different growth morphologies may result (1). Presently of interest is the parameter controlling this additional degree of freedom. One might expect the faster growing phase to select a morphology that would give a large growth area. In this case, the diffusion coefficients of the system may aid in predicting the morphology.

Schmalzried and Köhne (Institut für Physikalische und Elektrochemie, Technische Universität Hannover, Hannover, Germany) are currently investigating this possibility in ternary oxide systems. To observe the effect of the diffusion coefficients on the growth morphologies, it would be necessary to choose systems in which the diffusion rates are very similar, very different, and intermediate, and then compare the reaction interfaces for each type of system. Due to the lack of diffusion data available on oxides, many combinations must be investigated in order to find acceptable systems. Since diffusion coefficients in oxides generally change rapidly with composition, it may be possible to find a single system in which the diffusion coefficients vary with composition in the manner described above.

The purpose of this investigation is to calculate the interdiffusion coefficients in the Fe_3O_4 - Al_2O_3 and Mn_3O_4 - Al_2O_3 binary systems and plot the composition paths in the Fe_3O_4 - Mn_3O_4 - Al_2O_3 ternary system. The ternary diffusion experiments only include coupling the Al_2O_3 corner with Fe_3O_4 - Mn_3O_4 binary. The diffusion paths connecting the Fe_3O_4 - Al_2O_3 and Mn_3O_4 - Al_2O_3 binaries will be plotted later. The ternary diffusion coefficients may then be calculated using the proper assumptions for the ionic nature of the oxides.

Experimental Procedure

Diffusion couples were prepared with Al_2O_3 and mixtures of Fe_3O_4 and Mn_3O_4 . Due to the small solubilities of Fe_3O_4 and Mn_3O_4 in Al_2O_3 , (2, 3) a pure Al_2O_3 single crystal was used for the ternary as well as the binary diffusion couples. A single crystal of Fe_3O_4 was used in the Fe_3O_4 - Al_2O_3 diffusion couple. Sample preparation of the single crystals included cutting to size (avg $2 \times 5 \times 10$ mm) and polishing. The Al_2O_3 single-crystal samples were polished to $40 \mu\text{m}$ on the contact side and also the opposite side to ensure planar contact in the diffusion couple. The Fe_3O_4 single-crystal samples were polished to $3 \mu\text{m}$ on the contact side and $40 \mu\text{m}$ on the opposite side.

A single crystal of Mn_3O_4 could not be easily obtained; therefore, a sample prepared from Mn_3O_4 powder was used for the Al_2O_3 - Mn_3O_4 diffusion couple. The mixtures

for the ternary diffusion couples were also prepared from powders of the oxides.

The oxide powders were sintered separately at 1420°C in air. These powders were mixed in a ball mill in weight ratios (Fe_3O_4 : Mn_3O_4) of 85:15, 60:40, 40:60, and 20:80. The powder was cold-pressed, with the resulting pellets having densities 40% to 60% of the theoretical densities of the mixtures. The cold-pressed pellets were then enveloped in platinum foil, placed in a graphite matrix, and hot-pressed at 1000°C under a 300 kg load. The hot pressed pellets were 1 cm in diameter and 3-5 mm high with densities of 91% to 99% of the theoretical densities. The pellets were sintered at 1400°C in air for 24h. However, the pure Mn_3O_4 pellets were not sintered because a phase transition caused them to crumble. This phase transition occurred during the diffusion experiment, but due to the pressure applied to maintain contact between the oxides, only cracks appeared in the sample. After sintering, the pellets were cut to size and polished to $3 \mu\text{m}$ on the contact side and $40 \mu\text{m}$ on the opposite side.

The samples were washed in acetone and placed in the diffusion couple as shown in Fig. 1. The diffusion couple was then placed in the furnace at 1400°C in air. The ternary mixtures were allowed to react for 24h and the binary reactions were carried out for approximately 22 and 44h. After cooling rapidly in air, the samples were mounted perpendicular to the reaction plane. Often, the platinum foil and alumina slides could not be easily removed and were also mounted. The samples were polished to $1 \mu\text{m}$, and examined in an electron microscope. Finally, concentration profiles were measured using electron microprobe analysis.

Results of Ternary Diffusion Experiments

The results from the electron microprobe analysis were the x-ray counting rates of the various elements present at each point in the sample. The counting rates were converted to mass fraction and then mole fraction of the cat-

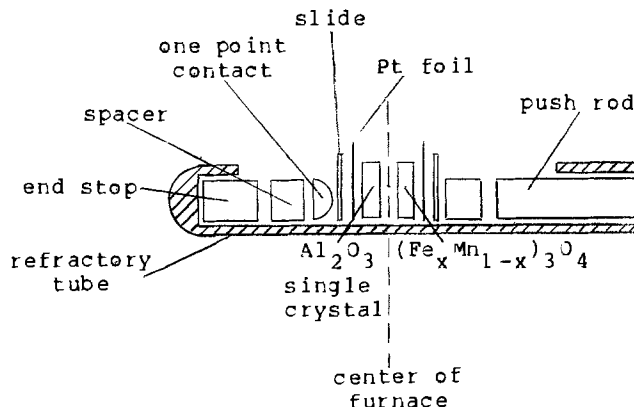


Fig. 1. Diffusion couple assembly

ions in the oxides according to the equations in the Appendix. It was assumed that the cations moved on a fixed oxygen lattice, that is, that the oxygen concentration at all points in the sample remained constant. Throughout the samples, there were many instances in which the sum of the cation mole fractions was greater or less than one. Therefore, this assumption, which provided the basis for the cation mole fraction calculation, proved to be inaccurate.

Ideally, when the three cation mole fractions are plotted on the Gibbs triangle, the result is a single path because the sum of the cation mole fractions should be one. However, there are usually small variations, and the points in the path are small triangles with each side representing a cation mole fraction. In these experiments, the variations were so large that these triangles would have rendered the diagram unintelligible. To avoid this, the iron and manganese mole fractions were plotted as a function of the aluminum mole fraction. In all the diagrams, the concentration profiles in the alumina were plotted as a point on the Al_2O_3 corner of the diagram because Fe_3O_4 and Mn_3O_4 have very small solubilities in Al_2O_3 .

The composition paths plotted on the Gibbs triangle are shown in Fig. 2-5. In all these diagrams, the path to the left represents the manganese mole fraction, and the one to the right is the iron mole fraction. As can be seen, the different mixtures produced very different paths. In Fig. 2, the manganese mole fraction appears fairly constant, and the iron mole fraction seems to vary linearly as a function of the aluminum mole fraction. In Fig. 3, the

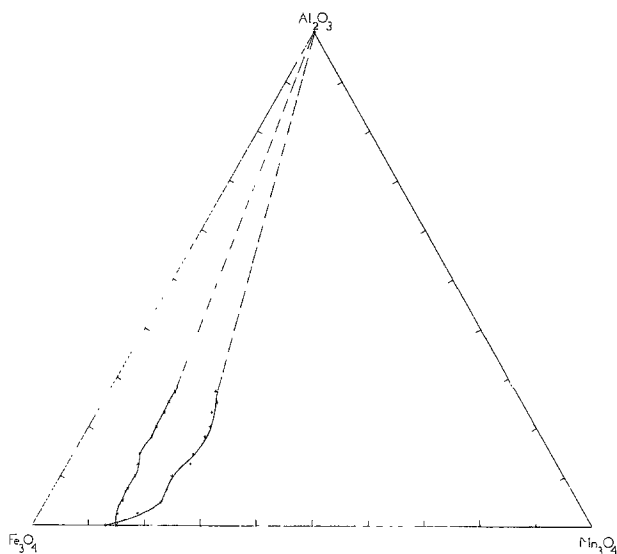


Fig. 2. Cation mole fraction, $(\text{Fe}_{0.85}\text{Mn}_{0.15})_3\text{O}_4\text{-Al}_2\text{O}_3$

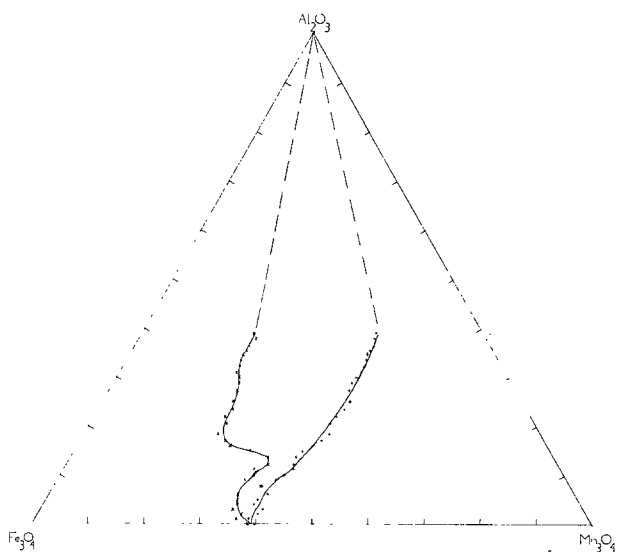


Fig. 3. Cation mole fraction, $(\text{Fe}_{0.6}\text{Mn}_{0.4})_3\text{O}_4\text{-Al}_2\text{O}_3$

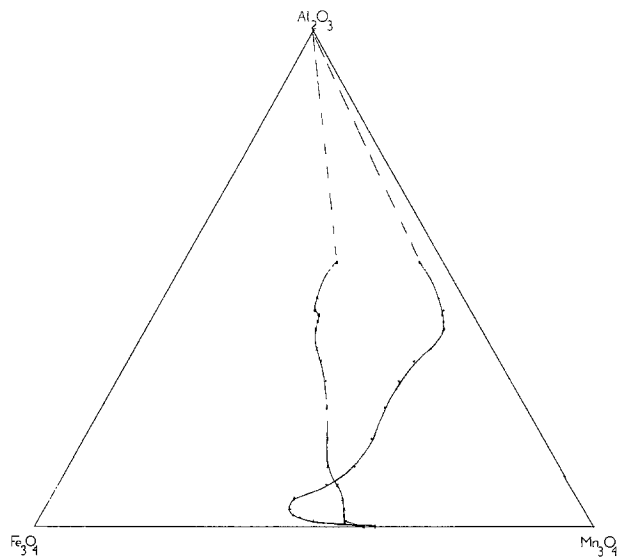


Fig. 4. Cation mole fraction, $(\text{Fe}_{0.4}\text{Mn}_{0.6})_3\text{O}_4\text{-Al}_2\text{O}_3$

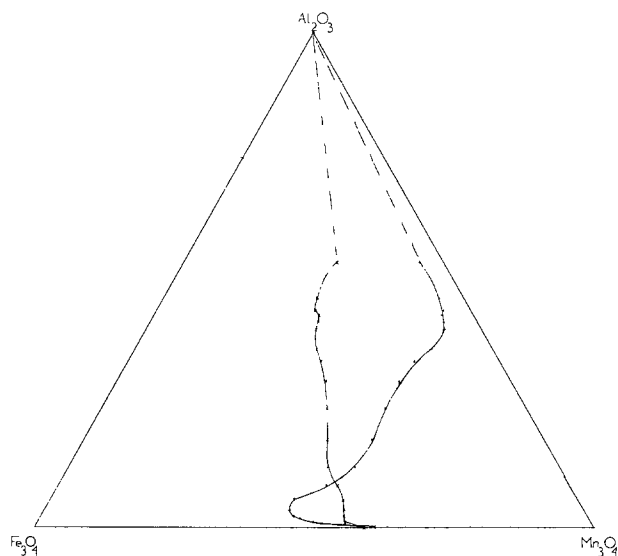


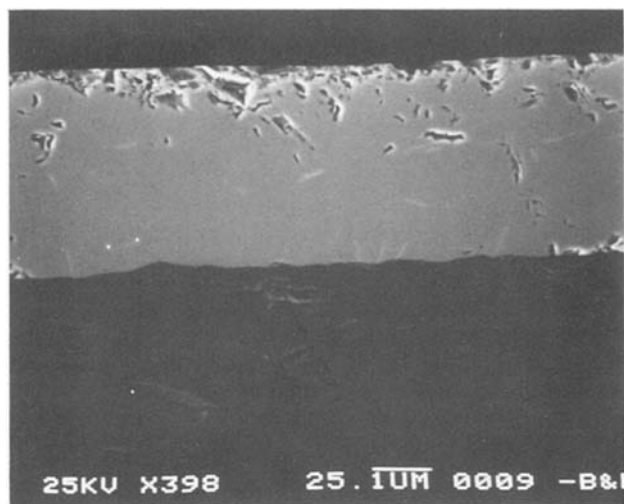
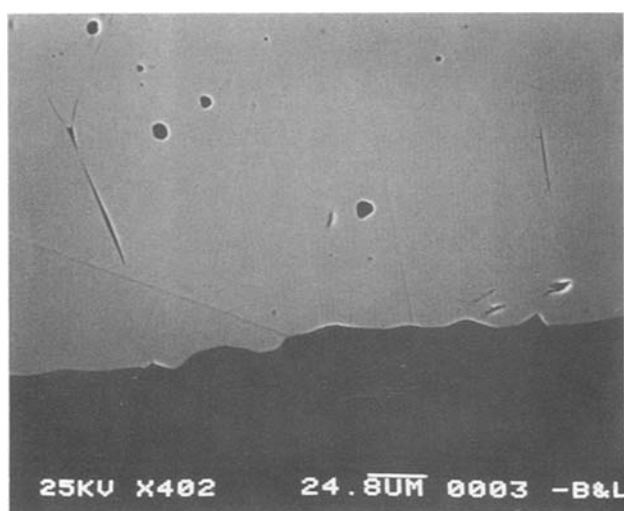
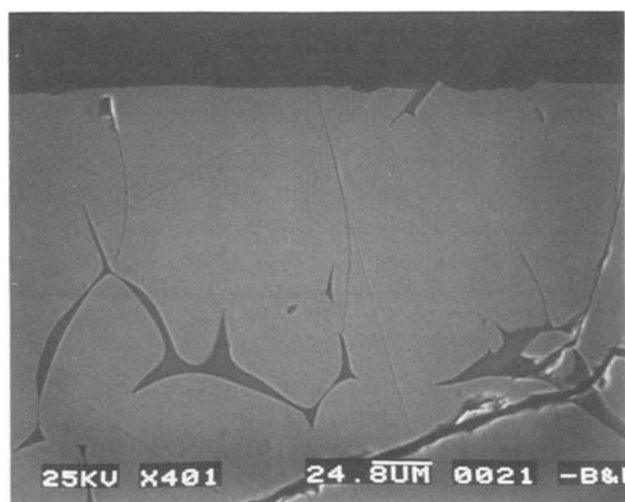
Fig. 5. Cation mole fraction, $(\text{Fe}_{0.2}\text{Mn}_{0.8})_3\text{O}_4\text{-Al}_2\text{O}_3$

manganese mole fraction is erratic except in the region between $X_{\text{Al}} = 0.2$ and $X_{\text{Al}} = 0.4$, in which it is nearly constant. Again, the iron mole fraction appears to vary linearly with the aluminum mole fraction. In Fig 4, the manganese and iron mole fractions seem to vary linearly over the entire range and from $X_{\text{Al}} = 0.1$ to $X_{\text{Al}} = 0.4$, respectively. The iron mole fraction also appears to remain almost constant from $X_{\text{Al}} = 0.4$ to $X_{\text{Al}} = 0.55$. In Fig. 5, the manganese and iron mole fractions are fairly regular and could be considered to be linear in different aluminum mole fraction ranges.

Figures 6-8 are representative electron micrographs of the ternary diffusion couples in the region of the phase boundary. The dark phase is Al_2O_3 , and the light phase is $(\text{Fe}_x\text{Mn}_{1-x})_3\text{O}_4$. The magnification is $400\times$. In the progression of micrographs, one can see the effect of the compositional variations on the phase boundary. The diffusion couples with higher iron contents developed less planar boundaries and more mixed precipitates in the diffusion region (dark areas in the light phase). In addition, there are very angular regions along these boundaries, possibly indicating a crystallographic relationship.

Results of Binary Diffusion Experiments

The raw data obtained from the electron microprobe analysis was the same as in the ternary experiments. The x-ray counting rates were converted using the same methods as described in the Appendix. Figures 9 and 10 show the aluminum mole fractions for $\text{Fe}_3\text{O}_4\text{-Al}_2\text{O}_3$ and $\text{Mn}_3\text{O}_4\text{-Al}_2\text{O}_3$ diffusion couples, respectively, as a function of dis-

Fig. 6. $(\text{Fe}_{0.2}\text{Mn}_{0.8})_3\text{O}_4\text{-Al}_2\text{O}_3$ Fig. 7. $(\text{Fe}_{0.6}\text{Mn}_{0.4})_3\text{O}_4\text{-Al}_2\text{O}_3$ Fig. 8. $(\text{Fe}_{0.85}\text{Mn}_{0.15})_3\text{O}_4\text{-Al}_2\text{O}_3$

tance. The origin of the coordinate system is arbitrary because the chosen method of calculating the interdiffusion coefficients does not require the determination of the location of the Matano interface.

Sauer and Freise (4) derived the equations describing the interdiffusion coefficients in binary systems involving a volume change. A simplified derivation, using molar instead of mass quantities, was given by Wagner (5-7). This approach was used for these calculations.

The general equation is given below

$$\bar{D}(N_2^*) = \frac{(N_2^+ - N_2^-) V_m (N_2^*)}{2t \left. \frac{\partial N_2}{\partial x} \right|_{x^*}} \left[(1 - Y^*) \int_{-\infty}^{x^*} \frac{Y}{V_m} dx + Y^* \int_{x^*}^{\infty} 1 - \frac{Y}{V_m} dx \right]$$

where

N_2^* = mole fraction of 2 at x^*

N_2^+, N_2^- = initial mole fractions on each side of interface

t = diffusion time

$\left. \frac{\partial N_2}{\partial x} \right|_{x^*}$ = derivative of concentration profile at x^*

$Y^* = \frac{N_2 - N_2^-}{N_2^+ - N_2^-}$ for two initially pure components
 $Y^* = N_2$

The molar volumes were assumed to be constant within the phases but different for each phase. Thus, $1/V_m$ could be extracted from the integrals. In Fig. 11, area 1 represents $\int_{-\infty}^{x^*} Y dx$ and area 2 is $\int_{x^*}^{\infty} 1 - Y dx$. The aluminum mole fraction was taken as N_2^* for all the diffusion couples because the concentration profiles obtained appeared to be smoother than those of the iron and manganese mole fractions. Either mole fraction could be used since N_1 and N_2 are not independent (i.e., $N_1 + N_2 = 1$).

Figure 12 is an electron micrograph of a $\text{Mn}_3\text{O}_4\text{-Al}_2\text{O}_3$ diffusion couple. It should be noted that three distinct regions are present, unlike the $\text{Fe}_3\text{O}_4\text{-Al}_2\text{O}_3$ binary and $(\text{Fe}_x\text{Mn}_{1-x})_3\text{O}_4$ ternary samples in which only two phases were distinguishable. The dark phase is Al_2O_3 , and the light phase is Mn_3O_4 . The intermediate phase was assumed to be MnAl_2O_4 , and its molar volume was used in the calculation of the interdiffusion coefficients.

In the $\text{Fe}_3\text{O}_4\text{-Al}_2\text{O}_3$ diffusion couples, the concentration profiles were very smooth, and polynomials were fit to the profiles on each side of the interface and used in the calculations. As a result, the plots of the interdiffusion coefficients as a function of composition are also smooth, as seen in Fig. 13 and 14.

The concentration profiles from the $\text{Mn}_3\text{O}_4\text{-Al}_2\text{O}_3$ diffusion couples were not as smooth. Many regions were approximated linearly for the calculations. The interdiffusion coefficients are therefore represented discretely as a function of aluminum mole fraction. These plots appear in Fig. 15 and Fig. 16. These interdiffusion coefficients appear somewhat erratic. This may be attributed to the discrete evaluation of the data, or possibly the diffusion time was not adequate, as evidenced in the narrow profiles. The interdiffusion coefficients in the MnAl_2O_4 were fairly constant; the average values were $D = 2.0 \times 10^{-9} \text{ cm}^2/\text{s}$ for $t = 23\text{h}$ and $D = 1.6 \times 10^{-9} \text{ cm}^2/\text{s}$ for $t = 45\text{h}$.

Conclusion

This study has provided a first approximation of the interdiffusion coefficients in the $\text{Fe}_3\text{O}_4\text{-Al}_2\text{O}_3$ and $\text{Mn}_3\text{O}_4\text{-Al}_2\text{O}_3$ binary systems. The calculations in the $\text{Fe}_3\text{O}_4\text{-Al}_2\text{O}_3$ system were relatively straightforward because the concentration profiles were smooth. With the $\text{Mn}_3\text{O}_4\text{-Al}_2\text{O}_3$ system, not only were more-involved calculations required due to the discrete nature of the data, but also those calculations are probably less accurate. A more complex curve might better describe these concentration profiles, or a spline-type method may be employed.

From the electron micrographs, it can be seen that the $\text{Mn}_3\text{O}_4\text{-Al}_2\text{O}_3$ diffusion couples formed a third phase. The phase was assumed to be MnAl_2O_4 and was taken into ac-

Fig. 9. Concentration profiles from $\text{Al}_2\text{O}_3\text{-Fe}_3\text{O}_4$ diffusion couples.

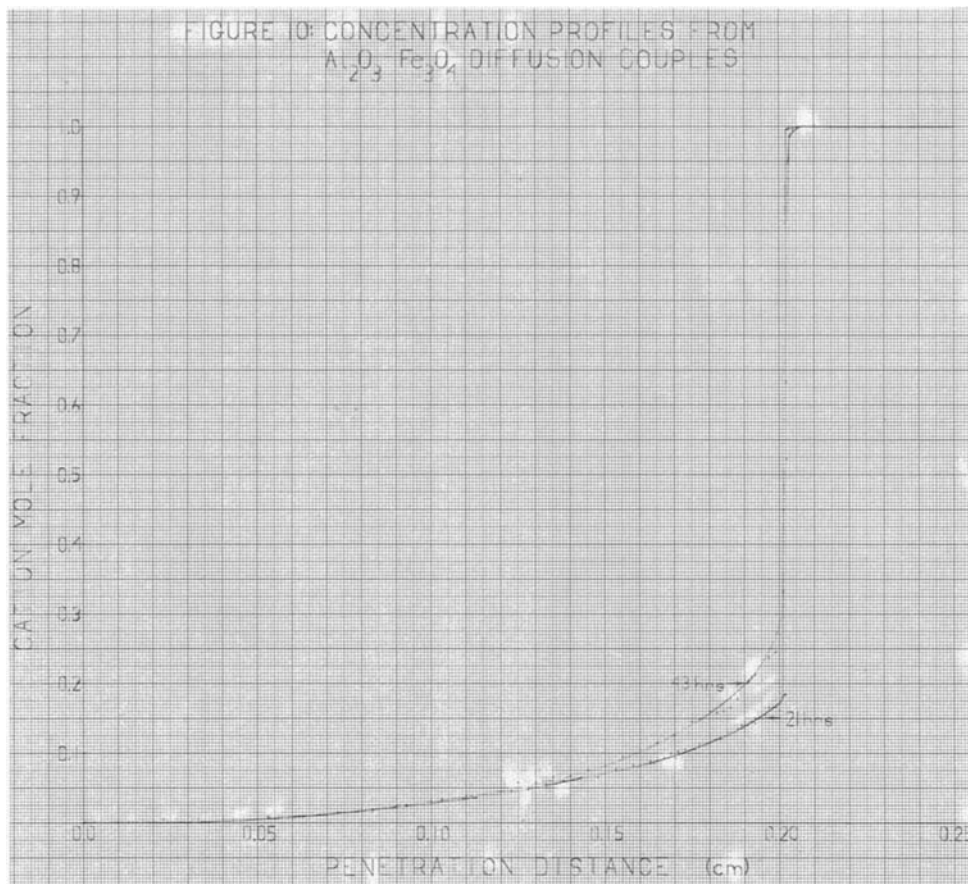
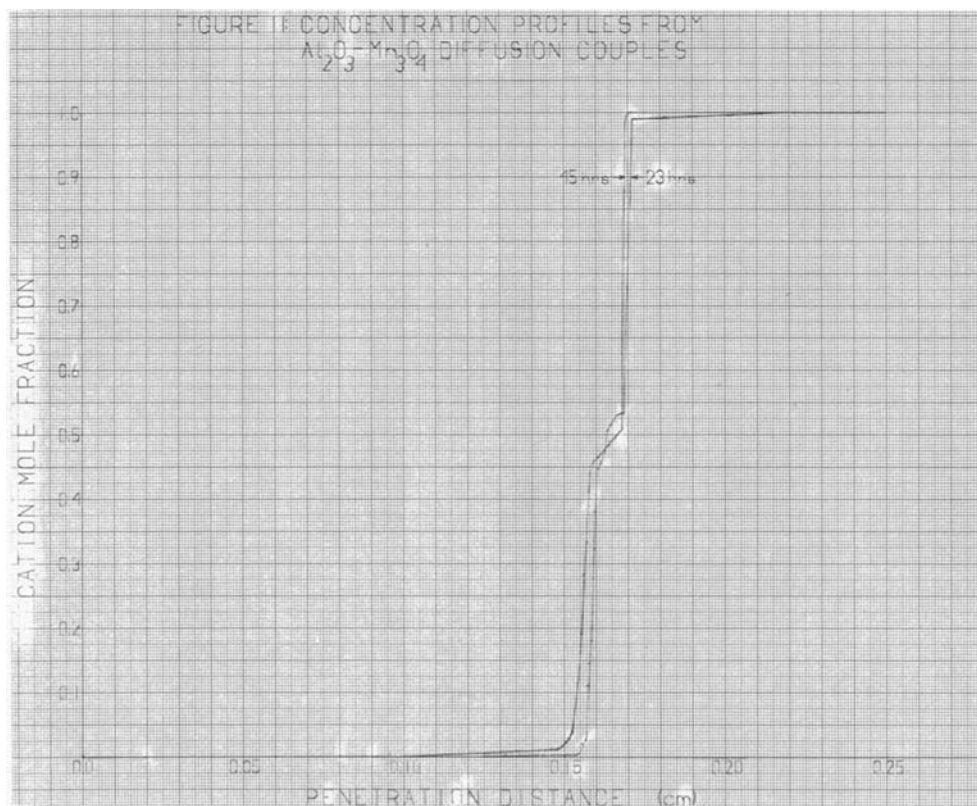


Fig. 10. Concentration profiles from $\text{Al}_2\text{O}_3\text{-Mn}_3\text{O}_4$ diffusion couples.



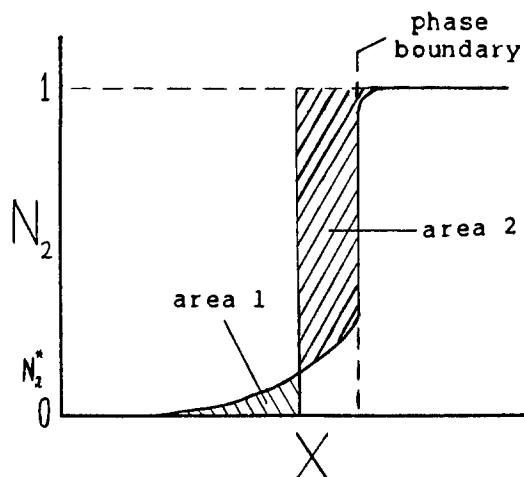
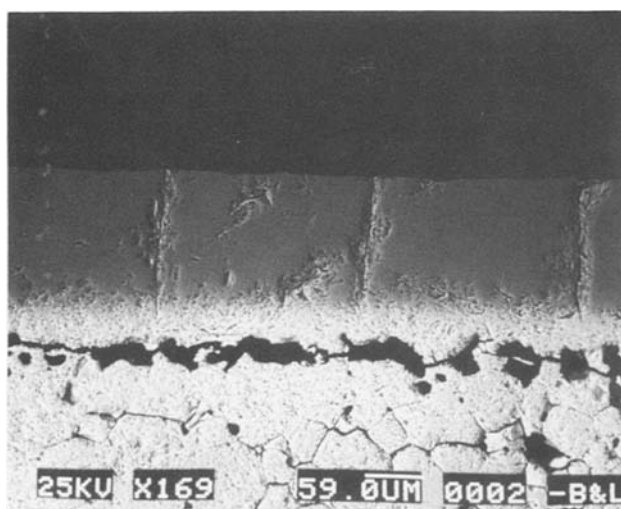


Fig. 11. Schematic concentration profiles

Fig. 12. $\text{Mn}_3\text{O}_4\text{-Al}_2\text{O}_3$

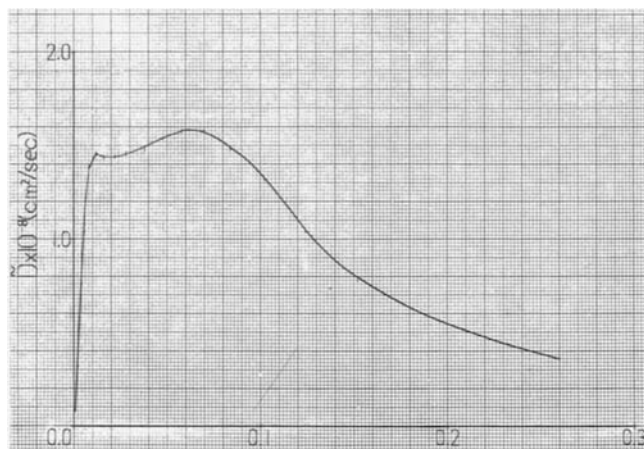
count in the calculations. The interdiffusion coefficients within this phase were fairly constant. Other mixed spinel phases may form in the other diffusion couples during longer reaction times, but, these were not observed in these experiments.

With the completion of additional ternary diffusion experiments, the diffusion coefficients in the ternary system may be calculated. At this point, it is not clear whether or not this system will be useful in predicting growth morphologies by comparing diffusion rates. However, the changes observed in the interfaces during the reaction of these few ternary diffusion couples are encouraging.

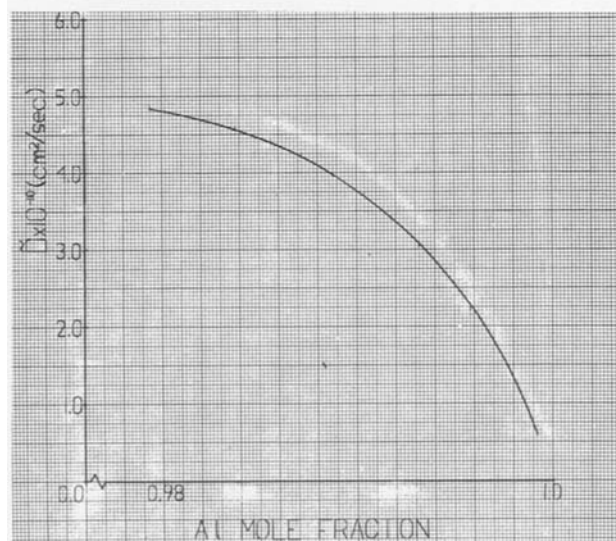
Acknowledgment

Sincere appreciation is extended to Professor Dr. H. Schmalzried and M. Köhne for their daily supervision, academic guidance, and gracious hospitality during my residence in Hannover, Germany. I am also indebted to The Electrochemical Society for selecting me as the 1983 F. M. Becket Memorial Award recipient and thereby providing me with this tremendous educational opportunity and the funding to study in Hannover. The experience and knowledge that I gained under Professor Dr. H. Schmalzried is invaluable. I am also extremely grateful to Mr. V. H. Braneky, Executive Secretary of The Electrochemical Society, for being very patient and helpful during my association with the Society involving the award.

Manuscript received Feb. 22, 1984.



(a)



(b)

Fig. 13. Interdiffusion coefficients $\text{Fe}_3\text{O}_4\text{-Al}_2\text{O}_3$. $t = 43\text{h}$

APPENDIX

The mass fraction, Y_i , is proportional to the x-ray counting rate, C_i . The proportionality factor, K_i for each cation i , is determined using a pure oxide sample. If $Y_{i, \text{std}}$ is the mass fraction in the pure oxide and $C_{i, \text{std}}$ is the average counting rate measured from the standard, then

$$K_i = \frac{Y_{i, \text{std}}}{C_{i, \text{std}}}$$

and the measured values were converted by

$$Y_{i, \text{meas}} = C_{i, \text{meas}} \times K_i$$

The mass fraction in terms of the number of moles, n_i , molecular weights of the cations and oxides, M_i and M_o is given by

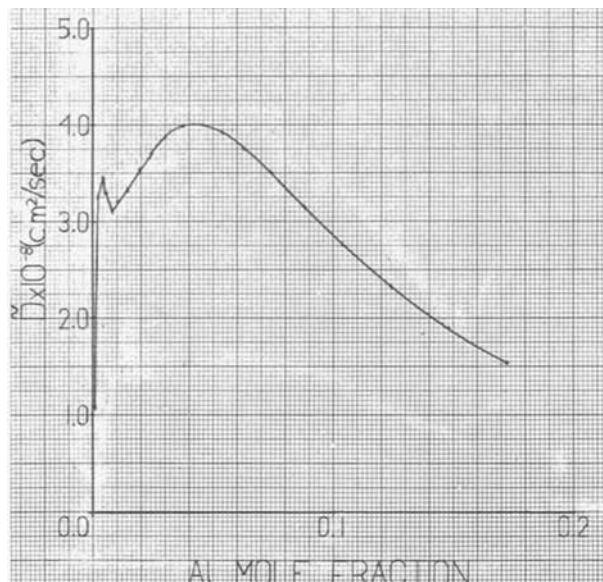
$$Y_i = \frac{n_i M_i}{M_o}$$

rearranging yields

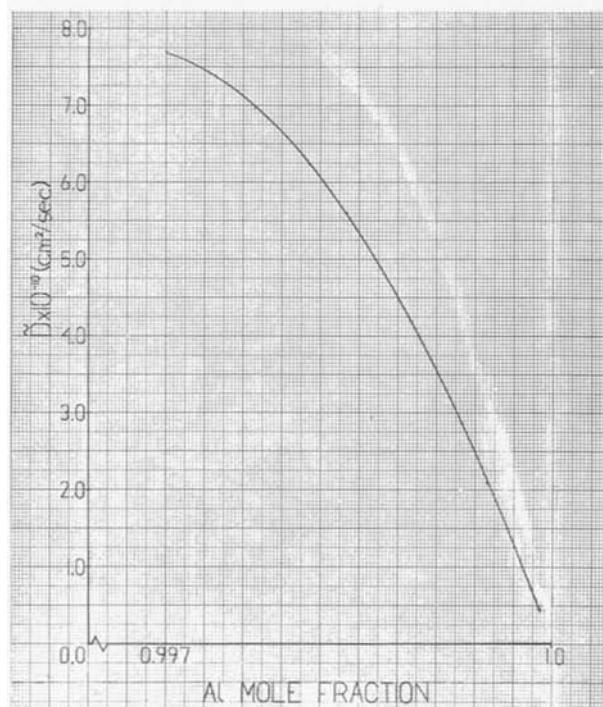
$$n_i = \frac{M_o Y_i}{M_i}$$

and from the definition of mole fraction, X_i

$$X_i = \frac{n_i}{\sum n} = \frac{Y_i}{\sum \frac{Y}{M}}$$



(a)



(b)

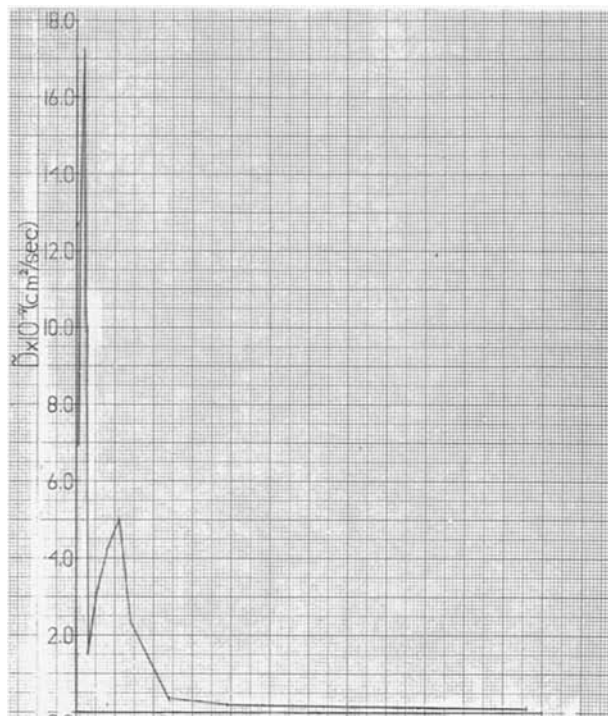
Fig. 14. Interdiffusion coefficients Fe₃O₄-Al₂O₃. t = 21h

where the M_o 's canceled and the sum of the unsubscripted variables is the sum of all the components. The cation mole fractions are then

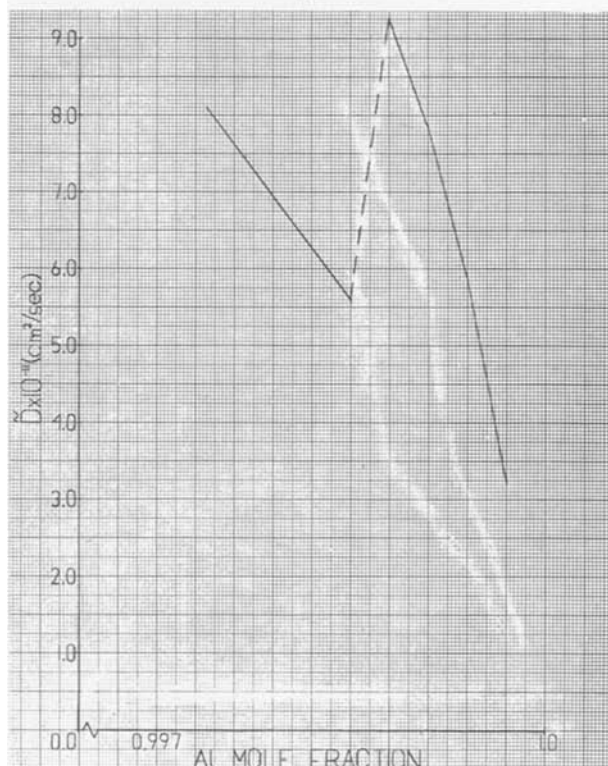
$$X_{Al} = \frac{\frac{Y_{Al}}{M_{Al}}}{\frac{Y_{Al}}{M_{Al}} + \frac{Y_{Fe}}{M_{Fe}} + \frac{Y_{Mn}}{M_{Mn}} + \frac{Y_O}{M_O}} \times 2.500$$

$$X_{Fe} = \frac{\frac{Y_{Fe}}{M_{Fe}}}{\frac{Y_{Al}}{M_{Al}} + \frac{Y_{Fe}}{M_{Fe}} + \frac{Y_{Mn}}{M_{Mn}} + \frac{Y_O}{M_O}} \times 2.333$$

$$X_{Mn} = \frac{\frac{Y_{Mn}}{M_{Mn}}}{\frac{Y_{Al}}{M_{Al}} + \frac{Y_{Fe}}{M_{Fe}} + \frac{Y_{Mn}}{M_{Mn}} + \frac{Y_O}{M_O}} \times 2.333$$



(a)



(b)

Fig. 15. Interdiffusion coefficients Mn₃O₄-Al₂O₃. t = 45h

The factors 2.500 and 2.333 are added to make the cation mole fractions in the pure oxides unity. Since Y_O was not measured, let $Y_O = 1 - Y_{Al} - Y_{Fe} - Y_{Mn}$ from the definition of mass fraction. The values used in the above equations were

- $Y_{Al, std} = 0.5292$
- $Y_{Fe, std} = 0.7236$
- $Y_{Mn, std} = 0.7203$
- $M_{Al} = 26.98 \text{ g/mol}$
- $M_{Fe} = 55.85 \text{ g/mol}$
- $M_{Mn} = 54.94 \text{ g/mol}$
- $M_O = 16.00 \text{ g/mol}$

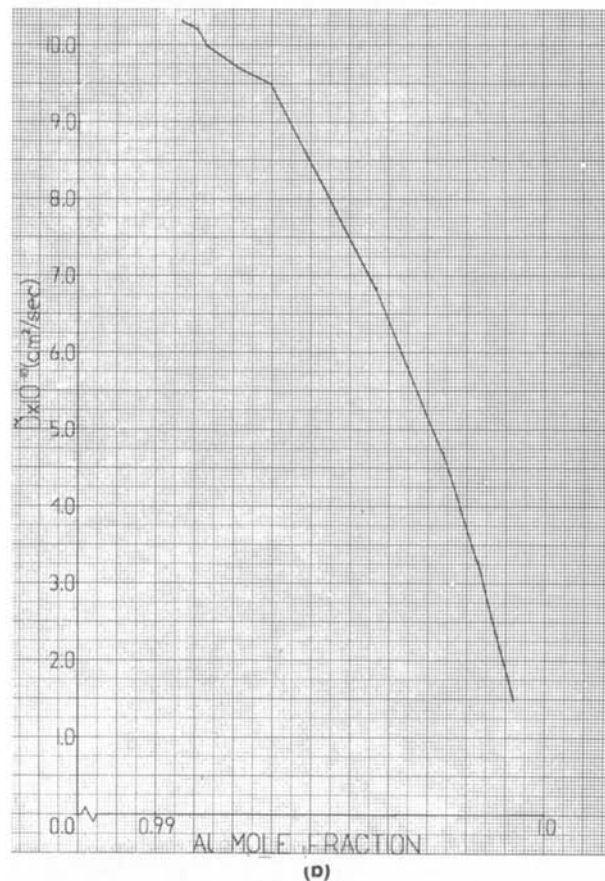
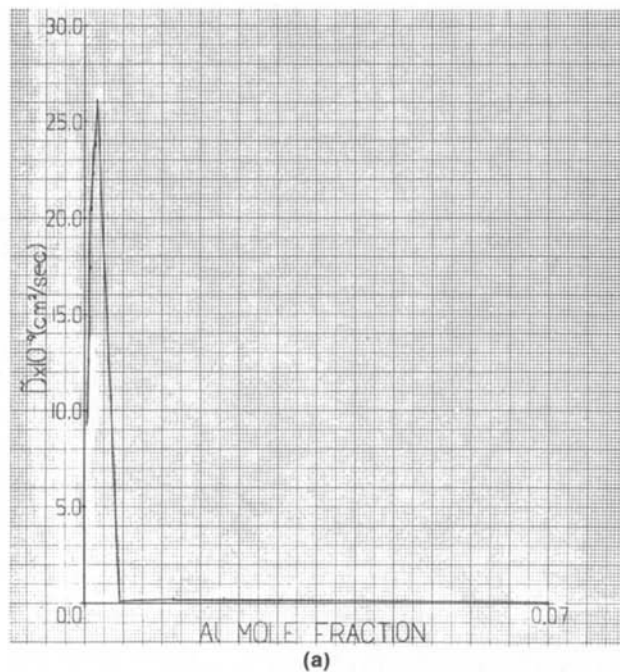


Fig. 16. Interdiffusion coefficients $\text{Mn}_3\text{O}_4\text{-Al}_2\text{O}_3$. $t = 23\text{h}$

REFERENCES

1. J. S. Kirkaldy and D. G. Fedak, *Trans. AIME*, **224**, 490 (1962).
2. A. Maun and C. L. Gee, *J. Am. Ceram. Soc.*, **39**, 207 (1956).
3. A. Maun, B. E. McKean, and T. Ranganathan, *ibid.*, **45**, 279 (1962).
4. F. Sauer and V. Freise, *Z. Elektrochem.*, **66**, 353 (1962).
5. C. Wagner, *Acta Metall.*, **17**, 99 (1969).
6. H. Schmalzried, "Solid State Reactions," pp. 115-116, Academic Press, New York, (1974).
7. C. Greskovich and V. S. Stubican, *J. Am. Ceram. Soc.*, **53**, 251 (1970).



Moderate Temperature Sodium Cells

V. Discharge Reactions and Rechargeability of NiS and NiS₂ Positive Electrodes in Molten NaAlCl₄

K. M. Abraham* and J. E. Elliot

EIC Laboratories, Incorporated, 111 Downey Street, Norwood, Massachusetts 02062

ABSTRACT

NiS₂ and NiS have been characterized as high energy density rechargeable positive electrodes for moderate-temperature Na batteries of the configuration, Na_{α/β}-Al₂O₃/NaAlCl₄(l), NiS_x. The batteries operate in the temperature range 170°-190°C. Positive electrode reactions during discharge/charge cycles have been characterized. Excellent rechargeability of the batteries has been demonstrated by extended cell cycling. A Na/NiS₂ cell, operating at 190°C, exceeded 600 deep discharge/charge cycles with practically no capacity deterioration. The feasibility of secondary Na/NiS_x batteries with specific energies ≥ 50 Wh/lb and cycle lives exceeding 1000 deep discharge/charge cycles has been demonstrated.

Sodium batteries which operate in the moderate temperature range of 125°-225°C have been pursued in recent times (1-6) as potential alternatives to the liquid Na/molten S system which operates in the range of 350°-400°C (7). The anode in both types of battery comprises liquid Na contained in a Na⁺ conducting solid electrolyte, usually Na-β- or Na-β'-Al₂O₃. A moderate temperature Na battery offers several advantages, including lower corrosion and easier thermal and materials management. A possible limitation is reduced discharge-rate capability due to a lowering of the Na⁺ conductivity in the Al₂O₃ solid electrolyte at the moderate temperature. Nevertheless, with advances in the technology to fabricate very thin Na-β'-Al₂O₃, and with the advent of novel and superior Na⁺ conducting solid electrolytes, a moderate temperature rechargeable Na battery could become a very attractive alternative to its high temperature counterpart.

A major aspect in the development of a high energy density moderate temperature rechargeable Na battery concerns the positive electrode. A useful cathode must exhibit a number of desirable properties including a low equivalent weight, good reversibility for the discharge reaction, long-term thermal stability at the operating temperature, and chemical compatibility with the solid electrolyte. Lately, we have investigated the feasibility of a number of cathode systems for 125°-175°C Na batteries. They include a soluble S cathode consisting of sodium polysulfides dissolved in organic solvents (2) and insoluble cathodes comprising Na intercalating layered transition metal chalcogenides such as TiS₂, VS₂, and VSe₂. The chalcogenide electrodes have been operated in conjunction with both an organic (1) and an inorganic (3) electrolyte. However, organic electrolytes have been found not to have the stability required for long cycle-life Na batteries (1).

In order to circumvent problems encountered with the organic electrolytes, we chose molten NaAlCl₄ as an alternative. This has opened up some new areas of chemistry. The Na intercalating chalcogenides, TiS₂, VS₂, VSe₂, etc., have been found to react with molten NaAlCl₄. In the case of VS₂, however, the reaction products formed during cathode cycling in molten NaAlCl₄ exhibited excellent

rechargeability, providing an extremely useful high energy density rechargeable Na cell (3, 4).

NiS₂ and NiS are non-Na intercalating materials, and we have found their chemistry and electrochemistry in molten NaAlCl₄ to be markedly different from those of Na intercalating TiS₂ and VS₂ in the same medium. Our results are presented in this paper.

There have been studies of other moderate temperature Na batteries utilizing molten NaAlCl₄ as the catholyte. These include a cell utilizing an acidic NaCl-AlCl₃ melt with SCl₃⁺AlCl₄⁻ as the positive electrode (6) and batteries employing a S₂Cl₂-AlCl₃ cathode (5). Our studies of VS₂ and MoS₃, reported elsewhere (1, 3, 4), and of NiS and NiS₂, presented in this paper, represent first examples of the utility of transition metal sulfide cathodes in molten NaCl-AlCl₃ electrolyte medium. It would be apparent from the data presented that these results may be of considerable scientific and technological importance.

Experimental

All air- and moisture-sensitive materials were handled using standard equipment and techniques designed for the manipulation of air-sensitive compounds. All electrochemical experiments were carried out in a glove box (Vacuum Atmospheres Corporation) maintained over an argon atmosphere, which was continuously circulated through a drying column.

Preparation of NaAlCl₄.—The NaAlCl₄ electrolyte was prepared by heating a NaCl (51 mole percent [m/o]) -AlCl₃ (49 m/o) mixture at 190°C to form a liquid. The melt was then purified by constant current electrolysis between two Al disk electrodes for 48-72h. The resulting clear liquid was cooled, and the solid was ground to a fine white powder and stored in a glove box until use.

Nickel sulfides.—NiS₂ and NiS were obtained from Alfa-Ventron, Beverly, Massachusetts. The NiS₂ is believed to have a cubic structure (ASTM File no. 11-29), and the NiS a hexagonal structure (ASTM File no. 2-1280).

Cell construction and tests.—A typical laboratory cell, having a tubular shape, consisted of an outer Pyrex compartment, which contained the cathode mix of the sulfide and NaAlCl₄, and an inner compartment fabricated from a β'-Al₂O₃ tube (Ceramatec Incorporated, Catalog no. CT16A), containing the Na anode. The cathode was fabricated in a graphite felt (Union Carbide, WDF

*Electrochemical Society Active Member.

EST

Felt) matrix by sifting a weighed amount of the sulfide powder into a known area of the felt. The latter, in turn, was wound around the β'' -Al₂O₃ tube. An amount of NaAlCl₄, sufficient to completely wet the carbon felt, was added. A tungsten (W) wire served as the positive electrode lead. The anode compartment contained an excess of Na, and a W wire served as the anode current collector. Before assembly into the cell, the β'' -Al₂O₃ tube containing Na was heated and maintained at 400°C for ~24h, in order to allow good wetting of the β'' -Al₂O₃ with liquid Na.

The cathode mix in a typical Na/NiS₂ laboratory cell consisted of 0.75g (6.1 mmol) of NiS₂, 0.15g of Ni, and 4.75g (24 mmol) of NaAlCl₄. (Early on in the investigation, we discovered that a small amount of Ni, ~20 m/o, initially incorporated in the cell would improve cathode discharge capacity. Therefore, NiS₂ cathodes contained a small amount of Ni powder.) Experiments were also performed with smaller capacity NiS₂ cathodes and with several NiS₂:NaAlCl₄ mole ratios.

Cells were also constructed in an inside-out configuration with the positive electrode contained inside the β'' -Al₂O₃ tube. The outer Na compartment was fabricated from a stainless steel tube. An advantage of the inside-out configuration is that it eliminates most hardware corrosion problems relating to molten NaAlCl₄. A 4 Ah nominal capacity Na/NiS₂ cell was constructed in the inside-out configuration. A schematic representation of this cell is given in Fig. 1. The cathode mix and graphite felt, placed inside the β'' -Al₂O₃ tube, had a height of ~10 cm. A vitreous carbon rod extending the full inside length of the β'' -Al₂O₃ tube served as the cathode lead. The cathode composition of the 4 Ah NiS₂ cell was as follows: 8.1g NiS₂, 1.62g Ni, and 29g NaAlCl₄.

Cells, after assembly, were placed in a thermostated oven, maintained at 170°C. Some of the extended cycling experiments were performed at 190°C. Galvanostatic cycling was carried out with standard cycling equipment. Data collection and retrieval were done with a Bascom-Turner 8000 Recorder equipped with microprocessor accessories.

Analysis of cycled cathodes:—X-ray analyses of cycled cathodes were carried out after washing off the molten salt with carefully distilled CH₃CN. Any adhering NaCl was subsequently removed by washing the cathode in aqueous NH₄OH and then dried in vacuum. X-ray diffraction data were obtained by the Debye-Scherrer method.

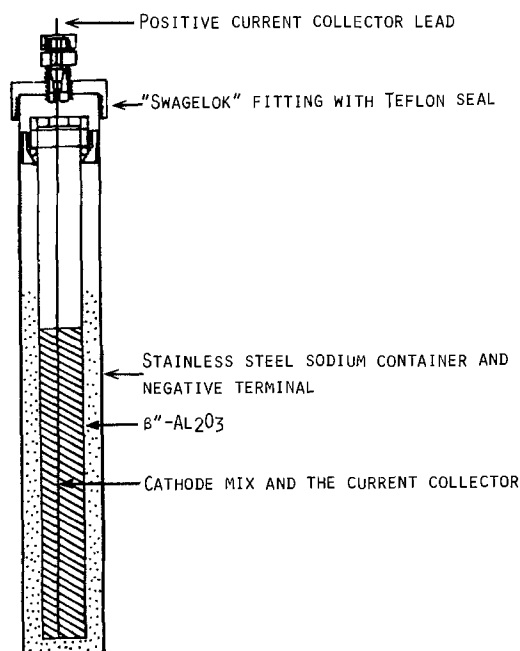
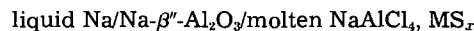


Fig. 1. Schematic representation of a Na cell

Results and Discussion

The Na cell being discussed has the configuration



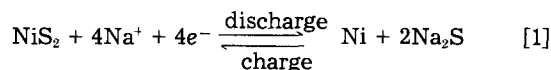
We have operated the cell in the temperature range of 170°-190°C. The MS_r cathode is NiS₂ or NiS. The electrolyte is the basic NaCl-AlCl₃ molten salt, NaAlCl₄, which melts at ~155°C. Acid-base properties of NaCl-AlCl₃ melts have been discussed by others (8). Advantages of the basic melt over the acidic melt for battery applications include lower volatility and fewer corrosion problems. The desirability of molten NaAlCl₄ as a high rate battery electrolyte is evident from the data in Table I, which compares some of its properties with those of Na- β'' -Al₂O₃. In the 170°-190°C range, the specific conductivity of molten NaAlCl₄ is significantly higher than that of Na- β'' -Al₂O₃.

Electrochemical behavior of NiS₂.—Figures 2 and 3 depict galvanostatic discharge/charge cycles of two Na/NiS₂ cells, 10 and 20, at ~170°C. In both cases, the current density is 1 mA/cm² of β'' -Al₂O₃, but the voltage limits in cell 10 are 1.7 and 3.0V and 1.7 and 3.5V in cell 20. The open-circuit voltage (OCV) of the Na/NiS₂ cell is ~3.0V. The first discharge proceeds through three potential plateaus, at 2.40, 2.25, and 2.0V, yielding a mid-discharge potential of 2.3V. The cathode utilization in the first discharge is 2.5 electrons per NiS₂ (e^-/NiS_2).

In cell 20, with a charge limit of 3.5V, a capacity approaching $3e^-/\text{NiS}_2$ is obtained in the second discharge. There is very little change in capacity in this cell after the second discharge.

When the charge limit is 3.0V, the cell capacity decreases by ~10% on going from the first to the second discharge, and by smaller amounts in the next few cycles. In this cycling regime the average rechargeable capacity is $\sim 2e^-/\text{NiS}_2$. The additional capacity obtained when the charge limit is 3.5V appears at the beginning of the second and later discharges at a plateau of 2.7V. The many voltage plateaus which appear in the discharge of NiS₂ most probably correspond to intermediate phases comprising lower nickel sulfides.

Intermediate phases in the discharge of NiS₂ and NiS.—Cathodes from NiS₂ cells after cycling to various depths were isolated and analyzed by x-rays. Some relevant data are given in Table II. The final discharge product is Ni. The data show also that the reduction of NiS₂ to Ni involves the intermediate phases, Ni₃S₄, NiS, and Ni₃S₂. The overall discharge/charge processes in the NiS₂ cathode which conform to the x-ray results are



Additional support for reaction [1] has been obtained by an independent demonstration of the charge part of this reaction in a cell setup with a cathode comprised of Ni and Na₂S, taken in a mole ratio of 1:2. The relevant cycling data are given in Fig. 4. A discharge of Na/NiS₂ cell 20 is included in Fig. 4 for comparison.

In order to verify the intermediacy of the NiS phase in the discharge of NiS₂, we have examined the discharge/charge behavior of Na/NiS cells. The cycles given in Fig. 5 clearly manifest the relationship in the electrochemical

Table I. Some properties of NaAlCl₄ and Na- β'' -Al₂O₃

Electrolyte	Temperature (K)	Viscosity (c.p.)	Density (g/ml)	Conductivity ($\Omega^{-1} \text{cm}^{-1}$)
NaCl:AlCl ₃ (1:1) or NaAlCl ₄	460	2.65	1.43	0.46
Na- β'' -Al ₂ O ₃ *	573	—	3.2	0.16

* From Ceramatec, Incorporated, Salt Lake City, Utah, Catalog no. CT16A.

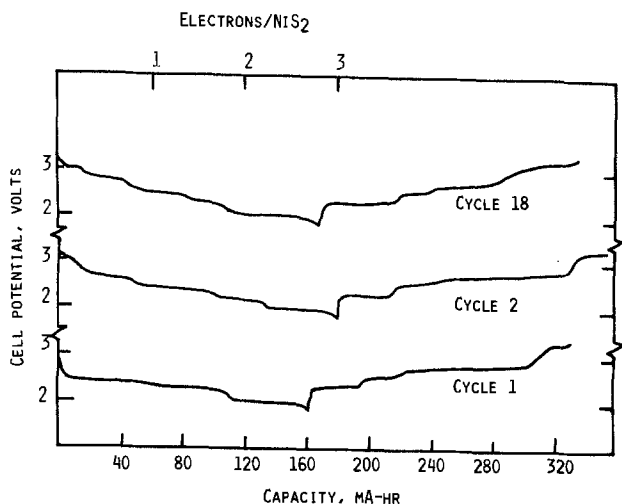


Fig. 2. Galvanostatic cycles of Na/NiS₂ cell no. 20 at 170°C. Current density: $i_d = i_c = 1 \text{ mA/cm}^2$. Voltage limits, 1.7-3.5V.

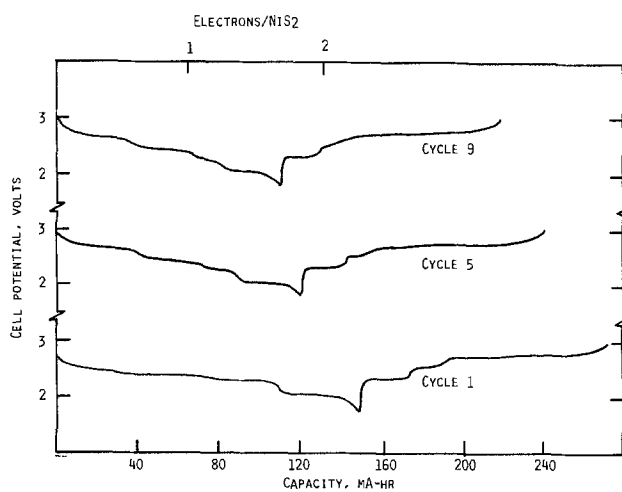


Fig. 3. Galvanostatic cycles of Na/NiS₂ cell no. 10 at 170°C. Current density: $i_d = i_c = 1 \text{ mA/cm}^2$. Voltage limits, 1.7-3.0V.

behavior of NiS₂ and NiS. The first discharge of NiS shows two voltage plateaus: the first at ~2.3V, encom-

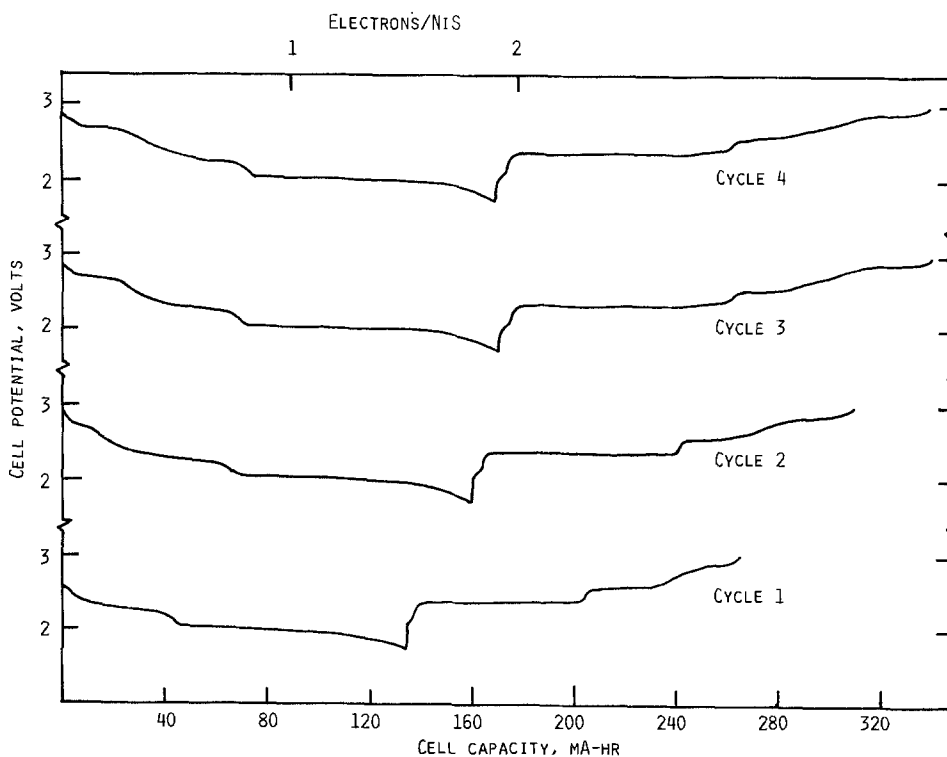
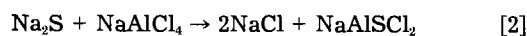


Fig. 5. First four cycles of a Na/NiS cell at 170°C. Current density $i_d = i_c = 1 \text{ mA/cm}^2$. Voltage limits, 1.7-3.0V.

passing $\sim 0.4e^-$ NiS, and the second at $\sim 2.0\text{V}$, yielding $\sim 1.1e^-$ NiS. These plateaus most probably correspond to the reduction of NiS to Ni₃S₂ and that of Ni₃S₂ to Ni. X-ray data obtained at the end of the tenth discharge of the cell in Fig. 5 strongly support this (see Table II). The products at the end of a discharge include Ni, Ni₃S₂, and small amounts of Ni₇S₆. Beginning with the second discharge of NiS, an additional plateau at $\sim 2.7\text{V}$, and a sloping voltage region between 2.7 and 2.4V, appear. The combined capacities in these two regions equal $\sim 20\%$ of the total material utilization. It appears that the charge of the NiS electrode to 3.0V oxidizes it to a composition slightly richer in S than that in NiS.

Cathode reactions in NiS₂ and NiS cells.—X-ray diffraction patterns of discharged NiS₂ or NiS cathodes showed no evidence of Na₂S. This is not surprising, since Na₂S would react with NaAlCl₄, forming NaAlS₂ and NaCl (9), Eq. [2]



Using available thermodynamic data (10, 11), we have calculated the equilibrium potentials at 500 K for the reactions, $\text{NiS}_2 + \text{Na} \rightarrow \text{NiS} + \text{Na}_2\text{S}$ and $\text{NiS} + 2\text{Na} \rightarrow \text{Ni} + \text{Na}_2\text{S}$, and found them to be ~ 1.60 and $\sim 1.30\text{V}$, respectively. These values are significantly ($\sim 0.8\text{V}$) lower than

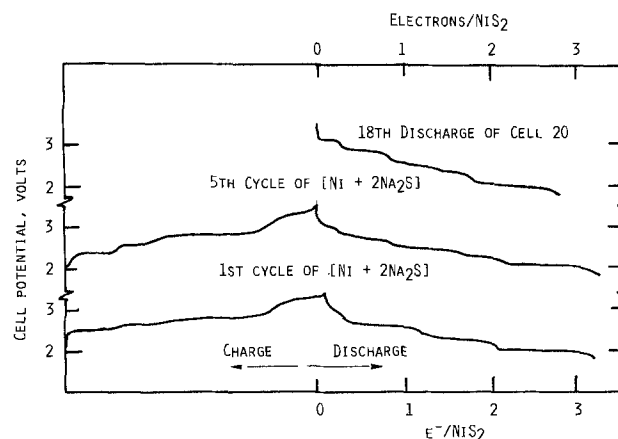


Fig. 4. Comparison of discharge of $[\text{Ni} + 2\text{Na}_2\text{S}]$ and NiS₂ cells. Temp. 170°C.

Table II. Phases identified in cycled NiS and NiS₂ cathodes

Cathode	Extent of cycling	Cathode composition calculated from net charge passed	Phases identified*
NiS ₂	One discharge to 1.7V	NiS _{0.51}	NiS (minor**), Ni ₃ S ₂ , Ni
NiS ₂	1.5 cycles, terminated prior to onset of 2.0V discharge plateau	NiS _{1.1}	Ni ₃ S ₄ (minor), NiS, Ni ₃ S ₂
NiS ₂	9 cycles, terminating at end of charge to 3.5V	NiS _{1.88}	NiS ₂ , Ni ₃ S ₄ (minor)
NiS	10 cycles, terminating at end of discharge to 1.7V	NiS _{0.025}	Ni ₃ S ₂ (minor), Ni

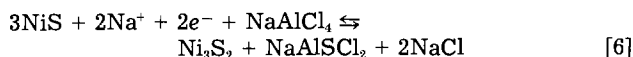
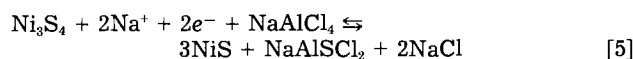
* By x-ray diffraction, Cu K α radiation.

** Approximate relative ratios based on the observed intensity of the x-ray lines.

the actual potentials observed by measuring the OCV's of NiS₂ and NiS cells during various stages of discharge at 170°C. The calculated equilibrium potential for the Na/S couple at 500 K is ~1.9V, while that observed in the NaAlCl₄ melt is ~2.9V (4, 5). It is clear that an interaction of the molten salt with either the cathode material or a reaction product of it also contributes to the overall free energy change in the cell. The most probable reaction involving the electrolyte is that given in Eq. [2]. Consequently, it is reasonable to assume that the overall electrode process in the cycling of the NiS₂ cathode is that in Eq. [3]



The various intermediate steps may be represented as shown in Eq. [4]-[7]



Reactions [6] and [7] are common to the NiS and NiS₂ electrodes. In extensively cycled cathodes, we have found small amounts of NiCl₂, probably formed from displacement reactions of the sulfide with NaAlCl₄. However, in separate experiments, we have found the reduction of NiCl₂ to Ni to be quite reversible and to occur at ~2.7V.

Most of the intermediate nickel sulfide phases we have identified in this work were found by Preto *et al.* in Li-Al/NiS₂ cells utilizing the LiCl-KCl molten salt electrolyte, at 400°C (11). However, the phase Ni₃S₄, which decomposes at ~300°C, was not detected in the higher temperature system. In the Li-Al/NiS₂ system, the molten salt does not take part in the discharge reaction, and the observed cell equilibrium potentials agree quite well with the calculated values. Electrolyte participation in discharge reactions is a characteristic which distinguishes the electrochemistry of NiS₂ and NiS in molten NaAlCl₄ from that in LiCl-KCl electrolytes.

A fraction of the specific energy lost by inclusion of NaAlCl₄ in the reaction stoichiometry in Na/NiS₂ cells is compensated for by the higher cell voltages achieved in this electrolyte.

Rate and rechargeability of NiS₂ and NiS cells.—Figure 6 gives cathode utilization, represented as electrons/NiS₂, at several current densities for two Na/NiS₂ cells. The NaAlCl₄:NiS₂ mole ratio in cell 30 is 3.5:1 and 2:1 in cell

40. The rate/capacity data were obtained at 190°C. In obtaining the data, each cell was successively discharged at current densities from 2 to 25 mA/cm² with each discharge followed by a charge to 3.5V at 2 mA/cm². Cathode utilizations show practically the same values in both cells at current densities ≥ 20 mA/cm². At lower current densities, the cathode with the smaller amount of NaAlCl₄ exhibits lower capacities. This is probably because of insufficient amounts of NaAlCl₄ in that cell, enabling only a partial utilization of NiS₂. The 25 mA/cm² discharge corresponds to a *c/2* rate. The NiS₂ utilization at the latter current density is nearly 60% of that realized at 2 mA/cm².

Rechargeability of NiS₂ and NiS cells have been evaluated by extended cycling of laboratory cells of 0.5–1 Ah capacities. Figure 7 displays capacity *vs.* cycle number for Na/NiS₂ cell 50. The cathode mix comprised 0.75g (6.1 mmol) of NiS₂, 0.15g of Ni, and 4.75g (24 mmol) of NaAlCl₄. In several initial cycles, the current was varied to arrive at optimum discharge and charge current densities for the extended cycling. Thus, the first four cycles were performed at a constant current of 25 mA (2 mA/cm²). Between cycles 5 and 54, the current was 50 mA (4 mA/cm²). In cycle 55, the current density was 8 mA/cm² for discharge and 4 mA/cm² for recharge. Thereafter, the current was unchanged. The temperature was maintained at 165°C until the 184th cycle, when it was raised to 190°C. All cycles subsequent to 184 were obtained at 190°C. The cell achieved 670, 100% depth-of-discharge cycles before the experiment was ended voluntarily. After the first 540 cycles, the cell was cooled to room temperature and then it remained at open circuit for about 2 months before the cycling was resumed at 190°C to obtain the additional 130 cycles. The cycle test took more than 1 yr. Some typical cycles are given in Fig. 8. The higher temperature of 190°C, at which the cell was maintained during the latter 10 months of cycling, helped increase the cathode utilization. This increase corresponded to an increase in the capacity involved in the 2.1V plateau. The average material utilization in the 650 cycles was ~2.6e⁻/NiS₂.

The excellent compatibility found between β' -Al₂O₃ and molten NaAlCl₄ appears to correlate with the free energies of formation of NaAlCl₄ and NaAlO₂ at 500 K of -233 and -244 kcal/mol, respectively. The observed stability is also in agreement with the estimated bond energies of 55 and 66 kcal for Al-Cl and Al-O_{1,2}, respectively.

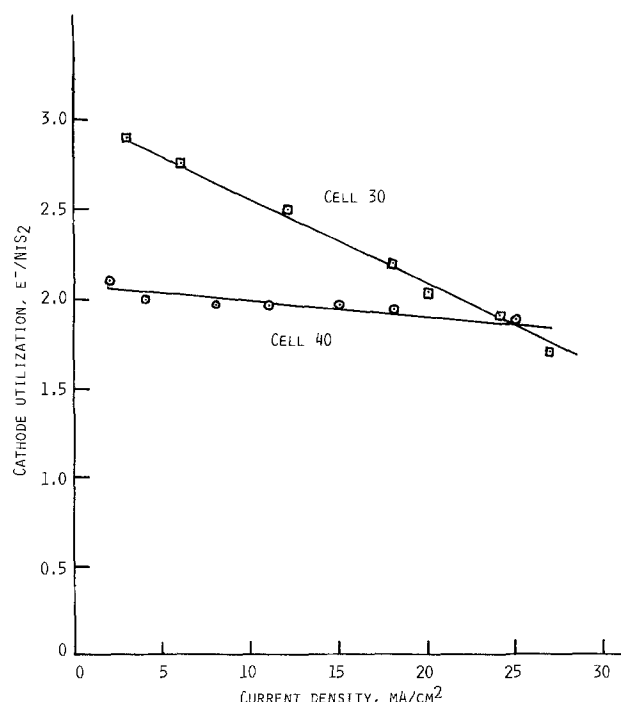


Fig. 6. Rate/capacity data for Na/NiS₂ cells 30 and 40. The NaAlCl₄:NiS₂ mole ratio in cell 30 is 3.5:1, and, in cell 40, it is 2:1.

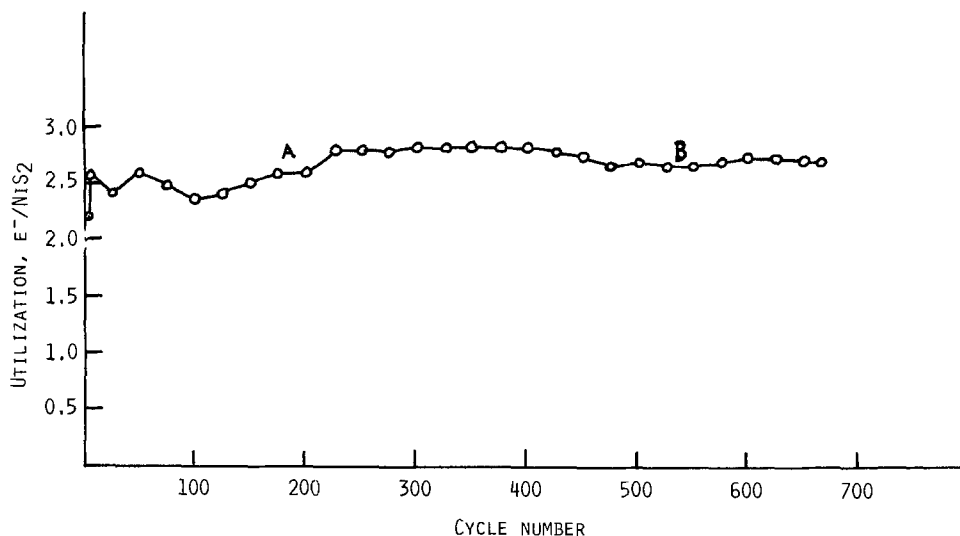


Fig. 7. Cathode utilization vs. cycle number for Na/NiS₂ cell 50. At A, the temperature was raised from 170° to 190°C. At B, the cell was left on open circuit for ~2 months at room temperature, prior to resumption of cycling.

In cell 60, the initial NaAlCl₄ to NiS₂ ratio was 2:1. The cathode mix comprised 1.53g (12.4 mmol) of NiS₂, 0.31g Ni, and 4.75g (24 mmol) of NaAlCl₄. The cell was subjected to more than 200 deep discharge-charge cycles. The average utilization obtained at current densities of 8 mA/cm² for discharge and 4 mA/cm² for charge, between 1.7-3.5V, was ~1.5e⁻/NiS₂. The data are given in Fig. 9. The 1.5e⁻/NiS₂ capacity in cell 60 corresponds to a specific utilization of 37 mAh/cm² of β'-Al₂O₃, which is slightly greater than the 33 mAh/cm² of β'-Al₂O₃ utilization realized in cell 50.

We believe that, with these experiments, we have demonstrated the feasibility of long cycle-life, high specific energy, and excellent system stability for the Na/NiS₂ battery. The results obtained from a 4 Ahr Na/NiS₂ preprototype cell further support these conclusions. That data will be discussed shortly, after presenting the long-term cycling results for a Na/NiS laboratory cell.

Na/NiS cell no. 70 was constructed with a cathode comprising 1.1g (12 mmol) of NiS and 4.7g (24 mmol) of NaAlCl₄. The cell exhibited an OCV of 2.9V at 190°C, the

temperature at which the entire cycling was performed. The cell was cycled between voltage limits of 1.5 and 3.0V, and at the currents of 50 mA (4 mA/cm²) for discharge and 25 mA (2 mA/cm²) for charge. More than 100 cycles have been obtained (see Fig 10 and 11), yielding an average cell capacity of 400 mAh or ~1.3e⁻/NiS. The corresponding specific utilization is 32 mAh/cm² of β'-Al₂O₃, which is of the same order as those realized in NiS₂ cells 50 and 60.

A 4 Ah nominal capacity NiS₂ cell having the specification given in the experimental section was operated at 190°C. The first eight cycles were obtained at a current of 100 mA or 2.5 mA/cm². Beginning with the ninth cycle, the discharge current was changed to 300 mA or 7.5 mA/cm² and the charge current to 3.75 mA/cm². The voltage limits were 1.5 and 3.5V. The cell was cycled more than 75 times (Fig. 12). The highest capacity of the cell was 3.7 Ah, corresponding to a utilization of 2e⁻/NiS₂.

Unlike in the laboratory cell, the capacity showed a tendency to fade gradually with cycling. We believe this was due to a relatively high cell resistance of ~1Ω which

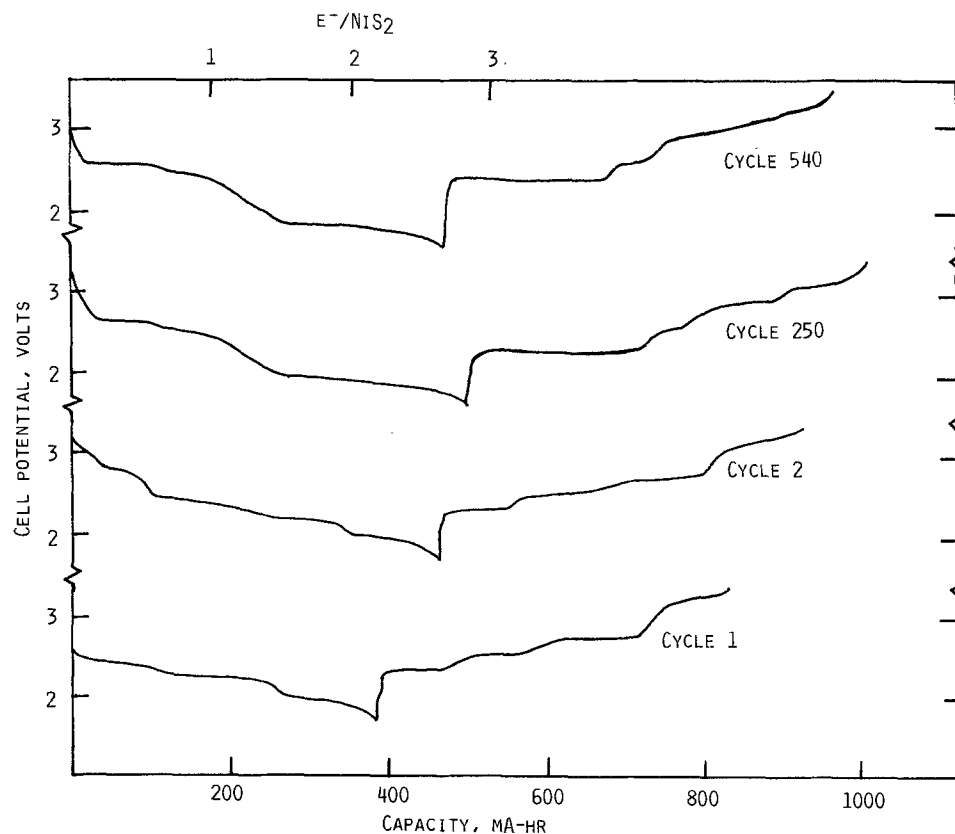


Fig. 8. Typical cycles of Na/NiS₂ cell 50. Current density: cycles 1 and 2, $i_d = i_c = 2 \text{ mA/cm}^2$; cycles 250 and 540, $i_d = 8 \text{ mA/cm}^2$, $i_c = 4 \text{ mA/cm}^2$.

Fig. 9. Cathode utilization vs. cycle number in Na/NiS₂ cell 60. NaAlCl₄:NiS₂ = 2:1. Temp. 190°C. Current density, *i_d* = 8 mA/cm², *i_c* = 4 mA/cm². Voltage limits: 1.7-3.5V.

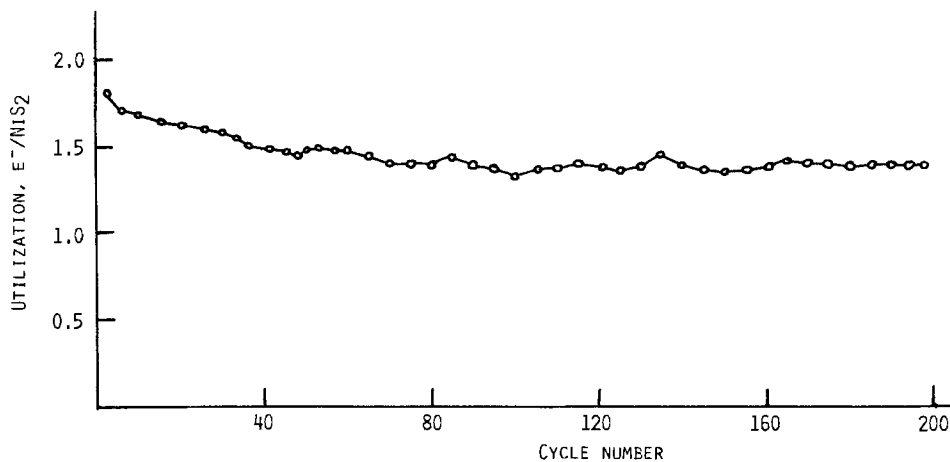
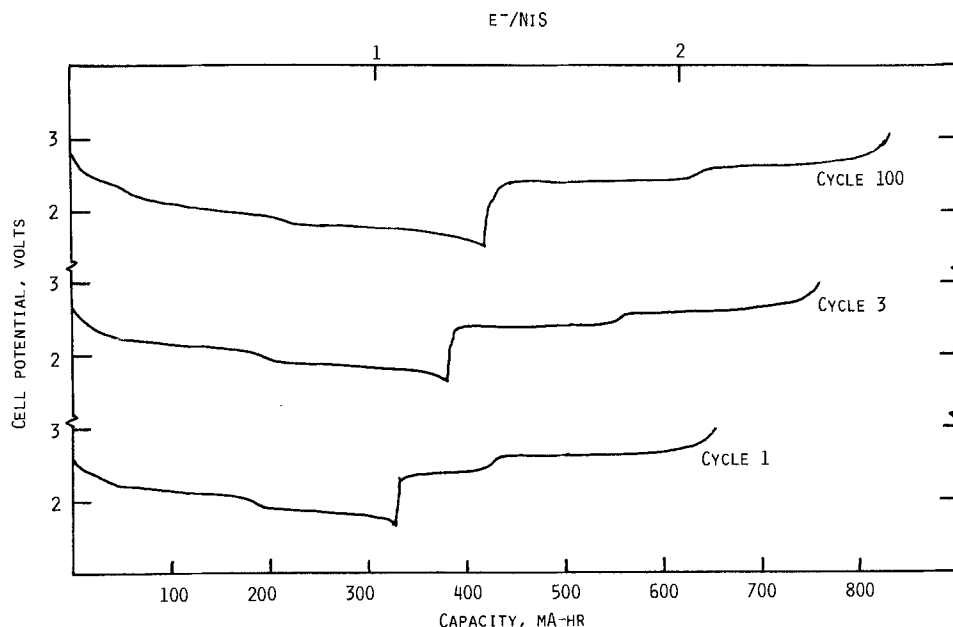


Fig. 10. Typical cycle of Na/NiS cell 70 at 190°C. Current density: cycles 1 and 3, *i_d* = *i_c* = 2 mA/cm²; cycle 100, *i_d* = 4 mA/cm², *i_c* = 2 mA/cm².



slowly increased with repeated cycling. As a result, only smaller and smaller fractions of the capacity involved in the 2V plateau became accessible in later cycles. The specific energy achieved based on the observed capacity of 3.7 Ah, a mid-discharge potential of 2.3V, and including all weights, except those of β -Al₂O₃ and the can, is ~200 Wh/kg. At least a 25% improvement over this should be possible with further optimization of electrode structures and cell configuration.

Overdischarge and overcharge.—Sodium cells utilizing NaAlCl₄ possess a remarkable overdischarge safety mechanism. When the cell is discharged down to ~1.6V vs. Na⁺/Na, a reversible process involving the reduction of the electrolyte occurs

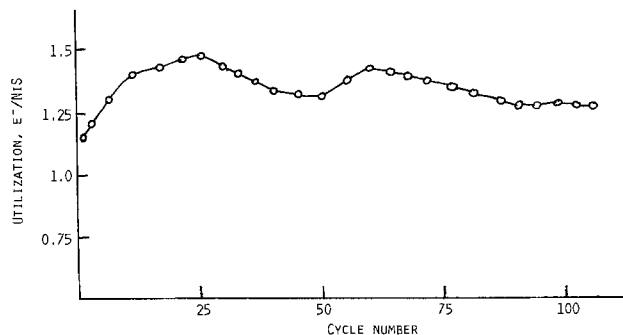
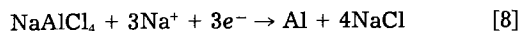


Fig. 11. Cathode utilization vs. cycle number in Na/NiS cell 70

We have found that these cells can be overdischarged for extended periods of time without any apparent deleterious effect on their subsequent cycle performance. In fact, the capacity corresponding to the overdischarge process can also be harnessed practically, thus increasing the energy densities of cells which contain an excess of the electrolyte.

The effect of overcharge was investigated by repeatedly charging a cell to a potential of 4.0V. This had no detrimental effects on the cell's subsequent cycle performance. The overcharge between 3.5 and 4.0V occurred with a sloping potential profile, and the associated capacity showed some variations from cycle to cycle. When the recharge potential limit was lowered to 3.5V after the overcharge cycles, the cell resumed cycling with capacity and voltage characteristics typical of cells which had never been overcharged.

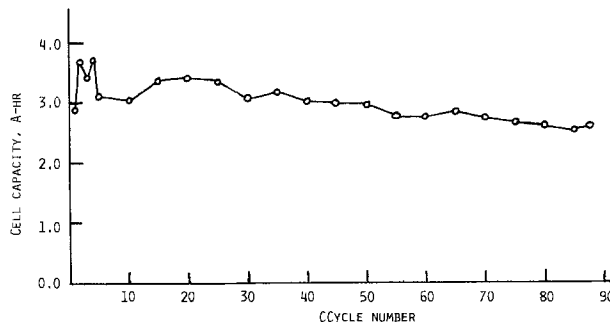


Fig. 12. Cathode utilization vs. cycle number in a pre-prototype Na/NiS cell. Temp. 190°C.

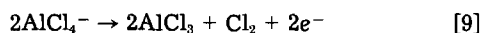
Table III. Energy densities of nickel sulfide cells

Cathode	Capacity (e ⁻ /metal)	Mid-discharge voltage (V)	Cycling regime (V)	Specific energy* (Wh/kg)
NiS	1.9	2.1	1.7-3.0	337
NiS ₂	1.7	2.4	1.7-3.0	336
NiS ₂	2.5	2.4	1.7-3.5	378
NiS ₂	4.0	2.4	1.7-3.5	424**

* Based on a discharge reaction involving NaAlCl₄, also. About 25%-35% of this should be achievable in a practical battery.

** Maximum, corresponding to reaction [3].

The most likely reaction at the cathode during overcharge to 4.0V is that in Eq. [9] (6, 12)



The Cl₂ would dissolve in the electrolyte, or it would react with the cathode material. Another possible reaction during overcharge is the oxidation of NiS₂ to form S and NiCl₂. In discharges following an overcharge to 4.0V, a fraction of the capacity appeared at a potential of ~3.4V. This, most likely, is associated with the reduction of Cl₂ dissolved in the electrolyte.

An overcharge to 4.5V also proceeds with a sloping potential profile similar to that seen in the region between 3.5 and 4.0V. The OCV of cell after the charge to 4.5V was 3.8V, indicating Cl₂ in solution. Again, no detrimental effect of any sort on cell performance was observed. We can conclude that Na/NiS_x cells utilizing NaAlCl₄ possess excellent built-in overdischarge and overcharge protection features due to reversible chemical processes in addition to those associated with the redox reactions of the sulfides.

Conclusions

The electrochemistry of the sulfides, NiS₂ and NiS, in molten NaAlCl₄ has been found to be different from that of Na intercalating chalcogenides such as TiS₂, VS₂, and VSe₂. The nickel sulfides undergo displacement reactions upon reduction, and these processes, forming Ni as

the final product, pass through the intermediate phases, Ni₃S₄, NiS, and Ni₂S₂. Despite the appearance of these intermediate phases, NiS₂ behaves as a highly reversible positive electrode in the Na battery, permitting high rate discharges. The mid-discharge voltage of the Na/NiS₂ cell is 2.4V. A cell with a mid-discharge voltage of 2.1V is obtained when NiS is used as the initial positive electrode. The specific energies calculated based on experimental data are given in Table III. Practical secondary Na batteries capable of delivering ≥50 Wh/lb and >1000 deep discharge/charge cycles appear feasible.

Acknowledgment

This work was supported by the National Aeronautics and Space Administration under Contract no. NAS3-21726.

Manuscript submitted April 13, 1984; revised manuscript received May 31, 1984.

REFERENCES

1. K. M. Abraham, *Solid State Ionics*, **7**, 199 (1982); and references therein.
2. K. M. Abraham, R. D. Rauh, and S. B. Brummer, *Electrochim. Acta*, **23**, 501 (1978).
3. K. M. Abraham, M. W. Rupich, and L. Pitts, *This Journal*, **128**, 2700 (1981).
4. K. M. Abraham, M. W. Rupich, L. Pitts, and J. E. Elliot, Final Report on NASA Contract NAS3-21726, Report no. NASA CR 168220, July 1983; available from NTIS, Springfield, VA 22161.
5. J. J. Auburn and S. M. Granstaff, *Proc. 15th IECEC*, 575 (1980).
6. G. Mamantov, R. Marassi, M. Matsunaga, Y. Ogato, J. P. Wiax, and E. J. Frazier, *This Journal*, **127**, 2319 (1980).
7. I. W. Jones, *Electrochim. Acta*, **22**, 681 (1977).
8. J. Robinson, B. Gilbert, and R. A. Osteryoung, *Inorg. Chem.*, **16**, 3040 (1977).
9. R. W. Berg, S. Von Winbush, and N. J. Bjerrum, *ibid.*, **19**, 2688 (1980).
10. D. R. Stull and H. Prophet, "JANAF Thermochemical Tables," NSRDS-NBS-37, National Bureau of Standards, Washington, DC (1971).
11. S. K. Preto, Z. Tomczuk, S. Von Winbush, and M. F. Roche, *This Journal*, **130**, 264 (1983).
12. K. M. Abraham and R. M. Mank, *ibid.*, **127**, 2091 (1980).

Molten Carbonate Fuel Cell Cathode Materials Study

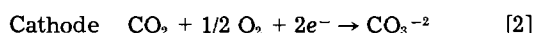
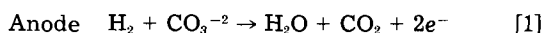
Charles E. Baumgartner,* Ronald H. Arendt,* Charles D. Iacovangelo,* and Bradley R. Karas*

General Electric Company, Corporate Research and Development, Schenectady, New York 12301

ABSTRACT

Data are presented on the electronic conductivity and molten alkali carbonate stability (Li:K binary of 62:38 mole ratio) of various materials at 923 K under a 30% CO₂/air atmosphere. Of the examined materials, only LaNiO₃ and La_xSr_{1-x}CoO₃ satisfied both criteria sufficiently for acceptable use as molten carbonate fuel cell cathode materials.

Molten carbonate fuel cells (MCFC's) have been under extensive development as high efficiency systems for directly converting gasified coal or natural gas into electricity. Relative to other liquid electrolyte fuel cells, the carbonate system offers the unique advantage of the electrolyte's composition remaining invariant during cell operation. The electrochemical reactions involved during H₂ oxidation at the anode and O₂ and CO₂ reduction at the cathode are shown below



Carbonate ion, consumed at the anode and generated at the cathode, is continuously transported between the

* Electrochemical Society Active Member.

electrodes through an alkali carbonate-filled, porous ceramic electrolyte structure. Conventional fuel cell components consist of a porous stabilized nickel anode, a porous lithium-doped NiO cathode, and a LiAlO₂-reinforced electrolyte structure typically containing a 62 mole percent (m/o) Li₂CO₃:38 m/o K₂CO₃ electrolyte.

A major MCFC problem is dissolution of the lithium-doped NiO (Li_{0.02}Ni_{0.98}O) cathode in the carbonate electrolyte (1-3). Following dissolution, the cathode material is transported diffusively into the electrolyte structure. In an operating cell, an oxygen concentration gradient exists within the electrolyte structure which decreases from the cathode to the anode interface. At some location between the two electrodes the P_{O₂} drops below the region where NiO is stable (4). The equilibrium nickel solubility at this location decreases resulting in the deposition of metallic

nickel from the electrolyte. These metallic nickel "sinks," located within the electrolyte structure, create a nickel concentration gradient which continually transports cathode material away from the cathode/electrolyte structure interface and, hence, facilitates further cathode dissolution. The consequence of such $\text{Li}_{0.02}\text{Ni}_{0.98}\text{O}$ corrosion is clearly evident in Fig. 1, which displays a Ni x-ray fluorescence map of a 0.18 cm thick electrolyte structure from a MCFC operated at 923 K and atmospheric pressure for 10,080h. Post-test analysis showed that approximately 10% of the cathode had dissolved, transported into the electrolyte structure, and precipitated as metallic nickel during the cell test. These nickel deposits are visible as bright spots in Fig. 1. While such a transport mechanism for NiO was not appreciated previously, a similar cathode corrosion was responsible for the abandonment of Ag and CuO as MCFC cathode materials (5-7).

In response to this acute problem, we have surveyed the molten alkali carbonate stability and high temperature electronic conductivity of selected materials in an attempt to identify a suitable replacement cathode material. The criteria of a successful candidate material were selected to be: (i) 923 K electronic conductivity ≥ 1 ($\Omega \text{ cm}$)⁻¹, (ii) stability in the MCFC cathode environment (923 K, O_2/CO_2 atmosphere, carbonate electrolyte), and (iii) reduced solubility under the cathode environment or, preferably, increased solubility in the anode environment relative to $\text{Li}_{0.02}\text{Ni}_{0.98}\text{O}$.

The third criterion satisfies the requirement that the cathode-to-anode material transport rate, and associated cathode fluxing, be reduced. Along this line, it is obviously preferable that no species derived from cathode dissolution precipitate within the cell since such "sinks" are directly associated with cathode fluxing. This would mandate that the material's solubility under the anode's environment be at least equal to, and preferably exceed, that under the operating cathode environment. However, since there is little quantitative published data on materials solubility in alkali carbonates (3-7), materials examined in this survey were not selected for their solubility characteristics. Instead, selection was based more on the anticipated material's stability in the oxidizing carbonate environment. Because of this, a few materials were included in our sampling which are thermodynamically stable as metals under the anode's environment (hence possessing a low solubility) when they were known to satisfy the stability requirement.

In addition to the above requirements, an acceptable replacement material must also be catalytically active towards O_2 electroreduction and fabricable into a porous electrode structure. These criteria, however, were not examined in this initial survey.

Experimental

Sample preparation.—Selected candidate materials were synthesized using either a molten salt (MS) mediated synthesis (8) or a more conventional high temperature solid-state synthetic route. The precise details of

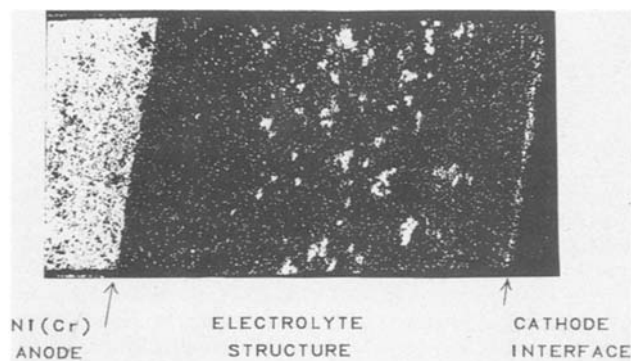


Fig. 1. Ni x-ray fluorescence map of a 0.18 cm thick electrolyte structure operated within a MCFC at 923 K and atmospheric pressure for 10,080h. The bright regions correspond to metallic nickel.

each sample's synthesis will not be given; the preparation of one material using each synthetic route will be covered instead. Materials prepared using a MS synthesis are typified by Ti-doped LiFeO_2 . The MS synthesis utilized molten 50 m/o NaCl-KCl as the solvent. This technique has the advantage of yielding a product of close compositional and particle-size uniformity. Ti-doped LiFeO_2 ($\text{LiFe}_{0.96}\text{Ti}_{0.04}\text{O}_2$) was synthesized by combining 1 mol each of KCl and NaCl, 0.48 mol Fe_2O_3 , 0.04 mol TiO_2 , and 1.25 mol LiOH; a 25% excess of LiOH was present to insure the final lithium ratio. These powders were well blended by dry roll milling, placed in a covered 500 ml $\alpha\text{-Al}_2\text{O}_3$ crucible, and heated in air for 16h at 1373 K. Following cooling, the chloride solvent was dissolved in deionized water and the product powder collected by filtration. X-ray diffraction (XRD) and chemical analysis were utilized to confirm product formation. Due to the survey nature of this study, no attempts were made to further identify minor constituents not detectable with XRD.

In addition to the MS synthetic route, materials were also prepared using a high temperature solid-state (SS) reaction. Reactants used in this synthesis were typically organometallics or hydroxides which were dissolved or dispersed in solution. An example of a cathode candidate synthesized by the SS reaction scheme is Ti-doped ZnO ($\text{Zn}_{0.97}\text{Ti}_{0.03}\text{O}$). Here 0.015 mol titanium tetra-butoxide [$\text{Ti}(\text{OBU})_4$] was dissolved in methanol to which was added 0.485 mol of ZnCO_3 powder. The materials were homogenized by ball milling with dense ZrO_2 media. The addition of dilute aqueous NH_4OH converted the $\text{Ti}(\text{OBU})_4$ to a $\text{Ti}(\text{OH})_4$ gel, which uniformly surrounded each ZnCO_3 particle. The mixture was dried under vacuum at 398 K. Conversion to the final composition was accomplished by a 16h air firing at 1373 K.

Material evaluation.—All candidates were evaluated for their stability in the molten 62:38 (mole ratio $\text{Li}_2\text{CO}_3:\text{K}_2\text{CO}_3$) carbonate electrolyte. The powdered material was combined with an approximately 50 \times molar excess of electrolyte in a 7.5 cm high, 1.6 cm diam gold crucible and heated for 50–100h at 923 K under a 30% CO_2 /air atmosphere. Following cooling, the electrolyte was dissolved in either dilute aqueous acetic acid or hot deionized water, the powder collected by filtration, and its identity determined by XRD and chemical analysis. Changes in either the XRD pattern or chemical composition were used as evidence of instability.

The sample's electrical conductivity was obtained using a standard four-probe ac impedance technique on pressed sintered pellets, as described previously (9). The conductivity apparatus is shown in Fig. 2. Pellets, 1.2 cm diam \times ~0.6 cm thick, were prepared by pressing the powders from between 70–120 MPa. Some powders required the addition of a few drops of a binder solution of 1% stearic acid in acetone to facilitate pellet formation. The pellets were air sintered from between 1023 and 1472 K, the actual temperature and time conditions depending on the particular material. Following sintering, the faces of the pellets were polished smooth, sputtered with 0.5–1.0 μm gold, and two gold wires were attached to each face using conductive silver paint (du Pont conductor composition 4922). The samples, held in an $\alpha\text{-Al}_2\text{O}_3$ frame (not shown in Fig. 2) and contained within an $\alpha\text{-Al}_2\text{O}_3$ tube furnace under a 30% CO_2 /air atmosphere, were heated to 773 K overnight to cure the silver paint. The above atmosphere was selected to simulate the in-cell cathode's environment; no atmospheric effects on electronic conductivity were examined. Sample conductivities were measured as a function of signal frequency (50–10,000 Hz) during both heating (773–1123 K) and cooling (1123–923 K) cycles using a PAR 5204 Lock-In Analyzer coupled to a PAR 371 signal source (Princeton Applied Research, Incorporated, Princeton, New Jersey).

Equilibrium solubility measurements were made on selected candidate materials in molten 62:38 electrolyte at temperatures between 923 and 1123 K according to the technique described in detail elsewhere (3, 14). Pellets

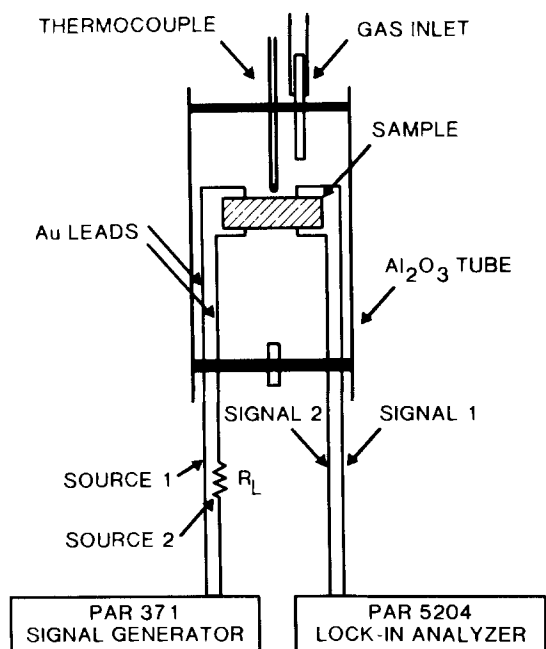


Fig. 2. Apparatus used to measure four-probe ac impedance on pressed samples.

prepared similarly to those described above were heated in a 7.5 cm tall \times 1.6 cm diam gold crucible with approximately 20g of electrolyte for between 250 and 500h under a room temperature humidified 30% CO_2 /air atmosphere. Electrolyte aliquots of between 1 and 2g were removed at temperature by inserting an $\alpha\text{-Al}_2\text{O}_3$ pipette into the upper portion of the carbonate melt. This electrolyte was transferred to a clean gold crucible, cooled, and analyzed for dissolved material by atomic absorption analysis. The sampling times were shown previously (14) to yield equilibrium solubility values, being defined here as the analyzed constituent not varying more than $\pm 5\%$ relative to a mean over a 3-day period. The limit of $\pm 5\%$ represents the typical reproducibility attained on identical samples and constitutes the cumulative deviation present in the solubility and analytical techniques. The fact that equilibrium was established here at the time of sampling was verified on several samples. An experimental blank containing electrolyte without any candidate material was processed occasionally with the experimental samples to insure that samples were not contaminated by the furnace environment.

Results and Discussion

Table I lists the candidate materials investigated, the synthetic scheme utilized in their preparation, the materials' electrolyte stability, and the electronic conductivity measured at 923 K and 1 kHz. The state-of-the-art cathode material, $\text{Li}_{0.02}\text{Ni}_{0.98}\text{O}$, is included for comparison. As can be seen from the data, several materials were found to be unstable in the electrolyte; the major source of instability being reactivity with Li_2CO_3 to yield a Li containing product. This is clearly demonstrated in the Fe- or Ti-based systems which always decomposed to yield LiFeO_2 or Li_2TiO_3 . Of those materials found to be stable in the carbonate fuel cell cathode environment, only the La containing perovskites, LaNiO_3 and $\text{La}_x\text{Sr}_{1-x}\text{CoO}_3$, exhibited electronic conductivities which exceeded the required 1 $(\Omega \text{ cm})^{-1}$.

The establishment of 1 $(\Omega \text{ cm})^{-1}$ as an acceptable pressed pellet conductivity minimum was based on the allowable IR drop associated with fuel cell operation. Although the relationship between conductivity and porosity was not determined here, Eq. [3] typifies the correlation found in the literature (10)

$$\sigma = \sigma_0 (1 - P)^x \quad [3]$$

Table I. Investigated candidate MCFC cathode materials

Material	Synthesis	Electrolyte stable	923 K electronic conductivity $(\Omega \text{ cm})^{-1}$
$\text{Li}_{0.02}\text{Ni}_{0.98}\text{O}$	SS	Yes	33
Fe-based			
LiFeO_2	MS	Yes	3×10^{-3}
$\text{LiFe}_0.98\text{O}_3$	MS	No	—
$\text{LiFe}_{0.99}\text{Ti}_{0.01}\text{O}_2$	MS	Yes	3×10^{-3}
$\text{LiFe}_{0.96}\text{Ti}_{0.04}\text{O}_2$	MS	Yes	1×10^{-3}
$\text{LiFe}_{0.94}\text{Ti}_{0.06}\text{O}_2$	MS	Yes	5×10^{-4}
$\text{LiFe}_{0.96}\text{Zr}_{0.04}\text{O}_2$	SS	Yes	2×10^{-3}
$\text{LiFe}_{0.94}\text{Zr}_{0.06}\text{O}_2$	SS	Yes	6×10^{-4}
NiFe_2O_4	MS	No	8×10^{-4}
$\text{Li}_{0.1}\text{Ni}_{0.5}\text{Fe}_2\text{O}_4$	MS	No	6×10^{-4}
$\text{Li}_{0.2}\text{Ni}_{0.4}\text{Fe}_2\text{O}_4$	MS	No	3×10^{-3}
$\text{Ni}_{0.5}\text{Fe}_{2.5}\text{O}_4$	MS	No	5×10^{-3}
$\text{Cu}_{0.1}\text{Ni}_{0.9}\text{Fe}_2\text{O}_4$	MS	No	5×10^{-4}
$\text{Fe}_{1.98}\text{Ti}_{0.01}\text{O}_3$	SS	No	3
$\text{Sr}_2\text{Fe}_2\text{O}_5$	MS	No	7×10^{-1}
Ti-based			
Li_2TiO_3	MS	Yes	4×10^{-5}
$\text{Li}_2\text{Ti}_{0.95}\text{Ta}_{0.05}\text{O}_3$	MS	Yes	2×10^{-3}
SrTiO_3	MS	No	—
$\text{SrTi}_{0.95}\text{Ta}_{0.05}\text{O}_2$	MS	No	—
NiTiO_3	MS	No	1×10^{-5}
$\text{Ni}_{0.2}\text{Sr}_{0.8}\text{TiO}_3$	MS	No	1×10^{-5}
$\text{Li}_{0.35}\text{Ni}_{0.67}\text{TiO}_3$	MS	No	—
La-perovskites			
LaNiO_3	SS	Yes	5
LaCoO_3	SS	Yes	—
$\text{La}_{0.6}\text{Sr}_{0.4}\text{CoO}_3$	SS	Yes	35
$\text{La}_{0.8}\text{Sr}_{0.2}\text{CoO}_3$	SS	Yes	20
$\text{La}_{0.5}\text{Sr}_{0.5}\text{MnO}_3$	SS	No	—
Others			
$\text{Li}_{0.01}\text{Cu}_{0.99}\text{O}$	MS	Yes	3×10^{-1}
ZnO	SS	Yes	7×10^{-3}
$\text{Zn}_{0.99}\text{Zr}_{0.01}\text{O}$	SS	Yes	1×10^{-4}
$\text{Zn}_{0.97}\text{Ti}_{0.03}\text{O}$	SS	Yes	2×10^{-3}
CeO_2	SS	Yes	1×10^{-3}
$\text{Ce}_{0.975}\text{La}_{0.025}\text{O}_2$	SS	Yes	3×10^{-4}
$\text{Ce}_{0.975}\text{Sr}_{0.025}\text{O}_2$	SS	Yes	1×10^{-3}
$\text{Ce}_{0.95}\text{Sr}_{0.05}\text{La}_{0.025}\text{O}_2$	SS	Yes	7×10^{-4}
$\text{Ce}_{0.9}\text{Nb}_{0.1}\text{O}_2$	SS	Yes	9×10^{-6}
$\text{SrSr}_{0.99}\text{Nb}_{0.01}\text{O}_3$	MS	No	3×10^{-5}
$\text{Li}_2\text{Sn}_{0.99}\text{Nb}_{0.01}\text{O}_3$	MS	Yes	—

where σ = actual conductivity

σ_0 = conductivity at theoretical density

P = pore fraction in sample

Literature values of x range between 1.5 and 3, with most references (10, 11) determining a value of $x = 1.5\text{--}2.0$. A fuel cell cathode structure possessing a 60% porosity, therefore, is expected to exhibit a conductivity $\sim 3\text{--}5$ times less than that measured using the nominally 80%–90% dense pressed pellets. A typical porous fuel cell cathode thickness is 0.038 cm. If it is assumed that the electrochemical reaction occurs predominantly near the electrode/electrolyte interface, all current must pass through the cathode thickness before reaching the current collector. For a cell current density of 160 mA/cm^2 , a porous cathode conductivity of 0.2 $(\Omega \text{ cm})^{-1}$ [comparable to a pressed pellet conductivity of $\sim 1 (\Omega \text{ cm})^{-1}$] would result in a one-dimensional IR loss of ~ 30 mV. Although the cathodic reaction most likely is not limited to a region close to the electrolyte interface, this approximation illustrates the importance of cathode conductivity on the cell's performance.

Referring to the results in Table I, LiFeO_2 and Li_2TiO_3 were shown to be stable in the MCFC's cathode environment; however, their 923 K electronic conductivities of 3×10^{-3} and $4 \times 10^{-5} (\Omega \text{ cm})^{-1}$, respectively, were considerably below the required cut off. Attempts to improve conductivity by doping with higher valency cations proved counterproductive for LiFeO_2 , the 923 K conductivity decreasing by a factor of ~ 5 upon substitution of 6% Zr or Ti for Fe. The conductivity-temperature curves obtained at 1 kHz for several Zr- and Ti-doped LiFeO_2 samples are shown in Fig. 3. Substitution of 5% Ta for Ti in Li_2TiO_3 did increase the 923 K conductivity by about a factor of 20; however, the conductivity remained orders of

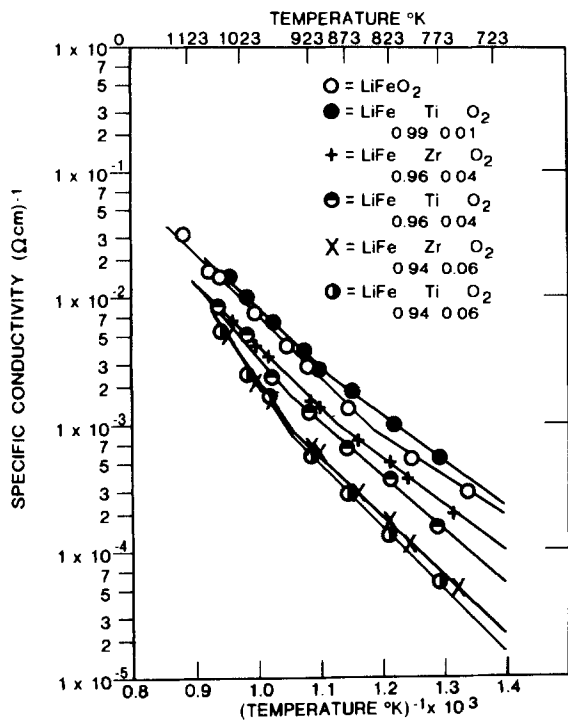


Fig. 3. Influence of Ti and Zr doping on the electrical conductivity of LiFeO_2 under 30% CO_2 /air atmosphere between 773 and 1123 K.

magnitude too low. Similar results were obtained with ZnO and CeO_2 , two other electrolyte-stable materials. As noted previously, only the La containing perovskites appear promising as candidates as a result of these data.

A minor drawback to the use of La-perovskites in MCFC applications is their reactivity towards the state-of-the-art electrolyte structure matrix material, LiAlO_2 . While found to be stable towards the carbonate electrolyte alone, the presence of both LiAlO_2 and the electrolyte leads to the metathetical reaction below



This necessitated the identification of an alternate matrix support material for use with a La-perovskite cathode structure. One promising candidate is SrTiO_3 (8), which has been shown to remain phase pure following exposure to both LaNiO_3 and molten electrolyte in a pot-test of several hundred hours duration.

In addition to an alternate cathode material possessing electrolyte stability and an acceptable electronic conductivity, the material must demonstrate a reduced corrosion rate in the electrolyte under cell operating conditions. This behavior can result from either a decreased solubility under cathode conditions or an increased solubility under anode conditions. Equilibrium solubility measurements were made on several materials as a function of temperature between 923 and 1123 K under a room temperature humidified 30% CO_2 /air atmosphere. These data are given in Fig. 4. Unfortunately, these solubility determinations are severely hindered by the presence of high background impurity levels in the nascent electrolyte. The impurity levels determined on various high purity electrolyte samples are listed in Table II and are also shown, in part, in Fig. 4.

Under experimental conditions where the nascent carbonate's impurity level exceeded the equilibrium solubility, no decrease in solute concentration was found with time up to 500h. The system's failure to approach equilibrium in the direction of decreasing concentration suggests that the solute species either remains supersaturated in solution or precipitates as a fine particulate suspension and was therefore sampled along with the dissolved form.

Despite the problematic impurity levels, however, the linear solubility/temperature relationships for NiO, ZnO,

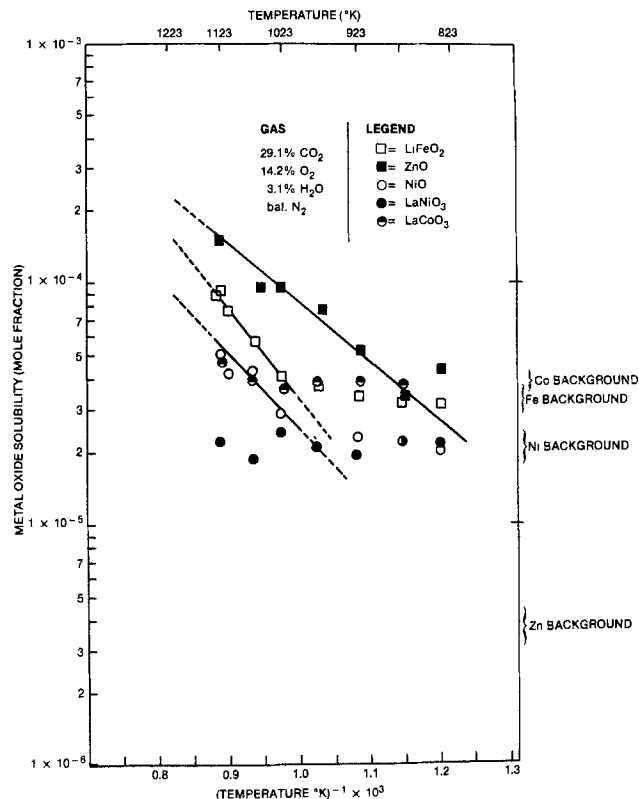


Fig. 4. Equilibrium solubility temperature dependence for NiO, ZnO, LaNiO_3 , LaCoO_3 , and LiFeO_2 in 62 m/o Li_2CO_3 :38 m/o K_2CO_3 under humidified 30% CO_2 /air atmosphere.

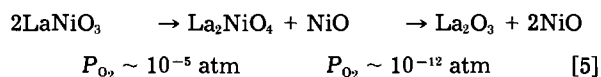
and LiFeO_2 are seen in Fig. 4. In each case, the solubility increased as a function of temperature in contrast to the retrograde NiO solubility-temperature dependence found by Sim *et al.* (12) under similar conditions. The magnitude of these solubilities at 923 K, the operating temperature of a MCFC, were relatively similar, with neither ZnO nor LiFeO_2 offering any particular advantage in equilibrium solubility relative to NiO under the experimental conditions. In contrast, the LaNiO_3 and LaCoO_3 solubilities were found to be temperature invariant, with the magnitude of the solubility not varying significantly from the electrolyte's background impurity levels. Complementary La analysis, performed on the electrolyte from LaNiO_3 samplings using x-ray fluorescence analysis, showed no La to be present, *i.e.*, the La concentration remained below the 5 ppm mole fraction detection limit. Since the LaNiO_3 and LaCoO_3 solubilities could not be measured, they may offer some reduced solubility advantages over NiO as MCFC cathode materials.

The transport rate, rather than the actual cathode environment solubility level, however, is important in determining the cathode dissolution rate. Attempts to determine the equilibrium solubility under simulated

Table II. Impurity levels determined in commercial "high purity" 62:38 (Li_2CO_3 : K_2CO_3) electrolyte

Impurity	Analyzed concentration (ppm mole fraction)
Ni	19-25
Fe	31-35
Co	33-40
Cr	2-7
Cu	0.3-1
Mn	2-7
Zn	2-6
Au	<1
Ti	<5
Al	<5
La	<5
Nb	<3

anode-side conditions (H_2/CO_2 mixture) were precluded by the high background impurity levels. Further studies along this line will require the synthesis of higher purity Li_2CO_3 and K_2CO_3 . It can be assumed, however, that neither $LaNiO_3$ nor $LaCoO_3$ will offer a significant advantage over NiO in anode side stability since both materials decompose to La_2O_3 and MeO ($Me = Ni$ or Co) at low oxygen partial pressures (13), as shown by the equation below



Therefore, dissolved $LaNiO_3$ or $LaCoO_3$ is expected to lead to metallic precipitation in the same fashion as the present cathode, and any advantage associated with this material will necessarily come from a reduced cathode-side solubility.

The results of this study demonstrate several points. First is the difficulty in finding materials which are chemically stable in the molten electrolyte under cathode gas environment. Second, there is the compounding difficulty of finding stable materials which possess a suitably high electronic conductivity. Of the materials examined, only $LaNiO_3$ and $La_{1-x}Sr_xCoO_3$ were found to satisfy these requirements. Third, there is the difficulty in evaluating equilibrium solubilities for materials in molten alkali carbonates. Although the measurements were complicated by high impurity background levels, temperature dependent solubilities were obtained for NiO , ZnO , and $LiFeO_2$ under a humidified 30% CO_2 /air atmosphere. The $LaNiO_3$ and $LaCoO_3$ solubilities were not determined because of the impurity levels in the base electrolyte.

Acknowledgments

This work was supported in part by the U.S. Department of Energy under contract no. DE-AC02-80ET17019. The Institute for Gas Technology, Chicago, Illinois, is thanked for supplying the electrolyte structure pictured in Fig. 1.

Manuscript submitted April 9, 1984; revised manuscript received June 4, 1984.

General Electric Company assisted in meeting the publication costs of this article.

REFERENCES

1. C. E. Baumgartner, in "Molten Carbonate Fuel Cells," The Electrochemical Society Softbound Proceedings Series, Pennington, NJ, To be published.
2. W. M. Vogel, L. J. Bregoli, S. W. Smith, and H. R. Kunz, in "Molten Carbonate Fuel Cells," The Electrochemical Society Softbound Proceedings Series, Pennington, NJ, To be published.
3. C. E. Baumgartner, *This Journal*, **131**, 1850 (1984).
4. M. D. Ingram and G. J. Janz, *Electrochim. Acta*, **10**, 783 (1965).
5. M. Schenke and G. H. J. Broers, in "Power Sources 1966," D. H. Collins, Editor, p. 459, Pergamon Press, Oxford, England (1967).
6. M. Schenke and G. H. J. Broers, in "Deuximes Journees Internationales a Combustible," p. 398, Brussels, June 19-23, 1967.
7. L. G. Austin, "Fuel Cells, A Review of Government Sponsored Research 1950-1964," NASA-SP-120, p. 68, NASA, Washington, DC (1967).
8. R. H. Arendt, *This Journal*, **129**, 979 (1982).
9. C. E. Baumgartner, R. H. Arendt, C. D. Iacovangelo, and B. R. Karas, p. 113, Abstracts of the 1982 National Fuel Cell Seminar, Newport Beach, CA, Nov. 14-18, 1982.
10. R. E. Meredith and C. W. Tobias, "Advances in Electrochemistry and Electrochemical Engineering," Vol. 1, pp. 15-47, Interscience, New York (1960).
11. D. A. G. Bruggeman, *Ann. Phys.*, **24**, 636 (1935).
12. J. W. Sim, C. H. Kucera, J. L. Smith, A. M. Breindel, and R. D. Pierce, p. 108, Abstracts of the 1982 National Fuel Cell Seminar, Newport Beach, CA, Nov. 14-18, 1982.
13. M. Tetsuro, G. Petzow, and L. J. Gauckler, *Mater. Res. Bull.*, **14**, 649 (1979).
14. C. E. Baumgartner, *J. Am. Ceram. Soc.*, **67**, 460 (1984).

Determination of the Thermoneutral Potential of $Li/SOCl_2$ Cells

N. A. Godshall*¹ and J. R. Driscoll

Altus Corporation, San Jose, California 95112

ABSTRACT

Heat generated during discharge of $Li/SOCl_2$ cells is an important consideration in the design of both active and reserve-activated batteries, and depends critically on the value of the enthalpic portion of the electrochemical reaction, or "thermoneutral potential" (E_H). The thermodynamic basis for the causes of heat generation in $Li/SOCl_2$ cells is described, and the importance of the thermoneutral potential is discussed. Good agreement was obtained between two experimental techniques used to measure E_H : (i) calorimetric studies and (ii) measurements of open-circuit potential as a function of temperature. Electrochemical discharge of $Li/SOCl_2$ cells was found to be exothermic at all discharge rates, with a thermoneutral potential of $3.72 \pm 0.02V$ and a $\partial E/\partial T$ value of -0.21 ± 0.03 mV/C.

The open-circuit voltage (E) of a faradaic electrochemical cell may be related to the thermodynamic free energy (ΔG_r) of the electrochemical reaction taking place within the cell by the relation

$$\Delta G_r = -zF \int_0^x E dx \quad [1]$$

where F represents the Faraday constant (23.06 kcal V^{-1} eq $^{-1}$), z is the charge transport number (eq mol $^{-1}$), and x is the extent of reaction (dimensionless). That is, the standard free energy of reaction (ΔG_r) is simply the area under a discharge curve of a cell discharged at an infinitely low rate. For an electrochemical couple having a

(nearly) flat discharge curve, such as lithium/thionyl chloride, Eq. (1) simplifies to

$$\Delta G_r = -zFE \quad [2]$$

The free energy of the electrochemical reaction is composed of enthalpic (ΔH_r) and entropic (ΔS_r) parts

$$\Delta G_r = \Delta H_r - T\Delta S_r \quad [3]$$

The combined statement of the first and second laws of thermodynamics states that

$$\partial \Delta G = \Delta V \partial P - \Delta S \partial T \quad [4]$$

So that at constant pressure

$$\frac{\partial \Delta G}{\partial T} = -\Delta S \quad [5]$$

* Electrochemical Society Active Member.

¹Present address: Sandia National Laboratories, Albuquerque, New Mexico 87185.

Substitution into Eq. (2) yields

$$\Delta S_r = zF \frac{\partial E}{\partial T} \quad [6]$$

Therefore, the entropy change of an electrochemical reaction at equilibrium may be derived from a knowledge of the way in which the open-circuit potential of the cell varies with temperature.

The enthalpy change of the electrochemical reaction (ΔH_r) follows directly from the above

$$E = \frac{-\Delta H_r}{zF} + \frac{T\Delta S_r}{zF} \quad [7]$$

$$\frac{-\Delta H_r}{zF} = E - \frac{T\partial E}{\partial T} \quad [8]$$

Equation [8] represents the thermoneutral potential, (E_H), and reflects that part of the cell voltage due only to the enthalpy term

$$E_H = \frac{-\Delta H_r}{zF} \quad [9]$$

E_H is that potential at which a cell would need to be operated such that no heat flowed into or out of the cell. It is also the theoretical open-circuit voltage of the cell at absolute zero. Because the enthalpy change of the electrochemical reaction (ΔH_r) is usually quite constant over the temperature range considered, the thermoneutral potential is also nearly independent of temperature.

Heat Analysis

The importance of the thermoneutral potential (E_H) to heat generation, and its derivation, may be found elsewhere (1, 2). The analysis in the previous section was concerned only with "equilibrium" phenomena (*i.e.*, open-circuit conditions). A complete heat analysis also includes nonequilibrium effects, such as those caused by finite discharge currents, corrosion of the lithium anode, etc. The total heat (q_T) generated during an electrochemical discharge is simply the sum of the heat generated by polarization (q_p), entropy affects (q_s), and other sources of heat such as self-discharge (*e.g.*, Li corrosion)

$$q_T = q_p + q_s + q_{\text{other}} \quad [10]$$

where a negative q_T represents a generation of heat by the cell, and a positive q_T represents an absorption of heat by the cell from its local surroundings.

The heat generated by cell polarization is given by the difference between the open-circuit potential (E) and the voltage under load (E_L)

$$q_p = -zF(E - E_L) \quad [11]$$

Likewise, the heat generated or absorbed due to the entropy effects described previously is given by

$$q_s = T\Delta S_r = zFT \frac{\partial E}{\partial T} \quad [12]$$

Considering only these two sources of heat results in

$$q_T = -zF \left(E - E_L - \frac{T\partial E}{\partial T} \right) \quad [13]$$

Substitution of Eq. [8] into Eq. [13] simplifies this result to terms involving only the thermoneutral potential and voltage under load

$$q_T = -zF(E_H - E_L) \quad [14]$$

Differentiation with respect to time renders this relation in terms of heating rate (\dot{q}_T), in watts, and the cell current (I), in amperes

$$\dot{q}_T = -I(E_H - E_L) \quad [15]$$

The behavior of an electrochemical cell, and its relation to heat generation, falls into one of the two cases outlined in Fig. 1-3. Most battery discharge reactions are of the

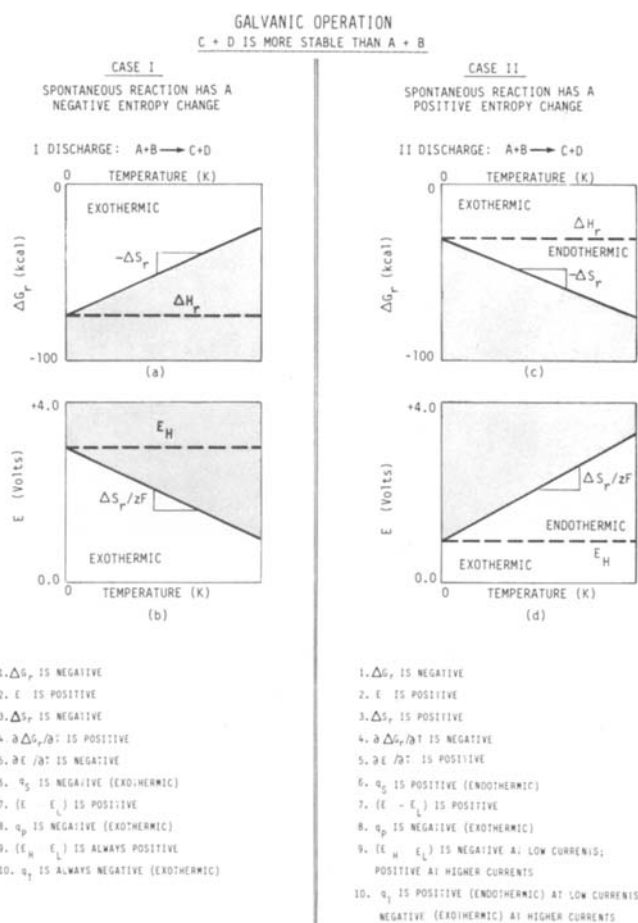


Fig. 1. Discharge of electrochemical cells having (I) negative and (II) positive entropies of reaction.

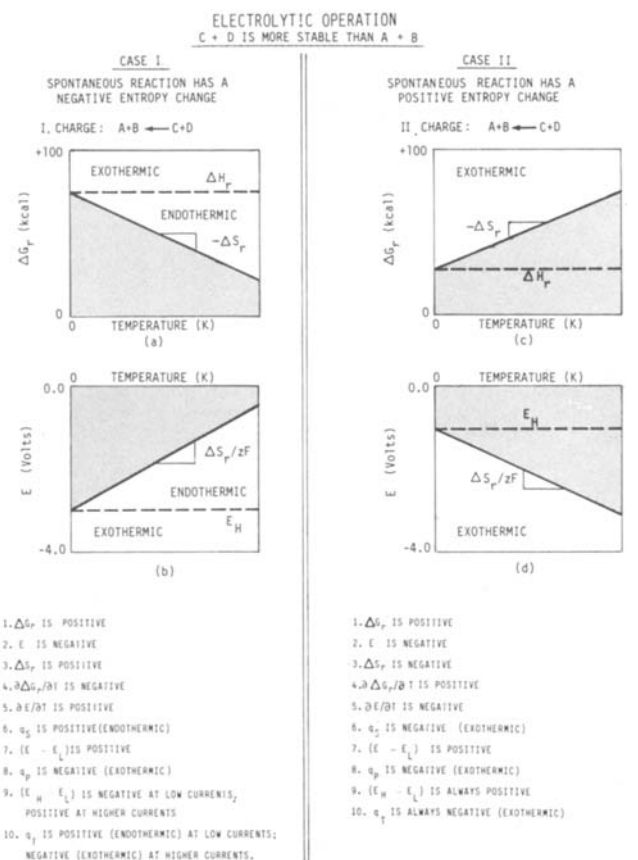


Fig. 2. Charging of electrochemical cells having (I) negative and (II) positive entropies of reaction.

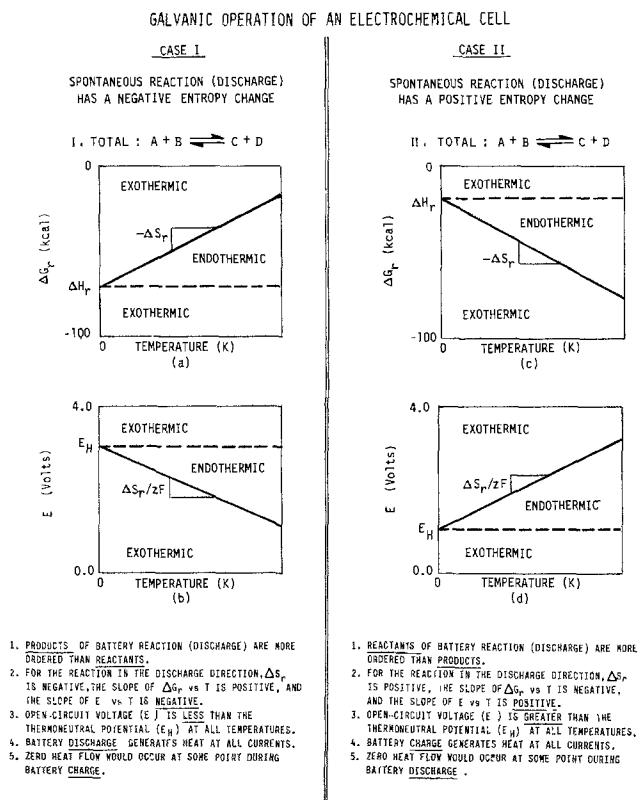


Fig. 3. Heat generation and absorption regions illustrated on idealized Ellingham and E vs. T diagrams for electrochemical reactions with (I) negative and (II) positive entropy changes during discharge (spontaneous reaction).

Case I type. That is, the free energy (ΔG_r) of the galvanic reaction (discharge) is less negative at higher temperatures, due to a negative entropy associated with the reaction (ΔS_r). That is, the products of the spontaneous electrochemical reaction are more ordered than the reactants. The tendency of all systems to increase in disorder (positive entropy) is therefore overridden by the large negative enthalpy of the reaction (ΔH_r). As the temperature increases, the entropy term of Eq. [3] becomes more dominant, and acts to decrease the overall energy (ΔG_r) of the cell, Fig. 1a.

The same behavior is illustrated in the temperature variation of a cell's open-circuit voltage, or equilibrium potential (E), Fig. 1b. The voltage due only to the enthalpic part (E_H) of the electrochemical reaction in Case I (dashed line) is larger than the actual open-circuit cell voltage (solid line) at all temperatures. That is, the negative ΔS_r term is manifested as a negative slope in E vs. T . Galvanic operation (discharge) of the cell is therefore exothermic at all rates. Electrolytic operation (charging of the cell) reverses the sign of most terms and the slope of E vs. T , Fig. 2. The combination of Fig. 1 and 2 is illustrated in Fig. 3 for the discharge direction. Therefore, only at a specific overpotential ($T\Delta S_r/zF$) during electrolytic operation (charge) would a "Case I" cell undergo zero heat flow into or out of the cell, Fig. 3b. This situation would therefore not occur in a primary system such as Li/SOCl₂.

Although occurring less frequently, some electrochemical systems exhibit the interesting properties associated with a positive entropy of reaction, Fig. 1c. That is, in Case II, the products of the spontaneous electrochemical reaction are less ordered than are the reactants. Thus, the cell's open-circuit potential (E) is made up of the typical enthalpic term (E_H) plus a small voltage ($E_s = T\Delta S_r/zF$) due solely to the increasing randomness of the electrochemical reaction, Fig. 1d.

Furthermore, galvanic operation (discharge) near equilibrium would be endothermic (i.e., would absorb heat from the surroundings). Only during a higher rate discharge (overpotential greater than $T\Delta S_r/zF$) would the cell

polarization generate more heat than the entropy of reaction would absorb, resulting in a net exothermic reaction, Fig. 3d. Once again, the point of zero heat flow would occur at a voltage equal to the enthalpic term, or thermoneutral potential (E_H). Charging a reversible "Case II" cell is exothermic at all rates.

The importance of the value of the thermoneutral potential and the sign of the slope of E vs. T are thus evident. Discharge or charge of a cell at a voltage E_L outside the limits of the thermoneutral (E_H) and open-circuit (E) potentials results in an overall exothermic process, or heat generation, Fig. 3. Note that such heat generation is independent of the open-circuit potential of the cell (E), Eq. [15]; it depends rather, on the enthalpic potential (E_H). Furthermore, for a given open-circuit potential (such as 3.65V for Li/SOCl₂ at 25°C), a larger negative E vs. T slope ($\Delta S_r/zF$) for a "Case I" electrochemical reaction results in a substantially higher thermoneutral potential ($E_H = E$ at 0 K); which, consequently, results in a substantially greater heat generation rate.

Conversely, discharge or charge of a cell at a voltage E_L between its thermoneutral (E_H) and open-circuit (E) potentials results in an overall endothermic process or heat absorption by the cell from its surroundings.

Experimental

Two methods were employed to determine the thermoneutral potential of Li/SOCl₂ cells: (i) calorimetric studies performed on discharging cells, and (ii) measurement of open-circuit potential as a function of temperature. Two independent quantities must be measured with each technique in order to calculate the thermoneutral potential (E_H).

Calorimetric measurements yield enthalpy of reaction (ΔH_r) data only; that is, the change in degree of order (entropy) of reactants and products cannot be measured in a calorimeter alone. The additional required information is obtained, then, by discharging the cell at a known current (I) and voltage (E_L) during the calorimetric measurements (\dot{q}_T). The entropy ($\partial E/\partial T$) and enthalpy (E_H) terms are then calculated from Eq. [13] and [15], respectively. In the calorimetry measurements, Li/SOCl₂ cells were equilibrated at temperatures between 0° and 53°C inside a Geosystems calorimeter and discharged at current densities between 1.0 and 20.0 mA/cm².

In the open-circuit potential technique, direct measurement of $\partial E/\partial T$ yields the entropy of reaction from Eq. [6]. The additional knowledge of the open-circuit potential at any temperature permits calculation of the enthalpy of reaction (ΔH_r) and thermoneutral potential (E_H) from Eq. [8]

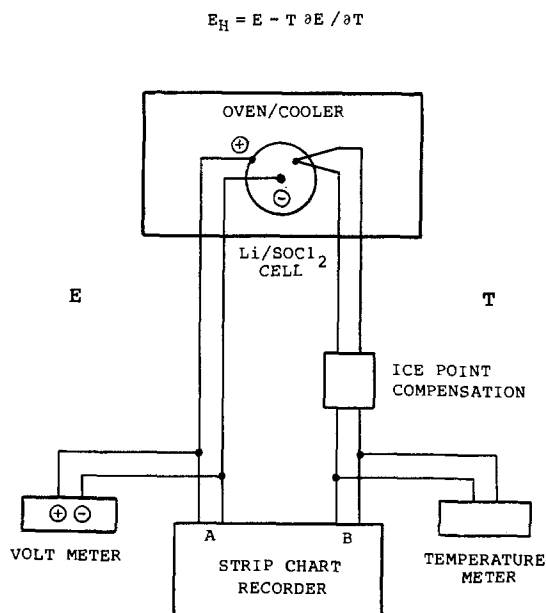


Fig. 4. Schematic of E vs. T experimental apparatus

and [9], respectively. In the $\partial E/\partial T$ measurements, all cells were first discharged at the C/24 rate for 2h (C/24 is that rate which would completely discharge a fresh cell in 24h) followed by equilibration at open-circuit conditions for 20h. This procedure was intended to minimize the effects of voltage delay, which is especially prevalent in undischarged cells. The cells were then placed inside an environmental chamber where the open-circuit potential (E) was measured as a function of incremental changes in temperature. A strip chart recorder was used to determine the steady-state equilibration of E (typically 1-5h) after a new temperature had been selected. The cell temperature was measured using a type "K" thermocouple and an electronic ice point to compensate for changes in ambient temperature. The temperature controller was found to maintain the temperature within $\pm 1^\circ\text{C}$ relative when the measurement temperature was greater than 20°C , and within $\pm 2^\circ\text{C}$ when less than 20°C .

Results

Typical calorimetric results are listed in Table I. The measured heating rates varied between 17 and 376 mW at currents between 58 and 664 mA, respectively. The thermoneutral potentials calculated from these data lie between 3.70 and 3.87V, and appear to be nearly independent of current, Fig. 5. The calorimetric results indicate a thermoneutral potential of $3.783 \pm 0.080\text{V}$, Eq. [15].

The above calorimetric analysis included only the polarization (q_p) and entropy (q_s) terms. Heat generation caused by significant Li corrosion (q_c) would result in erroneously high calculated thermoneutral potentials from Eq. (15). Therefore, lithium electrical efficiencies were measured in thionyl chloride electrolytes to determine their contribution to the total heating power (\dot{q}_T), Fig. 6. Lithium disks (2.5 cm^2 in area; 34 mg in weight) were completely discharged galvanostatically at currents between 2.5 and 120 mA/cm². Their electrical efficiency (ϵ) was calculated simply as the ratio of their integrated currents with respect to time *vs.* their theoretical capacity. Electrical efficiencies in neutral 1.6M LiAlCl₄ thionyl chloride electrolyte were approximately 98% at 21°C and 93% at 45°C below 25 mA/cm². Efficiencies were considerably lower using either higher current densities or acidic electrolyte, as expected (Fig. 6).

The heat generated solely by Li corrosion is given by the enthalpy of reaction between lithium and thionyl chloride (ΔH_r) and the inefficiency ($1 - \epsilon$)

$$q_c = \Delta H_r (1 - \epsilon) = -zFE_H (1 - \epsilon) \quad [16]$$

so that the heating rate due to Li corrosion is given by

$$\dot{q}_c = -I E_H (1 - \epsilon) \quad [17]$$

The total heating rate including polarization, entropy, and lithium corrosion is, therefore, given by

$$\dot{q}_T = -I (2E_H - \epsilon E_H - E_L) \quad [18]$$

Table I. Calorimetric measurements. $E_H = E_L - \dot{q}/I$

Temp. T (°C)	Current I (mA)	Heat \dot{q} (mW)	\dot{q}/I (V)	VUL E_L (V)	Calculated	
					E_H (V)	$\partial E/\partial T$ (mV/C)
0	333	-120	-0.360	3.33	3.69	-0.143
4	640	-376	-0.588	3.20	3.79	-0.491
4	640	-342	-0.534	3.20	3.73	-0.299
4	225	-92	-0.409	3.38	3.79	-0.494
4	115	-40	-0.348	3.40	3.75	-0.348
4	58	-17	-0.293	3.48	3.77	-0.439
25	660	-257	-0.390	3.35	3.74	-0.297
25	280	-73	-0.261	3.45	3.71	-0.201
25	117	-39	-0.333	3.50	3.83	-0.593
25	115	-38	-0.330	3.46	3.79	-0.465
25	59	-17	-0.288	3.53	3.82	-0.560
30	341	-94	-0.276	3.43	3.71	-0.185
53	664	-300	-0.452	3.32	3.77	-0.370
53	233	-83	-0.356	3.45	3.81	-0.473
53	118	-41	-0.348	3.50	3.85	-0.602
53	59	-21	-0.356	3.52	3.87	-0.665

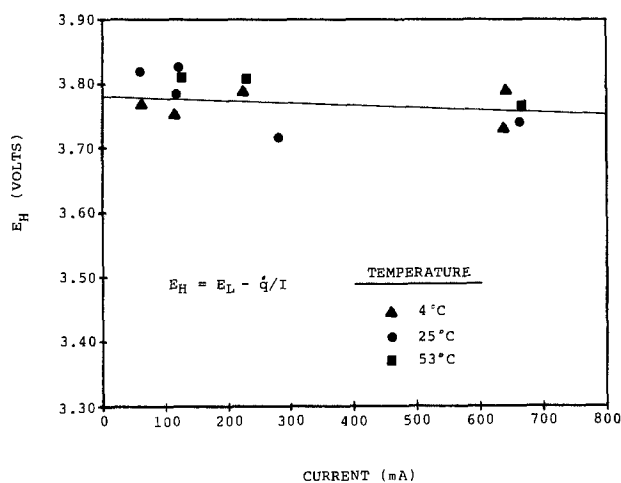


Fig. 5. Thermoneutral potentials obtained from calorimetric measurements.

$$E_H = \frac{E_L - \dot{q}/I}{2 - \epsilon} \quad [19]$$

Therefore, by including a lithium electrical efficiency of 98%, the thermoneutral potential calculated above (3.783V) is reduced to 3.71V.

The results of typical $\partial E/\partial T$ measurements are listed in Table II and illustrated in Fig. 7. These data reflect true E *vs.* T results; that is, the open-circuit potential was not determined from an extrapolation to zero current of various discharge voltages (2). Similar results were obtained regardless of whether the cell temperature was equilibrated from a higher or lower temperature. The open-circuit potential was found to vary with the temperature in a linear fashion over the temperature range -5° to 75°C . A least squares fit of the data resulted in a thermoneutral potential value of 3.723V and a $\partial E/\partial T$ value of negative 0.228 mV/C, indicating that lithium/thionyl chloride discharge is exothermic at all rates (Case I-type reaction).

The thermoneutral potential (E_H) of an electrochemical cell represents the enthalpic portion of the open-circuit potential

$$E_H = -\frac{\Delta H_r}{zF} = \frac{-\Delta G_r - T\Delta S_r}{zF} = E - \frac{T\partial E}{\partial T} \quad [20]$$

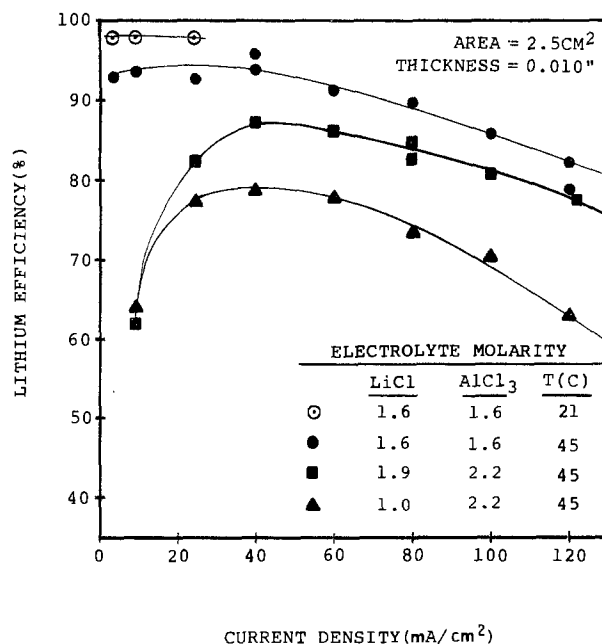


Fig. 6. Lithium electrical efficiency in thionyl chloride electrolytes

Table II. E vs. T measurement. $E_H = E - T\partial E/\partial T$

	Set point (°C)	"K" (mV)	Temperature		E (V)
			(°C)	(K)	
Heating					
	20	0.97	24.0	297.0	3.659
	35	1.50	37.5	310.5	3.654
	45	1.94	48.0	321.0	3.650
	55	2.40	59.0	332.0	3.647
	65	2.83	69.5	342.5	3.643
	70	3.06	75.0	348.0	3.641
Cooling					
	60	2.62	64.5	337.5	3.647
	50	2.18	54.0	327.0	3.652
	40	1.73	43.0	316.0	3.654
	30	1.26	31.5	304.5	3.655
	20	0.81	20.5	293.5	3.656
	10	0.33	8.5	281.5	3.659
Heating					
	0	-0.19	-5.0	268.0	3.663
	5	0.08	2.0	275.0	3.657
	15	0.57	14.5	287.5	3.656
	25	1.03	26.0	299.0	3.654
	32	1.37	34.0	307.0	3.651

Cell operation at the thermoneutral potential results in zero heat absorption or generation by the cell. Cell operation inside a region bounded by the free energy (ΔG_r) and

enthalpy (ΔH_r) terms, or by the open-circuit potential (E) and thermoneutral potential (E_H), always represents endothermic cell operation (heat absorption). Cell operation at voltages lying outside these regions results in exothermic cell operation (heat generation). Cell operation at the thermoneutral potential (E_H) represents a point of zero heat flow, and reflects a smooth transition between endothermic and exothermic cell operation. Conversely, the open-circuit potential (E) represents a discontinuous transition between endothermic and exothermic cell operation.

For an electrochemical reaction which has a negative entropy change (in the discharge direction), the slope of E vs. T will be negative, the open-circuit potential will be less than the thermoneutral potential at all temperatures, and the point of zero heat flow would occur during cell charging. Conversely, for an electrochemical reaction which has a positive entropy change (in the discharge direction), the slope of E vs. T will be positive, the open-circuit potential will be greater than the thermoneutral potential at all temperatures, and the point of zero heat flow would occur during cell discharge.

The thermoneutral potentials of LiSOCl₂ cells, calculated from the two different experimental procedures, exhibited reasonably good agreement. The calorimetric studies, performed on discharging cells and corrected for Li corrosion, yielded a thermoneutral potential of 3.710V

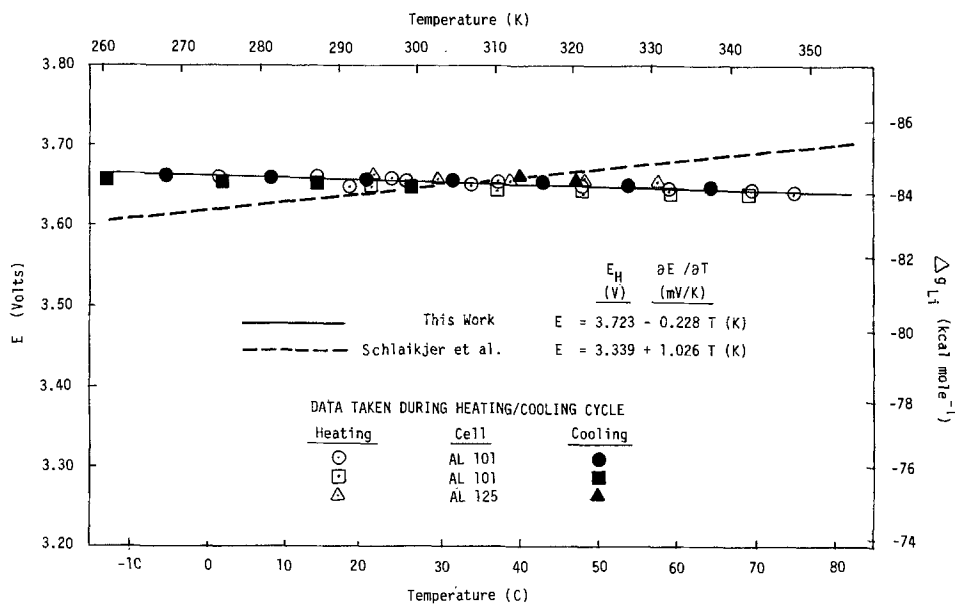


Fig. 7. Open-circuit potentials for lithium/thionyl chloride cells measured as a function of temperature.

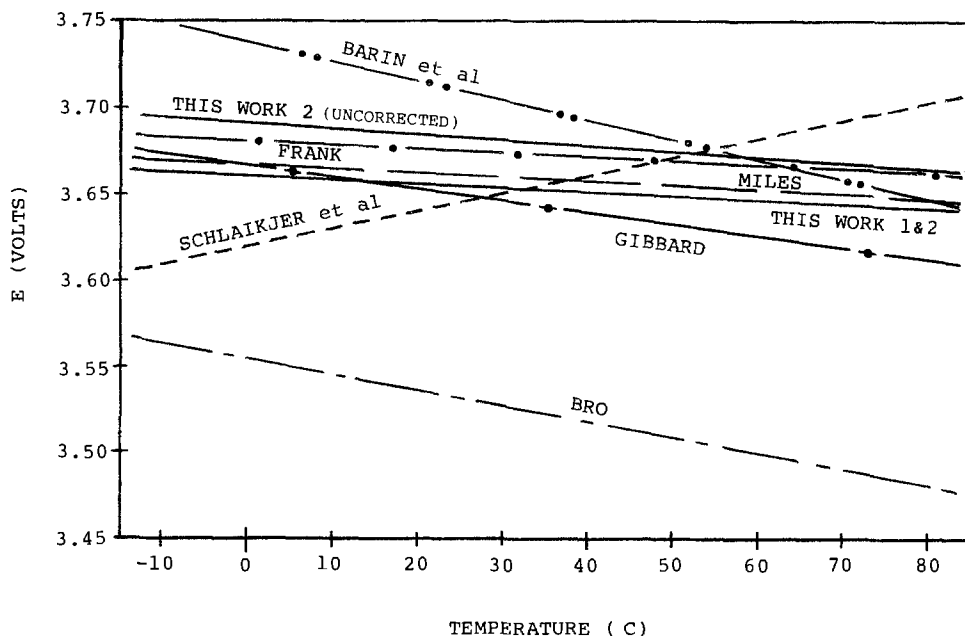


Fig. 8. Comparison of lithium/thionyl chloride thermodynamic data.

Table III. Summary of Li/SOCl₂ thermodynamic data at 25°C. 4Li_(s) + 2SOCl_{2(l)} → 4LiCl_(s) + S_(s) + SO_{2(g)}

Enthalpy		Entropy				Free energy		Ref. Method
ΔH_f (kcal/eq)	E_H (V)	ΔS_f (cal/K-eq)	$-T\Delta S_f$ (kcal/eq)	E_s (V)	$\partial E/\partial T$ (mV/K)	ΔG_f (kcal/eq)	E (V)	1 = $\partial E/\partial T$ 2 = Calorimetry 3 = Calculated
Calculated								
<u>-89.9</u>	3.897	<u>-12.85</u>	+3.83	-0.166	-0.557	-86.0	3.731	3 This work* (3)
<u>-86.1</u>	3.734	<u>- 5.62</u>	+1.68	-0.073	-0.244	-84.4	3.661	3 Miles (4)
Experimental								
<u>-77</u>	3.339	+23.7	-7.06	+0.306	<u>+1.026</u>	-84.1	<u>3.645</u>	1 Schlaikjer (2)
<u>-87.6</u>	3.80	-20.8	+6.2	-0.27	-0.90	-81.4	<u>3.53</u>	2 Bro (5)
<u>-90.4</u>	3.92	-11.3	+3.38	-0.145	-0.46	-83.9	<u>3.65</u>	2 Gibbard (6)
<u>-86.5</u>	3.75	- 5.8	+1.72	-0.08	-0.25	-84.6	<u>3.67</u>	2 Frank (7)
<u>-87.4</u>	3.783	- 7.74	+2.30	-0.10	-0.33	-83.9	<u>3.65</u>	2 This work
<u>-85.6</u>	3.710	- 4.64	+1.38	-0.06	-0.20	-83.9	<u>3.65</u>	2 Corrected
<u>-85.9</u>	3.723	- 5.26	+1.57	-0.068	<u>-0.228</u>	-84.3	<u>3.655</u>	1 This work

* Thermochemical data of Ref. (3) available for gaseous SOCl₂ only: $\Delta H_f^\circ = -50.75$ kcal/mol, $S^\circ = 73.6$ cal/mol K.

and a E vs. T slope of -0.20 mV/C. The $\partial E/\partial T$ measurements, performed under open-circuit conditions, yielded a thermoneutral potential of 3.723V and an E vs. T slope of -0.23 mV/C. Both values represent exothermic cell discharge, although the thermoneutral potential determined experimentally indicates less heat generation than that predicted by the values calculated thermodynamically ($E_H = 3.73$ - 3.90 V).

A review of the literature (3-7) for measured values of the enthalpic and entropic counterparts of the lithium/thionyl chloride reaction was made for comparison with these results (Table III). The underlined values in each line represent the original data obtained from the reference, from which all other values were calculated according to the above equations.

The first line reflects thermodynamic calculations of this work based on the thermochemical data of Barin *et al.* (3), while the second line reflects similar thermodynamic calculations performed by Miles (4). Calorimetric measurements were also performed on Li/SOCl₂ cells by Frank (7) (Table IV). The cell current (I), heating rate (\dot{q}_T), and voltage under load were taken directly from the original data at midpoint of discharge. Only the cell discharged at 0.1A exhibited results which would suggest endothermic behavior (*i.e.*, positive $\partial E/\partial T$ and E_H less than E). The remaining results of Table IV, though somewhat scattered, all indicate exothermic cell discharge with $3.66 < E_H < 3.84$ V. Similar calorimetric results indicating exothermic behavior were also obtained by Bro (5) and Gibbard (6).

A comparison of all the thermodynamic data is shown in Fig. 8. Only the work of Schlaikjer *et al.* (2) predicts a

positive $\partial E/\partial T$, or Case II (endothermic discharge) type of reaction for Li/SOCl₂. The corresponding E_H value of 3.34V is the only predicted value for the thermoneutral potential which is less than the open-circuit voltage (E) of the cell. In these $\partial E/\partial T$ measurements, the open-circuit voltage was not measured directly; rather, E was extrapolated from cell polarization data at different currents. It is possible that the irreversibilities associated with the lithium/thionyl chloride system might affect a $\partial E/\partial T$ value extrapolated from polarization data.

Conclusions

Electrochemical discharge of Li/SOCl₂ cells is believed to be exothermic at all rates, with a thermoneutral potential greater than the open-circuit potential and a negative E vs. T slope (Case I-type reaction). E_H was found to be 3.72 ± 0.02 V, with a corresponding $\partial E/\partial T$ of -0.021 ± 0.03 mV/C.

Acknowledgment

This work was supported by the United States Department of the Navy under Contract no. N00024-81-C-6124, Naval Sea Systems Command (NAVSEA).

Manuscript submitted Dec. 5, 1983; revised manuscript received May 21, 1984. This was Paper 40 presented at the Washington, DC, Meeting of the Society, Oct. 9-14, 1983.

Altus Corporation assisted in meeting the publication costs of this article.

REFERENCES

- H. F. Gibbard, *This Journal*, **125**, 353 (1978).
- C. R. Schlaikjer, F. Goebel, and N. Marincic, *ibid.*, **126**, 513 (1979).
- I. Barin, O. Knacke, and O. Kubaschewski, "Thermochemical Properties of Inorganic Substances," Springer-Verlag, Berlin (1977).
- M. H. Miles, *This Journal*, **126**, 2168 (1979).
- P. Bro, in "Power Sources 7," J. Thompson, Editor, p. 571, Academic Press, New York (1979).
- H. F. Gibbard, in "Power Sources for Biomedical Implantable Applications and Ambient Temperature Lithium Batteries," B. B. Owens and N. Margalit, Editors, p. 510, The Electrochemical Society Softbound Proceedings Series, Princeton, NJ (1980).
- H. A. Frank, JPL Publication 80-6, Feb. 1, 1980.

Table IV. Calorimetric measurements of Frank (7) at midpoint of discharge

Temp. T (°C)	Current I (A)	Heat \dot{q} (W)	q/I (V)	VUL E_1 (V)	Calculated	
					E_H (V)	$\partial E/\partial T$ (mV/C)
21	0.1	-0.06	+0.60	3.50	2.90	+2.517
21	0.2	-0.104	-0.52	3.25	3.77	-0.403
21	0.5	-0.20	-0.40	3.29	3.69	-0.134
21	1.0	-0.73	-0.73	3.11	3.84	-0.638
21	2.0	-1.06	-0.53	3.20	3.73	-0.268
21	5.0	-3.8	-0.76	2.9	3.66	-0.034

The Effect of Different Aluminum Alloy Surface Compositions on Barrier Anodic Film Formation

J. K. G. Panitz and D. J. Sharp

Sandia National Laboratories, Albuquerque, New Mexico 87185

ABSTRACT

We have grown barrier anodic coatings on samples of aluminum alloy with different elemental surface compositions. In one series of experiments, we characterized the surface composition present on 6061 aluminum alloy samples after different chemical treatments including (i) a detergent-water and methyl-ethyl ketone solvent clean, (ii) a 50% nitric acid-water etch, and (iii) a concentrated nitric acid-ammonium bifluoride etch. We anodized samples which were prepared similarly to those analyzed to evaluate the practical effects of the three different surface compositions. The anodization voltage rise time to 950V at constant current was used as a figure of merit. The solvent cleaned and the 50% nitric acid etched samples required, respectively, 113% and 41% more time to reach 950V than the concentrated nitric acid-ammonium bifluoride etched samples. In a second series of experiments, we alternately anodized groups of either 6061 or 1100 (commercially pure) aluminum alloy, observed rise times to 950V, and measured chloride ion concentrations in the electrolyte. Longer rise times and higher chloride ion concentrations were observed for the 1100 samples. It was observed that the chloride ion concentration fell from initially high levels when 6061 samples were anodized. The results of both series of experiments augment the results of other investigators, who report that the surface species initially present on aluminum have a significant effect on anodic film formation.

It is generally observed that the macroscopic characteristics displayed by barrier Al_2O_3 anodic coatings (e.g., growth rate, leakage current, and breakdown strength) are, in part, a manifestation of microscopic flaws which are incorporated in the coatings during anodization. One source of flaws in metal oxide coatings can be related to local topographical or compositional heterogeneities on the surface of the aluminum substrate material (1-3). Another source of flaws in barrier anodized coatings originates from contaminants in the electrolyte which can react with aluminum to form soluble by-products (4). Several groups have evaluated the efficacy of different chemical preparation sequences with regards to subsequent anodization processing (5-8). Shimizu *et al.* (3) have recently reported that flaw sites occur in barrier Al_2O_3 coatings in conjunction with the presence of silicon precipitates on the order of 0.3 nm or larger in the surface region of the Al-1.5% Si alloy which they anodized. Vermilyea (1) reports the formation of flaws in barrier anodized Ta_2O_5 coatings in conjunction with the presence of carbon on the original substrate surface. Badly flawed barrier aluminum oxide coatings are also observed on samples anodized in electrolyte contaminated with as little as 300 ppb chloride ions (4).

One macroscopic manifestation of a flawed barrier coating is slow growth rate (1, 4). Serious flaws in barrier coatings can be associated with locally degraded dielectric properties. The higher leakage currents typical of such coatings result in slower rise times to a desired anodization potential under constant current conditions. We have performed two series of controlled experiments and have observed the anodization voltage rise time to 950V. In interpreting this data, we assume that longer rise times are an indication of the presence of serious flaws which occur during coating growth.

In one series of experiments, we observed the species present on the surface of samples of 6061 aluminum alloy prepared with either: (i) a detergent-water scrub and a water rinse, followed by a methyl-ethyl ketone (MEK) rinse, (ii) a standard cleaning sequence (Fig. 1) terminated at the 50% HNO_3 step, or (iii) a standard cleaning sequence (Fig. 1) through to and including the concentrated HNO_3 - NH_4HF_2 step. Emission spectroscopy was used to determine the bulk composition of the alloy stock which was used. Auger electron spectroscopy (AES) and electron microprobe analysis (EMA) were used to determine what species remained on the surface after these treatments. Samples prepared similarly to those analyzed were anodized in an electrolyte consisting of a solution of ammonium tartrate in ethanol. The anodization voltage rise time to 950V was used as a figure of merit. Signifi-

cant variations in voltage rise time were regularly and reproducibly observed in conjunction with variations in sample surface composition, e.g., the amounts of carbon and silicon present.

In a second series of experiments, groups of samples of either 6061 or 1100 aluminum alloy were prepared using the complete etch sequence described in Fig. 1, and anodized in the ammonium tartrate-ethanol-based electrolyte. The electrolyte was reused for this entire series of experiments. Emission spectroscopy and AES were used to evaluate the bulk and surface compositions of the aluminum alloys. Samples of the electrolyte were taken after representative anodization runs and submitted for chemical analysis. The rise time to 950V was again observed as a figure of merit. Longer rise times and higher chloride ion concentrations were observed when the 1100 samples were anodized. The results of this second series of experiments strongly suggest that one or more of the alloying components in 6061 aluminum play a role in removing chloride ion contamination from the electrolyte.

Experimental

Different surface compositions on 6061 aluminum alloy.—We prepared and barrier anodized $2.5 \times 5.0 \times 0.15$ cm samples of 6061-T6 aluminum alloy sheet stock with an initial, as-received, surface finish of $0.25 \mu\text{m}$ (0.10 in.). The standard preparation sequence which we used (Fig. 1) employs the following etchants: (i) 5% AR-grade NaOH (by weight) in deionized water at 75°C for 2 min, (ii) a 1:1 solution of concentrated (70%) AR-grade HNO_3 (by volume) in deionized water at 27°C for 10 min, and (iii) concentrated (70%) HNO_3 with 63 g/l NH_4HF_2 at 27°C for 10 min. Deionized water with a resistivity of $18 \text{ M}\Omega\text{-cm}$ or higher was used for rinsing the samples and for preparing the chemicals used in these experiments. Absolute ethyl alcohol was used for a final rinse and for preparing the electrolyte.

We analyzed the surface elemental composition and anodized samples which had received either (i) detergent solution-MEK solvent cleaning, (ii) the standard cleaning

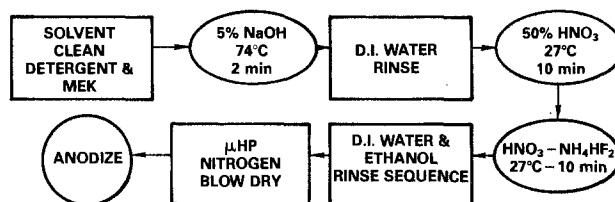


Fig. 1. Flow chart showing the alloy preparation sequence

sequence up to and including the 50% HNO₃ etch, or (iii) the complete standard cleaning sequence including the HNO₃-NH₄HF₂ etch (Fig. 1). We also analyzed and anodized samples which had been etched in the HNO₃-NH₄HF₂ bath for 2-15 min in addition to the standard 10 min etch time.

All samples were immersion-rinsed and spray-rinsed with deionized water, then spray-rinsed with ethyl alcohol, and finally blown dry with dry UHP nitrogen before being submitted for AES or EMA analysis, or before being anodized. The center line average (CLA) surface finish¹ of representative aluminum samples was measured with a Talysurf[®] stylus instrument.

The electrolyte consisted of 1 part by volume of a solution of 2.35g AR-grade ammonium tartrate in 470 ml deionized water added to 40 parts ethyl alcohol. These proportions result in an electrolyte with a resistivity varying from 55 to 70 kΩ-cm. Approximately 2 liters of the electrolyte were used in a cylindrical electrolytic trough equipped with a water cooling bath and a Teflon stirrer. Initial electrolyte temperatures of 21°-22°C, which rose to 27°-29°C at 950V, were typically observed during a run. The electrolytic trough contained three electrolytic cells, each with an identical platinized titanium mesh cathode and a sample of aluminum as the anode. Each cell was independently powered by a Fluke Model 330B "calibrator" power supply with an external voltmeter and ammeter (Fluke Model 86600 A digital multimeters). In a typical anodization run, three pieces of aluminum were anodized: two of which had been prepared with variations of the basic etchant sequence and one control which was prepared with the basic etchant sequence. By using a common electrolytic trough with independent power supplies to anodize several samples simultaneously, and by comparing the characteristics observed for the test samples to those observed for the control sample included in every run, we could compensate for experimental uncertainty arising from small variations in the condition of the electrolyte which occurred from one run to the next.

The aluminum samples were anodized to a cell potential of 950V at a constant current density of 1 mA/cm². For certain runs, when the cell voltage reached 950V, it was held constant; during this aging stage, the current drawn by a cell decreased as the oxide continued to grow, and the cell resistance continued to increase. For some representative runs, the coatings were leakage tested by reducing the cell voltage to 900, 800, and finally 700V; 2 min after the initial application of each of the above voltages, the current drawn by each cell was measured. Such wet leakage tests generally provide a good indication of subsequent dry dielectric leakage characteristics of a coating. For every run that we aged and leakage tested, the current drawn by a cell during leakage testing was proportional to the current drawn during aging which in turn was proportional to the rise time to 950V, i.e., the longer the rise time, the larger the leakage current. Because of this relationship, we used the rise time to 950V to establish a figure of merit for evaluating the different aluminum surface compositions. In the discussion which

follows, the percentage difference $\frac{T_r - T_c}{T_c}$ in the rise time of a test sample T_r , compared to the rise time of a control sample, T_c , included in the same run is used to make quantitative comparisons. From anodization runs in which we anodized three identically prepared alloy samples, we can estimate an experimental error of $\pm 2\%$. At least four different anodization runs were performed for each preparation variation studied.

Anodization of 6061 compared to 1100 (commercially pure) aluminum alloy.—In a separate, though similar,

series of experiments, we anodized samples of 6061-T6 aluminum alloy and 1100 (commercially pure) aluminum alloy. The bulk composition of both types of alloy stock were determined using emission spectroscopy. Samples of both types of alloy received the same standard preparation sequence (Fig. 1) and were anodized to 950V in the ammonium tartrate-ethyl alcohol-based electrolyte described above. Either 6061 or 1100 samples were anodized in a run. Representative samples were taken from the stock materials used for mixing the electrolyte and the electrolyte after either 6061 or 1100 alloy samples had been anodized and submitted for ion chromatography studies; chloride ions were one of the species observed in the chemical analysis of the electrolyte samples.

Results and Discussion

Different surface compositions on 6061 aluminum alloy.—Tables I and II and Fig. 2 and 3 exhibit data associated with the first series of anodization experiments. Tables I and II show the bulk composition of the 6061-T6 aluminum alloy stock used in the first series of experiments and the surface composition remaining on the alloy samples after different preparation steps. Figure 2 il-

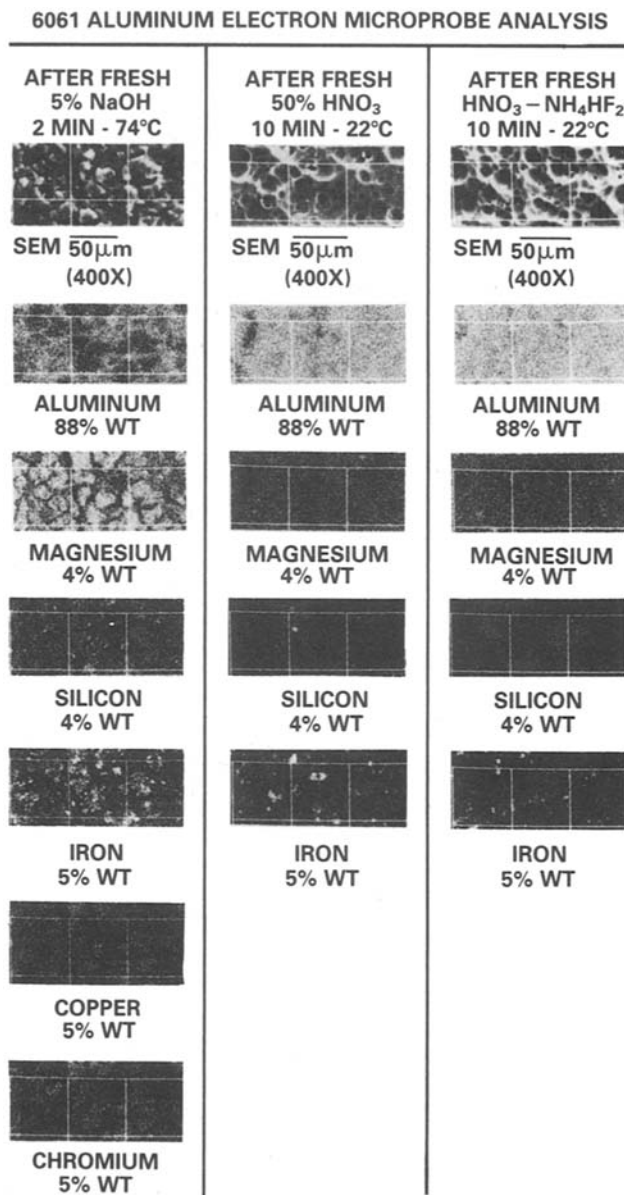


Fig. 2. Components present on the surfaces of 6061-T6 aluminum alloy determined by electron microprobe analysis. Here, the atomic concentrations given below the photomicrographs are the minimal atomic concentrations, which, if present, would result in a totally exposed picture for the gain factors used.

¹ "Center line average" is a surface finish designation which is similar to root mean square (RMS). The CLA is calculated from the integral of the absolute value of the displacement of a surface contour from its base line average value. The RMS is calculated from the square root of the integral of the square of the displacement of a surface contour from its base line average value.

Table I. Bulk and surface elemental compositions observed for 6061 aluminum alloy after different chemical treatments. Concentration (a/o)

Element	Emission spectroscopy [†] bulk alloy	Solvent clean surface	AES*					
			Solvent clean 200 nm deep	5% NaOH	50% HNO ₃	Concentrated HNO ₃ -NH ₄ HF ₂ Fresh 10 min std.	Fresh 5 min	Fresh 15 min
Al	97.31	6	19	44	46	30	35	33
Mg	0.88	10	13	14	0.7	0.8	0.8	0.8
Si	0.68	2	3	2.1	5	2	ND	ND
Fe	0.42	ND	ND	0.8	ND	ND	ND	ND
Cu	0.28	ND	<1	1.4	Trace	Trace	0.7	1
Cr	0.21	ND	ND	ND	ND	ND	ND	ND
Zn	0.13	ND	ND	Trace	ND	ND	ND	ND
Mn	0.07	ND	ND	ND	ND	ND	ND	ND
Sn	0.02	ND	ND	ND	ND	ND	ND	ND
Ni	<0.01	ND	ND	ND	ND	ND	ND	ND
Pb	<<0.01	ND	ND	ND	ND	ND	ND	ND
Ti	<<0.01	ND	ND	ND	ND	ND	ND	ND
C	—	63	10	1.4	11	35	36	35
Ca	ND	2	1	Trace	Trace	Trace	Trace	0.7
N	—	<1	<1	ND	Trace	0.6	Trace	1
S	—	<1	ND	ND	Trace	0.6	0.6	0.6
Na	ND	1	ND	Trace	ND	Trace	0.5	0.7
Cl	—	<1	ND	ND	Trace	Trace	ND	2
F	—	<1	ND	ND	Trace	5	5	6
O	—	14	34	37	36	25	21	21

* The measurement precision in these values is the larger of $\pm 10\%$ or 0.5 a/o. The electron excitation dose was 20 C/cm²; the consequences of electron beam induced effects were not investigated.

[†] Performed with direct reader.

ND = Not detected.

Table II. Sputter profile data observed for an alloy sample etched with freshly mixed HNO₃-NF₄HF₂ for 10 min at 22°C (from AES analysis*)

Element	Concentration (a/o)					
	Before sputter	≈ 10 nm	≈ 50 nm	≈ 70 nm	≈ 150 nm	≈ 250 nm
Al	30	43	72	78	88	92
Mg	0.8	2	0.8	0.7	0.6	Trace
Si	2	1	0.9	Trace	ND	0.5
Fe	ND [†]	ND	ND	ND	ND	ND
Cu	Trace	0.8	0.7	Trace	ND	Trace
Zn	ND	ND	ND	ND	ND	ND
Cr	ND	ND	ND	ND	ND	Trace
C	35	12	10	9	6	5
Ca	Trace	ND	ND	ND	ND	ND
N	0.6	ND	ND	ND	ND	ND
S	0.6	ND	ND	ND	ND	ND
Na	Trace	ND	ND	ND	ND	ND
F	5	6	2	1	0.5	Trace
Cl	Trace	ND	ND	ND	ND	ND
O	25	35	15	10	5	3

* The measurement precision in these values is the larger of 10% or 0.5 a/o. The electron excitation dose was 20 C/cm²; the consequences of electron beam induced effects were not investigated.

[†] ND = Not detected.

illustrates the results of EMA, micrographs showing the surface topographies of the samples and also the distribution of detectable alloying components present in the near-surface region.

Table III shows the surface finish observed for representative alloy samples which have been etched for 0 (as received), 2, and 4 min in the 5% NaOH etch, and similar samples which have received the complete standard etch sequence. The 5% NaOH etch dominates in determining the surface finish of the aluminum prepared by this etch sequence. The surfaces of samples etched with the 50% HNO₃ and with the HNO₃-NH₄HF₂ baths are only slightly rougher than the samples after the 5% NaOH step. As a general rule, if a group of substrates have similar surface compositions, the samples with rougher surfaces will anodize more slowly. There are two reasons for this: (i) topographic irregularities can initiate defect sites in the growing oxide during anodization, and (ii) the effective surface area of rougher samples is larger than the nominal surface area used to calculate the current which is supplied to each sample during the constant current density period of anodization.

Samples which have been solvent cleaned only are observed to take 113% more time to reach 950V than samples receiving the complete etch sequence. This dif-

ference in rise times must be a result of surface and/or near-surface composition effects since surface topography effects would tend to cause the smoother surfaced, solvent cleaned samples to anodize faster than the rougher surfaced, etched samples. Table I shows that the surfaces of the solvent cleaned samples contain almost twice as much carbon as the samples receiving the complete etch. Significant amounts of carbon are also detected in the near surface region of these samples. This carbon originates from external sources and/or surface segregation effects. (Metallurgical specifications allow no more than 0.05% atomic percent [a/o] carbon in bulk 6061 aluminum alloy, significantly less than was found in the surface region. Carbon could not be examined in the bulk 6061 aluminum alloy stock analyzed by emission spec-

Table III. Surface finish after chemical treatments

Etch time in 5% NaOH (min)	CLA [μm ($\mu\text{in.}$)]	
	After 5% NaOH etch only	After 5% NaOH etch + HNO ₃ + HNO ₃ -NH ₄ HF ₂
0	0.25 (10)	0.32 (13)
2	0.80 (32)	1.0 (40)
4	1.2 (47)	1.3 (53)

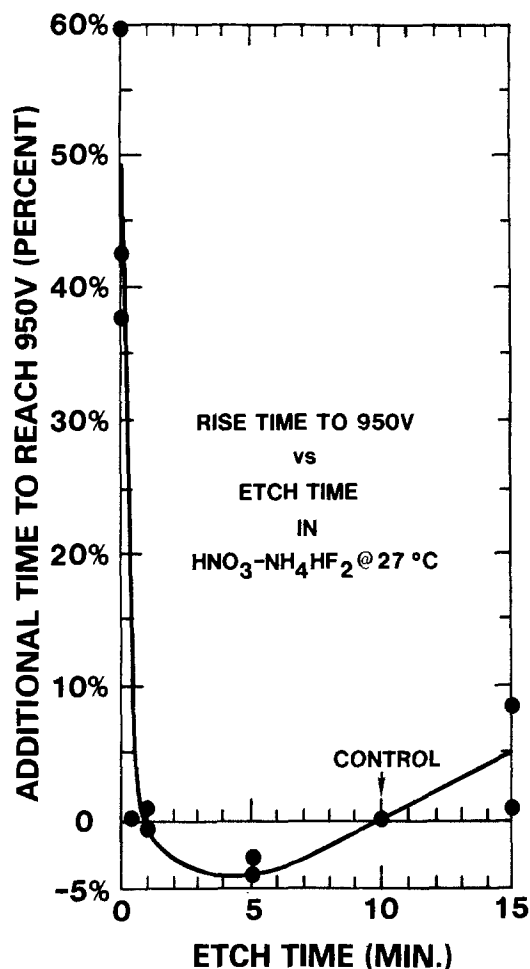


Fig. 3. Rise time as a function of etch time in $\text{HNO}_3\text{-NH}_4\text{HF}_2$ at 27°C

troscopy because carbon electrodes were used.) The fact that the surface region of the solvent cleaned samples consists of more carbon than aluminum may account for the observation that these samples are slow to anodize.

The surfaces of samples etched with 5% NaOH for 2 min at 74°C are covered with a dark powdery, poorly adhering deposit which is commonly called smut. One of the photomicrographs in Fig. 2 shows the surface topography associated with this smut. Electron microprobe analysis of the near (approximately $1\ \mu\text{m}$ deep) surface region of samples etched by 5% NaOH indicate this smut consists primarily of Mg, Si, Fe, Cu, and Cr. Auger electron spectroscopy sputter profiles of these samples indicate the mud-cake-like smut structures consist of a mixture of Al, Mg, Si, and their oxides and are at least $6\ \mu\text{m}$ thick. We did not attempt to anodize any of these samples.

Samples receiving the standard preparation sequence up to and including the 50% HNO_3 etch take 41% more time to anodize than samples receiving the complete etch sequence. The difference in the surface topographies for these two types of samples is small, but the slightly smoother surface of the HNO_3 etched samples would tend to favor faster anodization. The difference in rise times observed must therefore be dominated by surface composition effects. Auger electron spectroscopy indicates the $\text{HNO}_3\text{-NH}_4\text{HF}_2$ etched samples which anodize faster contain significantly less Si ($2 \pm 0.5\%$ a/o vs. $5 \pm 0.5\%$ a/o) and more C ($35 \pm 3.5\%$ a/o vs. $11 \pm 1.1\%$ a/o) than the samples etched with HNO_3 . Table II shows AES sputter profile data for an $\text{HNO}_3\text{-NH}_4\text{HF}_2$ -etched sample that indicates the higher levels of Si which are observed at the surface (2% a/o) diminish rapidly within 50 nm of the surface and approach the bulk concentration (0.68 a/o). These data indicate that the flaws which propagate in association with silicon degrade the dielectric properties of these barrier coatings more than the flaws associated with carbon. The

observation that samples containing less Si anodize faster agrees with the results reported by Shimizu *et al.*, who observe major flaws propagating through anodic Al_2O_3 coatings which originate from Si precipitates with grain sizes greater than approximately 30 nm (8).

Additional insight regarding the magnitudes of the reaction mechanisms involved here is provided by Fig. 3. Figure 3 shows the percentage difference in rise times which are observed as a function of etch time in the $\text{HNO}_3\text{-NH}_4\text{HF}_2$ solution. (Here samples etched for 10 min. The standard etch times were used as controls.) A small but significant minimum in rise time is observed for samples etched for approximately 5 min. The portion of the curve to the left of the minimum shown in Fig. 3 may be dominated by compositional effects. It is probable that some minimal amount of time is necessary for the etchant to chemically remove precipitates which affect or impede the formation of an anodic coating. Since Table I shows no significant differences in the surface composition of similar samples analyzed using AES, the curve on the right of the minimum may be dominated by surface topography effects. It is probable that preferential etching occurs along grain boundaries and for certain grain orientations and results in a rougher surface morphology for longer etch times.

Anodization characteristics of 6061 vs. 1100 aluminum alloy.—In a second sequence of experiments, we prepared and anodized samples of 6061-T6 and 1100 aluminum alloy using the same standard preparation sequence and electrolyte described above. Table IV shows the bulk composition of the aluminum alloy stock used for this series of experiments and the surface composition remaining on the surface of these samples after the complete etch sequence. No significant differences between the two types of samples are apparent over the sensitivity limitations of AES. Extrapolating from the composition data observed for the bulk samples would lead one to expect that less Mg, Si, Mn, Cu, Cr, and Zr and similar amounts of Fe are present in the surface region of the 1100 aluminum alloy samples.

Large variations in the percentage difference in rise time to 950V are observed when the 1100 samples are compared to the 6061 samples. In eight different anodization runs involving four different sets of anodization processing parameters, it was observed that the 1100 samples took 13%, 18%, 52%, and infinitely more time to reach 950V. Figure 4 shows the chloride ion concentration present in the electrolyte after either 1100 or 6061 samples were anodized. Figure 4 also shows the chloride ion concentration present in the stock chemicals used to prepare the electrolyte, and the chloride ion concentrations pres-

Table IV. Bulk and surface elemental composition observed for the samples used in the second series of experiments

Element	Elemental composition (a/o)			
	Bulk emission spectroscopy [†]		Surface after etch AES* [‡]	
	6061	1100	6061	1100
Al	97.5	99	52	53
Mg	0.8	0.3	ND	ND
Si	0.6	0.1	ND	ND
Mn	0.2	0.1	ND	ND
Cu	0.3	0.1	1.0	1.5
Fe	0.3	0.4	ND	ND
Cr	0.2	0	ND	ND
Zr	0.1	0	ND	ND
Ti	0	Trace	ND	ND
Ca	Trace	Trace	ND	ND
Li	Trace	Trace	ND	ND
C	—	—	7.5	8.5
F	—	—	3.8	3.0
O	—	—	37	34

[†] Precision within a factor of 2 (semiquant by photographic method).

* Precision is the larger of $\pm 10\%$ or 1.0 a/o; the consequences of electron beam induced effects were not investigated.

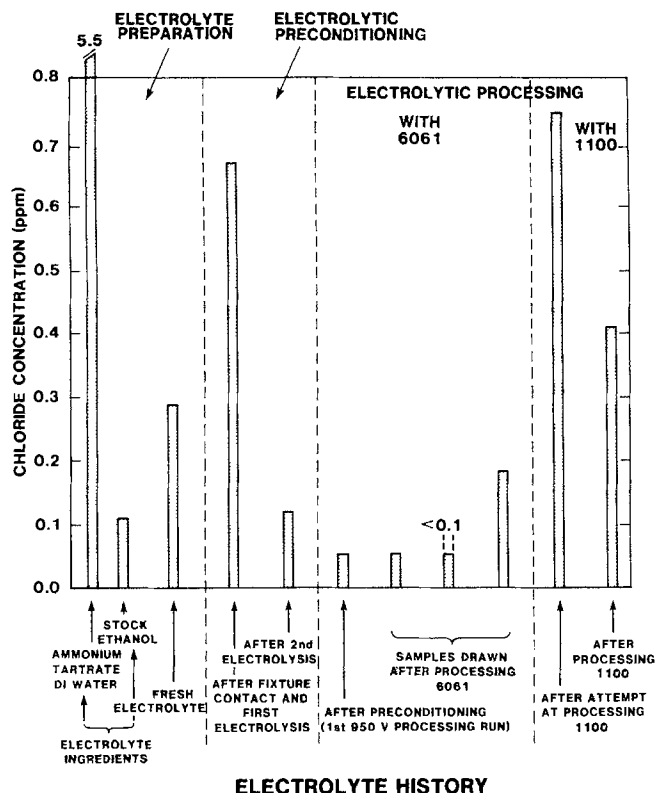


Fig. 4. Chloride ion concentration as a function of electrolyte history. Chloride ion concentrations are lower after preconditioning the bath by anodizing "dummy" 6061 samples. Chloride ion concentrations observed after anodizing 6061 alloy are significantly lower than those observed after anodizing 1100 alloy.

ent in samples of new electrolyte taken during the preliminary electrolyte preparation period while the electrolyte was being "dummied." It had previously been empirically observed that it is sometimes necessary to prepare or "dummy" the freshly mixed electrolyte by anodizing samples of 6061 aluminum alloy. It is typically observed that the maximum voltage attainable during the first break-in run is less than the 950V desired. High concentrations of chloride ions are observed in the fresh, unused electrolyte. We have documented that chloride ion contamination can impede or inhibit barrier coating formation on aluminum (4). Chloride ion contamination can be introduced into the electrolyte from (i) the stock ingredients used to prepare the electrolyte, (ii) contact with the anodization apparatus, and (iii) the samples of aluminum alloy themselves. Samples of electrolyte analyzed after successive break-in runs with 6061 show successively lower chloride ion concentrations. Relatively high levels of chloride ion contamination are observed in representative samples of electrolyte taken after 1100 aluminum alloy is anodized in the dummied electrolyte. Lower levels are observed in samples drawn after subsequent anodization runs, however, if 6061 aluminum alloy is anodized. These observations suggest one or more of the alloying components in the 6061 samples which are present in a smaller amount or absent from the 1100 samples react with Cl^- and remove it from solution. Most chloride compounds are known to be somewhat soluble in water and alcohol. However, some oxychloride compounds, such as $\text{CuCl}_2 \cdot 3\text{CuO} \cdot 4\text{H}_2\text{O}$ (Brunswick green) and $\text{Cu}_2(\text{OH})_3\text{Cl}$ (atacamite), exhibit limited solubilities. Additional work is necessary to identify which alloying component(s) causes this effect.

Summary and Conclusions

We have characterized the surface composition of 6061-T6 aluminum alloy samples prepared with different chemicals. We subsequently barrier anodized similar samples in a series of differential experiments. The anodization voltage rise time to 950V during constant cur-

rent density conditions was used to make semiquantitative comparisons of the effect of different surface compositions. From the experimental controls instituted, we can assume that the voltage rise times that were observed are related to the presence of flaws incorporated in the coatings during anodization.

Samples which are solvent cleaned only have a relatively large amount of carbon on the surface and require more than twice as much time to reach an anodization potential of 950V under constant current conditions, as compared to samples receiving the complete etchant sequence, which includes a concentrated nitric acid-ammonium biftuoride bath. Samples receiving a 50% nitric acid etch as the final chemical treatment have approximately twice as much surface silicon (and approximately one third as much surface carbon) and require 41% more time as compared to samples receiving the complete etchant sequence. Samples treated with the complete etch sequence concluded with the concentrated $\text{HNO}_3\text{-NH}_4\text{HF}_2$ treatment for different amounts of time ranging from 0-15 min exhibit reproducible voltage rise times with respect to control samples treated for 10 min. This relationship observed is interpreted as indicating that a certain minimal etch time is necessary to remove precipitates containing Si which impede anodic Al_2O_3 coating formation; beyond a certain optimal time, the rougher surface morphology which results from chemical etching appears to impede Al_2O_3 coating growth.

We also characterized the surface composition of 1100 (commercially pure) aluminum alloy prepared with the complete etch sequence and anodized these samples. Auger electron spectroscopy indicates similar surface compositions present on both the 6061 and the 1100 samples; however, extrapolating from the bulk compositions observed would imply that significantly less Mg, Si, Mn, Cu, and Cr are present on the 1100 surfaces. The voltage rise times and the chloride ion concentrations observed in the electrolyte after anodization for 1100 samples compared to 6061 samples strongly suggest that one or more of the alloying components which are present on the surface of the 6061 samples but not on the 1100 samples can remove Cl^- ions from the electrolyte. Most chloride compounds are very soluble in the electrolyte, i.e., ethyl alcohol and water. However, certain oxychloride compounds are relatively insoluble; the formation of these compounds may deplete the chloride concentration in the contaminated electrolyte coating growth on 6061 aluminum alloy.

In general, the behavior observed augments the work of other investigators, who report the surface composition which is initially present on aluminum significantly affects subsequent anodic coating formation.

Acknowledgments

We would like to express our gratitude for the support of many Sandia National Laboratory personnel who worked with us on this project. In particular, gratitude is due to Raymond Merrill, who dedicated a considerable effort towards developing a technique for chemically analyzing the electrolyte, Paul Hlava, who performed the electron microprobe analysis, Nora E. Campbell, who contributed the emission spectroscopy data, and finally Merrill Chamberlain and William Wallace, who did the AES analyses. This work was supported by the U.S. Department of Energy under Contract DE-AC04-76-DP00789.

Manuscript submitted March 11, 1983; revised manuscript received ca. March 20, 1984.

Sandia National Laboratories assisted in meeting the publication costs of this article.

REFERENCES

1. D. A. Vermilyea, *This Journal*, **110**, 250 (1963).
2. J. A. Richardson and G. C. Wood, *Corros. Sci.*, **10**, 313 (1970).
3. K. Shimizu, G. E. Thompson, and G. C. Wood, *Electrochim. Acta*, **27**, 245 (1982).

4. D. J. Sharp and J. K. G. Panitz, *This Journal*, **127**, 1412 (1980).
5. R. G. Dosch and T. S. Prevender, "Development and Characterization of a Pre-Barrier Anodizing Cleaning Process for 6061 Al Alloy," SLA-73-0199, Sandia National Laboratories, Albuquerque, NM (1973).
6. N. T. McDevitt, W. L. Baun, and J. S. Soloman, "Surface Analysis of 6061 and 7050 Aluminum Alloys After Conditioning By Chemical Treatment," AFML-TR-76-13, AFML/MBM, Wright-Patterson Air Force Base, OH (1975).
7. N. T. McDevitt and W. L. Baun, "Some Observations of the Relationship Between Chemical Surface Treatments and the Growth of Anodic Barrier Layer Films," AFML-TR-76-74, AFML/MBM, Wright-Patterson Air Force Base, OH (1975).
8. N. T. McDevitt and F. N. Weaver, "An Investigation of a Composite Oxide Film as a Corrosion Inhibitor for 2024 Aluminum," AFML-TR-80-4065, AFML/MBM, Wright-Patterson Air Force Base, OH (1979).

Kinetics and Mechanism of the Hydrogen Evolution Reaction on Titanium in Acidic Media

Eugene J. Kelly* and H. R. Bronstein*

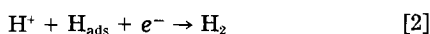
Oak Ridge National Laboratory, Chemistry Division, Oak Ridge, Tennessee 37831

ABSTRACT

The effects of potential and pH on the rate of the hydrogen evolution reaction on zone-refined titanium have been determined in acidic sulfate and chloride media over the pH range of 0 to 4.0. In all cases, the cathodic Tafel slope is equal to -120 mV, i.e., $(\partial E/\partial \log i_{H,\alpha})_{pH} = -2(2.303 RT/F)$. The reaction order with respect to proton activity, $(-\partial \log |i_{H,\alpha}|/\partial pH)_E$, exhibits a minimum value of 0.49 at $pH = 1.83$, and increases to a limiting value of 1.0 with increasing or decreasing pH. A mechanism in agreement with the aforementioned observations has been proposed. The mechanism consists of two parallel paths for rate-determining proton discharge, one path involving the usual solvated proton and the other involving the adsorbed surface species $(TiOH)_{ads}^+$, followed by the fast recombination reaction. Langmuir adsorption kinetics apply to the adsorbed hydrogen atoms. The proposed mechanism is consistent with what is known concerning the effect of potential upon the rate of absorption of hydrogen by the metal. The mechanism is also consistent with the mechanism of active-state dissolution and passivation of titanium in acidic media, i.e., the hypothetical existence of a 3-d phase oxide (as opposed to adsorbed oxy and hydroxy titanium species on the submonolayer level) on titanium in the active state is rejected.

Although the mechanism of active-state dissolution and passivation of titanium in acidic media has been thoroughly investigated and may be considered to be reasonably well understood, that of the hydrogen evolution reaction (HER) which accompanies corrosion of the metal has remained uncertain (1). In the following discussion, it will be shown that this uncertainty arises not only from the contradictory experimental results and conclusions reported by various investigators, but also from the conflicts which exist between the reported results and those to be expected on theoretical grounds.

Theoretical considerations.—The reactions normally considered in any discussion of the hydrogen evolution reaction are the following



The reactions are commonly referred to as the discharge reaction [1], the electrochemical desorption reaction [2], and the recombination reaction [3]. If one considers just reactions [1] and [2], the system may be described by Eq. [4] and [5]

$$\epsilon_H^{-1} (d\theta/dt) = \bar{k}_1 a_{(H^+)} (1 - \theta) - \bar{k}_{-1} \theta - \bar{k}_2 a_{(H^+)} \theta \quad [4]$$

$$-i_H/F = \bar{k}_1 a_{(H^+)} (1 - \theta) - \bar{k}_{-1} \theta + \bar{k}_2 a_{(H^+)} \theta \quad [5]$$

where i_H is the net current density, and $\bar{k}_{\pm j}$ are electrochemical rate constants for the $\pm j$ th reactions. In this paper, by convention, net and partial anodic (oxidation) current densities are positive, while net and partial cathodic (reduction) current densities are negative. If the Galvani potential difference between the pre-electrode plane (identified with the outer Helmholtz plane) and the bulk of the solution is negligible, as in the present work, then $\bar{k}_{\pm j} = k_{\pm j} \exp(\mp \alpha_{\pm j} FE/RT)$, where E is the electrode potential relative to an arbitrary reference electrode, $k_{\pm j}$ are

* Electrochemical Society Active Member.

chemical rate constants, $\alpha_{\pm j}$ are symmetry factors ($\alpha_{\pm j} = 1 - \alpha_{\mp j}$ and, generally, $\alpha_{\pm j} = 1/2$), and the other symbols have their customary significance. The fractional coverage by adsorbed hydrogen atoms is represented by θ , and ϵ_H is the proportionality constant between the surface concentration of adsorbed hydrogen atoms and θ , i.e., $\theta = \epsilon_H [H_{ads}]$. Initially, the chemical rate constants are assumed to be independent of θ , i.e., Langmuir kinetics prevail. Then, under steady-state conditions ($d\theta/dt = 0$), Eq. [4] may be solved for the steady-state coverage (θ_α) which, when substituted into Eq. [5], gives the steady-state current density ($i_{H,\alpha}$). The following limiting cases are obtained

$$\begin{aligned} \bar{k}_1 a_{(H^+)} &>> (\bar{k}_{-1} + \bar{k}_2 a_{(H^+)}), \\ i_{H,\alpha} &= -2Fk_2 a_{(H^+)} \exp(-\alpha_2 FE/RT), \\ \theta_\alpha &\approx 1, S = -120 \text{ mV}, n = 1 \quad [L-1] \end{aligned}$$

$$\begin{aligned} \bar{k}_{-1} &>> (\bar{k}_1 + \bar{k}_2) a_{(H^+)}, \\ i_{H,\alpha} &= -2Fk_2 K_1 a_{(H^+)}^2 \exp[-(1 + \alpha_2) FE/RT], \\ \theta_\alpha &= K_1 a_{(H^+)} \exp(-FE/RT) \ll 1, S = -40 \text{ mV}, n = 2 \quad [L-2] \end{aligned}$$

$$\begin{aligned} \bar{k}_2 a_{(H^+)} &>> (\bar{k}_1 a_{(H^+)} + \bar{k}_{-1}), \\ i_{H,\alpha} &= -2Fk_1 a_{(H^+)} \exp(-\alpha_1 FE/RT), \\ \theta_\alpha &= (\bar{k}_1/\bar{k}_2) \ll 1, S = -120 \text{ mV}, n = 1 \quad [L-3] \end{aligned}$$

If one considers only reactions [1] and [3], the system is described by Eq. [6] and [7]

$$\epsilon_H^{-1} (d\theta/dt) = \bar{k}_1 a_{(H^+)} (1 - \theta) - \bar{k}_{-1} \theta - 2k_3 \theta^2 \quad [6]$$

$$-i_H/F = \bar{k}_1 a_{(H^+)} (1 - \theta) - \bar{k}_{-1} \theta \quad [7]$$

For this system, under Langmuir conditions, the following steady-state limiting cases are obtained

$$\bar{k}_1 a_{(H^+)} \gg (\bar{k}_{-1} + 2k_3 \theta), i_{H,\alpha} = -2Fk_3, \theta_\alpha \approx 1 \quad [L-4]$$

$$\begin{aligned} \bar{k}_{-1} &\gg (\bar{k}_1 \alpha_{(\text{H}^+)} + 2k_3 \theta), \\ i_{\text{H},\alpha} &= -2\text{F}k_3 K_1^2 a_{(\text{H}^+)}^2 \exp(-2\text{F}E/RT), \\ \theta_{\alpha} &= K_1 \alpha_{(\text{H}^+)} \exp(-\text{F}E/RT) \ll 1, S = -30 \text{ mV}, n = 2 \quad [\text{L-5}] \\ 2k_3 \theta &\gg (\bar{k}_1 \alpha_{(\text{H}^+)} + \bar{k}_{-1}), \\ i_{\text{H},\alpha} &= -\text{F}k_1 \alpha_{(\text{H}^+)} \exp(-\alpha_1 \text{F}E/RT), \\ \theta_{\alpha} &= (k_1/2k_3)^{0.5} \alpha_{(\text{H}^+)}^{0.5} \exp(-\alpha_1 \text{F}E/2RT) \ll 1, \\ S &= -120 \text{ mV}, n = 1 \quad [\text{L-6}] \end{aligned}$$

If the free energy of adsorption of hydrogen atoms is a linear function of θ (Temkin adsorption)

$$\Delta F_{\text{ads}} = \Delta F_{\text{ads}, \theta=0} + m\theta \quad [8]$$

the free energies of activation may also be considered to be linear functions of θ , and, consequently, the chemical rate constants are functions of θ , i.e., $k_1 = k_{1, \theta=0} \exp(-\beta_1 m \theta / RT)$, $k_{-1} = k_{-1, \theta=0} \exp[(1 - \beta_1) m \theta / RT]$, $k_2 = k_{2, \theta=0} \exp(\beta_2 m \theta / RT)$, and $k_3 = k_{3, \theta=0} \exp(2\beta_3 m \theta / RT)$, where β_j are symmetry factors (for reactions [1] and [2], $\beta_j = \alpha_j$) which might be expected to assume values of (1/2), and where m is a constant (2). Temkin kinetics are only applicable in the intermediate coverage range ($0.2 < \theta < 0.8$) where one may assume that the coefficients $(1 - \theta)$ and θ in Eq. [4]-[7] are roughly constant. Then, one may write $k'_1 = k_{1, \theta=0} (1 - \theta)$, $k'_{-1} = k_{-1, \theta=0} \theta$, $k'_2 = k_{2, \theta=0} \theta$, and $k'_3 = k_{3, \theta=0} \theta^2$. Under these conditions, Eq. [4] and [5] yield the following limiting steady-state solutions

$$\begin{aligned} \bar{k}_{-1} &\gg \bar{k}_2 \alpha_{(\text{H}^+)}, \\ i_{\text{H},\alpha} &= -2\text{F}k'_2 (K'_1)^{\beta_2} \alpha_{(\text{H}^+)}^{(1+\beta_2)} \exp[-(\alpha_2 + \beta_2)\text{F}E/RT], \\ \theta_{\alpha} &= -(\text{F}/m)E + (RT/m) \ln K'_1 \alpha_{(\text{H}^+)}, \\ S &= -60 \text{ mV}, n = 1.5 \quad [\text{T-1}] \\ \bar{k}_2 \alpha_{(\text{H}^+)} &\gg \bar{k}_{-1}, i_{\text{H},\alpha} = -2\text{F}k'_2 (k'_1/k'_2)^{\beta_2/(1+\beta_2)} \alpha_{(\text{H}^+)} \\ &\exp[-(\alpha_2 \beta_1 + \alpha_1 \beta_2)\text{F}E/(\beta_1 + \beta_2)RT], \\ \theta_{\alpha} &= -(\alpha_1 - \alpha_2)\text{F}E/(\beta_1 + \beta_2)m \\ &+ [RT/(\beta_1 + \beta_2)m] \ln (k'_1/k'_2), S = -120 \text{ mV}, n = 1 \quad [\text{T-2}] \end{aligned}$$

Finally, under Temkin conditions, Eq. [6] and [7] give the following steady-state limiting cases

$$\begin{aligned} \bar{k}_{-1} &\gg 2k_3, i_{\text{H},\alpha} = -2\text{F}k'_3 (K'_1)^{2\beta_3} \alpha_{(\text{H}^+)}^{2\beta_3} \exp(-2\beta_3 \text{F}E/RT), \\ \theta_{\alpha} &= -(\text{F}/m)E + (RT/m) \ln K'_1 \alpha_{(\text{H}^+)}, S = -60, n = 1 \quad [\text{T-3}] \\ 2k_3 &\gg \bar{k}_{-1}, i_{\text{H},\alpha} = -2\text{F}k'_3 (k'_1/2k'_3)^{2\beta_3/(\beta_1+2\beta_3)} \alpha_{(\text{H}^+)}^{2\beta_3/(\beta_1+2\beta_3)} \\ &\exp[-2\beta_3 \alpha_1 \text{F}E/(\beta_1 + 2\beta_3)RT], \\ \theta_{\alpha} &= -[\alpha_1 \text{F}E/(\beta_1 + 2\beta_3)m] \\ &+ [RT/(\beta_1 + 2\beta_3)m] \ln (k'_1 \alpha_{(\text{H}^+)}/2k'_3), \\ S &= -180 \text{ mV}, n = (2/3) \quad [\text{T-4}] \end{aligned}$$

The diagnostic criteria of primary interest are the magnitudes of the Tafel slope (S) and the reaction order (n) with respect to the proton activity, $(\partial E/\partial \log[i_{\text{H},\alpha}])_{\text{pH}}$ and $(-\partial \log[i_{\text{H},\alpha}]/\partial \text{pH})_E$, respectively. The values of S ($T = 30^\circ\text{C}$) and n shown for each of the limiting cases were obtained by setting all symmetry factors equal to (1/2). In addition to the Temkin cases given above, Thomas discussed two more limiting solutions which one might label [T-3'] and [T-4']. These are given by [T-3] and [T-4] with $\beta_3 = 1$ (nonactivated adsorption of hydrogen atoms), and are characterized by (S, n) values of $(S = -30 \text{ mV}, n = 2)$ and $(S = -150 \text{ mV}, n = 0.8)$, respectively.

It should be emphasized that (S, n) data do not always suffice for the determination of the HER mechanism. As shown above, for example, the frequently observed set of values, $S = -120 \text{ mV}$ and $n = 1$, is generated by four of the limiting cases: [L-1], [L-3], [L-6], and [T-2]. In such a situation, one may, in principle, distinguish among the

four cases on the basis of the magnitude of θ and its variation with potential and/or pH. Such supplemental information enabled the HER mechanism to be uniquely determined for iron ($S = -120 \text{ mV}, n = 1$) in acidic sulfate solutions (3) and, as will be shown below is decisive for the present case involving titanium.

Results of earlier studies.—The experimental results which have been reported for the hydrogen evolution reaction on titanium in deoxygenated acidic media are shown in Table I. The wide diversity of reported (S, n) values, and a comparison of the (S, n) values with those to be expected on theoretical grounds, can only lead one to conclude that previous studies have failed to determine the HER mechanism on titanium.

Few mechanistic proposals have resulted from the data presented in Table I. Armstrong *et al.* stated that their results indicated that the rate-determining step in acidic sulfate media is slow discharge (10). They did not attempt to account for their anomalous Tafel slope. According to Thomas and Nobe (11), the rate-determining step in acidic sulfate media is slow electrochemical desorption. However, in order to account for the unusual reaction order ($n = 0.6$) and the anomalous Tafel slope ($S = -150 \text{ mV}$), they had to invoke both Temkin adsorption for H_{ads} and a dual-barrier model (20) based on the unwarranted premise that active-state titanium is covered with a 3-d oxide film. In analyzing their results for beta III titanium in acidic sulfate media, Dull and Nobe (14) retained Temkin adsorption behavior for H_{ads} , but abandoned the dual-barrier model, and concluded that the rate-determining step is slow recombination. Brynza *et al.* (13) invoked the dual-barrier model, but not Temkin adsorption of H_{ads} , and decided that the rate-determining step in acidic sulfate media is slow discharge followed by electrochemical desorption. Frayret *et al.* (18) noted the problem presented by their (S, n) data in acidic chloride media, $S = -186$ and $n = 0.88$, and merely pointed to the dual-barrier approach of Thomas and Nobe as a possible explanation. Finally, Petit and Dabosi (12) observed an abnormal Tafel slope ($S = -164 \text{ mV}$), but a normal value for the reaction order ($n = 1$) in acidic sulfate solutions. They concluded that Langmuir rather than Temkin kinetics apply, and that the rate-determining step is electrochemical desorption ($\theta \approx 1$). In order to account for their unusual Tafel slope, they rejected the dual-barrier model while accepting the hypothesis that an oxide film exists on active-state titanium in the cathodic potential region. They then assumed that the potential drop across the oxide film is a constant fraction (f) of the metal/solution potential difference. The Tafel slope then becomes equal to $[-2.303 RT/(1 - f)\alpha\text{F}]$ and, with $f = 0.26$ and $\alpha = 0.5$, one

Table I. HER parameters for titanium

S (mV)*	n	Media	T ($^\circ\text{C}$)	Ref.
-70	—	20% H_2SO_4	R.T.	(4)
-119	—	2N H_2SO_4	R.T.	(5)
-119	—	1N H_2SO_4	22	(6)
-120	—	0.5M [$\text{HSO}_4^- + \text{SO}_4^{2-}$] pH = ~1-3.0	30	(7)
-137	—	2N H_2SO_4	25	(8)
-142	—	1N H_2SO_4	25	(9)
-152	~1	0.1-10M H_2SO_4	70	(10)
-153	0.6	20N NaOH + 1N H_2SO_4 pH = 0.25-2.25	24	(11)
-164	1.0	1-10N H_2SO_4	22	(12)
-175	0.63	$\text{H}_2\text{SO}_4 + \text{K}_2\text{SO}_4$ pH = 0.1-2.32	25	(13)
-60**	1.0	1-10N H_2SO_4	23	(14)
-120	—	1M [Cl^-], pH = 0.7-2.3	30	(15)
-130	—	1N HCl	22	(6)
-153	—	4N HCl	24	(16)
-156***	1.0	0.5M [Cl^-], pH = 0.65-2.5	25	(17)
-186	0.88	1-10N HCl	21	(18)
-120	1.0	HCl - DMSO + ClO_4^-	25	(19)

* Adjusted to 30°C (except R.T. entries).

** Beta III titanium.

*** Ti 6 Al4V.

obtains the observed value of S . However, f must be regarded as little more than an arbitrary adjustable parameter (depending on f , one can obtain any value of S between -120 mV and $-\infty$). Indeed, there is no evidence to support the proposed model.

It is apparent that, excepting the proposal of Armstrong *et al.* (10), the mechanisms suggested for the hydrogen evolution reaction on titanium are those of Nobe and co-workers (11, 14), or closely related variations thereof. Consequently, their dual-barrier/Temkin adsorption model will be examined in detail in the "Discussion" section of this paper.

Experimental

The three-compartment cell assembly (test, reference, and counterelectrode compartments) was made of Pyrex glass and Teflon, and was so designed that solutions could be added to or removed from the cell without exposure to the atmosphere. All compartments were jacketed and maintained at a constant temperature of $30.00^\circ \pm 0.02^\circ\text{C}$. Hydrogen was passed through all compartments at all times. The hydrogen source was a Matheson generator which produces ultrapure gas via diffusion of electrolytically generated hydrogen through a palladium membrane. Stirring in the test compartment was achieved with a Teflon-coated magnetic stirrer.

The titanium electrodes employed in this study were made from zone-refined polycrystalline titanium (Materials Research Corporation). The cylindrical electrodes (length = 1.27 cm, diam = 0.635 cm) were polished successively with 320, 400, and 600 silicon carbide, followed by 1.0, 0.3, and $0.05 \mu\text{m}$ Al_2O_3 . The Teflon electrode holders exposed only the cylindrical surface of the electrodes. In order to ensure comparability of results, each electrode had to meet the following criteria in 1N H_2SO_4 : $E_{\text{corr}} = -745 \pm 5$ mV vs. SCE, $E_m = -530 \pm 3$ mV vs. SCE, and $i_m = 5.40 \times 10^{-5} \pm 4\%$ A cm^{-2} (E_m and i_m are defined in the "Results" section). All solutions were prepared from reagent-grade chemicals and triply distilled water. Acidic solutions having the desired pH were prepared by mixing 0.5M H_2SO_4 and 0.5M Na_2SO_4 , or 1M HCl and 1M NaCl. The test solutions were pre-electrolyzed for approximately 24h at -900 mV vs. SCE using a 10 cm^2 titanium cathode.

The titanium electrodes attained a stable active-state corrosion potential (E_{corr}) in all test solutions except that having the highest pH (4.04). Cathodic polarization curves were determined by maintaining each potential just long enough to obtain the minimum value of $|i_H|$ (~ 10 min), then returning to open circuit long enough to reestablish the original value of E_{corr} . Prolonged cathodic polarization was accompanied by a rise in the magnitude of the cathodic current density with time, the effect being more pronounced the more negative the potential and the lower the pH. Since the effect, one which might be attributed to hydriding of the surface layers, resulted in irreproducible and non-Tafel behavior, it was avoided. At the highest pH, titanium spontaneously passivates, and, consequently, a potential of -800 mV vs. SCE served as the reference state in place of E_{corr} .

The electrochemical measurements were made with a PAR potentiostat (Model 173), an Orion pH meter (Model 801-A), and a Hewlett-Packard/Moseley recorder (Model 7100 B, Model 17501 plug-ins).

All electrode potentials (E) were measured against a saturated calomel reference electrode, and all E values are given with reference to SCE.

Results

Typical polarization curves for titanium in acidic sulfate and chloride media are shown in Fig. 1. The cathodic Tafel lines corresponding to the HER have slopes of -120 mV, *i.e.*, $(\partial E/\partial \log |i_H|)_{\text{pH}} = -2(2.303 RT/F)$. Also, one observes that as the potential becomes increasingly positive (noble) relative to the active-state corrosion potential (E_{corr}), the anodic current density rises to a maximum (i_m) at the critical potential (E_m), and then decreases as the

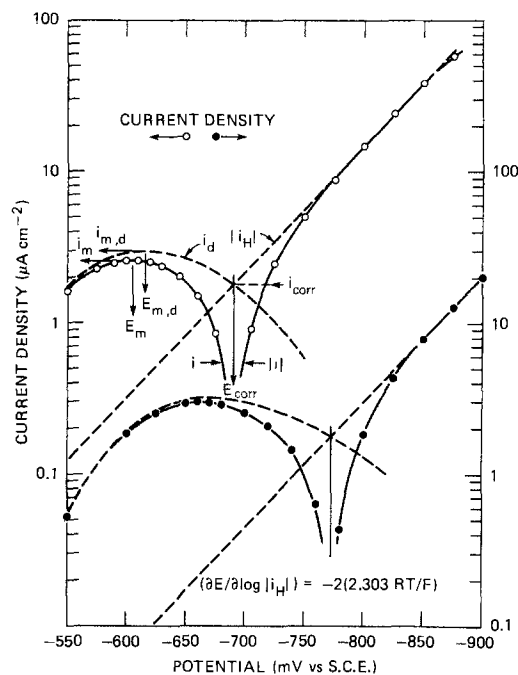


Fig. 1. Anodic and cathodic polarization curves for zone-refined titanium. —●—: 0.5M $[\text{HSO}_4^- + \text{SO}_4^{2-}]$, pH = 2.14. —○—: 1.0M $[\text{Cl}^-]$, pH = 1.00, from Ref. (15).

metal undergoes transformation from the active to the passive state. The partial anodic polarization curve (i_d) corresponding to just the oxidation of the metal to form Ti(III) ions in solution is obtained by adding $|i_H|$ to the observed (net) anodic polarization curve (i). As may be seen in Fig. 1, the current density maximum ($i_{m,d}$) in the i_d curve is greater than the observed value (i_m), and the corresponding value of the critical potential ($E_{m,d}$) is more negative than the observed value (E_m). Previous investigations (7, 15) have established the relationships

$$d \log i_{m,d}/dpH = -2/3 \quad [9]$$

and

$$dE_{m,d}/dpH = -(4/3)(2.303 RT/F) \quad [10]$$

These relationships have an important diagnostic significance in the determination of the mechanism of active-state dissolution and passivation of titanium (1). In addition, as will be shown in connection with Fig. 3, they are useful in the determination of n for the HER.

In Fig. 2, cathodic polarization curves are shown for 0.5M $[\text{HSO}_4^- + \text{SO}_4^{2-}]$ solutions in the pH range 1.03-4.04. For all solutions, the slope (S) of the cathodic Tafel line is equal to $-2(2.303 RT/F)$, *i.e.*, -120 mV. The reaction order (n) with respect to the proton activity, *i.e.*, $(-\partial \log |i_H|/\partial \text{pH})_E$, may be obtained from the data shown in Fig. 2. The values of $|i_H|$ at $E = -875$ mV vs. SCE (Fig. 2) are shown in Fig. 3 as open circles. Additional results obtained for the $[\text{HSO}_4^- + \text{SO}_4^{2-}]$ system in the present study (\square, ∇), as well as those presented in earlier publications (\square, Δ), are also shown in Fig. 3. The solid points in Fig. 3 correspond to the results obtained for the 1M $[\text{Cl}^-]$ system in the present (\bullet) and earlier studies (\blacktriangledown). In Fig. 2, one notes that the potential range in which Tafel behavior is observed, *i.e.*, in which $(\partial \log |i_H|/\partial E)_{\text{pH}}$ is constant, decreases with increasing acidity. In 1N H_2SO_4 , true Tafel behavior was not observed (1), and, consequently, i_H ($E = -875$ mV vs. SCE) for this medium was evaluated by determining i_{corr} and utilizing the relationship, $|i_H|_{(E=-875)} = i_{\text{corr}} \exp[-2.303(-875 - E_{\text{corr}})/120]$. A very sensitive electrochemical technique was used to measure i_{corr} (21). The method involves the use of a passive titanium sensor electrode to monitor changes in the concentration of Ti(III) ions in solution resulting from the dissolution of metal, and can be used to determine i_d at any potential in the active-state potential

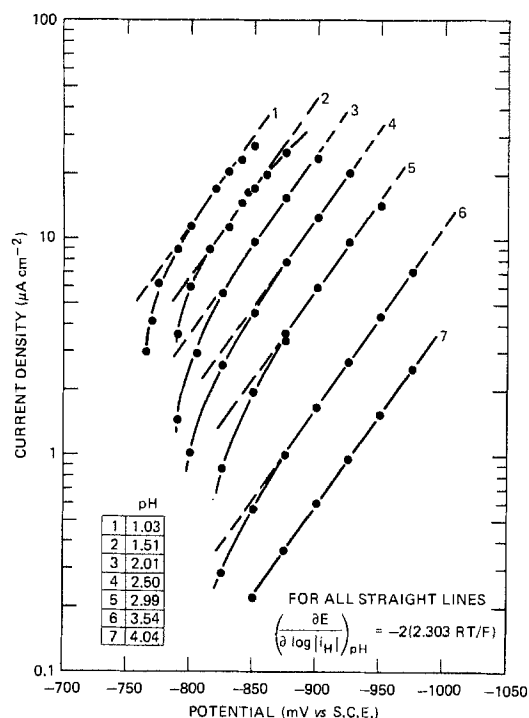


Fig. 2. Cathodic polarization curves for titanium in 0.5M $[\text{HSO}_4^- + \text{SO}_4^{2-}]$ at various pH values.

region, including E_{corr} . In the high pH region, where $|i_{\text{H}}|_{E=E_m}$ is significant compared to $i_{\text{m,d}}$, Eq. [9] and [10] provide a fast method for checking the values of $|i_{\text{H}}|_{E=-875}$ determined by direct cathodic polarization. For example, in 1N HCl (pH = -0.07) the values of $i_{\text{m,d}}$ and $E_{\text{m,d}}$ are 1.55×10^{-5} A cm^{-2} and -530 mV vs. SCE, respectively (15). Then, using Eq. [9] and [10], one finds that for pH = 2.01, $i_{\text{m,d}}$ and $E_{\text{m,d}}$ are equal to 6.36×10^{-7} A cm^{-2} and -696.4 mV vs. SCE, respectively. The observed anodic current density at $E_{\text{m,d}}$ was only 1.78×10^{-7} A cm^{-2} . Consequently, $|i_{\text{H}}|$ at $E_{\text{m,d}}$ is equal to 4.58×10^{-7} A cm^{-2} , i.e., $(6.36 \times 10^{-7} / 1.78 \times 10^{-7})$. With $S = -120$ mV, this value of $|i_{\text{H}}|$ at $E = -696.4$ mV vs. SCE corresponds to a value of 1.41×10^{-5} A cm^{-2} at $E = -875$ mV vs. SCE. The value obtained by cathodic polarization, and plotted in Fig. 3, is 1.46×10^{-5} A cm^{-2} . For use with acidic sulfate media, the values of $i_{\text{m,d}}$ and $E_{\text{m,d}}$ in 1N H_2SO_4 (pH = 0.32) are 5.40×10^{-5} A cm^{-2} and -530 mV vs. SCE, respectively (21).

The results presented in Fig. 3 show that the measured reaction order with respect to proton activity, $(-\partial \log |i_{\text{H}}| / \partial \text{pH})_E$, is a minimum (0.49) at pH 1.83, and approaches a limiting value of 1.0 with increasing or decreasing pH. The solid curve which fits the data over the entire pH range was calculated using Eq. [11]

$$|i_{\text{H}}|_E = [A / (1 + B a_{(\text{H}^+)}) + C a_{(\text{H}^+)}] \quad [11]$$

With $E = -875$ mV vs. SCE, the values of the constants in Eq. [11] are $A = 1.72 \times 10^{-5}$ A cm^{-2} , $B = 4.89 \times 10^{-3}$, and $C = 4.24 \times 10^{-4}$ A cm^{-2} . In practice, $a_{(\text{H}^+)}$ in Eq. [11] is obtained from the measured pH and the relationship, $\text{pH} = -\log a_{(\text{H}^+)}$. It is especially important to note that there is no significant difference in the kinetics of the hydrogen evolution reaction in the chloride and sulfate media. In either medium, the Tafel slope is -120 mV and, as shown in Fig. 3, Eq. [11] is equally applicable to either system. Consequently, the peculiar nature of the order plot cannot be attributed to media effects such as, for example, the pH-dependent ($\text{HSO}_4^- / \text{SO}_4^{2-}$) ratio. Instead, one must look to the surface for an explanation of the results.

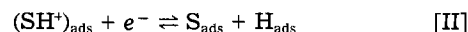
Discussion

Proposed mechanism for the HER.—The results shown in Fig. 2 and 3 immediately suggest a HER mechanism involving two parallel reaction paths of the ($S = -120$ mV, $n = 1$) type, i.e., of the [L-1], [L-3], [L-6], or [T-2] type. For

the sake of brevity, it is appropriate to anticipate the ultimate conclusion and derive the overall rate expression on the basis of just the [L-6] type mechanism (slow discharge—fast recombination). Justification for selecting [L-6] from the four possible ($S = -120$ mV, $n = 1$) limiting cases will be provided below. Of the two parallel reaction paths, one is that leading to [L-6], namely, reactions [1] and [3]. For titanium, it is proposed that one must also consider reactions [I] and [II]



and



where S_{ads} represents an adsorbed entity, the nature of which will be discussed below. The HER is then described by the following equations

$$\epsilon_{\text{H}}^{-1} (d\theta/dt) = \bar{k}_1 a_{(\text{H}^+)} (1 - \theta - \lambda) - \bar{k}_{-1} \theta - 2k_3 \theta^2 + \bar{k}_{\text{II}} \psi (1 - \theta - \lambda) - \bar{k}_{-\text{II}} \theta \phi \quad [12]$$

$$\epsilon_{\text{SH}}^{-1} (d\psi/dt) = -\epsilon_{\text{S}}^{-1} (d\phi/dt) = k_1 a_{(\text{H}^+)} \phi - k_{-1} \psi - \bar{k}_{\text{II}} \psi (1 - \theta - \lambda) + \bar{k}_{-\text{II}} \theta \phi \quad [13]$$

$$-i_{\text{H}}/F = \bar{k}_1 a_{(\text{H}^+)} (1 - \theta - \lambda) - \bar{k}_{-1} \theta + \bar{k}_{\text{II}} \psi (1 - \theta - \lambda) - \bar{k}_{-\text{II}} \theta \phi \quad [14]$$

where ψ and ϕ represent the fractional coverages by $(\text{SH}^+)_{\text{ads}}$ and S_{ads} , respectively, and ϵ_{SH} and ϵ_{S} are the proportionality constants between ψ and ϕ and surface concentrations of $(\text{SH}^+)_{\text{ads}}$ and S_{ads} . In addition, $\lambda = (\psi + \phi)$, and the other symbols retain their previous definitions. In the steady state, $(d\theta/dt) = 0$, the current density is equal to $-2Fk_3\theta^2$. Subject to the condition, $2k_3\theta_{\infty} \gg (\bar{k}_1 a_{(\text{H}^+)} + \bar{k}_{-1} + \bar{k}_{\text{II}}\psi + \bar{k}_{-\text{II}}\phi)$, the steady-state current density is given by Eq. [15]

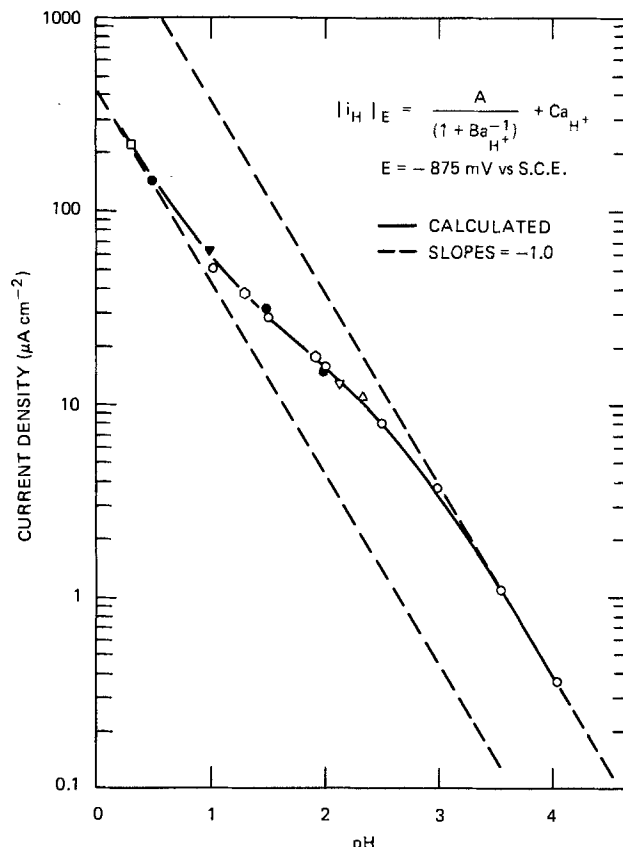


Fig. 3. Current density of the hydrogen evolution reaction on titanium as a function of pH at $E = -875$ mV vs. SCE. $[\text{HSO}_4^- + \text{SO}_4^{2-}] = 0.5\text{M}$. \circ : from Fig. 2. ∇ : from Fig. 1. \circ : additional data of present study. \square : from Ref. (21). \triangle : from Ref. (7). \square : from Ref. (15) or Fig. 1. \bullet : present study. \blacktriangledown : from Ref. (15) or Fig. 1.

$$|i_{H, \infty}| = F\bar{k}_1\alpha_{(H^+)}(1 - \lambda) + F\bar{k}_{II}\psi(1 - \lambda) \quad [15]$$

If reaction [I] is in virtual equilibrium, ψ is given by Eq. [16]

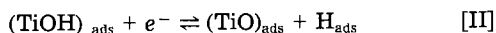
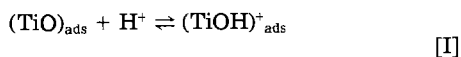
$$\psi = k_1\alpha_{(H^+)}\lambda/(k_1\alpha_{(H^+)} + k_{-1}) \quad [16]$$

Substitution of this expression for ψ into Eq. [15] gives the result

$$|i_{H, \infty}| = F\bar{k}_1\alpha_{(H^+)}(1 - \lambda) + F\bar{k}_{II}\lambda(1 - \lambda)/(1 + K_{-1}\alpha_{(H^+)})^{-1} \quad [17]$$

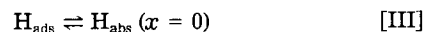
where $K_{-1} = k_{-1}/k_1$. Since $\bar{k}_1 = k_1 \exp(-\alpha_1 FE/RT)$ and $\bar{k}_{II} = k_{II} \exp(-\alpha_{II} FE/RT)$, it is apparent that, with $\alpha_1 = \alpha_{II} = 1/2$, and with λ constant, the Tafel slope given by Eq. [17] is equal to $-2(2.303 RT/F)$, i.e., -120 mV. Moreover, at constant potential and constant λ , Eq. [17] is identical with Eq. [11]. Thus, Eq. [17] is in complete agreement with the experimental results. For either of the parallel reaction paths, the mechanism is rate-determining slow discharge followed by fast recombination. When $\lambda = 0$, Eq. [17] reduces to the limiting current density equation presented for the limiting case [L-6]. An equation of the same form as Eq. [17] may be derived on the basis of reactions (I) and (II) with and [L-1]- or [L-3]-type mechanism and, consequently, S and n values again are insufficient to differentiate among these possibilities, and reference must be made to the effect of potential on θ (see below).

Nature of titanium surface species.—The generally accepted mechanism for the active-state dissolution of iron in acidic media involves the adsorbed surface intermediate $(FeOH)_{ads}$, with $\theta_{(FeOH)} \ll 1$. Since the surface of the metal is essentially an aquated one, it is not surprising that the HER on iron in acidic sulfate solutions ($S = -120$ mV and $n = 1$ throughout the entire pH range 0.32-3.50) is adequately described by reactions [1]-[3], with recourse to reactions [I] and [II] being unnecessary. The nature of the surface of titanium in the active and active-passive transition potential regions has already been discussed in great detail in connection with the so-called "monolayer" mechanism of active-state dissolution and passivation of the metal in acidic media (1). In contrast to iron, the surface of active-state titanium is not primarily an aquated surface, but one occupied predominantly by adsorbed oxy and hydroxy titanium species at the submonolayer level. These species, analogous to $(FeOH)_{ads}$, are of the form $(TiOH)_{ads}^{z-1}$ (with $z = 1, 2$, and 3) and $[Ti(OH)_2]_{ads}^{+2}$. The "monolayer" mechanism provides a quantitative description of the active-state dissolution and passivation processes. In particular, the experimentally confirmed relationships expressed by Eq. [9] and [10] derive directly from the mechanism. At $E_{m,d}$, coverages of the univalent and trivalent titanium species are negligible. If θ_2 and θ_4 represent the coverages by the divalent and quadrivalent species, then at $E_{m,d}$, $(\theta_2/\theta_4) = 2$ and $(\theta_2 + \theta_4) \approx 1$. With decreasing potential, at constant pH, θ_2 increases at the expense of θ_4 . Consequently, in the cathodic potential region, one may identify $(SH^+)_{ads}$ with $(TiOH)^+_{ads}$ and write reactions [I] and [II] in the form



where, it should be emphasized, $(TiO)_{ads}$ does not represent a 3-d phase oxide. Also, the total coverage (λ) by the divalent species remains virtually constant in the cathodic Tafel region.

Hydrogen absorption by titanium.—The question remains as to the justification for selecting a mechanism equivalent to [L-6], slow discharge-fast recombination, from among the four possible types of ($S = -120$ mV, $n = 1$) mechanisms. Justification for this selection derives primarily from information concerning the effect of potential on the coverage by H_{ads} . In addition to participating in reactions [1]-[3] and [II], electrolytically generated hydrogen atoms can penetrate into the metal, as represented by Eq. [III]



where H_{abs} ($x = 0$) refers to absorbed hydrogen atoms just inside the electrode. According to Brauer *et al.* (22), absorbed hydrogen atoms do not permeate significantly into the bulk of the metal, but, instead, concentrate in the near surface region in the form of a hydride layer having a concentration of 63 atom percent hydrogen ($TiH_{1.65}$). Further absorption simply results in an increase in the thickness of the $TiH_{1.65}$ layer by diffusion of hydrogen atoms through the hydride to the hydride/metal interface. This viewpoint is essentially the same as that proposed earlier by Brauer and Nann (23), Phillips *et al.* (24), and Tomashov and co-workers (25). All of the aforementioned investigators have observed that, at constant pH, the rate of absorption of hydrogen atoms increases with increasing magnitude of the applied cathodic current density. Phillips *et al.* (24), for example, found that the rate of absorption of hydrogen by initially hydrogen-free titanium increased with increasing $|i_H|$ in the region from 10^{-5} to 3×10^{-3} A cm $^{-2}$ in 0.05M H_2SO_4 ($T = 25^\circ C$). Others have noted a limiting cathodic current density above which further increases in $|i_H|$ have no effect on the absorption rate (22, 25). Regardless of the ultimate fate of hydrogen atoms once inside the metal, the rate of absorption of hydrogen atoms, r (mole cm $^{-2}$ s $^{-1}$), may be written, in accordance with reaction [III], in the form

$$r = k_{II}\theta(1 - \chi) - k_{-III}C_H^0(1 - \theta) \quad [18]$$

where C_H^0 is the concentration of H_{abs} ($x = 0$), χ is the fractional occupancy of absorption sites, and C_H^+ is proportional to χ . According to Eq. [18], an increase in θ results in an increase in r , i.e., $(\partial r/\partial \theta) > 0$. Consequently, the observed increase in r with increasing $|i_H|$ at constant pH reflects an increase in θ with increasing $|i_H|$. Actually, the investigators referred to above were mainly interested in the diffusion-controlled stage of the absorption process, i.e., the stage in which the absorption at constant cathodic current density followed a parabolic rate law. It was assumed that during this stage reaction [III] is in virtual equilibrium. According to Eq. [18], with $r \approx 0$, an increase in θ results in an increase in C_H^0 (in fact, if θ and χ are small, C_H^0 is directly proportional to θ). With C_H^0 serving as a boundary condition for diffusion of hydrogen atoms into the interior, the diffusion flux increases with increasing C_H^0 , i.e., with increasing θ . Consequently, the observed increase in the absorption rate with increasing $|i_H|$ at constant pH was attributed to an increase in θ , with θ attaining its maximum possible value at the limiting cathodic current density referred to above. At constant pH, an increase in $|i_H|$ corresponds to a decrease in potential, and, therefore, on the basis of the absorption studies, one may conclude that θ increases with decreasing potential at constant pH. Above, equations have been presented for θ_∞ for each of the limiting cases. For [L-1], $\theta_\infty \approx 1$ and, consequently, θ_∞ cannot increase with decreasing potential. For [L-3], $\theta_\infty \ll 1$, but θ_∞ is independent of potential. For [T-2], a Temkin case for which θ is restricted to a range of approximately 0.2 to 0.8, the expression for θ_∞ shows that if $\alpha_1 = \alpha_2$, as expected, then θ_∞ is independent of potential. For [L-6], in contrast to the other cases, θ_∞ increases with decreasing potential at constant pH, i.e., $(\partial \log \theta_\infty / \partial E)_{pH} = -(\alpha_1/2)(F/2.303 RT)$. Consequently, the results of the absorption studies are consistent only with the slow discharge-fast recombination mechanism, [L-6], or the modified [L-6] mechanism in which reactions [I] and [II] are added to reactions [1]-[3].

Phillips *et al.* (26) reported that the rate of absorption of hydrogen atoms at constant cathodic current density decreases with increasing pH. They attributed this decrease to a decrease in θ with increasing pH, and stated that this conclusion was in agreement with the HER mechanism proposed by Thomas and Nobe (11). In fact, the Temkin absorption-dual-barrier mechanism proposed by the latter authors requires that, at constant i_H , θ_∞ increase with an increase in pH, i.e.

$$(\partial \theta_\infty / \partial pH)_{i_H} = 2.303 RT (1 - \alpha_2)/(\alpha_2 + \beta_2)m \quad [19]$$

Equation [19] also applies to the simple [T-1] mechanism,

upon which the mechanism of Thomas and Nobe is based. However, according to the [L-6] mechanism, a constant $|i_{H,c}|$ corresponds to a constant θ_{α} , i.e., $|i_{H,c}| = 2Fk_3\theta_{\alpha}^2$, and, therefore, the absorption rate at constant i_H should be independent of pH. Tomashov and co-workers (25) found little effect of pH on the absorption rate in the pH region of interest in this study. In fact, in changing from pH = 0.3-1.3, Phillips *et al.*, also found a rather small effect, with a larger effect showing up at higher pH values. It seems possible that the effect noted might be attributed to the fact that the time required to activate titanium (remove the air-formed oxide film) increases markedly with increasing pH. The decrease in the absorption rate with increasing pH would then be attributed to the increased duration of the oxide film which serves as a barrier to hydrogen absorption.

3-d oxide film models.—In order to rationalize their abnormal (S, n) data, Thomas and Nobe (11) proposed that a 3-d oxide film exists on titanium in the active state, even under cathodic polarization in strongly acidic media, and that the hydrogen evolution reaction occurs at the oxide-dissolution interface. It was further assumed that the HER is described by just reactions [1] and [2], and that a Temkin adsorption isotherm applies to the adsorption of hydrogen atoms at the oxide surface. Consequently, in accordance with the definitions provided above, the rates of reactions [1] and [2] are given by Eq. [20]-[22]

$$r_1 = k'_1\alpha_{(H^+)} [\exp(-\beta_1 m\theta/RT)] [\exp(-\alpha_1 F\psi/RT)] \quad [20]$$

$$r_{-1} = k'_{-1} [\exp(1 - \beta_1)m\theta/RT] [\exp(1 - \alpha_1)F\psi/RT] \quad [21]$$

$$r_2 = k'_2\alpha_{(H^+)} [\exp(\beta_2 m\theta/RT)] [\exp(-\alpha_2 F\psi/RT)] \quad [22]$$

where ψ , the potential difference across the solution double layer at the oxide-solution interface, appears in place of E . If reaction [1] is assumed to be in quasiequilibrium, with reaction [2] rate-determining, then one may equate r_1 and r_{-1} to obtain a relation between θ_{α} and ψ

$$\theta_{\alpha} = -(F\psi/m) + (RT/m) \ln K'_1\alpha_{(H^+)} \quad [23]$$

Since the steady-state current density ($i_{H,c}$) corresponding to the HER is equal to $-2Fr_2$, one may substitute θ_{α} from Eq. [23] into Eq. [22] and obtain the result

$$i_{H,c} = -k_H\alpha_{(H^+)}^{(1+\beta_2)} \exp[-(\alpha_2 + \beta_2)F\psi/RT] \quad [24]$$

where k_H is equal to $2Fk'_2(K'_1)^{\beta_2}$. Except for ψ in place of E , Eq. [23] and [24] are identical to those given for the limiting Temkin case, [T-1]. (It should be noted in passing that Eq. [19] derives directly from Eq. [23] and [24].) The electrons participating in the HER must traverse the oxide film, and the electron current density through the oxide was presumed to be correctly described by Eq. [25]

$$i_t = k_t \exp(-\alpha_t F\psi_t/RT) \quad [25]$$

where α_t is the transfer coefficient for the activation-controlled electron transfer across the film, and ψ_t is the potential drop across the oxide. Under steady-state conditions, i_t must equal $|i_{H,c}|$, and, therefore, with the total potential difference (ψ_T) equal to $(\psi + \psi_t)$, Eq. [24] and [25] may be combined to yield the final result

$$\log |i_{H,c}| = C - [(1 + \beta_2)\alpha_t/(\alpha_2 + \beta_2 + \alpha_t)]pH - [\alpha_t(\alpha_2 + \beta_2)/(\alpha_2 + \beta_2 + \alpha_t)](F/2.303 RT)\psi_T \quad [26]$$

where C is a constant. According to Eq. [26], since $(d\psi_T/dE) = 1$, the Tafel slope (S) and reaction order (n) with respect to proton activity are given by the expressions

$$S = (\partial E/\partial \log |i_{H,c}|)_{pH} = -(2.303RT/F) [(\alpha_2 + \beta_2 + \alpha_t)/(\alpha_2 + \beta_2)\alpha_t] \quad [27]$$

and

$$n = (-\partial \log |i_{H,c}|/\partial pH)_E = [(1 + \beta_2)\alpha_t/(\alpha_2 + \beta_2 + \alpha_t)] \quad [28]$$

If the measured values, $S = -150$ mV and $n = 0.60$, are substituted into Eq. [27] and [28], then, assuming $\alpha_2 = \beta_2$, the calculated values of α_t and $\alpha_2 (= \beta_2)$ are 2/3 and 1/2, respectively. Similarly, the data of Brynza and Danilova (13) lead

to a value of 0.93 for α_t , while that of Frayret *et al.* (18) corresponds to values of 1.15 and 0.22 for α_t and $\alpha_2 (= \beta_2)$, respectively. Consequently, it is apparent that there are problems with the 3-d oxide model.

The only justification presented by Thomas and Nobe (11) for assuming that a stable 3-d oxide exists on titanium in the active state was that "... a mixed oxide film of TiO_2 and Ti_2O_3 is present on the surface of passive titanium. The thermodynamic data of these oxides indicate their possible presence even on active titanium in the Tafel region of the HER." The same authors subsequently invoked the concept of a 3-d oxide film on titanium in the active state in order to account for the results of their study of the active-state dissolution of titanium in acidic media (27). Unfortunately, one now finds such statements as "the presence of an oxide layer on the metal during both active dissolution and hydrogen evolution is indicated by... [the fact that]... both hydrogen evolution [Ref. (11) of this paper] and active dissolution [Ref. (27) of this paper] have been interpreted in terms of a dual-barrier model..." (28). With regard to whether an oxide layer exists on titanium in the active-state, thermodynamic considerations are basically useless since they also fail to preclude the possibility that the metal is preferentially oxidized to form Ti(III) ions in solution, with no oxide film present on the surface. Basically, it is a matter of kinetics, i.e., thermodynamics is useful as an indicator of what cannot occur, but not of what does occur when several options are thermodynamically possible. A recent study (i) found no definitive evidence to support the contention that a stable 3-d oxide layer exists on titanium in the active and transition states, (ii) demonstrated that the active-state dissolution and passivation of titanium in acidic media is not correctly described by mechanisms based on the presence of an oxide film, including that of Thomas and Nobe (27), and (iii) showed that active-state dissolution and passivation of the metal in acidic media is quantitatively described (including, for example, Eq. [9] and [10]) by the monolayer mechanism in which the surface is occupied by adsorbed oxy and hydroxy titanium reaction intermediates at the submonolayer level, and not a 3-d oxide film (1). Aside from the fact that a 3-d oxide layer on the surface of active-state titanium is likely nonexistent, it should be noted that, even if there were such an oxide layer, it is doubtful that Eq. [25] represents an accurate description of the electron current in the oxide (justification for Eq. [25] has not been provided, nor have the nature and properties of the oxide to which it supposedly applies ever been specified). This criticism applies whether the oxide be considered an insulator or a semiconductor (29). In the former case, one would expect a higher order dependency of the current density upon the potential drop across the oxide. In the latter case, the kinetics of the reduction reaction would be formulated quite differently, and limiting Tafel behavior would be expected (i) in the potential region in which ψ is constant and changes in ψ_t accompanying changes in ψ_T serve only to alter the surface concentration of electrons (tenfold change per 60 mV change in ψ_t), and (ii) at high cathodic current densities where $(d\psi/d\psi_T) \rightarrow 1$ as the semiconductor behaves increasingly like a metal (30). For a simple reduction reaction such as proton reduction, the Tafel slopes for cases (i) and (ii) would be -60 and -120 mV, respectively. One would not expect a Tafel region with $|S| > 120$ mV. Studies of redox reactions occurring on semiconducting oxide films formed on titanium typically yield abnormal anodic Tafel slopes, but normal cathodic Tafel slopes of -120 mV (30-32).

Although it is not incumbent upon the present authors to explain the diverse results of others, a plausible explanation for some of the reported values of n is afforded by the results of the present study. In Fig. 4, the points shown as triangles (\blacktriangle) were calculated by means of Eq. [11], and correspond to the solid curve in Fig. 3. The points shown as circles (\bullet) in Fig. 4 were abstracted from the paper of Thomas and Nobe (11). It is apparent that over the limited range of pH (0.25-2.25) encompassed by the data of Thomas and Nobe, one might reasonably but erroneously conclude that $(-\partial \log |i_{H,c}|/\partial pH)_E$ is constant, and that $n = 0.62$. The same

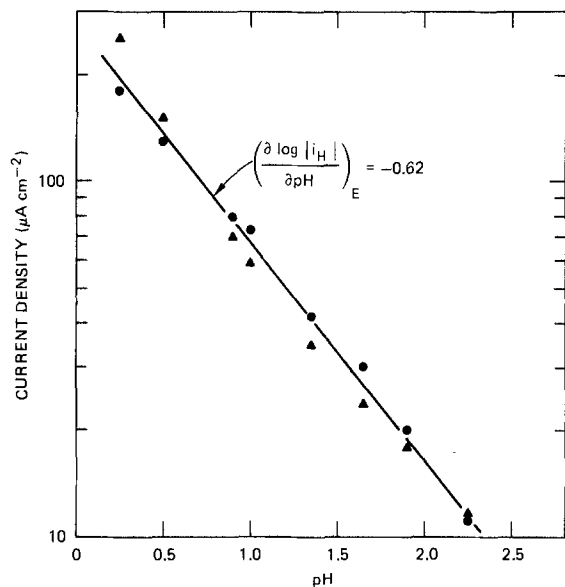


Fig. 4. Current density of the hydrogen evolution reaction on titanium as a function of pH in acidic sulfate media. ▲: Eq. [11] or solid curve in Fig. 2. ●: data of Thomas and Nobe (11). $E = -875$ mV vs. SCE.

explanation applies to the data of Brynza and Danilova (13), who reported a value of n equal to 0.63 over the pH range 0.1-2.32. In addition, Fig. 3 shows that in strongly acidic media one should expect n to equal 1.0, as reported by Petit and Dabosi (12) and by Armstrong *et al.* (10).

Summary

The rate of the hydrogen evolution reaction on zone-refined titanium in H_2 -saturated acidic sulfate and acidic chloride media ($T = 30.0^\circ\text{C}$) over the pH range 0-4.0 has been shown to be accurately described by the equation

$$|i_{H,ac}| = F(1 - \lambda) [k_1 a_{H^+} + k_2 \lambda / (1 + K_{-1} a^{-1}_{OH^+})] \exp(-FE/2RT)$$

i.e., by Eq. [17]. The rate equation may be derived on the basis of a mechanism invoking two parallel paths for proton reduction, one involving the usual solvated proton and the other involving the adsorbed titanium species, $(TiOH)_{ads}^+$. A consideration of the reported effect of potential on the rate of adsorption of hydrogen by the metal served to differentiate among the few HER mechanisms consistent with the rate equation, and led to the conclusion that the proton discharge reactions are rate determining, followed by the fast recombination reaction. The notion that a 3-d oxide layer (as opposed to adsorbed oxy and hydroxy titanium species on the submonolayer level) exists on titanium in the active state is rejected, as are HER mechanisms based upon its presumed existence.

Acknowledgment

The research reported in this paper was sponsored by the Division of Basic Energy Science, U.S. Department of En-

ergy, under Contract no. W-7405-eng-26 with the Union Carbide Corporation.

Manuscript received Feb. 6, 1984.

Oak Ridge National Laboratory assisted in meeting the publication costs of this article.

REFERENCES

1. E. J. Kelly, in "Modern Aspects of Electrochemistry," Vol. 14, J. O'M. Bockris, B. E. Conway, and R. E. White, Editors, chap. 5, Plenum Press, New York (1982).
2. J. G. N. Thomas, *Trans. Faraday Soc.*, **57**, 1603 (1961).
3. E. J. Kelly, *This Journal*, **112**, 124 (1965).
4. M. Stern and H. Wissenberg, *ibid.*, **106**, 755 (1959).
5. A. T. Petrenko, *Russ. J. Phys. Chem.*, **36**, 815 (1962).
6. V. I. Kichigin, N. I. Kavardakov, and V. V. Kuznetsov, *Sov. Electrochem.*, **18**, 940 (1982).
7. E. J. Kelly, in "Proceedings International Congress on Metallic Corrosion, 5th, Tokyo," 1972, p. 137, NACE, Houston (1974).
8. V. M. Artemova, *Sov. Electrochem.*, **3**, 1089 (1967).
9. T. Okada, *Electrochim. Acta*, **27**, 1273 (1982).
10. R. D. Armstrong, J. A. Harrison, H. R. Thirsk, and R. Whitfield, *This Journal*, **117**, 1003 (1970).
11. N. T. Thomas and K. Nobe, *ibid.*, **117**, 622 (1970).
12. J. A. Petit and F. Dabosi, *J. Chim. Phys. Phys.-Chim. Biol.*, **72**, 927 (1975).
13. A. P. Brynza and L. M. Danilova, *Sov. Electrochem.*, **9**, 336 (1973).
14. D. L. Dull and K. Nobe, *Corrosion*, **30**, 291 (1974).
15. E. J. Kelly, *This Journal*, **126**, 2064 (1979).
16. N. T. Thomas and K. Nobe, *Corrosion*, **29**, 188 (1973).
17. P. J. Aragon, *This Journal*, **120**, 1010 (1973).
18. J. P. Frayret, F. Del Ray, A. Moreau, and J. A. Petit, *Met. Corros. Ind.*, **51**, 426 (1976).
19. P. J. Aragon and R. E. Araujo, *Electrochim. Acta*, **20**, 649 (1975).
20. R. E. Meyer, *This Journal*, **107**, 847 (1960).
21. E. J. Kelly, *ibid.*, **123**, 162 (1976).
22. E. Brauer, R. Gruner, and F. Rauch, *Ber. Bunsenges. Phys. Chem.*, **87**, 341 (1983).
23. E. Brauer and E. Nann, *Werkst. Korros.*, **25**, 309 (1974).
24. I. I. Phillips, P. Poole, and L. L. Shreir, *Corros. Sci.*, **12**, 855 (1972).
25. N. D. Tomashov, V. N. Modestova, S. T. Galuznov, E. A. Borisova, and V. L. Zotov, "Corrosion of Metals and Alloys, Coll. No. 1," N. D. Tomashov, Editor, p. 196, N.L.L.S.T., Boston Spa, West Yorkshire, England (1964).
26. I. I. Phillips, P. Poole, and L. L. Shreir, *Corros. Sci.*, **14**, 533 (1974).
27. N. T. Thomas and K. Nobe, *This Journal*, **119**, 1450 (1972).
28. J. A. Harrison and D. E. Williams, *Electrochim. Acta*, **27**, 891 (1982).
29. H. Gerischer, in "Physical Chemistry, An Advanced Treatise," Vol. IXA, H. Eyring, Editor, chap. 5, Academic Press, New York (1970).
30. K. E. Heusler and K. S. Yun, *Electrochim. Acta*, **22**, 977 (1977).
31. E. N. Paleolog, A. Z. Fedotova, and V. D. Fityulina, *Sov. Electrochem.*, **4**, 625 (1968).
32. A. C. Makrides, *This Journal*, **111**, 392 (1964).

In Situ Laser Raman Spectroscopic Study of Anodic Corrosion Films on Nickel and Cobalt

C. A. Melendres* and S. Xu¹

Argonne National Laboratory, Argonne, Illinois 60439

ABSTRACT

In situ laser Raman spectra of anodic corrosion films formed on Ni and Co in 0.05M NaOH have been obtained for the first time and the composition of the surface films deduced. The Raman spectrum of the film found on Ni at about 0.6V vs. Hg/HgO corresponds closely to that of hydrated Ni₂O₃. The anodically formed film on Co at about 0.45V appeared to consist of a mixture of CoO and Co₃O₄.

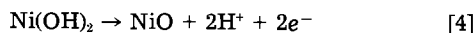
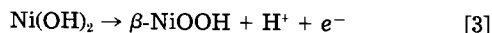
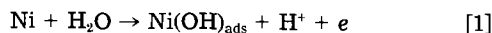
Laser Raman spectroscopy has been found to be a very valuable technique for the *in situ* identification of anodic corrosion films on metals such as Pb (1), Ag (2), and Cu (3), etc. This communication reports some results on a study of the composition of anodic corrosion films on Ni and Co using this technique in conjunction with electrochemical methods.

Experimental

Electrodes of Ni and Co were prepared from 0.010 in. thick foils of Marz grade material (99.999% purity) purchased from Materials Research Corporation, Orangeburg, New York. Counterelectrodes of the same metal were employed. The reference electrode was Hg/HgO in the same solution as the electrolyte. The 0.05M NaOH electrolyte solution was prepared from reagent-grade NaOH using four-times-distilled water. The corrosion specimens were anodized at constant potential in ambient air using a three-compartment spectroelectrochemical cell described previously (4). The applied potential was controlled with a Princeton Applied Research (PAR) Model 173 potentiostat while a PAR Model 179 Universal Programmer was used for potential scanning. The Raman measurements were carried out using a SPEX Model 1403 double monochromator fitted with a photomultiplier tube detector. Sample excitation was by an Ar⁺ laser (Coherent Model CR-6). Laser Raman spectra of standard samples, either obtained commercially or prepared by us, were taken to verify the assignment of the Raman bands to the appropriate compound. Additional confirmation of the composition of the corrosion films formed was attempted using x-ray diffraction (XRD) analysis.

Results and Discussion

Anodic corrosion films on Ni.—The electrochemistry of Ni has been studied fairly extensively in view of its practical application in alkaline batteries (5-8). The results, however, have not led to a general consensus on the composition of the anodic phases formed as a function of potential at different pH's. For Ni in basic solutions, it is widely held that the anodic corrosion proceeds in stages, resulting in the formation of Ni⁺, Ni²⁺, and higher valent oxides and hydroxides. Thus, Guzman *et al.* (8), for example, proposed the following electron transfer reactions for Ni in KOH solution



Further oxidation to NiO₂ is indicated by the Pourbaix (9) diagram (Fig. 1). The same diagram, however, does not show the existence of either NiO or β-NiOOH, which electrochemists have proposed; it indicates rather that

the stable phases are Ni₃O₄ and Ni₂O₃. However, it must be noted that Pourbaix diagrams show only which phases have been considered thermodynamically possible and not those which are preferred.

Figure 2 shows a typical cyclic voltammogram of Ni in 0.05M NaOH solution. Starting at an open-circuit potential of about 0.05V vs. Hg/HgO, potentiodynamic scans were made to the hydrogen evolution region at about -1.2V and to potentials as positive as 1.1V. After potential excursions to about -1.2V, we at times find an anodic wave at about -0.5V on the return sweep. This wave is, however, not always reproducible. Only the features shown in Fig. 2 appeared consistently during single-scan and cyclic voltammetric sweeps. We now consider the assignment of the observed waves on the basis of previous work by others (5-8). There seems to be general agreement that the wave at about -0.5V is due to the oxidation of Ni to form Ni(OH)₂ or what Davies and Barker (6) formulate as NiO · H₂O (*i.e.*, a hydrated nickel oxide). This assignment is consistent with the phases indicated in the Pourbaix diagram for our solution pH of about 11.9 (Fig. 1). There is a consensus in assigning the wave at about +0.5V to the further oxidation of Ni(OH)₂ to NiOOH or Ni₂O₃ · H₂O. However, there seems little agreement among various workers as to the degree of hydration or actual formulation of the NiOOH. MacArthur (7), for example, starting with the α modification of Ni(OH)₂, claimed that the oxidation product in KOH solution was 3NiOOH · 7/2 H₂O · 3/4 KOH. Bode *et al.* (10) have given the formula for the oxidized γ structure as [NiO(OH)]₃O₃(OH)K₂. Bourgault and Conway (11), probably starting with β-Ni(OH)₂, derived the formula 2NiOOH · 0.14KOH. Zedner (12), Forster (13), and Kornfeil (14) gave the formulations 2NiOOH · H₂O, 2NiOOH · 0.2H₂O, and 2NiOOH ·

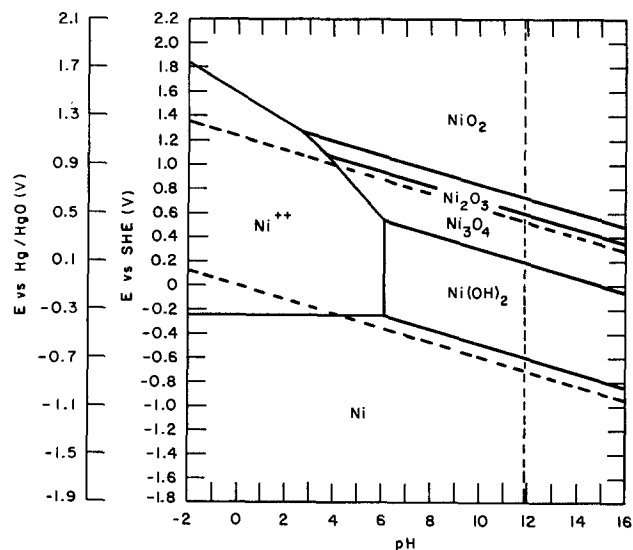


Fig. 1. Pourbaix diagram of the Ni-H₂O system at 25°C

* Electrochemical Society Active Member.

¹Present address: Department of Chemistry, University of Science and Technology of China, Hefei, Anhwei, China.

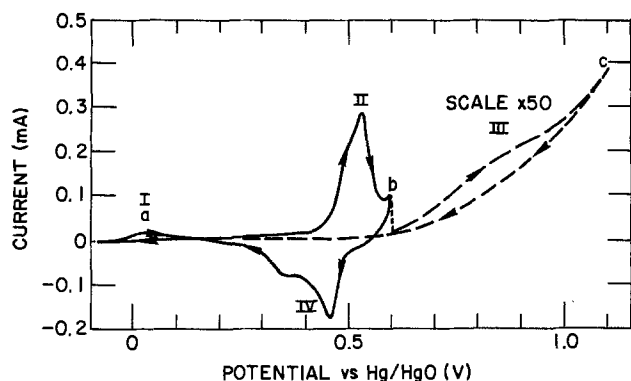


Fig. 2. Cyclic voltammogram of Ni in 0.05M NaOH solution. Scan rate: 10 mV/s.

$0.067\text{KOH} \cdot 1.16\text{H}_2\text{O}$, respectively. It is quite apparent that the electrochemistry of the nickel electrode is rather complex. Onset of oxygen evolution on the oxide coated surface occurs at about point b (Fig. 2), and massive O_2 evolution ensues beyond 0.8V. It is interesting to note other salient features of the voltammogram in Fig. 2, such as the shoulders on both anodic and cathodic portions of the wave at 0.5, the small wave at about 0 V, and one at about 0.8V.

Figure 3 shows typical laser Raman spectra of a Ni electrode in 0.05M NaOH as a function of potential. Spectra taken *in situ* at the open-circuit potential of about 0.05V exhibit a small background in the region of about 300-900 cm^{-1} that may be due to fluorescence from the glass window. On potentiostating the electrode past the wave (II) at 0.6V, two bands appear at about 477 and 555 cm^{-1} , respectively. These bands are relatively strong (signal:

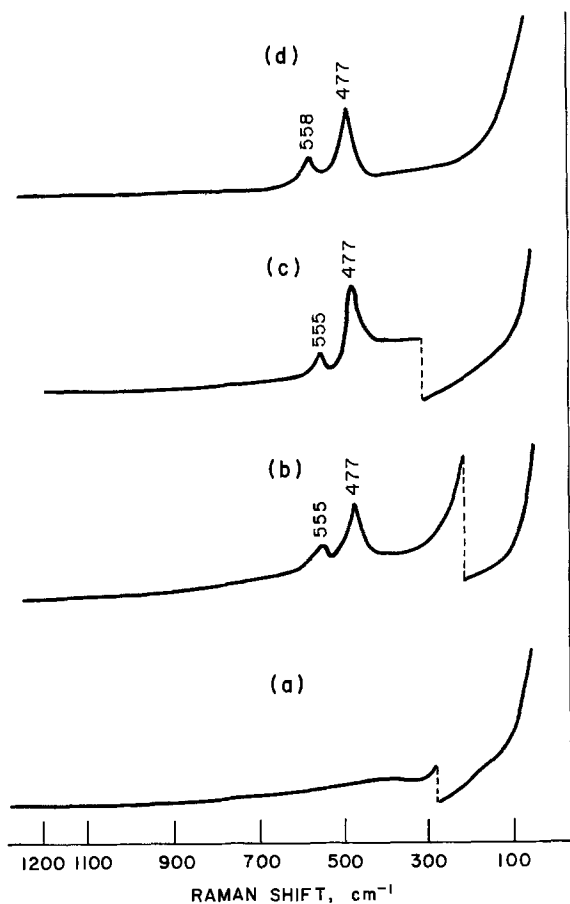


Fig. 3. Laser Raman spectra of Ni electrode at various potentials in 0.05M NaOH; Ar⁺ laser, $\lambda = 4880 \text{ \AA}$ line, $P = 80\text{-}150 \text{ mW}$. (a): At open circuit (OCV), $E = 0.05 \text{ V}$ vs. Hg/HgO. (b): $E = 0.6 \text{ V}$. (c): $E = 1.1 \text{ V}$. (d): *Ex situ* after anodization at $E = 0.7 \text{ V}$.

noise $\sim 3:1$), even with only 10 mC/cm^2 of charge passed (which would correspond roughly to about 20 layers of anodic film, assuming no film dissolution occurs). The bands disappear on scanning back to -0.1 V but persist if the potential is swept to more anodic values, e.g., 1.1V and held there for 2 or 3h, during which time oxygen is being evolved from the electrode surface. As might be expected, the electrode when potentiostated in the hydrogen evolution region (e.g., -1.2 V) did not show any apparent surface film. Figure 3d shows that the same bands are observed *ex situ* after removing the electrode from the cell at 0.7V. Repeated attempts to find other Raman bands in the potential range of -1.2 to $+0.4 \text{ V}$, where we had hoped to detect $\text{Ni}(\text{OH})_2$, have not been successful. Likewise, no other bands were found in the potential region of about $+0.7$ to 1.1 V , where higher oxides of Ni are expected to be formed. It is likely that whatever film is formed in these regions is neither thick enough nor a strong enough Raman scatterer to enable us to obtain a spectrum.

It is interesting to consider the probable origin of the observed bands at 558 and 477 cm^{-1} . As a first step, x-ray diffraction analysis was carried out on material scraped from electrodes following anodization at 0.6V. This, however, was not successful presumably due to the thinness of the film; the film may also have been amorphous, and, hence, would not have shown a diffraction pattern. As a further step towards film identification, Raman spectra were taken of standard samples of $\text{Ni}(\text{OH})_2$, Ni_2O_3 , NiO , and NiO_2 . The first was synthesized following the procedure prescribed by Hüttig and Peter (15), and the product obtained confirmed by x-ray analysis to be $\text{Ni}(\text{OH})_2$. The Ni_2O_3 , NiO , and NiO_2 were purchased from Alfa-Ventron (Danvers, Massachusetts). The first was reported to contain six waters of crystallization. Detailed elemental analysis indicated the composition to be $\text{Ni}_{1.2}\text{O}_{3.4} \cdot 2\text{H}_2\text{O}$ instead. X-ray analysis confirmed the composition of the NiO , but the NiO_2 was nearly amorphous with lattice parameters that somewhat resembled those given for $\beta\text{-NiOOH}$ or $\text{Ni}_3\text{O}_2(\text{OH})_4$. Spectra of the standard samples are shown in Fig. 4. We were unable to obtain the spectrum of NiO_2 which was a rather dark black sample. It is

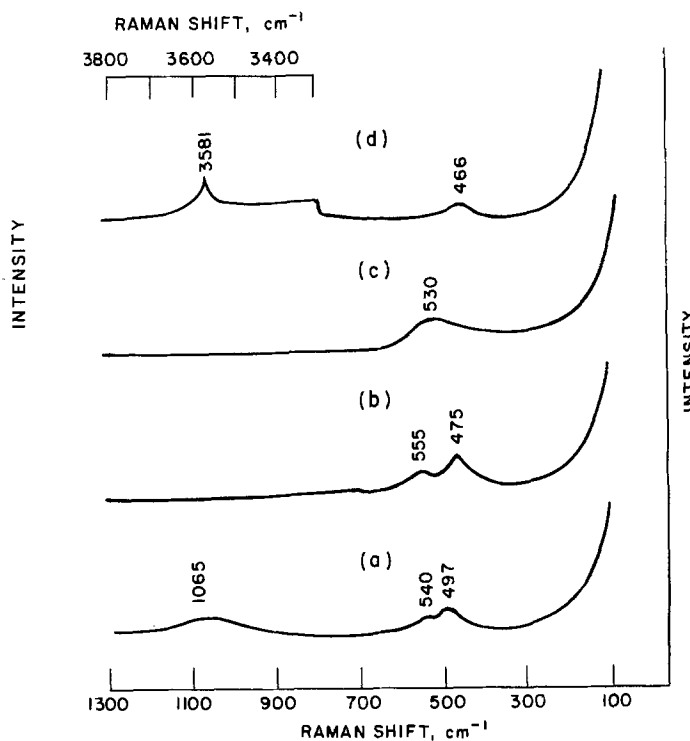


Fig. 4. Laser Raman spectra of standard samples of Ni compounds (20%/80% in KBr pellet); Ar⁺ laser, $\lambda = 4880 \text{ \AA}$ line, $P \approx 80\text{-}120 \text{ mW}$. (a): NiO . (b): $\text{Ni}_2\text{O}_3 \cdot 2\text{H}_2\text{O}$. (c): Charged Ni electrode for Ni/Fe battery. (d): $\text{Ni}(\text{OH})_2$.

evident from the results that the spectrum which corresponds most closely to what we observe for the anodized electrodes is that of $\text{Ni}_2\text{O}_3 \cdot 2\text{H}_2\text{O}$. As we have indicated in the beginning of this section, the anticipated product of anodic oxidation of Ni at about 0.5V is hydrated $\beta\text{-NiOOH}$ (8, 10). This compound is also generally accepted to be the active material in fully charged Ni electrodes in Ni/Cd or Ni/Fe alkaline batteries. Unable to purchase NiOOH commercially or to prepare it ourselves chemically, we examined the Raman spectrum of a charged Ni electrode obtained from the General Electric Company. The spectrum is shown in Fig. 4c. A broad band centered at about 530 cm^{-1} is observed. An electrode in the discharged state with composition corresponding to $\text{Ni}(\text{OH})_2$ was also charged electrochemically and then examined *ex situ*. A similar spectrum was obtained but a weak OH band at 3580 cm^{-1} was present, presumably owing to unconverted $\text{Ni}(\text{OH})_2$. If we assign the broad band at 530 cm^{-1} to NiOOH, we are led to the conclusion that the anodic film formed on Ni at 0.5V corresponds more closely to hydrated Ni_2O_3 than to $\beta\text{-NiOOH}$. Davies and Barker (6) have proposed the structural equivalence of NiOOH and $\text{Ni}_2\text{O}_3 \cdot \text{H}_2\text{O}$. Such equivalence, however, has not been experimentally established. Our results show a subtle difference between the two. The sharper bands for $\text{Ni}_2\text{O}_3 \cdot 2\text{H}_2\text{O}$ suggest a more crystalline structure compared to NiOOH. We searched for a difference in OH vibration for the two samples but were unable to find any OH or water vibrational frequency.²

The finding on the presence of Ni_2O_3 is in good agreement with that predicted by the Pourbaix diagram. However, we find no NiO or $\text{Ni}(\text{OH})_2$ as likewise predicted. This may be due to insufficient quantity of these compounds in the film. Davies, for example, calculates the thickness of the $\text{Ni}(\text{OH})_2$ film on Ni passivated in alkaline solutions to correspond to only one or two monolayers. The sensitivity of the Raman technique in the case of Ni is apparently not sufficient to detect this quantity of material. Finally, our study could not confirm the further oxidation of Ni^{+3} to Ni^{+4} to form NiO_2 because of our inherent inability to detect NiO_2 . Based on our experience, this is a problem commonly associated with Raman spectral determination of dark or black materials. Strong sample absorption of the incident light results in insufficient detectable scattered Raman light.

Surface corrosion films on Co.—A number of investigations have dealt with the electrochemical behavior of Co in basic and near-neutral solutions (16-19). Characterization of the nature and composition of the films formed was done notably by Sato (19, 21) and by Leidheiser (18, 20) using ellipsometry and Mössbauer spectroscopy, respectively.

Figure 5 shows an abbreviated Pourbaix diagram (9) for the Co/ H_2O system. The broken vertical line at pH 11.8 indicates the operating region corresponding to the 0.05M NaOH solution in which our electrodes were anodized. Depending on the applied potential, one sees that the phases that can be formed during the anodic corrosion of Co are $\text{Co}(\text{OH})_2$, Co_3O_4 , $\text{Co}(\text{OH})_3$, and CoO_2 .

Figure 6 shows a cyclic voltammogram of Co in 0.05M NaOH. The main features of the voltammogram appear to be the wave at about -0.5V and the set of reversible oxidation-reduction waves in the region of 0-0.4V prior to the onset of oxygen evolution at about 0.5V. The former has been assigned by Sato (19, 20) as due to the formation of a passive CoO film on the electrode. The range of potential from 0 to about 0.5V corresponds to what Sato has termed the primary and secondary passivation regions where $\text{Co}(\text{OH})_2$ and Co_3O_4 are formed, respectively. If waves II and III are associated with the formation of these compounds, waves VI and VII would correspond to their reduction. According to Sato, Co_2O_3 is formed beyond 0.5V, but there is no visible indication of an anodic wave in our voltammogram that could be attributed to

²The presence of water in the Ni_2O_3 sample has now been shown by infrared spectroscopy.

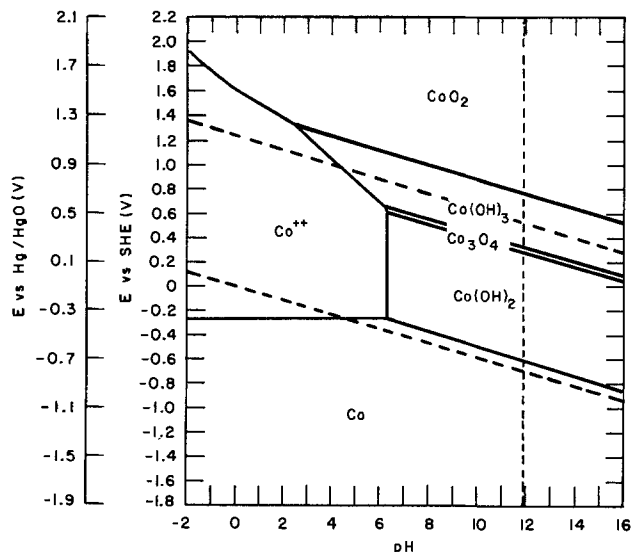


Fig. 5. Pourbaix diagram of the Co- H_2O system at 25°C

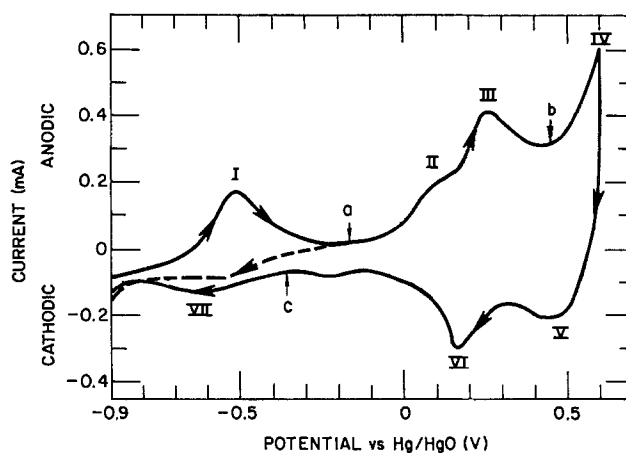


Fig. 6. Cyclic voltammogram of Co in 0.05M NaOH solution. Scan rate: 10 mV/s.

this. It may very well be masked by the large anodic current due to the other corrosion processes and the oxygen evolution reaction in this region.

Figure 7 shows the results of our Raman spectral measurements on Co electrodes. At the open-circuit potential of -0.16V, only background either from the glass window or the solution between the window and the electrode could be observed. On anodizing the electrode at 0.45V, four bands at 475, 515, 587, and 690 cm^{-1} , respectively, are observed. There is also an apparent increase in the background in the region of 400-900 cm^{-1} . The Raman bands disappear following a cyclic sweep and cathodic reduction at -0.35V (Fig. 7c). Spectral measurements in the interval between -1.1 to 1.2V did not yield additional Raman bands. *Ex situ* examination of the electrode surface following anodization at 0.45V yielded the result shown in Fig. 7d. It is obvious that there is an overlap of multiple vibrational bands in the relatively narrow frequency region of about 400-800 cm^{-1} . No bands were found in the OH^- stretching region, e.g., 3400-3700 cm^{-1} , for the film studied *ex situ*.

To facilitate interpretation of the observed spectra, an attempt was made to examine the films formed using x-ray diffraction. The films were, however, apparently so thin that a sufficient amount of material could not be scraped off the surface to get an XRD pattern. The material may have also been amorphous so that no pattern was obtained. We, therefore, concentrated on obtaining the spectra of standard samples of the possible and anticipated corrosion products of Co. Figure 8 shows results for the compounds $\text{Co}(\text{OH})_2$, CoO, and Co_3O_4 . The $\text{Co}(\text{OH})_2$ was prepared following the procedure of Hüttig

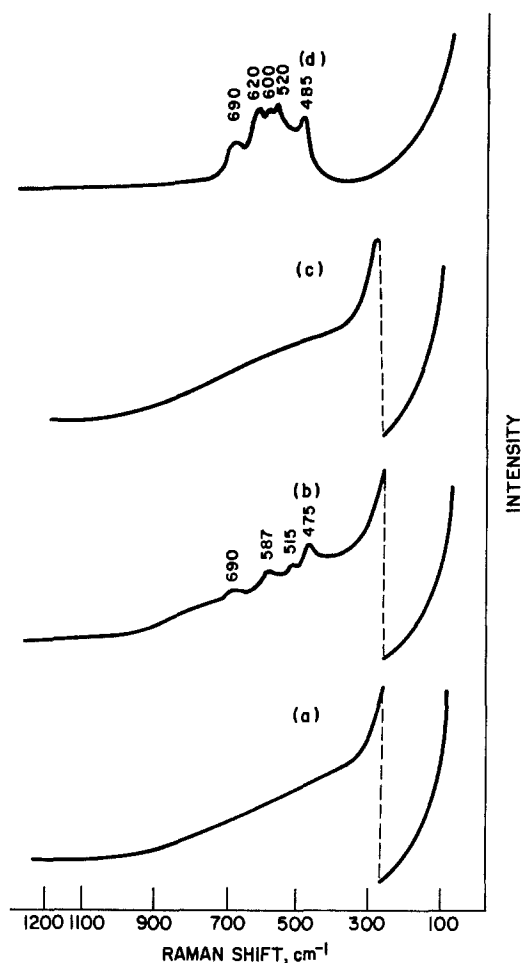


Fig. 7. Laser Raman spectra of Co electrode at various potentials in 0.05M NaOH; Ar⁺ laser, $\lambda = 4880 \text{ \AA}$ line, $P = 80\text{-}140 \text{ mW}$. (a): At open circuit (OCV), $E = -0.16 \text{ V}$ vs. Hg/HgO. (b): $E = 0.45 \text{ V}$. (c): $E = -0.35 \text{ V}$. (d): Ex situ after anodization at $E = 0.45 \text{ V}$.

and Kassler (22, 23); the composition of the product was confirmed by XRD analysis to be $\beta\text{-Co(OH)}_2$. The CoO

and Co_3O_4 were from Cerac (Milwaukee, Wisconsin). All the standard samples were pressed with KBr to make a pellet and rotated during the spectral measurement.

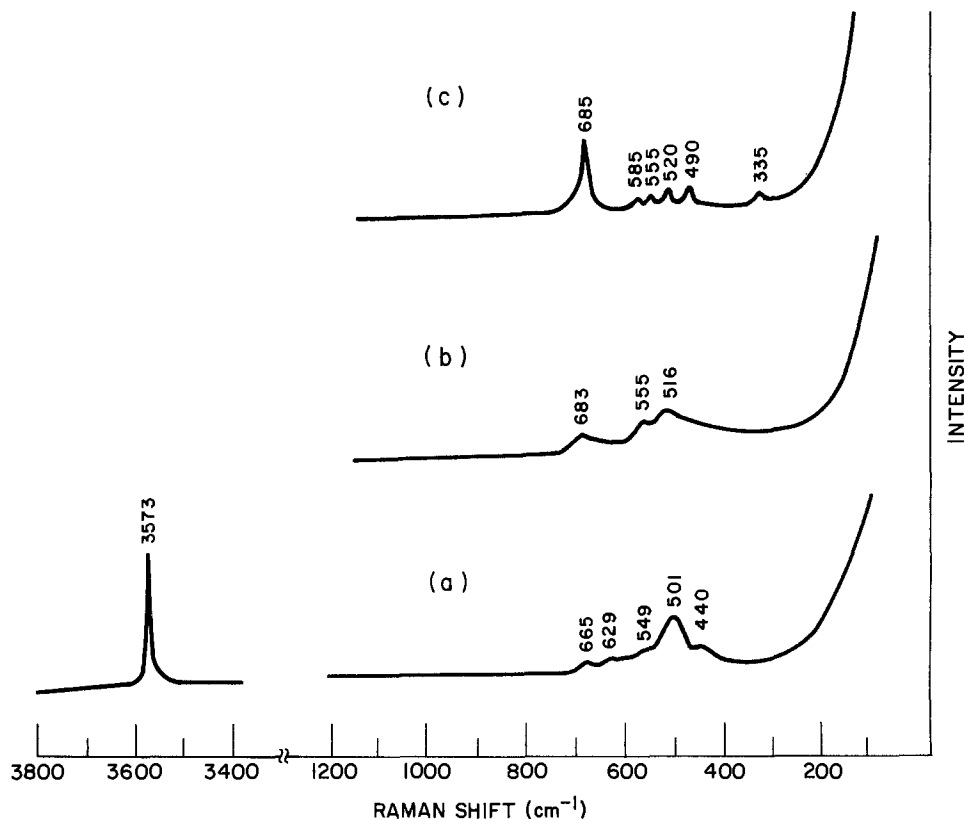
Comparing the *in situ* spectrum at 0.45V (Fig. 7b) with that obtained *ex situ* (Fig. 7d), one finds that there are more bands observed in the latter than in the former case. Two factors contribute to this: (i) the higher intensity obtainable when taking spectra outside the electrochemical cell, and/or (ii) masking of the spectra by the background fluorescence from the glass or solution is eliminated in the out-of-cell sample, resulting in better resolution and intensity. It is, however, unlikely that there would be more bands *ex situ* than *in situ*, so that it would be safe to assume that the bands observed *ex situ* are really also present *in situ*. The difference in peak frequencies between the corresponding bands may be more due to frequency shift associated with superposition of the spectrum on the high background. Comparing the *in situ* bands with the standards shows a one-to-one correspondence between the 515 and 516 cm^{-1} bands of the surface film and the CoO standard, respectively. Likewise, the 475 and 587 cm^{-1} bands of the electrode sample have counterparts in the Co_3O_4 spectrum. Further indication of the presence of Co_3O_4 in the film is the similarity in the gross features of the *ex situ* film spectrum with the Co_3O_4 standard. The absence of OH^- bands in the *ex situ* spectrum suggests that Co(OH)_2 is either not present in the film or is at a level below the detection sensitivity limits. One can then conclude that the anodic corrosion film formed at a cobalt electrode anodized at +0.45V consists of a mixture of CoO and Co_3O_4 . This is the first spectroscopic confirmation of Sato's finding of the existence of a bilayer CoO/ Co_3O_4 oxide film on Co in this potential region.

Acknowledgments

This research work was done under the auspices of the Division of Materials Sciences, Office of Basic Energy Sciences, U.S. Department of Energy. Thanks are due to B. Tani for the x-ray diffraction analysis of the samples and to Dr. D. Poa for supplying the Ni electrodes from alkaline Ni batteries.

Manuscript submitted Feb. 27, 1984; revised manuscript received May 21, 1984.

Fig. 8. Laser Raman spectra of standard Co compounds (20%/80% in KBr pellet); Ar⁺ laser, $\lambda = 4880 \text{ \AA}$ line, $P \sim 80\text{-}130 \text{ mW}$. (a): Co(OH)_2 . (b): CoO. (c): Co_3O_4 .



Argonne National Laboratory assisted in meeting the publication costs of this article.

REFERENCES

1. R. J. Thibeau, C. W. Brown, A. Z. Goldfarb, and R. H. Heidersbach, *This Journal*, **127**, 37 (1980).
2. R. Kötz and E. Yeager, *J. Electroanal. Chem.*, **111**, 105 (1980).
3. C. A. Melendres and S. Xu, *ibid.*, **162**, 343 (1984).
4. C. A. Melendres and F. A. Cafasso, *This Journal*, **128**, 755 (1981).
5. B. E. Conway and P. L. Bourgault, *Can. J. Chem.*, **37**, 292 (1959).
6. D. E. Davies and W. Barker, *Corrosion*, **20**, 47t (1964).
7. D. M. MacArthur, *This Journal*, **117**, 422 (1970).
8. R. S. Schreiber Guzman, J. R. Vilche, and A. R. Arvia, *Corros. Sci.*, **18**, 765 (1978).
9. M. Pourbaix, "Atlas D'Equilibres Electrochimiques," pp. 325, 333, Gauthier-Villars, Paris (1963).
10. H. Bode, K. Dehmelt, and J. Witte, *Electrochim. Acta*, **11**, 1079 (1966).
11. P. L. Bourgault and B. E. Conway, *Can. J. Chem.*, **38**, 1557 (1960).
12. J. Zedner, *Z. Elektrochem.*, **46**, 809 (1905).
13. F. Forster, *ibid.*, **13**, 414 (1907).
14. F. Kornfeil, in "Proceedings of the Annual Battery Research and Development Conference," p. 134, 12th Conference, U.S. Army Signal Corps, Fort Monmouth, NJ (1958).
15. G. F. Hüttig and A. Peter, *Z. Anorg. Allg. Chem.*, **189**, 183 (1930).
16. S. El-Wakkad and A. Hickling, *Trans. Faraday Soc.*, **46**, 1820 (1950).
17. W. K. Behl and J. E. Toni, *J. Electroanal. Chem. Interfacial Electrochem.*, **31**, 63 (1971).
18. H. Leidheiser, Jr., G. W. Simmons, and E. Kellerman, *This Journal*, **120**, 1516 (1973).
19. N. Sato and T. Ohtsuka, *ibid.*, **125**, 1735 (1978).
20. G. W. Simmons, E. Kellerman, and H. Leidheiser, *This Journal*, **123**, 1276 (1976).
21. K. Kudo, N. Sato, and T. Ohtsuka, in "Passivity of Metals," R. P. Frankenthal and J. Kruger, Editors, p. 918, The Electrochemical Society Monograph Series, Princeton, NJ (1978).
22. G. F. Hüttig and R. Kassler, *Z. Anorg. Allg. Chem.*, **187**, 16 (1930).
23. G. Brauer, Editor, "Handbook of Preparative Inorganic Chemistry," Vol. 2, p. 1521, Academic Press, New York (1965).

Electrochemical Deposition of CdS Thin Films on Mo and Al Substrates

E. Fatas, R. Duo, and P. Herrasti

Departamento de Electroquímica, Universidad Autónoma de Madrid, Cantoblanco, Madrid-34, Spain

F. Arjona and E. Garcia-Camarero

Departamento de Física Aplicada, Universidad Autónoma de Madrid, Cantoblanco, Madrid-34, Spain

ABSTRACT

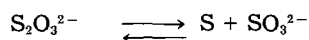
The formation of cadmium sulfide thin films by cathodic deposition of Cd²⁺ ions from a solution containing sulfur on different substrates (platinum, molybdenum, aluminum) is described along with the influence of the substrate on the formation and morphology. By evaporating a Cu₂S layer on the CdS films deposited on aluminum, a heterojunction which exhibits photovoltaic effect is formed.

Cadmium sulfide is one of the semiconductor materials widely used in solar cells. Together with copper sulfide, it forms the well-known CdS/Cu₂S solar cell (1, 2).

It is generally admitted that electrodeposition is an efficient method of film formation, allowing a more economical production and better control of properties and stoichiometry of the resulting layers than thermal evaporation, pyrolytic spraying, or sputtering.

Recent studies have shown that the anodization of cadmium in sulfur solutions can be used for preparing photoactive cadmium sulfide films (3-5). However, the films obtained in this way do not have a homogeneous composition because the surface is much more affected by the electrochemical reaction than the deep layers. A lack of macroscopic uniformity of these films is also observed.

In this work, we have followed the approach reported by Power *et al.* (6). The CdS film is cathodically deposited from a solution containing cadmium and thiosulfate ions. The thiosulfate ions disproportionate, depending on the pH, according to



Thus, the overall electrode reaction is



Although this process has been studied on platinum electrodes, we have extended the study to other electrode ma-

terials, which seem more appropriate for use in solar cell applications.

Experimental

The voltammograms presented were obtained with a potentiostatic system consisting of scan generator, X-Y recorder, and potentiostat, using a standard three-electrode electrochemical cell in which the reference electrode was a saturated calomel electrode (SCE) and the counterelectrode a cylindrical platinum grid. The electrode impedance was measured with a PAR Model 128A lock-in amplifier.

The plating solution was $2 \times 10^{-3}M$ CdSO₄, 0.1M Na₂S₂O₃. The pH was adjusted with H₂SO₄. All products were from Merck p.a. grade.

Solutions were prepared using twice-distilled water that had subsequently been passed through a Millipore Mili-Q system. The electrode surfaces were grazed with carborundum paper and then with alumina powders containing particles as small as 0.05 μm. After polishing, the electrodes were cleaned with doubly distilled water followed by acetone p.a. grade. All the measurements were performed at 25° ± 0.1°C.

In order to form the CdS/Cu₂S heterojunctions, a 1500Å Cu₂S film was evaporated at 10⁻⁵ torr on a CdS film previously grown.

The composition and morphology of the CdS thin films were analyzed by scanning electron microscopy (SEM) and x-ray dispersive analysis, with a Philips-EDAX scanning microprobe system.

Results and Discussions

The cyclic voltammetric curves obtained with a Pt electrode at neutral pH are shown in Fig. 1. From the results, it became evident that at potentials more negative than -550 mV a reduction process occurs due to deposition of cadmium metal. The anodic peak ($E_{ap} = -250$ mV) corresponds to the redissolution of the Cd. A reversible character became apparent by the constant value of the E_{ap} with sweep rate. The cathodic and anodic charges are different, and the excess cathodic charge may be due to hydrogen evolution rather than to the formation of a CdS film, which was not observed after subjecting the electrode to a potential of -850 mV for a few hours.

Figure 2 shows a voltammetric curve for an acid solution pH 2.3. In this condition, the $S_2O_3^{2-}$ is decomposed to colloidal sulfur, which is reduced to sulfide ions that together with the Cd^{2+} present in the interface form a CdS film on the electrode. The cathodic peak appears at more negative potentials ($E_{ap} = -750$ mV) and the cathodic currents are strongly increased, while the anodic peak has almost disappeared. These characteristics can be interpreted on the basis of the formation of a CdS film which is not redissolved until very anodic potentials are reached. The small anodic peak due to redissolution of cadmium appears at -250 mV vs. SCE.

The feasibility of forming CdS films on Pt by this method led us to investigate other metallic electrodes more suitable for the preparation of photovoltaic cells. We have initially investigated the cathodic deposition of CdS on molybdenum electrodes. Figure 3 shows the corresponding voltammogram. A rather higher cathodic current is observed, due partially to hydrogen evolution, and partially to the formation of a CdS film. The surface roughness of the metallic substrate prevented an exact determination of film thicknesses. However, it was never

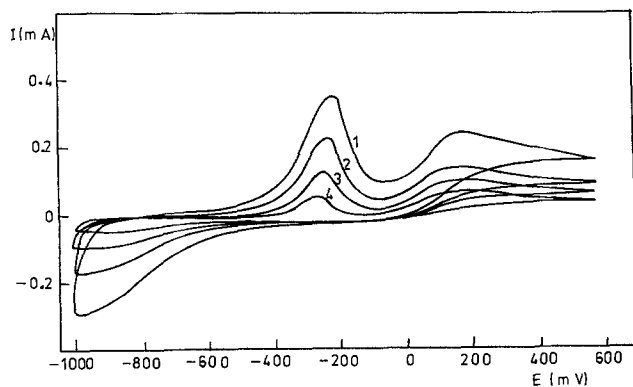


Fig. 1. Linear potential scans of a solution containing $2 \times 10^{-3}M$ $CdSO_4$ and $0.1M$ $Na_2S_2O_3$, pH = 6.7 at a Pt electrode. Scan rates: (curve 1) 200 $mV s^{-1}$, (curve 2) 100 $mV s^{-1}$, (curve 3) 50 $mV s^{-1}$, (curve 4) $mV s^{-1}$. Reference electrode: SCE.

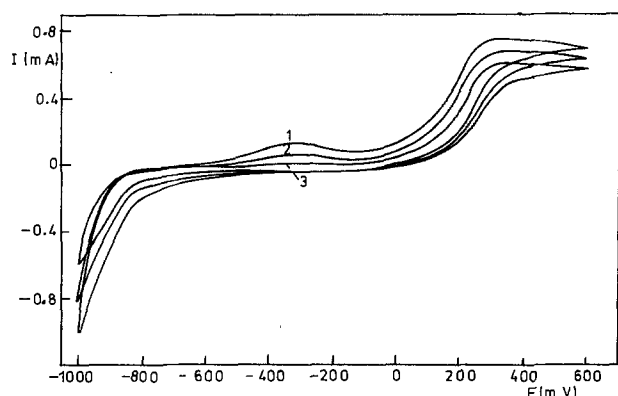


Fig. 2. Linear potential scans of a solution containing $2 \times 10^{-3}M$ $CdSO_4$ and $0.1M$ $Na_2S_2O_3$, pH = 2.3 at a Pt electrode. Scan rates: (curve 1) 200 $mV s^{-1}$, (curve 2) 100 $mV s^{-1}$, (curve 3) 50 $mV s^{-1}$. Reference electrode: SCE.

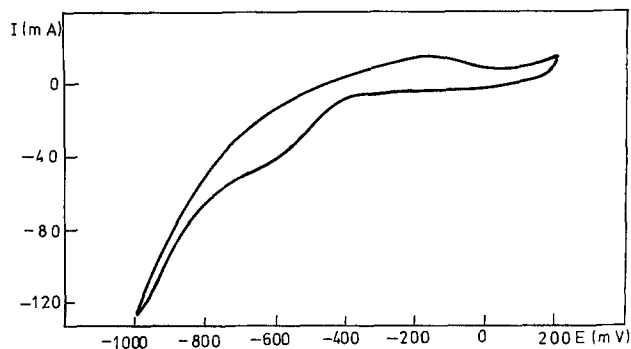


Fig. 3. Linear potential scans of a solution containing $2 \times 10^{-3}M$ $CdSO_4$ and $0.1M$ $Na_2S_2O_3$, pH = 2.3 at a Mo electrode. Scan rate: 200 $mV s^{-1}$. Reference electrode: SCE.

greater than about 1000\AA , which is clearly insufficient for applications in solar cells. If the CdS is so thin, the number of defects in the active region will probably increase and the collection efficiency will deteriorate (7).

These results led us to test aluminum as working electrode because of its good electrical characteristics. Figure 4 shows the voltammogram corresponding to the formation of CdS on this electrode at acid pH. The behavior of this system is qualitatively similar to the previous case, the cathodic current appearing at more negative potentials ($-1V$ vs. SCE). When this potential was applied for a

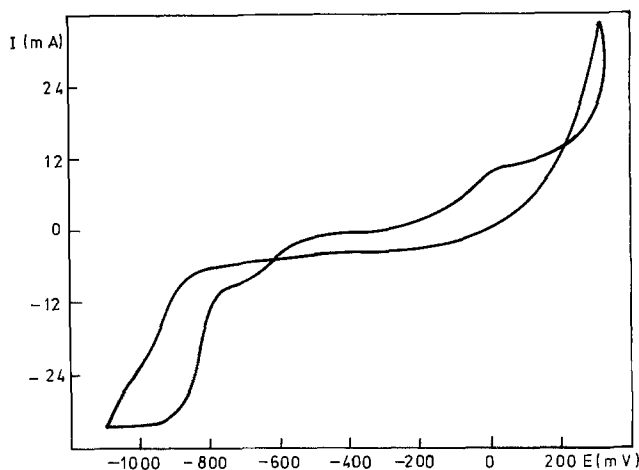


Fig. 4. Linear potential scans of a solution containing $2 \times 10^{-3}M$ $CdSO_4$ and $0.1M$ $Na_2S_2O_3$, pH = 2.3 at an Al electrode. Scan rate: 200 $mV s^{-1}$. Reference electrode: SCE.

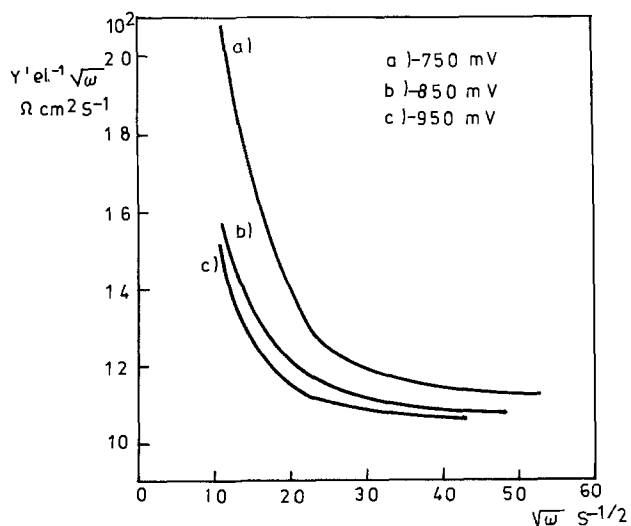


Fig. 5. Frequency dependence of the real component of the interfacial admittance Y'_{el} / \sqrt{w} vs. \sqrt{w} for indicated values of potential, at a Mo electrode.

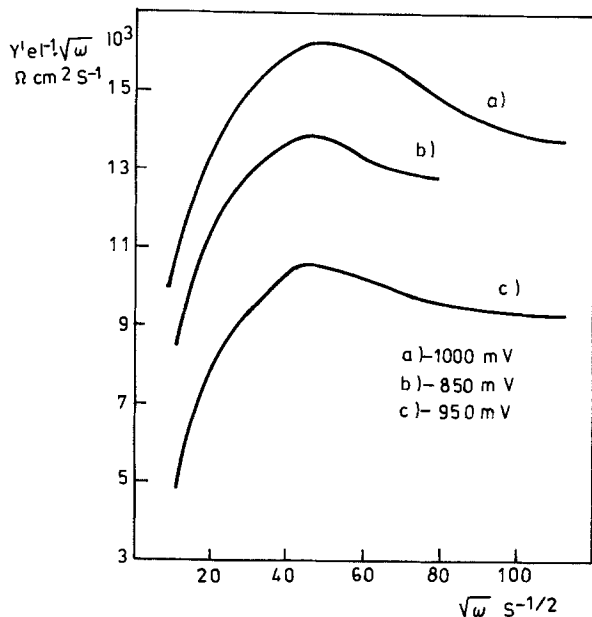


Fig. 6. Frequency dependence of the real component of the interfacial admittance $Y'_{el} \cdot \sqrt{w}$ vs. \sqrt{w} for indicated values of potential, at an Al electrode.

sufficiently long time, the electrode covered itself with a yellow, uniform, translucent, rather thick film. For shorter electrolysis times, thin, nonadherent CdS films were formed. Therefore long electrolysis times were used (1-2h). With the aim of producing thicker films, the cell solution was periodically changed, thus avoiding reduction of the sulfur concentration due to the precipitation of colloidal sulfur.

Molybdenum electrodes behaved somewhat differently. In order to investigate the difference in behavior of molybdenum and aluminum electrodes, we have performed ac impedance measurements, analyzing the real and imaginary components of the faradic admittance.

For the Mo electrode, Fig. 5 shows the variation of the real part of electroodic admittance (Y'_{el}) with frequency, w , at several potentials. The observed diminution of $Y'_{el} \cdot \sqrt{w}$ corresponds to anomalous values of the phase angle of the faradic impedance higher than 45° . This could be indicative of a faradic process with adsorption of an electroactive species (8). This effect can be the reason for the low thickness obtained and the impossibility of growing CdS films on Mo electrodes, now interpreted in terms of blocking of the electrode surface by adsorbed species.

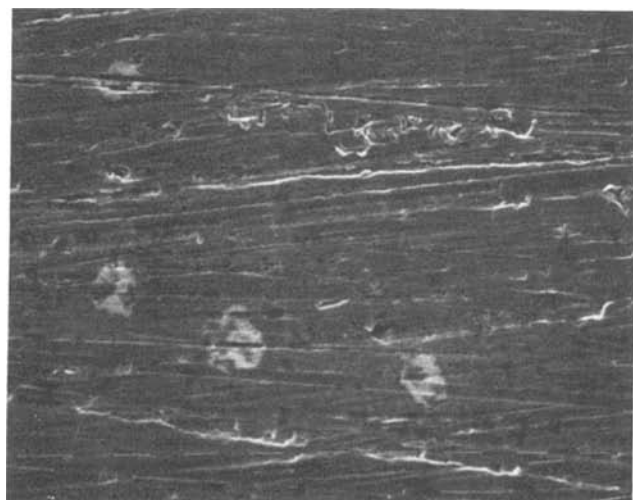


Fig. 7. Scanning electron micrograph of an electrode of molybdenum after 15 min deposition (640X).

The behavior of the parameter $Y'_{el} \cdot \sqrt{w}$ with frequency for an Al electrode is markedly different for all the studied potentials (Fig. 6). An increase with frequency is observed, followed by stabilization at a certain level, and in some cases by a slight diminution. This is not in agreement with Randles behavior in the whole frequency range, but can be explained by a chemical reaction coupling to charge transfer, which led to the described behavior of $Y'_{el} \cdot \sqrt{w}$.

Figure 7 shows the SEM micrograph of the film formed on molybdenum. Two zones can be seen. The first one consists of white stains whose composition is 98% sulfur and 2% cadmium. The second one is a large zone with less cadmium. These compositions are not very accurate due to the superposition of the sulfur K line at 2.3 keV, and the molybdenum L line at 2.29 keV, but, nevertheless, the data are significant. In every sample, the sulfur content is much greater than the cadmium content, indicating the preferential formation of a yellow layer of adsorbed sulfur instead of CdS. Figure 8 is a micrograph of a CdS film grown on the Al electrode. Three zones can be distinguished. The first one consists of white grains containing 91% sulfur and 9% cadmium. The second zone is made up of clusters the mean composition of which is 68% Cd and 32% sulfur, corresponding practically to stoichiometric CdS. The last zone is the uncovered substrate. A longer electrolysis time results in films with a lower cadmium content (58% Cd and 42% S) and the different morphology seen in Fig. 9. Thermal treatment *in vacuo* (200°C, 1h) leads to a higher degree of homogeneity demonstrated in Fig. 10.

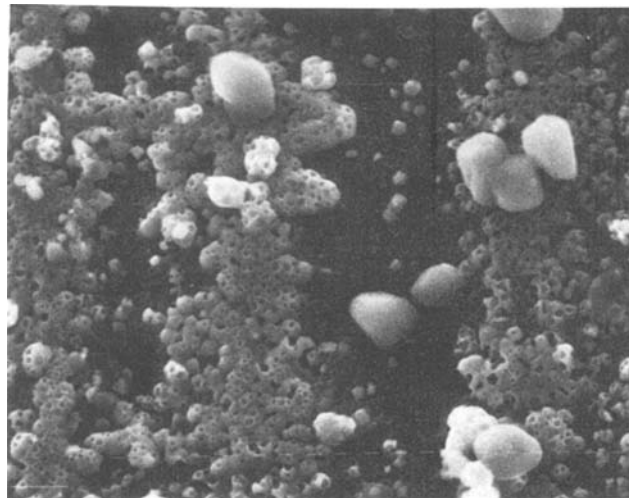


Fig. 8. Scanning electron micrograph of an electrode of aluminum after 2h deposition (2500X).

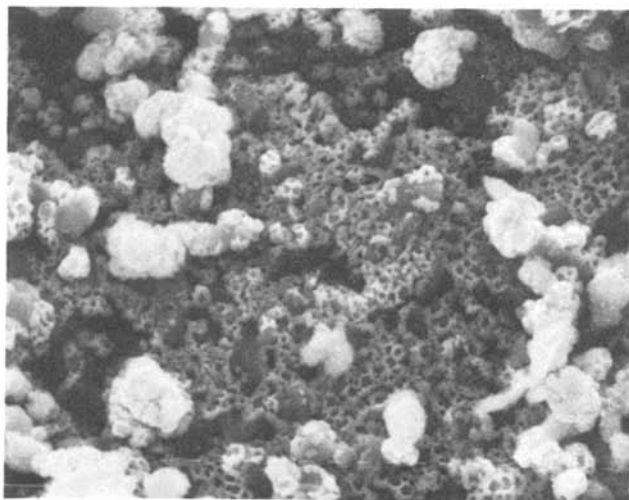


Fig. 9. Scanning electron micrograph of an electrode of aluminum after 2.5h deposition (2500X).

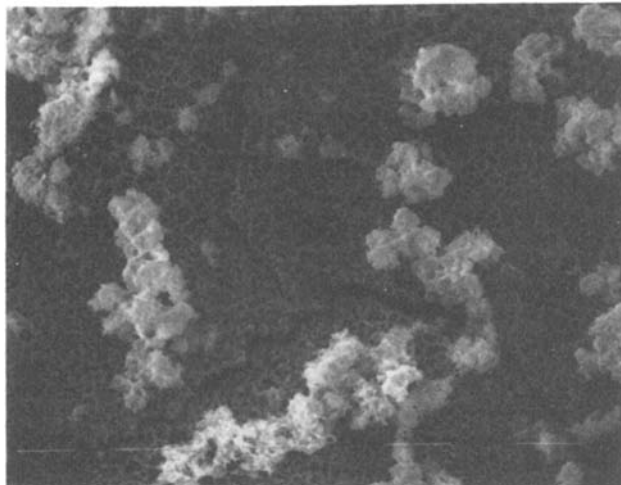


Fig. 10. Scanning electron micrograph of an electrode of aluminum after 2.5h deposition followed by thermal treatment (1500X).

A 1500Å Cu_2S film was deposited on CdS by vacuum evaporation. The heterojunction formed on a Mo substrate did not exhibit a photovoltaic effect due to the very small thickness and poor stoichiometry of the CdS film. However, the heterojunction formed on Al substrate exhibited a low photovoltaic effect, which was more evident in the heat-treated samples. Under 80 mW/cm^2 illumination, with a 300W General Electric ELH lamp, the open-circuit voltage was 10-15 mV, and the short-circuit current only a few microamperes.

Conclusions

The results reported above indicate that the metal used as a substrate has an important effect in the formation of

CdS films with suitable thickness and stoichiometry. Best results were obtained on aluminum. The different behavior of the metals studied has been attributed to different electrode mechanisms: surface blocking by adsorbed sulfur in the case of molybdenum, and chemical reaction coupled to charge transfer for aluminum.

Optimum conditions for the formation of a CdS layer on aluminum substrates were: pH = 2.3, potential -1V vs. SCE, and electrolysis time > 2h.

Thermal treatments improve the characteristics of the films and their photovoltaic properties.

These results are promising with regard to the feasibility of the electrochemical formation of CdS, for solar cell applications, where thicker and more adherent films are needed. Work is now in progress to achieve these objectives by trying electrodeposition at higher temperatures and different thermal treatments of the samples.

Manuscript submitted Jan. 4, 1984; revised manuscript received April 24, 1984.

Universidad Autónoma de Madrid assisted in meeting the publication costs of this article.

REFERENCES

1. A. G. Stanley, "Applied Solid State Science," Vol. 5, p. 251, Academic Press, New York (1975).
2. L. R. Shiozawa, F. Augustine, G. Sullivan, J. Smith, and W. Cook, Final Report AF33 (615)-5224, Clevite Corp., Cleveland, OH (1969).
3. L. M. Peter, *Electrochim. Acta*, **23**, 165 (1978).
4. L. M. Peter, *ibid.*, **23**, 1073 (1978).
5. B. Miller, S. Menezes, and A. Heller, *J. Electroanal. Chem.*, **94**, 85 (1978).
6. G. P. Power, D. R. Peggs, and A. J. Parker, *Electrochim. Acta*, **26**, 681 (1981).
7. H. J. Hovel, "Semiconductors and Semimetals," Vol. 11, p. 93, Academic Press, New York (1975).
8. M. Sluyters-Rehbach and J. H. Sluyters, *J. Electroanal. Chem.*, **39**, 136 (1982).

Detection of Gas Bubbles and Organic Molecules Included in Electrodeposited Films by Transmission Electron Microscopy

S. Nakahara*

AT&T Bell Laboratories, Murray Hill, New Jersey 07974

ABSTRACT

A transmission electron microscope method was developed for distinguishing the defocused images of organic inclusions from those of gas bubbles included in electrodeposited films. The method, in principle, utilizes a difference in the defocus contrast between the images of organic inclusions and gas bubbles. This contrast difference can be attributed to a difference in the mean inner potential between two types of inclusions. Experimental results of the defocus contrast from inclusions in copper electrodeposits were compared with theoretical image-intensity calculations. The results were found to be in good agreement with the theoretical predictions.

A recent transmission electron microscope (TEM) study (1) has established that electrodeposited films often contain small ($\approx 10\text{\AA}$) gaseous and/or organic inclusions. Gaseous inclusions, which are most likely to be hydrogen bubbles, result from the incorporation of hydrogen into a deposit at a cathode during electrocrystallization. The inclusion of hydrogen in a form of gas bubbles was previously found to cause the so-called "hydrogen embrittlement" in electroless copper films (2). Organic inclusions, however, originate primarily from addition agents deliberately added to an electrolyte.

In TEM, such small inclusions can be detected by a method known as the through-focus imaging (3). In this method, the images of inclusions may be seen with the defocus contrast, if the inclusions are sufficiently large

($\geq 10\text{\AA}$). The defocus contrast arises from phase contrast as a result of the interference at a chosen distance of defocus between electrons passing through an inclusion and those through its surrounding metal matrices. In TEM, therefore, such inclusions are regarded as "phase objects" (1).

Most recently, a simple method was developed (4) for distinguishing gas bubbles from organic inclusions ("polymer") in cobalt-hardened gold electrodeposits from their defocused images. An idea is to reveal statistical characteristics in the size distribution for two kinds of inclusions. It was found experimentally that gas bubbles exhibit a size-distribution curve much different from that of organic inclusions. Here, the size distribution of singly incorporated organic molecules in the gold deposits was quite uniform, whereas that of gas bubbles was random.

* Electrochemical Society Active Member.

Accordingly, the existence of organic inclusions in the deposit was manifested by the appearance of a relatively sharp peak in their size-distribution curve. This was the case for "polymer" inclusions in hard gold electrodeposits (4). The incorporation of gas bubbles, however, resulted in a broader curve, indicating a random size distribution. In this method, therefore, the presence of organic inclusions and gas bubbles and their relative amount can be estimated from their size-distribution curve. It is, however, obvious that this method cannot be applied to electrodeposits containing both organic molecules and gas bubbles, which happen to be comparable in size.

In this communication, we report another method for distinguishing organic inclusions from gas bubbles. The method is based upon the use of a significant difference present in the defocus contrast between organic inclusions and gas bubbles. The contrast difference was found to originate from the difference in the mean inner potential (MIP) between two types of inclusions, and to vary sensitively with the amount and sign of defocus. An optimum amount of defocus for distinguishing one type of inclusions from the other was determined from both experimental and theoretical results.

A Method of Intensity Calculation for Defocus Contrast

A simple method for computing the defocus contrast of "phase objects" having circular symmetry was previously described by Rühle (5). In this calculation, the effects of an incident beam divergence, lens aberration, and inelastic scattering were neglected. Furthermore, the presence of a finite objective aperture was not taken into account, which is equivalent to the aperture-free case. In order to describe the theoretical formulations based upon the above assumptions, we illustrate an electron-optic system in relation to the mathematical coordinate system. In an electron-optic system, there are four important planes, as shown in Fig. 1. These planes are object, objective lens, backfocal, and image planes. We consider a circular-phase object, the electron exit surface of which is located precisely at the object plane. Cartesian coordinates x , y , and z are defined in the object plane, where the origin is taken at the center of the phase object. When the object plane ($z = 0$) is focused by an objective lens, the focused image of the object is seen at the image plane. If a plane ($z \neq 0$) different from the object plane is focused, the defocused image of the phase object appears at the image plane. For example, the overfocused image can be seen if a plane below the object is focused (see Fig. 1). The distance between the object and the imaged planes is defined as an amount of defocus (Δf). The positive and negative signs of Δf imply the overfocused and underfocused conditions, respectively.

The theoretical formulation is based upon an information theory for image transfer, in which successive Fourier transforms are used to derive the wave function at the image plane. We assume that the wave function at the object plane (or more precisely at the electron exit surface of an object) is expressed as $\Psi(\vec{r})$, where \vec{r} is the position vector in the object plane x - y (see Fig. 1). The wave function, $\tilde{\Psi}(\vec{\xi})$, at the back-focal plane is then described as the Fourier transform of the function, $\Psi(\vec{r})$, where $\vec{\xi}$ is the Fourier wave vector at the back-focal plane which is defined by the cartesian coordinate ξ_1 and ξ_2 . The wave function, $\Psi_o(\vec{r})$, at the image plane is the inverse Fourier transform of the function, $\tilde{\Psi}(\vec{\xi})$, multiplied by an appropriate phase factor which accounts for a phase shift due to defocusing. The final intensity distribution, $I(\vec{r})$ at the image plane is expressed as the product, $\Psi_o(\vec{r}) \cdot \Psi_o^*(\vec{r})$, where the wave function, $\Psi_o^*(\vec{r})$, implies a complex conjugate of the function, $\Psi_o(\vec{r})$.

The function, $\Psi_o(r)$, was previously obtained (5, 6) to be

$$\Psi_o(\gamma, \Delta f) = C [1 - 2i\epsilon \exp(i\epsilon\gamma^2) \int_0^1 \{e^{i\gamma'^2} - 1\} \exp(i\epsilon\gamma'^2) J_0(-2\epsilon\gamma'\gamma)\gamma'd\gamma'] \quad [1]$$

where $C = \exp(2\pi i\Delta fK)$, K being the wave vector of an in-

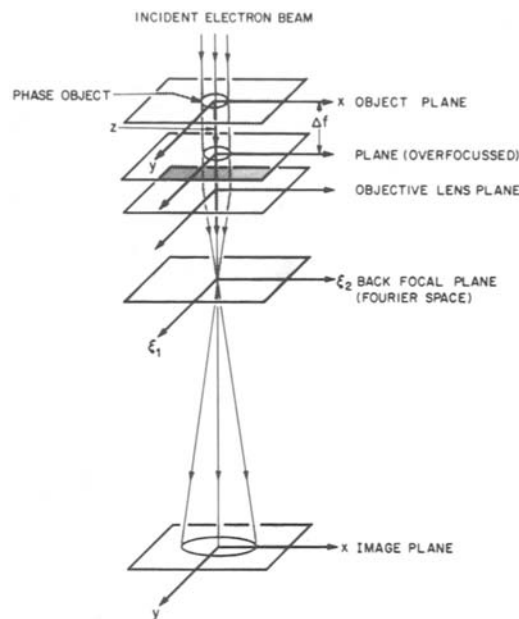


Fig. 1. Schematic illustration showing an electron-optic system for a transmission electron microscope.

cident electron beam, Δf the amount of defocus, $\gamma = |r|/r_0$, $\gamma' = r'/r_0$, $\epsilon = (\pi K/\Delta f) r_0^2$, r_0 the radius of the phase object, and J_0 the Bessel function of the 0th order. A function, $f(\gamma')$, represents a phase shift at the electron exit surface of a phase object. For spherical-phase objects

$$f(\gamma') = \Phi_0 \sqrt{1 - \gamma'^2} \quad (|\gamma'| \leq 1) \quad [2]$$

where Φ_0 is the phase shift at $\gamma' = 0$. The phase, Φ_0 , can be expressed in terms of MIP, V_0 , as

$$\Phi_0 = \pi t V_0 / \lambda E \quad [3]$$

where t is the thickness of an object along an electron-beam direction at $\gamma' = 0$, λ the wavelength of an electron beam, and E the accelerating voltage. The intensity distribution, $I(\gamma, \Delta f)$, at the image plane is obtained from the relation

$$I(\gamma, \Delta f) = \Psi_o(\gamma, \Delta f) \cdot \Psi_o^*(\gamma, \Delta f) \quad [4]$$

Experimental

Copper films were electrodeposited on annealed OFHC copper sheets in a sulfate electrolyte (200 g/l $\text{CuSO}_4 \cdot 5\text{H}_2\text{O}$, 50 g/l H_2SO_4) containing 5 mM/l O-phenanthroline as an organic additive. Plating was carried out at room temperature and at the current density of 5 mA/cm². The films plated in this condition were previously found (7) to contain O-phenanthroline molecules incorporated into the film without any decomposition. Furthermore, a selection of this particular organic as an additive was expected to be appropriate for studying by the defocus contrast, as O-phenanthroline molecules have previously been shown to be detectable in nickel electrodeposits by the defocus contrast using TEM (3).

Copper films used for TEM observations were jet polished in a mixture of 50 ml nitric acid and 100 ml methanol at room temperature. If a slow rate of polishing was required, the solution was chilled to the temperature of Dry Ice.

TEM micrographs were taken with a JEM 200 electron microscope operated at 200 kV. For through-focus sequences, an amount of defocus (Δf) was previously calibrated against the excitation current of an objective lens.

All the through-focus sequences for imaging inclusions were taken under the kinematical condition. This imaging condition allowed one to avoid the so-called amplitude contrast arising from multiple-diffraction events in a

crystal and thus provided pure phase contrast for inclusion images.

Results and Discussion

Observation of inclusions.—Through-focus sequences revealed numerous inclusion images in a copper deposit. Figures 2a and 2b show TEM micrographs of inclusions in the single grain, taken in the overfocused ($\Delta f = +3.9 \mu\text{m}$) and underfocused ($\Delta f = -3.9 \mu\text{m}$) conditions, respectively. Inclusions are seen as black dots surrounded by white rings in the overfocused condition (Fig. 2a) and as white dots surrounded by black rings in the underfocused condition (Fig. 2b). The density of these inclusions was $\sim 1 \times 10^{17}/\text{cm}^3$. As indicated by a dotted line in Fig. 2, all inclusions are seen to be distributed along a specific crystallographic direction. In order to insure that the inclusions were indeed distributed internally within the grain,¹ we took a stereo-pair, while keeping the identical defocus condition (8). Overfocus and underfocus stereo-pairs are shown in Fig. 3 and 4, respectively. A stereographic trace analysis made for several differently oriented grains indicated that the direction of the inclusion alignment lies along the $\langle 001 \rangle$. An origin of the directional alignment along the $\langle 001 \rangle$ will be discussed later. As shown previously by Wipper *et al.* (7), the inclusions are most likely to be O-phenanthroline molecules.² More information concerning these image features is, however, needed to determine whether or not all the inclusions are of organic origin.

As described in the earlier section, one of the indirect methods for determining the possible presence of organic inclusions or gas bubbles is to take the size-distribution curve of inclusions from their defocused images. Following this method, we made the size measurements from 200 inclusions visible in Fig. 2a. The number of inclusions *vs.* the image size³ is plotted in Fig. 5. A relatively well-defined peak is located at the size of $\sim 27 \text{ \AA}$. It is also seen from the curve that the majority of inclusions lies in the size range of $27 \pm 10 \text{ \AA}$. These inclusions are uniform in size, indicating the presence of O-phenanthroline molecules. This does not, however, insure that there are no gas bubbles in the deposit. Only a tentative conclusion here is that within 200 inclusions the deposit did not contain enough gas bubbles. A question then arises as to how one can recognize a small number of gas bubbles which are hidden inside a large number of organic inclusions, in

¹Unambiguous distinction cannot be made between inclusions at the surfaces and those inside a grain, unless the stereo-pair is taken.

²Inclusions in metal matrices, which are seen as white dots surrounded by black rings in the underfocused condition, consist of lower atomic elements than the metal. In an electrodeposited metal, only the possible inclusions of low atomic elements are organic molecules and/or gas bubbles.

³In defining the size of images taken in the overfocused condition, we took the outer diameter of black dot as a measure of the size. It has previously been shown (1) that the actual size of an inclusion is close to the outer diameter of black dot taken in the overfocused condition.

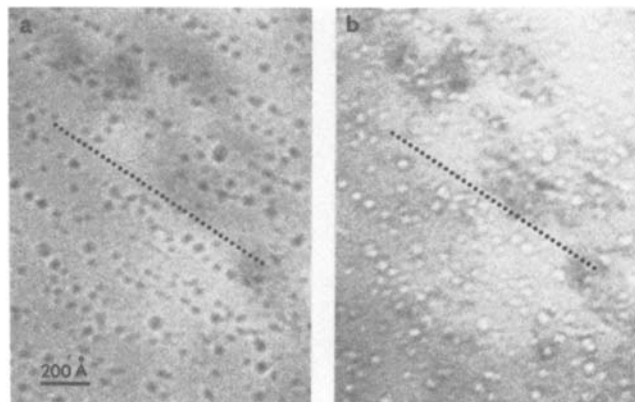


Fig. 2. Micrograph of a copper film taken in the (a) overfocused ($\Delta f = +3.9 \mu\text{m}$) and (b) underfocused ($\Delta f = -3.9 \mu\text{m}$) conditions.

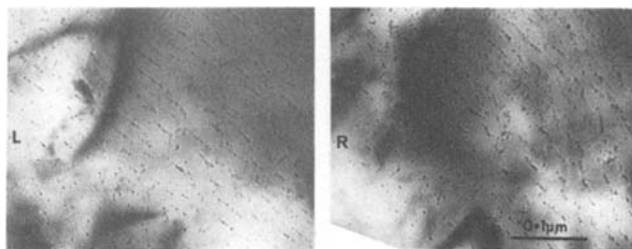


Fig. 3. A stereo-pair taken at $\Delta f = +3.9 \mu\text{m}$, showing a spatial alignment of inclusions.

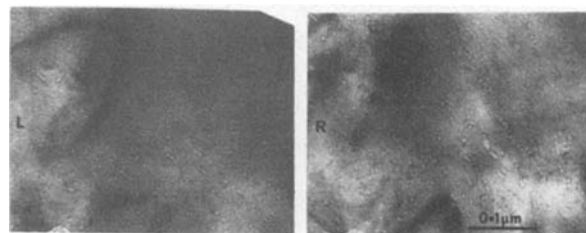


Fig. 4. A stereo-pair of the area corresponding to Fig. 3, taken at $\Delta f = -3.9 \mu\text{m}$.

particular if the size of gas bubbles is similar to that of organic inclusions. A method of taking the size distribution does not appear to be a reliable solution to this problem here.

So far, we have limited ourselves to an analysis of image size from a micrograph taken at one defocus. There is, in fact, one more important variable that has not yet been considered here. An additional variable is an intensity distribution of the image as a function of defocus distance. If there is a sufficient difference in MIP between two inclusions, it may be possible to observe a difference in the defocus contrast. Based on this consideration, we made a further systematic study on the image contrast of the inclusions by changing the amount and sign of defocus. Figures 6a and 6b are TEM micrographs of the inclusions, taken in focus and at the defocus distance of $+1.3 \mu\text{m}$ (overfocus), respectively. The images taken in the in-focus condition are practically invisible. At $\Delta f =$

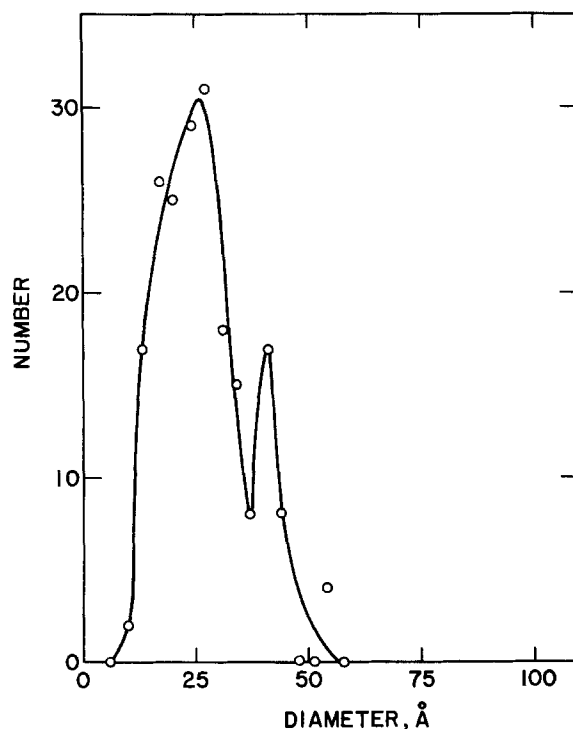


Fig. 5. A size distribution of inclusions in a copper deposit. The size represents a measured image size from micrographs obtained at $\Delta f = \pm 3.9 \mu\text{m}$.

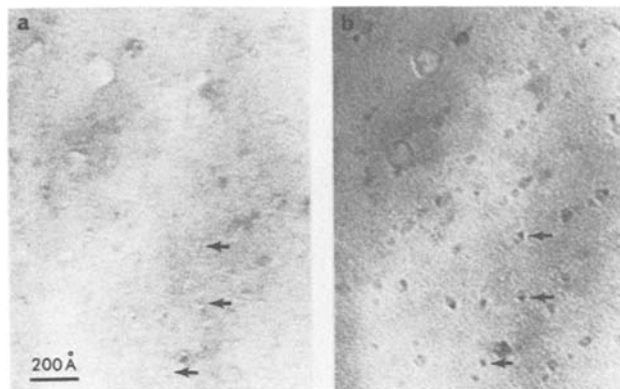


Fig. 6. Images of inclusions in a copper deposit. (a) $\Delta f \approx 0$ and (b) $\Delta f = +1.3 \mu\text{m}$.

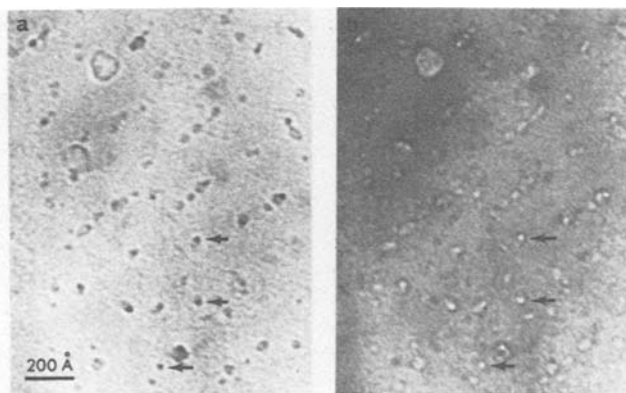


Fig. 7. Images of inclusions in a copper deposit. The area is the same as that shown in Fig. 6. (a) $\Delta f = +2.6 \mu\text{m}$, and (b) $\Delta f = -2.6 \mu\text{m}$.

+1.3 μm , it is noted that several inclusions (for example, those indicated by three arrows) exhibited slightly darker dots than the rest of inclusions. As most of inclusions in Fig. 6 are comparable in size, the difference in contrast should originate from that in MIP. Considering the fact that gas bubbles containing hydrogen should have a lower MIP than organic inclusions, it is suspected that these darker dots may originate from gas bubbles. The same area shown in Fig. 6 is further taken with $\Delta f = \pm 2.6 \mu\text{m}$ (see Fig. 7). Here, the corresponding inclusion images indicated by arrows can be recognized much more clearly than those in Fig. 6. In addition, the contrast difference between gas bubbles and organic inclusions is seen to be much more obvious here, but this difference tends to become smaller again with a further increase in defocus distance. For example, the images taken at $\Delta f = \pm 3.9 \mu\text{m}$ (see Fig. 2a and 2b) demonstrate this trend in a loss of contrast difference at a larger defocus distance.

These results strongly suggest that there is an optimum amount of defocus distance for obtaining the maximum difference in contrast between two types of inclusions. The optimum amount of defocus appears to lie between 1.3 and 2.6 μm . A quantitative analysis on the contrast difference is, however, needed to confirm this conclusion.

It should be mentioned here that the overlapped images of inclusions could also give rise to an enhanced contrast due to a linear superposition of phase shift along the electron-beam direction. For selecting probable gas bubbles (as indicated by three arrows in Fig. 6 and 7), care was taken to avoid overlapped inclusion images. A possible image overlap was further checked by taking a stereopair, which also supported the validity of our assumption that the inclusions are more or less spherical in shape.

Theoretical intensity calculation.—Based upon the above experimental observations, we made a theoretical analysis on the image contrast of inclusions. Equation [4] was used to compute an intensity profile as a function of radial distance, r . For this computation, the following parameters were used. From the size distribution curve shown in Fig. 5, we chose the average size of inclusions to be 27 Å diam. The shape of inclusions was assumed to be spherical. The MIP of copper was chosen to be 23.5V from the data obtained by Buhl (9). We assumed that gas bubbles contain hydrogen. Since hydrogen could readily diffuse out of the film at room temperature (2), gas bubbles could be effectively a spherical hole at the time of TEM observations. The MIP of hydrogen gas bubbles was therefore taken to be 0 V. Data for the MIP of O-phenanthroline are not available in literature. However, noting that its chemical formula is $\text{C}_{12}\text{H}_9\text{N}_2$, it is reasonable to assume that its MIP may not differ too much from that of other organic substances containing similar atomic elements. From published data (10), MIP's for stearic acid, $\text{C}_{30}\text{H}_{62}$, and $\text{C}_{31}\text{H}_{64}$ were 6.3, 6, and 7.2V, respectively. We chose 6V for the MIP of O-phenanthroline molecule. Equation [1] was numerically evaluated using a high-speed computer.

Figures 8a, 8b, and 8c are the intensity profiles of the hydrogen gas bubble (dotted line) and the organic molecule (solid line) computed for $\Delta f = +1.3$, +2.6, and +3.9 μm , respectively. Here, the vertical axis is normalized to the background intensity, I_0 , whereas the horizontal axis is normalized to the radius, r_0 , of an inclusion. As is evident in Fig. 8, a difference in primary intensity minimum at $r/r_0 = 0$ between two inclusions varies markedly with an amount of defocus. It is noted here that there is in fact 7% ~ 13% contrast difference at the peak ($r/r_0 = 0$) between the two inclusions. This contrast difference seems to be larger for a smaller amount of defocus. In Fig. 9, we plotted the intensity difference at $r/r_0 = 0$ between the gaseous and the organic inclusions as a function of defocus distance. From this curve, an optimum amount of defocus for distinguishing the images of organic inclusions from those of gas bubbles appears to lie between 1 and 3 μm , which is in good agreement with the experiment.

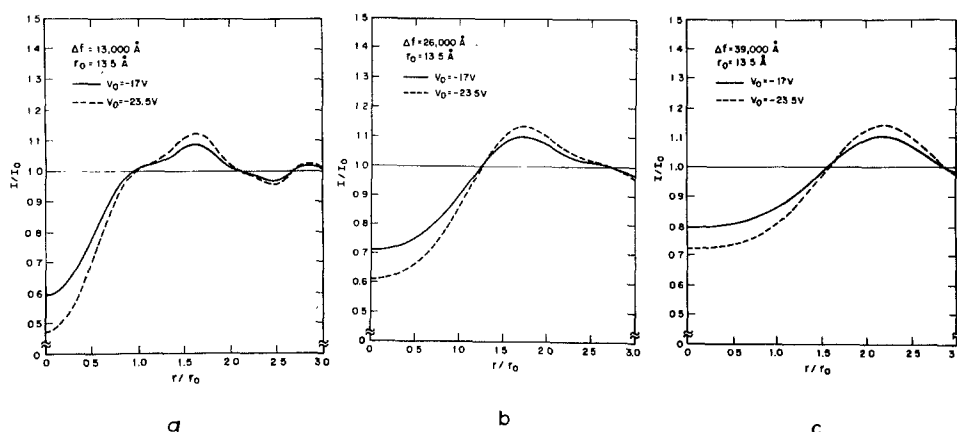


Fig. 8. Theoretical image intensity profile computed for spherical gaseous and organic inclusions in copper. Normalized intensity I/I_0 is plotted against normalized radial distance r/r_0 , where I_0 is the background intensity and r_0 is the radius of inclusion. The distance ($r/r_0 = 1$), therefore, represents the actual size of an inclusion. (a): $\Delta f = +1.3 \mu\text{m}$. (b): $\Delta f = +2.6 \mu\text{m}$. (c): $\Delta f = +3.6 \mu\text{m}$.

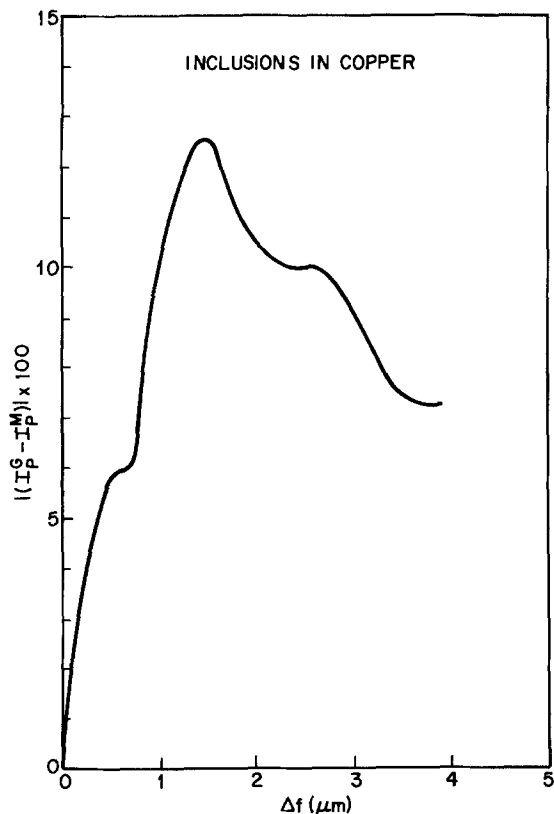


Fig. 9. Calculated intensity difference in primary intensity minimum at $r/r_0 = 0$ between gaseous (I_p^G) and organic (I_p^M) inclusions vs. the defocus distance (Δf).

Comparison of theoretical predictions with experimental results.—Our theoretical estimate shows a remarkable agreement with the experiment. This is rather surprising, considering the fact that identification of the nature of inclusions is still speculative here. Regardless of this experimental uncertainty, it is clear from the theoretical predictions that there is indeed a significant contrast difference expected between two types of inclusions. The contrast difference of course varies with the size of inclusions and the MIP of metal matrices. This contrast difference method may not be applicable to all situations, but at the present time there seem no other microscopic methods that provide further details on the nature of inclusions. Nevertheless, organic and gaseous inclusions generally play an important role in determining the physical prop-

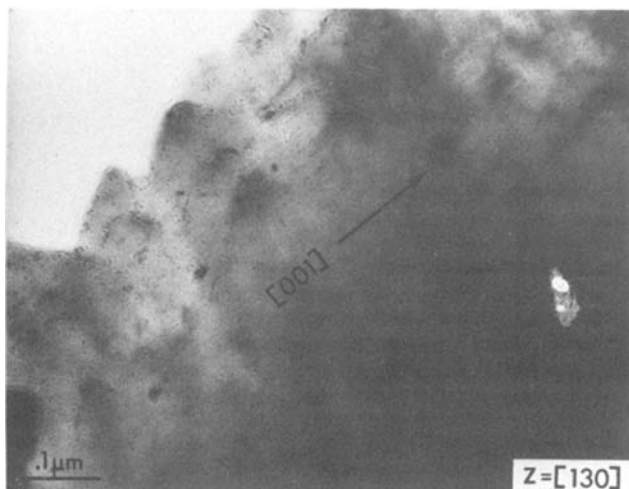


Fig. 10. TEM micrograph showing the overfocused ($\Delta f = +3.9 \mu\text{m}$) images of O-phenanthroline molecules lying along the $[001]$ direction in the $[130]$ -oriented copper crystal.

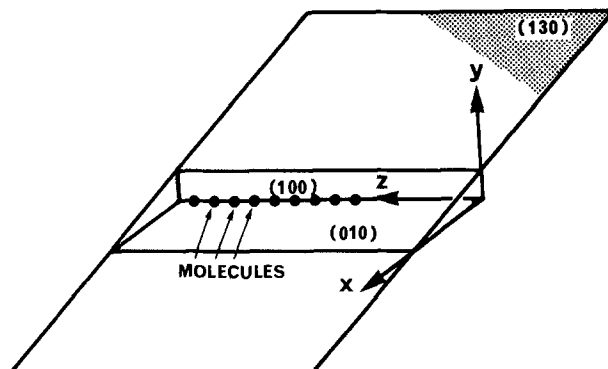


Fig. 11. A schematic illustration showing how O-phenanthroline molecules are trapped into copper crystal during crystallization (compare with Fig. 10).

erties of electrodeposited films. The present method should be useful in the TEM investigations of such films.

Origin of the Molecule Alignment along the $\langle 001 \rangle$ Direction

It was established from a stereographic trace analysis that lines of O-phenanthroline molecules lie along the $\langle 001 \rangle$ direction of copper lattice. This spatial alignment can be rationalized by the mode of impurity adsorption and subsequent incorporation during copper electrocrystallization. The adsorption of these molecules on the growth surface is expected to cause the inhibition of step movement, and this step slow-down eventually develops the formation of multi-atomic steps. Newly developed planes bounding these steps are expected to be of low index type. Once these steps are developed, they may even become convenient sites for additional incoming molecules to be trapped. Consequently, such incorporated molecules will be seen to lie along a specific crystallographic direction. One example is shown in Fig. 10, together with its probable incorporation model (see Fig. 11). It is seen that in the $[130]$ -oriented grain, the low index planes of (100) and (010) appear to develop after the adsorption, resulting in the molecular alignment along the $[001]$. We found the similar interpretation is applicable to the $[001]$ - and $[110]$ -oriented grains.

Acknowledgment

The author would like to thank Ms. Anne Marie Staudinger for her contribution to this project.

Manuscript submitted March 22, 1984; revised manuscript received June 14, 1984.

AT&T Bell Laboratories assisted in meeting the publication costs of this article.

REFERENCES

1. S. Nakahara and Y. Okinaka, in "Properties of Electrodeposits—Their Measurements and Significance," R. Sard, H. Leidheiser, Jr., and F. Ogburn, Editors, Chap. 3, The Electrochemical Society Soft-bound Proceedings Series, Princeton, NJ (1975).
2. Y. Okinaka and S. Nakahara, *This Journal*, **123**, 475 (1976).
3. L. Albert, R. Schneider, and H. Fischer, *Z. Naturforschung Bd. 19a*, **H. 9**, 1120 (1964).
4. S. Nakahara and R. J. Chesser, *Plat. & Surf. Finish.*, To be published.
5. M. Rühle, in "Radiation-Induced Voids in Metals," J. W. Corbett and L. C. Janniells, Editors, p. 255, Albany, New York (1971).
6. S. Nakahara, *This Journal*, **129**, 201C (1982).
7. P. Wipperfurth, G. Eichkorn, and H. Fischer, *Z. Metallkd.*, **63**, 38 (1972).
8. S. Nakahara, *This Journal*, **126**, 1123 (1979).
9. B. Buhl, *Z. Phys.*, **155**, 395 (1959).
10. R. D. Heidenreich, "Fundamentals of Transmission Electron Microscopy," p. 371, Interscience, New York (1964).

An Analysis of the Hydrodynamics of Aluminum Reduction Cells

R. Moreau

G. i. s MADYLAM, CNAS, Institut de Mecanique de Grenoble, Institut National Polytechnique de Grenoble, 38402 Saint-Martin D'Herès Cedex, France

J. W. Evans*

Department of Materials Science and Mineral Engineering, University of California, Berkeley, California 94720

ABSTRACT

An investigation of the flow of the two superposed liquids (the electrolyte and the molten aluminum) and of the interface shape has been carried out with the intention of revealing the main mechanisms and to clarify the hydrodynamic behavior of Hall-Héroult cells. The wide channels present around the anodes and between the two anodes rows in modern cells appear responsible, in the final analysis, for the electrolyte motion. The horizontal component of the current density in the aluminum layer largely determines the interface shape. It can also drive an organized motion when it is not a pure gradient. Two main ideas are at the source of this theory: (i) the shallow depth of the fluid layers (compared with their horizontal dimensions) justifies an approximation of zero inertia, and (ii) a linear approximation is proposed for the horizontal shear stresses. This almost explicit theory results in predictions that are not completely realistic, but it is shown how certain features of actual cell behavior can be revealed.

There is considerable interest in better understanding the general behavior of Hall-Héroult cells, because these large devices, in which aluminum oxide is reduced electrolytically to produce molten metal, are known as the major energy consumer in the production of aluminum from its ores. For a full description of these cells, the reader is referred to Lympny *et al.* (1). For the sake of brevity, it will only be mentioned that the electric current coming from the anodes (see Fig. 1) has to pass first through a horizontal liquid layer, the electrolyte (often known as "cryolite") before entering into the molten aluminum layer (where it is partially redirected in the horizontal direction), and thence through the carbon lining and into the collector bars.

Electromagnetics, hydrodynamics, heat and mass transfer, as well as electrochemistry, enter immediately into any complete description of the cell. Indeed, magnetohydrodynamic effects are responsible for the motion and the turbulence of the two liquids, and play a significant role in determining the current efficiency. In recent work (2), the development of a mathematical model, based on general equations of electromagnetics and hydrodynamics, has been attempted in order to compute the main behavior of these cells. The objective was to build a convenient tool for conception of new cells with better efficiency (3).

It has, however, been recently realized that the two-dimensional Navier-Stokes equations and the usual turbulence modeling ($k-\epsilon$) could not describe the true mechanisms involved in the motion of the two thin liquid layers. Using the $k-\epsilon$ model for turbulence in a supposed two-dimensional flow leads to neglect of the vertical transport of momentum, and this is unrealistic in this configuration, where it is, in fact, dominant over the horizontal one. Besides, a purely two-dimensional schema could not take into account the presence of channels between the anode blocks and around the cell periphery. These have, however, a strong influence on the flow of the electrolyte because they connect this flow with the atmospheric pressure, almost without head losses.

It is the purpose of this paper to propose a new basis of approximations to the hydrodynamics of the two superposed liquids, and to develop a better understanding of the influence of each parameter on the fluid flows and the interface shape. To do this, the concept of an ideal cell, in which the electromagnetic forces are pure gradients, is introduced. As a consequence, the cryolite is the only moving fluid. The pressure differences between the two liquids in different motion vary from one place to another, and this is responsible for the shape of the interface. It is also shown that second-order effects can easily

be superimposed on this state of reference predicted for the ideal cell, and an example is treated.

Each liquid layer may be characterized by its vertical thickness (under the anodes), H , its length, $2a$ and its width $2b$. It appears convenient to introduce also a typical horizontal length scale, L , which can be either a or b or some combination of them, in order to characterize the thinness of the layer by the ratio H/L . The thickness H is of the order of 0.04m in the cryolite and 0.16m in the aluminum. In typical modern cells, L may be of the order of 4m, so that H/L is of the order of 10^{-2} in the cryolite and $4 \cdot 10^{-2}$ in the aluminum. The smallness of H/L is of prime importance in the justification of the approximations proposed in the "Basic Equations" section below. Other important orders of magnitude are the typical electric current ($\approx 2 \cdot 10^6$ A) and the current density j_0 ($\approx 6 \cdot 10^3$ A m^{-2}).

The coordinates are defined in Fig. 2, with x in the long horizontal axis and y in the small one. The z axis is along the upward vertical, with its origin at the mean level of the interface between cryolite and aluminum. To illustrate the results, all the numerical computations have been done with a cell whose aspect ratio was $a/b = 2$. Unit vectors are denoted $\bar{e}_x, \bar{e}_y, \bar{e}_z$.

Basic Equations and Approximations

The relevant magnetic Reynolds number.—The question of a possible influence of the velocities in the two superposed liquids on the magnetic field has often arisen. Clearly, the relevant magnetic Reynolds number characterizing this effect must be the ratio between the diffusion time of the magnetic field through the whole cell and the

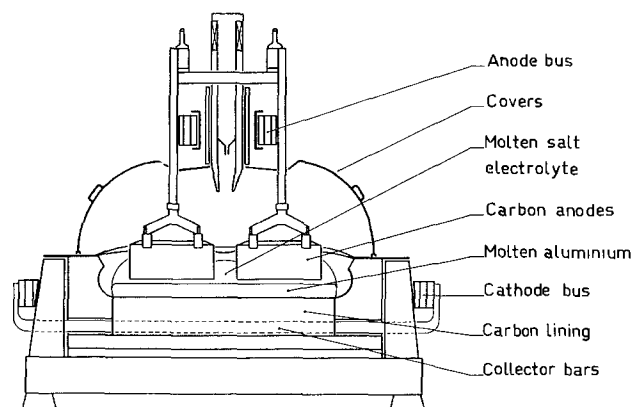
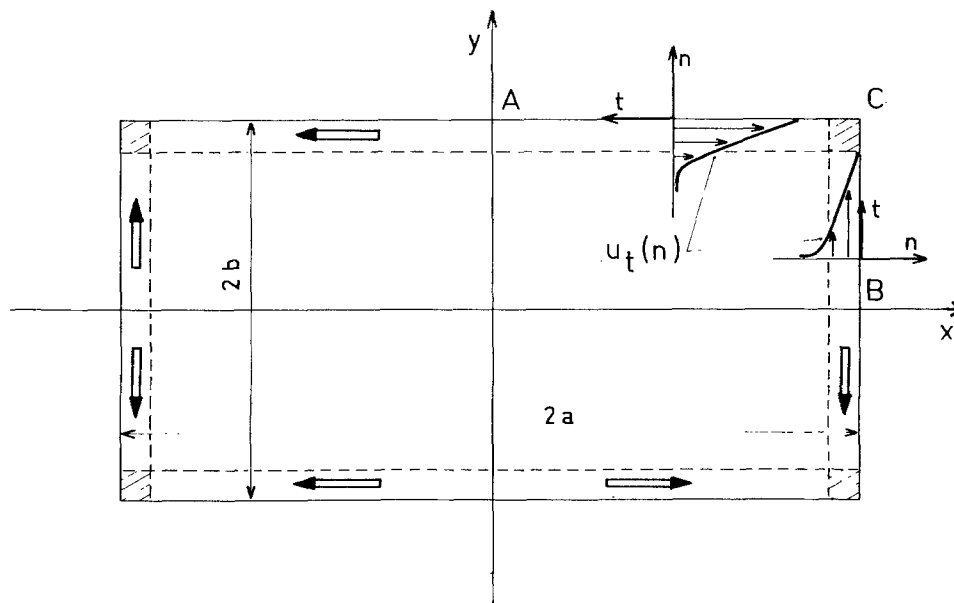


Fig. 1. Sectioned view of a Hall-Héroult cell as seen looking in the long horizontal direction.

*Electrochemical Society Active Member.

Fig. 2. Coordinates and main notations in a typical horizontal plane.



transit time of the fluid elements LV^{-1} . In the idealized configuration of a thin layer of conducting material located between two insulating media, any disturbance would diffuse instantaneously through these media, so that its diffusion time would be $\mu\sigma H^2$ (where μ and σ denote the permeability and the electrical conductivity of the conducting layer, respectively). The situation with which we are concerned is more complex because the media above and below the aluminum layer are conducting: they are thick (let H^* denote their total thickness) and they are conducting (let σ^* denote their conductivity). Forgetting the extremely short diffusion through the electrolyte layer, the total diffusion time through the cell may be estimated as $\mu(\sigma H^2 + \sigma^* H^{*2})$. Therefore, the relevant magnetic Reynolds number is

$$R_m = \mu\sigma VL \cdot \frac{H^2}{L^2} \left(1 + \frac{\sigma^* H^{*2}}{\sigma H^2} \right) \quad [1]$$

It appears that, although $\mu\sigma VL$ may be of the order of a few units, H^2/L^2 is extremely small ($\approx 3 \cdot 10^{-4}$). This means that the vertical diffusion time through the aluminum layer is extremely small compared with the transit time. Besides, the ratio σ^*/σ is sufficiently small ($\approx 2 \cdot 10^{-3}$) to also render negligible the diffusion time through the electrodes. Then it may be concluded that the classical approximation of a zero magnetic Reynolds number is valid.

The "shallow water" approximation.—Because of the shallowness of the two liquid layers and because of the very active mixing due to turbulence and to gas bubbles generated at the anode, the interest is essentially in describing the mean horizontal motion. If \bar{u}_H denotes the horizontal velocity field, the definition of this mean motion is

$$\langle \bar{u}_H \rangle = 1/H \int_{-H}^0 \bar{u}_H dz \quad [2]$$

The equations for such a two-dimensional flow are

$$\bar{\nabla}_H \cdot \langle \bar{u}_H \rangle = 0 \quad [3]$$

$$\rho \langle (\bar{u}_H \cdot \bar{\nabla}_H) \bar{u}_H \rangle = -\bar{\nabla}_H \langle p \rangle + \langle (\bar{j} \times \bar{B})_H \rangle + \frac{\partial}{\partial x_i} \left(\eta_e \frac{\partial}{\partial x_i} \langle \bar{u}_H \rangle \right) - \frac{\bar{\tau}}{H} \quad [4]$$

The subscript H stands for the horizontal vectors or operators, so that $\bar{\nabla}_H = (\partial/\partial x, \partial/\partial y, 0)$, $i = (1, 2)$, and p denotes the pressure, ρ the density, η_e the effective viscosity, and $\bar{\tau}$ the sum of the shear stresses at the top and bottom of the fluid layer.

To appreciate the consequences of the small values of H/L , let us write Eq. [4] in a nondimensional form. Since the driving mechanism is the difference between the Lorentz forces and the pressure gradient, it is convenient to introduce the nondimensional pressure

$$P = \frac{p}{\mu j_o^2 L^2} \text{ and the velocity scale } V = \left(\frac{\mu j_o^2 LH}{p} \right)^{1/2}$$

Then, with

$$X_i = \frac{x_i}{L}, \bar{U} = \frac{\bar{u}_H}{V}, T = \frac{\bar{\tau}}{\rho V^2}, \bar{F} = \frac{\langle \bar{j} \times \bar{B} \rangle}{\mu j_o^2 L}$$

the nondimensional equation is

$$\frac{H}{L} (\bar{U} \cdot \bar{\nabla}_H) \bar{U} = -\bar{\nabla}_H P + \bar{F} - \bar{T} + \frac{H}{L} \frac{\nu}{VL} \frac{\partial}{\partial X_i} \left(\frac{\eta_e}{\eta} \frac{\partial \bar{u}}{\partial X_i} \right) \quad [5]$$

With the typical values of H/L previously mentioned, for modern cells, with current of the order of $2 \cdot 10^5$ A, V is of the order of 0.1 ms^{-1} , and the Reynolds number VL/ν is of the order of $4 \cdot 10^6$. Therefore, even if η_e is much higher than the molecular viscosity η because of the intense mixing present in each liquid, it is clear that the two-dimensional friction (or the horizontal transport of momentum) cannot compete with the Lorentz forces. Inertia also appears unable to balance the driving forces. Consequently, the dominant equilibrium is between the difference $\bar{F} - \bar{\nabla}_H P$ (which is not exactly zero, as will be seen later) and the friction on the horizontal boundaries \bar{T} . Then the equations for the two-dimensional flow of each liquid reduce to

$$\bar{\nabla}_H \cdot \bar{U} = 0 \quad [6]$$

$$\bar{T} = \bar{F} - \bar{\nabla}_H P \quad [7]$$

Of course, this approximation still needs an assumption for the relation between the drag \bar{T} and the velocity \bar{U} . Two ideas suggest that a linear expression, *i.e.*

$$\bar{T} = \kappa \bar{U} \quad [8]$$

could be quite plausible, and certainly better than a quadratic expression (as in turbulent duct flows). One idea is the previously established fact that inertia is negligible in these shallow layers of liquids. The other derives from the fact that the typical scale of random eddies responsible for the vertical transport of momentum is H , which is much smaller than the typical horizontal length scale of the mean motion L . The situation appears then more similar to the kinetic theory of gases (with a mean free path much smaller than the macroscopic scales) than usual

turbulent flows (with an integral scale of the same order as the length scales of the mean flow). We will therefore retain this very simple expression [8]. It will be seen that it has also the advantage of allowing a clear illustration and understanding of the mechanism of stirring in each liquid.

The influence of the cryolite channels.—Since the cryolite is a poor conductor, compared to the carbon electrodes, the fraction of the electric current crossing the channels between the anode blocks may be neglected. Then the flow in these channels behaves like an open-channel flow, having the capability of exchanging mass and momentum with the neighboring two-dimensional flow underneath the anodes. In spite of this mass exchange, the mean flow in a straight channel is such that the pressure variation in the cross-section follows the law of hydrostatics. However, pressure differences develop underneath the anodes, in order to partially balance the Lorentz forces according to Eq. [7]. Because of the continuity of pressure between the cryolite layers and the channels, pressure gradients may also exist in the channels, where they would necessarily drive some flow and be balanced by friction and momentum transport.

Let S denote the area of the cross section, \mathcal{P} the wet perimeter, and q the flow rate which is a function of the abscissa ξ along the channel. If u_n and u_s stand for the outward normal and tangential velocity components of the two-dimensional cryolite flow along the anode edge, and if τ_w denotes the wall shear stress, the mass and momentum conservation equations can be written

$$\frac{dq}{d\xi} = u_n H \quad [9]$$

$$\frac{d}{d\xi} \left(\rho \frac{q^2}{S} \right) - \rho u_n u_s H = -S \frac{dP}{d\xi} - \mathcal{P} \tau_w \quad [10]$$

Because of the variations of the liquid depth, themselves related to the topology of the free surface and of the interface, and because of possible variations in the shape of the solidified ledge of cryolite (for the peripheral channel), the parameters S and \mathcal{P} may slowly vary from one place to another. However, in this theory they are supposed to be constant for the sake of simplicity. The wall friction τ_w is assumed to follow the usual quadratic law

$$\tau_w = \lambda \rho \frac{q^2}{S^2} \quad [11]$$

where the friction coefficient λ has still to be estimated.

Introducing the nondimensional quantities

$$Q = \frac{q}{VLH} \quad t = \frac{\xi}{L} \quad U_n = \frac{u_n}{V} \quad \text{etc.} \quad [12]$$

Eq. [10] and [11] reduce to

$$\frac{H^3 L}{S^2} \frac{dQ^2}{dt} - \frac{H^2}{S} U_n U_t = - \frac{dP}{dt} - \frac{\mathcal{P} L^2 H^3}{S^3} \lambda Q^2 \quad [13]$$

This equation exhibits three dimensionless numbers, essentially depending on the geometry, which characterize the three possibilities of balancing any longitudinal pressure gradient: momentum transport along the channel, or toward the horizontal layer of cryolite under the anodes, and friction.

There are two kinds of channels: the wide ones present around the cell periphery (or between the two rows of anodes in modern cells with automatic feeding of alumina), and the narrow ones between the anode blocks, 3 or 4 cm apart. In the wide channels typical values $S = 0.5 \text{ m}^2$ and $\mathcal{P} = 0.6 \text{ m}$ seem to be realistic and provide the following orders of magnitude

$$\frac{H^3 L}{S^2} \approx 10^{-3}, \quad \frac{H^2}{S} \approx 3 \cdot 10^{-3}, \quad \frac{\mathcal{P} L^2 H^3}{S^3} \lambda \approx 5 \cdot 10^{-3} \lambda$$

The consequence of these very small values is that any

pressure difference along the large channels could not be balanced. In other words, the channels are so large that their free surface must be horizontal. Therefore, the presence of these large channels is dictating the striking boundary condition that P must be constant at the edge of the anode rows.

In the narrow channels, with \mathcal{P} of the same order but S smaller ($\approx 0.1 \text{ m}^2$), the nondimensional numbers have the following orders of magnitude

$$\frac{H^3 L}{S^2} \approx 2.5 \times 10^{-2}, \quad \frac{H^2}{S} \approx 1.6 \times 10^{-2}, \quad \frac{\mathcal{P} L^2 H^3}{S^3} \lambda \approx 0.6 \lambda$$

It still appears that the momentum transport could not balance any pressure gradient. But the situation is not as simple with regard to friction because λ is very difficult to estimate. If these channels behaved like ordinary turbulent duct flows, λ would be in the range 10^{-2} – 10^{-1} . But the intense bubbling activity (carbon dioxide evolved from the anodes), particularly important in these channels because of their narrowness, would increase λ by a few orders of magnitude. Therefore, one has to accept the idea that some pressure differences (and variations in the height of the free surface) can take place. They could be modeled by the equation

$$\frac{dP}{dt} + \frac{\mathcal{P} L^2 H^3}{S^3} \lambda Q^2 = 0 \quad [14]$$

with a convenient guess for the λ coefficient. Since it is one of the aims of this paper to simplify rather than to inspect all the details, it will be considered that the friction term is dominant over the pressure gradient, as it would be if the gap between the anode blocks were smaller ($\leq 1 \text{ cm}$). Then, Eq. [14] reduces to $Q = 0$, and these channels may be ignored in this asymptotic limit.

It has still to be noticed that the cryolite channels have another consequence in allowing U_n to be nonzero at the boundary of the layer underneath the anodes. The flow rate in these channels Q follows from relations [8] and [12]. This is to be contrasted with the aluminum layer, at the border of which no such channels exist; U_n has to be zero at the aluminum boundary, but no restriction applies on the pressure.

The interface equation.—In each liquid, the vertical variation of pressure is of the form

$$p = -\rho_i g z + f_i(x, y) \quad [15]$$

where z is the upward vertical, g gravity, and where the values 1 and 2 will be used for the subscript i , respectively, in the cryolite and the aluminum. The functions $f_1(x, y)$ and $f_2(x, y)$ can only be determined by solving first Eq. [6] and [7] in each liquid with the relevant boundary conditions. Then the continuity of pressure at the interface $z = z_0$ gives the equation of this surface

$$(\rho_2 - \rho_1) g z_0 = f_2(x, y) - f_1(x, y) \quad [16]$$

A First Model for an Ideal Cell

Assumptions for currents and magnetic fields.—In each cell, the current density has a specific distribution depending on parameters like the geometry of each anode block, the particular design of the risers, the position of the collector bars, etc. The magnetic field also is dependent on many parameters (the effect of which is not easily taken into account explicitly), such as the position of the cell in a pot line or the shielding effect of the steel shell surrounding the cell. Therefore any distribution of the Lorentz forces $\vec{j} \times \vec{B}$ which could be considered as sufficiently exact for a given cell would certainly be imprecise for many others. Since a main goal of this study is to reach a general understanding of the hydrodynamics of cells, it has been chosen to use some "ideal" distributions of \vec{j} and \vec{B} , rather than to compute them. (Notice that even computed distributions would not be "exact.") Of course, such distributions have to be in agreement with some

first-order requirements, such as the respective positions and voltages of the anodes, the two liquids, the carbon cell lining, and the collector bars. They should also contain a small number of parameters which are to be adjusted by comparison with measurements or computed distributions such as those of Lypany and Evans (3). The first approximation developed in this section is based on the following assumptions: (i) the j_x component in the long horizontal direction is taken to be zero since the collector bars usually drive the horizontal current in the y direction, (ii) because of the very small electrical conductivity and depth of the cryolite layer, the current density is supposed purely vertical and uniform in this liquid ($j_z = -j_0$), (iii) in the aluminum the distribution of the current density is taken as

$$j_y = j_1 \frac{y}{H}, \quad j_z = -j_0 + j_2 \frac{z}{H} \quad [17]$$

where H is the depth of the aluminum layer; the level variations of the interface are neglected for electromagnetic calculations, and (iv) the magnetic field of all the external conductors is neglected by comparison with that of the internal current, which is itself assumed purely horizontal ($B_z \ll B_x, B_y$) and without variations with z in the gap of interest. Then the vector potential is purely vertical

$$B_x = \frac{\partial A}{\partial y}, \quad B_y = -\frac{\partial A}{\partial x} \quad [18]$$

and follows Ampere's law

$$\nabla_H^2 A = -\mu j_z \quad [19]$$

Clearly, these assumptions are open to discussion and improvements. For instance, the "Second-Order Improvement" section below shows an example of such an improvement obtained by adding a supplementary term and supplementary parameter in relations [17] in order to include a new effect. Indeed these relations [17] may be considered as the simplest combination of two conservative fields allowing the study of the influence of the horizontal current density via the parameter j_1 . Assumption (iv) may be understood as a tool to isolate the internal characteristics of the cell from external characteristics such as the arrangement of risers and collectors. Of course, an explicit approximation of the magnetic field induced in the two liquids by the external conductors could be added in Eq. [18] and [19]. But it follows from computed results (3) that this external magnetic field is definitely a second-order effect (a few gauss compared to 50G due to internal current).

Equation [19], together with $\nabla_H^2 A = 0$ outside the rectangle $2a \times 2b$, and the conditions of continuity of A and its two first derivatives on the boundary, has a solution of the form

$$A = (j_0 + j_1 \frac{z}{H}) \mu G(x, y) \quad [20]$$

where $G(x, y)$ is completely determined by equation

$$\nabla_H^2 G = \begin{cases} 1 & \text{inside the rectangle} \\ 0 & \text{outside the rectangle} \end{cases} \quad [21]$$

and by the continuity conditions. This solution, analogous to the distribution of the electric potential created by a charge density which is uniform in a rectangle and zero outside, is explicitly known (Durand, see Appendix A).

It follows from these assumptions that the Lorentz force has a simple expression in terms of A

$$\vec{j} \times \vec{B} = j_z \vec{\nabla}_H A = -\frac{1}{\mu} \nabla_H^2 A \cdot \vec{\nabla}_H A \quad [22]$$

Since we only need its mean value in each fluid layer, let us write

$$\vec{j} \times \vec{B} = -\mu j_0^2 C \vec{\nabla}_H G$$

where C is a nondimensional parameter representing the influence of the horizontal current j_y . It follows from our assumptions that $C = 1$ in the cryolite layer, whereas in the aluminum it has the value

$$C = 1 - \frac{j_1}{j_0} + \frac{1}{3} \frac{j_1^2}{j_0^2} \quad [24]$$

Motion and pressure in the cryolite layer.—The nondimensional form of Eq. [23] to use with Eq. [6], [7], and [8] in the electrolyte is $\vec{F} = -\vec{\nabla}_H G$. Therefore, the motion equations in this layer are

$$\vec{\nabla}_H \cdot \vec{U}_1 = 0 \quad [25]$$

$$\kappa_1 \vec{U}_1 = -\vec{\nabla}_H (P_1 + G) \quad [26]$$

Taking the divergence of [26] yields the equation for the pressure distribution

$$\nabla_H^2 P_1 = -1 \quad [27]$$

The solution satisfying the boundary condition that $P_1 = 0$ at the boundary of a rectangle is explicitly known; it is analogous to the temperature distribution in a rectangle with uniform heat production and boundaries at a constant temperature (Carslaw and Jaeger, see Appendix A).

This solution is illustrated in Fig. 3, and may be compared with the solution of Eq. [21] for G . It is clear that the boundary condition, imposing a stricter condition on P_1 than on G , makes all the difference between these two functions and prevents the two gradients from canceling each other. To emphasize this difference, which is the key to the mean flow in the cryolite, one could say that because of the presence of the wide channels, the isobars resemble rectangles, whereas the lines $G = \text{constant}$ look rather like circles.

The influence of a wide central channel appears very important when Fig. 3a is compared with Fig. 3b, where a center channel has been introduced. The center channel has essentially two main effects: (i) there are two symmetrical pressure domes, one under each anode row, when there is a wide central channel, rather than one bigger dome centered in the middle of the cell when no wide central channel is present (Fig. 3a), and (ii) in forcing $P_1 = 0$ at the center and along the x axis as well as at the boundary, the presence of a wide central channel reduces the pressure differences and the pressure forces, for the same given value of the Laplacian (by a factor 3.7 in the computed case).

It is straightforward to deduce the velocity field from Eq. [26] when P_1 and G are known. Figure 4 shows the streamlines of this potential flow deduced from equations

$$\kappa_1 U = \frac{\partial \Psi}{\partial y} = -\frac{\partial}{\partial x} (P_1 + G) \quad [28]$$

$$\kappa_1 V = \frac{\partial \Psi}{\partial x} = -\frac{\partial}{\partial y} (P_1 + G)$$

The influence of a wide central channel again appears dramatic since the nature of the main flow is completely different between Fig. 4a and 4b. It is, however, easy to interpret these flow patterns: when there is no central channel, the same pressure difference does exist along the small and the large axes, but the inward electromagnetic forces are dominant along the large axis, whereas the outward pressure gradient is dominant along the small axis. When a wide central channel is present, the general reduction of pressure differences makes the electromagnetic forces predominant everywhere and provides a velocity field almost parallel to the force field.

It is also of interest to notice that the value of the stream function Ψ is 3.5 times greater with, than without, a central channel in the computed case, and that the place where Ψ is maximum is not at all the same in the two cases. Also, the direction of the mean flow in the periph-

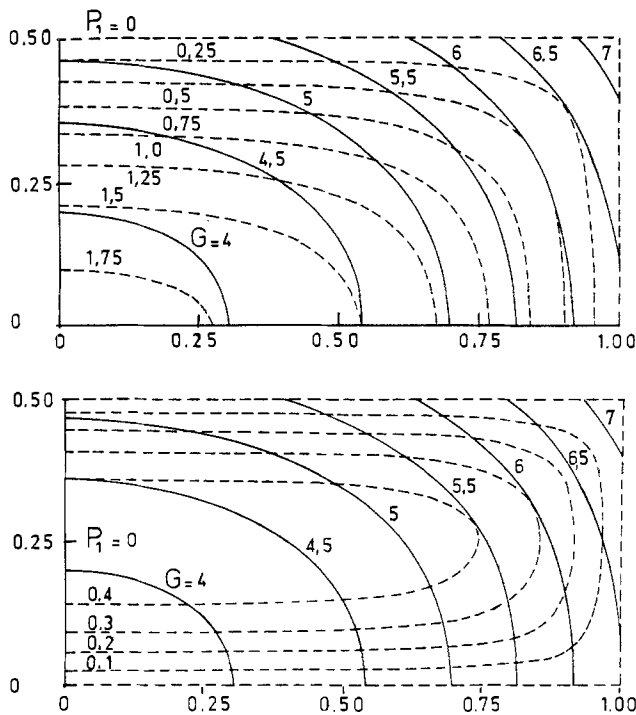


Fig. 3. Potential lines ($G = \text{const.}$) of the $\langle \vec{j} \times \vec{B} \rangle$ force field, and pressure lines ($P = \text{const.}$) a (top): For a cell without central channel. b (bottom): For a cell with central channel.

erent channel is changed when a wide central channel is present.

These predictions could be checked with direct observations on real cells since the wide channels are more accessible than the shadow of the anode (6). The flow rate in these channels is easily deduced from the values of Ψ at the boundary

$$q = \left(\frac{\mu j_0^2 H^3 L^3}{\rho} \right)^{1/2} \frac{\Psi}{\kappa_1} \quad [29]$$

and seems to be the first quantity to be checked with measurements.

It is remarkable that in this inertia-free approximation it is not necessary to give a numerical value to the friction

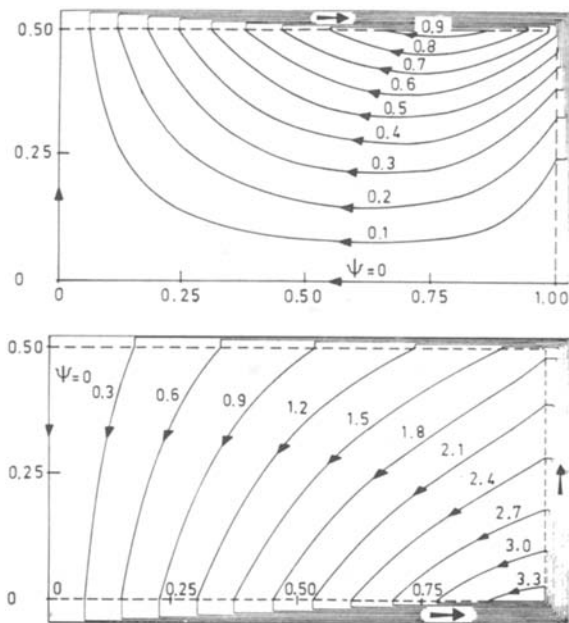


Fig. 4. Streamlines of the cryolite flow underneath the anode. a (top): For a cell without central channel. b (bottom): For a cell with central channel.

coefficient κ_1 to find out the flow pattern. This is, however, necessary to get some numerical value of the flow rates in the channel from Eq. [29]. Inversely, this relation could be used as an empirical way to determine κ_1 .

Pressure in the aluminum and interface shape.—In the aluminum layer, the motion equations are very similar to Eq. [25] and [26], with the only difference being that the velocity potential is now $P_2 + CG$. The important feature is the absence of channels or anything equivalent. The force distribution Eq. [23] is assumed to be valid everywhere, and the depth of the aluminum layer is assumed to be uniform. Then the only boundary condition demands that the normal component of the velocity be zero on the edge of the rectangle. The only irrotational plane motion satisfying this condition is $\vec{U}_2 = 0$. As a consequence, the pressure distribution in the aluminum is

$$p = -\rho_2 g z - \mu j_0^2 L^2 C G + \text{const.} \quad [30]$$

The analogous equation in the cryolite layer is

$$p = -\rho_1 g z + \mu j_0^2 L^2 P_1 \quad [31]$$

and it is straightforward to deduce from Eq. [30] and [31] the interface equation

$$(\rho_2 - \rho_1) g z_0 = -\mu j_0^2 L^2 (P_1 + C G) + \text{const.} \quad [32]$$

Our choice that the z origin be at the mean level of the interface determines the constant, and final equation of the interface is

$$\frac{(\rho_2 - \rho_1) g}{\mu j_0^2 L^2} z = \overline{P_1 + C G} - (P_1 + C G) \quad [33]$$

where the upper bar is used to designate the average value in the rectangle.

Figures 5, 6, and 7 show the results for our cell of reference (aspect ratio: 2), with and without a wide central channel, and for two values of the parameter C . The unrealistic case $C = 1$ has interest only as a reference to illustrate the influence of the horizontal current in the aluminum when C is smaller than one. It appears that the predicted shape looks like a dome, with deviations which are worthy of discussion.

To interpret these results, remember first that the overpressure which is developed under the anodes in the cryolite layer is the strongest when there is no central channel. Furthermore, the pressure differences which arise in the aluminum layer are exactly those necessary to balance the electromagnetic forces. In particular, the smaller $|j_y|$ ($C = 1$), the larger $|j_x|$, and the higher these pressure differences. The general dome shape is due to the fact that the central overpressure is generally smaller in the cryolite than in the aluminum; therefore, the only possibility of generating such a departure on a vertical line is to vary the height of the denser liquid. This is particularly clear along the boundaries of the rectangle where the interface is always like a dome, because $p = \text{const.}$ in the cryolite, whereas in the aluminum it has to be a maximum at the middle of each side and smallest at the corners in order to balance the inward electromagnetic forces. Therefore, one understands that in the four computed cases the dome is the most significant when $C = 1$ and when a large central channel is present. It is, on the contrary, the weaker when $C = 0.5$ and without any central channel.

From among the noticeable deviations from this dome shape, notice the central saddle or trough in the middle of a cell without a central channel. It comes from the fact that the central overpressure is higher in the cryolite than in the aluminum. It is remarkable that the depth of this trough increases when C decreases, thus illustrating the influence of increasing the horizontal current in the aluminum. Varying the coefficient C would also show that the lower point of the interface (still for a cell without central channel), which is at the corner when $C = 1$, moves along the small side to its middle and then along

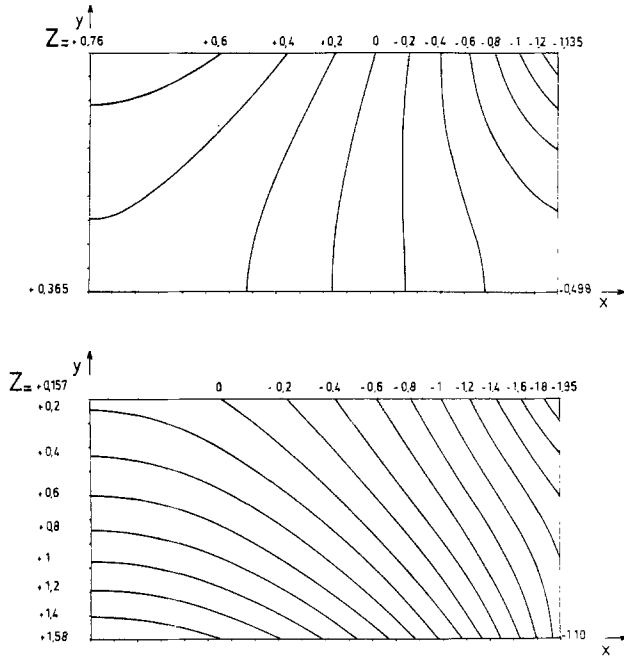


Fig. 5. Interface contour lines when $C = 1$ ($j_1 = 0$, i.e., no horizontal current in the aluminum). a (top): For a cell without central channel. b (bottom): For a cell with central channel.

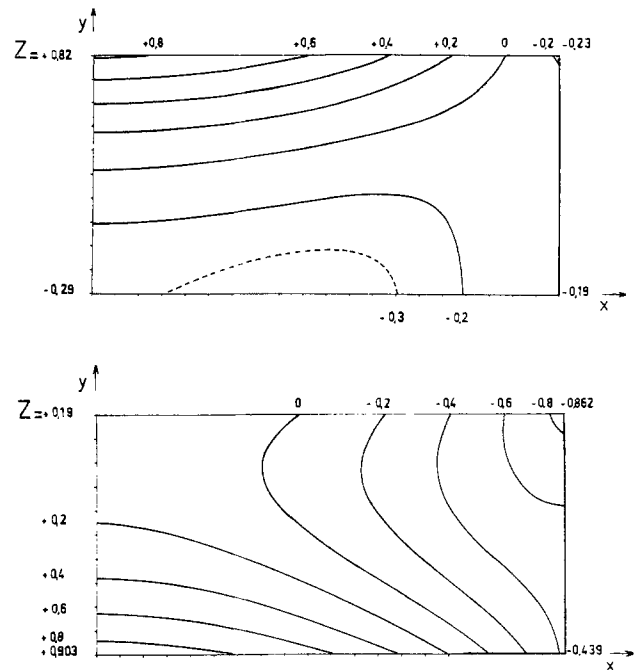


Fig. 6. Interface contour lines when $C = 0.5$ ($j_1/j_0 = 0.634$). a (top): For a cell without central channel. b (bottom): For a cell with central channel.

the large axis to the cell center as C decreases monotonically to its limit of 0.25 imposed by Eq. [24].

Example of a Second-Order Improvement

Correction of the electromagnetic data.—When expressions [17] are compared with plausible values such as those computed by Lympany and Evans (3), their linear variation with the coordinates does not seem to be correct for more than three-quarters of the cell width. It appears that in the outermost quarter some reduction should be introduced in relations [17]. This comes from the fact that the aluminum pool is wider than the anode. Indeed, the geometry of the external boundary of the aluminum layer is in itself a difficult question. The key point is the shape and the position of the ledge of solidified electrolyte all around the cell. It is, or course, strongly dependent on the thermal behavior of the cell, and it exhibits important variations from one cell to another, as well as in a given cell during its life.

In this section, consequences of this boundary phenomenon are studied as a disturbance of the reference state

described in the previous section. Because of the linearity of the motion Eq. [6], [7], and [8], this disturbance need not be supposed to be very small. However, the thickness of the region through which such a disturbance is concentrated is assumed to be small enough, so that ideas and techniques of the boundary layer theory apply.

The disturbance of the current density is supposed to take place in a plane (n,z) , where n is the outward normal to the rectangle edge (Fig. 2), and to have the following distribution

$$j_n = -j_2 \frac{\delta}{H} e^{n/\delta}, j_z = j_2 \frac{z}{H} e^{n/\delta} \quad [34]$$

Clearly, two new parameters (j_2 and δ) are thus introduced to characterize this disturbance. No restriction applies on j_2 , but the thickness δ of the disturbed layer is supposed to be much smaller than the width of the rectangle, so that the derivative $\partial/\partial t$ may be neglected in comparison with $\partial/\partial n$, except in the vicinity of the corners, where this theory fails.

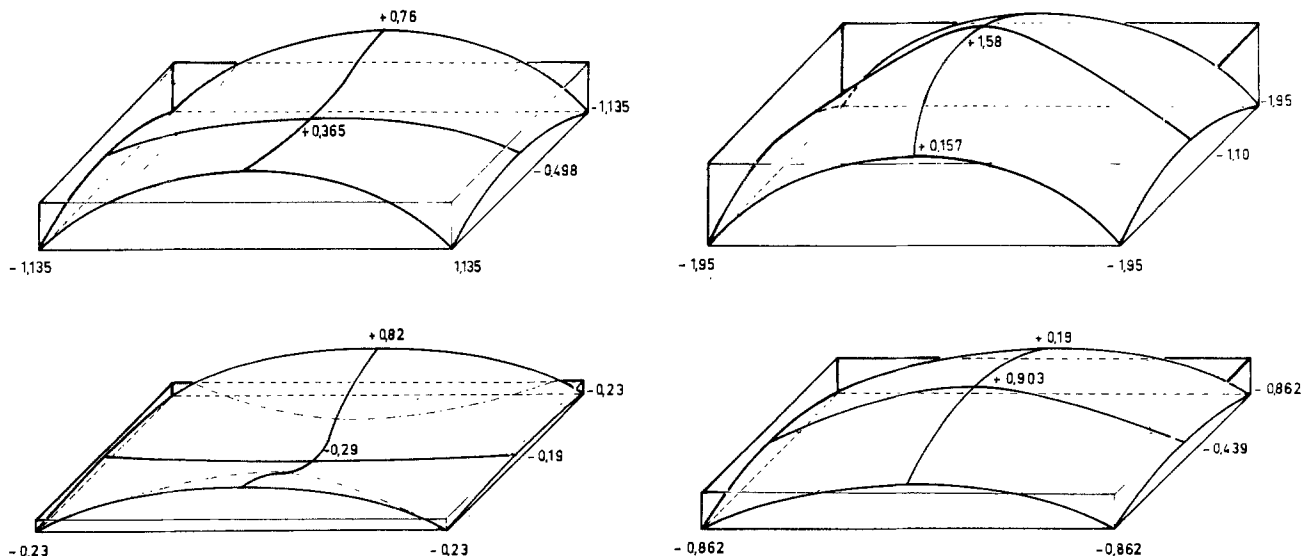


Fig. 7. Interface shape in the four computed cases. a (top left): $C = 1$, without central channel. b (top right): $C = 1$, with central channel. c (bottom left): $C = 0.5$, without central channel. d (bottom right): $C = 0.5$, with central channel.

The vector potential of the magnetic field may then be written

$$A = (j_0 + j_1 \frac{z}{H}) \mu G(x, y) - \mu j_2 \delta^2 \frac{z}{H} e^{n/\delta} \quad [35]$$

where the last term (the correction to [20]) is the solution of the simplified form of Eq. [19].

It follows that the mean value of the electromagnetic forces in the aluminum layer is now

$$\langle \bar{j} \times \bar{B} \rangle = -\mu j_0^2 \left[C \bar{\nabla}_H G - D \{ e^{n/\delta} \bar{\nabla}_H G + \delta^2 \bar{\nabla}_H (e^{n/\delta}) \} + E \frac{\delta^2}{2} \bar{\nabla}_H (e^{2n/\delta}) \right] \quad [36]$$

where nondimensional coefficients D and E , characterizing the importance of j_2 , have the definitions

$$D = \frac{j_2}{j_0} \left(-1/2 + 1/3 \frac{j_1}{j_0} \right), \quad E = 1/3 \frac{j_2^2}{j_0} \quad [37]$$

The two terms proportional to δ^2 in Eq. [36] can be neglected in comparison with $D e^{n/\delta} \bar{\nabla}_H G$, which appears as the essential correction. Notice also that they are pure gradients and could not drive any aluminum motion. It is then interesting to notice the distribution of the curl of the forces

$$\bar{\nabla}_H \times \langle \bar{j} \times \bar{B} \rangle = \frac{\mu j_0^2 D}{\delta} e^{n/\delta} \frac{\partial G}{\partial t} \cdot \bar{e}_z \quad [38]$$

Since $\delta G/\delta t$ is zero at the middle of each side and increases or decreases towards the corners as an odd function of the abscissa, it is clear that the flow driven along each side by this force has the directions and symmetries shown on Fig. 2.

The motion in the aluminum.—Let us introduce the decomposition

$$\bar{U} = \bar{U}_c + \bar{u}^*, \quad \bar{P} = \bar{P}_c + \bar{p}^* \quad [39]$$

where \bar{U}_c and \bar{P}_c stand for the dimensionless values of \bar{u} and \bar{p} in the central core of the aluminum rectangle, and vary on the typical length scale L . The corrections \bar{u}^* and \bar{p}^* are concentrated in the boundary region along the edge and vary along the normal on the short length scale δL . Clearly, \bar{U}_c and \bar{P}_c are no longer the values determined in the reference state, since the flow driven in the boundary region by the electromagnetic forces has to recirculate in the central core. Dimensionless Eq. [6] - [8] then become

$$\bar{\nabla}_H \cdot \bar{U}_c = 0 \quad [40]$$

$$\kappa_2 \bar{\nabla}_c = -\bar{\nabla}_H (P_c + CG) \quad [41]$$

$$\bar{\nabla}_H \cdot \bar{u}^* = 0 \quad [42]$$

$$\kappa_2 \bar{\nabla}_c^* = -\bar{\nabla}_H \bar{p}^* + D e^{n/\delta} \bar{\nabla}_H G \quad [43]$$

In the boundary region, the normal component u_n^* is negligible compared to the tangential component u_t^* . Therefore, with the matching condition $p(n \rightarrow -\infty) = 0$, the normal projection of Eq. [43] gives the disturbance of the pressure

$$p^* = D \int_{-\infty}^n e^{n/\delta} \frac{\partial G}{\partial n} dn = D \delta \left(\frac{\partial G}{\partial n} \right)_{n=0} e^{n/\delta} \quad [44]$$

Then after substitution of $\partial p^*/\partial t$, the tangential projection gives the u_t^* velocity component

$$\kappa_2 u_t^* = \frac{D}{\delta} \int_{-\infty}^n e^{n/\delta} \frac{\partial G}{\partial t} dn = D \left(\frac{\partial G}{\partial t} \right)_{n=0} e^{n/\delta} \quad [45]$$

Finally, the continuity equation and the matching condition $u_n^*(n \rightarrow -\infty) = 0$ give the u_n^* velocity component

$$\kappa_2 u_n^* = -D \delta \left(\frac{\partial^2 G}{\partial t^2} \right)_{n=0} e^{n/\delta} \quad [46]$$

It follows from the two last expressions that the non-dimensional flow rate driven by the electromagnetic forces in the boundary regions is $\frac{D \delta}{\kappa_2} \left(\frac{\partial G}{\partial t} \right)_{n=0}$

The core has essentially to feed these boundary regions. This demands

$$U_{cn} (n=0) = D \delta \left(\frac{\partial^2 G}{\partial t^2} \right)_{n=0} \quad [47]$$

in order that the total normal velocity component be zero at the boundary. Therefore, the molten aluminum cannot stay at rest in the core as in the reference state. The potential flow satisfying [40] and [41] may be determined in terms of a stream function Ψ_c . Taking account of the symmetries, in the cell quarter $x > 0$ and $y > 0$, this stream function, whose definition is

$$\kappa_2 U_{cx} = \frac{\partial \Psi_c}{\partial Y}, \quad \kappa_2 U_{cy} = -\frac{\partial \Psi_c}{\partial X} \quad [48]$$

is completely determined by the Laplace equation $\nabla_H^2 \Psi_c = 0$ together with the boundary conditions

$$\left\{ \begin{array}{ll} \Psi_c = 0 & \text{on the axes} \\ \Psi_c = -D \delta \left(\frac{\partial G}{\partial X} \right)_{y=b} & \text{on side AC} \\ \Psi_c = D \delta \left(\frac{\partial G}{\partial Y} \right)_{x=a} & \text{on side B} \end{array} \right. \quad [49]$$

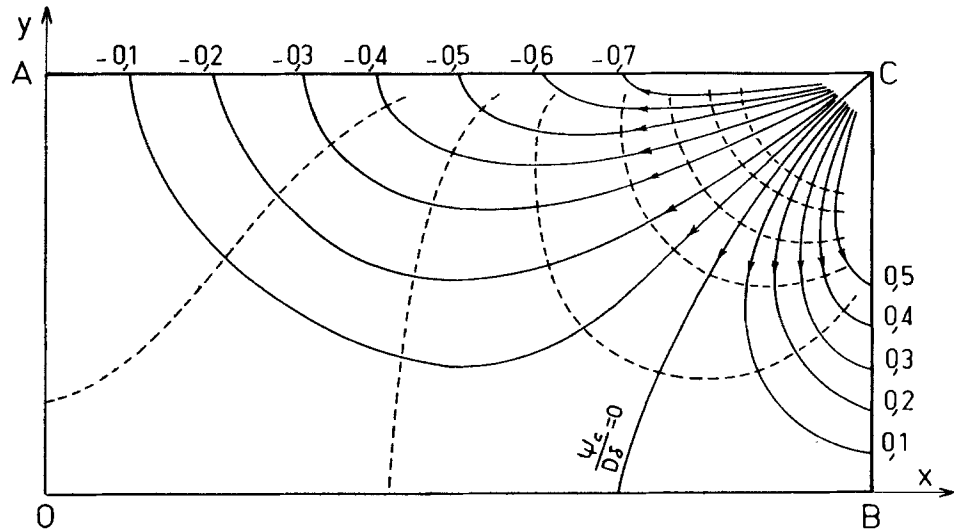
Some typical streamlines shown in Fig. 8 illustrate the main character of this flow. For the core flow, the corners are source points from which comes the flow rate necessary to feed the boundary regions. And, in return, they are the sink points to which goes all the flow of the boundary regions. Of course, this singularity of the corners is nothing but a consequence of the asymptotic character of this theory which is only rigorous in the limit of $\delta \rightarrow 0$.

It is also straightforward to calculate the pressure distribution. The velocity potential $\phi_c = P_c + CG$ which has also to satisfy the Laplace equation following [40] is completely determined by the Neumann boundary condition [47]. Some typical potential lines are also shown in Fig. 8. The pressure correction is proportional to $D \delta G$ and is therefore much smaller than the pressure differences found in the state of reference (proportional to CG). Therefore, it cannot introduce any important change into the interface topology. It is, however, interesting to notice that this second-order effect tends to compensate for the differences of level found at the state of reference, since the higher pressure correction takes place in the corners and tends to raise these lowest points of the interface.

Remarks and Discussion

The hydrodynamics of Hall-Héroult cells have been the subject of many investigations since the pioneering work by Givry (7). The fact that the governing mechanisms were still unclear, and that the numerical predictions [2] and [8] did not predict the same flow pattern, have given to this problem the reputation of being extremely difficult. In this context, this paper introduces a new point of view and some simplifications which provide an important clarification. From two main approximations (the way to model the channel's influence on the cryolite flow, and the shallow water approximation) arises an almost elementary solution for an ideal cell. This solution may be seen as a first-order solution and remains open to improvements. It shows that phenomena like the interface shape and the cryolite motion are controlled at the

Fig. 8. Typical streamlines of the core flow feeding the side boundary layers in the aluminum pool.



first order of approximation by the geometry of the channels between the anode blocks and around the cell, and by the distribution of the horizontal current in the aluminum layer.

This elementary theory still has, however, some weaknesses suggesting future work.

1. The analysis supposes that the channels are either very wide or very narrow, and that their width is not taken as a parameter. To remedy this first weakness, numerical solutions of the motion Eq. [6]-[8], together with relation [14] as a boundary condition at the edge of each anode block, should be used in the cryolite (see Appendix B).

2. Another resides in the fact that the idealized force distributions [23] or [36] do not coincide with those of a real cell. The remedy is obviously in the numerical computation of electric currents, magnetic fields, and force fields, as done by Evans *et al.* (2). It would permit the real distributions of $\langle \vec{j} \times \vec{B} \rangle_H$ to be introduced in the motion equations before computing the velocity fields.

3. It must also be pointed out that this first investigation is only concerned with a steady state, which is assumed to coincide with an average of the actual unsteady states. The unsteadiness and the turbulence are only taken into account through the friction coefficients κ_1 and κ_2 . To make significant progress in the understanding of the cell's behavior, it would be now important to study the mechanisms of instability of the interface. In this context, it is felt that the present concept of an ideal cell with an elementary steady state of reference offers the necessary basis into which small disturbances could be introduced and studied.

4. Assumption [8] that \bar{T} is proportional to the local velocity can only be justified in an ideal cell with mean velocities much smaller in the aluminum than in the cryolite. For cells with rotational Lorentz forces, relation [8] could be generalized under the form

$$\left\{ \begin{array}{l} \bar{T}_1 = \kappa_1 \bar{U}_1 + \gamma \bar{U}_2 \\ \bar{T}_2 = \kappa_2 \bar{U}_2 + \gamma \bar{U}_1 \end{array} \right\} \quad [50]$$

Such expressions that retain the linearity of the problem would not really make the numerical computation more difficult. The interest in their use would be to introduce some coupling between the two fluid flows. This coupling should not be ignored since each liquid tends to drive the neighboring one in the direction of its own motion.

5. In itself, this theory cannot give any idea of the numerical values of coefficients κ_1 , κ_2 , and γ . It is the hope of the authors that some comparison of measurements such as those made by Johnson (6) with numerical predictions deduced from equations of Appendix B could provide a good estimation for these parameters.

Acknowledgment

This work was supported by the Assistant Secretary for Conservation and Renewable Energy, Office of Energy Systems Research, Energy Storage Division of the U.S. Department of Energy under Contract no. De-AC03-76SF00098.

Manuscript received Jan. 16, 1984.

The University of California assisted in meeting the publication costs of this article.

APPENDIX A

Explicit Solutions of Equations [21] and [31]

With notations defined in Fig. 9 and $c = (a^2 + b^2)^{1/2}$, the solution of Eq. [21], such that the functions $G(x, y)$ and its two first derivatives be continuous on the edge of the rectangle, may be written

$$\begin{aligned} 2\pi G = & h_1 h_2 \log \left(\frac{r_1}{c} \right) + h_2 h_3 \log \left(\frac{r_2}{c} \right) + \\ & h_3 h_4 \log \left(\frac{r_3}{c} \right) + h_4 h_1 \log \left(\frac{r_4}{c} \right), \\ & + 1/2 [h_1^2 (\beta_1 - \beta_4) + h_2^2 (\beta_2 - \beta_1) \\ & + h_3^2 (\beta_3 - \beta_2) + h_4^2 (\beta_4 - \beta_3)] \\ & + \frac{\pi}{4} [h_1^2 + h_2^2 + h_3^2 + h_4^2] \quad [A-1] \end{aligned}$$

The last term is a particular solution of the Poisson equation $\nabla^2 G = 1$. The other terms are solutions of Laplace equation $\nabla^2 G = 0$. At the origin of coordinates, the value of G is

$$G(0) = \frac{1}{2\pi} \left[\pi b^2 + 2(a^2 - b^2) \arctan \left(\frac{b}{a} \right) \right] \quad [A-2]$$

It can be subtracted from [A-1] to get a zero value at the origin.

The solution of Eq. [27] such that P_1 is zero at the edge of the rectangle is

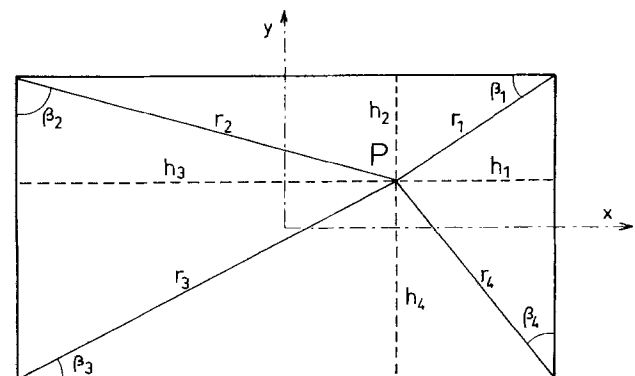


Fig. 9. Definition of notations used in Eq. [A-1]

$$P_1 = \frac{a^2 - x^2}{2} - \frac{16a^2}{\pi^3} \sum_{n=0}^{\infty} \frac{(-1)^n \cos [(2n+1) \pi x/2a] \cosh [(2n+1) \pi y/2a]}{(2n+1)^3 \cosh [(2n+1) \pi b/2a]} \quad [\text{A-3}]$$

APPENDIX B

Procedure for Computation of Velocity Fields and Interface Shape in Real Cells

When the distributions of the force fields \bar{F}_1 and \bar{F}_2 have been computed, the equations to solve to determine the velocity and pressure distributions in the two liquids are [6] and [7] with expressions [8] or [50] for the drag \bar{T}_i .

In the cryolite, the boundary condition to use on the edge of each anode block is

$$\left\{ \begin{array}{ll} P_1 = 0 & \text{in wide channels} \\ \frac{dP_1}{dt} + \Lambda Q^2 = 0 & \text{in narrow channels} \end{array} \right\} \quad [\text{B-1}]$$

where $Q = \int U_n(n=0) dt$ stands for the dimensionless flow rate in the channels, and where

$$\Lambda = \frac{\rho L^2 H^3}{S^3} \lambda$$

denotes the dimensionless friction coefficient. Taking the divergence of Eq. [7] gives a Poisson equation, the solution of which $P_1(x,y)$ is completely determined by Eq. [B-1]. Then Eq. [7] gives

$$\kappa_1 \bar{U}_1 + \gamma \bar{U}_2 = \bar{F}_1 - \bar{\nabla}_H P_1 \quad [\text{B-2}]$$

In the aluminum, the boundary condition to use on the edge of the metal pool is $U_n = 0$. Taking the curl of

the motion equation and eliminating $\bar{\nabla}_H \times \bar{U}_1$ with Eq. [B-2] gives

$$\left(\kappa_2 + \frac{\gamma^2}{\kappa_1} \right) \bar{\nabla}_H \times \bar{U}_2 = \text{curl } \bar{F}_2 - \frac{\gamma}{\kappa_1} \text{curl } \bar{F}_1 \quad [\text{B-3}]$$

The technique to solve Eq. [B-3] for a conservative velocity field ($\bar{\nabla}_H \cdot \bar{U}_2 = 0$) is quite straightforward. A stream-function is usually introduced, and appears to be determined by a Poisson equation together with the boundary condition that $U_n = 0$ at the edge of the aluminum pool. The velocity field \bar{U}_2 is thus determined. Then Eq. [B-2] gives the velocity field \bar{U}_1 , and the pressure distribution $P_2(x,y)$ follows from the motion equation.

Finally, the interface shape is given by

$$\frac{(\rho_2 - \rho_1) g z_0}{\mu_j^2 L_2} = P_2(x,y) - P_1(x,y) - (\bar{P}_2 - \bar{P}_1) \quad [\text{B-4}]$$

REFERENCES

1. S. D. Lympany, J. W. Evans, and R. Moreau in "Metallurgical Applications of Magnetohydrodynamics," The Metals Society, London (1983).
2. J. W. Evans, Y. Zundelevich, and D. Sharma, *Met. Trans.*, **12B**, 353 (1981).
3. S. D. Lympany and J. W. Evans, *ibid.*, **14B**, 63 (1983).
4. E. Durand, "Electrostatique," Tome 1, p. 350, Masson, France (1964).
5. H. S. Carslaw and J. C. Jaeger, "Conduction of Heat in Solids," 2nd ed., p. 171, Clarendon Press (1959).
6. A. F. Johnson, "Light Metals 1978," Vol. 1, pp. 45-58, The Metallurgical Society of AIME, New York (1978).
7. J. P. Givry, *Trans. Met. Soc. AIME*, **239**, 1161 (1967).
8. C. Cercignani, G. Solinas, B. Crudelle, and R. Bacchiega, Paper 23, presented at the AIME Conference, 1977.

Mass Transfer in Alternating Current Electrolysis

Anthony M. Pesco* and H. Y. Cheh**

Department of Chemical Engineering and Applied Chemistry, Columbia University, New York, New York 10027

ABSTRACT

A diffusion model was used to obtain an analytical solution for the mass transport to a rotating disk electrode under superimposed sinusoidal and triangular alternating current conditions for the case where the polarity of the applied current does not change. The analytical solution was compared to a numerical solution which resulted from a convective-diffusion model. Using the analytical solution, an expression for the instantaneous diffusion limiting current density was derived and verified experimentally using a ferri-ferrocyanide reaction system. Further, a quantitative comparison was made between the maximum rate of electrolysis under superimposed sinusoidal, triangular, and rectangular alternating current conditions with equal cycle times.

Electrolysis by a periodic variation of the applied current modifies the mass transport by producing a pulsating diffusion layer (1) in which the time-dependent concentration variation is important. This phenomenon is responsible for the fact that higher instantaneous rates of mass transport, without the initiation of a second reaction, are possible when compared to dc electrolysis.

Electrolysis by periodically varying currents has been used extensively in electrodeposition because of the changes produced in the morphology of the electrodeposits. The advantages most frequently cited by investigators are that smoother and more uniform deposits can be obtained with a better adherence to the substrate. Chin (2) presented a theory for the mass transport to a rotating disk electrode and the current-potential relationship during pulse electrolysis with rectangular current pulses, periodic pulse reversals, and double rectangular pulses with relaxations. The results indicated that the current pulses can change the current-potential relationship and thus af-

fect the properties of the electrodeposits. Electrolysis with a periodically varying current has also been used in anodic-dissolution, anodizing, and corrosion processes. A review of the fundamentals involved in alternating current electrochemical processes was given by Venkatesh and Chin (3).

An important quantity in the study of mass transport during electrolysis by alternating currents is the diffusion limiting current density, which is defined as the instantaneous current density that causes the lowest surface concentration of reacting species to reach zero. The limiting current density is a measure of the maximum rate of electrolysis for a particular system.

Using a simple diffusion model to study the mass transport of reacting species to a rotating disk electrode, Cheh (4, 5) derived an expression for the instantaneous diffusion limiting current density during electrolysis by rectangular current pulses, with and without periodically reversing the polarity of the applied current; Viswanathan and Cheh (6) derived an expression for the instantaneous diffusion limiting current density during electrolysis by

* Electrochemical Society Student Member.

** Electrochemical Society Active Member.

ramp and saw-tooth currents. Chin (2) used a simple diffusion model to obtain a solution for the fluctuating concentration of reacting species at the surface of a rotating disk electrode during electrolysis by rectangular current pulses, periodic pulse reversals, and double rectangular pulses with relaxations. Tokuda and Matsuda (7, 8) and Venkatesh (9) also used a diffusion model to study the fluctuating surface concentration of reacting species during electrolysis under ac conditions.

In this paper, a further study of the mass transport to a rotating disk electrode under superimposed sinusoidal ac conditions is presented. This study is limited to cases where the pulsating diffusion layer thickness remains much smaller than the steady-state diffusion layer thickness. In this case, a simple diffusion model is used to obtain an analytical solution for the surface concentration of reacting species. The analytical solution is compared to a numerical solution which results from a convective-diffusion model.

In an effort to demonstrate the effects of waveform characteristics on the mass transport, expressions for the instantaneous diffusion limiting current density are derived for electrolysis under superimposed sinusoidal as well as triangular and rectangular alternating current conditions, as a function of the fundamental properties of the system.

Theoretical

Assume that a rotating disk electrode is situated in an electrolyte of large extent and is rotating at a constant velocity. The radius of the disk and the distance from the disk to the counterelectrode are both large when compared to the thickness of the Nernst diffusion layer. The number of coulombs passed during an experiment is small, so that the concentration of the reacting species at the edge of the diffusion layer remains constant. An excess of supporting electrolyte is present, so electrical migration effects are negligible.

It has been shown by Viswanathan and Cheh (10) that the simple diffusion model used by Cheh (4) adequately predicts the concentration of reacting species at the electrode surface under pulse current electrolysis.

Using the diffusion model, the concentration of reacting species is governed by Fick's law of diffusion, which is expressed by the equation

$$\frac{\partial c}{\partial t} = D \frac{\partial^2 c}{\partial z^2} \quad [1]$$

with the boundary conditions

$$c = c_0 \text{ at } t = 0 \text{ and all } z \quad [2]$$

$$c = c_0 \text{ at } t > 0 \text{ and } z = 0 \quad [3]$$

$$D \frac{\partial c}{\partial z} = \frac{i}{nF} \text{ at } t > 0 \text{ and } z = \delta \quad [4]$$

where c is the concentration of the reacting species, c_0 is its concentration in the bulk of the solution, D is its diffusion coefficient, δ is the thickness of the Nernst diffusion layer, i is the applied current density, n is the number of electrons transferred during the reaction, F is Faraday's constant, t is time, and z is the axial coordinate extending from the edge of the boundary layer towards the disk surface.

The thickness of the Nernst diffusion layer was given by Levich (11) as

$$\delta = 1.612 \left(\frac{D}{\nu} \right)^{1/3} \left(\frac{\nu}{\Omega} \right)^{1/2} \quad [5]$$

where ν is the kinematic viscosity of the electrolyte, and Ω is the disk rotation speed.

DC electrolysis.—The solution of Eq. [1] subject to boundary conditions Eq. [2]-[4] was obtained by Rosebrugh and Miller (12). The surface concentration of the reacting species is given by the equation

$$c_s^* = 1 - \frac{i_{dc}}{(i_{dc})_l} \left[1 - \frac{8}{\pi^2} \sum_{j=1}^{\infty} \frac{1}{(2j-1)^2} \exp(-[2j-1]^2 \alpha t) \right] \quad [6]$$

where

$$c_s^* = c/c_0 \quad [7]$$

$$(i_{dc})_l = \frac{nFDc_0}{\delta} \quad [8]$$

$$\alpha = \frac{\pi^2 D}{4\delta^2} \quad [9]$$

$(i_{dc})_l$ is the limiting current density under dc conditions, and i_{dc} is the applied current density. When the transient term has vanished

$$c_s^* = 1 - \frac{i_{dc}}{(i_{dc})_l} \quad [10]$$

Sinusoidal ac electrolysis.—The solution of Eq. [1] subject to boundary conditions, Eq. [2]-[4] for alternating current electrolysis, when the applied current is of the form

$$i = I \sin(\omega t) \quad [11]$$

where I is the amplitude of the applied density and ω is the frequency, was solved by Warburg (13) for an infinitely large diffusion layer thickness, and by Rosebrugh and Miller (12) for a finite diffusion layer thickness.

The surface concentration of the reacting species can be expressed as

$$c_s^* = 1 - \frac{I}{2\delta(i_{dc})_l} \left(\frac{D}{\omega} \right)^{1/2} A \sin(\omega t + \gamma - \pi/4) + \frac{2I}{nF\delta} \sum_{j=1}^{\infty} \frac{\omega \exp(-[2j-1]^2 \alpha t)}{(2j-1)^4 \alpha^2 + \omega^2} \quad [12]$$

where

$$A = \frac{[\sinh^2(2\mu\delta) + \sin^2(2\mu\delta)]^{1/2}}{\sinh^2(\mu\delta) + \cos^2(\mu\delta)} \quad [13]$$

$$\mu = \left(\frac{\omega}{2D} \right)^{1/2} \quad [14]$$

$$\gamma = \tan^{-1} \left(\frac{\sin(2\mu\delta)}{\sinh(2\mu\delta)} \right) \quad [15]$$

When the transient term in Eq. [12] has vanished, the system reaches a periodic state, and the surface concentration of reacting species is given by the equation

$$c_s^* = 1 - \frac{I}{2\delta(i_{dc})_l} \left(\frac{D}{\omega} \right)^{1/2} A \sin(\omega t + \gamma - \pi/4) \quad [16]$$

Superimposed sinusoidal ac electrolysis.—If both the dc and sinusoidal alternating currents act simultaneously on the system, the applied current is of the form

$$i = \bar{i}_{dc} + I \sin(\omega t) \quad [17]$$

where \bar{i}_{dc} is the dc offset in alternating current electrolysis. The concentration change produced at the electrode surface is the sum of the concentration change that would be produced by the direct current, \bar{i}_{dc} , and the alternating current, $I \sin(\omega t)$.

The surface concentration, after the transient terms have vanished, is given by the equation

$$c_s^* = 1 - \frac{\bar{i}_{dc}}{(i_{dc})_l} - \frac{I}{2\delta(i_{dc})_l} \left(\frac{D}{\omega} \right)^{1/2} A \sin(\omega t + \gamma - \pi/4) \quad [18]$$

Mathematically, this analysis is valid regardless of whether the surface concentration is positive or negative, although, physically, its validity is limited to cases when the surface concentration is greater than or equal to zero.

Using Eq. [5], one readily obtains

$$\frac{1}{\delta} \left(\frac{D}{\omega} \right)^{1/2} = K\sigma \quad [19]$$

where

$$K = \frac{(Sc)^{-1/6}}{1.612} \quad [20]$$

and

$$\sigma = \left(\frac{\Omega}{\omega} \right)^{1/2} \quad [21]$$

Equation [18] can be transformed into

$$c_s^* = 1 - \frac{\overline{i_{dc}}}{(i_{dc})_l} - \frac{IAK\sigma}{2(i_{dc})_l} \sin(\omega t + \gamma - \pi/4) \quad [22]$$

Rosebrugh and Miller (12) demonstrated for sinusoidal ac electrolysis that with increasing values of $\mu\delta$, A approaches 2 and γ approaches 0. These limits can be substituted into Eq. [22] with an error of no more than one-half percent if $\mu\delta > 3$ where

$$\mu\delta = \frac{1}{2^{1/2}K\sigma} \quad [23]$$

For a system with a Schmidt number of 1000, the substitutions may be made when σ is less than 1.20.

When the appropriate substitutions are made, Eq. [22] is simplified to

$$c_s^* = 1 - \frac{\overline{i_{dc}}}{(i_{dc})_l} - \frac{IK\sigma}{(i_{dc})_l} \sin(\omega t - \pi/4) \quad [24]$$

The surface concentration was also obtained by performing a numerical integration of the convective-diffusion equation (see Appendix B). The results were compared with those obtained by using Eq. [24], for a particular set of experimental conditions. Very good agreement between the two results was obtained, as is shown in Fig. 1.

Electrolysis by superimposed ac may be performed in two ways. One way is such that the polarity of the applied current changes during a cycle. Another way is such that the current polarity remains the same throughout the cycle. In this investigation, only the latter will be considered.

Let us consider Eq. [22]. c_s^* reaches its lowest value for a particular current offset and amplitude when $\sin(\omega t - \pi/4) = 1$. In this case

$$c_s^* = 1 - \frac{\overline{i_{dc}}}{(i_{dc})_l} - \frac{IK\sigma}{(i_{dc})_l} \quad [25]$$

By setting Eq. [25] to zero and rearranging terms, an expression for the offset current required to reach the limiting current density is obtained. For a particular current amplitude, the equation is expressed as

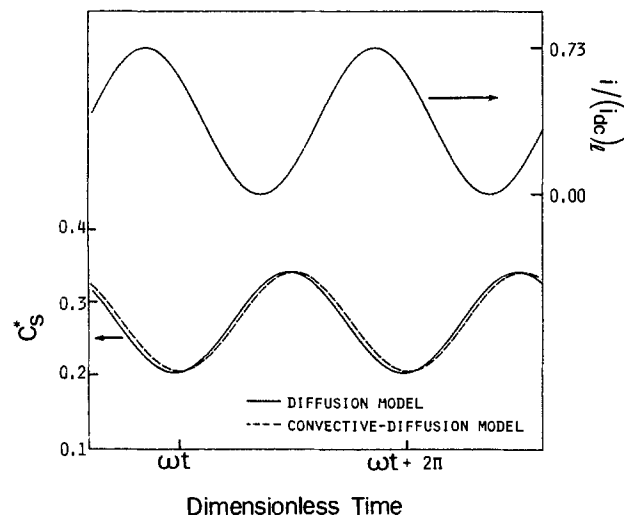


Fig. 1. Surface concentration at the periodic state in superimposed sinusoidal ac electrolysis ($Sc = 1000$, $\omega = 60$ Hz, $\Omega = 1640$ rpm).

$$(\overline{i_{dc}})_{l,s} = (i_{dc})_l - IK\sigma \quad [26]$$

where $(\overline{i_{dc}})_{l,s}$ is defined as the dc offset at the limiting current density in superimposed sinusoidal ac electrolysis. The corresponding limiting current density is the sum of the offset and the amplitude, and can be expressed by the equation.

$$(i_s)_l = (\overline{i_{dc}})_{l,s} + I \quad [27]$$

Rearranging Eq. [26] gives

$$\frac{(\overline{i_{dc}})_{l,s}}{(i_{dc})_l} = 1 - \frac{I}{(i_{dc})_l} K\sigma \quad [28]$$

$(\overline{i_{dc}})_{l,s}/(i_{dc})_l$ can also be defined as the ratio of the average rate of electrolysis under superimposed sinusoidal ac, at a particular value of I , σ , and K , to that under dc electrolysis. Even though higher instantaneous mass transfer rates can be achieved with superimposed sinusoidal ac, Eq. [28] implies that the average rate of electrolysis under superimposed sinusoidal ac is less than that which can be obtained under dc electrolysis. This is because $IK\sigma/(i_{dc})_l$ is always greater than zero.

Looking at the limiting cases for Eq. [28], we can clearly see that as I or σ approaches zero, the average overall rate of electrolysis by superimposed sinusoidal ac approaches that for dc electrolysis. The upper limit for I is bounded by the restriction placed on the applied current. Therefore, the maximum value for I occurs when $I = (\overline{i_{dc}})$. In this case, the applied current waveform is such that the lowest value of the current just reaches zero. Under this condition

$$\frac{(i_{dc})_l}{(\overline{i_{dc}})_{l,s,\max}} = 1 + K\sigma \quad [29]$$

and

$$\frac{(i_s)_{l,\max}}{(i_{dc})_l} = \frac{2}{1 + K\sigma} \quad [30]$$

where $(i_s)_{l,\max}$ is the maximum value for the limiting current density, and $(\overline{i_{dc}})_{l,s,\max}$ is the maximum value for the dc offset at the limiting current density.

Rectangular ac electrolysis.—The limiting current density for electrolysis with rectangular pulses separated by intervals of zero current is given by (4)

$$\frac{(i_p)_l}{(i_{dc})_l} = \frac{1}{1 - \frac{8}{\pi^2} \sum_{j=1}^{\infty} \frac{1}{(2j-1)^2} \frac{[\exp([2j-1]^2 a\theta_2) - 1]}{[\exp([2j-1]^2 a\theta) - 1]}} \quad [31]$$

where θ_2 is the off time of the applied current and θ is the cycle time (on time plus off time).

In order to compare the mass transport under pulse current conditions to that under superimposed sinusoidal ac conditions, the pulse characteristics will be restricted to cases where the off time equals the on time, or $\theta_2 = \theta/2$. By performing algebraic manipulations (as shown in Appendix A), Eq. [31] can be transposed into

$$\frac{(i_p)_l}{(i_{dc})_l} = \frac{2}{1 + 1.52K\sigma} \quad [32]$$

and

$$\frac{(i_{dc})_l}{(\overline{i_{dc}})_{l,p}} = 1 + 1.52K\sigma \quad [33]$$

where $(\overline{i_{dc}})_{l,p}$ is the dc offset at the limiting current density in pulsed current electrolysis.

Triangular ac electrolysis.—Rosebrugh and Miller (12) demonstrated that the concentration changes at the electrode surface produced by time varying currents can be expressed by the equation

$$c_s^* = 1 + \frac{2}{nF\delta C_0} \sum_{j=1}^{\infty} \exp(-m^2 at) \int_0^t \exp(m^2 au) i(\mu) du \quad [34]$$

where $m = 2j - 1$, and $i(\mu)$ is the expression for the time

varying current density. Consider a triangular shaped current wave which does not change polarity and is restricted so that the lowest value of the current just reaches zero. The expression for the current is written

$$i(t) = (\bar{i}_{dc}) \left[1 + \frac{8}{\pi^2} \sum_{l=1}^{\infty} \frac{(-1)^{l/2(p-1)}}{p^2} \sin(p\omega t) \right] \quad [35]$$

where $p = 2l - 1$, and (\bar{i}_{dc}) is the dc offset for the triangular current wave. By inserting Eq. [35] into Eq. [34] and performing the integration, an expression for the surface concentration is obtained in terms of an infinite series (see Appendix A). When the transient terms become negligible, the surface concentration is expressed by the equation

$$c_s^* = 1 - \frac{(\bar{i}_{dc})}{(i_{dc})_l} [1 + T] \quad [36]$$

where

$$T = \frac{64}{\pi^4} \sum_{j=1}^{\infty} \sum_{l=1}^{\infty} \frac{(-1)^{l/2(p-1)}}{p^2} \frac{m^2 \sin(p\omega t) - \frac{p\omega}{a} \cos(p\omega t)}{m^4 + \frac{p^2\omega^2}{a^2}} \quad [37]$$

The lowest concentration during a cycle occurs when T reaches its maximum value, T_{max} . The limiting current density and dc offset at the limiting current density can be written as

$$\frac{(i_l)}{(i_{dc})_l} = \frac{2}{1 + T_{max}} \quad [38]$$

and

$$\frac{(i_{dc})_l}{(i_{dc})_{l,t}} = 1 + T_{max} \quad [39]$$

where

$$T_{max} = 0.81K\sigma \quad [40]$$

(see Appendix A for details), (i_l) is the limiting current density, and $(i_{dc})_{l,t}$ is the dc offset at the limiting current density in electrolysis with a triangular current.

Summary.—A graphical representation of $(i_l)/(i_{dc})_l$ as a function of σ , for the three types of waveforms that were investigated, is shown in Fig. 2. The general solution for the limiting current density and dc offset at the limiting current density can be written as

$$\frac{(i_x)_l}{(i_{dc})_l} = \frac{2}{1 + AK\sigma} \quad [41]$$

$$\frac{(i_{dc})_l}{(i_{dc})_{l,x}} = 1 + AK\sigma \quad [42]$$

$x = (s, \max), p, t$

where A is a constant which appears to be dependent only on the current waveform.

Waveform	A
Rectangular	1.52
Sinusoidal	1.00
Triangular	0.81

Considering the pulsating diffusion layer in the same fashion as Viswanathan and Cheh (10), an expression for the maximum value for the thickness of the pulsating diffusion layer can be expressed as

$$\frac{(\delta_p)_{max}}{\delta} = \left[\frac{(i_l)}{(i_{dc})_l} \right]^{-1} = \frac{1}{2} + \frac{A}{2} K\sigma \quad [43]$$

By substituting the expressions for K and σ , Eq. [43] can be transposed into

$$\frac{(\delta_p)_{max}}{\delta} = \frac{1}{2} + \frac{A}{3.224} Sc^{-1/6} \left[\frac{Re_n}{\omega R^2} \right]^{1/2} \quad [44]$$

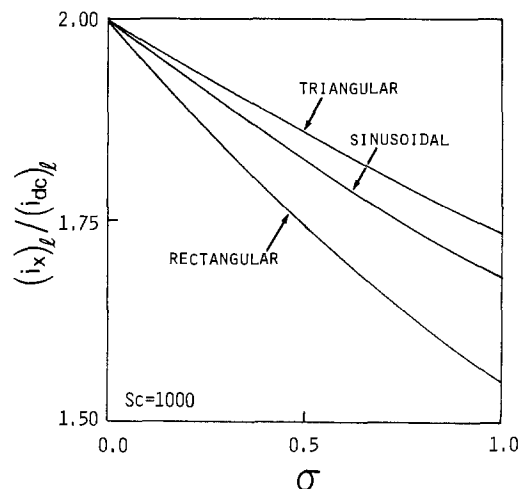


Fig. 2. Limiting current density for ac electrolysis by the three waveforms, as a function of σ .

where Re_n is the Reynolds number based on the disk rotational speed ($\Omega R^2/\nu$) and R is the disk radius.

Experimental Procedure

The reduction of ferricyanide ions in a ferri-ferrocyanide solution was chosen to study the mass transport to a rotating disk electrode under superimposed sinusoidal alternating current conditions.

The experiments were carried out in an experimental system consisting of a Pine Instrument Pt disk electrode with an area of 0.461 cm^2 , a Pt counterelectrode, and a Fisher Scientific saturated calomel electrode with a Luggin capillary. The electrolyte consisted of $0.01M \text{ K}_4\text{Fe}(\text{CN})_6$ and $0.01M \text{ K}_3\text{Fe}(\text{CN})_6$ in $1M \text{ KCl}$. Purified N_2 was bubbled for 0.5h prior to the experiments and passed over the solution during the experiments. All experiments were carried out at $22^\circ \pm 1^\circ\text{C}$. The kinematic viscosity of the electrolyte was measured with an Ostwald viscometer and found to be $0.00953 \text{ cm}^2/\text{s}$.

The dc limiting current densities for both the anodic and cathodic reactions were plotted as a function of $\Omega^{1/2}$, and the diffusion coefficients were calculated by using the Levich equation (11)

$$(i_{dc})_l = -0.6203 nFD^{2/3}\nu^{-1/6}\Omega^{1/2}C_0 \quad [45]$$

The diffusion coefficients for $[\text{Fe}(\text{CN})_6]^{-3}$ and $[\text{Fe}(\text{CN})_6]^{-4}$ were found to be 7.3×10^{-6} and $6.0 \times 10^{-6} \text{ cm}^2/\text{s}$, respectively. These values are in good agreement with those obtained by John and Vielstich (16).

For alternating current electrolysis, the current was supplied by feeding the sinusoidal wave output of a General Radio Three Phase Oscillator (1305-A) to an ECO Potentiostat (551). Both the offset and the amplitude of the potential difference between the rotating disk and reference electrodes were measured using a Keithley TRMS Multimeter (179-20A) and observed on a Tektronix Single Beam Storage Oscilloscope (5103N). Experiments were carried out at rotation speeds of 409, 920, and 1640 rpm, frequencies of 25, 60, and 120 Hz, and current amplitudes ranging from 0.9 to 6.0 mA/cm^2 .

The ac limiting current density was measured by using two methods. The first method consisted of observing the sudden increase in the amplitude of the potential difference and simultaneous distortion of the wave from its original sinusoidal shape on the oscilloscope, during a gradual increase of the current offset, for a particular applied current amplitude. In the second method, the root-mean-square of the overpotential, η_{rms} , was recorded and plotted as a function of the current offset normalized with respect to the dc limiting current density, as is shown in Fig. 3 for a particular rotation speed and various frequencies of the applied current. The current at which η_{rms} increases abruptly is the ac limiting current density, and

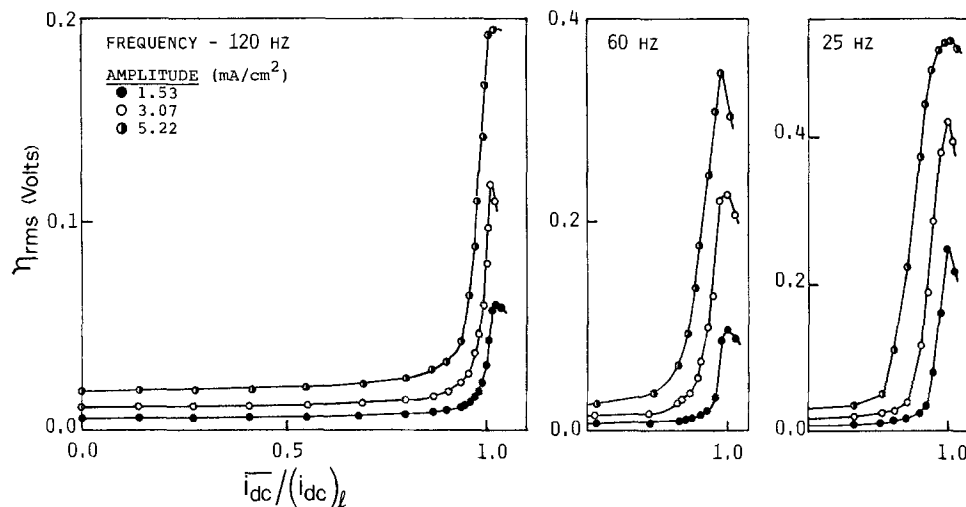


Fig. 3. Experimental results for the root-mean-square value of the overpotential as a function of current offset ($\Omega = 1640$ rpm).

the current at which η_{rms} reaches a maximum is identified to be the dc limiting current density.

The limiting current density for triangular and rectangular ac electrolysis was also measured in the same system by using the method that involves direct measure of the limiting current density from the oscilloscope. The current was supplied by feeding the triangular and rectangular wave outputs of a Tacussel (GSTP-3C) function generator to an ECO Potentiostat (551). Experiments were carried out at rotation speeds of 409, 920, and 1640 rpm and at frequencies of 25, 50, and 100 Hz.

Results and Discussion

Figure 4 is a graphical representation of the experimental results at a particular rotation speed of 1640 rpm, using both of the methods described for obtaining the limiting current density. The figure shows the current offset that was needed to reach the limiting current density at particular values of current amplitude in superimposed sinusoidal ac electrolysis.

According to Eq. [28], a linear relationship between the current amplitude and the current offset should exist at

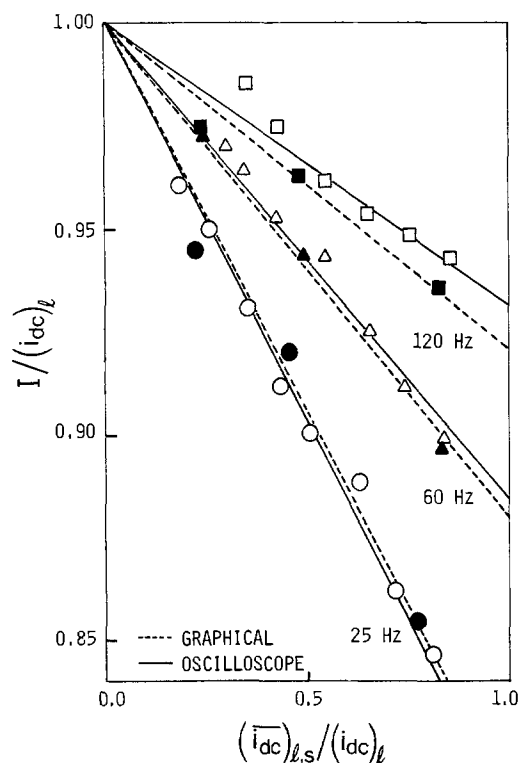


Fig. 4. Experimental results for the relationship between the current amplitude and current offset at the limiting current density ($\Omega = 1640$ rpm).

the limiting current density, and the slope equal to $-K\sigma$. A comparison between the experimental and calculated values for $-K\sigma$ is shown in Table I. The average error between the calculated values and the experimental values is approximately 7% for the graphical method and 4% for the method that involves a direct measure of the limiting current density from the oscilloscope.

The maximum limiting current density can be extrapolated from the experimental data by using the experimental values for $K\sigma$ in Eq. [30]. The results are plotted in Fig. 5 along with the calculated values.

Also plotted in Fig. 5 are the experimental results for the limiting current density during triangular and rectangular ac electrolysis along with the calculated values, as a function of σ . The average error between calculated and experimental values is approximately 2% for both of the waveforms.

Figure 5 indicates satisfactory agreement between the experimental and calculated results for all three cases studied in this investigation.

Conclusions

A solution based on a simple diffusion model was obtained for the concentration of a reacting species on the surface of a rotating disk electrode during electrolysis by sinusoidal and triangular alternating currents, which do not change polarity during a cycle. Using the solutions, as well as the solution for the surface concentration during electrolysis by rectangular currents separated by equal intervals of zero current, a simplified expression for the instantaneous diffusion limiting current density was derived based on four fundamental properties of the system: (i) Sc (Schmidt number) (ii) Re_n (Reynolds number based on Ω), (iii) a dimensionless group, $\omega R^2/\nu$, and (iv) A , a constant which is based on the waveform characteristics.

The expression for the instantaneous diffusion limiting current density during superimposed sinusoidal, triangular, and rectangular ac electrolysis was verified experimentally by using a ferri-ferrocyanide reaction system.

Table I. Comparison between calculated and experimental results

r (rpm)	ω (Hz)	$-K\sigma$		
		Calculated	Experimental	
			Oscilloscope	Graphical
409	25	0.096	0.098	0.085
	60	0.062	0.061	0.058
	120	0.044	0.045	0.048
920	25	0.143	0.144	0.145
	60	0.093	0.084	0.097
	120	0.065	0.065	0.058
1640	25	0.192	0.186	0.183
	60	0.124	0.124	0.125
	120	0.087	0.072	0.076

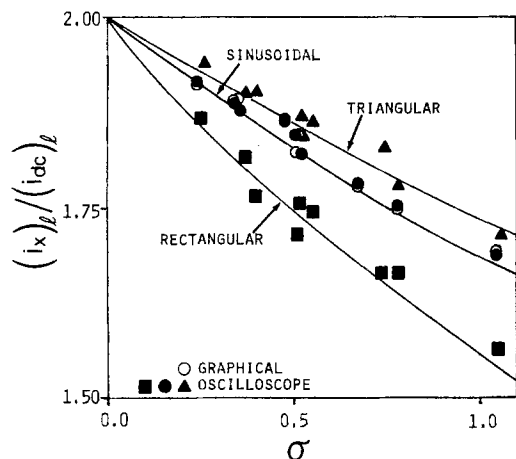


Fig. 5. Comparison between calculated and experimental values of the diffusion limiting current density for superimposed sinusoidal, triangular, and rectangular ac electrolysis, as a function of σ .

Good agreement was obtained between experimental and calculated results.

To summarize, the paper provides a unification in the theoretical analysis of mass transfer in the theory of transient electrolysis.

Acknowledgments

The authors wish to thank T. Cheng for making available his computer program for numerical integration. One of us (A.M.P.) would like to acknowledge partial support in the form of a fellowship from the U.S. Department of Energy.

Manuscript submitted Feb. 1, 1984; revised manuscript received May 23, 1984.

APPENDIX A

Limiting Current Density for Rectangular AC Electrolysis

Consider Eq. [31]. Upon substitution of $\theta_2 = \theta/2$, the equation can be expressed as

$$\frac{(i_p)_l}{(i_{dc})_l} = \frac{1}{1 - \frac{8}{\pi^2} \sum_{j=1}^{\infty} \frac{\left[\exp\left(m^2 \alpha \frac{\theta}{2}\right) - 1 \right]}{m^2 [\exp(m^2 \alpha \theta) - 1]}} \quad [\text{A-1}]$$

where

$$m = 2j - 1 \quad [\text{A-2}]$$

and

$$\alpha \theta = \frac{\pi^2 D \theta}{4 \delta^2} \quad [\text{A-3}]$$

By using Eq. [5] and substituting $\theta = 2\pi/\omega$ into Eq. [A1-3]

$$\alpha \theta = \frac{\pi^3 K^2 \sigma^2}{2} \quad [\text{A-4}]$$

If a variable q is defined such that

$$q = (\alpha \theta)^{1/2} = \left(\frac{\pi^3}{2}\right)^{1/2} K \sigma \quad [\text{A-5}]$$

$$\frac{(i_p)_l}{(i_{dc})_l} = \frac{1}{1 - \frac{8}{\pi^2} \sum_{j=1}^{\infty} \frac{\left[\exp\left(m^2 \frac{q^2}{2}\right) - 1 \right]}{m^2 [\exp(m^2 q^2) - 1]}}$$

and

$$\frac{(i_{dc})_l}{(i_{dc})_{l,p}} = 2 - \frac{16}{\pi^2} \sum_{j=1}^{\infty} \frac{\left[\exp\left(m^2 \frac{q^2}{2}\right) - 1 \right]}{m^2 [\exp(m^2 q^2) - 1]} \quad [\text{A-7}]$$

Differentiating Eq. [A-7] with respect to q yields

$$\frac{d \left[\frac{(i_{dc})_l}{(i_{dc})_{l,p}} \right]}{dq} = \frac{-16}{\pi^2} \sum_{j=1}^{\infty} q \left[\frac{\exp\left(m^2 \frac{q^2}{2}\right)}{[\exp(m^2 q^2) - 1]} - \frac{2 \exp(m^2 q^2) \left[\exp\left(\frac{m^2 q^2}{2}\right) - 1 \right]}{[\exp(m^2 q^2) - 1]^2} \right] \quad [\text{A-8}]$$

which was found numerically to be independent of σ .

$$\frac{d \left[\frac{(i_{dc})_l}{(i_{dc})_{l,p}} \right]}{dq} = \frac{d \left[\frac{(i_{dc})_l}{(i_{dc})_{l,p}} \right]}{\left(\frac{\pi^3}{2}\right)^{1/2} K d\sigma} = 0.3861 \quad [\text{A-9}]$$

$$\frac{d \left[\frac{(i_{dc})_l}{(i_{dc})_{l,p}} \right]}{d\sigma} = 1.52K \quad [\text{A-10}]$$

The ratio $(i_{dc})_l / (i_{dc})_{l,p}$ in Eq. [A-7] was found to approach unity as q approaches zero. Therefore, Eq. [A-6] and [A-7] can be expressed as

$$\frac{(i_p)_l}{(i_{dc})_l} = \frac{2}{1 + 1.52K\sigma} \quad [\text{A-11}]$$

and

$$\frac{(i_{dc})_l}{(i_{dc})_{l,p}} = 1 + 1.52K\sigma \quad [\text{A-12}]$$

Limiting Current Density for Triangular AC Electrolysis

The expression for the concentration changes produced at the electrode surface is given as

$$c_s^* = 1 + \frac{2}{nF\delta c_0} \sum_{j=1}^{\infty} \exp(-m^2 at) \int_0^t \exp(m^2 au) i(\mu) d\mu \quad [\text{A-13}]$$

where $i(\mu)$ is the time varying applied current density.

A triangular current waveform which does not change polarity during a cycle and is restricted so that the lowest value of the current just reaches zero, can be expressed by

$$i(t) = (\bar{i}_{dc}) \left[1 + \frac{8}{\pi^2} \sum_{l=1}^{\infty} \frac{(-1)^{1/2(p-1)}}{p^2} \sin(p\omega t) \right] \quad [\text{A-14}]$$

where $p = 2l - 1$ and (\bar{i}_{dc}) is defined as the offset current density. By combining Eq. [A-13] and [A-14], one readily obtains

$$c_s^* = 1 + \frac{2}{nF\delta c_0} \sum_{j=1}^{\infty} \exp(-m^2 at) \int_0^t \exp(m^2 au) (\bar{i}_{dc}) du + \frac{16(\bar{i}_{dc})}{\pi^2 nF\delta c_0} \sum_{j=1}^{\infty} \exp(-m^2 at) \int_0^t \exp(m^2 au) \sum_{l=1}^{\infty} \frac{(-1)^{1/2(p-1)}}{p^2} \sin(p\omega u) du \quad [\text{A-15}]$$

Upon further manipulation, Eq. [A-15] becomes

$$c_s^* = 1 - \frac{(\bar{i}_{dc})}{(i_{dc})_l} \frac{8}{\pi^2} \sum_{j=1}^{\infty} \frac{1}{m^2} [1 - \exp(-m^2 at)] + \frac{16(\bar{i}_{dc})}{\pi^2 nF\delta c_0} \sum_{j=1}^{\infty} \sum_{l=1}^{\infty} \frac{(-1)^{1/2(p-1)}}{p^2} \exp(-m^2 at) \int_0^t \exp(m^2 au) \sin(p\omega u) du \quad [\text{A-16}]$$

which, after the appropriate integration, becomes

$$c_s^* = 1 - \frac{\overline{(i_{dc})}}{(i_{dc})_1} \frac{8}{\pi^2} \sum_{j=1}^{\infty} \frac{1}{m^2} [-\exp(-m^2 at)] - \frac{64}{\pi^4} \frac{\overline{(i_{dc})}}{(i_{dc})_1} \sum_{j=1}^{\infty} \sum_{l=1}^{\infty} \frac{(-1)^{1/2(p-1)}}{p^2} \left[\frac{m^2 \sin(p\omega t) - \frac{p\omega}{a} \cos(p\omega t)}{m^4 + \frac{p^2\omega^2}{a^2}} + \frac{\frac{p\omega}{a} \exp(-m^2 at)}{m^4 + \frac{p^2\omega^2}{a^2}} \right] \quad [A-17]$$

When the transient terms have become negligible

$$c_s^* = 1 - \frac{\overline{(i_{dc})}}{(i_{dc})_1} [1 + T] \quad [A-18]$$

where

$$T = \frac{64}{\pi^4} \sum_{j=1}^{\infty} \sum_{l=1}^{\infty} \frac{(-1)^{1/2(p-1)}}{p^2} \left[\frac{m^2 \sin(p\omega t) - \frac{p\omega}{a} \cos(p\omega t)}{m^4 + \frac{p^2\omega^2}{a^2}} \right] \quad [A-19]$$

A graph of T during a cycle, for two values of σ , is shown in Fig. A-1 along with the applied current waveform.

The lowest surface concentration during a cycle occurs when T reaches its maximum value, T_{max} . The limiting current density and dc offset at the limiting current density can be expressed by the equation

$$\frac{(i_l)_1}{(i_{dc})_1} = \frac{2}{1 + T_{max}} \quad [A-20]$$

and

$$\frac{(i_{dc})_{l,t}}{(i_{dc})_{l,t}} = 1 + T_{max} \quad [A-21]$$

T_{max} was evaluated for various values of σ , and a linear relationship between them was found to exist.

Equations [20] and [21] can be rewritten as

$$\frac{(i_l)_1}{(i_{dc})_1} = \frac{2}{1 + 0.81K\sigma} \quad [A-22]$$

and

$$\frac{(i_{dc})_{l,t}}{(i_{dc})_{l,t}} = 1 + 0.81K\sigma \quad [A-23]$$

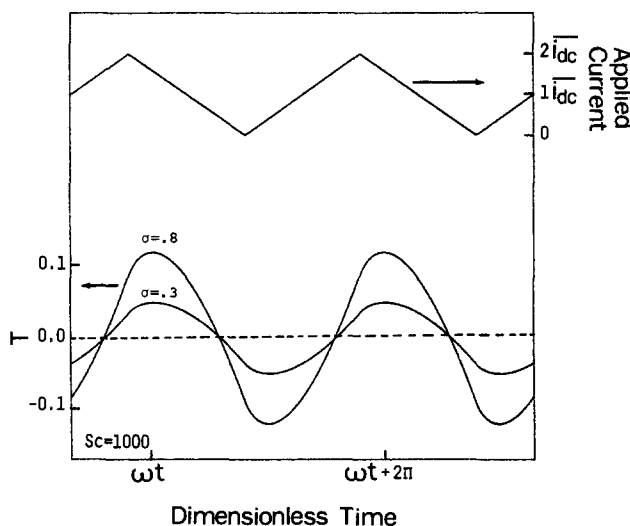


Fig. A-1. The behavior of T during a cycle for two values of σ .

APPENDIX B

Numerical Integration of the Convective-Diffusive Equation

If one considers the convective flux contribution to the mass transport, the equation which governs the concentration of the reacting species is of the form

$$\frac{\partial c}{\partial t} + v_z \frac{dc}{dz} = D \frac{\partial^2 c}{\partial z^2} \quad [B-1]$$

where v_z is the axial component of the velocity. Equation [B-1] can be rearranged into the dimensionless form

$$\frac{\partial c^*}{\partial \tau} = \frac{\partial^2 c^*}{\partial \xi^2} + K \xi^2 \frac{\partial c^*}{\partial \xi} \quad [B-2]$$

where

$$c^* = \frac{c}{c_0} \quad [B-3]$$

$$\tau = \frac{Dt}{\delta^2} \quad [B-4]$$

$$\xi = \frac{z}{\delta} \quad [B-5]$$

and

$$K = -\frac{v_z \delta^3}{z^2 D} = 2.136 \quad [B-6]$$

A time-independent spatial mesh can be formed which consists of a series of N equally spaced points which lie in the region from $\xi = 0$ to $\xi = 1$, such that for each ξ there exists a corresponding $c_i^*(\tau)$ where $i = 1, 2, 3, \dots, N$. At each ξ , there is also a corresponding $dc_i^*/d\tau$, such that

$$\begin{aligned} \frac{dc_1^*}{d\tau} &= f_1(\tau, c_1^*, c_2^*) & c^*(\tau) &= c_s^*(\tau) \\ \frac{dc_i^*}{d\tau} &= f_i(\tau, c_{i-1}^*, c_i^*, c_{i+1}^*) & c_i^*(\tau) & \\ \frac{dc_N^*}{d\tau} &= f_N(\tau, c_{N-1}^*, c_N^*) & c_N^*(\tau) &= 1 \end{aligned} \quad [B-7]$$

where f_i is the central finite difference approximation of the right-hand side of Eq. [B-2], in which

$$\frac{dc_i^*}{d\xi} = \frac{c_{i+1}^* - c_{i-1}^*}{2\Delta\xi} \quad [B-8]$$

$$\frac{d^2c_i^*}{d\xi^2} = \frac{c_{i-1}^* - 2c_i^* + c_{i+1}^*}{(\Delta\xi)^2} \quad [B-9]$$

By performing a spacial discretization, one partial differential equation [B-2], continuous in both space and time, was transformed into N ordinary differential equations of the initial value type [B-7], continuous in time only. The method used to solve this system of ordinary differential equations was developed by Hindmarsh (14), based on the backward differentiation formulas of Gear (15).

LIST OF SYMBOLS

- A defined by Eq. [13]
- a defined by Eq. [A-3]
- c concentration
- c_0 bulk concentration
- c_s^* surface concentration
- c_s^* dimensionless surface concentration
- D diffusion coefficient
- F Faraday's constant
- f_i defined by Eq. [B-7]
- i current density
- $\frac{i_{dc}}{i_{dc}}$ dc current density
- $\frac{i_{dc}}{i_{dc}}$ dc offset in electrolysis by periodic varying currents
- $(i_{dc})_1, (i_s)_1$ diffusion limiting current densities for dc, superimposed sinusoidal, rectangular, and triangular alternating current waveforms, respectively
- $(i_p)_1, (i_l)_1$

$(\bar{i}_{dc})_{l,ss}$, $(\bar{i}_{dc})_{l,p}$	dc offset at the diffusion limiting current density for superimposed sinusoidal, rectangular, and triangular alternating current waveforms, respectively
$(\bar{i}_{dc})_{l,t}$	
$(i_s)_{l,max}$, $(\bar{i}_{dc})_{l,max}$	the maximum value for the diffusion limiting current density and dc offset at the diffusion limiting current density that can be obtained in superimposed sinusoidal ac electrolysis for the case where the polarity of the applied current does not change
I	current amplitude in sinusoidal ac electrolysis
K	defined by Eq. [20]
N	number of spacial discretization points
n	number of electrons transferred in the electrochemical reaction
q	defined by Eq. [A-5]
R	disk radius
Re_n	Reynolds number based on disk speed ($\Omega R^2/\nu$)
Sc	Schmidt number (ν/D)
T	defined by Eq. [37]
T_{max}	the maximum instantaneous value of T , as defined by Eq. [37]
u	dummy variable of integration
v_z	axial component of fluid velocity
z	axial coordinate extending from the edge of the Nernst boundary layer ($z = 0$) towards the disk surface ($z = \delta$)
Greek letters	
γ	defined by Eq. [15]
δ	Nernst diffusion layer thickness
$\delta_{p,max}$	maximum value for the pulsating diffusion layer thickness
η_{rms}	root-mean-square overpotential in ac electrolysis
θ, θ_2	cycle time and off time in rectangular ac electrolysis

ξ	dimensionless axial coordinate defined by Eq. [B-5]
μ	defined by Eq. [14]
ν	electrolyte kinematic viscosity
σ	defined by Eq. [21]
τ	dimensionless time defined by Eq. [B-4]
ω	frequency of the applied current
Ω	rotation speed

REFERENCES

1. N. Ibl, J. Cl. Puipe, and H. Angerer, *Surface Tech.*, **6**, 287 (1978).
2. D. T. Chin, *This Journal*, **130**, 1657 (1983).
3. S. Venkatesh and D. T. Chin, *Isr. J. Chem.*, **18**, 56 (1979).
4. H. Y. Cheh, *This Journal*, **118**, 551 (1971).
5. H. Y. Cheh, *ibid.*, **118**, 1132 (1971).
6. K. Viswanathan and H. Y. Cheh, *ibid.*, **126**, 398 (1979).
7. K. Tokuda and H. Matsuda, *J. Electroanal. Chem.*, **82**, 157 (1977).
8. K. Tokuda and H. Matsuda, *ibid.*, **90**, 147 (1978).
9. S. Venkatesh, Ph.D. Thesis, Clarkson College of Technology, Potsdam, NY (1980).
10. K. Viswanathan and H. Y. Cheh, *This Journal*, **125**, 1772 (1978).
11. V. G. Levich, "Physicochemical Hydrodynamics," Prentice-Hall, Englewood Cliffs, NJ (1962).
12. T. R. Rosebrugh and W. L. Miller, *J. Phys. Chem.*, **14**, 816 (1910).
13. E. Warburg, *Ann. Physik*, **67**, 493 (1899).
14. A. C. Hindmarsh, "Gear: Solution of Ordinary Differential Equations Having Banded Jacobian," Lawrence Livermore Laboratory, Rept. UCID-30059, Rev. 1, March, 1975.
15. C. W. Gear, "Numerical Initial Value Problems in Ordinary Differential Equations," Prentice-Hall, Englewood Cliffs, NJ (1971).
16. D. Jahn and W. Vielstich, *This Journal*, **109**, 849 (1962).

Maximum Power Spectroscopy for Photovoltaic Devices

Barry Miller* and Joseph M. Rosamilia

AT&T Bell Laboratories, Murray Hill, New Jersey 07974

ABSTRACT

Maximum power spectroscopy for the study of photovoltaics is described. The technique is based on analyzing the modulated maximum power output of the photojunction cell for a controlled input spectrum in a dual beam (bias plus modulated monochromatic probe) arrangement. The differential power conversion efficiency is thus measured. The input spectrum is programmed by a computer and servo loop to be either neutral (wavelength independent) or solar in shape, from a stored reference table. The operation of the system, applicable to laboratory spectrum simulation, and the function of the bias beam are demonstrated. Spectra of a p-n Si diode with added series resistance simulate the differences between maximum power efficiency and the conventional short-circuit quantum efficiency. There are advantages to the power measurement in sensitivity to competitive kinetic processes governing cell conversion efficiency and to wavelength dependent effects on junction potential gradients.

The spectral response of solid-state photovoltaic and photoelectrochemical devices is usually taken as the set of monochromatic quantum efficiencies under short-circuit photocurrent (I_{sc}) collection. A less common alternative is based on the open-circuit voltage (V_{oc}) output. Both conditions correspond to measurement under zero power output since one of the current (I) or voltage (V) parameters is zero. Light-to-electrical conversion is, however, the raison d'être of the device. We have developed and describe herein the methodology of maximum power spectroscopy to capitalize on the evident advantages of measuring the power parameter.

We measure the modulated maximum power output response, ΔP_o , of the photovoltaic system of a chopped monochromatic power input, ΔP_i , which is superimposed on a steady beam of power, P_s . It must be noted that the spectral response of solar cells is a measurement with a long history of development and refinement whose status has been recently reviewed (1). Numerous references exist therein to spectroscopic response defined by differential short-

circuit current efficiency for chopped monochromatic beams superimposed on white or controlled-spectrum dc beams which bias the cell to some operating point. Previous experience in our laboratories with this technique (2) is illustrative of its possibilities in tracing the location and effects of surface and near-surface recombinative processes traceable to structural defects.

Nevertheless, there are a number of factors determining power conversion efficiency in solid-state cells and photoelectrochemical cells based on semiconductor-electrolyte junctions which do not influence spectral response under short-circuit conditions except when they are dominant. For the liquid junction cells, electrode kinetics, counterelectrode behavior, and internal resistance could be cited. Recombination processes will also likely have more dramatic effects on the maximum power output than the short-circuit current.

We have thus approached the power measurement in a dual beam mode yielding the differential efficiency $\Delta P_o/\Delta P_i$. The P_s source (either mono- or polychromatic) gives flexibility to the choice of operating level and allows probing of nonlinearity and saturation effects, as it does in

* Electrochemical Society Active Member.

traditional short-circuit current techniques. The important distinction is in the quantity controlled (ΔP_i) and measured (ΔP_o) differentially. By computer selection of reference voltages, we provide any chosen function of ΔP_i vs. wavelength, λ , from a constant value for all λ to a normalized duplication of the intensities of a solar spectrum in our region of interest here, 400-1000 nm. Appropriate analysis of this data can relate the solar responses of different systems in the laboratory, within the range restrictions.

To clarify the difference in response between this maximum power sensitive methodology and the conventional short-circuit approach, we use the experimental model of a junction device with variable added series resistance. The latter simulates, for these purposes, the effect on I-V curves of losses from the important photobarrier rate processes mentioned above (recombination of photogenerated hole-electron pairs and electron transfer kinetics). In this regard, we also show the relation of the total power output, P_o , as a function of the P_s level, to the corresponding $\Delta P_o/\Delta P_i$ derivative ratio for the same model experiments. This illustrates the enhanced sensitivity of the maximum power spectroscopy modulation technique to the junction loss factors and any consequent nonlinear and saturation effects of the P_s level. Applications to Schottky barrier metallizations and various liquid junction cells will follow separately.

Experimental

The central element of the new system is a servo scheme (3), which drives a photovoltaic device to its point of maximum power output, P_o . That instrumentation was primarily applied to fixed or relatively slowly changing light intensity measurements. The response was, however, also shown to follow accurately a modulated (~ 10 Hz) light input, and this capability is required for the present spectral application. Also essential is a means for generating the $\Delta P_i - \lambda$ relation, most simply for spectroscopy a constant ΔP_i . This programming is done with computer software and a light control servo loop. Such output intensity control has been initiated previously by means such as mechanical cams (4), function generators (5, 6), and step-by-step calibration and burn in of an EPROM (uv erasable programmable read only memory) (7).

The combination of functions is schematically shown in Fig. 1A and 1B. In path 1 on Fig. 1a the Apple IIe computer, through an 8-bit D-A converter (Interactive Structures, Incorporated, AO-03), outputs a stored set of voltages. These represent power outputs which are equated to the radiometer detector signal through the servo loop controlling the

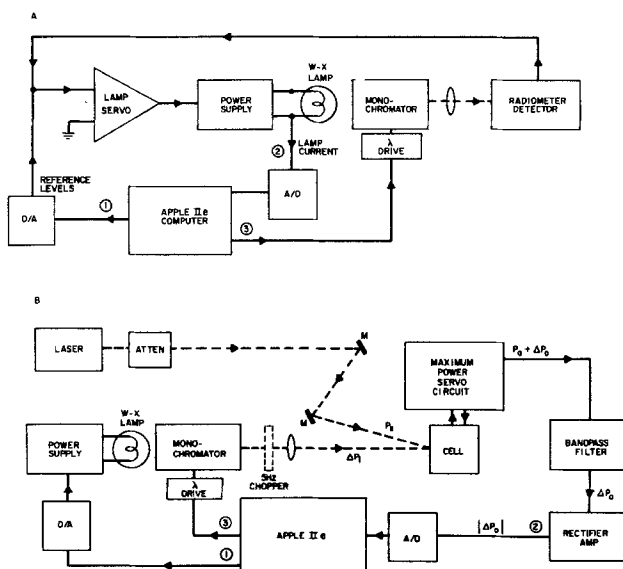


Fig. 1. A: Scheme for servo control and acquisition of lamp currents generated by a given set of computer reference voltages (powers). B: Schematic of maximum modulated power spectrometer. Computer program controls monochromator power output (path 1), data is acquired from cell (path 2), and wavelength is stepped (path 3).

lamp current. Thus, the monochromatic intensity incident on the detector follows the desired wavelength-power program. The necessary lamp current at each wavelength, in the form of a programming voltage that produces it, is read back to the computer via path 2 and a 12-bit A-D converter (Interactive Structures, Incorporated AI13). These values are then stored on disk.

If a constant power output from the monochromator is sought, the reference levels are identical at all wavelengths. Then the necessary lamp currents reflect the overall system light throughput at that wavelength. In that case, the wavelength of least efficiency determines the maximum constant ΔP_i attainable within the lamp operating limits. The light source for the monochromator (Oriol 7240) was a 100W tungsten-halogen bulb driven from a Hewlett-Packard 6024A 200W supply in a current-programmed by voltage mode.

The primary radiometer on which we rely as a neutral detector is a thermopile (Oriol 7102). For convenience in the lamp current control servo, we use a radiometric silicon detector (Metrologic 60-530) which is much faster and more stable, though nominally $\pm 10\%$ in spectral flatness (400-1000 nm). The Si detector is calibrated against the thermopile, and these factors are entered into the computer reference set in spectral programming. (The calibration is accomplished from the spectral data shown in Fig. 2, which are power spectra obtained for constant lamp current in this system.)

To obtain solar-shaped $\Delta P_i - \lambda$ spectra, the reference levels are a series of numbers in relative proportion to tabulated (8) values ($\text{mW cm}^{-2} \text{nm}^{-1}$) for the terrestrial solar power under different air mass conditions. The interval has been taken as 10 nm, and the tables have been interpolated to this increment where necessary. The monochromator drive (Oriol 7286) is indexed in 10 nm steps to computer command (path 3 in Fig. 1A or 1B) after steps 1 and 2 are completed. The spectral bandwidth has been kept about 10 nm throughout these experiments and is the limit to sharp resolution of any input spectral features.

If the optical elements in the system, particularly lamp characteristics, are stable, the stored lamp currents can repeatedly generate the desired $\Delta P_i - \lambda$ spectrum. The practical limits are determined by the 8-bit accuracy of the D-A converter (± 1 bit = ± 20 mV in the 5V equivalent to 10A lamp current).

Figure 1B shows the "playback" of lamp currents and the maximum power (ΔP_o) measuring mode. Path 1, then, is the lamp programming sequence operating in conjunction with the monochromator stepping (path 3). The P_s source was normally a Hughes 3235 H-PC He-Ne laser of about 12 mW output. Adjustment of P_s intensity was accomplished with a Karl Lambrecht KLOA series Optical Attenuator. The cell and maximum power circuitry blocks refer to the previously described system (3). In brief, it employs a small

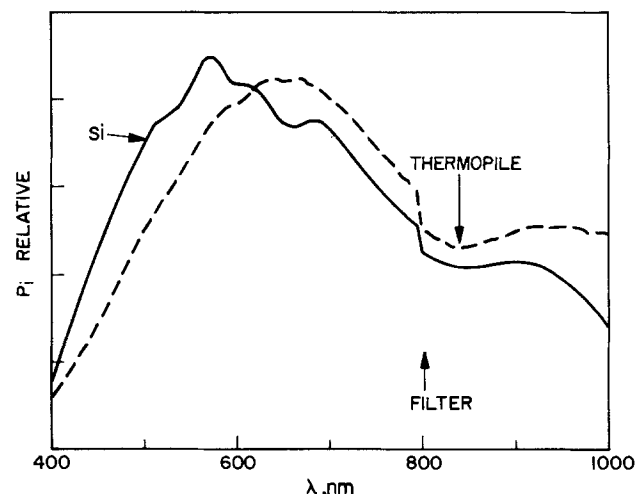


Fig. 2. P_i vs. λ at constant lamp current monitored by a radiometric silicon detector (—) and thermopile (---).

ac signal (5 mV) superimposed on the cell voltage and a lock-in amplifier to detect the synchronized component produced in the analog product of cell I and V. The lock-in output is part of a servo loop, and its dc level drives the cell voltage to the minimum $d(VI)/dV$ point. This makes the VI product a maximum. The superimposed ac signal is at 800 Hz and the light is square wave chopped (ΔP_i) at 5 Hz in the dual beam mode ($\Delta P_i + P_s$). Proper filter time constant and gain adjustment in the PAR 128 lock-in feedback loop allows the square wave output ΔP_o to be strictly followed.

The ΔP_o signal is passed through a bandpass filter (Wavetek-Rockland 452) set at two (low pass) and one-half (high pass) the chopping frequency, then full-wave rectified, filtered, and amplified by π to restore the peak-to-peak value if the signal was sinusoidal. These aspects are described in detail for another modulation context (9, 10). This data are acquired in path 2 by the A/D converter and the computer.

Figure 3 summarizes the input/output experiments to be described in this paper and the accompanying symbols. One or two sources may be superimposed on a sample or detector. If two, the P_s source may be combined with either the monochromator output P_i or its 5 Hz chopped version ΔP_i , P_s or P_i may be used separately. Thus dc (unvarying) incident beams are P_s , P_i , or $P_s + P_i$. The respective dc outputs are P_o and I_{sc} for maximum power or short-circuit current configurations of the cell electronics, respectively. With the dc + ac input, or $P_s + \Delta P_i$, which is the maximum power spectroscopy mode, we measure the ac output ΔP_o . For comparison to the conventional spectral response technique, we can measure the ac component ΔI_{sc} in that cell connection mode and the same bandpass filter-rectifying arrangement.

All timing sequences were adjusted to allow the light detectors, servo loops, and rectifier filtering to stabilize appropriately before data acquisition and 10 nm stepping. Experimental elapsed time was typically of the order of 1 s/nm in the wavelength stepping mode. An order sorting filter was manually inserted at 800 nm by programming an audible warning and sufficient delay in the software at that point. Since this was done in the lamp programming stage as well, there is no discontinuity in the spectral output because of the filter insertion.

It is to be noted that an alternative approach is use of a neutral beam splitter for illuminating a known response detector and a sample cell simultaneously, thus effectively combining the Fig. 1A and 1B functions. Our experience was that the problems of neutral beam splitting (7), and the managing of the monochromatic and bias beams in this more complex physical arrangement far outweighed any apparent advantages of such a "simplification."

Results and Discussion

The cell output measuring and light source input programming aspects are considered first separately, then in combination. For the photovoltaic output we test the measurements of P_o and ΔP_o for $P_i = \Delta P_i$ and fixed P_s . For input spectra generation, we compare their measured values to the desired flat or solar $\Delta P_i - \lambda$ relations.

The gain to a known square wave in the modulated output measuring system was calibrated. Then in the scheme of Fig. 3, this value of 1.27 was reproduced within $\pm 1\%$ with

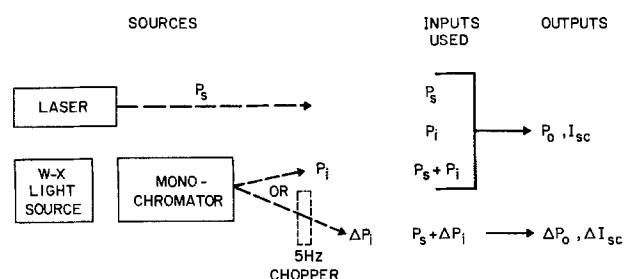


Fig. 3. Block diagram and symbology of the experimental sources and combinations of input light with the corresponding outputs.

Table I. Calculated and actual outputs

Input	Outputs	
$P_i + P_s$	$P_{o2} = 0.283$ mW	$I_{sc2} = 770$ μ A
P_s	$P_{o1} = 0.243$	$I_{sc1} = 662$
$\Delta P_i + P_s$	$\Delta P_o = 0.051$	$\Delta I_{sc} = 138$
Calc.	$\frac{\Delta P_o}{P_{o2} - P_{o1}} = 1.28$	$\frac{\Delta I_{sc}}{I_{sc2} - I_{sc1}} = 1.28$

a 5 Hz ΔP_i signal incident on a p-n Si diode. The outputs P_{o2} and P_{o1} were measured for inputs of $P_i + P_s$ and P_s , respectively. Next, ΔP_o was measured for the input $\Delta P_i + P_s$. Correspondingly, I_{sc2} , I_{sc1} , and ΔI_{sc} were also obtained. Table I shows the output measurements and calculations.

The excellent agreement of the $\Delta P_o/(P_{o2} - P_{o1})$ and $\Delta I_{sc}/(I_{sc2} - I_{sc1})$ ratios to the theoretical gain confirms the quantitative capability of the system to measure ΔP_o for a photovoltaic detector. The short-circuit data are obtained in a conventional zero voltage, current follower configuration. The number 1.27 is the ratio of outputs to square and sine wave inputs when such signals of the same amplitude are fed into the bandpass filter-rectifier- π gain circuit.

After the calibration of the radiometric Si detector against the thermopile (Fig. 2) and the subsequent generation of the lamp current set for flat power output, the spectrum was played back onto the reference thermopile and also onto a pyroelectric radiometer, an independent neutral detector. These outputs are shown in Fig. 4 (curves I and II). The flatness indicates the spectral neutrality achieved for ΔP_i vs. λ inputs. Curve III is the ΔP_i vs. λ solar spectrum generated as described above and measured by the thermopile. The solar air mass 1.0 reference levels [Table I in Ref. (8)] normalized to this scale are also shown on Fig. 4 as points. The fit between the tabulation and the playback values is illustrative of the software flexibility and calibration accuracy. The 1-bit (± 0.020 V) accuracy in lamp programming is $\pm 2-3\%$, typically, of ΔP_i . The variation in curves I and II at the 10 nm intervals is virtually all due to this 8-bit conversion limit, and further smoothing can be achieved by a better D-A.

A radiometric p-n Si diode (Oriol 7190, $\pm 8\%$ in A/W, 450-950 nm) was used to test the combined system, including modulated maximum power detection. Figure 5, curve I, shows P_o for P_i fixed, $P_s = 0$. ΔP_o , curve II, was obtained for the $\Delta P_i = P_i$, $\Delta P_i + P_s$ mode. These plots coincide experimentally when scaled as shown, confirming the circuit operation and the fact that the P_o/P_i ratio is constant through this level of P_i , which was controlled by the bias

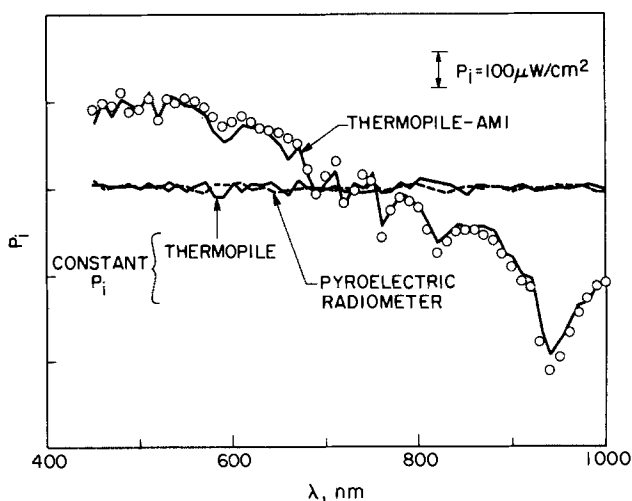


Fig. 4. P_i vs. λ programs. Curve I (—) and curve II (---) are constant power programs incident on a thermopile and pyroelectric radiometer, respectively. Curve III is the solar AM1 program onto thermopile with same total power, $\sum_{\lambda} P_{i\lambda}$, as others. Points are tabulated (relative) values for AM1.

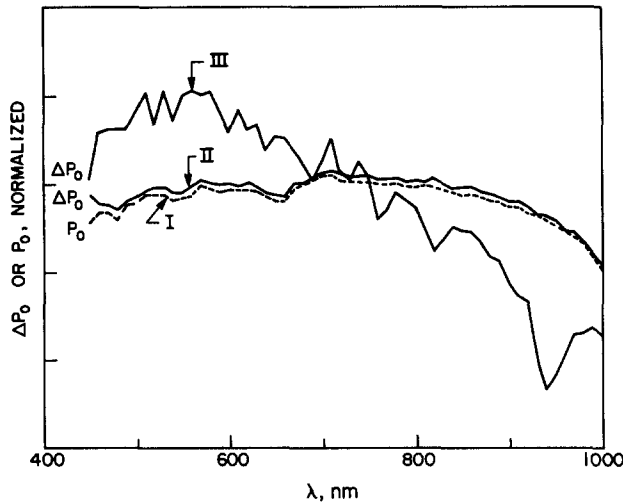


Fig. 5. Power spectra of radiometric Si diode. Curve I (---): P_0 spectrum with fixed P_1 and $P_s = 0$. Curve II: ΔP_0 spectrum with $P_s + \Delta P_1$ fixed. Curve III: ΔP_0 spectrum with P_s fixed and ΔP_1 follows AM1 program.

level, P_s . The ΔP_0 output corresponding to the $\Delta P_1 - \lambda$ solar spectrum of curve III, Fig. 4 follows in curve III.

A more rigorous test of the accuracy of modulated operation is shown as a function of λ in Fig. 6. There we compare the responses to a steady input level of P_1 , found by manually determining the maximum VI product, P_0 , and the values of ΔP_0 when the composite signal $\Delta P_1 + P_s$ is applied. In this case, $\Delta P_1 = P_1 = 0.5 \text{ mW/cm}^2$ and $P_s = 12 \text{ mW/cm}^2$. For the $\Delta P_1 + P_s$ mode, the ΔP_0 values were obtained automatically. The two spectra normalized are identical, as is required for the same inputs (P_1 and ΔP_1) and linear power response.

The effect of added series resistance on I-V curves for a blue enhanced p-n Si diode with active area = 0.05 cm^2 is shown for a fixed incident laser power in Fig. 7. Maximum power output is lowered without altering V_{oc} or I_{sc} until the load effect is very high. P_0 vs. P_1 plots from such sets with fixed laser input powers are shown in Fig. 8 with the corresponding values of I_{sc} . These latter do not vary except at the combination of high resistance (1 K) and high power ($P_1 > 1 \text{ mW}$).

The equivalent modulated spectrum from a $\Delta P_1 + P_s$ experiment is now repeated for P_s of 12 mW/cm^2 (0.6 mW on the Fig. 8 P_1 abscissa), with both ΔP_0 and ΔI_{sc} measured. The ΔP_0 spectra of Fig. 9 are sensitive at all wavelengths to the slopes of the $P_0 - P_1$ data at this fixed P_1 and varying resistance. Thus, as expected, the ΔI_{sc} spectra are virtually im-

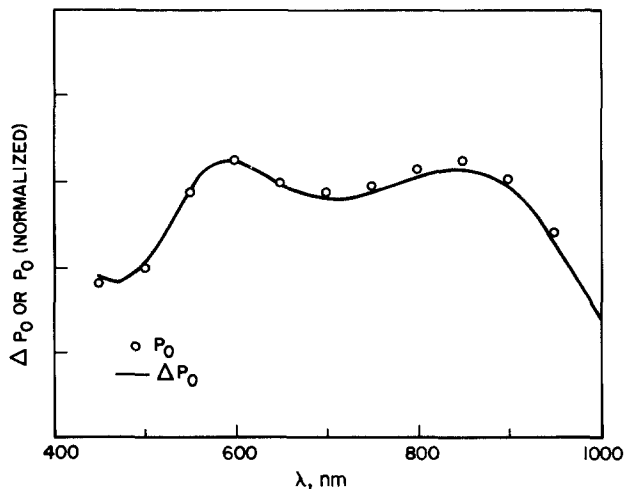


Fig. 6. ΔP_0 and P_0 [•] vs. λ for a p-n Si diode of 0.05 cm^2 active area. P_0 is manually measured maximum VI for fixed $P_1 = 0.5 \text{ mW/cm}^2$. ΔP_0 is measured with $\Delta P_1 = P_1, 12 \text{ mW/cm}^2$.

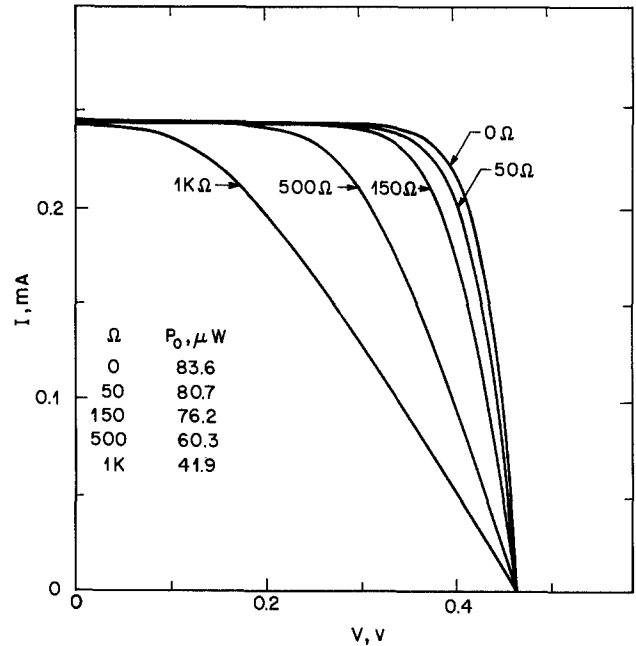


Fig. 7. Effect of added series resistance on I-V curves for p-n Si diode with $P_1 = 12 \text{ mW/cm}^2$. Maximum power values tabulated for each curve.

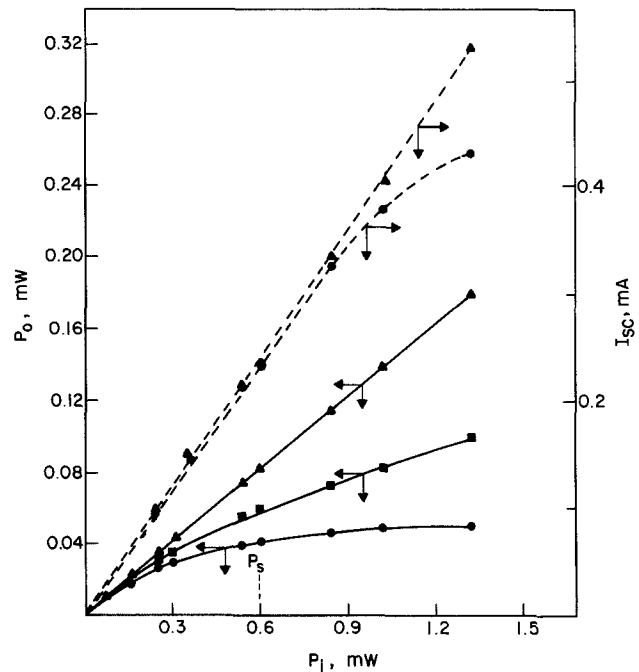


Fig. 8. I_{sc} (---) and P_0 (—) vs. P_1 as a function of added series resistance. [Δ], [■], and [•] represent 0Ω , 500Ω , and $1 \text{ k} \Omega$ series resistance, respectively.

immune to the added resistance, as they would be to any factor that affects the I-V curves only in the maximum power region.

From the individual wavelength data stored in the computer, the power output measurements may be summed for each 10 nm step over the spectrum to obtain a total power output $\sum_{\lambda} \Delta P_0$ at fixed $P_s + \text{fixed } \Delta P_1$. P_0 as a function of varying resistance at fixed input was calculated from Fig. 8 data. These are both displayed as a function of series resistance in Fig. 10. P_0 drops more slowly than the summed differential quantity $\sum_{\lambda} \Delta P_0$, as would be expected from Fig. 8; in the limit of saturation (horizontal, infinite resistance characteristic in a normal diode curve), $\Delta P_0 \rightarrow 0$, whereas P_0 remains a definite nonzero value.

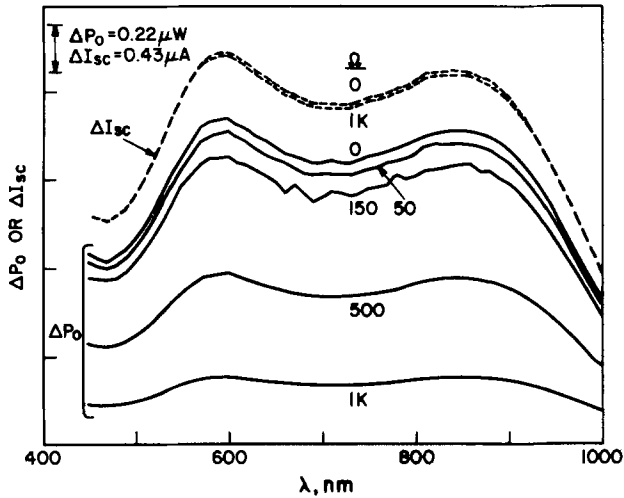


Fig. 9. Effect of added series resistance as marked on modulated spectra, ΔI_{sc} (---) and ΔP_o (—) vs. λ .

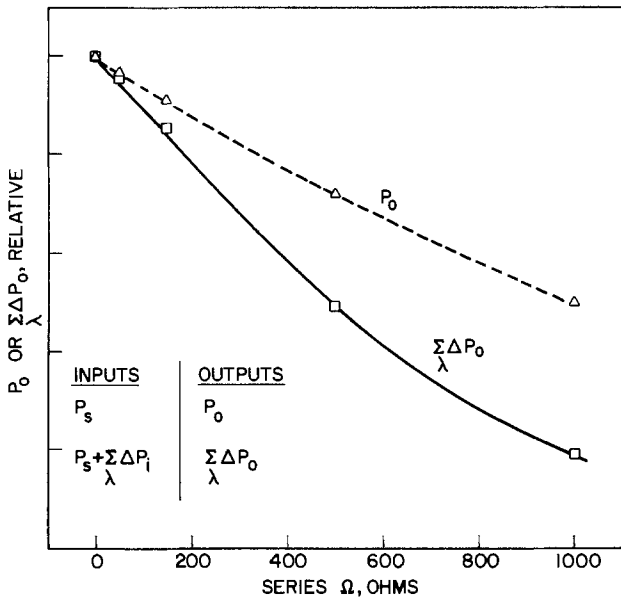


Fig. 10. Normalized plots of P_o (---) and $\sum P_o$ (—) vs. added series resistance with inputs of P_s and $P_s + \sum \Delta P_i$, respectively.

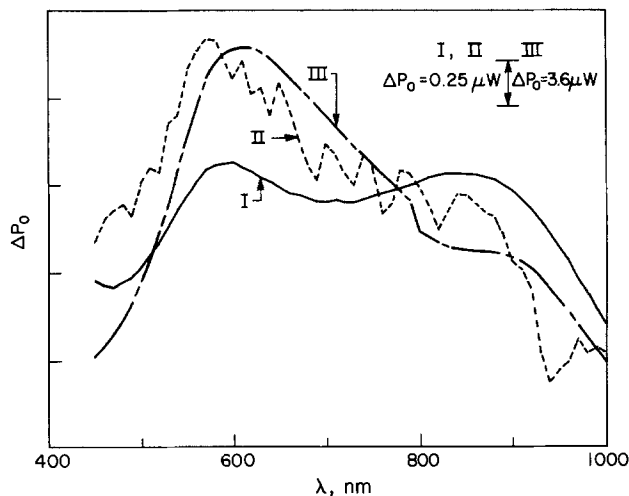


Fig. 11. Modulated power spectra, ΔP_o vs. λ , of a Si diode. Curve I (—): Modulated input, ΔP_i , flat. Curve II (---): ΔP_i follows AM1 solar spectrum with $\sum P_i$, flat at curve I equaling $\sum P_i$, solar of II. Curve III (---): Input with constant lamp current, $\Delta P_i - \lambda$ as in Fig. 2. P_s is fixed in all cases.

The response to solar shaped and flat power input spectra of the Si diode employed in Fig. 7-10 is given in Fig. 11 (curves I and II). The prior constraint here was $\sum_{\lambda} \Delta P_{i,flat} = \sum_{\lambda} \Delta P_{i,solar}$, applied by computing the right-hand member and then dividing by the number of intervals to calibrate $\Delta P_{i,flat}$.

This approach permits the relative efficiency of devices to be simply compared in the modulated mode for the same total power, $\sum_{\lambda} \Delta P_i$, incident in different spectral form. Curve III on Fig. 11 shows the spectral response (without total power constancy restriction) at constant lamp current, where ΔP_i vs. λ is shown in Fig. 2.

A corollary to this is the comparison of the response of different bandgap devices to the same source. Different bandgaps are simulated by running the Si diode with a set of shortwave transmitting interference filters (Melles Griot) intercepting ΔP_i . The $\sum_{\lambda} \Delta P_o$ will take on the appearance of the outputs of a series of progressively different bandgap semiconductors. This effect of "bandgap" on solar and flat spectra is shown in Fig. 12 for two cutoff wavelength (half-maximum transmission) values of the filters, under the equal total input restraint. The values of $\sum_{\lambda} \Delta P_i$ were corrected for filter transmission; this approximation has little effect on the point being demonstrated.

These data were treated under two measures of relative and absolute power conversion efficiencies. We define $Q_1 = \frac{\sum_{\lambda} \Delta P_{o,solar}}{\sum_{\lambda} \Delta P_{o,flat}}$ and $Q_2 = \frac{\sum_{\lambda} \Delta P_{o,solar}}{\sum_{\lambda} \Delta P_i}$. Plots of filter cutoff at half height (simulated bandgap) vs. Q_1 and Q_2 for Fig. 12-style spectra are given in Fig. 13.

The Q_1 plot, because of the cutoff values and the solar 550 nm irradiance peak, makes the solar spectral output relatively higher than that from a flat input spectrum. This effect is consistent with the Q_1 ratios paralleling the $\frac{\sum_{\lambda}^{cutoff} \Delta P_{i,solar}}{\sum_{\lambda}^{cutoff} \Delta P_{i,flat}}$ ratios, which are also shown on Fig. 13. Q_2 , a more conventional definition, shows the reduced efficiency of bandgaps greater than the 1.4 eV level, which best matches the solar spectrum (11).

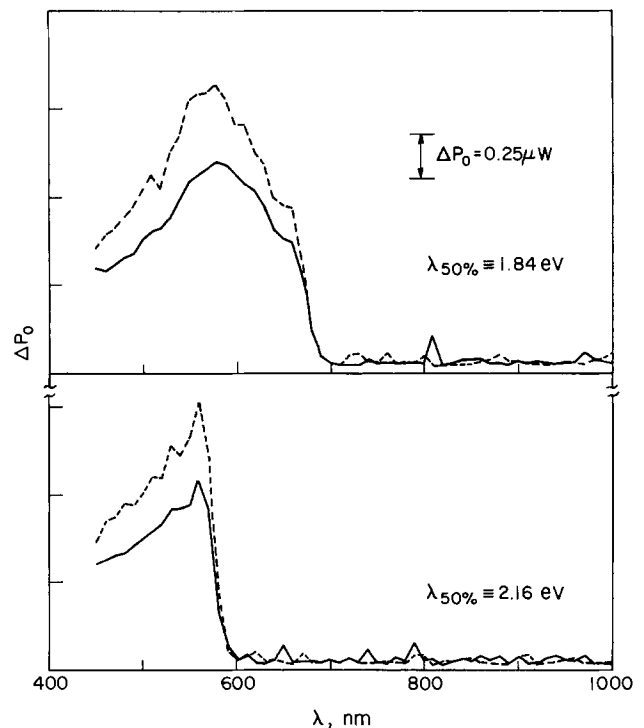


Fig. 12. Modulated power spectrum for a Si diode with two different short-wave transmitting filters, labeled by their wavelengths at 50% of maximum transmission, ΔP_i is flat as $f(\lambda)$ for the solid line and AM1 solar for the dash line.

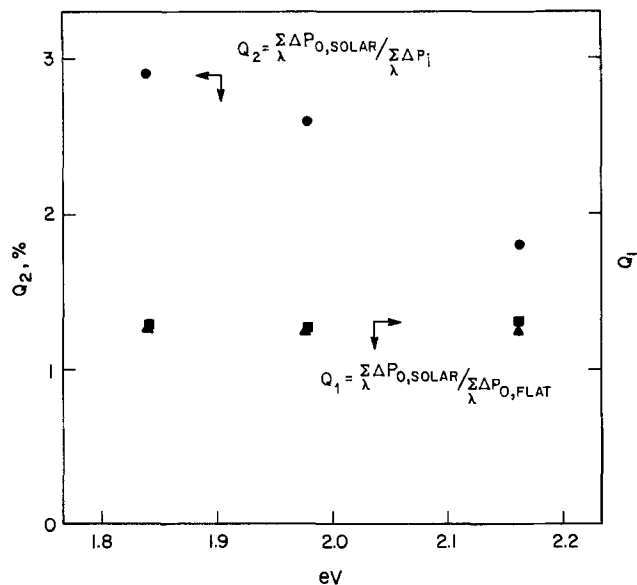


Fig. 13. Relative power efficiency, Q_1 , [■], absolute conversion efficiency, Q_2 , %, [•], and the ratio $\frac{\sum_{450} \Delta P_{1,solar}}{\sum_{450} \Delta P_{i,flat}}$ [△], vs. bandgap in eV.

Conclusions

Computer-controlled instrumentation for monitoring the maximum power delivered by a photovoltaic junction device under selectable input spectrum programming leads to the technique of maximum power spectroscopy. The input spectrum is applied in modulated form superimposed on an adjustable bias. The benefit of varying bias intensity as well as wavelength dependent parameters, in the manner

often applied to conventional spectral response (1), is also available to this methodology.

For photovoltaics, the relative sensitivity of maximum power output to loss factors is usually greater than that of short-circuit current, and our present method extends this to spectroscopic studies. A solar-derived or other selected input spectrum in the dual-input-beam mode permits inter-comparisons of wavelength response over any selected region for semiconductor cells. The differential scheme means the spectra also have enhanced sensitivity to intensity (bias) effects and the losses ascribable to high rate operation or concentration of light.

Manuscript submitted Dec. 19, 1984; revised manuscript received March 23, 1984. This was Paper 144 presented at the Cincinnati, Ohio, Meeting of the Society, May 6-11, 1984.

AT&T Bell Laboratories assisted in meeting the publication costs of this article.

REFERENCES

1. J. S. Hartman and M. A. Lind, "A Survey of Spectral Response Measurements for Photovoltaic Devices," PNL-3970, Richland, Washington (1981).
2. A. Heller, K.-C. Chang, and B. Miller, *J. Am. Chem. Soc.*, **100**, 684 (1978).
3. B. Miller, *This Journal*, **127**, 184 (1980).
4. R. H. Hill, R. Oechsli, and E. Marg, *J. Opt. Soc. Am.*, **51**, 1139 (1961).
5. D. A. Wayne and N. G. Dillman, *Appl. Opt.*, **8**, 603 (1969).
6. E. H. Stupp, *Rev. Sci. Instrum.*, **33**, 1215 (1962).
7. B. Ramadan, Y. K. Leung, and J. F. Kos, *ibid.*, **53**, 765 (1982).
8. R. E. Bird and R. L. Hulstrom, *Solar Cells*, **8**, 85 (1983).
9. B. Miller and S. Bruckenstein, *Anal. Chem.*, **46**, 2026 (1974).
10. J. M. Rosamilia and B. Miller, *J. Electroanal. Chem.*, **160**, 131 (1984).
11. H. J. Hovel, "Solar Cells, Vol. 11, Semiconductors and Semimetals," Chap. 4, Academic Press, New York (1975).

Energetics of Reaction of Al^{3+} with O^{2-} in an Alkali Halide Environment

Comparisons of *ab initio* Molecular Orbital Calculations with Molten Salt Data

L. A. Curtiss and M. Blander*

Argonne National Laboratory, Chemical Technology Division, Argonne, Illinois 60439

ABSTRACT

Ab initio molecular orbital calculations of the structures and energies of $LiAlF_4$, Li_2AlF_5O , $LiAlCl_4$ and Li_2AlF_5O are presented. These molecules were chosen so as to approximate Al^{3+} and O^{2-} in a molten salt environment. Calculated energies for vapor-phase reactions involving oxide addition to $LiAlX_4$ ($X = F, Cl$) are consistent with experimental data from molten halide melts. Comparison is also made between the quantum mechanical calculations and results from simple coulomb models.

The formation of complex species involving Al^{3+} and O^{2-} in molten salts is of fundamental scientific significance as well as of technological importance in current and advanced aluminum smelting processes and in batteries. Complex species of Al^{3+} with O^{2-} or S^{2-} have been extensively studied experimentally in fluoride and chloride solvents (1-10). Little experimental work (4, 6) and no quantum mechanical studies of the energetics of bonding have been published. In this paper, we report quantum mechanical calculations of the structures and energetics of gaseous molecules involved in reactions between Al^{3+} and O^{2-} ions. Insofar as is possible, the molecules were chosen so as to contain species which are expected or possible in molten halide melts. With a

* Electrochemical Society Active Member.

judicious choice of molecules, one might hope that the differences in solvation energies of reactants and products of the reaction can be minimized so that the energy changes for the reactions between gaseous molecules can represent the corresponding reaction in the liquid reasonably well. In addition to deducing reaction energies, we also calculate the structures of species, some of which exist in molten salt solutions.

We also compare our quantum mechanical calculations of the energetics of reactions between gaseous species with coulomb models. Our ultimate aim is to refine a simple coulomb model (4, 6) for predicting the energetics of complex species between Al^{3+} and O^{2-} in molten salts in order to make it accurate enough for reasonable predictions of the energetics of complexing.

Quantum Mechanical Calculations

In order to emulate the energetics of formation of solvated AlO^+ species in alkali chloride and fluoride melts, we chose the vapor molecules $\text{Li}_2\text{AlF}_3\text{O}$ and $\text{Li}_2\text{AlCl}_3\text{O}$ in which the AlO^+ species is coordinated by halide and alkali atoms. Because quantum mechanical calculations of the energies of ions, especially those with valences of two or more, are relatively inaccurate, we chose to perform calculations only for neutral species. In addition, electron correlation is an important factor which must be taken into account in calculations of energies of these molecules. However, if one calculates the energetics for reactions in which there are the same number of bonds in the reactants and products, there should be considerable cancellation of correlation energies and the error introduced into the calculated energy change, for the reaction is likely to be small (11, 12). Consequently, we considered the gas-phase reactions



and



Ab initio molecular orbital LCAO-SCF calculations (13) at the extended 3-21G (14) basis set level were carried out on the $\text{Li}_2\text{AlF}_3\text{O}$ and $\text{Li}_2\text{AlCl}_3\text{O}$ complexes. The structures of these complexes were optimized with respect to their total energy using the geometrical parameters illustrated in Fig. 1. The structures were optimized under a C_{3v} constraint which requires one of the Li atoms to be face-bridged with the Al (*i.e.*, three halide atoms in the bridge) and the Al-O-Li bridge to be linear. It is possible that structures having edge-bridges are more stable since similar calculations (15) on the related LiAlF_4 complex found the edge-bridged structure to be more stable by 9 kcal mol^{-1} . However, by using the face-bridged structures of LiAlF_4 and LiAlCl_4 on the left side of reactions [1] and [2], any error introduced by not using the lowest energy structure should nearly cancel. We have not investigated the other bridge structures for these oxide complexes because our interest here is in the strength of the Al-O bond compared to the Al-X ($X = \text{F}, \text{Cl}$) bond.

In order to determine energies for reactions [1] and [2], the energies of a number of other related molecules and complexes are needed. Table I contains the energies and optimized geometries of LiF , LiCl , Li_2O , AlF_3 , AlCl_3 , LiAlF_4 (face-bridged structure), and LiAlCl_4 (face-bridged structure) at the 3-21G level. The experimental geometries of LiF , LiCl , Li_2O , AlF_3 , and AlCl_3 are also given. The extended 3-21G basis set gives good agreement with experiment except for the bond lengths in LiCl and AlCl_3 , which are too long by 0.09 and 0.18 Å, respectively. A larger basis set with d-functions and, possibly, inclusion of correlation energy are necessary for better agreement with experiment for these bond lengths. These errors should be taken into account when considering the calculated oxide geometries.

The 3-21G optimized geometries of $\text{Li}_2\text{AlX}_3\text{O}$ ($X = \text{F}, \text{Cl}$) are given in Table I. The 3-21G geometries indicate that the LiX_3Al groups in the oxides have geometries which are very similar to the LiX_3Al groups in the LiX_3AlX complexes. Hence, the replacement of a halide by the OLi group does not significantly perturb the other end of the

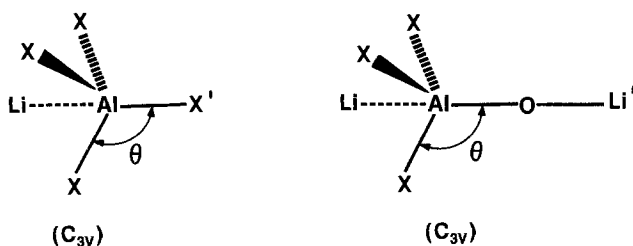


Fig. 1. Structures of species in reactions [1] and [2]. Assumed symmetries in parentheses ($X = \text{F}, \text{Cl}$).

Table I. Calculated 3-21G geometries and total energies

Structure ^a	Geometry ^b	Energy (a.u.) ^c
$\text{Li}_2\text{O}(\text{C}_{2v})^d$	$r(\text{Li-O}) = 1.58$ [1.59, 1.55] $\theta = 180$ [180]	-89.28714
LiF	$r(\text{Li-F}) = 1.52$ [1.564]	-106.35419
LiCl	$r(\text{Li-Cl}) = 2.11$ [2.021]	-464.79062
$\text{AlF}_3(\text{C}_{3v})$	$r(\text{Al-F}) = 1.63$ [1.63]	-537.52327
$\text{Li}_2\text{AlF}_3\text{O}(\text{C}_{3v})$	$r(\text{Al-F}) = 1.74$, $r(\text{Al-Li}) = 2.25$ $r(\text{Al-O}) = 1.65$, $r(\text{Al-Li}') = 3.24$ $\theta = 127$	-627.02952
$\text{LiAlF}_4(\text{C}_{3v})$	$r(\text{Al-F}) = 1.71$, $r(\text{Al-F}') = 1.63$ $r(\text{Al-Li}) = 2.26$, $\theta = 125$	-644.04689
$\text{AlCl}_3(\text{C}_{3v})$	$r(\text{Al-Cl}) = 2.24$ [2.06]	-1612.69055
$\text{Li}_2\text{AlCl}_3\text{O}(\text{C}_{3v})$	$r(\text{Al-Cl}) = 2.31$, $r(\text{Al-Li}) = 2.76$ $r(\text{Al-O}) = 1.65$, $r(\text{Al-Li}') = 3.26$ $\theta = 121^e$	-1702.17660
$\text{LiAlCl}_4(\text{C}_{3v})$	$r(\text{Al-Cl}) = 2.28$, $r(\text{Al-Cl}') = 2.16$ $r(\text{Al-Li}) = 2.83$, $\theta = 121$	-2077.56491

^a Assumed symmetries in parentheses.

^b Bond lengths in angstroms, bond angles in degrees. Experimental values [from Ref. (21)] in square brackets.

^c 1 a.u. = 627.5 kcal mol^{-1} .

^d Ref. (20).

^e Fixed at this value.

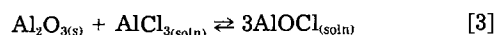
complex. In addition, the 3-21G geometries indicate that the Al-O bond is quite strong, as it has a bondlength of 1.65 Å in both complexes. The Li-O bond is apparently weakened somewhat in the complex as it lengthens by about 0.07 Å over its value in Li_2O .

The 3-21G energies for reactions [1] and [2] are -31.2 and -72.3 kcal mol^{-1} , respectively. They indicate that replacement of F or Cl by OLi is exothermic and that the reaction energy for the chloride reaction is more exothermic than that for the fluoride.

The calculational method used in this study does not include polarization functions or correlation energy. Higher level calculations on reactions involving small molecules including these factors have found that they are important in the determination of bond energies (16). However, at the present time such computations are not feasible for large molecules such as those we are considering. Hence, we have selected for this investigation only reactions in which the same number of formal type of bonds is retained on both sides of the reaction (isodesmic reaction). In an extensive study (11) of isodesmic bond separation reactions involving molecules containing first row atoms (C to F), it has been found that errors inherent in the theoretical treatment will cancel to a large extent. The mean absolute deviation between theory and experiment in that study of 21 reactions was 3.1 kcal mol^{-1} at the extended basis set level. We have carried out a limited investigation (17) of isodesmic bond separation reactions involving molecules containing Li, O, and second row atoms and have found a similar cancellation of errors to exist. Hence, the available evidence indicates that the 3-21G energies for reactions [1] and [2] should be reasonably accurate, since the reactions are isodesmic bond separation reactions. We now proceed to compare the calculated gas phase reaction energies with reaction energies in solution.

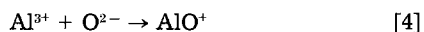
Comparisons of Calculated Energies with Measurements in Solution

The calculated energies of the two gas-phase reactions are now compared with energies deduced for the formation of Al-O bonds in molten salts. It is of particular interest to see if the large calculated difference between fluorides and chlorides is reflected in the molten salt data. Recent measurements of the solubility of Al_2O_3 in LiCl-KCl-AlCl_3 solutions at 723 K (18) are consistent with the reaction



having an equilibrium constant (in mole fraction units) of 8.0×10^{12} . (The dipolar AlO^+ ion is, of course, solvated by Cl^- and Li^+ ions.) From this value it can be shown (18) that

the equilibrium corresponding to formation of the solvated AlO^+ species in dilute solutions of Al^{3+} and O^{2-} in the LiCl-KCl eutectic



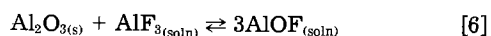
has a formation constant of 2.94×10^{22} . From a statistical mechanical expression for such formation constants (19)

$$K = Z[\exp(-\Delta A_1/RT) - 1] \quad [5]$$

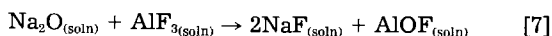
where Z is the coordination number, one can deduce the value of the specific bond free energy, ΔA_1 , for reaction [4] (18). For a coordination number of 4, ΔA_1 is -71.74 kcal mol $^{-1}$, (for $Z = 6$, it is -71.16 kcal mol $^{-1}$), a value which is remarkably close to the quantum mechanically calculated value of -72.3 kcal mol $^{-1}$ for formation of the Al-O bond in the gas-phase reaction.

Comparison of the calculated gas-phase reaction energy with the bond energy in the melt includes a number of assumptions: (i) the solvation of AlO^+ is emulated by the vapor molecules, (ii) the differences in vibrational energy are small; the zero point vibrational energy contribution to the reaction energy is not expected to be more than about 3 kcal mol $^{-1}$ (20), and (iii) the quantity ΔA_1 is a bond free energy and could contain contributions from nonconfigurational entropy. However, measurements in molten salts indicate that such nonconfigurational contributions are small for spherical ions (19). When one considers these assumptions and the uncertainties in the reaction energies themselves, a larger difference might have been expected between the calculated gas-phase value and the molten salt value. The relatively small difference may be due to fortuitous cancellation of factors. However, the results suggest the encouraging speculation that one might predict these bond free energies reasonably well from quantum mechanical calculations of vapor molecules, if isodesmic reactions are studied.

Unfortunately, experimental data for the fluorides are not complete enough to test this speculation. However, one can calculate a lower limit for the specific bond free energy of forming an Al-O bond in the NaF, AlF_3 , Al_2O_3 ternary system. One can perform this calculation using compositional data for the ternary eutectic at 881 K between Na_3AlF_6 , NaF, and $\beta\text{-Al}_2\text{O}_3$ at the composition (in mole percent) NaF-85.8, AlF_3 -13.1, and Al_2O_3 -1.1 (1). The largest uncertainty in the calculation stems from the lack of knowledge of the solution species. If one assumes that all of the oxide ions are present as AlO^+ species, then the apparent concentration of this species will be larger than it really is. As a consequence, this species will appear to be more stable, and the specific bond free energy deduced will be a lower limit, i.e., it will be more negative than a value calculated from the exact concentration of the AlO^+ species. From available information, AlO^+ is not likely to be the major species (2) and is hence less stable than is calculated here. If we assume that essentially all the oxygen is present as this species and that the reaction



is the only significant mode of solubilization of Al_2O_3 , then the concentrations of the three solution components (in mole percent) are NaF-84.4, AlF_3 -12.4, and AlOF -3.2, and the logarithm (base 10) of the equilibrium quotient for reaction [6] is -3.57 . From this quantity combined with data from the JANAF tables (21) and the activity of AlF_3 in the melt (22), we deduce a lower limit for the standard free energy of formation of the AlOF component in solution, $\Delta G_{\text{AlOF}}^\circ/2.3025RT = -38.234$. Using this quantity as well as data for $\text{Na}_2\text{O}_{(l)}$, $\text{AlF}_{3(s)}$, (21), and for the activity coefficients for AlF_3 (22), and if we also make the reasonable assumption that $\text{Na}_2\text{O}_{(l)}$ forms an essentially ideal solution with NaF, one can deduce that the upper limit to the equilibrium constant for the reaction



is 1.236×10^9 . This is also an upper limit for the formation constant of AlO^+ . From this, we calculate a lower limit to

the specific bond free energy using Eq. [5]. For $Z = 4$, $\Delta A_1 = -44.8$ kcal mol $^{-1}$ (for $Z = 6$, $\Delta A_1 = -43.9$ kcal mol $^{-1}$). This energy is expected to be somewhat more negative in a sodium salt melt than in a lithium containing melt (4, 6). The quantum mechanically calculated energy of -31.2 kcal mol $^{-1}$ is consistent with this lower limit. (A specific bond free energy of -31.2 kcal mol $^{-1}$ is consistent with a concentration of AlO^+ species, which is a factor of 380 lower than we used in the calculation.) In any case, it can be seen that as is calculated quantum mechanically, the Al-O bond in chlorides is relatively much more stable than that in fluorides. As an added indication of the strength of Al-O bonds in the fluoride vapor species, the Al-O bond length is much shorter than that of Al-F. The Al-O bond length is 1.65Å in the $\text{Li}_2\text{AlF}_5\text{O}$ species; whereas, the Al-F bond length is 1.74Å in the same species and 1.71Å in LiAlF_4 . This occurs despite the fact that the Pauling radius of O^{2-} is 0.04Å larger than that of isoelectronic F^- .

Discussion

The concept of coulomb complexing has been proposed as a means of predicting what types of complexes might form between polyvalent cations and anions. In this concept, polyvalent cations should associate with polyvalent anions in alkali halide solvents to form coulomb complexes (4, 6). Without considering charge compensation due to rearrangements of solvent ions when the coulomb complex is formed and without considering quantum mechanical effects, one can make predictions of the energetics of such associations based on simple coulomb models. Such predictions cannot be expected to be accurate, although they do lead to the correct prediction that coulomb complexing leads to stronger Al-O bonds in chlorides than in fluorides and that the Al-O bond is stronger than the Al-S bond. In order to try to make this model more quantitative, one should compare quantum mechanical results such as ours with a variety of coulomb models in order to see what properties coulomb models would need in order to be useful. We performed calculations on a very simple coulomb model in which pairs of ions interact with a coulomb potential and a soft repulsion of the form r^{-9} ($u_{ij} = Z_i Z_j e^2 / r_{ij} + A/r_{ij}^9$, where r_{ij} is the distance between the i th and j th ion, and u_{ij} is a pair potential between them). We chose the distances deduced from our quantum mechanical results and calculated a coulomb energy change for reaction [1] of -86.4 kcal mol $^{-1}$. Obviously, the coulomb model is too simple and needs modification. There are many ways to accomplish this. For example, softening the $\text{Al}^{3+} - \text{O}^{2-}$ repulsion by use of a $r^{-3.5}$ repulsion rather than a r^{-9} repulsion would make up the difference. However, because other possible modifications to the pair potential could also accomplish this, careful examination is needed in order to test the utility of the potentials which might make the concept of coulomb complexing a useful predictive tool.

Conclusions

Quantum mechanical calculations of the energies of formation of Al-O bonds in carefully chosen vapor molecules are strikingly similar to bond free energies in a chloride melt and consistent with data in a fluoride melt. Quantum mechanical calculations of well-chosen vapor molecules may be valuable for studying the energetics of bond formation in molten salts. Comparison of the quantum mechanical calculations with a very simple coulomb model supports our expectation that such models (although able to predict the relative effects of different solvents or of different ligands complexing Al^{3+}) cannot provide reasonably accurate predictions of the energetics without further development. More sophisticated coulomb pair potentials are needed to improve the utility of such models.

Acknowledgment

This work was performed under the auspices of the Materials Science Division, Office of Basic Energy Sciences, U.S. Department of Energy.

Manuscript submitted Feb. 23, 1984; revised manuscript received May 16, 1984.

Argonne National Laboratory assisted in meeting the publication costs of this article.

REFERENCES

1. K. Grjotheim *et al.*, "Aluminium Electrolysis," pp. 103-106, Aluminium Verlag GmbH; Duesseldorf, Germany (1977).
2. S. H. K. Ratkje, Dissertation; The University of Trondheim, Norway (1974).
3. B. Gilbert, G. Mamantov, and G. Begun, *Inorg. Nucl. Chem. Lett.*, **12**, 415 (1976).
4. Z. Nagy, J. L. Settle, J. Padova, and M. Blander; *This Journal*, **129**, 2034 (1982).
5. R. W. Berg, S. von Winbush, and J. J. Bjerrum, *Inorg. Chem.*, **19**, 2688 (1980).
6. M. Blander and Z. Nagy, *Z. Naturforsch., Teil A*, **38**, 116 (1983).
7. K. A. Paulsen and R. A. Osteryoung, *J. Am. Chem. Soc.*, **98**, 6866 (1976).
8. J. Robinson, B. Gilbert, and R. A. Osteryoung, *Inorg. Chem.*, **16**, 3040 (1977).
9. B. Gilbert and R. A. Osteryoung, *J. Am. Chem. Soc.*, **100**, 2725 (1978).
10. R. A. Osteryoung, in "Molten Salts," J. P. Pemsler, J. Braunstein, K. Nobe, D. R. Morris, and N. E. Richards, Editors, p. 240, The Electrochemical Society Softbound Proceedings Series, Princeton, NJ (1976).
11. R. Ditchfield, W. J. Hehre, J. A. Pople, and L. Radom, *Chem. Phys. Lett.*, **5**, 13 (1970).
12. L. Radom, W. J. Hehre, and J. A. Pople, *J. Am. Chem. Soc.*, **93**, 289 (1971).
13. P. N. van Kampen, G. F. Smits, F. A. M. de Leeuw, and C. Altona, Quantum Chemistry Program Exchange, Indiana University, Program no. 437.
14. J. S. Binkley, J. A. Pople, and W. J. Hehre, *J. Am. Chem. Soc.*, **102**, 939 (1980); M. S. Gordon, J. S. Binkley, J. A. Pople, W. J. Pietro, and W. J. Hehre, *ibid.*, **104**, 2797 (1982).
15. L. A. Curtiss, *Chem. Phys. Lett.*, **68**, 225 (1979).
16. J. A. Pople, J. M. Frisch, B. T. Luke, and J. S. Binkley, *Int. J. Quantum Chem.*, **S17**, 307 (1983); J. S. Binkley and M. J. Frisch, *ibid.*, **S17**, 331 (1983).
17. L. A. Curtiss, Unpublished work.
18. C. Wai and M. Blander, *Z. Naturforschung*, **39a**, 499 (1984).
19. M. Blander, in "Molten Salt Chemistry," M. Blander, Editor, John Wiley and Sons, New York (1964).
20. K. Raghavachari, *J. Chem. Phys.*, **76**, 5421 (1982).
21. D. R. Stull and H. Prophet, Editors, "JANAF Thermochemical Tables," 2nd ed., NSRDS-NBS37, Washington, DC (1971).
22. E. W. Dewing, *Metal. Trans. B*, **3**, 495 (1972).

Electrochemical Intercalation of Lithium into Transition Metal Compounds in Low Temperature Chloroaluminate Melts

Jacques Devynck,* Richard Messina, José Pingarron, and Bernard Trémillon*

Laboratoire d'Electrochimie Analytique et Appliquée, (Laboratoire associé au CNRS n° 216), ENSCP, 75231 Paris Cedex 05, France

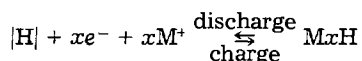
Luc Trichet

Laboratoire de Chimie des Solides, (Laboratoire associé au CNRS n° 279), Faculté des Sciences, 44072 Nantes Cedex, France

ABSTRACT

Investigation of the electrochemical intercalation of lithium into several high oxidation-state transition metal compounds (V_2O_5 , V_2O_3 , V_2O_4 , and TiS_2) has been undertaken in low temperature chloroaluminate melts: $AlCl_3$ -butyl pyridinium chloride-LiCl at 60°C and $AlCl_3$ -LiCl at 175°C. The reversibility of the different steps of intercalation and deintercalation has been examined. Cycling tests have shown a good stability and capacity of V_2O_5 and TiS_2 in these molten salt media.

Transition-metal sulfides like TiS_2 , NbS_2 , TaS_2 , etc., and oxides of high oxidation state (V_2O_5 , MoO_3 , CrO_3 , V_6O_{13}) which insert alkali ions during their reduction appear to be among the most promising cathode materials in rechargeable lithium batteries (1-3). Insertion of Li^+ ion in these materials has been widely investigated in recent years. The general intercalation-deintercalation reaction in a cathodic material can be presented as follows (4)



where $[H]$ is the host structure which inserts M^+ at a variable mole ratio (concentration) x , up to a maximum value x_{max} . The reversibility of this reaction seems to be linked to the existence of only a single solid phase. This reversibility has been demonstrated in many organic solvents such as propylene carbonate (6-8), 1,2-dimethoxyethane-propylene carbonate (80%-20% PC by volume) (5), methylacetate (8), N-N-dimethylformamide (9, 10), 1,2-dimethoxyethane (9, 10), and 2-methyltetrahydrofuran (9, 10).

The compatibility between lithium metal and the organic solvent appears to be the main impediment to the

development of Li/transition metal oxide or sulfide reversible batteries. A good solution would be to use a nonorganic electrolyte. Molten salts appear to be good candidates as electrolytes for these batteries (11-14).

$LiCl$ - KCl melts have been used with $LiAl$ and $LiSi$ alloys (15-17) at operating conditions where the number of charge-discharge cycles exceeds 500 (18). $NaAlCl_4$ at 165°C also seems to be compatible with these anodic materials (19).

Molten chloroaluminates present a large liquid temperature range, and mixtures of the $AlCl_3$ - RCl type, where R is an organic cation like butylpyridinium, are liquid at ambient temperature. These media, which combine the advantages of molten salts with those of relatively low temperature, have been widely studied during recent years, particularly by Osteryoung *et al.* (21, 22).

A major problem in the utilization of these electrolytes is the compatibility of the organic cation R^+ and a strongly reducing agent like Li or $LiAl$ alloy. A solution to this problem is the use of another ternary eutectic like $AlCl_3$ - $NaCl$ - $LiCl$ or $AlCl_3$ - $NaCl$ - KCl , but these mixtures are not liquid below 80°C (23, 24).

Whatever the anodic system, the most important condition for battery electrolyte utilization is that the cathodic materials must be insoluble in the electrolyte to avoid

*Electrochemical Society Active Member.

self-discharge. This condition limits the choice of convenient molten salt electrolytes in which the solubility of certain oxides has to be taken into account. There is very little in the literature concerning this point.

In this paper, we present the first results of an electrochemical study of lithium intercalation into several materials using low-temperature chloroaluminates as electrolytes.

Experimental

Solvents.—The melts used were the following: a ternary mixture N-n-butylpyridinium chloride (31.2 mole percent [m/o]), aluminum chloride (55.5 m/o), LiCl (13.3 m/o) at 60°C, and the mixture LiCl-AlCl₃ (49.25 m/o AlCl₃, *i.e.*, LiCl saturated LiAlCl₄) at 175°C.

N-n-butylpyridinium chloride (BpCl) was prepared according to the Osteryoung *et al.* procedure (25-27). AlCl₃ (Fluka AG) was purified by vacuum sublimation in the presence of pure aluminum wire. LiCl PROLABO (France) was dried according to the following procedure: (i) the LiCl was maintained overnight at 180°C, and then for 2h at 250°C under vacuum, (ii) Pure HCl (COOP LABO) was bubbled for 3h at 250°C, (iii) argon was bubbled for 2h at 250°C, (iv) LiCl was kept under vacuum for 3h at 250°C. All products dried and purified as above were kept in an argon-filled glove box (with less than 6 ppm of water inside).

The preparation of the ternary mixture BpCl-AlCl₃-LiCl was carried out as follows: the corresponding quantity of BpCl was slowly added to the stoichiometric quantity of AlCl₃. Once the mixture was molten, LiCl was added to obtain the expected concentration.

The preparation of LiCl (saturated)-LiAlCl₄ was done by weighing appropriate quantities of LiCl and AlCl₃, and introducing the mixture in a bulb in presence of pure aluminum wire. The bulb was sealed under vacuum and held at 240°C for 8h. After the melting of the mixture, the bulb was taken out of the furnace and the melt separated from the aluminum wire. The molten salt was allowed to crystallize slowly in the bulb and afterwards kept in an anhydrous argon-filled glove box. All weighings were carried out in the argon-filled glove box.

Products.—Oxides were Alfa-Ventron products. They were used without further purification and stored in a dry atmosphere.

The graphite for the working electrodes was supplied by Koch-Light (purity: 99.99%).

After some preliminary work with commercially supplied TiS₂ (Ventron), it was found that the material was not sufficiently pure, and, therefore, this compound was prepared and purified as follows.

TiS₂ was prepared by direct synthesis from the elements [Koch-Light titanium sponge (99.9%) and sulfur powder 99.99%]. 1% excess sulfur was used. The tube was placed in the oven in order to create a slight temperature gradient. The temperature was progressively increased from 200° to 550°C. On cooling, the excess sulfur gives a small amount of TiS₃ at the lower temperature end. The disulfide obtained by this method under a small sulfur pressure has the TiS_{1.988} stoichiometry determined by calcination.

The working electrode consisted of a platinum grid of 1 cm diam with a finely powdered mixture of the cathodic active materials and graphite (50% by weight). 10-16 mg of this mixture were pressed under 5 ton/cm² for 5 min over platinum grid. These electrodes were dried and sintered under vacuum at 220°C for 3h, then kept in an inert atmosphere of argon.

Important fluctuations in the results are observed when the content of the active material was higher than 50%, probably due to a bad contact between the graphite and electrode active material. Similar results were obtained by Tranchant and Messina (5, 6).

Aluminum wires were used as the reference and the auxiliary electrodes.

Experimental technique.—Experiments were performed using 25 ml of electrolyte and a three-electrode galvanostatic device permitting the control of the current during the determination of discharge-charge curves (potentiostat Tacussel PRT 10-0.05 L).

The electrode potential values were measured with a Tacussel Minisis 6000 millivoltmeter connected to a Tacussel EPL 1 potentiometric register.

All the experiments were carried out under argon in a dry glove box.

Voltage range.—It was determined by cyclic voltammetry that the available voltage range of the AlCl₃-BpCl-LiCl mixture, at 60°C, at a graphite disk microelectrode, lies between -0.03 and 2.0V with respect to the aluminum reference electrode (in the same medium). The potential range in LiAlCl₄ at 175°C is nearly the same (0.0-1.9V).

The galvanostatic curves without active material (*i.e.*, with only graphite in the electrode), recorded under identical operating conditions as those employed for discharge-charge voltage curves at constant current, have shown that no reduction or oxidation occurs in these voltage windows, either in BpCl-AlCl₃-LiCl at 60°C or in LiCl-saturated LiAlCl₄ at 175°C.

Results and Discussion

V₂O₅ in BpCl (31.2)-LiCl (13.3)-AlCl₃ (55.5 m/o).—The reduction of V₂O₅ with insertion of Li⁺ ion (that is, the electrochemical intercalation of lithium ion into V₂O₅) in BpCl-AlCl₃ + LiCl has been studied by voltammetry and by galvanostatic discharge-charge experiments.

The discharge curves of electrodes made of 50% graphite-50% V₂O₅, at various current densities and at 60°C, are reported in Fig. 1. Curve 4 shows that the reduction process implies the Li⁺ insertion: an electrode polarization appears at the beginning of the discharge when no Li⁺ ions are present in solution.

At low current densities (0.1 mA cm⁻²), the reduction proceeds in three steps. The first one begins at a potential value of about 1.2V (*vs.* Al) and needs about 1 F/mol of V₂O₅. At the end of this process, the oxidation state of vanadium is about 4.5. The second reduction process, which occurs at 0.3V, shows a large voltage plateau. It needs also 1 F/mol of V₂O₅. The last step appears at approximately 0.05V with another voltage plateau. At the end of this process, the mean oxidation state of vanadium is around 3.75.

The same three reduction steps were observed at a higher current density (0.5 mA cm⁻²). These results are in good agreement with previously reported results dealing with the electrochemical reduction of this oxide in organic solvent at ambient temperature.

The reversibility of the different processes has been studied by successive discharge-charge cycles at 0.5 mA cm⁻² for different discharge voltage cutoffs.

Figure 2a shows the results when the discharge was performed on the largest potential range (between 1.90

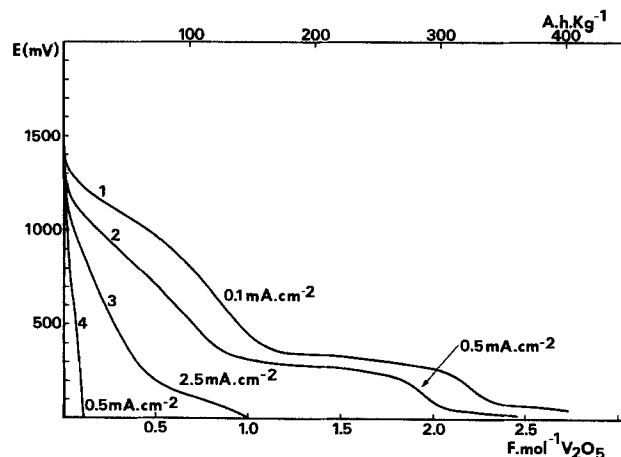


Fig. 1. V₂O₅ galvanostatic discharge at different current densities in BpCl (31.2)-LiCl(13.3)-AlCl₃(55.5 m/o) at 60°C (curves 1, 2, and 3) and in BpCl (45.5)-AlCl₃(55.5 m/o) (curve 4).

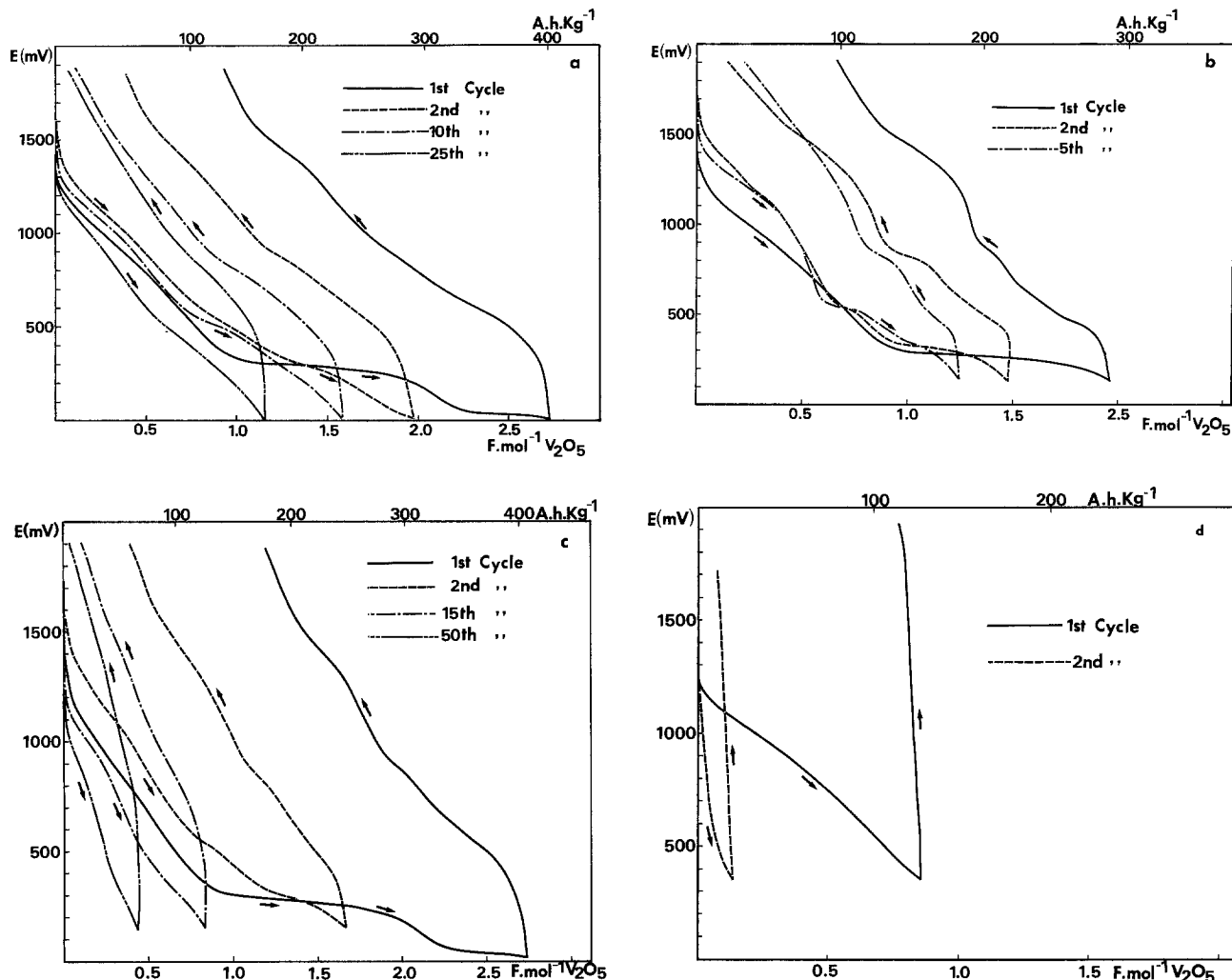


Fig. 2. Discharge-charge cycle of V_2O_5 in $BpCl(31.2)-LiCl(13.3)-AlCl_3(55.5 \text{ m/o})$ at $60^\circ C$, 0.5 mA cm^{-2} . Voltage cutoff: (a) 0.00 V , (b) 0.15 V , (c) 0.15 V , after a first discharge at 0.00 V voltage cutoff, and (d) 0.35 V .

and 0.00 V vs. Al). Cycling transforms the material, and the first cycle appears very different from the following ones. The large voltage plateau observed during the first discharge at 0.30 and 0.05 V have almost disappeared in the second cycle and completely in the following ones. Another modification was observed after the first cycle. The first part of the curve, between 1.90 and 0.3 V was divided into two steps at around 1.3 and 0.5 V .

The yield of the second cycle is 70% - 80% of the first discharge capacity. The decrease of yield becomes smaller after the second cycle and 95% - 99% of the preceding discharge capacity was obtained.

The nature of the phenomena was not greatly changed when the discharge voltage cutoff was raised to 0.15 V (Fig. 2b). However, the different reduction steps were better developed in the cycles following the first one up to 0.15 V . The yield of the second cycle is 70% - 75% of the first discharge capacity, and the following ones are 90% - 98% of the immediately preceding discharge capacity.

The successive discharge-charge cycles in the voltage window 1.90 - 0.15 V vs. Al are shown in Fig. 2c (after carrying out the first cycle at the discharge voltage cutoff of 0.00 V). Around 80% of the faradaic capacity of the first discharge is recovered at the second one. The yield is between 90% and 96% of the preceding discharge for the 15 following cycles, and very close to 100% thereafter.

These results suggest that the reduction step at 0.05 V does not significantly affect the cycling process. On the contrary, important changes appear when the discharge voltage cutoff was fixed at 0.35 V , which is before the first large voltage plateau. Then, the total amount of Li^+

ion inserted during the first reduction could not be recovered by the subsequent recharge process (Fig. 2d).

The normal capacity of 1 F/mol was recovered only when the first cycle was complete, from 1.90 to 0.00 or 0.15 V . The yield is then 95% for the third cycle, and 97% - 100% of the capacity of the immediately preceding discharge for the following cycles (Fig. 3).

V_2O_4 and V_2O_3 in $BpCl-LiCl-AlCl_3$.—Vanadium (IV) and (III) oxides have also been investigated in $BpCl(31.2)-LiCl(13.3)-AlCl_3(55.5 \text{ m/o})$.

The electrochemical reductions of V_2O_3 and V_2O_4 at 0.5 mA cm^{-2} take place, respectively, at 0.80 and 0.95 V at higher potentials than the V_2O_5 reduction step. Conse-

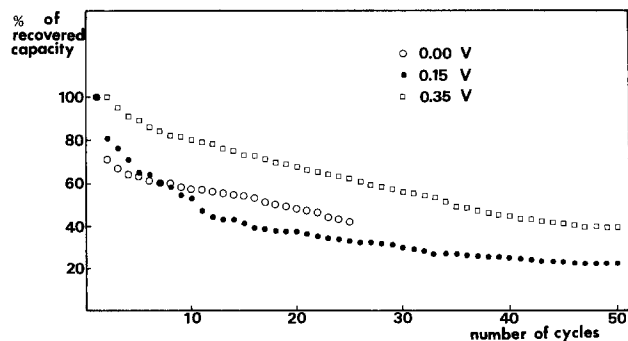


Fig. 3. Galvanostatic discharge capacity (percentage of the initial recovered capacity) of V_2O_5 as a function of the cycle number in $BpCl(31.2)-LiCl(13.3)-AlCl_3(55.5 \text{ m/o})$. $J = 0.5 \text{ mA cm}^{-2}$. $T = 60^\circ C$.

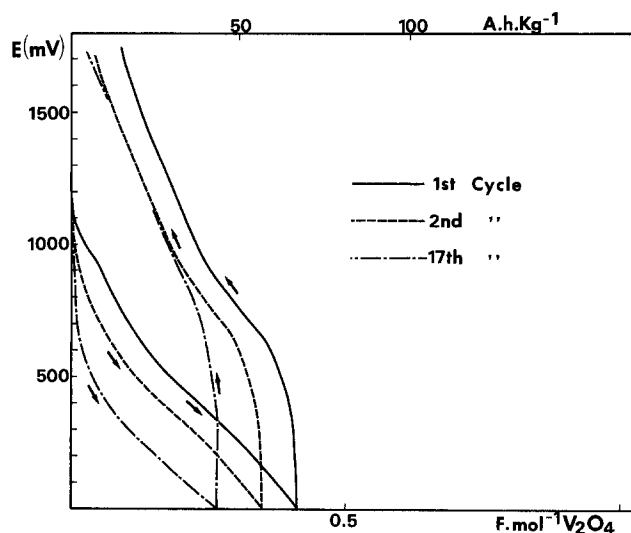


Fig. 4. V_2O_4 discharge-charge cycle at 0.5 mA cm^{-2} in $\text{BpCl}(31.2)\text{-LiCl}(13.3)\text{-AlCl}_3$ (55.5 m/o). $T = 60^\circ\text{C}$.

quently, the formation of V_2O_4 or V_2O_3 during the electrochemical reduction of V_2O_5 must be excluded.

Successive galvanostatic discharge-charge curves for V_2O_4 (Fig. 4) show that the cycling behavior of this material is reversible. The second discharge yield is 84% of the first cycle, and the following cycles recover 96%-100% of the capacity of their immediately preceding cycle. So, 77% of the faradaic capacity of the second discharge is recovered at the 17th cycle. However, this capacity is rather low, so that this material appears to be of little interest as reversible cathodic material.

In contrast, V_2O_3 behaves irreversibly, and a very small part of the initial faradaic capacity is recovered during the second cycle.

V_2O_5 in LiCl (saturated) LiAlCl_4 .—Attempts to electrochemically reduce V_2O_5 in LiCl (saturated) LiAlCl_4 at 175°C have failed because of the strong oxidizing power of V_2O_5 at this temperature. We have observed a chemical oxidation of LiAlCl_4 with chlorine evolution.

TiS_2 in $\text{BpCl}(31.2)\text{-LiCl}(13.3)\text{-AlCl}_3$ (55.5 m/o).—Electrochemical reduction of TiS_2 with Li^+ insertion was investigated in the $\text{BpCl-AlCl}_3\text{-LiCl}$ melt by voltammetry and galvanostatic reduction. Characteristic discharge curves at various current densities are represented in Fig. 5. For current densities between 0.1 and 2.5 mA cm^{-2} , the experimental curves show a horizontal plateau at 0.40 V (*vs.* Al reference electrode). The capacity is near to 1 F/mol at low current density.

As expected, the discharge curve obtained in BpCl-AlCl_3 (55.5 m/o) at 60°C , without Li^+ ions (curve 4), shows an important polarization similar to that of V_2O_5 . This confirms that the electrochemical process involves Li^+ intercalation.

Charge-discharge cycles have been performed for a current density of 0.5 mA cm^{-2} in the voltage window $1.60\text{-}0.00 \text{ V}$. Results are reported in Fig. 6. The general shape is the same for all curves. The faradaic capacity at the first discharge is about 0.86 F/mol of TiS_2 . 92%-96% yield is obtained in the second cycle, and the following discharges give between 96% and 100% yield with respect to the immediately preceding discharge. Figure 8 shows that the recovered capacity after 50 cycles is about 40% of the initial capacity. The reversibility of the process is rather good, and the aspect of the curves shows that TiS_2 behaves towards Li^+ ions in this medium in a way comparable to other (organic) media.

TiS_2 in LiCl (saturated) LiAlCl_4 .—The behavior of TiS_2 was also studied in LiAlCl_4 at 175°C , in the voltage window $1.28\text{-}0.15 \text{ V}$ (*vs.* Al). The material is stable in this medium, and at this temperature and no dissolution or chemical reaction was observed.

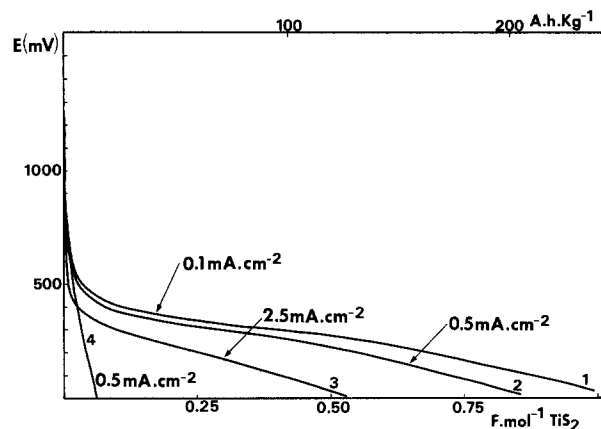


Fig. 5. TiS_2 (+ graphite 50%) galvanostatic discharge at different current densities in $\text{BpCl}(31.2)\text{-LiCl}(13.3)\text{-AlCl}_3$ (55.5 m/o) at 60°C (curves 1, 2, and 3) and without LiCl (curve 4).

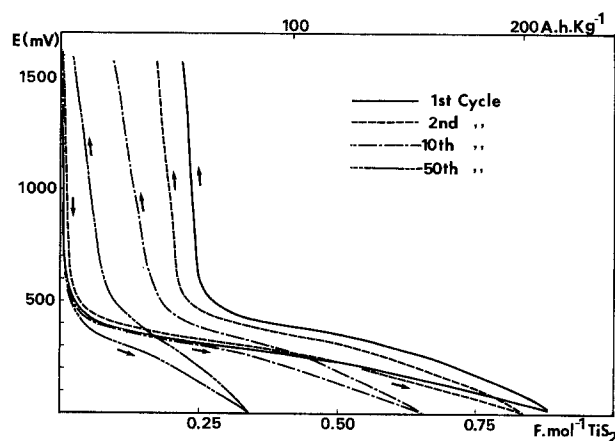


Fig. 6. Galvanostatic discharge-charge cycle of TiS_2 in $\text{BpCl}(31.2)\text{-LiCl}(13.3)\text{-AlCl}_3$ (55.5 m/o) at 0.5 mA cm^{-2} . $T = 60^\circ\text{C}$.

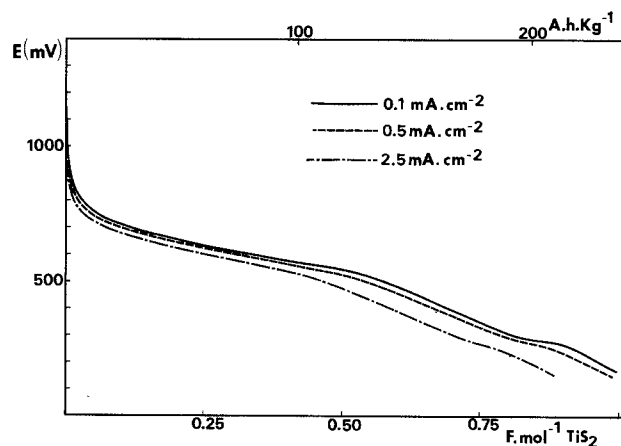


Fig. 7. TiS_2 galvanostatic discharge in LiCl (sat) + AlCl_3 at 175°C at various current densities.

The galvanostatic discharge curves of TiS_2 electrodes at various current densities are reported in Fig. 7. By comparison with the behavior of this material in an $\text{AlCl}_3\text{-BpCl-LiCl}$ mixture at 60°C , the effect of current densities is quite negligible and the faradaic capacity is the same (1 F/mol TiS_2) between 0.1 and 0.5 mA cm^{-2} . A decrease of capacity (11% smaller than in $\text{BpCl-AlCl}_3\text{-LiCl}$) is observed when the discharge is carried out at 2.5 mA cm^{-2} for the same voltage cutoff. A first voltage plateau appears at the middle-discharge voltage ($\sim 0.65 \text{ V}$), and another small plateau appears at about 0.28 V . This last one is better defined at low current densities.

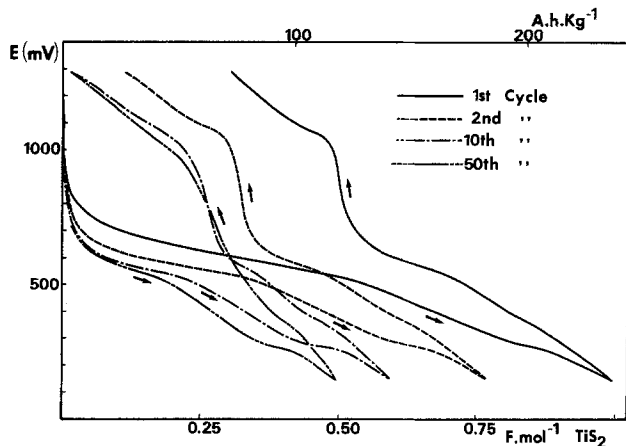


Fig. 8. Galvanostatic charge-discharge cycles of TiS_2 in LiCl (saturated) + AlCl_3 (49.5 m/o) at 0.5 mA cm^{-2} . $T = 175^\circ\text{C}$. Voltage window: 1.28-0.15V.

Discharge-charge cycles.—Discharge-charge cycle curves at 0.5 mA cm^{-2} in the voltage window 1.28-0.15V are shown in Fig. 8. The two plateaus at 0.70 and 0.28V are well defined in each cycle. The faradaic capacity is 1 F/mol^{-1} for the first discharge. It falls to about 77% in the second cycle, and then stays quite constant (between 98% and 100% of the preceding discharge) during the following ones.

A comparison between the results in $\text{BpCl}_3\text{-LiCl}$ at 60°C (Fig. 6) and in LiAlCl_4 (49.25 m/o AlCl_3) at 175°C (Fig. 8) is shown in Fig. 9. It shows that the yield is higher in the all-inorganic molten salt. As an example, the observed faradaic capacity at the fiftieth cycle is 120 Ah kg^{-1} in LiAlCl_4 and only 81 Ah kg^{-1} in $\text{BpCl-AlCl}_3\text{-LiCl}$. This comparison is illustrated by the decrease of the capacity of TiS_2 as a function of cycle number in both molten salts (Fig. 8). The capacity appears to be better in the first cycles in $\text{BpCl-AlCl}_3\text{-LiCl}$, but the higher reversibility observed in LiAlCl_4 shows that, after the 20th cycle, the faradaic capacity is higher in this medium.

The successive cycles of TiS_2 in LiAlCl_4 clearly show that the voltage plateau at around 0.27V is reversible. The shapes of the successive charge-discharge curves demonstrate that the voltage plateau at 0.27V has no influence on the earlier reduction step or on the subsequent recharge. Recovered capacity during the second discharge is 81% of the first. This means that the greatest part of the observed capacity loss during the second cycle is due to a relatively small irreversible process in the discharge. After the fifth cycle, the irreversible process appears to be insignificant and the recovered capacity at twentieth discharge is still 92% of the fifth cycle and 83% of the second one.

Conclusion

Experimental results show that, in spite of the strong ability of chloroaluminates to dissolve oxides and sulfur compounds, V_2O_5 and TiS_2 are stable enough to be used as cathodic materials in these molten salts. A chemical oxidation of chloroaluminate by the cathodic material was observed in only one case: V_2O_5 in LiCl-AlCl_3 at 175°C . Chemical oxidation at ambient temperatures has not been observed under the experimental conditions.

Whatever the cathodic material is, the reduction process with Li^+ insertion seems to occur the same in molten chloroaluminates as in organic electrolytes (5-10) or in LiCl-KCl (15-19). As has been reported, a complete initial reduction is always necessary in order to obtain good reversibility of the charge-discharge cycle.

In the case of V_2O_5 at low current density, the Li^+ insertion proceeds in four steps like in an organic solvent. These steps correspond to the following stoichiometry (reference: Al electrode)

- | | |
|--|--|
| (1) $\text{V}_2\text{O}_5\text{Li}_{0.25} \approx 1.3\text{V}$ | (3) $\text{V}_2\text{O}_5\text{Li} \approx 0.35\text{V}$ |
| (2) $\text{V}_2\text{O}_5\text{Li}_{0.5} \approx 1.0\text{V}$ | (4) $\text{V}_2\text{O}_5\text{Li}_3 \approx 0.10\text{V}$ |

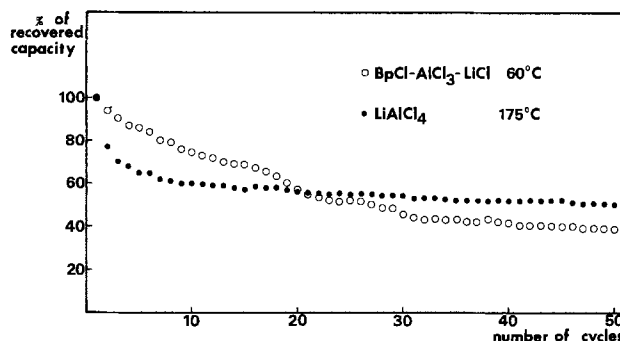


Fig. 9. Comparison of the galvanostatic discharge (as percentage of the initial recovered capacity) of TiS_2 in $\text{BpCl} + \text{LiCl}$ at 60°C and in LiAlCl_4 at 175°C . Current density: 0.5 mA cm^{-2} .

The maximum capacity is about 2.5 Li^+ per V_2O_5 unit.

Curves in Fig. 2 show that the modification of the crystal lattice which is necessary for the reversibility occurs at + 0.30V.

The decrease of the capacity with successive charge-discharge cycles becomes very small at high cycle numbers.

While it is still necessary to limit this decrease, V_2O_5 appears to be a good cathodic material in molten chloroaluminates at a temperature not far from the ambient.

As has been previously observed, the reversible insertion of Li^+ during the TiS_2 reduction is rigorously dependent on the quality of TiS_2 . With titanium sulfide prepared as described, the insertion process in both chloroaluminate melts (BpCl-LiCl-AlCl_3 and LiCl-AlCl_3) gives the same results as in organic media or in LiCl-KCl at 450°C . The capacity is about $1 \text{ Li}^+/\text{TiS}_2$.

Nevertheless, the best reproducibility is obtained in LiAlCl_4 at 175°C ; in this electrolyte, the loss of capacity during the successive cycles is lower than in the presence of BpCl . The Li^+ capacity is less dependent on the current density because of the combined effect of temperature increase and viscosity decrease.

Work is in progress to increase the yield of Li^+ cycling and to find anodic lithium compounds compatible with the cathodic lithium insertion compounds.

Acknowledgment

The financial support of the M.R.I. (Decision no. 82F0120) is gratefully acknowledged.

Manuscript submitted Nov. 16, 1983; revised manuscript received Feb. 13, 1984.

REFERENCES

- M. S. Whittingham, *Science*, **192**, 1126 (1976).
- M. S. Whittingham, *Prog. Solid State Chem.*, **12**, 41 (1978).
- D. W. Murphy and P. A. Christian, *Science*, **205**, 651 (1979).
- M. Armand, Thesis de doctorate d'Etat, Université de Grenoble, Grenoble, France (1978).
- A. Tranchant, R. Messina, and J. Perichon, *J. Electroanal. Chem.*, **113**, 225 (1980).
- A. Tranchant, Thesis 3d cycle, Université Pierre et Marie Curie, Paris (1980).
- D. W. Murphy, P. A. Christian, F. J. DiSalvo, and J. N. Carides, *This Journal*, **126**, 497 (1979).
- G. L. Holleck and J. R. Driscoll, *Electrochim. Acta*, **22**, 647 (1977).
- A. J. Vaccaro, T. Palanisamy, R. L. Kerr, and J. T. Maloy, *This Journal*, **129**, 677 (1982).
- A. J. Vaccaro, T. Palanisamy, R. L. Kerr, and J. T. Maloy, in "Proceeding of the 29th Power Sources Conference," Atlantic City, NJ, June 9-12, 1980, The Electrochemical Society, Inc., p. 215 (1982).
- E. J. Cairns, in "Materials for Advanced Batteries," D. W. Murphy, J. Broadhead, and B. C. H. Steele, Editors, p. 3, Plenum Press, New York (1980).
- G. Mamantov, in "Materials for Advanced Batteries," D. W. Murphy, J. Broadhead, and B. C. H. Steele, Editors, p. 11, Plenum Press, New York (1980).
- J. C. Nardi, J. K. Erbacher, C. L. Hussey, and L. A. King, *J. Power Sources*, **3**, 81 (1978).
- G. Mamantov, "Studies of High Energy Cathodes and

- Anodes for Molten Salts Batteries," DOE Report ORO 5053-12 (1979).
15. Y. M. F. Marikar and D. Inman, Abstract 153, p. 397, The Electrochemical Society Extended Abstracts, Vol. 79-2, Los Angeles, California, Oct. 14-19, 1979.
 16. M. Gauthier, G. Vassort, A. Belanger, and W. A. Adams, *This Journal*, **129**, 970 (1982).
 17. Z. Tomczuk, K. E. Anderson, D. R. Vissers, and M. F. Roche, *ibid.*, **127**, 1881 (1980).
 18. L. Redey and D. R. Vissers, in "Materials for Advanced Batteries," D. W. Murphy, J. Broadhead, and B. C. H. Steele, Editors, Plenum Press, New York (1980).
 19. K. M. Abraham, M. W. Rupich, and L. Pitts, *This Journal*, **128**, 2700 (1981).
 20. R. A. Carpio and L. A. King, *ibid.*, **128**, 1510 (1981).
 21. J. Robinson and R. A. Osteryoung, *ibid.*, **127**, 122 (1980).
 22. R. J. Gall, B. Gilbert, and R. A. Osteryoung, *J. Am. Chem. Soc.*, **101**, 2723 (1979).
 23. E. M. Levin, J. F. Kinney, R. D. Wells, and J. T. Benedict, *Res. Natl. Bur. Stand.*, **78A**, 505 (1974).
 24. F. Seon, Thèse de Doctorat d'Etat, Université Pierre et Marie Curie, Paris (1981).

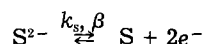
The Anodic Reaction of Sulfide Ions at Graphite Electrodes in Molten Cryolite

Nguyen Quang Minh* and Neng-Ping Yao*

Argonne National Laboratory, Chemical Technology Division, Argonne, Illinois 60439

ABSTRACT

The anodic reaction of sulfide ions at graphite electrodes in molten cryolite has been studied by cyclic voltammetry at 1323 K. The anodic reaction is found to proceed via a quasi-reversible mechanism, *i.e.*, one in which the current is controlled by both diffusion and charge transfer kinetics



The transfer coefficient β and the standard rate constant k_s are estimated to be 0.5 and 4.2×10^{-3} cm/s, respectively. The apparent diffusion coefficient for sulfide ions in cryolite at 1323 K is about 3.93×10^{-5} cm²/s.

Since the early work of Delarue (1, 2) on the anodic oxidation of sulfide ions in molten salts, many investigations and reviews (3-5) have been published on the subject. However, several important questions about the mechanism of the electrochemical reaction and the sulfide species present remain unanswered.

From the fundamental viewpoint, the electrochemical reaction of sulfide ions in molten salts offers an area of challenging research. The mechanism of the reaction is still controversial and cannot be interpreted in an unambiguous manner. It is also of technological interest since metal sulfides have been proposed as cathode materials in molten-salt batteries (6) and the extraction of metals by molten-salt electrolysis of sulfides (electrowinning) has long been of commercial interest and the subject of many investigations (5). Except for some electrochemical studies of the sulfide reaction at very high temperatures (1623-1823 K) in slags (as applied to electroslag remelting of metals) (7-11), most of the investigations on sulfide in melts were carried out in chlorides and in the temperature range 700-850 K. Recently, the present authors have investigated the anodic oxidation of sulfide in both molten chlorides and fluorides (12-14) at a temperature of 1023 K. These studies were carried out as part of the experimental work on the molten-salt electrolysis of Al_2S_3 for the production of aluminum. For MgCl_2 - NaCl - KCl eutectic (12) and AlCl_3 - MgCl_2 - NaCl - KCl melts (13), it has been found that the oxidation of sulfide proceeds via a mechanism based on two steps: $\text{S}^{2-} \rightleftharpoons \text{S} + 2e^-$ followed by $\text{S} + \text{S} \rightleftharpoons \text{S}_2$. The electrochemical reaction is diffusion controlled and reversible. The dimerization is very fast and very much displaced towards S_2 . However, the detailed analysis of the voltammetric results in LiF - NaF eutectic (14) suggests the following mechanism for the anodic oxidation of sulfide ions at 1023 K: $2\text{S}^{2-} \rightleftharpoons \text{S}_2^{2-} + 2e^-$. Since cryolite (Na_3AlF_6) was used as an electrolyte component in previous work (15, 16) on the electrolysis of Al_2S_3 , it is interesting to know how sulfide behaves electrochemically in this system. In the present work, the anodic reaction of sulfide was studied in cryolite at 1323

K using the technique of cyclic voltammetry. The experimental results obtained from the study are presented in this paper.

Experimental

The electrochemical cell for the voltammetric measurements consisted of three electrodes inserted into a pyrolytic boron nitride crucible (5.2 cm diam, 7.2 cm high, Union Carbide) containing molten cryolite (from NaF , ultrapure, Alfa Ventron, and AlF_3 , 99.9% pure, Pennwalt). The boron nitride crucible was dipped into alumina granules held in a stainless steel crucible. The steel crucible was placed inside a furnace tube. The top of the furnace tube was sealed to another flange consisting of inlet ports which provided access to the melt. The upper part of the furnace tube was cooled by water flowing through a soldered-on coil of copper tubing. The furnace tube was heated by a three-zone Mellen high temperature furnace (Model C-2-121) with Mellen temperature controller (Model 919).

A three-electrode system was used for all measurements. The working electrode was a graphite rod (0.63 cm diam, Union Carbide, grade ECV) insulated with hot-pressed boron nitride (Carborundum) so that only a defined surface area was exposed to the molten salt. Another graphite rod immersed in the melt served as the counterelectrode. A Pt wire immersed in the melt was used as a quasi-reference electrode.

The molten salt was prepared from accurately weighed and blended mixtures of cryolite and Al_2S_3 reagent (Cerac Pure) inside a helium atmosphere glove box (Vacuum Atmosphere). The mixture was then charged into the boron nitride crucible, brought out of the glove box, and the cell was quickly assembled under argon. Experiments were started by heating the cell assembly to the experiment temperature of 1323 K. The electrodes were then slowly lowered into the molten salt. An argon atmosphere was maintained above the cell in all experiments. The cell temperature was monitored with a Chromel/Alumel thermocouple. The tip of the thermocouple was placed adjacent to the wall of the boron nitride crucible.

*Electrochemical Society Active Member.

Standard cyclic voltammetric instrumentation was employed. A universal programmer (PAR Model 175) was used to provide an external control voltage for a potentiostat (PAR Model 173) which was connected to the cell. Voltammograms were recorded with an X-Y recorder (Hewlett-Packard Model 7044A).

Results and Discussion

To provide background information, voltammetry of pure cryolite was carried out. A typical voltammogram of the melt with a graphite working electrode at 1323 K is shown in Fig. 1. The voltammetric curves obtained with the graphite working electrode in this study resemble those reported previously in the literature for molten cryolite (17-20) and sodium fluoride (21). The steeply rising cathodic current observed at about -0.5V (all potentials given vs. Pt quasi-reference electrode) can be attributed to aluminum deposition (22). An anodic peak was observed at approximately $+2.5\text{V}$. This anodic peak current represents the critical current density. In general, when a graphite or carbon anode in a molten salt is subjected to a gradually increasing anode potential, the current will eventually reach a maximum, the so-called critical current density, and then decrease abruptly to a low value, which signals the beginning of the anode effect. (The anode effect can be described as a blockage effect which greatly inhibits the current transport between the anode and the melt due to dewetting of the anode by fluorocarbon compounds. Under potentiostatic conditions, it manifests itself by an abrupt decrease in cell current.) It has been suggested that the anodic maximum which leads to the onset of the anode effect corresponds to the electrochemical formation of fluorocarbon compounds, $(\text{CF}_x)_m$, with CF_4 being the predominant species (18-20).

The background current of the molten cryolite in the potential range $+0.6$ to -0.2V is shown in Fig. 2. Within this potential range, the background current is quite small. Voltammograms of the cryolite melt containing Al_2S_3 show two additional peaks associated with the behavior of sulfide ions: a peak representing the anodic oxidation of sulfide, and, on the reverse scan, one repre-

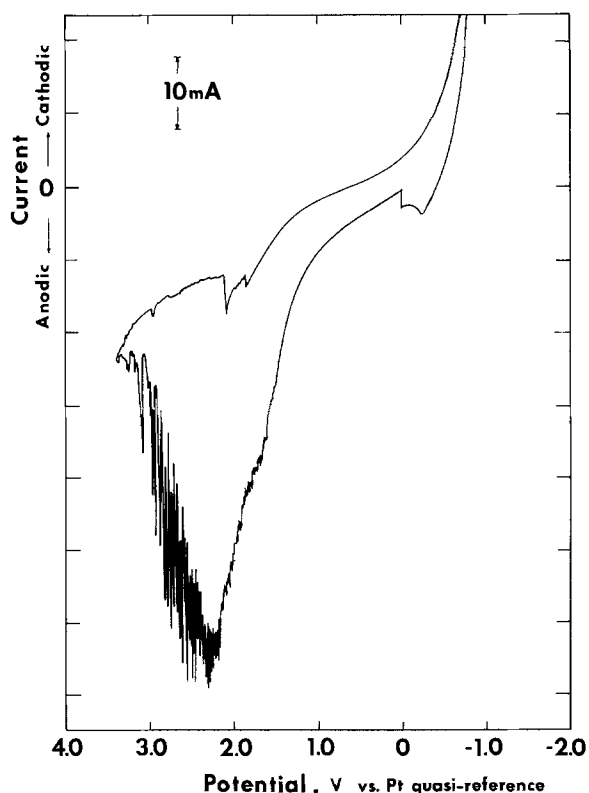


Fig. 1. Voltammogram of molten cryolite. T : 1323 K. Electrode area: 0.32 cm^2 . v : 100 mV/s .

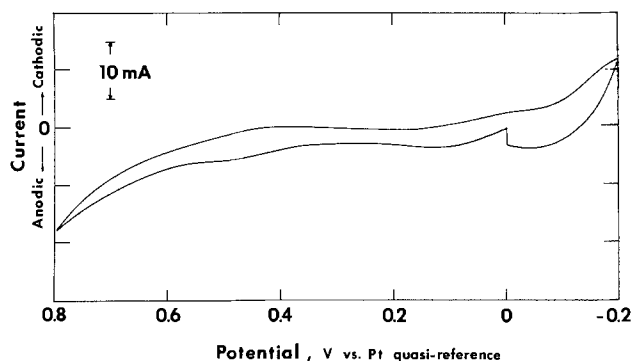


Fig. 2. Background current of molten cryolite in the potential range $+0.6$ to -0.2V . T : 1323 K. Electrode area: 0.32 cm^2 . v : 100 mV/s .

sented the cathodic reduction of its products. Typical voltammograms for sulfide ions are shown in Fig. 3. It can be seen from the figure that the peak potential for the sulfide oxidation shifts anodically with increasing potential sweep. Peak currents, i_p , at different sweep rates were measured and plotted against the square root of the sweep rate, $v^{1/2}$. Plots of i_p vs. $v^{1/2}$ are straight lines, as shown in Fig. 4, for two different Al_2S_3 concentrations. The separations between the anodic peak potential and the cathodic peak potential, $|E_p^a - E_p^c|$, at different sweep rates (uncorrected for ohmic drops) are presented in Table I. Potential separation values corrected for ohmic drops are also shown in Table I. In the present study, because the i_p values are large, it is necessary to correct the potential separations for the ohmic drops caused by uncompensated resistance R_u . This is to ensure that the effect of R_u on the peak separation is eliminated. (Since the ohmic drop at peak potential is approximately $i_p R_u$, each potential separation is corrected for $2i_p R_u$. For this cell, R_u was measured to be about 0.25Ω .) It can be seen from Table I that the separation increases as the sweep rate increases. The above properties of the voltammograms for the oxidation of sulfide ions are in agreement with the criteria for a quasi-reversible charge transfer mechanism (23). A quasi-reversible electrochemical reaction is one in which the current is controlled by both diffusion and charge transfer kinetics. For this type of reaction mechanism, if the sweep rate is slow enough, the reaction approaches reversible behavior (24). Thus, at slow sweep rates, the anodic-to-cathodic peak separation and the peak-to-half-peak separation (ΔE_p) of a quasi-reversible reaction are independent of the sweep rate and approach $2.22 RT/nF$ or $253/n\text{ mV}$ (at 1323 K) and $1.11 RT/nF$ or $126.5/n\text{ mV}$ (at 1323 K) (25), respectively, where R is the universal gas constant, T is the temperature, n is the number of electrons involved in the electrochemical reaction

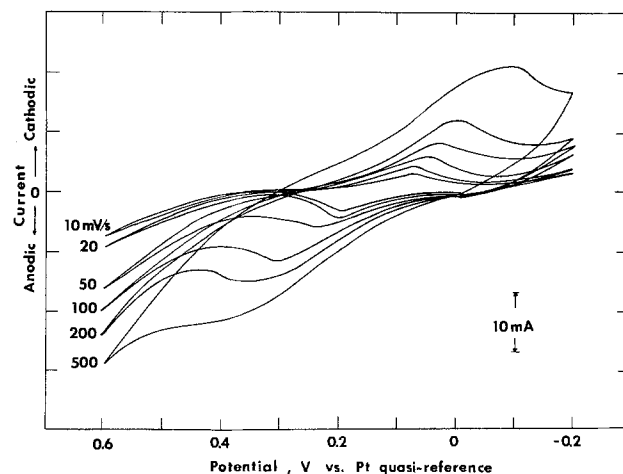


Fig. 3. Voltammograms of the oxidation of sulfide ions in molten cryolite at different sweep rates. T : 1323 K. Electrode area: 0.32 cm^2 . Al_2S_3 concentration: $1.3 \times 10^{-5}\text{ mol/cm}^3$.

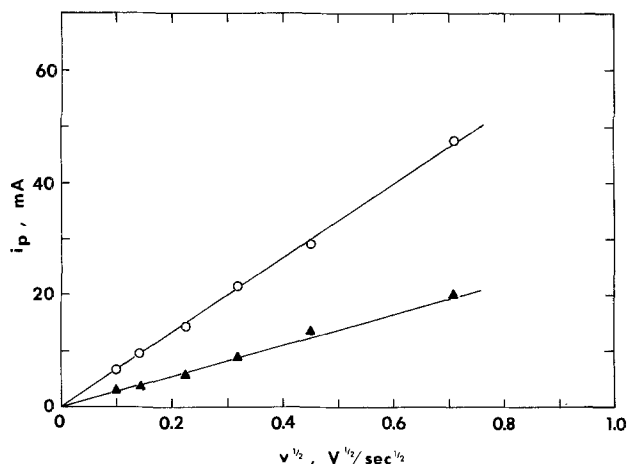


Fig. 4. Plots of i_p vs. $v^{1/2}$ for the anodic oxidation of sulfide ions in cryolite. T: 1323 K. Electrode area: 0.32 cm^2 . ▲: $1.3 \times 10^{-5} \text{ mol/cm}^3 \text{ Al}_2\text{S}_3$, ○: $3.1 \times 10^{-5} \text{ mol/cm}^3 \text{ Al}_2\text{S}_3$.

and F is the Faraday constant. It appears that at sweep rates of 10 and 20 mV/s, the voltammograms obtained for sulfide ions become reversible, and the experimental values for the potential separations (about 120-125 mV for $|E_p^a - E_p^c|$ and about 60-65 mV for ΔE_p) suggest two as the number of electrons involved in the anodic oxidation of sulfide ions.

As the reaction becomes reversible at sweep rates of 10 and 20 mV/s, the Randles-Sevcik equation applies

$$i_p = 0.446 \frac{n^{3/2} F^{3/2}}{R^{1/2} T^{1/2}} A_s D^{1/2} C^0 v^{1/2} \quad [1]$$

where A_s is the electrode area, D is the diffusion coefficient, and C^0 is the concentration of the electroactive species. The diffusion coefficient of sulfide ions can be estimated from i_p at 10 and 20 mV/s using Eq. [1]. The concentration of the diffusing species is the apparent concentration of sulfide ions (i.e., three times the Al_2S_3 concentration). The diffusion coefficients of sulfide ions in molten cryolite at 1323 K are calculated to be $3.95 \times 10^{-5} \text{ cm}^2/\text{s}$ at $1.3 \times 10^{-5} \text{ mol/cm}^3 \text{ Al}_2\text{S}_3$, and $3.92 \times 10^{-5} \text{ cm}^2/\text{s}$ at $3.1 \times 10^{-5} \text{ mol/cm}^3 \text{ Al}_2\text{S}_3$. No data have been reported in the literature on the diffusion coefficient of sulfide ions in cryolite. However, the above calculated values are not unreasonable considering previously reported values for diffusion coefficients of solute species in molten cryolite and other fluorides (26). For example, the diffusion coefficient of Al_2O_3 (2 weight percent) in cryolite is $2.24 \times 10^{-5} \text{ cm}^2/\text{s}$ at 1320 K. In cryolite-NaF melt, the diffusion coefficient of Fe^{3+} is $1.0 \times 10^{-5} \text{ cm}^2/\text{s}$ at 1273 K. The present authors obtained an average value of $1.47 \times 10^{-5} \text{ cm}^2/\text{s}$ for the apparent diffusion coefficient of sulfide in LiF-NaF eutectic at 1023 K (14).

Thus, the voltammetric results obtained suggest a quasi-reversible mechanism for the oxidation of sulfide ions in cryolite with two as the number of electrons involved in the reaction, i.e.



where k_s is the standard heterogeneous rate constant and β is the transfer coefficient.

Table I. Potential separation data for the oxidation of sulfide ions in molten cryolite at 1323 K

v (mV/s)	Al_2S_3 concentration $1.3 \times 10^{-5} \text{ mol/cm}^3$		Al_2S_3 concentration $3.1 \times 10^{-5} \text{ mol/cm}^3$	
	$ E_p^a - E_p^c $ (mV)		$ E_p^a - E_p^c $ (mV)	
	Uncorrected*	Corrected†	Uncorrected*	Corrected†
10	125	125	130	125
20	120	120	130	125
50	190	185	190	180
100	290	285	300	290
200	370	360	360	345
500	510	500	515	490

* Uncorrected for ohmic drops.

† Corrected for ohmic drops. Note: Because the error for potential separation is ± 5 , ohmic drop corrections have been rounded off to nearest multiple of 5; correction of 1 would be considered 0, a correction of 3 would be considered 5, etc.

Table II. Standard rate constants for the oxidation of sulfide ions in cryolite calculated from potential separation data

Al_2S_3 concentration	Sweep rate	$ E_p^a - E_p^c $ (1323 K)	$n E_p^a - E_p^c $ (298 K)	ψ	k_s (cm/s)
$1.3 \times 10^{-5} \text{ mol/cm}^3$	100 mV/s	285	128.4	0.31	0.0045
	200 mV/s	360	162.2	0.19	0.0040
$3.1 \times 10^{-5} \text{ mol/cm}^3$	100 mV/s	290	130.6	0.28	0.0041
	200 mV/s	345	155.4	0.20	0.0042

The shape of the voltammogram for a quasi-reversible oxidation reaction depends on β and k_s . The ratio of anodic to cathodic peak currents is affected by β . For larger values of β , the oxidation peak is much sharper and the peak current is larger than that of the corresponding cathodic peak. The opposite is true for small values of β . For $\beta = 0.5$, the anodic-to-cathodic peak current ratio is equal to 1. The ratios of anodic-to-cathodic peak currents obtained at different sweep rates and two Al_2S_3 concentrations in this study are approximately unity, suggesting that β is 0.5. For $\beta = 0.5$, the standard heterogeneous rate constant k_s can be derived from the data (at 298 K) given by Nicholson (24), showing variation of the peak separation $|E_p^a - E_p^c|$ with the kinetic parameter ψ , where ψ is defined as

$$\psi = \frac{k_s}{\left(\frac{nFv}{RT} D^{1/2}\right)^{1/2}} \quad [3]$$

The peak potential separations for the sulfide reaction presented in Table I were converted to equivalent values at 298 K (peak potential separations are proportional to the temperature), and the corresponding ψ values were determined. It was found that only the values of peak separation at 100 and 200 mV/s could be used to estimate k_s . The value of 500 mV/s fell outside the range of the data given by Nicholson (24), and the value at 50 mV/s was in the region where ψ is very sensitive to a small change in peak separation in such a way that k_s could not be determined with any confidence. From the peak separation values at 100 and 200 mV/s and the data given by Nicholson, k_s was calculated (Table II), and an average value of about $4.2 \times 10^{-3} \text{ cm/s}$ was obtained for the standard heter-

Table III. Standard rate constants for electrochemical reactions in molten salts

Electrochemical reactions	Solvent	Temperature (K)	k_s (cm/s)	Charge transfer coefficient	Ref.
Al^{3+}/Al	NaCl-AlCl_3	1093	0.2	—	(27)
$\text{Na}_3\text{AlF}_6/\text{Al}$	NaCl-KCl	1007	8.9×10^{-4}	0.66	(28)
Pb^{2+}/Pb	LiCl-KCl	723	1×10^{-2}	0.38	(29)
Bi^{3+}/Bi	LiCl-KCl	723	9×10^{-4}	0.5	(29)
Ag/Ag^+	$\text{LiNO}_3\text{-NaNO}_3\text{-KNO}_3$	438	2×10^{-2}	0.5	(30)
$\text{CO}_3^{2-}/\text{C}, \text{O}^{2-}$	NaCl-KCl	973	6.69×10^{-3}	0.46	(31)
S^{2-}/S	Na_3AlF_6	1323	4.2×10^{-3}	0.5	This work

ogeneous rate constant for the oxidation of sulfide ions in cryolite at 1323 K. This derived value for k_s for the sulfide reaction is compared in Table III with the published data on standard rate constants for some other electrochemical reactions in molten salts.

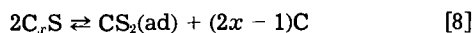
It should be noted that the use of Eq. [2] to represent the mechanism of the oxidation of sulfide ions at graphite electrodes in molten cryolite is a simplification. At the experimental temperature of the present work (1323 K), besides the formation of sulfur gas, the formation of CS_2 (32) is possible at the graphite electrode. It was not possible to determine the reaction steps for S_2 and CS_2 formation in this electrochemical study. A probable reaction scheme, however, might be



followed by



and/or



Acknowledgment

This work was performed under the auspices of the United States Department of Energy, Division of Electrochemical Energy Storage Systems. The authors would like to thank Professor G. Mamantov of the University of Tennessee for his helpful suggestions on ohmic corrections.

Manuscript submitted Nov. 14, 1983; revised manuscript received March 26, 1984. This was Paper 779 presented at the San Francisco, California, Meeting of the Society, May 8-13, 1983.

Argonne National Laboratory assisted in meeting the publication costs of this article.

REFERENCES

1. G. Delarue, *Bull. Soc. Chim. Fr.*, 906 (1960).
2. G. Delarue, *ibid.*, 1654 (1960).
3. R. P. Tischer and F. A. Ludwig, in "Advances in Electrochemistry and Electrochemical Engineering," Vol. X, H. Gerischer and C. W. Tobias, Editors, p. 391, John Wiley and Sons, New York (1977).
4. V. Plichon, A. de Guibert, and M. N. Moscard-Levelut, in "Ionic Liquids," D. Inman and D. G. Lovering, Editors, p. 387, Plenum Press, New York (1981).
5. N. Q. Minh and N. P. Yao, in "Advances in Molten Salt Chemistry," Vol. 5, G. Mamantov, Editor, p. 231, Elsevier, Amsterdam (1983).
6. E. J. Cairns, in "Comprehensive Treatise of Electrochemistry, Vol. III: Electrochemical Energy Conversion and Storage," J. O'M. Bockris, B. E. Conway, E. Yeager, and R. E. White, Editors, p. 341, Plenum Press, New York (1981).
7. A. I. Sotnikov, O. A. Esin, and Yu. P. Nikitin, *Izv. Akad. Nauk SSSR, Metall.*, 33 (1965).
8. B. N. Boronenkov, O. A. Esin, G. A. Toporitzev, and A. S. Chyrkin, *Izv. VUZ Chern. Metall.*, 10 (1967).
9. A. K. Strelischov, G. A. Toporitzev, and O. A. Esin, *ibid.*, No. 3, 12 (1968).
10. N. Q. Minh and T. B. King, in "Proceedings of Joint US-USSR Symposium on Electrosag Remelting," p. 30, Ukrainian Academy of Sciences, Kiev, USSR (1978).
11. N. Q. Minh and T. B. King, *Metall. Trans.*, 10B, 623 (1979).
12. N. Q. Minh, R. O. Loutfy, and N. P. Yao, *J. Electroanal. Chem. Interfacial Electrochem.*, 131, 229 (1982).
13. N. Q. Minh, R. O. Loutfy, and N. P. Yao, "Preliminary Study of the Electrolysis of Aluminum Sulfide in Molten Salts," Argonne National Laboratory Report ANL/OEPM-83-3 (1983).
14. N. Q. Minh and N. P. Yao, *This Journal*, 130, 1025 (1983).
15. E. I. Khazanov and A. I. Belyaev, *Legk. Met.*, 4, 1 (1935).
16. P. Röntgen and K. Giesen, in "Abhandlungen Institut für Metallhüttenwesen und Elektrometallurgie der Technischen Hochschule, Aachen," Vol. V, P. Röntgen, Editor, p. 32, Aachen, Germany (1940).
17. A. Kerouanton and V. Plichon, *C. R. Acad. Sci., Ser. C*, 280, 497 (1975).
18. J. Thonstad, F. Nordmo, and J. K. Rødseth, *Electrochim. Acta*, 19, 761 (1974).
19. A. J. Calandra, C. E. Castellano, and C. M. Ferro, *ibid.*, 24, 425 (1979).
20. A. J. Calandra, C. E. Castellano, C. M. Ferro, and O. Cobo, in "Light Metals 1982," J. E. Andersen, Editor, p. 345, Metallurgical Society of AIME, Warrendale, PA (1981).
21. A. J. Calandra, C. M. Ferro, and C. E. Castellano, *Electrochim. Acta*, 25, 201 (1980).
22. K. Grjothem, C. Krohn, M. Malinovsky, K. Matiasovsky, and J. Thonstad, "Aluminium Electrolysis, the Chemistry of the Hall-Heroult Process," p. 187, Aluminium-Verlag GmbH, Düsseldorf (1977).
23. E. R. Brown and R. F. Large, "Techniques of Chemistry, Volume I, Physical Methods of Chemistry, Part IIA, Electrochemical Methods," A. Weissberger and B. W. Rossiter, Editors, p. 452, Wiley-Interscience, New York (1971).
24. R. S. Nicholson, *Anal. Chem.*, 37, 1351 (1965).
25. P. Delahay, "New Instrumental Methods in Electrochemistry," p. 120, Interscience, New York (1954).
26. G. J. Janz and R. P. T. Tomkins, "Physical Properties Data Compilations Relevant to Energy Storage, IV, Molten Salts: Data on Additional Single and Multi-Component Salt Systems," NSRDS-NBS 61, Part IV, U.S. Department of Commerce, National Bureau of Standards, Washington, DC (1981).
27. R. Ødegard, A. Bjørgum, A. Sterten, J. Thonstad, and R. Tunold, *Electrochim. Acta*, 27, 1595 (1982).
28. M. M. Vetyukov, B. S. Dyblin, and Yu. V. Borisoglebskii, *Sov. Electrochem.*, 8, 332 (1972).
29. E. A. Úkshe and N. G. Bukun, *Zh. Neorg. Khim.*, 9, 944 (1964).
30. D. L. Hill, G. J. Hills, L. Young, and J. O'M. Bockris, *J. Electroanal. Chem. Interfacial Electrochem.*, 1, 79 (1959).
31. Yu. K. Delimarskii, V. I. Shapoval, and V. A. Vasilenko, *Ukr. Khim. Zh.*, 39, 617 (1973).
32. J. M. Eiselev, *J. Appl. Chem. USSR*, 42, 15 (1969).

Combined Forced and Natural Convection at Vertical Electrodes

Assisting and Opposing Flows

Jacob Jorné*

Department of Chemical Engineering, University of Rochester, Rochester, New York 14627

ABSTRACT

Many electrochemical processes involve combined forced and natural (free) convection. The superimposition of velocity gradients and the Lighthill transformation are used to calculate mass-transfer coefficients for large Schmidt numbers near vertical electrodes where forced and natural convection exist. A distinction should be made between assisting and opposing flows. For assisting flow near a vertical electrode, the third-order correlation for the Sherwood number is a good approximation

$$Sh^3 = Sh_F^3 + Sh_N^3$$

where subscripts F and N represent forced and natural convection if each acts alone. For opposing flow, points of zero shear stress are expected along the electrode length, resulting in flow reversals and boundary-layer separation. An explicit correlation to the limiting forced and natural convection appears more complicated. The combined forced and natural convection near an electrode embedded in a fully developed laminar flow channel is analyzed as well. Again, a distinction should be made between assisting and opposing flows.

Electrochemical processes are usually mass-transfer limited. In order to overcome mass-transfer overpotential, forced convection is introduced via electrolyte circulation, stirring, or gas introduction. However, natural convection (or free convection) is almost an inherent phenomenon in electrochemical systems and in many cases is sufficient to adequately supply and remove reactants and products to and from the electrode-solution interface. Natural convection is the hydrodynamic flow, which results from density variations. In heat-transfer systems, these density variations are the result of temperature differences. In mass-transfer cases, and especially in electrochemical systems, the density variations are due to concentration variations in the electrolyte solution adjacent to the electrode.

In many electrochemical systems, both forced and natural convections exist. The relative magnitudes of the individual convections determine which one dominates. McAdams (1) recommended that the higher transfer coefficient be used. Similarly, Newman (2) recommended that the rule to follow is to calculate the mass-transfer coefficient separately for free convection and again for forced convection and to assume that the higher value applies. Acrivos (3) analyzed the combined effect of natural and forced convection and found that the transition region between predominance of natural convection and predominance of forced convection is usually narrow. However, in many electrochemical reactors, the flow of the electrolyte is relatively low and is determined by the rate of supply and removal of reactants and products, *e.g.*, the chlor-alkali process. In such cases, the magnitudes of the natural and forced convection are quite similar, and a prediction of their combined effect is desirable. Furthermore, in some situations, a balance between opposing natural and forced convection is used in order to minimize undesirable corrosion reaction, such as in the zinc-chlorine battery (4).

In the present communication, the combined effect of natural and forced convection is treated by using the Lighthill (5) transformation which has been extensively used by Newman (2). This transformation is used for two-dimensional convective diffusion in laminar systems where the diffusion boundary layer is much thinner than the hydrodynamic boundary layer due to the large Schmidt number. Based on this solution, an attempt is made to relate, when possible, the combined mass-transfer coefficient (or Sherwood number) to the individual mass-transfer coefficients. The individual mass-transfer coefficients correspond to the two limiting cases where either forced or natural convection exists by itself. The analysis is demonstrated for assisting flow cases

*Electrochemical Society Active Member.

such as vertical wall (electrode) in a free stream, and electrode embedded in a wall of a flow channel in which the flow is fully developed and laminar.

An attempt is made to also include cases of opposed flows where the forced convection is opposed by the natural convection. The opposing flow cases are more complicated, as noted by Churchill (6), Weber (7), and Acrivos (3), because of the fact that at some point along the wall the shear stress (or the velocity gradient) at the wall vanishes, thus causing separation of the boundary layer and flow reversal. In such a case, the analysis is probably valid up to the point of zero shear stress.

Combined Natural and Forced Convection at Vertical Surfaces

The problem of combined natural and forced convection in heat- or mass-transfer has received relatively little attention, mainly because the transition region between the two mechanisms is relatively narrow. McAdams (1) simply recommended using the higher transfer coefficient. Newman (2) advises the same approach in combined convection at electrode surfaces, based on Acrivos' (3) analysis which shows that the transition region is narrow.

Most of the heat transfer correlations that have been proposed are based on the power sum of the individual Nusselt numbers (6)

$$Nu^n = Nu_F^n + Nu_N^n \quad [1]$$

Where the subscripts F and N indicate forced and natural convection, respectively. Churchill (6) chooses $n = 3$ for assisting flows using an empirical correlation procedure. Acrivos (3) proposes $n = 4$ based on his approximate analysis for both assisting and opposing flows. Ruckenstein (8-10) and Ruckenstein and Rajagopalan (11) use a simple algebraic method for obtaining heat- and mass-transfer coefficients under mixed convection. They also calculate the combined coefficients using a similarity solution for the case of assisting and opposing flows. The value $n = 3$ is predicted both from the algebraic method and the similarity transformation. Ruckenstein and Rajagopalan (11) use the algebraic method to correlate mixed convection at vertical plate, entrance region, horizontal cylinder, and magneto-convective mass transfer.

Ruckenstein and Rajagopalan (11) analysis for the opposing flows case is based on the similarity transformation and is limited up to the point of zero shear stress at the wall where flow reversal is expected. However, it appears that their analysis for opposing flows is somewhat oversimplified. It appears that the extension of the correlation to opposing flows is unsuccessful, as pointed out by Weber (7) and Churchill (6).

Attempts at solving the complete transport equations for mixed convection were done by expansions in terms of the ratio of the Grashof number to the square of the Reynolds number (Gr_r/Re_r^2) [Szewczyk, (12) and Eshghy 13]. Merkin (14) obtained a complete solution limited to a Prandtl (or Schmidt) number of 1. Lloyd and Sparrow (15) and Wilks (16) obtained local similarity solutions. The results of Lloyd and Sparrow (15) show in $n = 4$ for $Pr = 10$ and 100. Furthermore, their results break down for $(Gr_r/Re_r^2) > 2$ (11).

Mass-Transfer under Combined Forced and Natural Convection

Electrolytic solutions possess large Schmidt number; therefore, the mass-transfer boundary layer is much thinner than the hydrodynamic boundary layer. Consequently, it is permissible to approximate the velocity components by their first terms in Taylor's expansion in the distance y from the wall

$$u = y \beta(x) \quad v = -\frac{1}{2} y^2 \beta'(x) \quad [2]$$

where $\beta(x)$ is the velocity derivative, $\beta(x) = (\partial u / \partial y)_{y=0}$ at the wall.

The governing laminar boundary layer equations along a vertical plate are

$$u \frac{\partial u}{\partial x} + v \frac{\partial u}{\partial y} = \nu \frac{\partial^2 u}{\partial y^2} + \alpha g(C - C_\infty) \quad [3]$$

$$\frac{\partial u}{\partial x} + \frac{\partial v}{\partial y} = 0 \quad [4]$$

$$u \frac{\partial C}{\partial x} + v \frac{\partial C}{\partial y} = D \frac{\partial^2 C}{\partial y^2} \quad [5]$$

The following boundary conditions are assumed

$$\begin{aligned} u = 0, v = 0, C = C_w \text{ at } y = 0 \\ u = u_\infty, C = C_\infty \text{ at } y = \infty \\ u = u_\infty, C = C_\infty \text{ at } x = 0 \end{aligned}$$

These boundary conditions correspond to a potentiostatic condition where the wall concentration is fixed. Under limiting current condition, the wall concentration vanishes, $C_w = 0$.

Since the diffusion layer is very narrow, it can be further assumed that the actual velocities under combined convection are approximately the sum of the velocities of the forced and natural convection if they exist independently (9)

$$(u_F + u_N) \frac{\partial C}{\partial x} + (v_F + v_N) \frac{\partial C}{\partial y} = D \frac{\partial^2 C}{\partial y^2} \quad [6]$$

Again, the subscripts F and N represent forced and natural convection, respectively, if they exist alone. The velocities are well known for various geometries such as vertical wall in a free stream, and fully developed laminar flow in a vertical channel.

Based on the known superimposed velocities, the local mass-transfer coefficients can be calculated using the Lighthill transformation (2)

$$k_x = \frac{D \sqrt{\beta(x)}}{\Gamma(4/3) (9D)^{1/3} \left[\int_0^x \sqrt{\beta(x)} dx \right]^{1/3}} \quad [7]$$

Where $\Gamma(4/3) = 0.89298$ and

$$\beta(x) = \left(\frac{\partial u_F}{\partial y} + \frac{\partial u_N}{\partial y} \right)_{y=0} = \beta(x)_F + \beta(x)_N \quad [8]$$

x is the distance from the upstream leading edge. The corresponding local Sherwood number is given by

$$Sh_x = \frac{k_x x}{D} = \frac{\sqrt{\beta(x)} x}{\Gamma(4/3) (9D)^{1/3} \left(\int_0^x \sqrt{\beta(x)} dx \right)^{1/3}} \quad [9]$$

The average mass-transfer coefficient is obtained by integration over the length L

$$k_{av} = \frac{1}{6L\Gamma(4/3)} \left[9D \int_0^L \sqrt{\beta(x)} dx \right]^{2/3} \quad [10]$$

and the corresponding average Sherwood number is

$$Sh_{av} = \frac{1}{6L\Gamma(4/3)} \left[9D \int_0^L \sqrt{\beta(x)} dx \right]^{2/3} \quad [11]$$

In the following sections, this method will be applied to several important geometries, and the resultant Sherwood numbers will be interpreted in terms of the individual Sherwood numbers for forced and natural convections. The assisting flows and the opposing flows will be discussed separately.

Assisting Forced and Natural Convection near a Vertical Wall

This situation occurs when an electrode is placed in either an upward free stream and the natural convection is directed upward (e.g., electrodeposition), or in a downward free stream when the natural convection is directed downward (e.g., electrodisolution). The situation is schematically illustrated in Fig. 1.

The superimposed velocity derivative at the wall is given by

$$\beta(x) = \beta(x)_F + \beta(x)_N \quad [12]$$

where

$$\beta(x)_F = \frac{A}{x^{1/2}} \quad \beta(x)_N = Bx^{1/4}$$

and

$$A = \frac{0.332 U_\infty^{3/2}}{\nu^{1/2}} \quad B = 1.92\nu Sc^{-1/4} \left(\frac{g\alpha\Delta c}{4\nu^2} \right)^{3/4}$$

The integration in Eq. [7] can be performed, and the resultant local mass-transfer coefficient is given by

$$k_x = \frac{(B/D)^{1/3} D}{2\Gamma(4/3)} \frac{x^{-1/4}}{\left[1 - \left(x^{-1/2} + \frac{B}{A} x^{1/4} \right)^{-3/2} x^{-3/4} \right]^{1/3}} \quad [13]$$

The local Sherwood number is

$$Sh_x = \frac{(B/D)^{1/3}}{2\Gamma(4/3)} \frac{x^{3/4}}{\left[1 - \left(x^{-1/2} + \frac{B}{A} x^{1/4} \right)^{-3/2} x^{-3/4} \right]^{1/3}} \quad [14]$$

Forced convection alone gives, upon similar integration

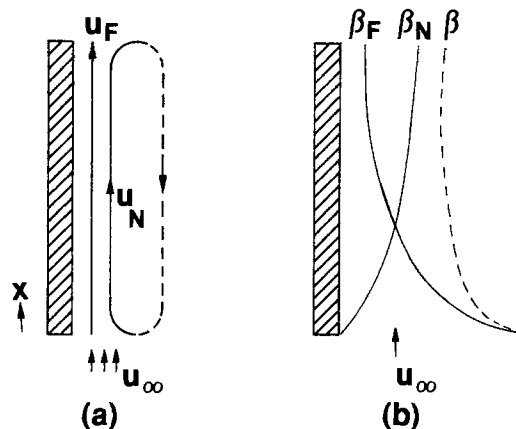


Fig. 1. Assisting forced and natural convection near a vertical wall (electrode). (a): Schematic flow pattern. (b): Velocity gradients at the wall.

$$k_F = \frac{D}{\Gamma(4/3) \left(\frac{12D}{A}\right)^{1/3} x^{1/2}} \quad [15]$$

$$Sh_F = \frac{x^{1/2}}{\Gamma(4/3) \left(\frac{12D}{A}\right)^{1/3}} \quad [16]$$

Natural convection alone gives, similarly

$$k_N = \frac{D}{2\Gamma(4/3) \left(\frac{D}{B}\right)^{1/3} x^{1/4}} \quad [17]$$

$$Sh_N = \frac{x^{3/4}}{2\Gamma(4/3) \left(\frac{D}{B}\right)^{1/3}} \quad [18]$$

By defining the ratio G as the cubic ratio between the natural and forced Sherwood numbers (11).

$$G = \left(\frac{Sh_N}{Sh_F}\right)^3 = \frac{3}{2} \frac{B}{A} x^{3/4} \quad [19]$$

and by comparing Eq. [14], [16], and [18], one obtains

$$\left(\frac{Sh_x}{Sh_N}\right)^3 = \frac{\left(1 + \frac{2}{3}G\right)^{3/2}}{\left(1 + \frac{2}{3}G\right)^{3/2} - 1} \quad [20]$$

For the case when

$$\left(1 + \frac{2}{3}G\right)^{3/2} \approx 1 + G \quad [21]$$

one obtains

$$Sh_x^3 = Sh_F^3 + Sh_N^3 \quad [22]$$

This result is identical to Ruckenstein and Rajagopalan's results (11) and in agreement with Churchill's correlation (6), in which the correlating power is $n = 3$. Therefore, for the region when the forced and natural convections are of similar magnitude along a vertical electrode, one can find the combined mass transfer by adding the cubic power of the individual Sherwood numbers. Similarly, the average Sherwood number, upon integration along the height of the electrode, is given by

$$Sh_{av}^3 = Sh_{Fav}^3 + Sh_{Nav}^3 \quad [23]$$

Therefore, the average Sherwood number, or the average mass-transfer coefficient, can be estimated from the corresponding limiting values where either forced or natural convection exist alone.

Opposing Forced and Natural Convection near a Vertical Wall

Consider the situation where the forced convection is opposing the natural convection. If the wall is of length L , the natural boundary layer is developing at the bottom $x = L$, and the forced boundary layer starts at $x = 0$ (see Fig. 2).

Two distinct situations should be considered: (i) when the velocity gradient (shear stress) does not change sign along the electrode height. This is the case when $\beta(x)_F > \beta(x)_N$ and the velocity direction at the wall is the same as that of the forced convection (see Fig. 2a and 2b). (ii) when the velocity gradient at the wall reaches 0 twice along the electrode height (see Fig. 2c and 2d). In this case, flow reversals can occur twice along the electrode surface, and the assumption of superimposition of velocities is probably unrealistic there.

Again, the derivative of the velocity at the wall is given by

$$\beta(x) = Ax^{-1/2} - B(L-x)^{1/4} \quad [24]$$

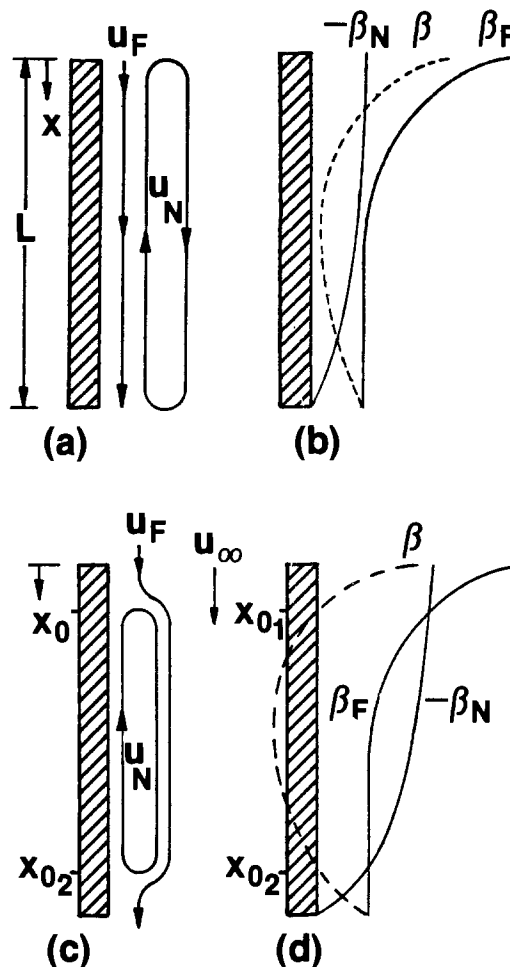


Fig. 2. Opposing forced and natural convection near a vertical wall (electrode). (a): Schematic flow pattern for no point of zero shear stress, $\beta_F > \beta_N$. (b): Velocity gradients at the wall for no point of zero shear stress. (c): Schematic flow pattern for two points of zero shear stress. (d): Velocity gradients at the wall for two points of zero shear stress.

where

$$A = \frac{0.332}{4} \frac{U_x^{3/2}}{\nu^{1/2}} \quad B = 1.92\nu \quad Sc^{-1/4} \left(\frac{g\alpha\Delta C}{4\nu^2}\right)^{3/4}$$

The local mass-transfer coefficient is given generally by

$$k_x = \frac{[Ax^{-1/2} - B(L-x)^{1/4}]^{1/2} D}{\Gamma(4/3)(9D)^{1/3} \left(\int_0^x [Ax^{-1/2} - B(L-x)^{1/4}]^{1/2} dx^{1/3}\right)} \quad [25]$$

However, this expression must be applied carefully for the opposing flows since the velocity derivative changes sign twice along the height of the electrode. The points of zero shear stress can be found by setting $\beta(x) = 0$

$$\beta(x) = Ax_0^{-1/2} - B(L-x_0)^{1/4} = 0 \quad [26]$$

or

$$x_0^2(L-x_0) = (A/B)^4 \quad [27]$$

The two real roots x_{01} and x_{02} represent the points of zero shear stress where flow reversal and separation of the boundary layer occur (see Fig. 2c and 2d). Therefore, the integration in Eq. [25] can be performed only for the upper region $0 < x < x_{01}$. The flow over the surface can be represented by Fig. 2c. For the regions $x_{01} < x < x_{02}$ and $x_{02} < x < L$, it appears unlikely to predict the local mass-transfer coefficients because of the flow reversals and internal circulation.

For the upper edge, the velocity derivative at the wall is given by

$$\beta(x) = Ax^{-1/2} - BL^{1/4} \left(1 - \frac{x}{L}\right)^{1/4} \quad [28]$$

For the case where $x \ll L$

$$\beta(x) = Ax^{-1/2} - BL^{1/4} \quad [29]$$

The integration in Eq. [25] gives

$$\begin{aligned} \int_0^x \sqrt{\beta(x)} dx &= \int_0^x (Ax^{-1/2} - BL^{1/4})^{1/2} dx \\ &= \left(x^{1/2} - \frac{A}{2BL^{1/4}}\right) (Ax^{1/2} - BL^{1/4}x)^{1/2} \\ &+ \frac{A^2}{4(BL^{1/4})^{3/2}} \left[\sinh^{-1} \left(\frac{2BL^{1/4}}{A} x^{1/2} + 1 \right) - \sinh^{-1} 1 \right] \quad [30] \end{aligned}$$

The mass-transfer coefficient is, therefore

$$\begin{aligned} k_x &= \frac{D(Ax^{-1/2} - BL^{1/4})^{1/2}}{\Gamma(4/3)(9D)^{1/3}} \\ &\left\{ \left(x^{1/2} - \frac{A}{2BL^{1/4}}\right) (Ax^{1/2} - BL^{1/4}x)^{1/2} \right. \\ &\left. + \frac{A^2}{4(BL^{1/4})^{3/2}} \left[\sinh^{-1} \left(\frac{2BL^{1/4}}{A} x^{1/2} + 1 \right) - \sinh^{-1} 1 \right] \right\}^{-1/3} \quad [31] \end{aligned}$$

The corresponding Sherwood number is given by

$$\text{Sh}_x = \frac{k_x x}{D} \quad [32]$$

This expression is valid only when $0 < x < x_{01}$, and when the electrode is long enough so the derivative of the velocity of the natural convection becomes almost constant. The mass-transfer coefficient in Eq. [31], or the corresponding Sherwood number (Eq. [32]), cannot be related easily to the limiting cases of individual forced or natural convection.

The individual mass-transfer coefficients (or Sherwood numbers) are calculated similarly to be for forced convection

$$k_F = \left(\frac{A}{12D}\right)^{1/3} \frac{D}{\Gamma(4/3)x^{1/2}} \quad [33]$$

$$\text{Sh}_F = \left(\frac{A}{12D}\right)^{1/3} \frac{x^{1/2}}{\Gamma(4/3)} \quad [34]$$

and for natural convection (in which the origin is at $x = L$)

$$k_N = \frac{D(B/D)^{1/3}}{2\Gamma(4/3)(L-x)^{1/4}} \quad [35]$$

$$\text{Sh}_N = \frac{(B/D)^{1/3}(L-x)^{3/4}}{2\Gamma(4/3)} \quad [36]$$

It appears that a simple relation between the local mass-transfer coefficient (Eq. [31] and [32]) and the individual mass-transfer coefficients (Eq. [33]-[36]) is not obvious as in the case of assisting flows.

The mass-transfer coefficient (Eq. [31]) can be related to the individual mass-transfer coefficients (Eq. [33] and [35]) by defining the ratio G_k , which represents the relative importance of the two individual mass-transfer coefficients

$$G_k = \left(\frac{k_N}{k_F}\right)^3 \approx \frac{3}{2} \frac{B}{A} \frac{x^{3/2}}{L^{3/4}} \quad [37]$$

The local mass-transfer coefficient is then related to the ratio $G_k L/x$ by

$$\left(\frac{k_x}{k_N}\right)^3 = \frac{4}{3G_k} \left(1 - \frac{2}{3} G_k \frac{L}{x}\right)^{3/2}$$

$$\begin{aligned} &\left\{ \left(1 - \frac{3}{4G_k} \frac{x}{L}\right) \left(1 - \frac{2}{3} G_k \frac{L}{x}\right)^{1/2} \right. \\ &\left. + \frac{1}{4} \left(\frac{3}{2G_k} \frac{x}{L}\right)^{3/2} \left[\sinh^{-1} \left(\frac{4G_k}{3} \frac{L}{x} + 1\right) - \sinh^{-1} 1 \right] \right\}^{-1} \quad [38] \end{aligned}$$

For the upper edge of the plate where $x \ll L$, the \sinh^{-1} term can be neglected, and Eq. [38] can be simplified to

$$\left(\frac{k_x}{k_N}\right)^3 \approx \frac{4}{3G_k} \frac{1 - \frac{2G_k}{3} \frac{L}{x}}{1 - \frac{4G_k}{3} \frac{L}{x}} \quad [39]$$

Further approximation when

$$\left(\frac{3}{4G_k} \frac{x}{L}\right) \ll 1$$

gives

$$k_x^3 \approx \frac{4}{3} k_F^3 - \frac{8}{9} k_N^3 \frac{L}{x} \quad [40]$$

It must be kept in mind that all the above correlations are for heights where the natural convection approaches a constant value.

The Sherwood number (Eq. [32]) can be related similarly to the individual Sherwood numbers (Eq. [34] and [36]) by defining the ratio G_{Sh}

$$G_{\text{Sh}} = \left(\frac{\text{Sh}_N}{\text{Sh}_F}\right)^3 = \frac{3}{2} \frac{B}{A} \frac{L^{9/4}}{x^{3/2}} \quad [41]$$

The local Sherwood number is then related to the ratio $G_{\text{Sh}} x^2/L^2$ by

$$\begin{aligned} \left(\frac{\text{Sh}_x}{\text{Sh}_N}\right)^3 &= \frac{4}{3G_{\text{Sh}}} \left(1 - \frac{2}{3} G_{\text{Sh}} \frac{x^2}{L^2}\right)^{3/2} \\ &\left\{ \left(1 - \frac{3}{4G_{\text{Sh}}} \frac{L^2}{x^2}\right) \left(1 - \frac{2}{3} G_{\text{Sh}} \frac{x^2}{L^2}\right)^{1/2} \right. \\ &\left. + \frac{1}{4} \left(\frac{3}{2G_{\text{Sh}}} \frac{L^2}{x^2}\right)^{3/2} \left[\sinh^{-1} \left(\frac{4}{3} G_{\text{Sh}} \frac{x^2}{L^2} + 1\right) - \sinh^{-1} 1 \right] \right\}^{-1} \quad [42] \end{aligned}$$

Again, for the upper section where $x \ll L$ and $3/4G_{\text{Sh}} L^2/x^2 \ll 1$, the correlation can be approximated by

$$\left(\frac{\text{Sh}_x}{\text{Sh}_N}\right)^3 \approx \frac{4}{3G_{\text{Sh}}} \frac{\left(1 - \frac{2}{3} G_{\text{Sh}} \frac{x^2}{L^2}\right)}{\left(1 - \frac{3}{4G_{\text{Sh}}} \frac{L^2}{x^2}\right)} \quad [43]$$

Further approximation yields

$$\text{Sh}_x^3 = \frac{4}{3} \text{Sh}_F^3 - \frac{2}{3} \text{Sh}_N^3 \frac{x^2}{L^2} \quad [44]$$

The above correlations are not as simple as in the case of assisting flow, partially because the natural convection starts at the downstream edge, $x = L$, and the characteristic length in Sh_N is L , while the characteristic length in Sh_x and Sh_F is x .

For both the lower edge of the electrode and the intermediate region, it is not appropriate to use the Lighthill transformation because of flow reversal and boundary layer separation.

The result in Eq. [31] is in disagreement with that of Ruckenstein and Rajagopalan (11) for opposing flows near a vertical wall

$$\left(\frac{Sh_x}{Sh_N}\right)^3 = \frac{(1 - 2/3 G)^{3/2}}{1 - (1 - 2/3 G)^{3/2}} \quad [45]$$

which, upon the simplification $(1 - 2/3 G)^{3/2} \approx 1 - G$, gives

$$Sh_x^3 \approx Sh_F^3 - Sh_N^3 \quad [46]$$

Equations [45] and [46] differ from the equations for assisting flow, Eq. [20] and [22], only by a minus sign. It is not clear how Ruckenstein and Rajagopalan (11) obtained the above results.

Furthermore, the limited experimental data available for opposing forced and natural convections do not agree with the simple relationship given by Ruckenstein and Rajagopalan (11), Eq. [45] and [46].

Vertical Flow Channel

Consider a vertical flow channel in which the flow is fully developed and laminar. An electrode of length L is embedded in the wall starting at point $x = 0$. Natural convection occurs at the electrode due to concentration depletion and density variation. For the case of assisting flows, both forced and natural convection are directed upward. For opposing flows the forced convection is downward while the natural convection is upward.

First consider the assisting flows case. See Fig. 3 for the schematic flow pattern and the velocity gradients at the wall.

The forced velocity is given by

$$u_F = 6\bar{u}_{av} \left(\frac{y}{d} - \frac{y^2}{d^2}\right) \quad v_F = 0 \quad [47]$$

where d is the gap of the flow channel. The velocity can be approximated near the wall to be

$$u_F \approx \left(\frac{6\bar{u}_{av}}{d}\right) y = Ay \quad v_F = 0 \quad [48]$$

The natural convection is given as before by

$$u_N = Bx^{1/4}y \quad [49]$$

and the velocity derivative is

$$\beta(x) = A + Bx^{1/4} \quad [50]$$

Integration gives the mass-transfer coefficient for the assisting flows

$$k_x = \frac{B^4 D z}{8\Gamma(4/3)(9D)^{1/3} \left(\frac{z^9}{9} - \frac{3A}{7} z^7 + \frac{3}{5} A^2 z^5 - \frac{A^3}{3} z^3 + \frac{16}{315} A^{9/2}\right)^{1/3}} \quad [51]$$

where

$$z = (A + Bx^{1/4})^{1/2} \quad [52]$$

The corresponding Sherwood number is

$$Sh_x = \frac{B^4 z x}{8\Gamma(4/3)(9D)^{1/3} \left(\frac{z^9}{9} - \frac{3A}{7} z^7 + \frac{3}{5} A^2 z^5 - \frac{A^3}{3} z^3 + \frac{16}{315} A^{9/2}\right)^{1/3}} \quad [53]$$

For the case of opposing flows, a distinction should be made between two cases: (i) when the velocity derivative at the wall $\beta(x)$ does not reach zero within the electrode length L , and (ii) when the point of zero shear stress occurs on the electrode and flow reversal is expected.

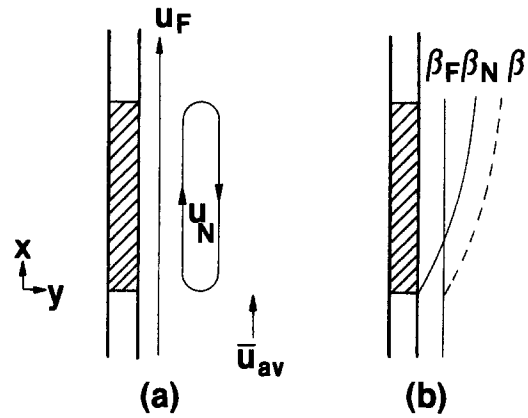


Fig. 3. Assisting forced and natural convection near an electrode embedded in a vertical flow channel. (a): Schematic flow pattern. (b): Velocity gradients at the wall.

The two cases are illustrated schematically in Fig. 4, where both the flow patterns and the corresponding velocity gradients are shown. For case (i), where no zero shear stress occurs at the electrode, the mass-transfer coefficient can be calculated in a similar way as for the case of assisting flows, except the integration starts at the top $x = L$ where the fresh solution approaches the electrode

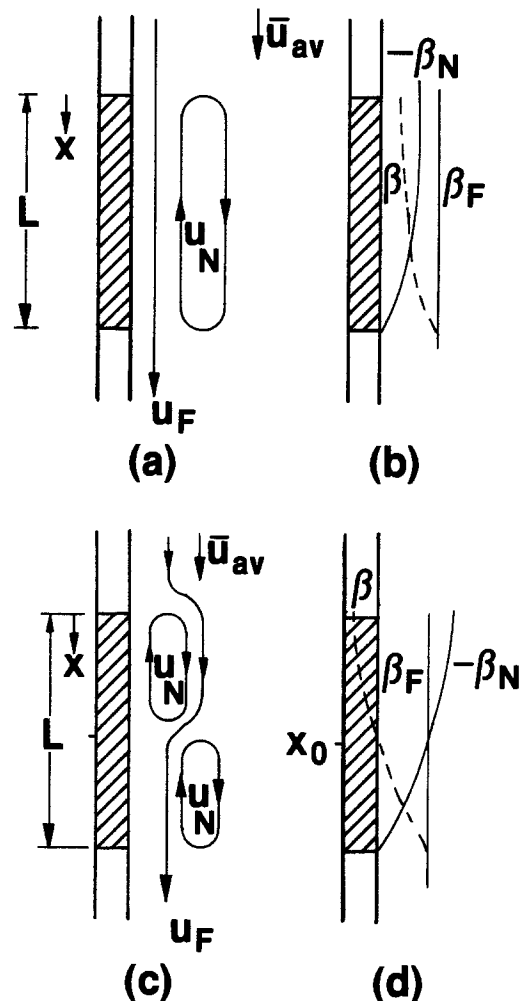


Fig. 4. Opposing forced and natural convection near an electrode embedded in a vertical flow channel. (a): Schematic flow pattern in the case of no zero shear stress at the electrode $\beta_F > \beta_N$. (b): Velocity gradients at the wall in the case of no zero shear stress at the wall. (c): Schematic flow pattern in the case of one point of zero shear stress at the wall. (d): Velocity gradients at the wall for one point of zero shear stress at the wall.

$$k_x = \frac{B^4 D [z(x) - z(L)]}{8\Gamma(4/3)(9D)^{1/3}} \left\{ \frac{z(x)^9 - z(L)^9}{9} - \frac{3A}{7} [z(x)^7 - z(L)^7] + \frac{3A^2}{5} [z(x)^5 - z(L)^5] - \frac{A^3}{3} [z(x)^3 - z(L)^3] \right\}^{-1/3} \quad [54]$$

where

$$z(x) = (Bx^{1/4} - A)^{1/2}$$

$$z(L) = (BL^{1/4} - A)^{1/2}$$

For case (ii), where the point of zero shear stress occurs within the electrode length, $0 < x_0 < L$, the situation is quite complicated, as shown in Fig. 4c and 4d. Flow reversal occurs which results in two circulation patterns. It appears that the present method is too oversimplified for such a case. Nevertheless, if one calculates the mass-transfer coefficients, two regions should be distinguished: the top region, $x_0 < x < L$, where natural convection dominates, and the bottom region, $0 < x < x_0$, where forced convection dominates.

Summary

It has been shown, theoretically, that the local and average mass-transfer coefficients along a vertical electrode where both forced and natural convection exist can be calculated using the superimposition of velocities and the Lighthill transformation. The case of vertical wall in a vertical free flow and the case of electrode embedded in the wall of a vertical flow channel have been treated. A distinction should be made between assisting and opposing flows. In the case of assisting flow, the integration in the Lighthill transformation is straightforward. However, for the cases of opposing flows, points of zero shear stress are expected accompanied by flow reversals. For such complicated cases, the local mass-transfer coefficients can be predicted only for the upstream regions, before flow reversal occurs.

Acknowledgments

The support of Energy Development Associates and the Electric Power Research Institute is gratefully acknowledged.

Manuscript submitted May 26, 1983; revised manuscript received Dec. 12, 1983.

LIST OF SYMBOLS

A	constant for forced convection
B	constant for natural convection
C	concentration (mol/cm ³)
D	diffusion coefficient (cm ² /s)
g	gravitational acceleration (cm/s ²)

G	ratio $(k_w/k_p)^3$ for assisting flow
G _k	ratio $(k_w/k_p)^3$ for opposing flow
Gr	Grashof number defined in terms of x
G _{sh}	ratio $(Sh_w/Sh_p)^3$ for opposing flow
k _x	local mass-transfer coefficient (cm/s)
L	length of vertical plate (cm)
Nu _{av}	average Nusselt number
Nu _x	local Nusselt number
Pr	Prandtl number
Sc	Schmidt number
Sh _{av}	average Sherwood number
Sh _x	local Sherwood number
u	velocity in x direction (cm/s)
u _{av}	average velocity in x direction (cm/s)
v	velocity in y direction (cm/s)
x	vertical position along vertical plate (cm)
y	position normal to the plate (cm)

Greek symbols

α	concentration coefficient of volumetric expansion (cm ³ mol ⁻¹)
β(x)	velocity derivative at the wall (s ⁻¹)
Γ(4/3)	0.89298, the gamma function of 4/3
μ	fluid viscosity, g cm ⁻¹ s ⁻¹
ν	kinematic viscosity, cm ² s ⁻¹
ρ	density of fluid, g cm ⁻³

Subscripts

av	average
F	forced convection
N	natural convection
w	at the wall surface
∞	in the bulk

REFERENCES

- W. H. McAdams, "Heat Transmission," 2nd ed., p. 217, McGraw-Hill, New York (1942).
- J. Newman, "Electrochemical Systems," Prentice-Hall, Englewood Cliffs, NJ (1973).
- A. Acrivos, *Chem. Eng. Sci.*, **21**, 343 (1966).
- J. Jorne, G. L. Henriksen, S. Kodali, and C. J. Warde, Abstract 374, p. 950, The Electrochemical Society Extended Abstracts, Vol. 79-1, Boston, MA, May 6-11, 1979.
- M. J. Lighthill, *Proc. R. Soc. A*, **202**, 359 (1950).
- S. W. Churchill, *A.I.Ch.E. J.*, **23**, 10 (1977).
- M. E. Weber, *ibid.*, **22**, 207 (1976).
- E. Ruckenstein, *ibid.*, **24**, 940 (1978).
- E. Ruckenstein, *ibid.*, **26**, 850 (1980).
- E. Ruckenstein, *Chem. Eng. Sci.*, **37**, 1505 (1982).
- E. Ruckenstein and R. Rajagopalan, *Chem. Eng. Commun.*, **4**, 15 (1980).
- A. A. Szewczyk, *J. Heat Transfer, Trans. ASME*, **86C**, 501 (1964).
- S. Eshghy, *ibid.*, **86C**, 290 (1964).
- J. H. Merkin, *J. Fluid Mech.*, **35**, 439 (1969).
- J. R. Lloyd and E. M. Sparrow, *Int. J. Heat Mass Transfer*, **13**, 434 (1970).
- G. Wilks, *ibid.*, **16**, 1958 (1973).
- J. Gryzgoridis, *ibid.*, **18**, 911 (1975).

Semiconductor Electrodes

LVII. Differential Photocurrent and Second Harmonic Techniques for *in situ* Monitoring of Surface States on n-MoSe₂ in Aqueous Solutions

Bob L. Wheeler, G. Nagasubramanian, and Allen J. Bard*

Department of Chemistry, The University of Texas at Austin, Austin, Texas 78712

ABSTRACT

Second harmonic ac impedance and differential photocurrent techniques are employed to monitor, *in situ*, the surface states on n-MoSe₂ electrodes in aqueous solutions containing the Fe(CN)₆^{3-/4-} couple. These two techniques are qualitatively more sensitive to the presence of surface states on single-crystal n-MoSe₂ than first harmonic ac techniques. Surface states on this semiconductor electrode were passivated by a thin layer of RuO_x. This film also increased the PEC efficiency of both single-crystal and polycrystalline n-MoSe₂.

Surface states, either intrinsic or extrinsic, are known to affect the performance of photoelectrochemical (PEC) cells and behavior of semiconductor electrodes by promoting Fermi level pinning, acting as recombination centers, and abetting dark current flow (1-3). Several techniques for the study of surface states at electrode surfaces contacting electrolyte solutions are available; these include (i) current-potential methods (3), (ii) photocapacitance spectroscopy (4), (iii) electroluminescence spectroscopy (5-7), (iv) photoluminescence spectroscopy (7), (v) measurements of the subbandgap photoresponse (8-10), (vi) interfacial capacitance (11), and (vii) surface photovoltage (12). Recently, we reported that the ac impedance technique can provide information about both the energy distribution and density of surface states (13, 14). This method could detect the presence of surface states even when their density was too small to cause Fermi level pinning on n-MoTe₂. We report here ac impedance studies of n-MoSe₂ and demonstrate the use of this method as a means of *in situ* monitoring of the semiconductor surface and the effects of surface treatments. In addition, two techniques are described which are qualitatively even more sensitive to the presence of surface states: the second harmonic ac impedance and the differential photocurrent techniques. Deposition of a thin layer of RuO_x on the surface of n-MoSe₂ was shown by all three techniques to passivate the surface states present. Concurrently, the photocurrent-voltage behavior showed a dramatic improvement. This provides strong evidence that all three techniques monitor the semiconductor surface, *in situ*, and that the surface states were responsible for the poor photocurrent-voltage behavior with the untreated surface. The improvement of the single-crystal behavior encouraged us to attempt to improve polycrystalline MoSe₂ films by the same method.

Experimental

Electrodes.—Single crystals of n-MoSe₂¹ were used. The van der Waals surface (\perp C axis) was the face exposed to the solution. Ohmic contacts were made to the back surfaces with Ga/In eutectic. A copper wire lead for electrical contact was attached to the ohmic contacts with silver conductive paint (Allied Product Corporation, New Haven, Connecticut) and then covered with 5 min epoxy cement (Devcon Corporation, Danvers, Massachusetts). A fresh surface was exposed by peeling off the top van der Waals layers with adhesive tape until the surface appeared free of edges or steps upon examination with a microscope. Assemblies were then mounted in 6 mm diam glass tubing and held in place by covering all except the front surface with silicone rubber sealant (Dow Corning Corporation, Midland, Michigan), which also served as a seal against the seepage of the electrolyte to the back contact. The exposed area was ~ 0.06 cm² for all electrodes

*Electrochemical Society Active Member.

¹The single crystals of n-MoSe₂ were obtained from Dr. Barry Miller and Dr. Frank DiSalvo of AT&T Bell Laboratories, Murray Hill, New Jersey.

used. The surfaces of the electrodes were treated with 6M HCl for 1 min and rinsed with distilled water prior to use. The electrolyte consisted of an aqueous solution of 0.2M K₂Fe(CN)₆, adjusted to pH 8 with KOH, and deaerated with prepurified N₂ prior to the experiment. A positive pressure of this N₂ was kept in the cell during the experiments.

Polycrystalline films of MoSe₂ were made from MoSe₂ powder, 99+% (Alfa, Danvers, Massachusetts) using I₂ vapor transport. A quartz tube, 1.5 cm diam + 15 cm length, was rinsed successively with 48% HF, distilled water, aqua regia, distilled water, 48% HF, and distilled water, then dried under vacuum at 150°C. Approximately 3g of the MoSe₂ powder was placed in the tube, and the tube was evacuated ($< 10^{-5}$ torr) for 1h. The tube was filled with He and I₂ was quickly added (~ 20 mg/g MoSe₂). Most of the He was removed and the tube was cooled in liquid N₂ and evacuated and sealed. The MoSe₂ and I₂ were distributed along the tube, which was placed in a split tube furnace (Hevi-duty Electric Company, Watertown, Wisconsin, length 18 in., diam 1.25 in.) and kept at 900°C. The ends of the furnace were plugged with spun alumina to minimize any temperature gradient which could cause growth of single crystals. After three weeks, the tube was removed from the furnace, and a suitable section was cooled under running water to condense the I₂, and then the rest of the tube was cooled. A polycrystalline mass of MoSe₂ had grown above and beneath the original charge. The side of the polycrystalline mass which faced the center of the quartz tube was covered with crystalline platelets protruding perpendicularly to the quartz walls; this was designated as the rough side. The opposite side, which was against the quartz tube, was shiny and was designated as the smooth side. The polycrystalline films were quite sturdy and could be removed easily from the quartz after the tube was broken. Contact to these films was made with silver paint and copper wire. The contact and the rest of the film, except for the area to be exposed to the solution, was covered with 5 min epoxy cement. Since the films had pinholes, the contact had to be kept above the solution level. The electrolyte solution used was an aqueous solution of 1M KBr, deaerated with N₂.

A conventional three-electrode single-compartment cell with a flat Pyrex window for illumination of the semiconductor electrode was used. The cell, which had a volume of about 30 ml, also contained a Pt gauze electrode (area > 40 cm²) which was used as the counterelectrode. The reference electrode was a saturated calomel electrode (SCE) separated from the cell by a KCl-saturated agar bridge. All potentials are reported *vs.* SCE.

Current-potential behavior was obtained with a PAR Model 173 potentiostat with Model 179 digital coulometer plug-in and Model 175 programmer (Princeton Applied Research, Princeton, New Jersey) and recorded with a Model 2000 X-Y recorder (Houston Instruments, Austin, Texas). Polychromatic illumination was obtained from a

450W Xe lamp (Oriel Corporation, Stamford, Connecticut) provided with a water filter. The intensity was 100 mW/cm².

Photodeposition of RuO_x ($x \leq 2$) on the MoSe₂ electrodes was accomplished by a modification of the procedure reported by Anderson and Warren (15). To a solution of 1.7g of RuCl₃ · 3H₂O in 100 ml of 98% aqueous EtOH, 6 ml of 1,3-cyclohexadiene was added (16). The solution was placed in a boiling flask fitted with a reflux condenser and heated to 45°C for 3h. The reflux condenser was then removed, and the solution volume was reduced to 30 ml. The red precipitate of [Ru(η^6 -C₆H₆)Cl₂]₂ was collected by filtration, washed with EtOH, and allowed to dry in air. This species was dissolved in a minimum amount of water, and 4 mol AgBF₄ were added per mole of Ru dimer to obtain Ru(η^6 -C₆H₆)(OH₂)₃²⁺ and a precipitate of AgCl. The solution was filtered, and the filtrate was diluted to give 0.04M Ru. The pH was adjusted to 5 and NaClO₄ was used as supporting electrolyte at a concentration of 0.1M. The aquated species can be oxidized on Pt at +0.9V vs. SCE to give a film of RuO_x (15). On illuminated n-MoSe₂, photo-oxidation starts at +0.2V vs. SCE. The films were produced by illuminating the n-MoSe₂ with white light and biasing at +0.5V while monitoring the charge passed with a coulometer.

AC impedance.—The lock-in technique (13, 14) was used to measure the ac impedance behavior as a function of applied potential. In this technique, a small amplitude sine wave, 12 mV peak to peak, from a wide-range oscillator (Model 200 CD, Hewlett-Packard, Palo Alto, California) is superimposed on a slow (≤ 5 mV/s) dc ramp from the PAR universal programmer by the PAR potentiostat and applied to the cell. The output of the current follower of the potentiostat is input to a lock-in amplifier (PAR Model 5204 or 5206) which separates the signal into the components in and out of phase (90°) with the ac signal from the oscillator. These signals were calibrated by using an RC circuit composed of a resistance substitution box checked with a digital multimeter and a precision decade capacitor (Hewlett-Packard Model 4440 B). The in and out of phase signals as a function of dc potential were plotted on an X-Y-Y recorder (Soltec, Sun Valley, California, Model 6432).

The second harmonic measurements were made by applying the same ac signal at a fundamental frequency (f) and setting the lock-in on the external $2f$ mode. The HP200 CD oscillator was found to have negligible harmonic distortion detectable at the sensitivities used, and, therefore, this oscillator was used for all ac measurements. All other instrumentation was the same as that used in the measurements at the fundamental frequency.

Differential photocurrent.—In this technique, the photocurrent is electronically differentiated with respect to potential as a function of potential (17). The method used the intermodulation frequency of chopped light and ac modulation of the electrode. This method has been described in detail elsewhere (18) and the results are plots of the photocurrent vs. voltage, as well as the differential photocurrent vs. voltage. Instrumentation is identical to that described previously (18).

Results and Discussion

Capacitance-voltage behavior of single-crystal n-MoSe₂.—Mott-Schottky (M-S) plots over the frequency range (f) 0.5-5 kHz are given in Fig. 1 for n-MoSe₂ in aqueous solution containing Fe(CN)₆⁴⁻³⁻ as the redox couple. In this frequency regime, the capacitance values (C) were generally free from the deleterious effects of surface states and yielded values of C which were only slightly dependent on f . The value of flatband potential (V_{FB}) and the average value of the doping density (N_D) obtained from the M-S plots are around $-0.1V$ vs. SCE and $2 \times 10^{17}/\text{cm}^3$. Taking the bandgap as 1.4 eV (19), we estimate that the valence band (VB) and conduction band (CB) edges are located, respectively, at +1.16 and $-0.24V$.

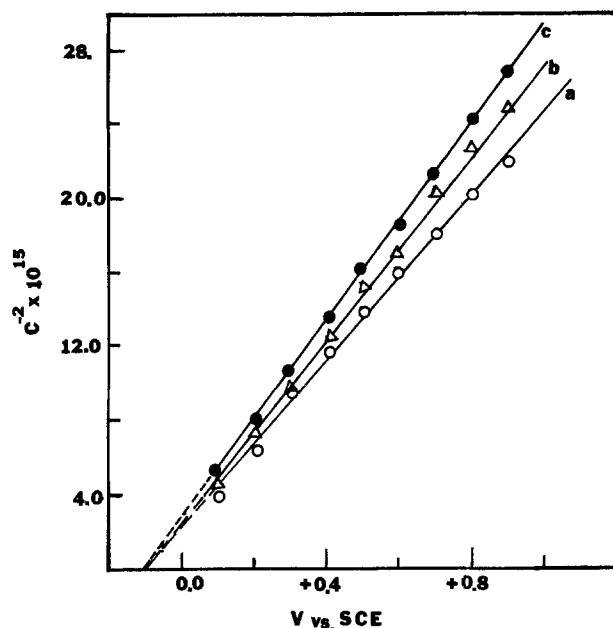


Fig. 1. Mott-Schottky plots for n-MoSe₂ in aqueous 0.2M K₄Fe(CN)₆. a: 500 Hz. b: 1 kHz. c: 5 kHz.

Inflections in the reverse bias region of capacitance (C) or conductance (G) vs. V plots are often associated with excess charge residing in surface states (20). Such inflections will be manifested as dips or humps in the C - V or G - V plots with frequency-dependent peak positions and heights. The shape and size of the humps are determined by the time constant (τ) associated with charge exchange and the density distribution as a function of potential energy (N_{ss} , cm⁻²eV⁻¹). The integrated area under the hump can be used to obtain quantitative information about the total density of surface states. This approach was used previously (14) to obtain a surface-state density of 1.4×10^{10} cm⁻² for n-MoSe₂. This density is too small for pinning the Fermi level (21, 22). In Fig. 2 are shown plots of the equivalent parallel conductance (G_p) and equivalent parallel capacitance (C_p) vs. V for two typical n-MoSe₂ electrodes in aqueous solution containing 0.2M K₄Fe(CN)₆ at two different frequencies, 100 and 500 Hz. While the C_p vs. V plots at 500 Hz show no hump in contrast to that at 100 Hz, the G_p vs. V plots exhibit humps with a frequency-dependent peak height. Different electrodes all gave similar results. This observation, that the in-phase component is more sensitive to the presence of surface states than the 90° component, is in accord with earlier observations (13, 23, 24). In Fig. 3 is shown the second harmonic of the ac impedance of n-MoSe₂ electrode of Fig. 2a in 0.2M K₄Fe(CN)₆ with ac modulation at 500 Hz. Note the absence of any dip or hump in the C_p vs. V at 500 Hz, while the second harmonic (which is related to dC/dV vs. V) exhibits a hump around +0.2V, roughly in the same potential region in which G_p vs. V exhibits a hump. In many devices, the capacitance changes much less rapidly than dC/dV (25, 26, 27) since, while $C_p \propto V^{1/2}$, $dC_p/dV \propto V^{-3/2}$. As with the dC_p/dV behavior, the small hump present in the G_p vs. V curve is greatly amplified in the second harmonic of the conductance (dG_p/dV) (Fig. 3).

Photocurrent and differential photocurrent behavior of n-MoSe₂.—In Fig. 4 are given the photocurrent (j) and the differential photocurrent (Δj) vs. V for two n-MoSe₂ electrodes with monochromatic illumination at 500 nm in aqueous solution containing K₄Fe(CN)₆ as redox couple. The plots in Fig. 4a are for the same electrode as Fig. 2a. Note that the current axis for Δj is given in a logarithmic scale. The $\log \Delta j$ vs. V plots exhibit a large hump in the potential regime in which j vs. V curves exhibit a dip. Similar results were obtained when the two modulating frequencies were varied by $\pm 20\%$ while maintaining the intermodulation frequency constant at 400 Hz for ease of

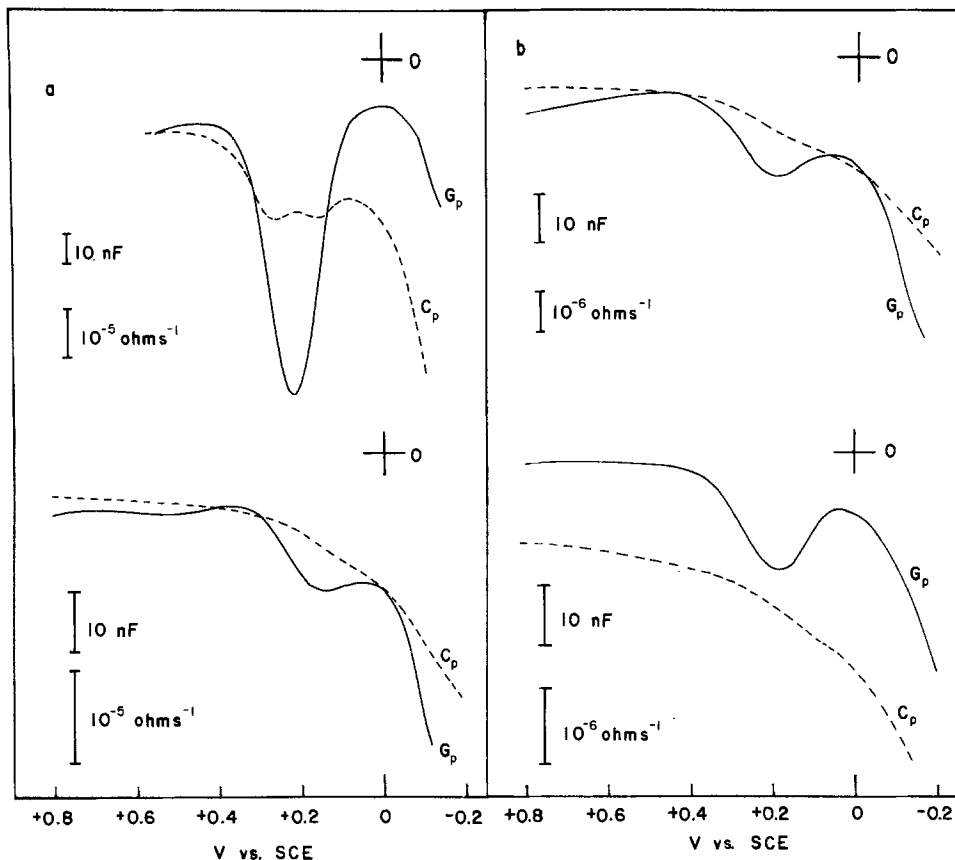


Fig. 2. AC impedance of n-MoSe₂ in 0.2M K₄Fe(CN)₆. (a) and (b) denote different electrodes. The upper plots are for 100 Hz, and the lower for 500 Hz. G_p , in-phase or equivalent parallel conductance, C_p ; quadrature or equivalent parallel capacitance.

filtering. Since Δj is the differential photocurrent at any potential, information concerning inflections in the photocurrent attributable, for example, to surface recombination and surface states, are amplified in Δj . Even a very small dip or hump in j vs. V will be apparent in Δj vs. V plots. Recall that the in-phase component (Fig. 2) exhibits a peak in the same potential regime in which the j and Δj vs. V plots exhibit a hump. This observation suggests that the differential photocurrent technique can be used as a diagnostic tool to probe the electrode surface for surface states.

The ac impedance and current-voltage behavior of n-MoSe₂ after surface modification with RuO_x.—These techniques, in conjunction with the ac impedance and current-voltage measurements, have been extended to regimes where surface states can be passivated by a thin layer of RuO_x. The thermodynamic potential for RuO_x deposition from Ru(η^6 -C₆H₆)(OH)₂²⁺ complex is about +0.9V vs. SCE. The VB edge of n-MoSe₂ is located at

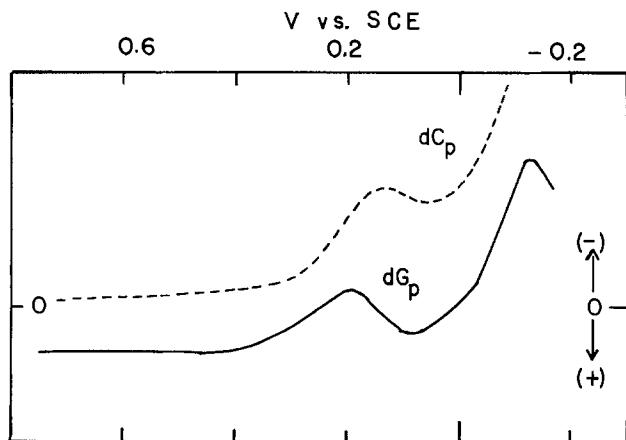


Fig. 3. Second harmonic ac impedance for n-MoSe₂ in aqueous 0.2M K₄Fe(CN)₆. Fundamental modulation frequency = 500 Hz. Sensitivity for dG_p (second harmonic of G_p) and dC_p (second harmonic of C_p) are 100x and 20x, respectively, G_p and C_p in Fig. 2b. Negative values are plotted upward.

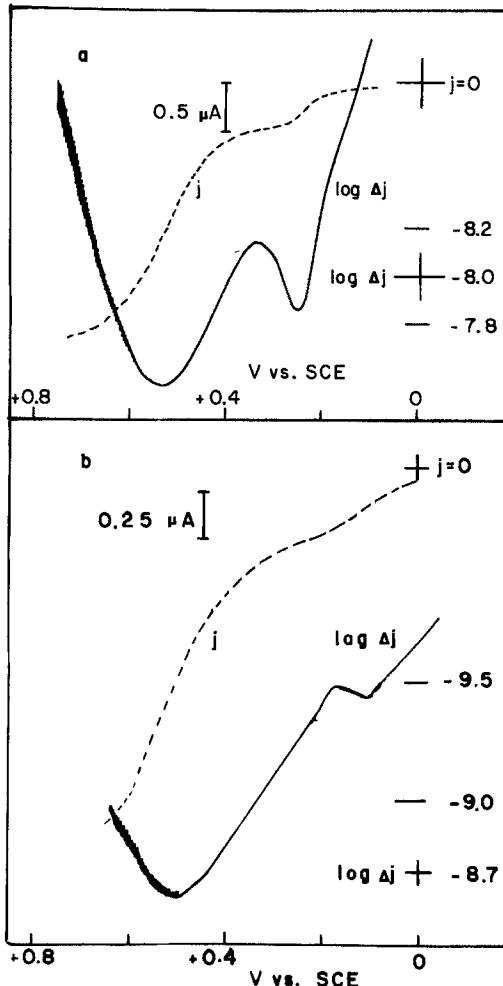
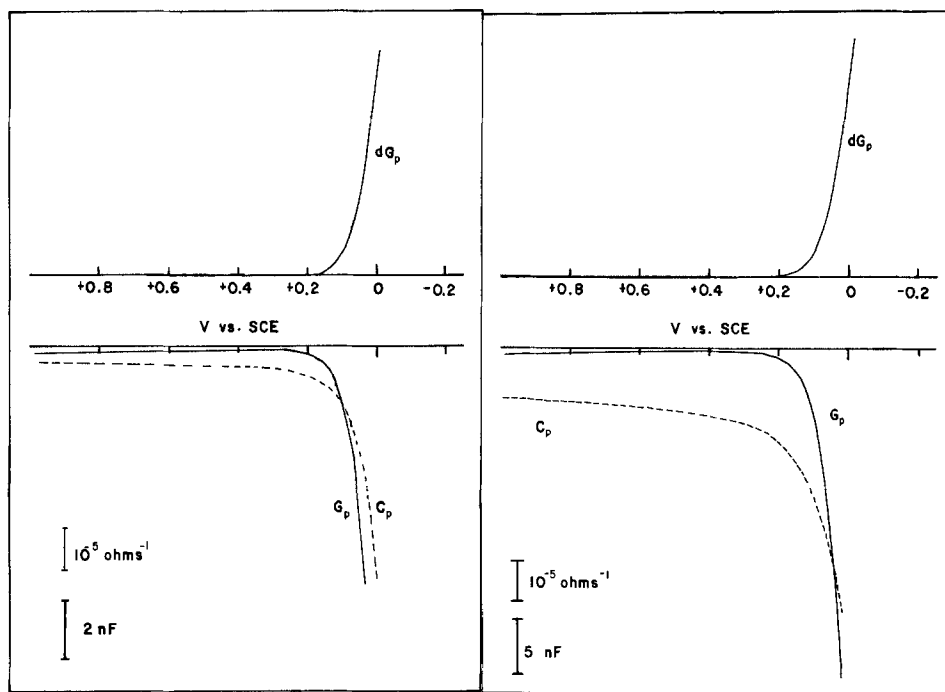


Fig. 4. Photocurrent (j) and log differential photocurrent (Δj) vs. potential for n-MoSe₂ in 0.2M K₄Fe(CN)₆. Monochromatic illumination at 500 nm, j obtained with light modulation at ~ 1.1 kHz, and Δj at the difference frequency (0.4 kHz) between the potential modulation (~ 1.5 kHz) and the light modulation. (a) and (b) denote different electrodes. The plots for (a) are for the electrode of Fig. 2a.

Fig. 5. AC impedance of $n\text{-MoSe}_2/\text{RuO}_x$ in $0.2\text{M K}_4\text{Fe(CN)}_6$. G_p = equivalent parallel conductance, C_p = equivalent parallel capacitance, dG_p = second harmonic of G_p (sensitivity = $5 \times G_p$). Modulation frequency is 25 Hz (left) and 100 Hz (right). Negative values of dG_p are plotted upward.



1.16V vs. SCE. We have photoelectrochemically deposited a thin layer of RuO_x on the surface of the $n\text{-MoSe}_2$ electrode of Fig. 2a held at +0.5V under white light illumination from a 450W Xe lamp. The film appeared golden yellow, and the amount of charge passed was equal to 1.9 mC ($\sim 30 \text{ mC/cm}^2$). In Fig. 5 are given plots of the impedance and the second harmonic ac impedance for two modulation frequencies in $\text{K}_4\text{Fe(CN)}_6$ solution. Both the ac impedance at the fundamental frequency and the more sensitive second harmonic exhibit smooth plots that are indicative of an improved surface. In Fig. 6 is shown the j and Δj vs. V for $n\text{-MoSe}_2$ after depositing RuO_x . Note the significant improvement in the shape of the current-voltage behavior. The photocurrent rises to saturation much more quickly than its counterpart in Fig. 4. This type of steep rise to saturation has been attributed to the absence of surface states and recombination effects (28, 29). At 0.3V, corresponding to the V_{redox} of $\text{Fe(CN)}_6^{4-/3-}$, the photocurrent (roughly corresponding to the short-

circuit photocurrent in a two-electrode PEC cell configuration) of the RuO_x -modified electrode is approximately double that of the untreated electrode. Consider the behavior of the differential photocurrent. Δj decreases more sharply with V than its counterpart in Fig. 4. Further, the hump attributable to the presence of surface states is absent, suggesting the passivation of the surface states. The RuO_x films were found to be stable in the presence of all mineral acids, but could be dissolved by sulfochromic acid. Short treatments in this acid of bare $n\text{-MoSe}_2$ electrodes were found not to affect the ac impedance behavior. In Fig. 7 is given the plot of j and Δj vs. V after partially removing the RuO_x layer by briefly dipping the electrode in chromic acid. Compare Fig. 6 and 7. In both cases, the j vs. V behavior is the same. The lower photocurrent in Fig. 6 is probably due to larger attenuation of the impinging light intensity by a thicker RuO_x

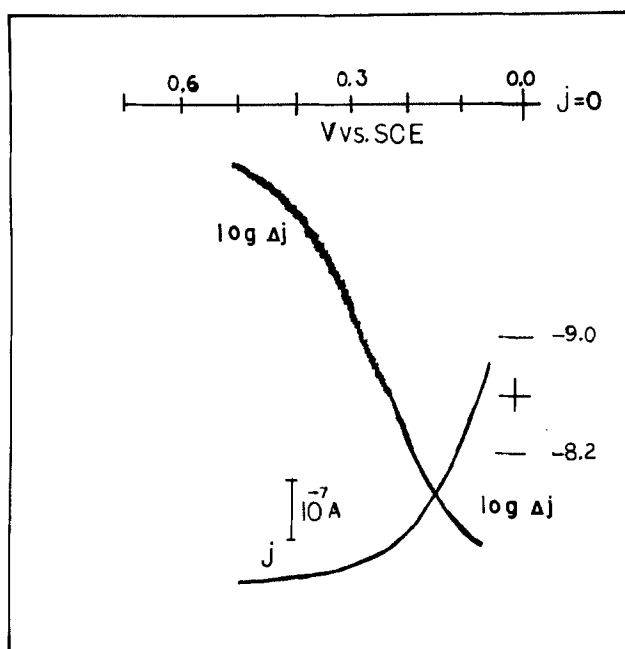


Fig. 6. Photocurrent (j) and log differential photocurrent (Δj) for $n\text{-MoSe}_2/\text{RuO}_x$ in $0.2\text{M K}_4\text{Fe(CN)}_6$. Illumination and frequencies are as in Fig. 4.

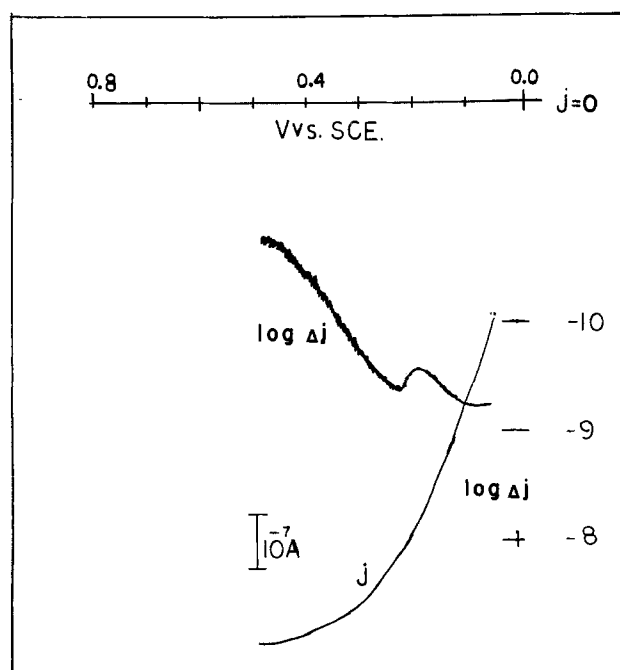


Fig. 7. Photocurrent (j) and log differential photocurrent (Δj) for $n\text{-MoSe}_2/\text{RuO}_x$ in $0.2\text{M K}_4\text{Fe(CN)}_6$ after etching RuO_x coating in chromic acid for 5s. Monochromatic illumination and frequencies are as in Fig. 4.

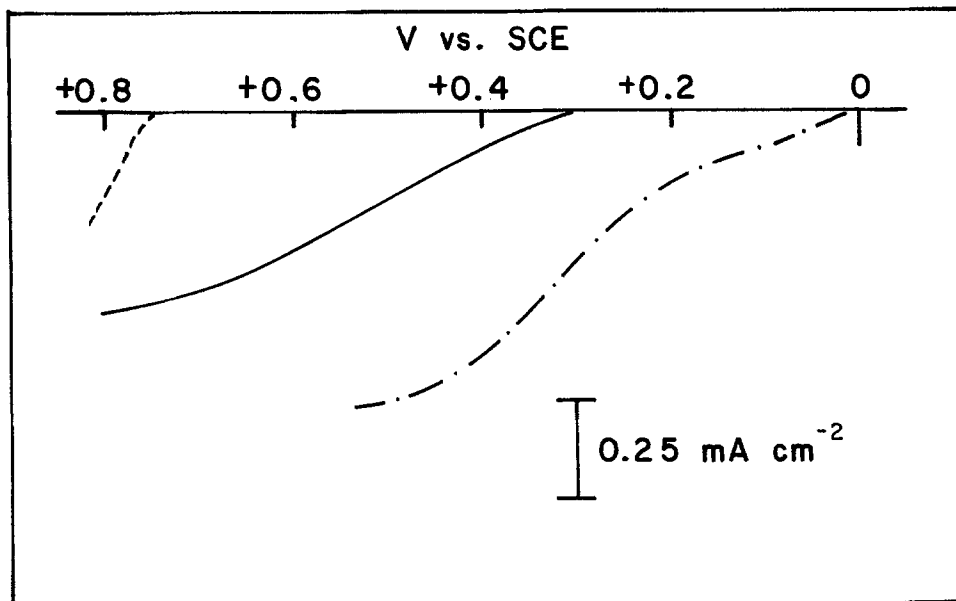


Fig. 8. Current-potential curves for smooth side of polycrystalline MoSe_2 in 1M KBr. Dark (---), illuminated with 450W Xe lamp ($\sim 100 \text{ mW/cm}^2$) (—), and after deposition of RuO_2 under illumination (-.-).

film. However, the Δj vs. V behavior is not the same. This plot exhibits a hump in the same potential regime in which both the ac impedance and differential photocurrent (before RuO_2 deposition) exhibit a hump. This observation indicates that the differential photocurrent method can be used to monitor the presence of surface states even at low levels, where the photocurrent behavior appears normal. In addition, even those states which cannot be charged in the dark but can be charged under illumination (30) are detectable by the differential photocurrent technique. In this respect it is even superior to the second harmonic impedance method for detecting surface states.

In a previous paper (14), we reported that the surface states existing on $n\text{-MoSe}_2$ were not present in sufficient density to cause pinning of the Fermi level in acetonitrile solutions. The possibility that a Schottky barrier exists between the $n\text{-MoSe}_2$ and the RuO_2 is ruled out by the constant onset potential of photocurrent in solutions of iodide, bromide, and ferrocyanide. Formation of insulating layers such as oxides could cause the measured impedance to be no longer equivalent to the combination of

space charge layer and surface states illustrated by Fig. A-1 of Ref. (14). The fact that RuO_2 is a conducting layer, as well as the values of the capacitance away from the potential regime of the surface states before and after RuO_2 deposition (compare Fig. 2a and Fig. 5), strongly suggests that the space charge layer capacitance is being measured. Additional support for this contention lies in the fact that even at frequencies as low as 100 Hz, the Mott-Schottky plots are linear; this would not be the case if the space charge capacitance were not approximately equivalent to the measured capacitance.

PEC behavior of polycrystalline $n\text{-MoSe}_2$.—Recent studies on polycrystalline films of $p\text{-WSe}_2$ (31) and $n\text{-WSe}_2$ (32) have been described. In the latter work, results of a modification procedure with silver and lanthanum ions were discussed. We report here work done on similar polycrystalline films of $n\text{-MoSe}_2$ and results of surface modification with photodeposited RuO_2 films. In Fig. 8 is shown the j - V behavior for the smooth side of polycrystalline $n\text{-MoSe}_2$ in aqueous solution containing 1.0M KBr as the redox couple before and after depositing

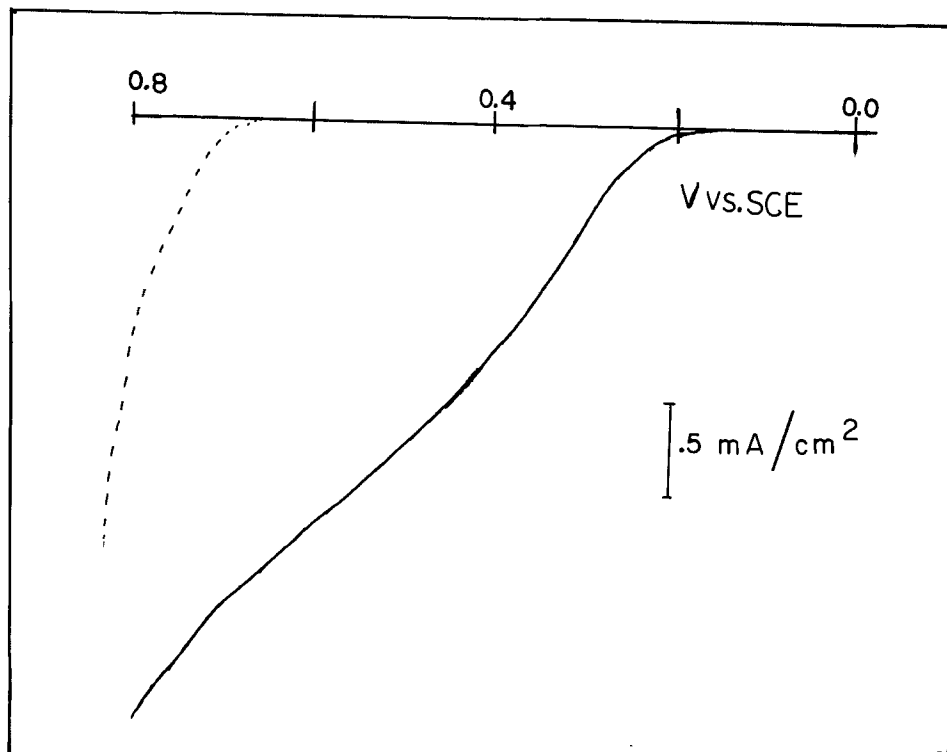


Fig. 9. Current-potential curves for rough surface of polycrystalline $n\text{-MoSe}_2$. Dark (---), illumination (—). Conditions are as in Fig. 8.

a thin layer of RuO_x. The conditions are the same as used for the single-crystal n-MoSe₂, except the number of coulombs passed in RuO_x deposition (~420 mC/cm² of projected surface area). (However, the actual surface area could be as much as an order of magnitude greater than the projected area.) The photoperformance is improved after RuO_x deposition; not only is the photocurrent increased, but the onset of photocurrent is located at least 0.3V more negative. Although the *j*-*V* performance appears to be improved after modifying the electrode surface with RuO_x, the photocurrent and efficiency of the polycrystalline material is still much smaller than that of treated single-crystal MoSe₂. Under similar conditions, the untreated rough side of the polycrystalline MoSe₂ gave better photocurrent than the RuO_x-coated smooth side (Fig. 9). However, deposition of the RuO_x on the rough side did not improve the behavior. Thus, the RuO_x treatment appears to help a poor surface more than a good one.

Conclusions

Both the second harmonic and the differential photocurrent methods can be used as diagnostic tools for monitoring the presence of surface states. Even under conditions where the presence of surface states cannot be detected by the photocurrent, the differential photocurrent can be used to detect them. Further, even those states which are not charged in the dark but can be charged under illumination can be detected by the differential photocurrent. In this respect, it is even superior to the second harmonic impedance method. The second harmonic is more sensitive than the ac impedance of the fundamental frequency.

Photoelectrodeposition of a thin film of RuO_x significantly improves both the potential for photocurrent onset as well as the short-circuit photocurrent for single-crystal n-MoSe₂ and the smooth side of polycrystalline MoSe₂. Attempts to study the behavior of similar n-MoTe₂ with RuO_x films were not successful. The Ru(η⁶-C₆H₆)(OH)₂²⁺ redox potential is more positive than the valence band-edge of this material (13) and, therefore, RuO_x films could not be formed by this method.

Acknowledgments

We are indebted to Dr. Barry Miller and Dr. Frank DiSalvo at AT&T Bell Laboratories for the gift of the sample of MoSe₂. The support of this research by the National Science Foundation (CHE8404666) and the Robert A. Welch Foundation is gratefully acknowledged. B. L. W. wishes to acknowledge the generous support of The Electrochemical Society, Inc., in the form of the Colin Garfield Fink Summer Fellowship.

Manuscript submitted Feb. 27, 1984; revised manuscript received May 14, 1984.

The University of Texas assisted in meeting the publication costs of this article.

REFERENCES

1. A. Heller and B. Miller, in "Interfacial Photoprocesses: Energy Conversion and Synthesis," M. S. Wrighton, Editor, p. 215, Advances in Chemistry Series 184, American Chemical Society, Washington, DC, (1980); M. S. Wrighton, in "Chemistry in Energy Production," symposium held December 10-12, 1980, New Orleans, LA, p. 25, Oak Ridge National Laboratory, Oak Ridge, TN (1982).
2. F.-R. F. Fan and A. J. Bard, *J. Am. Chem. Soc.*, **102**, 3677 (1980); A. J. Bard, F.-R. F. Fan, A. S. Gioda, G. Nagasubramanian, and H. S. White, *Discuss. Faraday Soc.*, **70**, 19 (1980).
3. S. N. Frank and A. J. Bard, *J. Am. Chem. Soc.*, **99**, 7427 (1975); P. Salvador and C. Gutierrez, *Chem. Phys. Lett.*, **86**, 131 (1982) and references therein; R. H. Wilson, *This Journal*, **127**, 228 (1980).
4. R. Haak and D. Tench, *ibid.*, **131**, 275 (1984).
5. R. N. Noufi, P. A. Kohl, S. N. Frank, and A. J. Bard, *ibid.*, **125**, 246 (1978).
6. H. Morisaki and K. Yazawa, *Appl. Phys. Lett.*, **33**, 1013 (1978).
7. Y. Nakato, A. Tsumura, and H. Tsubomura, *Chem. Phys. Lett.*, **85**, 387 (1982).
8. D. Laser and S. Gottesfeld, *This Journal*, **126**, 475 (1979).
9. H. Morisaki, M. Hariya, and K. Yazawa, *Appl. Phys. Lett.*, **30**, 7 (1977).
10. M. A. Butler and D. S. Ginley, *ibid.*, **42**, 582 (1983).
11. K. Kobayashi, Y. Aikawa, and M. Sukigara, *Chem. Lett.*, 679 (1981).
12. E. Kamieniecki, *J. Appl. Phys.*, **54**, 6481 (1983).
13. G. Nagasubramanian, B. L. Wheeler, G. A. Hope, and A. J. Bard, *This Journal*, **130**, 385 (1983).
14. G. Nagasubramanian, B. L. Wheeler, and A. J. Bard, *ibid.*, **130**, 1680 (1983).
15. D. P. Anderson and L. F. Warren, *ibid.*, **131**, 347 (1984).
16. R. A. Zelonka and M. C. Baird, *Can. J. Chem.*, **50**, 3063 (1972).
17. T. Sukegawa, T. Watanabe, T. Mizuki, and A. Tanaka, *IEEE Trans. Electron Devices*, **ed-27**, 1251 (1980).
18. B. L. Wheeler, G. Nagasubramanian, and A. J. Bard, *This Journal*, **131**, 1038 (1984).
19. H. Tributsch, H. Gerischer, C. Clemen, and E. Bucher, *Ber. Bunsenges. Phys. Chem.*, **83**, 655 (1979).
20. P. K. Vasudev, B. L. Mattes, E. Pietras, and R. H. Bube, *Solid State Electron.*, **19**, 557 (1976).
21. J. Bardeen, *Phys. Rev.*, **71**, 717 (1947).
22. A. J. Bard, A. B. Bocarsly, F.-R. F. Fan, E. G. Walton, and M. S. Wrighton, *J. Am. Chem. Soc.*, **102**, 3671 (1980).
23. E. H. Nicollan and A. Goetzberger, *Bell Syst. Tech. J.*, **46**, 1055 (1967).
24. M. Abe, H. Morisake, and K. Yazawa, *Jpn. J. Appl. Phys.*, **19**, 1421 (1980).
25. J. A. Copeland, *IEEE Trans. Electron Devices*, **ed-16**, 445 (1969).
26. C. L. Anderson, R. Baron, and C. R. Crowell, *Rev. Sci. Instrum.*, **47**, 1366 (1976).
27. K. H. Zaininger and F. P. Heiman, *Solid State Technol.*, **13**, 46 (1970).
28. M. P. Dare-Edwards and A. Hamnett, *J. Electroanal. Chem.*, **105**, 283 (1979).
29. J. Gobrecht and H. Gerischer, *Solar Energy Mater.*, **2**, 131 (1979); D. Laser and A. J. Bard, *This Journal*, **123**, 1828 (1976).
30. G. Cooper, J. A. Turner, B. A. Parkinson, and A. J. Nozik, *J. Appl. Phys.*, **54**, 6463 (1983).
31. H. D. Abruna and A. J. Bard, *This Journal*, **129**, 673 (1982).
32. D. S. Ginley, R. M. Biefield, B. A. Parkinson, and K. Keung-Kam, *ibid.*, **129**, 145 (1982).

The Voltammetric Response of Solutions of Electroactive Polymers

B. Lionel Funt* and P. M. Hoang

Department of Chemistry, Simon Fraser University, Burnaby, Vancouver, British Columbia, Canada V5A 1S6

ABSTRACT

A series of electroactive polymers was synthesized by incorporating pendant anthraquinone groups on a polystyrene backbone. The spacing between electroactive groups and the overall chain length were varied independently. Symmetrical, reversible cyclic voltammograms were obtained from polymer solutions. Linear plots of current *vs.* (sweep rate)^{1/2} were obtained whose slopes decreased with increase in chain length. Diffusion parameters thus evaluated agree with results obtained by viscometry. The Randles-Sevcik equation was modified to show the dependence of peak current upon polymer molecular weight. The predicted linear dependence of log *i_p* upon log \bar{M}_n was confirmed for polymers whose molecular weights were determined by gel permeation chromatography. The results clearly indicate the presence of independent, noninteracting centers.

The voltammetric behavior of solutions of polymers with pendant electroactive groups reflects the transfer of a large number of electrons to or from a single molecule. Although the electron transfer process may occur solely to the pendant groups, the chain configuration and structure can be expected to exert a profound influence on their diffusion to the electrode and to their interaction with neighboring groups. The size, shape, and location of voltammetric waves reflect the environment in which the electroactive centers are contained, and the extent to which interaction between neighboring groups hinders the process of electron transfer. Moreover, the electrochemical data may be used to characterize the polymers, because the voltammetric current is determined by the rate of diffusion of the macromolecule with its electroactive substituents.

Bard and co-workers investigated poly(2-vinylnaphthalene), poly(1-vinylanthracene) (1), and poly(vinylferrocene) (2), with triangular wave and pulse voltammetry, and found no interference between electroactive centers. We previously reported studies of a series of polymers of poly(vinylbenzophenone) and its copolymers with styrene (3, 4). These encompassed a range of molecular weights for which samples with differing spacings between electroactive groups were prepared. The electrochemical behavior indicated an absence of group-to-group interference for a wide range of copolymer compositions.

Examples of deviation from behavior explicable by this simple model have also been reported. Smith *et al.* (5) investigated poly(vinylferrocene) and estimated that only one in four ferrocene groups ($\bar{M}_n = 1.6\text{--}2.6 \times 10^4$) could be oxidized. Morishima *et al.* (6) investigated polymers and copolymers of 3-vinyl-10-methylphenothiazine (MPT) and found interference between neighboring groups in MPT but not in its copolymers. However, the latter could not be completely oxidized or reduced, and it is suggested that close proximity of electroactive groups is essential for electron self-exchange within the polymer chain and for the occurrence of complete oxidation.

Yap and Durst (7) developed a theoretical analysis of the effects of nearest neighbor interaction in order to quantify the current/potential relationship as a function of interaction parameters and chain length.

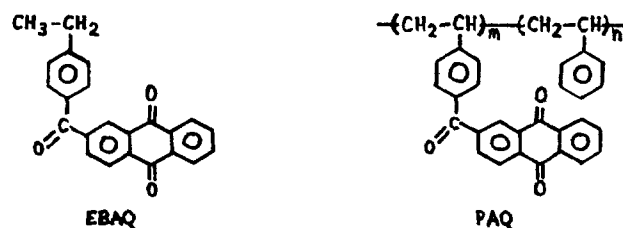
We have reported that noninteracting behavior in solution may be used to screen polymeric systems for possible utilization in polymer-modified electrodes (8). Systems which exhibit minimal group-to-group interference in solution are *a priori* expected to show similar tendencies when incorporated in thin films on electrodes.

In this work, we report the preparation and investigation of a series of polymers containing anthraquinone (AQ) and of a model compound for this polymer. The behavior of related quinones is well documented (9, 10), and their use as electrochemical mediators (11-15) prompted this choice.

*Electrochemical Society Active Member.

Experimental

A series of copolymers, of different anthraquinone (AQ) loading and with a range of chain lengths, was prepared.



2-Anthraquinonecarbonylchloride was prepared from 2-anthraquinone carboxylic acid and thionyl chloride by a standard procedure (16). 2-(p-Ethylbenzoyl)-9,10-anthraquinone (EBAQ) was synthesized by reaction of 2-anthraquinonecarbonylchloride (18.8 mM) and aluminum chloride (22.5 mM) with ethyl benzene (200 ml) at room temperature for 3 days. After recrystallization from methanol, the product was obtained as yellow crystals, yield 35%, m.p. 125°-126°C. Elemental analysis was: calculated C 81.18, H 4.71; found C 80.68, H 4.83. Mass spectrum *m/e* (%): 342 ($M^+ + 2$, 1.5), 341 ($M^+ + 1$, 10.5), 340 (M^+ , 35), 235 (9.5), 151 (17.1), 133 (100).

The IR spectrum showed a strong absorption of a quinone group at 1675 cm⁻¹, a β -carbonyl group at 1650 cm⁻¹, an ethyl group at 2970 cm⁻¹, 2930 cm⁻¹, and 2880 cm⁻¹, and a substituted benzene ring at 700 cm⁻¹.

The preparation of polystyrene of narrow dispersity and the determination of the chain length were described previously (3). Poly-[p-9,10-anthraquinone-2-carbonyl]styrene]-co-styrene (PAQ) was synthesized by reacting polystyrene with 2-anthraquinonecarbonylchloride and aluminum chloride in dry nitrobenzene. Polymers of different anthraquinone loading were prepared by changing the relative amounts of 2-anthraquinonecarbonylchloride and polystyrene. The product was purified by repeated precipitation in methanol and finally freeze-dried in vacuum. The IR spectrum showed a quinone band at 1675 cm⁻¹, a β -carbonyl band at 1650 cm⁻¹, a methylene band at 2920 cm⁻¹, and a substituted benzene ring at 700 cm⁻¹. Copolymer compositions were determined from infrared spectra and confirmed by elemental analysis.

Tetraethylammonium perchlorate (TEAP) (Kodak) was recrystallized twice from distilled water and dried under vacuum at 80°C for 3 days. Pyridine (Py) (BDH, analytical grade) was stored over molecular sieves in a nitrogen atmosphere. Dimethylformamide (DMF) (Fisher) was dried over BaO, vacuum distilled, and stored over molecular sieves.

Intrinsic viscosity measurements were performed at 25°C with an Ubbelohde viscometer, on solutions of polymer in 0.3M TEAP/Py-DMF (2/1, v/v). The choice of this solvent system was dictated by the poor solubility of polymers in conventional solvents. Molecular weights

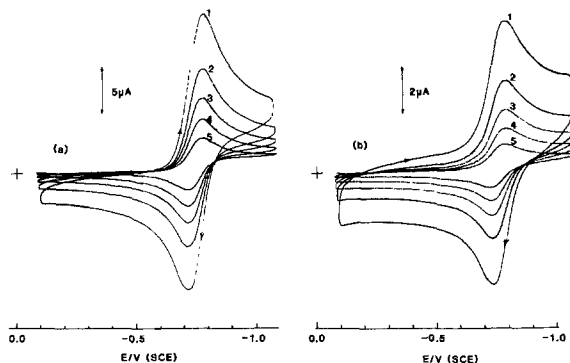


Fig. 1. Cyclic voltammety in 0.3M TEAP/Py-DMF (2/1, v/v) of (a) EBAQ (1.29 mM) and (b) PAQ 40 (1.55 mM anthraquinone residues). Scan rates: 500, 200, 100, 50, 20 mV s⁻¹ for curves 1-5, respectively.

were determined by gel permeation chromatography of the parent polymer. A Waters Model GPC/ALC 301 fitted with five capillary columns was employed.

Solutions of 0.3M TEAP/Py-DMF (2/1, v/v) were transferred to a three-compartment cell maintained under an argon atmosphere.

A ϕ 1.7 mm Pt disk (Bioanalytical Systems, Incorporated) was used as a working electrode with a Pt wire counterelectrode and an Ag/AgNO₃ reference. A PAR Model 170 Electrochemical System was employed for the voltammetric measurements. All potentials are reported relative to the saturated calomel electrode (SCE).

Results and Discussion

The cyclic voltammograms of the model compound EBAQ are shown in Fig. 1a. The peaks are symmetrical: E_{pc} and E_{pa} are independent of sweep rate (ν) for $\nu \leq 0.5$ V s⁻¹; the peak separation is ≈ 60 mV at all scan rates; i_{pa}/i_{pc} is unity, and i_{pc} is proportional to $\nu^{1/2}$. A similar pattern of ideal behavior is shown in Fig. 1b for the copolymer PAQ 40. For the further reduction of the dianion, EBAQ continued to show the characteristics of a simple system, whereas the polymer produces sharp anionic peaks indicative of strong adsorption on the electrode surface. Polymers with a high AQ content, such as PAQ 5(3) and PAQ 200(3), gave evidence of adsorption of the PAQ radical ion and of the PAQ polymer. These samples were excluded from further study, and the investigation on the remaining samples was confined to the first reduction step to the radical anion and of its reoxidation.

The data for a range of polymer chain lengths and for various average spacings of electroactive groups are presented in Table I and Fig. 2. A linear relationship between i_{pc} and $\nu^{1/2}$ is obtained even for samples whose AQ content differs greatly. For example, PAQ 5(1) and PAQ 5(2) each have an average of 51.9 repeat units (\overline{DP}_n) in the polymer chain but have 19.3% and 41.3%, respectively, of pendant AQ groups. The same pattern is evident with the high molecular weight samples [PAQ 200(1) and PAQ 200(2)] with 2170 repeat units in the chain and molecular weights in excess of 300,000. The lower slopes reflect the influence

Table I. Copolymer characterization

Polymers	AQ(%)	\overline{DP}_n	\overline{M}_n	$\overline{M}_w/\overline{M}_n$	$D \times 10^7$ (cm ² /s)	$[\eta]$ (g/100 ml)
EBAQ	1	338.2			78.7	
PAQ 5(1)	19.3	51.9	7.76×10^3	1.20	15.6	0.058
PAQ 5(2)	41.3	51.9	1.04×10^4	1.20	14.2	0.063
PAQ 5(3)	48.9	51.9	1.13×10^4	1.20	—	—
PAQ 8	21.6	72.2	1.12×10^4	1.22	13.4	0.066
PAQ 12	23.1	108	1.71×10^4	1.14	10.9	0.076
PAQ 40	18.0	413	6.06×10^4	1.16	5.84	0.166
PAQ 200(1)	19.5	2170	3.26×10^5	1.35	2.29	0.460
PAQ 200(2)	28.0	2170	3.69×10^5	1.35	2.00	0.483
PAQ 200(3)	47.4	2170	4.68×10^5	1.35	—	—

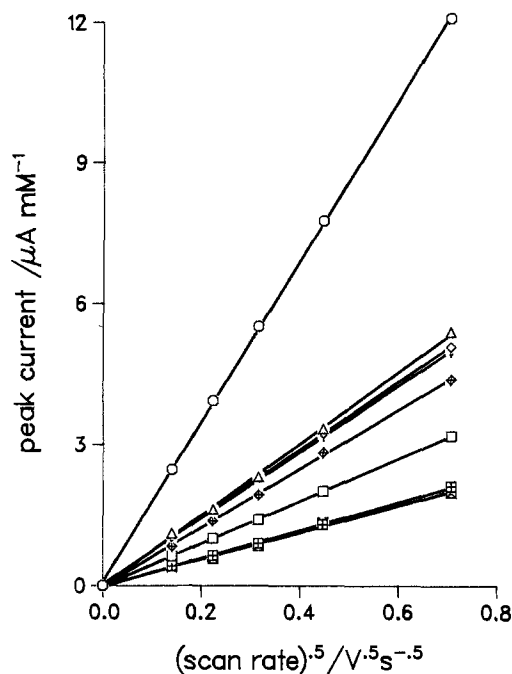


Fig. 2. Plots of cathodic peak current against (scan rate)^{1/2} for 1 mM anthraquinone residues. Curves from top: EBAQ, PAQ 5(1), PAQ 5(2), PAQ 8, PAQ 12, PAQ 40, PAQ 200(1), PAQ 200(2).

of chain length, but the curves are essentially independent of the number of electroactive groups on the chain.

The relationship between i_p and $\nu^{1/2}$ is given by the Randles-Sevcik equation (17, 18)

$$i_p = 2.69 \times 10^5 n^{3/2} A D^{1/2} C \nu^{1/2} \quad [1]$$

where n is the number of electrons transferred to each electroactive group, A the electrode area, D the diffusion coefficient, and C the bulk concentration of AQ residues (M cm⁻³).

The diffusion coefficients were calculated from the slopes of i_p vs. $\nu^{1/2}$ and are listed in Table I. However, the diffusion coefficients of polymers in solution are a function of the molecular weight and are given by

$$D = K_T M^{-b} \quad [2]$$

where K_T is a constant and the values of the exponent b range from 0.50 for a poor solvent to 0.55 for a good solvent (19). The variation in b results from the changes in chain conformation which occur as the chains coil or become extended in the solvent.

The values of D obtained from the electrochemical data were plotted against the number of average molecular weight, (\overline{M}_n) obtained from gel permeation chromatography of the parent polymers. A straight line whose slope

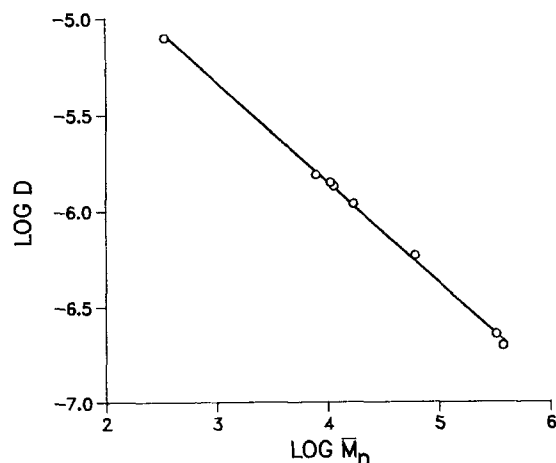


Fig. 3. Dependence of diffusion coefficient on molecular weight of PAQ copolymers and of EBAQ.

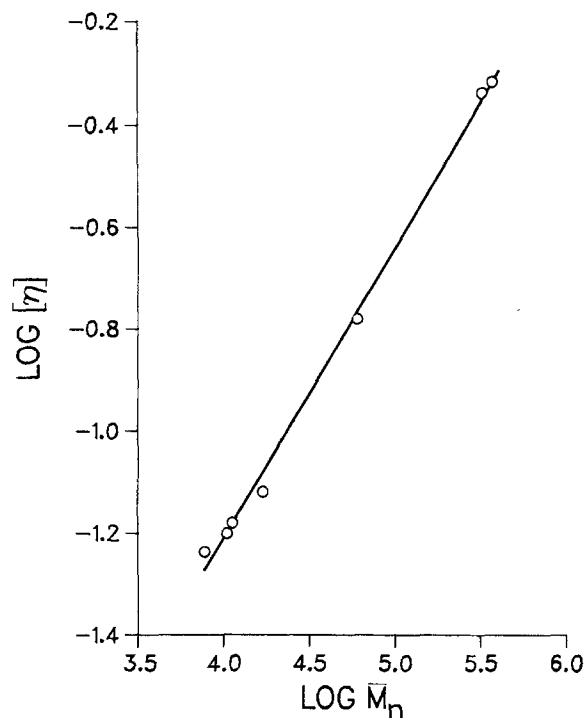


Fig. 4. Intrinsic viscosity-molecular weight relationship for PAQ

yielded $b = 0.52$ was obtained from the double logarithmic plot in Fig. 3.

A further comparison of hydrodynamic behavior may be made with the Mark-Houwink relationship which relates the limiting viscosity number, $[\eta]$ (intrinsic velocity), to the molecular weight

$$[\eta] = K M^a \quad [3]$$

where $b = (1 + a)/3$ (20).

The viscosities of each of the polymer samples were measured at four concentrations and extrapolated to zero concentration. The data in Fig. 4 yield $a = 0.57$ and $K = 3.27 \times 10^{-4}$. This is in remarkable agreement with $a = 0.56$ obtained from the voltammetric data.

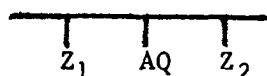
The Randles-Sevcik equation can be rewritten in a form which indicates the dependence of diffusion coefficient on the polymer molecular weight

$$i_p = 2.69 \times 10^5 n^{3/2} A \nu^{1/2} C K_T^{1/2} M^{-b/2} \quad [4]$$

A plot of $\log i_p$ vs. $\log \bar{M}_n$ is linear and is presented in Fig. 5. This again illustrates the feasibility of determining molecular weights from voltammetric measurements in these systems (4).

However, the conditions of ideality required for such an application predicate against the general use of this technique. Not only must a Nernstian electrode process occur to satisfy the assumptions of the Randles-Sevcik equation, but there must also be minimal interaction between electroactive centers. The ability to determine molecular weights, even for a limited group of polymers, is a reassuring manifestation of the essential soundness of the physical model.

On average, the electroactive groups were separated by at least one nonactive group along the chain. This does not imply a lack of opportunity for nearest neighbor interaction. The spacing along the chain is random, and it is instructive to calculate the number of sites in which AQ groups are adjacent to one another on a chain at neighboring positions Z_1, Z_2



Let X be the fraction of AQ groups in the polymer, and $(1 - X)$ the fraction of styrene groups. The probability for

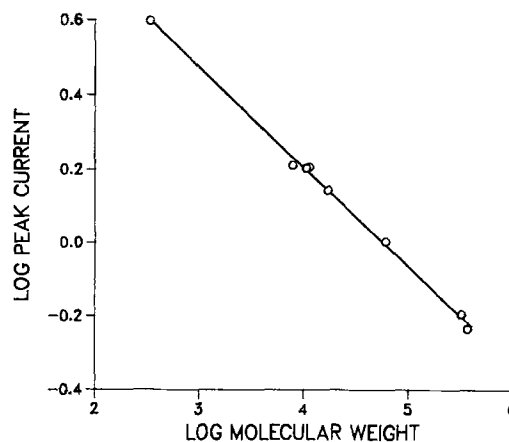


Fig. 5. Dependence of peak current at a scan rate of 50 mV s^{-1} on molecular weight of PAQ copolymers and of EBAQ.

structures such as AQ-AQ-AQ is X^2 ; AQ-AQ-STY is $2X(1 - X)$; and STY-AQ-STY is $(1 - X)^2$. Hence, the probability of an AQ group being adjacent to another AQ group is

$$P = 1 - (1 - X)^2 = X(2 - X) \quad [5]$$

For PAQ 5(2), $X = 0.413$ and thus $P = 0.655$. Hence, 65.5% of the AQ groups in the copolymer are adjacent to another AQ group and the opportunity for near-neighbor interaction is high. Despite this, the voltammetric data are indicative of noninteracting centers along the polymer chain. Although the diffusive motion of the electroactive groups is constrained by the relatively slow diffusion of the polymer molecule, the electrochemical behavior is otherwise unchanged from that of free, simple molecular species undergoing oxidation and reduction reactions at an electrode.

Acknowledgment

The authors thank the Natural Sciences and Engineering Research Council of Canada for their financial support of this work.

Manuscript submitted March 19, 1984; revised manuscript received ca. May 9, 1984. This was Paper 407 presented at the Cincinnati, Ohio, Meeting of the Society May 6-11, 1984.

Simon Fraser University assisted in meeting the publication costs of this article.

REFERENCES

1. T. Saji, N. F. Pasch, S. E. Webber, and A. J. Bard, *J. Phys. Chem.*, **82**, 1101 (1978).
2. J. B. Flanagan, S. Margel, A. J. Bard, and F. C. Anson, *J. Am. Chem. Soc.*, **100**, 4248 (1978).
3. B. L. Funt, L. C. Hsu, and P. M. Hoang, *J. Polym. Sci. Polym. Chem. Ed.*, **19**, 203 (1981).
4. B. L. Funt, L. C. Hsu, P. M. Hoang, and J. P. Martenot, *ibid.*, **20**, 109 (1982).
5. T. W. Smith, J. E. Kuder, and D. Wychick, *ibid.*, **14**, 2433 (1976).
6. Y. Morishima, Y. Itoh, and A. Koyagi, *ibid.*, **21**, 953 (1983).
7. W. T. Yap and R. A. Durst, *J. Electroanal. Chem.*, **130**, 3 (1981).
8. B. L. Funt and P. M. Hoang, *ibid.*, **154**, 229 (1983).
9. J. Q. Chambers, in "The Chemistry of the Quinonoid Compounds," S. Patai, Editor, Chap. 14, Wiley, London (1974).
10. A. S. Lindsey, in "The Chemistry of the Quinonoid Compounds," S. Patai, Editor, Chap. 15, Wiley, London (1974).
11. D. C-S. Tse and T. Kuwana, *Anal. Chem.*, **50**, 1315 (1978).
12. C. Ueda, D. C-S. Tse, and T. Kuwana, *ibid.*, **54**, 850 (1982).
13. C. Degrand and L. L. Miller, *J. Am. Chem. Soc.*, **102**, 5728 (1980).
14. K. J. Stutts and R. M. Wightman, *Anal. Chem.*, **55**, 1576 (1983).

15. C. S. Celabrese, R. M. Buchanan, and M. S. Wrighton, *J. Am. Chem. Soc.*, **105**, 5594 (1983).
16. P. C. Mitter and D. Banerjee, *J. Indian Chem. Soc.*, **9**, 375 (1932).
17. J. E. B. Randles, *Trans. Faraday Soc.*, **44**, 327 (1948).
18. A. J. Bard and L. R. Faulkner, "Electrochemical Methods Fundamentals and Applications," p. 218, John Wiley and Sons, New York (1980).
19. C. Tanford, "Physical Chemistry of Macromolecules," Chap. 6, John Wiley and Sons, New York (1961).
20. H. G. Elias, "Macromolecules," Vol. 1, p. 293, Plenum Press, New York (1977).

The Kinetics of Oxygen Reduction at Porous Teflon-Bonded Fuel Cell Electrodes

R. Holze*¹ and W. Vielstich**

Institute of Physical Chemistry, University of Bonn, D-5300 Bonn 1, Germany

ABSTRACT

Oxygen reduction on porous Teflon-bonded semihydrophobic electrodes has been investigated using the impedance method. Carbon-supported metals and activated carbon have been used as electrocatalysts in neutral and alkaline electrolytes. The results of the impedance measurements agree well with those of galvanostatic double-pulse experiments. Taking into account the internal structure, especially the large inner surface area of the catalyst particles forming the electrode, an attempt is made to calculate exchange current densities from the apparent charge transfer resistance. The values of i_0 support the assumption that hydrogen peroxide is the predominant reduction product formed on the electrocatalysts investigated. The measured polarization resistance is mainly caused by the slow diffusion of oxygen and its reduction products. The rather fast adsorption of oxygen and charge transfer reaction cause only a small contribution to the polarization. The results are discussed with respect to the electrode structure and compared with a general model describing the operation of a semihydrophobic porous electrode.

The reduction of oxygen is the most important cathodic reaction in fuel cells, reactive metal air batteries, and gas-sensitive devices. In the near future, oxygen electrodes may be used in chlor-alkaline electrolysis (1). Many papers related to the kinetics of the oxygen reduction on pure metal or carbon surfaces have been published, *e.g.*, (2).

There is still a lack of information concerning the kinetics of the reduction of oxygen on porous gas-diffusion electrodes, *e.g.*, on metal/carbon or catalyst/carbon electrodes. In recent years Teflon-bonded semihydrophobic electrodes, containing carbon or a catalyst supported on carbon as active material, have been shown to be promising candidates for a widespread application in electrochemical energy conversion. Therefore, it seems necessary to increase our knowledge about these electrodes, not only concerning technical aspects, *e.g.*, lifetime or performance (3), but also fundamental aspects, *e.g.*, exchange current densities, reaction mechanism, and relative influence of diffusion and reaction/adsorption on the overall electrode reaction. A general model of the oxygen reduction kinetics in porous electrodes must include oxygen diffusion, oxygen adsorption, or surface reaction on the active sites of the catalyst, charge transfer, and diffusion of the products.

Wabner demonstrated the possibilities of the impedance method for the investigation of hydrophilic porous gas-diffusion electrodes (4). He separated the polarization resistance of the working electrode into portions attributed to the various steps of the reaction and pointed out the great influence of diffusion polarization. The total electrode overpotential was described as the sum of a large diffusion overpotential due to the diffusion of oxygen and its reduction products, a small overpotential caused by an oxygen surface reaction, and a small charge transfer overpotential.

Using the impedance method, the galvanostatic double-pulse method, and other techniques we tried to develop an appropriate kinetic model describing oxygen reduction in semihydrophobic electrodes. In addition to

information on the kinetics of the electrode reaction, further information should be derived on structural aspects, *e.g.*, the location of the reaction in the porous electrode, the utilization of the electrode, and changes of electrode properties during extended operation.

Experimental

Porous electrodes were fabricated using platinum-carbon (Pt/C, 20 weight percent [w/o] Heraeus), activated carbon (Norit-BRX), silver/carbon (Ag/C, 10-30 w/o, prepared from activated carbon and AgNO₃-solution) and Teflon dispersion (Hoechst). The metal loading was 4 mg/cm² of platinum or 1.4-4.2 mg/cm² of silver with respect to the geometric electrode surface area. The electrodes were dried at 120°C (Pt/C) or 200°C (Ag/C and activated carbon). On one side of the catalyst layer, a silver screen current collector was pressed; on the other side, a porous Teflon backing layer (Berghof, Tuebingen, or Zitex) was pressed to prevent electrolyte leakage when the electrode was operated without feed gas overpressure (Fig. 1). For further details of the preparation, see Ref. (5). Additionally, commercial electrodes without backing layer (Prototech, Fig. 1) and sandwich electrodes, containing two layers of platinum/carbon and activated carbon were measured. Electrolyte solutions were prepared using water purified with a Millipore purification system and reagent-grade NaCl (3M) or KOH (6M). Electrodes were fed with unscrubbed air or oxygen. For electrodes without the porous Teflon backing layer a small feed gas overpressure of 3 kPa was applied. All experiments were performed at room temperature.

All experiments were carried out using a rectangular Plexiglas-cell. The test electrodes were mounted with a screw cap (for rapid replacement), and the counter-electrode was fixed at the opposite side of the cell. A small hole in the wall of the cell near the test electrode served as connection to the reference electrode compartment. In all experiments a saturated calomel electrode (+248 mV vs. SHE) served as a reference. For the impedance measurements, a transfer function analyzer (Model 1172 Solartron-Schlumberger), connected with a potentiostat (Model PCA 72 M, Bank), and a plotter interface (Model 1180 Solartron-Schlumberger) were used (Fig. 2). The measured impedance spectra were displayed on a X-Y plotter (Model HP 7035 B Hewlett-Packard) and

*Electrochemical Society Student Member.

**Electrochemical Society Active Member.

¹Present address: Case Center for Electrochemical Sciences, Case Western Reserve University, Cleveland, Ohio 44106.

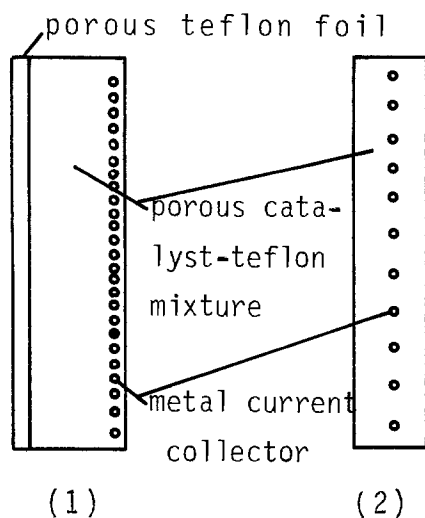


Fig. 1. Schematic cross section of porous gas-diffusion electrodes, (1) with porous Teflon backing layer, as described in Ref. (5), (2) without backing layer, as manufactured by Prototech.

stored on punch cards for further processing. Galvanostatic double-pulse experiments were done using the same cell and a rather simple circuit (Fig. 3), containing a pulse-galvanostat (Model MP-IM 400 Mega-Physik), a transient-recorder (Model B-C 104 Bruker), a CRT display (Model 702 Tektronix), and a custom-designed impedance converter, which contained a circuit for automatic iR_{dc} drop and rest potential correction. During the experiments, the dc current density i_{dc} and feed gas composition were varied. The influence of other experimental conditions is discussed elsewhere (6). To interpret the measured impedances, the equivalent circuit of an oxygen reducing electrode developed by Drossbach (7) was used. The typical properties of porous electrodes which may affect the measured impedance were taken into account according to the results of de Levie (9) and Drossbach (10). After separating the electrolyte resistance R_{so1} and the apparent double layer capacity $C_{D,app}$ from the measured electrode impedance by using a linear regression program, the faradaic impedance was obtained. The kinetic parameters of the elements in the faradaic impedance were fitted using the Marquardt-Levenberg algorithm. All programs were run on an IBM 370/168 computer. A description of the programs and further experimental details are given in Ref. (8).

BET surface areas were determined with a custom-designed apparatus via N_2 adsorption. The porosity of the electrodes was determined from the weight differences between a dry electrode and an electrode soaked with electrolyte.

Results

The polarization curves and the faradaic impedances measured at different dc current densities i_{dc} of electrodes containing platinum carbon in 3M NaCl solution are presented in Fig. 4 and 5. The apparent double-layer capacity

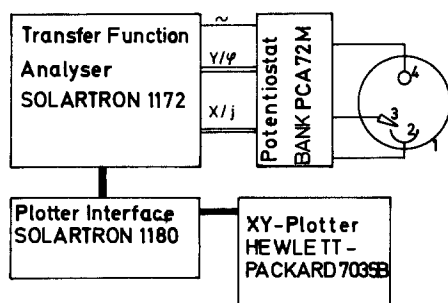


Fig. 2. Schematic wiring diagram of the circuit used for impedance measurements. 1: Cell. 2: Working electrode. 3: Reference electrode. 4: Counterelectrode.

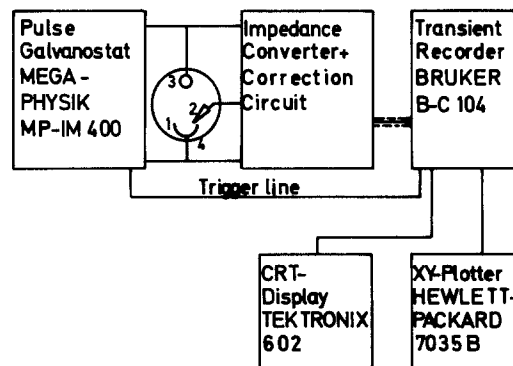


Fig. 3. Schematic wiring diagram of the circuit used for the galvanostatic double-pulse experiments. 1: Cell. 2: Working electrode. 3: Reference electrode. 4: Counterelectrode.

$C_{D,app}$ and the apparent charge transfer resistance $R_{ct,app}$ were measured independently with the impedance method and the galvanostatic double-pulse method, as described above. The results of both methods agreed within experimental error, and the results are given in Table I. Due to changes in the wetting of the electrode, these values were not constant, but time dependent. Using the approximation of the Butler-Volmer equation for small charge transfer overpotentials (*i.e.*, at low charge transfer resistances and small dc current densities) the apparent exchange current density was calculated

$$i_{0,app} = \frac{R \cdot T}{z \cdot F \cdot R_{ct,app}}$$

With $z = 2$ and $T = 298 \text{ K}$, $i_{0,app} = 390 \text{ mA/cm}^2$ (geometric electrode surface area) was obtained. The real inner surface area of the electrode exceeds the geometric surface area by orders of magnitude. In order to obtain a value of the exchange current density i_0 related to the electrochemical active fraction of the inner electrode surface, a surface factor S was calculated. This factor represents the ratio of the electrochemical active surface area of the electrode to the geometric electrode surface. It was obtained by dividing the apparent double layer capacity $C_{D,app}$ obtained for the geometrical electrode surface area by an assumed value of $C_{D,true} = 10 \mu\text{F/cm}^2$ for a smooth carbon electrode. The previously published results leading to the selection of this value will be discussed in detail later in this paper.

With $C_{D,app} = 1.4 \text{ mF/cm}^2$ a surface factor of $S = 140$ was calculated. The $i_{0,app}$ value can be corrected to give an exchange current density per unit true area, $i_0 = 2.85 \text{ mA/cm}^2$. Further interpretation of the impedance spectra is possible with the aid of an appropriate equivalent circuit, containing elements representing the steps of the electrode reaction. According to Drossbach (7), these are as follows. (i) Diffusion of oxygen through the gas phase in the pores and the electrolyte to the reaction sites. (Due

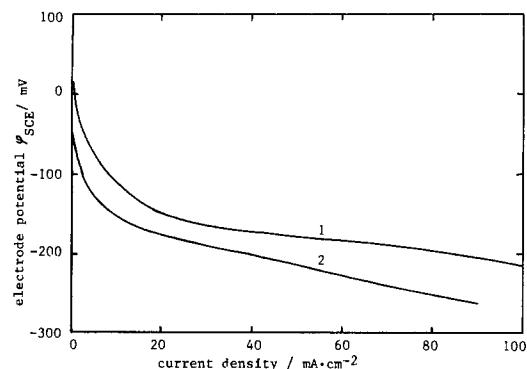


Fig. 4. Steady-state polarization curves for oxygen reduction at a Pt/C electrode in 3M NaCl electrolyte, room temperature, feed gas (1 atm): (1) oxygen, (2) air.

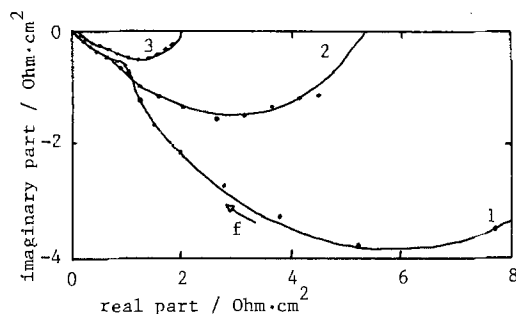


Fig. 5. Faradaic impedance of a Pt/C electrode at different dc current densities. Feed gas (1 atm): air. 3M NaCl electrolyte, room temperature. i_{dc} : (1) 5 mA/cm², (2) 10 mA/cm², and (3) 20 mA/cm². Frequency at the maximum of the complex plane plot: (1) 3.9 mHz, (2) 15.7 mHz, and (3) 39.7 mHz.

to the small solubility and low diffusivity of oxygen in water and the accumulation of inert gas in the pores, this step should cause a significant contribution.) (ii) Adsorption or heterogeneous surface reaction of the oxygen, coupled with oxygen diffusion. (iii) Charge transfer, reduction of oxygen to H₂O₂ or H₂O. (iv) Diffusion of reduction products into the bulk electrolyte.

These steps in the oxygen reduction process are represented in the faradaic branch of the equivalent circuit of the electrode impedance (Fig. 6). Both diffusion processes are described by diffusion impedances Z_{diff} according to the theory of the Nernstian diffusion impedance (11). They are determined by a diffusion factor $A = 2d/\sqrt{2D}$ (with the diffusion coefficient D and the thickness d of the Nernstian diffusion layer) and a diffusion resistance

$$R_{diff} = \frac{R \cdot T \cdot d}{z^2 \cdot F^2 \cdot a \cdot c_{sur} \cdot D}$$

where c_{sur} is the concentration of the diffusing species at the electrode surface area a . The reaction/adsorption impedance is represented by a resistor and a capacitor in parallel, where $R_{ad/react}$ is given by

$$R_{ad/react} = \frac{R \cdot T}{z^2 \cdot F^2 \cdot c_{sur} \cdot k \cdot a}$$

and $C_{ad/react}$ by

$$C_{ad/react} = \frac{z^2 \cdot F^2 \cdot c_{sur} \cdot a}{R \cdot T}$$

The rate constant of the adsorption/reaction k can be derived by $k = 1/[R_{ad/react} C_{ad/react}]$, and the surface concentration of the reacting/adsorbing species by

$$c_{sur} = \frac{R \cdot T \cdot C_{ad/react}}{z^2 \cdot F^2 \cdot a}$$

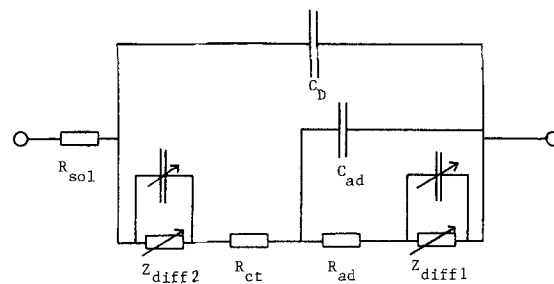


Fig. 6. Equivalent circuit of a working oxygen reduction electrode. For description of elements and parameters, see text.

The results of the fitting of the parameters are given in Table II for different values of i_{dc} .

The BET surface area was measured to be 192 m²/g, and the porosity of the electrode was 28%.

At electrodes prepared from silver/carbon, dried at 200°C, $C_{D,app} = 2.6$ mF/cm² and $R_{ct,app} = 0.01$ Ω · cm² were measured with the impedance and the galvanostatic double-pulse method in 3M NaCl electrolyte. With a surface factor $S = 260$, an exchange current density $i_0 = 4.9$ mA/cm² was calculated. The optimization of the parameters of the equivalent circuit yielded data similar to the results obtained at Pt/C electrodes.

At activated carbon electrodes dried at 200°C, much higher values of $C_{D,app}$ and higher values of $R_{ct,app}$ were measured in 6M KOH electrolyte. The current pulses necessary to charge the double-layer capacity of this electrode could not be supplied by the pulse generator used in these experiments; therefore, only the results of the impedance measurements are given in Table I. The relative magnitude of the polarization resistances attributed to the steps of the electrode reaction were nearly the same as they were in the case of the Pt/C electrode. Only the adsorption/reaction impedance was smaller.

The results obtained with the electrode manufactured by Prototech in 3M NaCl solution were $C_{D,app} = 1.5$ mF/cm² and $R_{ct,app} = 0.017$ Ω · cm², and the calculated exchange current density was $i_0 = 4.95$ mA/cm². No further information about metal content and composition of electrode was provided by the supplier, and thus a detailed discussion of the results is difficult. Comparing the data with the results obtained with our electrodes, this electrode seems to contain a rather active electrocatalyst. The thickness of the diffusion layer as well as the diffusion resistance R_{diff} calculated from the impedance attributed to the diffusion process are nearly equal, indicating a relative decrease of the influence of the oxygen diffusion on the total polarization resistance of the electrode (6). This is a result of the different construction of this electrode without the porous Teflon backing layer (Fig. 1). The inert gas accumulation which can take place in the pores of

Table I. Experimental results of impedance measurements

Electrode	Electrolyte	$C_{D,app}$ (mF · cm ⁻²)	$R_{ct,app}$ (Ω · cm ²)	Surface factor	i_0 (mA · cm ⁻²)	ϕ_{SCE} at $i_{DC} = 20$ mA cm ⁻² (mV)
Pt/C	3M NaCl	1.4	0.032	140	2.85	—
Ag/C	3M NaCl	2.6	0.01	260	4.9	—
Activated carbon	6M KOH	14.3	0.1	1430	0.08	—
Prototech	3M NaCl	1.5	0.017	150	4.95	—
Sandwich A	6M KOH	2.8	0.007	280	6.5	-197
Sandwich B	6M KOH	9.1	0.026	910	0.5	-281

Table II. Impedance parameters of the faradaic impedances of Fig. 5, obtained with the least squares fit program described

i (mA · cm ⁻²)	A1 (√s)	A2 (√s)	R_{diff1} (Ω · cm ²)	R_{diff2} (Ω · cm ²)	R_{ad} (Ω · cm ²)	C_{ad} (F · cm ⁻²)	$C_{D,app}$ (mF · cm ⁻²)	$R_{ct,app}$ (Ω · cm ²)
5	13.4	0.88	9.9	(0.18)	(0.33)	(0.025)	1.9	0.027
10	10.4	(5.5)	2.3	1.9	0.33	0.22	(3.6)	0.04
20	4.5	1.45	1.11	0.5	0.16	0.13	2.2	0.03

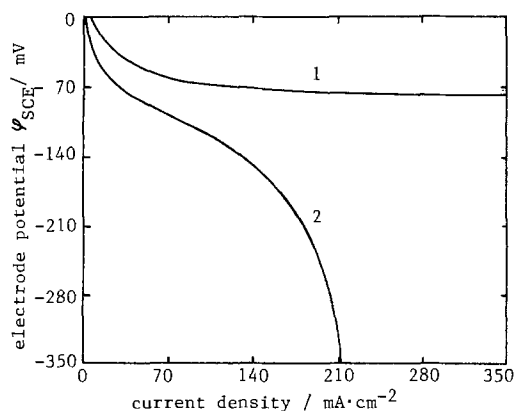


Fig. 7. Steady-state polarization curves for oxygen reduction at an Ag/C electrode in 3M NaCl electrolyte, room temperature, feed gas (1 atm): (1) oxygen, (2) air.

the backing layer, with the resulting hindrance due to limited gas transport through the layer, thus, was not observed. In addition, the air on the gas chamber in front of the electrode is exchanged rapidly due to the flowing feed gas.

In order to determine the location of the reaction zone within the porous system, the impedance of sandwich electrodes, containing two active layers in different arrangements, was measured. The thickness of these electrodes was nearly doubled: the usual thickness of a single-layer electrode was about 0.6 mm, while the thickness of the sandwich electrodes was about 1 mm.

A reaction zone near the gas-side surface will be favored by a shorter diffusion path for the oxygen, and a reaction zone near the electrolyte side surface will be favored by a shorter diffusion path for the products. Additionally, the reaction could take place in the vicinity of the current collector.

Two types of sandwich electrodes with different layer sequences were investigated: type A (foil-activated carbon-platinum/carbon-current-collector and type B (foil-platinum/carbon-activated carbon-current-collector).

The results are given in Table II. They indicate clearly that the typical properties of the layer at the electrolyte side were measured. The potential difference between electrode A and B demonstrates that the reaction takes place in this zone, since the potential of the electrode is more negative in case of electrode B with less active carbon near the electrolyte. These results were confirmed in experiments with stirred electrolyte. Especially at higher current densities, the potential was more positive if the electrolyte was stirred. This could be explained only by the assumption that the reaction zone must be located near the electrolyte-side surface of the electrode, where the stirring is effective.

Discussion

Although the charge transfer resistance was small for all of the electrodes investigated in our experiments, a detailed discussion of the results is necessary for the understanding not only of the reaction kinetics, but also of the electrode deterioration caused by reaction products.

Taking into account the generally accepted results of research on oxygen reduction catalysis (13) and our numerical values for the exchange current density, two pathways for the reduction of oxygen are important. The first is the $4e^-$ pathway, leading from O_2 directly to H_2O , characterized by low i_0 values ranging from 10^{-6} to 10^{-10} A/cm², with the number of electrons transferred z being 4. The second is $2e^-$ pathway, leading to H_2O_2 , characterized by higher i_0 values, ranging in alkaline electrolytes at carbon electrodes from 10^{-3} to 10^{-4} A/cm² with $z = 2$ (14). Obviously, at our electrodes, the $2e^-$ pathway predominates: calculating i_0 with $z = 4$ leads to i_0 values which are much too high for the $4e^-$ pathway. This verifies the assumed value of $z = 2$ in the calculations described above. In the

case of the activated carbon electrode, no other possibility exists, and the HO_2^- concentration, calculated from the diffusion impedance related to the transport of the product into the bulk electrolyte, confirmed this result. (The HO_2^- concentration calculated from the diffusion resistance is about $10^{-2}M$ in the reaction zone, as discussed below.) At metal/carbon electrodes, the interpretation is more difficult. Both platinum and silver catalyze the $4e^-$ pathway (15). The mechanism via a bridge-like adsorbed oxygen molecule is very sensitive to impurities adsorbed on the electrode surface. With respect to the values obtained i_0 for the metal/carbon electrodes, it has been concluded that oxygen is reduced on these catalysts mostly to H_2O_2 . Obviously, the metal acts as a very active hydrogen peroxide decomposing catalyst: no H_2O_2 could be detected in the bulk electrolyte. The $4e^-$ pathway cannot be excluded, but seems to be of minor importance and may be suppressed by impurities adsorbed on the metal during the preparation of the electrode. Based on our results, a separation of the currents generated at the carbon and at the metal surface is impossible.

The data presented confirm the assumption that the oxygen electrode potential is a mixed potential described by

$$\varphi = \varphi_0 \frac{RT}{zF} \ln \frac{[HO_2^-][OH^-]}{[O_2][H_2O]}$$

Potential differences between different electrocatalysts, e.g., between activated carbon and platinum carbon (e.g., at sandwich electrodes), measured under identical conditions, can be explained at least partially using this equation. With a very active peroxide decomposing catalyst (e.g., platinum), the peroxide concentration is low, resulting in less potential loss.

The most important part of the overpotential (the corresponding diffusion resistances are given in Table II) is due to the diffusion of oxygen to the reaction sites. Various items which are consistent with this view are: (i) low solubility of oxygen in water, about 10^{-3} to $10^{-4}M$ (16), (ii) a small diffusion coefficient, about 0.675×10^{-5} cm²/s (17), (iii) the limited oxygen concentration in air, and (iv) inert gas accumulation in the porous system. Together, these cause a diffusion overpotential of 48%-91% of the total overpotential. According to the theory of the Nernst diffusion impedance, the concentration of the diffusing species as well as the thickness d of the diffusion layer can be calculated with the equations already mentioned

$$d = \frac{A\sqrt{2D}}{2} \quad c_{sur} = \frac{R \cdot T \cdot d}{z^2 \cdot F^2 \cdot R_{diff} \cdot a \cdot D}$$

With the diffusion factors and the diffusion resistances measured in our experiments, values of d ranging from 1 to 275 μm were obtained (depending on i_{DC} , the electrode composition and other experimental conditions) [for details, see Ref. (8)]. These values are in some cases of the same order of magnitude as the thickness of the active layer of the electrode (300-400 μm). This is in disagreement with the classical theory [see e.g., Ref. (11)] of diffusion layers at electrode-electrolyte interfaces, although the values are plausible if one assumes an oxygen concentration gradient from the gas phase outside the electrode to the inner electrode surface. Nevertheless, it seems useful to discuss the diffusion layer theory again for the case of a porous gas-diffusion electrode.

The assignment of the diffusion impedance to the diffusion of the reduction products into the electrolyte is straightforward and depends only on the composition of the catalyst. At platinum/carbon and silver/carbon electrodes, the hydrogen peroxide is decomposed rather fast. The diffusion layer thickness and the concentration of the diffusing species calculated from the impedance parameters can only be associated with the OH^- transport into the bulk electrolyte (3M NaCl). (The OH^- concentration calculated from the results given in Table II is about $10^{-1}M$.) At activated carbon electrodes operating in 6M KOH electrolyte, this diffusion impedance cannot be at-

tributed to the diffusion of OH^- produced during the reduction of oxygen, since the concentration of OH^- obtained from the diffusion resistance would be below the concentration in the bulk electrolyte. Since the product of the reduction of oxygen at smooth carbon electrodes is only hydrogen peroxide (14), this impedance must be attributed to the diffusion of hydrogen peroxide. The concentration values calculated from the measured impedances range from 3.1×10^{-2} to $7.5 \times 10^{-2} M$ (depending on i_{dc}) and agree well with the results obtained at smooth electrodes (14).

Compared with the rather straightforward situation at a planar electrode (with well-defined transport of the reactants) the situation in a porous electrode is more complex. One of the most surprising results concerning the phase boundaries in the gas diffusion electrodes studied in this paper is the low utilization of the inner surface.

The comparison of the electrochemically active surface, the wetted surface, and the total surface area of the electrode obtained from BET measurements has been the subject of many papers published in recent years. Of particular interest are results obtained with activated carbons, graphites, charcoals, and related materials. BET surface areas of these materials range from values as low as $10 \text{ m}^2/\text{g}$ (SP-1 graphite) to as high as $1600 \text{ m}^2/\text{g}$ (Norit-BRX activated carbon). In order to obtain true double-layer capacities, many authors have assumed a complete wetting of the total surface area with the electrolyte. The measured apparent double-layer capacity, in most cases obtained from cyclic voltammograms, was divided by the BET surface area to calculate a true double-layer capacity related to the actual electrode surface. Some representative results are: $3.7 \mu\text{F}/\text{cm}^2$ for Ketjenblack (Armak) (18), $4.3 \mu\text{F}/\text{cm}^2$ for Carpack B, graphitized carbon black (Supelco) (19), $8 \mu\text{F}/\text{cm}^2$ for XC-72 (Cabot) (20), $9.5\text{--}10.7 \mu\text{F}/\text{cm}^2$ for FC-12 (St. Mary's Penn) (28), $10 \mu\text{F}/\text{cm}^2$ [several carbons (22)], $12 \mu\text{F}/\text{cm}^2$ for RB-activated carbon (Calgon) (18), and $19 \mu\text{F}/\text{cm}^2$ for Shawinigan black (Gulf) (18). Unfortunately, there are some inherent limitations and drawbacks in the application of dynamic methods for porous electrodes, as has already been discussed by de Levie (23).

Especially in experiments with high surface area carbons like Ketjenblack or RB, the long relaxation time caused by the extended internal structure of the porous electrode may have affected the results. The assumption of a totally wetted surface is also in obvious contradiction to the results of Momot *et al.* (24) and Lore *et al.* (25), which state that only a small fraction of the BET surface area of the activated carbons and graphites investigated was accessible to the electrolyte and, therefore, at least potentially electrochemically active.

Double-layer capacities obtained at smooth carbon electrodes are not useful in clarifying this contradiction. The published results depend very much on the type of the carbon and the pretreatment. Examples are: $3 \mu\text{F}/\text{cm}^2$ [basal plane of peeled stress annealed pyrolytic graphite (SAPG) (26, 27)], $12 \mu\text{F}/\text{cm}^2$ [ordinary pyrolytic graphite (OPG) basal plane, cleaved (28)], $25 \mu\text{F}/\text{cm}^2$ [glassy carbon, (29)], and $60 \mu\text{F}/\text{cm}^2$ [OPG, basal plane polished (28), and SAPG edge oriented polished (26)].

Using advanced BET-adsorption instruments, the pore volume distribution and the surface area distribution as a function of the pore diameter can be measured. The results can be used for the interpretation of changes in the electrochemical activity of a carbon as a function of changed surface area and surface area distribution for certain electrode reactions (30). However, they are only of limited value for the discussion of the ratio of BET surface area to wetted surface area, unless the microscopic structure of the carbon particle surface and the wetting properties are not well known (31). This situation is further complicated, when electrochemical measurements are done with Teflon-bonded electrodes, *e.g.*, as in Ref. (18), where parts of the carbon may have become hydrophobic.

An additional difficulty is introduced when the double

layer capacity of an operating electrode ($i_{dc} \neq 0$) is determined. According to Schwabe *et al.* (32), only pores of diameter greater than 100 \AA contribute to the current generation during the reduction of oxygen at activated carbon electrodes in alkaline solution. The penetration depth of the electrochemical reaction as well as the penetration depth of the ac signal used in the impedance method into the porous electrode are limited. A detailed discussion with respect to the electrodes used in our experiments is given in Ref. (33).

According to the results and conclusions obtained by Wabner (4) and Holze (33), it is assumed that the measured apparent double-layer capacity resembles the electrochemical active surface area involved in the reduction of oxygen. Since the assumption of a true double layer capacity of $C_D = 10 \mu\text{F}/\text{cm}^2$ seems reasonable with respect to the results published previously and the fact that the carbons used in our experiments are similar to the carbons used in some of the papers mentioned above (18, 19, 22), this value was used to calculate the surface factor S , the surface area involved in the electrochemical reaction, and the exchange current density i_0 .

Only about 0.5% of the BET surface area of the Pt/C electrode is involved in the electrochemical reaction. The wetted surface area may be greater; based on a porosity of 28% and a simplified model of the porous structures assuming cylindrical pores of 100 nm avg diam, it was concluded that about 5% of the BET surface area is wetted. This is in good agreement with, *e.g.*, the value of 2%–5% obtained with Teflon-bonded platinum-black in $1N \text{ H}_2\text{SO}_4$ reported by Austin and Almaula (34).

Kunz and Gruver discussed the utilization of an electrode prepared from carbon-supported platinum (35). From transmission electron microscopy, they calculated a surface area of the platinum of $175 \text{ m}^2/\text{g}$; from the hydrogen adsorption on the platinum, a surface of $70 \text{ m}^2/\text{g}$ was calculated. From the comparison of polarization curves obtained during oxygen reduction experiments in H_3PO_4 on the porous electrodes described with results obtained with smooth platinum electrodes, the authors concluded that about $70 \text{ m}^2/\text{g}$ of the platinum surface was electrochemically active. The discrepancy with the higher values estimated using transmission electron microscopy was attributed to several processes leading to the loss of active surface area. The double-layer capacity and the BET surface area of the electrodes under investigation were not determined; thus, a careful comparison with our results is not possible.

Although several other authors in addition to Austin and Almaula (4, 36, 37) have obtained low utilization values somewhat at variance with the results of Kunz and Gruver, a comparison between different porous electrodes is difficult due to the often poorly understood influence of parameters such as internal structure, surface distribution, degree of interaction between catalyst and Teflon, contact angle, etc., on the actual value of the surface area under discussion.

The active surface area of the electrode can be represented as a very thin reaction zone of, *e.g.*, $1.3 \mu\text{m}$ thickness in case of the Pt/C electrode described. This zone must be localized near the electrolyte-side surface of the electrode. Similar conclusions have been reached by other authors (4, 34, 36, 37).

The results obtained at our electrodes can be explained using the semihydrophobic porous electrode model described by Burshtein *et al.* (38). In this model, Teflon agglomerates form gas channels across the electrode which are surrounded by catalyst-Teflon mixture wetted with electrolyte. At variance with the results given by Burshtein *et al.* (38), in the electrodes investigated here, oxygen reduction obviously occurs preferentially in a small reaction zone located near the electrolyte-side surface of the electrode, probably at the electrolyte-side ends of the gas channels. In this case the diffusion pathways for oxygen and reduction products both are at a minimum. This situation is the most favorable one, since oxygen diffusion in the electrolyte is slower than in the gas-filled channels. If

the reaction zone moves toward the gas side, the diffusion overpotential due to the diffusion of the products will increase. This is demonstrated during the lifetime of the electrode when the loss of hydrophobicity results in flooding of the electrode and increased overpotential due to oxygen diffusion. Additionally, the applicability of this model is favored by the results of our C_p measurements at various Teflon-bonded electrodes of different composition (6).

The situation in the Prototech electrode is slightly different. In this electrode, no porous Teflon backing layer is used. The three-phase boundary is established by the hydrophilic properties of the active layer and a small overpressure of the feed gas. The feed gas was supplied in greater than stoichiometric amounts. This resulted in a diminution of the diffusion overpotential due to gas transport when air was used, since the accumulation of inert gas, which was observed at electrodes with a porous Teflon backing layer, cannot take place. The actual location of the reaction zone in this electrode depends both on the hydrophilicity of the electrode and the feed gas overpressure. Under the experimental conditions applied here, the thickness of the diffusion layer for oxygen as well as that for reduction products, as calculated from the diffusion impedances, is equal. This indicates that the location of the reaction zone is equidistant from both outer-electrode surfaces (6).

Conclusions

The kinetics of oxygen reduction at porous electrodes fabricated from dispersed Teflon and electrocatalysts (Pt/C, Ag/C, activated carbon) as described here are mainly diffusion controlled. In all cases, the reduction of oxygen to hydrogen peroxide prevails, followed by an effective decomposition to water and oxygen in the metal containing electrodes. If the electrode is covered with a porous Teflon backing layer on the gas side, oxygen reduction occurs in a small reaction zone located near the electrolyte side. The thickness of this zone is typically 1.3 μm (compared with a total thickness of the active layer of 0.3-0.4 mm). The utilization of the catalyst is poor.

These results indicate that further development of such electrodes should aim at thin electrodes with homogeneous distribution of the catalyst or at sandwich electrodes with a very thin active layer localized on the electrolyte-side surface. A similar approach has been described by Iliev *et al.* (39). The effectiveness of the electrocatalyst must be judged with respect to parameters such as electrode structure, wetting properties, and Teflon content. These influence the diffusion processes, which produce the major part of the still high overpotential of the porous oxygen electrode.

Acknowledgments

The valuable assistance of F. Barz and D. A. Tryk during the preparation of the manuscript is gratefully appreciated. One of the authors (R.H.) thanks the Studienstiftung des Deutschen Volkes for providing a generous graduation stipend.

Manuscript submitted July 22, 1983; revised manuscript received May 14, 1984.

The University of Bonn assisted in meeting the publication costs of this article.

REFERENCES

1. E. Yeager and P. Bindra, *Chem.-Ing. Tech.*, **52**, 384 (1980).
2. J. P. Hoare, "Encyclopedia of the Electrochemistry of the Elements," Vol. 3, p. 191, Dekker, New York (1974).
3. C. Fabian, *Proc. B.S.*, **3**, 233 (1980).
4. D. W. Wabner, *Metalloberfläche-Angew. Elektrochem.*, **28**, 21 (1974).
5. W. Vielstich, "Fuel Cells," p. 42, Wiley-Interscience, London (1970).
6. R. Holze and W. Vielstich, *Electrochim. Acta*, **29**, 607 (1984).
7. P. Drossbach, *ibid.*, **9**, 667 (1964).
8. R. Holze and W. Vielstich, in "Advances in Battery Materials and Processes," J. McBreen, D.-T. Chin, R. S. Yeo, and A. C. C. Tseung, Editors, p. 230, The Electrochemical Society Softbound Proceedings Series, Pennington, NJ (1984).
9. R. de Levie, *Electrochim. Acta*, **8**, 751 (1963) *ibid.*, **9**, 1231 (1964).
10. P. Drossbach, *ibid.*, **13**, 2089 (1968).
11. P. Drossbach and J. Schulz, *ibid.*, **9**, 1391 (1964).
12. A. A. Pilla, *This Journal*, **117**, 467 (1970).
13. E. Yeager, in "Electrode Materials and Processes for Energy Conversion and Storage," J. D. E. McIntyre, S. Srinivasan, and F. G. Will, Editors, p. 159, The Electrochemical Society Softbound Proceedings Series, Princeton, NJ (1977).
14. E. Yeager, P. Krouse, and K. V. Rao, *Electrochim. Acta*, **9**, 1057 (1964).
15. P. Fischer and J. Heitbaum, *J. Electroanal. Chem.*, **112**, 231 (1980).
16. K. E. Gubbins and R. D. Walker, *This Journal*, **112**, 469 (1965).
17. R. E. Davis, G. L. Horvath, and C. W. Tobias, *Electrochim. Acta*, **12**, 287 (1967).
18. J. A. Molla, Thesis, Case Western Reserve University, Cleveland, OH (1983).
19. Y. Oren and A. Soffer, *This Journal*, **125**, 869 (1978).
20. K. Kinoshita and J. A. S. Bett, *Carbon*, **11**, 403 (1973).
21. A. Soffer and M. Folman, *J. Electroanal. Chem.*, **38**, 25 (1972).
22. E. G. Gagnon, *This Journal*, **122**, 521 (1975).
23. R. de Levie, *Adv. Electrochem. Electrochem. Eng.*, **6**, 239 (1967).
24. E. Momot, M. Bonnemay, G. Bronoel, D. Doniat, and E. Levart, *C. R. Acad. Sci. Paris, Ser. C*, **265**, 444 (1962).
25. J. Lore, A. Jardy, A. Falguieres, and R. Rosset, *ibid.*, **274**, 1979 (1972).
26. J. P. Randin and E. Yeager, *This Journal*, **118**, 711 (1971).
27. J. P. Randin and E. Yeager, *J. Electroanal. Chem.*, **36**, 257 (1972).
28. H. H. Bauer, M. S. Spritzer, and P. J. Elving, *ibid.*, **17**, 299 (1968).
29. R. J. Taylor and A. A. Humffray, *ibid.*, **42**, 342 (1973).
30. L. A. Knerr and R. Holze, Unpublished results.
31. R. Holze and E. B. Yeager, Unpublished results.
32. K. Schwabe, W. Wiesener, E. Hollax, A. Tschoe, G. Anders, J. Schreiber, G. Meitzner, and L. Zollfrank, *Electrochem. Technol.*, **3**, 189 (1965).
33. R. Holze, Thesis, Universität Bonn, Bonn, Germany (1983).
34. L. G. Austin and S. Almaula, *This Journal*, **114**, 927 (1967).
35. H. R. Kunz and G. A. Gruver, *ibid.*, **122**, 1279 (1975).
36. H. H. Horwitz, *ibid.*, **113**, 650 (1967).
37. S. Srinivasan, H. D. Hurwitz, and J. O'M. Bockris, *J. Chem. Phys.*, **46**, 3108 (1967).
38. R. Kh. Burshtein, A. V. Dribinskii, M. R. Tarasevich, Yu. A. Chizmadzhev, and Yu. G. Chirkov, *Sov. Electrochem.*, **7**, 1762 (1971).
39. I. Iliev, S. Gamburgzev, A. Kaisheva, E. Vakanova, J. Muchovski, and E. Budevski, *Izv. Otd. Khim. Nauki, Bulg. Acad. Nauk*, **7**, 223 (1974); *ibid.*, **7**, 233 (1974).

Electrochemical Deposition, Optical Properties, and Photoelectrochemical Behavior of CdTe Films

Makoto Takahashi, Kohei Uosaki,* and Hideaki Kita

Department of Chemistry, Faculty of Science, Hokkaido University, Sapporo 060, Japan

ABSTRACT

Electrochemical deposition of cadmium telluride from acidic solutions containing CdSO_4 and TeO_2 is studied and the current-potential expression for this reaction is presented. The electrochemically deposited CdTe films are photoactive, and the maximum cathodic photocurrent due to hydrogen evolution is observed at CdTe films deposited at -0.40V . The photocurrents of the as-grown CdTe films are relatively small compared with those of CdTe single crystals. The major reason for this low efficiency is the effective recombination of hole-electron pairs at grain boundaries and at the surface. The photocurrents are increased significantly by the increase of crystallite diameter by the heat-treatment in a He atmosphere and by the removal of surface Te, which acts as a recombination center, by the etching treatment.

Since cadmium telluride (CdTe) is a direct gap semiconductor with a room temperature energy gap of 1.44 eV (1) and can readily be prepared in both n- and p-type form (2), it is considered to be a promising material for low cost thin film photovoltaic and photoelectrochemical cells. A variety of methods, such as liquid-phase epitaxial growth (3), vacuum evaporation (4), chemical transport (5), and direct combination method (6), have been employed to form CdTe thin films on foreign substrates. CdTe can also be deposited electrochemically from a solution containing CdSO_4 and TeO_2 (7). The electrochemical deposition has the following advantages. The thickness of the film can be controlled by the charge passed during the deposition, both n-type and p-type material can be formed by just changing the deposition potential, and the doping is performed easily by adding the foreign species other than CdSO_4 and TeO_2 in the solution.

Several papers on the photoelectrochemical behavior of CdTe single crystals (8-12) and CdTe thin films (13-16) have been published. Although one of us reported that p-CdTe is a stable photocathode for photoelectrochemical generation of hydrogen (8, 9), most of the work was on n-CdTe in solution containing redox couples as stabilizing agents. Photoelectrochemical studies on electrochemically deposited CdTe films published so far are all on n-CdTe (15, 16), except one, which we published recently as a preliminary note of this work (17).

In this paper, we investigate the electrochemical deposition of CdTe films and report the photoelectrochemical characteristics of the CdTe films deposited at several potentials ($-0.2 \sim -0.6\text{V vs. Ag/AgCl}$) and the effect of annealing and etching treatment on the optical and photoelectrochemical properties of the electrochemically deposited CdTe films.

Experimental

The CdTe films were deposited from aqueous solutions of pH 1.4 containing CdSO_4 and TeO_2 on Ti or Ni (The Japan Lamp Industrial Company, Limited) sheets which were degreased by chloroform and ethanol vapor and washed in purified water before use. The reagent-grade H_2SO_4 , NaOH, CdSO_4 (purity 99.5%), and TeO_2 (purity 99%) were used without further purification. Water was purified by Milli Q water purification system (Millipore Corporation). The usual three electrode cells were used both for the preparation of CdTe films and for the photoelectrochemical measurements. A platinum sheet and a Ag/AgCl electrode were used as a counter and a reference electrode, respectively. A Hokuto Denko HA-301 potentiostat with a Hokuto Denko HB-105 programmable function generator or a Wenking Model 68 FRO.5 potentiostat was used for the potentiostatic deposition of CdTe films and photoelectrochemical measurements. Photoelectrochemical measurements were carried

out in 1M NaOH. A 300 or 500W Xe lamp (Usio Denki Company, Limited) with an IR absorbing filter (Toshiba, IRA-20) was used as a light source. A monochromator (Ritsu Oyo Kogaku Company, Limited) was used to obtain photocurrent action spectra. In all the measurements, currents were recorded on a Rika Denki RW-11T X-Y-t recorder. The electrochemical deposition and photoelectrochemical measurements of the films were carried out at room temperature after the electrolyte solutions were deaerated by passing purified He gas for about 20 min. The heat-treatments of the films were carried out in a quartz tube under a He gas flow. The etching treatment of the films was carried out in a solution containing 0.6M $\text{Na}_2\text{S}_2\text{O}_4$ and 2.5M NaOH at 80°C (18).

The type of semiconductivity of the CdTe films was determined by measuring the potential difference between a hot and a cold contact. The thickness of the films was determined by using a Surfcom 300B surface roughness measuring instrument (Tokyo Seimitsu Company, Limited). The reflection spectra of the films were recorded by a Beckman DK-2 reflectometer. X-ray diffraction measurements were carried out by using a Toshiba XC-40 x-ray diffractometer.

Results

Electrochemical deposition of CdTe.—The current-potential (*i*-V) relation of a Ni sheet electrode in a solution containing 1M CdSO_4 , 1 mM TeO_2 , and 0.05M H_2SO_4 is shown in Fig. 1. Limiting current was observed at potentials between -0.30 and $-0.65\text{V vs. Ag/AgCl}$. The cathodic current increased significantly at potentials more negative than -0.65V . The *i*-V relations were affected by TeO_2 concentration very strongly, and a linear relation was observed between TeO_2 concentration and the limiting cur-

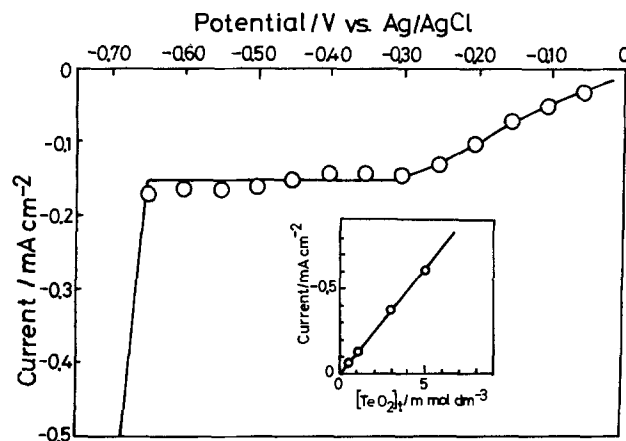


Fig. 1. Current-potential relation of Ni electrode in a sulfuric acid solution (pH 1.4) containing 1M CdSO_4 and 1 mM TeO_2 . Insert: TeO_2 concentration dependence of the current at $-0.35\text{V vs. Ag/AgCl}$.

* Electrochemical Society Active Member.

rent, as shown in Fig. 1. However, CdSO_4 concentration affected the i-V relations little. The limiting current was larger when the solution was stirred. The thickness of the film and the charge passed during the deposition, Q_{dep} , are linearly correlated as shown in Fig. 2. The film thickness was found to be uniform throughout the film ($\pm 5\%$). As already reported, x-ray diffraction patterns of the deposited films confirmed the formation of CdTe (19). The x-ray diffraction peak due to Te was also observed in the films deposited at relatively positive potentials. The more positive the deposition potential, the stronger the diffraction peak due to Te (19). Cd deposition was not observed at the potential region employed in this study ($-0.20 \sim -0.60\text{V vs. Ag/AgCl}$). CdTe films deposited at relatively positive potentials were p-type, and those deposited at relatively negative potentials were n-type.

Optical properties and photoelectrochemical behavior of as-grown CdTe films.—A typical example of the diffuse reflection spectra of as-grown CdTe films is shown in Fig. 3. The wavelength dependence of the reflectivity was very small, and the energy gap was not able to be determined.

The photocurrent-potential relations of CdTe films deposited at various potentials are shown in Fig. 4. The most efficient cathodic photocurrent-potential relation was observed at the CdTe films deposited at -0.40V . The films deposited at the potentials at either more negative or more positive than -0.40V gave lower photocurrent, and no cathodic photocurrent was observed at CdTe films deposited either more positive than -0.20V or more negative than -0.55V . Even the highest cathodic photocurrent observed was relatively small compared with that at p-CdTe single crystals (9). The observed cathodic photocurrent at relatively positive potential seemed to be due to hydrogen evolution reaction, as suggested by bubble formation. The photocurrent increased significantly when the potential became more negative than -0.85V , and it seemed to be due to the cathodic decomposition of CdTe, as color of the solution near the electrode became purple, suggesting Te_2^{2-} formation.

Effect of heat-treatment.—By the heat-treatment at 200°C in a He atmosphere, the x-ray diffraction peaks due

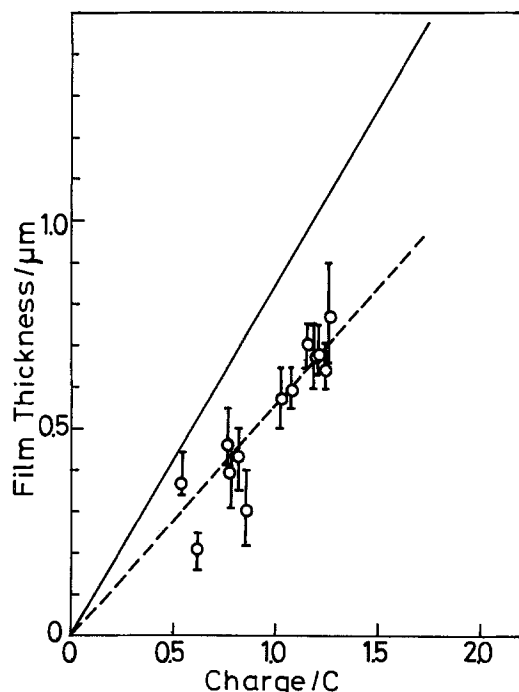


Fig. 2. The thickness of the electrochemically deposited films on Ni as a function of charge passed. The deposition was carried out at -0.35V (vs. Ag/AgCl) in a sulfuric acid solution (pH 1.4) containing 1M CdSO_4 and 1mM TeO_2 . Solid line shows the theoretical value calculated by assuming six-electron process.

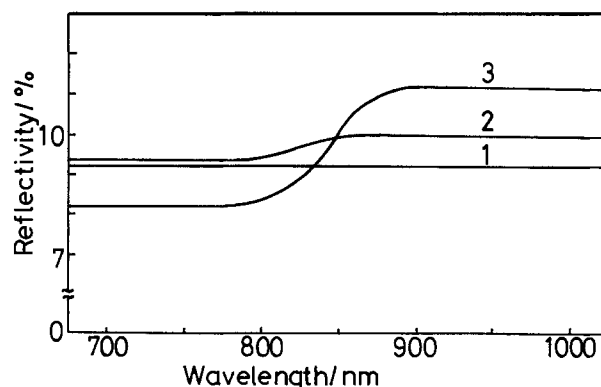


Fig. 3. Diffuse reflection spectra of the electrochemically deposited films ($3\ \mu\text{m}$ thick) on Ti substrate. The other deposition conditions are the same as those in Fig. 2. Curve 1: As grown. Curve 2: Heat-treated in a helium atmosphere at 200°C for 12h. Curve 3: Etched in a solution containing $0.6\text{M Na}_2\text{S}_2\text{O}_4$ and 2.5M NaOH at 80°C after heat-treatment in a He atmosphere at 200°C for 12h.

to CdTe became stronger and sharper by the increase of annealing time, but the peak due to Te was not affected by this treatment (17). The crystallite diameter calculated by using Scherrer equation (20) with the value of the full width at half maximum (FWHM) of x-ray diffraction peak due to (311) face of CdTe as well as the photocurrent increased with increase of annealing time, as shown in Fig. 5. By the heat-treatment, the reflection spectra of the CdTe films became clearer, as shown in Fig. 3. The band-edge energy determined from the reflection spectra is 1.45eV and is in good agreement with the value reported for CdTe single crystal (1). The photocurrent-wavelength relation also showed the same energy gap (17).

Effect of etching treatment.—The effect of the etching treatment was studied at p-CdTe films which were deposited at -0.35V and annealed at 200°C in a He atmo-

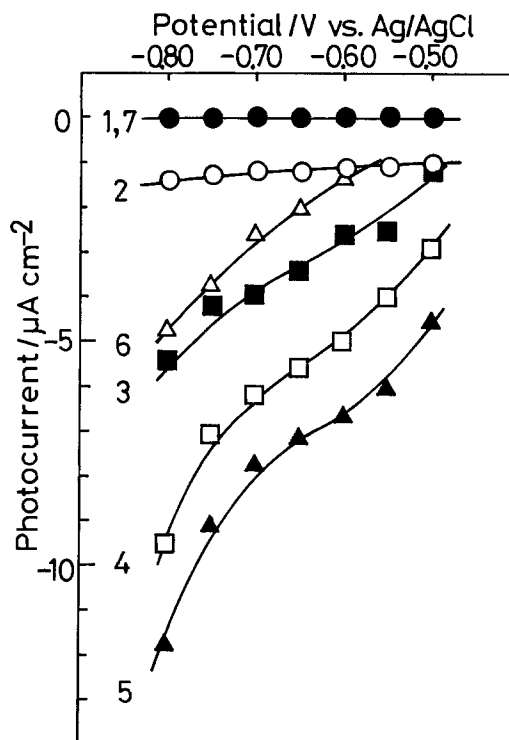


Fig. 4. Photocurrent-potential relations of the as-grown films deposited on Ti at several potentials, from a sulfuric acid solution (pH 1.4) containing 1M CdSO_4 and 1mM TeO_2 . Curve 1: -0.20V . Curve 2: -0.25V . Curve 3: -0.30V . Curve 4: -0.35V . Curve 5: -0.40V . Curve 6: -0.50V . Curve 7: -0.55V . All vs. Ag/AgCl. Photoelectrochemical measurements were carried out in 1M NaOH solutions. A 300W Xe lamp with an IR absorbing filter was used as a light source.

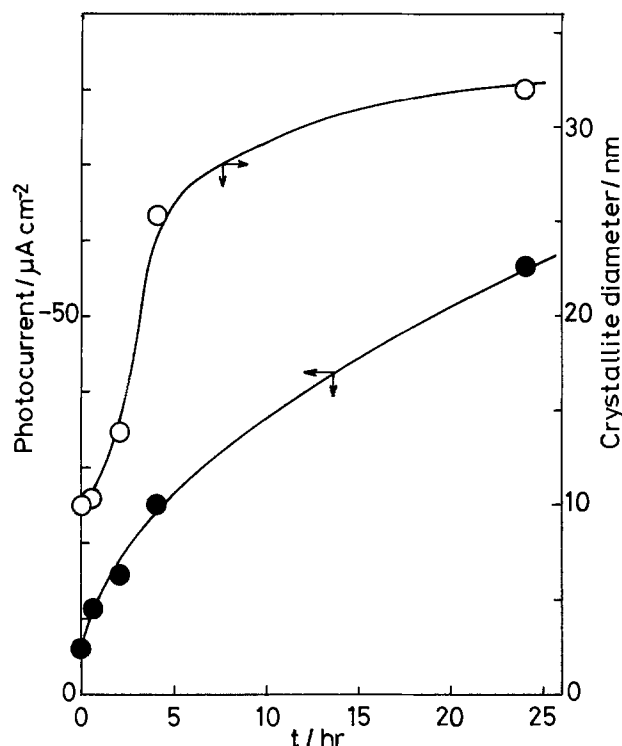


Fig. 5. Photocurrent at $-0.65V$ (vs. Ag/AgCl) in $1M$ NaOH under illumination of $300W$ Xe lamp and crystallite diameter of the electrochemically deposited films ($3 \mu m$ thick on Ti) as a function of annealing time. Deposition conditions are as same as those in Fig. 2.

sphere for 12h. As shown in Fig. 6, the intensity of x-ray diffraction peak due to Te decreased and that of x-ray diffraction peaks due to CdTe increased with the increase of the etching time. The FWHM of CdTe peaks was not affected by the treatment, suggesting the crystallite diame-

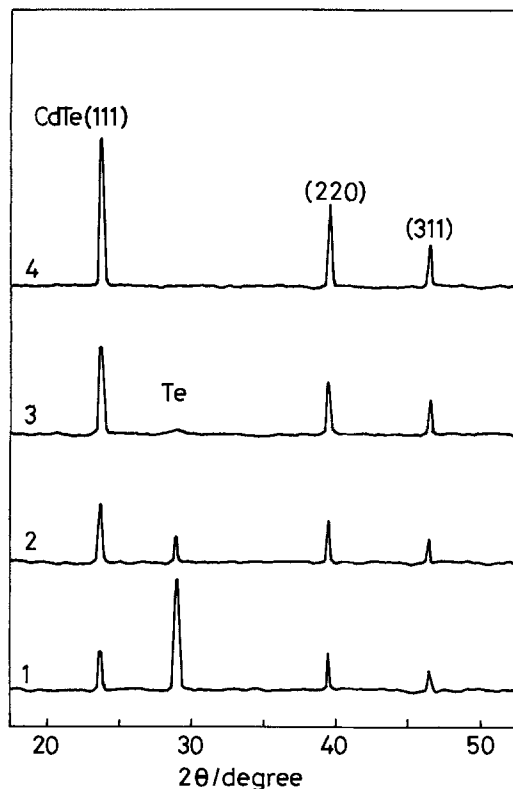
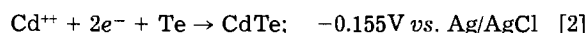
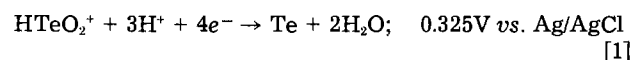


Fig. 6. X-ray diffraction patterns of the films deposited at $-0.35V$ (vs. Ag/AgCl), heat-treated at $200^\circ C$ in a He atmosphere for 12h and etched in a solution containing $0.6M$ $Na_2S_2O_3$ and $2.5M$ NaOH at $80^\circ C$ for several time periods. Curve 1: No etching treatment. Curve 2: 2s. Curve 3: 10s. Curve 4: 40s.

ter did not change during the treatment. The etching treatment also increased the photocurrent. The etching time dependence of the intensity of x-ray diffraction peaks and the photocurrent at $-0.70V$ are shown in Fig. 7. The effect of etching on the reflection spectra is shown in Fig. 3. The absorption edge became much clearer by this treatment. By the too-long treatment, however, the photocurrent as well as the intensity of x-ray diffraction peaks due to CdTe decreased, suggesting that, not only Te, but also CdTe dissolved during the etching treatment.

Discussion

Panicker *et al.* studied the cathodic deposition of CdTe mainly by galvanostatic method (7) and proposed that the following reactions were involved in the formation of CdTe



and that the diffusion of $HTeO_2^+$ preceding reaction [1] is the rate-determining step. The results of the present work also support this mechanism. The current due to reaction [1] at diffusion limited region, i_{Te} , is given by

$$i_{Te} = -\frac{4DFc_{HTeO_2^+}}{\delta} \quad [3]$$

where D and $c_{HTeO_2^+}$ are the diffusion coefficient and the bulk concentration of $HTeO_2^+$, and δ is the diffusion layer thickness. The current due to reaction [2], i_{CdTe} , is given by

$$i_{CdTe} = -2Fk'c_{Cd^{2+}}\theta_{Te}e^{-\alpha F\Delta\phi/RT} \quad [4]$$

where k is the rate constant, $c_{Cd^{2+}}$ is the concentration of Cd^{2+} , θ_{Te} is the surface coverage of Te, α is the transfer coefficient and $\Delta\phi$ is the potential difference across the interface. By considering mass balance, θ_{Te} is given by

$$\theta_{Te} = k'f_{Te} = k' \frac{i_{Te}/4 - i_{CdTe}/2}{i_{Te}/4} \quad [5]$$

where f_{Te} is the fraction of Te at the surface of the films and k' is a proportional constant. From Eq. [3], [4], and [5]

$$\theta_{Te} = \frac{k'Dc_{HTeO_2^+}/\delta}{(Dc_{HTeO_2^+}/\delta) + kk'c_{Cd^{2+}}e^{-\alpha F\Delta\phi/RT}} \quad [6]$$

By using Eq. [3], [4], and [6], the total current, i , is given by

$$i = i_{Te} + i_{CdTe} = -\frac{DFc_{HTeO_2^+}}{\delta} \left(4 + \frac{2kk'c_{Cd^{2+}}e^{-\alpha F\Delta\phi/RT}}{(Dc_{HTeO_2^+}/\delta) + kk'c_{Cd^{2+}}e^{-\alpha F\Delta\phi/RT}} \right) \quad [7]$$

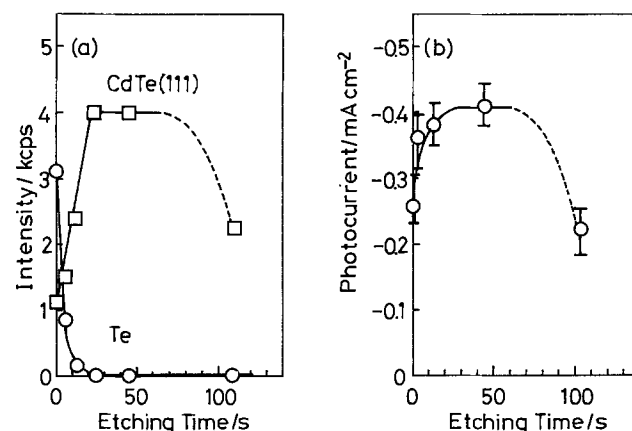


Fig. 7. Etching time dependence of (a) the intensity of x-ray diffraction peaks due to CdTe (111) face (\square) and Te (\circ) and (b) the photocurrent in $1M$ NaOH at $-0.70V$ (vs. Ag/AgCl) under illumination of $500W$ Xe lamp with an IR absorbing filter. Experimental conditions are the same as those in Fig. 6.

Thus, the current should be proportional to the bulk concentration of HTeO_2^+ , i.e., TeO_2 , as observed experimentally. The more negative the potential is, the higher f_{CdTe} and the less free Te are expected from Eq. [6]. Experimental results also confirmed this expectation. When $D_{\text{HTeO}_2^+}/\delta \ll k'c_{\text{Cd}^{2+}}e^{-\alpha F\Delta\phi/RT}$, i.e., the potential is very negative and $\theta_{\text{Te}} \approx 0$, then Eq. [7] becomes

$$i = - \frac{6DFc_{\text{HTeO}_2^+}}{\delta} \quad [8]$$

By assuming that the film is mainly CdTe, that the density of CdTe is 6.2, and that the deposition of CdTe is a six-electron process, as Eq. [8] shows, the current efficiency is calculated as 75% from the data of Fig. 2. The other reaction involved may include the reduction of oxygen, which is left in small amount despite the deaeration before the experiment. The other supporting evidence for this mechanism is that only the films deposited electrochemically at the potentials more negative than -0.25V were photoactive while the standard redox potential of reaction [2] is calculated as -0.155V (vs. Ag/AgCl).

As far as the films deposited at the potentials more positive than -0.40V were concerned, the more negative the deposition potential, the higher the photocurrent. One reason for this seems to be that the amount of free Te left is smaller, and another is that the amount of CdTe is larger in the films deposited at more negative potentials. Free metal is known to act as an electron-hole recombination center and reduce the photoconversion efficiency (21). The higher concentration of CdTe naturally increases the photoresponse. The films deposited more negative than -0.45 are n-type (19), and the more negative the deposition potentials, the lower the cathodic photocurrent.¹

As mentioned before, the photocurrents of the as-grown CdTe films were much smaller than those of CdTe single crystals. Since the usual cause of small efficiency is the effective recombination of hole-electron pairs at grain boundaries and at the surface, the increase of grain size by heat-treatment and removal of surface recombination center by etching treatment are considered to improve the photoconversion efficiency. As shown in Fig. 5, the heat-treatment increases the crystallite diameter as well as the photocurrent. Due to the increase of the crystallite diameter, the number of grain boundaries decreases, and therefore the photoconversion efficiency should be increased. In this case, since the amount of free Te was not affected, only the crystallite diameter affected the photocurrent.

The fact that no diffraction peak due to Te was observed in the x-ray diffraction patterns after the etching treatment suggests that the free Te existed mainly near the surface.² The Te at CdTe surface would act as a surface recombination center which should decrease the photocurrent. As shown in Fig. 7, the photocurrent was increased by removing the surface Te and, thus, it is confirmed that the surface Te was also responsible for the small photocurrent. The fact that the x-ray diffraction peaks due to CdTe were increased and the reflection spectra became much clearer by the etching treatment is explained by the removal of the surface Te-rich layer. This was supported by the fact that FWHM of x-ray diffraction peaks due to CdTe was not changed by the etching treatment.

Conclusion

1. The current-potential expression for the electrochemical deposition of CdTe films is presented.

¹ The anodic photocurrents were observed at potentials more positive than ca. -0.40V .

² The effect of Ar⁺ sputtering on Auger spectra also support this result (19).

2. The electrochemically deposited CdTe films are photoactive, and the maximum cathodic photocurrent which is due to hydrogen evolution reaction is observed at CdTe films deposited at -0.40V (vs. Ag/AgCl). The photocurrents at CdTe films deposited at more positive potentials than -0.40V are smaller because the amount of free Te, which acts as a surface recombination center, is larger, and, accordingly, the amount of CdTe is smaller. The photocurrents at CdTe films deposited at potentials more negative than -0.40V are smaller because the CdTe films deposited at these potentials are n-type.

3. The photocurrents of the as-grown CdTe films are relatively small compared with those of CdTe single crystals. The major reasons for this low efficiency are the effective recombination of hole-electron pairs at grain boundaries and at the surface. The photocurrents are increased significantly by the increase of crystallite diameter by the heat-treatment in a He atmosphere and by the removal of surface Te, which acts as a recombination center, by the etching treatment.

Acknowledgments

Thanks are due to Professor T. Yokokawa and Dr. T. Maekawa for the help in x-ray diffraction measurements and to Professor Y. Matsunaga for the help in reflection spectra measurements. This work was partly supported by Japan Securities Scholarship Foundation and a Grant-in-Aid for Scientific Research, Ministry of Education, Science, and Culture, 58045002.

Manuscript submitted Feb. 6, 1984; revised manuscript received April 18, 1984.

Hokkaido University assisted in meeting the publication costs of this article.

REFERENCES

1. K. W. Böer and A. Rothwarf, *Ann. Rev. Mater. Sci.*, **6**, 303 (1976).
2. S. S. Chern, H. R. Vydyanath, and F. A. Kröger, *J. Solid State Chem.*, **14**, 33 (1975).
3. J. Saraie, M. Kitagawa, and T. Tanaka, *This Journal*, **126**, 2226 (1979).
4. T. H. Myers, S. W. Edwards, and J. F. Schetzina, *J. Appl. Phys.*, **52**, 4231 (1981).
5. M. Weinstein, G. A. Wolff, and B. N. Das, *Appl. Phys. Lett.*, **6**, 73 (1965).
6. T. L. Chu, S. S. Chu, Y. Pauleau, K. Murthy, E. D. Stokes, and P. E. Russell, *J. Appl. Phys.*, **54**, 398 (1983).
7. M. P. R. Panicker, M. Knaster, and F. A. Kröger, *This Journal*, **125**, 566 (1978).
8. K. Ohashi, K. Uosaki, and J. O'M. Bockris, *Energy Res.*, **1**, 25 (1977).
9. J. O'M. Bockris and K. Uosaki, *This Journal*, **124**, 1348 (1977).
10. A. B. Ellis, S. W. Kaiser, J. M. Bolts, and M. S. Wrighton, *J. Am. Chem. Soc.*, **99**, 2839 (1977).
11. I. Taniguchi, B. Aurian-Blajeni, and J. O'M. Bockris, *J. Electroanal. Chem.*, **157**, 179 (1983).
12. J.-L. Sculfort and M. Herlem, *Electrochim. Acta*, **28**, 1439 (1983).
13. G. Hodes, J. Manassen, and D. Cahen, *J. Am. Chem. Soc.*, **102**, 5962 (1980).
14. F. Gaspard, F. Mondon, and F. Muller, *J. Chim. Phys.*, **77**, 69 (1980).
15. W. J. Danaher and L. E. Lyons, *Nature*, **271**, 139 (1978).
16. M. Skyllas-Kazacos, *J. Electroanal. Chem.*, **148**, 233 (1983).
17. K. Uosaki, M. Takahashi, and H. Kita, *Electrochim. Acta*, **29**, 279 (1984).
18. S. Tanaka, J. A. Bruce, and M. S. Wrighton, *J. Phys. Chem.*, **85**, 3778 (1981).
19. M. Takahashi, K. Uosaki, and H. Kita, *J. Appl. Phys.*, **55**, 3879 (1984).
20. J. R. Anderson, "Structure of Metallic Catalysts," p. 365. Academic Press, London (1975).
21. L. L. Kazmerski and P. E. Russell, *J. Phys.*, **43**, C1-171 (1982).



Thermal Decomposition of Dimethoxymethane Electrolyte Solution

J. S. Foos*

EIC Laboratories, Incorporated, Norwood, Massachusetts 02062

Ethereal solutions of LiAsF_6 have shown promise for use as electrolytes in lithium batteries. Solutions of LiAsF_6 in 2-methyltetrahydrofuran (2-MeTHF) and in ether blends with diethylether (DEE) have demonstrated the ability to cycle lithium in high efficiency in Li/TiS_2 laboratory cells (1, 2).

The ability of 2-MeTHF electrolyte to cycle Li well is reflected in its superior thermal stability toward Li in storage tests at 70°C (3). Other electrolytes which react in storage tests give lower Li cycling efficiencies in Li/TiS_2 cells (2, 4). Although the reactivity observed in the above tests can be attributed to reaction with Li, many ether electrolytes also react at elevated temperatures (100°C) in the absence of Li (5).

During the investigation of various ethers for use as electrolytic solvents in lithium batteries, dimethoxymethane (DMM) was chosen for testing. Solutions of LiAsF_6 in DMM allowed the cycling of the Li electrode in high efficiency (6). Unfortunately, this high efficiency was not realized in Li/TiS_2 cells (7). In order to rationalize this discrepancy, investigations into the thermal stability of DMM electrolytes were initiated. Storage tests at 70°C were conducted with solutions of LiAsF_6 in DMM in the presence and absence of Li. The visual results with this ether are similar to those previously reported for other ethers.

However, dramatic differences were observed in ether reactivity which are detected only through analysis of the reaction products. The simple structure of DMM and its decomposition products allow the use of NMR spectroscopy in determining the stoichiometry of its decomposition reaction. A mechanism for the decomposition is proposed based on the identity of the reaction products and the ratio in which they are produced.

Experimental

All purification procedures subsequent to distillation and storage test preparations were conducted at ambient temperature under Ar atmosphere in a Vacuum-Atmospheres Corporation dry box equipped with a Model He-493 Dri-Train. The DMM (Aldrich) was dried with MgSO_4 , followed by molecular sieves. The solvent was then distilled from Na benzophenone ketyl. The lithium hexafluoroarsenate (LiAsF_6) (U.S. Steel Agri-Chemicals, electrochemical-grade) was used as received. Lithium foil (15 mil) was obtained from Foote Mineral Company sealed under Ar.

Activated neutral alumina (Woelm 200 neutral, activity-grade Super 1) was used as received and exposed only to the dry box atmosphere. Approximately 1g desiccant per 5 ml solvent was used in a given purification procedure.

The electrolytes for storage tests were prepared by adding LiAsF_6 with cooling, using Cu shot previously cooled in Dry Ice. The solvents, if treated with alumina, were passed through a column of activated alumina, and the first 10% was discarded.

Generally, the stability tests were conducted by storing a sample of electrolyte (3-10 ml) at 70°C in the absence or presence of Li (1-2 cm^2). The samples were contained in

test tubes with Teflon-lined screw caps. The threads of the test tube were wrapped with Teflon tape. The DMM electrolyte storage test which was analyzed by NMR spectroscopy was conducted in a 5 mm (0.8 mm wall) NMR tube. The sample was placed in the tube in the dry box and then attached to a vacuum line. The sample was outgassed in three freeze-thaw cycles and then the tube sealed under vacuum while the sample was frozen in liquid nitrogen (LN_2).

The test tube storage samples were analyzed by IR spectroscopy (Beckman Acculab 5) using a 10 cm gas cell (at ~ 20 torr). The sample was first frozen (LN_2) and then quickly fitted with an adapter which could be attached to a vacuum line. The sample was then allowed to warm, and aliquots were collected in the IR cell.

The proton NMR analyses were done using a JEOL FX-90Q spectrometer (Biomeasure Incorporated, Hopkinton, Massachusetts). The sample in the 5 mm NMR tube was supported in a 10 mm NMR tube using a Teflon spacer. This outer tube contained the deuteriochloroform for the deuterium lock and the tetramethylsilane (TMS) external standard. The chemical shifts are reported as ppm downfield from TMS. To determine the effect of the external TMS on chemical shift values, spectra of DMM solvent were run with internal and external TMS. The chemical shifts were $\delta 3.26(6\text{H})$ and $\delta 4.47(2\text{H})$ [lit 3.23 and 4.40, Ref. (9)] with internal TMS; and $\delta 2.74(6\text{H})$ and $\delta 3.95(2\text{H})$ with external TMS, giving a change of -0.52 ppm with external TMS. This shift must be due to inhomogeneity in the magnetic field.

Results

Stability tests were carried out with solutions of 1.5M LiAsF_6 in DMM at 70°C with and without Li metal. The samples containing Li showed relatively little reaction, with the best samples showing no reaction after 30 days. The most stable samples appeared to be those prepared from distilled solvent which was subsequently treated with alumina (DA).

In contrast, when samples were stored without Li, the (DA) samples turned dark in 5-7 days. Samples which had not been treated with alumina (D) remained colorless from 11 to 17 days. In either case it is clear that the DMM electrolyte solution is stabilized by Li.

IR analysis.—A sample of DMM electrolyte that had turned dark due to storage at 70°C was analyzed by IR spectroscopy. This analysis was done by slowly warming the cooled sample which was attached to a vacuum line. Aliquots of the vapor which were collected in the vacuum line were then analyzed in an IR gas cell. Surprisingly, the sample was found to contain little or no DMM. The IR spectra contained only absorptions which are attributed to methyl formate and dimethyl ether. The methyl formate absorptions were identical to those obtained from an authentic sample (Eastman). The dimethyl ether absorptions were identical to a published spectrum (8).

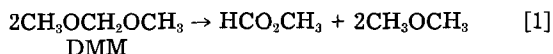
Proton NMR analysis.—In order to positively identify the products, to assess the stoichiometry of the reaction, and to search for minor products, the decomposition was

* Electrochemical Society Active Member.

repeated in an NMR tube. A sample of 1.5M LiAsF₆/DMM was sealed in a 5 mm NMR tube which was stored at 70°C. At time intervals, the sample was removed and analyzed by proton NMR spectroscopy. After decomposition, the spectrum show a small amount of residual DMM along with methyl formate and dimethyl ether. All chemical shift values, even after correction for external TMS, show considerable deviation from literature values. This can be attributed to the presence of 1.5M LiAsF₆ in solution.

The chemical shifts for DMM, methyl formate, and dimethyl ether observed above are listed in Table I. This table also shows that when authentic methyl formate is added to DMM electrolyte solution, the chemical shift values of the methyl formate are near those attributed to the methyl formate in the storage test. It can be noted that as the amount of DMM in the sample decreases, the chemical shifts decreases in value. At the end of the experiment, methyl formate and dimethyl ether were present in a 1:2 ratio, as determined from integration of the NMR absorptions. At 5 days storage at 70°C, there was no change in the appearance of the NMR sample and no change in the NMR spectrum. At 9 days, the sample was dark brown, and the NMR analysis showed that the decomposition was 35% complete. At 16 days, a white precipitate appeared, and the reaction was 90% complete (based on the ratio of DMM to methyl formate signals in the NMR spectrum).

This experiment establishes that the decomposition gives almost exclusively 1 mol methyl formate and 2 mol dimethyl ether. The balanced equation for this reaction is shown in Eq. [1]



The brown color may be associated with the beginning of the decomposition of DMM. In contrast, a sample of LiAsF₆/2Me-THF electrolyte solution, which had turned brown as a result of storage at 70°C, showed no trace of 2-MeTHF decomposition when analyzed by proton NMR spectroscopy.

Discussion

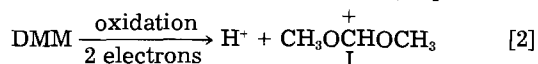
The dark coloration is typically observed when LiAsF₆ ether solutions are stored at elevated temperatures. This coloration is not observed in storage tests with LiClO₄ (5), implying that the color is associated with the salt rather than the ether. Additionally, it has been observed that the time of onset of color depends on the purification technique used in preparing solvent, e.g., DMM/LiAsF₆ (DA) reacts more rapidly than DMM/LiAsF₆ (D). These observations imply that the color is a result of decomposition of AsF₆⁻ and that the decomposition of the solution is affected by impurities remaining after solvent purification or due to solvent decomposition. The decomposition products of AsF₆⁻ are expected to be acidic and/or strongly oxidizing. The polymerization of dioxolane is rapid in the presence of LiAsF₆, due to the influence of the AsF₆⁻ anion (10). This polymerization presumably operates in a cationic mechanism.

The above considerations imply that a cationic mechanism might be used to explain the decomposition of

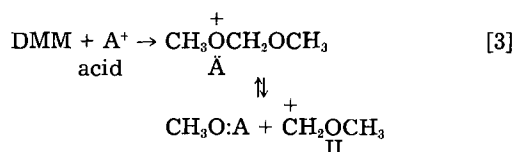
DMM to methyl formate and dimethyl ether. The observation that the presence of Li metal retards the decomposition reaction is consistent with this hypothesis.

Treatment of DMM with an oxidizing agent would be expected to give an oxygen stabilized cation, especially in the absence of a strong nucleophile (11). This oxidation, Eq. [2], as well as the reaction in Eq. [3], are initiation steps in a proposed chain reaction. The oxidation may result from the slow decomposition of LiAsF₆ or from trace impurities, such as O₂. In either case, only a very small amount of oxidation (initiation) can eventually destroy the total amount of DMM. The fact that the solution is stabilized by Li implies that the oxidizer is a trace impurity or produced very slowly.

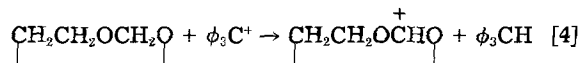
It is important to note that the prominent nucleophiles in the DMM-LiAsF₆ solution are the AsF₆⁻ anion, which would be poorly nucleophilic (the anion of a strong acid), and the ether itself. The expected cation, I, would be stabilized by the presence of two oxygen atoms, Eq. [2]



Alternately, the cation I could also be formed from acidic impurities. The instability of acetals like DMM is well known in acidic aqueous solution. In the absence of H₂O, an additional molecule of solvent might be expected to react with an acid-base (ether) complex, Eq. [3], to give the dimethyl ether cation (II)



This cation undoubtedly exists in solution in the form of an oxonium ion formed with a molecule of solvent (12). However, it also could react with DMM via hydride transfer to give the same stabilized intermediate, I, described above (see also Eq. [5]). A similar reaction was used to form the 1,3-dioxolan-2-ylum ion (12), (Eq. [4])



The cation I, although relatively stable, may decompose by methyl transfer to a solvent molecule, forming an oxonium ion (III). This oxonium ion could, in turn, decompose giving the intermediate II, which reacts with DMM (with a hydride transfer), regenerating the cation I. These reactions, shown in Eq. [5]-[7], constitute the propagation steps of a chain reaction

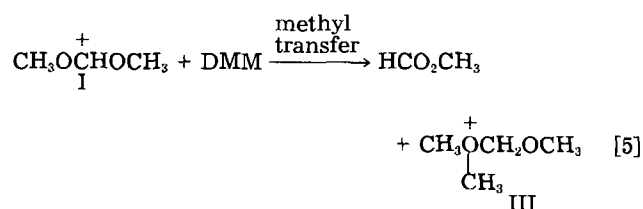
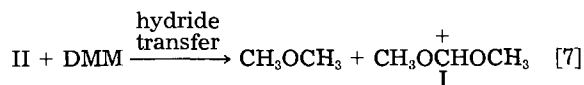
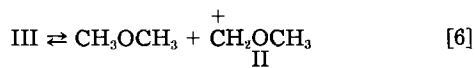


Table I. Chemical shifts (ppm, δ) for DMM, methyl formate, and dimethyl ether (corrected to internal TMS)* in 1.5M LiAsF₆/DMM storage test, reference sample, and DMM solvent only

	1.5M LiAsF ₆ /DMM storage sample (70°C)			Reference sample	
	Initial	35% Decomposed	90% Decomposed	Methyl formate added to 1.5M LiAsF ₆ /DMM	DMM solvent only
DMM	3.48(6H) 4.71(2H)	3.44(6H) 4.66(2H)	3.33(6H) 4.54(2H)	3.46(6H) 4.68(2H)	3.26(6H) 4.47(2H)
Methyl formate	—	3.91(3H) 8.22(1H)	3.77(3H) 8.11(1H)	3.93(3H) 8.27(1H)	—
Dimethyl ether	—	3.46(6H)	3.33(6H)	—	—

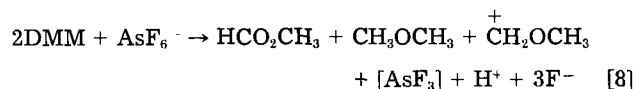
* A correction factor of 0.52 was added to each of the values observed using external TMS (see "Experimental" section).



This mechanism explains the products and stoichiometry observed. It also explains the reaction-retarding effect of Li metal. It would be expected that cation intermediates would be rapidly reduced on Li to anions which might be insoluble but which would at least disrupt the propagation of the chain reaction. Nucleophilic impurities such as H₂O would be expected to react rapidly with cations to disrupt the chain. Such reactions would be chain-terminating steps.

The alumina while being effective in removing impurities, such as H₂O and peroxides, simultaneously establishes the conditions for the chain reaction. In the presence of Li any residual impurities are scavenged. However in the absence of Li the electrolyte would be more reactive. In Li/TiS₂ secondary cells the electrolyte should be stabilized by the fresh plated Li.

An alternate mechanism for the reaction which might be proposed, is the direct oxidation of DMM by AsF₆⁻ (or by an AsF₆⁻ decomposition product)



It has been suggested that in the case of several ethers (not DMM) that the reactive agent may be AsF₅ produced from the thermal decomposition of LiAsF₆ (4, 5). This could be an initiation step in the proposed chain mechanism. This reaction may become the principal route of decomposition if suitably catalyzed or in the presence of an ether less amenable than DMM to a chain reaction. In our view, this mechanism fails to explain the observed DMM decomposition for several reasons. Although a small amount of white precipitate is observed, it is too little to be the LiF produced if direct oxidation were the major reaction. Actually, the amount of LiAsF₆ in 1.5M LiAsF₆/DMM is insufficient to oxidize the DMM present by this reaction. The IR spectrum of the residual salt left after the decomposition of DMM in a storage test showed a strong peak remaining at 700 cm⁻¹, which corresponds to the AsF₆⁻ absorption. Appreciable oxidation by LiAsF₆ would not be expected in view of its apparently good thermal and solution stabilities (13).

A free-radical mechanism might be proposed as an alternative to the cation mechanism suggested above. However, we do not believe that this is credible. Cation intermediates of the type proposed are known to be stable species, whereas similar free-radical species would be much less stable.

Conclusions

It is observed that DMM electrolyte decomposes thermally to give dimethyl ether and methyl formate. Since methyl formate is unstable towards Li (14), it might be expected that this reaction would seriously degrade the performance of DMM/LiAsF₆ electrolyte in a Li cell. This decomposition reaction may occur during electrolyte preparation or during storage prior to filling the cell.

In the cell, in the presence of the Li negative, the decomposition could be minimized. However, in the bulk

solution, away from the surface of the Li, some decomposition may be initiated by acidic, or oxidizing, impurities introduced during the construction of the cell. If a reaction in the cell, such as AsF₆⁻ decomposition, produces an acid or oxidizing agent, the effects of that reaction will be magnified by the DMM decomposition chain reaction.

Of more general importance, this reaction is an illustration of a type of reaction that can occur only in certain specialized conditions. Such conditions include the presence of a nonreactive, nonnucleophilic anion, i.e., AsF₆⁻, which may stabilize the carbocation intermediates. Required as well is the absence of a reactive nucleophile other than the solvent itself. These conditions are seldom achieved in synthetic organic chemistry but are typical in Li battery electrolytes.

Acknowledgment

We wish to acknowledge the support of the Office of Naval Research.

Manuscript submitted Feb. 6, 1984; revised manuscript received April 6, 1984. This is a part of Paper 684 presented at the Montreal, Quebec, Canada, Meeting of the Society, May 9-14, 1982.

REFERENCES

- G. L. Holleck, K. M. Abraham and S. B. Brummer, in "Power Sources for Biomedical Implantable Application and Ambient Temperature Lithium Batteries," B. B. Owens and N. Margalit, Editors, p. 384, The Electrochemical Society Softbound Proceedings Series, Pennington, NJ (1980).
- K. M. Abraham, J. L. Goldman, and D. L. Natwig, *This Journal*, **129**, 2404 (1982).
- J. L. Goldman, R. M. Mank, J. H. Young, and V. R. Koch, *ibid.*, **127**, 1461 (1980).
- K. M. Abraham and J. L. Goldman, *J. Power Sources*, **9**, 239 (1983).
- V. R. Koch, J. L. Goldman, J. T. Y. Maurand, and M. Mulvaney, in "Lithium Batteries," H. V. Venkatesetty, Editor, p. 165, The Electrochemical Society Softbound Proceedings Series, Pennington, NJ (1981).
- J. S. Foos and J. McVeigh, *This Journal*, **130**, 628 (1983).
- J. S. Foos, K. M. Abraham, J. McVeigh, J. L. Goldman, and V. Meltz, Abstract 38, p. 63, The Electrochemical Society Extended Abstracts, Vol. 82-2, Detroit, MI, Oct. 17-21, 1982.
- "Raman/IR Atlas of Organic Compounds," B. Schroder and W. Meier, Editors, Verlag Chemie, Weinheim, Germany (1977).
- "Sadtler Standard NMR Spectra," 10, no. 6313M, Sadtler Research Laboratories, Philadelphia, PA (1969).
- P. G. Glugla, in "Power Sources for Biomedical Implantable Applications and Ambient Temperature Lithium Batteries," B. B. Owens and N. Margalit, Editors, p. 407, The Electrochemical Society Softbound Proceedings Series, Pennington, NJ (1980).
- V. D. Parker, in "Organic Electrochemistry," M. M. Baizer, Editor, pp. 544-545, Dekker, New York (1973).
- P. Kubisa and S. Penczek, *Makromol. Chem.*, **144**, 169 (1971).
- R. C. Cannon, C. C. Stone, and R. A. Wiesboeck, in "Power Sources for Biomedical Implantable Applications and Ambient Temperature Lithium Batteries," B. B. Owens and N. Margalit, Editors, p. 321, The Electrochemical Society Softbound Proceedings Series, Pennington, NJ (1980).
- R. D. Rauh and S. B. Brummer, *Electrochim. Acta*, **22**, 85 (1977).

The Role of Oxygen in the Redox Chemistry of Lutetium Diphthalocyanine

M. M. Nicholson*

Rockwell International Science Center, Anaheim, California 92803

T. P. Weismuller

Rockwell International Corporation, Defense Electronics Operations, Anaheim, California 92803

Spectroscopic evidence on the role of oxygen in the redox chemistry of lutetium diphthalocyanine is reported here. The observations indicate an irreversible reaction of oxygen with vacuum-sublimed films of the dye material and a reversible reaction with its solution in dimethylformamide. This behavior can account for several apparent anomalies found in previous investigations.

Since the multicolor electrochromism of lanthanide diphthalocyanine electrode films was reported by Moskalev and Kirin (1), these compounds have been the subject of many chemical and electrochemical investigations (2-11). Although much now is known concerning electron-transfer reactions of the lutetium complex, the exact composition of the green vacuum-sublimed films remains in question. The formula LuHPc_2 , with one labile hydrogen atom, was anticipated from the acidic nature of metal-free phthalocyanine and the strong tendency of rare-earth elements to assume the oxidation state of three.¹ However, Corker *et al.* found that green preparations of lutetium diphthalocyanine were paramagnetic and suggested that this could be due to formation of a salt $\text{LuHPc}_2^+\text{A}^-$ containing an unidentified anion A^- (5). Chang and Marchon confirmed the paramagnetism and reported a mass spectrum corresponding to the composition LuPc_2 (7). For that species, they proposed a radical structure $\text{Lu(III)Pc}_2^{\cdot}$ in which, effectively, one of the organic rings has lost an electron. Collins and Schiffrin subsequently observed the parent masses of both LuHPc_2 and LuPc_2 by field-desorption mass spectroscopy, but they placed more emphasis on finding the mass of LuPc_2 only by the conventional electron-impact technique (9).

Other evidence of the labile hydrogen was obtained by Moskalev and Kirin in a spectrophotometric investigation of tetrasulfonated diphthalocyanines of lutetium, gadolinium, and yttrium in aqueous solutions (2). Spectral changes in the pH range of 6-12 were attributed to a simple acid-base equilibrium involving the imino hydrogen, with the sulfonic acid groups remaining completely ionized. Moreover, two forms of rare-earth diphthalocyanines, one green and the other blue, have been found in chromatographic separations of reaction products from the usual synthesis carried out by heating a rare earth salt with *o*-phthalonitrile. Mackay *et al.* noted that these forms were interconvertible but concluded that a simple acid-base equilibrium relationship between them could be an oversimplification (3).

We proposed, in a 1982 review (8), that the radical and hydrogenated forms could be related through the reaction



Then, in the presence of excess oxygen, the paramagnetic cation could form, in combination with the superoxide anion



Collins and Schiffrin actually found oxygen on the order of stoichiometric amounts in green lutetium diphthalocyanine films by x-ray fluorescence and x-ray photo-

electron spectroscopy (9). They too suggested that O_2^- or OH^- might be the anion in the initial green material. The results presented below offer new insight on the role of oxygen in this system and can be interpreted to account for its influence on certain faradaic processes in diphthalocyanine electrode films.

Film Spectra

Lutetium diphthalocyanine films 0.1-0.2 μm thick were deposited on glass by the usual vacuum-sublimation procedure at $\sim 10^{-5}$ torr. Such films were consistently green and showed no visible change on exposure to air. However, it was found that details of the absorption spectrum could change in air, depending on the substrate temperature during deposition of the film. This behavior is illustrated by Fig. 1 and 2. All spectra reported here were recorded at room temperature. To obtain the film spectrum prior to air exposure, nitrogen at 1 atm was first admitted to the deposition chamber. With an externally controlled manipulator, the dye specimen was then placed in a flat-sided glass cell, and a grease-sealed cover was attached. The protected specimen was promptly transferred to the spectrometer, and its absorption spectrum was determined.

Curve a of Fig. 1 is the typical spectrum of an air-exposed lutetium diphthalocyanine film deposited on an unheated glass substrate. It includes the prominent Q band at the wavelength (λ) of 666 nm, with vibrational

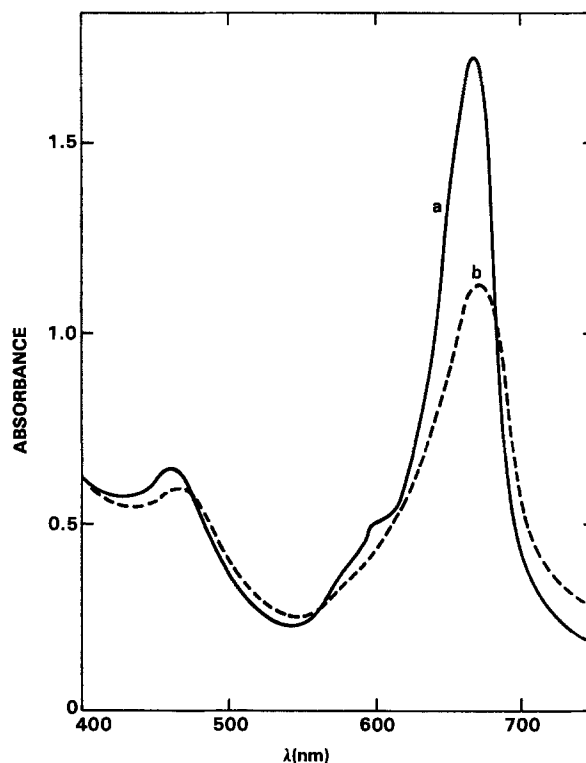


Fig. 1. Effect of air on spectrum of lutetium diphthalocyanine film vacuum-sublimed on an unheated glass substrate. Curve a: after exposure to air. Curve b: before exposure to air.

*Electrochemical Society Active Member

¹The symbol Pc represents the phthalocyaninato group $\text{C}_{32}\text{H}_{16}\text{N}_8$.

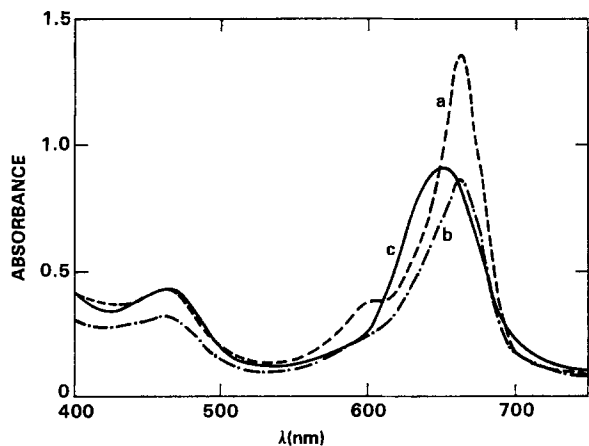


Fig. 2. Spectra of air-exposed lutetium diphthalocyanine films from three deposition runs with different substrate heating. Curve a: glass substrate preheated in vacuum, then cooled before deposition. Curve b: heated only until beginning of deposition. Curve c: heated before and during deposition.

transitions on the short-wavelength side at 575 and 605 nm. The weaker band at 462 nm lies between the Q band and the ultraviolet Soret band characteristic of phthalocyanines.² Curve b of Fig. 1 is the spectrum of the same film recorded under nitrogen before exposure to air. Here, the main peak is lower, at 671 nm, the vibrational transitions are not evident, and the weaker electronic band is slightly shifted to 467 nm. We propose that curve b is the spectrum of solid LuPc_2 , while curve a is that of the paramagnetic oxygen containing species.

Figure 2 indicates the effect of heating the substrate with an infrared lamp in the vacuum-deposition procedure. These data were from different deposition runs which produced somewhat different film thicknesses. Curve a again is for an unheated substrate. Curve b shows the result of preheating the glass under an infrared lamp. This curve, recorded in air, resembles rather closely the curve b spectrum of Fig. 1 for the unheated film before air exposure. When heating was continued during the deposition time of several minutes, the Q band was broadened and shifted slightly, as in curve c of Fig. 2.

The reaction of the fresh green film with air proved to be irreversible. Prolonged evacuation of the air-exposed film at room temperature failed to change the spectrum, subsequently observed under helium. Heating of the exposed film in air converted the spectrum, from curve a of Fig. 1 to one closely resembling curve b of Fig. 1, or curve b of Fig. 2, but the sensitivity to air was lost in the heating process. Briefly, the unheated green films were air-sensitive, while the heated ones were not. The spectral broadening and the loss of air sensitivity on heating may have been due to polymerization or crystallization of LuPc_2 . Unless heated excessively, however, the dye apparently returns to the monomeric vapor state on sublimation.

Solution Spectra

Figure 3 shows a typical spectrum of lutetium diphthalocyanine dissolved in reagent grade dimethylformamide (DMF). The solution was blue, with absorption maxima at 614 and 693 nm. Corker *et al.* noted that this blue form, which was not paramagnetic, could be a reduction product of the green, due to its reaction with aliphatic amine impurities in the DMF (5). In fact, their green solid preparation produced a paramagnetic green solution when dissolved in DMF that had been distilled over CuSO_4 or pre-electrolyzed.

In this investigation, we obtained the same result by adding a small amount of aqueous hydrochloric acid to the blue solution in unpurified DMF. The acidified-solution spectrum, curve a in Fig. 4, matches that of Corker's paramagnetic green. This curve also has features of the

²Electronic spectra of various monophthalocyanines are discussed, for example, in Ref. (12).

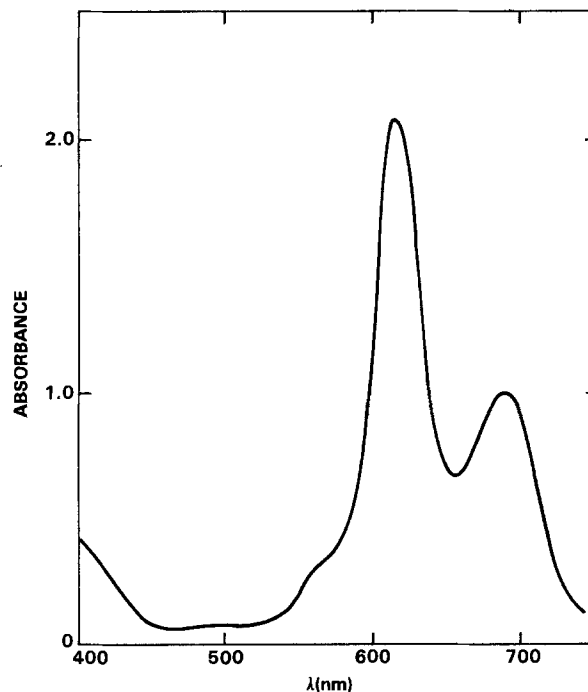


Fig. 3. Spectrum of lutetium diphthalocyanine solution in reagent-grade dimethylformamide before acidification.

air-exposed green-film spectrum, although the peaks at comparable heights are sharper for the solution than for the solid film.

A most interesting change occurred on removal of air from the acidified DMF solution. Over several hours, the spectrum shifted from curve a to curve b of Fig. 4, with a corresponding color change from green to blue. Significantly, the spectral change was reversible with addition and removal of oxygen. This appears to be the first clear evidence of reversible oxygen addition to a diphthalocyanine complex. Complete conversions between the

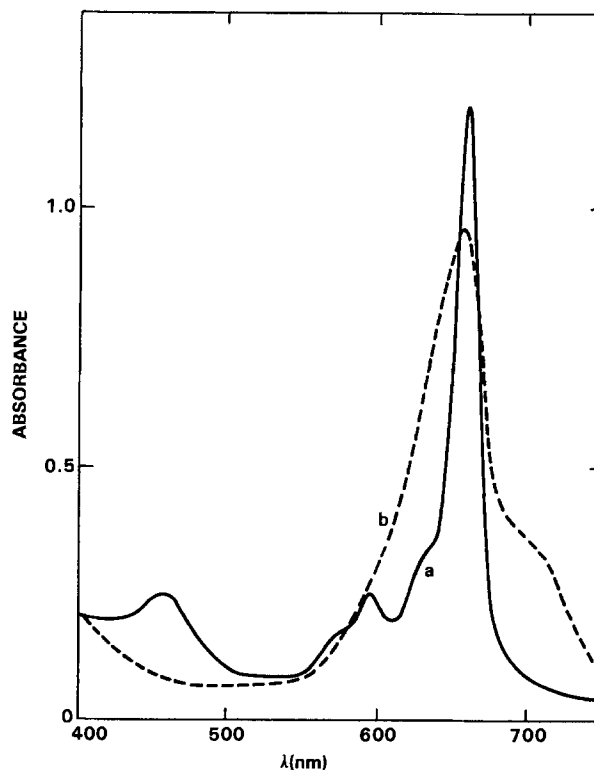


Fig. 4. Effect of oxygen on spectrum of lutetium diphthalocyanine solution in acidified reagent-grade dimethylformamide. Curve a: under oxygen. Curve b: under helium.

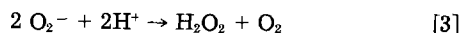
curve a and curve b forms occurred in several hours. The spectrum in nonacidified, unpurified reagent-grade DMF remained as in Fig. 3 and was unaffected by addition or removal of dissolved oxygen.

With lutetium diphthalocyanine dissolved in reagent-grade dimethylsulfoxide, a similar spectral change occurred on acidification, but the apparent addition of oxygen was not reversible. Related changes due to oxygen also occurred in acidified acetone, with possible formation of an intermediate state. The spectrum in dichloromethane, without acid, matched that of the oxygenated solution in Fig. 4. The same spectrum was observed in dichloromethane by Chang and Marchon (7).

Interpretations

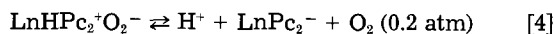
Before formulation of a unified reaction scheme, it is instructive to distinguish two types of blue-solution spectra and compare them with the spectra of cathodically reduced lutetium diphthalocyanine films, which now are known to be pH dependent (10). Curve b of Fig. 4, for the deoxygenated solution in acidified DMF, differs from the spectrum of the original blue nonacidified solution represented by Fig. 3. It closely resembles, however, the spectrum of a blue solid formed by the one-electron cathodic reduction of a cycled green lutetium diphthalocyanine film in an aqueous electrolyte near pH 3 (10). Moreover, the solution spectrum of Fig. 3, in nonacidified DMF, is similar to the reduced-film spectrum in a pH 7 electrolyte (10). These comparisons support the opinion that the dye was reduced by impurities in the reagent DMF.

For the green forms of lutetium diphthalocyanine, we note the similarity between the spectra of the air-exposed unheated green film, the paramagnetic green in solution with air present, and the electrochemically cycled green film with air absent (10). Several experimental observations can be correlated by assignment of the formula LuHPC_2^+ to the dye species in each of these cases. Reactions 1 and 2 account for its formation from LuPc_2 in the presence of water and oxygen. If LuPc_2 or LuHPC_2^+ is first reduced to LuHPC_2 in the unpurified DMF, the reversible addition of oxygen in solution also can be represented by reaction 2. In this proposed scheme, LuHPC_2 is blue, while LuPc_2 and its protonated form LuHPC_2^+ are both green. The other blue reduction product, obtained at higher pH, probably is the anion LuPc_2^- . The oxygen complex $\text{LuHPC}_2^+\text{O}_2^-$ proposed here is analogous to $\text{MnPc}_2^+\text{O}_2^-$ suggested by Lever *et al.* for the dioxygen adduct formed by MnPc in dimethylacetamide (13). Thermodynamically, the superoxide ion can disproportionate in acidic aqueous media through reaction [3] (14)



This reaction requires a catalyst to proceed rapidly, however, and O_2^- apparently is stabilized in the present system by pairing with the cation LuHPC_2^+ .

With this information, the acid-base equilibrium question can be re-examined. For titrations of the tetrasulfonated rare earth diphthalocyanines in water, the simple acid-base interpretation of Moskalev and Kirin (2) probably is correct, since the acidic anion $[\text{LuHPC}_2(\text{SO}_3)_4]^-$ would not be expected to pair with O_2^- . It appears possible, however, that the pK_a values reported by Moskalev and Alimova for unsubstituted diphthalocyanines of the lanthanide elements (Ln) in DMF-water solutions corresponded to the reaction



rather than the simple equilibrium.



Finally, a discrepancy in the faradaic n values from some of our previous work can be resolved. Nonintegral n 's approaching 2 were typical of anodic moving boundary experiments with the dye on an insulating substrate in air (6), while values close to 1.0 were found by an incremental potential-step technique, using cycled films on tin oxide in the absence of air (10). The color change was from green to orange (or reddish orange) in each case. The difference in the number of electrons lost per molecule of dye is readily explained on the basis that $\text{LuHPC}_2^+\text{O}_2^-$ was the predominant starting material in the boundary propagations. Since the superoxide ion is a relatively strong reducing agent (14), the overall anodic reaction for an air-exposed lutetium diphthalocyanine film in an electrolyte with the anion X^- should be



For a cycled green film in the absence of oxygen, however, the same color conversion would involve only one electron



Acknowledgment

This research was sponsored by the Air Force Office of Scientific Research (AFSC), under Contracts no. F49620-80-C-0060 and F49620-83-C-0088.

Manuscript submitted Dec. 28, 1983; revised manuscript received May 7, 1984.

Rockwell International Science Center assisted in meeting the publication costs of this article.

REFERENCES

1. P. N. Moskalev and I. S. Kirin, *Opt. Spectrosc.*, **29**, 220 (1970).
2. P. N. Moskalev and I. S. Kirin, *Russ. J. Phys. Chem.*, **16**, 57 (1971).
3. A. G. Mackay, J. F. Boas, and G. L. Troup, *Aust. J. Chem.*, **27**, 955 (1974).
4. P. N. Moskalev and N. I. Alimova, *Russ. J. Inorg. Chem.*, **20**, 1474 (1975).
5. G. A. Corker, B. Grant, and N. J. Clecak, *This Journal*, **126**, 1339 (1979).
6. M. M. Nicholson and F. A. Pizzarello, *ibid.*, **126**, 1490 (1979).
7. A. T. Chang and J. C. Marchon, *Inorg. Chim. Acta*, **53**, L241 (1981).
8. M. M. Nicholson, *Ind. Eng. Chem. Product R&D*, **21**, 261 (1982).
9. G. C. S. Collins and D. J. Schiffrin, *J. Electroanal. Chem.*, **139**, 335 (1982).
10. M. M. Nicholson and T. P. Weismuller, Final Report, Contract N00014-81-C-0264, AD-A120 483, Oct. 1982; C. A. 98:207469d.
11. M. L'Her, Y. Cozien, and J. Courtot-Coupez, *J. Electroanal. Chem.*, **157**, 183 (1983).
12. A. B. P. Lever, S. Licoccia, K. Magnell, P. C. Minor, and B. S. Ramaswamy, *ACS Symp. Ser.*, **201**, 237 (1982).
13. A. B. P. Lever, J. P. Wilshire, and S. K. Quan, *Inorg. Chem.*, **20**, 761 (1981).
14. J. Wilshire and D. T. Sawyer, *Acct. Chem. Res.*, **12**, 105 (1979).

Calcium/ $\text{Ca}(\text{AlCl}_4)_2$ —Thionyl Chloride High Rate Cell

E. Peled,* R. Tulman, A. Golan, and A. Meitav

Department of Chemistry, Tel Aviv University, Tel Aviv 69978, Israel

The lithium- SO_2 cell shows good performance over a wide range of temperatures and a good shelf life. In addition, it has the highest power density of all commercially available cells (1). For example, a C-size cell is capable of continuously delivering 1.5A at room temperature (2). However, because of hazard limitations, its recommended maximum continuous rate is only 0.36A (2). Recently, both the safety and rate capability of the Li- SO_2 system were improved (3-5), and the recommended maximum continuous rate was doubled. All of this was accomplished by, among other things, the use of balanced Li-to- SO_2 ratio and greater electrode area. The main hazard factors in high rate lithium cells are the deposition of very reactive high surface area lithium during reversal and charging abuses (6-8).

The calcium-thionyl chloride system has recently attracted attention, as a safer alternative to lithium high rate cells (9-17). Encouraging electrical performance was obtained for cells of various sizes - between 3.5 and 2000 Ah - containing LiAlCl_4 electrolyte (15-17).

Recent studies in our laboratory, with the use of small laboratory cells (10 cm^2 electrode area) containing $\text{Ca}(\text{AlCl}_4)_2$ electrolyte, have shown (9-12) good electrical performance and much better safety characteristics. Unlike lithium cells or the $\text{Ca}/\text{LiAlCl}_4$ -TC cell, the $\text{Ca}/\text{Ca}(\text{AlCl}_4)_2$ -TC cell successfully resists charging and reversal abuses (9-12). It behaves like an "electrochemical diode" (11, 12), *i.e.*, it delivers high current densities (up to 50 mA cm^{-2}) in the anodic direction, but operates as a high resistance in the negative direction, and during reversal tests. This seems to result from the facts that the SEI is almost a pure anionic conductor (9-11, 13) and that during cathodic polarization a blocking process of the ionic current takes place. This process most likely results from a sharp decrease in the ionic conductivity of the CaCl_2 -SEI due to depletion of the mobile ionic defects during continuous cathodic polarization. Corrosion tests of calcium in $\text{Ca}(\text{AlCl}_4)_2$ -TC solutions both at 70°C and at room temperature, indicate a projected shelf life of 1.5-2 yr (12). The average corrosion current density of 70°C is 12 $\mu\text{A cm}^{-2}$, and at room temperature it is 0.5 $\mu\text{A cm}^{-2}$ or less.

The goals of this work are: to demonstrate that the $\text{Ca}/\text{Ca}(\text{AlCl}_4)_2$ -TC cells can be scaled up by an order of magnitude with respect to electrode area, while preserving their excellent safety features, and to study the electrical performance of high rate laboratory prototype jelly-roll C-size cells.

Experimental

Details concerning materials and the preparation of solutions have been described in detail in Ref. (9). Calcium (99.9%) 0.5 mm thick foil was purchased from Pfizer. It was degreased in AR petroleum-ether and annealed at 600°-650°C for 2h. The laboratory prototype C-size cell is shown in Fig. 1. It consists of 0.5 mm calcium foil and 0.9-1.0 mm thick Teflon (10% by weight) bonded carbon cathode supported on nickel Exmet. Carbon loading was 1.8g per cathode. The anode and cathode were rolled together with a double 0.18 mm nonwoven glass separator. The effective electrode area was about 100 cm^2 . The cell case was a C-size stainless steel can, which was sealed inside a glass vessel. Connections to the anode and cathode were made with tungsten rods, which were sealed to the glass cap. A ground-glass joint was attached to a side arm of the glass vessel and served as a safety vent. Cells were vacuum filled (to the top of the can) with 1.0M $\text{Ca}(\text{AlCl}_4)_2$ -TC solution. The discharge tests were per-

*Electrochemical Society Active Member.

formed at room temperature by loading the cell with a suitable power resistor. Data were collected by a Fluke Data Logger. Charging and several tests were performed with the use of a Kepco regulated dc power supply.

Results and Discussion

The OCV of freshly filled cells was 2.8-2.9V and increased to 3.1-3.2V within 1-2 days. This OCV is somewhat lower than the OCV of the small glass laboratory cells (9). Cells were discharged through constant loads at current equivalent to 0.125-0.8A, a day or two after filling them with electrolyte. In all tests they exhibited a stable discharge voltage plateau over most of their service life. This plateau voltage decreased from 2.8V at 0.125A to 2.65V at 0.8A. Typical discharge curves are shown in Fig. 2. The initial increase of working potential ("voltage delay") is attributed mostly to the "cleaning" of the anode surface of calcium oxide. In recent experiments (9), a much smaller "voltage delay" was observed, probably

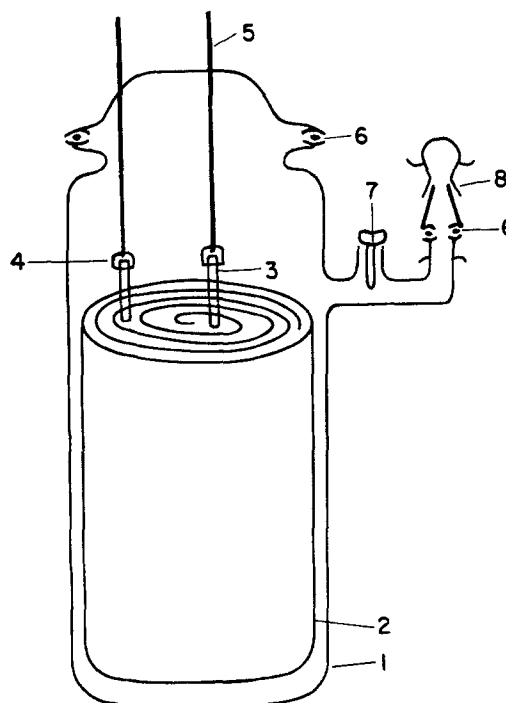


Fig. 1. A jelly-roll laboratory prototype C-size cell. 1: Glass cell. 2: C-size stainless steel can. 3: Connector to the anode. 4: Connector to the cathode. 5: Tungsten rod. 6: Viton O-ring. 7: Rotaflo stopcock. 8: Ground glass joint.

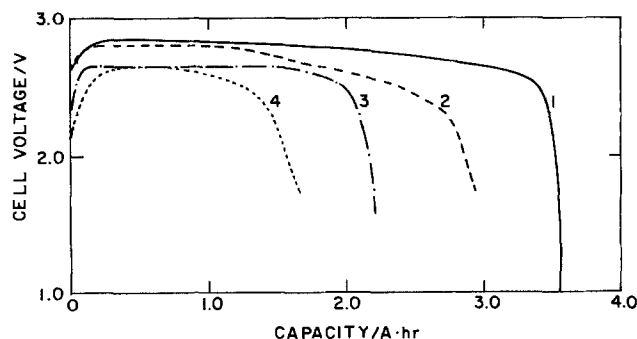


Fig. 2. Constant load discharge curves at room temperature. Curve 1: 2.2. Curve 2: 8.2. Curve 3: 5.5. Curve 4: 3.4.

due to the fact that the anodes were rubbed with sandpaper inside the glove box. This "voltage delay" diminished when the cells were stored for a week or more at room temperature prior to the discharge test. By this time, the thick calcium oxide layer had dissolved by reaction with TC. Cell capacity decreased linearly with current (Fig. 3). It was 3.5 Ah at 0.125A, 2.0 Ah at 0.6A, and 1.5 Ah at about 0.8A.

Capacity per unit area of cathode decreased from 35 mAh cm⁻² at 1.25 mA cm⁻² to 15 mAh cm⁻² at 8 mA cm⁻². These values are 10%-30% lower than those previously obtained for small, flat 10 cm² cells (9). However, the smaller cells had a 10%-20% thicker cathode and a higher concentration of electrolyte (1.3M instead of 1M, in this work).

The small cells exhibited excellent safety features as they resisted abuse charging and reversal tests. Figure 4, 5, and 6 show that these safety features are maintained even when the electrode area is scaled up by an order of magnitude. It should be noted that the initial short-circuit current of these cells is above 10A. Figure 4 describes an abuse "charging" test of a fresh C-size cell at 25V. The initial current is about 150 mA and it decreased to 50 mA after 10 min and to less than 20 mA after 60 min. In a 28V reversal test of a fully discharged C-size cell, the current dropped even faster (Fig. 5). It started at about 120 mA and dropped to 30 mA after 1 min, and then it slowly decreased to less than 20 mA after 200 min. Figure 6 describes the simulation of the reversal of a "weak" cell in a

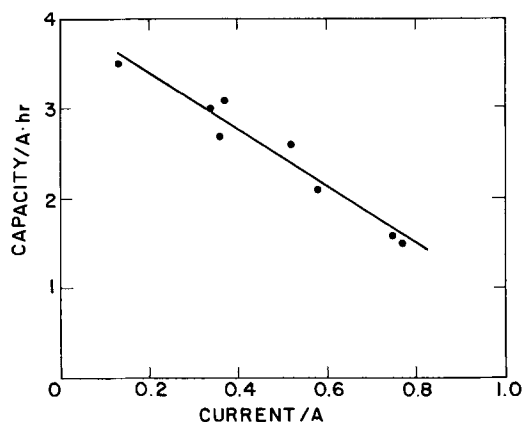


Fig. 3. The dependence of cell capacity on the discharge current

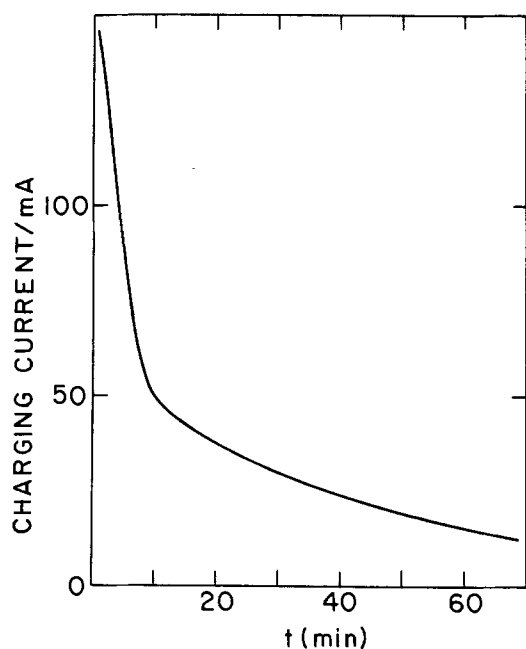


Fig. 4. Charging test of a fresh cell at 25V

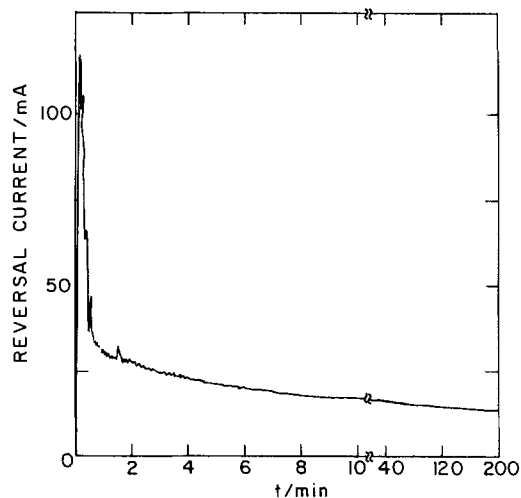


Fig. 5. Reversal test of a fully discharged cell at a constant voltage of 28V.

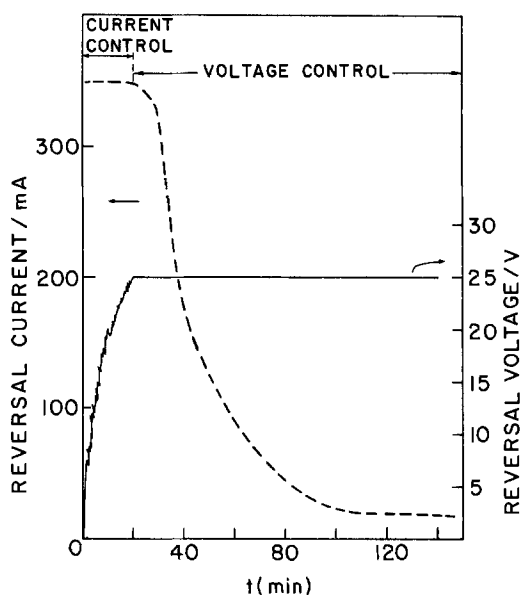


Fig. 6. Simulation of a reversal test of a weak cell in a ten cell in series battery, first forced-discharged at constant current and later at constant voltage of 25V.

30V series battery (ten cells in series). At the beginning, a fully discharged cell is forced to discharge at a constant current of 350 mA, till its reverse voltage reaches 25V. This takes about 20 min. Then it is force-discharged at a constant voltage of 25V. The current drops from 350 mA to less than 20 mA after 70 min and stays about constant at this level.

It should be emphasized that any other lithium cell or even a regular nonlithium cell would explode, or at least would vent, under charging or reversal at 25V.

Summary

The Ca/Ca(AlCl₄)₂-TC C-size laboratory cell (with 100 cm² electrode area) exhibits, at low rates, a volumetric energy density close to that of the Li-SO₂ cell. It can deliver a continuous current similar to that permitted for the Li-SO₂ cell. Its energy and power density can be further increased by increasing the electrode area of the cell. It exhibits an excellent safety feature: it successfully resists abuse charging and reversal tests. It is, therefore a very promising candidate for high power multicell battery applications.

Acknowledgment

The authors wish to thank the Israel National Council for Research and Development for supporting this work.

Manuscript submitted Feb. 18, 1983; revised manuscript received June 20, 1984.

Tel Aviv University assisted in meeting the publication costs of this article.

REFERENCES

- H. Hazkany, E. Peled, and B. Raz, in "Proceedings of the 29th Power Sources Conference," Atlantic City, NJ, June 9-12, 1980, The Electrochemical Society, Inc., p. 56 (1981).
- Duracell Battery Data Guide for Designers (1981).
- D. Linden and B. McDonald, *J. Power Sources*, **5**, 35 (1980).
- J. S. Cloyd, Report no. AFWAL-TR-81-2137 (May 1982).
- C. C. Crafts and S. C. Levy, Report no. SAN-0644 (April 1982).
- A. N. Dey, in "Proceedings of the 28th Power Sources Conference," Atlantic City, NJ, June 12-15, 1978, The Electrochemical Society, Inc., p. 251 (1979).
- K. M. Abraham, M. W. Rupich, and L. Pitts, in "Proceedings of the 30th Power Sources Conference," Atlantic City, NJ, June 7-10, 1982, The Electrochemical Society, Inc., p. 119 (1983).
- T. Voland and S. Eriksen, *J. Power Sources*, **7**, 365 (1982).
- A. Meitav and E. Peled, *This Journal*, **129**, 451 (1982).
- E. Peled, A. Meitav, and M. Brand, *ibid.*, **129**, 1936 (1981).
- A. Meitav and E. Peled, Paper 35, International Meeting on Lithium Batteries, Rome, 1982.
- R. Tulman, A. Golan, A. Meitav, and E. Peled, Paper 114, The 49th Meeting of the Israel Chemical Society, Tel Aviv, Israel, 1982.
- R. J. Staniewicz, *This Journal*, **127**, 782 (1980).
- A. Meitav and E. Peled, in "Proceedings of the 131st ISE Meeting," Venice, Italy (1980).
- R. Higgins and J. S. Cloyd, in "Proceedings of the 29th Power Sources Conference," Atlantic City, NJ, June 7-10, 1982, The Electrochemical Society, Inc., p. 147 (1983).
- R. Higgins, in "Proceedings of the 12th Power Sources Conference," Brighton, England (1980).
- R. L. Higgins, in "Proceedings of the 30th Power Sources Conference," Atlantic City, NJ, June 7-10, 1982, The Electrochemical Society, Inc., p. 157 (1983).

Photoelectrochemical Behavior of Indium Phosphide Arsenide Alloys in Acidic Electrolytes

S. Menezes,* A. Werner, and H. J. Lewerenz**

Hahn-Meitner Institut für Kernforschung, Berlin, Germany

F. A. Thiel

AT&T Bell Laboratories, Murray Hill, New Jersey 07974

P. Lange, M. Fearheiley, C. Morrison,**1 S. Bedair, B. Breithaupt, and K. J. Bachmann**

North Carolina State University, Raleigh, North Carolina 27650

Recently, we reported on electrodisolution and passivation phenomena on single crystal electrodes of the III-V compounds InP, InAs, InSb, GaP, GaAs, and GaSb in aqueous electrolytes (1). Considerable differences in the behavior are observed that are particularly pronounced in acid solutions. InAs and InP represent extreme cases: InAs does not passivate at $pH \sim 0$ except at very high current density (c.d.), but the films formed at high c.d. are too porous to prevent excessive surface corrosion. InP exhibits severe inhibition to anodic dissolution even in 4M HCl solution by the formation of a coherent film that can be removed only by extensive cathodic reduction.

Also, we reported previously on p-InP/ $V^{2+}-V^{3+}$, 4M HCl/C solar cells (2) that represent efficient EIS junctions (3). The function of this device is thus intimately linked to the passivation behavior of p-InP (1). A similar condition has been observed for p-InP-indium-tin oxide (ITO) solar cells that represent efficient SIS junctions (4) where the dielectric is a phosphorus oxide film of tunneling thickness (5). Investigations in InP_yAs_{1-y}/ITO solar cells show that the dielectric becomes porous at $y \geq 0.85$. At higher P concentration, the solar power conversion efficiency peaks presumably because of a reduction in the dielectric film thickness, but at lower P concentrations, the solar cell characteristic degrades steeply (6). In this paper, we report on the passivation and electrodisolution behavior of alloys at the InAs-InP pseudobinary that show complete solid solubility over the entire range of compositions InP_yAs_{1-y} , $0 \leq y \leq 1$. Also, we include information

on p-InP_yAs_{1-y}/ $V^{2+}-V^{3+}$, HCl/C and InP_yAs_{1-y}/ I_3^- , I^- , HCl/C junctions.

Experimental Results and Discussion

Both InP_yAs_{1-y} bulk single crystals and epitaxial layers were used for the fabrication of the electrodes. The bulk crystals were grown by zone leveling, as described elsewhere (7). The epitaxial layers were grown by liquid phase epitaxy on nominally undoped and semi-insulating InAs and InP substrates, respectively. The composition of the samples was checked by x-ray diffraction and x-ray fluorescence analyses. The n-type crystals and epilayers were nominally undoped with carrier concentrations $1 \times 10^{16} \leq N_D - N_A \leq 3 \times 10^{16} \text{ cm}^{-3}$. The p-type material was Zn doped to $N_A - N_D = 5 \times 10^{16} \text{ cm}^{-3}$. Au:Zn and In were used to make an ohmic contact to the p- and n-type material, respectively.

The contacts and substrates were embedded into epoxy so that only the InP_yAs_{1-y} was exposed to the electrolyte. The usual three-electrode potentiostatic arrangement was used, employing carbon counter and saturated calomel reference electrodes.

Figure 1 show cyclic voltammograms in 1M HCl solution for (a) bulk p-InP_{0.47}As_{0.53}, (b) bulk n-InP_{0.45}As_{0.55}, (c) n-InP_{0.57}As_{0.43} epitaxially grown on InP, and (d) n-InP_{0.37}As_{0.63} epitaxially grown on InAs. The solid and dashed lines correspond to measurement under simulated AM1 illumination and in the dark, respectively. Note that up to 55% InAs in the pseudobinary alloy the passivation characteristics of pure InP electrodes, i.e., passivity in potential range B, transpassive current flow in region C, and cathodic activation in region A, are retained. However, the passive region B extends over a nar-

* Electrochemical Society Student Member.

** Electrochemical Society Active Member.

¹ Present address: TRW, El Segundo, California.

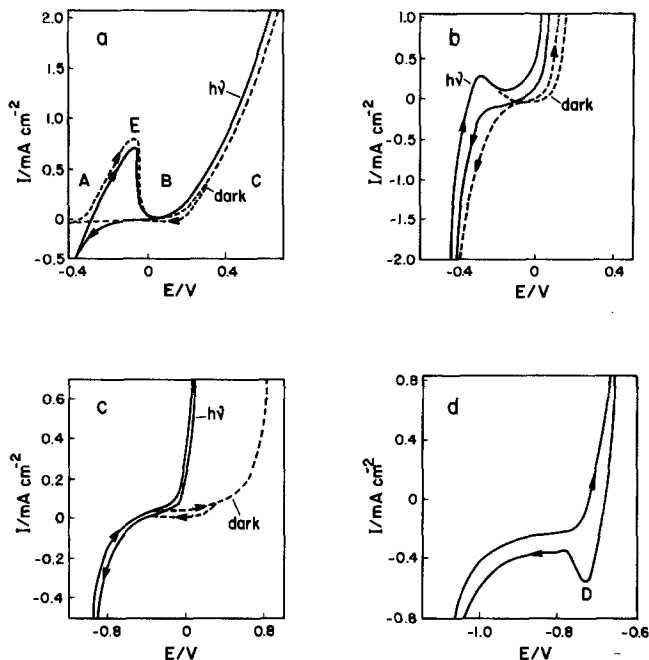


Fig. 1. Current-voltage curves at illuminated (-) and dark (---) in 1M HCl solution in (a) bulk $p\text{-InP}_{0.47}\text{As}_{0.53}$, (b) bulk $n\text{-InP}_{0.45}\text{As}_{0.55}$, (c) $n\text{-InP}_{0.57}\text{As}_{0.43}$ epitaxially grown on InP, and (d) $n\text{-InP}_{0.37}\text{As}_{0.63}$ epitaxially grown on InAs.

rower potential range and the transpassive anodic c.d.'s are larger than for pure InP. Also, on repeated cycling the oxidation wave (labeled E) decreases. For pure InP, this peak has been identified by ring-disk electrode measurements (1) to be partially related to the oxidation of In metal formed on the surface during the preceding reduction period in potential region A. The phenomenon in Fig. 1c may be either a reduction in the formation of In metal due either to the presence of other oxidation products formed in the transpassive cycle or to changes in surface composition related to the graded nature of the epitaxial film. Although the latter is indicated by the absence of a similar behavior for the n-type bulk material, the phenomenon is difficult to understand on the basis of a graded epitaxial structure alone, because under the conditions of LPE of $\text{InP}_y\text{As}_{1-y}$ the distribution coefficient of P is larger than unity. Therefore, corrosion of the epilayer should expose in successive cycles compositions that are richer in InP leading to a widening of passive region B that is not observed. For the largest As concentration (Fig. 1d), the epilayer shows InAs-like behavior.

Solar cells were measured using essentially the same $\text{V}^{2+} - \text{V}^{3+}$, HCl electrolyte as described in Ref. (2) and 0.05M I_2 , 1M CaI_2 , 1M HCl solution for the p-type photocathodes and n-type photoanodes, respectively. Figure 2 shows the spectral response of a $p\text{-InP}_{0.47}\text{As}_{0.53}$ photocathode in the spectral region between 800 nm and 1.5 μm . In accord with the decrease in the energy gap of the alloy as compared to pure InP, the long wavelength cutoff is shifted to larger wavelength. Also, the open-circuit voltage of the device is smaller than for pure InP, as expected from the decrease in the built-in voltage with decreasing energy gap. However, in contrast to expectations based on a consideration of the bandgap, the short-circuit c.d. of the alloy cell is, also, substantially smaller than for pure InP.

The latter observation is consistent with the behavior observed for the n-type $\text{InP}_y\text{As}_{1-y}$ photoanodes in I_3^-/I^- , HCl solution. Figure 3 shows a plot of the short-circuit current density (I_{sc}) relative to the value observed in the same solution for pure n-InP electrodes vs. the mole fraction of InAs in the pseudobinary alloy. For small additions of As to the anion sublattice, the short-circuit c.d. increases in accord with the extension of the spectral response to larger wavelength with decreasing energy

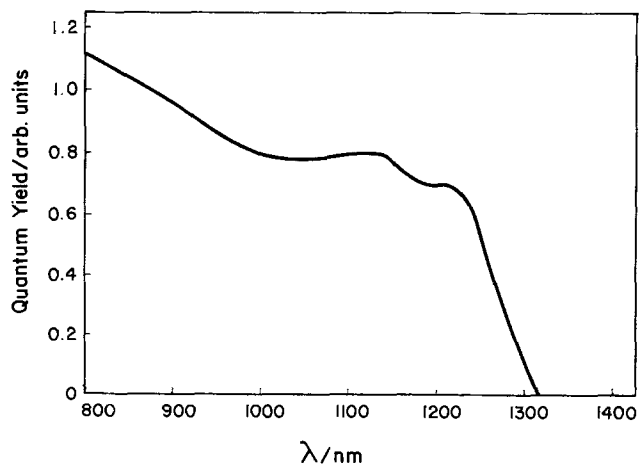


Fig. 2. Long wavelength edge of the spectral response of a $p\text{-InP}_{0.47}\text{As}_{0.53}/\text{V}^{2+}, \text{V}^{3+}, \text{HCl}/\text{C}$ junction.

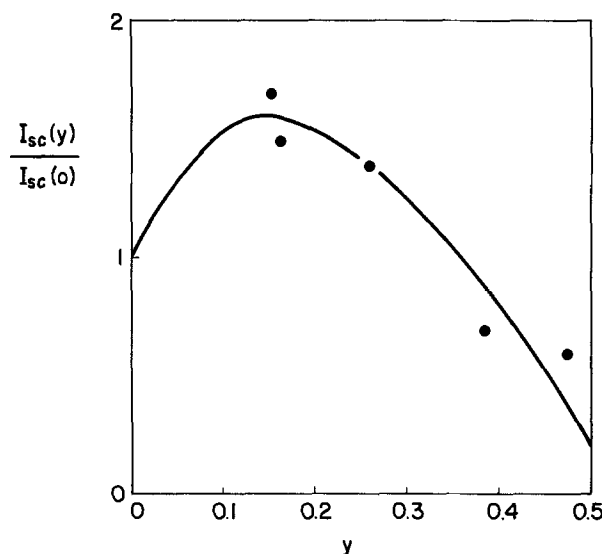


Fig. 3. Plot of $I_{sc}(y)$ vs. y of $\text{InP}_y\text{As}_{1-y}/\text{I}_3^-, \text{I}^-, \text{HCl}/\text{C}$ cells in units of the value of I_{sc} observed for pure n-InP electrodes in the same solution.

gap. However, at $\sim 16\%$ InAs, the short-circuit c.d. decreases, and no photoeffect is observed for $\text{InP}_y\text{As}_{1-y}$ epilayers for $y \leq 0.4$. This limit agrees with the observed threshold in the As concentration at which the passivation/electrodissolution behavior shifts from InP to InAs-like characteristic. Also, it is consistent with the earlier results on solid-state devices (6) where the gain in I_{sc} overcompensates the decrease in V_{oc} to $\sim 15\%$ InAs and photovoltaic activity vanishes at $0.4 \leq y \leq 0.5$. However, in the case of our liquid junctions, V_{oc} deteriorates more rapidly so that the efficiency of the alloy cells at the present stage of development is smaller than the efficiency of the pure InP cells. Whether this pattern may be affected by cyclic optimization or other manipulations of the interfacial chemistry is currently unknown. In view of the limited stability of n-InP photoanodes in I_3^-/I^- solutions a search for better redox partners for n-InP $_y$ As $_{1-y}$ photoanodes appears to be preferable to more extensive exploration of the $\text{InP}_y\text{As}_{1-y}/\text{I}_3^-, \text{I}^-, \text{HCl}$ system.

Summary and Conclusions

The electrodisolution and passivation behavior of $\text{InP}_y\text{As}_{1-y}$ alloys in acid solutions has been studied for both n- and p-type bulk single crystals and epitaxial alloy layers on InP and InAs substrates. InP-like passivation behavior is observed to $y \geq 0.45$, while larger As concentrations lead to electrodisolution behavior that is charac-

teristic of pure In As. The threshold in the passivation behavior coincides with the As concentration at which photovoltaic activity vanished in $\text{InP}_y\text{As}_{1-y}$ liquid junction solar cells, and similar characteristics in the short-circuit current density vs. alloy composition relation are observed, as previously reported for indium-tin oxide/ $\text{InP}_y\text{As}_{1-y}$ solar cells. This result strengthens the argument that the efficiency of InP-based liquid junction solar cells is closely linked to their passivation characteristics and points to close similarities between SIS and EIS solar cell device structures.

Manuscript submitted Jan. 9, 1984; revised manuscript received May 29, 1984.

North Carolina State University assisted in meeting the publication costs of this article.

REFERENCES

1. S. Menezes, B. Miller, and K. J. Bachmann, *J. Vac. Sci. Technol.*, **B1**, 48 (1983).
2. A. Heller, B. Miller, H. J. Lewerenz, and K. J. Bachmann, *J. Am. Chem. Soc.*, **102**, 6555 (1980).
3. S. Menezes, H. J. Lewerenz, F. A. Thiel, and K. J. Bachmann, *Appl. Phys. Lett.*, **38**, 710 (1981).
4. K. S. Sreeharsha, K. J. Bachmann, P. H. Schmidt, E. G. Spencer, and F. A. Thiel, *ibid.*, **30**, 645 (1977).
5. K. J. Bachmann, H. Schreiber, Jr., W. R. Sinclair, P. H. Schmidt, F. A. Thiel, E. G. Spencer, G. Pasteur, W. L. Feldmann, and K. S. Sreeharsha, *J. Appl. Phys.*, **50**, 3441 (1979).
6. K. J. Bachmann, F. A. Thiel, H. Schreiber, Jr., and W. R. Sinclair, in "Conference Record of the 14th IEEE Photovoltaic Specialists Conference," p. 1343, San Diego, CA, Jan. 7-10, 1980 IEEE, New York (1980).
7. K. J. Bachmann, F. A. Thiel, and H. Schreiber, *Prog. Cryst. Growth Characteriz.*, **2**, 171 (1979).



Thermoelectricity

VIII. The Thermal Conductivity Quality Factor, Q_k , A Semiconductor Characterization Tool

Donald Tuomi*¹

Roy C. Ingersoll Research Center, Borg-Warner Corporation, Des Plaines, Illinois 60018

ABSTRACT

Through surveys of the relationships between thermal conductivity and electrical conductivity in bismuth antimony telluroselenide alloys a pragmatic approach is used to define a thermal conductivity quality factor, Q_k , relating doping level to thermal conductivity. This empirical variable permits the evaluation of thermoelectric alloys in terms of materials parameters rather than the engineering design variables of the figure of merit, Z . Imperfection structure variables contribute to the optimization of both electron- and phonon-transport phenomena defined by the combined Seebeck and thermal conductivity quality factors, Q_s and Q_k .

Thermoelectric energy conversion for generating electric power or supplying refrigeration and air conditioning depends upon using heavily doped semiconductors (1). The engineering performance of the n- and p-type semiconductors must be optimized to the absolute solid-state limits in order to realize fully the business opportunities present. The materials are characterized by properties of both dielectrics and metals in a complex way (2, 3).

The engineering optimization depends upon doping proper structure and composition alloys to the largest figure of merit, Z . This is $Z = S^2\sigma/k$ where S is the Seebeck coefficient, σ electrical conductivity, and k the thermal conductivity. A challenge exists to optimize the materials processing and composition variables (4) in combination with device engineering (5) to the limits of the promised long life and reliability.

Simplifications are needed in the isolation and identification of the electronic and thermal energy transport variables. The identification of the power coefficient S_σ^2 with characteristics of the mobility-effective mass product, $\mu_0(m^*/m_0)^{3/2}$, for electrons led to introducing the Seebeck quality factor as a materials variable (5-9).

General device theory identifies the mobility-effective mass product divided by the lattice thermal conductivity, $\mu_0(m^*/m_0)^{3/2}/k_L$, as the critical material parameter to be maximized in order to attain high figures of merit (1, 10). With the introduction of the Seebeck quality factor, Q_s , the goal is maximizing Q_s/k_L .

The lattice thermal conductivity proves on closer examination to involve as many materials variables, as does the Seebeck quality factor. The challenge thus arose to devise a thermal conductivity quality factor Q_k for phonon transport equivalent Q_s for electron transport. This required an empirical evolution from the interaction of theory with experiment, much as did the Q_s .

The Thermal Conductivity of Materials

A brief scan through two volumes of thermal conductivity data compiled by the Thermophysical Properties Research Center (11) quickly emphasizes ranges and bounds on thermal conductivity variations in materials ranging from dielectrics to metals, and from perfect crys-

tals to amorphous structures. The total range extends from a low limit of 0.001 to a high range of 100 W/cm K.

The perfect crystals of diamond serve to define in combination with sapphire and silver the upper limits to heat flow at successively lower temperatures, as shown in Fig. 1. The lattice thermal conductivity of the dielectric materials maximizes at temperatures below 100 K, while metallic well-crystallized alloys maximize only at the temperature of liquid hydrogen and less.

Metallic alloys are characterized by thermal conductivities which are in the 0.3-8 W/cm K ranges for temperatures above 100 K. The temperature dependency is not very marked, as contrasted to the data for dielectric materials.

The relatively pure, intrinsic-class silicon and germanium semiconductors are characterized by temperature thermal conductivity curves similar to ordinary crystalline dielectrics. The heavily doped alloys show a dramatically decreased temperature dependence of thermal conductivity. This approaches a metallic characteristic above 100 K (12). The $1/T$ proportionality of the dielectrics is replaced by near T^0 behavior at ambient temperatures, or even an inversion to a positive temperature coefficient.

Classical theory describes the thermal conductivity as involving an electronic component described by the Wiedemann-Franz law, $k_e = L\sigma T$, where L is the Lorenz number, σ the electrical conductivity, and T the absolute temperature. Classical statistics assign the Lorenz number a value of $2(k/e)^2$ for nondegenerate electrons, and $(2\pi/3)(k/e)^2$ for the degenerate case, where k/e is the ratio of the Boltzmann constant, k , to the electronic charge, e . As noted by Drabble and Goldsmid (12), the electronic component dominates the thermal conductivity of metallic materials; but in semiconductors difficulties are encountered in identifying precisely the magnitudes of the electronic and lattice contributions to the thermal conductivities.

Thermal Conductivity Theory

The development of semiconductors as the route to useful thermoelectric alloys stimulated both experimental and theoretical investigations of the ways to alter the lattice thermal conductivity contribution to the figure of merit, Z . The existence of controllable contributions of electrons and phonons, k_e and k_L , to the thermal conduc-

*Electrochemical Society Active Member.

¹Permanent address: Donald Tuomi, Ph.D., and Associates, Limited, 221 South Illinois Drive, Arlington Heights, Illinois 60005

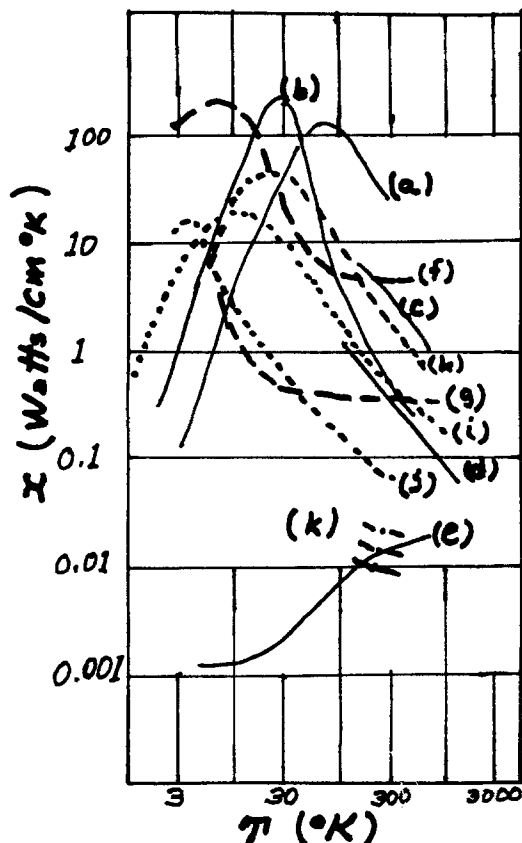


Fig. 1. Thermal conductivity ranges for: (a) diamond, (b) sapphire, (c) BeO, (d) Al₂O₃, (e) vitreous SiO₂, (f) Ag, (g) Pb, (h) Si, (i) Ge, (j) Bi, and (k) Bi₂Te₃ alloys. After Touloukian *et al.* (11).

tivity was recognized very early in the research and development effort (1). Since the mean free path of electrons was expected to be greater than that for phonons, performance enhancements were expected through use of high atomic weight alloys in combination with solid solution alloying as in PbTe-PbSe, Bi₂Te₃-Bi₂Se₃, or Bi₂Te₃-Sb₂Te₃.

The extensive review of thermal conductivity and lattice vibrational modes published by Klemens in 1958 (13) brought attention to the complex combinations of solid-state structural imperfections which were expected to influence the thermal conductivity of the lattice. The fundamental origin of thermal resistance is the increasing anharmonicity of the lattice vibrations with increasing temperature. Thus, in Fig. 1, the development of the low temperature maximum in thermal conductivity with increasing temperature of the crystalline insulators arises from increasing phonon scattering by anharmonicity of the lattice vibrations. The high temperature region beyond the maximum is dominated increasingly by "Umklapp" process scattering of the phonons. This lattice component of thermal conductivity exhibits a reciprocal of the absolute temperatures, $1/T$, dependence, with increasing temperature. However, at temperatures below the thermal conductivity maximum, the "normal" processes of phonon scattering dominate along with boundary scattering in the case of perfect crystals. The thermal conductivity no longer is an intensive property of the crystal, but is now a function of the dimensions since "normal" processes do not contribute to thermal resistivity, the lattice vibrations are simple harmonic oscillations.

Klemens' review brings attention to the diversity of imperfection phenomena in materials structures which alter the vibrational behaviors of the atoms. These range from the familiar isotope effect of changing the nuclear mass, to impurity substitutional alloying, to lattice vacancies, to lattice interstitials, to dislocations, to grain boundaries, and to more complex associated imperfection structures. The alteration of the crystal lattice from an ordered re-

peating perfect structure to the disordered amorphous state shifts the thermal conductivity into an imperfection-structure-dominated form. This is made evident in Fig. 1 by the vitreous silica curve defining a lower bound region for the thermal conductivity of dielectric solids.

Klemens' survey of the phenomena in metals, alloys, and semiconductors further emphasized the situation complexity in attempting to identify uniquely the electronic and lattice components of thermal conduction. The electron scattering arises from interactions with lattice vibrations as well as the imperfection structures. A parallel exists to the phonon scattering processes noted for dielectric materials. The semiconductors of the heavily doped class of interest in thermoelectrics present an extremely difficult situation for using theory to direct experiment except in a qualitative-semiquantitative context.

The later review by Drabble and Goldsmid (12) focused upon the characterization and theory evaluations of thermal conduction processes as applied to semiconductors. Emphasis is again given to the overall difficulties in utilizing theory to direct experiment. The doping process for altering the electrical conductivity introduces static point defects which themselves alter the thermal conductivity of the lattice as in iodine doping of Bi₂Te₃ (14).

Further complications are evident in attempts to analyze the thermal conduction processes in heavily doped lead telluride using classical statistics (15). The ambipolar electron contributions to thermal conductivity at ambient temperatures are evident at electrical conductivities below 500 mho/cm for both n- and p-type Bi₂Te₃. These data emphasize the difficulties in experimentally defining the lattice components of thermal conductivity for the two different alloys at ambient temperature (16).

A later review of thermal conduction in semiconducting materials by Steigmeier (17) focused upon studies of lattice thermal resistivity in elements, compounds, and alloys with particular attention to higher temperature behaviors, *i.e.* above the Debye temperature. The results, particularly for Ge-Si alloys, indicated progress in formulating theory to account for limited experimental observations. The discussions of Kudman (18) emphasize the importance of both mass fluctuation and lattice strain contributions to phonon scattering in III-V and IV-VI compounds, with strain effects possibly the dominant factor according to theory evolutions by Abeles.

More recently, Spitzer (19) described a chemical bond approach to the lattice thermal conductivity characteristics of crystals. This investigation identifies the crystalline structures of compounds as the critical variable determining the range of thermal conductivity. Surprisingly, all tetrahedrally bonded compounds had higher thermal conductivities than octahedrally bonded materials. Increasing the coordination number of the atoms in the unit cell decreases the thermal conductivity. The low thermal conductivity Bi₂Te₃ and PbTe alloys are octahedrally coordinated, as contrasted to the high thermal conductivity Ge-Si materials in the tetrahedral coordination class.

More recently still, Slack (20) reviewed the thermal conduction characteristics of pure nonmetallic crystals at high temperature. The discussion brings attention to the acoustic vibrational mode phonon dominance in rare gas crystals with one atom per unit cell. The more complex crystal structures will simultaneously involve both acoustic and optic modes in their vibrational energy spectrum with the acoustic modes transporting the thermal energy. Complex crystalline structures are needed with a multiplicity of optic modes to reduce the phonon transport in acoustic modes, thus reducing the lattice thermal conductivity.

Slack, in concluding, suggests that, as the number of atoms per unit cell is increased to very large values, the thermal conductivity of the lattice approaches the minimum limit of a room temperature glass. The challenge is identifying phonon scattering mechanism which will produce an equivalent result within a semiconducting alloy.

Clearly, theory and experiment suggest that many different imperfection structures may be used to modify both phonon and electron scattering behavior in alloys. The complexity requires recourse to experiments for identifying the presence of physically real effects which are directly related to the input variables.

Defining of the Thermal Conductivity Quality Factor

From the literature to 1962, varied graphs were prepared of the Seebeck coefficient vs. electrical conductivity and the thermal conductivity vs. electrical conductivity. For the 200-50 $\mu\text{V/K}$ Seebeck coefficient range, significant degeneracy effects were expected to be influencing the Lorenz number so that classical values should not be applicable. As noted by Drabble and Goldsmid (14), the Bi_2Te_3 class alloys showed consistently smaller values than expected for an alloy fitting acoustic-alloy scattering vibrational mode characteristics in the S - σ relationship (6-9). A need clearly existed to be able to define a thermal conductivity quality number which would be useful for comparing samples as better than or worse than others.

Theory did not readily provide a selection through, for example, the estimation of the lattice component by subtracting the electronic component. As shown in Fig. 2, the Lorenz number depends upon the relaxation time characteristics of the electron energy as well as the Fermi level as defined by the Seebeck coefficient. The observed fit of acoustic mode-alloy scattering of electrons to the Seebeck coefficient-electrical conductivity relationship defined through the Seebeck quality factor, Q_s , (9) did not provide an invariant lattice thermal conductivity component when the corresponding Lorenz numbers were used to estimate the electronic term to be subtracted from the measured thermal conductivity.

The graphical analysis of all available k - σ data for the better quality bismuth telluride n- and p-type alloys showed a greater internal consistency of the p-type results. This led to constructing the empirical curve of Fig. 3 utilizing the p-type Bi_2Te_3 alloy data as shown. This curve defined by the equation

$$k = 10 + 0.000372 \sigma$$

led to defining the thermal conductivity quality factor (21)

$$k = Q_k + 0.00372 \sigma$$

where the thermal conductivity is in units of (mW/cm K) and the electrical conductivity in (mho/cm).

The Q_k number has many of the characteristics classically identified with subtracting an electronic component from the thermal conductivity of a set of samples. Thus the curves a through f in Fig. 3 reflect varied options for the classical Lorenz number subtraction of the electron term k_e . In light of the Q_s characterization of the Seebeck coefficient-electrical conductivity relationship of, S to σ in terms of acoustic mode-alloy scattering and the relaxa-

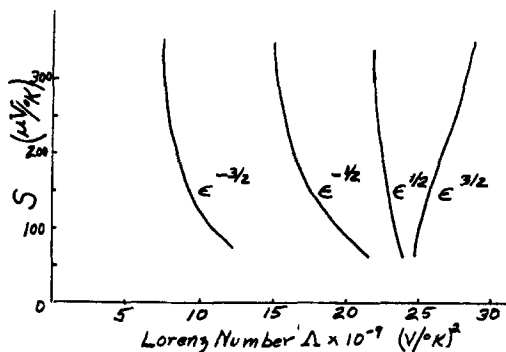


Fig. 2. The Lorenz number, L , in the Wiedemann-Franz law relationship of thermal conductivity to electrical conductivity, $k = L_o T$, dependence upon the Seebeck coefficient for variations in the energy dependence of the electron relaxation time (20).

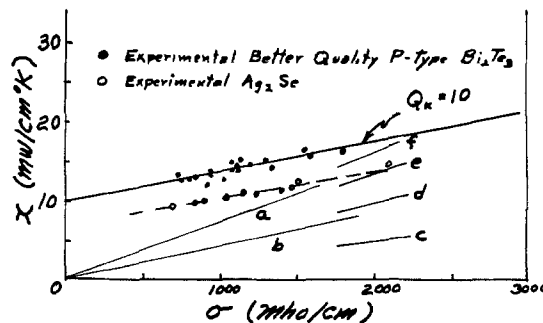


Fig. 3. The definition of the thermal conductivity quality factor reference line $Q_k = 10.0$ by experimental data on p-type better quality bismuth telluride-class alloys of similar chemical compositions. Reference electronic thermal conductivity curves are for (a) degenerate classical statistics, (b) nondegenerate classical statistics, (c) $\epsilon^{-3/2}$ electronic energy, ϵ , relaxation dependence, (d) $\epsilon^{-1/2}$, (e) $\epsilon^{1/2}$, and (f) $\epsilon^{3/2}$ case.

tion time relationship for L , the Lorenz numbers in Fig. 2, none of the theoretical identifications of a to f are justifiable as an experimental reference base defining a quality factor for the thermal conductivity.

A further insight into the relationship is provided by plotting the experimental points for the Ag_2Se thermal conductivity-electrical conductivity relationship (23). This alloy has a Seebeck quality factor of 100 Q_s and thermal conductivity quality factor of 7 Q_k , as defined by graphically constructing a family of parallel lines to the defined reference curve of 10.0 Q_k .

A summary of the better class alloy thermal conductivity data is given in Fig. 4. The distributions of quality among both Q_s and Q_k are as follows

- p-type: $360 \pm 37 Q_s$ and $10.0 \pm 0.77 Q_k$
- n-type: $337 \pm 68 Q_s$ and $11.69 \pm 1.77 Q_k$

with the $Q_s/Q_k = M$ ratios being 36.0 and 28.0, respectively, consistent with the higher reported figures of merit for the p-type. The variabilities noted among the different samples were interpreted as showing that either signifi-

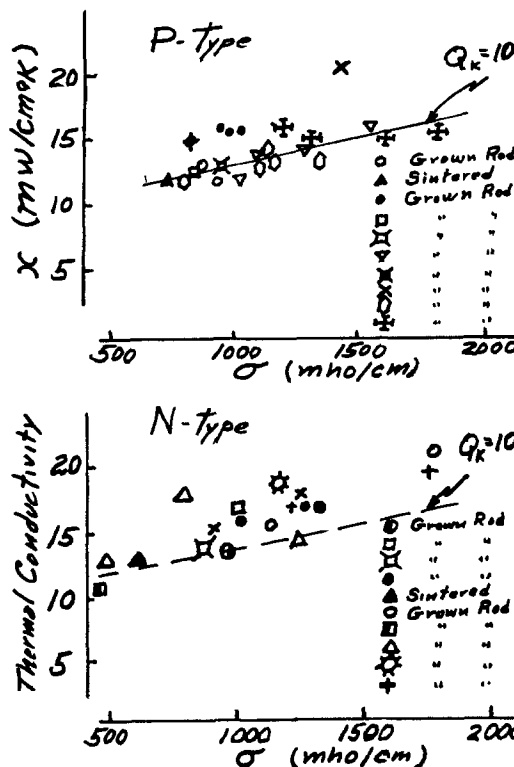


Fig. 4. Better quality n- and p-type Bi_2Te_3 -class alloy thermal conductivity-electrical conductivity data utilized in thermal conductivity quality factor, Q_k , evolution.

cant measurement errors existed or unique optimum alloy performances had not been attained experimentally.

The Seebeck quality factor, Q_s , had been found to be independent of temperature for the bismuth telluride alloys. Consequently, the available temperature-dependent thermal conductivity data were plotted on the reference curve figure defining Q_k . The results in Fig. 5 indicate that under some limited conditions the Q_k may be independent of temperature, or a second-order effect for 300-240 K, the temperature range for refrigeration alloys.

The complex interactions of point defects and alloying additions with the lattice and electron components of thermal conductivity produce surprising effects on the total thermal conductivity characteristics as well as the Seebeck coefficient-electrical conductivity relationship. The empirical definition of the thermal conductivity quality factor accepts this complex reality as an experimental fact. The assumption was made that as data accumulated a refinement of the modeling could be done in two ways. First, effects identified with process and composition variables could be related to the thermal conductivity quality number in an empirical way. Subsequent characterization of alloys in a structural chemical sense would provide at least conceptual views of the interacting factors. Second, as inadequacies of the Q_k concept became apparent, a revision of the graphical representation would be feasible.

The composite Q_s and Q_k curves used in data analysis are shown in Fig. 6. The characteristics commonly encountered for Bi_2Te_3 alloys maximize the figure of merit in the 700-1200 mho/cm range, but the power coefficient $S^2\sigma$ frequently maximizes at the higher ranges of electrical conductivity. Technology development goals involve an initial optimization of $Q_s/Q_k = M$ followed by controlled doping to maximize the figure of merit.

Extensive illustrations are not feasible on the use of Q_k to analyze published data. This reflects the historic difficulties in conveniently and accurately measuring all three parameters S , σ , and k on the same sample. The emphasis on the Z meter and power coefficient measurements frequently results in virtually no thermal conductivity data being available.

One example from the literature arises from the study of Cosgrove *et al.* (24) of thermoelectric effects of crystal growth conditions for $BiSbTe_3$ composition with 0.56 w/o selenium addition, or $BiSb(Te_{0.983}Se_{0.016})_{3.05}$. This nonstoichiometric composition is in the two-phase field region of the Bi-Sb-Te-Se tetrahedron between the $(Bi,Sb)_2(Te,Se)_3$ composition plane and the (Te,Se) eutectic solid solution. The anion-rich phase is n-type, while the cation-rich phase of the $BiSbTe_3$ solid solution is p-type.

The research identified the changes in thermoelectric properties on varying the crystal growth temperature gradient, G , from 25°, to 50°, to 250°C/cm while changing the crystal growth rate, R from 0.08 to 15.2 cm/h. The G/R ratio varied from 5 to 670. Measurements of S , σ , k , and Z

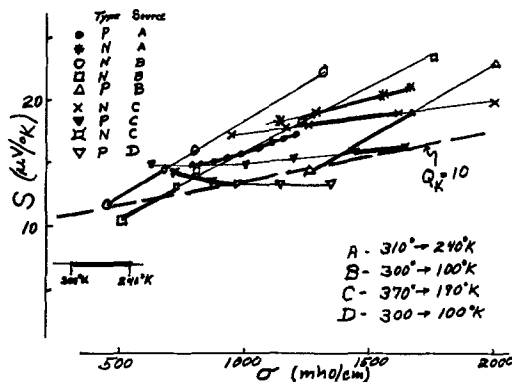


Fig. 5. Temperature-dependent thermal conductivity-electrical conductivity data for varied samples of n- and p-type Bi_2Te_3 alloys compared to the $Q_k = 10$ reference curve.

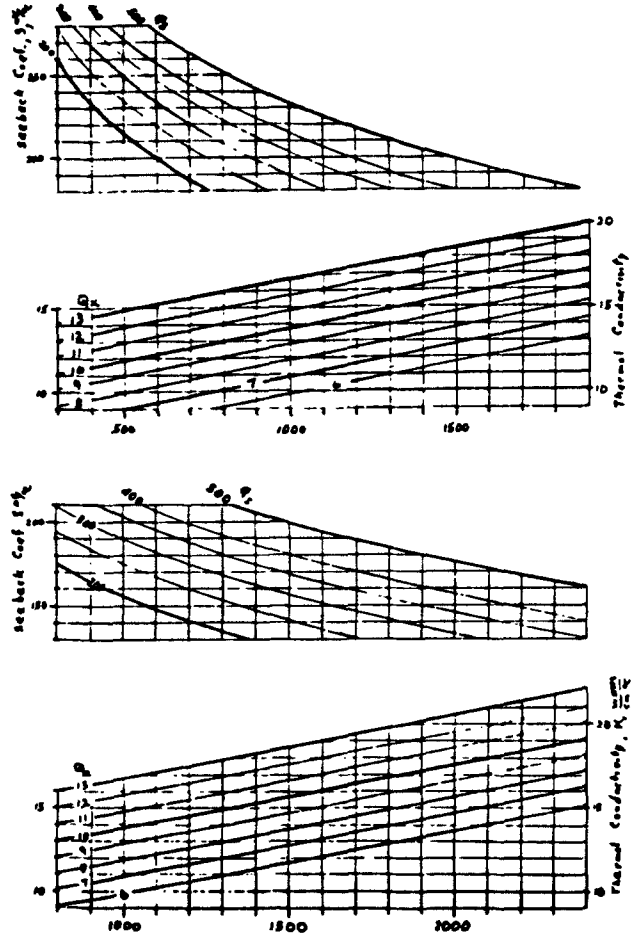


Fig. 6. Alloy optimization: S - σ - k , Q_s , Q_k interrelationships for laboratory data analysis.

permitted identifying the dependence of the variables on $G/R^{1/2}$.

The experimental results are presented in an unconventional way in Fig. 7 through 10 to illustrate phenomenologically the use of Q_s and Q_k descriptors. The relationship of the Seebeck coefficient to electrical conductivity in Fig. 7 shows how decreasing the crystal growth rate and increasing the temperature gradient to 250°C/cm with the growth rate at 0.435 cm/h improved alloy quality simultaneously with an apparent shift in the Fermi level as shown by increasing S and σ . The 50°C/cm gradient

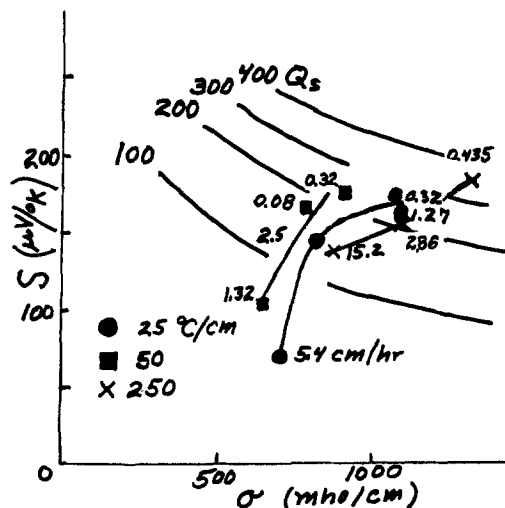


Fig. 7. The Q_s , Seebeck quality, characteristics of varying growth rate, R , and temperature gradient, G , samples of n-type $BiSbTe_3$ plus 0.56 w/o Se (24).

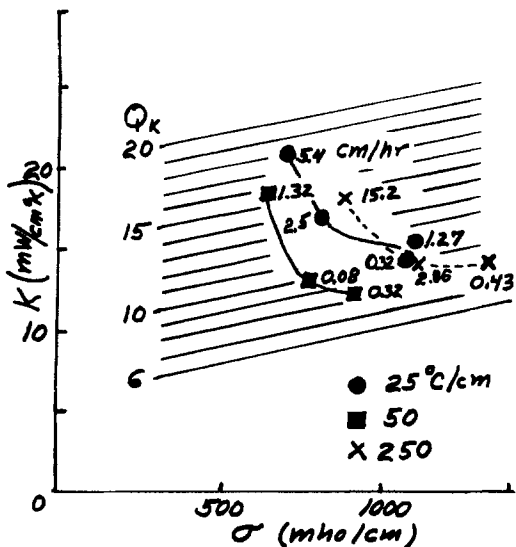


Fig. 8. The Q_{kT} thermal conductivity quality, characteristics of varying growth rate, R , and temperature gradient, G , samples of n-type BiSbTe_3 plus 0.56 w/o Se (24).

samples show anomalous characteristics compared to 25° and 250°C/cm.

The corresponding thermal conductivity curves shown in Fig. 8 illustrate the decrease in thermal conductivity paralleling the increase in Seebeck coefficient in Fig. 7. A minimum in Q_k near 8.7 is evident for the 50° and 250°C/cm temperature gradients, while a 10.0 Q_k range is reached at 25°C/cm.

The correlations of Q_s , Q_k , and $Q_s/Q_k = M$ with varying preparative conditions are in Fig. 9, and the correlation of Q_s to Q_k in Fig. 10. The outlier specimen at the steepest temperature gradient and slowest crystal growth rate is unusual as a 350 Q_s , 8.8 Q_k , and 39.8 M . The high figure of merit of $3.15 \times 10^{-3}/\text{K}$ represents an extreme in performance for an alloy at the BiSbTe_3 composition. The overall

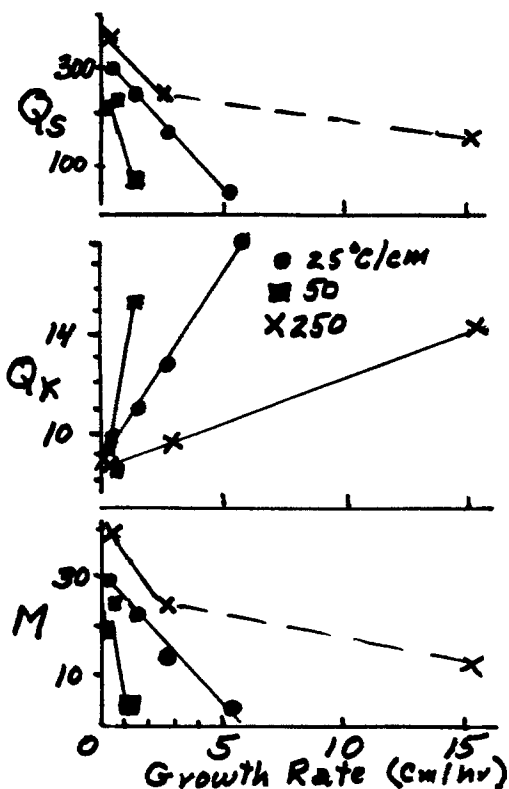


Fig. 9. The correlation of Q_s , Q_k , and $Q_s/Q_k = M$ with the variation of growth rate, R , and temperature gradient, G , in samples of n-type BiSbTe_3 plus 0.56 w/o Se (24).

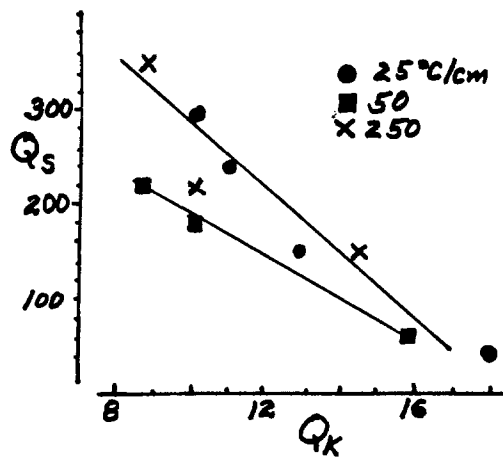


Fig. 10. The correlation of Q_s to Q_k for the sample series with variations of growth rate, R , and temperature gradient, G , in samples of n-type BiSbTe_3 plus 0.56 w/o Se (24).

internal consistency of the data would suggest this Q_s outlier more probably is in the 300 range and the figure of merit corresponds to $Q_s/Q_k = M$ of 30 or less rather than the higher value of Fig. 9.

Clearly, the samples of BiSbTe_3 doped with 0.56 w/o selenium incorporated a structural-chemical heterogeneity in the distribution of n- and p-type regions in the cross section. This gives rise to circulating current degradation of Q_s and Q_k .

Implications of Q_s and Q_k

Rather profound implications are present through the applicability of the Seebeck and thermal conductivity quality factors to the description of the thermoelectric properties of heavily doped semiconducting materials. This empirical, seemingly pragmatic approach provides a basis for value judgments critical to technology advancement. Furthermore, as experimental results are acquired in an organized framework, modifications of the quality factor concepts may be introduced in an evolutionary defined manner useful to advancing the technology as well as the science and engineering aspects.

An immediate consequence of using materials parameters to characterize alloys is the recognition and acceptance of the need for precise, accurate thermoelectric property measurements. The experimental designs must identify and distinguish between errors of thermoelectric parameter measurements and deviations introduced by materials variables. Careful planning of experimental designs is important, but failure to introduce the key variables is catastrophic. The objective is to develop commercial production technologies for the highest possible figure of merit n- and p-type alloys using compositions and procedures making commodity production of alloys feasible. Thus, a major program focus has been on developing adequate thermoelectric property measurements technology (25-26) to be used in adequately sophisticated statistical design approaches to experimentation.

A second consequence of the Q_s and Q_k parameter evaluation of materials is a recognition of the challenge complexity. A single or pair of samples preparative technology approach has limited justification for identifying likely candidate alloys. In general, the alloy performance must be optimized simultaneously for superior electron and phonon transport structural-chemical features. When the task is preparing a single-phase solid solution alloy with superior, reproducible properties, the phase rule defined bounds on the alloy are replaced by kinetic considerations. Sophisticated conceptual views to experimental design are important if the desired results are to come into reach of the experimentalist.

A third consequence is that the experimentation has a focus upon creating response surface relationships for the variables Q_s , Q_k , M , and Z connecting to the composition

and process variable space as well as to the structural-chemical descriptions for the solid state. This becomes crucial when technology transfer to production areas is undertaken. The new problems of scale-up must be identified and optimizable as a logical progression rather than becoming a mess of confounded variables. Too many variables exist for ease of sorting by simple experiments.

A fourth consequence of the application of Q_s and Q_k to experimental materials evaluation is a recognition of the difficulties in planning definitive studies. The literature contains thousands of publications relating to semiconductors for use in thermoelectrics. This accumulation of three decades is difficult to place into a rational perspective. The detailed analysis of one general case in depth and breadth is important for identifying the true character of both materials processing and materials characterization problems within a single relevant complex alloy system such as the $(\text{Bi,Sb})_2(\text{Te,Se})_3$, rhombohedral crystal system alloys. Many of the generally accepted paradigms prove to have limited validity.

A fifth consequence of defining the $Q_k = 10$ reference line is the introduction of an experimentalist view towards future options. The bismuth telluride alloys are in the thermal conductivity class for amorphous silica, a 13.7 mW/cm K thermal conductivity at room temperature. The lower value for Ag_2Se shown in Fig. 3 shows that an electrically conductive, 1000 mho/cm solid may be produced with significantly smaller lattice components. Thus, a critical aspect of progress towards higher figure of merit refrigeration alloys with improved efficiencies lies in the discovery and optimization of alloys giving access to high Q_s , which may be alloyed to minimum Q_k without degrading the thermoelectric performance. The existence of 500-600 Q_s Bi_2Te_3 samples as outlier materials with a 1500 Q_s approached by Bi-Sb alloys implies that the proposal has more than speculative merit.

The sixth implication emerging from the Q_s - Q_k approach to thermoelectric property characterization is that at elevated temperatures a greater promise exists for attaining improved alloy performance. The thermal conductivity of the crystal lattice is characterized by a $1/T$, reciprocal dependence upon temperature. Thus, a lower lattice component should be accessible at, say, 900K as compared to 300 K if the radiation terms remain small enough. The $ZT = 2$ gadolinium selenide alloy, Gd_2Se_3 , is characterized by a less than 100 Q_s electron transport feature, so the superior figure of merit from a low lattice thermal conductivity would be further benefited by improvements in the Seebeck quality (7). The existing Bi_2Te_3 , PbTe , Si-Ge , etc., alloys represent the beginning to a technology rather than the end to new options.

The discussion emphasized that progress depends upon the escalation of the breadth and depth of understanding on how the crystalline imperfection structures do control electron and phonon transport in solids. The three-dimensional structural chemistry of the space lattice interaction with the unit cell becomes critical to the optimization process. Achieving ultimate performance limits means the elimination of gross degrading phenomena on macro, micro, and submicro scales. This makes possible the recognition of optimizations in the atomic scale properties of the n- and p-type solid solution phases.

Summary

An empirical, pragmatic basis has been utilized to develop an approach to identifying the comparative qualities of experimental samples of thermoelectric materials. The approach emphasizes the need to learn how to manipulate imperfection structures in real solids so as to optimize the material performance, particularly for use in thermoelectric energy conversion. A route is created which permits a systematic approach to organizing experimental data in comparative ways. As data accumulate, the opportunity for undertaking more fundamental

studies emerges while efforts are continued to develop materials suitable for commercial developments.

The approach acknowledges the complexity of heavily doped semiconductors with regard to all aspects of materials science. Progress is dependent upon learning ways for coping constructively with this complexity. Subsequent papers will address various aspects in the study of bismuth telluride, $(\text{BiSb})_2(\text{Te,Se})_3$ -class materials relevant to the general challenges.

Acknowledgments

The continued support of Borg-Warner Corporation and the Roy C. Ingersoll Research Center management and staff is gratefully acknowledged. Without this, advances in the technology would not have been possible. Particular acknowledgments are given to Dr. D. W. Collier and Dr. L. V. Sloma's contributions along the way, and to Dr. D. F. Hoeg and W. H. Weltyk for the support making possible the documentation. Specific acknowledgment needs to be given to Dr. A. Reich, Stanley Cook, Bharat Kalsa, and John Horwath for varied contributions to the conceptual evolutions. Dr. Jack Madigan (deceased) was responsive to the original concept evolutions by teaching physics to a chemist. Throughout the support of many friends and colleagues near and far has been deeply appreciated.

Manuscript received Dec. 30, 1983.

Donald Tuomi, Ph.D. and Associates, Limited, assisted in meeting the publication costs of this article.

REFERENCES

1. A. F. Ioffe, "Semiconductor Thermoelements and Thermoelectric Cooling," pp. 1-182, Infosearch, Ltd., London (1957).
2. V. I. Fistul, "Heavily Doped Semiconductors," pp. 1-392, Plenum Press, New York (1969).
3. V. L. Bonch-Bruyevich, "The Electronic Theory of Heavily Doped Semiconductors," American Elsevier Publishing Co., Amsterdam (1966).
4. D. Tuomi, in "Proceedings of the 15th Intersociety Energy Conversion Engineering Conference, Seattle, WA, Aug. 18-22, 1980," no. 809314, American Institute of Aeronautics and Astronautics, New York (1980).
5. D. Tuomi, in "Proceedings of the 14th Intersociety Energy Conversion Engineering Conference, Boston, MA Aug. 5-10, 1979," no. 799396, American Chemical Society, Washington, DC.
6. D. Tuomi, Paper 573 RNP presented at the St. Louis, MO, Meeting of the Society, May 11-15, 1980.
7. D. Tuomi, Abstract 377, p. 941, The Electrochemical Society Extended Abstracts, Vol. 81-1, Minneapolis, MN, May 10-15, 1981.
8. D. Tuomi, in "Proceedings of the 4th International Conference on Thermoelectric Energy Conversion," K. R. Rao, Editor, pp. 130-132, University of Texas, Arlington, TX (1982).
9. D. Tuomi, *This Journal*, **131**, 2101 (1984).
10. R. P. Chasmar and R. Stratton, *J. Electron. Control*, **7**, 52 (1959).
11. Y. S. Touloukian, R. W. Powell, P. Y. Ho, and P. G. Klemens, in "Thermophysical Properties of Matter, Vol. 1 and 1 Thermal Conductivity," pp. A-1-A-46, IFI/Plenum, New York (1970).
12. J. R. Drabble and H. J. Goldsmid, "Thermal Conduction in Semiconductors," pp. 8-12, Pergamon Press, New York (1961).
13. P. G. Klemens, in "Solid State Physics: Advances in Research and Applications," F. Seitz and D. Turnbull, Editors, pp. 1-98, Academic Press, New York (1958).
14. J. R. Drabble and H. J. Goldsmid, in "Solid State Physics: Advances in Research and Applications," F. Seitz and D. Turnbull, Editors, pp. 123-125, 183, Academic Press, New York (1958).
15. J. R. Drabble and H. J. Goldsmid, in "Solid State Physics: Advances in Research and Applications," F. Seitz and D. Turnbull, Editors, pp. 120-122, Academic Press, New York (1958).
16. J. R. Drabble and H. J. Goldsmid, in "Solid State Physics: Advances in Research and Applications," F. Seitz and D. Turnbull, Editors, pp. 125-127, Academic Press, New York (1958).
17. E. F. Steigmeier, in "Thermal Conductivity," R. P.

- Tye, Editor, pp. 203-247, Academic Press, New York (1969).
18. I. Kudman, in "Proceedings of the 7th Conference on Thermal Conductivity," NBS Special Publication 302 (1968).
 19. D. P. Spitzer, *J. Phys. Chem. Solids*, **31**, 19 (1970).
 20. G. A. Slack, in "Solid State Physics: Advances in Research and Applications," H. Ehrenreich, F. Seitz, and D. Turnbull, Editors, pp. 1-73, Academic Press, New York (1979).
 21. D. Tuomi, "Thermoelectric Material Quality—The Seebeck Coefficient-Electrical Conductivity Relationship," Internal Report, Borg-Warner Research 3259-01, Nov., 1963.
 23. R. Simon, R. C. Bourke, and E. H. Lougher, *Adv. Energy Convers.*, **3**, 481 (1963).
 24. C. J. Cosgrove, J. P. McHugh, and W. A. Tiller, *J. Appl. Phys.*, **32**, 621 (1961).
 25. M. L. Stanley and A. D. Reich, U.S. Pat. 3,733,807 (1973).
 26. M. L. Stanley, A. D. Reich, and L. J. Ybarsondo, *Energy Convers.*, **13**, 7 (1973).

Plasma Etching of Refractory Gates for VLSI Applications

T. P. Chow*

General Electric Corporate Research and Development, Schenectady, New York 12345

A. J. Steckl*

Center for Integrated Electronics, Rensselaer Polytechnic Institute, Troy, New York 12181

ABSTRACT

The present status of plasma etching of refractory gates is reviewed in the context of high resolution patterning. Etching of various refractory metals (*cf.* Mo, W) and metal silicides (*cf.* MoSi₂, WSi₂, TaSi₂) is particularly emphasized and discussed in terms of etch rate, anisotropy, etch selectivity over SiO₂, resist, and other thin film materials. Key issues addressed include choice of etchant (*cf.* CF₄, NF₃, CCl₄), additive gas (O₂, Ar, He), and reactor configuration (planar plasma, RIE, flexible diode, triode). Factors influencing the control of edge profiles in single-level and composite gate structures are described. End-point detection of these plasma processes is reviewed and compared with that developed for silicon etching. Also, basic mechanisms in these processes, such as desorption of reaction products, are discussed with respect to their effect on the etching characteristics of these refractory materials.

Refractory metals, metal silicides, and other metal compounds are under active development as gate and interconnecting materials in VLSI circuits because of their low resistivity (as compared to doped poly-Si) and, in the case of the silicides, good oxidation properties. This rapid development is demonstrated by the large body of work reported in the last few years, as reviewed by several recent articles (1-6).

Fine line patterning for the small dimensional (~1 μm) features required by VLSI necessitates the use of plasma etching techniques, such as planar plasma etching and reactive ion etching. The salient feature of these plasma processes is the use of reactive gases *vs.* inert gases commonly used in conventional sputter etching. Dry etching of poly- and monocrystalline silicon has been studied extensively (7-10), both in terms of basic plasma chemistry and microelectronic applications. In contrast, relatively little work has been reported for refractory metals and metal silicides. In this paper, the present status of plasma etching of refractory metal silicides for VLSI is reviewed. To begin with, in the "General Considerations" section, the general considerations of plasma etching processes and the pertinent aspects of metal and silicide etching are discussed. The specific processes, as applied to various gate structures (single-level metal or silicide, polycide, and others), are described, respectively, in the three following sections, in terms of advantages and trade-offs. Then, the basic mechanisms that take place during the etching of these materials are discussed, with respect to the effect they exert on the etching behavior (etch rate, selectivity, etc.). Finally the results are summarized.

General Considerations

In Table I, a summary of refractory metals on which plasma etching has been reported in the literature (11-35) is presented along with the etching gases used for each. Both fluorinated and chlorinated gases as well as their mixtures have been studied. A similar table for silicides is shown in Table II (36-53). As is well known in silicon etching, one of the fundamental differences between

fluorine- and chlorine-based plasma is the higher volatility of the reaction products (*i.e.*, silicon fluorides) in the former. To facilitate the desorption of the silicon chlorides so that further etching can proceed, ion-assisted reactions are necessary in chlorine-based plasma. However, this enhances the etching anisotropy, since the sidewall of the etched film or substrate is not subjected to energetic ion bombardment. Also, oxygen is often added, particularly for the halocarbons (like CF₄ and CCl₄), to enhance the etch rate of many of these gases. Its effect is believed to be the more efficient generation of fluorine atoms or radicals (8). Also indicated in the two tables are the reactor configurations which have been used. As the plasma technology evolved, cylindrical (barrel-type) reactors have been replaced by planar (parallel-plate) reactors. This latter group can be categorized into planar plasma etching (PPE), reactive ion (or sputter) etching (RIE), and, most recently, flexible diode (FDE) and triode-type (TE) etching modes (54-56). Generally, PPE systems are operated at higher pressures (~100 mtorr to 1-5 torr) than RIE, FDE, and TE systems (10 to 100 mtorr). For comparison, conventional sputter etching uses inert gases at 1 to ~10 mtorr. The main configuration difference between the PPE and RIE modes is in the RF power coupling, with the power supply connected to the top electrode for PPE and to the bottom electrode (on which the wafers are situated) for RIE. The FDE and TE modes are further refinements of the first two. In FDE, the RF power can be switched between the two electrodes during the process, while, in TE, both of the electrodes are simultaneously powered (with the chamber wall grounded). For a more detailed discussion of plasma etcher design and etching modes, see Ref. (54-56). Since each type of reactor may be optimized for the specific application, any direct comparison among these etching modes is difficult and must take into account the system and operating parameters (such as pressure and electrode spacing).

Gate structures incorporating refractory metals and/or metal silicides are shown in Fig. 1 (4) and discussed in the following sections. Since the patterning of these refractory materials is intricately related to the MOS gate structures' being implemented, it is useful to first point out

* Electrochemical Society Active Member.

Table I. A summary of refractory metals along with the etching gases and modes used

	Mo	W	Ti	Ta	Nb	V	Ti:W
CF ₄	a (4, 12, 23)	a (12)		a (28)	a (29) c (29)		
CF ₄ /O ₂	a (11, 13, 31) b (1)	a (13, 31) b (1) c (14) c (14)	a (31)	a (31, 33)	a (13)		
CHF ₃ C ₂ F ₆			c (30)			c (30, 32)	
NF ₃ NF ₃ /Ar NF ₃ /He SF ₆ SF ₆ /O ₂	b (15-17) b (15, 16) b (16) c (19)						b (17)
CCl ₂ F ₂ CCl ₂ F ₂ CCl ₂ F ₂ /O ₂ C ₂ Cl ₂ F ₄ /O ₂	c (26) c (26) c (?) (25)		a (11)				
CCl ₄ /O ₂	b (20) c (21, 22)						
CF ₃ Br CF ₃ Br/O ₂ /He	c (24)		b (27) b (27)				

a: Barrel or downstream plasma etching.

b: Planar plasma etching.

c: Reactive ion etching, reactive sputter etching.

?: Reference ambiguous on reactor configuration and/or specific gas used.

Table II. A summary of refractory metal silicides along with the etching gases and modes used

	MoSi ₂	WSi ₂	TaSi ₂	TiSi ₂	NbSi ₂
CF ₄ /O ₂	a (36, 37, 47)		a (42) (?) b (43)		a (44)
CF ₄ /C ₂ F ₆ NF ₃ NF ₃ /Ar NF ₃ /He SF ₆ /O ₂	c (38) c (47) b (15, 16, 45) b (15, 16) b (16) c (46)	b (39) c (40, 41)			
CCl ₂ F ₂ CCl ₄ /O ₂ BCl ₃ /Cl ₂	c (22)	d (49)		b (50) (?)	
CF ₄ /Cl ₂ NF ₃ /CCl ₄ NF ₃ /HCl SF ₆ /Cl ₂ SF ₆ /HCl SF ₆ /CCl ₄ SiF ₄ /Cl ₂	c (52) c (52) c (52) c (52) c (52) c (52)		c (51) c (51) c (53)		c (52) c (52) c (52) c (52)

a: Barrel plasma etching.

b: Planar plasma etching.

c: Reactive ion etching, reactive sputter etching.

d: Triode etching.

?: Reference ambiguous on reactor configuration and/or specific gas used.

various gate structures that have been suggested and their related etching requirements (Table III). The simplest gate structure is a direct replacement of the poly-Si with a refractory metal or metal compound-like silicide. The patterning process, in this case, should etch the gate conductor anisotropically and selectively over the gate dielectric (SiO₂, Si₃N₄) and the masking material (photoresist). Despite the simplicity of the single-level gate approach, the reliability of the poly-Si gate has led to the implementation of various composite gates in which the poly-Si/SiO₂ interface is maintained while the conductivity is enhanced with a silicide overlayer. The most widely accepted approach is the silicide/doped poly-Si ("polycide") structure. However, because of the bilayer nature of the polycide, its etching is more demanding. The requirements include: anisotropic and selective etching of both the silicide and poly-Si over the masking layer

and selective removal of poly-Si over the gate dielectric. In the next three sections, the etching of single-level metal and silicide gates is discussed first, and then the patterning of the polycide and other gate structures are described.

Pattern Definition of Single-Level Gates

Metals.—Among the refractory metals, molybdenum and tungsten are most widely used as MOS gates and interconnections. One of the major conditions for a metal to be considered as a gate material is its stability with the gate dielectric, which is usually SiO₂ or Si₃N₄. The group consisting of molybdenum, tungsten, and rhenium is the most stable over both oxide and nitride (4, 58) and hence most appropriate for microelectronic applications. Other metals, such as titanium and tantalum, can react with the oxide or nitride at relatively low temperatures (~600°C)

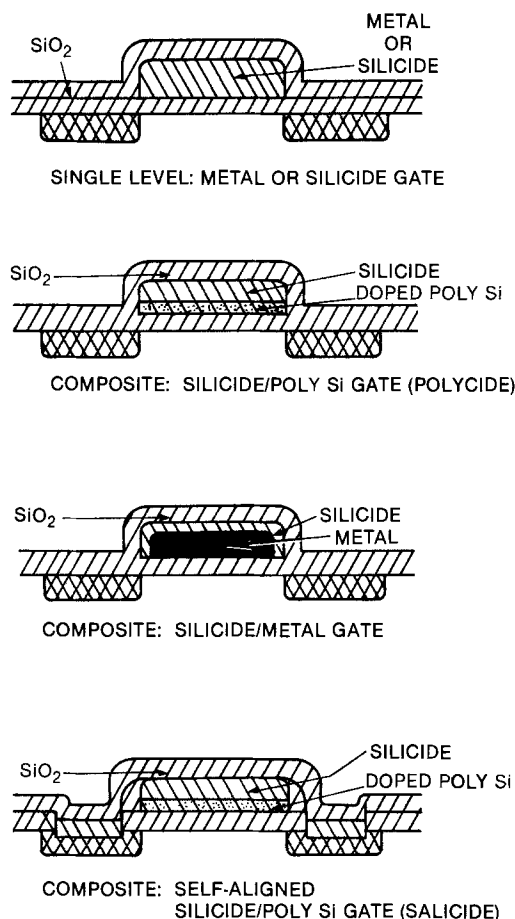


Fig. 1. Various gate structures incorporating refractory metals and metal silicides (4).

and thus may not be directly placed over the gate dielectric. However, these other refractory metals have been used in other applications, such as interconnections in hybrid circuits and superconductors in Josephson junctions. Therefore, the etching gases and modes used for their patterning have been included, for the sake of completeness, in Table I along with those for molybdenum and tungsten.

Fluorinated plasmas.—It has been known for some time now that fluorocarbon plasma can etch many refractory metals. Similar to silicon etching, addition of a small amount of oxygen to CF_4 substantially increase the etch rate of these metals. For example, adding 4% oxygen to CF_4 enhances the etch rate of molybdenum by about a factor of 4 (4). For high resolution patterning, planar-type reactors are usually utilized in either the planar plasma etching (PPE) (1) or reactive ion etching (RIE) mode (14). Recently, other fluorinated gases, most notably NF_3 and SF_6 , which can generate more fluorine atoms or radicals, have also been investigated (15-19), resulting in much higher etch rates. In Fig. 2, the etch rate of Mo and SiO_2 is

Table III. Etching requirements of various gate structures

	Metal or silicide	Polycide
Anisotropy		
Metal or silicide	X	X
Poly-Si		X
High selectivity		
Metal or silicide/resist	X	X
Poly-Si/resist		X
Metal or silicide/oxide	X	X
Poly-Si/oxide		X
Equal etch rate		
Silicide/Poly-Si		X

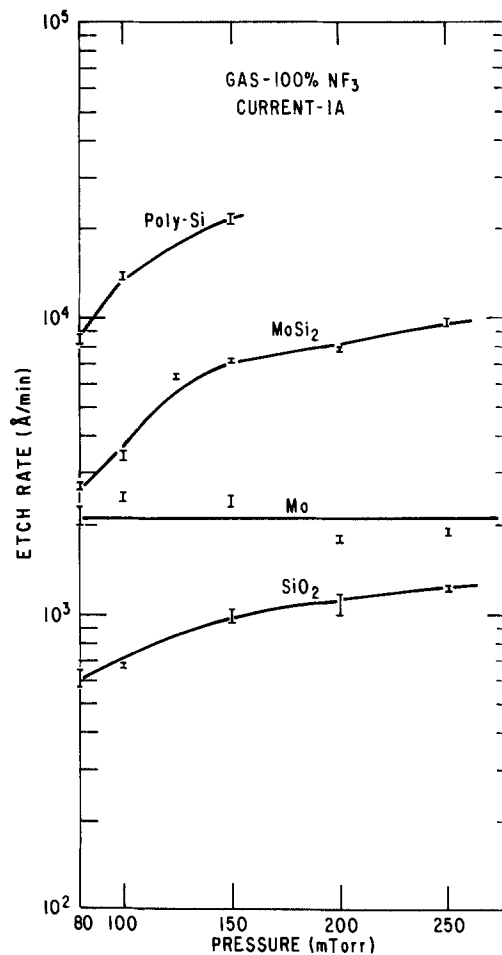


Fig. 2. Etch rates of Mo, $MoSi_2$, doped poly-Si, and SiO_2 as a function of pressure in NF_3 (16).

shown as a function of pressure for a planar reactor operating in the PPE mode. While the silicon and oxide etch rates increase with pressure, the metal etch rate remains fairly constant within the pressure range studied. Such a dependence is believed to be due to the lower volatility of molybdenum fluorides than the silicon fluorides. Diluting NF_3 or SF_6 with inert or oxidizing gases generally results in a decreased concentration of reactant species. Examples of this have been shown for NF_3/Ar or N_2 (57) and SF_6/O_2 (18). Therefore, addition of conventional dilutants (Ar , O_2 , He) only leads to a reduced metal etch rate. This trend is illustrated in Fig. 3 and 4 for the PPE of molybdenum in NF_3/Ar (15) and RIE of tungsten in SF_6/O_2 (18), respectively. Furthermore, while both molybdenum and tungsten can be selectively etched over SiO_2 , the etch rate of Si_3N_4 is usually faster than those of the metals in fluorine-based plasma (4).

Edge profiles of these metals have only been studied in a few of these plasmas. A vertical-to-horizontal etch ratio of 3 was measured for NF_3 etching of Mo at 100 mtorr in PPE (15), while very anisotropic profiles were obtained for both Mo and W in SF_6/O_2 using RIE at relatively low pressures (10-20 mtorr) and high power (18, 19).

Chlorinated plasmas.— CCl_4 has been most thoroughly studied among the chlorine-based compounds. Pure CCl_4 plasmas not only generate undesirable polymers in the etching chamber, but also etch Mo and W very slowly, and hence cannot be used. Addition of large amounts of oxygen (more than 50% by volume) greatly enhances the etch rate and selectivity over SiO_2 (60-100) (20-22). The reason for the large increase in etching is believed to be the formation of molybdenum oxychlorides, which have a much higher volatility than the chlorides. Obviously, because of the large amounts of oxygen added, the resist etch rate is also increased, but this is considered an acceptable tradeoff. For example, when the oxygen percent-

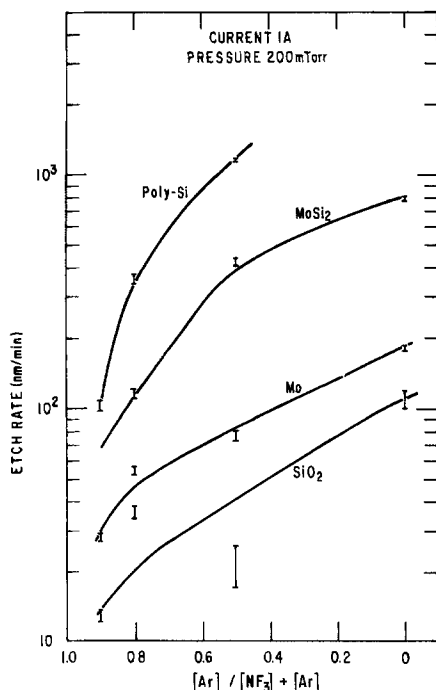


Fig. 3. Etch rates of Mo, MoSi₂, doped poly-Si, and SiO₂ as a function of argon percentage in NF₃/Ar mixtures (16).

age is varied from 20% to 80%, the photoresist (AZ1350J) etch rate is only tripled while the Mo etch rate is five times higher (21). Similar variations in etch rate with oxygen content were measured for oxygen percentage between 60% and 80% (Fig. 5) (22). Similar dependence on oxygen content was observed for negative electron beam resist (20). In addition, the silicon etch rate was sharply suppressed at over 70% oxygen, making selective etching of Mo over silicon feasible (21). As will be discussed in the "Mechanisms" section, similar characteristics are expected for tungsten, rhenium, and chromium, but only the case of chromium etching has been verified in the context of photomask fabrication (34, 35). Actually, in one case, carbon dioxide, instead of oxygen, was used as the oxidant so as to retard photoresist degradation (35).

The edge profiles obtained in CCl₄/O₂ plasmas were almost totally vertical. This may be due to molybdenum oxychlorides, which can only be formed or desorbed under energetic ion bombardment. In fact, traces of oxychlorides can be found on the electrode surfaces and the chamber walls after etching. Thus, precautions must be taken to prevent contamination of the exposed wafer surfaces. To clean up the chamber walls after etching, a fluorinated plasma (like CF₄) can be used (22).

Halide mixtures.—To improve the etching characteristics, combinations of fluorine- and chlorine-based gases can

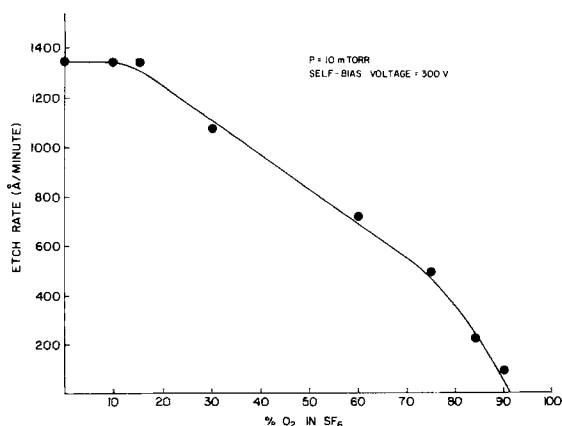


Fig. 4. Etch rate of tungsten as a function of oxygen content in SF₆/O₂ mixtures for a reactive ion etcher (18).

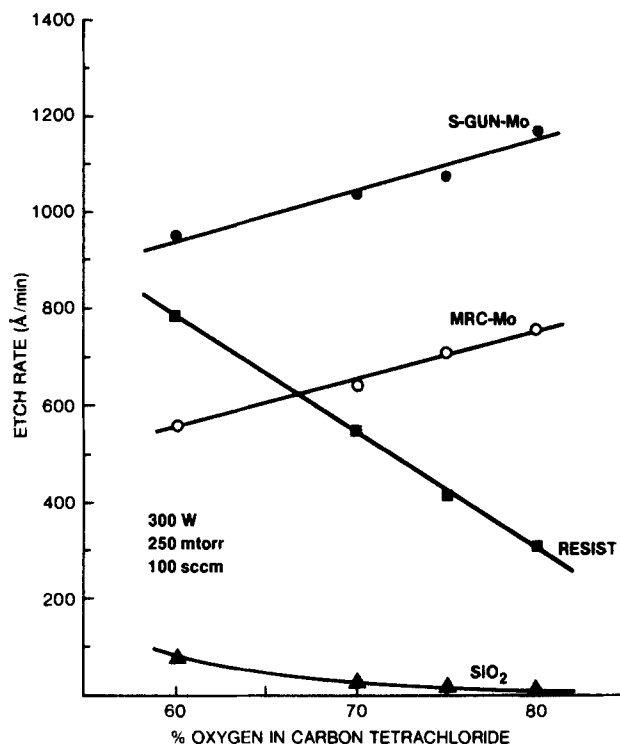


Fig. 5. Etch rate of molybdenum films deposited in two different sputtering systems as a function of oxygen percentage in CCl₄/O₂ mixtures (22).

be used. Basically, there are two ways of introducing two or more halide components into the etching reactions. The first is direct mixing of the gases at the inlet of the reaction chamber. Since the ratio of each component is controlled by the gas flow, it can be adjusted at will. The second is to use a molecule containing all of the halide components, such as fluorochloromethane.

As far as halide mixtures are concerned, the refractory metals have been mostly patterned using chlorofluorocarbons. For example, reactive sputter etching of Mo with CCl₂F₂ and C₂Cl₃F₃ has been reported in an early study (26). Using these reactive halide compounds, an etch rate four to five times higher than using argon was observed for molybdenum.

Metal silicides.—The stability trends mentioned earlier for refractory metals on SiO₂ and Si₃N₄ also apply to the metal silicides (2, 4). The situation is less critical for the silicides because, among the silicide compounds, only the disilicides which have a large percentage of silicon (66.7%) are commonly used. Nevertheless, the disilicides most often implemented in single-level structures are still those of molybdenum and tungsten. Etching gases and modes are listed in Table IV.

Fluorinated plasmas.—For silicide etching in fluorinated plasmas, the basic mechanisms involve the reaction of the silicide with the generated fluorine radicals to form metal and silicon fluorides. Similar to refractory metal etching, the initial plasma etching of silicides involved fluorocarbons (such as CF₄/O₂) in barrel reactors. This reactor/etchant combination resulted in acceptable silicide etch rate and selectivity (over SiO₂ and photoresist), but also in isotropic edge profiles. For example, etch rates of 800-1000 Å/min have been reported for MoSi₂ (37) and NbSi₂ (44) at 100W of RF power and a pressure of 0.2-0.3 torr with an etch rate selectivity over thermal oxide of ~15 to 1. To improve the linewidth control while increasing the etch rate, more advanced techniques using parallel-plate-type reactors in conjunction with other fluorinated compounds (such as NF₃ and SF₆) have been employed. An example of this is PPE of MoSi₂ over SiO₂ in NF₃-based plasmas. Diluting NF₃ with inert gases (argon, in this case) leads to a monotonic decrease in silicide etch rate (Fig. 3). For argon concentration as high as 50%

Table IV. The melting, boiling, and sublimation points of fluorides and oxyfluorides of several refractory metals and silicon (66, 67)

Fluoride or oxyfluoride	Melting point (°C)	Boiling point (°C)	Sublimation point (°C)
SiF ₄	-90.2	-86	—
TiF ₄	>400	—	284
TiF ₃	1200	1400, (1727) ^a	—
TiF ₂	(1277)	(2152)	—
ZrF ₄	—	—	~600, (903)
ZrF ₃	(1327)	(2127)	—
ZrF ₂	(1402)	(2277)	—
HfF ₄	—	—	(927)
HfF ₃	(1327)	(2127)	—
HfF ₂	(1377)	(2027)	—
VF ₅	19.5	111.2	—
VF ₄	—	—	(327)
VF ₃	(1127)	(1627)	—
VF ₂	(1327)	(2227)	—
VOF ₃	300	480	—
NbF ₅	72	236	—
TaF ₅	96.8	229.5	—
TaF ₄	(1477)	(2077)	—
TaF ₃	(1237)	(1977)	—
CrF ₃	>1000, 1100	(1427)	1100-1200
CrF ₂	1100	>1300, (2127)	—
MoF ₆	17.5	35	—
MoF ₅	67	213.6	—
MoF ₄	(557)	(617)	—
MoF ₃	Nonvolatile	—	—
MoO ₂ F ₂	—	—	270
MoOF ₄	98	180	—
WF ₆	2.5	17.5	—
WF ₅	(107)	(247)	—
WF ₄	(527)	(622)	—
WOF ₄	110	187.5	—
ReF ₇	48	74	—
ReF ₆	18.8	47.6	—
ReF ₅	125	221, (387)	—
ReF ₄	124.5, (427)	(687)	—
ReF ₃	(1107)	(1257)	—
ReOF ₄	39.7	62.7	—
ReO ₂ F ₂	156	—	—

^aEstimated values are in parentheses.

in NF₃/Ar, the selectivity over oxide did not significantly deteriorate.

Chlorinated plasmas.—Compared to fluorinated plasmas, fewer works have been reported on chlorinated plasmas. In one study (22), RIE of MoSi₂ using CCl₄/O₂ was reported. Generally, lower etch rates of both silicide and oxide were measured than in the NF₃ case. The relationship between etch rates (of MoSi₂, SiO₂, and photoresist) and pressure for 50% O₂ in CCl₄ is shown in Fig. 6. The silicide etch rate increases with pressure (as in NF₃ plasmas), whereas the oxide etch rate is constant (while it increases with pressure NF₃). For the same RIE system, CCl₄ diluted with oxygen (40%–70%) resulted (22) in a lowered etch rate for both MoSi₂ and SiO₂ (Fig. 7).

Fluorinated/chlorinated mixtures.—Recently, several combinations of fluorine/chlorine compounds have been investigated for a few silicides. However, most of the studies addressed the problem of polycide etching and hence concentrated on optimizing silicide/poly-Si etch rate ratio and edge profiles. These results will be discussed in the third part of the section below. In one recent study, RIE of MoSi₂ and NbSi₂ over oxide was investigated with SF₆ or NF₃/CCl₄ or HCl mixtures. The details will be published elsewhere (53). In general, the silicide and poly-Si etch rate increases with increasing fluorine content, RF power, and pressure. For example, at 100W in a 50/50 NF₃/HCl mixture, the etch rates of MoSi₂ and SiO₂ were 370 and 60 Å/min but were increased to 540 and 300 Å/min, respectively, when the RF power was raised to 300W. Also, HCl and NF₃ plasmas tend to have a higher

MOLYBDENUM SILICIDE ETCH RATE vs. PRESSURE

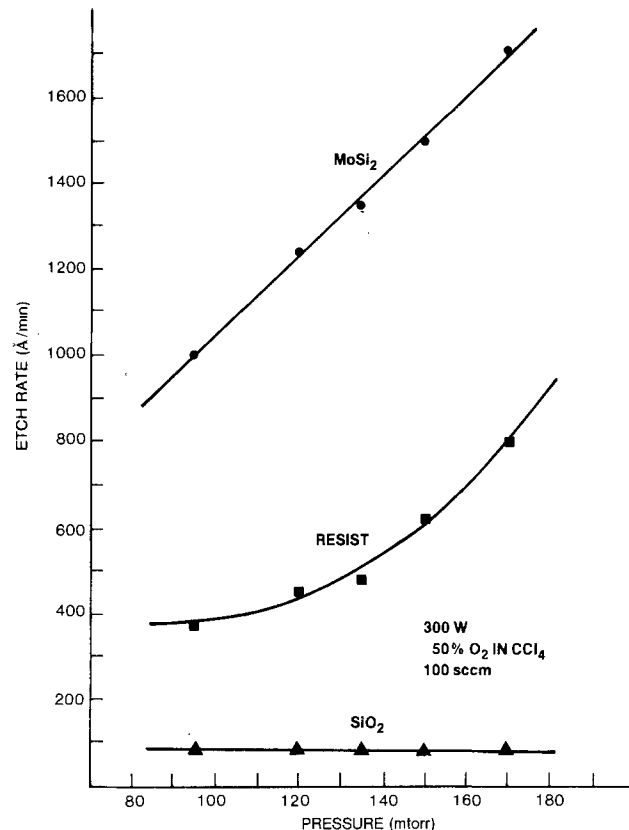


Fig. 6. Etch rates of MoSi₂, photoresist, and SiO₂ as a function of pressure in 50% oxygen in CCl₄ (22).

substrate dc bias (by about an order of magnitude) than CCl₄ or SF₆ plasmas under identical conditions.

Patterning of Polycide Gates

To preserve the reliable nature of poly-Si gate structures while enhancing the conductivity with silicides, a

MOLYBDENUM SILICIDE ETCH RATE vs. OXYGEN

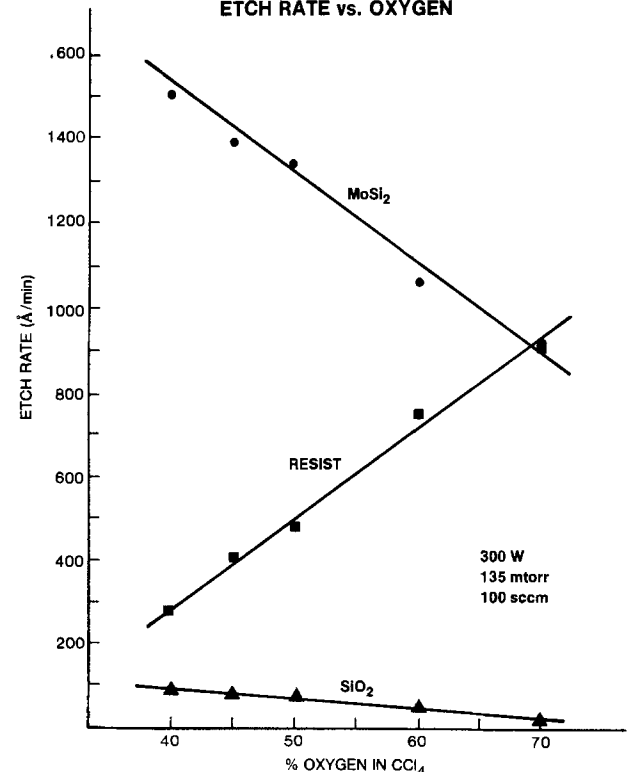


Fig. 7. Etch rates of MoSi₂, photoresist, and SiO₂ as a function of oxygen percentage in CCl₄ (22).

composite silicide/doped poly-Si (polycide) structure is widely used. The pattern definition of this bilayer structure is complicated by the possible undercut of either material. As discussed in the "General Considerations" section, the requirements for etching this structure are more stringent. In the ideal case, equal etch rates and perfect anisotropy under all conditions for both materials would yield the vertical profile shown in Fig. 8a. If the anisotropy for the two materials is not but equal, the dashed edge profile would result. To achieve a realistic optimal solution, one has to understand the interdependent relationships involving the loading dependence of etch rate and anisotropy of the materials exposed during etching. For example, severe silicide "pull-back" (Fig. 8b) can result from either (i) high silicide/poly-Si etch rate ratio ($\gg 1$) or (ii) increased lateral silicide etching upon the near completion of vertical silicide etching. If the second case is operative, separate vertical etch rate data for silicide and poly-Si would not predict the correct profile. However a silicide "roof" (Fig. 8c) can be formed only when the silicide/poly-Si etch rate ratio $\ll 1$. This discussion assumes that the etching cycle is terminated precisely at the point where the underlying oxide is exposed, and, therefore, there is no overetching. To obtain vertical edge profiles for this composite gate structure, two basic approaches have been taken. One is to optimize the choice of etchants and operating conditions, and the other is to design novel reactor configurations. In the following, both of these approaches will be described for the specific silicide/etchant combination reported.

Fluorinated plasmas.—Coevaporated tungsten silicide polycide edge profiles have been studied as a function of oxygen percentage in CF_4 for a planar reactor in the PPE mode (48). Figure 9 shows the etch rates of both WSi_2 and poly-Si and their etch rate ratio as a function of oxygen percentage in CF_4 . At low oxygen concentration ($<3\%$), the silicide is etched faster than the n^+ poly-Si, leading to a pull-back of the silicide layer. At higher O_2 contents, the doped poly-Si is removed faster, resulting in a silicide overhang. A similar trend was reported (41) for RIE of WSi_2 in a flexible diode reactor with CF_4/O_2 mixtures, but the oxygen percentage at which equal silicide/poly-Si etch rates were measured was $\sim 35\%$ (Fig.

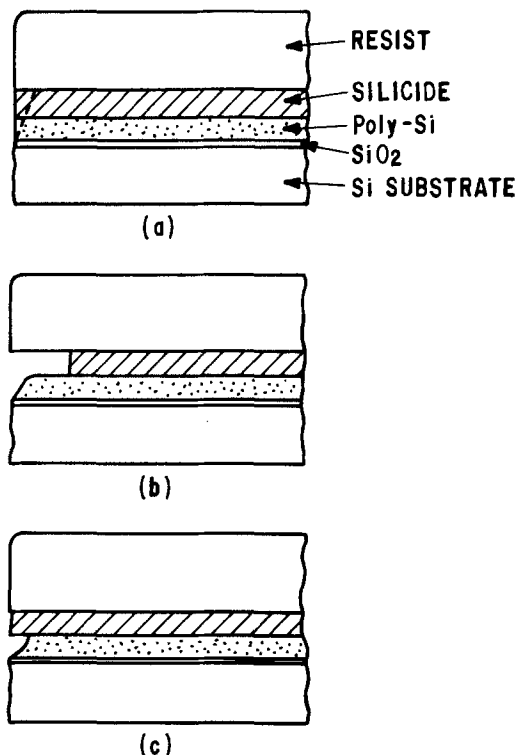


Fig. 8. Schematic drawings of three types of possible edge profiles for the polycide structure.

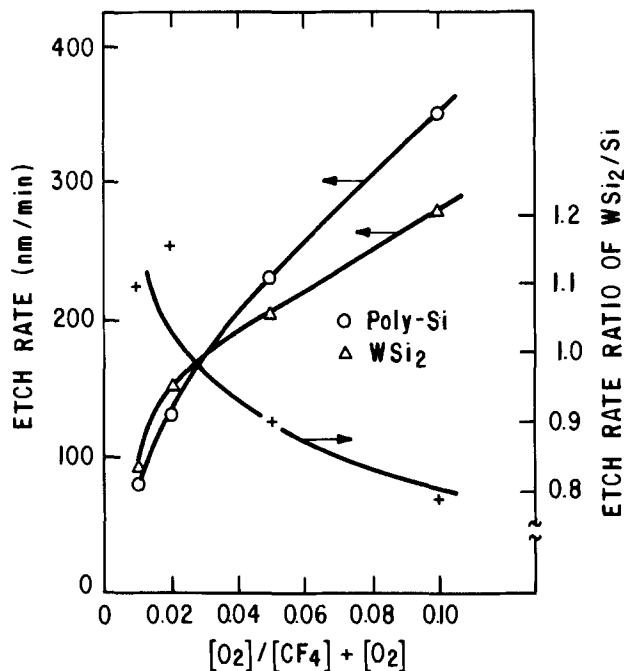


Fig. 9. Etch rates of WSi_2 and doped poly-Si and their etch rate ratios as a function of O_2 percentage in CF_4/O_2 mixtures for a PPE reactor (39).

10). In either study, micron-size WSi_2 polycide gates with acceptable profiles were realized. This cross-over point in tungsten silicide *vs.* poly-Si etch rates apparently cannot be found (48) when adding oxygen (up to 50%) to SF_6 (see Fig. 11).

For $MoSi_2$ polycide etching, both CCl_4/O_2 and NF_3 plasmas are usable. For example, in Fig. 2, the etch rate dependence on pressure is shown for poly-Si, $MoSi_2$, Mo, and SiO_2 in NF_3 . It is seen that the poly-Si-to-silicide etch rate ratio is about 3-4, leading to silicide roof formation. A similar overhang was reported (43) for the PPE in CF_4/O_2 of cosputtered $TaSi_2$ on doped poly-Si.

Fluorinated/chlorinated mixtures.—To improve or tailor the etching characteristics, combinations of gases can be used. The objective is to provide the optimum reactant gas for each layer of the polycide. Etching of refractory metal silicides in pure chlorinated plasmas usually yields a very low etch rate due to the limited volatility of the resulting metal chlorides. To enhance the silicide etch rate, either oxidants or fluorine components may be added. Oxidant additives are used when they can convert the metal chlorides to more volatile oxychlorides. Similarly, higher volatility can be achieved in many cases with metal fluorides obtained from the introduction of fluorine components. This latter approach is exemplified in Fig. 12 and 13 for RIE of

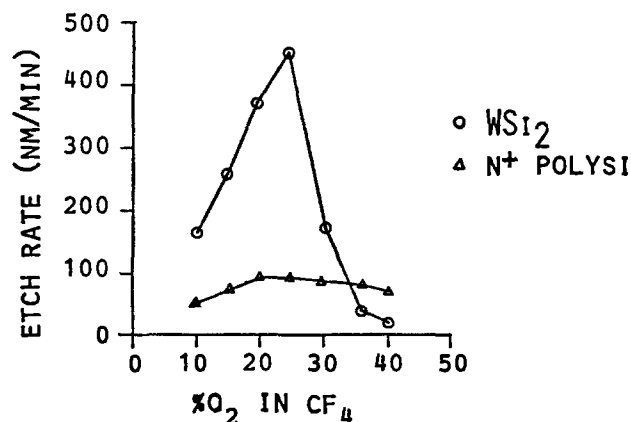


Fig. 10. Etch rates of WSi_2 as a function of oxygen in CF_4 for a planar reactor in the RIE mode (41).

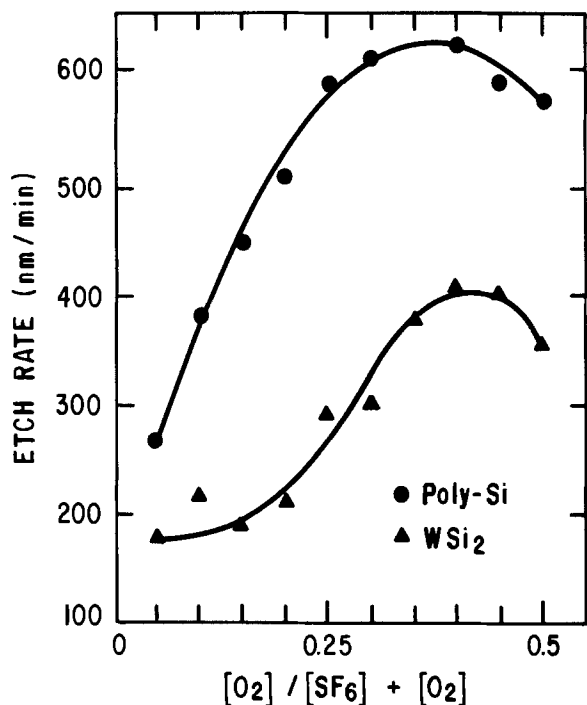


Fig. 11. Etch rates of WSi₂ and n⁺ poly-Si as a function of oxygen percentage in SF₆/O₂ mixtures for a PPE reactor (48).

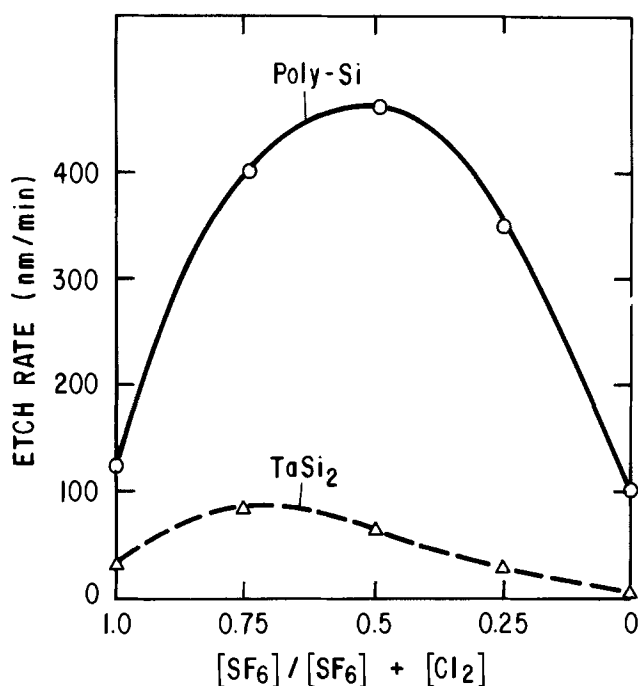


Fig. 12. Etch rates of TaSi₂ and n⁺ poly-Si as a function of gas composition for SF₆/Cl₂ mixtures (51).

TaSi₂ polycide (51). It is interesting to note that, in SF₆/Cl₂ mixtures (Fig. 12), while the poly-Si and TaSi₂ etch rates do not change uniformly with increasing SF₆ content, their ratio decreases monotonically but is always larger than unity (i.e., no crossover point). However, the addition of CF₄ to chlorine plasmas results in two apparent crossover points (Fig. 13).

An alternative method to introduce chlorine and fluorine species is the use of a molecule consisting of both components, such as fluorochlorocarbons. Only very limited data have been reported on this approach (49) using CCl₂F₂ in the triode-type etching mode on WSi₂ polycide. A third alternative employs a sequence of etching gases and modes for the silicide, interfacial region, and poly-Si (47).

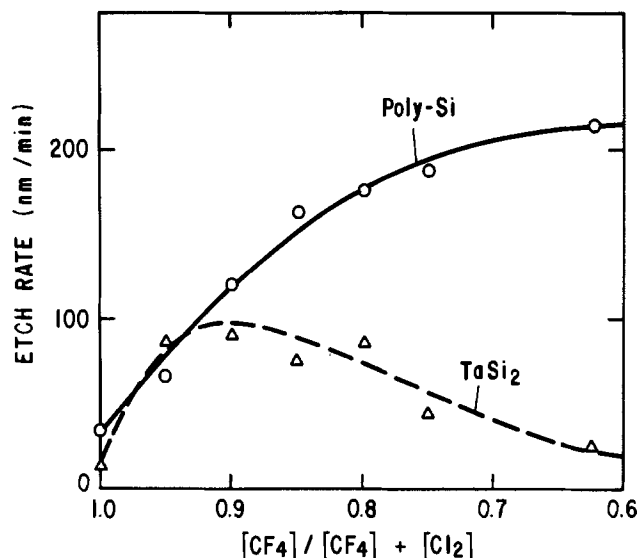


Fig. 13. Etch rates of TaSi₂ and n⁺ poly-Si as a function of gas composition for CF₄/Cl₂ mixtures (51).

Etching of Other Gate Structures

While the single-level metal or metal compound and composite polycide gate structures have been most extensively investigated, there are other novel structures which have also attracted considerable attention lately.

Self-aligned gate structures.—Realizing that the pattern definition of a composite silicide gate like the polycide requires stringent optimization and extensive development efforts, self-aligned silicide/poly-Si gate processes have been proposed recently (59-62). A variety of silicides (PtSi, TiSi₂, TaSi₂, CoSi₂, and others) have been incorporated into gates and contacts in this type of self-aligned processing. This approach involves patterning of the poly-Si gate and opening of the silicon substrate contacts, deposition of a metal layer, heat-treatment to form silicide only over the exposed silicon areas, and the selective removal of the unreacted metal. While no high resolution silicide patterning is needed in this process, plasmas may be used in the last step to selectively remove the unreacted metal.

Edge-defined structures.—To achieve submicron device structures without resorting to the use of advanced lithographic equipment, edge-defined patterning has been investigated. Many device features—oxide spacers and gates, just to mention two—have been realized with this maskless approach. The edge-defined approach usually involves the following steps: (i) definition of a vertical edge, (ii) conformal deposition of either a gate material (direct technique) or a material to be used as a transfer mask (indirect technique), (iii) anisotropic etching of the conformal film, resulting in a residue along the initial edge, (iv) selective removal of the initial step material, leaving only the residue, and (v) transfer of the pattern into the underlying gate material layer (indirect technique only). The direct technique has been applied to the realization of submicron MoSi₂ structures shown in Fig. 14 (45). The anisotropic etching was performed in a PPE reactor at relatively high power and low pressure with NF₃ plasma. The step material used was aluminum, which was patterned in a CCl₄ plasma. The molybdenum silicide layer was conformally deposited by dc magnetron sputtering and then anisotropically etched in a PPE reactor with NF₃.

Metal/metal nitride structures.—Recently, molybdenum gates overcoated with a layer of its own nitride have been studied to avoid dopant ion channeling. Unless the nitride layer is formed through self-aligned nitridation after the Mo patterning, patterning of the composite molybdenum nitride/Mo stack is needed. Only limited data have been reported in RIE with CCl₄/O₂ (22). The nitride etch

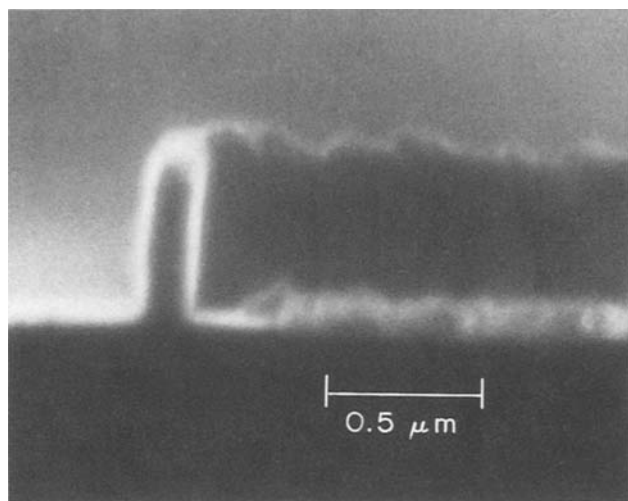


Fig. 14. SEM micrograph of a submicron MoSi_2 line fabricated with an edge-defined technique (45).

rate is generally about 40% higher than the Mo etch rate. For example, etch rates of 1460 and 1070 $\text{\AA}/\text{min}$ was obtained for Mo_2N and Mo, respectively, in 75/25 CCl_4/O_2 at 250 mtorr. Furthermore, lateral undercut of only 0.1 μm on each side was measured for a $\text{Mo}_2\text{N}/\text{Mo}$ composite.

Endpoint Detection

To selectively etch a single layer or multiple layers of thin films over underlying layers or substrates, the ability to detect the endpoint of the plasma etching process is essential. A variety of techniques have been developed to meet this need. Among them are optical emission spectroscopy, mass spectrometry, optical reflection, impedance monitoring, Langmuir probe, and pressure change (72). Mass spectrometry and optical emission spectroscopy are apparently the most popular. Both of these techniques involve the monitoring of reactive species and/or etch products. However, the product species are preferred because they originate solely from the etching reactions. For example, in plasma etching of silicon, silicon dioxide, and silicon nitride, the peak most often mon-

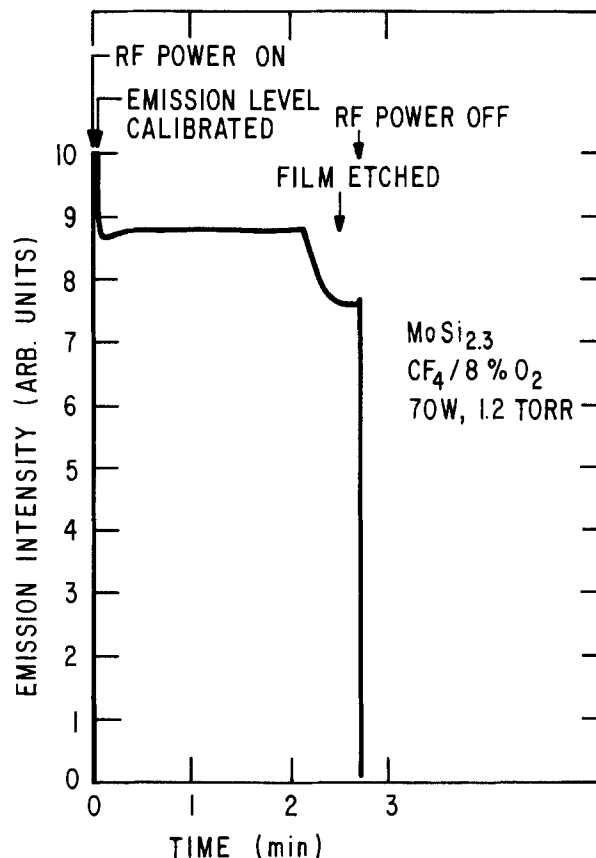
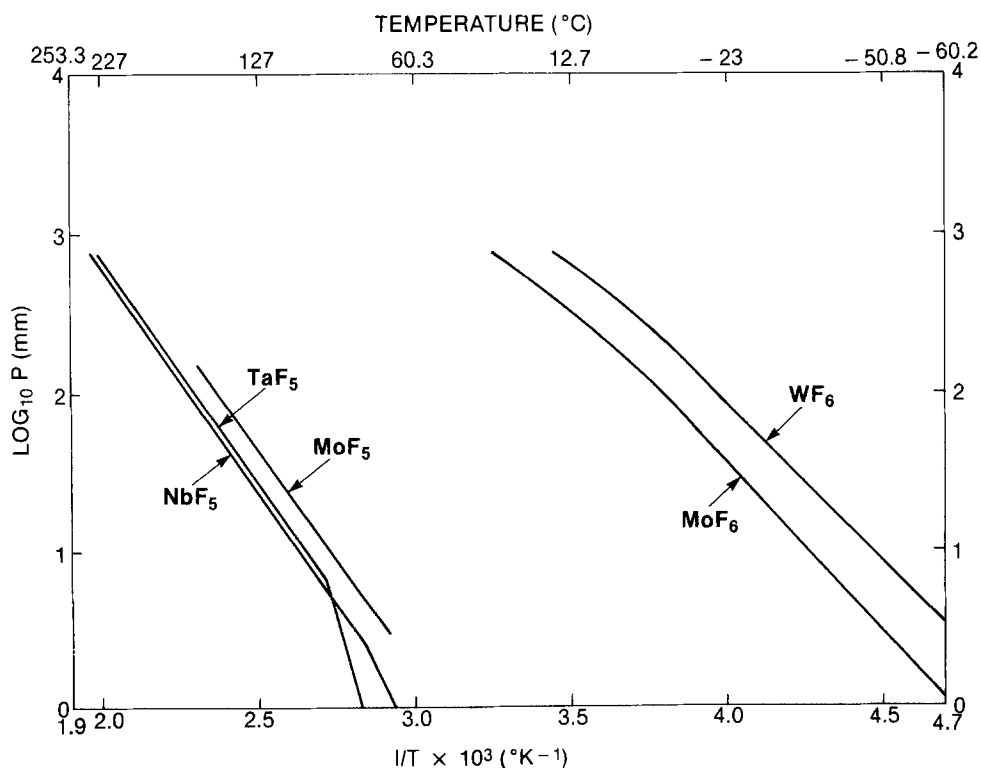


Fig. 15. Endpoint detection of PPE of sputtered MoSi_2 over oxide using a photodiode sensitive in the 300-700 nm region (peak sensitivity at 500 nm) (73). Etching conditions: $\text{CF}_4/4\% \text{O}_2$, 70W, 1.2 torr.

itored in mass spectrometry is SiF_3^+ ($M/e = 85$ amu) even though other species such as O^+ , Si^+ , and CO^+ have also been used (72). During the etching of these refractory materials, the product species generally have large M/e ratios (>200 amu) and hence harder to detect in quadrupole-type spectrometers (where transmission varies as $1/M$). Consequently, the reactant species are preferred, but very little

Fig. 16. Vapor pressures of some refractory metal fluorides (63-65).



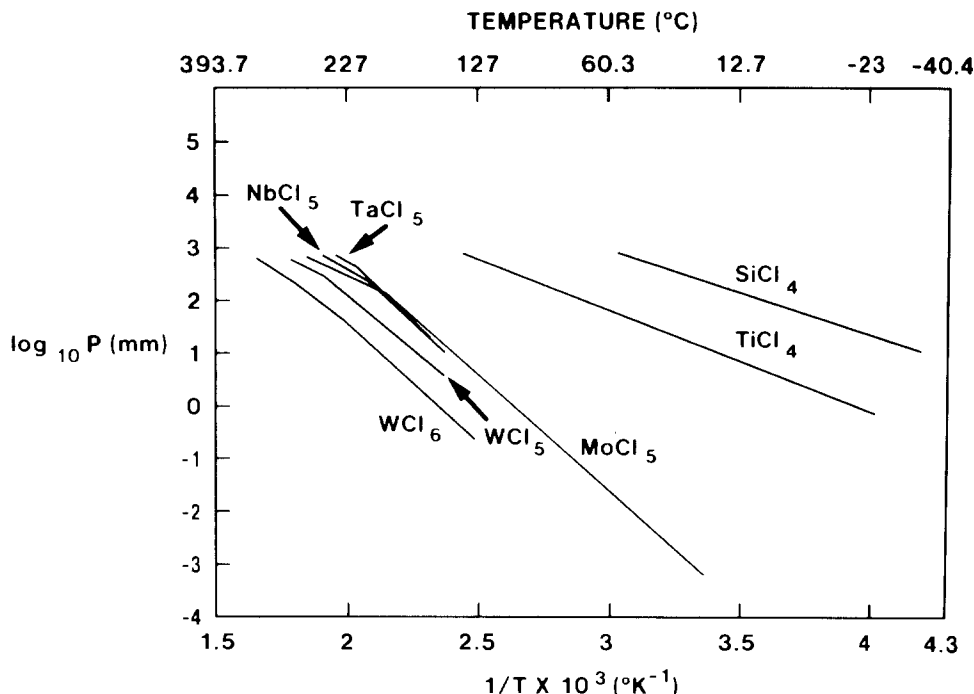


Fig. 17. Vapor pressures of some refractory metal chlorides (68-71).

work in this area has been reported. Unlike mass spectrometry, optical emission spectroscopy is nonintrusive and generally easier to set up, but the identification of the peak signals is more difficult. For fluorinated plasmas, atomic fluorine and CO (if fluorocarbons are used) are generally monitored for all silicon compounds because of their great sensitivity. Atomic silicon or SiCl_3 are usually measured for chlorine-based plasmas (72). Since the emission lines from either the metals or metal compounds within 200 and 700 nm are not strong enough for endpoint detection, the reactant species are usually used instead. For the metals, atomic fluorine line at 704 nm was monitored for CF_4/O_2 etching of LPCVD tungsten on oxide (70) and atomic chlorine line at 256 nm for RIE of sputtered Mo on oxide with CCl_4/O_2 (22). In the latter case, a loading effect on the 256 nm line intensity was observed (22). During the etching of refractory metal silicides, the peaks used for silicon (F, CO, etc.) can also be used, owing to the large percentage of silicon present. For example, a photodiode sensitive in the 300-700 nm region (which includes the CO peaks) and a maximum sensitivity at 500 nm has been found to be effective for endpoint detection during PPE of MoSi_2 and other silicides over oxide in an automated single-wafer etcher Fig. 15 (73). Because of the high reflectivity of the metals, the optical reflection method which measures the reflectivity changes as the etched layer gets thinner can also yield satisfactory results. In fact, this method was used in conjunction with optical spectroscopy during the plasma etching of tungsten on oxide mentioned earlier as well as etching molybdenum on oxide (72).

Mechanisms

To control the etching process, one must understand the fundamental mechanisms that occur. In the case of the silicides, this is complicated by the fact that they are binary compounds. In turn, polycide is an even more complex bilayer structure. Surface reactions during etching require the breaking of metal-silicon and metal-metal bonds as well as silicon-silicon bonds. Also, for binary compounds, there is a greater variety of possible reaction products, the desorption of which can affect the etch rate. The metal halides that are formed in this process are less volatile than the silicon halides. Therefore, only the former can be a rate-limiting step in the etching process. In Fig. 16, the vapor pressures of some of the pertinent metal fluorides are shown as a function of temperature (63-65). For comparison, silicon tetrafluoride, which is not included in the figure, has a vapor pressure of over 20

Table V. The melting, boiling, and sublimation points of chlorides and oxychlorides of several refractory metals and silicon (66, 67)

Chloride or oxychloride	Melting point (°C)	Boiling point (°C)	Sublimation point (°C)
SiCl_4	-70	57.57	—
TiCl_4	-25	136.4	—
TiCl_3	(927) ^a	(1327)	—
TiCl_2	(757)	(1327)	—
ZrCl_4	437*	—	331
ZrCl_3	(627)	(1207)	—
ZrCl_2	(727)	(1387)	—
HfCl_4	—	—	319
HfCl_3	(627)	(1227)	—
HfCl_2	(727)	(1477)	—
VCl_4	-28	148.5	—
VCl_3	dec >500	—	—
VCl_2	(1000)	(1377)	—
VOCl	—	127	—
VOCl_3	-77	126.7	—
NbCl_5	204.7	254	—
NbOCl_3	—	—	335
TaCl_5	216	242	—
TaCl_4	(297)	(777)	—
TaCl_3	(1027)	(1347)	—
TaCl_2	(937)	(1377)	—
CrCl_4	—	(162)	—
CrCl_3	1150	—	947, 1300
CrCl_2	824	1302	—
CrO_2Cl_2	-96.5	117	—
MoCl_5	(307)	(357)	—
MoCl_3	194	268	—
MoCl	dec 427	—	—
MoCl_2	dec	—	—
MoOCl_4	—	—	yes
MoOCl_3	—	—	100
MoO_2Cl_2	—	—	yes
WCl_6	275	346.7	—
WCl_5	248	275.6	—
WCl_4	dec	—	—
WCl_2	dec	—	—
WOCl_4	211	227.5	—
WO_2Cl_2	266	—	—
ReCl_4	(177)	500	—
ReCl_3	(727)	>550, (827)	—
ReO_2Cl	4.5	131	—
ReOCl_4	29.3	223	—

^aEstimated values are in parentheses.

* At 25 atm.

atm at room temperature. WF_6 is the most volatile fluoride in this group; TiF_4 is the least. Among the metal fluorides, the hexafluorides are more volatile than the pentafluorides and other lower fluorides. For example, MoF_6 vaporizes at $35^\circ C$, but MoF_5 boils at $214^\circ C$, while MoF_4 and MoF_3 are estimated to have higher boiling points. Thus, any lower fluorides formed will remain at the surface until further reactions convert them to the higher fluorides and eventually desorb from the surface. Consequently, the higher metal fluorides are the reaction products expected in the effluent.

The situation is slightly more complicated with the addition of oxygen. In Table V, the melting and boiling points and applicable sublimation temperatures (some of them estimated when experimental data not available) of the metal and silicon oxyfluorides are shown along with those of the fluorides (66, 67). It can be noted that the oxyfluorides are less volatile than the fluoride compounds. Thus, while, on one hand, adding oxygen can enhance the generation of fluorine atoms, on the other, it can also retard the etching with the formation of a surface layer of metal oxyfluoride.

For chlorinated plasmas, the addition of oxygen can enhance the etching when the metal oxychlorides are more volatile than the corresponding chlorides. The vapor pressures of several metal chlorides are shown in Fig. 17 as a function of temperature (68-71). In contrast to the fluorides, $TiCl_4$ is the most volatile and WCl_6 is the least. The melting and boiling points, and the sublimation temperatures (measured or estimated), whenever applicable, are shown in Table V (66, 67). It can be seen that the oxychlorides of Group VIA metals have higher vapor pressure than the corresponding chlorides, whereas the opposite is true for the Group IVA and VA metals. The importance of volatility of oxychlorides has been clearly demonstrated in the molybdenum and chromium etching in CCl_4/O_2 plasmas (20-22, 34, 35). Increasing oxygen from 30% to 70% in CCl_4/O_2 mixtures, the Mo etch rate is four times higher, while the underlying SiO_2 etch rate is halved, leading to an exceptionally high etch rate ratio (~ 60) (21).

Summary and Concluding Remarks

We have reviewed the plasma etching of refractory metal silicides, summarizing the etching gases used for the various gate structures implemented. The factors influencing the patterning of high resolution silicide gates and interconnects have been pointed out. Since both plasma etching and refractory metal silicides are key parts of VLSI technology, we expect the development in this area to continue to advance rapidly.

Acknowledgments

One of us (AJS) would like to acknowledge the Office of Naval Research for its partial support of this work. We also would like to thank Dr. J. W. Coburn for reviewing the manuscript.

Manuscript submitted Dec. 15, 1983; revised manuscript received May 30, 1984.

General Electric Corporation assisted in meeting the publication costs of this article.

REFERENCES

1. P. L. Shah, *IEEE Trans. Electron Devices*, **ed-26**, 631 (1979).
2. S. P. Murarka, "Silicides for VLSI Applications," Academic Press, New York (1983).
3. F. Mohammadi, *Solid State Technol.*, **24**, 65 (1981); F. Mohammadi, Ph.D. Thesis, Stanford University, Stanford, CA (1980).
4. T. P. Chow, Ph.D. Thesis, Rensselaer Polytechnic Institute, Troy, NY (1982); T. P. Chow and A. J. Steckl, *IEEE Trans. Electron Devices*, **ed-30**, 1480 (1983); T. P. Chow and A. J. Steckl, *IEEE IEDM Tech. Dig.*, 513 (1983).
5. F. M. d'Heurle, in "VLSI Science and Technology/1982," C. J. Dell'Oca and W. M. Bullis, Editors, p. 194, The Electrochemical Society Softbound Proceedings Series, Pennington, NJ (1982).
6. M.-A. Nicolet and S. S. Lau, in "VLSI Electronics: Microstructure Science," Vol. 6, N. G. Einspruch and G. B. Larrabee, Editors, Chap. 6, p. 329, Academic Press, New York (1983).
7. J. W. Coburn, *Plasma Chem. Plasma Process*, **2**, 1 (1982).
8. C. J. Mogab, A. C. Adams, and D. L. Flamm, *J. Appl. Phys.*, **49**, 3796 (1978).
9. G. J. Schwartz and P. M. Schaible, *J. Vac. Sci. Technol.*, **16**, 410 (1979).
10. C. J. Mogab and H. J. Levinstein, *ibid.*, **17**, 721 (1980).
11. W. H. Legat and H. Schilling, Abstract 130, p. 336, The Electrochemical Society Extended Abstracts, Vol. 75-2, Dallas, TX, Oct. 5-9, 1975.
12. K. Maeda and K. Fujino, *Denki Kagaku*, **43**, 22 (1975).
13. Y. Horiike and M. Shibagaki, Abstract 243, p. 619, The Electrochemical Society Extended Abstracts, Vol. 77-1, Philadelphia, PA, May 8-13, 1977.
14. H. W. Lehmann and R. Widmer, *J. Vac. Sci. Technol.*, **15**, 319 (1979).
15. T. P. Chow and A. J. Steckl, *IEEE IEDM Tech. Dig.*, 149 (1980).
16. T. P. Chow and A. J. Steckl, *J. Appl. Phys.*, **53**, 5531 (1982).
17. L. B. Roth and G. Hagen, Personal communication.
18. J. N. Randall and J. C. Wolfe, *Appl. Phys. Lett.*, **39**, 742 (1981).
19. A. Bensaoula, J. C. Wolfe, J. A. Oro, and A. Ignatiev, *ibid.*, **42**, 122 (1983).
20. K. Hirata, Y. Ozaki, M. Oda, and M. Kimizuka, *IEEE Trans. Electron Devices*, **ed-28**, 1323 (1981).
21. Y. Kurogi and K. Kamimura, *Jpn. J. Appl. Phys.*, **21**, 168 (1982).
22. B. Gorowitz and R. Saia, General Electric TIS Report 82CRD249 (1982).
23. S. Takahashi, F. Murai, and H. Kodera, *IEEE Trans. Electron Devices*, **ed-25**, 1213 (1978).
24. S. Matsuo, *Appl. Phys. Lett.*, **36**, 768 (1980).
25. M. Fukumoto, K. Inoue, S. Ogawa, S. Okada, and K. Kugimiya, 1st VLSI Symposium on VLSI Technology, Digest of Technical Papers, p. 28, IEEE Electron Devices Society and Japan Society of Applied Physics, Maui, HI, Sept. 8-11, 1981.
26. N. Hosokawa, R. Matsuzaki, and T. Asamaki, *Jpn. J. Appl. Phys.*, Suppl. 2, part 1, 435 (1974).
27. C. J. Mogab and T. A. Shanoff, *This Journal*, **124**, 1766 (1977).
28. H. H. Busta, R. E. Lajos, and D. A. Kiewit, *Solid State Technol.*, **22**, 61 (1979).
29. T. Harada, K. Gamo, and S. Namba, *Jpn. J. Appl. Phys.*, **20**, 259 (1981).
30. S. Matsuo, *ibid.*, **17**, 235 (1978).
31. R. G. Poulsen, *J. Vac. Sci. Technol.*, **14**, 266 (1977).
32. S. Matsuo, *ibid.*, **17**, 587 (1980).
33. G. L. Dybwad, Abstract 199, p. 324, The Electrochemical Society Extended Abstracts, Vol. 83-1, San Francisco, CA, May 8-13, 1983.
34. H. Nakata, K. Nishioka, and H. Abe, *J. Vac. Sci. Technol.*, **17**, 1351 (1980).
35. Y. Suzuki and T. Yamazaki, Abstract 183, p. 287, The Electrochemical Society Extended Abstracts, Vol. 82-2, Detroit, MI, Oct. 17-21, 1982.
36. T. Mochizuki, K. Shibata, T. Inoue, and K. Ohuchi, *Jpn. J. Appl. Phys.*, **17**, Suppl. 17-1, 37 (1978).
37. T. P. Chow and A. J. Steckl, *Appl. Phys. Lett.*, **37**, 466 (1980).
38. T. Mochizuki, T. Tsujimaru, M. Kashiwagi, and Y. Nishi, *IEEE Trans. Electron Devices*, **ed-27**, 1431 (1980).
39. F. R. White, C. W. Koburger, D. L. Harmon, and H. J. Geipel, *This Journal*, **129**, 1330 (1982).
40. B. L. Crowder and S. Zirinsky, *IEEE Trans. Electron Devices*, **ed-26**, 369 (1980).
41. R. S. Bennett, L. M. Ephrath, M. Y. Tsai, and C. J. Lucchese, Abstract 301, p. 750, The Electrochemical Society Extended Abstracts, Vol. 81-1, Minneapolis, MN, May 10-15, 1981.
42. F. Nepl and U. Schwabe, *IEEE Trans. Electron Devices*, **ed-29**, 508 (1982).
43. A. K. Sinha, W. S. Lindenburger, D. B. Fraser, S. P. Murarka, and E. N. Fuls, *ibid.*, **ed-27**, 1425 (1980).
44. C. D. Rude, T. P. Chow, and A. J. Steckl, *J. Appl. Phys.*, **53**, 5703 (1982).
45. S. Okazaki, T. P. Chow, and A. J. Steckl, *IEEE Trans. Electron Devices*, **ed-28**, 1364 (1981).
46. W. Beinvogl and B. Hasler, in "Semiconductor Silicon 1981," H. R. Huff, R. J. Kriegler, and Y. Takeishi, Editors, p. 648, The Electrochemical Society Softbound Proceedings Series, Pennington, NJ (1981).
47. E. C. Whitcomb and A. B. Jones, *Solid State Technol.*, **25**, 121 (1982).

48. M. E. Coe and S. H. Rogers, *ibid.*, **25**, 79 (1982).
49. L. M. Ephrath and R. S. Bennett, in "VLSI Science and Technology/1981," C. J. Dell'Oca and W. M. Bullis, Editors, p. 108, The Electrochemical Society Softbound Proceedings Series, Pennington, NJ (1981).
50. K. L. Wang, T. C. Holloway, R. F. Pinizzoto, Z. P. Sobczak, W. R. Hunter, and A. F. Tasch, Jr., *IEEE Trans. Electron Devices*, **ed-29**, 547 (1982).
51. H. J. Mattausch, B. Hasler, and W. Beinvoogl, *J. Vac. Sci. Technol. B*, **1**, 15 (1983).
52. R. W. Light and H. B. Bell, *This Journal*, **131**, 459 (1984).
53. M. Zhang, J. Z. Li, I. Adesida, and E. D. Wolf, *J. Vac. Sci. Technol. B*, **1**, 1037 (1983).
54. T. P. Chow and G. M. Fanelli, To be published.
55. J. L. Vossen, *This Journal*, **126**, 319 (1979).
56. L. M. Ephrath, *ibid.*, **129**, 62C (1982).
57. B. Chapman, "Glow Discharge Processes," John Wiley and Sons, New York (1980).
58. P. Pretorius, J. M. Harris, and M.-A. Nicolet, *Solid State Electron.*, **21**, 667 (1978).
59. T. Shibata, K. Heida, M. Sato, M. Konaka, D. L. M. Dang, and H. Iizuka, *IEEE Trans. Electron Devices*, **ed-29**, 531 (1982).
60. C. M. Osburn, M. Y. Tsai, S. Roberts, C. J. Lucchese, and C. Y. Ting, in "VLSI Science and Technology/1981," C. J. Dell'Oca and W. M. Bullis, Editors, p. 213, The Electrochemical Society Softbound Proceedings Series, Pennington, NJ (1982).
61. H. Okabayashi, E. Nagasawa, and M. Morimoto, *IEEE IEDM Tech. Dig.*, 556 (1982).
62. C. K. Lau, Y. C. See, D. B. Scott, J. M. Bridges, S. M. Perna, and R. D. Davies, *ibid.*, 714 (1982).
63. F. Fairbrother and W. C. Firth, *J. Chem. Soc.*, 3051 (1951).
64. G. H. Cady and G. B. Hargreaves, *ibid.*, 1563 (1961).
65. G. H. Cady and G. B. Hargreaves, *ibid.*, 1568 (1961).
66. "CRC Handbook of Chemistry and Physics," 60th Ed., pp. B51-B144, CRC Press, Cleveland, OH (1978).
67. A. Glassner, in "The Thermochemical Properties of the Oxides, Fluorides, and Chlorides to 2500 K," U.S. Government Report ANL-5750 (1959).
68. Y. Saeki, T. Takuma, R. Matsuzaki, and K. Funaki, *Denki Kagaku*, **39**, 384 (1971).
69. T. Takuma and S. Kawakubo, *Nippon Kagaku Kaishi*, **5**, 865 (1972).
70. K. M. Alexander and F. Fairbrother, *J. Chem. Soc.*, S223 (1949).
71. K. K. Kelley, "Thermodynamic Properties of Molybdenum Compounds," Chemical Data Bull. Ser., Bull. Cdb-2, (Climax Molybdenum Company), p. 7 (1954).
72. P. J. Marcoux and P. D. Foo, *Solid State Technol.*, **24**, 115 (1981).
73. T. P. Chow, Unpublished results.

An XPS and TEM Study of Intrinsic Adhesion Between Polyimide and Cr Films

N. J. Chou,* D. W. Dong, J. Kim, and A. C. Liu*,¹

IBM T. J. Watson Research Center, Yorktown Heights, New York 10598

ABSTRACT

An examination of the interface between Cr and cured polyimide (PI) was carried out using x-ray photoelectron spectroscopy and transmission electron microscopy. The results indicate that, after curing, the interface remains sharp and planar, at least on a submicron scale, with no discernible material mixing or mechanical interlocking. During Cr metallization of cured polyimide (PI) at room temperature, the first few monolayers of Cr appear to react with the pendant oxygen in the PI substrate. This layer of oxidized Cr atoms forms chemical bonds with PI on the one side, and metallic bonds with the subsequent Cr deposit on the other. It is estimated that the interfacial reaction may give rise to an eightfold increase in intrinsic adhesion strength of the Cr/PI system as compared to Cu/PI couples for which no interfacial reaction have been observed.

In the active development of an advanced VLSI packaging technology, polyimides have recently emerged as a strong contender for use as insulating and pattern delineating materials. Adhesion between the cured polyimide (PI) and wiring metallurgy thus becomes a topic of both theoretical and practical interest. It is well known that when two solids join to form a couple an intermediate region of mixing or mechanical interlocking may be produced between the bulk of the two solids depending on the nature of the solids and the joining process which is used. The adhesion properties of a couple depends therefore on the morphological and chemical physical nature of the interface.

To explore the intrinsic attributes of adhesion between cured PI and Cr metallurgy, we have used x-ray photoelectron spectroscopy (XPS) to monitor the interfacial reaction during metallization, and transmission electron microscopy (TEM) to examine the morphology of the interface. The former technique had been previously employed in a number of investigations involving metallization of polymer film (2).

Experimental

In order to obtain planar interfaces prior to processing, oxidized silicon wafers were used as substrates. 120 nm SiO₂ layers were obtained by thermal oxidation in dry ox-

ygen at 1000°C. Cr (200 nm), Cu (400 nm), and Cr (200 nm) layers were deposited sequentially in that order on the oxide layers from E-beam, heated evaporation sources. Polyamic acid (du Pont 5878) in a N-methylpyrrolidone (NMP) solvent was then spread on the Cr layers by spinning. Planar PI (200 nm) films were obtained by a standard curing procedure (350°C, 30 min). The thickness uniformity of the cured PI films was checked by ellipsometry (3) and was believed to be within ± 2.5 nm. The TEM study was carried out on a Philips 400-T electron microscope. The specimens for TEM examination were prepared by cementing together two cured PI samples face to face with epoxy. The epoxied samples were then sliced into strips of appropriate size, and the strips thinned down to a thickness of 5-7 μ m by polishing both sides of the strips. The Cr/PI interface was finally exposed by ion milling in a direction normal to the strips.

The XPS investigation was conducted in a UHV spectrometer system (PHI-1000), which consisted of a double-pass cylindrical mirror analyzer and a MgK _{α} x-ray source. Measurements were made *in situ* at a pass energy of $E_{\text{pass}} = 25$ eV when thin Cr films (one monolayer or less) were successively deposited at room temperature on a freshly cured PI film, prepared on a planar metal substrate as described above. The evaporation source was fabricated from tungsten filaments which were electroplated with a 2 μ m thick Cr layer in a chromic acid solution, followed by cleaning in H₂ at 1000°C for 30 min. The base pressure of the vacuum system was routinely maintained at 6 \times

*Electrochemical Society Active Member.

¹Permanent address: Department of Chemistry, Harvard University, Cambridge, Massachusetts.

10^{-10} torr. During the deposition runs, however, it rose to 1×10^{-9} torr. The oxygen partial pressure in these instances was estimated to be less than 5% or $<5 \times 10^{-11}$ torr from the mass-spectroscopic data obtained from our UHV system. The deposition pressure varied from 5×10^{-9} to 5×10^{-8} torr, depending on the rate of deposition used. The rate of deposition was calibrated with an Inficon 2000 thickness monitor for various regulated power inputs applied to the film source. It ranged from 0.1 to 0.5 \AA per second in our deposition runs. The exposure of the evaporated films to the UHV ambient at the deposition pressure was less than 5s in all cases. To minimize the possibility of carbon contamination, the electron flood gun was not used during measurement. In view of specimen charging, no attempt was made to determine accurately the absolute binding energies. The core level spectra associated with C, O, N, and Cr were measured in an expanded energy scale following a spectral survey scan after each deposition to locate the kinetic energies of core electrons under the conditions of surface charging. In analyzing our experimental data, we relied primarily on the C1s and Cr2p core electron spectra, although other core level spectra (N1s and O1s) were also used for monitoring the interfacial reactions (4). This is because the Cr2p spectra for the overlayer and the C1s spectra for the cured PI are better documented in the literature (5).² A Gaussian decomposition program (6) was used to resolve overlapping peaks in the C1s spectra. In addition, the spectra difference technique (4) was used to help remove the arbitrariness of the curve fitting procedure. The technique proves to be particularly advantageous in this investigation since it is not sensitive to energy shifts due to specimen charging.

Results

TEM examination revealed that the interface between the cured PI and Cr overlayer was sharp and planar at least on a submicron scale (Fig. 1A, 1B, and 1C). Note that the procedure for TEM specimen preparation is different from that for ESCA investigation. At higher magnification, the interface exhibited scaled irregularities which

²Supplied by R. H. Lacombe, IBM East Fishkill Facility, Hopewell Junction, New York.

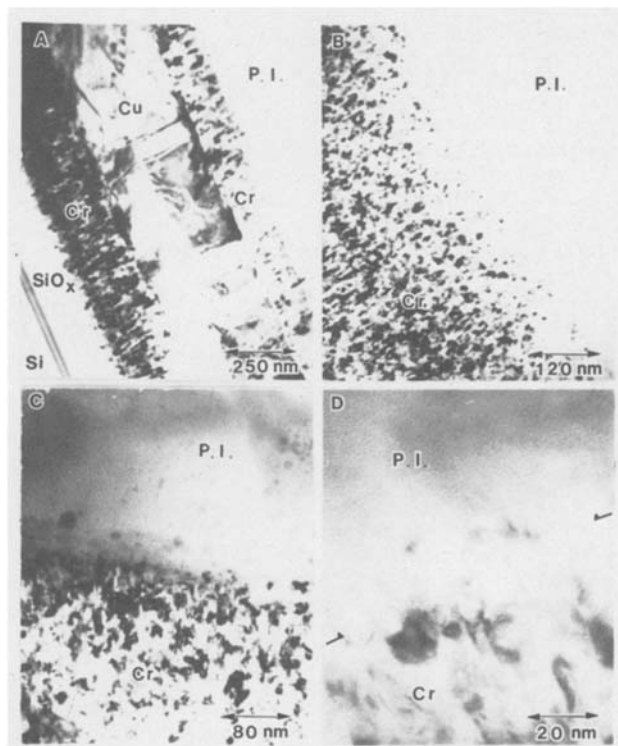


Fig. 1. TEM micrographs of the interface between Cr metal and cured PI at various magnifications. Note that the interfaces are marked with arrows.

were comparable in dimension to the crystallites in the Cr layer (Fig. 1D). There was no evidence of mixing or interpenetration at the interface as a result of PI curing. The observation lends support to the ellipsometric result regarding thickness uniformity of cured PI layers. It is thus reasonable to surmise that the interface of the Cr-metalized PI will be planar if the initial surface of the cured PI is planar.

The "full scan" XPS spectra of the freshly cured PI surface and those metallized with Cr films of varying thickness are shown in Fig. 2. It is evident that the signals associated with C, O, and N from the PI substrate attenuate with increased Cr overlayer thickness. At the same time, the Cr signal appears and grows in magnitude.

The C1s core level spectra of cured PI film consisted of three resolvable peaks prior to deposition. With successive deposition of Cr overlayers, the C1s spectra not only decreased in integrated intensity, but also exhibited changes in shape. Shown in the central column of Fig. 3 are the C1s spectra for a PI film with 0, 1.5, and 2.5 monolayer Cr coverage (spectra a, b, and c). It should be noted that the spectrum with 0.5 monolayer coverage was not included for analysis because of the uncertainties associated with extra-atomic relaxation processes attributable to submonolayer coverage. In Fig. 3d, 3e and 3f, spectra are shown to have been resolved into individual Gaussian peaks using the constraints obtained with the aid of the spectra difference technique and the previously published data (5). For example, the difference spectrum between 1.5L and zero coverage (Fig. 4a) indicates that there are at least two peaks present in the C1s spectra. The published XPS data on cured PI derived from polyamic acid resins (5) gave three C1s peaks at lower binding energy values with energy separations of 3.9 and 1.3 eV. These parameters were then used as the constraints in our Gaussian curve fitting for spectra a and b. At thicker Cr coverage (> 2.5 monolayers) the difference spectra (Fig. 4b) exhibited the presence of no more than two peaks. In such cases, 1.3 eV separation was used as a curve fitting constraint.

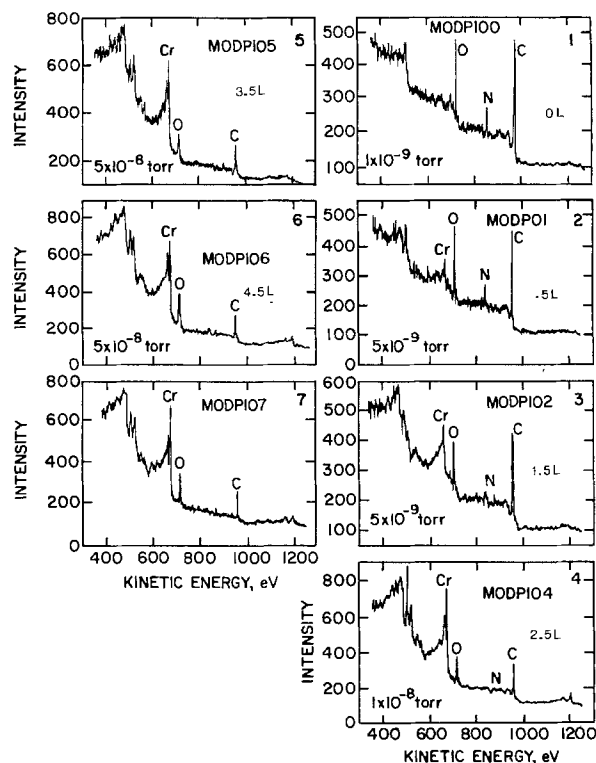


Fig. 2. X-ray photoelectron spectra of a bare PI surface with successively increased amount of Cr overlayer: 1-freshly cured PI; 2-1 monolayer(L) coverage; 3-1.5L; 4-2.5L; 5-3.5L; 6-4.5L; and, 7-same, but at a different spot of the surface. The deposition pressure is given for each deposition in the plot.

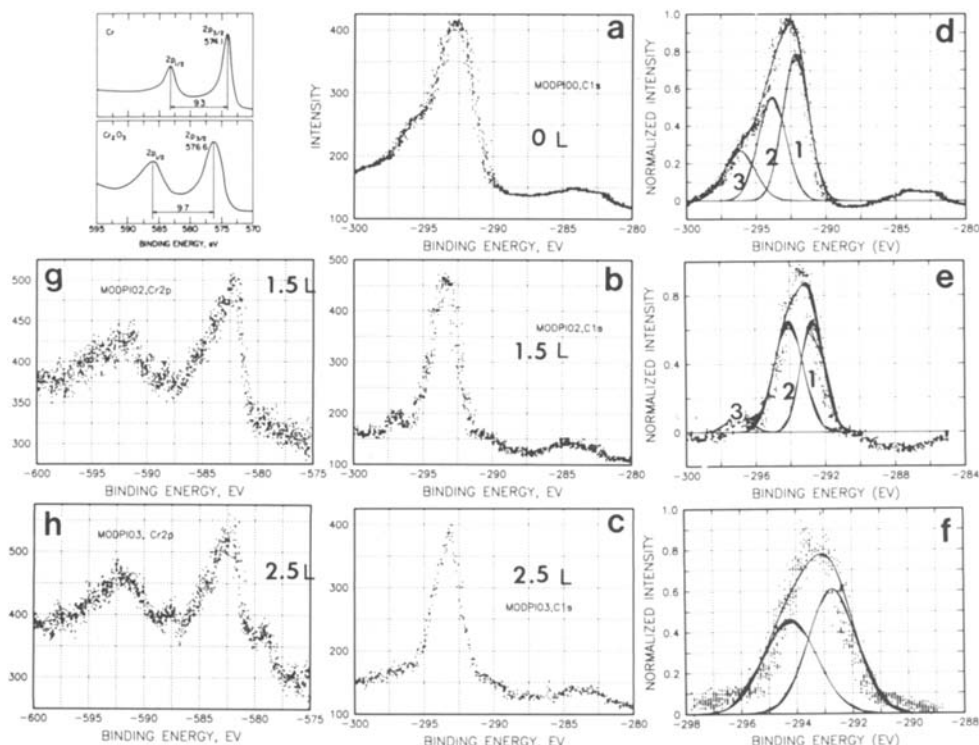


Fig. 3. C1s and Cr2p core level spectra of PI with 0L, 1.5L, and 2.5L Cr coverage. Note that peak 3, attributable to C atoms with carbonyl bonds, disappears in the background noise after 2.5 monolayers of Cr deposition while metallic Cr2p doublet emerges (Fig. 3h). See text.

As the C1s spectra indicate, the peak with the largest binding energy (labeled as peak 3) disappeared into the background after 2.5 monolayers of Cr deposit. At the same time, inspection of the corresponding Cr2p spectra (Fig. 3g and 3h) for these surfaces reveals that after 2.5 monolayers' deposition, additional peak attributable to the metallic doublet emerged against the background of those of the oxidized chromium. This is obvious when reference is made to the standard 2p spectra (6) for Cr and Cr₂O₃ reproduced in the upper left corner of Fig. 3. As a matter of fact, the metallic Cr peaks, though barely discernible, already exist in the spectrum with 1.5 monolayer coverage.

The O1s and N1s spectra of the freshly cured and metalized PI surfaces cannot be resolved with confidence by

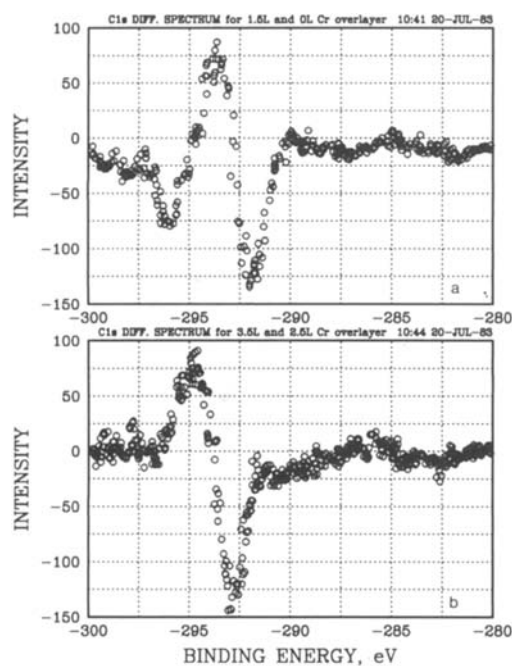


Fig. 4. C1s difference spectra: (a) between a PI surface with 1.5L Cr overlayer and o bare PI surface and (b) between PI surfaces with 3.5L and 2.5L Cr overlayer, respectively.

Gaussian fitting. The binding energies of O1s electrons have been reported to be 530.0 eV for Cr₂O₃ (6, 8) and 532.2 and 533.5 eV for cured PI (5). As shown in Fig. 5a, 5b, and 5c, the O1s peaks appear to have broadened with successive deposition of Cr overlayer. When the C1s peak is used as the internal reference for the energy scale, it is found that a steady-state surface charging was not achieved during our XPS measurement since the amount of charging fluctuated between 7.5 and 8.5 eV from one spectrum to another. Thus, the apparent broadening of the O1s spectra cannot be resolved with some physically meaningful constraints. Similar situation prevails for the N1s spectra in Fig. 5d, 5e, and 5f.

The O1s difference spectra (Fig. 6a, 6b, and 6c) also show that the O1s signal associated with the oxidized Cr cannot be readily distinguished from that originating from the PI substrate, as one would expect from the reported binding energy values (5, 6, 8). This is evident from the fact that the decrease and increase in O1s intensity occur practically at the same binding energy when the surface charging is taken into account (Fig. 6).

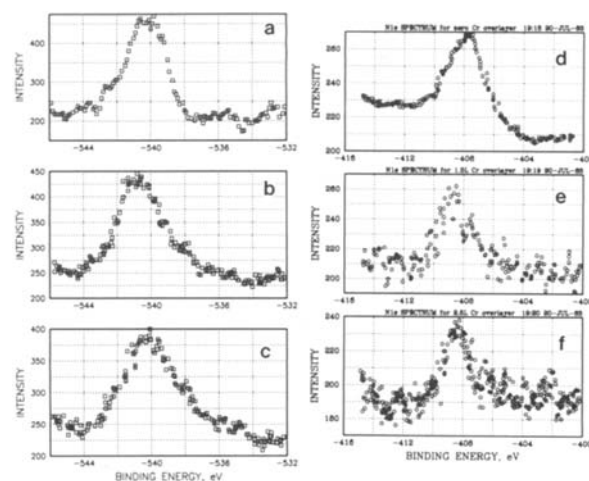


Fig. 5. O1s and N1s spectra for a PI surface with 0L, 1.5L, and 2.5L Cr overlayer. No useful information can be extracted because (i) the spectra are noisy, and (ii) surface charging effect makes it difficult to determine the absolute chemical shifts. See text.

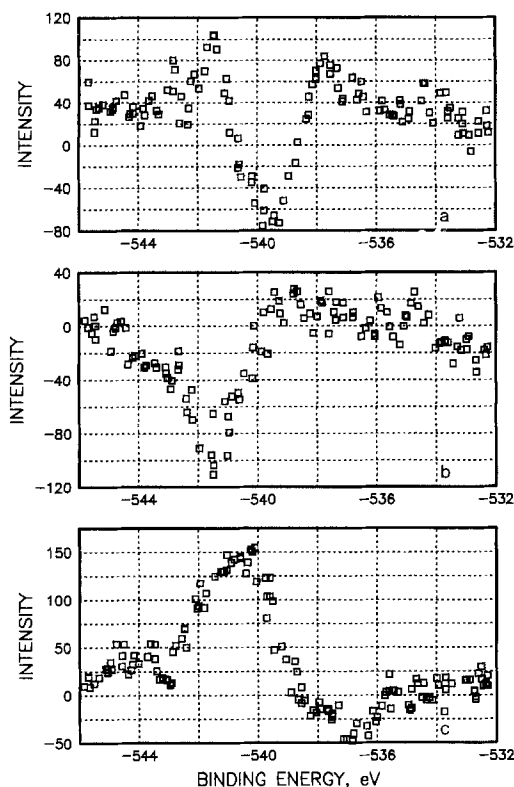


Fig. 6. O1s difference spectra (a) between a PI surface with 1.5L Cr overlayer and a bare PI surface, (b) between PI surfaces with 2.5L and 1.5L overlayers, and (c) between PI surfaces with 3.5 and 2.5L overlayers.

Discussion

When the total area of the C1s spectra and the areas of individual resolved peaks are plotted against the thickness of the Cr overlayer, it becomes clear that while the attenuation of the total peak area follows closely to the calculated escape length effect, those of the individual peaks do not (Fig. 7). In calculating the attenuation through Cr overlayer, we used 1.2 nm and 0.227 nm for the inelastic mean free path (IMFP) of C1s electrons and the effective monolayer thickness of Cr, respectively. Both of these parameters were determined according to Seah and Dench (8). Particularly noteworthy is the fact that during the first 1.5 monolayer deposit peak 3 decreased at a higher rate than the calculated whereas the neighboring peak 2 increased in magnitude.

Based on the published data (5) we can assign the three resolved C1s peaks as follows. A fully cured PI has 22 carbon atoms in its molecular unit (Fig. 8), of which 4 with carbonyl bonds ($=O$) (relative concentration: 18.2%) will be designated as peak 3. This particular peak assignment was established in a PI curing study reported in Ref. (5). The ten carbon atoms with H-bonds (45.5%) and the eight with $-N$, $-O$, or $-C$ bonds (36.3%) in the benzene rings will be assigned peaks 1 and 2, respectively. It will be noted that in addition to dissimilar atomic species, the difference in charge distribution about C atoms of groups 2 and 3 consists in the absence of a resonating carbon bond in the latter group. These peak assignments are substantiated by the agreement between the calculated relative concentrations and measured peak area ratios, and by the agreement with the reported spectra of cured PI (5) when specimen charging (approximately 7.5 eV) is taken into account. Thus, regrouping of C1s peaks and appearance of oxidized and metallic Cr2p peaks during metallization indicate that in the first few monolayers of deposition Cr was oxidized, resulting in a charge redistribution about the carbon atoms with carbonyl bonds ($=O$). This strongly suggests that the pendent oxygen in PI is involved in the reaction since no significant change in N1s spectra has been detected.

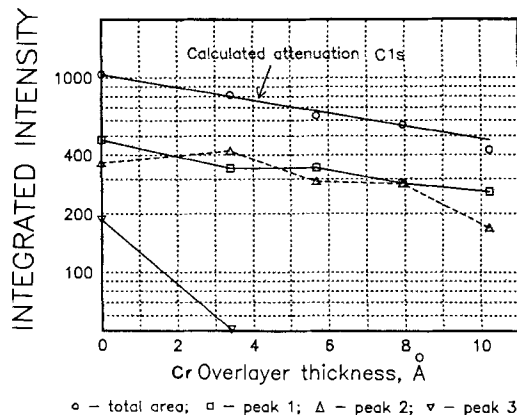
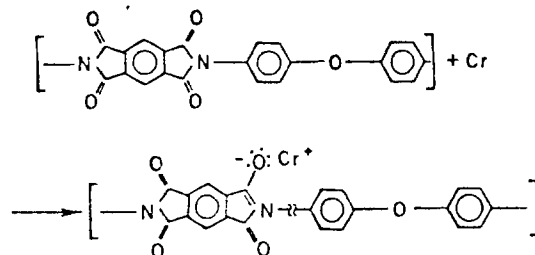


Fig. 7. Change in total and resolved C1s peak areas with Cr overlayer thickness.

Oxidation of Cr involving the pendent oxygen in PI can occur in one of the two likely ways: (i) formation of Cr oxygen complexes followed by the scission of C-N bonds depicted by the equation



(in this case, the binding energies of C1s, O1s, and possibly N1s electrons are expected to change after the first monolayer of Cr deposit) and (ii) formation of CrO , CrO_2 , or Cr_2O_3 with breakage of carbonyl ($\text{C}=\text{O}$) bonds, in which case only C1s and O1s electrons are expected to exhibit appreciable chemical shifts. Furthermore, we should anticipate the integrated O1s intensity to deviate from the expected attenuation behavior since formation of oxide alters the atomic density of oxygen, and growth of oxide may not be limited to one monolayer of deposit.

Shown in Fig. 9 is the change in integrated O1s signal intensity with successive Cr deposition. The attenuation calculated for O1s electrons in Cr (with IMFP=1.2 nm) is shown as a straight line for comparison (curve 1). In contrast to the behavior of C1s electrons, we note that after 1.5 monolayers' deposit, the integrated O1s intensity is

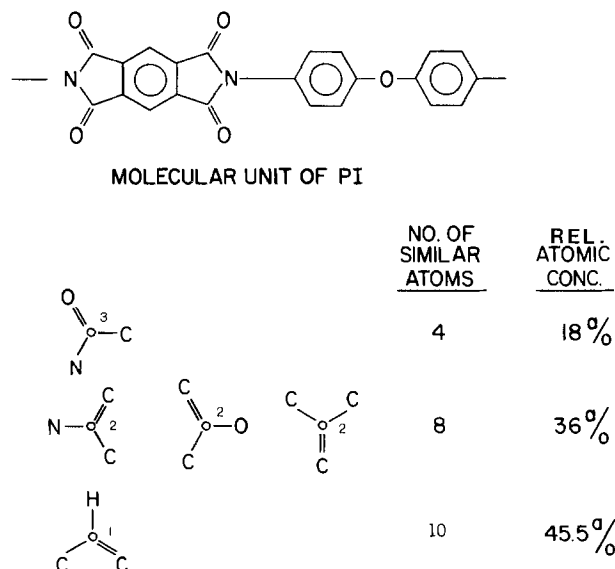


Fig. 8. Molecular unit of a fully cured PI and assignment of resolved C1s peaks.

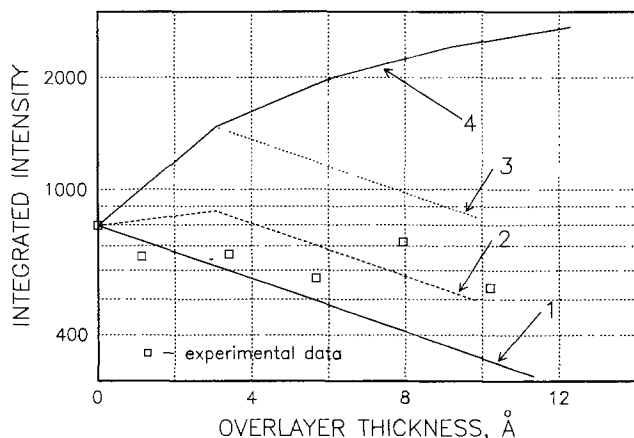


Fig. 9. Experimental and calculated variation of O1s integrated intensity with Cr overlayer thickness. Curve 1 gives the calculated attenuation for overlayers consisting of Cr metal. Curve 2 gives the calculated intensity variation for the case where the first monolayer of deposit is partially oxidized. Curve 3 shows where the first monolayer is completely oxidized. Curve 4 shows where each layer of deposit is oxidized. See Appendix.

consistently higher than the calculated, indicative of extraneous oxygen uptake. The uptake could arise either from oxygen incorporation from the UHV ambient or atomic rearrangement whereby oxygen from PI moved across the interface during oxide growth. Elementary calculation using available thermodynamic data (10) indicates that oxidation of Cr is possible at an oxygen partial pressure of 10^{-11} torr, corresponding to a base pressure of 1×10^{-10} torr in our system. The driving force for the Cr_2O_3 formation at an oxygen partial pressure of 10^{-13} atm, at 300 K, (8) is given by $\Delta G \approx -110$ kcal/g-at. Cr, where ΔG is the free energy of formation. This is consistent with the observation by Allen *et al.* (8) that it is not possible to produce and maintain Cr surfaces completely free of oxygen even at a base pressure of 10^{-10} torr. The amount of oxygen uptake from the UHV ambient can be readily estimated if a sticking coefficient of unity is assumed. Since the exposure of deposited film to deposition ambient ranged from 4 to 10s, the oxygen uptake will be no greater than 1% of a monolayer.

To inquire into the origin of the oxygen uptake, we have calculated the variation of O1s integrated intensity with increased overlayer for three hypothetical cases (see Appendix): (i) in which each successively deposited Cr film was completely oxidized to form Cr_2O_3 (curve 4, Fig. 9), (ii) in which only the first Cr overlayer was completely oxidized (curve 3), and (iii) in which the first overlayer was partially oxidized or oxidized to form suboxides (curve 2). Comparison of the experimental data with the calculated intensities indicates that consistent with the Cr2p data, oxidation is indeed limited to the first few monolayers of deposit. It also suggests that the supply of oxygen from the PI substrate was insufficient to fully oxidize the overlayer and that outdiffusion of oxygen from substrate to overlayer is confined to a rather localized scale. The O1s intensity data thus appear to favor the view that oxidation of Cr by the pendent oxygen occurs with breakage of carbonyl bonds. It should be pointed out, however, that our TEM electron diffraction study failed to identify any Cr_2O_3 phase at the interface. Furthermore, although the duration of exposure to deposition pressure was only of the order of a few seconds, one cannot completely rule out the possibility of larger than estimated oxygen uptake from the UHV ambient because there might be transient upsurge of oxygen partial pressure when the filament power is turned on. Nor can our O1s and N1s data provide sufficient collaborative information for us to determine unequivocally the consequence and products of the interfacial oxidation. In short, our investigation indicates that during metallization of PI at room temperature, the first few monolayers of Cr are

oxidized by the pendent oxygen in the substrate. Pending further investigation, the product of this interfacial oxidation cannot be exactly ascertained: it may result in the formation of either Cr-O-C complexes or a separate oxide phase at the interface. However, the extent of oxidation and subsequent charge transfer and, possibly, a slight atomic rearrangement to accommodate the structural mismatch must be limited to a few monolayers of material.

Adhesion between the two phases of a couple arises from molecular forces acting across surfaces differing in nature. In the case of flawless and stress-free intimate contact, a condition which is most likely fulfilled in the process of metallization, van der Waals' interaction must be always operative because of its universal nature (10). If interfacial reactions occur during the process of joining, then added to van der Waals' contribution to the adhesion strength are the contributions from either chemical bonds formed across the interface or the electrostatic forces associated with the formation of double charge layer as a result of charge transfer.

As our study suggests barring excessive oxygen contamination during metallization, the Cr/PI interface formed at room temperature shall consist of a few partially oxidized monolayers of Cr atoms sandwiched between the PI and Cr metal. The oxidized Cr atoms form chemical bonds with the pendent oxygen in the PI, on the one side, and metallic bonds with the Cr overlayer, on the other. Furthermore, dangling bonds produced the interfacial reaction may give rise to secondary reactions accompanied by the formation of additional bonds between the substrate and the overlayer.

When the interface is sharp and planar, as in the case of our Cr/PI system, van der Waals' forces are inversely proportional to the third power of the separation between the two parallel plates (11) and amounts to *ca.* 10^6 dyne-cm⁻² or 1.02×10^8 kg/m².

Various theoretical and experimental studies of bond fracture in polymers (12) indicate that the breaking stress of chemical bonds in polymers varies from 7×10^3 to 10^5 kg/cm². The formation of chemical bonds across the PI/Cr interface is therefore expected, by a conservative estimate, to increase the intrinsic adhesion strength at least by eightfold.

Conclusions

Our study has shown that Cr metallization of cured PI at room temperature results in a couple with a sharp and planar interface if the initial PI surfaces are planar and clean. Barring excessive oxygen contamination from the deposition ambient, the first few monolayers of Cr will react with the pendent oxygen atoms in the PI, forming either Cr oxygen complexes or Cr oxides at the interface. Consideration of the chemical bond contribution to the adhesion strength of the Cr/PI system suggests that the interfacial reaction between Cr and PI increases the intrinsic adhesion strength significantly. Other things being equal, metallization of PI with Cr will have at least an eight-fold increase in adhesion strength as compared to other metals such as Cu (13), which do not react interfacially with PI.

Acknowledgment

The authors are indebted to A. Tuttle and J. Santilli for fabrication of evaporation sources, and to R. Goldblatt for preparation of cured PI films. They benefited from many useful discussions with Dr. Chin-An Chang. They are also thankful to I. Ames for critical reading of the manuscript.

Manuscript submitted Jan. 6, 1984; revised manuscript received April 13, 1984.

IBM Corporation assisted in meeting the publication costs of this article.

Appendix

The intensity of photoelectrons of a given energy ejected by monochromatic x-ray from a homogenous bulk film is expressible by

$$I = \int_0^{\infty} F \alpha D k \exp(-x/\lambda) dx = F \alpha D k \lambda$$

where F is the x-ray flux, α the photoionization cross-section, D the density of the atoms from which the photoelectrons are produced, k the transmission coefficient of the spectrometer, and λ the IMFP of the photoelectrons in the film. In our *in situ* measurement, where the photon flux and other instrumental parameters are equal for the substrate and overlayer, the O1s integrated intensity of the overlayer (say, Cr_2O_3), I_{ox} , can be expressed in terms of the O1s integrated intensity of the substrate, I_{PI} (8)

$$\frac{I_{\text{ox}}}{I_{\text{PI}}} = \frac{D_{\text{ox}} \lambda_{\text{ox}}}{D_{\text{PI}} \lambda_{\text{PI}}}$$

The atomic densities of oxygen in Cr_2O_3 and fully cured PI, D_{ox} and D_{PI} , can be determined from their densities and molecular weights, and are found to be $6.22 \times 10^{22}/\text{cm}^{-3}$ and $8.05 \times 10^{21}/\text{cm}^{-3}$, respectively. For O1s electrons the IMFP's are nearly equal in Cr and Cr_2O_3 (8). The IMFP of O1s electrons in cured PI is not accurately known, but is estimated to be 1.6 times that in Cr or Cr_2O_3 based on the IMFP data on organic compounds (9). Thus

$$I_{\text{ox}} = 4.8 \times I_{\text{PI}}$$

which compares favorably with the experimental intensity ratio (4.0) for the bulk Cr_2O_3 and PI films. Given the O1s integrated intensity of the bare PI surface, we can therefore calculate the intensity variation with increasing overlayer thickness for various hypothetical cases (1). If the growing overlayer consists of Cr only, we have simply

$$I = I_{\text{PI}} \exp\left(-\frac{n d_{\text{Cr}}}{\lambda_{\text{Cr}}}\right)$$

where n is the number of monolayers deposited and d_{Cr} is the effective monolayer thickness of Cr.

If, during deposition, the overlayer has been completely oxidized to form Cr_2O_3 , we then have

$$I(n) = I_{\text{PI}} \exp\left(-\frac{n d_{\text{ox}}}{\lambda_{\text{ox}}}\right) + 4.8 \times I_{\text{PI}} \left[1 - \exp\left(-\frac{n d_{\text{ox}}}{\lambda_{\text{ox}}}\right)\right]$$

If only the first monolayer has been completely or partially oxidized and the subsequent deposit consists of Cr, then we have

$$I(n) = \left\{ I_{\text{PI}} \exp\left(-\frac{d_{\text{ox}}}{\lambda_{\text{ox}}}\right) + 4.8r \times I_{\text{PI}} \left[1 - \exp\left(-\frac{d_{\text{ox}}}{\lambda_{\text{ox}}}\right)\right] \right\} \exp\left(-\frac{(n-1)d_{\text{Cr}}}{\lambda_{\text{Cr}}}\right)$$

where $0 < r < 1$ is the extent of oxidation and $n \geq 1$.

For the calculated intensity variations shown as curves 1-4, Fig. 9, we have used the following physical parameters: $\lambda_{\text{Cr}} = \lambda_{\text{ox}} = 12\text{\AA}$, $d_{\text{ox}} = 0.307 \text{ nm}$, $I_{\text{PI}} = 796 \text{ eV counts}$, and $r \sim 0.3$, which is obtained from $(D_{\text{PI}}/D_{\text{ox}})^{2/3}$.

REFERENCES

1. See, for example, K. L. Mittal, *J. Vac. Sci. Technol.*, **13**, 19 (1976).
2. R. F. Roberts and H. Schonhorn, *Polym. Reprints*, **16**, 146 (1975); J. M. Burkstrand, *Appl. Phys. Lett.*, **33**, 387 (1978); K. S. Kiang, W. R. Salaneck, and I. A. Aksay, *Solid-State Commun.*, **19**, 329 (1976).
3. D. W. Dong and N. J. Chou, Unpublished data.
4. J. M. Burkstrand, *J. Appl. Phys.*, **52**, 4795 (1981).
5. H. J. Leary, Jr. and D. S. Campbell, "Photon, Electron and Ion Probes of Polymer Structure and Properties," p. 147 ACS Sym. Ser. 162 (1981).
6. C. D. Wagner, W. M. Riggs, L. E. Davis, J. F. Mouler, and G. E. Mullenberg, "Handbook of X-ray Photoelectron Spectroscopy," Perkin Elmer Corp. (1978).
7. M. P. Seah and W. A. Dench, *Surf. Interf. Anal.*, **1**, 1 (1979).
8. G. C. Allen, P. M. Tucker, and R. K. Wild, *J. Chem. Soc., Farad. Trans. 2*, **74**, 1126 (1978).
9. O. Kubaschewski and E. L. Evans, "Metallurgical Thermochemistry," John Wiley and Sons, New York (1956).
10. C. Weaver, *J. Vac. Sci. Technol.*, **12**, 18 (1975).
11. R. H. Ottewill, in "Aspects of Adhesion," 2, D. J. Aigner, Editor, p. 18 (1965).
12. S. N. Zhurkov, V. L. Vettegren, V. E. Korsukov, and I. I. Novak, in "Proceedings of the Second International Conference on Fracture," Brighton, 1969, p. 545, Chapman & Hall, Ltd.
13. N. J. Chou and C. H. Tang, *J. Vac. Sci. Technol. A*, **24**, 298 (1984).

A Comparison of Reactive Ion Beam Milling and Reactive Ion Etching for Multilevel Resist Patterning

R. N. Castellano¹

Stanford University, Stanford, California 94305

ABSTRACT

Several multilevel resist processes have been designed to overcome the problem of nonplanar surfaces during high resolution patterning. Reactive ion etching and plasma etching are the most commonly used methods for pattern delineation. In this study, reactive ion beam milling with an oxygen beam has been shown to generate highly anisotropic resist profiles at high (100 nm/min) etch rates.

As the size of the minimum features on integrated circuits decreases toward submicron geometries, there will not necessarily be a concomitant decrease in the height of these features. For example, as the width of Al(Si, Cu) interconnections decreases from 3 to 1 μm , the metal thickness must remain close to 1 μm in order to avoid excess electrical resistance and to minimize electromigration caused by high current densities. Thus, an increasingly difficult problem is the generation of resist patterns over a nonplanar surface because of highly stepped topographies. For most resists, high resolution can only be achieved with a thin resist on a featureless surface; x-ray

¹ Present address: Strategic, Incorporated, Cupertino, California 95015-2150.

and electron-beam resist thicknesses greater than approximately 0.5 μm lead to seriously degraded resolution during exposure. In response to this problem, a number of multilevel resist processes have been reported (1-5) in order to improve pattern fidelity by reducing proximity effects (6) and eliminate development time variations due to wafer topography (2). In general, a thick (1 μm) layer of an organic resist is spun onto the substrate to be etched and baked at high temperature ($T > 120^\circ\text{C}$) to flow the resist which tends to planarize the surface by presenting a relatively flat top surface. A thin (0.1 μm) intermediate layer such as Si or SiO_2 is deposited on this resist and serves as a pattern transfer mask. The uppermost layer is a thin (0.4 μm) resist material used for high resolution lithographic

patterning because of its planarity. The pattern is transferred into intermediate layer by a reactive plasma process. This layer, in turn, acts as an inert mask for the patterning of the thick resist layer by a second reactive plasma process.

Reactive ion etching (RIE) is the reactive plasma process most commonly employed for patterning the intermediate and bottom layers. Essentially, the lower pressure (larger mean free path) and physical-chemical etching mechanisms of the RIE method allow for more anisotropic patterning compared to plasma etching (PE) in which a chemical removal predominates and undercutting (isotropic etch) can result. Because of the high degree of anisotropic etching, along with acceptable etch rates and selectivities that have been demonstrated with fluoro- or chloro-carbon reactive gases in RIE during integrated circuit fabrication, it has been a natural course that this method should be utilized for multilevel resist processes. The ultimate resolution of RIE has not been ascertained, but Oro and Wolfe (7) have reactive ion etched 0.6 μm thick crosslinked poly(methylmethacrylate) with 50 nm resolution.

Ion beam milling (IBM) is a common method for the generation of high resolution patterns. The low mean free path of the sputtered species (250 cm at 8×10^{-5} torr) suggests that IBM is a viable method for high aspect ratio pattern delineation. Etch rates of photoresist as high as 200 nm/min using a beam of oxygen ions (8) are comparable to those obtained by RIE (9). Flanders *et al.* (10) have shown that reactive ion beam milling (RIBM) with an oxygen beam can produce 40 nm linewidths in 0.2 μm thick polyimide. A comparison of the properties of PE and RIE with RIBM is shown in Table I.

In this study, RIBM has been utilized to generate multilevel resist patterns in optical resist with 0.75 μm linewidth resolution. These results are compared to multilevel patterns generated by PE and RIE.

Experimental

The tri-level resist system used in this RIBM study consisted of 1 μm AZ1350J (Shipley) - 0.08 μm polysilicon - 1 μm AZ1350J layers. The substrates were thermally oxidized <100> Si wafers. After exposure (Canon optical projector) and development of the top resist layer, the polysilicon was patterned in a low frequency planar PE system (PlanarEtch IIA, Technics, Incorporated, San Jose, California) using CF_4 . Etching was carried out at 75W RF power at a pressure of 0.1 torr for 1 min. Subsequently, the planarizing resist was patterned with a RIBM system (MIM-TLA 20, Technics, Incorporated) which utilized a 20 cm Kaufman source. Argon was injected into the ion gun and oxygen introduced into the vacuum chamber. The percentage of O_2 was varied between 25% and 100% at a total operating pressure of 8×10^{-5} torr. The accelerating voltage was varied between 500-1000V at a current density of 0.5 mA/cm². The samples were rotated and the angle of incidence of the beam trajectory maintained at 90°. The etch rates of a polysilicon thin film and a bare thermally oxidized wafer were also measured after milling at the above parameters to determine the selectivity of the resist to the Si mask and SiO_2 underlayer.

Results and Discussion

Scanning electron micrographs of a sample milled at an accelerating voltage of 1000V with 75% oxygen concentra-

Table I. Comparison of dry etching characteristics

	Plasma etching	Reactive ion etching	Reactive ion beam milling
Pressure (torr)	0-0.1	10^{-1} - 10^{-2}	10^{-4} - 10^{-5}
Mechanism	chemical	chemical/physical	chemical/physical
Etch rate	high	medium	medium
Selectivity	very good	good	good
Anisotropy	low	high	high
Machine throughput	high	medium	medium

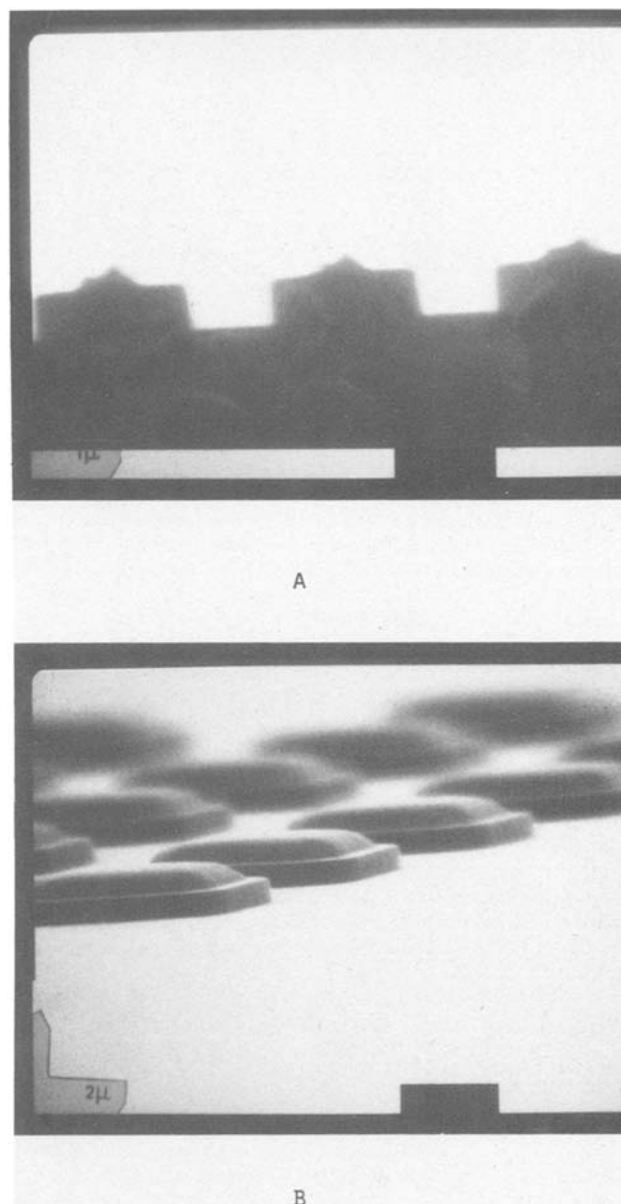


Fig. 1. Resist profiles after reactive ion beam milling. Conditions: 1000 eV, 0.5 mA/cm², 75% O_2 , 6 min.

tion are shown for a channel edge and a mesa structure in Fig. 1a and 1b, respectively. The bottom planarizing resist layer is characterized by vertical wall profiles. No undercutting, trenching, or redeposition is observed; problems sometimes observed in IBM using argon gas (11). The width of the channel is 0.75 μm . The top layer of resist has been faceted, resulting in changes in linewidth dimensions. Faceting is a result of the angular dependence of removal rate associated with physical sputtering due to the fact that, after a collision of an incident ion with a surface atom, the probability that the ejected atom acquires a momentum vector away from the sample surface increases as the angle of incidence decreases from 90° to 0°. At normal incidence, more than one collision is necessary for the atom to be ejected because the momentum vector must be changed by 90°. A maximum angle, θ_{max} , is associated with each material and is typically 40°-50° from normal incidence. Since the top resist layer tends to have a slightly rounded edge close to θ_{max} from baking, lateral etching occurs with loss of dimensional control. In this tri-level system, this faceting does not influence the profile of linewidth of the bottom resist layer, which will act as a mask for subsequent patterning of the substrate. The interlevel polysilicon layer also tends to isolate the bottom resist layer from the faceting effect of the top resist film.

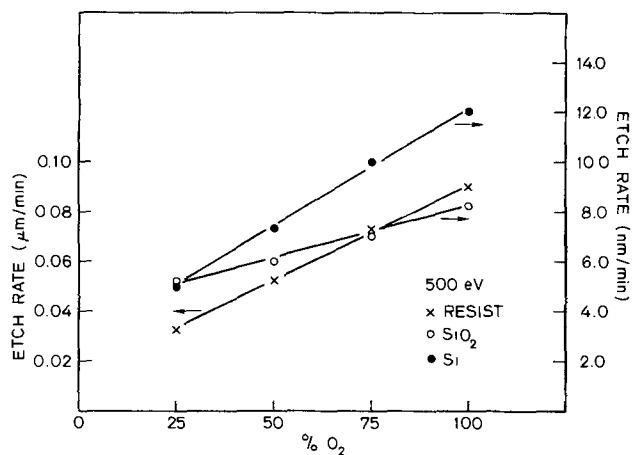


Fig. 2. Resist etch rate vs. oxygen concentration

Shown in Fig. 2 are the etch rates of resist, the polysilicon intermediate layer, and SiO₂ underlayer as a function of the percentage of oxygen at an accelerating voltage of 500V at a pressure of 8×10^{-5} torr. The observed increase in the etch rate for resist is straightforward; increasing the percentage of oxygen results in a greater number of activated oxygen species for chemical oxidation of the organic resist. It is not clear why the etch rates of polysilicon and SiO₂ increase with increasing O₂ concentration. It is possible that during the milling of the resist, a carbonaceous material was deposited on the polysilicon and SiO₂ test wafers as a result of decomposition of the resist. An increase in the O₂ concentration would facilitate removal of carbon by formation of CO and CO₂. The etch rates of resist, as high as 100 nm/min, are comparable to those obtained by RIE (9). Also of importance is the selectivity in etch rates between polysilicon and the resist. At 75% O₂, this ratio is 0.14, indicating that a minimum polysilicon thickness of 0.14 μm is necessary to prevent erosion of the bottom resist.

The etch rates of the resist, polysilicon, and SiO₂ also increase linearly with increasing accelerating voltage at constant (75%) O₂ concentration, as illustrated in Fig. 3. The slopes of these curves are 9, 7, and 16×10^{-6} μm/min/eV for polysilicon, SiO₂, and resist, respectively. The small changes in etch rates are consistent with physical sputtering under argon ion bombardment in which sputter yield increases at a slow rate above 300 eV and ac-

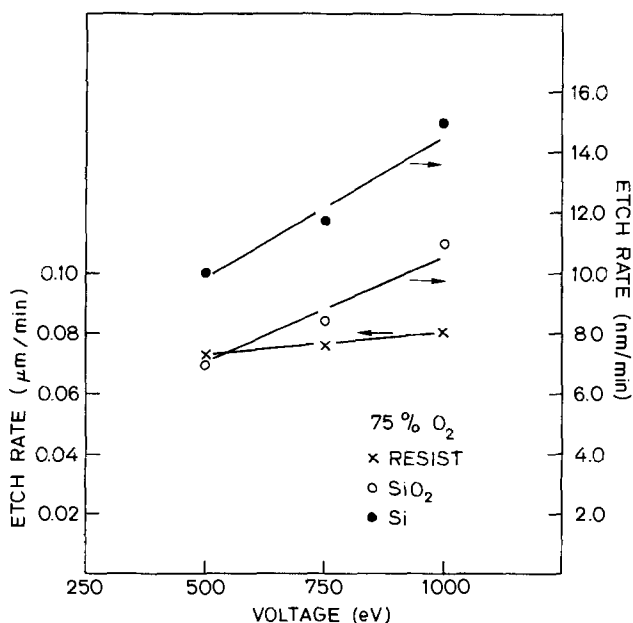


Fig. 3. Resist etch rate vs. accelerating voltage

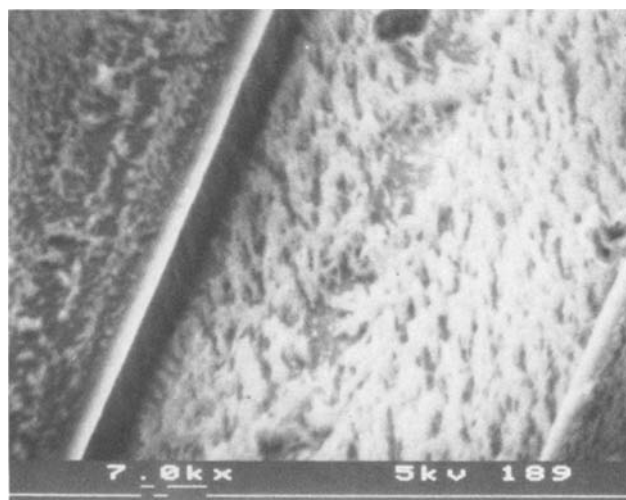


Fig. 4. Resist profile after reactive ion etching

tually decreases above 10⁴ eV (12, 13). At 1000V, the polysilicon/resist selectivity is 0.18.

The slopes of the curves in Fig. 2 are 9, 2, and 76×10^{-5} μm/min for each percentage point increase in O₂ for polysilicon, SiO₂, and resist, respectively. This order of magnitude enhancement in resist etching over polysilicon and SiO₂ is compared to only a factor of 2 increase vs. voltage in Fig. 3.

The experimental observations in this study are a result of combined chemical etching and physical sputtering of the resist material. Chemical etching predominates. It is apparent that resist etch rates increase linearly with increasing O₂, even though no Ar was injected into the gun while O₂ was injected into the chamber. This indicates significant backstreaming of the O₂ into the ion gun where it is ionized and accelerated as a beam of oxygen ions.

The physical sputtering component of the 1350J resist etch rate is minimal under these conditions. Indeed, extrapolation of the resist etch rate curve to 0% O₂ in Fig. 2 yields a sputter rate of only 14 nm/min, compared to etch rates of 100 nm/min with 100% O₂.

Another possible mechanism is ion-enhanced, gas-surface chemistry (14). Although neutral oxygen molecules do not spontaneously react with the resist, they may react with ion beam-activated sites. The number of these sites generally increases with energy. Because of the two-dimensional structures of resist, however, the collision cascade from an incident ion is terminated in this neighboring chain and the generation of activated sites may not be large. It is not possible to determine the contribution of this process to the total resist etch rate from these experimental conditions, but this mechanism had been confirmed by Geis *et al.* (15) for Cl₂ etching of GaAs.

Several planar diode PE and RIE systems were evaluated with respect to tri-level patterning under a variety of pressures, gas flows, and power levels using O₂ as the reactive species. In most cases, a grass-like residue at the bottom of the channel, several hundred nanometers thick, remained after etching. This is illustrated in Fig. 4. All the systems utilized Al electrodes, and it was determined by electron microprobe analysis that Al was present in the residue. It is probable that eroded electrode particulates are deposited on the resist and mask further removal. Attempts to cover the Al electrode with a Teflon layer were only partially successful. A comparison of Fig. 1 and 4 shows that no residue remains after RIBM. Previous studies have shown that no material from the ion gun was detected after ion beam milling with argon (16).

Conclusion

It has been demonstrated that RIBM is a viable technique for high resolution multilevel resist patterning.

Highly anisotropic edge profiles result with no undercutting and no residual deposited materials.

Manuscript submitted May 23, 1983; revised manuscript received April 23, 1984.

Stanford University assisted in meeting the publication costs of this article.

REFERENCES

1. K. L. Tai, W. R. Sinclair, R. G. Vadimsky, J. M. Moran, and M. J. Rand, *J. Vac. Sci. Technol.*, **16**, 1977 (1979).
2. J. M. Moran and D. M. Maydan, *ibid.*, **16**, 1620 (1979).
3. J. H. Bruning, *ibid.*, **17**, 1149 (1980).
4. M. M. O'Toole, E. D. Liu, and M. S. Chang, *IEEE Trans. Electron. Devices*, **ed-28**, 1405 (1981).
5. D. N. K. Wang, D. Maydan, and H. J. Levinstein, *Solid State Technol.*, **23**, 122 (1980).
6. P. Rissman and M. P. C. Watts, *Hewlett-Packard J.*, **14**, 21 (1982).
7. J. A. Oro and J. C. Wolfe, *J. Appl. Phys.*, **53**, 7379 (1982).
8. M. Itoh, H. Gokan, S. Esho, and K. Asakawa, *J. Vac. Sci. Technol.*, **20**, 21 (1982).
9. I. S. Goldstein and F. Kalk, *ibid.*, **19**, 743 (1981).
10. D. C. Flanders, A. M. Hawryluk, and H. I. Smith, *ibid.*, **16**, 1615 (1979).
11. R. N. Castellano, "Low-Energy Ion Beams 1980," pp. 241-245, Institute of Physics Conference Series 54, London, England, (1980).
12. N. Leagreid and G. K. Wehner, *J. Appl. Phys.*, **32**, 365 (1961).
13. R. J. MacDonalds, *Adv. Phys.*, **19**, 457 (1970).
14. H. F. Winters and J. W. Coburn, *Appl. Phys. Lett.*, **34**, 70 (1979).
15. M. W. Geis, G. A. Lincoln, N. Efremow, and W. J. Piacentini, *J. Vac. Sci. Technol.*, **19**, 1390 (1981).
16. P. H. Schmidt, R. N. Castellano, and E. G. Spencer, *Solid State Technol.*, **15**, 27 (1982).

The Solubility of Chromium in Gallium Arsenide

M. D. Deal*¹ and D. A. Stevenson**

Department of Materials Science and Engineering, Stanford University, Stanford, California 94305

ABSTRACT

The solubility of Cr in GaAs was investigated using well-defined Cr sources selected from specific regions of the Cr-Ga-As system and SIMS analysis. Using these sources, maximum solubilities and solid-liquid distribution coefficients were obtained. These results and the ternary information were used as a point of reference for correlating previous literature values of Cr solubility. The study of the dependence of Cr solubility upon donor concentration and concurrent capacitance voltage measurements were used to establish the electrical activity of Cr in GaAs.

Chromium is intentionally introduced in the growth of gallium arsenide (GaAs), both during bulk growth and epitaxial layer growth. The purpose of this addition is to compensate the electrically active residual defects and impurities in order to provide semi-insulating substrates for the growth of active layers. As a consequence, there is interest in the solubility of chromium (Cr) in GaAs for a wide variety of growth and processing conditions. However, the failure to recognize that the Cr solubility depends in a fundamental way on the temperature, Cr source, and extent of equilibrium in the system or process has led to considerable confusion. A major source of this confusion arises from a failure to consider fundamental ternary-phase equilibria principles in the design and interpretation of solubility experiments.

There is good agreement that the maximum solubility of Cr in otherwise undoped GaAs at or just below the melting point (1238°C) is about $2 \times 10^{17} \text{ cm}^{-3}$, as obtained from melt doping in bulk crystal growth (1-3). Values obtained from liquid-phase epitaxial (LPE) growth by Woodard (4) are often quoted as maximum solubilities for a specific temperature, without recognizing that these LPE solubility values correspond to equilibrium with a specific liquid composition and are not expected to be either a unique solubility for that temperature or the maximum value. Furthermore, solubilities from these LPE experiments have been compared to those obtained from indiffusion experiments using a pure Cr source in a closed ampul (5). However, there are three problems with such a comparison: the indiffusions were not performed long enough to establish equilibrium; the pure Cr source for the diffusion source and the liquid source in the LPE are clearly different; and, as noted in Ref.(5), the pure Cr diffusion source was changing significantly during the indiffusion.

*Electrochemical Society Student Member.

**Electrochemical Society Active Member.

¹Present address: American Microsystems, Incorporated, Santa Clara, California 95051.

Further confusion arises from the frequent use of non-equilibrium systems in relation to solubility levels. Morokoc *et al.* (6) propose a solubility of Cr in GaAs of $1 \times 10^{16} \text{ cm}^{-3}$ at 580°C from molecular beam epitaxy (MBE) experiments. This value is orders of magnitude higher than any others reported for that temperature. Bonnet *et al.* (7) state that the solubility limit of Cr in GaAs is around $5 \times 10^{16} \text{ cm}^{-3}$ (temperature not known) from their metal-organic chemical vapor deposition (MOCVD) results. Linh *et al.* (8) point out that their own MBE and MOCVD results for Cr solubility differ from each other as well as from other reported results. Both these methods of layer growth, however, are nonequilibrium techniques, and are not suitable for equilibrium solubility studies. These examples show the lack of concern for equilibrium considerations, and especially the ternary-phase relations, when measuring and interpreting the Cr solubility in GaAs. A major reason for this has been the complete lack of information on the ternary Ga-As-Cr system and, in fact, misleading information on the Cr-As binary system. With recent ternary information on this system (9), however, it has been possible to interpret previous solubility information and to design new solubility studies. We present an experimental study of Cr solubility in GaAs using this phase-equilibria information as a guide.

Experimental

General considerations.—The key consideration in designing the present solubility studies was the recently determined ternary Cr-Ga-As system (9). A representative isothermal section for 800°C is shown in Fig. 1 for $X_{As} < 0.5$. The most significant features of this diagram are: a Cr phase is never in equilibrium with GaAs, there is a broad liquid + GaAs_(s) region, and there is a ternary tie triangle including a GaAs_(s) phase. The latter two regions are suitable for Cr sources for solubility; however, it should be noted that when temperature is fixed, the remaining degrees of freedom are one and zero, respectively, in accord with the Gibbs phase rule. Thus, the solubility should be

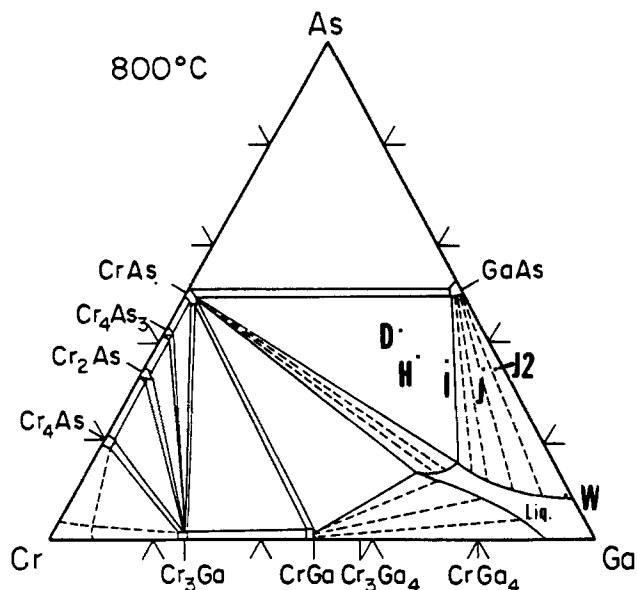


Fig. 1. Compositions of sources D, H, I, J, and W

identical for any points in the tie triangle, such as points D, H, and I in Fig. 1, whereas point J in Fig. 1 is in the $\text{Ga}_{(1)} + \text{GaAs}_{(s)}$ region and will correspond to a specific tie line, and the solubility will differ from that of the tie triangle source.

Experimental techniques.—For most of the experiments, the GaAs used was Cominco LEC high resistivity, undoped GaAs. According to Cominco, the resistivity was $\geq 10^7 \Omega \text{ cm}$ and the dislocation density was $\leq 10^4 \text{ cm}^{-2}$. This material was used in most cases, rather than Bridgman GaAs, because of its very low impurity level, which is the reason why it is semi-insulating without Cr additions. Other GaAs material used included: Crystal Specialties undoped GaAs (Bridgman); Hewlett-Packard Te-doped and undoped GaAs (LEC); and Morgan Semiconductor Si-doped GaAs. The GaAs wafers, 350–400 μm thick, were cut into approximately $1 \times 1.5 \text{ cm}$ squares. Before annealing, the squares were cleaned according to a 14-step schedule which was designed to remove particles, organic impurities, native oxides, and inorganic chemicals.

The Cr sources used were appropriate Ga-As-Cr phases which were made prior to the solubility anneals by mixing appropriate amounts of Cr, Ga, GaAs, and CrAs, and annealing these mixtures to establish an equilibrium Cr source. The source material was then crushed, and small samples of it were examined with x-rays to establish that the appropriate phases were present. The ampuls used were made from high purity quartz with a constriction in the ampul to separate the powder-source material and the GaAs substrate. The total interior volume of the ampul was $\approx 2 \text{ ml}$. A diagram is shown in Fig. 2.

Immediately after cleaning the GaAs wafer, the wafer and source were placed in the ampul, which was evacuated to $\approx 10^{-6}$ torr, and sealed. The vacuum inside the ampul was checked by a Tesla coil before and after each anneal. After annealing the samples for the appropriate time and temperature, the ampuls were quenched in water. The GaAs wafers were then ultrasonically cleaned in methanol, boiled in HCl to remove any loose particles and/or dissolve any precipitates from the surface, and then rinsed in isopropyl alcohol. The GaAs wafers were then analyzed by SIMS.

Composition analyses.—For this work, a Cameca "IMS 3F" SIMS system, at Charles A. Evans and Associates (San Mateo, California), was used. For Cr in GaAs, an O_2^+ primary beam was used, with an energy of 12.5 keV. The beam size was either 75 or 150 μm in diameter (which rastered out respective areas of 250×250 or $500 \times 500 \mu\text{m}^2$) and the sampling area, controlled by an aperture in front of the detector, was 75 μm^2 (or 150 μm^2). The usual pri-

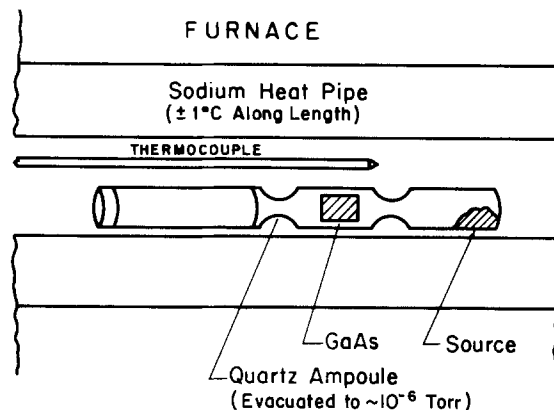


Fig. 2. Schematic diagram of the annealing system used for the solubility and diffusion experiments.

mary beam current, which determined the sputtering rate, was $\approx 6 \mu\text{A}$, resulting in a sputtering rate of $\approx 50 \text{ \AA/s}$.

The conversion of ion intensity to Cr concentration was established with a calibration using ion implantation of Cr and by use of the As matrix ion intensity as a reference. At the start of each set of analyses, a "low chromium" sample was analyzed by SIMS to determine the background level for that day. This was usually $\approx 1 \times 10^{15} \text{ cm}^{-3}$ and sometimes less.

The time-to-depth conversion was determined by measuring the depth of the SIMS crater after each analysis with a Dektak, which uses a very sensitive stylus to measure step distances, and then assuming that the sputter rate is constant throughout the profile (confirmed by periodically profiling of Ga and/or As to establish that they give constant concentration-depth profiles). There is an uncertainty factor in the absolute depth measurement of 15%. A depth measurement taken across the entire SIMS crater showed the crater to be very uniform. Micrographs were also taken which confirm that the SIMS sputtering of GaAs was uniform, in contrast to some matrix materials, which do not sputter uniformly.

Results and Discussion

Anneals of GaAs with a "D source," as shown in Fig. 1 were performed at 800°C for 6, 12, and 24h in order to determine the length of time needed to reach the Cr solubility level in the bulk of the GaAs (*i.e.*, $> 4 \mu\text{m}$ from the surface); SIMS Cr profiles indicated that 12h was sufficient time to establish equilibrium at 800°C. The Cr solubility was thus determined to be $3 \times 10^{16} \text{ cm}^{-3}$ ($\pm 1.5 \times 10^{16} \text{ cm}^{-3}$) at 800°C. Eight anneals were then done at that temperature using sources D, H, I, and J (Fig. 1) for 6, 12, or 24h as indicated in Fig. 3. As mentioned earlier, according to the phase rule and the Ga-As-Cr ternary-phase diagram, GaAs samples in equilibrium with sources D, H, and I should have the same Cr solubility, while a sample in equilibrium with source J should be different, and probably less. The SIMS Cr profiles, shown in Fig. 3, verify this. The bulk Cr levels for the D, H, and I samples are all around $3 \times 10^{16} \text{ cm}^{-3}$, while that for J is $\approx 4 \times 10^{15} \text{ cm}^{-3}$. (The unusual surface buildup of Cr is a result of surface effects and does not relate to equilibrium bulk solubility.) These results confirm the proposed ternary-phase diagram (9) and also confirm the applicability of the phase diagram and the phase rule for this type of study.

These results explain why Woodard's solubility values (4) are lower than those obtained for sources D, H, and I; his results are for GaAs in equilibrium with $\text{Ga}_{(1)}$, whose Cr content is 0.86 atom percent (a/o), which corresponds approximately to point W in Fig. 1. This is to the right of J in the $\text{GaAs}_{(s)}-\text{Ga}_{(1)}$ region and hence one would expect a lower Cr solubility in $\text{GaAs}_{(s)}$.

Solubility anneals were then performed with the H source at 700°, 750°, 900°, and 1000°C in order to obtain the temperature dependence of the Cr solubility for the

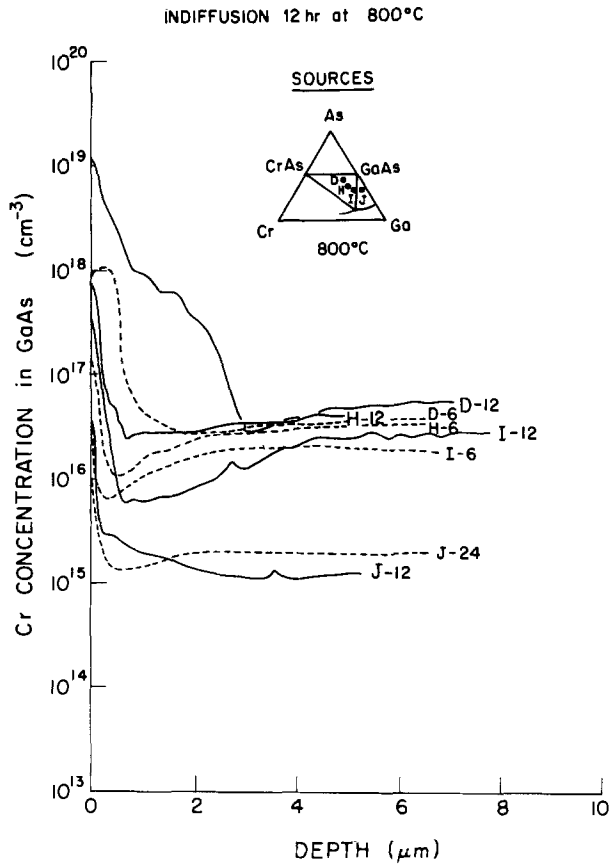


Fig. 3. Cr in GaAs concentration profiles from 800°C solubility experiments for various times and with various sources, as indicated in the profile designations.

GaAs_(s)-CrAs_(s)-Ga_(l) tie triangle Cr source. These were performed for 18, 18, 8, and 7h respectively—long enough to reach the maximum level in the bulk. The resulting SIMS Cr profiles, including that for 800°C, are shown in Fig. 4. The Cr solubility vs. 1/T is plotted in Fig. 5. As expected, the Cr solubility extrapolates to the maximum Cr solubility of $2 \times 10^{17} \text{ cm}^{-3}$ just below the melting point of GaAs.

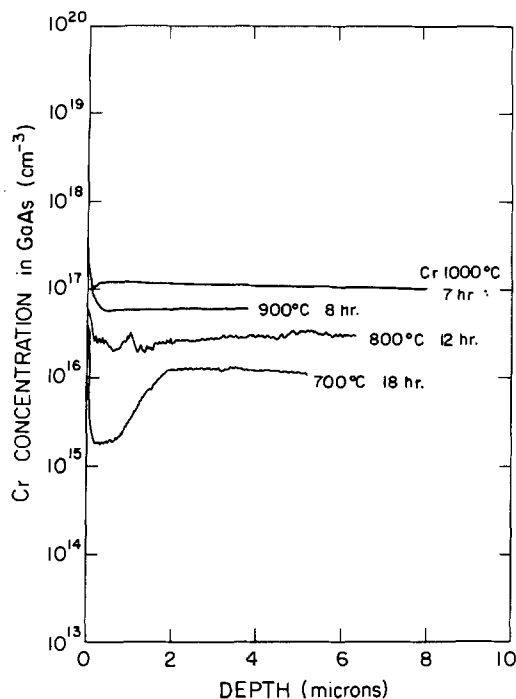


Fig. 4. Cr in GaAs concentration profiles from solubility experiments for times and temperatures indicated.

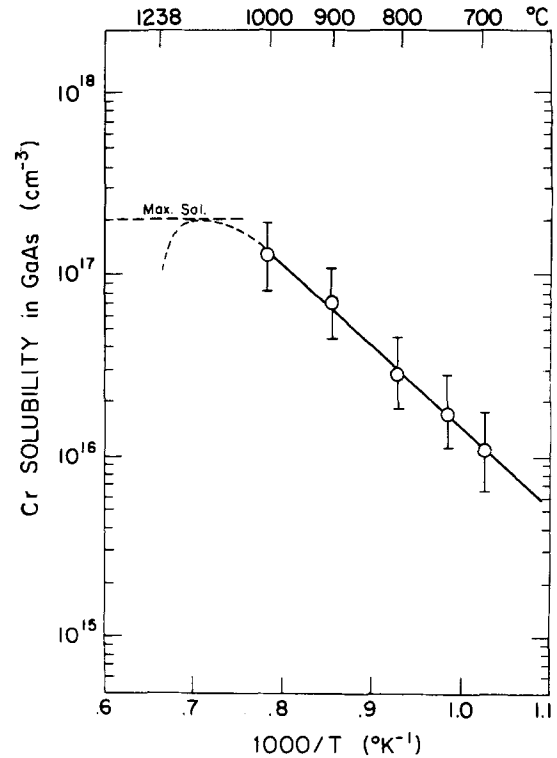


Fig. 5. Cr solubility in GaAs (for GaAs_(s)-CrAs_(s)-Ga_(l) region), with maximum solubility of Cr in GaAs as indicated.

As is the case with most impurities in semiconductors, Cr exhibits retrograde solubility in GaAs; the solubility increases with temperature above the 670°C eutectic point, between CrGa₃ and GaAs.

To confirm that the bulk levels reached in the solubility experiments correspond to equilibrium conditions, an experiment was done in which a GaAs wafer was annealed at 900°C (with the H source) for a long time (12h) and then annealed at 800°C (again with the H source). SIMS analysis was done after each anneal with the resulting Cr profiles shown in Fig. 6. As one can see, the bulk

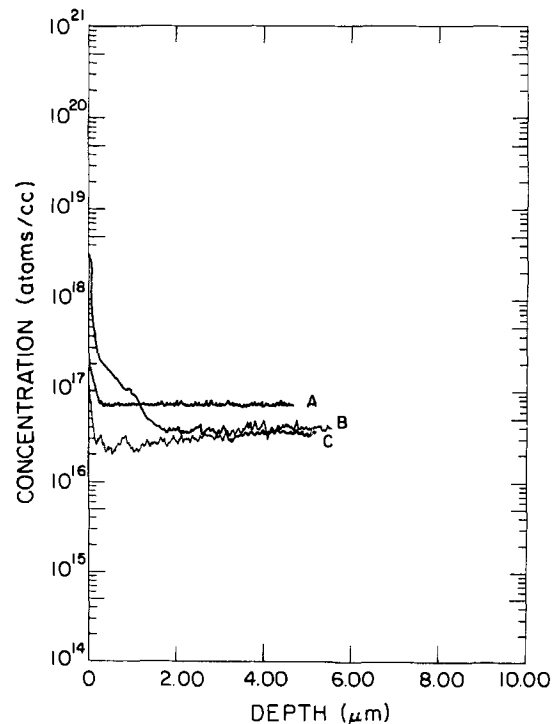


Fig. 6. Cr in GaAs concentration profiles, from solubility experiments. A: 900°C, 12h indiffusion with H source. B: subsequent 800°C, 12h anneal with H source. C: 800°C, 12h indiffusion into undoped GaAs, with H source.

Cr level after the 900°C anneal (curve A) was at $\approx 8 \times 10^{16}$ cm^{-3} , the determined solubility level for that temperature. The bulk Cr level after the subsequent 800°C anneal (curve C) is lower, $\approx 4 \times 10^{16}$ cm^{-3} . Also shown (curve B) is the profile of the original 800°C solubility determination, with a bulk level of 3.5×10^{16} cm^{-3} . This shows that the same Cr concentration (within experimental error) was reached both from above and from below, confirming that it is the equilibrium solubility.

From the solid solubility results, and from the Ga-As-Cr phase diagram (specifically, the Cr concentration in the Ga-rich liquid in equilibrium with $\text{CrAs}_{(s)}$ and $\text{GaAs}_{(s)}$), the distribution coefficient, k , of Cr in GaAs was determined for various temperatures; the distribution coefficient equals $[\text{Cr}]_s/[\text{Cr}]_l$, the solid being $\text{GaAs}_{(s)}$ and the liquid being $\text{Ga}_{(l)}$. These numbers, as well as the liquid and solid solubility values from which they were calculated, are tabulated in Table I. The distribution coefficients vs. $1/T$ are plotted in Fig. 7. The distribution coefficient at 800°C was also determined from sample J (GaAs in equilibrium with J source), and is the lower point at 800°C. The results show that k does not vary much with Cr concentration; even with a variation in solubility of an order of magnitude between J and D, k differed by only a factor of two. Also plotted in Fig. 7 are the results of Woodard (4), from his LPE studies (which are for $\text{GaAs}_{(s)}$ in equilibrium with a Ga-rich liquid of 0.86 a/o Cr concentration). These are consistent with the results for higher Cr concentrations. Therefore, while the solubilities vary as the total composition moves across the phase diagram, the ratio of solid solubility to liquid solubility remains approximately constant, as one would expect for dilute solutions. In addition, the distribution coefficients determined from Cr-doped GaAs crystal growth, which are for temperatures just below the melting point of GaAs, are shown [from Ref. (1, 10-13)]. As one can see, the results of the present work fill the gap nicely between the lower temperature results of Woodard for LPE conditions and the higher temperature results from bulk crystal growth. (Note: upon further examination of the "crystal growth" values, one observes the following trend: the more Cr in the melt, the smaller the k value. This is a logical trend since the melting point of GaAs decreases as the content in the melt increases. Therefore, the temperatures and the corresponding k values for those six cases would be different. Taking this into account, the six points should not be plotted at the same temperature, but for decreasing temperatures, and would follow the trend of k decreasing with decreasing temperature.)

To see if there is a difference in Cr solubility between one type of undoped GaAs and another, solubility anneals were done using GaAs substrates from different suppliers (Cominco, Hewlett-Packard, and Crystal Specialties). The differences between the resulting solubilities were within the expected error of the experiments. Therefore, the way the GaAs is produced apparently has no appreciable effect on the final equilibrium solubility.

To see the effect of doping on the solubility of Cr in GaAs, solubility anneals were performed at 800°C using the H source in Te-doped (n-type) GaAs. After an 18h anneal, 10 μm of the GaAs was etched off each surface (using a 16:1:1 $\text{H}_2\text{O}:\text{H}_2\text{O}_2:\text{H}_2\text{SO}_4$ solution) to ensure that any

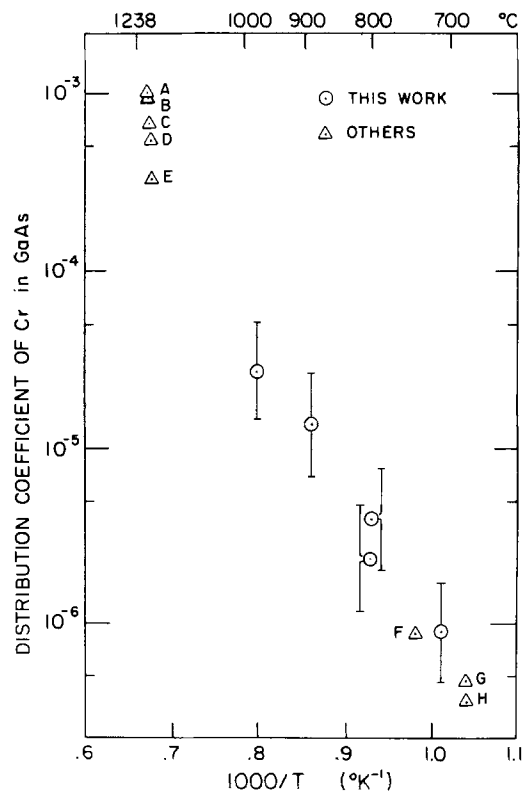


Fig. 7. Distribution coefficient, k , vs. $1/T$ for Cr in GaAs. Circled data are from this work; data with triangles are from others: A, C: Ref. (11); B: Ref. (10); D: Ref. (1) and (12); E: Ref. (13), and F, G, H: Ref. (4).

surface artifacts are removed and to remove any Te-depletion region caused by Te outdiffusion. (However, since the diffusivity of Te at 800°C is very small, this was not a problem.) SIMS analysis indicated a Cr solubility of 8×10^{16} cm^{-3} , almost three times that for undoped GaAs at that temperature. This is consistent with the model of Cr as a deep acceptor in GaAs (on a Ga site) (14-17), since the presence of a donor usually increases the solubility of an acceptor (18, 19), based on charge equilibrium considerations. (Likewise, the presence of another acceptor usually decreases the solubility of an acceptor.) These results are consistent with those of Brozel *et al.* (3), who found in their crystal growth experiments that the Cr solubility increases with increasing Si concentration, the Si acting as a donor. C-V carrier concentration measurements, using gold contacts to the GaAs surface and a Hewlett-Packard automated C-V measuring system, were made on the Te-doped sample both before and after the Cr indiffusion. Before Cr diffusion, the n-type carrier concentration was 3.8×10^{17} cm^{-3} , (consistent with the reported Te doping of $\approx 3 \times 10^{17}$ cm^{-3}), whereas after Cr diffusion, it was 2.4×10^{17} cm^{-3} . This means that 1.8×10^{17} cm^{-3} carriers were compensated by the chromium. If, as proposed by Brozel *et al.* (3), the Cr acts as a double acceptor in n-type GaAs with the donor concentration greater than twice the Cr concentration, then $1/2 \times (1.8 \times 10^{17})$ cm^{-3} , or 9×10^{16} cm^{-3} Cr atoms should be electrically active. This compares very well with the measured 8×10^{16} cm^{-3} chromium (the difference is well within the experimental error). This means that the bulk chromium seen in the SIMS profiles is in solution, and are not precipitates or clusters. It is also good evidence of the accuracy of the SIMS analysis in this work.

In heavily doped GaAs (n-type), all the Cr is probably ionized (3), and acts like a normal acceptor, and its solubility should increase with an increase in the n-type doping level. The increase in the Cr solubility should then be given by the model for the influence of the donor concentration on the acceptor solubility (18-20).

$$C_s'' \approx C_s' (1 + gn/n_i)(1 + g) \quad [1]$$

Table I. Distribution coefficient, k , of Cr in GaAs (Ga-rich side)

T	$[\text{Cr}]_l$	$[\text{Cr}]_s$	k
700°C	0.17	7×10^{15}	9×10^{-7}
800°C	0.16	3×10^{16}	4.5×10^{-6}
800°C	0.05	4×10^{15}	2.5×10^{-6}
900°C	0.15	9×10^{16}	1.2×10^{-5}
1000°C	0.12	1.3×10^{17}	2.5×10^{-5}

$[\text{Cr}]_l$: Concentration (mole fraction) in Ga-rich liquid.
 $[\text{Cr}]_s$: Cr concentration (cm^{-3}) in GaAs.
 k : $[\text{Cr}]_s/[\text{Cr}]_l/4.4 \times 10^{22}$.

where C_s'' is the new solubility level, C_s' is the solubility in the intrinsic, or undoped case, n is the electron concentration (due to the doping), n_i is the intrinsic carrier concentration, and g is the degeneracy factor, which according to Sze (21), is equal to 1/4 for acceptors in Ge, Si, and GaAs. Testing this for the case discussed above, at 800°C [$n_i = 7 \times 10^{16} \text{ cm}^{-3}$ (22)], a Te doping of 3.8×10^{17} , and an intrinsic Cr solubility of $3 \times 10^{16} \text{ cm}^{-3}$, one would predict from this equation a new solubility of $6 \times 10^{16} \text{ cm}^{-3}$. The actual solubility, from SIMS, is $8 \times 10^{16} \text{ cm}^{-3}$. A similar calculation at 850°C (with the same Te doping), would predict a solubility of $8 \times 10^{16} \text{ cm}^{-3}$. A solubility experiment was done at 850°C in the same way as in the previous case, and the SIMS Cr profile indicated a new solubility of $9 \times 10^{16} \text{ cm}^{-3}$. As predicted, at high temperatures, the relative increase is less because n_i increases. As a first-order approximation, Eq. [1] is adequate.

A similar experiment was done in n-type Si-doped GaAs at 800°C for 48h. The exact Si concentration was estimated to be in the low-to-mid 10^{17} cm^{-3} , as with the Te case, and the results were qualitatively similar. The Cr solubility was higher than in the undoped case: $7 \times 10^{16} \text{ cm}^{-3}$ vs. $3 \times 10^{16} \text{ cm}^{-3}$. Even though the donor was on a different site (on a Ga site, rather than an As site as is the case of Te), the effect was the same, indicating that it is an electrical effect, rather than a steric and/or lattice stress effect.

Summary

The solubility of Cr in GaAs was studied using Cr sources that were taken from two types of regions from isothermal sections of the Cr-Ga-As system: a ternary tie triangle region including $\text{Ga}_{(1)}$, $\text{GaAs}_{(s)}$, and a $\text{CrAs}_{(s)}$; and a $\text{GaAs}_{(s)}$ - $\text{Ga}_{(1)}$ region. The former values correspond to maximum solubilities, whereas the latter correspond to tie lines and corresponding distribution coefficient. The experimental values of the maximum Cr solubility determined for temperatures from 700° to 900°C extrapolated nicely to previously reported values of the maximum solubility of Cr near the melting point of GaAs. Distribution coefficients were also determined over the same temperature range and connect nicely with distribution coefficients obtained from liquid-phase epitaxy at lower temperatures and solubilities obtained from bulk crystal growth at higher temperatures. Enhanced solubility in Te- and Si-doped GaAs in combination with the deep double acceptor (electron trap) model for Cr in GaAs.

Acknowledgments

We thank Lisa Michael for assistance in the experiments and Dr. Richard A. Reynolds for his suggestions and guidance through all phases of this investigation. We

thank Charles A. Evans and Craig Hopkins for their skill in the SIMS analysis. We acknowledge financial support from the Advanced Research and Application Corporation (ARACOR) and the Defense Advanced Research Projects Agency.

Manuscript received May 2, 1984.

REFERENCES

1. G. R. Cronin and R. W. Haisty, *This Journal*, **111**, 874 (1964).
2. R. W. Haisty and G. R. Cronin, in "Proceedings of the 7th International Conference on the Physics of Semiconductors," M. Hulin, Editor, p. 1161, Dunod, Paris (1964).
3. M. R. Brozel, J. Butler, R. C. Newman, A. Ritson, D. J. Stirland, and C. Whitehead, *J. Phys. C.*, **11**, 1857 (1978).
4. D. W. Woodard, Ph.D. Thesis, Cornell University, Ithaca, NY (1979).
5. B. Tuck and G. A. Adegboyega, *J. Phys. D.*, **12**, 1895 (1979).
6. H. Morkoc, C. Hopkins, C. A. Evans, Jr., and A. Y. Cho, *J. Appl. Phys.*, **51**, 5986 (1980).
7. M. Bonnet, J. P. Duchemin, A. M. Huber, and G. Morillot, in "Semi-Insulating III-V Materials, Nottingham 1980," G. J. Rees, Editor, p. 68, Shiva, London (1980).
8. N. T. Linh, A. M. Huber, P. Etrenne, G. Morillot, P. Duchemin, and M. Bonnet, in "Semi-Insulating III-V Materials, Nottingham 1980," G. J. Rees, Editor, p. 206, Shiva, London (1980).
9. M. D. Deal, R. A. Gasser, and D. A. Stevenson, Submitted to *J. Phys. Chem. Solids*.
10. G. M. Martin, *J. Appl. Phys.*, **50**, 467 (1979).
11. M. R. Brozel, B. Tuck, D. Rumsby, and R. M. Ware, Submitted for publication.
12. R. K. Willardson and W. R. Allred, Institute of Physics Conference Series, p. 35, Institute of Physics, London (1967).
13. T. Udagawa and T. Nakanisi, *Jpn. J. Appl. Phys.*, **20**, 579 (1981).
14. B. Deveaud and P. N. Favennec, *Solid-State Commun.*, **24**, 473 (1977).
15. G. H. Stauss and J. J. Krebs, Institute of Physics Conference Series, 33A, p. 84, Institute of Physics, London (1976).
16. P. M. Asbeck, J. Tandon, B. M. Welch, C. A. Evans, Jr., and V. R. Deline, *IEEE Electron. Dev. Lett.*, **ed1-1**, 35 (1980).
17. U. Kaufmann and J. Schneider, *Appl. Phys. Lett.*, **36**, 747 (1980).
18. R. A. Swalin, "Thermodynamics of Solids," pp. 263-70, John Wiley and Sons, New York (1962).
19. F. A. Kröger, "The Chemistry of Imperfect Crystals," pp. 716-27, John Wiley and Sons, New York (1964).
20. R. A. Swalin, in "Atomic Diffusion in Semiconductors," D. Shaw, Editor, pp. 65-112, Plenum Press, New York (1973).
21. S. M. Sze, "Physics of Semiconductor Devices," p. 24, John Wiley and Sons, New York (1981).
22. J. S. Blakemore, *J. Appl. Phys.*, **53**, R123 (1982).

The Variation of Physical Properties of Plasma-Deposited Silicon Nitride and Oxynitride with Their Compositions

V. S. Nguyen,* S. Burton, and P. Pan*

IBM General Technology Division, Essex Junction, Vermont 05452

ABSTRACT

Silicon nitride and silicon oxynitride films with refractive indices varying from 1.60 to 1.95 were deposited on silicon substrates using plasma-enhanced chemical vapor deposition (PECVD) processing. Variation of the film's physical properties with composition is examined. Refractive indices, infrared, Auger analysis, and plasma etching of plasma-deposited films are studied before and after an annealing cycle. A direct correlation between etch rates and etch profiles of the deposited films with their composition was observed. Plasma etching, using a 92% CF_4 + 8% O_2 gas mixture, showed that the etch rate of oxynitride film increases with hydrogen concentration and decreases as the oxygen content increases. The length of the undercut, i.e., etch profile, depends on the amount of oxygen and hydrogen content in the films. Infrared data suggests that silicon oxynitride film with a refractive index of 1.75 is more stable under thermal annealing cycles, as compared to other silicon oxynitride films. Ellipsometric measurements showed that film thickness and refractive index uniformity are comparable with those of CVD processing. However, Auger depth profile analysis revealed poor compositional uniformity in all deposited films, especially at the silicon or silicon dioxide substrate interfaces.

Due to the demand for improvement in integrated circuit reliability, increased attention has recently been paid to the development of the final passivation layer which protects integrated circuits from contamination (e.g., alkaline ions and moisture). Silicon nitride films prepared by plasma-enhanced chemical vapor deposition (PECVD) processing were found to be a suitable material for final passivation. A recent study (1) indicated that converting a plasma-deposited silicon nitride to silicon oxynitride by introducing oxygen improves thermal stability, cracking resistance, and decreases film stress. In addition, low temperature plasma-deposited films also have many applications in multilayer resist lithography (2), interlevel dielectrics for multilevel metallization structures (3), and as a diffusion mask or photolithographic mask coating. However, the use of plasma-deposited films in electrically active regions of integrated circuits is still very limited (4) because the deposition is difficult to control and there is limited understanding of film properties.

In order to improve this situation, we have studied the deposition, bonding, composition, and plasma etching properties of PECVD silicon nitride and silicon oxynitride films. It has been reported that some physical properties of plasma-deposited silicon nitride are strongly dependent on composition ratio and hydrogen concentration (5-8). In this paper, we report the direct correlation between etching properties and etch profiles of both plasma-deposited (PECVD) silicon nitride and silicon oxynitride films with their composition and bonding. Fourier transformed infrared (FTIR) and Auger (AES) analysis techniques were used to analyze film compositions and bonding before and after the thermal annealing cycle.

Experimental Procedure

Films were deposited in a high frequency (13.56 MHz), parallel-plate plasma reactor with a ring-type gas injection system. The process parameters for the best uniformity ($\sigma = +3\%$) silicon nitride deposition are given in Table I. Silane and ammonia were used as reactants for this deposition process; ammonia instead of nitrogen was chosen as a reactant gas because it provides better thickness and refractive index uniformity. This is due to the comparable dissociation energy between N-H and Si-H. Helium was used as an inert carrier gas; its effect on plasma deposition has been discussed previously (9). Silicon oxynitride films were formed by reacting silane, ammonia, and nitrous oxide under the same process conditions as silicon nitride deposition. Nitrous oxide flow rate was varied from 8 to 18 standard cubic centimeters per minute (sccm) to change the oxygen concentration. The films

were deposited on both bare silicon and thermally grown silicon dioxide substrate surfaces.

Film thickness and refractive index were measured using a He-Ne laser ellipsometer (wavelength = 632.8 nm) together with Talystep techniques. FTIR studies were performed with 500 nm silicon nitride and silicon oxynitride films deposited on bare silicon substrates. Background absorption of the substrate was subtracted from the spectra to obtain the bulk film spectra. The maximum resolution of the spectrometer was 0.5 cm^{-1} wavenumber. Auger analyses for compositional depth profiles were performed with 100 nm films on both silicon and silicon dioxide substrate surfaces. The films were sputtered by 1 keV Ar^+ ion to determine the depth composition. The detection limit of this tool is 0.5 atomic percent (a/o). The films were examined as deposited and after annealing in an argon atmosphere for 20 min at 1000°C .

The plasma etching experiments were carried out in another parallel-plate radial flow etching reactor. The upper electrode is driven with a frequency of 13.56 MHz. The ground electrode, 56 cm diam, is temperature controlled. The conditions for etching were 0.16 W/cm^2 RF power, 250 mtorr, and 160 sccm total flow using 8% O_2 in CF_4 . The grounded substrate electrode was temperature controlled at 40°C during the process. Etch rates were determined as a function of oxynitride composition and annealing conditions. Etch rates were calculated using a laser interferometry end-point trace, dividing the cycle thickness by the time required to etch one cycle. The formula used to calculate cycle thickness is $\lambda/2n$, where λ is the wavelength of the laser and n is the film's refractive index.

Scanning electron microscopy (SEM) was used to study the etch profiles of photoresist/plasma films/silicon substrate structure. The etch profiles of plasma-deposited

Table I. Plasma deposition conditions of silicon nitride

Condition	Value
Power	300 W (0.12 W/cm^2)
Pressure	1.2 Torr
Temperature	300°C
Electrode Spacing	2 cm
Flow Rates	
— Silane (1.8% in He)	1550 sccm
— Ammonia (100%)	90 sccm
— Helium	800 sccm
Deposition Rate	7 nm/min

* Electrochemical Society Active Member.

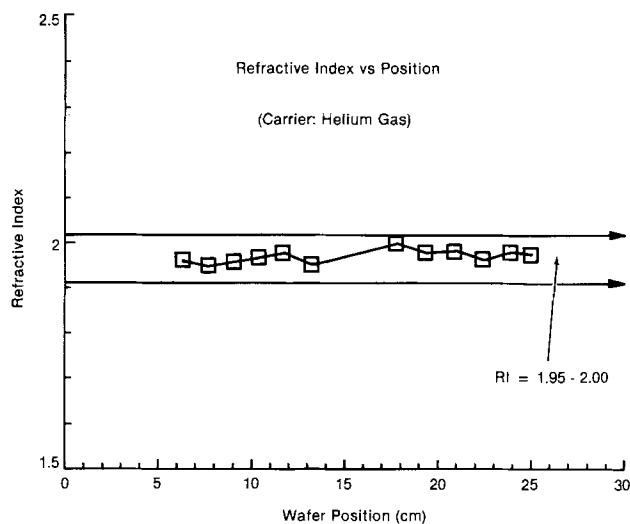


Fig. 1. Variation of refractive index vs. position of plasma-deposited silicon nitride in the parallel reactor.

films before and after annealing in argon for 20 min at 1000°C were examined.

Results and Discussion

Film deposition.—The results of silicon nitride deposition (Fig. 1) show that the film thickness and refractive index uniformity are good. The refractive index varied from 1.95 to 2.00 within a batch with a deposition rate of 7 nm/min.

Figure 2 shows the results of silicon oxynitride deposition at various nitrous oxide flow rates ranging from 8 to 18 sccm. At flow rates of 8, 12, and 18 sccm, the refractive indices were 1.85, 1.75, and 1.65, respectively. Silicon oxynitride films had relatively good thickness uniformity ($2\sigma = 5\%$) for each batch. The deposition rates of silicon oxynitride deposition varied only slightly, from 6.5 to 7 nm/min. We also used carbon dioxide and diatomic oxygen gas as oxygen sources for silicon oxynitride deposition under the same conditions. However, these oxygen sources resulted in poor refractive index ($RI = 1.46-2.00$) and thickness uniformity ($2\sigma = 100\%$). Nitrous oxide appeared to be a better oxygen source for silicon oxynitride deposition.

The film uniformity in this PECVD process has been attributed to a large penning effect of the helium inert carrier gas. We have examined and discussed the extent of this effect with various inert carrier gases in PECVD processing previously (9).

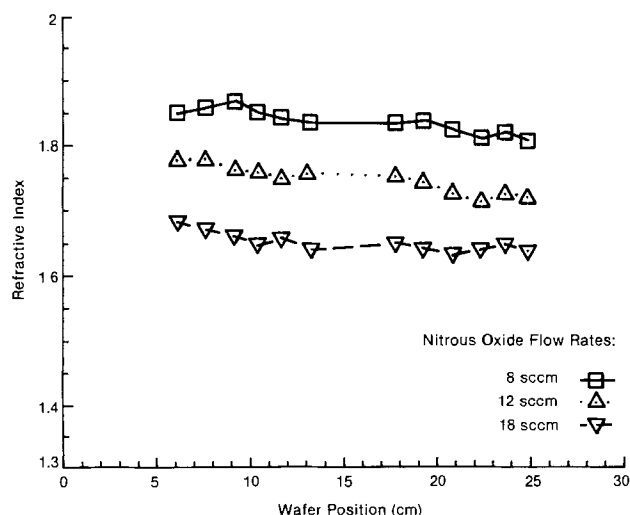


Fig. 2. Variation of refractive index vs. position of plasma-deposited silicon oxynitride in the parallel reactor.

Infrared and Auger analysis.—The IR spectrum of silicon nitride films with a refractive index of 1.95 showed the presence of N-H (3350 cm^{-1}), Si-H (2200 cm^{-1}), Si-N ($850-900\text{ cm}^{-1}$), and Si-O (1150 and 450 cm^{-1}) (Fig. 3) (10, 11). No oxygen was detected in this film with AES. This indicates that the amount of oxygen in the film is below the detection limit of our measurements (0.5 a/o). The silicon nitride sample was also found to be silicon rich with about 28 a/o excess silicon from the stoichiometric ratio of Si_3N_4 . Electron spectroscopy for chemical analysis (ESCA) data indicated the presence of a Si-(Si_3) phase in this silicon nitride film. Infrared spectra of silicon nitride films after annealing showed a marked reduction in the intensity of Si-H and N-H bands (Fig. 3a). The data appears to be consistent with both nuclear reaction analysis profiling and quadrupole mass analysis results (12, 13) of the hydrogen content in plasma-deposited silicon nitride films as deposited and after annealing. These results indicate that a significant amount of hydrogen was evaporated from the film during the annealing process. One expected that the density of as-deposited material is lower and the presence of hydrogen (and helium) gas in the film is higher than for standard CVD silicon nitride films. This explains why the refractive index of silicon-rich film is only 1.95. After annealing, a small amount of film would typically peel off, probably a result of trapped gases.

Infrared analysis of plasma-deposited silicon oxynitride films with the refractive index varying from 1.85 to 1.65 also showed the presence of N-H, Si-H, Si-O, and Si-N bonds at various intensities (Fig. 3b). However, no O-H bond was observed in either plasma-deposited silicon nitride or oxynitride films. Substantial overlap between Si-O and Si-N bands prevented an exact normalized intensity measurement. The intensity of the Si-O bands, *i.e.*, the number of Si-O bonds, increased as the film's refractive index decreased. This result corresponds well with our Auger analysis data which indicated the average oxy-

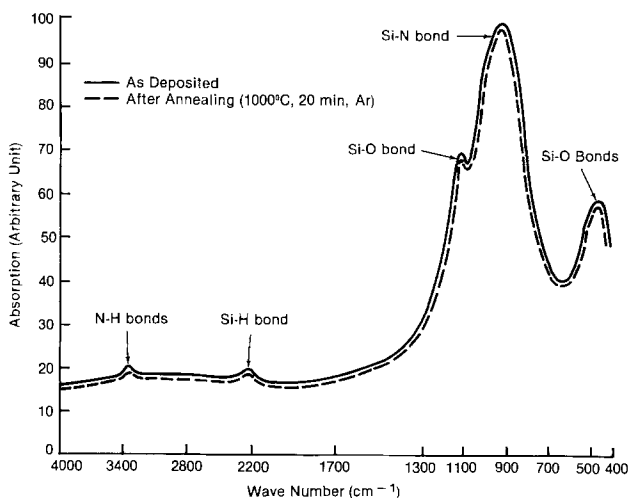
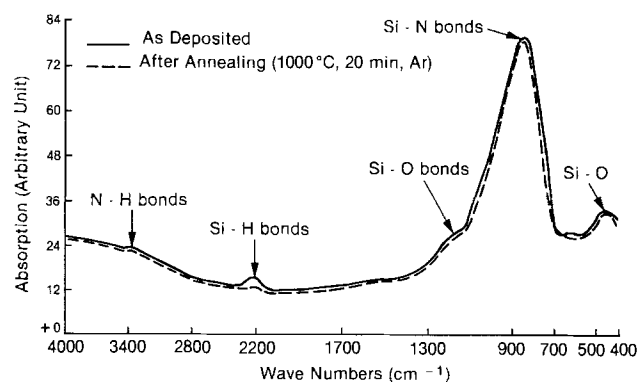


Fig. 3. Infrared absorption plasma-deposited silicon nitride (a, top) and silicon oxynitride (b, bottom) (refractive index = 1.75).

gen concentration increased from 2.1 to 35.8 a/o as the film's refractive index decreased from 1.85 to 1.65 (Table II). The compositional analysis data appear to be consistent with the reported results of PECVD films with a refractive index of 1.55 (14). Although positive identification of Si-N-O bonds cannot be confirmed due to band overlap, one may expect that these types of bonds must also exist. The IR spectral intensity analysis of Si-H and N-H bands indicated that significantly less hydrogen was evaporated from the silicon oxynitride with a refractive index of 1.75 during annealing (as compared to other plasma-deposited films).

Auger analyses of all films showed no significant change in silicon, nitrogen, or oxygen composition after the samples were annealed. Furthermore, Auger depth profiles showed poor compositional uniformity during the first 10-30 nm of deposition for all experimental films examined, *i.e.*, the result indicated the presence of a two-layer structure. The bottom 10-20 nm layer near the substrate interface was more silicon rich than the top layer (Fig. 4a-4d). For our typical plasma-deposited silicon nitride films, the ratio of the silicon content in the bottom layer to the top was 1.17. These two-layer structures are probably a result of the changes in electron temperature and density of silane reactive species concentration during the first few minutes of deposition processing. It appeared that more silane was dissociated to reactive species and deposited during the first few minutes of operation. The silicon-rich interface appeared to be an intrinsic property of plasma-deposited films and a direct result of initial transient phenomena observed in our PECVD processes.

Table II. Auger analysis data of silicon nitride and oxynitride films

Refractive Index	Average Atomic Percent Composition		
	Silicon	Nitrogen	Oxygen
1.95	71.4	28.6	0
1.85	43.7	54.2	2.1
1.75	31.2	52.3	16.5
1.65	38.5	25.7	35.8
1.45 (Silicon Dioxide)	32.9	0	67.1

Note: No Significant Change in Si, N, and O Composition Before and After Annealing

There are several factors that interrelated and enhanced each other to prolong the initial transient period in PECVD processing, such as the initial variation of RF power gas impedance. The RF power required a short period of time to reach its steady state. During this transient period, changes in electron temperature and density distribution will occur, thus varying the reactive species concentrations and the composition of deposited films. The reactant and inert carrier gases used in PECVD processes have different gas impedance which directly affect the electron density and temperature of the plasma. During the initial stages of the deposition process, some of the reactant gases are broken down to by-products of silane, for example, Si_2H_6 , SiH_2 , SiH_3 , SiH , and Si , and thereby change the total gas impedance. A

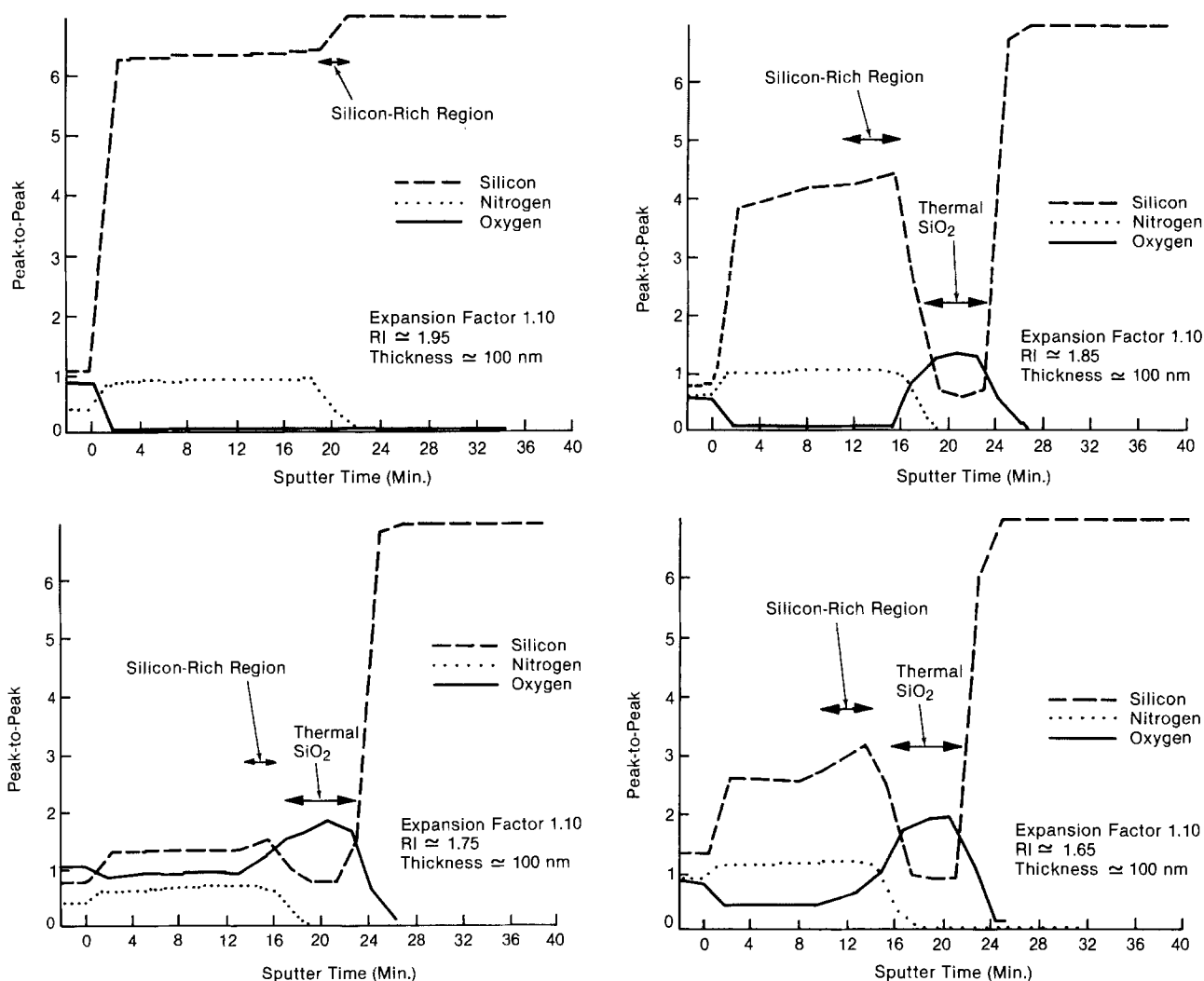
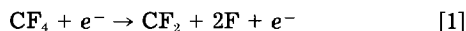


Fig. 4. Auger depth profiles for a (top left): silicon nitride (refractive index = 1.95), b (top right): silicon oxynitride (refractive index = 1.85), c (bottom left): silicon oxynitride (refractive index = 1.75), and d (bottom right): silicon oxynitride (refractive index = 1.65).

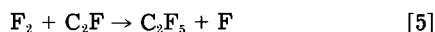
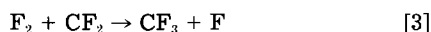
transient period is required to stabilize the plasma to steady state.

Due to the weaker Si-H bonds of silane as compared to N-H bonds of ammonia and N-O bonds of nitrous oxide, more silane is broken into reactive species during initial transient periods. This will substantially increase the concentration ratio of Si/N reactive species during initial transient periods compared to those of steady-state plasma. Therefore, more silicon will be deposited on the substrate during this period, thus creating the silicon-rich interface phenomena in all plasma-deposited silicon nitride and oxynitride films. In a previous presentation (15), we showed a direct correlation between Si-rich interfaces in plasma-deposited films and initial transient phenomena in PECVD processes.

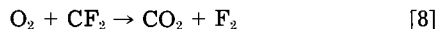
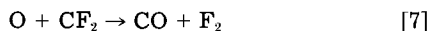
Plasma etching.—In pure CF₄ plasma under low pressure and high frequency conditions, reactive fluorine atoms (F) and fluorocarbon radicals are produced by electron-impact dissociation reaction as follows (16)



Other unsaturated species, such as C₂F₄, are formed in secondary reactions between fluorocarbon radicals, especially those involved with CF₂. In CF₄ plasma, both F and F₂ react with unsaturated species by the following reactions



With the addition of oxygen to the plasma, oxygen atoms will be generated in the plasma. Both O and O₂ will compete with free fluorine atoms for CF₂ by the following reactions



The addition of oxygen gas in CF₄ plasma will then increase the concentration of reactive fluorine atoms (17). In the absence of ion bombardment, fluorine atoms react slowly with SiO₂ (18). As we have shown, IR and AES data indicate all increased number of Si-O bonds and oxygen concentration as the silicon oxynitride film's refractive index decreases. In terms of bond energy, the relative strength of Si-O bonds is greater than that of Si-H, Si-Si, and Si-N bonds (11). Films with lower refractive indices will etch more like SiO₂, which requires ion bombardment of the surface for etching at reasonable rates (19-22). Under fixed etching conditions, *i.e.*, the same ion bombardment and reactive species concentrations, films with higher oxygen concentration will etch slower. This is consistent with the film etch rate results shown in Table III. A decrease in film refractive index from 1.95 to 1.65 corresponds to a decrease in etch rate for both as-deposited and after-annealed films.

Another factor strongly influencing the etch rate of plasma-deposited films is the amount of hydrogen incorporated in the film. Again, in terms of bonding, the Si-H is the weakest of the four types of silicon bonds present, and therefore has the highest probability of being broken by electron and ion bombardment, leaving the reactive Si sites available for fluorine atoms to attack during the plasma-etch process. Thus, in films with a large number of Si-H bonds, one would expect a greater number of reactive Si sites and faster etch rates. Films with more hydrogen content are also less dense and more easily penetrated by fluorine atoms. This phenomena is observed in the annealed *vs.* as-deposited films. The IR data indicate a large reduction in the number of Si-H bonds present after anneal, while Auger analysis showed

Table III. Plasma etching of silicon nitride and oxynitride films

*Etching Conditions:		
+ Power	= 400 watts	
+ Pressure	= 250 mmTorr	
+ Flow Rates:		
- CF ₄	= 147 sccm	(8% O ₂ in CF ₄)
- O ₂	= 13 sccm	

* Etch Rates (Average):		
Film Refractive Index	As Deposited (Å / Minute)	Annealed (Å / Minute)
1.95	1950	830
1.85	2100	520
1.75	930	400
1.65	510	370
LPCVD Si ₃ N ₄	200	

no significant change in Si, N, or O composition after annealing. The dramatic decrease in the film's etch rate observed after annealing is apparently due to loss of hydrogen during the anneal cycle. The loss of hydrogen translates to a decrease in the easily activated Si-H sites, a denser structure, and possibly more Si-N, Si-O, and Si-Si bonds. Low pressure chemical vapor deposition (LPCVD) silicon nitride films which contain much less hydrogen etched at slower rates of 20 nm/min.

Etch profiles of the plasma films also vary due to a different film composition. Figure 5 shows the photoresist-plasma film-silicon substrate structure under examination. The pictures in Fig. 6a and 7a show the difference in etch profile between the unannealed and annealed samples with refractive indices of 1.95. A large undercut is clearly observed for the unannealed sample. Since reactive species such as fluorine (F) and unsaturated CF_n radicals can etch Si-H sites readily without any ion bombardment, isotropic etching will occur (23). This isotropic mechanism will result in a larger undercut in unannealed films where substantial amounts of Si-H and N-H exist. As we have previously discussed, the number of Si-O bonds is significantly higher in the lower refractive index film, and films with these types of bonds require ion bombardment to achieve reasonable etch rates. Since ion bombardment is a directional process, higher etch rates will be observed in the vertical direction. Films with high oxygen concentration, therefore, have more anisotropic etching properties and less undercut. This is consistent with the observation that the undercut for silicon oxynitride samples with refractive indices of 1.65 (Fig. 6b and 7b) are slightly less than that for the silicon nitride samples (Fig. 6a and 7a). While substantial improvement in the undercut length was observed for silicon nitride (*n* = 1.95) samples after annealing (Fig. 6a and 7a), no significant difference in undercut profiles was found between annealed silicon oxynitride (RI = 1.65) samples (Fig. 7b). This indicates a larger influence of oxygen over hydrogen in relatively stoichiometric silicon oxynitride film. It is therefore possible to obtain a range of desirable

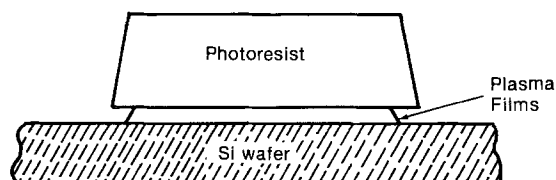


Fig. 5. Photoresist-plasma film-silicon substrate profiles

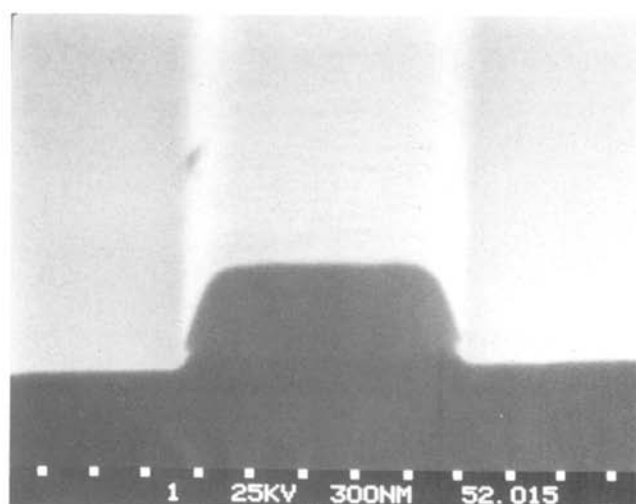
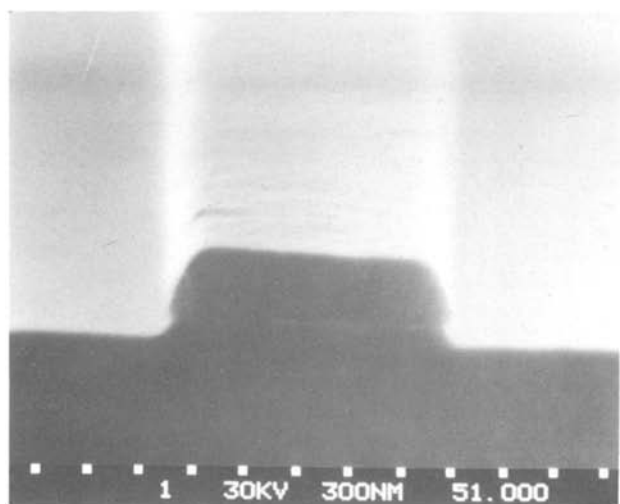
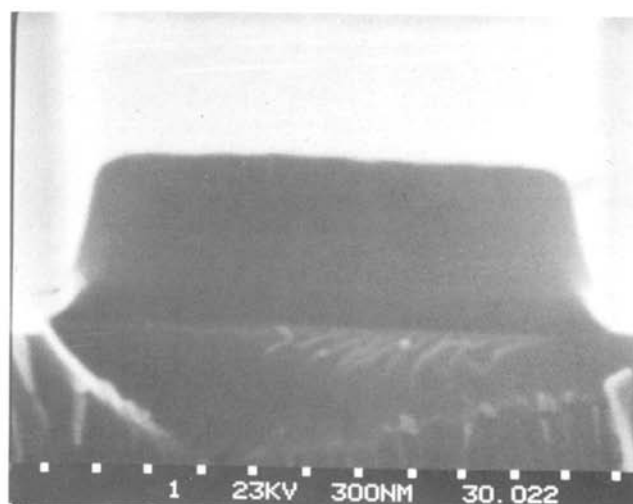
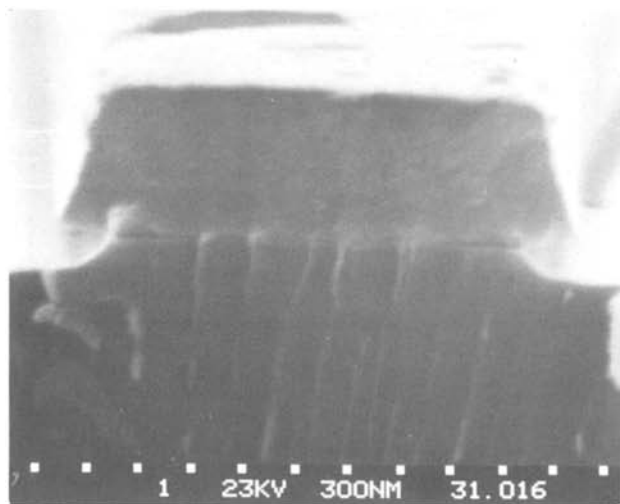


Fig. 6. SEM etch profiles of (a, top) PECVD film and (b, bottom) PECVD silicon nitride film with refractive index = 1.95.

Fig. 7. SEM profiles of (a, top) annealed PECVD silicon nitride film with refractive index = 1.95 and (b, bottom) annealed PECVD silicon oxynitride film with refractive index = 1.65.

etch profiles in plasma-deposited films not only by varying the etching conditions (plasma *vs.* reactive ion etching), but also by varying the film's oxygen and hydrogen compositions.

Conclusion

Good uniformity silicon nitride and silicon oxynitride films with refractive indices varying between 1.60 and 1.95 were deposited on silicon and silicon dioxide substrate surfaces using plasma-enhanced chemical vapor deposition (PECVD) processing. In terms of uniformity, nitrous oxide was found to be a better oxygen source for plasma silicon oxynitride deposition. In our previous study (9), He was found to be a very efficient carrier gas in the plasma compared to other inert gases at low silane concentration.

Infrared and Auger analyses show the films deposited under the described conditions contain significant amounts of hydrogen. Substantial loss of hydrogen was observed after annealing. The concentration of other species, such as Si, N, and O, however, remains unchanged. Infrared analysis of hydrogen band intensities suggests that silicon oxynitride films with a refractive index of 1.75 are probably more stable during thermal annealing. Although ellipsometer measurements showed that film thickness and refractive index uniformity are good, Auger depth profiles revealed poor compositional uniformity during the first 10-30 nm of deposition for all experimental films examined. This nonuniformity is due to the variation of electron temperature and silane reactive-species concentration during the first few minutes of

deposition processing, *i.e.*, the initial transient instability in RF power and gas impedances.

Direct correlation between etching properties of plasma-deposited films and their oxygen and hydrogen compositions was observed. Under identical etching conditions, plasma etch rates of plasma-deposited films decreased with decreased hydrogen concentration (upon annealing) and with increased oxygen concentration in film composition. Variations of etch profiles are also found to be directly correlated to hydrogen and oxygen concentration. Oxygen concentration appears to have a larger influence than hydrogen on etching properties of silicon oxynitride. The changes in etch rate and etch profiles corresponds well to the variation of hydrogen and oxygen concentration. These changes can be explained by the variation of bond energies and the etch-rate enhancement by ion bombardment.

Acknowledgments

The authors wish to thank Peggy Gibson of the Chemical Analysis Laboratory for infrared analysis and David Dobuzinsky for his special effort in tool maintenance. Invaluable discussions and advice from Dr. H. J. Geipel are also highly appreciated.

Manuscript submitted Jan. 6, 1984; revised manuscript received May 15, 1984.

IBM Corporation assisted in meeting the publication costs of this article.

REFERENCES

1. K. Takasaki, K. Koyama, and M. Takagi, Abstract 298, p. 767, The Electrochemical Society Extended Abstracts, Vol. 80-2, Hollywood, FL, Oct. 5-10, 1980.
2. K. Suzuki, J. Matsui, and T. Torikai, *J. Vac. Sci. Technol.*, **20**, 191 (1982).
3. H. Kotami, H. Harada, and K. Tsukamoto, Report no. 1A-R-5 at the 29th Meeting of the Japan Society of Applied Physics, April, 1982.
4. K. Tshibashu and M. Marsumura, *Appl. Phys. Lett.*, **41**, 454 (1982).
5. G. M. Samuelson and K. M. Mar, *This Journal*, **129**, 1773 (1982).
6. W. A. Lanford and M. J. Rand, *J. Appl. Phys.*, **49**, 2473 (1978).
7. P. S. Percy, H. J. Stein, B. L. Doyle, and S. T. Picaux, *J. Electron. Mater.*, **8**, 11 (1979).
8. H. J. Stein, V. A. Well, and R. E. Hampy, *This Journal*, **129**, 1750 (1979).
9. V. S. Nguyen, Abstract 136, p. 216, The Electrochemical Society Extended Abstracts, Vol. 83-1, San Francisco, CA, May 8-13, 1983.
10. M. Noda and H. Ishida, *Jpn. J. Appl. Phys.*, **21**, 195 (1982).
11. "C. R. C. Handbook of Chemistry and Physics," R. C. Weast, Editor, 62nd Edition, C. R. C. Press, Inc., Boca Raton, Florida (1982).
12. R. Chow, W. A. Lanford, and W. Ke-Ming, Abstract 299, p. 770, The Electrochemical Society Extended Abstracts, Vol. 80-2, Hollywood, FL, Oct. 5-10, 1980; R. Chow, R. S. Rosler, W. A. Lanford, and K.-M. Wang, Abstract 294, p. 732, The Electrochemical Society Extended Abstracts, Vol. 81-1, Minneapolis, MN, May 10-15, 1981.
13. T. Yoshima and K. Tanaka, Abstract 198, p. 531, The Electrochemical Society Extended Abstracts, Vol. 78-2, Pittsburgh, PA, Oct. 15-20, 1980.
14. D. Llic, *Solid State Technol.*, **25**, 91 (1982).
15. V. S. Nguyen, Extended Abstract B2, Electronic Material Conference, The Metallurgical Society of AIME, Burlington, VT, June 22-24, 1983.
16. D. L. Flamm, V. M. Donnelly, and D. E. Ibbotson, *Semiconductor International*, **4**, 108 (1983).
17. D. L. Flamm and V. M. Donnelly, *Plasma Chem. Plasma Proc.*, **1**, 371 (1981).
18. D. L. Flamm, V. M. Donnelly, and J. A. Mucha, *J. Appl. Phys.*, **52**, 3633 (1981).
19. J. W. Coburn and H. F. Winter, *J. Appl. Phys.*, **50**, 3189 (1979).
20. E. Kay and J. W. Coburn, *ibid.*, **43**, 4965 (1972).
21. Y. Y. Tun, T. J. Chuang, and H. F. Winters, *Phys. Rev.*, **23**, 823 (1981).
22. V. Gerlach-Meyer, J. W. Coburn, and E. Kay, *Surf. Sci.*, **103**, 177 (1981).
23. H. F. Winters, *J. Appl. Phys.*, **49**, 5165 (1978).

Device Processing Aspects of Ion Beam Nitridation

J. R. Troxell

General Motors Research Laboratories, Electronics Department, Warren, Michigan 48090-9055

D. E. Moss

Delco Electronics Division of General Motors Corporation, Advanced Engineering, Kokomo, Indiana 46902

ABSTRACT

Silicon nitride local oxidation masking layers fabricated by low energy nitrogen ion implantation into silicon have been employed in the fabrication of n-channel silicon-gate MOSFET's. Processing considerations which are unique to the application of these very thin (10 nm) silicon nitride films are detailed. The effects of oxygen contamination during implantation are described, as are those of subsequent wafer processing steps such as RCA cleaning and oxygen plasma photoresist stripping. It is also shown that resputtered material from the wafer holder can result in iron contamination of the resulting silicon nitride films. Finally, we show that careful attention to these possible problems can produce transistors with reasonable current-voltage characteristics, as compared to conventionally processed devices.

The implantation of low energy nitrogen ions into silicon has been shown to result in the formation of a thin film of silicon nitride in intimate contact with the underlying silicon. This silicon nitride layer forms a suitable mask to prevent oxidation of the underlying silicon during the local oxidation process which is typically employed in silicon integrated circuit processing to isolate adjacent devices.

Because no silicon dioxide is present between the silicon and silicon nitride layers, the lateral encroachment of silicon dioxide into active device regions (the "bird's beak" effect) is minimized (Fig. 1), allowing increased device packing densities. In this paper, we characterize the aspects of the implantation process which affect the properties of the resulting silicon nitride film when it is employed in integrated circuit fabrication processes.

Experimental

All samples described in this study were cleaned by the RCA procedure (1) prior to nitrogen implantation. Oxidations were performed either in steam or in burnt hydrogen. Both 5 and 7.5 cm diam silicon wafers of varying resistivity were used. Nitrogen implantations were performed in a commercial 15 cm diam beam ion mill (2, 3), with the ion beam incident perpendicular to the wafer surface, unless otherwise noted. The ion beam was neutralized with a hot wire (thoriated tungsten) filament in order to avoid surface charging and consequent nonuni-

formities in the implanted layer. The samples were mounted on a water-cooled stage and rotated within the ion beam in order to increase process uniformity. The presence or absence of sample cooling did not affect either the film thickness or its oxidation resistance. Silicon dioxide film thicknesses were measured using a surface profiler, while studies of the composition of the implanted silicon nitride film were performed using Auger electron spectroscopy. The fabrication of active transistors was achieved using a conventional n-channel MOS process, except for the local oxidation step. Details of the electrical characterization of these devices and process parameters will be covered in a subsequent publication.

Ion Beam Nitridation

In order to minimize the problems associated with lateral oxidation, it is necessary to eliminate any silicon dioxide which may be present between the silicon nitride layer and the silicon surface. This is achieved by forming the silicon nitride layer by nitrogen ion implantation into the silicon substrate (4-8). The nitride layer thus formed is beneath the silicon surface, its exact position and thickness being dependent upon the implantation parameters. With a Kaufman-type ion source (9, 10), it is possible to achieve nitrogen ion fluences of $8.01 \text{ E}17 \text{ cm}^{-2}$ in 2 min. (For the commercial ion mill used in this study, the actual typical cycle time, including vacuum pump-down and venting, is 15 to 20 min.)

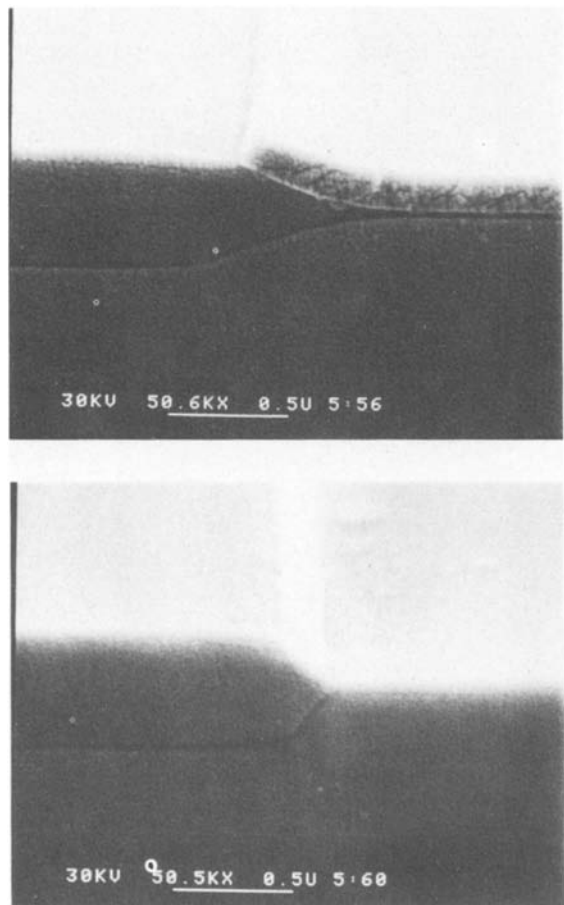


Fig. 1. Comparison of lateral oxidation during field oxide growth for (a, top) conventional deposited silicon nitride mask and (b, bottom) low energy ion-implanted silicon nitride mask. Samples were oxidized simultaneously at 1180 K for 320 min. The significant reduction of the bird's beak in (b) results from the absence of a silicon dioxide layer beneath the silicon nitride mask.

Because nitrogen can chemically bond to silicon, a significant portion of the incident nitrogen remains in the sample after implantation. Typical Auger spectroscopy concentration profiles of the resulting films are shown in Fig. 2. Essentially no change is observed in these profiles after the films have been subjected to nitrogen ambient anneals at 750° and 1050°C. Although the sputtering rate for nitrogen ions is less than that for argon, erosion of the substrate wafer will still occur, as will be demonstrated in the following discussion. Thus, the result of the nitrogen implantation process at these low energies involves a balance between the implantation and erosion processes.

The variation of silicon nitride film thickness with implantation energy is shown in Fig. 2. Film thickness is found to be relatively insensitive to implantation energy. For implantation energies of 1.9-2.1 keV, the resulting silicon nitride film thickness may be estimated at approximately 12 nm. This value is comparable to values reported by Chiu *et al.* (11). Ellipsometric measurements of as-implanted films yielded parameter values of $\Psi = 15.4$ and $\Delta = 151$. Following a nitrogen anneal at 750° or 1050°C, values of $\Psi = 13.9$ and $\Delta = 172$ were observed. Reduction of these values to yield nitride film thicknesses was hindered by the lack of an independently measured value for the index of refraction of the nitride film and by the presence of a silicon dioxide film at the surface. Similar difficulties have been reported by Chiu *et al.* (11), and for nitride films implanted at higher energies, by Tsujide and Nojiri (12). The effect of ion beam induced sputter erosion upon the silicon is shown in Fig. 3. Here, erosion rate data are presented for the case of a 2.1 keV, 1 mA cm^{-2} nitrogen ion beam. The ion beam-induced erosion

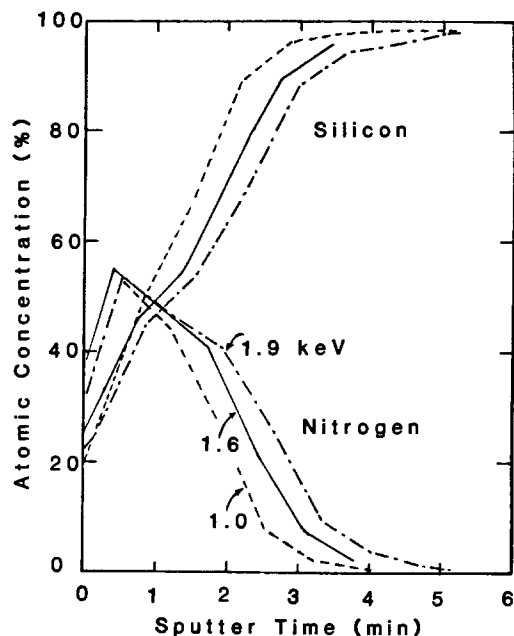


Fig. 2. Dependence of silicon nitride film thickness upon implantation energy. All implants were performed for 2 min with a 1.0 mA cm^{-2} beam. Auger spectroscopy sputtering rate was approximately 4 nm/min.

rate for silicon is found to be about 25 nm/min, while that for silicon dioxide is about 58 nm/min. These values may be compared to the erosion rate observed when 2.1 keV argon ions are employed, which is about 76 nm/min for both silicon and silicon dioxide. The dependence of implanted layer profile upon incident nitrogen ion dose is shown in Fig. 4. Reducing the implantation time (and therefore the dose) by a factor of 10 to $8.0 \text{ E}16 \text{ cm}^{-2}$ does not change the nitrogen concentration profile. Upon further reducing the implanted ion dose by a factor of ten (in this case, by reducing the ion beam current density to 0.1 mA cm^{-2}), a reduction in the implanted nitrogen profile is observed.

The resistance of these thin silicon nitride layers to thermal oxidation in steam is shown in Fig. 5. Although the silicon nitride films successfully mask the growth of 780 nm of silicon dioxide at 970°C, they are completely consumed prior to the growth of 420 nm of silicon dioxide at 1070°C. Using the oxidation model of Deal and Grove (13, 14), one can estimate the time required to grow the amounts of silicon dioxide shown in the three cases in which the silicon nitride layer was totally consumed. In turn, this provides an estimate of the amount of time required to break down the silicon nitride layers them-

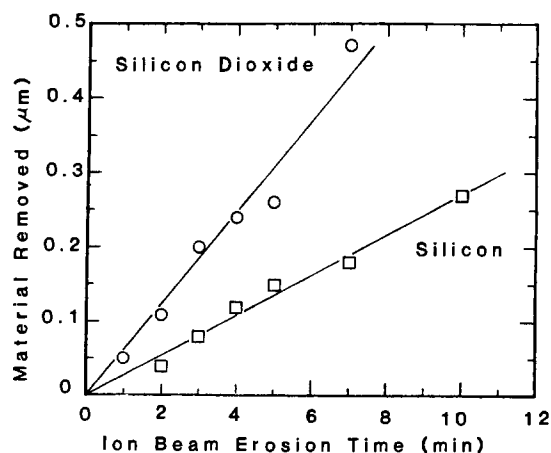


Fig. 3. Material erosion during low energy nitrogen implantation. Data taken for 2.1 keV, 1.0 mA cm^{-2} , 2 min implantations.

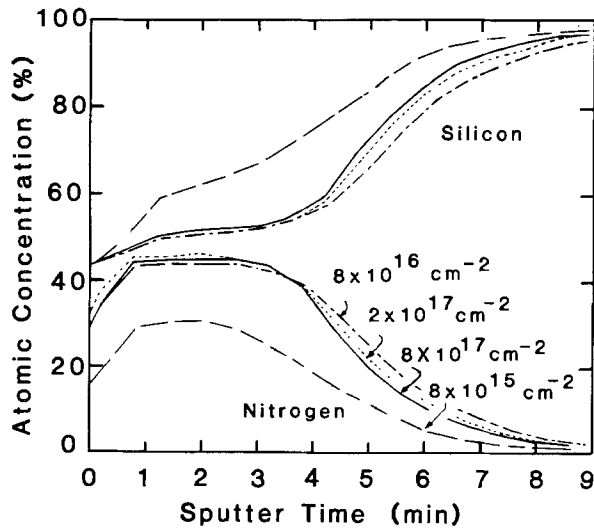


Fig. 4. Dependence of silicon nitride film profile upon nitrogen implant dose. Implants were performed at an energy of 2.1 keV and beam current density of 1.0 mA cm^{-2} (except 0.1 mA cm^{-2} for the total dose of 8.0 E15 cm^{-2}). Auger spectroscopy sputtering rate was approximately 2.5 nm/min.

selves. By then assuming a linear oxidation rate (5) for the silicon nitride layer, this data can be compared with the data of Hui *et al.* (5) and the linear oxidation rates of silicon in both wet and dry ambients (11, 12), as shown in Fig. 6.

The oxidation resistance of these silicon nitride films is also dependent upon their initial impurity content, the most obvious contaminant being oxygen. Oxygen contamination can arise from trace oxygen content in the nitrogen gas source or from air leaks in the vacuum system. The presence of oxygen during implantation results in a thinner silicon nitride layer being produced, with a resulting reduction in oxidation resistance. For example, when a partial pressure of 18% oxygen was maintained in the ion mill vacuum system during implantation, the silicon nitride layer was consumed after 1.6h of wet oxidation at 1210 K. This contrasts with a time of 3.2h, which is observed when no oxygen is intentionally introduced into the system. Conversely, a 40% partial pressure of oxygen during implantation reduced this time to 1.1h.

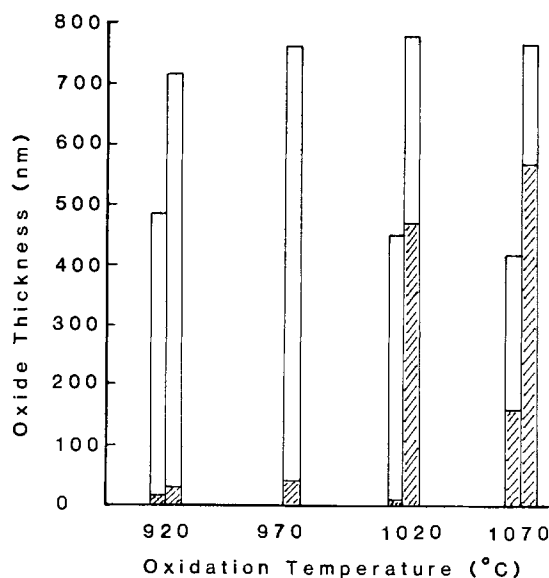


Fig. 5. Oxidation resistance of implanted silicon nitride films as a function of wet oxidation temperature for two sets of samples with nominal 450 and 750 nm field oxides, respectively. The crosshatched regions represent the resulting amount of silicon dioxide grown in the implanted regions following nitride breakdown, while the open regions represent the corresponding field oxide thickness.

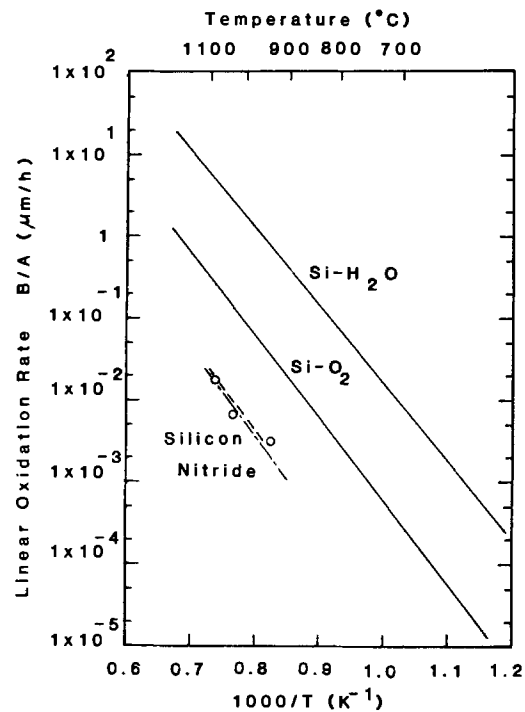


Fig. 6. Variation of oxidation rates with temperature for implanted silicon nitride films assuming an initial film thickness of 10 nm. Also shown is the oxidation rate data measured by Hui *et al.* (5), for both ion-implanted (— — —) and plasma-deposited (----) silicon nitride and the linear oxidation rates for $\langle 111 \rangle$ silicon (—), in both wet and dry ambients (13, 14). (More recent work by Deal (28) reports slightly different oxidation rates for $\langle 111 \rangle$ silicon, and notes that the oxidation rate for $\langle 100 \rangle$ silicon is a factor of 1.7 slower for both oxygen and water vapor ambients.)

Additional oxygen contamination in these thin silicon nitride films can result from the wafer cleaning procedures employed just prior to high temperature oxidation. Typically, an RCA-type cleaning procedure (1) is employed prior to inserting the wafers into the diffusion tube. This subjects the thin silicon nitride film to an oxidizing agent, hydrogen peroxide. In addition, in many cases, the silicon nitride film will have been exposed to the oxygen plasmas which are generally used to remove photoresist. In either case, atomic oxygen is available to attack the silicon-nitrogen bonds.

In the case of RCA cleaning, we have found that properly prepared basic and acidic cleaning solutions oxidize only the surface layers of the nitride films, and thus do not normally constitute a major problem. Figure 7 displays the atomic concentration profiles of three samples which were simultaneously implanted with nitrogen. Figure 7a represents a control sample which was not subjected to any subsequent processing, while each sample in Fig. 7b was exposed to one of the RCA solutions for 10 min. The samples characterized in Fig. 7c were not exposed to either of the RCA cleaning solutions, but had been exposed to an oxygen plasma for either 15 or 30 min. The oxygen plasma is more effective in attacking silicon nitride, but still leaves a significant portion of the silicon nitride film intact.

In addition to oxygen, carbon is typically detected in ion beam-nitrided silicon films. The carbon is detected primarily near the exposed surface of the silicon nitride, with its concentration dropping off farther into the film. The observed carbon profile is similar to that detected following argon ion bombardment of silicon, suggesting that it may, in part, result from material adsorbed onto the sample surface following nitrogen implantation. The carbon profiles do not change as the silicon nitride is oxidized, which suggests that it is not being driven into the silicon substrate, and thus may be removed when the silicon nitride layer is removed.

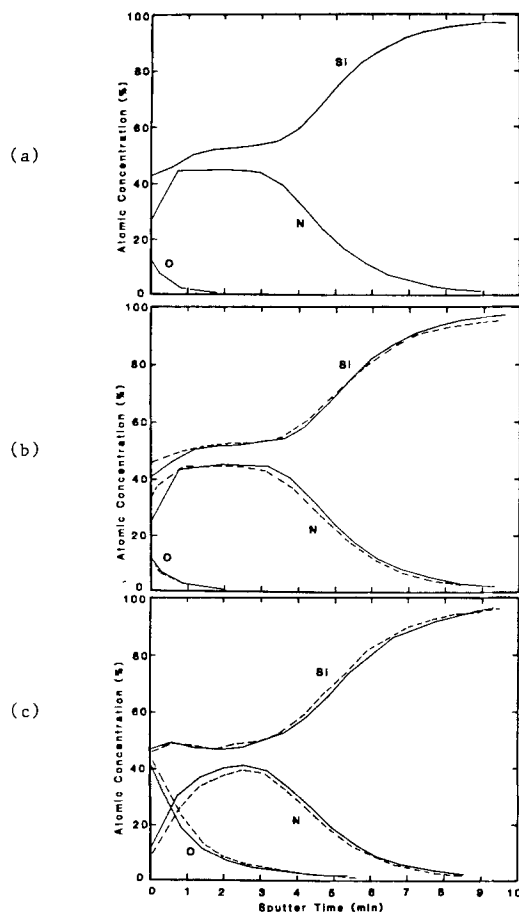


Fig. 7. Auger spectroscopy concentration profiles of ion-implanted silicon nitride films simultaneously prepared and subjected to various wafer cleaning procedures. (a): Control, as-implanted sample. (b): Samples cleaned for 10 min in basic (ammonium hydroxide, —) and acidic (hydrochloric acid, ---) RCA cleaning solutions at 360 K. (c): Samples exposed for 15 (—) or 30 min (---) to a photoresist stripping oxygen plasma (350W at 0.133 kPa oxygen pressure). Auger spectroscopy sputtering rate was approximately 2.5 nm/min.

A final source of contamination involves the platen on which the sample wafers are mounted. Because the ion beam-nitridation process is essentially a low energy sputtering process in which the incident ions "stick" to the substrate being bombarded, there is a potential problem associated with resputtering of the substrate holder material. In the present case, the wafer supporting platen was made of aluminum, while the hold-down clamp which is used to improve heat transfer from the wafers to the water-cooled substrate is fabricated in stainless steel. Thus, when the hold-down clamp is used, iron, chromium, and nickel traces are detected in the 10 nm thick silicon nitride film. Alternatively, when the hold-down clamp is not used, and the support platen is not completely covered with silicon wafers, aluminum is detected. In either case, peak concentrations of the contaminant metals can reach several atomic percent. The contaminant distributions shown in Fig. 8 are typical of those observed when the sample holder is not coated with silicon nitride. The fact that the iron concentration reaches a maximum near the silicon-silicon nitride interface is not understood, although it may result from a buildup of a relatively inert iron nitride film on the surface of the sample holder as the nitridation process continues. This could reduce the amount of iron which is resputtered, and serve to lower the contaminant concentration near the surface of the silicon nitride film.

Typical leakage-current measurements for $250 \times 250 \mu\text{m}$ junction diodes fabricated using both local oxidation processes are shown in Fig. 9. The enhanced leakage in the case of the ion beam-nitrided devices is not completely understood at present, since Wright etching of ion

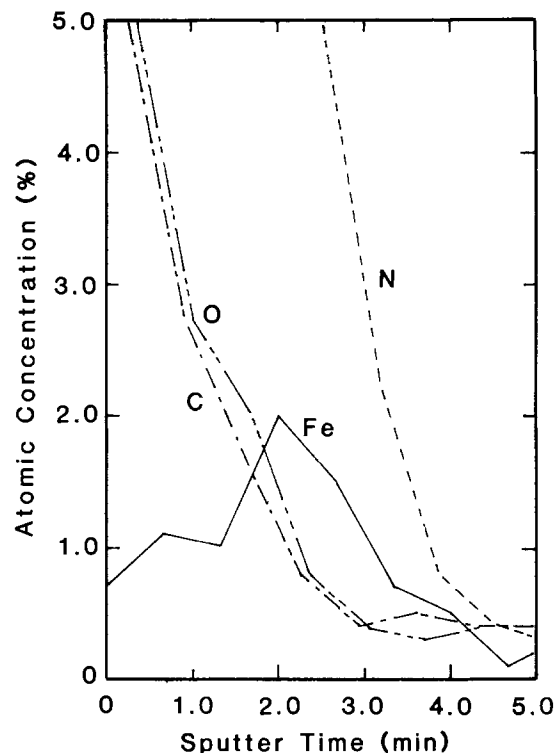


Fig. 8. Auger spectroscopy profile detailing presence of typical contaminants, oxygen (---), carbon (-.-.), and, when an untreated sample holder is used, iron (—), which was resputtered from the stainless steel platen. Sample was implanted with nitrogen (---) at 2.1 keV, 1.0 mA cm^{-2} , for 2 min. Auger spectroscopy sputtering rate was 4.0 nm/min .

beam-nitrided regions following local oxidation does not reveal an increased density of etch pits, as compared to similarly etched samples fabricated using the conventional local oxidation process. In addition, n-channel silicon gate MOSFET's were fabricated. Ion beam nitridation parameters for the local oxidation step included a beam

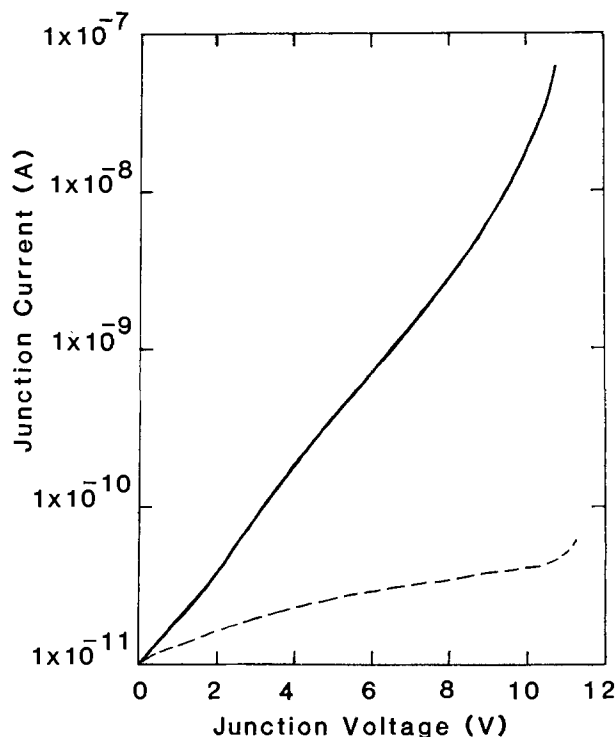


Fig. 9. Comparison of junction diode leakage currents for devices fabricated using either ion beam nitridation (—) or a conventional local oxidation process (---) during the growth of a 510 nm thick isolation oxide film. Diode junction area = 4.4 E4 cm^2 .

energy of 2.1 keV and a beam current density of 1.0 mA cm^{-2} . Some wafers were simultaneously processed using a conventional local oxidation process employing 80 nm of plasma-deposited silicon nitride on top of a thermally grown 60 nm thick silicon dioxide layer. All of the wafers were then etched in hot phosphoric acid to delineate the transistor mesa regions, and thermally oxidized at 900°C for 280 min in burnt hydrogen, yielding a field oxide layer 690 nm thick. All subsequent processing was identical for both the ion beam-nitrided and conventionally processed samples. The goal in this work was to evaluate the reduction of device channel width (from W to W' , see Fig. 10) resulting from the conventionally local oxidation process and any changes in effective device width (W') which result from the use of ion beam nitridation.

Discussion

As shown in Fig. 2, silicon nitride film thickness is relatively insensitive to the energy of the implanted nitrogen ions. For comparison, the mean range of nitrogen ions implanted into silicon with an energy of 2.1 keV is approximately 6.0 nm (15). Essentially doubling the incident ion energy is found to increase film thickness by less than 40%. This relative insensitivity to ion beam energy is primarily a result of the simultaneous physical erosion of the silicon surface due to sputtering. Samples implanted at an angle of 45° [the angle for which the sputter erosion rate approaches a maximum (16, 17)] show a significant reduction in nitride film thickness when compared to the results shown in Fig. 2. To be sure, implantation at a 45° angle will reduce the effective perpendicular range of the incident ions by about 30%, but this is not sufficient to explain the magnitude of the observed reduction in film thickness. Also, we obtain essentially identical Auger concentration profiles for samples implanted at angles of 0.0°, 7.0°, and 10.0° with respect to normal incidence.

These observations are confirmed by the data presented in Fig. 3, which show an erosion rate of about 25 nm/min for nitrogen implantation of silicon, as compared to a typical erosion rate of about 76 nm/min for argon ion bombardment under the same conditions. Part of this reduction in sputtering rate is a result of the reduced sputtering yield of nitrogen ions as compared to that of argon

ions (2), but a substantial amount of this difference is due to the bonding of the incident nitrogen ions into the silicon lattice when they come to rest. By comparison, the sputtering rate of silicon dioxide under 2.1 keV argon ion bombardment is also 76 nm/min (for a beam current density of 1.0 mA cm^{-2}), while the rate for nitrogen ion bombardment is about 58 nm/min. In this case, where there is less opportunity for the nitrogen atoms to find available bonding sites to silicon atoms, the sputtering rate is 2.3 times higher than that for a silicon substrate. This differential etching behavior has been used to develop a novel contact window opening process (18), which requires only a single photolithography step. Similar reductions in erosion rate have been documented for argon ion milling of metallic layers in an oxygen ambient (19-21), wherein the oxygen bonds to the metal atoms, forming a metallic oxide surface layer. Effectively, this results in an increase in the number of atoms which must be sputtered from the surface in order to remove a given number of metal atoms, and thus the sputtering rate is effectively reduced.

In addition to being relatively insensitive to implantation energy, the nitrogen concentration profile is also independent of the number of implanted ions, or implantation dose, as shown in Fig. 4. Implantation doses as low as 8.0 E16 cm^{-2} result in nitrogen profiles which are essentially identical to those for implantation doses a factor of ten larger. Further reductions in implantation dose below 8.0 E16 cm^{-2} , however, result in a reduction of the maximum nitrogen concentration within the films, leaving a silicon-rich silicon nitride film.

The oxidation resistance of these ion beam-nitrided silicon films (Fig. 5, 6) agrees well with the data of Hui *et al.* (5), having an oxidation activation energy of about 2.0 eV. The absence of any change in either nitrogen concentration profile or oxidation resistance following a nitrogen ambient anneal is consistent with results in the literature. Hezel and Lieske (7) find no change in Auger spectra following a nitrogen anneal, although they do observe a slight increase in silicon-nitrogen bonding, as measured by low energy electron spectroscopy. Similarly, Ramin *et al.* (22) find no change in infrared absorption with annealing, although they do observe "slightly improved" oxidation resistance. The reduction in this oxidation resistance as a result of oxygen contamination during implantation can be significant, and demonstrates the need for a leak-free vacuum system and a low oxygen content nitrogen source. A similar concern must be shown for any wafer cleaning processes employed while the silicon nitride layer is present. Although a properly performed RCA cleaning procedure does not seriously affect the silicon nitride layer, we have observed that, if the basic solution (hydrogen peroxide and ammonium hydroxide) becomes depleted of hydrogen peroxide, the silicon nitride layer will be rapidly etched, as will the underlying silicon, by the ammonium hydroxide. This is consistent with the observations of Kern and Puotinen (1), who point out the problem of hydrogen peroxide depletion, and suggest limiting the use of the basic solution to less than 40 min. Finally, it should be noted that although the proper application of typical cleaning processes may not seriously reduce the oxidation resistance of the silicon nitride films, the repeated application of these cleaning steps (for example, two exposures to the oxygen plasma as a result of poor photolithography results) can consume a major portion of the 10 nm thick silicon nitride film.

The problem of heavy metal contamination, as evidenced by the Auger data in Fig. 8, is potentially fatal to any semiconductor processing technique. However, the existing evidence suggests that the most likely source of this contamination is the wafer holder assembly. Thus, a relatively simple solution to this problem, then, is to coat both the hold-down clamp and the platen with a relatively inert material, such as plasma-deposited silicon or silicon nitride. Although this coating must be periodically renewed, this has essentially eliminated the metal contamination problem within the detection limits of Auger spectroscopy (less than 1 atomic percent). In addition,

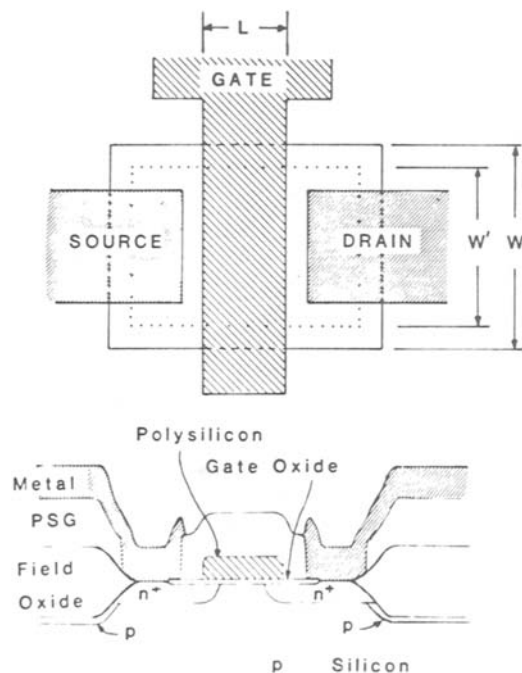


Fig. 10. Plan and cross-sectional views of a typical MOSFET transistor. Of importance for the present discussion are the channel length, L , and width, W , and the change in the latter (to W') which results from a change in the size of the device well (from — to) due to lateral oxidation.

transient capacitance measurements (23) of junction diodes fabricated in ion beam-nitrided device wells show no evidence of the relatively well-characterized iron-related defect levels (24, 25) in the underlying silicon. Thus, although it is necessary to exercise some caution in this regard, it appears that the metal contamination problem is controllable.

The effects of local oxidation-induced stress and/or contamination upon the performance of devices fabricated using ion beam nitridation is not well understood. Hui *et al.* (26) have reported enhanced leakage current in diodes fabricated using the SILO process with a plasma nitridation step, even though (4) they generally detect no increase in stress-induced defects associated with the use of these very thin nitrided-silicon films. Our results, measured on $250 \times 250 \mu\text{m}$ junction diodes (Fig. 10) show even larger leakage currents in ion beam nitrided samples. At present, we can offer no explanation as to the exact origin of the enhanced leakage current, although deeply penetrating nitrogen ions which were not removed along with the silicon nitride film and/or residual unannealed implantation damage could produce such effects.

The photomask set used to fabricate the devices for which current-voltage curves appear in Fig. 11, contains device patterns with mask dimension channel widths and lengths which vary from 4.0 to 10.0 μm . As shown in Fig. 10, the conventional local oxidation process results in a reduction in the dimensions of the active device well or mesa region. Only the channel width of the transistor is directly affected by this shrinkage, however, since the transistor channel length is determined by the dimension of the polysilicon gate. Having a mask set with both variable channel lengths (L) and widths (W), then, allows one to evaluate the effects of a change in channel width due to the local oxidation process used, while allowing for the possibility of other variations in photoresist processing or polysilicon etching between samples. Such an approach is necessary since the device drain current is proportional to the ratio of the effective channel width (W') to the effective channel length (L). A detailed analysis of the electrical properties of the devices fabricated in this study, using the analysis technique described by Chern *et al.* (27), will appear in a subsequent publication. These results are qualitatively described, however, by the current voltage characteristics shown in Fig. 11. For devices of similar (W/L) mask dimensions, the electrical characteristics of the ion beam-nitrided devices are generally similar to those which were fabricated using the conventional local oxidation process. Thus the fabrication of active de-

vices using the ion beam-nitridation process does result in devices with reasonable electrical characteristics.

Summary

Ion beam nitridation of silicon using a conventional ion milling machine is a quick, efficient way to form a thin silicon nitride layer on silicon, which may be employed to fabricate active devices with reasonable current-voltage characteristics. For typical nitrogen ion beam parameters of 2.1 keV acceleration potential and 1.0 mA cm^{-2} beam current density, incident ion doses of $8.0 \text{E}17 \text{ cm}^{-2}$ can be achieved in 2 min, resulting in the formation of a silicon nitride film approximately 10 nm thick. As a result of the simultaneous occurrence of implantation and sputter erosion, this process is very insensitive to variations in the implantation process, resulting in uniform, reproducible silicon nitride films. In addition, this coincidence of implantation and sputter erosion can be used to advantage in a novel contact opening process. Subsequent wafer processing steps such as RCA cleaning or oxygen plasma photoresist stripping can attack the resulting thin film, but their effects can be minimized with proper attention to the process parameters. Finally, the fabrication of active devices using the ion beam-nitridation process to mask the growth of a 690 nm thick field oxide results in transistors with reasonable current-voltage characteristics, being qualitatively comparable to those of devices fabricated simultaneously, but using a conventional local oxidation process.

Acknowledgments

The authors gratefully acknowledge the contributions of J. C. Erskine, K. C. Jain, D. Heilman, D. A. Butler, M. I. Harrington, and J. Biafora towards the completion of this work. Also, we would like to acknowledge the AES measurements of S. W. Gaarenstroom and R. A. Waldo and the SEM work of W. H. Lange.

Manuscript submitted Feb. 6, 1984; revised manuscript received May 31, 1984.

General Motors Corporation assisted in meeting the publication costs of this article.

REFERENCES

- W. Kern and D. A. Puotinen, *RCA Rev.*, **31**, 187 (1970).
- E. G. Spencer and P. H. Schmidt, *J. Vac. Sci. Technol.*, **8**, S52 (1971).
- W. Laznovsky, *Res./Dev.*, **26**, 47 (1975).
- J. C. Hui, T. Y. Chiu, S. Wong and W. G. Oldham, *IEEE Trans. Electron. Devices Lett.*, **ed1-2**, 244 (1981).
- J. C. Hui, T. Y. Chiu, S. W. S. Wong, and W. G. Oldham, *IEEE Trans. Electron. Devices*, **ed-29**, 554 (1982).
- N. Lieske and R. Hezel, *Thin Solid films*, **85**, 7 (1981).
- R. Hezel and N. Lieske, *This Journal*, **129**, 379 (1982).
- G. E. Thomas, L. J. Beckers, F. H. P. M. Habraken, and A. E. T. Kuiper, *Appl. Phys. Lett.*, **41**, 56 (1982).
- H. R. Kaufman, J. J. Cuomo, and J. M. E. Harper, *J. Vac. Sci. Technol.*, **21**, 725 (1982).
- J. M. E. Harper, J. J. Cuomo, and H. R. Kaufman, *ibid.*, **21**, 737 (1982).
- T. Y. Chiu, H. Bernt, and I. Ruge, *This Journal*, **129**, 408 (1982).
- T. Tsujide and M. Nojiri, *J. Appl. Phys.*, **51**, 1605 (1980).
- B. E. Deal and A. S. Grove, *ibid.*, **36**, 3770 (1965).
- E. H. Nicollian and J. R. Brews, "MOS Physics and Technology," pp. 667-681, John Wiley and Sons, New York (1982).
- K. Bruce Winterbon, "Ion Implantation Range and Energy Deposition Distributions," Vol. 2, IFI/Plenum, New York (1975).
- S. Hosaka and S. Hashimoto, *J. Vac. Sci. Technol.*, **15**, 1712 (1978).
- R. E. Lee, *ibid.*, **16**, 164 (1979).
- J. K. Bhagat and J. R. Troxell, *This Journal*, **130**, 2293 (1983).
- M. Cantagrel and M. Marchal, *J. Mater. Sci.*, **8**, 1711 (1973).
- M. Cantagrel, *IEEE Trans. Electron. Devices*, **ed-22**, 483 (1975).
- H. Dimigen and H. Luthje, *Philips Tech. Rev.*, **35**, 199 (1975).
- M. Ramin, H. Ryssel, and H. Kranz, *Appl. Phys.*, **22**,

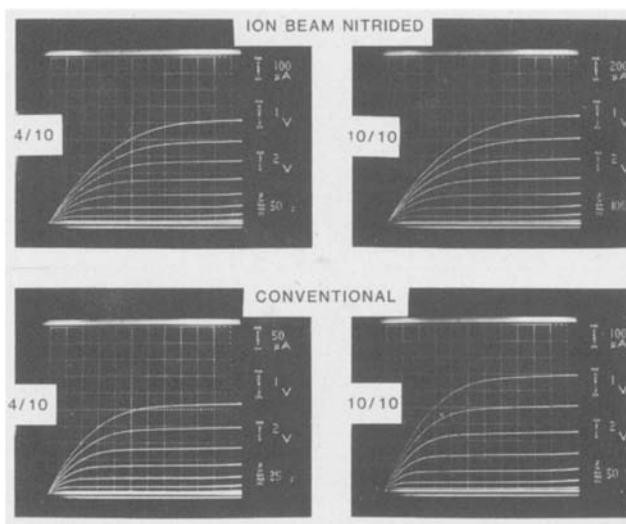


Fig. 11. Current-voltage characteristics for typical devices fabricated using either the conventional local oxidation process or ion beam nitridation. Data is shown for both narrow ($W/L = 4/10 \mu\text{m}$) and wide ($W/L = 10/10 \mu\text{m}$) devices. In each case, the maximum gate voltage is 20V.

- 393 (1980).
 23. J. R. Troxell, Unpublished data (1982).
 24. J. L. Benton and L. C. Kimerling, *This Journal*, **129**, 2098 (1982).
 25. K. Graff and H. Pieper, in "Semiconductor Silicon 1981," H. R. Huff, R. J. Kriegler, and Y. Takeishi, Editors, p. 331, The Electrochemical Society Softbound Proceedings Series, Princeton, NJ (1981).
 26. J. C. Hui, T. Y. Chiu, S. Wong, and W. G. Oldham, 1982 *IEDM*, **220**, Paper 9.2 (1982).
 27. J. G. J. Chern, P. Chang, R. F. Motta, and N. Godino, *IEEE Trans. Electron. Devices Lett.*, **edl-1**, 170 (1980).
 28. B. E. Deal, in "Semiconductor Technology," D. A. Doane, D. B. Fraser, and D. W. Hess, Editors, p. 15, The Electrochemical Society Softbound Proceedings Series, Pennington, NJ (1983).

Germanium Doping of InP Films Grown by Liquid Phase Epitaxy

B. H. Chin and R. E. Frahm

AT&T Bell Laboratories, Murray Hill, New Jersey 07974

ABSTRACT

We have investigated Ge doping at high concentrations in InP films grown at 648°-640°C on <100> InP by liquid phase epitaxy. Hall measurements show that the carrier concentration saturates at $\sim 9 \times 10^{18} \text{ cm}^{-3}$ for a mole fraction of Ge in the liquid (χ_{Ge}^l) greater than 0.10. In the carrier-saturation regime, the Ge concentration in the solid, as measured by secondary ion mass spectroscopy, increases superlinearly with χ_{Ge}^l . Transmission electron microscopy reveals no precipitate formation.

In the liquid phase epitaxy (LPE) of InP, tin is the usual n-type dopant. For strongly doped <100> layers, however, we have recently shown that tin is not suitable (1) because the carrier concentration ($N_D - N_A$) saturates at $\sim 6 \times 10^{18} \text{ cm}^{-3}$. As an alternative n-type dopant, germanium is particularly attractive on account of its high purity and low vapor pressure. Ge doping at high concentrations has received considerable attention in bulk InP crystals grown by liquid-encapsulated Czochralski (LEC) (2-4), highly doped LPE films, however, have not been well characterized. Rosztochy *et al.* (5) grew Ge-doped layers on <111> B substrates at a growth temperature of 650°-600°C. A linear relationship between ($N_D - N_A$) and χ_{Ge}^l , the mole fraction of Ge in liquid indium solution, was observed up to $\chi_{\text{Ge}}^l = 0.17$, corresponding to ($N_D - N_A$) = $2.6 \times 10^{19} \text{ cm}^{-3}$; the distribution coefficient was determined to be $k = 0.011$. Similar results were obtained by Astles *et al.* (6), who grew layers on <111> A, <111> B, and <100> substrates at $\sim 650^\circ\text{C}$. The doping behavior was essentially the same for all faces: ($N_D - N_A$) vs. χ_{Ge}^l was linear up to $\chi_{\text{Ge}}^l = 0.10$, corresponding to ($N_D - N_A$) = $8 \times 10^{18} \text{ cm}^{-3}$; the derived distribution coefficient was $k = 0.005$. Last, Kuphal (7) found a value of $k = 0.005$ for <100> layers grown at $\sim 700^\circ\text{C}$; the ranges of χ_{Ge}^l and ($N_D - N_A$) were not stated.

In this paper, we present a detailed study of <100> layers doped up to $\chi_{\text{Ge}}^l = 0.18$. The layers have been characterized by the following techniques: (i) Hall measurements to determine the carrier concentration ($N_D - N_A$), (ii) secondary ion mass spectroscopy (SIMS) to monitor the Ge concentration in the solid, c_{Ge}^s (atoms/cm³), and (iii) transmission electron microscopy (TEM) to probe for the presence of precipitates.

Experimental

Since we have previously described our experimental procedures in detail (1), we shall recap only the salient features here. The epitaxial layers were grown from two-phase, indium-rich, solutions onto <100>-oriented, Fe-doped, semi-insulating InP substrates. To minimize the variation of distribution coefficient with temperature, the layers were deliberately grown over a narrow temperature interval, 648°-640°C, at a cooling rate of 0.7°C/min. The carrier concentrations in the epitaxial layers were subsequently determined by Hall measurements in the van der Pauw configuration; for rapid, accurate data acquisition, a fully computer-controlled apparatus was utilized (8). To monitor actual Ge concentrations, SIMS depth profiles¹

were performed on the samples; a Cs⁺ ion source was used for sputtering, and the mass 72 Ge peak was monitored. Conversion of the SIMS signal levels to atomic concentrations was achieved by comparison with signals from an ion-implanted standard. For TEM analysis, a 3 mm diam disk was ultrasonically cut from a wafer. After the substrate had been polished down to $\sim 25 \mu\text{m}$ with bromine-methanol, a number of small holes were opened up near the center of the disk with a jet polish of bromine-methanol.

Results

In Fig. 1, we have plotted the room temperature values of ($N_D - N_A$) as a function of χ_{Ge}^l . [Note that χ_{Ge}^l has been calculated from $\chi_{\text{Ge}}^l \approx M_{\text{Ge}}/(M_{\text{In}}^0 + M_{\text{Ge}})$, where M_{Ge} and M_{In}^0 are, respectively, the number of moles of pure Ge and pure In in solution. A direct measurement of the solubility of InP verified that the dissolved InP may be neglected over the range of χ_{Ge}^l considered here.] The background level in nominally undoped layers was $< 1 \times 10^{17} \text{ cm}^{-3}$, an order of magnitude less than the lowest intentional doping level. For $\chi_{\text{Ge}}^l < 0.10$, ($N_D - N_A$) increases lin-

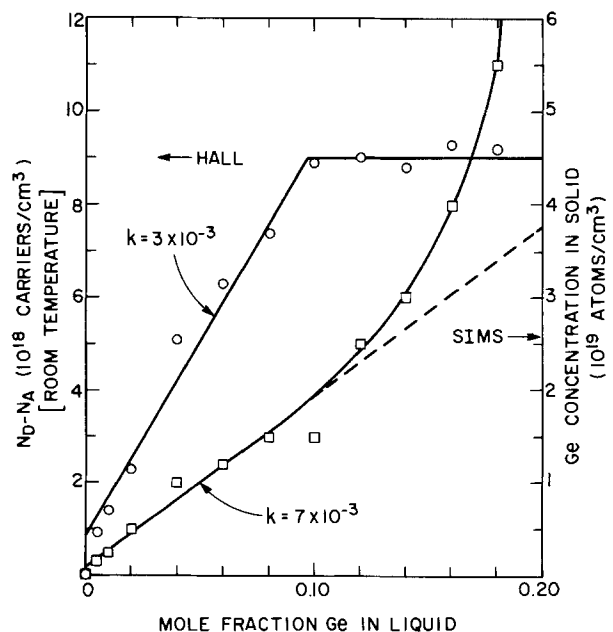


Fig. 1. Plot of room temperature carrier concentration and germanium concentration as a function of mole fraction germanium in liquid.

¹SIMS analysis performed by C. A. Evans and Associates, San Mateo, California.

early with χ_{Ge}^1 ; the extracted value of the distribution coefficient is $k = 0.003$. [Here, we use the definition of k found in Ref. (6) and (7).] For $\chi_{\text{Ge}}^1 > 0.10$, $(N_D - N_A)$ saturates at $\sim 9 \times 10^{18}/\text{cm}^3$.

Carrier saturation may be induced by a number of causes. The principal ones are: (i) a solubility limit of Ge in the liquid is attained, (ii) a solubility limit of Ge in the solid is attained, (iii) Ge is incorporated into neutral or acceptor sites as well as donor sites, and (iv) the background acceptor level from impurities increases with χ_{Ge}^1 . (More involved mechanisms, such as defect complexes, may, of course, also be invoked.) The trivial case, (i), may be dismissed because direct measurement of the Ge solubility in an InP solution indicated that, over the whole range of χ_{Ge}^1 considered here, the solutions were undersaturated with respect to Ge.

To distinguish among the remaining cases, the samples were analyzed by SIMS and TEM. First, wide-field SIMS scans of three samples, with $\chi_{\text{Ge}}^1 = 0, 0.020$, and 0.18 , respectively, showed no significant increase of background impurities with increasing χ_{Ge}^1 . Second, the values of c_{Ge}^s were measured by SIMS; they are plotted as a function of χ_{Ge}^1 in Fig. 1. For $\chi_{\text{Ge}}^1 < 0.10$, we see that c_{Ge}^s varies linearly with χ_{Ge}^1 . Within the accuracy of the SIMS calibration (\sim a factor of two), there is general agreement between the values of c_{Ge}^s measured by SIMS and those expected from the Hall measurements. The value of the distribution coefficient derived from the SIMS data is $k = 0.007$. In the carrier saturation regime, $\chi_{\text{Ge}}^1 > 0.10$, the SIMS results reveal a curious behavior: c_{Ge}^s does not saturate but, rather, increases superlinearly with χ_{Ge}^1 .

Since the SIMS data suggests the possibility of precipitate formation, the most highly doped samples, with $0.06 \leq \chi_{\text{Ge}}^1 \leq 0.18$, were examined by TEM. To a resolution of $\sim 20\text{\AA}$, however, the TEM analysis failed to reveal any precipitates. Our result is in accord with the analysis of highly Ge-doped InP grown by LEC. Although Brown *et al.* (2) first reported precipitates in bulk crystals doped to $\sim 10^{19}/\text{cm}^3$, they later attributed the features in their TEM images to etching artifacts (9).

Summary

We have investigated Ge doping in InP films grown on $\langle 100 \rangle$ InP by LPE over the temperature range $648^\circ\text{--}640^\circ\text{C}$. The net carrier concentration $(N_D - N_A)$ determined from Hall measurements varies linearly with χ_{Ge}^1 up to $\chi_{\text{Ge}}^1 = 0.10$; the extracted distribution coefficient is $k = 0.003$. For $\chi_{\text{Ge}}^1 \geq 0.10$, $(N_D - N_A)$ saturates at $\sim 9 \times 10^{18}/\text{cm}^3$. Measurements by SIMS show that the atomic concentration of Ge in the solid, c_{Ge}^s , also varies linearly with χ_{Ge}^1 up to $\chi_{\text{Ge}}^1 = 0.10$; the value of k determined from the SIMS data is 0.007 . For $\chi_{\text{Ge}}^1 \geq 0.10$, c_{Ge}^s varies superlinearly with χ_{Ge}^1 . At low doping levels, our measurements are in reasonable agreement with previous work (5-7). Our results for high doping levels, however, do not agree with those of Rosztochy *et al.* (5), who found no evidence of carrier saturation up to $\chi_{\text{Ge}}^1 = 0.17$, corresponding to $(N_D - N_A) = 2.6 \times 10^{19}/\text{cm}^3$. This discrepancy is probably due to the differences in the following growth conditions

which may affect dopant incorporation (10-12): (i) substrate orientation, (ii) growth temperature, (iii) cooling rate, and (iv) growth rate. In our work, films were grown on $\langle 100 \rangle$ substrates at a temperature of $648^\circ\text{--}640^\circ\text{C}$ and a cooling rate of $0.7^\circ\text{C}/\text{min}$; the resulting growth rate was typically $\sim 0.5 \mu\text{m}/\text{min}$. In the work of Rosztochy *et al.* (5), however, films were grown on $\langle 111 \rangle$ B substrates at a temperature of $650^\circ\text{--}600^\circ\text{C}$ and a cooling rate of $5^\circ\text{C}/\text{min}$ (growth rates were not given).

In conclusion, then, our data show that, under our particular growth conditions, Ge probably behaves as a simple donor at low doping levels ($\chi_{\text{Ge}}^1 \leq 0.10$). The Hall and SIMS measurements, however, may also indicate dopant incorporation at a fixed compensation ratio. At high doping levels ($\chi_{\text{Ge}}^1 > 0.10$), the mechanism of dopant incorporation is more complex and not determined. Although the superlinear variation of c_{Ge}^s vs. χ_{Ge}^1 , as measured by SIMS, is consistent with the nucleation and growth of precipitates (13), TEM failed to reveal precipitates. The possibility of precipitates not detected by TEM must, of course, be further explored.

Acknowledgments

We would like to thank T. T. Sheng and S. Nakahara for TEM analysis, W. A. Bonner for supplying the substrates, and R. H. Saul for helpful comments on the manuscript.

Manuscript submitted March 26, 1984; revised manuscript received May 14, 1984.

AT&T Bell Laboratories assisted in meeting the publication costs of this article.

REFERENCES

1. B. H. Chin, R. E. Frahm, T. T. Sheng, and W. A. Bonner, *This Journal*, **131**, 1373 (1984).
2. G. T. Brown, B. Cockayne, and W. R. MacEwan, *J. Cryst. Growth*, **51**, 369 (1981).
3. J. O. Williams, E. S. Crawford, G. T. Brown, and B. Cockayne, *J. Mater. Sci. Lett.*, **1**, 499 (1982).
4. B. Cockayne, G. T. Brown, W. R. MacEwan, and G. W. Blackmore *ibid.*, **2**, 309 (1983).
5. F. E. Rosztochy, G. A. Antypas, and C. J. Casau, in "1970 Symposium on GaAs and Related Compounds Aachen," K. Paulus, Editor, p. 86, Inst. Phys. Conf. Ser. 9, Institute of Physics, London (1971).
6. M. G. Astles, F. G. H. Smith, and E. W. Williams, *This Journal*, **120**, 1750 (1973).
7. E. Kuphal, *J. Cryst. Growth*, **54**, 117 (1981).
8. R. E. Frahm, Unpublished data.
9. G. T. Brown, B. Cockayne, W. R. MacEwan, and D. J. Ashen, *Mater. Sci. Lett.*, **2**, 667 (1983).
10. G. A. Antypas and L. Y. L. Shen, in "1976 Symposium on GaAs and Related Compounds, St. Louis," L. F. Eastman, Editor, p. 96, Inst. Phys. Conf. Ser. 33b, Institute of Physics, London (1977).
11. K. Akita, A. Yamaguchi, K. Nakajima, and T. Takanohashi, *Electron. Lett.*, **24**, 921 (1981).
12. K-H. Zschauer and A. Vogel, in "1970 Symposium on GaAs and Related Compounds, Aachen," K. Paulus, Editor, p. 100, Inst. Phys. Conf. Ser. 9, Institute of Physics, London (1971).
13. K. R. Lawless, *Rep. Prog. Phys.*, **37**, 231 (1974).

Phosphorus-Doped Polycrystalline Silicon via LPCVD

I. Process Characterization

B. S. Meyerson*

IBM T. J. Watson Research Center, Yorktown Heights, New York 10598

W. Olbricht

Cornell University, Ithaca, New York

ABSTRACT

We have studied the low pressure chemical vapor deposition (LPCVD) process as applied to the preparation of *in situ* phosphorus-doped polycrystalline silicon films. Thickness profiling, electron microprobe, and mass spectrometry have been utilized in the characterization of this process. The addition of phosphine (PH_3) as the dopant bearing precursor molecule was found to result in a factor of 25 decay in film growth rates relative to the intrinsic LPCVD process. The physical and chemical characteristics of samples prepared in this manner are shown to be a strong function of local reactor geometry, with growth-rate variations of a factor of two within a wafer commonly observed. Mass spectrometry data is presented supporting the proposal that phosphine passivates the silicon surface, and the implications of this phenomenon for altering silicon growth kinetics are discussed. A model is presented accounting for the growth-rate variations observed within individual wafers, as well as for the sensitivity of the phosphine-doped process to system geometry.

In recent years, as technology has made increasingly severe demands on the physical uniformity, conformality, and chemical homogeneity of materials for use in LSI and VLSI devices, significant advances have been made in the area of thin film deposition, particularly in the field of low pressure chemical vapor deposition (LPCVD) (1-4). LPCVD is especially attractive in that one may deposit large numbers (~200) of highly conformal, uniform films ($\pm 2\%$) in a single run. A chemical system where this technique works particularly well is the pyrolysis of silane (SiH_4) to yield intrinsic polycrystalline silicon films (1). A logical extension of the LPCVD technique would be to the preparation of *in situ* doped polycrystalline silicon by the introduction of the phosphorus bearing precursor phosphine (PH_3) into the intrinsic polysilicon LPCVD process. This technique offers a great reduction in complexity over more conventional doping technologies, which in general rely on the post-deposition implantation (5) of dopant, or the indiffusion of dopant from a dopant-rich layer applied to the sample surface (6). Although *in situ* doping is straightforward in concept, the introduction of silicon/phosphorus chemistry into this previously well-characterized technique causes a rapid degradation of the LPCVD process, with severe growth-rate suppression and film inhomogeneity two primary difficulties encountered. In this paper, the first in a set of two, macroscopic phenomena observed during the LPCVD preparation of *in situ* phosphorus-doped polycrystalline silicon are discussed. In the second paper of this set, a variety of surface science techniques are applied to study the microscopic interactions of silane and phosphine with silicon surfaces, and thus better understand the underlying mechanisms responsible for the problems observed in this paper.

Experimental

Samples were prepared in an LPCVD system configured as shown in Fig. 1. The LPCVD system consists of a 4 in. bore quartz furnace tube, pumped by a Leybold Haereus WS150 roots blower backed by a D30AC mechanical pump. An Inficon IQ200 mass spectrometer was used to analyze furnace effluent as well as initial process gas quality. Source gases supplied to the system were silane (SiH_4), phosphine (PH_3), and argon as an inert purge gas. Films were deposited on 2.25 in. diam Si substrates which had been thermally oxidized to a depth of 900Å, allowing thickness profiling of deposited films using interferometry (IBM Film Thickness Analyzer). Samples were placed in the twentieth slot of a 35 wafer

carrier, wafers mounted coaxially on 0.16 in. centers. Remaining slots were filled with blanks (wafers not removed run to run) to maintain carrier symmetry. Silane input was 30.0 sccm, with pressure maintained at 100 μm via a pressure feedback loop to a servo-controlled butterfly valve in series with the roots blower. Depositions were carried out at 623°C, for both the case of pure silane and a range of silane/phosphine mixtures. Subsequent to deposition, films were profiled for both thickness (using the FTA) and phosphorus content (by electron microprobe).

Results

We display in Fig. 2 the sharp contrast between films obtained from pure silane (A) vs. those obtained upon the addition of 2.5% phosphine (0.75 sccm) to the source gas (B). The addition of phosphine to the silane LPCVD process results in the suppression of film deposition rates by over an order of magnitude, and is accompanied by the onset of severe nonuniformity in thickness of the films deposited. The degree of growth rate inhibition as well as the uniformity of both film thickness and phosphorus content are strong functions of the interwafer spacing, and this is displayed, respectively, in Fig. 3 and 4. As the spacing upstream of the test wafer is increased, by the sequential removal of blanks immediately upstream, one observes a reduction in film thickness variation as well as an increase in deposition rate, but both remain at great variance to the intrinsic case. In addition, the bulk phosphorus content of the films drops from 3.0% to 1.8% with increasing interwafer spacing. Although inferior in uniformity, the phosphorus-doped films were of good quality otherwise, with pinhole densities and surface textures comparable with their intrinsic counterparts.

Figure 5 displays mass spectrometry data obtained while monitoring furnace effluent during film depositions from increasing ratios of phosphine to silane input gas at 623°C and 100 μm pressure. The partial pressure of unreacted silane in the reactor exhaust increased discontinuously by approximately 20% upon the addition of less

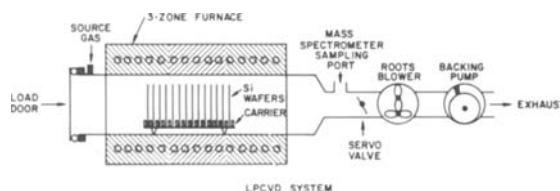


Fig. 1. Schematic of the LPCVD system

*Electrochemical Society Active Member.

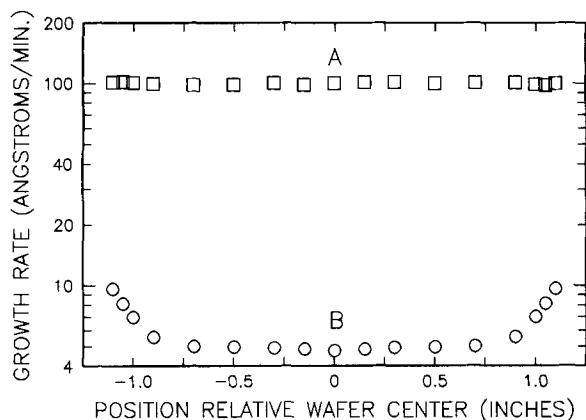


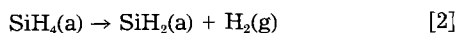
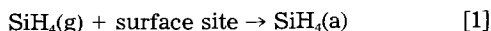
Fig. 2. Deposition rate profile across a wafer diameter for (A) $T_s = 623^\circ\text{C}$, $P = 0.1$ torr, $\text{SiH}_4 = 30.0$ sccm, and (B) as A with $\text{PH}_3 = 0.75$.

than two parts per thousand phosphine to the source gas. Above this phosphine level, the concentration of unreacted silane was found to be relatively insensitive to increased phosphine levels in the source gas. Apart from silane, peaks corresponding to a $1.0 \mu\text{m}$ partial pressure of disilane were also observed in the furnace effluent, although none was present in the source gas itself.

Discussion

During the attempt to produce phosphorus-doped polysilicon films by LPCVD, two serious process failures occurred. The reduction in film deposition rates by a factor of 20 results in unacceptably long time requirements for film deposition, and the lack of physical and chemical homogeneity in films so produced renders them unfit for use in VLSI technology. We consider first the mechanism resulting in the severe growth rate suppression.

To proceed with any form of analysis, it is necessary to establish a model framework for the LPCVD of silicon from silane. We propose, as others (7, 8) have, the reaction sequence



adsorption, decomposition to an intermediate state [the silylene (9) radical is a reasonable candidate], followed by the evolution of remaining hydrogen, Si incorporation, and the structural ordering of the lattice (10). It is unnecessary for the purpose of the following argument to establish the rate limiting step in silane LPCVD. However, examining the mechanism, we find that reaction [1] is the sole point where phosphine could trivially interdict silicon film growth, by preferential adsorption at surface sites. Gas-phase chemistry that one might propose wherein phosphine consumes silane by some mechanism,

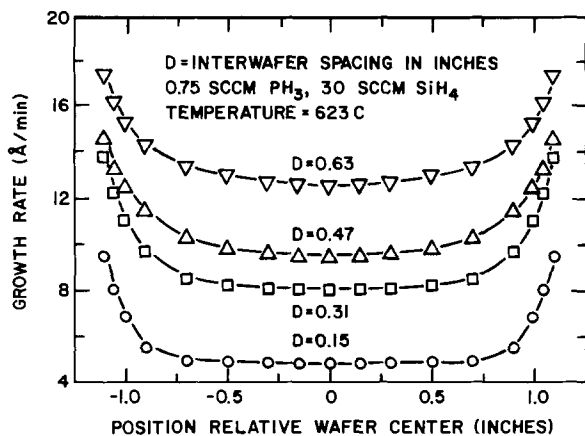


Fig. 3. Deposition rate profile vs. interwafer spacing (D)

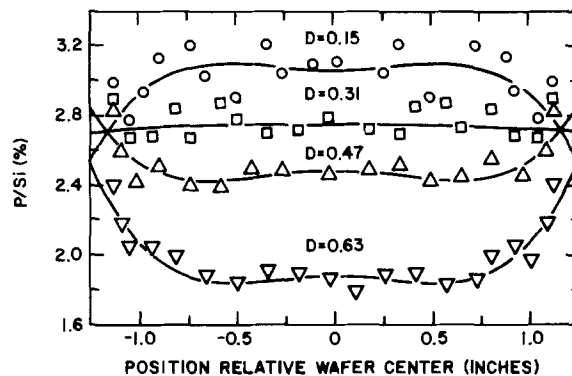


Fig. 4. Phosphorus distribution vs. interwafer spacing

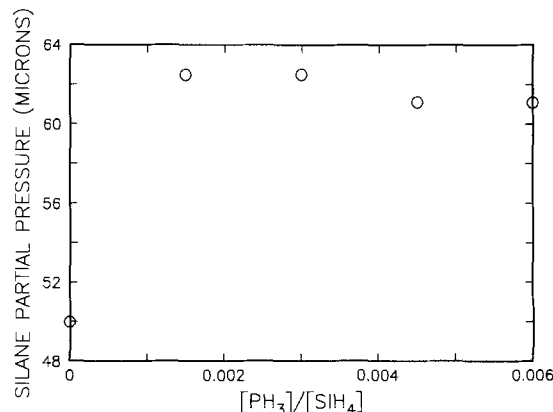


Fig. 5. Residual silane partial pressure vs. phosphine input

thus excluding it from the deposition process, could only produce effects of magnitude $[\text{PH}_3]/[\text{SiH}_4] = 2.5\%$, insufficient to explain the order of magnitude effects we observe. The formation of a stable layer of adsorbed phosphine is plausible as the presence of a lone pair of valence electrons on the phosphine molecule should enable phosphine to compete successfully with silane (a fully coordinated molecule) for available surface sites. One could then postulate the nondissociative adsorption of a stable layer of pentavalent phosphorus bridging adjoining silicon atoms, while one would have to propose a dissociative adsorption scheme for the silane molecule (*i.e.*, hydrogen loss occurs to allow the bonding of silane to the surface). In the second paper of this set, we will seek to demonstrate the validity of this argument by a detailed examination of the interactions of silane and phosphine with the silicon surface.

The second problem encountered upon phosphorus doping was the onset of significant inhomogeneities in films so deposited (Fig. 2 and 3). If we assume this deposition process is first order in reactant flux to the silicon surface, typical for LPCVD, observed growth-rate profiles (Fig. 3) mirror a steep concentration gradient in the active deposition species, having its minimum along the furnace axis in the interwafer region. To understand the origin of the aforementioned reactant concentration gradient, it is necessary to determine the role played in this process by reactant surface kinetics *vs.* reactant transport.

If a reaction is purely surface kinetic controlled, it should result in uniform film deposition, as kinetic control is defined to be the case where reactant flux to the growth surface greatly exceeds the reaction rates of the relevant heterogeneous (surface) chemistry. Thus, reactant transport is far more rapid than depletion, and reactant concentration is only slowly varying with position in the reactor. Conversely, when heterogeneous reaction rates are sufficiently rapid such that reactant transport is the rate limiting step, reactant concentration is a strong function of position within the reactor, as rapid depletion of the film forming species occurs. Hitchman (8)

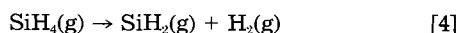
calculates that kinetic control dominates the LPCVD process when using a pure silane source, and states the criteria for uniform deposition (kinetic control) as

$$K \ll D/L, \text{ where } K = (Q/A)Ln(C_{(\text{initial})}/C_{(\text{final})})$$

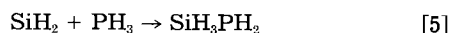
K is an effective heterogeneous rate constant, where D is the diffusion constant of the reactive species, L is the relevant system dimension (the wafer diameter is a good choice if one desires uniform deposition across this dimension), Q is the volume flow per unit time through the reactor, A is defined as the total surface area for the reaction, and C is the reactant concentration. The inequality above has been shown (8) valid for the case of silane LPCVD, so rather than compute anew the values of all terms, it is equally instructive to estimate the effect that the introduction of phosphine has on the terms of the inequality. Upon switching from the undoped to the phosphine-doped process, the quantity D/L remains unchanged, as pressure, temperature, and system geometry are unchanged. Taking C as the silane concentration, our mass spectrometry data show $C_{(\text{initial})}/C_{(\text{final})}$ to decrease by 20%, as silane consumption declines that amount upon the introduction of phosphine. Upon the addition of phosphine, Q/A is unchanged, as silane flow and system geometry are fixed. As defined above, we see K is thus reduced in magnitude as silane consumption falls off with the addition of phosphine. With the inequality above satisfied for the case of undoped silane LPCVD, using the assumptions just stated, it remains satisfied for the case of phosphorus-doped LPCVD as well. This implies that the deposition reaction should remain under kinetic control, with good film uniformity, contrary to experimental evidence.

The aforementioned inconsistency would not have come about had the effective heterogeneous reaction rate increased greatly upon the addition of phosphine. A method for resolving this impasse is to propose that the active species participating in film deposition is no longer predominantly silane. We have already discussed the suppression of silane's heterogeneous decomposition chemistry due to phosphine adsorption. Consequently, we should now consider the possibility that nominally less rapid homogeneous (gas-phase) reactions operating in parallel with the surface chemistry may play a more prominent role in the film forming process.

Utilizing a technique referred to as homogeneous chemical vapor deposition (HOMOCVD), Scott *et al.* (11) have demonstrated that when one quenches silane's rapid heterogeneous decomposition reactions by depositing on a cold ($T < 250^\circ\text{C}$) substrate from a heated silane source ($T_{\text{gas}} > 650^\circ\text{C}$), a film may be grown directly from silylene (SiH_2) produced by the homogeneous decomposition of silane



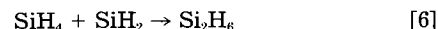
Silylene resulting from the pyrolysis of silane is believed to then insert into Si-H bonds on the silicon surface, resulting in silicon deposition. Both homo- and heterogeneous chemistries were shown to operate in parallel, but the more rapid heterogeneous silane decomposition processes dominate film growth unless they are quenched. In the instance of phosphorus-doped LPCVD, heterogeneous silane chemistry is also greatly suppressed, though in this case by the preferential adsorption of phosphine rather than by cooling the substrate. This effectively increases the fractional contribution of homogeneous chemistry (*i.e.*, deposition from homogeneously generated silylene) to the phosphorus-doped LPCVD process. Although the presence of adsorbed phosphine would quench silane surface chemistry, it would not be expected to interdict film growth due to silylene. Blazejowski and Lampe (12) investigated the insertion of silylene into phosphine's P-H bonds to form monosilylphosphine



and obtained reaction rate constants roughly equal those

found for the insertion of silylene into Si-H bonds. Thus, the substitution of P-H bonds for Si-H at the growth interface in the case of phosphorus-doped LPCVD would not be expected to interfere with film growth by silylene insertion at that surface. Also, in work by Meyerson *et al.* (13), phosphine was used to prepare phosphorus-doped films by HOMOCVD, and films were seen to deposit somewhat more rapidly in the presence of phosphine, leading us to conclude again that phosphine will not degrade the contribution of homogeneous chemistry to the silicon growth process.

In addition to contributing directly to film growth, silylene may also reinsert into silane, producing disilane via reaction [6]



Thus, a series of homogeneous reactions proceed, producing intermediate species such as silylene, disilane, and monosilylphosphine. These species are known to be highly reactive relative to silane. Silylene insertion reactions proceed at near gas kinetic rates (9, 14) (insertion rates equal to collisional frequencies), while disilane's instability relative to silane is well documented (9). Monosilylphosphine was shown (15) to be stable in the gas phase at up to 550°C , yet it is highly unstable in the presence of surfaces, and will decompose to film at ambient temperature. Therefore, the homogeneous generation of these highly reactive species in the reactor environment, in concert with the suppression of silane's heterogeneous contribution to the growth process, serves to enhance the effective reaction rate constant K . Hitchman, using an LPCVD system very similar to ours, obtained values for K and D/L of 1.5 and 3.0×10^3 , respectively, for silane LPCVD, thus satisfying the criteria for uniform deposition with $K \ll D/L$. If we now view the phosphorus-doped LPCVD process as controlled by homogeneously generated precursors such as silylene, we must use the appropriate K value, $K_{(\text{silylene})}$, in the inequality. We may obtain an order of magnitude estimate of the relationship between $K_{(\text{silylene})}$ and $K_{(\text{silane})}$ by noting that Farrow (7) and Janai (16) found values of 10^{-4} and 10^{-6} , respectively, for the decomposition probability of silane when impinged upon a 600°C silicon surface, while silylene reacts with near unity probability. Thus, we may estimate $K_{(\text{silylene})} \approx 10^4 K_{(\text{silane})}$. Consequently, $K_{(\text{silylene})} \sim 1.5 \times 10^4$, *i.e.*, $K_{(\text{silylene})} > D/L$, and one would expect the rapid depletion of this reactant to occur. Reactant transport, therefore, plays a major role in controlling the rate of phosphorus-doped film deposition, and the concentration of active film precursors is a strong function of position within the reactor. A similar argument is possible for disilane, or monosilylphosphine, in that they are all highly reactive relative to silane, but silylene is by far the most reactive and thus the best example.

Viewed as a transport-limited deposition process, phosphorus-doped silicon LPCVD behaves as expected. Depletion of the active species in the interwafer region results in film growth rate profiles as shown in Fig. 3. By symmetry alone it is apparent that film thickness minima will occur along the furnace axis. A variety of methods may be employed to qualitatively model (17) the functional form of the growth rate profiles obtained when deposition is carried out under transport control. In the Appendix, we have conducted a worst case calculation of the expected growth profiles for an LPCVD process operating in this regime. As expected, our model (see Fig. 6 and 7) predicts variations in excess of those observed, though the results are correct in their qualitative dependence of both uniformity and growth rate on the interwafer spacing. Our calculation allows only for the contribution to growth of reactive species generated in the annulus external to the interwafer region, as the transport properties of these species will determine the uniformity of resulting films. The complete process, however, is the sum of several mechanisms operating parallel. A residual contribution to deposition by heterogeneous silane decomposition is present, as well as the contribution by gas-phase reac-

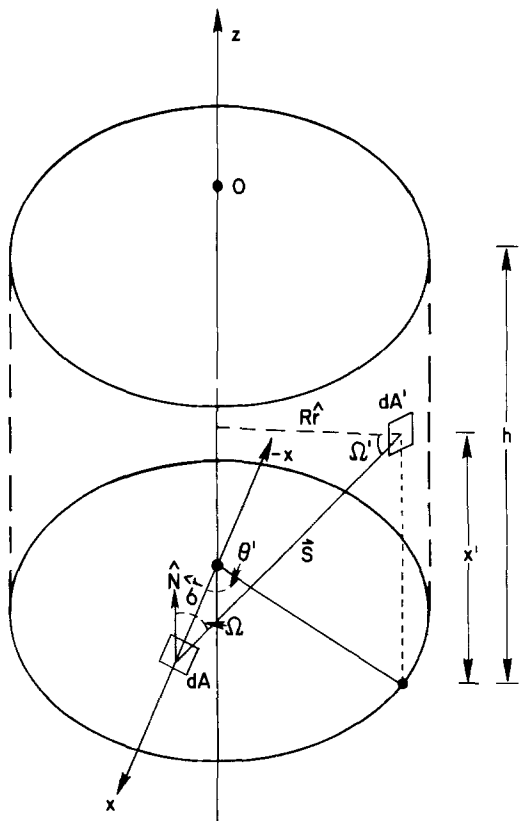


Fig. 6. Geometry of system considered in Appendix (see text)

tions in the interwafer region itself, and both add uniform background deposition rates to the total process. For the case of 0.15 in. wafer separation, taking 4 Å/min as the background, fitting the model curve (Fig. 8) at center and edge to our data results in reasonable agreement across the entire wafer. However, owing to the simplicity of the model, its extension beyond this demonstration cannot be made without an independent measure of the parameters utilized in fitting the curve to the data. This requires that one obtain spatially resolved data on the various gaseous components of the deposition source, and this technology is currently in its infancy.

We have seen in Fig. 4 that both the phosphorus content and its distribution across a given wafer are strong functions of wafer spacing. Workers in the field of gas-phase kinetics have demonstrated (12) the rapid conversion of phosphine to the unstable intermediate monosilylphosphine in the presence of the products of silane pyrolysis. Whether the rate of this conversion leads to the depletion of phosphine in the interwafer region (see Fig. 4), or, alternatively, the spatially varying flux of silicon bearing species to the growth interface interacts with ad-

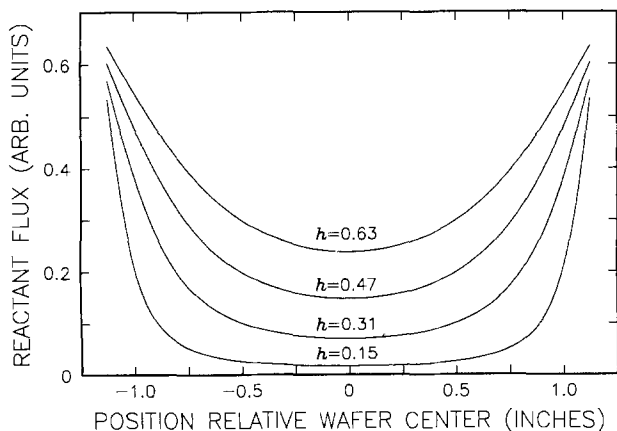


Fig. 7. Growth rate profiles expected for the case of a transport-limited LPCVD process.

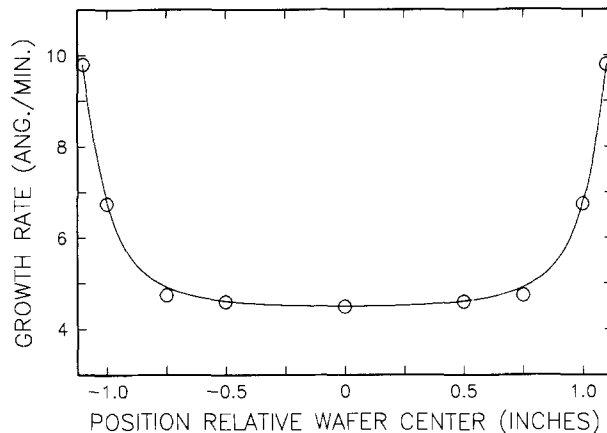


Fig. 8. Data for the case of 0.15 in. interwafer spacing vs. the predicted profile.

sorbed phosphine to produce the phosphorus distributions observed, we are not at present in possession of sufficient data to make a reasonable estimate of the relative importance of these potential mechanisms.

Conclusions

The intrinsic silicon LPCVD technique is not trivially transferable to the preparation of *in situ* doped polycrystalline silicon. The addition of phosphine to the well-characterized pure silane LPCVD process results in both the suppression of film deposition rates by a factor of 20, coupled with a severe degradation of film uniformity. Our results are consistent with the preferential adsorption of phosphine at the growth interface, thus inhibiting heterogeneous silane decomposition chemistry, accounting for the reduction in deposition rates. In the second paper we will examine the manner in which silane and phosphine compete for available surface sites, and therefore further test the conclusion above.

We observe the onset of severe uniformity problems upon the addition of phosphine as a dopant in the silane LPCVD process. This difficulty is attributed to the suppression of heterogeneous silane decomposition chemistry, which allows normally secondary homogeneous chemical processes to play a role of increased importance. The growth rate profiles observed indicate the LPCVD process has been shifted into a transport-controlled regime by the presence of these homogeneously generated film precursors. Mass spectrometry provides evidence for a 1.0 μm partial pressure disilane (Si_2H_6), a highly reactive by-product of the homogeneous decomposition of silane, and thus also supports the presence of its precursor, silylene (SiH_2). We have presented a straightforward model for the limiting case of an LPCVD process operating under transport control, and have demonstrated how this leads to growth rate profiles such as those observed here.

Acknowledgments

The authors wish to acknowledge the help of W. F. Kane in the preparation of the samples used in this study, and also J. Kuptsis for the microprobe analysis of these samples. In addition, we wish to thank J. Blum and B. A. Scott for many helpful discussions in the course of this work.

Manuscript submitted Dec. 9, 1983; revised manuscript received May 2, 1984.

IBM Corporation assisted in meeting the publication costs of this article.

APPENDIX

We will demonstrate the consequences of the presence of highly reactive species within the LPCVD reactor environment by considering the limiting case where the following conditions are met.

1. The molecular mean free path exceeds the interwafer dimension, *i.e.* molecular flow dominates in the interwafer region.

Table I. Predicted vs. observed wafer spacing

Wafer spacing	Variation (observed)	Variation (predicted)
0.15 in.	1.98	30.53
0.31 in.	1.71	8.08
0.47 in.	1.54	4.05
0.63 in.	1.37	2.65
2.0 in.	—	1.10

2. The reactant under consideration has a reaction probability of unity upon impact with the silicon surface.

Condition 2 is actually quite reasonable for a reactant such as silylene, which is known to insert into Si-H bonds at gas kinetics rates (with probability near unity). The conditions above will lead to a worst case prediction of thickness variations within a wafer undergoing LPCVD of an unspecified film, in that deposition is assumed to be due solely to species generated in the gas phase, with that generation process being rate limiting.

The large annular region external to the wafers $R_{\text{furnace tube}} > r > R_{\text{wafers}}$ is taken to be the source of the reactive species (reactant Q), which then enters the interwafer region and is removed by collisions at surfaces. Consider a flux F_0 of reactant Q crossing the differential area dA' on the cylindrical surface defined by the wafer edges (see Fig. 6), and then striking the lower wafer in the region dA . The total flux F_T of Q reaching the lower wafer is

$$\int_A \int_{A'} \frac{F_0}{4\pi s^2} \cos \Omega \cos \Omega' dA dA'$$

Integrating only over source (primed) terms, we calculate the flux of Q as a function of radial position ($r = \sigma$) across the wafer. Referring to Fig. 6

$$\cos \Omega = \frac{x'}{s} \quad \cos \Omega' = \frac{R - \sigma \cos \Theta'}{s}$$

$$F(\sigma) = \frac{F_0}{4\pi} \int_{\Theta'=0}^{\Theta'=2\pi} \int_{r'=0}^{r'=h} \left(\frac{1}{s^2} \right) \left(\frac{x'}{s} \right) \left(\frac{R - \sigma \cos \Theta'}{s} \right) R dx' d\Theta'$$

where

$$s = (\sigma^2 + R^2 + x'^2 - 2\sigma R \cos \Theta')^{1/2}$$

Integration over x yields

$$-\frac{F_0}{8\pi} \int_{\Theta'=0}^{\Theta'=2\pi} \left(\frac{R - \sigma \cos \Theta'}{\sigma^2 + R^2 + h^2 - 2\sigma R \cos \Theta'} \right) R d\Theta' + \frac{F_0}{8\pi} \int_{\Theta'=0}^{\Theta'=2\pi} \left(\frac{R - \sigma \cos \Theta'}{\sigma^2 + R^2 - 2\sigma R \cos \Theta'} \right) R d\Theta'$$

Defining the dimensionless (w.r.t. R) parameters

$$\sigma_d = \frac{\sigma}{R} \quad \text{and} \quad h_d = \frac{h}{R}$$

integration over Θ' yields

$$\text{flux}(\sigma) \propto F_0 \left(1 - \frac{1 - \sigma_d^2 - h_d^2}{((\sigma_d^2 + h_d^2 + 1)^2 - 4\sigma_d^2)^{1/2}} \right)$$

In Fig. 7, we plot flux vs. σ using $R = 1.125$ in., and h as shown. As expected for a worst case calculation, the computed ratios of edge growth rate vs. wafer center growth rates (see Table I) exceed those observed, but the qualitative dependence of both growth rate and deposition uniformity upon wafer spacing is correct. Increased interwafer spacing results in both increased net film growth rates and enhanced uniformity. As this calculation accounts only for those reactant molecules generated external to the interwafer region, a uniform background deposition rate may be summed with the deposition profiles obtained here, reducing the severity of predicted inhomogeneity (see Fig. 8 and main text). However, upon reaching 2.0 in. interwafer dimension, films are expected to vary within $\pm 10\%$ at worst, setting a general upper bound on the system dimensions required to produce films of adequate uniformity for electronic device purposes. To obtain other than a limiting case model for the LPCVD system is complex, and beyond the scope of this paper. As such, we will defer such a calculation to a paper to follow.

REFERENCES

1. S. Harbeke, L. Krausbauer, E. F. Steigmeier, A. E. Widmer, H. F. Kappert, and G. Neugebauer, *Appl. Phys. Lett.*, **42**, 249 (1983).
2. M. L. Hitchman and A. E. Widmer, *J. Cryst. Growth*, **55**, 501 (1981).
3. R. S. Rosler, *Solid State Technol.*, **20**, 63 (1977).
4. H. Kurokawa, *This Journal*, **129**, 2620 (1982).
5. M. M. Mandurah, K. C. Saraswat, and C. R. Helms, *J. Appl. Phys.*, **51**, 5755 (1980).
6. T. I. Kamins, *This Journal*, **126**, 833 (1979).
7. R. F. C. Farrow, *ibid.*, **121**, 899 (1974).
8. M. L. Hitchman, in "Chemical Vapor Deposition," T. O. Sedwich and H. Lydtin, Editors, p. 59, The Electrochemical Society Softbound Proceedings Series, Princeton, NJ (1979).
9. P. Neudorff, A. Jodhun, and D. P. Strausz, *J. Phys. Chem.*, **84**, 339 (1980).
10. E. K. Kinsbron, M. Sternheim, and R. Knoell, *Appl. Phys. Lett.*, **42**, 835 (1983).
11. B. A. Scott, R. M. Plecenick, and E. E. Simonyi, *ibid.*, **39**, 73 (1981).
12. J. Blazejowski and F. W. Lampe, *J. Photochem.*, **20**, 9 (1982).
13. B. S. Meyerson, B. A. Scott, and D. J. Wolford, *J. Appl. Phys.*, **54**, 1461 (1983).
14. P. John and J. H. Purnell, *J. Chem. Soc. Faraday Trans.*, **69**, 1455 (1973).
15. G. Z. Fritz, *Naturforsch.*, **86**, 771 (1953).
16. M. Janai, *Thin Solid Films*, **91**, 211 (1982).
17. M. L. Hitchman and J. Kane, *J. Cryst. Growth*, **55**, 485 (1981).

Phosphorus-Doped Polycrystalline Silicon via LPCVD

II. Surface Interactions of the Silane/Phosphine/Silicon System

B. S. Meyerson* and M. L. Yu

IBM Thomas J. Watson Research Center, Yorktown Heights, New York 10598

ABSTRACT

Secondary ion mass spectrometry (SIMS), low energy electron diffraction (LEED), and Auger electron spectroscopy (AES) have been employed to study the interactions of silane (SiH_4) and phosphine (PH_3) with the Si(100) surface. Phosphine adsorption and desorption were investigated at surface temperatures in the range $25^\circ \leq T \leq 700^\circ\text{C}$. At ambient temperature, phosphine saturated the bare Si(100) surface after 3-5L exposure, and fitting adsorption data to a Langmuir model yields the value $s = 1.0$ for the sticking coefficient. Phosphine adsorption was found to follow the 2×1 pattern of the underlying silicon. Competitive adsorption experiments set an upper bound of $s \leq 0.025$ for silane adsorption under like conditions. The silicon surface was observed to be passivated with respect to silane adsorption by prior exposure to phosphine, with a layer of preferentially adsorbed phosphine formed which served to preclude subsequent silane adsorption. The results obtained here are discussed in the context of their bearing upon the phosphorus-doped low pressure chemical vapor deposition process.

In this paper, we will study the interactions of silane, phosphine, and the silicon surface, in an effort to understand in detail the microscopic phenomena leading to the order of magnitude suppression of film growth rates during the LPCVD preparation of phosphorus-doped polycrystalline silicon. This phenomena, discussed in the first paper of this set, has been observed by others (1, 2). Detailed kinetic equations were devised (1) to test the consistency of the models proposed, after which novel inert gas diluents and/or alternative furnace and wafer carrier geometries were studied in an effort to ameliorate the difficulties associated with this particular chemistry. In modeling such a process kinetically, a limitation is that one may demonstrate the model to be consistent with observation, but not necessarily unique. For this reason, we pursue an alternative approach, that being the direct observation via surface probe techniques, of the interactions relevant to the phosphorus-doped LPCVD process.

Experimental

We have studied the interaction of silane and phosphine with the Si(100) surface using low energy electron diffraction (LEED), Auger electron spectroscopy (AES), photo emission spectroscopy (PES), and secondary ion mass spectrometry (SIMS). The detailed interaction of each adsorbate with the surface will be reported separately (3, 4), with the emphasis here placed on data relevant to the mutual interaction of these two adsorbates with the silicon surface.

The experiments were conducted in an ultrahigh vacuum (UHV) apparatus, baked, and then pumped to below 2×10^{-10} torr base pressure. A silicon (100) sample was cut from a 10 Ω -cm n-type silicon wafer, etched lightly in HF, then suspended in the sample chamber by Ta clamps of low thermal mass such that the sample could be heated resistively (using a dc current). Sample temperature was determined by a Chromel-Alumel thermocouple spot-welded to the clamps adjacent to the sample. Thermocouple readings were calibrated from 750° to 1100°C using optical pyrometry. Overlapping data from pyrometry and thermocouple measurements were found to be in good agreement. Once at base pressure, the sample was flashed to 1100°C for 15s thermal etching cycles. Surface contaminant levels were monitored by *in situ* AES until only negligible residual C or O was detected and LEED showed a clear $p(2 \times 1)$ pattern, consistent with the bare (100) surface. Between sequential adsorption studies, 600° - 900°C anneals sufficed to return the surface to its initial bare state as determined again via AES. Avoidance of repeated 1100°C cleaning is desirable to eliminate excessive thermal etching and accompanying changes in surface morphology. Controlled exposure of the silicon surface to PH_3 and SiH_4 was achieved using calibrated leak

valves to bring the system up to preset partial pressures. Mass spectrometry was utilized at various stages in the experiments to ensure source purity. All filaments (ion gauges and titanium sublimation pumps) as well as ion pumping equipment were turned off during these exposures to avoid introducing unwanted by-products of gas-phase chemistry (such as atomic hydrogen formation at the hot filaments) caused by the aforementioned equipment. We therefore employed a 170 liter/s turbomolecular pump to maintain the system at the desired exposure pressure.

Phosphine adsorption on Si at substrate temperatures in the range $25^\circ \leq T_s \leq 625^\circ\text{C}$ was monitored via observation of the 120 eV phosphorus LMM Auger line. Phosphine which had been adsorbed at $T = 25^\circ$ and 550°C was removed from the surface by subsequent annealing (1 min anneals at each temperature step), observing the evolution of phosphine using AES. Though suitable for monitoring phosphine, AES is unable to distinguish silicon atoms in adsorbed silane from the bulk silicon. Thus, to track silane adsorption we employed static mode SIMS, utilizing a 500 eV, 2 mm diam, 1 nA, Ne^+ primary beam generated by a differentially pumped ion gun to monitor both SiH_x^+ fragments and H^+ from adsorbed silane, thus quantifying the degree of silane surface coverage. The competitive adsorption of silane with phosphine required a modified detection scheme, as interference from the H^+ signal of phosphine as well as overlap of several SiH_x^+ and PH_y^+ peaks made silane detection unsure. Consequently, we substituted fully deuterated silane SiD_4 during competitive adsorption experiments, and found only negligible interference with the D^+ signal due to H_2^+ ($\text{H}_2^+/\text{H}^+ \sim 0.5\%$), allowing the straightforward detection of adsorbed silane in the presence of phosphine.

Competitive adsorption of silane and phosphine was examined in two distinct modes. Initially, the sample was exposed to sufficient phosphine concentration (20L) to ensure the presence of a phosphine-saturated silicon surface, subsequent to which SiD_4 was introduced into the chamber, tracking the displacement of phosphine by the SiD_4 via the SIMS D^+ signal. In the second mode, the sample was exposed to a 1:10 mixture of PH_3/SiD_4 , at 10^{-7} and 10^{-6} torr partial pressures respectively for 100s, observing the Si (LMM) Auger line in ratio to the phosphorus (LMM) Auger line. We report our findings in the following section.

Results

Figure 1 displays adsorbate surface coverage as a function of exposure for both silane and phosphine when the two gases are adsorbed independently on a clean silicon surface. It is apparent from the data that the saturation of surface sites proceeds to completion far more rapidly for phosphine, with the Auger signal saturating after expo-

*Electrochemical Society Active Member.

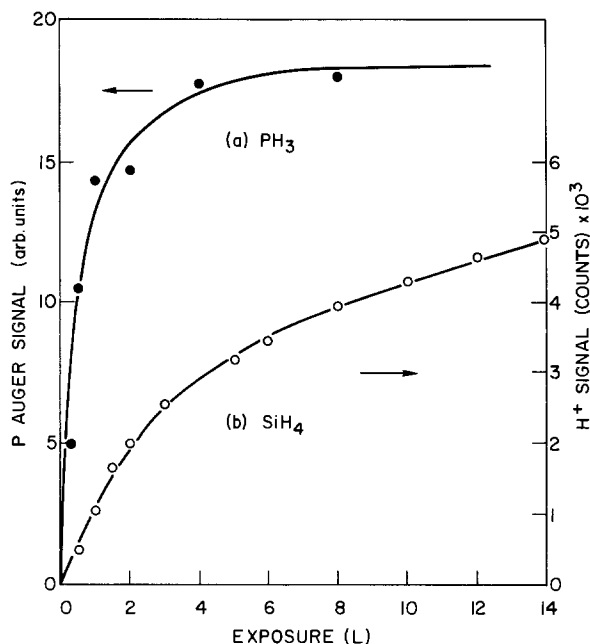


Fig. 1. Phosphine and silane adsorption on the bare Si(100) surface

sure to 3-4L ($1\text{L} \cong 10^{-6}$ torr/l/s) of gas. One may calculate¹ a value of $s = 1.0$ for phosphine's sticking coefficient on the bare silicon surface from this result. LEED patterns taken during phosphine adsorption remained typical of the underlying 2×1 silicon surface, indicating that an ordered adsorption of phosphine had occurred. In contrast to phosphine, silane adsorption reaches equilibrium on a far longer time scale, beyond 40L exposure, indicating a greatly reduced value of s relative that for phosphine. Calculation of an exact value of $s_{(\text{silane})}$ directly from a simple Langmuir adsorption scheme as was done for phosphine was not possible as silane adsorption is dissociative, yielding more than one site coverage per molecule adsorbed. Instead, bounds on $s_{(\text{silane})}$ are set using the method elaborated further on in this paper.

Saturation values for phosphine surface coverage were obtained over a range of adsorption temperatures as displayed in Fig. 2, and a broad maximum is seen at 550°C . Silane adsorption at elevated temperatures was avoided as its decomposition to form film on the silicon surface might result in sample morphology changes making run comparisons invalid.

In Fig. 3, AES data are given for the evolution of phosphine (adsorbed at $T_s = 25^\circ$ and 550°C .) from the silicon surface as a function of annealing temperature, along with accompanying hydrogen loss from the adsorbed (at $T_s = 25^\circ\text{C}$) phosphine. An interesting feature here was the disappearance of the hydrogen signal from the adsorbed phosphine at approximately 500°C , while the phosphorus signal remained unchanged. It is evident that phosphine dissociates at the surface, evolving hydrogen, and leaving bound phosphorus atoms on the surface.

Data taken at room temperature for the case of deuterated silane adsorption onto a phosphine-saturated silicon surface demonstrated that silane does not readily displace adsorbed phosphine. The D^+ signal from newly adsorbed SiD_4 failed to exceed 1.0% of the saturation value found for SiD_4 adsorption on a bare silicon surface, even after the phosphine-covered surface was exposed to the equivalent of 100 monolayers silane flux to the surface. Hence, in all cases, the presence of a phosphine saturated surface served to virtually exclude the subsequent adsorption of SiD_4 .

Three AES spectra are shown in Fig. 4; trace A for a bare silicon surface, trace B for phosphine adsorption on

¹Taking the normalized surface coverage as N , $dN/dt = F_s(1 - N)$, $N = 1 - e^{-Fst}$, $F = \text{flux in L/s}$, $s = \text{sticking coefficient}$, and $t = \text{time (s)}$. A semilog plot of $(1 - N)$ vs. Fst yields s for a known flux F .

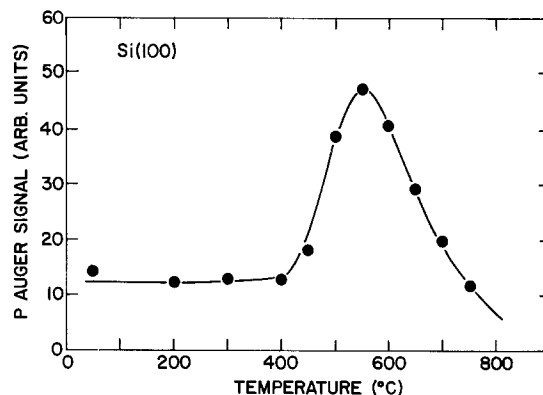


Fig. 2. Phosphine adsorption at elevated substrate temperature

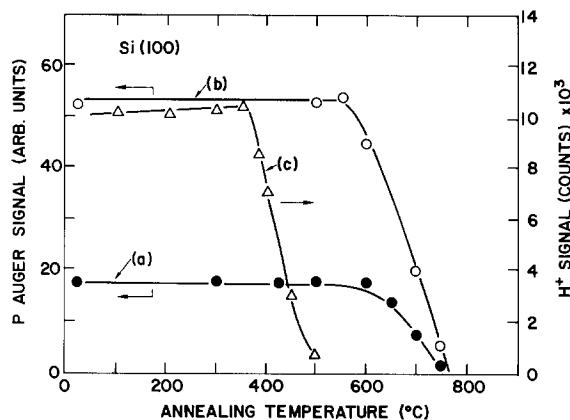


Fig. 3. Data from phosphine and hydrogen desorption experiments, curve A for PH_3 adsorbed at 25°C , B for phosphine adsorbed at 550°C , and C the hydrogen signal for phosphine adsorbed at 25°C .

bare silicon, and trace C the signal obtained from the competitive adsorption of the 1:10 phosphine/silane ratio gas source. Despite the presence of ten times the atomic flux of silane vs. phosphine to the Si surface, the phosphorus Auger peak reaches 80% of the value obtained in the instance of phosphine adsorption on the bare silicon surface. Assuming all other species on the surface are deuterated silane, using a straightforward Langmuir adsorption scheme we compute $s_{(\text{silane})} < 0.025s_{(\text{phosphine})}$. As it is probable that silane adsorption is a dissociative phenomenon, the value $s = 0.025$ must serve as an upper bound on silane's sticking coefficient, as deuterium freed by silane's dissociation may occupy surface sites directly, leading to a higher value of $s_{(\text{silane})}$ than is in fact the case.

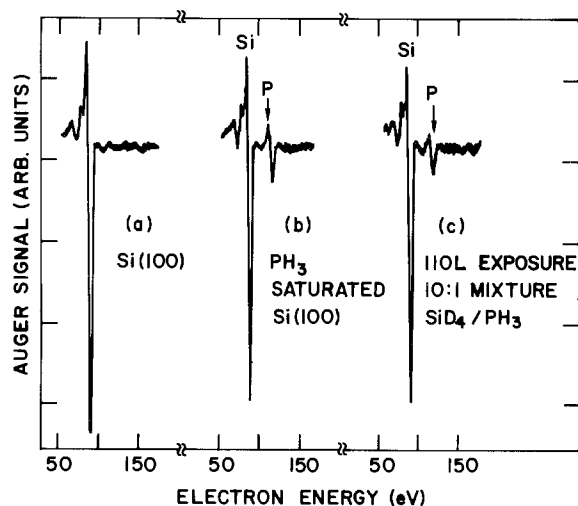


Fig. 4. AES spectra for (A) bare Si(100) surface, (B) PH_3 -saturated Si surface, and (C) competitively adsorbed PH_3 and SiH_3 (see text).

Discussion

We have determined the sticking coefficient of phosphine to be greater than 40 times that of silane. We find that once phosphine forms an adsorbed layer, its displacement by subsequent exposure to silane is extremely slow. Additionally, the adsorbed phosphorus is stable on the surface at temperatures typical of those at which LPCVD operates, although our data indicate the onset of hydrogen loss from the adsorbed phosphine above 400°C. Thus, we have direct evidence for the "poisoning" of the phosphorus-doped LPCVD process due to the preferential adsorption of phosphine *vs.* silane, resulting in the suppression of heterogeneous silane chemistry that is believed (5, 6) dominant in the silane LPCVD process. Although our measurements were conducted on the (100) silicon crystal face, others (7, 8) have examined the adsorption of phosphine on Si(111), and the adsorption of atomic phosphorus on Si(111) (9). In all cases, a sticking coefficient of near unity was deduced, and the rapid saturation of the silicon surface was observed. As our results are consistent with those for the (111) orientation, we feel it probable that our findings are general for the phosphine/silicon system, rather than specific to a particular silicon surface morphology.

In our earlier work (10), it was noted that one must invoke the presence of reactive intermediates to account for the observed film thickness variations. We have found here that phosphine, once adsorbed, virtually excludes silane from the silicon surface, yet we observed (10) film growth rates as high as 18 Å/min at the edges of test wafers. With silane's access to the surface sites reduced to the extent our Auger data indicate, growth rates approaching 20% of those for undoped silane LPCVD cannot be adequately accounted for in terms of heterogeneous silane chemistry. Thus, we must again invoke the presence of species, other than silane, which compete successfully with phosphine for the silicon surface. Though we have a strong existence theorem for the presence of such species, and have identified at least one such reactant (disilane) via mass spectrometry (10), *in situ* reactant detection and profiling in the LPCVD environment is essential to the further understanding of these processes, and will be undertaken shortly.

The maximum in phosphorus surface coverage observed at 550°C is attributable to two phenomena. During annealing experiments performed on phosphine saturated silicon surfaces, hydrogen loss from the surface was seen to occur above 400°C (Fig. 3). The hydrogen evolved during anneals could originate from two sources. One source is adsorbed phosphine, stripped of its hydrogen above 400°C, leaving behind bare adsorbed phosphorus atoms in the range $500^\circ < T_s < 650^\circ\text{C}$. Additional surface thus becomes available as phosphine molecules dissociate, allowing higher concentrations of adsorbed phosphorus at temperatures above 400°C. Alternatively, hydrogen bound directly to the silicon surface due to hydrogen transfer from adsorbed phosphine may also evolve, opening additional sites for phosphine adsorption. Photoemission studies failed to detect a significant signal for Si-H bonding on the phosphine-covered silicon surface, and we therefore believe that little hydrogen (<10% is our detection limit) is transferred to the surface from adsorbed phosphine molecules. Thus, though we cannot exclude the possibility that hydrogen removal directly from the silicon surface contributes to the maximum in phosphine adsorption observed, our failure to observe Si-H bonding implies it contributes less than 10% to the effect. Though the adsorption of in excess of one monolayer (at $T > 400^\circ\text{C}$) of phosphine would also result in an adsorption maximum, the constancy of the bulk silicon Auger peak under varying adsorption temperatures indicates that the adsorbed phosphine layer does not propagate outward from the surface. Above 600°C, the decrease in phosphorus surface coverage is due to evolution of the atomic phosphorus from the surface. We do not believe the disappearance of the phosphorus AES signal is due to diffu-

sion of phosphorus into the bulk, as the diffusivity of phosphorus in silicon at these temperatures is for our purposes negligible (11), and we observed no loss of Si Auger signal as would have occurred had P diffused into the bulk, displacing subsurface silicon atoms.

The outcome of these experiments has implications for the other dopant species one might employ in LPCVD. Alternative n-type dopant species for use in LPCVD will by definition share the basic electronic structure of phosphine (12), with arsine (AsH_3) an example. This similarity in valence electron configuration has the expected result, *i.e.*, arsine is also observed (2) to severely depress silicon growth rates, presumably owing to its preferential adsorption over silane. All the above assumes the arrival of the dopant molecules intact at the growth surface, as gas-phase pyrolysis clearly changes the nature of the species reaching the surface and thus alters the deposition chemistry. Phosphine (13) is known to be quite stable on the temperature/residence time scales in use during LPCVD, and we have verified this via mass spectrometry, finding no significant decomposition of pure phosphine at 625°C. Arsine stability has been investigated (14) as it relates to gallium arsenide CVD, and it too undergoes negligible decomposition on the LPCVD temperature/residence time scale.

Conclusions

By direct observation of the competition between silane and phosphine for adsorption sites on the silicon surface, we have verified the formation of a stable layer of adsorbed phosphorus during the phosphorus-doped LPCVD process. It has been demonstrated that phosphine, the phosphorus dopant source, has a sticking coefficient $s = 1.0$ when adsorbed on the bare silicon (100) surface, while the value for silane under identical conditions was found to be $s \leq 0.025$. We find that adsorbed phosphine will dissociate, evolving hydrogen, at temperatures below those necessary to desorb phosphorus itself, leading to a maxima in phosphorus adsorption at 550°C. Once adsorbed, phosphine is stable under a silane flux, and thus effectively passivates the silicon surface with respect to heterogeneous silane chemistry and is responsible for the suppression of growth rates in the phosphorus-doped LPCVD process.

Acknowledgments

The authors wish to thank Dr. B. A. Scott and Dr. J. Jasinski whose comments and suggestions added greatly to this study. This work was partially supported by the Office of Naval Research.

Manuscript submitted Dec. 9, 1983; revised manuscript received May 3, 1984.

IBM Corporation assisted in meeting the publication costs of this article.

REFERENCES

1. H. Kurokawa, *This Journal*, **129**, 2620 (1982).
2. F. C. Eversteyn and B. H. Put, *ibid.*, **120**, 106 (1973).
3. M. L. Yu and B. S. Meyerson, *J. Vac. Sci. Technol. A*, To be published.
4. M. L. Yu and R. Purtell, To be published.
5. M. L. Hitchman, in "Chemical Vapor Deposition," T. O. Sedgwick and H. Lydtin, Editors, p. 59, The Electrochemical Society Softbound Proceedings Series, Princeton, NJ (1979).
6. M. S. Sukhov, *Izv. Akad. Nauk SSSR Neorg. Mater.*, **18**, 1077 (1982).
7. A. J. Van Bommel and F. Meyer, *Surf. Sci.*, **8**, 381 (1967).
8. A. J. Van Bommel and J. E. Crombeen, *ibid.*, **36**, 773 (1973).
9. R. J. Bennet and C. Parish, *J. Phys. D*, **9**, 2555 (1976).
10. B. S. Meyerson and W. Olbricht, *This Journal*, **131**, 2361 (1984).
11. J. S. Makris and B. J. Masters, *ibid.*, **120**, 1252 (1973).
12. F. A. Cotton and C. Wilkinson, "Basic Inorganic Chemistry," p. 228, John Wiley and Sons, New York (1976).
13. J. Blazejowski and F. W. Lampe, *J. Photochem.*, **20**, 9 (1982).
14. J. Nishizawa and T. Kurabayashi, *This Journal*, **130**, 413 (1983).

The Apparent Activation Energy for the Electrochemical Oxidation of HCOOH at a Platinum Electrode Chemically Modified by Bi Adatoms in 0.5M H₂SO₄

Ronald W. Tsang¹ and Dennis C. Johnson*

Department of Chemistry and Ames Laboratory,² Iowa State University, Ames, Iowa 50011

Glenn R. Luecke

Department of Mathematics, Iowa State University, Ames, Iowa 50011

ABSTRACT

The enhancement by Bi adatoms of the anodic peak for oxidation of HCOOH at a Pt electrode in 0.5M H₂SO₄ was studied as a function of temperature. The results are interpreted on the basis of an increased value of the pre-exponential term in the Arrhenius rate equation, which is attributed to an increase in the frequency of the vibrational motion leading to desorption of the strongly adsorbed product of the organic oxidation. This increase is concluded to be the direct effect of the site-to-site surface migration of the freshly deposited Bi adatoms.

It is well known that the electrochemical oxidation of many organic compounds on noble metal electrodes in aqueous solutions is characterized by rapid fouling of the electrode surfaces by the strongly adsorbed intermediate and/or final products of the faradaic reactions. These adsorbed materials, call them "poisons," are desorbed very slowly or not at all, and the electrode current decays very rapidly for a constant applied electrode potential. The instantaneous electrode current and total faradaic charge which can pass before substantial fouling has occurred can be increased significantly by the *in situ* electrodeposition of certain metal adatoms on the electrode surface. Three prominent explanations for the apparent electrocatalytic activity of the ad-atoms are reviewed briefly, and we offer an alternative explanation based on results of a temperature study for oxidation of HCOOH at a Pt electrode in 0.5M H₂SO₄ containing Bi(III).

Explanations for the Apparent Electrocatalytic Activity of Adatoms

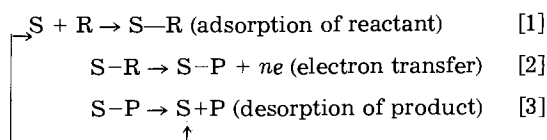
The third-body effect.—This model has as its basis the speculation that the strongly adsorbed poisons are formed by dimerization of less strongly adsorbed free radicals, *e.g.*, ·COOH in the case of the oxidation of HCOOH, on adjacent surface sites. Electrodeposited metal adatoms are presumed to be uniformly distributed on the electrode so as to occupy alternate surface sites. With such an arrangement of adatoms, the proximity of adsorbed radicals is not favorable for the dimerization reaction. Hence, a uniform surface coverage by the adatoms of 0.5 monolayer is predicted to yield the maximum catalytic benefit. Angerstein-Kozłowska *et al.* (1), Adzic *et al.* (2, 3), and Motoo and Watanabe (4) have concluded this mechanism is operative for adatoms of Hg, Bi, Pb, Tl, and Cd in the oxidation of HCOOH on Pt electrodes. The metal adatoms are referred to as the "third bodies." This model does not explain satisfactorily the quantitative differences observed in the enhancement effect of various metals. Furthermore, it has yet to be proved that adatoms are uniformly distributed rather than clustered for surface coverages less than the equivalent of one monolayer.

The suppression of hydrogen adsorption.—This model was proposed by Spasojevic *et al.* (5) for oxidation of HCOOH and presumes that the poisons are formed via interaction of adsorbed H atoms with ·COOH radicals. Electrodeposited metal adatoms inhibit the adsorption of H

atoms by site exclusion and thereby decrease the extent of the reaction supposed to produce the strongly adsorbed poisons. Numerous organic oxidations which lead to surface fouling occur in regions of electrode potential for which the equilibrium surface coverage by H atoms is virtually zero, *i.e.*, $E \gg E_{H^+,H_2}^0$, a fact which is counter to the basic presumption of this model.

The bi-functional model.—Motoo and Watanabe (6, 7) proposed this explanation of the enhancement effects of metal adatoms, which has been applied to the electrocatalysis by the adatoms Sn, Ge, As, and Ru of the oxidation of CH₃OH, HCHO, and CO on Pt (6-11). Oxygen atoms or oxygen containing species, *e.g.*, the ·OH radical, adsorbed on the metal adatoms catalyze the oxidation of organic molecules and radicals adsorbed on adjacent surface sites. Kock *et al.* (8) derived a mathematical expression based on this model relating the catalytic currents to the free energy of adsorption of oxygen on the metal adatoms. The theory was found to be in good agreement with experimental results. This model appears to be contradicted by data from alkaline solutions for which the catalytic current ceases on the positive scan of potential when the metal adatoms are oxidized to their insoluble oxides.

An alternate model.—We propose a mechanism which in its simplest form is given by Eq. [1]-[3]. In these equations, S represents a surface site, R a reactant molecule in the diffusion layer, and P the product of the faradaic reaction which functions as a poison when adsorbed at a surface site



Desorption of the reaction product (P) from a reaction site by reaction [3] is necessary for continuation of the faradaic signal. The metal adatoms are concluded to enhance the rate of desorption (k_3) in this mechanism. No bonding interaction is presumed to occur between the adatoms and R or P; consequently, a reaction is not shown which involves the direct chemical participation of adatoms. The faradaic signal is proportional to the molar surface coverage by adsorbed R, $\theta_R \Gamma_{\max}$, as given by

$$i = nFAk_2\theta_R\Gamma_{\max} \quad [4]$$

where Γ_{\max} is the maximum coverage (mol cm⁻²) corresponding to $\theta_R = 1$. It is observed that the voltammetric response is in the form of an anodic peak and, for the

*Electrochemical Society Active Member.

¹Present address: 43B Tai Hang Road, 1/F Causeway Bay, Hong Kong.

²Operated by the U.S. Department of Energy by Iowa State University under Contract no. W-7405-ENG-82.

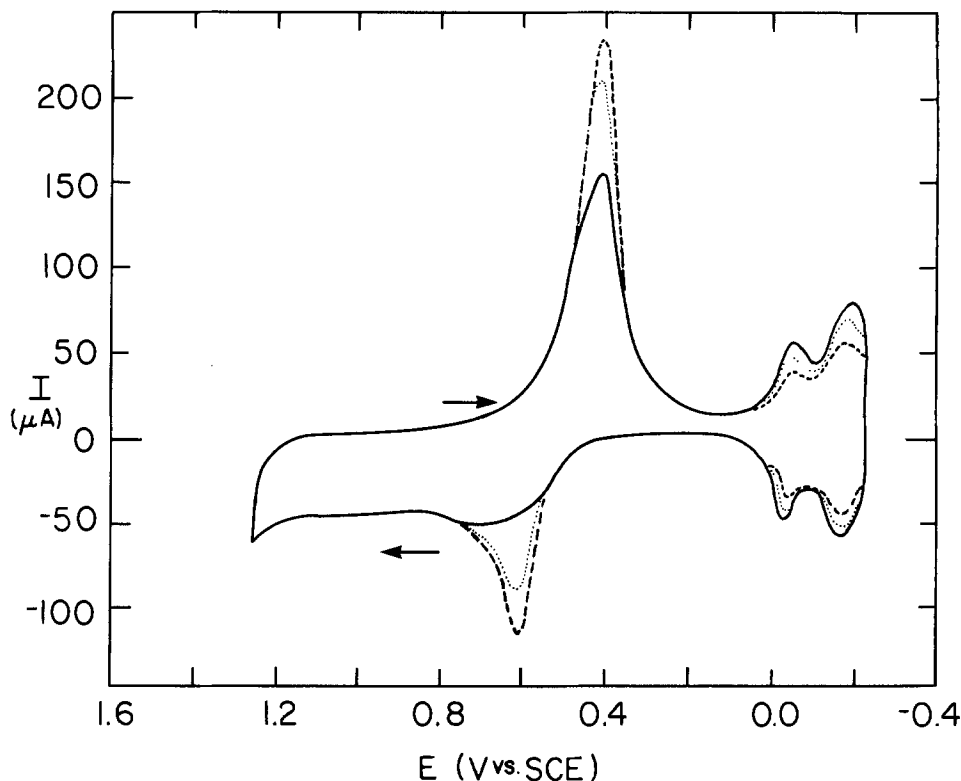


Fig. 1. i-E curves for Pt in 0.5M H_2SO_4 with and without Bi(III). $W = 400 \text{ rev min}^{-1}$, $\phi = 6.0 \text{ V min}^{-1}$. Curves: — 0.00 μM Bi(III), 0.40 μM Bi(III), - - - 0.40 μM Bi(III), - · - · 2.0 μM Bi(III).

peak current ($i = I_p$), a steady-state condition is momentarily satisfied. Hence

$$\frac{di}{dt} = 0 = nFA\Gamma_{\max} \left[k_2 \left(\frac{d\theta_R}{dt} \right) + \theta_R \left(\frac{dk_2}{dE} \cdot \frac{dE}{dt} \right) \right] \quad [5]$$

The symbol ϕ is substituted for the rate of potential scan, (dE/dt) , and we write

$$k_2 \left(\frac{d\theta_R}{dt} \right) = -\theta_R \phi \left(\frac{dk_2}{dE} \right) = \theta_R \phi k_2 \left(\frac{\alpha F}{RT} \right) \quad [6]$$

where α includes the symmetry factor and the number of electrons up to and including the rate-determining step.

We have as yet been unable to obtain a satisfactory rigorous solution to the system of equations, and we proceed instead with the assumption that for a large value of the bulk concentration of R (C_R^b), the concentration of R at the electrode surface equals the bulk concentration ($C_R^s \approx C_R^b$) and $\theta_R + \theta_p \approx 1$. The value of θ_{H_2O} is small but not zero and we apply the steady-state approximation for θ_{H_2O} , i.e., $d\theta_{H_2O}/dt \approx 0$, with the result

$$\theta_{H_2O} = \frac{k_3 - k_3\theta_R + k_{-1}\theta_R}{k_1 C_R^b} \quad [7]$$

The time derivative of θ_R is evaluated which, together with Eq. [7], yields

$$\frac{d\theta_R}{dt} = k_3 - k_3\theta_R - k_2\theta_R \quad [8]$$

Equations [6] and [8] are combined and the result is solved for θ_R to give

$$\theta_R = \frac{k_3}{k_2 + k_3 - \alpha F \phi / RT} \quad [9]$$

Hence, Eq. [4] can be written for the peak current as

$$I_p = -nFA\Gamma_{\max} \frac{k_2 k_3}{k_2 + k_3 - \alpha F \phi / RT} \quad [10]$$

The value of I_p is expected to be independent of C_R^b , on the basis of the assumption leading to Eq. [10], as is observed for large values of C_R^b .

Experimental

Voltammetric data was obtained with a Pt rotating disk electrode (RDE, 0.43 cm^2), Model PIR rotator and Model RDE-3 potentiostat (Pine Instrument Company, Grove City, Pennsylvania). The X-Y recorder was Model 7035B (Hewlett-Packard). The electrolysis cell (ca. 500 ml) had a double wall construction for circulation of thermostated water from a Model 2095 refrigerated and heated circulating bath (Forma Scientific, Incorporated, Marietta, Ohio). Temperatures were controlled in the range 10°-43°C with a precision of $\pm 0.1^\circ\text{C}$. All electrode potentials were measured in V vs. SCE.

Solutions were prepared from reagent-grade chemicals using triply distilled water. Solutions of Bi(III) were prepared from $\text{Bi}(\text{NO}_3)_3$.

Results and Discussion

Current-potential curves.—Typical i-E curves for Pt in 0.5M H_2SO_4 are shown in Fig. 1 with and without added Bi(III). Bismuth adatoms are deposited at $E < \text{ca. } 0.5\text{V}$, i.e., over the entire accessible range of values for which platinum oxide (PtO) is not present on the electrode surface. Bismuth adatoms are oxidized on the positive scan to produce the peak at 0.6V appearing on the wave for PtO production. Cadle and Bruckenstein (12) demonstrated that a significant fraction of the oxidized Bi(III) remains adsorbed on the Pt surface. The adsorbed Bi(III) is reduced simultaneously with reduction of PtO on the negative scan, i.e., $E \approx 0.4\text{V}$. The transport-limited current for the reaction $\text{Bi}(\text{III}) + 3e \rightarrow \text{Bi}^0$ is 0.2 μA in $4 \times 10^{-7}\text{M}$ Bi(III), which is not perceptible for the current sensitivity represented in Fig. 1. Several cyclic scans are necessary to reach the reproducible surface coverage by Bi adatoms for this low concentration, and the i-E curves shown are the reproducible curves obtained after 10-20 repetitive cycles.

The surface coverage by Bi adatoms, θ_{Bi} , is conveniently determined on the basis of the decrease in the cathodic charge for the reaction $\text{H}^+ + e \rightarrow (\cdot\text{H})_{\text{ads}}$ in the potential range 0.10 to -0.25V vs. SCE . Values of θ_{Bi} calculated for a 1:1 substitution of Bi for $(\cdot\text{H})_{\text{ads}}$ are given in Table I for several values of $C_{\text{Bi(III)}^b}$.

The effectiveness of Bi adatoms to enhance the anodic signals for HCOOH at the Pt electrode in 0.5M H_2SO_4 is il-

Table I. Values of θ_{Bi} for several values of $C_{\text{Bi(III)}}^b$

$C_{\text{Bi(III)}}^b$ (μM)	θ_{Bi}
2.0	0.08
5.0	0.16
10.0	0.25
20.0	0.38
30.0	0.52
40.0	0.62

Conditions: $W = 400 \text{ rev min}^{-1}$, $\phi = 6.0 \text{ V min}^{-1}$.

illustrated in Fig. 2. In the absence of Bi(III), the largest peak signal is obtained on the negative scan of potential (peak D) immediately following reduction of PtO. The products of the reaction for peak D which remain adsorbed on the electrode result in substantial loss of surface activity, and only a very small peak (A) is obtained for oxidation of HCOOH on the subsequent positive scan. The adsorbed organic poisons are oxidatively removed during formation of surface oxide for $E > 1.0\text{V}$. The addition of Bi(III) to the solution with subsequent formation of Bi adatoms results in a very substantial increase in peak A with only a modest effect on peak D. Values of the peak signals, $I_{p,A}$ and $I_{p,D}$, are shown in Fig. 3 as a function of $C_{\text{Bi(III)}}^b$. Again, the i-E curves in Fig. 2 and the peak values in Fig. 3 correspond to the reproducible data achieved after several cyclic scans of potential. Since the adsorbed product for the oxidation of HCOOH obliterates the cathodic peaks for formation of $(\cdot\text{H})_{\text{ads}}$ in the presence or absence of Bi(III), θ_{Bi} cannot be determined in the presence of HCOOH and we can only suppose that HCOOH has a negligible effect on θ_{Bi} for a given value of $C_{\text{Bi(III)}}^b$. On this basis, we conclude for peak A that the maximum enhancement observed for ca. $10 \mu\text{M}$ Bi(III) corresponds to $\theta_{\text{Bi}} \approx 0.25$ (see Table I). For $\theta_{\text{Bi}} \rightarrow 1.0$, the resultant decrease in surface sites available for adsorption of HCOOH is expected to cause a decrease in the peak current. The value of $I_{k,A}$ is observed to decrease for $C_{\text{Bi(III)}}^b > 10 \mu\text{M}$.

The value of $I_{p,D}$ continues to increase for $C_{\text{Bi(III)}}^b$ exceeding $10 \mu\text{M}$. Because only a portion of the Bi(III) produced by oxidation of Bi adatoms remains adsorbed to the surface oxide, the value of θ_{Bi} corresponding to peak D, obtained immediately after reduction of the surface oxide, is concluded to be less than 0.25. Provided Bi(III) is electro-deposited at a transport-limited rate, it is predicted that a period of approximately 15s is required to accumulate a 0.25-monolayer coverage by Bi adatoms under the condi-

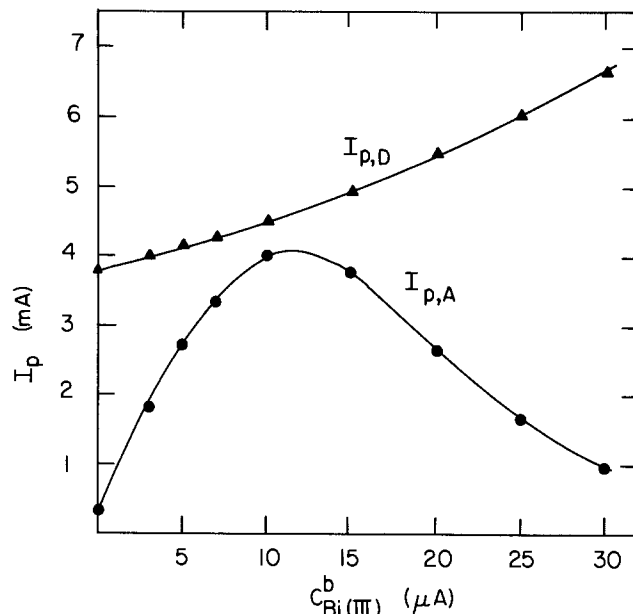


Fig. 3. $I_{p,A}$ and $I_{p,D}$ as a function of $C_{\text{Bi(III)}}^b$ for 0.25M HCOOH in 0.5M H_2SO_4 . $W = 400 \text{ rev min}^{-1}$, $\phi = 60 \text{ V min}^{-1}$.

tion $C_{\text{Bi(III)}}^b = 10 \mu\text{M}$ and $W = 400 \text{ rev min}^{-1}$, assuming $D = 1 \times 10^{-5} \text{ cm}^2 \text{ s}^{-1}$, $\nu^{-1/6} = 2.2 \text{ cm}^{1/3} \text{ s}^{-1/6}$ and $\Gamma_{\text{max}} = 2 \times 10^{-9} \text{ mol cm}^{-2}$. The time required for the applied potential to scan across the region from 0.5V , where peak D begins to appear, to 0.4V , the peak potential for peak D, is 1.0s for $\phi = 6.0 \text{ V min}^{-1}$. This is hardly sufficient for θ_{Bi} to increase substantially beyond the value of $\theta_{\text{Bi(III)}}$ characteristic of the oxidized surface for $E > 0.6\text{V}$.

In a separate experiment, Bi adatoms were deposited at 0.0V in the absence of HCOOH. After several minutes, HCOOH was added to the cell and the potential scanned in the positive direction. Very little enhancement of peak A was observed in comparison to the same experiment without Bi(III). In this case, the electrode surface had not become deactivated by the adsorbed products of HCOOH oxidation, and, according to the three models for adatom catalysis mentioned, the Bi-ad atoms should have retained their catalytic activity. Therefore, we conclude that existing models are not adequate and that it is essential, for observation of the enhancement phenomenon, that the equilibrium status of the Bi adatoms be disarranged periodically such as occurs for cyclic voltammetry in the presence of Bi(III).

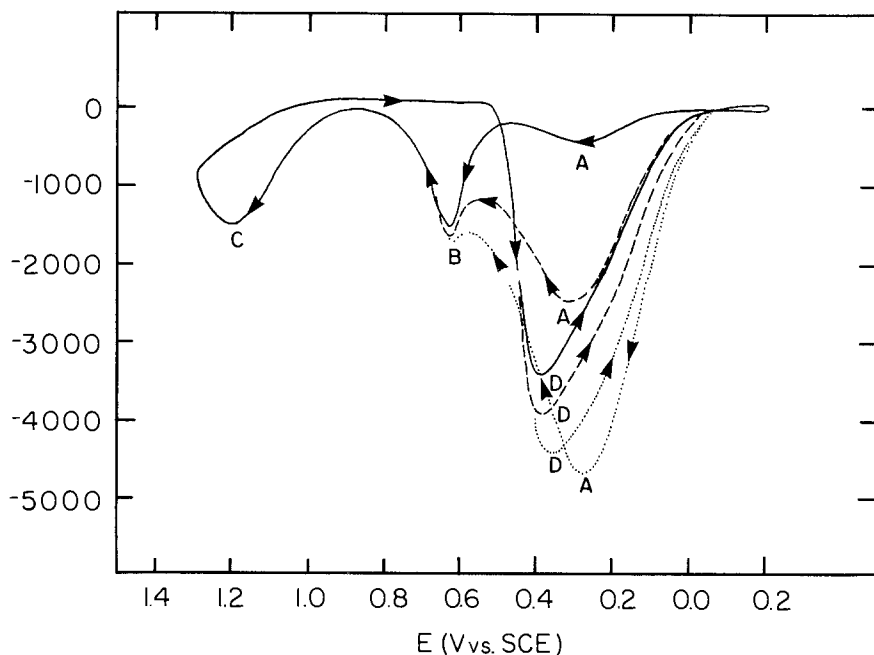


Fig. 2. i-E curves for Pt in 0.5M H_2SO_4 containing 0.25M HCOOH. $W = 400 \text{ rev min}^{-1}$, $\phi = 6.0 \text{ V min}^{-1}$. Curves: — $0.00 \mu\text{M}$ Bi(III), - - - $3.2 \mu\text{M}$ Bi(III), ···· $8.4 \mu\text{M}$ Bi(III).

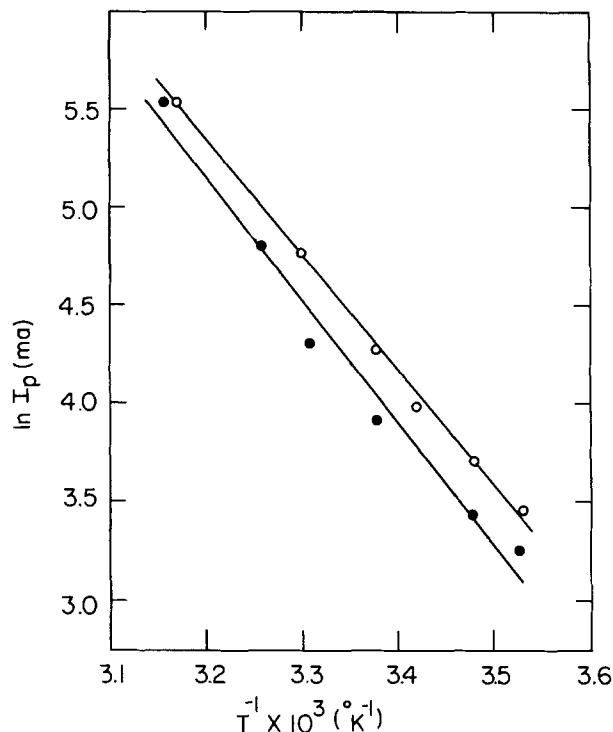


Fig. 4. Plot of $\ln \{I_p\}$ vs. $1/T$ for peak D. 0.25M HCOOH in 0.5M H_2SO_4 , $W = 400 \text{ rev min}^{-1}$, $\phi = 6.0 \text{ V min}^{-1}$. Curves: 0-0.0 μM Bi(III), \bullet -10.0 μM Bi(III).

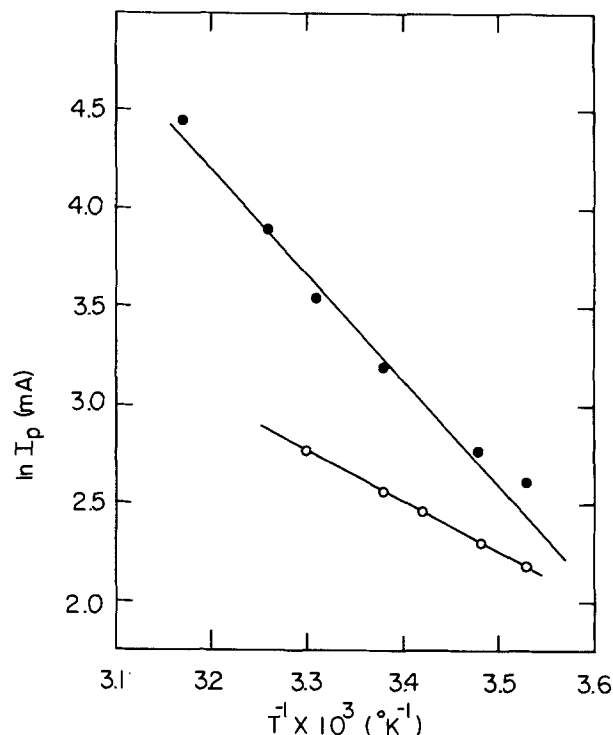


Fig. 5. Plot of $\ln \{I_p\}$ vs. $1/T$ for peak A. 0.25M HCOOH in 0.5M H_2SO_4 , $W = 400 \text{ rev min}^{-1}$, $\phi = 6.0 \text{ V min}^{-1}$. Curves: 0-0.0 μM Bi(III), \bullet -10.0 μM Bi(III).

Temperature effects.—The effect of variation in temperature was studied for 0.25M HCOOH in the presence and absence of 10 μM Bi(III). At this high concentration of HCOOH, $I_{p,A}$ and $I_{p,D}$ are nearly independent of C_{HCOOH}^b and Eq. [10] is presumed appropriate for describing I_p . The peak potential for peak A is virtually unchanged by the addition of Bi(III), and the enhancement mechanism is concluded not to involve a change in the rate of the electron-transfer reaction. Such an observation is consistent with Eq. [10], provided $k_2 \gg k_3 - \alpha F\phi/RT$. On that basis, we write

$$I_p = nFA\Gamma_{\text{max}}k_3 \quad [11]$$

The rate of desorption is expressed in the manner

$$k_3 = Z \cdot \exp \{-E_{\text{act},3}/RT\} \quad [12]$$

where $E_{\text{act},3}$ is the apparent activation energy for the reaction in Eq. [3]

$$\ln \{I_p\} = \ln \{nFA\Gamma_{\text{max}}Z\} - E_{\text{act},3}/RT \quad [13]$$

and plots of $\ln \{I_p\}$ vs. $1/T$ (K^{-1}) are expected to yield a slope of value $-E_{\text{act},3}/R$.

Experimental results are shown plotted in Fig. 3 and 4 and the results of linear regression analyses of the data are presented in Table II. Large uncertainties are expected for the intercept, *i.e.*, $\ln \{nFA\Gamma_{\text{max}}Z\}$, because of the rather narrow range of temperatures used and the large extrapolation required for evaluation at $1/T \rightarrow 0$. The differences in slope and intercept for peak D (negative scan) are not statistically significant for the presence and ab-

sence of Bi(III). This observation is consistent with our earlier conclusion that $\theta_{\text{Bi}} < 0.25$ for peak D even when $C_{\text{Bi(III)}}^b = 10 \mu\text{M}$ and the primary mechanism for reactivating the electrode during the negative scan is the reduction of surface oxide immediately prior to the appearance of peak D to produce a reduced Pt surface free of adsorbed organic poisons.

Values of slope and intercept in Fig. 5 are concluded to be statistically different for peak A in the presence and absence of Bi(III). Of great significance is the observation that the presence of Bi adatoms actually increases rather than decreases the apparent activation barrier. The experimental reality that Bi adatoms do, in fact, enhance the value of $I_{p,A}$ is explained by a substantial increase in the pre-exponential part (Z) of Eq. [12], *i.e.*, an increase of a factor of ca. 20,000. We interpret Z in the usual manner as representing the frequency of the vibrational process which leads to the desorption reaction. Correspondingly, the term $\exp \{-E_{\text{act},3}/RT\}$ represents the probability that a single vibrational event will successfully lead to desorption. We conclude that the large increase in the frequency factor for reaction [3] results from the site-to-site surface migration of freshly deposited Bi atoms as they move from the sites of electrodeposition to sites of maximum stability. This is consistent with the observation that the benefit of Bi adatoms to enhance the anodic signal for HCOOH decays rather rapidly with time at a constant potential when the surface arrangement of the Bi adatoms has reached its equilibrium state. For enhanced anodic reactions where the site hopping mechanism is operative, it cannot be expected that steady-state signals will be obtained for hydrodynamic electrodes at constant potential.

Conclusion

The effect of Bi(III) to enhance the rate of anodic oxidation of HCOOH at a Pt electrode in 0.5M H_2SO_4 during the positive scan of electrode potential results from a substantial increase in the frequency of the vibrational event leading to desorption of the adsorbed products of the oxidation of HCOOH rather than a decrease in the activation barrier of the rate controlling step. Hence, the Bi adatoms do not function in the role of a true catalyst in that their presence does not offer an alternate reaction pathway

Table II. Linear regression statistics for data in Fig. 4 and 5

Peak Scan	Bi(III)	Intercept*	Slope 10^{-3} (K)	$E_{\text{act},3}$ (kcal/mol $^{-1}$)	$S_{y,x}$
D	neg. absent	10 ± 1	-5.7 ± 0.4	11.3 ± 0.8	0.039
D	neg. present	12 ± 5	-6.3 ± 1.4	12.5 ± 2.8	0.149
A	pos. absent	-3 ± 1	-2.5 ± 0.3	5.0 ± 0.4	0.012
A	pos. present	7 ± 3	-5.1 ± 0.9	10.1 ± 1.8	0.098

* Confidence intervals calculated at the 90% level.

having a smaller activation energy. Use of the description "electrocatalysis" in this case is inappropriate, and we have carefully avoided its application to the description of the enhancement phenomenon.

Acknowledgment

This work was supported by the Office of Basic Energy Sciences, U. S. Department of Energy.

Manuscript submitted June 2, 1983; revised manuscript received April 3, 1984.

Ames Laboratory assisted in meeting the publication costs of this article.

REFERENCES

1. H. Angerstein-Kozłowska, B. MacDougall, and B. E. Conway, *This Journal*, **120**, 756 (1973).
2. R. R. Adzic, D. N. Simic, A. R. Despic, and D. M. Drazic, *J. Electroanal. Chem.*, **65**, 587 (1975); *ibid.*, **80**, 81 (1977).
3. R. R. Adzic, M. D. Spasojevic, and A. R. Despic, *ibid.*, **92**, 31 (1978).
4. S. Motoo and M. Watanabe, *ibid.*, **98**, 20 (1979).
5. M. D. Spasojevic, R. R. Adzic, and A. R. Despic, *ibid.*, **109**, 261 (1980).
6. M. Watanabe and S. Motoo, *ibid.*, **60**, 275 (1975).
7. S. Motoo and M. Watanabe, *ibid.*, **69**, 429 (1976).
8. D. F. A. Koch, D. A. J. Rand, and R. Woods, *ibid.*, **70**, 73 (1976).
9. S. Motoo, M. Shibata, and M. Watanabe, *ibid.*, **110**, 103 (1980).
10. S. Motoo and M. Watanabe, *ibid.*, **111**, 261 (1980).
11. K. Takamura and M. Sakamoto, *ibid.*, **113**, 273 (1980).
12. S. H. Cadle and S. Bruckenstein, *Anal. Chem.*, **44**, 1993 (1972).

Ion-Beam Etching of InP and Its Application to the Fabrication of High Radiance InGaAsP/InP Light Emitting Diodes

Osamu Wada

Fujitsu Laboratories Limited, 1677, Ono, Atsugi 243-01, Japan

ABSTRACT

A novel application of Ar ion-beam etching to the fabrication of microlenses on an InP substrate is described. Baking a positive acting photoresist layer was found to facilitate a very reproducible method of forming a spherical mask suitable for ion-beam etching. Characteristics of Ar ion-beam etching of InP are studied, and etching parameters such as the ion energy, the ion incident angle, and the target supporting technique are optimized for obtaining optically smooth etched surfaces. The generation of cones and other microfeatures previously reported on ion-beam-etched InP was completely eliminated, through this optimization, by choosing the energy of 1000 eV and the incident angle of 60°-70° as well as introducing a target supporter made of Ti. The geometry of a lens thus formed on an InP substrate was confirmed to be a sphere. The present technique was applied to fabricating InGaAsP/InP double heterostructure light emitting diodes at the wavelength of 1.3 μm which have monolithic lenses on the light extraction surfaces. The result showed an improvement in the light power coupled to a standard fiber by a factor as large as 1.8.

Ion-beam etching or ion milling technique, in which the bombardment of energetic ions such as Ar⁺ is utilized to sputter etch the target material, has been applied by now to a variety of semiconductor device as well as integrated circuit-fabrication processes. In comparison to wet chemical etching and other dry etching techniques such as plasma and reactive ion etching, the distinct characteristics of ion-beam etching involve a relatively small material selectivity in the etching rate and an ability of anisotropic etching with no mask undercut (1-3). The former makes it possible to etch any material even with a multilayer structure such as Ti/Pt/Au to which the application of chemical etching would be difficult. The latter characteristic is the dominant reason for the use of ion-beam etching in the fine pattern formation down to submicron dimensions in Si and, more recently, GaAs integrated circuits (4), optical waveguide, and grating devices, including distributed-feedback-type (DFB) injection lasers composed of AlGaAs/GaAs (5, 6) and InGaAsP/InP (7) heterostructures. The large area uniformity and the high etching depth controllability are also advantages of ion-beam etching which realizes the batch processing of semiconductor wafers.

Ion-beam etching can improve the pattern quality and complexity when it is applied within the existing semiconductor processes, as mentioned above. However, the extension of its advantages to a novel process would facilitate a drastic improvement in the device and circuit performance. In particular, there has been an accelerating need in the development of high performance light sources and detectors composed of InP and its related compounds for optical fiber communication systems at the wavelengths near 1.3 and 1.5 μm . We have previously reported a novel fabrication method of InGaAsP/InP double heterostructure (DH) light emitting diodes

(LED's) having monolithic InP lenses (8). This has been achieved by an extensive use of controlled and low material selective etching characteristics of the ion-beam etching, and a remarkable improvement in the LED-fiber optical coupling efficiency has been demonstrated. This method of lens formation consists of only two simple process steps: namely, photoresist mask preparation and ion-beam etching, both of which are suitable for batch processing. In addition, this method can eliminate elaborate assembling process required when a separate microlens made of a dielectric material (9) is attached to the individual LED chip.

The purpose of this paper is to describe the details of the lens formation on an InP substrate using Ar ion-beam etching technique. The process sequence is explained briefly in the next section, and the details of the mask preparation and ion-beam etching processes are described in the following two sections. Particularly, the ion-beam etching has been applied to etch the InP substrate down to 8 μm depth. Previous reports on ion-beam etching of InP have shown occasional degradations in the etched surface morphology, including the generation of a number of "cones" (10, 11). In the present study, a sequence of experiments has been carried out to improve the morphology as well as to precisely control the etch rate by the selection of etching parameters such as the ion energy, ion incident angle, and the target supporting technique. In the final part of this paper, the application of this process to the fabrication of LED's and the performance results are demonstrated.

Lens Formation on InP Substrate

Figure 1 illustrates the sequence of processes for forming spherical lenses on an InP substrate (8). Photoresist masks for ion-beam etching are first prepared on the

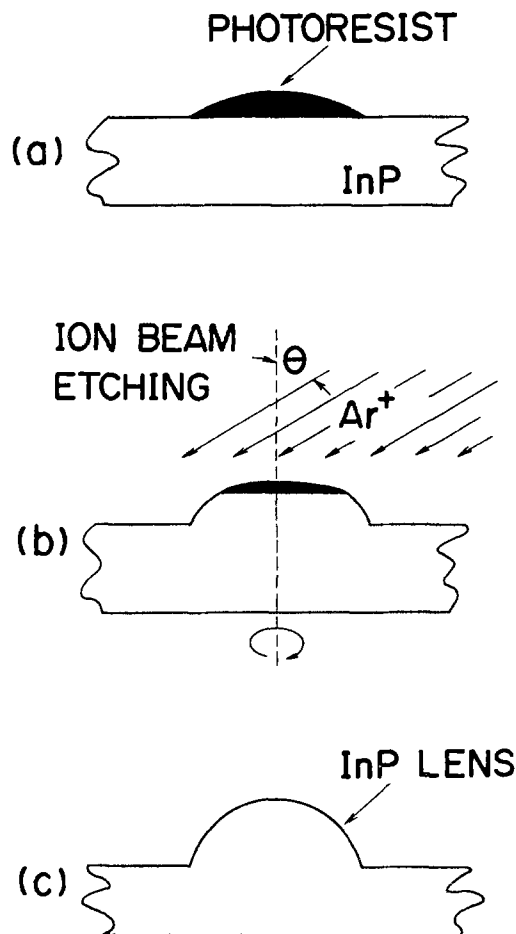


Fig. 1. Sequence of processes for InP lens formation. (a): Mask formation by patterning and baking a photoresist layer. (b): Ar ion-beam etching until complete removal of the mask. (c): Completed InP lens.

substrate surface (a). A commercial positive acting photoresist, Shipley AZ-1350J, has been used in our study. The photoresist patterns with the diameter appropriate to the device design in the range of 60-250 μm , in the present case, are delineated by conventional photolithographic technique. They are then baked at a temperature higher than the glass-transition point of photoresist so that spherical contours are generated by the effect of surface tension on the photoresist surface. Then the substrate is subject to Ar ion-beam etching (b) using, in this experiment, Veeco Microetch system in which Ar^+ ions are generated by a Kaufman ion gun, neutralized, and then fed to bombard a rotating target.

During the etching, the spherical mask contour is transferred to the InP substrate surface. The lens shape is dependent on the initial mask thickness and the mask to substrate ion-beam etch rate ratio which is a function of etching parameters, e.g., the ion energy and the ion incident angle θ .

The morphology of the lens surface is of the most importance in device applications, and it has to be optimized by choosing suitable etching conditions, as will be described in the applications section. By terminating the ion-beam etching when the whole photoresist mask is etched off, an InP lens can be obtained (c). If the etched surface exhibited microfeatures, slight etching by a chemical solvent could be introduced to improve the surface smoothness.

Photoresist Mask Preparation

The most important procedure in preparing the photoresist mask is the baking to generate spherical surfaces. Schematic cross sections of the photoresist layer baked at various temperatures are shown in the inset of Fig. 2. At a temperature just above the glass-transition point at which the flow initiates, the layer exhibits a concave with the

thickness at the center, d , smaller than the initial thickness d_0 , as shown in Ref. (2). By increasing the temperature, the photoresist viscosity decreases and the surface tension dominates in determining the surface geometry to generate a convex as shown in Ref. (3). It is theoretically proved that the geometry stabilized by the effect of surface tension is a sphere (12), and, actually, our stylus measurements have confirmed this.

Figure 2a shows a plot of the photoresist thickness at the center as a function of the baking temperature. The initial thickness d_0 was 3.2 μm . The baking was carried out under a nitrogen flow just after the photoresist development procedure, and the duration was fixed to be 2 min; no appreciable difference was found for longer bakings. As shown in the figure, the temperature required for generating a convex becomes lower for smaller diameter D . It is also found from this result that the convex formation can be achieved only for small diameters up to 80 μm . Figure 2b shows a plot similar to that of Fig. 2a, except that the photoresist layer was exposed to ultraviolet light, prior to the baking, for 220s using a conventional mask alignment equipment. By this exposure, the transition from concave to convex with respect to the temperature increase becomes more distinct; therefore, the stability of the process improves, and the maximum diameter for the convex generation increases to 150 μm . Such an effect is considered to be attributed to the decrease of the photoresist viscosity due to the lowering of the polymer molecular weight under the exposure. Figure 3 summarizes the maximum diameter of the photoresist pattern for which a spherical geometry can be generated as a function of the baking temperature for the duration of 2 min. For our application to the LED fabrication, the diameter of about 100 μm is appropriate. This can be achieved by a baking at the temperature above 190°C.

Our experiments showed that a negative acting photoresist OMR-83 (Tokyo Ohka) exhibits similar convex generation, but in only a narrow range of the baking temperature, the upper value of which is restricted due to the photoresist evaporation. The use of positive acting photoresist is therefore more suitable for this process. It is worth noting here that the generation of a spherical surface is an outcome of the effect of the surface tension, which is highly immune from most deviations in process conditions such as the baking temperature and duration.

Ion-Beam Etching of InP

Etch rate.—The etch rates of the photoresist layer and the (100)-oriented InP wafer were measured at a variety of the ion incident angle (θ) for different ion energies E_i . Figure 4 shows the data obtained at $E_i = 500$ and 1000 eV. The ion current density used is 0.57 mA/cm². The maximum etch rate occurs at smaller angle for InP than for photoresist, and this peak shifts to larger angle as the ion energy increases. This is interpreted by the fact that the chance of a primary ion-target atom collision resulting in the momentum being directed away from the substrate surface increases due to the increase in the primary ion penetration depth at larger incident angle. The detail of the incident angle and energy dependences of the sputtering yield will be discussed in a separate paper.

Figure 5 shows the dependence of the ratio at the etch rate of InP over that of photoresist on the ion incident angle for two ion energies. No appreciable difference in the dependence can be found within the experimental error for two ion energies. The etch-rate ratio monotonically decreases as the incident angle increases, particularly at a small gradient above $\theta = 60^\circ$; this is profitable to stabilize the etch-rate ratio and therefore the lens curvature in practical processes. As will be described in the next section, the incident angle more than 60° is used in the practice from the morphology point of view.

Etched surface morphology.—As the morphology of ion-beam-etched InP surface is one of the most important factors in determining the lens characteristics, a detailed experiment was conducted to study the causes for

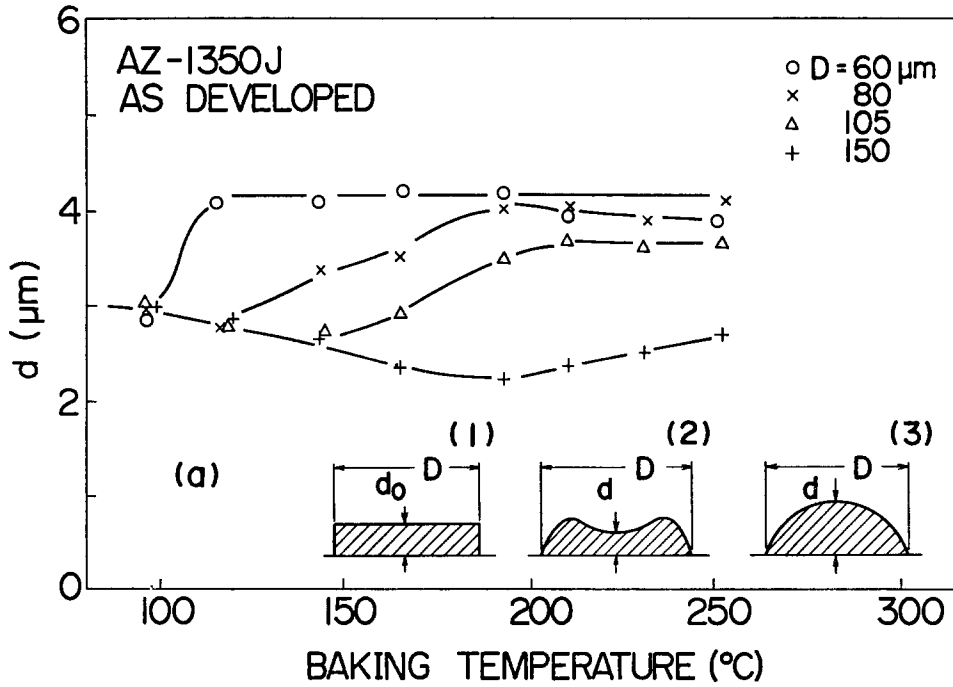


Fig. 2. Baking characteristics of positive-acting photoresist disk with various values of diameter D (a) without and (b) with exposure prior to baking. The thickness of the photoresist layer at its center d can be maximized when a sphere is generated at an elevated temperature. The exposure widens the diameter limit for sphere generation (b).

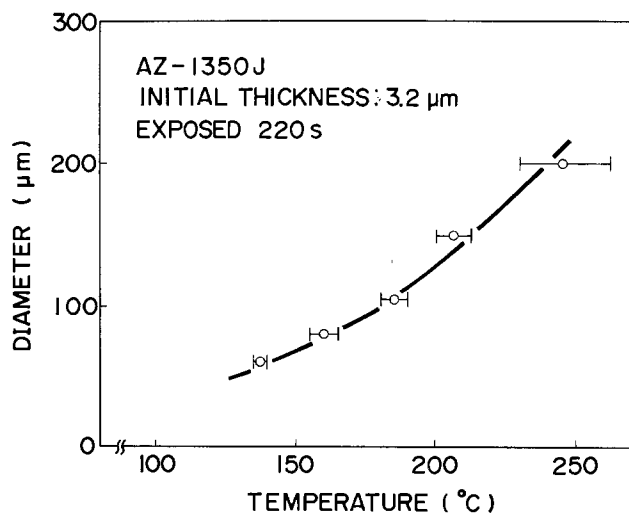
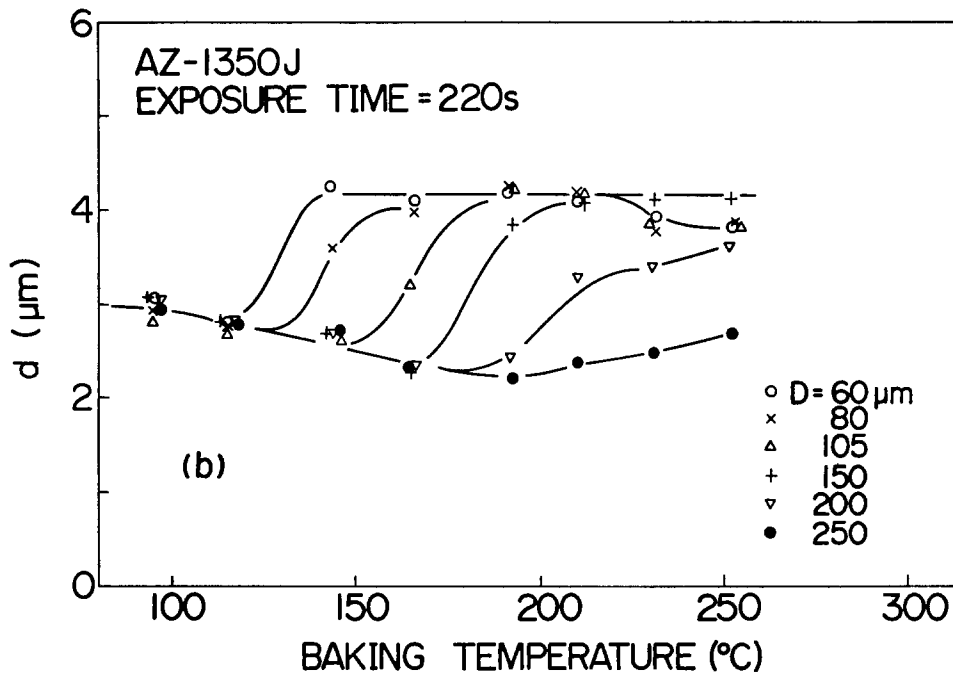


Fig. 3. Baking temperature dependence of maximum diameter for which spherical geometry can be obtained.

degradation of surface morphology. Some of previous works showed the occasional generation of "cones" on InP surfaces (10, 11). The elimination of these was the goal of this series of experiments.

The surface smoothness was compared on samples etched to about $1 \mu\text{m}$ depth using various values of the energy and the incident angle. InP wafers partially masked by photoresist were supported on a substrate holder made of stainless steel. The stylus measurements of smoothness revealed a slight improvement when using larger ion energy (1000 eV, in comparison to 500 eV) and a strong dependence on the incident angle. Figure 6 shows the incident angle dependence of the surface roughness together with scanning electron micrographs of the mask peripheries, gathered at the energy of 500 eV. At the angle of less than 30° , the etched surface exhibits the formation of fine globules and droplets all over the unmasked regions and cones at the mask peripheries. Auger electron spectroscopy measurements performed on some of these etched samples indicated an appreciable deficiency of P near the surface. Taking this into account, the droplets observed as white contrast particles, for example, in the

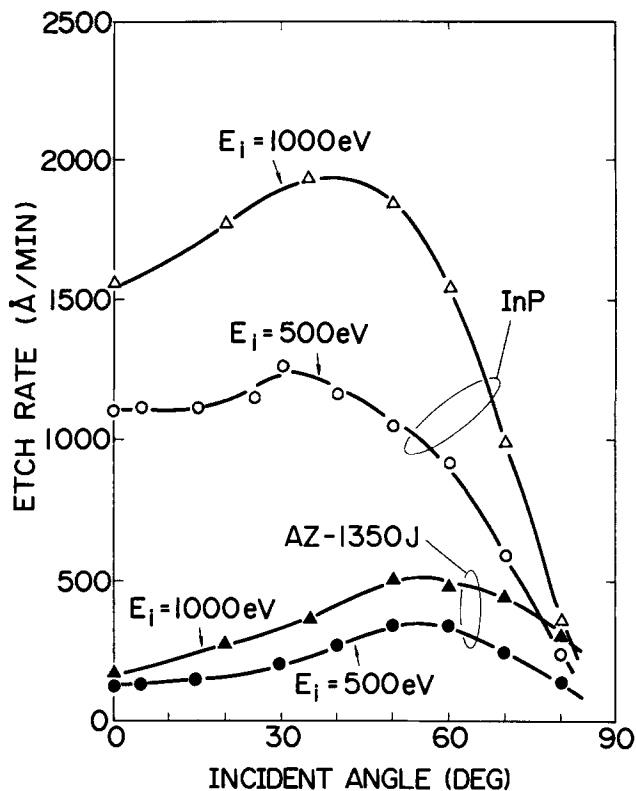


Fig. 4. Ar ion-beam etch rates of InP and positive acting photoresist as a function of ion incident angle for two different ion energies. The ion current density is 0.57 mA/cm^2 .

middle micrograph of Fig. 6, are considered to be composed of In precipitates. This is consistent with the previous reports (13). The geometries of cones at mask edges show no explicit dependence on the incident angle. The generation of cones is suspected to be related to the redeposition of atoms sputtered from the mask, the unmasked regions of the substrate, and even the substrate holder. More details will be discussed later. The morphology degradation is found to be suppressed at the incident angle at 60° , although the etched riser still has wavy feature as shown in the micrograph. The roughness below a few tens of angstroms can be achieved at the incident angle of greater than 50° . It is understood from this result that the use of a large incident angle at the sacrifice of

Fig. 6. Ion incident angle dependence of surface roughness of InP substrate after etching down to approximately $1.1 \mu\text{m}$. Insets are scanning electron micrographs showing the degradation of morphology at mask peripheries for the incident angles of 0° , 30° , and 60° .

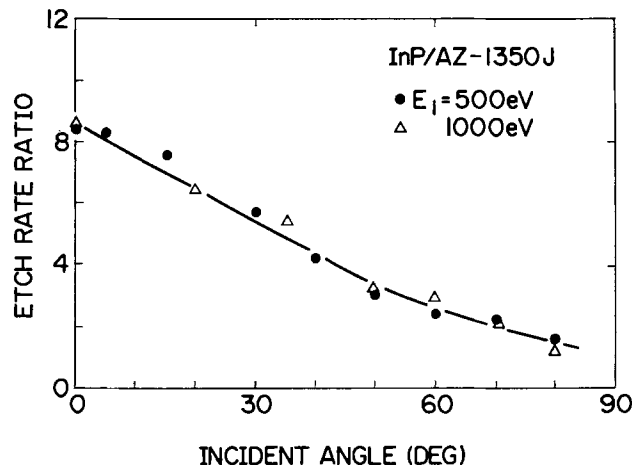
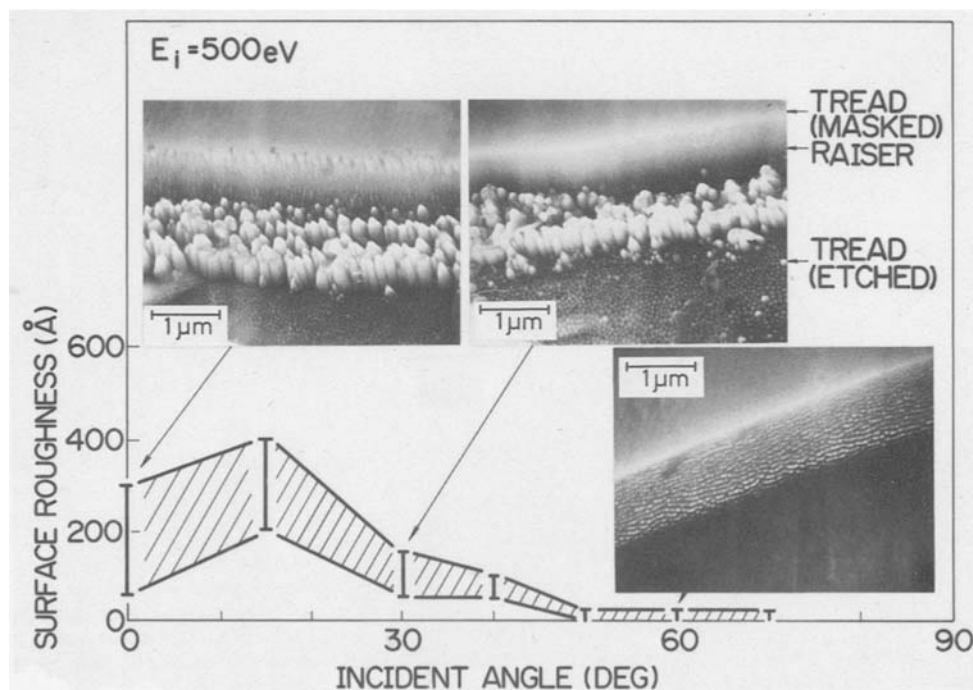


Fig. 5. Ratio of etch rate for InP over that for photoresist as a function of ion incident angle at two ion energies.

long etching time is effective for obtaining smooth etched surfaces.

To look further into the details of etched surface morphology, the effect of the redeposition was studied by varying the substrate supporting methods. The influence of the material supporting the substrate was tested by using photoresist and Ag as small and large sputtering rate (2, 14) materials, respectively. Scanning electron micrographs of both samples taken at tilted angles ($\sim 60^\circ$) are shown in Fig. 7. The ion incidence was normal to the substrate surface, and an ion energy of 500 eV was used. The etching duration was 10 min, which gave the average etching depth of approximately $1.1 \mu\text{m}$. The surface obtained for the photoresist case does not contain any large size cones and hillocks except small globules, but the sample supported on a Ag plate exhibits numerous sharp cones along the ion incident direction. This result may suggest that the redeposition of Ag atoms on the InP substrate during the etching brings about, regardless of its relatively high sputtering yield, the local masking effect to produce cones (15-17). Auger analysis carried out on the InP substrate supported and etched on the Ag plate showed no Ag atom presence on the etched surface. This would be, however, not surprising because it has been shown that extremely small amount of foreign atoms can give rise to the formation of cones on the surface being etched (17). Nevertheless, possibilities of not only the

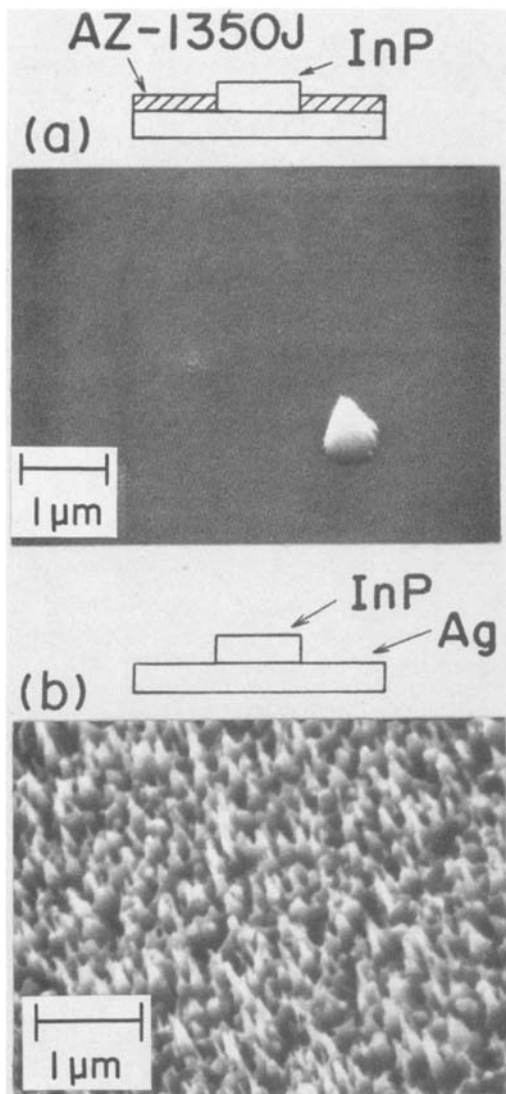


Fig. 7. Scanning electron micrographs indicating effect of material for substrate supporter. Etching has been carried out at $E_i = 500$ eV for 10 min. A cone observed in (a) is considered to be generated by some imperfection included in the original InP surface. Note that the sputter rate is much larger for Ag than for AZ-1350J.

chemical and/or metallurgical reaction of Ag with InP but also the incorporation of impurity atoms having the low sputtering yield and/or high melting point (20) should be considered in order to fully understand the cone generation. A marked difference in the surface feature observed within the present set of samples at least reveals a strong influence of the choice of the supporting material on the etched surface morphology.

The redeposition effect was examined also by using an InP substrate having a special structure (shown in Fig. 8). A part of the substrate of approximately 2 cm^2 area was surrounded by InP walls with a height of approximately 1.5 cm. This substrate was supported on a stainless steel holder, considering that the surface feature obtained by the stainless steel holder is similar to that observed in the experiment using photoresist (Fig. 7a). The ion-beam etching was performed with $E_i = 500$ eV at the normal incidence. The etching duration was selected to be as long as used in practice, 55 min, which corresponds to an etching depth of about $6 \mu\text{m}$. Scanning electron micrographs at two different positions within the wafer are shown in Fig. 8. The part of the surface surrounded by the walls (A) exhibits only small globules similar to that seen in Fig. 6 and Fig. 7a, whereas the outer part (B) suffers from having numerous cones which are aligned in the ion direction. The density of cones generated was found to increase at the edge of the substrate. The present result is

likely to be again consistent with the model in which the redeposition of atoms sputtered from the InP substrate as well as the substrate supporter on the InP substrate causes the generation of cones. The higher density of cones at the substrate edge is considered to suggest a stronger effect of the redeposition from the substrate supporter material rather than from the InP substrate itself. It is also found reasonable to say that the globules as observed in Fig. 6 grow to become larger size cones in the course of a prolonged etching.

The result described above indicates the importance of preventing the sputtered atoms from depositing on the surface of the substrate being etched. This can be achieved in the case of the normal incidence by the structure of Fig. 8, but a configuration to lift up the substrate, which is useful for any incident angles, was recently suggested by Williams *et al.* (18). We designed a substrate holder as shown in Fig. 9, in which titanium was chosen because of its low sputtering rate. The substrate surface is approximately 2 cm apart from the holder plane in this configuration, and a remarkable effect in eliminating the surface microfeature has been confirmed in etching down to $8 \mu\text{m}$ depth. An example of this will be given later in this paper (Fig. 13).

Spherical lens formation.—We first consider the geometry of a lens formed by ion-beam etching using a spherical photoresist mask. Figure 10 illustrates the substrate cross section before and after the etching. The aperture diameter of the lens is D , and the maximum height of the photoresist mask at its center is h_r . The radius of the mask is given by

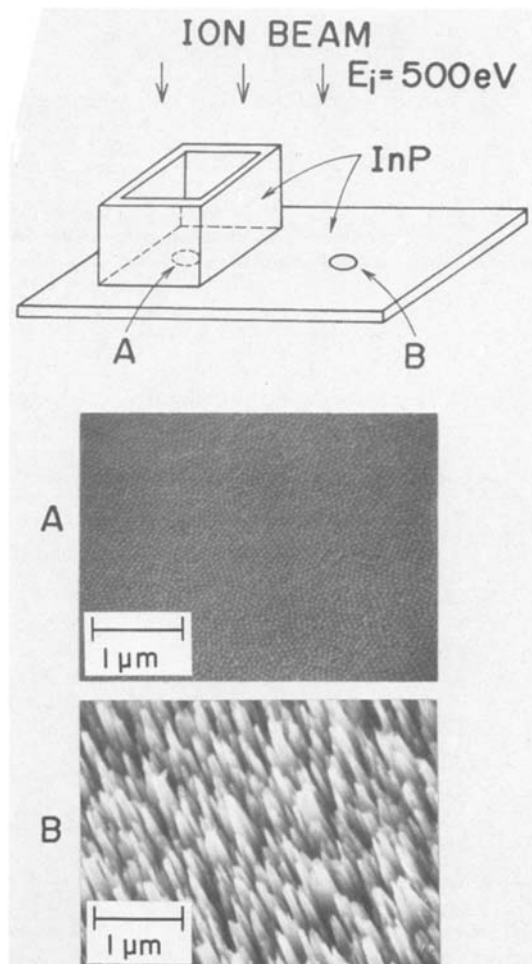


Fig. 8. Structure of target used for examining redeposition effect and scanning electron micrographs showing surface features obtained at different positions on the target. The generation of numerous cones at B indicates that the redepositing atoms enhance the cone generation. The ion incidence is normal to the substrate plane, and the etching time is 55 min.

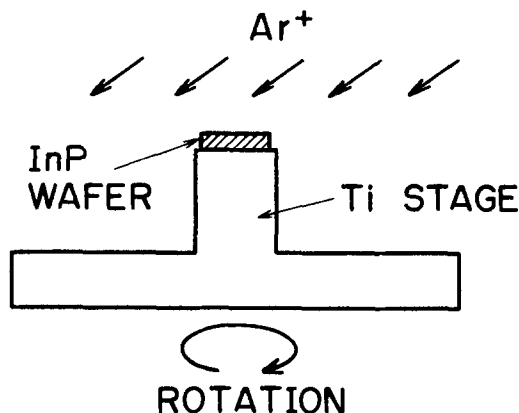


Fig. 9. Structure of target supporter made of Ti, in which target can be lifted up toward incident beam.

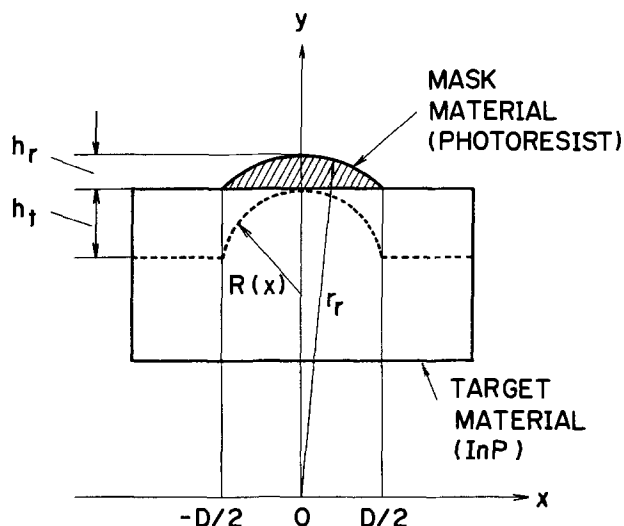


Fig. 10. Schematic cross section of InP substrate with spherical photoresist mask. A lens contour to appear is shown by a dotted line.

$$r_r = [h_r^2 + (D/2)^2]/2h_r \quad [1]$$

After the ion-beam etching, a lens shape as shown by the dotted line in Fig. 10, is generated and this becomes an ellipse expressed as

$$\frac{x^2}{r_r^2} + \frac{[y + (k-1)r_r + h_r]^2}{k^2 r_r^2} = 1 \quad [2]$$

with the radius at x of

$$R(x) = \frac{r_r}{k} \left[1 + (k^2 - 1)^{3/2} \left(\frac{x}{r_r} \right)^3 \right] \quad [3]$$

where k stands for the mask to target etch rate ratio. When the second term in the bracket of Eq. [3] is well smaller than unity, the lens geometry becomes a sphere with a constant radius of

$$R(x) = R = r_r/k \quad [4]$$

This applies at least to the near-axis radius in our practical case where the values of k and $D/2r_r$ are both less than 3 and 0.1, respectively.

The lens geometry was actually measured by stylus and compared with the calculation explained above. Figure 11 shows an example of the results, in which the height of the photoresist mask was $3.0 \mu\text{m}$ and the value of k of 2.3 was selected at the ion incident angle of 65° during the etching. The lens height h_l has been measured to be $7.0 \mu\text{m}$, and the calculation curve has been obtained with the assumption of a sphere with the radius determined from $R = [h_l^2 + (D/2)^2]/2h_l$. The agreement between the measurement and the calculation is considered to be excellent, taking into account the simplicity of the calculation. The present method has been thus confirmed to realize spherical lenses. The optical property of lenses with a variety of the radius has been previously demonstrated through the observation of images of patterns prepared on the substrate surface opposite to the lens, in which a good agreement has been seen between the measured and calculated magnification characteristics (8).

Application to InGaAsP/InP DH LED's

The present method was applied to improve the light coupling efficiency of InGaAs/InP DH LED to optical fiber. The structure of the LED is shown in Fig. 12. The fabrication method will be explained just briefly in the following, since it is essentially same as that already reported (19). The DH structure, which includes a low doped n-type InGaAsP active layer with the composition of a $1.3 \mu\text{m}$ wavelength emission and the thickness of about $1.5 \mu\text{m}$, was grown on a (100)-oriented n-InP substrate by conventional sliding boat system of liquid-phase epitaxy. A $40 \mu\text{m}$ diam p contact composed of a Au/Zn/Au multilayer was formed, and an isolating SiO_2 layer and subsequently a thick-plated Au layer were formed. The substrate was then polished to approximately $100 \mu\text{m}$ thickness, and the present lens formation procedures were applied. After the lens was formed, an n contact of AuGe/Ni film was prepared and a SiO_2 antireflection coating was deposited. The individual LED chip was mounted on a copper heat sink and assembled with a spherical-ended fiber.

An example of scanning electron micrograph of the lensed LED thus fabricated is shown in Fig. 13. The lens aperture and the lens height in this case are 90 and $8 \mu\text{m}$, respectively, giving a magnification of 2. In etching the InP substrate, the higher ion energy, 1000 eV , and the larger incident angle, 65° , were adopted together with the use of the target supporter made of Ti (Fig. 9). It is significant to note that the lens surface is completely free from any inhomogeneities and far improved in comparison with a surface that would be obtained without an optimization of etching conditions as has been performed in our experiment. The remarkable improvement of the surface smoothness, particularly observed outside the lens aperture, can be noticed by comparing Fig. 13 with the previous results, e.g., Fig. 7 of Ref. (8).

Figure 14 shows the characteristic of the light power coupled to a graded-index fiber as a function of the bias

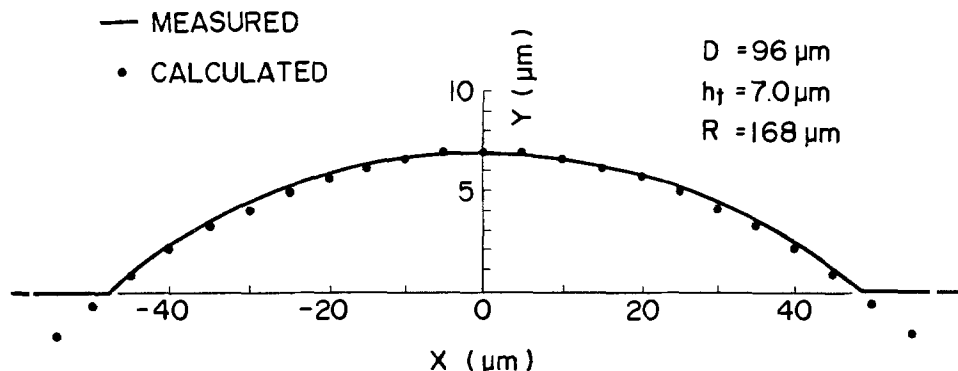


Fig. 11. Comparison of lens geometries obtained by stylus measurement and calculated by assumption of sphere. It is clear that a spherical lens is formed by the present technique.

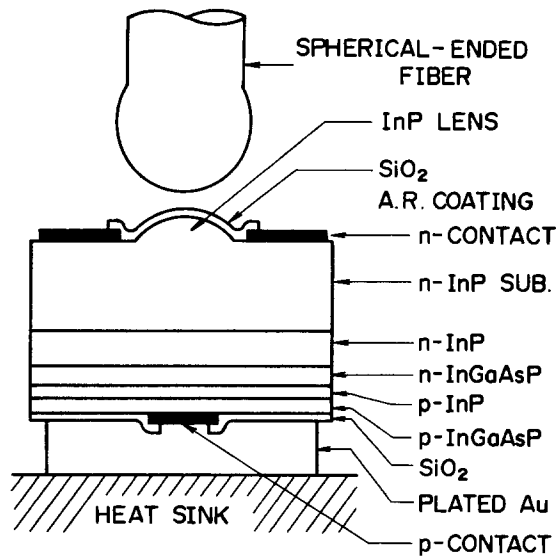


Fig. 12. Schematic illustration of InGaAsP/InP DH LED coupled to fiber. The InP lens can significantly improve the light coupling efficiency.

current for both the lensed and conventional flat-surface LED's prepared from the same epitaxial wafer. An improvement of the coupled power by a factor of 1.8 is estimated at the current of 100 mA, by introducing the lensed LED structure. The ultimate power of $35 \mu\text{W}$ at 100 mA is classified in the highest available power with the surface emitting-type LED at the $1.3 \mu\text{m}$ wavelength. It would be both interesting and important to point out another advantage of the lensed LED structure: the improvement in the frequency response characteristics (19). The lens makes the light generated near the p contact center, where a faster response can be realized than at the contact edge owing to the current crowding effect, to be coupled predominantly. This effect gives rise to more than 50% improvement in the cut-off frequency characteristics, and the maximum value of 120 MHz has been achieved in our experiment.

Summary

A technique for preparing spherical lenses on an InP substrate by means of Ar ion-beam etching using a thermally deformed photoresist layer as an etching mask was investigated and applied to the fabrication of high radiance InGaAsP/InP DH LED's. The mask, having a geometry of perfect sphere, was found to be formed easily and reproducibly by introducing the exposure prior to baking and choosing a suitable baking temperature. The conditions of Ar ion-beam etching were optimized in terms of the controllability of the etch depth into InP and the morphology of the etched surface. It was found that a very

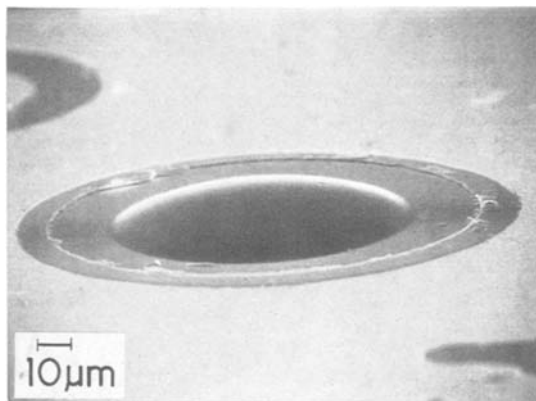


Fig. 13. Scanning electron micrographs showing lensed surface of completed LED chip. Note that the lens surface is free from any imperfections.

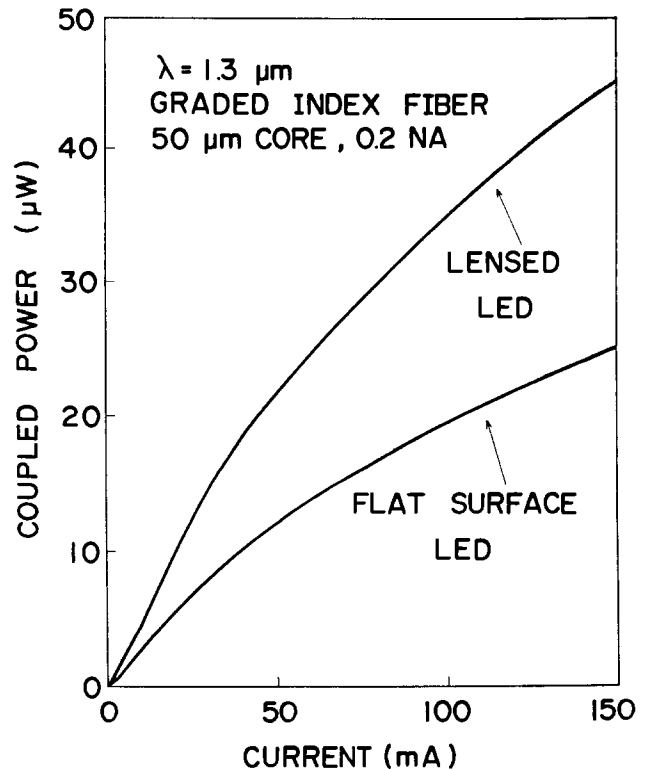


Fig. 14. Bias current dependences of light power coupled to fiber for both lensed and conventional flat-surface LED's. The lensed LED gives 1.8 times greater power than the conventional device.

smooth surface can be generated by using (i) a relatively high ion energy (1000 eV), (ii) a large ion incident angle (60° - 70°), and (iii) a titanium-made supporter which lifts up the InP substrate. The present substrate supporter was significantly effective in eliminating the redeposition effect and in producing microfeature-free lens surfaces. Experiments also confirmed the reproducible generation of InP lenses with smooth spherical surfaces. This technique was applied to fabricate surface emitting InGaAsP/InP DH LED's at $1.3 \mu\text{m}$. The device performance was measured, and a remarkable improvement in the coupling efficiency, namely, by a factor of 1.8, was demonstrated.

It is worth pointing out that the present technique exhibits a high reproducibility and a high controllability of lens geometry. Moreover, this technique is favorable to the batch processing. In view of further applications, the present technique can be suitable for preparing non-spherical lenses too, since the geometry of the lens can be varied by the selection of the mask to substrate ion-beam etch-rate ratio. This can be carried out by changing, for example, the ion incident angle during the etching. Such applications are considered to be interesting in fabricating various devices for fiber as well as waveguide optics.

Acknowledgments

The author would like to express his thanks to T. Ishiyama for processing LED's and to Y. Nishitani for growing epitaxial wafers. Thanks are also due to T. Sakurai, Y. Toyama, and K. Dazai (Fujitsu Laboratories) and T. Ikegami (Nippon Telegraph and Telephone Public Corporation) for their continuous encouragement during the work.

Manuscript submitted Nov. 28, 1983; revised manuscript received April 3, 1984.

Fujitsu Laboratories Limited assisted in meeting the publication costs of this article.

REFERENCES

1. P. G. Glöersen, *J. Vac. Sci. Technol.*, **12**, 28 (1975).
2. C. M. Melliar-Smith, *ibid.*, **13**, 1008 (1976).
3. J. M. E. Harper, J. J. Cuomo, and H. R. Kaufman,

- ibid.*, **21**, 737 (1982).
4. R. E. Lee, *ibid.*, **16**, 164 (1979).
 5. S. Somekh and H. C. Casey, Jr., *Appl. Opt.*, **16**, 126 (1977).
 6. L. F. Johnson and K. A. Ingersoll, *Appl. Phys. Lett.*, **35**, 500 (1979).
 7. Y. Yuba, K. Gamo, H. Toba, Xi Guan He, and S. Namba, *Jpn. J. Appl. Phys.*, **22**, 1206 (1983).
 8. O. Wada, S. Yamakoshi, M. Abe, Y. Nishitani, and T. Sakurai, *IEEE J. Quant. Electron.*, **qe-17**, 174 (1981).
 9. R. C. Goodfellow, A. C. Carter, I. Griffith, and R. R. Bradley, *IEEE Trans. Electron Devices*, **ed-26**, 1215 (1979).
 10. D. J. Barber, F. C. Frank, M. Moss, J. W. Steeds, and I. S. T. Tsong, *J. Mater. Sci.*, **8**, 1030 (1973).
 11. D. L. Kirk and C. Jones, *J. Phys. D*, **12**, 651 (1979).
 12. H. Marginau and G. M. Murphy, "The Mathematics of Physics and Chemistry," Chap. 6, Van Nostrand (1945).
 13. M. G. Dewsett, R. M. King, and E. H. C. Parker, *Appl. Phys. Lett.*, **31**, 529 (1977).
 14. Y. Okajima, *J. Appl. Phys.*, **51**, 715 (1980).
 15. A. D. G. Stewart and M. W. Thompson, *J. Mater. Sci.*, **4**, 56 (1969).
 16. M. J. Witcomb, *ibid.*, **9**, 551 (1974).
 17. G. K. Wehner and D. Najicek, *J. Appl. Phys.*, **42**, 1145 (1971).
 18. R. S. Williams, R. J. Nelson, and A. R. Schlier, *Appl. Phys. Lett.*, **36**, 827 (1980).
 19. O. Wada, H. Hamaguchi, Y. Nishitani, and T. Sakurai, *IEEE Trans. Electron Devices*, **ed-29**, 1454 (1982).
 20. G. K. Wehner, *Appl. Phys. Lett.*, **43**, 366 (1983).

Oxidation-Induced Defects at the Poly/Mono Silicon Interface

W. J. M. J. Josquin and M. J. E. Ulenaers

Philips Research Laboratories, 5600 JA Eindhoven, The Netherlands

ABSTRACT

The application of polycrystalline silicon in intimate contact with monocrystalline silicon can give rise to the growth of oxidation-induced stacking faults. When Si_3N_4 is employed on top of the polysilicon, the oxidation can also generate dislocations along Si_3N_4 edges. It appears that the key parameters in the defect generation mechanisms are the oxygen concentration at the poly/mono interface and, related to that, the epitaxial realignment of the polysilicon on the substrate. The experiments indicate which conditions are beneficial for the application of polysilicon on the back of silicon wafers for enhanced gettering purposes. They also indicate how oxidation-induced defects can be avoided when polysilicon is applied on the front side of silicon wafers as a gate material and/or as a diffusion source.

Polycrystalline silicon in intimate contact with monocrystalline silicon is extensively used in silicon IC technology for quite diverse purposes. On the one hand, polycrystalline silicon is applied to the back of silicon wafers to obtain an enhanced gettering effect. In this case, the presence of crystal defects at the back of the wafer is the key to an effective gettering action. It has been shown that the employment of patterned Si_3N_4 on top of the polysilicon further improves the gettering efficiency (1). On the other hand, polysilicon is applied to the front side of silicon wafers as a gate material and/or as a diffusion source. In this case, Si_3N_4 is often employed on top of the polysilicon so that local oxidation techniques can be used to pattern the polysilicon (2, 3). For these applications, the occurrence of any defect in the device area can be fatal for the device performance.

In both cases, two types of defects can be expected: oxidation-induced defects originating from the poly/mono interface (8) and stress-induced dislocations along Si_3N_4 edges. The present study deals with the defect-generation mechanisms and the elimination of defects in devices with polysilicon diffusion sources, but many of the results are also significant for the understanding of enhanced gettering mechanisms.

Experimental

The substrates used throughout the study were p-type, 15-25 Ω cm, <100> CZ silicon wafers, unless otherwise specified. The wafers were cleaned in fuming nitric acid and hot concentrated nitric acid, causing the wafers to be covered with a native oxide layer, which will be referred to as cleaning oxide. Subsequently, one set of wafers was dipped in a 1% HF solution to remove the cleaning oxide, a second set received no further treatment, and a third set was heat-treated at 850°C in dry nitrogen for 30 min to densify the cleaning oxide. RBS analysis has revealed that this results in oxygen concentrations at the poly/mono interface which are equivalent to 0.5, 1.4, and 2.0 nm SiO_2 , respectively (4). The various sets of wafers will be referred to as wafers with dipped, cleaning oxide, and densified cleaning oxide interfaces.

The wafers were covered with 0.1 μm of polycrystalline silicon deposited from SiH_4 at 625°C and a pressure of 140 mtorr. On top of the polysilicon, a Si_3N_4 layer 0.1 μm thick was deposited from SiH_2Cl_2 and NH_3 at 820°C and a pressure of 200 mtorr. Then a preoxidation annealing treatment was applied of either 20h at 850°C or 5h at 1000°C in dry nitrogen to simulate extensive low or high temperature processing. Next, a photomask was used to pattern the Si_3N_4 layer. On half of the wafers the polysilicon was also etched using anisotropic plasma etching. Then the wafers were oxidized in wet oxygen ($p_{\text{H}_2\text{O}} \sim 0.80$) to an oxide thickness of about 0.55 μm .

In this way, all the polysilicon was converted into SiO_2 . Oxidation was carried out at temperatures of 1000°, 950°, 900°, and 850°C. Finally, the oxide and nitride layers were stripped and Wright etch was applied to reveal oxidation-induced defects. The etched surfaces were examined in an SEM using a magnification of 5000 \times , unless otherwise specified.

From some of the wafers, TEM specimens were prepared by thinning stripped wafers from the back in an etchant composed of HNO_3 , HF, and CH_3COOH (4:1:1). Observations were made with a Philips EM400T microscope operated at 120 kV.

On some wafers, no Si_3N_4 was deposited, and the final oxide of 0.55 μm was etched back to 0.15 μm , which then served as the gate oxide of gate-controlled diodes fabricated on those wafers.

Results

Field defects.—The first results concern wafers with a dipped poly/mono interface which received a preoxidation anneal at 850°C. Figure 1 shows SEM micrographs of the samples after oxidation at four different temperatures (A: 850°C, B: 900°C, C: 950°C, and D: 1000°C) and Wright etching. After oxidation at 1000° and 950°C, very high densities of stacking faults were found ($\sim 10^8$ cm $^{-2}$); at 900°C a small number of small etch pits was observed, and at 850°C no crystal defects could be detected. These results were found to be reproducible both for <100>- and <111>-oriented wafers, with and without phosphorous gettering at the back of the wafers.

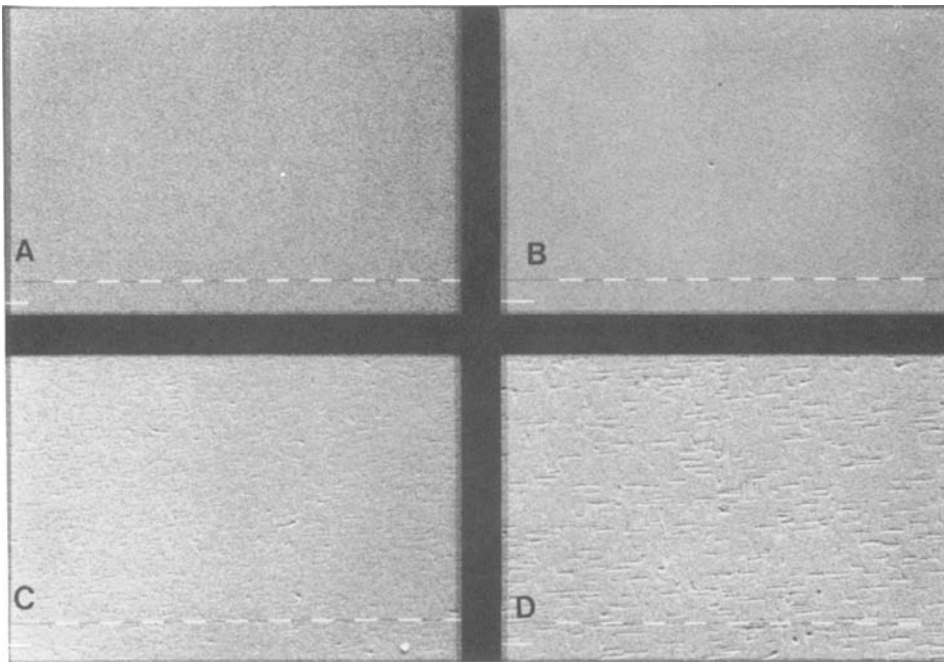


Fig. 1. SEM micrographs of Wright-etched samples with a dipped poly/mono interface and a preoxidation anneal at 850°C for different oxidation temperatures: A: 850°C, B: 900°C, C: 950°C, and D: 1000°C (5000x).

Figure 2 shows the corresponding TEM micrographs of the samples oxidized at 900° (A), 950° (B), and 1000°C (C). In the 850°C sample, again no defects could be detected. The other three samples show defect densities of about 10^8 cm^{-2} . At 900°C, the only observable defects are stacking faults, whereas at 950° and 1000°C, dislocations as well are observed which may be the result of an unfauling reaction of the stacking faults. The length of the stacking faults is 2.2 μm at 1000°C, 1.4 μm at 950°C, and about 0.75 μm at 900°C. Using weak beam imaging, we found no impurity decoration of the defects. The discrepancy between the defect densities observed in the 900°C

sample by TEM and by preferential etching suggests that the preferential etching technique may have failed to reveal the small stacking faults.

Figure 3 shows the corresponding SEM micrographs of the wafers with a cleaning oxide at the poly/mono interface and a preoxidation anneal at 850°C: there are now no defects to be seen, irrespective of the oxidation temperature.

Wafers with a dipped interface and with a cleaning oxide interface were processed to obtain gate-controlled diodes. About 0.15 μm of the oxide grown at the four different temperatures served as the gate oxide. Table I lists

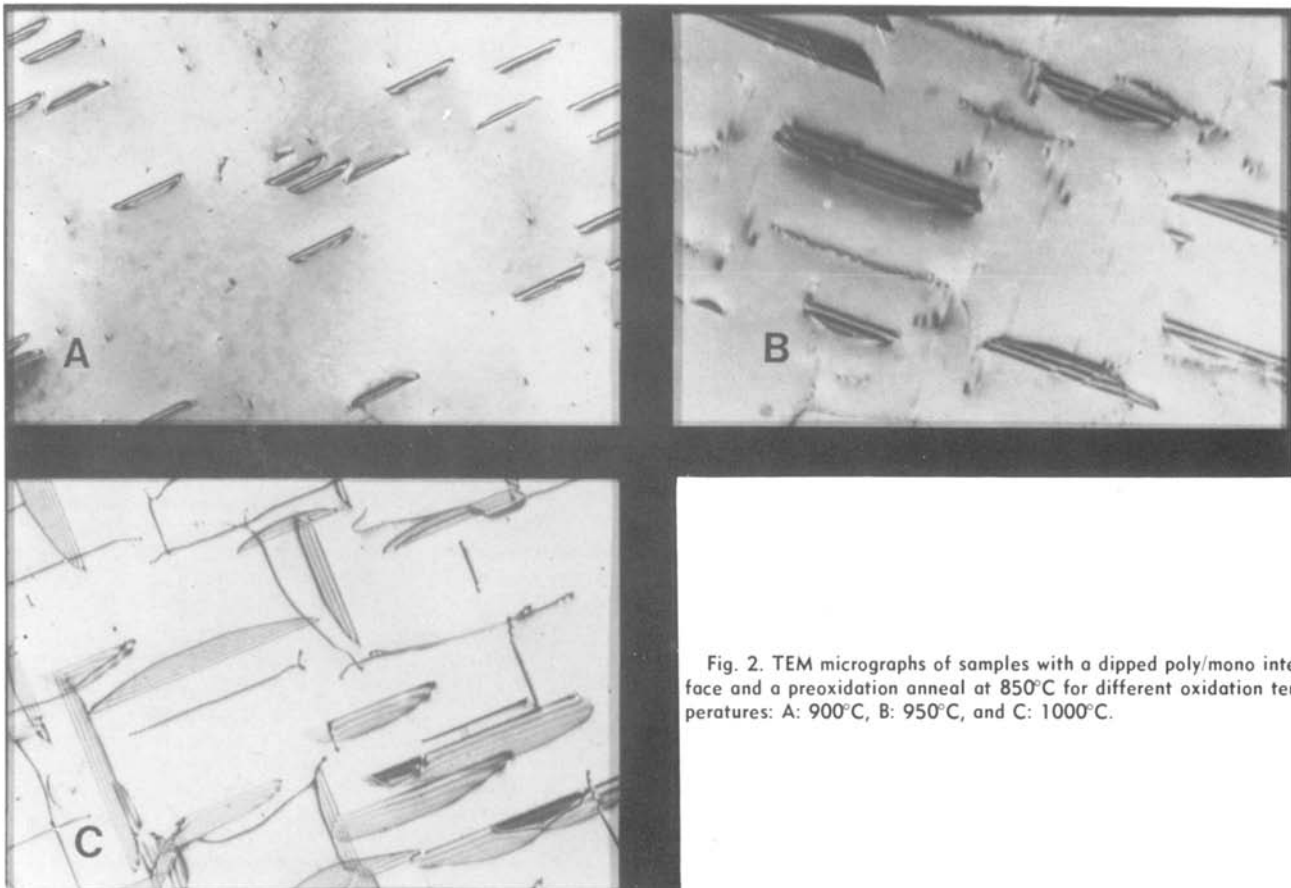


Fig. 2. TEM micrographs of samples with a dipped poly/mono interface and a preoxidation anneal at 850°C for different oxidation temperatures: A: 900°C, B: 950°C, and C: 1000°C.

Fig. 3. SEM micrographs of Wright-etched samples with a cleaning oxide interface and a preoxidation anneal at 850°C for different oxidation temperatures: A: 850°C, B: 900°C, C: 950°C, and D: 1000°C (5000x).

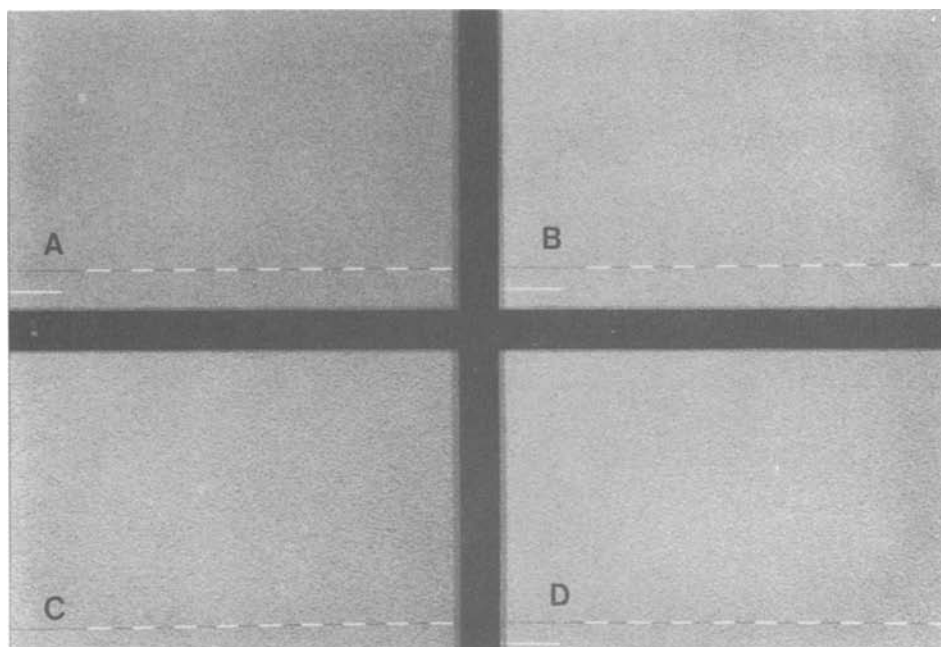
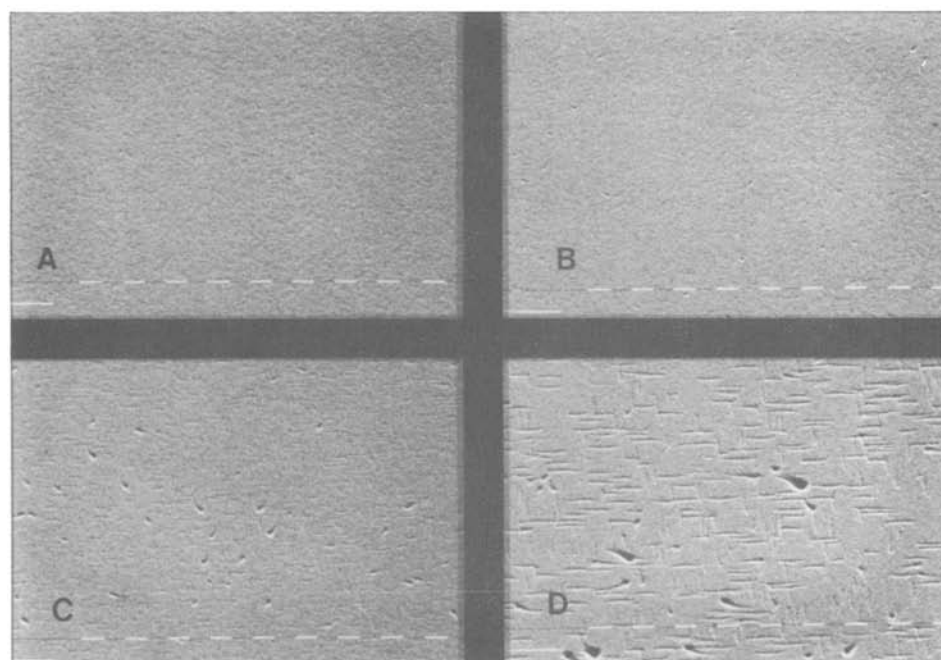


Fig. 4. SEM micrographs of Wright-etched samples with a cleaning oxide interface and a preoxidation anneal at 1000°C for different oxidation temperatures: A: 850°C, B: 900°C, C: 950°C, and D: 1000°C (5000x).



the reverse current densities for the depletion mode: for a dipped interface and an oxidation temperature of 850°C or for a cleaning oxide interface the current density is about 1 nA/cm², which is equal to the current level found on control wafers on which no polysilicon had been deposited. For a dipped interface and an oxidation temperature higher than 850°C, the current density is at least an order of magnitude higher and increases slightly with the oxidation temperature. The current densities were found to be independent of the substrate orientation (<100> or <111>) or the type of material (FZ or CZ). It is clear that there is a strong correlation between the reverse current densities and the observed defect densities.

Figure 4 shows the SEM micrographs for wafers with a cleaning oxide interface which received a preoxidation anneal at 1000°C: the defect densities are seen to be similar to the ones found for wafers with a dipped interface and an 850°C preoxidation anneal (Fig. 1). In fact, for wafers with a dipped interface, the temperature of the preoxidation anneal does not affect the final defect density. The field defect densities after Wright etching are summarized in Table II in a semi-quantitative way.

Wafers with a densified cleaning oxide interface show zero defect densities, independent of the preoxidation annealing temperature or the oxidation temperature.

When the polysilicon was removed prior to the oxidation by anisotropic etching in a Cl₂ plasma, using a 100% overetch to a depth of about 0.1 μm in the substrate, no defects were observed, irrespective of interfacial conditions, preoxidation anneal, or oxidation temperature.

Figure 5 shows SEM micrographs of the polysilicon surface morphology immediately after a preoxidation anneal at 1000°C for the three interface conditions: dipped

Table I. Reverse current densities (nA/cm²) of gate-controlled diodes in depletion mode

Oxidation temp.	Prior to poly-Si deposition	
	1% HF dip	No HF dip
1000°C	25-50	1.0
950°C	15-35	1.0
900°C	10-20	1.0
850°C	1.0	1.0

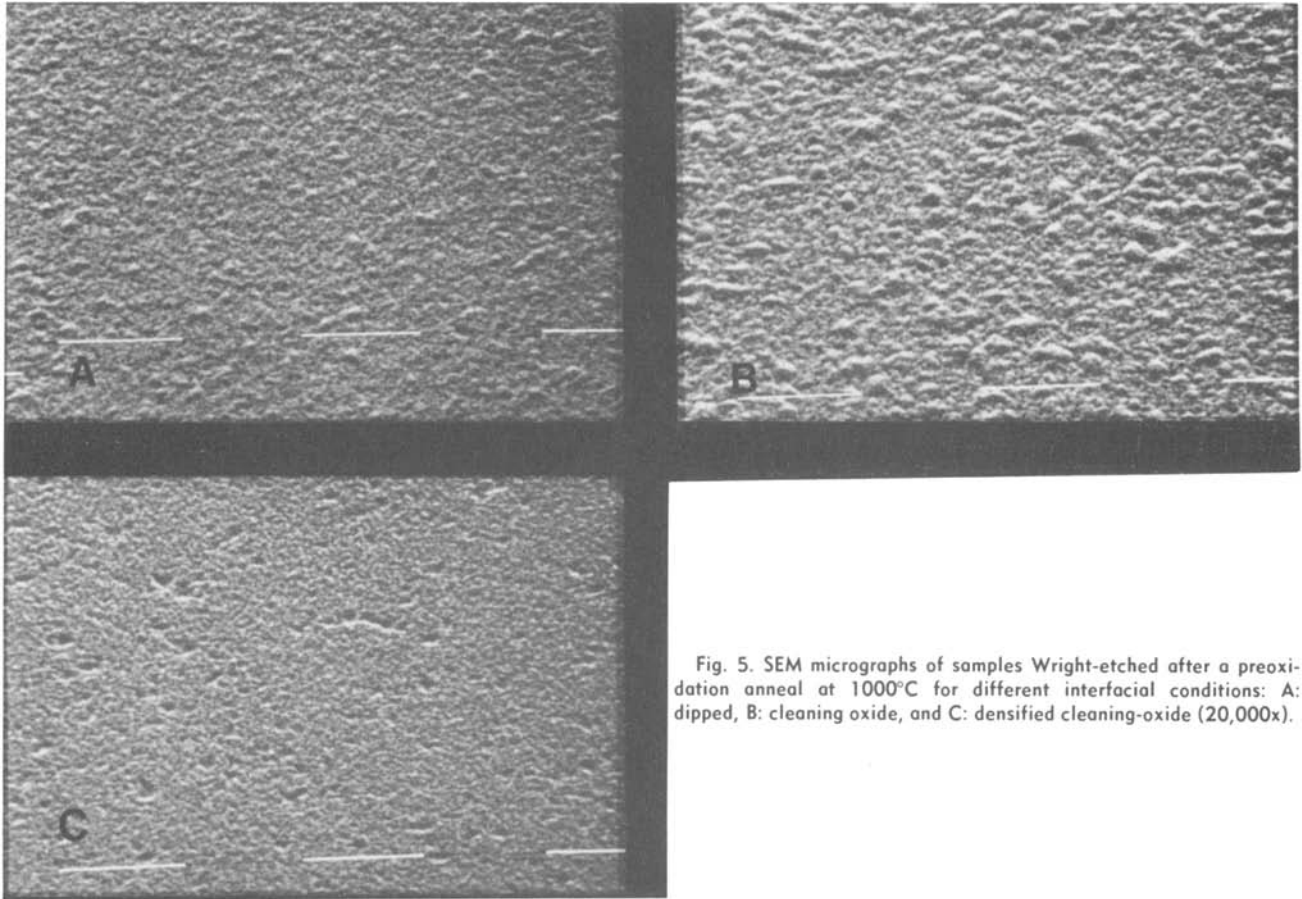


Fig. 5. SEM micrographs of samples Wright-etched after a preoxidation anneal at 1000°C for different interfacial conditions: A: dipped, B: cleaning oxide, and C: densified cleaning-oxide (20,000x).

(A), cleaning oxide (B), and densified cleaning oxide (C). The sample with a dipped interface shows a relatively smooth surface, the sample with the cleaning oxide interface gives a rougher surface, whereas the densified cleaning oxide interface results in a smoother surface.

Edge defects.—Edge defects can be observed most clearly when no field defects are present. Therefore, we will first discuss the results obtained on wafers where the polysilicon was removed by plasma etching prior to the oxidation to avoid field defects. Figure 6 shows the SEM micrographs of samples that were locally oxidized using $0.1 \mu\text{m Si}_3\text{N}_4$ as an oxidation mask on wafers with a

dipped poly/mono interface which received a preoxidation anneal at 850°C. The defect density along the Si_3N_4 edges is seen to be very high after oxidation at 850° (A), 900° (B), or 950°C (C), and only slightly lower at 1000°C (D).

Figure 7 shows the corresponding micrographs for wafers with a cleaning-oxide interface. At 850° (A), 900° (B), and 950°C (C) no defects are observed; at 1000°C (D), a considerable defect density is found. A comparison of Fig. 1 (field defects) and fig. 6 (edge defects) illustrates that whenever stacking faults occur after oxidation of polysilicon, defects along Si_3N_4 edges are found as well. The opposite is not true, however: when a wafer is free of

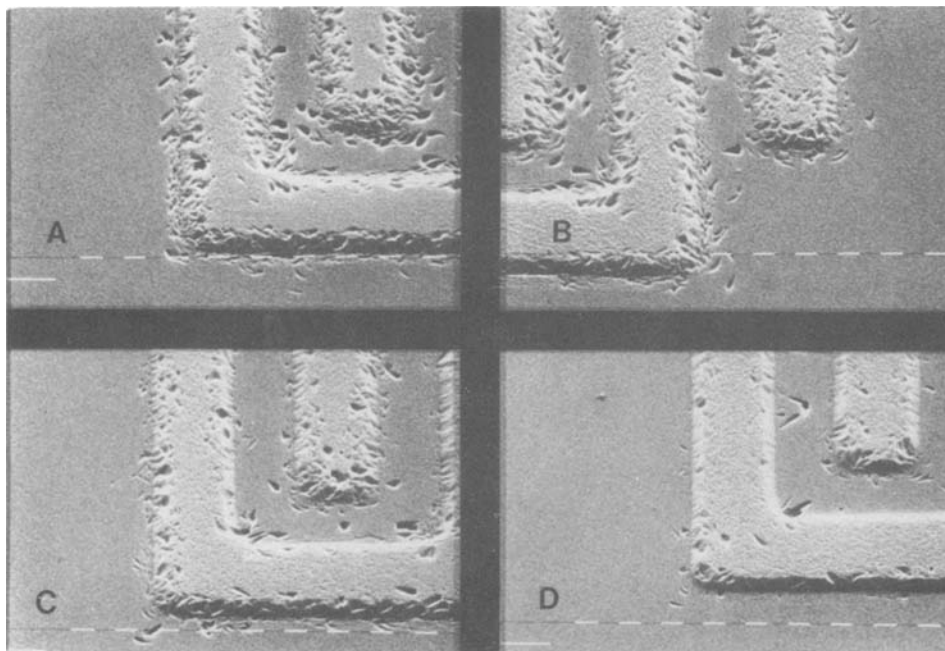
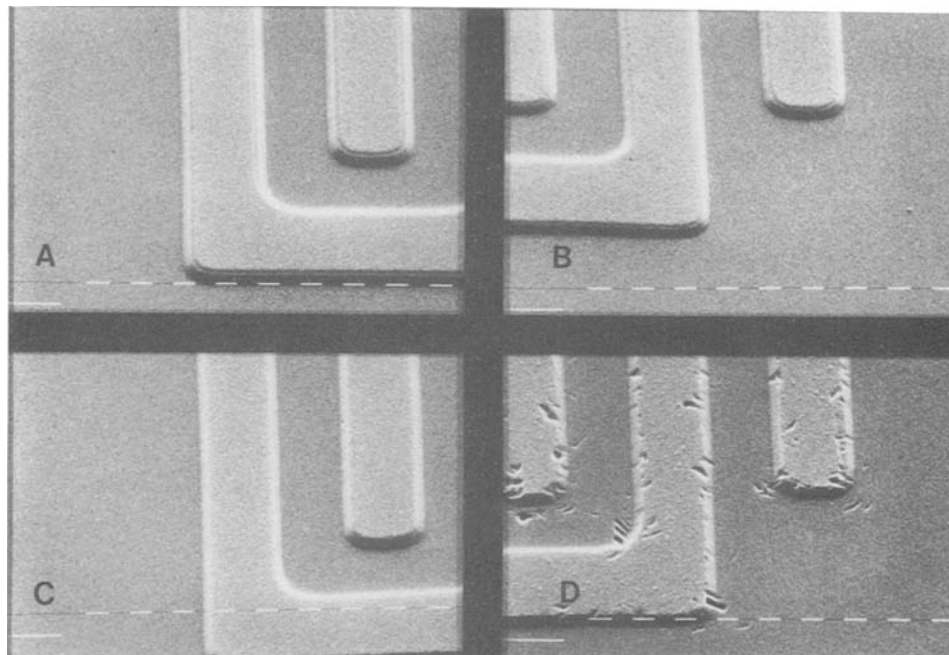


Fig. 6. SEM micrographs of Wright-etched samples with a dipped interface, a preoxidation anneal at 850°C, and polysilicon etched prior to oxidation at A: 850°C, B: 900°C, C: 950°C, and D: 1000°C (5000x).

Fig. 7. SEM micrographs of Wright-etched samples with a cleaning oxide interface, a preoxidation anneal at 850°C, and polysilicon etched prior to oxidation at A: 850°C, B: 900°C, C: 950°C, and D: 1000°C (5000x).



stacking faults, it may still contain edge defects. After an oxidation at 850°C, stacking faults are never observed; nevertheless, Fig. 6a shows a large number of edge defects.

Similarly, a wafer with a cleaning oxide interface does not show stacking faults after oxidation at 1000°C, but does show a considerable number of edge defects (cf. Fig. 3d and 7d).

When wafers with a cleaning oxide interface are preannealed at 1000°C, the same trend is observed as for wafers with a dipped interface: very high defect densities after oxidation at 850° (A), 900° (B), or 950°C (C) and only a slightly lower defect density at 1000°C (D). The edge defect densities observed after Wright etching are summarized in Table III in a semi-quantitative way.

Wafers with a densified cleaning-oxide at the poly/mono interface never show edge defects.

For the wafers where the polysilicon is not removed in a plasma prior to the local oxidation, one might expect

the final defect density to be the sum of the field defects [Fig. 1 (dipped) and 3 (cleaning oxide)] and the edge defects [Fig. 6 (dipped) and 7 (cleaning oxide)]. Figures 8 and 9 show the actual results for wafers with a dipped and a cleaning oxide poly/mono interface. It appears that there is a one-to-one correlation in the occurrence of edge defects between wafers with and without plasma etching of polysilicon. The edge defect density, however, can be very different from the case where the polysilicon was removed prior to the oxidation. The sample with the dipped interface oxidized at 850°C is the most striking example: the edge defect density in Fig. 8a (without poly-etching) is orders of magnitude smaller than the one observed in Fig. 6a (with poly-etching).

Discussion

Field defects.—RBS analysis has shown that a dipped poly/mono interface contains about 2.5×10^{15} O atoms/cm², which is equivalent to 0.5 nm SiO₂ (4). It was also found that such an interface is clean enough to allow an almost complete epitaxial realignment of the polysilicon at 1000°C. The minimum yield obtained in the 100 channeling direction is about 6%-7%, compared to 3% for an ideal crystal and to 100% for unrecrystallized polysilicon (4). Hence, the polysilicon layer in real intimate contact with the substrate and subjected to a heat-treatment at 1000°C, should be considered as imperfect monocrystalline material rather than as polycrystalline material. This may explain the observations on surface roughness (Fig. 5): the relatively smooth surface of the sample with the dipped interface is attributed to the high degree of crystallinity of the layer. The same heat-treatment of polysilicon on a cleaning oxide results in local nucleation on the substrate through pinholes in the interfacial oxide, followed by dendritic growth into a layer with a rough surface, similar to the results reported by Tsaur and Hung (5). The densified cleaning oxide is obviously dense enough to prevent nucleation of the polysilicon on the substrate: the layer recrystallizes only in itself with only a small increase in surface roughness.

From the fact that a densified cleaning-oxide at the poly/mono interface prevents the defect generation, we conclude that it is the partial or complete epitaxial realignment of the polysilicon on the substrate which creates the nucleation sites from which the stacking faults can grow during a subsequent oxidation. Stacy *et al.* (6) concluded from TEM observations that the stacking faults and microtwins in the polysilicon do not simply grow into stacking faults in the substrate, but that the

Table II. Field defect densities observed after Wright etching for various processing sequences

Interface T_{ox} (T_{preann})	Dipped 850°C	Dipped (1000°C)	Cleaning oxide 850°C	Cleaning oxide (1000°C)
850°C	—	—	—	—
900°C	+	+	—	+
950°C	++	++	—	++
1000°C	++	++	—	++

++: $\geq 10^8$ cm⁻².
+ : $< 10^8$ cm⁻².
—: No defects.

Table III. Edge defect densities observed after Wright etching for various processing sequences

Interface T_{ox} (T_{preann})	Dipped 850°C	Dipped (1000°C)	Cleaning oxide 850°C	Cleaning oxide (1000°C)
850°C	++	++	—	++
900°C	++	++	—	++
950°C	++	++	—	++
1000°C	+	+	+	+

++: ≥ 10 μm^{-1} .
+ : < 10 μm^{-1} .
—: No defects.

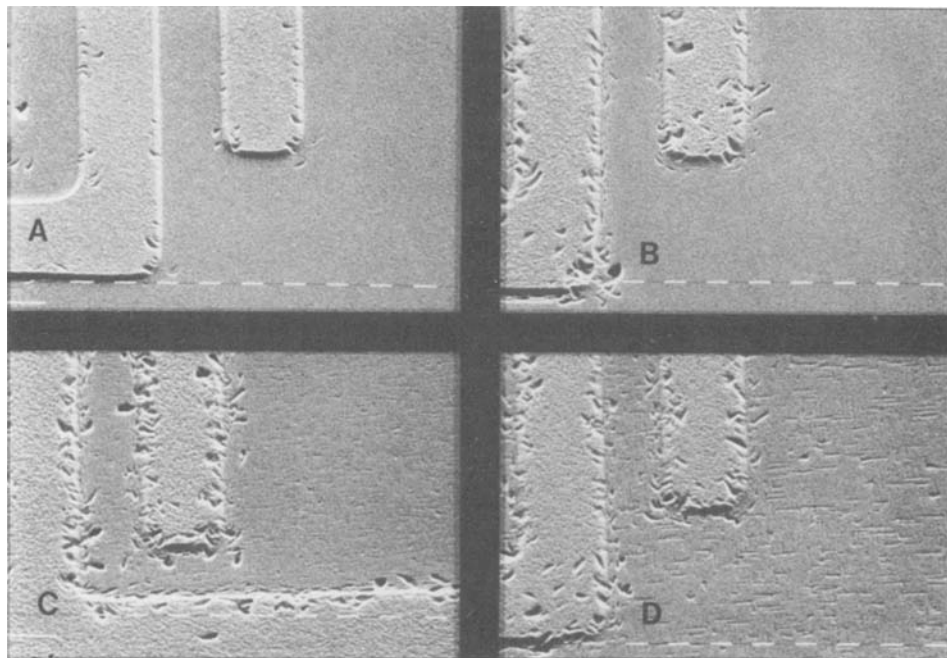


Fig. 8. SEM micrographs of Wright-etched samples with a dipped poly/mono interface and a preoxidation anneal at 850°C for different oxidation temperatures: A: 850°C, B: 900°C, C: 950°C, and D: 1000°C (5000x).

stacking faults in the substrate start to grow at the moment that the oxidation front reaches the poly/mono interface, from nucleation sites which are probably generated by the microtwins and stacking faults within the polysilicon. This is supported by the fact that the stacking faults in polysilicon which are bounded by $1/6 \langle 112 \rangle$ partials cannot simply develop into oxidation-induced stacking faults bounded by $1/3 \langle 111 \rangle$ Frank partials. The lengths of the stacking faults in our experiments seem to be in agreement with these observations. The stacking fault lengths, as determined from TEM, are 2.2, 1.4, and 0.75 μm for oxidations at 1000°, 950°, and 900°C, respectively. Theoretically, the oxidation time needed to obtain a certain stacking fault length can be estimated from

$$L_{\text{SF}} = K'' t^{0.66} \exp(-2.37 \text{ eV}/kT)$$

where L_{SF} is the stacking fault length, K'' is a constant, and t is the oxidation time (7). For the oxidation temperatures of 900°, 950°, and 1000°C, the calculated oxidation times are 132, 80, and 42 min, respectively, which does not

agree with the experimental times of 270, 150, and 90 min, but agrees rather with the time which elapses after the oxidation front has passed the poly/mono interface: 172, 96, and 58 min, respectively.

The calculation also explains the absence of defects after oxidation at 850°C even in cases where the defect nuclei must be present. The estimated stacking fault length is so small (0.3 μm) that the corresponding depth of the stacking fault is much less than the oxide thickness, so that an actual stacking fault cannot be expected.

We suggest that as long as the oxidation front has not reached the poly/mono interface, the excess concentration of silicon interstitials at the interface is negligible, because the remaining part of the polysilicon layer acts as an effective sink for interstitials. The stacking fault nuclei at the poly/mono interface can only start to grow when this polysilicon sink has been consumed by the oxidation.

Finally, if the epitaxial realignment of the polysilicon is avoided by having a sufficient amount of oxide at the poly/mono interface and by limited high-temperature treatments, the defect nuclei are absent and no stacking faults are observed in the oxidized area.

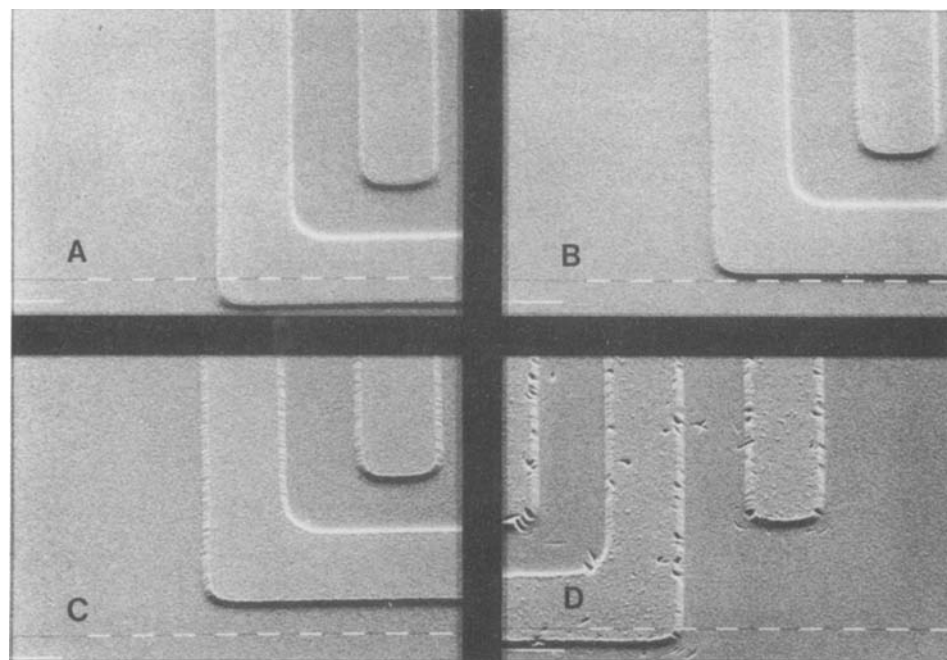


Fig. 9. SEM micrographs of Wright-etched samples with a cleaning oxide interface and a preoxidation anneal at 850°C for different oxidation temperatures: A: 850°C, B: 900°C, C: 950°C, and D: 1000°C (5000x).

Edge defects.—It is well known that excessive stresses during local oxidation can give rise to generation of dislocations along Si_3N_4 edges, extending along {111} planes in the silicon crystal. Generally the key factors in the generation of these oxidation-induced dislocations are the intrinsic stress in the Si_3N_4 layer, the viscoelastic behavior of the expanding SiO_2 (9, 10) and the occurrence of nonplanarities in the silicon surface (11). However, when dealing with polysilicon on top of monocrystalline silicon, the dominant parameters in the defect generation mechanism appear to be the oxygen concentration at the poly/mono interface and, closely related to that, the crystalline structure of the polysilicon layer, whereas the above-mentioned factors are only of secondary importance.

For those conditions where oxidation-induced stacking faults are observed in the field, the polysilicon has partly or completely realigned epitaxially on the substrate. As a consequence of this realignment, the Si_3N_4 is effectively in direct contact with monocrystalline silicon and dislocations along Si_3N_4 edges will be generated in the same way as for conventional local oxidation with Si_3N_4 in direct contact with silicon (9). For an oxidation at 1000°C, the dislocation density is somewhat lower than at 850°, 900°, 950°C because the viscoelastic flow of the SiO_2 at 1000°C relieves some of the stress.

From the fact that dislocations along Si_3N_4 edges are never observed on wafers with a densified cleaning oxide at the poly/mono interface, we conclude that these dislocations can only be transferred to the substrate when there is at least an onset of epitaxial realignment of the polysilicon on the substrate. The sample with the cleaning oxide interface oxidized at 1000°C (Fig. 9d) shows no stacking faults but a considerable number of dislocations. This suggests that some nucleation of the polysilicon on the substrate must have occurred, but that the amount of epitaxially realigned material is not sufficient to create oxidation-induced stacking faults.

The only phenomenon left to explain is the fact that the dislocation densities tend to be higher after plasma etching of polysilicon. The reason for this is that the oxidation of a shaped silicon surface gives an additional stress component because of the volume expansion of the SiO_2 at the foot of a step in the surface (11). However, it is clear that the stress induced by the Si_3N_4 is the dominant factor for the dislocation generation. If the epitaxial realignment of the polysilicon is completely avoided, the stress from the Si_3N_4 cannot act upon the substrate, and, in that case, even an oxidation of a shaped surface at a temperature of 850°C does not generate dislocations (Fig. 7a).

Finally, it should be noted that the use of a densified cleaning oxide at the poly/mono interface is a possible method of avoiding all kinds of defects, but such an inter-

facial oxide presents a significant barrier to dopant atoms which have to diffuse from the polysilicon into the substrate (4). It has been shown that an undensified cleaning oxide at the poly/mono interface is not a significant barrier to the diffusion of dopant atoms and is therefore a more realistic approach in eliminating defects (4).

Conclusion

From these observations the following conclusions can be drawn: if it is desired to have a high defect density at the interface between polycrystalline and monocrystalline silicon for enhanced gettering purposes, the amount of oxygen at the poly/mono interface should be as low as possible and prolonged processing steps at high temperatures are beneficial. The application of a Si_3N_4 pattern on top of the polysilicon will further increase the defect density.

However, when dealing with polysilicon diffusion sources, a small amount of oxygen at the poly/mono interface is beneficial and extensive high temperature processing should be avoided. In such a case, the best advice is: let poly be poly.

Acknowledgments

The authors are indebted to J. A. Appels and H. G. R. Maas for many valuable discussions, to M. P. A. Vieggers for the TEM measurements, and to Mrs. H. M. C. van der Linden for technological assistance.

Manuscript submitted Nov. 21, 1983; revised manuscript received March 20, 1984.

Philips Research Laboratories assisted in meeting the publication costs of this article.

REFERENCES

1. M. C. Chen and V. J. Silvestri, *This Journal*, **129**, 1294 (1982).
2. K. Okada, K. Aomura, T. Nakamura, and H. Shiba, *IEEE J. Solid-State Circuits*, **sc-14**, 307 (1979).
3. T. Hosoya, S. Muramoto, and S. Matsuo, *IEEE Trans. Electron. Devices*, **ed-28**, 77 (1981).
4. W. J. M. J. Josquin, P. R. Boudewijn, and Y. Tamminga, Submitted to *Appl. Phys. Lett.*
5. B. Y. Tsaur and L. S. Hung, *ibid.*, **37**, 648 (1980).
6. W. T. Stacy, M. C. Arst, K. N. Ritz, J. G. de Groot, and M. H. Norcott, Abstract 310, p. 484, The Electrochemical Society Extended Abstracts, Vol. 83-1, San Francisco, CA, May 8-13, 1983.
7. S. P. Murarka and G. Quintana, *J. Appl. Phys.*, **48**, 46 (1977).
8. Y. Tsunoda, *ibid.*, **19**, 209 (1980).
9. K. Shibata and K. Taniguchi, *This Journal*, **127**, 1383 (1980).
10. Y. Tamaki, S. Isomae, S. Mizuo, and H. Higuchi, *ibid.*, **128**, 644 (1981).
11. R. B. Marcus and T. T. Sheng, *ibid.*, **129**, 1278 (1982).

Modeling Rapid Thermal Diffusion of Arsenic and Boron in Silicon

R. B. Fair*

Microelectronics Center of North Carolina, Research Triangle Park, North Carolina 27709

J. J. Wortman* and J. Liu**

Department of Electrical Engineering, North Carolina State University, Raleigh, North Carolina 27650

ABSTRACT

Rapid thermal annealing (RTA) of high dose B and As implants is believed to produce large transients of point defects that may exist for the duration of the anneal (2-30s). Enhanced diffusion during RTA of boron implants $>10^{15}$ cm $^{-2}$ is related to damage clusters at the peak of the range which can grow into cross-grid dislocation networks. This process can create point defects through dislocation-dislocation reactions and by nonconservative climb processes. Enhanced diffusion during RTA of high dose As implants $>2 \times 10^{14}$ cm $^{-2}$ is related to the amorphous Si surface layer formed during implantation. Regrowth of this layer into a defect-free, crystalline layer is assumed to produce point defects which remain behind until they diffuse away. In the meantime, they contribute to enhanced As diffusion during the first 5-10s of the RTA cycle. Preamorphization at low temperature eliminates this enhanced diffusion of As by eliminating the source of point defects presumed to be vacancies because of the associated defect removal in the implanted layer. Enhanced dopant diffusion has been modeled by overlaying an empirical transient point defect model on thermally assisted diffusion models associated with steady-state furnace environments. A weighted exponential function was used to describe the transient process with a decay time of 4.4s.

Pulse and short-time annealing of ion-implanted Si have been receiving attention as potentially useful techniques for achieving shallow junctions free of extended defects. However, several observations have been made of significant dopant diffusion occurring as a result of rapid thermal annealing (RTA) using incoherent light sources (1-4). And, it has been observed that this enhanced diffusion occurs during the initial stage of the RTA cycle (4, 5). Hence, enhanced diffusion during RTA is observed to be a transient process, and therefore requires computer modeling in order to understand the important mechanisms that are operating. The purpose of this paper is to discuss RTA diffusion models for B and As in Si, and to describe the computer modeling effort required to simulate RTA diffusion profiles.

Experimental

Czochralski-grown (100) Si wafers, 8-15 Ω -cm p-type were implanted with As at liquid nitrogen temperature, room temperature, and 200°C at 1×10^{15} cm $^{-2}$, 50 keV. Room temperature As implants were also performed at 50 keV for doses of 2×10^{14} cm $^{-2}$ and 1×10^{16} cm $^{-2}$. n-Type As-doped wafers were implanted with 35 keV B $^{+}$ at a dose of 2×10^{15} cm $^{-2}$ (6). Samples were RTA processed in either air or N $_2$ in an AG Associates Heatpulse System Model 210M. Measurements of the temperature vs. time profiles obtained in the Heatpulse system are shown in Fig. 1. For a furnace set point temperature of 1100°C, the RTA cycle begins at 850°C. For a 2s RTA cycle, it can be seen that the temperature may only reach 1000°C. These profiles were approximated for computer modeling by 200 ms incremental time steps during which a constant average temperature is assumed. This allows the program to solve the finite difference equations for diffusion during constant temperature intervals.

Arsenic and B profile measurements were made on the North Carolina State University Cameca MS-3F ion probe. Reproducible wafer temperature measurements were performed by supporting wafers on a Chromel-Alumel thermocouple during RTA. No independent temperature measurements were made to verify the curves in Fig. 1. However, they agree generally with curves supplied by the manufacturer.

Diffusion Models

The approach taken in modeling RTA diffusion of dopants was to overlay a transient point defect calculation onto the steady-state, thermally assisted diffusion

models that existed in the program PREDICT. A detailed description of the models in PREDICT is beyond the scope of this paper, and will be presented elsewhere (7). Briefly, the PREDICT modeling program is based upon the multiple charge-state vacancy model of diffusion which assumes that under steady-state furnace conditions vacancies exist in Si in several ionization states. The total diffusion coefficient of a dopant in Si is the sum of the contributions to diffusion made by each type of vacancy (8). Overlaid on the vacancy model is the supplementary effect of self-interstitials on diffusion of dopants. In principle, both vacancies and self-interstitials may occur simultaneously, and somewhat independently. Thus, if both types of point defects are important, diffusion processes may involve both types (9, 10)

$$D_i = D_i^I + D_i^V \quad [1]$$

where D_i^I is the interstitial contribution and D_i^V is the vacancy contribution to the total measured intrinsic diffusivity, D_i . Recent analyses of diffusion data taken while the silicon surface was being oxidized correctly show that generated self-interstitials assist dopant diffusion, i.e., P, As, and B (11). However, simplified calculations are unable to correctly predict the fraction of diffusion flux due to the interstitial or vacancy mechanisms, since they ignore the many different kinds of point defect-impurity association and recombination processes that

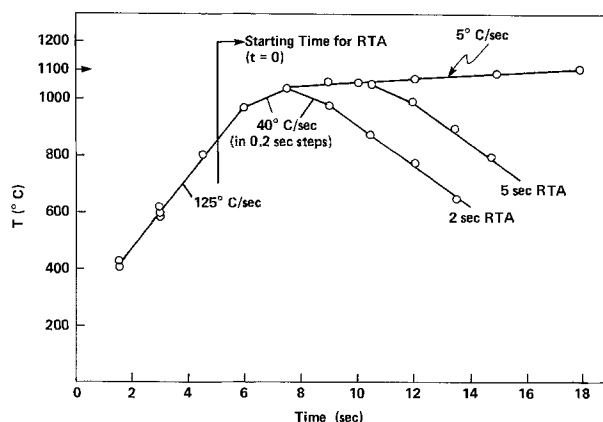


Fig. 1. Measured temperature vs. time data (O) for an undoped wafer with a thermocouple attached to the back side in the RTA furnace. The furnace set-point temperature was 1100°C. The straight line approximations were used in computer calculations of dopant diffusion with time steps of 0.2s.

*Electrochemical Society Active Member.

**Electrochemical Society Student Member.

Table I. Models included in PREDICT

Ion implantation

Gaussian based on experimental range statistics with measured exponential tails
Through oxide implants

Diffusion

Oxidation enhanced diffusion (OED)
Partial O₂ pressure dependence
Time dependence
Dopant concentration dependence
Concentration dependent diffusion
Stress effects
Electric field effects
Ion pairing
Orientation dependence
Clustering
Solubility limits
Segregation
Transient point defects (RTA)

can occur. This problem was recently solved by Mathiot and Pfister (12), who numerically solved all of the necessary continuity equations involving vacancies, self-interstitials, and dopant-defect complexes. Their results show that for P, As, and B diffusion below 1100°C, the interstitialcy components are less than 25%. Thus, we have assumed that D_1^v dominates in Eq. [1] under nonoxidizing conditions.

As-implanted profiles were assumed to be Gaussian, based on measured range statistics. However, exponential tails were included in the initial profiles as determined by direct profile measurements. The steady-state, thermally assisted diffusion effects that are included in PREDICT are listed in Table I. Effects that increase diffusion beyond the expected intrinsic diffusivity include time-dependent oxidation-enhanced diffusion (OED), concentration-dependent diffusion, and any other process that creates the supersaturation of point defects (vacancies or silicon self-interstitials). The retarded diffusion effects listed in Table I are associated with reduced point defect levels.

Boron diffusion during RTA.—Thermally assisted diffusion of B in Si is assumed to occur primarily by the monatomic species via neutral and donor point defects. During oxidation of the Si surface, vacancy-assisted diffusion is dominated by a partial interstitial process. Concentration-dependent diffusion is modeled as the increase in donor point defects as B concentration exceeds n_i . Concentration-dependent OED is treated as a reduction in Si self-interstitials due to increased vacancy concentration with doping above n_i (13).

A comparison of steady-state, thermally assisted diffusion calculations with RTA data of a 2×10^{15} cm⁻², 35 keV B implant is shown in Fig. 2. It can be seen that during the 1050°C, 5s RTA, a significant tail on the B profile is created. However, the model calculations are unable to predict the occurrence of this tail. In fact, this modeling predicts that little or no movement of the profile occurs.

In order to understand the origin of the enhanced diffusion of B during RTA, consider the TEM plan-view micrographs shown in Fig. 3. Sadana *et al.* (3) implanted B at a dose of 5×10^{15} cm⁻², 35 keV in (100) Si. Figure 3a shows the as-implanted sample which exhibits a single-crystal diffraction pattern, indicating that no amorphous layer is produced by the implanted B even at this high dose. A 1000°C, 30 min furnace-annealed sample in N₂ shows a high density of irregularly shaped loops in addition to a dislocation network. The RTA sample in Fig. 3c shows that after 10s at 1100°C in air, a dislocation network is forming. After a 30s 1100°C RTA, a well-defined cross-grid dislocation network was observed in the implanted region, as shown in Fig. 3d. The significance of these micrographs is that during the RTA cycle, a cross-grid dislocation network is being created and stabilized. As a result, point defects are being generated through dislocation reactions and cross-slip processes.

Sadana *et al.* (3) have shown through TEM cross

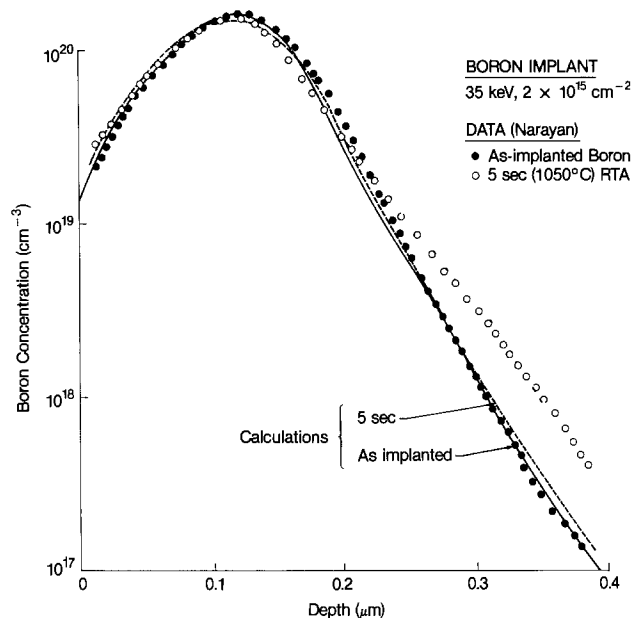


Fig. 2. As-implanted B data and 1050°C, 5s RTA in air data. The solid curve is the calculated implant distribution and the dashed curve is calculated on the basis of steady-state, thermally assisted diffusion of B during RTA.

sections that the dislocation network is formed at the peak of the implanted B profile. In general, it is found that if the implant dose exceeds 1×10^{15} cm⁻², the high B concentration in the peak will likely generate damage clusters (3). A TEM cross-sectional micrograph is shown in Fig. 4 along with the corresponding 5×10^{13} cm⁻², 35 keV B profile following a 1100°C 10s RTA. It can be seen that the B in the peak of the profile has diffused more slowly than the B external to the dislocation network. This network was sufficiently stable that even after a 1000°C 30 min N₂ furnace anneal, the dislocation network was still in place. In addition, the B outside of the dislocated region diffused quite rapidly compared to normal, thermally assisted diffusion.

The preceding results and the model assumptions can be summarized as follows.

1. The B⁺ implant is not sufficient to drive the Si surface amorphous. Thus, no solid-phase epitaxial regrowth occurs.

2. For doses greater than 10^{15} B/cm², networks of dislocations occur at the peak of the profile following annealing due to the high B concentration.

3. Point defects are generated during dislocation network stabilization which occurs within the first 30s of RTA.

4. The lifetime of generated point defects is very low within the network of dislocations. This dislocation region is an efficient generator and recombination area for point defects, and, as such, the crystal can easily maintain point defect equilibrium.

5. The lifetime of point defects is relatively high outside of the dislocated network. Thus, generated point defects can diffuse significant distances away from the network before they recombine.

6. Enhanced B diffusion occurs outside of the dislocation network where generated point defects can reach supersaturated levels.

A schematic diagram of the situation during RTA of implanted B is shown in Fig. 5. The dislocation network is indicated by the cross-hatched area in the figure. It is assumed that within this area diffusion can proceed almost normally (14) with no point defect supersaturation. However, during the first 30s of the creation of this network, a significant population of point defects is generated which diffuses out into the nondislocated crystal. These point defects contribute to enhanced diffusion outside of

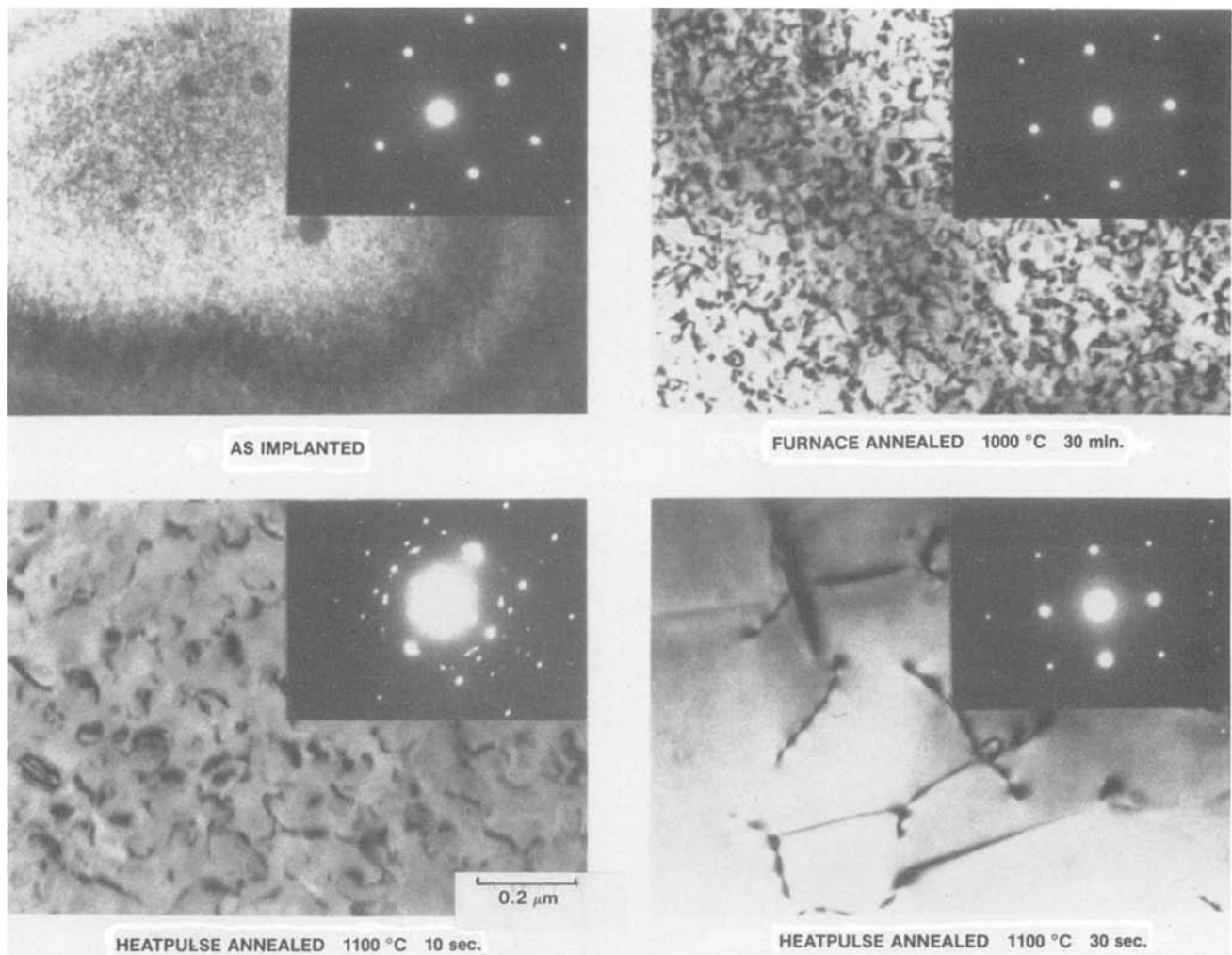


Fig. 3. TEM plan-view micrographs of 35 keV B implanted (100) Si, $5 \times 10^{15} \text{ cm}^{-2}$; (a, top left) as-implanted, (b, top right) furnace-annealed 1000°C/10s in air, (c, bottom right) RTA for 1100°C/10s in air, (d, bottom right) RTA for 1100°C/30s in air. After Sadana *et al.* (3).

the cross-hatched area. The time dependence of the density, C_{pd} , of this point defect supersaturation is represented by an equation of the form

$$C_{pd} = K(T) \exp(-t/\tau) \quad [2]$$

Inside the dislocated band, it is assumed that

$$C_{pd} = C_{equil} \quad [3]$$

where C_{equil} is the equilibrium concentration of point defects. The establishment of the dislocation network involves nonconservative processes such as climb which can be efficient vacancy generators (15). The intrinsic diffusion coefficient is multiplied by an enhancement factor of the form

$$D_B = D_i (1 + K'(T) \exp(-t/\tau)) \quad [4]$$

Over the RTA furnace setpoint range of 1000°-1100°C, it was found that

$$K'(T) = 5 \times 10^{-6} \exp\left(\frac{2.0 \text{ eV}}{kT}\right)$$

$$\tau = 4.4\text{s}$$

giving B diffusion coefficient enhancements of 100-400 at $t = 0$ outside of the dislocated region shown in Fig. 5.

Computer simulations of RTA of B implants are shown in Fig. 4, 6, and 7. Notice that in Fig. 6 little diffusion occurs within the first 0.22 μm of the B profile following a 5s RTA at 1050°C. It appears, in fact, that some negative diffusion has occurred back towards the surface. The model presented here cannot account for this. However, enhanced diffusion outside of the dislocated region can be accounted for by assuming the model in Fig. 5.

After 10s, the temperature in the RTA furnace has increased sufficiently to cause some diffusion to occur at the peak of the B profile. This level of diffusion is completely accounted for by steady-state thermally assisted diffusion processes. However, the bulk of the diffusion in the tail region of the profile is dominated by the assumed transient vacancy production associated with the formation of the dislocation network. The time dependence of this process is evident in Fig. 6 and 7, where movement of B in the tail region is greatest during the initial period of RTA when the temperature is lowest.

The rapid thermal anneals associated with Fig. 4, 6, and 7, were all performed in an air ambient. Calculations show that the OED associated with this air ambient is sufficient to cause some additional enhanced diffusion beyond that which occurs during the dislocation network formation. However, insufficient data were available to model this effect adequately. Other models, such as B precipitation and B clustering, were investigated to explain the profile shapes obtained. However, these attempts were not successful.

Arsenic diffusion during RTA.—The defect morphology introduced by high dose As implants is significantly different from the high dose B case. It is known that at room temperature, a $2 \times 10^{14} \text{ As/cm}^2$ implant is sufficient to create an amorphous surface layer in Si (16). In addition, such an amorphous layer can epitaxially regrow to a single-crystalline layer in milliseconds at 1000°C (17). Solid-phase epitaxy (SPE) of this amorphous layer produces defect-free material, although secondary defects below the amorphous/crystalline interface may still be present (3). However, it has been shown that these secondary defects also anneal out during RTA at 1100°C for

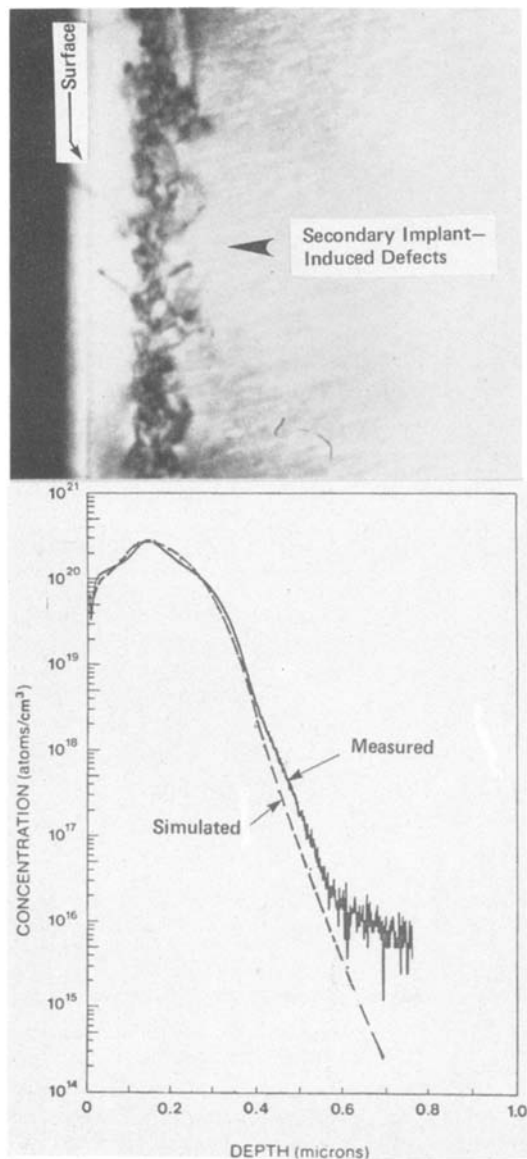


Fig. 4. Comparison of TEM cross-sectional micrographs corresponding to a measured B profile following RTA at 1100°C/10s in air. The simulated B profile is based upon the model depicted in Fig. 5. After Sadana et al. (3).

10s (3, 6). This suggests that a supersaturation of vacancies exists for a period of time to facilitate defect shrinkage following SPE.

The application of steady-state, thermally assisted diffusion calculations to RTA of implanted As in (100) Si is shown in Fig. 8. Arsenic was implanted at 100 keV, $1 \times 10^{16} \text{ cm}^{-2}$, and a 1150°C 5s anneal was performed in air. The solid circles and curves that pass through them are respectively the measured (6) and calculated as-implanted distribution of As. After the RTA anneal, the As has diffused more than predicted by calculations performed under the assumption of a constant 1150°C exposure at 5s. By using a time-dependent temperature ramp as actually measured in the RTA furnace, the calculated diffusion length at 10^{20} cm^{-3} is only 180Å. Thus, the steady-state calculations are insufficient to explain the enhanced diffusion that occurs during RTA of As (2).

Attempts were made to try to understand the origin of the enhanced diffusion of As during RTA. Shown in Fig. 9 are As diffusion profiles obtained by putting wafers in compressive or tensile stress during the RTA process. It can be seen that no significant difference exists in the As profiles measured in the stressed and the unstressed wafers.

In order to understand the role of the amorphous layer created during implantation on enhanced diffusion dur-

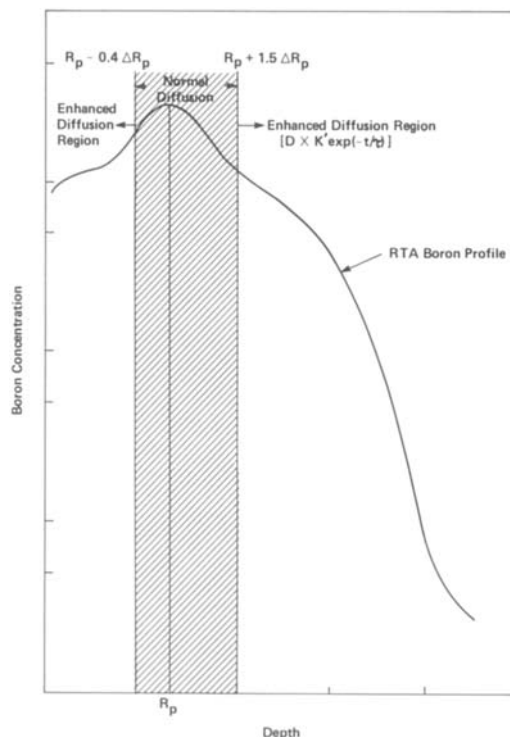


Fig. 5. Schematic diagram of the transient point defect model for B diffusion during RTA. The cross-hatched region corresponds to the implant-induced dislocation network where normal diffusion occurs.

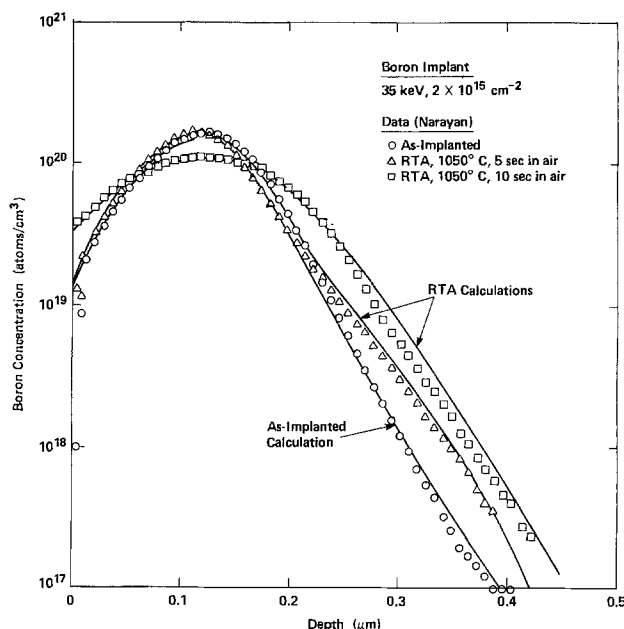


Fig. 6. Comparison of RTA B profile data with transient model diffusion calculations at 1050°C.

ing RTA, a $1 \times 10^{15} \text{ As/cm}^2$ 50 keV implant was performed at 200°C. This implant temperature is sufficient to insure that the implant would not create an amorphous layer (16). The wafer then underwent RTA at 1100°C for 10s in N_2 . The results are shown in Fig. 10. The effect of the 200°C anneal was to form an as-implanted profile with a long tail. During RTA, little or no diffusion occurs in the tail portion of the profile. However, some thermally assisted diffusion occurs in the higher concentration portion of the profile. This diffusion can be accounted for through steady-state modeling calculations as shown. By comparison, the same implants carried out at LN_2 temperature and room temperature produced amorphous layers. Following RTA, some enhanced diffusion is observed as shown in Fig. 11. No measurable difference is

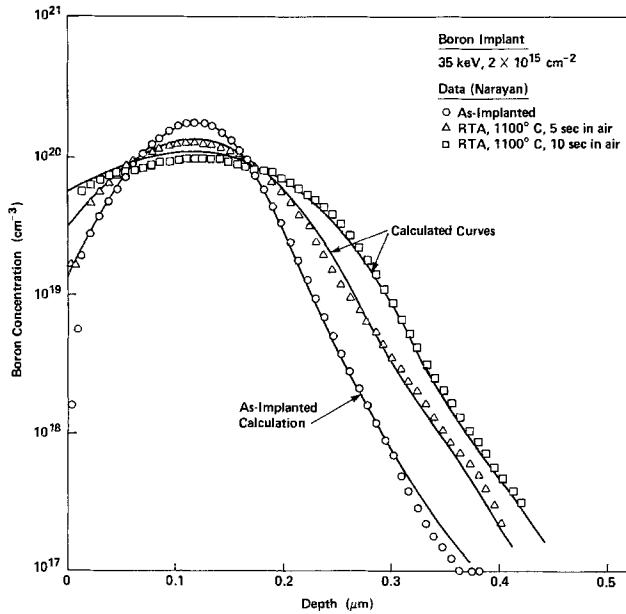


Fig. 7. Comparison of RTA B profile data with transient model diffusion calculations at 1100°C.

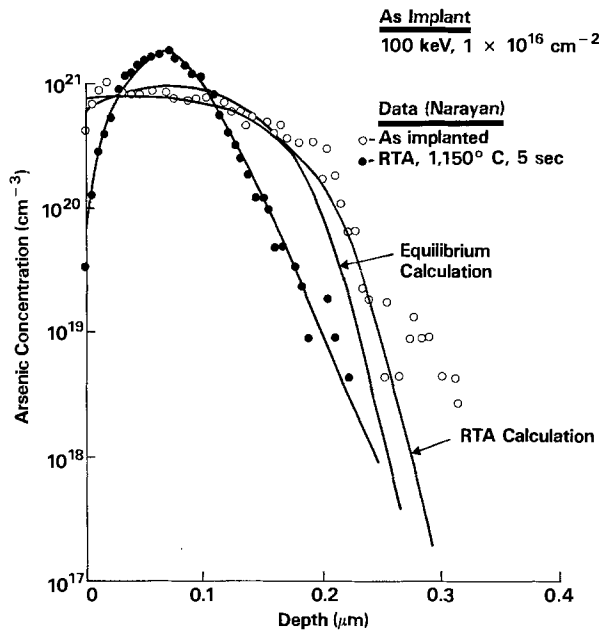


Fig. 8. Rapid thermal annealing of implanted As showing the comparison with steady-state, thermally assisted diffusion calculations which assume a constant 1150°C temperature during the 5s RTA. Also shown is a calculation based upon the transient point-defect generation model for As with K' (1150°C) = 7 and $\tau = 4.4s$.

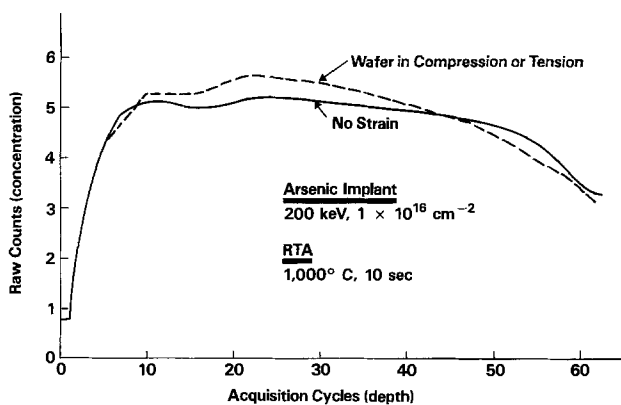


Fig. 9. The role of wafer stress on As diffusion during RTA. Wafers were intentionally bowed into compressive or tensile stress ($\sim \pm 10^9$ dyne/cm²) in the RTA furnace. Plotted is unreduced doping concentration vs. depth in the Si.

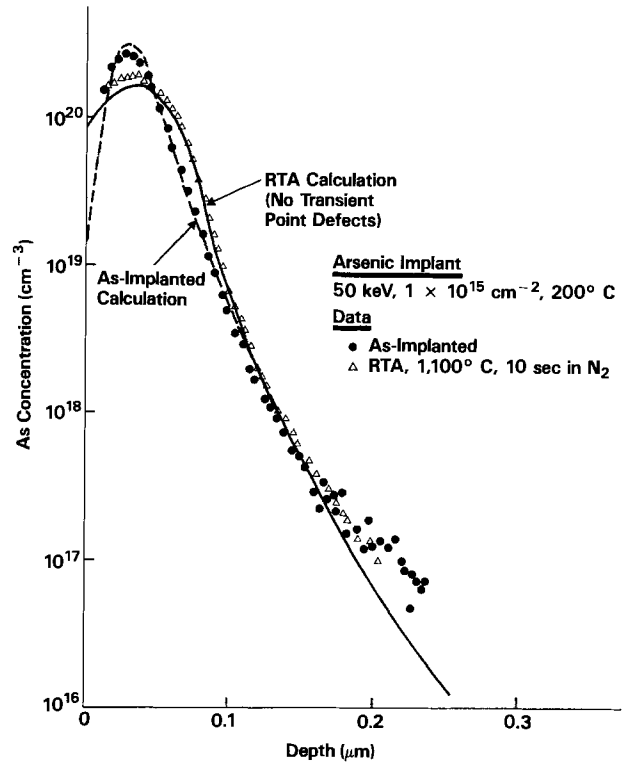


Fig. 10. Rapid thermal annealing of arsenic-implanted Si for a 200°C implant temperature. The solid curve is a steady-state, thermally assisted diffusion calculation.

seen between the profiles for the LN₂ and RT implants, even though the amorphous layer created by the LN₂ implant was deeper by $\sim 300\text{\AA}$ (18).

The following is known about As implantation in silicon: (i) arsenic doses greater than 2×10^{14} cm⁻² at room temperature drive the Si surface region amorphous (16);

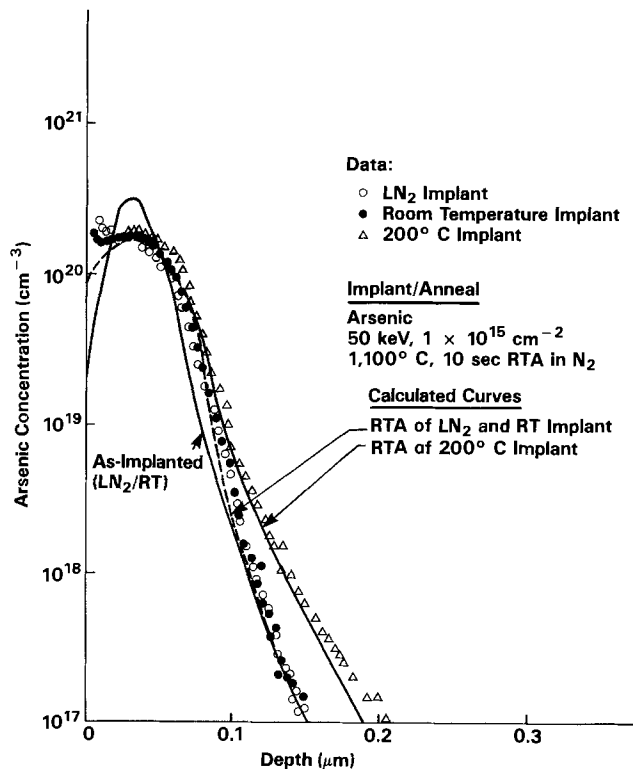


Fig. 11. Comparisons of RTA results for wafers arsenic-implanted at LN₂ temperature, room temperature, and 200°C. The LN₂ and RT implants leave the Si surface amorphous, and the dashed curve is calculated assuming transient point defects occur after SPE. The tail on the 200°C implant resulted from the hot implant, as shown in Fig. 10.

(ii) solid-phase epitaxial regrowth (SPE) occurs during RTA in milliseconds at high temperatures (17). Point defect generation during RTA may be caused by: (i) solid-phase regrowth where vacancies or self-interstitials are generated and diffuse from the regrown region. A typical diffusion length of vacancies would be $2 \mu\text{m}$ after 5s at 1050°C . (ii) Annealing of secondary implant damage also occurs in the 5-10s time frame at T greater than 1050°C (3, 5). This suggests that vacancies are the dominant, remnant point defect after SPE.

To study the effect of SPE on RTA, a 550°C anneal for 30 min was performed on as-implanted samples. Such an anneal is sufficient to regrow approximately 90% of the amorphous layer associated with a high dose As implant (19). The effect of a low temperature, recrystallization anneal on enhanced diffusion of As is demonstrated in Fig. 12. A $1 \times 10^{16} \text{ As/cm}^2$, 50 keV implant was performed in two Si wafers. One wafer was preannealed at 550°C for 30 min in N_2 . RTA was then performed on both wafers at 1100°C for 10s in N_2 . It can be seen in Fig. 12 and 13 that the preannealed wafer exhibited very little enhanced diffusion. The calculated curve shown in Fig. 12 is based on steady-state, thermally assisted diffusion calculations. In Fig. 13, a comparison is made between the results obtained on the two wafers. It can be seen that without the 550°C preanneal, significant enhanced diffusion of As has occurred.

Modeling of enhanced diffusion of As during RTA was achieved by overlaying a transient vacancy model onto the steady-state diffusion models in PREDICT II. These models assume As diffusion occurs primarily by V^- and V^+ vacancies. Thus diffusion coefficients were made to be directly proportional to the vacancy transient. At high concentrations, diffusion of electrically active As is reduced by clustering (20, 21), and clustering was assumed to occur instantaneously and independently of the vacancy transient. Diffusion coefficients of the form of Eq. [4] were used with

$$K'(T) = 1.3 \times 10^{-6} (E/200) \exp\left(\frac{2.0 \text{ eV}}{kT}\right)$$

$$\tau = 4.4\text{s}$$

for As doses $> 2 \times 10^{14} \text{ cm}^{-2}$ and temperatures in the 1000°C - 1150°C range. The parameter E is the As implant en-

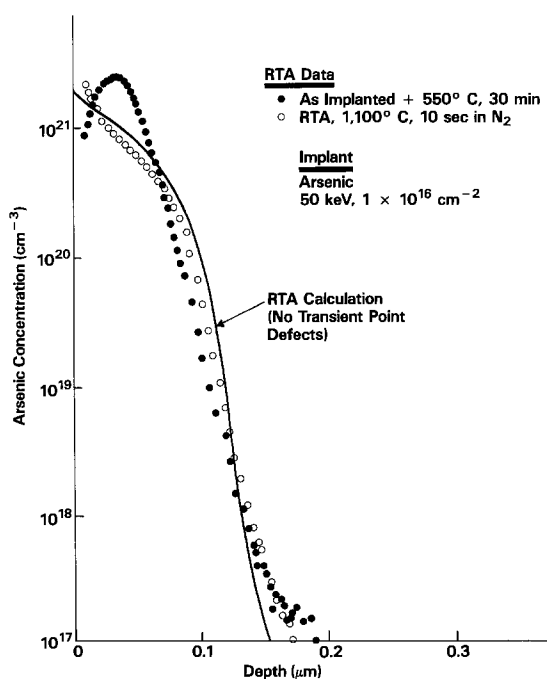


Fig. 12. Rapid thermal annealing of arsenic-implanted silicon that was preannealed at 550°C for 30 min to regrow 90% of the amorphous layer.

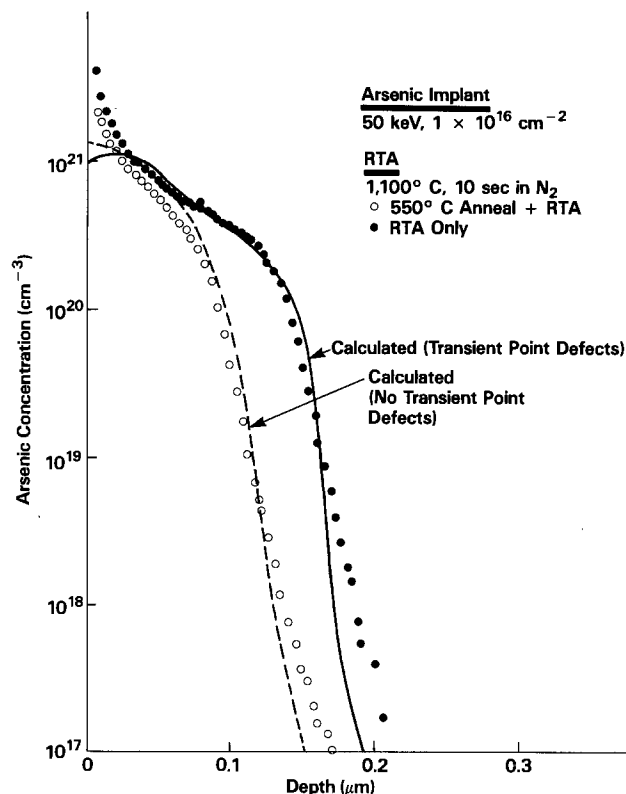


Fig. 13. Comparison of RTA data and calculations for 550°C preannealed and nonannealed arsenic-implanted silicon.

ergy and is included to account for the increased width of the amorphous region with implant energy for $50 \leq E \leq 200 \text{ keV}$. It is assumed, unlike the case of B, that enhanced diffusion occurs over the entire profile since no dislocation network is created. Examples of calculated profiles using the transient model are shown in Fig. 8, 11, and 13.

It should be pointed out that the "activation" energy associated with $K'(T)$ is somewhat fictitious, since we are dealing with temperature transients as shown in Fig. 1. For As the product $D_{\text{As}} \cdot K'(T)$ has an activation energy of 2.1 eV, where $D_{\text{As}} = 23 \exp(-4.1 \text{ eV}/kT)$ (8). Recently, Kalish *et al.* (4) found that the activation energy for enhanced As diffusion during RTA was $\sim 1.8 \text{ eV}$, in reasonable agreement.

Another comparison of RTA As data with transient model calculations is shown in Fig. 14. Here, $2 \times 10^{14} \text{ As/cm}^2$ 50 keV implants were performed at room temperature. Thus, the Si surface was driven amorphous. RTA was performed at 1100°C for 5 and 15s in N_2 . Enhanced diffusion is observed beyond that which is attributable to normal thermally assisted diffusion. The amount of this enhanced diffusion agrees with the transient model calculation.

The time evolution of the redistribution of a 50 keV, $1 \times 10^{16} \text{ As/cm}^2$ implant in Si during 1100°C RTA is shown in Fig. 15. The transient nature of enhanced diffusion is evident in this figure. Significant motion of the profile is observed after 2, 5, and 10s. However, much less diffusion occurs after 10s. Computer simulations are shown for comparison with $K'(1100^\circ\text{C}) = 7$ and $\tau = 4.4\text{s}$. The exponential time decay assumed for the vacancy supersaturation models the enhanced diffusion reasonably well. However, it is not possible to extract τ directly by plotting x_i vs. RTA time due to the fact that temperature is constantly changing as shown in Fig. 1. Extensive computer simulations were the only alternative. At concentrations above 10^{21} cm^{-3} agreement between theory and data is poor as a result of As precipitation which has not been modeled.

Arsenic and Boron Codiffusion during RTA

The application of RTA to the annealing of double-implanted As and B in Si is shown in Fig. 16. RTA was

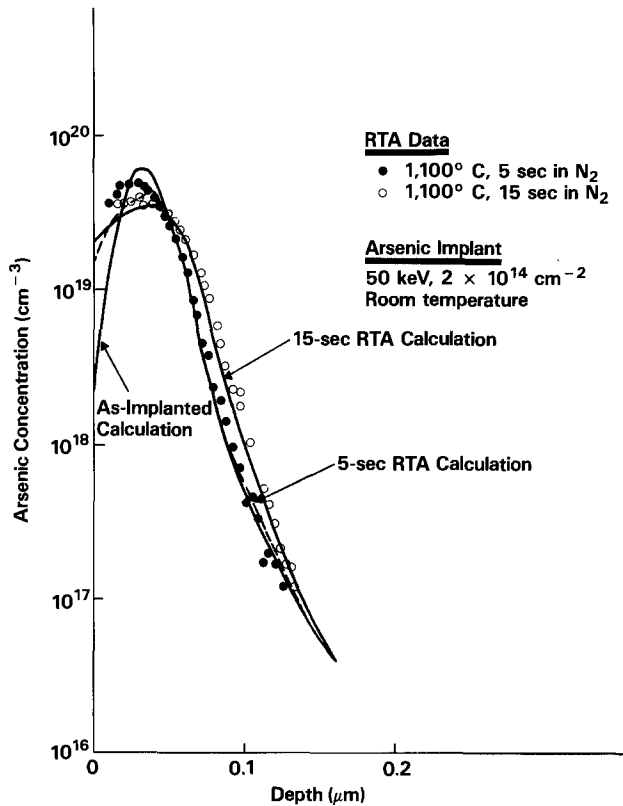


Fig. 14. Comparison of RTA As data with transient model calculations for $2 \times 10^{14} \text{ cm}^{-2}$, 50 keV implants.

performed at 1000°C for 10s in air (2). For comparison, model calculations assuming thermally assisted diffusion only are shown. The experimental profiles show that substantial movement of As has occurred beyond what would be expected at 1000°C for 10s. In addition, tails have formed on both the As and B profiles. The double implant using $1.2 \times 10^{16} \text{ cm}^{-2}$, 200 keV As and $2 \times 10^{15} \text{ cm}^{-2}$, 42 keV BF_2 into (100) Si present a substantially dif-

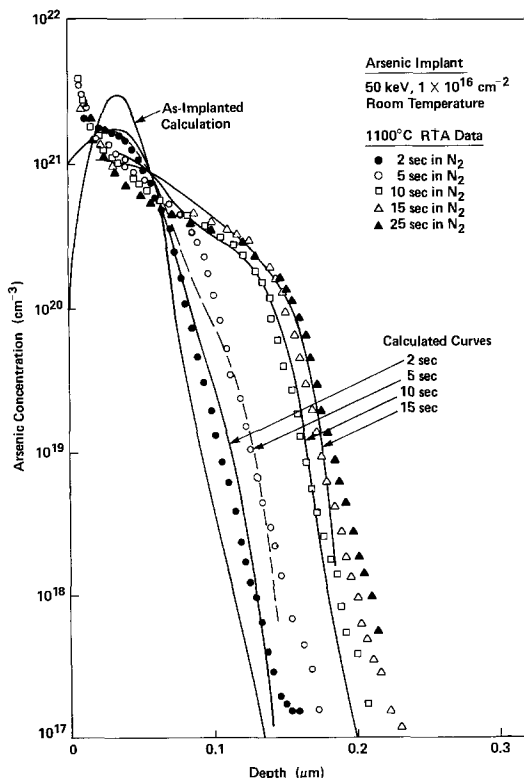


Fig. 15. Comparison of RTA data and calculations showing the time-dependent evolution of enhanced As diffusion during RTA.

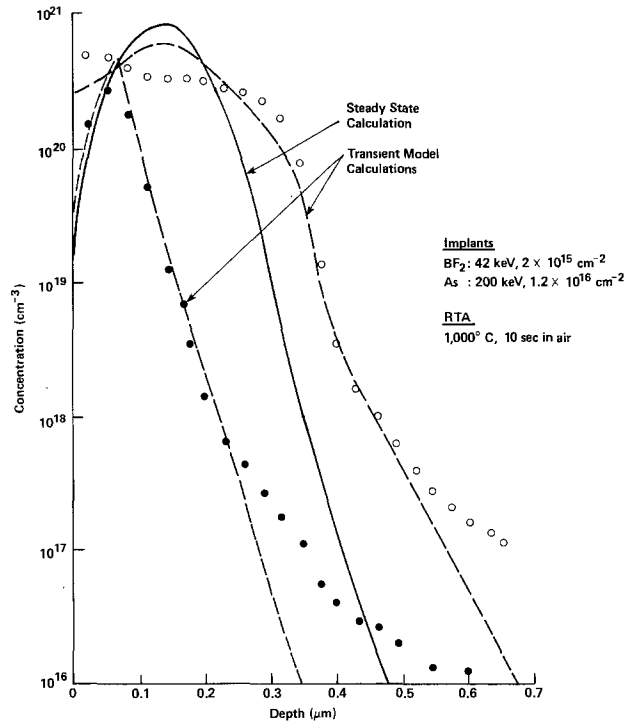


Fig. 16. The application of RTA to the annealing of a double-implanted layer (As into B implanted Si). Comparison of the SIMS data with steady-state model calculations shows significant As diffusion has occurred. Transient model calculations were made with K' (1000°C) = 105 and $\tau = 4.4s$.

ferent modeling environment for B diffusion during RTA. SPE of the amorphous layer created by the As implant is considered to be the dominant source of transient point defects.

The result of overlaying the transient point defect model on the thermally assisted diffusion calculations for the conditions described in Fig. 16 are also shown. In these calculations, K' (1000°C) = 105 for both As and B and $\tau = 4.4s$. Reasonably good agreement is obtained with the measured data except in the low concentration tail regions. It is not clear at this point whether these tails are measurement errors. It is interesting to note that the point-defect transient assumed to be created by SPE causes significant As diffusion, but the B profile essentially does not move from its as-implanted position. Thus, the presence of the heavily doped As layer is believed to control the charge state of the generated point defects (vacancies) such that few of these point defects are of the type that B needs to diffuse (8).

Summary and Conclusions

Modeling the diffusion of As and B during RTA presents a unique challenge, since point-defect generation mechanisms are believed to be operating during the short annealing intervals. In the case of high dose B implants, damage clusters created by the high concentration of B in the peak of the implant distribution grow into well-defined cross-grid dislocation networks during the first 10-30s of the anneal. Quantifying the concentration of point defects generated during this process requires knowledge of the types of dislocation reactions, climb processes, and cross-slip processes that may occur simultaneously. For the case of As implantation, it was assumed that the process of SPE leaves behind vacancies that participate in the shrinkage of secondary defects at the original amorphous/crystalline interface. Since the re-growth of amorphous layers leaves a crystalline layer that is practically defect free, the vacancies probably diffuse out of the recrystallized region rather than recombine within the region. The time required to do this is on the order of 5-10s at 1050°C, which corresponds to the period over which enhanced As diffusion is observed. Pre-

amorphization at low temperature eliminates this enhanced diffusion.

Calculations of diffusion during RTA were performed by overlaying a transient point defect model on thermally assisted diffusion models associated with steady-state furnace processes. A weighted exponential function was assumed to describe the transient process, and diffusion coefficients were directly multiplied by this function. Numerical integrations were performed over 200 ms constant temperature intervals to approximate the RTA environment.

The results of this study are at best semi-quantitative. The experimental data represent measurements of time-averaged phenomena with varying temperatures. More detailed modeling requires knowledge of wafer temperature vs. time, point defect generation mechanisms, and quantification of the transient processes involved.

Acknowledgment

This work was jointly supported by the Semiconductor Research Corporation and the Microelectronics Center of North Carolina.

Manuscript submitted Dec. 29, 1983; revised manuscript received May 15, 1984.

The Microelectronics Center of North Carolina assisted in meeting the publication costs of this article.

REFERENCES

1. J. L. Benton, G. K. Celler, D. C. Jacobson, L. C. Kimmerling, D. J. Lischner, G. L. Miller, and Mc. D. Robinson, "Laser and Electron Beam Interactions with Solids," B. R. Appleton and G. K. Celler, Editors, Vol. 4, p. 765, Elsevier, New York (1982).
2. R. B. Fair, J. J. Wortman, J. Liu, M. Tischler, N. A. Masnari, and K. Y. Duh, Paper III B-8 presented at Device Research Conference, IEEE, Burlington, VT, June 20-22, 1983.
3. D. K. Sadana, S. C. Shatas, and A. Gat, in "Microscopy of Semiconducting Materials," Institute of Physics, Physics Conference Series, Institute of Physics, London (1983).
4. R. Kalish, T. O. Sedgwick, S. Mader, and S. Shatas, *Appl. Phys. Lett.*, **44**, 107 (1984).
5. R. B. Fair, J. J. Wortman, and J. Liu, in "1983 International Electron Device Meeting, Technical Digest," p. 658, IEEE, New York (1983).
6. J. Narayan, O. W. Holland, R. Eby, J. Wortman, V. Ozguz, and G. A. Rozgonyi, *Appl. Phys. Lett.*, **43**, 957 (1983).
7. R. B. Fair, To be published.
8. R. B. Fair, in "Silicon Integrated Circuits," D. Kahing, Editor, Suppl. 28, Applied Solid-State Science Series, Academic Press, New York (1981).
9. A. Seeger and K. D. Chik, *Phys. Status Solidi*, **29**, 455 (1968).
10. S. M. Hu, *J. Appl. Phys.*, **45**, 1567 (1974).
11. U. Gösele and T. Y. Tan, in "Defects in Semiconductors," S. Mahajan and J. W. Corbett, Editors, p. 45, The Materials Research Society Symposium Proceedings, North Holland, Amsterdam (1983).
12. D. Mathiot and J. C. Pfister, *J. Appl. Phys.*, **55**, 3518 (1984).
13. R. B. Fair, *This Journal*, **128**, 1360 (1981).
14. V. A. Panteleev, R. S. Baryshev, L. V. Lainer, A. G. Zinina, and E. F. Pakkutina, *Fiz. Tverd. Tela*, **16**, 502 (1974).
15. S. M. Hu and T. H. Yeh, *J. Appl. Phys.*, **40**, 4615 (1969).
16. F. F. Morehead and B. L. Crowder, in "First International Conference on Ion Implantation, Thousand Oaks," F. Eisen and L. Chadderton, Editors, p. 25, Gordon and Breach, New York (1971).
17. L. Csepregi, J. W. Mayer, and T. W. Sigmon, *Appl. Phys. Lett.*, **29**, 92 (1976).
18. D. K. Sadana, J. Washburn, P. F. Byrne and N. W. Chaing, in "Defects in Semiconductors," S. Mahajan and J. W. Corbett, Editors, p. 511, Materials Research Society Symposium Proceedings Series, Vol. 14, North Holland, Amsterdam (1983).
19. J. S. Williams and R. G. Elliman, *Appl. Phys. Lett.*, **37**, 829 (1980).
20. J. Murota, E. Arai, K. Kobayashi, and K. Kudo, *J. Appl. Phys.*, **50**, 804 (1974).
21. R. B. Fair, in "Semiconductor Silicon 1981," H. R. Huff, R. J. Kriegler, and Y. Takashi, Editors, p. 963, The Electrochemical Society Softbound Proceedings Series, Pennington, NJ (1982).

Growth of Low Dislocation Density GaAs by As Pressure-Controlled Czochralski Method

K. Tomizawa, K. Sassa, and Y. Shimanuki

Perfect Crystal Growth Group, Nishizawa Perfect Crystal Project, Research Development Corporation of Japan, Central Research Institute, Mitsubishi Metal Corporation, 1-297 Kitabukuro, Omiya, Saitama, Japan

J. Nishizawa*

Nishizawa Perfect Crystal Project, Research Development Corporation of Japan, Semiconductor Research Institute, Kawauchi, Sendai, Japan

ABSTRACT

A new growth technique of the low dislocation density GaAs crystals is described. The ambient As vapor pressure was controlled through precise control of temperature in a quartz chamber in which a crystal was grown by the Czochralski method. The dislocation density in the undoped crystals ($2^\circ\phi$, $\langle 111 \rangle$) was as low as $2 \times 10^8 \text{ cm}^{-2}$, which was lower than the case of the commercial LEC method by a factor of ten. The origin of such a pronounced reduction of the dislocation density is discussed by taking into account the effects of the melt stoichiometry and the thermal stress exerted on the grown crystal.

Dislocations in GaAs crystals are known to exert a very considerable influence on the performance of devices such as microwave devices, IC's, and laser diodes. It is already clear that dislocations in substrates reduce the lifetime of the laser diodes (1), and it has been shown that the dislocation distribution affects the uniformity of the FET threshold voltage in the IC (2). Therefore, numerous at-

tempts have been made to develop the growth technique of dislocation-free GaAs crystals.

Nishizawa *et al.* (3) have revealed that the ambient As vapor pressure greatly affects the stoichiometry and therefore the defect density in GaAs crystals. On the basis of an extensive investigation of the liquid-phase epitaxy and annealing of GaAs, they reported the optimum As vapor pressure (P_{opt}) for growth of the stoichiometric GaAs crystal as follows

*Electrochemical Society Active Member.

$$P_{\text{opt}} = 2.6 \times 10^6 \exp\left(-\frac{1.05}{kT_g}\right) \quad [1]$$

where T_g is the growth temperature. In the case of crystal growth from the melt, putting the melting temperature of GaAs, 1238°C, into T_g in Eq. [1], one obtains the value of P_{opt} as 813 torr. The As pressure is determined by the lowest temperature, T_{As} , in the chamber in which the crystal is grown. By using the relationship between T_{As} and the vapor pressure (4), the temperature corresponding to the As pressure of 813 torr is obtained as 612°C.

Recently, Parsey *et al.* (5) grew GaAs crystals by the horizontal Bridgman (HB) method under a controlled As vapor pressure and succeeded in reducing the dislocation density in 1 cm diam crystals to 500 cm⁻².

In the case of the liquid-encapsulated Czochralski (LEC) method, it is much more difficult to obtain dislocation-free crystals than with the HB method because the excessive thermal stress caused by the high temperature gradient just above the encapsulant assists dislocation generation (6). For this reason, it has been proposed to grow crystals by the LEC method by elevating the ambient temperature (6). However, it has also been shown that higher ambient temperatures tend to generate Ga droplets on the surface of the crystal due to As escape (7).

Thus, growth of GaAs crystals by the Czochralski method (without the liquid encapsulant) under a controlled As vapor pressure will lead to a significant reduction of the defect density through the combined effects of improvement of the melt stoichiometry and reduction of the thermal stress without formation of Ga droplets. Steinemann *et al.* (8) and Leung *et al.* (9) have shown that low dislocation density crystals can be grown by the Czochralski method under an As atmosphere. However, because of the complexity and limitation of repeated use of their apparatus, their techniques have not been applied for industrial use.

In this study, a new apparatus for the Czochralski method (without the liquid encapsulant) is proposed for growth of large crystals under a controlled As vapor pressure. It is also shown that the crystals (2"φ, undoped) grown by this apparatus are characterized by a low dislocation density of 2 × 10³ cm⁻².

Apparatus

A schematic diagram of the crystal puller is shown in Fig. 1. Crystal growth is carried out under a controlled As vapor pressure in a quartz chamber. The quartz chamber is 60 cm high and 10.8 cm in inner diameter (id), and the quartz crucible is 8.4 cm id.

In order to grow crystals under a controlled As pressure, the following requirements should be fulfilled. First, the temperature within the quartz chamber must be precisely controlled. The As pressure is controlled by the temperature at the top portion of the quartz chamber and the temperature of the other parts must be maintained above this temperature to avoid As deposition onto the chamber wall. Furthermore, the portion indicated by the arrow in Fig. 1 must be kept transparent during growth in order to observe the growing crystal; the temperature at this portion must be such as to avoid GaAs deposition. These requirements are met by controlling temperatures of three separate carbon heaters shown in Fig. 1.

Second, an effective seal is required between the chamber and the pull rod as well as the crucible supporting rod. As a sealing material, molten B₂O₃ (9) in Mo lids is used. The third requirement is as follows. After the growth of the crystal, the crystal and the crucible must be taken out of the quartz chamber without fracture of the chamber and the crucible. To meet this, taper joints between the quartz chamber and Mo lids are used.

The growth operation is made as follows. First, after the metal chamber is evacuated, the heaters A and C are heated to melt the B₂O₃ and the upper and lower lids are sealed by the taper joints. Then, the heater B is heated to melt GaAs. During the melting process, N₂ gas is intro-

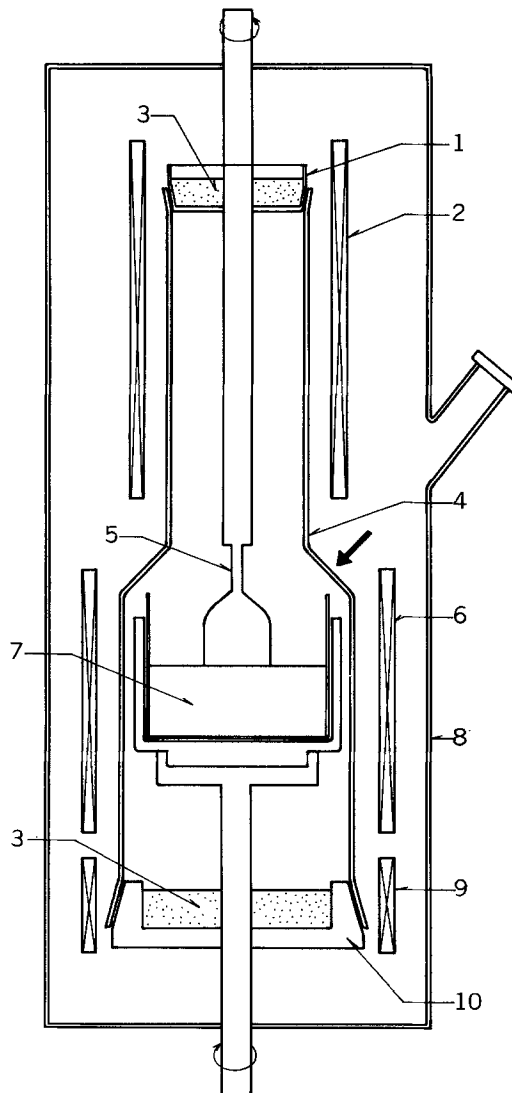


Fig. 1. Schematic diagram of the crystal puller. 1: Upper lid. 2: Heater A. 3: B₂O₃. 4: Quartz chamber. 5: Seed. 6: Heater B. 7: GaAs melt. 8: Metal chamber. 9: Heater C. 10: Lower lid.

duced into the metal chamber in order to balance the pressure outside of the quartz chamber against the As pressure within the quartz chamber. After melting the GaAs, the temperature of the heater A is so controlled that the desired As pressure within the quartz chamber is realized. After these processes, a seed is lowered, and a crystal is pulled by the ordinary Czochralski method.

Experimental Procedures

For the growth of each crystal, presynthesized GaAs (600g) and sufficient arsenic to give a required As vapor pressure over the GaAs melt were charged in a quartz crucible and a <111> seed was used. Two crystals, no. 1 and 2, were pulled under the As pressure controlling temperatures of 616° and 620°C, respectively. Pulling conditions such as the temperatures of the heaters B and C, and the position of the crucible with respect to the heater B were similar for the two crystals. In both cases, the temperature gradient just above the melt surface, which is mainly affected by the position of the crucible with respect to the heater, was about 10°C/cm. This value was much lower than the case of the commercial LEC method (~100°C/cm). Similar values of the carrier concentration and the Hall mobility at room temperature were obtained at the front portion of the two crystals and were 5 × 10¹⁶ cm⁻³ and 3.3 × 10³ cm²/V s, respectively.

From crystal 1, (111) slices were cut perpendicularly to the growth axis. After polishing, the dislocation density distribution was determined by EPD measurements on an etched surface and by x-ray topography. (110) slices

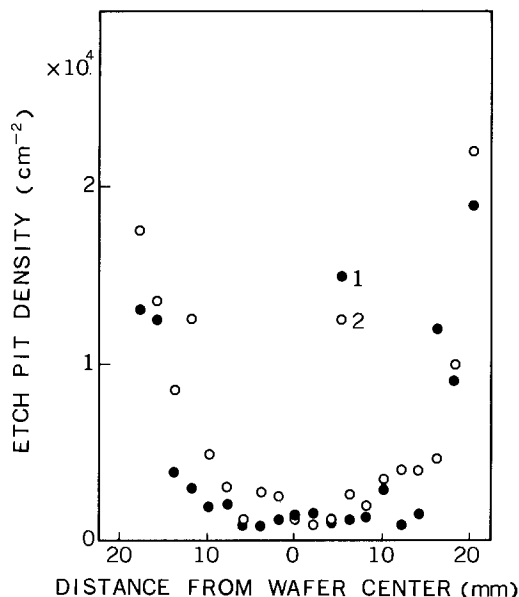


Fig. 2. Radial dislocation density profiles across wafers cut from the shoulder. Crystals 1 and 2 were pulled under the As pressure controlling temperatures of 616° and 620°C, respectively.

were cut longitudinally from crystal 2. The dislocation distribution in these slices were examined by x-ray topography. A (111) slice perpendicular to the growth axis was also cut to examine the EPD distribution for comparison with the case of crystal 1.

Results and Discussion

Radial etch-pit density distribution.—The radial etch-pit density distributions across wafers cut from the shoulder are shown in Fig. 2. The EPD distributions are U shaped, and the EPD's around the center of wafers cut from the two crystals are about $2 \times 10^8 \text{ cm}^{-2}$, which is lower than the case of the commercial undoped LEC crystals by a factor of ten. Another important result is that the EPD in crystal 1 is lower than that in crystal 2. This fact appears to show the dependence of the EPD on the As vapor pressure during the crystal growth.

Possible explanations for the pronounced reduction of the dislocation density achieved by this study are as follows. First, improvement of the stoichiometry of GaAs melt due to the As vapor pressure led to suppression of point defect formation and in turn dislocation formation. It is possible that dislocation loops are formed by aggre-

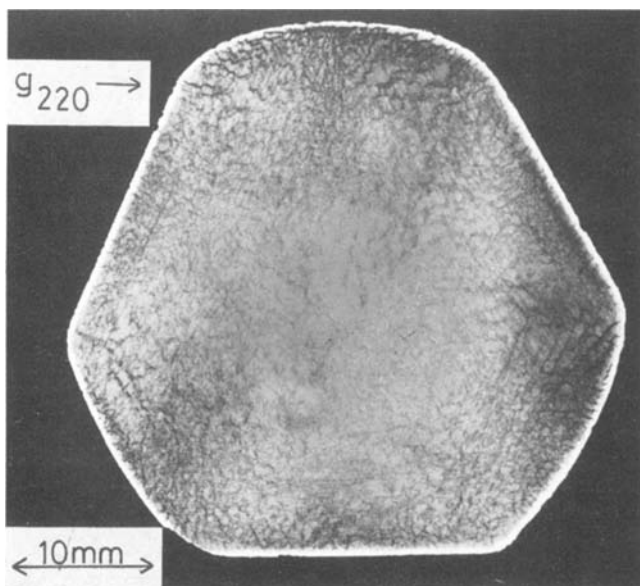


Fig. 3. X-ray topograph of a (111) wafer cut from the shoulder of a crystal which was pulled under an As pressure controlling temperature of 616°C.

gation of point defects (10). In addition, climb motion of dislocations, which is assisted by point defects (10), will reduce the back-stress acting on dislocation sources and lead to generation of new dislocations. The As pressure dependence of the EPD mentioned above appears to suggest the importance of the stoichiometry. Second, since As vaporization from the crystal surface was reduced by the As atmosphere, the growth of crystals under a low temperature gradient along the pulling axis was possible without formation of Ga droplets. As a result, generation of dislocations due to thermal stress was suppressed.

Results of x-ray topography.—Figure 3 shows an x-ray topograph of a (111) wafer cut from the shoulder of crystal 1 which was pulled under an As pressure controlling temperature of 616°C. Around the center of the wafer, isolated dislocations are observed. Dislocations form the cell structures only loosely, whereas toward the edge of the wafer dislocations begin to form distinct cell structures elongated along the $\langle 110 \rangle$ direction. These cell structures appear to be formed by the climb motion of dislocations glided in (111) planes.

A dislocation distribution in a longitudinal slice of crystal 2 is shown in Fig. 4. The temperature of the As source was kept constant during growth. Although the dislocation density is high around the seed end, it rapidly decreases toward the shoulder. It is to be noted that the dislocation distribution in the portion where the crystal diameter is increasing is different from that in another portion where the diameter is decreasing. In the former portion, dislocations around the center do not form distinct cell structures and the dislocation density decreases with pulling time. However, in the latter portion, dislocations form cell structures even in the center region; the dislocation density increases with pulling time. Such a variation in the dislocation distribution with the crystal diameter was observed over the whole length of this crystal. Since the pulling rate was kept constant during growth of the body, variation in the crystal diameter appeared to be caused by some variation in the temperature of the GaAs melt. It is possible that the temperature of the GaAs melt, as well as the temperature of the As source, affects the dislocation density. If this is the case, precise control of the temperature of the melt is necessary to reduce the dislocation density.

Summary

A new apparatus was developed to grow GaAs crystals by the Czochralski method under a controlled As pressure. The dislocation density in undoped, 2" ϕ crystals grown by this apparatus was as low as $2 \times 10^8 \text{ cm}^{-2}$. Such a pronounced reduction of the dislocation density seemed to be associated with both the improved melt stoichiometry resulting from the As vapor pressure control and the reduced thermal stress due to the low temperature gradient just above the melt. Further investigation based on the precise control of the As pressure is needed to evaluate the net effect of the stoichiometry on the defect density.

The apparatus described in this paper is applicable for industrial use to grow large GaAs crystals with low dislocation densities.

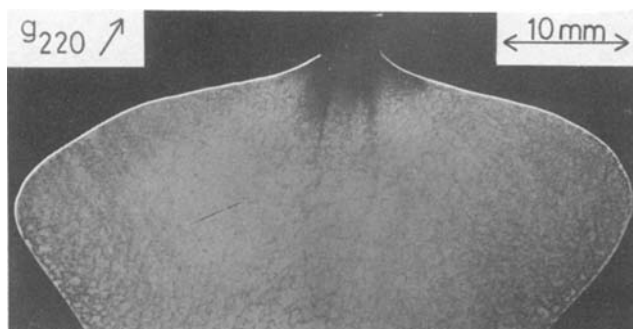


Fig. 4. X-ray topograph of a longitudinally cut slice of crystal 2 pulled under an As pressure controlling temperature of 620°C.

Manuscript submitted Jan. 16, 1984; revised manuscript received April 30, 1984.

Research Development Corporation of Japan assisted in meeting the publication costs of this article.

REFERENCES

1. P. Petroff and R. L. Hartman, *Appl. Phys. Lett.*, **23**, 469 (1973).
2. Y. Nanishi, S. Ishida, T. Honda, H. Yamazaki, and S. Miyazawa, *Jpn. J. Appl. Phys.*, **21**, L335 (1982).
3. J. Nishizawa, Y. Okuno, and H. Tadano, *J. Cryst. Growth*, **31**, 215 (1975); J. Nishizawa and Y. Okuno, in "Proceedings of the Second International School on Semiconductor Optoelectronics," Cetniewo, Poland (1978); J. Nishizawa, N. Toyama, and Y. Oyama, in "Proceedings of the Third International School on Semiconductor Optoelectronics," Cetniewo, Poland (1981).
4. J. Van den Boomgaard and K. Schol, *Philips Res. Rep.*, **12**, 127 (1957).
5. J. M. Parsey, Jr., J. Lagowski, and H. C. Gatos, Paper 325 presented at the Electrochemical Society Meeting, San Francisco, CA, May 8-13, 1983.
6. A. S. Jordan, R. Caruso, and A. R. Von Neida, *Bell Syst. Tech. J.*, **59**, 593 (1980).
7. R. T. Chen and D. E. Holmes, *J. Cryst. Growth*, **61**, 111 (1983).
8. A. Steinmann and U. Zimmerli, *J. Phys. Chem. Solids, Suppl. 1*, 81 (1967).
9. P. C. Leung and W. P. Allred, *J. Cryst. Growth*, **19**, 356 (1973).
10. J. Friedel, "Dislocations," pp. 92, 106, Pergamon, Oxford, England (1964).

Chlorine Content in Dry and Wet MOS Gate Oxides

W. A. Bösenberg

RCA Solid State Technology Center, Somerville, New Jersey 08876

C. W. Magee and E. M. Botnick

RCA Laboratories, Princeton, New Jersey 08540

ABSTRACT

Highly sensitive SIMS measurements of chlorine content in 1000-3000Å of silicon dioxide show that only very small amounts of chlorine (less than $6 \times 10^{11} \text{ cm}^{-2}$) can be found in steam-grown oxides in which gaseous or liquid HCl or TCA has been added during the oxide growth. Oxides grown in dry oxygen with gaseous HCl or TCA addition show a large range in chlorine content depending on the growth conditions. Chlorine can be incorporated into steam-grown oxides at temperatures as low as 750°C when the last 5%-10% of the desired oxide thickness is grown in dry O₂ and TCA atmosphere. The activation energy for this process is 2.3 eV. The increase in chlorine content is less than linear with TCA concentration and independent of oxide thickness.

In MOS processing, hydrogen chloride treatments are often performed by passing an excess of HCl over the silicon wafers during critical steps or piping HCl into the furnace during tube cleaning. The use of hydrogen chloride during the growth of the gate oxide of a MOS device is a well established technique (1-3). The chlorine reduces the sensitivity of the oxide to sodium-induced shifts of the threshold voltage; a total sodium content as low as $1 \times 10^{11} \text{ cm}^{-2}$ causes a shift of several tenths of one volt.

The analytical techniques for measurement of chlorine in silicon dioxide, i.e., secondary ion mass spectroscopy (SIMS) and nuclear backscattering, have not been sensitive enough for more detailed quantitative work at the 10^{11} - 10^{14} cm^{-2} level. This paper discusses a technique that has the required sensitivity and its application to various growth conditions for MOS gate oxides.

Conversion of Volume Concentration to Areal Density

For an investigation of oxide layers with chlorine content in the region of interest for MOS applications, the chlorine detection system should be able to detect levels of the order of 10^{10} at./cm^2 . This areal density is of the same order as the MOS interface charge density usually found in well-controlled oxide layers. It is more useful to express the values in terms of an areal density similar to the dose used in ion implantation of impurities into MOS devices.

Most of the measurement techniques, however, give the volume concentration of the species. Therefore, conversions between the two quantities are needed.

For uniformly distributed chlorine in 1000Å of SiO₂ with a volume concentration of $N = 1 \times 10^{15} \text{ cm}^{-3}$, the areal density or content C is $C = 10^{15} \text{ cm}^{-3} \times 10^{-5} \text{ cm} = 10^{10} \text{ cm}^{-2}$. For nonuniformly distributed layers, which is the normal case with most of the chlorine being found near the Si/SiO₂ interface, the integral over the oxide thickness

t_{ox} has to be taken

$$C = \int_0^{t_{\text{ox}}} N(x) dx \quad [1]$$

For actual MOS transistors, the areal density must be related to a shift in threshold voltage. For oxide layers which are 1000Å thick, an areal density of $1 \times 10^{11} \text{ ion/cm}^2$ corresponds to a threshold voltage shift of 0.5V. This value scales roughly with the areal density. VLSI circuits have up to factor five thinner oxides and are less sensitive to voltage shifts by the same factor.

Instrumentation

Auger sputtering.—Auger sputter analysis, which is based on a layer-by-layer removal technique combined with characteristic Auger electron energy analysis, is a useful technique for analyzing impurities in thin layers (4). The practical detection limit for this technique, however, is about $1 \times 10^{19} \text{ at./cm}^3$, and hence Auger analysis has a lower limit problem when analyzing practical chlorine-doped oxides.

Secondary ion mass spectrometry.—The technique of SIMS utilizes a beam of energetic ions to sputter away a solid surface producing ionized sputtered particles which can be mass spectrometrically detected. This analytical method can provide in-depth information on atomic constituents if one or more mass peaks are recorded as the sputtering process erodes the sample, thus producing the detected signal from continuously greater depths beneath the original sample surface.

The strength of the SIMS technique is its very high sensitivity for most elements. Previous SIMS analyses of chlorinated oxides (5, 6) have reported detection limits of $1 \times 10^{19} \text{ at./cm}^3$ or 170 ppm atomic. Previous SIMS instrumentation, however, was limited by the design that only

the positive ion Cl^+ could be monitored. It is obvious from the electron population of the Cl 3p orbital that this atom is much more likely to be sputtered as Cl^- than Cl^+ . If this species could be detected, then considerably higher sensitivity should be achievable than previously reported.

The primary ion beam used in these experiments was $^{40}\text{Ar}^+$. It is now well known (7) that negative ion yields (and thus sensitivities) can be greatly increased if Cs^+ ions are used as the primary bombarding species. While our SIMS instrument is equipped with a cesium ion source (8), we chose not to use it because the Cs which becomes implanted into the sample can create artifacts in the data as the profile approached the SiO_2/Si interface, just where most of the chlorine is located.

The unique design of the secondary ion optics of the SIMS instrumentation used for our studies (8-12) allows these negatively charged chlorine ions to be detected with high efficiency and low background. Volume detection limits of $1-3 \times 10^{17}$ at./ cm^3 are routinely achievable, with areal density sensitivities of $1-2 \times 10^{14}$ / cm^2 .

Calibration of SIMS

The large range in elemental sensitivities and the matrix or chemical effects encountered in SIMS require the use of a standard sample of chlorine in SiO_2 to calibrate the instrument for this particular analysis. The standard chosen was 180 keV $^{35}\text{Cl}^+$ implanted into thermally grown SiO_2 film of approximately 1 μm thickness (SIMS profile shown in Fig. 1). Such samples make ideal standards for SIMS due to the high accuracy ($\pm 1\%$) with which the dose (3×10^{14} cm^{-2}) can be controlled, and the localization of the implanted atoms in depth. No prior knowledge of the implant distribution is needed. The depth scale is determined by measuring the depth of the sputtered crater subsequent to the analysis by profilometry. Knowledge of the depth scale and the area under the measured profile (implanted dose) allows one to establish the concentration scale and thus to convert the counts/s into volume concentration. Previous calibrations have been done using Cl implants with doses of 1×10^{14} , 3×10^{14} , and 1×10^{15} cm^{-2} . The calibrations were so accurate that only one dose is needed.

The chlorine can move under the influence of an electric field. Since it is in a matrix of insulating SiO_2 , the

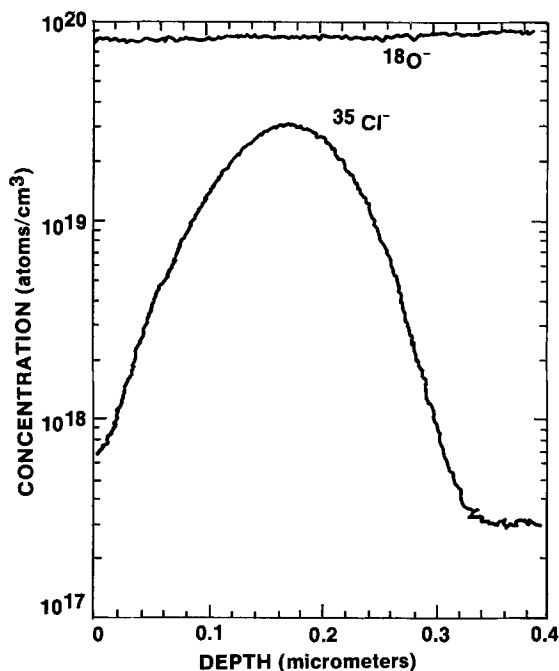


Fig. 1. Chlorine depth profile of an ion-implanted standard used for calibrating SIMS sensitivity for Cl in SiO_2 . The sample is a 10,000 Å thick thermally grown SiO_2 layer which has been implanted with $^{35}\text{Cl}^+$ ions at 180 keV to dose of 3×10^{14} at./cm^2 . Shown is the actual profile as measured by SIMS. Also shown is the $^{18}\text{O}^-$ concentration indicating constant sensitivity during the SIMS analysis.

charge built up during argon sputtering must be minimized by the use of a compensating electron beam (10).

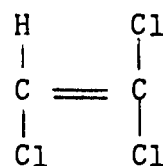
Also critically important to quantitative SIMS depth profiling of SiO_2 films is the ability to maintain constant instrument transmission (sensitivity) while sputtering through the layers. Previous efforts at SIMS analysis of SiO_2 films (13) have suffered from changes in sensitivity of two orders of magnitude during the analysis due to surface charging effects from the sputtering beam. Constant sensitivity throughout the analyses in this report can be inferred from the steady signal of the $^{18}\text{O}^-$ ion detected along with the $^{35}\text{Cl}^-$ signal (see Fig. 1).

Chlorine Sources

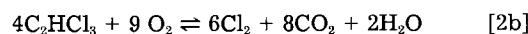
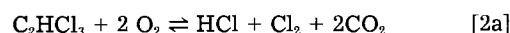
The handling of liquified chlorine and liquified hydrogen chloride from steel tanks is more troublesome than handling of other substances. A small amount of water vapor in the gas stream will cause metal corrosion of the connecting plumbing and transfer heavy metal impurities into the silicon dioxide. Azeotropic mixtures of hydrogen chloride and water have been in long use as HCl-steam boilers. The boiler is made of clean quartz glass, and Teflon tubing is used for connecting the boiler to the furnace tube. However, it is not always desirable to pass wet HCl through the oxidation tube.

More recently, HCl or Cl_2 have been generated from chlorinated hydrocarbons. This concept is not new. Most of the early literature shows data on trichloroethylene (TCE), then the most often used dry cleaning and degreasing fluid (14-19).

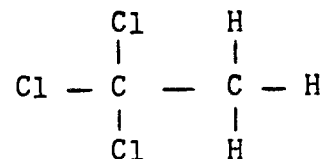
Trichloroethylene (TCE).—The formula is as follows



Decomposition in an oxygen atmosphere at elevated temperatures occurs according to the following two equations



(1,1,1) Trichloroethane (TCA).—The chemical formula is

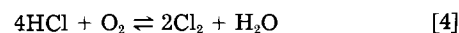


The decomposition in an oxygen atmosphere is



(1,1,2) TCA decomposes in the same fashion as (1,1,1) TCA, but is more toxic and since it has a lower vapor pressure tends to enrich in the evaporator when mixtures of (1,1,1) and (1,1,2) TCA are used. Some traces of (1,1,2) TCA can always be found in MOS-grade (1,1,1) TCA.

At high temperatures and in an excess of oxygen, the following reaction occurs



The beneficial component is Cl_2 . In the presence of steam, the equilibrium moves toward the left and less Cl is incorporated into the gate oxide.

TCE inherently would be better for the chlorination of gate oxides. However, in the USA the EPA restrictions on its use are severe and can only be overcome with difficulty. Therefore, all our work is presently performed using (1,1,1) TCA.

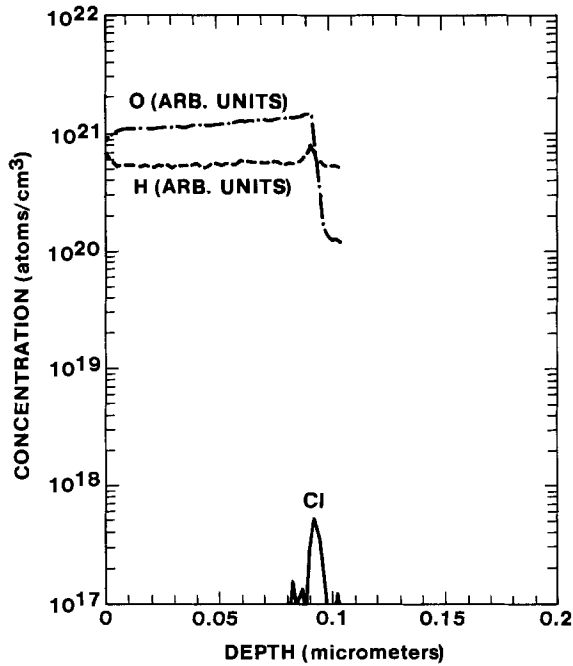


Fig. 2. Chlorine, oxygen, and hydrogen SIMS concentration profile for 900Å SiO₂ sample. The layer was grown for 55 min at 875°C in an azeotropic mixture of boiling hydrochloric acid and water (about 50% each by volume). Only a small amount of chlorine can be seen at the interface. The chlorine content is $3 \times 10^{11} \text{ cm}^{-2}$.

Early Results as a Function of Sample Preparation

Oxides grown with an azeotropic mixture of water and hydrochloric acid, a mixture that has been shown to be beneficial for MOS devices (20-21), show only traces of chlorine at the detection limit (see Fig. 2). The same is true for silicon dioxide grown in steam with additions of gaseous HCl (see Fig. 3) or with chlorine generated by the oxidation of (1,1,1) trichloroethane (TCA). From Eq. [4], it can be seen that the addition of H₂O will shift the equilibrium toward the left. Since Cl₂ is the active species, less gets into the oxide.

However, oxides grown in dry oxygen with the addition of gaseous HCl show appreciable chlorine content (see

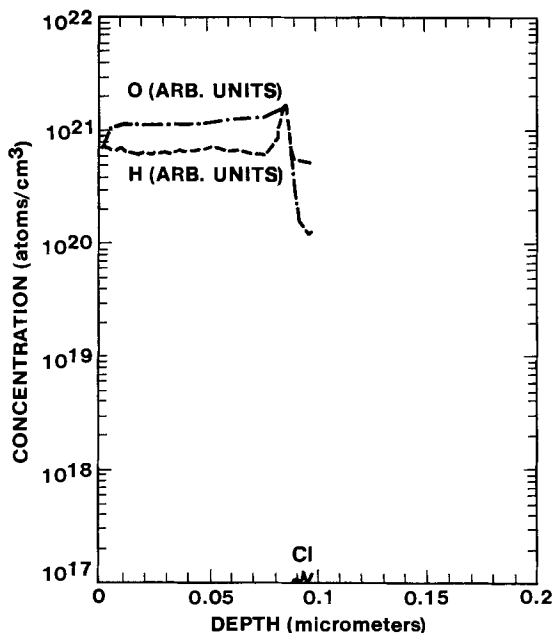


Fig. 3. Chlorine, oxygen, and hydrogen SIMS concentration profile for 950Å SiO₂ sample. The layer was grown for 30 min at 900°C in steam with the addition of 1% of gaseous HCl. Only a small amount of chlorine can be seen at the interface. The chlorine content is $3 \times 10^{11} \text{ cm}^{-2}$.

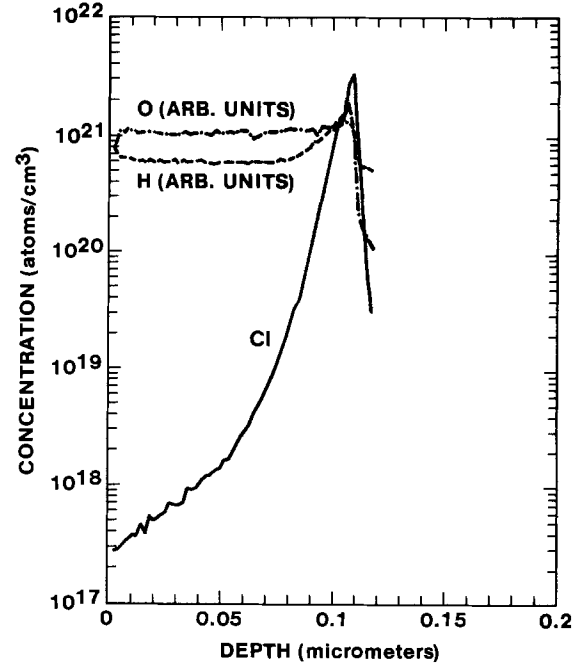


Fig. 4. Chlorine, oxygen, and hydrogen SIMS concentration profile for 1050Å SiO₂ sample. The layer was grown at 1100°C in oxygen with 3% gaseous HCl. The chlorine content is $2.8 \times 10^{15} \text{ cm}^{-2}$.

Fig. 4). A peak always occurs at the Si/SiO₂ interface, and, often, a second lower peak occurs at the SiO₂/air or metal interface. Under an electric field at elevated temperatures, the chlorine distribution will shift, but the areal density will remain constant. An anneal in forming gas (10% hydrogen, 90% nitrogen) at 1100°C will reduce the areal density by a factor of 2.

Lower Temperature Oxides with Chlorine

The dry oxidation method with O₂ and gaseous HCl is slow and requires, for a sufficient thickness, high temperature and/or a long time cycle. Unfortunately, a long oxidation cycle makes the boron and phosphorus junction depths deeper than desired.

We have investigated a process in which the first part of the oxide is grown in steam followed by a dry oxida-

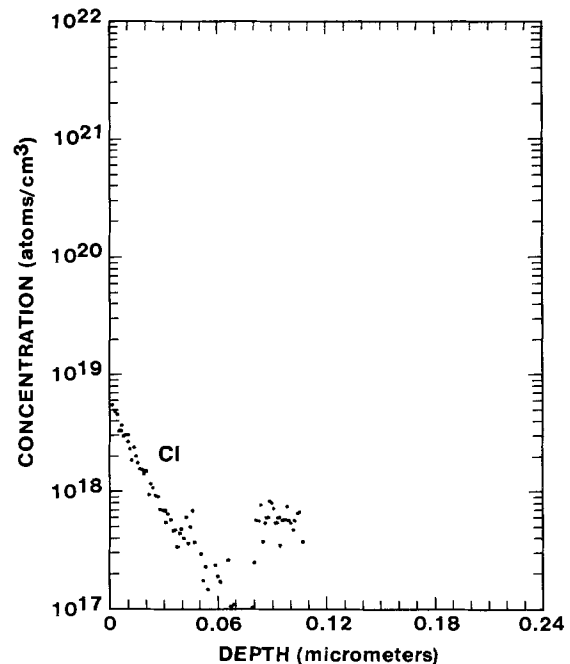


Fig. 5. Chlorine SIMS profile in 827Å of SiO₂ after 10 cm³ TCA had passed over the sample at 750°C for 60 min. The chlorine content is $7.5 \times 10^{12} \text{ cm}^{-2}$.

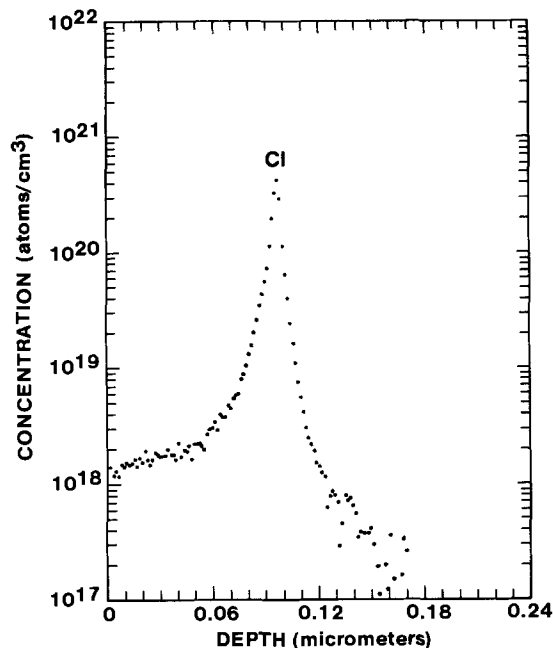


Fig. 6. Chlorine SIMS profile in 963 Å of SiO₂ after 10 cm³ TCA had passed over the sample at 950°C for 60 min. The chlorine content is 3.0×10^{14} cm⁻².

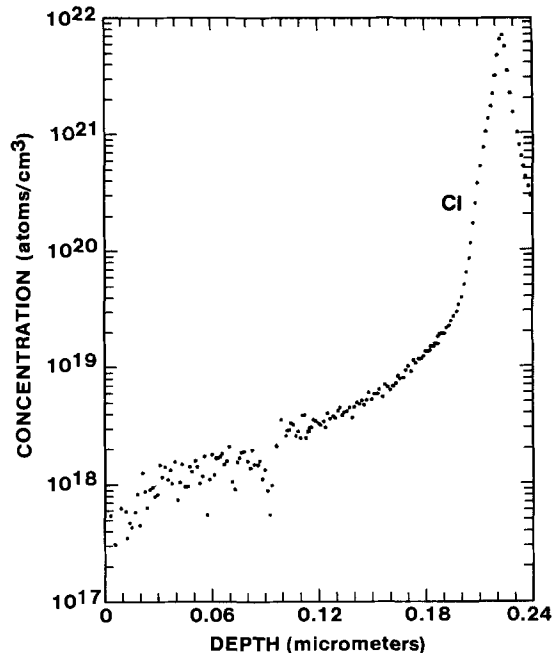


Fig. 7. Chlorine SIMS profile in 2097 Å of SiO₂ after 10 cm³ TCA had passed over the sample at 1150°C for 60 min. The chlorine content is 6.5×10^{14} cm⁻².

tion with a chlorine ambient. The dry oxidation can then be done at much lower temperatures, leaving the diffusion cycle almost unaffected.

The steam oxides were grown for 100 min (by combustion of hydrogen and oxygen) at a temperature of 875°C on (100) n-type silicon wafers of 5-10 Ω-cm resistivity. The ellipsometrically measured oxide thickness averaged 812 ± 12 Å.

The dry oxidations were done at 100°C intervals, from 750° to 1150°C. The first group of samples were subjected to a gas stream injection of 1 cm³ of TCA. This was done linearly over a period of 30 min. The second group of samples was subjected to the injection of 10 cm³ TCA over a 60 min period. An injection time of 30 min would have required a larger oxygen-gas flow than the 4 liter/min used. Table I shows the increase in oxide thickness with the TCA injections. It is appreciable at temperatures over 950°C.

The SIMS profiles show that the transport of chlorine to the silicon/silicon dioxide interface is slow at temperatures below 850°C. At higher temperatures, most of the chlorine will accumulate at this interface (see Fig. 4-7).

Table I. Oxide thicknesses t_{ox1} after 875°C 30 min pyrolytic steam oxidation, oxide thickness t_{ox2} after TCA treatment at temperatures between 750° and 1150°C. Two volumes of TCA were used 1 cm³ in 30 min and 10 cm³ in 60 min. The oxide thickness increases appreciably at the higher temperatures. The total chlorine increases with temperature and TCA volume

Temp. (°C)	1 cm ³ TCA, 30 min			10 cm ³ TCA, 60 min		
	t_{ox1} (Å)	t_{ox2} (Å)	Total Cl (cm ⁻²)	t_{ox1} (Å)	t_{ox2} (Å)	Total Cl (cm ⁻²)
750	766	785	1.0×10^{12}	812	827	7.5×10^{12}
850	804	829	8.4×10^{12}	815	853	5.9×10^{13}
950	811	881	6.6×10^{13}	813	963	3.0×10^{14}
1050	811	1059	5.2×10^{14}	813	1336	1.8×10^{15}
1150	824	1510	1.3×10^{15}	813	2097	6.5×10^{15}

Table II. Constants C_0 and E for an Arrhenius-type plot $C = C_0 \cdot \exp(\Delta E/kT)$ of Fig. 8 with R as the correlation coefficient of the linear regression

Curve	Conditions	C_0 (cm ⁻²)	ΔE (eV)	R
1	1 cm ³ TCA/30 min	2.750×10^{23}	-2.328	0.99743
2	10 cm ³ TCA/60 min	2.145×10^{23}	-2.129	0.99915

The oxide thicknesses and the total chlorine content for the ten samples are listed in Table I. The chlorine content vs. $1/T$ is shown as an Arrhenius plot in Fig. 8, with the numerical values given in Table II. An activation energy of 2.3 eV has been calculated from these measurements. The ratio of measured chlorine content of the two samples to TCA liquid volumes is less than predicted by linearity, and decreases with temperature.

A second set of samples was prepared to study how much chlorine is incorporated with increasing TCA volume and oxide thickness. The initial steam oxide was grown at 875°C of two thicknesses of 1000 and 2700 Å on

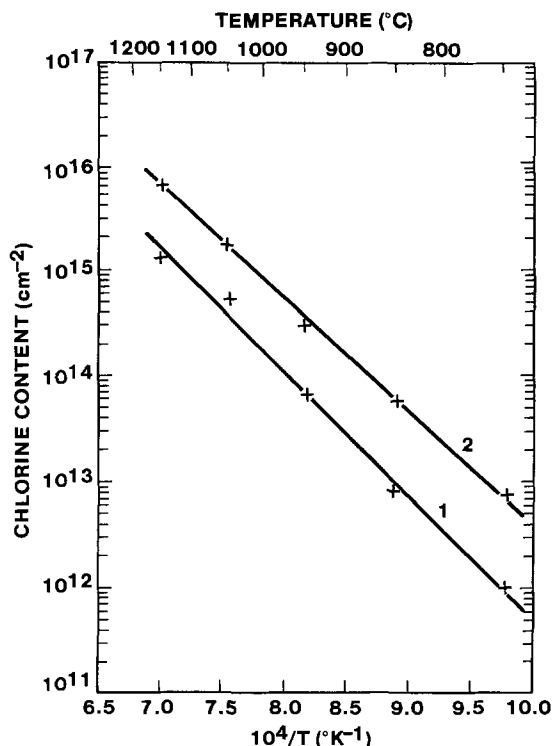


Fig. 8. Chlorine content C as a function of $1/T$. Least squares fit lines to the equation $C = C_0 \cdot \exp(E/kT)$ give a reasonable description. Curve 1 is for 1 cm³ TCA in 30 min, curve 2 is for 10 cm³ TCA in 60 min. The values C_0 and E are listed in Table II.

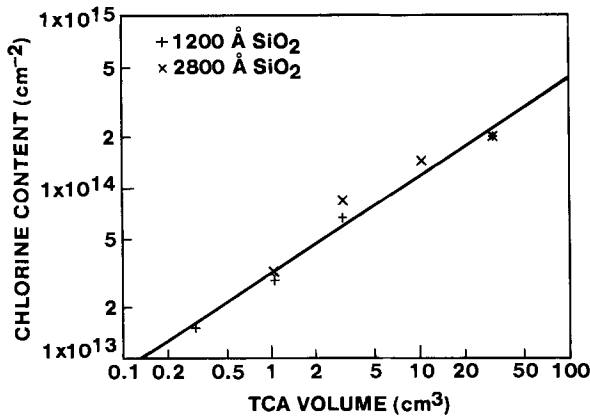


Fig. 9. Chlorine content C as a function of TCA volume. The TCA injection is for 120 min at 950°C . The data for 1200\AA SiO_2 are marked by +; the data for 2800\AA by x. The least squares fit line is representing data from both oxide thicknesses. The numerical values are given in Table IV.

5-10 $\Omega\text{-cm}$ n-type bulk silicon wafers. Precise amounts of TCA were injected into the oxidation tube from a motor-driven syringe system over a period of approximately 120 min at a temperature of 950°C . After this treatment, the oxide thicknesses increased to 1250 and 2800\AA .

Table III lists the total chlorine content in the samples. Figure 9 indicates a linear relationship when both the chlorine content and the TCA volume (and indirectly the Cl concentration) are plotted on a log-log scale. Table IV lists the constants and correlation coefficients of least squares fits.

Capacitance/Voltage Stability

Chlorinated oxides are extremely stable. Figure 10 shows the capacitance/voltage characteristics under $\pm 10\text{V}$ bias at 300°C . The total chlorine content is $1.0 \times 10^{14} \text{ cm}^{-2}$ after a 20 min 1150°C forming gas anneal. The total shift is less than 20 mV. The theoretical curve for $N_{ss} = 0$ coincides with these curves.

Discussion

SIMS analysis of chlorine in silicon dioxide has allowed a quantitative study of how chlorine is incorporated into SiO_2 . The sensitivity has been increased so as to permit quantitative measurement of low levels, thus the analysis can be applied to actual MOS gate oxides.

Oxides grown with an azeotropic mixture of hydrochloric acid and water are beneficial for reducing the sodium sensitivity, but chlorine cannot be detected in sufficient quantity in these oxides. The same is true for silicon dioxide grown in steam with additions of gaseous HCl or chloro-

Table III. SIMS chlorine constant (cm^{-2}) in silicon dioxide of various thicknesses as a function of TCA volume injected during a 120 min oxygen heat cycle at 1050°C

TCA volume (cm^3)	1200 \AA oxide	Repeat 1200 \AA	2800 \AA oxide
0.3	1.5×10^{13}		
1	2.9×10^{13}	2.83×10^{13}	3.24×10^{13}
3	6.7×10^{13}		8.25×10^{13}
10	1.2×10^{14}		1.43×10^{14}
30	2.1×10^{14}	2.08×10^{14}	2.07×10^{14}

Table IV. A least squares fit for the SIMS chlorine content C (cm^{-2}) as a function of the TCA volume V (cm^3) can be represented by the following equation: $\log(C) = A + B \cdot \log(V)$ and the following constants A and B

Oxide thickness (\AA)	A	B	R
1200	13.4904	0.5816	0.9940
2800	13.5358	0.6204	0.9209
both	13.5082	0.5747	0.9787

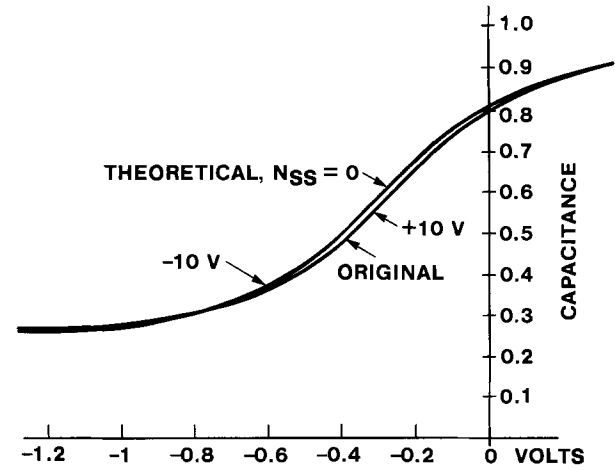


Fig. 10. Capacitance-voltage characteristics under bias-temperature stress of MOS capacitor with 1000\AA thick SiO_2 layer with $1 \times 10^{14} \text{ cm}^{-2}$ chlorine in it. All experimental curves with zero, $+1 \times 10^6$ and $-1 \times 10^6 \text{ V/cm}$ field fall within 20 mV of each other and the theoretical curve. This represents an extraordinary degree of stability.

rine generated by the oxidation of (1,1,1) trichloroethane. The beneficial results can only be explained by the chlorine cleaning action of the oxidation tube and/or by preventing the sodium from entering the SiO_2 .

At temperatures of 1200°C , the addition of HCl to the steam will substantially increase the minority carrier lifetime (22).

Oxides grown in dry oxygen with the addition of gaseous HCl show appreciable chlorine content. This method of oxide growth is slow and requires, for a sufficient thickness high temperature and/or a long time cycle. Unfortunately, such an oxidation cycle makes the boron and phosphorus junction depths deeper than desired.

We have developed a process in which the first part of the oxide is grown in steam, followed by a dry oxidation with a chlorine containing ambient. The dry oxidation can be done at much lower temperatures, leaving the diffusion cycle almost unaffected. The activation energy for the chlorine incorporation was found to be 2.3 eV. This allows practical chlorine incorporation at a temperature as low as 800°C .

Chlorinated oxides are electrically very stable. Capacitance voltage temperature bias stressing indicates total shifts of less than 20 mV. No negative instability that has been linked to chlorine in the oxide (23) has been found especially for polysilicon MOS capacitors that are shielded from deep UV irradiation common in sputtered-metal deposition systems. In our favor is the use of the (100) direction of the silicon substrate material and the low chlorine concentration in the oxide. In our opinion, chlorine is not harmful to MOS gate oxides. Very clean steam oxides without chlorine ambient have also shown similar stability. The addition of chlorine into the gas stream creates an extra margin useful in a production environment.

Experiments which were designed to show the sodium interaction with chlorine in the oxide did not show appreciable sodium passivation. In these experiments, well-quantitized levels of sodium have been implanted into chlorinated SiO_2 . SIMS measurements with sodium are very difficult to perform. Electrical measurements that rely on the sodium mobility in SiO_2 at temperatures of 300°C do not show reduced threshold voltage shifts for the chlorine levels and low chlorine incorporation temperatures used here. At high temperatures and very high chlorine levels that will form a liquid phase of $\text{Si}_x\text{Cl}_y\text{O}_z\text{H}_2$, sodium passivation occurs (24-26).

Acknowledgment

The authors are indebted to N. Ditrick for sample generation.

Manuscript submitted Sept. 16, 1983; revised manuscript received May 24, 1984. This was Paper 362 presented at the San Francisco, California, meeting of the Society, May 8-13, 1983.

RCA Corporation assisted in meeting the publication costs of this article.

REFERENCES

1. P. H. Robinson and F. P. Heiman, *This Journal*, **118**, 141 (1971).
2. R. J. Kriegler, Y. C. Cheng, and D. R. Colton, *ibid.*, **119**, 388 (1972).
3. A. Rohatgi, S. R. Butler, F. J. Feigl, H. W. Kraner, and K. W. Jones, *ibid.*, **126**, 143 (1979).
4. J. W. Rouse *et al.*, *J. Vac. Sci. Technol.*, **18**, 971 (1981).
5. B. E. Deal, A. Hurrle, and M. J. Shulz, *This Journal*, **125**, 2024 (1978).
6. I. S. T. Tsong *et al.*, in "Proceedings of the International Conference on the Physics of MOS Insulators, pp. 321-325, Raleigh, NC, June, 1980.
7. H. A. Storms *et al.*, *Anal. Chem.*, **49**, 2023 (1977).
8. C. W. Magee, *This Journal*, **126**, 660 (1979).
9. C. W. Magee, W. L. Harrington, and R. E. Honig, *Rev. Sci. Instrum.*, **49**, 477 (1978).
10. C. W. Magee and W. L. Harrington, *Appl. Phys. Lett.*, **33**, 193 (1978).
11. C. W. Magee and E. M. Botnick, *J. Vac. Sci. Technol.*, **19**, 47 (1981).
12. C. W. Magee and R. E. Honig, *Surf. Interface Anal.*, **4**, 35 (1982).
13. N. M. Johnson, D. K. Biegelsen, M. D. Moyer, V. R. Deline, and C. A. Evans, Jr., *Appl. Phys. Lett.*, **38**, 995 (1981).
14. M.-C. Chen and J. W. Hile, *This Journal*, **119**, 223 (1972).
15. G. J. Declerck, T. Hattori, G. A. May, J. Beaudou, and J. D. Meindl, *ibid.*, **122**, 436 (1975).
16. E. J. Janssens and G. J. Declerck, *ibid.*, **125**, 1696 (1978).
17. T. Hattori, *Jpn. J. Appl. Phys.*, **17**, 69 (1978).
18. R. Scot-Clark, *Solid State Technol.*, **80** (1979).
19. T. Hattori, *ibid.*, **83** (1982).
20. A. Mayer, U. S. Pat. 3,556,879 (1975).
21. B. E. Deal, D. W. Hess, J. D. Plummer, and C. P. Ho, *This Journal*, **125**, 339 (1978).
22. A. M. Goodman, L. A. Goodman, and H. F. Gossenberger, *RCA Rev.*, **44**, 326 (1983).
23. D. W. Hess, *This Journal*, **124**, 740 (1977).
24. J. Monkowski, R. E. Tressler, and J. Stach, *ibid.*, **125**, 1967 (1978).
25. M. D. Monkowski *et al.*, Paper presented at the Conference on Surfaces and Interfaces on Ceramic and Ceramic Metal Systems, Berkeley, CA, July 1980.
26. J. R. Monkowski *et al.*, in "Proceedings of the IEEE Electronic Components Conference, San Francisco, CA, April, 1980," IEEE, New York.

A New Silicone-Based Negative Resist (SNR) for Two-Layer Resist System

Masao Morita, Saburo Imamura, Akinobu Tanaka, and Toshiaki Tamamura

Nippon Telegraph and Telephone Public Corporation, Ibaraki Electrical Communication Laboratory, Polymers Section, Tokai, Ibaraki 319-11 Japan

ABSTRACT

A new silicone-based negative resist (SNR) for a two-layer resist system was synthesized by the chloromethylation of oligomeric diphenyl siloxane (ODPS), in which the polymerization of ODPS occurred simultaneously. The molecular weight of SNR could be controlled by the reaction conditions. SNR showed excellent dry etching resistance to O₂ RIE owing to the siloxane main chain structure and high sensitivity and high resolution to electron beam, x-ray, and deep UV radiation due to chloromethyl groups as the crosslinking units. The high glass transition temperature of SNR (150°C) due to diphenyl structure contributes to improving resolution and eliminates lithographic problems involved in low T_g conventional silicone resins. Submicron patterns with a high aspect ratio were fabricated in a two-layer system comprised of SNR on AZ1350 photoresist bottom layer.

As the minimum pattern size in VLSI reaches submicron dimensions, single-layer resist systems cannot satisfy all requirements in electron beam lithography or photolithography. A demand to establish practical multi-layer resist (MLR) systems has been growing, because the MLR has various advantages over single-layer resist systems, such as the planarization of surface topography, higher resolution and higher aspect ratio, proximity effect reduction in electron beam lithography, and so on (1-5). A decision to introduce a MLR system depends on the trade-off between these advantages and the substantial increase in the number of processing steps, which is a vital drawback for MLR systems.

With respect to resist materials for MLR systems, polymers containing certain amounts of inorganic elements are one of the most important class of resists, because they can possess a very high resistance against oxygen reactive ion-etching (O₂ RIE) (1, 5, 6). Two-layer resist (2LR) systems composed of this type of resist as a thin top layer and an organic polymer film as a thick bottom layer are now regarded as among the most promising for realizing a practical MLR system with a relatively small increase in the number of processing steps.

Several organometallic polymers or inorganic resists have been already proposed (7-10). Among them, silicone resins are particularly interesting, because of very high O₂ RIE resistance, and a wide variety of available raw materials to synthesize new resists. Hatzakis *et al.* (7) reported that commercially available, high molecular weight poly(vinyl methyl siloxane) and poly(dimethyl siloxane) act as high sensitivity (2 μC/cm²) and high resolution (contrast

of 2.0) inorganic polymer resists. The good wettability of silicone resins onto organic polymer layers, which prevents the formation of pinholes even in a thin layer of top resist, is also pointed out as another advantage of silicone resins. However, because of the extremely low glass transition temperature (T_g), aliphatic polysiloxanes are normally viscous liquid or gum at room temperature so that several problems arise such as adhesion of dust and control of resist thickness (11). Besides these problems, high T_g is an important factor for negative resist polymers from various aspects. We have pointed out that the degree of resist swelling during development can be substantially depressed in a high T_g polymer, forming resist patterns with a fine edge definition and a steep pattern profile (12). When synthesizing new resists, high T_g will make the chemical modification and purification of polymers much easier.

It is known that the substitution of the methyl groups of poly(dimethyl siloxane) by phenyl groups can improve the thermal stability of silicone resin. However, T_g of a silicone resin in which 75% of the methyl groups are substituted with phenyl groups is still about -30°C. When all methyl groups are completely replaced by phenyl groups, the resulting polymer is expected to have very high T_g, because commercially available oligomeric diphenylsiloxane has a T_g of about 150°C. However, poly(diphenylsiloxane) (PDPS) has not been produced in a high molecular weight form.

We have succeeded in synthesizing high molecular weight PDPS containing chloromethyl groups as a cross-linking functional group (13). The resist called silicone-

based negative resist (SNR), shown in Fig. 1, can provide very high resolution two-layer resist systems (14, 15). This paper deals with the synthesis and the resist performance of SNR.

Experimental

To synthesize high molecular weight PDPS, oligomeric diphenylsiloxane (ODPS) available from Petrarch Systems was used as a starting material. The ODPS with a molecular weight of 1400 (polymerization degree of about 7) had Si-OH groups at both ends. The chloromethylation of ODPS was carried out in chloromethylmethyl ether using SnCl_4 as a catalyst. The temperature and reaction times must be rigorously controlled so that polymers with various molecular weights are produced without forming gel. The typical reaction conditions are as follows: ODPS (30g) was dissolved in chloromethylmethyl ether (500 ml). Then, SnCl_4 (25 ml) was added to the solution. The reaction mixture was stirred for 17h at 0°C , and a white polymer was isolated by reprecipitation in methanol. The molecular parameters of polymers obtained were determined compared with polystyrene standards by gel permeation chromatography (GPC) using a Model HLC-802UR (Toyo Soda).

For the sensitivity measurements, the resist was spin-coated on a silicon wafer from a nominal 5% solution in methylisobutyl ketone. The initial thickness at 1000 rpm was about $0.2\ \mu\text{m}$. The resolution of SNR was evaluated in a two-layer resist system where a photoresist AZ-1350J (Shipley) was used as a bottom layer. $1.25\ \mu\text{m}$ thick AZ resist was spin-coated on Si wafers. $0.2\ \mu\text{m}$ thick SNR layer was coated on a hard-baked AZ layer. Monochlorobenzene was used as a spinning solvent for SNR when AZ is soft-baked at a temperature lower than 90°C . The resist film was so thin that no prebaking was carried out before exposure.

A computer-controlled electron beam exposure machine ELS-5000 (Elionix) operating at 20 kV was used for lithographic evaluation. After exposure, samples were developed by dipping in a suitable developer. Normally, methylethyl ketone:isopropanol mixed solvent and isopropanol were used as a developer and rinse solvent, respectively. The development of SNR on soft-baked AZ layer was carried out by the combination of xylene and cyclohexane. As electron beam sensitivity, $D_{n^{0.5}}$ and D_n^i were used, which are defined as a dose to leave half of the initial thickness and a minimum dose required to form insoluble gel on substrate. The contrast (γ) was defined as $\gamma = (1/2) [\log (D_{n^{0.5}}/D_n^i)]^{-1}$. Sensitivity curves for x-ray and deep UV exposure were determined with a step-and-repeat-type x-ray exposure machine SR-1 developed at NTT (16) using an Mo target and a 200W deuterium lamp (Ushio Electric Company), respectively.

Dry etching resistance of SNR was evaluated by reactive ion etching (RIE) with a parallel-plate etching ma-

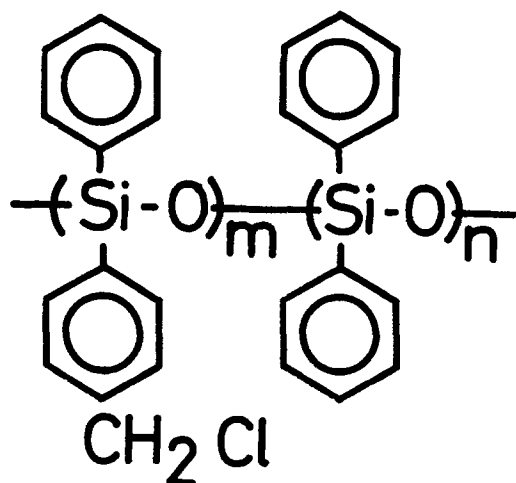


Fig. 1. Molecular structure of SNR

Table I. Molecular parameters of SNR

No.	$\overline{M}_w \times 10^4$	$\overline{M}_w/\overline{M}_n$	D_n^i ($\mu\text{C cm}^{-2}$)	γ
1	0.64	1.9	35	2.9
2	1.2	1.8	11	2.6
3	3.8	3.1	2.7	1.9
4	4.4	2.8	2.0	1.8
5	7.6	4.7	1.2	1.7
6	11.3	8.5	0.68	1.1

chine DEM-451 (ANELVA) using O_2 and CF_4 gases. In two-layer resist systems, the developed SNR patterns were transferred to the AZ layer by O_2 RIE. Typical O_2 RIE conditions were a gas pressure of 10 mtorr and a power of $0.1\ \text{W/cm}^2$. Patterns obtained were evaluated by scanning electron microscope (SEM) observation with JSM-35 (JEOL).

Results and Discussion

SNR syntheses.—Figure 2 shows the GPC curves of several polymers produced by the chloromethylation of ODPS. Table I summarizes the molecular parameters of SNR samples as well as their resist properties for electron beam exposure. So far, SNR's with a molecular weight range of 6,400-113,000 were produced, without forming gel. An average polymer yield was 60% after two reprecipitations with the tetrahydrofuran-methanol system. The chloromethyl group content is about 20%, which is enough for sensitizing SNR to high energy beams as was observed in chloromethylated polystyrene (CMS) (12).

A key point for SNR development is the finding that the polymerization reaction of ODPS occurs at the same time as the chloromethylation in the Friedel-Craft-catalyzed chloromethylation reaction of ODPS (13). The mechanism of the polymerization reaction is now under investigation. However, terminal OH bonds in ODPS and chloromethylmethyl ether seem to be deeply involved with the polymerization reaction, because methyl-terminated siloxane oligomer could not be polymerized under the same reaction conditions. Polymerization did not occur without chloromethylmethyl ether. The condensation of the OH group is also confirmed by NMR studies, where a small peak assigned to the OH group at 1.5 ppm observed in ODPS disappears in the resultant polymers (13).

Normally terminal OH groups in di- or mono-methyl substituted oligomeric siloxanes are very reactive, producing high molecular weight polysiloxanes by condensation, whereas the OH groups in ODPS seem to be stabilized by the diphenyl groups. When chloromethyl

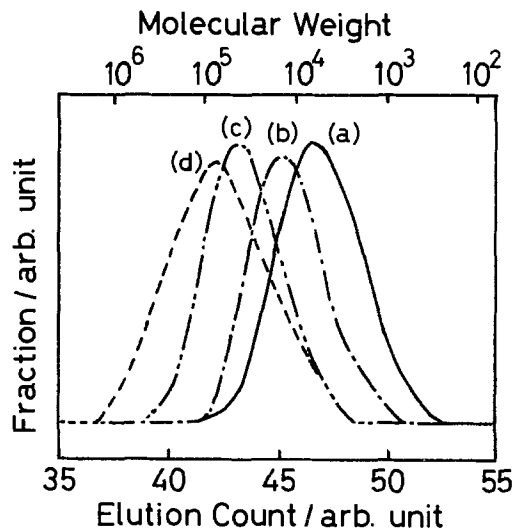


Fig. 2. Gel permeation chromatography curves of SNR. (a): $\overline{M}_w = 6.4 \times 10^3$. (b): $\overline{M}_w = 1.2 \times 10^4$. (c): $\overline{M}_w = 4.4 \times 10^4$. (d): $\overline{M}_w = 1.13 \times 10^5$.

groups are introduced into phenyl rings, the electronic states of ODPS are changed, making the terminal OH groups reactive. Another consideration is that the combination of chloromethylmethyl ether and SnCl_4 generates an active catalyst which can initiate condensation as well as chloromethylation. Consequently, SNR can be synthesized by only one reaction step from relatively cheap ODPS, suggesting a low resist cost when SNR is commercialized.

Resist performance of SNR.—Figure 1 shows a chemical structure of SNR. SNR consists of three important functional groups. First, a siloxane main chain makes SNR strongly resistant to O_2 RIE. Second, phenyl groups realize a high T_r (150°C). Third, the chloromethyl groups attached to the phenyl groups give SNR high sensitivity to high energy radiation such as electron beam, x-ray, and deep UV light. The obtained resist performances are as follows.

Sensitivity.—SNR has an almost equivalent structure to CMS except for its main chain structure. CMS is one of the representative negative electron resists with high sensitivity and high resolution, particularly applicable to dry-etching processes because of high dry-etching resistance. SNR also has a high sensitivity, as shown in Fig. 3, where several SNR sensitivity curves to electron beam are plotted. The starting material ODPS also exhibits negative-type behavior, but the chloromethylation clearly realizes a large sensitization. The sensitivities are in a range of $0.68\text{--}35 \mu\text{C}/\text{cm}^2$ for \overline{M}_w between 1.13×10^5 and 6.4×10^8 , as listed in Table I, and the relationship is almost linear as observed in another negative electron resist (15).

In comparing the cross-linking reactivity of negative electron resists, the product of molecular weight \overline{M}_w and the minimum dose D_n^1 has been used to eliminate the factor of molecular weight. The average $D_n^1 \overline{M}_w$ of SNR's is $0.12 \text{ C}/\text{cm}^2$ whereas that of a starting material, ODPS is $2.4 \text{ C}/\text{cm}^2$, indicating distinctively high cross-linking reactivity of the chloromethyl group. SNR reactivity is even higher than that of CMS with the same chloromethylation ratio ($0.2 \text{ C}/\text{cm}^2$). Though many reasons may be offered, such as the effect of residual OH groups and higher efficiency in energy transfer to reactive sites in SNR, it may be erroneous to compare \overline{M}_w of quite different types of polymers by using GPC with polystyrene standards. Absolute values of \overline{M}_w must be exactly determined before detailed arguments can be made. However, it cannot be denied that SNR shows high electron beam sensitivity compared with that of CMS.

Figure 4 plots the sensitivity curves of SNR-4 ($\overline{M}_w = 4.4 \times 10^4$) and CMS ($\overline{M}_w = 1.8 \times 10^5$) to x-ray from Mo target (5.4\AA). The $D_n^1 \overline{M}_w$ of SNR is $1500 \text{ J}/\text{cm}^2$, whereas that of CMS is $3600 \text{ J}/\text{cm}^2$, indicating high sensitivity of SNR to

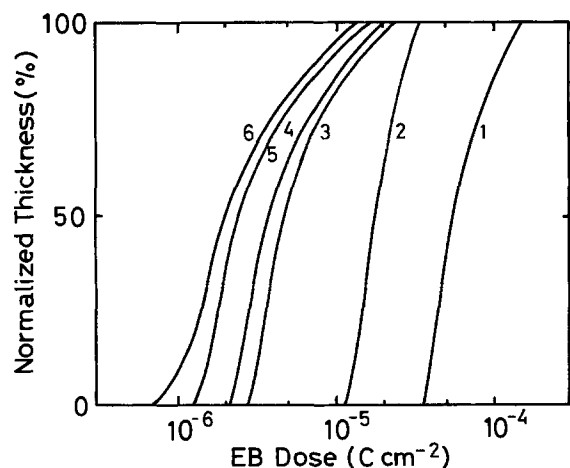


Fig. 3. Electron beam sensitivity curves of SNR. Accelerating voltage; 20 keV. The number of every curve corresponds to the sample number listed on Table I.

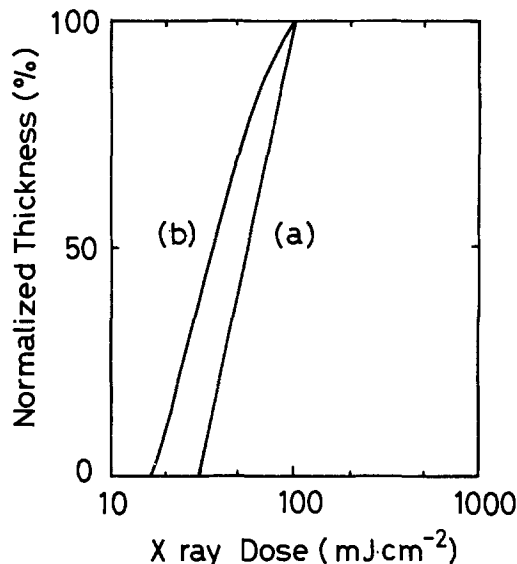


Fig. 4. X-ray sensitivity curves of SNR and CMS. (a): SNR, $\overline{M}_w = 4.4 \times 10^4$. (b): CMS, $\overline{M}_w = 1.8 \times 10^5$. Target: Mo.

x-rays as well as electrons. The $D_n^1 \overline{M}_w$ of SNR to x-ray showed a better value than expected from the comparison of SNR and CMS in electron beam sensitivity. This is because Si and O atoms contained in SNR absorb x-rays, particularly in the $5\text{--}6.7\text{\AA}$ wavelength region, as shown in Fig. 5, where the absorption coefficient of SNR is compared with those of CMS and PMMA. When Mo target is used, SNR has about three times larger absorption than CMS and two times greater than PMMA.

SNR is also useful in deep-UV lithography. In Fig. 6, the sensitivity curve of SNR-3 to a deuterium lamp is

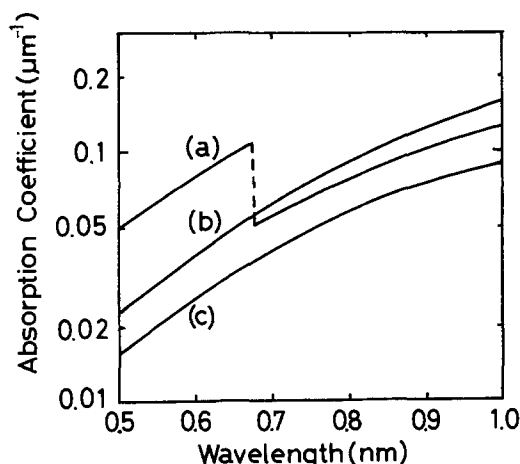


Fig. 5. X-ray wavelength dependence of absorption coefficients for (a) SNR, (b) PMMA, and (c) CMS.

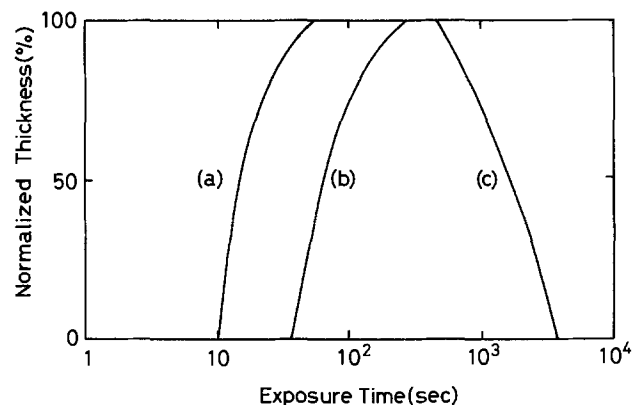


Fig. 6. Deep UV sensitivity curve of SNR (200 W deuterium lamp). (a): SNR, $\overline{M}_w = 3.8 \times 10^4$. (b): CMS, $\overline{M}_w = 6.0 \times 10^4$. (c): PMMA, elvacite 2041.

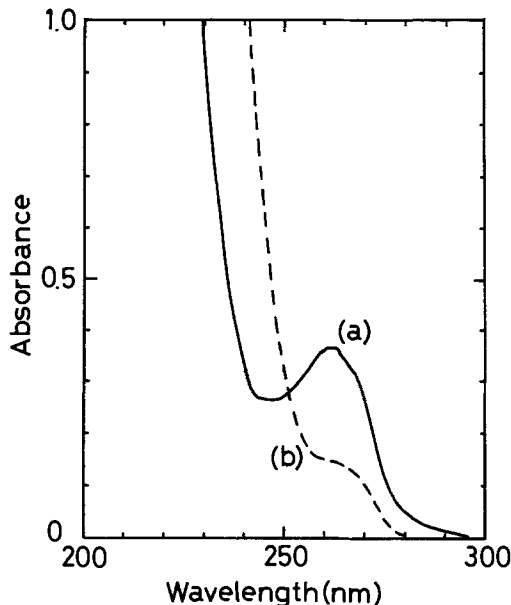


Fig. 7. UV spectro of (a) SNR and (b) CMS. Film thickness: both 1.0 μm .

compared with those of CMS ($\overline{M}_w = 6 \times 10^4$) and PMMA. Figure 7 shows UV absorption spectra of SNR and CMS. The strong absorption of phenyl groups around 260 nm gives SNR higher sensitivity than CMS. The self-filtering effect due to very strong absorption will be no problem because SNR used in lithography is usually very thin.

Contrast.—A contrast of SNR to electron beam exposure, listed in Table I as γ , is a function of \overline{M}_w and $\overline{M}_w/\overline{M}_n$, as is observed in many negative electron resists (12, 15). The contrast of SNR is lower than that of CMS because the molecular weight distribution of SNR is much greater than that of CMS. It would be improved by the fractionation of SNR polymers or the use of monodisperse poly(diphenyl siloxane) as a starting material, if a ring opening living polymerization of cyclic diphenylsiloxanes were possible. However, as SNR can be uniformly coated in a very thin film of about 0.1 μm , sufficiently high resolution is obtained without any modification of the polymers, as shown later.

Dry etching resistance.—SNR has high resistance against dry etching, especially against O_2 RIE. The etching rate of SNR is less than 5 nm/min for the RIE condition used (10 mtorr, 50 sccm, 0.1 W/cm^2 , bias of 500V), whereas that of AZ-1350 is more than 80 nm/min, as shown in Fig. 8.

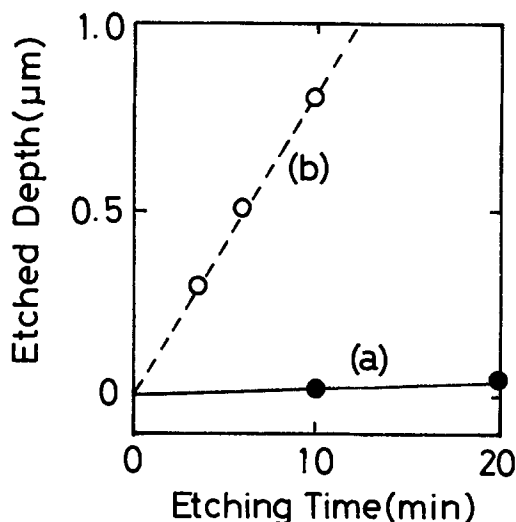


Fig. 8. Etching characteristics of (a) SNR and (b) AZ for O_2 RIE. Conditions: 10 mtorr, 50 sccm, 0.1 W/cm^2 , bias of 500V.

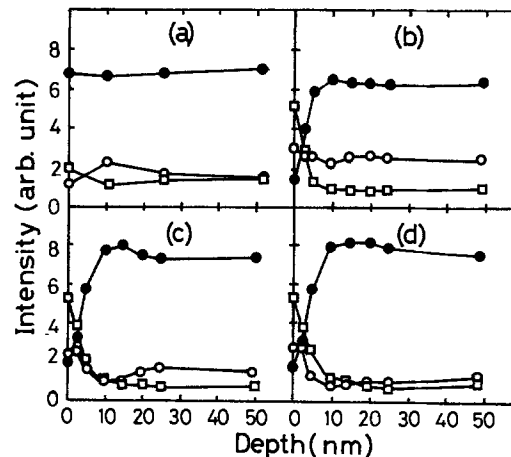


Fig. 9. Auger electron spectroscopy depth profiles of etched SNR. ●: Carbon. □: Oxygen. ○: Silicon. Etching time: (a) 0 min, (b) 1 min, (c) 5 min, and (d) 10 min. O_2 RIE condition: 10 mtorr, 0.1 W/cm^2 .

When relatively high O_2 gas pressure such as 100 mtorr is adopted, the etching rate of SNR is almost negligible.

The high O_2 RIE resistance of SNR is needed to accomplish high resolution lithography. Since SNR is hardly etched, the thickness can be as thin as possible, and a limit in thinning resist would depend on another factor, that is, the formation of pinholes. We confirmed that 0.1 μm is enough thickness to perform practical fabrications without increasing pinhole density. This could be due to the good wettability of silicone polymers.

We examined the oxidation of SNR to SiO_2 during O_2 RIE by means of Auger electron spectroscopy (AES). Auger electron intensities from silicon, oxygen, and carbon were measured in depth direction for SNR samples etched by O_2 RIE for various times. The samples were etched under the above conditions for 1, 5, and 10 min, respectively. Figure 9 shows AES depth profiles of SNR. In the unetched sample (Fig. 9a), a constant elemental composition which is equivalent to that of SNR was observed from the surface to bottom; whereas, the surface of etched samples (Fig. 9b to 9d) show a drastic decrease of carbon content and an increase of oxygen content, indicating the oxidation of SNR to SiO_2 . It should be noted that the oxidized regions were at most 10 nm from the surface and were independent of etching time. This means that the surface of SNR is immediately converted to SiO_2 by O_2 RIE. The SiO_2 layer formed on SNR is slightly etched by a sputtering effect, but SNR just under the SiO_2 layer is immediately oxidized to SiO_2 , so that the thickness of the surface SiO_2 is constant vs. etching time.

SNR is expected to show a high resistance against conventional RIE using halogenated carbon gases as judged by its aromatic structure and high T_g . The SNR etching rate against CF_4 RIE is compared with other resists, summarized in Table II. SNR shows much higher resistance to CF_4 RIE than poly(aliphatic methacrylates), but slightly lower resistance compared to CMS and AZ. This means that the SNR layer in two-layer resist systems is relatively easily removed when the substrate layer is etched by RIE using a two-layer mask. However, this property is an advantage for SNR, because after the etching, O_2 plasma ashing can be used for resist removal,

Table II. CF_4 RIE etching rate

Resist	Rate ($\text{nm} \cdot \text{min}^{-1}$)
SNR	38
AZ	30
CMS	25
PMMA	90
FBM	180

Etching condition: 80 mtorr, 0.1 W/cm^2 .

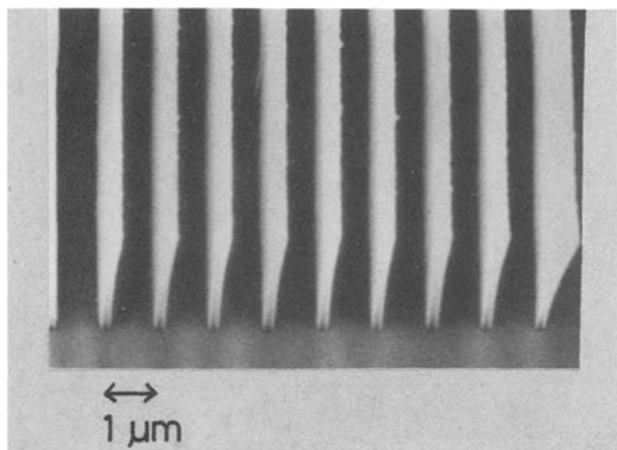


Fig. 10. SEM photograph of high aspect ratio submicron pattern formed by SNR on AZ-1350 two-layer resist. Accelerating voltage: 30 keV. Dose: $14.5 \mu\text{C}/\text{cm}^2$. Film thickness: SNR $0.2 \mu\text{m}$, AZ $1.3 \mu\text{m}$.

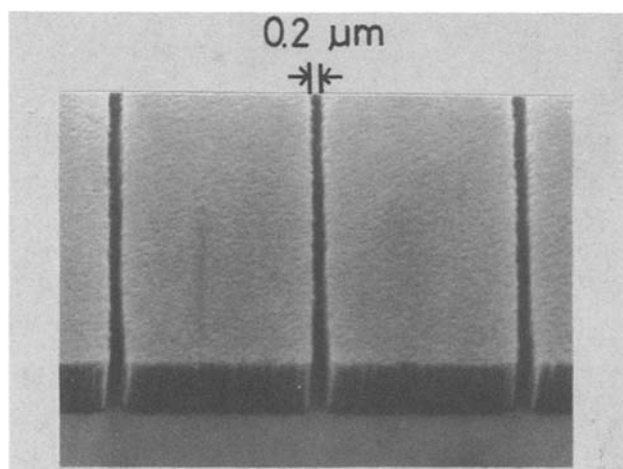


Fig. 11. SEM photograph of high resolution pattern formed by SNR on AZ-1350 two-layer resist. Accelerating voltage: 20 keV. Dose: $7.8 \mu\text{C}/\text{cm}^2$. Film thickness: SNR $0.2 \mu\text{m}$, AZ $1.05 \mu\text{m}$.

which is one of the few problems with multiple-layer resist systems.

SNR/AZ two-layer system.—A submicron pattern with high aspect ratio is demonstrated by the SNR/AZ two-layer resist system. It takes only six steps to accomplish the resist process by using SNR. These are AZ-1350J coating, baking at 200°C for 60 min, SNR coating, electron beam exposure and development, and O_2 RIE. This is only a two-step increase compared with a single-layer resist system. Figures 10 and 11 show SEM photographs of fabricated patterns using SNR-4. A $0.3 \mu\text{m}$ line and $0.7 \mu\text{m}$ space pattern and a $3 \mu\text{m}$ line and $0.2 \mu\text{m}$ space pattern are clearly formed. The proximity effect is efficiently reduced, indicating the high resolution capability of this resist system.

Furthermore, SNR shows good solubility in many solvents, including most ketones, esters, ethers, aromatic hydrocarbons, and many halogenated hydrocarbons. Plain hydrocarbons and alcohols are nonsolvents. As compared with CMS, SNR shows better solubility, perhaps due to the siloxane main chain structure. This provides a very wide variety of developers and spinning solvents. As a bottom layer in a two-layer resist system, various poly-

mers can be used even if that polymer is soluble in many solvents. For instance, the hard baking of AZ photoresist is not necessary with a suitable combination of spinning solvent and developers. Monochlorobenzene can be used as the spinning solvent, and xylene is one of the most excellent developers for SNR; both hardly dissolve soft-baked AZ resist. The use of a soluble bottom layer has another merit in stripping the resist. As the hard-baked AZ is normally stripped by O_2 plasma ashing, scums are sometime observed on the substrate when SNR layer is not completely removed. When soft-baked AZ resist was used as a bottom layer, SNR could be easily lifted off and no scum was observed.

Summary

New silicone-based negative resists (SNR's) for a two-layer resist system were synthesized by the chloromethylation of oligomeric diphenylsiloxane. SNR showed excellent dry etching resistance against O_2 RIE, and could be applied to an imaging resist of two-layer resist systems. Practical high sensitivities to electron beam, x-ray, and deep UV radiation were obtained. An excellent resolution was realized in a two-layer resist system using SNR.

Acknowledgment

The authors express their deep gratitude to Mr. K. Murase and Mr. O. Kogure for their valuable discussions, Mr. Okamoto for measuring Auger electron spectroscopy, and Miss K. Iimura for measuring the E-beam sensitivity of SNR.

Manuscript submitted Feb. 29, 1984; revised manuscript received June 4, 1984.

Nippon Telegraph and Telephone Public Corporation assisted in meeting the publication costs of this article.

REFERENCES

1. J. M. Moran and D. Maydan, *J. Vac. Sci. Technol.*, **16**, 1620 (1979).
2. M. J. Bowden, *Solid State Technol.*, **24**, 73 (1981).
3. M. Hatzakis, *ibid.*, **24**, 74 (1981).
4. B. J. Lin, *ibid.*, **26**, 105 (1983).
5. J. R. Havas, Abstract 279, p. 743, The Electrochemical Society Extended Abstracts, Vol. 76-2, Las Vegas, NV, Oct. 17-22, 1976.
6. B. J. Lin and T. H. P. Chang, *J. Vac. Sci. Technol.*, **16**, 1669 (1979).
7. M. Hatzakis, J. Paraszczak, and J. Shaw, in "Proceedings of the International Conference on Microlithography," p. 386, Lausanne, Switzerland, Sept. 28-30 (1981).
8. M. Suzuki, K. Saigo, H. Gokan, and Y. Ohnishi, *This Journal*, **130**, 1962 (1983).
9. K. L. Tai, W. R. Sinclair, R. G. Vadimsky, J. M. Moran, and M. J. Rand, *J. Vac. Sci. Technol.*, **16**, 1977 (1979).
10. S. A. MacDonald, A. S. Steinmann, H. Ito, W. Lee, and C. G. Willson, *Proc. ACS Div. Polym. Mater. Sci. Eng.*, 104 (1983).
11. M. Hatzakis, J. R. Maldonado, and J. Paraszczak, *IBM Tech. Discl. Bull.*, **26**, 479 (1983).
12. S. Imamura, T. Tamamura, K. Harada, and S. Sugawara, *J. Appl. Polym. Sci.*, **27**, 937 (1982).
13. S. Imamura, M. Morita, T. Tamamura, and O. Kogure, *Macromol.*, **17**, 1412 (1984).
14. M. Morita, A. Tanaka, S. Imamura, T. Tamamura, and O. Kogure, *Jpn. J. Appl. Phys.*, **22**, L659 (1983).
15. A. Tanaka, M. Morita, S. Imamura, T. Tamamura, and O. Kogure, "Radiation Chemistry of Polymers," ACS Symposium Series, L. F. Thompson, Editor, To be published.
16. T. Hayasaka, S. Ishihara, and H. Kinoshita, in "Electron and Ion Beam Science and Technology," R. Bakish, Editor, p. 347, The Electrochemical Society Softbound Proceedings Series, Pennington, NJ (1982).

Mixed Conduction and Defect Structure of $\text{ZrO}_2\text{-CeO}_2\text{-Y}_2\text{O}_3$ Solid Solutions

B. Calès and J. F. Baumard

Centre de Recherche sur la Physique des Hautes Températures, CNRS, 45045 Orléans Cédex, France

ABSTRACT

The electrical properties of the solid solutions between stabilized zirconia and ceria, $(0.9-y)\text{ZrO}_2\text{-}y\text{CeO}_2\text{-}0.1\text{Y}_2\text{O}_3$ with $0 < y < 0.9$, have been investigated, between 1273 and 1673 K, in a large range of oxygen partial pressures. The total electrical conductivity and the concentrations of the various charge carriers, determined through thermogravimetry and measurement of magnetic susceptibility at high temperature as a function of oxygen partial pressure, makes it possible to develop a model accounting for the transport properties as a function of temperature and oxygen partial pressure. On the basis of the present results, the materials in question appear to be suitable as membranes semipermeable to oxygen.

Refractory oxides with a fluorite-type structure, such as stabilized zirconia and pure or doped ceria, have been extensively studied in recent years (1, 2). Most of them are characterized by a predominant ionic-type conductivity, which proceeds through the motion of oxygen ions via vacancies (2). Owing to the electrolytic character of these materials, they can be potentially used at intermediate temperatures (of the order of 1273 K) in applications such as oxygen gauges (3, 4) or fuel cells and electrolyzers (5).

However, at temperatures higher than ≈ 1673 K, these oxide electrolytes may exhibit a partial electronic conductivity (6). The resulting oxygen flux through the electrolyte (7), although believed to have a detrimental effect on the property of the material as an oxygen gauge at temperatures higher than 1473 K, may be judiciously applied to the problem of selective oxygen pumping at high temperature. Thus stabilized zirconia walls have been recently used as oxygen semipermeable membranes for the extraction of the oxygen arising from steam decomposition (8). Such a membrane must be characterized by a mixed, ionic, and electronic, conductivity. Indeed, in a gradient of oxygen chemical potential, the ionic component of the conductivity allows the oxygen to diffuse as O^{2-} ions through the membrane, while the electronic component ensures a transfer, between the two electrolyte-gaseous phase interfaces, of the electrons required for the exchange of oxygen between the electrolyte and the gaseous phases. Furthermore, it has been shown (8) that the oxygen transfer is maximum when the ionic component of the conductivity is equal to the electronic component. This is not precisely the case for stabilized zirconia (9), the oxygen semipermeability of which is limited by the value of its electronic conductivity which is very low.

However, the electronic conductivity of stabilized zirconias may be enhanced by doping these materials with an oxide the cation of which may present different valence states. This is the case for cerium oxide, CeO_2 , which is characterized, at high temperature, by a redox equilibrium between the tetravalent Ce^{4+} and the trivalent Ce^{3+} states of cerium ions (10), accountable for an n-type electronic conductivity. Cubic solid solutions with a fluorite-type structure may be obtained between stabilized zirconias and ceria in large ranges of composition (11).

The aim of the present work was to investigate the electrical transport properties of solid solutions between stabilized zirconia $0.9\text{ZrO}_2\text{-}0.1\text{Y}_2\text{O}_3$ and CeO_2 in order to define the ability of such compounds to be used as oxygen semipermeable membranes. This has been achieved by the study of the electrical conductivity and the investigation of the high temperature defect structure of the solid solutions $(0.9-y)\text{ZrO}_2\text{-}y\text{CeO}_2\text{-}0.1\text{Y}_2\text{O}_3$, $0 < y < 0.9$. The properties of the two compositions corresponding to $y = 0$ and $y = 0.9$ have been reported elsewhere (9, 12) and will not be considered further here.

Experimental

Sample preparation.—The solid solutions were prepared by solid-state reaction between the oxide pow-

ders: monoclinic zirconia (Ugine-Kuhlman), ceria (Rhône-Poulenc), and yttria (Pechiney), with a level of purity above 99.9%. Appropriate proportions of ZrO_2 , CeO_2 , and Y_2O_3 powders were mechanically mixed in acetone and dried for 12h at 500°C. The calcined materials were then isostatically pressed into rods and fired for 5h at 2073 K in air, in a laboratory-built furnace (6).

X-ray diffraction shows that the solid solutions $(0.9-y)\text{ZrO}_2\text{-}y\text{CeO}_2\text{-}0.1\text{Y}_2\text{O}_3$, with $0 \leq y \leq 0.9$, are characterized by a cubic fluorite-type structure, the lattice parameter of which increases linearly with the ceria content y (Fig. 1)

$$a = (5.145 + 0.243 = y)\text{Å}$$

The first term corresponds to the lattice parameter of stabilized zirconia as reported in Ref. (1). The lattice expansion occurs as a consequence of the substitution of zirconium ions by cerium ions, the ionic radius of which is greater ($\text{Zr}_{\text{VI}}^{4+} = 0.79\text{Å}$, $\text{Ce}_{\text{VI}}^{4+} = 0.9\text{Å}$) (13). The value of a obtained for $y = 0.9$ is in good agreement with the lattice parameter previously reported for the solid solution $0.9\text{CeO}_2\text{-}0.1\text{Y}_2\text{O}_3$ (14).

Conductivity measurements.—The specimens used for total conductivity measurements were cut into cylinders.

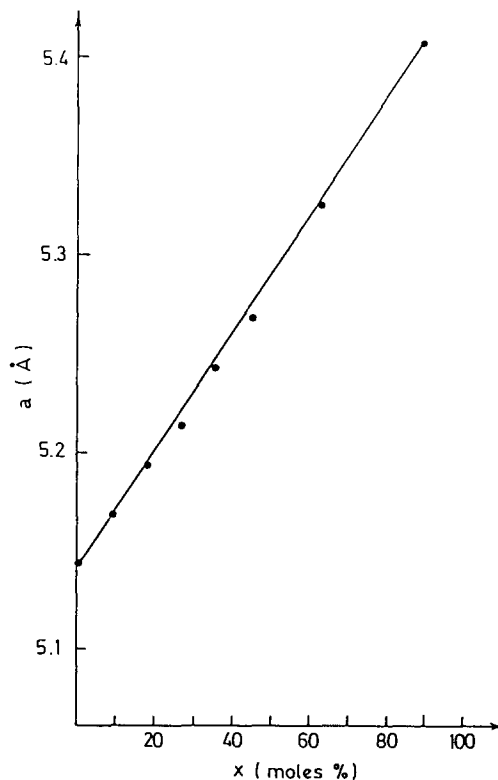


Fig. 1. Dependence of the lattice parameter of the solid solutions $(0.9-y)\text{ZrO}_2\text{-}y\text{CeO}_2\text{-}0.1\text{Y}_2\text{O}_3$ on composition.

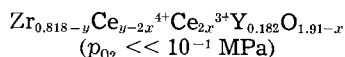
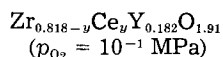
Small grooves were then cut in the cylindrical sample to define the position of the electrodes. Platinum wires are tightly wrapped in the grooves around the sample and coated with platinum paste. The whole assembly is fired to improve the contacts and provide a good adhesion. The conductivity measurements were carried out in a platinum furnace between 1273 and 1673 K, over a large range of oxygen partial pressures, using a standard four-probe dc method. High oxygen partial pressures (10^{-1} - 10^{-5} MPa) were achieved by using Ar-O₂ mixtures, while lower oxygen chemical potentials were obtained with CO-CO₂ mixtures.

Measurements of defect concentrations.—As previously reported (12), the specific electrical properties of solid solutions containing cerium dioxide arise from the formation, at low oxygen activities, of oxygen vacancies and the simultaneous reduction of cerium ions from the tetravalent Ce⁴⁺ to the trivalent state Ce³⁺. Such a behavior must give rise to a weight loss of the samples, which can be measured by thermogravimetric techniques, and to a noticeable variation of their magnetic susceptibility: Ce³⁺ ions are paramagnetic, while all the other anions and cations present only a diamagnetic contribution. In order to get the various defect concentrations involved in the transport properties of these compounds, a thermogravimetry and magnetic susceptibility equipment for use at high temperatures was built. Since this apparatus has been previously described in detail (12), only the principle of operation is summarized below.

The composition of the solid solutions in the (T , $p_{O_2} = 10^{-1}$ MPa) states is taken as a stoichiometric reference and may be explicitly written $Zr_{0.818-y}Ce_yY_{0.182}O_{1.91}$. Under these conditions, the solid solutions are characterized by a weight p_1 and a molar susceptibility $\chi_M(1)$. Assuming that the additivity law of magnetic susceptibilities is satisfied (15), the latter quantity is equal to the sum of the molar diamagnetic contributions $\chi_M^d(k)$ of the various species k

$$\chi_M(1) = (0.818-y)\chi_M^d(Zr^{4+}) + y\chi_M^d(Ce^{4+}) + 0.182\chi_M^d(Y^{3+}) + 1.19\chi_M^d(O^{2-}) \quad [1]$$

The oxygen partial pressure is then gradually lowered below 10^{-1} MPa, under isothermal conditions; when equilibrium has been reached, the composition of the solid solutions departs from the "stoichiometric" composition by a value x , according to



The deviation from stoichiometry follows from the relationship

$$x = \frac{2(p_1 - p_2)M}{p_1 M(O_2)} \quad [2]$$

where M and $M(O_2)$ denote the mean molar weight of the solid solution and the molar weight of oxygen molecules, respectively, and p_2 the sample weight for $p_{O_2} \ll 10^{-1}$ MPa.

Owing to the formation of paramagnetic Ce³⁺ centers, the molar susceptibility of the nonstoichiometric sample, $\chi_M(2)$, differs from $\chi_M(1)$, and the difference, $\chi_M(2) - \chi_M(1)$, allows one to define a molar susceptibility $\chi_M(3)$. Assuming that the variation of the sample molar weight can be neglected in a first approximation, $\chi_M(3)$ is found from

$$\chi_M(3) = x[2\chi_M^p(Ce^{3+}) + 2\chi_M^d(Ce^{3+}) - 2\chi_M^d(Ce^{4+}) - \chi_M^d(O^{2-})]$$

or

$$\chi_M(3) = x[2\chi_M^p(Ce^{3+}) + C] \quad [3]$$

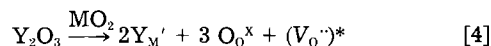
where $\chi_M^p(Ce^{3+})$ denotes the paramagnetic susceptibility

of the Ce³⁺ ion and C a correction for the diamagnetic contributions.

Results and Discussion

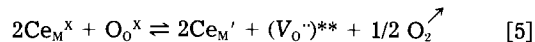
Electrical conductivity.—The general nature of the variations of the electrical conductivity with the oxygen partial pressure is similar for all compositions (Fig. 2-4), and three domains can be distinguished in the $\log \sigma - \log p_{O_2}$ plots. In the first one, for the highest oxygen partial pressures, the conductivity is constant or very slightly dependent on p_{O_2} . It has also been observed for the compositions $0.9ZrO_2-0.1Y_2O_3$ ($y = 0$) and $0.9CeO_2-0.1Y_2O_3$ ($y = 0.9$) (16). This domain shrinks as the ceria content y and/or the temperature increases. At lower oxygen partial pressures, the conductivity increases rapidly up to a maximum value and the rise of conductivity is the more important as the ceria content is higher. At low CeO₂ contents, for instance $y = 0.09$ (Fig. 2), the maximum is barely noticeable and disappears completely above 1573 K. Finally, for the lowest oxygen partial pressures, the conductivity strongly decreases down to a value lower than the conductivity level observed under oxidizing atmospheres.

At high oxygen activities, the conductivity is mostly ionic in nature, as found earlier for the compositions $y = 0$ and $y = 0.9$ (16). The conductivity takes place by motion of oxygen ions via vacancies and, for a given temperature, its value is fixed by the concentration of oxygen vacancies ($V_{O^{\cdot\cdot}}$)*, formed in the material as charge compensating defects when Y³⁺ ions substitute M⁴⁺ cations ($M = Zr^{4+}, Ce^{4+}$). According to the formalism of Kröger and Vink (17), this reaction is written as



The concentration of oxygen vacancies [$(V_{O^{\cdot\cdot}})^*$] is then only dependent on the yttria content.

Under reducing conditions, the increase of conductivity may be explained as in the case of doped ceria $0.9CeO_2-0.1Y_2O_3$ (12). In this domain, excess carriers, resulting from the displacement of the redox equilibrium between the two valence states of cerium ions



give rise to an electronic-type conductivity. The additional oxygen vacancies involved in this equilibrium are marked with a double asterisk, while those resulting from reaction [4] are marked with a single asterisk.

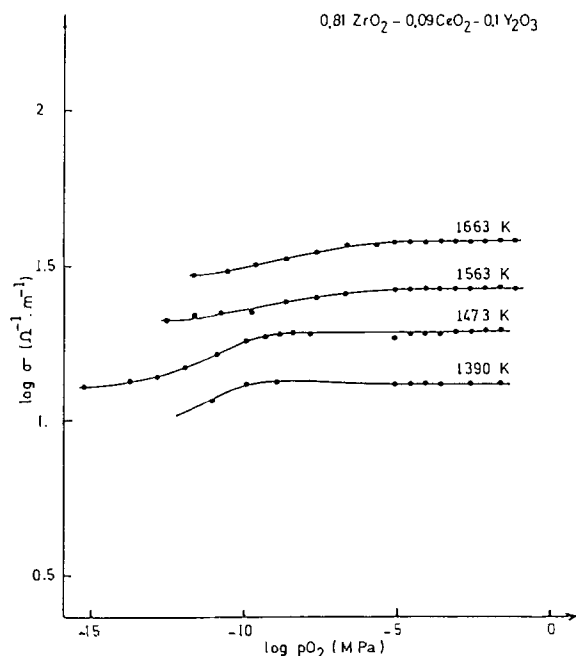


Fig. 2. Variation of the total electrical conductivity of $0.81ZrO_2-0.09CeO_2-0.1Y_2O_3$ vs. oxygen partial pressure.

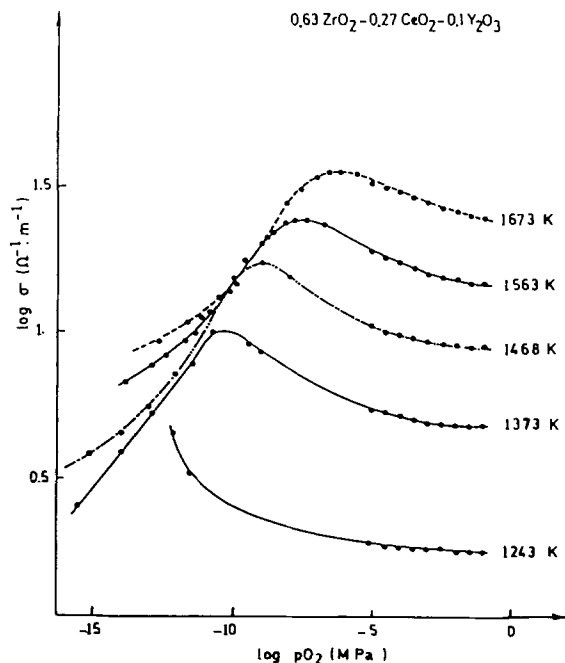


Fig. 3. Variation of the total electrical conductivity of 0.63ZrO₂-0.27CeO₂-0.1Y₂O₃ vs. oxygen partial pressure.

On assuming that, as for nonstoichiometric pure or doped ceria (10), the electrons are localized on cerium sites and move in the lattice between cerium ions through a hopping process, the electronic part of the conductivity should be roughly proportional to the product of charge carriers concentration $[Ce_M']$ and the concentration of available sites $[Ce_M^X]$. According to this assumption, a decrease of p_{O_2} should displace Eq. [5] towards the right-hand side and should lead to an increase of the product $[Ce_M'] [Ce_M^X]$ and thus should enhance the conductivity. When the oxygen partial pressure is low enough to reduce a large fraction of the cerium ions to the trivalent state, the product $[Ce_M'] [Ce_M^X]$ and therewith the partial electronic conductivity should go through a maximum. This occurs when the concentrations of cerium ions in the two valence states are equal, each being half of the total concentration of cerium ions which is constant.

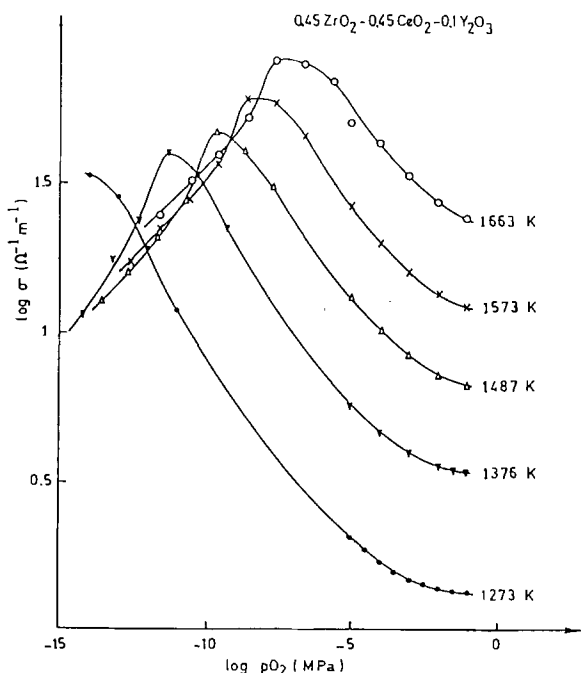


Fig. 4. Variation of the total electrical conductivity of 0.45ZrO₂-0.45CeO₂-0.1Y₂O₃ vs. oxygen partial pressure.

A maximum value is indeed observed in the $\log \sigma - \log p_{O_2}$ plots (Fig. 3 and 4). Similar results have been also reported for the binary solid solutions $(1-y)ZrO_2-yCeO_2$. For instance, in the case of 0.3ZrO₂-0.7CeO₂, a conductivity maximum has been observed by Gouet (18) and attributed to a $[Ce^{3+}]/[Ce^{4+}]$ ratio close to unity. According to Fehrenbacher and Tallan (19), the conductivity maximum of 0.8ZrO₂-0.2CeO₂ is once more related to the reduction of half the cerium ions to the trivalent state.

For the lowest oxygen partial pressures investigated here, it has been noticed that the conductivity level is lower than the value found for the ionic plateau in the vicinity of oxygen pressures of 10⁻¹ MPa. Nevertheless, under strongly reducing conditions, a major fraction of the cerium ions is reduced to the trivalent state and the value of the product $[Ce_M'] [Ce_M^X]$ should be very low. Then the conductivity should again present a predominant ionic character. This indicates that the ionic component of the conductivity is depressed by the presence of additional oxygen vacancies resulting from the reduction of the Ce⁴⁺ ions (Eq. [5]). Indeed, it has been clearly shown that, from a given content of dopant oxide [of the order of 10 mole percent (m/o) in the case of Y₂O₃ (20)], the ionic conductivity of stabilized zirconias decreases when additional heterovalent cations are added. In the present case, beyond the concentration of oxygen vacancies initially fixed by the yttria content (10 m/o), the ionic conductivity should gradually decrease during the reduction of the Ce⁴⁺ ions.

As a consequence, the observed maximum of the $\log \sigma - \log p_{O_2}$ plots does not necessarily correspond to a quantitative equipartition of cerium ions between the Ce⁴⁺ and Ce³⁺ states, since a decrease of the total conductivity may be partly induced by a lowering of the ionic component. Therefore, the knowledge of the reduction rate of cerium ions seems to be of prime importance in explaining the transport properties of the $(0.9-y)ZrO_2-yCeO_2-0.1Y_2O_3$ solid solutions. This will be treated below.

Structural considerations.—It is generally admitted that the decrease of the ionic conductivity of fluorite-type solid solutions for high contents of oxygen vacancies is related to the formation of associated defects or defect ordering (21). In the case of the cubic solid solutions between zirconia and trivalent lanthanide oxides Ln₂O₃, order-disorder transitions have been observed in a range of composition which depends, to a first approximation, on the ratio of the cationic radii of Zr⁴⁺ and Ln³⁺ ions (22). Moreover, the results obtained by Negas *et al.* (23) have shown that the reduction of Ce⁴⁺ ions at low oxygen activities may induce the ZrO₂-CeO₂ cubic solid solutions to form ordered compounds with a pyrochlore-type structure. Concerning the $(0.9-y)ZrO_2-yCeO_2-0.1Y_2O_3$ solid solutions, under low p_{O_2} , the reduction of cerium ions to the trivalent state generates, within the cationic and anionic sublattices, large amounts of atomic and electronic defects which may induce such order-disorder phenomena. The structure of these materials, quenched after an anneal under reducing conditions, therefore, has been analyzed by x-ray techniques.

For low ceria contents, for instance 0.81ZrO₂-0.09CeO₂-0.1Y₂O₃, after annealing under $p_{O_2} = 10^{-15}$ MPa at 1373 K, the x-ray diffraction patterns exhibit any characteristic line of a pyrochlore-type ordered phase. A similar result has been obtained for the composition 0.72ZrO₂-0.18CeO₂-0.1Y₂O₃ which consists of a single phase having a fluorite-type structure. However, its lattice parameter increases with the rate of reduction, owing to the fact that the cationic radius of Ce³⁺ is higher than that of Ce⁴⁺ (13); it rises from $a_F = 5.194\text{\AA}$ for $p_{O_2} = 10^{-1}$ MPa to $a_F = 5.197\text{\AA}$ for $p_{O_2} = 10^{-11}$ MPa and $a_F = 5.207\text{\AA}$ for $p_{O_2} = 10^{-17}$ MPa.

For higher concentrations of ceria, an ordered phase has been observed only after long time annealings (~100h). A second phase having a pyrochlore-type structure seems to gradually precipitate in the disordered fluorite-type matrix, the size of the pyrochlore domains increasing very slowly owing to the low kinetics of cation

diffusion (24). The lattice parameter of the pyrochlore-type phase $a_p = 10.530\text{\AA}$ is about twice the lattice parameter of the fluorite-type phase $a_f = 5.320\text{\AA}$, the defect ordering in the anionic and cationic sublattices inducing a double cell for the crystal structure.

The effect of such a second phase on the electrical transport properties should be taken into account. In the case of binary $\text{ZrO}_2\text{-Ln}_2\text{O}_3$ systems, the formation of a pyrochlore-type structure is generally related to a decrease of the ionic conductivity (25). Thus, in the present case, even if, for low CeO_2 content, there is a small decrease of the conductivity under low oxygen activities which may probably be explained on the basis of interactions between oppositely charged defects, for higher ceria contents, the very low kinetics for the solid-gas phase equilibria and the rapid decrease of the conductivity under reducing conditions must be partly related to the formation of pyrochlore-type domains. This result has been confirmed by the analysis of the high temperature defect structure.

Correlations between defect structure and transport properties.—As a result of the previous considerations, two distinct compositions have been investigated between 1273 and 1473 K, using the techniques of thermogravimetry and measurement of magnetic susceptibilities.

Solid solution with low ceria content: $0.81\text{ZrO}_2\text{-}0.09\text{CeO}_2\text{-}0.1\text{Y}_2\text{O}_3$.—The various defect concentrations have been measured as presented in the experimental section.

The departure from stoichiometry x of the $0.81\text{ZrO}_2\text{-}0.09\text{CeO}_2\text{-}0.1\text{Y}_2\text{O}_3$ solid solution has been deduced from the thermogravimetric measurements, using Eq. [2], and is plotted in Fig. 5 vs. the oxygen partial pressure. For a given temperature, in the whole range of oxygen partial pressure investigated here x varies closely as $p_{\text{O}_2}^{-1/4}$. Moreover, the deviation from stoichiometry is relatively small, and the charge balance relationship between the defect concentrations is

$$[\text{V}_{\text{O}^{\cdot\cdot}}] = [(\text{V}_{\text{O}^{\cdot\cdot}})^*] = 1/2 [\text{Y}_{\text{M}}'] \gg [(\text{V}_{\text{O}^{\cdot\cdot}})^{**}] = 1/2 [\text{Ce}_{\text{M}}'] \quad [6]$$

where $[\text{V}_{\text{O}^{\cdot\cdot}}]$ denotes the total oxygen vacancy concentration.

On assuming that the concentration of Ce^{3+} ions is low enough to obey the dilute solution laws, the equilibrium constant K relative to Eq. [5] may be written using the concentration of Ce_{M}' species instead of its activity

$$K = \frac{a_{\text{V}_{\text{O}^{\cdot\cdot}}} [\text{Ce}_{\text{M}}']^2}{a_{\text{O}_2} a_{\text{Ce}_{\text{M}}^x}} p_{\text{O}_2}^{1/2} \quad [7]$$

In the domain defined by the electroneutrality relation [6], the activities $a_{\text{V}_{\text{O}^{\cdot\cdot}}}$, a_{O_2} , and $a_{\text{Ce}_{\text{M}}^x}$ may be considered as essentially constant, and it follows from Eq. [7]

$$[\text{Ce}_{\text{M}}'] = 2 [(\text{V}_{\text{O}^{\cdot\cdot}})^{**}] \propto p_{\text{O}_2}^{-1/4} \quad [8]$$

The same $p_{\text{O}_2}^{-1/4}$ dependence is then expected for x , since

$$x = [(\text{V}_{\text{O}^{\cdot\cdot}})^{**}] = 1/2 [\text{Ce}_{\text{M}}'] \quad [9]$$

The susceptibility $\chi_{\text{M}}(3)$, deduced from magnetic measurements, should follow the same p_{O_2} dependence as x , and, according to Eq. [3], a direct proportionality should be observed between $\chi_{\text{M}}(3)$ and x . Indeed, the $\log \chi_{\text{M}}(3)$ vs. $\log x$ plots are straight lines with slopes close to unity (Fig. 6).

The concentration of the different defects, $\text{V}_{\text{O}^{\cdot\cdot}}$ and Ce_{M}' , involved in the transport properties have been deduced from the values of x and $\chi_{\text{M}}(3)$, using Eq. [9] and [3]. However, it is not allowed to relate the partial, ionic or electronic conductivity σ_k of these materials to their respective charge carrier concentration C_k , i.e., $[\text{V}_{\text{O}^{\cdot\cdot}}]$ or $[\text{Ce}_{\text{M}}']$, by the classical relationship

$$\sigma_k = Z_k q C_k v_k$$

where Z_k and v_k denote the valence and the mobility of species k and q the electronic charge.

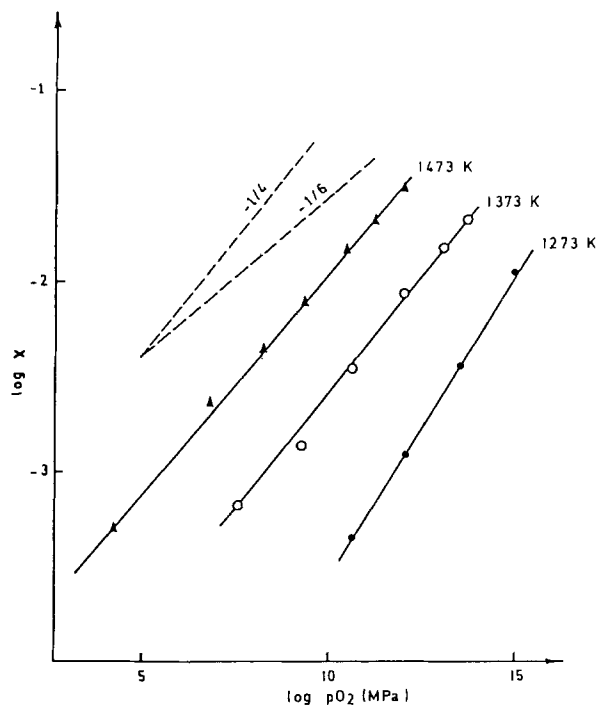


Fig. 5. Variation of the departure from stoichiometry of $0.81\text{ZrO}_2\text{-}0.09\text{CeO}_2\text{-}0.1\text{Y}_2\text{O}_3$ vs. oxygen partial pressure.

Indeed, it is now accepted (26) that the ionic conductivity σ_i of fluorite-type solid solutions does not depend linearly on the concentration of oxygen vacancies. Furthermore, in the present case, we have considered a decrease of σ_i when additional oxygen vacancies are created under reducing conditions. Nevertheless, it has been shown in a previous paper (12) that the decrease of the ionic conductivity in such fluorite-type solid solutions is analogous to that observed for stabilized zirconias when additional oxygen vacancies are generated by additions of trivalent Y^{3+} ions (20) and may be accurately approximated by the same empirical laws. Using the same treatment, the variations of σ_i vs. p_{O_2} have been deduced from the values of $[\text{V}_{\text{O}^{\cdot\cdot}}]$ given by the thermogravimetric measurements; the electronic part of the conductivity is then obtained by difference between the total conductivity σ_t and σ_i

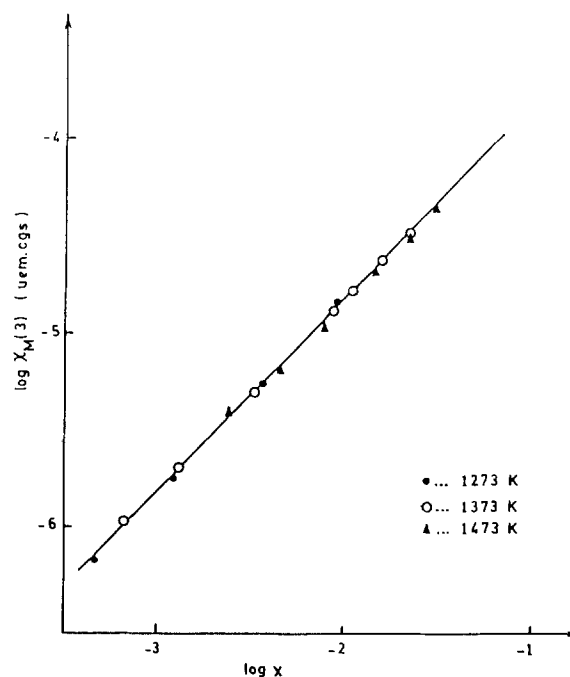


Fig. 6. Dependence of the magnetic susceptibility $\chi_{\text{M}}(3)$ on the departure from stoichiometry of $0.81\text{ZrO}_2\text{-}0.09\text{CeO}_2\text{-}0.1\text{Y}_2\text{O}_3$.

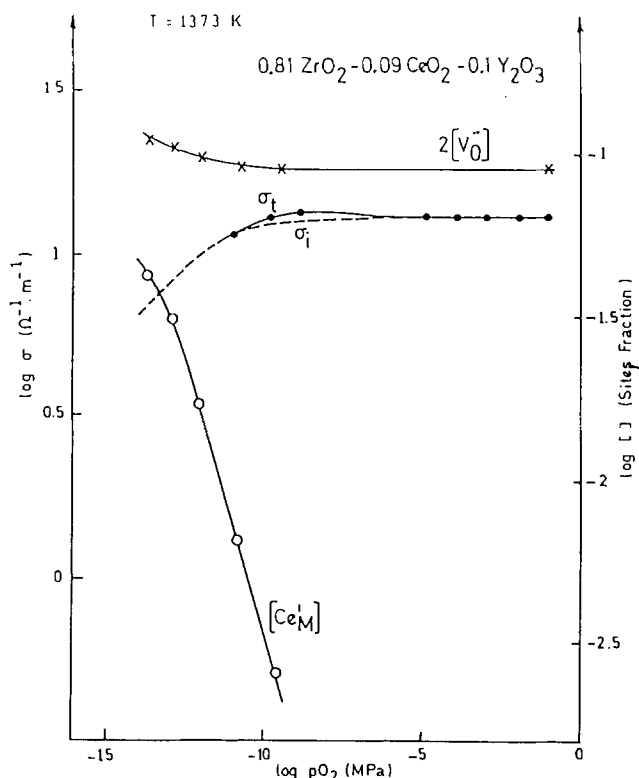


Fig. 7. Plots of the defect concentrations $[V_{O}^{\cdot-}]$ and $[Ce_M']$ and of the conductivities σ_t and σ_i vs. oxygen partial pressure, at 1373 K.

$$\sigma_e(p_{O_2}) = \sigma_t(p_{O_2}) - \sigma_i(p_{O_2})$$

Figures 7 and 8 show the p_{O_2} dependence of the concentrations of charge carrier $[V_{O}^{\cdot-}]$ and $[Ce_M']$ and the partial conductivities obtained according to this procedure at two temperatures, 1373 and 1473 K, for $0.81ZrO_2-0.09CeO_2-0.1Y_2O_3$.

For the highest oxygen partial pressures ($p_{O_2} > 10^{-6}$ MPa), the conductivity is mostly ionic and constant. In-

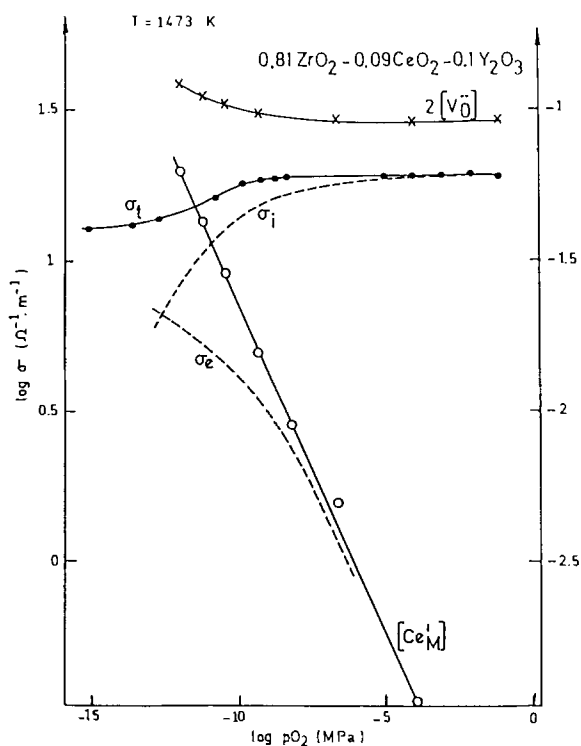


Fig. 8. Plots of the defect concentrations $[V_{O}^{\cdot-}]$ and $[Ce_M']$ and of the conductivities σ_t , σ_i , and σ_e vs. oxygen partial pressure, at 1473 K.

deed, in this domain, $[V_{O}^{\cdot-}]$ does not depend on p_{O_2} since the content of oxygen vacancies resulting from the reduction of Ce_M^x ions is negligible compared to that fixed by the Y_2O_3 content. Under reducing conditions, according to the relationship [8], deduced on the basis of a model of randomly distributed and noninteracting electronic defects, the concentration $[Ce_M^x]$ varies approximately as $p_{O_2}^{-1/4}$. The observed decrease of the total conductivity is here directly related to the decrease of its ionic component and, at 1373 K (Fig. 7), the values of σ_i calculated for the lowest oxygen partial pressures are in good agreement with the measured values of σ .

At higher temperatures, for instance, at 1473 K (Fig. 8), the effect of the electronic component σ_e on the variation of σ_t is no longer negligible. Furthermore, it will be noticed that, for the lowest oxygen partial pressures, the major part of cerium ions are reduced to the trivalent state and the ratio $[Ce_M^x]/[Ce_M^{\cdot}]$ is larger than unity. The electronic conductivity σ_e , which is proportional to $[Ce_M^x]/[Ce_M^{\cdot}]$, would then decrease for more reducing conditions. However, σ_e is of the same order of magnitude as σ_i for an oxygen partial pressure $p\theta$ of about 10^{-12} - 10^{-13} MPa. For $0.9CeO_2-0.1Y_2O_3$ ($y = 0.9$), the partial pressure $p\theta$ corresponding to the condition $\sigma_i = \sigma_e$ is equal to $\approx 10^{-8}$ MPa at the same temperature (12). Such a lowering of the parameter $p\theta$ results from a decrease of the electronic conductivity due to a lower electronic mobility. Indeed, for a deviation from stoichiometry $x = 1.7 \cdot 10^{-2}$, the electronic mobility in $0.81ZrO_2-0.09CeO_2-0.1Y_2O_3$ is equal to $v_e = 3.1 \cdot 10^{-8} m^2V^{-1}s^{-1}$, while under the same conditions the electronic mobility of $0.9CeO_2-0.1Y_2O_3$ is at least a factor of ten higher (12). Owing to the order of magnitude of v_e , one may reasonably attribute the electronic conductivity of the solid solutions $(0.9-y)ZrO_2-yCeO_2-0.1Y_2O_3$ to a small polaron mechanism with electrons localized on cerium sites, as in the case of pure or doped nonstoichiometric ceria (10). As a consequence, the variation of the electronic mobility with respect to the composition should be related to a change of the probability for an electron to jump from a localized site to another, which is expected to be a decreasing function of the jump distance (27).

Solid solution with high CeO₂ content: $0.45ZrO_2-0.45CeO_2-0.1Y_2O_3$.—The properties of the solid solution $0.45ZrO_2-0.45CeO_2-0.1Y_2O_3$ are in part similar to those of $0.81ZrO_2-0.09CeO_2-0.1Y_2O_3$. Indeed, in a limited range of oxygen partial pressure, the size of which shrinks when the temperature increases, the departure from stoichiometry x follows the same $p_{O_2}^{-1/4}$ dependence (Fig. 9), and the proportionality relationship between the susceptibility $\chi_M(3)$ and x is also observed. Beyond this domain, the deviation from stoichiometry increases rapidly and any solid-gas phase equilibrium has not been reached even after 100h. For this reason, the values of x reported in Fig. 9 for the lowest oxygen partial pressures, at 1373 and 1473 K, do not correspond to equilibrium conditions.

The lower limit of the domain with a $p_{O_2}^{-1/4}$ dependence is observed for an oxygen partial pressure of 10^{-12} MPa about at 1373 K and 10^{-10} MPa at about 1473 K. This is approximately equal to the oxygen partial pressure corresponding to the conductivity maximum of the $\log \sigma - \log p_{O_2}$ plots (Fig. 4). Owing to the results of x-ray analysis, which show an ordered phase with a pyrochlore-type structure for lower oxygen activities, the rapid increase of x can be reasonably attributed to the formation of a two-phase system which consists of a disordered fluorite-type matrix into which pyrochlore-type ordered domains gradually precipitate.

The defect concentrations $[V_{O}^{\cdot-}]$ and $[Ce_M^x]$ and the partial conductivities σ_i and σ_e were deduced or calculated using the same steps as in the case of $0.81ZrO_2-0.09CeO_2-0.1Y_2O_3$. Typical results obtained at 1373 K are plotted in Fig. 10. It should be observed that, in opposition with the previous case, the electrical conductivity of $0.45ZrO_2-0.45CeO_2-0.1Y_2O_3$ is mostly electronic in na-

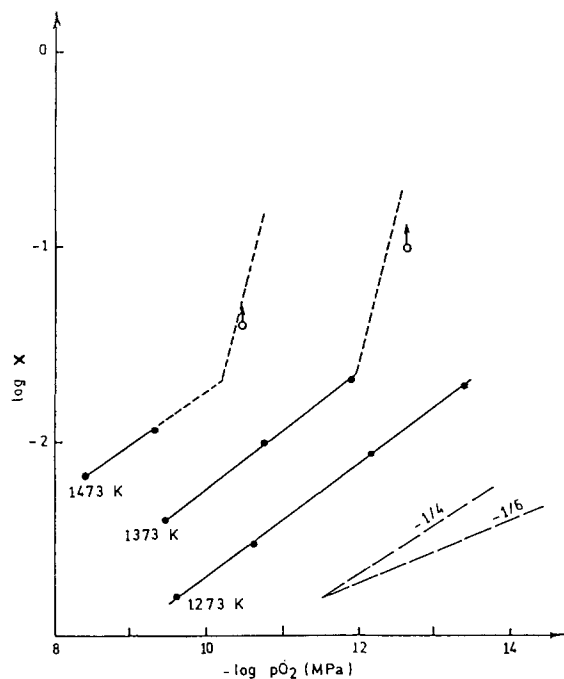


Fig. 9. Dependence of the departure from stoichiometry of $0.45\text{ZrO}_2\text{-}0.45\text{CeO}_2\text{-}0.1\text{Y}_2\text{O}_3$ on oxygen partial pressure.

ture, since the electronic component is equal to the ionic one for a higher oxygen partial pressure $p\Theta \approx 10^{-6}$ MPa. For oxygen partial pressures lower than about 10^{-12} MPa, the total conductivity rapidly decreases, although the concentrations of oxygen vacancies and Ce^{3+} ions strongly increase. This will be due to the formation of pyrochlore-type ordered domains, the conductivity of which would be lower. Indeed, the relation between the conductivity maximum and an equipartition of cerium ions between the two valence states Ce^{3+} and Ce^{4+} (the hypothesis proposed by various authors to explain the electrical properties of ceria-based solid solutions) is no longer accurate in the present case, since for the oxygen

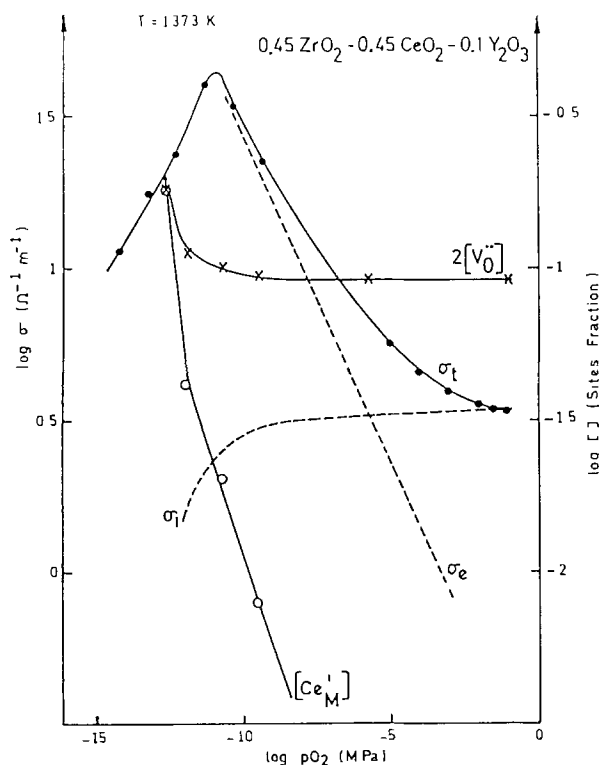


Fig. 10. Plots of the defect concentration $[\text{V}_{\text{O}}^{\cdot\cdot}]$ and $[\text{Ce}_{\text{M}}^{\cdot}]$ and of the conductivities σ_{iv} , σ_{iv} , and σ_{e} vs. oxygen partial pressure, at 1373 K.

partial pressure corresponding to a maximum of conductivity, $p_{\text{O}_2} \sim 10^{-11}$ MPa at 1373 K, only about 6% of cerium ions are reduced in the trivalent state. Furthermore, the decrease of σ_{e} cannot be simply explained on the basis of a decrease of the ionic component σ_{i} , since, close to the maximum, the total conductivity is practically equal to its electronic component σ_{e} . It must be then assumed that the formation of the ordered domains induces an important decrease of the electronic conductivity, and, more precisely, owing to the rapid increase of the charge carrier concentration $[\text{Ce}_{\text{M}}^{\cdot}]$ in this domain, a decrease of the electronic mobility.

Conclusion

The study of mixed ionic and electronic conductors belonging to the $\text{ZrO}_2\text{-CeO}_2\text{-Y}_2\text{O}_3$ system has been motivated by the potential applications of these materials as oxygen semipermeable membranes in various processes involving an oxygen extraction at high temperature. This is particularly the case for the production of gaseous fuels, such as H_2 or CO , by direct thermal splitting of H_2O or CO_2 and extraction of the oxygen arising from the dissociation reaction (25). At the temperatures of 1873-2273 K required for the decomposition reaction (25), it has been previously shown that the material used as semipermeable membrane should present, in a given range of oxygen partial pressure $[p_{\text{O}_2}(\text{I}), p_{\text{O}_2}(\text{II})] = (10^{-3}, 10^{-7}$ MPa) (25), a mixed electrical conductivity with equivalent ionic and electronic components. It is therefore interesting to compare the transport properties of the $(0.9-y)\text{ZrO}_2\text{-}y\text{CeO}_2\text{-}0.1\text{Y}_2\text{O}_3$ solid solutions to the requirements of such processes. The oxygen partial pressure $p\Theta$, for which these materials exhibit equal ionic and electronic partial conductivities, should be thus of the same order of magnitude as the partial pressures $p_{\text{O}_2}(\text{I})$ and $p_{\text{O}_2}(\text{II})$.

The conditions of temperature and oxygen partial pressure required for these techniques correspond to the hatched domain of Fig. 11. The different values of the parameter $p\Theta$, obtained for the $(0.9-y)\text{ZrO}_2\text{-}y\text{CeO}_2\text{-}0.1\text{Y}_2\text{O}_3$

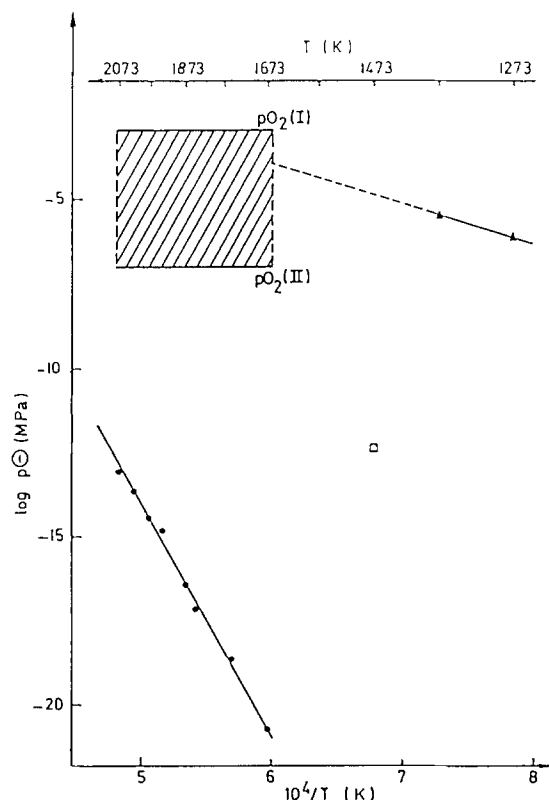


Fig. 11. Temperature dependence of the oxygen partial pressure $p\Theta$ in the case of stabilized zirconia (●) (9), $0.45\text{ZrO}_2\text{-}0.45\text{CeO}_2\text{-}0.1\text{Y}_2\text{O}_3$ (▲), and $0.81\text{ZrO}_2\text{-}0.09\text{CeO}_2\text{-}0.1\text{Y}_2\text{O}_3$ (□). The hatched domain corresponds to the temperature and oxygen partial pressure working conditions of oxygen semipermeable membranes.

solid solutions from the thermogravimetric and magnetic susceptibility measurements, are reported in the same figure. As a reference, the temperature dependence of $p\theta$ of the stabilized zirconia, primarily used as oxygen semipermeable membrane (9), is also plotted in Fig. 11.

As previously stated (9), stabilized zirconia is not an attractive material for applications as oxygen semipermeable membranes, since the corresponding values of $p\theta$ are much lower than the oxygen partial pressures $p_{O_2}(I)$ and $p_{O_2}(II)$. The solid solutions (0.9- y)ZrO₂- y CeO₂-0.1Y₂O₃ appear to be more appropriate. For the composition $y = 0.45$, the values of the partial pressures $p\theta$ extrapolated at high temperature are of the same order of magnitude as the pressures $p_{O_2}(I)$ and $p_{O_2}(II)$. However, the solid solution 0.45ZrO₂-0.45CeO₂-0.1Y₂O₃ gives rise, under reducing conditions, to large departures from stoichiometry and to pyrochlore-type ordered domains which have a detrimental effect on the electrical properties. The oxygen partial pressure for which this second phase has been observed increases rapidly with the temperature, and, consequently, this composition is not suitable for such applications.

The formation of an ordered phase has been observed also for solid solutions with higher concentrations of ceria, for instance, $y = 0.63$ (25), so that it seems more advisable to use solid solutions with a ceria content low enough to keep the structure disordered, in ranges of temperature and oxygen partial pressure of interest for such processes.

The use of a composition with about 20 m/o of cerium oxide appears to be a good solution, since the values of the parameter $p\theta$ will be appreciably higher than in the case of $y = 0.09$, about $10^{-11.5}$ MPa at 1473 K, owing to the increase of the electronic conductivity level arising from a higher ceria content. Moreover, such a solid solution does not correspond to the composition range for which the pyrochlore-type phase is observed (25). Indeed, the x-ray analysis of the solid solution 0.72ZrO₂-0.18CeO₂-0.1Y₂O₃, annealed under various reducing atmospheres ($p_{O_2} = 10^{-11}$ - 10^{-17} MPa), clearly shows that this material is a single, fluorite-type, phase.

For these reasons, the composition 0.72ZrO₂-0.18CeO₂-0.1Y₂O₃ has been used to prepare oxygen semipermeable membranes, which are presently under investigation. Preliminary results show that the oxygen semipermeability of such membranes is higher by about a factor of 50 than the oxygen semipermeability of membranes made of "classical" stabilized zirconia (28).

Manuscript submitted April 3, 1984; revised manuscript received June 12, 1984.

CNRS assisted in meeting the publication costs of this article.

REFERENCES

1. T. H. Etsell and S. N. Flengas, *Chem. Rev.*, **70**, 339 (1970).
2. R. M. Dell and A. Hooper, in "Solid Electrolytes," P. Hagenmuller and W. Van Gool, Editors, p. 291, Academic Press, New York (1978).
3. W. A. Fischer and D. Janke, *Arch. Eisenhüttenwesen*, **39**, 89 (1968).
4. E. M. Logothetis, in "Science and Technology of Zirconia," A. H. Heuer and L. W. Hobbs, Editors, p. 388, The American Ceramic Society, Columbus, OH (1981).
5. H. S. Isaacs, in "Science and Technology of Zirconia," A. H. Heuer and L. W. Hobbs, Editors, p. 406, The American Ceramic Society, Columbus, OH (1981).
6. B. Calès and A. M. Anthony, in "Progress in Solid Electrolytes," T. A. Wheat, A. Ahmad, and A. K. Kuriakose, Editors, p. 413, Energy Mines and Resources, Ottawa (1983).
7. J. Fouletier, P. Fabry, and M. Kleitz, *This Journal*, **123**, 204 (1976).
8. B. Calès and J. F. Baumard, *High Temp. High Press.*, **14**, 681 (1982).
9. B. Calès and J. F. Baumard, *J. Mater. Sci.*, **17**, 3243 (1982).
10. H. L. Tuller, in "Nonstoichiometric Oxides," O. T. Sorensen, Editor, p. 271, Academic Press, New York (1981).
11. M. Forestier, G. Robert, M. Caillet, and C. Desportes, *Mater. Res. Bull.*, **4**, 727 (1969).
12. B. Calès and J. F. Baumard, *J. Phys. Chem. Solids*, To be published.
13. R. D. Shannon and C. P. Prewitt, *Acta Crystallogr. Sect. B.*, **25**, 925 (1969).
14. R. T. Dirstine, R. N. Blumenthal, and T. F. Kuech, *This Journal*, **126**, 264 (1979).
15. L. F. Bates, in "Modern Magnetism," Cambridge University Press, Cambridge, England (1961).
16. B. Calès and J. F. Baumard, *Rev. Int. Hautes Temp. Refract.*, **17**, 137 (1980).
17. F. A. Kröger and H. J. Vink, in "Solid State Physics," Vol. 3, F. Seitz and D. Turnbull, Editors, Academic Press, New York (1957).
18. M. Gouet, Thesis, University of Paris Val de Marne, Paris (1979).
19. L. L. Fehrenbacher and N. M. Tallan, *Am. Ceram. Soc. Bull.*, **48**, 409 (1969).
20. D. W. Strickler and W. G. Carlson, *J. Am. Ceram. Soc.*, **47**, 122 (1964).
21. C. R. A. Catlow, in "Nonstoichiometric Oxides," O. T. Sorensen, Editor, p. 61, Academic Press, New York (1981).
22. M. Perez Jorba, *Ann. Chim. Paris*, **7**, 479 (1962).
23. T. Negas, R. S. Roth, C. L. McDaniel, H. S. Parker, and C. D. Olson, *Proc. Rare Earth Res. Conf. 12th*, **2**, 605 (1976).
24. W. H. Rhodes and R. E. Carter, *J. Am. Ceram. Soc.*, **49**, 244 (1966).
25. B. Calès, Thesis, University of Orléans, Orléans, France (1983).
26. J. A. Kilner and B. C. H. Steele, in "Nonstoichiometric Oxides," O. T. Sorensen, Editor, p. 233, Academic Press, New York (1981).
27. N. F. Mott and E. A. Davis, in "Electronic Processes in Non-Crystalline Materials," Clarendon Press, Oxford (1971).
28. J. Lédé, C. Braun, F. Lapique, J. Villermaux, B. Calès, Y. Nigara, A. M. Anthony, C. Abdul-Aziz, D. Puechberty, and M. Ledoux, *Entropie*, To be published.

Reactions of NaCl with Gaseous SO₃, SO₂, and O₂

W. L. Fielder, C. A. Stearns, and F. J. Kohl

National Aeronautics and Space Administration, Lewis Research Center, Cleveland, Ohio 44135

ABSTRACT

Hot corrosion of gas turbine engine components involves deposits of Na₂SO₄ which are produced by reactions between NaCl and oxides of sulfur. For the present investigation, NaCl single crystals were exposed at 100°–850°C to gaseous mixtures of SO₃, SO₂, and O₂. The products formed during this exposure depend, primarily, on the temperatures. The four product films were NaCl · SO₃, Na₂S₂O₇, Na₂SO₄, and NaCl-Na₂SO₄. The kinetics of the reactions were measured.

Hot corrosion degradation of components of gas turbine engines burning relatively clean fuels usually involves deposits of only Na₂SO₄. Two processes have been proposed to account for the deposits: (i) deposition by impaction of NaCl particles on the turbine surfaces and subsequent reaction of the condensed NaCl with oxides of sulfur, and (ii) reaction in the hot combustion stream to form Na₂SO₄ with subsequent deposition. Some previous investigators have observed the conversion of NaCl to Na₂SO₄ under real or simulated combustion atmospheres in the presence of oxide scales on turbine-type substrates (1-3). Such experiments, while verifying that conversion of NaCl to Na₂SO₄ does occur, did not clearly differentiate between processes (i) and (ii). Furthermore, the influence of the substrates, used in these experiments, upon the rates of conversion was still unclear.

The present study was concerned primarily with observing the surface reactions occurring when solid NaCl is exposed to oxides of sulfur (*i.e.*, the reaction in process (i) that might occur after NaCl impaction) over a broad temperature range without the influence of oxide scales or turbine-type substrates. Therefore, NaCl, either as single crystal or as a 1:1 powder mixture with Na₂SO₄, was exposed to gaseous mixtures of SO₃ in SO₂-O₂ between 100° and 850°C. The products and kinetics of the reactions were determined.

Experimental

Samples of single-crystal NaCl were obtained by cleaving from a high purity boule grown from the melt. For a few runs, samples of anhydrous powder mixtures of 1:1 molar NaCl and Na₂SO₄ were prepared by melting high purity NaCl and Na₂SO₄ at 700°C. Anhydrous, high purity mixtures of SO₂ in O₂ were obtained commercially or were prepared in-house by pressure dilutions from commercial SO₂ and O₂.

The sample was suspended (inside a quartz tube) from a sensitive electrobalance. The sample was maintained at the desired temperature, exposed to the SO₂-O₂ mixture, and the weight change was followed with time. For most of the runs, the flow rates of the mixtures were about 17 cm³ s⁻¹ (3.4 cm s⁻¹). A Pt catalyst was used to produce the desired concentration of SO₃ in the SO₂-O₂ mixture.

For the anhydrous runs, the H₂O contents in the gaseous atmospheres were less than 20–40 ppm as indicated by hydrometric analyses. For a few runs, the influence of H₂O was observed by introducing it into the system by dilution by passing a parallel O₂ flow through an H₂O bubbler. For these runs, the H₂O content was determined with sufficient accuracy using vapor pressure data and measured flow rates.

High pressure mass spectrometric sampling techniques were used to analyze the gaseous reactant compositions and to identify the gaseous products. The apparatus and techniques have been discussed previously (4). This technique facilitates determination of the concentrations of the gaseous reactants and/or products being produced under the actual experimental conditions because it effectively "freezes" the chemical composition of the gas flow. For the mass spectrometer SO₂ calibration curves, mixtures of SO₂ and O₂ of known compositions were used. A commercial SO₃ analyzer was used initially to determine

the absolute SO₃ concentration produced in a mixture of SO₂-O₂ flowing over the Pt catalyst. At the same time, the mass spectrometer calibration curve was obtained using these SO₃ results and recorded mass peak intensities for SO₃, SO₂, SO, and O₂.

Results and Discussion

The product films formed on the NaCl surface, when it is exposed to oxides of sulfur, depend primarily upon the temperature of exposure. The four films observed were solid NaCl · SO₃, molten Na₂S₂O₇, solid Na₂SO₄, and molten Na₂SO₄-NaCl.

Solid NaCl · SO₃.—A solid film of NaCl · SO₃ forms when NaCl at 100°–150°C is exposed to SO₃



This reaction has been previously used as an analytical method for determining SO₃ concentrations in the presence of SO₂ and O₂ (5).

The rate of formation of the solid product film of NaCl · SO₃ at 150°C was obtained by exposing a NaCl sample to a SO₂-O₂ mixture containing 0.1 mole percent (m/o) SO₃. The weight of the sample initially increased linearly with time (at about 2.7 × 10⁻⁴ mg cm⁻² s⁻¹) for about 1 h. Then, the sample weight increased parabolically (as shown in Fig. 1) with a rate constant, *k*, of about 2.4 × 10⁻¹⁰ g² cm⁻⁴ s⁻¹ suggestive of a mass-transfer control process.

The rate-limiting process for the formation of the NaCl · SO₃ film is still uncertain. A solid-state diffusion process does not seem likely because it should be characterized by smaller parabolic rate constants. And, even though a reasonable value of about 2 × 10⁻⁵ cm² s⁻¹ can be calculated for a diffusion coefficient, *D*, mass transfer of SO₃ through a liquid film (as the rate-limiting process) also does not seem likely since no evidence of a liquid film was observed at 150°C. This value of 2 × 10⁻⁵ was calculated by assuming the approximate relation of *k* = 2*DCd* where the concentration of SO₃ in the gas, *C*, was

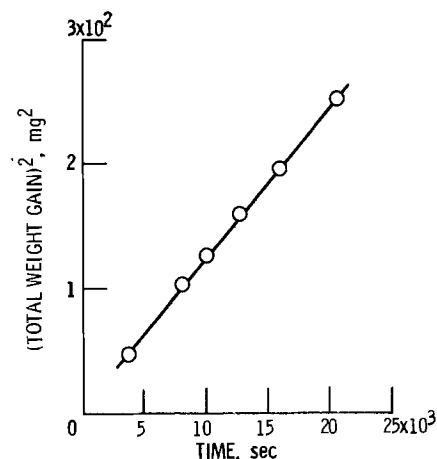
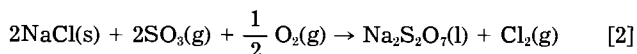


Fig. 1. Plot of (weight gain)² with time for the exposure of single-crystal NaCl to 0.1 m/o anhydrous SO₃ at 150°C (flow rate of 17 cm³ s⁻¹).

$3.6 \times 10^{-6} \text{ g cm}^{-3}$ and a value of 2 g cm^{-3} was estimated for the density of the film, d .

Molten $\text{Na}_2\text{S}_2\text{O}_7$.—Between 400° and 450°C , molten $\text{Na}_2\text{S}_2\text{O}_7$ is the principal film product formed when NaCl is exposed to oxides of sulfur

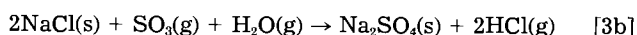
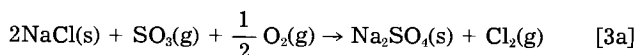


Based on weight gain measurements, a mass-balance calculation showed that the film produced at 420°C , after about 10 min, was molten $\text{Na}_2\text{S}_2\text{O}_7$, with only a slight excess of SO_3 . The sample was exposed for 1.5h at 420°C (i.e., to build up a film for analysis) and then quenched to minimize any further change in the film composition. Examination of the sample after quenching indicated that the film had been molten. X-ray analysis of a small portion of the film showed only $\text{Na}_2\text{S}_2\text{O}_7$, Na_2SO_4 , and the NaCl substrate. After reheating this film to about 500°C in flowing O_2 for about 12h, the $\text{Na}_2\text{S}_2\text{O}_7$ was converted to a porous nonadhering film of Na_2SO_4 as indicated by x-ray analysis. Therefore, for the temperature range of 400° to about 450°C , molten $\text{Na}_2\text{S}_2\text{O}_7$ is the principal film product that is formed.

The rate of formation of the $\text{Na}_2\text{S}_2\text{O}_7$ (and Na_2SO_4) film was determined at 415°C by exposing a NaCl single crystal to an anhydrous mixture of 0.1 m/o SO_3 in SO_2 - O_2 . As shown in Fig. 2, the rate of weight change was parabolic with a rate constant of $5.8 \times 10^{-9} \text{ g}^2 \text{ cm}^{-4} \text{ s}^{-1}$ from which a diffusion coefficient of about $4 \times 10^{-4} \text{ cm}^2 \text{ s}^{-1}$ was calculated. This value is in reasonable agreement with those values usually obtained for diffusion processes in liquids and in particular with the value of about $2 \times 10^{-4} \text{ cm}^2 \text{ s}^{-1}$ reported for the diffusion of $\text{S}_2\text{O}_7^{2-}$ ions in molten Na_2SO_4 (6), and for SO_3 in a chloride melt (7).

The exact mechanism for the $\text{Na}_2\text{S}_2\text{O}_7$ film formation is still unclear. However, it seems reasonable to propose that, initially, a very thin film of Na_2SO_4 may form at the NaCl surface. Subsequently, as suggested by the thermodynamic data (8) for the equilibrium between SO_4^{2-} and $\text{S}_2\text{O}_7^{2-}$, the ratio of $\text{Na}_2\text{S}_2\text{O}_7$ to Na_2SO_4 at equilibrium should be of the order of 10:1 for a SO_3 concentration of 0.1 m/o. Consequently, Na_2SO_4 formed at the NaCl surface at 415°C should convert, essentially, to molten $\text{Na}_2\text{S}_2\text{O}_7$.

Solid Na_2SO_4 .—The reactions that occur when NaCl is exposed at 450° to 625°C to SO_2 and O_2 mixtures containing SO_3 are



High pressure mass spectrometry showed that Cl_2 is the principal gaseous product produced during the reaction under anhydrous conditions while HCl is evolved when

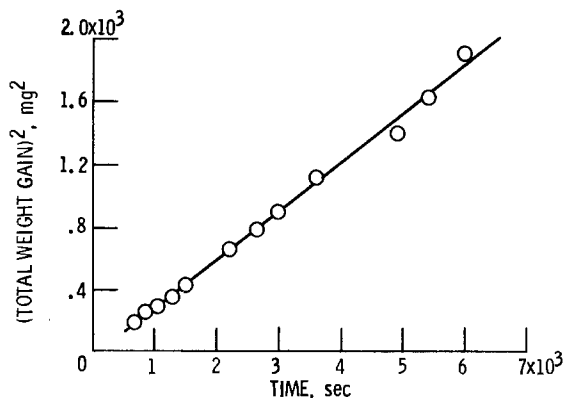


Fig. 2. Plot of (weight gain)² with time for the exposure of single-crystal NaCl to 0.1 m/o anhydrous SO_3 at 415°C (flow rate of $17 \text{ cm}^3 \text{ s}^{-1}$).

reasonable quantities of H_2O are present. Chemical and x-ray analyses revealed that solid Na_2SO_4 is the principal film product that forms on the NaCl surface in this temperature range. These films, unlike the $\text{Na}_2\text{S}_2\text{O}_7$ films at 420°C , are porous and are removed easily from the NaCl crystal upon cooling. This predominance of Na_2SO_4 over $\text{Na}_2\text{S}_2\text{O}_7$ for this temperature range is in agreement with the Na_2SO_4 - $\text{Na}_2\text{S}_2\text{O}_7$ concentrations as calculated from the thermodynamic data. For example, for a SO_3 concentration of 0.1 m/o, the calculated Na_2SO_4 concentration exceeds that of $\text{Na}_2\text{S}_2\text{O}_7$ at about 450°C and becomes increasingly larger with increasing temperature.

Experiments showed that SO_3 was the key reactant rather than SO_2 . For example, the rate of formation of Na_2SO_4 at 500°C was almost three orders of magnitude faster for the anhydrous system when a Pt catalyst was present. For both of these systems, the SO_2 levels were comparable, but the SO_3 concentration was negligible for the system without the catalyst.

Weight gain rates were obtained at varying flow rates. A typical curve is shown in Fig. 3. Both the anhydrous and the H_2O containing systems gave similar types of curves except that the rates of weight gain were larger when H_2O was present. For the system shown in Fig. 3, the rates of weight gain became independent of flow rate above $5 \text{ cm}^3 \text{ s}^{-1}$. Therefore, for this system shown in Fig. 3, mass transfer in the gas phase above the sample should not be rate limiting for flow rates greater than about $5 \text{ cm}^3 \text{ s}^{-1}$.

The weight gains were measured with time (at flow rates where the rates of weight gains are independent of flow rates). A typical curve for an anhydrous system is shown in Fig. 4 (at a flow rate of $10 \text{ cm}^3 \text{ s}^{-1}$) for the exposure at 465°C . Similar types of curves were obtained for the system containing 0.1 m/o H_2O , for comparable quantities of SO_3 , except that the weight gains were almost an order of magnitude larger than for the anhydrous system. As seen in Fig. 4, the weights for the anhydrous systems increased linearly with time (i.e., the rate was essentially constant with time). Also, mass spectrometry results showed that the rates of formation of Cl_2 and HCl were essentially constant with time.

The rates of weight gain were first order with SO_3 pressure for the anhydrous systems and first order with H_2O content for those systems containing varying concentrations of H_2O . Typical curves are shown in Fig. 5. Likewise, the rates of formation of HCl were shown by mass spectrometry to be first order with H_2O concentrations.

Arrhenius-type plots are shown for both systems in Fig. 6 where the data has been normalized to 0.1 m/o SO_3 . For the anhydrous systems, the rate K , expressed in units of $\text{mg cm}^{-2} \text{ s}^{-1}$, is

$$K = 0.6 P_{\text{SO}_3} \exp(-22,000/RT) \quad [4]$$

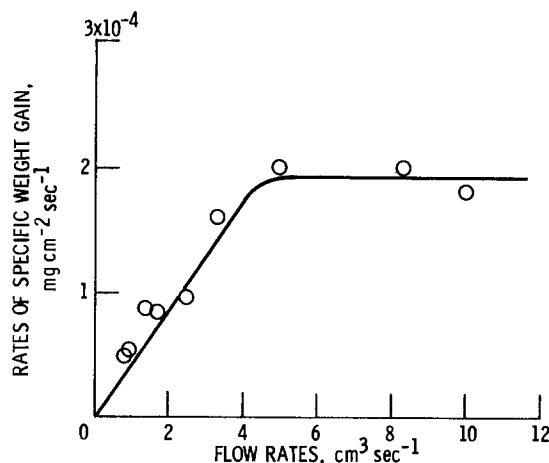


Fig. 3. Plot of rates of specific weight gain with flow rates for the exposure of single-crystal NaCl to 0.3 m/o H_2O and 0.01 m/o SO_3 at 550°C .

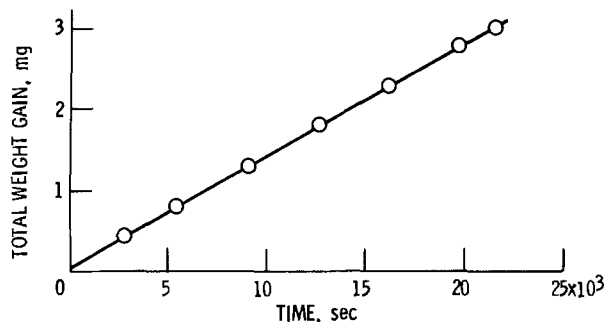


Fig. 4. Plot of total weight gain with time for the exposure of single-crystal NaCl to 0.1 m/o anhydrous SO_3 at 465°C (flow rate of $10 \text{ cm}^3 \text{ s}^{-1}$).

where pressure is in units of atmospheres. The values for the activation energy and pre-exponential factor are quite small, being about $22 \text{ kJ mol}^{-1} \text{ K}^{-1}$ and $0.6 \text{ mg cm}^{-2} \text{ s}^{-1} \text{ atm}^{-1}$, respectively. For the systems containing 0.09 m/o H_2O , the rates of weight gain were almost an order of magnitude faster than for the anhydrous systems, but the slope was essentially zero.

It is proposed that the limiting process for the formation of a solid Na_2SO_4 film between 450° and 625°C , under anhydrous conditions, is the kinetics of the reaction of SO_3 at the NaCl surface since the rate of formation of the product film was constant with time (e.g., Fig. 4). This is in agreement with a chemical control process where the rate of reaction should be independent of the product layer thickness. A mass-transfer control process (in pores or solid state) seems unlikely since this process is characterized by diminishing reaction rates with time as the product layer becomes thicker. Furthermore, a boundary-layer diffusion process in the gas phase does not seem likely because the measurements were made at flow rates where the rates of weight gain were independent of flow rate. Furthermore, boundary layer diffusion rates should not change radically as the temperature was increased from 620° to 640°C , but the rates of weight gain of a NaCl single crystal were found to increase rather sharply at about 630°C (to be discussed later).

Because the observed activation energy value is small, it is believed that no strong bonds are being broken, and, indeed, a low energy process has been proposed for the formation of Na_2SO_4 (9). For this process a planar SO_4 species (produced from SO_2 and O_2) and SO_3 are absorbed

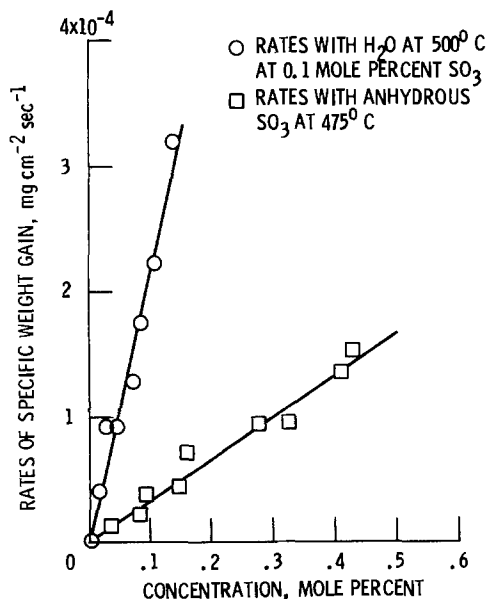


Fig. 5. Plot of rates of specific weight gain with concentration for the exposure of single-crystal NaCl to SO_3 and H_2O (flow rate of $17 \text{ cm}^3 \text{ s}^{-1}$).

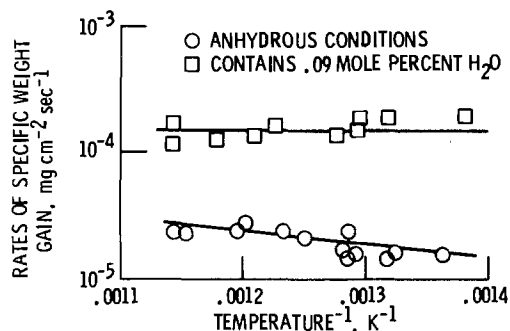


Fig. 6. Plot of rates of the specific weight gain with t^{-1} for the exposure of single-crystal NaCl to 0.1 m/o SO_3 under anhydrous and moisture conditions (flow rate of $17 \text{ cm}^3 \text{ s}^{-1}$).

upon the NaCl surface to form a S_2O_7 transition species where the SO_3 and SO_4 are connected by an O—O bond. Rearrangement and Cl_2 oxidation (i.e., electron transfer) leads to a trigonal pyramidal $\text{S}_2\text{O}_7^{-2}$. It was suggested that the rate-limiting step, which requires only a relatively small energy, may involve the transformation of this species to the tetrahedral $\text{Na}_2\text{S}_2\text{O}_7$. Any $\text{Na}_2\text{S}_2\text{O}_7$ so produced is in equilibrium with Na_2SO_4 . Because Na_2SO_4 is the more stable species at these temperatures, the $\text{Na}_2\text{S}_2\text{O}_7$ will then decompose to give solid Na_2SO_4 at the NaCl surface.

As indicated previously (Fig. 6), the rates of weight gain with temperature for the systems containing 0.09 m/o H_2O could be fitted to one straight line with a slope of essentially zero (at about $1.5 \times 10^{-4} \text{ mg cm}^{-2} \text{ s}^{-1}$). No postulate can be put forward at this time to explain the observed lack of an activation energy for this process.

Molten Na_2SO_4 -NaCl.—Initial experiments showed that the rates of weight gain increased sharply (by at least an order of magnitude) when the single-crystal NaCl temperature was raised above 625°C during exposure to SO_3 - SO_2 - O_2 atmospheres. Samples held at temperatures above 640°C for short intervals and then quenched showed a molten film mixture of Na_2SO_4 and NaCl on the surface, as determined by sulfate and chloride analyses. This is in agreement with the phase diagram which shows that a eutectic is formed at about 625°C (10).

Similar results were obtained when solid mixtures of 1:1 Na_2SO_4 and NaCl were exposed to SO_3 . For example, upon exposing this sample mixture to 0.1 m/o SO_3 between 620° and 630°C , the sample melted and the rate of weight gain above 625°C increased rather sharply by almost an order of magnitude. For data taken after relatively short times, the rate of weight gain remained essentially constant at about $10^{-3} \text{ mg cm}^{-2} \text{ s}^{-1}$ over the range of 650° - 850°C .

The reaction of SO_3 with the NaCl in the molten 1:1 mixture of NaCl and Na_2SO_4 (contained in a crucible) was studied by exposing it between 700° and 750°C to SO_2 - O_2 mixtures, containing 0.1 m/o SO_3 , at flow rates of about $17 \text{ cm}^3 \text{ s}^{-1}$. The data, normalized to 0.1 m/o SO_3 , is shown in Fig. 7. A rate constant of $7.0 \times 10^{-10} \text{ g}^2 \text{ cm}^4 \text{ s}^{-1}$ was obtained from the parabolic curve suggestive of a mass-transfer control process. It is proposed, that for temperatures above 625°C , SO_3 reacts with NaCl at its surface to produce Na_2SO_4 , which can then form a molten phase with the NaCl. Presumably, mass transfer of one of the reacting species (i.e., SO_3) becomes rate limiting as SO_3 continues to react with NaCl in the melt to produce additional Na_2SO_4 .

An order of magnitude estimate can be made for the time required to consume NaCl particles under simulated gas turbine conditions operating at 800°C . A rate of about $10^{-4} \text{ mg cm}^{-2} \text{ s}^{-1}$, is assumed for a combustion atmosphere, containing about 0.01 m/o SO_3 (a rate of about 10^{-3} was obtained for this molten phase region for 0.1 m/o SO_3). If we assume compressor shedding, it is not unreasonable to assume that NaCl cubes of $10 \mu\text{m}$ on a side might transit to the hot turbine blade. This particle, when

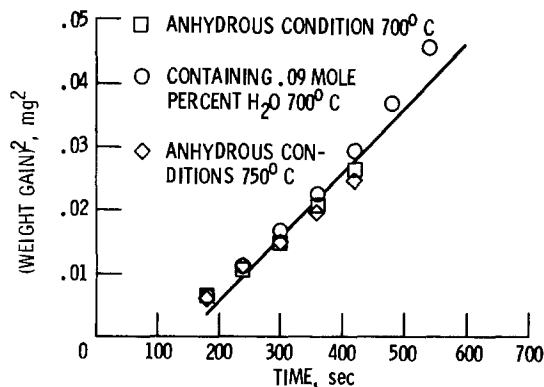


Fig. 7. Plot of (weight gain)² with time for the exposure of a molten mixture of 1:1 Na₂SO₄ and NaCl to 0.1 m/o SO₃ (flow rate of 17 cm³ s⁻¹).

exposed to the simulated gas turbine conditions, would require of the order of an hour to be converted to Na₂SO₄. This rather lengthy time interval suggests that the deposits formed on the component parts should show some NaCl. This is contrary to what is actually observed on scrapings from turbine blades. As a consequence, processes involving impaction of NaCl particles upon the component parts with subsequent reaction to form Na₂SO₄ appear to be of less significance than processes involving a conversion to Na₂SO₄ in the hot combustion stream with subsequent deposition (11).

Summary

1. A series of product films were obtained upon exposure of NaCl to SO₃ in SO₂-O₂ gas mixtures: (i) solid NaCl SO₃; (ii) molten Na₂S₂O₇; (iii) solid Na₂SO₄; and (iv) a molten mixture of Na₂SO₄ and NaCl.

2. Experimentally measured rates indicated that processes (i), (ii), and (iv) of the above are mass-transfer controlled. The formation of solid Na₂SO₄ (iii), however, is a reaction kinetic process with a small activation en-

ergy of about 22 kJ mol⁻¹ K⁻¹. Mechanisms for this process, involving the transformation of a S₂O₇ transition structure to a tetrahedral SO₄⁻² ion, are proposed.

3. The relatively slow rates at 800°C suggest that the process where Na₂SO₄ forms in the hot combustion atmosphere and then deposits on the turbine component parts may be of greater significance than the process where NaCl impacts on the component surfaces and reacts there to form Na₂SO₄.

REFERENCES

1. J. F. G. Condé, N. Birks, M. G. Hocking, and V. Vasantaree, in "Proceedings of 4th Conference on Gas Turbine Materials in the Marine Environment," Vol. II, p. 385, Naval Sea Systems Command, Washington, DC (1979).
2. C. G. McCreath, in "Proceedings of 4th Conference on Gas Turbine Materials in the Marine Environment," Vol. II, p. 339, Naval Sea Systems Command, Washington, DC (1979).
3. E. R. Duffy and A. R. Stetson, in "Proceedings of 4th Conference on Gas Turbine Materials in the Marine Environment," Vol. II, p. 543, Naval Sea Systems Command, Washington, DC (1979).
4. C. A. Stearns, F. J. Kohl, G. C. Fryburg, and R. A. Miller, "A High Pressure Modulated Molecular Beam Mass Spectrometric Sampling System," National Aeronautics and Space Administration, NASA TM-73720, Washington, DC (1977).
5. V. A. Roiter, N. A. Stukanovskaya, G. P. Korneichuk, N. S. Volikovskaya, and G. I. Golodets, *Kinet. Catal. (Engl. Transl.)*, **1**, 379 (1960).
6. D. A. Shores and W. C. Fang, *This Journal*, **128**, 346 (1981).
7. D. Inman, in "Electromotive Force Measurements in High Temperature Systems," C. B. Alcock, Editor, p. 163, Institution of Mining and Metallurgy, London (1968).
8. L. P. Kostin, L. L. Pluzhnikov, and A. N. Ketov, *Russ. J. Phys. Chem. (Engl. Transl.)*, **49**, 1313 (1975).
9. A. B. Anderson, Personal communication.
10. P. I. Federov and K. A. Bol'shakov, *Russ. J. Inorg. Chem. (Engl. Transl.)*, **4**, 405 (1959).
11. D. E. Rosner, B. K. Chen, G. C. Fryburg, and F. J. Kohl, *Combust. Sci. Technol.*, **20**, 87 (1979).

The Homogeneous Nucleation of Condensed Silicon in the Gaseous Si-H-Cl System

Carlyle S. Herrick* and David W. Woodruff*

General Electric Company, Corporate Research and Development, Schenectady, New York 12345

ABSTRACT

The chemical vapor deposition of semiconductor silicon by pyrolysis of SiH₄ and SiH₂Cl₂ often produces undesirable silicon powder in the reactor, owing to homogeneous nucleation in the gas phase. Experiments reported herein show the temperature-composition dependence of powdered silicon formation from SiH₂Cl₂-H₂ mixtures. Classical nucleation theory has been applied to the Si-H-Cl system to calculate nucleation rates for liquid or solid silicon from each silicon containing homolog. In general, these rates are dual valued, there being both a higher and a lower temperature associated with each. The lower temperature values compared favorably with literature values reported by Eversteijn and with experimental measurements reported here.

The high purity silicon required for transistors, most integrated circuits, and allied electronic circuitry is obtained at the present time from the pyrolysis of a silicon containing homolog selected from the Si-H-Cl system. By the term homolog, we mean any compound in the series SiH₄, SiH₃Cl, SiH₂Cl₂, SiHCl₃, and SiCl₄.

Those homologs containing the most chlorine usually produce desirable deposits of void-free solid silicon, while homologs containing the most hydrogen often produce some fine powder of particulate silicon. Powder generally has significant deleterious effects on product

*Electrochemical Society Active Member.

quality. It may cause undesirable surface roughness, or may limit yield or reduce the deposition rate. In bulk quantities, silicon powder may suffer due to the large surface area and the impurities which adsorb on it.

The same high hydrogen content homologs which produce undesirable silicon powder also produce higher conversions and yields than do the high chlorine content homologs at the same operating conditions (1). In bulk silicon production as well as in silicon epitaxy, this translates into higher deposition rates and faster production. There is, therefore, considerable interest attached to the problem of understanding silicon powder formation.

Powder formation is generally acknowledged to result from homogeneous nucleation in silicon vapor to produce fine particles of solid silicon. Homogeneous nucleation is described by a classical theory which was developed mainly by Volmer, Weber, Becker, and Doring (2) and modified by Katz and Wiedersich (3) as well as by a statistical mechanical theory of Lothe and Pound (4) and Binder and Stauffer (5). At the present time, the latter theory does not agree well with experimental measurements. However, the classical theory has recently enjoyed considerable success in describing closely the experimental results for a number of systems near room temperature (6). In no published study has the classical theory been applied at the high temperatures required for the chemical vapor deposition of solid silicon nor has it been applied to a system in which chemical reaction takes place.

This paper describes the homogeneous nucleation of solid silicon as measured experimentally in mixtures of SiH_2Cl_2 with hydrogen and as calculated for all of the Si-H-Cl system homologs using the classical theory. Calculated results are compared with experimental values reported here as well as with values from the several sources reported in the literature.

Experimental Measurements

Gas-phase nucleation experiments were conducted in a tube furnace using a gaseous mixture of dichlorosilane (DCS) and hydrogen as the feed. After mixing in a bed of glass beads, the feed was introduced into a 1.27 cm (0.5 in.) od, 1.02 cm (0.4 in.) id quartz tube having a hot zone 30.5 cm (1 foot) long. The outlet end was connected to a small Ehrlemeyer flask with a loose glass wool plug placed in the side port. This side port was connected to a scrubber to remove residual chlorosilane.

During the course of an experiment the individual gas flow rates were set to produce the predetermined compositions and total flows indicated in Table I. The initial furnace temperature was set low enough not to cause gas-phase nucleation of silicon. Temperature was increased stepwise 10° every 10 min until brown silicon powder was observed either at the tube outlet or on the glass wool plug. The experiments were repeated at a variety of concentrations between 0.02 and 0.20 mole fraction DCS in H_2 . The temperature uncertainty was about ± 5 K.

Table I is a list of the results for the various concentrations and flow rates of DCS tested. The correlation between inlet composition and the onset temperature for

Table I. Results of gas-phase nucleation experiments

Mole fraction SiH_2Cl_2	Flow rate (std ml/s)	Nucleation onset temperature (K)
0.02	16.7	1078
0.02	16.7	1198
0.02	8.35	1148
0.02	8.35	1158
0.02	8.35	1138
0.02	8.35	1138
0.02	8.35	1108
0.03	16.7	1198
0.03	16.7	1108
0.03	8.35	1108
0.04	16.7	1088
0.04	16.7	1068
0.05	16.7	1058
0.05	16.7	1058
0.10	16.7	918
0.10	16.7	1008
0.10	16.7	988
0.10	16.7	1008
0.10	8.35	1038
0.15	16.7	978
0.15	16.7	968
0.20	16.7	958
0.20	16.7	958

visible homogeneous nucleation of solid silicon is shown in Fig. 1. The four points with the greatest scatter were all measured at the higher total gas flow rate, which appeared to be less sensitive to the experimental conditions than the lower rate. Also contributing to data scatter at the lower compositions was the difficulty in detecting smaller amounts of silicon. These data are the first attempt to establish the onset of homogeneous nucleation for DCS- H_2 mixtures.

Nucleation Rate Calculations

Nucleation rates are calculated here by the straightforward application of classical nucleation theory without invoking adjustable parameters of any kind. For nucleation in the gas phase, the theory proceeds from the assumed existence in the gas phase of a distribution of "clusters" of associated gas molecules, each of which will in time dissociate to gas-phase monomers. Gas-phase clusters containing the maximum number of molecules are of "critical size" because the addition of a single gas-phase monomer molecule creates a new entity, a stable

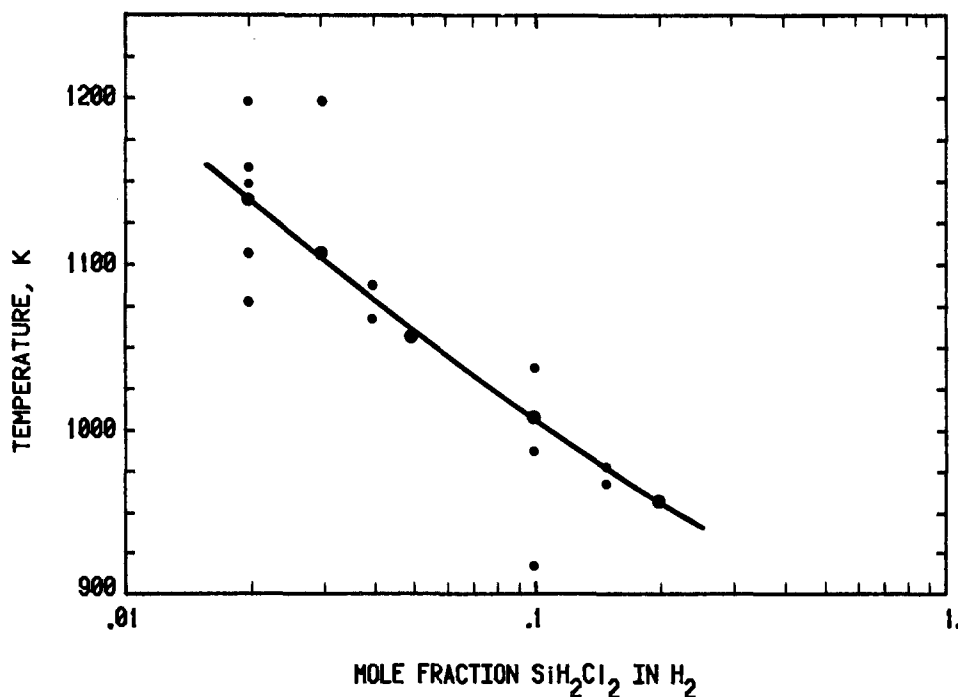


Fig. 1. Experimental temperatures for the onset of homogeneous nucleation of solid silicon from mixtures of SiH_2Cl_2 and H_2 . Larger dots indicate two coincident points.

nucleus, having a monomer evaporation rate lower than the monomer condensation rate. Its continuing future existence in associated form is assured either as a liquid or as a solid. Equation [1] expressed these ideas in mathematical notation (see list of symbols).

$$I = awn \exp \left(\frac{\Delta G_{cs}}{kT} \right) \quad [1]$$

where the quantity $n \exp \Delta G_{cs}/kT$ represents the concentration of critical-size clusters in the gas, and the quantity (aw) represents the condensation rate of monomer on a cluster. Approximately

$$\Delta G_{cs} = \frac{16\pi}{3} \frac{\sigma^3}{\Delta G_v^2} \quad [2]$$

and

$$\Delta G_v = -\frac{kT}{V_c} \ln \frac{P}{P_0} \quad [3]$$

also

$$r_{cs} = -\frac{2\sigma}{\Delta G_v} \quad [4]$$

Then for an ideal gas, the kinetic theory of gases gives

$$w = 4\pi r_{cs}^2 P (2\pi mkT)^{-1/2} \quad [5]$$

The accommodation coefficient α is taken to be unity, an appropriate assumption in view of Langmuir's extensive measurements on similar systems at similar temperatures. The ratio P/P_0 is the supersaturation which, because α is assumed independent of the partial pressure, is equal to the condensation ratio, the driving force promoting nucleation (3). Values for the vapor pressure of silicon, P_0 , are subject to disagreement. The values used in this work are those published by the American Institute of Physics (7). They can be correlated by different straight lines above and below the melting point.

$$\log_{10} P_0 = 5.8225 - 2.0483 \times 10^4/T \quad T > 1685 \text{ K} \quad [6]$$

$$\log_{10} P_0 = 7.5341 - 2.3399 \times 10^4/T \quad T < 1685 \text{ K} \quad [7]$$

These data suggest a boiling point of 3518 K for silicon, higher than other sources, and consequently somewhat lower vapor pressures at the operating temperatures.

The partial pressures of silicon, P in Eq. [3] and [5] and n in Eq. [1] are obtained from equilibrium calculations for the gaseous single-phase Si-H-Cl system. The algorithm employed in Ref. (1) was used here with the output constrained to the vapor phase. The surface energies of condensed-phase silicon nuclei are taken to be equal to the surface tensions, which are estimated by the method suggested in Ref. (8).

Nucleation rates were calculated for all of the silane homologs using Eq. [1]-[7] over a range of temperatures and composition. Table II and Fig. 2 are typical of the re-

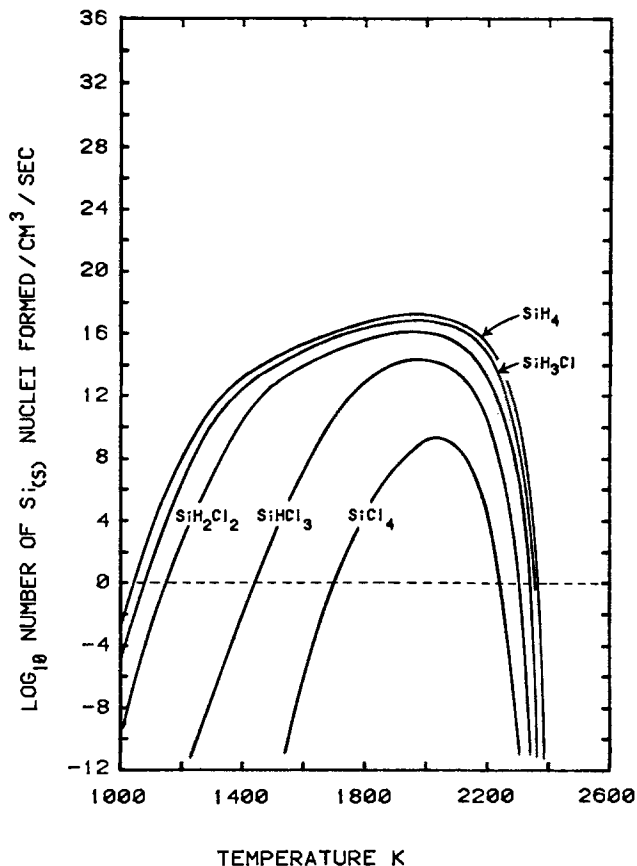


Fig. 2. Homogeneous nucleation rates for silicon from the silane homologs at various temperatures. Inlet composition is 0.01 mole fraction homolog and 0.99 mole fraction hydrogen. Total pressure is 1 atm.

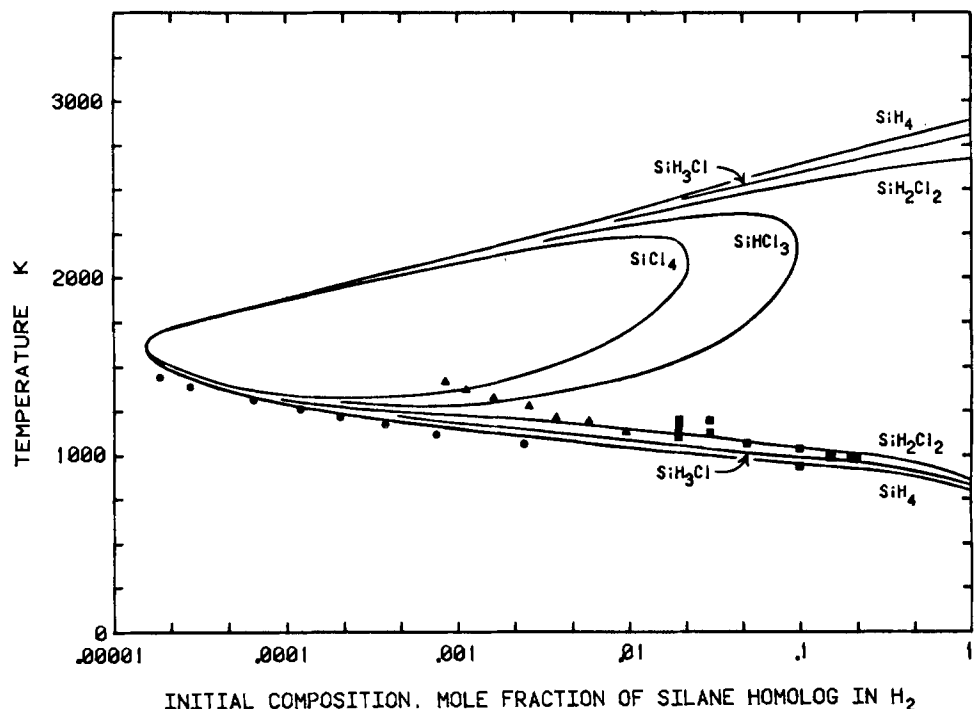
sults. The rates cover a range greater than 53 decades, more at higher homolog concentrations. Each homolog exhibits a maximum in the nucleation rate vs. temperature curve. Therefore, there are usually two temperatures at which one can obtain a given nucleation rate. At the lower temperature, the nucleation rate is determined by a very large supersaturation and a very small concentration of silicon vapor. The reverse condition occurs at the higher temperature, where the supersaturation is small and the concentration of silicon vapor is large (see Table II).

Instead of concentration of silicon atoms in the vapor, Table II lists the mean free path between Si-Si collisions, a quantity directly proportional to the reciprocal of concentration, for the additional insight which that quantity provides. In addition, Table II lists fractional numbers of atoms in a critical size cluster. Of course, the use of fractional atoms is an entirely artificial device. It results from

Table II. Calculated nucleation rates for the inlet composition 0.01 mole fraction SiH_4 , 0.99 mole fraction H_2 , 1 atm total pressure

Temp. (K)	Supersaturation (P/P_0)	Si-Si mean free path (cm)	Atoms in a critical cluster	Nucleation rate (nuclei/cm ³ /s)
900	4.3×10^4	1.5×10^9	5.6	1.0×10^{-11}
1000	3.5×10^4	5.6×10^8	4.1	1.2×10^{-3}
1100	3.0×10^4	5.9×10^4	3.0	1.4×10^3
1200	2.6×10^4	1.4×10^3	2.3	7.3×10^7
1300	1.7×10^4	7.7×10^1	2.0	1.5×10^{11}
1400	6.1×10^3	1.3×10^1	2.0	9.7×10^{12}
1500	2.1×10^3	3.2	2.3	1.8×10^{14}
1600	7.9×10^2	1.0	2.7	1.8×10^{15}
1700	3.3×10^2	3.7×10^{-1}	3.3	1.1×10^{16}
1800	1.5×10^2	1.5×10^{-1}	4.0	4.4×10^{16}
1900	7.1×10^1	7.2×10^{-2}	5.1	1.1×10^{17}
2000	3.6×10^1	3.7×10^{-2}	7.0	1.3×10^{17}
2100	1.9×10^1	2.1×10^{-2}	10.4	4.9×10^{16}
2200	9.6	1.4×10^{-2}	18.3	1.4×10^{15}
2300	4.8	1.0×10^{-2}	45.3	1.1×10^{10}
2400	3.3	9.3×10^{-3}	258.0	$< 1.0 \times 10^{-36}$

Fig. 3. The locus of all points at which the homogeneous nucleation rate is one nucleus/cm³/s for each silane homolog. In the enclosed regions nucleation rates are greater; elsewhere they are lower. Below the silicon melting point (~1685 K), nuclei are solid; above that temperature, nuclei are liquid. Solid lines are calculated from classical nucleation theory, symbols are experimental. ■: This work, SiH₂Cl₂. ●: SiH₄, Ref. (9). ▲: SiH₄, Ref. (10).



treating Eq. [4] as a continuous function rather than as a function limited to those discrete values corresponding to whole numbers of atoms per cluster. So doing greatly reduces the amount of effort required to solve Eq. [1]-[7] simultaneously. The solutions (Fig. 2 and 3) become continuous functions which consist of a number of real values periodically interspersed in a monotonic continuum of imaginary ones.

It is apparent from Fig. 2 that there is no unique value for the onset of homogeneous nucleation. It is common practice to select a rate of one nucleus per cubic centimeter per second to mark the onset, and that value will be used here. It is indicated by the horizontal dashed line in Fig. 2. In that neighborhood, a factor of 10 change in nucleation rate is created by approximately a 17 K temperature change in the lower temperature level and by a 2 K change in the upper level. Uncertainties in determining nucleation onset temperatures experimentally are likely to be near these magnitudes. At the conditions chosen for Fig. 2 and Table II, the low temperature nucleation onset for SiH₄ occurs at a temperature of about 1046 K, a supersaturation of about 33,000, a Si-Si mean free path of about 6.2 km, and 3.5 atoms in a critical-size cluster. Some values for other conditions are given later in this paper.

Repeating the calculations (Eq. [1]-[7]) a large number of times permits one to construct Fig. 3, which traces the loci of all points in the system at which the nucleation rate is 1 nucleus/cm³/s. Selected values of temperature and composition from Fig. 3 are given in Table III for convenience including the upper and lower limiting compositions. The loci for SiCl₄ and SiHCl₃ form closed paths, while the other homologs bound closed areas in combination with a mole fraction of 1.0, an impenetrable boundary even though it is not part of the loci. Nucleation rates inside the closed areas are greater than one while rates outside are lower. Figure 2, a cross section of Fig. 3 at 0.01 mole fraction, illustrates nucleation rate behavior inside and outside of the closed areas.

At high initial concentrations, between 0.1 and 1.0 mole fraction, only SiH₄, SiH₃Cl and SiH₂Cl₂ are able to generate supersaturations large enough to nucleate 1 nucleus/cm³/s. As initial concentration decreases below 0.1 and 0.01 mole fraction, SiHCl₃ and SiCl₄ become able to generate the necessary supersaturations, but, at first, only at high temperatures. Convergent behavior becomes evident with further decreases in actual composition as differences in constitution between homologs diminish in importance and concentration becomes the dominant fac-

tor. The lower functional values of concentration differ very slightly among the homologs. This difference is not visible in Fig. 3, but is detailed in Table III. Although the precision of Table III is not quite good enough to demonstrate the fact, it appears that there are no points of coincidence between the loci for the various homologs. Instead, they constitute a set of nested curves which never quite coincide with one another.

There is no previous work of comparable scope with which to compare the Fig. 3 result. Calculations by others have been confined to narrow temperature ranges; hence, they never explored the geometry of the nucleation onset locus. Figure 3 is characterized by two principal shapes; a left pointing V shape with a high temperature leg and a low temperature leg, which describes the behavior of materials with only nominal thermal stability, and an inverted air-foil shape, which describes the behavior of materials with greater thermal stability. These shapes are nested and nearly coincident at the lowest

Table III. Temperatures corresponding to a homogeneous nucleation rate of 1 nucleus/cm³/s for mixtures of various silane homologs with hydrogen at 1 atm total pressure

Inlet mole fraction of silane homolog	Temperature (K)				
	SiH ₄	SiHCl ₃	SiH ₂ Cl ₂	SiHCl ₃	SiCl ₄
1.0	816	822	842	*	*
0.1	917	995	1042	*	*
0.09765	—	—	—	2186	*
0.02226	—	—	—	—	2108
0.01	1046	1079	1148	1434	1704
0.001	1144	1178	1226	1290	1366
0.0001	1302	1310	1321	1334	1348
0.0000162	—	—	—	—	1610
0.0000161	—	—	—	1609	*
0.0000160	—	1609	1609	*	*
0.0000159	1608	*	*	*	*
0.0000158	*	*	*	*	*
0.0001	1873	1873	1872	1871	1870
0.001	2102	2100	2096	2090	2084
0.01	2362	2352	2331	2298	2242
0.02226	—	—	—	—	2108
0.09765	—	—	—	2186	*
0.1	2651	2613	2541	*	*
1.0	2876	2812	2634	*	*

* Temperature not calculated at this composition.

* Homogeneous nucleation rates as high as 1 nucleus/cm³/s cannot be reached at any temperature.

Table IV. Supersaturation values corresponding to a homogeneous nucleation rate of 1 nucleus/cm³/s for mixtures of various silane homologs with hydrogen at 1 atm total pressure

Inlet mole fraction of silane homolog	Supersaturation (P/P_0)				
	SiH ₄	SiH ₃ Cl	SiH ₂ Cl ₂	SiHCl ₃	SiCl ₄
1.0	1.9 × 10 ⁹	1.2 × 10 ⁹	3.3 × 10 ⁸	*	*
0.1	4.5 × 10 ⁵	1.7 × 10 ⁵	3.7 × 10 ⁴	*	*
0.09765	—	—	—	3.9	*
0.02226	—	—	—	—	4.5
0.01	3.3 × 10 ⁴	1.3 × 10 ⁴	2.5 × 10 ³	63	14
0.001	2.8 × 10 ³	1.4 × 10 ³	650	260	110
0.0001	230	210	180	160	140
0.0000162	—	—	—	—	21
0.0000161	—	—	—	21	*
0.0000160	—	21	21	*	*
0.0000159	21	*	*	*	*
0.0000158	*	*	*	*	*
0.0001	7.7	7.6	7.7	7.7	7.7
0.001	4.5	4.5	4.6	4.6	4.7
0.01	3.0	3.1	3.1	3.3	3.6
0.02226	—	—	—	—	4.5
0.09765	—	—	—	3.9	*
0.1	2.2	2.3	2.4	*	*
1.0	1.9	2.0	2.2	*	*

— Supersaturation not calculated at this composition.

* Homogeneous nucleation rates are high as 1 nucleus/cm³/s cannot be reached at any temperature.

functional concentration. There is reason to expect that this general behavior may be exhibited by many other materials when the full range of nucleation behavior is explored.

Table IV lists calculated values for the supersaturations corresponding to Fig. 3 and Table III. It is noteworthy that the maximum and minimum values of supersaturation differ by nine orders of magnitude. Broadly speaking, one finds from Table IV that along the high temperature leg of the V-shaped characteristic curve that supersaturations are always less than 10. Along the low temperature leg of the V, supersaturations are always greater than 100. By this criterion, all work reported in the literature for other materials appears to fall along the high temperature leg of the respective systems. For silane homolog pyrolysis, on the other hand, temperatures along the high temperature leg (2300-2400 K for the more reactive homologs at a 0.01 initial mole fraction) are clearly much higher than those employed in silicon processing practices, so the region of interest appears to fall along

the low temperature leg. This is confirmed by the comparison with experimental data shown in Fig. 3.

In Fig. 3, the data of Eversteijn (9) is in excellent agreement with the calculated values for the onset of nucleation in SiH₃-H₂ mixtures. The onset data for SiH₄Cl₂-H₂ mixtures reported earlier in this paper is also in excellent agreement with the calculated values. On the other hand, the data of Murthy *et al.* (10) shows a substantial deviation. Had Murthy *et al.* corrected their data to find effective concentrations (as did Eversteijn), satisfactory agreement might well have been obtained.

Table V lists values for the critical nucleus size to demonstrate that the classical calculation involves size values that are in a reasonable range. Tables III, IV, and V all follow the same order, with values for the low temperature leg being listed first.

Nucleation calculations must fulfill several difficult conditions if they are to be significant in a high temperature system such as Si-H-Cl. The first requires that the amount of "jitter" in the calculated results be limited, otherwise much of what might be revealed by the method could instead be obscured. Jitter refers to seemingly random changes in calculated result arising from small changes in an input variable and the uncertainties introduced by using calculational techniques involving convergence in some form. The criteria for satisfying convergence must permit calculating the smallest necessary converged result with reasonable reproducibility. In this case, the partial pressures of silicon involve a convergence calculation and values as low as 1.4×10^{-12} atm occur. The Table III nucleation onset temperatures are reported using four significant figures as an indicator of the absence of calculational "jitter" at that level. As a result, one can make the necessary comparisons between homologs that clearly indicate nested curves rather than some less definite conclusion.

The second condition for significance is some form of demonstrated accuracy, preferably the form arising from comparison with experimental data. Enough criticism has been raised against the classical nucleation theory (2-5) to create substantial doubt about every application to a new system. A comparison is therefore necessary if the doubt is to be eliminated.

Acknowledgment

The authors gratefully acknowledge the assistance of D. K. Dietrich with the experimental work.

Manuscript submitted April 2, 1984; revised manuscript received June 7, 1984.

Table V. Critical nucleus sizes corresponding to a homogeneous nucleation rate of 1 nucleus/cm³/s for mixtures of various silane homologs with hydrogen at 1 atm total pressure

Inlet mole fraction of silane homolog	Si atoms per critical nucleus				
	SiH ₄	SiH ₃ Cl	SiH ₂ Cl ₂	SiHCl ₃	SiCl ₄
1.0	1.0	1.0	1.1	*	*
0.1	2.4	2.7	3.5	*	*
0.09765	—	—	—	86.9	*
0.02226	—	—	—	—	76.6
0.01	3.5	4.2	5.9	17.4	35.4
0.001	5.8	6.7	8.2	10.7	14.0
0.0001	11.1	11.4	11.9	12.5	13.2
0.0000162	—	—	—	—	28.3
0.0000161	—	—	—	28.3	*
0.0000160	—	28.0	28.3	*	*
0.0000159	28.1	*	*	*	*
0.0000158	*	*	*	*	*
0.0001	50.6	50.8	49.7	50.0	49.8
0.001	75.4	75.2	74.3	73.1	73.8
0.01	113	112	108	103	94.9
0.02226	—	—	—	—	76.6
0.09765	—	—	—	86.9	*
0.1	168	162	156	*	*
1.0	222	205	174	*	*

— Critical nucleus size not calculated at this composition.

* Homogeneous nucleation rates are high as 1 nucleus/cm³/s cannot be reached at any temperature.

General Electric Company assisted in meeting the publication costs of this article.

LIST OF SYMBOLS

a	accommodation coefficient for condensation of impinging gas-phase monomer
I	rate of formation of stable nuclei
ΔG_{cs}	free energy of formation of critical-size clusters
ΔG_v	free energy change per unit volume of condensed phase
k	Boltzmann's constant
m	mass of one unit of gas-phase monomer
n	concentration of gas-phase monomer
P	partial pressure of monomer in the gas phase
P_0	equilibrium vapor pressure of monomer
r_{cs}	radius of a critical-size cluster
T	absolute temperature
V_c	molar volume of condensed phase
w	impingement rate of monomer on critical-size cluster
σ	surface free energy per unit area

REFERENCES

1. C. S. Herrick and R. A. Sanchez-Martinez, *This Journal*, **131**, 455 (1984).
2. W. J. Dunning, in "Nucleation," A. C. Zettlemoyer, Editor, p. 1, Marcel Dekker, New York (1969); R. P. Andres, in "Nucleation," A. C. Zettlemoyer, Editor, p. 69, Marcel Dekker, New York (1969).
3. J. L. Katz and H. Wiedersich, *J. Colloid Interfac. Sci.*, **61**, 351 (1977).
4. J. Lothe and G. M. Pound, in "Nucleation," A. C. Zettlemoyer, Editor, p. 109, Marcel Dekker, New York (1969).
5. K. Binder and D. Stauffer, *Adv. Phys.*, **25**, 343 (1976).
6. J. L. Katz and T. L. Virkler, *Faraday Disc. Chem. Soc.*, **61**, 83 (1976).
7. "American Institute of Physics Handbook," 3rd Ed., D. E. Gray, Editor, pp. 4-300, McGraw Hill, New York (1972).
8. C. L. Yaws, L. L. Dickens, R. Lutwack, and G. Hsu, *Solid State Technol.*, **24**, 87 (1981).
9. F. C. Eversteijn, *Philips Res. Rep.*, **26**, 134 (1971).
10. T. U. M. S. Murthy, N. Miyamoto, M. Shimbo, and J. Nishizawa, *J. Cryst. Growth*, **33**, 1 (1976).

Growth of InSb and InAs_{1-x}Sb_x by OM-CVD

P. K. Chiang and S. M. Bedair

Department of Electrical and Computer Engineering, North Carolina State University, Raleigh, North Carolina 27695-7911

ABSTRACT

Organometallic chemical vapor deposition (OM-CVD) growth of InSb and InAs_{1-x}Sb_x has been obtained using triethylindium (TEI), trimethylantimony (TMS), and arsine (AsH₃) on (100) GaAs, (100) InSb, and (111)-B InSb substrates. InSb with excellent morphology was achieved on both (100) InSb and (111)-B InSb substrates. The measured electron mobility at 300 K of undoped InSb grown on (100) GaAs semi-insulating substrates was 40,000 cm²/V-s at a carrier concentration of $N_D - N_A = 2.0 \times 10^{16}$ cm⁻³. Carrier concentration of $N_D - N_A = 1.2 \times 10^{15}$ cm⁻³ has been measured at 77 K. InAs_{1-x}Sb_x (0.07 $\leq x \leq$ 0.75) with mirror-like surfaces have been grown on (100) InSb and InAs substrates. This composition range of 0.55 $< x <$ 0.75 ($E_g \approx$ 0.1 eV) has been successfully achieved for the first time. Solid composition variations as a function of growth temperature and InSb substrate orientations are also discussed.

There are two wavelength ranges, 3-5 and 8-12 μ m, which cover the atmosphere window where minimum absorption is present. The InSb infrared detector has significant application for the detection of 3-5 μ m radiation. This material has received increasing attention over the past few years. Epitaxial growth of InSb has been reported by LPE (1); however, there are several problems associated with the surface morphology. MBE growth of InSb (2) has been also recently reported; however, the electrical properties of the epitaxial layers have not been reported. Organometallic chemical vapor deposition (OM-CVD) is a potential technique for the epitaxial growth of InSb on large area substrates with surface morphology and electrical properties suitable for infrared focal plane arrays. Relatively little work has been reported on the growth of InSb and its alloys by OM-CVD. Manasevit (3) reported the growth of InSb on Al₂O₃ by OM-CVD with a room temperature mobility of 15,000 cm²/V-s and a carrier concentration of $(2-3) \times 10^{16}$ cm⁻³; however, no discussion of optimized growth parameters and the growth of epitaxial layers on InSb substrates has yet been reported.

InAs_{1-x}Sb_x with $x = 0.6$ has the lowest bandgap (\approx 0.1 eV) of the III-V compounds. This bandgap can be suitable for detectors in the 8-12 μ m wavelength region. InAs_{1-x}Sb_x epilayer growth by LPE is difficult because of the very wide separation of liquidus and solidus curves in the phase diagram (4). There have been several reports of OM-CVD growth of InAs_{1-x}Sb_x on InAs and insulating substrates (5, 6); however, poor surface morphology of the epitaxial layers has always been a problem especially for high value of x . We are not aware of any reported epitaxial growth of InAs_{1-x}Sb_x, with 0.5 $< x <$ 0.7, where the bandgap is about 0.1 eV.

In this paper, we report for the first time the epitaxial growth of InSb on InSb substrate by OM-CVD. Optimum growth conditions for mirror-like surfaces and the electrical properties of the epitaxial layers will be presented. Also, we report here the growth of InAs_{1-x}Sb_x on InSb and InAs substrates with mirror-like surfaces over the composition range 0 $< x \leq$ 0.75.

Experimental

Epitaxial layers were grown in a vertical quartz reactor (9.5 cm id and 30 cm long) using 300 kHz RF induction for heating the graphite susceptor. Triethylindium (TEI) (Alfa), trimethylantimony (TMS) (Alfa), and arsine (AsH₃) (5% in H₂, Matheson or Phoenix Research) were used as indium, antimony, and arsenic sources, respectively. Palladium-diffused H₂ was used as the carrier gas at a nominal flow rate of 3.6 l/min. Substrates included (100), (111)-B InSb, and (100) 2° toward [110] InAs and Cr-doped semi-insulating GaAs.

Both InSb and GaAs substrates were prepared by cleaning with TCE, acetone, and methanol. Final treatments included an 8:1 (lactic acid:HNO₃) etching for InSb, and a 7:1:1 (H₂SO₄:H₂O₂:H₂O) etching for GaAs substrates.

The deposition temperature for InSb was varied from 375° to 480°C. Both TEI and TMS flows were started when the substrate temperature reached the growth temperature for InSb deposition. No group V overpressure was maintained during the preheat.

InAs_{1-x}Sb_x growth on (100) InSb substrates showed mirror-like surface morphology with different III/V ratios. However, it had not shown satisfactory surface morphology on (111)-B InSb substrates; therefore, we concentrated our experiments on (100) InSb substrates.

Conventional van der Pauw method on clover leaf samples cut from the epitaxial layers grown on Cr-doped GaAs substrates was used with alloyed In contacts for the electrical characterization. X-ray diffraction was used for determining the solid composition of InSb in InAs_{1-x}Sb_x.

Results and Discussion

InSb.—The optimum growth conditions which produced the best surface morphology on both (100) and (111)-B InSb substrates are 460°C growth temperature with flow rates of 1.45×10^{-5} mol/min and 1.13×10^{-5} mol/min for TEI and TMS, respectively. Figure 1 shows the surface morphologies of InSb epi-layers grown on (100)- and (111)-B InSb substrates under optimum growth conditions. The best results were obtained with a slightly In-rich gas phase (TMS/TEI = 0.78 partial pressure ratio) similar to the OM-CVD growth of GaSb under Ga-rich gas phase done by Cooper *et al.* (7). This is different from most arsenic containing growth, such as GaAs, which are grown with a group V-rich gas phase. It is more difficult to grow GaAs because excess As is very volatile at the growth temperature for GaAs; therefore, it is easily separated from the binary during growth (8). However, In and Sb have a relatively low vapor pressure at growth temperatures less than 480°C. Excess In or Sb will deposit on the substrate and incorporate into the layer as In or Sb droplets.

Figure 2 shows that the growth rate is proportional to the TMS flow rate with a constant TEI flow rate and growth temperature. Growth rate varies from 0.01 to 0.043 $\mu\text{m}/\text{min}$ while maintaining good surface morphology.

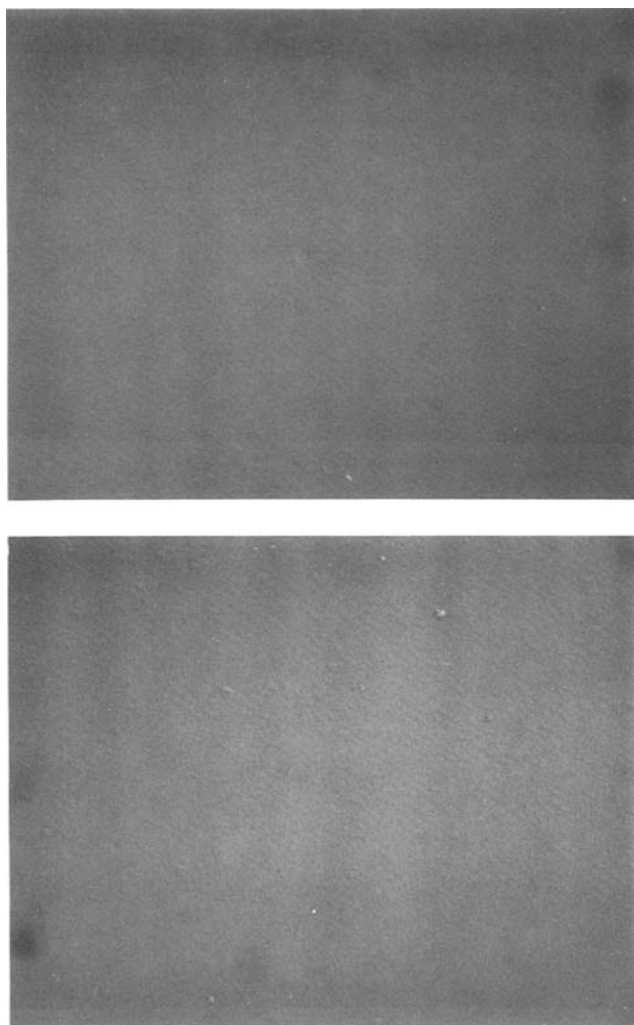


Fig. 1. Surface morphologies of InSb epilayers grown on two InSb substrate orientations. a (top): (100) InSb substrate (300 \times). b (bottom): (111)-B InSb substrate (300 \times).

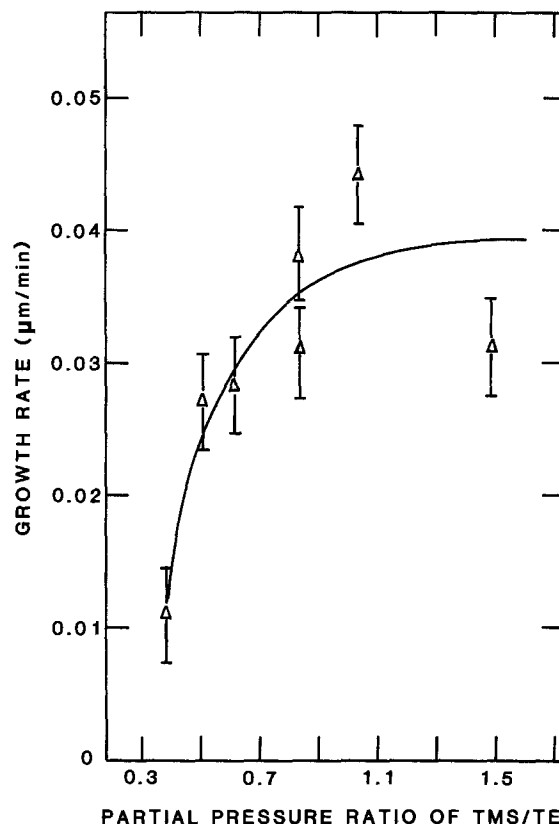


Fig. 2. Growth rate of InSb as a function of partial pressure ratio of TMS/TEI with TEI = 2.90×10^{-5} mol/min and growth temperature 450°C.

This growth rate of 2.5 $\mu\text{m}/\text{h}$ makes OM-CVD a very practical method for the epitaxial growth of InSb.

The dependence of growth rate on growth temperature with constant TMS/TEI partial pressure ratio is shown in Fig. 3. Both higher growth rate and better surface morphology have been obtained at a high growth temperature. At growth temperatures above 480°C, local melting of the InSb substrate was observed (InSb mp = 525°C). In addition, there was no growth when temperature was decreased to 375°C, probably owing to the insufficient dissociation of the OM sources. Because of the lack of available InSb semi-insulating substrates, we used GaAs (100) 2° toward [110] Cr-doped semi-insulating substrates to study the electrical properties of the InSb epilayer. It could be estimated (9) that there exists 10^{14} cm^{-2} dislocation density at the interface between the InSb epilayer and the (100) GaAs substrate due to their 14% lattice mismatch. The InSb epilayers grown on GaAs were shown to be single crystal by x-ray diffraction, however, with poor surface morphology. Figure 4 shows the room temperature electron mobility *vs.* the partial pressure ratio of TMS/TEI with constant TEI flow rate at two different growth temperatures. All samples show n-type conductivity at partial pressure ratios of TMS/TEI from 0.4 to 1.5. At room temperature, carrier concentrations in the range 2×10^{16} to $8 \times 10^{16} \text{ cm}^{-3}$ have been obtained. This range is close to what can be achieved since at room temperature the intrinsic carrier concentrations for InSb, n_i , is about $2 \times 10^{16} \text{ cm}^{-3}$. At liquid nitrogen temperature, the lowest measured carrier concentration is about $1 \times 10^{15} \text{ cm}^{-3}$. This indicates the presence of N_D-N_A background impurity of the order of magnitude 10^{15} cm^{-3} since n_i for InSb at liquid nitrogen temperature is in the 10^9 cm^{-3} range. We have not yet identified the nature and sources of these impurities.

Our best room temperature electron mobility is 40,000 $\text{cm}^2/\text{V}\cdot\text{s}$ at a carrier concentration of $N_D-N_A = 2.0 \times 10^{16} \text{ cm}^{-3}$ (thickness = 1 μm) grown at 400°C with a 2.9×10^{-5} and 2.47×10^{-5} mol/min flow rate of TEI and TMS, respectively. This result is comparable with what has been

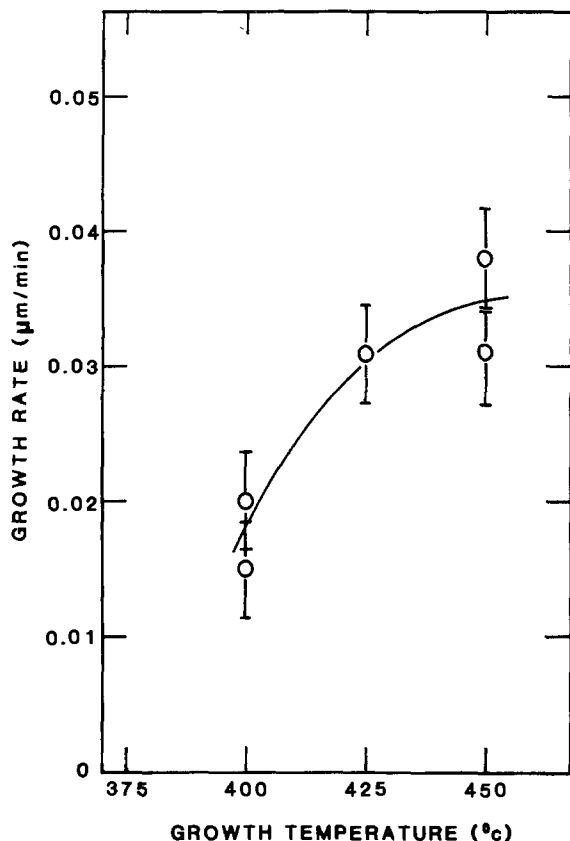


Fig. 3. Growth rate of InSb as a function of temperature with flow rate of TEI:TMS = 2.9×10^{-5} : 2.47×10^{-5} mol/min.

obtained using infinite solution liquid-phase epitaxy by Holmes and Kamath (1). They reported electron carrier

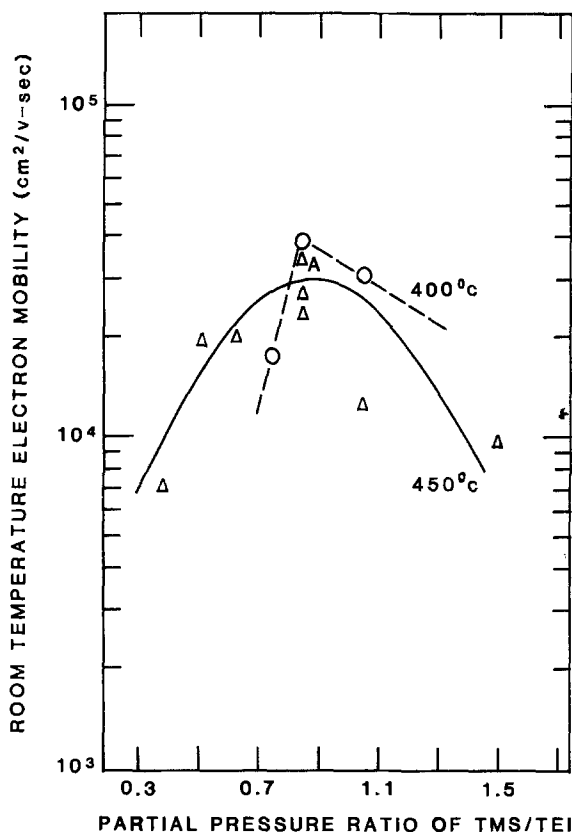


Fig. 4. Room temperature electron mobility of InSb as a function of TMS/TEI partial pressure ratio (flow rate of TEI fixed at 2.9×10^{-5} mol/min) at growth temperatures 400°C (O) and 450°C (Δ). The thickness of all the samples are 1-2 μm except sample A ($\approx 4 \mu\text{m}$). Substrates are (100) GaAs Cr-doped semi-insulators.

concentrations and mobilities for 20 μm thick InSb epilayers ranging from 2 to $4 \times 10^{16} \text{ cm}^{-3}$ and from 5 to $6 \times 10^4 \text{ cm}^2/\text{V-s}$, respectively. In Fig. 4, we also find that the electron mobilities increase from 25,000 $\text{cm}^2/\text{V-s}$ for a 2 μm thick epilayer to 35,000 $\text{cm}^2/\text{V-s}$ for a 4 μm thick epilayer, which were grown at the same growth conditions. This indicated that mobility is dependent on the thickness of the epilayer as has been previously observed in the OM-CVD growth of GaAs (10). Figure 5 shows the temperature dependence of the electron mobility. The electron mobility tends towards a maximum value in the vicinity of 300 K and decreases monotonically with increasing temperature. This result is similar to that reported by Wieder's study of dendritic films of InSb (11). Such mobility temperature dependence can be partially explained to be a result of the presence of high dislocation density in the InSb epilayer on GaAs substrates. Ehrenreich (12) has shown that lattice scattering dominates above 200 K and has a temperature dependence of the electron mobility $\mu \propto T^{-1.7}$. In addition, Dexter and Seitz (13) have indicated that the density of dislocations, N , necessary to give dislocation scattering at temperature T equal to the lattice scattering is $N = 6 \times 10^4 T^{5/2} \text{ cm}^{-2}$ which is $\approx 10^{11} \text{ cm}^{-2}$ at 300 K. Since there exists 10^{14} cm^{-2} dislocation density at the interface between InSb epilayer and (100) GaAs substrate, dislocation scattering has to be considered as well as impurity and lattice scattering effects. Dexter and Seitz also indicated that dislocation scattering effect increases with decreasing temperature. The reciprocal mobility can be described as

$$\frac{1}{\mu} = \frac{1}{\mu_i} + \frac{1}{\mu_l} + \frac{1}{\mu_d} \quad [1]$$

where μ , μ_i , μ_l , and μ_d represent the experimentally measured mobility, impurity scattering mobility, lattice scattering mobility, and dislocation scattering mobility, respectively. From Putley's paper (14), we estimated that the impurity scattering mobility, at carrier concentration,

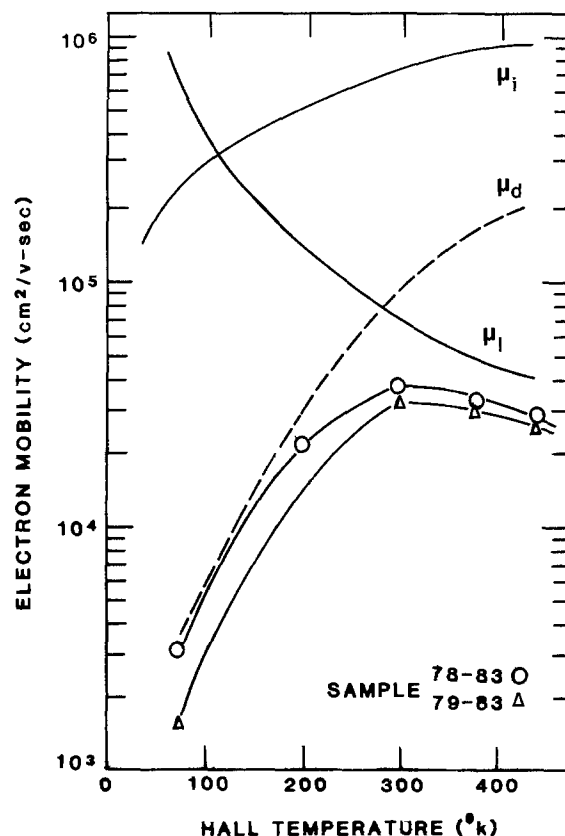


Fig. 5. Temperature dependence of the InSb electron mobility. The measured values of μ were used in conjunction with lattice scattering mobility μ_l and impurity scattering mobility μ_i to determine the dislocation scattering mobility μ_d .

$n = 10^{16} \text{ cm}^{-3}$, $\mu_i \approx 1.1 \times 10^4 T^{0.73}$. For the two curves shown in Fig. 5, the measured values of μ were used in conjunction with $\mu_i = 1.1 \times 10^4 T^{0.73}$ and $\mu_i = 1.09 \times 10^9 T^{-1.68}$ (11) to determine μ_d as a function of temperature by means of Eq. [1]. The results indicate that μ_d increases linearly with temperature. Thus, Eq. [1] can be expressed as

$$\frac{1}{\mu} = \frac{T^{-0.73}}{1.1 \times 10^4} + \frac{T^{1.68}}{1.09 \times 10^9} + \frac{1}{\mu_d}$$

letting $\mu_d = \beta T$ where β is constant ($\approx 330 \text{ cm}^2/\text{V}\cdot\text{s/K}$).

This result shows that the Dexter-Seitz's dislocation scattering mechanism represents the mobility limiting process. Finally, we believe that much higher mobility can be achieved both at 77 and 300 K if InSb is grown on a lattice matched semi-insulator such as CdTe.

InAs_{1-x}Sb_x-InAs_{1-x}Sb_x ternary layers have been grown in the composition range of $0 < x \leq 0.75$ on (100) InSb substrates, with mirror-like surface morphologies. The variations of the solid composition at growth temperature of 460°C with constant TEI and AsH₃ flow rates is shown in Fig. 6. As shown in this figure, the mole percent of InSb in the solid phase cannot be increased substantially upon further increase in TMS flow rates. Values of x higher than 0.6 can be achieved by decreasing the mole fraction of AsH₃ in the gas phase. This has also been observed in the case of OM-CVD growth of GaAs_{1-x}Sb_x, where reducing the AsH₃ partial pressure was found to be more effective in obtaining higher GaSb in the solid phase than increasing the TMS partial pressure as being reported by Bedair *et al.* (15). Data shown in Fig. 6, however, are obtained for the minimum AsH₃ partial pressure that can be obtained from our OM-CVD system. Another way to increase the value of x is to decrease the growth temperature and to increase the TEI flow rate. Figure 7 shows the dependence of the InSb percent in the solid phase on the TEI flow rate at two different growth temperatures. As shown in this figure, growth at 440°C resulted in higher values of x than that at 460°C for

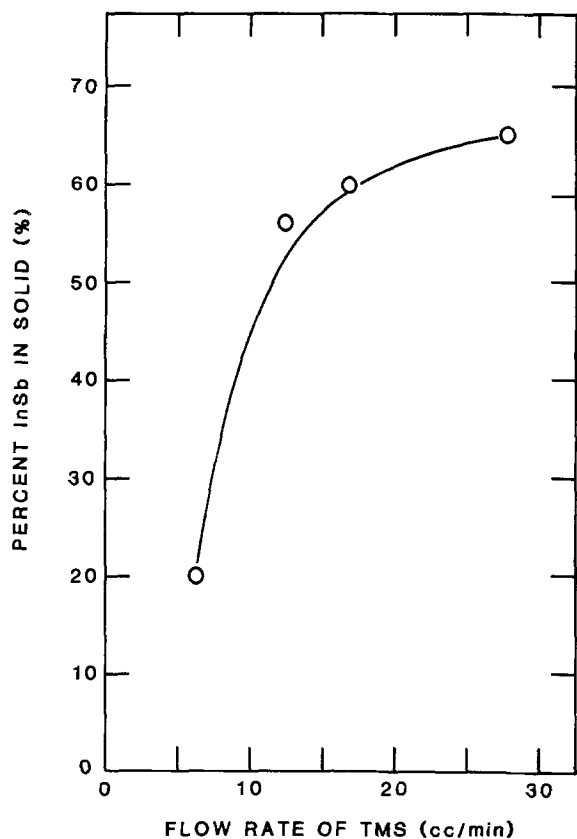


Fig. 6. Mole percent of InSb in the InAsSb epilayer as a function of the flow rate of TMS with the flow rate of TEI:AsH₃ = 2.03×10^{-5} : 1.22×10^{-5} mol/min at growth temperature 460°C using (100) InSb substrates.

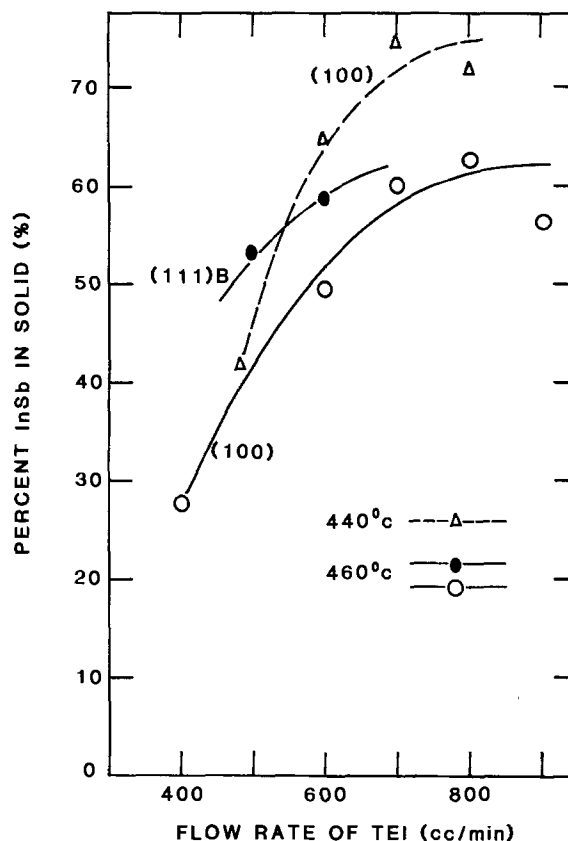


Fig. 7. Mole percent of InSb in the InAsSb epilayer as a function of the flow rate of TEI with the flow rate of TMS:AsH₃ = 2.96×10^{-5} : 1.22×10^{-5} mol/min at growth temperature 460°C using (100) InSb (-o-o-) and (111)-B InSb (-•-•-) substrates. This figure also shows the mole percent of InSb in the InAsSb epilayer as a function of the flow rate of TEI with the flow rate of TMS:AsH₃ = 2.96×10^{-5} : 1.22×10^{-5} mol/min grown on (100) InSb substrates at two different growth temperatures, 460°C (-o-o-) and 440°C (-Δ-Δ-).

the same flow rate of reacting gases. A possible explanation is that AsH₃ dissociates more efficiently at higher temperatures and As is preferentially incorporated into the crystal over Sb (7). Under this circumstance, lower InSb percent in the solid phase was obtained at higher temperatures. In this figure, we also show the dependence of the solid composition on the substrate orientations. With each substrate orientation, the InSb percent in solid phase is proportional to the flow rate of TEI. The growth on (111)-B InSb substrates has a higher percent of InSb in the solid composition as compared to the growth on (100) InSb substrates. This result may indicate that the growth is controlled by surface reaction kinetics rather than by mass transport.

Finally, we had grown InAs_{1-x}Sb_x with $x = 0.63$ on (100) 2° toward [110] InAs substrates at growth temperature 460°C with very good surface morphology. This InSb percentage in the solid is higher than what had been previously achieved on InAs substrates by OM-CVD (5, 6). However, further study of the growth on InAs substrates has not been done yet.

Conclusion

OM-CVD epitaxial growth of high quality InSb has been demonstrated. This was achieved by careful control of growth temperature and the TMS/TEI partial pressure ratio. A room temperature mobility of 40,000 cm²/V·s has been measured even with 14% lattice mismatch between the InSb epilayer and GaAs substrate. Dislocation scattering mechanism has been used to explain the variations of mobility with temperature.

InAs_{1-x}Sb_x growth on (100) InSb substrates has been obtained from 7% to 75% InSb in the solid phase with good surface morphologies. The dependence of the InSb percent in the solid phase on growth temperature and gas

partial pressures can be explained by preferential incorporation of As over Sb. In addition, the variation of the InSb percent in the solid phase as a function of substrate orientation was studied. Thus OM-CVD technique can be a potential technique of the epitaxial growth of InSb and $\text{InAs}_{1-x}\text{Sb}_x$ for infrared focal plane arrays covering the 3-5 and 8-12 μm ranges.

Acknowledgments

This work was supported by NASA and Army Office of Research. The authors would like to thank Dr. J. R. Hauser, R. Sillmon, T. Katsuyama, R. J. Markunas, Cherie Winston, and J. H. Wang for their fruitful discussions and help.

Manuscript submitted Nov. 17, 1983; revised manuscript received May 29, 1984.

North Carolina University assisted in meeting the publication costs of this article.

REFERENCES

1. D. E. Holmes and G. S. Kamath, *J. Electron. Mater.*, **9**, 95 (1980).
2. A. J. Noreika, M. H. Francombe, and C. E. C. Wood, *J. Appl. Phys.*, **52**, 7416 (1981).
3. H. M. Manasevit, *J. Cryst. Growth*, **55**, 1 (1981).
4. G. B. Stringfellow and P. E. Greene, *This Journal*, **118**, 805 (1971).
5. T. Fukui and Y. Horikoshi, *Jpn. J. Appl. Phys.*, **19**, L53 (1980).
6. G. Nataf and C. Verie, *J. Cryst. Growth*, **55**, 87 (1981).
7. C. B. Cooper III, R. R. Saxema, and M. J. Ludowise, *Electron. Mater.*, **11**, 1001 (1982).
8. H. M. Manasevit and K. L. Hess, *This Journal*, **126**, 2031 (1979).
9. D. B. Holt, *J. Phys. Chem. Solids*, **27**, 1053 (1966).
10. P. D. Dapkus, H. M. Manasevit, and K. L. Hess, *J. Cryst. Growth*, **55**, 10 (1981).
11. H. H. Wieder, *Solid State Electron.*, **9**, 373 (1966).
12. H. J. Ehrenreich, *Phys. Chem. Solids*, **2**, 131 (1957).
13. D. L. Dexter and F. Seitz, *Phys. Rev.*, **86**, 964 (1952).
14. E. H. Putley, *Proc. Phys. Soc.*, **73**, 280 (1959).
15. S. M. Bedair, M. L. Timmons, P. K. Chiang, L. Simpson, and J. R. Hauser, *J. Electron. Mater.*, **12**, 959 (1983).

Low Resistivity Thin Film Refractory Silicides Grown in Ultrahigh Vacuum at Low Temperature

R. Pantel, Y. Campidelli, and F. Arnaud d'Avitaya

Centre National d'Etudes des Télécommunications, 38243 Meylan Cedex, France

ABSTRACT

Refractory metal silicides, MoSi_2 and WSi_2 , have been grown successfully on (100) silicon wafers in ultrahigh vacuum. It is demonstrated that an MBE-like growth technique, *i.e.*, metal evaporation on a clean heated monocrystal, yields device-worthy thin film silicides of excellent electrical conductivity. For silicide films from 50 to 150 nm thick and substrate temperatures ranging from 750° to 900°C, resistivities as low as 65 $\mu\Omega$ cm for MoSi_2 and 30 $\mu\Omega$ cm for WSi_2 are obtained. Similar resistivities for cosputtered silicides would require films 200–500 nm thick annealed at 1100°C for 30 min.

Refractory silicides have long been considered the most likely candidates for interconnections and electrical contacts in VLSI (1, 2). Molybdenum and tungsten silicides have attracted special attention because their metallurgical, chemical, and electrical properties are good and compatible with the usual fabrication processes. However, all the studies on molybdenum and tungsten have pointed out the difficulties inherent in obtaining silicides from them. The presence of impurities such as carbon and oxygen can hinder and even block the reaction between these metals and silicon (3-5). In addition, their mechanical properties seem to be responsible for the very rough surface of the silicides obtained via metal deposition and subsequent sintering with silicon. As a consequence, the only fabrication method used at present is codeposition of both metal and silicon. This technique leaves two major problems unsolved, however: poor resistivity when the silicides film is less than 150 nm thick and cracking when the thickness of the film exceeds 350 nm for tungsten and 500 nm for molybdenum (6). Moreover, such films require annealing at high temperatures (1000°–1100°C for 0.5-1h) to improve their resistivity.

In this paper, we present a process for the fabrication of thin film molybdenum and tungsten silicides which overcomes the above-mentioned drawbacks. The process consists in metal evaporation on a hot silicon substrate in ultrahigh vacuum. Films 30-150 nm thick were grown at temperatures between 600° and 800°C. The films, whether as grown or post-annealed at 900°C, are smooth, adhere well to the silicon substrate, and have low resistivities.

Experimental

The experiment was carried out in a Riber MBE 2300 ultrahigh vacuum (UHV) system. Silicon wafers are intro-

duced via a loading chamber at 2×10^{-10} torr base pressure. In the evaporation vessel after bakeout, the ultimate pressure of 5×10^{-11} torr is obtained by means of an ionic pump. The refractory metals are evaporated using a 2 kW electron gun. This gun is outgassed for several hours prior to metal deposition. During evaporation, pumping is speeded up by titanium sublimation and liquid nitrogen cooling of the condensation panels. The deposition rate is monitored by a quartz balance previously calibrated by other thickness measurement techniques (RBS and mechanical stylus).

The system is equipped with a low energy electron diffractometer (LEED) to check surface crystallinity and an Auger electron spectrometer for analysis of chemical composition. Oven and sample holder have been designed to heat 2 in. silicon wafers uniformly up to 1200°C without warpage. The temperature is measured by an optical pyrometer, and a thermocouple located at the back side of the wafer. Reproducible temperatures are obtained by using a stabilized power supply.

The substrates used in this experiment were 2 in. (100)-oriented p-type silicon wafers having a resistivity $> 10^8 \Omega$ cm. Before loading in the UHV system, the samples were chemically cleaned according to Shiraki's method (7) for preparing silicon wafers in molecular beam epitaxy (MBE). The most critical steps in such sample preparation are (i) removal of residual carbon by repetitive oxidation in boiling nitric acid followed by a HF dip, and (ii) growth of a very thin monoxide film which protects the surface of the wafer until its introduction into the vacuum chamber. Once the wafer has been loaded in the UHV system, this oxide layer is removed via a gradual temperature increase up to 750°C followed by a flash anneal at 950°C for 90s. When it has cooled down to room tempera-

ture, the surface is observed by LEED. The diffraction patterns show the sharp over structure (2×1) typical of a clean (100) Si surface. The absence of any contaminants, such as carbon or oxygen, is further checked by AES. The samples are now ready to receive the evaporated metal. The refractory source metals are 99.999% pure (Marz, MRC) molybdenum and tungsten ingots, which are outgassed at a temperature higher than their evaporation temperatures. Molybdenum and tungsten layers 15 nm to 60 nm thick were evaporated at 0.1 nm/s onto silicon substrates heated to a temperature of 650°–750°C in the case of molybdenum and 600°–800°C in the case of tungsten. The temperature elevation due to metal evaporation is calculated from the radiation power intercepted by the wafer and found to be approximately 50°C for molybdenum and 100°C for tungsten. Once the desired silicide thickness is attained, evaporation is stopped and the samples are allowed to cool.

The silicide films were subsequently observed *in situ* by AES. RBS measurements, SEM observations, and electrical measurements were also carried out. Finally, the films were annealed in forming gas at 900°C for one hour in a classical furnace (previously evacuated to 10^{-6} torr) to observe the evolution of their resistivities.

For comparison purpose, some evaporations were also made onto silicon substrates at room temperature and the silicides were formed by post-annealing *in situ* for 10 min at 650°C for molybdenum and 750°C for tungsten.

Results

Figure 1a shows the Auger spectrum of the cleaned silicon surface before metal deposition. Neither carbon nor oxygen was detected.

Figures 1b and 1c show typical Auger spectra of the surface obtained after deposition of molybdenum and

tungsten on hot silicon substrates (650° and 750°C, respectively). These spectra likewise exhibit an absence of contaminants and provide clear evidence of reaction of the metals with silicon. The Si/Mo and Si/W ratios of both silicides, however, suggest a surface composition rich in silicon. Previous studies have shown that silicides annealed in UHV are generally coated with a monolayer of silicon (8-9). Whatever that may be, all the molybdenum and tungsten silicides presented in this paper were found (by x-ray diffraction) to be pure disilicides.

Figures 2a and 2b show the corresponding typical RBS spectra. A simple calculation shows that the silicides are slightly silicon enriched ($\text{MoSi}_{2.1}$ and $\text{WSi}_{2.15}$). These profiles also suggest that the films are continuous and of uniform thickness: 70 nm for MoSi_2 and 150 nm for WSi_2 . This uniformity is confirmed by SEM observations. Figures 3a and 3c show the surfaces of MoSi_2 and WSi_2 films grown on hot substrate at 650° and 750°C, respectively. For comparison, we also present the SEM images of the above-mentioned silicides obtained by metal deposition on substrates at room temperature and subsequently annealed at 650° and 750°C for molybdenum and tungsten, respectively (Fig. 3b and 3d). This comparison gives evidence of the higher quality of the films obtained by the MBE-like method.

Figures 4a and 4b show the electrical resistivities of as-grown MoSi_2 and WSi_2 films for various temperatures in the 600°–800°C range. The evolution of resistivity after annealing at 900°C for 1h in forming gas is also reported. We note that the gain in resistivity is not significant for samples reacted at 750° and 800°C for MoSi_2 and WSi_2 films, respectively. The best result is around $65 \mu\Omega \text{ cm}$ for 58 nm thick MoSi_2 films and $30 \mu\Omega \text{ cm}$ for 150 nm thick WSi_2 films. The curve shown as a continuous line is from Denison (6), who has published the best resistivity

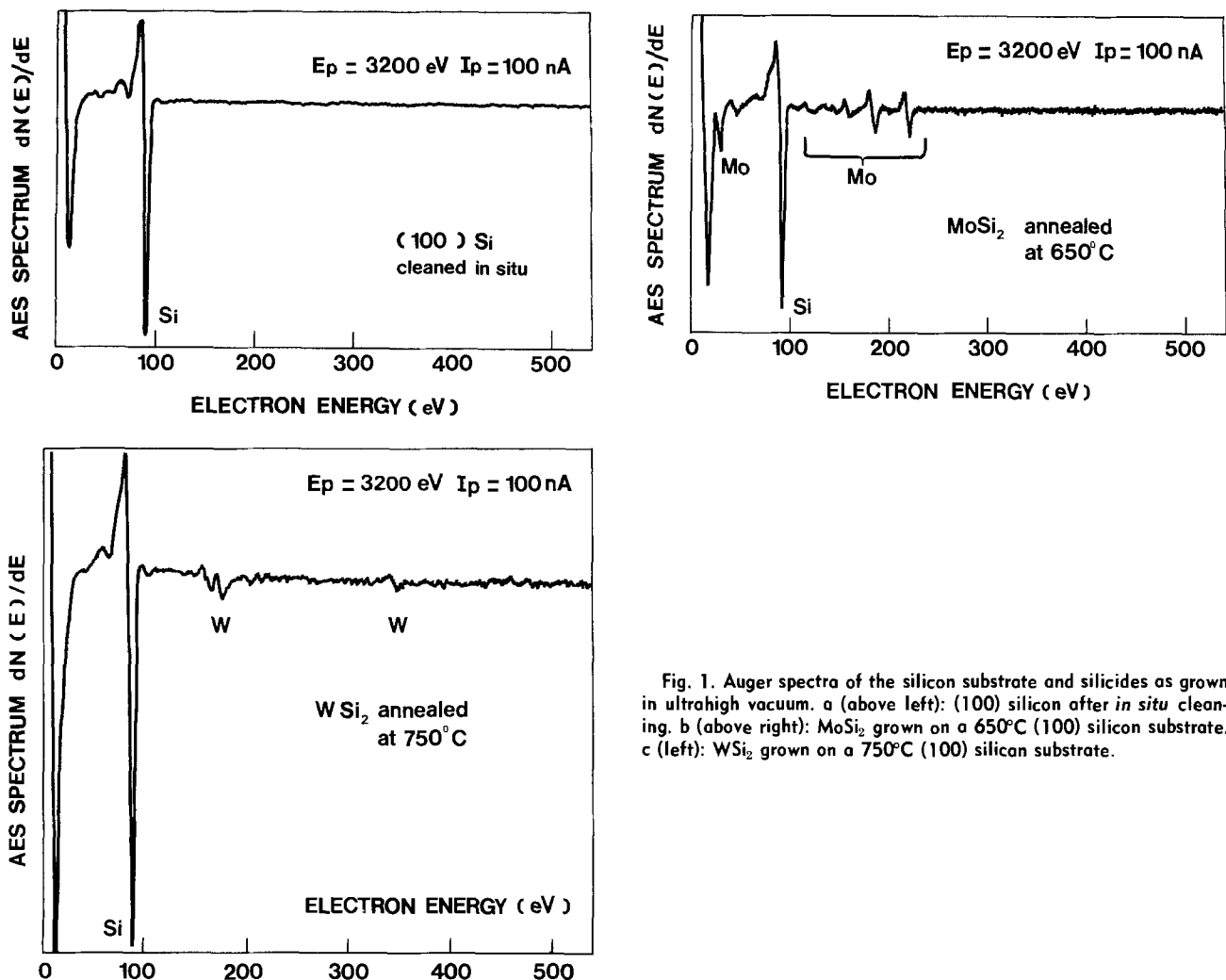


Fig. 1. Auger spectra of the silicon substrate and silicides as grown in ultrahigh vacuum. a (above left): (100) silicon after *in situ* cleaning. b (above right): MoSi_2 grown on a 650°C (100) silicon substrate. c (left): WSi_2 grown on a 750°C (100) silicon substrate.

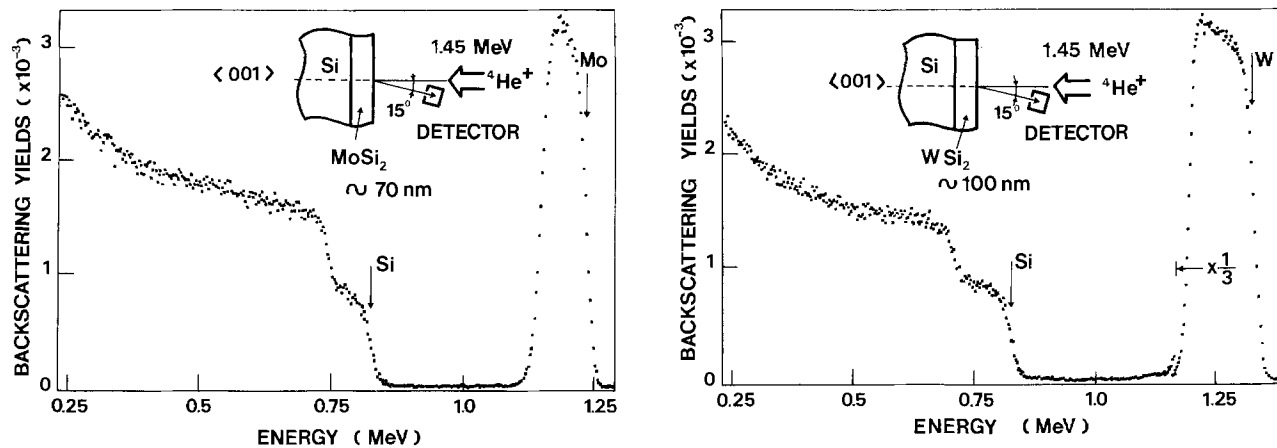


Fig. 2. Rutherford backscattering spectra of MoSi_2 and WSi_2 thin film silicides grown in ultrahigh vacuum on heated (100) silicon substrate. a (left): MoSi_2 on 650°C silicon. b (right): WSi_2 on 600°C silicon.

obtained to date on cosputtered films of MoSi_2 ($50 \mu\Omega$ cm) and WSi_2 ($26 \mu\Omega$ cm).

Discussion

The cleaning of silicon wafers under ultrahigh vacuum conditions has eliminated impurities both at the interface and in the silicide, as Auger analysis has shown. This absence of impurities explains the low temperature reaction

between silicon and the refractory metals. However, elimination of impurities is not the only determining factor for obtaining good, *i.e.*, smooth and continuous, thin silicide films. Actually, we reported earlier (4) that MoSi_2 thin films obtained by evaporation in ultrahigh vacuum on substrates at room temperature followed by a 950°C annealing leads to nodular discontinuous films. Since, in the present study, the substrate is kept at the actual tem-

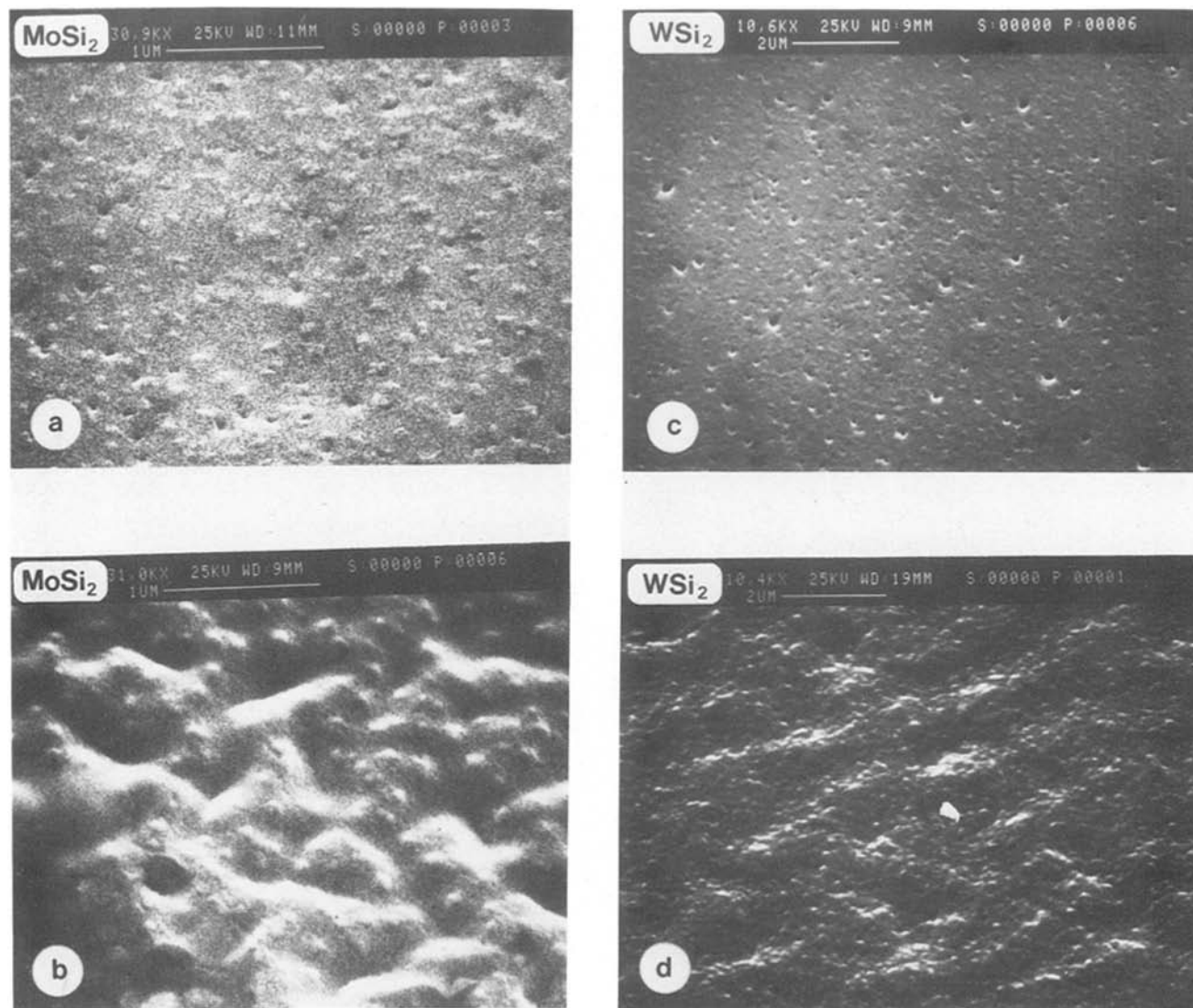


Fig. 3. SEM images of the surfaces of the silicides. All pictures were obtained at the same incidence angle of 45°. a: MoSi_2 grown on a 650°C silicon substrate. b: MoSi_2 grown by reacting a Mo film on silicon (650°C). c: WSi_2 grown on a 750°C silicon substrate. d: WSi_2 grown by reacting a W film on silicon (750°C).

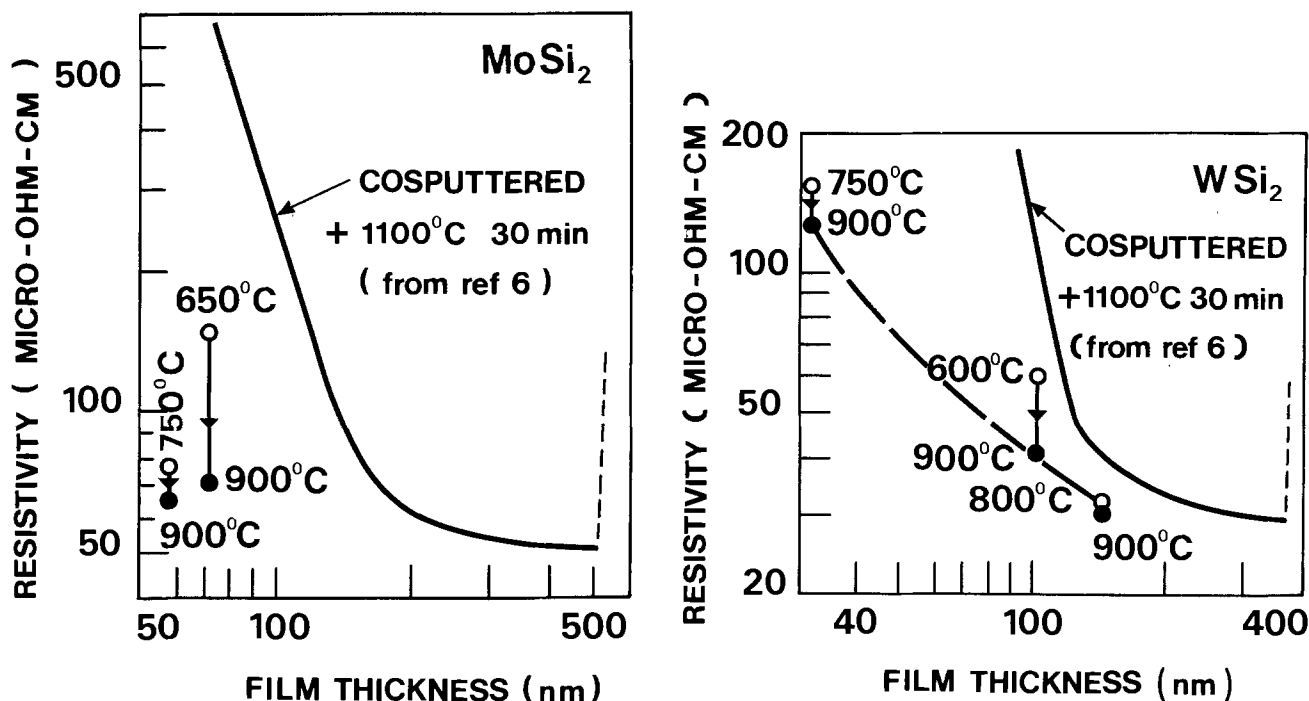


Fig. 4. Resistivities of thin film silicides grown in ultrahigh vacuum at various temperature (\circ), annealed at 900°C for 1h (\bullet). a (left): MoSi_2 . b (right): WSi_2 .

perature of silicide formation, one might almost say that the silicide grows as if one were depositing not only the refractory metal but the silicide compound. This process is not very far from equilibrium, and stresses are minimized. As shown by SEM, the result is a smooth surface. On the contrary, when metal is deposited on room temperature substrates and the silicide is formed by post thermal annealing, stresses due to temperature elevation and silicide formation are created. The result is quite rough surface.

The RBS profiles of the MBE-like-grown silicides show a continuous film with a silicon stoichiometry slightly greater than two, and Auger spectra indicate a silicon enrichment of the surface. These two characteristics ensure the stability of the silicide during thermal processing (oxidation and thermal annealing), especially if the silicides are to come in contact with silicon (polycide, self-aligned silicide). This is not the case for some metal-rich refractory thin films such as W_4Si or Mo_3Si , which have been found to be highly conductive (10-11) but incompatible with VLSI processing (11).

The stability of our silicides is also observed in the evolution of resistivity with thermal annealing. The films, with the exception of MoSi_2 grown at 650°C , are only slightly improved by 900°C treatment. In this particular case, it is known that a hexagonal-to-quadratic crystalline transition occurs around 700°C , and this may explain the improvement in resistivity we observed.

So far, the best resistivities for molybdenum and tungsten silicides have been obtained by Denison on cosputtered films. However, his films were treated at 1100°C for 30 min, and only the thick films (200–500 nm) exhibited good resistivities. Denison observed a drastic increase in resistivity when film thicknesses went below 150 nm. In fact, it has already been shown that the resistivity limitation of cosputtered WSi_2 films is due to grain boundary scattering (12), which may be caused by segregation of impurities. Thus, the only way to improve the resistivity of cosputtered films is via an increase in grain size, and for that purpose a 1100°C anneal is necessary. However, where very thin films are concerned, grain size cannot be increased beyond that of the film thickness; otherwise, the film will become discontinuous resulting in poor conductivity.

In the case of our UHV-grown films, one does not observe a drastic limitation of resistivity for slight thick-

nesses. TEM observation shows grains of uniform dimensions (around 50 nm) arranged in a mosaic which minimizes the total surface of boundaries. The layers are free of impurities. This explains the good resistivities as well as the thermal stability since grain size is not significantly modified by annealing at 900°C .

It has been reported in the literature that impurities induce surface topography effects (3, 13) when thin film silicides are grown by reaction of metal with a silicon substrate. This explains the quite smooth surfaces we have obtained, the best silicides being those grown on hot substrates. This would indicate that stress is also a factor which creates rough surfaces.

UHV silicides also exhibit good adhesion. This is due to the reaction of metal with the silicon substrate which ensures effective silicide-silicon interface bonding. On the contrary, cracking of thick cosputtered films during thermal annealing has been reported (6). Indeed, those films grown without reaction with the substrate are insufficiently bound.

Conclusion

The first important result of working in UHV and following a special procedure for cleaning wafers has been the elimination of impurities. This is, of course, conducive to low temperature reactions of metal with silicon and leads to pure silicides. By contrast, we have shown that if the silicides are formed via metal evaporation and post annealing, the films present serious limitations (surface roughness, among others). A significant improvement has been made by choosing a MBE-like growth technique involving a thermally assisted reaction during a slow rate evaporation of the refractory metal. The good quality of the films obtained in this way confirms that impurities and stresses were the causes of problems previously encountered when reacting a metallic film with silicon.

The method is versatile and still further improvements in such silicide films can be expected by adjustment of growth conditions. Experiments are now in progress to explain the high conductivities, which are in all likelihood due to the particular crystallographic properties of the films.

We feel that the results presented here make these silicides very attractive for the technological process involved in VLSI and particularly for the purpose of self-aligned silicide devices. This technique consists in

selective deposition of the silicides on sources, drains, and gates of MOS transistors (14) and involves very thin layers of silicides, low temperature annealing, and the lowest possible resistivities. The thin film silicides we have presented in this paper quite satisfy these criteria.

Acknowledgments

Thanks are due to G. Jacob, D. Bois, and M. Brillouet for stimulating discussions. We also thank J. Torres for x-ray diffraction experiments and J. C. Oberlin for RBS measurements.

Manuscript received March 7, 1984.

Centre National d'Etudes des Télécommunications assisted in meeting the publication costs of this article.

REFERENCES

1. S. P. Murarka, *J. Vac. Sci. Technol.*, **17**, 775 (1980).
2. F. Mohammadi, *Solid State Technol.*, **1**, 65 (1981).
3. L. D. Locker and C. D. Capio, *J. Appl. Phys.*, **44**, 4366 (1973).
4. F. Arnaud d'Avitaya, G. Bomchil, and C. Arena, *This Journal*, **130**, 637 (1983).

5. F. Nava, G. Najni, P. Cantoni, G. Pignatelli, G. Ferla, P. Cappeletti, and F. Mori, *Thin Solid Films*, **94**, 59 (1982).
6. D. R. Denison, *J. Electron. Mater.*, **11**, 1023 (1982).
7. A. Ishizaka, K. Nakagawa, and Y. Shiraki, Collected papers of 2nd International Symposium on Molecular Beam Epitaxy and Related Surfaces Techniques, p. 183, The Japan Society of Applied Physics, Tokyo, Japan, August 27-30 (1982).
8. K. Oura, S. Okada, and T. Hanawa, *Appl. Phys. Lett.*, **35**, 705 (1979).
9. J. Küppers and A. Rodriguez Gonzales Elipe, in "Proceedings of the Fifth International Conference on Solid Surfaces," p. 32 Madrid, Spain, Sept. 26-30 (1983).
10. E. M. King and K. E. Osteiger, *J. Vac. Sci. Technol. A.*, **1**, 614 (1983).
11. F. Neppi, G. Menzel, and U. Schwabe, *This Journal*, **130**, 1174 (1983).
12. D. R. Campbell, S. Mader, and W. K. Chu, *Thin Solid Films*, **93**, 341 (1982).
13. C. A. Crider, J. M. Poate, J. E. Rowe, and T. T. Sheng, *J. Appl. Phys.*, **52**, 2860 (1981).
14. C. K. Lau, Y. C. See, D. B. Scott, J. M. Bridges, S. M. Perma, and R. D. Davies, in "IEDM 82 (IEEE Conference)," p. 714, IEEE, New York (1982).

Plasma-Enhanced Chemical Vapor Deposition of Silicon Epitaxial Layers

R. Reif*

Department of Electrical Engineering and Computer Science, Massachusetts Institute of Technology, Cambridge, Massachusetts 02139

ABSTRACT

Silicon epitaxial layers are conventionally deposited by atmospheric or reduced pressure chemical vapor deposition (CVD) at temperatures of 1050°-1200°C. This relatively high processing temperature limits the minimum thickness and conductivity of epitaxial films deposited on substrates containing heavily doped regions near the surface because of solid-state outdiffusion and autodoping. In order to minimize outdiffusion and autodoping, the epitaxial process step needs to be carried out at lower temperatures. Plasma-enhanced CVD (PECVD) is a technique capable of depositing silicon epitaxial layers at relatively low temperatures (700°-800°C) and with reasonable deposition rates (200-2000 Å/min). This article discusses the PECVD process and its application to the low temperature deposition of silicon epitaxial films.

Silicon epitaxy is an important processing step in the implementation of several integrated circuit technologies such as bipolar, CMOS, and VMOS (1), as well as many memory (2), microwave, and photonic devices (3). The preferred technique for the fabrication of silicon epitaxial layers is chemical vapor deposition (CVD), which is conventionally carried out at atmospheric or reduced (40-100 torr) pressure, and at temperatures of 1050°-1200°C.

An important drawback of the conventional CVD technique is the relatively high processing temperature (1050°-1200°C) required for silicon epitaxial growth. This high temperature causes significant dopant redistribution near the film-substrate interface (4). This dopant redistribution limits the minimum thickness and conductivity of lightly doped films deposited on substrates containing heavily doped regions near the surface. Consequently, it imposes restrictions on the level of on-chip integration that can be achieved by active down scaling, *i.e.*, by scaling down lateral and vertical device dimensions. It is for this reason that alternative epitaxial deposition techniques which minimize this undesired dopant movement during the epitaxial process are desirable.

The CVD of silicon epitaxial layers requires two high-temperature processing steps: (i) a predeposition *in situ* cleaning of the wafer surface, which is usually carried out at a temperature of 1150°-1200°C in a H₂ or HCl/H₂ ambient. This step is needed to remove the native silicon dioxide film and any other undesired film or contaminants from the wafer surface, and (ii) the actual deposition step,

which is normally carried out at a temperature of 1050°-1200°C, depending on the silicon source used.

The high predeposition temperature releases dopant atoms from the wafer surface by evaporation, and these dopant atoms are later incorporated in the epitaxial layer during growth. Such unintentional doping of the epitaxial film is usually referred to as autodoping (5). In addition, the high deposition temperature causes further dopant movement because of solid-state outdiffusion. Both autodoping and outdiffusion are responsible for the undesired redistribution of impurities commonly associated with silicon epitaxy by CVD.

In order to minimize autodoping, the predeposition cleaning step must be carried out at lower temperatures to limit impurity evaporation, and/or lower pressures to quickly remove from the system any evaporated impurities. In order to minimize solid-state outdiffusion, the epitaxial deposition step must be carried out at lower temperatures. Several techniques have been proposed as possible low temperature, low pressure alternatives for the silicon epitaxial process: molecular beam epitaxy (MBE) (6), ion cluster beam deposition (7), ion beam epitaxy (8), and plasma-enhanced CVD (PECVD) (9-14). One potential advantage of PECVD is that it requires low (0.01-1 torr) pressures for operation, while all the other beam-related techniques need high vacuums. Consequently, PECVD appears more compatible with manufacturing requirements, *i.e.*, easy operation and maintenance and high wafer throughput.

This article reviews the PECVD of epitaxial silicon. The physics and chemistry of the PECVD process are briefly

*Electrochemical Society Active Member.

discussed in the next section. Following this, the most important advances in the PECVD of silicon epitaxy are reviewed.

Plasma-Enhanced Chemical Vapor Deposition

Glow discharge.—A simple model of a glow discharge consists of a partially ionized gas containing equal volume densities of positive and negative charged species (mostly ions and electrons, respectively) and different volume densities of ground-state and excited species (15, 16). Most of the glow discharges used in microelectronics are generated by the application of a radio frequency (RF) electric field to a gas. The energy from the field accelerates free electrons in the gas, while the ions are relatively unaffected because of their much heavier mass. The accelerated electrons lose little energy in elastic collisions with atoms or molecules because of the large difference in mass, and initially lose little energy in inelastic collisions (*e.g.*, excitation and ionization). Once these electrons acquire sufficiently high energies, their collisions with gas species lead to excitations and ionizations, the latter generating additional electrons which are, in turn, accelerated by the RF field. In steady state, the glow gains electrons from ionizations and other mechanisms (*e.g.*, electron emission from positive ion bombardment on the electrodes and other surfaces within the chamber), and loses a numerically equal number of electrons and ions to the electrodes and walls.

The inelastic collisions between high energy electrons (which obtained their energy from the applied electric field) and gas molecules produce highly reactive species such as excited neutrals and free radicals, besides more electrons and ions. In this manner, the applied electric field supplies the energy used to create highly reactive species without significantly raising the gas temperature. PECVD uses these reactive species to deposit thin films (16) (*e.g.*, silicon nitride, silicon dioxide, amorphous silicon, and polycrystalline silicon) at temperatures lower than those possible by thermally activated CVD. In addition, the energy from the RF field might also be used to modify the structure, stoichiometry, and other properties of the deposited films. This can be done by controlling the bombardment of ions into the substrate surface; the importance of ion bombardment is discussed below.

The glow discharges currently used in microelectronics are relatively low pressure (0.1-1 torr) plasmas. The plasma density (*i.e.*, density of free electrons and ions) is typically about $10^{19}/\text{cm}^3$. The degree of ionization is typically $\leq 10^{-4}$, *i.e.*, the gas consists mostly of neutrals. The Maxwell-Boltzmann distribution is usually used to approximate the energy distribution of free electrons in the glow, with the fastest electrons having energies as high as 10-30 eV (17). These high energy electrons are responsible for excitation and ionization, since the corresponding threshold energies are typically ≥ 10 eV (*e.g.*, the threshold energies for excitation and ionization are 11.56 and 15.8 eV, respectively, for argon). In a typical room temperature glow discharge environment, the ground-state species in the gas may have energies corresponding to temperatures slightly above 300 K, the excited species and ions may have energies corresponding to 400 K up to thousands of degrees Kelvin, and the free electrons may have energies corresponding to 10^4 - 10^5 K. Consequently, the glow discharge environment is not in thermal equilibrium, and thermodynamics cannot be used to predict the outcome of a plasma deposition experiment.

Potentials in RF glow discharges.—Several potentials are important in the RF glow discharges used in microelectronics: the plasma potential, the floating potential, and the sheath potentials. The plasma potential (V_p) is the potential of the glow region of the plasma, which is normally considered nearly equipotential. It is the most positive potential in the chamber and is the reference potential for the glow discharge. The floating potential (V_f) is the potential at which equal fluxes of negative- and positive-charged species arrive at an electrically floating

surface in contact with the plasma. If the chamber walls are electrically insulated, $q(V_p - V_f)$ is the maximum energy with which positive ions bombard the walls, where q is the unit electron charge (18). Most sputtering threshold energies are 20-40 eV (15). Therefore, $V_p - V_f \leq 20$ -40 eV is normally desired to avoid sputtering walls, which may lead to film contamination.

As mentioned above, the plasma potential is always positive with respect to all surfaces in contact with the plasma. This is because the electron mobility in the plasma is much greater than the ion mobility and, consequently, the initial electron flux to all surfaces is always greater than the ion flux. As a result, the surfaces in contact with the plasma become negatively charged, and a positive space charge layer or sheath forms near these surfaces. Because there are fewer electrons in the sheath, fewer atoms are excited by electron collisions, and fewer atoms relax to give off radiation. Consequently, the sheath region is dark relative to the glow region. The sheath regions extract positive ions from the glow region and accelerate them into the electrodes and other surfaces in contact with the plasma. Similarly, the sheath regions accelerate secondary electrons emitted from surfaces (*e.g.*, due to positive ion bombardment) into the glow region. Therefore, the sheath voltages are very important because they determine the maximum energy with which positive ions bombard the electrodes, and help estimate the maximum energy with which secondary electrons emitted from electrodes enter the glow region. It can be shown that in an asymmetric plasma system with a "blocking" capacitor, the ratio of the sheath voltages is proportional to the reciprocal of the ratio of their corresponding electrode areas (19-21). If the blocking capacitor is absent or the plasma system is symmetric, then the sheath voltages at each electrode are the same.

Qualitative model.—A qualitative model for PECVD now becomes apparent. Inelastic collisions between high energy electrons in the plasma and gas-phase reactants help establish a steady-state population of highly reactive species. The rate of these inelastic collisions is a function of the reactant partial pressure, the collision cross section (which is energy dependent), and the electron energy distribution (15-17). The latter is a function of plasma power and system pressure (17). The glow discharge also acts as a source of positively charged species, mostly ions. The highly reactive species in the glow have a relatively high sticking coefficient and adsorb readily on the substrate surface (16). These reactants, once adsorbed, and because of their relatively weak internal binding, are easily broken down by the thermal energy provided by the substrate into their constituent atoms yielding a solid film. This surface decomposition reaction is enhanced by positive ion bombardment on the substrate surface.

Ion bombardment not only affects deposition rates, but also the structure, composition, and other properties of the film (22). Furthermore, ion bombardment is particularly important when the glow discharge is used to enhance the deposition of crystalline films. On one hand, it can be used to clean substrate surfaces by sputtering contaminants, including native oxides (this feature is important in silicon epitaxy). But, ion bombardment can also be used to create adsorption sites [thereby reducing the distance the average adatoms must travel (23)], and to enhance adatom surface mobility (24).

PECVD of Epitaxial Silicon

Table I summarizes the results obtained by researchers in this field (9-14).

Townsend and Uddin (9) carried out their work in a conventional horizontal water-cooled reactor. An RF generator was used to inductively heat the silicon carbide-coated susceptor, and a 350W, 27 MHz generator was used to create a glow discharge. The 27 MHz generator was connected to a pair of external aluminum ring electrodes. The silicon source used was 1% silane in pure hydrogen.

Table I. Summary of results for the PECVD of silicon epitaxy

Authors	Deposition temp (°C)	Deposition rate (Å/min)	Discharge power (W)	Gas ambient	Operating pressure (torr)
Townsend and Uddin (9)	800-900	200-400	350 (27 MHz)	SiH ₄ /H ₂	0.2-0.6
Pons <i>et al.</i> (11)	760	600	500 (13.56 MHz)	SiH ₄	0.03-0.1
Shanfield and Reif (12)	750-900	200-400	25 (dc)	SiH ₄ /H ₂	0.02
Suzuki and Itoh (13)	600-850	1200-2400	200 (13.56 MHz)	GeH ₄ /SiH ₄	1×10^{-2} - 3×10^{-2}
Donahue <i>et al.</i> (14)	775	450	20 (13.56 MHz)	SiH ₄	1.5×10^{-2}

The operating pressure was 0.2-0.6 torr. A hydrogen glow discharge was established immediately before the start of the plasma enhanced deposition step and maintained for a few minutes to clean the substrate surface. This pre-deposition clean-up was found to give epitaxial layers of very high surface quality. When the deposition was not carried out in the presence of a glow discharge, the pre-deposition clean-up consisted of a 30 min hydrogen treatment at 1100°C. Layers deposited at 850°C without plasma enhancement (*i.e.*, with the 27 MHz generator turned off) were single crystal but contained about 200 stacking faults/cm². The stacking fault density decreased with increasing deposition temperature. The authors reported that all attempts to deposit epitaxial silicon without plasma enhancement at temperatures below 850°C were unsuccessful. When the glow discharge was used, however, the layers deposited at 800°C and above were epitaxial. The deposition rate at 800°C was about 200Å/min. The deposition rates obtained with and without the aid of the glow discharge were similar, *i.e.*, these authors did not find evidence of plasma enhancement in the deposition rate. [As is shown below, Donahue *et al.* (14) did observe plasma enhancement of deposition rates at even much lower RF power, 20W, but also at much lower operating pressures, 1.5×10^{-2} torr.] The layers deposited with the aid of the glow discharge exhibited lower stacking fault densities and better surface quality. This improved quality was attributed to a more effective predeposition clean-up provided by the glow discharge compared to the normal heat-treatment in hydrogen.

Pons *et al.* (11) reported the deposition of silicon epitaxial layers at a substrate temperature of 760°C. They used a 0.5 MHz generator to inductively heat the susceptor and a 13.56 MHz generator to create the glow discharge. Both sapphire and silicon substrate wafers were used. The silicon source was 100% silane, and the operating pressures were in the range of 0.03-0.1 torr. Silicon epitaxial layers were deposited at a rate of 600 Å/min using 500W of RF power supplied to the plasma.

Shanfield and Reif (12) used a direct current (dc), low pressure plasma discharge system (see Fig. 1) to deposit silicon epitaxial layers in the temperature range of

750°-900°C. Deposition rates of 200-400 Å/min were obtained using a silane/hydrogen discharge of 25W at an operating pressure of 0.02 torr.

Suzuki and Itoh (13) used a different plasma CVD geometry to deposit silicon epitaxial layers at 750°C. They used a vertically aligned system with RF (13.56 MHz) excitation to generate a glow discharge. The glow was confined between two horizontal, parallel mesh electrodes, which were perpendicular to the gas flow. The wafer was located downstream, parallel to the mesh electrodes, and 150 mm below the lowest electrode. Pure silane and germane were used as the source of silicon and germanium, respectively, and pure hydrogen chloride was used for surface etching. Experiments were carried out at operating pressures of 1×10^{-2} and 3×10^{-3} torr, which resulted in deposition rates of 1980 and 840 Å/min, respectively. All these deposition experiments were carried out in the presence of a glow discharge, *i.e.*, the results of experiments carried out without plasma enhancement were not reported. The power level supplied to the discharge was 200W. The gas ambient consisted of silane, but germane was added to the plasma at the beginning of the deposition. The addition of germane was found to be essential, and it was proposed that it cleaned the wafer surface by removing the native silicon dioxide layer coating the substrate. This would occur by the reaction of Ge + SiO₂ to form GeO₂, which is reduced at this temperature (750°C) in the presence of hydrogen to Ge, or reduced by Ge to GeO, which is volatile. The oxygen would volatilize

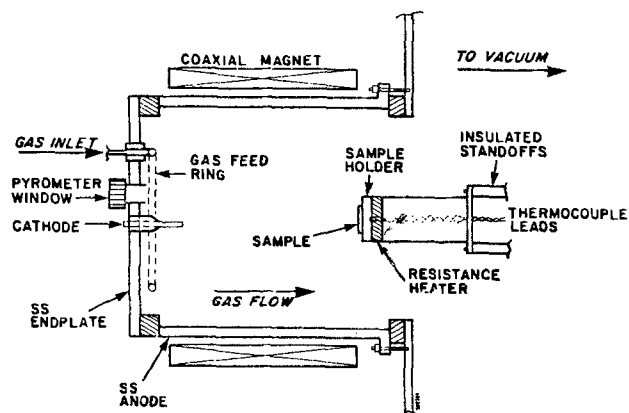


Fig. 1. Schematic diagram of PECVD chamber with dc excitation. [After Shanfield and Reif (12).]

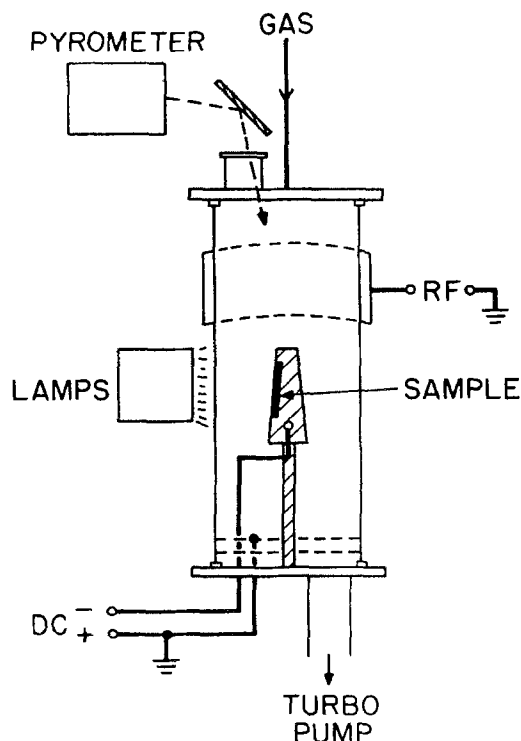


Fig. 2. Schematic diagram of PECVD chamber with RF excitation. [After Donahue *et al.* (14).]

as a gas or would react with H_2 to form H_2O , which would also etch Si and volatilize. The addition of germane, however, resulted in the formation of a Si-Ge alloy in the first 1000Å of the epitaxial film. Predeposition cleaning consisting of hydrogen chloride gas (850°C, 10 min) was found unsuitable because it yielded nonspecular epitaxial surfaces. The films were *in situ* doped by adding phosphine diluted in helium to the plasma, but they had to be annealed (1000°C, 60 min) to electrically activate most of the phosphorus in the film. Hall effect measurements indicated that the film electron mobility was similar to bulk values for carrier concentrations in the range of $(2 \times 10^{16}) - (3 \times 10^{18} \text{ cm}^{-3})$.

Donahue *et al.* (14) have deposited silicon epitaxial layers at 775°C using a low pressure CVD system both with and without plasma enhancement using silane. A schematic diagram of this system is shown in Fig. 2. The system consists of a gas distribution system, the chamber, the heating system, the pumping system, and the RF circuit. "Research purity" gases (less than 0.1 ppm each of O_2 , H_2O , etc.) are delivered to the chamber through stainless steel welded lines, and the flows are controlled using mass flow controllers. The available gases are argon, nitrogen, hydrogen, silane, and arsine. The chamber consists of a quartz tube sealed to stainless steel endplates by silicone gaskets. A single wafer sits on a silicon-carbide-coated graphite susceptor facing a radiant heater (six infrared lamps of 6 kW each). The wafer temperature is monitored by an infrared pyrometer that looks through a window in the top of the chamber, and a feedback loop controls the lamp power. A mesh is needed between the window and the plasma to prevent deposition on the window. The chamber is pumped on by a turbomolecular pump which is backed by a mechanical pump. The RF circuit consists of a 1 kW, 13.56 MHz generator and an automatic matching network, and it is coupled to the gas by an external copper plate wrapped around the top third of the chamber. The RF current return path is through a silicon-coated stainless steel false bottom located above the bottom endplate. Direct current bias can be applied between the false bottom and the graphite susceptor. By

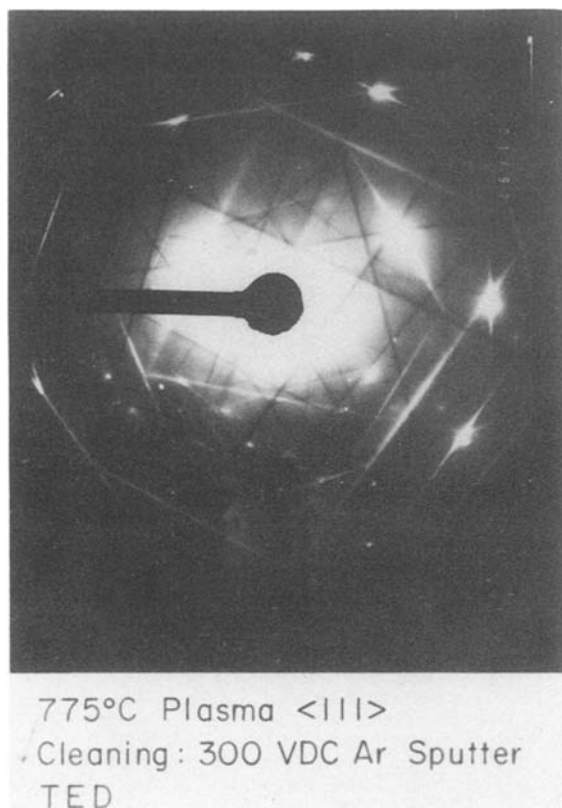


Fig. 3. Transmission electron diffraction micrograph of an epitaxial film deposited at 775°C with plasma enhancement (14).

using pure silane during deposition at an operating pressure of 1.5×10^{-2} torr, deposition rates of 450 and 340 Å/min were obtained with and without plasma enhancement, respectively. The power level supplied to the discharge during the PECVD experiments was only 20W, which probably explains the lower deposition rate observed here compared to that reported by Suzuki and Itoh (13). These results also disagree with those of Townsend and Uddin (9), in that they did not observe any plasma enhancement in the deposition rate; however, they worked at much higher operating pressures.

Donahue *et al.* (14) found that the predeposition *in situ* cleaning of the substrate surface to remove the native silicon dioxide film was essential for achieving epitaxial growth at this low temperature (775°C). Surface cleaning was done by sputtering the wafer in a 50W argon plasma at 775°C for 5 min with a dc bias applied between the false bottom and the susceptor. A polycrystalline deposit resulted when either the argon plasma cleaning or the dc bias during the predeposition argon plasma was not included in the procedure. Hazy epitaxial films resulted when only 100 or 200V of dc bias were used, but only if the plasma was used during the deposition. This suggests that the silane plasma is capable of cleaning away enough of the native silicon dioxide film to allow epitaxial growth. The plasma may also be providing energy to enhance the mobility of adsorbed silicon species. Finally, if a 300V bias was applied during the argon cleaning, smooth, specular epitaxial films of identical quality were obtained with or without plasma enhancement during the deposition (see Table II and Fig. 3 and 4).

The results obtained by Donahue *et al.* (14) clarify two important issues: (i) the presence of a glow discharge enhances the silicon epitaxial deposition rate even at relatively high temperatures (775°C) and low RF discharge power (20W). Similar results were observed by Shanfield and Reif (12) using a dc discharge. (ii) The predeposition *in situ* cleaning of the substrate surface determines the structure, quality, and morphology of these low temperature epitaxial films. Table III compares the different predeposition cleaning treatments used by different researchers.

The low temperature epitaxial films reported in Ref. (14) had an intrinsic resistivity of 40 Ω cm. Cs/SIMS measurements in these films found oxygen and carbon levels of $10^{18}/\text{cm}^3$ and $2 \times 10^{19}/\text{cm}^3$, respectively. An oxygen donor level located 0.147 eV below the conduction band was found by plotting the log of carrier concentration *vs.* temperature obtained from Hall measurements.

Epitaxial layers of GaAs have also been obtained by plasma-enhanced techniques (25, 26). Deposition temperatures of 350°C and deposition rates of 0.2 μm/min have been reported (25). Plasma cleaning of the substrate sur-

Table II. Influence of predeposition substrate bias on film structure and morphology. Process temperature: 775°C (14)

DC bias (V)	Non-plasma CVD	Plasma-enhanced CVD
0	Polycrystalline	Polycrystalline
100	Polycrystalline	Epitaxy (hazy)
200	Polycrystalline	Epitaxy (hazy)
300	Epitaxy (specular)	Epitaxy (specular)

Table III. Predeposition *in situ* cleaning of substrate surfaces immediately prior to silicon epitaxial growth (— means no information available)

Authors	Gas ambient	Temp (°C)	Discharge
Townsend and Uddin (9)	H_2	800-900	on
Pons <i>et al.</i> (11)	—	—	—
Shanfield and Reif (12)	H_2	750-900	on
Suzuki and Itoh (13)	GeH_4/SiH_4	600-850	on
Donahue <i>et al.</i> (14)	Ar	775	on

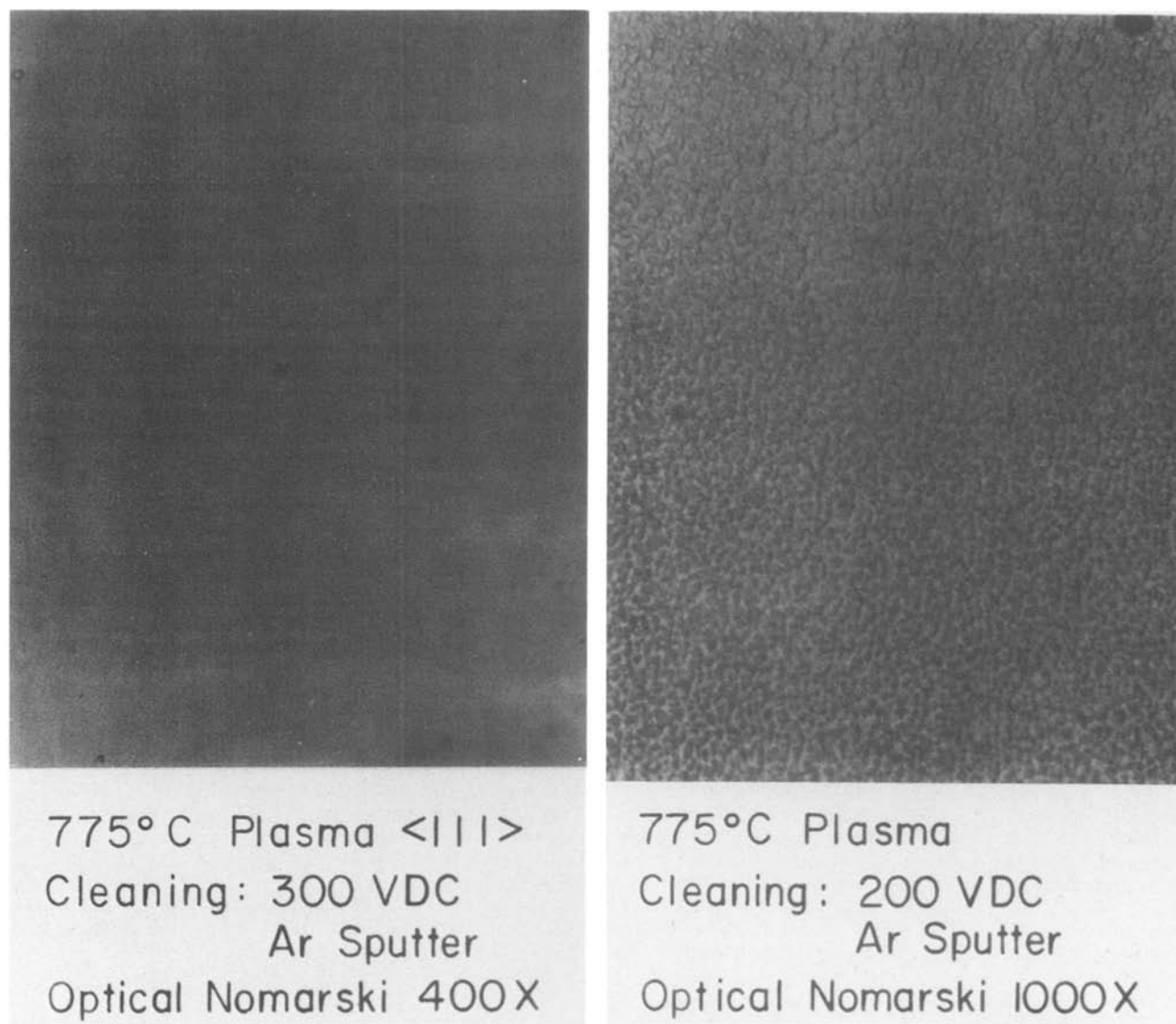


Fig. 4. Nomarski optical micrographs of films grown at 775°C both (a, left) with and (b, right) without sufficient predeposition *in situ* cleaning (14).

face to remove native oxide layers prior to epitaxial deposition is also believed to be essential for GaAs epitaxy at these low temperatures.

Summary and Conclusions

This article briefly discussed the physics and chemistry of the PECVD process, the importance of low temperature silicon epitaxy for the fabrication of VLSI chips, and the most recent advances in the PECVD of silicon epitaxial films. It is shown that the most important step to achieve silicon epitaxy at low (700°-800°C) temperatures is the predeposition *in situ* cleaning of the substrate surface. Although this low temperature process represents an attractive alternative to MBE, much more work is still needed to evaluate the quality of these low temperature films. In particular, issues such as defect density, *in situ* doping, pattern shift, pattern distortion, carrier mobilities, and carrier lifetimes are currently being investigated and will determine the impact of this technology.

Acknowledgment

The author gratefully acknowledges the financial support provided by the Semiconductor Research Corporation (Contract no. 83-01-033), which made the writing of this article possible.

Manuscript submitted Jan. 20, 1984; revised manuscript received May 29, 1984. This was Paper 204 presented at the Cincinnati, Ohio, Meeting of the Society, May 6-11, 1984.

Massachusetts Institute of Technology assisted in meeting the publication costs of this article.

REFERENCES

1. F. E. Holmes and C. A. T. Salama, *Solid State Electron.*, **17**, 791 (1974).
2. D. S. Yaney and C. W. Pearce, *Proc. Int. Electron Devices Meet. IEEE*, 236 (1981).
3. J. C. Bean, *Proc. Int. Electron Devices Meet. IEEE*, 6 (1981).
4. R. Reif and R. W. Dutton, *This Journal*, **128**, 909 (1981).
5. G. R. Srinivasan, *ibid.*, **125**, 146 (1978).
6. Y. Ota, *J. Appl. Phys.*, **51**, 1102 (1980).
7. T. Takagi, I. Yamada, and A. Sasaki, *Thin Solid Films*, **39**, 207 (1976).
8. P. C. Zalm and L. J. Beckers, *Appl. Phys. Lett.*, **41**, 167 (1982).
9. W. G. Townsend and M. E. Uddin, *Solid State Electron.*, **16**, 39 (1973).
10. S. Suzuki, H. Okuda, and T. Itoh, *Jpn. J. Appl. Phys.*, **19**, Suppl. 19-1, 647 (1979).
11. M. Pons, D. Bourgeat, J. Trilhe, and B. Bourdon, *Le Vide, Les Couches Minces*, **200**, 3 (1980).
12. S. R. Shanfield and R. Reif, Abstract 144, p. 230, The Electrochemical Society Extended Abstracts, Vol. 83-1, San Francisco, CA, May 8-13, 1984.
13. S. Suzuki and T. Itoh, *J. Appl. Phys.*, **54**, 1466 (1983).
14. T. J. Donahue, W. R. Burger, and R. Reif, *Appl. Phys. Lett.*, **44**, 346 (1984).
15. B. Chapman, "Glow Discharge Processes," p. 374, John Wiley and Sons, New York (1980).

16. M. J. Rand, *J. Vac. Sci. Technol.*, **16**, 420 (1979).
17. J. R. Hollahan and A. T. Bell, Editors, "Techniques and Applications of Plasma Chemistry," p. 1, John Wiley and Sons, New York (1974).
18. J. L. Vossen, *This Journal*, **126**, 319 (1979).
19. J. W. Coburn and E. Kay, *J. Appl. Phys.*, **43**, 4965 (1972).
20. C. M. Horwitz, *J. Vac. Sci. Technol. A*, **1**, 60 (1983).
21. H. R. Koenig and L. I. Maissel, *IBM J. Res. Dev.*, **14**, 276 (1970).
22. J. E. Greene and S. A. Barnett, *J. Vac. Sci. Technol.*, **21**, 285 (1982).
23. L. N. Aleksandrov, A. S. Lutovich, and E. D. Belorusetz, *Phys. Status Solidi A*, **54**, 463 (1979).
24. M. Marinov, *Thin Solid Films*, **46**, 267 (1977).
25. T. Hariu, K. Takenaka, S. Shibuya, Y. Komatsu, and Y. Shibata, *ibid.*, **80**, 235 (1981).
26. K. P. Pande, Abstract 340, p. 531, The Electrochemical Society Extended Abstracts, Vol. 83-1, San Francisco, CA, May 8-13, 1983.

Ferromagnetic Iron Oxides from Synthetic β -FeOOH by Vacuum Thermal Decomposition

Katsuya Inouye, Kiyohito Shibata, Sumio Ozeki, and Katsumi Kaneko

Department of Chemistry, Faculty of Science, Chiba University, Chiba 260, Japan

ABSTRACT

The synthetic β -FeOOH (Akaganeite) was dehydrated at 300°-500°C for 1-20h under vacuum of 10^{-3} and 10^{-5} torr. The magnetic properties of the obtained dehydration products have been measured for saturation magnetization (M_s), residual magnetization (M_r), and coercive force (H_c). M_s and M_r were proportional to the chemically analyzed Fe^{2+} content in the samples. With reference to the x-ray diffraction results, it was found that the dehydrated products of β -FeOOH *in vacuo* are the oxides in the Fe_3O_4 series containing different amounts of Fe^{2+} in the range 1-3 mmol g^{-1} , and with a certain amount of α - Fe_2O_3 . The oxidation of the dehydrated β -FeOOH in air at 225°C for 20h gave oxides of the γ - Fe_2O_3 series, which are entirely different in magnetic properties but almost similar in x-ray reflections in comparison with those of the dehydrated β -FeOOH. The variations of H_c and the reduced remanence (M_r/M_s) with the Fe^{2+} content are also discussed.

The decomposition product of synthetic β -FeOOH (Akaganeite), particularly under vacuum or in an inert atmosphere, has recently been the subject of interest in different problems: first for a possibility of producing ferromagnetic acicular powder material suitable for magnetic tapes (1, 2), and, second, for the investigation of pore formation by dehydration which is relevant to the adsorbability of gaseous molecules such as N_2 , CCl_4 (3), H_2O (4), and NO (5).

The present work deals with the first problem, particularly to discussion of whether the dehydration product is γ - Fe_2O_3 (maghemite) as commonly believed by the preceding authors. As is well known, acicular microparticles embracing maghemite are useful material for electronic purposes. It was Mackay (6) who first suggested from electron diffraction evidence that γ - Fe_2O_3 is the decomposition product of β -FeOOH under a vacuum of the electron microscope condition, although he reserved the possibility that it is Fe_3O_4 (magnetite). Watson *et al.* (7) also reported that the dehydration of β -FeOOH in an electron microscope gives γ - Fe_2O_3 on the basis of selected-area electron diffraction measurements. In a similar study on pore formation in β -FeOOH by Galbraith *et al.* (8), the product in the electron microscope was mentioned as γ - Fe_2O_3 . Gonzalez-Calbet *et al.* (4) asserted more recently that the dehydration product of β -FeOOH at 10^{-3} torr and 350°C for 1h is γ - Fe_2O_3 , a conclusion mainly based on the x-ray diffraction patterns which are characteristic of γ - Fe_2O_3 . Naono *et al.* (3) examined the "micropore" formation in dehydrated β -FeOOH at 10^{-5} torr and 25°-500°C for 10-20h, but their dehydration products at higher temperature range appeared to be α - Fe_2O_3 (hematite). In our previous experiment (5), β -FeOOH changed at 10^{-5} torr and 350°-500°C to a black strongly magnetic product. Although this product was distinguished by a high adsorption capacity for NO molecules, its properties and structure remained to be investigated.

It has become practically important that the raw material of magnetic iron oxide power is expected in the future to be iron chloride obtained as an acid-washing waste in the steel industry. It is also widely known that the hydrolysis of iron chloride gives β -FeOOH easily. It is

hence envisaged that the preparation of a magnetic oxide from β -FeOOH is promising. In this report, we will provide the magnetic properties of the dehydration product of β -FeOOH *in vacuo*, and its oxidation product as well, and will also discuss the kinds of products obtained, with reference to the examinations by x-ray diffraction, chemical analysis, and electron micrography.

Experimental

Synthetic β -FeOOH and other materials.— β -FeOOH was prepared by the hydrolysis of 0.1M FeCl_3 at 95°-100°C for 5h (9). The precipitates were filtered, washed with distilled water until no chloride ions were detected, and dried at 110°C for 1h. The BET surface area by nitrogen adsorption was 25 $\text{m}^2 \text{g}^{-1}$. The Fe_3O_4 and γ - Fe_2O_3 used as reference materials are commercial pure-grade reagents ex. Wako Chemical Industries and Toda Chemical Industries, respectively; each showed sharp x-ray diffraction patterns without considerable impurities.

Vacuum dehydration.—Approximately 10 mg sample was situated in a glass cell connected with a vacuum system and temperature controller. The sample was evacuated at 10^{-3} or 10^{-5} torr, and then heated at a rate of 3.3°C min^{-1} up to temperatures in the range 300°-500°C. The temperature deviation at 380°C was +5° and -10°C. The time of heating was 1-20h at each final temperature. The dehydrated sample was cooled to room temperature under the same vacuum. The preliminary experiments revealed that the magnetic values (see next section) elevate during heating to approach constant values with the heating temperature in the range 300°-500°C and with the heating time between 1 and 20h, irrespective of the degree of vacuum. The typical heating conditions for comparison of the magnetic properties of the products were: 380°C, 10^{-3} torr, and 3h.

Magnetic measurement.—A tablet composed of a 10 mg sample and 300-400 mg KBr was used for the measurements to prevent movement of sample powders in the magnetic field. The tablet was formed with a compression pressure of $8 \times 10^3 \text{ kg cm}^{-2}$. The magnetic hysteresis curve was drawn at room temperature by means of a Far-

aday balance with the magnetic field ranging from -720 to $+5740\text{G}$ (10^{-4} T). From the hysteresis curve, the saturation magnetization (M_s), the residual magnetization (M_r), and the coercive force (H_c) were obtained.

Oxidation of dehydrated sample.—The oxides obtained by heating at different temperatures *in vacuo* were further subjected to oxidation in air in an electric furnace regulated at $225^\circ \pm 7^\circ\text{C}$ for 20h. This oxidation condition was selected as appropriate for the oxidation of Fe_3O_4 to $\gamma\text{-Fe}_2\text{O}_3$ in the industrial production of acicular magnetic powder as described in numerous patents.

Chemical analysis and sample characterization.—The content of Fe^{2+} in the samples was determined by the Zimmerman-Reinhardt oxidation-reduction titration by use of a standard $\text{K}_2\text{Cr}_2\text{O}_7$ solution for the sample solution in HCl. The x-ray diffraction patterns were obtained by an automatic diffractometer (Rigakudenki 2028) with Mn-filtered $\text{Fe K}\alpha$ radiation at 35 kV and 10 mA. JEM 50B (Japan Electron Optics) was employed for the electron microscopic examinations of carbon-coated samples at 50 kV. Observation at a low voltage was preferable to avoid sintering between microcrystals.

Results and Discussion

As already reported by Gonzalez-Calbet *et al.* (4), as well as by the present authors (5), a strongly magnetic oxide is formed from $\beta\text{-FeOOH}$ in the limited temperature range between 300° and 500°C under a vacuum of $10^{-3}\text{-}10^{-5}$ torr. Above 500°C , $\alpha\text{-Fe}_2\text{O}_3$ is the sole product, which is known to be antiferromagnetic.

Figure 1 shows the x-ray diffraction patterns of the samples obtained by heating at 380°C and 10^{-3} torr for 3h and by air oxidation at 225°C for 20h, in comparison with the patterns of Fe_3O_4 and $\gamma\text{-Fe}_2\text{O}_3$. It appears that the dehydration product is composed of $\alpha\text{-Fe}_2\text{O}_3$ (marked with h in Fig. 1), $\gamma\text{-Fe}_2\text{O}_3$, and/or Fe_3O_4 . The reflections of $\gamma\text{-Fe}_2\text{O}_3$ and Fe_3O_4 are very similar to each other as compared in Fig. 1. Numerous studies have been published on the distinguishability between $\gamma\text{-Fe}_2\text{O}_3$ and Fe_3O_4 based on the magnetic and crystallographic examinations. The surveys of those reports can be found in Shieber's book (10) and more recently in Datta's review (1). It is apparent that no single technique can characterize unambiguously each oxide. Gonzalez-Calbet *et al.* (4) asserted that lattice parameters at $d_{(102)}$, 0.7085 nm, $d_{(110)}$, 0.5955 nm, and $d_{(104)}$,

0.5094 nm are characteristic of $\gamma\text{-Fe}_2\text{O}_3$, which are marked with small filled circles in Fig. 1. However, it seems doubtful if these weak diffraction patterns can be the basis for the reasoning of $\gamma\text{-Fe}_2\text{O}_3$ formation by dehydration, if one compares the patterns of the dehydrated product with those of $\gamma\text{-Fe}_2\text{O}_3$ and Fe_3O_4 .

It is noticeable that the chemical analysis of the oxides clearly gives evidence of Fe^{2+} in the concentration range $1\text{-}3$ mmol g^{-1} , as is described later. This fact means that the presence of an iron oxide like Fe_3O_4 containing Fe^{2+} cannot be denied. We recall that the presence of Fe^{2+} has been observed in iron oxide hydroxides and iron oxides by heating *in vacuo* (11).

However, the saturation magnetization (M_s) and the residual magnetization (M_r) increase linearly with the Fe^{2+} concentration, as shown in Fig. 2 and 3. The coercive force (H_c) appears to be almost independent of the Fe^{2+} concentration or increases slightly in the middle range of the Fe^{2+} concentration, and it tends to decrease towards the value of Fe_3O_4 (shown by triangle) in a higher concentration range than 3 mmol g^{-1} , as illustrated in Fig. 4. The samples, for which magnetic data are shown in Fig. 2, 3, and 4 by open circles, are the oxides obtained by heating the $\beta\text{-FeOOH}$ at various temperatures ($350^\circ\text{-}500^\circ\text{C}$) and $10^{-3}\text{-}10^{-5}$ torr for various durations (1-20h).

The samples after the oxidation of dehydrated products in air at 225°C still have some amounts of Fe^{2+} and their values of M_s , M_r , and H_c increase linearly with the Fe^{2+} concentration. However, it is apparent that the dependence of magnetic values upon Fe^{2+} concentration is entirely different between the dehydrated oxides and their air-oxidation products. The dependencies of M_s , M_r , H_c , and M_r/M_s on the Fe^{2+} concentration of the oxidation products (see the filled circles in Fig. 2, 3, 4, and 5) are greater than those of the dehydrated oxides. The M_s , M_r , and H_c of the $\gamma\text{-Fe}_2\text{O}_3$ sample as the reference are also shown in each figure by double circles on horizontal dashed lines. From the intersections of the full lines and dashed lines in Fig. 2-5, the Fe^{2+} concentration in the oxidation product having magnetic values of $\gamma\text{-Fe}_2\text{O}_3$ is estimated as 0.17 ± 0.05 mmol g^{-1} . The Fe^{2+} concentration by chemical analysis in this $\gamma\text{-Fe}_2\text{O}_3$ was 0.15 ± 0.01 mmol g^{-1} . The fairly close agreement for the content of Fe^{2+} from the chemical analysis and the magnetic experiments implies that the magnetic properties of oxidation products are characteristic of $\gamma\text{-Fe}_2\text{O}_3$. We call them the $\gamma\text{-Fe}_2\text{O}_3$ series, in con-

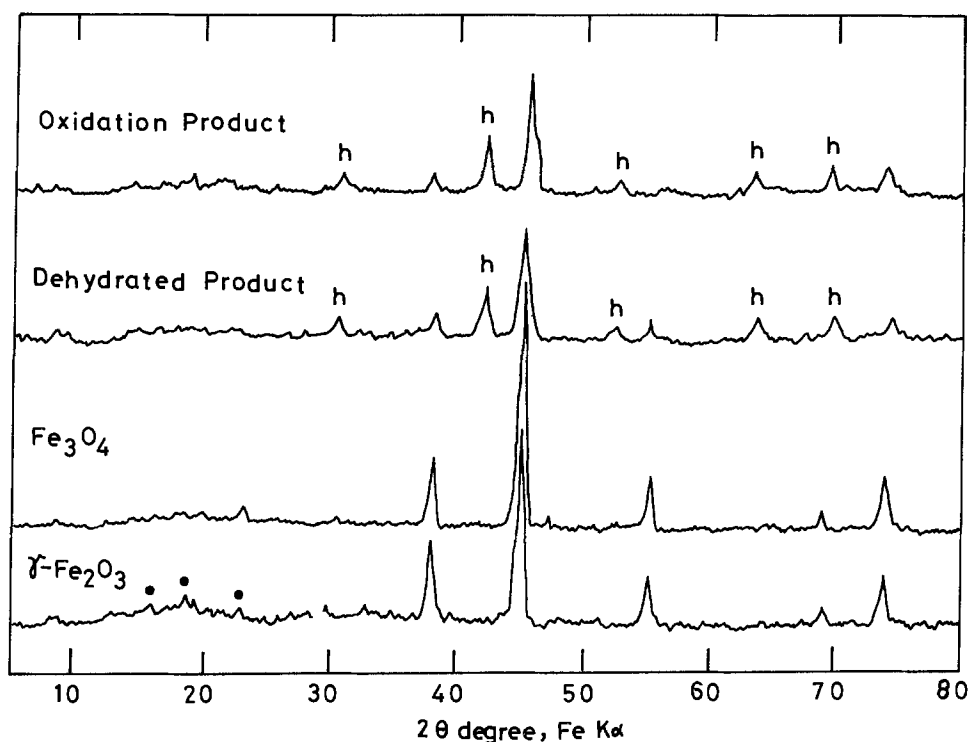


Fig. 1. X-ray diffraction patterns of $\gamma\text{-Fe}_2\text{O}_3$, Fe_3O_4 , dehydrated $\beta\text{-FeOOH}$ (380°C , 10^{-3} torr for 3h), and its air-oxidation product (225°C for 20h). As for the symbols in figure, see text.

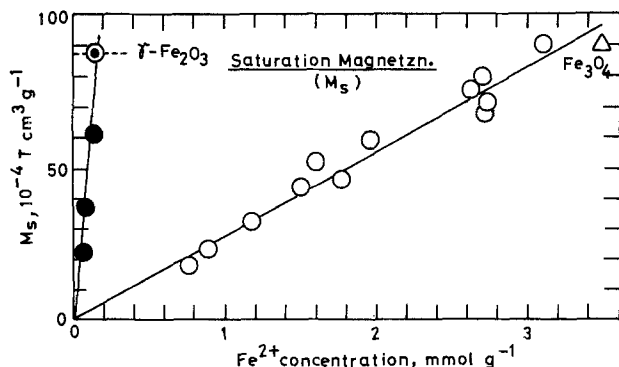


Fig. 2. Correlation of saturation magnetization with Fe^{2+} content in dehydration products (open circles) and their oxidation products (filled circles).

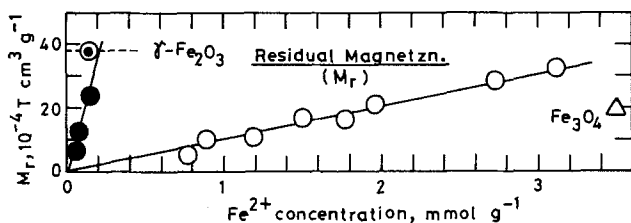


Fig. 3. Correlation of residual magnetization with Fe^{2+} content in dehydration products (open circles) and their oxidation products (filled circles).

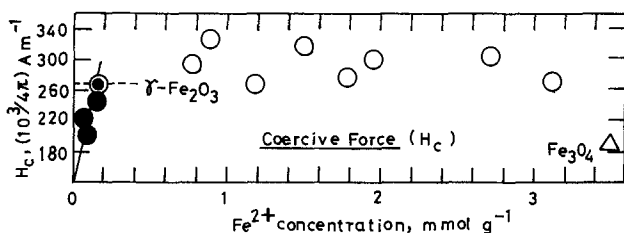


Fig. 4. Variation of coercive force with Fe^{2+} content in dehydration products (open circles) and their oxidation products (filled circles).

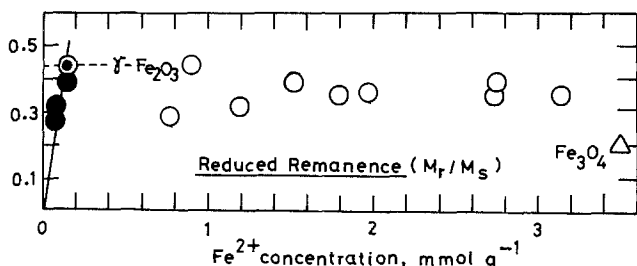


Fig. 5. Variation of reduced remanence with Fe^{2+} content in dehydration products (open circles) and their oxidation products (filled circles).

trast to the dehydration products, denoted as the Fe_3O_4 series.

The x-ray diffraction patterns of an oxidized sample in air at 225°C for 20h are illustrated also in Fig. 1. The spinel-structure reflections observed in the dehydration product remain identifiable. Both the dehydrated product and its oxidation product show the x-ray patterns indicating the coexistence of $\alpha-Fe_2O_3$, marked with h in the figure. The sample after the air oxidation appears therefore to be composed of defective $\gamma-Fe_2O_3$ and $\alpha-Fe_2O_3$. It seems significant that the magnetic properties of the Fe_3O_4 series, *viz.*, the dehydrated $\beta-FeOOH$, are entirely different from those of the $\gamma-Fe_2O_3$ series, *viz.*, the air-oxidation products. It may well be that the dehydrated products of $\beta-FeOOH$ *in vacuo* are of the Fe_3O_4 series with different amounts of "insufficient" Fe^{2+} and that the air oxidation of the dehydration products gives the oxides of the $\gamma-Fe_2O_3$ series still with a small amount of Fe^{2+} . It may

appear strange that the linear relationships between M_s (and M_r) and the Fe^{2+} concentration pass through the zero points of magnetic values (Fig. 2 and 3), but it can be related to the structural transformation of the oxides of the $\gamma-Fe_2O_3$ series into nonferromagnetic $\alpha-Fe_2O_3$ by a rather extensive air oxidation.

Gonzalez-Calbet and Alario-Franco (12) examined recently the decomposition of $\beta-FeOOH$ within several minutes to suggest that the nucleation of $\gamma-Fe_2O_3$ initiates its growth, during which a single macropore, as observed by the electron microscope, is formed. According to the theoretical treatment by Knowles (13), the acicular particles of partially oxidized Fe_3O_4 , showing higher H_c and reduced remanence (M_r/M_s) relative to typical Fe_3O_4 or $\gamma-Fe_2O_3$, is considered to comprise an inner core of Fe_3O_4 with an outer layer of $\gamma-Fe_2O_3$. The volume change with oxidation results in a stress field interacting with the magnetization. Our results for H_c and M_r/M_s for "partially oxidized" Fe_3O_4 samples containing less Fe^{2+} than Fe_3O_4 (Fig. 4 and 5) seem to support, though vaguely, the view by Knowles. It should be mentioned that the values of H_c and M_r are highly structure sensitive, influenced by morphological properties of the particles, so that the meaning of comparison of these values between samples is complex and limited.

The particle images by electron microscope have been abundantly provided in various papers, especially those discussing pore structure in $\beta-FeOOH$ microcrystals and their dehydration products *in vacuo* (3, 4, 6, 8, 9, 11). Our electron microscopic observations are by no means different from those so far published. The average particle size of 300 nm length and 50 nm width did not considerably alter with the vacuum dehydration (250 × 40 nm) and the air oxidation (280 × 40 nm). No sintering between particles has been observed throughout the heat-treatments.

The direct use of dehydrated $\beta-FeOOH$ or its oxidation products as an acicular powder for magnetic tapes still seems to be unfavorable as far as the H_c values in the range of 200-350 ($10^3/4\pi$) $A m^{-1}$ of the products described in the present paper are concerned. Suitable means to improve the magnetic properties should be found up to a commercially attractive level for H_c of at least 500 ($10^3/4\pi$) $A m^{-1}$. Furthermore, the length to width ratio should be increased up to 10-15 for the original $\beta-FeOOH$ crystals by a better procedure of synthesis. Further investigations may yet find a useful magnetic material from $\beta-FeOOH$ by means of a more direct path than the complicated routine procedure using $\alpha-FeOOH$.

Conclusion

By the measurement of saturation magnetization, residual magnetization, and coercive force of the dehydration products of a synthetic $\beta-FeOOH$ at 300°-500°C under a vacuum of 10^{-3} - 10^{-5} torr for 1-20h and of their oxidation products in air at 225°C for 20h, and with reference to the x-ray diffraction patterns and chemical analysis of Fe^{2+} concentration in each product, the following conclusions have been reached.

1. The dehydrated $\beta-FeOOH$ is a mixture of oxides in the Fe_3O_4 series containing different amounts of Fe^{2+} and $\alpha-Fe_2O_3$. It is unlikely that the dehydration of $\beta-FeOOH$ *in vacuo* gives, as believed by the authors of most of the preceding reports, $\gamma-Fe_2O_3$.

2. The oxidation of the above dehydration products in air at 225°C for 20h produces a mixture of oxides in the $\gamma-Fe_2O_3$ series, which show entirely different magnetic properties from those of the Fe_3O_4 series, and $\alpha-Fe_2O_3$.

3. The saturation magnetization and residual magnetization of both the dehydration products and the oxidation products are proportional to the Fe^{2+} concentration in the oxides. The dependence of the magnetic values on the Fe^{2+} content is steeper for the $\gamma-Fe_2O_3$ series than that for the Fe_3O_4 series.

Acknowledgment

The financial support by the Special Grant for Molecular Assemblies Research of the Ministry of Education,

Science, and Culture, Japanese Government, for this work is gratefully acknowledged.

Manuscript submitted Nov. 24, 1983; revised manuscript received May 25, 1984.

Chiba University assisted in meeting the publication costs of this article.

REFERENCES

1. N. C. Datta, *J. Sci. Ind. Res.*, **40**, 571 (1981).
2. B. Hendel, M. Lorenz, and K. Stopperka, *J. Signallaufzeichnungsmaterialein*, **9**, 381 (1981).
3. H. Naono, R. Fujiwara, H. Sugioka, K. Sugiya, and H. Yanazawa, *J. Colloid Interf. Sci.*, **87**, 317 (1982).
4. J. M. Gonzalez-Calbet, M. A. Alario-Franco, and M. Gayaso-Andrade, *J. Inorg. Nucl. Chem.*, **43**, 257 (1981).
5. T. Hattori, K. Kaneko, T. Ishikawa, and K. Inouye, *J. Chem. Soc. Jpn.*, 423 (1979).
6. A. L. Mackay, in "Reactivity of Solids," p. 571, Elsevier Publishing Co., Amsterdam (1961).
7. J. H. L. Watson, R. R. Cardel, and W. Heller, *J. Phys. Chem.*, **66**, 1757 (1962).
8. S. T. Galbraith, T. Baird, and J. R. Fryer, *Acta Crystallogr., Sect. A*, **35**, 197 (1979).
9. A. L. Mackay, *Mineral. Mag.*, **32**, 545 (1960).
10. M. M. Shieber, in "Experimental Magnetochemistry," Chap. 4, North-Holland Publishing Co., Amsterdam (1967).
11. K. Kaneko and K. Inouye, *This Journal*, **122**, 451 (1975); *J. Chem. Soc., Faraday Trans. 1*, **72**, 1258 (1976).
12. J. M. Gonzalez-Calbet and M. A. Alario-Franco, *Thermochim. Acta*, **58**, 45 (1982).
13. J. E. Knowles, *J. Magnetism Magnetic Mater.*, **22**, 263 (1981).

Investigation of Liquid Dopants for the Production of High Efficiency Solar Cells from Dendritic Web Silicon

K. S. Tarneja and R. B. Campbell*

Westinghouse Electric Corporation, Pittsburgh, Pennsylvania 15236

P. Alexander

Jet Propulsion Laboratory, Pasadena, California 91109

ABSTRACT

Conventional gaseous BBr_3 and CVD SiO_2 are presently used in the Westinghouse baseline process for the production of high efficiency (13%-15%) dendritic web solar cells. The objective of this study was to replace the CVD SiO_2 mask and the subsequent BBr_3 diffusion step with a liquid SiO_2 /liquid boron dopant diffusion process. The number of process steps are reduced significantly with the use of the liquid process. Data on time-temperature relationship on sheet resistance, junction depth, etc., were obtained and are presented. Various application techniques for the liquid process were investigated. As a first step, a manually applied sponge-squeegee applicator was used, which was later replaced with a meniscus coating machine. This equipment permitted the application of uniform layers of liquid dopants of controlled thickness on the dendritic web. Various runs were made to make direct comparison of the liquid and baseline processes. The results of cell efficiencies achieved using the liquid process indicate that high efficiencies (13%-15%) can be achieved with this process. Results of V_{oc} , I_{sc} , fill factor, etc., are presented in detail and compared with the baseline process. Dark IV measurements made on liquid-processed cells indicate excellent quality junctions and high lifetime values. The series and shunt resistance measurements on typical cells show no difference as compared with the baseline process. Junction profiles are presented for both a gaseous diffused cell and a liquid processed cell. The profiles show no dissimilarities.

The purpose of this paper is to present results on the doping of dendritic web silicon with liquid metallo-organics to produce an n^+pp^+ solar cell structure.

Dendritic web silicon is crystalline silicon grown in long strips. In the as-grown condition, it is thin, generally 120-150 μm thick, and requires no sawing or lapping prior to the cell fabrication process.

Figure 1 shows the Westinghouse baseline process sequence in block form. The original Westinghouse baseline process sequence required gaseous diffused back and front junctions, each junction formation step being preceded by a chemical vapor deposition (CVD) applied oxide masking step. The development work being conducted at Westinghouse and reported herein involves the substitution of liquid-applied oxide masks for the CVD-applied masks and substitution of liquid-applied dopants for gaseous diffused dopants.

Figure 2 shows a length of dendritic web silicon and a solar cell fabricated from this material. The edges (dendrites) and the center section (web) are one single crystal with a re-entrant twin plane. The dendrites are generally left on the strip until the final processing steps. The material is normally processed in 33 cm long strips.

Figure 2 also shows a typical solar cell fabricated on dendritic web silicon. Its natural rectangular shape permits a high packing factor of active cell area in the solar modules.

In the experiments reported here, we used a p-type web with a resistivity of 4-8 $\Omega\text{-cm}$. The cell sizes are a nominal 2×10 cm, with ten contact pads per cell. The double doping process sequence uses a boron containing liquid for the back surface field diffusion and a phosphorus containing liquid for the n^+p front junction producing an n^+pp^+ junction structure.

Because of the different diffusion constants of B and P in silicon and the requirements for shallow front junctions, the process sequence requires two diffusions. The first is a boron diffusion to form the p^+p back surface field, followed by a phosphorus diffusion at lower temperature to form the front n^+p junction.

Baseline Process Comparisons

In the work reported here, the liquid dopant experiments were carried out in conjunction with a baseline gaseous diffusion process using BBr_3 and POCl_3 . In this way, the efficacy of the liquid dopant process could be determined.

*Electrochemical Society Active Member.

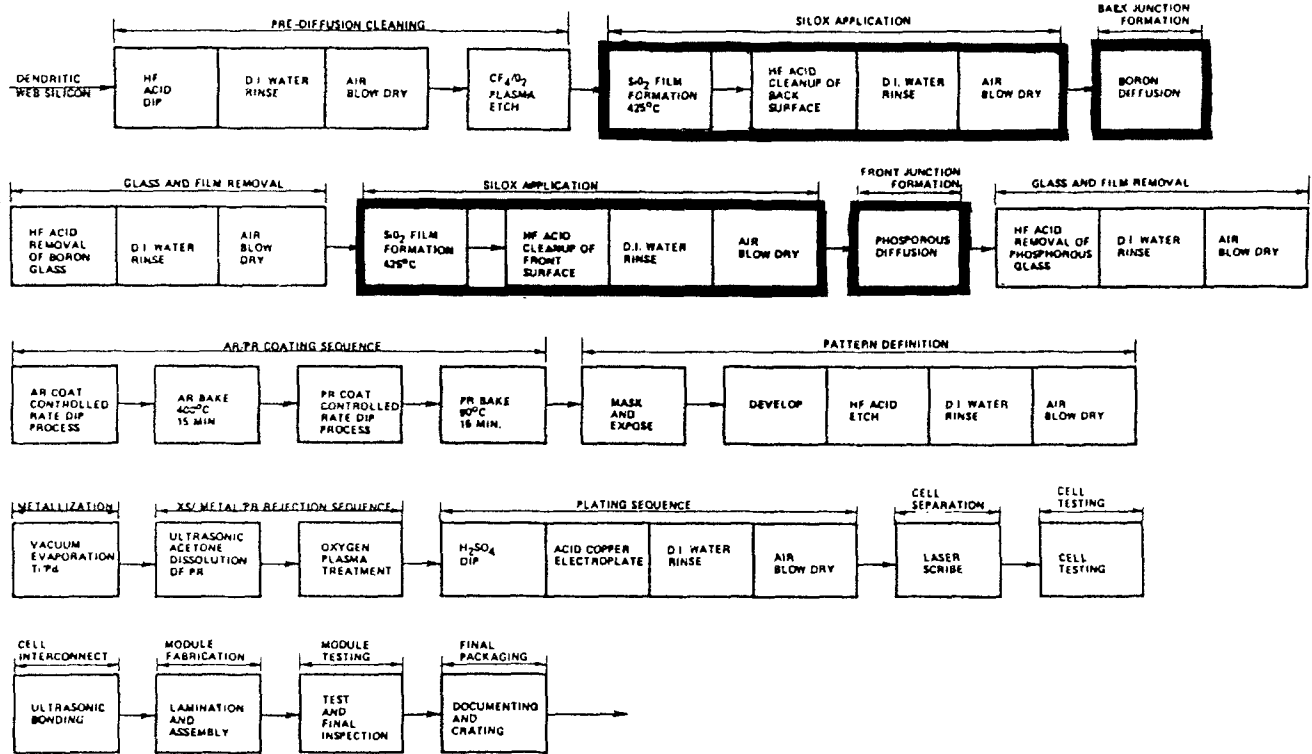


Fig. 1. Westinghouse baseline process sequence flow chart

Since two diffusions were required to form the n^+pp^+ structure, an SiO_2 layer was used as a diffusion mask. In the baseline process, the mask was a CVD SiO_2 layer, while in the liquid process, we used a solution containing SiO_2 .

Table I shows the process steps required for three different junction formation techniques used. The first column is the baseline gaseous BBr_3-POCl_3 process. The second column is a liquid mask/liquid boron + liquid mask/ $POCl_3$ process, while the third column is the liquid mask/liquid boron + liquid mask/liquid phosphorus process. The work reported herein describes the results of column 2, back junction, p^+ . The work of column 3, front junction, n^+ , is not completed.

Due to the long lengths of dendritic web processed in the Westinghouse facility (33 cm), the liquids were manu-

ally applied using a sponge-squeegee rather than the normal spin-on method used for wafers.

This method of application was generally satisfactory. After the coated strip was baked (before diffusion), the surface showed the normal oxide colors. The thickness of the layers was 0.25 to 0.5 μm .

Table II shows the results of a diffusion time-temperature study to determine conditions for the desired $40 \Omega/\square$ sheet resistivity for the back junction, p^+ . The underlined $980^\circ C$ temperature for 30 min was chosen for all further work.

Figure 3 shows junction profiles of the liquid produced p^+p junction as compared to a gaseous BBr_3 -produced p^+p junction. There is no essential difference.

Lighted and dark IV measurements made on the two types of cells, liquid applied p^+ vs. gaseous p^+ , are shown

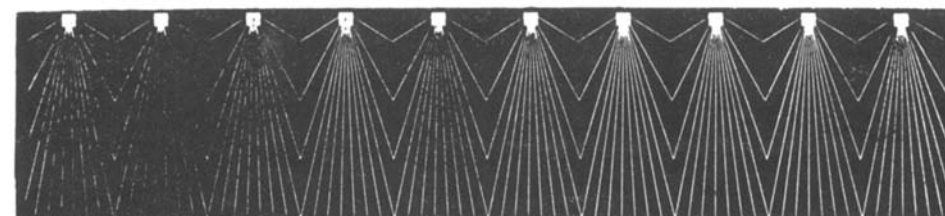


Fig. 2. A length of dendritic web silicon and a solar cell fabricated from it.

Table I. Solar cell junction formation process steps: baseline vs. various liquid dopant sequences

Step no.	Process	Baseline	Liquid mask/liquid B + POCl ₃	Liquid mask/liquid B + liquid mask/liquid P
1A	CVD SiO ₂ n ⁺ side	X		
1B	Apply liquid mask and bake		X	X
1C	Apply liquid boron and bake		X	X
2	HF etch	X		
3	Prediffusion clean	X		
4	Diffuse p ⁺	X	X	X
5	Oxide etch	X	X	X
6A	Apply liquid mask and bake		X	X
6B	Apply liquid phosphorus and bake			X
6C	CVD p ⁺ side	X		
7	HF etch	X		
8	Prediffusion clean	X	X	
9	Diffuse n ⁺	X	X	X
10	Oxide etch	X	X	X

Table II. Liquid boron diffusion-time/temperature study

Diffusion temp. (°C)	Diffusion time (min)	Sheet resistivity (Ω/□)
925	20	90
925	30	80
960	20	65
960	30	50
960	40	48
980	15	75
980	30	55*
980	45	45
980	60	30

Baseline BBr₃ gaseous diffusion carried out at 960°C for 20 min. 80% N₂, 20% O₂ ambient diffusion environment.

Baseline process specification for boron-doped p⁺p junction = 40 Ω/□ ± 10 Ω/□.

* Liquid dopant diffusion carried out at 980°C for 30 min. 80% N₂, 20% O₂ ambient diffusion environment. Actual run data produces 40 Ω/□ nominal instead of 55 Ω/□ indicated by research data.

in Table III. Again, there is no essential difference between the two types of cells, with both cells having excellent lifetimes and junction depletion regions having very few recombination centers.

The efficiency of these cells (liquid mask/liquid boron and liquid mask/POCl₃) is comparable to the baseline-processed cells.

To demonstrate the feasibility of using belt furnaces (which are highly automatable) for liquid dopant drive-in diffusion, a series of experiments were conducted at Radiant Technologies Incorporated, Cerritos, California, using one of their belt furnaces. Using web material from the same run, one-half of the liquid boron dopant cells were diffused using a belt furnace, and the second half were diffused using a standard diffusion tube furnace. The data presented in Table IV indicate that the performance of cells processed with the belt furnace was equal to those processed with a diffusion tube furnace. These fur-

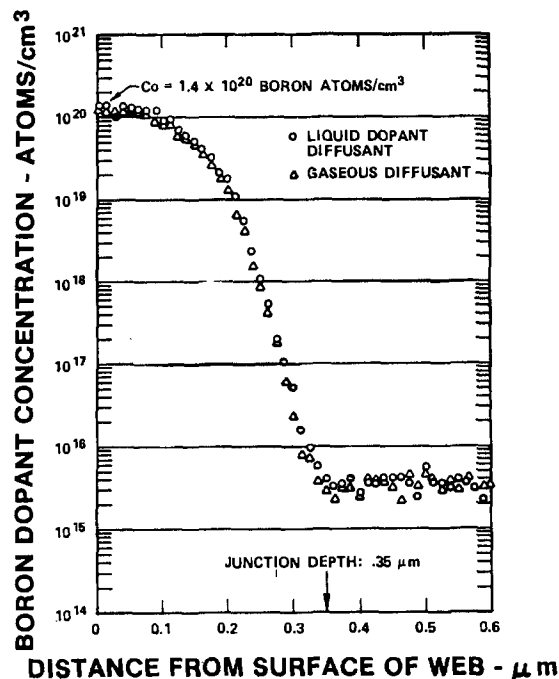


Fig. 3. Liquid vs. gaseous p⁺p junction profiles

nance experiments were significant in that they demonstrated that liquid dopant cells are amenable to being processed with automatable equipment, which, in turn, can be reflected in lower processing costs.

Table V shows the average efficiency of baseline processed cells vs. the liquid boron p⁺p junction cells fabricated over a 3 month period. These data indicate that the liquid process is indeed a suitable replacement for gaseous diffusion.

The next series of experiments, which is continuing, is to verify that a n⁺p junction can be produced using a liquid phosphorus dopant and can be used to replace the gaseous POCl₃ diffusion.

The same procedure has been used to determine the proper diffusion time, diffusion temperature, and ambient gas for the liquid phosphorus study as was done for the liquid boron reported herein. To obtain the required 60 Ω/□ sheet resistivity, a diffusion temperature of 890°C for 20 min in an ambient of 100% O₂ is being used for the phosphorus dopant studies.

Our present plans are to develop a statistically significant data base with the liquid phosphorus dopants the same as was done with the liquid boron dopants. From our study, we conclude that an n⁺pp⁺ junction structure can be formed on p-type dendritic web silicon using liquid-applied dopants and liquid-applied diffusion masks. The cells produced with liquid dopants perform at least equal to or better than the baseline gaseous process. Cost analyses conducted on the gaseous process using the Solar Array Manufacturing Industry Costing Standards (SAMICS) developed at the Jet Propulsion Laboratory indicate front and back junction formation costs at 37.3 and 5.7 ¢/W, respectively, for a 1 and a 25 MW/yr production volume. Although costing studies have not been completed for liquids, it is expected that the junction forma-

Table III. Lighted and dark I-V measurements

Cell id	Bulk (μs)	J _{sc} (mA/cm²)	V _{oc} (V)	Fill factor	η%	R _s series resistance (Ω-cm²)	R _{sh} shunt resistance (kΩ-cm²)	J ₀₂ (A/cm²)	Remarks
2102-15C	434	33.8	0.578	0.798	15.6	0.31	68	3.2 × 10 ⁻⁷	Liquid boron/POCl ₃ process
2090-36C	339	32.5	0.578	0.802	15.1	0.44	31	6.2 × 10 ⁻⁸	Standard B(BBr ₃)/POCl ₃ process

Table IV. Belt furnace feasibility data

	Belt furnace run	Diffusion furnace run
No. of cells	96	86
V_{oc} (V)	0.544 + 0.010	0.542 + 0.008
I_{sc} (A)	0.578 + 0.027	0.578 + 0.028
Fill factor	0.780 + 0.023	0.778 + 0.029
Avg. efficiency (%)	12.7	12.5

tion costs using liquid dopants can be reduced by at least one-third.

Acknowledgments

The dopants used in this study were obtained from Allied Chemical, Diffusion Technology, Incorporated, Emulsitone Company, and Filmtronics, Incorporated. We wish to thank these suppliers for helpful discussions. The work described in this paper was done at Westinghouse and supported in part under Contract 955909 with the Jet

Table V. Comparison of baseline process with liquid SiO₂/liquid boron process

Baseline process		Liquid SiO ₂ /liquid boron process	
No. of cells	Avg. efficiency (%)	No. of cells	Avg. efficiency (%)
6161	12.6	9265	12.7

Period covered: 3 months production in late 1982.
Baseline process: CVD SiO₂ + BB_{r3}; CVD SiO₂ + POCl₃.
Liquid process: liquid SiO₂ + liquid boron; liquid SiO₂ + POCl₃.

Propulsion Laboratory, California Institute of Technology, as part of the FSA (Flat-Plate Solar Array) Project funded by the Department of Energy (DOE) through an agreement with NASA.

Manuscript submitted June 12, 1983; revised manuscript received June 12, 1984.

Westinghouse Electric Company assisted in meeting the publication costs of this article.

Technical Notes



Effect of Photoirradiation of GaAs Surface during HF Treatment

Masayoshi Ohno

Nippon Telegraph and Telephone Public Corporation, Ibaraki Electrical Communication Laboratory, Tokai-mura, Ibaraki 319-11, Japan

Yasunobu Ishii and Shintaro Miyazawa

Nippon Telegraph and Telephone Public Corporation, Atsugi Electrical Communication Laboratory, Atsugi-shi, Kanagawa 243-01, Japan

Much interest has been centered on the surface of compound semiconductors such as GaAs (1). Controlling the chemical, crystallographic, and electrical properties of the surface has become indispensable for realizing GaAs integrated circuits (2). One of the problems in GaAs IC fabrication, however, is to obtain uniformity of the electric properties for each device as well as a reproducibility from wafer to wafer. It is thus necessary to find primary factors affecting surface change, so as to be able to achieve homogeneity and reproducibility for the surface.

Recently, the effects of various etchants on the GaAs surface have been reported (3-6). Chang *et al.* reported that the etching with HCl or NH₄OH results in As-rich surface (3). In the case of etching with HCl, exposure of the etched surface to a small amount of air allows not formation of oxide nor hydrated oxide, but oxygen chemisorption. After prolonged exposure to air, however, the etched surface is oxidized (5). The mechanism of oxidation needs further clarification.

The oxidation process for a cleaved surface has been also studied (7-8). Room temperature oxidation of the cleaved surface can be induced through exciting the oxygen molecules (7). It seems important that the oxidation of the cleaved surface needs exciting energy provided by discharge.

Photoetching phenomena have themselves been studied for the last several decades (9-11). Etching can be accomplished in very dilute electrolytes assisted by photoirradiation (9). These reports suggest that photoirradiation has considerable effect on the chemical properties of semiconductor surfaces.

This paper reports some preliminary results of investigations into photoirradiation effect, during and after acid treatment, on GaAs surface chemical composition and morphology.

Horizontal Bridgman (HB) grown and liquid encapsulation Czochralski (LEC) grown Cr-doped semi-insulating GaAs (100) wafers were washed in boiling trichloroethylene, then chemically etched of about a 0.2 μm in a solution of 1(1N)NaOH:1(1N)H₂O₂, rinsed in deionized water ($\rho > 18 \text{ M}\Omega \text{ cm}$), and dried by blowing dry N₂. Samples were immersed in several kind of acids, mainly HF, for 3 ~ 600 min, were rinsed in deionized water, and were dried by dry N₂ (acid treatment). After exposure of the samples to air, the GaAs surface was observed under an optical microscope and a scanning electron microscope (SEM), and was examined by Auger electron spectroscopy (AES). In particular, effects of photoirradiation during acid treatment and exposure to ambient air were investigated.

Figure 1 shows a typical HF-treated GaAs (100) surface. The acid treatment was carried out in a solution of 1 (50%) HF + 1H₂O:(1:1)HF, for 20 min in bright light. After it was rinsed in deionized water for 3 min and dried in dry N₂, the surface was partially irradiated using the illuminator of a microscope for 60 min during exposure to air. The micrograph indicates the difference in surface features (morphology) between the irradiated and nonirradiated regions. The appearance of fine particles on the irradiated region could clearly be observed. Consequently, photoirradiation after HF treatment has a particular influence on the appearance of fine particles. The appear-

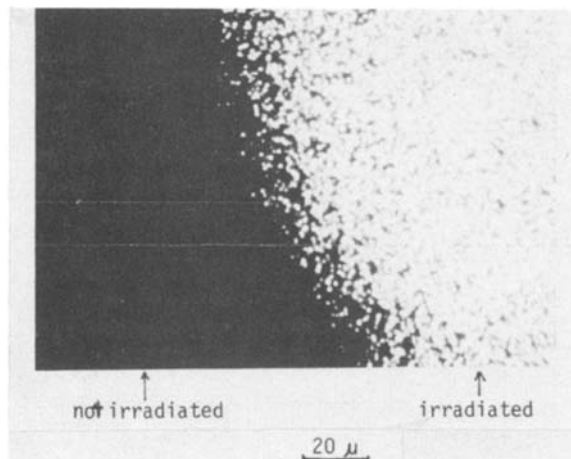


Fig. 1. Micrograph showing HF-treated GaAs surface in bright room light. Right-hand side (bright) area was photoirradiated in air for 60 min using the illuminator of an optical microscope.

ance of fine particles could be observed in the case of HF treatment in (1:1) HF for 3 min and photoirradiation using room light during exposure to air.

Observation using SEM (Fig. 2) made it clear that the fine particles were crystalline material. As the HF-treatment time increased to several hours, the number of the fine crystalline particles increased.

This phenomenon could be observed after acid treatments with sulfuric acid or phosphoric acid, when the acid treatment was carried out for 24h in bright room light using each concentrated acid, respectively. But in the case of hydrochloric acid, this phenomenon could not be observed when GaAs surface was photoetched in bright room light for 24h using concentrated acid. These results agreed well with a study using ellipsometry (12).

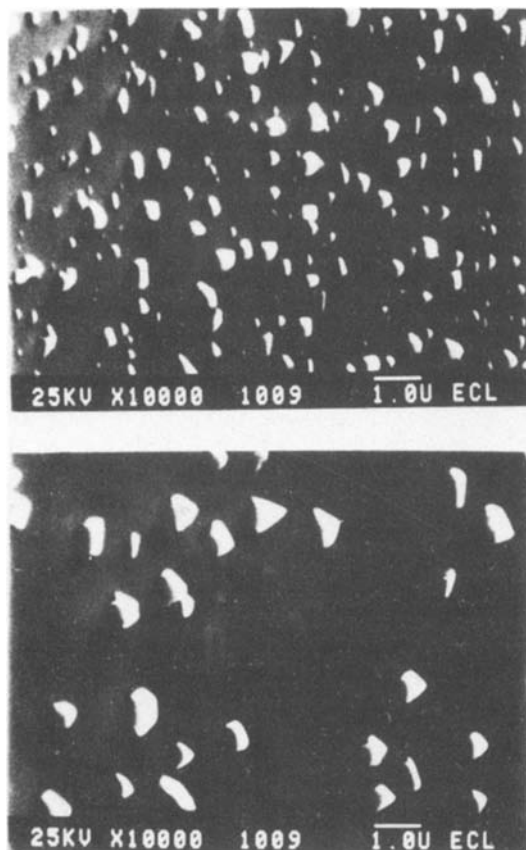


Fig. 2. SEM micrographs of fine particles appearing on GaAs surface after HF treatment in bright light and exposure to air. a (top): Heavily photoirradiated region during exposure to air. b (bottom): Lightly photoirradiated region.

Table I. Dependence of photoirradiation and atmosphere on appearance of fine crystalline particles. HF treatment was done in (1:1)HF for 15 min

Method of etching	Method of air exposure	Fine particles
Etched in bright light	In bright light	Appeared
	Exposed to air	None
Etched in dark	In dark	None
	Exposed to air	None
Etched in dark	In bright light	None
	Exposed to air	None

The effect of photoirradiation and atmosphere on the appearance of fine crystalline particles is summarized in Table I. It can be noted that the appearance of fine crystalline particles on the surface might be assisted by a photoirradiation, during both acid treatment and following exposure to oxygen in ambient air.

The composition of the fine crystalline particles was studied. The particles were found to be sublimated at about 100°C in air and also dissolved in room temperature water in about 15 min. On the basis of these observations, it was speculated that the fine crystalline particles are diarsenic trioxide arsenorite, which is composed of As_2O_3 units (13). From Ref. (13), the rate of vaporization of a crystalline arsenorite As_2O_3 at about 100°C is about 10^0 mg/cm² min. Using this value, the time for the disappearance of 1 μm diam crystals was estimated to be about 10^{-1} min. This estimate agreed well with the observation.

If the particle is diarsenic trioxide claudetite, the time for the disappearance of 1 μm diam crystals was similarly estimated at about $10^6 \sim 10^7$ min. So, the particles do not seem to be claudetite. Furthermore, the particles do not seem to be diarsenic pentoxide; As_2O_5 is deliquescent and easily dissolved in water. A sublimation of gallium oxide is difficult, so the particles do not seem to be gallium oxide.

The results analyzed by AES for surface under various exposure conditions are shown in Fig. 3. The HF treatment was carried out in (1:1)HF for 270 min in bright light. The HF-treated wafers were then stored about 1 day in dark and bright light. One sample was heated up to about 100°C for 30 min after the storage under bright light. In the case of HF treatment in bright light and followed by storage in the dark, the surface was covered with almost arsenic only, and no fine crystalline particles appeared. This indicated that acid treatment in bright light made the surface rich in As (3). However, with storage under photoirradiation, oxygen and gallium increased, while arsenic decreased, and fine crystalline particles appeared. After the sample was heated up to about 100°C for 30 min, arsenic and oxygen decreased, while gallium did not vary and the fine crystalline particles vaporized. This change indicates that the photoirradiation under air exposure brought about oxidation of the

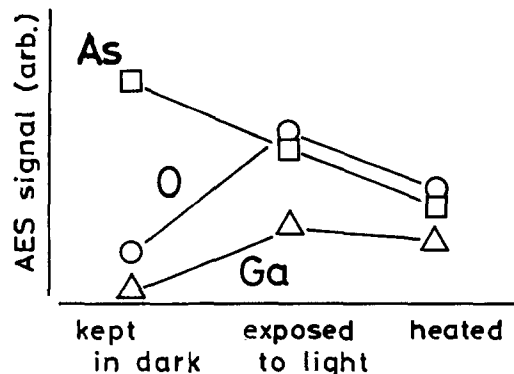


Fig. 3. Results of AES for various treatments after HF treatment. HF treatment was carried out in (1:1) HF for 270 min in bright light.

Table II. Dependence of irradiated light wavelength upon appearance of fine crystalline particles

Wavelength (nm)	Fine particles
350 < λ < 600	Appeared
690 < λ	Appeared
900 < λ	None

As-rich surface, resulting in a production of As₄O₆ fine crystalline particles. The density (in number) of the fine particles increased with HF treatment time; this may be due to the increment of the As layer. The oxidation of the arsenic layer brought about the appearance of the GaAs layer under the initial As layer, and thus the gallium content was increased.

The mechanism of the fine particles' formation is related to the dependence of irradiated light wavelength on the phenomenon. Then, the dependence was investigated as follows in order to identify the mechanism. HF treatment was done in (1:1)HF for 15 min in bright light. The photoirradiation under air exposure was carried out under filtered illumination for 60 min using an optical microscope. The dependence of irradiated light wavelength on this phenomenon is shown in Table II. It seems that electron-hole pairs creation by the photoirradiation play an important role in the phenomenon (14). This is because the threshold of photoirradiation effect exists between 690 and 900 nm regions. It was speculated that the threshold wavelength may be around the bandgap energy of GaAs.

In conclusion, HF etching treatment under photoirradiation resulted in an As-rich surface for GaAs crystal. The As-rich surface could be oxidized in air by means of photoirradiation, and fine crystalline particles were formed on the surface. The particles were thought to be As₄O₆ (arsenorite). Based on the above results, much attention has to be paid to the photoirradiation in both etching process and air exposure of the GaAs surface in the GaAs IC process.

Acknowledgments

The authors would like to express their thanks to Y. Watanabe for the AES experiments. They are also indebted to M. Ohmori, Y. Nanisi, H. Yamazaki, and T. Honda for their support and valuable comments during this experiment. One of the authors (M.O.) in particular would like to thank Y. Katayama, T. Kurokawa, T. Okada, H. Hiratsuka, and T. Yamada for their helpful discussions and much administrative support.

Manuscript submitted March 7, 1984; revised manuscript received June 1, 1984.

Nippon Telegraph and Telephone Public Corporation assisted in meeting the publication costs of this article.

REFERENCES

- O. Leistiko, Jr. and C. A. Bittman, *Solid State Electron.*, **16**, 1321 (1973)
- E. H. Nicollian, *J. Vac. Sci. Technol.*, **8**, S-39 (1971).
- C. C. Chang, P. H. Citrin, and B. Schwartz, *ibid.*, **14**, 943 (1977).
- N. Bottka and J. H. Dancy, *This Journal*, **127**, 2521 (1980).
- P. A. Bertrand, *J. Vac. Sci. Technol.*, **18** 28 (1981).
- D. E. Aspnes, G. P. Schwartz, G. A. Gualtieri, A. A. Studna, and B. Schwartz, *This Journal*, **128**, 590 (1981).
- P. Pianetta, I. Lindau, C. M. Garner, and W. E. Spicer, *Phys. Rev. B*, **18**, 2792 (1979).
- H. Iwasaki, Y. Mizokawa, R. Nishitani, and S. Nakamura, *Jpn. J. Appl. Phys.*, **18**, 525 (1979).
- R. W. Haisty, *This Journal*, **108**, 790 (1961).
- F. Kuhn-Kuhnenfeld, *ibid.*, **119**, 1063 (1972).
- K. W. Frese, Jr., M. J. Madou, and S. R. Morrison, *J. Phys. Chem.*, **84**, 3172 (1980).
- A. C. Adams and B. R. Pruniaux, *This Journal*, **120**, 408 (1973).
- K. A. Becker, A. Plieth, and I. N. Stranski, *Prog. Inorg. Chem.*, **4**, 1 (1962).
- G. Goldbach and K. Graff, *Wiss. Ber. AEG-Telefunken*, **42**, 156 (1969).

Stress Effects in Boron-Implanted Polysilicon Films

Min S. Choi* and Eric W. Hearn*

IBM Corporation, General Technology Division, East Fishkill Facility, Hopewell Junction, New York 12533

Polycrystalline silicon films are used throughout the semiconductor industry in the fabrication of both metal-oxide-semiconductor (MOS) and bipolar products. For example, in MOS products, doped polysilicon is used for gate and interconnection materials. In bipolar products, polysilicon is used for device isolation, passive resistors, or active base elements.

While these films are usually used with different ranges of doping, stress measurement of doped polysilicon is not well reported.

Earlier reports of thick (up to 500 μm) intrinsic polysilicon films gave tensile stress properties (1). Later reports using thinner films (4000-6000 \AA) showed compressive stress properties (2). The thinner films were deposited under different conditions than the thick films, and were both intrinsic and boron diffused.

The purpose of conducting this study was to determine quantitative stress measurements made on boron-implanted and annealed polycrystalline films to assess the possible effect of stress on device fabrication, such as pattern distortion and change in the electrical property of a substrate. Comparative warpage measurements were made treating various film structures as substrates.

The effect of doping concentrations and annealing temperatures on the film stress was also studied.

*Electrochemical Society Active Member.

Film stress was determined using comparative warpage measurements on oxide, polysilicon, and nitride films.

Experimental Procedures

Sample preparation.—The substrates used were p-type (10-20 Ω cm), 82.5 mm diam and 0.4 mm thick. After 2000 \AA thermal oxide was grown, polysilicon was deposited to a thickness of 2000-5000 \AA by low pressure chemical vapor deposition (LPCVD) at 625°C by the decomposition of silane. A 500 \AA LPCVD oxide cap was deposited at 430°C, and two-thirds of the samples were ion implanted with boron (1×10^{14} - $5 \times 10^{15}/\text{cm}^2$, 45-100 keV) and annealed. All films except nitride were simultaneously deposited on both sides of wafer. Dose and energy of the implantation were adjusted so that the doping concentration after annealing was 5×10^{18} or $1 \times 10^{20}/\text{cm}^3$. The peak dopant concentration is located near the middle of the films as determined by published data (3). This approach assumes that boron spreads quickly at annealing temperatures greater than 925°C. This was verified by SIMS analysis in a separate experiment.

After annealing (925°-1100°C, 60 min), back-side reactive ion etching (RIE) of oxide or of oxide and polysilicon was done on some wafers. Subsequently, 2000 \AA nitride was deposited on some of these wafers at 1000°C using SiH₄, NH₃, and H₂ carrier gas. This series of procedures resulted

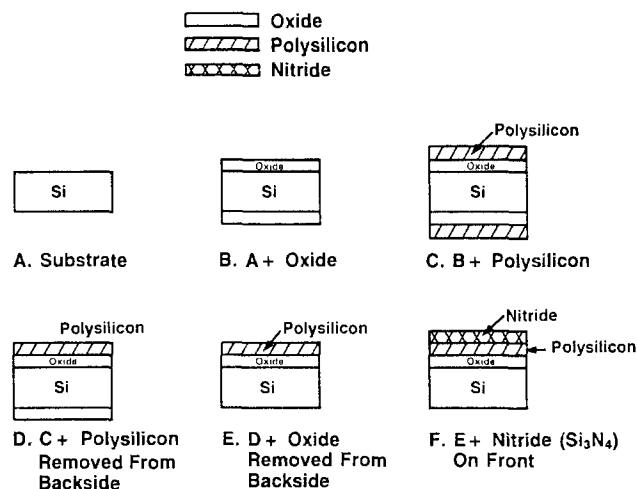


Fig. 1. Sequence of oxide, polysilicon, and nitride film depositions used in this experiment.

in the film configurations shown in Fig. 1. Table I gives the details of the respective wafer splits for doping, film thicknesses, and annealing temperatures.

Warpage measurements.—The warpage of wafers was measured on a Mikrokator thickness gauge (see Fig. 2). This measurement resulted in the warpage values used in the modified stress equation (4) for small bending due to film stress (σ_f)

$$\sigma_f = \pm \alpha \frac{1}{3} \frac{t_s^2 \Delta h}{t_f r^2} \frac{E_s}{1 - \nu} \quad [1]$$

where t_s is the substrate thickness, t_f the film thickness, r the radius of wafer, Δh the deviation of wafer from optical flat (warpage), E_s Young's modulus of the silicon substrate (1.805×10^{12} dyne/cm²), ν Poisson's ratio for the substrate, α a correction factor (1.5) for deflection measurement,¹ + the tensile or concave warpage, and - the compressive or convex warpage.

Results

Warpage measurements.—From the experimental data represented in Fig. 1 and 2 and Table I, stress was calculated using the following hypothesis.

Warpage values may be compared interchangeably between any composite structure by defining the substrate to be that portion of the wafer cross section containing the greatest number of symmetric top and bottom layers.

This assumption is valid under the condition that the film thickness is negligible compared to the wafer thickness, so the elasticity of the wafer is not affected. After

widely-accepted experimental x-ray warpage data (5) were compared to the present "disk" warpage measurement and resulted in a correction factor of 1.5.

Table I. Experimental parameters for each wafer

Wafer #	Doping	Thickness	Temp. (60 Min. Anneal)			
1	No Doping	3000Å Polysi	Rm.	All Films Have 2000Å Oxide		
2			925°C			
3			1000°C			
4			1100°C			
5	5 × 10 ¹⁹ /cm ³	2000Å Polysi	1100°C		Si ₃ N ₄ (2000Å)	
6			4000Å Polysi			
7			5000Å Polysi			
8	5 × 10 ¹⁹ /cm ³	3000Å Polysi	Rm.		All Films Have 2000Å Oxide	
9			925°C			
10			1000°C			
11			1100°C			
12	1 × 10 ²⁰ /cm ³	2000Å Polysi	1100°C			Si ₃ N ₄ (2000Å)
13			4000Å Polysi			
14			5000Å Polysi			
15	1 × 10 ²⁰ /cm ³	3000Å Polysi	Rm.			All Films Have 2000Å Oxide
16			925°C			
17			1000°C			
18			1100°C			
19	2000Å Polysi	5000Å Polysi	1100°C			
20			5000Å Polysi			

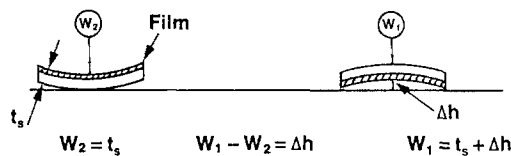


Fig. 2. Warpage measurement

the warpage for a particular film or film composite was measured, the stress was calculated using Eq. [1].

For example (from Fig. 1), the substrate warpage caused by the polysilicon film is calculated from the warpage difference between two cross sections: $D_{(\text{warpage})} - B_{(\text{warpage})} = \text{Polysilicon}_{(\text{warpage})}$ by using B as the substrate. Equivalent results were obtained using levels D and C . For the stress values of silicon nitride, good correlation was found between direct and indirect level comparisons, i.e., $F_{\text{warpage}} - E_{\text{warpage}}$ (direct) as compared to $(F-A) - \{(E-C)\}$ (indirect).

To show the effectiveness of the hypothesis, Fig. 3 illustrates the correlation of polysilicon stress calculated using two different structures.

Figure 4 shows similar results for polysilicon + oxide, and Fig. 5 shows the results for Si₃N₄.

Standard linear regression (6) method was used to get the correlation coefficients. As seen in Fig. 3-5, the correlations are good and give assurance that the warpage

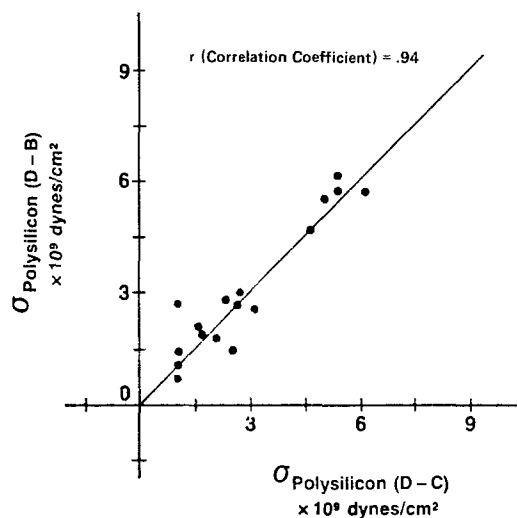


Fig. 3. Correlation of comparative warpage measurements on polysilicon films.

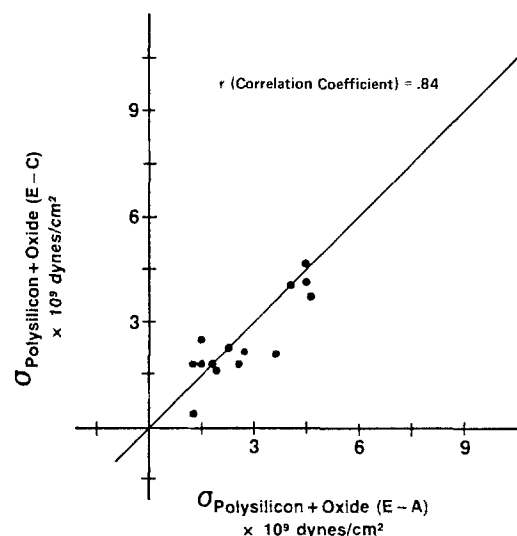


Fig. 4. Correlation of comparative warpage measurements on polysilicon + oxide films.

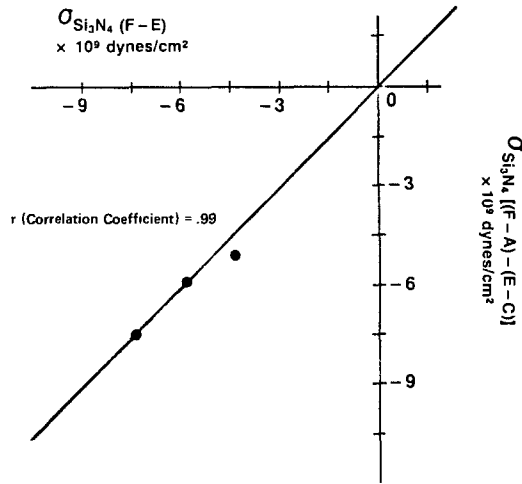


Fig. 5. Correlation of comparative warpage measurements on Si₃N₄ films.

values are true indicators of stress changes associated with processing.

These data indicate that the stress of the polysilicon on top of the oxide is compressive and varies between approximately -1×10^9 and -6×10^9 dyne/cm² over the entire range of doping and heat-treatments used in this experiment.

Polysilicon + oxide stress (Fig. 4) was also compressive, and varied between -1×10^9 and -5×10^9 dyne/cm². This is comparable to either SiO₂ or polysilicon.

The nitride stress in Fig. 5 is tensile and ranges between 4.0 and 8.0×10^9 dyne/cm². This value is slightly lower than unannealed nitride films on bare substrates reported in Ref. (5). The difference could be a result of the nitride films' being deposited under different conditions.

Undoped polysilicon and nitride films were deposited on bare substrates; their respective stress values were 4.0×10^9 and 7×10^9 dyne/cm². This compares favorably with the undoped polysilicon and nitride values on top of oxide films. This lends credence to the relative film comparative technique.

Effect of annealing temperature on stress.—Figure 6 is a plot of stress calculated for samples with 3000Å polysilicon films that were exposed to various doping levels and heat-treatments.

The results show that there is a temperature threshold near 1000°C, where the stress decreases. Unfortunately, one of the samples (no. 16) broke, and the second data point for the 10^{20} /cm³ curve is missing. However, stress and grain size (and morphology) do not change appreciably for the different concentrations and annealing tem-

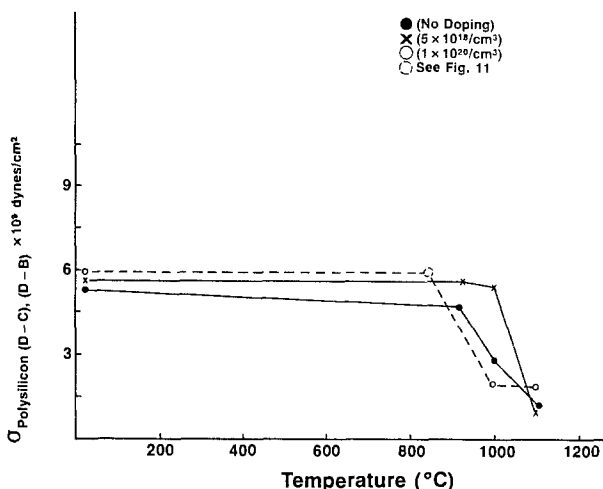


Fig. 6. Annealing temperature vs. polysilicon film stress (3000Å) for different doping levels.

peratures up to 1000°C [see Fig. 6 and Ref. (11)]. Based on these findings, we feel justified in assuming the graphed qualities for the missing data point. The entire data base is sparse. However, the trend is clear, and the correlation of the earlier data (Fig. 3-5) is encouraging.

It is also noted that for unannealed samples, the stress is higher in the implanted case than in those samples without implantation.

This trend seems to continue up to where the stress obviously changes (relaxation temperature). This is a reasonable trend, considering that the implantation damage may not be annealed thoroughly at temperatures lower than the relaxation temperature.

The relaxation of the 5×10^{18} /cm³ sample occurs at a higher temperature than does the intrinsic polysilicon. This is probably due to a concentration effect, and will be explained in the discussion section.

Discussion

It has been reported that the compressive stress of thermal oxide can be explained by a thermal mismatch between the oxide and the silicon substrate (2). The observed tensile stress for the CVD nitride films is largely caused by the intrinsic film stress (7). For the 60-500 μm thick polysilicon films grown on oxidized wafers using different reaction gases and temperatures above 1100°C, some authors report tensile stresses (1, 8). However, for the thin film case (4000-6000Å) (2) compressive stress is in agreement with the observations reported here.

The nature of the observed compressive stress of the polysilicon film is believed to be due to the intrinsic properties of the film because the difference in the coefficients of expansion between polysilicon and single-crystal silicon is small (1, 2).

The stress relaxation near 1000°C, observed for different ranges of doping (Fig. 6), is assumed to be due to the annealing effect. The grain-size measurement of a transmission electron microscope (TEM) showed that substantial grain growth occurs above 1000°C.

The relaxation temperature of the higher doped (5×10^{18} /cm³) sample is higher than that of the undoped sample. This could be attributed to the ion-implantation damage rather than the doping effect. TEM results show that film morphology and grain size look about the same in the three samples at 1000°C. However, for the highest doped samples (1×10^{20} /cm³), the stress near the relaxation temperature appears lower than the undoped or the 5×10^{18} /cm³ samples. This may be explained as follows.

Brotherton *et al.* (9) report a relationship exists between the substrate lattice constant and the stress in the lattice (σ_s).

Also, the lattice constant of silicon is shown to decrease (resulting in a tensile stress) as a function of boron concentration (10) (see Fig. 7). Assuming a lattice constant corresponding to the 1×10^{20} /cm³ doping concentration used in this experiment, Fig. 8 shows the resultant change in stress due to boron concentration using Brotherton's equation in Ref. (9).

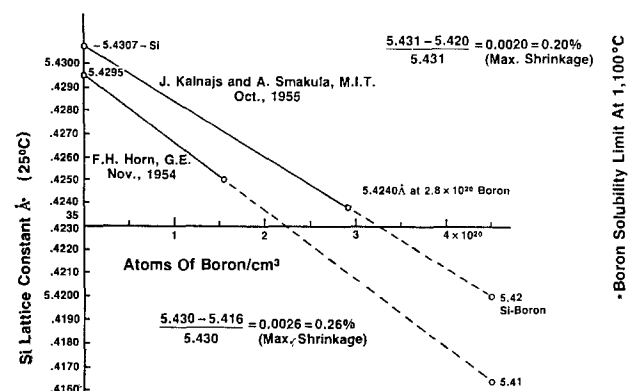


Fig. 7. Silicon lattice constant vs. boron concentration

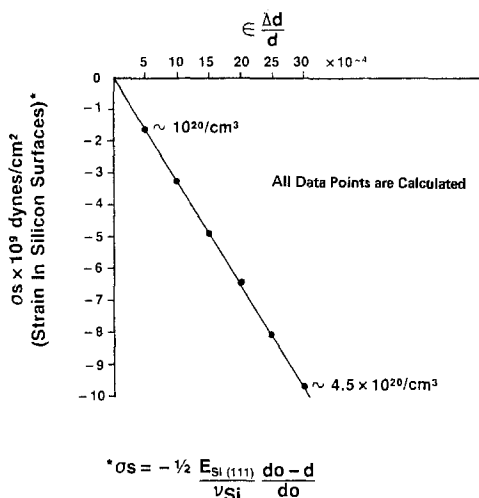


Fig. 8. Stress induced by change in silicon lattice constant as a result of boron in the lattice. From Ref. (9).

This calculation shows that at $1 \times 10^{20}/\text{cm}^3$ boron concentration, the stress can change 2×10^9 dyne/cm² in the tensile direction. If we assume a similar behavior for the polycrystalline films, the magnitude of the induced tensile stress is comparable to the measured compressive stress in these polysilicon films and can, therefore, partially compensate for the film stress.

Summary

Comparative warpage measurements were used to measure the film stress of polysilicon and nitride. The film stress of polysilicon (2000-5000Å) on top of oxide was found to be approximately $-(1-5) \times 10^9$ dyne/cm² (compressive) over the range of doping from intrinsic to $10^{20}/\text{cm}^3$, and of annealing temperature from 25° to 1100°C. Temperature effects on polysilicon film stress were

larger than the doping effects. The film stress of nitride deposited on oxide plus polysilicon was found to be $+(4-8) \times 10^9$ dyne/cm² (tensile). Stress relaxation was observed near 1000°C annealing temperature for the polysilicon films.

Acknowledgments

The authors wish to thank R. Hallock, T. Hansen, and A. Ferguson for their processing support, K. Yang for his TEM work, and K. Yang and M. Poponiak for their valuable discussions.

Manuscript submitted March 7, 1984; revised manuscript received ca. May 7, 1984. This was Paper 374 RNP presented at the Detroit, Michigan, Meeting of the Society, Oct. 17-21, 1984.

IBM Corporation assisted in meeting the publication costs of this article.

REFERENCES

1. T. Suzuki, A. Mimura, and T. Ogawa, *This Journal*, **124**, 1776 (1977).
2. I. T. Toncheva and I. S. Vassilev, *Thin Solid Films*, **60**, 353 (1979).
3. W. Johnson and J. Gibbons, "Projected Range Statistics in Semiconductors," Stanford University Book Store, Palo Alto, CA (1969).
4. G. G. Stoney, *Proc. R. Soc. (London)*, Ser. A., **82**, 172 (1909).
5. E. Hearn, *Adv. X-Ray Anal.*, **20**, 273 (1977).
6. H. D. Brunk, "Introduction to Mathematical Statistics," Ginn Blaisdell, New York (1965).
7. M. Tamura and H. Sunami, *Jpn. J. Appl. Phys.*, **11**, 1097 (1972).
8. T. I. Kamins, *This Journal*, **121**, 681 (1974).
9. S. D. Brotherton, T. G. Read, D. R. Lamb, and A. F. W. Willoughby, in "Semiconductor Silicon," H. R. Huff and R. R. Burgess, Editors, p. 385, The Electrochemical Society Softbound Proceedings Series, Princeton, NJ (1973).
10. G. H. Schwuttke, "Epitaxial Growth, Part A," p. 281, Academic Press, San Francisco (1975).
11. L. Mei, M. Rivier, Y. Kwark, and R. W. Atton, *This Journal*, **129**, 1791 (1982).

Short Time Annealing of Coevaporated Tungsten Silicide Films

T. O. Sedgwick,* F. M. d'Heurle,* and S. A. Cohen

IBM T. J. Watson Research Center, Yorktown Heights, New York 10598

Short time annealing (STA) which is thermal processing for times short compared to standard furnace annealing is being explored as a means of reducing the time-temperature exposure of device structures in silicon technology (1). Early efforts in STA employed pulsed or CW laser or electron beams to heat samples for times of milliseconds down to nanoseconds. These energy sources, however, usually require scanning of a small area spot over a large sample with the disadvantages of nonuniform exposure, high localized thermal stresses, and low sample throughput. Many recent STA studies employ incoherent light sources to anneal large-area samples (~10 cm) which are spatially uniform in temperature for time intervals of 1-100s. The technique is best referred to as isothermal STA. These heat sources include arrays of tungsten halogen lamps, high intensity argon or xenon discharge lamps, and resistance-heated graphite blackbody radiation sources. This technique is meant to acquire the additional advantage of a full wafer isothermal process while retaining the known advantage of a reduced thermal cycle.

As device dimensions shrink and the degree of integration increases in VLSI technology, refractory metal silicides have found important application as device interconnections because of their metallic-like conductivity,

ability to be oxidized, and thermal stability (2, 3). For many applications, a silicide/polycrystalline Si (poly-Si) double layer called a polycide structure is used (4) as a gate electrode and interconnection.

The silicides of Ta, Mo, and W, all of which are being investigated as potential high conductivity interconnects can, in principle, be formed by direct reaction. However, the reaction of the metal with Si occurs at high temperatures and with poor reproducibility. Thus, direct reaction has not been the preferred fabrication method for device applications. We note, however, that Wakita *et al.* and others (5) have formed Mo and W silicide by CW argon laser annealing of the metal/silicon structure.

Reproducible formation of refractory silicide may be obtained by coevaporation or cosputtering of the elements or sputtering of the compound, or CVD of suitable precursors. All these techniques are finding application in practical device fabrication. Even with this initial degree of premixing, an additional thermal cycle in the range of 1000°-1200°C is required to crystallize the compounds and produce highly conducting films. Tsai *et al.* (6) reported the dependence of film resistance on annealing time and temperature, but did not investigate annealing times less than 3 min because of standard furnace process limitations. Recently, Sedgwick *et al.* (7) and McPherson *et al.* (8) have reported on the STA of WSi₂ and MoSi₂, respectively.

*Electrochemical Society Active Member.

In the fabrication of small devices in VLSI, there are four important requirements on this thermal anneal process: (i) the silicide should become homogeneous and well adherent, (ii) the silicide should become as conductive as possible, (iii) the time-temperature cycle should not perturb the dopant distribution in any underlying partly fabricated device, and (iv) the dopant in the polycrystalline Si (poly-Si) of a polycide structure should not be grossly depleted.

In the present study, we present results of the STA of WSi_2 with reference to the above items. With regard to item (ii), we have studied annealing down into the few second time range. With regard to (iii), we compare the properties of the silicide after a STA at $1200^\circ C$, 6s with those after a standard furnace anneal at $950^\circ C$, 30 min. With respect to diffusion in Si, these two thermal treatments are equivalent; from a standard diffusion calculation, they lead to minimal dopant motion of B in a submicron FET technology where the B implant is already present in the channel region of the device. The results for item (iv) are as yet only qualitative and preliminary.

Experimental

Figure 1 shows a schematic of the graphite resistance heater used for the STA experiments. The horizontally arranged resistance heater has a free standing area of 4×5 in. and is 0.050 in. thick. It is made of graphite from POCO. Rapid heating is achieved by passing up to 600A alternating current at 14V through the graphite using the water-cooled clamps. The polycide samples about 1 cm^2 , were placed on small quartz chips 0.020 in. thick in the center of the graphite plate. The temperature of the sample was monitored *in situ* using a Irtroic Model 3100 IR pyrometer focused to a $1/2$ mm diam spot. It was positioned to look vertically down, through a quartz window and small holes in horizontal Ta shields (not shown in Fig. 1), at the sample top surface. The ambient was dry N_2 and the heating apparatus was carefully purged at room temperature and at $450^\circ C$ before high temperature annealing.

Typical time temperature curves are shown for nominal $1200^\circ C$, 3s exposures in Fig. 2, and a $1200^\circ C$, 60s exposure in Fig. 3. The IR pyrometer was calibrated by focusing it close to a Pt-PtRd thermocouple bonded to the chip surface and allowed to equilibrate for at least 15s. Figure 4 shows that the thermocouple and the pyrometer read the source temperature within $12^\circ C$ over the range 900° - $1200^\circ C$. STA experiments in the time range of a few seconds still resulted in overall agreement within $12^\circ C$. The furnace anneal at $950^\circ C$, 30 min was carried out in a standard furnace with argon or N_2 ambient.

GRAPHITE STRIP HEATER

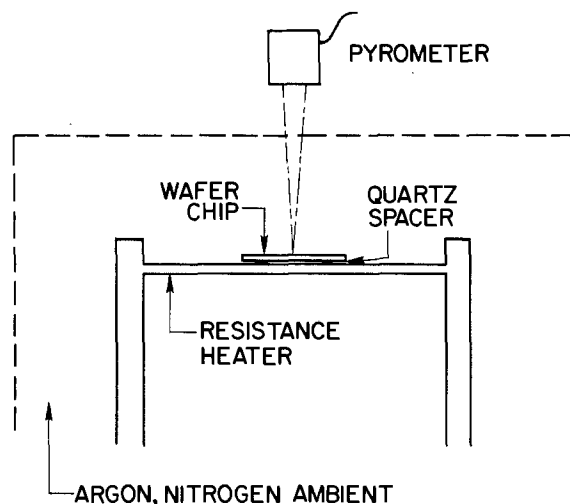


Fig. 1. Schematic of graphite resistance STA apparatus

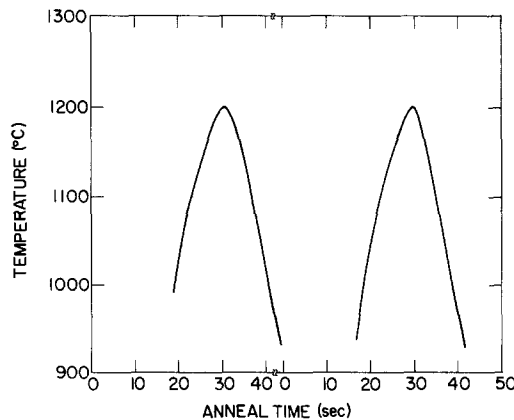


Fig. 2. Pyrometer trace of time-temperature nominal 3s anneal at $1200^\circ C$ in graphite resistance apparatus.

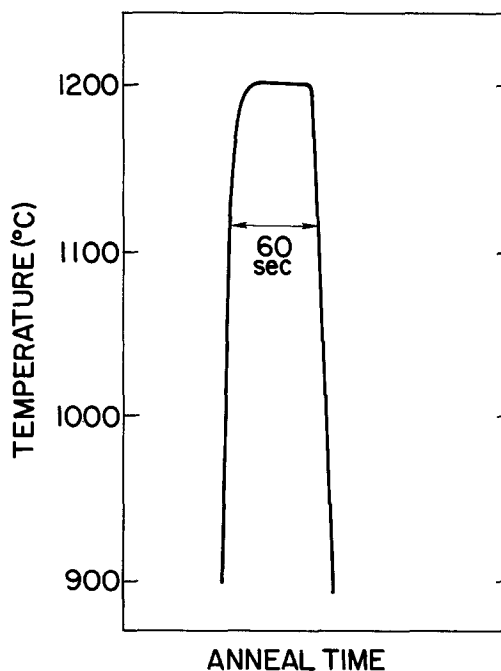


Fig. 3. Pyrometer trace of time-temperature for a 60s anneal at $1200^\circ C$.

The polycide structures I, II, and/or III in Fig. 5 were used in the experiments. The silicide was deposited by coevaporation with a stoichiometry of $WSi_{2.1-2.3}$. Structure I was 1300\AA silicide on a Si (100) wafer. Structure II was 1300\AA coevaporated WSi_2 on 1500\AA of heavily doped P-, As-, or B-doped LPCVD or CVD poly-Si on 1000\AA dry wet thermal SiO_2 . Structure III was an RIE patterned film with submicron dimensions. This structure was 300\AA evaporated silicon on 1500\AA coevaporated WSi_2 on 1000\AA of $POCl_3$ -doped polysilicon on 100\AA thermal SiO_2 .

Sample resistance was measured with a four-point probe. B, P, and As profiles were measured by secondary ion mass spectrometry (SIMS) and W profiles were measured with Rutherford backscattering spectroscopy (RBS).

Results and Discussions

Figure 6 shows an RBS profile of the W in a structure II sample with B-doped polycide as deposited, both after a $950^\circ C$, 30 min furnace anneal and after a $1200^\circ C$, 6s STA exposure. The unintentional (but useful for the present experiment) W concentration minimum (corresponding to a Si concentration maximum) just below 2.07 MeV in the as-deposited film is not removed by the furnace anneal, but good homogenization is apparent after the STA process. [This is in agreement with the previous observations (6, 9) that while excess W can be annealed out at tempera-

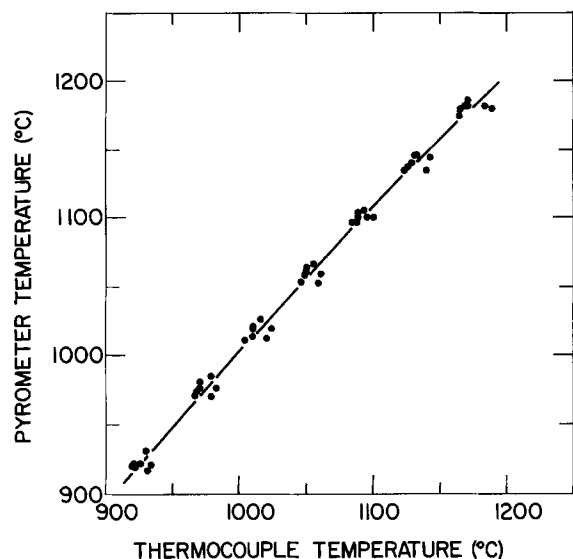


Fig. 4. Calibration showing pyrometer vs. thermocouple measured temperature.

POLYCIDAL STRUCTURES

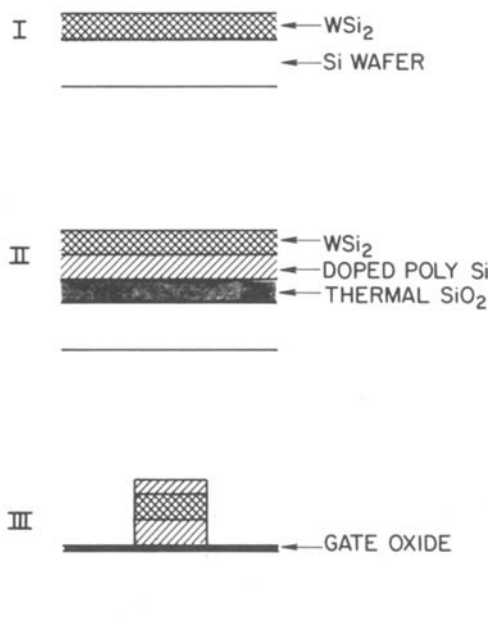


Fig. 5. Schematic of various polycide structures, I, II, and III (see text for detailed fabrication).

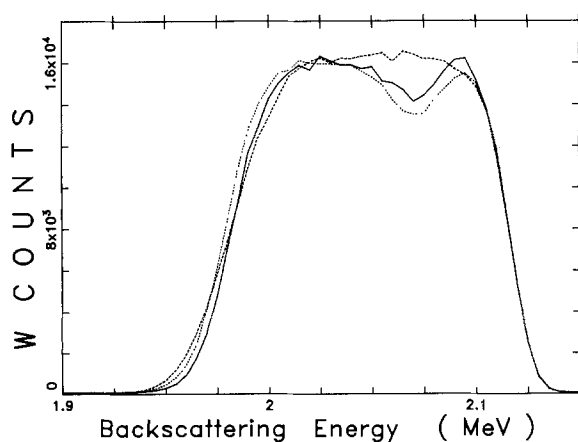


Fig. 6. W content by RBS of structure II. Solid curve: as deposited. Dotted curve: after 950°C, 30 min furnace anneal. Dashed curve: after 1200°C, 6s STA treatment.

tures as low as 800°C, the elimination of excess Si requires temperatures of the order of 1000°C.]

Figures 7a and 7b show samples of structure III after STA at 1200°C, 6s. The perfectly intact lines exhibit no adverse effect of STA.

The variations of resistance with annealing time and temperature for polycide samples of structures I and II are displayed, respectively, in Fig. 8 and in Fig. 9, 10, and 11. Within a small variation, all the results are very similar even though the poly-Si in Fig. 9, 10, and 11 is heavily doped with P, As, and B, respectively. The major result is that the resistance is a fairly strong function of the temperature. The resistance decreases only weakly as a function of increasing time in the range 3s to 5 min at both 1000° and 1100°C. At 1200°C, the resistance is independent of time. Apparently, at 1200°C, the silicide annealing process is fast compared to 3s.

Table I compares the minimum resistance observed in samples of structure II for both STA at 1200°C, 6s and fur-

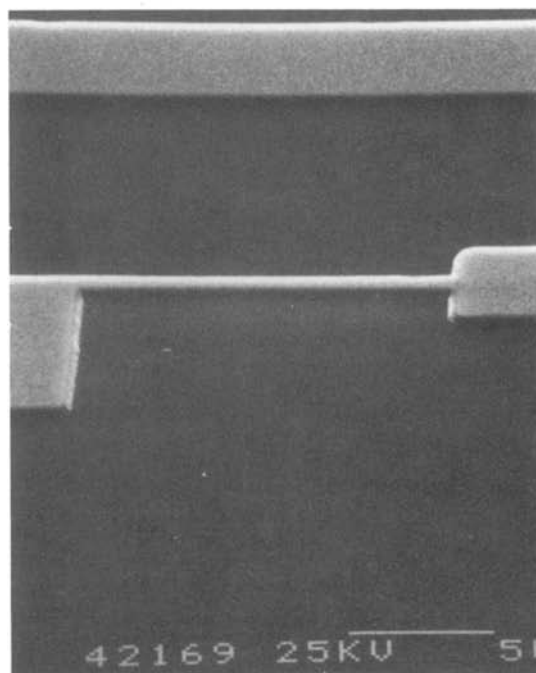
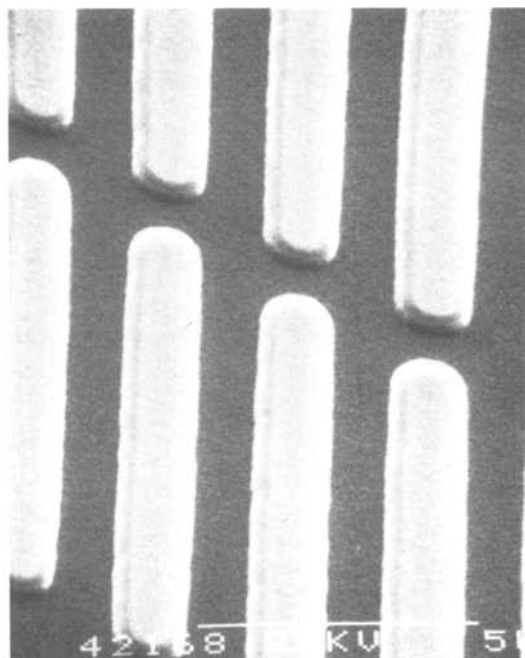


Fig. 7. Etched polycide structure II samples after 1200°C, 10s anneal

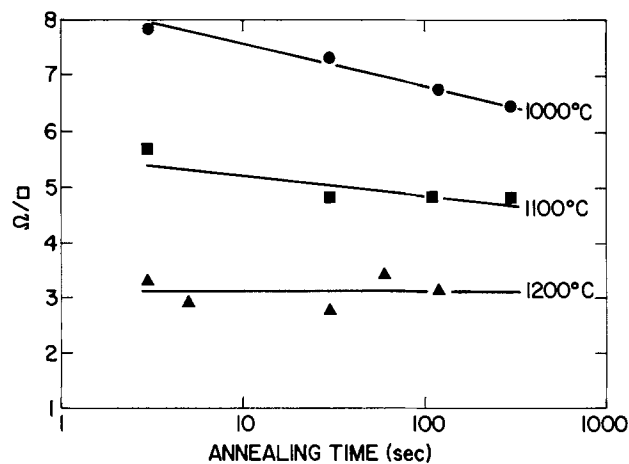


Fig. 8. Four-point probe sheet resistance of 1300Å coevaporated WSi_2 on single-crystal $\langle 100 \rangle$ Si surface as a function of annealing time and temperature.

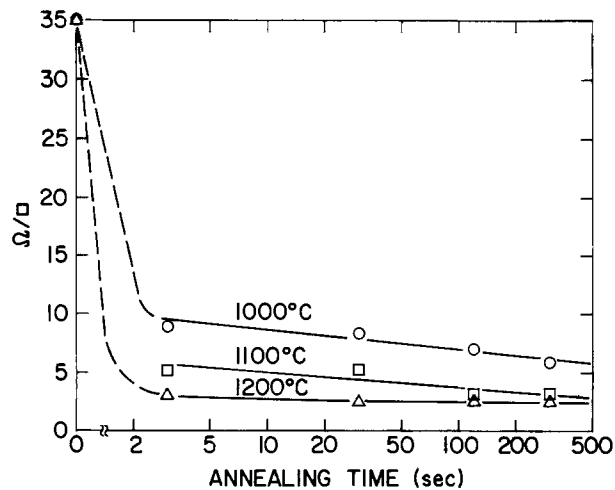


Fig. 11. Sheet resistance of 1360Å WSi_2 and B-doped poly-Si after annealing at various times and temperatures.

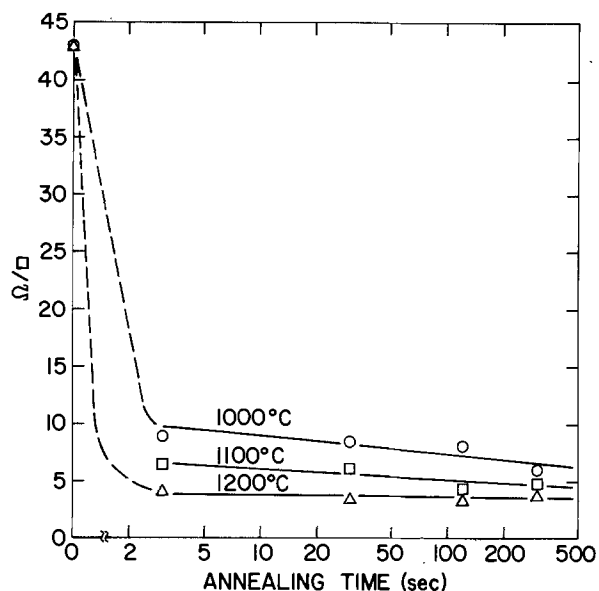


Fig. 9. Sheet resistance of 1360Å WSi_2 on P-doped poly-Si after annealing at various times and temperatures.

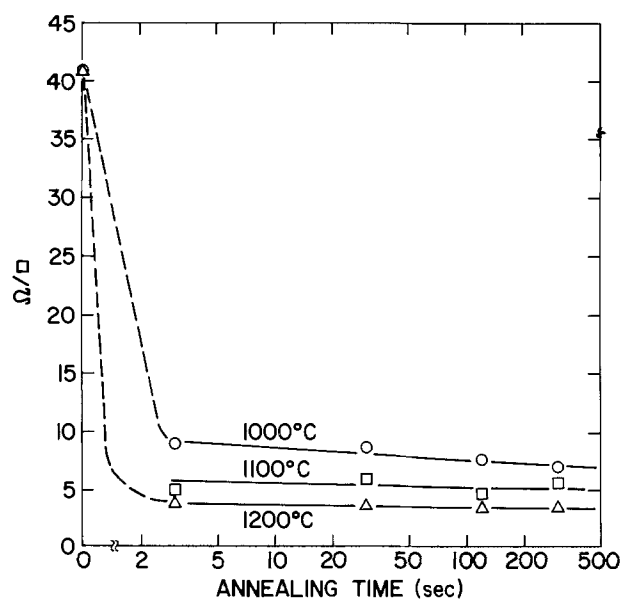


Fig. 10. Sheet resistance of 1360Å WSi_2 on As-doped poly-Si after annealing at various times and temperatures.

nance anneal at 950°C, 30 min. The principal result is that the STA process yields resistances of two to three times less than for the furnace anneal. We will touch on this fact again at a later point. The small differences between samples with differently doped poly-Si underlayers are judged not significant without further supporting data.

At this time, we offer some qualitative comments but do not present a quantitative explanation for the silicide resistivity as a function of time and temperature, a phenomena which we believe is quite complex. The grain size of the silicide films has not been measured in this work, although it no doubt increases as a function of annealing time and temperature. In general, there exists a positive correlation between grain size and conductivity in silicide films. However, this is not enough to justify the often-encountered statement that the decrease in resistivity is due solely to grain growth. The attempt to relate quantitatively grain sizes and resistivities in silicide films leads to material parameters which appear too extreme to be physically valid (2, 10). The lowest resistivity achieved, about 35 $\mu\Omega$ cm (Fig. 8, 11), appears to be in good concordance with the minimum published value for WSi_2 .

The data of Table I clearly show the factor of 2 to 3 advantage in lowered resistance when using a 1200°C, 6s *vs.* a 950°C, 30 min anneal. As pointed out above, these two widely different thermal treatments were chosen to lead to a minimal and equivalent B diffusion in any underlying device. Figure 12 shows an Arrhenius-like plot of B diffusion in Si where the area with vertically hatched lines corresponds to the acceptable process region. For the limiting B-diffusion line, we have used a SUPREME calculation, where the shallow-channel B is required not to move significantly. The actual device requirement is that the substrate sensitivity not be degraded significantly in a submicron FET technology (11). In terms of the dopant motion, this corresponds to a B diffusion less than 700Å at a C/C_0 value of 3.3×10^{-2} . On the same Fig. 12, one also finds the apparent temperature *vs.* time region (hatched with horizontal lines) required to obtain a silicide sample resistance less than 4 Ω/\square . Only the data at 1100° and 1200°C were used. The very high apparent thermal activation of the silicide annealing process defines a new processing region, at high temperatures

Table I. Resistance of WSi_2 polycide structure II

	STA anneal	Furnace anneal
Structure	1200°C, 6s	950°C, 30 min
WSi_2 /B-doped poly-Si	2.8 Ω/\square	10.5 Ω/\square
WSi_2 /P	3.7	8
WSi_2 /As	3.7	8.8
Resistivity of silicide	38-50 $\mu\Omega$ cm	109-143 $\mu\Omega$ cm

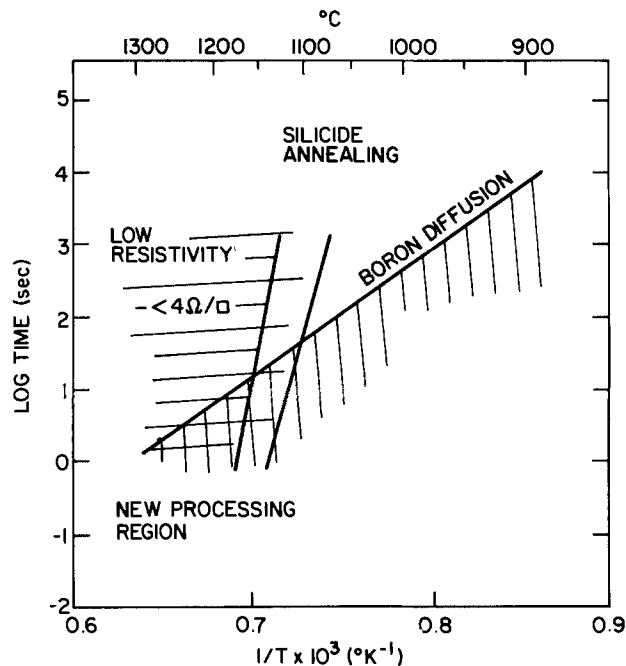


Fig. 12. Arrhenius-type plot showing overlap regions (cross-hatched) where minimal B diffusion occurs (line-hotched) and where sufficient silicide annealing (lines hatched) to achieve a resistance less than $4 \Omega/\square$.

and short times, where both sufficient silicide conductivity is obtained and minimal diffusion is expected.

The definition of such a satisfactory new region for thermal treatment in the present case is possible because of the wide range of temperatures and times available currently in thermal annealing, and because the thermal activations for the two processes are widely different.

Figure 13 shows SIMS profiles of the B concentration in a polycide sample structure II as deposited, after STA, and after furnace annealing. The depth scale is not calibrated because of the differing sputtering rates but the step-like B concentration in the as-deposited trace corresponds to the doped poly-Si layer and the region to the left corresponds to the WSi_2 layer. Upon STA or furnace annealing, the B redistributes throughout both the silicide and poly-Si layers. Unfortunately, because of the matrix effect on the SIMS sensitivity in the different layers, the actual concentration of B in each layer may not be equal, even though the B levels have the same relative height. Samples of WSi_2 on both P- and As-doped poly-Si were measured, but are not shown here. In these cases, there was a significant decrease in dopant in the poly-Si layer after the 950°C , 30 min furnace anneal and an even greater decrease after the 1200°C , 6s STA cycle. There was clearly a net loss of dopant in the P and As cases, presumably by evaporation from the WSi_2 surface.

Overall, the present furnace annealing results are consistent with those previously reported (12, 13). The

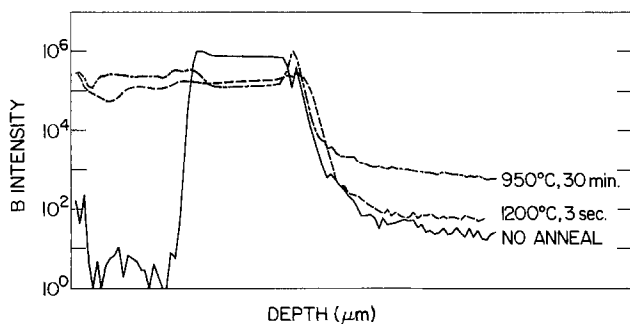


Fig. 13. SIMS plot of B concentration in a structure II sample as a function of annealing. Depth and vertical scales vary in each material (WSi_2 on the left, poly-Si on the right, see text).

motion of B from poly-Si into WSi_2 has been observed as low as 800°C , and the accumulation of B in WSi_2 up to 1000°C has also been reported (9, 14). Similarly, the rapid diffusion of P and As through poly-Si and WSi_2 and evaporation have been observed (9, 14). [During furnace annealing, the evaporation of As (9), and probably also of P, can be avoided by the deposition of a CVD silicon oxide cap.] More recently, the motion of P through cosputtered TaSi_2 has been investigated by Pelleg and Murarka (15), and the rapid diffusion of As through doped poly-Si has been studied by Arienzo *et al.* (16). Rough estimates of diffusion in our samples annealed at 1200°C , 6s using the published data (15, 16) indicate that significant out diffusion of As and P is at least plausible during STA. Yet, we note with interest that McPherson *et al.* report essentially no loss of P in a polycide structure of sputtered MoSi_2 annealed at 1250°C , 16s (8). Because of the very marked similarity between MoSi_2 and WSi_2 [see, for example, Ref. (2)], the reported different behaviors of P in the two compounds during STA is quite surprising. Could it be that a residual layer of SiO_2 (or other impurity) at the interface between MoSi_2 and poly-Si hindered the out diffusion of P?

Summary

Short time annealing (STA) of coevaporated WSi_2 on single-crystal and polycrystalline Si (poly-Si) doped with B, P, and As has been carried out with a graphite resistance heater up to 1200°C for times as short as 3s.

STA at 1200°C for 6s resulted in good film homogenization and fine line patterns down to submicron dimensions, which remained intact and well adherent. STA at 1200°C for 6s yielded a silicide resistivity 2 to 3 times lower than furnace annealing at 950°C , 30 min. These two anneals would produce a calculated minimal and equivalent B diffusion in an underlying partially fabricated device. Dopants in the poly-Si of the polycide structure move rapidly through both the poly-Si and the WSi_2 for both STA and furnace annealing. The B redistributes throughout the polycide, but the As and P are lost from the WSi_2 surface by evaporation.

Acknowledgments

We would like to acknowledge the helpful consultations of April Schweighart and the consultations and SUPREME calculations of Matt Wordeman.

Manuscript received March 19, 1984.

IBM Corporation assisted in meeting the publication costs of this article.

REFERENCES

1. T. O. Sedgwick, *This Journal*, **130**, 484 (1983).
2. F. M. d'Heurle, in "VLSI Science and Technology 1982," C. J. Dell'Oca and W. M. Bullis, Editors, p. 194, The Electrochemical Society Softbound Proceedings Series, Pennington, NJ (1982).
3. F. Mohammadi, *Solid State Technol.*, **24**, 65 (1981).
4. M. Y. Tsai, H. H. Chao, L. Ephrath, B. L. Crowder, A. Cramer, R. Bennett, C. Lucchese, and M. R. Wordeman, *This Journal*, **128**, 2207 (1981).
5. A. S. Wakita, T. W. Sigmon, and J. F. Gibbons, in "Laser and Solid Interactions and Transient Thermal Processing of Materials," J. Narayan, W. L. Brown, and R. A. Lemons, Editors, p. 721, Proceedings of the 1982 Materials Research Society Conference in Boston, Vol. 13, North-Holland, New York (1983); H. Ishiwara, S. Saitoh, K. Mitsui, and S. Furukawa, in "Laser and Electron Beam Solid Interactions and Materials," J. F. Gibbons, L. A. Hess, and T. W. Sigmon, Editors, p. 525, Proceedings of the 1980 Materials Research Society Conference in Boston, Vol. 1, Elsevier/North-Holland, New York (1981); T. Shibata, T. W. Sigmon, J. L. Regolini, and J. F. Gibbons, *This Journal*, **128**, 637 (1981).
6. M. Y. Tsai, F. M. d'Heurle, C. S. Petersson, and R. W. Johnson, *J. Appl. Phys.*, **52**, 5350 (1981).
7. T. O. Sedgwick, F. M. d'Heurle, and S. A. Cohen, Paper 391 presented at The Electrochemical Society Meeting, San Francisco, CA, May 8-13, 1983.
8. J. McPherson, T. Kaeriyama, and J. Keenan, Paper 0-2 presented at the Electronic Materials Committee Conference in Burlington, VT, June 22-24, 1983.

9. F. Jahnel, J. Biersack, B. L. Crowder, F. M. d'Heurle, D. Fink, R. D. Isaac, C. Lucchese, and C. S. Petersson, *J. Appl. Phys.*, **53**, 7372 (1982).
10. D. Campbell, S. R. Mader, and W. K. Chu, *Thin Solid Films*, **93**, 341 (1982).
11. M. Wordeman, Calculations and private communications.
12. H. Norstrom, F. Rumore, P. Buchta, W. Wiklund, M. Ostling, and C. S. Petersson, *J. Vac. Sci. Technol. A*, **1**, 463 (1983).
13. J-S. Maa, C. W. Magee, and J. J. O'Neill, *J. Vac. Sci. Technol. B*, **1**, 1 (1983).
14. P. Pan, N. Tsieh, H. Geipel, and G. Slusser, *J. Appl. Phys.*, **53**, 3059 (1982).
15. J. Pelleg and S. P. Murarka, *J. Appl. Phys.*, **54**, 1337 (1983).
16. M. Arienzo, Y. Komen, and A. E. Michel, *ibid.*, To be published.



COMMENTS

Each issue of the **Journal** will have a section of "Comments." In this section, we provide a means via short pieces, *i.e.*, one column or less, to applaud, dispute, or otherwise discuss the papers published in the **Journal**. Space will be provided for one response by the paper's author(s) to each comment.

Since space available in each issue for the "Comments" section is limited, it is important to be concise.

Comments should be sent to the Editor, Dr. Norman Hackerman, President's Office, Rice University, P.O. Box 1892, Houston, TX 77251.

This is the first appearance of the "Comments" section.

Norman Hackerman
Editor

Effects of the Helmholtz Layer Capacitance on the Potential Distribution at Semiconductor/Electrolyte Interface and the Linearity of the Mott-Schottky Plot

K. Uosaki and H. Kita
pp. 895-897, Vol. 130, No. 4

H. Gerischer:¹ The paper of the above authors contains some serious errors in the equations quoted. The last term in the numerator of Eq. [4] must read $n_0 \cdot e^{y_s}$, not n_0 . Equations [8] and [9] represent the approximation for the case of a depletion layer in an n-type semiconductor and should read correctly

$$Q_{sc} = \left(2e\epsilon\epsilon_0 N_D \right)^{1/2} \left(\Delta\psi_{sc} - \frac{kT}{e} \right)^{1/2} \quad [8]$$

$$C_{sc} = \left(\frac{e\epsilon\epsilon_0 N_D}{2} \right)^{1/2} \left(\Delta\psi_{sc} - \frac{kT}{e} \right)^{-1/2} \quad [9]$$

Besides this, the paper gives a misleading impression of the relation between the space-charge layer capacitance and the Helmholtz double-layer capacitance of normal semiconductor electrodes since the calculations are made with an unusually high carrier concentration in the bulk ($n_0 = N_D = 10^{19} \text{ cm}^{-3}$) and an exceptionally large dielectric constant ($\epsilon = 173$). Most semiconductors such as ZnO, CdS, CdSe, GaP, GaAs, Si, MoS₂, MoSe₂, WS₂, and WSe₂, have static dielectric constants in the order of 6-12. Usual carrier concentrations are in the order of 10^{16} - 10^{18} . With such values, the space-charge capacity is by far smaller than for the example given in this paper. Consequently, the relation between the variation of the voltage drop in the Helmholtz double layer and the voltage applied to the whole interface (referred to the flatband potential) is drastically reduced in comparison to the data given in Fig. 1 of this paper.

More realistic data are shown in Fig. 1a and b, which was derived for depletion layers in the absence of surface states from the following relations, being valid for $y_{sc} > 4$

$$Q_{sc} = (2e\epsilon_0 k T N_D)^{1/2} (y_{sc} - 1)^{1/2} \quad [1]$$

$$C_{sc} = e \left(\frac{\epsilon_0 N_D}{2kT} \right)^{1/2} (y_{sc} - 1)^{-1/2} \quad [2]$$

$$y_{sc} = \frac{e\Delta\psi_{sc}}{kT} \text{ with } \Delta\psi_{sc} = \psi_b - \psi_s \quad [3]$$

$$y_H = \frac{e\Delta\psi_H}{kT} = 2 \frac{C_{sc}}{C_H} (y_{sc} - 1) \quad [4]$$

The voltage drop in the space-charge layer $\Delta\psi_{sc}$ and in the Helmholtz layer $\Delta\psi_H$ is represented in Eq. [3] and [4] in terms of kT/e units (25 mV at $T = 298 \text{ K}$). With $\epsilon_0 = 8.854 \cdot 10^{-14} \text{ As/V} \cdot \text{cm}$ and $C_H = 10 \mu\text{F}$, the relation $[y_H/(y_H + y_{sc})]$ has been calculated and is plotted against $y_H + y_{sc}$ in Fig. 1a for $N_D = 10^{19}$ and 10^{17} with $\epsilon = 173$, and in Fig. 1b for the same donor concentrations with $\epsilon = 10$. One sees that the relative contribution of y_H to the whole potential drop $y_H + y_{sc}$ is very small for $N_D = 10^{17}$ and $\epsilon = 10$, representing the usual situation in semiconductor electrochemistry.

The necessary correction for the variation of $\Delta\psi_H$ in the extrapolation to the flatband potential in a Mott-Schottky plot has been correctly derived in the paper of DeGryse *et al.*² and quoted as Eq. [10] in the above paper. It is, however, also drastically reduced, if the dielectric constant has a normal value and the donor density is

²R. De Gryse, W. P. Gomes, F. Cordon, and J. Vennik, *This Journal*, 123, 711 (1975).

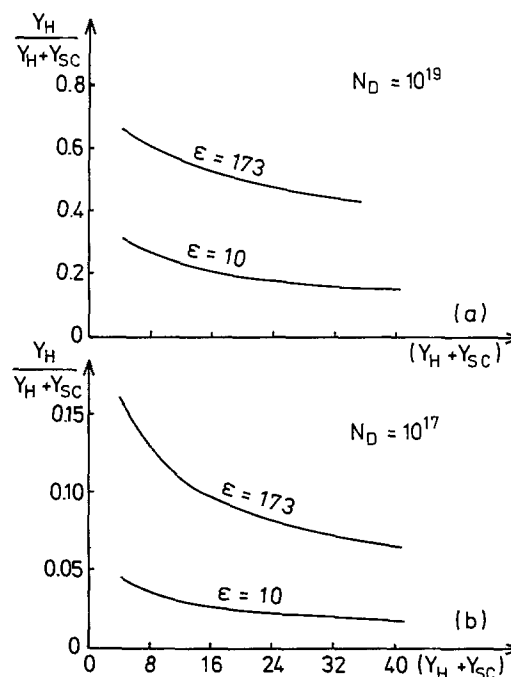


Fig. 1. Relative contribution of the voltage drop variation in the Helmholtz double layer, y_H , to the whole voltage variation over the semiconductor/electrolyte interface, $y_H + y_{sc}$, for two different donor concentrations and two different dielectric constants of the semiconductor. Helmholtz double-layer capacity: $10 \mu\text{F}$.

¹Fritz-Haber-Institut der Max-Planck-Gesellschaft, Berlin 33, Germany.

smaller than 10^{19} . DeGryse *et al.* have found with $C_H = 10 \mu\text{F}$ as correction for the extrapolated value of V_{FB} at an n-type semiconductor with $\epsilon = 173$ and $N_D = 10^{19}$ the large value of -0.12V . From the correction formula, $\Delta V_H = -[\epsilon\epsilon_0 e N_D / 2C_H^2]$, one obtains with $\epsilon = 10$, instead of 173, only -7 mV , and with $N_D = 10^{17}$ instead of 10^{19} , this correction is fully negligible.

It is certainly important to be aware of the possibility that the potential drop in the Helmholtz double layer can vary with the applied voltage. However, one should also see that the importance of this effect depends very critically on the doping level and the magnitude of the dielectric constant. A variation in $\Delta\psi_H$ will much more often be due to the presence of surface states with a density in the order of 10^{13} cm^{-2} within a narrow range of energies.

K. Uosaki and H. Kita:³ We must admit that Eq. [4], [8], and [9] of our paper contain misprints, as Professor Gerischer has pointed out. But note all the calculations have been carried out by using proper equations.

Although Gerischer commented that our calculations were made only with an unusually high carrier concentration in the bulk ($n_0 = N_D = 10^{19} \text{ cm}^{-3}$), we calculated the potential distribution with a wide range of carrier concentrations ($10^{16} \text{ cm}^{-3} \sim 10^{20} \text{ cm}^{-3}$) as shown in Fig. 1 of our paper.

Gerischer said this paper gives a misleading impression of the relation between the space-charge layer capacitance and the Helmholtz double-layer capacitance of normal semiconductors. However, we think it is important to stress the effects of the Helmholtz double-layer capacitance on the potential distribution and linearity of the Mott-Schottky plot because many semiconductor electrochemists simply ignore the Helmholtz layer capacitance without considering its physical significance.

As far as the effect of the Helmholtz layer capacitance on the linearity of the Mott-Schottky plot is concerned, we supported the general conclusion of De Gryse *et al.*⁴ but pointed out that the real Mott-Schottky plot deviates from the linear line calculated by using Eq. [10] of our paper, which was derived by De Gryse *et al.* with the Mott-Schottky approximation,⁴ near the flatband potential.

Galvanostaircase Polarization

S. T. Hirozawa

pp. 1718-1721, Vol. 130, No. 8

F. Mansfeld:⁵ Hirozawa's paper gives an interesting application of a very simple experimental technique. However, some discussion of the conclusions by the author concerning pitting of aluminum is necessary to avoid even more confusion in the general topic of "critical potentials" than there exists now. There is no theoretical justification in the paper for the claim that extrapolation of the E-I curves to $I = 0$ leads to the breakdown potential E_b for increasing I and to the protection potential E_{prot} for decreasing I . The statement " E appears to have no direct relevance to localized corrosion; however, it seems to have indirect relevance" is quite puzzling in the light of the previous claim concerning E_b and E_{prot} .

In analyzing Hirozawa's experiment, one could conclude that the application of the first constant-current step produces pitting. The corresponding potential maximum is probably the pitting potential. While the current is increased stepwise, the kinetics in the growing pits are measured, since there is not much contribution from the passive surface. The observed small hysteresis in uninhibited solutions is due to changes in the pit growth kinetics, pit size, conductivity in the pits, etc. In the inhibited solutions, the electrochemical kinetics in the growing pit are altered, owing to the presence of the inhibitor. As the pits grow (which they do even when the current is de-

creased), hysteresis occurs because the inhibitor concentration in the pit decreases and for other, presently unknown reasons. As can be seen from Hirozawa's data (his Fig. 3 and 4), the electrochemical kinetics in this case tend to return to those for the uninhibited case.

In summary, the galvanostaircase method applied to Al shows some promise for the study of electrode kinetics in growing pits. However, the claim that the breakdown and protection potentials can be determined from Hirozawa's data cannot be accepted unless it is substantiated by further theoretical and experimental work.

S. T. Hirozawa:⁶ Mansfeld claims that extrapolation for E_b and E_{prot} from GSCP curves has not been theoretically justified and would only increase the confusion presently existing concerning the critical potentials. Others (7-9) using galvanokinetic or galvanostatic polarization techniques have used terms that are analogous to E_b and E_{prot} (paragraph 1 of my paper).

It is true that we have no theoretical justification for the use of the E_b and E_{prot} , but we do have experimental justification using long term constant potential corrosion tests (second paragraph of my paper). The two main causes for the confusion concerning the critical potentials are nomenclature and the use of potential-controlled polarization techniques under highly passivating conditions which lead to induction time effects and current hysteresis.

For Al under highly passivating conditions, *e.g.*, in anti-freeze coolants, E_b (which is often considered to be the pitting potential) appears to have no direct relevance to localized corrosion because E does not have to be raised above E_b , to initiate pitting: one only needs to raise E above E_{prot} to initiate pitting. Hence, E_b is not a critical potential, but it does have indirect relevance because the greater the difference between E_{prot} and E_b , the greater is the tendency for crevice corrosion.

Mansfeld's statement that "in analyzing Hirozawa's experiment, one could conclude that the application of the first current step produces pitting" is true for Fig. 3 and 4, where the evidence for pitting is quite apparent. Pitting occurs on metals that are passivated, preferably by a layer of insoluble salts. In Fig. 1 and 2, pitting is not evident. Chloride is nonpassivating; therefore, the corrosion is general and not localized. The passivation of Al by nitrate is unique. The first current step does not break down the passive layer, but rather it builds it up further. Hence, the use of the term, E_b , is not appropriate; it is used here for the want of a better name. The gradual change of potential during the first two steps probably indicates changes in the resistance of the inner oxide layer as well as the distribution of nitrate within the passive layer under the influence of the electric field.

In conclusion, the GSCP method should dispel some of the confusion related to the critical potentials, induction effects, and the scan rate, hysteresis, and charge effects on the value of E_{prot} .

The Effect of Stress on the Redistribution of Implanted Impurities in GaAs

J. Kasahara, Y. Kato, M. Arai, and N. Watanabe

pp. 2275-2279, Vol. 130, No. 11

C. Blaauw:¹⁰ The authors analyze the effect of stress, induced by a plasma silicon nitride capping film, on the diffusion constants for Si and Se implants in GaAs. Several incorrect assumptions are made, which affect analysis of the results. For example, Eq. [1] implies that the intrinsic stress of the capping film is taken to be zero, whereas it is well known that plasma silicon nitride films

⁶BASF Wyandotte Corporation, Wyandotte, Michigan 48192.

⁷S. Smialowska and M.Czachor in "Localized Corrosion," R. W. Staehle, B. F. Brown, J. Kruger and A. Agrawal, Editors, p. 353, NACE-3, Houston (1974)

⁸A. Broli, H. Holtan, and K. L. Prestud, *Corrosion*, **30**, 427 (1974).

⁹K. Nisancioglu and H. Holtan, *Corros. Sci.*, **18**, 835 (1978).

¹⁰Bell-Northern Research, Ottawa, Ontario, Canada K1Y 4H7.

³Department of Chemistry, Faculty of Science, Hokkaido University, Sapporo 060, Japan.

⁴R. De Gryse, W. P. Gomes, F. Cardon, and J. Vennik, *This Journal*, **123**, 711 (1975).

⁵Rockwell International Science Center, Thousand Oaks, California 91360.

are deposited in a state of tensile stress (11, 12). More seriously, the analysis of the diffusion coefficients in terms of jump frequency and vacancy concentration rests on the assumption that the substrate-induced stress at 850°C is proportional to the thickness of the capping film. This assumption is not justified, as the properties of plasma silicon nitride are not necessarily uniform throughout the film. We have carried out stress measurements as a function of film thickness, for plasma silicon nitride on GaAs, which show that both the intrinsic stress and the temperature dependence of the stress depend on film thickness (2). Extrapolating stress *vs.* temperature curves to 850°C, we find that the substrate-induced stress for a 0.4 μm film is only approximately 40% larger than that of a 0.1 μm film deposited under the same conditions. If a similar relationship were to apply for the work under discussion, this would move the data points at $\approx 0.3 \mu\text{m}$ in Fig. 7, of the paper in question well to the left on the corresponding stress scale, in good agreement with the linear solid line of this figure. This would imply that there is no need

¹¹A. K. Sinha, H. J. Levinstein, and T. E. Smith, *J. Appl. Phys.*, **49**, 2423 (1978).

¹²C. Blaauw, *J. Appl. Phys.*, **54**, 5064 (1983).

to assume a stress-dependent vacancy concentration within the region of investigation.

J. Kasahara:¹³ I appreciate the interest and useful reading of our paper.

Basically, I agree with the comments, which pertain mainly to our Fig. 7. Although further quantitative study is necessary, if the intrinsic stress and thickness-dependent temperature dependence of the stress have some influence, the scale of the lower axis for the stress might be modified. Dr. Blaauw discussed this subject in his Ref. (2), which was not available when our manuscript was being prepared. Also, it is difficult to apply his data directly to our data, because the deposition system for SiN is different. Further, considering the behavior of the stress dependence of the diffusion of Zn, known to be by an interstitial-substitutional mechanism, and the result of Se with about 0.6 μm of thicker SiN, I think it is too important to ignore the effect of the vacancy concentration. Further discussion probably requires measuring the stress *in situ* at the annealing temperature investigated.

¹³Sony Corporation Research Center, Yokohama 240, Japan.



Further Evidence for Monoatomic Hydrogen as a Darkening Agent in Chemography

I. A. Blech and J. Kruger

Department of Materials Engineering, Technion, Haifa 32000, Israel

INTRODUCTION

It has been demonstrated recently that freshly etched or abraded silicon surfaces in contact with photographic plates in the dark will produce visible images⁽¹⁾. The process to obtain such images was named chemography. It was suggested that the images were produced by a gas, probably atomic hydrogen, emitted from the silicon surface. Hydrogen evolution was thought to occur as a result of the reaction of water vapor present in the air with the fresh silicon surface forming silicon hydride and atomic hydrogen. The sensitivity of photographic plates to atomic hydrogen was demonstrated previously by placing such plates in a stream of atomic deuterium which caused a considerable darkening⁽¹⁾. It was also shown that molecular hydrogen does not darken the photographic plates.

The present paper provides further evidence that atomic hydrogen is responsible for the darkening of photographic plates in chemography by producing atomic hydrogen through the electrolysis of water.

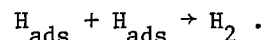
EXPERIMENTAL

The experimental apparatus is shown schematically in Fig.1. Two stainless steel electrodes were immersed in an electrolyte. Each electrode was 1.1 cm wide, 0.4 cm thick and 7.5 cm long. The photographic plates (Ilford nuclear plates type L4, 50 μ m) were masked off from the electrodes by an adhesive tape and were mounted with their emulsion facing the electrodes leaving a gap of

0.5–1.0 mm between the emulsion and the surface of the electrodes. Sufficient electrical current was supplied to produce copious evolution of hydrogen at the cathode. After a selected time the current was stopped and the photographic plates were removed and rinsed. Dark images were already clearly visible on the plates that were facing the cathode even without development. The plates were developed in D19 Kodak developer for 2 minutes at room temperature. Prints with the same contrast as the original plates were made using an intermediate negative.

RESULTS AND DISCUSSION

The electrolytes used were the following: (1) 0.1N H₂SO₄, (2) 0.1N H₂SO₄ containing 0.05 g/l NaAsO₂ (3) 0.1N H₂SO₄ containing 0.1 g/l NaAsO₂. The rationale behind using solutions (1),(2) and (3) was to produce varying amounts of atomic hydrogen by electrolyzing water in solutions containing different amounts of an arsenic compound, NaAsO₂. It is known⁽²⁾ that arsenic compounds poison the hydrogen recombination reaction,



Therefore, if monoatomic hydrogen is responsible for the darkening of photographic plates, solutions with varying degrees of efficiency in the production of stable atomic hydrogen should exhibit varying degrees of darkening. This is exactly what is demonstrated in Fig.2. It can readily be seen that, when no NaAsO₂ is present in the sulfuric acid solution (Fig.2a), darkening was observed at the bottom of the plate near the edge of the masking tape where the plate was nearest to the electrode surface. There is apparently some atomic hydrogen in bubbles rising along the cathode and the spray above the solution surface as indicated by the darkened areas observed in Fig.2a.

* Electrochemical Society Active Member

¹ Lady Davis Fellow - Technion.
Present address: Dept. of Materials Sci. and Engr., Johns Hopkins Univ. Baltimore MD.

Key words: hydrogen, chemography, photographic emulsion

Fig.2b shows the considerable enhancement in darkening that occurs when a recombination reaction poison is added. When the concentration of the poison is increased, Fig.2c shows increased darkening over that shown in Fig.2b.

Apparently, after the atomic hydrogen has left the cathode surface, it has a sufficiently long lifetime to migrate over to the anode. There it darkens the photographic plate on its edges which are less shielded by the oxygen evolving at the anode. This can be seen in Fig.2d.

In order to be certain that the NaAsO_2 in the 0.1N H_2SO_4 was not responsible for the darkening effects, we exposed photographic plates to solutions (2) and (3) in absence of an electrolyzing current. Virtually no darkening was observed for periods of exposure longer than those used during electrolysis.

The possibility of AsH_3 , formed by the reduction of AsO_2^- at the cathode, being responsible for the darkening was ruled out by producing such darkening at potentials where hydrogen is evolved but where the production of significant amounts of AsH_3 is precluded by thermodynamics. Also, three different solutions containing no arsenic compounds produced darkening.

The foregoing experiments clearly support the conclusion that monoatomic hydrogen causes darkening of photographic plates. This strongly suggests that it is the agent responsible for the darkening observed in chemography.

ACKNOWLEDGEMENT

This research was supported by the fund for the promotion of research at the Technion.

REFERENCES

1. I.A. Blech and E.S. Meieran, *Appl. Phys. Letters*, **43**, 396 (1983).
2. P. Poole in *Corrosion, Vol.1, Metal Environment Reaction*, 2nd Edition, L.L. Shreir, Ed., Newnes-Butterworths, London, 1976, p.8:64.

Manuscript submitted June 15, 1984.

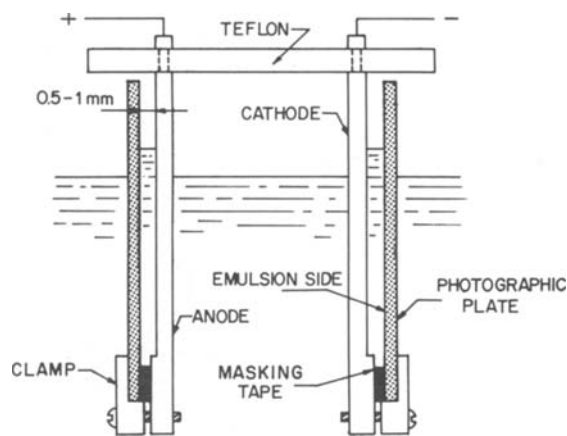


Fig.1. Schematic drawing of the experimental apparatus used for exposure of photographic plates to monoatomic hydrogen.

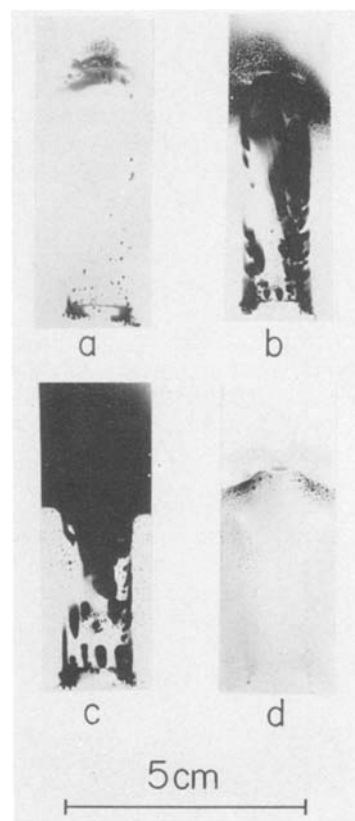


Fig.2. Chemographs of the anode and the cathode produced by the electrolysis of:
 (a) 0.1N H_2SO_4 , cathode side, 10 min.
 (b) 0.1N H_2SO_4 +0.05 g/l NaAsO_2 , cathode side, 10 min.
 (c) 0.1N H_2SO_4 +0.1 g/l NaAsO_2 , cathode side, 5 min.
 (d) 0.1N H_2SO_4 +0.1 g/l NaAsO_2 anode side. 5 min.

Crystallographic Orientation Dependence of Transition Layer at Magnetron-Sputtered Ta₂O₅/Si Interface

S. Seki, T. Unagami, and O. Kogure

*Nippon Telegraph and Telephone Public Corporation,
Ibaraki Electrical Communication Laboratory, Tokai, Ibaraki 319-11, Japan*

In recent years, tantalum pentoxide (Ta₂O₅) films have received particular interest for use in electronic devices. The higher dielectric constant of Ta₂O₅ films, compared with that of SiO₂, makes them attractive as gate insulators for MOS devices. For these applications, Ta₂O₅ films were prepared by chemical vapor deposition (1) and thermal oxidation of a deposited Ta film (2,3). More recently, it has been indicated that a Ta₂O₅ gate insulator with relatively good interface properties can be obtained by RF-magnetron sputtering (4). Based upon this result, Si-TFT's with this magnetron-sputtered Ta₂O₅ film as a gate insulator have been fabricated on quartz (5). These investigations have clarified that the dielectric constant of deposited Ta₂O₅ becomes lower than that of the bulk of Ta₂O₅, due to the existence of the low dielectric constant transition layer at the Ta₂O₅/Si interface.

In device applications, it has become important to obtain Ta₂O₅ with higher dielectric constant on Si. The present work explores roles of Si substrate in determining dielectric constant of Ta₂O₅ deposited on Si, and indicates that crystallographic orientation has an influence on the dielectric constant of Ta₂O₅.

The transition layer at the interface was studied by dielectric constant variation with deposited Ta₂O₅ thickness. Dielectric constant was calculated from the capacitance of an Al/Ta₂O₅/Si capacitor in accumulation. Single-crystalline silicon wafers with different specifications ((a) p-type, <100>-oriented and 9 to 11 ohm-cm, (b) p-type, <100>-oriented and 0.07 to 0.13 ohm-cm, (c) p-type, <111>-oriented and 1.2 to 1.8 ohm-cm, and (d) p-type, <110>-oriented and 0.07 to 0.13 ohm-cm) were used as substrates. These substrates were cleaned by a mixture of H₂SO₄ and H₂O₂, and then rinsed

in deionized water. Immediately before being installed into the sputtering chamber, wafers were dipped into dilute HF to remove the oxide formed during the previous processing steps. Ta₂O₅ films were fabricated using an RF-magnetron sputtering system. The Ta₂O₅ target was 10 cm in diameter and 5 mm thick. The target to substrate distance was 5 cm. The sputtering chamber was evacuated to less than 1x10⁻⁷ Torr prior to sputtering, and then backfilled with sputtering gas, which consisted of a mixture of argon and oxygen (partial pressure ratio of Ar/O₂ = 90/10). The sputtering pressure was 5x10⁻³ Torr. Electron-beam evaporated aluminum was used as electrodes. Prior to capacitance measurement, these MOS capacitors were annealed at 450°C for 30 minutes in a hydrogen ambient. Capacitance measurements were performed at 1 MHz in the dark, shielded box.

Figure 1 shows variations in deposited Ta₂O₅ dielectric constant with changes in thickness. Variations for three Si substrates with different crystallographic orientation are compared. For each substrate, the dielectric constant of deposited Ta₂O₅ increases monotonically with Ta₂O₅ thickness. At the same time, the dielectric constant depends on the crystallographic orientation of the silicon substrate. At every thickness, the dielectric constant follows the sequence ε(110) > ε(111) > ε(100). On the other hand, dielectric constant plots of Ta₂O₅ deposited on <100>-oriented silicon substrates with the resistivity of 0.07 to 0.13 ohm-cm and 9 to 11 ohm-cm were found to be on the same curve. Hence, the results shown in Fig. 1 are due to the crystallographic orientation of the substrate.

To clarify the reason for this variation depending on the crystallographic orientation, the dielectric constant profile within the Ta₂O₅ film was calculated from the results shown in Fig. 1. Figure 2 (a) and (b) indicate the dielectric constant profiles of Ta₂O₅ deposited on <100>-oriented Si and on <110>-oriented Si, respectively.

Key words: transition layer, crystallographic orientation, Ta₂O₅, interface.

The bars represent the average value of the dielectric constant for each layer. The lowest average value was taken as the dielectric constant for the sample with the minimum thickness. The dielectric constant for the second layer was then obtained by reevaluating the dielectric data, using a multilayer model consisting of the first and second layer (4). This calculation was repeated for each successive layer. The results shown in Fig. 2 indicate that both Ta_2O_5 layers consist of two regions: a low dielectric constant transition layer at the interface and the higher dielectric constant homogeneous layer. The dielectric constant of the homogeneous layer on $\langle 100 \rangle$ -oriented Si is the same as that on $\langle 110 \rangle$ -oriented Si. The values are about 24.5, close to that of the bulk of Ta_2O_5 . The dielectric constant of the homogeneous layer on $\langle 111 \rangle$ -oriented Si was also calculated to be about 24.5. This indicates that the crystallographic orientation has no influence on the homogeneous layer formation. This has been confirmed by etch rate experiments, performed by reactive ion etching using CF_4 as a reactive gas (6). A typical etch rate was measured to be 150 Å/min for each homogeneous layer, independent of the crystallographic orientation. These results indicate that dielectric constant variation shown in Fig. 1 is attributed to the transition layer at the interface.

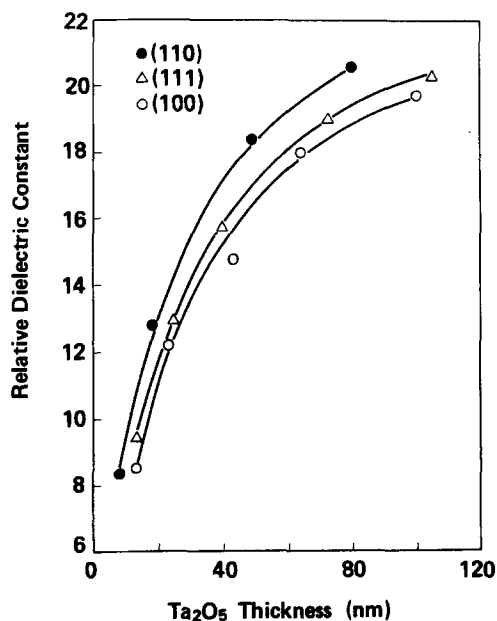
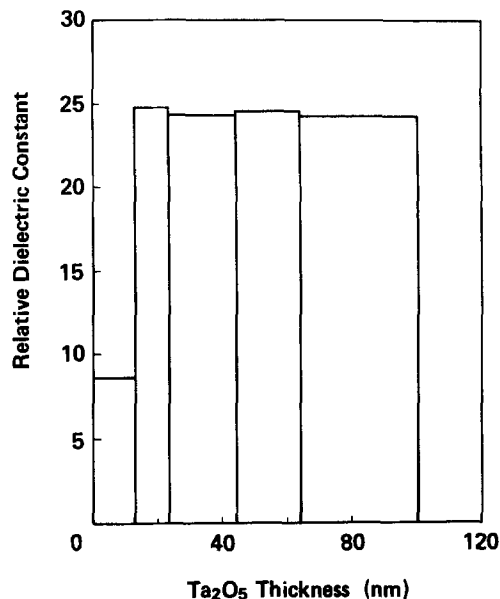
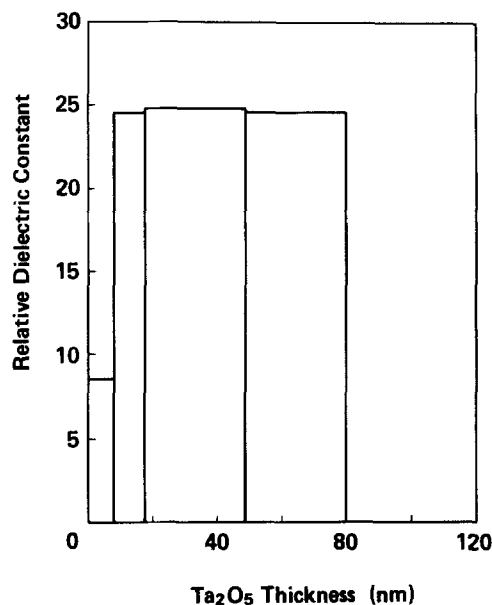


Figure 1 Relative dielectric constant versus Ta_2O_5 thickness for Si substrates with different crystallographic orientation.

Though the Si was etched with HF just before sputtering in these experiments, oxide would reform very quickly during subsequent exposure to air before installing into the sputtering chamber. If we assume that the transition layers are ascribed to air-oxidized SiO_2 grown on Si, and that total



(a)



(b)

Figure 2 Variations in relative dielectric constant with changes in distance from the Ta_2O_5/Si interface. (a) on $\langle 100 \rangle$ -oriented Si, (b) on $\langle 110 \rangle$ -oriented Si.

insulator on Si consists of this SiO₂ ($\epsilon=3.4$) and homogeneous Ta₂O₅ layer ($\epsilon=24.5$), the SiO₂ thickness can be calculated from the results shown in Fig. 2 to be 26.5 Å for <110>-oriented silicon and 39.2 Å for <100>-oriented silicon. These values are much larger than the air-oxidized film thickness grown on Si substrate by exposure to air before sputtering, which is estimated to be less than 10 Å (7). This indicates that the transition layer is not solely attributed to the air-oxidized film on Si, and that this transition layer is the result of the interaction of silicon and sputtered particles in the early stage of Ta₂O₅ formation on Si. Based upon the results described above, it can be concluded that the crystallographic orientation has a great influence on the transition layer formation at the Ta₂O₅/Si interface.

In summary, influences of the resistivity and crystallographic orientation of Si substrate on dielectric constant of Ta₂O₅ deposited on Si have been investigated. The present study has indicated dielectric constant of Ta₂O₅ deposited on <110>-oriented Si becomes higher than that of Ta₂O₅ deposited on <111>-oriented and on <100>-oriented Si, independent of substrate resistivity. This variation is due to the transition layer at the interface, and the crystallographic orientation has an influence on the transition layer formation.

ACKNOWLEDGEMENTS

The authors would like to thank Dr. B. Tsujiyama for his encouragement during the course of this work.

REFERENCES

1. E. Kaplan, M. Balog, and D. Frohman-Bentchkowsky, *This Journal*, 123, 1570 (1976).
2. A. G. Revesz and J. F. Allison, *IEEE Trans. Electron Devices*, ED-23, 527 (1976).
3. D. J. Smith and L. Young, *IEEE Trans. Electron Devices*, ED-28, 22 (1981).
4. S. Seki, T. Unagami, and B. Tsujiyama, *This Journal*, to be published.
5. S. Seki, T. Unagami, and B. Tsujiyama, *IEEE Electron Device Lett.*, EDL-5, 197 (1984).
6. S. Seki, T. Unagami, and B. Tsujiyama, *This Journal*, 130, 2505 (1983).
7. M. Tabe, K. Arai, and H. Nakamura, *Surface Sci.* 99, L403 (1980).

Manuscript submitted July 9, 1984.

Nippon Telegraph and Telephone Public Corporation assisted in meeting the publication costs of this article.

Thin Thermal Oxide on Silicon

E. A. Taff*

General Electric Company, Corporate Research and Development, Schenectady, New York 12301

INTRODUCTION

The growth kinetics of thermal oxide on silicon were detailed by Deal and Grove (1) with a resulting development of a linear-parabolic relationship. The silicon-oxygen surface reaction constitutes a linear part and the diffusing oxidant gives the parabolic part of the defining equation. Thin dry oxides (<250A) were not discussed. A sampling of the literature (2-7) shows that experimental data and physical modeling continues to appear. Hauffe (8) gives a discussion of a model of very thin (<100A) film growth proposed by Mott and Cabrera. In this treatment space charge effects are ignored, electrons are transferred by electron tunneling and charged ions are transported by high fields in the very thin dielectric layer. This model also has been applied to silicon (9-10). Fehlner (9,11) dealt with low temperature films of not more than 30A thickness to fit the Mott-Cabrera model. Van der Meulen, Irene and Hopper et. al (2-4) present data which is generally for higher temperature oxides. Their analyses did not readily fit any simple model. Apparently, as yet, there is no consensus on the major factors governing the growth of thin oxides on silicon. The purpose of this note is to present data for support of a model of oxide growth while detailed studies continue.

EXPERIMENTAL

Silicon wafers of 1-10 ohm-cm resistivity of <111> and <100> orientation were cleaned, HF acid dipped, and

fired at 1200C in hydrogen. The initial measured thicknesses of film on the silicon were 3-4 Angstroms. Further oxidations were done in a temperature controlled furnace in dry oxygen. The oxidized wafers were cooled and removed from the furnace from time to time. A Rudolf Research Auto-El ellipsometer was used for the thickness measurements.

RESULTS AND DISCUSSION

Film growth results are shown in Fig. 1 for temperatures of 450C, 612C and 821C. These curves, for <111> and <100> silicon orientations, have been selected to illustrate the premise that the usual linear-parabolic model holds for the lower temperatures as well as for higher temperatures. The additional factor is a Mott-Cabrera mechanism as is discussed by Hauffe (8). The 450C points of Fig. 1a were obtained over the course of several months though they extend to only 40A. The solid line is the exponential equation $t = \exp(14.1 - 101/x)$ where x is the thickness in Angstroms and the time is in minutes. This is a simplified form of reciprocal logarithmic film growth from Hauffe (8). Extrapolation of data from activation energies for the linear-parabolic model given by Deal and Grove or derived from my own curves indicates that there should be no oxide growth at this temperature. All the growth must be due to the Mott-Cabrera mechanism and the excellent curve fit to the data should be expected. The 612C points of Fig. 1b fit well, up to 40A, a reciprocal logarithmic equation $t = \exp(8.3 - 75/x)$. As in Fig. 1a there is no orientation effect observed thus far. However, at 612C the two orientations are different for oxide growth above 50A, and the linear-parabolic mechanism becomes a

*Electrochemical Society Active Member
Keywords: films, ellipsometry,
transport

larger factor.

Extrapolated activation energy data again lends credence as the expected growth rates from the linear parabolic model are of the correct amplitude for 612C. At 821C in Fig. 1c, the orientation difference is readily apparent; the growth curves can be approximately analyzed as before (1-4). However, the rapid orientation independent growth for 25A taking only about five minutes seems to be quite normal when considered with Fig. 1a and Fig. 1b. At higher temperatures, this initial growth will be more difficult to detect as the linear-parabolic model coefficients becomes larger.

It is postulated that only two basic oxygen transport mechanisms control silicon oxidation. Up to 25A at 821C, and observably beyond at lower temperatures, the Mott-Cabrera scheme prevails. The charged oxygen species involved in quickly forming the initial film diminish very rapidly with film thickness, although a 40A oxide has been shown where competing processes have not been active. At longer times or a higher temperatures where the rate constants become larger, the linear-parabolic oxidation scheme becomes dominant. Also, these linear-parabolic rate constants as in the low pressure study or Kamigaki and Itoh (9) could be so greatly reduced that at the lowest pressures only the reciprocal logarithmic growth remains.

REFERENCES

1. B. E. Deal and A. S. Grove, J. Appl. Phys., 86, 3770 (1965).
2. Y. J. van der Meulen, This Journal, 119, 530 (1972).
3. M. A. Hopper, R. A. Clarke, L. Young, *ibid*, 122, 1216 (1979).
4. E. A. Irene and Y. J. Van der Meulen, *ibid*, 123, 1380 (1976).
5. S. M. Hu, Appl. Phys. Lett., 42, 872 (1983).
6. A. Fargeix and G. Ghibaudo, J. Appl. Phys., 54, 7153 (1983).
7. K. K. Ng, W. J. Polito, and J. R. Ligenzza, Appl. Phys. Lett., 44, 626 (1984).
8. Hauffe, "Oxidation of Metals", p. 125, Plenum Press, NY (1965).

9. Y. Kamigaki and Y. Itoh, J. Appl. Phys., 48, 2891 (1977).
10. Francis P. Fehlner, This Journal, 119, 1723 (1972).
11. Francis P. Fehlner, This Journal, 131, 1645 (1984).

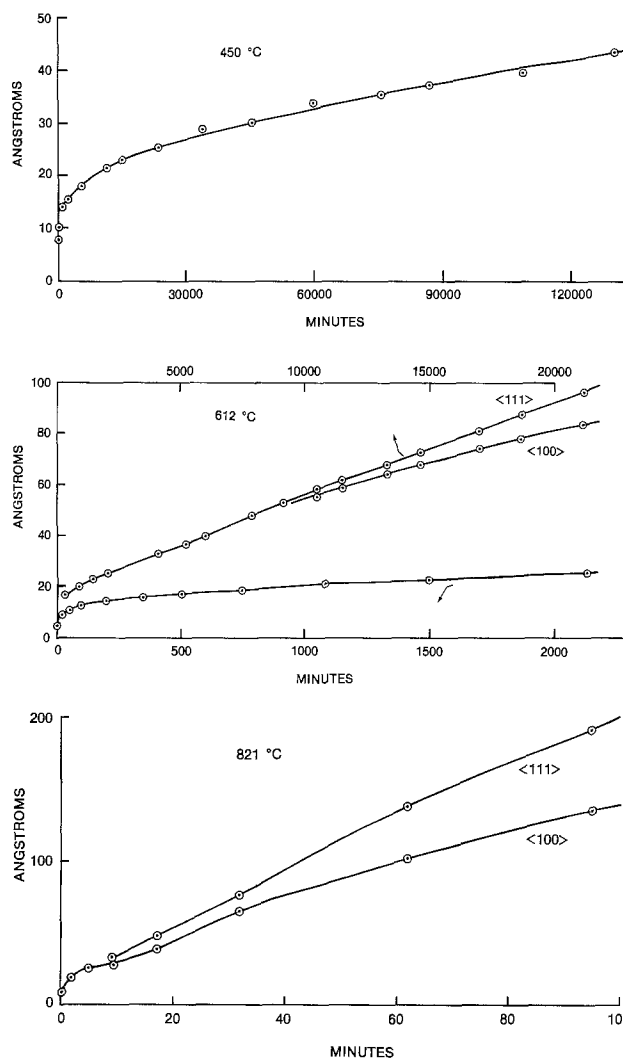


Fig. 1. Growth curves of dry oxide on two orientations of silicon for three temperatures. For 450C the data for both orientations fits $t = \exp(14.1 - 101/x)$. For 612C the linear-parabolic growth is apparent at $>40\text{A}$. At $<40\text{A}$ $t = \exp(8.3 - 75/x)$ is a good fit to the data. For 821C larger linear-parabolic coefficients affect the growth at $>25\text{A}$.

Manuscript submitted July 9, 1984.
General Electric Co. assisted in meeting the publication costs of this article.

Heterojunction by Photoelectrochemical Surface Transformation: n:CuInSe₂/p - CuISe₃Se^o

*Hahn-Meitner-Institut für Kernforschung Berlin,
Bereich Strahlenchemie, D-1000 Berlin 39, Germany*

Heterojunction formation by photoelectrochemical alteration of semiconductor surfaces is reported. Growth of a new semiconducting phase at the n-CuInSe₂/I⁻-I₂-Cu⁺ interface is achieved by controlling electrochemical parameters. The interfacial layer is identified as CuISe₃Se^o and exhibits p-type conductivity. Under illumination the interphase mediates efficient charge transfer between CuInSe₂ and the I⁻/I₂ redox couple while inhibiting semiconductor dissolution.

Current interest in CuInSe₂ systems from its exceptional optoelectronic properties, resulting in the development of efficient solid state (1) and photoelectrochemical (2) solar cells. Performance of the latter pivots on the growth of an interfacial layer induced by specific electrolyte composition, resulting in a substrate-film-electrolyte structure. In this note we explore the location of the photoactive junction and the circumstances leading to the CuInSe₂ surface transformation.

Interfacial films were grown on back ohmic contacted, epoxy insulated and etched (112) faces of n-CuInSe₂ by operation as photoanodes in an electrolyte consisting of 1 M I⁻, 0.05 M I₂, 0.02 M CuI and 2 M HI. This involved, cyclic polarization of the electrode between the potential limits of short circuit and open circuit or leaving it at the maximum power point. Film quality was monitored by the photocurrent-voltage output. Generally 3 - 4 intermediary etches were required to optimize the film performance.

Scanning electron micrographs of the electrochemically treated CuInSe₂ electrodes show that a polycrystalline film consisting of randomly oriented, flat, hexagonal crystallites is grown on the CuInSe₂ substrate (3). Crystallite sizes range between 2 - 5 microns. A cross-section of a cleaved electrode evidences that the film does not penetrate deeper than 2 microns into the substrate even after pro-

key words: Semiconductor Interfaces, Solar Energy, Photoelectrochemistry

longed operation (5 weeks) in a solar cell, but appears to completely cover the substrate growing into microscopic cavities.

The distinct crystallite geometry suggests that a chemically well defined compound is grown at the CuInSe₂/electrolyte interface. X-ray diffraction analysis of the crystallites identifies the new phase as consisting of mainly CuISe₃ and up to 30 % elemental Se. No evidence for formation of polycrystalline CuI was found.

Chemical reactions of illuminated CuInSe₂ with the electrolyte constituents obviously transform the semiconductor surface to generate the CuISe₃-Se^o phase. In the absence of Cu⁺ in the electrolyte, elemental Se^o and triangular crystallites of CuI have been detected on photocorroded CuInSe₂ surfaces (3). CuI is partly soluble in iodide solution forming CuI₂⁻. Addition of Cu⁺ to the solution probably raises the surface concentration of CuI₂⁻ to a critical value required to initiate CuISe₃ film growth. CuISe₃ crystals have been previously prepared by reacting stoichiometric mixtures of CuI and Se in HI medium under hydrothermal conditions (4). The reactants employed in the hydrothermal synthesis of CuISe₃ are thus provided by the electrolyte and the semiconductor components in our cell while the reaction enthalpy is probably supplied by the photopotential.

Fig. 1 compares UPS energy distribution curves, N(E) of the untreated CuInSe₂ single crystal and the CuInSe₂/CuISe₃-Se^o structure, with the Fermi levels E_Fⁿ aligned to the edges of the valence band. E_Vⁿ and E_V^p for the two samples differ by 0.65 eV. |E_Vⁿ-E_Fⁿ| is 0.85 eV for CuInSe₂ and 0.2 eV for the film. With a bandgap, E_g^p of 2 eV for CuISe₃ (5) and for Se (6), the film is thus a p-type semiconductor. Measurement of the relative work functions, φ, of the two samples with the vacuum levels aligned also indicate that the E_Fⁿ's differ by 0.65 V. Hence E_Vⁿ(CuInSe₂)=E_V^p(film). Adding the electron affinity, χⁿ of 4.58 eV (7) to the E_gⁿ of 1 eV for CuInSe₂ the absolute value of E_Vⁿ is estimated to be 5.58 eV.

The energetics of the structure are given in Fig. 2. Experimental and literature values for various electronic parameters indicated with superscripts n and p refer to n-CuInSe₂ and p-CuISe₃-Se⁰, respectively. An estimate for the work function of the I⁻-I₂-Cu⁺-HI electrolyte of $\phi^e=5.1$ eV is obtained by adding the measured redox potential of +0.2 V (SCE) to the more recent value of (NHE)=4.7 eV (8). Comparison of E_F^n , E_F^p and ϕ^e yields a potential of at least 0.65 eV at the substrate/film junction and of 0.2 eV ($\Delta\phi$) at the film/electrolyte interface. This implies a p-n junction between the solids and a rectifying junction at the electrolyte contact. The spectral response and the anodic photocurrent, however, attest the light absorption and photogeneration of h^+ in the n-CuInSe₂ (2,3). A barrier at the film/electrolyte interface would impede h^+ transfer to I⁻. The high quantum efficiency and the photovoltage of 0.42 V (2) argue against such a barrier and suggest that the principal potential drop occurs in the p-n junction with the electrolyte providing an ohmic contact. Interactions between the semiconductor and electrolyte upon immersion may account for the energetic difference, $\Delta\phi$, as the scheme in Fig. 2 disregards the effects of pH and specific adsorption.

References

1. J.L. Shay, S.Wagner, and H.M. Kasper, Appl. Phys. Lett., 27, 89 (1975).
2. S.Menezes, H.J.Lewerenz, and K.J.Bachmann, Nature, 305, 615 (1983).
3. K.J.Bachmann, S.Menezes, R.Kötz, M.Fearheily, and H.J.Lewerenz, Surface Sci., 138 (1984).
4. A.Rabenau, H.Rau and G.Rosenstein. Z.Anorg. Allgem. Chem., 374, 43 (1970).
5. A. Rabenau and H. Rau, Solid State Commun. 1, 1281 (1969).
6. W.H. Strehlow and E.L. Cook, J. Phys. Chem. Ref. Data, 2, 183 (1973).
7. K.J. Bachmann, E.Buehler, J.C.Shay, and S.Wagner, Appl.Phys.Lett., 29, 121 (1976).
8. R.Gomer and G.Tryson, J.Chem.Phys., 66, 4413 (1977).

Manuscript submitted July 7, 1984.

Hahn-Meitner-Institut für Kernforschung
Berlin assisted in meeting the publication costs of this article.

* Electrochemical Society Active Member.

** Electrochemical Society Student Member.

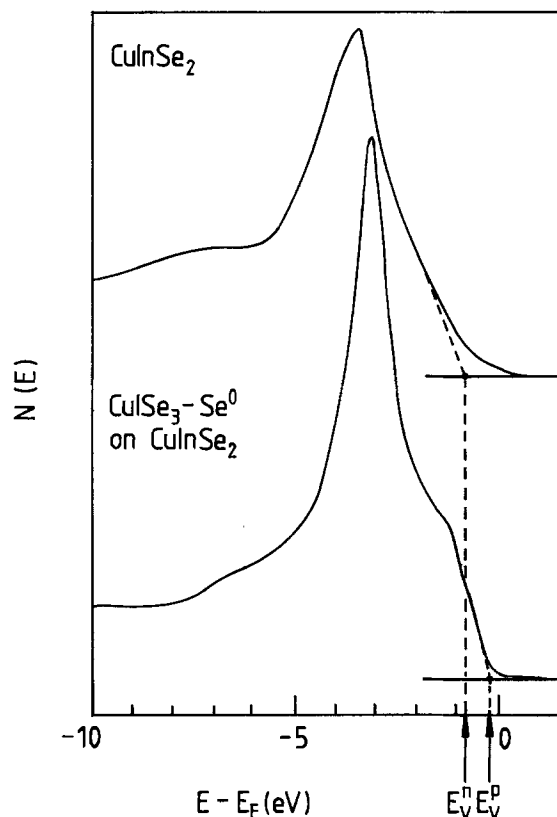


Fig.1 Energy distributions $N(E)$ obtained by UPS using He(II) excitation ($h\nu = 41.8$ eV).

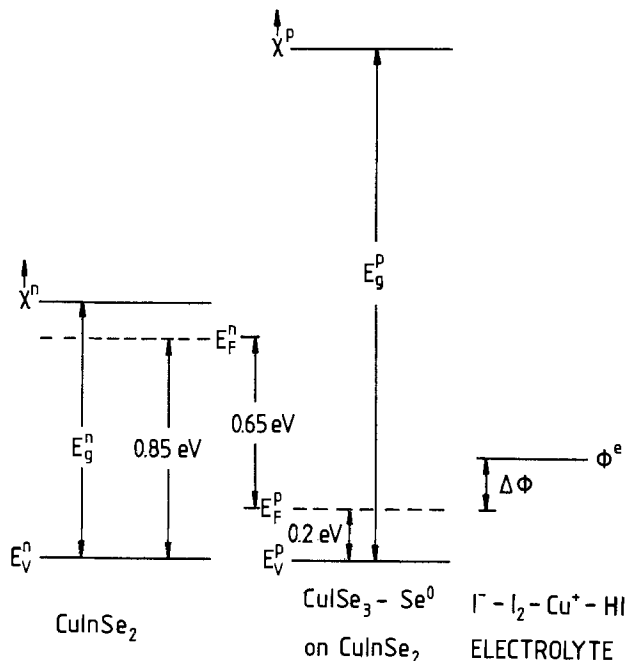


Fig.2 Schematic of energy levels of n-CuInSe₂, p-CuISe₃ and redox electrolyte.

Adsorption of Trifluoromethane Sulfonic Acid on Pt by FTIR and Radiotracer Methods

P. Zelenay,* M. A. Habib,† and J. O'M. Bockris†

Department of Chemistry, Texas A&M University, College Station, Texas 77843

The oxygen reduction rate on Pt was found to increase two orders of magnitude in trifluoromethane sulfonic acid (TFMSA) than in H_3PO_4 electrolyte (1,2). Petrii et al. (3) found adsorption of the $CF_3SO_3^-$ ion on platinum to be small and to have no effect (compared with H_2SO_4) on the catalytic activity of Pt in methanol electrooxidation. Recently, Habib and Bockris (4,5) reported the adsorption of H_3PO_4 on Pt as measured by in-situ FTIR and radiotracer techniques. Hyde et al. (6) concluded that phosphoric ion is physisorbed on Pt but the TFMSA is not. However, the latter compound was found to be unstable on Pt after 72 hours and some kind of degradation product seemed to be present (6). We report here the adsorption of $CF_3SO_3^-$ ion on Pt and compare with that of H_3PO_4 .

The IR Spectra for the adsorbed layer, as reported here, were obtained by subtracting from spectra obtained at a series of potentials at which adsorption was expected, the spectrum taken in a region of more cathodic potential, where adsorption was judged to be absent. The detailed experimental set up and the procedure are described elsewhere (5). The electrode was polarized potentiostatically in the range of $-0.2V$ and $1.6V$ (NHE).

TFMSA, one of the strongest of all known acids (7), is completely dissociated to $CF_3SO_3^-$ and H_3O^+ ions in aqueous solutions. The IR adsorption band at 1250 to 940 cm^{-1} consists of several peaks due to the resonance vibration of the $S=O$ bond (8) (Fig. 1). The peak observed at 1155 cm^{-1} is caused by asymmetric stretching vibration of the $S=O$ bond and the peaks at 1080 , 1045 and 1005 cm^{-1} are ascribed to the symmetric stretching vibration of the $S=O$ bond. Another adsorption band occurs at ca 1380 to 1290 cm^{-1} and is due to the vibration of the C-F bond (see e.g., peak at 1345 and 1295 cm^{-1}). All these peaks observed at $0.0V$ are found to increase with anodic potential (Fig. 1).

†Electrochemical Society Active Member

*On leave of absence from the Department of Chemistry, Warsaw University, Warsaw, Poland.
Key Words: Adsorption, Trifluoromethane-sulfonic acid, Platinum.

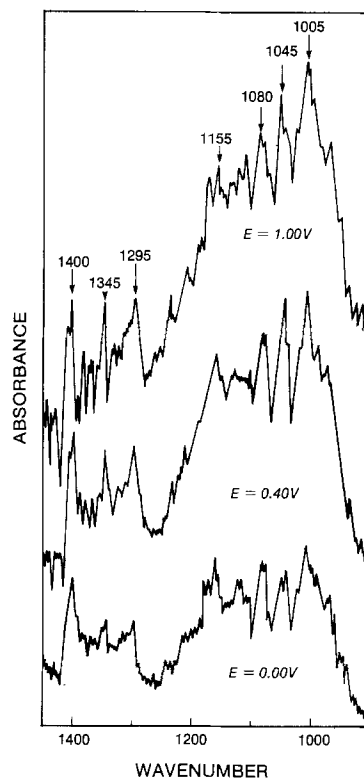


Fig. 1: Differential spectra of adsorbed $CF_3SO_3^-$ ion on platinum at various potentials; $C_{CF_3SO_3} = 2 \times 10^{-2}\text{ mole}\cdot\text{dm}^{-3}$

The adsorption bands originated in TFMSA were confirmed by the fact that no bands were observed in the absence of the acid. That the bands were due to the adsorbed $CF_3SO_3^-$ ion was confirmed by the disappearance of the bands at 1250 to 940 cm^{-1} and 1380 to 1390 cm^{-1} when the incident light was perpendicularly polarized.

The area under the adsorption bands which corresponds to the amount of $CF_3SO_3^-$ ions on the surface is normalized to the surface excess at $0.8V$ as measured by radiotracer method. The results obtained both by FTIR and the radiotracer technique are shown in Fig. 2. The agreement is good up to $1.2V$. At anodic potentials higher than $1.2V$ a slight decrease

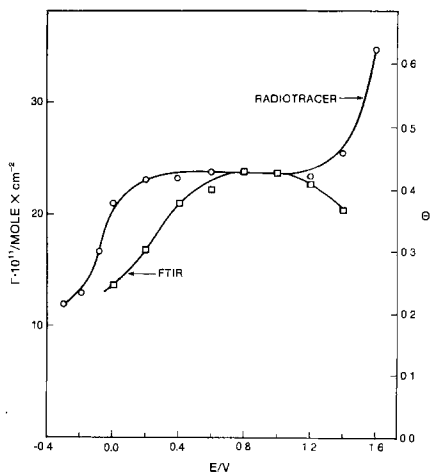


Fig. 2: Γ and θ of CF_3SO_3^- ion as a function of potential; $C_{\text{CF}_3\text{SO}_3^-} = 2 \times 10^{-2} \text{ mole} \cdot \text{dm}^{-3}$

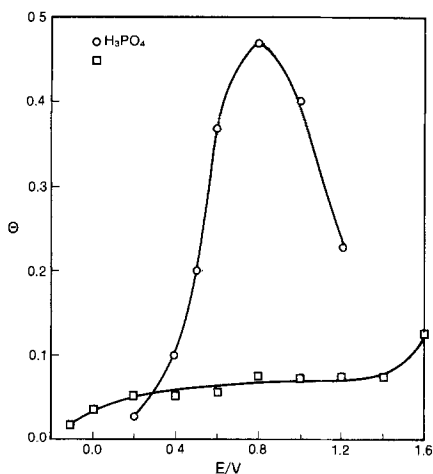
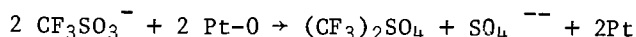


Fig. 3: Comparison of the fractional coverages of H_3PO_4 (4) and CF_3SO_3^- ion on Pt

in the intensity of the IR bands was observed, presumably due to oxidation of the sulfonate ions. One of the possible reaction paths is:



If the adsorbed CF_3SO_3^- ions are oxidized then the bands due to the $\text{S}=\text{O}$ and C-F bonds vibration in sulfonate ions will not appear in the spectrum and hence a decrease in the area of the corresponding IR bands will result as found in the present work. But in the radiotracer experiment, since carbon in the CF_3 group is tagged (^{14}C radionuclide), the increase in the radiotracer signal is expected as confirmed in Fig. 2.

The increase of the radiotracer signal

being observed at high anodic potentials may also be attributed to the "trapping" of CF_3SO_3^- ions in the growing oxide layer on Pt. Such an effect would be detectable in the radiotracer experiment only since the FTIR technique is limited to the outer layer of the adsorbed species.

The fractional surface coverage, θ , in Fig. 2 has been calculated on the basis of a molecular model of CF_3SO_3^- , in which the ions are assumed to adsorb with their SO_3^- ends towards the surface occupying 30.4 \AA^2 area per ion. The surface coverage around 0.8V is thus 0.43. The solution used in this case was $2 \times 10^{-2} \text{ mole} \cdot \text{dm}^{-3} \text{ CF}_3\text{SO}_3\text{H (aq)}$.

A comparable maximum coverage for H_3PO_4 on Pt was reported from a solution of $10^{-2} \text{ mole} \cdot \text{dm}^{-3} \text{ H}_3\text{PO}_4$ in $1 \text{ mole} \cdot \text{dm}^{-3} \text{ HClO}_4 \text{ (aq)}$ (5). For the sake of comparison of CF_3SO_3^- adsorption with that of H_3PO_4 , the adsorption of CF_3SO_3^- ion was measured by the radiotracer method using a solution of $2 \times 10^{-2} \text{ mole} \cdot \text{dm}^{-3} \text{ CF}_3\text{SO}_3^-$ in $1 \text{ mole} \cdot \text{dm}^{-3} \text{ HClO}_4 \text{ (aq)}$. The surface coverages for the CF_3SO_3^- ion and H_3PO_4 on Pt as a function of potential are shown in Fig. 3.

The measurements under the same experimental conditions suggest greater adsorption of H_3PO_4 compared to that of CF_3SO_3^- .

ACKNOWLEDGEMENTS

Discussions with Dr. A.J. Appleby and Dr. S.G. Canagaratna are gratefully acknowledged. Thanks are also due to the Electric Power Research Institute for financial support.

REFERENCES

1. A.J. Appleby and B.S. Baker, *J. Electrochem. Soc.*, **125**, 404 (1978).
2. A.J. Appleby, *J. Electrochem. Soc.*, **117**, 328 (1970).
3. O.A. Petrii, S. Va. Vasina and L. Yu Lukyancheva, *Elektrokhimiya*, **17**, 1383 (1981).
4. M.A. Habib and J.O'M. Bockris, *J. Electrochem. Soc.*, submitted for publication.
5. M.A. Habib and J.O'M. Bockris, *J. Electrochem. Soc.*, **130**, 2510 (1983).
6. P.J. Hyde, S. Srinivasan and S. Gottesfeld, *J. Electrochem. Soc.*, in preparation.
7. R.D. Howells and J.D. McCown, *Chem. Rev.*, **77**, 69 (1977).
8. G. Socrates, *Infrared Characteristic Group Frequencies*, Wiley-Interscience, Chichester, 1980.

Manuscript submitted June 11, 1984

Texas A&M University assisted in meeting the publication costs of this article.



Development and Commercialization of the Monsanto Electrochemical Adiponitrile Process¹

D. E. Danly*

Monsanto Fibers and Intermediates Company, Pensacola, Florida 32575

Mr. President, I would like to begin this Vittorio de Nora-Diamond Shamrock Award address by expressing my sincere appreciation to the members of the Board of Directors of The Electrochemical Society for naming me the award recipient. When I learned several months ago that I had been selected for this honor, I was immensely pleased, but also surprised; I really consider myself more a conventional chemical engineer than an electrochemical technologist. My assignment with Monsanto over the past 26 years has been to seek cost-effective processes for synthetic fiber intermediates, employing whatever type of technology best gets the job done. Fortunately, as a result of Manual Baizer's 1960 discovery of an efficient electrochemical method for reductively coupling acrylonitrile to form adiponitrile (which is an important nylon intermediate), I have been able to spend much of the past 20-plus years in the area of technology of primary interest to this Society.

Before I get into the description of the development and commercialization of the Monsanto electrochemical adiponitrile process, I must say that I could not possibly accept this award without making it very clear that I had a tremendous amount of able help in this successful venture. The team responsible for the laboratory and pilot plant development of our electrohydrodimerization process (or, as we called it, EHD) consisted of about 20 chemists and engineers working in our technical center at Pensacola, Florida. Many others in our Engineering and Manufacturing organization also made significant contributions as we moved from laboratory to pilot plant to an operating commercial facility. So as I stand before you this afternoon, please consider that, in a very real sense, I am acting rather as the captain of a ball club representing his team.

The story of the Monsanto EHD process begins in our St. Louis research labs, where Dr. Baizer had been asked to investigate the possibility of converting acrylonitrile (AN) to adiponitrile (ADN). The impetus for this work stemmed from Monsanto's projections at that time of high growth rates for nylon and acrylic fibers, which translated into a need for additional ADN and AN production capability. If adiponitrile could be made from acrylonitrile, the size of the new AN plant could be increased, improving plant economics, and adipic acid capacity formerly required to provide feed for the existing ADN process would be freed up for use in producing additional nylon 66 salt.

The reductive coupling of AN had been examined by a number of prior investigators, but only with modest success. The highest selectivity to ADN was about 60% for a reaction system using potassium amalgam, as reported by Knunyants and Vyazankin in the USSR. While falling far short of acceptable yields, this work did lead Baizer to

think in terms of an electrochemical approach, and he began to experiment with various electrolyte/electrode systems. I do not plan to relate the details of this research effort, although it is a fascinating story in itself. Let me simply summarize the very significant discovery stemming from Baizer's study — namely, that electrolysis of AN in relatively concentrated aqueous solutions of certain quaternary ammonium salts gave nearly quantitative yields of ADN. Cathodes of mercury or lead gave the best results.

Once the feasibility of the EHD chemistry had been demonstrated in Baizer's 500 ml lab cell, the question was addressed of how to best proceed with the process development. After much discussion and debate at headquarters in St. Louis, it was decided (and I firmly believe correctly so) that the operating division expected to commercialize the process should carry out the scale-up studies. Thus, the task fell to the Chemstrand Division (now Monsanto Fibers and Intermediates Company), which had in-place at Pensacola, Florida, a chemical process development group under Dr. Frank Riordan. I had joined this organization three years previously, following completion of my graduate work in chemical engineering at the University of Florida. None of the group had any real experience in electrochemistry. I was probably the only one who had ever been to a national Electrochemical Society meeting, that a single event as a result of a part-time job at the University in battery research. Being perfectly frank, my background in electrochemistry went little beyond familiarity with the Nernst equation, and I actually found little opportunity to use it in the following days. Since I was eager to be involved in development of this unique process, I may have been guilty of overselling my expertise, but for whatever reason, I found myself appointed project leader for the pilot plant EHD studies.

This was late 1961, and since our forecasts indicated we needed additional ADN capacity by early 1965, we determined that we only had a little over a year to prove out the process. Thus, I need not have worried about getting on the project, since before long the entire research and development group was working on one aspect or another of the process. The chemists began screening electrode materials, diaphragms, alternate electrolytes, and operating conditions, while the mechanical engineers began to consider the cell design. Baizer's lab cell was a glass resin flask containing a platinum wire anode and a mercury pool as cathode, with an aluminum cup serving to separate the anolyte and catholyte. Having calculated that it would take 350,000 of these cells to give the targeted plant capacity of 15,000 metric tons per year, we began to appreciate the magnitude of the scale-up challenge facing us.

Electrode Selection

The selection of a cathode material was relatively easy. Baizer had shown that either lead or mercury was suitable, and we were so horrified by the anticipated envi-

*Electrochemical Society Active Member.

¹Vittorio de Nora-Diamond Shamrock Award address delivered May 8, 1984 at the Cincinnati, Ohio, Meeting of the Society.

Old Process

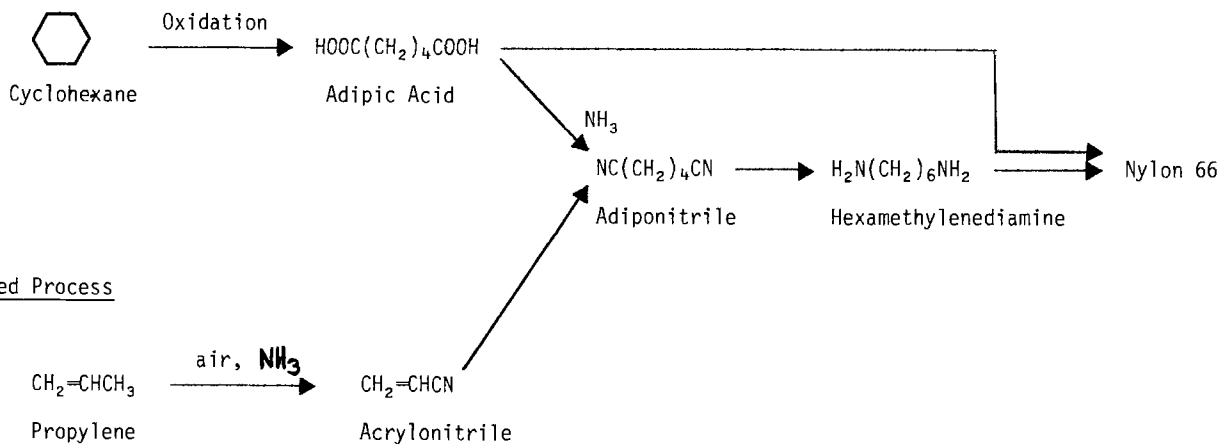


Fig. 1. Routes to adiponitrile

ronmental and cell design problems with mercury that we quickly settled on lead. We tested a long list of other materials reported to give high hydrogen overvoltages, but none was found superior to lead.

Anode selection proved to be considerably more difficult. We began our studies using platinized titanium, but the platinum loss was clearly intolerable. With a switch from Baizer's anolyte of toluene sulfonic acid to dilute sulfuric acid, the use of lead alloys was made possible. Tainton's alloy of 1% Ag in lead had been used successfully in aqueous H_2SO_4 for the manufacture of electrolytic zinc, and this was our early choice, although we tested a number of other lead alloys reported in the literature to have greater stability.

The real surprise in anode development came during the first attempts to operate a pilot-scale cell. While anode corrosion rates as low as 3 mm/yr were measured in short lab tests, we found that in extended pilot-plant runs the corrosion rate would increase by 20-fold over a 24h operating period. Our analytical folks were able to place the blame on a buildup of nitrates and various chlorine containing anions in the anolyte. The nitrate anions were evidently being formed by oxidation of AN diffusing through the membrane into the anolyte compartment, while the chlorine was entering the system in small amounts in the sulfuric acid and quaternary ammonium salt. The problem was solved by putting tight chloride specifications on the raw materials and instituting a continuous purge and makeup of anolyte to hold the nitrate concentration below a critical level.

Selection of Supporting Electrolyte

Baizer's recommended catholyte was a 40% aqueous solution of tetraethylammonium p-toluenesulfonate. This electrolyte possessed two properties which at that time were believed to be necessary for high ADN selectivity: (i) the cation was not reduced at the cathode, and (ii) the salt greatly enhanced the solubility of AN in the solution. Other factors considered important for a commercial process were the electrolyte cost, electrical conductivity, and ease of removal of ADN from the electrolyte. More than 30 quaternary ammonium salts were prepared for measurement of these properties. Four of these were selected for extensive benchscale and pilot plant testing, from which it was determined that the yield of electrolysis by-products (propionitrile and high-boiling AN oligomers) decreased with increasing size of the quaternary ammonium cation. Salts with cations larger than tetraethylammonium were not felt to be practical because their aqueous solutions exhibited poor electrical conductivities and very high AN and ADN solubilities, making extraction of product difficult. Tetraethylammonium ethylsulfate was a clear choice, since it not only gave the best ADN selectivity, but also could be simply prepared by combination

of two low-cost intermediates, triethylamine and diethylsulfate.

In attempting briefly to outline our research and development studies, I am greatly oversimplifying the story. I have made it sound as though we tested cathodes, ... picked one, ... tested anodes, ... picked one, ... tested electrolytes, ... picked one, and so forth. It really was not that straightforward. For example, we solved the problem of poor stability of pure lead as an anode by adding a small amount of silver, only to discover the Ag cation introduced into the anolyte by corrosion of the anode passed through the membrane, deposited on the cathode, and sharply depressed the ADN selectivity. This particular problem was ultimately resolved by electrodeposition of the silver ions contained in the recycled quaternary ammonium salt on a lead-shot cathode of a packed-bed electrolyzer. We also found that the best anode alloy when using a p-toluene sulfonate anion in the catholyte was not the best one when we switched to ethylsulfate anion. Small amounts of these anions migrating from the catholyte into the anolyte had a significant impact on anode stability.

Membrane Development

The selection of a diaphragm for separation of anolyte and catholyte required something more than the cut-and-try approach used with electrodes and supporting electrolyte. We did begin our search by testing samples of all of the commercial cation-permselective membranes, but the majority of these failed in less than a day. Unfortunately, the perfluorinated membranes now proving so successful in chloralkali cells were not around in 1962. Of the materials available, the most encouraging results were with a membrane made by Ionics, Incorporated, composed of sulfonated polystyrene/divinylbenzene polymer and a glass fiber reinforcing cloth. With these, benchscale runs of a week or so were possible. Since considerable improvement in durability was needed to achieve the targeted 1000h service life, we entered into a joint membrane development program with Ionics. They provided numerous test samples, varying such parameters as degree of

Table I. Pilot-plant electrolyte evaluations (50 A/dm², 50°C)

Cation	Electrolyte Anion	Selectivities (%)	
		EHD by-products	ADN ¹
Me ₄ N	p-Toluenesulfonate	9.0	89.8
MeEt ₃ N	p-Toluenesulfonate	7.1	89.2
Et ₄ N	Benzenesulfonate	7.2	90.9
Et ₄ N	Ethyl sulfate	4.9	93.4

¹ ADN selectivity corrected for AN recoverable from cyanoethylation by-products.

Table II. Benchscale membrane screening tests

Supplier/Designation		Service life (h)
AMF	C-60	76*
	C-110	5
	C-313	2
Asahi Glass	GSG-10	<24
	GMG-10	<24
	CMV-10	<24
Asahi Chemical	DK-1	<24
Tokuyama Soda	CHR-4	190*
	CL-2.5T	133*
Ionac Chemical	MC3142	2
Permutit/U.K.	C-20	15
Radiation Applications	320	2
	1010 (paired)	115
Ionics	AZG	255*

* Using Ionics AZG membrane for support.

polymer cross-linkage, type of reinforcing fabric, and membrane thickness. We geared up for performance testing, setting up six 1 dm² flow cells, which we operated around the clock at typical EHD operating conditions.

When we began pilot plant operation with an 80-fold scale-up in membrane area, we found, to our dismay, that the formulation that had given several hundred hours service life in the 1 dm² benchscale cells did not even last for a day. In pilot operation, the ion-exchange resin was randomly spalling off, forming small windows for movement of anolyte into the catholyte. As an expedient solution, we simply installed dual membranes, banking on the odds against the windows' lining up, and this allowed run lengths of a week or two.

This rather brute-force solution was not very elegant, but at least allowed us to stay on line with our pilot plant cell to try to answer other unresolved process and cell design questions. Some months later, our friends at Ionics developed a membrane incorporating two layers of glass cloth in the same resin matrix. These exhibited operating lives of up to 2000h in lab cells and were adopted as the standard.

Cell Design

Since the process as we knew it at that time required separation of anolyte and catholyte, we thought in terms

of a plate-and-frame design for the commercial cell from the outset. This decision was reinforced when, in the early days of process development, we called in the renowned consultant, Dr. Robert B. MacMullin. Bob, as many of you know, was the second recipient of the Society's Electrochemical Engineering and Technology Award. He was asked to provide a design for a 250A lab cell and then to make a preliminary design and cost estimate for the electrolysis portion of a commercial EHD plant. Although we never constructed the MacMullin cell, his detailed design calculations were extremely valuable in educating us in the techniques of voltage balances, electrolysis system heat balances, cellhouse layout, and a multitude of other electrochemical engineering considerations.

The other distinguished advisor we enlisted was Dr. Vittorio de Nora. Following discussions with us in Pensacola during one of his frequent trips to the U.S., it was agreed that the de Nora firm in Milan would design and build us a prototype cell. I was immediately dispatched to Italy to provide the de Nora engineers with what little process information we had.

At the time of Dr. de Nora's visit, the development team at Pensacola had already moved well into the design of the first pilot-plant cell. We decided early-on that this cell should be the same size as visualized for the full-scale facility. Surely if we could make a bank of 3-5 cells work in the pilot plant, operation of a plant using several hundred identical units *should* pose no problem. The size of the cell was set by the dimensions of the largest membrane then offered by Ionics: roughly 90 × 100 cm. Since we were trying to develop all the required plant design data in the space of 12 months, we pushed forward simultaneously with both the Monsanto and de Nora cell designs.

The first Monsanto design was a single cell unit with the electrodes mounted on polyethylene plates, into which were machined cavities for electrolyte distribution (Fig. 2). Anolyte flow was vertically upward, while catholyte was introduced through a central vertical plenum, where it split and flowed horizontally to the two sides. Dividing of the catholyte flow was aimed at reducing the length of the catholyte flow path in order to minimize the pressure differential across the membrane. This cell was used briefly in the initial pilot-plant operation, but problems in sealing of the membrane gaskets and evidence of uneven distribution of electrolyte across the cathode led us to install the de Nora cell unit as soon as it arrived by air from Italy.

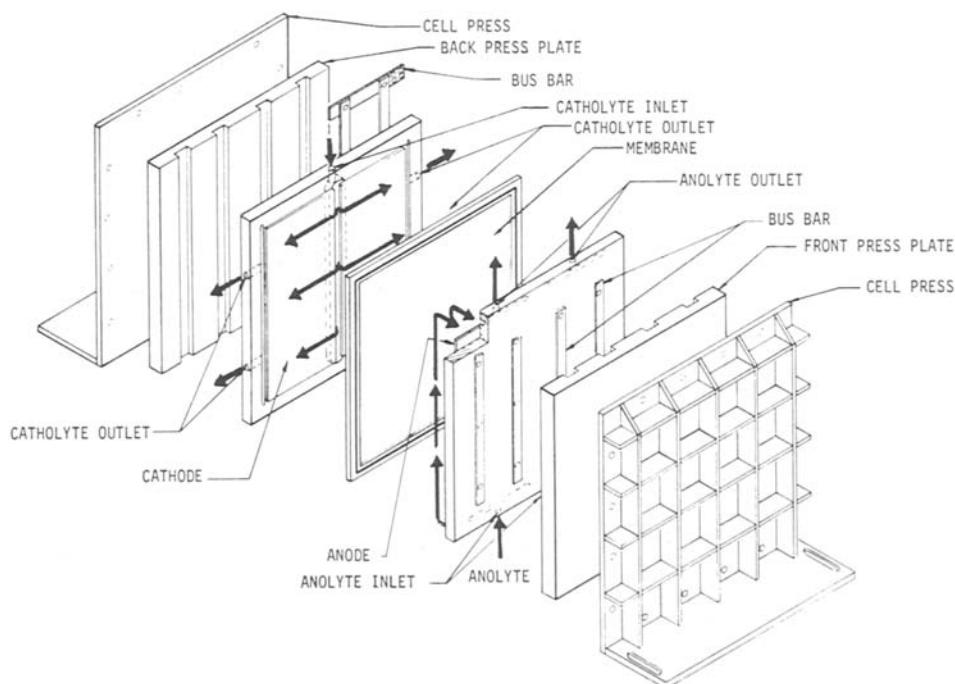
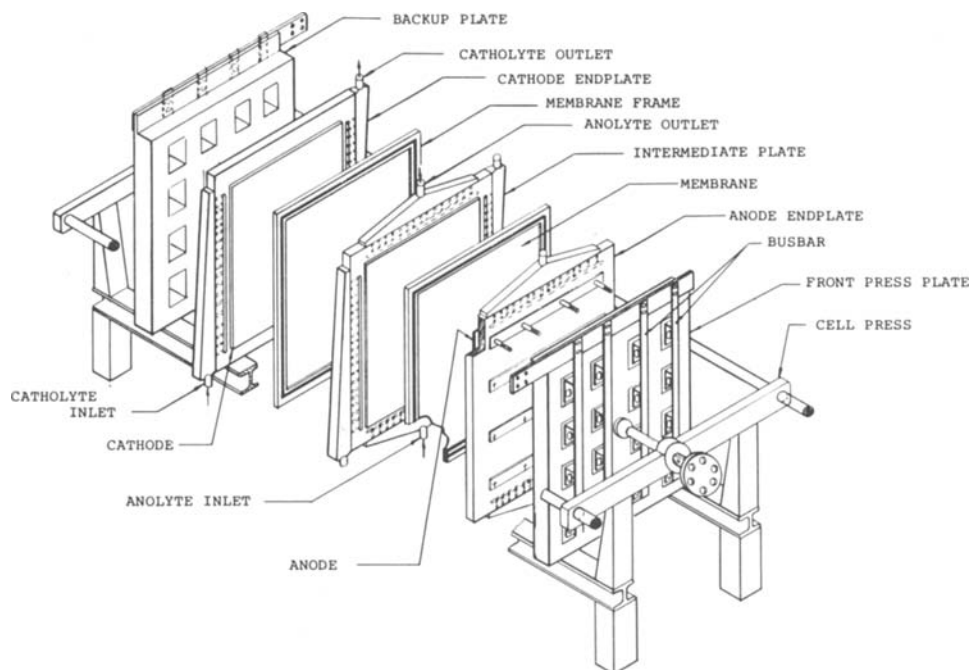


Fig. 2. Monsanto Mark I EHD cell.

Fig. 3. de Nora cell

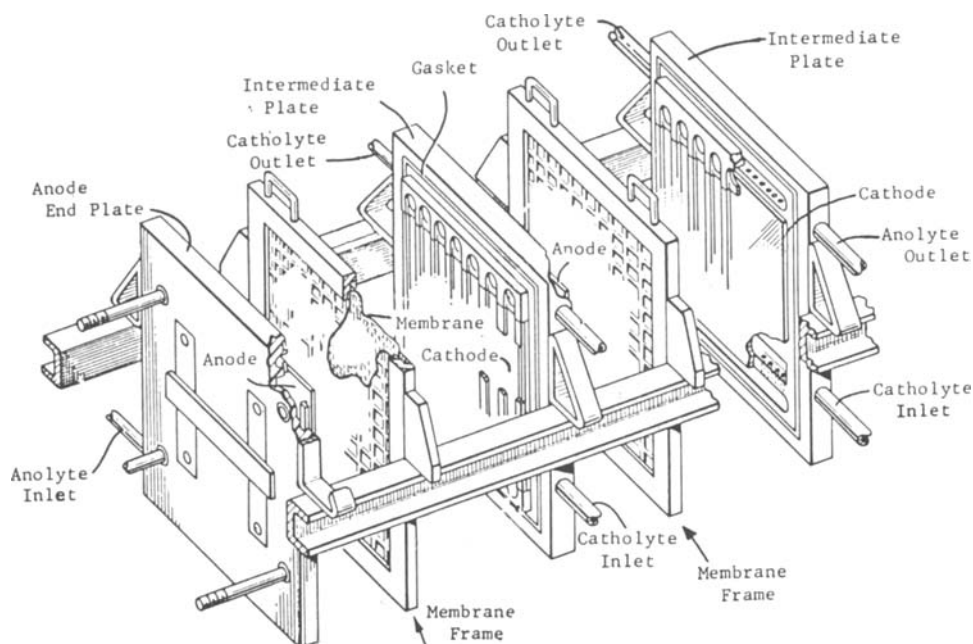


The de Nora unit (Fig. 3) contained five bipolar cells. The electrolyte streams were introduced through tapered, external distribution boxes, then passed through a series of small holes into internal plenum chambers in the cell plates. This design provided greatly improved uniformity of electrolyte flow compared to the first Monsanto design. This cell was operated for several months to conduct studies of spacer design and the effects of catholyte velocity, composition, and temperature. The chief problems with the cell were the integrity of the hydraulic seals and recurring failures of the external distribution boxes, which were made by welding together sections of polypropylene sheeting.

These problems were overcome in the third-generation design (Fig. 4), which employed tapered electrolyte distribution cavities machined into polypropylene plates behind the electrodes. The membranes were held between two mated polypropylene frames for convenience in handling. The fluid leakage problem was solved by the use of a beaded gasket, which markedly lowered the required sealing force. This proved to be a reliable assembly, and with minor modifications it was ultimately adopted for use in the commercial plant.

Probably one of the most important electrochemical engineering concerns we faced was that of achieving high mass-transfer rates at the cathode surface. The transfer of AN across the diffusion layer from bulk catholyte to the cathode turned out to be less critical than neutralization of the hydroxyl ions produced at the cathode (Fig. 5). Acrylonitrile reacts very rapidly with water under alkaline conditions to form the cyanoethylation by-products hydroxypropionitrile and bis-cyanoethylether. These side reactions represented a very significant AN-yield loss in early experiments at low catholyte flow velocities. Our first approach was to employ turbulence promoters, such as plastic webbing or baffles, similar to the types proven effective in electro dialysis devices. While several of these significantly lowered losses of AN due to cyanoethylation, buildup of AN polymer on the plastic spacers in time gave rise to an intolerable pressure drop along the catholyte flow path. Various means of in-place cleaning were tested, but we finally concluded that only fully open channels offered any chance for reasonable on-stream time. After many aborted efforts, we found the most dependable way to form the open channels was to attach narrow plastic ribs directly to the Pb cathode in

Fig. 4. Mork II Monsanto cell



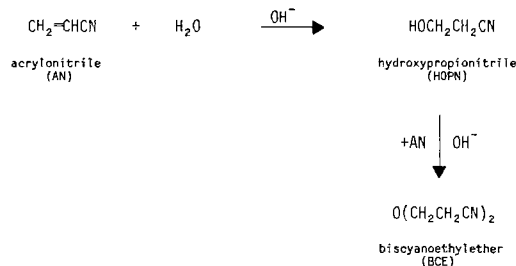


Fig. 5. Cyanoethylation reactions

much the same way the chrome strip is fastened to one's automobile fender. We tested different gauges, widths, and thicknesses of the parallel strips, and most importantly, the catholyte velocity needed to control the cyanoethylation side reaction (Fig. 6). A velocity of 2 m/s was selected as giving the optimum balance between AN-yield loss and catholyte pumping cost.

While definition of the cell design and optimization of the electrolysis conditions were paramount to the success of the process development, a substantial effort was also needed to define the product recovery and purification systems. Processing downstream of the cells (Fig. 7) consisted of extraction of ADN from catholyte with AN, stripping of the AN to produce a crude ADN, and final clean up in a four-column distillation train. We felt it was imperative to demonstrate the process in the pilot plant with all the recycle loops closed. Had we not done this, the serious consequences of silver ion buildup in the recycle QAS might never have been recognized. We also felt obliged to show that our refined ADN could be satisfactorily hydrogenated to hexamethylene diamine and converted into standard-quality nylon polymer. All of these steps were demonstrated in the pilot plant.

In scaling up a new process, one generally prefers to complete laboratory demonstration and then prepare the plant-design documents. Our tight timetable for commercialization of the process did not allow us this luxury. A very preliminary design of the full-scale facility was developed even before the first pilot-plant run by a member of the Engineering Department assigned to work with the

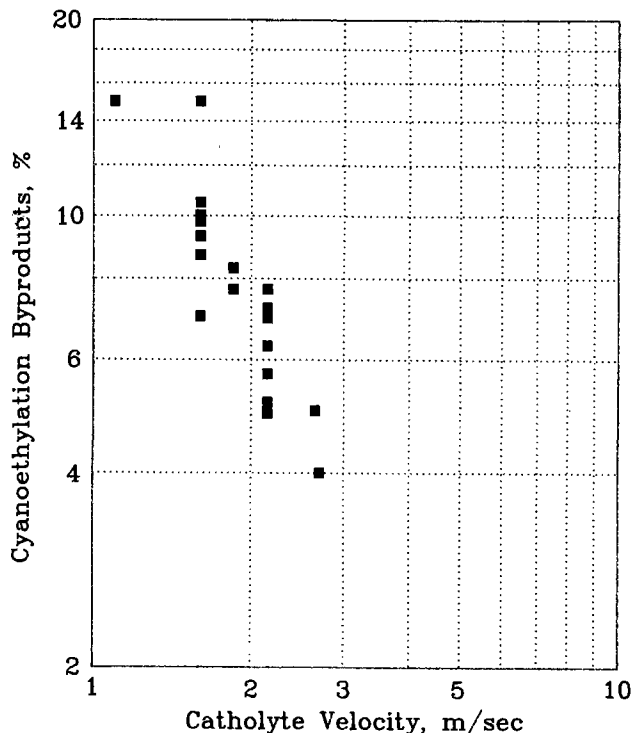


Fig. 6. Effect of catholyte velocity on cyanoethylation by-products

Development team. Our first pass through the projected process economics was based on operation at a cathode current density of 20 A/dm², and we discovered the investment in cells would be enormous. We examined higher current densities on paper and found the optimum balance between electrolysis operating costs and capital burden occurred in the current density range 40-60 A/dm² (Fig. 8). Fortunately, lab studies showed no measurable decline in electrolysis performance below 100 A/dm², provided the catholyte flow was 2 m/s. This early conceptualization and evaluation of the proposed commercial process thus proved to be most valuable in guiding our development efforts.

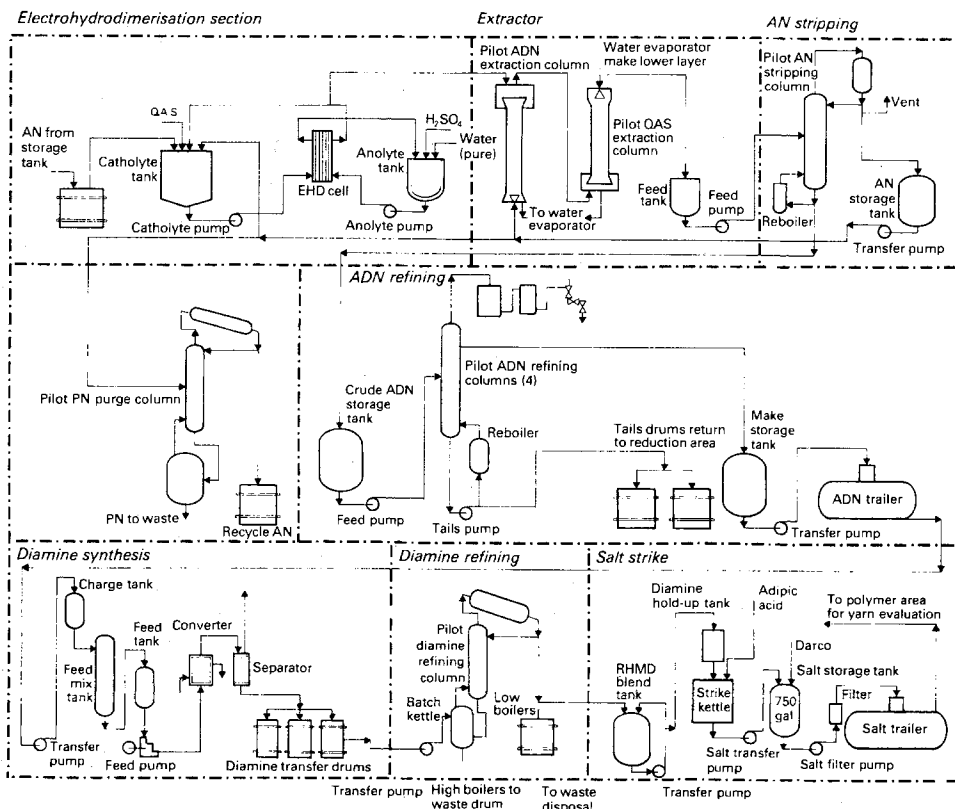


Fig. 7. Complete pilot plant system.

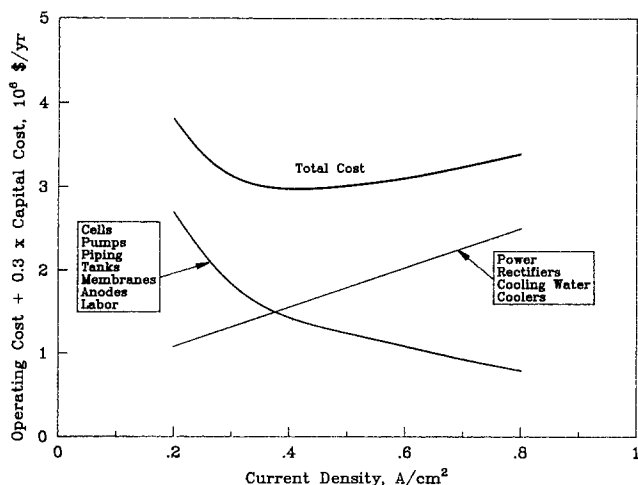


Fig. 8. Current density optimization

The preliminary plant design was modified repeatedly as we learned more about the process and cell requirements, and a final document was approved almost exactly one year from the initial pilot plant run. The first EHD facility (Fig. 9) was constructed at our Decatur, Alabama, plantsite and had a design capacity of 14,500 MT/Y ADN. The electrolysis system consisted of 16 cell presses, each housing 24 bipolar cells and operating at about 3000A. Four independent catholyte circulating systems were employed to minimize the impact of a major membrane failure on total plant operations.

I wish I could tell you the plant was built, started up, and ran like a Swiss watch from the outset. However, I must confess that initial plant operation was plagued by short membrane lives, deterioration in ADN selectivity due to a buildup of previously unidentified impurities in the recycle QAS, and several small fires stemming from ruptured catholyte hoses supplying feed to the cells. These problems were largely resolved during the first

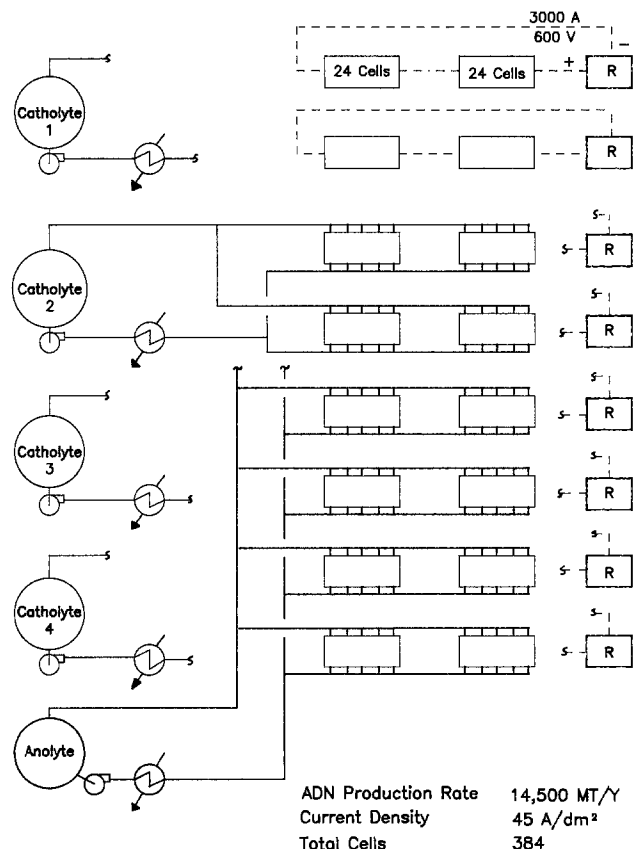


Fig. 9. Original EHD plant layout

year of operation by use of improved membranes from Ionics, installation of a supplemental QAS cleanup system, and a change-over to steel-reinforced hoses.

Meanwhile, back at the labs in Pensacola, we were busy seeking ways to make a step-change improvement in the process. The divided-cell technology we had commercialized had three serious drawbacks: the electrical power usage was high (7-8 kWh/kg), the cells were complicated and expensive, and membrane replacement still remained a significant operating cost. Clearly, if we could devise a workable undivided cell system, we would avoid or reduce all of these penalties. In 1965, the same year as our plant startup, some Russian investigators (Tomilov, Varshavskii, and Knunyants) reported ADN selectivities as high as 90% in an undivided cell using an emulsion of AN in an aqueous electrolyte of 1N sodium hydrogen phosphate containing about 1 weight percent tetraethylammonium phosphate. Their cell employed a graphite cathode and a magnetite anode, and was operated at 18°C to minimize cyanoethylation side reactions. While the fragile nonmetallic electrodes used in this work seemed ill-suited to a commercial cell, the high electrical conductivity of the aqueous alkali phosphate electrolyte seemed most appealing. We initiated studies of alternate cathode and anode materials, targeting an all-metal electrode system capable of operation at higher temperatures, in order to avoid refrigeration.

I will not go through the long laundry list of electrode and electrolyte systems we examined, but will summarize several years of testing by saying that carbon steel proved to be a very satisfactory anode, provided small amounts of Na₄EDTA and Na₂B₄O₇ were added to the phosphate electrolyte as corrosion inhibitors. These additives reduced the anode corrosion rates from about 10 mm/yr in uninhibited electrolyte to a quite acceptable level of 0.5 mm/yr.

Of all the solid metals tested as cathodes, cadmium was found to give the best performance with respect to ADN selectivity and electrode stability. Aided some by serendipity, we discovered that the Na₄EDTA added to enhance anode stability led to mild corrosion at the cadmium cathode, thus serving to keep it free from accumulation of anode corrosion products (Fig. 10). In the absence of EDTA, hydrogen evolution at the cathode increased over a day's operation to the point where it represented greater than 10% loss in cathodic current efficiency. We ultimately found it desirable to introduce sufficient EDTA to chelate all the Cd and Fe cations entering the electrolyte via electrode corrosion.

The other absolutely essential electrolyte component is the quaternary ammonium salt. We screened a number of candidates and found the higher molecular weight analogs to give better results than the tetraethylammonium compounds used in our divided-cell process. Hexamethylene bis(ethyldibutylammonium) phosphate

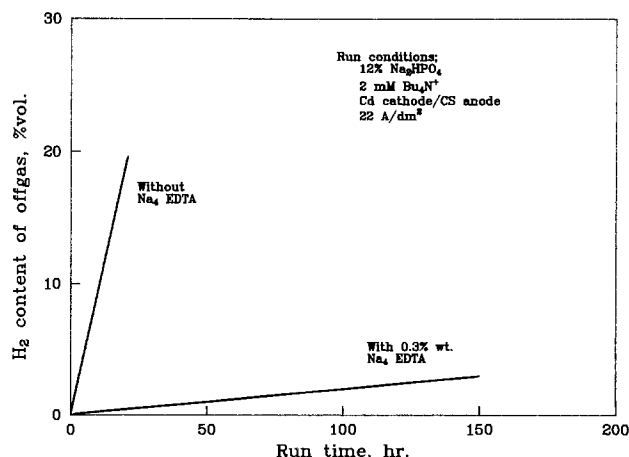


Fig. 10. Effect of EDTA as cathode stabilizer

Table III. Quaternary ammonium salt evaluation, undivided cell

QAS cation	ADN selectivity (%)
10% Na ₂ HPO ₄ Cd cathode 0.002M QAS	
Et ₄ N ⁺	85
EtPr ₃ N ⁺	87
MeBu ₃ N ⁺	88
EtBu ₃ N ⁺	89
EtPe ₃ N ⁺	89
EtHx ₃ N ⁺	87
Pr ₃ N(CH ₂) ₄ NPr ₃ ⁺⁺	88
EtBu ₂ N(CH ₂) ₆ NBu ₃ Et ⁺⁺ (Preferred QAS)	89

Me = CH₃, Et = C₂H₅, Pr = C₃H₇, Bu = C₄H₉, Pe = C₅H₁₁, Hx = C₆H₁₃.

performed best in terms of ADN selectivity and ease of extraction from the organic products.

Elimination of the membrane vastly simplifies cell design (Fig. 11). Bipolar electrodes are prepared from 1.5 mm thick sheets of carbon steel by electroplating 50-100 μm of Cd on one side. These are stacked together using plastic spacers to set the electrode distance. The total thickness of an individual cell is only about 3 mm; thus, a 100-cell bipolar stack has a thickness of only 30 cm. The electrode stack is fitted with a polypropylene housing and is contained in a cylindrical vessel, which provides a leak-free means of circulating electrolyte through the stack. Plastic electrode extensions at the inlet and outlet ends of the cell serve to limit current bypassing through the electrolyte in the vessel heads. The cost per square meter of cathode area for the undivided stack assembly is less than one-tenth that of the earlier plate-and-frame cell. Our Mechanical Engineering group at Pensacola deserves most of the credit for this accomplishment.

Another major advantage of the undivided cell is the markedly reduced cell voltage and power usage (Table IV). The voltage reduction is due to the use of a significantly more conductive catholyte and elimination of the membrane- and anolyte-IR drops. In addition, the low cell cost shifts the economic optimum current density to lower values, further reducing the total voltage. Cell power usage is cut by almost two-thirds.

However, we were not yet "home free," even though we had a workable electrolyte system and cell design. In the

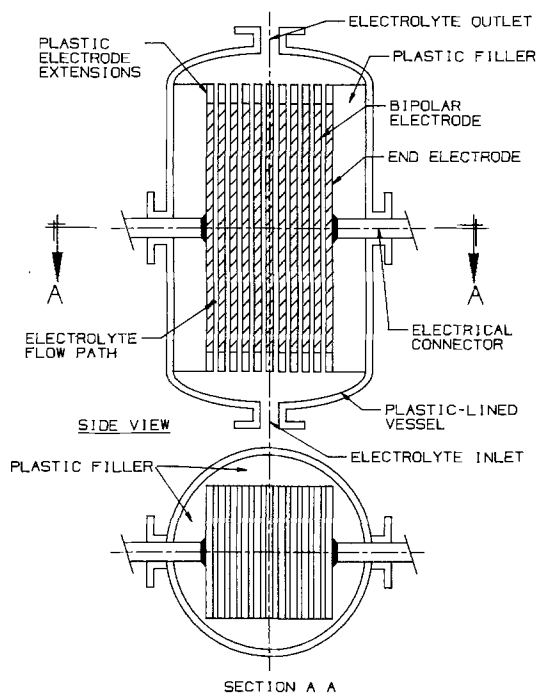


Fig. 11. Undivided EHD cell

Table IV. Comparison of EHD cell voltages

	Divided cell	Undivided cell
Current density (A/dm ²)	45	20
Voltage drops		
Reaction EMF	2.50	2.50
Overpotential	1.22	0.87
Catholyte IR drop	5.47	0.47
Anolyte IR drop	0.77	—
Membrane IR drop	1.69	—
Cell voltage	11.65	3.84
Power usage (kWh/kg)	6.6	2.4

undivided-cell EHD process, the offgas from the cells is an oxygen stream saturated with acrylonitrile vapor and may also contain 5%-10% H₂. This represented a serious explosion hazard. We felt we were safe within the cell itself, since the gas was present as small, discreet bubbles. But somewhere in the circulating system we had to face up to handling large volumes of this explosive gas mixture.

The proposed solution (Fig. 12) involves the use of a cone-capped electrolyte surge vessel, fitted with a scrubbing column at the apex. The liquid level is maintained several meters up into the column, and the gas bubbles rising through the cone and into the column create an aerated zone, which acts as a shock-absorber in the event of an explosion in the gas phase above. This small-diameter column is designed to withstand a H₂-O₂ explosion, while the rest of the system is not. AN is scrubbed from the offgas with ADN in the upper section of the column, which is packed with plastic Pall rings. The concept of protecting a large, thin-walled vessel from an explosion by a column of aerated liquid was proven out in a small-scale system, and it works.

The improved EHD process is capable of producing ADN at a significantly lower cost than the adipic-acid-based route practiced by many nylon manufacturers, and we believe it is fully competitive with the newer technology involving direct hydrocyanation of butadiene. Monsanto currently has installed EHD capacity of about 180,000 MT/Y ADN, divided roughly equally between the plant at Decatur, Alabama, and a newer facility at Seal Sands, England, brought on-stream in 1978. This is clearly the world's largest example of electro-organic processing.

In conclusion, I would like to try to summarize what I believe to be the key to the success of the EHD process development. Certainly, dedication and innovation were

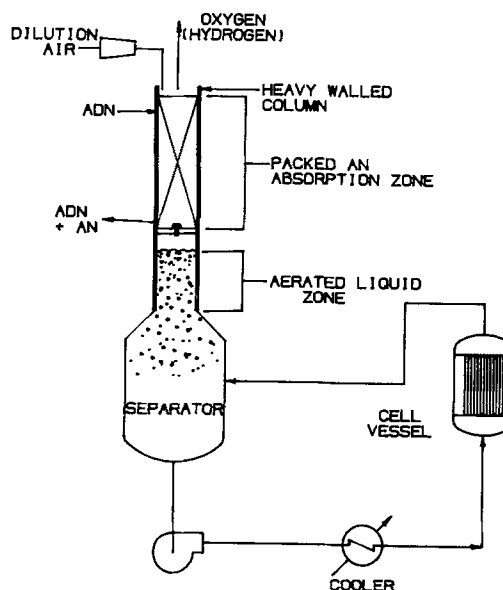


Fig. 12. EHD offgas system

required on the part of the entire technical team, but the resources surely would have been cut off at an early stage had we not committed capital to that first commercial installation. It really was a gamble on unproven technology, and there were times in those early years when even *I* had some doubts. But with the plant sitting there, we had to

make it work and, as electricity and capital costs rose, we had to make the process better. One seldom can see all the potential improvements at the outset, but as the experience-curve philosophy tells us, with work they will come.

Thank you.



The Mechanisms of Thionyl Chloride Reduction at Solid Electrodes

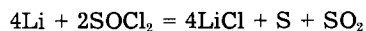
W. K. Istone^{*1} and R. J. Brodd^{*2}

Ray O Vac Corporation, Madison, Wisconsin 53711

ABSTRACT

An experimental technique has been devised which allows *in situ* sampling of electrolyte from a functioning Li-SOCl₂ cell, followed by rapid FTIR analysis for soluble reaction products. Disulfur monoxide (S₂O) is observed as an intermediate discharge product. The half-life of S₂O is estimated to be about 20 min. The presence of S₂O is consistent with sulfur chemistry, as well as the accepted stoichiometry of the Li-SOCl₂ battery system. A possible safety hazard for low temperature discharges of Li-SOCl₂ cells is identified.

There has been great interest in the thionyl chloride-lithium battery system because of its high energy density and good high rate capability. There is general agreement that the overall discharge reaction for the system is



The details of the reaction are not yet known with certainty. Previous studies of the reaction mechanism have proposed various reaction pathways. Intermediates such as SO, S₂Cl₂, etc., have been postulated (1-4). It is important to know all aspects of the reaction characteristics in order to properly design the electrode structures (e.g., porosity) to accommodate reaction products, and to select materials of construction that are stable in SO, S₂Cl₂, SOCl₂, etc. It is also likely that the safety questions concerning thionyl chloride battery systems are related to the identity and stability of the reaction intermediates. Safety aspects include constructional features of the anode, the cathode, and the complete cell; they also prevent conditions such as internal shorts and the direct reaction of lithium and the sulfur reaction product.

In order to better understand the detailed steps and intermediates of the reaction mechanism, a technique described below has been devised to allow *in situ* sampling of electrolyte at the electrolyte surface. The materials present in the electrolyte are analyzed immediately utilizing Fourier transform infrared spectroscopy (FTIR). It is believed that the technique and relatively short analysis time (30s) have allowed us to confirm the existence of some reaction intermediates not previously observed.

Experimental

Thionyl chloride from Aldrich Chemical Company was redistilled in a glass and in Teflon still at ambient pressure under dry argon by the method of Wetter (5), with 160 ml additions of triphenyl phosphite to 1 liter of thionyl chloride. Care was taken to keep the pot below 82°C and column temperature below 78°C to prevent thermal decomposition of thionyl chloride. Fluka "puriss."-grade aluminum chloride was used as received. LiCl from Alpha Chemical Company was dried at 150°C *in vacuo* for 48h. The 1.6M LiAlCl₄ solutions were prepared in the argon dry box by slowly adding AlCl₃ to thionyl chloride to avoid heating and then slowly adding LiCl in slight excess. The resulting solutions were a very pale straw color.

* Electrochemical Society Active Member.

¹ Present address: St. Regis Technical Center, West Nyak, New York 10994.

² Present address: Standard Oil Company, Amoco Research Center, Naperville, Illinois 60566.

All pure chemicals and solutions were stored in glass inside an argon dry box.

Linear-sweep voltammetry experiments utilized a PAR Model 173 potentiostat and Model 175 waveform generator. Cell discharges were at constant current using a Keithley Model 227 constant current source.

The molar extinction coefficients are not known with certainty for the various reaction-product compounds in thionyl chloride. As a result, the absolute concentrations of the compounds cannot be determined. The amounts of materials were estimated on a relative basis. Since thionyl chloride is present in excess in all solutions, the peak for thionyl chloride at 2400 cm⁻¹ was used as a reference. The height of the peak for a particular compound, relative to the height of the 2400 cm⁻¹ peak, was used to follow changes in concentrations. This normalization procedure was used to eliminate errors due to changes in cell path length or instrumental conditions.

The experimental cell and sampling techniques were described previously (1). The FTIR cell was a Barnes micro flow-through cell having a path length of 0.1 mm. The cell material was KBr, with a total cell volume of 0.4 μl. The cell was connected by Teflon tubing to a syringe, which was used to draw samples of electrolyte into the FTIR cell. A valve prevented siphoning. A second piece of Teflon tubing connected the FTIR cell to the electrochemical cell, utilizing a stainless steel needle as a probe. The SOCl₂ slowly attacked the KBr cell, slightly changing its optical path. Therefore, the results reported here are semiquantitative in nature.

The electrochemical cell was contained in a glass vial containing 5 ml of 1.6M LiAlCl₄ in SOCl₂. A glass fiber mat separated the negative electrode (Foote Chemical Company pure lithium foil of 1 cm² area pressed into expanded stainless steel mesh) from the positive electrode (90% Shawinigan black, 10% PTFE, hot pressed at 275°C into expanded stainless steel grid to form a 1 cm² area electrode). The positive electrode made in this fashion had a porosity of about 60%. The stainless steel sampling probe was placed with its opening pressed against the face of the positive electrode. Experiments were also carried out with PTFE-bonded positive electrodes, using copper powder mixed with the Shawinigan black, as well as other solid planar materials, including glassy carbon, platinum, gold, nickel, and Type 316 stainless steel. The cell was assembled, filled, and sealed under argon atmosphere in a glove box, then transferred to the FTIR for discharge experiments.

The test cell was discharged at 5 mA/cm² constant current, with electrolyte samples of about 1 μl drawn for

Table I. Infrared spectral assignments for thionyl chloride and related species (5-10)

Compound	Assignment (cm ⁻¹)
SOCl ₂	<u>1229*</u> , 490, 443, 344, <u>284</u> , 194
SO ₂ Cl ₂	<u>1414*</u> , 1182, 560, 405, 388, 380, 362, 282, 218
SO ₂	<u>1332*</u> , 1157
SO ₃	1330, 1069*, 652, 532
SO	1124
S ₂ O	1165, 679*, 388
(SO) _x	1125
S ₂ Cl ₂	<u>538</u> , 448, <u>438*</u> , <u>242</u> , 203
SCl ₂	<u>535*</u> , 514, 208
(AlCl ₃) _x	575*, 349, 180, 146
HCl	2886* (broad)
S	1290, 932, <u>841*</u> , 686, <u>465</u>

Underscoring denotes strong band.

* Denotes principal frequency for analytical purposes.

analysis before discharge began to establish base line and at 15 min intervals during discharge. The FTIR is a Nicolet MX-1. The 27 scans between 4400 and 225 cm⁻¹, taken to establish each spectrum, required 30s. Most experiments were carried out at a room temperature of 298 K (25°C). Some experiments were carried out at low temperatures of 273 K (0°C) and 260 K (-13°C) to establish the effect of temperature on the reaction rate and, if possible, to stabilize fast reacting species.

Results and Discussion

The infrared correlation chart (Table I) of species pertinent to sulfur oxyhalide chemistry was used to interpret the experimental results. The spectra obtained from the cell electrolyte were analyzed to determine which compounds are observed in analyzed electrolyte, whether these compounds are present as impurities or as the result of electrochemical discharge, and how the compounds' relative concentrations change as a function of experimental stand time and depth of discharge. The electrolytes are spiked with compounds of interest to confirm their presence, with the exception of SO₃ and S₂O.

Figure 1 shows a typical IR spectra taken during discharge of a Shawinigan-black, PTFE carbon cathode. The location of the significant peaks is noted during the experiments. An analysis of the spectra shows that small amounts of SO₂Cl₂, SO₂, S₂Cl₂, SCl₂, and HCl are present in the electrolyte as impurities at the beginning of the experiment. The HCl and SO₂ concentrations increase

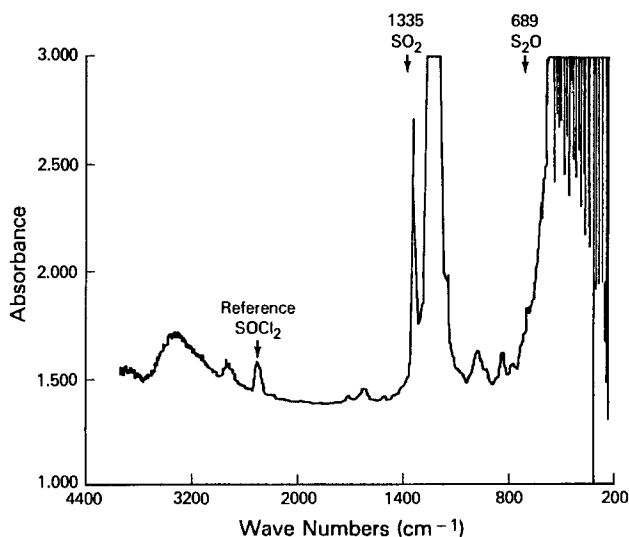
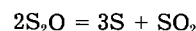


Fig. 1. Typical IR spectra showing S₂O, SO₂, and thionyl chloride reference peaks.

slightly with stand time, presumably as a result of moisture pickup from the cell walls. SO₃ is not observed initially and does not appear during stand time or during discharge. The SO and (SO)_x species are difficult to detect because the proximity of the large SOCl₂ bands tend to mask them. The peak heights for S₂Cl₂ and SCl₂ remain constant throughout the experiments. Only the intensities of peaks assigned to SO₂ and S₂O are observed to change as a function of cell discharge. Matrix effects can result in wavelength shifts from the values reported for pure compounds, as opposed to the compound dissolved in 1.6M LiAlCl₄ in SOCl₂. For instance, the SO₂ peak reported at 1332 cm⁻¹ appears at 1335 cm⁻¹, and the S₂O peak of 679 cm⁻¹ appears at 689 cm⁻¹ in SOCl₂ media. The other peaks for these compounds are also detected with similar matrix shifts, though the 1332 and 679 cm⁻¹ are the easiest to monitor.

Figure 2 shows the change in relative concentration of SO₂ and S₂O as a function of cell discharge. It may be noted that the S₂O concentration increases to a maximum and then begins to decrease with time (mAh), whereas the SO₂ concentration increases and then appears to level off. We believe that the plateau in Fig. 2 is related to the steady-state concentration of SO₂ at the electrode surface under the experimental discharge conditions. Companion experiments run at a significantly higher discharge rate (50 mA/cm²) show that the amount of SO₂ increases as a function of discharge time. Hence, the plateau of Fig. 2 may simply be related to the SO₂ diffusion away from the electrode surface in a steady-state situation. No new compounds were found at the higher current density. The results are similar to the results reported at lower current density, but with slightly higher concentrations of the S₂O intermediate. When an electrolyte sample from a discharged electrode is allowed to stand in the FTIR cell for a prolonged period (*e.g.*, 30 min), analyses show that the SO₂ concentration increases and the S₂O is deposited on the FTIR cell walls. Sulfur is a reaction product, and the S₈ species could be found as a reaction product. However, though S₈ has a weak absorption band at 686 cm⁻¹, it has a medium absorption band at 841 cm⁻¹ which would not be interfered with in the observed spectra. Experimentally, no change around 841 cm⁻¹ occurred, as would be expected. Also, on stand, no change should occur if S₈ is responsible for the 690 cm⁻¹ band. This is consistent with the reported decomposition reaction for S₂O (7)



Copper powder added to the positive electrode has been reported to improve the high rate capability of the Li-SOCl₂ cell (11). The copper reacts with SOCl₂ to produce insoluble CuCl. No new soluble materials were observed in thionyl chloride of cells containing copper. Only peaks for SO₂ and S₂O were observed. Figure 3 shows the change in relative concentrations of SO₂ and S₂O, using

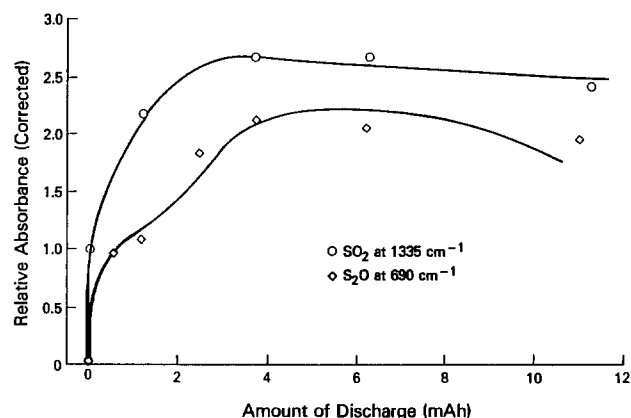


Fig. 2. Changes in the concentrations of SO₂ and S₂O as a function of thionyl chloride discharge (Shawinigan black cathode in 1.6M LiAlCl₄ (SOCl₂) at 25°C; discharge rate: 5 mA cm⁻²).

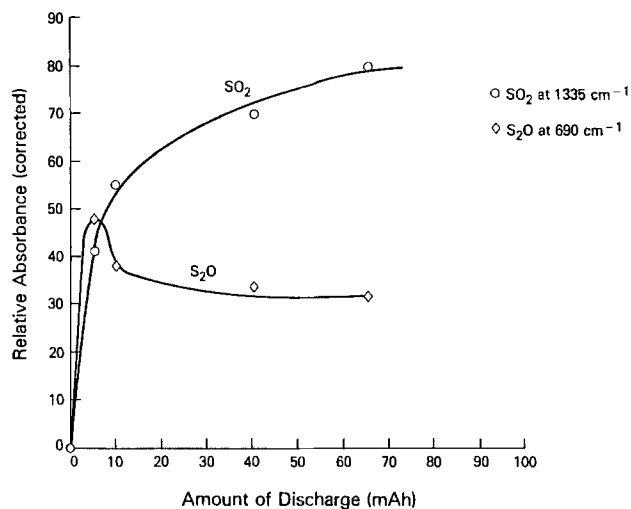


Fig. 3. Change in relative concentrations of SO₂ and S₂O using copper containing cathodes at 25°C (discharge rate: 5 mA cm⁻²).

copper containing cathodes. The results are similar to those with only Shawinigan black.

Figures 4 and 5 show the effect of discharge at low temperature on the relative amounts of SO₂ and S₂O produced. The S₂O material is stabilized at the lower temperatures, and its concentration builds up to higher concentration levels at the lower temperature. It decomposes much more slowly at 273 and 260 K than at room temperature. From our results, we estimate that the half-life of S₂O at room temperature is of the order of 20 min.

Figure 6 shows a linear sweep for a glassy carbon cathode. The results are very similar to those reported for py-

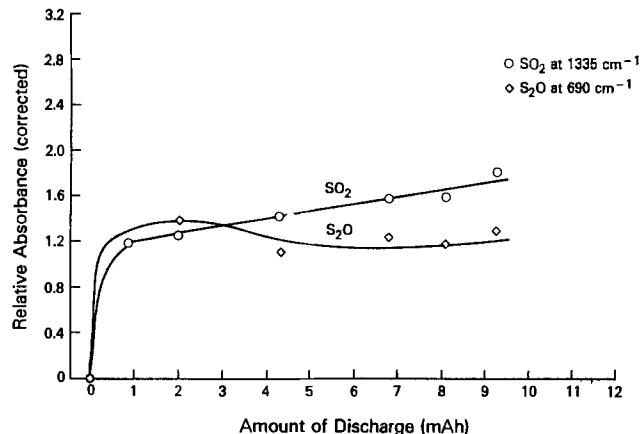


Fig. 4. Relative amounts of SO₂ and S₂O produced at 0°C (Shawinigan black cathode discharge rate: 5 mA cm⁻²).

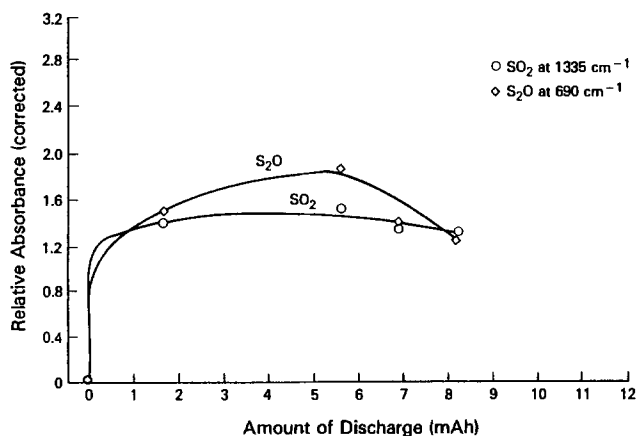


Fig. 5. Relative amounts of SO₂ and S₂O produced at -13°C (Shawinigan black cathode discharge rate: 5 mA cm⁻²).

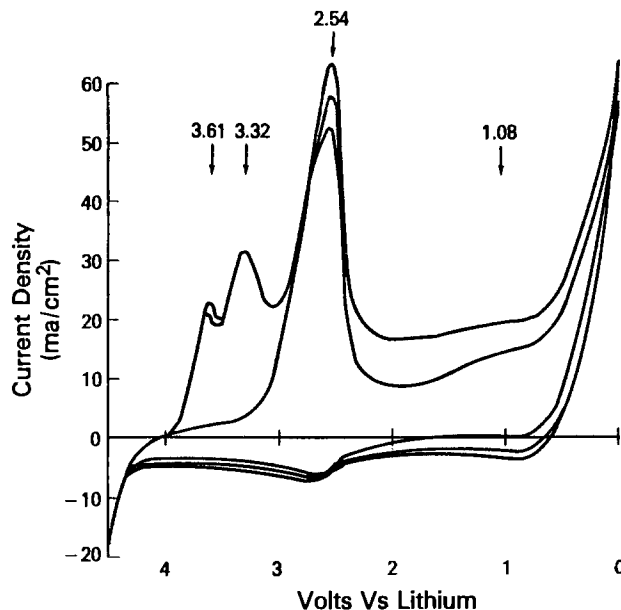
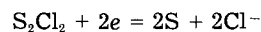
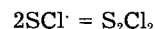
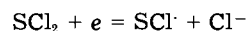
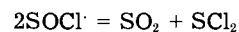
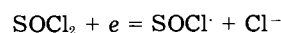


Fig. 6. Linear sweep voltammetry of a glassy carbon electrode in 1.6M LiAlCl₄ (SOCl₂).

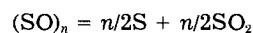
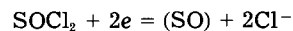
rolytic carbon (4). The main peak for SOCl₂ reduction is at 2.54V vs. Li, with some reaction at 1.1V vs. Li, presumably due to SO₂ reduction. On the second and third sweeps after the excursion into Cl₂ evolution, peaks at 3.61 and 3.32V were also observed. The peak at 3.61V is usually associated with Cl₂, but could be due in part to SO₃. The peak at 3.32V is thought to be due to SO₂Cl₂ formed during the excursion to higher voltages.

The results reported here are not consistent with previous reports of reaction mechanism. Blomgren *et al.* (4) reported SCl and S₂Cl₂ as intermediates in SOCl₂ reduction. Both of these materials are active in the IR region under observation, but no changes in peak heights were observed in these compounds in the present study. None of the cells took on the blood red color usually associated with sulfur chlorides. Since their time frame for analysis was long, previous studies would not have observed the S₂O reported above. Blomgren *et al.* (4) proposed the following mechanism



The results here do not support the presence of sulfur chlorides as reaction intermediates. The reason for this difference is not obvious. Pure materials were used in both experiments. The only obvious difference is the different carbon electrode materials used in each study. Blomgren *et al.* did not use Shawinigan black, but a black produced by Union Carbide Corporation. They also used pressure-annealed pyrolytic graphite electrodes for linear sweep experiments. It is not clear why this difference should influence the reaction mechanism, if indeed it does.

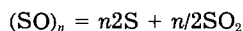
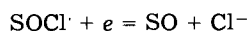
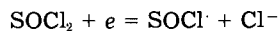
Schlaikjer *et al.* (4) propose the following mechanism, which uses Teflon-bonded Shawinigan black electrode structures.



They also report the possible formation of solid Li₂SO₃ in small amounts at low temperature discharge.

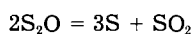
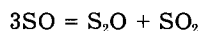
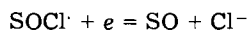
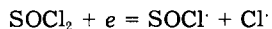
Dey *et al.* (3) proposed a mechanism somewhat similar to that of Blomgren *et al.*, involving the SO radical, but

with formation of SOCl as the first step of the reduction. They did not report S₂Cl₂ and SCl₂ as intermediates



The SO radical could follow the proposed reaction. However, according to Nickless, the usual path for SO reaction involves S₂O formation.

The identification of S₂O formation reported here would suggest the following mechanism



The observation that S₂O is produced can be taken as proof that SO is formed in the thionyl reduction process. The formation of solid products such as Li₂SO₃ would not be expected unless there were excessive impurities in the SOCl₂ or there was a potential excursion of 4.0V vs. Li. If such an excursion occurred, SO₃ and SO₂Cl₂ could form, giving Li₂SO₃ and Li₂S₂O₃ on discharge. In the discharge of large cells, the IR spectra of discharged electrolyte indicates the presence of SO₃ when cells are held at 4.0V for a short period of time.

The formation of S₂O intermediate could explain some previous observations concerning the rate of SO₂ formation during discharge. It would be expected that smaller-than-stoichiometric quantities of SO₂ would be generated during the initial stages of cell discharge, owing to the stability of S₂O. Only toward the end of discharge, when S₂O production corresponds to the discharge rate, would the SO₂ production be directly proportional to discharge rate. As the stability of S₂O varies with temperature, low temperature discharges (especially at high rates) could lead to buildup of large S₂O concentrations. Warming these cells to room temperature could quickly lead to rapid decomposition of S₂O with rapid heat release and SO₂ pressure buildup.

Conclusions

1. It is possible to detect short-lived intermediates in thionyl chloride reduction using an *in situ* sampling technique, coupled with FTIR apparatus.
2. S₂O specie was identified and, therefore, by implication, the SO specie was identified as intermediates in electrochemical reduction of thionyl chloride.
3. The half-life of S₂O in thionyl chloride is about 20 min.
4. S₂O was identified as an intermediate with carbon, carbon-copper mixture, platinum, gold, nickel, and stainless steel electrodes.

Acknowledgments

This work was carried out at Inco Sterling Forest, with the financial support of Ray O Vac Corporation. The authors gratefully acknowledge the helpful discussions of N. Margalit, R. B. Roe, B. C. Bergum, and J. R. Thomas, as well as the assistance of D. Kerstanski and T. Gardinier in carrying out the experiments reported here. The authors also thank INCO, Limited and Ray O Vac Corporation for permission to publish this work.

Manuscript submitted Jan. 5, 1984; revised manuscript received June 26, 1984.

REFERENCES

1. J. C. Bailey and J. P. Kohut, "Power Sources 8," J. H. Thompson, Editor, p. 17, Academic Press, New York (1981).
2. C. R. Schlaikjer, T. Goebel, and N. Marimer, *This Journal*, **126**, 513 (1979).
3. A. M. Dey and P. Bro, *ibid.* **125**, 1574 (1978).
4. G. E. Blomgren, V. Z. Leger, T. Kalnoki, M. L. Kronenberg, and R. J. Brodd, "Power Sources 7," J. H. Thompson, Editor, p. 583, Academic Press, New York (1979).
5. L. Friedman and W. P. Wetter, *J. Chem. Soc.*, 36 (1967).
6. K. Nakamoto, "Infrared Spectra of Inorganic and Coordination Compounds," John Wiley and Sons, New York (1963).
7. "Inorganic Sulfur Chemistry," G. Nickless, Editor, Elsevier, New York (1968).
8. D. L. Chua, S. L. Despande, and H. V. Venkatesetty, in "Battery Design and Optimization," S. Gross, Editor, p. 365, The Electrochemical Society Softbound Proceedings Series, Princeton, NJ (1979).
9. M. M. Yanak and W. K. Istone, Unpublished results.
10. H. G. Bernstein and J. Powling, *J. Chem. Phys.*, **18**, 1018 (1950).
11. L. R. Giattino, U.S. Pat. 4,262,065 (1981).

Investigation of SOCl_2 Reduction by Cyclic Voltammetry and AC Impedance Measurements

M. J. Madou*

SRI International, Menlo Park, California 94025

S. Szpak*

Naval Ocean Systems Center, San Diego, California 92152

ABSTRACT

Cyclic voltammetry and ac impedance measurements, covering the range 10^{-3} - 10^4 Hz, were employed to investigate the reduction of thionyl chloride on glassy carbon surfaces and to determine the associated elementary processes. The quasi-exchange current density of the electroreduction of SOCl_2 is 6.4×10^{-7} A cm^{-2} and becomes larger in the presence of dissolved chlorine. Also, in the presence of Cl_2 , the rest potential shifts to more positive values. At low overpotentials, the reduction of SOCl_2 is kinetically controlled. However, as the overpotentials are increased, a transition to mass-transport control occurs, even before the onset of passivation at +2.7V. The rate of mass transport is governed by the thickness and quality of the LiCl film.

The lithium thionyl chloride battery is one of the most energetic systems reduced to practice thus far and is well developed for lower power density requirements (1). However, to achieve high discharge rates, a new set of problems must be resolved, which requires a more detailed knowledge of the elementary processes that take place within the battery. In particular, reference is made to those processes that occur within the porous structure of the positive electrode.

The reduction of SOCl_2 was studied quite extensively (2-7). The reported results, however, are incomplete inasmuch as they do not provide useful data for electrode modeling which is essential for the rational design of high power output batteries (8, 9). In an attempt to provide this information, we will emphasize the description of the elementary processes rather than concentrate on the identification of reactive species (10, 11).

Experimental

Solutions.—Stock solutions having a composition of 1M AlCl_3 , 1M LiAlCl_4 , 1.6M LiAlCl_4 , 2.2M AlCl_3 , plus 1.9M LiAlCl_4 in SOCl_2 were used as supplied (source: Altus Corporation, San Jose, California 95112). Typical impurity levels, certified by the supplier, were Fe 1.8 ppm, SCl_2 0.1%, and OH 84 ppm in neutral solutions. The acidic solutions usually contained more OH (up to 251 ppm for the 1M AlCl_3 in SOCl_2).

Electrochemical cell and apparatus.—The electrochemical cell used in this investigation is shown in Fig. 1. A porous vitreous carbon and a flat glassy rod, press-fitted into a Teflon screw, were employed as the counter and working electrodes, respectively. Metallic Li and Mo were used interchangeably as reference electrodes. The cell volume was ca. 2 cm^3 .

A Princeton Applied Research potentiostat/galvanostat, Model 173/176, and Universal Programmer, Model 175, were used to perform cyclic voltammetry. Measurements of the electrochemical transfer function were carried out using a Solartron Frequency Response Analyzer (FRA) Model 1172/1183/1185 in an experimental configuration described elsewhere (12).

Procedure.—All measurements were carried out in a dry box under a positive argon pressure. Before each measurement, the working electrode was polished with an Al_2O_3 aqueous slurry (particle size 1 μm) on a polishing cloth, followed by methanol wash, and then wiped dry with a lense paper. A fresh Li reference electrode was used for each set of impedance measurements and between sets of cyclic voltammograms. The porous vitreous

carbon counterelectrode was replaced before each set of experiments.

Results and Discussion

The results and discussion section covers five topics: the choice of reference electrode, the concept of mixed potential and the quasi-exchange current density, the cyclic voltammetry data, the results of impedance measurements, and their relevance to battery modeling.

Choice of reference electrode.—Metallic Li is the reference electrode of choice in neutral solutions. It is not suitable in acidic electrolytes because of the dissolution of the protective LiCl film, which, for small cells, would substantially change the composition of the electrolyte phase. To avoid these difficulties, we have selected Mo as the reference electrode for most of the work in acidic solutions (13). These two reference systems were compared by measuring open-circuit potentials between a Mo electrode and a Li electrode in a U-type cell provided with a fritted glass disk between the cell compartments (e.g., 1.6M LiAlCl_4 in SOCl_2), a V_{oc} of approximately 3.60V was measured. Upon the addition of an aliquot of 1M AlCl_3 solution in SOCl_2 to the Mo compartment, the V_{oc} increased to about 3.95V. Interestingly, these potentials are close to those reported for the carbon/lithium couple in neutral and acidic solutions (14). Such a relationship suggests that the Mo electrode acts as an electrode of the first kind and not as one of second kind, as concluded by Spandau and Brunneck (13), i.e., it responds to the electron transfer associated with the fastest reaction, just as does the carbon electrode (15).

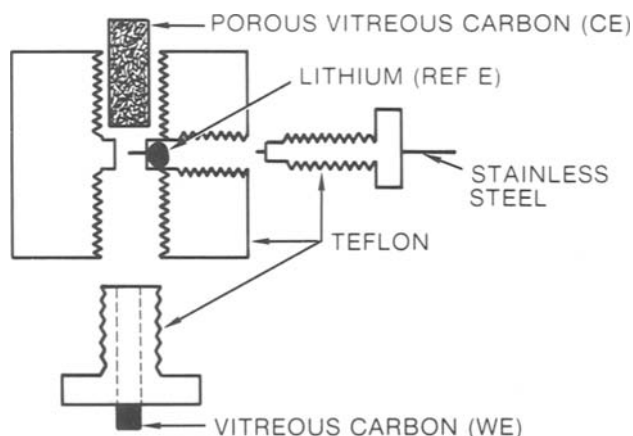


Fig. 1. Electrochemical cell, exploded view

* Electrochemical Society Active Member.

Table I. Summary of postulated overall cell reactions in neutral Li/SOCl₂ system (24)

Overall reaction	(F/mol)	E _o , (V) (calc.)
4Li + 2SOCl ₂ → 4LiCl + S + SO ₂	2.00	3.72
8Li + 3SOCl ₂ → 6LiCl + 2S + Li ₂ SO ₃	2.67	3.60
8Li + 4SOCl ₂ → 6LiCl + S ₂ Cl ₂ + Li ₂ S ₂ O ₄	2.00	3.50
14Li + 6SOCl ₂ → 12LiCl + 4S + Li ₂ S ₂ O ₆	2.33	3.70
10Li + 4SOCl ₂ → 8LiCl + 2S + Li ₂ S ₂ O ₄	2.50	3.57
10Li + 4SOCl ₂ → 8LiCl + 3S + Li ₂ SO ₄	2.50	3.73
8Li + 3SOCl ₂ → 6LiCl + S + Li ₂ S ₂ O ₃	2.67	3.56
6Li + 4SOCl ₂ → 6LiCl + S ₂ Cl ₂ + 2SO ₂	1.50	3.68
10Li + 6SOCl ₂ → 8LiCl + 2S ₂ Cl ₂ + Li ₂ S ₂ O ₆	1.67	3.64
7Li + 4SOCl ₂ → 5LiCl + 3/2S ₂ Cl ₂ + Li ₂ SO ₄	1.75	3.68
6Li + 3SOCl ₂ → 4LiCl + S ₂ Cl ₂ + Li ₂ SO ₃	2.00	3.52
7Li + 3SOCl ₂ → 5LiCl + 1/2S ₂ + Li ₂ S ₂ O ₃	2.33	3.52

Open-circuit potential and quasi-exchange current density.—The calculated values of open-circuit potential, listed in Table I, range from 3.52 to 3.73V for cells employing neutral electrolytes, with higher values in acidic electrolytes, e.g., ca. 4.0V (14), i.e., the same values that were recorded for the C/Li and Mo/Li couples. The gain in the open-circuit potential of ca. 0.4V in acidic electrolytes was attributed by Klinedinst and Domeniconi (14) to the difference in the Gibbs' free energy associated with the respective reactions. Using the available data for the equilibrium constant for the complexation reaction (i.e., formation of LiAlCl₄), they estimated this gain to be between 0.53 and 0.63V. Experimentally, however, the gain is somewhat less, viz., 0.35-0.4V.

A possible explanation for the discrepancy between the theoretical and experimental data is that, in adding the AlCl₃, not only the reaction product has changed (i.e., LiAlCl₄ rather than LiCl) but also the reactant (i.e., AlCl₃·SOCl₂ adduct rather than SOCl₂). There is, indeed, substantial evidence for the existence of the AlCl₃·SOCl₂ and 2AlCl₃·SOCl₂ adducts by Raman spectroscopy (16), and for AlCl₃·SOCl₂ adduct by infrared spectroscopy (17). By taking the reaction of adduct formation, i.e., starting with a more stable reactant, ΔG, and thus also ΔE, will be lowered, in contrast to the situation where no complexation has been taken into account.

In what follows, we will show that the experimentally determined cell potential is not the reversible potential, but is a mixed one, with a cathodic current involving the reduction of SOCl₂ or Cl₂ and the anodic current involving evolution of Cl₂ from either SOCl₂, AlCl₄⁻, or LiCl.

An Evans-type representation of log *i* vs. *V* curves for the reduction and oxidation in neutral electrolyte is shown in Fig. 2. The cathodic and anodic branches were constructed with the aid of potential sweeps commencing at potentials slightly negative to the V_{oc} for the cathodic branch (curve a) and at 4.00V for the anodic branch (curve b). The development of a curvature and hysteresis indicates that the activation-controlled region is relatively narrow (between +3.55 and +3.00V), with a region for the reduction of both Cl₂ and SOCl₂ being between +3.55 and +3.25V only.

The anodic branch arises because of Cl₂ evolution generated by oxidation of SOCl₂, AlCl₄⁻, or LiCl. The Cl₂ generated by the anodic excursion is subsequently reduced during the returned sweep with the amount of cathodic current depending on the anodic charge consumed.

Processes determining the V_{oc} and the quasi-exchange current density, *i*₀^a, are complex. Assuming that the amount of Cl₂ present (or generated) in the solution is small, it follows that the intersection of curves a and b determines both the V_{oc} and *i*₀^a. Extrapolation of data in Fig. 2 yields V_{oc} = +3.55V and *i*₀^a = 6.4 × 10⁻⁷ A cm⁻². Extrapolation of curves c and a yields higher values for the *i*₀^a and a more positive open-circuit potential. The sensitivity of both these quantities to the dissolved chlorine is an expected behavior, provided that the reduction of SOCl₂ is a rapid reaction.

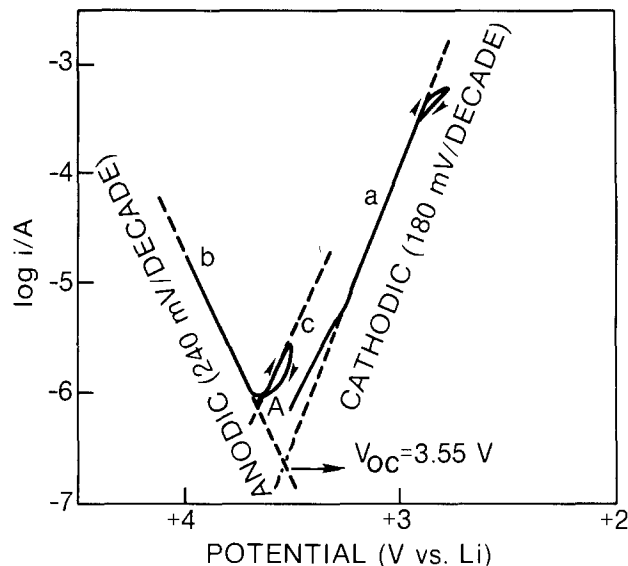


Fig. 2. Evans plot (log *i* vs. *V*). Electrolyte: 1.6M LiAlCl₄ in SOCl₂. Temperature: room. Electrode area: 0.314 cm². Reference Electrode: Li. Sweep rate: 10 mV s⁻¹.

Additional information concerning the magnitude of the electrode transfer resistance associated with the reduction of thionyl chloride can be extracted from data in Fig. 2. Using *i*₀^a = 6.4 × 10⁻⁷ A cm⁻² and substituting into the Stern-Geary relationship, Eq. [1]

$$R_p = \bar{\beta} = \bar{\beta}/2.303 \times i_0^a \times A \times (\bar{\beta} - \bar{\beta}) \quad [1]$$

a value of $R_p = 7 \times 10^4 \Omega \text{cm}$ is calculated. Here $\bar{\beta}$ and $\bar{\beta}$ are the anodic and cathodic Tafel coefficients, respectively, and *A* is the electrode area.

Cyclic voltammetry.—A typical voltammogram in a neutral electrolyte exhibits a large reduction peak (peak I), a rather broad peak located between +2.0 and +1.0V (peak II), followed by a rapid increase in current at ca. +1.0V (peak III). Upon reversal of the sweep, two anodic peaks appear at potentials of ca. +1.1 and +2.9V (peaks IV and V).

There is no disagreement in the identification of peak I and current onset III. However, the origin and structure of peaks II and V have not been resolved as yet. In fact, Behl (2) reported two barely perceptible peaks at +1.7 and +1.3V rather than one broad peak. The existence of these peaks has not been confirmed in this work or in work by others (4, 10, 19). The broad peak II is most likely due to the reduction of SO₂ (10, 19). However, even in SO₂-saturated neutral electrolytes, the peak height remains about the same because, to be reduced, SO₂ must diffuse through the passive film (2). As expected, the effect of SO₂ bubbling on the peak height is more evident in acid solutions since the excess of AlCl₃ partially dissolves the precipitated LiCl, thus making the surface accessible to the electroreduction of SO₂.

Commencing a cyclic voltammogram at a potential positive to the V_{oc} (e.g., at +4.50V) and terminating the sweep at a potential positive to the appearance of peak II, two additional cathodic current peaks, peaks A and B, appear before the SOCl₂ reduction peak (Fig. 3, curve a). The first peak, peak A, at +3.60V, was attributed to the reduction of SCl₂ (8), and peak B, at +3.25V, to the reduction of Cl₂. To confirm this assignment, we have used a Cl₂-saturated electrolyte and commenced the sweep at potentials slightly cathodic to the V_{oc}. As illustrated in Fig. 3, curve b, peak B is substantially increased, i.e., attributable to the reduction of Cl₂. Peak A, although present, was not affected by the presence of dissolved chlorine.

Figure 4 shows the dependence of reduction peak I on the scan rate. The substantial shift of the peak potential with the scan rate is indicative of the highly irreversible character of the SOCl₂ reduction. A plot of peak height *i*

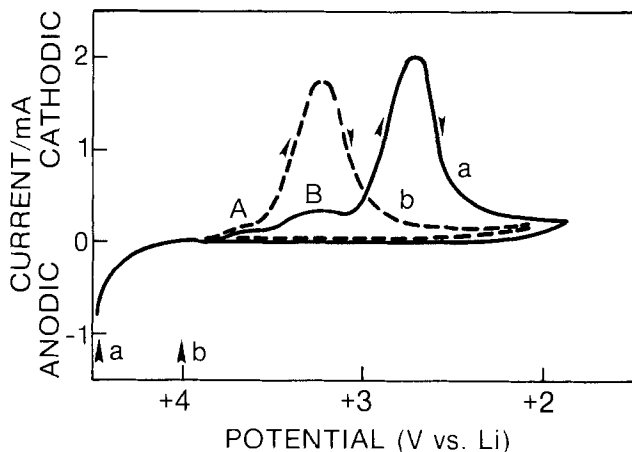


Fig. 3. Cyclic voltammograms on glassy carbon. Scan rate: 100 mV s^{-1} . Electrode area: 0.314 cm^2 . Temperature: room. Reference electrode: Li. Electrolyte: 1M LiAlCl_4 in SOCl_2 (curve a) and $1\text{M LiAlCl}_4 + \text{Cl}_2$ in SOCl_2 (curve b). Scan initiation: (curve a) $+4.5\text{V}$, (curve b) $+4.0\text{V}$.

vs. \sqrt{v} results in a straight line passing through the origin indicating a diffusion-controlled process, in agreement with results of Behl (20) and Doddapaneni (22). Since we did not find the usual effect of stirring of the electrolyte, the diffusion limitation suggested by the *i vs. \sqrt{v}* plot cannot be due to the concentration polarization in the liquid phase. We conclude, therefore, that the diffusion limitation has its origin in the transport of species through the film produced on the electrode surface. The limiting diffusion current density in the electrolyte phase would have been much larger, on the order of Acm^{-2} (23).

Impedance measurements.—Impedance measurements were employed by Meitav and Peled (6) to study the behavior at the open circuit of stainless steel immersed in 1M LiAlCl_4 in SOCl_2 electrolyte. They concluded that the charge transfer reaction resistance is very high. Phillips *et al.* (7) found that also the reduction of SOCl_2 on vitreous carbon surfaces is slow. Qualitatively, these results are in agreement with the i_0 and R_p values determined with the aid of the Evans plot (Fig. 2).

In an attempt to provide additional information, two sets of impedance measurements were made. In the first

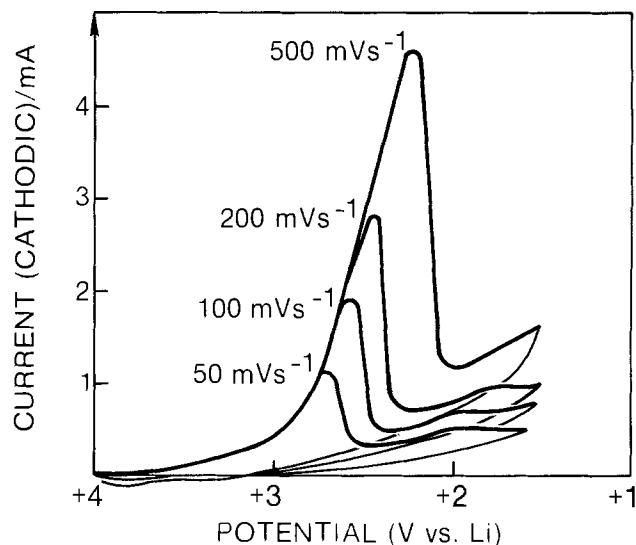


Fig. 4. Cyclic voltammograms as function of scan rate. Electrode: glassy carbon, area 0.314 cm^2 . Electrolyte: 1M LiAlCl_4 in SOCl_2 . Temperature: room. Scan rates indicated. Reference electrode: Li.

set, repetitive impedance data (with a 2 min delay time) were obtained at the V_{oc} and at very low cathodic overpotentials in neutral and acidic solutions. In the second set, impedance data were collected at higher cathodic overpotentials, also in neutral and acidic solutions.

A typical Nyquist plot (*i.e.*, a plot of the real *vs.* imaginary part of the electrode impedance) in acid solutions is shown in Fig. 5a, while the corresponding Bode plot (*i.e.*, a plot of the logarithm of the total electrode impedance *vs.* the ac frequency) is shown in Fig. 5b. A straightforward mathematical treatment shows that a semicircle intersecting the real axis at 90° in the Nyquist plot is indicative of a kinetically controlled reaction and can be represented by a simple RC parallel equivalent circuit. However, when a diffusional process is controlling the impedance factor, the Nyquist plot yields a straight line intersecting the real axis at 45° . The corresponding Bode plots are straight lines with slopes -1 and $-1/2$.

The separation and identification of contributing processes is clear in acid solutions (Fig. 5a and 5b). The Nyquist and Bode plots in neutral solutions are similar

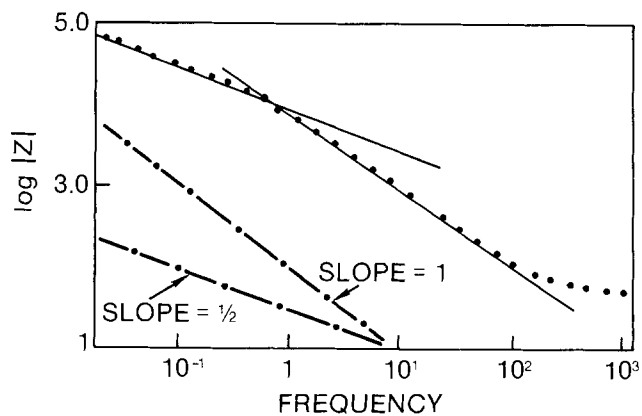
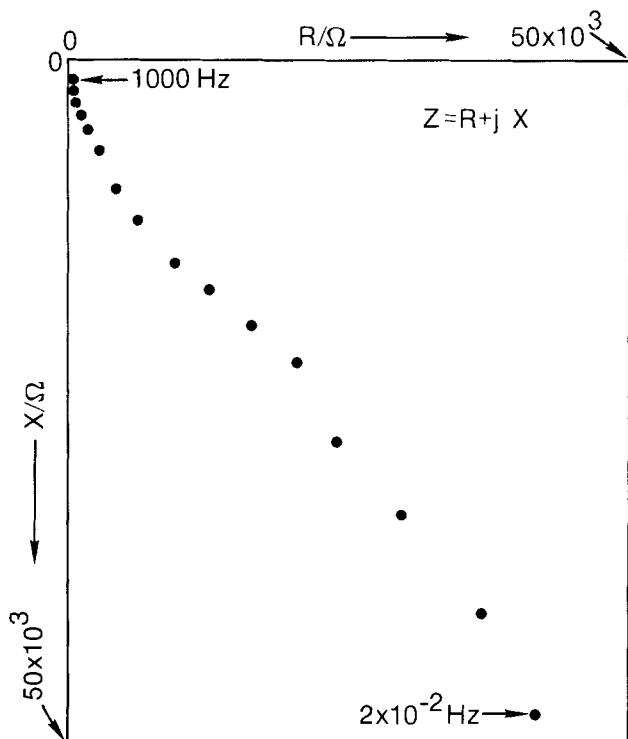


Fig. 5. Nyquist (a, left) and Bode (b, above) plots. Electrode: glassy carbon, area 0.314 cm^2 . Electrolyte: $2.2\text{M LiAlCl}_4 - 1.9\text{M AlCl}_3$ in SOCl_2 . Temperature: room.

except that the kinetic and transport controlled processes are less clearly resolved. Here, the Nyquist plot in Fig. 6 is a large "depressed" semicircle, with its center below the real axis. The Bode plot (not shown) is a straight line with slopes approaching -1 and $-1/2$ at the highest and lowest frequencies, respectively. The diffusional process, we believe is associated with switch-on of Cl_2 in the solution.

Consecutive measurements at the V_{oc} or at low overpotentials were reproducible in the acidic electrolytes, while in neutral electrolytes, the impedance increased with each successive measurement. Such a behavior indicates that, in acid solutions, the electrode surface remains free from deposited LiCl , whereas in neutral solutions, the deposited LiCl changes the electrode impedance even at the open circuit. The presence of the deposited LiCl accounts for the difficulty in clearly separating and identifying participating processes.

Fitting the high frequency points in the Nyquist plot (Fig. 5a) to a semicircle yields a R_p of ca. $9.4 \times 10^3 \Omega \text{cm}^{-2}$ and a value of C_p from the imaginary component of the impedance between 60 and $70 \mu\text{Fcm}^{-2}$, the latter being about twice that measured by Meitav and Peled on stainless steel (6).

Results of impedance measurements at different cathodic overpotentials are presented in Fig. 7, with the Nyquist plots on the left-hand side and the Bode plots on the right-hand side. These measurements were taken in steps at 200 mV starting at +3.3V (Fig. 7a) and terminating at +2.5V (Fig. 7e). In contrast to the electrode behavior of the open-circuit potential, no clear evidence for the dominance of transport properties can be presented at low cathodic overpotentials. This is an expected behavior because the diffusional process at low frequencies is associated with the reduction of Cl_2 , which must disappear at potentials negative to the V_{oc} .

Results of the ac impedance measurements, summarized in Fig. 7a-7d, indicate that the electroreduction of SOCl_2 on glassy carbon is complex. The diameter of the single semicircle in Fig. 7a, *i.e.*, at 3.3V is almost the same as at the V_{oc} . If there were only one reduction process involved at V_{oc} , *e.g.*, the SOCl_2 reduction, we would expect the R_p to decrease exponentially with increasing overpotential. This clearly is not the case here and indicates that R_p at the V_{oc} is relatively small because of the contribution due to the reduction of Cl_2 at the V_{oc} . The diameter of the single semicircle in Fig. 7a and 7b decreases as the potential decreases from +3.3 to +3.1V. The approach to the real axis of the semicircles at high frequency is close to 90° , but the centers of the semicircles are found some-

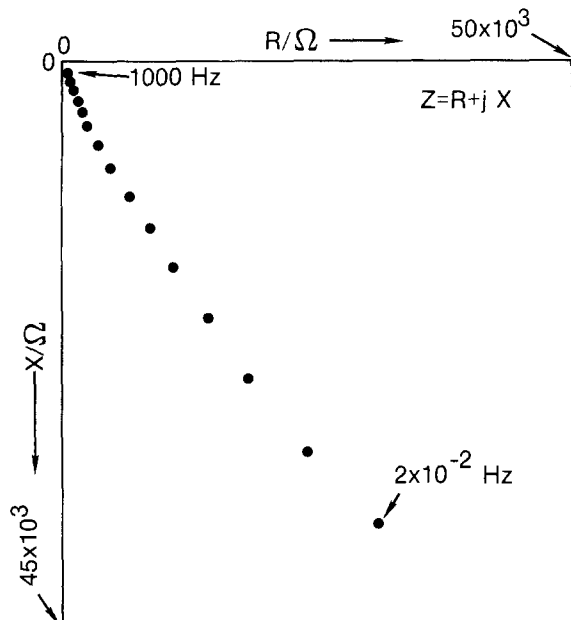


Fig. 6. Nyquist plot at rest potential. Electrode: glassy carbon, area 0.314 cm^2 . Electrolyte: 1M LiAlCl_4 in SOCl_2 . Temperature: room.

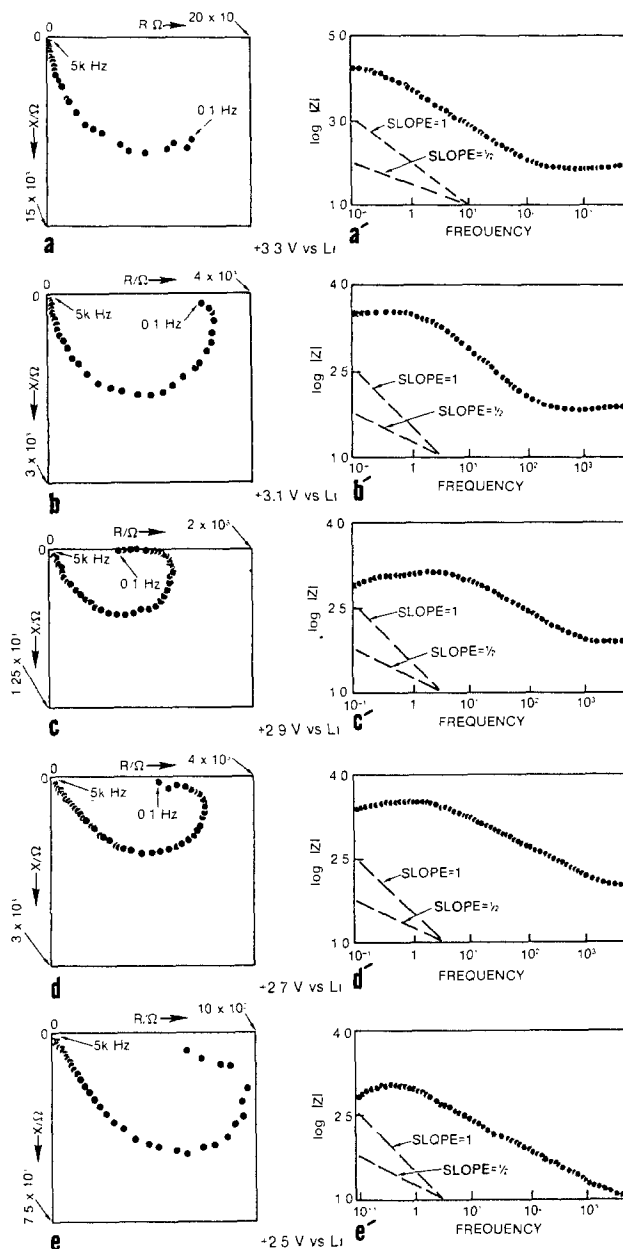


Fig. 7. Nyquist and Bode plots as function of overpotential. Electrode: glassy carbon, area 0.314 cm^2 . Electrolyte: 1M LiAlCl_4 in SOCl_2 . Temperature: room. Reference electrode: Li. Curve a: at +3.3V. Curve b: at +3.1V. Curve c: at 2.9V. Curve d: at +2.7V. Curve e: at +2.5V.

what below the real axis. The Bode plots, Fig. 7a' and 7b', exhibit a slope approaching -1 over a wide frequency range. Taking the point at 0.1 Hz in these figures as representative for the R_p of a relatively LiCl -free surface, we can see that R_p has decreased over almost one order of magnitude with a change of 200 mV in electrode potential.

At electrode potentials close to the reduction peak of SOCl_2 , the impedance spectra indicate diffusional behavior. The Nyquist plots, shown in Fig. 7c and 7d at +2.9 and +2.7V, respectively, exhibit an approach to the real axis at high frequencies of approximately 45° , and the corresponding Bode plots show lines with a slope approaching $-1/2$. The high frequency range, in which the diffusional character of the impedance becomes apparent, sets it apart from the diffusional process in solution, which has been discussed in connection with Fig. 5a and 5b. We note that within the low frequency range of the Nyquist plot in Fig. 7c, 7d, and 7e some points are lying along the real axis, indicating that R_p is increasing during the measurement. This change in R_p is due to the reduction of available area on the electrode surface because of deposition of LiCl .

Relevance to battery modeling.—In the “Cyclic voltammetry” section, we propose that a quasi-diffusional process arises during the SOCl₂ reduction, with its origin being the transport of species to or from the surface of the carbon electrode through voids in the LiCl film. The impedance spectra in Fig. 7a-7e support this picture. The approach of the intercept of the low frequency points toward the real axis in a Nyquist plot, for diffusion-controlled systems, is equal to the sum of series resistance R_s , here equal to the electrolyte resistance, R_p , the electron transfer resistance, and R_d diffusion layer resistance. The magnitude of the diffusion layer resistance is proportional to the thickness of a layer through which diffusion takes place. Here, the thickness of the diffusion layer is that of a LiCl film deposited on a glassy carbon surface. Evidently, the cathodic polarization of carbon electrode reduces R_p but increases R_d owing to an increase in thickness of a LiCl film. The dominance of the R_d with the increase in cathodic polarization is clearly shown in Fig. 7d, where the diameter of the Nyquist plot begins to increase. As cathodic overpotentials are increased, to +2.5V (Fig. 7e), the electrode surface is completely covered, as evidenced by a sudden expansion of the Nyquist plot.

Upon starting the ac impedance measurements at +2.9V and stepping the dc bias towards more anodic potentials (again with 2 min delay) it was found that the quasi-diffusional behavior dominated the impedance even at +3.3V (vs. Li). Obviously, the thicker film formed at +2.9V was permanent and was not removed by reducing the cathodic polarization.

The quasi-diffusional behavior, *i.e.*, transport through solid LiCl film, similar to that in neutral solution, was never observed in acidic solutions, not even at potentials in the passive region. Despite this, the Nyquist plots showed points at low frequency lying along the real axis, indicating, again, the reduction in active area during the measurement. Evidently, in contrast to neutral solutions, in acidic electrolyte, the LiCl film remains sufficiently thin and does not result in quasi-diffusional behavior. The passivation of the electrode surface is likely to occur if the rate of LiCl complexation is slower than LiCl formation.

Conclusions

1. Metallic Li is a suitable reference electrode for measurements in neutral solutions, while Mo is preferable in acidic electrolytes.
2. The rest potential of a carbon electrode, immersed in SOCl₂, is a mixed potential, with the cathodic partial reaction being the reduction of SOCl₂ and the anodic branch arising from the oxidation of SOCl₂, AlCl₄⁻, and Cl⁻.
3. Reduction of SOCl₂ on a glassy electrode is a slow process with the quasi-exchange current density of 6.4×10^{-7} A cm⁻².
4. The reduction of SOCl₂ is kinetically controlled at low overpotentials. However, as these overpotentials are increased, a transition to diffusion control occurs, even before the onset of passivation at +2.7V.
5. All reactions, including SO₂ reduction, that take place at potentials more negative than +2.7V, are controlled by mass transport. The controlling factor is the thickness and porosity of the LiCl film rather than the conditions in the bulk electrolyte.
6. Once formed, the LiCl film cannot be removed by holding the electrode negative to the V_{oc} . Removal of this film requires potentials more positive than the V_{oc} .

7. In acidic solutions, the electrode surface remains free from deposited LiCl. Diffusional control through a LiCl film is possible only if the dissolution of the LiCl film is slower than its formation.

Acknowledgments

This work was funded by Naval Sea Systems Command (NAVSEA 63R-32) and constitutes a fraction of a program to establish a technology base for high discharge rate Li/SOCl₂ batteries. We thank M. F. Romano (NAVSEA 63R-32) for his interest and support.

Manuscript submitted Aug. 4, 1983; revised manuscript received June 4, 1983.

The Naval Ocean Systems Center assisted in meeting the publication costs of this article.

REFERENCES

1. J. A. Christopoulos and S. Gilman, *IEEC '75 Rec.*, 437 (1975).
2. W. K. Behl, *This Journal*, **101**, 367 (1979).
3. W. L. Bowden and A. N. Dey, *ibid.*, **127**, 1419 (1980).
4. D. L. Chua, S. L. Deshpande, and H. V. Venkatesetty, in “Battery Design and Optimization,” S. Gross, Editor, p. 365, The Electrochemical Society Softbound Proceeding Series, Princeton, NJ (1979).
5. W. K. Behl, in “Proceedings of the 27th Power Sources Conference,” Atlantic City, NJ, June 21-24, 1976, p. 30.
6. A. Meitav and E. Peled, *J. Electroanal. Chem.*, **134**, 49 (1982).
7. J. Phillips, J. C. Hall, and H. F. Gibbard, Abstract 65, p. 169, The Electrochemical Society Extended Abstracts, Vol. 80-2, Hollywood, FL, Oct. 5-10, 1980.
8. K.-C. Tsaur and R. Pollard, *This Journal*, **131**, 975 (1984).
9. K.-C. Tsaur and R. Pollard, *ibid.*, **131**, 984 (1984).
10. K. M. Abraham and R. M. Mank, *ibid.*, **127**, 1091 (1980).
11. S. Dullek, S. A. James, and W. P. Kilroy, *ibid.*, **128**, 508 (1981).
12. M. Madou and M. C. H. McKubre, *ibid.*, **130**, 1056 (1983).
13. H. Spandau and E. Brunneck, *Z. Anorg. Allg. Chem.*, **278**, 197 (1955).
14. K. A. Klinedinst and M. J. Domeniconi, *This Journal*, **127**, 530 (1980).
15. J. Devynck, A. Petit, M. C. Brage, and J. P. Descroix, Abstract 263, p. 423, The Electrochemical Society Extended Abstracts, Vol. 82-2, Detroit, MI, Oct. 17-21, 1982.
16. D. A. Long and R. T. Bailley, *Trans. Faraday Soc.*, **59**, 594 (1963).
17. J. P. Gabano and P. Lenfant, Abstract 37, p. 101, The Electrochemical Society Extended Abstracts, Vol. 72-2, Los Angeles, Oct. 14-19, 1979.
18. M. Stern, and A. L. Geary, *This Journal*, **104**, 56 (1957).
19. G. E. Blomgren, T. Leger, M. L. Kronenberg, T. Kalnoki-Kio, and R. J. Brodd, in “11th International Power Sources Conferences,” Brighton, England (1978).
20. W. K. Behl, *This Journal*, **127**, 1444 (1980).
21. J. R. Driscoll, G. L. Holleck, and D. E. Tolland, in “Proceedings of the 27th Power Sources Conference,” Atlantic City, NJ, June 21-24, 1976, p. 28.
22. N. Doddapaneni, “Final Report for Period 10 April to 9 May 1982,” ERADCOM, Fort Monmouth, NJ (1982).
23. G. L. Holleck and M. J. Turchan, in “Record of the Tenth Intersociety Energy Conversion Engineering Conference,” Newark, Delaware, Aug. 18-22, 1975.
24. M. Domeniconi, K. Klinedinst, N. Marincic, C. Schlaikjer, R. Staniewicz, and L. Swette, Contract no. N-00014-76-C-0524, Oct. 1977.

Pore Development during Selective Leaching

A. D. Tomsett, D. J. Young,* and M. S. Wainwright

School of Chemical Engineering and Industrial Chemistry, University of New South Wales, Kensington, New South Wales 2033, Australia

ABSTRACT

The leaching kinetics of a Cu-50 weight percent Al alloy in aqueous NaOH have been studied. The product of the reaction, known as Raney copper, an important industrial catalyst, consists almost entirely of highly porous copper. In forming this material, the Al is selectively dissolved from the alloy, the rate of the leaching reaction being controlled by liquid-phase diffusion within the pores of the leach residue. At constant temperature, the spacing of these pores increases as the leaching rate decreases. As the temperature decreases, so does the pore spacing. The conversion of the original alloy phase, CuAl₂, to porous copper is considered as an example of a phase transformation, and the pore spacing is taken as a measure of the distance over which Cu-Al segregation must occur within the alloy. Models based on volume diffusion adjacent to the reaction front and on boundary diffusion at the front are used to describe the relationship between pore spacing and reaction rate. Application of these models to the experimental data, for a temperature of 20°C, yields estimates of $D = 6 \times 10^{-12} \text{ cm}^2\text{s}^{-1}$ with an activation energy of $53 \pm 2 \text{ kJ}$ for volume diffusion and $D_b = 5 \times 10^{-10} \text{ cm}^2\text{s}^{-1}$ with an activation energy of $62 \pm 4 \text{ kJ}$ for boundary diffusion. It is concluded that alloy segregation takes place at the leach reaction front by a mechanism of boundary diffusion.

The selective leaching in alkaline solution of aluminum from alloys to leave a porous, spongy residue is a well-known, but incompletely understood, phenomenon. Reactions of this type have been exploited since the days of Raney (1, 2) in the manufacture of high surface-area metal catalysts. The widespread use of Raney catalysts in a variety of chemical processes adds practical interest to fundamental questions about the nature of the leaching mechanism. Since the leach reaction determines the product morphology, it is possible that an understanding of the leaching mechanism will lead to the ability to control the morphology and, hence, the catalyst properties. The purpose of this study is to examine the relationships between leaching kinetics and product morphology.

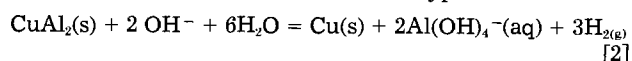
A series of studies (3-6) has shown that caustic leaching of aluminum and zinc from alloys based on copper, nickel, and cobalt proceeds according to parabolic kinetics

$$X^2 = k_p t \quad [1]$$

where X is the thickness of the reaction-product rim formed in time, t . The magnitude of k_p is found to be independent of the orientation of the parent alloy with respect to reaction direction. From these observations, it is concluded that the leach reaction rate is controlled by diffusion through the liquid occupying the pores of the reaction product. This conclusion is consistent with the magnitude of k_p and its activation energy.

During these reactions, the microstructure of the precursor alloy is reproduced in the reaction product. An example is shown in Fig. 1, where a Cu-Al alloy consisting of CuAl₂ grains separated by frozen Al-CuAl₂ eutectic is seen to produce grains of porous copper separated by void space. This observation, together with the fact that copper solubility in strong alkali is negligible, leads to the conclusion that the mechanism is one of selective dissolution and not dissolution reprecipitation. Similar findings apply to Ni-Al and Co-Al alloys.

In all cases, the product material is almost entirely composed of noble metal and is highly porous. The question therefore arises as to how rearrangement occurs within the solid to accommodate the loss of a large fraction of its constituent atoms in a reaction of the type



The reaction is presented schematically in Fig. 2. The highly ordered product morphology depicted is based on the observation (7) that pore sizes are very similar.

Theory

The transformation of a homogeneous parent phase into a highly ordered two-phase structure in which the re-

*Electrochemical Society Active Member.

action products appear in lamellar or rodlike form is a phenomenon familiar to metallurgists. Reaction morphologies of this sort are observed in eutectic and eutectoid transformations (8, 9)



and in discontinuous precipitation (10)



where α , β , and γ denote different phases and α' denotes a distinctly different composition of a solid-solution phase α . In addition, reactions leading to the production of these cellular morphologies have been observed (11-13) in cases of reaction of the parent phase with an externally supplied gaseous reactant, R. Reactions of this type may be written



Although selective dissolution reactions have not hitherto been described in these terms, they appear to fall within this latter class. A brief review of the theory of cellular phase-transformation kinetics is therefore pertinent.

A simple description of transformation kinetics was first provided by Zener (14) on the supposition that segregation of the parent-phase constituent elements toward the tips of the advancing α and β lamellae occurs by diffusion within the parent phase itself. Assuming further that α - β - γ triple-phase junctions are at mechanical equilibrium, then the velocity, v , at which the reaction front advances into the parent phase, is given by

$$v = \frac{D}{S} \frac{A}{a} \left(1 - \frac{S_c}{S} \right) \quad [6]$$

where D is the chemical diffusion coefficient in γ , S is

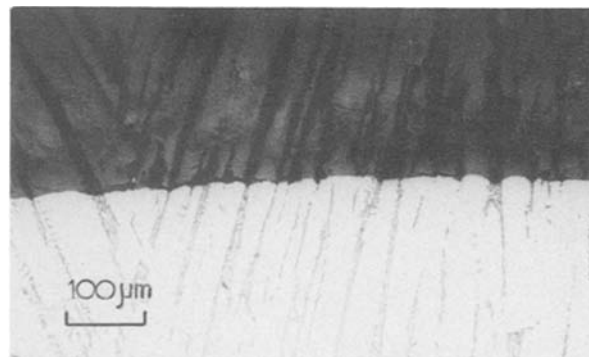


Fig. 1. Micrograph of section through partially leached Al-50Cu alloy

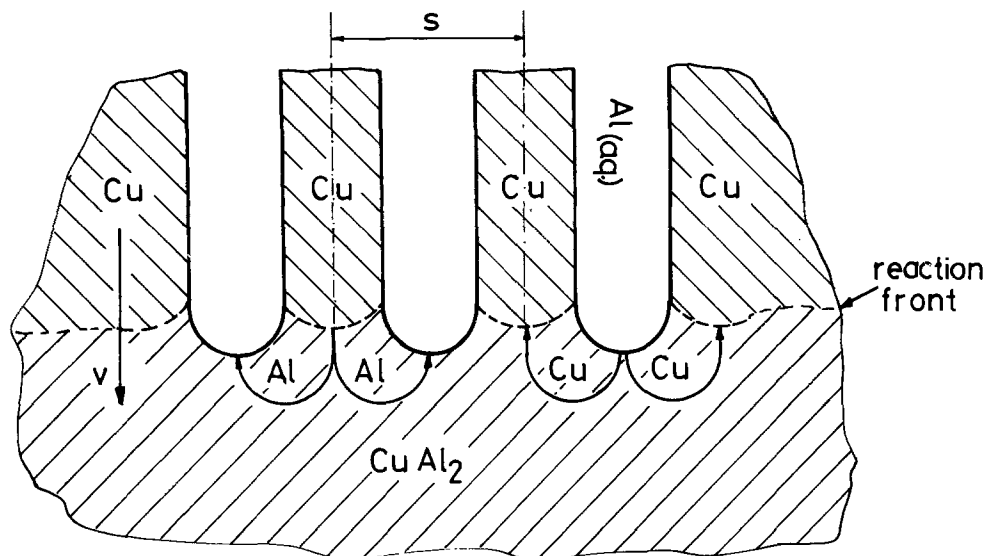


Fig. 2. Schematic representation of a CuAl_2 -Cu grain and the alloy-reaction product interface.

the combined width of α and β lamellae, A is the relative supersaturation within the parent phase, and α is a geometric constant of order unity. The quantity S_c is a critical lamellar spacing at which the free energy per unit volume of two-phase product equals that of the parent phase and at which reaction ceases. This term arises through the surface free energy associated with the α - β interfaces which are created in the reaction. A complete local-equilibrium solution for eutectoids was provided by Hillert (15) by incorporating the Gibbs-Thompson effect for the pressure-composition variation in the parent phase along the curved interfaces, thereby evaluating the compositional differences driving the diffusion. Hillert in this way shows that

$$A = \frac{1}{f^\alpha f^\beta} \frac{C^{\gamma\alpha} - C^{\gamma\beta}}{C^\beta - C^\alpha} \quad [7]$$

where $(C^{\gamma\alpha} - C^{\gamma\beta})/(C^\beta - C^\alpha)$ is the ratio of the lateral concentration difference in front of limiting flat interfaces to that between the product phases. The constants f^α and f^β are, respectively, the ratios S^α/S and S^β/S ; they are determined by the parent-phase composition.

Because the relationship between ν , S , and relative supersaturation permits an infinite number of solutions, a further condition must be imposed. Zener (14) and Hillert (15) suggest that the system stabilizes at a value of S for which ν is a maximum. If so, then

$$S = 2S_c = \frac{2\sigma^{\alpha\beta}}{RT(C^{\gamma\alpha} - C^{\gamma\beta})} \quad [8]$$

where R is the gas constant and $\sigma^{\alpha\beta}$ is surface energy of the α - β phase boundary.

Alternatively, it has been proposed (16-18) that the rate of entropy production is a maximum, whence

$$S = 3S_c = 3\sigma^{\alpha\beta}/RT(C^{\gamma\alpha} - C^{\gamma\beta}) \quad [9]$$

The consequences of the two optimizations are seen to be similar. Substitution from Eq. [7] and [9] to Eq. [6] leads to the result

$$\nu = \frac{2D}{\alpha f^\alpha f^\beta RT} \frac{\sigma^{\alpha\beta}}{C^\alpha - C^\beta} \frac{1}{S^2} \quad [10]$$

A preferred mechanism of alloy segregation may be diffusion along the interface between the parent and product phases. In the present case, where CuAl_2 of tetragonal symmetry is converted to Cu of cubic symmetry, a discontinuous boundary between the two phases will certainly be formed. Boundary-diffusion theories were developed for discontinuous-precipitation reactions by Turnbull (10) and Cahn (16) and have been adapted to the eutectoid transformation by others (19-21). The resulting

kinetic expression is

$$\nu = \frac{24D_B \delta K}{\alpha RT} \frac{f^\alpha f^\beta \sigma^{\alpha\beta}}{C^\alpha - C^\beta} \frac{1}{S^3} \quad [11]$$

where maximum entropy production has been adopted as the reaction constraint. In Eq. [11], D_B is the boundary diffusion coefficient, δ is the boundary width, and K is the coefficient representing partition of solute between bulk and boundary.

In the selective dissolution process represented by Eq. [2], the product phases are the liquid solution which fills the newly created pores and the copper which separates the pores. In terms of the foregoing theory, the spacing, S , which characterizes the product morphology, is given by the sum of the pore diameter and the width of the intervening copper region. Both size parameters are measurable, as is the reaction velocity, ν .

This paper reports measurements of pore spacings as a function of the selective-dissolution reaction rate. The relationship between pore spacing and reaction velocity is used to test the applicability of phase-transformation theory to the leaching process.

Experimental

An alloy of composition Cu-50.3 weight percent (w/o) Al was prepared by induction melting aluminum (99.9% pure) and copper (99.5% pure) using the method of Marsden *et al.* (22). For the leaching kinetic experiments, the homogeneous melt was cast onto a chilled copper mold to form a plate from which rectangular prisms were cut. The cast alloy consisted of CuAl_2 , plus frozen Al-CuAl₂ eutectic. The prisms were reacted with thrice the amount of 20% w/w aqueous NaOH required to completely react with the aluminum in the alloy. This reaction was carried out isothermally at various temperatures. Partially extracted alloy pieces were removed after various reaction times of up to 24h and thoroughly washed with distilled water until the pH of the wash water was seven. The samples were then mounted in cold setting resin, cross sectioned at right angles to an original face of the specimen, and polished to a 1 μm finish. The depth of chemical attack was measured under an optical microscope using a graduated eyepiece.

Since the leaching reaction kinetics were parabolic, the average reaction rate over the complete course of leaching was lower for a large alloy particle than for a small one. It was therefore possible to investigate reaction morphology as a function of average leaching rate by using alloy samples having discrete particle size ranges. Samples consisting of a large number of particles were prepared by crushing and screening the alloy to yield approximately spherical particles in the size ranges

Table I. Surface and pore structure data for particles of alloy that are fully leached at 293 K

Particle size (μm)	Surface area (m^2g^{-1})		Pore diam (\AA)		V_p (cm^3g^{-1})	Crystallite size (\AA)	Interpore distance (\AA)
	S_{BET}	S_{BET}	$2r_p$	$2r_a$			
105-180	31.44	236	268	0.214	88,85	129	
353-420	25.28	316	316	0.203	84,79	177	
710-850	23.48	342	330	0.197	87	194	
1000-1180	23.96	338	328	0.197	89,81	192	
1400-1676	23.89	342	324	0.197	85	194	
2000-2360	21.35	382	366	0.195	79,85	218	

specified in Table I. These samples were leached to completion at 20°C.

The extraction method used was similar to that reported by Friedrich *et al.* (4). A 40% w/w NaOH solution was added to the alloy pieces over a period of 0.75h so that the reaction temperature was kept to $20^\circ \pm 2.5^\circ\text{C}$. After extraction was complete, as determined by hydrogen evolution, the catalyst was thoroughly washed with distilled water until the pH of the wash water was seven.

The temperature dependence of the diffusion coefficient was also studied by leaching 1-1.18 mm particles at the temperatures given in Table II.

The composition of the alloy and leach residues was determined by atomic-absorption spectroscopy of acid-digested samples. The BET surface areas of the extracted materials were determined by a single-point chromatographic method (23).

Pore size distributions were calculated from nitrogen isotherms measured at -195°C , using a Micromeritics 2100E ORR surface area and pore-volume analyzer. Samples were transferred to the adsorption flask under water and evacuated at 130°C overnight. The degassed samples were weighed after completion of each experiment.

The crystallite size of the leach residues was estimated from x-ray line broadening of the Cu(200) diffraction line using the Scherrer equation, with corrections for instrumental broadening obtained from the silicon (220) diffraction line. The powdered catalysts were pyrophoric, and it was necessary to coat them with collodian prior to examination. CuK_α radiation was used, and the diffraction patterns were compared with those in the ASTM files to identify the compounds present.

Results

The interface between the unaffected alloy and the leach residue of the alloy (reacted at 50°C for 12h) is shown in Fig. 1. A clearly defined boundary which is parallel to the original alloy surface is discovered. As noted earlier, the CuAl_2 grains have leached to yield porous copper, and the eutectic material has been completely removed.

The thickness of the reaction-affected rim around the partially extracted alloy pieces, as a function of leaching time, is shown at various temperatures in Fig. 3. After an

Table II. The effect of the temperature of extraction on the surface area and pore structures of completely, leached 1.0-1.18 mm alloy particles^a

Extraction temp (K)	Surface areas (m^2g^{-1})		Pore diam (\AA) $2r_p$	Crystallite size (\AA)	Interpore distance (\AA)
	S_{BET}^b	S_{BET}			
275	25.4	23.1	302	75	170
293	24.0	18.6	338	85	192
308	22.6	15.6	550	112	310
323	18.5	15.0	610	120	343
343	16.9	11.3	750	137	422
363	12.7	9.8	1076	146	606

^a Data are for particles washed with 40% NaOH prior to washing with distilled water, unless otherwise stated.

^b Particles washed with distilled water with no caustic wash.

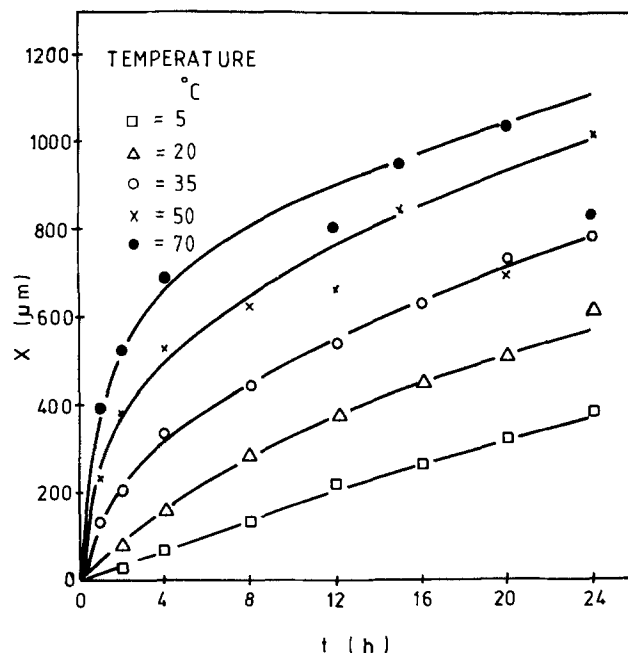


Fig. 3. Average thickness of reaction-affected rim as a function of leaching time.

initial period of chemical-reaction control, the shapes of the curves indicate parabolic leaching kinetics. Therefore, the data have been replotted in Fig. 4, where the straight lines are the results of regression on Eq. [1]. An activation energy is determined from an Arrhenius plot for k_p , and found to be $29 \pm 2 \text{ kJmol}^{-1}$.

Table I gives the BET surface areas, pore radii, pore volumes, and crystallite sizes of the reaction product obtained from samples of various particle sizes. The pore volumes and mean pore radii are calculated from the nitrogen isotherm. The pore volume, V_p , is estimated from the amount of nitrogen adsorbed at a relative pressure of 0.99 and calculated as a normal liquid. The values of r_p correspond to the maxima in plots of $\Delta V_p/\Delta r_p$ vs. r_p . The pore size-distribution consists of a single, narrow peak. The average pore radius, r_a , is calculated by the equation for nonintersecting cylindrical pores, $r_a = 2V_p/S_{\text{BET}}$ (24).

The effect of extraction temperature on these properties is shown in Table II. Pore volumes are not measured in these experiments, and the average pore radius is calculated assuming $V_p = 0.2 \text{ cm}^3/\text{g}$. The surface areas of

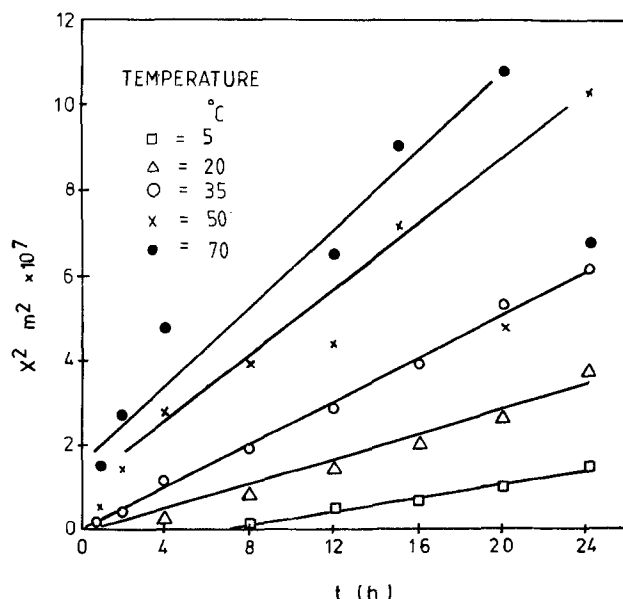


Fig. 4. Parabolic plots from Fig. 3

the copper are reported for samples with 40 w/o NaOH after washing with distilled water. The lower areas obtained after washing with NaOH are assumed to be due to removal of alumina produced in the reaction procedure. The atomic-absorption spectroscopy results show that in all leach residues, there is less than 3% aluminum, assumed to be present as alumina and evenly distributed over the reaction-product surface (15).

Discussion

The selective dissolution in alkali of aluminum from a Cu-50 w/o Al alloy proceeds according to parabolic kinetics, the reaction being controlled by liquid-phase diffusion within the reaction-product layer. Increasing the particle size of the alloy, which corresponds to decreasing the average reaction rate, results in a decrease in the surface area and an increase in the pore radius. However, the pore volume is approximately constant. Thus, the decrease in the average reaction rate results in an increase in the average diffusion distance, \bar{S} , at a fixed temperature. We now examine this correlation.

From Eq. [10] and [11], it is seen that the instantaneous reaction rate is related to $1/S^2$ for volume diffusion and $1/S^3$ for boundary diffusion. Because this rate varies with extent of reaction, the value of S also is predicted to vary. Because the measurements of pore size and copper crystallite size are obtained from the entire sample, they represent volume averages. It is therefore necessary to relate these averages to the instantaneous qualities. By definition

$$\bar{S}^2 = \frac{\int S^2 dV}{\int dV}$$

where V represents volume. For spherical particles of radius B

$$\bar{S}^2 = 3 \int_0^B S^2 r^2 dr / B^3 \quad [12]$$

where r is the radial coordinate within the sphere.

From Eq. [10], the diffusion distance is related to the diffusion coefficient and the velocity of the reaction front by

$$S^2 = \frac{\mathcal{H}D}{\nu} \quad [13]$$

where

$$\mathcal{H} = 2\sigma^{\text{CuP}}/f^{\text{Cu}}f^{\text{P}}aRT(C^{\text{Cu}} - C^{\text{P}})$$

From Eq. [1] it follows that

$$\nu = \frac{dX}{dt} = \frac{k_p}{2X} \quad [14]$$

Combining Eq. [13] and [14] yields

$$S^2 = \frac{2\mathcal{H}D}{k_p} X$$

which for a spherical particle becomes

$$S^2 = \frac{2\mathcal{H}D}{k_p} (B - r) \quad [15]$$

Combination of Eq. [12] and [15], followed by integration, yields

$$\bar{S}^2 = \frac{\mathcal{H}D}{2k_p} B \quad [16]$$

The corresponding expression for boundary diffusion is found to be

$$\bar{S}^3 = \frac{\mathcal{H}'D_B\delta K}{2k_p} B \quad [17]$$

where

$$\mathcal{H}' = 24 f^{\text{Cu}}f^{\text{P}}\sigma^{\text{CuP}}/aRT(C^{\text{Cu}} - C^{\text{P}})$$

Equations [16] and [17] predict rather simple dependencies of \bar{S} on B .

In order to calculate \bar{S} , both the pore diameter, \bar{S}^{P} , and the copper width, \bar{S}^{Cu} are required. Knowing the pore volume and S^{P} , S^{Cu} is calculated on the presumption that the pores are uniform, cylindrical, and parallel. These presumptions are borne out by the shape of the N_2 desorption isotherms and by the agreement between r_p and r_a . Proceeding, then, on the basis that the pores' axes are arrayed on a square grid and that the intervening regions of solid are composed of pure, theoretically dense copper, the average interpore distances shown in Tables I and II are calculated. Similar values for \bar{S}^{Cu} are calculated for hexagonally arrayed pores. Comparison of these numbers with the measured average crystallite sizes indicates poor agreement, although the trends with temperature are the same. Since average crystallite size is measured by x-ray line broadening, the average may be biased toward the smaller crystals in the total population. Because no analysis of the diffraction line shape has been performed, the values of \bar{S}^{Cu} calculated from pore data are preferred.

Plots of \bar{S}^2 and \bar{S}^3 vs. B are shown in Fig. 5 and 6. In these plots, the first point, corresponding to a radius of 71 μm , is disregarded because the leaching kinetics (Fig. 4) show that the leaching reaction is under chemical-reaction control at this time. In both plots, the remaining data conform reasonably well with the predicted straight-line relationship. The good fit achieved by the two models does not differ at a statistically significant level. It is therefore concluded that pore spacing is indeed related to leaching rate through the alloy-segregation process. The two possible mechanisms of segregation, however, cannot be distinguished on this basis.

The volume diffusion coefficient is calculated from the slope of the \bar{S}^2 vs. B plot using Eq. [16] and the following values: $a = 1$; $f^{\text{Cu}} = 0.36$; $f^{\text{P}} = 0.64$; $\sigma^{\text{CuP}} = 300 \text{ erg cm}^{-2}$; $C^{\text{Cu}} = 0.13 \text{ mol cm}^{-3}$; $C^{\text{P}} = 0$; and $k_p = 3.97 \times 10^{-8} \text{ cm}^2\text{s}^{-1}$. The value obtained is $D = 6 \times 10^{-12} \text{ cm}^2\text{s}^{-1}$. Values for the diffusion coefficient in CuAl_2 are given by Smithells (26). Extrapolation of this high temperature data to 20°C yields a calculated value of $1 \times 10^{-23} \text{ cm}^2\text{s}^{-1}$. In comparison, the value suggested by the application of the volume diffusion mechanism to the present results is seen to be rather high. A value of $1 \times 10^{-12} \text{ cm}^2\text{s}^{-1}$ has been deduced by Pickering and Wagner (27) for the diffusion of copper in a copper-gold alloy at 25°C and has been attributed to a divacancy mechanism. Such a mechanism might be oper-

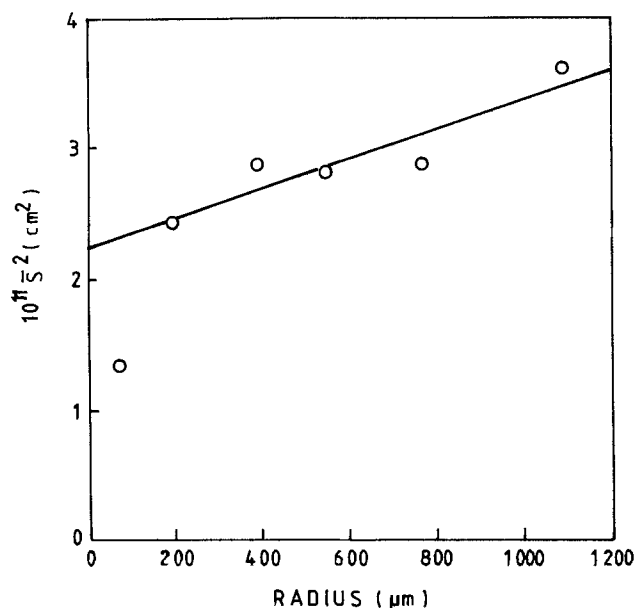


Fig. 5. Average diffusion distance squared as a function of particle radius.

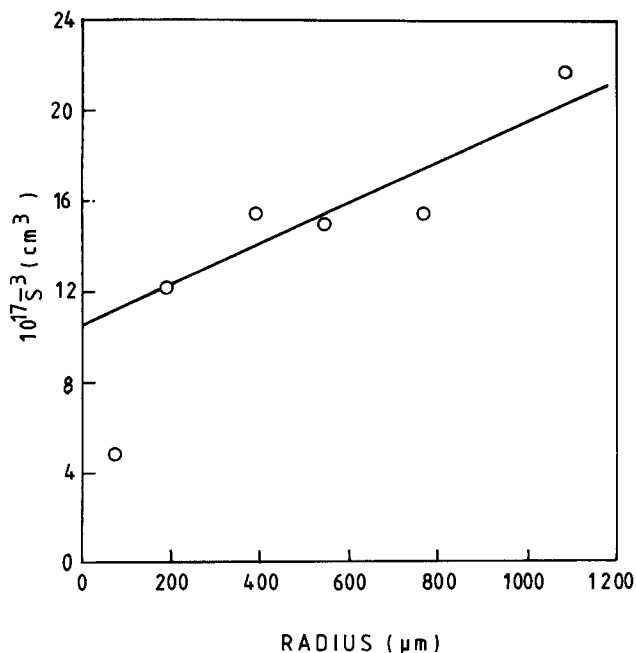


Fig. 6. Average diffusion distance cubed as a function of particle radius.

ative in the present case, but no independent evidence for it exists.

If alloy segregation occurs via boundary diffusion, then Eq. [17] applies. In this case, the slope of the \bar{S}^3 vs. B plot leads to the estimate

$$D_B \delta K = 1 \times 10^{-16} \text{ cm}^3 \text{ s}^{-1}$$

Using the values $\delta = 10 \text{ \AA}$ and $K = 2$, it is found that $D_B = 5 \times 10^{-10} \text{ cm}^2 \text{ s}^{-1}$. Because of the absence of information on the CuAl_2/Cu boundary diffusion properties, it is difficult to comment on this value.

The temperature dependence of \bar{S} can be deduced from Eq. [16] and [17] for the two modes of alloy segregation. Logarithmic differentiation for particles of fixed size leads to

$$\frac{\partial \ln \bar{S}^2}{\partial (1/T)} = -(Q_V - E_A)/R \quad [18]$$

$$\frac{\partial \ln \bar{S}^3}{\partial (1/T)} = -(Q_B - E_A)/R \quad [19]$$

where the linear term in T has been neglected. Here, Q_V is the activation energy for volume diffusion, Q_B the activation energy for boundary diffusion, and E_A the activation energy for the leaching reaction. The results in Table II for alloy particles of the same size, leached to completion at different temperatures, yield \bar{S} as a function of T . These data are used to construct the Arrhenius plot shown in Fig. 7. From the slope of this plot and the measured value $E_A = 29 \text{ kJ}$, it is calculated that if volume diffusion is operative, then $Q_V = 53 \pm 2 \text{ kJ}$; whereas, if boundary diffusion is in effect, then $Q_B = 62 \pm 4 \text{ kJ}$.

Activation energies for volume diffusion in CuAl_2 and Cu have been reported (26) as 127 and 211 kJ, respectively. The value estimated from the application of the volume diffusion model to the present results is seen to be quite inconsistent with these values. On the other hand, the value of Q_B estimated from the boundary diffusion model is about half the value expected for volume diffusion in CuAl_2 , and is therefore quite reasonable.

The volume diffusion model has been found to lead to an inordinately low estimate of the activation energy. It also yields a remarkably high diffusion coefficient, for which no independent supporting evidence exists. For these reasons, the hypothesis that alloy segregation occurs via volume diffusion is rejected. Conversely, the boundary diffusion model has been found to yield an acti-

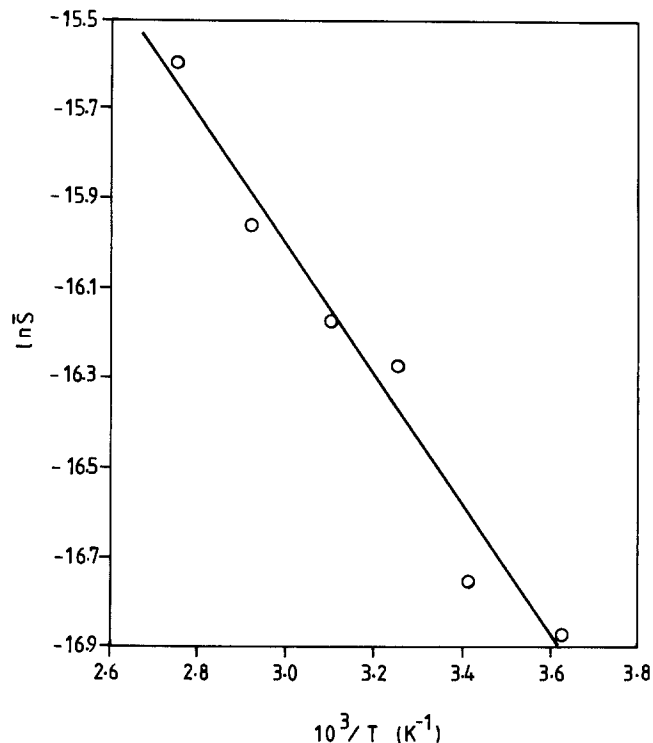


Fig. 7. Arrhenius plot according to Eq. [18] and [19]

vation energy of the expected magnitude and a diffusion coefficient for which there is no reason to reject. In addition, the model correctly predicts the relationship between spacing and reaction rate. It is therefore concluded that alloy segregation at the leach reaction front occurs by a mechanism of boundary diffusion.

The qualitative consequences are clear. At a given temperature, the alloy diffusion coefficient is fixed, and the pore spacing is controlled by the leach reaction rate. An increase in reaction rate leads to a decrease in pore spacing. Because the pore volume is fixed by the leachable content of the alloy, a decrease in pore spacing leads to an increase in the number of pores and, hence, an increase in surface area. These effects have been demonstrated in the present work by varying the average leaching rate through particle size control. Other methods of controlling the reaction rate would presumably achieve the same purpose.

Changing the reaction temperature affects the leaching rate and the alloy diffusion coefficient. Because the activation energy for alloy diffusion is significantly greater than for leach reaction, the effect on solid diffusion outweighs the other. Thus, an increase in temperature increases the alloy segregation distance more than it does the leaching rate. Consequently, a decrease in pore spacing and an increase in surface area is achieved for alloy particles of fixed size by lowering the temperature. These effects have also been demonstrated in the present work.

Acknowledgments

The financial assistance of the Australian Research Grants Scheme is gratefully acknowledged. A. D. Tomsett acknowledges support from the Commonwealth Government Postgraduate Scheme.

Manuscript received Nov. 29, 1983.

The University of New South Wales assisted in meeting the publication costs of this article.

REFERENCES

1. M. Raney, U.S. Pat. 1,563,587 (1925).
2. M. Raney, *Ind. Eng. Chem.*, **32**, 1199 (1940).
3. D. J. Young, M. S. Wainwright, and R. B. Anderson, *J. Catal.*, **64**, 116 (1980).
4. J. B. Friedrich, D. J. Young, and M. S. Wainwright, *This*

- Journal*, **128**, 1840 (1981).
5. J. B. Friedrich, D. J. Young, and M. S. Wainwright, *ibid.* **128**, 1845 (1981).
 6. J. P. Orchard, A. D. Tomsett, M. S. Wainwright, and D. J. Young, *J. Catal.*, **84**, 189 (1983).
 7. J. B. Friedrich, M. S. Wainwright, and D. J. Young, *ibid.*, **80**, 1 (1983).
 8. P. G. Shewman, "Transformations in Metals," p. 185, McGraw-Hill Book Company, New York (1969).
 9. V. F. Zackay and H. I. Aaronson, Editors, "Decomposition of Austenite by Diffusional Processes," pp. 39, 131, Interscience Publishers (1962).
 10. D. Turnbull, *Acta Metall.*, **3**, 55 (1955).
 11. D. J. Young, W. W. Smeltzer, and J. S. Kirkaldy, *This Journal*, **123**, 1758 (1976).
 12. J. Fridberg and M. Hillert, *Acta Metall.*, **25**, 19 (1977).
 13. H. H. Hindam and W. W. Smeltzer, *This Journal*, **127**, 1419 (1980).
 14. C. Zener, *Trans. AIME*, **167**, 550 (1946).
 15. M. Hillert, *Jernkont. Ann.*, **141**, 757 (1957).
 16. J. W. Cahn, *Acta Metall.*, **7**, 18 (1959).
 17. M. P. Puls and J. S. Kirkaldy, *Metall. Trans.*, **3**, 2777 (1972).
 18. J. S. Kirkaldy and R. C. Sharma, *Acta Metall.*, **28**, 1009 (1980).
 19. J. M. Shapiro and J. S. Kirkaldy, *ibid.*, **16**, 579 (1968).
 20. M. Hillert, Monograph and Report Series No. 33, p. 231, Institute of Metals, London (1969).
 21. B. Sundquist, *Acta Metall.*, **16**, 1413 (1968).
 22. W. L. Marsden, M. S. Wainwright, and J. B. Friedrich, *Ind. Eng. Chem. Prod. Res. Dev.*, **19**, 551 (1980).
 23. J. W. Evans, M. S. Wainwright, A. J. Bridgewater, and D. J. Young, *Appl. Catal.*, **7**, 75 (1983).
 24. S. J. Gregg and K. S. W. Sing, "Adsorption, Surface Area and Porosity," p. 165, Academic Press, New York (1978).
 25. S. D. Robertson and R. B. Anderson, *J. Catal.*, **23**, 286 (1971).
 26. C. J. Smithells, "Metals Reference Book," Vol. 2, Butterworths, London (1955).
 27. H. W. Pickering and C. Wagner, *This Journal*, **114**, 698 (1967).

Surface Dislocation Pinning by Adsorbed Ions and Water Molecules

C. J. van der Wekken

Laboratory of Metallurgy, Delft University of Technology, 2628 AL Delft, The Netherlands

ABSTRACT

Gold wire specimens were subjected to creep tests under constant load in various salt solutions. The effect of cathodic or anodic polarization on the creep behavior in deaerated acid solutions was found to depend on the nature of the ions present in the solution. Specific adsorption is a necessary but not sufficient condition for the pinning of surface dislocations by ions. A simple model for the observed rebinder effects is proposed.

It has been shown previously (1, 2) that the effects of cathodic polarization on the creep rate of gold wire specimens cannot be explained in terms of changes in the surface stress. Instead, it was concluded from the experimental observations that in deaerated alkaline solutions specifically adsorbed hydroxyl ions have a strong pinning effect on surface dislocations in the metal. As the OH⁻ ions are desorbed during cathodic polarization near and beyond the point of zero charge (pzc), unpinning occurs which results in extra strain. Similar extra strain effects confirming the role of adsorbed OH⁻ ions were observed to occur when the pH was decreased by adding acid to the test solutions (2).

Measurements in acid NaClO₄ solutions (2) suggested that perchlorate ions are also able to pin dislocations. The effects were much smaller, however, than the effects caused by hydroxyl ions. In contrast Cl⁻ ions were concluded not to pin dislocations (1) since no extra strain was measured at potentials near the pzc in acid chloride solutions.

Extra strain effects ascribed to dislocation pinning by adsorbed water molecules (2) have been measured at potentials below -1000 mV vs. SCE. However, in the present study of effects due to adsorbed ions, the attention is focused on potentials above -1000 mV. The specimen is loaded at a potential E_{def} and subsequently polarized in the direction of the pzc. Dislocation pinning by anions is detected during cathodic pulsing after loading at $E_{def} > pzc$. Pinning by cations may occur at $E_{def} < pzc$ and gives rise to extra strain during subsequent anodic pulsing. A variety of test solutions was employed in order to gain more insight into the nature of the dislocation pinning processes at the metal surface.

Experimental Procedure

The test apparatus has been described previously (1). The experimental procedure was essentially similar to that followed earlier (2). The annealed 99.999% pure gold wires of 0.15 μm diam and an average grain size of 15 μm

were loaded in deaerated solutions to a stress of 85 MPa. The test solutions employed, prepared from reagent grade chemicals and high purity deionized (Milli-Q) water, are listed in Table I. The pH values of the solutions were measured at room temperature. The concentrations employed were 1M except for a 0.2M TlAc solution. The reasons for this lower concentration were the high cost of the chemical and its toxicity. Since earlier measurements (2) showed that larger effects could be expected at ~50°C than at room temperature, the present tests were performed at 50°C. After deaerating the test solutions and before applying the load, the specimen surface was pre-reduced for 1 min at -1300 mV, followed by a 1 min pulse at -800 mV vs. SCE.

Possible anion pinning was investigated by loading at either +400 or 0 mV and subsequently subjecting the specimen to a series of 1 min pulses of increasing magnitude in the cathodic direction, similar to the procedure employed earlier (1, 2).

In order to measure dislocation pinning by cations, the specimens were loaded at -800 mV vs. SCE and subjected to 1 min potential intervals following the sequence

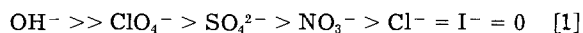
Table I. Experimental test conditions and conclusions regarding dislocation pinning by various ions

Test solution	pH	E_{def} vs. SCE	Direction of potential pulses	Conclusion: extra strain due to dislocation pinning by
1M NaClO ₄	0.6	0 mV	cathodic	ClO ₄ ⁻
1M Na ₂ SO ₄	0.6	0 mV	cathodic	SO ₄ ²⁻ (HSO ₄ ⁻)
1M NaNO ₃	0.6	+400 mV	cathodic	NO ₃ ⁻
1M CsCl	0.6	+400 mV	cathodic	—
1M K I	0.6	0	cathodic	—
0.2M Tl Ac	4.2	+400 mV	cathodic	—
1M NaClO ₄	0.6	-800 mV	anodic	—
1M CsCl	0.6	-800 mV	anodic	Cs ⁺
0.2M Tl Ac	4.2	-400 mV	anodic	—

-800, -600, -800, -400, -800, -200, -800, 0, -800, +200, -800, +400 mV. In the TlAc solution the specimen wire was loaded at $E_{\text{def}} = -400$ mV.

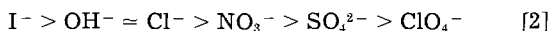
Results and Discussion

The extra strain effects resulting from the applied potential changes were measured in accordance with the definition given earlier (1) and plotted in extra strain-potential pulse (ES-PP) diagrams as shown in Fig. 1. A comparison between the extra strains measured previously in alkaline solutions (2) and the results presented in Fig. 1 shows that the effects measured in all the acid test solutions presently investigated are much smaller. If the present effects are also associated with surface dislocation pinning by adsorbed anions or cations, the pinning species can be identified. A list of pinning and non-pinning ions based on Fig. 1 can be derived. The result is shown in Table I. Considering the magnitude of the observed peaks in the ES-PP diagrams of Fig. 1 and taking into account the large effects caused by OH^- ions in previous studies, the dislocation pinning strength of adsorbed anions can be concluded to decrease as follows



Literature data (3, 4) suggest that hydroxyl ions and Cl^- ions are adsorbed on gold with similar strength.

Taking the change in the pzc in 0.1M solutions (5) as a measure for the strength of specific adsorption on polycrystalline gold, then, yields the following sequence for the anions



Comparing the pinning strength [1] and the strength of specific adsorption [2], it is observed that the sequences are reversed except for the position of OH^- . The observations for the CsCl solution constitute the first example of a rehbinder effect occurring during anodic polarization. Cs^+ cations, which are known to adsorb specifically on Hg, can be concluded from the present observations to adsorb

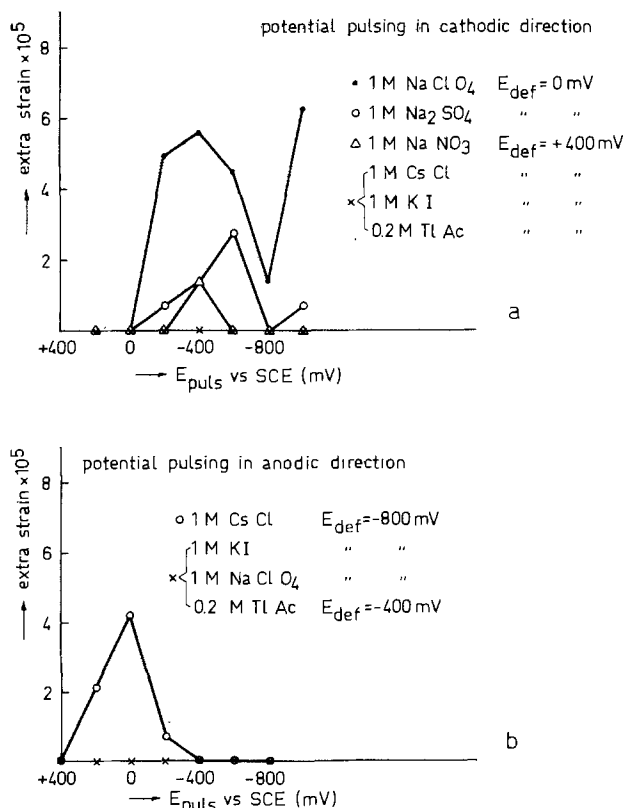


Fig. 1. Extra strain effects measured in deaerated acid salt solutions. a: Loading at a potential E_{def} above pzc and potential pulsing in cathodic direction. b: Loading at a potential E_{def} below pzc and potential pulsing in anodic direction.

specifically on gold as well. The large Tl^+ ions are probably adsorbed stronger than Cs^+ . The fact that no extra strain effect was observed in the (less concentrated) TlAc solution suggests that, probably, the sequences of pinning strength and specific adsorption strength for cations are also reversed. Earlier observations (1) indicated that not specifically adsorbed ions, e.g., the cations in KCl and NaCl solutions, have some influence on the observed rehbinder effects. However, a necessary condition for any extra strain effect in the potential region around the pzc is the occurrence of specific adsorption. If cathodic polarization is applied beyond -1000 mV SCE, a second peak is measured in the ES-PP diagram. This peak has been attributed to pinning by adsorbed water molecules (2).

It can be concluded from the available information that the observed rehbinder effects are primarily determined by contact adsorbed species in the first layer next to the metal surface.

A simple model for surface dislocation pinning in electrolyte solutions.—Figure 2 represents an example of a dislocation with Burgers vector b emerging at the metal surface. As the dislocation moves under the influence of a stress, a slip step is formed. Adsorbed ions I and water molecules W are present in the first adsorbed layer on the metal surface. As the area of the slip step is extended, the dislocation will disrupt the structure of the adsorbed layer. This implies that various interactions between metal atoms, ions, and water molecules will be broken (see Fig. 2). Previous explanations (6, 7) of rehbinder effects were based on the assumption that the energy necessary for the creation of a new surface area would determine the formation rate of new slip steps. The surface stress was considered to be a rate-determining parameter for the deformation process in the surface layer of the specimen. It is clear, however, that the surface stress is a macroscopic quantity which is related to some average value of the interactions mentioned above. It is to be expected that a surface dislocation moving under a certain stress will be stopped (pinned) by the strongest obstacles on its path. Let us consider a situation as represented in Fig. 2 and let the interactions I-Me and W-Me be strong. In that case, in addition to Me-Me bonds, I-W and W-W bonds across the slip plane must be broken if the dislocation is to move. The strongest of the latter two interactions will be likely to function as a barrier (pinning point) for further movement. Suppose that I-W bonds are pinning certain dislocations at a certain electrode potential. The pinning will be released as the ions I are desorbed by a change in electrode potential. The dislocation will then continue its movement in the slip plane and further on experience a weaker pinning by W-W interactions across

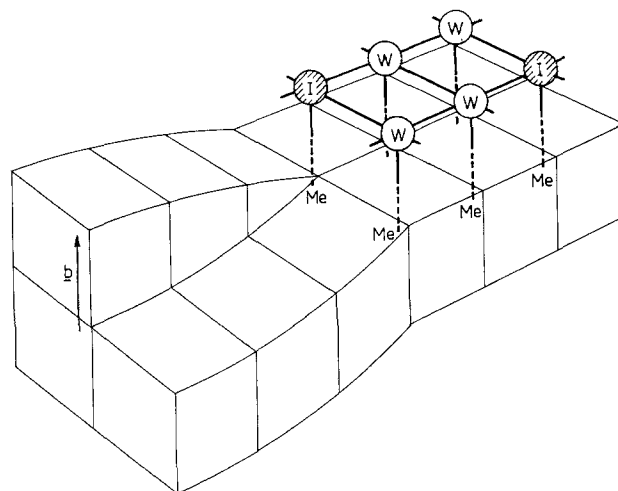


Fig. 2. Screw dislocation with Burgers vector b emerging at the surface of a metal electrode covered with contact adsorbed ions and water molecules.

its path. This type of pinning will be released as the adsorbed water is decomposed at potentials below -1000 mV. If the I-W interactions at the surface are weaker than the W-W bonds, pinning will only occur by the W-W interactions and no first peak will be measured in the ES-PP diagram. This is observed in the case of chloride solutions after loading at potentials anodic to the pzc and subsequent pulsing in the cathodic direction. Stronger I-W interactions can be expected for ions, which are known to be more strongly hydrated in the bulk of the solution. It is known that the strength of specific adsorption of ions and the strength of their interaction with hydration water molecules tends to be complementary (8). At the specimen surface, the I-W interaction may similarly increase as the strength of specific adsorption decreases. This could explain the reversed sequences [1] and [2] noted above. OH^- ions constitute an exception. These ions fit very well in the water structure. They are known as order producing ions (8, 9) in solutions, as is the case with F^- . However, the nature of their interactions with water molecules is different. Busing and Hornig (10) concluded that OH^- ions in aqueous solutions form a strong hydrogen bond with at least one water molecule. Not all surrounding water molecules are bonded with equal strength. Strong hydrogen bonds are expected to be retained in the case of specific adsorption. OH^- ions are thus strongly adsorbed, and simultaneously they have strong interactions with surrounding adsorbed water molecules. The strong I-W interactions in this case are probably the explanation for the large extra strain effects found in alkaline solutions.

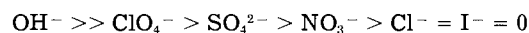
Figure 2 represents only one possible example of the configuration of the lattice at the specimen surface around an emerging dislocation. Other situations are possible: for example, with the Burgers vector parallel to the specimen surface. What will happen in detail at the surface during slip depends on the relative strength of the various interactions between metal, adsorbed ions, and adsorbed water molecules, as well as on the local geometry of the slip process. It seems reasonable and in accordance with the experimental observations to conclude that the I-W and W-W interactions largely control the extra strain effects. The strength of the W-Me interactions is potential dependent. This has consequences for the magnitude of the second peak in the ES-PP diagram, as shown earlier (2). We may expect, for example, in the case of very weak Me-W interactions during loading—for gold at potentials near the pzc (2)—that during loading Me-W interactions will be broken before W-W interactions. Dislocation pinning will consequently be less, and a smaller second peak will be the result. This was indeed observed (2).

In the above discussion, the use of the term dislocation pinning is not necessarily meant to imply that dislocation movement is permanently blocked. It may well be that the stressed dislocations jump from one barrier to the next one of a similar type. Instead of "pinning," we could

speak of "drag" in that case. From the present tests, it is not clear which term is more appropriate. Both more or less permanent pinning of dislocations as well as drag may play a role. While during loading the stress on the specimen is continually increased, the effective stress on dislocations during the primary creep stage after loading will decrease due to continuing work hardening of the specimen. The decreasing effective stress will lead to conditions where the dislocations become really pinned during longer periods at certain barriers. The removal of these barriers at the metal surface by means of variations in the potential is at the origin of the observed extra strain effects.

Conclusions

1. Specific adsorption is a necessary, but not a sufficient condition for dislocation pinning by ions.
2. The dislocation pinning strength of anions on gold has been observed to decrease according to the sequence



3. Cs^+ cations have been found to pin dislocations.
4. The pinning strength of adsorbed ions has been attributed to the strength of the interactions between the adsorbed ions and adsorbed water molecules. No extra strain effects due to the ions are observed when these interactions are weaker than the water-water interactions in the contact adsorbed layer.
5. The second peak in the ES-PP diagrams is due to interactions between adsorbed water molecules.
6. Dislocations are mechanical microprobes which can be used for the study of the structure of the compact double layer.

Manuscript submitted Oct. 11, 1983; revised manuscript received May 29, 1984.

Delft University of Technology assisted in meeting the publication costs of this article.

REFERENCES

1. C. J. van der Wekken, *This Journal*, **129**, 706 (1982).
2. C. J. van der Wekken, in "Extended Abstracts, 33rd ISE Meeting," M. Costa, Editor p. 28, ISE Lyon, (1982).
3. K.-F. Lin, *This Journal*, **125**, 1077 (1978).
4. D. D. Bodé, Jr., T. N. Anderson, and H. Eyring, *J. Phys. Chem.*, **71**, 792 (1967).
5. G. M. Schmid and M. E. Curley-Fiorino, in "Encyclopedia of Electrochemistry of the Elements," Vol. IV, A. J. Bard, Editor, p. 122, Dekker, New York (1975).
6. A. Pfützenreuter and G. Masing, *Z. Metallk.*, **42**, 361 (1951).
7. V. I. Likhtman, L. A. Kochanova, D. I. Leikis, and E. D. Shchukin, *Elektrokhimiya*, **5**, 729 (1969).
8. B. E. Conway, *Adv. Colloid Interf. Sci.*, **8**, 91 (1977).
9. G. R. Choppin and K. Buijs, *J. Chem. Phys.*, **39**, 2042 (1963).
10. W. R. Busing and D. F. Hornig, *J. Phys. Chem.*, **65**, 284 (1961).

AES/XPS Study of Transpassive Films on Iron in Nitrate Solution

M. Datta,* H. J. Mathieu, and D. Landolt*

Department of Materials, Swiss Federal Institute of Technology, CH-1007 Lausanne, Switzerland

ABSTRACT

Anodic films on iron formed in a forced convection system in the transpassive potential region in nitrate electrolytes at current densities up to 40 A/cm² have been studied by *in situ* coulometry and *ex situ* Auger electron spectroscopy (AES) and angle-resolved x-ray photoelectron spectroscopy (XPS). Qualitatively similar results on the variation of film thickness with applied current density are obtained by different methods. The transition from transpassive oxygen evolution to transpassive metal dissolution coincides with a marked decrease in film thickness and with the appearance of nitrogen in a reduced state at the metal-film interface.

Transpassive dissolution of iron and nickel in passivating electrolytes takes place at high current densities in the potential region beyond oxygen evolution and involves breakdown of passive films (1-3). Anodic films formed on iron and nickel in nitrate and chlorate electrolytes were investigated by Hoare and co-workers using potentiostatic polarization and coulometry in a stationary system (4-8). Their results showed that the film thickness increased in the passive potential region then decreased at the onset of the transpassive potential region. The behavior was attributed to an ion exchange mechanism (9), according to which electrolyte anions are incorporated into the film lattice by exchanging positions with oxygen ions leading to film dissolution. However, most of the data showing film thinning refer to a low current density region of exclusive oxygen evolution, and, therefore, their relation to transpassive dissolution, which occurs at much higher current densities, is not evident.

In a recent study, the present authors employed AES (Auger electron spectroscopy) and coulometry to investigate anodic films formed on nickel in the transpassive potential region in nitrate electrolytes under controlled hydrodynamic conditions in a flow channel cell (10). Results indicated that the passive film thickness reached its maximum as a function of current density in the oxygen evolution region. At higher current densities, nitrate ions were observed at the metal-oxide interface (10). In the present study, anodic films formed on iron in a concentrated nitrate electrolyte over a wide current density range in the transpassive potential region were investigated using XPS, AES, and coulometry. In particular, the study obtained information on the relationship among thickness, chemical nature of the films, and transpassive metal dissolution behavior. In addition to depth profiling, angle-resolved XPS was used for characterizing the films.

Experimental

Galvanostatic experiments were performed in a flow channel cell (11), through which the electrolyte was pumped at a constant linear velocity of 2.5 m/s. Cylindrical iron anodes (99.99%, single crystal, [111] orientation), 8 mm diam were mechanically polished to 0.25 μ m finish using diamond spray and ethanol as coolant. Only a part of the anode corresponding to the width of the channel (3 mm) was exposed to the electrolyte, while the remaining part was insulated by a Teflon spacer constituting the flow channel.

The applied anodic current density ranged from 1 mA/cm² to 40 A/cm². Anode potentials were recorded against a mercury sulfate electrode connected to the channel by a back-side capillary. The electrolyte solution (6M NaNO₃ + 0.1M NaOH) was prepared from analytical-grade chemicals and double-distilled water. An alkaline solution was employed to avoid self-activation of the anode after current interruption.

* Electrochemical Society Active Member.

¹ Supplier: Johnson Matthey Chemicals Limited, London, England.

In coulometric studies, anodic oxide films formed at different current densities were reduced by a constant cathodic current (20 mA/cm²), and the quantity of charge for oxide reduction was evaluated from the measured potential-time traces. A switching system with mercury relays was employed for presetting anodic polarization time and for switching between anodic and cathodic currents. The anodic charge passed was kept small (0.5 C/cm²) to minimize possible changes in surface roughness due to dissolution. A digital oscilloscope (Explorer III, Nicolet Instruments) recorded anodic and cathodic potential transients.

For AES and XPS studies, anodically polarized electrodes were quickly removed from the cell, washed with distilled water, rinsed in ethanol, and dried in a cold air stream. They were kept in a desiccator until introduced into the UHV chamber of a combined XPS/AES system with double pass cylindrical mirror analyzer, differentially pumped raster ion gun, and x-ray source (Perkin-Elmer, Physical Electronics Division, Model 590/550 A). All samples were analyzed in the same position, corresponding to an angle of $\alpha = 42^\circ$ between surface normal and CMA axis. In the XPS mode, the Mg x-ray source was operated at 10 keV and 40 mA with a pass energy of 50V. Binding energy calibration of the instrument was based on the measurement of the Au 4f_{7/2} peak at 83.8 eV. Depth profiling was performed by rastering a Kr⁺ beam over an area of 1.5 \times 1.5 mm or 6 \times 7 mm in the AES or XPS mode, respectively. The ion gun, operated at 2 keV, was positioned at an angle of 39° with respect to the surface normal. For calibration purposes, a depth profile of a standard 10 nm Ta₂O₅ film was measured with each series of experiments (12).

Angle-dependent measurements with the CMA were performed using a drum with an angle resolving aperture of 12° (13). The take-off angle of electrons could be varied between 0° and 84° with respect to the surface normal without moving the sample. In these measurements, an Al x-ray source was employed.

Current efficiency for metal dissolution was determined from weight loss measurements using Armco iron (99.9%) anodes. The applied charge corresponded to a maximum dissolution depth of 20 μ m.

Results

The galvanostatic anodic polarization curve for iron in 6M NaNO₃ + 0.1M NaOH at 2.5 m/s is shown in Fig. 1 as is the current efficiency calculated from weight loss measurements assuming divalent iron formation (14). At current densities below 8 A/cm², current efficiency is low because oxygen evolution is the main reaction. The current-potential curve exhibits Tafel behavior, with a slope of ~ 100 mV up to 0.2 A/cm², where the limiting current for OH⁻ discharge is reached (10). Measured potentials at higher current densities are strongly influenced by ohmic drops, which explains the shape of the current voltage curve above ~ 2 A/cm².

Figure 2 shows the charge necessary for reduction of films formed at different current densities. From the measured charge, the apparent film thickness was esti-

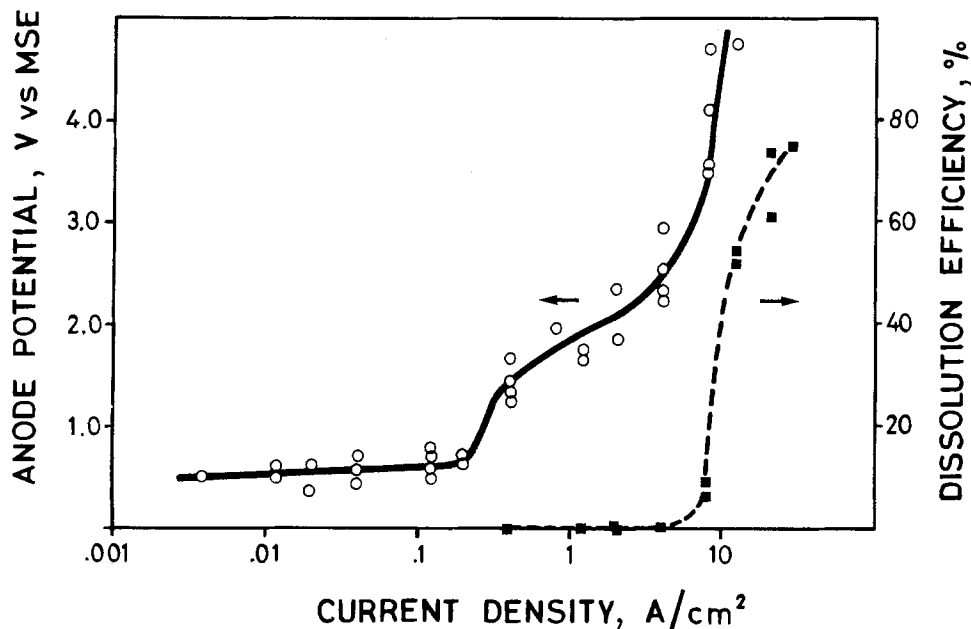


Fig. 1. Anodic potential (○) and current efficiency for iron dissolution (■) as a function of current density. Electrolyte: 6M NaNO₃ + 0.1M NaOH.

mated assuming that the film is Fe₂O₃ with a density of 5.24 g/cm³ (15) and that it is reduced at 100% current efficiency. The apparent film thickness as a function of current density exhibits two maxima: one at approximately 0.2 A/cm² corresponding to the limiting current density for the OH⁻ discharge, and the other at approximately 8 A/cm², beyond which the metal dissolution efficiency increases (Fig. 1).

Figure 3 shows Auger depth profiles of films formed at 0.042 A/cm² and 12.5 A/cm². The amplitude of the 703 eV iron, 503 eV oxygen, 272 eV carbon, and 379 eV nitrogen peaks were monitored as a function of time while sputtering the sample with Kr⁺. The important difference between the two films is in their nitrogen profiles. For the films formed at 0.042 A/cm², the nitrogen peak amplitude decreases rapidly with sputtering, in a similar manner as for air-formed films (not shown). The observed surface nitrogen is due to adsorption from air. For the film formed at 12.5 A/cm², however, the nitrogen peak amplitude increases with time reaching a maximum at the oxide-metal interface.

The apparent film thickness was calculated from the sputter time corresponding to a decrease of the oxygen peak amplitude to 50% of its maximum value, assuming that the sputter rate of the film is the same as that of bulk Fe₂O₃. The relative sputter rate of Fe₂O₃ with respect to the Ta₂O₅ standard was determined from a single-crystal sample to be 0.92. The variation of the apparent film thickness as a function of applied current density (Fig. 4a) is qualitatively similar to that obtained by coulometry

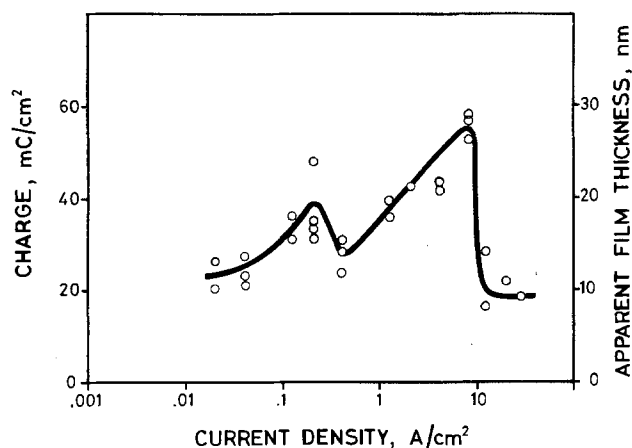


Fig. 2. Coulometrically measured charge for film reduction and estimated apparent film thickness as a function of current density.

(Fig. 2), i.e., two maxima are observed. Above 12 A/cm², the film thickness is independent of current density.

Using elemental sensitivity factors (16), the atomic concentration of nitrogen at the metal-oxide interface was estimated from AES depth profiles. The results (Fig. 4b) show that up to a current density of 1 A/cm² the nitrogen concentration is close to the AES detection limit, but beyond 1 A/cm², it increases with increasing current density to a value close to 5 atom percent (a/o) in the high rate metal dissolution region. A similar behavior was previously observed for nickel (10).

Films formed at different current densities were also analyzed by XPS without sputtering. The binding energies of different peaks were determined with respect to C 1s = 284.6 eV. The binding energy of the Fe 2p_{3/2} peak was 710.5 ± 0.2 eV, independent of applied current density, and the N 1s peak was at 398.1 ± 0.4 eV. Comparing the binding energies of the N 1s electrons for different com-

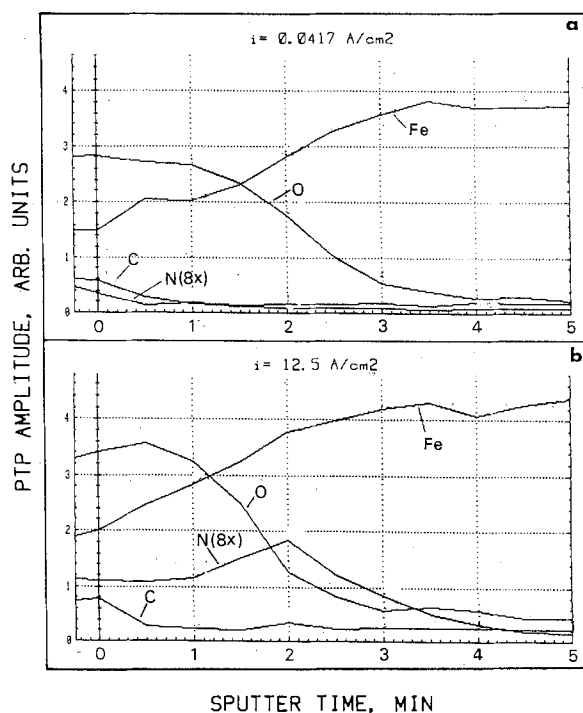


Fig. 3. AES depth profiles of films formed on iron at two different anodic current densities. Sputter rate of a standard Ta₂O₅ film is 1.86 nm/min under identical experimental conditions.

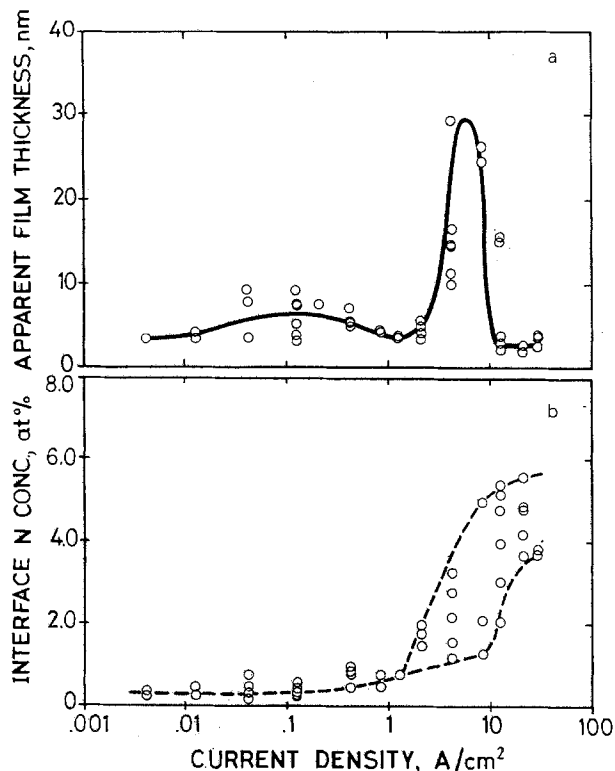


Fig. 4. Apparent film thickness (a) and nitrogen concentration at the metal-film interface (b) determined from AES depth profile data as a function of current density.

pounds from the literature (17-20), it is concluded that the nitrogen in the transpassive film corresponds to the reduced form, N^{3-} .

Experiments described so far investigated the influence of applied current density on film properties. Further experiments were aimed at the more detailed characterization of transpassive films formed under high rate metal dissolution conditions. Samples polarized at 20 A/cm² were subjected to XPS sputter profiling and angle-resolved XPS measurements. The latter technique, in which the analysis information depth is varied by changing the take-off angle of emitted electrons, permits the characterization of very thin surface layers as a function of depth without the use of ion sputtering (21).

Figure 5 shows XPS sputter depth profiles of transpassive (a) and air-formed (b) films on iron. The data are qualitatively similar to those obtained by AES depth profiling of films formed under similar conditions. The nitrogen at the surface of the air-formed film is due to adsorption from air and disappears rapidly upon sputtering. Transpassive films exhibit nitrogen at the metal-oxide interface. From the XPS depth profiles, the thicknesses of the transpassive and air-formed films were estimated to be 3.7 and 2.4 nm, respectively, and compare well with the AES depth profile data (Table I).

The shapes of the Fe 2p_{3/2} spectra for transpassive and air-formed films depend on the take-off angle (Fig. 6). At

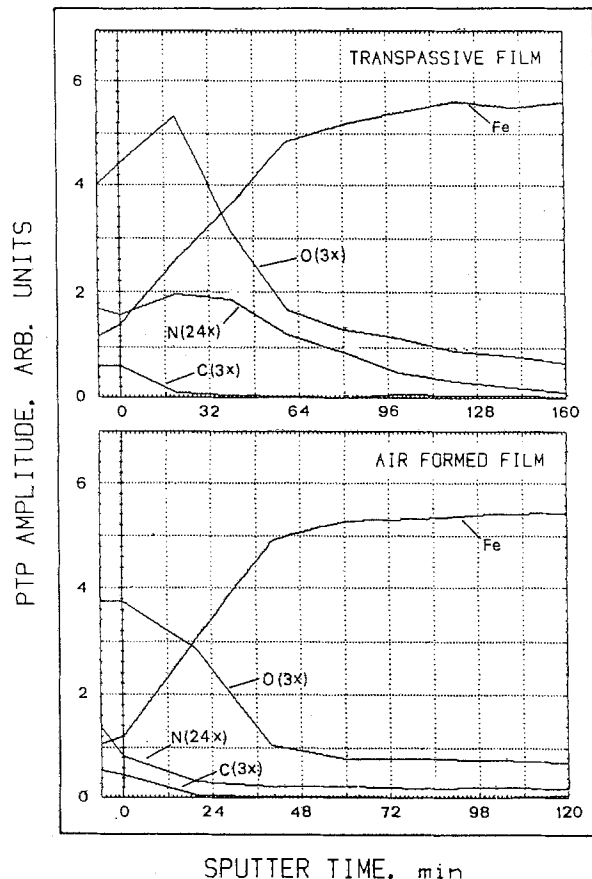


Fig. 5. XPS depth profiles of transpassive and air-formed films on iron. Sputter rate of a standard Ta₂O₅ film is 0.09 nm/min under identical experimental conditions.

$\phi = 0^\circ$, a main peak at 710 eV and a shoulder at 707 eV are observed; these are attributed to oxidized iron and metallic iron, respectively (22-25). The intensity of the metallic iron peak decreases with increasing take-off angle and is almost completely absent at 57°, since at this angle most of the information is derived from the surface film.

The ratio of the signal intensity of oxidized and of metallic iron can be used to estimate the film thickness (12, 20). For a homogeneous oxide film (f) covering a flat substrate (m), the signal intensity ratio, $I_{Fe,f}/I_{Fe,m}$, is related to the film thickness, l , by (20)

$$l = -\lambda_{Fe,f} \cos \phi \ln \left[\frac{K}{K + \frac{I_{Fe,f}}{I_{Fe,m}}} \right] \quad [1]$$

with

$$K = \frac{\lambda_{Fe,f} n_{Fe,f}}{\lambda_{Fe,m} n_{Fe,m}} \quad [1a]$$

Here the iron ionization cross-sectional ratio between film and metal is taken as unity, $I_{Fe,f}$ and $I_{Fe,m}$ are the intensities of iron in the film and in the metal substrate, re-

Table I. Apparent film thickness on iron determined by different methods

Film	AES depth profiling*	Estimated film thickness (nm)		Coulometry**
		XPS depth profiling*	Angle resolved XPS*	
Transpassive (at $i = 20$ A/cm ²)	3.5 ± 0.3 ^a	3.7 ± 0.2 ^b	5.1 ± 0.5 ^c	11.5 ± 0.5 ^a
Exposed to electrolyte flow	2.8 ± 0.2 ^b	—	—	10.1 ± 0.4 ^d
Air-formed	2.1 ± 0.4 ^a	2.4 ± 0.3 ^b	4.5 ± 0.7 ^c	—

* Referred to the sputter rate of Fe₂O₃ single crystal.
 ** Assuming the film to be Fe₂O₃.
 Average of (a) 5, (b) 2, (c) 12, and (d) 8 measurements.

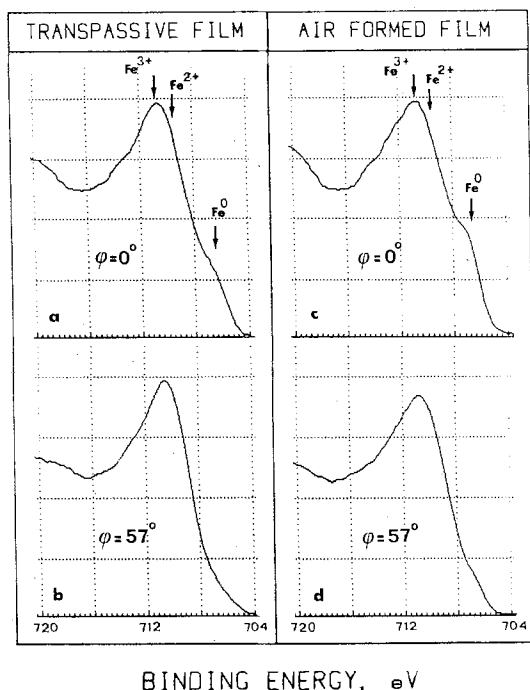


Fig. 6. Fe $2p_{3/2}$ spectra of transpassive (a, b) and air-formed (c, d) films on iron at different take-off angles. (a and c): $\phi = 0^\circ$, (b and d): $\phi = 57^\circ$.

spectively, $\lambda_{Fe,f}$ and $\lambda_{Fe,m}$ are mean free paths, $n_{Fe,f}$ and $n_{Fe,m}$ are atomic concentrations, and ϕ is the take-off angle of photoelectrons with respect to the surface normal. The values of constants used in Eq. [1] to evaluate film thickness are given in Table II.

To evaluate the signal intensity ratio, $I_{Fe,f}/I_{Fe,m}$, the Fe $2p_{3/2}$ spectra from 704 to 718 eV were resolved into four peaks (Fig. 7) at 706.6, 709.5, 710.6, and 714 eV that are attributed to Fe^0 , Fe^{2+} , Fe^{3+} , and a shake-up satellite signal of oxidized iron, respectively (23, 25, 27). The sum of the area intensities of Fe^{2+} and Fe^{3+} peaks was taken as a measure of the intensity of oxidized iron species. The contribution from the relatively small shake-up satellite signal was neglected. The transpassive and the air-formed film thicknesses thus determined from Eq. [1] are 5.1 ± 0.5 and 4.5 ± 0.7 nm, respectively (Table D).

The O 1s spectra of an air-formed and of a transpassive film were measured at different take-off angles. Three different peaks at 529.2, 530.9, and 532.2 eV were attributed to oxide (O^{2-}), hydroxide (OH^-), and water (H_2O), respectively (22-25, 28). Area intensities of these species were determined and are shown in Fig. 8 as a function of take-off angle. Little difference is observed between the two films. This behavior differs from that observed previously with nickel, where transpassive films contained significantly more O^{2-} than air-formed films (20). At the largest take-off angle, the ratio O^{2-}/OH^- decreases (Fig. 8), suggesting that the surface of the film contains more OH^- than the interior.

The energy of the N 1s peak measured at different take-off angles was the same and corresponded to that measured on an air-formed film. This indicates that the

Table II. Physical parameters used to calculate mean free path of Fe $2p_{3/2}$ photoelectrons in XPS

Material	Atomic density, n (mol/cm ³)	Binding energy, E_b (eV)	Kinetic energy, E_k (eV)	λ^* (nm)
Fe	0.141	706.6	775.4	1.24
Fe ₂ O ₃	0.066	710.5	771.5	2.01

* Mean free path calculated using the empirical equations by Seah and Dench (26) for elements and inorganic compounds, respectively.

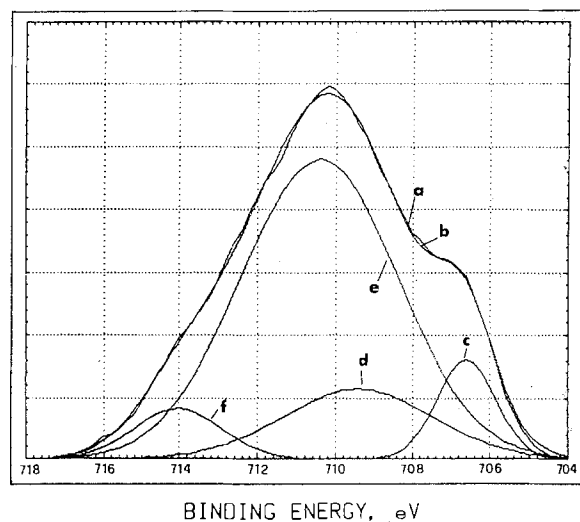


Fig. 7. Deconvoluted Fe $2p_{3/2}$ spectrum after background subtraction. a: Raw data. b: Fitted curve. c: Metallic iron. d: Fe^{2+} . e: Fe^{3+} . f: Satellite shake up signal of oxidized iron.

interface and the surface nitrogen are in the same chemically reduced state. The intensity of the N 1s signal on transpassive films showed no appreciable change with the variation of take-off angle, although one would have expected this based on the AES and XPS sputter profiles shown in Fig. 3 and 5. This is attributed to nitrogen adsorbed on the surface of the film; a high take-off angle the loss of intensity from the nitrogen at the film-metal interface is compensated by the increased intensity from adsorbed nitrogen.

Discussion

Characterization of anodic films by coulometry and by surface analytical techniques is subject to several limitations inherent in each method (10, 20). For example, coulometric data may include contributions from side reactions, and their interpretation requires a knowledge of film stoichiometry, density, and true surface area. AES/XPS analysis may be affected by sample transfer and contamination problems. In addition, the sputter rate is known approximately only, and the deconvolution procedures in XPS involve some degree of uncertainty. Therefore, data obtained for air-formed and transpassive

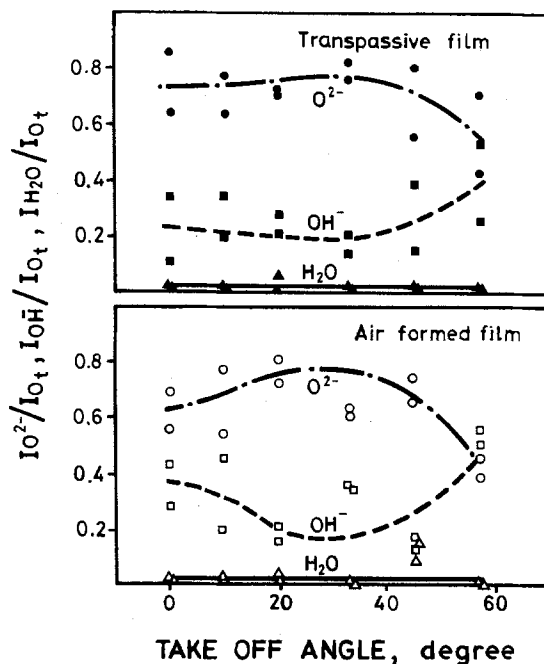


Fig. 8. Relative intensity of O^{2-} , OH^- , and H_2O XPS signals as a function of take-off angle for a transpassive and an air-formed film.

films at different current densities are of interest mostly on a comparative basis.

Film thickness as a function of current density shows two maxima (Fig. 2 and 4a). The first maximum lies close to the limiting current for OH^- discharge (Fig. 1), at which the local pH at the film-solution interface is diminished, favoring dissolution of surface hydroxyl species. This explains the decrease in film thickness in this region. Assuming film growth by high field conduction (29), the film thickness should increase with increasing potential resulting from higher applied current density. This leads to the observed increase in film thickness beyond the first maximum in Fig. 2 and 4a. At sufficiently high current density (anode potential), film breakdown occurs leading to high rate metal dissolution. This is evident in Fig. 9, which shows a scanning electron micrograph of iron dissolved at 10 A/cm^2 for 0.7s. At a current efficiency of 20% (cf. Fig. 1), this corresponds to an average dissolution depth of $0.5 \mu\text{m}$. The photograph confirms that the transpassive dissolution of iron takes place by local breakdown of the passive film at random sites, similar to observations for nickel in nitrate electrolytes (1). The apparent film thickness in the metal dissolution region is independent of current density.

Because of unavoidable transfer effects, the determination of transpassive film composition from XPS measurements is rather uncertain. However, AES and XPS depth profiles do exhibit a distinct nitrogen maximum at the metal-oxide interface at current densities corresponding to transpassive metal dissolution. This nitrogen originates from nitrate ions present in the electrolyte that might have penetrated through faults in the film (10).

The results of the present investigation provide new insight into the high rate transpassive dissolution behavior of iron in nitrate electrolytes. Under conditions of present experiments, transpassive dissolution in $6\text{M NaNO}_3 + 0.1\text{M NaOH}$ sets in at a current density of approximately 8 A/cm^2 , and the metal dissolution efficiency is an increasing function of current density up to 30 A/cm^2 . The apparent film thickness, however, remains constant beyond 12 A/cm^2 (Fig. 2 and 4a). The transpassive dissolution efficiency, therefore, is independent of film thickness, contrary to previous conclusions (4-8). The presence of nitrogen in the interior of the film suggests that passive films under these conditions are highly defective, so that electrolyte anions can penetrate locally up to the metal surface. It is probable that metal dissolution occurs at these sites, while oxygen evolution occurs on the rest of the surface. Micropits formed in this way, may grow until repassivation, e.g., due to ohmic drop, occurs or until different micropits merge together. The current efficiency for transpassive dissolution, thus, would be governed by

the kinetics of depassivation and repassivation phenomena, which determine the average surface fraction available for oxygen evolution and metal dissolution, respectively.

Conclusions

1. For iron polarized in nitrate solution in the transpassive potential region, two states with respect to surface films have to be distinguished: oxygen evolution, where film thickness is a function of applied current density, and metal dissolution, where film thickness is independent of current density. This follows from both *in situ* coulometry and *ex situ* AES/XPS data.

2. In the metal dissolution region, current efficiency for metal dissolution is independent of apparent film thickness, and nitrogen in a reduced state is observed at the film-metal interface.

3. Obtained data suggest that the transition from transpassive oxygen evolution to high rate metal dissolution involves film breakdown initiated by penetration of anions through flaws.

Acknowledgments

The authors thank N. Xanthopoulos for experimental assistance. Thanks are also due to Dr. R. P. Frankenthal of AT&T Bell Laboratories for his valuable comments. This work was financially supported by the Fonds National Suisse de La Recherche Scientifique, Bern, Switzerland.

Manuscript submitted Oct. 17, 1983; revised manuscript received June 1, 1984.

The Swiss Federal Institute of Technology assisted in meeting the publication costs of this article.

REFERENCES

1. M. Datta and D. Landolt, *This Journal*, **124**, 483 (1977).
2. M. Datta and D. Landolt, *Electrochim. Acta*, **25**, 1263 (1980).
3. D. T. Chin and K. W. Mao, *J. Appl. Electrochem.*, **4**, 155 (1974).
4. J. P. Hoare, *This Journal*, **117**, 142 (1970).
5. K. W. Mao, M. A. LaBoda, and J. P. Hoare, *ibid.*, **119**, 419 (1972).
6. J. P. Hoare, *Nature (London) Phys. Sci.*, **241**, 44 (1973).
7. M. A. LaBoda, A. J. Chartrand, J. P. Hoare, C. R. Weise, and K. W. Mao, *This Journal*, **120**, 643 (1973).
8. J. P. Hoare, in "Passivity of Metals," R. P. Frankenthal and J. Kruger, Editors, p. 505, The Electrochemical Society Monograph Series, Princeton, NJ (1978).
9. T. P. Hoar, *Corros. Sci.*, **7**, 341 (1967).
10. M. Datta, H. J. Mathieu, and D. Landolt, *Electrochim. Acta*, **24**, 843 (1979).
11. M. Datta and D. Landolt, *ibid.*, **25**, 1255 (1980).
12. H. J. Mathieu and D. Landolt, *Surf. Interf. Anal.*, **6**, 82 (1984).
13. H. J. Mathieu and D. Landolt, *Appl. Surf. Sci.*, **10**, 455 (1982).
14. K. W. Mao, *This Journal*, **118**, 876 (1971).
15. "Handbook of Chemistry and Physics," 53rd Ed. p. B-99, CRC Press, Cleveland, OH (1972).
16. L. E. Davis, N. C. MacDonald, P. W. Palmberg, G. E. Riach, and R. E. Weber, "Handbook of Auger Electron Spectroscopy," 2nd Ed., p. 11, Physical Electronics Industries, Inc., Eden Prairie, MN (1976).
17. B. Folkesson, *Acta Chem. Scand.*, **27**, 287 (1973).
18. H. Schultheiss and E. Fluck, *J. Inorg. Nucl. Chem.*, **37**, 2109 (1975).
19. W. D. Wagner, W. M. Riggs, L. E. Davis, J. F. Moulder, and G. E. Muilenberg, "Handbook of X-ray Photoelectron Spectroscopy," Perkin Elmer Corp., Eden Prairie, MN (1979).
20. M. Datta, H. J. Mathieu, and D. Landolt, *Appl. Surf. Sci.*, **18**, 299 (1984).
21. C. S. Fadley, *Prog. Solid State Chem.*, **11**, 265 (1976).
22. K. Asami and K. Hashimoto, *Corros. Sci.*, **11**, 559 (1977).

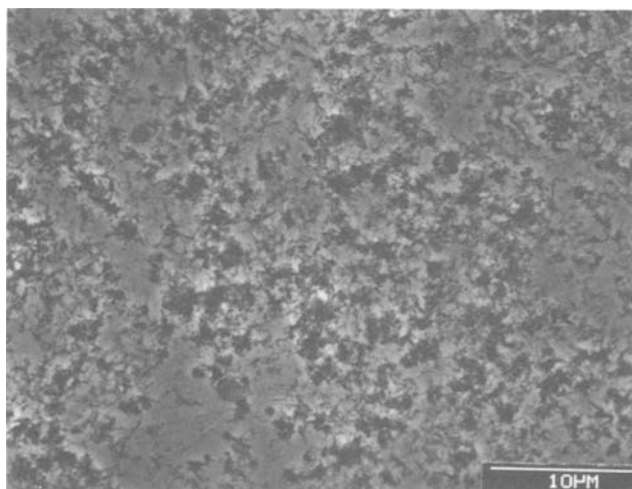


Fig. 9. SEM photograph of an iron sample after anodic dissolution in $6\text{M NaNO}_3 + 1\text{M NaOH}$ at 10 A/cm^2 for 0.7s.

23. N. S. McIntyre and D. G. Zetaruk, *Anal. Chem.*, **49**, 1521 (1977).
24. H. Konno and M. Nagayama, in "Passivity of Metals," R. P. Frankenthal and J. Kruger, Editors, p. 585, The Electrochemical Society Monograph Series, Princeton, NJ (1978).
25. C. R. Brundle, T. J. Chuang, and K. Wandelt, *Surf. Sci.*, **68**, 459 (1977).
26. M. P. Seah and A. W. Dench, *Surf. Interf. Anal.*, **1**, 2 (1979).
27. T. J. Chuang, C. R. Brundle, and K. Wandelt, *Thin Solid Films*, **53**, 19 (1980).
28. R. Kötz, H. Neff, and S. Stucki, *This Journal*, **131**, 72 (1984).
29. K. J. Vetter, "Electrochemical Kinetics," p. 759, Academic Press, New York (1977).

Development of Silver-Palladium Alloy Plating for Electrical Contact Applications

U. Cohen*,¹ K. R. Walton,² and R. Sard*,³

AT&T Bell Laboratories, Murray Hill, New Jersey 07974

ABSTRACT

Silver-palladium alloys were electroplated as high quality coatings from a concentrated chloride bath. Adherent, uniform, and coherent deposits were obtained with thicknesses of up to 20 μm . The alloys were found to be homogeneous, single-phase solid solutions, with palladium content ranging from about 30% to 60%, depending on the operating variables. The microstructure of the plated Ag-Pd alloys consists of very fine grains (100-300 \AA). These alloys have a fcc crystal structure, and the lattice parameter varies continuously with composition. The useful plating rate with moderate agitation was found to be about 0.44 $\mu\text{m}/\text{min}$ at 10 mA/cm^2 , which is almost twice that of conventional cobalt-hardened gold, due to the current efficiency of nearly 100%. Alloys containing about 40% Pd were obtained with these conditions. High speed plating of the Ag-Pd alloy was achieved in a forced flow cell up to rates of about 9 $\mu\text{m}/\text{min}$. To achieve satisfactory deposits, it was generally necessary to use a thin (0.2-0.4 μm) soft gold underplating. Preliminary tests of electrical contact properties revealed that the Ag-Pd coatings possessed low contact resistance (about 1 $\text{m}\Omega$ at 100g load). Other relevant properties include intermediate Knoop microhardness (about 200 kg/mm^2 at 25g load) and an excellent resistance to formation of corrosion films in accelerated tests using flowers of sulfur. The present study indicates that the plated Ag-Pd coatings are superior in contact resistance stability to the bulk wrought alloy R156 (40%Ag-60%Pd). Finally, these coatings show satisfactory wear response in the selected tests provided a hydrocarbon lubricant is present.

The development of a suitable process for electroplating Ag-Pd would provide an attractive alternative to hard gold plating in a variety of electrical contact applications. The material cost per unit volume of a 40%Ag-60%Pd alloy is currently less than 20% that of pure gold.⁴ The properties of metallurgically prepared Ag-Pd alloys are known to be suitable for contact materials (1, 2). In particular, savings in material costs and comparable corrosion behavior in tarnishing environments have led to the conversion of Bell System wire spring relays from pure Pd to this material (1).

The Ag-Pd alloy system consists of a homogenous solid solution phase over its entire composition range. The mechanical and electrical properties, therefore, should be easy to control and to reproduce. Problems associated with precipitation of a second phase in a multiphase alloy, such as erratic, abrupt, or irreproducible changes in the properties, are thus eliminated. Small fluctuations in the alloy composition have only a minor effect on such properties because, in a homogeneous phase, properties vary gradually with the composition.

In his comprehensive treatise (3), Brenner reviewed the unsuccessful attempts up to that time to electroplate the Ag-Pd alloy from various baths. He commented, however, that the concentrated chloride bath, investigated by Graham *et al.* (4) for Ag-Pt alloy plating, should also be feasible for Ag-Pd alloy plating. Although the latter (4) mentioned briefly that they had obtained Ag-Pd alloy from a

similar bath, they gave no details. Andreeva *et al.* (5) then reported Ag-Pd alloys using conditions similar to those specified by Graham *et al.* (4) for plating Ag-Pt alloys. Electrodeposition of the Ag-Pd alloy was also reported from a buffered ammoniacal electrolyte containing EDTA by Kudryavtsev *et al.* (6, 7). The ammoniacal plating system, however, appears to operate under conditions of silver diffusion-limited current, which adversely affects the deposition, composition, morphology, thickness, and rate of growth. We have chosen to work with the concentrated lithium chloride bath, which is simple and contains no additives or hazardous components. This electrolyte relies on the anomalous solubility of AgCl in the presence of chloride ion. At high concentrations of the latter, the solubility increases with the concentration of the chloride ion. The bath, however, is very aggressive towards base metals, causing vigorous displacement reactions with them. An intermediate layer of a more noble metal must thus be applied to protect the base metals against these reactions (8).

This paper describes our preliminary investigation related to: (i) the feasibility of electroplating high quality coatings of Ag-Pd alloy from the concentrated lithium chloride bath and (ii) initial characterization of the plated Ag-Pd coatings and their testings as contact materials. Desirable properties of an electrical contact include a low and stable contact resistance throughout service life and the ability to resist friction and wear. These requirements were discussed by Holm (9), and the contact resistance and wear resistance test methods were described by Antler (10). Comparative studies have been made here of the corrosion resistance, the electrical contact resistance, and the wear performance of the plated Ag-Pd alloys *vs.* the properties of a wrought Ag-Pd alloy (R156) and also *vs.* the properties of hard gold plating. This paper also briefly

* Electrochemical Society Active Member.

¹ Present address: Magnetic Peripherals, Incorporated, Santa Clara, California 95051.

² Present address: Exxon Research and Engineering Company, Linden, New Jersey 07036.

³ Present address: Oxy Metal Industries, Warren, Michigan 48089.

⁴ The product of a density factor (11.3/19.3 = 0.59) and a price factor \$130/\$390.

summarizes the results of a study of the morphology and microstructure of the plated Ag-Pd coatings (11). In another related study (12), the feasibility of a new method of plating cyclic multilayered alloys (CMA) was demonstrated by plating a wide variety of Ag-Pd structures.

Experimental

In the present work, the electrolyte for Ag-Pd alloy plating consisted of 500g of LiCl, 12g of AgCl, 3g of PdCl₂, 20 ml HCl, and 1000 ml of H₂O. After dissolving the salts, the bath was heated and brought to boiling (~130°C) to ensure complete dissolution of all salts, filtered (when hot), and cooled to the operating temperature (typically, 85°C). Moderate stirring was used during the plating, and the current density range studied initially was 0.5-20 mA/cm². Most samples, however, were plated at 5 ± 0.5 mA/cm².

Figure 1 illustrates the electroplating cell and associated electronics. The cell was a 500 ml reaction flask with an O-ring fitted cover that contained five standard tapered joints. Three electrodes, a thermometer, and a glass-stirrer were inserted through Teflon glands to the plating bath. The flask was immersed in a dark heating oil bath to provide uniform heating and to prevent photodissociation of wet solid AgCl. A stable plating bath temperature (within ± 0.5°C) was maintained with this arrangement.

Chemical analysis of the alloys was usually done with a nondispersive x-ray fluorescence (XRF) analyzer mounted on a scanning electron microscope (SEM). These analyses were corrected by comparison with several standard samples analyzed by wet chemical techniques and by electron microprobe. X-ray diffraction (XRD) was used for phase and texture analyses and for the determination of the lattice parameter. The coating morphology was studied by SEM and metallographic

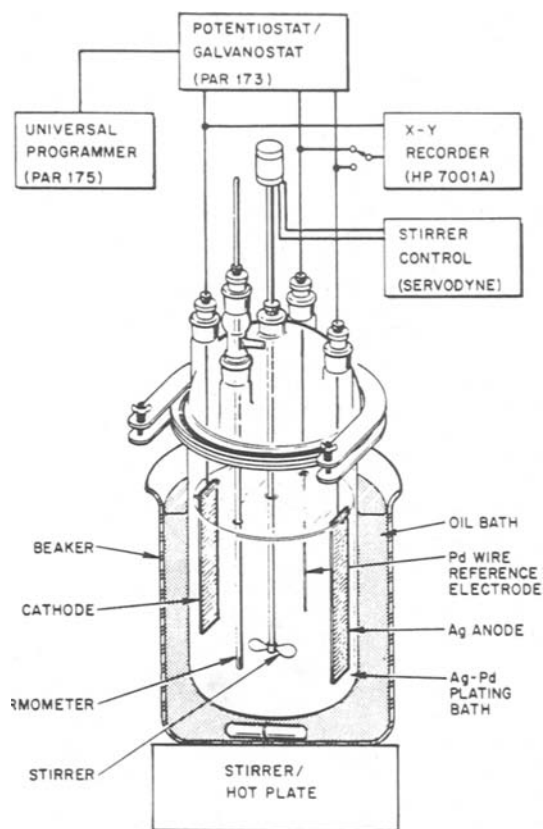


Fig. 1. Schematic of the experimental setup. The plating cell is immersed in a bath of oil. The oil bath is heated on a hot plate/stirrer equipped with a control thermistor sensor, which is immersed in the oil bath. A Pd wire immersed in the plating solution serves as an internal secondary reference electrode. A large plate (~25 cm²) of Ag metal serves as the anode. Electrical signals are provided to the cell from a potentiostat/galvanostat, PAR 173, combined with a signal programmer, PAR 175. The signals are recorded on an (HP-7004B) X-Y recorder.

cross sections. Transmission electron microscopy (TEM) was used to study the grain size and microstructure (11). Knoop microhardness was tested at 25g force (with a Tukon instrument) on polished cross sections of coatings ≥ 10 μm thick.

Electrical contact resistance was measured using a four-wire technique. In the measuring system (13), a 0.05 cm diam gold wire bent around a 60° Teflon wedge is used as the contact member. With this system, contact closure takes place with virtually no contact wipe. Measurements were performed at 100g load both on samples and standards prior to and after exposure to aggressive environments.

Wear and friction behavior was studied using a rider/flat wear test fixture, which simulates the sliding of separable connectors. The wear behavior with actual connector hardware plated with an Ag-Pd finish was also evaluated. The rider/flat tester is shown schematically in Fig. 2. In this tester, a flat coupon slides back and forth (on the same track) under a 0.25 in. diam spherical rider. The latter is loaded with a known weight. The resulting frictional force is sensed by a transducer through a shaft coupled to the rider assembly and monitored on a chart recorder. The coefficient of friction, μ_f , for a given cycle in the rider/flat experiment, is obtained by dividing half the total swing in the frictional force during each cycle by the load on the rider. The implicit assumption here is that the sliding events in both directions are equivalent. For the accuracy of about 20% sought in this work, this assumption is believed valid. Rider/flat tests were conducted for 200 cycles at a rate of 27 cycles/min (about 1 cm/s). The load on the rider was either 70 or 255g. However, only the results at 255g load are reported here; the results at 70g load are similar and lead to the same interpretations and conclusions. The depth and width of the wear tracks on the flat coupon were determined quantitatively by a Dektak microprofiler equipped with a 5 μm diam diamond-tipped stylus. Qualitative examination of the degree of wear on the coupons was done using optical and scanning electron microscopy.

Results and Discussion

Substrate compatibility.—To determine the compatibility of base metal substrates to the concentrated chloride plating bath, Cu and Ni strips were immersed with no external current in a simulated plating bath (but milder and not including the PdCl₂, for simplicity). The bath contained 50g of LiCl, 0.4g of AgCl, 2 ml of HCl, and 100 ml of H₂O, and was held in the temperature range 70°-80°C. No stirring was used. A vigorous displacement reaction was observed when a Cu strip was immersed in the solution. The strip was soon covered with a very loose and spongy white silver deposit and, at the same time, the Cu strip partially dissolved. After a 60 min immersion, the strip was removed from the solution, the Ag deposit

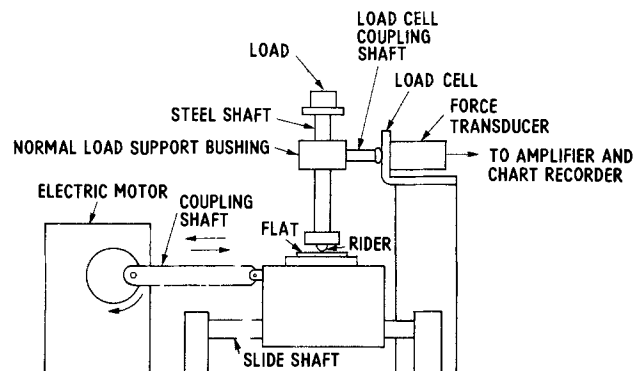
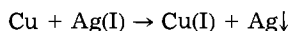
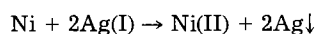


Fig. 2. Schematics of the wear tester. The load support is coupled by a shaft to a load cell (Statham UL4) and a force transducer (Statham UC3). Frictional forces experienced by the rider during sliding are transmitted to this unit. The transducer output is amplified and calibrated to read the frictional force in grams (accuracy to 0.1g) by a bridge amplifier (Statham SC1105).

scraped off, washed, and dried. The Ag deposit weight gain was 107.8 mg, and the Cu strip weight loss was 62.9 mg. These numbers may be compared with the respective atomic weights (107.87 for Ag, 63.54 for Cu), which indicate that the displacement reaction was



A more moderate displacement reaction was observed with a Ni strip. It was slowly covered with white Ag deposit of poor adherence. After an immersion of 17.5h, the strip was removed from the solution (which had become yellow-green in color). SEM examination of the deposit revealed individual Ag crystallites (10-20 μm) over most of the flat substrate surface and large Ag dendrites (400-600 μm on the strip edges). A total weight gain (strip plus deposit) of 110.1 mg was found. It may be noted that the Ag atom is almost twice the weight of the Ni atom, and that, for the displacement reaction

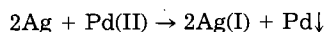


two Ag atoms are deposited for every dissolving Ni atom. Thus, a net weight gain is evidence of a displacement reaction.

Immersion of bare Cu and Ni substrates in the regular Ag-Pd alloy plating bath, under cathodic current, yielded loose powdery and spongy Ag-Pd deposits on Cu, and spontaneous peeling of the deposit from the Ni substrates. Current efficiencies, based on weight gain and Faraday's law, were much greater than 100%, indicating spontaneous displacement reactions had again occurred. These tests clearly demonstrate that the bare Cu and Ni substrates are incompatible with the concentrated chloride bath, containing Ag (or Pd) ions.

Substrates of Cu and Ni, with protective Ag films 1 μm thick (especially if immersed under cathodic current), showed a significant improvement over the bare substrates. However, they still contained some unacceptable rough areas.

Bulk noble metal substrates, such as Pd, Au, and Ag, were generally found compatible and suitable for the plating of the Ag-Pd alloy. However, it was found that prolonged immersion of Ag metal in the plating bath with no external current could have deleterious effects, probably owing to the slow displacement reaction



This reaction could result in poor adhesion and occasional cracking of the Ag-Pd coatings, probably owing to undercutting. The slow displacement reaction of Ag metal with the plating bath was also indicated by the observation that Ag strips, when immersed with no external current in the plating bath, exhibited immediate darkening of the Ag surface in contact with the bath. The metal surface when analyzed by XRF confirmed the presence of Pd metal. Further evidence was provided from SEM analysis of cross sections (12) and electrochemical potential measurements. The electrode potential gradually changed to less negative values *vs.* a Pd metal reference electrode. All these results indicate that Pd is more noble than Ag in this alloy plating system. By starting the plating of the alloy on Ag substrates immediately following immersion, or, preferably, by immersing under cathodic current; it was possible to eliminate the deleterious effects associated with these substrates.

It was found that the application of very thin (0.2-0.4 μm) protective undercoatings of soft gold could provide the most reliable protection to the base metal substrates against the displacement reactions. Soft gold plated from the citrate-buffered bath (14) provided better protection than hard-gold or gold-strike platings. This is believed to be due to the higher density (and lower porosity) of the soft gold. Without adequate substrate preparation, exposed pits or holes to the base metal will, of course, result in extensive displacement. Both unpolished and mechanically polished substrates of Cu, CDA725 alloy (89 w/o Cu-9 w/o Ni-2 w/o Sn), and Ni, when properly prepared

and coated with 0.2-0.4 μm soft gold, proved to be excellent substrates for Ag-Pd alloy plating. The substrate preparation procedure outlined in Table I was developed to give reproducible results for the plating of the Ag-Pd coatings.

The plated Ag-Pd coatings, under favorable conditions, closely reproduced the substrate surface features. Figure 3a depicts the surface of a 2.5 μm thick Ag-Pd coating which was deposited at 5 mA/cm² on an unpolished CDA725 alloy substrate, with a nominal 0.3 μm soft gold undercoating. Another sample, prepared under identical conditions except that the alloy substrate was mechanically polished (0.3 μm alumina was the last abrasive) proved to be so smooth that it was featureless on the scale of 1 μm (*cf.* Fig. 3b). This type of surface finish is similar to that typically found with carefully prepared hard gold deposits.

Effects of current density and waveform.—DC plating.—The effects of current density were studied for the bath composition given above. Ag strips were used as substrates for these experiments. They were chemically etched in a mixture NH₄OH/H₂O₂ (1:1) for 5-10s, rinsed, and dried. They were then masked with adhesive plating tape to prevent nonuniformity stemming from edge effects, and to prevent plating of the strip back side. Coatings ~10 μm thick were deposited to facilitate characterization. Increasing the current density was found, in general, to produce Ag-Pd alloys with increased Ag content, as described more fully below. Table II summarizes the various effects of the current density; and the various surface morphologies are shown in the SEM photographs of Fig. 4. At the lowest current density, 0.5 mA/cm², the deposits were dark gray matte due to the three-dimensional growth features evident in Fig. 4a. At 2 mA/cm², the overall general appearance was similar. However, the microstructure was quite different, as shown in Fig. 4b. This structure gives rise to unfavorable properties, such as high contact resistance. At 5 mA/cm², the surface appeared much lighter, and the morphology was noticeably smoother (*cf.* Fig. 4c). At 10 mA/cm², similar deposits to those obtained with 5 mA/cm² were observed (*cf.* Fig. 4d). Plating with moderate stirring (about 10 cm/s flow rate) and with current density in the range of 5-10 mA/cm² was judged most favorable. A standard condition at 5 mA/cm² was thus adopted to prepare samples for additional measurements, as described below. At a current density of 20 mA/cm², deterioration of the coating was evident close to the edges, where the effective current density was highest. Spontaneous cracking was sometimes observed (*cf.* Fig. 4e and 4f). Thus, under the conditions used (*i.e.* moderate stirring), the useful plating current density is less than 20 mA/cm². It should be noted that, at 10 mA/cm², the plating rate of Ag-Pd was about 0.44 $\mu\text{m}/\text{min}$, which is almost twice that of hard gold plating.

Table I. Substrate preparation for plating

1. Degrease in acetone and trichloroethylene
2. Ultrasonic cleaning in Neutra-Clean 68 solution for about 1 min
3. Rinse in deionized (DI) water
4. Activate in dilute (1:1) HCl for about 30-60s
5. Rinse in DI water
6. Soft gold plate, 0.2-0.4 μm thick*
7. Rinse in DI water and dry**
8. Introduce to the Ag-Pd alloy plating bath under cathodic current†

* Procedure was to immerse (wet) substrates under cathodic current in a bath containing potassium gold cyanide (20 g/l), dibasic ammonium citrate (50 g/l), ammonium sulfate (50 g/l). Conditions were 65° ± 5°C, 8 ± 2 mA/cm², 30-45s, and moderate stirring.

** The substrates must not be introduced wet into the alloy plating bath since precipitation of AgCl due to local chloride dilution may occur on the surface, yielding coatings with poor adhesion (4). The preferred procedure is to dip the substrate, prior to plating, in a concentrated chloride solution.

† This is to insure that the thin gold layer is protective. Substrates with ≥0.4 μm soft gold undercoatings could be immersed in the plating bath with no external current for several minutes without deleterious effects.

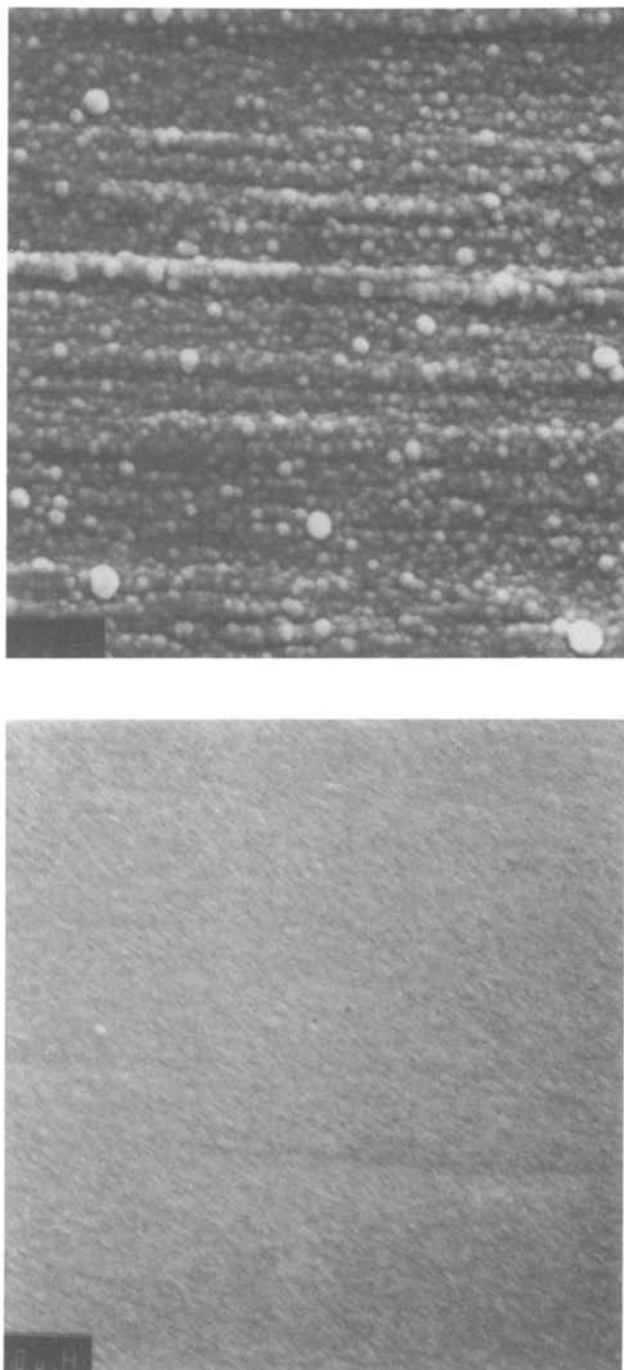


Fig. 3. SEM photographs of the surface of 2.5 μm thick Ag-Pd coatings plated at 5 mA/cm^2 using (a, top) unpolished CDA725 alloy substrate and (b, bottom) mechanically polished (with 0.3 μm alumina) CDA725 alloy substrate. Both substrates were plated with 0.3 μm soft gold prior to the Ag-Pd plating.

Much higher current densities were used in preliminary experiments with high speed plating of the Ag-Pd alloy in a forced flow cell (14). The solution velocity in the latter is estimated to be about an order of magnitude higher than in the stirred beaker. A precise value of the cathodic current density could not be determined because of some uncertainty regarding the plated area. Measurements of coating thickness on metallographic cross sections of a series of platings, obtained with a constant current and varying deposition time, revealed a linear thickness increase with plating duration. Assuming 100% current efficiency, an effective surface area of $\sim 9.5 \text{ cm}^2$ was estimated. Smooth coatings could be obtained with total currents up to $\sim 2000 \text{ mA}$. These conditions correspond to a current density of up to $\sim 210 \text{ mA}/\text{cm}^2$ (or $\sim 9 \mu\text{m}/\text{min}$),

which is roughly equivalent to rate attainable with high speed hard gold plating (14). Examination of the cross sections showed that even the very thin ($\sim 0.7 \mu\text{m}$) coatings were continuous over the entire substrate surface. Some thick ($> 7 \mu\text{m}$) coatings showed initiation of nodular growth at locations of relatively higher current densities. The composition of a typical coating obtained at $\sim 105 \text{ mA}/\text{cm}^2$ (or $\sim 4.5 \mu\text{m}/\text{min}$), was found by XRF analysis to be 62%Ag-38%Pd. The surface morphology of the coating, as revealed by SEM examination, was also very similar to the high quality coatings obtained with the much lower current density of 5 $\text{mA}/\text{cm}^2 \sim 0.22 \mu\text{m}/\text{min}$ under moderate stirring. Thus, the deleterious effects of high current densities on the morphology (cf. Fig. 4e and 4f) and excessive Ag content of the deposit, can be overcome by using a high speed flow cell.

Characterization of the plated Ag-Pd coatings.—Composition.—The composition of the coatings varied from about 70%Ag-30%Pd to about 42%Ag-58%Pd, depending on the current density and the rate of stirring. Generally, decreasing the current density or increasing the amount of stirring yielded alloy coatings with higher Pd content. This fact is further evidence that Pd is more noble than Ag in the alloy plating system. Data depicting the effect of dc current density on the alloy composition (for a constant stirring rate) are shown in Fig. 5.

Microstructure.—Transmission electron microscopy (TEM) examination revealed a microstructure of very fine grains (100-300 \AA). Voids of about 20-30 \AA in size were also noted at the grain boundaries. No second phase precipitates were observed. Electron and x-ray diffraction patterns indicated that the alloy coatings were homogeneous, single-phase solid solutions. These measurements also indicated that the fcc lattice parameter varies continuously with the composition in a similar manner to wrought Ag-Pd alloys (15). This dependency is shown in Fig. 6. The Ag-Pd coatings obtained with dc current had a strong fiber texture (preferred orientation) with the [100] direction perpendicular to the surface. As described elsewhere (11), plating of CMA coatings with cyclic current modulation tended to reduce degree of the preferred orientation. In particular, coatings with dense (or thin) multilayers exhibited more random orientation.

Microhardness.—Knoop microhardness was measured with a 25g load on polished cross sections of coatings with at least 10 μm thickness. A nominal value of about 200 kg/mm^2 was observed for optimal conditions. Some results are given in Table II.

Internal stress.—The internal macrostress of the Ag-Pd alloy coatings was continuously monitored using an electronic spiral contractometer (16, 17). The spirals were made of stainless steel 0.020 in. thick. They were plated with 2 μm Ni and with 2 μm soft gold. The gold, applied prior to the measurements, served to protect the spirals from the displacement reactions with the alloy plating bath.

Increasing the current density was found, in general, to decrease the tensile stress or to shift it to a compressive stress. The range of stress values observed for deposits 2.5 μm thick varied from slightly less than 1 kg/mm^2 tensile stress for coatings obtained at 2 mA/cm^2 , to about the same magnitude of compressive stress for coatings obtained at 20 mA/cm^2 . Temperature variations of $\pm 10^\circ\text{C}$ (from the standard 85 $^\circ\text{C}$) had little effect on the macrostress. Thus, the magnitude of the internal macrostress found in the Ag-Pd coatings is rather small and is comparable to pure silver and other widely used electroplatings, such as acid-copper and sulfamate nickel. Moreover, these stress levels are substantially lower than the high values associated with such brittle platings as cobalt-hardened gold (16) and tin-nickel alloy.

Contact resistance.—Effects of tarnishing.—Contact resistance was measured with a four-point probe instrument with a 100g load. The contact resistance of the as-plated Ag-Pd coatings was typically about 1 $\text{m}\Omega$. One

Table II. Results of dc experiments

Current density (mA/cm ²)	Coating thickness (μm)	Composition XRF* (w/o)	KHN ₂₅ ** (kg/mm ²)	CR† (mΩ)	Remarks
0.5	~ 5.0	Ag 43.2 Pd 56.8	—	1.5	Dark gray matte deposits of uniform appearance and composition (see Fig. 4a).
2.0	~16.4	Ag 45.8 Pd 54.2	155-165	25	Uniform gray matte color. Unusual morphology responsible for high CR (see Fig. 4b).
5.0	~10.0	Ag 53.9 Pd 46.1	168-220 avg 200	1.3	Uniform light gray matte color (see Fig. 4c).
10.0	~10.0	Ag 54.6 Pd 45.4	192-212	3.0	Light gray matte color (see Fig. 4d).
20.0	~10.0	Ag 69.6 Pd 30.4	—	—	Very light gray color. Surface appears badly cracked and deteriorated with loose powdery spots (see Fig. 4e and 4f).

* Based on x-ray fluorescence intensity measurements relative to metallurgical alloy standard of 40%Ag-60%Pd. Also, checked with microprobe and wet chemical analysis.

** Knoop microhardness, 25g load.

† Four-wire contact resistance measurements at 100g force with soft gold probe (0.020 in. diam wrapped around 60° wedge).

week exposure at 50°C in an environment containing flowers of sulfur and 85% relative humidity (RH) had hardly any effect on this contact resistance with the plated Ag-Pd coatings. Wrought R156 alloy (40Ag-60Pd) exposed to the same environment exhibited a significant increase in its contact resistance. Whereas the mean change in contact resistance, ΔR , of the plated alloy was less than about 0.2-0.3 mΩ, the corresponding value of the R156 alloy was 4-6 mΩ. In these tests, 2.5 μm thick alloy deposits of about 40%Pd were plated on CDA725 substrates with a soft gold undercoat about 0.25 μm thick. Additional results are given in Ref. (12). Indeed, the corrosion resistance of the plated Ag-Pd coatings in this test was found quite similar to that of plated hard gold.

The superior corrosion resistance and contact resistance stability (CRS) of the plated alloys over the wrought alloy, R156, is quite surprising, since the latter contains more palladium. However, the plated alloys differ substantially from the wrought alloy in many respects. For example, the grain size of the wrought alloy is in the neighborhood of several micrometers (about two orders of magnitude larger than the grain size of plated alloys). Also, the plated alloys are more homogeneous in their composition than the wrought material. Wrought alloys may have a composition variation of several weight percent from grain to grain (18), owing to the influence of the anisotropic distribution coefficient during solidification. The finer grain size, as well as the homogeneity of

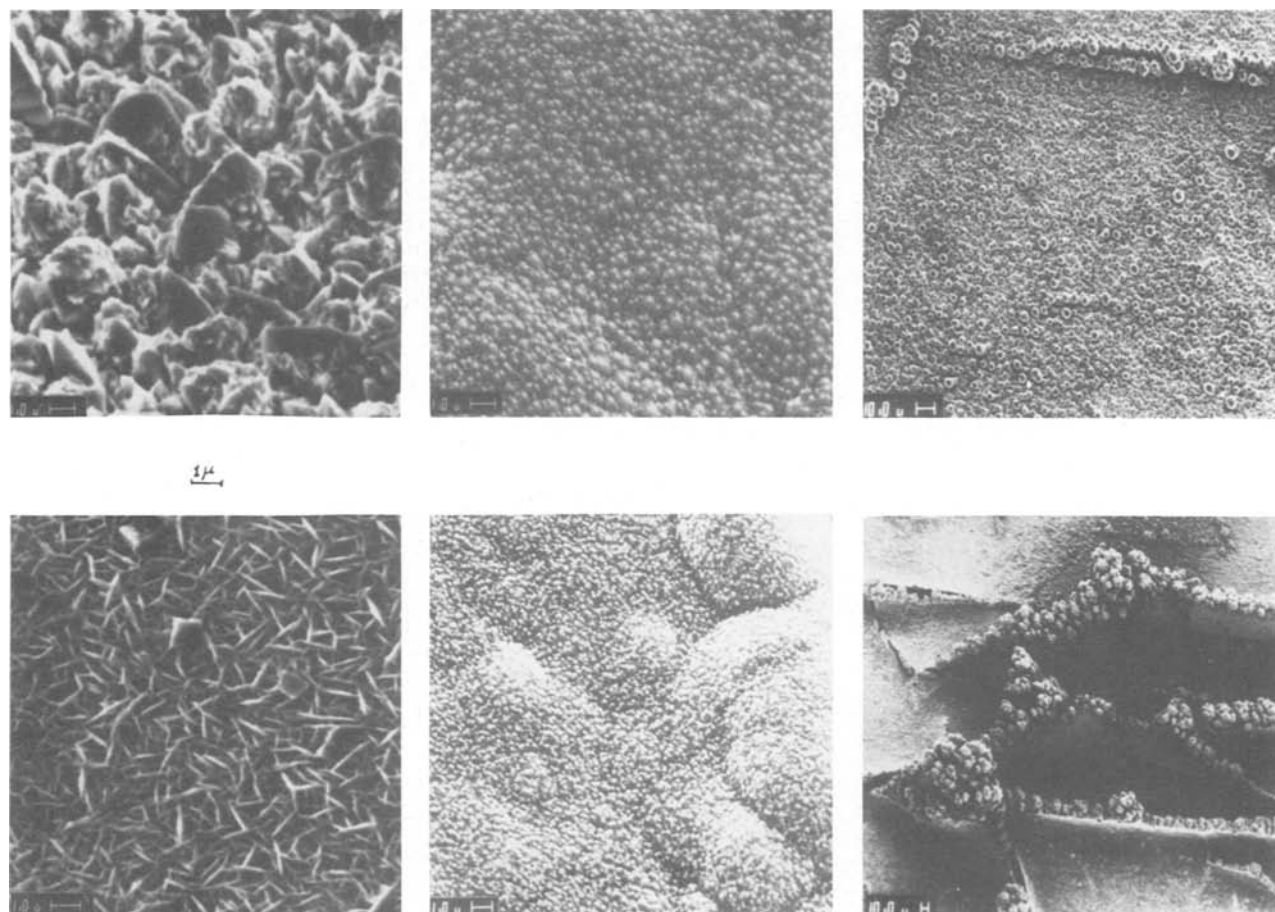


Fig. 4. SEM photographs of Ag-Pd alloy coatings obtained on Ag substrates with (a, top left) 0.5 mA/cm², (b, bottom left) 2 mA/cm², (c, top center) 5 mA/cm², (d, bottom center) 10 mA/cm², and (e, top right, and f, bottom right) 20 mA/cm². Figure 4e shows surface area in the center of the sample; 4f shows cracks closer to the sample edge, where there was higher current density. Note also the smaller magnifications of Fig. 4e and 4f.

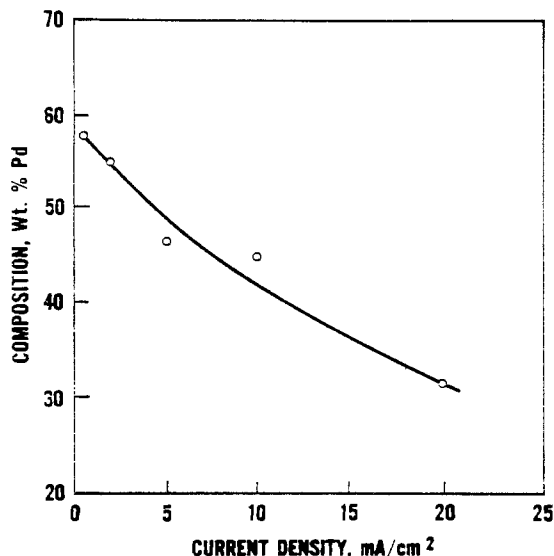


Fig. 5. Plated alloy composition vs. dc current density for low speed plating conditions.

the plated alloys, are likely to reduce the mobility of Ag atoms towards the surface, thereby reducing the formation of tarnish films in the sulfiding environment. It is also conceivable that certain impurities which are incorporated in the plated alloys help to reduce the mobility of Ag atoms towards the surface. The presence of incorporated Cl impurity in electroplated Ag-Pd CMA coatings was established by Auger electron spectroscopy (12). Incorporation of Cl in the plated Ag-Pd alloys could also contribute to their superior tarnish resistance over that of the wrought alloy.

Wear and friction.—Polished (rms surface roughness less than $0.5 \mu\text{m}$), and unpolished (rms less than $5 \mu\text{m}$) substrate coupons of CDA725 alloy were used as flats for the rider/flat wear tests. These were plated with either $2.5 \mu\text{m}$ of hard gold or with $2.5 \mu\text{m}$ of Ag-Pd alloy having a composition of $40 \pm 2\%$ Pd (preceded, as usual, by the $0.25 \mu\text{m}$ soft gold undercoating). The riders were hardened steel ball bearings (0.25 in. diam) plated first with $4 \mu\text{m}$ of nickel (Sel Rex 10-03S), then $0.25 \mu\text{m}$ of soft gold undercoating, and finally $5 \mu\text{m}$ of either the hard gold finish, or $5 \mu\text{m}$ of the Ag-Pd finish. Immediately prior to wear tests, both members of the test pair were carefully vapor degreased and then lubricated by dipping into a solution of Bareco wax (KS19416) in trichloroethane or a 2% synthetic hydrocarbon oil (Mobil RM109F).

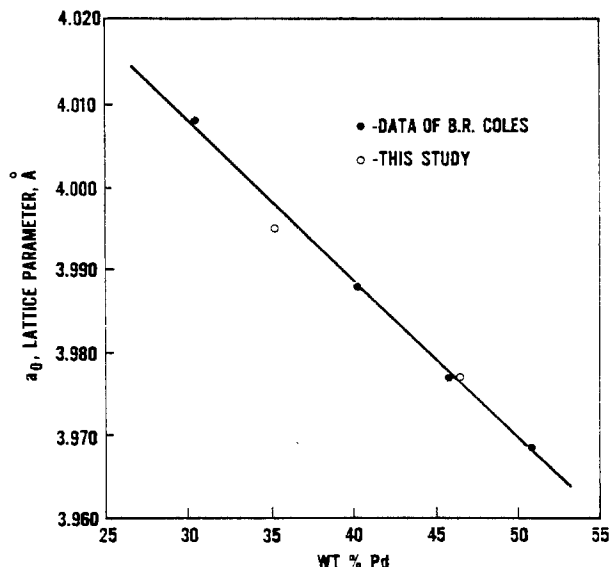


Fig. 6. Lattice parameter, a_0 , vs. alloy composition. Plated (this study) and thermally prepared Ag-Pd alloys.

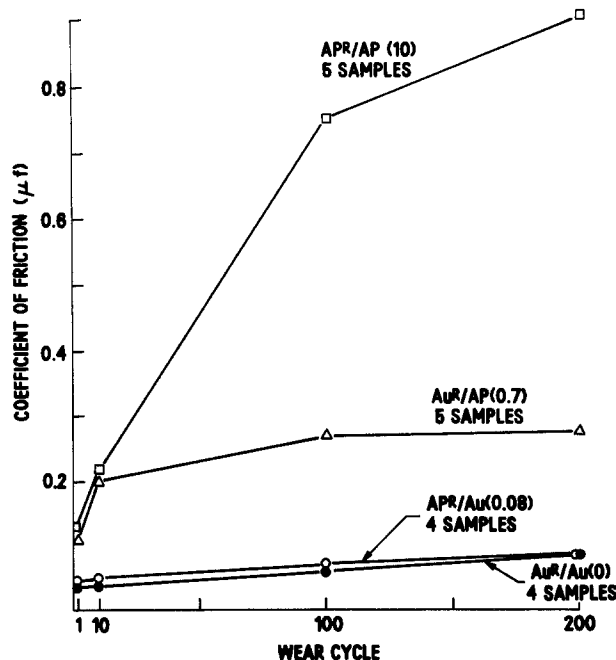


Fig. 7. The effect of contact finish variation on the wear and friction of rider/flat systems with microcrystalline wax lubrication, 225g load, 200 cycles, and polished CDA725 alloy substrates. Each data point represents the median value of 4 or 5 wear tests. $\text{AP}^{\text{R}}/\text{AP}$ is alloy-plated rider/alloy-plated flat. $\text{Au}^{\text{R}}/\text{AP}$ is gold-plated rider/alloy-plated flat. $\text{AP}^{\text{R}}/\text{Au}$ is alloy-plated rider/gold-plated flat. $\text{Au}^{\text{R}}/\text{Au}$ is gold-plated rider/gold-plated flat. The median wear depth in micrometers is indicated in parentheses.

The key results are summarized in Fig. 7 and 8 for the microcrystalline wax and hydrocarbon oil lubricants, respectively. It is clear from Fig. 7 that, with the solid lubricant (the microcrystalline wax), the hard gold-plated flats are superior to those with Ag-Pd-plated flats. In particular, the test pair with both rider and flat plated with Ag-Pd behaved very poorly. It is evident, however, that the pair with Ag-Pd-plated rider and hard gold-plated flat shows a wear response equivalent to the hard gold-plated pair. Figure 8 indicates that, with the liquid lubricant, all the test pair combinations are satisfactory and have essentially similar wear response (although there appears to be slightly better performance for the hard gold-plated

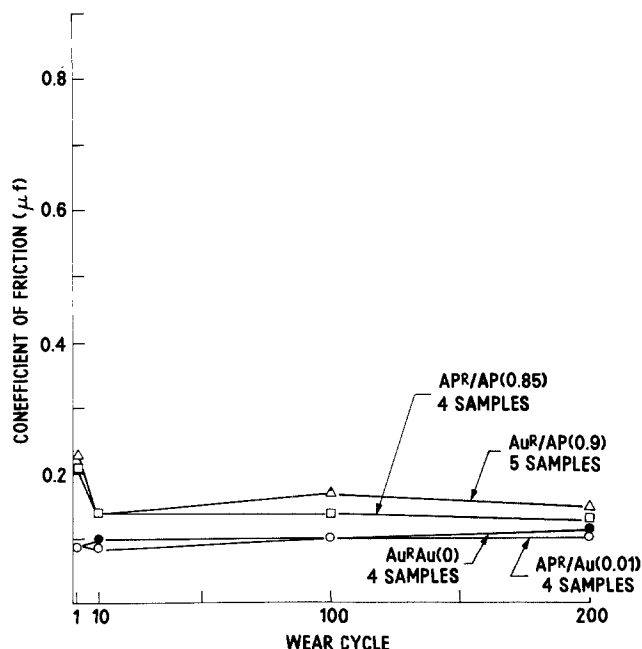


Fig. 8. As in Fig. 7, but with the synthetic hydrocarbon oil lubricant

flats). Surface roughness, in the range tested, appears to have little significance on the wear and friction performance. With both lubricants, the smoother substrates revealed a somewhat improved median wear response over the rougher substrates, but essentially identical friction coefficients. Coupons of bulk R156 alloy, when tested as flats with both lubricants under similar conditions, revealed significantly higher friction and wear than the plated Ag-Pd alloys. It should be noted that, without lubrication, both hard gold and the Ag-Pd alloys exhibited high coefficients of friction ($\mu_f \geq 0.6$) and disastrous wear (track depth up to 16 μm).

Some limited wear tests were also done with actual two-piece connector hardware of the type used in electronic switching systems. Standard 946/947 connectors with a mating load of 250g were the test vehicles. The male connector contact finish was 2.5 μm of hard gold plating. It was lubricated with the hydrocarbon oil prior to the testing. The female connectors were first plated with 2.5 μm of the Ag-Pd alloy finish and then tested by 200 mate/unmate cycles at a rate of 27 cycles/min, or about 1 cm/s as with the rider/flat tests. The median force of insertion was 1.8 kg for couples with Ag-Pd plated females (slightly higher than the 1.6 kg value for the reference pairs with soft gold inlay in place of the Ag-Pd alloy). Analysis by SEM and XRF mapping revealed some transfer of Ag-Pd to the male connector surface. However, there was no exposure of the base metal and no indication of unacceptable damage to any of the contacts after the 200 insertion cycles.

Summary

A simple, concentrated chloride electrolyte containing no additives or excessively hazardous components was used to demonstrate the potential benefits of Ag-Pd alloy plating. A very thin soft gold preplate (*i.e.*, 0.20-0.4 μm) was necessary to prevent displacement reactions with base metal substrates. Dense, uniform, single-phase alloys with Ag content of 40%-70% can be obtained at ~100% current efficiency. Decreasing the current density and increasing the amount of agitation increase the Pd content of the plated alloy. The lattice parameters, a_0 , increase continuously with the Ag content of the alloy, in agreement with previous studies of Ag-Pd alloys (15).

Under optimal conditions, the following Ag-Pd alloy properties appear to be favorable for contact applications: (i) microhardness of ~200 (KHN₂₅), (ii) very low internal stresses (<1 kg/mm² compressive), (iii) with a hydrocarbon lubricant, wear and friction characteristics similar to hard gold plating, and (iv) the corrosion resistance in flowers of sulfur is better than R156 alloy and similar to hard gold plating.

The Ag-Pd alloy plating system appears to be an attractive potential substitute for hard gold in certain con-

tact applications. However, more detailed study of the coating properties is required, as is continued development of a fully satisfactory plating process. The bath stability and aging due to photodissociation should be also studied in more detail.

Acknowledgments

The authors are indebted to F. B. Koch, R. A. Maher, S. Nakahara, G. J. Russ, and T. T. Sheng of Bell Laboratories for their help in various stages of this work.

Manuscript submitted June 11, 1982; revised manuscript received May 14, 1984. This was Paper 309 presented at the Denver, Colorado, Meeting of the Society, October 11-16, 1981.

AT&T Bell Laboratories assisted in meeting the publication costs of this article.

REFERENCES

1. T. R. Long and K. F. Bradford, in "Proceedings of the 8th International Conference on Electrical Contact Phenomena," Tokyo, Japan (1976).
2. W. A. Crossland and E. Knight, in "Proceedings of the Seminar on Electrical Contacts," p. 247, Chicago (1973).
3. A. Brenner, "Electrodeposition of Alloys: Principles and Practice," Academic Press, New York (1963).
4. A. K. Graham, S. Helman, and H. L. Pinkerton, *Plating*, **35**, 1217 (1948); *ibid.*, **36**, 47, 79 (1949).
5. G. P. Andreeva, N. P. Fedot'ev, and P. M. Vyacheslavov, in "Protective Metallic and Oxide Coatings, Metal Corrosion and Electrochemistry," N. P. Fedot'ev, Editor, Akademiya Nauk SSSR (1965); trans. published by Israel Program for Scientific Translations, Jerusalem, pp. 226-231 (1968).
6. N. T. Kudryavtsev, I. F. Kushevich, and N. A. Zhandarova, *Z. Metallov.*, **7**, 206 (1971).
7. I. F. Kushevich and T. Kudryavtsev, *ibid.*, **10**, 78 (1974).
8. U. Cohen and R. Sard, U.S. Pat. 4,269,671 (1981).
9. R. Holm, "Electric Contacts," New York (1967).
10. M. Antler, in "Properties of Electrodeposits—Their Measurement and Significance," R. Sard, H. Leidheiser, Jr., and F. Ogburn, Editors, p. 353, The Electrochemical Society Softbound Proceedings Series, Princeton, NJ (1975).
11. U. Cohen and S. Nakahara, "The Microstructure of Plated Ag-Pd Alloy Coatings," To be published.
12. U. Cohen, F. B. Koch, and R. Sard, *This Journal*, **130**, 1987 (1983).
13. G. J. Russ, *IEEE Trans. Compon. Hybrid. Manuf. Technol.*, **chmt-2**, 317 (1979).
14. D. E. Koontz and U. Landau, U.S. Pat. 4,001,093 (1977); D. Bacon, U. Landau, and R. L. Meek, *West. Elec. Eng.*, April 1978.
15. B. R. Coles, *J. Inst. Metals*, **84**, 364 (1956).
16. F. B. Koch, R. A. Maher, D. L. Simms, and R. Sard, *Plating*, **63**, 45 (1976).
17. R. A. Maher, Personal communication (1974).
18. J. E. Bennett and M. R. Pinnel, Personal communication (1973).

A Quantitative Investigation of the Open-Circuit Photovoltage at the Semiconductor/Liquid Interface

Nathan S. Lewis*

Department of Chemistry, Stanford University, Stanford, California 94305

ABSTRACT

A quantitative analysis of the theoretical value for the open-circuit photovoltage, V_{oc} , of a semiconductor/liquid junction reveals that control of bulk carrier transport properties is crucial to interpreting the observables at the semiconductor/liquid interface. Use of characterized semiconductor samples yields quantitative agreement between the maximum theoretical V_{oc} and experimentally observed values for both n-Si and p-Si surfaces in nonaqueous solvents. This accord between theory and experiment rules out deleterious effects of charged surface states on the V_{oc} of these interfaces. Lower than ideal V_{oc} values in other systems might reflect poor diffusion lengths in the semiconductor, classical tunneling over the barrier, or the effects of surface states. The observation of large photovoltages from n- and p-type-based semiconductor interfaces (n-Si, p-Si, n-GaAs, p-GaAs) in the same solvent is used to rule out a fixed density of charged surface states as the mechanism for obtaining constant photovoltages at these junctions. Direct support for this interpretation is obtained by techniques which verify the presence of mobile surface charge on p-type Si cathode surfaces in the inversion condition. Thus, control and investigation of bulk semiconductor properties that has been eminently significant to the understanding of p-n junction solar cells is also crucial to developing a rational understanding of the observables at the semiconductor/liquid interface.

The aim of this paper is to present a clarified treatment of the energetics at semiconductor/liquid interfaces. Recently, substantial effort has been directed into revision of the model which describes the relevant observables at a semiconductor/liquid junction. Rationales for junction properties include carrier inversion (1-3), pinning of the surface Fermi level by gap states (4-6), and hot carrier injection (7). Each of these models has been proposed to explain the behavior of a particular semiconductor/liquid combination. The specific conditions under which hot carrier injection may be observed have been discussed recently by Nozik (7), and this effect will not be the main focus of our discussion. Surface states have been frequently invoked to explain nonideal junction behavior at a variety of electrode surfaces (4-6). A key difference between carrier inversion and Fermi-level pinning by surface states is that the latter can (in principle) be manipulated by chemical treatment of gap states, while carrier inversion should not be sensitive to such effects.

We have previously demonstrated that modest interface parameters may not be intrinsic to the semiconductor/liquid junction, but can arise from nonideal bulk semiconductor properties (8) or from poor photoelectrochemical cell design (9). In the present work, the open-circuit photovoltage (V_{oc}), an especially important property of a semiconductor/liquid junction, is treated quantitatively. The ideal photovoltage for a semiconductor of bandgap E_g has been claimed to be the value of E_g itself (3, 4a, 10). Thus, constant photovoltages, less than $(1/q)E_g$ in value, have been stated to be diagnostic of surface states which pin the semiconductor Fermi level (3-6, 11). However, a quantitative analysis of the factors involved in the separation of photogenerated carriers indicates that at moderate light intensities (1 Sun), intrinsic bulk recombination kinetics of the semiconductor will prevent attainment of a photovoltage close to the value of $(1/q)E_g$. This maximum restriction on V_{oc} holds even in the absence of any other sources of recombination, and rigorously applies for all surface barrier devices (semiconductor/liquid junctions) and all p-n diodes (12, 13). In addition to presenting a theoretical framework within which to interpret experimental data for semiconductor/liquid interfaces, we describe experiments which rule out a fixed density of surface states as the dominant factor in determination of V_{oc} at p-type Si photocathodes, and present data which establish the presence of mobile surface charge (carrier inversion) at p-type Si surfaces in nonaqueous solvents.

Experimental

The mounting and characterization of semiconductor electrodes has been described previously (8, 9).

*Electrochemical Society Active Member.

Characterization of relevant samples is as follows: n-type Si, (100)-oriented, phosphorus-doped, 4-9 Ω -cm (Wacker Siltronic) ohmic contact with Ga-In eutectic or with phosphorus diffusion (950°C) followed by Al contact; p-type Si, (100)-oriented, boron-doped, 5-10 Ω -cm (Wacker Siltronic) ohmic contact by evaporation of Al and alloying at 650°C for 5 min; n-type GaAs, (100)-oriented, Si-doped, donor density = 8×10^{15} cm^{-3} ohmic contact by evaporation of In and annealing under N_2 at 450°C for 15 min; p-type GaAs, (100)-oriented, Zn-doped, acceptor density = 2×10^{16} cm^{-3} (Laser Diode Company) ohmic contact by evaporation of 98% Au/2% Ge alloy, followed by annealing under H_2 at 450°C for 5 min. Si surfaces were etched before use with 48% HF for 10s, followed by a rinse with H_2O , then by a rinse with solvent, and were air dried. GaAs surfaces were etched with 3:1:1 $H_2SO_4:H_2O_2:H_2O$, 1:1 $H_2O_2:H_2SO_4$, or 12M HCl, rinsed with H_2O , then rinsed with solvent, and air dried before use.

All open-circuit photovoltages were obtained by direct measurement of the voltage between the semiconductor electrode and a large area Pt counterelectrode. Measurements were conducted through a high input impedance voltmeter, and were recorded on a Houston Instruments Model 2000 X-Y chart recorder. The accuracy of these measurements was verified by recording current-voltage curves in a three-electrode configuration *vs.* a Pt wire reference electrode poised at the solution potential. Semiconductor surface conductivity measurements on Si cathodes were performed by monitoring the voltage drop across a calibrated 10 k Ω resistor placed in series with the conductivity cell. Voltage detection was performed with a Princeton Applied Research Model 124A Lock-In Amplifier. The lock-in amplifier supplied the applied voltage, which was a sine wave with a 10 mV amplitude and a frequency of 1 kHz. The output signal was recorded on a Linear Instruments Model 555 Strip Chart Recorder. Negligible changes in conductance were recorded when the semiconductor shunt was omitted from the apparatus.

The CH_3OH solvent was distilled in a nitrogen atmosphere from Mg, and was stored over activated 3Å molecular sieves until use. CH_3CN was distilled from P_2O_5 and stored over 3Å sieves until use. Cobaltocene was purchased from Strem Chemical, Incorporated, and was purified by sublimation. All manipulations with cobaltocene were performed in a Vacuum Atmospheres, Incorporated glove box because of the extreme air sensitivity of this compound. N,N' -dimethyl-4,4'-bipyridinium dichloride dihydrate was used as received from Aldrich Chemical Corporation. N,N' -dibenzyl-4,4'-bipyridinium dibromide was synthesized by addition of benzyl bromide to 4,4'-bipyridine in CH_3CN solvent, and was isolated by addition of diethyl ether. Decamethylferrocene was used as received from Strem Chemical Corporation. N,N,N',N' -

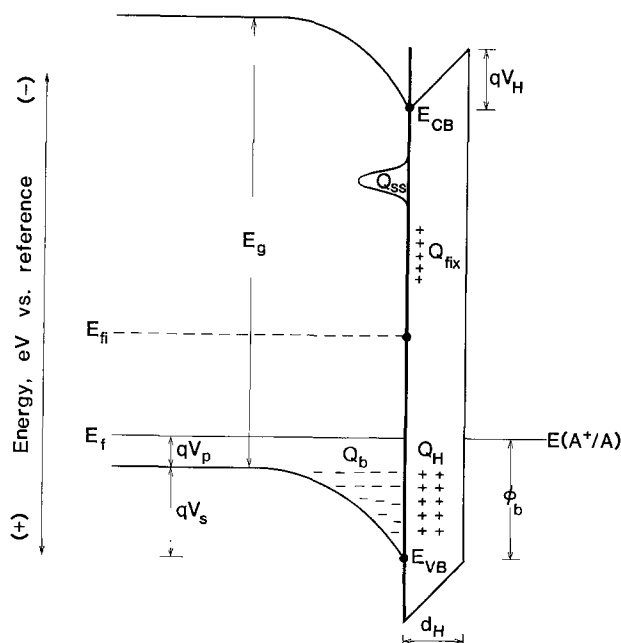
tetramethylphenylenediamine, 1,1'-dimethylferrocene, ferrocene, and acetylferrocene were purchased from Aldrich Chemical Corporation, and were recrystallized before use. Other oxidation states of all redox couples were obtained by constant potential electrolysis in a three-compartment electrochemical cell.

Expectations for the dependence of photovoltage upon solution redox potential.—A model of interface parameters at a p-type semiconductor/liquid junction is represented in Scheme I. Properties of interest include the energies of the semiconductor conduction and valence bandedges, E_{cb} and E_{vb} , the position of the Fermi level of the semiconductor, E_f , the position of the Fermi level of the intrinsic semiconductor when the band bending is zero, E_{fi} , the bandgap of the semiconductor, E_g , and the redox potential of the solution, $E(A^+/A)$. All potentials are defined in accord with the electrochemical scale where more negative potentials are closer to the vacuum level. The energy of the semiconductor Fermi level before equilibration with $E(A^+/A)$ is defined as the "flatband" condition, $E_{FB} \equiv E_{vb} + kT \ln(N_A/N_v)$, where N_A is the bulk equilibrium hole concentration in the doped semiconductor and N_v is the effective density of states in the valence band. We assume that the back contact to the semiconductor is an ohmic or selective (for majority carriers) ohmic contact.

Equation [1] is appropriate to relate the band bending in the semiconductor, V_s , to $E(A^+/A)$, given values of fixed interfacial charge density, Q_{fix} , charge in surface states, Q_{ss} , and charge in the bulk semiconductor, Q_b

$$(qV_s = E_{vb} - q)E(A^+/A) - qV_p + q(d_H/\epsilon_H)(Q_b + Q_{fix} + Q_{ss}) \quad [1]$$

For values of V_s such that $E_f > E_{fi}$, Eq. [1] reduces to the conventional model of the semiconductor/liquid junction. For band bending such that E_f is negative of $2E_{fi} - E_{FB}$, a substantial contribution to the space charge in the semiconductor will come from accumulation of minority carriers. In this regime, the semiconductor is said to be in the strong inversion condition (1, 13), which can lead to V_{oc} values which are insensitive to the actual magnitude of



Scheme I. Representation of the energetic parameters of a semiconductor/liquid interface at charge transfer equilibrium. The energy scale is depicted using the electrochemical potential convention, where increasing negative potentials indicate energies closer to the vacuum level. The diagram is appropriate for a moderately doped, p-type semiconductor, and neglects image force effects or Schottky barrier lowering. The potential drop in the electrolyte is assumed to occur entirely across the Helmholtz layer, which is characterized by a thickness d_H with dielectric constant ϵ_H .

$E_{vb} - qE(A^+/A)$. Under these conditions, the maximum band bending can reach $E_g - qV_p$ ($V_p \equiv (1/q)(E_{vb} - E_f)$ at zero band bending).

The maximum band bending under conditions where Q_{ss} dominates Q_b and Q_{fix} in Eq. [1] will be determined by the energetic distribution of the charged states relative to E_{vb} and E_{cb} . Thus, in the absence of surface chemistry with the electrolyte (a change in Q_{fix}), if the barrier height, ϕ_b , is limited by surface states, the maximum value of ϕ_b for a p-type semiconductor/liquid junction and the maximum value of ϕ_b for the corresponding n-type semiconductor/liquid junction will add up to no greater than $(1/q)E_g$ (3, 12, 13). In the absence of field shaping in an interfacial layer (15), V_{oc} at moderate light intensities will be substantially less than ϕ_b . Within this framework, if the maximum V_{oc} at a photocathode and at the corresponding photoanode should exceed (or even closely approach) $(1/q)E_g$, we can rule out Fermi-level pinning by a fixed surface-state density as the source of constant V_{oc} values with variation in $E(A^+/A)$. We discuss the experimental observation of such conditions below.

Maximum attainable photovoltages at a semiconductor/liquid interface.— V_{oc} values which are significantly less than $(1/q)E_g$ have been interpreted to indicate Fermi level pinning by interface states (3-6, 11, 16). Furthermore, the maximum V_{oc} value is commonly associated with the value of ϕ_b ($\pm 0.1V$) (3, 4, 10c, 17), and nonidealities of V_{oc} are thus taken as indications of lower than theoretical ϕ_b values. In order to develop an explicit relationship between V_{oc} and ϕ_b at the semiconductor/liquid interface, we apply the procedures commonly used by physicists and physical electrochemists to relate E_g and V_{oc} in p-n junction cells and in electrolyte cells (12, 13).

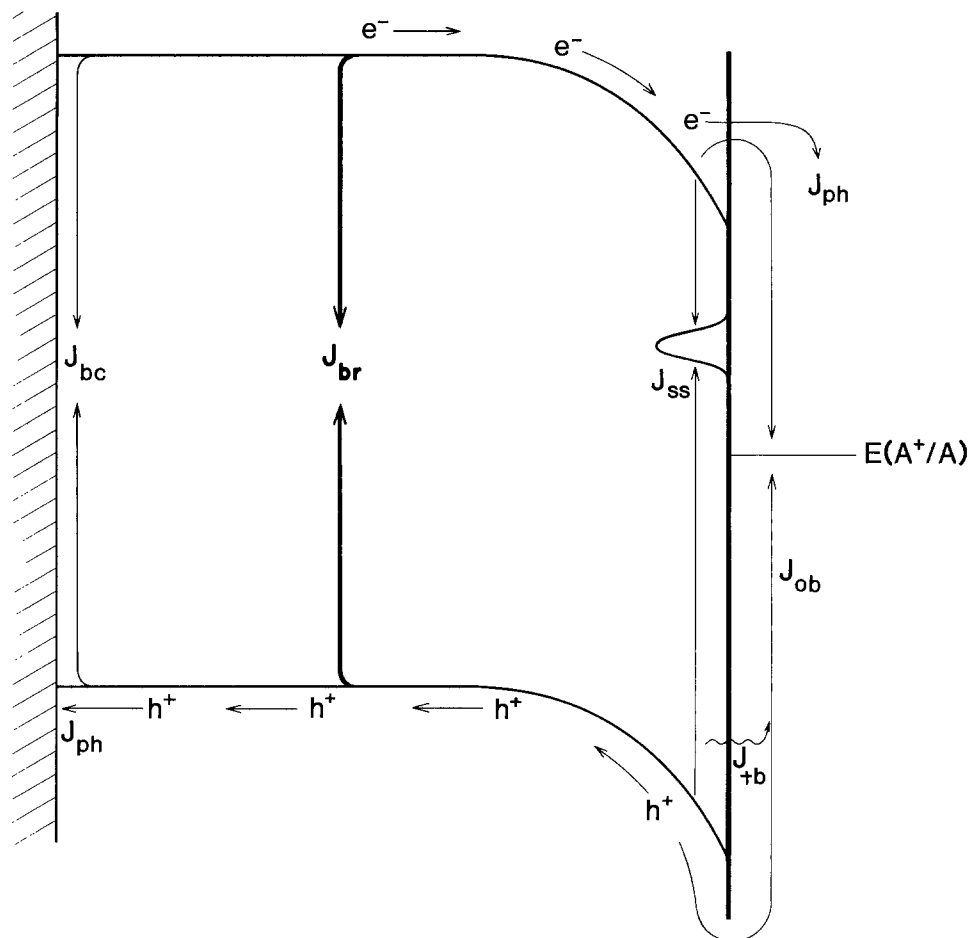
The key notion is that V_{oc} is not an energetic parameter of the interface, but is determined by the generation, recombination, and transport of the minority and majority carriers throughout the semiconductor. Scheme II outlines most of the pertinent mechanisms for recombination of electron-hole pairs at a semiconductor/liquid interface. Depicted are mechanisms for loss of photo-generated carriers: direct and indirect bulk recombination, J_{br} ; recombination at the back contact, J_{bc} ; recombination via surface states, J_{ss} ; thermionic emission of majority carriers over the barrier, J_{ob} ; and tunneling or leakage (perhaps at chemical imperfections) through the barrier, J_{lb} . Most of these current densities are dependent upon the voltage developed in the cell. Additionally, the overall voltage profile of the recombination components yields the dark current-voltage curve for the interface. Also depicted is the current density for capture of photo-generated minority carriers by the electrolyte, J_{ph} , which will lead to useful energy extracted from the system.

The V_{oc} is defined as the potential at which the net collected current is zero; thus, recombination by any of the mechanisms indicated in Scheme II can lower V_{oc} . If no recombination occurred by any of the pathways indicated, then the maximum V_{oc} might approach $(1/q)E_g - V_p$. However, for real solids with finite mobilities of charge carriers and finite diffusion lengths, J_{br} will not approach zero. Collection of any photogenerated current by the electrolyte will necessarily lead to a change in the quasi-Fermi level for electrons from its value in the dark. This change in population will be "resisted" by the finite values of the minority carrier diffusion coefficient, D_n , (for a p-type semiconductor), and the minority carrier diffusion length, L_n . Thus, in the absence of surface recombination or leakage across the barrier, bulk recombination processes will define an upper limit on V_{oc} at a given photocurrent density.

The expression relating J_{br} to these bulk materials parameters is represented in Eq. [2] (12, 13)

$$J_{br}(V) = \frac{qD_n n_0}{L_n} (e^{\frac{qV}{kT}} - 1) = qN_c \frac{D_n}{L_n} e^{-(E_g - qV_p)/kT} (e^{\frac{qV}{kT}} - 1) \quad [2]$$

Scheme II. Representation of the kinetic parameters involved in separation of charge carriers at an illuminated semiconductor/liquid interface. Recombination by any of the mechanisms depicted can contribute to low open-circuit photovoltages in the system. If all other sources of recombination are suppressed, bulk recombination (by both direct and indirect mechanisms) will determine the upper limit on the attainable photovoltage at a given light intensity. Thus, the ultimate limit on the photovoltage represents a bulk property of the semiconductor itself, not a parameter of the semiconductor/liquid junction. Poor bulk properties can thus yield low photovoltages without implying the presence of surface states.



D_n is related to the mobility by $D_n = (kT/q)\mu$, and is thus a function of the semiconductor (the effective density of states in the conduction band), while L_n is a function of the particular crystal under study. N_c is the density of states in the conduction band, n_0 is the electron concentration in the bulk semiconductor before equilibration with the solution, and the other parameters have their usual meanings. Setting $J_{br} = J_{ph}$ will define the maximum possible V_{oc} at photocurrent density J_{ph} for a p-type semiconductor/liquid interface with fixed values of D_n , L_n , N_A , and E_g , and yields the approximate expression in Eq. [3] for V_{oc} . Similar treatments would apply to any semiconductor surface barrier device where photocurrent is to be collected

$$V_{oc} \cong \frac{kT}{q} \ln \frac{J_{ph} L_n}{q N_c D_n} + (1/q) E_g - V_p$$

$$= \frac{kT}{q} \ln \frac{J_{ph} L_n N_A}{q D_n n_i^2} \quad [3]$$

At a semiconductor/liquid junction, under the usual conditions of low level injections, V_{oc} can never exceed the value determined from Eq. [3] (the "diffusion limit") without having an electrochemical corrosion reaction in series with stable photoelectrochemical power production. Table I indicates calculations of typical values of V_{oc} (max) for several common semiconductors under particular experimental conditions. Appropriate modifications can be made for the parameters in Eq. [2] or [3] to predict the theoretical V_{oc} at any photocurrent density given the appropriate materials parameters. It is emphasized that Eq. [2] and [3] refer specifically to p-type semiconductors, but analogous equations apply equally rigorously to n-type materials (replacing D_n with D_p , L_n with L_p , N_A with N_D , etc). The typical experimental variable which must be determined for a p-type crystal is L_n , with larger values of L_n indicating higher quality material. Notably, low L_n or N_A values can yield a low V_{oc} without surface states contributing to recombination. For accurate studies of the

Table I. Typical values of V_{oc} (max)

Semiconductor	Solvent	J_{ph} (mA/cm ²)	N_{maj} (cm ⁻³)	D_{min} (cm ² /s)	n_i (cm ⁻³)	L_{min} (μm)	V_{oc} (theory) ^a (V)	V_{oc} (obs.) (V)	Ref.
n-Si	CH ₃ OH	17.0	7.7×10^{15}	11.65	1.45×10^{10}	300	0.60	0.57-0.58	This work
n-Si	CH ₃ OH	17.0	9.3×10^{14}	11.65	1.45×10^{10}	700	0.56	0.51-0.52	(9)
p-Si	CH ₃ CN	21.0	2.1×10^{16}	34.97	1.45×10^{10}	400	0.55	0.48-0.50	(40)
n-GaAs	CH ₃ CN	22.0	8.0×10^{15}	10.9	1.8×10^6	2	0.94	0.72-0.75	(8a)
n-GaAs	H ₂ O	22	10^{16}	10.9	1.8×10^6	2	0.94	0.70-0.75	(41)
p-InP	H ₂ O	25	2.4×10^{17}	119	1.5×10^7	2	0.86	0.66-0.68	(24)
n-CdTe	CH ₃ CN	15	10^{16}	1.7	6.9×10^5	1	1.01	0.65-0.72	This work
n-MoSe ₂ ^b	CH ₃ CN	20	7×10^{16}	5	1.3×10^{10}	5	0.6	0.6	(1, 42)
n-MoSe ₂ ^b	H ₂ O	25	10^{17}	5	1.3×10^{10}	5	0.6	0.6	(42, 43)
n-WSe ₂ ^b	H ₂ O	15	10^{17}	5	1.9×10^{10}	5	0.6	0.7	(44)

^a Calculated based on Eq. [3]. Relevant semiconductor parameters taken from Ref. (12, 13) and references therein. The theoretical value is calculated for an infinite crystal thickness, and thus ignores any further lowering of V_{oc} owing to the large surface recombination velocity of the back ohmic contact in typical experimental systems. The correction is on the order of 5%, and is not significant to the accuracy of the present values available for semiconductor/liquid junctions.

^b The accuracy of these values are limited both by the dispersion in experimental V_{oc} values (1, 42, 43) and some uncertainty concerning the value of n_i for these crystals. We have used $E_g(\text{MoSe}_2) = 1.06$ eV, $E_g(\text{WSe}_2) = 1.16$ eV and approximate $N_c = N_v = 10^{19}$ for these materials (44).

semiconductor/liquid junction, it has been demonstrated that L_n (or L_p) must be sufficient to insure the collection of photogenerated carriers (8, 19). However, even values of L_n or L_p sufficient to produce unit quantum yields at short circuit with 632.8 nm irradiation might not suffice to obtain the V_{oc} values calculated for the highest quality material in Table I. Thus, although V_{oc} values have been interpreted to represent the chemical nature of the semiconductor/liquid interface (3-6, 10, 11, 17), it is seen that these V_{oc} values might in many cases primarily reflect the bulk properties of the semiconductor.

Although we have not considered any of the other recombination mechanisms depicted in Scheme II, we note that in most surface barrier devices the dominant recombination terms are leakage across the barrier and J_{ob} , the thermionic emission term (13, 20). For a finite barrier height, ϕ_b , classical emission over the barrier will ideally have a dependence on the cell potential as given in Eq. [4] and [5]

$$J_{ob} = J_o (e^{\frac{qV}{kT}} - 1) \quad [4]$$

$$J_o = A^* T^2 e^{-\frac{q\phi_b}{kT}} \quad [5]$$

The effective Richardson's constant, A^* , is related to the free electron value by the ratio of effective electron (hole) mass in the semiconductor to the value in vacuum. If the dark current is dominated by J_{ob} , for a barrier height of $(1/q)E_g$, V_{oc} will be less than $(1/q)E_g$, and can be less than the V_{oc} value obtained from the diffusion limit of Eq. [3]. Use of the A^* appropriate for n-GaAs in Eq. [5] reveals that if V_{oc} for an n-GaAs anode is 0.90V at photocurrent densities of 20 mA/cm², this may be entirely consistent with a V_{oc} controlled by thermionic emission, and does not necessarily imply the presence of surface states. We note that use of expression [5] is predicated on the assumption of rapid carrier capture available in a metal, and liquids might require substantially different descriptions for the over-barrier component than given in Eq. [4] and [5]. The main point is that there are several mechanisms for obtaining low photovoltages at the semiconductor/liquid interface which do not require postulation of charge in surface states. Thus, in cases where V_{oc} is found to be substantially lower than the bulk diffusion limit, a detailed analysis of the junction properties is necessary in order to identify the dominant recombination term at the particular semiconductor/liquid interface.

Results and Discussion

Comparison of theory and experiment: open-circuit photovoltage.—A comparison of the theoretical maximum V_{oc} values calculated from Eq. [3] with accurate experimental data indicates close agreement with ideal behavior in several systems. Listed in Table I are the calculated $V_{oc}(\text{max})$ from Eq. [3] and the experimental values of V_{oc} for semiconductor/liquid junctions where approximate estimates of the photocurrent density and the minority carrier diffusion length are possible. The quantitative comparison in Table I indicates that several of the common semiconductor/liquid junctions previously suggested to have severe limitations of V_{oc} due to Fermi-level pinning (3-5) actually display photovoltages which are close to the maximum possible values. As an example, p-type Si photocathodes have been stated to be Fermi-level pinned because V_{oc} is only 0.35-0.50V with laser excitation of up to 50 mW/cm² (11c, 21). At photocurrent densities of 25 mA/cm² on characterized silicon samples (Table I), we measure a V_{oc} of 0.48-0.52V for p-type Si in the cobaltocene^{+/0}/CH₃CN system. The theoretical value calculated from Eq. [3] (0.55V) is thus within 10% of the observed V_{oc} . Similar agreement between theory and experiment can be observed for n-Si/ferrocene junctions in CH₃OH solvent, where theory and data differ by less than 4% (9). We emphasize that the ideal values as-

sume no losses from any of the other mechanisms depicted in Scheme II, and entirely neglect any contribution from the thermionic emission component or from recombination at the back contact. In view of the fact that we have not searched for conditions to optimize the performance of our liquid junctions, we are highly encouraged by the close accord between ideal expectations and actual experimental results.

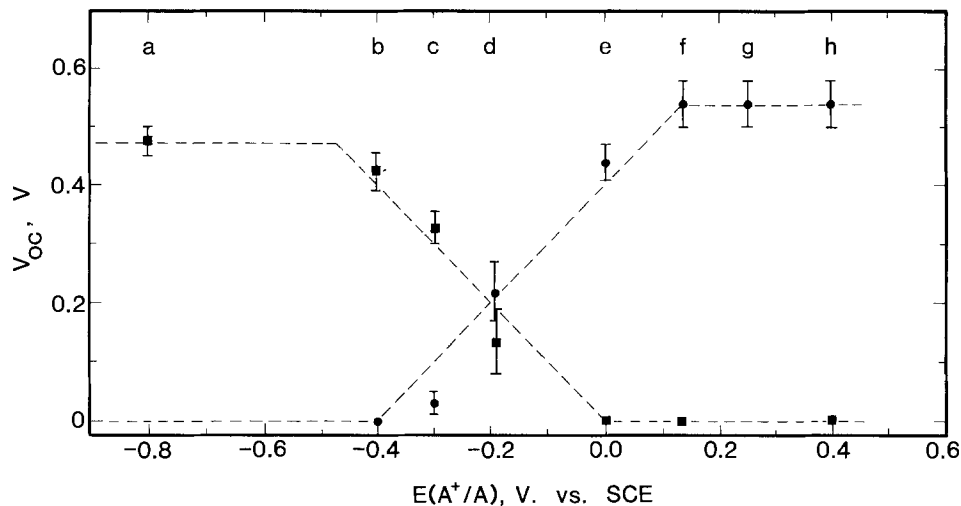
It is interesting to compare the V_{oc} values obtained on these Si/liquid systems to the V_{oc} values obtained with Si p-n junctions. It has been suggested that when no surface states are present at a semiconductor/liquid interface, that the value of V_{oc} would approach that of a p-n junction. At 35 mA/cm² photocurrent density, typical p-n junctions (NASA Si secondary standard cells) exhibit a V_{oc} of 0.55-0.57V, and active area efficiencies of 12.5% (22). The n-Si/CH₃OH/ferrocene^{+/0} photoelectrode system ($\rho \approx 5 \Omega\text{-cm}$) yields $V_{oc} = 0.52\text{-}0.56$ at 25 mA/cm², and total area efficiencies of 10.0% (without elimination of residual solution absorption or series resistance losses) (9). Thus, if similar substrates are employed, the photocurrent-voltage parameters attainable at the semiconductor/liquid interface compare favorably in V_{oc} to technologically advanced silicon solid-state systems.

A similar analysis can be applied to p-InP, where V_{oc} values of 0.80V have been obtained and assigned to surface states (3, 23). The bulk diffusion limit on V_{oc} for p-InP with an extremely long diffusion length ($L_n \approx 5 \mu\text{m}$) is approximately 0.9V. In the absence of leakage, and if the thermionic emission limit applies, a barrier height of $E_g - qV_p \approx 1.2$ eV might yield a $V_{oc}(\text{max})$ of only 0.8V. Although there is some discrepancy between the maximum bulk-diffusion-limited V_{oc} and the experimentally reported V_{oc} values, clearly indicating some other dominant recombination pathway at this junction, reference to Eq. [3] indicates that ideal junctions could not yield substantial (> 0.2V) improvements in V_{oc} over the reported data; thus, we conclude that surface-state pinning is not a severe limitation on the value of V_{oc} for p-InP cathodes in aqueous or nonaqueous solvents. This is consistent with the observation by Heller that the oxide on p-type InP will prevent surface states from significantly reducing the attainable V_{oc} value (24). Changes in stoichiometry at n-InP surfaces (owing to chemical reactions with the etchant, atmosphere, etc.) may prevent attainment of the maximum V_{oc} in photoanode-based systems, however, this does not necessarily mandate restrictions on V_{oc} for the p-InP system. The important concept is that Eq. [3] provides a quantitative framework to assess bulk *vs.* surface recombination effects at semiconductor/liquid interfaces.

For the systems listed in Table I (other than the Si-based junctions), it is clear that some improvement in experimental V_{oc} can be attained, and that bulk recombination does not limit the junction properties in all cases. Clearly, when surface etching is found to change junction properties, or when photocorrosion processes dominate the photovoltage, the surface will play an important role in determining the observed V_{oc} . In these cases, Fermi-level pinning may dominate the junction behavior, and this pinning can lead to lower than optimum V_{oc} values. However, Table I demonstrates that in some semiconductor/liquid systems, substantial improvements in V_{oc} could not be attained even if surface-state effects were minimized. We conclude that V_{oc} should be compared to the bulk-diffusion-limited value (and possibly to the ideal thermionic-emission-limited value) and not to the value of E_g , in order to ascertain a potential role for surface recombination at the semiconductor/liquid junction.

We also note that some reported values of V_{oc} significantly exceed the value calculated from the bulk diffusion limit (25, 26). We suggest that these particular interfaces must involve a parallel corrosion reaction which yields artificially high V_{oc} values. It is possible, of course, that the value of ϕ_b might actually exceed E_g if a fixed surface charge of the appropriate sign and density or an

Fig. 1. Open-circuit photovoltage vs. solution redox potential for n-Si and p-Si photoelectrodes in 1.0M KCl/CH₃OH solution. The redox couples used were: (a) cobaltocene^{2+/0}, (b) N,N'-dimethyl-4,4'-bipyridinium dichloride^{2+/+}, (c) N,N'-dibenzyl-4,4'-bipyridinium dibromide^{2+/+}, (d) decamethylferrocene^{2+/0}, (e) N,N,N',N'-tetramethylphenylenediamine^{+/0}, (f) dimethylferrocene^{+/0}, (g) ferrocene^{+/0} and (h) acetylferrocene^{+/0}. A tungsten-halogen bulb was used to provide light intensities which yielded short-circuit photocurrent densities of 25-30 mA/cm².



oxide were present at the interface. This might produce suppression of the J_{ob} component, and other mechanisms might then dominate the dark current. Under no conditions, however, can the dark current be less than the bulk diffusion limit of Eq. [2]; therefore, higher V_{oc} values than those calculated from Eq. [3] must indicate chemical reactions with the electrolyte.

It can also be seen that V_{oc} measurements at any accessible light intensity generally will not provide an accurate estimate of ϕ_b . It has been stated that measurement of V_{oc} by cyclic voltammetry indicates ϕ_b to within 0.1V (3, 4, 21). Furthermore, it has been stated that V_{oc} measurements to determine ϕ_b are analogous to photoresponse measurements in the solid state (17). Photoresponse measurements on Schottky barriers are based upon internal photoemission from the metal into the semiconductor, and are a direct measure of ϕ_b , not V_{oc} (12, 27). We also emphasize the distinctions in Scheme I between ϕ_b , V_s , and V_{oc} .¹ Even in the absence of temperature effects and of recombination kinetics which are nonlinear with light intensity, plots (on linear axes) of the logarithmic dependence of the V_{oc} vs. incident light intensity can appear to exhibit a saturation value which does not reflect ϕ_b . Within the framework described above, V_{oc} should be correlated with V_s or ϕ_b only with a detailed understanding of the interfacial kinetics at the particular semiconductor/liquid junction system.

Comparison of maximum photovoltages for n-type and p-type semiconductors: distinguishing between Fermi-level pinning and carrier inversion.—Having established the theoretical upper limit on V_{oc} , it still remains of interest to determine the mechanism for constant photovoltages over a wide range of solution potentials, $E(A^+/A)$. In this work, two methods have been applied to differentiate between carrier inversion and Fermi-level pinning. One method, discussed below, is based on measurement of the near-surface conductivity of the semiconductor. Additionally, if the sum of the maximum barrier heights for an n-type semiconductor, ϕ_{bn} , and a p-type semiconductor, ϕ_{bp} , in the same solvent should substantially exceed E_g , then Fermi-level pinning by a fixed distribution of surface states inherent to the semiconductor/solvent interface can be ruled out. An even more severe restriction is that the sum of the maximum V_{oc} for the n- and p-type combination should not exceed $(1/q)E_g$. In principle, differential capacitance data can be used to extract the value of E_{FB} ; however, frequency dependences of the measured capacitance generally complicate the analysis (29). The

For an ideal Si/Au Schottky diode (ideal diode quality factor, $n = 1.0$; dark current dominated by thermionic emission), V_{oc} at 30 mA/cm² photocurrent density will underestimate ϕ_b by 0.5V (28). Furthermore, light intensities of over 2000 W/cm² would be needed to obtain a 0.2V agreement between V_{oc} and ϕ_b . Lack of change in V_{oc} with increases in incident light intensity can reflect the onset of recombination processes in the bulk semiconductor or recombination at the interface, and need not imply that the flatband potential has been approached.

onset of photocurrent has also been used in some instances (5a, 30); however, it has not been unambiguously determined how to relate the kinetic parameters measured under these conditions (no well-defined solution redox potential, artificial suppression of dark current due to low concentrations of electroactive species) to the energetic parameter ϕ_b . We have thus carried out direct measurements of V_{oc} as a function of photocurrent density in various solutions (A^+/A) in both CH₃OH and CH₃CN solvent. The values of V_{oc} will determine lower limits of the sum of $\phi_{bn} + \phi_{bp}$ for the pairs of n- and p-type semiconductors.

For the redox couples (A^+/A), in order to insure rapid interfacial kinetics at the semiconductor/liquid interface, we choose outer sphere redox reagents which exhibit reversible electrochemistry at metal electrodes. Typical V_{oc} data for the n-type Si ($N_D = 9 \times 10^{14}$ cm⁻³), and p-type Si ($N_A = 2 \times 10^{15}$ cm⁻³) electrode system are depicted in Fig. 1. The incident light intensity is sufficient to produce photocurrent densities of 25-30 mA/cm² in all cases, and the solutions contain high concentrations of both forms of the redox couple (where possible). We observe V_{oc} values of 0.54 ± 0.02 V for n-Si in the ferrocene^{+/0} system, and 0.45 ± 0.02 V for p-Si in the cobaltocene^{+/0} system. Further changes in redox potential do not yield higher value of V_{oc} at this photocurrent density in methanol solvent.

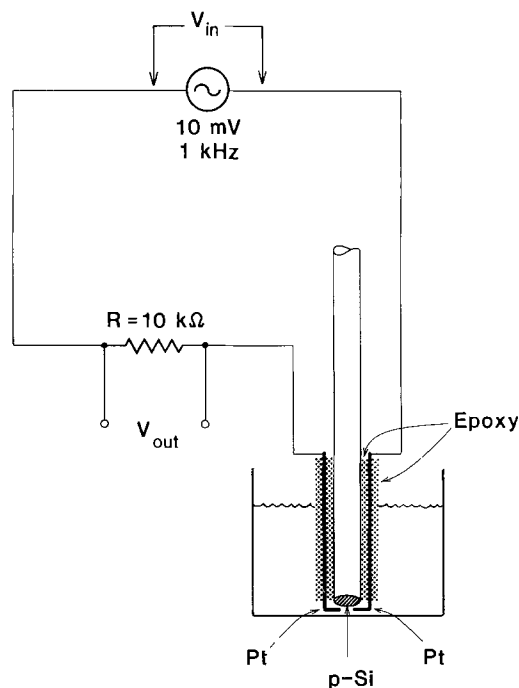
Similar photovoltage data, obtained by cyclic voltammetry for p-type Si in CH₃CN solvent (6a) and for n-type Si in C₂H₅OH (31) and CH₃CN solvent (6a), have been associated with ϕ_b , and have been used to propose Fermi-level pinning of the Si by surface states. In direct measurement of V_{oc} in a full cell configuration, at higher incident light intensities we observe $V_{oc} > 0.65$ V for n-Si and $V_{oc} > 0.55$ V for p-Si, for a sum of V_{oc} values of > 1.2 V (E_g for Si at 300 K = 1.12 eV). The fact that the sum of the V_{oc} values exceeds $(1/q)E_g$ contradicts the notion that severe restrictions on V_{oc} are present due to a fixed set of charges in surface states.

Data interpreted as evidence for surface states have been obtained previously for n- and p-type GaAs in CH₃CN solvent (5a). p-Type GaAs is reported to yield low V_{oc} values (0.2-0.3V) in both aqueous and nonaqueous solvents (32). In addition, constant (0.55-0.62V) photovoltages have been measured for n-type GaAs in CH₃CN solvent (33, 34). Therefore, it has been stated that n-GaAs and p-GaAs are Fermi-level pinned by surface states (4a, 5a). This is proposed to be consistent with the "1/3 rule" in semiconductor physics which empirically generalizes that surface states tend to reside at $E_{vb} - (1/3)E_g$ (12, 35). At light intensities ≈ 10 Suns, we observe V_{oc} values for n-type GaAs in ferrocene^{+/0} > 0.85 V, and V_{oc} values for p-type GaAs in the cobaltocene^{+/0} system of > 0.75 V. We thus conservatively estimate $\phi_{bn} + \phi_{bp} > 1.6$ eV, which is in excess of E_g for GaAs (1.42 eV). Additionally, the barrier height for n-GaAs in CH₃CN (based on V_{oc} measurements) has been proposed to be in excess of 1.1 eV (34),

implying that surface states should be within 0.3 eV of the valence band, and should thus prevent substantial V_{oc} values at p-GaAs. The observation of $V_{oc} > 0.75V$ in the p-GaAs/cobaltocene^{+/0} system is inconsistent with these predictions. We thus conclude that Fermi level pinning by charge in a fixed density of interface states cannot account for the V_{oc} behavior of GaAs in CH_3CN solvent, and does not necessarily prevent design of efficient semiconductor/liquid junctions with these systems (8a).

We also note that the V_{oc} values for n-Si, p-Si, n-GaAs, and p-GaAs interfaces can substantially exceed those reported for direct Schottky contacts to noble metals such as Pt or Au (12). This cannot be simply due to Fermi-level pinning of ϕ_b , with more favorable interfacial kinetics resulting in higher V_{oc} values at liquid junctions. This possibility is excluded by the observation of V_{oc} values for liquid systems which exceed ϕ_b values for Au Schottky barriers. In contrast to the V_{oc} values of 0.54V for n-Si and 0.46V for p-Si CH_3OH junctions, surface-state pinning in Schottky barriers yields V_{oc} values of only 0.30V for n-Si/Pt interfaces, and yields low barrier height, "ohmic" contacts for p-Si/Pt and p-Si/Au junctions. In addition, we note that analogies (4a, 21) to the commonly quoted Schottky Fermi-level pinning behavior for covalent vs. ionic solids (36) clearly do not apply to the semiconductor/liquid interface, as evidenced by data showing extensive regions of ideal behavior for V_{oc} vs. $E(A^+/A)$ for liquid junctions with n-Si, p-Si (37), p-InP (24), n-CdTe (21a), a-Si:H (8b), and other small E_g semiconductors. Pinning of the Fermi level in solid-state systems can be associated with changes in surface stoichiometry upon formation of the Schottky barrier (38). The recombination induced by surface states which pin the Fermi level can only lower V_{oc} from the theoretical value defined by the diffusion limit of Eq. [3]. Different chemical interactions at liquid interfaces [including formation of surface oxides (9a)] may allow formation of more ideal junctions, and will preclude proposed generalizations of V_{oc} or ϕ_b values observed in Schottky systems to semiconductor/liquid junctions.

Surface conductivity measurements to verify carrier inversion.—An obvious difference between Q_b and Q_{ss} is that increases in Q_b should produce increases in mobile



Scheme III. Diagram of cell arrangement for determination of near-surface conductivity of p-type silicon electrodes. The current response to an oscillating voltage signal applied between the two Pt wires is sensitive to the conductivity of the intermediate Si surface shunt. The method is only sensitive to mobile charge carriers. Thus, it will not detect charge in surface states, and will provide a method to distinguish between carrier inversion and Fermi-level pinning by surface states.

charge, while surface-state charge is essentially fixed. Thus, measurement of the near-surface conductivity should lead to a direct evaluation of the contribution of Q_b to the potential drop across the Helmholtz layer. Our measurement of the near-surface conductivity for p-Si photocathodes in CH_3CN solvent involves detection of the ac conductance between two Pt electrodes which are in close proximity to the semiconductor surface (Scheme III). If the semiconductor develops an inverted, conduct-

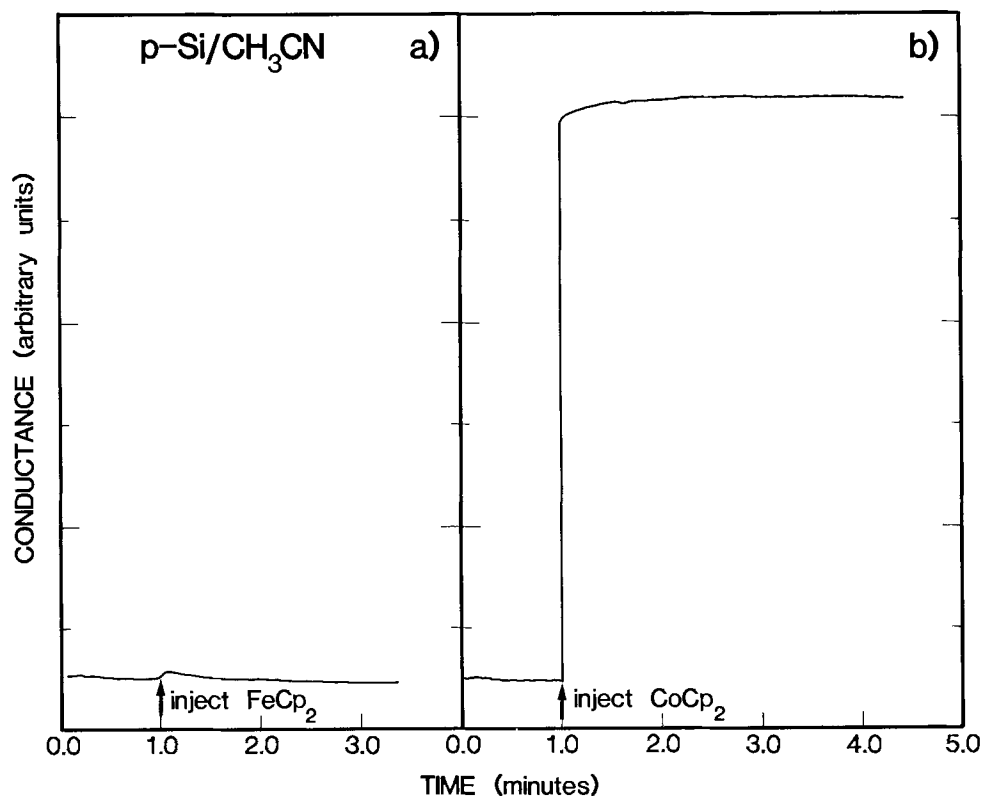


Fig. 2. Conductance between two Pt wires arranged as a Scheme III, under various experimental conditions. (a) Injection of 10 mM ferrocene into a 1.0 mM $LiClO_4/CH_3CN$ solution yields no detectable change in measured conductance. (b) Injection of 1.0 mM cobaltocene yields a large, sustained change in measured conductance owing to the shunt formed by injection of mobile surface charge from the cobaltocene into the p-Si surface. Under our circuit conditions, the relationship between the measured change in conductance and the electron concentration in the semiconductor can be approximated by $N_e = (\Delta G)/(Ae\mu)$. Assumption of a 5×10^{-7} cm thick inversion layer in our 0.2×0.3 cm electrode yields $A = 1 \times 10^{-7} \text{ cm}^2$, $l = 0.3$ cm, and thus $N_e \approx 10^{17} \text{ cm}^{-3}$ for a change in conductance of $5 \times 10^{-6} \Omega^{-1} \text{ cm}^{-1}$, as indicated.

ing surface layer, the conductance of the "cell" will change dramatically, and Q_b can thus be estimated directly. In our experiments, the reduced form of the redox couple A^+/A is injected into the solution, and the conductance between the Pt probe electrodes is monitored. This technique is similar to a method recently proposed by Gerischer (1c), which has roots in early field effect experiments on semiconductor surfaces. Because the semiconductor should be in depletion upon injection of the appropriate A, any increase in conductivity can be associated with the presence of mobile minority carriers near the surface, and would therefore imply the presence of carrier inversion.

Figure 2 displays the measured change in conductance between two Pt wires with a p-type Si surface ($N_A = 2 \times 10^{15} \text{ cm}^{-3}$) as the possible shunt. The experiments are performed in dry $\text{CH}_3\text{CN}/1.0 \text{ mM LiClO}_4$. Injection of ferrocene yields little change in the conductance, but injection of cobaltocene produces a pronounced, stable increase in the signal. Because we have injected a neutral molecule into the solution, yet have produced an increase in the measured conductance, we associate this phenomenon with the formation of an inversion layer at the p-type Si cathode. Ferrocene is not a sufficiently strong reductant to effect carrier inversion in p-Si, and no increase in conductivity occurs.

Analysis of the geometry of our cell allows a rough estimate of the carrier concentration in the inversion layer. Assuming a 50\AA inverted region, and a mobility of $480 \text{ cm}^2/\text{V}\cdot\text{s}$, an electron concentration of $10^{17} \text{ carriers}\cdot\text{cm}^{-3}$ is calculated. This is consistent with the presence of strong inversion in the semiconductor, as might be expected for a redox couple with a formal potential as negative as cobaltocene^{+/0}.

Both carrier inversion ($Q_b > Q_{ss}$) and Fermi-level pinning ($Q_b < Q_{ss}$) have been proposed to explain the photoelectrochemistry of p-type Si in CH_3CN solvent (2, 39). The similarity of V_{oc} values for the cobaltocene^{+/0} system in CH_3CN , and CH_3OH , the direct detection of mobile charge carriers at p-Si surfaces in CH_3CN , and the high efficiency of p-Si photocathodes in CH_3CN solvent (40) leads us to propose that carrier inversion is the dominant mechanism of developing charge across the Helmholtz layer for redox couples where $E(A^+/A) < -0.7 \text{ V}\cdot\text{vs. SCE}$ (40).² Carrier inversion can provide a situation where design of efficient photoelectrodes is possible for both carrier types in the same solvent, and is consistent with accurate current-voltage data using high quality Si semiconductor samples.

Conclusions

The ultimate limit on the open-circuit photovoltage at a semiconductor/liquid interface can reflect the bulk recombination kinetics of the semiconductor itself. A quantitative treatment of these kinetics indicates that typical electrode samples may exhibit open-circuit photovoltages substantially below the value of the semi-

² Differential capacitance measurements have been suggested to rule out carrier inversion for p-Si in CH_3CN solvent (39) because the apparent E_{FB} position was found to change before a band bending of $(1/2)E_b$ had been achieved. In this analysis, it is stated that qV_p of the p-Si ($N_A = 2 \times 10^{15} \text{ cm}^{-3}$) is 0.05 eV . However, for this doping level, we calculate $qV_p = 0.24 \text{ eV}$ (12, 13), and can thus use the original data to place E_{vb} at $+0.4 \text{ V}\cdot\text{vs. SCE}$. At this doping level, weak inversion could onset at $-0.15 \text{ V}\cdot\text{vs. SCE}$, strong inversion could then occur at $-0.4 \text{ V}\cdot\text{vs. SCE}$, and the data might be consistent with carrier inversion. Ideal behavior would predict that the reported analysis (39) of a straight line of slope ~ 0.5 for E_{FB} vs. $E(A^+/A)$ might actually be properly described as two distinct regions, each exhibiting a linear dependence of E_{FB} vs. $E(A^+/A)$. Other workers have noted the anomalous behavior of differential capacitance data for p-Si in CH_3CN (6a), and additional data might be warranted to unambiguously describe the dependence of ϕ_s upon potential in this system. We also note that at the highest measured value of V_{ss} , $q(\phi_s)$ is approximately 0.9 eV (if the proper E_{vb} is employed). Thus, if surface states do pin the Fermi level, they must be very close to E_{cb} , and should not appreciably limit V_{oc} . This notion is consistent with the excellent agreement between theory and experiment in Table I, and is strongly supported by other results in our laboratory, which describe the design of efficient p-Si-based photoelectrochemical cells in nonaqueous solvents (40).

conductor bandgap, yet not possess any deleterious effects assignable to Fermi-level pinning. Lower than ideal open-circuit photovoltages may occur because of poor diffusion lengths in the bulk semiconductor, classical carrier emission over the surface barrier, or leakage across low barrier chemical imperfections at the semiconductor/liquid interface. Characterization and control of bulk semiconductor properties is thus crucial to obtaining meaningful data at the semiconductor/liquid interface. Saturation in open-circuit photovoltage with increases in incident light intensity can reflect recombination kinetics of the semiconductor, and may not yield the barrier height. Constant values of the open-circuit photovoltage with changes in solution redox potential can be consistent with carrier inversion at ideal semiconductor/liquid interfaces. The observation of large photovoltages for n- and p-type-based semiconductor interfaces in the same solvent can rule out pinning by a fixed density of charged surface states as the mechanism for obtaining constant photovoltages. Direct evidence for mobile minority charge carriers in the semiconductor can be obtained by ac conductivity techniques, and verifies the presence of an inversion layer for p-type Si cathodes in nonaqueous solvents. Application of the "1/3 bandgap" rule to p-type GaAs/liquid junctions is inappropriate, and in general, behavior of liquid contacts may not correlate with measured properties of Schottky barriers. Fermi-level pinning will prevent design of the most efficient semiconductor/liquid junctions, while carrier inversion may lead to interfaces which operate near the theoretical diffusion-limited photovoltage.

Acknowledgment

We acknowledge helpful discussions with C. Gronet and R. Bube of Stanford University, as well as G. Cogan, J. Gibbons, and G. Moddel of SERA Solar Corporation, Santa Clara, California. This work was partially supported by the NSF through Stanford Center for Materials Research. N.S.L. also wishes to thank the IBM Corporation for generous support through receipt of a Young Faculty Development Award and support from NSF grant CHE-8312692.

Manuscript submitted Dec. 2, 1983; revised manuscript received Jan. 24, 1984.

REFERENCES

- (a) J. Gobrecht and H. Gerischer, *Ber. Bunsenges, Phys. Chem.*, **82**, 1331 (1978); (b) W. Kautek and H. Gerischer, *ibid.*, **84**, 645 (1980); (c) C. D. Jaeger, H. Gerischer, and W. Kautek, *ibid.*, **86**, 20 (1982).
- (a) J. A. Turner, J. Manassen, and A. J. Nozik, *Appl. Phys. Lett.*, **37**, 488 (1980); (b) ACS Symposium Series 146, "Photo effects at semiconductor—Electrolyte Interfaces," A. J. Nozik, Editor, p. 253, American Chemical Society, Washington, DC (1981).
- J. A. Baglio, G. S. Calabrese, D. J. Harrison, E. Kamieniecki, A. J. Ricco, M. S. Wrighton, and G. D. Zoski, *J. Am. Chem. Soc.*, **105**, 2246 (1983).
- (a) A. J. Bard, A. B. Bocarsly, F.-R. F. Fan, E. G. Walton, and M. S. Wrighton, *ibid.*, **102**, 3671 (1980); (b) L. F. Schneemeyer and M. S. Wrighton, *ibid.*, **101**, 6496 (1979).
- (a) A. J. Bard, F.-R. F. Fan, A. S. Gioda, G. Nagasubramanian, and H. S. White, *Discuss. Faraday Soc.*, **70**, 19 (1980); (b) F.-R. F. Fan, H. S. White, B. L. Wheeler, and A. J. Bard, *J. Am. Chem. Soc.*, **102**, 5142 (1980); (c) R. E. Malpas, K. Itaya, and A. J. Bard, *ibid.*, **103**, 1622 (1981); (d) A. J. Bard and S. N. Frank, *ibid.*, **97**, 7427 (1975); (e) P. A. Kohl and A. J. Bard, *ibid.*, **99**, 7531 (1977); (f) H. S. White, H. D. Abruna, and A. J. Bard, *This Journal*, **129**, 265 (1982); (g) D. Laser and A. J. Bard, *J. Am. Chem. Soc.*, **80**, 459 (1976).
- H. J. Byker, V. E. Wood, and A. E. Austin, *This Journal*, **129**, 1983 (1982); (b) L. Nadjo, *J. Electroanal. Chem.*, **108**, 29 (1980); (c) J. L. Shulfort and A. M. Batirole, *Rev. Phys. Appl.*, **15**, 1209 (1980).
- (a) A. J. Nozik, D. S. Boudreaux, R. R. Chance, and F. Williams, *Adv. Chem. Ser.*, **184**, 155 (1980); (b) D. S.

- Boudreaux, F. Williams, and A. J. Nozik, *J. Appl. Phys.*, **51**, 2158 (1981).
8. (a) C. M. Gronet and N. S. Lewis, *Appl. Phys. Lett.*, **43**, 115 (1983); (b) C. M. Gronet, N. S. Lewis, G. W. Cogan, J. F. Gibbons, G. R. Moddel, and H. Weismann, *This Journal*, To be published.
 9. (a) C. M. Gronet, N. S. Lewis, G. Cogan, and J. Gibbons, *Proc. Natl. Acad. Sci. USA*, **80**, 1152 (1983); (b) N. S. Lewis, R. Dominguez, C. M. Gronet, C. M. Lieber, M. D. Rosenblum, G. W. Cogan, J. F. Gibbons, and G. R. Moddel, in "Electrocatalysis," J. McIntyre, Editor, The Electrochemical Society Softbound Proceedings Series, Pennington, NJ, To be published.
 10. (a) A. B. Ellis, S. W. Kaiser, J. M. Bolts, and M. S. Wrighton, *J. Am. Chem. Soc.*, **99**, 2893 (1977); (b) K. D. Legg, A. B. Ellis, J. M. Bolts, and M. S. Wrighton, *Proc. Natl. Acad. Sci. USA*, **74**, 4116 (1977); (c) M. S. Lin, N. Hung, and M. S. Wrighton, *J. Electroanal. Chem.*, **135**, 121 (1982).
 11. (a) H. S. White, F.-R. F. Fan, and A. J. Bard, *This Journal*, **128**, 1045 (1981); (b) P. A. Kohl and A. J. Bard, *ibid.*, **126**, 59 (1979); (c) A. B. Boscarsly, D. C. Bookbinder, R. N. Dominey, N. S. Lewis, and M. S. Wrighton, *J. Am. Chem. Soc.*, **102**, 3683 (1980).
 12. (a) S. M. Sze, "Physics of Semiconductor Devices," 2nd Ed., John Wiley and Sons, New York (1981); (b) A. L. Fahrenbruch and R. H. Bube, "Fundamentals of Solar Cells," Academic Press, New York (1983); (c) A. J. Hovel, "Solar Cells," Vol. 11 of Semiconductors and Semimetals, Academic Press, New York (1975); (d) S. J. Fonach, "Solar Cell Device Physics," Academic Press, New York (1981).
 13. (a) V. A. Myamlin and Yu. V. Pleskov, "Electrochemistry of Semiconductors," Plenum Press, New York (1967); (b) W. Shockley, *Bell Syst. Tech. J.*, **28**, 435 (1949); (c) "Electrons and Holes in Semiconductors," Van Nostrand, Princeton, NJ (1950); (d) C. T. Sah, R. N. Noyce, and W. Shockley, *Proc. IRE*, **45**, 1128 (1957); (e) W. Shockley and H. J. Queisser, *J. Appl. Phys.*, **26**, 535 (1955); (f) M. Wolf, *IEEE Trans. Electron Devices*, **ed-27**, 751 (1980); (g) J. C. Fossum, *Solid State Electron.*, **19**, 269 (1976); (h) W. Van Roosbroeck, *J. Appl. Phys.*, **26**, 380 (1955).
 14. H. Gerischer, *J. Electroanal. Chem.*, **58**, 263 (1975).
 15. S. J. Fonash, *J. Appl. Phys.*, **47**, 3597 (1976).
 16. (a) M. S. Wrighton, *Acc. Chem. Res.*, **12**, 303 (1979); (b) L. F. Schneemeyer and M. S. Wrighton, *J. Am. Chem. Soc.*, **102**, 6964 (1980).
 17. (a) J. A. Baglio, G. S. Calabrese, E. Kamieniecki, R. Kershaw, C. P. Kubiak, A. J. Ricco, A. Wold, M. S. Wrighton, and G. C. Zoski, *This Journal*, **129**, 1961 (1982); (b) A. Aruchamy and M. S. Wrighton, *J. Phys. Chem.*, **84**, 2848 (1980); (c) S. Tanaka, J. A. Bruce, and M. S. Wrighton, *ibid.*, **85**, 3778 (1981).
 18. W. R. Brandhorst, Jr., "Terrestrial-Photovoltaic Measurement Procedures," ERDA-NASA Technical Report 1022-77116, June 1977.
 19. A. Heller, K. C. Chang, and B. Miller, *J. Am. Chem. Soc.*, **100**, 684 (1978).
 20. W. A. Anderson, S. M. Vernon, A. E. Delahoy, J. K. Kim, and D. Mathe, *J. Vac. Sci. Technol.*, **13**, 1158 (1976).
 21. (a) J. A. Bruce, T. Murahashi, and M. S. Wrighton, *J. Phys. Chem.*, **86**, 1152 (1982); (b) R. N. Dominey, N. S. Lewis, D. C. Bookbinder, J. A. Bruce, and M. S. Wrighton, *J. Am. Chem. Soc.*, **104**, 467 (1982); (c) D. C. Bookbinder, J. A. Bruce, N. S. Lewis, R. N. Dominey, and M. S. Wrighton, *Proc. Natl. Acad. Sci. USA*, **77**, 6280 (1980).
 22. R. B. Godfrey and M. A. Green, *Appl. Phys. Lett.*, **34**, 790 (1979).
 23. R. N. Dominey, N. S. Lewis, and M. S. Wrighton, *J. Am. Chem. Soc.*, **103**, 1261 (1981).
 24. A. Heller, B. Miller, H. J. Lewerenz, and K. J. Bachmann, *ibid.*, **102**, 6555 (1980).
 25. R. Noufi, D. Tench, and L. F. Warren, *This Journal*, **128**, 2596 (1981).
 26. Y. Kamprakash, S. Basu, and D. N. Bose, *J. Indian Chem. Soc.*, **58**, 153 (1981).
 27. D. L. Pulfrey and R. F. McQuat, *Appl. Phys. Lett.*, **24**, 167 (1974).
 28. J. P. Ponpon and P. Siffert, *J. Appl. Phys.*, **47**, 3248 (1976).
 29. (a) H. S. White, F.-R. F. Fan, and A. J. Bard, *This Journal*, **128**, 1045 (1981); (b) G. Nagasubramanian, B. L. Wheeler, G. A. Hope, and A. J. Bard, *ibid.*, **130**, 385 (1983); (c) E. C. Dutiot, R. L. Van Meirhaeghe, F. Cardon, and W. P. Gomes, *Ber. Bunsenges. Phys. Chem.*, **79**, 1206 (1975); (d) LaFlere, R. L. Van Meirhaeghe, F. Cardon, and W. P. Gomes, *Surf. Sci.*, **59**, 401 (1976); (e) J. N. Chazalviel, *This Journal*, **129**, 963 (1982).
 30. F.-R. F. Fan, H. S. White, B. L. Wheeler, and A. J. Bard, *J. Am. Chem. Soc.*, **102**, 5142 (1980).
 31. A. B. Boscarsly, E. G. Walton, M. G. Bradley, and M. S. Wrighton, *J. Electroanal. Chem.*, **100**, 283 (1979).
 32. F.-R. F. Fan and A. J. Bard, *J. Am. Chem. Soc.*, **102**, 3677 (1980).
 33. P. A. Kohl and A. J. Bard, *This Journal*, **129**, 603 (1979).
 34. J. M. Bolts and M. S. Wrighton, *J. Am. Chem. Soc.*, **100**, 5257 (1978).
 35. C. A. Mead and W. G. Spicer, *Phys. Rev. Lett.*, **10**, 471 (1963).
 36. McGill, *J. Vac. Sci. Technol.*, **11**, 936 (1974).
 37. A. Heller, H. J. Lewerenz, and B. Miller, *J. Am. Chem. Soc.*, **103**, 200 (1981).
 38. R. J. Williams, *J. Vac. Sci. Technol.*, **8**, 929 (1981).
 39. G. Nagasubramanian, B. L. Wheeler, F.-R. F. Fan, and A. J. Bard, *This Journal*, **129**, 1742 (1982).
 40. C. M. Lieber, C. M. Gronet, and N. S. Lewis, *Nature (London)*, To be published.
 41. B. A. Parkinson, A. Heller, and B. Miller, *This Journal*, **126**, 954 (1979).
 42. J. Gobrecht, H. Tributsch, and H. Gerischer, *ibid.*, **125**, 2085 (1978).
 43. G. Kline, K. Kam, D. Canfield, and B. A. Parkinson, *Solar Energy Mater.*, **4**, 301 (1981).
 44. (a) J. A. Wilson and A. D. Yoffe, *Adv. Phys.*, **18**, 193 (1969); (b) W. Kautek, H. Gerischer, and H. Tributsch, *This Journal*, **127**, 2471 (1980); (c) F. Levy, Ph. Schmid, and H. Berger, *Philos. Mag.*, **34**, 1129 (1976).

Electrode Heat Balances of Electrochemical Cells

Application to Water Electrolysis

Y. Ito*

Department of Nuclear Engineering, Faculty of Engineering, Kyoto University, Sakyo-ku, Kyoto 606, Japan

H. Kaiya and S. Yoshizawa*

Department of Industrial Chemistry, Faculty of Engineering, Kyoto University, Sakyo-ku, Kyoto 606, Japan

S. K. Ratkje and T. Førland

Laboratory of Physical Chemistry, Norwegian Institute of Technology, University of Trondheim, Trondheim, Norway

ABSTRACT

Irreversible thermodynamics has been used to describe electrode heat balances of electrochemical cells. The specific example of electrolysis of water in molten sodium hydroxide is chosen for the purpose of illustration. Experimental data are presented for this system. The importance of a distinction between time and charge-dependent changes in entropy is pointed out. Only changes of the last type contribute to cell EMF's. The relation between EMF of thermocells, the temperature coefficient of an isothermal cell, and the electrode heat balances are discussed particularly. Results show a reasonably good agreement between theoretical predictions and experimental observations. With partial pressures of hydrogen and water vapor in the cathodic compartment of 0.8 and 0.2 atm, respectively, 63 kJ is evolved, and with partial pressures of oxygen and water vapor in the anodic compartment of 0.8 and 0.2 atm, respectively, 72 kJ is absorbed during the passage of 1F of current at 623 K.

When it is desired to improve the energy conversion efficiency or the temperature control of an electrochemical reactor, it is important to consider the overall energy flow through the reactor.

For example, if heat is not supplied to electrodes where an endothermic process takes place, a drop in temperature may result. This may lead to an increase in cell voltage, or, in molten salt electrochemical reactors, even freezing of the electrolyte. Conversely, if heat is not conducted from electrodes where exothermic processes take place, a rise in temperature may result. This may lead to a breakdown of the cell or electrolyte boiling. In order to maintain constant temperature at the electrodes, it is helpful to know the magnitude of the reversible heat changes during electrolysis. This includes the Peltier heat for each electrode (1).

It is the purpose of this article to show how reversible heat changes are related to electromotive forces of thermogalvanic cells, and how they can be estimated from EMF measurements. Experiments related to electrolysis of water in NaOH (1) are used to illustrate the theory, since this electrolytic process is promising for the future hydrogen energy system and the accumulation of thermodynamic and electrochemical data are desired for the further engineering development. The results are obtained using nonequilibrium thermodynamics (2). The approach by Førland and Ratkje (2) is chosen, since this describes electrochemical cells directly by local energy conversion processes. This is in contrast to conventional approaches which describe EMF by local electric potential differences due to charge separation (3, 4). The main features of the theory of Førland and Ratkje, in addition to the above, are (i) the use of single ion activities or electrochemical potentials is avoided. This is because energy changes are only defined and measurable with respect to electroneutral processes. (ii) The components of the system are components according to the phase rule. Components involved in electrode reactions are included. This ensures independent mass variables. (iii) The electric current is an independent flux of the system, since this can be controlled externally. (iv) The frame of reference is the wall of the cell container.

For isothermal systems, the superposition of time (diffusion) and charge-(migration) dependent processes has been pointed out (5, 6). In the nonisothermal case, we will

*Electrochemical Society Active Member.

show that a similar superposition is essential when characterizing entropy changes. This superposition separates irreversible (time dependent) and reversible heat changes. Furthermore, the nonisothermal transport processes will be described without using single ion entropies or electronic entropies.

Entropy Production by Heat, Mass and Charge Transfer in a Continuous System

According to Førland and Ratkje (2) and Ratkje (7), the entropy production θ per unit volume and unit time at any point in the electrochemical system can be written

$$\theta = \nabla \left(\frac{1}{T} \right) J_{q'} - \frac{1}{T} \sum_{i=1}^k \nabla \mu_{iT} J_i - \frac{1}{T} \nabla \phi^{\text{obs}} I \quad [1]$$

Current density is assumed to be constant through the system, so no local charge accumulation takes place. $J_{q'}$ is the measurable heat flux. $J_{q'}$ is equal to the heat flow which is required from two heat reservoirs on either side of a volume element to keep constant temperatures. J_i denotes the component fluxes of the k independent components, and I is the electric current density. The chemical potential gradient $\nabla \mu_{iT}$ contains only pressure and composition dependent terms. The symbol $\nabla \phi^{\text{obs}}$ denotes the differential EMF, measured with defined identical electrodes across the volume element. By integration across all volume elements the EMF of the system is obtained. This is illustrated in Fig. 1. T is the absolute temperature.

Fluxes of some components which form parts of the electrodes are completely coupled to the electric current

$$J_i = k_i \cdot I \quad [2]$$

where k_i is an integer or ratio of integers. By inserting this condition into Eq. [1], we obtain

$$\theta = \nabla \left(\frac{1}{T} \right) J_{q'} - \frac{1}{T} \sum_{i=1}^n \nabla \mu_{iT} J_i - \frac{1}{T} \left(\nabla \phi^{\text{obs}} + \sum_{i=n+1}^k \nabla \mu_{iT} k_i \right) I \quad [3]$$

This defines the electric force conjugate to the current as

$$\frac{1}{T} \nabla \phi = \frac{1}{T} \left(\nabla \phi^{\text{obs}} + \sum_{i=n+1}^k \nabla \mu_{iT} k_i \right) \quad [4]$$

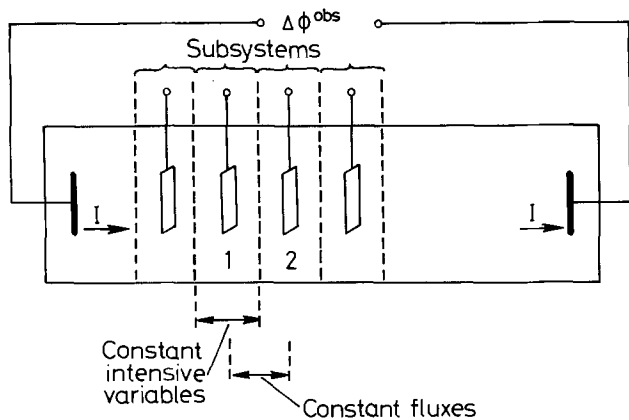


Fig. 1. Scheme of the electrochemical system

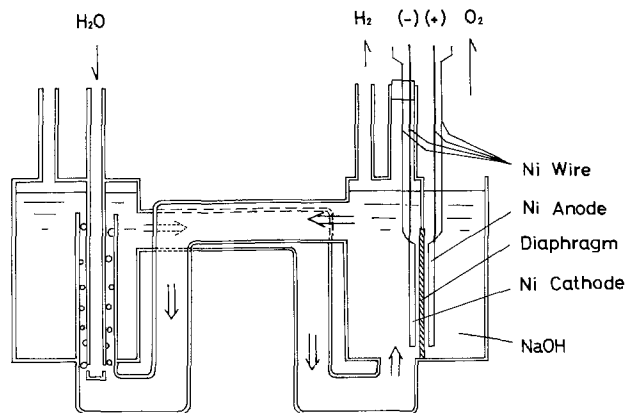
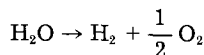


Fig. 2. Prototype cell for water vapor electrolysis

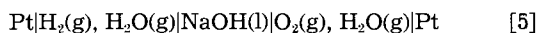
The quantity $\nabla\phi$ can be regarded as the effective electric potential gradient. The expression [3] for the entropy production can be used to define independent fluxes. This will be done below for our special systems, the water electrolysis system developed by Ito and co-workers (8, 9), and electrochemical systems related to this. The use of equations for specific systems is chosen on purpose to simplify reading. Generalizations to include more components are straightforward and will not give further physical insight.

The System

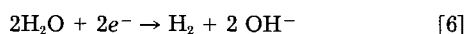
The electrolysis of water can be efficiently performed in the temperature range 330°-450°C by dissolving water vapor in molten sodium hydroxide (8, 9). The overall reaction is



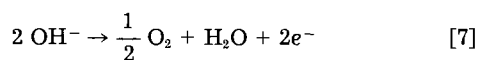
This cell can be expressed as



The cathodic and anodic reactions are written, respectively, as



and



One possible cell construction is shown in Fig. 2. The cell is made entirely of nickel, and, in order to avoid bipolar effects, the inside of the anodic compartment is covered by an α -alumina wall. A porous α -alumina plate is used as a diaphragm. Water vapor is supplied to the left-

hand side of the cell, and the electrolyte saturated with water circulates by a gas lift of both water vapor bubbles and evolved hydrogen gas in the direction given by the arrows in the figure.

During electrolysis heat will be evolved at the cathode and absorbed at the anode. In order to quantify this, the electrodes have been studied separately in the thermocell shown in Fig. 3: A gas mixture of either H_2O and H_2 or H_2O and O_2 was used for the right-hand side Pt-electrode of this figure. A sodium/ β -alumina electrode at temperature T_1 was used as the constant reference electrode. The temperature T_2 of the gas electrode was varied. Porous α -alumina was used as a bridge between the two half cells. By subtracting the resulting EMF for two values of T_2 , the EMF of the following thermocells are obtained

$$(T) Pt|H_2O(g), H_2(g)|NaOH(l)|H_2(g), H_2O(g)|Pt (T + \Delta T) \quad [8]$$

$$(T) Pt|H_2O(g), O_2(g)|NaOH(l)|O_2(g), H_2O(g)|Pt (T + \Delta T) \quad [9]$$

Fluxes and Forces of the Experimental System of Fig. 2 and 3

Apart from the gas components forming the electrodes ($H_2(g)$, $H_2O(g)$, $O_2(g)$), there is one component present in these systems, *i.e.*, NaOH. Using the general expression [3] for the entropy production, this gives for the fluxes and forces of the system

$$J_{q'} = L_{11}\nabla\left(\frac{1}{T}\right) - L_{12}\frac{1}{T}\nabla\mu_{1T} - \frac{1}{T}L_{13}\nabla\phi \quad [10]$$

$$J_{NaOH} = L_{21}\nabla\left(\frac{1}{T}\right) - L_{22}\frac{1}{T}\nabla\mu_{1T} - \frac{1}{T}L_{23}\nabla\phi \quad [11]$$

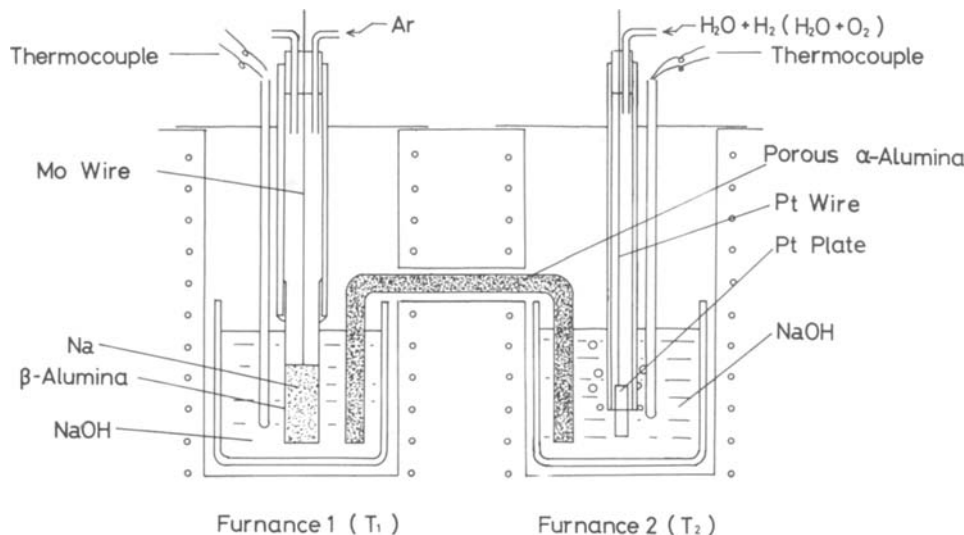


Fig. 3. Thermogalvanic cell arrangement.

$$I = L_{31} \nabla \left(\frac{1}{T} \right) - L_{32} \frac{1}{T} \nabla \mu_{1T} - \frac{1}{T} L_{33} \nabla \phi \quad [12]$$

The problem is to find the meaning of the coefficients L_{ij} in each case. Furthermore, $\nabla \phi$ needs clarification when the electrodes are different, e.g., during electrolysis.

One simplification may be introduced: we assume that the solubility of all gas components H_2O , H_2 , and O_2 is so low (9) that the chemical potential, μ_{1T} , of NaOH is not significantly influenced by these components, so that $\nabla \mu_{1T} = 0$.

Superposition of Time and Charge Dependent Processes

For the interpretation of L_{ij} , it is important to acknowledge that the heat transferred consists of one time-dependent term $\Delta q'(t)$ and one charge-dependent term $\Delta q'(Q)$. This superposition can be seen as follows: by elimination of $\nabla \phi$ in Eq. [10] by Eq. [12], and setting $\nabla \mu_{1T} = 0$, we obtain

$$J_{q'} = \left(L_{11} - \frac{L_{13}L_{31}}{L_{33}} \right) \nabla \left(\frac{1}{T} \right) + \frac{L_{13}}{L_{33}} \cdot I \quad [13]$$

The condition $\nabla \mu_{1T} = 0$ corresponds to the situation in which no concentration and/or pressure gradient exists in the system. The total heat transferred ($\Delta q'$) and the charge transferred (ΔQ) during a short time interval, Δt , are $J_{q'} \cdot \Delta t$ and $I \cdot \Delta t$ respectively. Thus

$$\Delta q' = \left(L_{11} - \frac{L_{13}L_{31}}{L_{33}} \right) \nabla \left(\frac{1}{T} \right) \cdot \Delta t + \frac{L_{13}}{L_{33}} \cdot \Delta Q \quad [14]$$

This equation shows that the transferred heat consists of one time-dependent term, which is the first term on the right-hand side, and one charge-dependent term. The latter is time independent, its sign reversed by reversing the sign of ΔQ . This part of the heat transfer is reversible. The heat balance is

$$\Delta q' = \Delta q'(t) + \Delta q'(Q) \quad [15]$$

The presence of gradients in chemical potentials will not change the general form (15), but will merely give an additional contribution to both the time-dependent and charge-dependent parts of $\Delta q'$.

The entropy change per Faraday corresponding to $\Delta q'(Q)$ is

$$S'(Q) = \frac{q'(Q)}{T \cdot \Delta Q} \quad [16]$$

The heat $\Delta q'(Q)$ will contain the heat associated with the electrode reactions, but $\Delta q'(Q)$ will also contain contributions from the reversible transport process through the electrolyte and metal leads. This means that the coefficient ratio L_{13}/L_{33} is also determined by the mechanism of transport

$$L_{13}/L_{33} = TS'(Q) \quad [17]$$

Furthermore, by expressing $\nabla \phi$ by Eq. [12], we obtain

$$(\nabla \phi)_{I=0}, \nabla \mu_{1T=0} = - \frac{L_{31}}{L_{33}} \frac{\nabla T}{T} \quad [18]$$

By application of Onsager relations, we see that the coefficient ratio (17) determines the electric work that can be obtained from the system

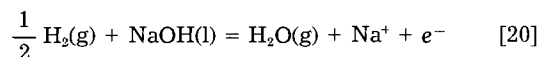
$$(\Delta \phi)_{I=0}, \nabla \mu_{1T=0} = -\Delta T S'(Q) \quad [19]$$

For a temperature difference ΔT , it is thus only the heat $\Delta T S'(Q)$ which can be reversibly converted to electric work or vice versa. Equation [19] will next be used to find contributions to EMF or electric work done in the outer circuit.

Reversible Entropy Changes during Electrolysis or EMF Measurements

Consider first the thermocell given by Eq. [8], and a small volume element, as given by Fig. 1. When electrons

pass from left to right in the outer circuit, the following reaction takes place at the left-hand side electrode



The entropy change due to formation of $H_2O(g)$ and removal of $H_2(g)$ and $NaOH(l)$ is equal to

$$\Delta S_1 = S_{H_2O(g)} - \frac{1}{2} S_{H_2(g)} - t_{NaOH} S_{NaOH}^{\circ} \quad [21]$$

where $t_{NaOH} = t_{Na^+}$ (transport number of Na^+) is the number of moles of NaOH transferred from left to right per Faraday. All entropies on the right-hand side of Eq. [21] are state functions. By inserting the experimental values of $P_{H_2O} = 0.2$ atm and $P_{H_2} = 0.8$ atm and using literature data (10), we obtain the entropy change of the left-hand region of the cell per Faraday transferred

$$\Delta S_1 = 150.0 JK^{-1}F^{-1} - t_{NaOH} S_{NaOH(l)}^{\circ} \quad [22]$$

This is the entropy change of the left-hand part of the system due to composition changes caused by charge transfer. Since this is a reversible entropy change, it is equal to the entropy transferred from a heat reservoir at the left-hand side, $S'_{(Q1)}$, minus the transported entropy $\bar{S}_{(Q)}$, due to the charge transport process in the electrolyte. The term corresponding to $\bar{S}_{(Q)}$ due to transport of charge in metallic leads will be neglected here (Peltier heat for metals is small). The terminology is according to Agar (4). The entropy balance is shown in Fig. 4. We have

$$\Delta S_1 = S'_{(Q1)} - \bar{S}_{(Q)} \quad [23]$$

or

$$S'_{(Q1)} = \Delta S_1 + \bar{S}_{(Q)} \quad [24]$$

For the present system, measurements show that $S'_{(Q1)}$ is positive, which means that a negative Peltier heat $TS'_{(Q)}$ is transferred reversibly over a temperature interval of dT . For dT positive, electric work must be supplied, i.e., the EMF is negative. Combining Eq. [18], [24], and [22], one obtains in the one dimensional case

$$\frac{d\phi_1}{dT} = -(\Delta S_1 + \bar{S}_{(Q)}) \quad [25]$$

$$\frac{d\phi_1}{dT} = -150.0 JK^{-1}F^{-1} + t_{NaOH(l)} S_{NaOH(l)}^{\circ} - \bar{S}_{(Q)} \quad [26]$$

The second type of cell investigated, given by Eq. [9],

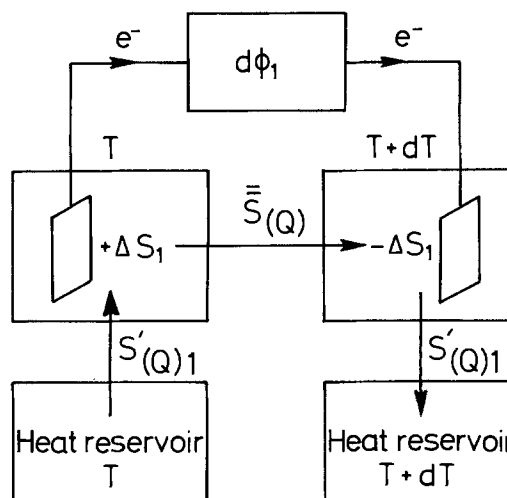
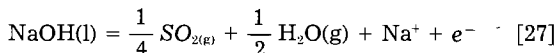


Fig. 4. Entropy balance for a thermogalvanic cell. ΔS_1 is entropy change due to change in composition. ΔS_1 is obtained from changes in state functions. $\bar{S}_{(Q)}$ is transported entropy caused only by the transport of electric charge in the electrolyte. $\bar{S}_{(Q)}$ depends on mechanism of charge transport. $S'_{(Q1)}$ is entropy supplied to or from heat reservoirs in equilibrium with sections of the cell. $S'_{(Q1)} \cdot T$ is the Peltier heat.

can be treated in a similar way. The reaction at the left-hand side electrode is now



The entropy change at the left-hand side of the cell is

$$\Delta S_2 = \frac{1}{4} S_{\text{O}_{2(\text{g})}} + \frac{1}{2} S_{\text{H}_2\text{O(g)}} - t_{\text{NaOH}} S_{\text{NaOH}}^\circ \quad [28]$$

where the last term is the same as the last term in Eq. [22]. With $P_{\text{O}_2} = 0.8$ atm and $P_{\text{H}_2\text{O}} = 0.2$ atm, we have

$$\Delta S_2 = 170.2 \text{ JK}^{-1} \text{ F}^{-1} - t_{\text{NaOH}} S_{\text{NaOH}}^\circ \quad [29]$$

An entropy balance gives (compare Eq. [23])

$$S'_{(\text{Q})2} = \Delta S_2 + \bar{S}_{(\text{Q})} \quad [30]$$

where $\bar{S}_{(\text{Q})}$ has the same value as in Eq. [24]. Thus, the thermoelectric EMF $d\phi_2/dT$ is given by

$$\begin{aligned} \frac{d\phi_2}{dT} &= -(\Delta S_2 + \bar{S}_{(\text{Q})}) \\ &= -170.2 \text{ JK}^{-1} \text{ F}^{-1} + t_{\text{NaOH}} S_{\text{NaOH}}^\circ - \bar{S}_{(\text{Q})} \end{aligned} \quad [31]$$

This completes the analysis of the heat change at the separate electrodes and how this change can be obtained experimentally by EMF measurements. When we need to know the details of the thermoelectric power, additional experiments must be performed to obtain t_{NaOH} and $\bar{S}_{(\text{Q})}$, but, at present, the analysis given above is sufficient for our purpose.

It remains to be shown how the thermoelectric powers of the thermocells [8] and [9] are related to the EMF of the formation cell [5].

Thermogalvanic Electric Power and Isothermal Temperature Coefficient

It will be shown below that the EMF of the two thermocells [8] and [9] are related to the temperature coefficient $d\phi_3/dT$ of the isothermal cell [5]. Consider for this purpose the simple combination of cells given by Fig. 5. In this case, all electrodes contain the same metal, Pt. If, further, the junctions between Pt and other leads (e.g., Cu) are all at the same temperature, one can see that the reversible heats absorbed both at T_1 and T_2 cancel. It is shown in Fig. 5 how the transfer of charge results totally in zero transfer of heat. This heats Δq_{1T_1} in Fig. 5, corresponding to the last term $\Delta q'(Q)$ in Eq. [15]. This gives for the complete circuit

$$\Delta\phi_1 + \Delta\phi_3 + \Delta\phi_2 + \Delta\phi_4 = 0 \quad [32]$$

under the condition for the junctions given above. Further

$$\Delta\phi_1 = \frac{d\phi_1}{dT} \Delta T; \quad \Delta\phi_2 = -\frac{d\phi_2}{dT} \Delta T \quad [33]$$

and

$$-\Delta\phi_3 = \Delta\phi_4 + \frac{\partial\phi_3}{\partial T} \Delta T \quad [34]$$

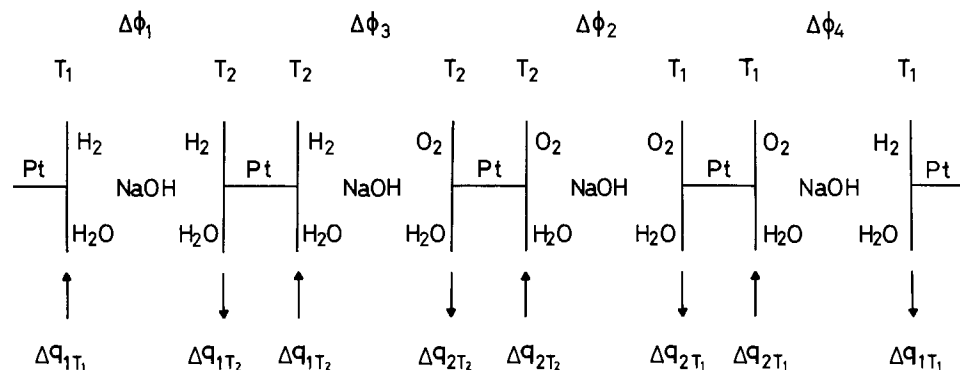


Fig. 5. A combination of thermocells and formation cells which together give zero EMF, T_1 and T_2 are temperatures while q_1 and q_1 are absorbed heats.

Thus

$$\frac{d\phi_1}{dT} - \frac{d\phi_2}{dT} = \frac{d\phi_3}{dT} \quad [35]$$

This relation makes possible a consistency check on separate measurements, since all terms in Eq. [35] can be measured independently of each other.

Interpretation of Flux Equations for the Formation Cell

The results obtained from the analysis of the thermogalvanic cells [8] and [9] can be related to electrolysis—conditions in the isothermal cell given by Eq. [5]. Since the electrolyte is almost pure NaOH(l), $\nabla\mu_{\text{NaOH}} = 0$. The electric force of Eq. [10]-[12] is now related to the observed EMF by Eq. [4]

$$\nabla\phi = \nabla\phi^{\text{obs}} - \left(-\nabla\mu_{\text{H}_2\text{O}} + \frac{1}{2} \nabla\mu_{\text{H}_2} \right) \quad [36]$$

with traces of H_2 and O_2 present anywhere along with local test electrodes, we can assume local equilibrium and

$$\frac{1}{2} \mu_{\text{H}_2} = \frac{1}{2} \mu_{\text{H}_2\text{O}} - \frac{1}{4} \mu_{\text{O}_2} \quad [37]$$

We are then obliged to reduce the number of components by one, and have chosen to exclude O_2 . Formation of $1/4 \text{ O}_2$ is then described as formation of $1/2 \text{ H}_2\text{O}$ and removal of $1/2 \text{ H}_2$. This means that we may regard the total electrode reaction as a transfer of H_2O and H_2 . The limits for the chemical potential of H_2 are the value at the cathode and given from Eq. [37] at the anode. This means by inserting into Eq. [36] and integrating for isothermal conditions that

$$\begin{aligned} \Delta\phi &= \Delta\phi^{\text{obs}} - \left[-\Delta\mu_{\text{H}_2\text{O}} \right. \\ &\quad \left. + \frac{1}{2} \left(\mu_{\text{H}_2(2)} - \mu_{\text{H}_2\text{O}(1)} + \frac{1}{2} \mu_{\text{O}_2(1)} \right) \right] \end{aligned}$$

or

$$\Delta\phi = \Delta\phi^{\text{obs}} - \Delta G \quad [38]$$

where ΔG is the Gibbs free energy change of the formation cell, and $\Delta\mu_{\text{H}_2\text{O}} = 0$. By inserting Eq. [38] into Eq. [12], we can find an expression for $\Delta\phi^{\text{obs}}$. An equation like [34] cannot be written for the entropy, and it is thus not possible to eliminate O_2 as a component when reversible entropy changes are considered. The reversible transfer of entropy is as before the sum of the entropy changes at the electrodes and the entropy of transport in the electrolyte and metallic leads.

With a temperature gradient across the cell [5], the processes taking place will in total be identical to the processes taking place in a cell [8] with the temperature gradient in series with an isothermal cell [5]. The processes in both these cells can then be described by Eq. [10]-[12]. Alternatively, the entropy balance may be analyzed in a way similar to that shown in Fig. 4. It should be noticed, however, that, since the transport mechanism in the electrolyte is different in cell [5] from that in cells [8] and [9],

t_{NaOH} , ΔS_1 , ΔS_2 , and $\bar{S}_{(Q)}$ will have different values and thus the reversible entropy $S_{(Q)}$ absorbed from the heat reservoirs will be different. For this type of thermogalvanic cell with different electrodes, the entropy absorbed from the left-hand side heat reservoir is different from the entropy donated to the right-hand side heat reservoir.

In this section, we have focused attention on the effect of heat transport, and how this can be described when no concentration gradients are present. The presence of concentration gradients will give irreversible heat changes. Soret equilibrium is defined when migration balances diffusion ($J_i = 0$). This condition can easily be introduced in the flux Eq. [10]-[12], and can be used to quantify diffusional heat effects. This is outside the practical scope of this case.

Experimental

The thermogalvanic cell was constructed as shown in Fig. 3. Molten sodium hydroxide was contained in two separate high purity α -alumina beakers (SSA-S, 99.5%), and their electrolytic contact was achieved by a porous α -alumina bridge, which was completely wetted by molten sodium hydroxide.

A gas mixture of either H_2O and H_2 or H_2O and O_2 was supplied through a high purity α -alumina pipe to make a three-phase zone on the platinum working electrode submerged in the molten sodium hydroxide in the right-hand-side beaker. A gas mixture was prepared by passing H_2 or O_2 gas through a water pool maintained at a fixed temperature. The composition was determined by the flow rate measurement of H_2 or O_2 before passing through the water pool, together with the weight gain of a CaCl_2 column due to the absorption of the water in the gas mixture coming out from the cell. The composition determined in these ways coincided well with the value estimated from the vapor pressure data of the water. A sodium/ β -alumina reference electrode was prepared by making a liquid sodium pool at the bottom of the β -alumina tube. This tube was connected to a high purity β -alumina pipe by using alumina cement. Argon gas was supplied into the tube as a cover gas to prevent the oxidation of the liquid sodium. To obtain reversibility of the reference electrode, cathodic and anodic currents were applied alternatively through the reference electrode before thermoelectric power measurements. By this pre-treatment, wetting of the inner and outer surface of the β -alumina tube by liquid sodium and molten sodium hydroxide, respectively, was achieved to ensure good electrolytic contact.

The temperature of furnace 1 was set at a constant temperature T_1 and the temperature T_2 of furnace 2 was raised, and the electromotive force between the platinum working electrode and the sodium/ β -alumina reference electrode was measured at various T_2 values.

Results and Calculations

The results are presented in Fig. 6 and 7. From these figures, we obtain

$$\frac{d\phi_1}{dT} = -1.05 \pm 0.02 \text{ mV K}^{-1} = -101 \pm 2 \text{ JK}^{-1} \text{ F}^{-1} \quad (T_1 = 340.5^\circ\text{C}) \quad [39]$$

and

$$\frac{d\phi_2}{dT} = -1.19 \pm 0.04 \text{ mV K}^{-1} = -115 \pm 4 \text{ JK}^{-1} \text{ F}^{-1} \quad (T_1 = 336^\circ\text{C}) \quad [40]$$

These results can be checked for internal consistency by application of Eq. [35]. The isothermal temperature coefficient is

$$\frac{d\phi_3}{dT} = \frac{1}{4} S_{\text{O}_2} + \frac{1}{2} S_{\text{H}_2} - \frac{1}{2} S_{\text{H}_2\text{O}} = \Delta S \quad [41]$$

where ΔS refers to 1F. For the present conditions ($P_{\text{O}_2} =$

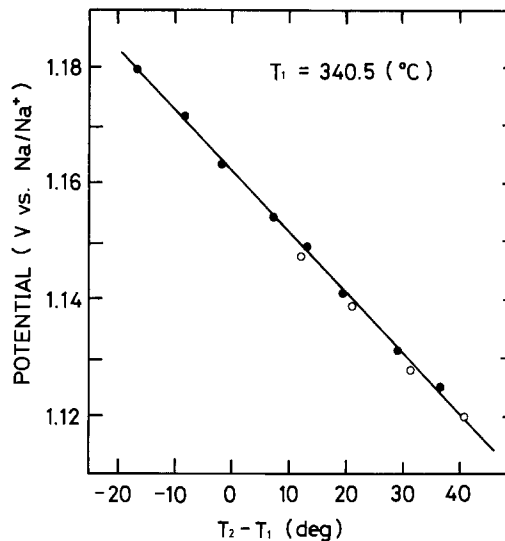


Fig. 6. Electromotive force of thermogalvanic cell consisting of two hydrogen electrodes (cell 8). \circ : Measured when $(T_2 - T_1)$ was increased. \bullet : Measured when $(T_2 - T_1)$ was decreased.

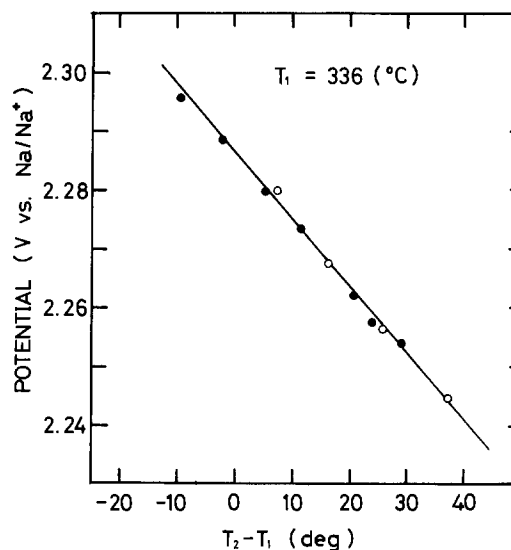


Fig. 7. Electromotive force of thermogalvanic cell consisting of two oxygen electrodes (cell 9). \circ : Measured when $(T_2 - T_1)$ was increased. \bullet : Measured when $(T_2 - T_1)$ was decreased.

0.8 atm, $P_{\text{H}_2} = 0.8$ atm, $P_{\text{H}_2\text{O}} = 0.2$ atm)

$$\begin{aligned} \Delta S &= \frac{1}{2} \left(150.7 + R \ln \frac{1}{0.8} \right) + \frac{1}{4} \left(226.3 + R \ln \frac{1}{0.8} \right) \\ &\quad - \frac{1}{2} \left(212.9 + R \ln \frac{1}{0.2} \right) = 20.2 \text{ JK}^{-1} \text{ F}^{-1} \end{aligned}$$

This result may be compared to the difference between the experimental results $115 - 101 = 14 \text{ JK}^{-1} \text{ F}^{-1}$ (see Eq. [35]).

A more complete analysis of the thermogalvanic cells would include independent measurements of t_{NaOH} and the entropy of transport $\bar{S}_{(Q)}$. The most important thing is, however, to estimate the single electrode heat changes at each electrode and not their difference. When the entropy of transport is to be included in the calculation of electrode compartment heat changes, they are found from Eq. [31] and [26]. Partial pressures of hydrogen and water vapor in the cathodic compartment of 0.8 atm and 0.2 atm, respectively, give 63 kJ F^{-1} evolved at the cathode. Partial pressures of oxygen and water vapor in the anodic compartment of 0.8 and 0.2 atm, respectively, give 72 kJ F^{-1} absorbed at the anode. In both cases the charge transferral is 1F at 623 K.

Conclusion

A theoretical procedure has been developed for the purpose of calculating the heat evolution at each electrode in electrochemical reactors. The heat change at the electrode includes the Peltier heat and heat reversibly transferred by the electrolyte. Thermoelectric power measurements can be interpreted by the sum of these heat changes and the heat change due to the entropy of transport.

The procedure has been illustrated by using the results obtained for water electrolysis in molten sodium hydroxide. For the conditions given, the total heat changes in the electrode compartments are 63 kJ F⁻¹ at the cathode and -72 kJ F⁻¹ at the anode.

Acknowledgment

This work was carried out under support from Grant no. 320 from the Japanese Ministry of Education, Science and Culture.

Manuscript submitted Nov. 4, 1983; revised manuscript received June 15, 1984.

Kyoto University assisted in meeting the publication costs of this article.

LIST OF SYMBOLS

I	current density (F · s ⁻¹ · m ⁻²)
J_i	mass flux of component i (mol · s ⁻¹ · m ⁻²)
$J_{q'}$	thermal flux (J · s ⁻¹ · m ⁻²)
k_i	complete coupling coefficient between mass flux of component i ($i = n + 1 \sim k$) and current density (mol · F ⁻¹)
L_{11}	Onsager coefficient (J · m ⁻¹ · s ⁻¹ · K)
L_{12}	Onsager coefficient (mol · m ⁻¹ · s ⁻¹ · K)
L_{13}	Onsager coefficient (F · s ⁻¹ · m ⁻¹ · K)
L_{21}	Onsager coefficient (mol · m ⁻¹ · s ⁻¹ · K)
L_{22}	Onsager coefficient (J ⁻¹ · mol ² · m ⁻¹ · s ⁻¹ · K)
L_{23}	Onsager coefficient (mol · m ⁻¹ · s ⁻¹ · V ⁻¹ · K)
L_{31}	Onsager coefficient (F · m ⁻¹ · s ⁻¹ · K)
L_{32}	Onsager coefficient (J ⁻¹ · F · mol · m ⁻¹ · s ⁻¹ · K)
L_{33}	Onsager coefficient (F · m ⁻¹ · s ⁻¹ · V ⁻¹ · K)
Q	charge (F = 96487 Cmol ⁻¹)
q'	heat transferred through unit area (J · m ⁻²)

$S'(Q)$	Peltier entropy (J · F ⁻¹ · K ⁻¹)
\bar{S}	transported entropy (J · F ⁻¹ · K ⁻¹)
S_i	partial molar entropy of component i (J · mol ⁻¹ · K ⁻¹)
S_i°	standard partial molar entropy of component i (J · mol ⁻¹ · K ⁻¹)
T	temperature (K)
t	time (s)
t_i	transference number of component i (mol · F ⁻¹)

Greek letters

ϕ	"effective" potential (J · F ⁻¹)
ϕ^{obs}	observed potential (J · F ⁻¹)
μ_i	chemical potential of component i (J · mol ⁻¹)
θ	entropy production per unit volume per unit time, (JK ⁻¹ · s ⁻¹ · m ⁻³)
∇	grad operator (m ⁻¹)

Subscripts

i, j, l	mass component i, j, l
Q	charge
q'	heat

REFERENCES

1. Y. Ito, F. R. Foulkes, and S. Yoshizawa, *This Journal*, **129**, 1936 (1982).
2. T. Førland and S. K. Ratkje, *Electrochim. Acta*, **25**, 157 (1980).
3. T. Jacobsen and G. H. J. Broers, *This Journal*, **124**, 207 (1977).
4. J. N. Agar, "Advances in Electrochemistry and Electrochemical Engineering," Vol. 3, P. Delahay, Editor, p. 31, Interscience, New York, (1963).
5. T. Førland, L. Thulin, and T. Østvold, *J. Chem. Ed.*, **48**, 741 (1971).
6. A. Ekman, S. Liukkonen, and K. Kontturi, *Electrochim. Acta*, **23**, 243 (1978).
7. S. K. Ratkje, *K. Norske Vidensk. Selsk. Skr.*, **6** (1982).
8. Y. Ito, H. Kaiya, and S. Yoshizawa, in "Proceedings of the 3rd World Hydrogen Energy Conference," 221 (1980).
9. Y. Ito, H. Kaiya, and S. Yoshizawa, *Energy Dev. Jpn.*, **3**, 153, (1981).
10. I. Barin and O. Knacke, Editors, "Thermochemical Properties of Inorganic Substances," Springer Verlag, Berlin (1973).

The Mechanism of Electrodeposition of Cadmium Sulfide on Inert Electrodes from Diethylene Glycol Solutions

A. S. Baranski* and W. R. Fawcett*¹

Guelph-Waterloo Centre for Graduate Work in Chemistry, University of Guelph, Guelph, Ontario, Canada N1G 2W1

ABSTRACT

The mechanism of electrodeposition of CdS from diethylene glycol solutions containing a cadmium salt and elemental sulfur was investigated. At fresh gold and platinum electrodes, the potential at which CdS is formed is strongly dependent on Cd²⁺ concentration and independent of sulfur concentration; the opposite is true at an electrode covered with a coherent layer of CdS. The properties of the electrodeposited films are strongly dependent on the nature of the anion in the electrolyte. In the presence of Cl⁻ and Br⁻ anions, mixed Cd-CdS films are formed under specified conditions. A detailed analysis of the effect of Cl⁻ anion showed that the results obtained were due to a change in the nature of the predominant form of Cd(II) in solution from Cd²⁺ to CdCl₂⁻.

Recently, a simple electrochemical method for depositing thin polycrystalline films of metal sulfides and selenides on conducting substrates was developed in this laboratory (1-4). In this technique, metal chalcogenides are electrodeposited at the cathode in a cell containing a solution of the metal salt and elemental chalcogen at an elevated temperature. There is a limited choice of solvents from which deposition is possible. Moreover, as one would expect, the structural and electrical properties of

the deposit are strongly dependent on the nature of the electrolyte and solvent, and composition of the solution. In a previous paper (2), it was shown that CdS grown from dimethylsulfoxide (DMSO) solutions exhibits high specific resistivity and has a tendency to crack. Similar problems exist if DMSO is replaced by other highly basic solvents such as N,N-dimethylformamide, pyridine, hexamethylphosphoramide or 1-methyl-2-pyrrolidone. However, deposition from solvents of low basicity, such as propylene carbonate, acetonitrile, or ethanol, results in the formation of a Cd-CdS mixed film. It was subsequently discovered that CdS could be grown from ethyl-

* Electrochemical Society Active Member.

¹ Present address: Department of Chemistry, University of California, Davis, California 95616.

ene glycol (EG) or diethylene glycol (DEG) solutions with much better physical properties suitable for use in photovoltaic devices. DEG is more convenient in this regard because of the higher solubility of sulfur.² The physical properties of CdS film grown from DEG solutions containing 10% water by volume and saturated with sulfur have been characterized (5). In the present paper, we report the results of a study of the mechanism of CdS deposition from DEG solutions.

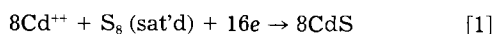
Experimental

The electrochemical measurements were carried out with a PAR Model 173 potentiostat. In most cases, the working electrode was a Pt wire, 0.25 mm diam and 1.5 cm long. In some experiments, a gold electrode with an area of 0.12 cm² or a glassy carbon electrode with an area of 0.3 cm² was employed. The counterelectrode was a Pt cylinder with an area of 3 cm². The reference electrode was constructed from a Cd rod immersed in a 0.05M Cd(ClO₄)₂ solution in DEG. The reference electrode system was kept at the same temperature as the main cell and was connected to it through a sintered glass disk. The temperature was maintained constant to within ±0.1°C by circulating paraffin oil from a constant temperature bath through a jacket surrounding the cell and reference electrode.

The solvent, diethylene glycol, was dried for 24h over 4Å molecular sieves and then distilled under argon at reduced pressure from a Vigreux column 1m high. The purified salts, Cd(ClO₄)₂, CdCl₂, LiClO₄, and NaI were dried for 24h at 120°C under vacuum. NH₄Cl, NH₄Br, and NH₄ClO₄ were dried for 24h at 60°C under vacuum. Sublimated sulfur was recrystallized from benzene and dried at 60°C.

Results and Discussion

The electrochemical studies of the mechanism of CdS deposition were carried out by cyclic voltammetry in DEG solutions containing LiClO₄ as supporting electrolyte in the temperature range 70°-130°C. In this medium, sulfur is reduced quasi-reversibly at gold and glassy carbon electrodes and irreversibly at platinum. The current-voltage curves were similar to those observed in other nonaqueous media for the reduction of S₈ (6): accordingly, it is assumed that the first step in the reduction process is the formation of the S₈^{•-} anion. The standard potential for the reaction S₈ + 2e → S₈^{•-} in DEG at 100°C was 0.055V against the Cd/Cd²⁺ reference electrode. Noting that the potential for the reaction Cd²⁺ + 2e → Cd is 0 V against the same reference electrode when the concentration of Cd²⁺ is 0.05M, and that the free energy of formation of CdS from metallic Cd and sulfur in a saturated DEG solution at 100°C is -139.6 kJ mol⁻¹, the reversible potential for the reaction



is 0.72V at 100°C. The potential for this process and the reduction of sulfur both depend very little on temperature.

Typical current-voltage curves observed in a DEG solution containing 0.05M Cd(ClO₄)₂ and 0.2M LiClO₄, and saturated with S₈ at various electrodes at 120°C are shown in Fig. 1. At a fresh Au electrode, a distinct prepeak is observed at 0.56V. At Pt, the peak occurs at a less positive potential and is not as sharp. In addition, the potential of the prepeak depends strongly on Cd²⁺ concentration, the potential shift being 80 mV for a tenfold increase in Cd²⁺ concentration at Pt. However, the peak potential is virtually independent of sulfur concentration (Fig. 2). If the metallic electrode is already covered with a coherent layer of CdS, the prepeak does not appear. Similar observations were made earlier for deposition from DMSO solutions (7). On the basis of the present results and those obtained earlier (7), it is concluded that the prepeak is due to the reduction of Cd²⁺ at a pre-existing layer of metal sulfide formed by reaction of the metal electrode with

² The solubility of sulfur at 120°C is 0.62 and 0.14g per 100 ml of DEG and EG, respectively.

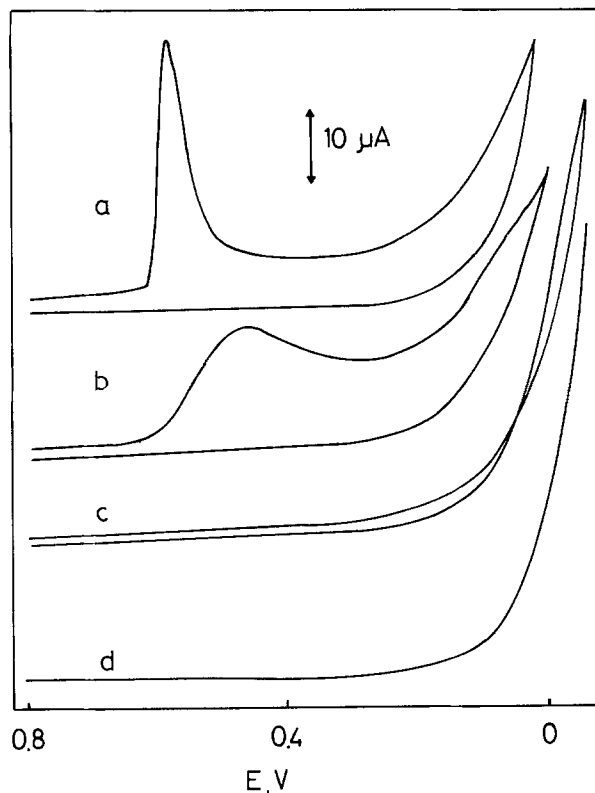
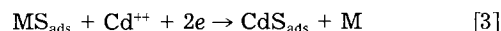
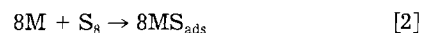


Fig. 1. Cyclic voltammograms for the electrodeposition of CdS at (a) gold, (b) platinum, (c) glassy carbon, and (d) CdS (thickness ~1 μm) on Pt. The electrolyte solution contained 0.05M Cd(ClO₄)₂, 0.2M LiClO₄, and saturated sulfur in diethylene glycol; the sweep rate was 50 mV s⁻¹, and temperature 120°C. The electrode areas were 0.12 cm² for Pt, Au, and CdS, and 0.3 cm² for glassy carbon.

sulfur in solution; the electrode reaction results in the metal sulfide being converted to CdS. Representing the metal composing the electrode (Au or Pt) as M, the reaction scheme may be written



Strong chemisorption of sulfur on Au and Pt from DEG solutions was demonstrated experimentally in the same way as described previously for DMSO solutions (7). However, this process does not occur at glassy carbon, no prepeak being observed at this electrode.

The present investigation was chiefly directed to determination of the mechanism of CdS deposition on an electrode already covered with a coherent film of CdS. In this case, the nature of the substrate electrode has no influence on the electrode process. The study was carried out by analyzing Tafel plots (ln *i* against electrode potential) obtained for different solution compositions and at various temperatures. The electrode was prepared by covering a Pt wire (surface area ~0.12 cm²) with a layer of CdS ~1 μm thick;³ the CdS layer was deposited from the system under investigation at a constant current density of 0.25 mA cm⁻². Then, the electrode was polarized with a linearly changing potential, typically at a rate of 20 mV s⁻¹, and the current-potential curve recorded. During the experiment, the solution resistance was carefully compensated, and concentration polarization avoided by stirring the solution using a magnetic stirrer. Furthermore, only currents less than one-tenth of the limiting current were considered in the analysis. Under these conditions, the current-voltage curves were independent of the thickness of the CdS layer, the potential sweep rate, and the rate of solution stirring.

³ The thickness of the deposit was estimated assuming that the electrodeposition process consumed 100% of the charge passed, and that the density of the CdS film is the same as bulk CdS (4.82 g cm⁻³).

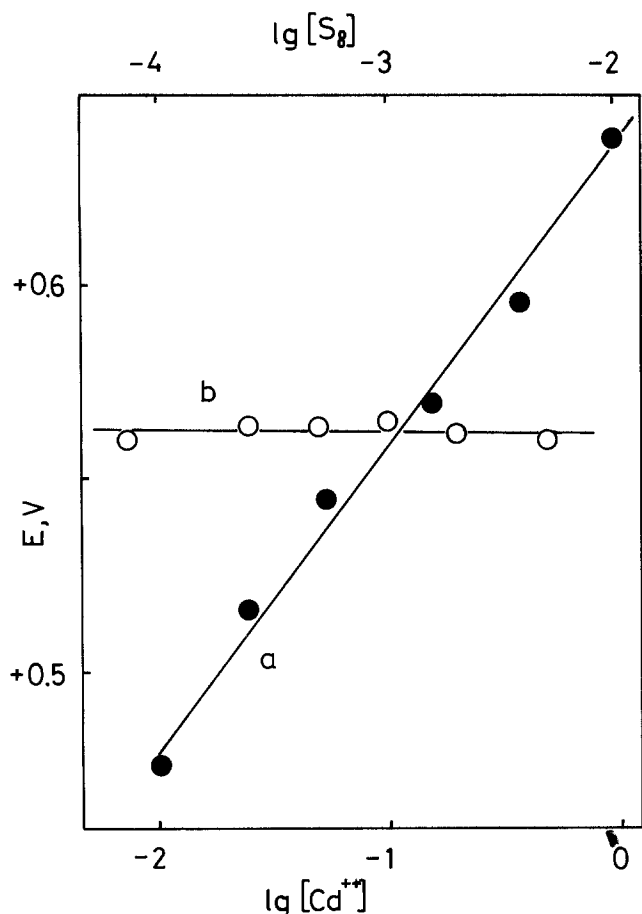


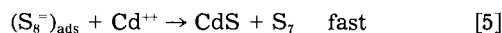
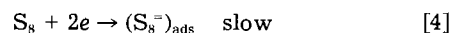
Fig. 2. The dependence of the half-peak potential on (a) Cd^{2+} concentration and (b) sulfur concentration for the prepeak corresponding to CdS deposition on Pt at 120°C in a DEG solution containing (a) 0.2M LiClO_4 , saturated with sulfur and varying concentrations of Cd as indicated or (b) 0.1M $\text{Cd}(\text{ClO}_4)_2$, 0.2M LiClO_4 , and varying concentrations of S_8 as indicated.

In all cases, it was found that the electrode process was controlled by irreversible electron transfer. The experimental transfer coefficient calculated from the slope of the Tafel plots was 0.57 ± 0.05 . Tafel plots obtained for

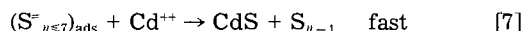
different sulfur concentrations in DEG solutions containing 0.02M $\text{Cd}(\text{ClO}_4)_2$ and 0.24M LiClO_4 are shown in Fig. 3. As the sulfur concentration increases, the plots are shifted in the direction of positive potentials. The change in the logarithm of the current density was linear with that of the sulfur concentration at constant potential; the order of the electrode process with respect to sulfur, determined from the slope of this plot, is 1.05 ± 0.1 .

In another experiment, the concentration of sulfur was kept constant and that of $\text{Cd}(\text{ClO}_4)_2$ varied from 0 to 0.1M , the ionic strength of the solution being maintained constant by addition of the appropriate concentration of LiClO_4 . The resulting Tafel plots showed no effect of Cd^{2+} concentration on the electrode process (Fig. 4). However, when the solution contained no Cd^{2+} ions, a decrease in the Tafel slope was observed at high currents. The latter result is probably due to strong adsorption of the $\text{S}_8^{=}$ anion on the CdS electrode. This adsorption may have an auto-inhibiting effect on further sulfur reduction. The Tafel plot for the reduction of sulfur on Pt from a DEG solution containing 0.3M LiClO_4 is also shown in Fig. 4. It is interesting to note that the reduction of sulfur is much more irreversible on CdS than on Pt.

On the basis of the data presented in Fig. 3 and 4, the following mechanism for CdS deposition on CdS is proposed



S_7 and other sulfur species containing less than eight sulfur atoms are expected to be more reactive than S_8 (8), and may undergo subsequent electron transfer processes



The deposition of CdS from DEG solutions was very strongly temperature dependent. Tafel plots obtained for deposition of CdS from DEG solutions containing 0.1M $\text{Cd}(\text{ClO}_4)_2$, 0.1M LiClO_4 , and saturated with sulfur are shown at various temperatures in Fig. 5. On the basis of these data, the enthalpy of activation of the electrodeposition process was found to be $95 \pm 20 \text{ kJ mol}^{-1}$.

It is interesting to note that, except at the highest temperatures, the deposition of CdS occurs at potentials more negative than the reversible potential for the

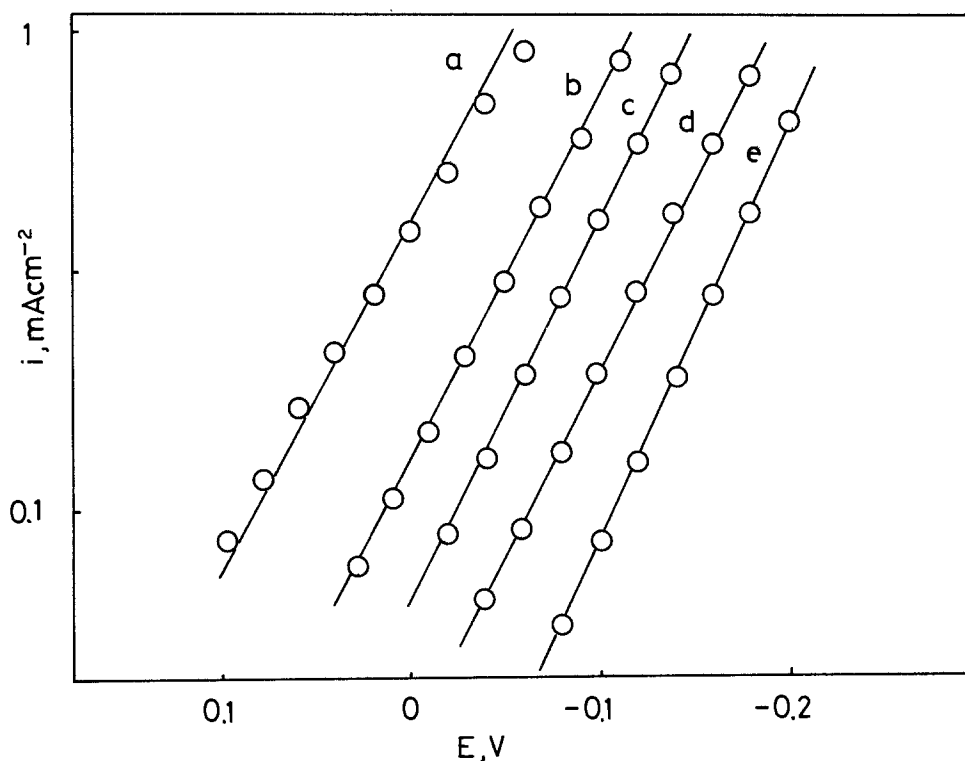
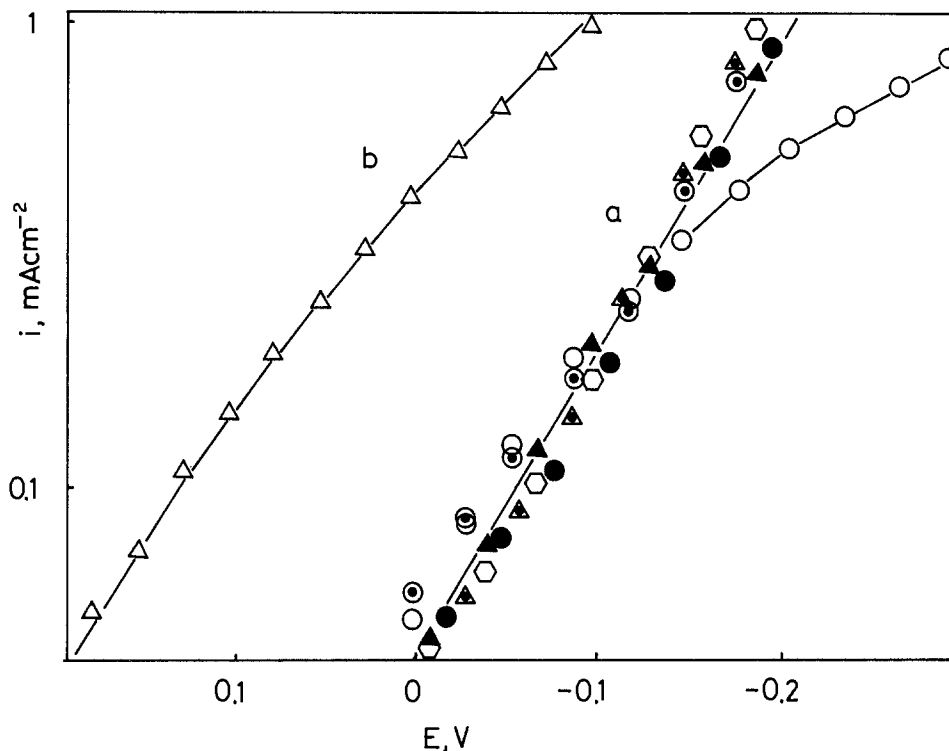


Fig. 3. Tafel plots for the deposition of CdS on a Pt electrode covered with a coherent film of CdS at 130°C from a DEG solution containing 0.02M $\text{Cd}(\text{ClO}_4)_2$, 0.24M LiClO_4 , and various concentrations of S_8 : (a) 0.007M ; (b) 0.003M ; (c) 0.0016M ; (d) 0.0008M ; and (e) 0.0004M . The ordinate scale is logarithmic.

Fig. 4. Tafel plots for the deposition of CdS on (a) a Pt electrode covered with a coherent film of CdS at 130°C from a DEG solution containing 0.001M S_8 and various concentrations of $Cd(ClO_4)_2$: (○) 0; (▲) 0.005M; (◐) 0.01M; (●) 0.02M; (◑) 0.005M; and (△) 0.1M. The ionic strength was maintained constant at 0.3M by adding $LiClO_4$. Curve b is the Tafel plot for the reduction of sulfur at a fresh Pt electrode at 130°C in a DEG solution containing 0.001M S_8 and 0.3M $LiClO_4$. The ordinate scale is logarithmic.



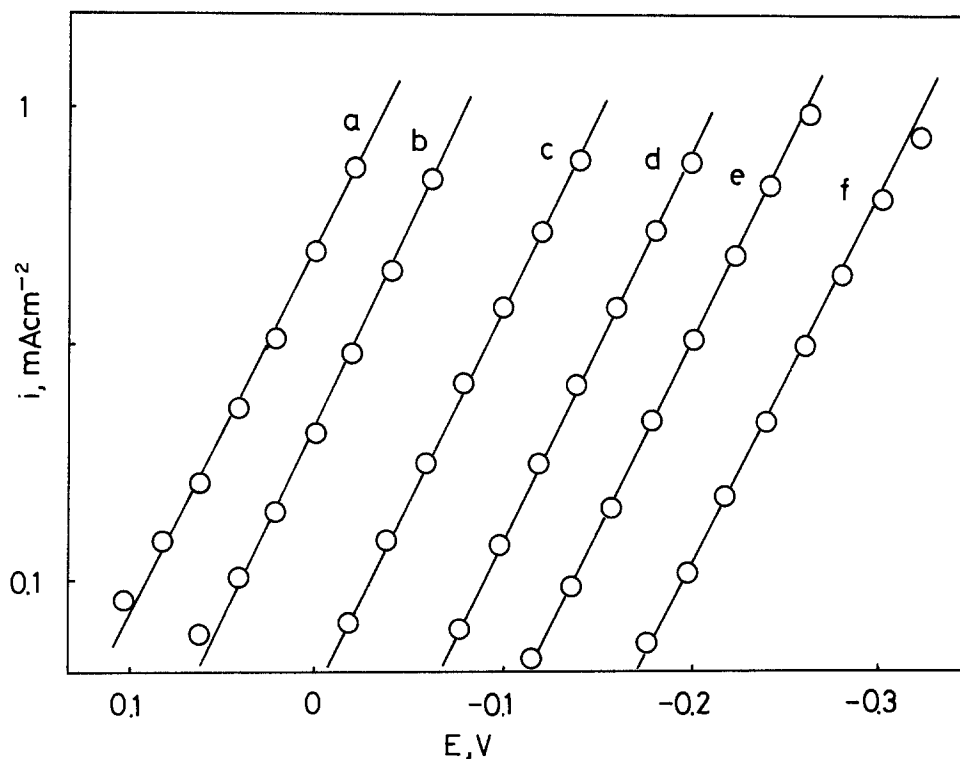
Cd/Cd⁺⁺ system. It was found that the deposition of Cd on CdS in the absence of sulfur is a fast diffusion-controlled process in this potential region. However, x-ray analysis of deposits obtained from DEG solutions at 90°C containing 0.002M S_8 , 0.1M $LiClO_4$, and varying concentrations of $Cd(ClO_4)_2$ in the range from 0.005-0.1M showed no excess of Cd in the CdS deposit. Apparently, when sulfur is present in solution, the reduction of Cd⁺⁺ is strongly inhibited by the adsorption of molecular sulfur on the surface of the CdS electrode.

In previous work (5), it was found that addition of small amounts of water to the electroplating solution significantly improved the adhesion of the electrodeposited CdS film to the substrate. In the present study, it was shown that addition of water in quantities up to a mole fraction of 0.57 (~20% H_2O by volume) had a surprisingly

small effect on the deposition process (Fig. 6). The observed change in the slope of the Tafel plots is probably caused by a change in double layer structure at the semiconductor/solution interface.

The role of the supporting electrolyte in the electrode process was also studied. It was shown that the cation does not play any significant role, the same Tafel plots being obtained when Li^+ was replaced by Na^+ , K^+ , or NH_4^+ . However, the role of the anion is very important. Replacement of ClO_4^- by BF_4^- , $CH_3SO_3^-$, Cl^- , or Br^- usually resulted in the formation of a dark dendritic deposit composed of a mixture of Cd and CdS. The effect of halide ions was particularly interesting and was studied in more detail. In this regard, the percentage of metallic Cd in a mixed Cd-CdS deposit was determined by chronopotentiometry. When a mixed film is deposited at

Fig. 5. Tafel plots for the deposition of CdS on a Pt electrode covered with a coherent film of CdS from a DEG solution saturated with sulfur and containing 0.1M $Cd(ClO_4)_2$ and 0.1M $LiClO_4$ at various temperatures: (a) 130°C; (b) 123°C; (c) 108°C; (d) 95°C; (e) 82°C; and (f) 70°C. The ordinate scale is logarithmic.



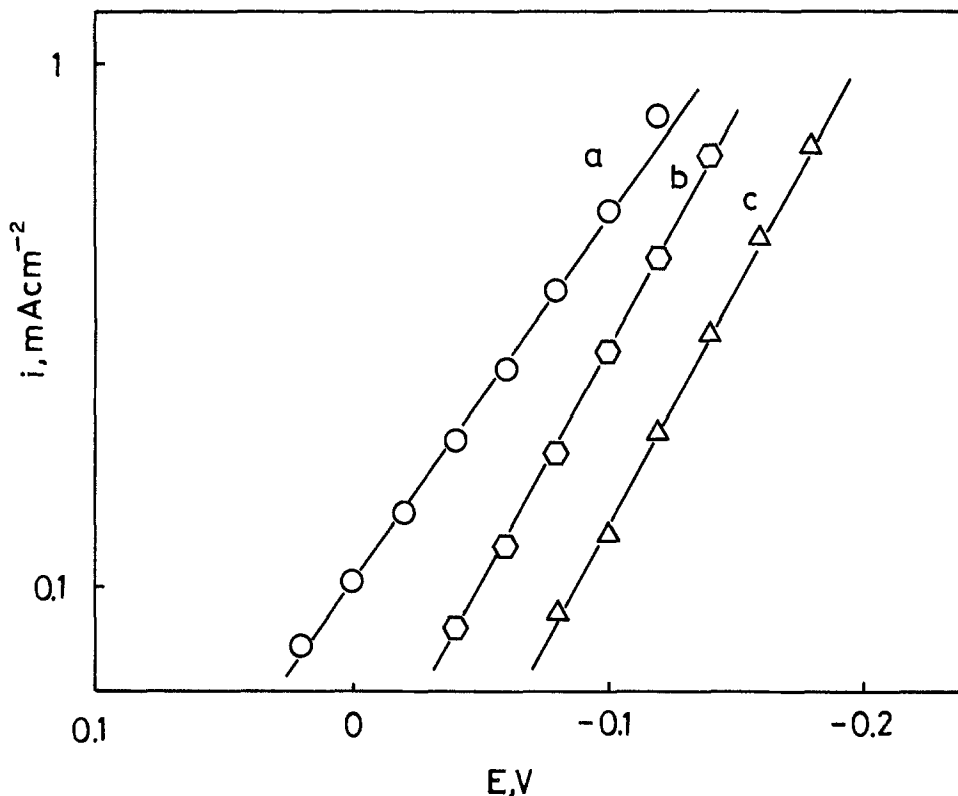
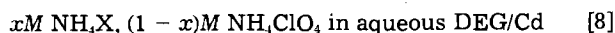
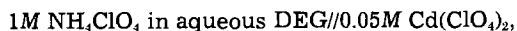
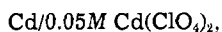


Fig. 6. Tafel plots for the deposition of CdS on a Pt electrode covered with a coherent film of CdS at 110°C from a DEG solution saturated with sulfur and containing 0.1M $\text{Cd}(\text{ClO}_4)_2$, 0.1M LiClO_4 , and different amounts of water: (a) 0; (b) 5%; and (c) 20% by volume. The ordinate scale is logarithmic.

constant current by reduction, only the metallic Cd is oxidized when the current is reversed. Thus, the ratio of the transition time in the oxidation process to the reduction time is equal to the mole fraction of Cd in the deposit. This experiment was carried out under conditions for which the mixed deposit is not too thick, thereby ensuring that all available Cd was oxidized on current reversal. Chronopotentiometric experiments were run with varying concentrations of NH_4Cl , NH_4Br , NaI , and water at different temperatures. Some of the results are presented in Fig. 7. The addition of iodide anion had no effect on the ratio of Cd to CdS in the deposit, pure CdS being formed over the entire concentration range studied. However, in the cases of Cl^- and Br^- anions, pure CdS can be electrodeposited only when the concentration of these ions is very low or very high. Lowering the temperature, or adding water to the deposition bath results in a slight decrease in range of concentrations over which pure CdS can be deposited, but the general characteristics of the dependence remain the same.

In order to investigate the role of halide ions further, the stability constant for formation of the CdX_4^{2-} ion was determined on the basis of EMF measurements using the following cell



where X represents Cl^- , Br^- , or I^- , and the solvent contained 10% H_2O by volume. In the presence of the large excess of halide ions the tetrahalocadmium(II) ion (CdX_4^{2-}) was formed with the logarithm of the stability constant ($\log \beta_4$) equal to 8.4, 9.0, and 9.9 for Cl^- , Br^- , and I^- , respectively, at 110°C. In Fig. 8, the equilibrium potentials for the $\text{Cd}/\text{CdCl}_r^{2-r}$ system (curve a) and the potentials for deposition of CdS at a current density of 0.5 mA cm^{-2} (curve b) are shown as a function of the Cl^- ion concentration in the DEG solution. It is noteworthy that for Cl^- concentrations less than $0.002M$, the deposition of pure CdS occurs at a potential about 100 mV more negative than the equilibrium potential for the $\text{Cd}/\text{CdX}_r^{2-r}$ system. This was attributed to strong inhibition of Cd^{++} reduction by adsorbed molecular sulfur on the CdS sur-

face. However, as the Cl^- ion concentration increases, the inhibition by sulfur becomes less effective, probably because Cl^- ions are coadsorbed on the CdS surface and provide bridging sites for the adsorption of Cd^{++} (9). As a result, a mixture of Cd and CdS is formed in the electrode process, and the overpotential decreases. For higher Cl^- ion concentrations, a substantial shift in the $\text{Cd}/\text{CdCl}_r^{2-r}$ equilibrium potential in the negative direction is observed due to formation of the complex ions CdCl^+ , CdCl_2 , CdCl_3^- , and CdCl_4^{2-} . Finally, when the $\text{Cd}/\text{CdCl}_r^{2-r}$ potential becomes more negative than the potential for CdS formation, pure CdS is deposited in the electrode process. The higher overpotential for CdS formation in the presence of high Cl^- ion concentrations is attributed to the inhibiting effect of adsorbed Cl^- ions on the reduction of sulfur.

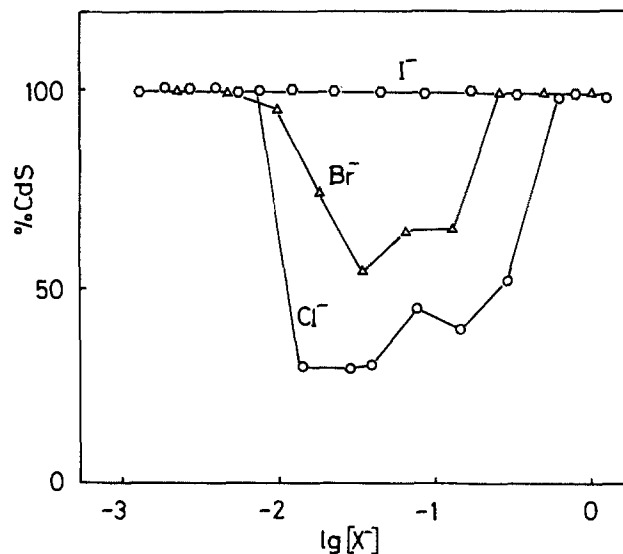


Fig. 7. The percentage of CdS in mixed Cd-CdS deposits obtained from solutions containing halide ions against the logarithm of the halide ion concentration. The electrolyte solution in DEG was saturated with sulfur and contained 0.05M $\text{Cd}(\text{II})$ and 10% H_2O by volume. The deposition current was 0.5 mA cm^{-2} , and the temperature 110°C.

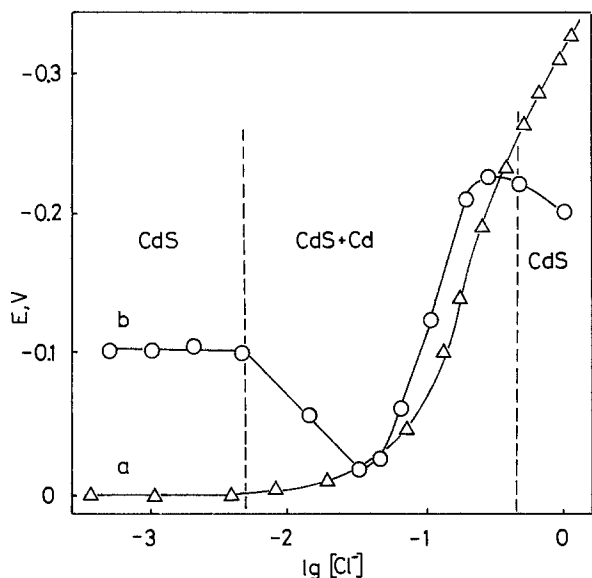


Fig. 8. A plot of (a) the equilibrium potential for the $\text{Cd}/\text{CdCl}_x^{2-x}$ couple and (b) the deposition potential for mixed Cd-CdS films against the logarithm of chloride ion concentration in the electroplating bath. The electrolyte solution in DEG was saturated with sulfur and contained 0.05M Cd(II) and 10% H_2O by volume. The deposition current was 0.5 mA cm^{-2} , and the temperature 110°C .

The addition of Cl^- ions to the electroplating bath causes marked changes in the orientation of the electrodeposited CdS crystallites (5). For Cl^- ion concentrations less than 0.005M, the crystallites are randomly oriented, but for Cl^- ion concentrations greater than 0.5M, they are strongly oriented with the c-axis perpendicular to the substrate. It is reasonable to assume that the extent of Cl^- ion adsorption varies with the crystallographic orientation of the exposed CdS face. This will result in differences in the rate of growth of different faces of the crystallites, and consequently, the promotion of one orientation in thicker deposits.

Conclusions

The growth of CdS during electrodeposition from DEG solution at a CdS surface is controlled by the reduction of sulfur. The anion formed in the electrode process, presumably S_8^{2-} , subsequently reacts with Cd^{2+} , causing the deposition of CdS. The process is strongly affected by the nature of the anions in the electrolyte. In the case of ClO_4^- anion, which is probably not strongly adsorbed on the electrode, the deposition of CdS occurs at potentials more negative than the standard potential of the Cd/Cd^{2+}

system. However, the reduction of Cd^{2+} and subsequent formation of a Cd-CdS mixture is inhibited, most likely, by the adsorption of molecular sulfur on the CdS surface. This inhibition is not as effective in the presence of Cl^- or Br^- anions. In this case, the deposition of pure CdS is only possible if the equilibrium potential of the $\text{Cd}/\text{Cd(II)}$ system is shifted by complex ion formation to a potential more negative than the reduction potential of S_8 at CdS.

The formation of the first monolayer of CdS on metallic electrodes occurs by a different mechanism. In this case, the rate of reaction is independent of sulfur concentration but depends strongly on Cd^{2+} concentration. These observations are attributed to the initial formation of a monolayer of metallic sulfide on the metal electrode which is reduced to CdS at the appropriate potential in the presence of Cd^{2+} ions. The initial stages of the formation of CdS in DMSO were also studied at gold electrodes by Roe *et al.* (10), who concluded that the first monolayer was formed by reaction of sulfur with cadmium already on the electrode as a result of underpotential deposition. No evidence in support of their proposal was obtained in our earlier work (7) or in that reported here.

Acknowledgments

The financial support of the Natural Sciences and Engineering Research Council, Canada (NSERC) and of the Technology Development Corporation, Canada through operating grants is gratefully acknowledged.

Manuscript submitted March 5, 1984; revised manuscript received June 13, 1984.

The Natural Sciences and Engineering Research Council, Canada, assisted in meeting the publication costs of this article.

REFERENCES

1. A. S. Baranski and W. R. Fawcett, *This Journal*, **127**, 766 (1980).
2. A. S. Baranski, W. R. Fawcett, A. C. McDonald, R. M. de Nobriga, and J. R. MacDonald, *ibid.*, **128**, 963 (1981).
3. A. S. Baranski, W. R. Fawcett, K. Gatner, A. C. McDonald, J. R. MacDonald, and M. Selen, *ibid.*, **130**, 579 (1983).
4. A. S. Baranski, W. R. Fawcett, and C. Gilbert, *ibid.*, **130**, 2423 (1983).
5. A. S. Baranski, M. S. Bennett, and W. R. Fawcett, *J. Appl. Phys.*, **54**, 6390 (1983).
6. J. Badoz-Lambling, R. Bonnaterre, G. Cauquis, M. Delamer, and G. Demange, *Electrochim. Acta*, **21**, 119 (1976).
7. A. S. Baranski, W. R. Fawcett, and A. C. McDonald, *J. Electroanal. Chem.*, **160**, 271 (1984).
8. F. N. Tebbe, E. Wasserman, W. G. Peet, A. Vatvars, and A. C. Hayman, *J. Am. Chem. Soc.*, **104**, 4971 (1982).
9. F. C. Anson, *Acc. Chem. Res.*, **8**, 400 (1975).
10. D. K. Roe, Li Wenzhao, and H. Gerischer, *J. Electroanal. Chem.*, **136**, 323 (1982).

Thin Film CdSe Electrodeposited from Selenosulfite Solution

Michael Cocivera,* Andrzej Darkowski, and Bruce Love

Guelph Waterloo Center for Graduate Work in Chemistry, University of Guelph, Guelph, Ontario, Canada N1G 2W1

ABSTRACT

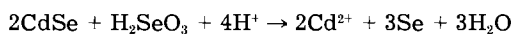
Thin film CdSe on titanium is electrodeposited by reduction of an aqueous solution containing the selenosulfite anion and a nitrilotriacetate complex of cadmium ion. Films having thickness between 1.3 and 2.6 μm and surface areas of 1 cm^2 give photoconversion efficiencies between 5.5% and 5.9% when used in a photoelectrochemical cell and illuminated with an ELH lamp.

A number of workers (1-4) have reported the preparation of thin film CdSe for solar cells by means of electrodeposition from an aqueous solution containing Cd^{2+} and H_2SeO_3 . A substantial excess of selenium is detected in

*Electrochemical Society Active Member.

films prepared in this manner (1, 3). To remove a major portion of this excess, the films must be annealed at temperatures as high as 750°C (3).

It has been suggested that selenium incorporation occurs according to the reaction



Consequently, use of a selenium precursor that is formally in a lower valence state might avoid undesirable side reactions of this type. For this purpose, we have developed (5) an electrodeposition process that involves the reduction of selenium, which is in the form of the selenosulfite anion SeSO_3^{2-} . This species is prepared *in situ* by dissolving elemental selenium in an aqueous sodium sulfite solution. The selenosulfite anion has also been employed to form CdSe films by a chemical process rather than an electrochemical process (6). In addition, thin film CdSe has been electrodeposited from cyanide solution in which elemental selenium has been dissolved; however, the reported efficiencies are low (7).

We find that electrodeposition of CdSe from aqueous selenosulfite solutions results in films having a Cd/Se ratio close to 1. The process consistently provides 1 cm² films having efficiencies between 5.5% and 5.9% for conversion of light power into electrical power using unfiltered light from an ELH lamp. Furthermore, the solution seems fairly stable since a 24h old solution provides films that also have efficiencies around 5.5%. Selenosulfite electrodeposited films appear to adhere quite well to titanium, whereas flaking has been reported for films electrodeposited from H_2SeO_3 solutions (4). A similar problem has been found for films grown by the chemical bath process using selenosulfite solution unless the film is grown in stages (6). In addition, the chemical bath solutions apparently cannot be used for periods longer than about 1h (6). Selenosulfite has been used previously under conditions that are different from those presented below to electrodeposit CdSe films, which were reported to be of inconsistent quality and had a maximum of only 1% light conversion efficiency (8).

Experimental

Electrodeposition of CdSe.—Thin film CdSe is deposited at a titanium cathode at room temperature using a two-electrode cell in which the anode is cadmium metal. A constant potential of 0.30V between these electrodes was maintained using a Bioanalytical Systems (BAS) CVIB. Under these conditions, there is an initial transient reduction current that decays to near zero in about 10s. The current density then gradually increases to 0.34 mA/cm² over a period of ca. 100s and continues to increase gradually to 0.47 mA over a period of 15 min. By including a saturated calomel electrode (SCE) in the cell, we find that the titanium electrode potential is -1.07V vs. SCE .

The electrodeposition solution is prepared by mixing 30 ml of aqueous selenosulfite solution with 10 ml of aqueous cadmium nitilotriacetate solution. The selenosulfite solution is prepared by dissolving 0.120g of elemental selenium powder (0.050 molar) in an aqueous solution containing 3.0g of sodium sulfite (0.75 molar) at pH 9. The cadmium solution was prepared by dissolving 0.20g of $\text{CdCl}_2 \cdot 2.5\text{H}_2\text{O}$ (0.088 molar) into an aqueous solution containing 0.103M sodium nitilotriacetate (NTA) at pH 8. After mixing, the combined solution remains clear and colorless over a period of about 8h. Over a period of 24h, a very thin redish brown film of either CdSe or Se forms on the walls of the flask; however, the solution remains clear and colorless. The electrodeposition is performed at pH 9 and room temperature using an air-saturated solution. The anode is not isolated from the cathode. Magnetic stirring is maintained during deposition.

Preparation of the titanium electrode prior to film deposition involved abrading the rectangular titanium plates using no. 400 emery paper. The plate was then soaked in chromic acid at 90°C for 3 min, rinsed in distilled water, and soaked in ca. 1M sodium hydroxide at 80°C for 5 min. It was then rinsed in distilled water and dried.

Electrolysis for 1h provides a film thickness of 1.3-1.6 μm . This thickness is determined in two ways. First, the weight of the film scraped from molybdenum foil was compared with the tabulated density of CdSe (9). Second, a Sloan Dektak stylus-type device was used at two posi-

tions on a CdSe film deposited on indium tin oxide-coated glass. Based on the weight of the film and the number of coulombs passed, the electrodeposition appears to be 88% efficient. The weight of the film was determined after the film has been annealed at 500°C. At this temperature, vaporization of the film does not appear to be extensive.

Cyclic voltammetry.—Cyclic voltammetry (CV) at the titanium electrode was performed with the BAS CVIB in a three-electrode cell containing the SCE as the reference electrode and cadmium metal as the auxiliary electrode. In addition to the electrodeposition solution, measurements were made at room temperature on a solution containing only the selenosulfite, on a solution containing only the cadmium complex, and on a solution of cadmium ion in the absence of NTA.

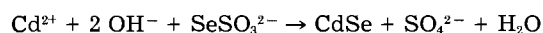
Composition of CdSe film.—Two methods were used to determine the composition of the film: polarography and Rutherford backscattering spectroscopy (RBS). For the polarographic determination, the analytical solution was prepared by treating the film on titanium with nitric acid at 50°C to dissolve cadmium as Cd^{2+} and selenium as H_2SeO_3 . The $E_{1/2}$ for the reduction waves for Cd^{2+} and H_2SeO_3 occur at -0.745 and -1.500 (SCE). The polarographic analysis gives a Cd/Se ratio of 1.2. Preliminary RBS analysis of the surface composition of the CdSe film indicates a similar ratio (1.1 ± 0.1). More extensive studies of surface and depth profiles will be reported later. For this analysis, a 3 MV Van de Graaff accelerator provided 1.6 MeV helium nuclei.

Surface morphology.—An Etec Autoscan scanning electron microscope that employs the backscattered electron technique was used to observe the surface structure of the film before and after various annealing treatments. Photographs of the micrographs were taken on Kodak FXP/20 film using a Graphex lens and aperture.

Performance.—The photoresponse of the CdSe film was determined in a photoelectrochemical cell (PEC) using an aqueous solution containing 1/1/1M $\text{Na}_2\text{S}/\text{S}/\text{NaOH}$. The two-electrode cell contained the CdSe photoanode connected by a variable resistor (EICO resistance decade box) to a cathode that consisted of brass wire mesh coated with Cu_2S (10). No external bias was applied. The voltage across the load was measured with a digital voltmeter. Unfiltered light from a 300W CGE Quartzline ELH lamp was used. Power output from the lamp was determined with an Eppley thermopile. Prior to power measurements, the films were etched in 9N HCl, soaked in 1N NaCN, and treated with 1M ZnCl_2 (11).

Results and Discussion

The selenosulfite anion and the cadmium complex are made *in situ* in separate solutions, which are then mixed. The selenosulfite anion is prepared by dissolving elemental selenium in 0.6M sodium sulfite. The cadmium complex is prepared by dissolving cadmium chloride in 0.028M sodium nitilotriacetate. The cadmium complex [stability constant $10^{9.8}$ (12)] is used to reduce the concentration of free cadmium ion. Otherwise, the chemical reaction (6, 13)



occurs to an appreciable extent during the time of the electrolysis. By means of this complex, the solution remains stable for at least 24h. Furthermore, control experiments indicate that this chemical reaction provides no detectable CdSe film on the titanium during the period used for the electrolysis.

The CdSe film is electrodeposited at a titanium cathode from an air-saturated aqueous solution containing 0.02M selenosulfite anion and 0.02M cadmium cation complexed to nitilotriacetate anion. This deposition is performed at room temperature and pH 9 using a two-electrode cell in which cadmium metal is employed as the anode. A constant potential of 0.30V is maintained be-

tween the electrodes, giving a current density that gradually rises from 0.34 to 0.47 mA/cm² during the deposition period. A time period of 1h provides a film thickness between 1.3 and 1.6 μm . So far, these conditions provide the CdSe film with the best light power to electrical power conversion efficiency (5.5-5.9%) for this system. Furthermore, these conditions provide consistent quality films from one solution to the next. Five solutions gave films having efficiencies between 5.5% and 5.9%. An added advantage is that the solutions are sufficiently stable so that electrolyses can be repeated several times. In addition, solutions left overnight without any special protection provide films with photoconversion efficiencies as good as those obtained from fresh solutions.

The film on titanium appears dark gray with a slight sheen. It adheres well to titanium. Adhesion to other substrates, such as molybdenum, platinum, and indium tin oxide-coated glass, is not as good. Polarographic analysis indicates that the ratio Cd/Se is 1.2 in the film, and Rutherford backscattering spectroscopy indicates a ratio of 1.1 ± 0.1 using the surface energy approximation (14). Based on this composition, comparison of the weight of the films with the number of coulombs passed indicates that the efficiency of the electrodeposition process is 88%. For this determination, the film was annealed at 500°C for 30 min.

Prior to photoconversion efficiency measurements, the CdSe film was annealed in air to 550°C for 30 min to activate it. We found that this temperature provided suitable activation without causing substantial loss of material due to vaporization. A similar observation has been reported earlier (6). Careful temperature control seems to be important since films annealed at 500° and 550°C give photoconversion efficiencies of 4.5% and 5.8%, respectively, at 70 mW insolation. Above 550°C, vaporization appears to become significant. After annealing, the surface of the film was prepared by etching with 9N HCl, soaking in 1N NaCN, and treatment with 1M ZnCl₂ (10).

The efficiency for the conversion of light power into electrical power was determined using a photoelectrochemical cell (PEC) that contained an aqueous solution of Na₂S/S/NaOH in the molar ratio 1/1/1. In this cell, the CdSe photoanode was connected by a variable resistor to the counter electrode, which consisted of brass mesh coated with Cu₂S (11). No external biasing was applied. The photovoltage across the resistor was measured using a digital voltmeter. Unfiltered light from a Quartzline ELH lamp was used for excitation. The photovoltage measured in this manner for the film were quite stable with no appreciable variation during irradiation for periods up to 15 min. Dark voltages were negligible at all loads below 1 k Ω . Above 1 k Ω , the dark voltage increased with resistance to a maximum value around 50 mV at open circuit.

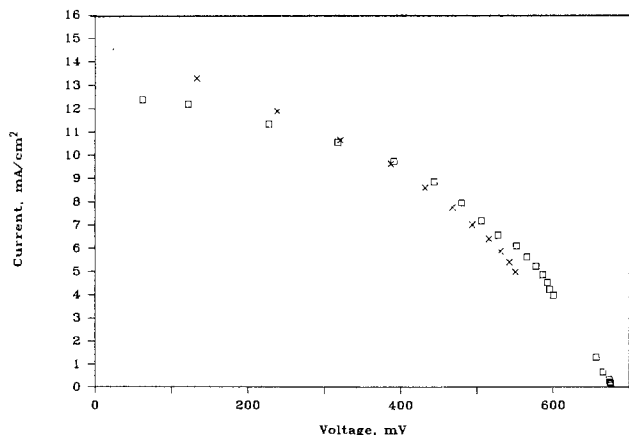


Fig. 1. Photocurrent/photovoltage results for 1 cm² CdSe films at two thicknesses: (□) 1.3 and (X) 2.6 μm . Conditions: PEC containing aqueous polysulfide; 70 mW unfiltered light from an ELH lamp; no externally applied bias.

Figure 1 illustrates the photocurrent/photovoltage characteristics for two CdSe films having thicknesses of ca. 1.3 and 2.6 μm . There appears to be little difference between the results at the two thicknesses. For three 1 cm² CdSe films (ca. 1.3 μm thick) deposited from three separate fresh solutions, the average efficiency for the conversion of light power to electrical power is $5.74 \pm 0.09\%$ for 70 mW insolation. For these samples and those discussed below, the dark voltages were usually negligible, *i.e.*, no more than one or two millivolts except at open circuit, for which the dark voltage could be as large as 50 mV. Open-circuit photovoltages at 70 mW insolation are typically between 600 and 700 mV. Variation between 40 and 100 mW insolation gave open-circuit photovoltages in this range also. The photoresponse of each film was quick; response time appeared to be limited by the response of the voltmeter. At all loads, the photovoltage/photocurrent was stable during the illumination period, typically about 15 min. Short-circuit current density at 70 mW insolation was in the range 12.4-14.4 mA/cm² and fill factors were in the range 0.40-0.47. Figure 2 illustrates the photoresponse as a function of light power. The conversion efficiency decreases somewhat as the light intensity increases. Thus at 40, 70, 80, and 100 mW insolation, the conversion efficiency is 5.9%, 5.9%, 5.1%, and 4.7%, respectively, for a film having a surface area of 1 cm². When the surface area was increased to 3.2 cm², the efficiency decreased to 4.0% at 70 mW. Aging the electrolysis solution does not appear to adversely affect the quality of the film. Thus a conversion efficiency of 5.4% is obtained for a film grown from a solution that has been exposed to air for 24h at room temperature.

The effect of other conditions on the properties of the CdSe film are currently under study. Preliminary results indicate that current densities higher than 0.500 mA/cm² give films having efficiencies somewhat lower (ca. 5.0%). Larger selenosulfite anion concentrations have a similar effect.

Scanning electron microscopy reveals the effect of temperature on the surface morphology of the CdSe film. Figure 3A illustrates the surface morphology of the CdSe film on titanium after deposition for 1h and prior to any temperature treatment. At the present time, it is not clear if the cracks occur during electrodeposition or if they result when the film is dried at room temperature. The characteristic cauliflower appearance (3) found for H₂SeO₃-grown CdSe is not evident with our film. Annealing at 500°C for 30 min followed by 9N HCl etch gives the surface illustrated in Fig. 3B. The consequences of the annealing on the surface are not clear at this time.

A cyclic voltammogram (CV) of the deposition solution at room temperature is illustrated in Fig. 4. Second and subsequent scans exhibit currents higher than the first one given in Fig. 4, and the first peak shifts 70 mV in the positive direction. The CV's were obtained under condi-

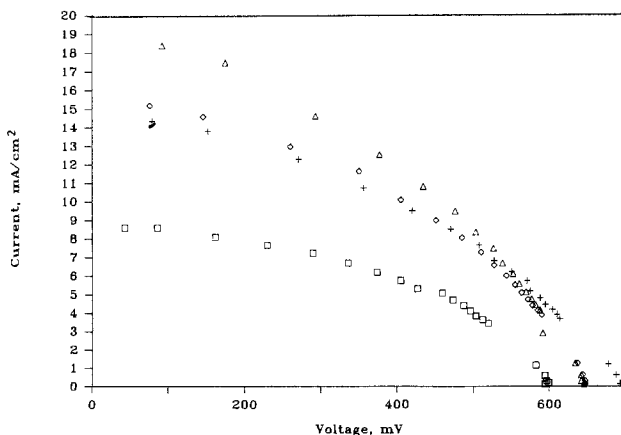


Fig. 2. Photocurrent/photovoltage results as a function of light flux for 1 cm² CdSe film 1.3 μm thick in PEC containing aqueous polysulfide. □: 40 mW + 70 mW. ◇: 80 mW. △: 100 mW.

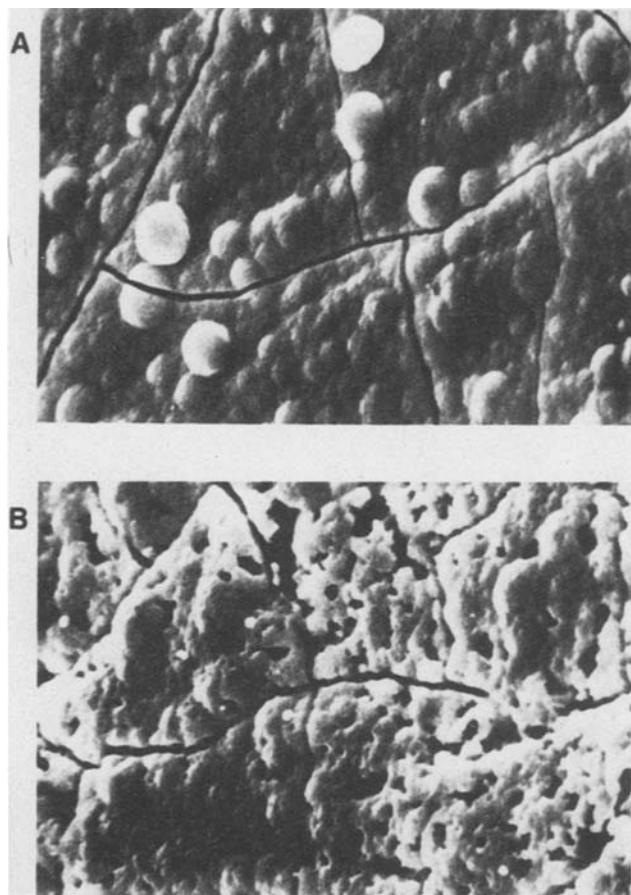


Fig. 3. Scanning electron micrographs of electrochemically deposited CdSe films on titanium. Magnification, 3250X; angle, 45°. A: As deposited. B: Annealed at 500°C for 30 min in air.

tions very close to those employed for film preparation, *i.e.*, same concentrations and electrode except the surface area of the titanium was reduced to 0.08 cm².

For several reasons, the details of the electrodeposition process are not clear at this time. First, CV of Cd²⁺ + NTA exhibits a peak at potential close to that in Fig. 4. Second, CV of SeSO₃²⁻ exhibits peak 200 mV more negative than first peak in Fig. 4. Third, in both these cases, the current is not enhanced on the second and subsequent scans. Fourth, polarographic studies of the reduction of the various species alone and when mixed indicates that the mixture exhibits an additional wave that may result from an interaction between SeSO₃²⁻ and either free or complexed cadmium ion. Consequently, the results thus far indicate several possibilities that are currently under study.

Acknowledgments

We thank Professor W. R. Fawcett for sharing the polarographic analyzer and the Sloan Dektak with us, and Professor J. R. MacDonald for allowing the use of the Van

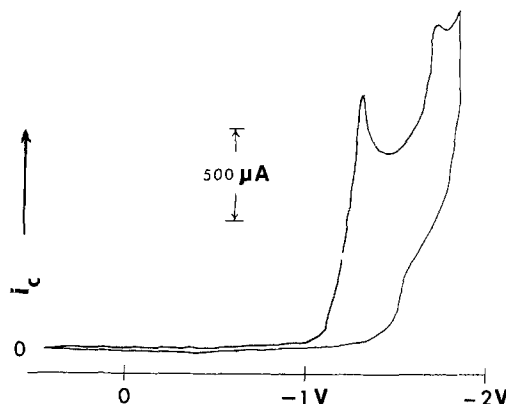


Fig. 4. Cyclic voltammogram at room temperature and 100 mV/s for an aqueous solution containing 0.6M sulfite, 0.02M selenosulfite, 0.022M cadmium chloride, and 0.28M sodium nitrilotriacetate at pH 9. Titanium electrode area is 0.08 cm². Reference is SCE.

de Graaff accelerator. We are pleased to acknowledge helpful discussions with Dr. A. S. Baranski. This work was supported in part by the Natural Sciences and Engineering Research Council of Canada.

Manuscript submitted April 9, 1984; revised manuscript received June 20, 1984.

The University of Guelph assisted in meeting the publication costs of this article.

REFERENCES

1. M. Skyllas-Kayacos and B. Miller, *This Journal*, **127**, 869 (1980).
2. G. Hodes, J. Manassen, and D. Cahen, *Nature (London)*, **261**, 403 (1976); *Bull. Isr. Phys. Soc.*, **22**, 100 (1976).
3. M. Tomkiewicz, I. Long, and W. S. Parsons, *This Journal*, **129**, 2016 (1982).
4. R. A. Boudreau and R. D. Rauh, *Solar Energy Mater.*, **7**, 385 (1982).
5. Preliminary report: M. Cocivera, *Chem. Commun.*, 938 (1984).
6. R. A. Boudreau and R. D. Rauh, *This Journal*, **130**, 513 (1983).
7. M. Skyllas-Kazacos, *J. Electroanal. Chem.*, **148**, 233 (1983).
8. M. Skyllas Kazacos and B. Miller, *This Journal*, **127**, 2378 (1980).
9. "CRC Handbook of Chemistry and Physics," 46th Ed., R. C. Weast, Editor, p. B161, Chemical Rubber Co., Cleveland, OH (1965).
10. G. Hodes, D. Cahen, J. Manassen, and M. David, *This Journal*, **127**, 2252 (1980).
11. G. Hodes, J. Manassen, and D. Cahen, *ibid.*, **127**, 544 (1980).
12. T. S. West, "Complexometry with EDTA and Related Reagents," 3rd Ed., p. 221, BDH Chemicals Ltd., Poole (1969).
13. G. S. Klevonov and N. A. Ostrapkevich, *Zh. Prikl. Khim.*, **35**, 1199 (1962).
14. W. K. Chu, J. W. Mayer, and M. A. Nicolet, "Backscattering Spectrometry," Chap. 2, Academic Press, New York (1978).

Reduction of CO₂ on n-GaAs Electrodes and Selective Methanol Synthesis

K. W. Frese, Jr.* and D. Canfield

SRI International, Materials Research Laboratory, Menlo Park, California 94025

ABSTRACT

Faradaic efficiencies and current voltage characteristics for the reduction of CO₂ to CH₃OH on n-GaAs (111 As) single-crystal electrodes have been determined. The yield of CH₃OH is ~ 100% for current densities of ~ 140 μA/cm² at -1.2 to -1.4V vs. SCE. The excess current due to CO₂ was found to have a threshold at pH ~ 3.6 and a maximum at pH ~ 4.3. The current also exhibited a rotation-independent *j/v* characteristic that is interpreted as a rate-determining surface chemical combination step involving adsorbed H atoms and a carbon containing intermediate. The pH dependence of the saturation current is modeled with a kinetic scheme involving the parallel reduction of H⁺ and CO₂.

Over the past 40 years, there have been a number of studies dealing with CO₂ reduction at metal electrodes (1, 2). Recently, we have been investigating the reduction of CO₂ at semiconductor electrodes. One goal of the semiconductor approach is to utilize the electrochemical properties of p-type photocathodes to convert sunlight and CO₂ into useful fuels. It is known that CO₂ can be reduced to methanol and small amounts of methane on certain semiconductor electrodes in aqueous solutions (3-6). Our results (7) on electrolysis of CO₂ solutions using n- or p-GaAs and p-InP electrodes show that methanol is the major product (pH 4-6). These studies involving semiconductor electrodes, however, have mainly concerned product identification and yield.

Our purpose is to investigate aspects of the kinetics of CO₂ reduction on semiconductor electrodes. In this paper, we report measurements of the current voltage characteristics of a rotating disk n-GaAs electrode as a function of pH and rotation rate in the presence of N₂ and CO₂.

The faradaic efficiency for CH₃OH as a function of current density has also been determined. The results, especially the saturation current for CO₂ reduction, are modeled by kinetic analysis of a set of tentative elementary steps.

Experimental

Single-crystal disks, 5 mm diam, were mounted in a Pine Rotating-ring disk arrangement. Rotation speed was controlled by means of a Pine analytical rotator.

The crystal face was n-GaAs (111 As). The electrodes were first etched with 1% Br₂/CH₃OH and rinsed for 10s with 1M HCl. The GaAs electrodes were further etched in 1% sodium hypochlorite/0.1M Na₂ EDTA at pH 10. All etching was done with a wet cotton tip applicator. Finally, all electrodes were rinsed with distilled water.

All solutions were prepared with distilled, deionized water and reagent-grade chemicals, unless otherwise noted. High purity N₂ was passed through the electrolyte to remove dissolved oxygen. The electrode potential was swept at 1 V/min by means of a Pine RDE-3 potentiostat. The initial voltage for all sweeps was -0.5V SCE. All experiments were performed at room temperature, 22°C.

Electrolyte pH was controlled by addition of H₂SO₄ or NaOH solutions. When pH was varied, it was checked before and after each scan to make sure it had not changed.

Experimental Results

Current-voltage curve.—Current-voltage curves for n-GaAs (111)As in N₂-saturated and CO₂-saturated 0.2M Na₂SO₄ electrolyte (pH = 4.0) are shown in Fig. 1. Before these curves were obtained, the rotating disk electrode was held at -1.2V vs. SCE in the same N₂-saturated electrolyte but with pH = 3.4 and 1600 rpm rotation speed. It was observed that the current increased with time until a steady current of 2.5 mA/cm² was reached after a period of about 10 min. A typical current-time curve is shown in the inset

in Fig. 1. This pretreatment was chosen because we wanted to make measurements with the surface conditions close to those obtained in our extended electrolysis experiments (7) that are performed at -1.2 to -1.4V vs. SCE in a similar electrolyte (pH = 4-5). In those experiments, we always observed changes in the initial current voltage characteristics for about 30-60 min, then steady conditions are found for at least 70h. The probable cause for the longer current transient is that the pH is higher than in the present case.

Returning to Fig. 1, the onset for excess current due to CO₂ is -0.95V. Both curves with N₂ or CO₂ showed saturation behavior starting to -1.1 to -1.2V. This portion of the curve corresponds to diffusion-limited H⁺ reduction, and in the case of CO₂ solution to the simultaneous reduction of H⁺ and CO₂. Beyond -1.4V, a steep rise in current was observed with either gas present. This current is apportioned between H₂O and CO₂ reduction. It should be noted that the pH of the electrolyte was constant before and after each measurement. The saturation currents (N₂ present) depended on rotation speed, but the magnitude of the excess current due to CO₂ was almost constant up to -1.4V at pH 4.

Effect of rotation speed.—Figure 2 illustrates the dependence of the excess current in the presence of CO₂ as a function of rotation rate and electrode potential. These curves were constructed by direct subtraction of points on the N₂ and CO₂ curves at each voltage. The rotation rate was varied from 100 to 2500 rpm. This electrode was also pretreated as in Fig. 1. It can be seen that at pH 4.2, the excess CO₂ current was independent of rotation speed and showed saturation behavior over a voltage range between -1.15 and -1.40V. The saturated current density was ~ 1.4 × 10⁻⁴ A/cm². At potentials negative of -1.4V,

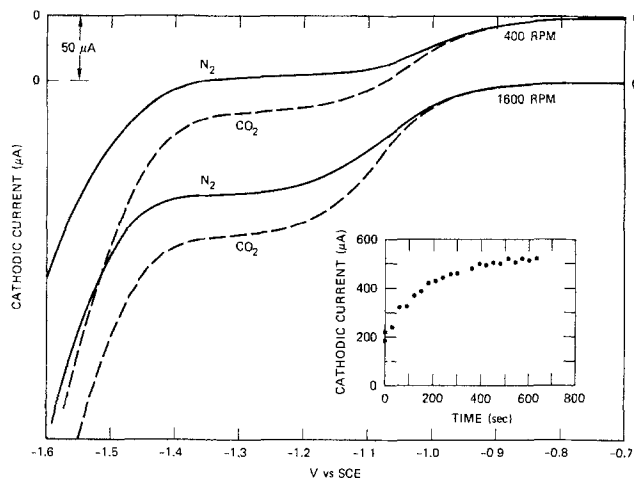


Fig. 1 Current-voltage curves in N₂ and CO₂ saturated 0.2M Na₂SO₄ solution, pH = 4.0, for n-GaAs (111) As face disk at two rotation speeds. Inset shows pretreatment current as function of time at -1.2 vs. SCE, pH = 3.4 same electrolyte (N₂). Area 0.2 cm².

*Electrochemical Society Active Member.

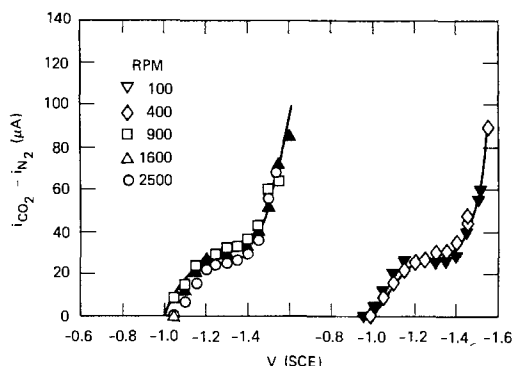


Fig. 2. Excess cathodic current due to CO₂ vs. electrode potential and rotation speed. n-GaAs, (111) As, in CO₂-saturated 0.1M Na₂SO₄, pH = 4.2. Area, 0.2 cm². Pretreatment as in Fig. 1.

an increase in excess current was observed. This characteristic also appeared to be independent of rotation rate.

A more detailed study of the rotation dependence of the cathodic current in the presence of N₂ or CO₂ was made. The results are shown in Fig. 3. With only N₂ present at pH = 4.2, a diffusion-limited H⁺ reduction wave was obtained as shown by the linear plot of i vs. (rpm)^{1/2}. A diffusion coefficient of 7.0×10^{-5} cm²/s was calculated from the slope assuming a proton activity coefficient (8) of 0.76. This diffusion coefficient was obtained at 22°C; correction to 25°C using 3.1 kcal/mol (9) activation energy yields 7.4×10^{-5} cm²/s, in good agreement with data obtained in KCl electrolyte (9). When the electrolyte was saturated with CO₂, plots of i vs. (rpm)^{1/2} were again linear with nearly the same slope as in the N₂-saturated case. Importantly, the intercepts of these plots were nonzero and depended on the electrode potential. A plot of the intercept vs. potential is shown in the inset to Fig. 3. Note the similarity of this i-V curve obtained in CO₂-saturated solution and those shown in Fig. 2 that were calculated by difference from data pairs in CO₂ and N₂ saturated electrolytes at constant rotation speed.

Effect of pH.—Cathodic current vs. pH and electrode potential was measured in both N₂- and CO₂-saturated electrolytes. The results for a rotation speed of 400 rpm are shown in Fig. 4. The lower curves in each panel correspond to the N₂ case, and the upper curves to the CO₂ case. In order to obtain reproducible results over the whole pH range that we investigated, we had to etch the

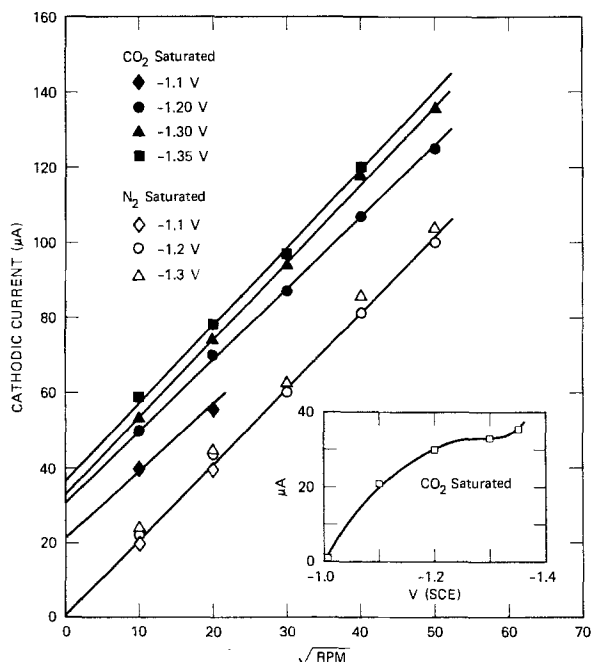


Fig. 3. Cathodic current vs. rotation speed and electrode potential for n-GaAs (111)As face in 0.2M Na₂SO₄. Pretreatment as in Fig. 1. pH = 4.2. Area = 0.2 cm². Inset shows i-V curve from i vs. RPM intercepts with CO₂ present.

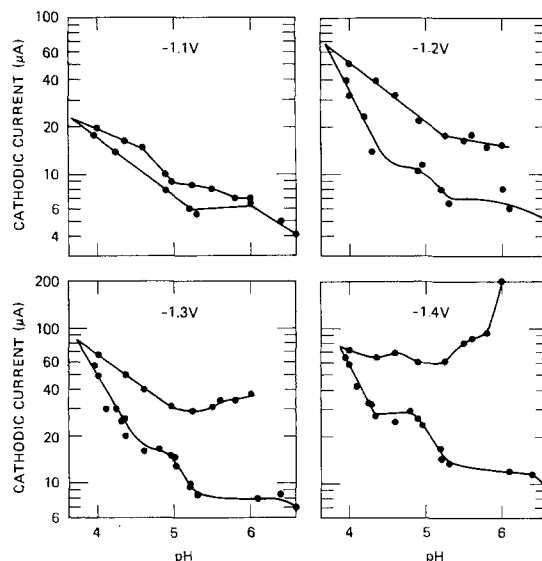


Fig. 4. Current vs. pH at various electrode potentials for n-GaAs (111)As in N₂- (lower curve) and CO₂- (upper curve) saturated electrolytes. 0.2M Na₂SO₄. Etch pretreatment only. Rotation speed, 400 RPM. Electrode area, 0.2 cm².

crystal before each i-V scan at a given pH. Therefore, the electrode was given the same etch pretreatment before each data point in Fig. 4. This treatment consisted of a 2s rinse in 1M HCl, 10s distilled H₂O rinse, followed by a 20s etch with 1% v/v sodium hypochlorite in pH 9 aqueous solution, and final H₂O rinse. In all cases, the etched electrodes shed rinse water immediately on contact. Generally, these surfaces are considered to be much closer to stoichiometric than the cathodically pretreated ones (Fig. 1-3). In the pretreated case, some surface roughening and cathodic corrosion giving at least a Ga monolayer is expected.

Inspection of the curves in Fig. 4 reveals that excess CO₂ current was first detected at pH values of 3.6, 3.7, 3.7, and 3.9 for -1.1, -1.2, -1.3, and -1.4V, respectively. The reaction orders for H⁺ reduction with N₂, $d \log i/dpH$ were 0.37, 0.95, 0.91, and 0.97 for the same electrode potentials. The numbers were calculated from the straight lines in the most acid region of the plot. These unit reaction orders are consistent with diffusion-controlled reduction of hydrogen ions. Another approximate calculation of D_{H^+} was performed by extrapolation of the current at -1.3V (N₂ present) to pH = 0. A diffusion coefficient of 7.0×10^{-5} cm²/s was found, in good agreement with our earlier determination. Under less acidic conditions, the reaction order approached zero and then came close to unity again. The deviation in reaction order with respect to the hydrogen ion may be caused by reduction of a thin (perhaps mono) layer of adsorbed species which are more stable at certain pH values. We assume this effect is constant for both N₂- and CO₂-saturated electrolytes. The electrolyte was saturated with CO₂, and the i-V curves at each pH were determined, again, after a standard etch for each pH value. The general pattern was that the apparent reaction order with respect to hydrogen ion decreased when CO₂ was present.

Then, plots of $i_{CO_2} - i_{N_2}$ vs. pH at a fixed potential were constructed; the results are shown in Fig. 5. The excess current began at a pH of 3.5-3.9 and increased to a maximum at pH 4.3 and then, depending on voltage, increased sharply again.

Finally, the $i_{CO_2} - i_{N_2}$ data were plotted vs. electrode potential with pH as a variable, as shown in Fig. 6. Strikingly different i-V curves at each pH were observed. The onset potential was similar to that already observed in Fig. 1 and 2, namely, $\sim -1.0V$. At pH 4.0, a saturation current was also found between -1.2 and -1.4V. As the pH increased, the saturation portion narrowed and a sharp increase became very noticeable. At pH 6, the saturation characteristics completely disappeared. Tafel plots of the

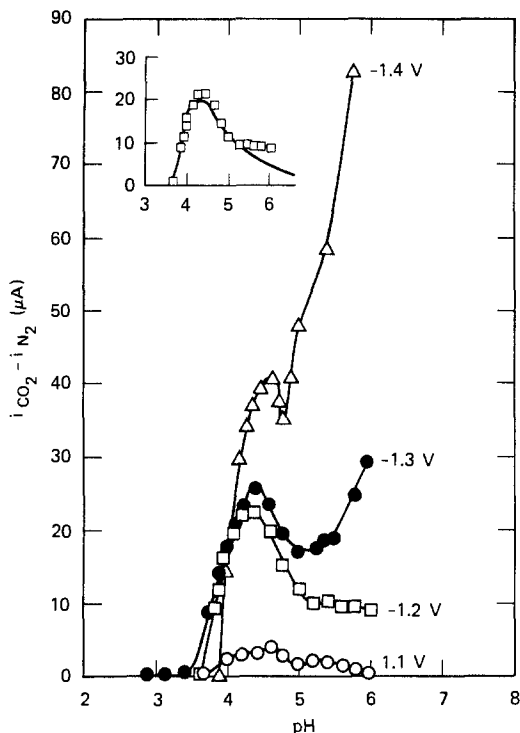


Fig. 5. Excess current due to CO_2 vs. pH, electrode potential. n-GaAs (111) As. Rotation speed, 400 rpm. Area, 0.2 cm^2 . $0.2M \text{ Na}_2\text{SO}_4$. Inset shows kinetic model fit for pH variation of saturation current, $i_{CO_2} - i_{N_2}$. Solid line calculated, data squares from $-1.2V$ curve below.

i-V curves for pH 5.8-6.0 and the more cathodic portion of the pH 5.5 curve are shown in the inset. The Tafel slopes were 220-230 mV.

Electrolysis and chemical analysis.—We performed long-term (17-20h) electrolysis experiments using two dif-

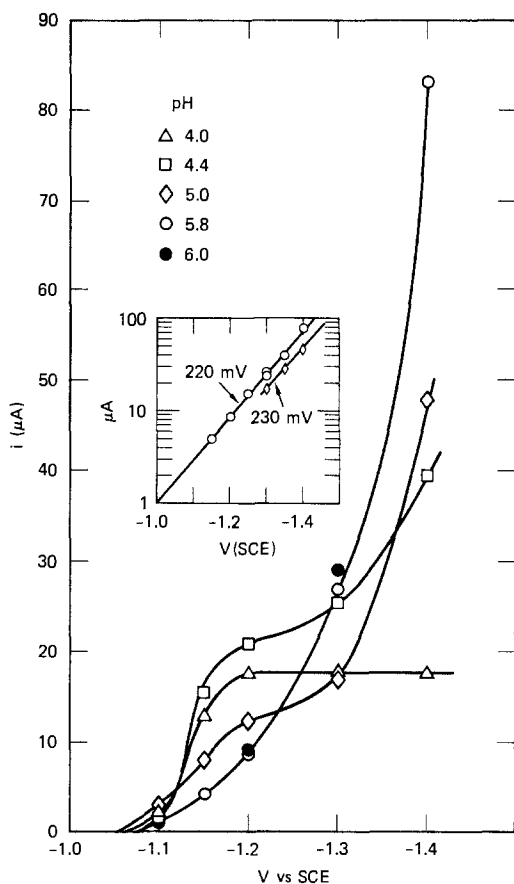


Fig. 6. Current-voltage curves for CO_2 reduction at various pH values using n-GaAs (111)As in $0.2M \text{ Na}_2\text{SO}_4$. Inset shows Tafel plots for most alkaline pH values. Area, 0.2 cm^2 .

ferent Na_2SO_4 electrolytes that were saturated with CO_2 , initial pH 4.2. The details of these experiments, analytical procedures, and more complete results have been tabulated (7). The objective was to determine the reduction products and obtain faradaic efficiencies.

Analysis for methane, methanol, formaldehyde, and CO was performed. The electrolysis was conducted at various current densities (based on geometrical area) using n-GaAs (111)As crystals similar to those that were used in the *i-V* measurements reported above.

Occasionally, only traces of CH_4 were observed. Faradaic efficiencies for formaldehyde were always very low, $< 1\%$. Also, efficiencies for CO were usually $\sim 1\%$. However, the efficiencies for methanol were high and depended on current density, as shown in Fig. 7. Note that in an electrolyte made from 99.999% Na_2SO_4 and high purity water, no methanol was formed. This effect will be discussed more fully in later reports. The results with the Ga (111) face were similar except that methanol was produced in either reagent-grade or high purity electrolyte.

At a current density of $\sim 1.4 \times 10^{-4} \text{ A/cm}^2$, the efficiency for methanol was 100%. At $5 \times 10^{-4} \text{ A/cm}^2$, the methanol efficiency dropped to low values with either face.

Electrolysis of similar electrolytes at pH 5.8-6, gave some formate ion product, as shown by qualitative analysis using the mercuric chloride test (10). Formate has been shown to be the major product on Hg electrodes (11) in this same pH range. Methanol has also been found at pH up to 6.7 with current efficiencies $> 10\%$.

Discussion

In this section, we will discuss our results in light of a plausible reaction mechanism for CO_2 reduction. A number of key experimental observations can be summarized as follows. The excess current due to CO_2 saturates at $\sim 140 \mu A/cm^2$ (cathodically pretreated surface, Fig. 2 and 3) and at $\sim 90 \mu A/cm^2$ on an as-etched surface (Fig. 6). This saturation current is independent of rotation speed from 100 to 2500 rpm. This behavior suggests that the current is controlled by a chemical surface reaction with nearly saturation coverage with adsorbed intermediates. The faradaic efficiency for CH_3OH reaches 100% at a current density of $\sim 140 \mu A/cm^2$. This value is remarkably close to the saturation current for a similarly activated electrode. Also, the pH has a pronounced influence on the excess current, $i_{CO_2} - i_{N_2}$. Two critical pH values were found (Fig. 5); a low value when the excess current is immeasurably small, and a higher value where a maximum occurs. Finally, the reduction of H^+ is diffusion controlled in the presence of CO_2 (Fig. 3). According to the analysis of Pleskov (12), plots of current density vs. $(rpm)^{1/2}$ like those in Fig. 3 (CO_2 present) indicate that rapid diffusion-controlled H^+ reduction occurs in parallel with a slower

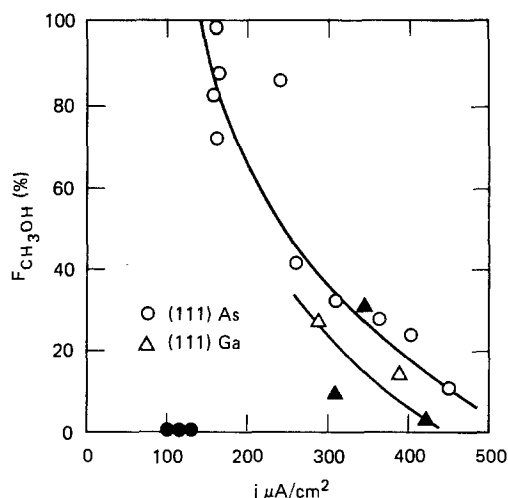


Fig. 7. Faradaic efficiency for CH_3OH on n-GaAs in CO_2 -saturated $0.2M \text{ Na}_2\text{SO}_4$. Open symbols = reagent grade salt/distilled water. Solid symbols = 99.999% salt/ $1.7 \times 10^7 \Omega \cdot \text{cm}$ water. $10^{17} \text{ donors/cm}^2$.

activation-controlled process. This factor is used in formulating the parallel reaction mechanism below. An increase in current at more cathodic voltages (Fig. 2 and 6) indicates a change in mechanism. At pH values 5-6, Tafel slopes of 220-230 mV/decade were observed. We will first focus on the saturation current and the effect of pH.

The data presented here do not, of course, allow for identification of the chemical species involved in all the mechanistic steps. However, the data do provide important clues concerning the overall reaction sequence and the rate-determining step in CO₂ reduction to methanol.

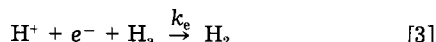
In the following discussion, we will assume that under reaction conditions, the GaAs rotating disk electrode surface contains adsorbed hydrogen atoms. It is further assumed that the steady-state coverage with hydrogen, θ , is mainly controlled by the convective diffusion of H₃O⁺ ions. The value of θ will depend on the rate of removal of H atoms and the diffusion properties. In the following, the subscript "a" indicates adsorbed on the surface. When the combination reaction is rate determining in the hydrogen evolution reaction, HER, we have



By equating the current for Eq. [1] with the Levich equation (12), we obtain

$$\theta = \left(\frac{A}{k_c} \right)^{1/2} (\text{rpm})^{1/4} (\text{H}^+)^{1/2} \quad [2]$$

where $A = 0.017 (D_{\text{H}^+})^{2/3}$, D and H^+ are expressed in units of 10⁻⁵ cm/s and mol/liter, respectively. Similarly, when the electrochemical desorption is rate determining

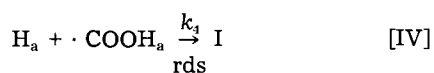
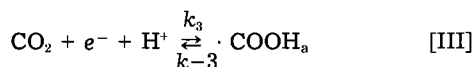
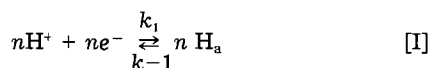


and

$$\theta = \frac{A(\text{rpm})^{1/2}}{k_g} \quad [4]$$

According to Eq. [2], the hydrogen coverage depends on the square root of the proton concentration and depends slowly on rotation rate. For the second case of electrochemical desorption, θ is independent of H^+ and varies more strongly with stirring.

Now, consider the following elementary scheme of steps to account for the saturation of $j_{\text{CO}_2} - j_{\text{N}_2}$ and its pH dependence.



followed by four additional hydrogenation steps to give methanol via additional intermediates, I. We have no specific evidence for the identity of these intermediates, I. For example, I in step [IV] could be CO_{ad}. For H₂ and CH₃OH reduction products, n would equal seven. Adsorbed formate radicals are believed to be the precursor to CO₂ in the oxidation of formic acid (13) and to be the product of the one electron reduction of CO₂ on Hg electrodes (11, 14).

The key to explaining the saturation current and its pH dependence is the assumption that the rate of CO₂ reduction (methanol formation) is limited by a surface chemical reaction involving H_a. For simplicity let us say that step [IV] is rate limiting. The total current in the presence of CO₂ is then given by

$$j_{\text{CO}_2} = 2k_c\theta^2 + 6k_4\theta\gamma \quad [5]$$

where γ is the surface coverage with formate radicals. An expression for γ can be obtained by the usual steady-state method. Under saturation conditions, we simply write $\theta + \gamma = 1$. Other analogous rate-determining steps involving H_a and species I would lead to a relation similar to Eq. [5] (consecutive step reaction). Using our expression for θ (combination reaction) Eq. [2], and conservation of sites, we obtain the following expression for the experimentally determined $j_{\text{CO}_2} - j_{\text{N}_2}$

$$j_{\text{CO}_2} - j_{\text{N}_2} = 6k_3B(\text{H}^+)^{1/2} [1 - B(\text{H}^+)^{1/2}] \quad [6]$$

where

$$B = [A/k_c]^{1/2} (\text{rpm})^{1/4}$$

According to Eq. [6], the excess current should go to zero when $(\text{H}^+)_0 = k_c/A(\text{rpm})^{1/2}$; and it should be maximum at $(\text{H}^+)_{\text{max}} = k_c/4A(\text{rpm})^{1/2}$. In addition, the model predicts $\text{pH}_{i=\text{max}} - \text{pH}_{i=0} = \log 4$. From Fig. 5, we see that for -1.2V, the excess current is maximum at pH = 4.3 and goes to zero at pH = 3.6. Therefore $\Delta\text{pH} = 0.7$ agrees with the predicted value $\log 4 = 0.6$.

We can calculate a value for k_c in current density units by applying the equation for $(\text{H}^+)_{\text{max}}$ just mentioned above. Using the appropriate constants for A , and an activity coefficient of 0.76, we obtain $k_c = 3.2 \times 10^{-4}$ A/cm². Using this value of k_c , we can calculate $B = 62.4M^{-1}$. Returning to Eq. [6] and noting the saturation current at pH = 4.2 of 90 $\mu\text{A}/\text{cm}^2$ (Fig. 6), we can calculate that $k_4 = 6.1 \times 10^{-5}$ A/cm².

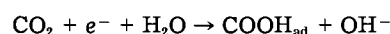
It is of interest to compare the surface combination rate constants determined here with those deduced (15) from limiting current behavior for Cl₂ evolution. Here, the reaction rate is limited by combination of Cl atoms on the surface. On oxide-free Pt electrodes in anhydrous trifluoroacetic acid, k_c ranges from 300 to 1500 $\mu\text{A}/\text{cm}^2$, depending on coverage of Cl atoms. Our values, particularly for the H atom combination are in the same range. A more realistic comparison would involve rate calculations based on details of the energy surfaces for the adsorbed H_a and COOH_a on the GaAs electrode. Unfortunately, these are not available.

At this stage, we can calculate the complete pH dependence of the saturation current using Eq. [6] and our rate constants. The inset to Fig. 5 shows the model prediction (solid line) and the data points for -1.2V. The fit is seen to be good. If θ were determined by the electrochemical desorption in the HER Eq. [4], no maximum is predicted in the saturation current vs. pH. At pH > 5, the observed current is slightly above the calculated curve; this is probably due to a faster process taking over. This also explains why the -1.4V peak (Fig. 5) appears larger than the -1.2 and -1.3V peaks.

We now consider some other features of the $j_{\text{CO}_2} - j_{\text{N}_2}$ curve. As we have seen, at more cathodic potentials (Fig. 2, 5, and 6), different i-V characteristics were observed. At pH 4.2, a rotation-independent increase in excess current was found, beginning at -1.4V (Fig. 2). The Tafel shapes for these two plots are 152 and 134 mV/decade. It is not clear if these slopes depend on rotation rate or if the data is imprecise. At pH 5-6, the i-V curves are dominated by characteristics with Tafel slopes of 220-230 mV/decade (400 rpm) and no saturation effect is observed.

From the earlier discussion concerning the saturation current, it is clear that under our reaction conditions the surface is nearly saturated with adsorbed intermediates. Therefore, Temkin-type analysis with the possibility of activated adsorption must be applied (16).

We have not done a complete analysis of these effects, and, therefore, a detailed interpretation of the Tafel slopes must be postponed. However, we note that Tafel slopes of 224 mV/decade were already observed (14) for CO₂ reduction on Hg electrodes in NaHCO₃ solution. In that case (11, 14), the rate-determining step ($j > 10^{-5}$ A/cm²) was concluded to be



The reaction product was stated to be formate (98% current efficiency). At $\text{pH} > 5$, it is reasonable to expect that the coverage on GaAs with H_{ad} is also low and hydrogen has to be obtained from H_2O .

Now consider the effect of current density on the faradaic efficiency, $F_{\text{CH}_3\text{OH}}$, for methanol. These measurements were made at -1.3 to -1.4V (SCE) in CO_2 -saturated solutions with an initial pH of 4.1-4.2. There is a close correspondence between this current density of $F_{\text{CH}_3\text{OH}} = 100\%$ and the saturation current in Fig. 2 for a cathodically pretreated electrode. Both these values are $\sim 140 \mu\text{A}/\text{cm}^2$. If the total current is increased beyond this value, the yield of methanol should drop if the limiting rate of methanol formation corresponds to the saturation current. This appears to be the case as shown in Fig. 7. Apparently, another CO_2 reduction product is formed at high current densities as demonstrated by the drop in methanol yield and the simultaneous rise in excess current, as shown in Fig. 2. This current may correspond to the reduction of the adsorbed formate radicals that were postulated to be reactants in the surface chemical rate-limiting step of methanol synthesis.

According to our model, the yield of CH_3OH will depend on the coverage of H atoms. Recall that we assume only H_a and I, which may be $\cdot\text{COOH}$, are the only important intermediates in the mechanism. Using Eq. [5] and the observed rate constants, k_c and k_3 , we can write

$$F_{\text{CH}_3\text{OH}} = \frac{6k_4\theta\gamma}{j_{\text{CO}_2}} = \frac{1}{1 + 1.75 \left(\frac{\theta}{1 - \theta} \right)} \quad [7]$$

It may be seen that methanol yield increases as θ decreases. For $\theta = 0.5$ and 0.1 , $F_{\text{CH}_3\text{OH}}$ is 0.36 and 0.84, respectively. Even though $k_4 < k_c$, the yield of methanol can reach high values as found experimentally. In the limit of $\theta = 0$, Eq. [7] is undefined.

The question of the acidity of the postulated adsorbed formate radicals is not completely answerable at this time. It has been suggested that adsorbed CO_2^- is the dominant first electron product based on the reported pK_a of 1.4 (18) for free aqueous formate radicals. However, the value of 3.9 has also been reported (19) for the same radical. We reason that is more appropriate to estimate the acidity of adsorbed formate radicals by analogy to organic acids. There appears to be little quantitative data on the pK_a 's of metalcarboxylic acids (20, 21); however, many organic acids with different hydrocarbon substituents have been studied. In many cases (22), the pK_a 's are in the range of 4.7 to 5.0. In addition, substituent effects can change the K_a 's by an order of magnitude. If bonding of radicals occurs to the more electropositive Ga atoms on the surface, then the pK_a of the adsorbed radical might exceed 5.0. The negative charge at the cathodic surface may also act to further increase the pK_a . For example (22), introduction of the $-\text{CO}_2^-$ group for a methyl hydrogen in acetic acid raises pK_a from 4.76 to 5.69. Finally, adsorbed CO_2^- would be less favorable, owing to lateral repulsions on the surfaces. In summary, because of the above chemical and physical effects, protonated CO_2^- radicals are a distinct possibility as suggested in our mechanism, step [III], for $\text{pH} \leq 5$.

Summary

Carbon dioxide can be reduced to methanol on n-GaAs (111 As) electrodes with high faradaic efficiencies for current densities of $\sim 150 \mu\text{A}/\text{cm}^2$. Methanol synthesis appears to be limited by a surface chemical step involving adsorbed hydrogen and an unidentified surface intermediate. Possible intermediates are CO_{ad} ; formyl, $-\text{COH}$; hydroxycarbene, $-\text{CH}-\text{OH}$; hydroxymethyl, CH_2-OH ; or methoxy, $-\text{O}-\text{CH}_3$.

Analysis of the pH dependence of the saturation current led to information on the HER. We used the assumption that hydrogen is formed by the combination reaction. This step was already proposed as part of the HER on GaAs electrodes (17). A chemical rate constant of $3.2 \times 10^{-4} \text{A}/\text{cm}^2$ for the H_2 combination was obtained. The pH dependence of the saturation current in the presence of CO_2 could be fit with parameters derived from the data. The analysis gave a chemical rate constant of $6.1 \times 10^{-5} \text{A}/\text{cm}^2$ for the rate-determining step.

The results given here show that very complex catalytic reactions can be performed on semiconductor surfaces in electrochemical cells. A start has been made towards understanding such mechanisms as CH_3OH synthesis. There appears to be pH and voltage range for certain mechanisms or products.

The onset potentials for CH_3OH synthesis are quite cathodic, which means, the energy efficiency, for the process is low. The use of p-type cathodes and/or n-type photoanodes in electrolysis cells could significantly alter this situation.

Manuscript submitted July 11, 1983; revised manuscript received June 8, 1984. This was Paper 517 presented at the San Francisco, California, Meeting of the Society, May 8-13, 1983. This work was supported by the Gas Research Institute.

SRI International assisted in meeting the publication costs of this article.

REFERENCES

1. P. G. Russel, N. Kovac, S. Srinivasan, and M. Steinberg, *This Journal*, **124**, 1329 (1977) and references therein.
2. S. Kapusta and N. Hackerman, *ibid.*, **130**, 607 (1983).
3. M. Halmann, *Nature*, **275**, 115 (1978).
4. T. Inoue, A. Fujishima, S. Konishi, and K. Honda, *ibid.*, **277**, 637, (1979).
5. B. Aurian-Blajeni, M. Halmann, and J. Manassen, *Solar Energy*, **25**, 165 (1980).
6. K. W. Frese, Jr. and D. G. Canfield, SRI Quarterly Report no. 1 July (1982) and SRI Quarterly Report no. 2 October (1982), "Reduction of CO_2 to Methanol and Methane by Photo and Dark Reactions on Semiconductor Electrodes," Sponsored by Gas Research Institute, 1982.
7. D. Canfield and K. W. Frese, Jr., *This Journal*, To be published.
8. R. A. Robinson and R. H. Stokes, *Trans. Faraday Soc.*, **612** (1949).
9. Von B. Gostisa-Mihelcic, W. Veilstick, and A. Heindrichs, *Ber. Bunsenges. Phys. Chem.*, **76**, 21 (1972).
10. F. Feigl, V. Amger, and R. Oesper, "Spot Tests in Organic Analysis" p. 453 Elsevier Publishing, Amsterdam (1966).
11. W. Paik, T. N. Andersen, and H. Eyring, *Electrochim. Acta*, **14**, 1217 (1969).
12. F. Opekar and P. Beran, *J. Electroanal. Chem.*, **69**, 1 (1976).
13. J. Horiuti, in "Physical Chemistry, An Advanced Treatise", Vol. IXB, H. Eyring, Editor, p. 1, Academic Press, New York (1970).
14. J. Ryu, T. N. Andersen, and H. Eyring, *J. Phys. Chem.*, **76**, 3278 (1972).
15. B. E. Conway and D. M. Novak, *J. Electroanal. Chem.*, **99**, 133 (1979).
16. B. E. Conway, "Principles of Electrode Kinetics," Ronald Press (1965).
17. K. D. N. Brummer, *This Journal*, **114**, 74 (1967).
18. G. V. Buxton and R. M. Sellers, *J. Chem. Soc. Faraday Trans.*, **69**, 555 (1973).
19. A. Fojtik, G. Czapski, and A. Henglein, *J. Phys. Chem.*, **74**, 3204 (1970).
20. R. Laine and R. B. Wilson, in "Aspects of Homogeneous Catalysis," Vol. 5, R. Ugo, Editor, D. Reidel Publishing Co. (1984).
21. N. Grice, S. C. Kao, and R. Pettit, *J. Am. Chem. Soc.*, **101**, 1627 (1979).
22. H. C. Brown, D. H. McDaniel, and O. Haflinger, in "Determination of Organic Structure by Physical Methods," E. A. Braude and F. C. Nachod, Editors, Academic Press, New York (1955).

Anode-Limited Cell Reversal in Lithium-Sulfur Oxyhalide Cells

Alan I. Attia*,¹ and Christian Sarrazin

Gould Research Center, Rolling Meadows, Illinois 60008

Kenneth A. Gabriel and Richard P. Burns

Department of Chemistry, University of Illinois at Chicago, Chicago, Illinois 60680

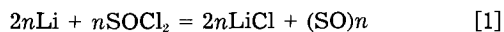
ABSTRACT

In situ infrared spectroscopy and mass spectrometry were used to investigate the gas and liquid phases in lithium-sulfur oxyhalide cells driven into anode-limited reversal at 1.5 mA/cm². In the lithium-thionyl chloride system the species HCl, CS₂, SO₂, S₂O, SCl₂, and SO₂Cl₂ were identified in the gas phase and HCl, AlCl₃OH⁻, SO₂, SO₂Cl₂, and SOCl⁺ AlCl₄⁻ in the liquid phase. A species giving rise to three absorption bands at 1337, 1070, and 665 cm⁻¹ was observed in the liquid phase of that system during anode-limited reversal only, and in the lithium sulfuryl chloride system during normal discharge and during reversal; this compound was tentatively identified as Li(SO₂, SO₂Cl₂)⁺ AlCl₄⁻ and is analogous to the well-known complexes involving LiAlCl₄, SO₂, and SOCl₂. The lithium-sulfuryl chloride cell behaved similarly to the thionyl chloride cell, specifically with respect to formation of SO₂- and SOCl⁺-like species—the latter tentatively identified as SO₂Cl⁺. Indirect evidence suggests that chlorine may accumulate in both systems at -20°C, but at 25°C its accumulation in the cells is prevented by its reaction with SO₂ to form SO₂Cl₂.

In the ten years since the feasibility of lithium-sulfur oxyhalide cells was first recognized (1), remarkable progress has been made in hardware development; however, their widespread use has been impeded, owing to the safety hazards associated with their relatively high energy density. Conflicting reports exist as to the cause of several explosions involving the lithium-thionyl chloride system. Explosions have been observed in anode-limited cells driven into reversal (2); a hazard also exists in cathode-limited cells since they contain both lithium and sulfur at the end of discharge, and the highly exothermic formation of Li₂S may be possible at elevated temperatures (3, 4). In addition, poor mechanical design is suspected in some cases.

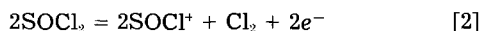
The lithium-sulfuryl chloride cell which does not form any sulfur during discharge is potentially safer than Li/SOCl₂ (5). However, the relatively high corrosion rate of lithium in that system limits its use to special high rate reserve applications.

Resolution of the unpredictable safety hazards associated with these systems may only be possible by analytical determination of their causes, and several investigations have been conducted along these lines. Istone and Brodd (6) have performed an *in situ* infrared study of the electrolyte of Li/SOCl₂ cells and observed that only two absorption bands change in intensity during normal discharge, one at 1335 cm⁻¹ due to SO₂ formation, the other at 689 cm⁻¹ which they assigned to S₂O. Elemental sulfur was also seen to deposit on the spectroscopic cell walls. These authors proposed a mechanism involving formation of SO₂ and S₂O with subsequent decomposition of the S₂O to sulfur and SO₂. This mechanism had been previously rejected on the basis of stoichiometry by Schlaikjer *et al.* (7), who postulated instead the formation of a sulfur monoxide polymer according to the reaction

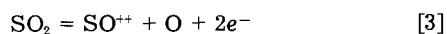


followed by decomposition of the polymer to produce elemental sulfur and SO₂.

Spectroelectrochemical studies first carried out by Abraham and Mank (8) then by Salmon *et al.* (9) have provided evidence that the principal reaction at the anode current collector on reversal is

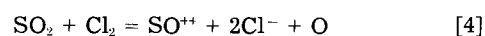


Salmon *et al.* further speculated that several electrochemical reactions involving SO₂ were also occurring



*Electrochemical Society Active Member.

¹Present address: Gould, Incorporated, Micro Power Products Division, Eagan, Minnesota 55121.



IR absorption bands at 1070 and 690 cm⁻¹ were assigned by these authors to SO⁺⁺ and Cl₂O, respectively. Abraham and Mank had observed the 1070 cm⁻¹ band in their investigation but assigned it to an S-O stretching vibration of a sulfur-oxy compound. Under the same conditions, they also observed a band at 1415 cm⁻¹, which they assigned to SO₂Cl₂.

Evidence for a significant involvement of aluminum chloride species in the IR absorption spectrum was obtained by Bailey and Blomgren (10), who identified several aluminates in Li₂CO₃-AlCl₃/SOCl₂ electrolyte giving rise to absorptions at 3200-3400 (AlCl₃OH⁻), 800, and 695 cm⁻¹. The last two bands were assigned to the oxychloroaluminate species with the suggested structure Li₂(AlCl₃)₂O. They corroborated their results using ²⁷Al NMR spectroscopy.

More recently, McDonald (11) was able to show by mass spectroscopy the generation of substantial amounts of hydrogen and nitrogen in Li/SOCl₂ batteries.

In order to clarify these issues, we have re-examined the IR absorption spectrum of the electrolytes of lithium thionyl chloride and lithium-sulfuryl chloride cells during normal discharge and anode-limited reversal, at current densities between 1 and 5 mA/cm², and temperatures between -20° and 25°C. Furthermore, we have carried out a mass spectrometric analysis of the gases evolved from a Li/SOCl₂ cell during discharge and anode-limited reversal at 25°C.

Experimental

The cell.—The electrochemical cell used for all our experiments is shown in Fig. 1. It consists of two concentric electrodes supported within a nickel cylinder. The cathode is a thin (20 cm² × 20 mil) carbon-Teflon porous electrode pressed on a nickel grid spot welded to the wall of the cylinder. The lithium anode (8 cm² × 5 mil) is pressed on a nickel foil substrate spot welded around a stainless steel central post. The electrodes are about 0.5 cm apart and separated by a double layer of 0.005 in. glass mat. The cell can be coupled directly to a mass spectrometer via a valve system, as shown in Fig. 2, or to an IR spectroscopic cell via a pump to circulate the electrolyte between the electrochemical cell and the spectroscopic cell. The volume of solution in the cell is 14 ml. An additional volume of 2 ml is circulating through the pump and spectroscopic cell. The head space volume is 1 ml.

Mass spectra.—A Perkin-Elmer (PE270) mass spectrometer with a home-built all-glass gas inlet system was used

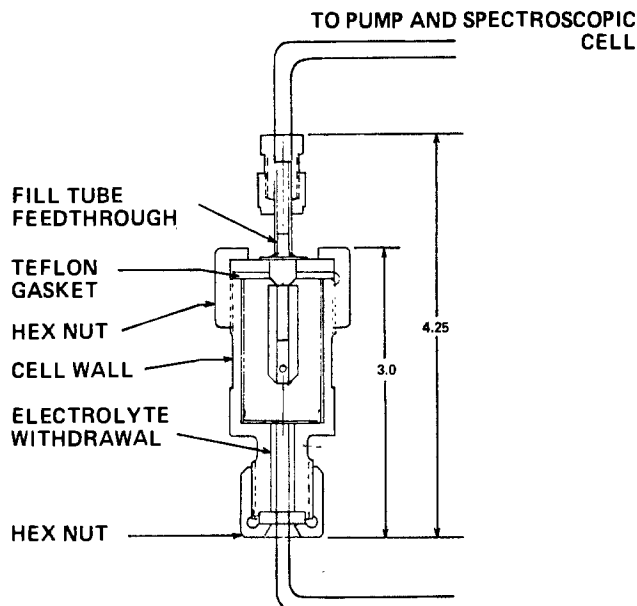


Fig. 1. Electrochemical cell for flowing electrolyte system

for *in situ* gas-phase analysis (Fig. 2). This sampling system consists of two (V_1 and V_2) stainless steel shut-off nonrotating stem valves from Circle Seal. The sampling volume contained between V_1 and V_2 is approximately 0.5 cm^3 . The glass inlet system includes four Teflon stopcocks (V_3 - V_6), with V_4 providing access to a roughing pump and V_6 leading to the mass spectrometer ion source. V_5 gives access to a perfluorokerosene (PFK) reservoir, which is used in the calibration of the mass scale. Exact mass experiments were performed on an AEI MS-30 double focusing mass spectrometer equipped with an Anatron peak matching unit. These measurements were carried out with known perfluorokerosene fragments as the mass reference (12). Intensity *vs.* time data were obtained with 80 eV electron energy on the PE270 mass spectrometer and with 70 eV electron energy on the MS-30 mass spectrometer.

Infrared spectra.—The IR absorption spectra were obtained with a Nicolet 5MX/1200S FTIR spectrometer. Silver chloride windows were used for the spectroscopic cell with a 0.1 mm optical path length. All spectral fre-

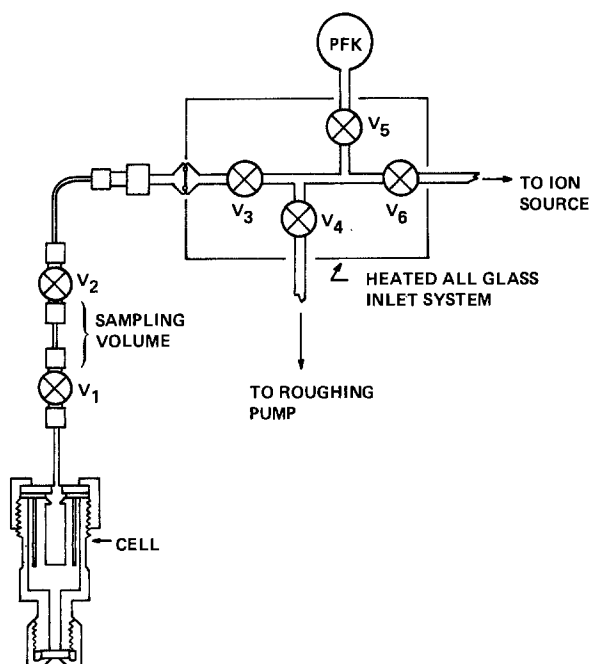


Fig. 2. Mass spectrometric sampling system

quencies are accurate to within $\pm 4 \text{ cm}^{-1}$; for the purpose of quantitative analysis, peak heights above the base line were measured. For badly overlapping bands, we used the tangent line technique to obtain reproducible results, or spectral subtractions.

Chemicals.— SOCl_2 and SO_2Cl_2 were double-distilled before use. LiAlCl_4 was used as received from Anderson Physics.² The electrolyte solutions, 1.4M LiAlCl_4 in SOCl_2 and 1.5M LiAlCl_4 in SO_2Cl_2 were prepared in a dry room shortly before filling the electrochemical cell.

Spiking and calibration experiments.—Mixtures of known composition were used for calibration and identification of possible products of discharge. These mixtures were prepared in a dry room or glove box and transferred to the spectroscopic cells in a dry environment. The calibration for SOCl_2 was obtained by dissolving known amounts of AlCl_3 in pure thionyl chloride, assuming 100% conversion of the AlCl_3 to $\text{SOCl}^+\text{AlCl}_4^-$.

S_2O synthesis.—We attempted to synthesize S_2O in a vacuum line using the reaction between SOCl_2 and Ag_2S at 160°C , as described by Nickless (13).

Results and Discussion

Qualitative IR studies.—Typical spectra of electrolyte from Li/SOCl_2 and $\text{Li}/\text{SO}_2\text{Cl}_2$ cells driven into anode-limited reversal are shown in Fig. 3(a) and 3(b). The most prominent absorption bands are tabulated in Table I together with their most likely assignment based on previously published results (6-10, 14) or the present work. The spectra for these electrolytes during normal discharge show only the formation of SO_2 at these relatively low current densities of 1-5 mA/cm².

To identify the various absorption bands, we spiked several solutions of SOCl_2 or SO_2Cl_2 with known compounds and compared the resulting IR spectra with the electrolyte spectra during normal discharge and reversal. The results of these tests are shown in Table II.

Water has a substantial effect on the absorption spectrum of SOCl_2 . Addition of water to pure SOCl_2 results in the formation of HCl (2790 cm^{-1}) and SO_2 (1335 and 1144 cm^{-1}). However, the same addition to 1.4M $\text{LiAlCl}_4/\text{SOCl}_2$

²Anderson Physics Laboratory, Urbana, Illinois 61801.

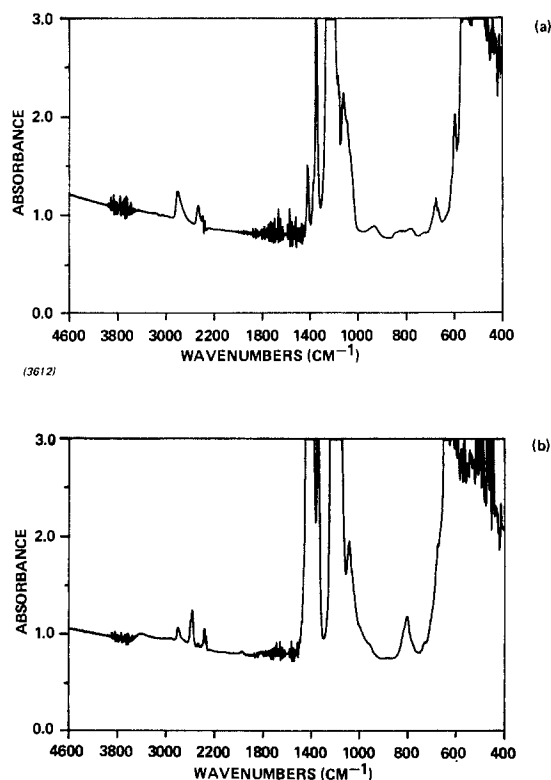


Fig. 3. IR absorption spectra during anode-limited reversal. (a): Li/SOCl_2 system. (b): $\text{Li}/\text{SO}_2\text{Cl}_2$ system.

Table I. Observed frequencies and assignments for Li/SOCl₂ and Li/SO₂Cl₂ systems in reversal

Frequency (cm ⁻¹)	Assignment	Ref.
Li/SOCl ₂ - 1.4M LiAlCl ₄		
3400	AlCl ₃ OH ⁻	(10)
2790	HCl	(14)
2450, 1225, 775, 927	SOCl ₂	(14)
1408, 1160, 570	SO ₂ Cl ₂	(14)
1335, 1144	SO ₂	(13)
1115	SOCl ⁺ AlCl ₄ ⁻	(8)
1337, 1070, 665	Li(SO ₂ , SO ₂ Cl ₂) ⁺ AlCl ₄ ⁻	This work
822	Oxychloroaluminate	(10)
694	Oxychloroaluminate	(10)
Li/SO ₂ Cl ₂ - 1.5M LiAlCl ₄		
3444	AlCl ₃ OH ⁻	(10)
2811, 2569, 2360, 1413, 1180, 1000, 796, 575	SO ₂ Cl ₂	(14)
1335	SO ₂	(13)
1337, 1068, 668	Li(SO ₂ , SO ₂ Cl ₂) ⁺ AlCl ₄ ⁻	This work
692	Oxychloroaluminate	(10)
1084, 1059	SO ₂ Cl ⁺ AlCl ₄ ⁻	This work

Table II. Spiking experiment

	Observed frequencies (cm ⁻¹)
SOCl ₂ neat	2450, 1225, 927, 776, 722, 636, 616, 590, 569, 549
Water added to SOCl ₂	2790, 1335, 1144 ^a
SOCl ₂ /1.4M LiAlCl ₄	2445, 1225, 924, 777, 722, 638, 617, 591, 577
Water added to SOCl ₂ /1.4M LiAlCl ₄	3400, 2790, 1333, 1144, 694 ^b
SO ₂ Cl ₂ added to SOCl ₂	1412, 1169, 800, 570 ^a
HCl to SOCl ₂	2790 ^a
SO ₂ to SOCl ₂	1144, 1335 ^a
AlCl ₃ to SOCl ₂	1117, 557 ^a
SO ₂ and SO ₂ Cl ₂ SOCl ₂ /1.4M LiAlCl ₄	1070, 668, 1337, 1408, 594 ^b
SOCl ₂ or S ₂ Cl ₂ to SOCl ₂ /1.4M LiAlCl ₄	1070, 668, 1337, 1408, 594 ^b
Water to SOCl ₂ /AlCl ₃	1335, 1144, 1115, 822 ^a
SO ₂ Cl ₂ neat	2814, 2586, 2368, 1415, 1180, 996, 793, 775, 723, 570
SO ₂ Cl ₂ /LiAlCl ₄	2811, 2569, 2360, 1413, 1180, 1000, 796, 775, 723, 575
AlCl ₃ to SO ₂ Cl ₂	1090, 1053 ^c
SO ₂ + SO ₂ Cl ₂ /LiAlCl ₄	1335, 1068, 668 ^d

^a Frequencies observed in addition to those in SOCl₂.

^b Frequencies observed in addition to those in SOCl₂/1.4M LiAlCl₄.

^c Frequencies observed in addition to those in SO₂Cl₂.

^d Frequencies observed in addition to those in SO₂Cl₂/LiAlCl₄.

electrolyte gives rise to two more absorption bands at 694 and 3400 cm⁻¹ (AlCl₃OH⁻). The addition of AlCl₃ and water to SOCl₂ results in the formation of AlCl₃OH⁻ (3400 cm⁻¹), but the absorption band at 694 cm⁻¹ does not appear, while two other poorly resolved bands at 803 and 822 cm⁻¹ appear instead.

Absorption bands at 3400, 800-820, and occasionally 694 cm⁻¹ are evident in both the LiAlCl₄/SOCl₂ and LiAlCl₄/SO₂Cl₂ electrolyte spectra, indicating water contamination (HCl is not formed in the Li/SO₂Cl₂ system) (13). The same absorptions have been observed by Bailey and Blomgren in the Li₂CO₃-AlCl₃/SOCl₂ system and were assigned to AlCl₃OH⁻ (3400 cm⁻¹) or oxychloroaluminate species (800, 695 cm⁻¹). With great precaution, we were able to reduce considerably the absorption at 694 cm⁻¹ during normal discharge, but it was nearly impossible to eliminate water contamination completely, and its effects were more noticeable towards the end of the relatively long period of reversal.

The addition of AlCl₃ to SOCl₂ gives rise to strong absorption bands at 1115 and 557 cm⁻¹ owing to the complex SOCl⁺AlCl₄⁻ (2). On reversal, the Li/SOCl₂ cell shows the same absorption bands, indicating formation of SOCl⁺AlCl₄⁻. An analogous SO₂Cl⁺AlCl₄⁻ (15) compound is formed in the Li/SO₂Cl₂ system upon addition of AlCl₃

or during anode-limited reversal, with characteristic absorption bands at 1090 and 1053 cm⁻¹ reflecting the two S-O stretching frequencies expected from SO₂Cl⁺. Any absorption band at the lower frequency range would be hidden under the strong SO₂Cl₂ absorption band at 570 cm⁻¹.

Addition of SCl₂ or S₂Cl₂ to LiAlCl₄/SOCl₂ in the presence of SO₂ results in a slow increase in the IR absorptions at 1070, 665, and 1337 cm⁻¹, together with the formation of SO₂Cl₂, as evidenced by the characteristic absorption bands at 1408 and 570 cm⁻¹. [The IR absorptions due to the sulfur chlorides (13) occur below 550 cm⁻¹ and cannot be detected by our instrument.] The same effect is observed with addition of SO₂Cl₂ and SO₂ to LiAlCl₄/SOCl₂. This characteristic triplet (1070, 665, 1337 cm⁻¹) appears only during anode-limited reversal in the Li/SOCl₂ system, while it is observed during normal discharge in the Li/SO₂Cl₂ system.

A compound with this characteristic IR spectrum was isolated from SO₂Cl₂ or SOCl₂ electrolytes following evaporation of the solvent. This compound decomposes abruptly at 40°C, releasing SO₂. It appears that its formation requires the presence of SO₂Cl₂, SO₂, and either LiAlCl₄ or AlCl₃. A reasonable assignment for the bands might be the S-O stretching vibrations and Al-Cl stretching modes of a complex similar to those observed by Barbier (16) between SO₂, SOCl₂, and LiAlCl₄. Subsequently, we refer to this complex as Li(SO₂, SO₂Cl₂)⁺AlCl₄⁻.

In our attempt to synthesize S₂O, we were only able to observe one (1168 cm⁻¹) of the three absorption bands characteristic of this compound (13). Attempts to condense S₂O in SOCl₂ at 77 K resulted only in the formation of a red polysulfur oxide which decomposed to S and SO₂ upon heating to room temperature. We concluded that the absorption which Istone and Brodd (6) observed at 688 cm⁻¹ and assigned to S₂O, in effect, must have been due to the interaction of water with neutral electrolyte. Salmon's assignment of a 690 cm⁻¹ absorption to Cl₂O (9) also overlooks the strong interaction of water with the electrolyte, which may, if excessive, mask the absorption band at 665 cm⁻¹ formed only during anode-limited reversal in the Li/SOCl₂ system. Actually, mass spectrometry shows the presence of small amounts of S₂O in the gas phase but no trace of Cl₂O (see below).

In situ mass spectrometry.—The Li/SOCl₂ systems was studied mass spectrometrically using the apparatus shown in Fig. 2. The *in situ* experiment, which lasted 69.25h, involved the discharge of a single cell at 8 mA (1 mA/cm² based on the anode) for a period of about 20h, followed by a period of reversal at 50 mA which lasted approximately 50h (Fig. 4).

The quantity of gas used in sampling was significant with respect to the head space, and the effect is shown in Fig. 4 as the short-term "sampling spikes." There was no

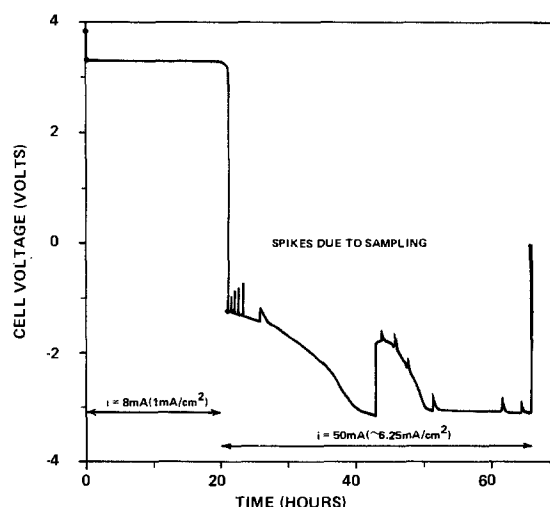


Fig. 4. Discharge curve of Li/SOCl₂ cell used for mass spectrometric analysis.

pause between end of discharge and the onset of cell reversal. The rate of discharge was increased sixfold during reversal in order to accelerate reaction progress. Infrared analysis had already shown that this change in current density did not affect the reaction mechanism, but rather simply accelerated the reaction progress.

Fifteen sets of mass spectra were recorded from time zero at the beginning of the discharge through time 69.25h at the end of the experiment. No spectra were recorded on the complete cells stored without discharge. Reversal occurred at time $t = 21$ h, and the reversal process was continued through $t = 66$ h. The last set of spectra was recorded at time $t = 69.25$ h. Tabulated intensities for nominal masses appearing between masses 35 and 138 are given in Table III.

Masses below mass 35 were not included because these masses primarily arise from residual gases in the mass spectrometer and inlet system. The cell used in this study contained SOCl_2 in excess, and the vapor pressure remained essentially constant during the experiment reported here. Therefore, the partial pressures of the various species can be estimated using the known vapor pressure of SOCl_2 , the ion intensities reported in Table III, and estimates of the relative ionization cross sections. All intensity data are relative to the intensity of mass 83 (SOCl^{35+}) which is set arbitrarily at 100. The uncertainty in the intensity data is estimated to be $\pm 20\%$.

Pure samples of SCL_2 , SOCl_2 , and SO_2Cl_2 were introduced into the mass spectrometer, their spectra recorded and the peak intensities were entered in Table IV. The inlet system used in these experiments contributed to the peak at mass 36. This peak arises from the reaction between the chlorine containing sample and adsorbed water and/or hydrocarbons in the inlet system. Under the carefully controlled inlet conditions used with these samples, the intensity of mass 36 remained constant to within 20%. Thus, in subsequent experiments, it will be assumed that the inlet reactions are constant to within 20% and that large changes in the intensity of mass 36 are due to factors other than the inlet system. All of these spectra were recorded with an electron energy of 80 eV.

Three exact mass experiments at nominal masses 50, 76 and 80 yielded the following exact mass values: 49.99597 (± 30 ppm), 75.94528 (± 20 ppm), and 79.94057 (± 20 ppm), respectively.

The results clearly show the presence of molecular HCl, SO_2 , CS_2 , S_2O , SCL_2 , SOCl_2 , and mass 134 species (mainly SO_2Cl_2 , with, probably, some S_2Cl_2). The data also reveal the presence of high levels of chlorine fragments as well as low concentrations of CF_2^+ fragments. Species with nominal mass exceeding 140 were also observed toward the later stages of reversal.

The plots of intensity vs. time of HCl and Cl^+ (Fig. 5 and 6) indicate that their concentrations remain constant in the gas phase during normal discharge but increase during anode-limited reversal after an induction period of 5h. We have investigated the contribution to mass 36 and have found that the intensity of the mass 36 (HCl) signal can be reduced by improving the inlet system to the mass spectrometer. However, not all of the mass 36 can be removed by the improved inlet; thus, part of mass 36 may arise from cell components containing chlorine and hydrogen. Water contamination may, in part, be introduced from the cathodes which are formed by an aqueous process.

The plots of CS_2 and S_2O (Fig. 7 and 8) show little variation in the concentration of these species with time during both discharge and reversal, while the plots for SCL_2 (Fig. 9) and SO_2Cl_2 (Fig. 10) indicate that these compounds are only formed during reversal, also following a 5h induction period.

The increase in the concentration of HCl following reversal indicates a source of hydrogen which may be the residual water in the electrolyte or, more likely, the adsorbed water on the carbon cathode.

The mass spectrometric analysis of SO_2 confirms our infrared results: SO_2 appears to be the major product of discharge. If the data for SO^+ and SO_2^+ intensities are plotted (Fig. 11), interesting results are obtained. This figure clearly shows that the SO_2^+ rate of increase is larger than that for SO^+ fragments. Furthermore, it is seen that the difference in concentration between SO_2^+ and SO^+ increases rapidly after the onset of reversal and then reaches a steady value. It is worth noting that the ratio of SO^+ to SO_2^+ intensities is approximately 0.5 for pure SO_2 (18). Thus, it is clear that the SO^+ intensity in the discharge mode is higher than that accounted for by SO_2 fragmentation alone. Upon reversal, the $\text{SO}^+/\text{SO}_2^+$ ratio decreases and approaches its limiting value predicted by SO_2 fragmentation only.

Table III. Mass intensity vs. time data for the *in situ* experiment

Mass	Time (h)															
	0	0.1	1.25	2.33	18.5	20.33	21.00 ^a	24.00	26.00	42.33	45.00	48.75	50.25	66.00 ^b	69.25	
35	18.2	—	25.0	13.2	23.8	16.3	12.2	12.1	20.7	51.3	93	55.9	57.6	52.9	47.4	
36	34.7	27.3	37.6	43.3	165	50.5	54.3	40.3	85.5	212	224	385	395	376	357	
37	6.5	5.1	8.9	4.8	10.2	5.9	4.1	4.9	6.0	16.7	29.5	17.8	19.2	18.7	17.1	
38	27.7	19.1	23.1	14.5	52.5	18.0	18.2	15.6	31.5	69.1	72.1	129	135	120	108	
48	92.8	—	68.8	48.1	87.8	—	115	163	170	171	238	256	302	146	128	
50	6.9	5.9	8.3	2.4	5.0	11.6	6.5	8.6	12.0	10.5	27.5	12.6	6.1	10.2	9.7	
64	93.4	—	62.4	65.2	111	—	145	279	292	307	444	565	648	340	320	
67	8.5	9.7	11.6	5.9	5.1	6.6	5.1	7.2	8.5	6.8	28.4	12.5	19.2	11.4	13.2	
69	0	4.4	4.9	2.5	3.3	2.8	2.7	2.1	3.7	5.0	12.1	4.8	7.0	9.1	9.1	
76	9.7	11.9	27.0	9.6	14.3	25.0	16.3	17.3	14.9	13.7	14.7	15.0	7.9	8.6	8.4	
78	0.8	1.1	2.4	0.7	1.2	2.6	1.4	1.5	1.1	1.5	1.0	1.1	0.5	0.6	0.7	
80	23.8	27.2	23.7	20.6	16.0	19.9	15.9	19.1	22.2	19.8	28.4	31.9	22.0	19.3	20.0	
82	2.0	2.5	2.6	2.0	1.3	1.8	2.0	1.6	1.7	1.7	2.5	2.8	1.8	1.5	1.7	
83	100	100	100	100	100	100	100	100	100	100	100	100	100	100	100 ^c	
85	35.6	37.5	37.5	39.0	35.3	38.9	39.1	39.4	44.4	37.6	42.4	39.5	40.0	42.3	38.9	
99	0	0	0	0	0	0	0	0	0	2.11	1.39	1.34	1.10	0.77	0.87	
101	0	0	0	0	0	0	0	0	0	1.05	0.70	0.58	0.56	0.32	0.40	
102	0	0	0	0	0	0	0	0	0	1.95	9.12	7.21	7.21	6.39	4.15	
104	0	0	0	0	0	0	0	0	0	1.26	6.60	5.33	5.00	5.05	2.99	
106	0	0	0	0	0	0	0	0	0	0.49	1.12	0.94	0.98	1.24	0.71	
118	20.0	18.7	19.1	14.6	14.3	15.9	14.2	14.6	15.0	15.3	16.9	14.8	14.6	12.2	14.7	
120	13.8	13.1	14.2	11.6	11.0	12.4	10.6	10.6	9.6	11.4	11.4	11.3	11.0	8.9	10.9	
122	2.0	2.1	2.1	2.4	2.2	2.0	2.0	2.0	2.1	2.1	2.7	2.0	2.1	2.0	2.0	
134	0	0	0	0	0	0	0	0	0	1.43	1.14	1.17	0.67	0.52	0.64	
136	0	0	0	0	0	0	0	0	0	0.78	0.80	0.80	0.37	0.34	0.38	
138	0	0	0	0	0	0	0	0	0	0.25	0.22	0.21	0.14	0.07	0.07	

^a Time at onset of reversal.

^b Last data set obtained before conclusion of reversal.

^c All intensities are relative to the intensity of mass 83, which is set arbitrarily to 100.

Table IV. Mass spectral intensities for pure SCl_2 , SOCl_2 , and SO_2Cl_2

Mass	SCl_2	SOCl_2	SO_2Cl_2	Mass	SCl_2	SOCl_2	SO_2Cl_2
30	0	0	0	86	0	0	0
31	0	0	0	87	0	0.62	0
32	64.4	100*	36.5	88	0	0	0
33	0	0	0	89	0	0	0
34	1.34	1.13	0.93	90	0	0	0
35	12.1	17.7	6.67	91	0.96	0	0
36	75.3	91.4	18.7	92	0	0	0
37	4.10	6.55	2.76	93	1.09	0	0
38	26.2	27.7	9.41	94	0	0	0
39	1.92	0	1.46	95	4.76	0	0
40	4.45	7.25	3.58	96	1.11	0	0
41	4.5	0	0.93	97	3.70	0	0
42	1.86	0	1.46	98	0	0	0
43	1.95	2.23	2.50	99	0	0	35.3
44	1.73	2.80	3.63	100	0	0	1.17
45	0	0	0	101	0	0	12.9
46	0	0	0	102	67.8	0	0
47	0	0	0	103	0.83	0	1.17
48	1.74	49.8	53.5	104	43.7	0	0
49	0	0.92	0.93	105	0.96	0	0
50	0	2.81	4.09	106	8.60	0	0
51	2.85	0	0.93	107	0.91	0	0
52	2.21	0	0	108	0	0	0
53	0	0	0	109	0	0	0
54	0	0	0	110	0	0	0
55	6.69	0	0.90	111	0	0	0
56	2.15	0	0	112	0	0	0
57	5.24	0	0.98	113	0	0	0
58	0	0.75	0.91	114	0	0	0
59	0	0	0	115	0	0	0
60	0	0.63	0.78	116	0	0	0
61	0	0	0	117	0	0	0
62	0	0	0	118	0	3.6	0
63	0	0	0	119	0	0	0
64	4.00	31.1	100*	120	0	2.5	0
65	0	0	2.28	121	0	0	0
66	0	2.06	7.54	122	0	0.58	0
67	100*	3.44	0.92	123	0	0	0
68	0.95	0	0	124	0	0	0
69	36.4	1.32	6.27	125	0	0	0
70	9.72	0	1.27	126	0	0	0
71	2.71	0	0	127	0	0	0
72	5.56	0	1.17	128	0	0	0
73	0	0	0	129	0	0	0
74	1.03	0	0	130	0	0	0
75	0	0	0	131	0	0	0
76	2.54	2.56	2.16	132	0	0	0
77	0	0	0	133	0	0	0
78	0	0	0	134	0	0	6.84
79	1.05	0	0	135	0	0	0
80	0	3.00	0	136	0	0	5.08
81	3.63	0.23	0	137	0	0	0
82	1.30	0	0	138	0	0	1.17
83	3.5	41.5	0	139	0	0	0
84	0	0	0	140	0	0	0
85	1.79	14.5	0				

*Most intense peak.

Thus, the foregoing analysis indicates that during discharge SO^+ intensity results from at least two major contributions. The first is from SO_2 fragments, and the second arises from SOCl_2 fragmentation. However, as the cell is brought into reversal, the SO_2 becomes the major source of SO^+ production.

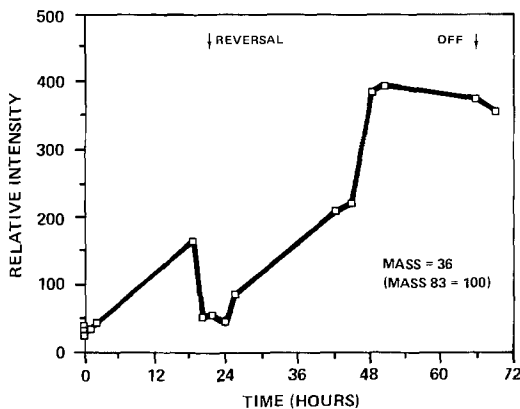


Fig. 5. Mass 36 (HCl^{35}) vs. time (h)

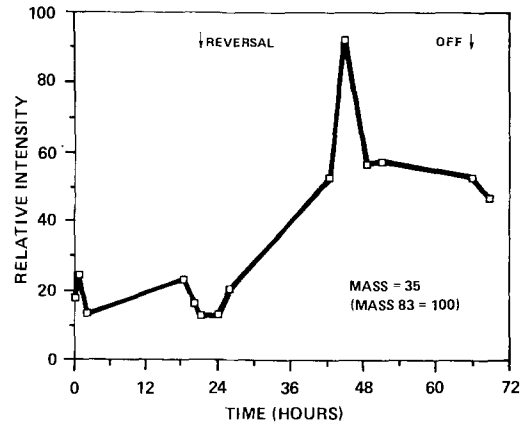


Fig. 6. Mass 35 (Cl^{35}) vs. time (h)

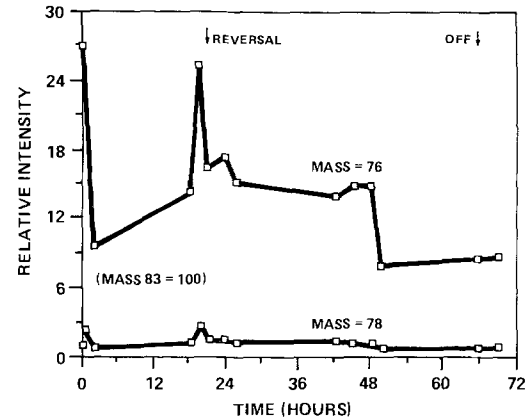


Fig. 7. Mass 76 and 78 (CS_2) vs. time (h)

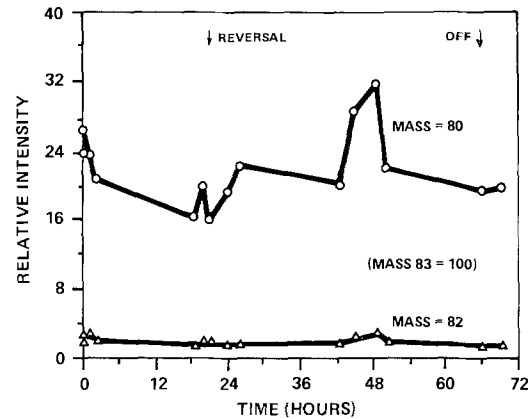


Fig. 8. Mass 80 and 82 (S_2O) vs. time (h)

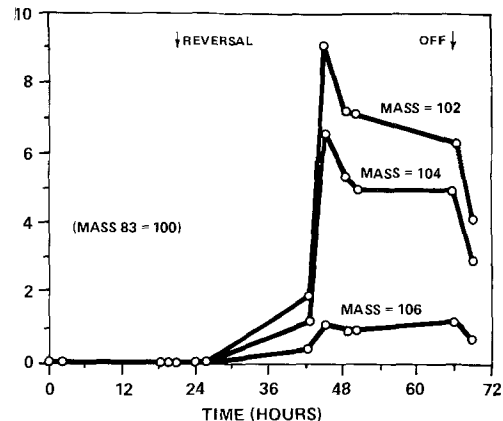


Fig. 9. Mass 102, 104, and 106 (SCl_2) vs. time (h)

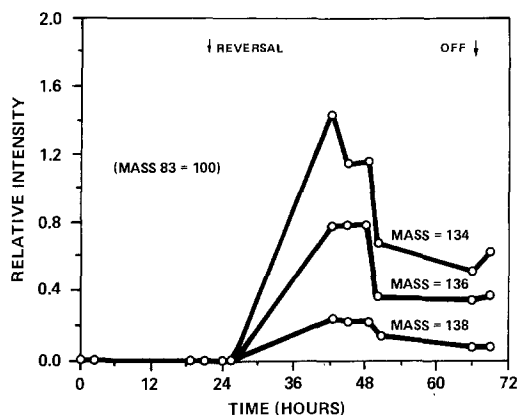
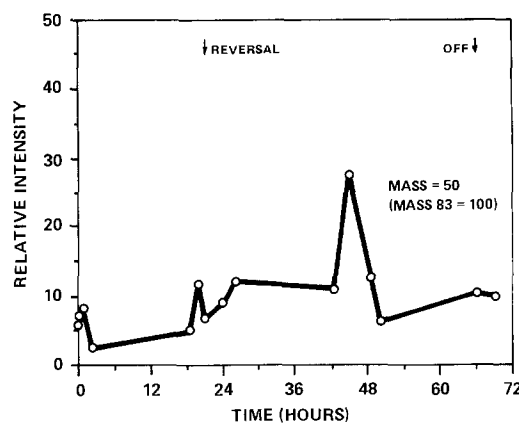
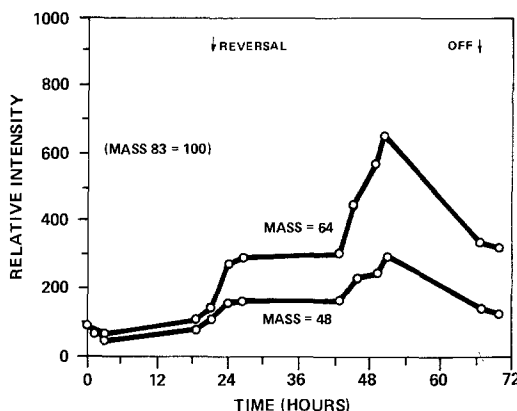


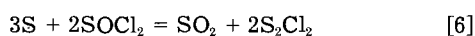
Fig. 10. Mass 134, 136, and 138 vs. time (h)

Fig. 12. Mass 50 (CF₂⁺) vs. time (h)Fig. 11. Mass 48 and 64 (SO⁺ and SO₂⁺) vs. time (h)

Mass 80 was identified as S₂O by exact mass measurements. This is not surprising, as Meshi and Myer (17) had previously identified both S₂O and CS₂ as products in a discharge-tube reaction between elemental sulfur and SO₂. Furthermore, thermal decomposition of SOCl₂ has been shown to yield S₂O as a product (17). It is worth noting, however, that the amount of S₂O in the gas phase remains fairly constant throughout the experiment and appears independent of any electrochemical process.

The mass triplet 102, 104, and 106, characteristic of SCl₂, appears only in reversal after an induction period of 5h. The species giving rise to masses 67 and 69 (Table III) can arise from fragmentation of SCl₂. However, since no SCl₂ parent is detected at and prior to *t* = 26h, the intensities measured for this doublet at and prior to *t* = 26 do not arise from SCl₂. This result also implies that species other than SCl₂ give rise to masses 67 and 69 in the cell. It is important to note that chlorine dioxide (ClO₂, mass 67, 69) can give rise to these masses. However theoretical isotopic abundance considerations neither confirm nor rule out ClO₂ as species giving rise to masses 67 and 69. It is also noteworthy that the absence of both parent (masses 86, 88, and 90) peaks and fragments (masses 51, 53) in the mass spectrum strongly suggests that Cl₂O is not present in measurable concentration in this system.

The mass triplet 134, 136, 138 also detected during reversal after a 5h induction period could arise from either S₂Cl₂ or SO₂Cl₂. S₂Cl₂ has been suggested as a possible reaction product by Schlaikjer *et al.* (7) as follows



Thus S₂Cl₂ may be present in this system, but our infrared results suggest that SO₂Cl₂ is the major component. Mass 50 (Fig. 12) was positively identified as CF₂⁺ by exact mass analysis. Its presence throughout the periods of discharge and reversal implies a chemical or electrochemical attack on the Teflon binder at the cathode during both discharge and reversal.

Quantitative FTIR studies.—Li/SOCl₂, normal discharge.—A total of eight cells were discharged and driven into reversal under various conditions ranging from -20° to +25°C and 1.5 mA/cm².

During normal discharge, the only noticeable change is the increase in SO₂ concentration. At 25°C, SO₂ appears to increase linearly until the cell is fully discharged then levels off. At -20°C, a slight curvature is noticeable at the beginning of the discharge. This also holds true for the Li/SO₂Cl₂ system. Typical results are shown in Fig. 13. Average results for four of the cells are tabulated in Table V. In every case, the amount of SO₂ produced during normal discharge was always found to be only a fraction of that predicted by the usually accepted equation for the discharge of this cell



Li/SOCl₂, anode-limited reversal.—On reversal, the most noticeable changes in the IR spectrum are due to formation of SO₂Cl₂ (1408 and 580 cm⁻¹), SOCl⁺ (1115 and 557 cm⁻¹), and what we tentatively identified as the weakly bound complex Li(SO₂, SO₂Cl₂)⁺AlCl₄⁻ absorbing at 1070, 665, and 1337 cm⁻¹ (this last band appears as a shoulder on the very large SO₂ peak). Typical results are plotted in Fig. 14 and 15 for ambient temperature operation, and in Fig. 16 and 17 for operation at -20°C.

A small amount of water contamination is always present and is the cause for the three broad bands at 3400 cm⁻¹ (AlCl₃OH⁻), 2900 cm⁻¹ (HCl), and 800-820 cm⁻¹ (oxychloroaluminate).

At room temperature, SO₂Cl₂ increases steadily after a short induction period then appears to level off. SOCl⁺ starts increasing immediately, levels off to a steady-state value, and disappears fairly rapidly after the current is turned off. The peaks at 1070 and 665 cm⁻¹ also show an initial increase, then an apparent leveling off.

At low temperature (-20°C), one should note the immediate and sharp increase in the SOCl⁺ species (0.65 mol/Faraday) (see Fig. 17). Obviously, at room temperature regenerative processes are fast and prevent accumulation of large amounts of SOCl⁺. The SO₂Cl₂ concentration (see

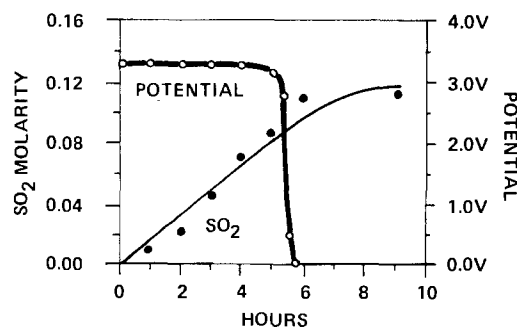
Fig. 13. SO₂ formation during discharge of anode-limited Li/SOCl₂ cells: *i* = 40 mA (5 mA/cm²).

Table V. SO₂ production during normal discharge

Cell	Discharge conditions	SO ₂
SC-69	(5 mA/cm ² , 25°C)	0.14 mol/Faraday
SC-71	(5 mA/cm ² , 25°C)	0.17 mol/Faraday
SC-77	(1 mA/cm ² , 25°C)	0.17 mol/Faraday
SC-81	(1 mA/cm ² , -20°C)	0.13 mol/Faraday

Fig. 17) levels off at a fairly low value. However, upon heating to room temperature, a dramatic jump in SO₂Cl₂ concentration occurs, pointing to the accumulation of unstable species (most likely Cl₂) during the reversal period at low temperature. Water contamination and the large SOCl⁺ concentration precluded our plotting the increases in absorption of 665 and 1070 cm⁻¹ for the low temperature run.

Li/SO₂Cl₂.—As with the *Li/SOCl₂* system, the major reaction product during normal discharge is SO₂. Its concentration appears to increase linearly at room temperature, but somewhat nonlinearly at -20°C. The SO₂ concentration levels off after reversal (see Fig. 18).

Qualitatively, the results are identical at room temperature and at -20°C, but at -20°C an analysis of the potential evolution, especially during reversal, shows a small plateau at -2.8V and a larger one not very flat at -5.5/-6V followed by a sharp decrease after about 15h to -12V at which point the current is cut off (see Fig. 19). When the cell is allowed to recover, the voltage stabilizes at -0.8/-0.6V, then goes to 0V upon warming up to room temperature. This small polarization left on recovery at low temperature could be attributed to the formation of a species stable at -20°C.

Absorption bands at 1070, 1337, and 665 cm⁻¹ appear during normal discharge and continue increasing slowly in intensity during reversal (see Fig. 20). The three peaks appearing during the normal discharge as they do in a

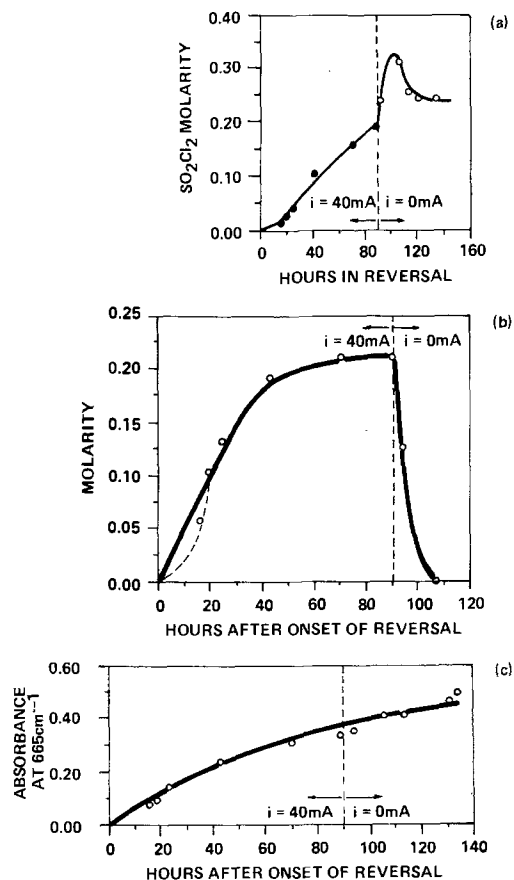


Fig. 14. Formation of (a) SO₂Cl₂, (b) SOCl⁺, and (c) Li(SO₂, SO₂Cl₂)⁺AlCl₄⁻ during reversal of anode-limited Li/SOCl₂ cell. *i* = 40 mA (5 mA/cm²). *T* = 25°C.

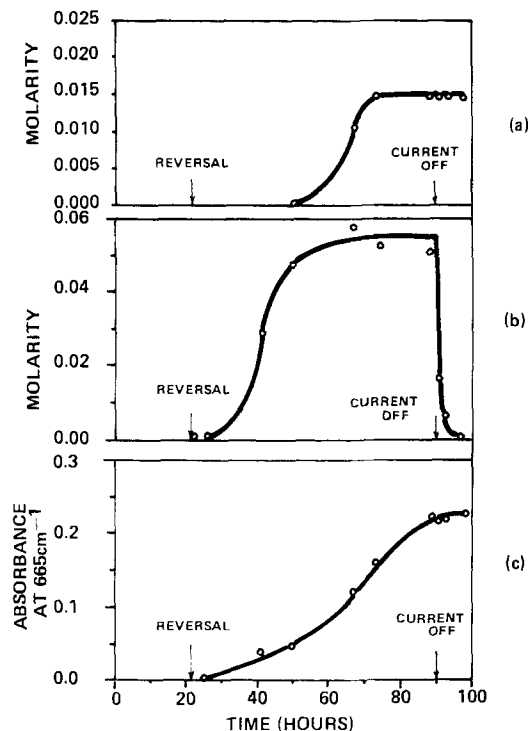


Fig. 15. Formation of (a) SO₂Cl₂, (b) SOCl⁺, and (c) Li(SO₂, SO₂Cl₂)⁺AlCl₄⁻ during reversal of anode-limited Li/SOCl₂ cell. *i* = 7.4 mA (1 mA/cm²). *T* = 25°C.

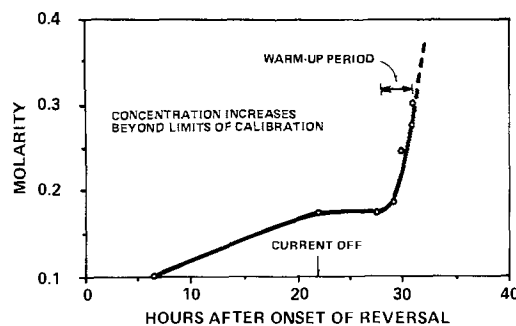


Fig. 16. Formation of SO₂Cl₂ during reversal of anode-limited Li/SOCl₂ cell at -20°C and warm-up to 25°C. *i* = 40.5 mA (5 mA/cm²).

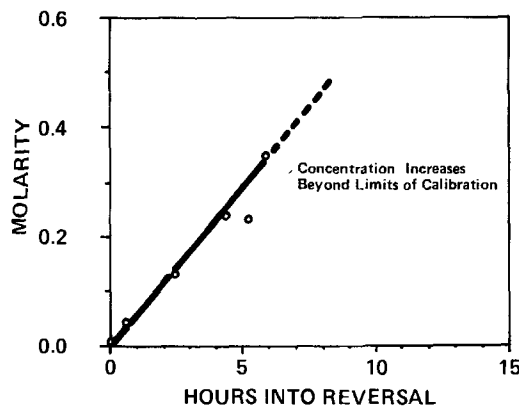


Fig. 17. Formation of SOCl⁺ during reversal of anode-limited Li/SOCl₂ cell at -20°C. *i* = 40.5 mA (5 mA/cm²).

mixture of SO₂, LiAlCl₄, and SO₂Cl₂ without the passage of current suggest a chemical reaction. The appearance of the same peaks in the Li/SOCl₂ cells on reversal is probably due to the formation of SO₂Cl₂ during the over-discharge and its subsequent reaction with LiAlCl₄ and SO₂. The product of this reaction has been tentatively identified as Li(SO₂, SO₂Cl₂)⁺AlCl₄⁻.

Additional peaks appear on reversal at 1090 and 1059 cm⁻¹, which quickly disappear on recovery. Those facts

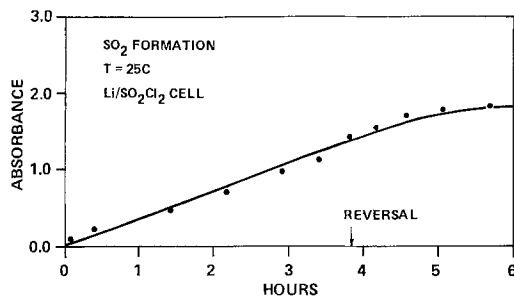


Fig. 18. Formation of SO_2 during discharge and reversal of anode-limited $\text{Li}/\text{SO}_2\text{Cl}_2$ cell at 25°C . $i = 40 \text{ mA}$ ($5 \text{ mA}/\text{cm}^2$).

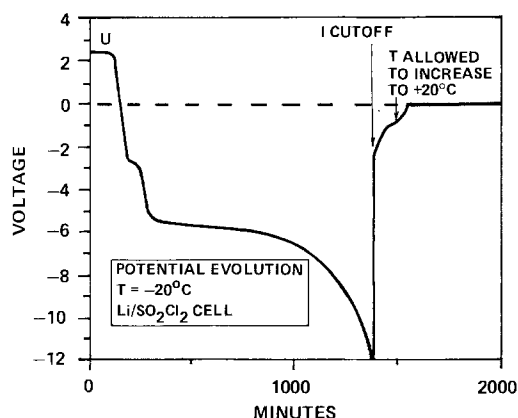


Fig. 19. Potential evolution for $\text{Li}/\text{SO}_2\text{Cl}_2$ cell during discharge and anode-limited reversal at -20°C . $i = 40 \text{ mA}$ ($5 \text{ mA}/\text{cm}^2$).

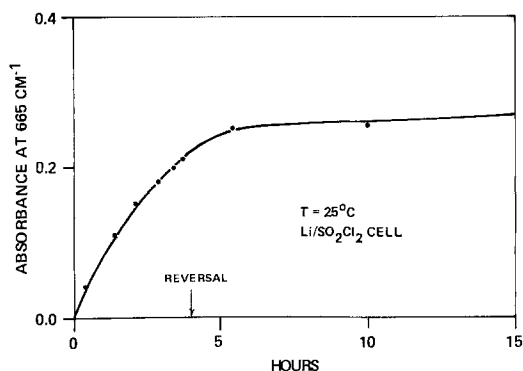
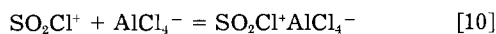
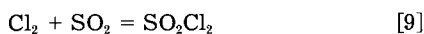
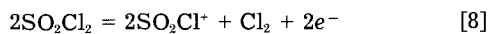


Fig. 20. Formation of $\text{Li}(\text{SO}_2, \text{SO}_2\text{Cl}_2)^+\text{AlCl}_4^-$ during discharge and reversal of $\text{Li}/\text{SO}_2\text{Cl}_2$ cell at 25°C and $i = 40 \text{ mA}$ ($5 \text{ mA}/\text{cm}^2$).

suggest the formation of a complex analogous to $\text{SOCl}^+\text{AlCl}_4^-$ in the Li/SOCl_2 system. This complex is proposed to be $\text{SO}_2\text{Cl}^+\text{AlCl}_4^-$ (15) and may be formed as follows



Conclusions and Summary

Mass spectrometry and infrared spectroscopy have been used to investigate both the gas and liquid phases in lithium-sulfur oxyhalide cells during normal discharge and anode-limited reversal.

By measuring the spectra *in situ*, we were able to minimize the interaction of moisture with the electrolyte. Quantitative and reproducible results have been obtained and definite trends have been demonstrated. With the two techniques, we were able to corroborate our results.

In the lithium-thionyl chloride system, the species HCl , CS_2 , SO_2 , S_2O , SOCl_2 , and SO_2Cl_2 were identified in the gas phase, and HCl , AlCl_3OH^- , SO_2 , SO_2Cl_2 , $\text{SOCl}^+\text{AlCl}_4^-$ in

the liquid phase. A species giving rise to absorptions at 1337 , 1070 , and 665 cm^{-1} was observed in the liquid phase during anode-limited reversal; this last compound is tentatively identified as $\text{Li}(\text{SO}_2, \text{SO}_2\text{Cl}_2)^+\text{AlCl}_4^-$ and is analogous to the complexes characterized by Barbier (16) involving LiAlCl_4 , SO_2 , and SOCl_2 instead of SO_2Cl_2 .

The gas phase concentrations of CS_2 and S_2O were essentially constant throughout the experiment. These species may not necessarily arise from electrochemical processes but are probably minor products of chemical reactions either in the cell or the inlet system. Fragments identified as CF_2^+ were observed in measurable amounts. The origin of these fragments is most likely the Teflon binder used in the construction of the porous carbon electrode.

The sulfonyl chloride cell behaved similarly to the thionyl chloride cell, specifically with respect to formation of SO_2 and the formation of SOCl^+ -like species tentatively identified as SO_2Cl^+ . Moreover, this system exhibited the same sensitivity to water and the same behavior at -20°C as the thionyl chloride system. During normal discharge a compound absorbing at 665 , 1070 , and 1337 cm^{-1} was formed immediately upon generation of SO_2 . This compound was isolated from SO_2Cl_2 solutions containing LiAlCl_4 and SO_2 , it decomposes at approximately 40°C with evolution of SO_2 , and is the same as the $\text{Li}(\text{SO}_2, \text{SO}_2\text{Cl}_2)^+\text{AlCl}_4^-$ complex observed in the thionyl chloride system.

The formation of chlorine in both systems is quite likely but its accumulation in the cells at room temperature is prevented by reaction with SO_2 to form SO_2Cl_2 . At low temperatures, chlorine does accumulate but reacts quite rapidly on warming up to form SO_2Cl_2 .

Finally the effect of water contamination was characterized. Water tends to form strongly IR absorbing species with AlCl_3 or AlCl_4^- . This fact should be taken into account in interpreting the results of previous investigations.

Acknowledgments

This work was supported in part by the Naval Surface Weapons Center under Contract no. N60921-81-C-0363. Portions of the material contained in this article were prepared in collaboration with Mr. Christian Sarrazin, a French scientist working at Gould, Incorporated, Gould Research Center under a cooperative agreement of the governments of the United States of America and France through the Foreign Science/Engineer Exchange Program, administered by the Department of Defense. Mr. Sarrazin is a staff member of Direction des Recherches Etudes et Techniques/G7-1, 75015 Paris, France.

Manuscript submitted Nov. 18, 1983; revised manuscript received July 9, 1984.

Gould, Incorporated assisted in meeting the publication costs of this article.

REFERENCES

1. J. Auburn, K. W. French, S. I. Lieberman, U. K. Shan, and A. Heller, *This Journal*, **120**, 1613 (1973).
2. K. M. Abraham, P. G. Gudrais, G. L. Holleck, and S. B. Brummer in "Proceedings of the 28th Power Sources Symposium," Atlantic City, NJ, June 12-15, 1978, The Electrochemical Society, Inc. p. 255 (1979).
3. A. N. Dey, in "Proceedings of the 28th Power Sources Symposium," Atlantic City, NJ, June 12-15, 1978, The Electrochemical Society, Inc., p. 251 (1979).
4. S. Dallek, S. D. James, and W. P. Kilroy, *This Journal*, **128**, 508 (1981).
5. W. K. Behl, *ibid.*, **127**, 1444 (1980).
6. W. K. Istone and R. J. Brodd, *ibid.*, **129**, 1853 (1982).
7. C. R. Schlaikjer, F. Goebel, and N. Marincic, *ibid.*, **126**, 513 (1979).
8. K. M. Abraham and R. M. Mank, *ibid.*, **127**, 2091 (1980).
9. D. J. Salmon, M. E. Peterson, L. L. Henricks, L. L. Abels, and J. C. Hall, *ibid.*, **129**, 2496 (1982).
10. J. C. Bailey and G. E. Blomgren, in "Electrocatalysis," W. E. O'Grady, P. N. Ross, Jr., and F. G. Will, Editors, p. 485, The Electrochemical Society Softbound Proceedings Series, Pennington, NJ (1982).
11. R. C. McDonald, *This Journal*, **129**, 2453 (1982).

12. "Perfluorokerosene Mass Spectral Table," PCR Research Chemical, Inc., Gainesville, FL.
13. G. Nickless, "Inorganic Sulfur Chemistry," p. 409 Elsevier, Amsterdam (1978).
14. R. J. Gillespie and E. A. Robinson, *Can. J. Chem.*, **39**, 2171 (1961).
15. J. C. Bailar, Jr., H. J. Emeleus, Sir R. Nyholm, A. F. Trotman-Dickenson, Editors, "Comprehensive Inorganic Chemistry," Vol. 2, p. 858, Pergamon Press, New York (1973).
16. Y. Bedfer, J. Corset, M. C. Dhumelincourt, F. Wallart, and P. Barbier, *J. Power Sources*, **9**, 267 (1983).
17. D. J. Meshi and R. J. Myers, *J. Am. Chem. Soc.*, **78**, 6220 (1956).
18. "EPA/NIH Mass Spectral Data Base," Vol. 1, p. 11, Dec. 1978.

Electrochemical Behavior of Water in Immobilized Salt Electrolytes

I. Electrical Conductivity and Thermal Measurements

Rachel Parash, Frederico Broitman, Uri Mor, Dan Ozer, and Armand Bettelheim

Nuclear Research Center-Negev, Beer-Sheva, Israel

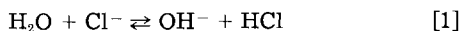
ABSTRACT

The meaning of moisture content of a pelletized LiCl-KCl-MgO mixture is discussed in terms of different states of interaction in which water may exist in the specimen. According to electrical conductivity measurements, differential thermal analysis, and thermogravimetric experiments in the ambient to $\approx 400^\circ\text{C}$ range, water comes off the pellet by an endothermic process that involves the migration of water to the surface of the pellet where it vaporizes ($T = 25^\circ\text{--}130^\circ\text{C}$). Exothermic reactions involving oxide ions and traces of water and hydrogen chloride are suggested to exist in the $130^\circ\text{--}250^\circ\text{C}$ range. This is followed ($T > 250^\circ\text{C}$) by a hydrolytic and endothermic reaction, which converts chloride ions to hydroxide ions and hydrogen chloride.

The investigation of water in pelletized LiCl-KCl-MgO mixtures is of interest for the development of primary as well as secondary batteries for load leveling and electric vehicle applications. The presence of water as well as contaminants formed near the electrodes during exposure to humid air could affect cell performance and accelerate self-discharge (1).

To prevent direct reaction between the anolyte and catholyte, a separator must be employed to physically separate the anode from the cathode, which in most cases consists of a lithium alloy and FeS_x ($x = 1$ or 2), respectively (2). An effective separator must be ionically conducting and chemically inert to all the cell components. Two concepts were considered for the separators (2, 3): (i) a refractory powder compact composed of the electrolyte (usually a LiCl-KCl eutectic mixture) and binder (such as SiO_2 or MgO) and (ii) separator pads fabricated from boron nitride or yttria fiber pads impregnated with electrolyte. The choice of the binder is based upon its ability to gel or immobilize the electrolyte, which would otherwise flow when subjected to the battery operation temperature, some 150°C above the electrolyte melting point. In the present study, the separator is a pelletized mixture of electrolyte composed of LiCl + KCl (64:36 mole percent [m/o]) in the presence of MgO (50 weight percent [w/o]) as binder.

The most troublesome aspect of preparing a pure electrolyte fusion arises from the highly deliquescent property of the lithium chloride. Unless special precautions are taken, hydrolytic decomposition occurs as the temperature is raised



Consequently, the melt becomes contaminated with alkaline products (4-7). Various methods have been proposed and used to prevent hydrolytic decomposition during the preparation of anhydrous and fused alkali metal chlorides. The difficulty of removing the last traces of residual moisture from the salts has often necessitated rather arduous drying procedures (8, 9). A high degree of purity of the LiCl-KCl melts has been achieved by treating the fused salt with hydrogen chloride gas (10) or chlorine (11).

The extreme sensitivity of electrical methods of analysis to chemical and structural transformations has been highlighted in several publications (12-14). From an application viewpoint, the practical potential of electrochem-

ical methods such as electrical conductivity measurements has been demonstrated in a wide variety of geological problems related to underground resources (15). It is the purpose of this paper to seek a correlation between the trends observed in the electrical and thermal behavior of pelletized LiCl-KCl-MgO mixtures containing various amounts of water. A wide variety of techniques, an electrical conductivity (EC), thermogravimetric analysis (TGA), and differential thermal analysis (DTA), was employed for the detection and characterization of the different states of water in the specimen.

Experimental

AR-grade LiCl, KCl, and MgO (Merck) were used.

The water content of the LiCl-KCl-MgO mixtures after weighing, blending, and mixing was determined by Karl Fisher titrations (16). Pellets of variable water concentrations were obtained by heating the pellet at $\approx 150^\circ\text{C}$ for several hours in a dry glove box ($\text{RH} \leq 0.5\%$). Water concentration after pelletizing was calculated by weight-loss measurements.

A schematic diagram of the electrical conductivity (EC) apparatus and furnace arrangement are illustrated in Fig. 1. The apparatus described here can be used for EC measurements on pressed disks up to a maximum temperature of about 500°C . The furnace is a ceramic block, and temperature is detected by two Chromel-Alumel thermocouples. One of them controls the rate of temperature rise via a proportional band temperature programmer; the other measures the temperature of the pellet and its EMF output is recorded on the X-axis of a Type 3078 Yokogawa X-Y recorder.

The samples were pressed in the form of disks using a stainless steel piston and die and a Beckman 30 ton hydraulic press. The disks, 28.6 mm diam and 4.5 mm thick, were held by a spring between two stainless steel electrodes.

AC electrical conductivity (EC) measurements were carried out using a Wayne Kerr B642 or B605 bridge. No control of the sample chamber atmosphere was necessary because of its geometry, the atmosphere surrounding the sample was essentially a "self-generated" one containing water vapor (17).

Differential thermal analysis (DTA) and thermogravimetric analysis (TGA) were performed on a Netzsch differential thermo-analyzer 404 and a Setaram thermo-

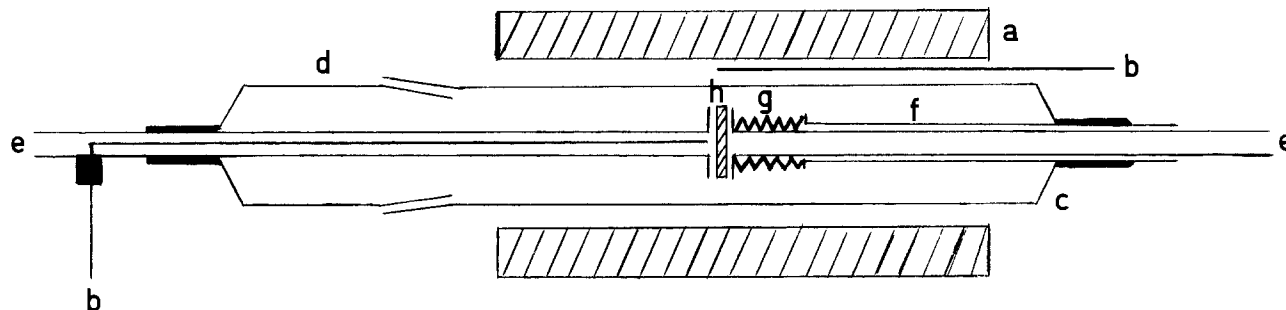


Fig. 1. Cell for EC measurements. a: Furnace. b: Thermocouples. c: Glass cell. d: Glass joint. e: Stainless steel electrodes. f: Stainless steel electrodes guide. g: Stainless steel spring. h: Pellet.

balance, respectively. Dehydration conditions in the sample chamber of the DTA and TGA were similar to those used in the EC measurements, *i.e.*, a self-generated atmosphere of water vapor. Alumina crucibles containing small portions (< 20 mg) of the pelletized salts were used for the thermal methods.

A Shaw hygrometer (Model Sha-3) with a medium (yellow spot) sensor range was used to detect water vapor evolved from a pellet subjected to heat-treatment in the apparatus shown in Fig. 1.

Results and Discussion

Room temperature measurements made at 1.5 kHz between two metallic collectors positioned at opposite sides of a pellet (Fig. 1) showed an increase in the ac conductance when the pellet was exposed to ambient atmosphere (RH = 50%). Passing a dry gas (air or argon, RH < 0.5%) through the porous structure of the pellet at ambient temperature caused a decrease in conductance, as shown in Fig. 2. Moreover, this procedure caused a gradual decrease in weight, probably due to loss of surface adsorbed water. A total weight loss of about 0.3 w/o was detected for a pellet initially containing 2 w/o water.

Figure 3 shows the electrical conductance of a LiCl-KCl-MgO pellet as function of temperature, measured at three different frequencies. The increase in electrical conductivity with temperature can be related to ohmic conduction which follows the well-known relationship (18)

$$\sigma_{\text{ohmic}} = \sigma_0 \exp(-E_a/RT) \quad [2]$$

where E_a is the activation energy for the mobility of the current carriers, and σ_0 , the pre-exponential factor, is related to the lattice vibration frequency. Conductivity in alternating current fields, however, is the sum of ohmic and polarization components expressed as

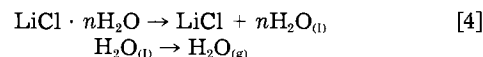
$$\sigma_{\text{total}} = \sigma_{\text{ohmic}}(T) + \sigma_{\text{pol}}(\nu, T) = \sigma_0 \exp(-E_a/RT) + 2\pi\nu\epsilon'' \quad [3]$$

where σ_{pol} represents the contribution of polarization current to the total conductivity σ_{total} , ν is the operating frequency, and ϵ'' is the loss factor. As can be seen from Fig. 3, the conductivity in the temperature range 25°-250°C increases by a factor of about two when the frequency is increased by two orders of magnitude. This indicates that the ohmic conductivity is the dominant factor in the total conductivity of the pellet. Polarization effects superimposed on the ohmic contribution to the conductivity are found only at temperatures below 70°C, as indicated by the small peaks in the conductivity curves at low frequencies (19).

As with other dynamic thermoanalytical techniques, the EC curve of a sample was influenced by the heating rate. At higher heating rates, the peaks were much smaller and broader. Low heating rates allow more time for the dissociation of hydrates and for bulk water vapor to diffuse to the vicinity of the electrodes.

Peaks I and II (appearing at 60°-65° and 80°-110°C, respectively) are correlated with the loss of absorbed water (peak I) and vaporization of liquid water which is in equilibrium with hydrates (peak II). Similar EC results were reported for the $\text{CuSO}_4 \cdot 5\text{H}_2\text{O}$ salt (17). For lithium chlo-

ride, the dehydration process could be described by the following scheme



According to Duval (20), a water molecule is associated with two lithium chloride molecules, *i.e.*, $n = 1/2$. The presence of liquid water, as given in reaction [4], forms a saturated solution, which permits an increase in current flowing through the sample. As this water vaporizes, the current decreases to the level of the original substance (17).

The process taking place at region III in the EC curve (Fig. 3) will be described in the context of the DTA and TGA results. The conductance rises at $T > 250^\circ\text{C}$ (not shown in the figure) until a steady value is obtained at the melting point of the electrolyte (about 370°C for the present composition of LiCl-KCl). At 450°C, the conductivity of the LiCl-KCl-MgO mixture is about one order of magnitude lower than the reported value in the absence of binder (21): 0.13 and 1.5 $\text{mho} \cdot \text{cm}^{-1}$, respectively. It should be noted that part of the samples showed a tendency to exhibit conductivity that "smeared" over a broad temperature region extending from 200° to 400°C. The loss of resolution in region III is presumably due to overlapping of the temperature regimes of the processes contributing to the electrical conductivity in the intermediate region 200°-250°C (processes II, III, and high ionic mobility above 250°C).

The EC curves in the 25°-125°C range for pellets containing various initial water concentrations are shown in Fig. 4. Conductivity in this temperature range increases when the water content in the pellet is increased and decreases in subsequent heating cycles. The disappearance of peaks I and II in the absence of water seems to be related to the lack of mobility of the current carriers ($\sigma_{\text{ohmic}} \rightarrow 0$ in Eq. [2]). As it can be seen from Fig. 4, the relative heights of peaks I and II vary independently on the total

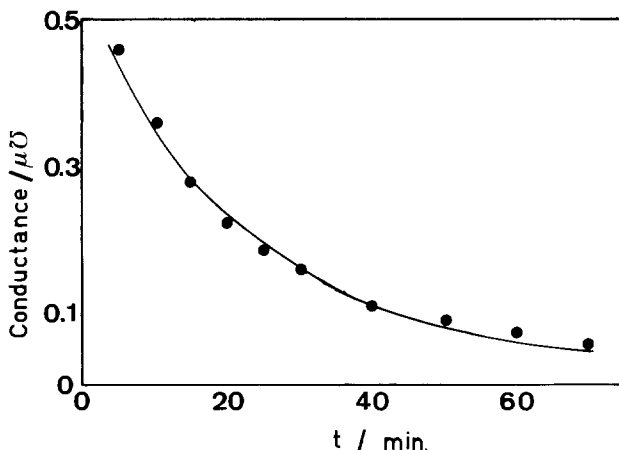


Fig. 2. The decrease of conductance at 1.5 kHz as function of time for a pellet (50 w/o electrolyte + 50 w/o MgO) at room temperature when a dry (RH = 0.5%) gas (air or Ar) is allowed to flow (rate = 1 liter/min⁻¹) through the sample (initial water concentration \approx 2 w/o).

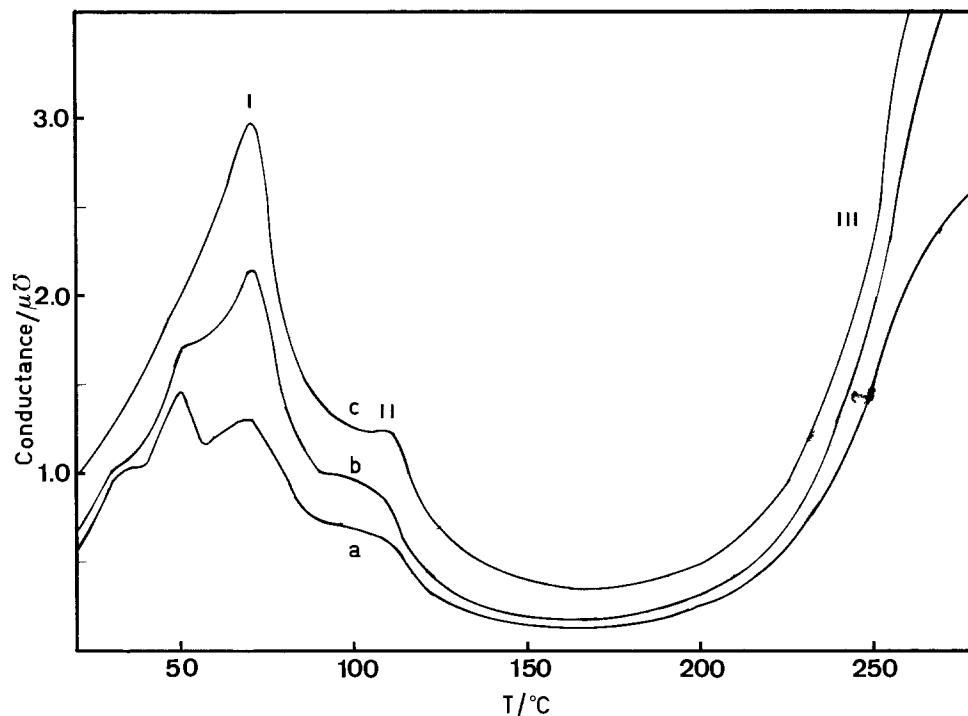


Fig. 3. Conductance vs. temperature at different frequencies, (a) 0.1, (b) 1, (c), 10 kHz, for a pellet (50 w/o electrolyte + 50 w/o MgO) containing an initial water concentration of 3 w/o.

water content in the various pellets. This is probably due to the variation of the time required to prepare the different samples, and hence to the different amounts of adsorbed water in the specimen.

For comparison of the trends observed in the electrical behavior, DTA experiments were carried out on pellets of the same composition (50 w/o electrolyte and 50 w/o magnesia). The first heating cycle yielded (Fig. 5) endothermic

mic effects at 80°, 120°, 320°, and 382°C (peaks I, II, IV, and V, respectively). The last endothermic peak (peak V), appearing at 382°C in the first heating cycle and 370°C in the second cycle, and the reverse (exothermic) process at 320°C (peak V') are attributed to the solid-liquid and liquid-solid transitions, respectively. The shift of the electrolyte melting point to a higher temperature in the heating part of the first cycle could arise from changes of thermal conductivity or strain effects in nucleation. The first heating-cooling treatment probably eliminates effects arising from sample compaction due to sintering (12). The hysteresis in the transformation temperature in

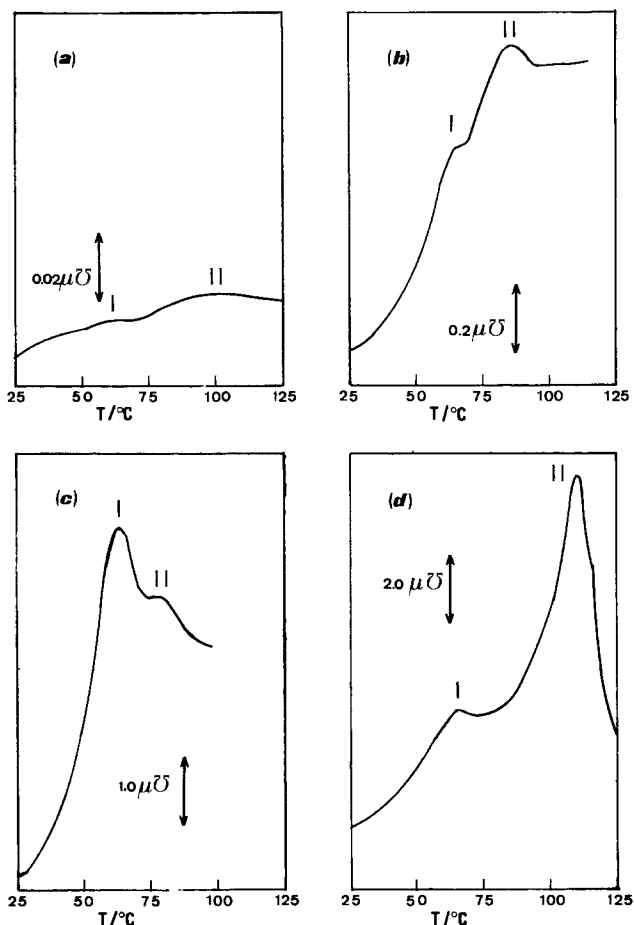


Fig. 4. Conductance vs. temperature at 1.5 kHz for pellets initially containing (a) 0.5, (b) 1.3, (c) 1.8, and (d) 2.6 w/o water.

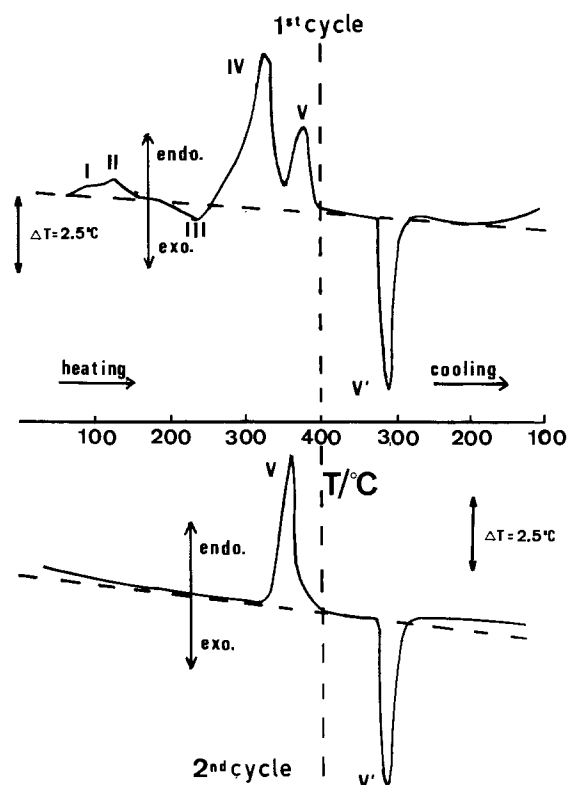
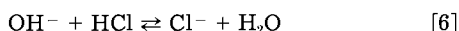
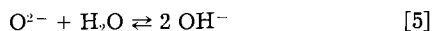


Fig. 5. DTA curves (first and second heating-cooling cycles) for a 50 w/o electrolyte + 50 w/o MgO mixture (heating-cooling rate = $5^{\circ}\text{C} \cdot \text{min}^{-1}$).

the two directions could be reduced by reducing the heating-cooling rate.

Since the endothermic peaks at 80° and 120°C (peaks I and II) appeared only in the first heating cycle, they seem to be due to processes involving water being expelled during the first heating cycle. The origin of the first two effects is the same as described for the EC behavior in regions I and II (Fig. 3 and 4). The exothermic broad effect at 200°-250°C (region III in Fig. 5) seems also to be related to an increase in electrical conductance (region III in Fig. 3). The following exothermic reactions are consistent with the EC and DTA results and are known to occur in similar electrolytes (10, 11)



Moreover, for LiCl-KCl mixtures in the absence of MgO, only endothermic peaks corresponding to the loss of adsorbed water (peak I), vaporization of liquid water (peak II), and to the electrolyte solid-liquid transition (peak V) were observed. This is in accordance with the suggestion that the exothermic effect (peak III) is related to reactions involving oxide and hydroxide ions (such as reactions [5] and [6]). The endothermic process IV taking place between regions III and V is suggested to be the result of the hydrolytic decomposition, in which the electrolyte becomes contaminated with alkaline products and HCl is lost from the system, *i.e.*, reaction [6] from right to left. Such reaction occurring at temperatures near fusion has been reported in several publications (10, 11).

The weight loss temperature dependence of the alkali chlorides has been investigated by Duval (20) using a thermogravimetric balance. An almost horizontal stretch between 80° and 96°C in the TGA curve of lithium chloride was interpreted to correspond to the composition $\text{LiCl} \cdot \frac{1}{2}\text{H}_2\text{O}$ (20). A typical TGA curve for the LiCl-KCl-MgO mixture is shown in Fig. 6. The lost weight processes found at 50°-70°C and 70°-130°C correspond to the loss of surface adsorbed water and the evolution of water vapor after hydrate dissociation. Moreover, the overall weight loss in the ambient-130°C range is quite identical to the initial water content of the sample, determined by a Karl Fisher titration to be 2.5 w/o. The surprisingly large weight loss (≈ 6 w/o) found in the 130°-170°C region seems to correspond to the conductance increase in region III (Fig. 3) and to the exothermic activity (peak III in Fig. 5) observed after dehydration. Since this TGA effect in region III was neither reported for LiCl (20) nor detected in the present study for LiCl-KCl in the absence of MgO, it seems to be related to a reaction consuming oxide ions and converting to a volatile product, *i.e.*, water. This suggestion is also consistent with the EC results, since electrical conductivity is sensitive to water evolution.

To detect water vapor in the gas evolved from pellets subjected to heat-treatment, a hygrometer was connected to the apparatus shown in Fig. 1 and relative humidity

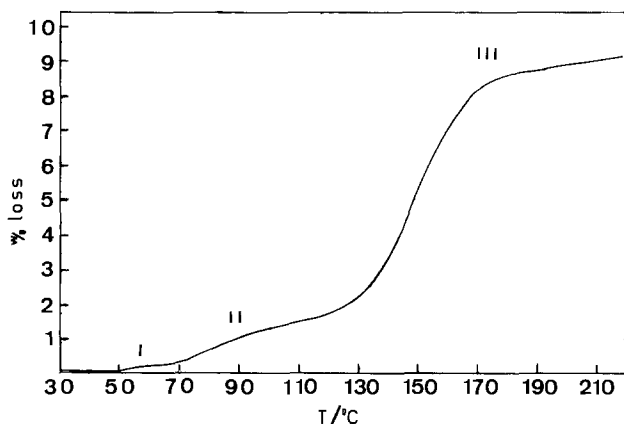


Fig. 6. TGA curve for a sample (50 w/o electrolyte + 50 w/o MgO) initially containing ≈ 2.5 w/o water.

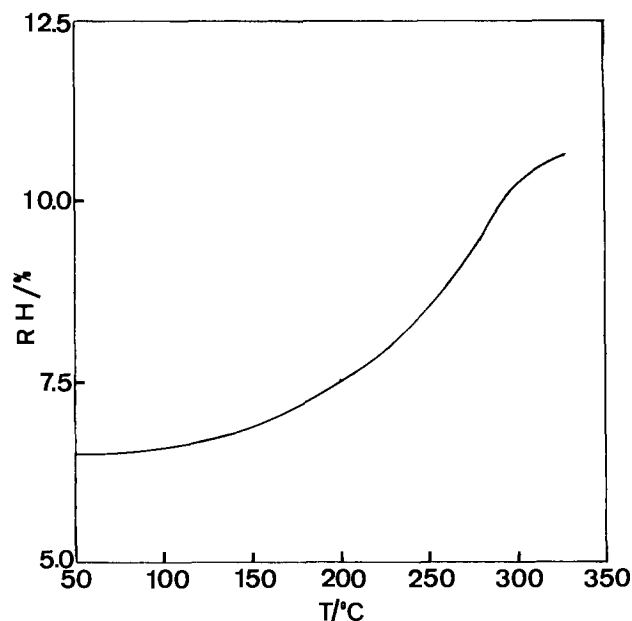


Fig. 7. Relative humidity vs. temperature of the gas evolved from a pellet (50 w/o electrolyte + 50 w/o MgO) which has been preheated and cooled (150°-25°C) several times. The system was continuously flushed with dry argon ($\text{RH} < 0.5\%$, flow rate = $2 \text{ cm}^3 \cdot \text{min}^{-1}$).

was recorded as function of temperature. Contrary to the EC, DTA, and TGA experiments, a small and constant flow of dry argon ($\text{RH} < 0.5\%$) was allowed to flush the system (the electrodes also serving as gas inlets). To eliminate the contribution of water evolved in the 25°-150°C region to the relative humidity, several heating-cooling cycles were applied until a constant value of RH was obtained in this temperature range. The RH vs. temperature curve obtained (Fig. 7) showed an increase in relative humidity at $T > 150^\circ\text{C}$, confirming water vapor evolution in this temperature range.

Conclusions

Electrical conductance as function of temperature of several eutectic mixtures has been reported in the literature. However, all reported data concern temperatures above melting point of the electrolyte (21). In the present study, ac conductivity measurements were particularly conducted below the melting temperature of the pelletized LiCl-KCl (64-36 m/o) mixture in the presence of MgO. The electrochemical data were compared to those obtained using differential thermal and thermogravimetric analysis and were related to the various states of water present in the pelletized mixture. There are distinct changes taking place at temperatures right from the ambient value, and at least three main different processes seem to be related to the presence of water in the pellet; the processes are listed below.

1. Initially, the pellet dries by a process that involves the migration of water to the surface of the pellet, where it vaporizes ($T = 25^\circ\text{-}130^\circ\text{C}$).

2. In the temperature region 30°-250°C, exothermic reactions give rise to an increase in electrical conductivity and to a large weight loss effect. Hygrometric measurements indicate the evolution of water in this temperature range. This is suggested to be the product of the thermochemically favorable reaction between oxide or hydroxide ions and hydrogen chloride (reaction [6] from left to right). However, the intensity of the EC, DTA, and TGA effects in region III is much larger than expected to arise from the small amounts of HCl present in the electrolyte (5). Further studies are needed to investigate the exact nature of the processes involved in these temperatures.

3. Further heating ($T > 250^\circ\text{C}$) causes hydrolytic decomposition of the electrolyte, *i.e.*, equilibrium [6] is shifted from right to left, yielding hydrogen chloride and hydroxide ions. The voltammetric detection of water as well as

hydrolytic products in fused pelletized electrolytes ($T > 370^{\circ}\text{C}$) will be described in a future publication (22).

REFERENCES

- W. Borger, D. Kunze, and H. S. Panesar, *Prog. Batt. Solar Cells*, **3**, 251 (1980).
- D. R. Vissers, *NATO Conf. Ser., Ser. 6*, **2**, 47 (1980).
- J. P. Mathers, T. M. Olszanski, and J. E. Battles, *This Journal*, **124**, 1149 (1977).
- K. W. Fung and G. Mamantor, *Adv. Molten Salt Chem.*, **2**, 199 (1973).
- S. H. White, in "Ionic Liquids," D. Inman and D. G. Lovering, Editors, Chap. 12 Plenum Press, New York (1981).
- R. Combes, in "Ionic Liquids," D. Inman and D. G. Lovering, Editors, Chap. 15, Plenum Press, New York (1981).
- A. A. El Hosary, D. H. Kerridge, and A. M. Shams El Din, in "Ionic Liquids," D. Inman and D. G. Lovering, Editors, Chap. 16, Plenum Press, New York (1981).
- S. Senderoff and A. Brenner, *This Journal*, **101**, 16 (1954).
- H. J. Gardner, C. T. Brown, and G. J. Janz, *J. Phys. Chem.*, **60**, 1458 (1946).
- H. A. Laitinen, W. S. Ferguson, and R. A. Osteryoung, *This Journal*, **104**, 516 (1957).
- D. L. Maricle and D. N. Hume, *ibid.*, **107**, 354 (1960).
- R. Nottenburg, K. Rajeshwar, M. Freeman, and J. Du Bow, *Anal. Chem.*, **51**, 1149 (1979).
- K. Rajeshwar, R. Nottenburg, M. Freeman, and J. Du Bow, *Thermochim. Acta*, **33**, 157 (1979).
- K. Lonvik, K. Rajeshwar, and J. B. Du Bow, *ibid.*, **42**, 11, (1980).
- G. V. Keller and F. C. Frischknecht, "Electrical Methods in Geophysical Prospecting," Pergamon Press, New York (1966).
- A. I. Vogel, "A Textbook of Quantitative Inorganic Analysis Including Elementary Instrumental Analysis," 3rd Ed., p. 944, Longmans, London (1961).
- W. W. Wendlandt, *Thermochim. Acta*, **1**, 11 (1970).
- A. B. Lidiard, in "Encyclopedia of Physics, Vol. 20, Electrical Conductivity II," S. Flugge, Editor, p. 246 Springer-Verlag, Berlin, (1957).
- K. Rajeshwar, R. Nottenburg, J. Du Bow, and R. Rosenvold, *Thermochim. Acta*, **27**, 357 (1978).
- C. Duval, "Inorganic Thermogravimetric Analysis," p. 165, Elsevier, Houston, (1953).
- E. R. Van Artsdalen and I. S. Yaffe, *J. Phys. Chem.*, **59**, 118 (1955).
- F. Broitman, R. Parash, U. Mor, D. Ozer, and A. Bettelheim, In preparation.

Corrosion of the Wet-Seal Area in Molten Carbonate Fuel Cells

I. Analysis

R. A. Donado, L. G. Marianowski, and H. C. Maru¹

Institute of Gas Technology, Chicago, Illinois 60616

J. R. Selman*

Department of Chemical Engineering, Illinois Institute of Technology, Chicago, Illinois 60616

ABSTRACT

Severe corrosion can occur in the seal area between the cell housing and the electrolyte tile of a molten carbonate fuel cell even if an optimal selection of the active cell materials has been made. Thermodynamic calculations and an approximate mixed-potential analysis indicate that several minor corrosion cells are active at open circuit, and a major corrosion cell is established when the cell is under load. Extensive corrosion can be expected on the anode side of the wet seal, although effects at the cathode side are minor.

The available literature related to gas-seal techniques and methods of minimizing corrosion, particularly in the seal area of a molten carbonate fuel cell, is very limited. In early work on cell development, several types of assemblies comprising all-ceramic components were used, e.g., by Broers *et al.* (1), Salvadori (2), and Kronenberg (3), but such assemblies are bulky and have low resistance to thermal shock. More recently, investigators have used cells and cell stacks formed by pressing together a series of flat-plate cell components (filter-press arrangement) and utilizing a wet seal (4, 5).

In the wet-seal technique, metal flanges are pressed against the flat surface of an electrolyte "tile," i.e., a porous, inert matrix filled with electrolyte. At the cell operating temperature, sufficient free liquid is present to wet the metal surfaces and form a gas seal, as schematically represented in Fig. 1. The concept was first applied by Davtyan (6) when working with "solid electrolyte" fuel cells in 1946. Later investigations by Broers (6) revealed that the electrolyte was not really a solid but contained molten salts such as phosphates and tungstates. Chambers and Tantram (7), using a eutectic mixture of lithium and sodium carbonates held in a porous, sintered magnesia disk, formed a cell or battery by sandwiching the disk, with its attached electrodes, to metal flanges. Similar sandwich-type cells were investigated by Peattie and

Trachtenberg (8). The wet-seal approach was also used in a previous project carried out at IGT (9). Critical improvements in seals and seal design for single, flanged cells are described in patent citations (10, 11). A review of more recent developments is given by Pigeaud *et al.* (5).

Because the wet-seal technique involves metal-electrolyte contact in a gas-deficient region of the cell, one may expect one or more corrosion cells to form. Experience with single, flanged cells has shown that corrosion of the seal-area metal can be severe and may lead to a poor seal and rapid deterioration of cell performance as a result of gas leakage. Severe corrosion in the wet-seal area also aggravates carbonate loss from the tile and may cause catastrophic failure (4). In fuel-cell stacks the cells are separated by a bipolar plate, which forms a wet seal with the electrolyte tile in each cell of the stack. The bipo-

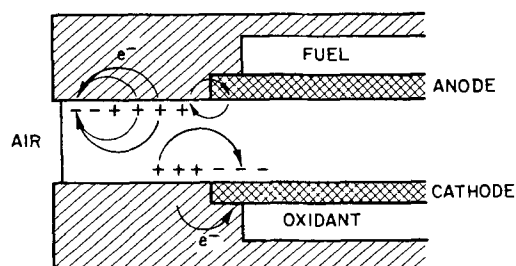


Fig. 1. Schematic of a wet-cell area of a molten carbonate fuel cell

*Electrochemical Society Active Member.

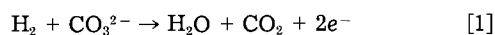
¹Present address: Energy Research Corporation, Danbury, Connecticut 06810.

lar plate, for which stainless steel is a candidate material, experiences similar corrosion problems as the anode and cathode flanges in a single cell.

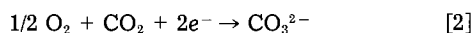
Although wet-seal corrosion and its prevention have received some attention in the electrochemical literature (12), no systematic study has been made of the corrosion mechanism and of the corrosion rates at various points in the wet-seal area. In this paper, we compare thermodynamically the corrosion cells operating in the wet-seal area and report corrosion rates under conditions simulating those in a fuel cell. A further objective is to clarify how corrosion can be prevented and to determine the level to which corrosion rates can be reduced. In this paper, the possible mechanisms of corrosion are presented and analyzed. This analysis cannot predict the actual corrosion rates, for which experiments are necessary. The experimental results are presented in the following paper (13).

Conversion and Corrosion Reactions

The main electrode reactions occurring in a molten carbonate fuel cell are at the fuel (negative) electrode or anode



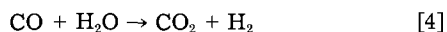
and at the oxygen (positive) electrode or cathode



The overall cell reaction is



Although the cell also converts CO, the direct electrochemical oxidation of CO, analogous to Eq. [1], appears to be very slow. It is generally assumed that CO oxidation takes place via the water-gas shift equilibrium



The fuel electrode and the negative flange of the cell housing (Fig. 1) are continuously in contact with fuel gas containing H₂, CO, H₂O, and CO₂, with N₂ constituting the balance. The oxygen electrode and the positive flange are continuously in contact with oxidant gas containing O₂, CO₂, and a small amount of H₂O, with N₂ constituting the balance. The gas compositions used here to illustrate corrosion processes are shown in Table Ia; they correspond to reformed naphtha as fuel and standard oxidant (70% air, 30% CO₂) as oxidant gas.

A large cell operating under an electrical load has an appreciable degree of conversion, typically 75% for the fuel gas and 50% for the oxidant. The resulting outlet compositions of fuel and oxidant are also shown in Table Ia.

The local driving force for conversion, Eq. [3], is determined by the equilibrium potentials of electrode reactions [1] and [2], which depend on the local gas compositions. This is illustrated in Table Ib, based on standard thermodynamic data (14, 15). The reference potential is that of oxygen reduction, Eq. [2], the reference oxidant consisting of 33% oxygen and 67% CO₂. Because the equilibrium potentials of Eq. [1] and [2] vary from point to point along the electrodes, the driving force for conversion, Eq. [3], varies correspondingly. Consequently, the distribution of the current in a cell with appreciable conversion is nonuniform. Analyses of current distribution in scaled-up cells have been presented by Sampath *et al.* (16) and Wilemski *et al.* (17).

Variations in local gas composition also cause variations in the local driving force for corrosion. The negative half (flange) of the cell housing is in contact, over its entire interior surface, with fuel gas of varying composition. Likewise, the inside of the positive half contacts oxidant of varying composition. In addition, both halves are in contact with ambient air, at and around the open end of the wet seal, where some electrolyte creepage usually occurs. The equilibrium potential of oxygen reduction from air is included in Table Ib.

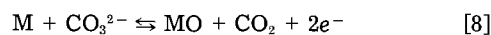
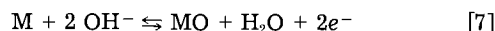
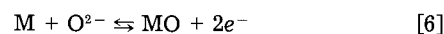
Table Ia. Compositions of gases used in this work (m/o)

	H ₂	CO ₂	H ₂ O	CO	N ₂	O ₂
Fuel inlet	60.9	8.4	21.6	9.1	—	—
Fuel outlet	10.3	39.6	45.4	4.6	—	—
Air	—	0.03	2.5	—	Bal	20.5
Oxidant inlet	—	29.2	2.8	—	53.7	14.3
Oxidant outlet	—	18.7	3.6	—	68.8	9.0
Reference gas	—	66.7	—	—	—	33.3

Table Ib. Equilibrium potentials of reactions [1] and [2] with respect to standard oxygen electrode (33.3% oxygen, 66.7% CO₂)

	Reaction	Potential at 923 K
Fuel inlet	1	-1121
Fuel outlet	1	-960
Air	2	-310
Oxidant inlet	2	-50
Oxidant outlet	2	-76

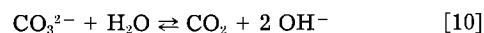
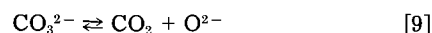
Corrosion cells are formed by local oxidation (dissolution) and reduction reactions occurring in adjacent areas of the same, electronically conducting surface. In the present case, these adjacent areas are located on the inside surface of the anodic or cathodic flange and on the porous electrode enclosed by the flange. The oxidation (dissolution or corrosion) reactions can be represented in a general way by the following equations written for a two-valent metal



Similar reactions may be written for a trivalent metal. The reduction reactions contributing to corrosion cells are gas-electrode reactions, principally oxygen reduction, Eq. [2], and possibly reduction of H₂O by the reverse reaction of Eq. [1].

In the treatment of corrosion presented here, the possibility of carbide formation (carburization) is not considered, although carbides can form in the metal phase beneath the oxide scale, if the oxygen activity is very low. Rapp *et al.* (21) have analyzed the conditions for carbide formation in detail and confirmed their predictions experimentally. Shores and Singh (22) have demonstrated the presence of carburization in laboratory cell current collectors. However, it is unlikely that the oxygen activity in the wet seal area will be low enough to cause carburization, except possibly very close to the inner edge of the anode-side flange, at open-circuit conditions or at very small conversions. The experimental results to be presented in Part II (13) show that this assumption is correct.

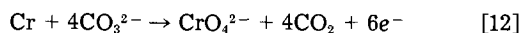
The electrode reactions, Eq. [5]-[8], are not independent. They involve dissolved gases and ionic species which locally participate in dissociation and hydrolysis equilibria



The water-gas shift equilibrium, Eq. [4], is also applicable. All of these reactions are rapid, at least compared with the rate of corrosion reactions [5]-[8], so that local equilibrium may be assumed. Thus, at any point of the flange surfaces, the equilibrium potentials of electrode reactions [5]-[8] are identical, and we may evaluate the potential by the Nernst equation applied to one of them; for example, Eq. [8]

$$E = E^0(\text{MO}, \text{CO}_2/\text{M}, \text{CO}_3^{2-}) + RT/2F \ln \frac{(\text{MO})(\text{CO}_2)}{(\text{M})(\text{CO}_3^{2-})} \quad [11]$$

The oxide MO is assumed to be insoluble, or sparingly soluble, so its activity is equal to, or close to, unity. In fact, stainless steel passivates; that is, it forms a coherent, conducting oxide layer that reduces the corrosion rate appreciably (18). This oxide layer may consist in part of mixed oxides such as LiFeO_2 and LiCrO_2 , which are also insoluble or sparingly soluble and do not significantly affect the electrode potential. In the transpassive region, these surface layers disintegrate under formation of loosely adherent metal oxides; in a strongly oxidizing, basic (*i.e.*, alkali oxide-rich) environment, such as exists at the cathode under load, chromium may be oxidized further to the very soluble chromate ion



$$E = E^0(\text{CrO}_4^{2-}, \text{CO}_2/\text{Cr}, \text{CO}_3^{2-}) + RT/6F \frac{(\text{CrO}_4^{2-})(\text{CO}_2)^4}{(\text{Cr})(\text{CO}_3^{2-})^4} \quad [13]$$

In Table II, the equilibrium potentials of various metals according to Eq. [11], based on standard thermodynamic data (14, 20), are collected; the gas compositions are those of Table Ia. Iron, chromium, and nickel are of interest not only as constituents of Type 300 stainless steels, but also as electrode materials. In the latter category, copper and cobalt are of interest. The table also includes structural materials such as tantalum, vanadium, and other refractory metals. Among the light metals included are aluminum and titanium, which form insulating oxides.

From Tables Ib and II, one can immediately ascertain which corrosion cells are thermodynamically possible. For example, all three components of stainless steel will have a tendency to corrode at those points of the flange where contact with air and electrolyte occurs. The driving force for these corrosion cells is, from Tables Ib and II

Chromium	-310 -(-1834) = 1524 mV
Iron	-310 -(-1346) = 1036 mV
Nickel	-310 -(-1087) = 777 mV

However, whether corrosion really takes place and, if so, at what rate, depends on the actual electrode potential at the point in question. Corrosion takes place only if the actual electrode potential is more positive than the equilibrium potential of the anodic (dissolution, corrosion) reaction. The rate of corrosion depends on the available driving force (actual potential minus equilibrium potential of the anodic reaction). Therefore, one may expect important differences in the corrosion picture when the cell is under load, as compared to that at open circuit. Thus, it is well known that at high current densities the porous anode material, mainly consisting of nickel, may become oxidized. Table II indicates that this is only possible if the actual electrode potential of the anode, with respect to a 33% oxygen, 67% CO_2 reference electrode, is more positive than, for example, -862 mV if the CO_2 partial pressure is 0.084 atm, as for reformed naphtha at inlet conditions. Such an electrode potential, though unacceptably high (positive) for state-of-the-art fuel cell anodes under standard operating conditions (4), may occasionally be

reached at very high current densities. However, from Table Ib it can be seen that in a cell at open circuit, oxidation of nickel by the reverse reaction of Eq. [1] is thermodynamically impossible unless the H_2O and CO_2 partial pressures in the fuel gas are increased far in excess of those in reformed naphtha at 75% conversion.

In a cell at open circuit, the negative and positive flanges are not electronically connected. Each flange then assumes a mixed potential corresponding to zero net current of the various electrochemical reactions that exchange electrons via the flange. The mixed potential is the result of a complex interaction between the electrochemical reactions (corrosion and reduction) and the supply, by diffusion, of dissolved gases to various points of the wet-seal area. In the carbonate fuel cell at open circuit, a small fraction of the feed gas on both sides is continually being consumed by chemical reaction; that is, there is a small but stationary flux of dissolved gas into the tile toward the opposing electrode or toward the air interface of the wet seal. Hydrogen diffusing from the fuel electrode toward the oxygen electrode and the air/tile interface reacts with oxygen and is consumed (chemical discharge). Furthermore, a small fraction of the feed gases on either side may be involved in corrosion cells (circuits); on the cathode side, some oxygen is reduced, and on the anode side, some H_2O may be reduced. These corrosion cells are parasitic or cooperative, depending on whether or not they consume part of the feed gases. At open circuit, the changes in gas composition are usually of no practical significance. Corrosion cells involving oxygen from air are indifferent with respect to conversion.

In all of the above cases, only those corrosion reactions (dissolution or oxidation) can take place whose equilibrium potential is more negative than the mixed potential assumed by the flange.

The same applies to a fuel cell under load, that is, producing a current. However, the analysis is easier because the electrode potential is controlled externally through the load rather than through the spontaneous interaction of diffusion and reactions in the wet-seal area. The corrosion cells (circuits) are now superimposed on the main cell current, due to fuel conversion, as schematically shown in Fig. 2. One may still distinguish cooperative, parasitic, and indifferent corrosion cells. Thus, a corrosion cell restricted to the anode flange, in which some H_2O is reduced to hydrogen, decreases fuel conversion for a given cell current; it is, therefore, cooperative. Corrosion cells that involve both flanges may also be established, as shown in Fig. 2; such cells parallel the main cell reaction and increase the external current, while also increasing oxidant conversion for a given main cell current due to fuel conversion.

In reality, of course, the various corrosion cells (circuits) do not exist as separate entities in the overall current distribution between the flanges. The resulting current distribution at the flanges can be interpreted in terms of corrosion cells. This is convenient in cases like the present one, where the exact, quantitative analysis of the potential distribution would require much mathematical effort.

Table II. Equilibrium potentials at 925 K vs. standard oxygen reference electrode (33.3% oxygen, 66.7% CO_2)

Material	Reaction	Potential (mV)				
		Air 0.03% CO_2	Fuel inlet 8.4% CO_2	Fuel outlet 39.6% CO_2	Oxidant inlet 29.2% CO_2	Oxidant outlet 18.7% CO_2
Cu	$\text{Cu}(c) + 1/2 \text{O}_2(g) = \text{CuO}(c)$	-674	-449	-388		
Ni	$\text{Ni}(c) + 1/2 \text{O}_2(g) = \text{NiO}(c)$	-1087	-862	-801	-813	-830
Co	$\text{Co}(c) + 1/2 \text{O}_2(g) = \text{CoO}(c)$	-1156	-931	-872	-882	-899
Fe	$0.947\text{Fe}(c) + 1/2 \text{O}_2(g) = \text{Fe}_{0.947}\text{O}(c)$	-1346	-1121	-1060	-1072	-1090
Cr	$2\text{Cr}(c) + 3/2 \text{O}_2(g) = \text{Cr}_2\text{O}_3(c)$	-1834	-1609	-1548	-1560	-1578
Nb	$2\text{Nb}(c) + 5/2 \text{O}_2(g) = \text{Nb}_2\text{O}_5(c)$	-1836	-1611	-1550		
Ta	$2\text{Ta}(c) + 5/2 \text{O}_2(g) = \text{Ta}_2\text{O}_5(c)$	-1980	-1755	-1694		
V	$2\text{V}(c) + 3/2 \text{O}_2(g) = \text{V}_2\text{O}_5(c)$	-2014	-1789	-1728		
Ti	$\text{Ti}(\alpha) + \text{O}_2(g) = \text{TiO}_2(c)$	-2296	-2071	-2010		
Zr	$\text{Zr}(\alpha) + \text{O}_2(g) = \text{ZrO}_2(\alpha)$	-2665	-2440	-2379		
Al	$2\text{Al}(c) + 3/2 \text{O}_2(g) = \text{Al}_2\text{O}_3(\text{Cor})$	-2675	-2450	-2389		

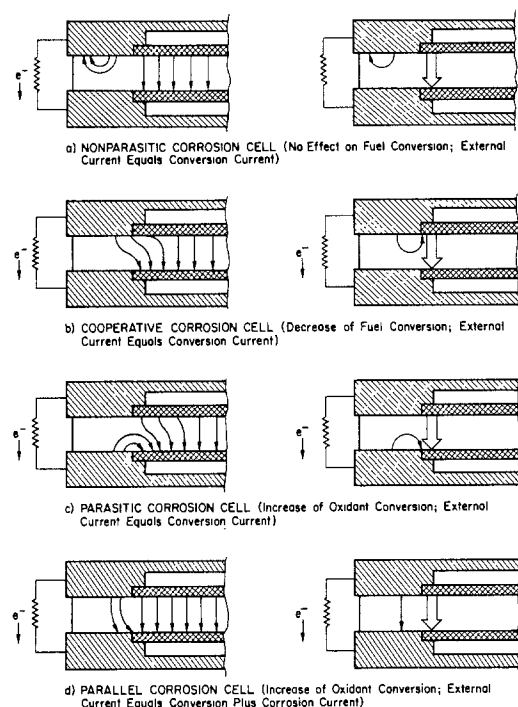


Fig. 2. Types of corrosion cells existing in the wet-cell area. Left: current distribution in the electrolyte. Right: schematic in terms of corrosion cells. The bold arrow represents the main cell current due to fuel conversion in the absence of corrosion.

Corrosion Regions and Solute Fluxes

To distinguish the various corrosion cells in the wet-seal area, we identify first the approximate gas compositions adjacent to various regions of the cell housing. These are schematically indicated in Fig. 3.

Surrounding the anode is region A, which has a high concentration of H_2 and CO , and which also contains a considerable amount of H_2O (see Table Ia). From this region, H_2 and CO diffuse toward the edge of the flange. From the edge of the flange (regions C and F), O_2 (as air) diffuses toward region A. H_2 and O_2 react in a zone (indicated by a dotted line) at region B where, consequently, the H_2O concentration is high. Because the solubility and diffusivity of H_2 are appreciably larger than those of O_2 in molten carbonate (17), the location of region B is closer to the outer edge of the seal area than to the inner edge.

The reaction zone between H_2 (or CO) and O_2 within the tile is schematically indicated by the dotted line in Fig. 3. From region B, this line curves toward that part of the tile that lies between the electrodes. The reaction zone is region G, which is closer to the cathode than to the anode.

Region D, near the edge of the cathode, contains a relatively high concentration of O_2 and CO_2 , while region F, near the outer edge, contains a high concentration of O_2 but is low in CO_2 . The concentration of H_2O goes from relatively low in region D to very low in region F. This is schematically indicated in Table III. Region E, unlike the opposite region at the anode side (region B), is characterized by conditions that are not very different from adjacent regions.

To analyze the corrosion effects, it is desirable next to assess the relative importance of the various fluxes of

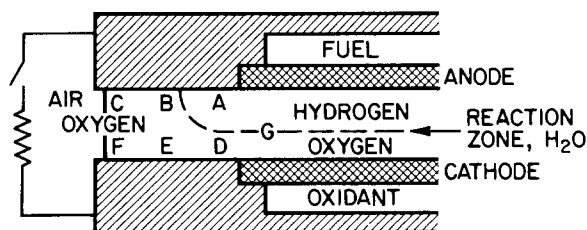


Fig. 3. Regions in the wet seal according to major dissolved-gas species

Table III. Dissolved gas concentrations in various regions of the wet seal (schematically) in percent of total gas pressure

Region	$H_2 + CO$	CO_2	O_2	H_2O
A	70	8	0	22
B	0	(8)*	0	(92)
C	0	0.1	19	0.1
D	0	29	14	3
E	0	(10)	(17)	(1)
F	0	0.1	19	0.1

* The concentrations in regions B and E are determined by the reaction of converging fluxes, and could be estimated by a rather involved mathematical analysis. The values in parentheses are rough estimates only for purpose of illustration.

dissolved gas in the wet-seal area. These fluxes may reinforce or may counteract the corrosion cells that arise spontaneously. The concentration differences (Table III) and the distances between various regions lead us to conclude that certain fluxes are very important and others secondary, as indicated by solid and dashed arrows in Fig. 4. It should be noted that the tile thickness is only about one-fifth of the length dimension of the flange, so fluxes across the tile are relatively more important than those along the flanges. Also, H_2O fluxes are in first approximation equivalent to CO_2 fluxes because of the hydrolysis equilibrium (Eq. [10]).

Analysis: Corrosion at Open Circuit

The corrosion picture at open circuit is simplified by the observation that in cells of reasonably large size, the open-circuit potentials of the fuel electrode and the oxidant electrode are practically equal to the equilibrium potentials of the respective conversion reactions, that is, H_2 oxidation (reaction [1]) and O_2 reduction (reaction [2]). Therefore, we can make use of Table IV, in which are collected the equilibrium potentials of the primary corrosion and reduction reactions in the various regions.

At the anode side, little iron dissolution should be expected in regions A and B. Only if the fuel gas is richer in H_2O and CO_2 than assumed in Table Ia will it be likely that there is a strong corrosion cell between regions A and B. However, between regions B and C, the conditions are fulfilled for dissolution of iron under simultaneous reduction of O_2 . The driving force for this cell, indicated by i_1 in Fig. 5, is considerably larger than that for corrosion between regions A and B (i_3).

Chromium dissolution can occur over the entire anode wet seal, compensated for by reduction of O_2 from air in region C. Corrosion of chromium, like that of iron, will be most intense just outside region B.

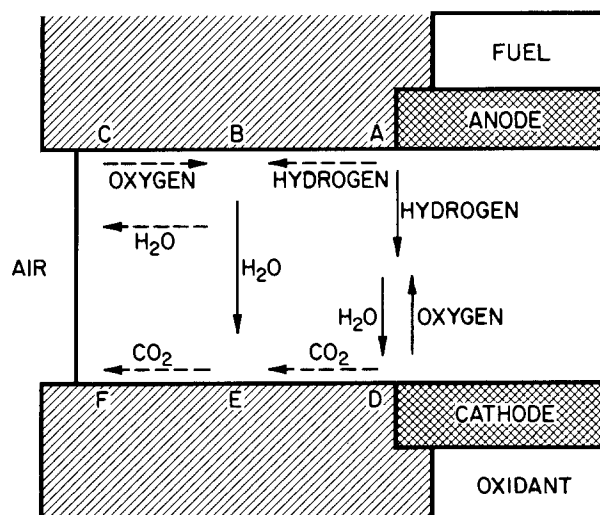


Fig. 4. Primary fluxes (solid arrows) and secondary fluxes (dashed arrows) of dissolved gas at open circuit.

Table IV. Equilibrium potentials of electrode reactions in various regions of the wet seal (in mV at 925 K vs. the 33% oxygen, 66.7% CO₂ reference electrode)

Region	H ₂ O/H ₂	O ₂ , CO ₂ /CO ₃ ²⁻	FeO/Fe	Cr ₂ O ₃ /Cr	NiO/Ni
A	-1120		-1120	-1610	-860
B			-1050	-1611	-864
C		-310	-1350	-1830	-1090
D		-50	-1070	-1560	-810
E		-50	-1110	-1603	-856
F		-310	-1350	-1830	-1090

Figure 5 indicates schematically how the positive and negative areas on the anode side of the wet seal are distributed, corresponding to the prevailing fluxes (H₂O from B to C and E; CO₂ from B to C; O₂ from C to B; and H₂ from A to B).

At the cathode side, where the open-circuit potential is very close to -50 mV, metal dissolution compensated by oxidant reduction is possible everywhere. It is most likely to be intense in region D, where the distance to the cathode itself is shortest. The distribution of positive and negative sites indicated in Fig. 5 is in agreement with a CO₂ flux from region D to E. In region D, one would expect corrosion to be serious, since the driving force for metal oxidation is very large (Table IV). However, the compensating oxygen reduction apparently proceeds at a very small rate: the cathode open-circuit potential is close to equilibrium for this reaction. This suggests that the corrosion rate may, after all, be quite small compared to that at the anode because the kinetics of O₂ reduction in molten carbonate are known to be very much slower than those of H₂ oxidation (15).

Analysis: Corrosion under Load

In a cell under load, some changes may be expected in the picture of Fig. 3. Region B, where H₂ from (A) combines with O₂ from (C), will be located closer to (A) because the concentration of H₂ at (A) is now lower, except at the fuel inlet. At the cathode, the flux of CO₂ from region D, via (E) to (F), will be smaller than at open circuit for similar reasons. The flux of H₂O across the tile, although still very prominent, will be smaller than at open circuit and shifted toward the inner edge of the wet seal.

Again considering the equilibrium potentials shown in Table IV, we note that these are valid only at the feed gas inlet points. The potentials at outlet may be found from Tables I and II; they are graphically illustrated in Fig. 6.

The most important differences, however, have to do with the actual electrode potentials of anode and cathode. These are considerably different from the open-circuit

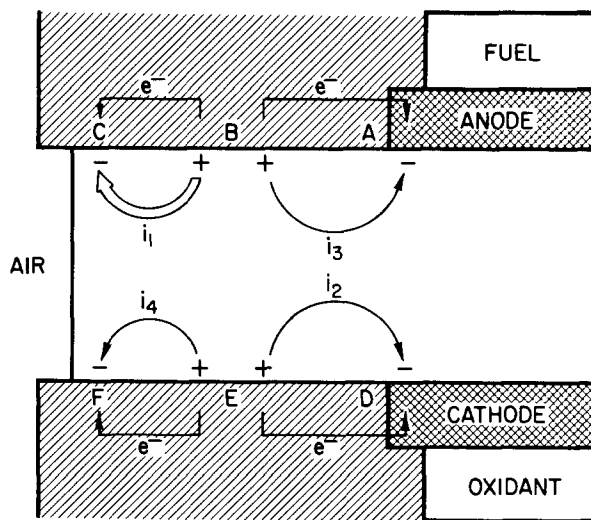


Fig. 5. Corrosion cells in the wet-seal area as open circuit

values (Fig. 6). Also, anode and cathode are connected electronically through the load, thereby opening the possibility of cross-tile corrosion cells. The consequences of the new situation are shown schematically in Fig. 7.

At the anode side, where the operating potential is -950 mV, corrosion cell i₁, in region C, is likely to extend further toward the inner edge of the wet seal. Also, under fuel outlet conditions the H₂O concentration at (A) may be high enough to make the anodic leg of corrosion cell i₃, at and near (B), extend further toward the inner edge of the seal. This is equivalent to an increase of corrosion current i₃ and a decrease of fuel conversion (cooperative corrosion). Nevertheless, i₃ remains quite small because the driving force is small.

The salient feature of Fig. 7, however, is the corrosion cell across the tile, between regions B and E. This is a major corrosion cell because the driving force is large and the distance over which it operates is small. Cell i₅ is made possible by the electronic connection between the flanges. The current is in first approximation inversely dependent on the load, as is the main conversion current of the fuel cell. We note also that the corrosion current i₅ is reinforced by the flux of H₂O, and equivalently of CO₂ by equilibrium (10), across the tile from region B to E.

At the cathode side, the corrosion cell i₂ is weakened or suppressed, as is cell i₄, by the negative shift of the electrode potential under load (cathodic protection).

To quantify the various corrosion tendencies in first approximation, we observe that the driving force for cor-

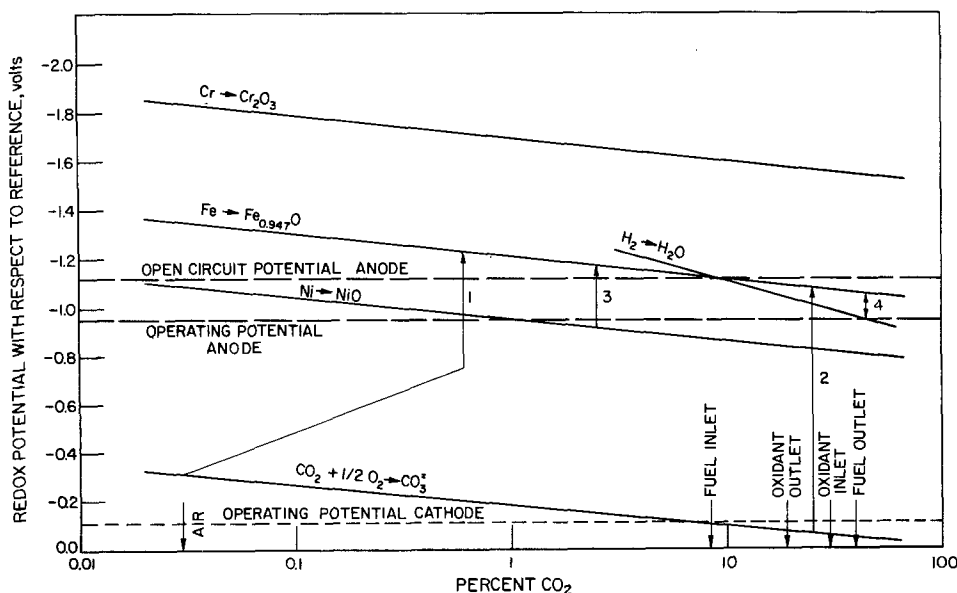


Fig. 6. Equilibrium potentials of electrode reactions vs. the 33.3% oxygen and 66.7% CO₂ reference electrode as a function of CO₂ partial pressure. Operating potentials of anode and cathode, as well as anode open-circuit potential, are indicated.

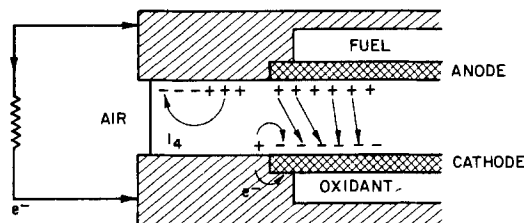


Fig. 7. Corrosion cells in the wet-seal area under load

rosion cell i_2 of Fig. 7 is, for iron corrosion, approximately $-50 - (-1110) = +1060$ mV at open circuit, but decreases to $-100 - (-1110) = 1010$ mV under load, similarly for cell i_4 . The principal corrosion cell on the anode side is at open-circuit cell i_1 , which has a driving force of $-310 - (-1050) = +740$ mV; however, under load the principal corrosion cell is i_5 , with driving force $-100 - (-950) = +850$ mV over a much smaller distance.

Thus, corrosion at the cathode side of the wet seal should be decreased and the anode side should experience more intense corrosion. Correspondingly, the corroded area of the anode side may be expected to increase under load, although the cathode side should be largely immune.

Corrosion of Various Metals in an Operating Cell

At the anode operating potential of -950 mV, chromium and iron will be oxidized (Fig. 6), but nickel, cobalt, and copper will not (Table II). The thermodynamic data also indicate that somewhat less corrosion of iron should be observed at the fuel outlet side of the cell because the equilibrium potentials for metal oxidation become more positive with increasing partial pressure of CO_2 (Fig. 6). In terms of the corrosion cells of Fig. 7, this means a strong cathodic component of i_3 (H_2O being reduced in region A) and possibly a shift of the anodic leg of i_3 , as well as i_5 , toward the outer edge of the wet seal. However, this does not necessarily imply that the total rate of corrosion in the wet-seal area is less.

For the corrosion of chromium, fuel inlet or outlet conditions make little difference because the driving force for corrosion is large. If, as has been suggested (19), corrosion of stainless steel takes place by intergranular attack of chromium, there would not be any significant effect of fuel gas composition. However, the picture is complicated by the formation of mixed oxides, such as LiCrO_2 and LiFeO_2 , whose solubility and conductivity are influenced by the basicity of the melt and by the relative concentrations of the alkali ions. For lack of adequate information about these fundamental chemical aspects of corrosion in molten carbonates, the present approximate analysis must suffice.

The analysis in this paper is based primarily on tendencies indicated by thermodynamic equilibria combined with a semi-quantitative assessment of the actual corrosion cells in the wet-seal area. A more exact prediction of the intensity of corrosion and its distribution would follow from a complete mathematical model of the potential, current, and species concentration distributions in the wet-seal area and adjoining regions. Solving such a model would require not only extensive computational effort, but also reliable kinetic information, for example, on the dissolution and passivation of stainless steel and the reduction of oxygen at steel or various metal oxides.

Under these conditions, it is easier to simulate wet-seal conditions experimentally in a model cell. The results of model experiments are reported in the second part of this paper (13).

Summary

A semi-quantitative analysis of the mixed-potential conditions in the wet-seal area of a molten carbonate fuel cell leads to the following conclusions.

1. At open circuit, the anode side will corrode mostly near the center of the wet seal compensated by reduction

of atmospheric O_2 near the outer edge. Corrosion close to the inner edge of the seal is only expected if the fuel is very rich in H_2O and CO_2 . The cathode side will corrode near the inner edge of the seal, compensated by reduction of oxidant in the porous cathode.

2. Under load, anode wet-seal corrosion will take place much more intensively than at open circuit and over a greater area. The compensating reaction is reduction of oxidant gas, or atmospheric oxygen, at the cathode flange. Corrosion of the cathode side is less intensive than at open circuit owing to cathodic protection under load.

3. Under higher H_2O and CO_2 partial pressures at fuel outlet conditions, somewhat more corrosion should be observed at the inner edge of the anodic wet seal near the fuel outlet than at fuel inlet. This effect should be very clear if the corrosion process involves iron oxidation directly, if it takes place via chromium oxidation, the differences should be minor.

Acknowledgments

The work reported here was sponsored by the U. S. Department of Energy through Argonne National Laboratory. Guidance and suggestions by the program manager, Dr. John P. Ackerman, are very much appreciated. One of the authors (J. R. Selman) also acknowledges support by the Office of Basic Energy Sciences, U. S. Department of Energy.

Manuscript submitted June 14, 1984; revised manuscript received Feb. 27, 1984.

The Institute of Gas Technology assisted in meeting the publication costs of this article.

REFERENCES

- G. H. J. Broers, M. Schenke, and G. G. Piepers, *Adv. Energy Convers.*, **4**, 127 (1964).
- A. Salvadori, P. Lovy, and M. Beigelman, U.S. Pat. 3,359,134 (1967).
- M. L. Kronenberg, U.S. Pat. 3,216,911 (1965).
- J. R. Selman and L. G. Marianowski, in "Molten Salt Technology," D. H. Lovering, Editor pp. 323-393, Plenum Press, New York, (1982).
- A. Pigeaud, A. J. Skok, P. S. Patel, and H. C. Maru, *Thin Solid Films*, **83**, 449 (1981).
- G. H. J. Broers, Thesis, University of Amsterdam, Amsterdam (1958).
- H. H. Chambers and A. D. S. Tantram, in "Fuel Cells," Vol. 1, G. Y. Young, Editor, pp. 94-108, Reinhold, New York (1960).
- C. J. Peattie, I. Trachtenberg, and J. K. Truitt, in "Proceedings of the First Australian Conference Electrochemistry," J. A. Friend and F. Gutmann, Editors, pp. 683-688, Pergamon Press, Oxford, England (1963).
- Institute of Gas Technology, "Development of Molten Carbonate Fuel Cells," A. G. A. Project DC-4-1 Final Report, Chicago, March 1967.
- C. R. Schroll, U. S. Pat. 3,855,002 (1974).
- A. Z. Borucka, U. S. Pat. 3,723,186 (1973).
- R. B. Swaroop, J. W. Sim, and K. Kinoshita, *This Journal*, **125**, 1799-1800 (1978).
- R. A. Donado, L. G. Marianowski, H. C. Maru, and J. R. Selman, *ibid.*, **131**, 2541 (1984).
- D. R. Stull and H. Prophet, "JANAF Thermochemical Tables," 2nd Ed., p. 37, NSRDS-NBS, Washington, DC (1971).
- J. R. Selman and H. C. Maru, in "Advances Molten Salt Chemistry 4" G. Mamantov and J. Braunstein, Editors, pp. 157-389 (1981).
- V. Sampath, A. F. Sammells, and J. R. Selman, *This Journal*, **127**, 79 (1980).
- T. L. Wolf and G. Wilemski, *ibid.*, **130**, 48 (1983).
- G. J. Janz and A. Conte, *Electrochim Acta*, **9**, 1277 (1964).
- B. K. Anderson, Thesis, Technical University of Denmark, Lyngby, Denmark (1975).
- I. Barin, O. Knacke, and O. Kubaschewski, "Thermochemical Properties of Inorganic Substances" (1973) and Supplement (1977), Springer Verlag, Dusseldorf.
- R. A. Rapp, in "Proceedings of the DOE/EPRI Workshop on Molten Carbonate Fuel Cells," EPRI-WS-78-135, Nov. 1979, p. 230 (1979).
- D. A. Shores and P. Singh, Papers 254 and 387 presented at the Electrochemical Society Meeting, Montreal, Quebec, Canada, May 9-14, 1982.

Corrosion of the Wet-Seal Area in Molten Carbonate Fuel Cells

II. Experimental Results

R. A. Donado, L. G. Marianowski, and H. C. Maru¹

Institute of Gas Technology, Chicago, Illinois 60616

J. R. Selman*

Department of Chemical Engineering, Illinois Institute of Technology, Chicago, Illinois 60616

ABSTRACT

Experimental results for anode wet-seal corrosion in molten carbonate fuel cells generally agree with postulated mechanisms that involve corrosion couples acting along or across the seal area. The corrosion rate of Type 316 stainless steel in the anode wet-seal area under all test conditions is unacceptably high. Substitution of an aluminum containing alloy, such as Kanthal A-1, reduces the anode wet-seal corrosion by at least two orders of magnitude. The corrosion rate of Type 316 stainless steel in the cathode wet seal is about two orders of magnitude lower than in the anode wet seal.

In Part I (1), we presented an approximate thermodynamic analysis of the mechanisms that cause corrosion of the molten carbonate fuel cell hardware. Two corrosion cells of relatively minor intensity should be active at open circuit: flange metal/air at the anode side and flange metal/oxidant gas at the cathode side. A major corrosion cell, anode-side flange metal/cathode-side oxidant, should be established under load. The analysis predicted a greater corrosion rate of the anode wet seal than of the cathode wet seal.

In this part, we present the results of corrosion experiments carried out to test the thermodynamic predictions, and we identify practical solutions to the wet-seal corrosion problem. The experiments were carried out at varying electrode potential (cell at open circuit or under load), fuel utilization (inlet or outlet), and material (316 stainless steel or Kanthal A-1).

Apparatus and Experimental Conditions

As discussed in Part I, several corrosion cells may be expected to operate in the wet-seal area of molten carbonate fuel cells (1). Because of the design limitations of scaled-up cells, such as the difficulty of access for reference electrodes, the corrosion mechanism cannot be studied quantitatively in actual operating cells. Therefore, out-of-cell testing is required. However, great care must be taken to assure that the characteristic design parameters controlling corrosion rates, for example, tile thickness, diffusion path lengths, and local gas compositions, are comparable to those in actual cells. Several test configurations were evaluated and tested before the design shown in Fig. 1 was adopted. In the test-stand design of Fig. 1, the test-specimen (J) for the anode wet seal, 3.8 cm diam, was welded to a ring (L) previously welded to a Type 316 stainless-steel tube. An electrolyte tile (I) was placed on the specimen. The test specimen was 0.64 cm larger in diameter than the electrolyte and was welded around the edge of the ring to minimize any changes in the grain structure that could occur during the welding operation. The specimen was then machined to accommodate a ring-shaped anode. Perforations in the specimen provided fuel access to the electrode. The cathode compartment was similar to that of the anode, except that a hole in the center of the cathode and a cathode current collector was provided for the reference electrode. The electrolyte and the wet-seal area, 0.64 cm wide, had the same thickness and width, respectively, as in a working cell. The active cell area was 2.5 cm²; the electrodes were 1.91 cm diam with a 0.66 cm diam center hole.

The corrosion tests were operated at 923 K (650°C) for 1000h using electrolyte tiles 0.178 cm thick. The carbonate content of the electrolyte tiles was approximately 60

Table I. Gas compositions (m/o)

	H ₂	CO ₂	H ₂ O	CO	O ₂	N ₂
Fuel inlet*	60.9	8.4	21.6	9.1	—	—
Fuel outlet**	31.5	21.9	37.0	9.6	—	—
Oxidant†	—	29.2	2.8	—	14.3	53.7
Reference electrode	—	66.7	—	—	33.3	—

* Reformed naphtha fuel.

** Reformed naphtha fuel (37% H₂ utilization).

† Standard oxidant.

weight percent (w/o). A Li₂CO₃/K₂CO₃ eutectic carbonate mixture (62 mole percent [m/o] Li₂CO₃/38 m/o K₂CO₃) was used. The compositions of the test gases are presented in Table I. In the tests operated under load, the anode potential was potentiostatically kept constant at -1000 mV with respect to the 67% CO₂/33% O₂-gold reference electrode described by Borucka (2) and Argano *et al.* (3).

Results

Corrosion at open circuit.—Tests at open circuit were carried out to observe the corrosion caused at the anode side by the metal/air and the metal/fuel corrosion cells (i₁ and i₃ in Fig. 5 of Part I). Both cells cause corrosion in the wet-seal area of the test cell, but the metal/fuel cell would cause more corrosion near the inner edge of the wet-seal area.

Typical corrosion results at open circuit are shown in Fig. 2. The sampling locations are indicated in Fig. 3. Figure 2 demonstrates that the most severe corrosion occurs at sites 3 and 4, which are at the edge of the tile and

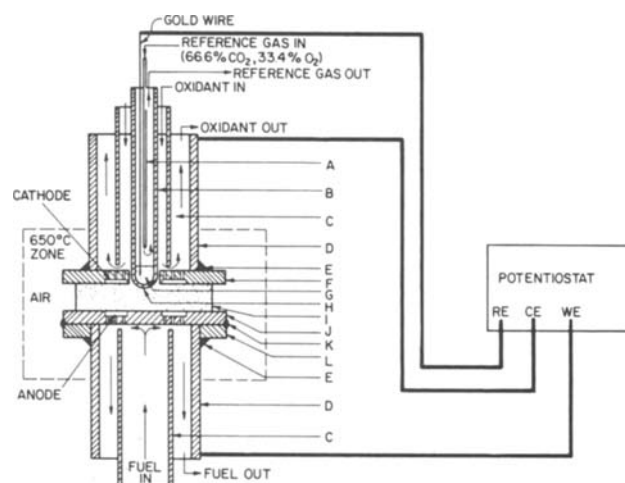


Fig. 1. Corrosion test cell. F: Cathode specimen. I: Tile. J: Anode test specimen. L: Support ring.

*Electrochemical Society Active Member.

¹Present address: Energy Research Corporation, Danbury, Connecticut 06810.

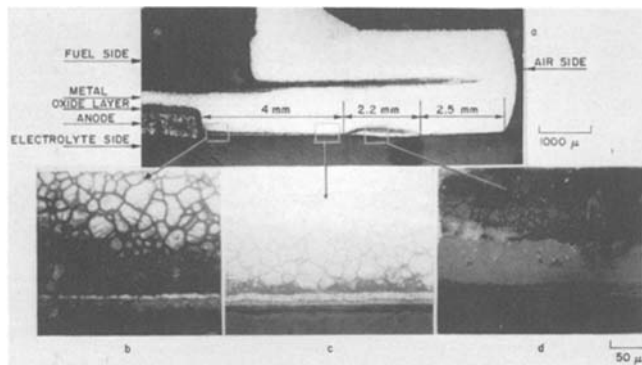


Fig. 2. Test results for Type 316 SS at open circuit. a: Cross section of entire anodic wet-seal flange and support ring. b, c, and d: Photomicrographs of coupons at indicated locations.

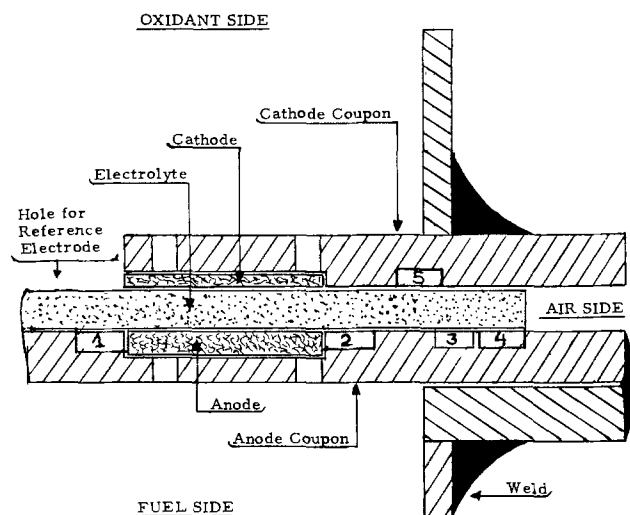


Fig. 3. Sampling sites (1-5)

nearest to the ambient air environment. This agrees with the analysis (1), which predicted that the affected area would be beyond the center of the wet seal: the metal/air corrosion cell, i_1 , is stronger than the metal/ H_2O cell, i_3 . The corrosion in areas 3 and 4 is very similar to that caused by excess OH^- and O^{2-} ions, as described by Andersen (4), who worked with basic alkali carbonates and alkali oxides. Corrosion at the center (site 1) and the inside (site 2) of the wet seal is much less severe.

Corrosion under load.—Corrosion testing under load conditions was carried out at fuel inlet and fuel outlet conditions. Photomicrographs from test cells are shown in Fig. 4 and 5. In both types of tests, very severe corrosion is observed. A much greater rate of corrosion is observed at the inside of the anode wet seal (site 2) and its central portions (site 1) than at the outer edge; repeat tests showed similar results. Corrosion rates at these same sites (1 and 2) were much smaller in our experiments at open circuit, where the metal/air cell (i_1) had a limited operating range. Clearly, there is a shift in potential distribution in

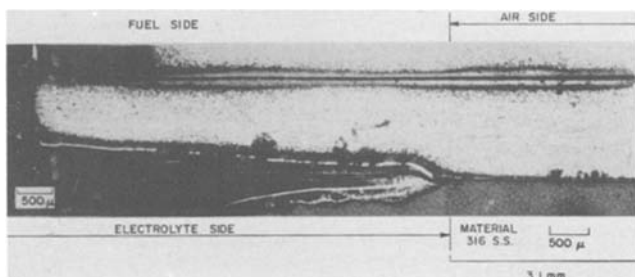


Fig. 4. Test results for Type 316 SS under load at fuel inlet conditions

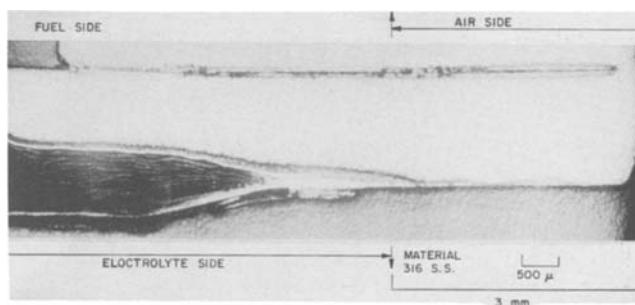


Fig. 5. Test results for Type 316 SS under load at fuel outlet conditions

the wet-seal area upon electrically loading the cell; this is caused by a new, across-tile metal/oxidant corrosion cell (i_5). The latter is the principal corrosion-causing cell when an external current is drawn.

The test cells also show somewhat greater corrosion rates at fuel outlet conditions than at fuel inlet. As our analysis predicted (1), at fuel inlet conditions corrosion cell i_3 (metal/ H_2O) is relatively ineffective because of the high H_2 activity in the gas phase. This protection decreases with the conversion of the fuel, and at the fuel-outlet conditions iron will tend to corrode over a much wider area adjacent to the porous anode. Therefore, it is likely that the somewhat greater corrosion observed at fuel-outlet conditions in our experiments is indeed the result of the much lower H_2/H_2O ratio than at fuel inlet (0.85, compared to 2.82 at inlet).

Careful visual examination of the cathode coupon was carried out after termination of each test. In all the tests, a brownish, rust-like, apparently thin, oxide layer covered the surface of the coupon; the oxide layer was very uniform, with almost no sign of corrosion. To verify this, we sectioned the cathode wet-seal coupon from one test operated at open circuit. Corrosion (caused by the metal/oxidant cell, i_2) is expected to be at a maximum under these conditions. The corrosion observed at the cathode wet seal (Fig. 6) is not severe and is uniform across the sample. The corrosion morphology of the specimen nearest the porous cathode did not differ significantly from that closer to the tile-air interface.

Rates of Corrosion

Experiments under load at -1000 mV vs. the 67% $CO_2/33\%$ O_2 reference electrode show that the most severe corrosion of the Type 316 stainless-steel wet seal occurs at the anode side and at the inner portion of the seal. The rate of corrosion caused by the metal/oxidant cell, i_5 , across the tile, was an order of magnitude greater than

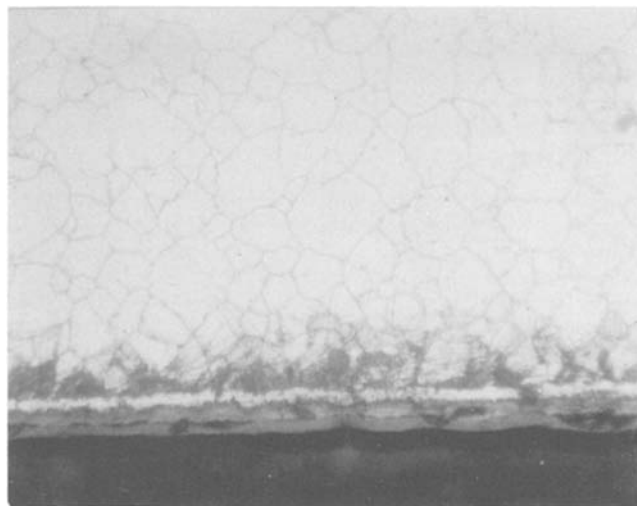


Fig. 6. Typical corrosion of the cathode wet-seal area

Table II. Corrosion of Type 316 stainless steel as a wet-seal material

	Site ^a	Open circuit	Load
		(mm/1000h)	
Anode	1	0.035-0.041	0.43-0.60 ^c
	1		0.970 ^d
	2	0.035-0.041	0.470-0.62 ^c
	2		0.45 ^d
Cathode	3	0.015 ^b	
	4	0.079-0.109	
	5	0.008-0.010	0.008-0.010

^a See Fig. 3 for location.

^b Minimum corrosion.

^c Maximum for fuel inlet gas conditions.

^d Maximum for fuel outlet gas conditions.

that caused by the metal/air cell, i_1 , and the metal/H₂O cell, i_3 , at open circuit. The corrosion rate under load at the anode side was two orders of magnitude greater than that by the metal/oxidant cell, i_2 , at the cathode wet seal under open-circuit conditions.

Corrosion rates measured in 1000h of testing under the same gas environment are collected in Table II. The metal/oxidant cell across the tile, i_5 , combined with the metal/H₂O cell, i_3 , under load causes 0.43-0.62 mm of corrosion. This is to be compared with the metal/H₂O cell, i_3 , alone at open circuit, which is responsible for 0.036-0.040 mm, and the metal/air cell, i_1 , alone at open circuit, which causes 0.08-0.11 mm of corrosion in 1000h. A somewhat greater rate of corrosion of Type 316 stainless steel is observed under fuel outlet conditions (0.45 to 0.97 mm) than under inlet conditions (0.43 to 0.62 mm). On the cathode side, at open circuit, the metal/oxidant cell, i_2 , does not cause more than 0.01 mm. The latter, very low corrosion rate indicates that most of the driving force of this cell (1022 mV at open circuit) is spent in overcoming a high ohmic resistance caused by the oxide layer.

Corrosion Protection by Alumina

The corrosion rates reported above for the anode side of the wet seal are prohibitive, both at open circuit and under load. Since the largest amount of corrosion is clearly associated with the metal/oxidant cell, i_5 , across the tile, corrosion protection by means of an insulating gasket covering the wet-seal faces would be an obvious solution. Such a gasket would function as a barrier to the ions and dissolved gas molecules diffusing or migrating across the tile in the wet-seal area. However, a gasket would not offer long-term protection unless it was intimately bonded to the base metal of the wet-seal flanges. Various possibilities were explored, of which alumina or compounds derived from alumina appeared most promising.

In long-term laboratory cell testing, dense alumina has been shown to be stable for over 40,000h (5). However, its direct use in the wet-seal area would be impractical from the viewpoint of thermal expansion matching in scaled-up cells, and it would also be expensive. Therefore, indirect means of forming a protective oxide layer

based on Al₂O₃ were explored. Alloys known to form protective layers of aluminum oxide and aluminized metals were tested. At 923 K, the redox potential of aluminum in an air atmosphere (0.03% CO₂) is -2675 mV with respect to the (67% CO₂, 33% O₂) reference electrode. In a fuel inlet or outlet atmosphere (Table I), its potential is -2450 or -2389 mV, respectively. These potentials indicate that in an operating cell (anode potential -950 mV or more positive), aluminum will readily be oxidized, possibly at a faster rate than chromium, because the latter has a more positive redox potential. To investigate this possibility, we operated test cells with a Kanthal A-1 (Fe-Cr-Al alloy containing 5% aluminum) anode wet seal.

Visual examination of the Kanthal wet seal revealed no points of high, localized corrosion; this was confirmed by photomicrographs (Fig. 7). An almost-uniform corrosion from the fuel side to the air side of the wet seal is observed; the intensity of the corrosion is small, even though the cell was accidentally operated at 1098-1123 K for 8-15h, during which time corrosion might be expected to be accelerated by the higher temperature.

Thus, Fe-Cr-Al alloys are definitely more suitable than austenitic stainless steels as anode wet-seal material. A further possibility would be that corrosion protection could be achieved by a metallic diffusion coating of aluminum on stainless steel. This was investigated next in assemblies in which the flange surfaces had been treated by aluminum diffusion (5). Aluminized wet seals, which form an insulating layer of Al₂O₃ and or LiAlO₂ *in situ* during the thermal start-up of the cell, have shown negligibly small corrosion rates (less than 0.025 mm in 5000h of testing) (6). This indicates that the cell endurance desired for economic viability (40,000h) can be achieved inasmuch as wet-seal corrosion is concerned.

Summary

The experimental results presented in this paper confirm the validity of the thermodynamic and mixed-potential analysis presented earlier (1). Much greater corrosion of the anode wet seal than of the cathode wet seal is observed; for Type 316 stainless steel, the corrosion rates in a cell under load are greater by two orders of magnitude than open-circuit values. Typically, anode wet-seal corrosion of 316 stainless steel proceeds at a rate of 0.5-1 mm/1000h.

Kanthal A-1 steel (Fe-Cr-Al alloy containing 5% aluminum) was tested to assess the effectiveness of an alumina or aluminate barrier interrupting the principal, cross-tile, metal/oxidant corrosion cell. The rate of corrosion of Kanthal A-1 was small and almost uniformly distributed (0.02 mm/1000h). The results indicate that aluminum diffusion coatings are effective corrosion barriers. In long-term tests of aluminized wet seals, negligible corrosion (less than 0.025 mm in 5000h) was observed (6). This satisfies economic viability requirements.

The low rate of corrosion at the cathode side of the wet seal indicates that Type 316 stainless steel satisfies endurance requirements for molten carbonate fuel cell stacks without further modifications.

Acknowledgments

The work reported here was sponsored by the U. S. Department of Energy through Argonne National Laboratory. Guidance and suggestions by the program manager, Dr. John P. Ackerman, are very much appreciated. One of the authors (J. R. Selman) also acknowledges support by the Office of Basic Energy Sciences, U. S. Department of Energy.

Manuscript submitted June 14, 1982; revised manuscript received Feb. 27, 1984.

The Institute of Gas Technology assisted in meeting the publication costs of this article.

REFERENCES

1. R. A. Donado, L. G. Marianowski, H. C. Maru, and J. R. Selman, *This Journal*, **131**, 2535 (1984).
2. A. Borucka, "Fuel Cells," Paper presented at the 154th

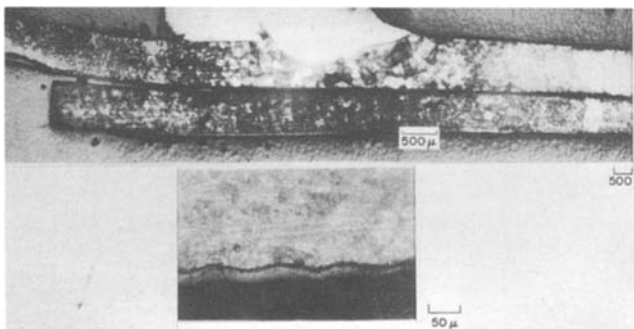


Fig. 7. Test results for Kanthal A-1 (anode wet seal) at fuel inlet conditions. The oxide coating is clearly visible in the photomicrograph at high magnification.

- National Marketing Division, Fuel Chemistry, American Chemical Society, Chicago, Sept. 10-15, 1967.
- E. S. Argano and J. Levitan, *This Journal*, **116**, 153 (1969).
 - B. K. Anderson, Ph.D. Thesis, Technical University of Denmark, Lyngby, Denmark (1975).

- J. R. Selman and L. G. Marianowski, in "Molten Salt Technology," D. H. Lovering, Editor, pp. 323-393, Plenum Press, New York (1982).
- E. H. Camara, L. G. Marianowski, and R. A. Donado, U. S. Pat. 4,160,067 (1979).

Styrene Production from Ethylbenzene on Platinum in a Zirconia Electrochemical Reactor

J. N. Michaels*¹ and C. G. Vayenas²

Department of Chemical Engineering, Massachusetts Institute of Technology, Cambridge, Massachusetts 02139

ABSTRACT

The vapor-phase electrochemical oxidative dehydrogenation of ethylbenzene on platinum-paste electrodes was studied at 575°-600°C in a stabilized-zirconia electrochemical reactor. Styrene and carbon dioxide were the major products. The dehydrogenation rate increased markedly with anodic current, reaching an ethylbenzene-concentration-dependent asymptote at large current densities. The rate of deep oxidation of ethylbenzene to CO and CO₂ was linear in current density. Both rates were strongly inhibited by gas-phase hydrogen. These results can be rationalized by an electrode mechanism in which the dominant charge-transfer reaction is exchange between chemisorbed oxygen on the electrode and oxygen ions in the electrolyte lattice. Styrene and CO₂ were formed primarily by catalytic reactions of ethylbenzene and neutral dissociatively adsorbed oxygen, although at least one other parallel charge-transfer reaction was evident. The current dependence of the dehydrogenation rate results from an oxidative dehydrogenation reaction on the surface whose rate is sensitive to the amount of oxygen on the electrode surface. A simple kinetic model is presented which quantitatively describes these experimental observations.

Styrene is presently produced commercially by the vapor-phase dehydrogenation of ethylbenzene over promoted iron oxide, molybdenum oxide, or mixed iron-oxide/molybdenum-oxide catalysts (1, 2). The reaction is endothermic and equilibrium-limited; under operating conditions of 580°C and atmospheric pressure, the equilibrium constant is 0.19 (3). Ethylbenzene is, therefore, diluted 1:15 in steam to increase the equilibrium conversion to styrene and to maintain the reaction temperature. Under these conditions, conversion is 55%-60% per pass (2).

A significant fraction of the cost of styrene manufacture lies in the separation of styrene from unreacted ethylbenzene. For this reason, alternative processes have been sought which increase the per-pass yield of styrene. The most widely studied among these is oxidative dehydrogenation with a suitable oxidant, such as oxygen or sulfur dioxide (4-10). A second alternative is coproduction of styrene and propylene oxide via the Oxirane process (11).

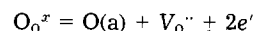
This work is part of an investigation of a third alternative, electrochemical oxidative dehydrogenation of ethylbenzene. In this process, ethylbenzene is fed to a solid-oxide electrolytic cell, reacting with electrochemically supplied oxygen to form styrene and water. This process offers three potential advantages over the conventional dehydrogenation process. First, because the overall reaction in this cell is the oxidative dehydrogenation of ethylbenzene by oxygen, the equilibrium limitation is eliminated. Second, electricity can be directly cogenerated with styrene production at an efficiency which is not Carnot-limited. Third, because of the absence of equilibrium or flammability limits, dilution of ethylbenzene is unnecessary, permitting construction of smaller reactors.

It should be noted that the economic desirability of cogenerating electricity is not obvious. Recent work by Spillman *et al.* (28) suggests that net expenditure of electrical energy to boost styrene production might be preferable to power cogeneration. Our work does not aim to evaluate the economics of electro-oxidative dehydrogenation. Rather, it attempts to illustrate the physical feasibility

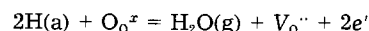
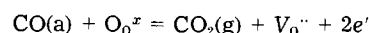
of the process and to understand the electrochemical kinetics of partial and complete oxidation of ethylbenzene. For this reason, no effort has been made to optimize the electrochemical reactor, nor to characterize the sources of electrical inefficiency.

The electro-oxidative dehydrogenation process is shown schematically in Fig. 1. The electrochemical reactor consists of two porous electrodes flanking a section of an oxygen-ion conducting solid electrolyte, such as yttria-stabilized zirconia. At the cathode, molecular oxygen is reduced to oxygen ions. These ions pass through the electrolyte to the anode, where they subsequently react with ethylbenzene to form styrene, water, and other by-products.

This work is an investigation of the anodic kinetics and reaction mechanism of electro-oxidative dehydrogenation of ethylbenzene. Such a study is useful in guiding the choice of suitably active and selective electrocatalysts for this process. We believe that the anodic electrode mechanism in such a system is likely to be a complex combination of electrochemical and purely catalytic steps. The simplest type of mechanism is one in which the sole charge-transfer reaction is exchange between chemisorbed oxygen on the electrode and oxygen ions in the electrolyte. In Kroger-Vink notation, this electrochemical step is



where O_o^x is a lattice oxygen, $V_o^{\cdot\cdot}$ is an oxygen ion vacancy in the electrolyte, $O(a)$ is a chemisorbed oxygen atom on the electrode surface, and e' is an electron. In this mechanism, the oxidation of ethylbenzene and other reactive species occurs by reactions with neutral chemisorbed oxygen. On the other hand, multiple charge-transfer reactions of other chemisorbed, oxidizable species with oxygen ions may occur simultaneously. For example, chemisorbed carbon monoxide or hydrogen may participate in the following reactions



Such charge-transfer reactions have been observed in similar electrochemical systems (19, 24).

*Electrochemical Society Active Member.

¹Present address: Department of Chemical Engineering, University of California, Berkeley, California 94720.

²Present address: Department of Chemical Engineering, University of Patras, Patras, Greece.

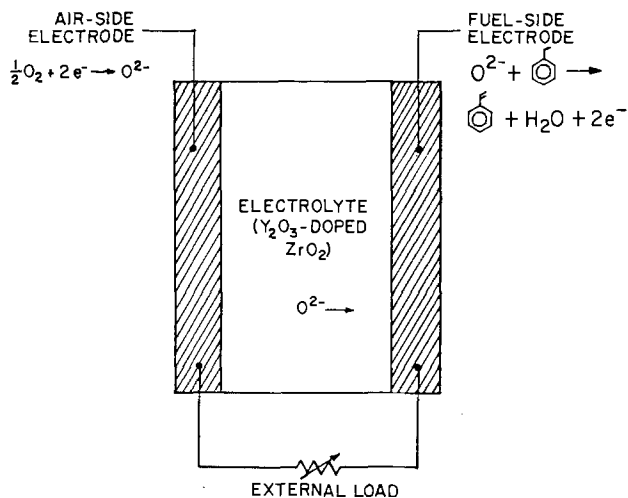


Fig. 1. Schematic of electro-oxidative dehydrogenation

This paper discusses the anode kinetics of the electrochemical cell



Platinum has been chosen as the electrocatalyst in this investigation because of its activity for ethylbenzene dehydrogenation (12) and the simplicity of depositing porous, conductive films onto zirconia (13). The kinetics of styrene formation and carbon dioxide formation are discussed, and a simple electrode mechanism is proposed which quantitatively models these results. Particular attention is paid to determining the major steps in the electrode mechanism and whether multiple charge-transfer reactions occur on platinum.

Experimental

Two electrochemical reactors were constructed from 8 weight percent (w/o) yttria-stabilized zirconia tubes (Zircona Products) having dimensions 46 cm long, 1.9 cm od, and 1.6 cm id. One of these reactors, shown schematically in Fig. 2, was designed to minimize the occurrence of homogeneous reactions of ethylbenzene; it was used in all experiments at 600°C. The active volume of this reactor was reduced from 19.5 to 2.13 cm³ by insertion of a 44 cm long, 1.5 cm diam fused-quartz rod; the rod was centered in the zirconia tube with gold shims. Platinum-paste working electrodes were deposited on the center 10 cm of the inside and outside tube surfaces. Each working electrode was flanked by two 1 cm² platinum-paste reference electrodes. Platinum-paste leads were deposited from each electrode to the appropriate ends of the zirconia tube. The second reactor, used in all experiments below 600°C, had neither reference electrodes, nor a quartz rod. The active volume of this reactor was 19.5 cm³. Each reactor was heated by a Lindberg Sola Basic tubular furnace controlled by a Love Controls Corporation Model 49 proportioning temperature controller.

Platinum-paste electrodes were deposited by painting the cleaned, masked-zirconia surfaces with one to three coats of Engelhard A-3788 fluxed platinum ink. Each coat was air dried at 60–70°C, then calcined in air at 850°C for 30 min. The temperature was raised from room temperature to 850°C at approximately 200°C/h. Freshly deposited electrodes were dull gray in color and adhered well to the electrolyte surface. Their specific surface area was approximately 300 cm²/(cm² superficial area) (13). The end-to-end resistance of the working electrodes at 25°C ranged between 1 and 2.5Ω. External connections to these electrodes are discussed in detail elsewhere (14).

Each reactor was shielded from extraneous electrical noise by insertion into a grounded 30 cm long, 3.8 cm od stainless steel tube. Air flowed through the annular space between the shield and reactor at a nominal flow rate of 100 cm³ (STP)/min. At this flow rate, both the pressure drop and external mass transfer resistance were negligi-

ble, and the oxygen partial pressure at the cathode surface remained constant at 0.21 atm.

The reactors were controlled galvanostatically by an AMEL Model 549 potentiostat/galvanostat. The current and voltages between any pair of electrodes were measured with Fluke Model 8600A digital multimeters (voltmeter input impedance 10⁷Ω). The cell working voltage and the anodic overpotential were monitored continuously with a two-pen chart recorder (input impedance 10⁶Ω). The anodic overpotential was measured using the adjacent downstream reference electrode. Because these electrodes were made of the same material and, therefore, catalyzed the same electrode reactions, the measured overpotential was insensitive to the overall conversion of ethylbenzene.

In a typical experiment, feed conditions and the cell current density were set, and the system was allowed to reach steady-state conditions. The approach to steady state was followed by monitoring the cell working voltage and, when possible, the anodic overpotential. When the voltages stabilized, the feed and product-stream compositions were analyzed by on-line gas chromatography, and the cell current, the feed and product volumetric flow rates, and all relevant voltages were measured. All results discussed below are steady-state results.

The reactors were differential with respect to ethylbenzene conversion; total conversion was limited to 15% or less in all experiments. Reaction rates, therefore, were calculated directly from product flow rates. Reaction rates, rate constants, and cell current are normalized by the area of active electrolyte.

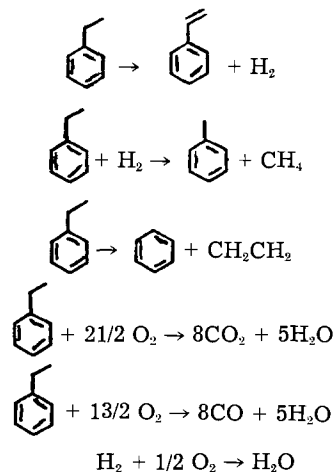
The experimental flow system and gas-chromatographic analytical system are discussed in detail elsewhere (14, 15).

Results

Three experiments are discussed below. In the first, ethylbenzene diluted with helium was fed to the reactor, and the rates of product formation were measured as a function of current density. In the second, hydrogen was added to the ethylbenzene/helium feed stream, and the same measurements repeated. In the third, oxygen was added to the ethylbenzene/helium feed stream, and the rates of product formation were measured at open circuit.

In all experiments, detectable products included H₂, CO, CO₂, water, methane, ethylene, benzene, toluene, and styrene. Neither working electrode lost electrochemical activity during the duration of the experiments. The carbon atom balance closed to within ±2%, suggesting that coke formation on the anodic surface is insignificant.

The overall reactions which occur in the electrolytic cell may be summarized as follows



This list is not exhaustive; rather, it represents the predominant reactions responsible for the final product distribution. Because this reaction system is so complex, it is convenient to lump the production of CO and CO₂ and that of benzene and toluene in the analysis of the rate data. The rate of formation of CO and CO₂ is termed the

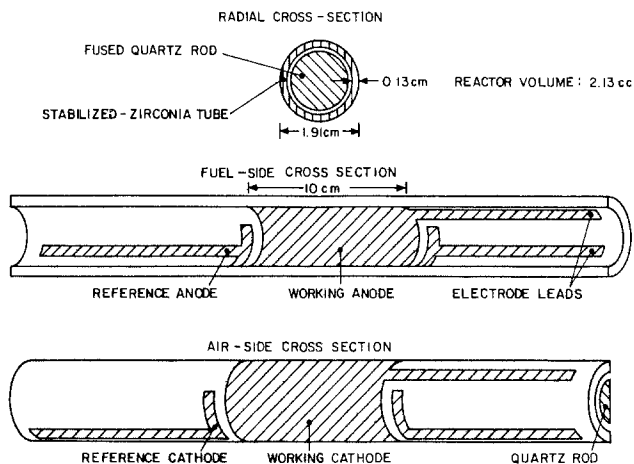


Fig. 2. Stabilized-zirconia electrochemical reactor: annular geometry

“deep oxidation” rate and is designated by r_{DO} ; the rate of benzene and toluene formation is called the “dealkylation” rate and is designated by r_{DA} . The rate of styrene production is synonymous with the “dehydrogenation” rate and is designated by r_{DH} .

Due to the diversity of the experimental measurements, the discussion of results is divided into two subsections. The division is based on the primary goals of this work: elucidation of the prominent steps in the electrode mechanism; and detection of the predominant charge-transfer reactions. The behavior of the dehydrogenation, deep oxidation, and dealkylation rates are discussed in the first subsection. These measurements are summarized in Fig. 3-6. The current-voltage characteristics of the anode and the effect of gas-phase oxygen on the reaction rates, summarized in Fig. 7 and 8, are discussed in the second subsection.

Electrode mechanism.—Dehydrogenation.—When no hydrogen or oxygen is present within the feed, the dehydrogenation rate is strongly current dependent, as shown in Fig. 3a. At low ethylbenzene concentrations and moderate current densities, the rate of styrene production is as much as six times larger than that at open circuit; the enhancement of the dehydrogenation rate saturates at large current densities. This behavior suggests that dehydrogenation of ethylbenzene occurs by two pathways on the platinum electrode. The first pathway is a nonoxidative reaction which produces styrene and hydrogen. The second pathway is an oxidative pathway which ultimately produces styrene and water, whose rate is dependent on the supply of oxygen to the electrode surface.

Further evidence of this dual-pathway dehydrogenation mechanism is furnished by the experiments with hydrogen/ethylbenzene mixtures. As shown in Fig. 4a, the dehydrogenation rate at a given current density decreases as the hydrogen concentration in the feed increases. This indicates that dehydrogenation of ethylbenzene is inhibited by hydrogen. This inhibition is evident only at nonzero current densities; the open-circuit dehydrogenation rate is independent of the hydrogen concentration. These results suggest that styrene is formed in two parallel, independent surface reactions: a nonoxidative pathway which is insensitive to current density and hydrogen concentration; and an oxidative pathway which is current dependent and strongly inhibited by gas-phase hydrogen.

Deep oxidation.—The deep oxidation rate in the absence of gas-phase hydrogen is linear in current density and zero order in ethylbenzene, as shown in Fig. 3b. Oxygen atom balances indicate that all of the electrochemically supplied oxygen is accounted for by the formation of CO, CO₂, and water; no oxygen is detected in the gas phase. The linearity of the rate, therefore, is simply a consequence of Faraday's law. The rate of production of all oxygenated species must be proportional to the current density and independent of gas-phase composition. Although

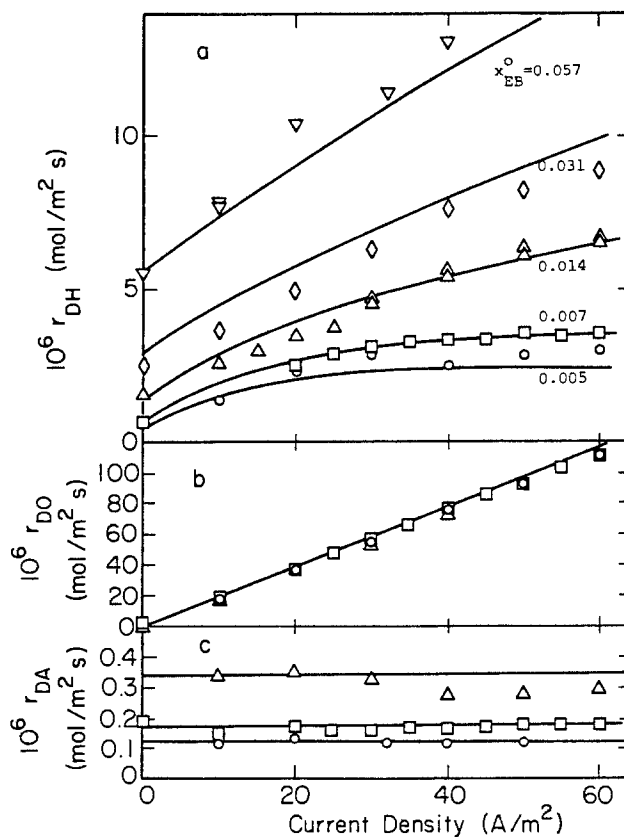


Fig. 3. Reaction rates at 575°C. Feed ethylbenzene mole fraction: ○ 0.48%; □ 0.70%; △ 1.44%; ◇ 3.12%; ▽ 5.72%. (a, Top) dehydrogenation rate; (b, middle) deep oxidation rate; (c, bottom) dealkylation rate. — Calculated rate.

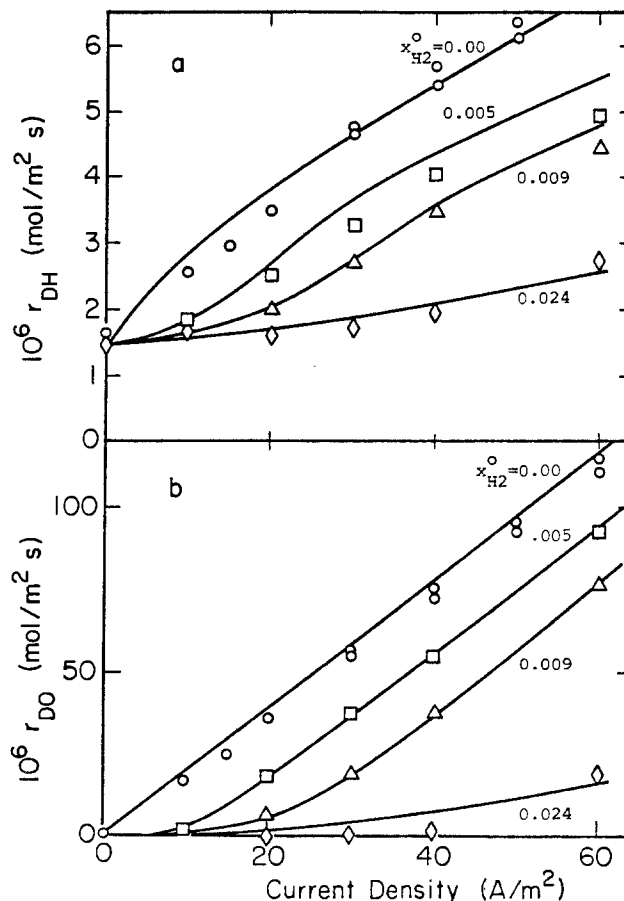


Fig. 4. Hydrogen inhibition of reaction rates at 575°C. Feed ethylbenzene mole fraction: 1.48%. Feed hydrogen mole fraction: ○ 0.00%; □ 0.51%; △ 0.94%; ◇ 2.36%. (a Top) dehydrogenation rate; (b bottom) deep oxidation rate. — Calculated rate.

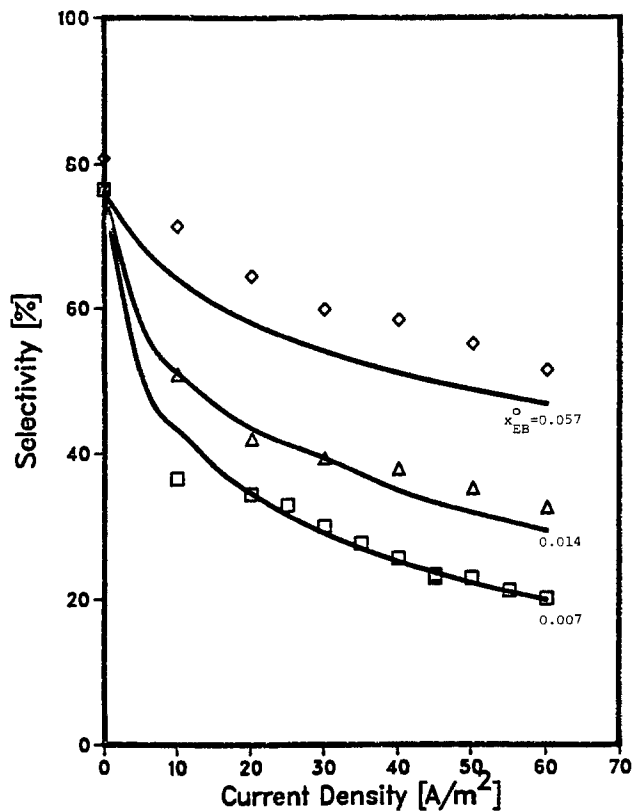


Fig. 5. Selectivity to styrene at 575°C. Feed ethylbenzene mole fraction: □ 0.70%; △ 1.44%; ▽ 5.72%. — Calculated selectivity.

small amounts of water are produced by oxidative dehydrogenation of ethylbenzene, all of the oxides of carbon and most of the water are produced by deep oxidation. Therefore, the deep oxidation rate should be nearly linear in current and independent of ethylbenzene concentration, as observed. It is interesting to note that the absence

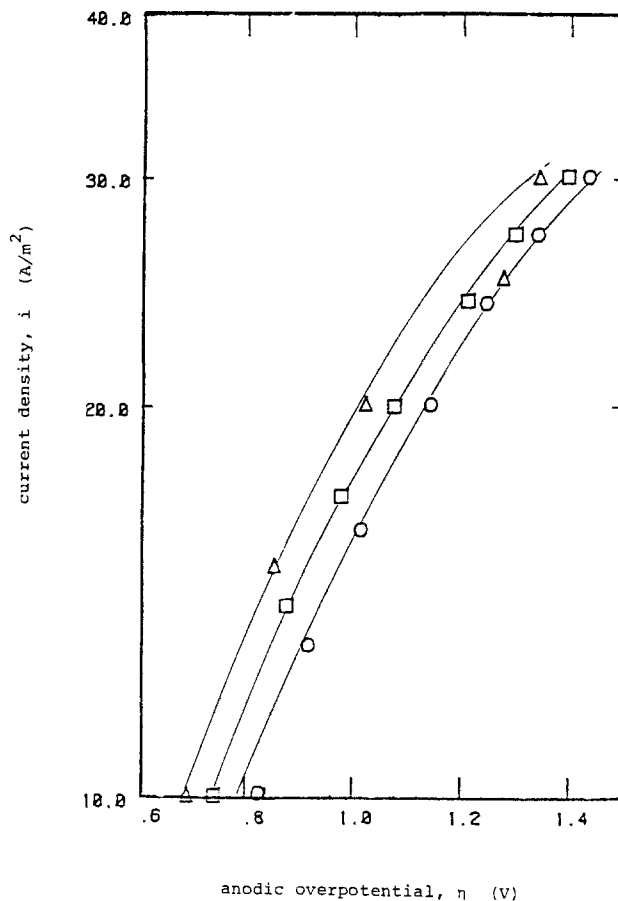


Fig. 7. Anodic overpotential at 600°C. Feed ethylbenzene mole fraction: ○ 0.47%; □ 0.86%; △ 1.94%. — Calculated overpotential.

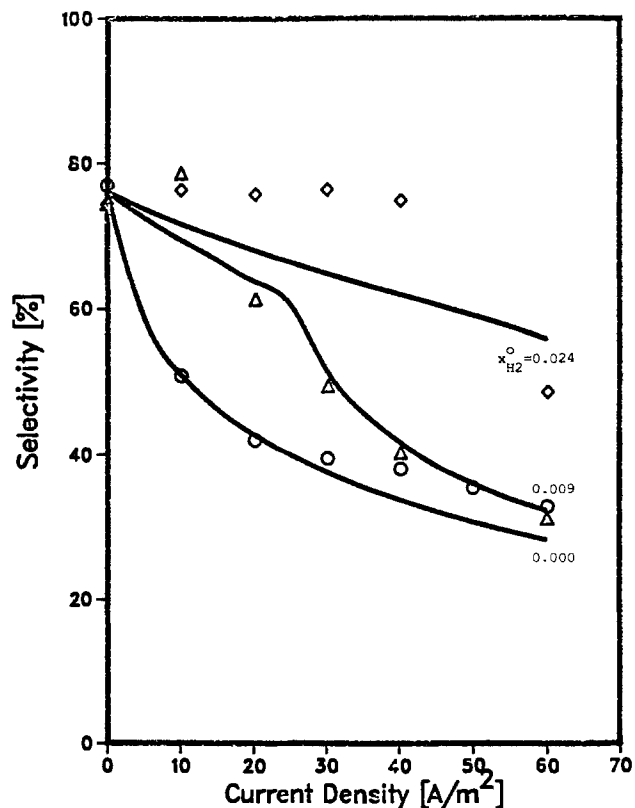


Fig. 6. Hydrogen enhancement of selectivity to styrene at 575°C. Feed ethylbenzene mole fraction: 1.48%. Feed hydrogen mole fraction: ○ 0.00%; △ 0.94%; ◇ 2.36%. — Calculated selectivity.

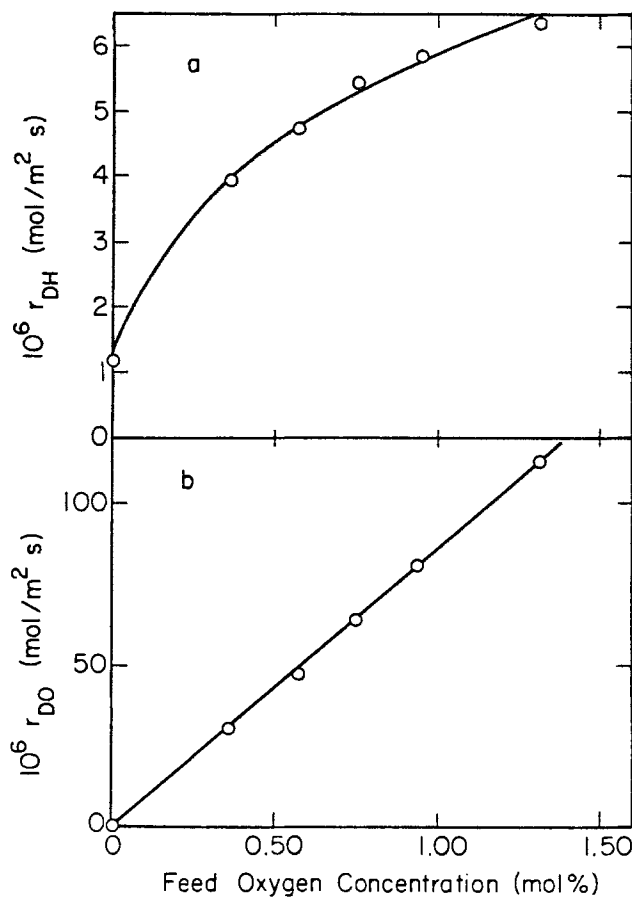


Fig. 8. Effect of gas-phase oxygen on open-circuit reaction rates at 575°C. Feed ethylbenzene mole fraction: 1.42%. (a) Top) dehydrogenation rate; (b) bottom) deep oxidation rate.

of oxygen evolution at the anode implies that the deep oxidation of ethylbenzene is oxygen limited.

As shown in Fig. 4b, the deep oxidation rate is strongly inhibited by addition of hydrogen to the gas phase. In contrast to the dehydrogenation rate, the deep oxidation rate is reduced to zero by large hydrogen concentrations. This behavior is suggestive of simple competition between hydrogen and ethylbenzene for available oxygen on the electrode surface in parallel surface reactions. The large inhibition of r_{do} implies that oxidation of hydrogen on the surface is significantly faster than that of ethylbenzene.

Dealkylation.—In contrast to the dehydrogenation and deep oxidation rates, the dealkylation rate is independent of current density. This is shown in Fig. 3c. This behavior suggests that dealkylation is a nonelectrochemical, catalytic reaction which occurs in parallel with dehydrogenation and deep oxidation of ethylbenzene.

Selectivity to styrene.—The experimental results shown in Fig. 3 and 4 may be simply summarized by plotting the selectivity to styrene as a function of current density. This has been done in Fig. 5 and 6, respectively, where some of the data shown in Fig. 3 and 4 have been removed for clarity. The selectivity to styrene in these figures is defined as the ratio of the dehydrogenation rate to the total rate of consumption of ethylbenzene.

In the absence of gas-phase hydrogen, the selectivity decreases markedly with current density, as shown in Fig. 5. This current dependence is the result of deep oxidation of ethylbenzene. The selectivity decreases with decreasing ethylbenzene concentration at nonzero current densities because the deep oxidation rate is zero order in ethylbenzene, while the dehydrogenation rate is positive order. At open circuit, no CO_2 is formed, and the selectivity is 78% and is concentration independent; this value is determined by the relative rates of dehydrogenation and dealkylation, which are each first order in ethylbenzene.

The selectivity in the presence of significant amounts of gas-phase hydrogen is shown in Fig. 6. The selectivity increases and becomes less sensitive to changes in current density as the hydrogen concentration increases. Both of these effects are due primarily to the inhibition of the deep oxidation rate by hydrogen.

Charge-transfer reactions.—The results discussed above present an overview of the important steps in the anode reaction mechanism. It is clear that some steps in this mechanism are nonoxidative and, therefore, purely catalytic. However, among the oxidative reactions, it is not possible to distinguish between catalytic reactions with neutral chemisorbed oxygen and charge-transfer reactions with oxygen ions. This question is addressed most directly by measurement of the anodic overpotential. Tafel plots of the anodic overpotential measured at 600°C are shown in Fig. 7. These measurements are not compensated for the ohmic drop between the reference and working electrodes; this is the source of the curvature of the plots. Unfortunately, the ohmic resistance was not determined by current interruption; therefore the data were fit by the high-field limit of the Butler-Volmer equation, modified to account for the significant ohmic contribution to the overpotential.

$$\eta_m = \frac{RT}{\alpha F} \ln(i/i_0) + IR_E$$

where η_m is the measured overpotential, η is the activation overpotential, α is the transfer coefficient, i_0 is the exchange-current density, F is the Faraday constant, R is the gas constant, T is the absolute temperature, I is the total cell current, and R_E is the uncompensated resistance. The solid lines in Fig. 7 are calculated with $\alpha = 1.0$, $R_E = 5.5\Omega$, and exchange-current densities of 0.015, 0.028, and 0.060 A/m² at feed ethylbenzene mole fractions of 0.0047, 0.0086, and 0.0194, respectively. As discussed in detail in the following section, a transfer coefficient of unity is consistent with oxygen oxidation/reduction's being the major anodic charge-transfer reaction. On the other hand,

the ethylbenzene-concentration dependence of i_0 suggests that an additional exchange reaction also occurs in the electrode mechanism.

The variation of the open-circuit dehydrogenation and deep oxidation rates with oxygen partial pressure also suggests that oxygen exchange is the dominant anodic charge-transfer reaction. As shown in Fig. 8, the dehydrogenation rate increases rapidly to a constant value as the oxygen pressure increases, and the deep oxidation rate is first order in oxygen. Furthermore, oxygen is fully consumed in the production of CO , CO_2 , and water. These results are qualitatively similar to the electrochemical results shown in Fig. 3. This similarity suggests that the reactions of oxygen and ethylbenzene are insensitive to the source of oxygen. This is consistent with an electrode mechanism in which ethylbenzene reacts with neutral chemisorbed oxygen in nonelectrochemical steps.

Discussion

These results strongly suggest that electro-oxidation of ethylbenzene on platinum occurs mainly by chemical, rather than electrochemical, steps. Oxygen ions are rapidly oxidized to neutral adatoms, and these subsequently react with ethylbenzene and hydrogen to form styrene, CO_2 , and water. Dehydrogenation of ethylbenzene occurs by two parallel surface reactions, one nonoxidative, the other oxidative. Deep oxidation of ethylbenzene and hydrogen are rate limited by oxygen supply to the electrode surface. Small amounts of toluene and benzene are formed in parallel, purely catalytic reactions.

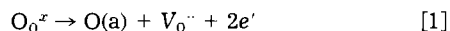
These ideas are incorporated into the following kinetic model, which quantitatively describes the observed electrode kinetics. This model does not attempt to describe all of the reaction steps and intermediates involved in ethylbenzene dehydrogenation and deep oxidation. That would be a formidable task and is not justified by the extent of the data. Rather, emphasis is placed on developing the simplest model which captures the important aspects of the qualitative mechanism described above and adequately describes the experimental observations. Additional details of this model are presented in Ref. (15). For simplicity, the dealkylation reactions are ignored due to their small contribution to the overall conversion of ethylbenzene. Deep oxidation of styrene and production of carbon monoxide are also neglected.

This model contains three major assumptions. First, oxygen exchange is the sole charge-transfer reaction. Second, two forms of uncharged oxygen coexist on the platinum surface. The first form is mobile, chemisorbed oxygen, which reacts with adsorbed hydrocarbons and hydrogen to form CO_2 and water. The second form is a surface "oxide" which oxidatively dehydrogenates adsorbed ethylbenzene to styrene and water. This assumption is supported by studies of cyclohexane dehydrogenation on platinum single crystals; these studies show the dehydrogenation rate to be enhanced by preoxidation of the crystal surface (15, 27). The third assumption is that interchange between the two forms of oxygen is rapid and can be modeled as an equilibrium. Thus, an increase in the coverage of chemisorbed oxygen increases the coverage of the oxide and concomitantly increases the oxidative-dehydrogenation rate.

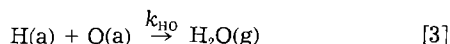
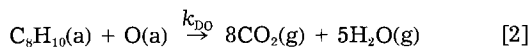
The catalytic surface is therefore modeled to have two types of sites, S1 and S2. All gas-phase species adsorb and react on S1 sites. Nothing in the gas-phase adsorbs on S2 sites. Rather, S2 sites are "oxidized" by available chemisorbed oxygen and subsequently react with adjacent adsorbed ethylbenzene molecules to form styrene and water. Ethylbenzene and styrene are assumed to be in adsorption equilibrium on S1 sites at suitably low coverages such that their isotherms are linear. This assumption appears to be justified by the low desorption temperature of benzene on clean and carbon-covered platinum surfaces (18). Hydrogen and oxygen adsorb dissociatively on the S1 sites; hydrogen is assumed to be in adsorption equilibrium and at low coverage (25, 26).

Because the deep oxidation reactions are oxygen limited, oxygen is not in adsorption equilibrium.

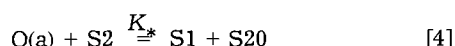
In the absence of gas-phase oxygen, the sole source of oxygen atoms to S1 sites on the anode is the oxygen-exchange reaction



Since this is the only charge-transfer step in the mechanism, Faraday's law requires that the rate of oxygen adsorption on S1 sites equals the oxygen ion flux to the anode, $j_o = i/2F$. Once adsorbed on the anode, the oxygen atoms can react with adsorbed ethylbenzene and hydrogen to produce CO_2 and water. It is assumed that the rate-determining step in each reaction is first order in the adsorbed reactants with the rate constants shown in Eq. [2] and [3]

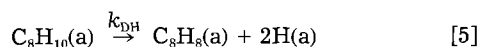


These reactions are written nonstoichiometrically to emphasize the molecularity of their rate-determining steps. Furthermore, chemisorbed oxygen can oxidize S2 sites. It is assumed that surface oxidation is rapid and that equilibrium between adsorbed oxygen and the oxidized surface is achieved at steady state. If the oxide has stoichiometry S20, this equilibrium is written

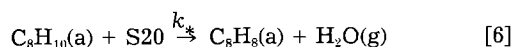


where K_* is the oxidation equilibrium constant.

Finally, ethylbenzene dehydrogenation is assumed to occur by two parallel reactions. The first is a nonoxidative surface reaction whose rate-determining step is first order in adsorbed ethylbenzene



The second is an oxidative reaction which is first order in ethylbenzene and oxidized sites



k_{DH} and k_* are the rate constants of the nonoxidative and oxidative dehydrogenation rate-determining steps, respectively.

Reaction rates and selectivities calculated with this model are shown by the solid lines in Fig. 3-6. Because hydrogen conversion in most measurements is large, calculation of the rates required integration of the appropriate rate expressions over the hydrogen profiles in the reactor. Details of these calculations are presented elsewhere (14, 15). The model correctly predicts the "Langmuir-type" behavior of the dehydrogenation rate and the ethylbenzene-concentration independence of the deep oxidation rate at low hydrogen concentrations. The inhibitory effect of hydrogen is also correctly described. The "break" in the selectivity at the intermediate hydrogen concentration shown in Fig. 6 is a real effect. This occurs at the current density at which the hydrogen conversion first reaches 100%. At larger current densities, the hydrogen concentration is zero in an increasing fraction of the reactor, and the deep oxidation rate is uninhibited in the same region. Because the uninhibited rate is so much greater than the rate in the presence of hydrogen, quantitative conversion of hydrogen in the latter stages of the reactor results in a dramatic loss of selectivity to styrene. The large discrepancy between the measured selectivity and calculated selectivity at the highest hydrogen concentration is caused by inaccurate measurement of very small carbon dioxide concentrations.

This model oversimplifies the electrochemistry at the platinum anode by assuming a single charge-transfer re-

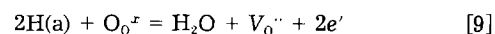
action. If the only exchange reaction at the electrode-electrolyte interface were oxygen exchange (Eq. [1]), the anodic overpotential would be well described by the Butler-Volmer equation with transfer coefficients of unity (19-23)

$$i = i_o [\exp(\eta F/RT) - \exp(-\eta F/RT)] \quad [7]$$

This agrees well with the measured overpotential. However, the exchange current density should vary with the surface coverage of chemisorbed oxygen, according to (20)

$$i_o = 2eK_r[\theta_o(1 - \theta_o)]^{1/2} \quad [8]$$

where e is the electronic charge, K_r is the geometric average of the forward and reverse rate constants of reaction [1], and θ_o is the oxygen surface coverage at open circuit. At the temperatures of interest, the coverage of chemisorbed oxygen should be small (18), and the exchange current should decrease monotonically with decreasing oxygen coverage. Since deep oxidation of ethylbenzene is oxygen limited, increasing the ethylbenzene concentration should decrease the steady-state oxygen coverage by increasing the surface reaction rate. Thus, i_o should decrease with increasing ethylbenzene concentration. The measured exchange current density displays the opposite behavior. Therefore, it appears that a second exchange reaction occurs in parallel with reaction [7]. Because of the extent of deep oxidation and dehydrogenation of ethylbenzene, it is likely that there is a significant amount of hydrogen on the electrode surface. Thus, a possible charge-transfer reaction is direct oxidation of adsorbed hydrogen atoms



This exchange reaction has been observed previously on nickel electrodes (24). When the surface coverage of hydrogen is small, the exchange current of this reaction should increase with increasing hydrogen coverage. Thermal programmed desorption results suggest that hydrogen is in dissociative-adsorption equilibrium and is at low coverages under conditions of interest (25, 26); therefore, hydrogen coverage increases with increasing hydrogen partial pressure. Because the dehydrogenation rate is positive order in ethylbenzene, the average hydrogen concentration in the reactor increases and increasing ethylbenzene concentration. For this reason, the exchange current of reaction [1] also should increase with increasing ethylbenzene mole fraction.

Conclusion

The dehydrogenation rate of ethylbenzene is significantly enhanced by electrochemical supply of oxygen to a platinum-paste anode. In the absence of significant amounts of gas-phase hydrogen, the major by-product is CO_2 . Addition of hydrogen to the reactor feed inhibits dehydrogenation and deep oxidation; in the limit of large hydrogen partial pressures, the dehydrogenation rate approaches its value at open circuit, and the deep oxidation rate approaches zero.

The anodic electrode kinetics are well described by a model which assumes that the sole electrochemical reaction is exchange of dissociatively adsorbed oxygen and oxygen ions in the electrolyte lattice. Electrochemically supplied oxygen adatoms subsequently react with adsorbed ethylbenzene and hydrogen to form carbon dioxide and water, or with the platinum surface to form a surface oxide. Adsorbed ethylbenzene reacts with this oxide in an oxidative-dehydrogenation reaction to form styrene and water. This surface reaction is responsible for the electrochemical enhancement of the dehydrogenation rate.

This kinetic model oversimplifies the anodic electrode mechanism by assuming oxygen exchange is the sole charge-transfer reaction. The current-voltage characteristics of the anode suggest that oxygen exchange is indeed an important step in the mechanism. However, at least one other parallel charge-transfer reaction is apparent.

From a practical standpoint, the performance of these reactors is hampered by platinum's activity as a non-specific oxidation catalyst. A better choice for the anodic material might be an active and selective oxidative-dehydrogenation catalyst with suitably large electrical conductivity. Another possible improvement is suggested by the inhibitory effect of hydrogen. If a hydrogen-rich mixture of styrene and ethylbenzene were produced in the vicinity of a platinum anode, hydrogen could be selectively oxidized from the mixture electrochemically, shifting the equilibrium toward styrene and potentially generating electricity. This could be accomplished by packing a platinum-anode solid-oxide fuel cell with a commercial dehydrogenation catalyst. Preliminary work with both of these approaches is reported elsewhere (14).

Acknowledgments

The authors thank Professor James Wei at MIT and Ms. Karrie Hanson at University of California, Berkeley for their contributions to this work. The project was supported by the Department of Energy, Grant no. DE-AC02-80ER10694.

Manuscript submitted Feb. 27, 1984; revised manuscript received June 8, 1984.

LIST OF SYMBOLS

(a)	chemisorbed species
(g)	gas-phase species
e	electronic charge
F	Faraday's constant
I	total current
i	current density
i_0	exchange-current density
j_0	oxygen ion flux to anode
K_f	geometric-average rate constant for oxygen exchange
K_*	surface oxidation equilibrium constant
k_i	rate constant of ith reaction
k_*	surface oxidation-dehydrogenation rate constant
R	gas constant
R_E	uncompensated electrode resistance
r_i	rate of ith reaction
T	absolute temperature
Greek Symbols	
α	transfer coefficient
η	activation overpotential
η_m	measured overpotential
θ_0	surface coverage of chemisorbed oxygen

Subscripts

DA	dealkylation
DH	dehydrogenation
DO	deep oxidation
HO	hydrogen oxidation

REFERENCES

- W. W. Kaeding, *Catal. Rev.*, **8**(2), 307 (1973).
- C. L. Thomas, "Catalytic Processes and Proven Catalysts," pp. 47-48 Academic Press, New York (1970).
- L. Gutman, E. F. Westrum, and K. S. Pitzer, *J. Am. Chem. Soc.*, **95**, 1246 (1943).
- T. G. Alkhozov, A. E. Lisovskii, M. G. Safarov, and A. M. Dadsheva, *Kinet. Katal.*, **13**, 509 (1972).
- A. Cortes and J. L. Seoane, *J. Catal.*, **34**, 7 (1974).
- Z. Dziewiekie and A. Makawski, *React. Kinet. Catal. Lett.*, **13**, 51 (1980).
- K. Fujimoto and T. Kunugi, *Ind. Eng. Chem., Proc. Des. Dev.*, **20**, 319 (1981).
- C. R. Adams and T. L. Jennings, *J. Catal.*, **17**, 152 (1970).
- N. J. Gaspar, A. D. Cohen, M. Vadekar, and I. S. Pasternak, *Can. J. Chem. Eng.*, **53**, 79 (1975).
- M. Vadekar, I. S. Pasternak, and N. J. Gaspar, *ibid.*, **52**, 788 (1974).
- "SRI International Chemical Economics Handbook," Stanford Research Institute, Menlo Park, CA, (1982).
- F. E. Shepard and J. J. Rooney *J. Catal.*, **3**, 129 (1964).
- R. D. Farr, MS. Thesis, MIT, Cambridge, MA (1979).
- J. N. Michaels, Sc.D. Thesis, MIT, Cambridge, MA (1983).
- C. G. Vayenas and J. N. Michaels, *J. Catal.*, **85**, 477 (1984).
- R. C. Reid, J. M. Prausnitz, and T. K. Sherwood, "The Properties of Liquids and Gases," pp. 629-65 McGraw Hill, New York (1977).
- C. G. Vayenas, B. Lee, and J. N. Michaels, *J. Catal.*, **66**, 36 (1980).
- J. L. Gland, *Surf. Sci.*, **93**, 487 (1980).
- T. H. Etsell and S. N. Flengas, *Chem. Rev.*, **70**, 339 (1970).
- D. Y. Wang and A. S. Nowick, *This Journal*, **126**, 1159 (1979).
- T. H. Etsell and S. N. Flengas, *ibid.*, **118**, 1890 (1971).
- D. Braunstein, D. S. Tannhauser, and I. Riess, *ibid.*, **128**, 82 (1981).
- D. Y. Wang and A. S. Nowick, *ibid.*, **126**, 1166 (1979).
- E. J. L. Schouler, M. Kleitz, E. Forest, E. Fernandez, and P. Fabry, *Solid State Ionics*, **5**, 559 (1981).
- R. W. McCabe and L. D. Schmidt, *Surf. Sci.*, **60**, 85 (1976).
- S. M. Davis and G. A. Somorjai, *ibid.*, **91**, 73 (1980).
- C. E. Smith, J. P. Biberian, and G. A. Somorjai, *J. Catal.*, **57**, 426 (1979).
- R. W. Spillman, R. M. Spotnitz, and J. T. Lundquist Jr., *Chemtech*, **14**, 176 (1984).

A Theoretical Comparison of Flow-Through and Flow-By Porous Electrodes at the Limiting Current

Tim Risch*,¹

Acurex Corporation, Aerotherm Division, Mountain View, California 94039

John Newman**

Materials and Molecular Research Division of Lawrence Berkeley Laboratory, and Department of Chemical Engineering, University of California, Berkeley, California 94720

ABSTRACT

A limiting current model for the potential and concentration distribution for a flow-by porous electrode of infinite length to width ratio is developed and compared to previous models of Alkire and Ng and Fedkiw. For flow-by electrodes of practical interest, the maximum solution phase potential drop is shown to be dependent upon one relevant parameter: the product of the electrode width and the reciprocal of the penetration depth, αd . Criteria delineating the optimal electrode configuration are given using this potential difference as a basis for comparison. Results of the comparison show that the criteria are dependent upon reactant conversion but independent of any specific mass-transfer correlation.

Packed-bed porous electrodes have become increasingly attractive in the past several years for use in a number of industrially important processes. These electrodes have been suggested for such diverse applications as removal of dilute metal ions from waste streams (1), electro-organic synthesis (2), and off-peak energy storage (3).

Two principal configurations for packed-bed electrodes have been developed: the flow-through configuration, where fluid flow and current are parallel; and the flow-by configuration, where the fluid flows perpendicularly to the current. Both configurations are illustrated in Fig. 1, where the porous electrodes are represented by rectangles and the separators by dashed lines. For simplicity, we choose to represent the counterelectrodes as planar electrodes; however, in general, the counterelectrodes can also be porous electrodes.

Figure 1a illustrates a flow-through electrode with an upstream counterelectrode. An upstream counterelectrode is favored over a downstream counterelectrode in the flow-through configuration, because it gives a lower ohmic potential drop, particularly at high conversions (4). The Y direction denotes the direction of fluid flow in the figure. For the flow-through configuration, the flow is divided as it enters and flows in different directions through the working electrode and counterelectrode. Current generated within the porous electrode flows in the same spatial direction as the fluid flow.

Figure 1b illustrates a flow-by configuration. For the flow-by configuration, the fluid flow is again divided, but here the flow to the working electrode and counterelectrode remains in the same direction. In this configuration, current generated within the porous electrode travels generally in the X direction, which is perpendicular to the direction of the fluid flow.

Bennion and Newman (1) developed a one-dimensional model for the flow-through electrode assuming its performance to be limited only by the transport of reactants from the bulk stream to the surface of the electrode. More realistic one-dimensional models for the flow-through electrode not restricted to this "limiting current" assumption have subsequently been developed (5). These models incorporate equilibrium constraints, finite rate kinetics, and parasitic side reactions in addition to the transport of reactants.

Because the fluid and current travel in the same direction in the flow-through configuration, the analysis remains one-dimensional even in the general case. In the

flow-by configuration, however, the general analysis is necessarily two-dimensional. The absence of a common space variable for the fluid and current flow requires that the analysis be formulated in terms of partial differential equations, unless simplifications are made.

Alkire and Ng (6, 7) simplified the analysis of the flow-by electrode by assuming current flow to travel directly perpendicular to the fluid flow. This assumption reduces the equation for the potential distribution from a partial differential equation to an ordinary differential equation. Recently, Fedkiw (8) analyzed the special case of a flow-by electrode at the limiting current by including the two-dimensional nature of the current distribution and the effects of the finite electrode length. However, he included in his analysis a single specific dependence of the mass-transfer coefficient on velocity. Stork *et al.* (8, 9), in two recent papers, give theoretical and experimental results for the potential distribution in a flow-by electrode. The theoretical model they present is essentially the same limiting current analysis given by Fedkiw. Some experimental measurements of the potential distribution inside a flow-by electrode are also given which compare well with results of their calculations.

Alkire and Ng (6, 7), Trainham and Newman (2), and Fedkiw (8) have all considered the selection of the optimum electrode configuration for a given application. Trainham and Newman developed a method, applicable below the limiting current, to select the optimum con-

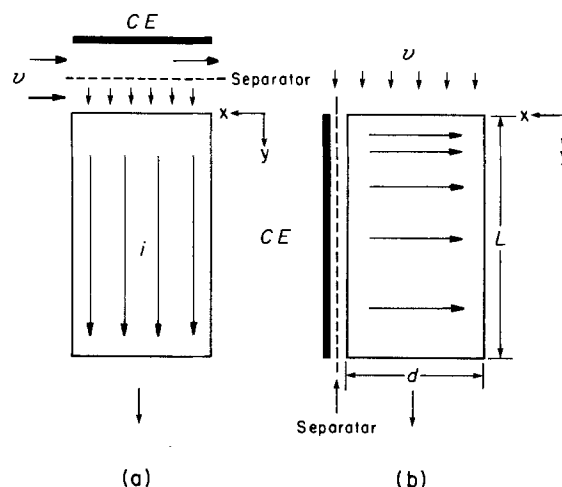


Fig. 1. Porous electrode configurations (a): flow-through electrode, upstream counterelectrode. (b): Flow-by electrode.

*Electrochemical Society Student Member.

**Electrochemical Society Active Member.

¹Present address: Acurex Corporation, Aerotherm Division, Mountain View, California 94039.

figuration. Alkire and Ng, followed by Fedkiw, considered the choice of the optimum configuration at the limiting current. Alkire and Ng maximized the volumetric current density to compare the two configurations. Fedkiw compared the maximum solution-phase potential drop for the flow-through configuration to the maximum solution phase potential for the flow-by electrode. Equal electrode volumes and identical flow velocities were chosen as fixed quantities for these two comparisons. At the limiting current, the maximization of the volumetric current density or the minimization of the maximum ohmic potential drop lead to the same result.

The results of Alkire and Ng and Fedkiw can be reconciled by an order-of-magnitude analysis. This can be useful in determining the approximate conditions under which the flow-by configuration is superior to the flow-through configuration at the limiting current. Consider a flow-through and a flow-by electrode of equal dimensions and feed flow rates and with identical packings and feed compositions. Each reactor has a length L , width d , and height W . At the limiting current, the reactant flows through the electrode and reacts at a rate determined solely by the type of packing and the magnitude of the fluid flow. The distribution of the reaction and the total current will therefore be identical in the two reactors. For high conversions of reactant to product, most of the reactant will be depleted in a region very near the front of the electrode. The characteristic length of this region is the penetration depth, denoted by $1/\alpha$. Most of the current in the flow-through electrode with an upstream counter-electrode, must travel an approximate distance $1/\alpha$, through an area of Wd . The majority of the current in the flow-by electrode, however, need only travel a distance comparable to the width of the electrode d , through an area of W/α . The superior electrode configuration is the configuration that yields a lower ohmic potential drop. The ohmic potential drop is the product of the total current times the length of travel divided by the cross sectional area to current flow. A comparison of the ohmic drop shows that the flow-by electrode configuration is preferred for high conversions if the approximate condition

$$\alpha d < 1 \quad [1]$$

is satisfied. This result is identical to the result obtained by Alkire and Ng when they maximized the volumetric current density to compare configurations.

At low conversions, however, the penetration length eventually becomes comparable to the electrode length. In this limit, the current in the flow-through electrode now flows a distance L , rather than $1/\alpha$. Likewise, in the flow-by electrode, the current flows through an area of WL . Equating the ohmic potential drop in the low-conversion limit results in the criterion that the flow-by configuration is favored for

$$\frac{L}{d} > 1 \quad [2]$$

Equation [1] shows that, at high conversions, the parameter αd is of primary importance in distinguishing the optimum electrode configuration and in determining the maximum potential drop in the flow-by configuration. At low conversions, Eq. [2] shows L/d can be expected to be the parameter of primary importance in determining the optimum configuration.

In this paper, we propose a limiting form solution to the two-dimensional potential distribution for large αd . This solution shows that the maximum solution-phase potential drop for the flow-by electrode is primarily dependent upon the parameter αd , with only a secondary dependence upon L/d . We then reexamine potential distribution derived by Fedkiw to determine the conditions under which the two-dimensional nature of the current distribution and the effects of the finite electrode should be included. This new solution, along with the expressions derived by Fedkiw and Alkire and Ng, is presented in a

form that is not restricted to the single mass-transfer correlation presented by Fedkiw.

Finally, the flow-by and flow-through configurations are compared using the maximum solution phase potential drop as a basis for comparison. Criteria are given delineating the optimum electrode configuration which depend upon reactant conversion. Results of this comparison show that the two configurations can be compared independent of any specific mass-transfer relationship.

Potential Distribution

The starting point for the analysis will be the theoretical framework for porous electrodes developed by Benion and Newman (1) and extended by Newman and Tiedemann (11). The porous electrode is treated as a superposition of two continua, representing the fluid phase and the solid phase. A single reaction of the form



will be assumed to occur within the electrode. Under these assumptions, the electrode reaction appears as a homogeneous source or sink term within the conservation of species equation. A solution with excess supporting electrolyte and a uniform solution conductivity will be assumed as well as a dilute solution of reacting species. Diffusion and dispersion will be neglected. Also, the velocity within the electrode is assumed to be plug-flow, one-dimensional in the Y direction only. Under these conditions, at steady state, conservation of the reactant species for both the flow-through and flow-by electrode can be expressed as

$$v \frac{dc}{dy} = -ak_m c \quad [4]$$

with the boundary condition

$$\text{at } y = 0, c = c_f \quad [5]$$

Solution of Eq. [4] subject the boundary condition of Eq. [5] yields

$$c = c_f e^{-\alpha y} \quad [6]$$

where

$$\alpha = \frac{ak_m}{v} \quad [7]$$

The reciprocal of the parameter α can be thought of as a penetration length. The penetration length defines the distance where the reactant is depleted to $1/e$ of its inlet composition, or, as an order of magnitude, the length of the region where most of the reaction occurs within the electrode.

At the end of the bed ($y = L$), the concentration of the flowing stream will have reacted to the largest extent. Here, the concentration of the reactant will be denoted as c_L . Equation [6] then gives at the end of the bed

$$c_L = c_f e^{-\alpha L} \quad [8]$$

This may be rearranged for αL in terms of the inlet and outlet concentrations as

$$\alpha L = \ln \frac{c_f}{c_L} \quad [9]$$

Equation [9] shows that the parameter αL effectively specifies the conversion of reactant within the electrode.

Now that the concentration distribution has been established, the solution to the potential distribution may proceed. For a uniform conductivity and negligible diffusion potential, Ohm's law governs the potential distribution within the fluid phase

$$i_2 = -\kappa \nabla \Phi_2 \quad [10]$$

Faraday's law relates the transfer current to the local rate of mass transfer within the electrode

$$j = \frac{nFak_m c}{s_R} \tag{11}$$

One must also employ the relationship

$$\nabla \cdot i_2 = j \tag{12}$$

which defines the transfer current as the divergence of the total current. Substituting the concentration distribution obtained in Eq. [6] into Eq. [11] and using Eq. [10] and [12], we obtain

$$\nabla^2 \Phi_2 = - \frac{nFak_m c_F}{s_R \kappa} e^{-\alpha y} \tag{13}$$

In contrast to the solution for the concentration distribution, the solution to the potential distribution depends upon the electrode configuration.

Bennion and Newman (1) solved Eq. [13] for a one-dimensional flow-through electrode. Alkire and Ng (6) solved Eq. [13] for the flow-by electrode assuming potential variation only in the direction perpendicular to fluid flow. This assumption reduces Eq. [13] from a partial differential equation to an ordinary differential equation. Fedkiw (8) solved Eq. [13] for two-dimensional current flow in a flow-by electrode of finite length.

Here, we propose to examine the limiting case of a flow-by electrode with an infinite aspect ratio. Thus, our case will reflect the condition

$$R = \frac{L}{d} \rightarrow \infty \tag{14}$$

The potential distribution is obtained by solving Eq. [13] subject to the boundary conditions

$$\text{at } y = 0, \frac{\partial \Phi_2}{\partial y} = 0 \tag{15}$$

$$\text{as } y \rightarrow \infty, \frac{\partial \Phi_2}{\partial y} \rightarrow 0 \tag{16}$$

$$\text{at } x = 0, \frac{\partial \Phi_2}{\partial x} = 0 \tag{17}$$

and

$$\text{at } x = d, \Phi_2 = V \tag{18}$$

Solution to Eq. [13] by separation of variables subject to the boundary conditions in Eq. [15] through [18] yields

$$\frac{\Phi_2 - V}{\frac{nF c_F V^2}{s_R \kappa a k_m}} = \left(\frac{\cos \alpha x}{\cos \alpha d} - 1 \right) e^{-\alpha y} + 2\alpha d \sum_{n=0}^{\infty} (-1)^n \left(\frac{1}{\lambda_n^2} - \frac{1}{\lambda_n^2 - (\alpha d)^2} \right) e^{-\lambda_n y/d} \cos \lambda_n x/d \tag{19}$$

where

$$\lambda_n = \frac{(2n + 1)\pi}{2} \tag{20}$$

To the designer, the maximum variation in solution phase potential may be a quantity of greater interest rather than the potential distribution within the electrode. To relate the relevant design variables to the maximum variation in solution potential, the results of the potential distribution will be used. For the flow-by electrode configuration, the semi-infinite potential distribution indicates that the maximum solution phase potential drop occurs at the front of the electrode, $y = 0$, between the two electrode boundaries, $x = 0$ and $x = d$. This is the position where the greatest current is flowing. The maximum solution phase potential difference in dimensionless form is given as

$$\frac{\Phi_2(x = 0, y = 0) - V}{\frac{nF c_F V^2}{s_R \kappa a k_m}} = \frac{\Delta \Phi_2}{nF c_F V^2} = \frac{\Delta \Phi_2}{\epsilon n F c_F D_0} \frac{Sh}{Pe^2} = \frac{1}{\cos \alpha d} - 1 + 2\alpha d \sum_{n=0}^{\infty} (-1)^n \left(\frac{1}{\lambda_n^2} - \frac{1}{\lambda_n^2 - (\alpha d)^2} \right) \tag{21}$$

This result can be compared to the results obtained by other investigators. The Alkire-Ng approximation gives for the maximum solution phase potential difference

$$\frac{\Phi_2(x = 0, y = 0) - V}{\frac{nF c_F V^2}{s_R \kappa a k_m}} = \frac{\Delta \Phi_2}{\epsilon n F c_F D_0} \frac{Sh}{Pe^2} = \frac{1}{2} (\alpha d)^2 \tag{22}$$

The solution obtained by Fedkiw, which includes the effects of the finite electrode length, can be represented as

$$\frac{\Phi_2(x = 0, y = 0) - V}{\frac{nF c_F V^2}{s_R \kappa a k_m}} = \frac{\Delta \Phi_2}{\epsilon n F c_F D_0} \frac{Sh}{Pe^2} = f(\alpha d, \alpha L) \tag{23}$$

where $f(\alpha d, \alpha L)$ represents a complicated function of the variables αd and αL previously derived by Fedkiw (8).

For the flow-through electrode, the maximum solution-phase potential drop occurs between the front and the rear of the electrode, $y = 0$ and $y = L$. From Bennion and Newman (1), this is

$$\frac{\Phi_2(y = 0) - \Phi_2(y = L)}{\frac{nF c_F V^2}{s_R \kappa a k_m}} = \frac{\Delta \Phi_2}{\epsilon n F c_F D_0} \frac{Sh}{Pe^2} = 1 - e^{-\alpha L} (1 + \alpha L) \tag{24}$$

In Fig. 2, we have plotted the dimensionless maximum potential drop times the ratio of the Sherwood number to the square of the Péclet number for a flow-by electrode. The variable αd has been chosen as the independent variable. We have included curves for a semi-infinite electrode and curves for electrodes of finite aspect ratio. Curves for the finite aspect ratio electrodes were obtained from the work of Fedkiw. In addition, the solution given by Alkire and Ng is shown. These curves are independent of any specific mass-transfer relationship.

The dotted lines plotted on Fig. 2 represent the limiting behavior of the flow-by electrode potential distribution for large values of αd . We have determined these by solving the following problem which is suggested by the limiting physical behavior of the electrode. For a fixed bed aspect ratio R , a large value of αd implies a large value of αL , and consequently a high conversion. Reactants are therefore consumed in a region very near the front of the electrode. For a reactor of very large αL , the volume of the reactor where a significant portion of

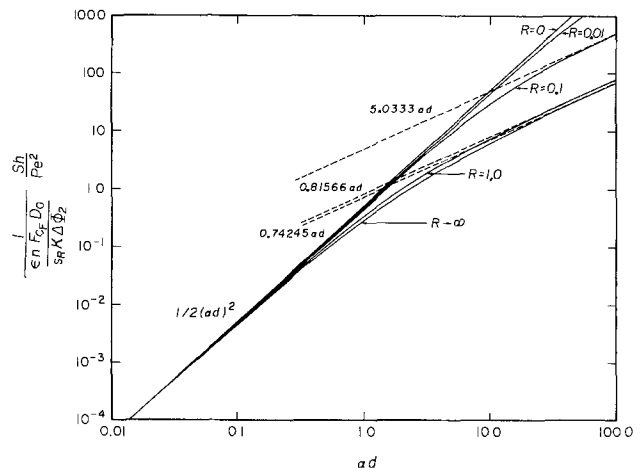


Fig. 2. Dimensionless maximum potential drop times the ratio of the Sherwood number to the square of the Péclet number for the flow-by electrode of various aspect ratios as a function of αd .

the reaction occurs approaches zero. The current generated within the bed can then be approximated as a uniform line source of current along the front of the reactor, and Laplace's equation can be used to solve for the potential distribution within the bed. Details of the problem formulation and the calculations are given in the Appendix.

Figure 2 clearly demonstrates five points.

1. The dimensionless maximum potential drop times the ratio of the Sherwood number to the square of the Péclet number calculated by the finite-electrode solution, the semi-infinite-electrode solution, and the Alkire and Ng solution all approach the same limit as αd becomes small.

2. The maximum dimensionless potential drop times the ratio of the Sherwood number to the square of the Péclet number approaches a limit for R becoming large. At large values of αd and large aspect ratios this relationship becomes proportional to αd . In the limit of small αd , this relationship approaches a value given by $1/2(\alpha d)^2$.

3. The maximum dimensionless solution phase potential drop times the ratio of the Sherwood number to the square of the Péclet number for finite R asymptotically becomes proportional to αd at large values of αd . The value of this proportionality constant is determined by the magnitude of R .

4. The effect of the finite electrode length is important only for values of R approximately less than one and then only at large values of αd .

5. The Alkire and Ng one-dimensional solution is seen to reflect the limit as the aspect ratio of the flow-by electrode tends toward zero for all values of αd . This contrasts with earlier work, which has suggested the Alkire and Ng solution results only as the aspect ratio R goes to infinity (8).

If the maximum dimensionless solution phase potential drop times the ratio of the Sherwood number to the square of the Péclet number for the flow-through electrode were plotted on this graph, the resulting curves would be horizontal straight lines. Equation [24] shows that for the flow-through electrode this quantity is not dependent upon the parameter αd .

Comparison of Configurations

As a first approximation, the optimum electrode configuration for a specified conversion might be found by assuming that the dimensionless potential drops times the ratio of the Sherwood number to the square of the Péclet number are equal. We satisfy this requirement by fixing equal potential drops for each configuration and by assuming that each electrode is constructed from the same materials and processes solutions with identical properties. Additionally, we restrict the comparison to equal ratios of the Sherwood number to the square of the Péclet number. This last constraint requires both the flow-through and flow-by electrodes to have identical volumes, flow rates, and consequently, equal pressure drops. In Fig. 3, we have plotted the values of αd and R (as functions of αL) which give equal dimensionless maximum potential drops times the ratio of the Sherwood number to the square of the Péclet number for the flow-through electrode and for the flow-by electrode. We have also designated the regions where each type of configuration is preferred. Again, the variable αL can be used to represent the reactor conversion. The maximum dimensionless potential drop times the ratio of the Sherwood number to the square of the Péclet number for the flow-through electrode has been calculated using Eq. [24]. We have included the three possibilities for evaluating this quantity for the flow-by electrode. First, the flow-by electrode is assumed to be infinitely long, and Eq. [21] is used. We can also assume the one-dimensional potential variation of Alkire and Ng might be appropriate and use Eq. [22]. Finally, the effects of the finite electrode length also can be included. The relationship given by Fedkiw could also be used. For this finite electrode case, an additional constraint must be imposed since this function ex-

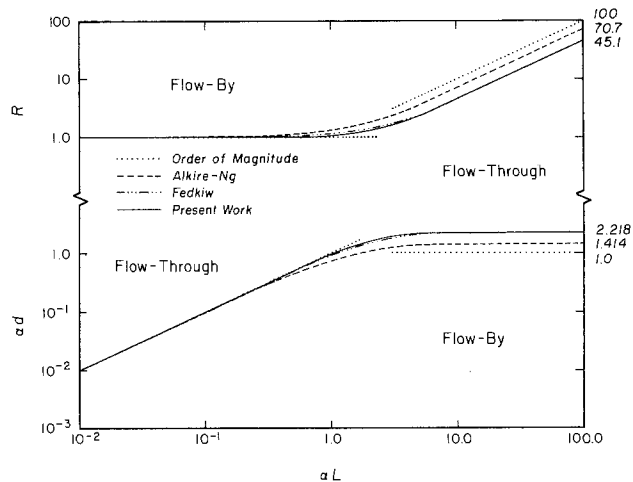


Fig. 3. Values of αd and R for equal dimensionless potential drops times the ratio of Sherwood number to the square of the Péclet number for the flow-through electrode and the flow-by electrode using: order-of-magnitude expressions, Alkire and Ng expression, semi-infinite electrode, and Fedkiw expression. These two representations are equivalent since $R = \alpha L/\alpha d$.

PLICITLY depends on the aspect ratio. The value of R is computed from

$$R = \frac{L}{d} = \frac{\alpha L}{\alpha d} \quad [25]$$

Thus, the value of αd and the value of R are found for each value of αL such that the maximum dimensionless potential drops times the ratio of the Sherwood number to the square of the Péclet number are equal. For comparison, we have also included the results of the order of magnitude analysis which were derived in the introduction.

We emphasize here that this comparison of the two electrode configurations does not require that we specify a mass-transfer coefficient relationship. This comparison does not depend upon the Sherwood-Péclet number relationship. Fedkiw compared the two configurations in a similar way, except that he introduced a specific Sherwood-Péclet number relationship in his comparison. The comparison presented here is considered to be preferable because it is not restricted to a single correlation.

Figure 3 establishes several important points. At low values of αL and, consequently, low conversion, the aspect ratio and the value of αd for equal potential drops are independent of the flow-by potential drop relationship. The Alkire and Ng one-dimensional approximation, the semi-infinite electrode approximation, and the finite electrode relationship all predict the same geometry. In this low conversion range, $\alpha L < 1$, the aspect ratio for equal potential drops is seen to approach one. The value of αd , given equal electrode cost, is seen to approach a limiting relationship of

$$\alpha d = \alpha L \quad [26]$$

The conclusion to be made here is that a flow-by electrode is favored at low conversions if it can be constructed with an aspect ratio greater than one. Otherwise, a flow-through electrode would be a better choice. Equation [26] is identical to Eq. [2], obtained by the order-of-magnitude analysis in the introductory section.

At higher conversions, values of αL greater than about 2, the criterion that specifies the optimum configuration changes. In this region, the value of R delineating the optimum electrode configuration no longer is constant. Also, the one-dimensional Alkire and Ng approximation deviates from the two-dimensional solutions. Since the one-dimensional approximation overpredicts the potential drop, it results in a criterion giving a lower flow-by aspect ratio. The two-dimensional potential distributions

are thus seen to affect the choice of electrode configurations only at high conversions. From Fig. 3, we can see that at high conversion one would choose a flow-by electrode only if the resulting aspect ratio is greater than 0.45 times αL . According to Fedkiw (8), the flow-by configuration was preferred over the flow-through configuration for

$$R \geq 5 \quad [27]$$

One can see, however, that this relationship holds only for values of αL near 10. In terms of αd , the flow-by electrode is superior at high conversions only if

$$\alpha d < 2.218 \quad [28]$$

Except for the factor of 2.218, Eq. [28] is consistent with Eq. [1], obtained by an order-of-magnitude estimate in the introductory section. This factor accounts for the variation of current across the flow-by electrode and the two-dimensional current flow, which was not included in the earlier analysis.

Figure 3 also demonstrates another significant point. The curves for the optimum electrode configuration given by the finite length electrode or the semi-infinite electrode are very nearly the same. At high and low conversions, the criterion becomes independent of whether one considers the finite electrode length. Only for a region of αL near one, does the effect of the finite electrode length on the criterion become noticeable. From Fig. 2, one can see that only when the aspect ratio approaches one at high conversions does the effect of the finite electrode length on the potential drop become noticeable. But at large conversions, or large αL , it is impractical to construct a flow-by electrode with an aspect ratio near one. Consequently, considering the potential distribution in a flow-by electrode of finite length is not really important for practical flow-by designs when the maximum potential drop is used as a basis for comparison. The potential distribution for an electrode with an infinite aspect ratio gives results which are practically identical, but in a less complicated expression.

Conclusions

The two-dimensional potential distribution for a flow-by porous electrode of infinite length to width ratio operating at the limiting has been derived. It is shown that the maximum solution-phase potential drop depends primarily on the ratio of the electrode width and the penetration depth αd . The potential drop for practical flow-by designs depends only weakly upon the length-to-width ratio. This result has been compared to the potential drop for a finite length electrode given by Fedkiw and the one-dimensional potential drop of Alkire and Ng.

The flow-through and flow-by electrode configurations have been compared at the limiting current using the maximum solution-phase potential difference as a basis for comparison. This comparison is independent of any specific mass-transfer coefficient correlation. Criteria delineating the optimal electrode configuration have been given which depend upon the reactant conversion. At low conversion, a flow-by electrode is favorable, providing that it can be constructed with a length-to-width ratio greater than one. At high conversions, however, a flow-by electrode is favorable if the ratio of the electrode width and penetration depth is less than 2.218.

Acknowledgment

This work was supported by the Assistant Secretary of Conservation and Renewable Energy, Office of Energy Systems Research, Energy Storage Division of the U. S. Department of Energy under Contract DE-AC03-76SF00098.

Manuscript submitted Feb. 13, 1984; revised manuscript received June 14, 1984.

The University of California assisted in meeting the publication costs of this article.

APPENDIX

Asymptotic Solutions for Large Values of αd

Consider a flow-by reactor with a given aspect ratio R . For large enough values of αd and large αL , most of the reactant will be consumed in a region very close to the electrode entrance. Consequently, the current will appear to be generated from a uniform line source near the front of the electrode. The applicable differential equation is thus Laplace's equation

$$\nabla^2 \Phi_2 = 0 \quad [A-1]$$

subject to the boundary conditions

$$\text{at } y = 0, \quad \frac{\partial \Phi_2}{\partial y} = -\frac{i_2}{\kappa} \quad [A-2]$$

$$\text{at } y = L, \quad \frac{\partial \Phi_2}{\partial y} = 0 \quad [A-3]$$

$$\text{at } x = 0, \quad \frac{\partial \Phi_2}{\partial x} = 0 \quad [A-4]$$

and

$$\text{at } x = d, \quad \Phi_2 = V \quad [A-5]$$

The solution to the above problem is

$$\begin{aligned} \frac{\Phi_2(x=0, y=0) - V}{\frac{nF c_F v^2}{s_R \kappa \alpha k_m}} &= \frac{\Delta \Phi_2}{\frac{\epsilon n F c_F D_0}{s_R \kappa}} \frac{\text{Sh}}{\text{Pe}^2} \\ &= \alpha d \sum_{n=0}^{\infty} \frac{2(-1)^n}{\lambda_n^2 \tanh \lambda_n R} \quad [A-6] \end{aligned}$$

where

$$\lambda_n = \frac{(2n+1)\pi}{2} \quad [A-7]$$

The above equation thus shows that at fixed R , the dimensionless potential drop times the ratio of the Sherwood number to the square of the Péclet number becomes proportional to αd at large αd . The constant of proportionality is determined the value of R . These are the dotted lines plotted in Fig. 2.

LIST OF SYMBOLS

a	specific interfacial surface area (cm^2/cm^3)
c	pore averaged concentration (mol/cm^3)
d	flow-by electrode bed width perpendicular to fluid-flow direction (cm)
D_0	free stream diffusion coefficient of reacting species (cm^2/s)
F	Faraday constant (96,485 C/eq)
i_2	total current density within electrolyte phase (A/cm^2)
j	transfer current density (A/cm^2)
k_m	mass transfer coefficient (cm/s)
L	bed depth in direction of fluid flow (cm)
M	arbitrary species
n	number of electrons transferred in reaction
Pe	Péclet number ($V/\alpha D_0$)
R	bed aspect ratio (L/d)
Sh	Sherwood number ($\epsilon k_m/\alpha D_0$)
s_R	stoichiometric coefficient of reactant
v	superficial fluid velocity (cm/s)
V	reference potential of flow-by electrode at $y = d$ (V)
z	charge number (eq/mol)

Greek characters

α	reciprocal of penetration length ak_m/v (cm^{-1})
$\Delta \Phi_2$	maximum allowable solution potential drop (V)
ϵ	bed porosity or void fraction
κ	conductivity of fluid phase in bed ($(\Omega \text{ cm})^{-1}$)
λ	dimensionless eigenvalue
Φ_2	solution potential, V

Subscripts

i	species number
n	eigenvalue number
F	feed condition
L	exit condition

REFERENCES

1. D. Bennion and J. Newman, *J. Appl. Electrochem.*, **2**, 113 (1972).
2. J. L. Fitzjohn, *Chem. Eng. Prog.*, **71**, 85 (1975).
3. J. A. Trainham and J. Newman, *Electrochim. Acta*, **26**, 455 (1981).
4. J. A. Trainham and J. Newman, *This Journal*, **125**, 58 (1978).
5. J. A. Trainham and J. Newman, *ibid.*, **124**, 1528 (1977).
6. R. Alkire and P. Ng, *ibid.*, **121**, 95 (1974).
7. R. Alkire and P. Ng, *ibid.*, **124**, 1220 (1977).
8. P. Fedkiw, *ibid.*, **128**, 831 (1981).
9. A. Stork *et al.*, *Electrochim. Acta.*, **27**, 293 (1982).
10. A. Stork *et al.*, *ibid.*, **27**, 301 (1982).
11. J. Newman and W. Tiedemann, in "Advances in Electrochemistry and Electrochemical Engineering", Vol. 11, Heinz Gerischer and Charles Tobias, Editors, Wiley Interscience, New York (1978).

Electrochemical Studies of Antitumor Antibiotics

V. An Electrochemical Method of Measurement of the Binding of Doxorubicin and Daunorubicin Derivatives to DNA

James A. Plambeck* and J. William Lown

Department of Chemistry, University of Alberta, Edmonton, Alberta, Canada T6G 2G2

ABSTRACT

A procedure has been developed for the measurement in aqueous solution of the association constant with native DNA of an agent which is electrochemically reducible. A fresh mercury drop is extruded into a solution containing both the agent and DNA, surface adsorption is reproducibly conditioned ($-0.4V \leq E \leq -1.0V$, 90s, followed by $-0.4V$, 90s), and the peak current is measured during a rapid voltage scan. A suitable plot of current as a function of DNA concentration yields the desired constant. Data are given for a significant series of substituted daunorubicin and doxorubicin compounds and for control compounds.

Since the concept of intercalation into DNA was first formulated by Lerman (1) in 1961, it has become widely recognized that many compounds of pharmacological interest, including anticancer drugs and antibiotics as well as certain carcinogens, function by binding to duplex nucleic acids (2). The anthracyclines (*e.g.*, adriamycin, daunorubicin, aclacinomycin) constitute one of the most widely studied types of such drugs owing to their established clinical efficacy against a wide range of malignancies; they are regarded as amongst the most promising of anticancer drugs (3, 4). The molecular mechanism of action of the anthracyclines is complex and appears to involve free radical generation (5, 6), lipid peroxidation (7), DNA damage (8, 9), and possible covalent attachment (10), as well as intercalative binding (2-4, 11). Nevertheless, the ability of anthracyclines to undergo intercalative binding to DNA has shown a consistent correlation with antitumor properties (3, 4, 11).

One of the parameters which characterizes this phenomenon is the binding constant K_b (12), also known as the apparent association constant K_{app} . Other parameters include sequence preference or specificity and spatial and functional group parameters determining molecular recognition (2, 3, 11, 12). Consequently, there is an urgent need for a direct, sensitive, and accurate method to quantify the binding to DNA of the growing number of new anthracyclines which are being prepared in order to improve their therapeutic index or especially to combat their main clinical limitation, severe cardiotoxicity (13, 14).

The methods which have been developed to measure binding constants of anthracyclines and other drugs fall into two categories (i) those that follow changes in properties of the drug, and (ii) those that monitor changes in the polynucleotide (12). Methods of the first type include measurement of (i) changes in the UV and visible absorption characteristics of the anthracycline chromophore (2, 15-17), (ii) changes in the fluorescence of the chromophore (15, 18-20), and (iii) circular dichroism characteristics (21-23). In addition, those methods for determining K_b values which depend on properties of the DNA include (i) viscosity changes (15, 16, 24), (ii) buoyant density and sedimentation coefficient differences (15, 16, 24), (iii) melting temperature changes (11, 24, 25), (iv) equilibrium dial-

ysis (16, 22, 26), and (v) removal of the supercoiling in native covalently closed circular DNA (2, 27).

Many of these methods are tedious experimentally or require either rather large amounts of the anthracyclines or expensive circular DNA's. Moreover, the reported association constants for daunorubicin (12) cover the range 1.3 to 9.3×10^6 liter/mol, indicating a lack of agreement using the different methods. In this paper, we describe a new method based on the electrochemical characteristics of both free and intercalatively bound drugs. The method is experimentally convenient and sensitive so that it requires only small amounts of materials. In principle, it can be applied to a wide range of intercalating drugs, provided they bear an electrochemically active moiety. We report also further studies upon DNA and the drugs required to establish this technique.

Early applications of electroanalytical techniques to solutions of nucleic acids have been reviewed (28, 29). Of the four bases present in deoxyribonucleic acid (DNA), adenine and cytosine are reducible at mercury electrodes whether free or bound to the nucleotide chain. Native DNA is not reducible at the dropping mercury electrode because the stability of the intact double helix makes the reducible bases inaccessible to the electrode. When the integrity of the double helix is altered, as by heating above the melting point or by induced breaks in the helix, reduction of bases can be observed.

AC methods have been employed by Barker (30) and Malfroy and Reynaud (31-33). Valenta and Nürnberg (34-44) have employed dc voltammetric methods in the fast sweep mode at a stationary mercury electrode and reviewed the results (45-47). Of significance to this work is their finding that native DNA can be reduced at mercury electrodes after adsorption and unwinding of the double helix (39, 47). Less extensive studies have also been carried out by Berg and co-workers (48, 49).

Theory

The constant to be measured is the equilibrium constant for the formation of the anthracycline-DNA complex (ADNA) from unbound anthracycline (A) and uncomplexed DNA (DNA), which in terms of concentrations may be written as

$$K = c(\text{ADNA})/c(\text{A}) c(\text{DNA})$$

*Electrochemical Society Active Member.

None of these species is easily measured directly, but the total concentration of anthracycline, $cT(A)$, and the total concentration of DNA, $cT(DNA)$, are established as conditions of the experiment and by definition

$$cT(A) = c(A) + c(ADNA)$$

$$cT(DNA) = c(DNA) + c(ADNA)$$

To express units consistently, if $cT(A)$ is in units of mol/dm^3 , and each molecule of anthracycline is understood to occupy one binding site, then $cT(DNA)$ must be expressed in units of binding sites/ dm^3 rather than mol/dm^3 . The number of binding sites/ dm^3 will depend upon the molecular weight of the DNA and its concentration, which are expressible as $\text{mol bases}/\text{dm}^3$, and the number of bases required to form a binding site. Since the molecules are intercalated in the helix, a minimum of four bases (two pairs) is required to form a binding site. However, it is improbable that the intrinsic binding to all types of four-base sites with different base pair compositions is identical, and the effect of bases other than nearest neighbors upon the binding may be significant (2). At the very low levels of saturation used in this study, only the most favorable sites should be occupied, and as a consequence the constants measured here should refer to an average of only the most favorable sites. Thus, the interaction constants measured by this method should be smaller than those measured by methods involving saturation of the DNA and should be more comparable to clinically realizable conditions.

When the concentration of DNA is expressed in this way and only a small proportion of the possible binding sites are occupied, then $c(ADNA)$ is much less than $cT(DNA)$ so that $c(DNA)$ is approximately equal to $cT(DNA)$. Thus measurement of the $c(ADNA)/c(A)$ ratio establishes the value of the binding constant K

$$K cT(DNA) = c(ADNA)/c(A)$$

Experimentally, we find that for at least all of the antibiotics reported here, and for others of different structure but containing at least one group reducible at a potential not more negative than -1.25V against SCE, application of the method described in this paper yields a curve of current against sweep potential having one (occasionally more) peaks at approximately the polarographic or cyclic voltammetric reduction potential of the anthracycline. The current I at this peak is directly proportional to $cT(A)$ in the absence of DNA, and thus to $c(A)$. In no case is an additional peak observed in the presence of DNA save for the reduction of DNA itself and consequent hydrogen evolution, but these are too negative to interfere with measurement of I ; addition of DNA reduces the value of I , but the potential of the peak remains unaffected.

Since the current I arises from reduction of A whether bound or unbound

$$I = k'c(A) + k''c(ADNA)$$

In the presence of A and absence of DNA, there can be no contribution from the bound anthracycline and such a value $I(0)$ equals $k'c(A)$ which is also $k'cT(A)$. At the other extreme of an infinite excess of DNA, the concentration of unbound anthracycline must go to zero and thus such a value $I(\text{inf.})$ equals $k''c(ADNA)$. Then

$$I(0) - I = k'cT(A) - (k'c(A) + k''c(ADNA))$$

$$I(0) - I = (k' - k'') c(ADNA)$$

$$I - I(\text{inf.}) = k'c(A) + k''c(ADNA) - k''c(ADNA) = k'c(A)$$

$$[I(0) - I]/[I - I(\text{inf.})] = c(ADNA)/c(A) = K cT(DNA)$$

Experimental

The experiments were carried out using a Princeton Applied Research (PAR) Polarographic Analyzer Model 174A, PAR Controller Model 315, and Static Mercury Drop Electrode Model 303, a Biomation Model 805 Waveform Recorder, and a Houston Instrument Type

2000 X-Y recorder. Both McIlvane and acetate buffers were used; 0.1M McIlvane buffers of pH 5.6 and 6.0 were prepared using reagent-grade dibasic sodium phosphate and citric acid. The ionic strength of the McIlvane buffers was adjusted to 1.0M using reagent-grade potassium chloride (29). The 0.1M acetate buffers of pH 5.6 and 6.0 were prepared using sodium acetate, acetic acid, and 10^{-4}M disodium EDTA dihydrate in 0.1M KCl. All buffers were prepared from triply distilled water. The acetate buffer of pH 5.6 so prepared was used in all experiments unless otherwise specified.

Calf thymus DNA was obtained from Sigma Chemical Company, *E. coli* DNA from Aldrich Chemical Company, and *B. subtilis* DNA (Grade A) from Calbiochem. The antibiotic daunorubicin **1b** was obtained from Sigma Chemical Company; its anhydrous molecular weight was 564.0. Compound AD32, **1o**, was kindly provided by Dr. M. Israel of the Sidney Farber Cancer Institute. Other anthracyclines were obtained from Dr. E. M. Acton of SRI International. Their structures are given in Fig. 1.

The procedure used was similar to those established by Nürnberg *et al.* (50). The "conditioning" potential E_c , the "deposition" potential E_s , and the final potential E_f were set on the potentiometers of the Model 315. The "deposition" potential and time are so noted on the Model 315, which was designed for use in anodic stripping voltammetry, but here represent only a second stage of conditioning. Both the "conditioning" time t_c and "deposition" time t_s were 90s. The internal switch in the PAR Model 174A was set to the position for 10 times higher sweep rates, which permits sweep rates of up to 5 V/s.

The Model 303 was set to HMDE mode with large drop size, each drop having a surface area of $2.83 \times 10^{-2} \text{cm}^2$. A fresh drop was used for each measurement. The reference electrode was AgCl/Ag-saturated KCl in a glass frit; all potentials were measured and are given with respect to this reference. A platinum wire served as an auxiliary electrode. All measurements were made at room temperature under an atmosphere of purified nitrogen after deaeration with nitrogen.

For 90s, the mercury drop was subjected to a constant applied "conditioning" potential whose values could be varied between -0.40 and -1.60V . After 90s, the potential was stepped to a constant "deposition" potential of -0.40V and was held there for a further 90s. Finally, the potential was driven by a rapid cathodic sweep with a rate of 1 or 5 V/s to the negative limit of potential at about -1.8V . The current values were stored in the Biomation Model 803 which was set for pretriggered recording with 1800 delay interval and single triggering mode. The stored voltammogram was plotted, using the Houston recorder in x-t mode, as provided by the Biomation Model 803; typical curves are shown in Fig. 2. The Biomation unit was triggered from the pen-drop switch closure of the Model 315 using an external battery. Similar results, though with less precise output, were obtained using an R564B storage oscilloscope (Tektronix).

For all of the solutions studied, the experimental curves were superimposable for successive fresh drops of the same size (as provided by the mechanical operation of the Model 303) in the same solution. Drops of nonreproducible size, or use of the same drop twice, gave totally nonreproducible results. Replicate runs on new solutions and using fresh drops were within $\pm 4\%$ - 5% on the basis of peak height.

The functions of peak current derived in the theory section of this paper were calculated and plotted against the concentration of DNA either manually or by computer (Amdahl 470/V7, Calcomp plotter, *IG package at University of Alberta Computing Services). Typical plots are given in Fig. 5 and 6. The association constant is obtainable from the linear portion of the slope of Fig. 5. In terms of originally measured quantities, this slope has the units of μg anthracycline complexed per cm^3 of DNA stock solution added, but use of the original anthracycline concentration (nominally $5.0 \times 10^{-6} \text{mol}/\text{dm}^3$), the concentration of the DNA stock solution (nominally $1.050 \text{mg}/\text{cm}^3$

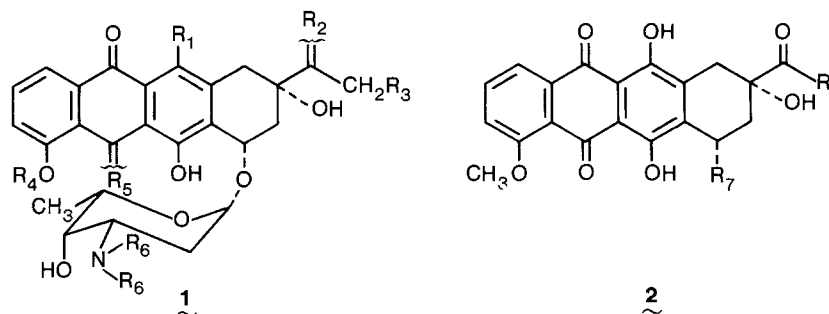


Fig. 1. Structures of anthracyclines (1) and aglycones (2).

1a	$R_1=OH, R_2=O, R_3=OH,$	$R_4=CH_3, R_5=O, R_6=H$
1b	$R_1=OH, R_2=O, R_3=H,$	$R_4=CH_3, R_5=O, R_6=H$
1c	$R_1=H, R_2=O, R_3=OH,$	$R_4=CH_3, R_5=O, R_6=H$
1d	$R_1=H, R_2=O, R_3=H,$	$R_4=CH_3, R_5=O, R_6=H$
1e	$R_1=H, R_2=O, R_3=OH,$	$R_4=H, R_5=O, R_6=H$
1f	$R_1=H, R_2=O, R_3=H,$	$R_4=H, R_5=O, R_6=H$
1g	$R_1=OH, R_2=(H,OH) R_3=OH,$	$R_4=CH_3, R_5=O, R_6=CH_2Ph$
1h	$R_1=OH, R_2=(H,OH) R_3=H,$	$R_4=CH_3, R_5=NH, R_6=H$
1i	$R_1=OH, R_2=(H,OH) R_3=H,$	$R_4=CH_3, R_5=O, R_6=-(CH_2)_2CHOCH_3(CH_2)_2-$
1j	$R_1=OH, R_2=O, R_3=H,$	$R_4=CH_3, R_5=O, R_6=(CH_2)_2O(CH_2)_2-$
1k	$R_1=OH, R_2=O, R_3=H,$	$R_4=CH_3, R_5=O, R_6=-(CH_2)_5-$
1l	$R_1=OH, R_2=O, R_3=H,$	$R_4=CH_3, R_5=O, R_6=(2'-tetrahydropyranyl)$
1m	$R_1=OH, R_2=O, R_3=H,$	$R_4=CH_3, R_5=O, R_6=-(CH_2)_2CHOCH_3(CH_2)_2-$
1n	$R_1=OH, R_2=O, R_3=H,$	$R_4=CH_3, R_5=O, R_6=-(CH_2)_2S(CH_2)_2-$
1o	$R_1=OH, R_2=O, R_3=OCO(CH_2)_4CH_3,$	$R_4=CH_3, R_5=O, R_6=(H,COCF_3)$
1p	$R_1=OH, R_2=(H,OH) R_3=H,$	$R_4=CH_3, R_5=O, R_6=H$
2a	$R_3=OH, R_7=OH$	
2b	$R_3=H, R_7=OH$	
2c	$R_3=OH, R_7=H$	
2d	$R_3=H, R_7=H$	

calf thymus DNA of od 21 measured at 260 nm), and the relationship that one od unit is equivalent to $50 \mu\text{g}/\text{cm}^3$ or 1.49×10^{-4} mol phosphate/dm³ or mol bases/dm³ permits calculation of the association constant in molar quantities, liter/mol phosphate or liter/mol bases.

Coulometric measurements were made upon the recorder output curves using a planimeter and converted to the original input time base. The method of obtaining the base line for the peaks near -1.5V was that of Valenta and Grahmann (37). In the peaks at -0.65V , the base line of the output curves with base electrolyte alone and the base

lines of the curves with DNA and/or daunorubicin **1b** were the same. Planimeter measurements were also made upon molecular models of **1b** to establish the area they would occupy. A single molecule of **1b** can occupy a surface area of ca. 1.50 nm^2 (flat) and ca. 0.64 nm^2 (on edge).

Results

Preliminary tests were made using 1.0×10^{-4} mol/dm³ Cd(II) in pH 5.6 McIlvane buffer. At a conditioning potential of, or positive of, -1.0V , a single sharp asymmetric peak (sharp rise, exponential fall) was observed at a peak

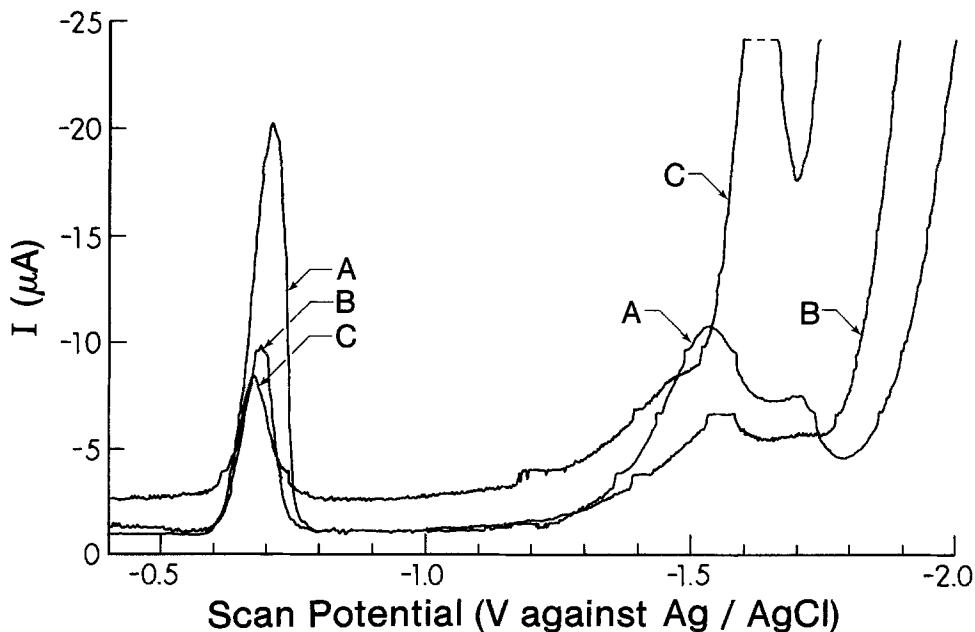


Fig. 2. Typical biomation output plots. Data for 5×10^{-6} mol/dm³ doxorubicin (**1a**) in acetate buffer, conditioning potential -0.4V . Curve A: no added DNA. B: calf thymus DNA concentration $10.4 \mu\text{g}/\text{cm}^3$. C: calf thymus DNA concentration $59.4 \mu\text{g}/\text{cm}^3$. Vertical scale of C, only, exaggerated by a factor of 2.5.

potential (E_p) of $-0.63 \pm 0.01V$. At "conditioning" potentials more negative than $-1.0V$, the current no longer fell exponentially. This is expected because the conditioning potential is now sufficiently negative to deposit more cadmium onto (or into) the HMDE than is removed during the "deposition" time at $-0.4V$. Addition of sufficient EDTA to give a 0.02 mol/dm^3 solution shifted the cadmium reduction peak negative to $-1.70V$; its fall then merged with the solvent discharge current. In the EDTA solution, the peak shape and height were not affected by the "conditioning" potential. This behavior is expected for aqueous Cd(II) and its EDTA complex, which are reversibly reduced on mercury.

DNA.—Calf thymus DNA was used both in McIlvane and acetate buffer. The addition of DNA to buffer caused the appearance of a single sharp asymmetric peak at about $-1.5V$ and a positive shift of the onset of hydrogen evolution from ca. $-1.83V$ (pH 6.0, $0.1M$ acetate buffer + $0.1M$ KCl) to ca. $-1.6V$ (same system + DNA). The bacterial DNA gave sharper peaks, as expected, owing to its lower molecular weight. All three forms of DNA gave only a single peak at about $-1.5V$ at all values of the conditioning potential less than $-1.5V$. Its height increased with scan rate, and varied with the type and concentration of DNA used (Table I). This peak is attributed to the reduction of the adenine and cytosine bases of the adsorbed DNA (34-47); for DNA alone, our results are comparable to those of Nürnberg *et al.*

Anthracyclines.—Solutions of **1b** in the absence of DNA gave a single, sharp, well-defined, approximately symmetric peak at $-0.625 \pm 0.005V$ (full width at half-maximum $0.08 \pm 0.02V$, except for extremely low concentrations). The peak potential did not change with **1b** concentration or with scan rate. The peak current was directly proportional to the concentration of **1b** up to about 2 mol/dm^3 , at which point the current increase be-

Table I. Effect of conditioning potential upon reduction of DNA

Calf thymus DNA; $84 \mu\text{g/cm}^3$ McIlvane buffer, pH 6.0; scan from "deposition" potential of $-0.4V$.				
E_c (V)	E_p (V) (5 V/s)	Q ($\mu\text{C/cm}^2$) (5 V/s)	E_p (V) (1 V/s)	Q ($\mu\text{C/cm}^2$) (1 V/s)
-0.4	-1.605	9.6	-1.525	17.6
-0.6	-1.605	12.3	-1.525	15.8
-0.8	-1.610	14.2	-1.525	12.9
-1.0	-1.655	12.1	-1.525	18.8
-1.2	-1.625	18.0	-1.535	24.9
-1.3	-1.620	18.1	-1.540	27.4
-1.35	-1.605	10.4	-1.530	25.6
-1.4	-1.595	5.5	-1.6?	4.0

Calf thymus DNA; $84 \mu\text{g/cm}^3$ acetate buffer, pH 6.0, scan rate 1 V/s from $-0.4V$ "deposition" potential, EDTA when present $1 \times 10^{-4} \text{ mol/dm}^3$.				
E_c (V)	E_p (V) (w/o EDTA)	Q ($\mu\text{C/cm}^2$) (w/o EDTA)	E_p (V) (w/EDTA)	Q ($\mu\text{C/cm}^2$) (w/EDTA)
-0.4	-1.535	5.08	-1.535	4.51
-0.6	-1.535	5.64	-1.540	5.16
-0.8	-1.535	5.57	—	—
-1.0	-1.540	6.77	—	—
-1.2	-1.530	10.64	-1.550	8.95
-1.3	—	—	—	—
-1.35	-1.540	9.35	-1.560	8.79
-1.4	-1.545	3.14	—	—

Bacterial DNA; *E. coli* DNA $40 \mu\text{g/cm}^3$, *B. subtilis* DNA $66.7 \mu\text{g/cm}^3$; scan rate 1 V/s from "deposition" potential of $-0.4V$; acetate buffer pH 5.6.

E_c (V)	<i>E. coli</i> DNA		<i>B. subtilis</i> DNA	
	E_p (V)	Q ($\mu\text{C/cm}^2$)	E_p (V)	Q ($\mu\text{C/cm}^2$)
-0.4	-1.515	2.66	-1.530	8.87
-0.6	-1.520	2.82	-1.530	8.38
-0.8	-1.525	3.07	-1.510	8.46
-1.0	-1.525	2.90	-1.520	9.11
-1.2	-1.525	3.30	-1.525	9.59
-1.3	-1.525	4.67	-1.525	11.20
-1.35	-1.525	4.28	—	—
-1.4	-1.530	2.58	-1.525	6.21

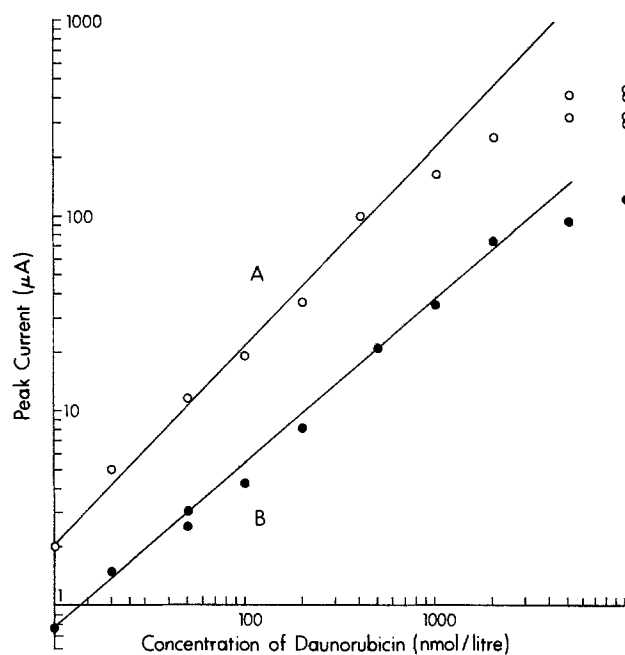


Fig. 3. Effect of concentration upon daunorubicin (**1b**) reduction. Aqueous buffer. Open circles (A) obtained at 5 V/s. Closed circles (B) obtained at 1 V/s. Log-log plot. Peak potential: $-0.65V$.

came less than proportional (Fig. 3). Direct proportionality is found from 10 nmol/dm^3 to over 500 nmol/dm^3 (Fig. 4); the lower limit is due to inability to easily distinguish the peak from base-line noise. Solutions of **1b** which contained no DNA also gave a peak or shoulder at the approximate potential of reduction of the bases of DNA, $-1.535V$. This is due to the additional reduction of **1b** at these more negative potentials (53, 54). The behavior of the other anthracyclines studied paralleled that of daunorubicin. In all cases, the easiest reduction of the anthracyclines is sufficiently positive of either their own second reduction or the reduction of DNA that the current returns to the base line before these processes begin.

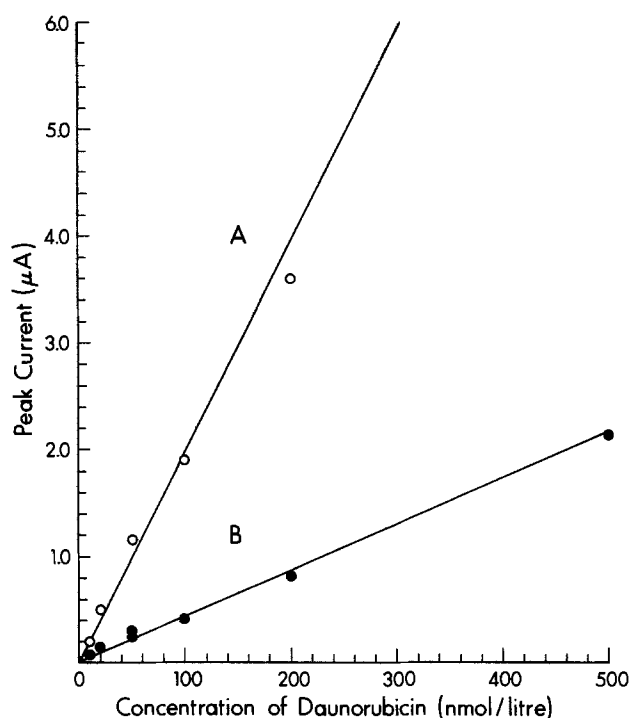


Fig. 4. Effect of low concentrations of daunorubicin (**1b**) upon peak current. Aqueous buffer. Open circles (A) obtained at 5 V/s. Closed circles (B) obtained at 1 V/s. Peak potential: $-0.65V$. Point on A at 500 nmol/liter is at $10.0 \mu\text{A}$, offscale.

DNA-anthracycline complexes.—The electrochemical behavior of solutions containing both DNA and the individual anthracycline is similar to the sum of the behavior of separate solutions of the two components. The first reduction of **1b** at $-0.625V$ shifts negative in the presence of DNA by not more than 50 mV; the peak is broadened and slightly reduced in height as compared to **1b** alone. The second reduction of **1b** is indistinguishable from the reduction of the adsorbed adenine and cytosine bases of DNA near $-1.55V$. As a consequence, we are unable to measure the effect of the anthracycline upon the DNA present, although at relatively low levels of anthracycline that effect is, within experimental error, absent. The sharp drop-offs in peak current and charge as the "conditioning" potential becomes more negative than $-1.3V$ are due to partial reduction of the adsorbed material while the "conditioning" potential is still held, well before the onset of the recorded voltammetric sweep. These observations apply to all of the other anthracyclines studied as well.

The association constants of the anthracyclines with DNA were calculated according to the procedure described from the values of the peak current as a function of DNA concentration. These are given in Tables II-V. The values reported in Tables II-IV are arbitrarily given to three places following the decimal point to ensure that any real differences in potential dependence are not lost. The reproducibility of completely separate experiments on different solutions is of the order of 5%, and the

Table II. Association constants in aqueous solution

Compound	K (l/mol phosphate $\times 10^3$)					$I(\infty)^1$ [% I(0)]
	-0.4V	-0.6V	-0.8V	-1.0V	Mean	
1a	0.688	0.755	0.889	0.856	0.797	4
1b	0.638	0.477	0.433	0.513	0.515	8
1c	0.765	0.738	0.792	0.738	0.758	3
1d	0.463	0.463	0.470	0.490	0.472	14
1e	0.366	0.460	0.436	0.315	0.394	2
1f	0.299	0.144	0.174	0.179	0.199	2
1h	0.342	0.329	0.409	0.403	0.371	4
1i	2.070	1.805	1.362	1.342	1.645	0
1j	1.644	1.752	1.299	1.393	1.522	0
1k	1.611	2.460	1.342	1.483	1.474	0
1l	0.359	0.352	0.466	0.366	0.378	7
1m	3.215	2.685	2.725	2.547	2.793	0
1n	1.812	1.342	1.544	1.409	1.527	0
1o	NS	NS	NS	NS	NS	—
1p	0.268	0.208	0.235	0.188	0.225	6

¹ Percent response in effectively "infinite" DNA excess as compared to total absence of DNA.
NS = not soluble.

Table III. Association constants in 3% CH₃CN

Compound	K (l/mol phosphate $\times 10^3$)					$I(\infty)^1$ [% I(0)]
	-0.4V	-0.6V	-0.8V	-1.0V	Mean	
1a	0.839	0.805	0.966	1.037	0.912	5
1b	0.698	0.839	0.923	0.883	0.836	6
1c	0.503	0.738	0.718	0.691	0.663	3
1d	0.389	0.470	0.383	0.463	0.426	9
1e	0.322	0.228	0.352	0.362	0.316	3
1f	0.262	0.322	0.329	0.430	0.336	8
1g ²	0.072	0.109	0.050	0.071	0.076	15
1h	0.356	0.383	0.456	0.443	0.411	5
1i	1.628	2.070	1.970	1.718	1.847	0
1j	1.883	1.570	1.386	1.319	1.540	0
1k	1.779	1.594	1.678	1.594	1.661	0
1l	0.416	0.440	0.473	0.466	0.449	7
1m	1.342	1.812	1.846	1.826	1.706	0
1n	1.544	1.805	1.715	2.577	1.910	0
1o	0.060	0.128	0.077	0.091	0.089	47
1p	0.208	0.201	0.268	0.221	0.225	8
2a ²	0.215	0.174	0.141	0.142	0.168	36

¹ Percent response in effectively "infinite" DNA excess as compared to total absence of DNA.

² 5% CH₃CN.

Table IV. Association constants in 30% CH₃CN

Compound	K (l/mol phosphate $\times 10^3$)					$I(\infty)^1$ [% I(0)]
	-0.4V	-0.6V	-0.8V	-1.0V	Mean	
1a	0.446	0.436	0.544	1.517	0.486	9
1b	0.503	0.560	0.537	0.356	0.489	10
1c	0.336	0.329	0.201	0.282	0.287	10
1d	0.218	0.255	0.228	0.181	0.221	18
1e	0.074	0.114	0.107	0.181	0.119	2
1f	0.228	0.255	0.228	0.299	0.253	8
1h	0.044	0.034	0.040	0.067	0.046	29
1i	0.356	0.336	0.302	0.292	0.322	0
1j	0.923	1.047	0.859	0.953	0.946	0
1k	0.560	0.604	0.423	0.128	0.429	0
1l	0.453	0.299	0.208	0.201	0.290	7
1m	1.117	1.235	1.510	0.775	1.159	0
1n	0.537	0.537	0.205	0.369	0.412	0
1o	0.054	0.060	0.027	0.037	0.044	12
1p	0.141	0.154	0.154	0.134	0.146	29
2b	0.255	0.201	0.195	0.148	0.200	40
2d	0.050	0.034	0.040	0.054	0.045	20

¹ Percent response in effectively "infinite" DNA excess as compared to total absence of DNA.

smaller number of figures given in the summary of Table V reflect this.

This procedure has been optimized for daunorubicin by adjusting the DNA increments and values to give a slope of about 50° in the plots of the type given in Fig. 5. For association weaker or stronger than that of daunorubicin by a factor greater than ten, the line approaches horizontal or vertical. Classes of compounds with much stronger association than daunorubicin, which may be those of greatest anticancer interest, are better studied with smaller or more dilute DNA additions.

The number of moles of bases of DNA per mole of anthracycline can be calculated from the total stoichiometric ratio in the solution. A plot of this ratio against the signal due to unbound anthracycline, which can be taken as proportional to the ratio of the peak current, less the peak current at an infinite excess of DNA, to the peak current measured in the absence of DNA, can give an indication of the number of base pairs of the DNA involved in direct interaction with the antibiotic (Fig. 6). This is essentially a titration of the anthracycline with DNA; the estimation of the number of bases/binding site uses only the initial rapid decrease.

In all cases, the number of bases per anthracycline calculated from the intercept of diagrams such as Fig. 6 was between 5 and 8.

Table V. Summary of mean association constants

Compound	Mean K ¹ (l/mol phosphate $\times 10^3$)		
	Aqueous	3% CH ₃ CN	30% CH ₃ CN
1a	0.80	0.91	0.49
1b	0.52	0.84	0.49
1c	0.76	0.66	0.29
1d	0.47	0.43	0.22
1e	0.39	0.32	0.12
1f	0.20	0.34	0.25
1g	NS	0.08 ²	—
1h	0.38	0.41	0.05
1i	1.65	1.85	0.32
1j	1.52	1.54	0.95
1k	1.47	1.66	0.43
1l	0.38	0.45	0.29
1m	2.79	1.71	1.16
1n	1.53	1.91	0.41
1o	NS	0.09	0.04
1p	0.23	0.23	0.15
2a	—	0.17 ²	—
2b	NS	NS	0.20 ⁴
2d	NS	NS	0.04

NS = not soluble.

¹ Value in table should be multiplied by 10⁵ to give K in l/mol phosphate.

² 5% CH₃CN.

³ No detectable complexation; value \ll 0.05.

⁴ Scattered data plots.

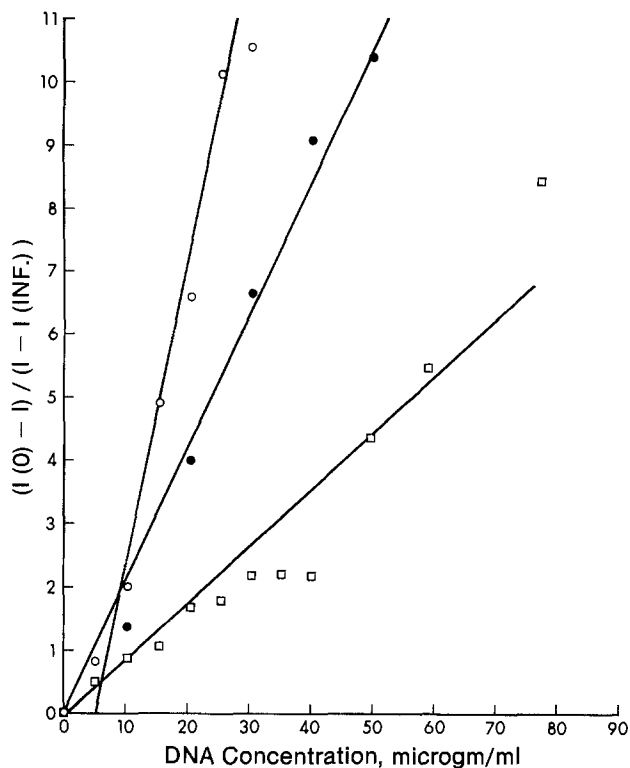


Fig. 5. Typical plots used to obtain association constants. Strong association, open circles (1j); moderate association, closed circles (1a); weaker association, open squares (1f). All in aqueous solution, conditioning potential $-0.4V$, scan rate 5 V/s.

Additional electrochemical studies of these compounds are given elsewhere (59).

Discussion

The interfacial mercury/aqueous electrolyte region has been used as a model for electrically charged biological membranes, the interactions of DNA with the electrode being then taken as relevant to the interactions of cellular DNA with cell membranes. While doubly helical native DNA is not reducible from solution, it can undergo the sequence adsorption, dehydration, strand separation, and base reorientation which renders the reducible adenine

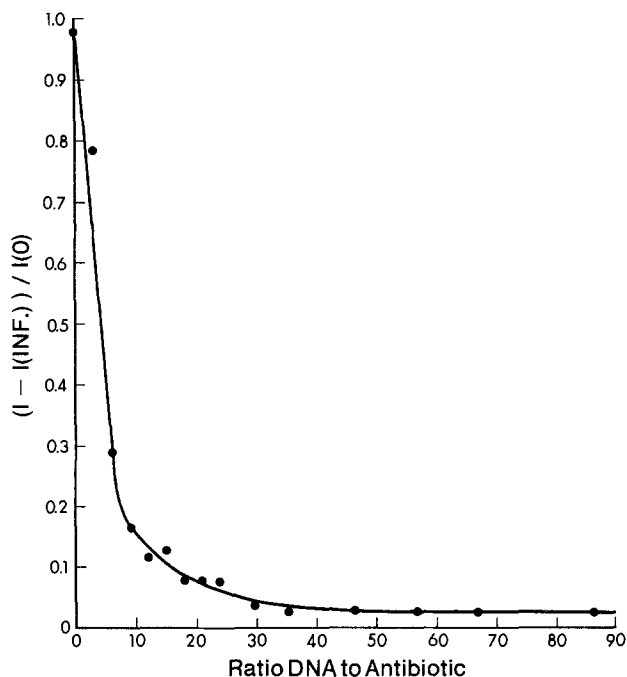


Fig. 6. Typical plot of moles of DNA base/mol agent. Data for 1a, aqueous solution, conditioning potential $-0.4V$, scan rate 5 V/s.

and cytosine bases accessible to electron transfer (43). Their irreversible reduction to strongly adsorbed products blocks the surface of the electrode to further adsorption of DNA. These products, in common with other nitrogen heterocyclic compounds, are catalysts for hydrogen evolution on mercury. The parameters known to affect the adsorption, and hence observable reduction, of DNA on fresh mercury electrodes include ionic strength, pH, percentage of A-T content in the DNA, and molecular weight, in addition to the experimentally adjustable parameters of adsorption time, potential of the electrode during adsorption, and rate of the voltammetric scan (43). Denatured DNA, in which the bases are already accessible, and mononucleotides are reducible through the latter part of the same mechanism. The data of this study for solutions of DNA alone are consistent with previous studies (43) and the above mechanism.

Anthracyclines.—Generation of fresh drops in the solution containing both the DNA and the anthracyclines known (51-54 and references therein) to interact with it, followed by the double potential step-sweep method under the conditions already established (50) as appropriate for study of DNA itself should demonstrate any effect of interaction with DNA upon the reduction of DNA. At the lowest anthracycline concentrations used, no such effect is observed.

If the behavior of the anthracyclines alone under the same conditions is established, any effect of interaction with DNA upon the redox properties of the anthracyclines should also be noticeable. This second factor is relevant to the possible reductive activation of an anthracycline once bound to DNA (51-54). We find no evidence of any such effect. The results obtained show that for anthracyclines alone the initial reduction studied by this method occurs at the same potential as is observed in the more conventional techniques of polarography and cyclic voltammetry. For daunorubicin either alone or in the presence of DNA, the peak current gives a linear response to concentration down to about 10 nmol/dm³, suggesting further development of this technique as a clinical analytical method.

DNA-anthracycline complexes.—The data presented by Berg and co-workers on the association constant of actinomycin with DNA obtained by pulse polarography (49) and of other anthraquinones with DNA obtained by classical polarography (55) employed experiments in which the decrease of polarographic response to a fixed total concentration of the antibiotic upon successive additions of calf thymus DNA was interpreted as being due to the complexation of the antibiotic with DNA. The complex was taken as having no polarographic response (55) or (49) as having a response at the same potential as the uncomplexed antibiotic with, however, a much slower rate of diffusion due to the attachment of DNA. This interpretation seems unlikely; it is more probable that the effects observed are due to time-dependent (and possibly also potential-dependent) competitive adsorption of the antibiotic and DNA, which would also account for the observed diminution of antibiotic response with increasing DNA concentration. Such effects, while necessarily present in dc polarographic techniques, are not a complication in the present procedure only because the equilibration time at constant potential is long enough to achieve equilibrium (or at least a highly reproducible steady state), while the scan rate is fast enough to prevent significant change from equilibrium before the measurement is complete. We have found 90s a practical minimum equilibration time and 1 V/s the minimum useful scan rate to obtain reproducible results with calf thymus DNA.

Molinier-Jumel *et al.* (58) gave a value of 0.78×10^5 liter/mol phosphate for 1b with sonicated calf thymus DNA using ac polarography in aqueous solution. The compound was added in increments to a solution with a fixed DNA concentration. Our comparable value using

the reverse procedure described here is 0.52×10^5 , in reasonable agreement.

Electrode coverage by mononucleotides is undoubtedly greater than for DNA, if only because the guanine and thymine bases in DNA are not reducible though they are presumably also adsorbed. In acid (pH 3.0 ± 0.5) aqueous solution, the protonated mononucleotide adenosine gives a reduction charge of $40 \mu\text{C}/\text{cm}^2$ for the adsorbed material between -0.2 and -0.4V (36); values higher than this are obtained for the compact stage of adsorption. Protonated cytidine has about half the occupied area of adenosine (56, 57). Our values are at or below these limits (Table I).

The charge expected for a two-electron reduction of a complete or maximum daunorubicin monolayer with molecules oriented parallel to the electrode surface is $21.4 \mu\text{C}/\text{cm}^2$, while $50 \mu\text{C}/\text{cm}^2$ could be expected for the less likely perpendicular orientation. This is quite consistent with the values of 13-17 $\mu\text{C}/\text{cm}^2$ actually obtained for daunorubicin in the absence of DNA.

Conclusion

The method described herein seems well suited to studies of the influence of structural variations in both anthracycline and sugar to the binding of the anthracyclines to DNA. The association constants do not vary significantly with potential when the conditioning potential ranges from -0.4 to -1.0V against SCE, nor does the addition of 3% acetonitrile alter their values (although 30% decreases them significantly). The configuration of DNA on the electrode surface is therefore reproducibly established by the experimental conditions used and it is to that configuration that the binding occurs.

The association constant reported herein for doxorubicin (**1b**) is significantly higher than that for daunorubicin (**1a**). The same difference is found for the corresponding pairs **1d**, **1c** and **1f**, **1e**, leading to the conclusion that replacement of the hydroxyl group at R3 with hydrogen reduces binding to DNA. This is in accord with the greater ΔT_m value observed for doxorubicin than for daunorubicin, but not in accord with all of the values reported by other methods (12), which generally give values for doxorubicin of 20% lower than for daunorubicin. Values obtained with solution rather than electrode methods also tend to be consistently higher and may refer to DNA of a considerably more accessible (to anthracyclines) configuration than that on electrode surfaces.

Binding of the aglycones **2a-2d** is much less than for the anthracyclines with attached sugars. The ratio of $I(\text{inf})/I(0)$ is greater than 30%, indicating that much of the aglycone remains unbound even at mole ratios greater than 300:1 bases:aglycone. It is clear that the sugar materially assists in the binding of the anthracyclines to DNA.

Acknowledgments

The authors are grateful to Z. Kherani for experimental measurements. This work was supported by grants from the Natural Science and Engineering Research Council of Canada (to J.A.P. and to J.W.L.), and by a grant from the National Cancer Institute of Canada and a contract with the National Foundation for Cancer Research (to J.W.L.).

Manuscript submitted Nov. 28, 1983; revised manuscript received July 2, 1984.

The University of Alberta assisted in meeting the publication costs of this article.

REFERENCES

- L. S. Lerman, *J. Mol. Biol.*, **3**, 18 (1961).
- M. J. Waring, in "The Molecular Basis of Antibiotic Action," E. F. Gale, E. Cundliffe, P. E. Reynolds, M. R. Richmond and M. J. Waring, Editors, p. 173, John Wiley and Sons, New York (1972).
- F. Arcamone, in "Topics in Antibiotic Chemistry," Vol. 2, P. Sammes, Editor, p. 102, John Wiley and Sons, New York (1978).
- A. Di Marco, F. Arcamone, and F. Zunino, in "Antibiotics III—Mechanism and Action of Antimicrobial and Antitumor Agents," J. W. Corcoran and F. E. Hahn Editors, pp. 101-128, Springer, New York (1975).
- N. R. Bachur, S. L. Gordon, and M. V. Gee, *Molec. Pharmacol.*, **13**, 901 (1977).
- J. W. Lown, H. H. Chen, J. A. Plambeck, and E. M. Acton, *Biochem. Pharmacol.*, **28**, 2563 (1979).
- T. Goodman and P. Hochstein, *Biochem. Biophys. Res. Commun.*, **77**, 797 (1977).
- V. Berlin and W. A. Haseltine, *J. Biol. Chem.*, **256**, 4747 (1981).
- J. W. Lown, S. K. Sim, K. C. Majumdar, and R.-Y. Chang, *Biochem. Biophys. Res. Commun.*, **76**, 705 (1977).
- B. K. Sinha and C. F. Chignell, *Chem. Biol. Interact.*, **28**, 301 (1979).
- D. W. Henry, in "Cancer Chemotherapy," A. C. Sartorelli, Editor, ACS Symposium Series 30, American Chemical Society (1976).
- S. Neidle, in "Topics in Antibiotic Chemistry," Vol. 2, P. Sammes, Editor, p. 230, John Wiley and Sons, New York (1978).
- G. Bonadonna and S. Monfardini, *Lancet*, **1**, 837 (1969).
- B. Smith, *Br. Heart J.*, **31**, 607 (1969).
- E. Calendi, A. Di Marco, M. Reggiani, B. Scarpinato, and L. Valentini, *Biochim. Biophys. Acta*, **103**, 25 (1965).
- F. Zunino, R. Gambetta, A. Di Marco, and A. Zaccara, *ibid.*, **277**, 489 (1972).
- A. Di Marco, F. Zunino, R. Silverstrini, C. Gambarracci, and R. A. Gambetta, *Biochem. Pharmacol.*, **20**, 1323 (1971).
- A. Di Marco, A. M. Casazza, R. Gambetta, R. Supino, and F. Zunino, *Cancer Res.*, **36**, 1962 (1976).
- F. Zunino, R. Gambetta, A. Di Marco, G. Luoni, and A. Zaccara, *Biochem. Biophys. Res. Commun.*, **69**, 744 (1976).
- K. C. Tsou and K. F. Yip, *Cancer Res.*, **36**, 3367 (1976).
- D. G. Dagleish, G. Fey, and W. Kersten, *Biopolymers*, **13**, 1752 (1974).
- G. J. Baggay, D. Grier, R. E. Fingeole, R. Reimer, S. Levy, S. W. Pearce, and W. D. Wilson, *Biochem.*, **15**, 2062 (1976).
- T. R. Kough and M. A. Young, *Nature*, **269**, 627 (1977).
- W. Kersten, H. Kersten, and W. Szybalski, *Biochem.*, **5**, 236 (1966).
- A. Di Marco and F. Arcamone, *Arzneim. Forsch.*, **25**, 368 (1975).
- Y. M. Huang and D. R. Phillips, *Biophys. Chem.*, **6**, 363 (1977).
- M. J. Waring, *J. Mol. Biol.*, **54**, 247 (1976).
- B. Janik and P. J. Elving, *Chem. Rev.*, **68**, 295 (1968).
- E. Palecek, in "Progress in Nucleic Acid Research and Molecular Biology," Vol. 9, J. N. Davis and W. E. Cohn, Editors, p. 31, Academic Press, New York (1969).
- G. C. Barker and D. McKeown, *Bioelectrochem. Bioenerg.*, **3**, 373 (1976).
- B. Malfoy, J. A. Reynaud, and P. J. Sicard, *ibid.*, **1**, 126 (1974).
- B. Malfoy and J. A. Reynaud, *J. Electroanal. Chem.*, **67**, 359 (1976).
- B. Malfoy, J. A. Reynaud, and P. J. Sicard, *Bioelectrochem. Bioenerg.*, **1**, 126 (1974).
- D. Krznaric, P. Valenta, and H. W. Nürnberg, *J. Electroanal. Chem.*, **65**, 863 (1975).
- P. Valenta, H. W. Nürnberg, and D. Krznaric, *Bioelectrochem. Bioenerg.*, **3**, 418 (1976).
- D. Krznaric, P. Valenta, H. W. Nürnberg, and M. Branica, *J. Electroanal. Chem.*, **93**, 411 (1978).
- P. Valenta and P. Grahmann, *ibid.*, **49**, 41 (1974).
- P. Valenta and H. W. Nürnberg, *ibid.*, **49**, 55 (1974).
- P. Valenta, H. W. Nürnberg, and P. Klahre, *Bioelectrochem. Bioenerg.*, **1**, 487 (1974).
- P. Valenta, H. W. Nürnberg, and P. Klahre, *ibid.*, **2**, 204 (1975).
- B. Malfoy, J. M. Sequaris, P. Valenta, and H. W. Nürnberg, *ibid.*, **3**, 440 (1976).
- J. M. Sequaris, B. Malfoy, P. Valenta, and H. W. Nürnberg, *ibid.*, **3**, 461 (1976).
- H. W. Nürnberg and P. Valenta, *Croat. Chem. Acta*, **48**, 623 (1976).
- H. W. Nürnberg and P. Valenta, in "Proceedings of the Colston Conference No. 29 (Bristol 1978)," pp. 201-229, Scientifica, Bristol (1979).
- J. M. Sequaris, P. Valenta, H. W. Nürnberg, and B. Malfoy, *Bioelectrochem. Bioenerg.*, **5**, 483 (1978).
- J. M. Sequaris, P. Valenta, H. W. Nürnberg, and B. Malfoy, in "Proceeding of the Colston Conference No. 29 (Bristol 1978)," pp. 230-234, Scientifica, Bristol (1979).
- P. Valenta and H. W. Nürnberg, *Biophys. Struct. Mech.*, **1**, 17 (1974).
- J. Flemming and J. Berg, *Bioelectrochem. Bioenerg.*, **1**, 459 (1974).

49. H. Berg and H. Schütz, in "Proceedings of the Second Conference on Applied Physical Chemistry," Vol. 1, Ilova Buzas, Editor, pp. 497-489, Akad. Kiado, Budapest (1971).
50. B. Malfoy, J. M. Sequaris, P. Valenta, and H. W. Nürnberg, *J. Electroanal. Chem.*, **75**, 455 (1977).
51. G. M. Rao, J. W. Lown, and J. A. Plambeck, *This Journal*, **124**, 195 (1977).
52. G. M. Rao, A. Begleiter, J. W. Lown, and J. A. Plambeck, *ibid.*, **124**, 199 (1977).
53. G. M. Rao, J. W. Lown, and J. A. Plambeck, *ibid.*, **125**, 534 (1978).
54. G. M. Rao, J. W. Lown, and J. A. Plambeck, *This Journal*, **125**, 540 (1978).
55. H. Berg and K. Eckhardt, *Z. Naturforsch.*, **25B**, 362 (1969).
56. Y. M. Temerk, P. Valenta, and H. W. Nürnberg, *J. Electroanal. Chem.*, **100**, 77 (1979).
57. Y. M. Temerk and P. Valenta, *ibid.*, **93**, 57 (1978).
58. C. M. Molinier-Jumel, B. Malfoy, M. A. Reynaud, and G. Aubel-Sadrom, *Biochem. Biophys. Res. Commun.*, **84**, 441 (1978).
59. J. A. Plambeck, J. W. Lown, S. F. Yen, E. M. Acton, and J. H. Peters, Submitted to *Biochem. Pharmacol.*

Quantitative Comparison of Fermi Level Pinning at GaAs/Metal and GaAs/Liquid Junctions

G. Horowitz

CNRS, Laboratoire de Photochimie Solaire, 94320 Thiais, France

P. Allongue and H. Cachet

G.R.4 du CNRS, "Physique des Liquides et Electrochimie," associé à l'Université Pierre et Marie Curie, 75230 Paris Cedex 05, France

ABSTRACT

Flatband potential (V_{FB}) of (100)-oriented n-GaAs electrodes in various aqueous solutions have been determined by ac impedance measurements. The Nernstian variation of V_{FB} with pH (-60 mV/pH) was verified in both indifferent electrolytes and redox-couple solutions. Taking into account this pH dependence, the barrier height ϕ_B of the n-GaAs/liquid junction with various redox couples could be calculated. ϕ_B was determined at the point of zero zeta potential (PZZP), where the voltage drop due to specific adsorption of OH groups vanishes. A pH (PZZP) of 2.8 was estimated from published data for the electron affinity of GaAs. The variation of ϕ_B as a function of redox potential at the GaAs/liquid junction could then be quantified through the slope S of the ϕ_B (V_{redox}) straight line. A value of $S \approx 0.8$ was found, showing that Fermi level pinning is much weaker than at the GaAs/metal junction, at which one has $S \approx 0.05$. The behavior is confirmed by published data on p-GaAs and polymer-coated n-GaAs. We discuss these results within the framework of recent works on the semiconductor/metal Schottky barrier.

Considerable attention has been brought recently to the problem of Fermi level pinning at semiconductor/liquid junctions. A recent report of the Institute for Science Information on the 1980 Chemistry papers most cited in 1980-1982 (1) showed that an article by Bard *et al.* (2) devoted to this problem has been cited 60 times during that period. In this article, was presented a model to account for the fact that the photovoltage measured on semiconductor electrodes (n-GaAs, p-GaAs, and p-Si) in acetonitrile solutions of various redox couples did not follow a linear variation as a function of the redox potential as would be expected according to the classical (Schottky) model for semiconductor/liquid junction, in which the band-edge positions at the semiconductor surface are fixed with respect to the solution levels (3). The modified model advanced by Bard *et al.* referred to the concept of Fermi level pinning due to surface states, which had been first proposed by Bardeen (4) to explain the observation that for most covalent semiconductors (Si, Ge, GaAs, InP, ...) the semiconductor/metal barrier height is independent of the metal.

More recently, measurements have been reported on n-GaAs photoanodes protected against photocorrosion with various polymer films: polypyrrole (PPy) (5), polystyrene pendant $\text{Ru}(\text{bpy})_3^{2+}$ (PSt-bpy-Ru) (6), and poly-3-methylthiophene (PMeT) (7). Open-circuit voltages V_{oc} greater than 1V have been reached with such electrodes. Furthermore, a quasi-linear variation of V_{oc} with redox potential is observed, suggesting that Fermi level pinning does not occur. The question then arises whether this behavior is characteristic of the n-GaAs/liquid junction or comes from modifications in the surface states when a conducting polymer is put between the semiconductor and the solution.

However, recent investigations on the semiconductor/metal interface led to the conclusion that the phenom-

enon responsible for the narrow range of barrier heights observed on GaAs/metal junctions is not the presence of intrinsic surface states (the so-called Tamm and Shockley surface states) at the semiconductor surface. Brillson (8) attributes this narrow range to a microscopic charge redistribution at the semiconductor/metal interface that depends on the chemical reactivity of the metal coverage. More recently, measurements on (110)-cleaved GaAs in ultrahigh vacuum (UHV) led Spicer *et al.* (9) to think that the pinning is due to extrinsic surface states due to defects produced at the semiconductor surface by the presence of the metal adatoms. Bolmont *et al.* (10) think that these surface states are rather due to a reconstruction of the GaAs surface by chemical bondings of the metal atoms with the semiconductor atoms. It thus seems established that the presence of the metal is necessary to induce the surface-state distribution leading to Fermi level pinning. Since the chemical reactivity of a liquid electrolyte is different from that one of a metal, one can expect a different behavior between the two kinds of junctions as far as the barrier formation is concerned. In this paper, we report flatband potential and open-circuit potential measurements performed on PMeT-coated and bare n-GaAs in contact with aqueous solutions of various redox couples. The results suggest that Fermi level pinning is much less important at the n-GaAs/liquid junction than at the n-GaAs/metal junction. This result is compared to recently published data on p-GaAs/liquid junctions and discussed within the framework of recent theories on the semiconductor/metal junction.

Experimental

Nonintentionally doped n-type (100)-oriented GaAs single-crystal slices were purchased from RTC (Caen, France). Ohmic contacts were made by vacuum evaporating Ge (12 weight percent [w/o]) Au alloy and annealing at

400°C under N_2 . The electrodes were then mounted on glass tubes with Torr Seal (Varian) resin and the active surface polished with 1 μm diamond paste. Before each measurement, the electrode surface was chemically etched in either $H_2SO_4:H_2O_2:H_2O$ (1:1:1 volume ratio) mixture or in Br_2 -MeOH solution. Both of these etching procedures led to similar experimental results.

Electrodeposition of polymer films was performed under illumination in 0.1M supporting salt, 1M distilled 3-methylthiophene, acetonitrile solutions, as described in a previous paper (7). The thickness of the film was monitored by measuring the charge with a digital coulometer. Typical thickness was about 0.1 μm .

Electrolytic solutions were prepared with reagent-grade chemicals and doubly distilled water. The various redox couples employed are listed in Table IV. For $[Fe(CN)_6]^{4-/3-}$ and $Fe^{2+/3+}$ couples, the concentrations were 0.1M. I^-/I_3^- and Br^-/Br_2 couples were obtained by adding 0.01M I_2 and 0.1M KI, and 0.01M Br_2 and 0.1M KBr, respectively, to 0.1M H_2SO_4 solutions. $Fe^{II/III}$ citrate was prepared by adding 0.1M $Fe(ClO_4)_2$ to a solution containing 1M NaH_2 citrate and 1M $NaClO_4$. The solution was then buffered to pH 9.4 by adding ammonia. S^{2-}/S_n^{2-} solutions were obtained by equimolar dissolution of Na_2S and S in KOH or NaOH solutions. The preparation of Se^{2-}/Se_2^{2-} solutions has been described elsewhere (11).

Impedance measurements were made in a classical three-electrode cell with a saturated calomel (SCE) reference and a Pt counterelectrode. Impedance was determined over a wide frequency range by using a 1174 Solartron frequency response analyzer equipped with a data management system.

Results

The correlation between the open-circuit voltage (taken as the difference between the photocurrent onset potential V_{on} and the redox potential V_{redox}) and V_{redox} for polymer-coated n-GaAs-based PEC cells is shown in Fig. 1. The data were taken from Ref. (6) for PSt-bpy-Ru- and Ref. (7) for PMeT-protected electrodes. The slope of the least squares fit straight line is 0.81, a value close to unity. This suggests that very weak Fermi level pinning occurs at polymer-coated n-GaAs/liquid junction. A similar behavior has been reported for n-GaAs/PPy electrodes (5), although no data were given for this system.

In order to determine whether this behavior is brought by the polymer film or is characteristic of the n-GaAs/liquid junction, measurements of the flatband potential V_{FB} were carried out on PMeT-coated and bare

electrodes in various redox couples. V_{FB} was obtained by ac impedance measurements over a wide frequency range (25 Hz-250 kHz). Impedance data were analyzed by means of a nonlinear least squares fit method, according to the equivalent circuits given in Fig. 2. In the complete circuit (Fig. 2a) the Helmholtz layer capacitance C_H is generally omitted since it is at least two orders of magnitude greater than the space charge layer capacitance C_{sc} . Analyses according to this complete circuit led to low values for the dispersion capacitance C_{ss} ($C_{ss}/C_{sc} < 0.1$), suggesting a low density of surface states. Consequently, most of the impedance data could be analyzed according to the simplified circuit given in Fig. 2b. Typical values for the series and parallel resistances R_s and R_p are 10 $\Omega \cdot \text{cm}^2$ and 10,000 $\Omega \cdot \text{cm}^2$, respectively. Good linear Mott-Schottky (M-S) plots for C_{sc} were obtained in all cases, for both polymer-coated and bare electrodes. The average of the slopes gave a donor concentration of $2.8 (\pm 0.2) \times 10^{16} \text{ cm}^{-3}$. The value given by the manufacturer is $1.9 \times 10^{16} \text{ cm}^{-3}$. This slight increase corresponds to a roughness factor of 1.2.

Table I gives the values for V_{FB} obtained on bare and PMeT-coated n-GaAs in I^-/I_3^- , $Fe^{2+/3+}$, and Br^-/Br_2 solutions. If we discard the measurement on coated electrode in $Fe^{2+/3+}$ solution, a mean value of $-0.88 \pm 0.04 \text{ V/SCE}$ is obtained. The mean deviation is inside the range of experimental error (a mean deviation of $\pm 0.5 \text{ V}$ is generally taken for impedance determinations of V_{FB}) and two main results can then be deduced from the data given in Table I: (i) V_{FB} is equivalent at bare and PMeT-covered electrodes. Again, a similar invariance has been observed on PPy- (5) and PSt-bpy-Ru-coated n-GaAs (6). (ii) V_{FB} does not depend upon the redox potentials, at least over the potential range covered by the three redox couples used.

It was, of course, necessary to extend the potential range of our V_{FB} determinations towards more negative values of V_{redox} , but some preliminary measurements had to be done in order to check the dependence of the flatband potential upon two other parameters of the solution: pH and redox-ion concentration.

The variation of V_{FB} with pH in indifferent electrolyte solutions is shown in Fig. 3. Data were obtained on (100)-oriented n-GaAs. Other data on the same orientation reported by Janietz *et al.* (12) and Haroutiounian *et al.* (13) are also drawn in Fig. 3, together with data reported by Lafere *et al.* (14) on (111)-oriented GaAs surface. The slope of the least squares fit straight line is -60 mV/pH with a correlation factor of 0.997. The well-known Nernstian behavior (3) is then observed on both surface orien-

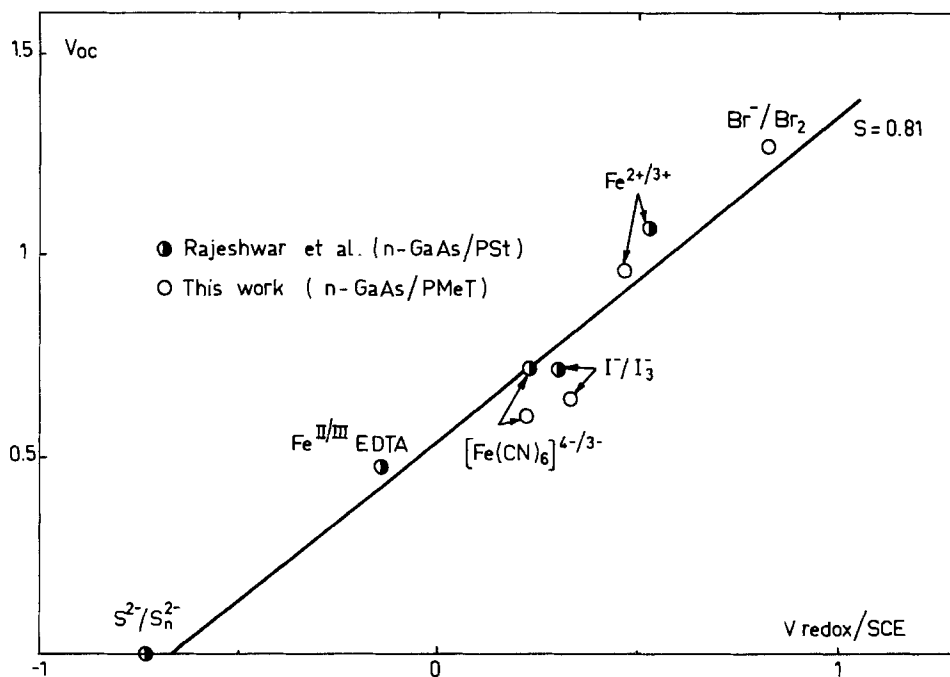


Fig. 1. Variation of the open-circuit potential V_{oc} (taken as the difference between the onset potential and redox potential) at PMeT- and PSt-bpy-Ru-coated n-GaAs in aqueous solutions of various redox couples. Data for GaAs/PSt taken from Rajeshwar *et al.* (6).

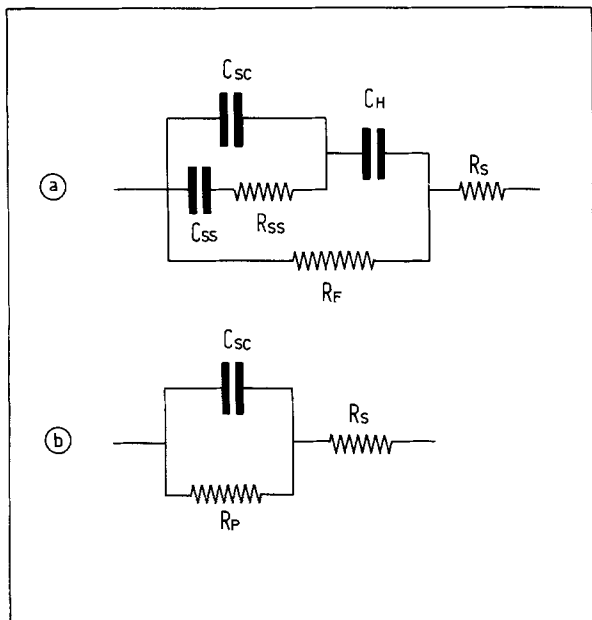


Fig. 2. (a): Equivalent circuit of a semiconductor/liquid junction. C_{sc} : space charge layer capacitance; C_H : Helmholtz layer capacitance; C_{ss} and R_{ss} : surface-state capacitance and resistance; R_F : Faradaic resistance; R_s : series resistance. (b): Simplified equivalent circuit used for analyzing impedance data.

tations. This result disagrees with that one reported by Rajeshwar and Mraz (15), who found a slope of -15 mV/pH on (100)-oriented n-GaAs.

The pH variation of V_{FB} was also measured with a redox couple added to the solution. The ideal redox couple for such a measurement is $[\text{Fe}(\text{CN})_6]^{4-/3-}$, which is soluble at all pH. Furthermore, its redox potential remains constant at $+0.22$ V/SCE, except at $\text{pH} < 2$, where it shifts towards positive potentials. Figure 3 shows that V_{FB} is shifted to positive potentials in the presence of $[\text{Fe}(\text{CN})_6]^{4-/3-}$ couple. Importantly, V_{FB} still follows a Nernstian behavior:

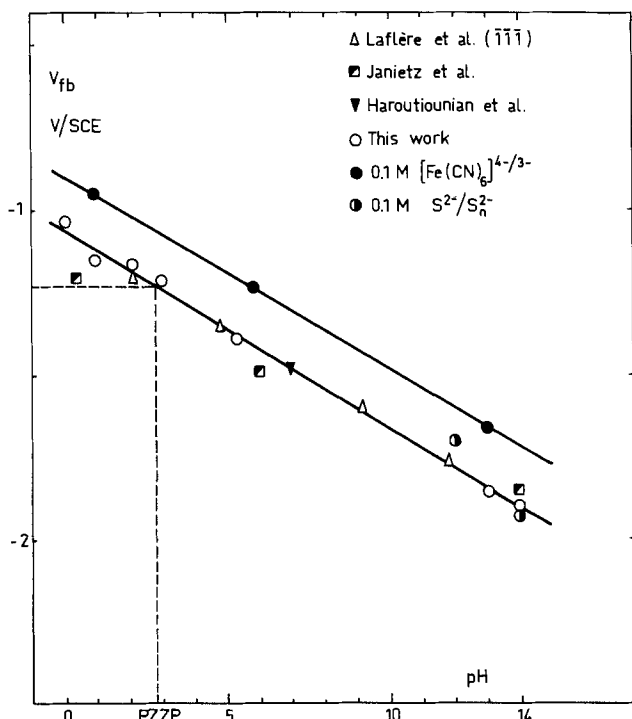


Fig. 3. Variation of the flatband potential V_{FB} as a function of the pH of the solution, for redox-free, and $[\text{Fe}(\text{CN})_6]^{4-/3-}$ and $\text{S}^{2-}/\text{S}_n^{2-}$ containing solutions. Dotted line shows the determination of the PZZP (see text). Data were taken from Ref. (12-14). All data on (100) GaAs unless otherwise stated.

Table I. Redox and flatband potentials of bare and PMeT-covered n-GaAs in three different redox couples. All solutions have a pH of 0.9 (0.1M H_2SO_4)

Redox couple	$V_{\text{redox}}/\text{SCE}$	V_{FB}/SCE	
		Bare	PMeT-coated
I^-/I_3^- $\text{Fe}^{2+}/\text{Fe}^{3+}$ (H_2SO_4 0.1M)	0.33	-0.81	-0.87
	0.42	-0.89	-0.71
	0.83	-0.91	-0.92

the slope of the least squares fit straight line is -59 mV/pH, which is the exact theoretical value. The variation of V_{redox} at low pH does not induce any deviation of V_{FB} . This confirms the independence of V_{FB} with V_{redox} .

Similar experiments were made with $\text{S}^{2-}/\text{S}_n^{2-}$ couple at pH 12 and 14. No significant shift of V_{FB} is observed when this redox couple is added to the solution, and a similar pH dependence is obtained. We shall then assume in the following that the flatband potential always follows a Nernstian variation with pH for all redox couples added to the solution.

The last preliminary verification was to check the variation of V_{FB} with redox-ion concentration. Experiments were made with various concentrations of $[\text{Fe}(\text{CN})_6]^{4-/3-}$ at pH 13 (0.1M KOH) and $\text{S}^{2-}/\text{S}_n^{2-}$ at pH 14 (1M KOH). Results are given in Table II and III. A mean value of -1.90 ± 0.04 V/SCE is obtained with $\text{S}^{2-}/\text{S}_n^{2-}$ couple: this variation is within the experimental error. As far as $[\text{Fe}(\text{CN})_6]^{4-/3-}$ couple is concerned, the variation occurring between 10^{-3} and 10^{-4} M corresponds to the shift observed in Fig. 3: the flatband potential behaves as if the effect of the redox-couple disappears when its concentration is lower than 10^{-3} M. Anyhow, we are still far from the -59 mV/decade variation reported by Ginley and Butler (16) for the CdS/ Na_2S junction, which was attributed to an adsorption of HS^- ions at the CdS surface. We can then assume that V_{FB} is insensitive to the redox ion concentration.

The flatband potential was determined for two more redox couples: $\text{Se}^{2-}/\text{Se}_2^{2-}$ (pH 14) and $\text{Fe}^{\text{III}}/\text{citrate}$ (pH 9.4). All our results are gathered in Table IV. The value corresponding to H_2/H^+ couple was taken from Fig. 3. In order to compare the results obtained for all redox couples, V_{FB} data were recalculated at $\text{pH} = 2.8$ by assuming a variation of -59 mV/pH. The reasons for this choice will be explicated in the discussion section. All data obtained on bare electrodes are plotted in Fig. 4, together with the values measured on PMeT- and PSt- [from Ref. (6)] coated n-GaAs. The redox-potential range is now almost 2V, and a slight variation of V_{FB} can be noted, with a slope of ca. 0.2.

Discussion

The classical model of the semiconductor/metal barrier was first developed by Schottky (17). This model pre-

Table II. Flatband potential of n-GaAs in 0.1M KOH (pH 13) with various concentrations of $[\text{Fe}(\text{CN})_6]^{4-/3-}$ ions

$[\text{Fe}(\text{CN})_6]^{4-/3-}$	V_{FB}/SCE
10^{-1}M	-1.66
10^{-2}M	-1.63
10^{-3}M	-1.83
10^{-5}M	-1.89

Table III. Flatband potential of GaAs in 1M KOH (pH 14) with various concentrations of $[\text{S}^{2-}/\text{S}_n^{2-}]$ ions

$[\text{S}^{2-}/\text{S}_n^{2-}]$	V_{FB}/SCE
1M	-1.85
10^{-1}M	-1.92
10^{-3}M	-1.93
10^{-4}M	-1.88

Table IV. Redox potentials, flatband potentials, and barrier heights of bare n-GaAs in various redox couple aqueous solutions. Data for H_2/H^+ couple taken from Fig. 3. Barrier height ϕ_B calculated from Eq. [3] with $\Delta V_{fc} = 0.07V$ (see text)

Redox couple	V_{redox}/SCE	ϕ_{redox} (eV)	V_{FB}/SCE	pH	V_{FB}/SCE	ϕ_B (eV)
Se^{2-}/Se_2^{2-}	-0.95	3.95	-2.05	14	-1.39	0.51
S^{2-}/S_n^{2-}	-0.73	4.17	-1.90	14	-1.24	0.58
$Fe^{II/III}$ citrate	-0.43	4.47	-1.70	9.4	-1.31	0.95
$[Fe(CN)_6]^{4-}/3-$ (0.1M KOH)	+0.22	5.12	-1.66	13	-1.06	1.35
$[Fe(CN)_6]^{4-}/3-$ (0.1M H_2SO_4)	+0.30	5.20	-0.95	0.9	-1.06	1.41
I^-/I_3^-	+0.33	5.23	-0.81	0.9	-0.92	1.32
$Fe^{2+}/3+$ (0.1M H_2SO_4)	+0.42	5.32	-0.89	0.9	-1.00	1.49
Br^-/Br_2	+0.83	5.73	-0.91	0.9	-1.02	1.92
H_2/H^+ (pH 2.8)	-0.41	4.49	-1.23	2.8	-1.23	0.86

dicts that the barrier height ϕ_B should be given (for an n-type semiconductor) by the difference between the metal work function ϕ_m and the semiconductor electron affinity χ_s . The concept of Fermi level pinning was first introduced by Bardeen (4) to explain the observed independence of the barrier height upon the metal work function for some semiconductors. This phenomenon was believed to result from a significant density of intrinsic (Tamm and Shockley) surface states at the semiconductor surface. Later, Cowley and Sze (18) showed that the Schottky and Bardeen models are the limiting cases of a more general expression for the barrier height that can be reduced to Eq. [1]

$$\phi_B = S\phi_m + \text{const.} \quad [1]$$

where S is dimensionless parameter depending on the semiconductor. From the study of the value of S for a large number of semiconductors, Kurtin *et al.* (19) showed that S can be quantitatively related to the ionicity of the semiconductor, which they measured as the difference ΔX in the electronegativities of the two constituents

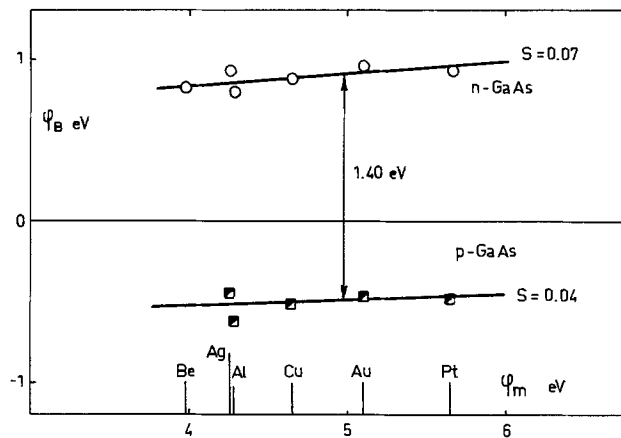
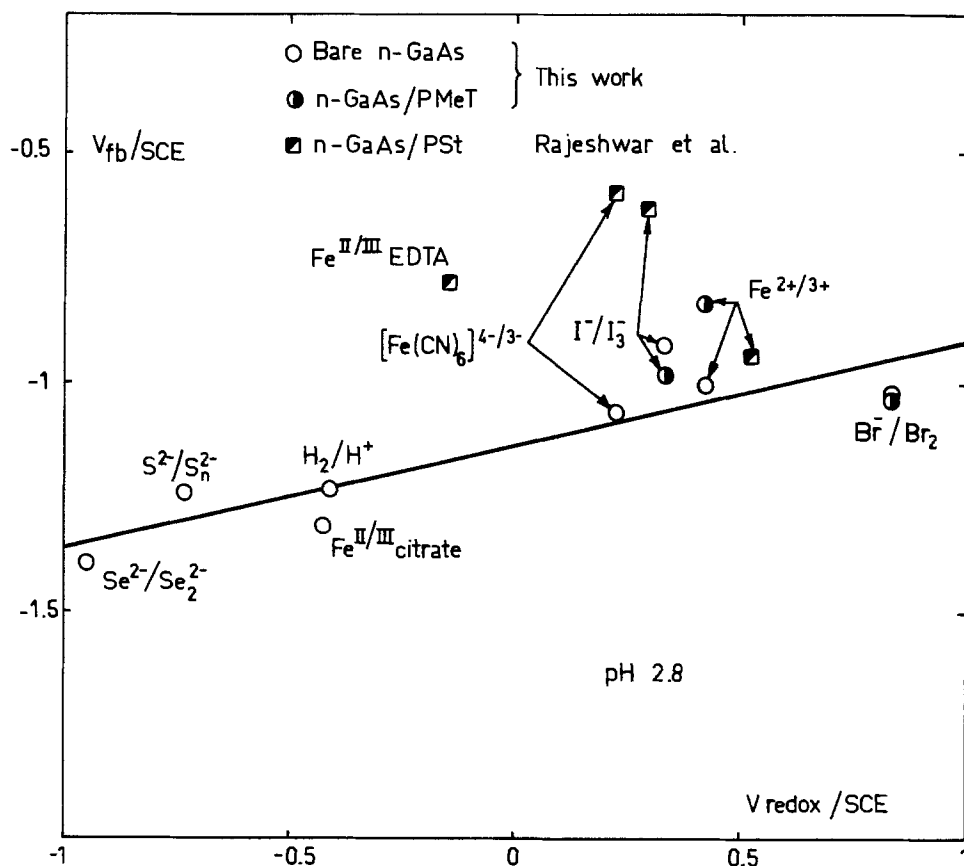


Fig. 5. Variation of the Schottky barrier height ϕ_B of a GaAs/metal junction as a function of the metal work function ϕ_m . Data for ϕ_B taken from Ref. (20), and for ϕ_m from Ref. (21).

of the semiconductor compounds (ΔX is taken as 0 in the case of an element semiconductor): S remains small for $\Delta X < 0.7$ and then changes rapidly to a value equal to unity when $\Delta X > 0.7$. A fundamental difference was then shown between ionic (*e.g.*, oxide) and covalent (*e.g.*, III-V compound) semiconductors. A similar result was obtained by Brillson (8) by taking the heat of compound formation as the measure of the ionicity.

The variation of ϕ_B with ϕ_m for GaAs is shown in Fig. 5. Data for ϕ_B were taken from Ref. (20). They were obtained by capacitance measurements on vacuum-cleaved surfaces. Recent determinations of metal work functions were taken from Ref. (21). A value of S of 0.07 is obtained for n-type and 0.04 for p-type GaAs. A quantitative comparison of Fermi level pinning at GaAs/metal and GaAs/liquid junctions can be made by calculating the value of S at the GaAs/liquid junctions. Figure 6 shows how ϕ_B can be determined from the value of V_{FB} . The dependence of the flatband potential as a function of the

Fig. 4. Variation of the flatband potential with the redox potential at bare and polymer-coated GaAs. Values of V_{FB} recalculated for a pH of 2.8 by assuming a variation -59 mV/pH. Data for PSt-coated GaAs taken from Ref. (6).



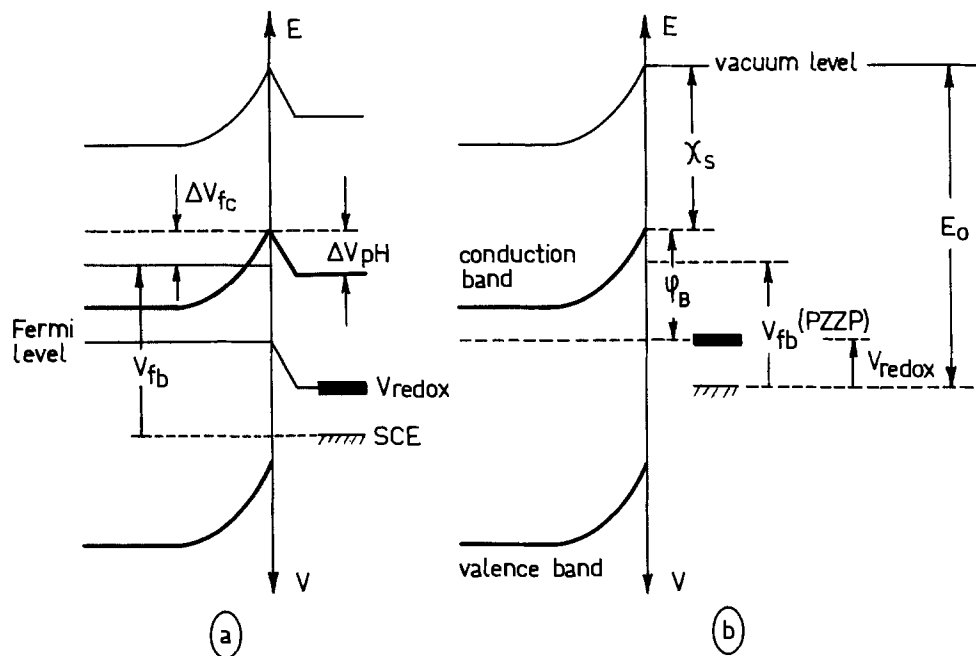


Fig. 6. Energetic diagram of an n-type semiconductor/liquid junction at equilibrium (a) general case and (b) at the point of zero zeta potential. Flatband (V_{FB}) and redox (V_{redox}) potentials are referred to SCE level; semiconductor electron affinity χ_s is defined with respect to the vacuum level. Energy and potential scales may be related through the equation: $E = E_0 + qV$, where q is the absolute electron charge. The meaning of other symbols is given in text. The variations of the vacuum level represent the existence of local electric fields.

pH is taken into account through a potential drop ΔV_{pH} due to specific OH groups adsorption (Fig. 6a). As pointed out by Butler and Ginley (22), there exists a value of the pH where $\Delta V_{pH} = 0$, called the point of zero zeta potential (PZZP) (Fig. 6b). This point can be determined from the value of the electronic affinity of the semiconductor χ_s through Eq. [2]

$$\chi_s = E_0 + q[V_{FB}(PZZP) - \Delta V_{fc}] \quad [2]$$

where E_0 is a constant relating the reference electrode to the vacuum level and $\Delta V_{fc} = (kT/q) \ln(N_c/N_d)$ the difference between the Fermi and the bottom of the conduction band (N_c is the density of states at the bottom of the conduction band, and N_d the donor impurity concentration). For n-GaAs and $N_d = 10^{16} \text{ cm}^{-3}$, one has $\Delta V_{fc} = 0.07 \text{ V}$. ϕ_B can then be calculated by using Eq. [3]

$$\phi_B = q[V_{redox} - V_{FB}(PZZP) + \Delta V_{fc}] \quad [3]$$

For the SCE a value of 4.75 eV is often taken for E_0 (23). More recent determinations gave $E_0 = 4.97 \text{ eV}$ (24). We shall take a value of 4.9 eV for E_0 . The electron affinity of GaAs has been reported from photoelectric measurements to be 4.07 eV for the (110) face (25) and 3.63 eV for the (111) face (26).

A discussion on Schottky-barrier height measurements by Geppert *et al.* led to a value of 3.57 eV (27). However, a theoretical value for χ_s can be calculated according to Mulliken (28) and Nethercot (29) by using the following relations

$$\chi_s = E_F^i - 1/2 E_g \quad [4]$$

$$E_F^i = (M_A M_B)^{1/2} \quad [5]$$

$$M_A = 1/2 (I_1 + A_r) \quad [6]$$

where E_F^i is the intrinsic Fermi level, E_g the bandgap, M_A the Mulliken potential of element A, I_1 the first ionization potential, and A_r the atomic electron affinity. Values for I_1 and A_r can be found in Ref. (21) and (30). We calculated an electron affinity of 3.40 eV for GaAs. From these four different determinations, a reasonable value of 3.60 eV can be assumed for χ_s . It can now be seen that at the PZZP we have $V_{FB} = (\chi_s - E_0)/q + \Delta_{fc} = 3.60 - 4.9 + 0.07 = -1.23 \text{ V/SCE}$. By carrying this value in Fig. 3, the point of zero potential is found to occur at pH = 2.8.

Values for ϕ_B calculated from Eq. [3] are given in Table IV, along with the redox "work function" ϕ_{redox} , which we define as

$$\phi_{redox} = E_0 + qV_{redox}$$

A plot of these data is given in Fig. 7. A value of $S = 0.78$ is obtained. This value is very close to that one deduced from V_{oc} measurements (Fig. 1) and again suggests a very slight Fermi level pinning at the n-GaAs/aqueous solution interface.

Also shown in Fig. 7 are values of the barrier height at a p-GaAs/acetonitrile-solution junction, calculated from flatband potential measurements recently reported by Nagasubramanian *et al.* (31). Equation [3] was used for this calculation, with $\Delta V_{fc} = 0.12 \text{ V}$. Data were not corrected for a ΔV_{pH} because this kind of correction is not likely to occur in acetonitrile solutions. A value of $S = 0.69$ is obtained. The mean difference between the two straight lines for n- and p-type GaAs is 1.40 eV, a value very close to the bandgap (1.43 eV). However, this result may be fortuitous because of the uncertainty on the values for χ_s and E_0 . Moreover, the SCE scale may be shifted from water to acetonitrile solutions.

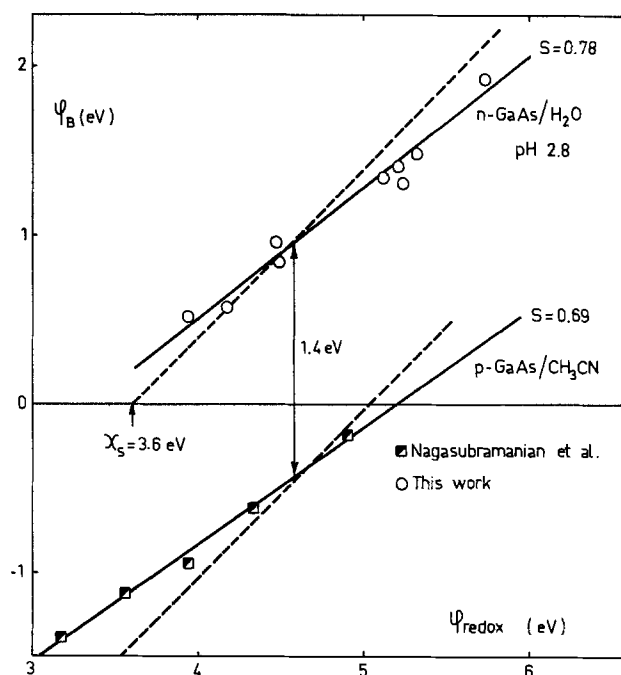


Fig. 7. Same as Fig. 5 for a GaAs/liquid junction. ϕ_B taken from Table IV for n-GaAs and calculated from data in Ref. (31) by using Eq. [2] for p-GaAs. Dotted line gives the values of ϕ_B that would be expected in the absence of Fermi level pinning.

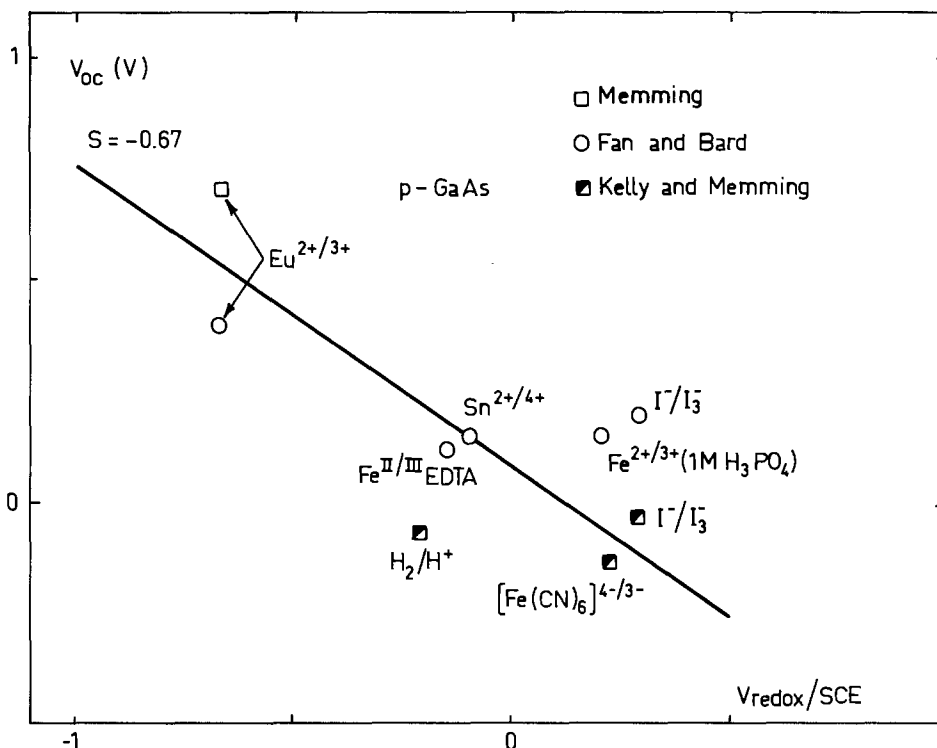


Fig. 8. Same as Fig. 1 for a bare p-GaAs electrode. Data taken from Ref. (32-34).

Finally, Fig. 8 shows the variation of the open-circuit potential for a p-GaAs/aqueous solution junction. Data were taken from Ref. (32-34). As previously, V_{oc} was taken as $V_{on} - V_{redox}$. Negative values of V_{oc} correspond to systems unable to work as energy converters. The slope of the straight line is -0.67 (this slope is negative because we are now dealing with a p-type semiconductor), in excellent agreement with the value deduced from flatband potential measurements.

The dispersion of the data in Fig. 8 can be explained by the fact that the onset potential of a semiconductor/liquid junction is not uniquely determined by the position of the bandedges at the semiconductor surface but also by the kinetics of electron transfers at the interface. A similar dispersion may be observed in Fig. 1.

A quantitative comparison of Fermi level pinning between GaAs/metal and GaAs/liquid junctions can now be made with the help of the parameter S . Figures 5 and 7 unambiguously show that Fermi level pinning at GaAs/liquid junction is considerably less pronounced than at GaAs/metal junction. This is the main result of this paper and it will now be discussed. From the classical Bardeen theory of Fermi level pinning by intrinsic surface states, one should expect from Fig. 5 a distribution of surface states centered at about 0.5 eV above the top of the valence band. From results of several experimental groups, it now appears firmly established that there is no intrinsic surface states in the bandgap of GaAs [see, e.g., Ref. (9) and references therein]. This is explained by a lattice rearrangement (or relaxation) of the surface, which moves the surface states out of the bandgap. The Fermi level pinning is then attributed to extrinsic surface states brought by the metal deposition, either through defects produced at the semiconductor surface (9) or by a restoration of the initial (nonrelaxed) surface (10). However, Brillson (8) suggests that the concept of Fermi level pinning should be replaced by that of microscopic charge redistribution at the semiconductor/metal junction, controlled by the degree of chemical reactivity between the semiconductor and metal atoms. The common characteristic of these models is that the "Fermi level pinning" at the semiconductor/metal junction is mainly induced by chemical reactions between the semiconductor and the metal overlayer. From our results and the preceding models, it can be concluded that the chemical reactivity of an aqueous electrolyte with GaAs sur-

faces is not able to induce a surface-state distribution sufficiently high to promote full Fermi level pinning.

However, a slight degree of Fermi level pinning is observed at GaAs/liquid junctions. Some ideas can be put forward to give the beginning of an explanation for this phenomenon: (i) Recent investigations on the kinetics of charge transfer at both n-type (35) and p-type (34) GaAs/liquid junctions under illumination suggest that (extrinsic or intrinsic) surface states do exist at the GaAs surface, but that the occupation rate of these states depends on kinetic factors. This is proved particularly by the shift of V_{FB} under illumination, and the fact that no surface states can be detected in the dark. (ii) A GaAs surface in contact with an aqueous or acetonitrile solution is far more "dirty" than a UHV-cleaved face. The formation of oxides has been shown to occur by simply dipping GaAs in water (36). The presence of extrinsic surface states is then likely, since it has been shown that the chemisorption of a submonolayer of oxygen suffices to induce such states (9).

As a final remark, the weak Fermi level pinning at the GaAs/liquid junction should permit high open-circuit voltages. Such high values have been already observed at polymer-protected n-GaAs electrodes with oxidizing redox couples such as $Fe^{2+/3+}$, I^-/I_3^- , or Br^-/Br_2 . Similar results can be expected with p-GaAs and reducing redox systems. This idea is supported by a value of 0.7V measured by Memming (32) on a p-GaAs/ $Eu^{2+/3+}$ cell. This result is noteworthy since the barrier height at p-GaAs/metal junction is always lower than 0.5V.

Acknowledgments

The authors are very grateful to Dr. C. A. Sebenne (Laboratoire de Physique des Solides, Université Pierre et Marie Curie, Paris, France) and Dr. F. Garnier (Laboratoire de Photochimie Solaire, CNRS, Thiers, France) for valuable discussions. This work was supported by the GRECO 130061 of the CNRS.

Manuscript submitted March 15, 1984; revised manuscript received June 4, 1984.

REFERENCES

1. E. Garfield, *Current Contents*, **35**, 5 (1983).
2. A. J. Bard, A. B. Bocarsly, F.-R. F. Fan, E. G. Walton, and M. S. Wrighton, *J. Am. Chem. Soc.*, **102**, 3671, (1980).
3. H. Gerischer, in "Physical Chemistry: An Advanced

- Treatise," Vol. IXA, H. Eyring, D. Henderson, and W. Sost, Editors, p. 467, Academic Press, New York (1970).
4. J. Bardeen, *Phys. Rev.*, **71**, 717 (1947).
 5. R. Noufi, D. Tench, and L. F. Warren, *This Journal*, **127**, 2310 (1980).
 6. K. Rajeshwar, M. Kaneko, and A. Yamada, *ibid.*, **130**, 38 (1983).
 7. G. Horowitz, G. Tourillon, and F. Garnier, *ibid.*, **131**, 151 (1984).
 8. L. J. Brillson, *Phys. Rev. Lett.*, **40**, 260 (1978); *J. Vac. Sci. Technol.*, **16**, 1137 (1979).
 9. W. E. Spicer, P. W. Chye, P. R. Skeath, C. Y. Su, and I. Lindau, *ibid.*, **16**, 1422 (1979).
 10. D. Bolmont, P. Chen, V. Mercier, and C. A. Sebenne, in "Proceedings of the 16th International Conference on Physics of Semiconductors," Montpellier, France, Sept. 6-10, 1982; *Physica B&C*, **117**, **118**, 816 (1983).
 11. A. Bourrasse, H. Cachet, G. Horowitz, and S. Le Crom, *Rev. Phys. Appl.*, **17**, 801 (1982).
 12. P. Janietz, R. Weiche, J. Westfahl, R. Landsberg, and R. Dehmlow, *J. Electroanal. Chem.*, **106**, 23 (1980).
 13. E. Haroutiounian, J.-P. Sandinu, P. Clechet, P. Lamouche, and J.-R. Martin, *This Journal*, **131**, 27 (1984).
 14. W. H. Laflere, F. Cardon, and W. P. Gomes, *Surf. Sci.*, **59**, 401 (1976).
 15. K. Rajeshwar and T. Mraz, *J. Phys. Chem.*, **87**, 742 (1983).
 16. D. S. Ginley and M. A. Butler, *This Journal*, **125**, 1968 (1978).
 17. W. Schottky, *Naturwiss.*, **26**, 843 (1938).
 18. A. M. Cowley and S. M. Sze, *J. Appl. Phys.*, **36**, 3212 (1965).
 19. S. Kurtin, T. C. McGill, and C. A. Mead, *Phys. Rev. Lett.*, **22**, 1433 (1969); T. C. McGill, *J. Vac. Sci. Technol.*, **11**, 935 (1974).
 20. C. A. Mead and W. G. Spitzer, *Phys. Rev.*, **134**, A713 (1964).
 21. "CRC Handbook of Chemistry and Physics," 61st ed., R. C. Weast, Editor, pp. E83-84, CRC Press, Cleveland, OH (1981).
 22. M. A. Butler and D. S. Ginley, *This Journal*, **125**, 228 (1978).
 23. F. Lohmann, *Z. Naturforsch., Teil A*, **22**, 813 (1967).
 24. R. Gomer and G. Tryson, *J. Chem. Phys.*, **66**, 4413 (1977).
 25. G. W. Gobeli and F. G. Allen, *Phys. Rev. A*, **137**, 245 (1965).
 26. J. Wojas, *Acta Phys. Polonica*, **35**, 1025 (1969).
 27. D. V. Geppert, A. M. Cowley, and B. V. Dore, *J. Appl. Phys.*, **37**, 2458 (1966).
 28. R. S. Mulliken, *J. Chem. Phys.*, **2**, 782 (1934); *ibid.*, **3**, 373 (1935).
 29. A. H. Nethercot, Jr., *Phys. Rev. Lett.*, **33**, 1088 (1974).
 30. H. Hotop and W. C. Lineberger, *J. Phys. Chem. Ref. Data*, **4**, 539 (1975).
 31. G. Nagasubramanian, B. L. Wheeler, and A. J. Bard, *This Journal*, **130**, 1680 (1983).
 32. R. Memming, *ibid.*, **125**, 117 (1978).
 33. F.-R. F. Fan and A. J. Bard, *J. Am. Chem. Soc.*, **102**, 3677 (1980).
 34. J. J. Kelly and R. Memming, *This Journal*, **129**, 730 (1982).
 35. P. Allongue, H. Cachet, and G. Horowitz, *ibid.*, **130**, 2352 (1983).
 36. H. Cachet, R. Calsou, M. Froment, and H. Mathlouthi, *J. Microsc. Spectrosc. Electron.*, **7**, 9 (1982).

Mathematical Modeling of Liquid-Junction Photovoltaic Cells

I. Governing Equations

Mark E. Orazem¹ and John Newman*

Materials and Molecular Research Division of Lawrence Berkeley Laboratory and Department of Chemical Engineering, University of California, Berkeley, California 94720

ABSTRACT

The equations which govern the liquid-junction photovoltaic cell are presented in the context of a one-dimensional mathematical model. This model treats explicitly the semiconductor, the electrolyte, and the semiconductor-electrolyte interface in terms of potentials and concentrations of charged species. The model incorporates macroscopic transport equations in the bulk of the semiconductor and electrolyte, coupled with a microscopic model of the semiconductor-electrolyte interface. Homogeneous and heterogeneous recombination of electron-hole pairs is included within the model. Recombination takes place at the semiconductor-electrolyte interface through interfacial sites, which can enhance the recombination rate. The coupled nonlinear ordinary differential equations of the model were posed in finite-difference form and solved numerically. The results are presented in succeeding papers.

The liquid-junction photovoltaic cell is an electrochemical system with one or two semiconducting electrodes. This system has undergone intense study since the early 1970's as a means of converting solar energy to chemical or electrical energy (1-8). A number of articles review the physics of the liquid-junction cell, the role of the semiconducting electrode, and the literature [see e.g., Ref. (9-19)].

A mathematical model is presented here which treats explicitly all components of the liquid-junction photovoltaic cell. The results of the model, obtained through numerical computation, are used to gain insight into the cell behavior and into the factors influencing cell design.

Development of a mathematical model constitutes an important step toward understanding the behavior and predicting the performance of the liquid-junction photovoltaic cell. Coupled phenomena govern the system, and the equations describing their interaction cannot, in general, be solved analytically. Two approaches have been

taken in developing a mathematical model of the liquid-junction photovoltaic cell: approximate analytic solution of the governing equations and numerical solution. These are reviewed elsewhere (20).

The use of a digital computer in the numerical solution of the equations governing the liquid-junction cell eliminates the need for restrictive assumptions. The numerical approach was taken in this work (20) and has been used in the modeling of solid-state devices (21-26). Laser and Bard (27-30) developed a computer program which was used to calculate open-circuit photopotentials, the transient behavior of the system following charge injection, and the time dependence of photocurrents in liquid-junction cells. Time-dependent material balances of holes and electrons and Poisson's equation described the semiconductor. The interface was included in terms of charge and flux boundary conditions. The model was limited by lack of convergence for electrode thicknesses greater than that of the space-charge region and did not treat explicitly the electrolyte and counterelectrode.

A number of computer programs related to the liquid-junction photovoltaic cell have been developed. Leary et al. (31), for example, calculated carrier concentrations in

* Electrochemical Society Active Member.

¹ Present address: Department of Chemical Engineering, University of Virginia, Charlottesville, Virginia 22901.

polycrystalline films using a numerical solution of Poisson's equation coupled with overall charge neutrality within spherical grains. Their model was used for analysis of semiconductor gas sensors. A computer program has been presented by Davis and colleagues (32-34) which uses simultaneous calculation of surface and solution equilibrium states to obtain the equilibrium condition of electrical double layers.

Physical Model

A one-dimensional representation of the liquid-junction photovoltaic cell is presented in Fig. 1. This model includes macroscopic representations of the counterelectrode, the electrolytic solution, and the semiconductor coupled with a microscopic representation of the interface between the semiconductor and the solution. The semiconductor-electrolyte interface couples the macroscopic equations which govern the adjacent bulk phases.

The interface is represented by four planes, inner and outer Helmholtz planes on the electrolyte side of the interface and inner and outer surface states on the semiconductor side. The outer Helmholtz plane (OHP) is the plane of closest approach for (hydrated) ions associated with the bulk solution. The inner Helmholtz plane (IHP) passes through the center of ions specifically adsorbed on the semiconductor surface. The outer surface state (OSS) represents the plane of closest approach for electrons (and holes) associated with the bulk of the semiconductor. The inner surface state (ISS) is a plane of surface sites for adsorbed electrons.

This model of the semiconductor-electrolyte interface is an extension of the classical diffuse-double-layer theory (35-37). Charge adsorbed onto the IHP and the ISS planes is balanced by charge in the diffuse region of the electrolyte and the space-charge region of the semiconductor. The net charge of the interface, including surface planes and diffuse and space-charge regions, is equal to zero.

Within the model, single-step reactions relate concentrations and potentials at interfacial planes. A continuous spectrum of energy levels at the ISS is represented by three discrete energy levels (designated *v*, *t*, and *c*). Conduction electrons are adsorbed via reaction [1] (see the interface in Fig. 1) from the OSS to high-energy sites at the ISS, via reaction [10] to intermediate energy sites at the ISS, and via reaction [11] to low energy sites at the ISS. Via reaction [2], low-energy electrons at the ISS can oc-

cupy vacancies in the valence band, or holes, at the OSS. Intermediate energy electrons can transfer from the ISS to the OSS through reaction [12], and high energy electrons can transfer through reaction [13]. Reactions [3] and [4] allow the shifting of electrons from one energy level to another.

Ionic species from the solution are adsorbed into the IHP by reactions [8] and [9]. Two adsorbed species are considered here. It is assumed that other ionic species in the solution do not adsorb and do not participate in the electrochemical reactions. Relaxation of this assumption involves the inclusion of additional ion-adsorption and charge-transfer reactions. Reactions [5], [6], and [7] are the charge-transfer reactions that take place among adsorbed ions at the IHP and adsorbed high, intermediate, or low energy electrons at the ISS. Charge-transfer reactions allow passage of electrical current from the semiconductor to the solution.

Theoretical Development

The equations governing the liquid-junction photovoltaic cell in the dark or under steady-state illumination are developed here in terms of the model presented above. The governing relationships can be developed separately for the semiconductor and the electrolyte. The microscopic model of the semiconductor-electrolyte interface couples the equations governing the macroscopic systems.

Semiconductor.—The electrochemical potential of a given species can arbitrarily be separated into terms representing a reference state, a chemical contribution, and an electrical contribution

$$\mu_i = \mu_i^0 + RT \ln (c_i f_i) + z_i F \Phi \quad [2]$$

where Φ is a potential which characterizes the electrical state of the phase and can be arbitrarily defined. The potential used here is the electrostatic potential which is obtained through integration of Poisson's equation (38). Equation [2] can be viewed as the defining equation for the activity coefficient, f_i .

The flux of an individual species within the semiconductor is driven by a gradient of electrochemical potential, which corresponds to gradients of potential and concentration [see *e.g.*, Chap. 11 in Ref. (39) and Gerischer (40)]. Under the assumption that the individual ionic activity coefficients are constant with a value of one,² the flux of holes is given by

$$N_{h^+} = -u_{h^+} F p \frac{d\Phi}{dy} - D_{h^+} \frac{dp}{dy} \quad [3]$$

and the flux of electrons by

$$N_{e^-} = u_{e^-} F n \frac{d\Phi}{dy} - D_{e^-} \frac{dn}{dy} \quad [4]$$

The concentrations of electrons and holes are represented by n and p , respectively, and the mobilities u_i are related to the diffusivities D_i by the Nernst-Einstein equation

$$D_i = RT u_i \quad [5]$$

Homogeneous reaction takes place in the semiconductor; thus a material balance for a given species, say holes,³ yields

² The assumption of constant activity coefficients, valid for dilute solutions, is appropriate for most semiconductors. The carrier concentrations in semiconductors is usually less than 0.0001M, which is low as compared to dilute aqueous solutions. The assumption of constant activity coefficients is in harmony with a Boltzmann distribution of electrons and holes. Use of Fermi-Dirac distributions for these charged species results in activity coefficients that are functions of concentration [see Ref. (46)].

³ The development presented here, while applicable to p-type semiconductors, is oriented toward analysis of an n-type semiconductor in which holes are the minority carrier. Material balances of holes and electrons are not independent, and conservation of the minority carrier was chosen to improve the numerical computational accuracy.

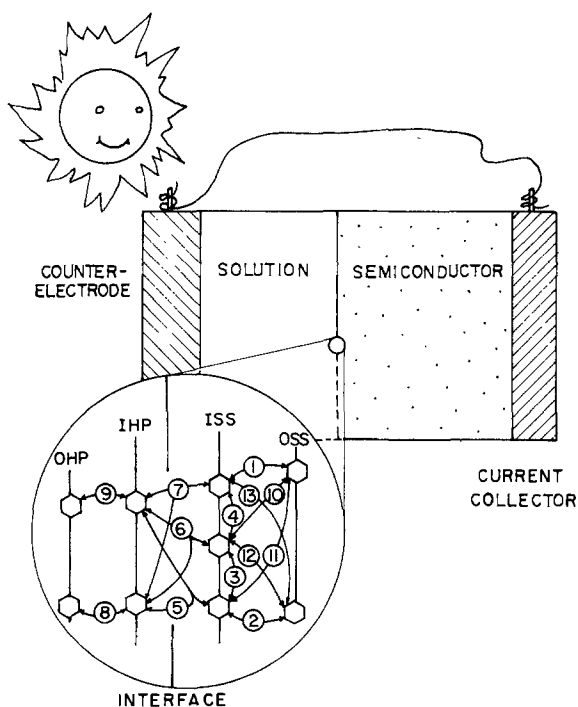


Fig. 1. Mathematical model of the liquid-junction photovoltaic cell

$$\frac{dN_{h^+}}{dy} = R_{h^+} \quad [6]$$

where R_{h^+} is the net rate of production of holes under steady-state conditions.

The rate of production of holes is, by stoichiometry, equal to the rate of production of electrons and is governed by three concurrent processes: generation by absorption of light, generation by absorption of heat, and recombination of electrons and holes (*i.e.*, transfer of an electron from the conduction band to the valence band)

$$R_{h^+} = G_L + G_{th} - R_{rec} \quad [7]$$

Mathematical models of the homogeneous recombination process have been developed which incorporate single-step electron transfer from one energy level to another. They differ in the assumption of the presence or absence of impurities within the semiconductor which allow electrons to have energies between the conduction and valence-band energies (41, 42).

Most semiconducting materials contain impurities or imperfections within their lattice structure which may be described as fixed sites with valence-band electron energies within the semiconductor bandgap. The trap-kinetics model allows recombination to occur through these sites (see Fig. 2). Absorbed radiation drives an electron from the valence band to the conduction band, and all recombination and thermal generation reactions are assumed to occur through trap sites. This model results in

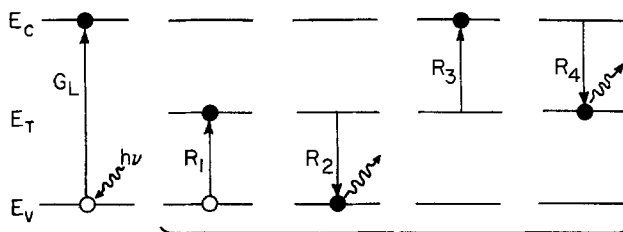
$$R_{h^+} = \eta m q_0 e^{-m\nu} - \frac{N_t k_2 (np - n_i^2)}{\frac{k_1(N_v - p) + k_3(N_c - n)}{k_4} + \frac{k_2}{k_4} p + n} \quad [8]$$

where k_1 , k_2 , k_3 , and k_4 are the rate constants for the corresponding reactions shown in Fig. 2. The intrinsic concentration is given by

$$n_i = \left[\frac{k_1 k_3 (N_c - n)(N_v - p)}{k_2 k_4} \right]^{1/2} \quad [9]$$

The electron and hole concentrations are generally small as compared to the respective conduction and valence-band site concentrations. The intrinsic concentration is therefore constant, and the reaction rate can be characterized with three lumped rate constants [$N_t k_2$, $(k_1 N_v + k_3 N_c)/k_4$, and k_2/k_4]. Homogeneous electron-hole recombination was assumed in the mathematical model to occur through trap sites (Eq. [8] and [9]).

The expression for the intrinsic concentration (Eq. [9]) is consistent with the expression derived through statistical-mechanical models (see Eq. [32] of Chap. 6, Ref.



Thermal Generation and Recombination Through Trap Sites

Individual Reaction Rates

$$G_L = \eta m q_0 e^{-m\nu}$$

$$R_1 = k_1(N_v - p)(N_T - n_T)$$

$$R_2 = k_2 n_T p$$

$$R_3 = k_3 n_T (N_c - n)$$

$$R_4 = k_4 n (N_T - n_T)$$

Fig. 2. Schematic representation of single-trap recombination kinetics in the semiconductor.

(20)). The intrinsic concentration can be considered to be a constant for a given semiconductor only if the ratios n/N_c and p/N_v are negligibly small as compared to unity. This condition is consistent with the assumption of unity activity coefficients for electrons and holes. The value of the intrinsic concentration derived from statistical-mechanical arguments serves as a relationship among the kinetic parameters in Eq. [9].

The divergence of the current is zero at steady state; therefore the fluxes of holes and electrons are related by

$$\frac{dN_{e^-}}{dy} - \frac{dN_{h^+}}{dy} = 0 \quad [10]$$

A material balance on electrons, analogous to Eq. [5], could be used to replace Eq. [10].

Poisson's equation

$$\frac{d^2\Phi}{dy^2} = - \frac{\mathbf{F}}{\epsilon_{sc}} [p - n + (N_d - N_a)] \quad [11]$$

relates the potential to the charge distribution. The concentrations of ionized electron donors and acceptors are represented by N_d and N_a , respectively. The Debye length

$$\lambda_{sc} = [\epsilon_{sc} RT / \mathbf{F}^2 (N_d - N_a)]^{1/2}$$

characterizes the distance over which the potential varies in the semiconductor. It typically has a value of 1×10^{-6} to 2×10^{-5} cm.

The degree of ionization of donors or acceptors is dependent upon the concentrations of charged species within the semiconductor and upon the temperature. Complete ionization has been assumed in this work. This assumption is reasonable at room temperatures and is consistent with the assumption of unity activity coefficients.

Electrolyte.—For a one-dimensional case, neglecting convective effects, the flux of an ionic species is governed by potential and concentration gradients

$$N_i = -z_i u_i c_i \mathbf{F} \frac{d\Phi}{dy} - D_i \frac{dc_i}{dy} \quad [12]$$

Under the assumption that homogeneous reactions do not take place, conservation of mass yields a uniform flux at steady state, *i.e.*

$$\frac{dN_i}{dy} = 0 \quad [13]$$

The potential and concentrations of charged species are related by Poisson's equation

$$\frac{d^2\Phi}{dy^2} = - \frac{\mathbf{F}}{\epsilon_{sol}} \sum_i z_i c_i \quad [14]$$

Electroneutrality of the electrolyte is not assumed here because the diffuse region near the interface plays an important role in the microscopic model of the interface. The Debye length in the solution is given by

$$\lambda_{sol} = [\epsilon_{sol} RT / \mathbf{F}^2 \sum_i z_i^2 c_{i,\infty}]^{1/2}$$

and typically has a value of 1×10^{-8} to 1×10^{-7} cm.

The relationships presented above are sufficient to describe the electrolytic solution. An additional relationship yields the current density as a function of the ionic fluxes

$$i = \mathbf{F} \sum_i z_i N_i \quad [15]$$

Within the semiconductor, this can be regarded as an integrated form of Eq. [10].

Semiconductor-electrolyte interface.—A general interfacial reaction can be expressed as



where s_i is the stoichiometric coefficient of species i , M_i is a symbol for the chemical formula of species i , and n is the number of electrons transferred. [See Chap. 8 in Ref. (39).] For single-step reactions, n is equal to one.

The rate of a single-step reaction 1 at the interface is given by

$$\begin{aligned} r_l = & k_{f,l} \exp \left[\frac{(1 - \beta_l) F \Delta \Phi_l}{RT} \right] \prod_i c_i^{p_{i,l}} \\ & - k_{b,l} \exp \left[\frac{-\beta_l F \Delta \Phi_l}{RT} \right] \prod_i c_i^{q_{i,l}} \end{aligned} \quad [17]$$

where β_l is a symmetry factor (usually assumed to be equal to 1/2), $k_{f,l}$ and $k_{b,l}$ are forward and backward reaction rate constants, respectively, and $\Delta \Phi_l$ is the potential driving force for the given reaction, l . The potential driving force enters into reactions involving charge transfer from locations of one potential to locations of another.

The reaction orders for a given species i in the forward and reverse directions are $p_{i,l}$ and $q_{i,l}$, respectively. They are determined from the stoichiometric coefficients, $s_{i,l}$

$$\text{If } s_{i,l} = 0; p_{i,l} = 0, \text{ and } q_{i,l} = 0$$

$$\text{If } s_{i,l} > 0; p_{i,l} = s_{i,l}, \text{ and } q_{i,l} = 0$$

$$\text{If } s_{i,l} < 0; p_{i,l} = 0, \text{ and } q_{i,l} = -s_{i,l}$$

The reaction rates are written in terms of the equilibrium constants as

$$\begin{aligned} r_e = & k_{b,l} \left\{ K_l \exp \left[\frac{(1 - \beta_l) F \Delta \Phi_l}{RT} \right] \prod_i c_i^{p_{i,l}} \right. \\ & \left. - \exp \left[\frac{-\beta_l F \Delta \Phi_l}{RT} \right] \prod_i c_i^{q_{i,l}} \right\} \end{aligned} \quad [18]$$

The equilibrium constant used here is the ratio of the forward and backward rate constants

$$K_l = \frac{k_{f,l}}{k_{b,l}} \quad [19]$$

Six of the 13 equilibrium constants are independent and can be calculated as functions of equilibrium interfacial concentrations and potentials

$$K_l = \exp \left[-\frac{F}{RT} \Delta \Phi_l \right] \prod_i c_i^{-s_{i,l}} \quad [20]$$

A discussion of the calculation of equilibrium concentrations and potentials and the subsequent calculation of equilibrium constants is presented elsewhere [see Chap. 6, Ref. (20)]. The remaining constants can be calculated from Eq. [20] or from the following identities

$$K_4 = \frac{K_3(N_d - N_a)^2}{K_1 K_2 n_i^2} \quad [21a]$$

$$K_6 = K_7 / K_3 \quad [21b]$$

$$K_7 = K_8 / K_4 \quad [21c]$$

$$K_{10} = K_1 K_4 \quad [21d]$$

$$K_{11} = K_{10} / K_3 \quad [21e]$$

$$K_{12} = K_8 / K_3 \quad [21f]$$

and

$$K_{13} = K_{12} K_4 \quad [21g]$$

Within the parametric studies which follow (44), one independent rate constant is assumed to be characteristic of each of four groups of interfacial reactions. The four groups, shown in Fig. 1, are reactions [1], [2], [10]-[13]

(OSS-ISS), reactions [3] and [4] (ISS), reactions [5]-[7] (ISS-IHP), and reactions [8] and [9] (IHP-OHP). The individual rate constants for each reaction l are related to the characteristic rate constant by

$$k_{b,l} = k_l^0 K_l^{-1/2} \quad [22]$$

and

$$k_{f,l} = k_{b,l} K_l = k_l^0 K_l^{1/2} \quad [23]$$

where k_l^0 is the pre-exponential part of the rate constant, with a characteristic value for a given reaction type, and β was given a value of one-half. These equations are consistent with Eq. [18] and [19].

Material balances govern the interface under steady-state conditions. These are expressed by continuity of flux at the OSS and the OHP

$$N_{e^-}|_{\text{oss}} = \sum_l -s_{e^-} r_{l,\text{iss}} \quad [24]$$

$$N_{\text{H}^+}|_{\text{oss}} = \sum_l -s_{\text{H}^+} r_{l,\text{iss}} \quad [25]$$

and

$$N_i|_{\text{ohp}} = \sum_l -s_{i,l} r_l \quad [26]$$

and material balances for each adsorbed species i at the ISS and the IHP

$$\sum_l s_{i,l} r_{l,\text{iss}} = 0 \quad [27]$$

and

$$\sum_l s_{i,l} r_{l,\text{iHP}} = 0 \quad [28]$$

Gauss's law can be applied to the region between the OSS and ISS

$$(\Phi_{\text{oss}} - \Phi_{\text{iss}}) = \frac{\delta_1}{\epsilon_{\text{sc}}} \left[\frac{\epsilon_2}{\delta_2} (\Phi_{\text{iss}} - \Phi_{\text{iHP}}) + \mathbf{F} \left(\sum_{\text{iss}} \gamma_i - g_{\text{iss}}^+ \right) \right] \quad [29]$$

and between the ISS and the IHP

$$(\Phi_{\text{iss}} - \Phi_{\text{iHP}}) = \frac{\delta_2}{\epsilon_2} \left[\frac{\epsilon_{\text{sol}}}{\delta_3} (\Phi_{\text{iHP}} - \Phi_{\text{ohp}}) - \mathbf{F} \left(\sum_{\text{iHP}} z_i \gamma_i \right) \right] \quad [30]$$

The evaluation of Gauss's law in the region between the OSS and the ISS includes a term for a fixed positive charge at the ISS, q_{iss}^+ , which was set equal to zero in this study.

Boundary conditions.—The semiconducting electrode is bounded at one end by the electrolyte and at the other end by a metallic current collector. The boundary conditions at the semiconductor-electrolyte interface are incorporated into the model of the interface. The boundary conditions at the semiconductor-current collector interface are that the potential is zero, the potential derivative is equal to a constant, determined by the charge assumed to be located at the semiconductor-current collector interface (this constant was set equal to zero in this study), and all the current is carried by electrons (the flux of holes is zero). The boundary conditions in the electrolytic solution are set a fixed distance (10 Debye lengths) from the interface. This distance may be considered to be a diffusion layer. The boundary conditions are that the potential gradient is continuous and that all concentrations have their bulk value.

Counterelectrode.—In the region sufficiently far from the interface that electroneutrality holds, the potential distribution is linear and is a function of current density. The potential drop in the region between the counterelectrode and the outer limit of the diffusion layer is given by

$$V_{IR} = \frac{Li}{\kappa} \quad [31]$$

where κ is the solution conductivity and L is the distance between the counterelectrode and the outer edge of the diffusion layer. The conductivity of dilute solutions is related to ionic mobilities and concentrations by

$$\kappa = F^2 \sum_i z_i^2 u_i c_i \quad [32]$$

The potential drop across the counterelectrode-electrolyte interface is given by

$$V_{CE} = V_{CE}^0 + \eta_{CE} \quad [33]$$

where V_{CE}^0 is the equilibrium potential drop across the interface and η_{CE} is the total counterelectrode reaction overpotential. The total overpotential is related to the current density through the Butler-Volmer reaction model (39, 43)

$$i = i_0 \left\{ \left[1 - \frac{i}{i_{a,lim}} \right] \exp \left[\frac{(1 - \beta)nF}{RT} \eta_{CE} \right] - \left[1 + \frac{i}{i_{c,lim}} \right] \exp \left[- \frac{\beta nF}{RT} \eta_{CE} \right] \right\} \quad [34]$$

where i_0 is the exchange current density associated with the bulk concentrations of reactants, $i_{k,lim}$ is the diffusion-limited current density associated with species k , and n is the number of electrons transferred in the counterelectrode reaction.

Conclusion

The equations which govern the liquid-junction photovoltaic cell are presented in the context of a one-dimensional mathematical model. This model treats explicitly the semiconductor, the electrolyte, and the semiconductor-electrolyte interface in terms of potentials and concentrations of charged species. The model incorporates macroscopic transport equations in the bulk of the semiconductor and electrolyte, coupled with a microscopic model of the semiconductor-electrolyte interface. Homogeneous and heterogeneous recombination of electron-hole pairs is included within the model. Recombination takes place at the semiconductor-electrolyte interface through interfacial sites, which can enhance the recombination rate. The coupled nonlinear ordinary differential equations of the model were posed in finite-difference form and solved numerically (44). Such numerical solution of the governing equations reduces the number of restrictive assumptions needed to solve the problem. The model can be used to gain insight into the effect of cell parameters on cell performance (44) and can be coupled with primary resistance calculations to optimize cell configurations (45).

Acknowledgment

This work was supported by the United States Department of Energy under Contract no. DE-AC03-76SF00098 through the Director, Office of Energy Research, Office of Basic Energy Sciences, Chemical Sciences Division, and through the Assistant Secretary of Conservation and Renewable Energy, Office of Advanced Conservation Technology, Electrochemical Systems Research Division.

Manuscript submitted June 24, 1983; revised manuscript received May 11, 1984. This was Paper 471 presented at the Minneapolis, Minnesota, Meeting of the Society, May 10-15, 1981.

The University of California assisted in meeting the publication costs of this article.

LIST OF SYMBOLS

c_i molar concentration of species i (mol/cm³)
 D_i diffusivity of species i (cm²/s)
 E_i energy of species or site i (eV)
 ΔE_i ionic adsorption energy (J/mol)

f_i molar activity coefficient of species i
 F Faraday's constant, 96,487 C/eq
 G_{th} rate of thermal electron-hole pair generation (mol/s-cm³)
 G_L rate of photo electron-hole pair generation (mol/s-cm³)
 i current density (mA/cm²)
 i_0 exchange current density (mA/cm²)
 $k_{r,l}$ forward reaction rate constant for reaction l
 $k_{b,l}$ backward reaction rate constant for reaction l
 k_k rate constants for homogeneous reaction k
 K_l equilibrium constant for reaction l
 m solar absorption coefficient (1/cm)
 M_i symbol for chemical formula of species i
 n number of electrons involved in electrode reaction
 n electron concentration (mol/cm³)
 n_i intrinsic electron concentration (mol/cm³)
 N total site concentration (mol/cm³)
 N_a total bulk electron-acceptor concentration (mol/cm³)
 N_d total bulk electron-donor concentration (mol/cm³)
 N_i flux of species i , (mol/cm²s)
 p hole concentration (mol/cm³)
 $p_{i,l}$ heterogeneous reaction order
 $q_{i,l}$ heterogeneous reaction order
 q_0 incident solar flux (mol/s-cm²)
 r_l heterogeneous reaction rate (mol/s-cm²)
 R universal gas constant, 8.3143 J/mol-K
 R_i net rate of production of species i (mol/s-cm³)
 R_{rec} net rate of electron-hole recombination (mol/s-cm³)
 $s_{i,l}$ stoichiometric coefficient of species i in an electrode reaction
 T absolute temperature (K)
 u_i mobility of species i (cm²-mol/J-s)
 V potential drop across depletion layer (V)
 W depletion layer thickness (cm)
 y distance variable (cm)
 z_i charge number of species i

Greek characters

β symmetry factor
 γ_k surface concentration of energy or species k (mol/cm²)
 Γ_k total surface-site concentration of energy or species k (mol/cm²)
 δ_k distance between interfacial planes (gap denoted by k) (cm)
 ϵ permittivity (C/V-cm)
 η photon efficiency
 η_k total overpotential at interface k (V)
 Θ fractional occupation of surface sites
 κ conductivity (mho/cm)
 λ Debye length (cm)
 μ_i electrochemical potential of species i (J/mol)
 Φ electrical potential (V)

Superscripts

\circ equilibrium
 θ secondary reference state at infinite dilution
 $*$ secondary reference state in semiconductor

Subscripts

bulk associated with the bulk
 c associated with conduction band in semiconductor
 CE associated with the counterelectrode
 $cell$ associated with the cell
 e^- relating to electrons
 h^+ relating to holes
 ihp associated with inner Helmholtz plane
 iss associated with inner surface states
 k dummy subscript
 l associated with reaction l
 o equilibrium value or initial value
 ohp associated with outer Helmholtz plane
 oss associated with outer surface states
 sc associated with semiconductor
 sol associated with solution
 t associated with trap band in semiconductor
 v associated with valence band in semiconductor
 1 associated with the region between the OSS and the ISS
 2 associated with the region between the ISS and the IHP
 3 associated with the region between the IHP and the OHP

REFERENCES

1. A. Fujishima and K. Honda, *Nature*, **238**, 37 (1972).
2. J. Manassen, D. Cahen, and G. Hodes, *ibid.*, **263**, 97 (1976).
3. A. J. Bard, *J. Photochem.*, **10**, 59 (1979).
4. H. Ehrenreich and J. H. Martin, *Phys. Today*, **32**, 25 (1979).
5. M. S. Wrighton, *Acc. Chem. Res.*, **12**, 303 (1979).
6. H. Gerischer, *Pure Appl. Chem.*, **52**, 2649 (1980).
7. A. J. Bard, *Science*, **207**, 139 (1980).
8. A. Heller, *Acc. Chem. Res.*, **14**, 154 (1981).
9. M. Green, in "Modern Aspects of Electrochemistry," Vol. 2, J. O'M. Bockris, Editor, Chap. 5, Academic Press, New York (1959).
10. H. Gerischer, in "Advances in Electrochemistry and Electrochemical Engineering," Vol 1, P. Delahay, Editor, Chap. 4, Interscience, New York (1961).
11. M. D. Archer, *J. Appl. Electrochem.*, **5**, 17 (1975).
12. K. Rajeshwar, P. Singh, and J. Dubow, *Electrochim. Acta*, **23**, 1117 (1975).
13. L. A. Harris and R. H. Wilson, *Ann. Rev. Mater. Sci.*, **8**, 99 (1978).
14. A. J. Nozik, *Ann. Rev. Phys. Chem.*, **29**, 189 (1978).
15. M. Tomkiewicz and H. Fay, *Appl. Phys.*, **18**, 1 (1979).
16. R. H. Wilson, in "CRC Critical Reviews in Solid State and Materials Science," p. 1, CRC Press, Cleveland, OH (1980).
17. R. Memmings, *Electrochim. Acta*, **25**, 77 (1980).
18. S. R. Morrison, "Electrochemistry at Semiconductor and Oxidized Metal Electrodes," Plenum Press, New York (1980).
19. S. U. M. Kahn and J. O'M. Bockris, in "Modern Aspects of Electrochemistry," Vol. 14, J. O'M. Bockris, B. E. Conway, and R. E. White, Editors, Chap. 3, Plenum Press, New York (1982).
20. M. E. Orazem, Ph.D. Thesis, University of California, Berkeley, CA (1983).
21. J. R. Macdonald, *Solid State Electron.*, **5**, 11 (1962).
22. A. De Mari, *ibid.*, **11**, 33 (1968).
23. A. De Mari, *ibid.*, **11**, 1021 (1968).
24. S. C. Choo, *IEEE Trans. Electron Devices*, **ed-18**, 574 (1971).
25. S. C. Choo, *ibid.*, **ed-19**, 954 (1972).
26. J. E. Sutherland and J. R. Hauser, *ibid.*, **ed-24**, 363 (1977).
27. D. Laser and A. J. Bard, *This Journal*, **123**, 1828 (1976).
28. D. Laser and A. J. Bard, *ibid.*, **123**, 1833 (1976).
29. D. Laser and A. J. Bard, *ibid.*, **123**, 1837 (1976).
30. D. Laser, *ibid.*, **126**, 1011 (1979).
31. D. Leary, J. O. Barnes, and A. G. Jordan, *ibid.*, **129**, 1382 (1982).
32. J. A. Davis, R. O. James, and J. O. Leckie, *J. Colloid Interface. Sci.*, **63**, 480 (1978).
33. J. A. Davis and J. O. Leckie, *ibid.*, **67**, 91 (1978).
34. J. A. Davis and J. O. Leckie, *ibid.*, **74**, 32 (1980).
35. D. C. Grahame, *Chem. Rev.*, **41**, 441 (1947).
36. J. F. Dewald, in "Semiconductors," N. B. Hannay, Editor, Chap. 17, Reinhold, New York (1959).
37. M. J. Sparnaay, "The Electrode Double Layer," Pergamon Press, New York (1972).
38. R. Parsons, in "Modern Aspects of Electrochemistry," Vol. 1, J. O'M. Bockris, Editor, pp. 103-179, Academic Press, New York (1954).
39. J. Newman, "Electrochemical Systems," Prentice-Hall, Englewood Cliffs, NJ (1973).
40. H. Gerischer, in "Physical Chemistry: An Advanced Treatise," Vol. IX, H. Eyring, Editor, Chap. 5, Academic Press, New York (1970).
41. J. L. Moll, "Physics of Semiconductors," McGraw-Hill, New York (1964).
42. R. A. Smith, "Semiconductors," Cambridge University Press, London (1959).
43. P. Delahay, "Double Layer and Electrode Kinetics," Interscience, New York (1965).
44. M. E. Orazem and J. Newman, *This Journal*, **131**, 2574 (1984).
45. M. E. Orazem and J. Newman, *ibid.*, **131**, 2582 (1984).
46. M. E. Orazem and J. Newman, *ibid.*, **131**, 2715 (1984).

Mathematical Modeling of Liquid-Junction Photovoltaic Cells

II. Effect of System Parameters on Current-Potential Curves

Mark E. Orazem¹ and John Newman*

Materials and Molecular Research Division of Lawrence Berkeley Laboratory, and Department of Chemical Engineering, University of California, Berkeley, California 94720

ABSTRACT

The one-dimensional mathematical model presented in a previous paper was used to calculate the effect of system variables on the performance of an n-type GaAs semiconducting anode in contact with an 0.8M K₂Se, 0.1M K₂Se₂, 1.0M KOH electrolytic solution. The performance of the semiconductor electrode is influenced by kinetic limitations to interfacial reactions, dopant concentration, semiconductor thickness, the direction of illumination, and the amount of light absorbed in the semiconductor. An optimal dopant concentration and semiconductor thickness can be calculated for a given system.

The liquid-junction photovoltaic cell is an electrochemical system with one or two semiconducting electrodes. This system has undergone intense study since the early 1970's as a means of converting solar energy to chemical or electrical energy (1-8). A number of articles review the physics of the liquid-junction cell, the role of the semiconducting electrode, and the literature. See *e.g.*, Ref. (9-19).

A mathematical model of the liquid-junction photovoltaic cell was presented in a previous paper (20). The results of the model, obtained through numerical computation, are used here to gain insight into the cell behavior and into the factors influencing cell design. This model can also be coupled with primary resistance calculations to optimize the design of cell configurations (21).

A one-dimensional mathematical model of the liquid-junction photovoltaic cell has been developed (20) which treats explicitly the semiconductor, the electrolyte, and the semiconductor-electrolyte interface in terms of potentials and concentrations of charged species. A one-dimensional representation of the model is presented in Fig. 1 of the first paper in this series (*This Journal*, p. 2569). This model includes macroscopic representations of the counterelectrode, the electrolytic solution, and the semiconductor coupled with a microscopic representation of the interface between the semiconductor and the solution. The semiconductor-electrolyte interface couples the macroscopic equations which govern the adjacent bulk phases.

Semiconductor-electrolyte interface.—A description of the semiconductor-electrolyte interface appears on page 2571 of *This Journal*.

Numerical method.—The coupled nonlinear ordinary differential equations of the model were posed in finite-

*Electrochemical Society Active Member.

¹Present address: Department of Chemical Engineering, University of Virginia, Charlottesville, Virginia 22901.

Table I. Input parameters for the semiconductor

Semiconductor: n-GaAs	N_v	$1.16 \times 10^{-5} \text{ mol/cm}^3 (7 \times 10^{18} \text{ cm}^{-3})$
Valence band site concentration	N_c	$7.80 \times 10^{-7} \text{ mol/cm}^3 (4.7 \times 10^{17} \text{ cm}^{-3})$
Conduction band site concentration	E_g	1.4 eV
Bandgap	$N_d - N_a$	$9.96 \times 10^{-8} \text{ eq/cm}^3 (6 \times 10^{16} \text{ cm}^{-3})$
Dopant concentration	D_{e-}	222.0 cm ² /s
Electron diffusivity	D_{h+}	6.46 cm ² /s
Hole diffusivity	ϵ_{sc}	$1.06 \times 10^{-12} \text{ C/V-s}$
Permittivity	m	$4.40 \times 10^5 \text{ cm}^{-1}$
Solar absorption coefficient	η	0.3735
Solar spectrum efficiency	q_0	$7.139 \times 10^{-7} \text{ mol/cm}^2\text{-s}$
Total incident radiation (AM-2)		882 W/m ²
	N/k_2	$1.89 \times 10^9 \text{ s}^{-1}$
Homogeneous recombination rate constants	$(k_1 N_v + k_2 N_c)/k_4$	100
	k_2/k_4	$2.56 \times 10^{-3} \text{ cm}^3/\text{mol}$

difference form and solved numerically for the cell under equilibrium and steady-state conditions (25). The equations were properly linearized, posed in finite-difference form, and solved using Newman's BAND method (28), coupled with Newton-Raphson iteration. Calculation of a current-potential curve involved iterative solution of the system of coupled equations for input values of solar illumination and current density. Numerical accuracy was enhanced by definition of concentration variables that are uniform under equilibrium conditions. The concentration and potential variables in the semiconductor were²

$$AN = \frac{n}{N_d - N_a} e^{-\phi}$$

and

$$P = \frac{p}{N_d - N_a} e^{\phi}$$

where

$$\phi = \frac{F\Phi}{RT}$$

Under equilibrium conditions, the dimensionless potential varied in the semiconductor from zero to around 40.

Numerical accuracy was further improved by partial decoupling of the three equations governing the semiconductor. The large number of equations associated with the semiconductor-electrolyte interface involve variables that appear only at that location. These equations were transformed into a smaller number of equations involving only bulk phase variables in a local inversion routine. A general method for local inversion is presented by White (48).

Results

Computed results for the mathematical model of the liquid-junction photovoltaic cell are presented in the following section. The parameter values chosen for the model are consistent with an n-type GaAs anode in contact with a 0.8M K₂Se, 0.1M K₂Se₂, 1.0M KOH solution. The redox couple was assumed to be Se₂²⁻/Se²⁻, and the semiconductor was illuminated at the semiconductor-electrolyte interface. Input parameter values are as presented in Tables I-III unless stated otherwise. Dependent parameters calculated from the input data are presented in Table IV.

The n-type GaAs system was chosen for analysis to allow comparison to the experimental work of Heller and Miller (8, 27, 28). Their cell achieved a 12% power efficiency based upon incident radiation, an open-circuit potential of 0.7V, and a closed circuit current of 24 mA/cm². A description of their experimental electrodes, cell, and measuring techniques is presented in Ref. (29). Their cell efficiency includes the effects of reflection losses and electrolyte resistance. The influence of kinetic

²A list of symbols appears on page 2573 of *This Journal*.

Table II. Input parameters for the semiconductor-electrolyte interface

ISS site	k	v	t	c
ISS site energy	E_k	1.3	1.4	1.5 eV
ISS site density	γ_k	0.3334	0.3333	0.3333
Total ISS site concentration	Γ_{iss}			$4.019 \times 10^{-12} \text{ mol/cm}^2$ ($2.42 \times 10^{12} \text{ cm}^{-2}$)
Total IHP site concentration	Γ_{ihp}			$1.200 \times 10^{-13} \text{ mol/cm}^2$ ($7.23 \times 10^{10} \text{ cm}^{-2}$)
IHP adsorption energy	ΔE_3			0.0 J/mol
	ΔE_4			0.0 J/mol
Equilibrium OSS potential	Φ_{oss}			5.93 mV
Equilibrium charge on interface				-0.1298 $\mu\text{C/cm}^2$
Distance between OSS and ISS	δ_1			$1.0 \times 10^{-8} \text{ cm}$
Distance between ISS and IHP	δ_2			$2.0 \times 10^{-8} \text{ cm}$
Distance between IHP and OHP	δ_3			$2.0 \times 10^{-8} \text{ cm}$
Permittivity between ISS and IHP	ϵ_2			$6.93 \times 10^{12} \text{ C/V-cm}$
Rate constants (OSS-ISS)	k_{etr}			$1.0 \times 10^{25} \text{ cm}^3/\text{mol-s}$
(ISS)	k_{stf}			$1.0 \times 10^{29} \text{ cm}^2/\text{mol-s}$
(ISS-IHP)	k_{cht}			$1.0 \times 10^{29} \text{ cm}^2/\text{mol-s}$
(IHP-OHP)	k_{ads}			$1.0 \times 10^{23} \text{ s}^{-1}$

Table III. Input parameters for the electrolyte

Electrolyte: 0.8M K ₂ Se, 0.1M K ₂ Se ₂ , 1.0M KOH					
Species index	k	1	2	3	4
Species		K ⁺	OH ⁻	Se ₂ ²⁻	Se ²⁻
Charge number	z_k	+1	-1	-2	-2
Bulk concentration	$c_{k,\infty}$	0.0028	0.0010	0.0001	0.0008
					mol/cm ³
Diffusivity ($\times 10^5$)	D_k	1.957	5.260	1.000	1.000 cm ² /s
Permittivity	ϵ_{sol}				$6.930 \times 10^{-12} \text{ C/V-cm}$
Conductivity	κ				0.3 ($\Omega\text{-cm}$) ⁻¹
Temperature	T				300 K

Table IV. Values calculated from input parameters

Semiconductor		
Fermi level	E_f	1.347 eV
Intrinsic concentration	n_i	$5.228 \times 10^{-18} \text{ mol/cm}^3$ ($3.15 \times 10^6 \text{ cm}^{-3}$)
Minority carrier diffusion length	L_p	5.846 $\times 10^{-4} \text{ cm}$
Debye length	λ_{sc}	$1.689 \times 10^{-6} \text{ cm}$
Electrolyte		
Debye length	λ_{sol}	$1.967 \times 10^{-8} \text{ cm}$

and mass-transfer limitations to current flow at the counterelectrode were reduced by using a counterelectrode to semiconductor area ratio of 50. The Se₂²⁻/Se²⁻ redox couple was chosen to limit the corrosion of GaAs under 1000 W/m² illumination to a few micrometers per year (approximately 0.04 mA/cm²) (30-32).

The discussion of the effect of kinetic, bulk semiconductor, and interfacial parameters does not include the effect of IR drop in the electrolyte or kinetic and mass-transfer limitations at the counterelectrode (see the "Counterelectrodes" section of the previous paper). The

contribution of these phenomena is discussed in the "Cell Design" section (see also the next paper).

Interfacial kinetic limitations.—The values of the interfacial rate constants can affect the open-circuit cell potential, the value of the limiting current, and the shape of the current-potential curve. Most (> 99%) of the recombination under open-circuit illumination occurs at the interface. Homogeneous recombination is included in the model, but does not play a major role for the range of parameters studied.

Ion-adsorption reactions.—Current-potential curves are presented in Fig. 1 with the interfacial rate constant for adsorption and desorption of ions onto the inner Helmholtz plane as a parameter (reactions [8] and [9] in Fig. 1 of the first paper). In each case, the cell potential is a maximum at open circuit (700.5 mV) and decreases as the anodic current increases. A limiting current is observed due to limitations of mass transfer and generation of holes in the semiconductor.

The ion-adsorption rate constant influences the limiting current and the shape of the current-potential curve. A dramatic decrease in the maximum power obtained from this system is observed for the cases with small ion-adsorption rate constants. Kinetic limitations to ion adsorption are seen to have a major effect on cell performance.

Concentration distributions of holes and electrons in the semiconductor are presented in Fig. 2 and 3 for a system with no interfacial kinetic limitations and for a system with kinetic limitations to ion adsorption, respectively. The equilibrium and illuminated open-circuit concentration distributions for the two cases are identical. Under equilibrium conditions, the concentration of holes (curve a) is essentially zero in the bulk of the semiconductor and increases near the negatively charged interface. Conduction electrons are depleted near the interface and reach a value of 0.328 dimensionless units at the current collector, where the concentrations are scaled by the dopant concentration ($N_d - N_a$). The electron concentration in a neutral region of the semiconductor would have a value essentially equal to 1.0. The equilibrated semiconductor of Fig. 2 can therefore be described as having an inversion region extending from the semicon-

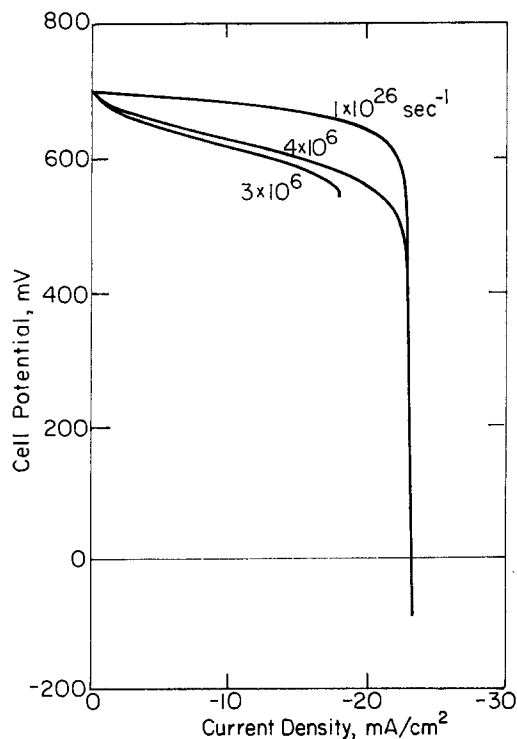


Fig. 1. Computed current-potential curves for an n-type GaAs anode with ion-adsorption rate constant as a parameter.

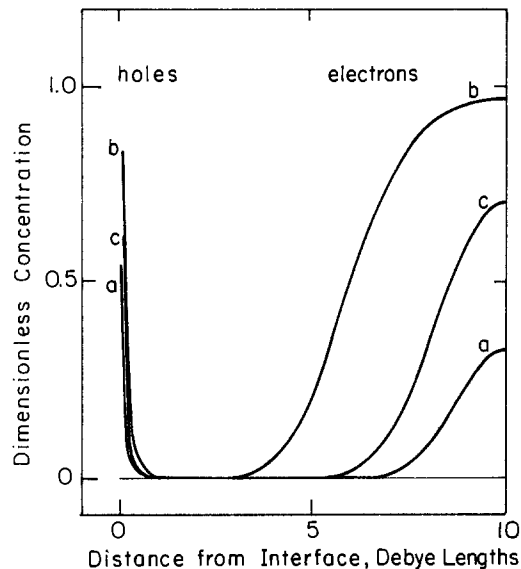


Fig. 2. Concentration distribution for the liquid-junction cell with no kinetic limitations ($k_{ads} = 1.0 \times 10^{26} \text{ s}^{-1}$). Curve a, open circuit in the dark; curve b, open circuit under illumination; and curve c, near short circuit ($i = -23.1 \text{ mA/cm}^2$) under illumination.

ductor-electrolyte interface to 0.5 Debye lengths from the interface and a depletion region extending to the current collector.

The positive background charge density has a value of 1.0; the semiconductor has a net positive charge which is balanced by charge associated with the diffuse region of the electrolyte and the interface. System electroneutrality is maintained. The potential gradient, the driving force for migration of charged species, is balanced by the concentration gradient, which drives diffusion. The net flux of each species in the semiconductor is equal to zero at equilibrium.

Illumination under open-circuit conditions produces electron-hole pairs, which are separated by the potential

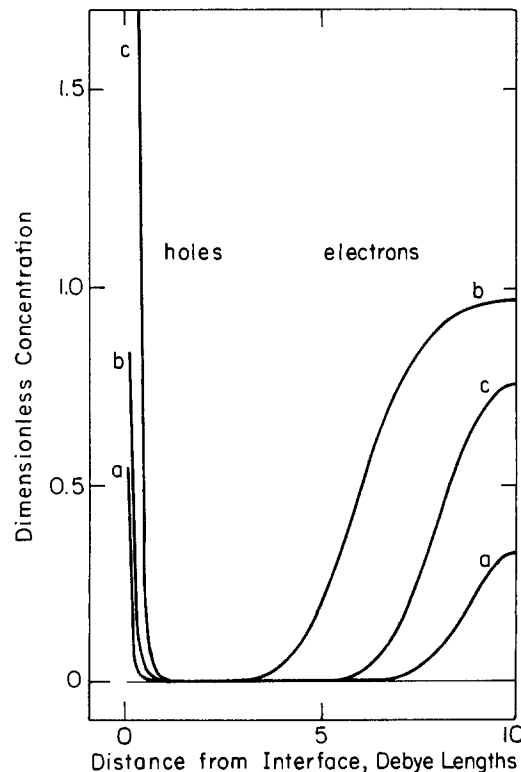


Fig. 3. Concentration distribution for the liquid-junction cell with kinetic limitations to ion adsorption ($k_{ads} = 4.0 \times 10^6 \text{ s}^{-1}$). Curve a, open circuit in the dark; curve b, open circuit under illumination; and curve c, near short circuit ($i = -23.1 \text{ mA/cm}^2$) under illumination.

gradient. The concentration of holes increases near the interface, and the concentration of electrons increases near the current collector (curve b). As the system without kinetic limitations approaches short circuit (curve c in Fig. 2), the concentrations of holes and electrons approach the equilibrium distributions. The system under kinetic limitations to ion adsorption, in contrast, experiences an increase in hole concentration at large current densities (curve c in Fig. 4).

The model also allows calculation of the potential distribution in the semiconductor and throughout the cell. Kinetic limitations at the interface are compensated by increased changes of potential across the reaction planes. A small ion-adsorption rate constant is therefore compensated by increased potential and concentration driving forces at the interface. In this way, kinetic limitations influence the cell performance.

Charge-transfer reactions.—Current-potential curves are presented in Fig. 4 with the rate constant for charge transfer from the inner surface states of the semiconductor to the inner Helmholtz plane as a parameter (reactions [5], [6], and [7] in Fig. 1 of the previous paper). The cell potential has a maximum value under open-circuit illumination and decreases as the anodic current increases. Kinetic limitations to charge transfer adversely influence the power performance of the cell. A small charge-transfer rate constant is compensated by increased potential and concentration driving forces.

Electron-adsorption reactions.—The influence of electron-adsorption rate constants (reactions [1], [2], [10], [11], [12], and [13] in Fig. 1 of the previous paper) upon the current-potential curve is presented in Fig. 5. A small electron-adsorption rate constant reduces the net rate of recombination of holes and electrons at the surface and thus increases both the cell potential and the value of the limiting current.

Surface-shift reactions.—The rate constants for reactions which allow electrons to move from one energy level at the interface to another (reactions [3] and [4] in Fig. 1 of the previous paper) do not have any independent effect upon the cell potential or the value of the limiting current.

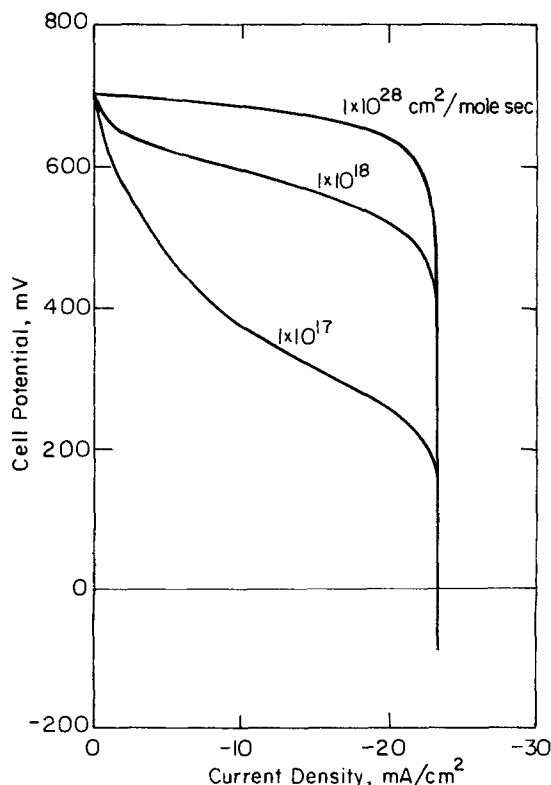


Fig. 4. Computed current-potential curves for an n-type GaAs anode with charge-transfer rate constant as a parameter.

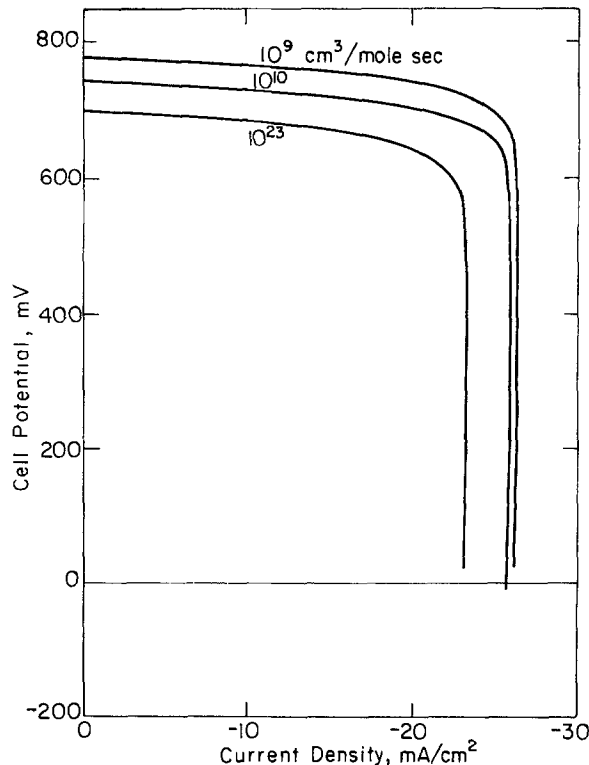


Fig. 5. Computed current-potential curves for an n-type GaAs anode with electron-adsorption rate constant as a parameter.

rent. These rate constants affect only the path by which recombination may take place.

Bulk semiconductor properties.—Bulk semiconductor properties can greatly influence the performance of the liquid-junction photovoltaic cell. Some properties which can be controlled in semiconductor manufacture and cell design are the dopant concentration, the thickness of the semiconductor, and the amount of light absorbed in the semiconductor. The influence of the solar absorption coefficient is also presented. This parameter is generally fixed for a given semiconductor.

Dopant concentration.—Current-potential curves are presented in Fig. 6 for concentrations of positive background charge ranging from 0.0396×10^{-7} to 2.500×10^{-7} eq/cm³ (2.4×10^{15} to 1.5×10^{17} cm⁻³) and for a semiconductor thickness of 10 Debye lengths. For low to moderate levels of doping, the open-circuit cell potential is independent of dopant concentration. The open-circuit cell potential decreases with very large doping levels due to a decrease in the equilibrium flatband potential. For low to moderately large levels of doping, the charged portion of the equilibrated semiconductor adjacent to the interface consists of an inversion region and a depletion region. Electroneutrality of the interfacial region can be satisfied in the very highly doped semiconductor by a region of low electron concentration. No inversion layer is observed, and the potential variation in the semiconductor (*i.e.*, the flatband potential) is reduced.

The short-circuit current is independent of dopant concentration for the highly doped semiconductor and is reduced at very low dopant levels because of enhanced homogeneous recombination of electron-hole pairs. This effect is dependent upon the rate constants for homogeneous recombination.

The semiconductor Debye length is inversely proportional to the square root of the dopant concentration. If the semiconductor thickness were held constant at a value of 1.69×10^{-5} cm, as opposed to 10 Debye lengths, similar results would be observed for high dopant concentrations. At low dopant concentrations, the semiconductor thickness would be smaller than the space-charge region thickness, and the cell potential would be reduced

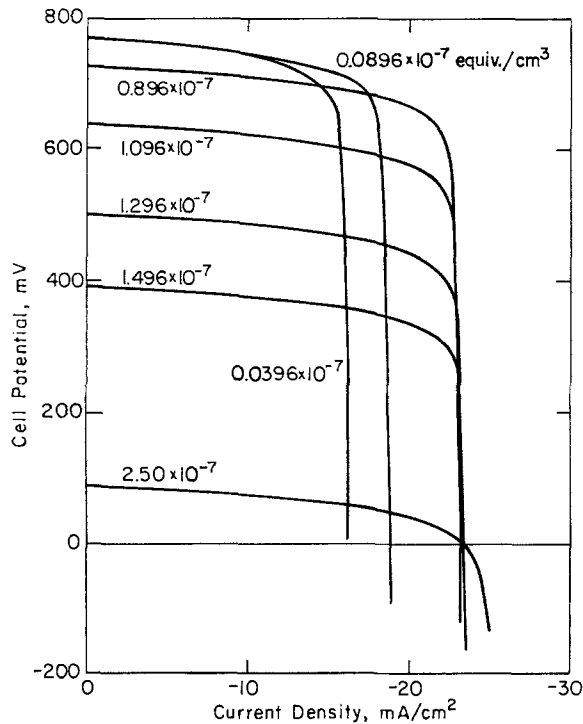


Fig. 6. Computed current-potential curves for an n-type GaAs anode with dopant concentration as a parameter.

(see next section). A change in the Debye length influences the utilization of the incident radiation (see the "Solar absorption coefficient" section below), but the change in cell performance due to this effect is small.

Maximization of power density yields an optimal dopant concentration for the n-GaAs system of about 9.0×10^{-8} eq/cm³. The donor concentration in the work presented by Heller and Miller (27,28) was 6×10^{16} carriers/cm³ (or 9.96×10^{-8} eq/cm³).

Semiconductor thickness. The effect of semiconductor thickness on the cell performance is presented in Fig. 7 for a characteristic depth of light adsorption of 228.2 Å

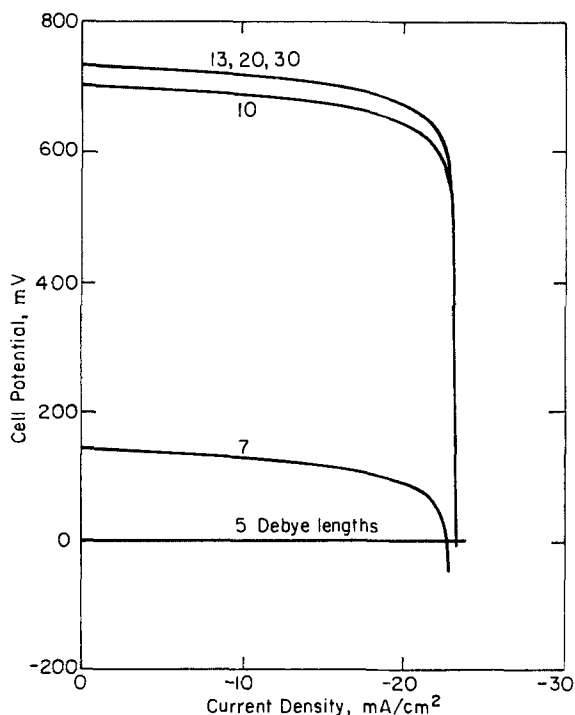


Fig. 7. Computed current-potential curves for an n-type GaAs anode with semiconductor thickness as a parameter.

(corresponding to 1.35 Debye lengths). The cell potential increases as the thickness increases from 5 to 13 Debye lengths. The current-potential curve is essentially unchanged for an increase in thickness from 13 to 30 Debye lengths. A very thick semiconductor is expected to decrease the system performance because of resistive losses in the semiconductor. For the system described here, however, the resistance losses should be insignificant, even for 1 mm thick crystals. A semiconductor thickness less than the normal space-charge region is associated with saturation of charge in the semiconductor. All mobile electrons are driven from the semiconductor in response to the negatively charged interface, and a large potential gradient across the semiconductor cannot be sustained. This may be regarded to be a limitation to the flatband potential and, therefore, a limitation to the cell potential.

Solar absorption coefficient.—The characteristic length for absorption of light can be compared to the Debye length by the dimensionless absorption coefficient $m\lambda_{sc}$. The open-circuit cell potential is presented in Fig. 8 as a function of the dimensionless absorption coefficient. A maximum in cell potential is observed in the region where the characteristic length for absorption of light is of the same order as the Debye length. The cell potential is relatively insensitive to the dimensionless absorption coefficient within the range of 0.2 to 3.0. Variation of dimensionless absorption coefficient from 0.04 to 10 (two-and-one-half orders of magnitude) results in a deviation from an average open-circuit cell potential of only 14 mV. The optimal value for the dimensionless absorption coefficient was around 0.425, where the characteristic length for light absorption is 2.4 Debye lengths. The absorption coefficient for single-crystal GaAs, averaged over photons with energy greater than the bandgap energy, is 4.4×10^5 cm⁻¹. This value corresponds to a dimensionless absorption coefficient of 0.743 and to a characteristic absorption depth of 1.35 Debye lengths.

Solar flux.—The amount of light absorbed within the semiconductor has a strong effect on cell performance. As seen in Fig. 9, light scattering or reflective losses can reduce the limiting current from -23.2 mA/cm² under full AM-2 irradiation (modeled here with a single mean absorption coefficient) to -14.0 mA/cm² under 60% AM-2 irradiation. The 40% decrease in limiting current is accom-

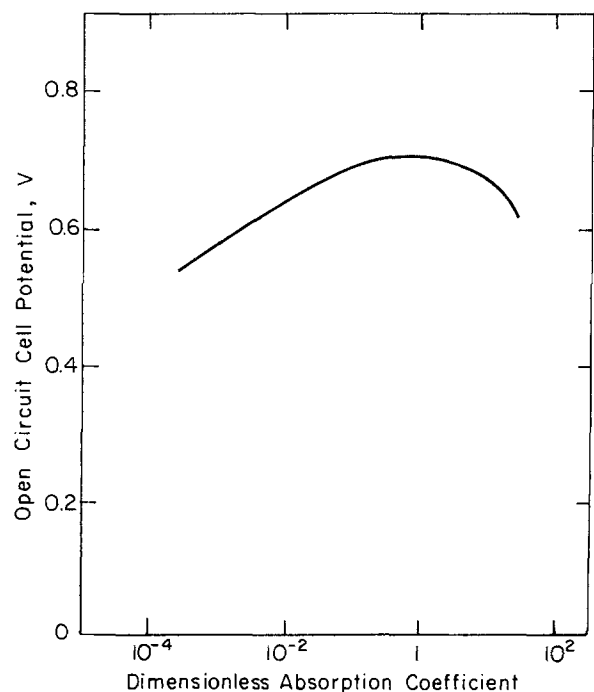


Fig. 8. Open-circuit cell potential as a function of dimensionless solar absorption coefficient.

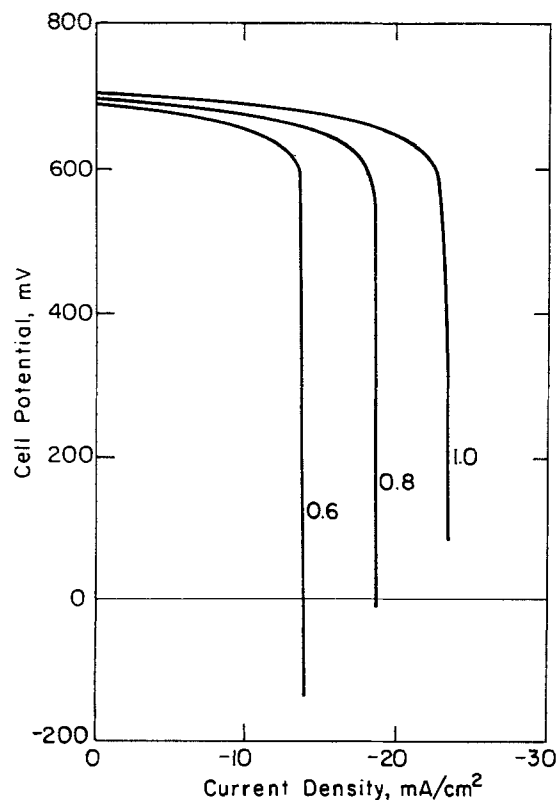


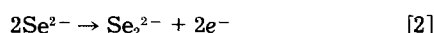
Fig. 9. Computed current-potential curves for an n-type GaAs anode with fractional absorption of incident AM-2 radiation as a parameter.

panied by a 1% decrease in open-circuit cell potential. The amount of light absorbed within the semiconductor is directly related to the generation of the limiting species, holes, and therefore primarily affects the limiting current.

Cell design.—Under electrolyte-side illumination and without interfacial kinetic limitations, electrolyte resistance, and counterelectrode effects, the maximum power efficiency of the cell was calculated to be 15.0%. This is the value that one might observe if the power density is calculated using a potential drop measured between the semiconductor electrode and a reference electrode reversible to the redox reaction and located just outside the diffusion region. The resistance of the electrolyte, mass-transfer and kinetic limitations at the counterelectrode, and the choice of front- or back-illumination will affect this value.

Electrolyte and counterelectrode.—Resistance in the electrolyte and kinetic and mass-transfer effects at the counterelectrode decrease the maximum power-density of the liquid-junction photovoltaic cell. The current-potential curve for a system with no interfacial kinetic limitations (see Fig. 2) is presented in Fig. 10 with electrolyte resistance included. The conductivity of the electrolyte was assumed to be $0.3 \Omega^{-1} \text{ cm}^{-1}$. The cell potential at a given current is reduced by an amount which is proportional to the current density and to the distance L between the counterelectrode and the semiconductor. A 10 cm separation between the counterelectrode and the semiconductor reduces the maximum power efficiency of the cell to 4.0%.

The same base current-potential curve is presented in Fig. 11 and 12 with the effect of kinetic and mass-transfer limitations at the counterelectrode included. The reaction



was assumed to follow the sequence

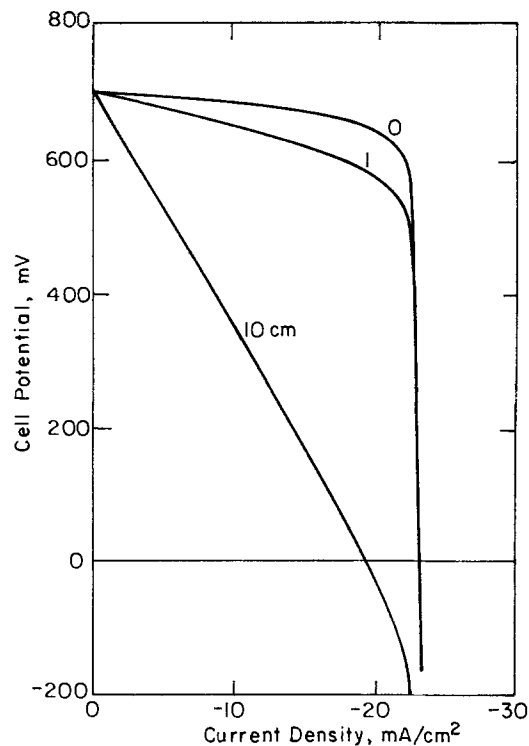
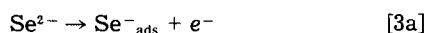


Fig. 10. Computed current-potential curves for an n-type GaAs anode with the separation between the counterelectrode and the semiconductor as a parameter. Solution resistance has been included.

Under the assumption that the second step is equilibrated, the current density at the counterelectrode can be expressed by

$$i = i_0 \left\{ \left[1 - \frac{i}{i_{4,\text{lim}}} \right] \exp \left[\frac{(1-\beta)F}{RT} \eta_{\text{CE}} \right] - \left[1 + \frac{i}{i_{3,\text{lim}}} \right]^{1/2} \exp \left[-\frac{\beta F}{RT} \eta_{\text{CE}} \right] \right\} \quad [4]$$

where i_0 is the exchange current density associated with the bulk concentrations of reactants

$$i_0 = F k_{\text{a},\text{f}} c_{\text{a},\text{f}} c_{4,\infty}^{\beta} \left[\frac{k_{\text{a},\text{b}} k_{\text{c},\text{b}}^{1/2}}{k_{\text{b},\text{f}}^{1/2}} c_{3,\infty}^{1/2} \right]^{(1-\beta)}$$

$i_{3,\text{lim}}$ is the diffusion-limited current density associated with species Se_2^{2-} , $i_{4,\text{lim}}$ is the diffusion-limited current density associated with species Se^{2-} , and n is equal to one.

The effect of diffusion limitation to currents at the counterelectrode is presented in Fig. 11 with diffusion-limited current density at the counterelectrode as a parameter. Diffusion-limited current densities of 20 mA/cm² for Se_2^{2-} and 80 mA/cm² for Se^{2-} correspond to a Nernst stagnant diffusion layer thickness of about 0.010 cm. An exchange-current density of 100 mA/cm² was assumed. The influence of the exchange current density on the current-potential curve is presented in Fig. 12. Diffusion-limited currents of 20 and 80 mA/cm² were assumed for the Se_2^{2-} and the Se^{2-} species, respectively. Kinetic limitations, either at the counterelectrode or the semiconductor, cause an inflection point in the current-potential curve.

The calculated maximum power efficiency is 11.8% for a cell with a 1.0 cm gap between the semiconductor and the counterelectrode, an exchange current density of 100 mA/cm², and diffusion-limited currents of 20 and 80 mA/cm² at the counterelectrode for the Se_2^{2-} and the Se^{2-} species, respectively. Reduction of illumination due to absorption in the electrolyte and reflection were not included.

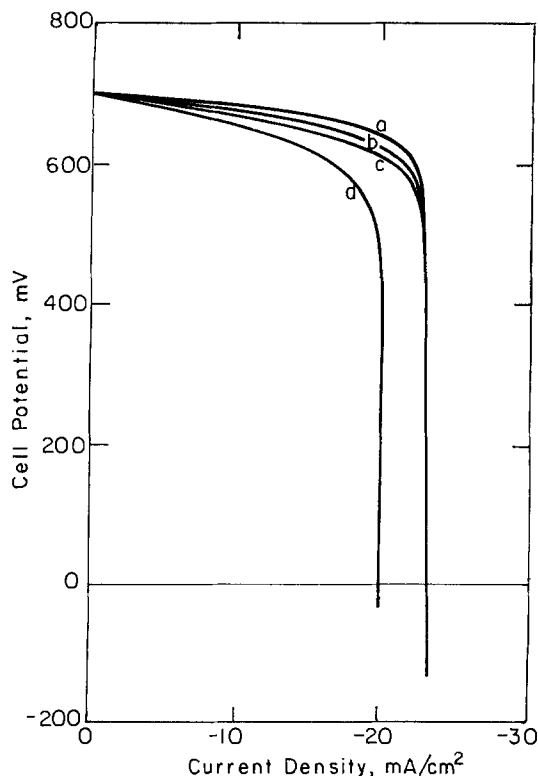


Fig. 11. Computed current-potential curves for an n-type GaAs anode with diffusion-limited current density at the counterelectrode as a parameter. Curve a, counterelectrode effects not included; curve b, $i_{lim,3} = 20 \text{ mA/cm}^2$ and $i_{lim,4} = 20 \text{ mA/cm}^2$; curve c, $i_{lim,3} = 10 \text{ mA/cm}^2$ and $i_{lim,4} = 40 \text{ mA/cm}^2$; curve d, $i_{lim,3} = 5 \text{ mA/cm}^2$ and $i_{lim,4} = 20 \text{ mA/cm}^2$.

Front- and back-illumination.—The semiconductor can be illuminated at the semiconductor-electrolyte interface (front illumination) or at the semiconductor-current collector interface (back illumination). The influence of the

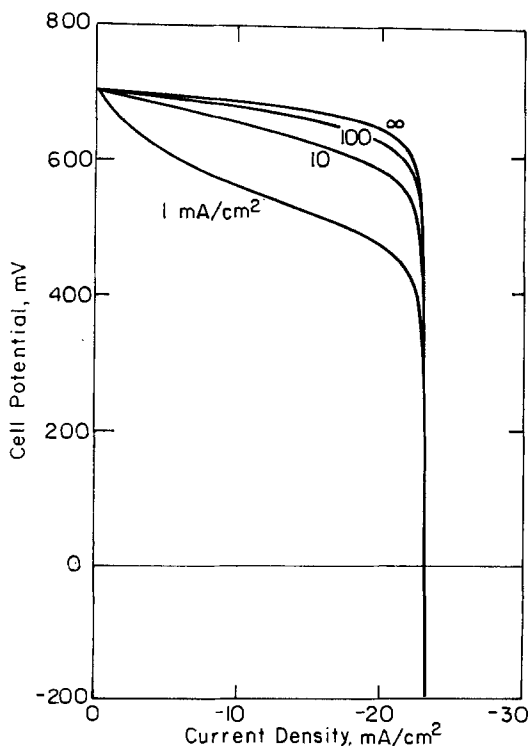


Fig. 12. Computed current-potential curves for an n-type GaAs anode with counterelectrode exchange-current density as a parameter. Kinetic and mass-transfer effects at the counterelectrode have been included.

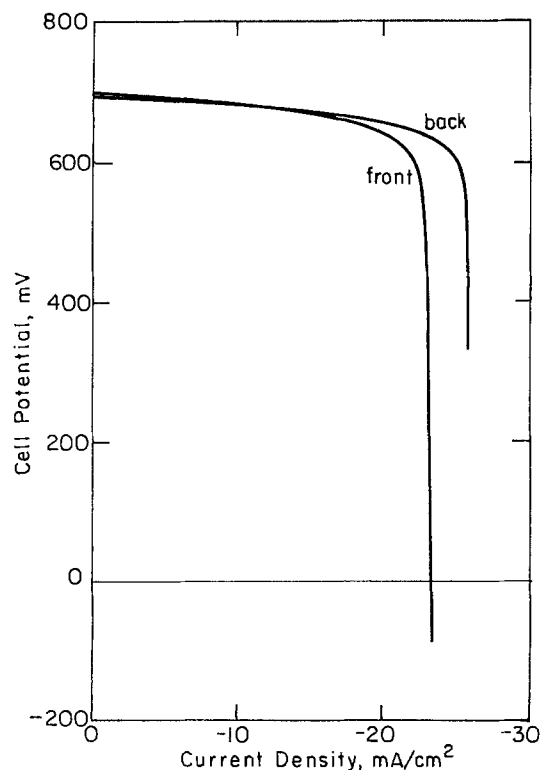


Fig. 13. Computed current-potential curves for an n-type GaAs anode with the direction of illumination (front or back illumination) as a parameter.

direction of illumination is strongly dependent upon the relative rates of recombination in the bulk and at the interfaces involved.

Under the conditions of a negligible surface recombination at the semiconductor-current collector interface and of a small rate of homogeneous recombination as compared to the rate of recombination at the semiconductor-electrolyte interface, back-illumination increases the power output. This effect is illustrated in Fig. 13, where current-potential curves for the case with no interfacial kinetic limitations are presented for the semiconductor under front and back-illumination. The limiting current under back-illumination is -25.6 mA/cm^2 , and the maximum power efficiency is 17.0%. The limiting current under front-illumination is -23.2 mA/cm^2 , and the maximum power efficiency is 15.0%. Generation of electron-hole pairs in regions where recombination is facilitated reduces the power output.

Discussion

Experimental results reported in the literature show the general shape of the current-potential curves presented in this paper. Small scale systems are generally designed with large counterelectrode areas (to minimize any limitation to current flow at the counterelectrode) and a small depth of electrolyte over the semiconductor surface (to minimize losses of illumination by absorption in the electrolyte). Current-potential curves thereby obtained include effects of electrolyte resistance and illumination losses.

Inflection points are observed for many experimental systems, e.g., TiO_2 in 1.0M NaOH (33), TiO_2 in 0.1M Na_2SO_4 at pH less than 10 (adjusted with NaOH and H_2SO_4) (34), $\text{PbFe}_{12}\text{O}_{19}$, $\text{Hg}_2\text{Ta}_2\text{O}_7$, CdFe_2O_4 , and $\text{Pb}_2\text{Ti}_{1.5}\text{W}_{0.5}\text{O}_{6.5}$ in 0.2M NaOH (35), n- and p-type GaP in liquid ammonia (36), p-GaP in 0.5M H_2SO_4 (37), WO_3 in 1M sodium acetate (38), KTaO_3 in 8.6M NaOH (39), CdS in 0.1M NaOH (40), CdS in 1.0M NaI, 1.0M $\text{Na}_2\text{S}_2\text{O}_3$, and 0.1M I_2 (41), and untreated polycrystalline GaAs with a selenium redox couple (8). These inflection points are indicative of kinetic limitations to charge-transfer or to ion-adsorption reactions at the semiconductor-electrolyte interface (as shown by the

parameter variation in Fig. 1 and 2 in the "Interfacial kinetic limitations" section). Other systems, e.g., ruthenium-treated polycrystalline GaAs (8, 42) and single-crystal GaAs (43) in contact with a selenium redox couple, CdS and Bi₂S₃ in contact with a sulfide-polysulfide redox couple (44), CdS in 1M KCl, 0.8M CH₃COOH, and 0.2M CH₃COOH (45), and p-InP in contact with a vanadium redox couple (8), do not exhibit inflection points. The interfacial reactions are equilibrated for these systems.

The results of the mathematical model presented in this paper are compared to experimental results in Fig. 14. The solid line represents the experimental current-potential curve for a ruthenium-treated n-GaAs photoanode in contact with a selenium redox couple (27, 28). The dashed lines are calculated results in which interfacial reactions were assumed to be equilibrated. Both calculated curves include a 7% loss of illumination; the lower curve includes an electrolyte resistance of 3 Ω-cm². The model parameters are presented in Tables I, II, and III. Bulk transport properties were obtained from the literature; values were assumed for properties characteristic of the semiconductor-electrolyte interface. The model agrees with the experimental results near open circuit, but exhibits a sharper limiting current plateau than the experimental results indicate. This discrepancy may be due to convective overpotential losses due to the textured surface of the semiconductor electrode. An increase in the homogeneous recombination rate constants decreases the sharpness of the potential drop near limiting current but also decreases the cell potential.

Some of the model parameters are associated with characteristics of the current-potential curve. In the absence of counterelectrode effects, the magnitude of the limiting current is determined by the intensity of illumination, and the shape of the curve is determined by kinetic parameters. Kinetic limitations to charge-transfer and to ion-adsorption reactions result in an inflection point. Kinetic limitations at the counterelectrode can also cause an inflection point. The magnitude of the open-circuit potential is a function of the equilibrium potential difference between the semiconductor and the solution. Within the model, this parameter is represented by the equilibrium OSS potential. The surface site energy distribution also influences the open-circuit cell potential. These parameters could be varied by selection of different semiconductor-electrolyte combinations. The open-circuit cell potential is also affected by semiconductor properties, such as bandgap energy and absorption coefficient.

Analytic models of the liquid-junction cell are described in Ref. (46). These models can match experimental current-potential curves but show maxima in electron and hole concentrations near the boundary between space-charge and neutral regions. These maxima were

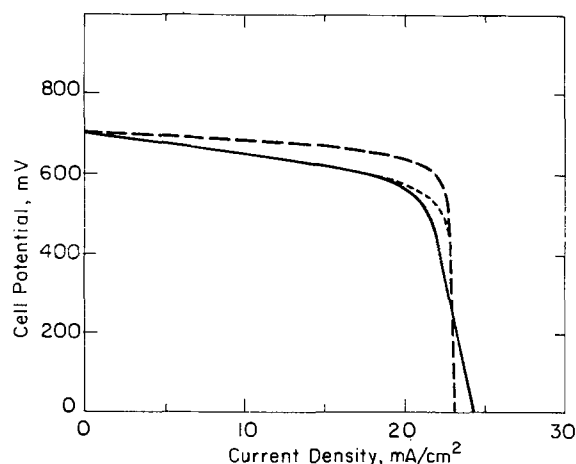


Fig. 14. Comparison of computed current-potential curves (dashed lines) to experimental results (solid line) for an n-type GaAs anode in contact with a selenium redox couple.

not seen in the results of the mathematical model and are probably due to imposition of boundary or matching conditions between those regions.

Conclusions

Kinetic limitations to interfacial charge-transfer and ion-adsorption reactions drastically reduce the power output of the liquid-junction cell. A small interfacial rate constant is compensated by increased potential and concentration driving forces, thus influencing the cell performance.

The cell performance is strongly influenced by bulk-semiconductor and cell-design properties such as the dopant concentration, the semiconductor thickness, and the amount of light adsorbed in the semiconductor. An optimal dopant concentration and semiconductor thickness can be calculated for a given semiconductor system. The resistance of the electrolyte and kinetic and mass-transfer limitations at the counterelectrode influence cell performance and may play an important role in the optimal design of a liquid-junction photovoltaic cell.

Acknowledgment

This work was supported by the United States Department of Energy under Contract no. DE-AC03-76SF00098 through the Director, Office of Energy Research, Office of Basic Energy Sciences, Chemical Sciences Division, and through the Assistant Secretary of Conservation and Renewable Energy, Office of Advanced Conservation Technology, Electrochemical Systems Research Division.

Manuscript submitted June 24, 1983; revised manuscript received May 11, 1984. This was Paper 471 presented at the Minneapolis, Minnesota, Meeting of the Society, May 10-15, 1981.

The University of California assisted in meeting the publication costs of this article.

REFERENCES

1. A. Fujishima and K. Honda, *Nature*, **238**, 37 (1972).
2. J. Manassen, D. Cahen, and G. Hodes, *ibid.*, **263**, 97 (1976).
3. A. J. Bard, *J. Photochem.*, **10**, 59 (1979).
4. H. Ehrenreich and J. H. Martin, *Phys. Today*, **32**, 25 (1979).
5. M. S. Wrighton, *Acc. Chem. Res.*, **12**, 303 (1979).
6. H. Gerischer, *Pure Appl. Chem.*, **52**, 2649 (1980).
7. A. J. Bard, *Science*, **207**, 139 (1980).
8. A. Heller, *Acc. Chem. Res.*, **14**, 154 (1981).
9. M. Green, in "Modern Aspects of Electrochemistry," Vol. 2, J. O'M. Bockris, Editor, Chap. 5, Academic Press, New York (1959).
10. H. Gerischer, in "Advances in Electrochemistry and Electrochemical Engineering," Vol. 1, P. Delahay, Editor, Chap. 4, Interscience, New York (1961).
11. M. D. Archer, *J. Appl. Electrochem.*, **5**, 71 (1975).
12. K. Rajeshwar, P. Singh, and J. DuBow, *Electrochim. Acta*, **23**, 1117 (1975).
13. L. A. Harris and R. H. Wilson, *Ann. Rev. Mater. Sci.*, **8**, 99 (1978).
14. A. J. Nozik, *Ann. Rev. Phys. Chem.*, **29**, 189 (1978).
15. M. Tomkiewicz and H. Fay, *Appl. Phys.*, **18**, 1 (1979).
16. R. H. Wilson, in "CRC Critical Reviews in Solid State and Materials Science," p. 1, CRC Press, Cleveland, OH (1980).
17. R. Memming, *Electrochim. Acta*, **25**, 77 (1980).
18. S. R. Morrison, "Electrochemistry at Semiconductor and Oxidized Metal Electrodes," p. 10, Plenum Press, New York (1980).
19. S. U. M. Kahn and J. O'M. Bockris, in "Modern Aspects of Electrochemistry," Vol. 14, J. O'M. Bockris, B. E. Conway, and R. E. White, Editors, Chap. 3, Plenum Press, New York (1982).
20. M. E. Orazem and J. Newman, *This Journal*, **131**, 2569 (1984).
21. M. E. Orazem and J. Newman, *ibid.*, **131**, 2582 (1984).
22. D. C. Grahame, *Chem. Rev.*, **41**, 441 (1947).
23. J. F. Dewald, in "Semiconductors," N. B. Hannay, Editor, Chap. 17, Reinhold, New York (1959).
24. M. J. Spernaay, "The Electrode Double Layer," Pergamon Press, New York (1972).
25. M. E. Orazem and J. Newman, Paper 471 presented at

- the Minneapolis, MN, Meeting of the Society, May 10-15, 1981.
26. J. Newman, *Ind. Eng. Chem. Fundam.*, **7**, 514 (1968).
 27. A. Heller and B. Miller, in "Interfacial Photoprocesses: Energy Conversion and Synthesis," M. S. Wrighton, Editor, Chap. 12, *Advances in Chemistry Series 184*, The American Chemical Society, Washington, DC (1980).
 28. B. A. Parkinson, A. Heller, and B. Miller, *Appl. Phys. Lett.*, **33**, 521 (1978).
 29. A. Heller, K. C. Chang, and B. Miller, *This Journal*, **124**, 697 (1977).
 30. K. C. Chang, A. Heller, B. Schwartz, S. Menezes, and B. Miller, *Science*, **196**, 1097 (1977).
 31. A. B. Ellis, J. M. Bolts, S. W. Kaiser, and M. S. Wrighton, *J. Am. Chem. Soc.*, **99**, 2848 (1977).
 32. M. S. Wrighton, J. M. Bolts, A. B. Bocarsly, M. C. Palazzotto, and E. G. Walton, *J. Vac. Sci. Technol.*, **15**, 1429 (1978).
 33. Y. Nakato, N. Takamori, and H. Tsubomura, *Nature*, **295**, 312 (1982).
 34. W. Gissler, P. L. Lensi, and S. Pizzini, *J. Appl. Electrochem.*, **6**, 9 (1976).
 35. H. H. Kung, H. S. Jarrett, A. W. Sleight, and A. Ferretti, *J. Appl. Phys.*, **48**, 2463 (1977).
 36. J. Belloni, G. Van Amerongen, M. Herlem, J.-L. Sculfort, and R. Heindl, *J. Phys. Chem.*, **84**, 1269 (1980).
 37. M. P. Dare-Edwards, A. Hamnett, and J. B. Goodenough, *J. Electroanal. Chem.*, **119**, 109 (1981).
 38. M. A. Butler, R. D. Nasby, and R. K. Quinn, *Solid-State Commun.*, **19**, 1011 (1976).
 39. A. B. Ellis, S. W. Kaiser, and M. S. Wrighton, *J. Phys. Chem.*, **80**, 732 (1977).
 40. R. Memming, *Ber. Bunsenges. Phys. Chem.*, **81**, 732 (1977).
 41. H. Gerischer and J. Gobrecht, *ibid.*, **80**, 327 (1976).
 42. W. D. Johnston, Jr., H. J. Leamy, B. A. Parkinson, A. Heller, and B. Miller, *This Journal*, **127**, 90 (1980).
 43. H. Gerischer, *J. Electroanal. Chem.*, **82**, 133 (1977).
 44. B. Miller and A. Heller, *Nature*, **262**, 680 (1976).
 45. R. A. L. Vanden Berghe, W. P. Gomes, and F. Cardon, *Ber. Bunsenges. Phys. Chem.*, **77**, 289 (1973).
 46. M. E. Orazem, Ph.D. Thesis, University of California, Berkeley, CA (1983).

Mathematical Modeling of Liquid-Junction Photovoltaic Cells

III. Optimization of Cell Configurations

Mark E. Orazem¹ and John Newman*

Materials Molecular Research Division of Lawrence Berkeley Laboratory, and Department of Chemical Engineering, University of California, Berkeley, California 94720

ABSTRACT

A one-dimensional mathematical model of the liquid-junction photovoltaic cell was coupled with primary resistance calculations to predict the optimal performance of three cell configurations. Two cells are considered in which the semiconductor is illuminated from the electrolyte side and one in which the semiconductor is illuminated from the current-collector side. An economic analysis is presented based upon these results. The performance of the liquid-junction photovoltaic cell is dependent upon the design, surface area, and placement of the counterelectrode and current collectors.

Most studies of the liquid-junction photovoltaic cell have been oriented toward developing an understanding of the semiconducting electrode which characterizes the cell [see, e.g., Ref. (1-19)]. This work describes the design and optimization of liquid-junction photovoltaic devices. The advantages and problems inherent in the liquid-junction cell are reviewed, and a mathematical model of the liquid-junction cell (20, 21) is used to predict the optimal performance of various cell configurations. An economic analysis is presented based upon these results.

The liquid-junction photovoltaic cell has appeal because, in contrast to solid-state junctions, the junction between electrolyte and semiconductor is formed easily and allows use of polycrystalline semiconductors. The electrochemical nature of the cell allows both production of electricity and generation of chemical products which can be separated, stored, and recombined to recover the stored energy. These features could make the liquid-junction cell an economical alternative to solid-state photovoltaic devices for solar energy conversion.

Liquid-junction cells also have the advantages that are attributed to other photovoltaic devices. Photovoltaic power plants can provide local generation of power on a small scale. The efficiency and cost of solar cells is independent of scale, and overall efficiency is improved by locating the power plant next to the load. Nuclear and fossil-fuel burning plants, in contrast, are economical only if built on a large scale (on the order of 1000 MW) (22).

The design of a liquid-junction photovoltaic cell requires selection of an appropriate semiconductor-

electrolyte combination and design of an efficient cell configuration. The selection of a semiconductor is based upon the bandgap, which provides an upper limit to the conversion efficiency of the device, and the choice of electrolyte is governed by the need to limit corrosion. The optimal design of the liquid-junction photovoltaic cell is aided by use of mathematical models.

Bandgap.—Photovoltaic cells rely on the unique properties of semiconductors to convert incident radiation to electrical current. The semiconductor property of interest is the moderate gap between the valence and the conduction-band energy levels. Incident photons of light with energy greater than or equal to the bandgap energy transfer their energy to valence-band electrons, producing conduction-band electrons and vacancies in the valence band.

An upper limit to the efficiency of photovoltaic devices can be established, based upon the bandgap and the solar spectrum, without consideration of cell configuration. This "ultimate efficiency" is given by (11)

$$\eta_{\text{ult}} = \frac{E_g \int_{E_g}^{\infty} N(E) dE}{\int_0^{\infty} E N(E) dE} \quad [1]$$

where E_g is the semiconductor bandgap energy, E is the photon energy, and $N(E)$ is the number density of incident photons with energy E . The fraction of the power in the solar spectrum that can be converted to electrical power is a function of the bandgap of the semiconductor. Photons with energy less than the bandgap cannot produce electron-hole pairs. Photons with energy greater than the bandgap yield the bandgap energy (23-25).

* Electrochemical Society Active Member.

¹Present address: Department of Chemical Engineering, University of Virginia, Charlottesville, Virginia 22901.

The "ultimate efficiency" of Eq. [1] represents an upper limit to conversion of solar energy (11, 26, 27); factors such as reflection and absorption losses of sunlight, kinetic and mass-transfer limitations, and recombination will reduce the efficiency. These effects are included in the "cell configuration" section. A bandgap between 1.0 and 1.5 eV is generally considered to be appropriate for efficient conversion of solar energy.

Corrosion.—The application of liquid-junction technology to photovoltaic power conversion is limited by problems associated with the semiconductor-electrolyte interface. Primary among these problems is corrosion. Efficient conversion of solar energy requires a bandgap between 1.0 and 1.5 eV and most semiconductors near this bandgap corrode readily under illumination. Semiconductors with large bandgaps (4-5 eV) tend to be more stable, but cannot convert most of the solar spectrum.

Among the approaches taken to solve this problem, the most successful concern the matching of an electrolyte to the semiconductor. The rate of corrosion is reduced if the semiconductor is in equilibrium with the corrosion products. The rate of corrosion can also be reduced by using a redox couple which oxidizes easily. The oxidation of the redox couple $\text{Se}_{r+2-}/\text{Se}_{r2-}$, for example, has been shown to compete successfully with photocorrosion reactions for holes in n-type GaAs electrodes (8, 28).

p-Type semiconductors used as cathodes are more stable than the more common and generally more efficient n-type semiconducting anodes. The inefficiency of p-type photocathodes has been attributed to the presence of surface states near the valence band energy. A stable p-type photocathode has been developed, however, with a solar conversion efficiency of 11.5% (29). Protective films have been proposed to be a solution to electrode corrosion. The electrode, in this case, would be a small bandgap semiconductor covered by a film composed of either a more stable large bandgap semiconductor, a conductive polymer, or a metal. A large Schottky barrier is frequently present at such semiconductor-metal and semiconductor-semiconductor interfaces which blocks the flux of holes from the semiconductor to the electrolyte. In cases where the photocurrent is not blocked, corrosion can take place between the semiconductor and the protective film (17, 30). Menezes *et al.* (31) discuss the difficulties in avoiding absorptive losses in the metal film while maintaining sufficient integrity to serve the semiconductor corrosion protection function. Frese *et al.* (32) have, however, reported a measurable improvement in the stability of GaAs with less than a monolayer gold metal coverage. Thin conductive polypyrrole films appear to be successful in inhibiting corrosion in some electrolytes (33-38). In addition, insulating polymer films deposited on grain boundaries can improve the performance of polycrystalline semiconductors by reducing surface recombination rates (39).

Mathematical model.—Development of a mathematical model constitutes an important step toward design and optimization of the liquid-junction photovoltaic cell. A one-dimensional mathematical model has been developed (20, 21) which treats explicitly the semiconductor, the electrolyte, and the semiconductor-electrolyte interface in terms of potentials and concentrations of charged species. The model incorporates macroscopic transport equations in the bulk of the semiconductor and electrolyte. Homogeneous and heterogeneous recombination of electron-hole pairs is included within the model. Recombination takes place at the semiconductor-electrolyte interface through interfacial sites, which can enhance the recombination rate. Surface sites at the semiconductor-metal interface were not included within the model.

The coupled nonlinear ordinary differential equations of the model were posed in finite-difference form and solved numerically. The mathematical model can be used to gain insight into the operation of cells with semiconducting electrodes, and to optimize their design. The model was used here to calculate the effect of cell design

Table I. Counterelectrode parameters

Diffusion-limited current density	$i_{s,lim}$	20.0 mA/cm ²
	$i_{e,lim}$	80.0 mA/cm ²
Exchange current density	i_0	100.0 mA/cm ²

on the performance of an n-type GaAs semiconducting anode in contact with an 0.8M K_2Se , 0.1M K_2Se_2 , 1.0M KOH electrolytic solution. The choice of this semiconducting electrode system was based upon the work of Heller and associates (8, 40-42). Cell design parameters are presented in Table I, and the parameters used in modeling the liquid-junction cell are presented elsewhere (20, 43).

Cell Configuration

The optimal design of liquid-junction photovoltaic cells shares constraints with solid-state photovoltaic cells (44, 45). Current collectors cast shadows and can reduce the amount of sunlight absorbed in the semiconductor. A constraint unique to the liquid-junction cell is the placement of the counterelectrode relative to the semiconductor-electrolyte interface. Mass-transfer and kinetic limitations at the counterelectrode and resistance of the electrolyte can play important roles in the optimal design of the liquid-junction photovoltaic cell. These considerations are treated qualitatively by Parkinson (46).

Under electrolyte-side illumination and without illumination losses, interfacial kinetic limitations, electrolyte resistance, and counterelectrode limitations, the maximum power efficiency of the cell was calculated (43) to be 15.3%. The corresponding value under back (or current-collector) side illumination was calculated (43) to be 17.2%. These are the values that one might calculate using a potential drop measured between the semiconductor electrode and a reference electrode reversible to the redox reaction and located just outside the diffusion region. The resistance of the electrolyte, illumination losses, and mass-transfer and kinetic limitations at the counterelectrode affect these values and are influenced by cell design. The difference between front and back illumination is due to the assumption that facilitated recombination does not take place at the semiconductor-current collector interface.

The performance of three cell configurations was calculated for operation under AM-2 solar illumination (882 W/m²). The semiconductor was assumed to be in the form of a thin film [see Mitchell for a review of thin-film photovoltaic technologies (47)]. Interfacial kinetic limitations were not included (20, 43). The one-dimensional model of the liquid-junction cell was coupled with the resistance to current flow associated with the two-dimensional systems. Some methods for calculation of this resistance were reviewed by Fleck *et al.* (48).

System 1: wire counterelectrode.—The liquid-junction photovoltaic cell with a wire-grid counterelectrode is presented in Fig. 1a. The cell consists of a semiconductive film supported on a metallic current collector, a wire-grid counterelectrode, and a transparent glass cover plate. The space between the cover plate and the semiconductor is filled with the electrolyte. The glass plate is an essential part of the cell because it keeps the system clean and allows optimal orientation of the cell for collection of sunlight. This cell is designed for conversion of solar energy into electrical energy; no provision is made for separation of chemical products. A two-dimensional representation of the cell is presented in Fig. 1b.

Sunlight absorbed in the semiconductor must pass through the cover plate, past the counterelectrode, and through the electrolyte. Reflection at each of the interfaces (air-glass, glass-electrolyte, and electrolyte-semiconductor), absorption in the glass and electrolyte, and screening by the counterelectrode decrease the amount of light which can be used for generation of electron-hole pairs. Absorption losses in the electrolyte can be limited by maintaining a small gap between the counterelectrode and the semiconductor. A wide spacing

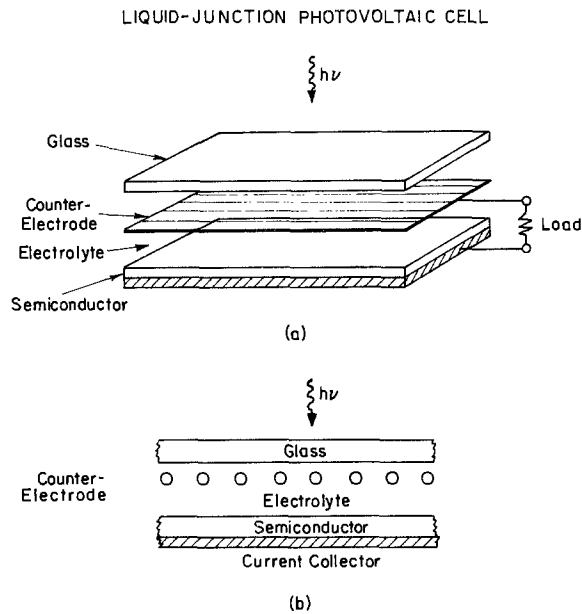


Fig. 1. Design of the liquid-junction photovoltaic cell. System 1: wire counterelectrode.

of counterelectrode elements reduces the screening of the semiconductor but also increases the influence of kinetic and mass-transfer effects at the counterelectrode as well as ohmic drop.

The one-dimensional model of the liquid-junction photovoltaic cell was used with averaged uniform current density and solar flux. The shadow of the counterelectrode was implicitly assumed to be diffuse. Resistive losses in the electrolyte were calculated from a two-dimensional solution of Laplace's equation (49-53). The potential drop in the electrolyte was given by Eq. [14] in Ref. (53). The current density at the counterelectrode was assumed to be uniform and was related to the semiconductor current density by

$$i_{ce} = i_{sc} \left(\frac{L}{\pi D} \right) \quad [2]$$

and the counterelectrode shadow was assumed to reduce the magnitude of incident light by a factor of $(1 - D/L)$. The effective solar flux was therefore given by

$$q_{sc} = q_0 \left(1 - \frac{D}{L} \right) (1 - \rho_{air-glass}) e^{-(m_x)_{glass}} (1 - \rho_{glass-soln}) e^{-(m_x)_{soln}} (1 - \rho_{soln-sc}) \quad [3]$$

where ρ_{j-k} is the reflectance associated with the interface $j - k$ and m is the extinction coefficient for a given phase of depth x .

The design parameter for this cell design is the ratio of the counterelectrode element spacing to the counterelectrode element diameter, L/D . When L/D has a value of one, the semiconductor is completely shaded from illumination; when L/D is very large, counterelectrode limitations dominate.

The power density of the cell with a counterelectrode radius of 0.05 cm is presented in Fig. 2 as a function of current density with L/D as a parameter. The maximum power density is presented in Fig. 3 as a function of L/D . The separation between the cover plate and the counterelectrode was 0.5 cm, and the separation between the semiconductor and the counterelectrode was 0.5 cm. The electrolyte depth was therefore 1.1 cm. The optimal value of L/D is 14, and the maximum power density obtained is 63.5 W/m². The current density under the optimal condition is 11.8 mA/cm² delivered at a cell potential of 538.7 mV. The maximum power efficiency of the wire-counterelectrode cell was 7.2%.

Kinetic limitations at the counterelectrode further reduce this efficiency. An exchange current density of

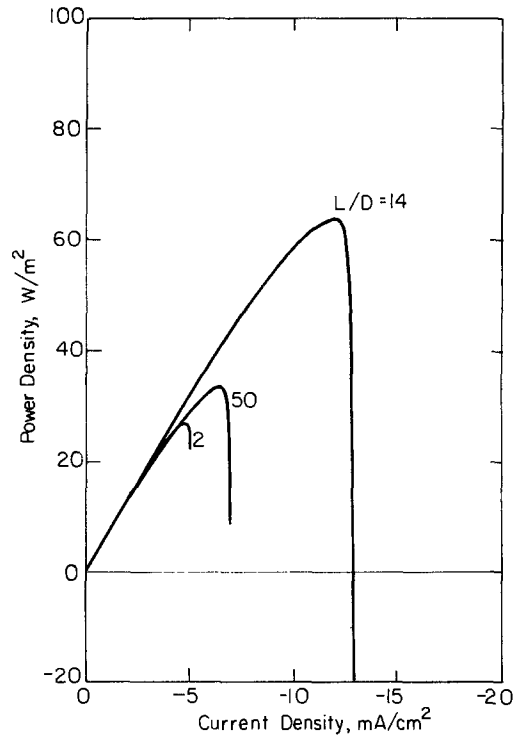


Fig. 2. Power density as a function of current density for system 1 with a counterelectrode element diameter of 0.10 cm.

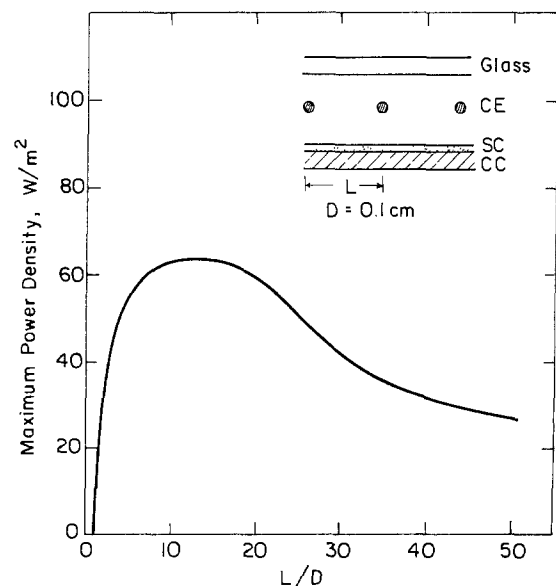


Fig. 3. Maximum power density as a function of L/D for system 1 with a counterelectrode element diameter of 0.10 cm.

1 mA/cm² leads to a 5.5% power efficiency at an optimal L/D of 10.

System 2: slotted semiconductor.—The liquid-junction cell configuration with a slotted-semiconductor electrode is presented in Fig. 4. A glass cover plate protects the cell. Sunlight passes through the cover plate and the electrolyte to illuminate the semiconductor surface. Electrical current passes between the semiconductor and the counterelectrode through slots cut in the semiconductor. This configuration has the advantage that no shadows are cast upon the semiconductor; furthermore, reaction products can be separated if a membrane is placed between the semiconductor and the counterelectrode.

The primary current distribution and the resistance of a cell containing a slotted electrode were calculated using numerical methods coupled with the Schwarz-Christoffel transformation (20, 54). The cell resistance is a function of three geometric ratios, chosen to be t/G , h/G , and L/h

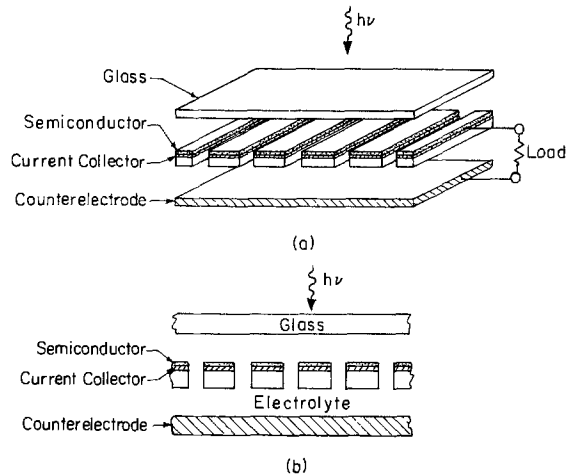


Fig. 4. Design of the liquid-junction photovoltaic cell. System 2: slotted semiconductor.

where L is the half-length of the protruding electrode assembly, t is the thickness of the protruding electrode assembly, G is the half-gap between the electrode assemblies, and h is the separation between the electrode and the upper insulating wall. h is also the separation between the counterelectrode and the lower edge of the semiconductor-electrode assembly.

The performance of this cell is a function of four geometric parameters. The distance between the counterelectrode and the semiconductor assembly was chosen to be 0.5 cm, and the semiconductor assembly thickness was assumed to be 0.1 cm. The primary resistance for this system is presented in Fig. 5 as a function of L/D with h/G as a parameter. The maximum power density is presented in Fig. 6 as a function of L/h and h/G as a parameter. L/h was varied by varying the half-length; h/G by varying the half-gap. The maximum power density for this system is obtained with a small gap. For $h/G = 0.5$ ($G = 1$ cm), the maximum power density was 47.8 W/m^2 , and the maximum power efficiency was 5.4%. The current density under maximum power conditions was 15 mA/cm^2 delivered at 477.6 mV. For $h/G = 10$ ($G = 0.05$ cm), the maximum power density was 67.7 W/m^2 , and the maximum power efficiency was 7.7%. At maximum power, the current density 15.2 mA/cm^2 delivered at 534.6 mV.

System 3: back-illuminated semiconductor.—A cell design is presented in Fig. 7, in which the semiconductor is illuminated from the current-collector side. The semiconducting film is deposited on a pane of transparent conducting glass. A current collecting grid is used to offset the low conductivity of the glass. The semiconductor is separated from the counterelectrode by a gap

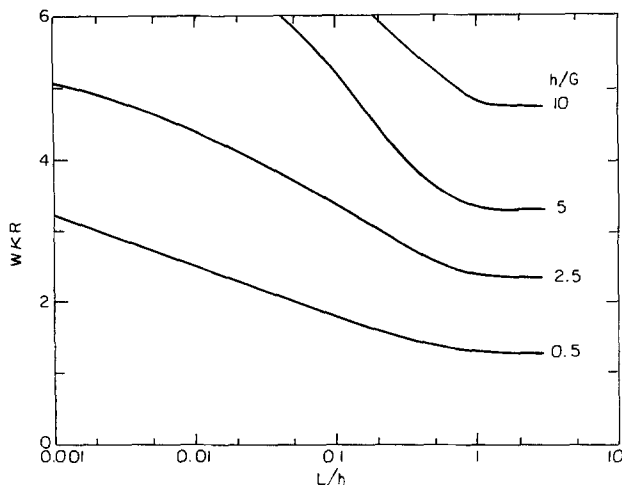


Fig. 5. Primary cell resistance as a function of L/h for system 2 with h/G as a parameter.

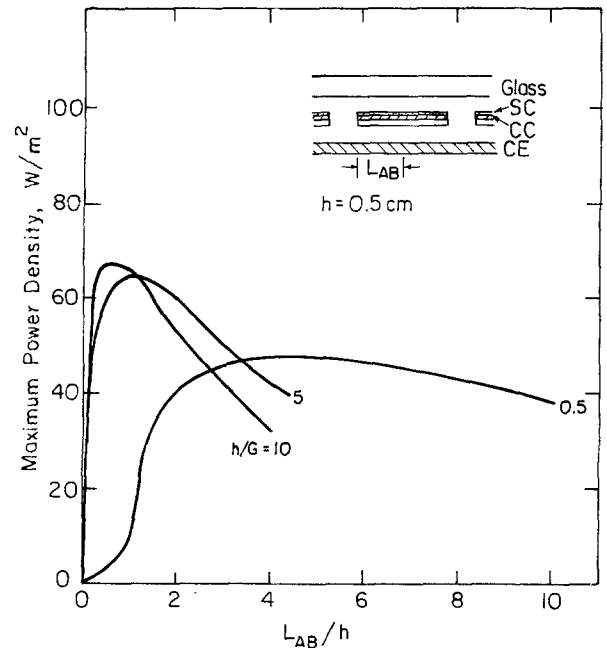


Fig. 6. Maximum power density as a function of L/h for system 2 with h/G as a parameter.

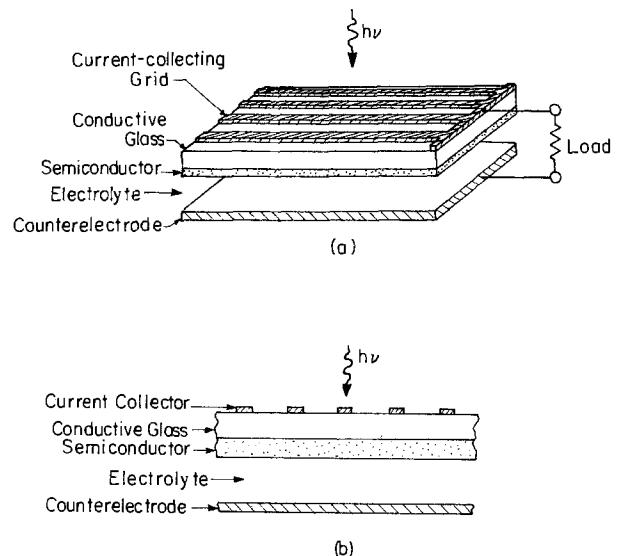


Fig. 7. Design of the liquid-junction photovoltaic cell. System 3: back-illuminated semiconductor.

filled with electrolyte. This design could be used with a membrane within the gap, which would allow separation of reaction products at each of the electrodes.

The potential drop between the semiconductor and the current collecting grid can be obtained through application of the general solution to the resistance of a rectangular conductor with arbitrarily placed electrodes presented by Moulton (55, 56).

The transparent conducting support for the semiconducting film was assumed to be SnO_2 , which is commonly used as a transparent electrode. SnO_2 is a large bandgap semiconductor and is essentially transparent to light with energy below 3.7 eV. The properties of SnO_2 have been reviewed by Jarzebski and Marton (57-59). The conductivity of the transparent material was assumed to be 50 mho/cm, and the total absorption and reflection losses at the air- SnO_2 interface for a 1/8 in. thick plate were assumed to be 8%. The reflectance at the SnO_2 -GaAs interface was assumed to be 5%. The separation between the counterelectrode and the semiconductor was 0.5 cm.

The maximum power density is presented in Fig. 8 as a function of the ratio of the current-collector-element

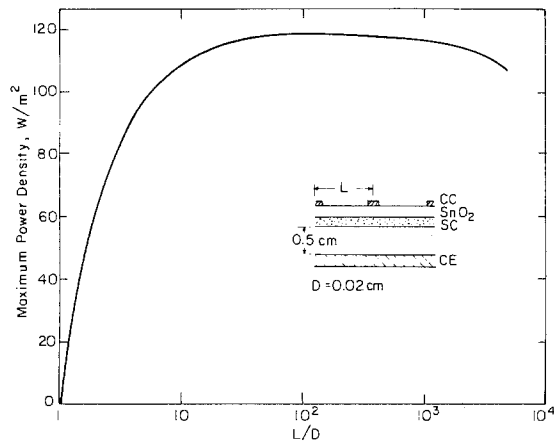


Fig. 8. Maximum power density as a function of L/D for system 3 with a current-collector element thickness of 0.01 cm.

spacing to the element width L/D . When L/D is equal to one, the semiconductor is completely blocked, and the power density is zero. When L/D is large, the resistance of the SnO_2 becomes important. The optimal value of L/D is around 100; the maximum power density is 118.5 W/m^2 , and the power efficiency is 13.4%. The current density under optimal operating conditions is 21.0 mA/cm^2 delivered at a cell potential of 564.3 mV.

The excellent performance of this cell design as compared to systems 1 and 2 can be misleading. Facilitated recombination at the semiconductor-metal interface was not included in the model. The back-illuminated system does have inherent advantages over front-illuminated cells. Optical losses, for example, can be smaller, and separation of electrochemical products is feasible. The relative rates of electron-hole recombination at the semiconductor-metal and the electrolyte-semiconductor interfaces, however, will influence the relative merit of front and back illumination.

Intensity of Illumination

The intensity of solar illumination varies with location, cloud cover, day of year, and time of day. In addition, mirrors and lenses can be used to concentrate the sunlight and reduce the amount of semiconducting material incorporated into the cell. The prediction of the performance of a given design of the liquid-junction photovoltaic cell must therefore consider the effect of the intensity of illumination.

The maximum power efficiency is presented as a function of illumination intensity in Fig. 9, 10, and 11 for systems 1, 2, and 3, respectively. The cells were designed with the design parameters calculated to be optimal under AM-2 illumination. The power efficiency decreases with increasing illumination due to the influence of electrolyte resistance and kinetic and mass-transfer limitations at the counterelectrode. These phenomena become increasingly important as current densities increase, and mass-transfer limitations at the counterelectrode result in an upper limit for cell currents.

The maximum power efficiency for systems 2 and 3 without counterelectrode limitations is also presented in Fig. 10 and 11. These results are appropriate for cells with porous counterelectrodes. A porous counterelectrode may not be feasible for system 1 because of the need in this system to pass sunlight through the counterelectrode. The efficiency still decreases with illumination intensity due to electrolyte resistance.

The maximum cell current obtained under large magnitudes of illumination depends upon the ratio of the counterelectrode area to the semiconductor area. This ratio must be large for liquid-junction photovoltaic cells designed for large intensities of illumination. Replacement of the flat-plate counterelectrode with a porous electrode (60) can increase the counterelectrode area of systems 2 and 3. Inclusion of a cooling system in the cell design be-

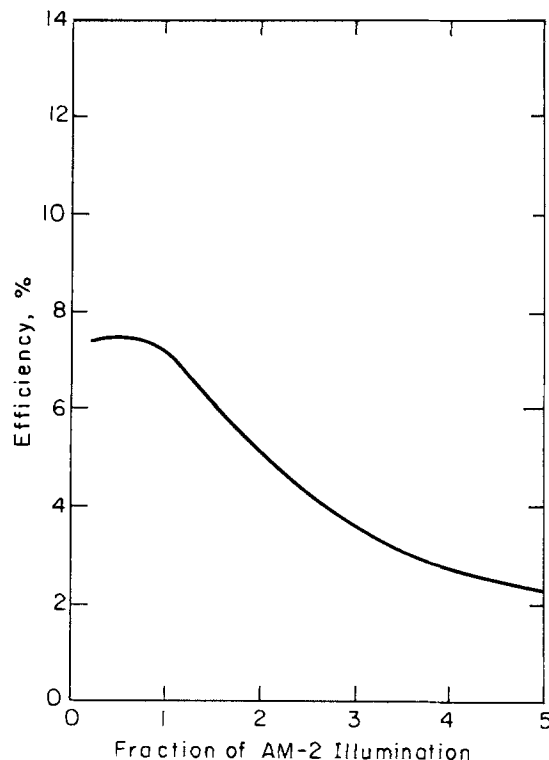


Fig. 9. Maximum power efficiency as a function of the fraction of AM-2 illumination (882 W/m^2) for system 1 with $L/D = 14$.

comes important under these conditions. The electrolyte itself can serve as a heat-exchange medium in photoelectrochemical systems.

Discussion and Economic Analysis

The cells discussed in the previous sections can be divided into two groups, front and back illuminated, within which they can be compared fairly. The comparison of front- and back-illuminated cells depends upon the relative rates of recombination at the semiconductor-metal

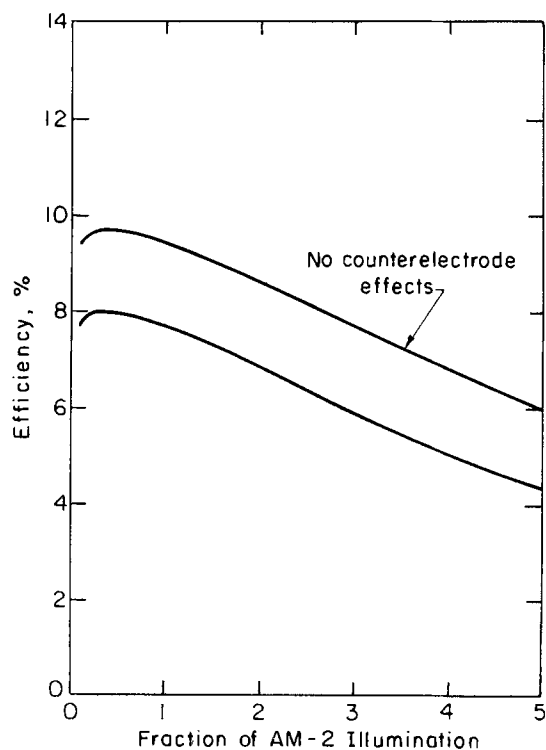


Fig. 10. Maximum power efficiency as a function of the fraction of AM-2 illumination (882 W/m^2) for system 2 with $h/G = 10$ and $L/h = 0.5$.

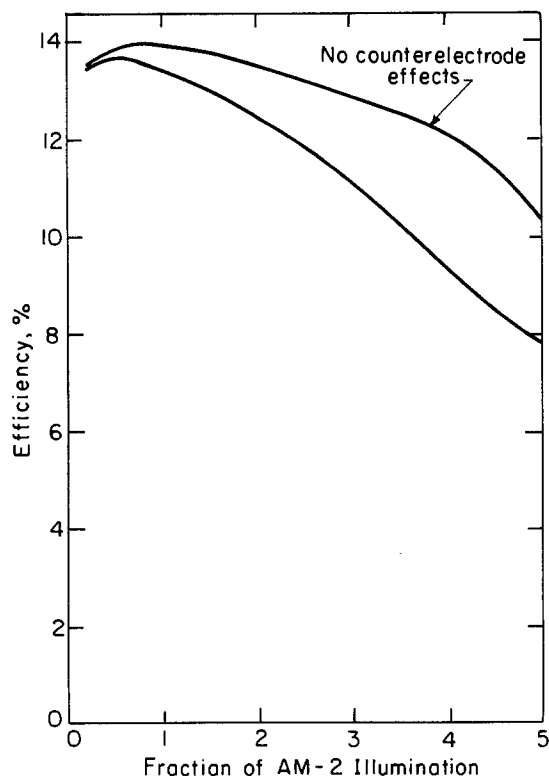


Fig. 11. Maximum power efficiency as a function of the fraction of AM-2 illumination (882 W/m^2) for system 3 with a current-collector half-width of 0.01 cm and with $L/D = 100$.

and electrolyte-semiconductor interfaces, and these rates will differ from one system to another.

The calculated power efficiencies are presented in Table II for the front-illuminated systems. Semiconductor effects, such as recombination, reduce the power efficiency from a value of 37%, based solely upon bandgap, to 15.3%. Reflection losses, with an arbitrarily chosen 8% efficiency of illumination, reduce this value to 12.2%. This value can be compared to the 12% efficiency obtained in the experimental work of Heller and Miller (8, 40, 41). The effect of cell design and illumination losses is to reduce the performance to 7.2% for system 1 and 7.7% for system 2.

The calculated power efficiencies are presented in Table III for the back-illuminated system. Semiconductor effects reduce the power efficiency from a value of 37%, based solely upon bandgap, to 17.2%. Enhanced recombination at the semiconductor-current collector interface was not included in these calculations. The effect of cell design and illumination losses is to reduce the power efficiency to 13.4%.

The calculated performance could be improved by making distances between semiconductor and counter-

Table II. Power efficiency under front illumination

	No illumination losses	Illumination losses*	Experimental results
Optimal bandgap	45	36 (80%)	
GaAs bandgap	37	30 (80%)	
Semiconductor-electrolyte junction	15.3	12.2 (80%)	12.0
Cell design (1)	10.1	7.2 (55.4%)	
Cell design (2)	9.8	7.7 (71.6%)	

* In some cases, the number in parenthesis represents the fraction of AM-2 illumination (above the bandgap) which actually enters the semiconductor, after accounting for reflection, shadowing, and absorption in the intervening phases. In other cases, where detailed calculations were not made, it represents the ratio to column 1 because the nonlinear effect of illumination could not be assessed.

Table III. Power efficiency under back illumination

	No illumination losses	Illumination losses*
Optimal bandgap	45	36 (80%)
GaAs bandgap	37	30 (80%)
Current collector and semiconductor-electrolyte junction	17.2	13.8 (80%)
Cell design (3)	15.4	13.4 (86.5%)

* In some cases, the number in parenthesis represents the fraction of AM-2 illumination (above the bandgap) which actually enters the semiconductor, after accounting for reflection, shadowing, and absorption in the intervening phases. In other cases, where detailed calculations were not made, it represents the ratio to column 1 because the nonlinear effect of illumination could not be assessed.

electrode smaller, reducing the effect of electrolyte resistance. The values chosen for this analysis were based primarily on mechanical considerations. A spacing of 0.5 cm was used between all cell elements. A smaller spacing could result in shorting of the counterelectrode and the semiconductor and/or trapping of gas bubbles. The influence of the counterelectrode could be reduced by increasing the flow rate or degree of mixing near the counterelectrode, thereby increasing the limiting current. Kinetic limitations at the semiconductor-electrolyte interface were not considered here and may greatly reduce the performance of some semiconductor systems.

Current-potential curves are presented in Fig. 12 for the front-illuminated cells. The optimally designed cells of systems 1 and 2 are compared to the cell without interfacial kinetic limitations, counterelectrode limitations, and electrolytic resistance. The cell with a slotted semiconductor has a larger power efficiency than the wire-grid counterelectrode cell and can be designed for separation of chemical products. The analysis of the system designed for separation of chemical products would include the electrical resistance of the membrane.

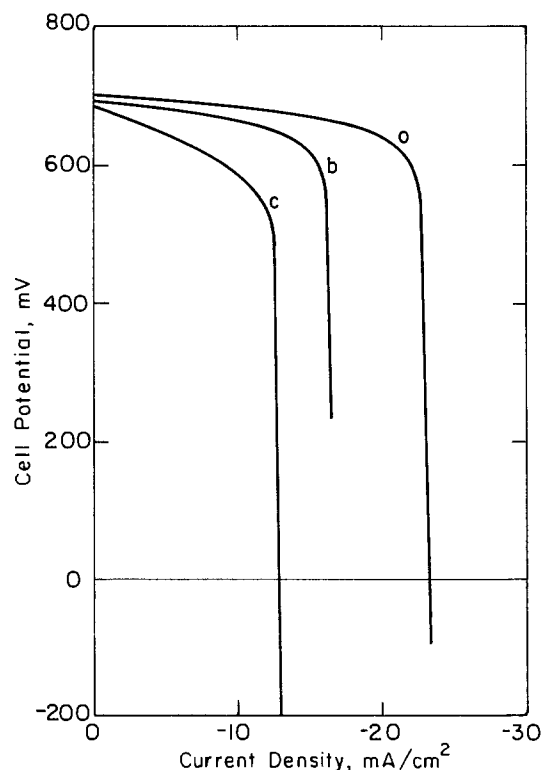


Fig. 12. Cell potential as a function of current density for (a) a front-illuminated semiconductor without kinetic, electrolyte-resistance, and counterelectrode limitations; (b) system 1 with a counterelectrode element diameter of 0.10 cm and with $L/D = 14$; and (c) system 2 with $h/G = 10$ and $L/h = 0.5$.

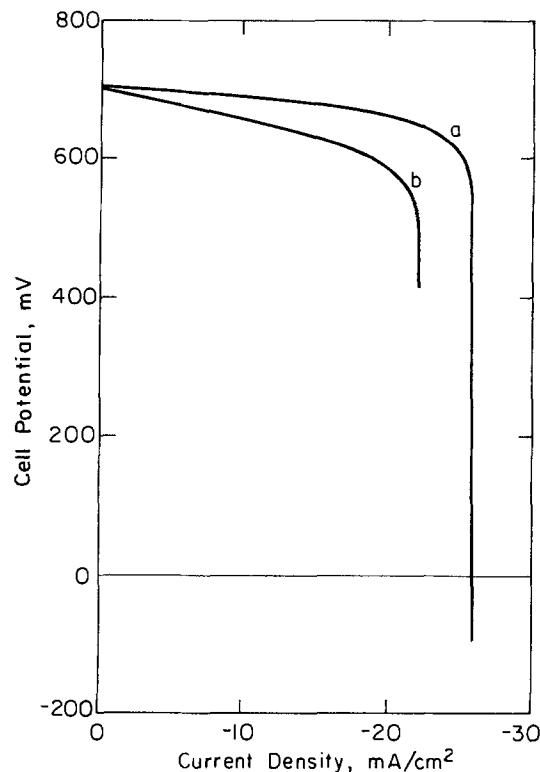


Fig. 13. Cell potential as a function of current density for (a) a back-illuminated semiconductor without kinetic, electrolyte-resistance, and counterelectrode limitations; and (b) system 3 with a current-collector element half-thickness of 0.01 cm and with $L/D = 100$.

Current-potential curves are presented in Fig. 13 for the back-illuminated cell. The optimally designed cell of systems 3 is compared to the cell without interfacial kinetic limitations, counterelectrode limitations, and electrolytic resistance. The back-illuminated design is appealing because chemical products can be separated and because of reduced losses of illumination.

The following discussion of cell economics is appropriate for all photovoltaic devices. The allowable capital investment for the cell is given by

$$I = 8.76 P_{in} \eta \Delta c y_e \quad [15]$$

where P_{in} is the annual incident illumination intensity average over 24h in watts per square meter, η is the cell efficiency, Δc is the difference in selling price and operating cost in dollars per kilowatt-hour, and y_e is the break-even point in years. This equation is presented as a nomogram in Fig. 14. The power output of the liquid-junction cell is presented in Fig. 14a as a function of the incident solar illumination with the average efficiency of the device as a parameter. The incident solar illumination is averaged over a 24h period. On this basis, the average insolation of the continental United States is 200-250 W/m^2 (11). Lenses or mirrors could be used to increase the amount of sunlight striking the semiconductor surface. The annual return on investment is presented in Fig. 14b as a function of the power output with power cost as a parameter. The total initial investment is presented in Fig. 14c as a function of the averaged annual investment with cell break-even period as a parameter.

Based upon a 7.7% power efficiency (averaged over 24h), 250 W/m^2 incident illumination (averaged over 24h), 0.05 dollars/kWh profit, and a break-even period of 5 yr, an investment of 42 dollars/ m^2 is justified for the complete cell. Based upon a 13.4% power efficiency (averaged over 24h) an investment of 73 dollars/ m^2 is justified for the complete cell.

An increase of solar illumination by a factor of five while reducing the efficiency to 6% (system 2 with a porous counterelectrode) yields an acceptable initial investment of 164 dollars/ m^2 . An efficiency of 10.4% (sys-

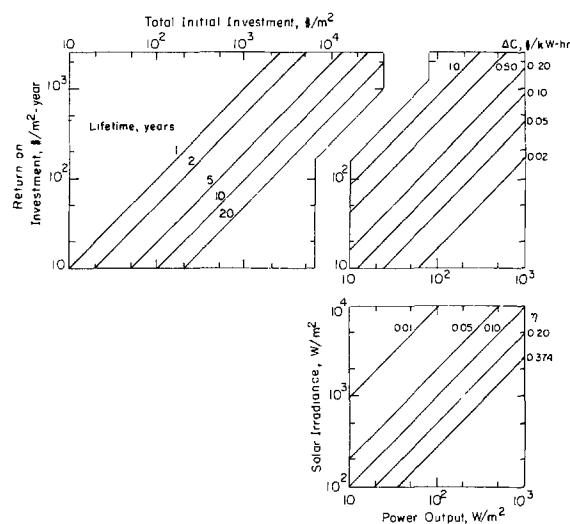


Fig. 14. Economic analysis of the liquid-junction photovoltaic cell. a (bottom): Power output as a function of the incident solar illumination with power efficiency as a parameter. b (top right): Averaged annual return on investment as a function of the power output with power cost as a parameter. c (top left): Total initial investment as a function of averaged annual return on investment with cell lifetime as a parameter.

tem 3 with a porous counterelectrode) yields an acceptable initial investment of 285 dollars/ m^2 . If the mirrors and lenses needed to concentrate sunlight are cheaper than the semiconducting film, the cell may be most economical under high illumination. Maintenance of a high efficiency under high illumination is possible only with the back-illuminated cell of Fig. 7 and the front-illuminated cell of Fig. 4, both coupled with porous counterelectrodes.

The values presented here can be compared to the estimate presented by Weaver *et al.* (61) of 0.34 dollars/peak W. This estimate is based on materials cost and assumes a cell efficiency of 13%. Under AM-2 illumination, this value corresponds to 39 dollars/ m^2 .

Conclusions

The optimization of the liquid-junction photovoltaic cell depends upon the choice of semiconductor, electrolyte, and cell design. The system studied in this work, n-GaAs with a Se_2^{-2}/Se^{-2} redox couple, is close to optimal with respect to utilization of solar irradiation and therefore provides a best-case estimate of liquid-junction cell efficiency. This system, however, exhibits a small rate of corrosion under illumination (a few micrometers per year) (62).

The performance of the liquid-junction photovoltaic cell is strongly dependent upon the design, surface area, and placement of the counterelectrode and current collectors. This system may be economical under concentrated illumination or where the power produced has high value.

Acknowledgment

This work was supported by the United States Department of Energy under Contract no. DE-AC03-76SF00098 through the Director, Office of Energy Research, Office of Basic Energy Sciences, Chemical Sciences Division, and through the Assistant Secretary of Conservation and Renewable Energy, Office of Advanced Conservation Technology, Electrochemical Systems Research Division.

Manuscript submitted June 24, 1983; revised manuscript received May 11, 1984.

The University of California assisted in meeting the publication costs of this article.

REFERENCES

1. A. Fujishima and K. Honda, *Nature*, **238**, 37 (1972).
2. J. Manassen, D. Cahen, and G. Hodes, *ibid.*, **263**, 97 (1976).

3. A. J. Bard, *J. Photochem.*, **10**, 59 (1979).
4. H. Ehrenreich and J. H. Martin, *Phys. Today*, **9**, 25 (1979).
5. M. S. Wrighton, *Acc. Chem. Res.*, **12**, 303 (1979).
6. H. Gerischer, *Pure Appl. Chem.*, **52**, 2649 (1980).
7. A. J. Bard, *Science*, **207**, 139 (1980).
8. A. Heller, *Acc. Chem. Res.*, **14**, 154 (1981).
9. M. Green, in "Modern Aspects of Electrochemistry," Vol. 2, J. O'M. Bockris, Editor, Chap. 5, Academic Press, New York (1959).
10. H. Gerischer, in "Electrochemistry and Electrochemical Engineering," Vol 1, P. Delahay, Editor, Chap. 4, Interscience, New York (1961).
11. M. D. Archer, *J. Appl. Electrochem.*, **5**, 71 (1975).
12. K. Rajeshwar, P. Singh, and J. Dubow, *Electrochim. Acta*, **23**, 1117 (1975).
13. L. A. Harris and R. H. Wilson, *Ann. Rev. Mater. Sci.*, **8**, 99 (1978).
14. A. J. Nozik, *Ann. Rev. Phys. Chem.*, **29**, 189 (1978).
15. M. Tomkiewicz and H. Fay, *Appl. Phys.*, **18**, 1 (1979).
16. R. H. Wilson, in "CRC Critical Reviews in Solid State and Materials Science," pp. 1-41, CRC Press, Cleveland, OH (1980).
17. R. Memming, *Electrochim. Acta*, **25**, 77 (1980).
18. S. R. Morrison, "Electrochemistry at Semiconductor and Oxidized Metal Electrodes," p. 10, Plenum Press, New York (1980).
19. S. U. M. Khan and J. O'M. Bockris, in "Modern Aspects of Electrochemistry," Vol. 14, J. O'M. Bockris, B. E. Conway, and R. E. White, Editors, Chap. 3, Plenum Press, New York (1982).
20. M. E. Orazem, Ph.D. Thesis, University of California, Berkeley, CA (1983).
21. M. E. Orazem and J. Newman, *This Journal*, **131**, 2569 (1984).
22. H. Oman and J. W. Gelzer, in "Energy Technology Handbook," D. M. Considine, Editor, pp. 6.56-6.80, McGraw-Hill, New York (1977).
23. J. J. Loferski, *J. Appl. Phys.*, **27**, 777 (1956).
24. J. J. Loferski, *Proc. IEEE*, **51**, 667 (1963).
25. J. J. Wysocki, *Solar Energy*, **6**, 104 (1962).
26. M. Wolf, *Proc. IRE*, **48**, 1246 (1960).
27. W. Shockley and H. J. Queisser, *J. Appl. Phys.*, **32**, 510 (1961).
28. K. C. Chang, A. Heller, B. Schwartz, S. Menezes, and B. Miller, *Science*, **196**, 1097 (1977).
29. A. Heller, B. Miller, and F. A. Thiel, *Appl. Phys. Lett.*, **38**, 282 (1981).
30. H. Gerischer, in "Proceedings of the 2nd International Photovoltaic Solar Energy Conference," R. van Overstraeten and W. Palz, Editors, pp. 408-431, D. Reidel, Boston (1979).
31. S. Menezes, A. Heller, and B. Miller, *This Journal*, **127**, 1268 (1980).
32. K. W. Frese, Jr., M. J. Madou, and S. R. Morrison, *ibid.*, **128**, 1939 (1981).
33. R. Noufi, D. Tench, and L. F. Warren, *ibid.*, **127**, 2310 (1980).
34. R. Noufi, D. Tench, and L. F. Warren, *ibid.*, **128**, 2596 (1981).
35. T. Skotheim, I. Lundstrom, and J. Prejza, *ibid.*, **128**, 1625 (1981).
36. F.-R. F. Fan, B. L. Wheeler, A. J. Bard, and R. N. Noufi, *ibid.*, **128**, 2042 (1981).
37. R. A. Bull, F.-R. F. Fan, and A. J. Bard, *ibid.*, **129**, 1009 (1982).
38. T. Skotheim, L.-G. Petersson, O. Inganas, and I. Lundstrom, *ibid.*, **129**, 1737 (1982).
39. H. S. White, H. D. Abruna, and A. J. Bard, *ibid.*, **129**, 265 (1979).
40. A. Heller and B. Miller, in "Interfacial Photoprocesses: Energy Conversion and Synthesis," M. S. Wrighton, Editor, Chap. 12, Advances in Chemistry Series 184, The American Chemical Society, Washington, DC (1980).
41. B. A. Parkinson, A. Heller, and B. Miller, *Appl. Phys. Lett.*, **33**, 521 (1978).
42. K. C. Chang, A. Heller, B. Schwartz, S. Menezes, and B. Miller, *Science*, **196**, 1097 (1977).
43. M. E. Orazem and J. Newman, *This Journal*, **131**, (1984).
44. H. J. Hovel, "Solar Cells," Vol. 11 of Semiconductors and Semimetals, R. K. Willardson and A. Beers, Series Editors, Academic Press, New York (1975).
45. P. A. Iles, Paper 1 presented at the 9th IEEE Photovoltaic Specialists Conference, Silver Springs, MD, 1972.
46. B. Parkinson, *Solar Cells*, **6**, 177 (1982).
47. K. W. Mitchell, *Ann. Rev. Mater. Sci.*, **12**, 401 (1982).
48. R. N. Fleck, D. N. Hanson, and C. W. Tobias, "Numerical Evaluation of Current Distribution in Electrochemical Systems," Lawrence Berkeley Laboratory Report UCRL-11612 (1964).
49. C. Kasper, *Trans. Electrochem. Soc.*, **77**, 353 (1940).
50. C. Kasper, *ibid.*, **77**, 365 (1940).
51. C. Kasper, *ibid.*, **78**, 131 (1940).
52. C. Kasper, *ibid.*, **78**, 147 (1940).
53. C. Kasper, *ibid.*, **82**, 153 (1942).
54. M. E. Orazem and J. Newman, *This Journal*, To be published.
55. H. F. Moulton, *Proc. London Math. Soc. Ser. 2*, **3**, 104 (1905).
56. F. Bowman, "Introduction to Elliptic Functions with Applications," John Wiley and Sons, New York (1953).
57. Z. M. Jarzebski and J. P. Marton, *This Journal*, **123**, 199C (1976).
58. Z. M. Jarzebski and J. P. Marton, *ibid.*, **123**, 299C (1976).
59. Z. M. Jarzebski and J. P. Marton, *ibid.*, **123**, 333C (1976).
60. D. Canfield and S. R. Morrison, "Electrochemical Storage Cell Based on Polycrystalline Silicon," Lawrence Berkeley Laboratory Report LBL-14639 (1982).
61. N. L. Weaver, R. Singh, K. Rajeshwar, P. Singh, and J. DuBow, *Solar Cells*, **3**, 221 (1981).
62. M. S. Wrighton, J. M. Bolts, A. B. Bocarsly, M. C. Palazzotto, and E. G. Walton, *J. Vac. Sci. Technol.*, **15**, 1429 (1978).

Electrochemical Studies of Chromium in Molten LiF-NaF-KF (FLINAK)

Toshinobu Yoko¹ and Ronald A. Bailey

Department of Chemistry, Rensselaer Polytechnic Institute, Troy, New York 12181

ABSTRACT

The mechanism of the reduction of Cr(III) in molten FLINAK was studied using cyclic voltammetry and chronopotentiometry over a temperature range of 612°-983°C and a Cr(III) concentration of 0.07 to 0.13 mol/l. Two reduction and two oxidation steps were observed, but extensive differences in the electrochemistry were seen over the measured temperature range. Cr(III) is reduced to Cr(II) followed by a two-electron reduction of Cr(II) to Cr metal and both reduction processes are quasi-reversible. The product of the first reduction process is soluble at 983°C, but is insoluble at lower temperatures.

Electroplating of refractory metals (IV, V, and VI transition groups) from molten salts has been explored for several years, most notably in the work of Senderoff and Mellors in the 1960's (1-8). More recently, there has been renewed interest in this technique (9, 10). In spite of the earlier work (2, 3, 4, 8), however, it is hard to say that the mechanisms of the electroplating of these refractory metals from molten salts are completely understood, especially for chromium (8, 11-14). The primary objective of this research is to elucidate the mechanisms of the electrode reduction of Cr(III) in molten LiF-NaF-KF eutectic (46.5 mole percent [m/o] LiF, 11.5 m/o NaF, 42.0 m/o KF, [FLINAK]) based on the results of cyclic voltammetry and chronopotentiometry.

Experimental

Each fluoride salt used was reagent grade. After being well mixed and dried in a vacuum oven at 160°C for over a week, the powdered mixture was melted, then filtered in an argon atmosphere to remove black material using a nickel crucible which had many layers of platinum screen welded over a hole in its bottom. The filtered salt was pre-electrolyzed at about 1.5V using a vitreous carbon anode and a stainless steel cathode until the current density of the cathode dropped to around 0.3 mA/cm²; this eliminated metal ion impurities. After pre-electrolysis, the background voltammograms for pure melts were flat between +1.0 and -1.0V. That is, there were no reduction or oxidation waves detectable at the highest sensitivity used over the voltage range scanned in the experiments.

Cr(III) was added either as CrF₃ (Cerac, 99.5%), or as K₃CrF₆, which was prepared by the method of Christensen (15). The K₃CrF₆ was examined using x-ray diffraction analysis, and no other lines were detected. Analysis of one preparation gave 18.5% Cr (18.4% calculated). Both materials gave identical electrochemical behavior.

Figure 1 shows a schematic diagram of the cell assembly used. To minimize the effect of cell resistance between the electrodes, a three-electrode system was employed. For both measurements, a vitreous carbon (Atomergic Chemicals Corporation) auxiliary electrode (1/4 in. diam) and a small Pt plate (1 × 1 cm, area 2 cm²) quasi-reference electrode were used. A very fine Pt microelectrode (0.12 mm diam, 5 mm long) and a Pt cylindrical working electrode (2.3 mm diam, 11.3 mm long) were used as the working electrodes for cyclic voltammetry and chronopotentiometry, respectively.

Although attempts were made to use a boron nitride insulator for the working electrode to obtain a precise area, this failed because of the conductivity of the BN above 600°C, probably as a result of porosity due to leaching of the binder.

The controlled potential cyclic voltammeter used was designed and built in this laboratory. With this instrument, scan rates from 0.01 to 80 V/s are available, and cell

¹Present address: Department of Industrial Chemistry, Faculty of Engineering, Mie University, Tsu, Mie-Ken, 514, Japan.

currents up to 500 mA can be measured. A constant current power supply (HP Model 6212A) was used for chronopotentiometry. Waves were recorded by means of either a Tektronix Type 564 storage oscilloscope or an Omnigraphic Series 2000 X-Y recorder. Data were measured either from the large X-Y recorder chart or from enlarged photographs; transition times were evaluated according to Kuwana's method (16), and those reported for the second wave are measured from the end of the first wave.

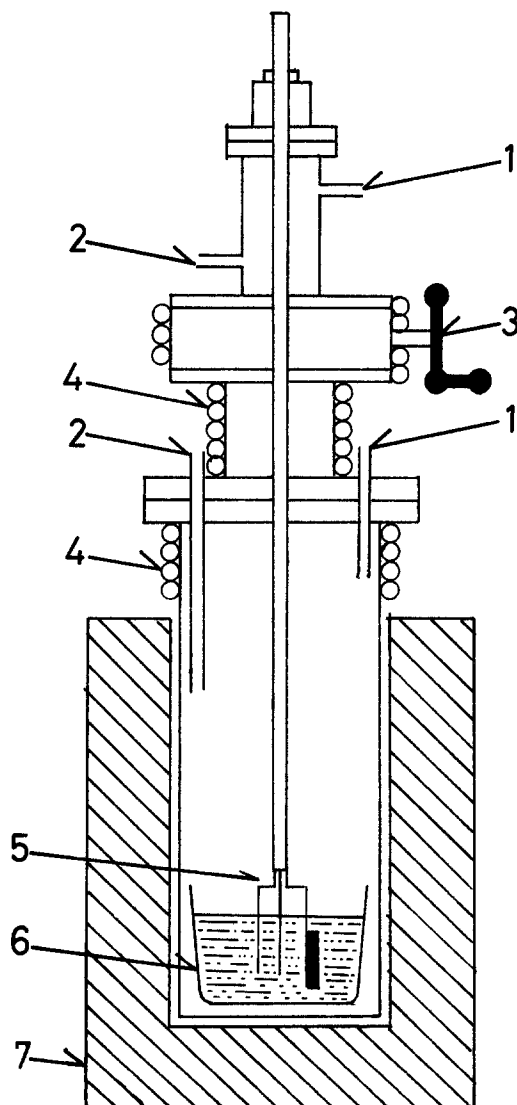


Fig. 1. Schematic diagram of the electrochemical cell. 1: Gas outlet. 2: Gas inlet. 3: Gate valve. 4: Water cooling coil. 5: Electrodes. 6: Ni crucible and molten salt. 7: Furnace.

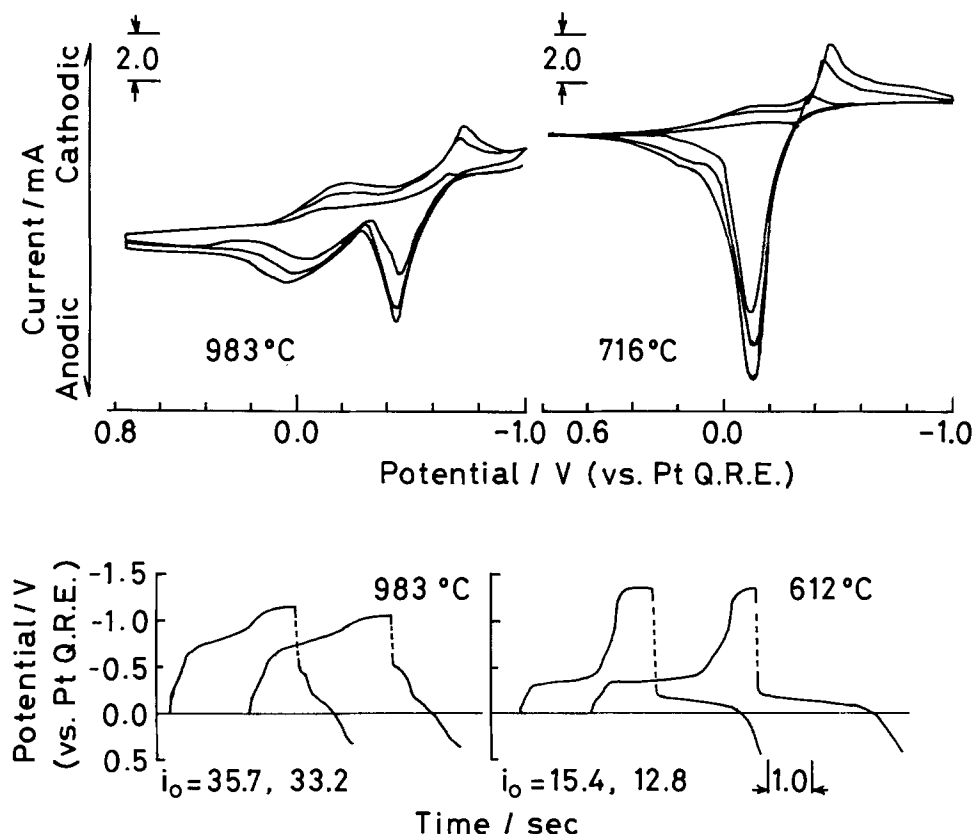


Fig. 2. Top: cyclic voltammograms for the reduction of Cr(III) in molten FLINAK. Scan rate: 8.0, 5.0, and 1.0 V s⁻¹. Concentration of Cr(III): 0.10 mol l⁻¹. Bottom: chronopotentiograms for the reduction of Cr(III) in molten FLINAK. Concentration of Cr(III): 0.10 mol l⁻¹. i_0 : current density/10⁻² mA m⁻².

All measurements were done in an argon atmosphere.

Results and Discussion

Both cyclic voltammetry and chronopotentiometry were performed over a temperature range of about 600° to 1000°C and a Cr(III) concentration of 0.07-0.13 mol/l. Figure 2 shows typical results taken at a Cr(III) concentration of 0.1 mol/l at temperatures of 983°, 716°, and 612°C. As shown in all of these figures, two reduction and two oxidation steps are evident. The first reduction step and the second oxidation step became indistinct at lower temperatures and lower scan rates, eventually almost merging with the others. This is mainly due to the tendency of the second reduction and first oxidation peaks to shift anodic with decreasing scan rate, decreasing temperature, and increasing concentration of Cr(III).

The shape of the first reduction wave in cyclic voltammetry is not in the form of a peak, but is a simple plateau at lower scan rates and lower temperatures. However, at higher scan rates, and especially at higher temperatures, it develops into a peak. The nature of the first reduction wave will be discussed later in more detail.

In Fig. 3, relationships between $i_0\tau^{1/2}$ and current density i_0 obtained from chronopotentiometry are shown for both reduction steps at different temperatures; $i_0\tau^{1/2}$ varies with current density at higher temperature and lower current density values, especially for the second reduction step, but becomes constant at higher current density. In Fig. 4, transition time constants, $i_0\tau^{1/2}/C$, where C is the concentration of Cr(III), at different temperatures are shown plotted against concentration of Cr(III) for both reduction steps. It is seen from Fig. 4 that the transition time constant of the first reduction step is substantially invariant at each temperature, in spite of some scatter of the data. The data for the second step show more deviation. In view of the high temperatures involved and the consequent possibility of convection, we do not consider that these deviations from constant values are unreasonable or represent real trends. That is, these results do not provide any indication that the electrode reaction of either reduction step has complications related to adsorption or coupled homogeneous chemical reactions (17, 18), although a reversible charge transfer followed by a re-

versible chemical reaction (ErCr) would also give a constant value. The deviation of $i_0\tau^{1/2}$ from the constancy observed at lower current density in Fig. 3 probably also is due to the convection of the bath melt. This is supported by the results from cyclic voltammetry.

In Fig. 5, relationships between peak current, i_p , of the cyclic voltammograms and the square root of the scan rate, $V^{1/2}$, are shown for both reduction steps at different temperatures. The value of i_p for the second wave was ob-

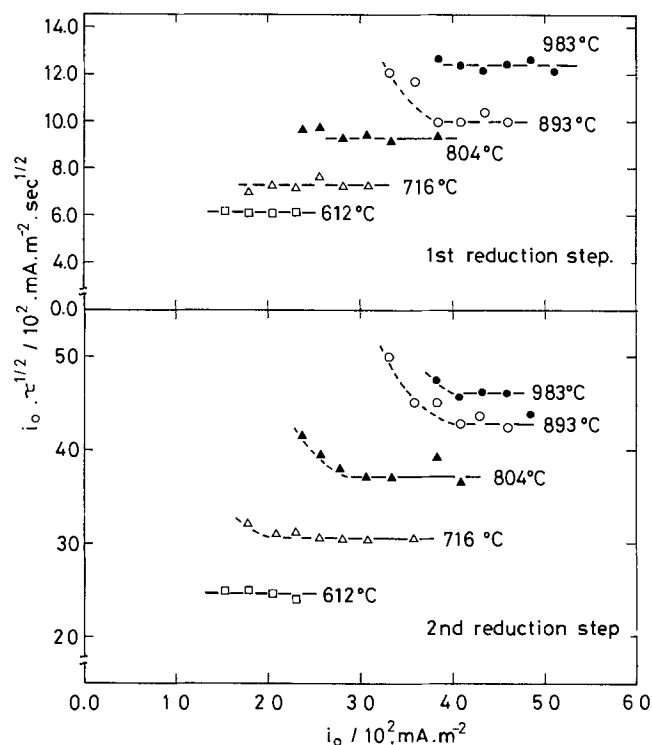


Fig. 3. Plots of $i_0\tau^{1/2}$ vs. i for the first and second reduction steps of Cr(III) in molten FLINAK. Concentration of Cr(III): 0.11 mol l⁻¹. Pt working electrode area: 0.98×10^{-4} m².

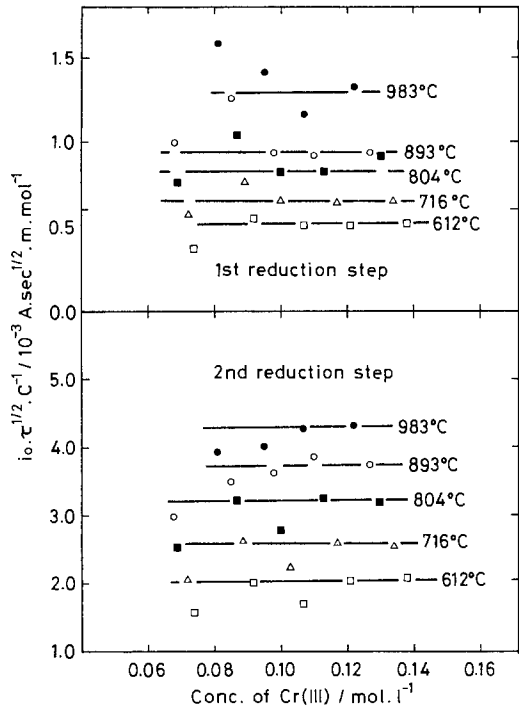


Fig. 4. Plots of $i_0\tau^{1/2}/C$ vs. C [concentration of Cr(III)] for the first and second reduction steps.

tained by extrapolating the first wave to provide a new base line; this was relatively straightforward at low scan rates, but involved more uncertainty at high scan rates and high temperatures, where a peak appeared on the first wave. A good linear relationship between i_p and $V^{1/2}$ is observed for the first reduction step, except at higher temperatures and lower scan rates. However, for the second reduction, the deviation from this relationship becomes significant at both lower and higher scan rates. The deviation of i_p at lower scan rates seems to be due to

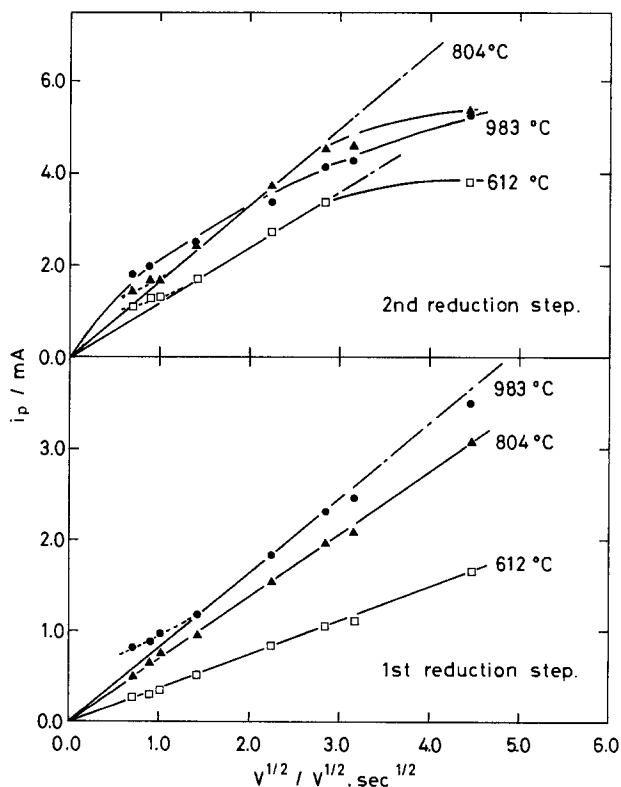


Fig. 5. Plots of i_p vs. $V^{1/2}$ for the first and second reduction steps of Cr(III) in molten FLINAK. Concentration of Cr(III): 0.11 mol l^{-1} . Pt microelectrode area: $2.02 \times 10^{-6} \text{ m}^2$.

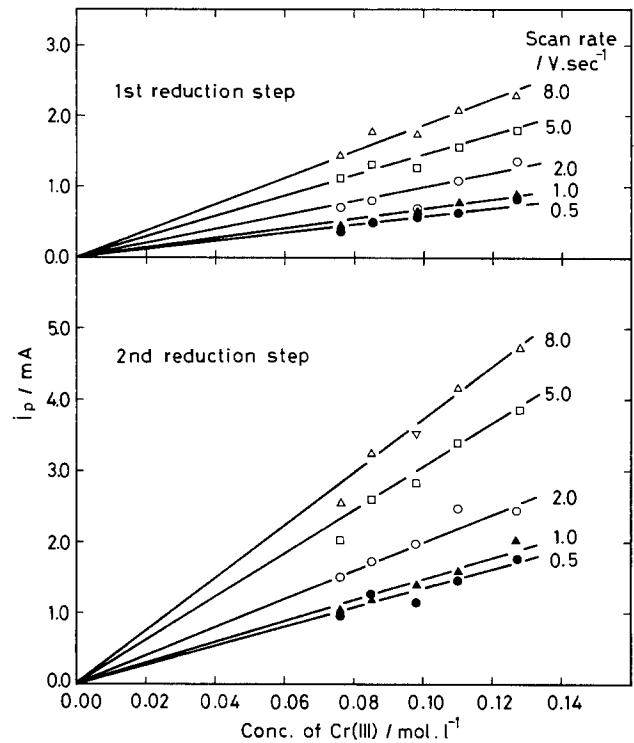


Fig. 6. Plots of peak current i_p vs. concentration of Cr(III) for the first and second reduction steps at 893°C .

the same cause as that of $i_0\tau^{1/2}$ at lower current density. The deviation of i_p at higher scan rates might suggest a slower reaction in the second reduction step, but may also reflect more uncertainty in the extrapolated base line for the second wave. The dependence of i_p on the concentration of Cr(III) for both reduction steps is shown in Fig. 6; i_p at each scan rate satisfies a linear function of Cr(III) concentration which goes through the origin over a wide range of concentrations of Cr(III). These observations mean that both reduction processes are diffusion or kinetically controlled, but are not adsorption or catalytic ones as just mentioned above (19). At the same time, this fact shows that there is no significant effect of uncompensated resistance between the electrodes (19).

In Tables I and II, scan rate and concentration dependence of the peak potentials (E_p) and current density and

Table I. Concentration dependence of peak potentials and quarter-wave potentials. Scan rate (voltammetry): 2.0 V s^{-1} . Current density (chronopotentiometry): $45.9 \times 10^2 \text{ mA m}^{-2}$. Temperature: 983°C

Concentration of Cr(III) (mol l^{-1})	E_p/V		$E_{1/4}/\text{V}$	
	First wave	Second wave	First wave	Second wave
0.07	-0.186	-0.774	—	—
0.08	-0.164	-0.762	-0.32	-0.782
0.10	-0.156	-0.746	-0.259	-0.792
0.11	-0.192	-0.734	-0.202	-0.764
0.12	—	—	-0.206	-0.752

Table II. Scan rate dependence of peak potentials (voltammetry) and current density dependence of quarter-wave potential (chronopotentiometry). Concentration of Cr(III): 0.11 mol l^{-1} , 983°C

Scan rate (V s^{-1})	E_p (V)		Current density (mA m^{-2})	$E_{1/4}$ (V)	
	First wave	Second wave		First wave	Second wave
1.0	-0.126	-0.738	33.2	-0.135	-0.610
2.0	-0.152	-0.749	35.8	-0.145	-0.616
5.0	-0.162	-0.786	38.4	-0.156	-0.628
8.0	-0.173	-0.796	40.9	-0.178	-0.637
10.0	-0.186	-0.815	43.5	-0.194	-0.646
20.0	-0.234	-0.857	46.0	-0.244	-0.656

concentration dependencies of the quarter-wave potential ($E_{p/4}$) are shown for both reduction steps. As seen from these tables, for both reduction steps, E_p and $E_{p/4}$ shift cathodic with increasing scan rate and current density and anodic with increasing concentration of Cr(III). None of logarithmic plots of cyclic voltammograms and chronopotentiograms such as $\log(i_p/i - 1)$, $\log(i - i_p)$, $\log(\tau^{1/2}/t^{1/2} - 1)$, and $\log(\tau^{1/2} - t^{1/2})$ are linear with potential, and it is clear that neither reduction step can be reversible.

As we cannot estimate from the slopes of such plots how many electrons are involved in each reduction step, we have to resort to another means to determine this. Berzins and Delahay (20) derived the equation which predicts the number of electrons involved in the stepwise diffusion-controlled electrode process

$$\frac{\tau_2}{\tau_1} = 2 \frac{n_2}{n_1} + \left(\frac{n_2}{n_1}\right)^2 \quad [1]$$

where τ_1 and n_1 are the transition time and number of electrons in each step, respectively. As $n_1 + n_2$ equals 3 in our case, the two different values of n_1 and n_2 are considered as follows

$$\text{Case I: if } n_1 = 1 \text{ and } n_2 = 2 \text{ then } \frac{\tau_2}{\tau_1} = 8$$

$$\text{Case II: if } n_1 = 2 \text{ and } n_2 = 1 \text{ then } \frac{\tau_2}{\tau_1} = 1.25$$

The average values measured at different temperatures are listed in Table III. The values at higher temperatures are nearly 8 and correspond to case I. Indeed, this is the expected mode of behavior of Cr(III), and has been observed earlier in this melt (8). However, while the behavior at 983°C is as expected, at lower temperature reduction must occur in a more complicated manner as considered later. Equation [1] applies strictly only to diffusion-controlled electrode processes.

In order to clarify the nature of the first reduction step further, reversal techniques were employed for both chronopotentiometry and cyclic voltammetry. Ratios of the forward to the reverse transition time, τ_f/τ_r , for the first wave measured at various temperatures are listed in Table IV. This value is a very powerful tool for determining whether the product of the electrode reaction is soluble or insoluble (18). At 983°C, the ratio τ_f/τ_r is nearly 3, which means that the reduced product is soluble. However, this value becomes nearly unity below 893°C, so the product of the first reduction step is considered to be insoluble. This result agrees with the result previously mentioned: that is, at lower temperatures the ratio τ_2/τ_1 ,

Table III. Temperature dependence of the ratio of the transition time of the second to the first reduction step, τ_2/τ_1 . Concentration of Cr(III): 0.09 mol l⁻¹

Temp. (°C)	983	893	804	716	612
τ_2/τ_1	8.0	8.6	9.3	11.3	13.4

Table IV. Ratio of the forward to the reverse transition time for the first wave at different temperatures. Concentration of Cr(III): 0.13 mol l⁻¹

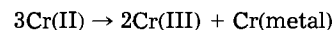
Temp. (°C)	Current density (10 ² mA m ⁻²)	Transition time		τ_f/τ_r
		Forward τ_f (s)	Reverse τ_r (s)	
983	51.0	0.102	0.039	2.6
	40.8	0.156	0.047	3.3
893	46.0	0.067	0.071	0.93
	35.8	0.110	0.098	1.1
804	30.7	0.157	0.126	1.2
	25.6	0.201	0.193	1.0
716	25.6	0.114	0.112	1.0
	20.5	0.186	0.169	1.1
612	20.6	0.119	0.123	0.97
	18.0	0.158	0.150	1.1

shown in Table III gets larger than 8 with decreasing temperature, owing to the formation of the insoluble product of the first reduction step. There is less diffusion of the product of step 1 from the electrode surface, therefore leading to a larger amount of material available for the second reduction step. Smith (21) has obtained similar chronopotentiometric behavior in this system.

Cyclic voltammograms of only the first wave were taken at 893° and 983°C. Following Nicholson's semiempirical method (22), ratios of the anodic to the cathodic peak current, i_{ap}/i_{cp} , were obtained and given in Table V with the peak separation potentials. As seen from this table, peak separation gets larger with increasing scan rate, although at lower scan rates it approaches the value which is predicted for the reversible system. The ratio of i_{ap}/i_{cp} increases to more than unity with increasing scan rate, and shows the value of about 1 at lower scan rates. Both quantities show smaller values than expected for reversible behavior at the lowest scan rates examined, especially at 983°C. Peak current ratios of less than 1 can be rationalized on the basis of nonreversible behavior, while the cause of small peak separations may arise from uncertainties in determining peak position as the wave becomes flatter and less well defined at low scan rates.

When the results obtained for the first reduction wave are compared with the diagnostic criteria for typical electrode processes (Table VI), it is seen that the closest agreement is with either a quasi-reversible case, or with an ErCr process (for example, a reaction of Cr(II), perhaps with F⁻, to form a metal cluster compound). Behavior of the i_{ap}/i_{cp} and τ_f/τ_r ratios is not consistent with the latter mechanism, however, so that a quasi-reversible process is considered most probable on the basis of the discrepancy of these ratios.

We cannot overlook the possibility that the Cr(II) might disproportionate by the following reaction



as pointed out by Mellors and Senderoff (8), and Redman (23). We also found that 8 weight percent of CrF₂ added into molten FLINAK for electrolysis did disproportionate and small amounts of Cr metal deposited on the surface of the Ni container after a week's experiment. The electrochemical results for a solution made from CrF₂ were qualitatively the same as when Cr(III) was used. However, it is believed that this disproportionation reaction is slow and is not detected within the range of the scan rates used in our experiments. Since our experiments have been carried out at a relatively high temperature (600°-1000°C) and the effect of convection in the melt becomes significant, reproducible measurements cannot be obtained at lower scan rates (≤ 1.0 V/s) and lower current density where the detection of a catalytic reaction might be feasible.

Table V. Ratios of the anodic to the cathodic peak current i_{ap}/i_{cp} , peak potentials and their peak separation at different scan rates. Concentration of Cr(III) = 0.11 mol l⁻¹

Temp. (°C)	Scan rate (V s ⁻¹)	i_{ap}/i_{cp}	E_{cp} (V)	E_{ap} (V)	$E_{cp} - E_{ap}$ (V)
983	20	1.27	-0.286	-0.091	-0.377
	10	1.18	-0.236	-0.085	-0.321
	8	1.12	-0.226	-0.075	-0.301
	5	1.02	-0.213	-0.070	-0.283
	2	0.95	-0.186	-0.051	-0.237
	1	0.92	-0.157	-0.049	-0.201
893	50	1.34	-0.339	-0.206	-0.545
	20	1.22	-0.226	-0.135	-0.351
	10	1.17	-0.199	-0.109	-0.308
	5	1.22	-0.173	-0.091	-0.264
	1	1.02	-0.152	-0.073	-0.225
					-0.234*

* Theoretical values calculated based on the reversible process (as $n = 1$).

E_{ap} , E_{cp} : Anodic and cathodic peak potential, respectively.

Table VI. Comparison of the results obtained for the first reduction step with the diagnostic criteria for typical electrode processes

Electrode process	$i_p/V^{1/2}$ vs. V	$i \tau^{1/2}$ vs. i	i_{ap}/i_{cp} vs. V	E_p vs. V	E_{η_1} vs. i	E_{η_1} vs. C	τ_d/τ_c vs. i
Observed	const.	const.	increasing	cathodic	cathodic	anodic	1 ^a 3 ^b
Reversible	const.	const.	1 ^c	const.	const.	anodic ^c const. ^d	1 ^c 3 ^d
Quasi-rev.	const.	const.	> 1 ^d	cathodic	cathodic	anodic	1 ^c 3 ^d
Irrev.	const.	const.	0	cathodic	cathodic	anodic	0 or 1 ^c 0 or 3 ^d
Cr.Er.	decreasing	decreasing	increasing from 1 at low V	anodic	—	—	3
Er.Cr.	const.	const.	decreasing from 1 at low V	cathodic	cathodic	anodic	increasing
Catalytic	*	increasing from 1	*	anodic or const.	anodic	—	—

Cr.Er.: Reversible chemical reaction preceding a reversible charge transfer.

Er.Cr.: Reversible charge transfer followed by a reversible chemical reaction.

* Decreasing at low V and constant at high V .

^a Below 893°C.

^b At 983°C.

^c Insoluble product.

^d Soluble product.

Table VII. Temperature dependence of the ratio of the transition time of the second reduction to the first oxidation step τ_{2d}/τ_{1r} . Concentration of Cr(III): 0.09 mol l⁻¹

Temp. (°C)	983	893	804	716	612
τ_{2d}/τ_{1r}	0.58	0.66	0.86	0.98	1.1

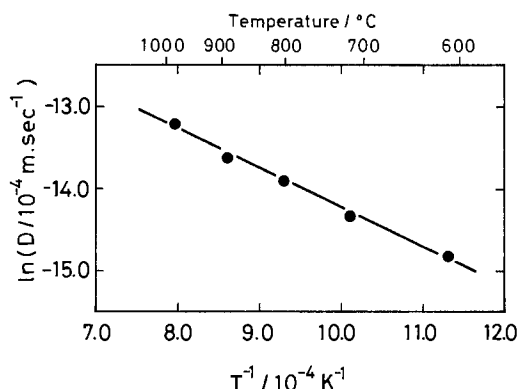
The ratios of the transition times of the second reduction to the first oxidation step, τ_{2d}/τ_{1r} , obtained at different temperatures are listed in Table VII. At lower temperatures, this ratio is very close to unity, but decreases with increasing temperature. Since the second reduction step has been found to be a quasi-reversible reduction of Cr(II) to Cr metal, this value should be unity. Possibly, alloy formation of deposited Cr metal with the Pt electrode might be responsible for the reduction of the ratio at higher temperatures.

Manning and Dale (11) have carried out voltammetric measurements on Cr(II) (as CrF₂) in LiF-BeF₂-ZrF₄ at 500°C and found that the reduction of Cr(II) to Cr metal in this melt is a quasi-reversible process. Their result reasonably agrees with ours.

The diffusion coefficient, D , of the electroactive species can be estimated from the Sand equation (24)

$$i_0 \tau^{1/2} = \frac{nFC(DD)^{1/2}}{2} \quad [2]$$

where i_0 is the current density, τ the transition time, C the concentration of electroactive species, and the re-

Fig. 7. Plots of $\ln D$ vs. $1/T$ for Cr(III) in molten FLINAK

maining terms have their usual significance. The result is shown plotted as the logarithm against the reciprocal of absolute temperature in Fig. 7; the result is a straight line. The diffusion coefficients of Cr(III) obtained in molten FLINAK seem to be low (983°C: 1.84×10^{-6} , 893°C: 1.19×10^{-6} , 804°C: 0.95×10^{-6} , 716°C: 0.59×10^{-6} , 612°C: 0.36×10^{-6} cm²/s), even allowing for some uncertainty ($\pm \sim 20\%$), mainly in the surface area of the working electrode and the concentration of Cr(III). The activation energy for the diffusion of Cr(III) calculated from the slope in Fig. 7 is 9.5 kcal/mol. Although small diffusion coefficients and large activation energies have been found for some other transition metals in molten FLINAK, the diffusion coefficients are still a factor of 5 or more greater than those obtained here (25, 26). This may suggest the existence of a large and stable complex anion like CrF₆³⁻ in the melt; Cr(III) does exhibit a maximum in ligand field stabilization energy and consequently in complex stability and inertness to ligand exchange.

In summary, Cr(III) in molten FLINAK is reduced in two steps over the temperature range 600°-983°C. The first step is the relatively slow reduction of Cr(III), to give a product which is soluble at 983°C and insoluble, but still electroactive, below 893°C. This step is most probably quasi-reversible, although the behavior of some parameters is not totally straightforward and some complications from chemical reactions are possible. The second step is the reduction of Cr(II) to Cr(O). This is also quasi-reversible, with indications from voltammetric peak currents that it is slow especially at higher temperatures.

In electroplating of Cr from molten FLINAK, there is a correlation between the physical nature of the electrodeposited metal and the changing nature of the electrochemistry with temperature. At low temperatures, the deposit consists of extensive dendrites imbedded in the salts. At high temperatures, dendrite formation is reduced and smoother plates are obtained. The results of the Cr electroplating will be reported separately.

Acknowledgments

The authors wish to thank Dr. George J. Janz (R.P.I.) for his helpful discussions and other assistance through the course of this study. Financial support was provided by the Army Research Office under Contract no. DAAG29-79-C-0035.

Manuscript submitted Oct. 10, 1982; revised manuscript received June 29, 1984. This was Paper 490 presented at the Minneapolis, Minnesota, Meeting of the Society, May 10-15, 1981.

REFERENCES

- G. W. Mellors and S. Senderoff, *Plating*, **51**, 972 (1964).
- G. W. Mellors and S. Senderoff, *This Journal*, **112**, 266 (1965).
- S. Senderoff, G. W. Mellors, and W. J. Reinhard, *ibid.*, **112**, 840 (1965).
- G. W. Mellors and S. Senderoff, *ibid.*, **113**, 60 (1966).
- S. Senderoff and G. W. Mellors, *ibid.*, **113**, 66 (1966).
- S. Senderoff and G. W. Mellors, *ibid.*, **114**, 556 (1967).
- S. Senderoff and G. W. Mellors, *ibid.*, **114**, 586 (1967).
- G. W. Mellors and S. Senderoff, in "Applications of Fundamental Thermodynamics to Metallurgical Processes," G. R. Fitterer, Editor, p. 81, Gordon and Breach Science Publishers, New York (1967).
- I. Ahmad, W. A. Spiak, and G. J. Janz, *J. Appl. Electrochem.*, **11**, 291 (1981).
- D. Inman and S. H. White, *ibid.*, **8**, 375 (1978).
- D. L. Manning and J. M. Dale, in "Molten Salts," G. Mamantov, Editor, p. 563, Marcel Dekker, New York (1969).
- I. I. Naryshkin, V. P. Yurkinskii, and P. T. Stangrit, *Elektrokhimiya*, **5**, 1043 (1969).
- K. Cho and T. Kuroda, *Denki Kagaku*, **39**, 206 (1971).
- D. Inman, J. C. L. Legey, and R. Spencer, *J. Electroanal. Chem.*, **61**, 289 (1975).
- O. T. Christensen, *J. Pract. Chem.*, **35**, 161 (1887).
- R. N. Adams, "Electrochemistry at Solid Electrodes," p. 183, Marcel Dekker, Inc., New York (1969).
- I. J. Bard and L. R. Faulkner, "Electrochemical Methods—Fundamentals and Applications," Chap. 7, 11, John Wiley and Sons, New York (1980).
- D. D. Macdonald, "Transient Techniques in Electrochemistry," Chap. 5, Plenum Press, New York (1977).
- A. M. Bond, "Modern Polarographic Methods in Analytical Chemistry," Chap. 3, 5, Marcel Dekker, New York (1980).
- T. Berzins and P. Delahay, *J. Am. Chem. Soc.*, **75**, 4205 (1953).
- J. F. Smith, Materials Research Corp., Orangeburg, NY, Private communication.
- R. S. Nicholson, *Anal. Chem.*, **37**, 1406 (1965).
- J. D. Redman, O.R.N.L. 2626 M.S.R.P., Q.P.R. 94 (1958).
- P. Delahay, "New Instrumental Methods in Electrochemistry," pp. 117, 180, Interscience Publishers, Inc., New York (1954).
- D. L. Manning, *J. Electroanal. Chem.*, **6**, 227 (1963); *ibid.*, **7**, 302 (1964).
- F. R. Clayton, G. Mamantov, and D. L. Manning, *This Journal*, **120**, 1193 (1973); *ibid.*, **121**, 86 (1974).

Cathodic Polarization of Aluminum in Alkylbenzene Electrolytes

G. A. Capuano*

Department of Chemistry, University of Quebec in Montreal, Montreal, Quebec, Canada H3C 3P8

W. G. Davenport

Department of Metallurgical Engineering, University of Arizona, Tucson, Arizona, 85721

ABSTRACT

Cathode overpotentials for the plating of aluminum from ethylbenzene toluene 1:1, 50 weight percent AlBr_3 electrolytes have been measured as a function of current density, temperature, and specific conductances. The exchange current density (i_0) and the heat of activation (ΔH), were determined to be 10^{-3} A/cm² and 2.6 to 4.5 kcal/mol, respectively. Stoichiometries of plating are proposed, and the observed transfer coefficient of 1.3 is shown to be consistent with monomeric aluminum complexes as the active plating species. Solutions prepared from anhydrous alkyl benzene and AlBr_3 are shown to be insufficiently conductive for aluminum plating. HBr increases the conductivities for optimal plating conditions.

The use of alkylbenzene electrolytes for the electro-deposition of aluminum and aluminum-copper alloys has been extensively studied in our laboratories during the past few years (1-10).

The plating solution consists of a 1:1 mixture (by volume) of ethylbenzene and toluene, containing 50 weight percent (w/o) AlBr_3 . Some gaseous HBr is added to insure a specific conductance of $2.4 \times 10^{-3} \Omega^{-1} \text{cm}^{-1}$ and to provide bromide ions to complex the excess of aluminum ions obtained whenever cathode efficiencies are lower than 100%.

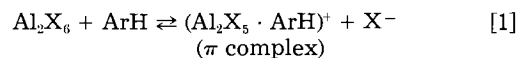
From the faradaic cathodic efficiencies obtained in our electroplating work (3, 8), the range of conductivities mentioned above is considered optimal for plating. All our kinetic data were determined, therefore, over this conductivity range.

The object of this paper is to describe and interpret cathode polarization experiments on the above-described system. The basic measurements were cathode overpotential as a function of current density, temperature, and specific conductance. The results are interpreted in terms of the exchange current density (i_0), the heat of activation (ΔH), and the transfer coefficient α . Plating stoichiometries are proposed.

Some aromatic complexes of aluminum.—When aluminum halides are dissolved in aromatic hydrocarbons, dif-

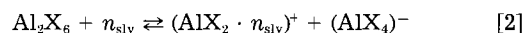
ferent types of complexes are formed, depending on the number and type of constituents used for their formation.

Binary mixture.—Brown and Wallace (11) and Brown and Brady (12) suggested that π complexes form when aluminum bromide is dissolved in an aromatic solvent such as benzene or toluene, *i.e.*



where ArH is an aromatic hydrocarbon and X a halide.

These complexes have a very low degree of dissociation because their saturated solutions have specific conductances of the order of $10^{-9} \Omega^{-1} \text{cm}^{-1}$ when prepared from rigorously dried AlBr_3 and aromatic solvents (13). Lebedev and Korshak (14-16) suggested that the formula for the complex compound of aluminum halides with an organic solvent is



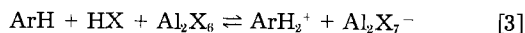
where slv denotes solvent.

Kessler and co-workers (17) considered this scheme to be the most probable and adopted the value of 2 for n .

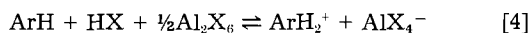
Ternary mixtures.—Brown and Wallace (18) reported on the basis of vapor pressure compositions-phase studies the formation of σ complexes or salts of carbonium ions (ArH_2^+) and Al_2X_7^- or AlX_4^- when hydrogen bromide and

*Electrochemical Society Active Member.

aluminum bromide react with the aromatic hydrocarbons, *i.e.*



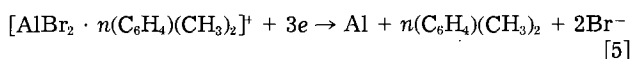
or



However, benzene and toluene could only produce dimeric complexes at room temperature as in Eq. [3], whereas solvent molecules having more or larger lateral chains such as *m*-xylene, and mesitylene, produced more readily the monomeric form of the aluminum complex as in Eq. [4].

The formation of these ions can explain the good conductivity of the solution when the hydrogen halide is added to an electrolyte containing aluminum bromide dissolved in an aromatic solvent.

Electrodeposition of aluminum from aromatic hydrocarbons.—Levinskieve and Simanavicius (19) suggested the following scheme for the electrodeposition of aluminum from a xylene-AlBr₃-HBr system



This is in agreement with the Lebedev and Korshak suggestion (Eq. [2]) and the Brown and Wallace findings (Eq. [4]).

This paper is essentially an investigation into cathode overpotentials at different current densities, temperatures, and specific conductances, with the aim of understanding to a greater extent the aluminum electroplating process.

Experimental

The experimental cell and auxiliary equipment used in the experiments have been described in a previous paper (5). The cell consists essentially of a cylindrical glass body with (i) working electrodes occupying the cross section of the cell at each end and (ii) a reference electrode behind the cathode, penetrating to the front through a 0.8 mm glass-lined hole. The thickness of the glass lining has been measured to be 0.001 cm, and it represents the distance between the capillary tip and the cathode surface. The amount of IR voltage drop for electrolytes having conductivities of 2 and 4 × 10⁻³ Ω⁻¹ cm⁻¹ at current densities of 10 mA cm⁻² are 5 and 2.5 mV, respectively, from the equation

$$E_{\text{IR}} = \frac{i_c \delta}{K} \quad [6]$$

where *i*_c is the cathodic current density, δ the glass wall thickness, and *K* is the specific conductance of the electrolyte (20). However, no corrections were made since the actual values of the *E*_{IR} are likely to be considerably lower due to edge effects which tend to increase the potential around the cathode hole due to field distortion (21, 22) and also because the capillary tip is displaced horizontally from rather than in front of the cathode.

Materials.—Aluminum bromide was prepared from super-pure aluminum (99.99%) and Fisher reagent-grade bromine. Ethylbenzene and toluene were both Fisher reagent-grade products. Preparation of the electrolyte has been described elsewhere (1-4). The conductivity of the plating solution was adjusted by bubbling gaseous HBr through the solution.

Procedure.—One liter of freshly prepared electrolyte, conditioned by 5-8h of aluminum plating at 10 mA/cm² in order to remove traces of more noble metals (impurities), was used in all the experiments. The cathode area was 30 cm². Four anodes of the same surface area were placed around the cathode (3).

The cell was protected from moisture in a closed system. After filling the cell, the first experimental step was to plate aluminum onto the platinum cathode and reference electrode for 30-60 min. Once this was done, the elec-

trodes were connected in their working and measuring circuits and plating was begun under controlled current density conditions. The electrolyte near the cathode was stirred by means of a micromagnetic Teflon-covered bar. The overpotentials were measured by a galvanostatic (point by point) procedure. Plating was carried out for 1 min before the cathode overpotential was measured.

Following each measurement, the current density was increased and the procedure was repeated at the new current density. After each set of experiments at one temperature, the cell was emptied, cleaned, filled with fresh electrolyte (from the 1 liter batch), and the experiments were repeated at a higher temperature. All the overpotentials reported were measured against a reference (reversible) aluminum electrode (RAI) located behind the cathode, containing the same solution under study and at the same temperature (5).

Results and Discussion

The polarization studies showed (Fig. 1) that the cathode overpotential (η) as a function of current density is significantly lowered with increasing specific conductance. However, at specific conductance greater than 8 × 10⁻³ Ω⁻¹ cm⁻¹, under galvanostatic conditions, the aluminum coating on the platinum cathode redissolved. At specific conductances of 1 × 10⁻³ Ω⁻¹ cm⁻¹, however, there was such an ohmic drop across the cell that it was impossible to reach the 15 mA/cm² current density with the potentiostat maximum output of 20V. Furthermore, when the aluminum bromide and the alkylbenzene were rigorously dried by redistillation under nitrogen in a dry box, current densities were not higher than 1 mA/cm² even for potentials up to 20V applied between the anode and the cathode. The specific conductance was of the order of 10⁻⁹ Ω⁻¹ cm⁻¹.

Thus, the polarization study complements that on the beneficial effect of HBr on the faradaic cathode efficiency in the region of conductances from 2 to 4 × 10⁻³ Ω⁻¹ cm⁻¹, as reported in previous papers (3, 8).

The effect of specific conductance on overpotentials.—The observed decrease in cathode overpotential

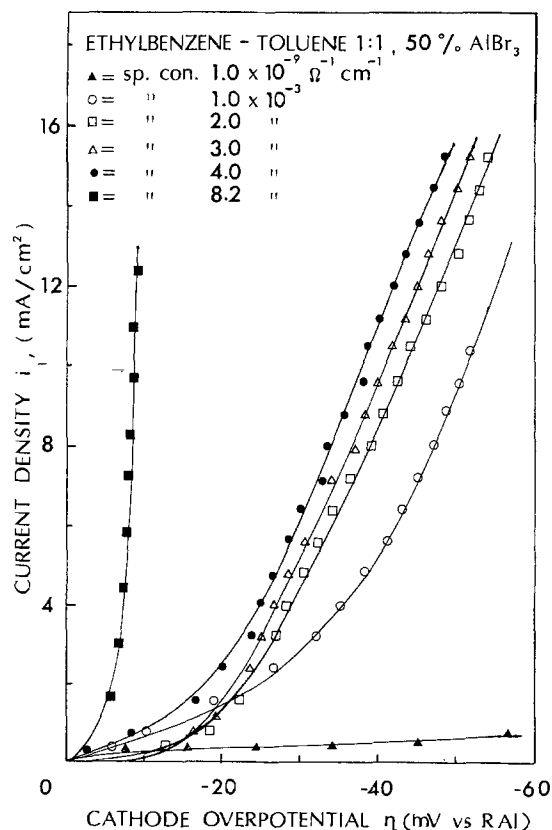
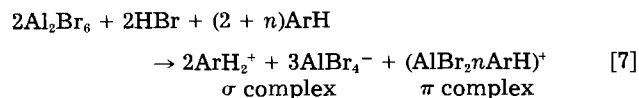


Fig. 1. Cathode overpotentials vs. current density for ethylbenzene-toluene 1:1 vol:50 w/o AlBr₃-HBr at the specific conductances shown.

with increasing specific conductance (Fig. 1 to 4) can be explained in terms of an increase in the concentration of the active aluminum bearing ions, *i.e.*, π complexes (Eq. [7]). These complexes are formed by the addition of HBr on the alkylbenzene and AlBr_3 electrolyte, as shown in Eq. [7], which is a combination of Eq. [2] and [4]



The Butler-Volmer equation gives

$$i = i_0(e^{\alpha F\eta/RT} - e^{-\alpha F\eta/RT}) \quad [8]$$

where

$$i_0 = \text{FKc} \text{CA}^{n+} e^{-\alpha F\eta/RT} = \text{FKcCD} e^{\alpha F\eta/RT}$$

and i is the net current density, i_0 the exchange current density, Kc the rate constant, CA^{n+} the positive

electroactive ion concentration, CD the reduced ions concentration, α the cathodic transfer coefficient, $\bar{\alpha}$ the anodic transfer coefficient, η the $\Delta\phi - \Delta\phi_e$ overpotential, $\Delta\phi_e$ the equilibrium potential, $\Delta\phi$ the applied potential, and F , R , and T have their usual significance.

Equation [8] predicts that an increase in the concentration species " CA^{n+} ," *i.e.*, the π complex in Eq. [7], causes an increase in current density at any applied cathodic potential, $\Delta\phi$. Similarly, an increase in CA^{n+} means that a lower potential $\Delta\phi$ is required to achieve any desired current density. Since $\eta = \Delta\phi - \Delta\phi_e$, where $\Delta\phi_e$ is the equilibrium rest potential across the electrode interface, the lower required applied potential $\Delta\phi$ (for any current density) is equivalent to the presence of a lower overpotential η at the cathode.

Tafel plots.—Figures 2, 3, and 4 present the (point by point) galvanostatic current overpotential relationship, for the cathodic reduction of aluminum at four different temperatures in alkylbenzene- AlBr_3 -HBr electrolytes,

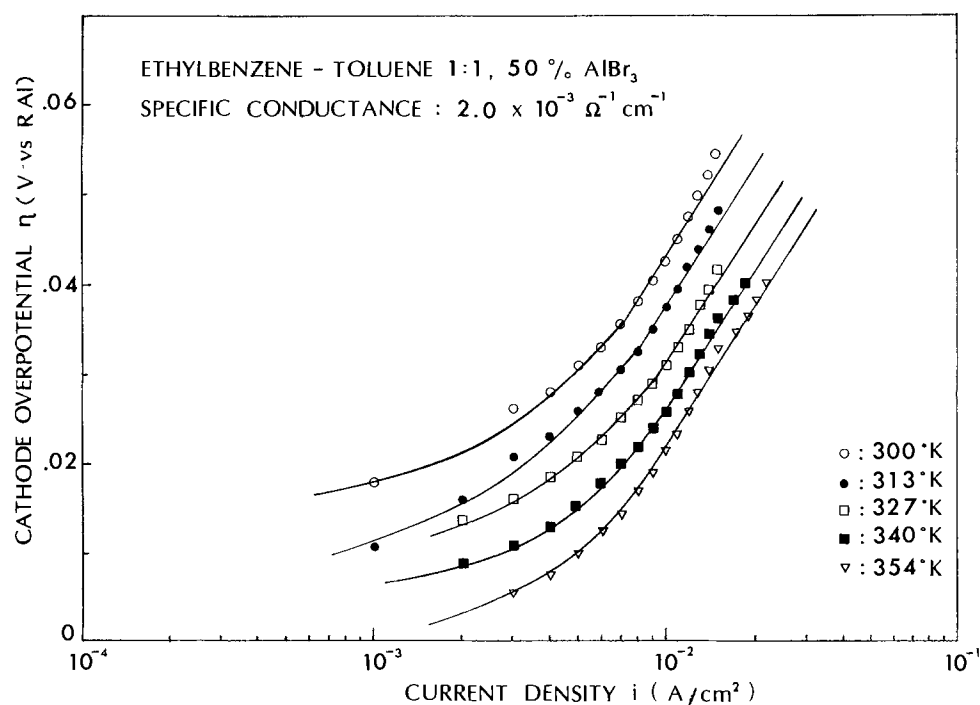


Fig. 2. Tafel plot of the temperatures shown, for ethylbenzene-toluene 1:1 vol:50 w/o AlBr_3 -HBr at a specific conductance of $2.0 \times 10^{-3} \Omega^{-1} \text{cm}^{-1}$.

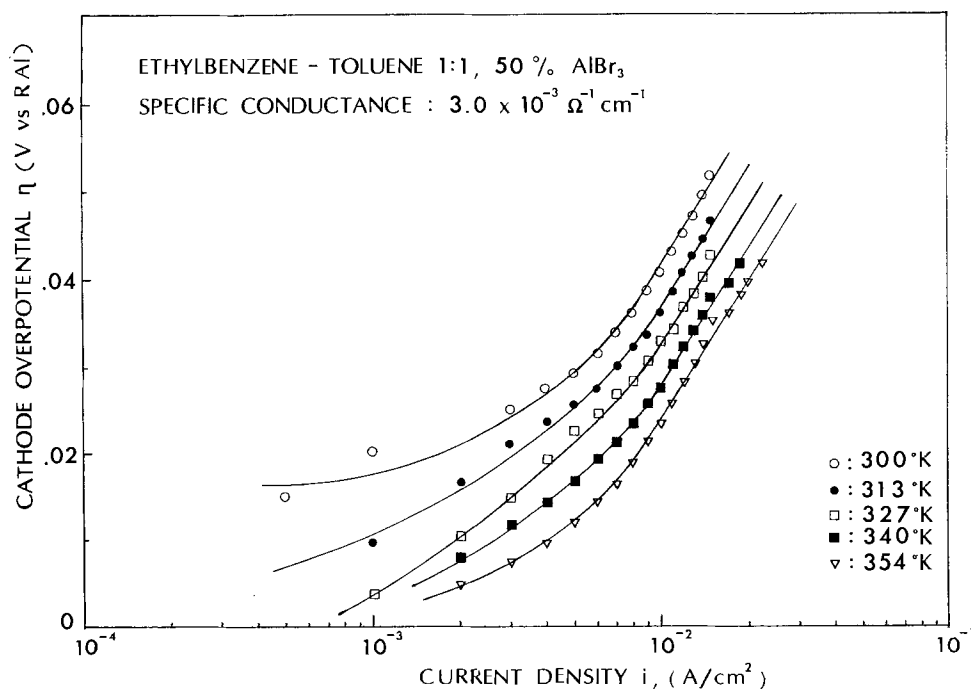


Fig. 3. Tafel plot at the temperatures shown, for ethylbenzene-toluene 1:1 vol:50 w/o AlBr_3 -HBr at a specific conductance of $3.0 \times 10^{-3} \Omega^{-1} \text{cm}^{-1}$.

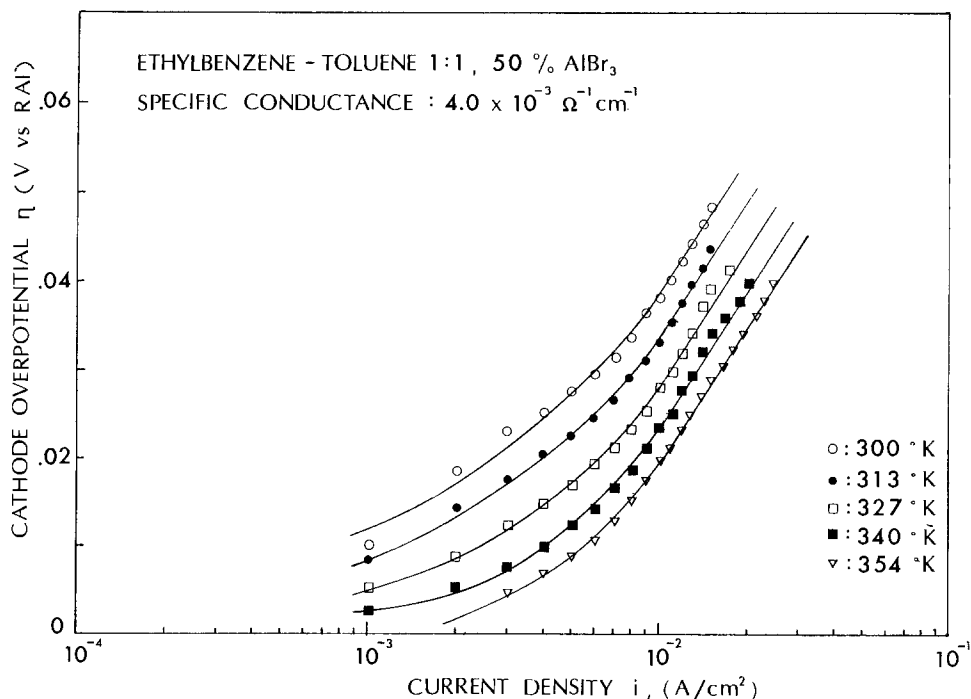


Fig. 4. Tafel plot at the temperatures shown, for ethylbenzene-toluene 1:1 vol:50 w/o $\text{AlBr}_3\text{-HBr}$ at a specific conductance of $4.0 \times 10^{-3} \Omega^{-1} \text{cm}^{-1}$.

having HBr added to yield specific conductances of 2, 3, and $4 \times 10^{-3} \Omega^{-1} \text{cm}^{-1}$, respectively.

These plots display a linear relationship between the cathode overpotentials and the log of the current density, above overpotential values of 30 mV. This is to be expected if the Tafel equation

$$\eta = \frac{2.30RT}{\alpha F} \log i_0 - \frac{2.30RT}{\alpha F} \log i_c \quad [9]$$

is obeyed and there is a controlling charge-transfer step.

Exchange current density.—The values of the exchange current density (i_0) were calculated by extrapolating the Tafel line to $\eta = 0$. For the three experimental electrolytes studied (specific conductance 2.0, 3.0, and $4.0 \times 10^{-3} \Omega^{-1} \text{cm}^{-1}$) and the data at 40°C (Fig. 2, 3, and 4), the i_0 values were found to be approximately $2 \times 10^{-3} \text{A/cm}^2$ (Table I).

Mechanism of aluminum deposition.—It is difficult to isolate the precise mechanism of aluminum deposition as there are numerous views on the types of complexes which can form between aluminum halides and aromatic hydrocarbons. However, the basic differences between the structures suggested are that, in one case, aluminum bromide exists in a monomeric form exemplified by the complex $(\text{AlBr}_2 \cdot n\text{ArH})^+$ (Eq. [2]) and, in the other, aluminum bromide would combine into a dimeric form, e.g., $(\text{Al}_2\text{Br}_5 \cdot n\text{ArH})^+$ (Eq. [1]).

Brown and Wallace (18) and Choi and Brown (23) found that unbranched or lower branched aromatic solvent molecules such as benzene and toluene produced mostly dimeric complexes (Eq. [3]). Solvent molecules with more or larger lateral chains, such as xylene and mesitylene, or alkyl benzenes having a higher basicity than toluene, generate mainly monomeric complexes, as shown in Eq. [4].

Table I. Calculated kinetic parameters from Tafel lines (40°C)

Specific conductance ($\Omega^{-1} \text{cm}^{-1}$)	i_0 (mA cm^{-2})	Tafel slope (V decade)	Cathodic transfer coefficient* (α)
4.0×10^{-3}	2.2	0.046	1.35
3.0×10^{-3}	2.0	0.048	1.3
2.0×10^{-3}	1.9	0.050	1.25

* Transfer coefficient: $\alpha = 2.3 RT/bF$, where b is Tafel slope.

Ethylbenzene provides highly basic alkylbenzenes such as diethylbenzene, ethylmethylbenzene, etc., through disproportionation reactions (10).

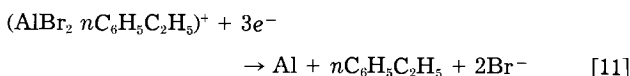
Capuano and Davenport, in an early publication (1), presented photographs showing the effects of several aromatic solvents on the quality of aluminum coatings. In fact, one can notice in Fig. 2 in Ref. (1) that no acceptable aluminum coatings are obtained from unbranched or lower branched solvents such as benzene or toluene. The quality of the aluminum coating improved, however, with xylene, and became excellent with ethylbenzene. This is consistent with the formation of monomeric aluminum complexes in solvent molecules having more or larger lateral chains than benzene and toluene. This supports the hypothesis that the presence of an aluminum complex in its monomeric form is prerequisite for aluminum electrodeposition in alkylbenzene- $\text{AlBr}_3\text{-HBr}$ electrolytes.

The slope of the experimental Tafel lines yields an average cathodic transfer coefficient $\bar{\alpha}$ of 1.3, close to 1.5. Similar values for the anodic transfer coefficient $\bar{\alpha}'$, are then predicted for Eq. [10]

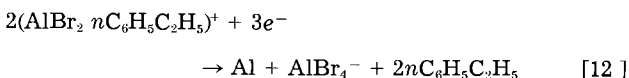
$$\bar{\alpha} + \bar{\alpha}' = \frac{n}{\nu} \quad [10]$$

These results indicate that if n (the total number of electrons transferred in the overall reaction) is equal to 3, i.e., if aluminum is present in a monomeric form, ν (the number of times the rate-determining step takes place for the overall reactions to occur once) equals 1.

Assuming then from the foregoing discussion that an ethylbenzene-toluene- $\text{AlBr}_3\text{-HBr}$ electrolyte produces monomeric aluminum complexes, the following plating reaction is proposed



Considering the fact that the Br^- is not likely to be in a free state, Eq. [11] can be written as



This is in agreement with Brown and Wallace (18) (Eq. [4]), Lebedev and Korshak (14-16) (Eq. [2]), and Levinskieve and Simanavicius (19) (Eq. [5]).

Heat of activation.—An electrochemical Arrhenius plot at some typical electrode overpotentials as derived from

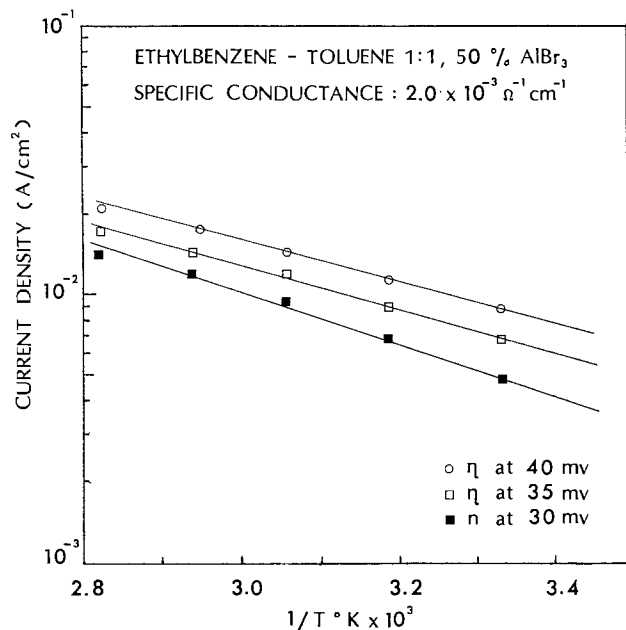


Fig. 5. Current density vs. $1/T$ (where T is the absolute temperature) plot adopted from Fig. 2, in order to determine the heat of activation (ΔH) _{η} at the overpotentials shown.

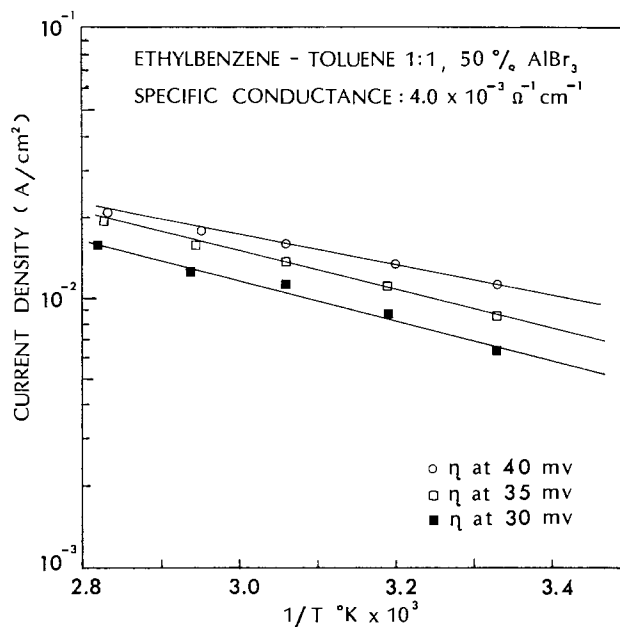


Fig. 6. Current density vs. $1/T$ (where T is the absolute temperature) plot adopted from Fig. 4, in order to determine the heat of activation (ΔH) _{η} at the overpotentials shown.

Fig. 2 and Fig. 4 is presented in Fig. 5 and Fig. 6. The heat of activation as given by the differential $(\partial \log i/\partial 1/T)_{\eta_0}$ lies between 2.6 and 4.5 kcal, depending on the electrode potential and the specific conductance. The complete results are given in Table II. These results compare well with the values obtained (4 kcal/mol) by Simanavicius *et al.* (24) for the Hurley and Wier (25) electrolyte (aluminum bromide and an ethyl-pyridinium bromide in toluene). It has been generally agreed (26) that the heat of activation in the electrodeposition of metals from aqueous solution is of the order of 10-30 kcal/mol. The values from the present work and values obtained by Simanavicius *et al.* (24) indicate, however, that the activation energies for plating metals from organic electrolytes are almost an order of magnitude less than the heats of activation for plating from aqueous electrolytes.

This result suggests that the bond energy of aluminum bromide in the alkylbenzene complexes is considerably lower than the hydration energy of metal ions in aqueous solutions.

Conclusions

1. A study of cathodic overpotentials of ethylbenzene-toluene $\text{AlBr}_3\text{-HBr}$ electrolyte showed that charge-transfer overpotentials were of the order of 40 mV at current density of 10 mA/cm². The overpotentials decrease with increasing specific conductances and temperature of the electrolyte.

2. Exchange current density (i_0) at specific conductances of $2.4 \times 10^{-3} \Omega^{-1} \text{cm}^{-1}$ and a temperature of 40°C are approximately $2 \times 10^{-3} \text{A/cm}^2$, and the heat of activation (ΔH) _{η} varies from 2.6 to 4.5 kcal/mol. The relatively high values of exchange current density and the relatively low value of heat of activation indicate that aluminum is

Table II. Calculated heat of activation for some typical electrode overpotentials at different specific conductances for the temperature range of 300-354 K

Specific conductance ($\Omega^{-1} \text{cm}^{-1}$)	Cathode overpotentials (mV)	Heat of activation (kcal/mol)
2×10^{-3}	30	4.5
	35	4.2
	40	3.5
4×10^{-3}	30	3.5
	35	3.1
	40	2.6

released rather easily from its organic complexes to plate on an aluminum cathode.

3. A cathodic transfer coefficient α of 1.3 is consistent with monomeric aluminum complexes being the active species during plating.

4. Solutions prepared from anhydrous alkylbenzene and aluminum bromide are not conductive enough for electroplating aluminum.

HBr is a suitable reagent for adjusting the conductivity of the solution to its optimum operating condition.

Acknowledgment

The authors wish to thank the Natural Sciences and Engineering Research Council of Canada and the Quebec Ministry of Education for financial support of this work.

Manuscript submitted July 11, 1983; revised manuscript received May 7, 1984.

The University of Quebec assisted in meeting the publication costs of this article.

REFERENCES

- G. A. Capuano and W. G. Davenport, *This Journal*, **118**, 1688 (1971).
- G. A. Capuano and W. G. Davenport, *Plating*, **60**, 251 (1973).
- G. A. Capuano, R. Lafortune, and C. Gobeil, *Plating Surf. Finish.*, **64**, 59 (1977).
- G. A. Capuano, J. Caza, and N. Homsy, in "1st International Symposium on Electrodeposition of Aluminum," Proceedings Session G-3, pp. 1-7 (1981).
- G. A. Capuano and W. G. Davenport, *This Journal*, **122**, 453 (1975).
- G. A. Capuano and W. G. Davenport, Canadian Pat. 945,935 (1974); U.S. Pat. 3,775,260 (1973).
- R. Lafortune, J. T. Bourret, and G. A. Capuano, *Can. J. Chem.*, **56**, 2375 (1978).
- G. A. Capuano, R. Ducasse, and W. G. Davenport, *J. Appl. Electrochem.*, **9**, 7 (1979).
- R. Ducasse and G. A. Capuano, *Plating Surf. Finish.*, **68**, 78 (1981).
- H. Antoun, A. Hade, and G. A. Capuano, *This Journal*, **129**, 40 (1982).
- H. C. Brown and W. J. Wallace, *J. Am. Chem. Soc.*, **75**, 6265 (1953).
- H. C. Brown and J. D. Brady, *ibid.*, **74**, 3570 (1952).
- D. D. Eley and P. J. King, *J. Chem. Soc.*, 2517 (1952).
- N. N. Lebedev, *JOCH*, **22**, 1505 (1948).
- V. V. Korshak and N. N. Lebedev, *ibid.*, **18**, 1766 (1948).

16. N. N. Lebedev, *ibid.*, **21**, 1780 (1951).
17. O. M. Kessler, N. M. Alpatov, and O. R. Orpow, *Adv. Chem.*, **33**, 261 (1964).
18. H. C. Brown and W. J. Wallace, *J. Am. Chem. Soc.*, **75**, 6268 (1953).
19. L. Simanavicius and A. Levinskieve, *Liet: TSR Mokslu Akad. Darb. Ser. B*, **4**, 39 (1966).
20. S. Barnartt, *This Journal*, **108**, 102 (1961).
21. S. Barnartt, *ibid.*, **99**, 549 (1952).
22. R. Piontelli, *Gazz. Chim. Ital.*, **83**, 357, 370 (1953).
23. S. V. Choi and H. C. Brown, *J. Am. Chem. Soc.*, **88**, 903 (1966).
24. L. Simanavicius and P. Dobrovolskis, *Issled. Obl. Ogazhdeniya Metal, Water. Respubl. Kouf. Ele. Kirochium. Litkov. S.S.R.*, **11**, 192 (1971).
25. F. H. Hurley and T. P. Wier, *This Journal*, **98**, 207 (1951).
26. J. O'M. Bockris, in "Modern Aspects of Electrochemistry," Vol. 2, J. O'M. Bockris, Editor, Butterworth Scientific Publication, London (1954).

Electrochemical Properties of $\text{WO}_3 \cdot x(\text{H}_2\text{O})$

III. Complex Plane Analysis of the Film on SnO_2

Nobuyuki Yoskiike, Masatake Ayusawa, and Sigeo Kondo

Matsushita Electric Industrial Company, Limited, Central Research Laboratory, Moriguchi, Osaka 570, Japan

ABSTRACT

Complex plane analysis of evaporated WO_3 films on SnO_2 coated glass substrate has been performed in propylene carbonate electrolytes as a function of frequency from 100 kHz to 100 mHz at various applied voltages. It has been confirmed that the electron injection process at the SnO_2 electrode/ WO_3 film interface, the electrochemical charge-transfer process in the WO_3 film and a diffusion-controlled process in the bulk are important processes at high ($f > 1$ kHz), medium ($1 \text{ kHz} > f > 3 \text{ Hz}$), and low frequencies ($f < 3 \text{ Hz}$), respectively. The change of electrochromic activity of various $\text{WO}_3 \cdot x(\text{H}_2\text{O})$ films depends mainly on the charge-transfer process in the film; the charge-transfer impedance increases with hydroxylation of WO_3 layer and, furthermore, increases drastically with hydrated crystallization.

WO_3 is one of the most useful materials for electrochromic displays (ECD) (1-6). A model for coloration by Faughnan *et al.* (3) explained reasonably well that double injection of electrons and protons into the film accompanies the formation of tungsten bronze. (The bronze has a stable memory effect and can be switched back into the original colorless state by reversing the current.) Recent studies (7-13) have confirmed that water in the film plays an important role for the coloration and bleaching mechanism.

The states of water in the WO_3 film may be classified into three groups: physisorbed water, chemisorbed water as hydroxylation, and hydrated water having a crystal structure. We (14, 15) have recently confirmed the influence of these three states on the electrochemical properties of evaporated WO_3 films. In particular, we have reported that water adsorbed on the film from ambient air after the ventilation of the vacuum evaporation chamber not only provides a fast electrochromic reaction at first, but also reacts gradually with WO_3 by hydroxylation and/or hydrolysis to shift the potential of the cathodic reaction to negative potentials. Then the hydroxylated film loses the electrochromic coloration density at the same applied voltage as before (14). We have also reported that the formation of tungstate crystals ($\text{WO}_3 \cdot \text{H}_2\text{O}$ and/or $\text{H}_2\text{WO}_4 \cdot \text{H}_2\text{O}$) by storing in high humidity air causes remarkable deterioration of the electrochromic activity of the film (15). The relationship between the electrochromic activity and the state of the water in $\text{WO}_3 \cdot x(\text{H}_2\text{O})$ has been clarified, but it is still not clear what kind of processes in the electrochromic reaction are being affected.

The mechanism and the coloration dynamics of the WO_3 film have been roughly clarified by many authors. Faughnan *et al.* (3, 16) measured a $t^{-1/2}$ dependence of current flow during the coloration reaction of the WO_3 film in H_2SO_4 aqueous solutions under low applied voltage and suggested a barrier-limited current of proton transport across the WO_3 /electrolyte interface as controlling. They (17) found $t^{-3/4}$ and $V^{1/2}$ dependence of current flow during the bleaching process under other constant applied voltages and suggested a field-driven space-charge-limited current of proton in those cases.

Mohapatra (18) also reported similar dynamics in the $\text{Li}_x\text{WO}_3/\text{Li}$ system. Green *et al.* (19-20) studied the thermo-

dynamics of the diffusion process with WO_3 /solid electrolyte and WO_3 /liquid electrolyte junctions using the galvanostatic method. However, although complex plane analysis is a most useful method, there are few studies of WO_3 film using this method. Ho *et al.* (21) have reported kinetic data such as chemical diffusion coefficient, partial ion conductivity, and thermodynamic enhancement factor, with $\text{Li}_x\text{WO}_3/\text{LiAsF}_6$ in propylene carbonate/Li system using this method. They suggested that the interfacial charge-transfer reaction at the WO_3 /electrolyte interface is important at short time ($t < 0.5\text{s}$), but at longer times the rate of Li injection is determined by the diffusion kinetics.

This paper describes studies on $\text{WO}_3 \cdot x(\text{H}_2\text{O})$ using complex plane techniques. The relationships between reaction processes and various states of water in $\text{WO}_3 \cdot x(\text{H}_2\text{O})$ are discussed for the actual operating conditions of display devices.

Experimental

Preparation of WO_3 films.— WO_3 films were deposited on SnO_2 -coated glasses ($100 \Omega/\text{cm}^2$) by an electron beam evaporation method. WO_3 targets (99.99%) were supplied by Furuuchi Kagaku Company, Limited. The deposition rate was 4 to 5 Å/s, the deposition angle was varied within 40° with a planetary rotation, and the substrate temperature was usually maintained at 80°C after being kept at 110°C for 5 min. The total gas pressure in the chamber during the evaporation process was controlled by a gas-introduction method at $4\text{-}5 \times 10^{-5}$ torr. Deposited WO_3 films were analyzed by electron diffraction and found to be amorphous. Packing density of the film calculated from film thickness and weight was $5.3\text{-}5.7 \text{ g/cm}^3$. The refractive index deduced from the interference patterns of visible absorption and film thickness was 1.85.

For the purpose of investigating the influence of humidity on the evaporated films, the films were stored in humidity- and temperature-controlled air at different conditions (Nagano Kagakukikai, Model NEW LH-20).

Electrochemical measurements.—Complex plane analyses were made using a pseudo-three-electrode configuration. The working electrode was the WO_3/SnO_2 electrode, in which the WO_3 film thickness and area were 3000Å and 0.3 cm^2 , respectively. In order to avoid interference arising from the SnO_2 /electrolyte interface, the SnO_2 elec-

trode surface was coated by a thin glass-plate insulator exposing only a part of the WO₃ film (0.3 cm²). The counterelectrode was a carbon electrode plate having a large surface area (the specific surface area of the carbon was 220 m²/g). The potential drift of the electrode during the measurements was negligibly small ($\Delta V < 1$ mV), so that the counter and reference electrode leads were combined (hence, pseudo-three electrode). The potential of the counterelectrode was monitored by a saturated calomel electrode (SCE).

The electrolytes were propylene carbonate (PC) solutions containing 0.3M LiClO₄ and 0.03M LiBF₄. PC (Wako Junyaku) was freshly distilled under vacuum. LiClO₄ (purity 99%, Mitsuwa Kagaku) and LiBF₄ (purity > 98%, Morita Kagaku) were used. Ar gas was bubbled before measurements.

Frequency response analysis was performed with the working electrode held at constant voltage by an electrochemical interface (Solartron Model 1186, England). A small alternating signal from a frequency response analyzer (Solartron Model 1170) was then superimposed on the constant voltage.

The amplitude of the signal which was applied to the sample was always 5 mV, and the frequency range covered extended from 100 kHz down to 100 mHz. Output data were the average values of ten sampling times and were plotted through a plotter interface (Solartron Model 1180).

Cyclic voltammetry measurements were performed with a potentiostat (Hokuto Denko, Model HA-301), which was supplied with voltage from a function generator (same company, Model HB-104). The counterelectrode was a Pt plate and the reference a SCE. The electrolyte was the same as the electrolyte used for complex plane measurements.

H₂O content of the electrolytes was checked in each case by an aquacounter (Hiranuma Seisakusho, Model AQ-3B). The concentrations were typically 0.03-0.05M.

Results and Discussions

Complex impedances of the WO₃ (3000Å thick) film on SnO₂ stored in air at 25°C for 1h after the evaporation were measured under various applied voltages, as shown in Fig. 1 and 2.

Figure 1 shows the complex impedance data under conditions of working electrode potentials from +500 to +300 mV vs. SCE, and counterelectrode potential constant at +370 mV vs. SCE. Figure 2 shows the complex impedance data for more negative working electrode potentials between +250 and -200 mV vs. SCE. In Fig. 1 and Fig. 2, the first semicircle was observed from 100 down to 1 kHz. It became small at more negative potentials of the working electrode and too small to be recognized at potentials more negative than +100 mV vs. SCE. The second semicircle was observed clearly from 1 kHz down to 3 Hz at potentials more negative than +400 mV and corresponds to a charge-transfer-controlled process. The second one also became small with more negative potential conditions.

The impedance plots for frequencies lower than 3 Hz approached a line parallel to the imaginary axis and were therefore assigned to finite diffusion control rather than a semi-infinite diffusion-controlled process.

These impedance results can be represented, as a rule, by the circuit of Fig. 3 (21-25). In Fig. 3, R_1 is the uncompensated ohmic resistance of the electrolyte and electrode. C_1 and θ_1 are the capacitance and the resistance associated with the first semicircle, respectively. C_2 and θ_2 are the capacitance and the charge-transfer resistance, respectively, associated with the second semicircle, and Z_w is a complex impedance arising from the diffusion of the electroactive species, associated with the straight line for lower frequencies.

Furthermore, θ_1 can be obtained from the following equation

$$\left(R - R_1 - \frac{\theta_1}{2}\right)^2 + X^2 = \left(\frac{\theta_1}{2}\right)^2 \quad [1]$$

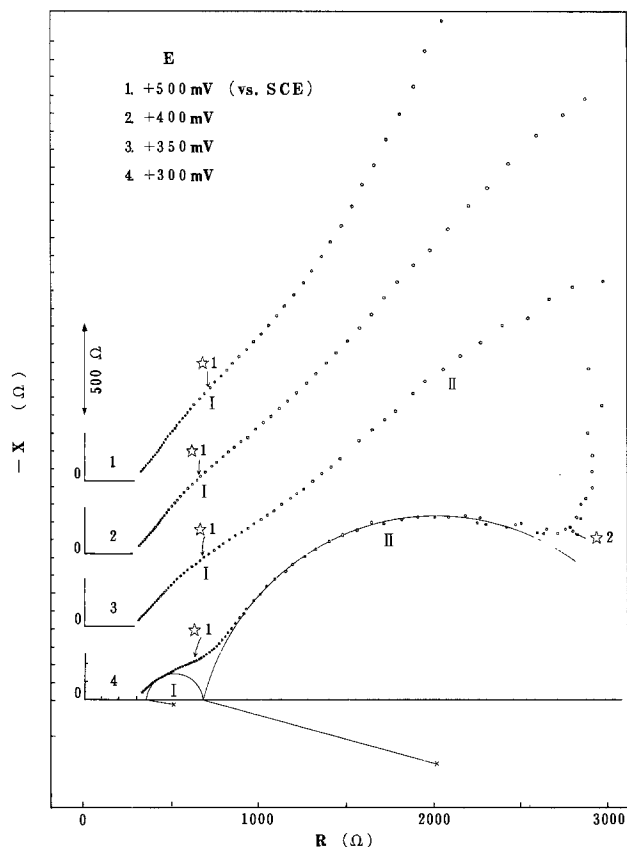


Fig. 1. Complex impedance data of the WO₃ film (3000Å thick, 0.3 cm²) stored in air at 25°C for 1h. I is the first semicircle, and II is the second semicircle. *1 and *2 are 1.1 kHz and 3.5 Hz, respectively.

where R and X are the real and imaginary parts of the complex impedance, respectively.

C_1 can be obtained from the following equation

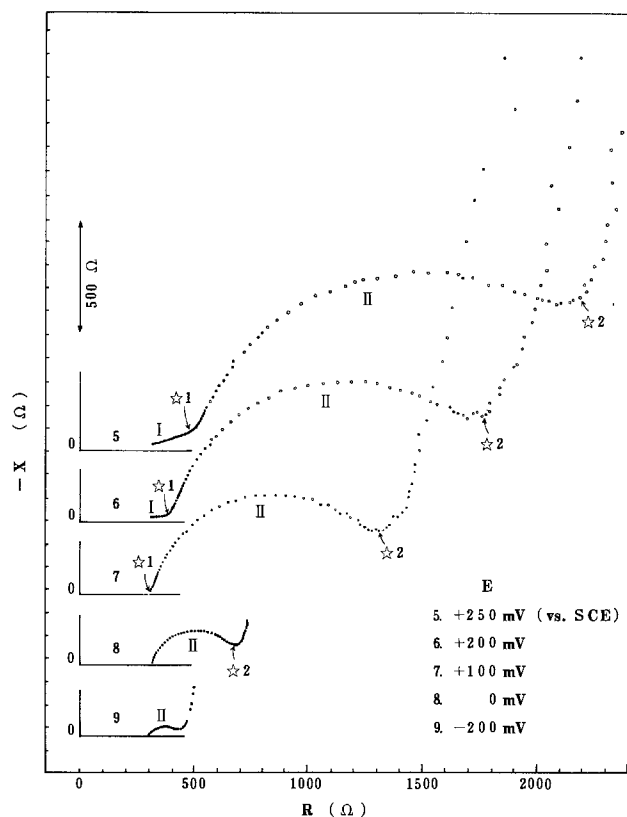


Fig. 2. Complex impedance data of the same sample as shown in Fig. 1.

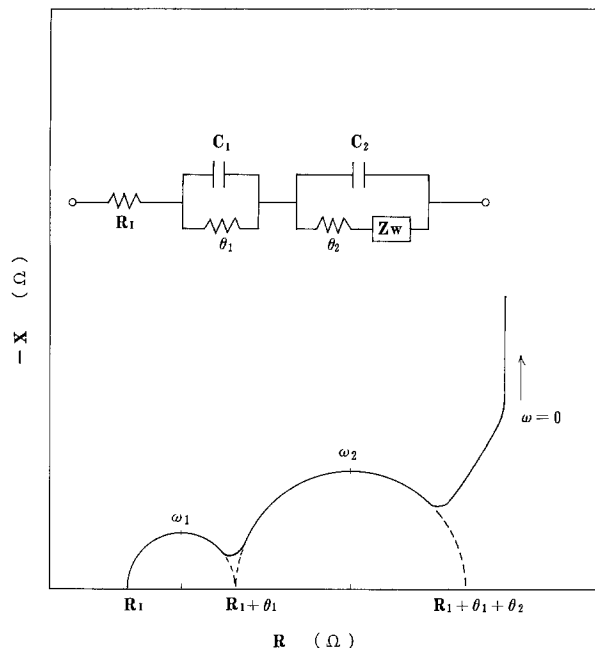


Fig. 3. Admittance plots for the circuit containing two R-C circuits and a finite diffusion-controlled process.

$$C_1 = \frac{1}{\theta_1 \omega_1} \quad [2]$$

where ω_1 is the radial frequency corresponding to the top of the first semicircle.

θ_2 can be obtained from

$$\left(R - R' - \frac{\theta_2}{2}\right)^2 + X^2 = \left(\frac{\theta_2}{2}\right)^2 \quad [3]$$

where $R' = R_1 + \theta_1$.

C_2 can be obtained from

$$C_2 = \frac{1}{\theta_2 \omega_2} \quad [4]$$

where ω_2 is the radial frequency corresponding to the top of the second semicircle.

The equivalent circuit shown in Fig. 3 is independent of the counterelectrode, because the counterelectrode was a large surface carbon electrode having a large double layer capacity (more than 1 mF). Thus, the complex impedance is determined by the reaction processes on the WO_3 electrode only. R_1 was about 290Ω , and was independent of the electrode potential.

In order to clarify the properties of the two semicircles, complex impedances of various WO_3 films having different thickness (500–5000Å) were measured. R_1 and θ values for each semicircle were calculated using a computer method in which three ideal plots for the semicircle were chosen and Eq. [1] and/or [3] were used. R_1 was $270 \pm 30\Omega$ and was independent of the thickness of the WO_3 films. The θ values for films of various thickness are shown in Fig. 4 and 5 as a function of the WO_3 electrode potential. In Fig. 4, the θ_1 values, corresponding to the first semicircle observed from 100 kHz down to 1 kHz, increase with the potential of the WO_3 electrode. The θ_1 value of 5000Å thickness WO_3 film was not obtained because of unstable plots.

The θ_1 values were independent of the WO_3 film thickness between 500 and 3000Å, so that θ_1 can be assigned to the charge-transfer impedance at the SnO_2 electrode/ WO_3 interface or the WO_3 /electrolyte interface, but not to a bulk property.

We consider the following four points: (i) the coloration of WO_3 is caused by the double injection of electrons from the electrode and cations from the electrolyte (3), and not caused by an electrochemical reaction such as a reaction $\text{W} = 0$ to W-O-H at the WO_3 /electrolyte interface; (ii) the

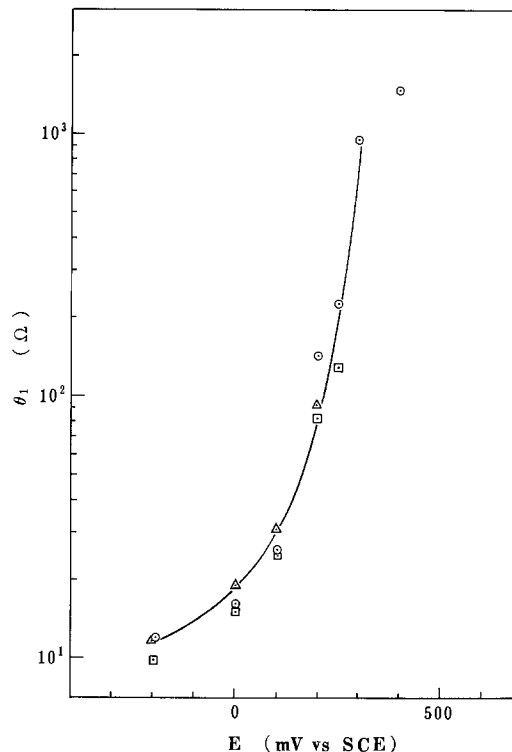


Fig. 4. Potential dependence of the resistance (θ_1) corresponding to the first semicircle (I). The thickness of the WO_3 films (0.3 cm^2) are 500 (Δ), 1000 (□), and 3000Å (○).

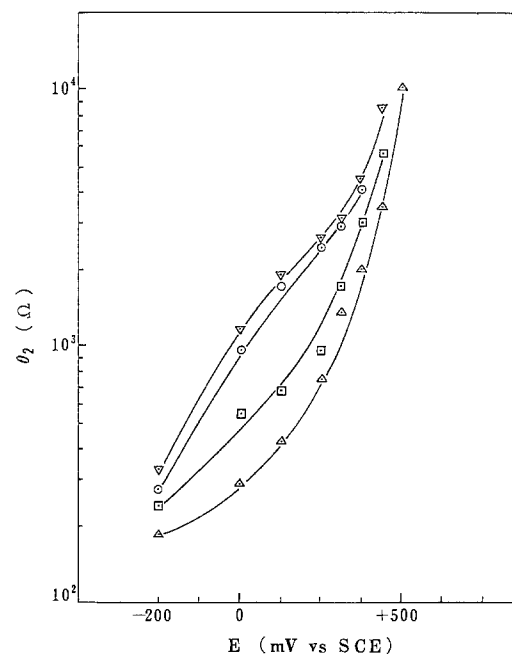


Fig. 5. Potential dependence of the resistance (θ_2) corresponding to the second semicircle (II). The thickness of the WO_3 films (0.3 cm^2) are 500 (Δ), 1000 (□), 3000 (○), and 5000Å (▽).

first semicircle is found at high frequency (1 kHz to 100 kHz); (iii) the interface of the WO_3 /electrolyte is not a flat plane, but a porous xerogel structure (12), so that the interface taking part in the cation injection process will increase with the WO_3 film thickness; and (iv) the small capacitance can exist at the electrode/ WO_3 interface in which WO_3 was evaporated as grains on the electrode surface (25) because of the following two reasons: the energy level of the conduction band of n- SnO_2 does not overlap the level of n- WO_3 , and, strictly speaking, the contact of n- SnO_2 /n- WO_3 may not be an ohmic contact; electron transfer from the SnO_2 electrode to the WO_3 layer may be slightly blocked at grain boundaries of WO_3 (25). There-

fore, it may be reasonable to say that the first semicircle results from a circuit involving the capacitance (C_1) and the resistance (θ_1) corresponding to the electron injection process at the electrode/WO₃ interface.

In Fig. 5, the θ_2 , corresponding to the second semicircle observed from 1 kHz down to 3 Hz, increases with the potential of the WO₃ electrode and increases with film thickness. However, the injection of cations into the WO₃ film would not only occur at the WO₃ surface interface, but also occur at voids in the porous WO₃ film (12). Then the semicircle corresponding to the cation injection process would be dependent on the WO₃ film thickness.

Therefore, θ_2 would be the charge-transfer impedance corresponding to an electrochemical reaction process such as the cation injection.

Various WO₃ · x(H₂O).—We prepared the following four kinds of WO₃ · x(H₂O) films after evaporation on SnO₂ electrodes: (i) as-deposited WO₃ film containing small amount of H₂O; (ii) WO₃ · x(H₂O) film containing much physisorbed water by storing in air at 25°C 50% (relative humidity) for 16h (14); (iii) hydroxylated WO₃ · x(H₂O) film having many OH groups by storing in air at 25°C 50% (RH) for 168h (14); and (iv) hydrated WO₃ · x(H₂O) film having WO₃ · H₂O and/or H₂WO₄ · H₂O crystal structures by storing in air at 40°C 95% (RH) for 24h (15).

Cyclic voltammograms of these WO₃ · x(H₂O) films were measured in PC electrolyte and are shown in Fig. 6. The cathodic current is associated with coloration of the film and the anodic current is associated with bleaching. WO₃ · x(H₂O) films containing much physisorbed water have a fast electrochromism (EC) and both hydroxylated WO₃ · x(H₂O) films and hydrated WO₃ · x(H₂O) films having crystal structures lose EC activity. We earlier discussed these properties in more detail (14, 15).

Complex impedances of these films were measured at various working electrode potentials. Both C_1 and C_2 values were calculated by Eq. [2] or [4] and are shown in Fig. 7. The capacitance of the WO₃ thin film bulk layer (C_2) was several μF , which was about 30 times the magnitude of the capacitance (C_1) of the electrode/WO₃ interface. The θ values of each process were calculated and are shown in Fig. 8 and 9.

Compositions (x) of M_xWO₃ bronze (M: H⁺ or Li⁺) under the various working electrode potentials were calculated from the injected charge and are shown in Fig. 10 as a function of the electrode potential. Both θ_1 and θ_2 are represented as a function of composition (x) in Fig. 11.

From these results, we conclude first concerning the fast electron injection process at the electrode/WO₃ interfaces that (i) the interface of an as-deposited film may be in a nonequilibrium state, thus giving rise to unstable complex impedances; (ii) the impedance decreases to

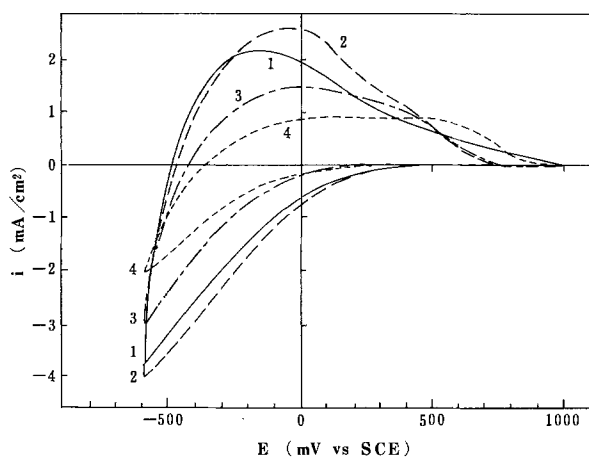


Fig. 6. Cyclic voltammograms of the WO₃ films (3000Å thick, 0.3 cm²). Scan rate: 200 mV/s. 1: As-deposited film. 2: WO₃ containing physisorbed water. 3: Hydroxylated film. 4: Hydrated film.

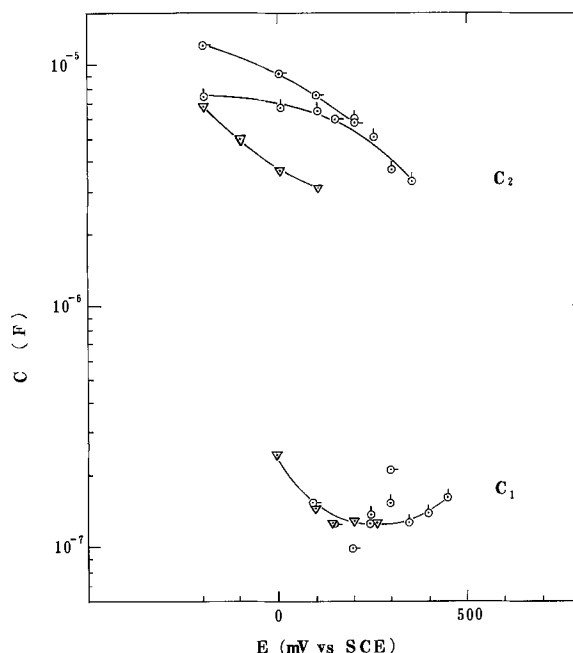


Fig. 7. Potential dependences of the equivalent circuit capacitances. WO₃ films (3000Å, 0.3 cm²) are the film containing physisorbed water (○), the hydroxylated film (△), and the hydrated film (▽).

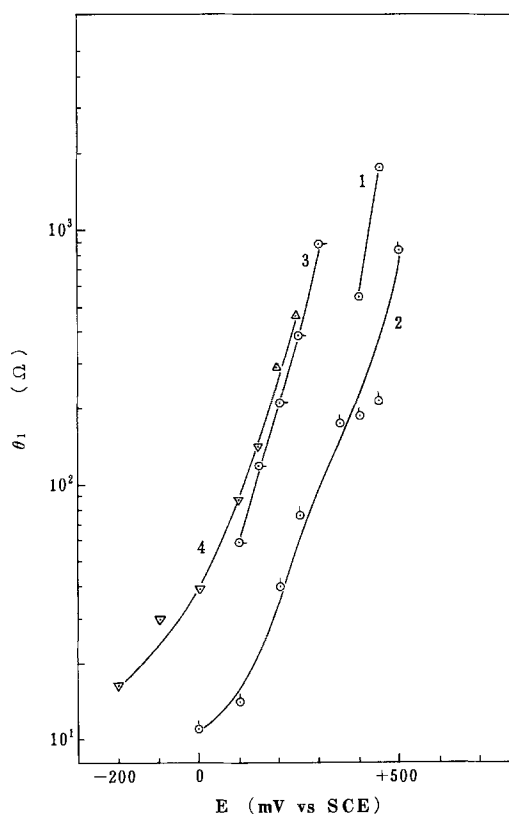


Fig. 8. Potential dependences of θ_1 . 1: As-deposited WO₃ film (○). 2: WO₃ film (3000Å, 0.3 cm²) containing physisorbed water (○). 3: Hydroxylated film (△). 4: Hydrated film (▽).

one-half with an increase of physisorbed water in the WO₃ film and doubles with hydroxylation of the film and is relatively insensitive to hydrated crystallization; (iii) there is a linear relationship between the impedance and the composition, x , of M_xWO₃ bronze; and (iv) the capacitance is about 10⁻⁷ F and not strongly dependent on the condition of water in the WO₃ · x(H₂O).

Second, concerning the charge-transfer process such as the cation injection process in the WO₃ film: (i) the as-deposited film is unstable; (ii) the electrochemical charge

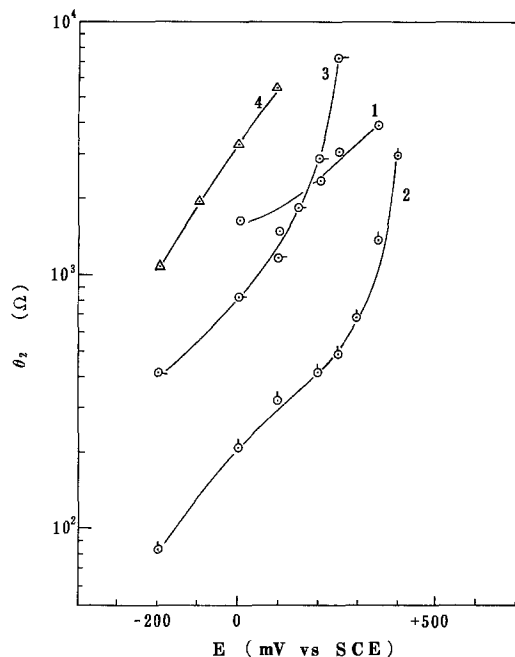


Fig. 9. Potential dependences of θ_2 . Sample numbers represent the same samples shown in Fig. 8.

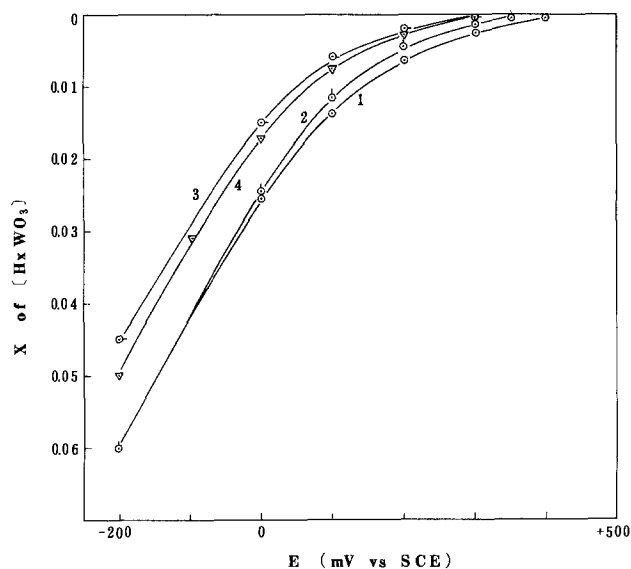


Fig. 10. Coulometric titration curve for M_xWO_3 . Sample numbers represent the same samples shown in Fig. 8.

transfer impedance in the film is about one order of magnitude larger than the electron injection impedance; and (iii) it decreases to about one-sixth to one-seventh with an increase of physisorbed water and increases about three times with hydroxylation of the film and about ten times with hydration. θ_2 values for four kinds of $WO_3 \cdot x(H_2O)$ films, in case of a composition $x = 0.01$ of M_xWO_3 bronze, are tabulated in Table I.

Conclusion

The coloration reaction process was separated into three processes using complex plane analysis; the electron injection process at the electrode/ WO_3 interface hav-

Table I. θ_2 values in case of a composition $x = 0.01$ of M_xWO_3 bronze

	$WO_3 \cdot x(H_2O)$	θ_2 (Ω)
1	As-deposited film	1.6×10^3
2	Containing physisorbed water	4×10^2
3	Hydroxylated film	9×10^2
4	Hydrated film	4.5×10^3

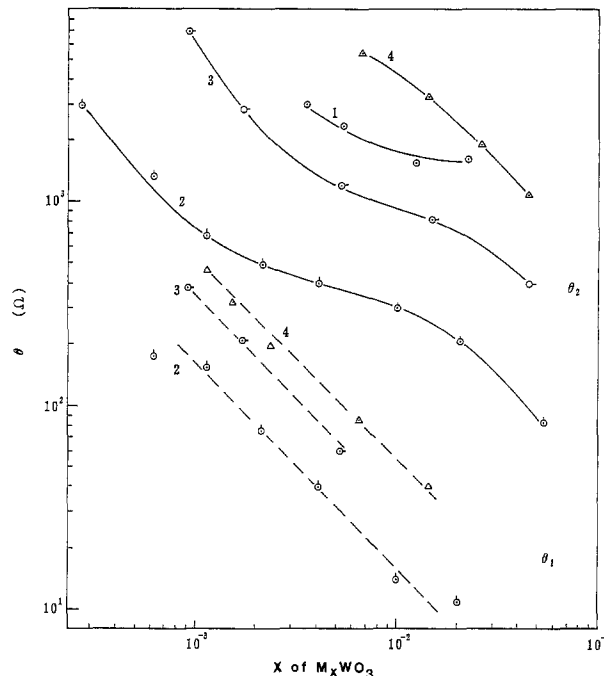


Fig. 11. Composition dependences of θ_1 and θ_2 . Sample numbers represent the same samples shown in Fig. 8.

ing the double layer capacitance ($10^{-7}F$) ($100 \text{ kHz} > f > 1 \text{ kHz}$), the electrochemical charge transfer through the cation-injection process in the WO_3 film having an impedance one order of magnitude larger than the electron injection impedance ($1 \text{ kHz} > f > 3 \text{ Hz}$), and a slow diffusion-controlled process in the bulk ($f < 3 \text{ Hz}$).

Remarkably, the fast electron injection process at the interface is not influenced by the condition of the water incorporation in the WO_3 films, but the electrochemical charge-transfer process in the WO_3 film clearly is. The electrochemical charge-transfer process in the WO_3 is the most important process in determining EC reaction speed for display devices.

Acknowledgments

The authors thank Dr. E. Hirota, the assistant director of Central Research Laboratory, for support in this work and Dr. S. Sekido for helpful discussions.

Manuscript submitted Dec. 21, 1983; revised manuscript received June 25, 1984.

Matsushita Electrical Industrial Company, Limited assisted in meeting the publication costs of this article.

REFERENCES

- S. K. Deb, *Appl. Opt. Suppl.*, **3**, 192 (1969).
- C. J. Schoot, J. J. Ponjee, H. T. Van dam, R. A. Van doorn, and P. T. Bolwijn, *Appl. Phys. Lett.*, **23**, 64 (1973).
- B. W. Faughnan, R. S. Crandall, and P. M. Heyman, *RCA Rev.*, **36**, 177 (1975).
- J. D. E. McIntyre, G. Beni, and J. L. Shay, Abstract of the 20th EMC, Santa Barbara, 1978.
- M. M. Nicholson and R. V. Galiardi, *SID 1978 Digest*, p. 24.
- N. Yoshiike, S. Kondo, and M. Fukai, *This Journal*, **127**, 1496 (1980).
- R. Hurditch, *Electron. Lett.*, **11**, 142 (1975).
- H. R. Zeller and H. V. Beyeller, *Appl. Phys.*, **13**, 231 (1977).
- B. Reichman and A. J. Bard, *This Journal*, **126**, 583 (1979).
- A. Deneuve, P. Gerard, and P. Billat, *Thin Solid Films*, **70**, 203 (1980).
- Y. Hajimoto, M. Matsushita, and S. Ogura, *J. Electron. Mater.*, **8**, 301 (1979).
- L. Pickelmann and P. Schlotter, Eurodisplay '81, München, FRG, Sept. 16-18, 1981.

13. T. C. Arnoldussen, *This Journal*, **128**, 117 (1981).
14. N. Yoshiike and S. Kondo, *ibid.*, **130**, 2283 (1983).
15. N. Yoshiike and S. Kondo, *ibid.*, **131**, 809 (1984).
16. R. S. Crandall and B. W. Faughnan, *Appl. Phys. Lett.*, **28**, 95 (1976).
17. B. W. Faughnan, R. S. Crandall, and M. A. Lampert, *ibid.*, **27**, 275 (1975).
18. S. K. Mohapatra, *This Journal*, **125**, 284 (1978).
19. M. Green, *Thin Solid Films*, **50**, 145 (1978).
20. M. Green, W. C. Smith, and J. A. Weiner, *ibid.*, **38**, 89 (1976).
21. C. Ho, I. D. Raistrick, and R. A. Huggins, *This Journal*, **127**, 343 (1980).
22. J. E. B. Randles, *Discuss. Faraday Soc.*, **1**, 11 (1947).
23. J. E. Bauerle, *J. Phys. Chem. Solids*, **30**, 2657 (1969).
24. S. Haruyama, *Denki Kagaku*, **39**, 536 (1971); *ibid.*, **39**, 658 (1971).
25. T. Takahashi, H. Iwahara, and Y. Suzuki, *ibid.*, **39**, 665 (1971).

Technical Notes



The Decomposition of Propylene Carbonate in a Lithium/Metal Phthalocyanine Cell

M. Arakawa, J. Yamaki,* and T. Okada

Nippon Telegraph and Telephone Public Corporation, Ibaraki Electrical Communication Laboratory, Tokai, Ibaraki-ken, 319-11, Japan

Recently, considerable attention has been focused on batteries composed of lithium anodes, cathodes, and organic electrolytes. This has been particularly true of lithium secondary batteries employing topochemical reactions (1-3).

We have reported on metal phthalocyanine (MPc) as a cathode active material, and its charge and discharge characteristics (4). Gas evolution, however, was observed in lithium batteries using MPc as the cathode active material. Gas evolution from the graphite electrode in lithium batteries was first reported by Dey *et al.* (5). However, the electrochemical characteristics and the gas evolution reaction mechanism were not clarified sufficiently.

Studies of the effect of MPc on electrocatalysis have been widely carried out for O₂ reduction reactions in aqueous electrolytes (6, 7). The decrease of electrocatalytic activity was reported in the order: Fe > Co > Ni > Cu > H₂ (8). This indicates a significant dependence of the central metal on electrocatalytic activity, though its role is not yet sufficiently understood.

In this paper, we report the catalytic effect of MPc on the gas evolution reaction.

Experimental

The experimental setup is schematically shown in Fig. 1. Test cell is set in the vacuum line and evacuated. A constant current discharge and stepwise potentiostatic discharge were then carried out, using a constant current and a constant voltage source (Hokuto Denko Company). The volume of gas evolved during the discharge test was measured using the oil manometer of the vacuum line, and its components were identified with a mass spectrometer.

The test cell was composed of a lithium anode, a cathode, and a reference electrode as shown in Fig. 2. The cathode was made up of MPc (M = H₂, Li₂, Na₂, CrF, Mn, Fe, Co, Cu, GaCl, Ag, Cd) (Eastman Kodak Company), carbon powder (Akzo Corporation, Ketjenblack EC), and polytetrafluoroethylene (PTFE, Daikin Kogyo Company Limited, F103). The mixing ratio of MPc, carbon powder, and PTFE was 49, 48, and 3 weight percent (w/o), respectively. The mixture (0.05g) was pressed at 30 kg/cm² to form a 13 mm diam disk. The lithium electrode was 13

mm diam and 0.24 mm thick disk. Lithium metal was also used for the reference electrode. Propylene carbonate (PC) containing 1M LiClO₄ (Tomiyama Pure Chemical Industries Limited) was used as the organic electrolyte. Water content was less than 20 ppm. All test cells were constructed in a dry box filled with dry argon gas.

Results and Discussion

Discharge tests were carried out galvanostatically at 3 mA for cathodes containing several kinds of MPc. Gas evolution volume during discharge down to 0.5V is summarized in Table I. A typical gas evolution curve is shown in

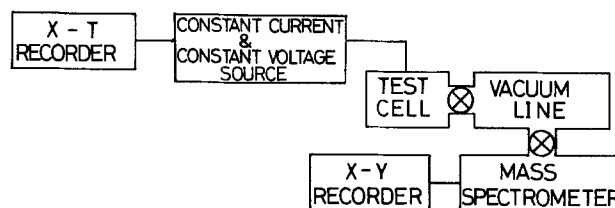


Fig. 1. Block diagram of gas evolution measurement system

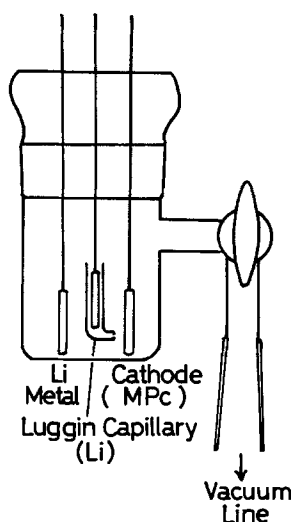


Fig. 2. Cell for gas evolution measurement.

* Electrochemical Society Active Member.

Fig. 3. A typical gas evolution characteristic in Li/MPc cell. M = Fe, 3 mA constant current discharge.

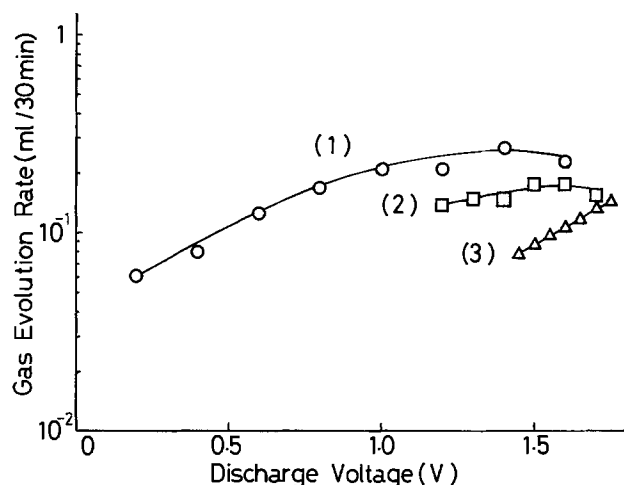
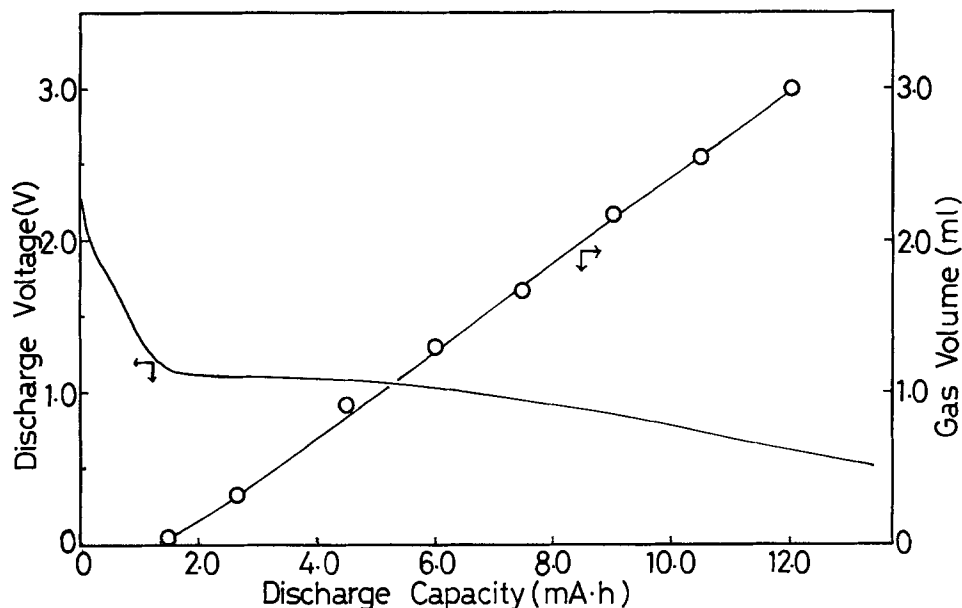


Fig. 4. Dependence of gas evolution rate on discharge voltage in Li/FePc cell with 1M LiClO₄/PC. (1): 0.2V stepwise discharge. (2): 0.1V stepwise discharge. (3): 0.05V stepwise discharge.

Fig. 3. The principal component of the evolved gas was identified as propylene from mass peaks ($m/e = 39, 41,$ and 42). In the cells containing FePc, CoPc, or MnPc, the evolved gas volume was very large. The effect of carbon on gas evolution cannot be neglected in the low voltage region. However, under the conditions reported here, the contribution from the carbon is estimated from the blank test to be less than 0.30 ml. A detailed study of the effect of carbon is now being carried out.

Table I. Gas evolution characteristics of various MPc's

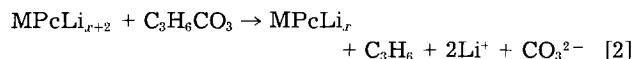
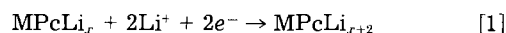
MPc	Gas volume (V _g)* (ml)	Ratio (R)** (%)	Discharge capacity (Q _d) (mA·h)	Net capacity (mA·h)
H ₂ Pc	0.19	5.05	9.0	8.55
Na ₂ Pc	0.08	4.25	4.5	4.31
Li ₂ Pc	0.02	0.90	5.3	5.25
CrFPc	0.58	15.88	8.7	7.31
MnPc	1.27	24.70	11.1	8.36
FePc	3.15	55.42	13.6	6.06
CoPc	1.75	46.50	9.0	4.82
NiPc	0.85	20.41	10.0	7.96
CuPc	0.12	4.42	6.5	6.21
GaClPc	0.03	0.89	3.5	3.47
AgPc	0.64	11.89	12.8	11.28
CdPc	0.04	0.89	5.3	5.25

* V_g is converted into the volume at 0°C, 1 atm.

** R is derived from Eq. [3].

A lithium cell containing FePc (Li/FePc) was employed to investigate the gas evolution reaction more closely. Stepwise potentiostatic discharge (0.05, 0.1, and 0.2V, respectively) was carried out at intervals of 30 min. The results are shown in Fig. 4. A simple relation was not observed between the gas evolution rate and discharge voltage. The rate varied according to the changes in the constant voltage step width. Namely, the gas evolution rate depends on not only the cathode voltage, but also the discharge condition. This indicates the electrochemical charge transfer process is not the rate-determining step for the gas evolution reaction.

This view is supported by the results of discharge tests performed galvanostatically at 1, 3, and 6 mA for Li/FePc cells. The evolved gas volume was plotted against discharge capacity (Fig. 5). The gas volume was proportional to the discharge capacity and independent of discharge current. This indicates that the rate-determining step of the gas evolution reaction is a reaction product formation process. The electrochemical reaction product (FePcLi_r) from FePc and Li⁺ may react chemically with PC and produce gas (Eq. [1] and [2])



This was confirmed by adding PC to the FePcLi_r, which was formed by the reaction of FePc with n-butyl lithium.

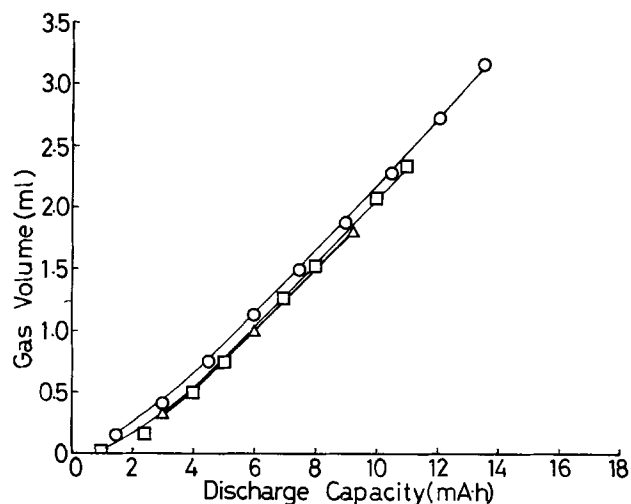


Fig. 5. Dependence of evolved gas volume on discharge capacity. □: 1 mA constant current discharge (CCD). ○: 3 mA CCD. △: 6 mA CCD.

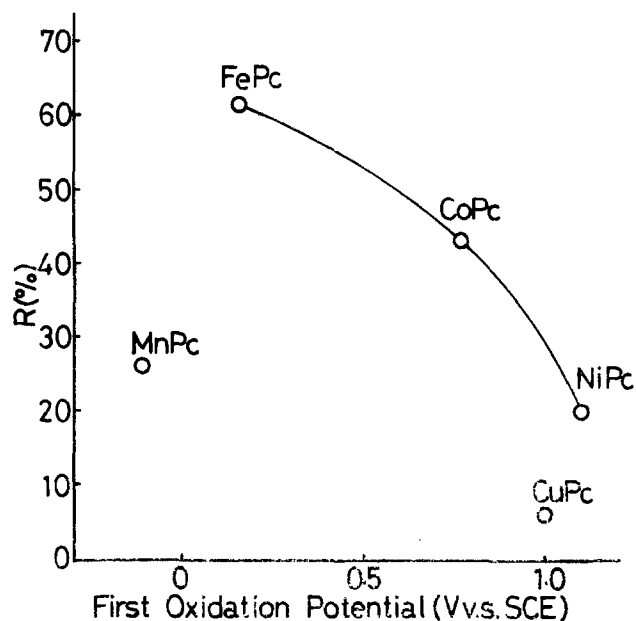


Fig. 6. Gas evolution ratio (R) derived from Eq. [3] plotted against the first oxidation potential of MPc taken from Ref. (9).

PC was added, and it immediately reacted to generate propylene gas.

Based on these results, the activity of MPcLi_x was estimated using the ratio (R) given by Eq. [3]. R means the ratio of the quantity of electricity for gas evolution to discharge capacity

$$R = \frac{2 \times 26.8 V_g / 22.4}{Q_d} \quad [3]$$

where V_g and Q_d represent gas volume and discharge-capacity, respectively. The ratios for several MPc are shown in Table I. Remarkable activity is observed for FePc and CoPc.

Gas evolution ratios (R) were plotted against the first oxidation potentials of MPc (Fig. 6). The data reported by Manassen and Bar-Ilan were used for first oxidation po-

tential values of the various MPc's (9). The relation shows that group VIII central metal MPc's have higher gas evolution activity than the other group. However, the reason for this activity difference has not been investigated in this work. Within the same group, the gas evolution activity increased with a decrease of oxidation potential. This may indicate that the order of the first oxidation potential of MPcLi_x is similar to that of MPc, and that the reactivity of reaction represented by Eq. [2] depends on the first oxidation potential of MPcLi_x ; that is, the reaction (Eq. [2]) proceeds more easily when the charge transfer from MPcLi_x to PC occurs more easily.

Conclusion

Gas evolution from the phthalocyanine electrode in lithium batteries was observed. During the discharge tests, the evolved gas volume was proportional to the discharge capacity. The principle component of the gas was identified as propylene. The activity of MPc was estimated based on discharge capacity. The activity decreased in the order of $\text{FePc} > \text{CoPc} > \text{MnPc} > \text{NiPc} > \text{CrPc} > \text{AgPc}$. H_2Pc , Li_2Pc , Na_2Pc , GaClPc , and CdPc did not have much activity. Propylene gas is probably generated by the chemical reaction between PC and the discharge product of phthalocyanine.

Manuscript submitted April 30, 1984; revised manuscript received ca. June 13, 1984.

Nippon Telegraph and Telephone Public Corporation assisted in meeting the publication costs of this article.

REFERENCES

1. B. Scrosati, *Electrochim. Acta*, **26**, 1559 (1981).
2. K. M. Abraham, *J. Power Sources*, **7**, 1 (1981).
3. K. M. Abraham, P. B. Harris, and D. L. Natwig, *This Journal*, **130**, 2309 (1983).
4. J. Yamaki and A. Yamaji, *ibid.*, **129**, 5 (1982).
5. A. N. Dey and B. P. Sullivan, *ibid.*, **117**, 222 (1970).
6. M. Savy, P. Andro, C. Bernard, and G. Magner, *Electrochim. Acta*, **18**, 191 (1973).
7. J. Zagal, P. Bindra, and E. Yeager, *This Journal*, **127**, 1506 (1980).
8. J. P. Randin, *Electrochim. Acta*, **19**, 83 (1973).
9. J. Manassen and A. Bar-Ilan, *J. Catal.*, **17**, 86 (1970).

Electronic Conductivity Decrease in Porous NiO Cathodes during Operation in Molten Carbonate Fuel Cells

Charles E. Baumgartner*

General Electric Company, Corporate Research and Development, Schenectady, New York 12301

The electronic conductivity of nascent and doped NiO has been extensively examined over the past several decades (1-16). Stoichiometric NiO is an insulator at room temperature with a specific resistivity of $\sim 10^{13} \Omega \text{ cm}$ (1, 5). The introduction of monovalent ions, such as lithium, into the NiO lattice on Ni lattice sites can decrease the room temperature resistivity by as much as 13 orders of magnitude. This pronounced effect was first explained by Verwey *et al.* (1-3), who postulated that coincident with the incorporation of each Li^+ ion was the formation of a trivalent nickel ion (Ni^{3+}) located on a Ni^{2+} lattice site, thereby reserving the overall crystal charge neutrality. The observed conductivity enhancement results from the mixed valency of nickel atoms located on equivalent, adjacent lattice sites. Following this mechanism, it was postulated, and later proven by Verwey (3), that doping NiO with equimolar concentrations of both a monovalent and a foreign trivalent species would yield an electronic con-

* Electrochemical Society Active Member.

ductivity resembling undoped NiO. This result has been subsequently demonstrated by other authors (6, 15) and is, in part, responsible for the differences in absolute Li-doped NiO conductivity values found in the literature. A recent review by Jarzebski (17) historically details the published NiO electronic conductivity data.

A state-of-the-art molten carbonate fuel cell (MCFC) utilizes a porous Li-doped NiO cathode. The structure is typically prepared by the oxidation of a porous nickel plaque *in situ* to the fuel cell cathode compartment, the lithium dopant originating from the $\text{Li}_2\text{CO}_3 \cdot \text{K}_2\text{CO}_3$ electrolyte. The resulting porous structure, containing an equilibrium Li concentration of approximately 0.02 cation fraction, possesses a 923 K (MCFC operating temperature) specific conductivity of $\sim 2 (\Omega \text{ cm})^{-1}$. In most present fuel cell designs, the cathode is in intimate contact with a ribbed stainless steel current collector which, during cell operation, oxidizes to form a scale containing predominantly Fe_2O_3 , LiFeO_2 , Li_2CrO_4 , and K_2CrO_4 . The chromates

are highly soluble in the molten alkali carbonate electrolyte and therefore dissolve from the cathode/current collector interface to leave behind a predominately iron oxide scale. The incorporation of either Fe^{+3} or Cr^{+3} into the NiO structure, from either the current collector or its dissolved corrosion products, would be expected to significantly decrease the cathode's electronic conductivity and thereby increase, with time, the voltage drop associated with cell operation.

This communication quantifies the specific conductivity penalty associated with Fe^{+3} addition to 0.02 cation fraction Li-doped NiO samples (i.e., $\text{Li}_{0.02}\text{Fe}_x\text{Ni}_{0.98-x}\text{O}$) and estimates this mechanism's impact on MCFC performance from Fe and Cr analysis of post-cell-tested NiO cathodes.

Experimental

Fe_2O_3 -doped $\text{Li}_{0.02}\text{Ni}_{0.98}\text{O}$ powders were prepared by the thermal decomposition (823 K) of reagent-grade $\text{FeOH}(\text{C}_2\text{H}_3\text{O}_2)_2$, $\text{Li}(\text{C}_2\text{H}_3\text{O}_2) \cdot \text{H}_2\text{O}$, and NiCO_3 powders which were previously well mixed in an acetone/acetic acid vehicle. Following decomposition, samples were air fired for 10h at 1023 K and washed in dilute acetic acid to remove nonincorporated Li salts. Elemental analysis was performed by atomic absorption spectroscopy, and the Ni^{+3} content obtained independently using the method described by Goodenough *et al.* (18).

Electronic conductivity measurements were made using a standard four-probe, ac impedance technique on pressed, sintered pellets using the apparatus diagrammed in Fig. 1. The pellets, 1.25 cm diam \times \sim 0.6 cm thick, were prepared by pressing the powders at \sim 120 MPa and sintering under a blanket of powder of the same composition in air at 1325 K for 1h. Chemical analysis showed the pellets' composition to be unchanged by sintering. Following sintering, the faces of the pellets were polished smooth, sputtered with \sim 1 μm gold, and two gold wires were attached to each face using silver paint (du Pont conductor composition 4922). The samples, supported using alumina holders (not shown in Fig. 1) and contained within an alumina tube furnace under a 30% CO_2 /air atmosphere, were heated to 823 K overnight to cure the silver paint. Sample conductivities were obtained as a function of signal frequency (50-20,000 Hz) during both heating (823-1123 K) and cooling (1123 K to ambient) cycles using a PAR 5204 Lock-In Analyzer coupled to a PAR 371 Signal Source (Princeton Applied Research, Princeton, New Jersey).

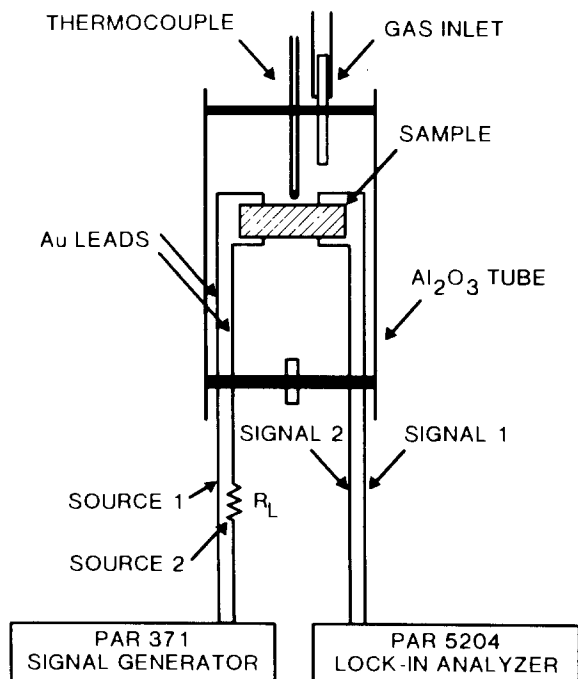


Fig. 1. Four-probe ac impedance measurement apparatus

Post-cell-tested NiO cathodes were obtained from MCFC's operated at 923 K for times between 50-10,080 h.¹ All cells were assembled using a Ni (10 weight percent [w/o] Cr) anode, a hot-pressed $\text{LiAlO}_2/\text{Li}_2\text{CO}_3/\text{K}_2\text{CO}_3$ electrolyte structure, and a porous nickel cathode. The cathode oxidized during heat-up to the 923 K cell operating temperature to form a porous NiO structure; lithium incorporated into the NiO lattice from the Li_2CO_3 containing electrolyte gave a final cathode composition of 0.02 ± 0.002 cation fraction Li (i.e., $\text{Li}_{0.02}\text{Ni}_{0.98}\text{O}$). Cathode current collectors were fabricated using 316 stainless steel in all cases.

Cathodes, obtained following cell testing, were thoroughly freed of $\text{Li}_2\text{CO}_3 + \text{K}_2\text{CO}_3$ electrolyte by washing with 50% aqueous acetic acid under a vacuum of $\sim 10^{-2}$ torr. The cathodes were then sectioned according to their structural location within the cell and analyzed for Fe and Cr by Auger electron spectroscopy (Physical Electronics Industries Model 548 ESCA/Auger spectrometer).

Results and Discussion

The composition of prepared Fe^{+3} -doped $\text{Li}_{0.02}\text{Ni}_{0.98}\text{O}$ samples (i.e., $\text{Li}_{0.02}\text{Fe}_x\text{Ni}_{0.98-x}\text{O}$) are given in Table I. Total Fe, Ni, and Li concentrations were obtained by atomic absorption spectroscopy, and the Ni^{+3} content obtained titrimetrically using the method of Goodenough *et al.* (18). Lithium concentrations were maintained at 0.02 cation fraction while iron was varied between 0.00 and 0.02 cation fraction. Samples prepared with Fe concentrations exceeding \sim 0.015 cation fraction possessed a Ni^{+3} concentration below the quantitative detection limit; however, it is apparent from the results presented in the table that Fe enters the NiO lattice as Fe^{+3} , thereby quantitatively reducing the Ni^{+3} concentration. This is in agreement with Verwey and others (1, 3, 12, 15).

The specific conductivity measured at 1 kHz as a function of temperature for the various samples is shown in Fig. 2. Frequencies between 50 and 20,000 Hz were scanned at each temperature with less than 2% frequency dependence observed, confirming that the measured values were indeed the samples' bulk conductivity. The measured 923 K specific conductivity at 1 kHz decreased from 33.0 to 3.5×10^{-2} ($\Omega \text{ cm}$)⁻¹ as the Fe^{+3} concentration increased from 0.00 to 0.02 cation fraction. In addition to a decrease in the magnitude of the conductivity, Fe^{+3} addition also resulted in changes to both the nature and the slope of the conductivity/temperature relationship. Prior to Fe^{+3} addition, two activation energies are apparent, with the transition from one to the other occurring at \sim 625 K. Activation energies of 0.68 and 3.9 kcal/mol obtained at temperatures above and below the transition temperature, respectively, are in reasonable agreement with Nowotny and Wagner's results (15) of 1.56 and 5.4 kcal/mol obtained for a 0.008 cation fraction Li-doped NiO sample.

It is evident from the data presented above that the incorporation of current collector corrosion products (e.g., Fe^{+3} , Cr^{+3}) into the lattice of a Li-doped NiO cathode would impact significantly on fuel cell performance. The measured porous cathode specific conductivity of $2(\Omega \text{ cm})^{-1}$ presently leads to a one-dimensional IR loss at a

¹The 10,080h sample was supplied by the Institute of Gas Technology, Chicago, Illinois.

Table I. Compositional analysis of $\text{Li}_{0.02}\text{Fe}_x\text{Ni}_{0.98-x}\text{O}$ powders, in cation fraction

[Li]	[Fe] _{total}	[Ni ⁺³] _{theoretical}	[Ni ⁺³] _{experimental}
0.020	0.000	0.020	0.021
0.021	0.006	0.015	0.015
0.020	0.010	0.010	0.010
0.019	0.013	0.006	0.006
0.020	0.014	0.006	0.005
0.020	0.017	0.003	—
0.020	0.019	0.001	—
0.020	0.020	0.000	—

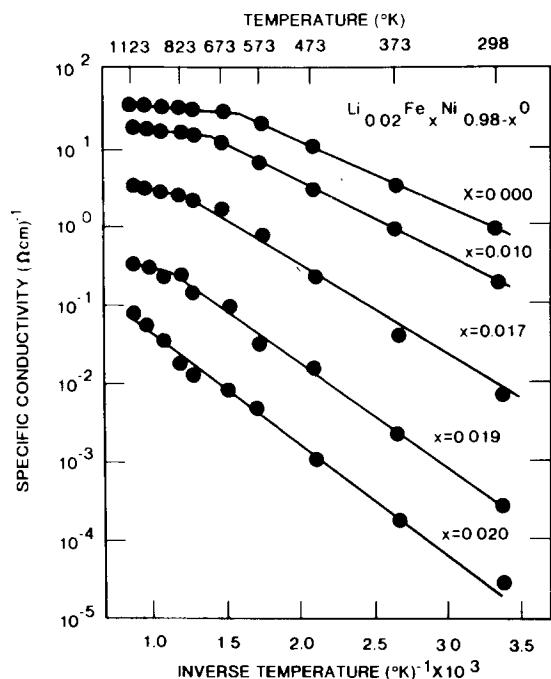


Fig. 2. Temperature dependence of specific conductivity for various compositions of Fe^{3+} , doped $\text{Li}_{0.02}\text{Ni}_{0.98-x}\text{O}$.

current density of 160 mA/cm^2 of about 3 mV for the 0.038 cm thick cathode. Conductivity decreases, as determined above for samples doped with 0.02 cation fraction Fe^{3+} , would increase this resistive drop by almost three orders of magnitude if the dopant were uniformly distributed throughout the structure. Both the iron and chromium content of porous NiO cathodes obtained from MCFC's were analyzed via Auger electron spectroscopy (AES) following alkali carbonate removal from the cathode structure by acetic acid washings. Chromates, present in the electrolyte by dissolution of Li_2CrO_4 and K_2CrO_4 corrosion products, are also entirely removed from the porous structure during this washing. Following washing, the cathodes were sectioned into four distinct areas according to their location within the cell. These areas were: region 1, in direct contact with the stainless steel current collector; region 2, adjacent to region 1, in contact with the open gas passage; region 3, located within the body of the cathode; and region 4, in contact with the electrolyte structure.

Nine cathodes were analyzed, encompassing cells operated between 50 and $10,080 \text{ h}$. All samples showed similar results in that all regions in direct contact with the current collector (region 1) contained iron within the NiO lattice. No iron was found in regions 2, 3, or 4, and no chromium was observed in any specimen. Chromates were, however, present in the electrolyte of several samples, as noted by the yellow color of the acetic acid wash solutions. Figure 3 displays a typical AES result, Fig. 3A showing the spectrum obtained on region 1 of a cathode on test for 2485 h , and Fig. 3B showing the spectrum obtained from region 2 of the same sample. The two spectra are virtually identical with the exception of the iron peak in area 3A. From this spectrum, an iron concentration of between 0.03 and 0.04 cation fraction was estimated; such a concentration is more than sufficient to neutralize the conductivity gain associated with the 0.02 cation fraction Li incorporation. No correlation was found between the observed iron level and the length of cell test.

The cathode AES results, coupled with the previous conductivity determinations, would lead to the prediction that a fairly resistive interface could exist between the cathode and current collector in operating MCFC's. The thickness of this resistive layer was determined for several cathodes from cells operated for various lengths of time by repetitive Auger analysis following argon ion etching. The results obtained on cathodes from cells

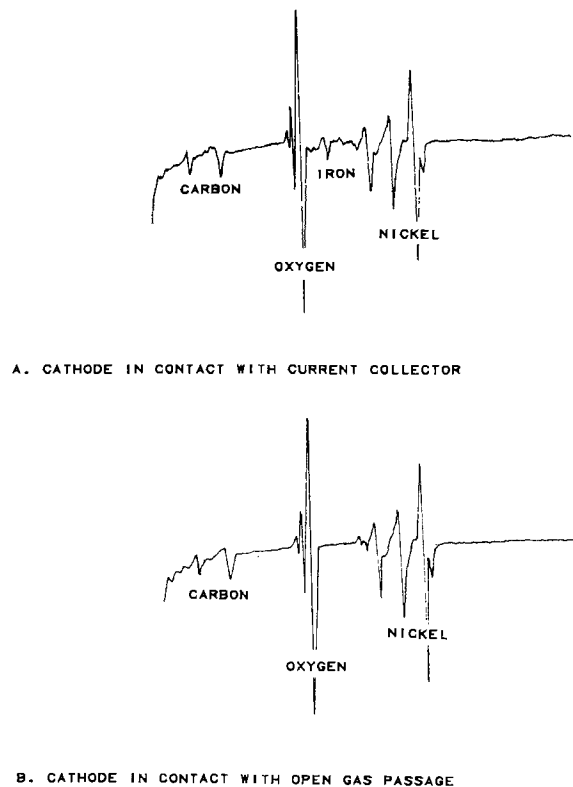


Fig. 3. Auger electron spectra of Li-doped NiO cathode from MCFC operated 2485 h . Region 1 was in contact with stainless steel current collector: region 2 was the adjacent location in contact with open gas channel.

tested for 515 , 2485 , and $10,080 \text{ h}$ are shown in Fig. 4. All samples possessed initial Fe levels similar to that shown in Fig. 3, and the depth profiles are therefore plotted on a relative ordinate. Whereas the absolute Fe level found at the NiO surface could not be correlated with the duration of cell test, longer cell tests did show a greater Fe penetration depth. However, even after $10,080 \text{ h}$ on test, iron has penetrated only superficially into the NiO grains, diffusing to a depth of $\sim 10 \text{ nm}$. Therefore, even though Fe^{3+} or Cr^{3+} incorporation into a $\text{Li}_{0.02}\text{Ni}_{0.98}\text{O}$ MCFC cathode

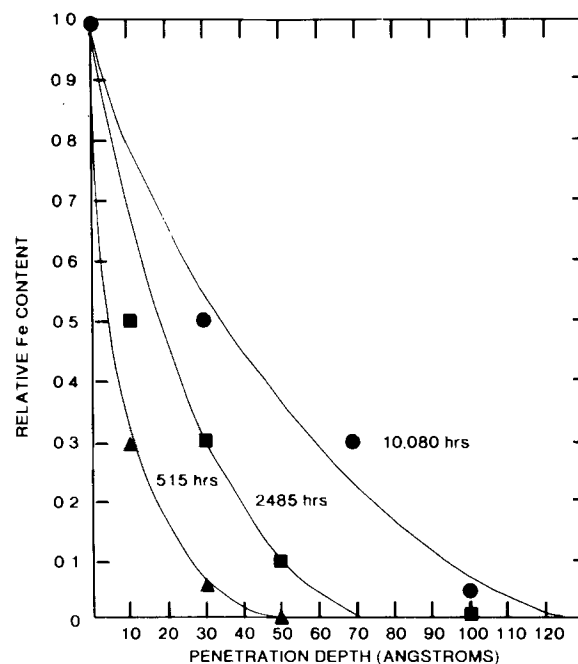


Fig. 4. Fe penetration profiles into the NiO lattice obtained by AES with Ar^+ milling. All samples were cathode regions in direct contact with the stainless steel current collectors.

could dramatically reduce fuel cell performance by decreasing cathode conductivity, such a mechanism apparently plays an insignificant role as neither impurity readily enters the Li-doped NiO cathode structure under experimental fuel cell operating conditions.

Conclusions

The 923 K specific electronic conductivity of 0.02 cation fraction Li-doped NiO ($\text{Li}_{0.02}\text{Ni}_{0.98}\text{O}$) was shown to decrease from 33.0 to $3.5 \times 10^{-2} (\Omega \text{ cm})^{-1}$ upon the addition of an equivalent doping level of Fe^{+3} . However, the impact of this conductivity degradation mechanism on the performance of MCFC's containing $\text{Li}_{0.02}\text{Ni}_{0.98}\text{O}$ cathodes was shown to be insignificant from iron and chromium analyses of post-tested cathodes. Although appreciable iron impurity levels were found within the NiO lattice in regions where the cathode contacted the stainless steel current collector, iron penetration into the grains was restricted to a distance of only 10 nm in 10,080h. The results indicate that impurity diffusion into the cathode should have little or no impact on fuel cell performance.

Acknowledgments

The author wishes to acknowledge the assistance of Mr. K. P. Zarnoch for the conductivity measurements. The Department of Energy is acknowledged for its support of this work under contract no. DE-ACO2-80ET17019.

Manuscript submitted May 19, 1983; revised manuscript received May 28, 1984. This was Paper 371 presented at the Montreal, Quebec, Canada, Meeting of the Society, May 9-14, 1982.

General Electric Company assisted in meeting the publication costs of this article.

REFERENCES

1. E. J. W. Verwey, *Chem. Weekblad*, **44**, 705 (1948).
2. E. J. W. Verwey, P. W. Haaijman, F. C. Romeijn, and G. W. van Oosterhout, *Philips Res. Rep.*, **5**, 173 (1950).
3. E. J. W. Verwey, "Semiconducting Materials," pp. 151-161, Butterworths, London (1951).
4. F. J. Morin, *Phys. Rev.*, **83**, 1005 (1951).
5. F. J. Morin, *ibid.*, **93**, 1195, 1199 (1954).
6. W. D. Johnson, *J. Chem. Ed.*, **36**, 605 (1959).
7. S. van Houten, *J. Chem. Phys. Solids*, **17**, 7 (1960).
8. S. Fujime, M. Murakami, and E. Hirahara, *J. Phys. Soc. Jpn.*, **16**, 183 (1961).
9. S. P. Mitoff, *J. Chem. Phys.*, **35**, 882 (1961).
10. A. J. Bosman, H. J. Van Daal, and G. F. Knuvers, *Phys. Lett.*, **19**, 372 (1965).
11. S. Koide, *J. Phys. Soc. Jpn.*, **20**, 123 (1965).
12. A. J. Bosman and C. Crevecoeur, *Phys. Rev.*, **144**, 763 (1966).
13. Ya. M. Ksendzov, B. K. Avdeenko, and V. V. Makarov, *Sov. Phys. Solid State*, **9**, 828 (1967).
14. I. G. Austin, A. J. Springthorpe, B. A. Smith, and C. E. Turner, *Proc. Phys. Soc.*, **90**, 157 (1967).
15. J. Nowotny and J. B. Wagner, Jr., *Bull. Acad. Pol. Sci.*, **21**, 931 (1973).
16. N. G. Eror and J. B. Wagner, Jr., *Phys. Status Solidi*, **35**, 641 (1969).
17. Z. M. Jarzebski, "Oxide Semiconductors," Engl. transl., B. R. Pamplin, Editor, International Series, Monographs in Science and Solid State, Vol. 4, pp. 150-189, Pergamon Press, 1973.
18. J. B. Goodenough, D. G. Wickham, and W. J. Craft, *J. Appl. Phys.*, **23**, 382 (1958).

Improved H_3PO_4 Corrosion Resistance of Graphite/Phenolic Composites Suitable for 190°C Hydrogen/Air Fuel Cells

J. T. Hoggins and M. L. Deviney

Ashland Chemical Company, Ventures Research Division, Dublin, Ohio 43017

Electrocatalyst life, bipolar plate chemical resistance to hot H_3PO_4 , and bipolar plate mechanical strength and dimensional stability have been identified as the major obstacles to the long-term service life of the hydrogen-air fuel cell (1-3). Composite bipolar plates prepared by molding graphite powder with phenol-formaldehyde resin binder have been studied by the Army and its contractors (4-6).

In an earlier Ashland investigation (7) concerned with fabrication of improved bipolar plates, two phenolic resins, Arofene® 877LF (Ashland Chemical Company) and A-33 (an experimental styrenated resin), were shown to exhibit good corrosion resistance to hot H_3PO_4 . A near optimum graphite powder loading for the composite was established along with a high density blend composition. In addition, an improved two-step molding technique was developed. The purpose of the present study was to further investigate the fabrication processes for the resin/graphite composite bipolar plates. As part of this investigation, we examined methods of treating bipolar plates so that essentially all etchable substances and possible poisons could be removed prior to fuel cell operation.

It was suspected that corrosion products from the phenolic resin could leach from the acid reservoir in the bipolar plate and be deposited on the catalyst. These could block the active sites, thus poisoning the catalyst.

Experimental

The initial experimental program consisted of monitoring the corrosion of test composite coupons fabricated

from C^{14} labeled resins and the graphite powder mixture. This was done by liquid scintillation counting of solution extracts from composite plates immersed in hot H_3PO_4 . The radiochemical procedure for monitoring corrosion offered two advantages. First, different positions of the resin molecular structure could be labeled; thus, the point of attack could be determined. Second, by monitoring the concentration of resin products in acid, problems in measuring accurate weight losses in these graphite composites were avoided.

Later in the program, an alternative method to monitor corrosion was developed to eliminate the costly and time consuming step of radio-labeled resin synthesis. It was observed that the color of the acid samples corresponded well with the concentration of resin in the acid. Therefore, optical (visible) spectrometry was studied as a potential method for measuring the concentration of resin in the acid. The optical spectrometry method was calibrated using the samples from the test with radio-labeled coupons. There was a linear correspondence between optical spectrometric absorption and radiochemically determined concentration. This good agreement allowed the use of commercially available resins in corrosion studies. Another advantage of visible spectrometry over the radio-tracer method is that visible spectrometry takes advantage of the color quenching which must be corrected for in the radiochemical method.

Synthesis of C^{14} labeled Arofene 877LF and A-33 resins.—The methylene "bridging" position was chosen as the C^{14} labeling position because the "bridge" was con-

sidered a likely point of attack (probably leading to polymer chain scission) by hot H₃PO₄.

The laboratory synthesis procedures used were scaled-down versions of commercial Ashland procedures. About 700g of resin was synthesized in each batch. The only significant synthesis modification was the addition of the C¹⁴ labeled formaldehyde earlier, and at a lower temperature, than the main formaldehyde charge. The purpose of this modification was to minimize volatility losses and to insure complete utilization of the C¹⁴ labeled formaldehyde. Radiochemical yields were about 90%. The physical property data on the Arofene 877LF and A-33 resins related to the present study are presented in Table I. The test methods used were all ASTM procedures.

Molding coupons and bipolar plates.—The conditions for fabrication of the coupons were as described in Ref. (7). A vacuum (~10⁻¹ torr) postcuring was applied on some coupons.

Corrosion tests.—These coupons (25 × 75 × 3 mm) were suspended by Teflon (trademark of E. I. du Pont de Nemours and Company) strings into a Teflon cup containing 93.5 ml of (85.6%) H₃PO₄ (Baker Chemical Company). The assembly was placed in an oven at 190°C for extended periods of time (up to 2000h). At various intervals, 0.3 ml of acid was removed for measurement of the concentration of resin dissolved in the acid and was replenished by 0.3 ml of fresh preheated acid.

Counting procedures for corrosion tests.—The 0.3 ml acid sample was diluted 9 to 1 with H₂O. Then 1 ml of diluted etching product was placed in 10 ml dioxane scintillation cocktail (for more concentrated samples, less of the diluted acid was used to reduce color quenching). The dioxane solutions were counted in a Beckman LS-100 liquid scintillation counter. A spiking procedure was used to determine the counting efficiency. This procedure required 50 μl of C¹⁴ radiochemical standard (New England Nuclear lot no. 697-242, containing 4.5 × 10⁶ dpm/ml activity) in each sample cocktail solution. Counting efficiency was calculated by comparison of the spiked solution counts with raw counts from the sample.

Table I. Physical properties of resin

Resin	Melt point (°C)	150°C Melt time (s)	125°C Flow* (mm)	150°C Cure time* (s)
C ¹⁴ labeled 877LF	92	165	44	73
Arofene 877LF lot 7198F	78	140	52	72
C ¹⁴ labeled A-33 batch 1	74	142	152	222
C ¹⁴ labeled A-33 batch 2	76	256	25	154
A-33 pilot plant lot 7214	77	264	60	114

* Determined with 10% hexamethylenetetramine added to the resin.

Visible optical spectrometry.—The 0.3 ml samples from the corrosion test were diluted with 9.7 ml of fresh H₃PO₄. A portion of the diluted sample was put in a cuvette and then placed in a Bausch and Lomb Spectrometer Model 100 tuned to 590 nm. This wavelength was determined to be the optimum wavelength by a broad scan of the sample. Fresh acid was used as a reference. The absorbance of the sample was then measured. For calibration, the absorbances were measured on samples of known concentrations. These concentrations were determined from C¹⁴ radiochemical measurements of corrosion extracts.

Results and Discussion

The results for several coupons from the initial tests are shown in Table II. First, it was apparent that some coupons exhibited very good corrosion resistance (less than 0.2% weight loss of the resin), while others, supposedly molded under identical conditions, showed poor corrosion resistance (more than 5% weight loss). Physical examination of the coupons after corrosion tests showed that the more corroded coupons had swelled considerably (up to about 17% increase in thickness). The scatter in

Table II. Results of etching

Coupon	Binder	w/o Furfural	Postcure	Final % etched	Total time (h)	Remarks
T-16	C ¹⁴ 877LF	0	Regular	0.13	271	
T-22	C ¹⁴ 877LF	0	Regular	5.50	281	9% HMTA
T-59	C ¹⁴ A-33 (B2)	0	Regular	0.75	2011	
T-60	C ¹⁴ A-33 (B1)	0	Regular	0.30	2011	
L-1	C ¹⁴ A-33 (B2)	0	Regular	2.86	750	
L-2	C ¹⁴ A-33 (B2)	0	Vacuum	0.10	750	
L-3	C ¹⁴ A-33 (B2)	0	Regular	3.30	750	9% HMTA
L-4	C ¹⁴ 877LF	0	Regular	5.37	750	
L-5	C ¹⁴ 877LF	0	Regular	9.10	750	9% HMTA
L-6	C ¹⁴ A-33 (B1)	0	Vacuum	0.40	750	
L-7	C ¹⁴ A-33 (B1)	0	Regular	4.80	750	Prolonged molding
L-8	C ¹⁴ A-33 (B1)	0	Regular	4.25	750	Prolonged molding, 9% HMTA
L-9	C ¹⁴ A-33 (B2)	0	Regular	3.08	456	
L-10	C ¹⁴ A-33 (B2)	0	Regular	3.42	456	
M-1	Arofene 877LF	0	Regular	12.71	456	Molding: Held at 220°C (20 min) → outgas
M-2	Arofene 877LF	0	Vacuum	2.65	456	Molding: Outgas → Held at 220°C (20 min)
M-3	Arofene 877LF	1	Regular	3.45	456	
M-4	Arofene 877LF	1	Regular	1.22	456	
M-5	Arofene 877LF	0	Vacuum	3.35	456	
M-8	Arofene 877LF	0	Regular	4.95	456	
M-9	Arofene 877LF	0	Regular	3.10	456	Molding: Outgas held at 220°C (20 min)
M-10	Arofene 877LF	0	Regular	12.30	456	
M-11	A-33 pilot plant	1.5	Regular	6.00	538	11.5% HMTA
M-12	A-33 pilot plant	1.5	Vacuum	0.21	538	
M-13	A-33 pilot plant	1.5	Vacuum	1.45	538	
M-14	Arofene 877LF	1.5	Vacuum	0.28	538	
M-15	Arofene 877LF	1.5	Vacuum	0.33	538	
M-16	C ¹⁴ A-33 (B2)	1.5	Vacuum	0.31	538	
M-17	C ¹⁴ A-33 (B2)	1.5	Vacuum	0.40	538	
M-18	Arofene 555	0	Vacuum	0.43	528	Purified by steam
M-19	Arofene 877LF	0	Regular	4.20	528	
M-20	Arofene 877LF	0	Vacuum	7.10	528	
M-21	Arofene 877LF	1.5	Vacuum	1.75	528	
M-22	Arofene 877LF	1.5	Vacuum	0.38	528	
M-30	Arofene 877LF	0	Vacuum	>10.0	96	Extracted with acetone before acid etch

these early results prompted a more thorough investigation into optimizing the curing conditions for the composites and more careful control over the molding and curing processes.

A second observation was that the corrosion process is complete in about 300h, regardless of the amount of total etching. A possible mechanism for this passivation is that H_3PO_4 attacks both low molecular weight resin and resin with a low cross-link density. Apparently, the etching ceases when low molecular weight resin materials are depleted, and only fully cross-linked material remains in the coupon. The total amount leached may be a function of both the total amount of low cross-link density resin and the total surface area in contact with the phosphoric acid. To minimize the exposed surface area, it is necessary for the resin to wet the graphite particles as well as possible. Two methods to achieve better wetting were investigated. The first was through enhanced flow characteristics of the resin, and second involved the use of a wetting agent. Molding techniques were varied to increase the flow during curing, but to no avail (see Table II).

Other possible sources of corrosion products are unreacted phenol and formaldehyde, and impurities such as low molecular weight phenol-formaldehyde reaction species. To minimize these, post curing was done in a vacuum furnace. This vacuum curing treatment resulted in some improvement in corrosion resistance. However, the corrosion of some coupons was unacceptably high: > 2.5% in two cases.

It was apparent from the data that an improvement in resin flow properties during molding (in the early stages of cure where the cross linking degree is low) was very desirable. Resin flow is usually enhanced when the free phenol content of the resin is low. The phenol was removed from the resin by steam stripping as a last step during synthesis. The coupon, M-18, prepared from low phenol resin (Arofene 555) showed good corrosion resistance.

The use of a chemical additive, furfural, to improve particle wetting resin flow during molding was another approach investigated. Initial results indicated much lower corrosion of test coupons in $190^\circ C H_3PO_4$. To check reproducibility, several additional coupons containing this flow enhancing additive were tested, and results were very favorable. Fairly consistent, low (< 0.3% weight loss) results were obtained in most cases. The earlier problems of higher corrosion rates and inconsistent results thus appeared to have been due to insufficient resin flow in the mold before cross linking becomes the dominant factor. Use of the resin formulations with slower cure rate properties and an additive for improved particle wetting and resin flow appear to be the keys to enhanced corrosion resistance for bipolar plates.

The mechanism for passivation is unknown, but, as noted before, essentially all corrosion takes place in the first 300h as shown in Fig. 1. This was also observed in a test where the acid was changed for each sampling (coupon T-22). Therefore, pre-etching the bipolar plate acid reservoir with H_3PO_4 could be beneficial. However, pre-etching with an organic solvent, acetone (note coupon M-30, Table II), was extremely deleterious. The coupon severely cracked and corrosion was very pronounced.

Conclusions

Arofene A-33 and 877LF, when molded and cured using the improved techniques developed in this study, are promising candidates for use in preparing composite (graphite powder/phenolic resin) bipolar plates, which are highly resistant to corrosion by $190^\circ C H_3PO_4$. These results suggest that a hot H_3PO_4 pretreatment of the bipolar plate reservoir area could result in little or no etching by H_3PO_4 in subsequent fuel cell operations. The main features of the modified curing/molding procedure developed (but not fully optimized) here for bipolar plate fabrication are the use of a chemical additive, furfural, molding techniques to improve particle wetting and resin flow properties during cure, and the employment of an

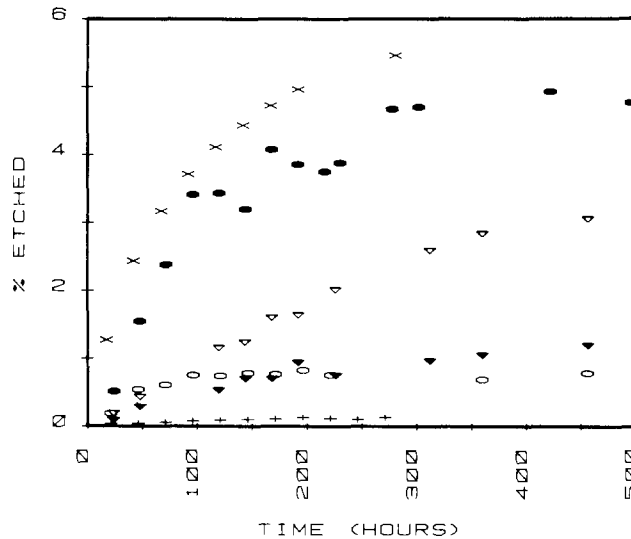


Fig. 1. w/o Resin leach from typical test coupons vs. time in H_3PO_4 at $190^\circ C$. +: Coupon T-16 (see Table II), coupon L-7. ∇: Coupon L-9. ∇: Coupon M-4. o: Coupon T-59. x: Coupon T-22.

extended (20h) vacuum oven postcure of the plates. Improved particle wetting and resin flow during molding can lead to a stronger, less permeable composite. Therefore, it may be possible to lower the bipolar plate resin content below 25% (the amount used in this study). This could result in greater electrical conductivity for the bipolar plate, without introducing increased plate porosity (which would lead to increased H_2 permeability and greater susceptibility to H_3PO_4 attack). This would require verification.

Steam stripping of the phenolic resin to remove excess phenol and reaction by-products may be a useful technique for improving test coupon resistance to hot H_3PO_4 . This approach is suggested by the limited results obtained here, but considerably more work is needed for verification.

Acknowledgments

The authors wish to express their gratitude to several persons whose assistance contributed greatly to the success of this project: Corbett L. Taylor, for performing the majority of the experimental work, particularly in the radiochemical analysis and resin curing areas; G. Fred Watts, for his expert counseling services in phenolic resins chemistry area; Alan H. Boyer, who carried out most of the synthesis of radio-labeled resins; and John E. Martin, who provided important counsel concerning experimental techniques developed during their previous related fuel cell contract.

Manuscript submitted Dec. 9, 1982; revised manuscript received March 28, 1984.

Ashland Chemical Company assisted in meeting the publication costs of this article.

REFERENCES

1. S. G. Abens, B. S. Baker, and I. Michalko, "Fuel Cell Stacks," Final Technical Report, Contract no. DAAK02-74-C-0367, June, 1977, Sponsored by U.S. Army Mobility Equipment R&D Command, Ft. Belvoir, VA.
2. A. Kaufman, "Phosphoric Acid Fuel Cell Stack and System Development," Technical Progress Report for Quarter Ending Sept. 30, 1979, Contract no. DE-AC-03-78-ET 15366, Sponsored by U.S. Dept. of Energy, Administered by NASA Lewis Research Center, Cleveland, OH.
3. G. A. Gruver, R. F. Pascoe, and H. R. Kunz, *This Journal*, **127**, 1219 (1980).
4. P. Stonehart, J. MacDonald, V. Jalan, and J. Baris, pp. 102-105, Extended Abstracts of the National Fuel Cell Seminar, Bethesda, MD, June 26-28, 1979.
5. L. G. Christner, "Technology Development for Phos-

- phoric Acid Fuel Cell Powerplant (Phase II)," 3rd Quarterly Report for Contract no. DEN 3-67, June, 1979, Sponsored by U.S. Dept. of Energy, Administered by NASA Lewis Research Center, Cleveland, OH (DOE/NASA/0067-79-2), NASA Report no. CR-159705.
6. H. C. Maru, L. G. Christner, S. G. Abens, and B. S. Baker pp. 86-90, Extended Abstracts of the National Fuel Cell Seminar, Bethesda, MD, June 26-28, 1979.
7. P. M. Colling, J. E. Martin, and R. V. Norton, "Selection and Evaluation of Carbon-Resin Composites for Bipolar Plates for Hydrogen Fuel Cells," Final Technical Report, Contract no. DAAK70-77-C-0151, Completed Sept. 1978, Sponsored by U.S. Army Mobility Equipment R&D Command, Ft. Belvoir, VA.



Adsorption of Hydroxide and Sulfide Ions on Single-Crystal n-CdSe Electrodes

K. W. Frese, Jr.* and D. G. Canfield

SRI International, Menlo Park, California 94025

ABSTRACT

Flatband potentials were determined for n-CdSe (11 $\bar{2}$ 0) electrodes as a function of OH⁻ and SH⁻ concentrations. Surface coverage was calculated from the observed flatband potential shift. The Frumkin isotherm was applied to the data, and thermodynamic parameters were determined. The standard free energies of adsorption for OH⁻ and S⁻ were found to be -2.3 and -6.9 kcal/mol, respectively. At high SH⁻ concentrations, there was evidence for a decrease in the repulsive interactions of the S⁻ and OH⁻ ions.

The n-CdSe/sulfide electrolyte redox system has been studied extensively in relation to solar-to-electrical energy conversion devices. Although it is known that this system possesses a high degree of stability with respect to photoanodic corrosion, the details of the corrosion-redox competition processes are not completely understood.

An important detail of the electron-transfer process in this system is surface adsorption and dissolution of sulfide and sulfur species, respectively. We have begun a study of the adsorption properties of the CdSe/sulfide electrolyte system. Because the alkaline polysulfide electrolyte can be complicated by different polysulfide species with perhaps different adsorption characteristics, we thought it useful to first study the adsorption process under simpler conditions. These conditions obtain in NaOH/Na₂SO₄ electrolytes and in NaOH/Na₂S electrolytes without dissolved sulfur. In this report, we focus on measurements of flatband potentials at room temperature in the dark. A distinction has to be made between measurements in the dark and under illumination. In the former case, the corrosion of the electrode and thus changes in the surface caused by the measurements are minimized, whereas in the latter case, corrosion products and the effect of illumination could significantly complicate the characteristics of the system.

Experimental

All measurements were made on single-crystal n-CdSe (11 $\bar{2}$ 0) electrodes (Cleveland Crystals). The donor densities were 1×10^{17} cm⁻³. The electrode surface was chemomechanically polished with 1% (V/V) Br₂/CH₃OH. After mounting in epoxy (Epoxy Patch) and in between capacitance/voltage measurements, the crystals were rinsed with 1M HCl to remove sulfide layers, and then cleaned with a cotton-tip applicator soaked in 1% Br₂/CH₃OH mixed with 50% by volume 1M HCl. This cleaning was followed by rinsing with distilled deionized water. All chemicals were reagent grade.

Capacitance/voltage sweep measurements were made at 50 kHz using a lock-in amplifier. A constant ac current was passed through the cell, and the 90° out-of-phase component of the voltage across the CdSe-Pt foil electrode was measured. AC voltages were typically 1-10 mV. Previous capacitance measurements (1) on these same crystals showed that the space-charge capacitance was independent of frequency (10³-10⁵ Hz). High purity N₂ was

*Electrochemical Society Active Member.

passed through the electrolyte before and during the measurements. All capacitance measurements were made within 15 min of the time of introduction of the electrode into the electrolyte.

Theory

Flatband potential and surface coverage.—The flatband potential, V_{FB} , is a property of a semiconductor-electrolyte system that is essentially a measure of the energy of the conduction band of the material. In general, the measured flatband potential can be related to its value when no excess charge exists on the surface, V_{FB}^0 , and the voltage drop across the Helmholtz double layer when net charge resides on the electrode surface. We can express this relationship as

$$V_{FB} = V_{FB}^0 \pm \frac{Q_{ad}}{C_H} \quad [1]$$

where C_H is the integral capacitance of the Helmholtz double layer. The chemical and physical structure of this interfacial region at the semiconductor-liquid junction is not fully known. It is expected that the concepts of inner and outer Helmholtz planes (2) that were developed for metal/electrolyte interfaces apply in the semiconductor electrode case. The shift in V_{FB} relative to the neutral condition is positive or negative, depending on the sign of the net surface charge. The quantity Q_{ad} (C/cm²) is assumed to be given by

$$Q_{ad} = q_0 (\sum z_i n_i^+ - \sum z_j n_j^-) \quad [2]$$

where n is the number of adsorbed species per square centimeters and q_0 is the elementary charge. z is the integral charge on the ion. If there are N total sites for adsorption, the surface coverage, θ , for the i th species is given by $\theta_i = n_i/N$. When $n_i = N$, θ is θ_{sat} , the saturation coverage.

Now consider the simplification that only one negatively charged species adsorbs on the electrode surface, e.g., OH⁻, with surface coverage, θ .

Then

$$V_{FB} = V_{FB}^0 - \frac{q\theta N}{C_H} \quad [3]$$

and the flatband potential saturates at

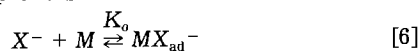
$$V_{FB}^{sat} = V_{FB}^0 - \frac{qN}{C_H} \quad [4]$$

By solving Eq. [3] for θ , and eliminating qN/C_H by means of Eq. [4], we find

$$\theta = \frac{V_{FB} - V_{FB}^0}{V_{FB}^{sat} - V_{FB}^0} \quad [5]$$

This simple result states that the fractional occupancy of surface sites is given by the ratio of the shift in flatband potential relative to the neutral condition to the total shift from neutral to saturation condition. Application of Eq. [5] assumes that V_{FB}^{sat} can be observed experimentally. Calculation of V_{FB}^{sat} appears to be unreliable at present. However, V_{FB}^0 values can be predicted with reasonable accuracy (3).

Isotherms.—The thermodynamic equilibrium constant for the adsorption process



is

$$K_0 = \frac{a_s}{a_v a_{el}} \quad [7]$$

where a_s and a_{el} are the activities of the adsorbing species on the surface and in the electrolyte, respectively, and a_v is the activity of vacant sites. According to the general isotherm of Frumkin (4), $a_s = \theta e^{f\theta}$, $a_v = (1 - \theta)$, and $a_{el} = a_{x-}$. For simple adsorption such as reaction [6], the Frumkin isotherm is

$$\ln \left(\frac{\theta}{1 - \theta} \right) + f\theta = \ln K_0 + \ln a_{x-} \quad [8]$$

The parameter f , in units of kT , represents the interaction energy between adsorbed particles. This energy may be repulsive ($f > 1$) or attractive ($f < 1$).

The parameter, f , generally depends on coverage and the density of electrons or holes on the electrode surface. In the case of semiconductors in the dark, the electrode charge is normally quite small (low density of ionized electronic surface states). At the flatband condition, the space charge is zero by definition. To a first approximation, neglect of electronic (as opposed to adsorbed) charge is permissible. If so, then f may be related to various models of the interface. For example, according to the induced dipolar heterogeneity model of Boudart (5)

$$f = \frac{2\pi q_0 N M_0}{kT \left(1 + \frac{9\alpha}{a^3} \theta \right)} \quad [9]$$

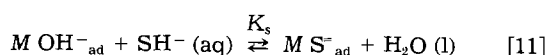
where N is the density of available sites, M_0 is a dipole moment normal to the surface, α is the polarizability of the adsorbing particles, and a is the distance between dipoles. For 10^{14} particle/cm², $M_0 = 1.0$ Debye, and $\alpha = 0$, $f = 7.3$, a very reasonable value (6, 7). Mutual polarization effects will lower f depending on α , a , and the coverage.

The Bockris-Devanathan-Müller isotherm (2, 8), that describes ion-ion interactions, can also provide an estimate of f . When the electrode charge is negligible

$$f = \frac{M' q_0^2 \tau_{ion}^2 (z N)^{3/2}}{\epsilon kT} \theta^{1/2} \quad [10]$$

where M' is a geometrical factor, τ is the radius of the adsorbing ion, and the dielectric constant, $\epsilon \approx 6$. Using $M = 15.3$ (8), $N = 10^{14}$ cm⁻², $z = 1$, and $\tau_i = 2.5 \times 10^{-8}$ cm, we find $f = 8.9$ for $\theta = 1$. Both models predict reasonable values of f and are useful for rationalizing and predicting changes in adsorption characteristics as system properties vary.

Surface substitution reaction.—Now consider a situation where the electrode is saturated with an adsorbed charged species and another more strongly adsorbing species is introduced into the electrolyte. Specifically, consider the equilibrium



where M stands for an adsorption site.

The equilibrium constant for this substitution reaction may be written

$$K_s = \frac{\theta_2 e^{f_2 \theta_2} a_{H_2O}}{\theta_1 e^{f_1 \theta_1} a_{SH^-}} \quad [12]$$

where the subscript 2 refers to adsorbed S^- ion and 1 refers to adsorbed OH^- ion. According to our data (see Fig. 2 and the results below), the CdSe surface is saturated with OH^- at the time SH^- ions were introduced into the 1M NaOH electrolyte. Therefore we describe the system by reaction [11]. Accordingly, it is assumed that $\theta_1 + \theta_2 = 1$. When the surface contains two interacting species, such as S^- and OH^- , the f 's have a more complicated meaning than that implied in Eq. [9] or [10]. A theory that counts the interaction between different kinds of particles is needed to describe the system.

For the present, we have to assume that like and unlike ion interactions are included in the f 's in Eq. [12]. Assuming a_{H_2O} is unity and $\theta_1 + \theta_2 = 1$, Eq. [12] may be written using θ_{S^-} for θ_2

$$\theta_{S^-} + \frac{1}{f_1 + f_2} \ln \left(\frac{\theta_{S^-}}{1 - \theta_{S^-}} \right) = \frac{1}{f_1 + f_2} \ln a_{SH^-} + \frac{f_1}{f_1 + f_2} + \ln K_s \quad [13]$$

This equation will be applied below.

Results

Adsorption of OH^- .—Typical Mott-Schottky plots for CdSe (11 $\bar{2}0$) in 0.1M Na₂SO₄ are shown in Fig. 1. The concentration of OH^- was varied by the addition of NaOH. The plots were linear over a wide voltage range. The measured capacitance followed the $1/C^2$ relation for surface barriers as small as 0.2V. This behavior suggests that the density of active electronic surface states in the upper part of the bandgap is quite low. Our previous measurements (1) with the same crystals in neutral Na₂SO₄ solution indicated interface state densities of 10^{12} - 10^{13} cm⁻² at 0.1-0.5 eV below the conduction bandedge. The interface is assumed to be formed by the CdSe and a thin (perhaps permeable and chemically active) layer of elemental Se. The Se results from the oxidative etch with Br₂. Apparently, the more-alkaline conditions, as in Fig. 1, play a role in reducing the interface state density. A possible explanation is that OH^- ions bond to sites with Cd²⁺ character and thus remove the postulated acceptor-state levels.

The flatband potentials determined from Fig. 1 were plotted against OH^- concentration, and the results are shown in Fig. 2. The inset to Fig. 2 shows how V_{FB} varies with $\log [OH^-]$. Interpolated values of V_{FB} are listed at various OH^- concentrations in Table I. The flatband po-

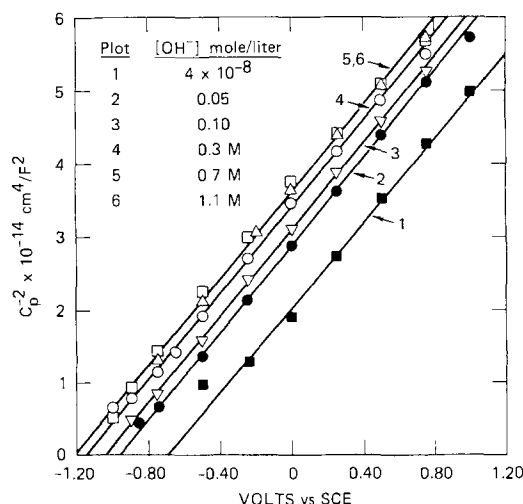


Fig. 1. Mott-Schottky plots for n-CdSe (11 $\bar{2}0$) in 0.1M Na₂SO₄ at 50 kHz. NaOH added. $N_0 = 7.6 \times 10^{16}$ cm⁻³.

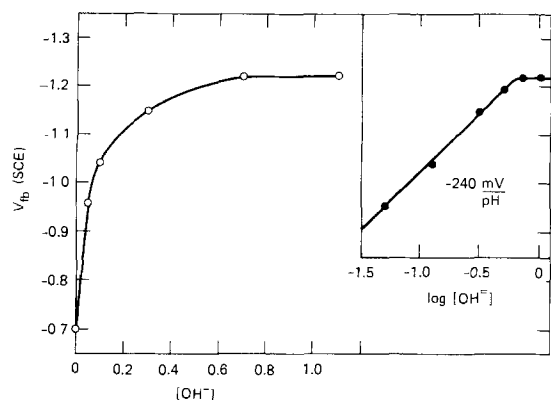


Fig. 2. Flatband potential vs. $[\text{OH}^-]$ for n-CdSe (11 $\bar{2}$ 0) in 0.1M Na_2SO_4 . Data from Mott-Schottky plots at 50 kHz.

tential was strongly dependent on $[\text{OH}^-]$, and at sufficiently large concentrations, a saturation V_{FB} of -1.22V vs. SCE was observed. The results suggest a strong adsorption of OH^- ions on the CdSe surface.

The behavior of V_{FB} in the pH range 4-11 is unusual. We (1) and others (9) have reported that V_{FB} is -0.7V vs. SCE and is independent of $[\text{OH}^-]$ in this intermediate pH range. Therefore, in the discussion to follow we will assume that OH^- or H^+ are not strongly adsorbing for $[\text{OH}^-] < 10^{-3}\text{M}$. And accordingly, we will assume that $V_{\text{FB}} = -0.7\text{V}$ corresponds to the neutral surface charge (adsorbed) condition, i.e., $V_{\text{FB}}^0 = -0.7\text{V}$ (see below).

Adsorption of S^{2-} .—The adsorption of sulfide ions was studied by measuring the flatband potential shift as a function of Na_2S in 1M NaOH. Mott-Schottky plots are shown in Fig. 3. These parallel plots of $1/C^2$ vs. V indicate that the addition of Na_2S leads to a further negative shift in V_{FB} . We assume that S^{2-} replaces OH^- on the surface until saturation is reached.

The results of V_{FB} determinations are plotted in Fig. 4 as a function of Na_2S concentration. Interpolated values are given in Table II.

Discussion

OH^- adsorption.—The surface coverage with OH^- was calculated using Eq. [5] and $V_{\text{FB}}^0 = -0.70$ and $V_{\text{FB}}^{\text{sat}} = -1.22\text{V}$. The results are plotted in Fig. 5 according to the logarithmic form of the Frumkin isotherm, Eq. [8]; the interaction parameter was calculated from the slope, $d\theta/d \ln c$ and found to be 1.7. This value indicates a weak interaction between the adsorbed OH^- ions. A value of the equilibrium constant for adsorption can be made by direct calculation by means of Eq. [8], for $\theta = 0.5$. Using an

Table I. Flatband potentials and derived values of surface coverage of OH^- on n-CdSe (11 $\bar{2}$ 0)

$[\text{OH}^-]$ (M)	V_{FB} (SCE)	θ
0.00	-0.700	0.0
0.01	-0.765	0.13
0.02	-0.840	0.23
0.03	-0.865	0.32
0.04	-0.915	0.41
0.05	-0.955	0.49
0.06	-0.980	0.54
0.07	-1.005	0.59
0.08	-1.020	0.62
0.09	-1.030	0.63
0.10	-1.040	0.65
0.15	-1.080	0.73
0.20	-1.110	0.81
0.30	-1.150	0.86
0.40	-1.176	0.92
0.50	-1.195	0.95
0.60	-1.210	0.98
0.70	-1.220	1.00

Electrolyte: 0.1M Na_2SO_4 with NaOH added.
Calculations based on Eq. [5] with $V_{\text{FB}}^0 = -0.70\text{V}$ (SCE).

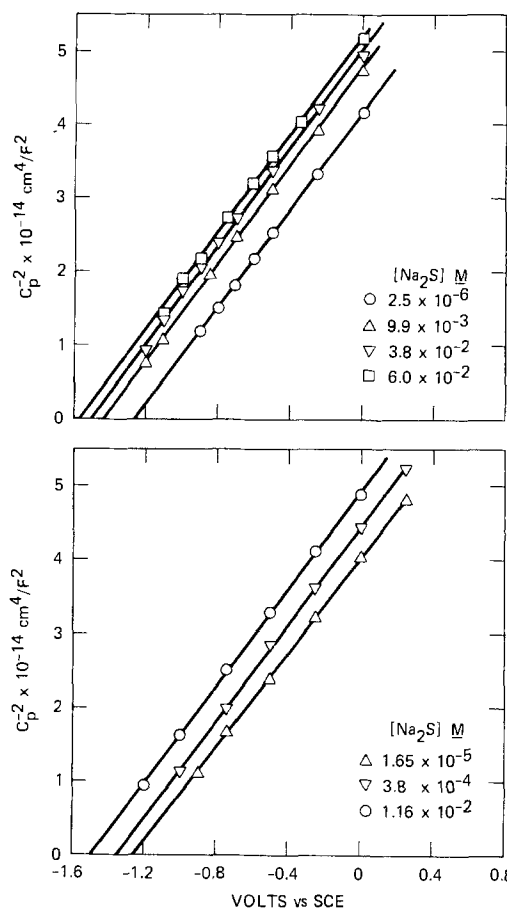


Fig. 3. Typical Mott-Schottky plots for n-CdSe (11 $\bar{2}$ 0) in 1M NaOH with added Na_2S . 50 kHz.

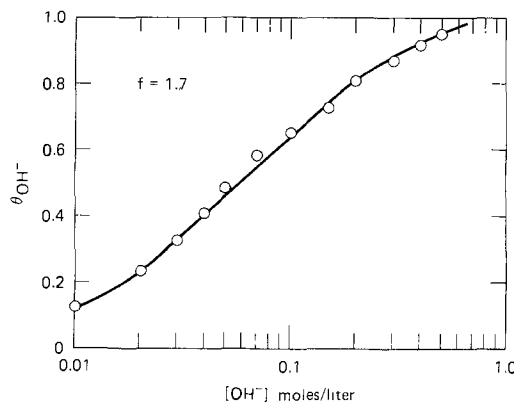


Fig. 4. Logarithm plot of θ_{OH^-} vs. concentration of OH^- for n-CdSe (11 $\bar{2}$ 0) in 0.1M Na_2SO_4 .

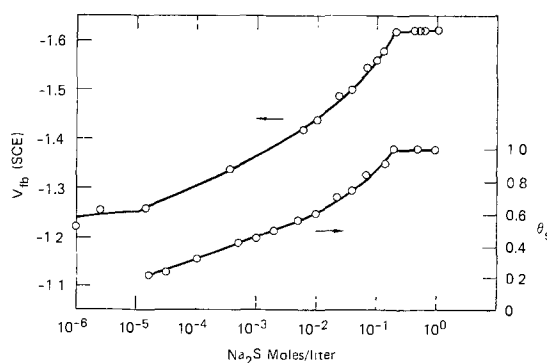


Fig. 5. Logarithm plot of flatband potential and surface coverage with sulfide for n-CdSe (11 $\bar{2}$ 0) vs. concentration of Na_2S .

Table II. Flatband potentials and derived values of surface coverage of S^{2-} on n-CdSe (1120)

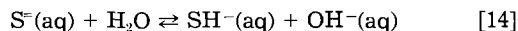
[Na ₂ S] (mol/liter)	V _{FB} (SCE)	θ*
0.00	-1.220	0
1.5 × 10 ⁻⁵	-1.260	0.22
3.0 × 10 ⁻⁵	-1.280	0.24
1.0 × 10 ⁻⁴	-1.310	0.33
5.0 × 10 ⁻⁴	-1.356	0.43
1.0 × 10 ⁻³	-1.370	0.46
2.0 × 10 ⁻³	-1.390	0.50
5.0 × 10 ⁻³	-1.420	0.57
1.0 × 10 ⁻²	-1.440	0.61
2.2 × 10 ⁻²	-1.490	0.72
4.0 × 10 ⁻²	-1.505	0.75
7.0 × 10 ⁻²	-1.550	0.85
1.0 × 10 ⁻¹	-1.561	0.87
1.5 × 10 ⁻¹	-1.580	0.91
2.0 × 10 ⁻¹	-1.620	1.0
5.0 × 10 ⁻¹	-1.620	1.0
1.0 × 10 ⁻¹	-1.620	1.0

Electrolyte: 1M NaOH with Na₂S added.

* Calculated using $qN/C_H = 0.46V$.

activity coefficient of 0.8 for 0.058M OH⁻ (Fig. 5), K_0 is found to be 50.4. The standard free energy change was calculated to be -2.3 kcal/mol. This value can be compared with $\Delta G^\circ = -3.7, -3.4,$ and $+2.6$ calculated (10) for adsorption of OH⁻ on Au, Ag, and Hg electrodes, respectively.

Aqueous sulfide chemistry.—Before detailed interpretation of the flatband potential data, the chemistry of Na₂S solutions has to be briefly considered. The addition of Na₂S to an aqueous solution results in nearly complete hydrolysis leading to an essentially equimolar solution of SH⁻ and OH⁻. The equilibrium constant for the hydrolysis (11)



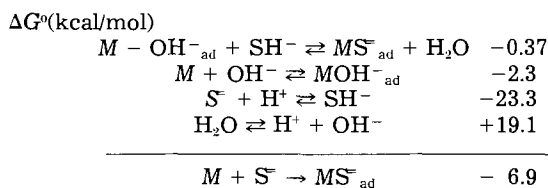
is $\sim 1.1 \times 10^3$. In 1M OH⁻, $\sim 0.1\%$ of sulfide is present as S²⁻. This means that SH⁻_(aq) is the dominant precursor to adsorbed S²⁻.

Another important aspect is the very probable large increase in acidity of SH⁻ when adsorbed on the surface. The chemical evidence for this expectation is the following. First, the pK_a for SH⁻ is 17.1 at room temperature (11). The pK_a of AgSH is 5.3 (12). Thus, the K_a increases by ~ 12 orders of magnitude by interaction of SH⁻ with a metal that is adjacent to Cd in the periodic table. Next, consider the enhancement in acidity of SH⁻ when it complexes with sulfur atoms to form polysulfide species. The pK_a 's for HS₂⁻, HS₃⁻, HS₄⁻, and HS₅⁻ were calculated to be 9.5, 7.4, 6.2, and 5.6, respectively (13). Clearly, complexation of SH⁻ with metals or nonmetals greatly increases its acidity. The above discussion allows us to conclude that any adsorbed SH⁻ will be nearly quantitatively converted to S²⁻_{ad} in 1M NaOH.

The coverage with sulfide was calculated on the assumption that $\theta_{OH^-} + \theta_{S^{2-}} = 1$, and the results are shown in Table II. Equation [3] was used with $qN/C_H = 0.46V$ and θ was replaced by $(1 + \theta_{S^{2-}})$. The value 0.46 is one-half the shift in V_{FB} from -0.70 to -1.62V, the saturation value for S²⁻. Saturation with S²⁻ with a double-negative charge should cause a shift twice that for saturation with OH⁻, a single-negative species, if the number of sites is constant. Comparison of ΔV_{FB} of 0.52 (OH⁻) with 0.92 (S²⁻) shows that this expectation is found experimentally. The coverage values, $\theta_{S^{2-}}$, were plotted vs. log [SH⁻], as shown in Fig. 4. The slope of the linear portion gives a first approximation to $(f_1 + f_2)^{-1}$. Various values of $f_1 + f_2$ were chosen until Eq. [13] was satisfied. The best fit was obtained for $f_1 + f_2 = 12.4$. For $\theta_{S^{2-}} > 0.6$, the data did not fit Eq. [13], as discussed below. This large $f_1 + f_2$ value compared to $f_{OH^-} \approx 2$ is not too surprising. The large negative charge and size of S²⁻ causes $f_{S^{2-}}$ to be larger (Eq. [10]). In addition, f_{OH^-} is increased because OH⁻ ions interact with some S²⁻ on

the surface. However, S²⁻ ions interact with OH⁻, and thus $f_{S^{2-}}$ is probably decreased. In order to calculate the equilibrium constant for the surface substitution reaction [11], an estimate of f_{OH^-} in the presence of S²⁻_{ad} is needed. We reasoned that this number should be greater than 2 but less than 1/2 ($f_1 + f_2$) = 12.4. A midrange value of 5 was assumed to be a reasonable compromise. Now K_s can be calculated using Eq. [13], $\theta = 0.5$, $C_{SH} = 2.0 \times 10^{-3}$, and an activity coefficient of 0.75 for SH⁻ ion in 1M NaOH solution. The calculation gives $K_s = 1.9$ and $\Delta G_s^\circ = -0.37$ kcal/mol.

A calculation of the free energy change for adsorption of S²⁻ can also be made using the thermodynamic data derived here. Consider the following series of reactions and corresponding standard free energy changes.



The value of ΔG° for adsorption of S²⁻ is found to be -6.9 kpm.

There is one other aspect of the sulfide coverage data that is of interest that is not predicted by Eq. [13]. The increase in slope of the θ vs. log C plot for $\theta \geq 0.6$ is unusual. Normally, the Frumkin isotherm with repulsive interaction shows a decrease in slope, leading to saturation for $\theta \geq 0.8$. Evidently, the nature of the interaction between the adsorbed ions changes in the direction of less repulsion as θ increases before saturation of the surface. A possible explanation is that a new phase forms on the surface, such as CdS or a sulfur layer. The former may require removal of Se, while the later may require at least partial oxidation of the adsorbed sulfide ions. Both of these processes, sulfur-selenium exchange and sulfur layer formation, are thought to occur on CdSe surfaces in contact with sulfide electrolytes in photoelectrochemical solar cells.

Summary

The adsorption of OH⁻ and S²⁻ ions on n-CdSe single-crystal electrodes was studied. Both ions reach saturation coverage for concentrations of 0.1-0.7M. Standard free energies of adsorption were -2.3 and -6.9 kcal/mol for OH⁻ and S²⁻, respectively. The corresponding quantity for the substitution reaction involving OH⁻_{ad} and S²⁻_{ad} was -0.37 kcal/mol. The repulsive interaction of S²⁻ (and possibly OH⁻) appears to weaken at high Na₂S electrolyte concentrations. The formation of a new phase in the near surface region may be implicated.

Acknowledgment

This research was supported by the Solar Energy Research Institute under Contract XE-2-0273-1.

Manuscript submitted Feb. 16, 1983; revised manuscript received July 9, 1984.

SRI International assisted in meeting the publication costs of this article.

REFERENCES

1. K. W. Frese, Jr., *J. Appl. Phys.*, **53**, 1571 (1982).
2. J. O'M. Bockris, M. A. V. Devanathan, and K. Müller, *Proc. R. Soc. A*, **274**, 55 (1963).
3. K. W. Frese, Jr., *J. Vac. Sci. Technol.*, **16**, 1042 (1979).
4. "Electrosorption," E. Gileadi, Editor, Plenum Press, New York (1967).
5. M. Boudart, *J. Am. Chem. Soc.*, **74**, 3556 (1952).
6. B. E. Conway and E. Gileadi, *Trans. Faraday Soc.*, **58**, 2493 (1962).
7. B. E. Conway, "Theory and Principles of Electrode Processes," Ronald Press, New York (1965).
8. H. Wroblowa and K. Müller, *J. Phys. Chem.*, **73**, 3528 (1969).
9. A. B. Ellis, S. W. Kaiser, J. M. Bolts, and M. S. Wrighton, *J. Am. Chem. Soc.*, **99**, 2839 (1977).
10. D. D. Bode, Jr., *J. Phys. Chem.*, **76**, 2915 (1972).

11. W. Giggenbach, *Inorg. Chem.*, **10**, 1333 (1971).
12. W. L. Freyberger and P. L. DeBruyn, *J. Phys. Chem.*, **61**, 586 (1957).
13. M. C. M. McKubre and D. D. Macdonald, "Electrochem-

ical Removal of Dissolved Sulfide from Geothermal Brines," Final Report from SRI International to the Environmental Protection Agency, EPA Contract no. 63-07-2778 (1981).

Effects of Additives on ZnO-B₂O₃-SiO₂ Passivation Glasses

Yutaka Misawa

Hitachi Limited, Hitachi Research Laboratory, Hitachi, Ibaraki, Japan

ABSTRACT

The addition of BaO, Sb₂O₃, or Bi₂O₃ to glass A with composition (weight percent [w/o]) 65.4 ZnO-24.5 B₂O₃-10.1 SiO₂ resulted in more negative surface charge density and increase in the thermal expansion coefficient (α). The glass B, 63 ZnO-29 B₂O₃-8 SiO₂ (w/o) showed finer crystals by the addition of ZnO (1 w/o) or glass A without affecting the surface charge density or α . The effects of additives on the DTA characteristic temperatures of the two glasses are also presented.

ZnO-B₂O₃-SiO₂ glasses are suitable passivants for high voltage silicon power devices such as thyristors, transistors, and diodes. One advantage of using this glass is that surface charge density of the glass/Si system can be controlled by changing the glass composition (1), i.e., the surface electric fields of the devices can be modified on demand. However, a new problem occurred when the ratios of B₂O₃ to SiO₂ were increased to shift the surface charge density in the negative direction (2). The problem consisted of an increase in crystal size.

Thus, to produce the passivation glass with a large negative surface charge density and fine crystals for high power devices, two approaches have been considered.

In method 1, a shift to more negative surface charge density of the glass with a small negative surface charge density and fine crystals is achieved by addition of another material. In method 2, forming finer crystals of the glass with a large negative surface charge density and large crystals is also achieved by addition of another material. For ZnO-B₂O₃-SiO₂ glass, Moriguchi *et al.* (3) reported that Sb₂O₃, CeO₂, and PbO were additives which lower the flowing point and crystallization point for the DTA curve and make the thermal expansion coefficient larger. However, Ta₂O₅ was an additive which did not change the flowing point, crystallization point, or thermal expansion coefficient, but did shift the surface charge density slightly in the positive direction.

In this report, method 1 was examined adding various metal oxides to glass A (ZnO:65.4, B₂O₃:24.5, SiO₂:10.1 w/o). Method 2 was investigated adding glass A or ZnO to glass B (ZnO:63, B₂O₃:29, SiO₂:8 w/o).

Experimental

Glass preparation.—In method 1, metal oxide components of glass A and 5 w/o of BaO, Al₂O₃, Ga₂O₃, SnO, PbO, ZrO₂, Sb₂O₃, Bi₂O₃, TiO₂, V₂O₅, Nb₂O₅, or Ta₂O₅ additive were mixed in a revolving mixer and used as glass materials. V₂O₅, Sb₂O₃, and PbO, which are low melting point materials, were heated at 500°C, while other materials were heated at 850°C to remove water and organic contaminations before weighing. Subsequent preparation procedures were the same as reported before (1, 2).

In method 2, glass A, with crystallized glass A or ZnO as additive, was mixed with glass B in a revolving mixer. Crystallized glass A was prepared as follows. Glass A powder was fired at 740°C for 40 min in air and then ground to give the same mean particle size distribution as glass A. ZnO was used like the glass materials.

Measurements.—Physical properties of glasses were measured by differential thermal analysis (DTA), thermal expansion coefficient measurements, and scanning electron microscope (SEM) observations.

Surface charge densities of the glass/silicon system were measured with metal-glass-silicon (MGS) capacitors.

Sample preparation and measurement methods have been reported previously (1, 2).

Results and Discussion

The effects of additives for glass A with a small negative surface charge density and fine crystals are shown in Fig. 1. as DTA curves of glass A and glass A with added Sb₂O₃. For the latter, a second crystallization point (T_{c2}) was not distinctly observed. Table I shows characteristic points for DTA curves of glass A with various metal oxides added. Characteristic points such as softening point (T_s), crystallization starting point (T_{cs}), and first crystallization point (T_{c1}) shift to lower temperatures on addition of any of the metal oxides. The oxides seemed to act as nucleating agents. Furthermore, the second crystallization points were not distinctly observed for all additives except TiO₂. Glass A with added TiO₂ showed distinct DTA characteristics. The boundary between T_c and T_{cs}

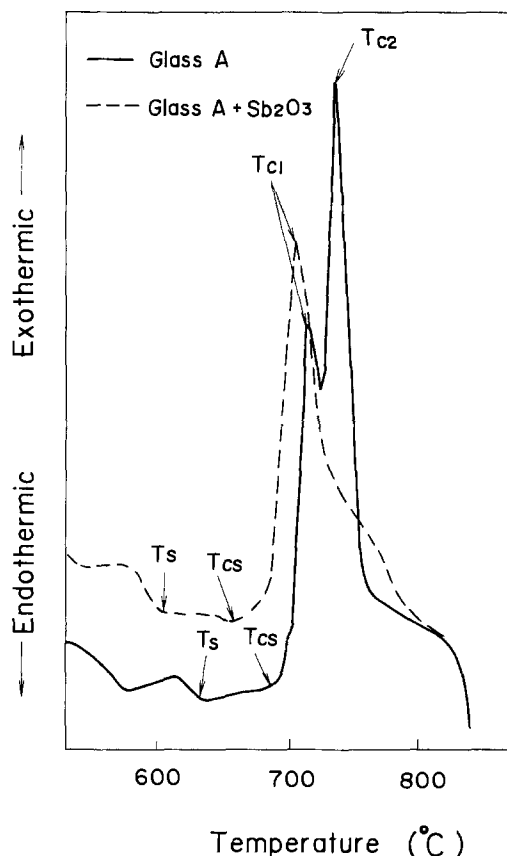


Fig. 1. DTA curves of glass A with and without added Sb₂O₃.

Table I. Characteristic points for DTA curves of glass A with various metal oxides added

Additive	T _s (°C)	T _{cs} (°C)	T _{ct} * (°C)	T _{cz} * (°C)
BaO	603	657	693 (133)	
Al ₂ O ₃	620	673	710 (150)	
Ga ₂ O ₃	590	645	690 (138)	
SnO	618	665	715 (125)	
PbO	600	654	690 (165)	
TiO ₂	595	595	635 (2)	700 (48)
ZrO ₂	600	650	703 (130)	
Sb ₂ O ₃	610	665	714 (75)	
Bi ₂ O ₃	600	656	700 (110)	
V ₂ O ₅	600	650	710 (60)	
Nb ₂ O ₅	595	653	700 (95)	
Ta ₂ O ₅	604	667	703 (100)	
None	636	690	724 (93)	755 (163)

* Numbers in parentheses are peak height in arbitrary units.

was unclear, and T_{ct} was very low in comparison with those of other glasses. Figure 2 shows typical photomicrographs for glasses fired on silicon at 700°C. Crystals in these glasses were different; they were larger than those in glass A and finer than those in glass B. Table II shows thermal expansion coefficients of glasses fired at 680° or 700°C. The thermal expansion coefficients for glass A with added metal oxide were all larger than that of glass A alone, except for ZrO₂ and Ga₂O₃ additives. It was expected that the thermal expansion coefficients of glass A with added metal oxide would be lower than that of glass A alone, because the crystallization points of these modified glasses were all lower than that of glass A alone. However, the results contradicted the expectations. The effects of metal oxides on the thermal expansion coefficients were larger than that of the degree of crystallization.

Table III shows the surface charge densities of glasses fired on n-type silicon at 680° or 700°C. The additives which shifted the surface charge density in the positive direction and accumulated the surface of n-type silicon are Al₂O₃, Ga₂O₃, SnO, PbO, TiO₂, ZrO₂, Nb₂O₅ and Ta₂O₅. These additive metals are from groups IIIB, IV, and VA of the periodic table. The additives which shifted the surface charge density in the negative direction and inverted the surface of n-type silicon are BaO, Sb₂O₃, and Bi₂O₃. These are from groups IIA and VB of the periodic table.

The effects of additives on the properties of glass B with large negative surface charge density and large crystals are shown in Fig. 3 as determined from DTA curves.

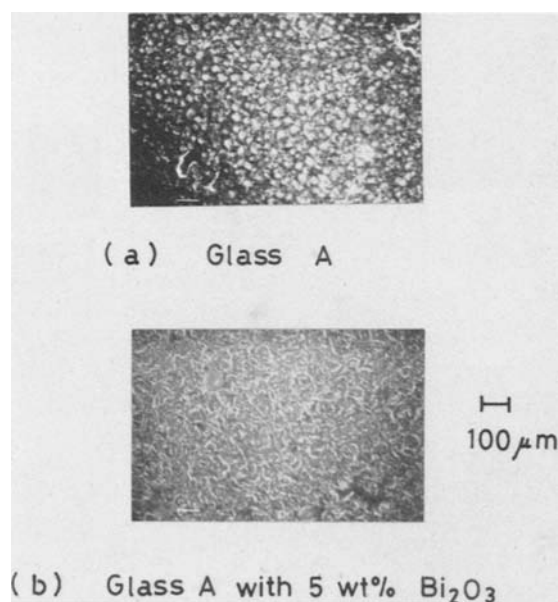


Fig. 2. Typical micrographs for glasses fired on silicon at 700°C for 40 min.

Table II. Thermal expansion coefficients of glass A with various metal oxides added

Glass firing Additive	Thermal expansion coefficient (10 ⁻⁷ /°C)	
	temperature 680°C	700°C
BaO	39.5	38.9
Al ₂ O ₃	42.6	
Ga ₂ O ₃	38.9	
SnO	42.4	
PbO	42.8	
TiO ₂	44.5	
ZrO ₂	34.8	
Sb ₂ O ₃	43.0	39.6
Bi ₂ O ₃	40.0	39.4
V ₂ O ₅	45.8	39.8
Nb ₂ O ₅	42.9	
Ta ₂ O ₅	42.4	
None	39.0	34.0

Table III. Surface charge densities of glass A with various metal oxides added

Glass firing Additive	Surface charge density (10 ⁻¹¹ cm ⁻²)	
	temperature 680°C	700°C
BaO	-1.0 to -1.2	-3.4 to -3.7
Al ₂ O ₃	+1.6 to +2.4	
Ga ₂ O ₃	+2.2 to +3.9	
SnO	+1.6 to -3.6	
PbO	+2.2 to +3.9	
TiO ₂	+4.1 to +5.7	
ZrO ₂	+3.0 to +3.8	
Sb ₂ O ₃	-1.7 to -3.4	-7.4 to -8.6
Bi ₂ O ₃	-2.0 to -2.8	-6.4 to -8.9
V ₂ O ₅	-0.4 to +0.3	-1.4 to -2.1
Nb ₂ O ₅	+2.0 to +2.4	
Ta ₂ O ₅	+2.3 to +2.5	
None	0 to -1.0	-1.0 to -3.0

Softening points of all the glasses changed hardly at all with additions. Crystallization starting point, first, and second crystallization point first decreased sharply and then by a slow increase by the addition of the additives. This tendency is independent of additives. Thus the additives were functioning as nucleating agents as stated before. However, T_{cz} did not disappear. And in particular,

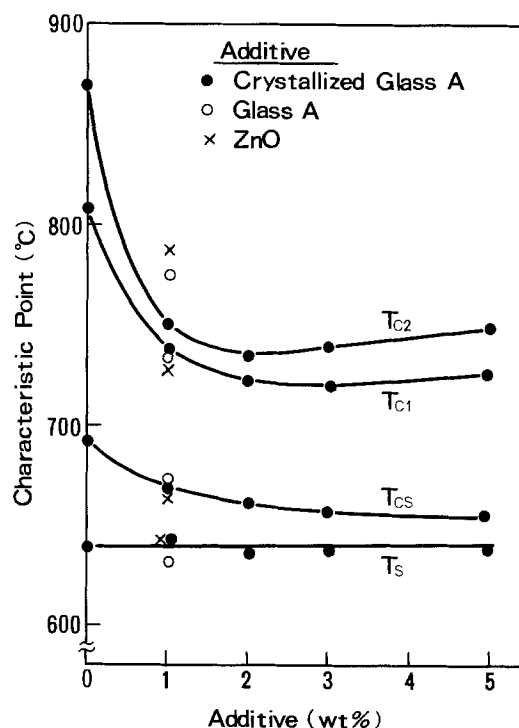


Fig. 3. Effects of additives on characteristic points of glass B as determined from DTA curves.

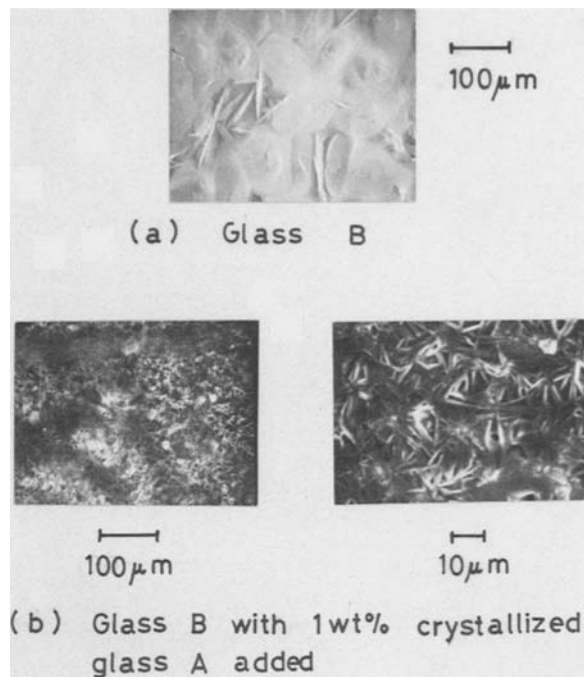


Fig. 4. Typical micrographs for glasses fired on silicon at 680°C or 700°C for 40 min.

variations of T_{c1} and T_{c2} were large with addition of only a small amount of additive. For 1 w/o additive, T_{c3} and T_{c1} did not differ for different additives. However, the variation of T_{c2} for glass B with crystallized glass A added was the largest. That is, crystallized glass A was most effective as a nucleating agent.

Phases of crystallization were observed by SEM. Figure 4 shows several photomicrographs for the glasses fired on silicon at 680° or 700°C. Large needlelike crystals were observed in glass B, as reported before (2). However, in glass B with additives, fine crystals were observed, as in glass A alone. Fine crystals formed because crystallization proceeded easily.

Figure 5 shows the relationship between the ratio of additives and thermal expansion coefficient of glass B fired at 680° or 700°C. Thermal expansion coefficients of glass B with added ZnO or crystallized glass A decreased with the ratio of additive. The thermal expansion coefficient of glass B with crystallized glass A was smaller than that with ZnO. This could be attributed to the difference in T_{c2} . The effect of the additive on the thermal expansion coefficient of glass B was opposite of

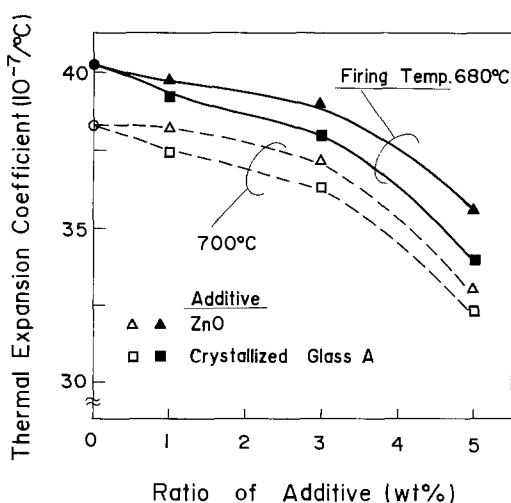


Fig. 5. The relationship between amount of additive and thermal expansion coefficient of glasses fired at 680° or 700°C.

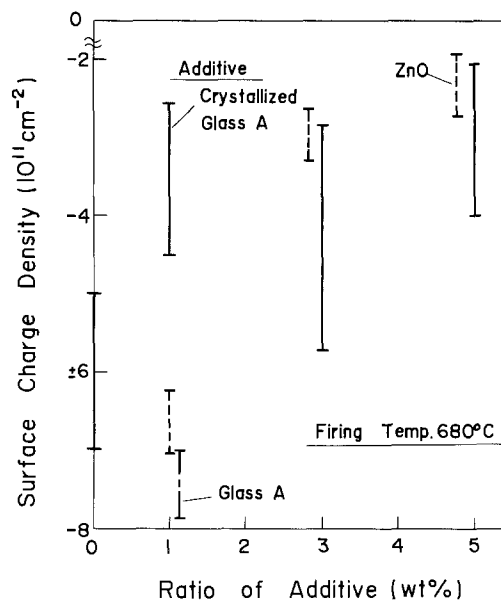


Fig. 6. The effect of amount of additive and surface charge density of glasses fired at 680°C.

that for glass A. This could be assumed to originate from the difference in the addition methods.

Figures 6 and 7 show the relationships between ratio of additive and surface charge density of the glass fired on silicon at 680° or 700°C. Surface charge density shifted in the positive direction with increasing ratio of additive. The shift was smallest for the glass B with added glass A.

Figure 8 shows the relationship between surface charge density and glass firing temperature. Surface charge density shifted to a more negative charge with higher firing temperature. This tendency was the same as that of glasses with no additive (1).

Conclusions

The effects of additives on DTA characteristics, crystal morphology, thermal expansion coefficient, and surface charge density of ZnO-B₂O₃-SiO₂ glasses were investigated.

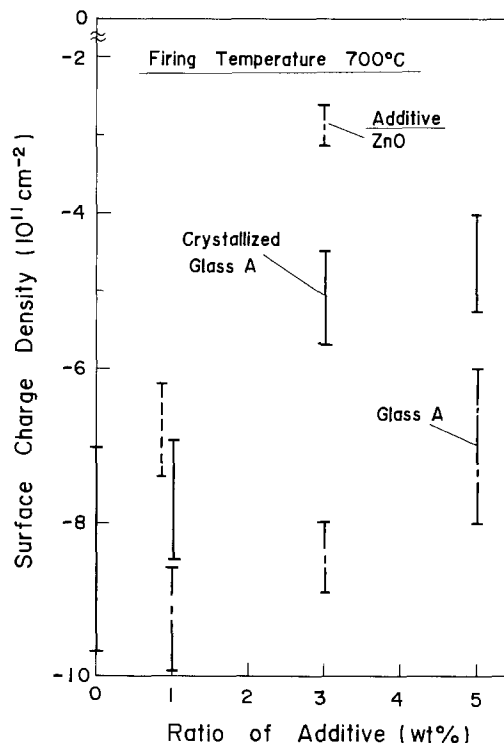


Fig. 7. The effect of amount of additive and surface charge density of glasses fired at 700°C.

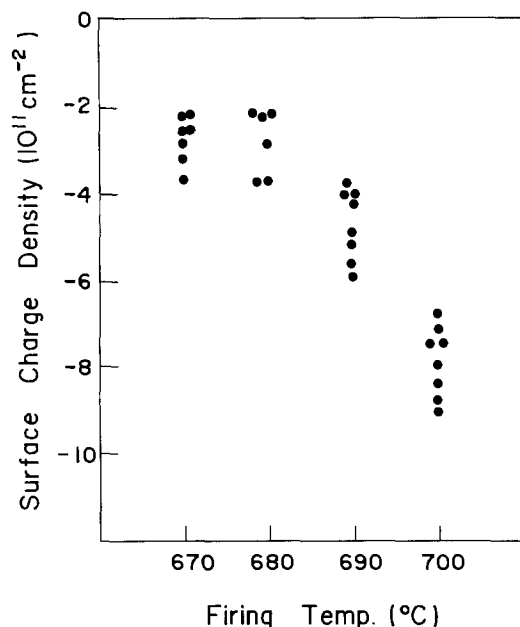


Fig. 8. The effect of firing temperature on surface charge density of glass B with 1 w/o crystallized glass A added.

The addition of metal oxides influenced the properties of glass A, which had a small negative surface charge density and fine crystals, as follows. Characteristic points such as T_s , T_{cs} , and T_{c1} of glass A decreased, and T_{c2} was not distinctly observed on addition of metal oxide. The thermal expansion coefficients of glass A increased. The surface charge density of the glass/silicon system shifted negatively with the addition of metal oxides, if the metal

belonged to groups IIA or VB (e.g., BaO, Sb₂O₃, or Bi₂O₃). It shifted to positive with the addition of metal oxides, if the metal belonged to groups IIIB, IV, or VA (e.g., Al₂O₃, Ga₂O₃, SnO, PbO, TiO₂, ZrO₂, V₂O₅, Nb₂O₅, or Ta₂O₅).

The addition of glass A or ZnO influenced the properties of glass B, which had a large negative surface charge density and large crystals, as follows. T_{cs} , T_c , and T_{c2} of glass B decreased, and the crystals in the glass were finer. The thermal expansion coefficient of glass B decreased with increasing ratio of additive. The surface charge density shifted positively with increasing ratio of additive. However the shift was negligible in the case of the glass with 1 w/o additive. Hence, glass B with 1 w/o additive meets the objectives of this work, which was the development of a glass with large negative surface charge and fine crystals.

Acknowledgments

The author wishes to thank Mr. Y. Ikeda and Drs. M. Okamura, H. Hackino, and M. Monma for their helpful suggestions and encouragement during this study and Mr. M. Takahashi for technical assistance.

Manuscript submitted April 16, 1984; revised manuscript received July 9, 1984.

Hitachi Limited assisted in meeting the publication costs of this article.

REFERENCES

1. Y. Misawa, H. Hackino, S. Hara, and M. Hanazono, *This Journal*, **131**, 359 (1984).
2. Y. Misawa, *ibid.*, To be published.
3. Y. Moriguchi, K. Miwa, M. Kanno, H. Kawamura, and T. Shibuya, in "Proceedings of First Symposium on Semiconductors and Integrated Circuits Technology, Tokyo," p. 10 (1971).

Electrical Characteristics of the RF Magnetron-Sputtered Tantalum Pentoxide-Silicon Interface

Shunji Seki, Takashi Unagami, and Bunjiro Tsujiyama

Nippon Telegraph and Telephone Public Corporation, Ibaraki Electrical Communication Laboratory, Tokai, Ibaraki 319-11, Japan

ABSTRACT

Tantalum pentoxide (Ta₂O₅) films were deposited onto single-crystalline silicon as gate insulators by RF magnetron sputtering. Capacitance-voltage characteristics were measured to determine the interface properties between Ta₂O₅ and Si. After annealing at 450°C in H₂ ambient, a negative interface charge that is fully localized in the low dielectric constant transition layer at the interface was observed. It has also been clarified that the rest of the film is homogeneous, whose dielectric constant is almost close to that of the bulk of Ta₂O₅. It has been shown that Ta₂O₅ gate insulator with relatively good interface properties can be fabricated at low temperatures using RF magnetron sputtering.

In recent years, tantalum pentoxide (Ta₂O₅) film is of interest for use as a gate insulator in MOS devices. The higher dielectric constant of Ta₂O₅, compared with that of SiO₂, makes it attractive for the fabrication of high quality MOS devices with high transconductance and low threshold voltage. Furthermore, since high quality Ta₂O₅ films can be fabricated at low temperatures using RF magnetron sputtering (1), it also offers the opportunity for removing some of the problems encountered with conventional MOS devices with thermally grown SiO₂ as a gate insulator.

The characteristics of MOS devices will be strongly dependent on the interface properties between the gate insulator and the silicon layer, in addition to the quality of the gate insulator itself. Because of its excellent properties, thermally grown SiO₂ has been used for years as gate insulators in MOS devices. However, since the thermal

oxidation is performed at 900°C or higher, the oxidation process prohibits the use of the thermal oxide on devices fabricated on a low melting point substrate. Furthermore, the high temperature oxidation generates stacking faults and dislocations in the silicon substrate, and it also changes the impurity distribution previously formed in the substrate. These structural defects and the variation of the impurity profiles induce the degradation in the performance of MOS devices. In order to remove these problems, gate insulator fabrication processing at low temperatures becomes necessary.

Several attempts have been made to employ Ta₂O₅ films as gate insulators in MOS devices, using chemical vapor deposition (2) and thermal oxidation of a deposited Ta film (3, 4). However, the interface properties between Ta₂O₅ and Si fabricated by these processes were inferior to those between SiO₂ and Si. More than -5 to -10×10^{11}

cm^{-2} interface charge density remained at flatband condition, which was much higher than that between SiO_2 and Si. In order to obtain high quality MOS devices, it is necessary to reduce the interface charge density between Ta_2O_5 and Si.

The authors have investigated the interface properties between the silicon layer and the Ta_2O_5 gate insulator formed by RF magnetron sputtering. This paper reports the results of these experiments, and also shows the ability to produce a relatively good quality Ta_2O_5 gate insulator at low temperatures using RF magnetron sputtering.

Experimental

Al/ Ta_2O_5 /Si structure devices were used to investigate the interface behavior. All of the MOS capacitors were fabricated on p-type, $\langle 100 \rangle$ -oriented, 1.2-1.8 $\Omega\text{-cm}$ silicon wafers. Si wafers were chemically cleaned using mixtures of H_2O_2 and H_2SO_4 (volume ratio of $\text{H}_2\text{O}_2/\text{H}_2\text{SO}_4 = 1/4$). Then, they were rinsed in deionized water. Immediately before being installed into the sputtering chamber, the wafer was dipped into dilute HF to remove the oxide formed during previous processing steps. Sputtering was performed using an ULVAC SBH-2204 RS RF magnetron sputtering system. Instead of a conventional oil diffusion pump, a 3000 liter/s cryogenic pump was used to eliminate contamination. The Ta_2O_5 target was 10 cm diam and 5 mm thick. The target to substrate distance was kept at 5 cm. The sputtering gas consisted of mixtures of argon and oxygen (partial pressure ratio of $\text{Ar}/\text{O}_2 = 8/2$). The sputtering chamber was evacuated to less than 1×10^{-7} torr prior to sputtering, and then backfilled with the sputtering gas. The sputtering pressure was varied from 4×10^{-3} to 2×10^{-2} torr. The Ta_2O_5 target was presputtered for at least 1h. Typical deposition rate ranged from 2 to 6 nm/min. Aluminum dot electrodes of 300 μm diam were electron-beam deposited onto the sputtered Ta_2O_5 surface. To minimize the radiation damage produced during the MOS capacitor fabrication steps, the wafers were annealed in the hydrogen ambient. After a final H_2 anneal, the high frequency capacitance-voltage characteristics were measured with automatic capacitance meters (HP 4275A and HP 4274A). These measurements were performed for more than 20 MOS capacitors fabricated on the same silicon substrate.

In-depth composition profiles of the deposited Ta_2O_5 were measured by Auger electron spectroscopy (AES) with simultaneous Ar sputtering. For the AES measurements, samples were taken from the sputtering chamber and were then mounted in an ultrahigh vacuum chamber of the AES measurement equipment (Φ 590). Measurements were performed under conditions of a 5 kV excitation voltage and a 0.5 μA beam current. Typical sputtering rate of Ta_2O_5 films was 3 nm/min for a 3 kV sputtering voltage and a 5 mA emission current.

Experimental Results

H_2 annealing effect.—To find H_2 annealing effect on the interface charge density, capacitance-voltage characteristics of MOS capacitors, which had been annealed in the hydrogen ambient at different temperatures, were measured at frequencies ranging from 1 kHz to 1 MHz. In these cases, annealing was performed after the aluminum electrode deposition, which is hereafter referred to as the postmetallization annealing. Annealing temperatures were varied from 350° to 450°C, and the annealing time was retained for 30 min. Figure 1 shows capacitance-voltage characteristics for MOS capacitors which were not annealed. A strong frequency dispersion was observed in their C-V curves. This is due to the existence of the high density of interface states with various response time constants. Two parameters were used to indicate the H_2 annealing effect: the interface charge density calculated from the flatband voltage measured at 1 MHz, and the flatband voltage difference between the low frequency C-V curve taken at 1 kHz and the high frequency C-V curve taken at 1 MHz.

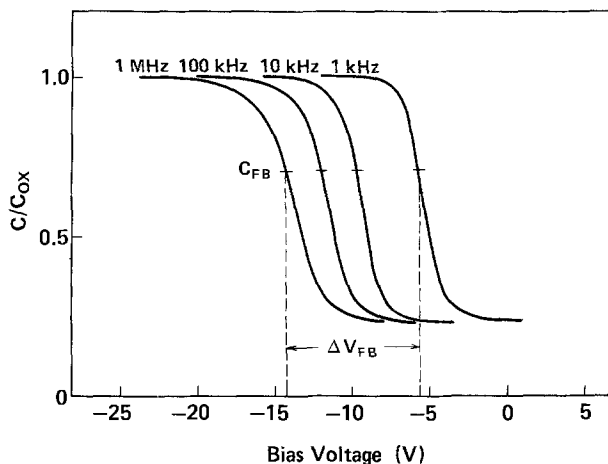


Fig. 1. Frequency dispersion in capacitance-voltage characteristics for MOS capacitors without the postmetallization annealing. The Ta_2O_5 thickness is 110 nm. The interface charge density, calculated from the V_{FB} measured at 1 MHz and the ΔV_{FB} inserted in the figure, were used to indicate the annealing effect.

Figure 2 shows variations in the interface charge density and the flatband voltage difference with annealing temperatures. The interface charge density decreases monotonically as the annealing temperature goes up from 350° to 450°C. After annealing at 450°C, the interface charge polarity changed to negative, and the value of $-3.1 \times 10^{11} \text{ cm}^{-2}$ was obtained. Flatband voltage difference also decreases uniformly with increasing annealing temperature. After annealing at 450°C, the flatband voltage difference in between low and high frequency C-V curves was reduced to less than 0.04V. It has been clarified that H_2 annealing has a great effect on the reduction in the interface charge density in Al/ Ta_2O_5 /Si structures.

In order to make the interface charge density much lower, the annealing process was newly introduced after the Ta_2O_5 deposition process. The purpose of this annealing process, hereafter referred to as the postsputtering annealing, is to reduce the radiation damage produced during the sputtering process. In these cases, wafers were annealed at 450°C in the hydrogen ambient for 30 min before the aluminum metallization, and the postmetallization annealing temperature was varied.

Figure 3 shows the variations in the interface charge density and the flatband voltage difference with postmetallization annealing temperatures. The interface

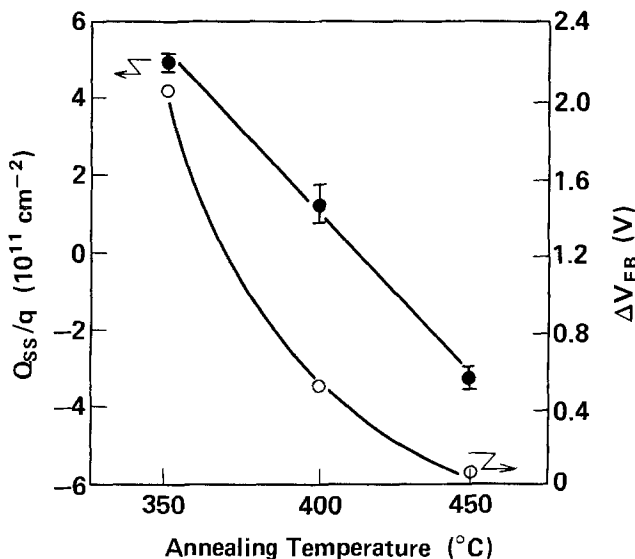


Fig. 2. Variations in interface charge density Q_{ss}/q and flatband voltage difference ΔV_{FB} with changes in postmetallization annealing temperature. The Ta_2O_5 thickness is 80 nm.

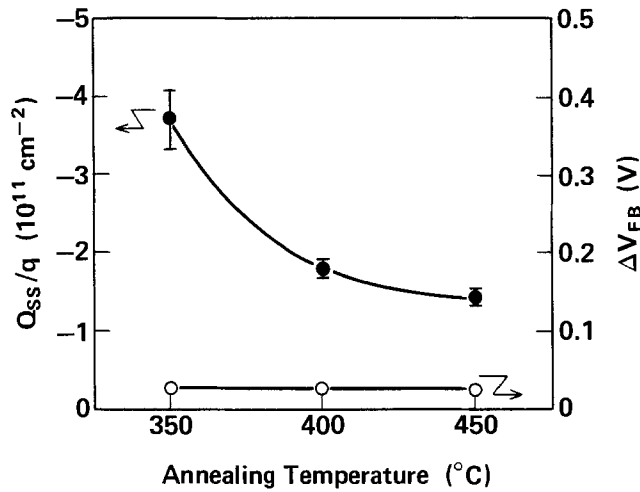


Fig. 3. Variations in Q_{ss}/q and ΔV_{FB} with changes in postmetallization annealing temperature. Samples had been annealed at 450°C in the hydrogen ambient before metallization. The Ta_2O_5 thickness is 80 nm.

charge density and the flatband voltage difference on the case involving postsputtering annealing without postmetallization annealing were $4.2 \times 10^{11} \text{ cm}^{-2}$ and 0.19V, respectively. Differing from the results shown in Fig. 2, the interface charge polarity changed to negative, even though the postmetallization annealing temperature was 350°C. The value of interface charge density decreases as the postmetallization annealing temperature rises from 350° through 450°C. After annealing at 450°C, the interface charge density was reduced to as low as $-1.4 \times 10^{11} \text{ cm}^{-2}$. Flatband voltage difference was made as low as 0.03V almost invariable in the postmetallization annealing temperature over 350°C. And the reproducibility of these results was good. It has become clear that the interface charge density can be reduced to as low as $-1.4 \times 10^{11} \text{ cm}^{-2}$ by the optimum combination of postmetallization annealing with postsputtering annealing. These are the lowest values which have been reported so far. These results imply that postsputtering annealing has an effect on the reduction of the radiation damages induced during the sputtering process.

The surface-state density was calculated from the high frequency (1 MHz) capacitance-voltage characteristics using the Terman method (5). The surface-state density distributions, before and after annealing in the hydrogen ambient, are compared in Fig. 4. The surface-state density for as-deposited samples was on the order of 10^{12} states $\text{cm}^{-2} \text{ eV}^{-1}$ in the middle of the energy gap and increased rapidly toward the bandedges. After the samples had been annealed at 450°C in the hydrogen ambient, the surface-state density was reduced to as low as 1.5×10^{11} states $\text{cm}^{-2} \text{ eV}^{-1}$ near the midgap, which is one order of magnitude lower than that reported previously (3).

Interface charge density dependence on gate insulator thickness.—It has become clear from the results mentioned in the previous section that the interface charge after annealing at 450°C in the hydrogen ambient is characterized by a negative charge and behaves like fixed charges in the Al/ Ta_2O_5 /Si structures. To clarify the charge distribution in the gate insulator, variations in the interface charge density with changes in the gate insulator thickness were investigated. Results are shown in Fig. 5. The interface charge density is within the range from -3.0×10^{11} to $-3.8 \times 10^{11} \text{ cm}^{-2}$ as varying the gate insulator thickness from 17 to 110 nm. The interface charge density is independent of the gate insulator thickness in the thickness range studied. If the charge distribution were uniform in the gate insulator, the interface charge density would increase monotonically with increasing gate insulator thickness. Hence, these results indicate that the charge distribution is not uniform in the gate insulator.

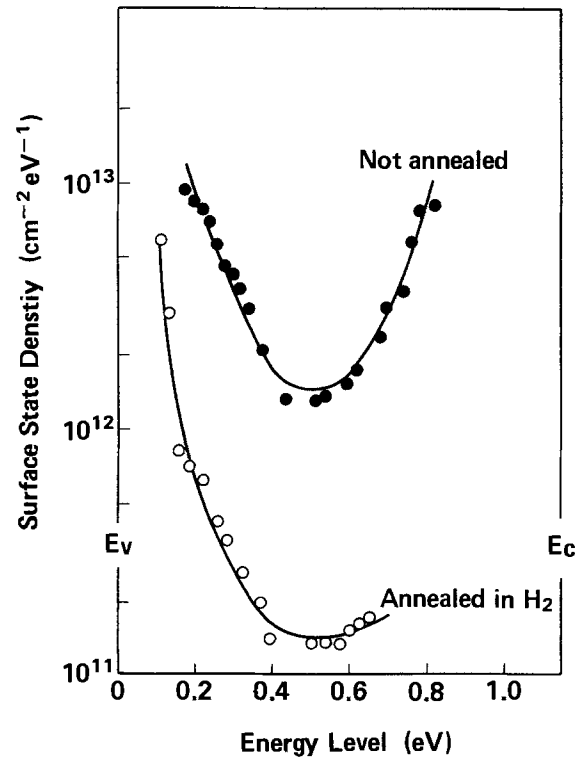


Fig. 4. Surface-state density distribution for Al/ Ta_2O_5 /Si MOS capacitors. Combination of postsputtering annealing with postmetallization annealing reduced the surface-state density to as low as $10^{11} \text{ cm}^{-2} \text{ eV}^{-1}$. The Ta_2O_5 thickness is 110 nm.

Dielectric constant dependence on gate insulator thickness.—In order to clarify dielectric properties of Ta_2O_5 sputtered on single-crystalline Si, the relationship between the dielectric constant of the gate insulator and the gate insulator thickness was studied. The dielectric constant of the gate insulator was calculated from the capacitance of MOS capacitors in the accumulated region measured at 1 MHz. Figure 6 shows the variations in gate insulator dielectric constant with changes in thickness. The dielectric constant increases monotonically with increasing gate insulator thickness. For the sample 17 nm thick, the dielectric constant is 3.9, which is much lower than that of Ta_2O_5 itself and is close to that of SiO_2 . As the thickness increases, the dielectric constant becomes higher and reaches 12.5 for the 110 nm thick sample. These results imply that the dielectric constant is not uniform throughout the whole thickness of deposited Ta_2O_5 .

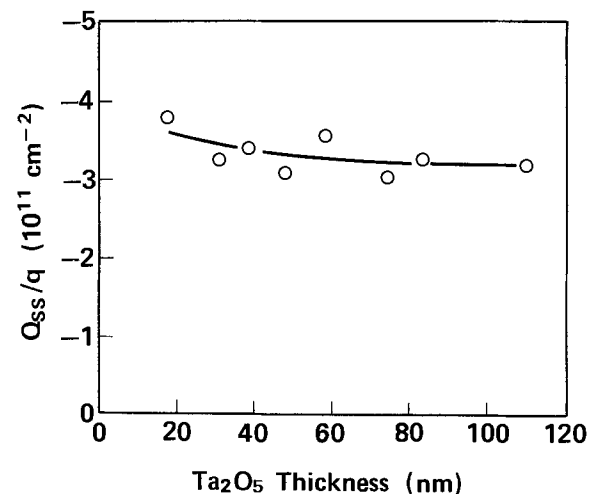


Fig. 5. Variation in interface charge density with changes in Ta_2O_5 gate insulator thickness. The interface charge density was calculated from the flatband voltage measured at 1 MHz.

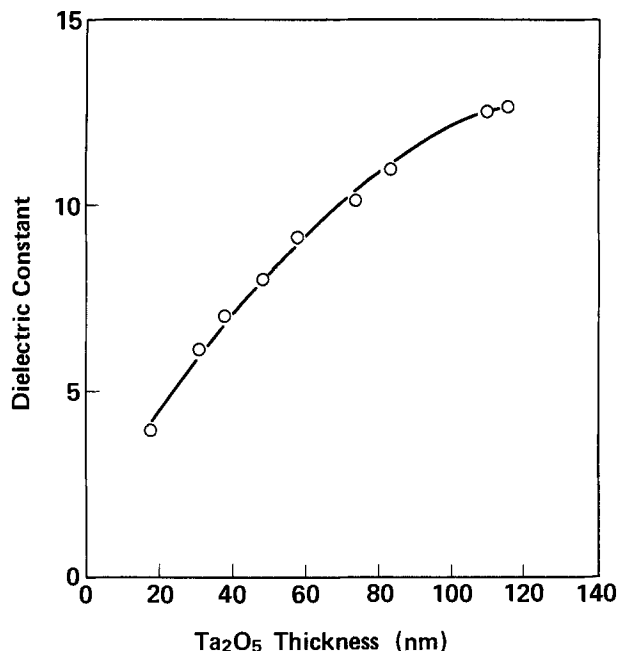


Fig. 6. Variation in Ta_2O_5 gate insulator dielectric constant with changes in the gate insulator thickness. Dielectric constant was calculated from the capacitance in the accumulated region at 1 MHz.

To clarify the reason for the variation in the dielectric constant, the dielectric constant profile within the deposited film was calculated from the results shown in Fig. 6. Figure 7 shows the dielectric constant profile, which was obtained by approximating the film with a series of discrete homogeneous layers. The bars shown in Fig. 7 represent the average value of the dielectric constant for each layer. The lowest average value was taken as the dielectric constant for the sample with the Ta_2O_5 thickness of 17 nm. The dielectric constant for the second layer was then obtained by reevaluating the dielectric data, using a multilayer model consisting of the first layer and the second layer. This calculation was repeated for each successive layer. The results indicate the existence of low dielectric constant layer near the $\text{Ta}_2\text{O}_5/\text{Si}$ interface. It has also been shown that the dielectric constant is almost uniform throughout the rest of the film and is almost close to that of the bulk of Ta_2O_5 .

To confirm the correctness of the model, etch-back experiments were performed. The sample with the oxide

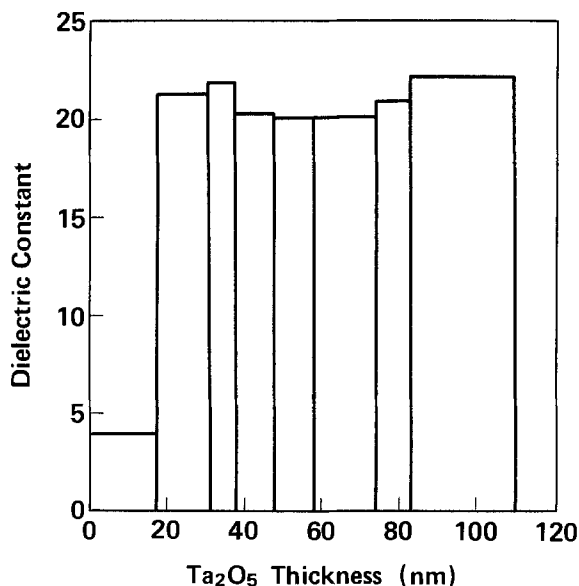


Fig. 7. Variation in dielectric constant with changes in distance from gate insulator/silicon interface. Data were obtained by approximating the Ta_2O_5 film with a series of discrete homogeneous layers.

thickness of 110 nm was etched back to 50 nm. Following the etch-back step, aluminum electrodes were deposited on it to fabricate the MOS capacitor. From the measurement of the capacitance, the dielectric constant of the oxide was calculated to be 8.5. This value fits well with the results shown in Fig. 6. It is, therefore, concluded that the outer part of the film is homogeneous, and that the thickness of the transition layer is independent of the total thickness of gate insulator.

Composition profiles.—AES measurements of in-depth composition profiles are shown in Fig. 8. The vertical axis is proportional to the relative concentration, and the sputtering time indicated by the horizontal axis is related to the depth counted from the outer surface.

A remarkable feature is that the relative composition ratio of Ta/O is fairly constant through the whole thickness of the film, except for near the silicon interface, where the relative composition ratio becomes larger. This is not unique to the case of this film, but has been observed for other films with different thicknesses as well. The variation of the relative composition ratio of Ta/O near the interface is assumed to be related to the formation mechanism of tantalum oxide on silicon.

Discussion

The results shown in Fig. 7 can be explained by a model with a relatively narrow transition layer at the interface, where the rest of the film is homogeneous. This transition layer is considered to be attributed to the imperfect tantalum compound formed in the early stage of Ta_2O_5 formation on silicon. It is assumed that the dielectric constant becomes lower in this transition layer, owing to its structure imperfection. Following the transition layer formation, nearly perfect tantalum oxide will form on it. Hence, the outer part of the film becomes homogeneous, and the value of the dielectric constant in this region is close to that of the bulk of Ta_2O_5 .

This model is confirmed by in-depth composition profiles obtained from the AES measurements. As shown in Fig. 8, the composition profile of the film is divided into two regions based on the relative composition ratio of Ta/O: (i) the outer part of the film, where the relative composition ratio of Ta/O is constant, and (ii) the region near the silicon interface, where the relative composition ratio becomes larger. Results shown in Fig. 8 indicate that the deposited film is homogeneous except for transition region near the interface. From the composition profiles, the thickness of this transition region is estimated to be in the range from 10 to 15 nm. Based on the assumption that the composition of the outer part of the film is Ta_2O_5 , the larger relative composition ratio implies the existence of the imperfect tantalum compound or lower tantalum oxide in the transition region.

It has already been reported by Revez *et al.* (2) and Smith *et al.* (3), that the interface charge is also negative

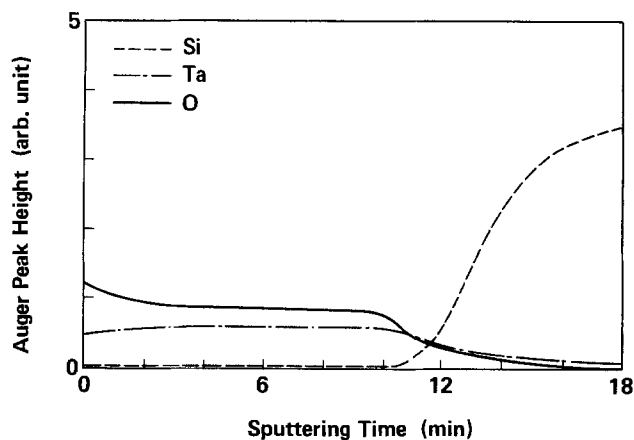


Fig. 8. In-depth composition profiles of Ta_2O_5 deposited on silicon. The sample was annealed at 450°C in the hydrogen atmosphere. Sputtering rate for Ta_2O_5 was 3 nm/min.

in the Ta₂O₅/Si system, when Ta₂O₅ gate insulator is fabricated with thermal oxidation of deposited Ta on Si. They investigated variations in refractive index of the film with changes in the film thickness in detail. However, the spatial distribution of these negative charges and the origin of these negative charges have not been clarified. The results shown in Fig. 5 indicate the fully localized distribution of the negative charge near the interface. As the interface charge density for the sample with 17 nm gate insulator thickness is almost the same as that for the sample with thicker gate insulator, the negative charge distribution will be localized within a thin layer at the Ta₂O₅/Si interface, which is less than 17 nm thick.

Taking the aforementioned results into consideration, it has become clear that the negative charges are fully localized in the low dielectric constant, narrow transition layer formed at the silicon interface. Even though the Si wafer is etched with dilute HF just before sputtering, oxide will reform quickly. The transition layer will be formed as the result of the interaction of this initial Si oxide film and/or Si surface with sputtered particles. If the transition layer consists of imperfect tantalum compound and/or lower tantalum oxide, it is suspected that the negative charge is due to the structure imperfections, such as the nonbridging oxygens, which are known to act as electron traps (6).

Conclusion

In the present study, Ta₂O₅ films have been deposited onto single-crystalline Si wafers using RF magnetron sputtering, and capacitance-voltage characteristics have been measured to determine the interface properties between Ta₂O₅ and Si. After annealing at 450°C in the hydrogen ambient, the interface charge in Al/Ta₂O₅/Si structures is characterized by a negative charge and is found to behave like a fixed charge. To obtain good quality interface, the postsputtering annealing has been newly introduced in addition to the conventional postmetallization annealing. At the optimized annealing conditions, the interface charge density was reduced to as low as $-1.4 \times 10^{11} \text{ cm}^{-2}$ at flatband, and the surface-state density of $1.5 \times 10^{11} \text{ cm}^{-2} \text{ eV}^{-1}$ was obtained near the midgap. These

are the lowest values in the Ta₂O₅/Si system which have been reported so far.

It has been clarified that the deposited oxide consists of two regions: a low dielectric constant, narrow transition layer at the silicon interface, and the higher dielectric constant, homogeneous layer. The thickness of this transition layer is in the range 10-15 nm, which is independent of the total thickness of Ta₂O₅ film. Moreover, it has been shown that the negative charges are fully localized in this transition layer. From the results of the present work, it has been pointed out that the negative charge in the Ta₂O₅/Si system results from imperfect tantalum compound formed in the early stage of Ta₂O₅ formation on single-crystalline silicon.

In the present Ta₂O₅ gate insulator fabrication processes, the highest temperature was restrained to under 450°C in the postannealing process. The present work demonstrates that a relatively good quality Ta₂O₅ gate insulator can be fabricated at low temperatures using RF magnetron sputtering.

Acknowledgments

The authors would like to thank Mr. K. Murase for his encouragement during the course of this work. The authors are also grateful to Dr. M. Ojima for the AES measurements.

Manuscript submitted Aug. 1, 1983; revised manuscript received June 22, 1984.

Nippon Telegraph and Telephone Public Corporation assisted in meeting the publication costs of this article.

REFERENCES

1. S. Seki, T. Unagami, and B. Tsujiyama, *J. Vac. Sci. Technol. A*, **1**, 1825 (1983).
2. E. Kaplan, M. Balog, and D. Frohman-Bentchkowsky, *This Journal*, **123**, 1570 (1976).
3. A. G. Revesz and J. F. Allison, *IEEE Trans. Electron Devices*, **ed-23**, 527 (1976).
4. D. J. Smith and L. Young, *ibid.*, **ed-28**, 22 (1981).
5. L. M. Terman, *Solid State Electron.*, **5**, 285 (1962).
6. A. Szekeres, S. Alexandrova, and K. Kirov, *Phys. Status Solidi A*, **62**, 727 (1980).

Wetting Angles and Surface Tension in the Crystallization of Thin Liquid Films

Eli Yablonovitch and Tom Gmitter

Exxon Research and Engineering Company, Annandale, New Jersey 08801

ABSTRACT

The behavior of thin liquid films is known to be dominated by surface tension forces. We show that the crystallization of thin liquid films requires that two wetting angle conditions be simultaneously satisfied: (i) relating to the liquid-vapor interface, and (ii) relating to the crystal-liquid interface. The balance between capillary pressure and thermal gradient forces shows that the equilibrium freezing point of thin films is actually depressed below the bulk freezing point. The magnitude of the effect is 1 K in an 800Å thick film. These observations suggest that small-scale thickness fluctuations may be responsible for the initiation of subgrain boundaries in the growth of crystalline silicon films.

The crystallization of thin liquid silicon films is a promising method (1) for producing single-crystal films of good electronic quality. These films will have important device applications in radiation hardening, dielectric isolation, high voltage integrated circuits, etc.

It is well known (2) that capillary forces, surface tension, and wetting play a vital role in the behavior of thin liquid films. In this article, we will derive the wetting angle requirements which permit the crystallization of thin liquid films to proceed. We will see that the success with liquid silicon films encapsulated in silicon dioxide is the result of a particularly fortuitous combination of wetting angles for those two materials.

Wetting Angle Requirements

In general, there is no assurance that a thin liquid film will be stable. There is the well-known tendency for the liquid film to "ball up" and form droplets on the surface of the substrate. The condition for spreading of the liquid film on a substrate is that its wetting angle should be identically zero. Since this is very rare, a different approach is used. We will show that a solid capping layer on the liquid film greatly relaxes this severe wetting angle constraint, and permits wetting under more easily satisfied conditions.

For practical stability, the liquid film should spread to fill any possible voids in the film, as shown in Fig. 1. Let

Capping Layer

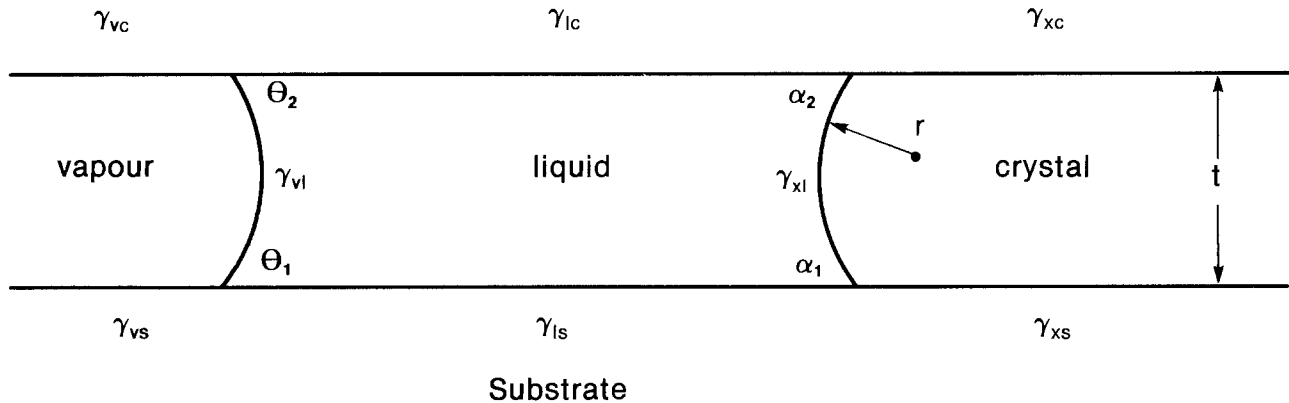


Fig. 1. A vertical cross-section through the thin liquid film. The liquid-vapor wetting angle, θ , is required to provide absolute stability against any voids which might be present in the film. The crystal-liquid angle α is required for high quality crystal growth and to prevent heterogeneous nucleation on the substrate. Note the radius of curvature r .

γ_{ls} and γ_{lc} be the surface energy (or tension) of the liquid with respect to the substrate and capping layer. Let γ_{vs} and γ_{vc} be the surface energy of the bare substrate and capping layer, respectively. The spreading of the liquid film should result in a net reduction of surface energy. Therefore

$$\gamma_{ls} + \gamma_{lc} - (\gamma_{vs} + \gamma_{vc}) < 0 \quad [1]$$

The Young-Dupre equation (2) for wetting angles, $\gamma_{vs} - \gamma_{ls} = \gamma_{vl} \cos \theta$, may be used to simplify inequality [1]

$$\cos \theta_1 + \cos \theta_2 > 0 \quad [2]$$

Inequality [2] states the wetting condition; the sum of the cosines of the wetting angles with respect to the substrate and the capping layer must be greater than zero. If the substrate and capping layer are made of the same material, then inequality [2] simply says that the wetting angle θ must be less than 90° . The wetting angle of liquid silicon on silica at the melting point has been independently measured (3) to be 87° , i.e., barely within the regime of stability! This must be regarded as extremely fortuitous. Of course, without a capping layer we go back to the condition $\theta_1 = 0$, i.e., wetting would be almost hopeless.

Since the surface tension γ_{vs} of the silica surface is thought to drop with increasing temperature, the angle θ_1 is thought (4) to become $> 90^\circ$ at temperatures 50-100 K above the silicon melting point. This probably explains the very narrow temperature window of stability in the crystallization of liquid silicon films on pure fused silica substrates. As a practical matter, it was found that the addition of a small amount of nitrogen (1) to the SiO_2 permitted the wetting conditions to be satisfied much more readily. The wetting angle of liquid silicon on Si_3N_4 is much less than 90° , having been measured (5) to be around 25° . It is understandable then that the addition of a small amount of Si_3N_4 to the SiO_2 might lower the wetting angle away from the condition of borderline stability, therefore broadening the temperature window of stability.

Thus far, we have considered wetting angles at the liquid-vapor interface, which controls the stability of the liquid film. Now we want to consider the crystal-liquid wetting angles, which will control the quality of crystal growth. It is a maxim (6) among crystal growers that the growth front should be convex away from the crystal. This permits any spurious crystal orientations to grow out to the edge and terminate there. A convex shape is guaranteed by wetting angles α_1 and α_2 both less than 90° . When α is greater than 90° , the Young-Dupre equation implies that γ_{xs} , the crystal-substrate interfacial energy, would be small, permitting easy heterogeneous nucleation of spurious grains at the surface of the substrate. In addition, the leading edge of the crystal growth would be

a cusp at one or both interfaces. Good crystalline quality is inherently unstable at such a cusp.

Therefore, the wetting angle requirement for good crystalline quality is that the angle α_1 enclosed by the liquid at the interface between the crystal and the substrate should be less than 90° . Likewise, the angle α_2 with respect to the capping layer should be less than 90° .

Recently, Celler (8) observed the angle formed by liquid silicon between crystalline silicon and silica. The angle he observed is $60^\circ < \alpha < 90^\circ$, again fortuitously in the favorable range for good crystal growth. The two wetting angle conditions may now be summarized as (i) $\cos \theta_1 + \cos \theta_2 > 0$, and (ii) $\alpha_1 < 90^\circ$ and $\alpha_2 < 90^\circ$.

Capillary and Thermal Gradient Forces

The convex interface in Fig. 1 between the crystal and the liquid experiences a pressure due to its curvature. This is a type of capillary pressure which can be computed from the equation of Young and Laplace (2)

$$P = \gamma_{xl} \left[\frac{1}{r} + \frac{1}{R} \right] \quad [3]$$

where γ_{xl} is the interfacial tension between crystalline and liquid silicon, r is the radius of curvature in the plane of Fig. 1, and R is the radius of curvature in the orthogonal plane coming out of the page. The smaller radius, r , may also be written as $r = t/2 \cos \alpha$, where t is the thickness of the film.

If the growth front is straight (looking down at the film from above) then $R = \infty$. A top view of the growing crystal-liquid interface in Fig. 2(a) shows not that the growth front is straight, but, rather that it is scalloped. The growing front is made up of a series of curved sections joined at cusps. The grain boundaries between adjacent crystal domains meet the growth interface at the tip of the cusps, as indicated schematically in Fig. 2(b). Because of this scalloped structure, the convex radius of curvature R of each scallop is finite.

The structure we observe differs from the faceted structure seen in the beautiful photographs by Geis *et al.* (1). We have found that the structure of the crystallization front depends on the speed of growth. At low speeds, $\approx 10^{-3}$ cm/s, the growth front is scalloped, as shown in Fig. 2(a). At higher speeds, some fraction of the cusps become deep, V-shaped facets. As the growth speed increases, more of the cusps become faceted. At a speed of 3×10^{-2} cm/s, the entire growth front is faceted, similar to Fig. 6 of Ref. (1). The facets are $\langle 111 \rangle$ crystal faces which form because of the kinetic barrier against crystal growth on that face. When the sample scanning direction is reversed, the facets disappear, but the scalloped structure remains. The reversibility of the scalloped structure indicates that it is

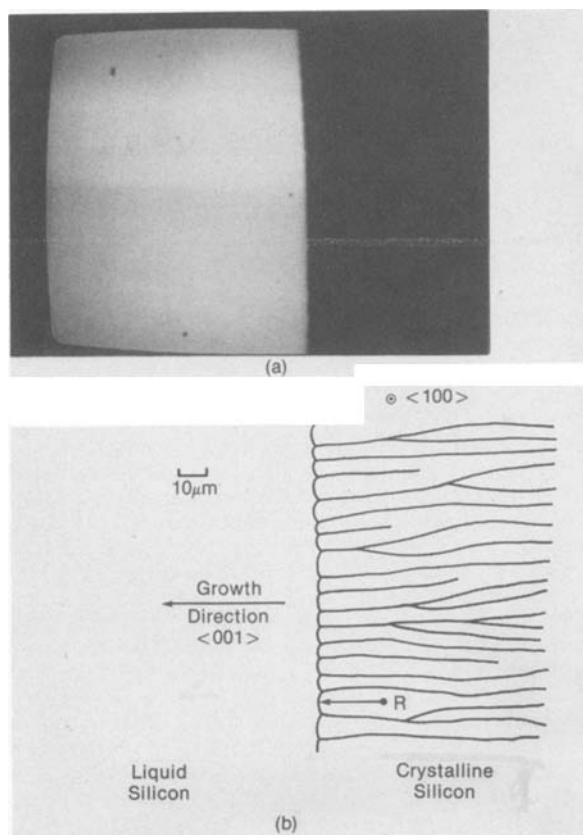


Fig. 2. (a) A video photograph of the crystal-liquid interface as seen in top view of the film. The crystal is the dark region on the right. Notice the presence of "scallop" on the growth front. The scallops join together at small pointed cusps, which are also seen on the growth front. (b) A schematic illustration of the grain boundary structure which might be visualized behind the growth front of Fig. 2(a). This grain boundary structure is typical of thin film crystal growth and has been observed in our experiments as well as others. It is implicit that the grain boundaries meet the growth front at the cusps. Note that R is the radius of curvature of a "scallop." A key question is: what is responsible for the nucleation of fresh grain boundaries in single-crystal material?

a minimum free energy configuration. In this article, we will explore mostly the regime of slow crystal growth. Nevertheless, we expect that many of the conclusions will apply equally well to more rapid crystal growth, where kinetic growth limitations begin to play a role.

In addition to the interfacial pressure due to the two radii of curvature r and R , Eq. [3], there is also a pressure term associated with the thermal gradient. Let z be the direction of crystal growth. The free energy associated with supercooling a layer of material of thickness dz is

$$\Delta G = \Delta S (T - T_m) dz dA \quad [4]$$

where ΔS is the entropy of melting per unit volume, T_m is the melting temperature, and dA is the area of the growth front. Assuming a linear temperature gradient, $(T - T_m) = (z - z_m)dT/dz$, Eq. [4] may be rewritten as an equation for interfacial pressure

$$P = \Delta S \frac{dT}{dz} (z - z_m) \quad [5]$$

where z_m defines the melting temperature isotherm. The pressure in Eq. [5] tends to push the crystal-liquid interface toward the position of the macroscopic melting point. That force is counteracted by the curvature pressure of the Young-Laplace Eq. [3], which pulls in the direction of supercooling. The actual amount of supercooling to be expected can be obtained by combining Eq. [3] and [5]

$$\Delta S \frac{dT}{dz} (z - z_m) = \gamma_{sl} \left[\frac{1}{r} + \frac{1}{R} \right] \quad [6]$$

Equation [6] gives the balance between capillary pressure and thermal gradient forces. Of the two terms on the right-hand side, the most important is $1/r$, since it is largest. If the other term is temporarily neglected, and $r = t/2 \cos \alpha$, then Eq. [6] simplified to

$$\Delta S \frac{dT}{dz} (z - z_m) = \gamma_{sl} \frac{2 \cos \alpha}{t} \quad [7]$$

Equation [7] shows that the equilibrium freezing point is depressed by surface tension forces in thin films. This may be seen even more clearly by substituting for the right-hand side of Eq. [7] using the Young-Dupre equation

$$\Delta S \frac{dT}{dz} (z - z_m) t = 2(\gamma_{xs} - \gamma_{ls}) \quad [8]$$

Equation [8] shows that the difference in surface free energy on the substrate between crystal and liquid is balanced by the volume free energy of supercooling. The equilibrium freezing point of thin films is therefore depressed by surface energy contributions. In the next section, we describe an experimental determination of the magnitude of this effect.

Freezing Point Depression

Equation [8] shows that fluctuations in thickness t can lead to variations in the positioning of the crystal growth front. Because of the importance of this phenomenon, we have made direct experimental confirmation of the effect and its magnitude.

In our experiment, thin films of silicon are deposited on top of fused quartz substrates and capped with SiO_2 . As shown in Fig. 3, the substrates are heated from below by CO_2 laser radiation, and the melt front is observed from above by a high power optical microscope. Since SiO_2 is opaque to CO_2 laser radiation, the silicon films are heated only indirectly by conduction. A knowledge of the thermal conductivity of quartz and the gaussian mode parameters of the laser beam permits a calculation of the radial temperature distribution on top of the substrate. We observe the effect of thickness variations on the microscopic position of the melting front and the freezing front of the thin film. In order to make a more precise measurement, we found it advantageous for both a thick film and a thin film to be present simultaneously. The thick film was 7000Å of polycrystalline Si deposited by chemical vapor deposition (CVD). This was capped by 2000Å of CVD SiO_2 . A second thin silicon layer only 800Å thick was then deposited and patterned by photolithography into stripes 35 μm wide. The whole structure was then capped again by 2000Å of CVD SiO_2 . A cross section of the final structure is shown in Fig. 4(b). By making the upper layer

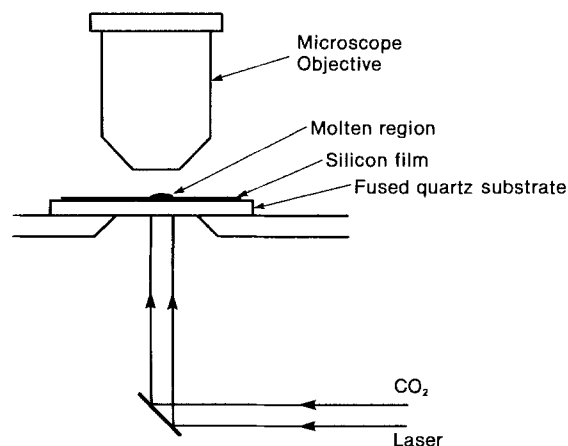


Fig. 3. The experimental arrangement used to produce the photographs in Fig. 2(a) and 4(a) was very simple. The CO_2 laser was fully absorbed in the fused quartz substrate, and the heating was by conduction.

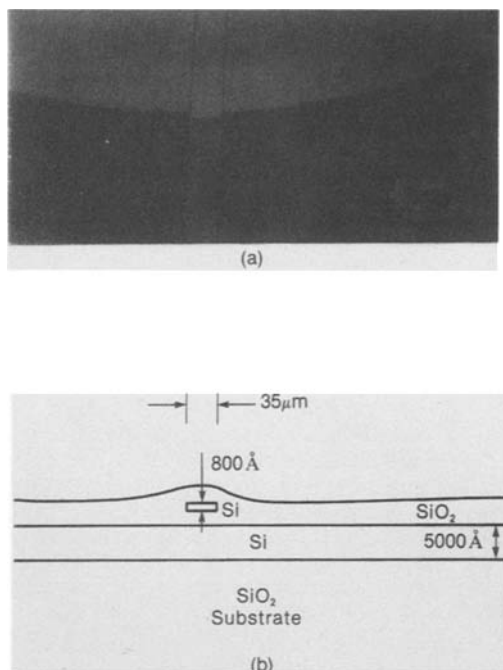


Fig. 4. (a) This photograph shows the depression of the freezing point in a thin film stripe in comparison to the thick film on which it rests. The dark region is crystalline silicon, and its crystallization front lags behind by approximately 1 K in the thin region relative to the thick region. The overall curvature is due to the round laser spot. (b) The cross section of the double layer structure of the film in Fig. 4(a). The Si, SiO₂, and Si layers were deposited in sequence. Then the thin silicon layer was patterned, and a final SiO₂ layer was applied.

in the form of narrow thin stripes, the position of the melt front in both the thin film and the thicker film can be observed simultaneously. Since the SiO₂ interlayer is only 2000 Å thick, the temperature difference between the two films due to thermal radiation from the top surface is only 0.02 K, which is much smaller than the temperature shift we are seeking.

A micrograph of the position of the two crystallization fronts is shown in Fig. 4(a). The overall curvature of the growth front is indicative of the round melted spot produced by the laser beam. Away from the center of the melted region the temperature drops. From Fig. 4(a) the freezing point temperature is clearly lower in the thin stripe than in the thicker material beneath it.

The shift in the freezing point of the thin stripe relative to the thick film was a strong function of the thickness of the stripe. There was no shift if the stripe had the same thickness as the underlying thick film. As the stripe thickness was reduced, the temperature shift rose roughly as the reciprocal of thickness t , in good agreement with Eq. [7].

Owing to the opacity of the substrate to the CO₂ laser, strong thermal gradients are produced, and thermal conductivity rather than radiation is the dominant thermal transport mechanism. We present a calculation of the radial thermal conductivity of a disk heated by a gaussian laser beam in the Appendix to this article. The result of that calculation is that the radial temperature gradient is given by

$$\frac{dT}{dr} = \frac{2r}{\omega^2} \frac{K_{av}}{RK(T)} \Delta T \quad [9]$$

where r is the radial distance from the center of the heated spot, ω is the gaussian radius of the laser beam, $K(T)/K_{av} = 1.17$ is the ratio of the thermal conductivity (9) of fused quartz at the melting point to the average thermal conductivity up to the melting point, $R = 2.02$ is the numerical value of an exponential integral, and ΔT is the overall temperature difference between the center of the heated spot and the edge of the fused quartz disk. The

temperature gradient in Fig. 4(a) is approximately 0.15 K/ μ m.

As the molten zone in Fig. 4(a) was moved back and forth, for example by moving the sample relative to the laser beam, a hysteretic effect was observed, *i.e.*, the thickness-induced shift in freezing point was different from the corresponding shift in melting point. Upon freezing of a stripe about 800 Å thick, the freezing point was depressed by 1 K relative to the thicker film beneath it. Upon remelting that same stripe, the melting point was virtually unchanged relative to the thicker film beneath it. Such hysteresis is common (2) in wetting angle measurements. An important distinction is therefore made between advancing wetting angles and receding wetting angles.

Such hysteresis is thought to be due to a change in surface energy of an interface due to its previous history. A freshly made crystal-SiO₂ interface has fairly high energy. After a period of time, there is probably significant reconstruction which lowers the surface energy. This may play the following role in our experiment. When the crystal advances into the liquid, it is forced to make a fairly energetic interface with the SiO₂, lowering the freezing point. When the liquid silicon advances into the crystal, it eliminates a low energy reconstructed crystal-SiO₂ interface. In that case, there is little or no melting point depression. Since we are interested in the crystallization of thin films, we will deduce the surface energies from freezing measurements rather than melting measurements.

Substituting the observed freezing point shift of thin stripes into Eq. [8] and using $\Delta S = 2.5 \text{ J/K cm}^3$ for the entropy of melting, we obtain for $(\gamma_{ss} - \gamma_{ls})$ the value of 80-100 erg/cm². As far as we know, there are no previous measurements that this numerical value might be checked against.

There are two precautions that should be mentioned in making this measurement. At the melting temperature of silicon, amorphous SiO₂ is a glass with a finite viscosity and is not absolutely rigid. We found that it was necessary to complete the measurements fairly quickly (< 10s at the melt) in order to avoid severe thickness distortions of the thin stripe. The thickness was double-checked after freezing by profilometry and interferometry. The second precaution has to do with the initial melting of the polycrystalline film. As we have mentioned, there is little or no melting point depression of the crystallized film. Nevertheless, there is a large melting point depression of the as-deposited polycrystalline silicon. This is probably due to the excess free energy associated with the large grain boundary density in the as-deposited film. These observations, which monitor the initial polycrystalline film rather than the crystallized film, are not incorporated with the data in this paper. Only the results on the crystallized film are summarized in Table I.

Instability of the Crystallization Front

We have learned from the previous section that the freezing point is a function of film thickness. Equation [8] connects the film thickness with the position z of the crystal growth front. A local fluctuation in film thickness can cause the crystal growth front to move forward or backward locally relative to the rest of the front. The key question in thin film crystal growth is how to produce the largest possible single-crystal domains. In this

Table I. The hysteresis between freezing and melting is thought to be due to reconstruction of the crystalline silicon-SiO₂ interface, lowering its surface energy

	Temperature depression in an 800 Å thick film relative to bulk ΔT	Surface energy difference with respect to SiO ₂ substrate $(\gamma_{ss} - \gamma_{ls})$
Freezing	1 K	80-100 erg/cm ²
Melting	≈ 0 K	≈ 0 erg/cm ²

section, we suggest that locally concave regions of the growth front caused by local thickness fluctuations may be the birthplace of fresh subgrain boundaries. This would tend to limit the maximum possible crystal-domain size.

As indicated schematically in Fig. 2(b), and has been observed in virtually all thin film crystallization experiments, grain boundaries run together and recombine during crystal growth. Simultaneously, fresh grain boundaries initiate in previously single-crystal material. Both processes are shown schematically in Fig. 2(b), which is representative of typical (1,10) photographs of grain boundary structure. It is the second of these two processes, the birth of fresh grain boundaries, which we must confront.

In the second section of this article, we mentioned the crystal grower's maxim (6) that the growth front should always be convex away from the crystal. It is very difficult to visualize how a fresh subgrain boundary may nucleate from single-crystal material. What we propose here is that concave regions of the growth front are the birthplace of fresh subgrain boundaries. In these regions, dislocations would tend to become locked into place and lead eventually to small-angle grain boundaries.

Although the growth front might be concave in top view, nevertheless, a cross-section view as shown in Fig. 1 would still remain convex, as demanded by the second wetting angle condition. Therefore, the actual three-dimensional geometry of that region is a saddle point. We are actually proposing that crystal growth at saddle points permits the initiation of small-angle grain boundaries.

As discussed in the third section and shown in Fig. 2(a), the growth front itself is scalloped, meeting the pre-existing subgrain boundaries at cusps. Each scallop represents a single crystal domain and has a finite radius of curvature R . This convex curvature tends to stabilize the domain structure and inhibit the birth of fresh subgrain boundaries. A local thickness fluctuation will have no effect unless it is deep enough to retard the growth front sufficiently to change it from convex curvature to locally concave. If the scallop radius of curvature R is very small, it would take an extremely deep and spatially localized thickness fluctuation to change it from convex to concave. Conversely, if the scallop is wide, representing a large crystal grain, the scallop radius of curvature R is large indicating a relatively straight growth front. In that case, even a small thickness fluctuation can change R from convex to concave. Thus, large grains are relatively unstable to grain boundary nucleation and they tend to split in two. Meanwhile, small grains tend to be stable and to avoid further subdivision. Therefore, the grain boundary structure represented in Fig. 2(b) tends to be stabilized around a certain crystal-domain width.

In conclusion, we have shown that thickness fluctuations could be responsible for the initiation of subgrain boundaries by producing locally concave regions of the growth front. A scalloped growth front, consisting of a series of domains of convex curvature, tends to be stable against growth front fluctuations. The balance between these two tendencies produces the actual grain structure that is observed.

Conclusions

The crystallization of thin liquid films demands that two wetting angle conditions be simultaneously satisfied: (i) regarding the liquid-vapor interface on the substrate, and (ii) regarding the crystal-liquid interface on the substrate.

The position of the crystal growth interface is determined by the balance between capillary forces, which tend to push the growth front to temperatures below the bulk freezing point, and thermal gradient forces which tend to pull the growth front toward the freezing point. The balance between these forces results in an equilibrium depression of the freezing point of thin films of about 1 K for an 800Å thick film. This implies a surface

tension difference ($\gamma_{xs} - \gamma_{ls}$) of approximately 80-100 erg/cm².

The coupling between thickness and growth front position provides a mechanism for a crystal-growth instability. Thickness fluctuations can produce locally concave regions of the growth front, where subgrain boundaries could initiate. The convex curvature of the scalloped growth front counteracts this effect and tends to stabilize the crystal domain structure.

Acknowledgments

We gratefully acknowledge the assistance of Mike Schneider, Bob Weinberger, Harry Deckman, and John Dunsmuir. We also thank Professor Hank Smith for his comments on the manuscript.

Manuscript received April 23, 1984.

Exxon Research and Engineering Company assisted in meeting the publication costs of this article.

APPENDIX

In this Appendix, we derive the thermal gradient produced in a thermally conducting disk by a gaussian laser beam. The CO₂ laser is absorbed within 10 μm of the surface of fused quartz. In principle, both conduction and radiation could play a role in transporting this heat. For the $t = 0.75$ mm thickness fused quartz plates used in these experiments, radial thermal conduction plays the major role, owing to the strong thermal gradient induced by the laser beam with radiative heat loss being only a small correction.

The power per unit area absorbed from a gaussian laser beam is

$$P(r) = \frac{2P_0}{\pi\omega^2} \exp\left\{-\frac{2r^2}{\omega^2}\right\}$$

where ω is the gaussian radius of the laser beam, about 2.8 mm in our case. P is its total power, about 30W and r is the distance from the central axis of the beam. The total power inside a spot of radius r is

$$H(r) = P_0 \left(1 - \exp\left\{-\frac{2r^2}{\omega^2}\right\}\right)$$

The thermal conduction equation in the radial direction is

$$H(r) = \frac{K(T) 2\pi r t dT}{dr} \quad [\text{A-1}]$$

where $K(T)$ is the temperature dependent thermal conductivity of fused quartz. Integrating Eq. [A-1] yields

$$\frac{P_0}{2\pi t} \int_0^r \left(1 - \exp\left\{-\frac{2r'^2}{\omega^2}\right\}\right) \frac{dr'}{r'} = \int_{T_{\max}}^{T_{\min}} K(T) dT \quad [\text{A-2}]$$

The integral in Eq. [A-2] is an "Exponential Integral," which is (11) approximately $R = [\ln(2r^2/\omega^2) + 0.577]/2 = 2.02$ in our geometry. Let us write the difference between the temperature T_{\max} at the center of the laser spot and T_{\min} the temperature at the edge of the fused quartz disk as $\Delta T = T_{\max} - T_{\min}$. Then the integrated heat flow equation can be written

$$\frac{P_0}{2\pi t} = \frac{K_{av} \Delta T}{2.02} \quad [\text{A-3}]$$

Simplifying [A-1] by taking $r < \omega$ we obtain

$$\frac{dT}{dr} = \frac{P_0}{2\pi t} \frac{2r}{K(T) \omega^2} \quad [\text{A-4}]$$

Substituting [A-4] in [A-3]

$$\frac{dT}{dr} = \frac{2r}{\omega^2} \frac{K_{av}}{RK(T)} \Delta T$$

which is the same as Eq. [9] in the text.

REFERENCES

1. M. W. Geis, H. I. Smith, D. J. Silversmith, R. W. Mountain, and C. V. Thompson, *This Journal*, **130**, 1178 (1983).
2. A. W. Adamson, "Physical Chemistry of Surfaces," Third ed., John Wiley and Sons, New York (1976).

3. K. M. Kim, S. Berkman, H. E. Temple, and G. W. Cullen, *J. Cryst. Growth*, **50**, 212 (1980).
4. S. Berkman, Private communication.
5. T. J. Whalen and A. T. Anderson, *J. Am. Ceram. Soc.*, **58**, 396 (1975); E. Kuroda, M. Matsuda, and M. Maki, *Phys. Status Solidi A*, **48**, 105 (1978).
6. J. C. Brice, "The Growth of Crystals from Liquids," see especially p. 209, North-Holland, Amsterdam (1973).
7. D. P. Woodruff, "The Solid-Liquid Interface," see especially p. 31, Cambridge University Press, London (1973).
8. G. K. Celler, Private communication.
9. "Handbook of Thermophysical Properties of Solid Materials," Vol. III, "Ceramics," A. Goldsmith, T. E. Waterman, and H. J. Hirschhorn, Editors, see especially p. 893, Pergamon Press, New York (1961).
10. M. W. Geis, H. I. Smith, B. Y. Tsaun, J. C. C. Fan, D. J. Silversmith, and R. W. Mountain, *This Journal*, **129**, 2812 (1982).
11. M. Abramowitz and I. A. Stegun, "Handbook of Mathematical Functions," see especially p. 228, Dover, New York (1965).

Effect of Group V/III Flux Ratio on Lightly Si-Doped $\text{Al}_x\text{Ga}_{1-x}\text{As}$ Grown by Molecular Beam Epitaxy

Y. Nomura, M. Mannoh, M. Mihara, S. Naritsuka, K. Yamanaka, T. Yuasa, and M. Ishii

Optoelectronics Joint Research Laboratory, Nakahara, Kawasaki, 211 Japan

ABSTRACT

Optical and electrical properties of lightly Si-doped $\text{Al}_x\text{Ga}_{1-x}\text{As}$ ($x \approx 0.2$) layers grown by molecular beam epitaxy under various V/III flux ratios (1 to 4) and at various substrate temperatures ($720^\circ\text{--}780^\circ\text{C}$) have been studied by low temperature ($\approx 4\text{ K}$) photoluminescence and Hall measurements. Bound exciton (BE) peak intensity and Hall mobility increase with decreasing flux ratio and increasing substrate temperature. An excess reduction in the flux ratio causes the condensation of group III metals on epilayers. An optimum flux ratio was found to be 2.3 for the highest substrate temperature investigated here, 780°C . The peak intensity of the defect complex has been shown to be correlated with the growth conditions. It is suggested that the defect complex includes defects dominant under excess arsenic population. Reflection electron diffraction patterns from the growing $\text{Al}_{0.2}\text{Ga}_{0.8}\text{As}$ layers have been related to the growth conditions and the qualities of the epitaxial layers. A sample with the highest BE peak intensity and smooth surface has been grown with a metal-rich structure (3×1) present on the surface. A structure (1×1) has reproducibly been observed at intermediate amounts of group V/III composition on the surface between those for the (3×1) and the arsenic-stabilized (2×4) structures. Growth conditions which result in surfaces with a (1×1) structure are found to cause surface roughening on the epilayers.

Novel devices with $\text{Al}_x\text{Ga}_{1-x}\text{As}/\text{GaAs}$ heterostructures, such as the high electron mobility transistor and lasers with extremely low threshold current density, have been fabricated by virtue of excellent controllability of film thickness and doping profile of molecular beam epitaxy (MBE) (1, 2).

The quality of $\text{Al}_x\text{Ga}_{1-x}\text{As}$ is important for high performance devices (3). The substrate temperature during growth affects optical properties of $\text{Al}_x\text{Ga}_{1-x}\text{As}$ layers grown by MBE (4, 5). The group V/III flux ratio is also an important growth parameter because it influences formation of nonstoichiometric defects that act as nonradiative centers (6). From a view of device applications of MBE-grown $\text{Al}_x\text{Ga}_{1-x}\text{As}$, in-depth understanding of the effect of the growth conditions on optical and electrical properties and surface morphologies is necessary, but little information has been available, particularly about the relation between the V/III flux ratio and the properties of $\text{Al}_x\text{Ga}_{1-x}\text{As}$.

Reflection electron diffraction (RED) patterns have often been used as indicators of growth conditions for GaAs growths on (001)-plane GaAs substrates by MBE. By real-time observation of RED patterns, empirical relationships have been established between the relative and absolute incident fluxes of Ga atoms and arsenic molecules and the surface reconstruction as a function of the substrate temperature (7, 8). This has enabled conditions to be defined for growth of stoichiometric epitaxial GaAs. In contrast, the relation between RED patterns and the growth conditions for $\text{Al}_x\text{Ga}_{1-x}\text{As}$ has not been reported.

In this paper, we report the effect of the V/III flux ratio and the substrate temperature on the optical and electrical properties of lightly Si-doped $\text{Al}_x\text{Ga}_{1-x}\text{As}$ layers grown by MBE. The layers were characterized by low temperature ($\approx 4\text{ K}$) photoluminescence (PL) and Hall measurements. The results show that both the optical and electrical qualities improve with decreasing flux ratio and increasing substrate temperature. We have also inves-

tigated RED patterns from growing $\text{Al}_{0.2}\text{Ga}_{0.8}\text{As}$ layers and have related these patterns to the growth conditions and the qualities of the epitaxial layers. We have found that high quality $\text{Al}_x\text{Ga}_{1-x}\text{As}$ layers with smooth surfaces are grown with the appearance of a (3×1) reconstruction pattern on the surface.

Experimental

The $\text{Al}_x\text{Ga}_{1-x}\text{As}$ layers were grown on semi-insulating (001)-plane GaAs substrates in a Varian MBE/GEN II system. The structure of samples consisted of a $2\ \mu\text{m}$, undoped GaAs buffer; a $1\ \mu\text{m}$, Si-doped $\text{Al}_x\text{Ga}_{1-x}\text{As}$ layer ($n \approx 1 \times 10^{16}\ \text{cm}^{-3}$); and a $250\ \text{\AA}$, undoped GaAs cap layer. Elemental Al, Ga, As, and Si were used as source materials. All the $\text{Al}_x\text{Ga}_{1-x}\text{As}$ layers were grown under group V/III flux ratios, $\gamma = \text{As}_4/(\text{Al} + \text{Ga})$, from 1 to 4 by changing the arsenic pressure and at substrate temperatures from 720° to 780°C . The molecular beam fluxes were estimated from pressure readings of an ion gauge that could be placed at the growth position of the substrate (9). The Al and Ga pressures were determined before elevating the cell temperature of the arsenic source. The growth rate of $\text{Al}_x\text{Ga}_{1-x}\text{As}$ layers was approximately $1\ \mu\text{m}/\text{h}$. The Al mole fraction, x , in the $\text{Al}_x\text{Ga}_{1-x}\text{As}$ layers was determined from the energy of the BE emission and was found to be 0.19–0.25. The substrate temperature was measured by a spring-loaded thermocouple (W-Re) pressed to the rear of a Mo heating block, on which the substrate was mounted. The substrate temperature was also checked by a pyrometer with emissivity setting at 0.6. To assure the accuracy of the temperature, we observed the removal temperature of the native oxides from GaAs substrates and determined it to be about 590°C , which is close to previously reported datum, 580°C (10). Peak heights of the dominant residual gasses of $^{16}\text{H}_2\text{O}^+$ and $^{28}\text{CO}^+$ in the growth chamber, determined by a quadrupole mass analyzer, were always kept low during growth.

Table I. The electron concentrations and Hall mobilities of lightly Si-doped $\text{Al}_x\text{Ga}_{1-x}\text{As}$ layers grown under various growth conditions

Sample	x	Substrate temp ($^{\circ}\text{C}$)	Flux ratio	n (10^{15} cm^{-3})	μ ($\text{cm}^2 \text{ V}^{-1} \text{ s}^{-1}$)
(a)	0.22	750	1.1	1.4	3870
(b)	0.21	750	1.4	1.4	1820
(c)	0.19	750	1.9	Highly resistive	
(d)	0.22	780	2.3	8.8	3520
(e)	0.23	780	2.8	9.4	3030
(f)	0.21	780	3.8	10	3010

PL measurements were made at liquid helium temperature ($\approx 4 \text{ K}$). The 6471\AA line of a Kr ion laser was used as the excitation source. The incident excitation intensity was approximately 1 W/cm^2 . Luminescence was analyzed by a 1-m monochromator and detected with a cooled photomultiplier with an S-1 response. The slit width was adjusted to $100 \mu\text{m}$ or less, resulting in a resolution of less than 1\AA .

Hall measurements (van der Pauw technique) were made on cloverleaf-shaped samples at room temperature.

Surface structures were examined *in situ* by glancing incidence reflection electron diffraction at an accelerating voltage of 8 keV .

Results and Discussion

Table I summarizes measured free electron concentrations and mobilities of the samples grown under various V/III flux ratios and at substrate temperatures, 750°C and 780°C . Si atoms are dominantly incorporated as donors in MBE-grown $\text{Al}_x\text{Ga}_{1-x}\text{As}$ layers. Although the Si cell temperature of 1050°C was maintained over the growths, the electron concentrations for the samples (d), (e), and (f) grown at 780°C were higher than those for the samples (a), (b), and (c) grown at 750°C , indicating a decrease of compensation of the donors by acceptors. The dependence of electron concentration on the flux ratio is small at 780°C . On the contrary, the samples grown at 750°C and under high flux ratios ($\gamma > 1.9$) were highly resistive, and Hall measurements were not possible. This is probably caused by a full depletion of the $\text{Al}_x\text{Ga}_{1-x}\text{As}$ layer owing to low carrier concentrations (11).

The principal result shown in Table I is that lower flux ratios yield higher electron mobilities. The dependence of mobility on the flux ratio is small at 780°C , whereas the mobility for samples grown at 750°C decrease rapidly with the flux ratio. We attribute the reduction in the mo-

bility of the relatively compensated sample (b) to the scattering of free electrons by increased space-charge regions at the heterostructure interface and the surface, as suggested by Stringfellow (12).

PL spectra in Fig. 1(a)-1(f) are from the samples (a) to (f) in Table I. The PL spectra show peaks due to the BE transition, the Si donor to carbon acceptor (DA) pair recombination, and the defect complex in order of increasing wavelength. These assignments have been made according to our previous work (13).

The half-widths of the BE peaks, 4 meV in Fig. 1(a) and 1(d), are comparable to the half-widths observed in high quality GaAs with a similar carrier concentration, indicating the high quality of the $\text{Al}_x\text{Ga}_{1-x}\text{As}$ layers. The BE peak intensities are dominated by excitons bound to silicon donors. We assume that high BE peak intensities reflect high qualities of $\text{Al}_x\text{Ga}_{1-x}\text{As}$ layers. It is known that the intensity of the BE peak relative to intensity of the other recombination peaks depends on doping concentration and the laser excitation (14). Since the doping and laser excitation were not changed in this work, only residual impurities and defects that act as nonradiative recombination centers and deep level emission centers will reduce the peak intensity.

We studied the BE intensity as a function of the flux ratio and the substrate temperature to determine the optimum growth condition. The results are shown in Fig. 2, including additional data with x ranging from 0.19 to 0.25. Figure 2 shows that the BE peak intensity increases with decreasing flux ratio and increasing substrate temperature. We note that the curve for $T_s = 780^{\circ}\text{C}$ exhibits a maximum at the flux ratio of 2.3. The degradation at the lower flux ratio, 1.2, is caused by condensation of group III metal on the surface due to extremely high evapora-

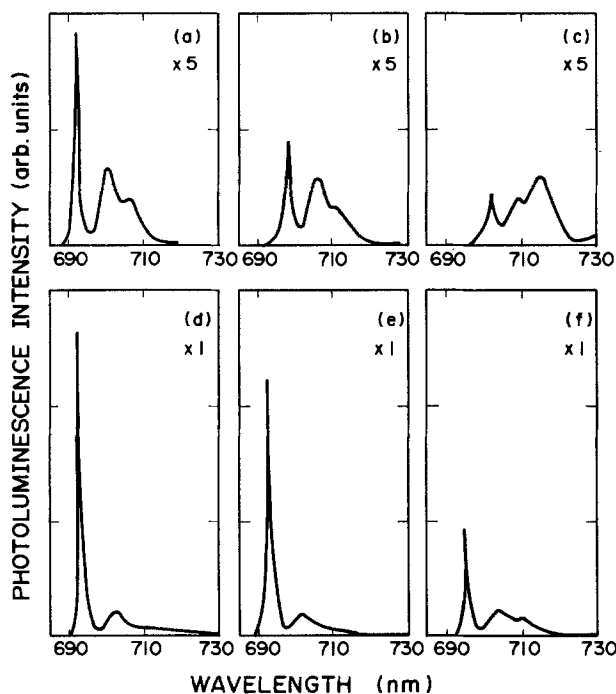
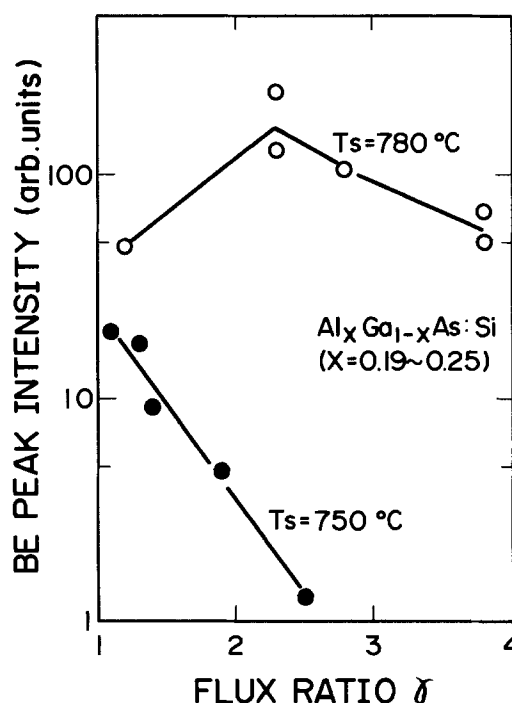


Fig. 1. PL spectra from the samples (a) to (f) from Table I

Fig. 2. BE peak intensity as a function of the flux ratio for substrate temperatures of 750°C and 780°C .

tion of arsenic molecules. Thus, in order to obtain high quality $\text{Al}_x\text{Ga}_{1-x}\text{As}$, the flux ratio should be adjusted to near 2.3. The results are consistent with the results of the Hall measurements; sample (d) among the samples grown at 780°C has the highest electron mobility. Samples grown at a substrate temperature, 720°C , and under flux ratios ranging from 1 to 2.5, had lower PL intensities than those in Fig. 1.

The carbon acceptor-related emission intensity increases monotonically with decreasing flux ratio and increasing substrate temperature, as shown in Fig. 1. This is mainly due to reduction of nonradiative centers, as indicated by BE intensity changes in Fig. 2. This reveals that the carbon incorporation rate is relatively insensitive to the growth conditions but gradually increases with decreasing flux ratio and increasing substrate temperature. The flux ratio dependence of the carbon incorporation rate agrees with the case of GaAs (15).

The defect complex luminescence in GaAs has been suggested to be associated with carbon impurities (16). However, the detailed nature of the defect complex has not been determined even in the case of GaAs (16). Figure 1 shows that the defect complex peak intensity closely correlates with the growth conditions; the intensity decreases with decreasing flux ratio and is not observed at high substrate temperatures and low flux ratios. A slight shift of the complex peak toward a higher energy with an increased excitation intensity is observed, indicating that the peak is due to DA pair recombination (17). It is natural to attribute the donor to Si. The acceptor could be attributed to defects dominant under excess arsenic conditions.

Figure 3 shows RED patterns in $[\bar{1}\bar{1}0]$ azimuth from $\text{Al}_{0.2}\text{Ga}_{0.8}\text{As}$ surfaces which were grown at T_s equal to (a) 700° , (b) 750° , and (c) 780°C and under a constant flux ra-

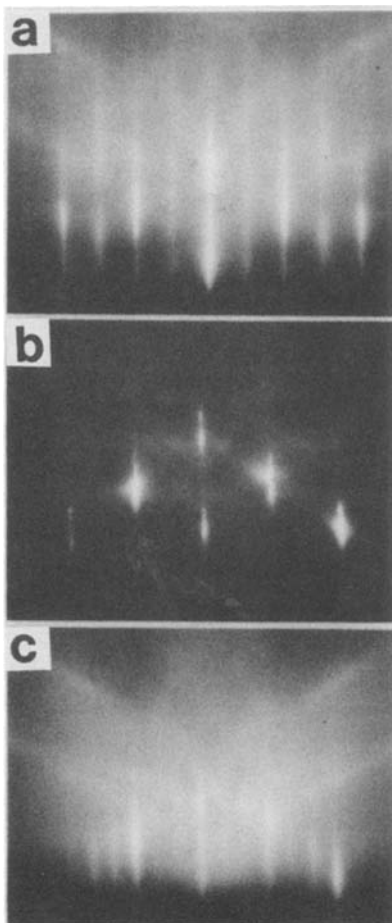


Fig. 3. RED patterns in $[\bar{1}\bar{1}0]$ azimuth, for $\text{Al}_{0.2}\text{Ga}_{0.8}\text{As}$ surfaces growing at a rate of $1 \mu\text{m/h}$ and under a flux ratio of 1.7. The substrate temperatures are (a) 700° , (b) 750° , and (c) 780°C .

tio of 1.7. To determine the structures, RED patterns in $[\bar{1}\bar{1}0]$ azimuth were also observed. It was revealed that the RED patterns in Fig. 3 corresponded to (a) (2×4) , (b) (1×1) , and (c) (3×1) structures. However, it was difficult to distinguish diffraction features associated with centered structures in common with other RED work (8). Thus, we will refer only to primitive two-dimensional lattice structures. This does not mean that centered structures were not present, only that RED did not distinguish, for instance, $c(2 \times 8)$ and (2×4) (8).

The structures shown in Fig. 3 could be reversibly changed from one to another by changing the substrate temperature only. These structures could be reproducibly observed from wafer to wafer. The metal-rich reconstruction (4×2) commonly observed for (001)-plane GaAs surfaces was not observed for $\text{Al}_x\text{Ga}_{1-x}\text{As}$ surfaces in the temperature range studied here. It could, however, be observed by depositing Al and Ga without the arsenic flux on the (3×1) surface but immediately changed to a (1×1) structure due to the lack of surface mobility of metal atoms (18).

The structures shown in Fig. 3 also depend on the flux ratio. Figure 4 shows the map where the flux ratios that provide the structures are plotted as a function of the substrate temperature. In Fig. 4, points A and D correspond to the growth conditions of samples (a) and (d) in Table I that have the highest mobilities and BE peak intensities for substrate temperatures of 750° and 780°C , respectively. The surface of sample (d) is smooth, as is shown in Fig. 5a. The samples grown at the point marked by an asterisk, only 15% below the flux ratio at point D, exhibit matt surfaces due to condensation of group III metals. Therefore, we believe that excess arsenic evaporates during growth under the conditions corresponding to the (3×1) structure.

The (1×1) structure shown in Fig. 3(b) has not been observed for GaAs, but is common with surfaces including Al (18). The (1×1) structure suggests roughness of the surface. Figure 5 shows surface morphologies of $\text{Al}_x\text{Ga}_{1-x}\text{As}$ layers ($x \approx 0.2$) grown under conditions of (T_s , γ) equal to 780°C , 2.3 (a), 750°C , 2.3 (b), and 720°C , 3.0 (c). These growth conditions are found, in Fig. 4, to be associated with (a) (3×1) , (b) (1×1) , and (c) (2×4) structures.

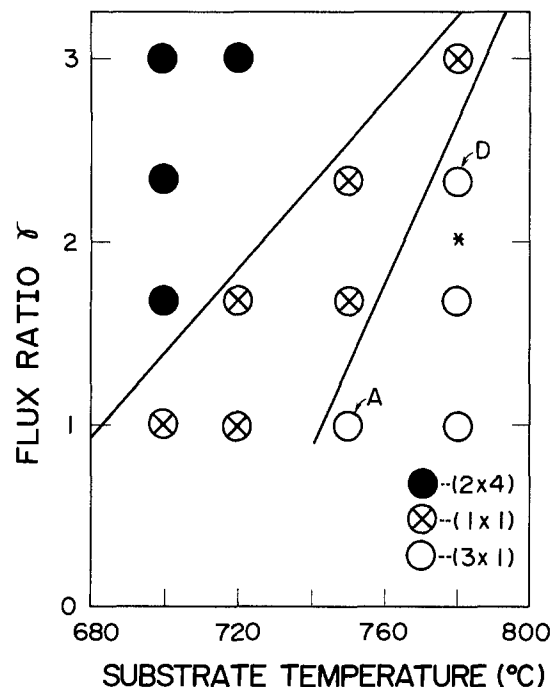


Fig. 4. Relationship between surface structures of growing $\text{Al}_{0.2}\text{Ga}_{0.8}\text{As}$ and growth conditions. The structures are $\bullet = (2 \times 4)$, $\otimes = (1 \times 1)$, and $\circ = (3 \times 1)$, as indicated. Characters A and D indicate the growth conditions for samples (a) and (d) in Table I and Fig. 1. Samples grown under the condition marked by the asterisk exhibit matt surfaces.

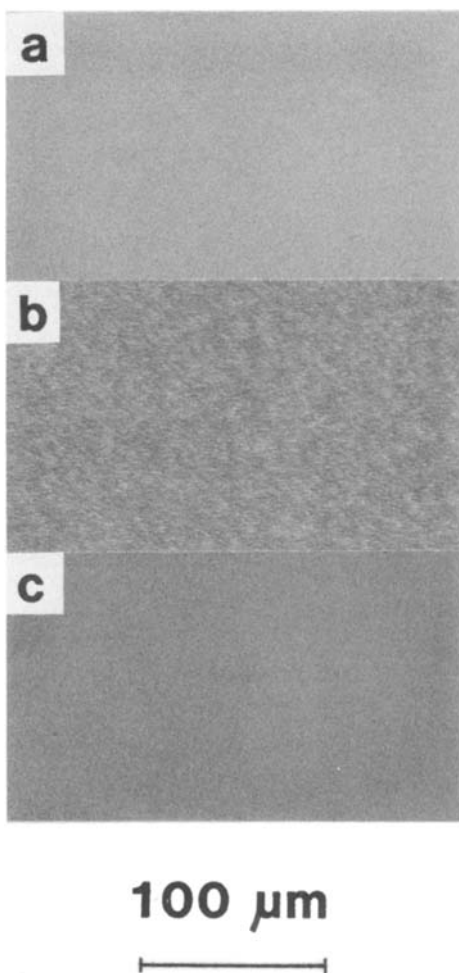


Fig. 5. Phase contrast photomicrographs of $1\ \mu\text{m}\ \text{Al}_x\text{Ga}_{1-x}\text{As}$ ($x \approx 0.2$) layers grown under the conditions of (T_s, γ) equal to (a) $(780^\circ\text{C}, 2.3)$, (b) $(750^\circ\text{C}, 2.3)$, and (c) $(720^\circ\text{C}, 3.0)$.

The (2×4) and (3×1) structures correspond to the smooth surfaces, but surface roughening is observed for the (1×1) structure, as shown in Fig. 5. Morkoc *et al.* have demonstrated that the surface morphology first degrades and later improves with increasing substrate temperature from 620° to 700°C for $x > 0.4$ and a constant V/III flux ratio of 4 (19). Our results show that such degradation occurs also for $x \approx 0.2$ under flux ratios lower than 3. These results now manifest that the growth condition for high quality $\text{Al}_x\text{Ga}_{1-x}\text{As}$ layers with smooth surfaces is rather critical and is restricted to the vicinity of point D in Fig. 4.

Conclusions

The effect of the growth conditions, V/III flux ratio, and substrate temperature on low temperature PL spec-

tra and Hall mobilities of lightly Si-doped $\text{Al}_x\text{Ga}_{1-x}\text{As}$ layers ($x \approx 0.2$) grown by MBE has been investigated. The Hall mobility and PL intensity increase with decreasing flux ratio increasing substrate temperature. The optimum flux ratio, 2.3, was obtained at a substrate temperature of 780°C . The peak intensity of the defect complex has been shown to be correlated with the growth conditions. It is suggested that the defect complex includes defects dominant under excess arsenic population.

The RED patterns from the growing $\text{Al}_{0.2}\text{Ga}_{0.8}\text{As}$ layers have been investigated and related to the growth conditions and the qualities of the epitaxial layers. The results show that the sample with the highest BE peak intensity and smooth surface has been grown with the (3×1) structure present on the surface.

Acknowledgment

This work was supported by the Agency of Industrial Science and Technology, MITI, of Japan in the frame of the National Research and Development Project "Optical Measurement of Control Systems."

Manuscript submitted Jan. 9, 1984; revised manuscript received June 22, 1984. This was Paper 335 presented at the San Francisco, California, Meeting of the Society, May 8-13, 1983.

Optoelectronics Joint Research Laboratory assisted in meeting the publication costs of this article.

REFERENCES

1. T. Mimura, S. Hiyamizu, T. Fujii, and K. Nanbu, *Jpn. J. Appl. Phys.*, **19**, L225 (1980).
2. W. T. Tsang, *Appl. Phys. Lett.*, **40**, 217 (1982).
3. W. T. Tsang, *ibid.*, **33**, 245 (1978).
4. G. Wicks, W. I. Wang, C. E. C. Wood, L. F. Eastman, and L. Rathbun, *J. Appl. Phys.*, **52**, 5792 (1981).
5. V. Swaminathan and W. T. Tsang, *App. Phys. Lett.*, **38**, 347 (1981).
6. W. T. Tsang and V. Swaminathan, *ibid.*, **39**, 486 (1981).
7. A. Y. Cho, *J. Appl. Phys.*, **42**, 2074 (1971).
8. J. H. Neave and B. A. Joyce, *J. Cryst. Growth*, **44**, 387 (1978).
9. C. E. C. Wood, D. Desimone, K. Singer, and G. W. Wicks, *J. Appl. Phys.*, **53**, 4230 (1982).
10. A. Y. Cho, *Thin Solid Films*, **100**, 291 (1983).
11. A. Chandra, C. E. C. Wood, D. W. Woodard, and L. F. Eastman, *Solid State Electron*, **22**, 645 (1979).
12. G. B. Stringfellow, *J. Appl. Phys.*, **50**, 4178 (1979).
13. M. Mihara, Y. Nomura, M. Mannoh, K. Yamanaka, S. Naritsuka, K. Shinozaki, T. Yuasa, and M. Ishii, Paper presented at the 1983 Electronic Materials Conference, University of Vermont, Burlington, VT.
14. E. Hanamura, *J. Phys. Soc. Jpn.*, **28**, 120 (1970).
15. O. Tejayadi, Y. L. Sun, J. Klem, R. Fischer, M. V. Kleivn, and H. Morkoc, *Solid-State Commun.*, **46**, 251 (1983).
16. F. Briones and D. M. Collins, *J. Electron. Mater.*, **11**, 847 (1982).
17. R. Dingle, *Phys. Rev.*, **184**, 788 (1969).
18. W. I. Wang, *J. Vac. Sci. Technol. B*, **1**, 574 (1983).
19. H. Morkoc, T. J. Drummond, W. Kopp, and R. Fisher, *This Journal*, **129**, 824 (1982).

Behavior of the Evaporated WO₃ Film in Li-Salt PC Electrolytes

Nobuyuki Yoshiike, Yasuo Mizuno, and Shigeo Kondo

Matsushita Electric Industrial Company, Limited, Central Research Laboratory, Moriguchi, Osaka 570, Japan

ABSTRACT

Electrochemical properties of evaporated amorphous WO₃ films on conductive glass substrates have been studied in propylene carbonate electrolytes, and the degradation of the electrochromic activity of the WO₃ film on storage in the electrolyte and the prevention of the degradation of the film have been investigated by cyclic voltammetry. The WO₃ films have also been analyzed by XPS, SIMS, and FT-IR spectra. We have confirmed that the thermodynamic degradation is accelerated by H₂O and LiClO₄ in the electrolyte. It is proposed that: first, H₂O contributes to the change of WO₃ into W(OH)_x; second, Li⁺ exchanges with the H⁺ of W(OH)_x; and then these reactions result in the formation of Li₂WO₄; and, consequently, in the negative shift of the cathodic reaction potential of the film. We have also confirmed that the degradation is prevented by addition of an acid, such as H₃PO₄ or acrylic acid, to the LiClO₄ PC electrolyte and by using LiBF₄ as a supporting electrolyte in place of LiClO₄.

Since the important paper of Deb (1), there have been numerous studies (2-8) of the electrochromic (EC) properties of WO₃ films. Electrochromic displays (ECD) using WO₃ thin films will be classified into three groups: WO₃/liquid electrolyte, WO₃/solid electrolyte, and WO₃/dielectric layer systems. The WO₃/liquid electrolyte systems have been studied frequently, and EC properties of this system, such as response and memory, are superior to other systems. Faughnan (5) reported a WO₃/glycerol-H₂SO₄ liquid electrolyte system which had a fast response, but it had problems of the dissolution of the WO₃ film on the shelf and the corrosion of transparent electrode during color/bleach cycling (9). In order to overcome these problems, nonaqueous organic solvents have been investigated as the electrolyte solvent. Randin (9) reported that evaporated WO₃ film dissolved about 10% under storage for 90 days at 50°C in acetonitrile and dimethylformamide, etc., but the film dissolution was negligibly small in γ -butyrolactone and propylene carbonate (PC) under the same conditions. Furthermore, Li salts have been used in the supporting electrolytes as a cation source in place of protons because the mobility of Li is the next highest. Problems of the dissolution and the corrosion have been solved by using LiClO₄ PC electrolyte.

However, even in the WO₃/LiClO₄ PC system, the problem of degradation of electrochromic activity on storage for long time and/or cyclic drive still remained.

Schlottter *et al.* (10) reported that the degradation with cycling was caused by ion exchange between Li and protons of W(OH)_x. Morita *et al.* (11) also reported that the origin of the mechanism dominating the degradation was essentially the accumulation of Li in the film with SIMS data and Auger analysis.

In this paper, the mechanism of degradation of the WO₃ film on storage in Li salt-PC electrolytes and preventive methods for the degradation will be described.

Experimental

Preparation of WO₃ films.—WO₃ films were deposited by an electron beam evaporation method. WO₃ targets (99.99%) were supplied by Furuuchi Kagaku Company, Limited. The deposition rate was 4-5 Å/s the deposition angle was varied within 40° with a planetary rotation, and the substrate temperature was usually maintained at 80°C after keeping at 110°C for 5 min. The total gas pressure in the chamber during the evaporation process was controlled by N₂ gas-introduction method to be 5-6.5 × 10⁻² Pa. Deposited WO₃ films were analyzed by electron diffraction and found to be amorphous. The packing density of the film calculated from film thickness and weight was 5.38 g/cm³, and the refractive index evacuated from the interference patterns of visible absorption and film thickness was 1.85.

The substrates were In₂O₃-coated glass (20 Ω/cm²) used for electrochemical measurements, XPS, and SIMS analyses, and Si wafers for IR spectra.

Electrochemical measurements.—Cyclic voltammetry measurements were performed with a potentiostat (Hokuto Denko, Model HA-301), which was supplied with voltage from a function generator (same company, Model HB-104). Coulometric measurements were performed with a coulomb meter (same company, HF-201). The WO₃ film thickness and area were 3000 Å and 0.3 cm², respectively. The counterelectrode was a Pt plate, and the reference electrode was a saturated calomel electrode (SCE). The electrolytes were propylene carbonate (PC) solutions containing 0.3M LiClO₄. PC (the first grade, Wako Junyaku) was freshly distilled under vacuum, LiClO₄ (purity 99%, Mitsuwa Kagaku) was used. Ar gas was bubbled before measurements.

H₂O content in the electrolytes was checked in each case by the Karl-Fisher method with an Aquacounter (Hiranuma Seisakusho, Model AQ-3B), and these concentrations were typically 0.01-0.03M.

Analyses of WO₃ films.—IR spectra were taken with a FT-IR spectrometer (Nihon Denshi, Model JIR-40D). For these measurements, the film thickness of WO₃ on a Si wafer was 3000 Å. Resolution was 8 cm⁻¹, and the number of sampling for one measurement was 400 cycles.

X-ray photoelectron spectroscopy (XPS) measurements were performed using a VG ESCALAB-5 electron spectrometer with Al K α x-ray sources (10 kV, 20 mA). The energy resolution for the Ag 3d_{5/2} photopeak was 1.1 eV at 20 eV pass energy. The normal pressure in the analyzer chamber was below 6 × 10⁻⁸ Pa.

Three kinds of powder, WO₃ (99.9%, Mitsuwa Kagaku) H₂WO₄, and Li₂WO₄ (Superfine grade, Kanto Kagaku), were used for IR and XPS analyses as reference samples.

Secondary ion mass spectrometry (SIMS) measurements were performed using a CAMECA IMS-3F, the primary ion was O₂⁺, and its ion beam current and energy were 500 nA and 8 keV, respectively.

Preparation of ECD cells.—ECD cells used for life test were constituted as follows: In₂O₃ (20 Ω/cm²)/WO₃ (3000 Å, 1.9 cm²)/Li salt-PC electrolyte (2 ml)/carbon counterelectrode.

Results and Discussions

Degradation of WO₃ film in LiClO₄ PC electrolytes.—The electrochemical properties of the WO₃ films which were stored in 0.3M LiClO₄ PC electrolytes containing H₂O less than 0.01M were investigated. The storage experimental conditions were as follows: WO₃ films (3000 Å thick, 0.3 cm²) evaporated on In₂O₃-coated glass were dipped completely in 1 ml of PC electrolytes in glass tubes (8 mm diam), air in the tubes was replaced by Ar gas, the glass tubes were sealed by melting and stored at 70°C for various storage times. After storage, the WO₃ films were taken out from the tube and rinsed quickly with acetone, then dried with a N₂ gas blower. Cyclic voltammograms of the WO₃ films were measured in

freshly prepared 0.3M LiClO₄ PC electrolyte, and shown in Fig. 1.

In Fig. 1, the cathodic current is associated with the coloring process of the film and the anodic current following scan reversal with the bleaching process. The starting potential (E_c) where the cathodic current of the WO₃ film begins to flow, was about +360 mV vs. SCE for the as-deposited WO₃ film, whereas that of the WO₃ film stored in the LiClO₄ PC electrolyte for 20h at 70°C was +50 mV vs. SCE; that is, the starting potential (E_c) was drastically shifted to the negative side by storage in the LiClO₄ PC electrolyte at high temperature for relatively short time. The shift continued gradually with storage time after the initial drastic shift. These cathodic shifts result in the decrease of the injection charge in the coloration reaction, which contributes to the degradation of electrochromic activity of the WO₃ film. With respect to the anodic oxidation of the colored WO₃ film, the anodic reaction become fast with the storage.

The thickness of the WO₃ film stored in the electrolyte at 70°C for 500h (Fig. 1, curve 5) was confirmed to be unchanged, so that the dissolution of the WO₃ film was negligibly small. In spite of various kinds of WO₃ films having various E_c corresponding to the states of water in WO₃ (12 ~ 13), the potential shifts of these WO₃ films had the same tendency.

The relationship between the cathodic reaction potential shift and the quantity of LiClO₄ PC electrolyte in glass tubes was investigated and shown in Fig. 2. It is shown that the potential shift is increased with increase of amount of LiClO₄ PC electrolyte used for storage. There-

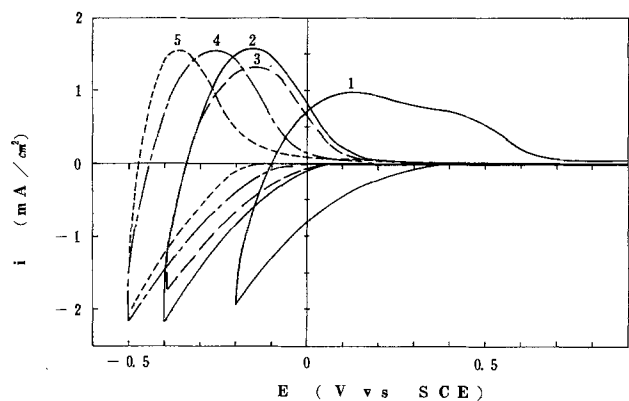


Fig. 1. Cyclic voltammograms for WO₃ films (3000Å, 0.3 cm²) in the freshly prepared 0.3M LiClO₄ PC electrolyte at 0.2 V/s scan rate. 1: As-deposited. 2: Stored in 3 ml 0.3M LiClO₄ PC electrolyte at 70°C for 20h. 3: Stored for 43h. 4: Stored for 113h. 5: Stored for 500h.

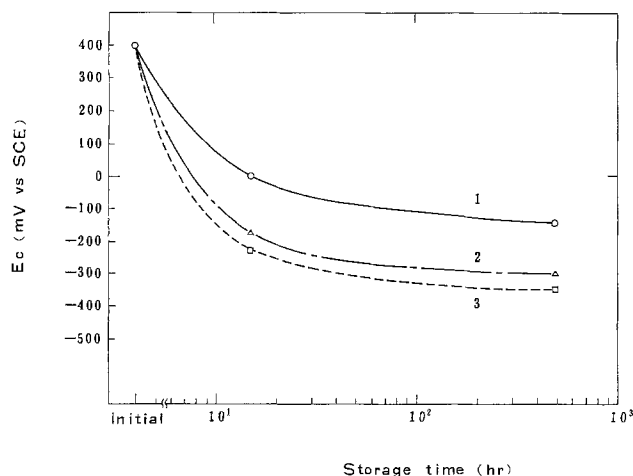


Fig. 2. Plots of starting potentials of cathodic reactions for WO₃ films at 0.2 V/s scan rate as a function of storage time at 70°C in 0.3M LiClO₄ PC electrolyte. The quantity of the electrolyte for the storage was (1) 0.3, (2) 3, and (3) 15 ml.

fore, the degradation of electrochromic activity the WO₃ film is accelerated with the quantity of the electrolyte.

The decrease of the injected charge on storage in PC electrolyte also depends on the concentration of the supporting electrolyte (LiClO₄), as shown in Fig. 3. In Fig. 3, Q_w is the cathodic injected charge of the WO₃ film stored in PC electrolytes for 15h at 70°C under the condition of the cyclic voltammetry from +1.0V to -600 mV vs. SCE with 200 mV/s scan rate, and Q_{w0} is the initial value.

In actual electrochromic display (ECD) cells, the degradation of electrochromic activity on storage at high temperature was observed and is shown in Fig. 4. In Fig. 4, Q_w is the cathodic injected charge, which is proportional to coloration optical density under the condition of applied pulse voltage between the WO₃ working electrode and the counterelectrode for 1s and Q_{w0} is the initial value, after the aging of cells at 70°C for 15h.

We confirmed that the potential shift of the counter-electrodes of the cells after the aging was negligibly small, so that the degradation of the electrochromic activity of ECD cells on storage at high temperature corresponds to the cathodic potential shift of the WO₃ film. Therefore, the degradation is accelerated with H₂O in PC electrolyte, as shown in Fig. 4.

The temperature dependence of the degradation of ECD cells is shown in Fig. 5. In Fig. 5, there is a linear relationship between $\log(t)$ and $1/T$, where t is storage time and T is storage temperature (K).

However, the Arrhenius equation for the rate constant k is

$$k = Ae^{-E_a/RT} \quad (1)$$

where A is a constant, R is the gas constant, and E_a is the activation energy of the reaction.

If we postulate that the degradation function $f(x)$ is represented as follows

$$f(x) = kt \quad (2)$$

we obtain

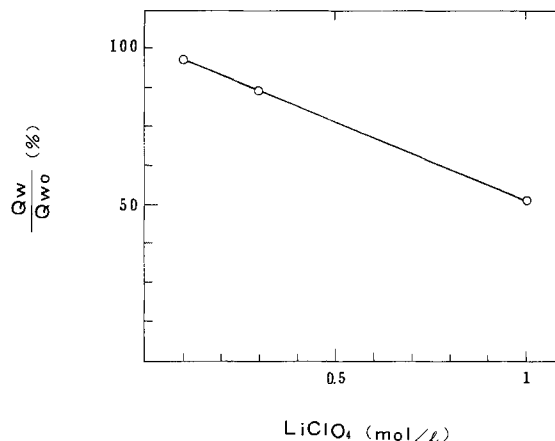


Fig. 3. Plots of Q_w/Q_{w0} as a function of LiClO₄ concentration in the electrolyte used for the storage.

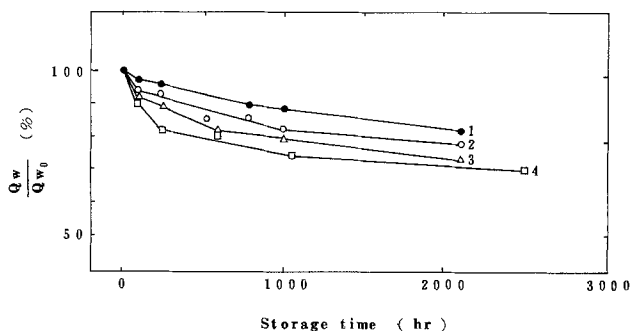


Fig. 4. Plots of Q_w/Q_{w0} of various ECD cells as a function of storage time at 60°C. H₂O concentration in the 0.3M LiClO₄ PC electrolyte was (1) 0.014, (2) 0.017, (3) 0.035, and (4) 0.072M.

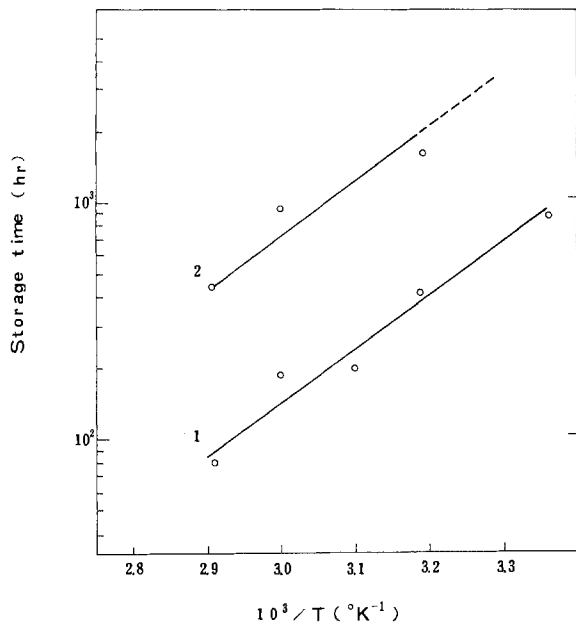


Fig. 5. $1/T$ dependence of lifetime of ECD cells until (1) the degradation $Q_w/Q_{w0} = 0.9$ and (2) $Q_w/Q_{w0} = 0.8$. Storage in $0.3M$ $LiClO_4$ + $0.036M$ H_2O PC electrolyte at $70^\circ C$.

$$t = \frac{1}{A} f(x) e^{E_a/RT} = ce^{E_a/RT} \quad [3]$$

where $c = 1/A f(x)$, and $f(x)$ is equal to Q_w/Q_{w0} , so that we can obtain the quantity of E_a using Eq. [3]. From the slope in Fig. 5, E_a was estimated to be 4.5 kcal/mol.

Consequently, from the results mentioned above, the degradation of the electrochromic activity on storage corresponds to the cathodic potential shift, which is caused by some thermodynamic reactions of the WO_3 layer with Li content and H_2O content.

Mechanism of degradation.—SIMS of the WO_3 films stored in PC electrolyte were measured, and their depth profiles are shown in Fig. 6. In Fig. 6, sample 1 was only washed with PC solvent and acetone successively, and it was dried by a N_2 gas blower. Sample 2 was dipped in $0.3M$ $LiClO_4$ PC electrolyte containing $0.01M$ H_2O for 10s and then treated the same as sample 1. Sample 3 was stored in $0.3M$ $LiClO_4$ PC electrolyte containing $0.01M$ H_2O in a sealed glass tube for 120h at $70^\circ C$, and then treated the same as sample 1.

A molecular ion of OLi^+ (mass = 22) was used for the evaluation of Li content in WO_3 film, because of two facts that secondary ion intensities of Li^+ (mass = 7) and Li^+ isotope (mass = 6) were too strong to get a good linearity between Li content and the signal intensity, and that OLi^+ (mass = 23) overlaps Na (mass = 23).

Each signal intensity of OLi^+ was normalized using a signal intensity of a main component, W^+ isotope (mass = 184). It can be said that Li^+ permeates smoothly into the WO_3 layer by quick dipping in the electrolyte for relatively short time (10s) and accumulates homogeneously in the film, and that the permeation of Li into the layer is accelerated by storing at high temperature.

It was difficult to wash away Li in the layer, even in the case of sample 2.

In spite of smooth permeation of Li, ClO_4^- did not permeate into the WO_3 layer (see the Cl depth profiles in Fig. 6). From these results, the degradation of the WO_3 film would correspond to an accumulation of Li in the film, but the degradation will not directly depend on Li concentration in the film. This is because if the degradation which associates with the negative potential shift of the cathodic reaction potential were only caused by accumulation of Li in the film, the negative potential shift of the WO_3 film by quick dipping in $LiClO_4$ PC electrolyte would be observed, compared with the potential of the WO_3 film in non-Li electrolyte (e.g., H_2SO_4 solution); but,

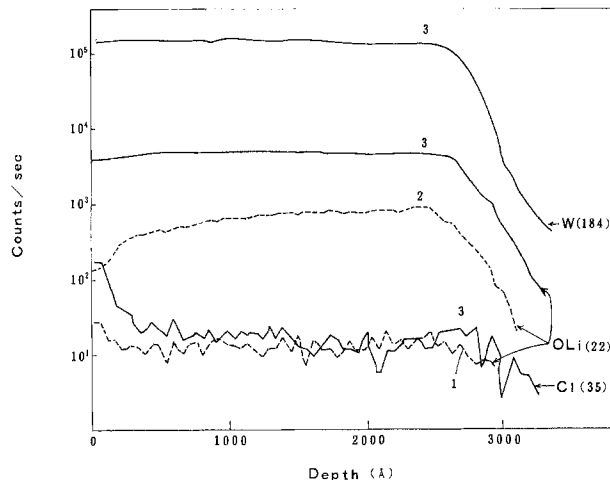


Fig. 6. SIMS depth profiles of WO_3 films. 1: No treatment. 2: Dipped in the $LiClO_4$ PC electrolyte for 10s. 3: Stored in the electrolyte for 120h at $70^\circ C$.

in fact, the cathodic reaction potential of as-deposited WO_3 film in $LiClO_4$ PC electrolyte is located at the more positive side about 250 mV more than that of same film in H_2SO_4 electrolyte (12). Therefore, it is better for the degradation process to be discussed on the basis of Li which can be separated from free Li^+ , remains in the void of the film, and/or is injected in Xerogel structure (10) and has a interaction with W-O such as W-O-Li.

FT-IR spectra of the WO_3 film stored in $0.3M$ $LiClO_4$ PC electrolyte at $70^\circ C$ for 500h in a sealed glass tube are shown in Fig. 7.

The O-H stretching broad peak at 3400 cm^{-1} was decreased, and the W-O stretching broad peak (~ 650 cm^{-1}) changed to a broad peak having several shoulders on storage.

IR spectra of WO_3 , H_2WO_4 , and Li_2WO_4 powders are shown in Fig. 8 for comparison.

From these results, IR spectrum of the degraded WO_3 film may be similar to a mixed spectrum of H_2WO_4 and a small amount of Li_2WO_4 , so that it seems that the internal surface of $W(OH)_x$ would change to Li_2WO_4 on storage in $LiClO_4$ PC electrolyte.

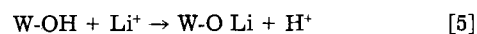
The $W_{4f_{7/2}}$ electrons binding energy and O_{1s} electrons binding energy of WO_3 film and powders of WO_3 derivatives were measured using XPS analysis and are shown in Fig. 9-10 with reference data of WO_3 , H_2WO_4 , and Li_2WO_4 (14-21).

The uncertainty of measured binding energy was estimated to be ± 0.3 eV, and the electron escape depth of $W_{4f_{7/2}}$ electrons was estimated approximately to be 20Å by Penn's equations (22).

The $W_{4f_{7/2}}$ and O_{1s} electrons binding energies of the WO_3 film which was stored in air for 144h after the evaporation will be in agreement with those of $WOOH$ (14) within the experimental error. The surface of the WO_3 film before dipped in PC electrolyte will be a $W(OH)_x$ structure as shown in Fig. 9, 10 and Ref. (10, 12).

The $W_{4f_{7/2}}$ electrons binding energy of the WO_3 film stored in $0.3M$ $LiClO_4$ PC electrolyte for 144h at $70^\circ C$ is essentially identical with that of WO_3 and Li_2WO_4 powder measured in our laboratory. It can be said that the surface of the degraded WO_3 film is constructed with WO_3 or Li_2WO_4 ; however, if we consider the SIMS and IR experimental results, the surface of the degraded WO_3 film will be constructed with Li_2WO_4 .

Consequently, it seems reasonable to assume that the surface state of the WO_3 film is changed by the H-Li ion exchange in $LiClO_4$ PC electrolyte such as in the following thermodynamic reaction



and this exchange reaction will result in the formation of Li_2WO_4 .

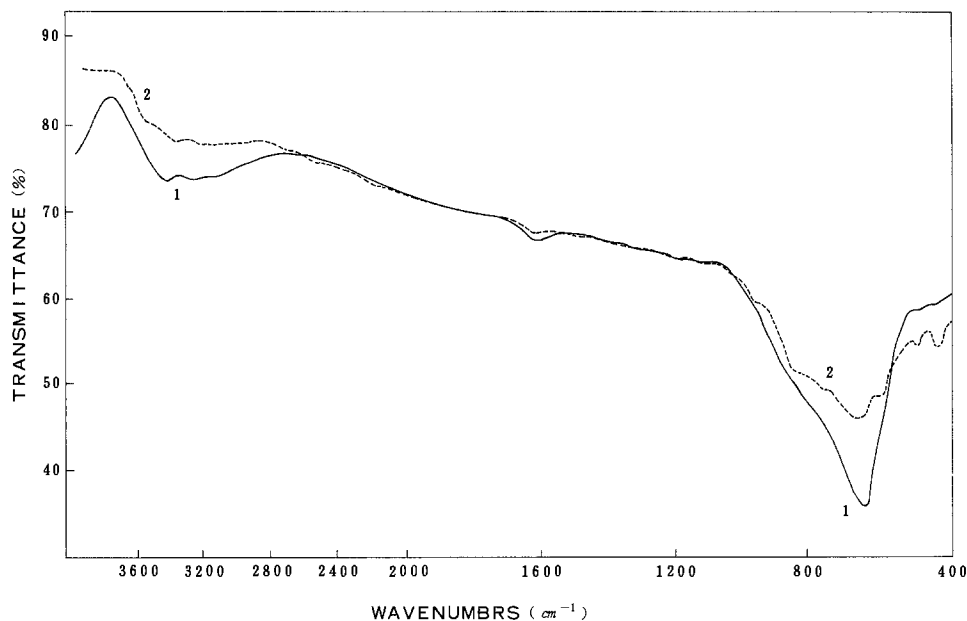


Fig. 7. FT-IR spectra of WO₃ films (1) as-deposited and (2) stored in 0.3M LiClO₄ PC electrolyte at 70°C for 500h.

Prevention of degradation.—Cyclic voltammograms of WO₃ films which were stored in various kinds of electrolytes in sealed glass tubes were measured and are shown in Fig. 11-12. The storage experimental conditions were as follows: WO₃ films (3000Å thick, 0.3 cm²) on In₂O₃-coated glass were dipped completely in PC electrolytes in glass tubes (8 mm diam), air in the tubes was replaced by Ar gas, the glass tubes were sealed by melting, and then stored at 70°C for various storage times. After storage, the WO₃ films which were taken out from the electrolyte were rinsed quickly with acetone and dried with a N₂ gas blower.

In Fig. 11, the starting potential (E_c) of the cathodic reduction of the WO₃ film was shifted to negative side about 300 mV on storage in 0.3M LiClO₄ PC electrolyte at 70°C for 1000h, but that of the WO₃ film stored in 0.3M LiClO₄ PC electrolyte containing 0.01 volume percent (v/o) H₃PO₄ under the same condition was scarcely shifted and the degradation of electrochromic activity was not observed.

In Fig. 12, the starting potential (E_c) of the cathodic reduction of the WO₃ film stored in 0.3M LiClO₄ PC electrolyte containing 5 v/o acrylic acid was also scarcely shifted to negative side.

From these results, the degradation of the WO₃ film in Li salt PC electrolyte, corresponding to the ion exchange between Li and H of W(OH)_x, will be prevented by the addition of an acid to the electrolyte. However, propylene carbonate is easy to decompose under coexistence of acids; therefore, it is undesirable to add a strong acid to the electrolyte.

Furthermore, we have found that the degradation of the WO₃ film is also prevented by using LiBF₄ as a supporting electrolyte.

Cyclic voltammograms of the WO₃ films stored in 0.3M LiBF₄ PC electrolyte containing 0.01M H₂O in sealed glass tubes at 70°C were measured and are shown in Fig. 13. The storage experimental conditions were as same as mentioned above.

In Fig. 13, compared to the case of LiClO₄ supporting electrolyte, as shown in Fig. 11, curve 2, the starting potential (E_c) of the cathodic reduction of the WO₃ film was rarely shifted to negative side by the storage at 70°C for 1000h. Moreover, there was no observation of gas evolution by decomposition of PC solvent.

The preventive effect on the degradation of the WO₃ film in LiBF₄ PC electrolyte can be attributed to the facts that LiBF₄ is especially effective in this regard, as can be

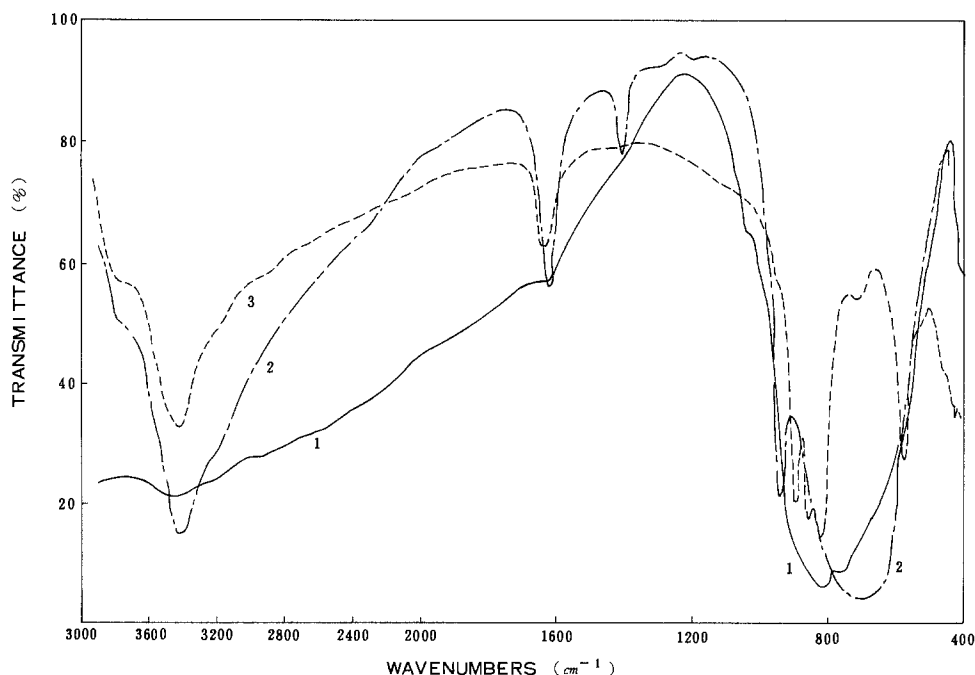


Fig. 8. FT-IR spectra of (1) WO₃ powder, (2) H₂WO₄ powder, and (3) Li₂WO₄ powder.

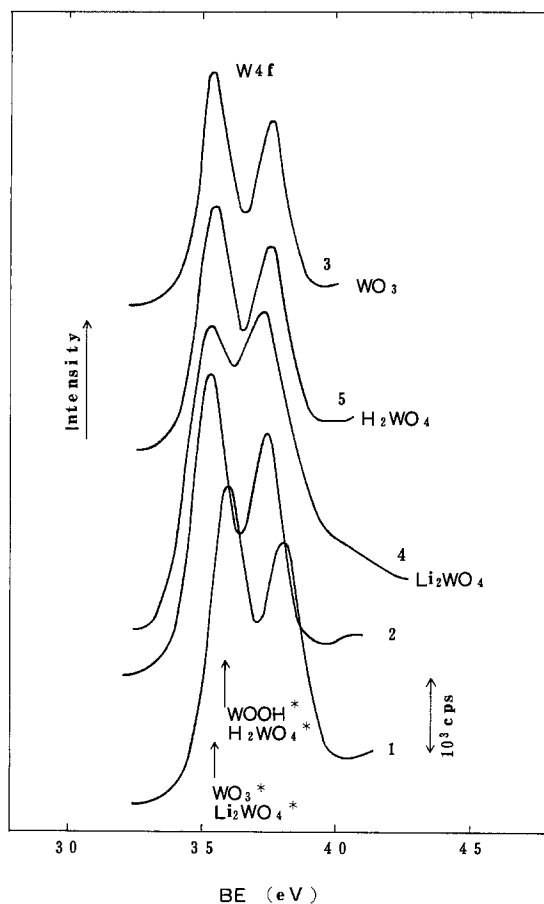


Fig. 9. XPS spectra of W_{4f} . 1: As-deposited WO_3 films. 2: Stored in $0.3M LiClO_4$ PC electrolyte at $70^\circ C$ for 144h. 3: WO_3 powder. 4: Li_2WO_4 powder. 5: H_2WO_4 powder. Reference data (14-21).

seen from aqueous PH determination (generally acidic, if hydrolyzed) (23), and that $LiBF_4$ is able to dissociate H^+ from H_2O containing in the electrolyte.

An FT-IR spectrum of the WO_3 film on a Si wafer stored in $0.3M LiBF_4$ PC electrolyte in a sealed glass tube at $70^\circ C$ for 500h is shown in Fig. 14 with reference IR data.

In Fig. 14, showing long-time storage in $LiBF_4$ PC electrolyte, the shoulder of O-H stretching broad peak at 3400 cm^{-1} was decreased as same as in $LiClO_4$ PC electrolyte, while the W-O stretching broad peak at 650 cm^{-1} was rarely changed. WO_3 film in $LiBF_4$ PC electrolyte was more stable than in $LiClO_4$ PC electrolyte.

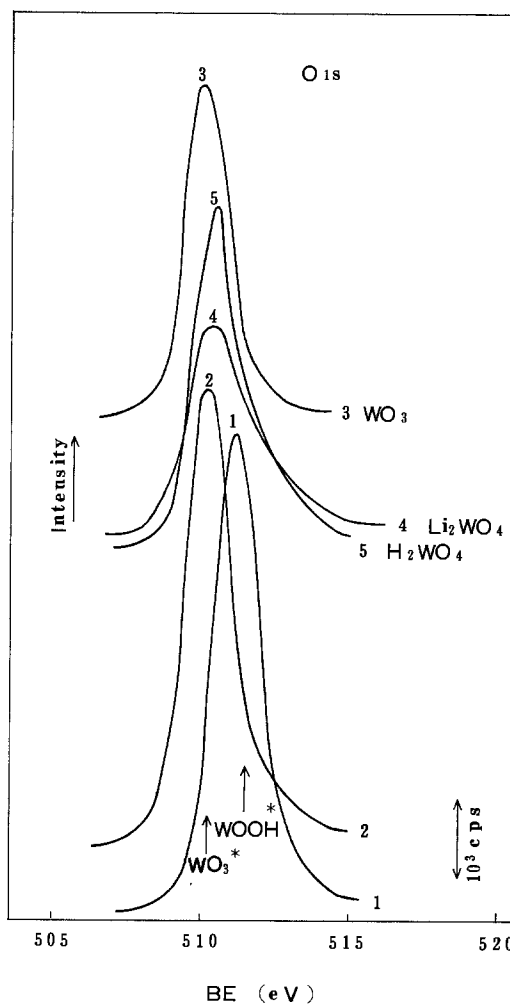


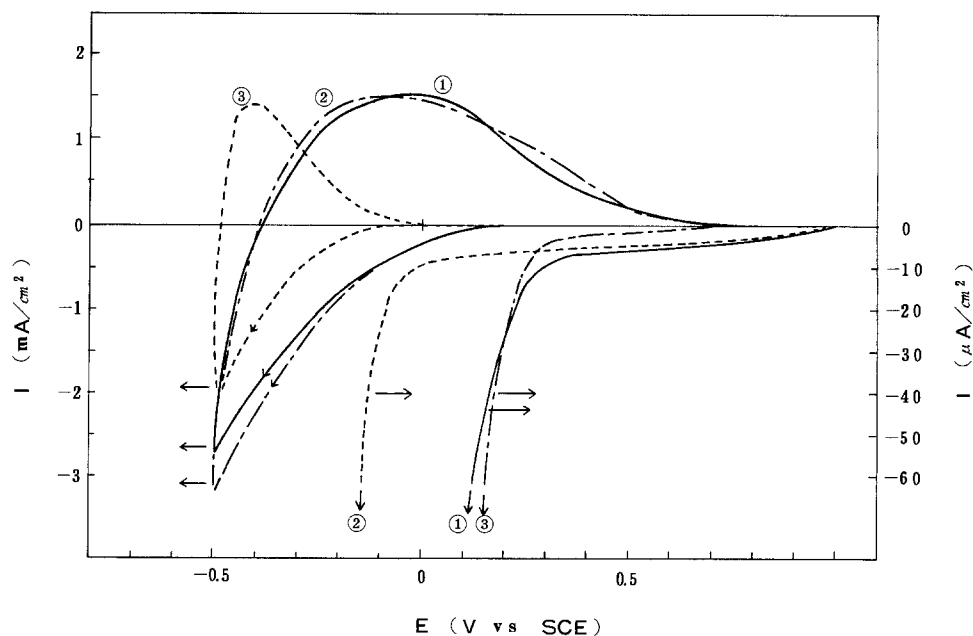
Fig. 10. XPS spectra of O_{1s} of the same samples as shown in Fig. 9. Reference data (14-21).

A SIMS depth profile of the WO_3 films stored in $0.3M LiBF_4$ PC electrolyte is shown in Fig. 15.

Sample 1 was merely dipped in $0.3M LiClO_4$ PC electrolyte for 10s; sample 2 was stored in $0.3M LiBF_4$ PC electrolyte for 120h at $70^\circ C$; and sample 3 was stored in $0.3M LiClO_4$ PC electrolyte for 120h at $70^\circ C$.

Molecular ion of OLi^+ (mass = 22) was used for the evaluation of Li content in WO_3 films, and each signal inten-

Fig. 11. Cyclic voltammograms for WO_3 films (3000 \AA , 0.3 cm^2) in freshly prepared $0.3M LiClO_4$ PC electrolyte at 0.2 V/s scan rate. 1: As-deposited. 2: Stored in $1\text{ ml } 0.3M LiClO_4 + 0.3M H_2O$ PC electrolyte at $70^\circ C$ for 1000h. 3: Stored in $1\text{ ml } 0.3M LiClO_4 + 0.01\text{ v/o } H_3PO_4$ PC electrolyte at $70^\circ C$ for 1000h.



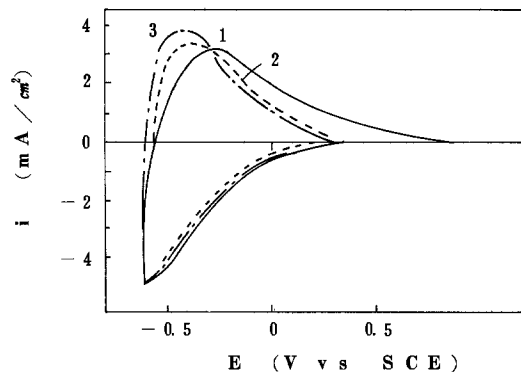


Fig. 12. Cyclic voltammograms for WO₃ films (3000Å, 0.3 cm²) in freshly prepared 0.3M LiClO₄ PC electrolyte at 0.2 V/s scan rate. 1: As-deposited. 2: Stored in 0.3 ml 0.3M LiClO₄ + 5 v/o acrylic acid PC electrolyte at 70°C for 500h 3: Stored for 1000h.

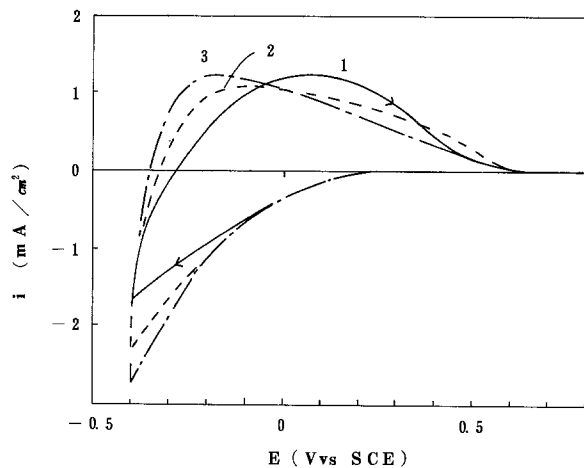


Fig. 13. Cyclic voltammograms of WO₃ films (3000Å, 0.3 cm²) in freshly prepared 0.3M LiClO₄ PC electrolyte at 0.2 V/s scan rate. 1: As-deposited. 2: Stored in 0.3M LiBF₄ + 0.01M H₂O PC electrolyte at 70°C for 500h. 3: Stored for 1000h.

sity of OLi was normalized using a signal intensity of a main component W⁺ (mass = 184).

Li content of the WO₃ film stored in LiBF₄ PC electrolyte was about one-half smaller than that of the case of LiClO₄ (Fig. 15). Considering the free Li⁺ remaining in the void of the WO₃ film by merely dipping in LiClO₄ PC electrolyte (Fig. 15, curve 2), it can be assumed that the ion exchange between Li⁺ and H⁺ of W(OH)₂ is depressed in LiBF₄ PC electrolyte.

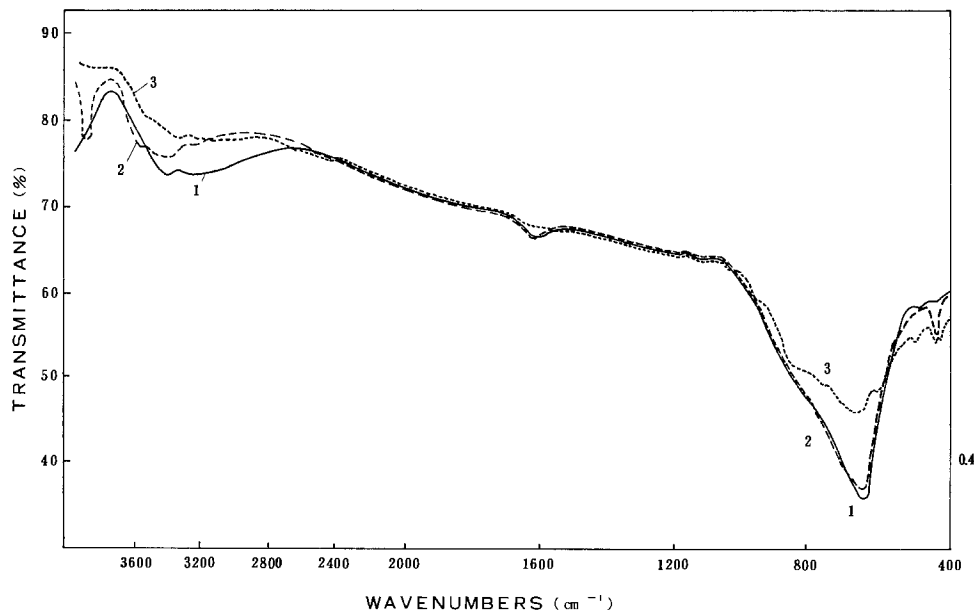


Fig. 14. FT-IR spectra of WO₃ films on Si wafers. 1: As-deposited. 2: Stored in 0.3M LiBF₄ PC electrolyte at 70°C for 500h. 3: Stored in 0.3M LiClO₄ PC electrolyte at 70°C for 500h.

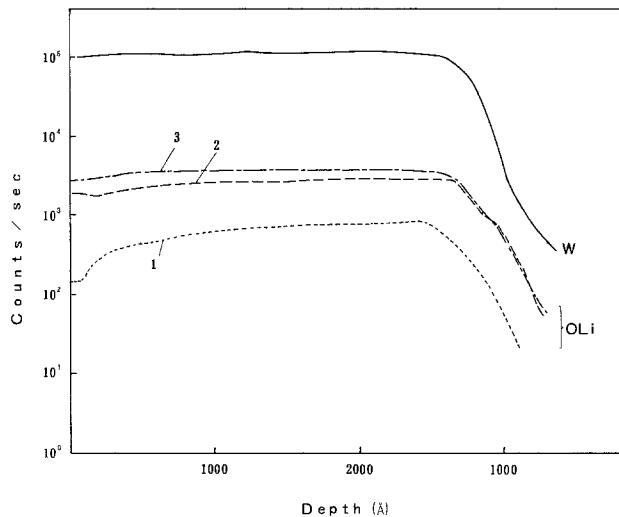


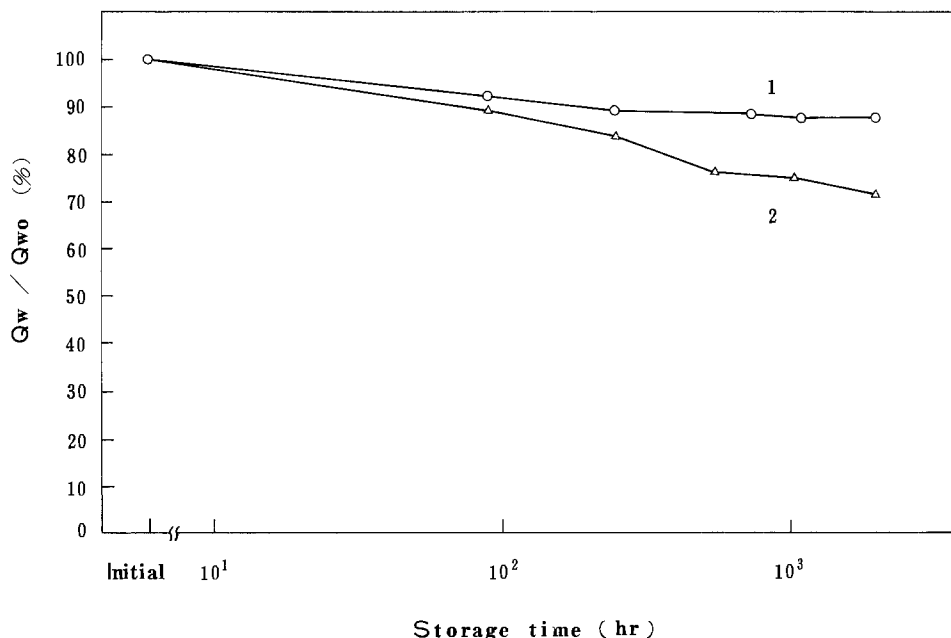
Fig. 15. SIMS depth profiles of WO₃ films. 1: Dipped in 0.3M LiClO₄ PC electrolyte for 10s. 2: Stored in 0.3M LiBF₄ PC electrolyte for 120h at 70°C. 3: Stored in 0.3M LiClO₄ PC electrolyte for 120h at 70°C.

In actual ECD cells, the degradation of electrochromic activity on storage at 70°C was investigated and is shown in Fig. 16.

The electrolytes of samples 1 and 2 were 0.3M LiBF₄ and 0.3M LiClO₄ PC solutions, respectively. The quantities of cathodic injected charge into the WO₃ films were measured under the condition of applied pulse voltages between the WO₃ electrode and the counterelectrode for 1s. Q_{w0} is the initial value of the quantity of cathodic injected charge into the WO₃ film after aging for 15h at 70°C, and Q_w is that of stored for various storage times after aging, in which Q_w is approximately proportional to coloration optical density. The potential drift of counterelectrode of the cells on storage at 70°C for 1000h after the aging was negligibly small. In Fig. 16, it is confirmed that the degradation of the electrochromic activity of ECD cells using LiBF₄ as the supporting electrolyte was remarkably small, compared with that of using LiClO₄.

The temperature dependence of the degradation of the ECD cells is shown in Fig. 17. There are linear relationships between $\log t$ and $1/T$, where t is storage time until $Q_w/Q_{w0} = 0.9$, and T is storage temperature (K). From the slopes of straight lines in Fig. 17, the activation energies of the degradation reaction of ECD cell using LiBF₄ PC electrolyte and LiClO₄ PC electrolyte were estimated 7.0 and 4.5 kcal/mol, respectively. Therefore, LiBF₄ PC sys-

Fig. 16. Plots of Q_w/Q_{w0} of ECD cells as a function of storage time at 70°C in the electrolyte. 1: 0.3M LiBF_4 + 0.2M H_2O . 2: 0.3M LiClO_4 + 0.3M H_2O .



tem has a larger amount of the activation energy for the degradation reaction corresponding to the ion exchange between Li^+ and H^+ of $\text{W}(\text{OH})_x$ than that of LiClO_4 PC system. It is, therefore, preferable to use LiBF_4 as the supporting electrolyte for ECD cells using WO_3 film.

Conclusion

The cathodic reduction potential of the evaporated WO_3 film is shifted to negative side on storage in LiClO_4 PC electrolyte, and this causes the degradation of the electrochromic activity of the film.

The degradation depends not only on the H_2O concentration, but also on the LiClO_4 supporting electrolyte concentration.

It seems reasonable, for the degradation, to assume that H_2O in the electrolyte contributes at first to the change of WO_3 into $\text{W}(\text{OH})_x$ and then Li^+ exchanges with the H^+ of $\text{W}(\text{OH})_x$, and that the exchange results in the formation of Li_2WO_4 .

The degradation of the WO_3 film in Li salt PC electrolyte caused by the ion exchange between Li^+ and H^+ of $\text{W}(\text{OH})_x$ can be prevented by the addition of acids and/or acidity compounds (e.g., LiBF_4) to PC electrolyte; however, an acid is undesirable for an additional agent because it causes decomposition of PC, then LiBF_4 is a preferable supporting electrolyte to prevent not only the ion exchange, but also the decomposition of PC.

Acknowledgments

We are grateful to Dr. E. Hirota, the Assistant-Director of Central Research Laboratory for permission to publish the paper and for encouragement. We thank S. Kohiki, K. Tsukamoto, and M. Kamikawaji, members of TechnoResearch Department, for performing the XPS, SIMS, and FT-IR observations and for helpful discussions.

Manuscript submitted Jan. 9, 1984; revised manuscript received June 1, 1984.

Matsushita Electrical Industrial Company, Limited assisted in meeting the publication costs of this article.

REFERENCES

1. S. K. Deb., *Philos. Mag.*, **27**, 801 (1973).
2. R. Hurditch, *Electron Lett.*, **11**, 142 (1975).
3. R. S. Crandall and B. W. Faughnan, *Appl. Phys. Lett.*, **26**, 120 (1975).
4. I. F. Chang, B. L. Gilbert, and T. I. Tan, *This Journal*, **122**, 955 (1975).
5. B. W. Faughnan, R. S. Crandall, and P. M. Heyman, *RCA Rev.*, **36**, 177 (1975).
6. B. W. Faughnan, R. S. Crandall, and A. M. Lampert, *Appl. Phys. Lett.*, **27**, 275 (1975).
7. R. S. Crandall and B. W. Faughnan, *ibid.*, **28**, 95 (1976).
8. N. H. Hersh, W. E. Kramer, and J. H. McGee, *ibid.*, **27**, 646 (1975).
9. J. P. Randin, *J. Electro. Mater.*, **7**, 47 (1978).
10. P. Schlotter and L. Pickelmann, *ibid.*, **11**, 207 (1982).
11. H. Morita and H. Washida, *Oyo Butsuri*, **51**, 488 (1982).
12. N. Yoshiike and S. Kondo, *This Journal*, **130**, 2283 (1983).
13. N. Yoshiike and S. Kondo, *ibid.*, **131**, 809 (1984).
14. T. L. Barr, *J. Phys. Chem.*, **82**, 1801 (1978).
15. P. Biloen and G. T. Pott, *J. Catal.*, **30**, 169 (1973).
16. C. D. Wagner, D. A. Zatko, and R. H. Raymond, *Anal. Chem.*, **52**, 1445 (1980).
17. T. L. Barr, *J. Phys. Chem.*, **82**, 1801 (1978).
18. G. E. McGuire, G. K. Schweitzer, and T. A. Carlson, *Inorg. Chem.*, **12**, 2450 (1973).
19. C. D. Wagner, *J. Vac. Sci. Technol.*, **15**, 518 (1978).

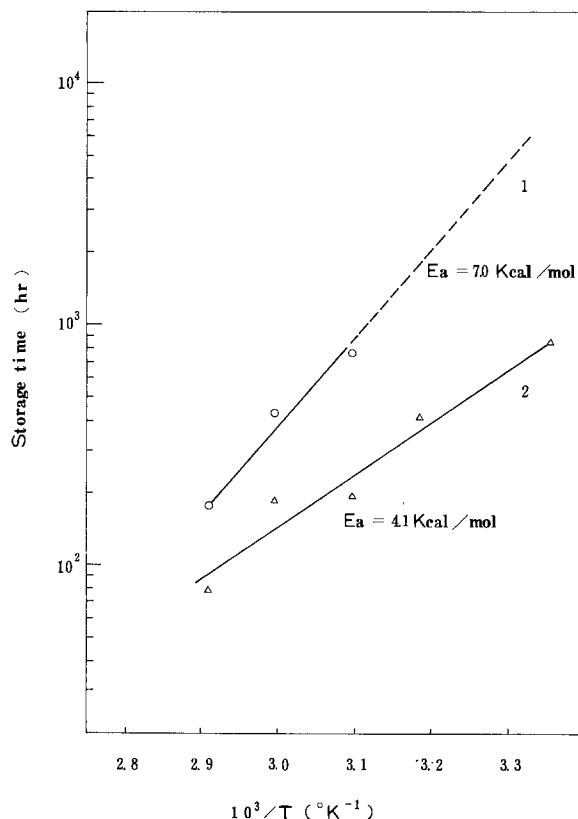


Fig. 17. $1/T$ dependence of lifetimes of ECD cells until $Q_w/Q_{w0} = 0.9$. Electrolyte, (1) 0.3M LiBF_4 + 0.02M H_2O and (2) 0.3M LiClO_4 + 0.3M H_2O .

20. R. J. Cotton and J. W. Rabalais, *Inorg. Chem.*, **15**, 236 (1976).
 21. K. T. Ng and D. M. Hercules, *J. Phys. Chem.*, **80**, 2094 (1976).
 22. D. R. Renn, *J. Electron. Spectro. Relat. Phenom.*, **9**, 26 (1976).
 23. J.-P. Gabano, "Lithium Batteries," p. 27, Academic Press, New York (1983).

The Etching of InP in HCl Solutions: A Chemical Mechanism

P. H. L. Notten

Philips Research Laboratories, 5600 JA Eindhoven, The Netherlands

ABSTRACT

The etch rate of InP in solutions of high HCl concentration was shown to be independent of the applied potential in a wide potential range negative with respect to the flatband value. Dissolution of the solid led to the formation of PH₃. The etch rate, which was not mass-transport controlled, was first order in molecular HCl concentration. The results lead us to conclude that, in HCl etchants, InP is dissolved by a purely chemical mechanism. The influence of chemical etching on the anodic behavior of InP in these electrolytes is described.

Aqueous etching of III-V materials is often an important step in device technology (1, 2). While anodic etching is sometimes used (3), the necessity of making electrical contact to slices of small dimensions is invariably a disadvantage. Methods not involving an external current or voltage source are therefore favored (1, 2). Such methods can be divided into two classes: "electroless" and "chemical" dissolution. Electroless dissolution involves two separate potential-dependent electrochemical reactions: the oxidation of the solid and the reduction of an oxidizing agent. The principle is illustrated in Fig. 1 for the etching of a p-type III-V semiconductor (4). For these materials, holes in the valence band are required at the surface for bond breaking. As a result, the anodic dissolution current increases at potentials close to the flatband value (V_{fb}) as shown in curve (a). For electroless dissolution, holes must be supplied by an oxidizing agent in solution. If the distribution function of the oxidizing agent overlaps with the valence band of the semiconductor, then reduction via hole injection into the valence band is expected [curve (b)]. Here, we have assumed that the reduction reaction is diffusion controlled, i.e., the cathodic partial current is independent of potential. Curve (c) represents the total measured current-potential curve in the electrolyte containing the oxidizing agent. At the rest potential, the anodic and cathodic partial currents are equal. If the potential is changed from this value using an external source, then the etch rate of the semiconductor will, of course, also change.

Gerischer and co-workers (5, 6) have shown that semiconductors can be dissolved by a purely chemical mechanism, which is characterized by the absence of any influence of the surface carrier concentration on the etch rate. Such behavior is observed with bifunctional agents, such as halogen or H₂O₂ molecules, which are capable of forming two new bonds with the semiconductor surface more or less simultaneously. For GaAs dissolution in bromine solution, for example, they suggest a coordinated reaction sequence involving the breaking of Ga-As and Br-Br bonds and the simultaneous formation of Ga-Br and As-Br bonds.

Etchants based on HCl are widely used for InP semiconductor devices (7, 8). The presence of other acids in the HCl solution has a significant influence on the etch rate. However, InP does not dissolve in conventional etchants involving simple oxidizing agents. In order to resolve the question of the dissolution mechanism, we studied both the etching and electrochemistry of p-InP in various HCl solutions.

Experimental

The p-type InP slices used in this work were made from liquid-encapsulated Czochralski material with a carrier

density in the range $1-2 \times 10^{18} \text{ cm}^{-3}$. The (100) face was exposed to the solution. The diameter of the electrodes was 3 mm, with the exception of the InP rotating disk, which had a diameter of 4 mm.

The current-potential measurements were carried out under potentiostatic control in a conventional cell using a Pt counterelectrode and a saturated calomel electrode (SCE) as reference. All potentials are given with respect to this SCE. A Solartron 1172 Frequency Response Analyser was employed for determining the flatband potentials. All impedance measurements were carried out at a frequency of 10 kHz.

The total dissolution rate of InP at various potentials was determined analytically by measuring the indium concentration in the etching solution by inductively-coupled-plasma (ICP) emission spectrometry. The etchant was passed over the InP electrode, which was mounted in a glass microelectrochemical flow cell as described by Haroutiounian *et al.* (9). Indium concentrations as low as 0.5 ppm could be determined with a relative accuracy of about 5%. An LKB Varioperpex peristaltic pump was used to pump the solution through the flow cell. The flow rate of the solution, mainly deter-

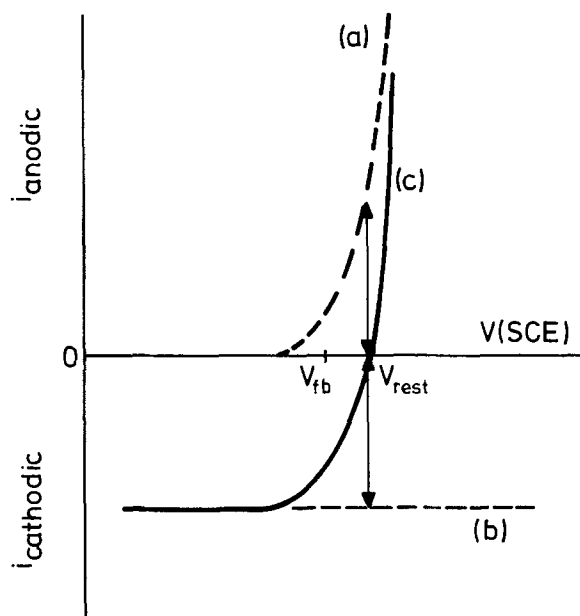


Fig. 1. Curve (a) represents the theoretical partial anodic dissolution current of a p-InP electrode in the dark, and curve (b) the diffusion-limited reduction current of an oxidizing agent as a function of the potential. Curve (c) gives the total current-potential curve.

mined by the lower limit of the indium detection, was in the range from 0.2 to 1.0 ml/min.

The gas was analyzed qualitatively using the color-detector tube method ("Dräger" tube), which in our case gave a color reaction specific for phosphine. A gas burette was used for the quantitative gas analysis.

Results

Flow-cell experiments.—In Fig. 2, results are given for the potentiostatic etching of p-InP in the dark in HCl solutions. Figure 2a shows the current-potential curves of this electrode in 3M and 6M HCl. At negative potentials the current is very low in both cases. In the vicinity of the flatband potential ($V_{FB} = 0.73V$ vs. SCE) the anodic current increases, as expected. It should be noted that the anodic curve for the 6M HCl solution is shifted slightly in the cathodic direction with respect to that for the 3M solution.

The total dissolution rate, according to the ICP analysis, is shown in Fig. 2b as a function of the potential. For the 3M HCl solution, the dissolution rate follows the current closely. At negative potentials the etch rate (r_t) is very low and increases considerably near the flatband potential. If we assume that in this case etching is due solely to anodic dissolution, then it can be easily shown that six holes are required to dissolve one InP entity. The total etch rate potential curve for the 6M HCl case differs markedly from that of the corresponding current-potential curve. This difference is most obvious at negative potentials, at which the InP dissolves at a rate essentially independent of applied potential. Since no cathodic reaction occurs in this range, we must conclude that InP is chemically dissolved by HCl. If we assume that anodic dissolution in 6M HCl here also requires six holes per InP, then the chemical etch rate can be calculated from the total etch rate and the measured anodic current. Figure 2c shows that the chemical etch rate (r_{chem}) remains

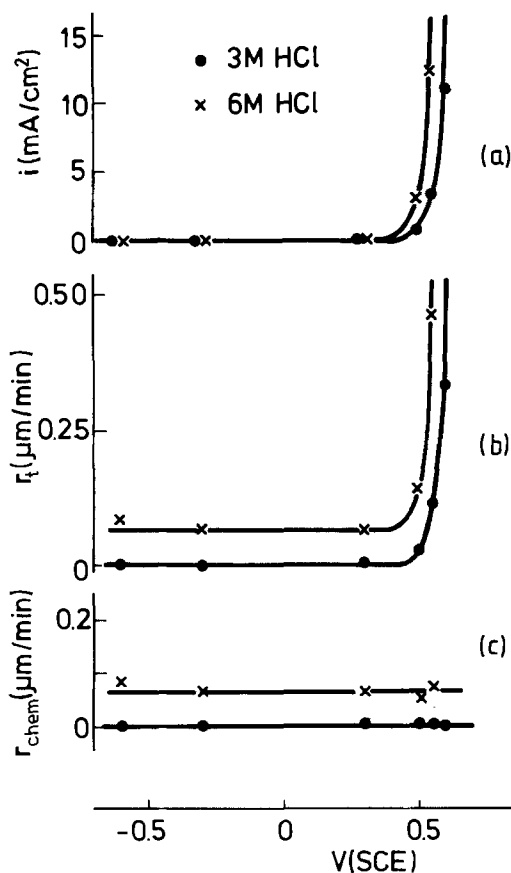


Fig. 2. Potentiostatically measured current-potential curves (a), total etch rate as a function of the electrode potential (b), and chemical etch rate as a function of the electrode potential (c) for a p-InP electrode in the dark in a 3M HCl (●) and 6M HCl (x) solution in water.

constant, even at potentials at which the electrode dissolves anodically.

A further example is shown in Fig. 3 for 1.5M HCl in concentrated acetic acid solution. Etchants based on HCl and acetic acid are often used in InP technology (7). Figure 3a shows the current-potential curve, and Fig. 3b the calculated chemical etch rate as a function of the electrode potential. The results in the cathodic region are similar to those found with 6M HCl solution; the current is low and a high chemical etch rate is found. The slow increase of the chemical etch rate with potential is probably due to a roughening of the electrode surface during the experiment. The increase in the anodic current at potentials near V_{FB} is considerably lower than that found in a HCl solution of the same concentration but without acetic acid. A dramatic decrease of the chemical dissolution rate is observed when the anodic dissolution starts. In this potential range, we observed the formation of an orange-colored film at the electrode surface. Phosphorus was found in this film by EDAX analysis. Obviously, a passivating film is formed during anodic dissolution. This film inhibits both the anodic and the chemical dissolution reactions.

It should be noted that the chemical dissolution rate depends markedly on the surface condition of the InP electrode. Since induction effects are observed, care must be taken to ensure a constant dissolution rate before measurements are made. This can be done by pre-etching the electrode in the same etching solution.

The results shown so far suggest that the chemical etch rate of InP is strongly dependent on HCl concentration. This dependence was studied by varying the HCl concentration over a wide range for two different systems. An InP crystal was chemically etched in these solutions in the flow cell (the measured current was zero), and the chemical dissolution rate was again analytically determined by ICP emission spectrometry. The results are shown in Fig. 4. For curve (a), the concentration was varied by diluting concentrated HCl with water. At 9M HCl, the chemical dissolution rate is high and decreases rapidly as the HCl concentration is lowered. For a 5M HCl

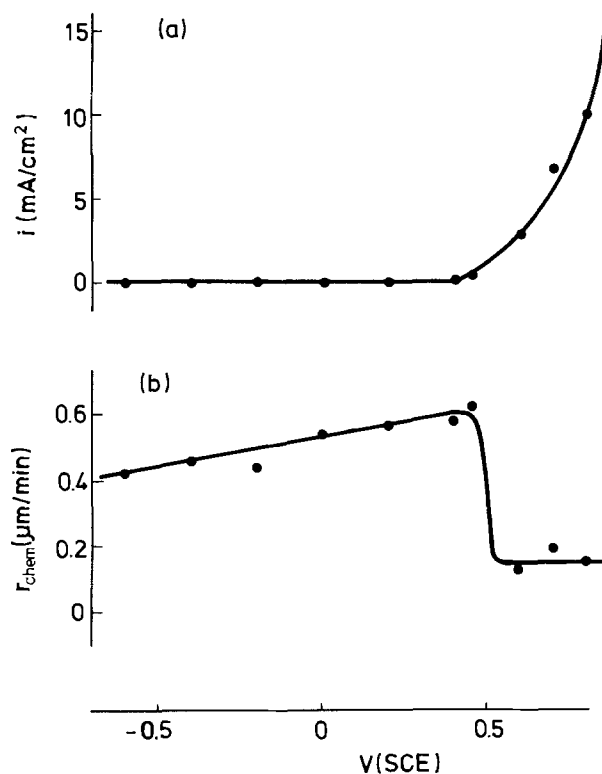


Fig. 3. Potentiostatically measured current-potential curve (a) and chemical etch rate as a function of the electrode potential (b) in the dark for a p-InP electrode in a solution of 1.5M HCl in concentrated acetic acid.

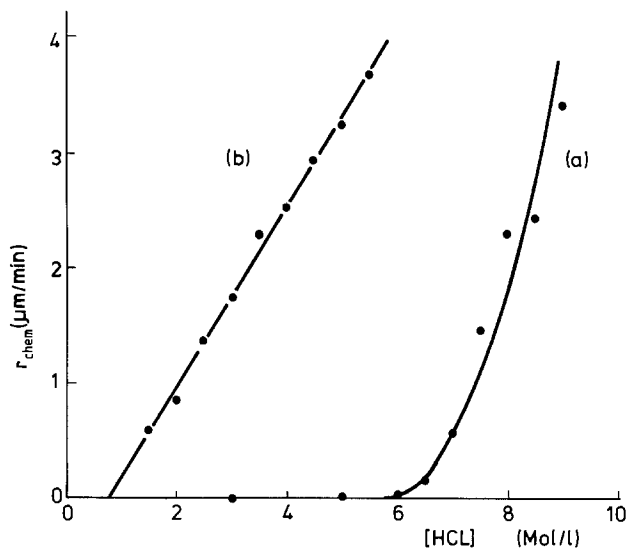


Fig. 4. Chemical etch rate as a function of the HCl concentration for a p-InP crystal in the dark. The HCl concentration was varied by diluting with water [curve (a)] and concentrated acetic acid [curve (b)].

concentration, the etch rate is less than 40 Å/min and even lower for more dilute solutions. For curve (b), concentrated HCl was diluted with concentrated acetic acid. It is striking that here a linear relationship between etch rate and HCl concentration is observed and that the etch rate is significantly higher than in the corresponding HCl-H₂O solutions.

To decide whether the dissolution is a diffusion or a kinetically controlled process, the etch rate was measured as a function of the rotation rate using a p-InP rotating disk electrode at open circuit. Figure 5 shows that the chemical etch rate measured in a 3M HCl in concentrated acetic acid solution is essentially independent of the rotation rate (N). This means that the rate of the dissolution reaction is kinetically controlled.

Gas analysis.—When an InP crystal was dissolved at the rest potential in a concentrated HCl solution, gas evolution was observed at the solid surface. Using the color-detector method, we showed that this gas was phosphine. A clear color change was indeed observed even with the most insensitive tubes. We determined the gas

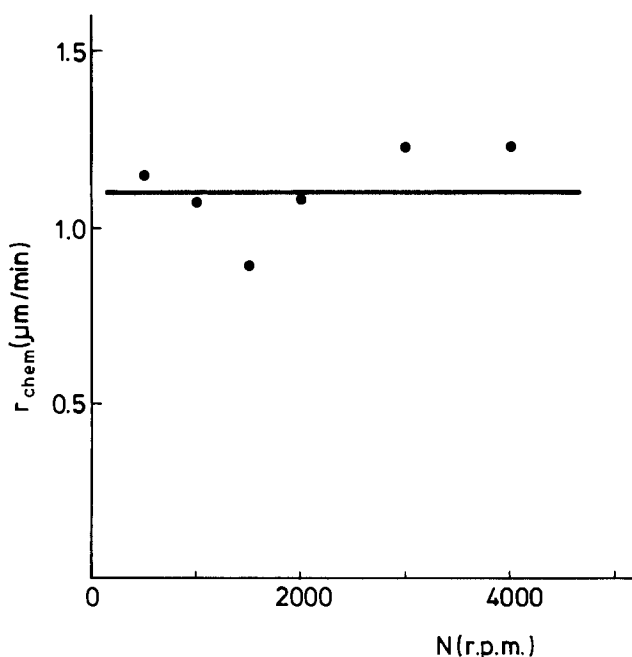


Fig. 5. Chemical etch rate in the dark as a function of the rotation speed of a p-InP electrode in a solution of 3M HCl in concentrated acetic acid.

quantitatively with a gas burette and showed that the phosphorus is converted for 100% ($\pm 1\%$) as PH₃.

Electrochemical measurements.—The current-potential curves of p-InP in 1N H₂SO₄ and in different HCl solutions in the dark are shown in Fig. 6. In all cases, the blocking current in the cathodic region was very low (< 0.02 mA/cm²). The onset of the anodic current in the case of 1N H₂SO₄ [curve (a)] occurs near the flatband potential ($V_{FB} = 0.73$ V), as expected. The anodic current for 1M HCl [curve (b)] is shifted some 150 mV in the negative potential direction with respect to the H₂SO₄ case. With an increase in the HCl concentration, this effect becomes more pronounced. For the 9M HCl solution, the shift amounts to about 350 mV. When the curve was measured again in 1N H₂SO₄ after the HCl experiments, exactly the same result was obtained as in the first measurement [curve (a)].

We also measured the Mott-Schottky plots for each of the solutions used in Fig. 6. The flatband potential did not depend on the HCl concentration: $V_{FB} = 0.725 \pm 0.050$ V in all cases. The slope of the Mott-Schottky plots decreased somewhat as the HCl concentration was increased. This is probably due to an increase in the surface area of the electrode due to roughening as a result of etching. A similar effect can also be seen in Fig. 3b.

Discussion

From Fig. 2 and 4, it is obvious that chemical dissolution occurs in aqueous solution when the HCl concentration exceeds a certain critical value. The rate is strongly dependent on the HCl concentration and becomes very low at values lower than 5M [see Fig. 4, curve (a)]. This suggests that the etch rate depends on the degree of dissociation of HCl molecules. Although it is clear that at low concentrations the dissolution of HCl is complete, there is a considerable discrepancy in the literature with respect to higher concentrations (10). Calculations based on vapor pressure measurements and on Hammett functions show that the concentration of undissociated HCl begins to increase significantly above 5 mol/l (11, 12). In order to avoid the uncertainty involved when HCl is diluted with water, we studied the dissolution rate in HCl-acetic acid solutions. The dissociation constant of HCl in acetic acid ($K_a = 10^{-8.55}$) is much lower than in water ($K_a = 10^{-3}$) (13). Consequently, the degree of dissociation of HCl in acetic acid is negligible, even at low HCl concentrations. The chemical etch rate could therefore be studied as a function of the molecular HCl concentration. The linear dependence of the chemical dissolution rate on the HCl concentration in concentrated acetic acid [Fig. 4, curve (b)] indeed confirms that chemical dissolution is determined by the molecular HCl concentration. The

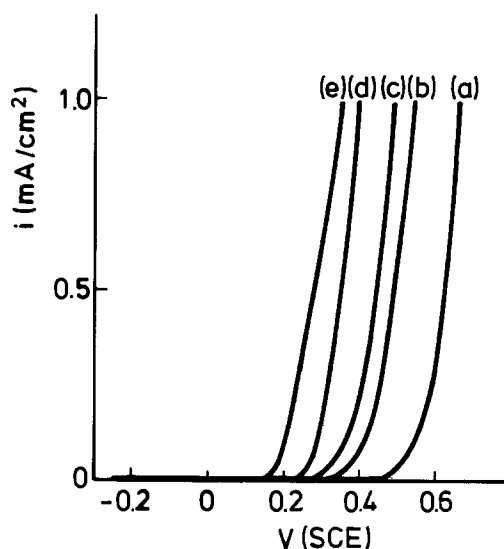
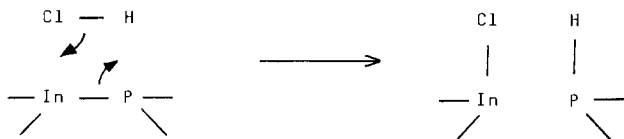


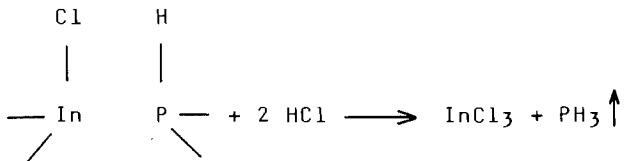
Fig. 6. Current-potential curves for a p-InP electrode in the dark in 1N H₂SO₄ (a), 1M HCl (b), 5M HCl (c), 7M HCl (d), and 9M HCl (e) in water. Scan rate: 10 mV/s.

high etch rate of HCl solutions diluted with concentrated acetic acid compared to that for aqueous solutions, also found by Adachi (7), can be understood in this way. Figure 5 shows that the etch rate is independent of the rotation rate of an InP electrode meaning that the chemical etch rate is kinetically determined by these HCl molecules.

The mechanism presented by Gerischer and Wallem-Mattes for the chemical dissolution of semiconductors involves symmetrical bifunctional etching agents such as H_2O_2 and halogen molecules (5, 6). Although we are, in the present work, dealing with an asymmetrical HCl molecule, we propose a reaction scheme similar to that for symmetrical agents. The first step involves a synchronous exchange of bonds: In-Cl and P-H bonds replace the original H-Cl and In-P bonds. This is very likely the rate-determining step

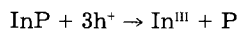


Since the indium and phosphorus atoms at the surface are triply bonded to neighboring atoms, two further bonds must be broken in an analogous manner to remove each atom from the lattice



Indium is therefore dissolved as hydrolyzed $InCl_3$ and PH_3 is evolved as a gas. Such a mechanism can account for the etching results observed.

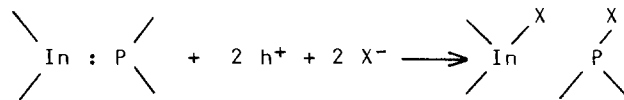
The chemical etch rate of InP in HCl solution is independent of potential. At potentials near the flatband value (Fig. 2 and 3) the p-InP electrode dissolves anodically. The rate of the anodic etching increases as the surface hole concentration is increased, *i.e.*, as the potential is made more positive. In aqueous HCl solutions, we have shown that six holes are required to dissolve one In-P entity. This means that both In and P are oxidized to the trivalent state, as is common for III-V materials (3-6). With a considerable concentration of acetic acid in the HCl solution, however, a film is formed on the electrode which inhibits both the chemical and anodic dissolution (Fig. 3). EDAX measurements have shown that this layer contains phosphorus but no indium or chlorine. We suspect that, in this case, phosphorus is not oxidized directly during anodic dissolution



A similar three-hole mechanism has been shown for GaP (14).

It is obvious from Fig. 6 that the chemical dissolution rate strongly influences the electrochemical behavior of InP. Anodic dissolution starts at a more negative potential as the HCl concentration is increased, although the flatband potential does not change. This must mean that the activation energy for electrochemical dissolution is lowered by chemical etching. A similar effect has been demonstrated by Gerischer and Wallem-Mattes (6) for the dissolution of GaAs in bromine solution. As in the GaAs case, this result can be explained if we assume that rup-

ture of the first In-P surface bond is rate determining for anodic dissolution



If this bond is broken during a chemical attack by HCl, then the remaining bonds are more easily attacked anodically and the onset potential for anodic dissolution is consequently lowered, indicating that it is, indeed, likely that the first step is the rate-determining dissolution step.

Conclusions

The dissolution of InP in concentrated HCl solutions follows a chemical mechanism in which undissociated HCl molecules play a decisive role. It seems likely that other etchants for InP, such as HBr and Br_2 (7, 8), are based on a similar mechanism. The reason why InP does not undergo electroless dissolution in conventional etchants containing oxidizing agents is probably related to the presence of a thin, highly resistant oxide layer on the semiconductor (15). Such a layer, which can inhibit either the dissolution of the solid or hole injection from the oxidizing agent, is unlikely to be present at the high HCl concentrations used here.

Acknowledgment

The author wishes to thank Dr. J. J. Kelly, Mr. J. E. A. M. van den Meerakker, and Dr. R. Memming (Philips Forschungslabor, Hamburg, Germany) for helpful discussions, and the Analytical Department of Ir. P. J. Rommers for the indium analyses.

Manuscript submitted March 19, 1984; revised manuscript received June 11, 1984.

Philips Research Laboratories assisted in meeting the publication costs of this article.

REFERENCES

1. W. Kern, *RCA Rev.*, **39**, 278 (1978).
2. R. P. Tjburg and T. van Dongen, *This Journal*, **123**, 687 (1976).
3. M. M. Faktor, T. Ambridge, C. R. Elliott, and J. C. Regnault, *Curr. Top. Mater. Sci.*, **6**, 1 (1980).
4. H. Gerischer and I. Mattes, *Z. Phys. Chem. N.F.*, **49**, 112 (1966).
5. H. Gerischer and W. Mindt, *Electrochim. Acta*, **13**, 1329 (1968).
6. H. Gerischer and I. Wallem-Mattes, *Z. Phys. Chem. N.F.*, **64**, 187 (1969).
7. S. Adachi and H. Kawaguchi, *This Journal*, **128**, 1342 (1981).
8. S. Adachi, Y. Noguchi, and H. Kawaguchi, *ibid.*, **129**, 1053 (1982).
9. E. Haroutiounian, J. Sandino, P. Clechet, D. Lamouche, and J. Martin, *ibid.*, **131**, 27 (1984).
10. "Gmelins Handbuch der Anorganischen Chemie," Chlor (6), *Ergänzungsband, Teil B - Lieferung 1*, p. 223, Verlag Chemie, GmbH, Weinheim, Germany (1968).
11. A. Eucken, *Z. Elektrochem.*, **52**, 255 (1948).
12. W. Kangro, *Z. Phys. Chem.*, **32**, 273 (1962).
13. W. Huber, "Titrations in Nonaqueous Solvents," pp. 215, 226, Academic Press, New York (1967).
14. R. Memming and G. Schwandt, *Electrochim. Acta*, **13**, 1299 (1968).
15. A. Heller, R. Vadimsky, W. Johnston, Jr., K. Strega, H. Leamy, and B. Miller, in "Proceedings of the 15th IEEE Photovoltaics Specialists Conference, Kissimmee, Florida, May 1980," p. 1422, IEEE, New York (1981).

Diffusion of Ion-Implanted Arsenic in Thermally Grown SiO₂ Films

R. Singh,¹ M. Maier, H. Kräutle, D. R. Young,² and P. Balk*

Institute of Semiconductor Electronics, Technical University Aachen, D-5100 Aachen, Germany

ABSTRACT

The diffusion of As implanted in thermally grown SiO₂ was studied at temperatures in the range 1000°-1200°C using N₂ and O₂ as ambients. Concentrations were between 3×10^{15} and 3.5×10^{16} As⁺ ions cm⁻². Energies of 60 and 340 keV were used. Because of As loss due to evaporation, significant quantitative data could only be obtained for deep implants. N₂-annealed samples exhibit low diffusion rates at high concentrations (above the middle of the 10^{19} cm⁻³ range). Larger diffusion rates are observed at lower concentrations. In the samples treated in O₂, the opposite concentration dependence of the diffusivity is observed. The shape of the profiles suggests that in both cases a high and a low concentration phase exists. A model is presented assuming that in O₂ a fully oxidized structure and in N₂ an oxygen deficient network is obtained as a first step in the annealing process. There are indications that the ambient also affects the diffusion rate during further high temperature treatment of these structures, probably through the concentration of oxygen vacancies.

Dopants introduced into gate oxide films during implantation of the channel in MOSFET devices or by out-diffusion from a polysilicon gate may act as trapping centers for charge carriers (1). For this reason, it is of interest to know the diffusion behavior and understand the trapping properties of such elements in thermally grown SiO₂.

In a recent study in this laboratory (2) on electron trapping in As-implanted SiO₂, different trapping states were found after annealing depending on the nature of the co-implant (O⁻ or Si⁺) or on the annealing ambient (O₂ or N₂). This was interpreted to mean that the conditions under which the implantation damage is being annealed determine the "microscopic location" of the As in the oxide structure. It may be expected that the diffusion mechanism of As will also depend on its mode of incorporation into the SiO₂ network.

Indeed, it had been reported by Wada and Antoniadis (3) that the diffusion rate of As implanted in SiO₂ is concentration and ambient dependent. Specifically, an enhancement of the As diffusion (compared to that in a N₂ ambient) was reported for the case that the process was carried out in O₂ and the silicon substrate was being oxidized simultaneously. The enhancement was attributed to the flow of oxygen through the oxide or, as a more likely cause, to the generation of some point defect at the Si-SiO₂ interface during oxidation. However, it was concluded that the mere presence of excess oxygen in the oxide does not suffice to create the faster rate of diffusion.

In the present study, we have attempted to shed some further light on the question of the diffusion mechanism of As in SiO₂. With some exceptions, we have confirmed the observations of Wada and Antoniadis. However, to arrive at a correct interpretation of the data, it is necessary to recognize that diffusion of implanted As is a two-step process: incorporation of As into the SiO₂ network and diffusion of the incorporated As. Both steps may, in principle, be affected by the experimental conditions, specifically by the annealing ambient. It will be shown in this paper that, even though a number of questions remain open, a consistent picture of the overall process is obtained by taking these aspects into account.

Experimental

To study the diffusion of implanted As in SiO₂, concentration profiles were determined for four groups of diffusion experiments. In the first two, some of the experiments of Wada and Antoniadis were repeated to clarify the role of the rate of oxidation in O₂ on the diffusion process. In the third experiment, the effects of implanted dose, annealing temperature, and ambient, and in the fourth that of "mixed" annealing treatments, using O₂ and N₂ consecutively, were studied. Annealing temperatures were 1000°, 1100°, and 1200°C.

*Electrochemical Society Active Member.

¹Present address: Solid State Physics Laboratory, Delhi, India.

²Present address: IBM Research Center, Yorktown Heights, New York 10598.

All substrates were (100)-oriented 22-32 Ωcm p-type silicon wafers. For the first experiment, to determine the effect of an ongoing oxidation process, these substrates were first oxidized in dry O₂ at 1000°C to approximately 100 nm. Subsequently, some of these samples were implanted with a dose of 10^{16} As⁺ ions (60 keV) cm⁻². Half of the latter group was additionally implanted with 5×10^{15} N₂⁺ ions (80 keV) cm⁻², giving a nitrogen profile with centroid at the Si-SiO₂ interface to block further oxidation. The inhibition or retardation of oxidation by this method, caused by the formation of a nitride layer near the interface and first demonstrated by Josquin and Tamminga (4), was confirmed by us. For example (Fig. 1), starting with an initial oxide of 102 nm, after 8h of further oxidation at 1000°C the N₂⁺-implanted oxide had become thicker by only 15 nm, and that of the sample implanted with As⁺ but not with N₂⁺ had increased by an amount more than ten times larger, i.e., 177 nm. Since for oxidation times > 10h the oxide thickness started to increase significantly, we limited the diffusion experiment at 1000°C to 8h only. All values of SiO₂ film thickness quoted were determined by ellipsometry with an accuracy of ± 1%.

For the second experiment, to explore the interaction between the oxidation and diffusion processes, samples with different oxide thicknesses (177 and 1040 nm) and

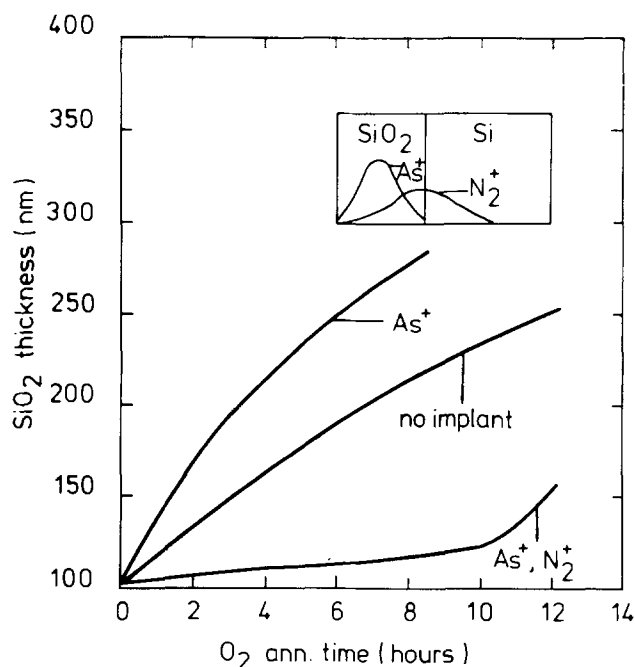


Fig. 1. Inhibition of oxidation by N₂⁺ implantation (5×10^{15} cm⁻³ at 80 keV) for samples with and without As⁺ implant (10^{16} cm⁻² at 60 keV). Insert: as-implanted profiles.

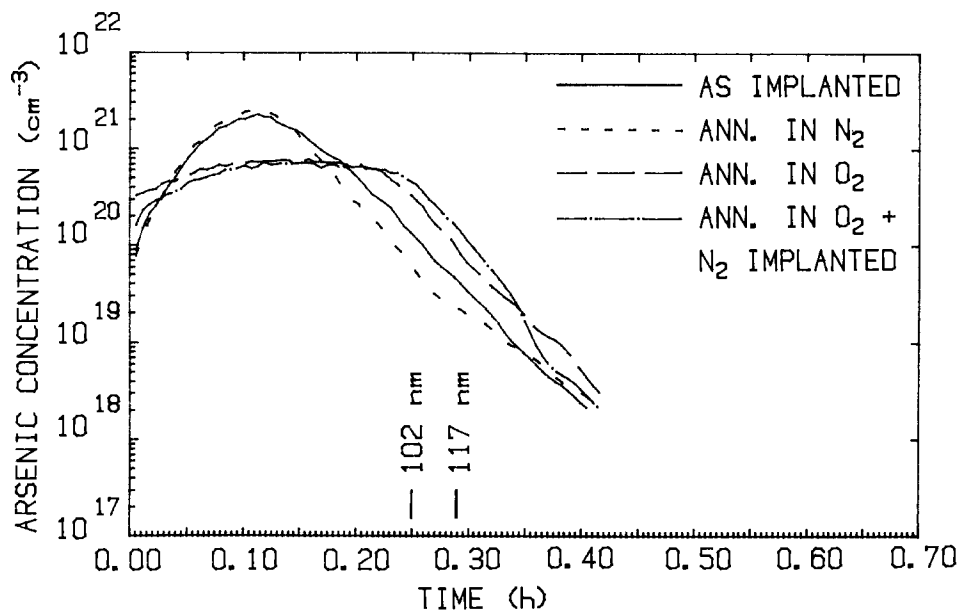


Fig. 2. As concentration vs. sputtering time for as-implanted (10^{16} cm^{-2} at 60 keV) sample and upon annealing in N_2 or O_2 at 1000°C (8h); the fourth sample had additionally been implanted with N_2^+ (5×10^{15} cm^{-2} at 80 keV) to inhibit oxidation. Position of SiO_2/Si interface is indicated (as-implanted and annealed in N_2 : 102 nm, N_2 implanted and annealed in O_2 : 117 nm).

thus different rates of oxidation during O_2 annealing were prepared. The oxidation was carried out in wet O_2 at 1000°C and was followed by 30 min of N_2 annealing at the same temperature. The As^+ implant was again of the same dose (10^{16} cm^{-2}) and at the same energy (60 keV) as in the first case.

The samples used for the third and fourth experiments had a 934 nm thick oxide, grown at 1000°C in wet O_2 ; they were again given a preimplantation N_2 anneal at 1000°C . As implants As^+ doses of 3.5×10^{16} and 3×10^{15} cm^{-2} at 340 keV were selected.

Concentration-depth profiles were determined from SIMS measurements using an Atomika instrument. A 10 keV O_2^+ primary ion beam, incident at an angle of 10° with respect to the surface normal, was employed for sputter erosion of the samples. The quadrupole mass spectrometer of the SIMS instrument was tuned to $^{75}\text{As}^+$ secondary ions and to $^{28}\text{Si}_2^+$ secondary ions of the matrix for reference purposes. The interference of $^{29}\text{Si}^{30}\text{Si}^{16}\text{O}^+$ molecular ions (mass 75) with the $^{75}\text{As}^+$ ions was suppressed by appropriate energy filtering. To minimize the charge up of the SiO_2 surface, the oxide was simultaneously bombarded with 2 keV electrons incident at 60° with respect to the surface normal. The change of intensity of the Si_2^+ ion signal at the SiO_2/Si interface was used to calibrate the sputter-time scale in terms of a depth scale. The error in the depth scale is about $\pm 5\%$. A calibration of the $^{75}\text{As}^+$ signal intensity normalized to the $^{28}\text{Si}_2^+$ signal was obtained by equating the integrals of the background-subtracted depth profiles to the implanted dose of the unannealed samples, which is known with an accuracy of $\pm 5\%$. The integrals of the depth profiles of unannealed samples were reproducible within $\pm 15\%$. The resulting error in the As concentration scale is $\pm 20\%$. As a check, some RBS measurements were also carried out. Even though the RBS analysis yields a somewhat poorer depth resolution than SIMS, all qualitative features of the profiles were confirmed. However, for determination of the total amount of As present in the samples, the RBS method offers greater accuracy. The RBS data led to the conclusion that the loss of As due to outdiffusion was underestimated in some cases (by as much as 10% of the total amount present) in the SIMS study.

Results and Discussion

Effect of ongoing oxidation process.—Results from the first group of experiments, where we studied the effect of retarded oxidation by a nitride layer prepared by N_2^+ ion implantation near the $\text{Si}-\text{SiO}_2$ interface, are presented in Fig. 2. The energy of the implanted As^+ ions had been chosen to place the maximum of the distribution in the middle of the oxide film at a projected range of 46 nm.

This value is close to the values of 47 nm from photo I-V measurements and 46 nm from a SIMS analysis for samples with the same implant as reported by earlier workers (1). The profile obtained after an 8h N_2 anneal at 1000°C shows some narrowing at higher concentrations compared to the As-implanted distribution and exhibits a pronounced tail in the lower concentration range. It should be noticed that the tail lies mainly in the Si substrate. This tailing, but also the narrowing at higher concentrations, could possibly be explained from the relatively high value of the diffusion coefficient of As in the Si substrate [4×10^{-15} cm^2s^{-1} at 1000°C (5), compared to 3×10^{-17} cm^2s^{-1} for As in SiO_2 (3)], which acts as a sink for the dopant.

The profile for the samples annealed for the same length of time at the same temperature in O_2 exhibit a strikingly different appearance. They are broad and flat at the top and do not show a corresponding smear-out at low concentrations. The profile for the sample without N_2^+ implant is somewhat narrower at high concentrations, which cannot be explained from out-diffusion into the substrate, since the interface has moved outside the range of the figure (from 102 to 279 nm) as a consequence of the oxidation process taking place during the O_2 anneal. Comparing the profiles for samples with and without N_2^+ implantation, which exhibit oxidation rates differing by more than an order of magnitude during the diffusion process in O_2 , it must be concluded that, even though we do observe the speed up compared to a N_2 anneal, as reported by Wada and Antoniadis, there is no evidence in our data that the rate of the oxidation process affects the diffusion.

To exclude the possibility that the presence of nitrogen or the damage caused by implantation of this element in the SiO_2 would enhance the diffusion rate, thereby "compensating" for a very slow rate of diffusion in pure and defect-free SiO_2 , the diffusion of implanted As in a thin (177 nm) and thick (1040 nm) sample were compared (Fig. 3). In this case, the average oxidation rates of the samples during O_2 annealing differed by a factor of nearly three, and in the early stages of the process by even more. However, again any indication of a correlation between oxidation rate and diffusion rate fails. Also, during the N_2 anneal (in this experiment annealing times of 30h at 1000°C were used, instead of 8h, as in the first experiment), there is a distinct change of profile, but certainly not so pronounced as upon O_2 annealing.

It is difficult to derive quantitative information from the data in Fig. 2 and 3 since our measurements indicate that during some of the diffusion experiments considerable amounts of As are lost, most likely because of evapo-

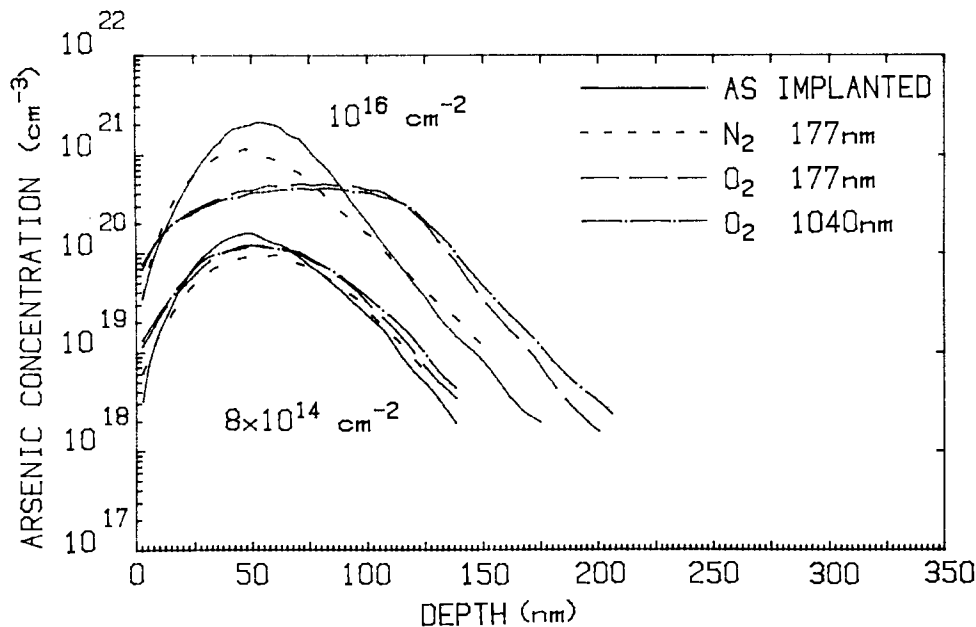


Fig. 3. Diffusion of As (10^{16} cm^{-2} and 8×10^{14} cm^{-2} at 60 keV) in thin (177 nm) and thick (1040 nm) oxides in O_2 at 1000°C (30h). For comparison, diffusion in N_2 at same conditions is also shown.

ration, as also mentioned by Wada and Antoniadis (3). This loss is particularly pronounced for the shallow implants used in experiments 1 and 2. It amounts to 50% (0%) for the O_2 -annealed samples and 30% (25%) for the N_2 -annealed sample with high (low) As dose of Fig. 3, to 35%-40% for the samples annealed in O_2 in Fig. 2, whereas upon the N_2 treatment, no loss could be detected. For this reason, we used in the experiments described below considerably deeper As⁺ implants (340 keV) and consequently thicker oxide films (934 nm).

Ambient dependence.—Having established that the diffusion rate of As in SiO_2 does not depend on the rate of an oxidation process of the silicon taking place simultaneously, we will deal with the difference in diffusion rate for N_2 and O_2 ambients. Figures 4-7 show profiles observed for different annealing temperatures (1000°, 1100°, and 1200°C) and for two (3.5×10^{16} and 3×10^{15} As ions cm^{-2}) deep (340 keV) implants.

The profiles obtained upon N_2 anneal at 1000°C (30h), 1100°C (17h), and 1200°C (5h) (Fig. 4 and 5) clearly show two regions: one at higher concentrations (for example, $> 3 \times 10^{19}$ cm^{-3} at 1200°C), where the profile narrows down, and a second region at concentrations below these limits, where relatively rapid diffusion occurs. The concentration around the maximum does not change at all, or, for the lower concentration implant, only in a modest

fashion. This behavior suggests the presence of a stable high concentration phase, as also proposed by Wada and Antoniadis (3), which acts as a source for the diffusion into the low concentration range. The diffusion coefficients in the low concentration range amount to 6.2×10^{-17} cm^2s^{-1} at 1000°C, to 1.0×10^{-15} cm^2s^{-1} at 1100°C, and to 1.1×10^{-14} cm^2s^{-1} at 1200°C. Contrary to the samples of Fig. 4, where there was no measurable loss of As due to evaporation (RBS yielded 6% outdiffusion), in Fig. 5 the loss amounted to 6% at 1000°, 15% at 1100°, and 30% at 1200°C. This ties in with the change of profile near the surface in the latter case.

The corresponding data for O_2 annealing are shown in Fig. 6 and 7. Particularly striking is the flat appearance of the distribution obtained for the high concentration implant; at 1000°C, only diffusion near the top of the distribution is visible. Apparently, at all temperatures the rate decreases towards lower concentrations. The measured loss of As is quite in line with these observations: for the 3.5×10^{16} cm^{-2} implant, it increases from 7% to 1000°C to 24% at 1100°C and 35% at 1200°C. For the 3×10^{15} cm^{-2} implant (Fig. 7), it ranged from 0% at 1000°C and 1100°C to 14% at 1200°C. The diffusion coefficients at lower concentrations are 4.0×10^{-16} cm^2s^{-1} at 1100°C and 2.7×10^{-15} cm^2s^{-1} at 1200°C.

It thus appears that the concentration dependences of the diffusion rates in O_2 and N_2 show opposite trends.

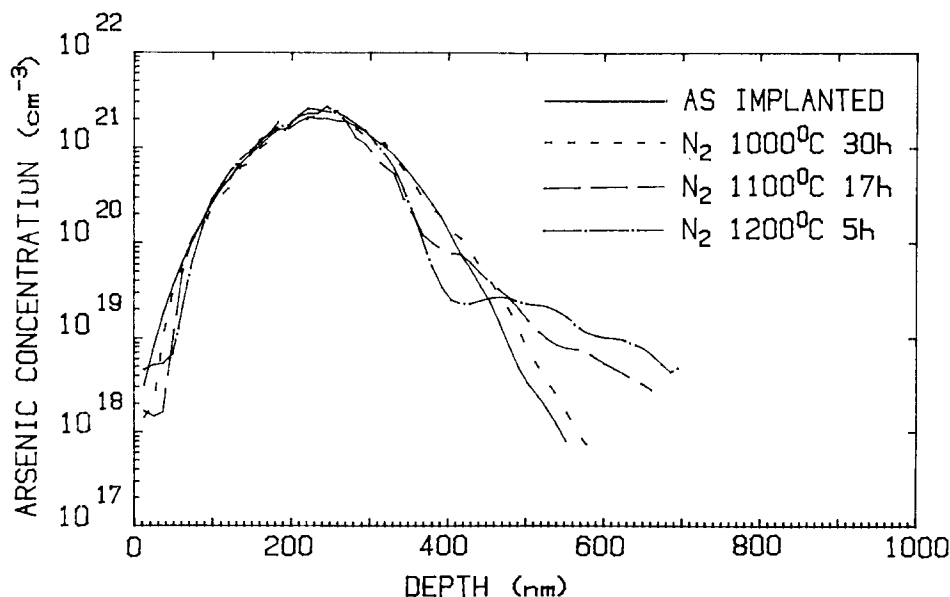


Fig. 4. As diffusion in 934 nm oxide in N_2 at 1000° (30h), 1100° (17h), and 1200° (5h). Implant: 3.5×10^{16} cm^{-2} at 340 keV.

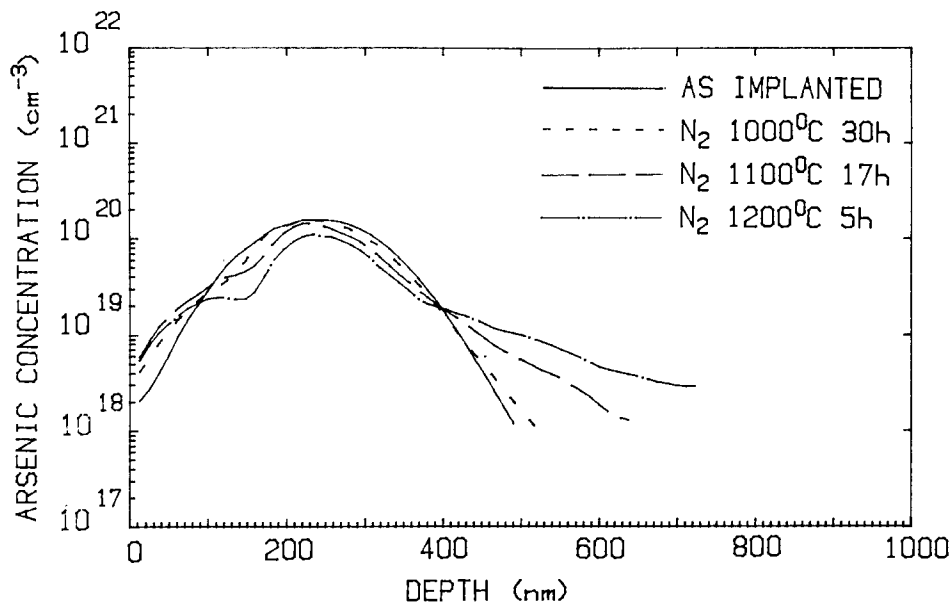


Fig. 5. As diffusion in 934 nm oxide in N₂ at 1000° (30h), 1100° (17h), and 1200°C (5h). Implant: $3 \times 10^{15} \text{ cm}^{-2}$ at 340 keV.

This complex behavior was further investigated in the fourth group of experiments.

The diffusion mechanism of implanted As.—In order to obtain a better understanding of the diffusion mechanism of As implanted in SiO₂ it is important to consider the following: upon implantation of As in SiO₂, the solid has become disordered. The oxygen available in the material does not suffice to reach the fully oxidized stage for both Si and As. This can only be achieved by introducing additional oxygen into the structure, for example, by annealing in O₂, which would lead to the formation of an arsenic silicate ((As₂O₃)_x-(SiO₂)_{1-x}) ($x \approx 0.04$, 1200°C) glass. In contrast, when annealing in N₂, Si and As will compete for oxygen. It is not clear whether here an arsenic silicate glass plus interstitial Si and As will form or if an incompletely oxidized network containing configuration like O₃ ≡ As-Si ≡ O₃³ with direct bonding between As and Si are obtained. However, it appears likely that the rate of diffusion should depend on the manner in which the As has been built into the network. Once a thermodynamically stable atomic configuration has been attained, there

³Here and in the following, the symbol O₃ ≡ As-Si ≡ O₃ is used to indicate an oxygen-deficient silicon oxide configuration O₃ ≡ Si-Si ≡ O₃ (fully oxidized oxide: O₃ ≡ Si-O-Si ≡ O₃), where one Si atom has been replaced by an As atom. The question of the different valency of As (3 to 5) compared to that of Si (4) is not being discussed; only the presence of direct As-Si and Si-Si bonds (or possibly also of As-As bonds) is being alluded to.

could, in principle, be a second effect of the ambient, namely, on the diffusion of the As built into the network, via the stoichiometry (vacancy content) of the oxide structure.

To explore this question, a fourth set of experiments was carried out. Again, implants of 3×10^{15} and 3.5×10^{16} As⁺ ions cm⁻² in thick oxide films (934 nm) were used, and annealing for 5h at 1200°C was studied. It may be seen that for the 3.5×10^{16} cm⁻² implant (Fig. 8), a 5 min O₂ anneal followed by a 5h N₂ treatment has nearly the same effect as a treatment for 5h in O₂ only. Apparently, a very brief O₂ anneal is sufficient to reach a fully oxidized state of the oxide system. In fact, such a transition requires only the presence of a slight amount of O₂ in the neutral ambient: it was observed that starting the annealing step in a neutral ambient without previously thoroughly flushing the furnace tube after introducing the sample led to oxygen-saturated behavior. The subsequent diffusion step appears to be nearly independent of the ambient. Even though a 5 min N₂ anneal may be able to restore the network in a manner typical for the N₂ ambient, the following 5h O₂ anneal appears to first turn the system into the more stable fully oxidized state. Consequently, again the profile characteristic for the network structure obtained for an O₂ treatment is observed.

The loss by evaporation was 35% for 5h O₂ anneal only, 47% for 5 min O₂ + 5h N₂, and 43% for 5 min N₂ + 5h O₂; these values are relatively large but hardly distinguishable.

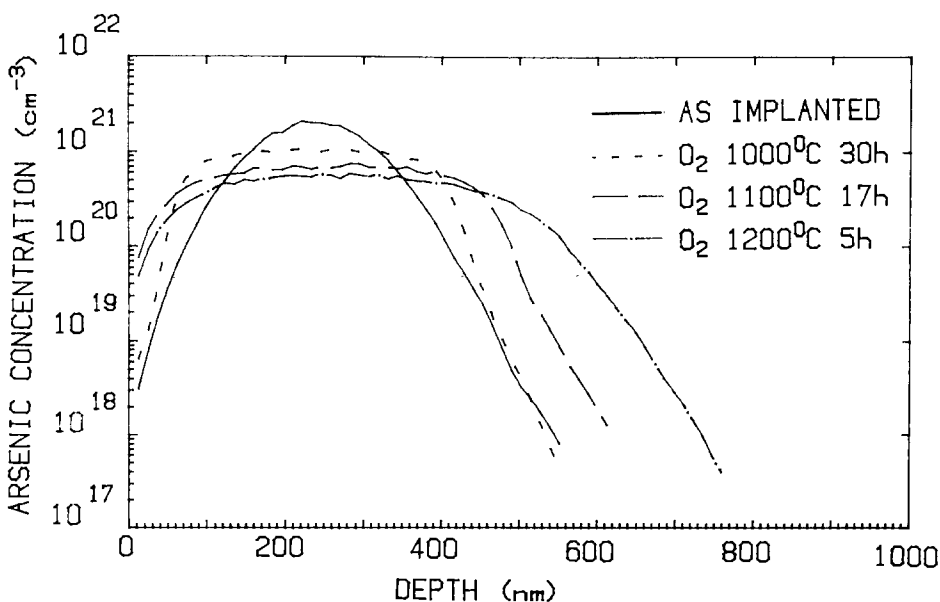


Fig. 6. As diffusion in 934 nm oxide in O₂ at 1000° (30h), 1100° (17h), and 1200°C (5h). Implant: $3.5 \times 10^{16} \text{ cm}^{-2}$ at 340 keV.

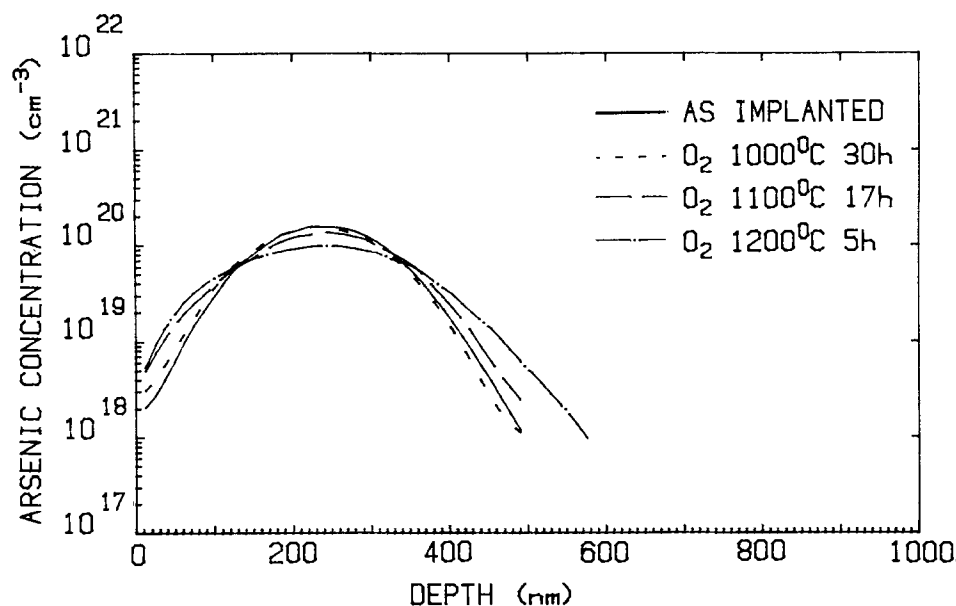


Fig. 7. As diffusion in 934 nm oxide in O_2 at $1000^\circ C$ (30h), $1100^\circ C$ (17h), and $1200^\circ C$ (5h). Implant: $3 \times 10^{15} \text{ cm}^{-2}$ at 340 keV.

ble. For the case of 5h annealing in N_2 only, in the sample of Fig. 4 could no loss be detected. During 5 min treatment in O_2 or N_2 , no measurable diffusion could be observed; the profiles were identical to the as-implanted distribution.

In the samples with lower concentration implants (Fig. 9), slight differences between the "mixed annealing" and O_2 annealing steps become visible. The samples which had been exposed to N_2 in a "mixed anneal" exhibit a somewhat wider profile (*i.e.*, faster diffusion at lower concentrations) than those which had been treated with O_2 only. Thus, the slope of these profiles is less steep and becomes closer to that of the samples annealed in N_2 only. Accordingly, the diffusion coefficient of the "mixed annealed" samples lies between O_2 and N_2 ($3.7 \times 10^{-15} \text{ cm}^2 \text{ s}^{-1}$). The samples which had been exposed to O_2 experienced a smaller loss of As (22% for 5 min O_2 + 5h N_2 , 19% for 5 min N_2 + 5h O_2 , 12% for the sample treated in O_2 only) compared to 30% for treatment in N_2 only.

The diffusion constants derived from our data in the lower concentration range have been plotted in Fig. 10. They show the lower values for the O_2 than for the N_2 ambient (by roughly a factor of three). An intermediate value is found for mixed ambients. It may be seen that this behavior is opposite to that reported in Ref. (3). The reason for this discrepancy is not clear to us.

Summing up, the findings of this section support the concept that upon annealing in N_2 or O_2 implanted As^+

ions are incorporated into the oxide system in a different fashion. In fact, it appears that N_2 anneal gives rise to two types of structures. One of these is observed only if As concentrations in the 10^{20} cm^{-3} range or higher are introduced. In this structure, the dopant is effectively immobilized. Parallel to the dopant incorporated in the first type of structure, As is also taken up in a second "site," where it diffuses at relatively high speeds. In the case of O_2 anneal, the situation is reversed: here there is a strong broadening of the profile at high concentrations, but slower diffusion at low concentrations. The behavior during N_2 anneal is suggestive of the presence of two phases; this could also be the case in the O_2 -treated samples.

It is worth noting that the diffusion behavior of As using a N_2 ambient is not specifically related to this ambient; annealing in Ar for 5h at $1200^\circ C$ led to a profile indistinguishable from that obtained in N_2 . Moreover, N incorporation into the bulk of the oxide film was not found within the detection limit (10^{18} cm^{-3}) for this element in SiO_2 using SIMS.

Incorporation of As on different sites upon O_2 or N_2 anneal was also suggested in Ref. (2): for an O_2 anneal, formation of an "As-O complex" was proposed, whereas the two centers found upon N_2 anneal were tentatively equated with As incorporated on Si sites, since their concentrations were reduced when Si was implanted simultaneously with As. It was assumed that the remaining As would occupy interstitial sites in the latter case. In

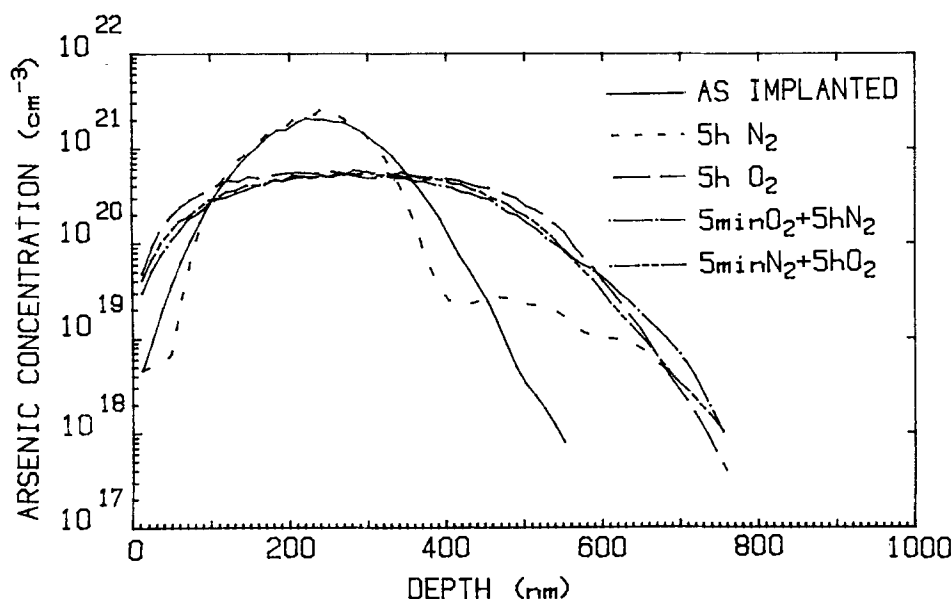
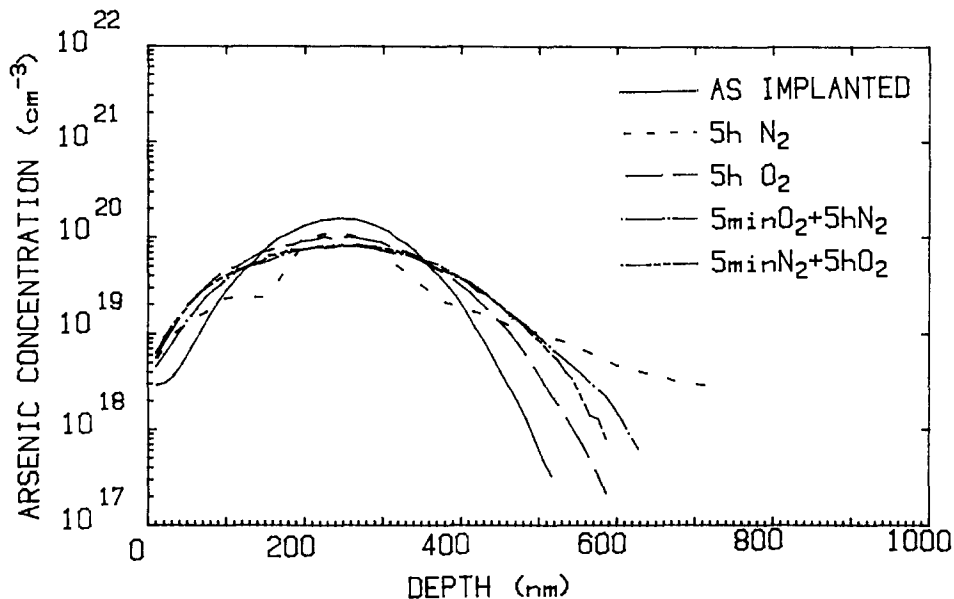


Fig. 8. As diffusion in 934 nm oxide at $1200^\circ C$ in N_2 (5h), O_2 (5h), O_2 (5 min) plus N_2 (5h) or N_2 (5 min) plus O_2 (5h). Implant: $3.5 \times 10^{16} \text{ cm}^{-2}$ at 340 keV.

Fig. 9. As diffusion in 934 nm oxide at 1200°C in N₂ (5h), O₂ (5h), O₂ (5 min) plus N₂ (5h) or N₂ (5 min) plus O₂ (5h). Implant: 3×10^{15} cm⁻³ at 340 keV.



comparing these data with ours, it should be remembered that the implantations in Ref. (2) were done at a dose of only 8×10^{12} cm⁻² at 80 keV, leading to maximum concentrations at least two orders of magnitude smaller than the lowest in our experiments. Thus, the conclusions in Ref. (2) are only relevant for the low concentration range in our data.

From a study of As₂O₃-SiO₂ glasses, used as diffusion sources, it is known that phase separation occurs when the As₂O₃ concentration in the arsenic silicate layer reaches a few mole percent (6). This suggests that, like observed for the phosphosilicate (7, 8) and borosilicate glasses (9), the high concentration phase is probably a liquid at the annealing temperature. It should be noted that one is dealing here with fully oxidized systems, like in our case of O₂ annealing.

Finally, it has been reported (10) from an XPS study of P-implanted SiO₂ that N₂ and O₂ annealing lead to differ-

ent spectra. In both cases, P appears to be incorporated in the lattice in PO₄ configurations; upon N₂ annealing an additional peak, indicative of P-Si bonds, appears. In Ref. (10), this peak is attributed to interstitial phosphorus, but in our opinion these data do not exclude the possibility of the occurrence of O₃ = Si-P = O₃ configurations.

The above considerations lead to the following tentative interpretation of our experimental data: upon O₂ annealing of As-implanted SiO₂, the system becomes fully oxidized and an arsenic silicate glass forms. Since there is no direct evidence that As exists in the form of As₂O₃ in this glass, its composition will be designated by (As₂O₃)_v-(SiO₂)_v. In analogy to the phosphosilicate glass system, we will assume that As replaces Si in the oxide network. This would also explain its low diffusivity. At higher concentrations, a second phase will form, which presumably is liquid at the temperature of annealing. During annealing, this phase will dissolve SiO₂ from both sides until it reaches the composition of the liquidus resulting in the flat and broad profile observed in our data.

We propose that the N₂-annealed samples most likely contain direct Si-As bonds in the form of O₃ = Si-As = O₃ configurations. Such bonds are probably relatively weak, so that O₃ = Si and O₃ = As dangling bond configurations are obtained. As atoms should be able to move through the network by reaction of O₃ = As with O₃ = Si-Si = O₃ configurations to form O₃ = Si-As = O₃ and O₃ = Si. This is responsible for the relatively rapid diffusion at lower As concentrations. Even though diffusion via interstitial As atoms cannot be excluded, the rather similar values obtained for the activation energies for diffusion in N₂ and O₂ appear to support the above mechanism. The immobile phase observed at high concentrations should also be oxygen deficient. Because of the very low diffusivity of As in this phase, it should be a solid, with As incorporated in the network. However, at the present time, we have no clear ideas about the structure of this phase.

It appears feasible that the ambient will additionally affect the rate of diffusion once the O-deficient or fully oxidized systems have formed. Most likely, a N₂ anneal creates a small concentration of oxygen vacancies (2) of the form O₃ = Si - Si = O₃. Such "stretched Si-Si-bonds" (11) are of the same nature as the O₃ = Si-As = O₃ configuration and should enhance the rate of As diffusion in the system. This should become particularly apparent in the fully oxidized system where the initial concentration of vacancies is low. Indeed, the data of the region of low As concentration for the samples submitted to a "mixed" 5 min O₂ plus 5h N₂ anneal suggest that this enhancement does indeed occur. However, further experiments would be necessary to substantiate this point.

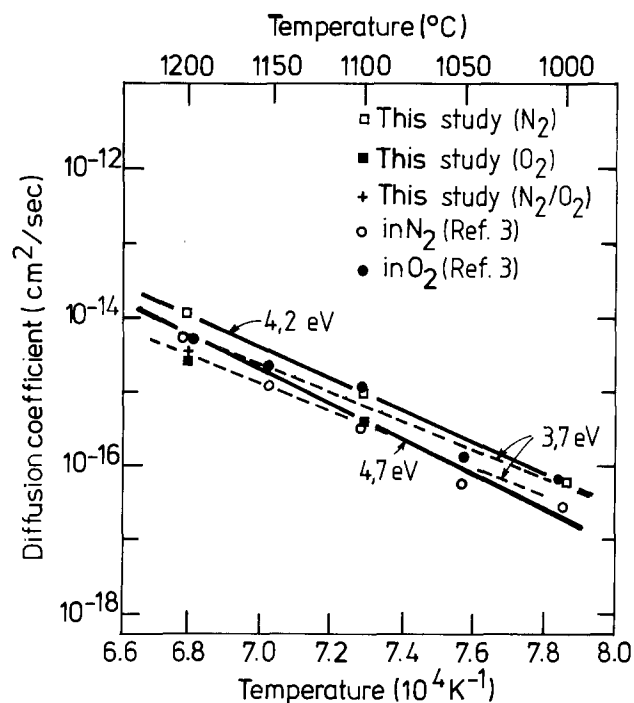


Fig. 10. Arrhenius plot of diffusion constants for As diffusion in SiO₂ in different ambients. For comparison, data from Ref. (3) are also shown. Full lines connect open symbols (N₂ ambient), dashed lines closed symbols (O₂ ambient). Dashed line through O₂ squares from this study was drawn parallel to the corresponding line from Ref. (3).

Conclusions

Our study shows that the diffusion of As in thermally grown SiO₂ is a complex phenomenon. In agreement with expectations from a simple model, one has to consider two consecutive process steps: restoration of the network structure damaged by implantation, and diffusion of As in the restored network. Both steps are likely to be ambient dependent.

The data presented in this paper suggest that two different oxide structures are obtained: an oxygen deficient one in N₂ (or Ar), and a fully oxidized structure in O₂. In both cases, As is incorporated into the network of the glassy oxide, and for N₂-annealed samples possibly additionally on interstitial sites.

The observation of a relatively high diffusion rate at high As concentrations and a very low one at lower concentrations in O₂-annealed samples leads to the conclusion that a separate high concentration liquid phase is formed in fully oxidized samples. The opposite behavior is exhibited by the N₂ heated samples. Again, a two-phase model is proposed, in this case with an immobile high concentration solid phase.

A report in the literature, claiming that a considerably enhanced rate of diffusion in O₂ is observed when simultaneously oxidation of the substrate takes place, could not be confirmed. However, we did find indications that the ambient affects the diffusion rate via the oxygen vacancy concentration in the system.

Acknowledgments

The authors like to thank Dr. O. Meyer, Kernforschungszentrum, Karlsruhe, Germany, for performing a number of RBS measurements. Mrs. D. Laschet has given valuable support in preparing the samples.

Manuscript submitted Dec. 29, 1983; revised manuscript received June 14, 1984.

Technical University Aachen assisted in meeting the publication costs of this article.

REFERENCES

1. R. F. Dekeersmaeker and D. J. DiMaria, *J. Appl. Phys.*, **51**, 1085 (1980).
2. S. Alexandrova and D. R. Young, *ibid.*, **54**, 174 (1983).
3. Y. Wada and D. A. Antoniadis, *This Journal*, **128**, 1317 (1981).
4. W. J. M. J. Josquin and Y. Tamminga, *This Journal*, **129**, 1803 (1982).
5. D. A. Antoniadis, A. M. Lin, and R. W. Dutton, *Appl. Phys. Lett.*, **33**, 1030 (1978).
6. M. Ghezzi and D. M. Brown, *This Journal*, **120**, 110 (1973).
7. T. Y. Tien and F. A. Hummel, *J. Am. Ceram. Soc.*, **45**, 422 (1962).
8. J. M. Eldridge and P. Balk, *Trans. Metall. Soc. AIME*, **242**, 539 (1968).
9. T. J. Rocket and W. R. Forster, *J. Am. Ceram. Soc.*, **48**, 75 (1965).
10. K. Hoh, M. Saitoh, and Y. Miura, *This Journal*, **128**, 1613 (1981).
11. K. L. Ngai and C. T. White, *J. Appl. Phys.*, **52**, 320 (1981).

Characteristics of Ion-Implantation Damage and Annealing Phenomena in Semiconductors

J. Narayan* and O. W. Holland

Solid State Division,¹ Oak Ridge National Laboratory, Oak Ridge, Tennessee 37831

ABSTRACT

The nature of ion-implantation damage in silicon and gallium arsenide as a function of implantation and substrate variables has been investigated using electron microscopy and Rutherford backscattering techniques. With no annealing effects, the crystalline-to-amorphous transition occurs at a critical energy of 12 eV/atom for silicon. By increasing the dose rate or the substrate temperature, "defect-free" regions with no dopant redistribution are obtained. There is a dose rate or substrate temperature window in which voids are formed, producing undesirable effects. The annealing effects at high dose rates are interchangeable with substrate temperature. A high fraction of dopants in both Si and GaAs is found to be in electrically active substitutional sites after high dose rate or high temperature implants. The origin and thermal annealing of underlying dislocation bands have been examined in detail. Subsequent annealing behavior of underlying dislocation bands is critically determined by the nature of the as-implanted states.

Ion implantation is now a well-established technique for a controlled introduction of dopants in semiconductors. Ion-implantation-induced damage must be removed in order to achieve a "complete" electrical activation of dopants and to recover carrier mobility (1). The conventional method of removing ion-implantation damage involves isothermal annealing treatments in a furnace in the temperature range of 900°-1000°C for about 30 min. Recently, more advanced methods based on rapid heating or annealing have been developed for removing ion-implantation damage. The annealing methods based on solid-phase and liquid-phase crystallization (2-6) have been successfully utilized to remove the damage. In both conventional and advanced annealing methods, the nature of ion-implantation damage before annealing is thought to determine the amount of residual damage and concomitant electrical activation and mobility achieved after annealing.

*Electrochemical Society Active Member.

¹Operated by Martin Marietta Energy Systems, Incorporated, under Contract no. DE-ACO5-84OR21400 for the U.S. Department of Energy, Oak Ridge, Tennessee 37831.

The purpose of this paper is twofold. The first purpose is to show that the nature of residual damage after ion implantation is a strong function of ion implantation and substrate variables. The ion-implantation variables of particular interest are the total dose, dose rate, and mass and energy of the incident ions. The substrate variables include the temperature and the mass. The second purpose of this paper is to show that different ion-implantation states exhibit different annealing behavior and electrical recovery of dopants. The mechanisms of dynamic *in situ* annealing during ion implantation and of subsequent annealing behavior are discussed for Si and GaAs. The correlations between residual ion-implantation damage and concentration of substitutional (electrically active) dopants in Si and GaAs specimens are presented. The paper is divided into the following sections: ion-implantation fundamentals; dose rate and substrate temperature effects in silicon; dose rate effects in different orientations; dose rate and substrate temperature effects in GaAs; thermal annealing of different ion-implantation states; and annealing effects in underlying dislocation bands and gettering.

Experimental

Single crystals of silicon having $\langle 100 \rangle$ and $\langle 111 \rangle$ orientations (500 μm thick, 2-6 $\Omega\text{-cm}$, Czochralski grown) were implanted with $^{28}\text{Si}^+$, $^{30}\text{Si}^+$, $^{75}\text{As}^+$, and $^{208}\text{Bi}^+$ ions. Implantation current varied from 1-500 $\mu\text{A cm}^{-2}$, ion energy from 100-250 keV, total dose from $1.0 \times 10^{14} \text{ cm}^{-2}$ to $5.0 \times 10^{16} \text{ cm}^{-2}$, and substrate temperature from liquid helium (He) to room temperature. No effort was made to heat-sink the samples during implantation. The $\langle 100 \rangle$ GaAs specimens were implanted with $^{28}\text{Si}^+$ ions using a similar range of implant and substrate variables. For some Si and GaAs specimens, *in situ* heating was applied while ion implantation was carried out at low dose rates. The ion-implanted silicon and gallium arsenide samples were analyzed by cross-sectional electron microscopy and Rutherford backscattering/channeling techniques at room temperature for a detailed determination of residual damage and lattice location of dopants. Lattice location of dopants is directly related to their electronic properties. The Si^+ -implanted GaAs samples were analyzed by MeV proton-induced x-ray excitation (PIXE) to determine the lattice location of silicon (7). For other studies, an analysis of the energy spectra of light ions backscattered from the sample under channeling and nonchanneling conditions is used for lattice-site determination. However, backscattering techniques are sensitive only to heavy impurities in light substrates and, therefore, are not suitable for GaAs work. The distinct separation of the Si characteristic x-rays from those of the host lattice makes lattice location studies possible in this material through the analysis of x-ray spectra (otherwise impossible using other ion scattering techniques). High resolution electron microscopy studies were conducted using a JEOL 200CX electron microscope operated at 200 kV with a spherical aberration coefficient (C_s) of 1.2 mm. The images were taken under axial illumination with optimum defocus, which is about 1.2 times the Scherzer defocus limit of -65 nm .

Results and Discussion

Ion-implantation fundamentals.—During ion implantation, when an energetic ion penetrates a solid, it collides with the electrons and nuclei of the solid. The energy lost in electronic excitations ultimately appears as heat. The initial energy of the primary ion can be partitioned into the amount lost in electronic excitations, and the remaining energy (E_D) goes into production of displacements. This displacement or ion-implantation damage is created as Frenkel (vacancy and interstitial) pairs, whose number is given by the modified Kinchin and Pease (8) expression $\kappa E_D/2E_d$, where κ (~ 0.8) is the displacement efficiency and E_d is the displacement threshold energy ($\sim 15 \text{ eV}$ for silicon) (9). The vacancies and interstitials accumulate as a function of implanted dose, and at a critical value of 12 eV/atom for E_D , there is a first-order phase transition from crystalline to amorphous phase. This value of 12 eV/atom, or $6.0 \times 10^{23} \text{ eV/cm}^3$ in silicon, is determined near 4 K, where annealing effects are negligible (10, 11). At higher temperatures, mobility of vacancies and interstitials becomes high enough that they annihilate each other or cluster to form dislocation loops. During ion implantation, if the regions of crystals exceed the critical energy for amorphization, they undergo a first-order phase transformation. It has been shown that for self-ions in silicon, overlap of damage produced by several ions is required because individual ions can deposit only about 3 eV/atom (11, 12). The ions, having mass equal to higher than that of antimony, can deposit 12 eV/atom or higher and, therefore, produce amorphous regions directly (11).

Figure 1A is a high resolution micrograph showing an amorphous region in a silicon specimen implanted with 100 keV, $1.0 \times 10^{14} \text{ cm}^{-2}$, $^{30}\text{Si}^+$ ions at liquid He temperature. The specimens that were implanted with $5.0 \times 10^{13} \text{ cm}^{-2}$ Si^+ (100 keV), at liquid He temperature or at room temperature, showed the presence of dislocation loops and not of amorphous regions. As the implanted dose was increased to $2.0 \times 10^{14} \text{ cm}^{-2}$, the small amorphous regions overlapped and created a large band of amorphous re-

gion. However, in this amorphous phase, the presence of microcrystallites is clearly delineated, as indicated by the arrow in Fig. 1B. Figure 1C shows a micrograph just below the critical dose of amorphization. There are many amorphous regions present at this dose, including a twinning partial dislocation, the core region of which is encircled in the micrograph. The line in the micrograph shows the trace of a twinning plane. Figure 1D shows a cross-section micrograph from a specimen implanted with a dose of $4.0 \times 10^{14} \text{ cm}^{-2}$, where the interface between crystalline and amorphous phase appears to be atomically sharp, confirming the first-order phase transition. Some microcrystallites (as shown by the arrow) are also present in this specimen. It is interesting to note that the amorphous-crystalline interface is fairly undulated, presumably because of ion-range straggling.

The displacements below the amorphous-crystalline interface are created because of ion-range straggling. The interstitials in this region can cluster at higher temperatures to form visible dislocation loops. The average size of the vacancy loops has been shown to be much smaller ($\sim 5\text{-}10\text{\AA}$) than that of interstitial loops (13), normally below the resolution limit of the strain-contrast imaging mode of the microscope.

The sequence of ion implantation as a function of increasing dose, discounting the annealing effects, can be described as follows. First, the region corresponding to the Gaussian damage peak turns amorphous after attaining 12 eV/atom of damage energy. This band then expands toward both the surface and deeper regions of the crystal with increasing implanted dose as these regions accumulate the critical energy for amorphization. Figure 2A shows a buried amorphous layer after a dose of $2.0 \times 10^{14} \text{ cm}^{-2}$ (100 keV, $^{30}\text{Si}^+$ ions). A high resolution micrograph from the near-surface region is shown in Fig. 2B, where the crystalline and amorphous boundary is clearly delineated. Although the amorphous-crystalline boundary is jagged, it is atomically sharp. The microcrystallites are present in the amorphous region. As the implanted dose is further increased, the amorphous-crystalline boundaries at both ends expand, ultimately creating amorphous layers followed by a band of dislocation loops. Figure 3 shows such layers for two different doses, 5.0×10^{14} and $5.0 \times 10^{15} \text{ cm}^{-2}$ (100 keV, $^{30}\text{Si}^+$). The thickness of the amorphous layer was found to increase from 2200-2660 \AA as the dose increased from 5.0×10^{14} (Fig. 3A) to $5.0 \times 10^{15} \text{ cm}^{-2}$ (Fig. 3B). Figure 3C is a microdiffraction pattern from $5.0 \times 10^{14} \text{ cm}^{-2}$ specimens, showing two clear rings, which correspond to the first and second neighbor distances, and a faint third ring. For a dose of $1.0 \times 10^{16} \text{ cm}^{-2}$, the thickness of the amorphous layer was found to be 2830 \AA . With further increase in dose, however, the increase in thickness was small because of saturation and the importance of sputtering effects.

Dose rate/substrate temperature effects in Si $^{28}\text{Si}^+$ implantation.—It has been shown that by increasing the ion-implantation current, the substrate temperature can be raised. Therefore, the annealing effects achieved by high dose rate implants (without additional sample heating) can be simulated by *in situ* heating of the substrate while implanting at low dose rates. By increasing the dose rate (ion-implantation current), it is possible to create "defect-free" regions near the surface, followed by a broad band of dislocation loops and tangles. An example is shown in Fig. 4A for a 200 keV Si^+ implant at 200 $\mu\text{A cm}^{-2}$ to a dose of $1.0 \times 10^{16} \text{ cm}^{-2}$. In this case, no additional heating was applied during implantation. The cross-sectional TEM micrograph shows a top 2100 \AA wide "defect-free" region, followed by a 3000 \AA wide region containing dislocation loops and tangles. The annealed layer has the same orientation as the underlying substrate. Figure 4B shows a random and $\langle 110 \rangle$ -aligned spectrum from these specimens. The aligned yield in the top 2100 \AA region is close to that of virgin crystals, which is in good agreement with TEM observations. The aligned yield increases below 2100 \AA , because of the presence of disloca-

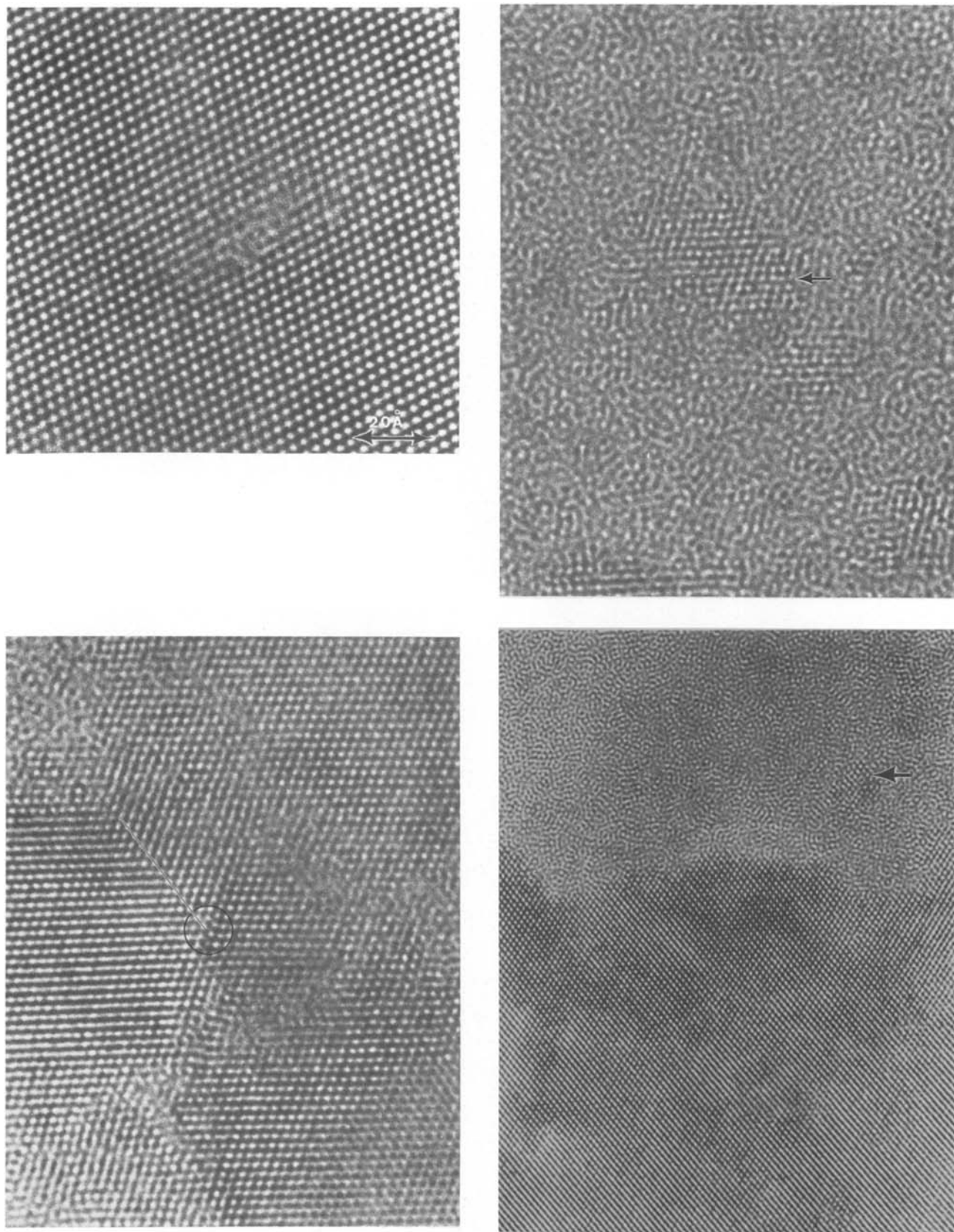


Fig. 1. A (top left): High resolution electron micrograph showing an amorphous cascade region in a specimen implanted with 100 keV $^{30}\text{Si}^+$ ions to a dose of $1.0 \times 10^{14} \text{ cm}^{-2}$. B (top right): High resolution micrograph of amorphous silicon implanted with 100 keV $^{30}\text{Si}^+$ ions to a dose of $2.0 \times 10^{14} \text{ cm}^{-2}$. C (bottom left): High resolution micrograph showing amorphous regions and a twinning partial dislocation (encircled) below the critical dose of amorphization. D (bottom right): High resolution electron micrograph (cross-sectional) showing the interface between the amorphous and crystalline silicon. Notice the presence of a microcrystallite in the amorphous region (indicated by arrow).

tions, but it does not reach the random or amorphous value. These results should be contrasted with low dose-rate Si^+ implants (see Fig. 19), where an amorphous layer followed by a band of dislocation loops is observed.

Figure 5 shows results from 80 keV $^{28}\text{Si}^+$ implants in silicon. After implantation to a dose of $1.0 \times 10^{16} \text{ cm}^{-2}$ at an implantation current of $120 \mu\text{A cm}^{-2}$, we found a buried amorphous layer, as shown in Fig. 5A. The cross-sectional

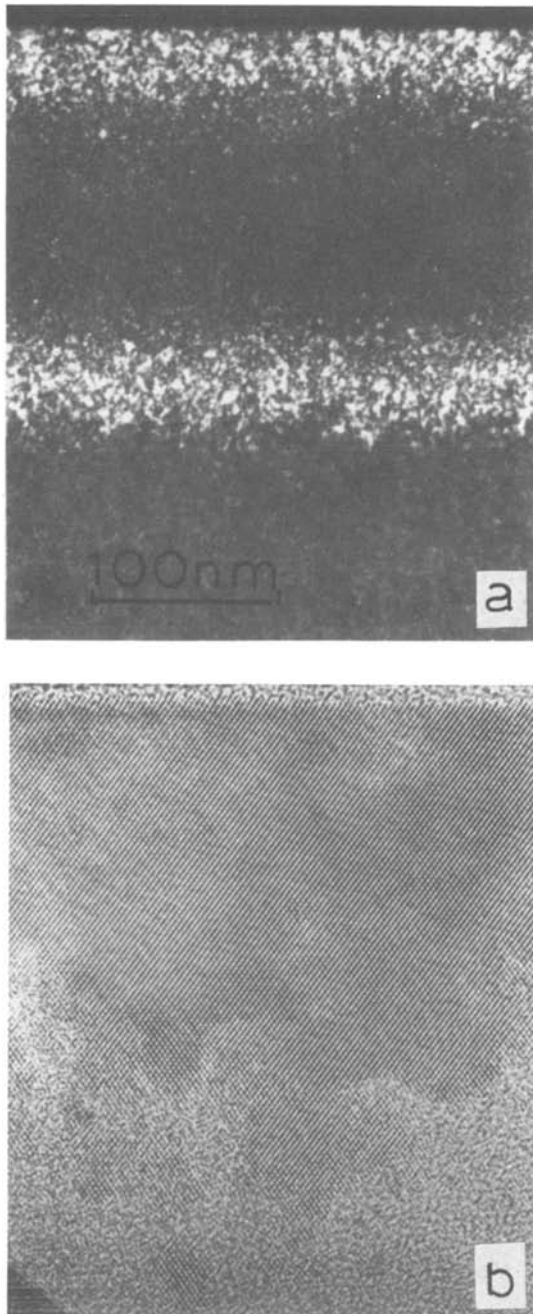


Fig. 2. Cross-sectional electron micrographs showing buried amorphous layers in specimens implanted with 100 keV $^{30}\text{Si}^+$ (dose $2.0 \times 10^{14} \text{ cm}^{-2}$). A: Dark-field. B: High resolution micrograph.

micrograph shows about a 350Å wide "defect-free" region, followed by a 700Å wide amorphous region. Below the amorphous layer, a 200Å wide defect-free layer is formed, which is followed by a 600Å wide region of dislocation loops and tangles. The RBS results from these specimens are shown in Fig. 5B. From the comparison of $\langle 110 \rangle$ -aligned spectra and random spectra, we find that the reduced yield in the top layer in as-implanted specimens is consistent with TEM observations. Below this region, the aligned yield approaches the random yield, corresponding to the presence of a 700Å wide amorphous layer. The aligned yield drops again, corresponding to the defect-free region below the amorphous layer. The yield increases again, owing to the presence of dislocations; however, the yield does not drop to a virgin value in the substrate, owing to previous dechanneling events. The as-implanted specimens containing buried amorphous layers were annealed at 550°C, and it was found that two amorphous-crystalline interfaces moved toward each other and ultimately produced a band of dislocation loops

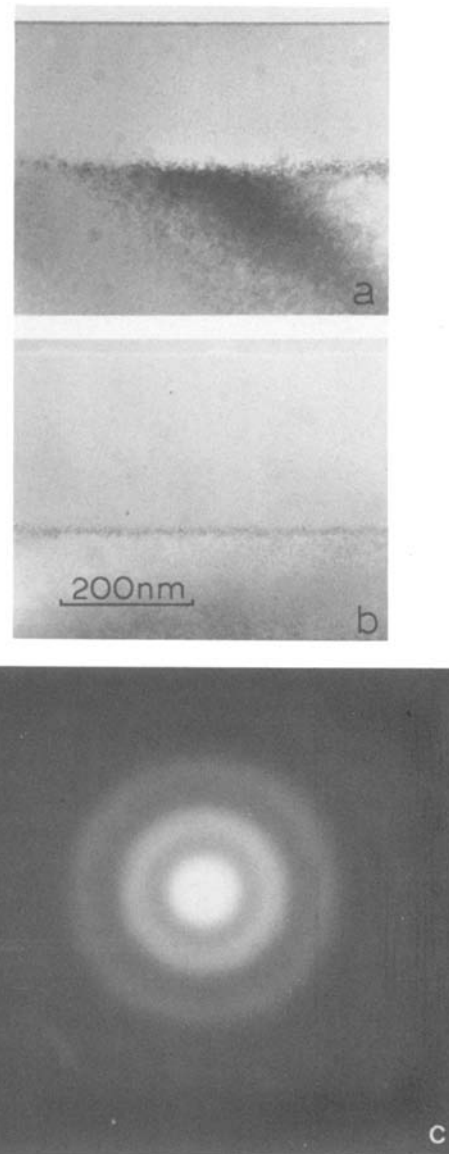


Fig. 3. Cross-sectional electron micrographs showing an increase in amorphous layer thickness with dose. A: 100 keV $^{30}\text{Si}^+$, dose = $5.0 \times 10^{14} \text{ cm}^{-2}$. B: Dose = $5.0 \times 10^{15} \text{ cm}^{-2}$. C: Microdiffraction pattern corresponding to A.

near the center. This is consistent with a small peak in the aligned spectrum at a 700Å depth after annealing the as-implanted specimens for 50 min at 550°C. This peak was reduced or almost annealed out by further annealing at 850°C for 10 min, but the large dislocation loops in this layer, particularly in the underlying layer, remain. This is consistent with increased dechanneling in the aligned spectrum below 1200Å.

$^{75}\text{As}^+$ implantation.—Figures 6-9 show results from high dose-rate, 100 keV As^+ implants in $\langle 100 \rangle$ silicon. Figure 6A is a TEM cross-sectional micrograph at $200 \mu\text{A cm}^{-2}$ to a dose of $1.0 \times 10^{16} \text{ cm}^{-2}$; it shows a defect-free region ($\sim 500\text{Å}$ wide), followed by a band of dislocation loops and tangles ($\sim 1000\text{Å}$ wide). A microdiffraction pattern from the implanted layers of these specimens is shown in Fig. 6B, in which diffraction spots are sharp and regular, corresponding to a $\langle 110 \rangle$ orientation. At $40 \mu\text{A cm}^{-2}$, there is a 1100Å wide amorphous layer followed by a 150Å wide defect-free region and a 300Å wide dislocation band, as shown in Fig. 6C. A microdiffraction pattern from the amorphous band is shown in Fig. 6D, which contains the characteristic rings of amorphous phase. The defect-free region is formed by a solid-phase epitaxial growth process at this dose rate because of beam heating. It is apparent that by increasing the dose rate, the SPE

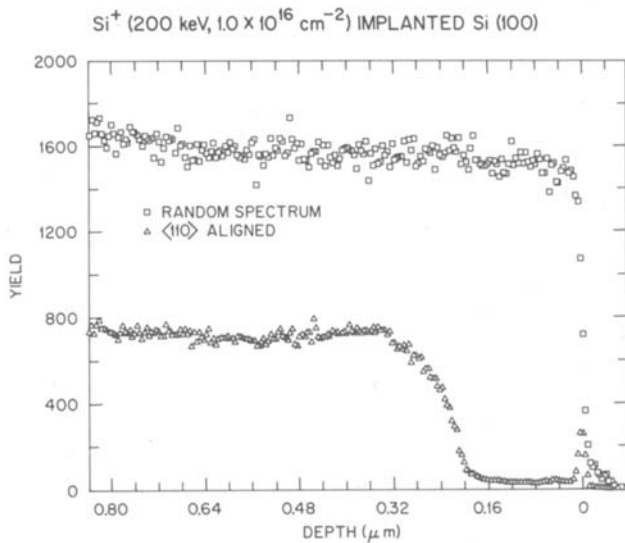
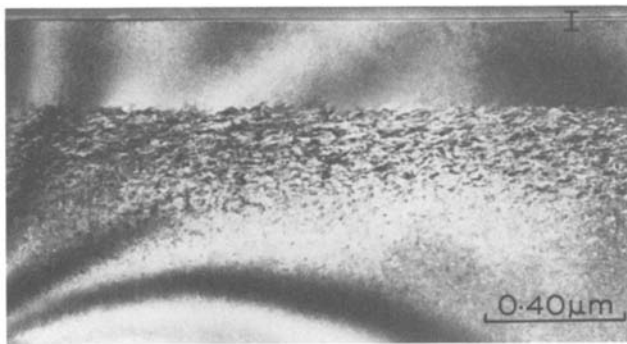


Fig. 4. A(top): Cross-sectional electron micrograph showing the formation of defect-free region in silicon-implanted (100) silicon (200 keV $^{30}\text{Si}^+$, $1.0 \times 10^{16} \text{ cm}^{-2}$, $200 \mu\text{A cm}^{-2}$). B(bottom): 2.0 MeV He^+ RBS spectra (random and $\langle 110 \rangle$ -aligned) from the specimen shown in A.

growth rate can be enhanced and annealing in the top region achieved. The dislocation loops and tangles are formed by clustering of point defects with number densities below that required for amorphous phase transformation. Figure 7 shows 2.0 MeV $^4\text{He}^+$ random and $\langle 110 \rangle$ -aligned spectra from high (Fig. 6a) and low (Fig. 6c) dose-rate implants and virgin crystals. The low dose-rate implants show $\sim 1500\text{\AA}$ thick defective layers. It should be noted that the 1500\AA wide defect-free band below the amorphous layer is not resolved in the aligned silicon spectrum for low dose-rate implants, presumably because of limited system resolution. The aligned silicon spectrum from high dose-rate implants shows reduced

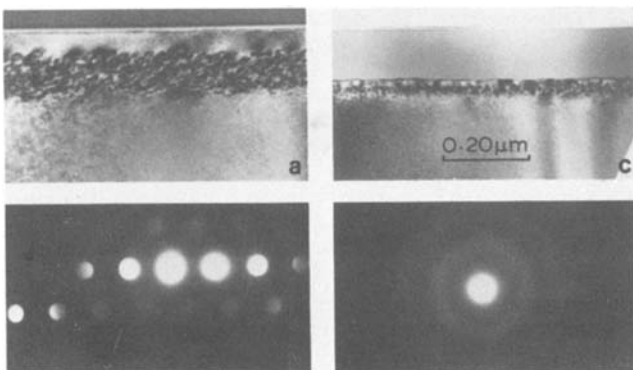


Fig. 6. Dose-rate effects in arsenic-implanted (100) silicon. A: $1.0 \times 10^{16} \text{ cm}^{-2}$ at $200 \mu\text{A cm}^{-2}$. B: Microdiffraction pattern corresponding to A. C: $1.0 \times 10^{16} \text{ cm}^{-2}$ at $40 \mu\text{A cm}^{-2}$. D: Microdiffraction pattern from C.

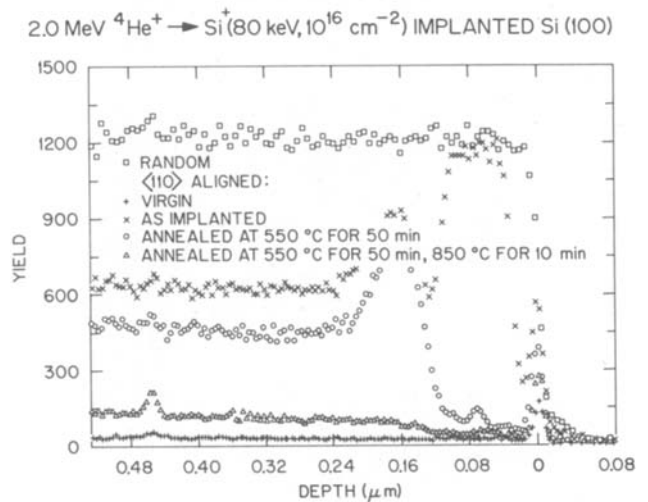
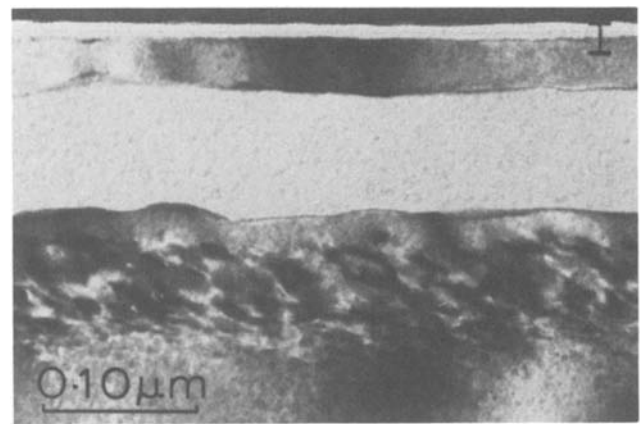


Fig. 5. A(top): Cross-sectional electron micrograph showing a buried amorphous layer in silicon-implanted (100) silicon (80 keV $^{30}\text{Si}^+$, $1.0 \times 10^{16} \text{ cm}^{-2}$ with a dose rate of $120 \mu\text{A cm}^{-2}$). B(bottom): 2.0 MeV He^+ RBS spectra (random and $\langle 110 \rangle$ -aligned) after annealing at 550° and 850°C (from specimen shown in 1A).

yield in the top 500\AA wide region corresponding to the defect-free region in the cross-sectional TEM micrograph. From the aligned and $\langle 110 \rangle$ random spectra of arsenic, it was found that up to 90% of the arsenic in substitutional sites were in certain regions. It is most interesting to note that the arsenic depth distribution remains Gaussian and largely unchanged during high dose-rate implants. Hall measurements showed a high electrical activation of arsenic of up to 70%.

When the dose rate was increased to $400\text{--}500 \mu\text{A cm}^{-2}$, we observed the formation of voids in the top 500\AA wide region with a 50\AA average diameter. The voids in Fig. 8a exhibit a characteristic light contrast for overfocus conditions and a characteristic dark contrast for underfocus

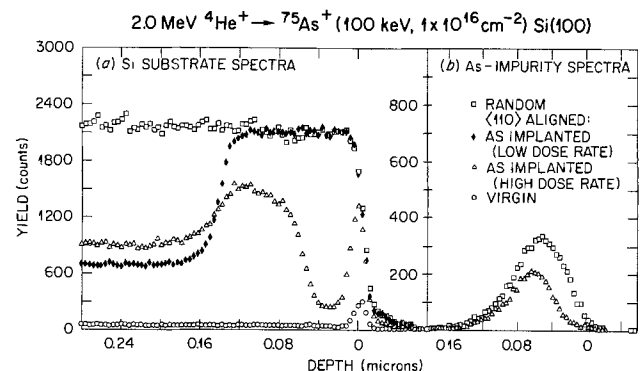


Fig. 7. 2.0 MeV He^+ RBS spectra (random and $\langle 110 \rangle$ -aligned) from the high and low dose-rate specimens shown in Fig. 6.

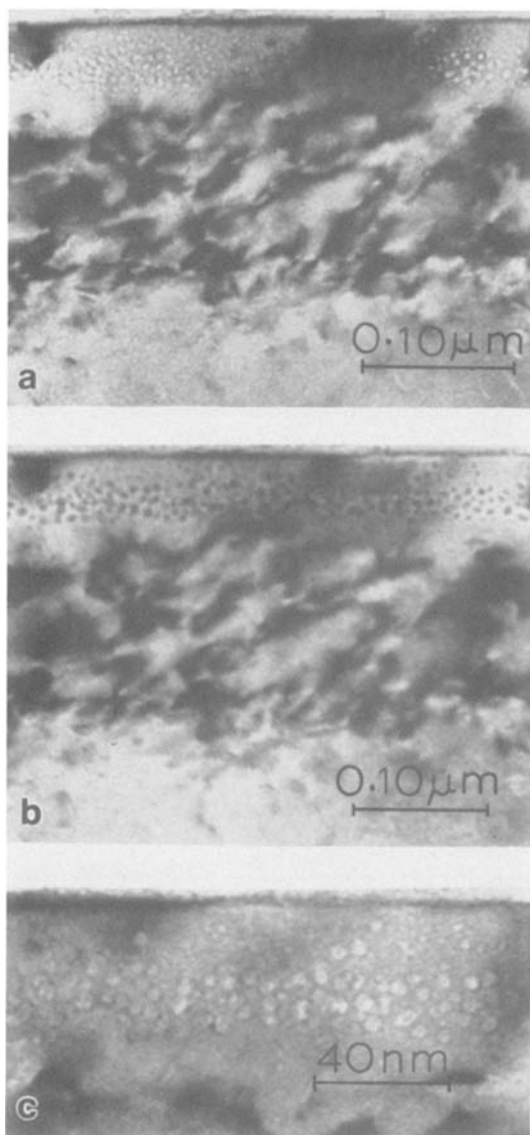


Fig. 8. Formation of voids in high dose-rate implanted (100) silicon specimen (100 keV As^+ , 1.0×10^{16} , $\sim 400 \mu\text{A cm}^{-2}$) under different focusing conditions. A: Cross-sectional electron micrograph showing voids in overfocus (light contrast) conditions. B: Underfocus (dark contrast) conditions. C: Voids with light contrast in overfocus conditions at a higher magnification.

conditions (15) [Fig. 8b]. A small area at a higher magnification is shown in Fig. 8c, where voids are shown under a light contrast. Figure 9 is a plan-view micrograph showing voids in light contrast (overfocus conditions) in the top region. The formation of voids occurs because the in-

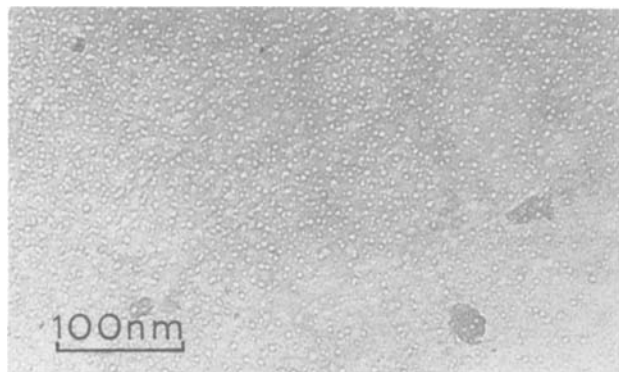


Fig. 9. Plan-view electron micrograph showing voids in light contrast (overfocus) conditions.

terstitials have faster mobility and are lost to the surface or other sinks. The vacancies, which in comparison with interstitials represent the slower moving species, cluster to form voids (16).

From these observations and a previous work (14), we have derived the following mechanism of annealing at high dose rates. During the initial phase of the ion implantation, buried amorphous layers or near-surface amorphous layers are formed, depending upon energy and mass of the incident ions and upon mass of the substrate. These variables determine the profile of the deposited damage energy. Lower energy of the incident ions and higher mass of the incident ions and substrate create amorphous layers near the surface. Buried amorphous layers are formed by higher energy of the incident ions and lower mass of the incident ions and substrate. For example, $100 \text{ keV } ^{28}\text{Si}^+$ tend to form buried amorphous layers, whereas $^{75}\text{As}^+$ ions form near-surface amorphous layers. The amorphous layers anneal by solid-phase epitaxial growth as the implantation is continued. The heat generated by the ion beam raises the substrate temperature. A typical substrate temperature of 750°C was measured during a $200 \mu\text{A cm}^{-2}$ (120 keV) Si^+ implant. Thus, SPE growth at high temperatures provides a primary mechanism of annealing at high dose rates. The kinetics of SPE growth have been extensively studied by RBS, TEM, and time-resolved reflectivity techniques (17). The interface velocity follows an Arrhenius relation $V = V_0 \exp(E_i/kT)$, where $V_0 \langle 100 \rangle = 3.07 \cdot 10^8 \text{ cm s}^{-1}$, and $E_a = -2.68 \text{ eV}$. The pre-exponential factor V_0 is orientation dependent, given by $(V_0 \langle 111 \rangle = 24 V_0 \langle 100 \rangle = 4 V_0 \langle 110 \rangle)$ (3). If the amorphous layers are not formed because the regions could not attain the critical energy of 12 eV/atom for amorphization, the recombination of interstitials and vacancies is a dominant mechanism of annealing. The cascades representing vacancy-rich regions may provide nuclei for void formation. It is noted that dopant depth profiles remain unchanged during high dose-rate implants. This is consistent because the average dopant diffusion distance ($\sqrt{2D\tau}$) during ion implantation (using the typical values of diffusion coefficients of arsenic in silicon at elevated temperatures, and using diffusion time, τ , the time of the ion implantation as the upper limit) is estimated to be less than 10 \AA .

Dose-rate effects in different orientations.—Since *in situ* solid-phase epitaxial (SPE) growth is a primary mechanism of annealing at high dose rates for high dose implants, it is interesting to study dose-rate effects in different orientations. The $\langle 111 \rangle$ Si specimens implanted with $^{75}\text{As}^+$ ions at a dose rate of $200 \mu\text{A cm}^{-2}$ contain an amorphous layer followed by a small defect-free region, similar to the microstructure obtained at $40 \mu\text{A cm}^{-2}$ in $\langle 100 \rangle$ specimens (shown in Fig. 6c). These results reflect a much smaller growth rate in $\langle 111 \rangle$ orientations than that in $\langle 100 \rangle$ orientations. The experimental results and theoretical models predict SPE growth rates to be slower by a factor of 24 in $\langle 111 \rangle$ orientations and a factor of 6 in $\langle 110 \rangle$ orientations, as compared with $\langle 100 \rangle$ orientations. Figure 10 shows a comparison between $\langle 100 \rangle$ and $\langle 111 \rangle$ orientations. These samples were implanted with 40 keV , $^{30}\text{Si}^+$ to $1.5 \times 10^{16} \text{ cm}^{-2}$ dose at liquid-nitrogen temperature at $\sim 5 \mu\text{A cm}^{-2}$ and then implanted with $120 \text{ keV } ^{28}\text{Si}^+$ to $1.0 \times 10^{16} \text{ cm}^{-2}$ dose at $\sim 200 \mu\text{A cm}^{-2}$. In $\langle 100 \rangle$ orientations, we found a 1700 \AA wide region to be fairly "defect free," except for a few polycrystalline regions near the surface. This region was followed by a 2000 \AA wide band of dislocation loops and tangles (Fig. 10a). A microdiffraction pattern from the recrystallized region is shown in Fig. 10c, where regularity and sharpness of diffraction spots are indicative of the perfection of the lattice.

The $\langle 100 \rangle$ Si results are in contrast to those of the $\langle 111 \rangle$ orientations, where we found 1700 \AA wide polycrystalline followed by a 2000 \AA wide band of dislocation loops and tangles (Fig. 10b). In the second region, a high number density of microtwins were also present.

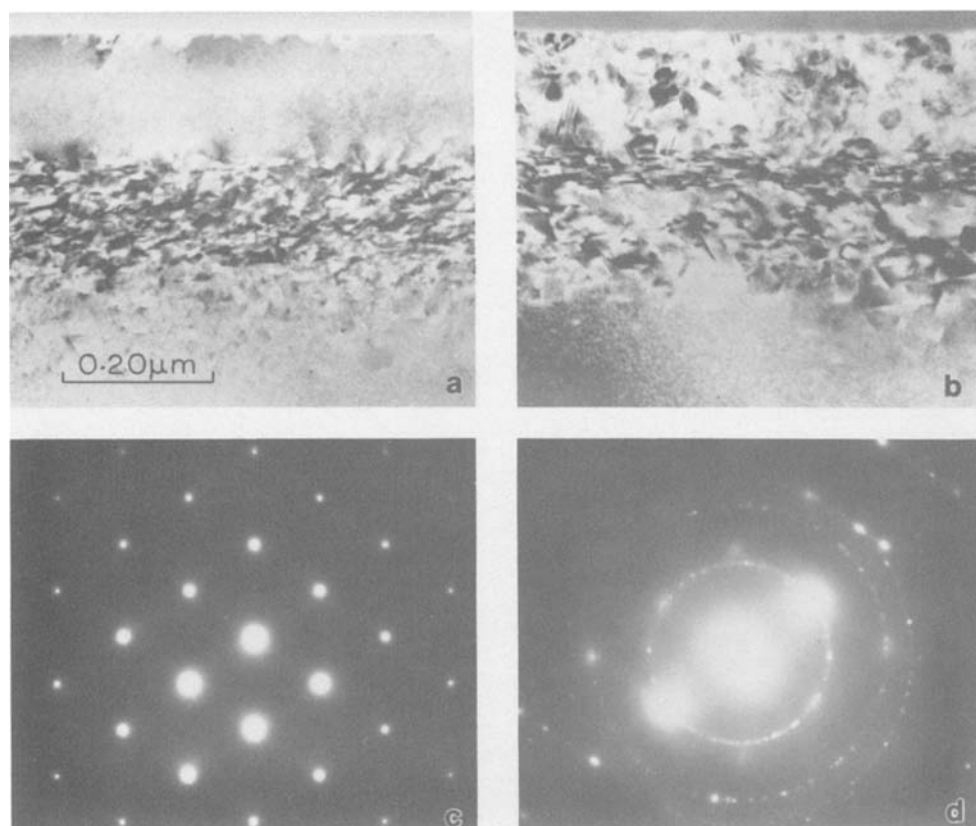


Fig. 10. Comparison of high dose-rate effects in $\langle 100 \rangle$ - and $\langle 111 \rangle$ -oriented silicon specimens implanted with 40 keV $^{30}\text{Si}^+$ to $1.5 \times 10^{16} \text{ cm}^{-2}$ dose at LN_2 ($\sim 5 \mu\text{A cm}^{-2}$) and then implanted with 120 keV $^{28}\text{Si}^+$ to $1.0 \times 10^{16} \text{ cm}^{-2}$ dose. A: Cross-sectional electron micrograph, $\langle 100 \rangle$ Si specimens. B: $\langle 111 \rangle$ specimens. C: Microdiffraction pattern from A. D: Microdiffraction pattern from B.

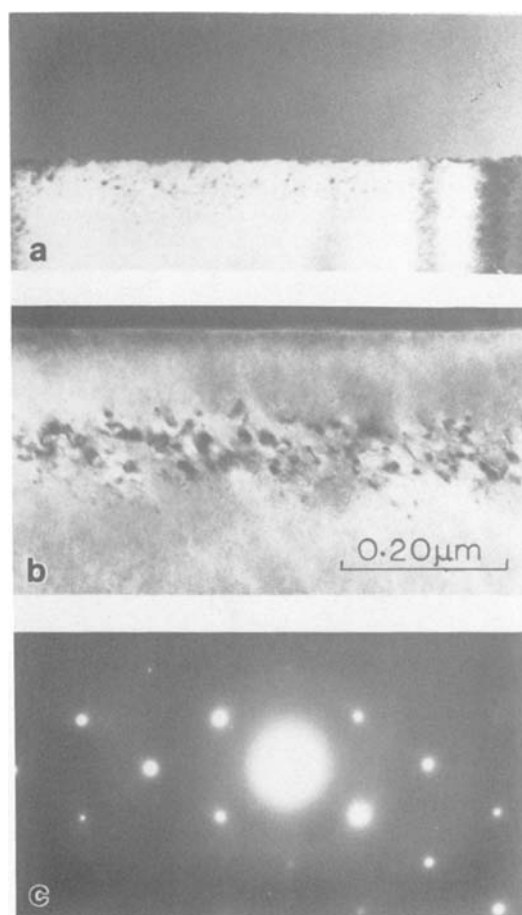


Fig. 11. Substrate temperature effects in $\langle 100 \rangle$ GaAs after ion implantation with 120 keV $^{28}\text{Si}^+$ to a dose of $5.0 \times 10^{15} \text{ cm}^{-2}$. A: $\langle 110 \rangle$ cross-sectional electron micrograph with a dose rate $\sim 5 \mu\text{A cm}^{-2}$ while substrate is at room temperature. B: $\sim 5 \mu\text{A cm}^{-2}$ while substrate is at 200°C . C: $\langle 110 \rangle$ microdiffraction pattern from the specimens shown in B.

Figure 10d shows a microdiffraction pattern from the top layer, where diffraction rings are consistent with the polycrystalline structure of Fig. 10b. It is envisaged that SPE growth in $\langle 100 \rangle$ orientations is rapid enough to be completed before the nucleation of polycrystalline regions ahead of the crystallizing interface can occur (17). However, in $\langle 111 \rangle$ orientations, since the SPE growth rate is 24 times slower than that in $\langle 100 \rangle$ orientations, the crystallites can nucleate ahead of the crystallizing interface (3). Once these crystallites nucleate, interface-controlled growth cannot occur, and the whole layer turns polycrystalline.

Dose rate and substrate temperature effects in GaAs.—We have studied dose rate effects in $\langle 100 \rangle$ GaAs and compared the results with those obtained by heating the substrate during ion implantation. The ion implantation at low dose rates of $\sim 5\text{--}10 \mu\text{A cm}^{-2}$ typically results in the formation of amorphous layers followed by bands of dislocation loops. A typical example is shown in Fig. 11a, after 120 keV $^{28}\text{Si}^+$ implantation to a dose of $5.0 \times 10^{15} \text{ cm}^{-2}$. The number density of dislocation loops in the underlying dislocation band is found to be lower in this case than that found in silicon for the same implant condi-

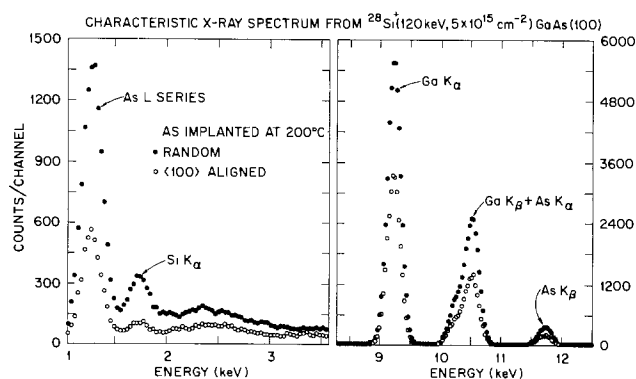


Fig. 12. Characteristic x-ray spectrum from specimens shown in Fig. 11b, showing random and $\langle 100 \rangle$ -aligned x-ray yields.

tions. By heating the substrate to 200°C during implantation, we found a 1100Å wide, defect-free region followed by a 900Å wide band of dislocation loops, as shown in Fig. 11b. Figure 11c is a microdiffraction pattern from the annealed region; it shows sharp and regular diffraction, as corresponded with a $\langle 110 \rangle$ orientation.

Figure 12 shows a characteristic x-ray spectrum taken in random and $\langle 100 \rangle$ -aligned directions. The differences in aligned and random spectra of Ga and As confirm good annealing of the lattice. The $\text{SiK}\alpha$ yield in random and $\langle 100 \rangle$ -aligned directions shows that more than 90% of Si is in substitutional sites. Thus, these results indicate that high electrical activation of dopants can be achieved by implantation at high temperatures. The silicon profiles were found to be Gaussian from SIMS-measurements, similar to the as-implanted profile, which indicates that annealing does not involve long-range migration of defects. This is consistent with SPE growth and close-pair recombination of vacancies and interstitials.

The annealing results similar to those obtained by heating the substrate can also be obtained by increasing the dose rate. Figure 13 shows a TEM cross-sectional micrograph from specimens implanted at $160 \mu\text{A cm}^{-2}$ to a dose of $5.0 \times 10^{15} \text{ cm}^{-2}$ ($100 \text{ keV } ^{28}\text{Si}^+$ ions). The micrograph shows a $\sim 1100\text{\AA}$ wide, defect-free region followed by a 1000\AA wide band of dislocation loops. As is shown in Fig. 11, heating the sample to 200°C produces qualitatively similar results. Figure 14 shows RBS results from speci-

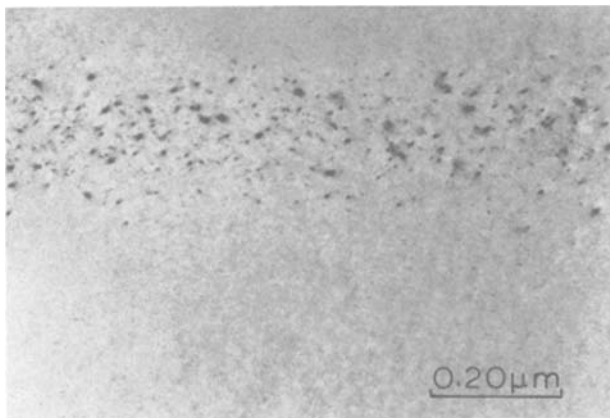


Fig. 13. Cross-sectional electron micrograph from (100) GaAs specimens implanted with $100 \text{ keV } ^{28}\text{Si}^+$ ions to a dose of $5.0 \times 10^{15} \text{ cm}^{-2}$ (dose rate = $160 \mu\text{A cm}^{-2}$).

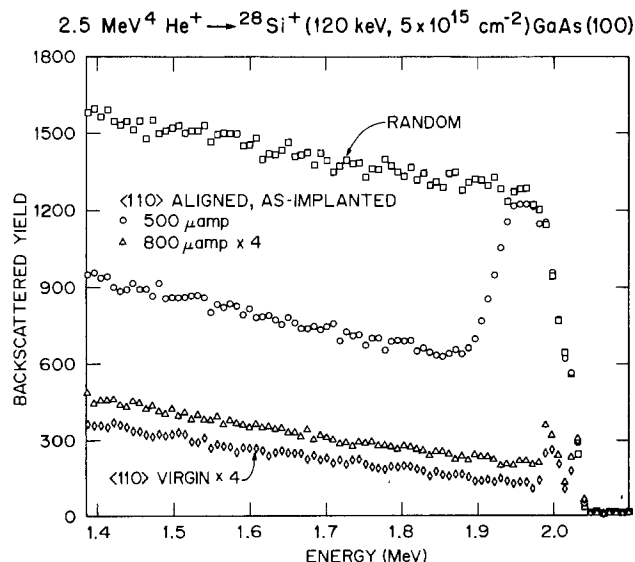


Fig. 14. 2.0 MeV He^- RBS spectra (random and $\langle 110 \rangle$ -aligned) from $^{28}\text{Si}^+$ (120 keV , $5.0 \times 10^{15} \text{ cm}^{-2}$) implanted specimens at 120 and $160 \mu\text{A cm}^{-2}$ specimens.

mens implanted at high currents ranging from 120 to $160 \mu\text{A cm}^{-2}$. The dechanneling as a function of depth decreases with increasing dose rate, and the yields are close to virgin crystals for specimens implanted with $160 \mu\text{A cm}^{-2}$.

Thermal annealing of different ion implantation states.—We now present a detailed characterization of some ion implantation states and their subsequent annealing behavior. At low dose rates, we produce buried amorphous layers, which expand toward the surface and into the deeper regions of the crystal as the implanted dose is increased. At a certain dose, which is critically determined by the ion implantation and substrate variables, we obtain a continuous amorphous layer, which extends from the surface to a certain depth and is followed by a band of dislocation loops. In this section, we divide the discussion into two parts: (i) annealing of amorphous layers; and (ii) annealing of dislocation loops in the underlying dislocation band.

The annealing of amorphous layers occurs by an interface-controlled crystallization process commonly referred to as solid-phase epitaxial (SPE) growth. An example is shown in Fig. 15, where by annealing at 550°C for 25 min, the interface moved toward the surface by a distance of 1050\AA . The specimens after ion implantation ($100 \text{ keV } ^{30}\text{Si}^+$ to $5.0 \times 10^{15} \text{ cm}^{-2}$ dose) contained a 2830\AA amorphous layer followed by a band of dislocation loops. This band of dislocation loops is left behind during SPE growth.

Figure 16 shows an implantation state ($100 \text{ keV } ^{30}\text{Si}^+$ to $5.0 \times 10^{14} \text{ cm}^{-2}$ dose at liquid nitrogen temperature) where the amorphous layer does not extend to the surface entirely. Figure 16a shows a bright-field, cross-sectional TEM micrograph in which dark regions near the surface represent crystalline islands. The sample contains a 2150\AA wide amorphous layer followed by a band of dislocation loops. Figure 16b shows a high resolution micrograph of the near-surface region. The crystalline islands contain two sets of fringes corresponding to (111) and $(\bar{1}\bar{1}\bar{1})$ planes in $\langle 01\bar{1} \rangle$ orientation. The size of crystalline islands varies from 6 to 30\AA . It is interesting to note the presence of a 15\AA thick oxide layer above the crystalline islands. The structure of the oxide is noncrystalline. If such samples are annealed, the SPE growth occurs both from the front and back sides of the specimens, as shown in Fig. 16c. The thickness of the SPE-grown back and front layers is 750\AA and 450\AA , respectively. The front amorphous-crystalline interface is considerably more undulated than the back interface. However, both the front and back SPE-grown layers have exactly the same orientation as the substrate, as shown by the microdiffraction patterns in Fig. 17. Figures 17a and 17b are microdiffraction patterns of front and back SPE-grown layers, respectively, both of which have identical $\langle 110 \rangle$ diffraction patterns. A microdiffraction pattern from the amorphous layer is shown in Fig. 17c, which contains characteristic amor-

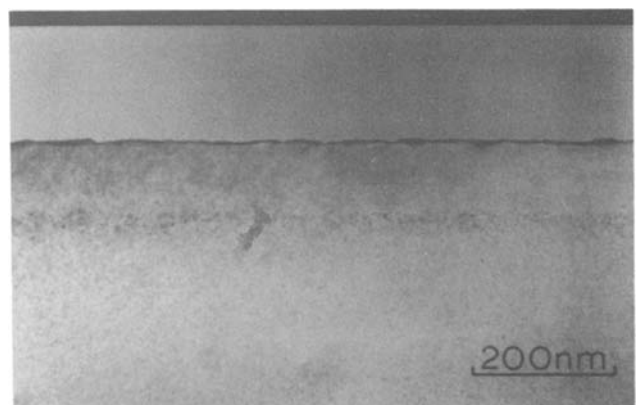


Fig. 15. Cross-sectional electron micrograph from $^{30}\text{Si}^+$ -implanted (100) Si specimen after annealing at 550°C for 20 min. The substrate was kept close to liquid He temperature and implanted with $100 \text{ keV } ^{30}\text{Si}^+$ to a dose of $5.0 \times 10^{15} \text{ cm}^{-2}$.

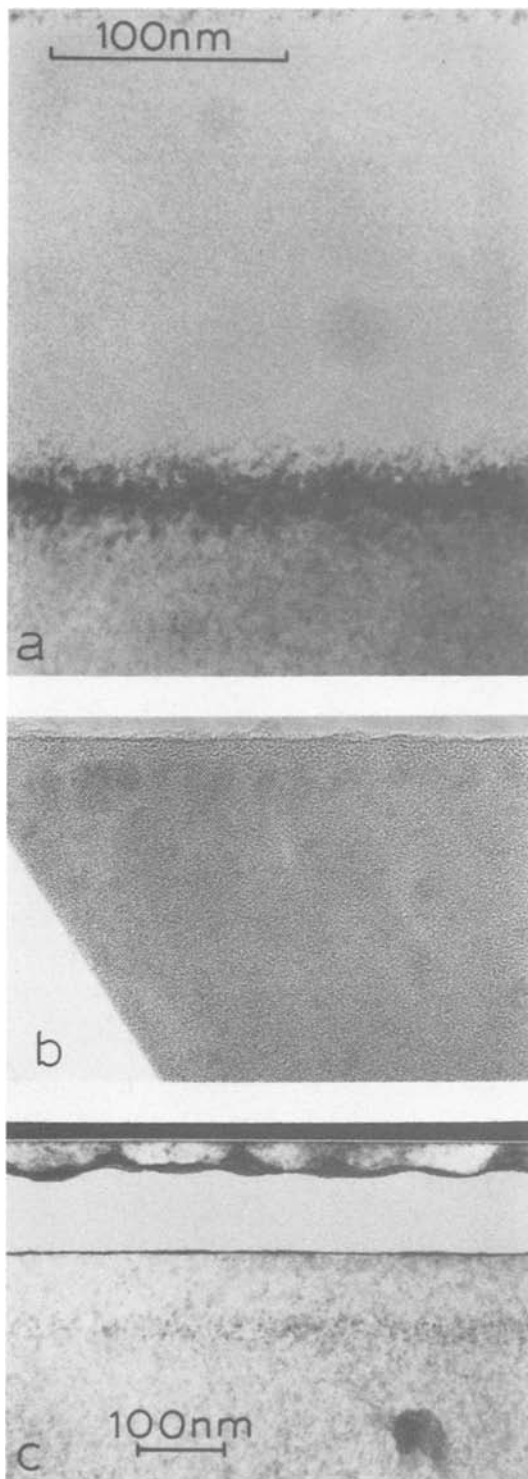


Fig. 16. A: Cross-sectional electron micrograph of as-implanted (100) Si specimens ($100 \text{ keV } ^{30}\text{Si}^+$, $5.0 \times 10^{14} \text{ cm}^{-2}$) containing crystalline islands near the surface. B: High resolution micrograph of A showing crystalline islands and the native oxide $\sim 15\text{\AA}$ thick. C: After isothermal annealing at 550°C for 10 min.

phous rings. As the time of isothermal annealing was increased to 40 min at 550°C , the front and back crystallizing interfaces were found to meet at a depth of about 880\AA . The dark line in Fig. 18a shows that defects associated with the interface at 880\AA are limited to within a 10\AA wide region. The nature of these defects was analyzed by plan-view electron microscopy, and the results are shown in Fig. 18b. The defects in this band consist of defect clusters and dislocation loops of interstitial nature. An approximate determination of concentration of point defects showed that the number of interstitials is equal to

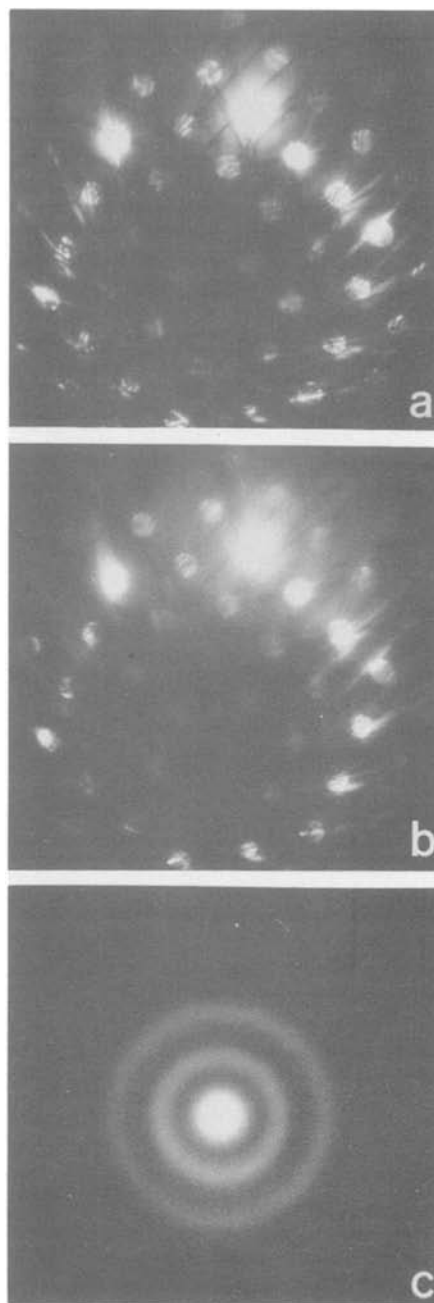


Fig. 17. Microdiffraction patterns of the different regions of specimens shown in Fig. 16C. A: Front layer. B: Back layer. C: Middle amorphous layer.

the number of implanted Si^+ ions. Recent RBS experiments (14) on high dose-rate annealing have shown that if buried amorphous layers are formed during early states of ion implantation, the annealing occurs by SPE growth from both front and back sides.

Annealing effects in underlying dislocation bands and gettering.—We now discuss the nature and annealing of dislocation bands below the amorphous layers. The dislocation loops in the region are formed as a result of clustering of point defects that escape amorphous regions. Due to ion-range straggling, the number density of displacements in this region does not reach the critical value needed for amorphization. The number density of dislocation loops in this region is critically determined by ion implantation and substrate variables. The specific damage-energy density (the number of displacements per unit volume) and ion range straggling are primarily determined by the atomic mass of the projectile and substrate and the energy of the projectile. This, in turn, determines the number of point defects that can escape the amor-

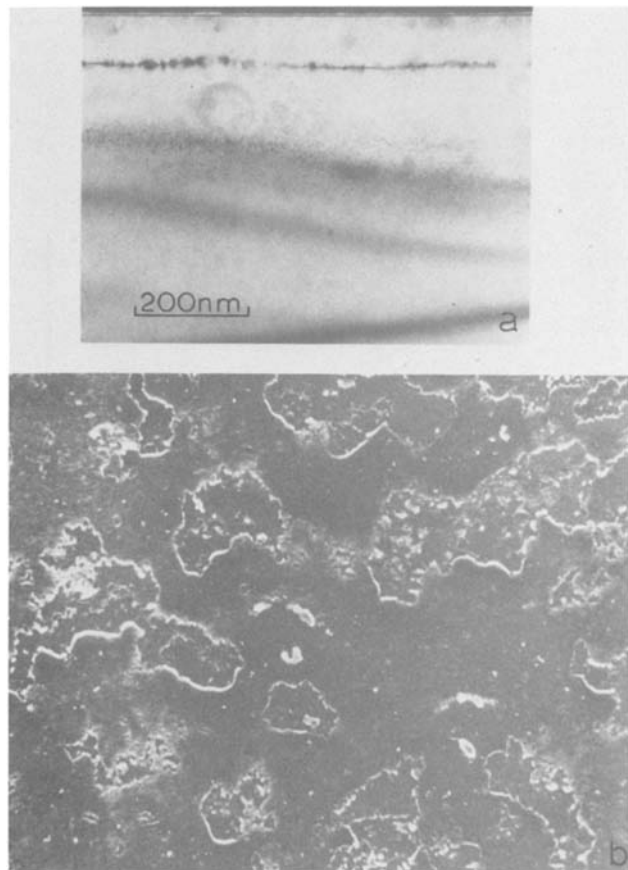


Fig. 18. Defect microstructures of specimens shown in Fig. 16C after thermal annealing at 550°C for 40 min. A: Cross-sectional micrograph. B: Plan-view micrograph of dislocation loops and tangles.

phous regions. The mobility of defects and subsequent clustering into dislocation loops are determined by the substrate temperature. The dislocation loops are observed (by conventional TEM imaging techniques) to be of an interstitial nature. The size of vacancy loops is usually much smaller (5-10Å) than that of interstitial loops. The number density of dislocation loops decreases with decreasing substrate temperature. Figures 19a and 19b show a comparison between room temperature and liquid nitrogen temperature implants (200 keV $^{28}\text{Si}^+$ to $1.5 \times 10^{16} \text{ cm}^{-2}$ dose). These specimens were annealed at 550°C/5 min so that underlying dislocation bands could be delineated. The nature of the dislocation band also affects the defect density in the SPE-grown layers. In room temperature implants, the amorphous-crystalline interface intersects dislocation loops whose average size is much larger than that in the liquid nitrogen temperature implants. As a result, during SPE growth, these dislocations continue to grow with the interface and create a network of high number density of hairpin dislocations. The number density of loops in the underlying dislocation band also decreases with increasing mass of the projectile or the substrate. An example is shown in Fig. 19c for a bismuth implant (200 keV, $1.0 \times 10^{16} \text{ cm}^{-2}$ dose) in silicon. With increasing mass of the projectile, specific deposited damage energy increases, resulting directly in amorphous cascades and allowing the escape of a smaller number of defects to form loops.

The dislocation loops should be minimized or, preferably, removed because they are detrimental to electrical characteristics of p-n junctions. The dislocations with energy levels close to the middle of the bandgap provide efficient recombination centers. The dislocations are also known to provide trap centers via electronic and elastic interactions. The dislocations in these bands are particularly undesirable, owing to their close proximity to the metallurgical junction. The annealing characteristics of dislocation loops during heat-treatment are determined

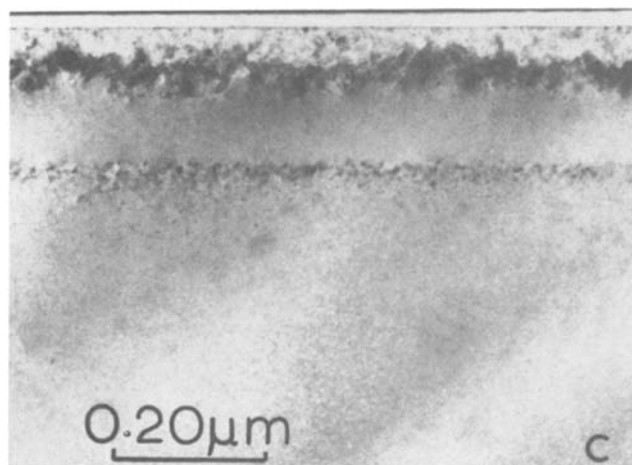
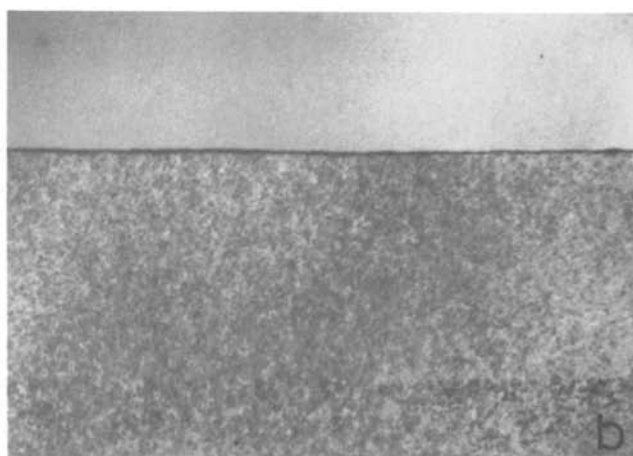
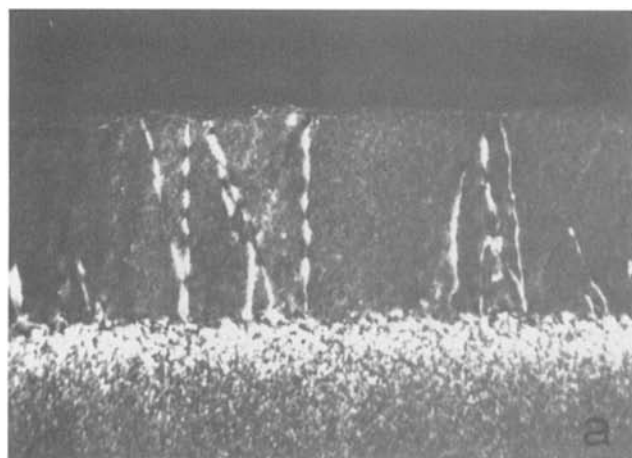


Fig. 19. Cross-sectional electron micrographs showing defect microstructures as a function substrate temperature and incident mass. A: 200 keV $^{28}\text{Si}^+$, $1.5 \times 10^{16} \text{ cm}^{-2}$ at room temperature after isothermal annealing at 550°C/5 min. B: 200 keV $^{28}\text{Si}^+$, $1.5 \times 10^{16} \text{ cm}^{-2}$ at liquid nitrogen temperature after similar annealing treatment. C: 200 keV $^{208}\text{Bi}^+$, $1.0 \times 10^{16} \text{ cm}^{-2}$ at room temperature after 550°C/40 min annealing treatment.

by the average size and number density of loops. If the distance between two loops is less than twice the diameter of the larger loops, these two loops may coalesce by glide and climb processes and form larger loops (18). If the loops are farther apart, they shrink by a normal bulk diffusion process (19). Figure 20 illustrates the subsequent annealing behavior of two different ion implantation (100 keV As⁺, 1.0×10^{16} cm⁻² dose) states shown in Fig. 6a (high dose rate) and Fig. 6c (low dose rate). The dislocation tangles in the high dose-rate samples evolve into a complicated network of dislocations upon subsequent thermal annealing (at 850°C/30 min). It was found that the carrier concentration and mobility are degraded after the above annealing treatment, presumably because of segregation and trapping of dopants at the dislocations. In the case of low dose-rate samples, the amorphous layers grow by a solid-phase epitaxial growth process, and the loops coarsen by loop coalescence. Sometimes a network is generated by a well-known dislocation reaction: $a/2\langle 101 \rangle + a/2\langle 01\bar{1} \rangle \rightarrow a/2\langle 110 \rangle$, as shown by the 1 in Fig. 20b. The electrical properties (carrier concentration and mobility) of these specimens were found to improve continuously with subsequent annealing treatment after SPE growth.

The dislocations in the underlying dislocation bands provide effective impurity/dopant traps via elastic and electronic interactions. The dislocations can also be used to tie up or remove unwanted impurities by trapping them at the dislocations. We illustrate antimony trapping or segregation at the dislocations in Fig. 21. The (100) Si specimens were implanted with 200 keV, 4.4×10^{15} Sb⁺ cm⁻² dose; they were annealed at 550°C/20 min for SPE growth of the amorphous layers and subsequently heat-treated at 900°C for 30 min. After the latter heat-treatment, large precipitates were formed at the dislocations, making

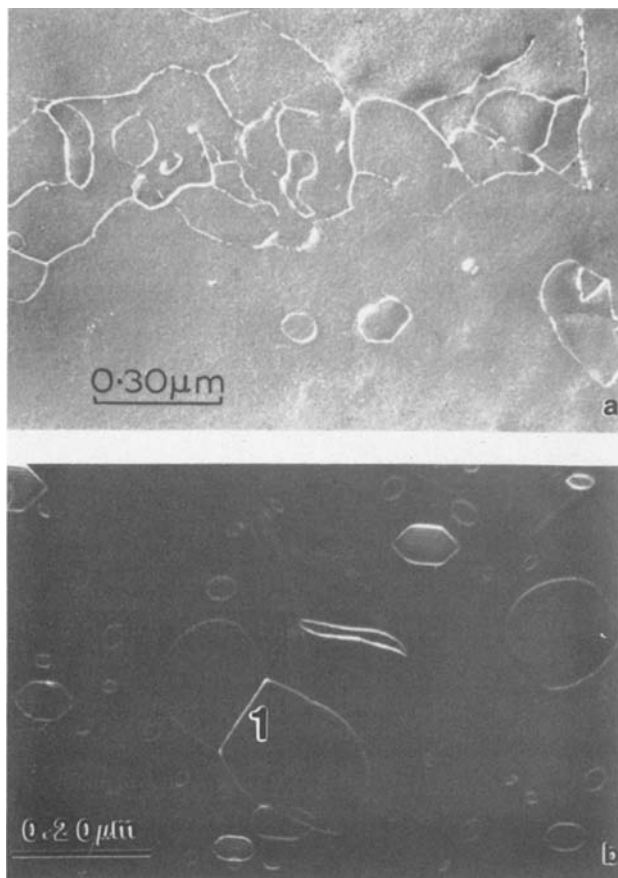


Fig. 20. Comparison of subsequent annealing behavior of high and low dose-rate As⁺-implanted specimens. A: High dose-rate specimens of Fig. 6A after isothermal annealing at 850°C/30 min. B: Low dose-rate specimens of Fig. 6B after the same heat-treatment.

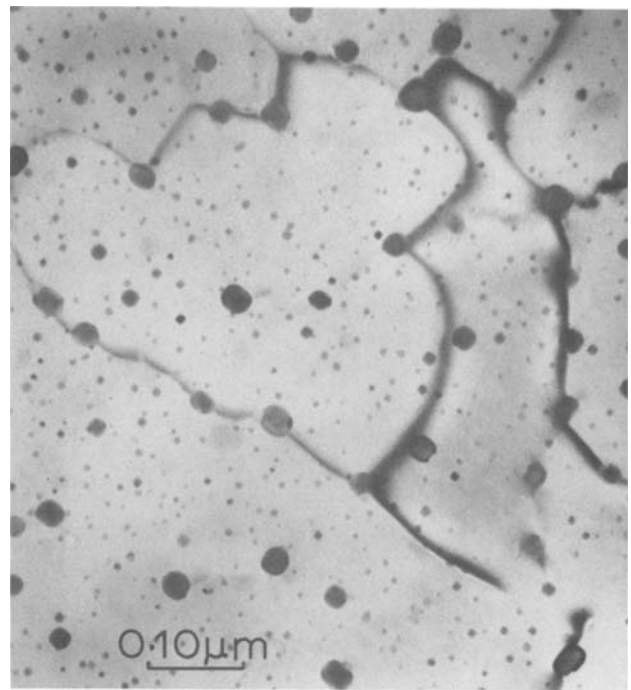


Fig. 21. Plan-view electron micrograph showing gettering of antimony by dislocations after heat-treatment of Sb⁺-implanted (200 keV, 4.4×10^{15} cm⁻²) specimens, 550°C/20 min and 900°C/30 min.

them efficient traps for dopants. Figure 22 illustrates gettering of fluorine by dislocations in a BF₃⁺-implanted (100) Si, which was annealed at 1100°C for 5s in a rapid thermal annealing apparatus. The as-implanted specimens (50 keV BF₃⁺, 1.0×10^{15} cm⁻² dose) contained a 500Å wide amorphous layer followed by a band of dislocation loops. After the rapid thermal annealing treatment, the loops coarsened and gettered the fluorine, as indicated by the formation of fluorine bubbles near the dislocations (see bubbles as white spots in the micrograph). The secondary ion-mass spectrometry results on fluorine

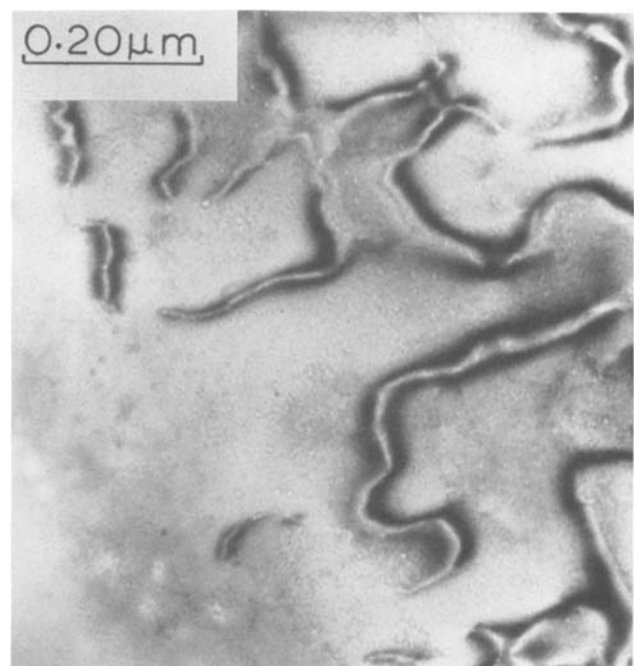


Fig. 22. Plan-view electron micrograph showing gettering of fluorine by dislocations after rapid thermal annealing (1100°C for 5s) of BF₃⁺-implanted specimens (50 keV BF₃⁺, 1.0×10^{15} cm⁻²).

profiles show a peak corresponding to the dislocation band. It is interesting to note that loops are confined in a rather narrow band because the segregation of fluorine inhibits the glide of dislocations. It was found that, by further annealing, the dislocations and fluorine are removed simultaneously.

Conclusion

We have shown that the nature of ion implantation damage is a strong function of implantation and substrate variables. In silicon, crystalline to amorphous phase transformation occurs above a critical damage energy of 12 eV/atom if there are negligible annealing effects. This value is very close to the displacement threshold. For other materials, the critical specific damage energy is expected to scale according to the displacement threshold energy. By increasing the dose rate, the substrate temperature is increased, which enhances the SPE growth rate of amorphous layers and/or the recombination of close pairs of vacancies and interstitials. The as-implanted profiles in high dose-rate implants were found to be unchanged because of negligible diffusion distances of dopants, as estimated from time and temperature of implants. The specimens implanted at high dose rates contain defect-free, self-annealed layers followed by a wide band of dislocation loops. In the defect-free, self-annealed layers, up to 90% of the arsenic was found to be in substitutional (electrically active) sites. During high dose-rate implants, buried or near-surface amorphous layers are formed, the annealing of which involves SPE growth from both the front and back sides (buried layers) or growth from the back side (near-surface layers). At still larger dose rates, there is a region in the implantation current where we obtain undesirable void structure. A comparison of microstructures obtained at high dose rates and high substrate temperatures shows that these two parameters are interchangeable. The number density of dislocation loops in the underlying dislocation band can be manipulated by ion implantation and substrate variables. The average size and number density of loops play a critical role in the development of network of dislocations during subsequent annealing. These dislocations provide strong recombination and trap centers for impurities and dopants. By moving their locations away from the junctions, these dislocations can be used to getter unwanted impurities that adversely affect the p-n junction characteristics.

Acknowledgments

We are grateful to D. Fathy, S. J. Pennycook, and O. S. Oen for useful discussions.

Manuscript submitted April 4, 1984; revised manuscript received July 10, 1984.

Oak Ridge National Laboratory assisted in meeting the publication costs of this article.

REFERENCES

1. K. A. Pickar, *Appl. Solid State Sci.*, **5**, 152 (1975).
2. J. Narayan and O. W. Holland, *Appl. Phys. Lett.*, **41**, 239 (1982).
3. J. Narayan, O. W. Holland, and B. R. Appleton, *J. Vac. Sci. Technol. B*, **1**, 871 (1983).
4. T. O. Segwick, *This Journal*, **130**, 484 (1982).
5. C. W. White, J. Narayan, and R. T. Young, *Science*, **204**, 461 (1981).
6. J. Narayan, J. Fletcher, C. W. White, and W. H. Christie, *J. Appl. Phys.*, **52**, 7128 (1981).
7. P. P. Pronko, A. K. Rai, O. W. Holland, B. R. Appleton, and J. Narayan, *ibid.*, **53**, 5621 (1982).
8. G. H. Kinchin and R. S. Pease, *Rep. Prog. Phys.*, **18**, 1 (1955); M. J. Norgett, M. T. Robinson, and I. M. Torrens, *Nucl. Eng. Des.*, **33**, 50 (1975).
9. J. W. Corbett and J. C. Bourgoin, in "Point Defects in Solids," J. H. Crawford and L. M. Slifkin, Editors, p. 1, Plenum Press, New York (1975).
10. J. R. Dennis and E. B. Hale, *J. Appl. Phys.*, **49**, 1119 (1978).
11. K. B. Winterbon, P. Sigmund, and J. B. Sanders, *Mat. Fys. Medd. Dan. Vid. Selsk.*, **37** (1970).
12. P. Sigmund, *Appl. Phys. Lett.*, **25**, 169 (1974).
13. B. C. Larson, R. T. Young, and J. Narayan, in "Neutron Transmutation Doping in Semiconductors," J. M. Meese, Editor, p. 281, Plenum Press (1979).
14. O. W. Holland and J. Narayan, *Appl. Phys. Lett.*, **44**, 748 (1984).
15. M. R. Rulhe, in "Radiation-Induced Voids in Metals," J. W. Corbett and L. C. Ianniello, Editors, p. 255, National Technical Information Service (CONF-710601), Washington, DC (1972).
16. R. Bullough and R. C. Perrin, in "Radiation-Induced Voids in Metals," J. W. Corbett and L. C. Ianniello, Editors, p. 769, National Technical Information Service (CONF-710601), Washington, DC (1972).
17. S. A. Kokorowski, G. L. Olson, and L. D. Hess, *J. Appl. Phys.*, **53**, 921 (1982).
18. J. Narayan and J. Washburn, *ibid.*, **43**, 4862 (1972); *Philos. Mag.*, **26**, 1179 (1972).
19. I. R. Sanders and P. S. Dobson, *J. Mater. Sci.*, **9**, 1987 (1974).

TEM Cross Section Sample Preparation Technique for III-V Compound Semiconductor Device Materials by Chemical Thinning

S. N. G. Chu* and T. T. Sheng

AT&T Bell Laboratories, Murray Hill, New Jersey 07974

ABSTRACT

A cross section sample preparation technique is described for the TEM studies of III-V compound semiconductor device materials. In this technique, a grid-masking method is introduced for selective-area perforation using chemical etching. By epoxy bonding a TEM specimen grid onto the surface of a face-to-face or face-to-back epoxy-bonded thin cross section sample stack, perforations by chemical etching are confined to the regions inside the meshes. Selective-area perforation can easily be achieved by accurately positioning the masking grid and monitoring the perforation under a microscope. Since many perforations can be made in the selected area, the chance of obtaining a cross section sample containing the device structure is greatly increased. Furthermore, the masking grid mechanically reinforces the perforated sample and hence eliminates problems associated with sample handling. Examples of the use of this technique for InP/InP(substrate) single-layer and p⁻-InGaAsP/p-InP/InGaAsP/n-InP/InP(substrate), multilayer laser device structures, grown by vapor-phase epitaxy, are demonstrated. The technique is also applicable to GaAlAs/GaAs multilayer structures, and, in addition, greatly facilitates the selective-area perforation of plan-view TEM samples.

Cross-sectional transmission electron microscopy (XTEM) has proven itself to be a powerful technique for the study of the generation and evolution of defect structures during heteroepitaxy of III-V compound semiconductor device materials (1, 2). In silicon integrated-circuit processing, XTEM is now routinely used for the characterization of process-related problems (3). The essential part of the XTEM technique, however, is the preparation of cross section samples containing the desired device structure.

Because most semiconductor devices consist of layers with thicknesses ranging from a few hundred angstroms to several microns near the surface of the wafer, reproducible XTEM samples are generally difficult to prepare. For example, sample preparation requires that the perforation, by ion milling or chemical etching, occur not only near the edge of the cross section, but right at where the desired device structure is located as well. Edge erosion of the sample is another problem. Unless the edge is well protected, the device structure is usually eroded before a perforation occurs.

These difficulties in the preparation of XTEM sample of silicon integrated circuits were overcome by Sheng *et al.* (3) using an epoxy embedding technique combined with large area ion milling. Direct application of this technique to InGaAsP/InP heterostructure-device materials, however, was found to be difficult simply because of the extreme fragility of the III-V materials compared with silicon. In this work, we report a new chemical thinning technique for the preparation of XTEM samples for III-V compound semiconductor device structures. We also introduce a grid masking method that allows us to control precisely the selected-area perforation. Finally, the XTEM for InP/InP single-layer and InGaAsP/InP multilayer structure materials are demonstrated.

Sample Preparation Technique

Thin cross section samples were cleaved from device wafers along a (011) plane. The cleaving process was facilitated by thinning the device wafer, from the back side, to less than 0.3 mm, using chemical-mechanical polishing in 2% Br₂-methanol solution. The cross section samples were epoxy bonded to form a stack with the device structures either face to face or face to back, as shown in Fig. 1, using extra-fast setting epoxy by Hardman, Incorporated (Belleville, New Jersey 07109). Excess epoxy was squeezed out between the samples. For best results in the subsequent thinning process, the thickness of the epoxy film was kept to a minimum. The cross section sample stack was then thinned by polishing it from both sides to a final thickness of about 20 μm.

*Electrochemical Society Active Member.

The details of the polish thinning process are as follows. The cross section stack was first bonded to a slide cover-glass, which in turn was bonded to a titanium disk (part of the sample polishing holder). A transparent crystal bond or soft wax can be used as a bonding material. The sample stack was surrounded with InP substrate wafers, as shown in Fig. 2, to prevent the edges of the stack from being rounded off during the polishing process. The stack was polished on one side to smooth the cross section surface and then turned over and polished to a final thickness of around 20 μm. Figure 3 shows Nomarski interference micrograph of a polished cross section sample stack.

Perforation by chemical etching immediately adjacent to the epoxy joint in the device region was accomplished by using a grid masking technique. A 100-mesh molybdenum grid was epoxy bonded onto the cross section stack, as shown in Fig. 4, using the same epoxy described before. Such grid masking requires careful alignment of the openings in the epoxy-coated grid to expose the device region, and can be done by using the grid-mounting jig shown in Fig. 5. With the cross section stack still on the titanium disk (Fig. 5), the disk is attached to the alignment block using double-sided adhesive tape. The sample

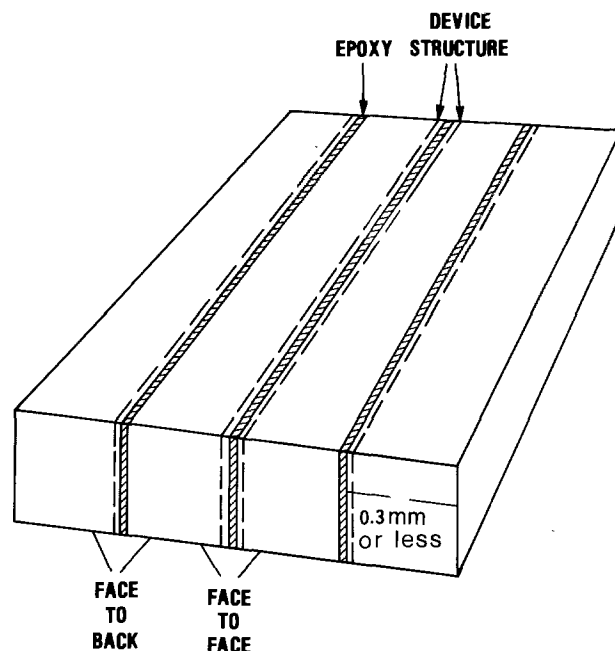


Fig. 1. Schematic diagram of face-to-face and face-to-back cross section sample stack bonded by epoxy.

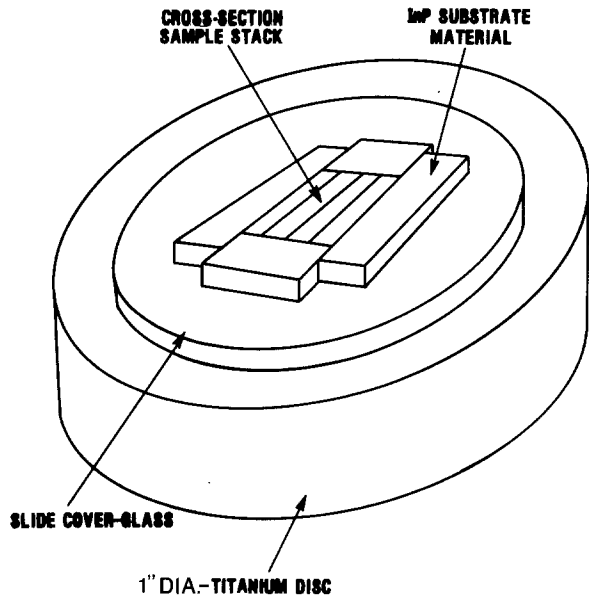


Fig. 2. Schematic diagram of a cross section sample stack surrounded by InP substrate wafer, ready for initial polish thinning.

stack is centered by adjusting the four alignment screws on the grid mounting device. It is then visually aligned by moving one of the epoxy-bonded interfaces to the center of the device using the transparent alignment cover. An epoxy-coated 3 mm diam molybdenum grid is placed over a 2 mm diam hole inside the grid mounting cover, and is lightly held in place by the epoxy on the grid to the edge of the hole. The grid mounting cover is then turned over and slid onto the grid mounting device until it contacts the stop ring which prevents the grid from contacting the sample surface.

Precise alignment of the grid to expose the desired area is then accomplished under a stereo microscope by adjusting the position of the sample with respect to the grid. The stop ring is released and the grid mounting cover lowered until the grid rests on the surface of the sample. Gentle pressure on the grid mounting cover transfers the grid onto the surface of the cross section stack.

Two important points should be noted: (i) only a thin layer of epoxy should be applied to the grid. Excess epoxy tends to smear out and cover the openings of the

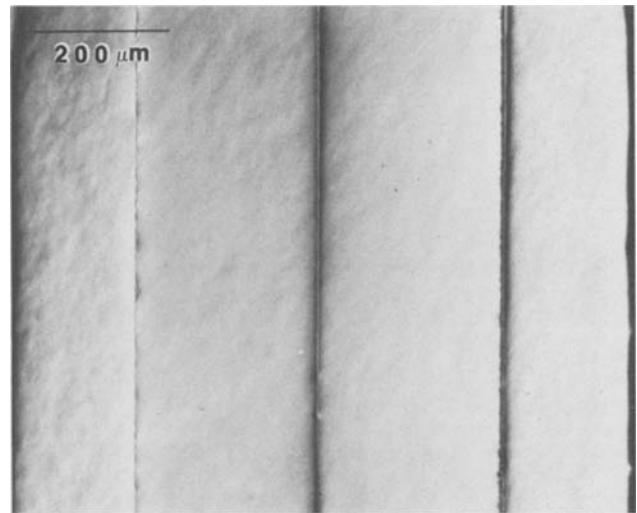


Fig. 3. Optical micrograph of the surface of a polished cross section couple. The dark strip is the epoxy.

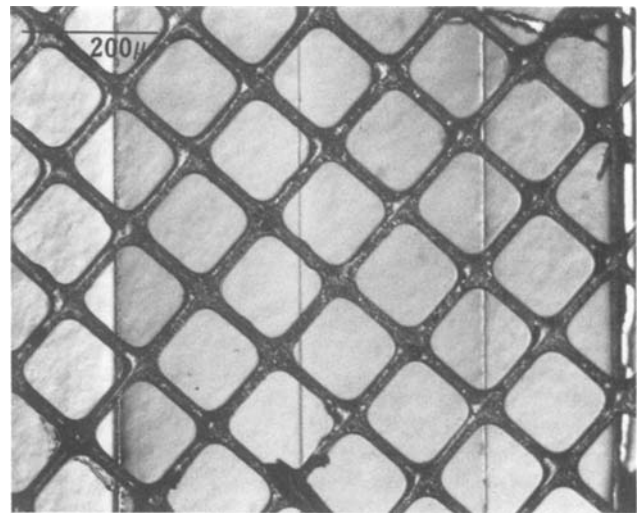


Fig. 4. Optical micrograph of a masking grid epoxy bonded to the surface of a thin cross section sample stack.

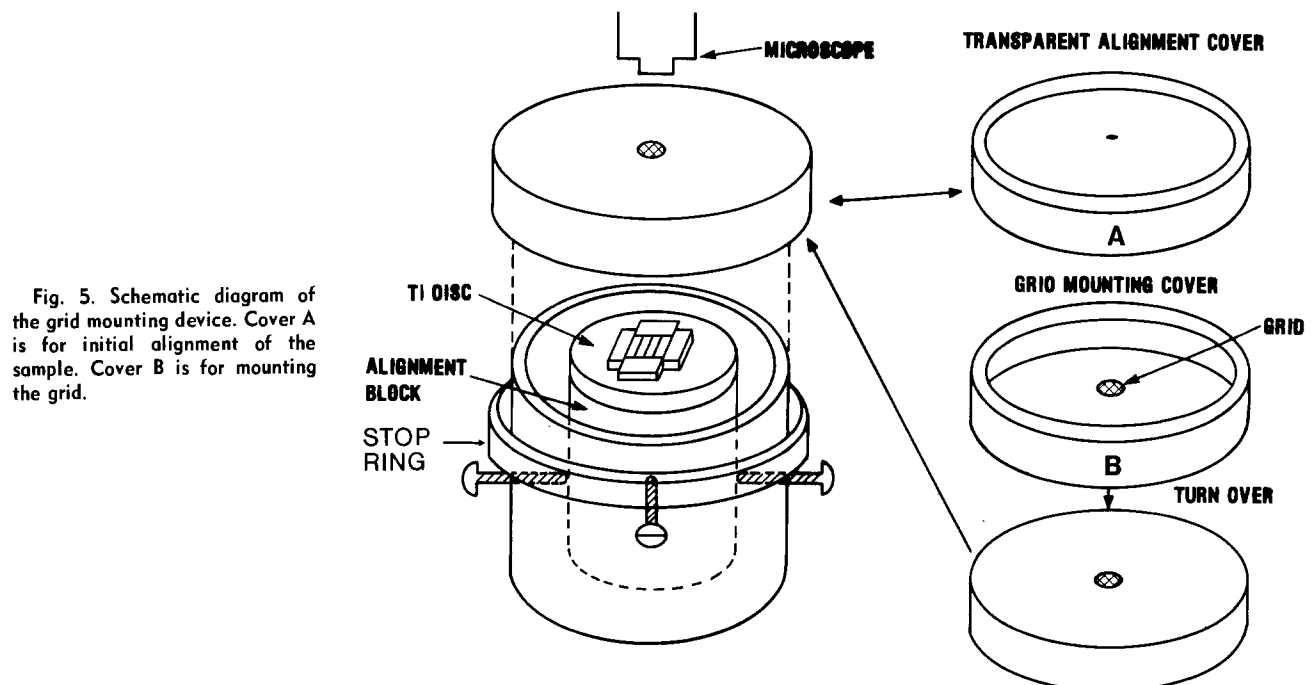


Fig. 5. Schematic diagram of the grid mounting device. Cover A is for initial alignment of the sample. Cover B is for mounting the grid.

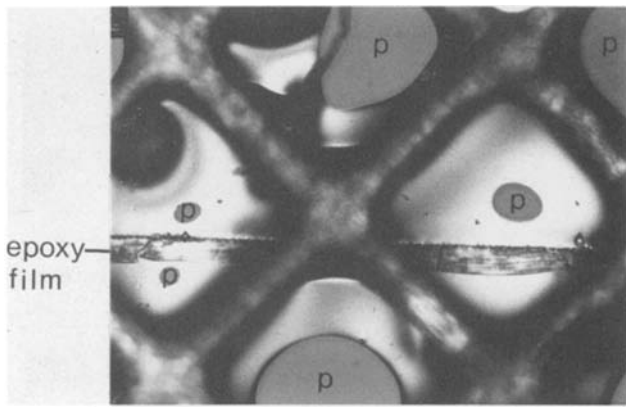


Fig. 6. Optical micrograph showing typical perforations occurring inside the mesh near the device structure. The dark ribbon is the epoxy film; perforations are labeled P.

grid. (ii) Any movement of the grid parallel to the surface must be prevented after the grid is transferred to the cross section stack. To avoid having the grid accidentally cover the entire device region, the edge of the cross section is aligned along the diagonal of the square mesh as shown in Fig. 4. The sample is then transferred with the cover glass onto a quartz disk.

The final perforation is done inside a crystalline dish by dripping 0.5% Br₂-methanol solution onto the masked-sample surface. A stereo microscope equipped with both reflection and transmission illumination is used to monitor the perforation. Because perforations are made only inside the meshes, each mesh becomes an individual sample. Grid masking, therefore, greatly increases the

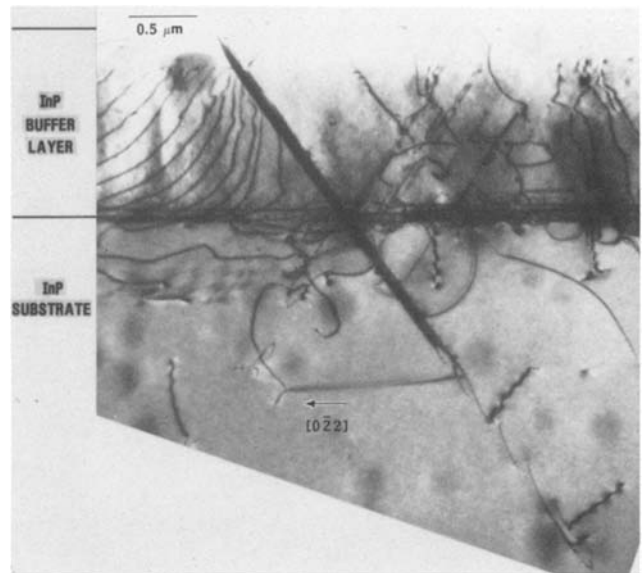


Fig. 7. XTEM of 1.3 μm InP buffer grown by VPE on InP substrate

success of obtaining a good XTEM sample. The etching process is stopped by applying a jet of methanol to the sample using a squeeze bottle. Small variations in thickness always exist across the polished cross section sample stack. As a result, perforations inside the mesh normally occurred progressively from mesh to mesh, starting from the thinnest area. It is important to stop the etching at the right moment, since the thin area around the perforation tends to be etched away very rapidly. The

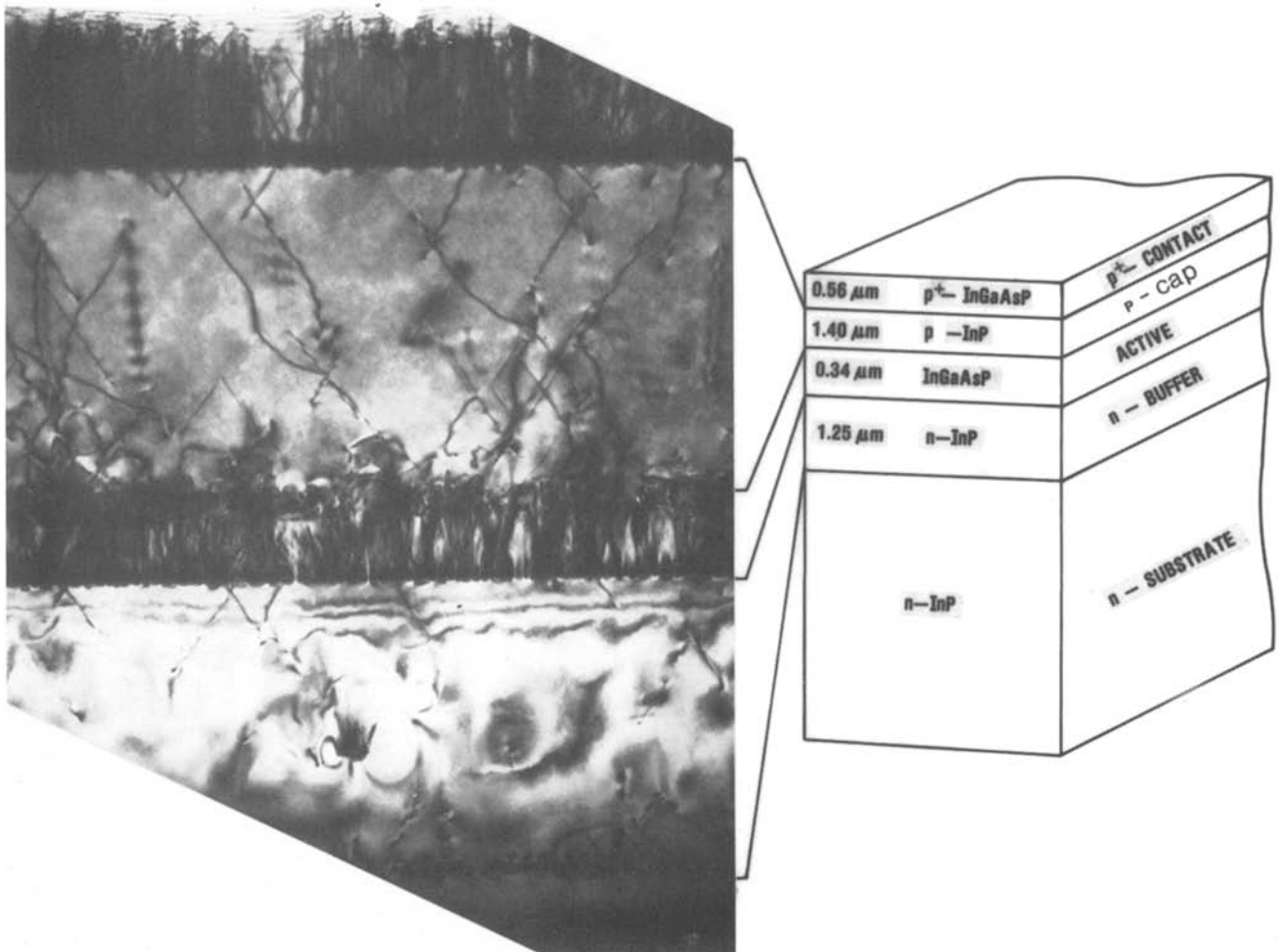
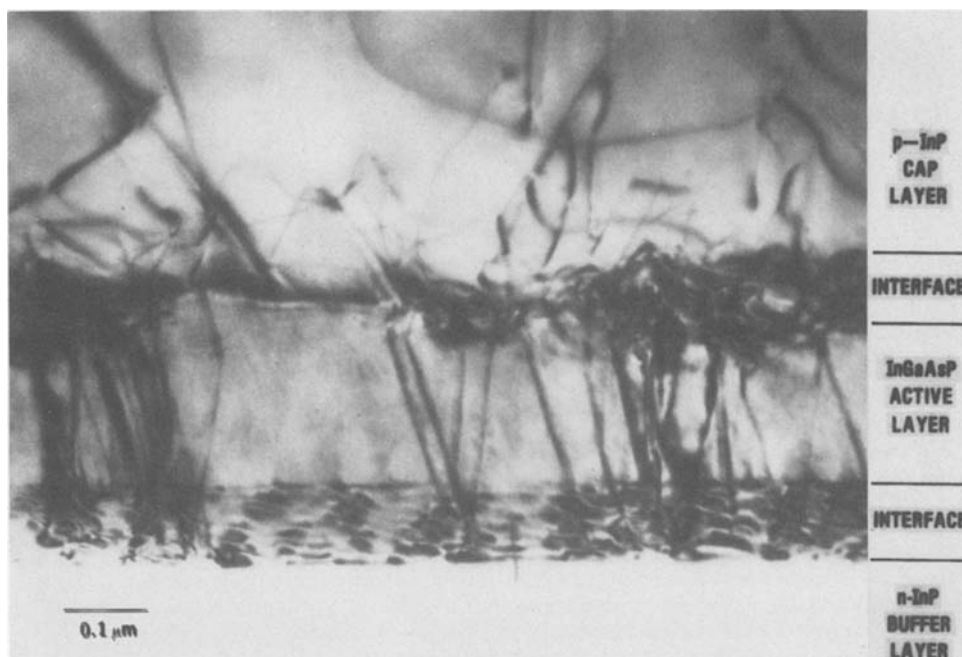


Fig. 8. XTEM of a four-layer InGaAsP/InP laser structure grown by VPE

Fig. 9. A tilted cross section view of the p-InP/InGaAsP (active) n-InP regions, showing the interfaces.



proper thickness at which to stop etching was judged by the transparency of the film as observed under the microscope using transmission illumination. When the proper transparency was achieved, the sample bonded to the grid was removed from the cover glass by soaking in acetone or trichlorethylene. Finally, the cross section sample is examined in the transmission electron microscope. Micrographs reported in this paper were taken using a JEOL 200-A instrument.

Results and Discussion

Figure 6 is an optical micrograph showing perforations that occur successively inside two meshes near the device structures. The semitransparent regions surrounding some of the perforations extend all the way to the device regions — a condition that is ideal for TEM studies. Since epoxy does not react with Br_2 -methanol, the epoxy film between the cross section remained as the semiconductors on both sides were etched away. The dark ribbon in Fig. 6 is the epoxy film that fell and covered one of the face-to-face epoxy-joined device structures.

A TEM cross section view of a $1.3 \mu\text{m}$ InP buffer layer grown by vapor-phase epitaxy on a (100) InP substrate is shown in Fig. 7. The InP epitaxial layer was contaminated by gallium during growth. It is therefore lattice mismatched to the InP substrate. This is shown by the presence of the straight interfacial-misfit dislocations oriented along the $[0\bar{1}1]$ direction. The dislocation networks on both sides of the interface were generated at the interface and propagated along the $\{111\}$ planes. Furthermore, the dark band oriented along the $[\bar{1}12]$ direction was verified to be a stacking fault. The detailed study of the gallium contamination of InP grown by vapor-phase epitaxy will be discussed in another paper (4).

The TEM cross section view of an InGaAsP/InP laser structure grown by vapor-phase epitaxy on a (100) InP substrate is shown in Fig. 8. The multilayer structure consists of $1.25 \mu\text{m}$ thick n-type InP buffer layer, a $0.34 \mu\text{m}$ thick undoped InGaAsP active layer, a $1.4 \mu\text{m}$ thick p-type InP cap layer, and a $0.56 \mu\text{m}$ thick p⁺-InGaAsP contacting layer. High density threading dislocations generated at the binary/quaternary interface, and threading through the quaternary layers can be seen in both active and p-contacting layers. These dislocations lie either in the $\{111\}$ planes or along a direction close to $[100]$. Furthermore, areas of diffuse dark contrast close to the $[100]$ orientation are also present, similar to those observed by Al-Jassim *et al.* (1) in InGaAs/InP VPE structures. An examination of the threading dislocation density between

the active layer and p-InP shows that the majority of the dislocations are either bent into the interface or recombined at the interface.

This bending and recombining is also seen in the tilted cross section view shown in Fig. 9. The threading dislocations recombine and form large dislocation tangles, only a few of which are propagated into the p-InP region. The lower interface shows a network of strain fields where the threading dislocations originate. The detailed characterization of the defect structure and the interfaces will be discussed in another paper. Similar quality of cross-sectional TEM samples have been achieved using the same technique on GaAlAs/GaAs and InAlAs/InGaAs/InP multilayer structures.

Conclusion

We have described a technique for preparing cross section samples for TEM studies of III-V compound semiconductor device materials using a chemical thinning technique. An essential aspect of the technique is the use of a grid masking method that makes it possible to exercise precise control over the selected-area perforation in the device regions. Since the perforation is confined to the area inside the mesh, each mesh becomes an individual sample, greatly increasing the probability of obtaining a good XTEM sample. The masking grid also mechanically reinforces the thin cross section of the sample, thereby alleviating sample handling problems. We have used the technique to prepare XTEM samples for InP/InP single-layer and InGaAsP/InP multilayer laser structures. The technique can also be applied to GaAlAs/GaAs and InAlAs/InGaAs/InP device structures, and, in addition, greatly facilitates the preparation of plan-view TEM samples.

Acknowledgments

The authors are grateful for the support and encouragement of W. D. Johnston, Jr., R. B. Marcus, and J. V. DiLorenzo. Appreciation is also due to S. Mahajan for the technical instruction of TEM, K. E. Stregge for providing us with the VPE sample, and C. M. Jodlauk for technical assistance. The valuable discussion with T. Boone on the polishing technique is acknowledged.

Manuscript submitted April 2, 1984; revised manuscript received May 18, 1984.

AT&T Bell Laboratories assisted in meeting the publication costs of this article.

REFERENCES

1. M. M. Al-Jassim, M. Hockly, and G. R. Booker, in "Defects in Semiconductors," J. Narayan and T. Y.

- Tan, Editors, p. 521, North-Holland, Amsterdam (1981).
2. G. H. Olsen, and M. Ettenberg, in "Crystal Growth," Vol. 2, C. H. L. Goodman, Editor, p. 1, Plenum Press, New York (1974).
3. T. T. Sheng and R. B. Marcus, *This Journal*, **127**, 738

- (1980).
4. S. N. G. Chu, F. A. Stevie, A. T. Macrander, R. F. Karl-icek, C. C. Chang, C. M. Jodlauk, K. E. Strege, D. L. Mitcham, and W. D. Johnston, Jr., Submitted to *This Journal*.

Mass Spectrometric Transient Study of DC Plasma Etching of Si in NF_3 and NF_3/O_2 Mixtures

T. Honda¹ and W. W. Brandt

Department of Chemistry and Laboratory for Surface Studies, University of Wisconsin-Milwaukee, Milwaukee, Wisconsin 53201

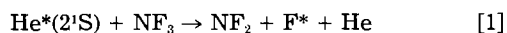
ABSTRACT

DC plasma etching experiments were performed on thin wafers of polycrystalline Si, using a pulse injection technique developed earlier, with NF_3 or NF_3/O_2 mixtures as etchants. The addition of O_2 was found to have no measurable effect on the etching rate, and steady-state concentrations of various radicals present in the plasma shifted relatively little. A fairly simple reaction scheme is presented which is consistent with these results. The NF_3 etching rates measured after oxidizing or nitriding the Si surface by plasma methods were explored to some extent as well.

It is very clear from the literature that plasma etching rates and related data obtained in different laboratories can normally not be compared in a quantitative fashion, since the experimental procedures, and, in fact, the quantities measured in each case, may differ. To arrive at reliable comparisons, the procedures must be standardized. At present, because of the large parameter space involved (1), this uniformity is an immediate and realistic objective only if the results which are to be compared are obtained in a single laboratory, using identical procedures, in short succession.

The present study represents such an attempt; the experimental procedures, including the sample preparation, were exactly the same as those used in several preceding studies (2, 3); only the etchant was changed, using NF_3 and NF_3/O_2 mixtures. The fragmentation of NF_3 in the plasma is likely to yield very few fragments, in contrast to SF_6 or SF_6/O_2 mixtures used earlier, judging from the published mass spectra of this gas (4-6). The tedious mass spectrometric fragmentation corrections needed to determine the concentrations of various excess species in the plasma are thus expected to be much simpler than those encountered in the earlier studies (2, 3, 7).

A second important reason for this study lies in that actinometric methods, based on optical emission measurements, are sometimes of no help in establishing the reaction mechanism of a system. For example, the plasma-etch rate of Si in NF_3/He mixtures fails to correlate with the concentration of electronically excited fluorine present in the plasma. Presumably the excitation transfer from $\text{He}^*(2^1\text{S})$ to NF_3 , with the simultaneous formation of excited F



becomes relatively important in certain mixtures, compared to direct electron impact excitation. There seem to be no actinometric results available on NF_3/O_2 mixtures thus far, but, eventually, such data, together with the results from this study, could help in determining the scope and reliability of actinometry in plasma etching studies (9, 10).

As an important by-product of this study, further information has been gathered concerning the detailed mass spectrometric procedures used in this and in previous studies (2, 3, 7), notably with respect to the unavoidable

random errors, and minor systematic errors which have been identified earlier.

Experimental

Most of the procedures used in this work are exactly the same as those used in the earlier studies (2, 3). Only the exposure of the polycrystalline Si sample to active O_2 and N_2 plasmas constitutes new types of experiments. The conditions are as shown in Table I.

Results and Discussion

Early during this study, it was recognized that the $m/e = 71$ and 52 signals, which are the major peaks in the NF_3 mass spectrum, and represent NF_3^+ and NF_2^+ , respectively, were always proportional to each other, and that their ratio was within the range of literature values (4-6). If plasma-generated NF_2 radicals were present, henceforth termed "excess NF_2^+ ," the NF_2^+ peak should be larger than that found in the standard NF_3 mass spectra. There was no such excess NF_2 outside the experimental errors, and, as a consequence, only the 52 peak was measured in the bulk of this study and taken to be a convenient measure of unfragmented or produced NF_3 present in the plasma.

The peak at $m/e = 85$, representing SiF_3^+ , served as a simple measure of the etch rate, as in earlier studies (2, 3). As illustrated in Fig. 1, this peak was found to be proportional (i) to the NF_2^+ signal, representing the unfragmented NF_3 in the plasma cell, and (ii) to the difference in the NF_2^+ peak before and after igniting the plasma, and thus to the amount of NF_3 fragmented in the plasma.

The signals at $m/e = 33$ and 14, representing NF^+ and N^+ , respectively, were corrected for the contributions from the NF_3 mass spectrum, and are also plotted in Fig. 1. The signals thus represent "excess NF^+ " and "excess N^+ ," respectively, which arise from NF and N radicals or ions formed in the plasma. The excess N^+ is seen to be proportional to the NF_2^+ and SiF_3^+ signals, and therefore to the etch rate, while the excess of NF^+ varies with the square of the NF_2^+ peak height (see Fig. 2).

Table I. Experimental conditions for O_2 - and N_2 -plasma treatment. Discharge voltage: 900V

Plasma gas	Pressure (torr)	Time (min)	Current (mA)
O_2	0.7	120	6.7
N_2	2.4	60	7.0

¹Present address: Department of Chemical Engineering, Tokyo Institute of Technology, O-Okayama, Meguro-Ku, Tokyo, Japan.

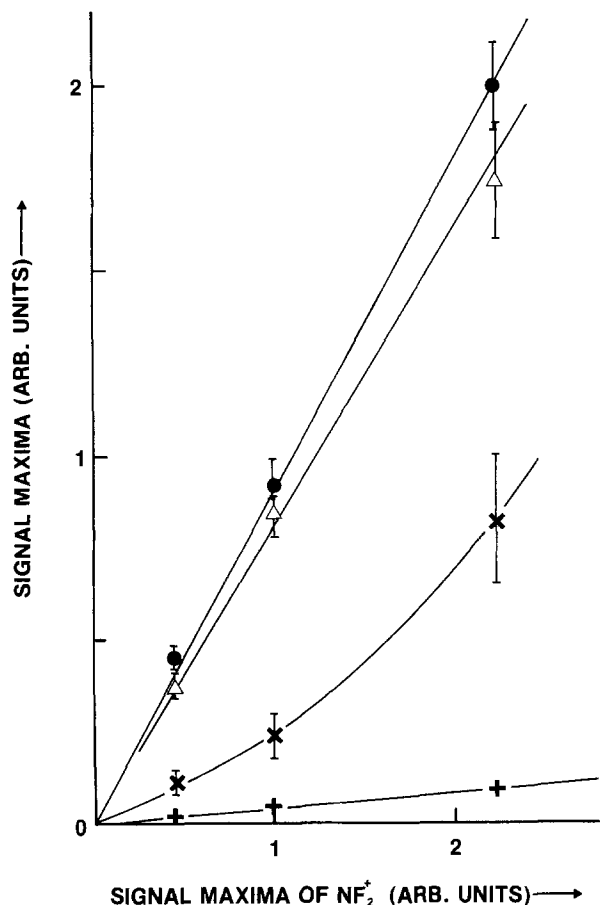
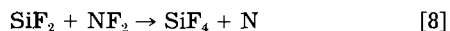
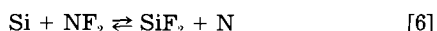


Fig. 1. Mass spectrometric signal maxima as a function of the amount of NF_3 injected with each pulse, as measured by the maximum of the NF_2^+ signal. \bullet : SiF_3^+ . \times : NF^+ . $+$: N^+ . Δ : (NF_2^+ signal maximum from the inactive cell) - (same quantity where plasma is ignited). The NF^+ and N^+ signals are corrected for the contributions arising from the mass spectrometric fragmentation of NF_3 .

Except for the last finding, one can summarize this as follows: there is essentially no measurable excess NF_2^+ , little excess NF^+ , and a somewhat larger excess N^+ —in short, the F-depleted fragments tend to accumulate in the plasma, as one would expect.

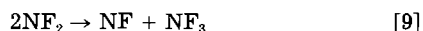
The results presented here are consistent with a relatively simple reaction scheme



Reactions [5] and [7] may well involve two separate steps which need not be discussed at length; the SiF_2 intermediate in the etching process has been documented by several spectroscopic studies (11, 12).

Reactions [6] and [8] are consistent with the fact that there is no measurable excess of NF_2 radicals in the plasma.

From the results analyzed in Fig. 2, one may postulate that in addition to the above reactions the disproportionation of NF_2



plays an important role. There are possible variations of this scheme which cannot be eliminated from the present data alone, such as a modified reaction [8]

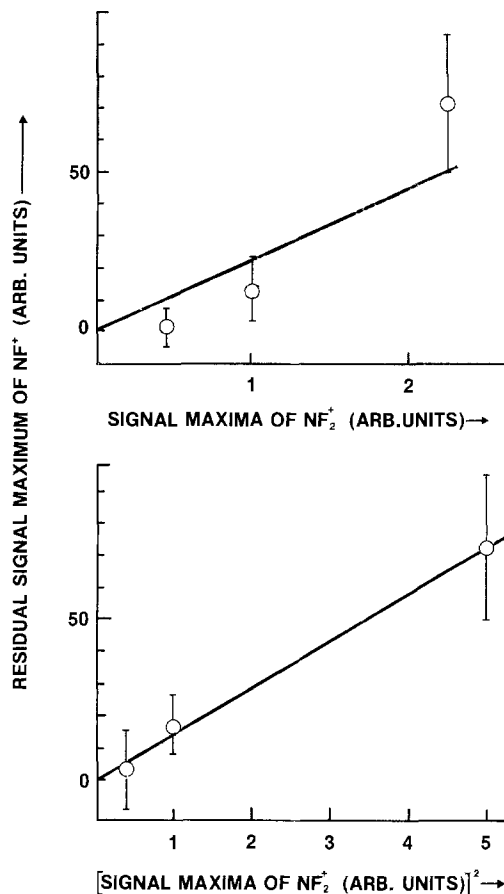
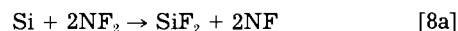


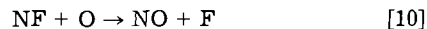
Fig. 2. Residual signal maximum of NF^+ , after subtracting the estimated SiF_2^{++} contribution to the $m/e = 33$ signal from the measured signal height (see text), against the signal maxima of NF_2^+ (top), and against the same quantities squared (bottom).



Next, measured SiF_3^+ signal heights, which are considered a simple measure of the etch rate, are independent of the amount of oxygen added to the plasma, within experimental errors, as shown in Fig. 3. There is a slight decrease of the $m/e = 52$ signal, i.e., of the amount of unfragmented NF_3 present. A corresponding slight increase of the SiF_3^+ signals is to be expected, but this effect is smaller than the experimental uncertainties.

Related to this, the changes in mass signals 33, 14, and 19, representing NF^+ , N^+ , and F^+ , respectively, must be considered. Unfortunately, the F concentrations are too low to be measurable, but the trends in the 33 and 14, as shown in Fig. 3, lead to some insight.

The 33 peak has contributions from NF (radicals or ions) and SiF_2^{++} . NF probably reacts with plasma-generated O when O_2 is present, according to



The NF contribution to the $m/e = 33$ signal initially present in O_2 -free plasmas is thus expected to vanish as O_2 is added while the $m/e = 30$ peak, representing NO , increases at the same rate, as seen in Fig. 3. The $m/e = 33$ signal, which remains at high O_2 concentrations, presumably arises from the SiF_2^{++} peak in the SiF_4 mass spectrum; this is consistent with the measured SiF_3^+ signals and the literature spectra (4-6). The $m/e = 30$ signal continues to increase with increasing O_2 concentration in the plasma, balancing the previously mentioned increase in NF_3 fragmentation (decrease of NF_2^+ signal). In view of reaction [10], and within the experimental uncertainties, NF and F seem to be equally effective in the etching process.

The $m/e = 14$ signal as plotted in Fig. 3 is practically constant throughout this series; either reactions [6] and [8] are not shifted by the addition of oxygen, or the contri-

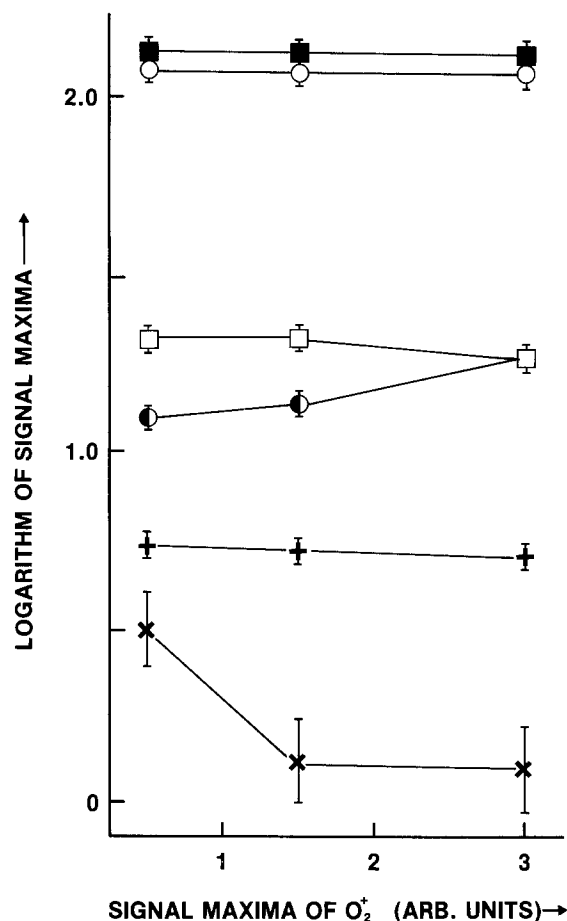


Fig. 3. Logarithm of signal maxima of various species against the signal maxima of O_2^+ , as a measure of the strength of the O_2 pulses injected. \circ : SiF_3^+ , \blacksquare , \square : NF_2^+ from the nonenergized plasma cell and in the presence of the plasma, respectively. \times , $+$, and \odot : signals at $m/e = 33, 14$, and 30 , respectively.

Contributions to the signal height from NO and NF are about equal, per unit concentration. In this context, one must recall that the contribution to the mass 14 signal arising from unfragmented NF_3 was subtracted earlier, and that NF_2 radicals are not present to a measurable extent.

Small $m/e = 44$ and 82 peaks were found in this study, both decreasing with increasing O_2 pressure. One can expect a small amount of $SiOF_2$ to form in this system, giving rise to SiO^+ and $SiOF_2^+$ signals, at 44 and 82 , respectively, but the concentrations of $SiOF_2$ should increase with O_2 concentration. Other unidentified traces may be involved here.

The sample surface and plasma cell walls remain very clean during the NF_3 and NF_3/O_2 etching experiments, so only volatile products are formed, except perhaps for small amounts of SiF_2 and $SiOF_2$.

Further support for the above interpretation is found in the kinetic results as presented in Fig. 4. As discussed in the earlier study (3), the apparent first-order constants determined from the slopes of the descending branches of the signal transients (2, 3) reflect the rate of the effusion process whenever one is dealing with chemically inert species. The NF_2^+ signals, representing unfragmented NF_3 present in the plasma cell, decay quickly, even somewhat faster than other inert species measured earlier regardless of whether the plasma indicated is ignited or not (see range b in Fig. 4). The SiF_3^+ apparent rate constants, by contrast, seem to be somewhat lower than the new NF_2^+ reference values, indicating some delay in the release of SiF_4 from the sample surface. This effect was just barely noticeable in the SF_6/Si system (2) and in the SF_6/O_2-Si system studied earlier (3).

NF^+ and N^+ signals also decay slowly, on this basis, and conceivably a portion of these species are formed, while the etching activities are dying down, after each injection

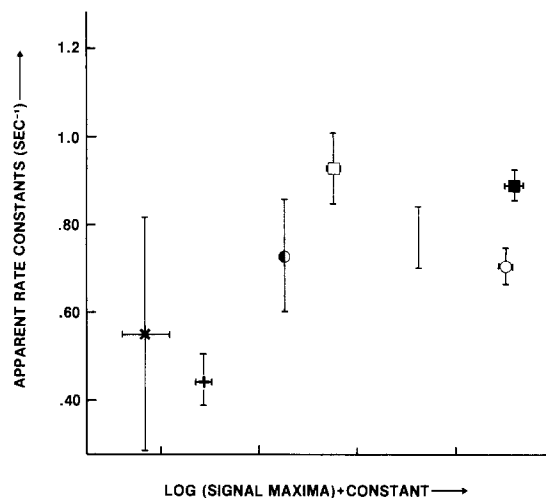
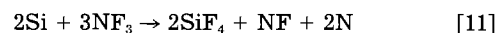


Fig. 4. Apparent rate constants, obtained from descending branches of transient signals, against natural logarithm of maximum signal. Data for low oxygen concentrations, corresponding to data near ordinate of Fig. 2. \blacksquare , \square : NF_2^+ before and after ignition of the plasma, respectively. \times , $+$, \odot : signals at $m/e = 33, 14$, and 30 , respectively. \circ : SiF_3^+ . B designates the range of other apparent rate constants in the absence of a plasma is shown, w.o. data point symbol. All data are corrected, according to Graham's law, to account for the different effusion rates. For this purpose, NF_2^+ is assumed to arise from NF_3 , NO^+ from NO , SiF_3^+ from SiF_4 , NF^+ from NF , and N^+ from N [see text, and Ref. (3)]. All corrections are relative to SiF_4 , as in Ref. (3).

of etchant gas. Possibly, NF_2 radicals, while present in the gas phase only in negligibly small amounts, are adsorbed at the surface undergoing etching, and cause reactions such as [6], [8], and/or [8a] to continue in the forward direction, even after the plasma activity ceased. Correspondingly, a small component of the SiF_3^+ signals, measured to evaluate the descending branches of the transient curves and to calculate the apparent rate constants, arises from that SiF_4 which is formed at the end of etching pulses. The fraction concerned is small: from Fig. 4, one obtains about 5%.

On the basis of these considerations, the overall reaction can be summarized approximately as



where NO appears in place of NF, whenever a sufficient amount of O_2 is present.

Finally, to gain some insight concerning the Si surface events, some plasma experiments were carried out to modify this surface. From Fig. 5, it appears that an oxide layer was created by exposure of the Si sample to an O_2 plasma, as described above. The layer is slowly removed by subsequent NF_3 etching, while Ar sputtering, under the conditions used, is quite ineffective for this purpose.

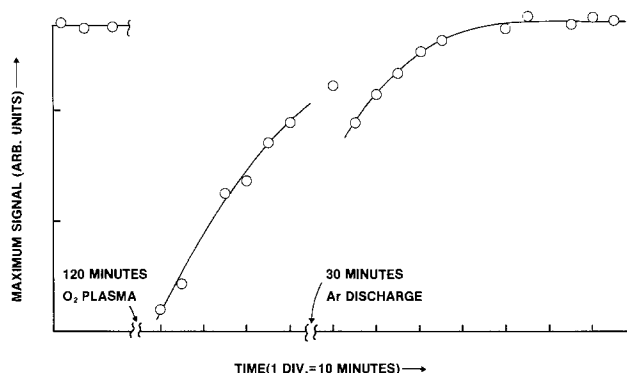


Fig. 5. Logarithms of maximum signals of SiF_3^+ , representing the etch rate, as a function of time. After the initial etching an O_2 plasma was produced for 120 min, at a pressure of 0.7 torr (see Table 1). Later on, a continuous Ar discharge was applied, modified by pulses of NF_3 , which resulted in the measured points. One ordinate division corresponds to a signal increase by a factor of 1.65.

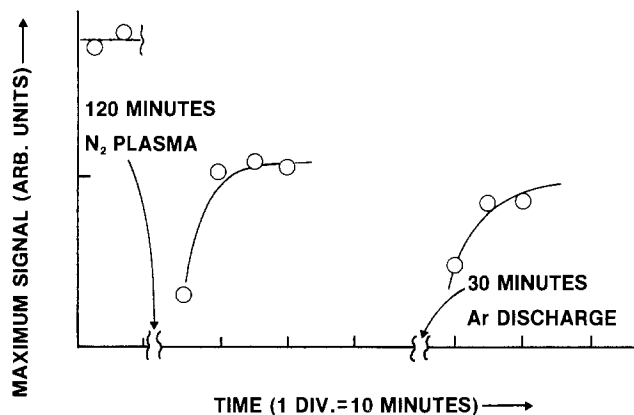


Fig. 6. Same as Fig. 5, for N_2 plasma exposure, for 60 min at 2.4 torr (see Table I). Ordinate scale factor: 1.29.

The exposure to a N_2 plasma leads to the formation of a nitride layer which appears to be even more tenacious under NF_3 etching, except initially, where there is a rapid increase in etching rate after N_2 -plasma exposure (see Fig. 6). Intermittent Ar sputtering appears to render this layer even more resistant to etching.

The exploratory experiments described here essentially show the versatility and scope of the pulse etching procedure.

Conclusions

The pulse injection procedure developed earlier was used to gain some detailed insight into the chemistry of the plasma etching of polycrystalline Si under NF_3 or NF_3/O_2 mixtures.

As shown in reaction [11], aside from the principal product SiF_4 , small amounts of NF and N were formed during that process, and in addition NO , whenever O_2 was present in the mixture. NF_2 radicals were not present in the gas phase in measurable amounts, but from a consideration of probable reaction steps, reactions [2]-[10], and the apparent first-order rate constants for the disappear-

ance of various species after each pulse, it was concluded that NF_2 is probably adsorbed at the surface, during etching. Oxygen additions have no measurable effect on the etching rates, and little effect on the concentrations of most species measured, with the important exceptions of NF which decreases, and of NO which increases, with oxygen concentrations.

Acknowledgments

The authors are indebted to the National Science Foundation for support of these studies, and to Professor d'Agostino for valuable comments concerning the reaction mechanism.

Manuscript submitted Feb. 28, 1984; revised manuscript received July 16, 1984.

REFERENCES

1. J. W. Coburn, *Plasma Chem. Plasma Proc.*, **2**, 1 (1982).
2. W. W. Brandt and T. Honda, in "Proceedings of the Sixth International Symposium on Plasma Chemistry," M. I. Boulou and R. J. Munz, Editors, p. 604, IUPAC, McGill University, Montreal, Que., Canada (1983).
3. W. W. Brandt and T. Honda, Submitted to *Plasma Chem. Plasma Proc.*
4. W. H. Beattie, *Appl. Spectrosc.* **29**, 334 (1975).
5. A. Cornu and R. Massot, "Compilation of Mass Spectral Data," Vol. 1, Heyden & Son, London (1975); E. Stenhagen, S. Abrahamsson, and F. W. McLafferty, Editors "Atlas of Mass Spectral Data," Wiley-Interscience, New York (1969).
6. W. H. Dibeler and F. L. Mohler, *J. Res. Natl. Bur. Stds.*, **40**, 25 (1948).
7. J. J. Wagner and W. W. Brandt, *Plasma Chem. Plasma Proc.*, **1**, 201 (1981).
8. N. J. Ianno, K. E. Greenberg, and J. T. Verdeyen, *This Journal*, **128**, 2174 (1981).
9. R. d'Agostino, V. Colaprico, and F. Cramacrossa, *Plasma Chem. Plasma Proc.*, **1**, 365 (1981); references therein.
10. R. d'Agostino, Personal communication.
11. T. J. Chuang, *J. Appl. Phys.*, **51**, 2614 (1980).
12. C. I. M. Beenakker, J. H. J. van Dommelen, and J. Dieleman, in "Plasma Processing," R. G. Frieser and C. J. Mogab, Editors, p. 302, The Electrochemical Society Softbound Proceedings Series, Pennington, NJ (1981).

Photosensitivity and Contrast Determination of Photoresist by Laser Interferometry

T. R. Pampalone,^{1,*} M. R. Hannifan, S. Jain, and C. D. Krieger

American Hoechst Corporation, AZ Photoresist Products, Somerville, New Jersey 08876

ABSTRACT

A laser interferometry technique was used to determine the photosensitivity and contrast values of positive photoresist. The precision of the technique was determined to be 2.7% (1 σ) for photosensitivity and 2.1% (1 σ) for contrast. The linear correlation of photosensitivity with film thickness was used to normalize the data. The utility of the technique as a quality control tool was demonstrated by analysis of 52 serially produced lots of 1350J photoresist.

Linewidth control during microlithographic fabrication of devices is critically dependent on the inherent photosensitivity of the resist. Some lot-to-lot variability in resist photosensitivity is expected by the device fabricator, and adjustments in exposure dose are routinely made on the line to compensate for this variability, most often using the critical dimensions of the device as the basis for the adjustment (1). Resist manufacturers do their best to minimize this lot-to-lot variability in photosensitivity by blending of raw materials or finished product to average out individual differences. However, one of the dif-

ficulties in achieving uniformity of photosensitivity is the variability of the test itself.

Several attempts to quantify the photosensitivity of a positive resist have been reported. One method measures the rate of photobleaching of the resist sensitizer, using monochromatic UV light as the irradiating source (2). The method assumes that the rate of photochemical conversion of sensitizer is a predictor of resist photosolubility, independent of processing conditions. This assumption is valid if the composition of the nonphotochemical components of the resist remain absolutely consistent so as not to change the physicochemical characteristics of the system. In practice, the latter situation seldom occurs. In or-

* Electrochemical Society Active Member.

¹ Present address: RCA Corporation, Solid State Division, Somerville, New Jersey 08876.

der to maintain consistent functional performance of the resist, resist manufacturers purposefully choose resins of varying molecular weight and developer solubility in the formulation to compensate for a particularly fast or slow sensitizer.

A functional measure of the photosensitivity of a resist is the "depth-of-penetration test" (3), which measures the thickness of resist film removed for a given amount of exposure energy under specific and controlled processing conditions. Recommended development time is 5 min. The thickness removed can be measured by a stylus measuring device if a ruled grating is used as the optical mask, and a plot of depth of penetration vs. exposure energy is constructed. From the plot, the minimum exposure energy to achieve complete dissolution of the film can be extrapolated. The precision associated with the test is $\pm 5\%$ (3), although for development times in the more-realistic 1-2 min range, the precision of the method is considerably less. A slight modification of the depth-of-penetration technique flood-exposes the sample and measures the thickness of film with an optical film thickness analyzer before and after development (4).

Rather than measure the thickness of film removed for a given exposure, one can measure the rate of film dissolution as a function of sensitizer photobleaching (5). Since for every resist there are inherent solubility rates for the dissolution of nonexposed and fully exposed resist, under fixed processing conditions, these solubility rates can be expressed as parameters to characterize the resist photosensitivity. A parameter related to contrast can then be calculated from the solubility parameters.

Although the approach has a good theoretical basis and generates functional data, it does not appear to be easily applicable to rapid resist characterization or have the rigor necessary for quality control.

In order to be useful to device fabricators, techniques to characterize the photosensitivity and contrast of photoresist must meet these criteria: (i) the results must be functional, derived under processing conditions the device actually undergoes; (ii) the results must be directly applicable to some device fabrication need, such as closely predicting the linewidth and edge acuity; (iii) the results must have good precision under production support conditions, which often differ considerably from the laboratory; and (iv) the technique must be responsive to small photoresist variations.

The laser interferometry technique described within has been under evaluation for over a year and meets these criteria. It functionally measures the dissolution properties of the total resist film, rather than the photochemical change of one component. In contrast, the Dill (7) procedure measures parameters (called "ABC") associated only with the photobleachability of the sensitizer (called photoactive compound, PAC) and neglects the contribution of the other components to dissolution rate. The Neureuther (5) technique uses laser interferometry to monitor development rate of the resist and generates data which can provide theoretical comparisons of resist lots. However, the data provided are not easily translated into the process-control parameters of interest to device makers. By comparison, the most useful application of the laser interferometry technique presented here appears to be quality control of photoresist on device fabrication lines. Contrast values indicate the attainable image resolution of the resist lot. Photosensitivity values provide a measure of lot-to-lot photosensitivity uniformity and can be used as a straightforward basis for making on-line exposure adjustments, if necessary. For instance, a $\pm 10\%$ variation in photosensitivity values determined by this technique results in linewidth variation of approximately $\pm 0.1 \mu\text{m}$ for a pattern generated with a Perkin-Elmer 220 Projection Aligner and consisting of $2 \mu\text{m}$ equal lines and spaces (6). The IC manufacturer, knowing that the photosensitivity value of a particular lot of photoresist is 10% higher than average, can increase exposure dose by 10% to maintain the same critical dimensions of the device.

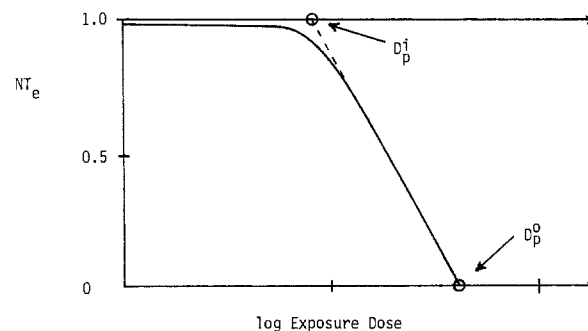


Fig. 1. Exposure curve for determining photosensitivity and contrast values. D_p^o = Exposure dose where $NT_e = 0$ (mJ/cm^2). D_p^i = Exposure dose where $NT_e = 1.0$ (mJ/cm^2). NT_e = Normalized film thickness. Contrast = $|\log D_p^o/D_p^i|^{-1} = |\text{slope}|$. Photosensitivity = D_p^o (mJ/cm^2).

The purpose of this paper is to review the laser interferometry procedure for determining photosensitivity and contrast of photoresist and show application of the technique for quality control. The laser inter-

Table I. Photosensitivity and contrast values for 1350J

Lot no. 1350J	T_o (μm)	Contrast	D_p^o (mJ/cm^2)	D_{pc}^o (mJ/cm^2)
1	1.701	1.447	100	107
2	1.732	1.540	98	101
3	1.816	1.558	105	99
4	1.707	1.547	99	105
5	1.806	1.554	106	101
6	1.766	1.471	98	97
7	1.680	1.598	102	111
8	1.837	1.467	106	97
9	1.814	1.506	104	98
10	1.790	1.534	106	103
11	1.799	1.507	105	101
12	1.785	1.467	106	103
13	1.806	1.583	105	100
14	1.805	1.647	100	95
15	1.792	1.587	101	97
16	1.764	1.513	108	108
17	1.741	1.405	97	99
18	1.797	1.435	95	91
19	1.761	1.487	93	93
20	1.783	1.350	104	101
21	1.807	1.589	102	97
22	1.808	1.549	102	97
23	1.756	1.462	87	88
24	1.798	1.442	101	97
25	1.770	1.473	91	90
26	1.765	1.633	108	107
27	1.765	1.570	103	102
28	1.785	1.513	111	108
29	1.771	1.521	108	107
30	1.786	1.570	106	103
31	1.773	1.428	112	110
32	1.779	1.517	108	106
33	1.716	1.598	98	103
34	1.765	1.559	101	100
35	1.779	1.561	99	97
36	1.762	1.563	100	100
37	1.733	1.677	93	96
38	1.733	1.678	94	97
39	1.746	1.616	93	95
40	1.743	1.590	95	97
41	1.739	1.526	96	98
42	1.770	1.416	109	108
43	1.747	1.563	101	103
44	1.714	1.613	101	106
45	1.748	1.510	105	106
46	1.735	1.620	98	101
47	1.719	1.574	89	94
48	1.757	1.663	100	100
49	1.723	1.781	86	90
50	1.761	1.518	108	108
51	1.746	1.494	110	112
52	1.747	1.645	94	95
\bar{x}	52	52	52	52
\bar{x}	1.764	1.543	100.9	100.4
σ	0.033	0.080	6.2	5.7
% RSD = $100\sigma/\bar{x}$	1.89	5.2	6.1	5.7

ferometry technique has been used widely by other workers (7) to characterize photoresist, and has been drafted into an ASTM test method (8).

Experimental

Determination of photosensitivity and contrast values.—The laser interferometry procedure is described fully in the ASTM method (8). Twelve 2 in. polished silicon wafers were spin coated at 4000 rpm with the 1350J photoresist and soft-baked 30 min at 90°C in an air circulating oven. The thickness variability for 12 wafers prepared in this manner was typically 0.008 μm (1σ). Each of the 12 wafers was exposed with a UV dose in the range 25-100 mJ/cm^2 , using an Oriel Corporation broadband 200W UV illuminator. The thickness of coated resist was measured in the center of each wafer using a Rudolf FTM (film thickness monitor). The wafers were each developed in 1:1 AZ Developer at 24°C, without agitation, and the loss of film was monitored by laser interferometry. From the resultant exposure curve of normalized film thickness remaining after 1 min development and the log exposure dose (Fig. 1), the photosensitivity and contrast values were determined for each of the 52 lots analyzed (Table I). The photosensitivity value (D_p^0) is the minimum UV dose required for complete film dissolution in the specified development time. In practice, the photosensitivity value is the exposure value when the linear portion of the exposure curve is extrapolated to zero normalized thickness. Contrast is the slope of the linear portion of the exposure curve (Fig. 1). Points within the linear limits of the exposure curve typically have a correlation coefficient of 0.98 or better. A reference 1350J resist was analyzed periodically to verify the reproducibility of the exposure and processing conditions.

Correlation of photosensitivity values with film thickness.—The photosensitivity values of 1350J (lot A), spin-coated at varying thicknesses, were determined and correlated with film thickness. Thicknesses from 3.3 to 1.6 μm were attainable by adjusting spin speed. After dilution to 26.5% solids, with AZ Thinner, coating thicknesses of 1.7-0.9 μm were attainable, and after dilution to 16.5% solids, coating thicknesses of 0.9-0.4 μm were attainable. The photosensitivity values obtained were recorded as a function of film thickness (Table II and Fig. 2). The correlation of photosensitivity value with film thickness was repeated for nine additional, randomly chosen lots of 1350J. For these additional runs, only six thicknesses were used, spanning the range of from 2.06 to 1.57 μm . The slope ($\text{mJ}/\text{cm}^2 \mu\text{m}$) of the least squares fit for each correlation, as well as the corresponding correlation coefficient, were calculated and statistically analyzed (Table III).

The contribution of substrate reflectivity to photosensitivity values.—The development rates of exposed resist

Table II. Photosensitivity values (D_p^0) as a function of film thickness (T_0)

1350J (30.5% solids)		(26.5% solids)		(16.5% solids)	
T_0 (μm)	D_p^0 (mJ/cm^2)	T_0 (μm)	D_p^0 (mJ/cm^2)	T_0 (μm)	D_p^0 (mJ/cm^2)
3.270	330	1.697	114	0.883	52
3.080	268	1.562	96	0.569	40
2.543	208	1.466	82	0.469	36
2.500	197	1.366	81	0.415	34
2.056	145	1.176	69	0.408	33
1.915	131	1.051	65		
1.906	126	0.959	56		
1.823	121	0.893	51		
1.814	116				
1.751	114				
1.745	107				
1.661	94				
1.576	90				
1.421	74				
1.382	73				
1.345	70				
1.305	68				
1.202	59				

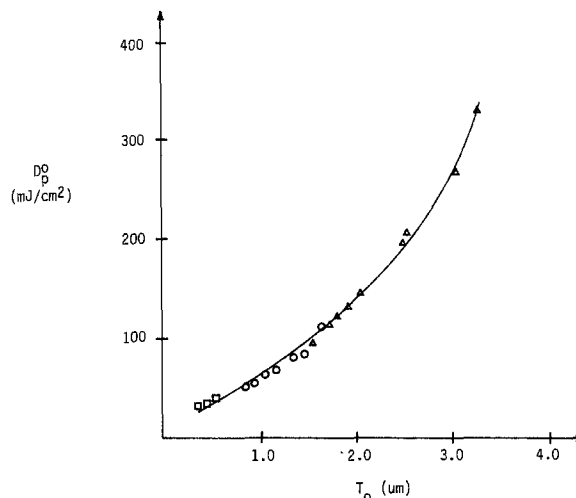


Fig. 2. Photosensitivity values (D_p^0) vs. film thickness (T_0). Δ : 30.5% solids. \circ : 26.5% solids. \square : 16.5% solids.

were monitored by laser interferometry to determine the contribution of the silicon substrate reflectivity to the photosensitivity values. The 1350J resist (lot A) was coated to thicknesses of 2.20, 1.45, and 0.49 μm on silicon wafers, with and without a proprietary antireflective coating. The antireflective coating was 1.88 μm thick and absorbed all of the normal incident light in the actinic range as determined by percent transmission measurements. After UV exposure with 25 mJ/cm^2 , the development rate of each wafer was monitored by laser interferometry, and the result plotted as film thickness removed vs. time (Fig. 3 and 4).

Results and Discussion

Photosensitivity values corrected for film thickness.—In Table III are listed the photosensitivity values obtained as a function of film thickness for 1350J (lot A) at 30.5% solids and after dilution to 26.5% and 16.5% solids. T_0 is the mean thickness of resist coated on the 12 wafers used for each photosensitivity determination. These results are plotted in Fig. 2. The slope of the least squares fit for a thickness range of 2.06-1.57 μm is statistically consistent for randomly chosen lots of 1350J, as shown in Table III. This consistency is not unexpected since the sensitizer and resin components are individually characterized and selected in formulating each resist lot. From the average

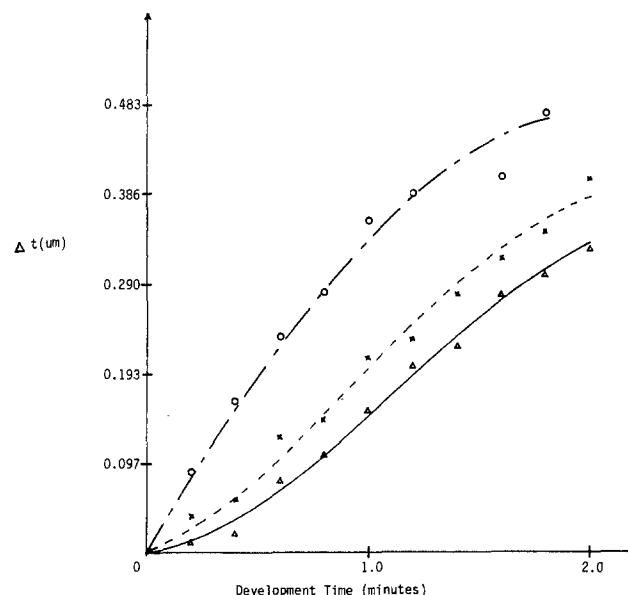


Fig. 3. Film thickness removed (μm) vs. development time (min). Polished silicon substrate, 25 mJ/cm^2 exposure. —: 0.49 μm film. - - - - -: 1.45 μm film.: 2.20 μm film.

Table III. Linear slope of photosensitivity values (D_p°) vs. film thickness (T_0) for random lots of 1350J

Lot no. of 1350J	Slope* (mJ/cm ²)(μ m)	Correlation coefficient
A	115.2	0.992
B	118.2	0.999
C	111.9	0.999
D	115.9	0.989
E	112.2	0.999
F	108.6	0.980
G	113.0	0.980
H	114.3	0.983
I	111.2	0.986
J	118.2	0.995
\bar{x}	113.8	0.990
σ	3.3	
% RSD = 100 σ/\bar{x}	2.9	

* 2.06-1.57 μ m thickness range.

slope value of 113.8 mJ/cm² μ m for 1350J are calculated the photosensitivity values corrected for film thickness (D_{pc}°). For AZ 1350J spun at 4000 rpm, the average dry coating thickness is formulated to 1.760 μ m. Therefore, the corrected photosensitivity value (D_{pc}°) for 1350J is derived from the relationship

$$D_{pc}^\circ = D_p^\circ + (1.760 \mu\text{m} - T_0) (113.8 \text{ mJ/cm}^2 \mu\text{m})$$

where D_p° is the uncorrected photosensitivity value and T_0 is the mean film thickness for the 12 wafers used in the determination. The correction is best suited to small film thickness variations. The inherent 3% error in the correction factor (Table III) corresponds to an error in correction of less than 1 mJ/cm² for the thickness range under consideration. The thickness range for the 52 lots reported in this study (Table I) is 1.85-1.65 μ m.

Photosensitivity and contrast values for 1350J.—Presented in Table I are the photosensitivity and contrast values for 52 serially produced lots of 1350J resist. Each lot of resist was spun on 12 silicon wafers at 4000 rpm and the resultant mean thickness (T_0) was recorded. The photosensitivity values (D_p°) of all the lots were corrected (D_{pc}°) to a 1.760 μ m film thickness using the correction formula given above. From Table I, the mean corrected photosensitivity value (D_{pc}°) for the 52 lots is 100.4 mJ/cm² with a 5.7% (% RSD) lot-to-lot variability.

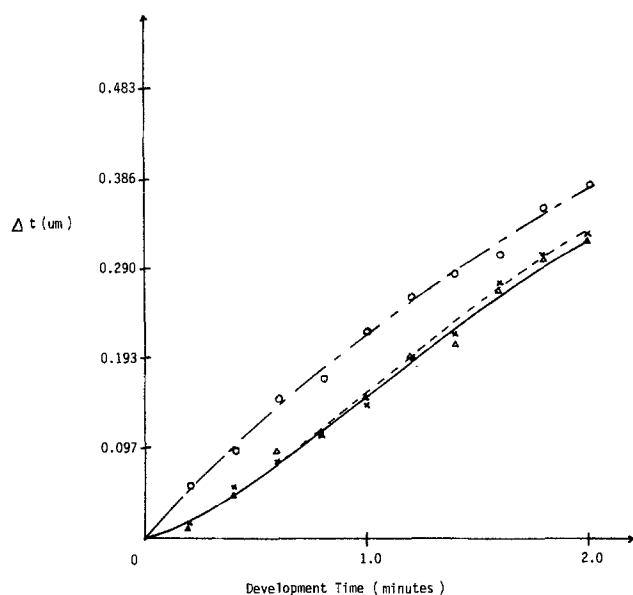


Fig. 4. Film thickness removed (μ m) vs. development time (min). Antireflective substrate. 25 mJ/cm² exposure. —: 0.49 μ m film. - - - -: 1.45 μ m film. —: 2.20 μ m film.

Precision of laser interferometry technique.—The repeatability precision of the laser interferometry technique was determined for 1350J (lot A) by the same operator using the same equipment. The statistical data and results are given in Table IV. The technique is shown to have a 1 σ precision of 2.7% (% RSD) for photosensitivity and 2.1% for contrast values.

Substrate reflectivity contribution to photosensitivity values.—As pointed out by Willson (9), the choice of method of defining resist sensitivity requires careful interpretation. His major concern is the contribution of substrate reflectivity, necessary to monitor film thickness loss, to the photosensitivity value. It is interesting to know how much, if any, of the reflected, actinic light affects the photosensitivity measurement. A direct observation of the reflectivity contribution was observed by analyzing the laser interferograms of 0.49, 1.45, and 2.20 μ m resist films after 25 mJ/cm² exposure. The plot of film thickness removed vs. development time (Fig. 3) illustrates the differential dissolution rates for the three films. (Deviation of the points from the curves is due mainly to standing wave effects.) The development rates for the 2.20 and 1.45 μ m films are similar; however, the 0.49 μ m film dissolves considerably faster. When the experiment is repeated, using an antireflective coating (Fig. 4), the dissolution rates of the 2.20 and 1.45 μ m film are unchanged; the 1.45 μ m film is now dissolving at the same rate as is the 2.20 μ m film, and the 0.49 μ m film is dissolving slower than before. Internal reflections and partial reflection at the photoresist-antireflective coating interface may still affect the dissolution rates despite the elimination of the reflection of normal incident light. The effect is more pronounced with thinner films owing to the higher relative intensity of incident light throughout the film and the interface. Residual solvent content of resist films after soft-bake is well known to affect dissolution rates (10). However, analysis of residual solvent in the 0.49 and 1.45 μ m resist films by quantitative infrared analysis (using transparent double-polished silicon wafers and scanning the 1720 cm⁻¹ carbonyl frequency) (11) showed that both films after soft-bake contained no detectable differences in percent ethoxyethyl acetate.

The data in Table II (photosensitivity value vs. film thickness) can be plotted as film thickness vs. log photosensitivity value. Each point on this curve represents a measured photosensitivity value for the respective film thickness on a substrate. In contrast, an exposure curve plot represents the film thickness removed after development for the respective log exposure dose. The plot of film thickness vs. log photosensitivity value (from Table II) superimposed upon an exposure curve of film loss vs. log exposure dose for a thick (3.2 μ m) film illustrates the contribution of substrate reflectivity to photosensitivity (Fig. 5).

In Fig. 5, the film thickness vs. log photosensitivity value plot (line no. 1) is superimposed upon the mean exposure curve for triplicate analyses of a 3.20 μ m film (line

Table IV. Precision of the laser interferometry technique

Trial no.	T_0 μ m	D_p° mJ/cm ²	D_{pc}° mJ/cm ²	Contrast
1	1.751	99	100	1.61
2	1.732	96	99	1.65
3	1.708	98	104	1.66
4	1.723	98	102	1.63
5	1.741	95	97	1.67
6	1.760	99	99	1.62
7	1.713	95	100	1.68
8	1.757	100	100	1.66
9	1.737	104	107	1.58
10	1.727	95	99	1.68
11	1.732	96	99	1.69
\bar{x}	1.735	98	101	1.65
σ	0.017	2.8	2.7	0.03
% RSD = 100 σ/\bar{x}	0.98	2.8	2.7	2.1

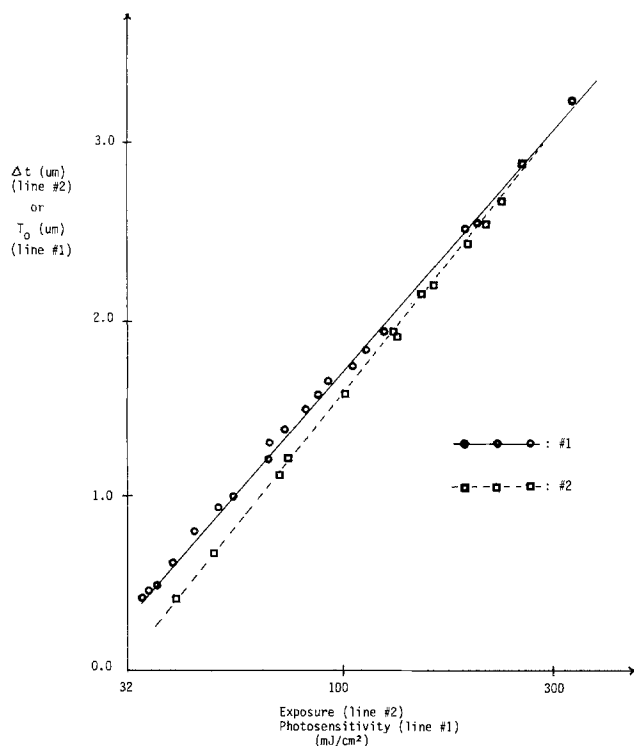


Fig. 5. No. 1: Initial film thickness (T_0) vs. exposure required for complete dissolution in 1.0 min development. No. 2: Film loss (Δt) in 1.0 min development vs. exposure given a "thick" film.

no. 2). The divergence of the two lines reflects the magnitude of the contribution of substrate reflectivity to photosensitivity. Reflectivity contribution to resist photosensitivity has been well documented, especially for thin films on highly reflective substrates (12). Quantifying reflectivity effects is possible in this case because the light source is broadband and standing wave effects are minor. This would not be so for narrow bandwidth light sources such as projection aligners or steppers.

Determination of lot-to-lot photosensitivity uniformity.—From Table I, the standard deviation of corrected photosensitivity values (D_{pc}^0) is 5.7 mJ/cm², and from Table IV, the standard deviation of the laser interferometry technique is 2.7 mJ/cm². Using analysis of variance (13), which assumes the total variance is the sum of separate variances

$$\sigma_{\text{Total}}^2 = \sigma_1^2 + \sigma_2^2$$

the variance for resist photosensitivity (σ_R^2) can be approximated

$$(5.7)^2 = \sigma_R^2 + (2.7)^2$$

$$\sigma_R^2 = 25.2$$

The standard deviation for resist photosensitivity is

$$\sigma_R = 5.0 \text{ mJ/cm}^2$$

Therefore, the lot-to-lot photosensitivity uniformity for 1350J resist at the 1σ level is approximately $\pm 5 \text{ mJ/cm}^2$, or $\pm 5\%$ (σ), since $x = 100.4 \text{ mJ/cm}^2$. By the same analysis of variance procedure, the lot-to-lot contrast uniformity for 1350J at the 1σ level is ± 0.074 , or $+4.8\%$, since $x = 1.543$.

Conclusions

The laser interferometry technique can be successfully used to characterize the photosensitivity and contrast of positive resist. The 1σ precision for the technique was found to be 2.7% for photosensitivity and 2.1% for contrast values. A correction for film thickness can be applied in the normal working range of 1350J to improve the measurement. The technique is particularly well suited for lot-to-lot quality control (QC) testing of photoresist. QC analysis of 52 lots of 1350J photoresist showed the percent relative standard deviation (% RSD) for photosensitivity and contrast to be 5.7% and 5.2%, respectively. The % RSD for photosensitivity and contrast corrected by analysis of variance was 5.0% and 4.8%, respectively.

Research work is now underway to improve the precision of the laser interferometry technique and correlate photosensitivity and contrast values with critical dimensions, wall angles, and other lithographic outcomes. The techniques described here are being used to monitor and qualify raw materials and manufactured lots of photoresist.

Manuscript submitted Dec. 9, 1983; revised manuscript received May 20, 1984.

American Hoechst Corporation assisted in meeting the publication costs of this article.

REFERENCES

1. J. N. Helbert, C. C. Walker, P. A. Seese, and A. J. Gonzales, *SPIE Semicond. Microlithogr.*, **275**, 182 (1981); K. Kadota, Y. Taki, and S. Shimizu, *ibid.*, **275**, 173 (1981).
2. D. F. Iltgen and R. J. Sutton, *This Journal*, **119**, 539 (1972); F. J. Loprest and E. A. Fitzgerald, *Photogr. Sci. Eng.*, **15**, 260 (1971).
3. D. J. Elliot, in "Integrated Circuit Fabrication Technology," Chap. 13, p. 325, McGraw-Hill Book Company, New York (1982).
4. M. J. Bowden, *This Journal*, **128**, 195C (1981).
5. D. J. Kim, W. G. Oldham, and A. R. Neureuther, in "Kodak Microelectronics Seminar, Proceedings of Interface '82," p. 100 (1982).
6. T. R. Pampalone, M. R. Hannifan, S. Jain, and C. D. Krieger, In preparation.
7. F. H. Dill, W. P. Hornberger, P. S. Hauge, and J. M. Shaw, *IEEE Trans. Electron Devices*, **ed-22**, 445 (1975); F. H. Dill, A. R. Neureuther, J. A. Tuttle, and E. J. Walker, *ibid.*, **ed-22**, 456 (1975); K. L. Konnerth and F. H. Dill, *Solid State Electron.*, **15**, 371 (1972); M. Exterkamp, W. Wong, H. Damar, A. R. Neureuther, C. H. Ting, and W. G. Oldham, *SPIE*, **334**, 182 (1982).
8. T. R. Pampalone and R. F. Doll, "Recommended Practice for Determining Contrast and Photosensitivity of a Photoresist," ASTM Document no. 8A60, Subcommittee Fl.08, American Society for Testing and Materials, Philadelphia.
9. G. C. Willson, in "Introduction to Microlithography," Chap. 3, p. 105, American Chemical Society, Washington, DC (1983).
10. J. M. Shaw, M. A. Frisch, and F. H. Dill, *IBM J. Res. Dev.*, **21**, 219 (1977).
11. T. R. Pampalone, M. R. Hannifan, S. Jain, and C. D. Krieger, In preparation.
12. F. Jones, M. Hatzakis, and H. Rothmann, in "Kodak Microelectronics Seminar, Proceedings of Interface '79," p. 113 (1979).
13. ICI Staff, in "Statistical Methods in Research and Production," O. L. Davis and P. L. Goldsmith, Editors, Chap. 8, Longman Group Limited, London (1972).

Nonlinear Two-Step Diffusion in Semiconductors

D. Anderson

Institute for Electromagnetic Field Theory, Chalmers University of Technology, S-412 96 Göteborg, Sweden

K. O. Jeppson

Research Laboratory of Electronics, Chalmers University of Technology, S-412 96 Göteborg, Sweden

ABSTRACT

At high concentrations, impurity diffusion in semiconductors tends to be governed by nonlinear diffusion processes. Using similarity analysis, analytical solutions are here found for the impurity profile resulting from a two-step diffusion process where the drive-in step involves a nonlinear diffusion process. Comparison with previously published experimental results shows very good agreement.

In the fabrication of many semiconductor devices, solid-state diffusion is a common method for the introduction of impurities into the semiconductor material. The desired impurity profile is often established by means of a two-step process. In the first predeposition step, a certain total number of impurities is deposited in a shallow region close to the surface of the material, either by ion implantation or by an initial diffusion process. The second drive-in step involves a diffusive redistribution of the impurities, usually resulting in much deeper penetration into the material (1).

For low impurity concentration, the diffusion processes are governed by linear diffusion equations and exact solutions in terms of Gaussian or erfc functions are available. Although there has recently been some discussion about the most convenient approximation for the final impurity profile resulting from two-step diffusion processes (2, 3), the analytical understanding of the evolution of the impurity profiles is generally very good, owing to the extensive knowledge existing for the linear diffusion equations, cf. Ref. (4).

However, many modern semiconductor applications involve high impurity levels, in which case the corresponding diffusion processes may become strongly nonlinear, and the simple linear diffusion equation is well known to give results which are not in agreement with experimental results (5).

The physical mechanism causing nonlinear diffusion of impurities in, e.g., silicon has recently been summarized by Fair (6, 7). According to the vacancy model, the diffusion of substitutional impurities is a result of the interaction with vacant states in the silicon. These vacancies may be neutral or charged. The concentration of neutral states at any temperature is independent of the impurity concentration, C , while the number of charged vacancies depend on the impurity concentration. The intrinsic diffusion coefficient D_i , at low doping levels ($C < n_i$) may be written as

$$D_i = D^0 + D^+ + D^- + D^- \quad [1]$$

where D^0 , D^+ , D^- , and D^- represent the effective diffusivities under intrinsic conditions for the neutral, positive, singly, and doubly negative charged states, respectively. For extrinsic conditions, the diffusion coefficient may be written as

$$D = h[D^0 + D^+(n_i/n) + D^-(n/n_i) + D^-(n/n_i)^2] \quad [2]$$

where n is the electron concentration

$$n = \frac{C}{2} \left\{ 1 + \left[1 + \left(\frac{2n_i}{C} \right)^2 \right]^{1/2} \right\} \quad [3]$$

and h is the self electric-field enhancement factor

$$h = 1 + \frac{C}{2n_i} \left[\left(\frac{C}{2n_i} \right)^2 + 1 \right]^{-1/2} \quad [4]$$

Usually, at high doping levels, one of the charged-state diffusivities becomes dominant, so the effective diffusion coefficient may be written

$$D = 2D_i(C/n_i)^\gamma \quad [5]$$

where $\gamma = 1$ for boron and arsenic, and $\gamma = 2$ for phosphorous. However, the diffusion of phosphorous in silicon is complicated by the dissociation of the doubly negative charged vacancies at doping levels of about 10^{20} cm^{-3} . At lower levels, this dissociation results in an enhanced tail diffusion.

As compared to the linear case, the analytical understanding of nonlinear diffusion processes is strikingly poor, and resort is mostly taken to numerical computations (6). As far as we know, within the context of semiconductor applications, the only attempt towards an analytical investigation of nonlinear diffusion processes has been made by Nakajima *et al.* (9), Fair (10, 11), and Fair and Tsai (12, 13) for arsenic and boron diffusion. This approach relies on the approximation of the impurity profile by Chebyshev polynomials in the variable $x/t^{1/2}$ suggested by Nakajima *et al.* where x and t denote space and time coordinates, respectively (see Appendix A). This is a good approach for diffusion involving a constant surface concentration, but is not appropriate in the case of a two-step diffusion, where the diffusive redistribution occurs under the condition of a constant total number of impurities. The proper variable in this case turns out to be $x/t^{1/(\gamma+2)}$, i.e., $x/t^{1/3}$ and $x/t^{1/4}$ for $\gamma = 1$ and $\gamma = 2$, respectively.

The purpose of the present work is to demonstrate that similarity methods (14) provide a powerful and flexible tool for a systematic study of the nonlinear diffusion equations which occur in solid-state high concentration impurity diffusion. Furthermore, the analytic solutions which are obtained are exact, attractively simple, and yield very good agreement with experimental results.

Analysis

We restrict the present analysis to the case of a two-step process where the first step establishes a very shallow impurity profile containing a given total dose, Q_0 . For high impurity concentration, the second drive-in step is assumed to be governed by a diffusion equation of the form

$$\frac{\partial C}{\partial t} = \frac{\partial}{\partial x} \left(D \frac{\partial C}{\partial x} \right) \quad [6]$$

where the diffusion coefficient, D , depends nonlinearly on the impurity concentration, C , as given by Eq. [5], i.e., $D_0 = 2D_i$,

$$D = D_0 \left(\frac{C}{n_i} \right)^\gamma \quad [7]$$

A systematic and very powerful tool for analyzing diffusion equations is similarity methods (14), which have the

attractive advantage of being equally applicable to linear and nonlinear equations. Following the similarity approach, we look for solutions of Eq. [6] and [7] in the form

$$C(x, t) \sim t^\alpha \phi(\xi) \quad [8]$$

where the similarity variable, ξ , is given by

$$\xi = \frac{x}{t^\beta} \quad [9]$$

The unknown function, $\phi(\xi)$, as well as the parameters α and β , are determined by inserting the expression into the diffusion equation and using the appropriate boundary or initial conditions. If the initial shallow impurity profile can be approximated as a delta function and the total number of diffusing impurities is assumed constant, the exact solution of Eq. [6] and [7] can be written in the suggestive form (see Appendix B)

$$C(x, t) = C_s(t) \left(1 - \frac{x^2}{x_F^2(t)}\right)^{1/\gamma} \quad [10]$$

where the surface concentration, $C_s(t)$, and the penetration depth, $x_F(t)$, are given by

$$C_s(t) = \left(\frac{\gamma}{2(\gamma+2)I_\gamma} \cdot \frac{Q_0^2 n_1^\gamma}{D_0 t}\right)^{1/(\gamma+2)}$$

$$x_F(t) = \left(\frac{2(\gamma+2)}{\gamma I_\gamma} \cdot \frac{Q_0^\gamma D_0 t}{n_1^\gamma}\right)^{1/(\gamma+2)} \quad [11]$$

In Eq. [10] and [11], I_γ is a numerical factor given by $I_1 = 2/3$ and $I_2 = \pi/4$.

In particular, we find from Eq. [10] and [11] for $\gamma = 1$ and $\gamma = 2$, respectively

(i) $\gamma = 1$

$$C(x, t) = C_s \left(1 - \frac{x^2}{x_F^2}\right) \quad [12]$$

where

$$C_s = \frac{3^{1/3}}{2} \left(\frac{Q_0^2 n_1}{D_0 t}\right)^{1/3} \cong 0.57 \left(\frac{Q_0^2 n_1}{D_0 t}\right)^{1/3}$$

$$x_F = 9^{1/3} \left(\frac{Q_0 D_0 t}{n_1}\right)^{1/3} \cong 2.62 \left(\frac{Q_0 D_0 t}{n_1}\right)^{1/3} \quad [13]$$

(ii) $\gamma = 2$

$$C(x, t) = C_s \left(1 - \frac{x^2}{x_F^2}\right)^{1/2} \quad [14]$$

where

$$C_s = \left(\frac{2}{\pi}\right)^{1/2} \left(\frac{Q_0^2 n_1^2}{D_0 t}\right)^{1/4} \cong 0.67 \left(\frac{Q_0^2 n_1^2}{D_0 t}\right)^{1/4}$$

$$x_F = \left(\frac{8}{\pi}\right)^{1/2} \left(\frac{Q_0^2 D_0 t}{n_1^2}\right)^{1/4} \cong 1.90 \left(\frac{Q_0^2 D_0 t}{n_1^2}\right)^{1/4} \quad [15]$$

We emphasize the characteristic time dependence of C_s and x_F involving $t^{1/3}$ and $t^{1/4}$ for $\gamma = 1$ and $\gamma = 2$, respectively, as opposed to the ordinary $t^{1/2}$ dependence of the conventional Boltzmann transformation. This feature has caused some confusion in previous investigations of nonlinear diffusion in semiconductors, cf. Ref. (11-13, 15).

The delta function approximation for the initial impurity distribution is a good approximation when the final width of the profile, as resulting from the drive-in step, is much larger than the width of the initial profile. Actually, the drive-in profile asymptotically approaches the similarity profile as t increases, irrespective of the form of the first impurity deposition. In situations where the width of the initial profile does play a non-negligible role, it can easily be incorporated into the analysis (see Appendix B).

In particular, Eq. [10]-[15] are still valid, provided we redefine the surface concentration and the penetration depth according to (cf. eq. [13] and [15])

(i) $\gamma = 1$

$$C_s = \frac{3^{1/3}}{2} \left(\frac{Q_0^2 n_1}{D_0 t}\right)^{1/3} \left(1 + \frac{x_0^3}{9Q_0 D_0 t/n_1}\right)^{-1/3}$$

$$x_F = 9^{1/3} \left(\frac{Q_0 D_0 t}{n_1}\right)^{1/3} \left(1 + \frac{x_0^3}{9Q_0 D_0 t/n_1}\right)^{1/3} \quad [16]$$

(ii) $\gamma = 2$

$$C_s = \left(\frac{2}{\pi}\right)^{1/2} \left(\frac{Q_0^2 n_1^2}{D_0 t}\right)^{1/4} \left(1 + \frac{\pi^2}{64} \frac{x_0^4}{Q_0^2 D_0 t/n_1^2}\right)^{-1/4}$$

$$x_F = \left(\frac{8}{\pi}\right)^{1/2} \left(\frac{Q_0^2 D_0 t}{n_1^2}\right)^{1/4} \left(1 + \frac{\pi^2}{64} \frac{x_0^4}{Q_0^2 D_0 t/n_1^2}\right)^{1/4} \quad [17]$$

and x_0 is the width of the initial profile.

Discussion

The general shape of the doping profile given by Eq. [10] is shown in Fig. 1 for $\gamma = 1$ and $\gamma = 2$, together with the Gaussian profile and the Chebyshev polynomial approximation (9-13). In this plot, the impurity concentration is normalized to the surface concentration and plotted against normalized junction depth. (For the Gaussian and Chebyshev profiles, the junction depth was chosen as the depth at which the concentration falls to 1% of the surface concentration.) As expected analytically, and also observed experimentally (8-13), the solutions to the nonlinear diffusion equations are much steeper, giving more abrupt junctions than the linear Gaussian profile.

For arsenic, only the neutral and singly negative charged vacancies are responsible for the impurity diffusion. The diffusivity of arsenic may then be written

$$D = D^0 + D^- \frac{n}{n_i} \quad [18]$$

but since $\beta = D^-/D^0 \cong 1$, the diffusion process is strongly nonlinear for $C \gg n_i$, and the resulting profile may be described by Eq. [10] and [11] where $\gamma = 1$. In Fig. 2, the

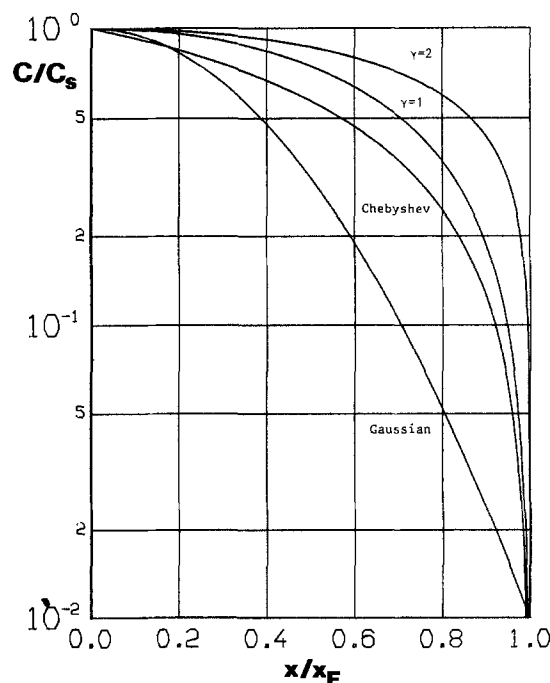


Fig. 1. Normalized doping profiles for $\gamma = 1$ and $\gamma = 2$. The Gaussian profile is given for comparison together with the Chebyshev polynomial approximation (9-13).

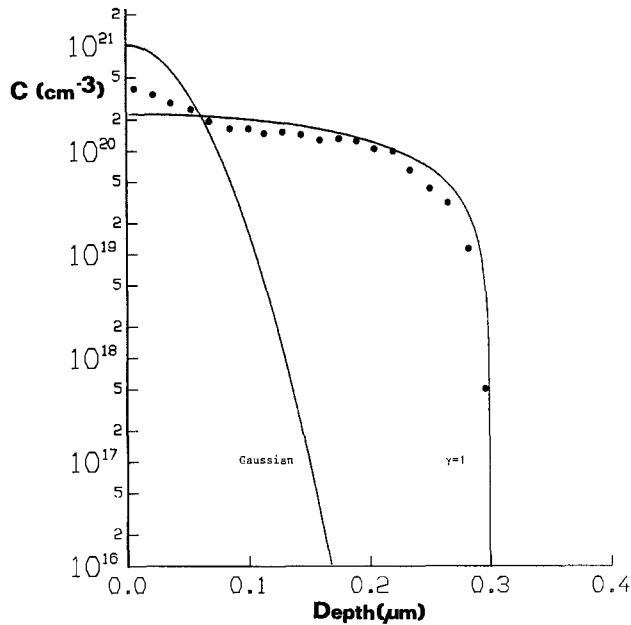


Fig. 2. Doping profile for shallow implanted arsenic compared with experimental results of Hill (16). The Gaussian profile for a constant diffusion constant is given for comparison.

doping profile of shallow ion-implanted arsenic, after 30 min of diffusion in argon at 1000°C , measured by Hill (13), has been compared to our theoretical curve calculated from Eq. [10] and [11]. Excellent agreement is found between the two curves. The Gaussian profile for the same conditions is also shown for comparison. In this plot, the value of $D_i = 24 \exp(-4.08/kT)$ has been used together with the value of n_i according to Morin and Maita (17).

The diffusion of ion-implanted arsenic in silicon has also been extensively studied by Fair and Tsai (12, 13), using secondary ion mass spectroscopy (SIMS). In Fig. 3, their experimental data for the surface concentration as a function of $(Q_0^2 n_i / D_i t)^{1/3}$ is compared to our theoretical result as given by Eq. [13]. Very good agreement is found. In particular, we note that for a given dose and temperature, the surface concentration will decrease as $t^{-1/3}$, as theoretically predicted by Eq. [13].

In Fig. 4, the junction depth, x_f , as described theoretically by Eq. [13], is plotted against $(Q_0 D_i t / n_i)^{1/3}$, together with the experimental data of Fair and Tsai (12, 13), in the

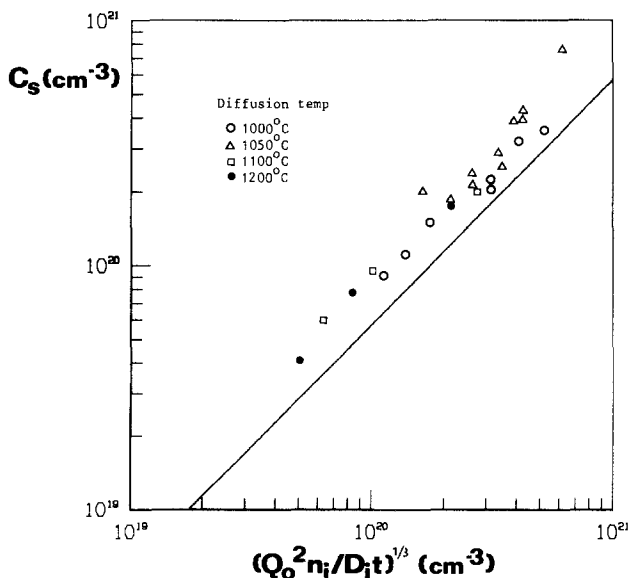


Fig. 3. The dependence of the surface concentration on time, temperature, and dose (Eq. [13]) for implanted As compared with experimental results of Fair and Tsai (13).

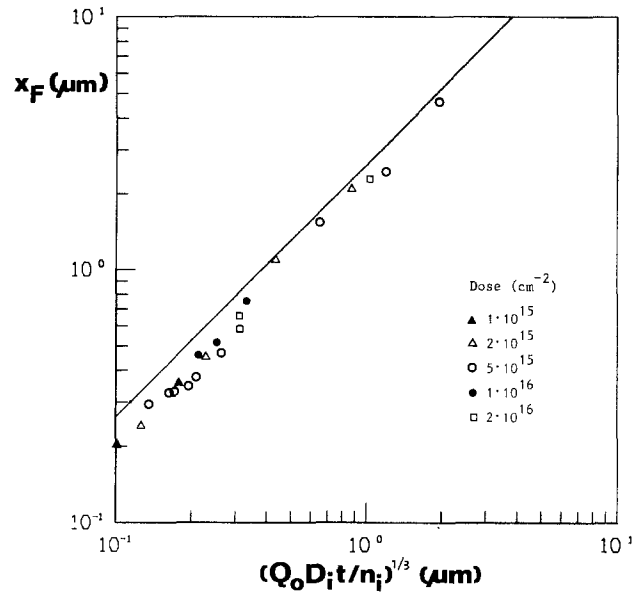


Fig. 4. The dependence of the junction depth of time, temperature, and dose (Eq. [13]) for implanted As compared with experimental results of Fair and Tsai (13) for dry ambients.

temperature range 1000°C - 1250°C . Again, good agreement is found, especially for deeper junction depths. In particular, the junction depth is clearly seen to increase as $t^{1/3}$.

Finally, Eq. [13] may also be rewritten as the following simple relation between surface concentration, dose, and junction depth, viz.

$$C_s = 1.5 Q_0 / x_f \quad [19]$$

This relation, together with the experimental data of Fair and Tsai, is shown in Fig. 5, again with good agreement.

The characteristic scaling of surface concentration and junction depth has previously been pointed out by Fair and Tsai (13), using a semiempirical approach. However, in this paper, we have demonstrated that the observed scalings are exact consequences of the properties of the nonlinear diffusion equation. The similarity method clearly shows that, for arsenic and boron diffusion at high impurity concentrations when the diffusion constant is concentration dependent (with $\gamma = 1$), the impurity profile is a function of $x/(D_i t)^{1/2}$ for diffusion with constant surface concentration and a function of $x/(D_i t)^{1/3}$ for diffusion with a constant number of shallow implanted impu-

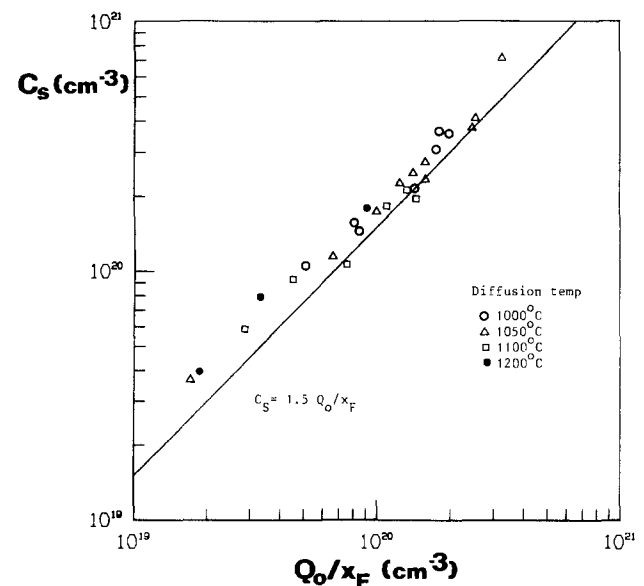


Fig. 5. The surface concentration of implanted As vs. average doping compared with experimental data from Fair and Tsai (13).

urities. In earlier papers, this fact has only been obtained indirectly, as shown in Appendix A. Any function of $x/(C_s D_1 t/n_1)^{1/2}$, describing a doping profile with a constant surface concentration (and $\gamma = 1$), will be turned into a function of $x/(Q_0 D_1 t/n_1)^{1/3}$ if instead the total number of impurities are assumed constant, since integration of the impurity profile over x yields

$$Q_0 = \text{const.} \cdot C_s x_j \quad [20]$$

This constant is empirically determined by Fair and Tsai (13) to be 0.53 for arsenic, as compared to our theoretical value of 0.67 from Eq. [19], which is a 20% difference. For boron, this constant is 0.4 (11).

As shown in Fig. 2, the exact solution of the nonlinear diffusion equation is an excellent description of the arsenic doping profile, except very close to the surface. In this region, the theoretical profile tends to underestimate the surface concentration. This is also evident from the experimental data in Fig. 3. This is probably due to the reduced arsenic diffusivity at concentrations above 10^{20} cm^{-3} (6, 7). Hence, the implanted profile close to the surface is not redistributing as fast as theoretically expected, owing to complex impurity-vacancy pair formation, clustering, and strain effects. This effect is also more evident at lower diffusion temperatures.

This is probably also the explanation for why the Chebyshev approximation, with its nonvanishing slope at the surface, may result in just as good, or even better, doping profiles as compared to the theoretical solution in this paper. This is, then, not a natural result of the nonlinear diffusion itself, but rather a consequence of the deviations from ideal conditions, such as reduced surface diffusivity. The nonvanishing slope is, then, a residue of the originally implanted profile.

Manuscript submitted Feb. 9, 1984; revised manuscript received July 16, 1984.

Chalmers University of Technology assisted in meeting the publication costs of this article.

APPENDIX A

For nonlinear diffusion with $\gamma = 1$ and a constant surface concentration C_s , Nakajima *et al.* (9) approximated the doping profile with the Chebyshev polynomial

$$C/C_s = 1.00 - 0.87 Y - 0.45 Y^2 \quad [A-1]$$

where $Y = x/(8C_s D_1 t/n_1)^{1/2}$. This profile approximation may be simplified to

$$C/C_s = 1 - 0.70 \frac{x}{x_j} - 0.30 \left(\frac{x}{x_j} \right)^2 \quad [A-2]$$

where $x_j = 2.3 (C_s D_1 t/n_1)^{1/2}$ is the junction depth. This expression does not include the background concentration because of the large doping gradient at the diffusion front. Integrating Eq. [A-2] over x gives the total amount of dopants as

$$Q_0 = K C_s x_j \quad [A-3]$$

where K is a constant. This approximation is used by Fair and Tsai (13) also for the case of implanted arsenic diffusion with a constant amount of impurities. In this case, Q_0 is assumed constant in Eq. [A-3] instead of C_s , which is now assumed slowly varying. Insertion of Eq. [A-3] into the junction depth expression yields

$$x_j = 2(Q_0 D_1 t/n_1)^{1/3} \quad [A-4]$$

$$C_s = 0.94 (Q_0^2 n_1 / D_1 t)^{1/3} \quad [A-5]$$

which has turned the doping profile in Eq. [A-2] into a $t^{1/3}$ dependence instead of the original $t^{1/2}$ dependence.

For boron diffusion with $\gamma = 1$ and a constant surface concentration C_s , the doping profile may be approximated by (11)

$$C/C_s = 1 - \left(\frac{x}{x_j} \right)^{2/3} \quad [A-6]$$

where the junction depth $x_j = 2.45 (C_s D_1 t/n_1)^{1/2}$. Integrating Eq. [A-6] over x yields the total amount of boron im-

purities

$$Q_0 = 0.4 C_s x_j \quad [A-7]$$

Now assuming Q_0 constant for implanted boron diffusion, yields

$$C_s = 0.53 (Q_0^2 n_1 / D_1 t)^{1/3} \quad [A-8]$$

where 0.53 is an empirical constant.

APPENDIX B

The purpose of this Appendix is to give a more detailed presentation of the similarity approach as applied to the nonlinear diffusion equation obtained by combining Eq. [6] and [7], *i.e.*

$$\frac{\partial C}{\partial t} = D_0 \frac{\partial}{\partial x} \left(\left(\frac{C}{n_1} \right)^\gamma \frac{\partial C}{\partial x} \right) \quad [B-1]$$

It is convenient to normalize Eq. [B-1] by introducing $\tilde{C} = C/n_1$ and $\tau = D_0 t$. Equation [B-2] then becomes

$$\frac{\partial \tilde{C}}{\partial \tau} = \frac{\partial}{\partial x} \left(\tilde{C}^\gamma \frac{\partial \tilde{C}}{\partial x} \right) \quad [B-2]$$

In order to investigate Eq. [B-2] by similarity methods, we write the solution as (11)

$$\tilde{C}(x, \tau) = \tau^\alpha \phi(\xi)$$

$$\xi = \frac{x}{\tau^\beta} \quad [B-3]$$

Inserting this ansatz into Eq. [B-2] we find that the powers of τ match if α and β are related by

$$\alpha = \frac{2\beta - 1}{\gamma} \quad [B-4]$$

and the resulting equation for $\phi(\xi)$ is then

$$\alpha \phi - \beta \xi \frac{d\phi}{d\xi} = \frac{d}{d\xi} \left(\phi^\gamma \frac{d\phi}{d\xi} \right) \quad [B-5]$$

A further relation between α and β is obtained from the fact that the total number of diffusing particles is conserved, *i.e.*

$$\int_0^\infty \tilde{C}(x, \tau) dx = \tau^{\alpha+\beta} \int_0^\infty \phi(\xi) d\xi = \tilde{Q}_0 = \text{const.} \quad [B-6]$$

This obviously requires $\alpha = -\beta$, which, together with relation [B-4], determines α and β to be

$$\alpha = -\beta = -\frac{1}{\gamma + 2} \quad [B-7]$$

Note that constant surface concentration requires $\alpha = 0$ and consequently $\beta = 1/2$. With α and β given by Eq. [B-7], Eq. [B-5] for $\phi(\xi)$ can be integrated explicitly to yield

$$\phi(\xi) = \phi_0 \left(1 - \frac{\xi^2}{\xi_0^2} \right)^{1/\gamma} \quad [B-8]$$

where the characteristic penetration depth, ξ_0 , is related to the integration constant, ϕ_0 , by

$$\xi_0^2 = \frac{2(\gamma + 2)}{\gamma} \phi_0^\gamma \quad [B-9]$$

Furthermore, ϕ_0 is determined from the conservation condition, Eq. [B-6]. This yields

$$\phi_0 = \left(\frac{\gamma}{2(\gamma + 2) I_\gamma} \tilde{Q}_0^2 \right)^{1/(\gamma+2)} \quad [B-10]$$

where I_γ denotes the integral

$$I_\gamma = \int_0^1 (1 - x^2)^{1/\gamma} dx = \frac{\sqrt{\pi}}{2} \frac{\Gamma(1 + 1/\gamma)}{\Gamma(3/2 + 1/\gamma)} \quad [B-11]$$

and $\Gamma(x)$ is the complete elliptic integral. In particular, $I_1 = 2/3$ and $I_2 = \pi/4$.

Using Eq. [B-10] in Eq. [B-9], ξ_0 is obtained as

$$\xi_0 = \left(\frac{2(\gamma + 2)}{\gamma I_\gamma^\gamma} \bar{Q}_0^\gamma \right)^{1/(\gamma+2)} \quad [\text{B-12}]$$

Collecting our results, we find that $C(x, \tau)$ can be written

$$\bar{C}(x, \tau) = \bar{C}_s(\tau) \left(1 - \frac{x^2}{x_F^2(\tau)} \right)^{1/\gamma} \quad [\text{B-13}]$$

i.e., in terms of a decaying maximum concentration, $\bar{C}_s(\tau)$, given by

$$\bar{C}_s(\tau) = \left(\frac{\gamma}{2(\gamma + 2)I_\gamma^2} \frac{\bar{Q}_0^2}{\tau} \right)^{1/(\gamma+2)} \quad [\text{B-14}]$$

and a well-defined diffusion front at $x = x_F(\tau)$, where

$$x_F(\tau) = \left(\frac{2(\gamma + 2)}{\gamma I_\gamma^\gamma} \bar{Q}_0^\gamma \tau \right)^{1/(\gamma+2)} \quad [\text{B-15}]$$

In order to incorporate the feature of a finite width of the initial profile, we note that the fundamental nonlinear diffusion equation, Eq. [B-2], is invariant under time translations. This implies that a more general similarity solution is obtained through an arbitrary time translation of the previously obtained solution, i.e.

$$\bar{C}(x, \tau) = \phi_0(\tau + \tau_0)^{-1/(\gamma+2)} \left(1 - \frac{x^2}{\xi_0^2(\tau + \tau_0)^{2/(\gamma+2)}} \right)^{1/\gamma} \quad [\text{B-16}]$$

The arbitrary constant, τ_0 , can be related to the width of the original profile as follows: As $\tau \rightarrow 0$, the solution given by Eq. [B-16] does not approach a delta function, but rather

$$\lim_{\tau \rightarrow 0} \bar{C}(x, \tau) = \bar{C}(x, 0) = \phi_0 \tau_0^{1/(\gamma+2)}$$

$$\left(1 - \frac{x^2}{\xi_0^2 \tau_0^{2/(\gamma+2)}} \right)^{1/\gamma} \quad [\text{B-17}]$$

This implies that, for an initial profile of the form given by Eq. [B-17], the subsequent diffusive evolution is determined exactly by Eq. [B-16]. Admittedly, we cannot expect the initial profile to correspond to a similarity profile, as given by Eq. [B-17]. However, it is possible to approximate realistic initial profiles by functions of the form of Eq. [B-17], provided we choose τ_0 properly. Thus, Eq. [B-16] yields an approximate solution for the subsequent development, and, furthermore, this solution asymptotically approaches the correct solution, as the influence of the original profile width diminishes.

To be more specific, we note that if we characterize the initial profile simply by its width, x_0 , this determines τ_0 as

$$\tau_0 = (x_0/\xi_0)^{\gamma+2} = \frac{\gamma}{2(\gamma + 2)} \left(\frac{I_\gamma}{\bar{Q}_0} \right)^\gamma x_0^{\gamma+2} \quad [\text{B-18}]$$

which implies that the maximum concentration, C_s , and the location of the diffusion front, x_F , can be written as

$$C_s = \left(\frac{\gamma}{2(\gamma + 2)I_\gamma^2} \frac{\bar{Q}_0^2}{\tau} \right)^{1/(\gamma+2)} \left(1 + \frac{\tau_0}{\tau} \right)^{1/(\gamma+2)}$$

$$x_F = \left(\frac{2(\gamma + 2)}{\gamma I_\gamma^\gamma} \bar{Q}_0^\gamma \tau \right)^{1/(\gamma+2)} \left(1 + \frac{\tau_0}{\tau} \right)^{1/(\gamma+2)} \quad [\text{B-19}]$$

REFERENCES

1. A. B. Glaser and G. E. Subak-Sharpe, "Integrated Circuit Engineering," Addison-Wesley, Reading, England (1979).
2. R. Shrivastava and A. Marshak, *Proc. IEEE*, **65**, 1614 (1977).
3. W.-S. Wang, *ibid.*, **71**, 179 (1983).
4. J. Crank, "The Mathematics of Diffusion," Chap. 2, 2nd ed. Clarendon Press, Oxford, England (1975).
5. A. S. Grove, "Physics and Technology of Semiconductor Devices," p. 58, John Wiley and Sons, New York (1967).
6. R. B. Fair, in "Impurity Doping Processes in Semiconductors," F. F. Y. Wang, Editor, Chap. 7, North-Holland Publishing Co., Amsterdam (1981).
7. R. B. Fair, in "Silicon Integrated Circuits," Part B, D. Kahng, Editor, Applied Solid State Science, Supplement 2, pp. 1-108, Academic Press, New York (1981).
8. See e. g. G. J. Declerck, in "Large Scale Integrated Circuits Technology; State of the Art and Prospect," L. Esaki and G. Soncini, Editors, p. 112, NATO Advanced Study Institutes Series, Vol. E55, Martinus Nijhoff Publishers, The Hague (1982).
9. Y. Nakajima, S. Ohkawa, and Y. Fukukawa, *Jpn. J. Appl. Phys.*, **10**, 162 (1971).
10. R. B. Fair, *J. Appl. Phys.*, **43**, 1278 (1972).
11. R. B. Fair, *This Journal*, **122**, 800 (1975).
12. R. B. Fair and J. C. C. Tsai, *ibid.*, **122**, 1689 (1975).
13. R. B. Fair and J. C. C. Tsai, *ibid.*, **123**, 583 (1976).
14. W. F. Ames, "Nonlinear Partial Differential Equations," p. 133, Vol. 1, Academic Press, New York (1965).
15. M. Ghezzi, *This Journal*, **119**, 977 (1972).
16. C. Hill, Lecture notes, see p. 124 in Ref. (8).
17. F. J. Morin and J. P. Maita, *Phys. Rev.*, **96**, 28 (1954).

Carrier Lifetime Reduction in Silicon by Proton Implantation Through MOS Structures

A. Mogro-Campero* and R. P. Love

General Electric Research and Development Center, Schenectady, New York 12301

ABSTRACT

Ion implantation provides a versatile technique for lifetime control in silicon. Localized penetration and damage profiles provide means for the creation of regions of low lifetime within device structures. Protons of 80 keV were implanted 0.5 μm into silicon through a MOS structure, with doses up to 10^{14} cm^{-2} . The generation lifetime can be reduced by several orders of magnitude, and varies linearly with dose. Changes in oxide quality, surface generation velocity, and doping concentration were also studied. Low temperature annealing repairs the oxide degradation while maintaining substantial lifetime reduction.

The methods currently used to reduce carrier lifetime in silicon (the diffusion of gold or platinum, and electron irradiation) produce effects throughout the silicon wafer. Because of their well-defined range, implanted ions make possible the spatial localization of regions of reduced lifetime. Masking can be used to provide planar

*Electrochemical Society Active Member.

selectivity; depth control can be attained by energy selection or epitaxial overgrowth. Argon implantation provides an effective way of reducing lifetime, and is resistant to high temperature annealing (1-3). This makes it particularly appropriate for use during the early steps of device processing. In this paper, we explore the use of ion implantation to reduce lifetime in silicon during the late

stages of device processing. Depth control can be implemented by varying the energy of the ion. Most of the damage occurs near the end of range, so that a considerable degree of localization is still possible. Protons were used in our study; for singly ionized atoms and a given maximum implanter energy, they provide the greatest choice of depth. Since MOS structures are present in many of the devices of interest, the implantation was performed into the silicon through the metal and oxide layers.

Procedure

n-Type CZ silicon wafers of (111) orientation and doping density of 10^{15} phosphorus atoms cm^{-3} were used. The backs of the wafers were implanted with 10^{15} cm^{-2} phosphorus of 100 keV to ensure a low resistance contact to the back-side aluminum. 100 nm of dry oxide were grown at 1000°C. A set of 300 nm thick aluminum dots was then evaporated to form MOS capacitors, and sintered at 450°C for 30 min in nitrogen.

Using energy-loss and range tables (4), we calculate that the 80 keV protons implanted through the MOS structures penetrated $0.5 \mu\text{m}$ into the silicon. The maximum depletion depth under inversion is $1 \mu\text{m}$, so that the high frequency (1 MHz) capacitance-voltage and capacitance-transient measurements used in this experiment should be affected by the implantation. A portion of each sample was left unimplanted to serve as a control area. The damage produced by the protons has been estimated (5) to be such that at $0.35 \mu\text{m}$ into the silicon, the fraction of silicon atoms displaced from their crystalline positions is about 4×10^{-4} for the maximum proton dose of 10^{14}cm^{-2} used in this experiment.

Generation lifetime was measured at room temperature by the Zerbst technique (6, 7). A MOS capacitor is pulsed into deep depletion, and the formation of the inversion layer is observed via the capacitance transient. By this method it is possible to deduce the generation lifetime (τ_g) in the depleted zone, and the parameter s due to minority carriers whose current is independent of the time varying depth of the depletion zone. Because the lifetime is not constant with depth within the sampling volume, an average value dependent on depletion voltage will be obtained (3). The lifetime values reported here have been obtained with a -10V depletion pulse. The parameter s is the sum of the surface generation velocity and a term corresponding to diffusion of carriers into the depletion zone from the quasi-neutral regions (3). A typical variation of τ_g by a factor of 2 and parameter s by a factor of 3 was found across a given sample.

Results

Generation lifetime as a function of proton dose is shown in Fig. 1. Functional dependence with dose is close

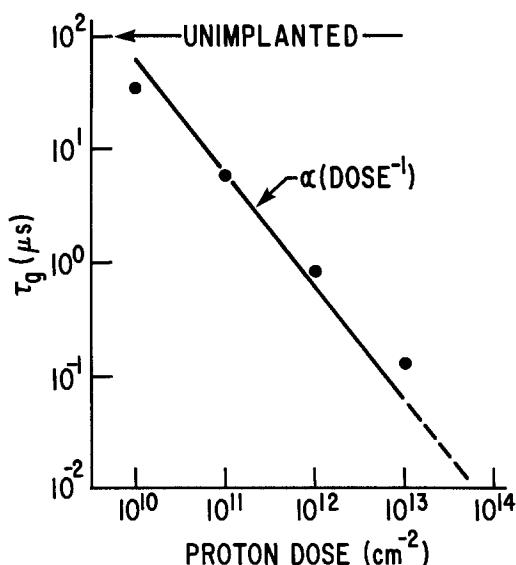


Fig. 1. Generation lifetime vs. proton dose

to linear. At 10^{14}cm^{-2} , analysis by the capacitance transient technique was no longer reliable, but the duration of the capacitance transient continued to follow an inverse dose dependence, as shown by the dotted line extension in the figure. The superlinear dependencies (reverse leakage current of diodes approximately proportional to dose squared) for helium and carbon implantation within the range of doses in our experiment (8) were not observed.

The generation lifetime as a function of proton dose has been reported to drop more than three orders of magnitude in the dose range 10^{12} - 10^{13}cm^{-2} for similar experimental conditions (9). We find no evidence for this precipitous drop in lifetime. In that experiment, the lifetime was also deduced from a capacitance transient analysis, but the surface contribution was not taken into account. It has been shown that for irradiated samples, this procedure can lead to large errors (3).

The parameter s as a function of proton dose is shown in Fig. 2. Since the implantation damage region includes the oxide/Si interface, a linear dose dependence suggests the predominance of the surface generation velocity in the parameter s [the diffusion term would be either independent of dose if arising from deeper than the implant range, or proportional to the square root of dose if related to the lateral component (3)]. In a separate study of the temperature variation of τ_g and s for the sample with a dose of 10^{11}cm^{-2} , we have also come to the conclusion that the surface generation velocity is the dominant term in s at room temperature.

Doping profiles were obtained by a pulsed C-V method (10), using a pulse width of 1 ms. The result is shown in Fig. 3. The rise in doping density at shallow depths is most likely due to the interface proximity limitation (10). The rise in doping density due to the redistribution of

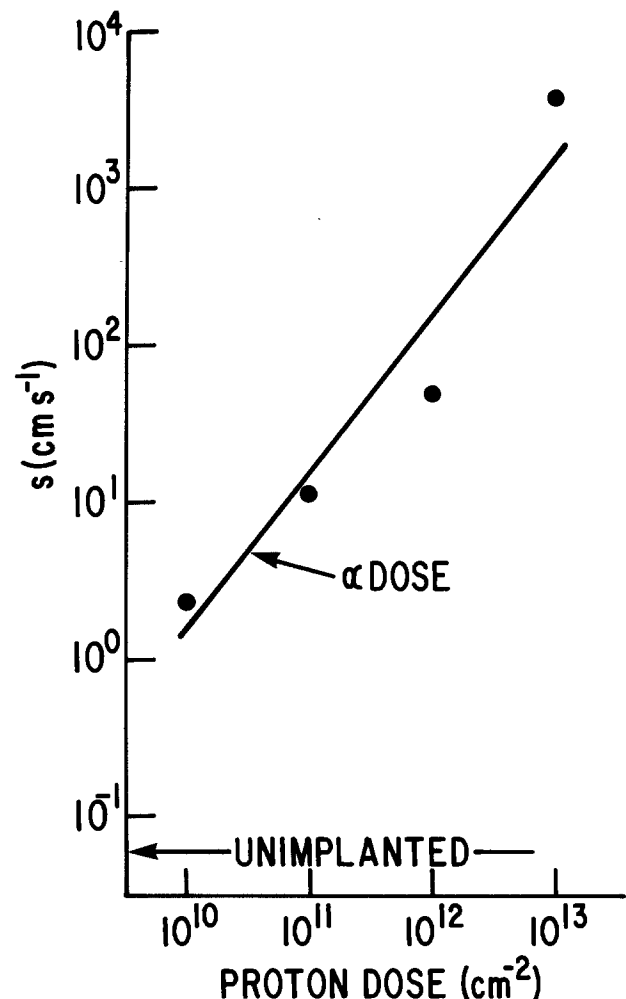


Fig. 2. Parameter s vs. proton dose

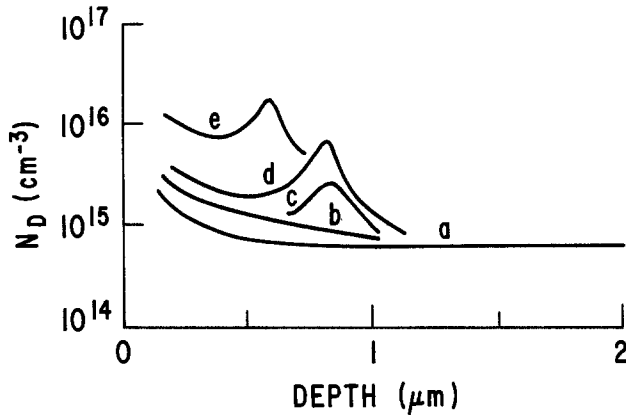


Fig. 3. Donor density vs. depth from C-V measurements. Portions of the curves have been omitted for clarity. All curves merge at depths $> 1.3 \mu\text{m}$. Curve a corresponds to a control sample and to a sample with a proton dose of 10^{10} cm^{-2} . Curves b-e correspond to proton doses 10^{11} - 10^{14} cm^{-2} .

phosphorus during thermal oxidation (11) is only a small effect in our case. The peaks in Fig. 3 correspond approximately to the expected range of the protons, and they indicate an increase in doping density with proton dose. However, interface traps can produce apparent changes in doping density profiles (10). Therefore, an average value of doping density within the equilibrium depletion depth under inversion (0.3 - $0.8 \mu\text{m}$ for doping densities 10^{16} - 10^{15} cm^{-3}) was obtained by the maximum-minimum C-V method, which is free of interface trap effects (10). A doping density increase is again observed (Fig. 4), but only for the highest proton dose.

Doping concentration changes after proton implantation into n-type silicon have been reported; carrier concentration decreases were found after implantation, but increases appeared after annealing at around 300°C (12). This indicates a competition between the dominance of deep and shallow levels, which should depend on the energy level spectrum within the silicon bandgap. Since various point defect complexes and/or defect-impurity associations are probably responsible for the levels, the details in a particular situation are bound to be different. It is important to note in this respect that we have used Czochralski samples, whereas the other experimenters (12) have worked with float-zoned material. It is well known that there is a large difference in impurity concentrations in these two types of crystals, notably with respect to oxygen concentration, which in Czochralski samples is many orders of magnitude higher (in the 10^{18}

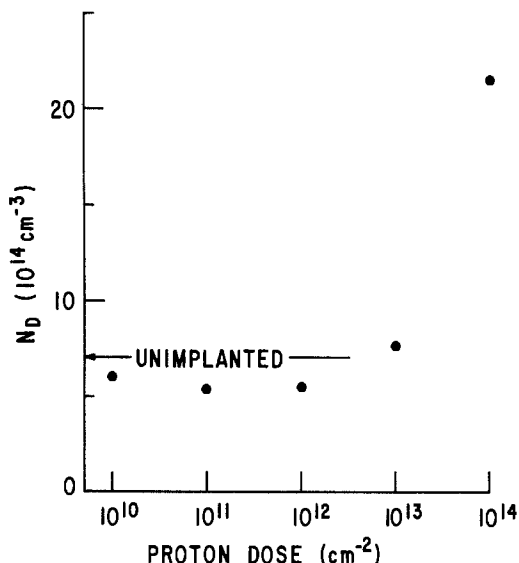


Fig. 4. Doping density within the equilibrium depletion depth vs. proton dose (from C-V measurements).

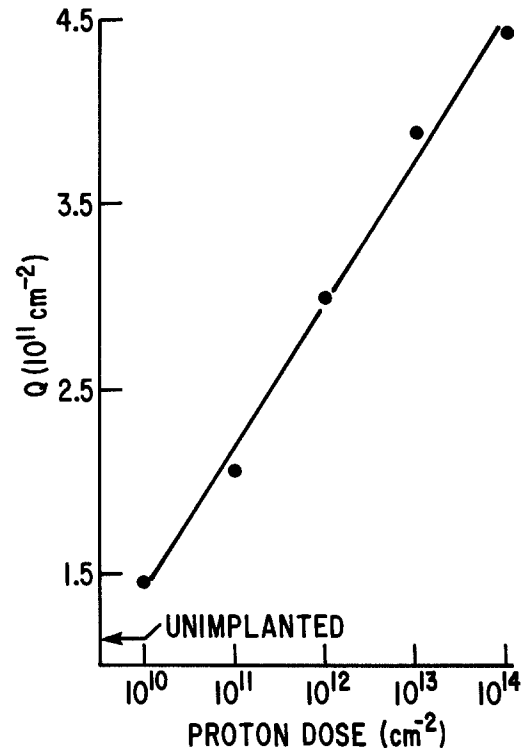


Fig. 5. Charge associated with the oxide in units of the electron charge as a function of proton dose.

cm^{-3} range). Sample differences are presumably also partly responsible for the variety of energy levels reported by different investigators after proton bombardment (13).

Charge associated with the oxide was computed from flatband voltage shift (14); the results are shown in Fig. 5. The associated shift in threshold voltage for inversion is 2V for a dose 10^{14} cm^{-2} . C-V curves for a control sample, and one with a dose of 10^{14} cm^{-2} are shown in Fig. 6. The

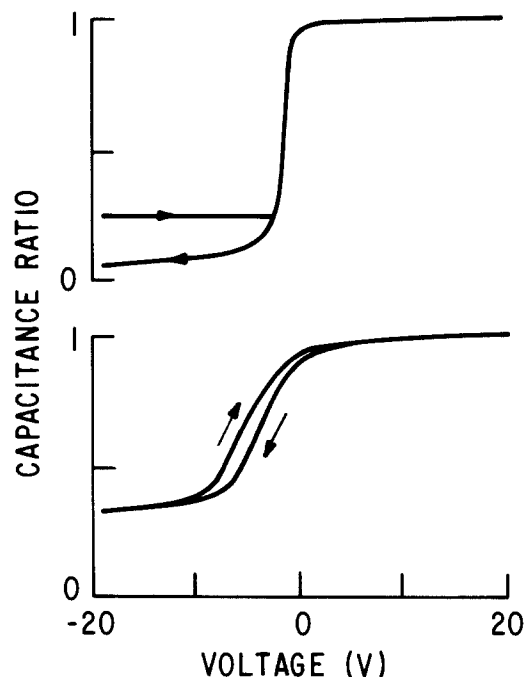


Fig. 6. Capacitance normalized to the oxide capacitance vs. voltage. The arrows indicate the direction of the voltage sweeps (at a rate of 0.4 V s^{-1}). The top graph is for the control region of the sample, and the bottom one for a proton dose of 10^{14} cm^{-2} . Measurements are carried out in the dark, except that the sample is brought to equilibrium by a brief exposure to light after the positive-to-negative voltage sweep.

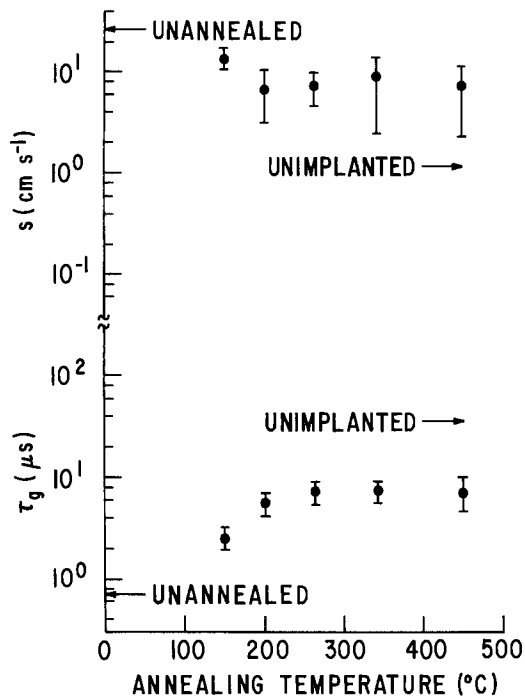


Fig. 7. Surface generation velocity and generation lifetime as function of annealing temperature for samples implanted with 10^{12} protons cm^{-2} . All anneals for 30 min. Average values are indicated with arrows for an unimplanted sample annealed at 450°C and for an implanted sample prior to annealing.

hysteresis and stretch out after irradiation are characteristic of interface charge trapping near the oxide/Si interface (15).

Annealing experiments in nitrogen were carried out for samples with a proton dose of 10^{12} cm^{-2} . Half-hour anneals showed that the oxide parameters referred to in the previous paragraph returned to their preimplanted condition after the 350°C anneal. The doping density increase deduced from the pulsed C-V method discussed earlier was reduced by the 150°C anneal, and disappeared after the higher temperature annealing treatments.

The results for annealing of the generation lifetime and surface generation velocity are shown in Fig. 7. Both parameters achieve stable values, but do not regain the unimplanted levels. It is interesting to note that the lifetime in the case of electron irradiation has returned to the unirradiated value after a 450°C anneal step for 30 min (16). Lifetime reduction by proton implantation is thus more thermally stable.

Further evidence for persistent lifetime reduction after annealing is provided in Fig. 8. For longer annealing times both τ_g and s move further away from the unimplanted values. This phenomenon of negative annealing has been observed in the reverse leakage current after carbon ion implantation in a similar temperature regime (8), and attributed to complexes that do not act to suppress lifetime annealing out at these temperatures, and freeing mobile defects which can recombine to form lifetime-active centers.

Conclusions

The generation lifetime of silicon samples can be reduced by several orders of magnitude by proton implantation, as deduced from measurements prior to annealing treatments. The implantation can be carried out near the end of the device processing sequence, so that only low temperature steps are left. Oxide degradation in MOS structures can be repaired with low temperature annealing treatments, which also serve to stabilize the lifetime. The relatively high value of surface generation velocity will tend to increase surface leakage current and decrease channel mobility. The severity of oxide and interface related effects will also depend on the ion energy used,

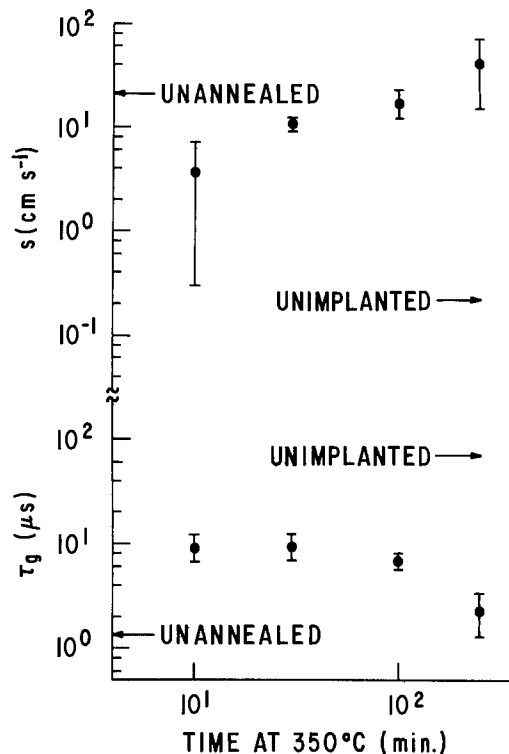


Fig. 8. Surface generation velocity and generation lifetime as a function of time at 350°C for samples implanted with 10^{12} protons cm^{-2} . Average values are indicated by arrows for an unimplanted sample annealed for 250 min and for an implanted but unannealed sample.

since ion energy-loss rates depend on energy. Well-defined range and damage profiles allow localization of regions of low lifetime within device structures, so that ion implantation is emerging as a versatile tool for lifetime control in silicon.

Acknowledgments

We are indebted to G. Gidley and M. Lazzeri for carrying out various processing steps; phosphorus implantations were performed by W. Whitney, and proton implantation at the State University of New York at Albany with Professor H. Bakhru. We thank P. Chow for making us aware of Ref. (9).

Manuscript submitted May 18, 1984; revised manuscript received July 26, 1984. This was Paper 81 presented at the Cincinnati, Ohio, meeting of the Society, May 6-11, 1984.

General Electric Company assisted in meeting the publication costs of this article.

REFERENCES

- H. F. Kappert, G. Sixt, and G. H. Schwuttke, *Phys. Status Solidi A*, **52**, 463 (1979).
- A. Mogro-Campero and R. P. Love, in "Defects in Semiconductors," W. M. Bullis and L. C. Kimerling, Editors, p. 595, The Electrochemical Society Soft-bound Proceedings Series, Pennington, NJ (1983).
- A. Mogro-Campero and R. P. Love, *This Journal*, **131**, 655 (1984).
- B. Smith, "Ion Implantation Range Data for Silicon and Germanium Device Technologies," Research Studies Press, Inc., Forest Grove, OR (1977).
- A. Mogro-Campero and R. P. Love, in "Ion Implantation and Ion Beam Processing of Materials," G. K. Hubler, O. W. Holland, C. R. Clayton, and C. W. White, Editors, p. 537, Elsevier, New York (1984).
- M. Zerbst, *Z. Angew. Phys.*, **22**, 30 (1966).
- D. K. Schroder and J. Guldborg, *Solid State Electron.*, **14**, 1285 (1971).
- K. A. Pickar and J. V. Dalton, *Rad. Eff.*, **6**, 89 (1970).
- Y. Wada and M. Ashikawa, *Jpn. J. Appl. Phys.*, **14**, 1405 (1975).
- E. H. Nicollian and J. R. Brews, "MOS Physics and Technology," pp. 380-408, John Wiley and Sons,

- Inc., New York (1982).
11. A. S. Grove, O. Leistiko, Jr., and C. T. Sah, *J. Appl. Phys.*, **35**, 2695 (1964).
 12. Y. Ohmura, Y. Zohata, and M. Kanazawa, *Phys. Status Solidi A*, **15**, 93 (1973).
 13. J.-W. Chen and A. G. Milnes, *Ann. Rev. Mater. Sci.*, **10**, 157 (1980).
 14. S. M. Sze, "Physics of Semiconductor Devices," p. 395, John Wiley and Sons, Inc., New York (1981).
 15. P. V. Gray, *Proc. IEEE*, **57**, 1543 (1969).
 16. R. O. Carlson, Y. S. Sun, and H. B. Assalit, *IEEE Trans. Electron Devices*, **ed-24**, 1103 (1977).

The System AgI-AgBr: Energetic Consequences of Defect Equilibria in Single-Phase and Two-Phase Regions

A. Khandkar,* V. B. Tare, A. Navrotsky, and J. B. Wagner, Jr.**

Center for Solid State Science, Arizona State University, Tempe, Arizona 85287

ABSTRACT

The enthalpy of solution of various single- and two-phase AgI-AgBr compositions in AgNO_3 at 518 K has been determined using a Calvet-type twin microcalorimeter. The enthalpy ($H_{518} - H_{298}$) of melted and unmelted mixtures of AgI and AgBr of various compositions within two-phase regions of the phase diagram has also been obtained using the same calorimeter. The effect of AgBr on the temperature and enthalpy of transformation of β -AgI to α -AgI has been investigated using a Perkin Elmer Differential Scanning Calorimeter. The terminal compositions at 518 K of the two-phase region of AgI-AgBr system has been found to be $\text{AgI}_{0.85}\text{Br}_{0.15}$ and $\text{AgI}_{0.3}\text{Br}_{0.7}$. The excess enthalpy, the difference in ($H_{518} - H_{298}$) values of the unmelted and melted mixtures in the two-phase region of the AgI-AgBr system, has been found to be maximum at the equivolume concentration of the two terminal phases and is suggested to be due to the generation of silver ion vacancies at the interfaces due to a space-charge layer.

During the past few years, several investigators have reported anomalous electrical conduction in materials containing finely divided particles dispersed as a second phase. The systems investigated include the dispersion of submicron-sized insulating particles in an ionically conducting matrix [$\text{LiI} + \text{Al}_2\text{O}_3$ (1), $\text{AgI} + \text{Al}_2\text{O}_3$ (2), $\text{AgCl} + \text{Al}_2\text{O}_3$ (3)], of insulating particles in materials with predominant electronic conduction [SiO_2 in TiO_2 (4)], of metallically conducting particles in a semiconductor [Ni_3S_2 (5) or Ni (6) in NiO], and of ionically conducting materials in an ionically conducting matrix [AgBr in AgI (7)]. The observed changes in the electrical conductivity could not be explained on the basis of classical theories alone. Several alternative explanations have been proposed (8-10); however, the explanation based on the presence of additional defects at the interface because of the space-charge layer appears to be most satisfactory (8). The AgI-AgBr system was chosen for the present study because of its relative physical and chemical simplicity and because of the extensive investigations carried out in this laboratory regarding its electrical conductivity (2, 7, 11). Silver iodide is known to exist in at least two stable crystallographic modifications with a transition at 420 K from a low temperature wurtzite β form to a high temperature, body-centered cubic α form. Silver bromide, on the other hand, is stable only in the rocksalt-type cubic structure up to its melting temperature.

Electrical conductivity of α -AgI is several orders of magnitude higher than that of β -AgI and AgBr. Partial replacement of iodine in AgI with bromine has been found to lower the transition temperature (11). Anomalous changes in electrical conductivity of several single-phase and two-phase compositions in the AgI-AgBr system have also been reported (7). Since the changes in the electrical conductivity are presumably associated with the changes in number and the mobility of the transporting species, present investigations were undertaken to see whether these changes are reflected in the energetics of this system as well.

Experimental

Sample preparation.—AgI and AgBr, (99.999% pure from Apache Chemicals) in powder form, were mixed together in appropriate proportions and sealed in 6 mm

* Electrochemical Society Student Member.

** Electrochemical Society Active Member.

diam evacuated silica tubes. The mixture was melted at 873 K for 1h. To ensure complete solution and homogenization, the melt was shaken from time to time. The sample was then quenched to room temperature, removed from the silica tube, and cut into small pieces of 500-600 mg each. Some of these pieces were annealed in air at 533 K for times varying from 2 to 15h before using them for drop calorimetry. Other pieces were ground to a fine powder (~200 mesh), and 50-60 mg of the powder was used for solution calorimetry in molten AgNO_3 . A few milligrams of the same powder was used in a Perkin-Elmer DSC-2 Differential Scanning Calorimeter.

Compositions of the samples were assumed to be the same as those of the starting mixtures. X-ray powder diffraction technique was used on samples at 298 K to confirm that no phases other than wurtzite-type AgI and rocksalt-type AgBr were present.

Calorimetry

Solution calorimetry.—A Calvet-type twin-microcalorimeter as described elsewhere (12), was used. Samples were dissolved in molten AgNO_3 at 518 K. 50g of AgNO_3 were premelted in silica crucibles and then put in each calorimeter chamber. The Ag(I, Br) samples (about 50 mg of powder) were placed in a platinum cup, which was suspended just above the solvent by means of a movable quartz assembly. After the system attained thermal equilibrium (as seen by a steady baseline signal), the platinum cup with the powder was immersed in the solvent and, after a quick up-and-down stirring action, raised to the original level above the solvent. This procedure was repeated several times until the baseline returned to the original value. The area under the peak representing the enthalpy changes associated with the dissolution process was proportional to the heat generated. Calibration was achieved by dropping pieces of platinum, of known weight and heat content, into the melt.

To check whether the stirring contributed to the heat, several experiments were performed using empty platinum cups. No change in baseline was detected, indicating negligible heat due to stirring. The heat effects in each experiment were approximately 0.1 cal; the heat of solution ranged from +1000 to -4200 cal/mol.

Heat content measurement.—($H_{518} - H_{298}$) was measured by dropping ~250 mg cylindrical samples from 298 K into

the same calorimeter at 518 K using empty crucibles. The calorimeter was calibrated by dropping Al_2O_3 rods of similar dimensions, the heat content of which is tabulated by Barin and Knacke (13).

Differential scanning calorimetry (DSC).—A Perkin-Elmer Differential Scanning Calorimeter Model DSC-2 was used to obtain the temperature and enthalpy of transformation of various AgI-AgBr samples. Since the transformation occurs at temperatures close to the melting of indium (429.6 K), the instrument was calibrated using the melting point of indium, which was found to be within ± 0.5 K of the reported value (13).

The heating rate of 5 K/min was found to be most suitable. The temperature was varied from 350 to 450 K at this rate. The enthalpy changes associated with the transformation were recorded on a strip chart recorder and integrated using a planimeter. The reproducibility of the temperature measurement was ± 0.5 K and of the enthalpy measurement ± 50 cal for at least ten different indium samples.

Results

The data ($H_{518} - H_{298}$) obtained by drop calorimetry for pure AgI and various AgI-AgBr compositions are listed in Table I. To see any effects of change in grain size or grain boundary structure during annealing, some of the samples were annealed for periods varying from 2 to 15h at 533 K. The enthalpy values obtained for annealed and unannealed samples were the same within experimental error. Our value of 4720 ± 125 cal/mol for pure AgI is comparable to 4558 cal/mol reported by Barin and Knacke (13).

Table II lists the excess enthalpy values which were obtained for two-phase mixtures by taking the difference between the experimentally determined ($H_{518} - H_{298}$) values for various compositions obtained by melting and the values estimated for the same composition by taking the weighted average of the experimentally determined values for the terminal solid solutions. The phase diagram of the AgI-AgBr system has been reported by Stasiw and Teltow (14). However, subsequent investigations are not consistent with the solubility limits reported in the phase diagram. Shahi and Wagner (11) suggested from the conductivity measurements that the end members of the two-phase region of the AgI-AgBr system are $AgI_{0.9}Br_{0.1}$ and $AgI_{0.3}Br_{0.7}$. These terminal compositions were therefore used to estimate excess enthalpy. The excess enthalpy values are shown in Fig. 1 as a function of mole percent (m/o) $AgI_{0.3}Br_{0.7}$. A maximum in excess enthalpy is observed at about 50 m/o $AgI_{0.3}Br_{0.7}$. The unmelted samples (mechanical mixtures) show no excess heat content.

The enthalpies of solution of various compositions in $AgNO_3$ at 518 K are listed in Table III. For some composi-

Table I. Values of ($H_{518} - H_{298}$) in cal/mol for various AgI-AgBr compositions

Mole fraction of AgI	Annealing time at 533 K (h)	$H_{518} - H_{298}$ cal/mol of composition	Average with standard deviation
1.0	0	4740	4720 ± 125
	0	4924	
	0	4564	
	0	4712	
0.9	0	4658	4720 ± 125
	0	4450	
	0	4532	
	0	4459	
0.8	0	4517	4489 ± 55
	0	4399	
	15	4556	
	15	4511	
0.7	0	4495	4399 ± 66
	15	4422	
	15	4359	
	15	4320	
0.6	2	4627	4638 ± 11
	15	4645	
	0	4366	
	0	4506	
0.5	15	4616	4508 ± 124
	15	4645	
	15	4526	
	15	4393	
0.4	0	4308	4259 ± 113
	2	4423	
	5	4114	
	15	4301	
0.3	15	4151	3907 ± 25
	0	3883	
	2	3932	
	0	3424	
0.3	0	3467	3430 ± 28
	15	3389	
	15	3442	

tions in the two-phase region, the enthalpies of solution were also obtained by preparing mechanical mixtures (without melting) of the end compositions. These values are also shown in this table. The difference in enthalpies of solution between the two-phase melted and unmelted compositions is within the experimental scatter.

The enthalpies of solution are plotted in Fig. 2 as a function of m/o AgBr. This figure indicates that the variation of the enthalpy of solution with composition shows some curvature in the AgBr-rich single-phase region, while it is approximately linear in the AgI-rich single-phase region. The enthalpy values of the compositions in the two-phase region fall approximately on a straight line joining the enthalpy values of the two terminal compositions.

The enthalpy and temperature of the β to α transformation of various compositions, as determined by

Table II. Excess enthalpy for various two-phase AgI-AgBr compositions

	1	2	3	4	5	6	7	8	9
A. m/o AgI	1.0	0.90	0.85	0.80	0.70	0.60	0.50	0.40	0.30
B. $H_{518} - H_{298}$ cal/mol	4720	4489	4364*	4339	4638	4508	4529	3907	3430
C. $H_{518} - H_{298}$ cal/mol		4489		4313	4136	3959	3783	3606	3430
Assuming mixing of 2 and 9									
D. $H_{518} - H_{298}$ cal/mol			4364*	4279	4109	3905	3765	3599	3430
Assuming mixing of 3 and 9									
E. Mol fraction $AgI_{0.9}Br_{0.1}$		1.00		0.83	0.67	0.50	0.33	0.166	0
F. Mol fraction $AgI_{0.35}Br_{0.15}$			1.00	0.91	0.73	0.54	0.36	0.18	0
G. Excess enthalpy cal/mol									
(B-C)		0		86	502	549	476	301	0
(B-D)			0	120	529	603	490	308	0

* Estimated by linear extrapolation.

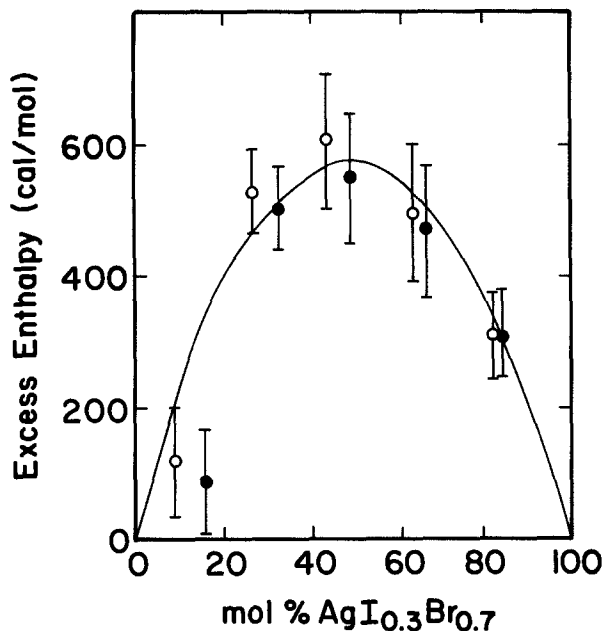


Fig. 1. Excess enthalpy, $[(H_{518} - H_{298})_{\text{melted}} - (H_{518} - H_{298})_{\text{unmelted}}]$ as a function of $\text{AgI}_{0.3}\text{Br}_{0.7}$ in $\text{AgI}_{0.9}\text{Br}_{0.1}$ (●), and $\text{AgI}_{0.85}\text{Br}_{0.15}$ (○).

differential scanning calorimetry are listed in Table IV. For pure AgI, these values are 1420 ± 30 cal/mol and 420 ± 0.5 K, respectively, in excellent agreement with the literature value (13).

A plot of transformation temperature as a function of composition is shown in Fig. 3. The temperature varies linearly up to 15 m/o AgBr in AgI and then remains constant. A plot of transformation enthalpy per mole of composition shown in Fig. 4 also indicates that the enthalpy varies linearly with a change in slope occurring at 15 m/o AgBr. No transformation was detected for the composition 30 m/o AgI-70% AgBr. These data indicate that the terminal compositions of the two-phase region of AgI-AgBr system at 518 K are $\text{AgI}_{0.85}\text{Br}_{0.15}$, which undergoes the $\beta \rightarrow \alpha$ transformation at 403.5 K with a transformation enthalpy of 1200 cal/mol, and $\text{AgI}_{0.3}\text{Br}_{0.7}$, which does not undergo a crystalline transformation. The enthalpy values obtained for the composition in the two-phase region are therefore entirely due to the $\beta \rightarrow \alpha$ transformation of $\text{AgI}_{0.85}\text{Br}_{0.15}$ and are converted to values per mole of

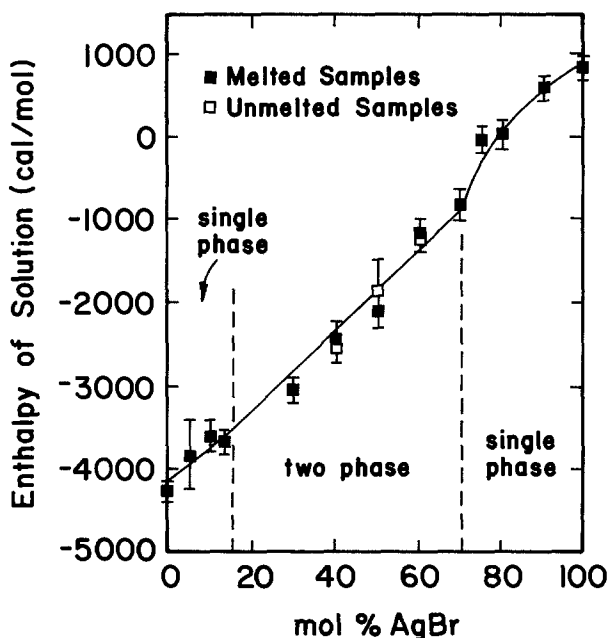


Fig. 2. Enthalpy of solution in AgNO_3 as a function of composition at 518 K.

Table III. Enthalpy of solution of various AgI-AgBr compositions in AgNO_3 at 518 K

Mole fraction of AgI	Enthalpy of solution (cal/mol)	
	Melted	Unmelted
1.00	-4150 -4343 -4087 -4501 avg. -4270 (± 188)	
0.95	-3623 -3237 -4438 -4085 avg. -3846 (± 525)	
0.90	-3299 -3714 -3557 -3356 -3936 avg. -3572 (± 262)	
0.87	-3599 -3796 -3636 avg. -3677 (± 105)	
0.60	-2432 -2581 avg. -2506 (± 105)	-2553 -2543 avg. -2548 (± 7)
0.50	-1717 -2051 -1893 -2267 avg. -1982 (± 233)	-1598 -1316 -2247 -2241 avg. -1850 (± 469)
0.40	-1216 -996 avg. -1106 (± 155)	-1271 -973 avg. -1122 (± 211)
0.30	-605 -884 -625 -787 -688 avg. -718 (± 116)	
0.25	-162 +275 -108.25 +75 avg. +20 (± 198)	
0.20	0 +89 +159 +123 avg. +93 (± 68)	
0.10	+777 +678 +609 +519 avg. +646 (± 109)	
0.00	+716 +1012 +692 +1075 +896 avg. +878 (± 172)	

$\text{AgI}_{0.85}\text{Br}_{0.15}$ and plotted in Fig. 4. These values are constant within experimental error.

Discussion

The results obtained by differential scanning calorimetry and solution calorimetry indicate that at 518 K the terminal compositions in the two-phase region of the AgI-AgBr system correspond to 15 m/o AgBr for the α -AgI type cubic phase and 70 m/o AgBr for the AgBr-type cubic phase. The excess enthalpy values shown in Fig. 1, therefore, need to be modified. Assuming a linear variation with composition in the AgI-rich single-phase region, the enthalpy of solution for the $\text{AgI}_{0.85}\text{Br}_{0.15}$ terminal composition was calculated. This value was used to estimate the modified excess enthalpy values which are also shown in the same figure. The maximum in excess enthalpy value is still around 50 m/o. $\text{AgI}_{0.85}\text{Br}_{0.15}$ and 50 m/o $\text{AgI}_{0.3}\text{Br}_{0.7}$. However, whatever terminal compositions are assumed for the solid solutions, the rather surprising observation remains that the enthalpy ($H_{518} - H_{298}$) is much larger for the melted and solidified two-phase mixture

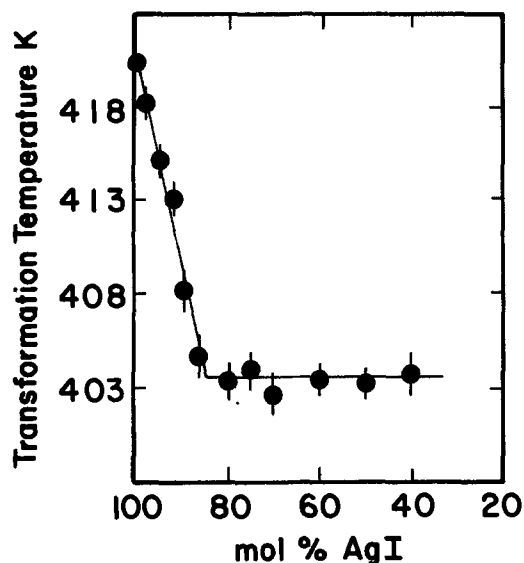


Fig. 3. Transformation temperature as a function of composition. The break in the curve corresponds to the solubility limit of AgBr in AgI.

than for a mechanical mixture of the two terminal solid solutions, while the enthalpies of solution at 518 K are similar for both types of two-phase compositions. Since the maximum in excess heat content occurs near an equimolar mixture of the two-terminal solid solutions, and since their densities are not very different, the maximum also corresponds to 50 volume percent (v/o) of each. Because of the identical methods of preparation, the grain sizes in different compositions are expected to be similar. The maximum in excess enthalpy at equivalent concentrations of each of the terminal compositions suggests that the excess enthalpy may be related to changes at the interface between these two phases. Since interfacial enthalpies reported for other systems in the literature (15) are two to three orders of magnitude smaller than the values measured in the present investigation, an additional explanation for the origin of this enthalpy is necessary.

The measured enthalpy ($H_{518} - H_{298}$) for various compositions may be considered to be the sum of (i) the enthalpy change associated with the heating of the sample from 298 K to the transformation temperature, (ii) the enthalpy of the $\beta \rightarrow \alpha$ transformation, and (iii) the enthalpy change associated with heating the sample from the transformation to the calorimetric temperature, 518 K.

The measurement of the $\beta \rightarrow \alpha$ transformation enthalpy by DSC and the enthalpy of solution in AgNO_3 of melted

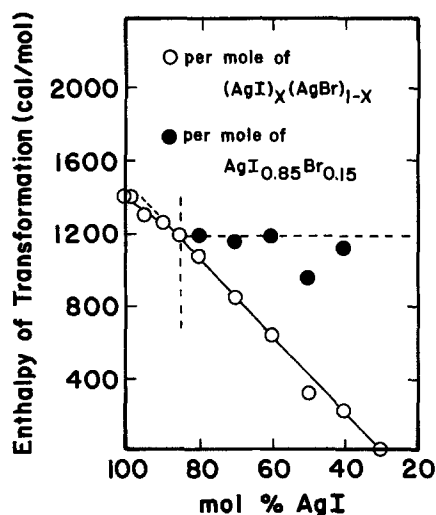


Fig. 4. Enthalpy of transformation as a function of m/o AgI in AgBr

Table IV. Temperature and enthalpy of transformation of various AgI + AgBr compositions

Mol fraction of AgI	Transition temperature K [± 0.5 K]	Enthalpy of transformation (cal/mol)
1.00	420.75	1461
	420.25	1413
		1411
		1433
0.98		1412
		1411
		1306
		1376
0.95	416	1348
	414.25	1335
0.92	413.2	1116
	413.6	1135
0.90	407.75	1093
	407.75	1368
	407.25	993
	408.4	1277
	409	1350
		1198
0.85		1180
		946
0.80	402.5	1060
	402.5	997
	402.75	878
0.70	404	693
	401.75	656
0.60	402.5	619
	404.2	647
	404	582
0.50	402.75	347
	403	184
0.40	403.6	323
	403.5	161
	405.2	226

and unmelted samples in the two phase region at 518 K indicates that contributions from (ii) and (iii) are small. The excess enthalpy may therefore be considered to be predominantly due to the effects below the $\beta \rightarrow \alpha$ transition in the AgI-rich phase.

An anomalous increase in electrical conductivity in the two-phase region of the system at temperatures below the $\beta \rightarrow \alpha$ transformation was observed by Shahi and Wagner (2). The maximum in conductivity was reported to be at 20 m/o AgI-80 m/o AgBr. This enhanced conduction was suggested to be due to the presence of additional defects generated at the two-phase interface due to the space charge layer. AgI is an ionic conductor in which Frenkel-type defects predominate (16). Although the enthalpy of formation of silver interstitials and silver vacancies in AgI is not known, a comparison of similar values reported for AgCl suggests that the enthalpy of formation of silver vacancies is smaller than that of silver interstitials. The presence of silver vacancies as the predominant transporting species at lower temperatures has been suggested by Khandkar and Wagner (3) in the case of $\text{AgCl-Al}_2\text{O}_3$ composites and by Shahi and Wagner (2) in the case of $\text{AgI-Al}_2\text{O}_3$ composites. The latter authors inferred the predominance of silver vacancies from the sign of thermoelectric EMF.

The definite qualitative correlation observed between the anomalous conductivity enhancement and the excess enthalpy in the two-phase region suggests that the same mechanism may be responsible for both effects. It is suggested that the origin of this excess enthalpy is the excess vacancy concentration at the interface in the melted two-phase compositions of the AgI-AgBr system.

The observation that maxima in the electrical conductivity and in the excess enthalpy occur at different compositions suggests that the presence of a second phase not only affects the concentration of mobile species taking part in conduction, but also affects their mobility as well. Changes in mobility would not be reflected in the measured excess enthalpy, but could shift the maximum conductivity away from the composition of presumed maximum defect concentration and maximum enthalpy.

Enthalpies of solution of the AgI and the AgBr-rich single-phase compositions can be used to obtain enthal-

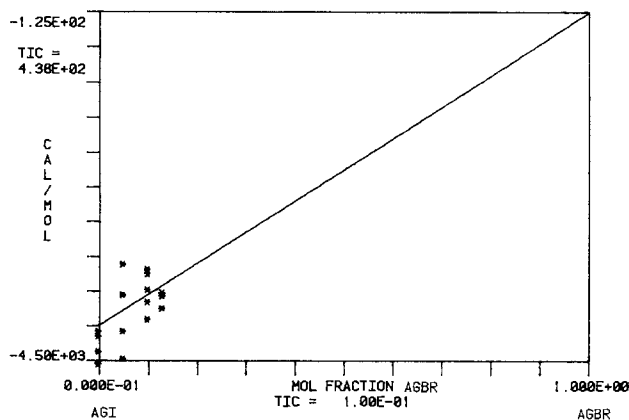


Fig. 5. Linear extrapolation of the enthalpy of solution of AgI-rich single-phase compositions to pure AgBr.

pies of solution of their metastable polymorphs by a method similar to that described by Davies and Navrotsky (17) for NiO-ZnO solid solutions. In this approach, one fits the enthalpy of solution within a single-phase region by an appropriate polynomial. Extrapolation to mole fraction of the solute equal to one gives the enthalpy of solution of the solute in the hypothetical polymorph having the structure of the terminal solid solution. The difference between that value and the heat of solution of the pure solute in its normal structure gives the enthalpy of transformation. A linear fit to the enthalpy of solution data implies that the solid solution is ideal when referred to standard states having the same structure; a quadratic fit that the solution is regular. The least squares computer fit for the data is shown in Fig. 5 and 6 for AgI-rich and AgBr-rich compositions, respectively. In each case the fit was obtained using all the data points for each composition rather than averages for each composition. Linear extrapolation of the data to pure AgBr gives a value for the enthalpy of solution of AgBr with the α -AgI-type cubic structure as -125 ± 150 cal/mol. From Table III, the enthalpy of solution of AgBr having rocksalt-type cubic structure is 870 ± 170 cal/mol. Therefore, the enthalpy of transformation of AgBr from its stable rocksalt-type cubic structure to α -AgI-type bcc structure is estimated to be 1000 ± 300 cal/mol. The variation of enthalpies of solution of AgBr-rich single phases with composition shows a small curvature. Because of the large scatter in the data obtained and small composition range of the single-phase region, the extrapolation of the data to pure AgI is quite uncertain. The linear fit (ideal solution) gives a near-zero enthalpy of transformation for AgI ($\alpha \rightarrow$ rocksalt). A quadratic fit implies negative heats of mixing in the rocksalt solid solutions and an enthalpy of transformation of 12,500 cal/mol. These two fits may represent an underestimate and overestimate, respectively, of the curvature of the data and may place a lower and upper bound on the enthalpy of transformation. Thus, ΔH for AgI ($\alpha \rightarrow$ rocksalt) may lie in the range 0-12 kcal/mol. No data are available for comparison.

Conclusions

1. The excess enthalpy, as defined by the difference in ($H_{518} - H_{298}$) values between the melted and solidified two-phase compositions and the mechanical mixtures of the terminal solid solutions of the AgI-AgBr system, exhibits maxima at equivolume concentrations of the terminal compositions and is suggested to be due to the excess silver ion vacancies generated at the interfaces due to the space-charge layer.

2. The terminal composition of the two-phase region of AgI-AgBr system at 518 K are $\text{AgI}_{0.85}\text{Br}_{0.15}$ and $\text{AgI}_{0.3}\text{Br}_{0.7}$.

3. The enthalpy of transformation of AgBr from its stable rocksalt-type cubic structure to α -AgI-type bcc structure is estimated to be 1000 ± 300 cal/mol, while the

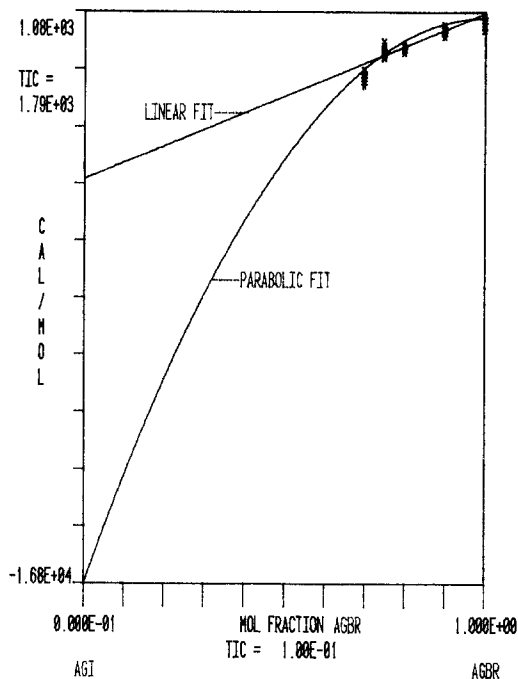


Fig. 6. Linear and quadratic extrapolations of the enthalpy of solution of AgBr-rich single-phase compositions to pure AgI.

enthalpy for the transformation of α -AgI to the rocksalt structure lies between 0 and 12 kcal/mol.

Acknowledgments

The authors thank DOE for providing financial support to A. Khandkar under Contract DE-ACO2-82ER12091, NSF for Grant DMR8106027 to A. Navrotsky, and The Center for Solid State Science for providing funds to V. B. Tare and J. B. Wagner, Jr. to carry out this research.

Manuscript submitted March 26, 1984; revised manuscript received June 15, 1984. This was Paper 832 presented at the San Francisco, California, Meeting of the Society, May 8-13, 1983.

Arizona State University assisted in meeting the publication costs of this article.

REFERENCES

1. C. C. Liang, *This Journal*, **120**, 1289 (1973).
2. K. Shahi and J. B. Wagner, Jr., *ibid.*, **128**, 6 (1981).
3. A. Khandkar and J. B. Wagner, Jr., Abstract 833, p. 1236, The Electrochemical Society Extended Abstracts, Vol. 83-1, San Francisco, CA, May 8-13, 1983.
4. G. Crosbie, *J. Solid State Chem.*, **25**, 367 (1978).
5. V. B. Tare and J. B. Wagner, Jr., *J. Appl. Phys.*, **154**, 252 (1983).
6. V. B. Tare and J. B. Wagner, Jr., *ibid.*, **154**, 6459 (1983).
7. K. Shahi and J. B. Wagner, Jr., *Appl. Phys. Lett.*, **37**, 757 (1980).
8. J. B. Wagner, Jr., *Mater. Res. Bull.*, **15**, 1691 (1980).
9. T. Jow and J. B. Wagner, Jr., *This Journal*, **126**, 1963 (1972).
10. A. Hooper, Paper 76 presented at the International Conference on Fast Ionic Transport in Solids, Gatlinburg, TN, May 18-22, 1981.
11. K. Shahi and J. B. Wagner, Jr., *Phys. Rev. B*, **23**, 6417 (1981).
12. A. Navrotsky, *Phys. Chem. Min.*, **2**, 89 (1977).
13. "Thermochemical Properties of Inorganic Compounds," compiled by I. Barin and O. Knacke, Springer-Verlag, Berlin (1973).
14. O. Stasiw and J. Teltow, *Z. Anorg. Allg. Chem.*, **259**, 150 (1949).
15. J. J. Kramer, G. M. Pound, and R. F. Mehl, *Acta Metall.*, **6**, 763 (1958).
16. K. Shahi, *Phys. Status Solidi A*, **41**, 11 (1977).
17. P. Davies and A. Navrotsky, *J. Solid State Chem.*, **38**, 264 (1981).

Phase Relations and Thermochemistry of Iron-Aluminum-Sulfur System at 1173 K

P. C. Patnaik* and W. W. Smeltzer**

Department of Metallurgy and Materials Science, McMaster University, Hamilton, Ontario, Canada L8S 4M1

ABSTRACT

The compositions were determined of alloy and sulfide phases in the Fe-Al-S system equilibrated with one another at 1173 K. These evaluations were used to construct the ternary Fe-Al-S isotherm, which was comprised of three sulfide phases coexisting with alloy: FeS containing up to 0.61 atomic percent (a/o) Al, FeAl_2S_4 of Fe/Al ratio 0.766 to 0.518 in the alloy composition range 0.84 to 5.86 a/o Al, and Al_2S_3 containing 0.30 a/o Fe. These results were combined with available thermodynamic data to determine the ternary equilibrium diagram in the form of sulfur activity vs. aluminum metal atom fraction of the alloy and sulfide phases. The sulfur activity over the ternary univariant coexistence alloy + FeAl_2S_4 + Al_2S_3 is 5.35×10^{-6} .

Phase relations and thermodynamic properties of the Fe-Al-S solid-gas system at high temperatures are not known. In this investigation, the ternary Fe-Al-S isotherm at 1173 K is constructed using the compositions of equilibrated phases. The sulfur activities coexisting with aluminum sulfide and alloys were evaluated using the value for the standard free energy of formation of Al_2S_3 (1) and the available aluminum activity data for the binary Fe-Al alloys (2, 3). These sulfur activity evaluations, in conjunction with compositions of the sulfide and alloy phases, were utilized to construct the ternary equilibrium sulfur activity diagram.

Experimental

A number of ternary compositions in the Fe-Al-S system were synthesized from the elements. The starting materials were powders of iron and aluminum of 99.99% purity and sulfur of 99.999% purity supplied by Cerac, Incorporated. Several overall compositions (P1 to P6), as shown in Fig. 1, were chosen. In each case, the elements were thoroughly mixed, compressed to a pellet, and then placed in a high purity (99.9%) alumina crucible which was sealed in a quartz tube under vacuum (1-2 Pa). This method avoided SiO_2 contamination of the sample pellet resulting from its bonding to the quartz wall, which has been shown previously to occur (4).

Previous workers using aluminum and sulfur to obtain Al_2S_3 in a quartz ampul have encountered explosions while determining a suitable heating schedule (5). This behavior was due to the autocatalytic nature of aluminum sulfidation by which the exothermic sulfidation reaction increased the sulfur pressure in the ampul. With an increased sulfur pressure, the reaction rate increased, releasing additional heat, which led to excessive sulfur pressures and rupture of the quartz tube. This problem was not encountered in the present case, owing to rapid reaction between iron and sulfur. However, for a successful experiment, combinations of slow and step heatings were used.

Figure 2 shows a typical heating schedule of samples placed in alumina crucibles encased in quartz ampuls. Initially, they were heated for 2 days in steps at 423 and 509 K (total P_{S_2} at 509 K = 10^3 Pa) to permit combination of the sulfur with metals. All the samples contained 35 atomic percent (a/o) sulfur with varying amounts of the metals. The completeness of reaction was indicated by the absence of visible sulfur in the quartz tube. After approximately 240h at 1173 ± 2 K, the ampuls were quenched in water. The quenched samples were mounted for metallographic observation. In addition to metallography, x-ray powder diffraction with Ni-filtered CuK_α radiation was also employed to identify the various phases present in each sample. Compositions of various phases were determined using electron probe microanalyses (EPMA) with Fe-Al alloys, FeS, and FeAl_2S_4 of known

compositions as standards. These compositions could be determined to within ± 0.05 a/o.

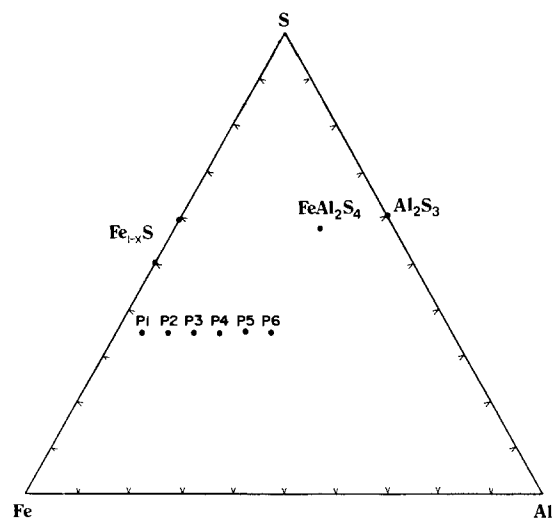


Fig. 1. Overall compositions of Fe, Al, and S (P1-P6) considered for the analysis of the ternary Fe-Al-S isotherm.

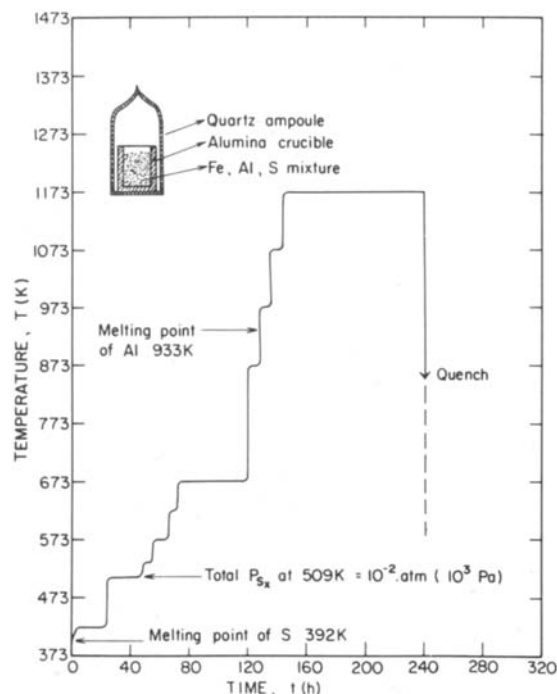


Fig. 2. Sample heating schedule for phase equilibration to determine the ternary Fe-Al-S isotherm.

*Electrochemical Society Student Member.

**Electrochemical Society Active Member.

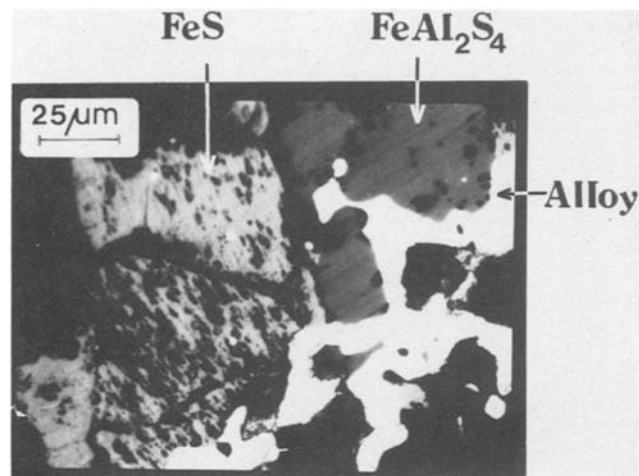


Fig. 3. Optical photomicrograph of polished-annealed alloy + FeS + FeAl₂S₄ pellet.

Results

Figure 3 shows three equilibrated phases, FeS + Fe-0.84Al (a/o) + FeAl₂S₄. Table I summarizes the equilibrated phases in pellets P1 through P6 as identified by metallography and x-ray diffraction. The x-ray intensity plots *vs.* diffraction angle 2θ for several pellets are shown in Fig. 4. The correspondence of these diffraction patterns to ASTM standards for FeS, Al₂S₃, and Fe-Al alloys and to independent diffraction measurements made on synthesized FeAl₂S₄ support the inferences drawn from the metallographic observations (4, 6).

Compositions of alloys and coexisting sulfide phases determined by EPMA are reported in Table II. These analyses demonstrated the following findings of phase equilibria at 1173 K: (i) in the FeS + alloy + FeAl₂S₄ univariant equilibrium, FeS contained 0.61 a/o Al and the alloy contained 0.84 a/o Al, (ii) the double sulfide phase, (Fe_{1.24}Al_{1.618})S₄, in equilibrium with (Fe_{0.96}Al_{0.012})S and the Fe-0.84 Al alloy was rich in iron, and its iron content decreased to (Fe_{0.99}Al_{1.91})S₄ as the double sulfide was equilibrated with higher aluminum containing alloys, and (iii) the solubility of iron in Al₂S₃ equilibrated with double sulfide and alloy containing 5.86 a/o Al was 0.30 a/o. This solubility of iron in Al₂S₃ was found to decrease with increasing aluminum contents of the alloy.

Discussion

The Fe-Al-S isotherm, Fig. 5, was constructed from results of this investigation using the binary Fe-Al, Fe-S, and Al-S phase extents (3). Pure iron and aluminum dissolve up to 0.05 and 5 a/o of sulfur, respectively. These concentrations were used to represent the sulfur solubility in the alloy, as indicated by a dotted line on the ternary isotherm. Solubilities of aluminum and iron in FeS and Al₂S₃ were determined to be 0.61 and 0.3 a/o, respectively, when each phase was equilibrated with alloy and FeAl₂S₄. The phase field of double sulfide, (Fe_{1.24}Al_{1.618})S₄-

Table I. Summary of phase identification by metallographic observations and powder x-ray diffraction of the equilibrated pellets

Points on isotherm	Overall composition			Inference
	S	Al	Fe	
P1	35	5	60	Three-phase region: alloy, FeS and FeAl ₂ S ₄
P2	35	10	55	Three phases: alloy + FeS + FeAl ₂ S ₄
P3	35	15	50	Two-phase region: alloy + FeAl ₂ S ₄
P4	35	20	45	Two-phase region: alloy + FeAl ₂ S ₄
P5	35	25	40	Three-phase region: alloy + Al ₂ S ₃ + FeAl ₂ S ₄
P6	35	30	35	Two-phase region: alloy + Al ₂ S ₃

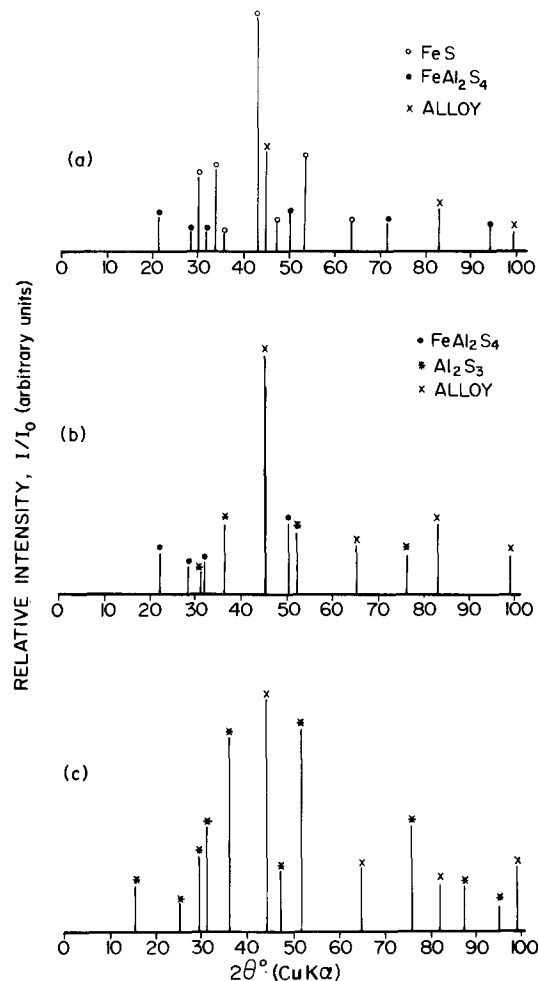


Fig. 4. Powder x-ray diffractograms of various sulfide phases in the pellets P1-P6 (Fig. 1) of increasing Al content. (a): FeS + FeAl₂S₄ + alloy. (b): FeAl₂S₄ + Al₂S₃ + alloy. (c): Al₂S₃ + alloy.

(Fe_{0.99}Al_{1.91})S₄, was obtained from the microprobe analyses. Construction of two-phase regions containing alloy + FeAl₂S₄, alloy + Al₂S₃, and three-phase triangles consisting of alloy + FeS + FeAl₂S₄, alloy + FeAl₂S₄ + Al₂S₃ were made using the compositions as given in Table II of the appropriate equilibrated phases. The tie lines (dotted) shown in the two-phase regions are those determined experimentally. Dotted lines in the upper portion of the isotherm are schematic.

Aluminum activities in solid Fe-Al alloys over the range 5-80 a/o at 1173 K were determined by Eldridge and Komarek (2) and the values are recorded in Table III. Sulfur activities upon equilibrating Al₂S₃ with alloys containing

Table II. Electron probe microanalyses of equilibrated phases in the Fe-Al-S system

Pellet no. (Fig. 1)	Phases	Al and Fe a/o in the alloy		Chemical formula of the sulfide
		Al	Fe	
2	Alloy	0.84	99.15	(Fe _{0.96} Al _{0.012})S
	Iron sulfide			
3	Alloy	2.73	97.25	(Fe _{1.24} Al _{1.618})S ₄
	Double sulfide			
4	Alloy	3.42	96.54	(Fe _{1.10} Al _{1.846})S ₄
	Double sulfide			
5	Alloy	5.86	94.11	(Fe _{0.99} Al _{1.91})S ₄
	Double sulfide			(Fe _{0.015} Al _{1.955})S ₃
	Aluminum sulfide			
6	Alloy	21.05	78.94	(Fe _{0.009} Al _{1.962})S ₃
	Aluminum sulfide			

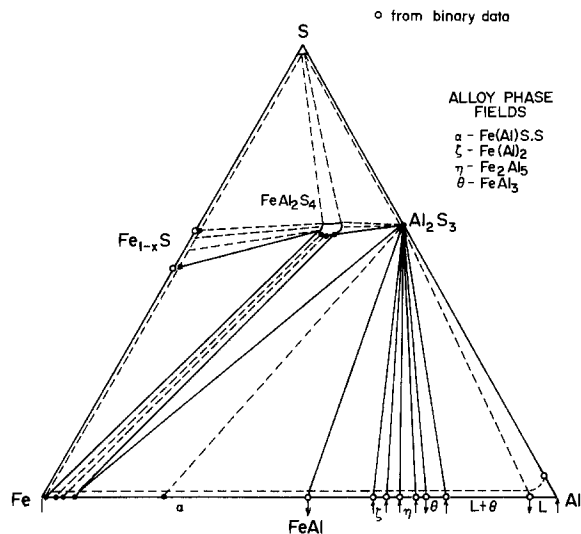
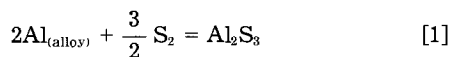


Fig. 5. The experimentally determined ternary Fe-Al-S isotherm at 1173 K.

6-80 a/o Al can be calculated as follows. If one considers the reaction



the equilibrium constant is given by

$$K = \exp - \frac{\Delta G_f^\circ}{RT} = \frac{a_{\text{Al}_2\text{S}_3}}{a_{\text{Al}}^2 P_{\text{S}_2}^{3/2}} \quad [2]$$

where $a_{\text{Al}_2\text{S}_3}$ and a_{Al} are the activities of Al_2S_3 and aluminum in the alloy, respectively, P_{S_2} is the dissociation pressure of Al_2S_3 , and ΔG_f° is the standard free energy of formation of Al_2S_3 . Since $a_{\text{Al}_2\text{S}_3} \approx 1$, the sulfur pressure relationship is given by

$$\log P_{\text{S}_2} (\text{Pa}) = \frac{2}{3} \left(\frac{\Delta G_f^\circ(\text{Al}_2\text{S}_3)}{2.303 RT} - 2 \log a_{\text{Al}} \right) + \log (101,300) \quad [3]$$

Upon substituting the most recently determined value for $\Delta G_f^\circ(\text{Al}_2\text{S}_3) = -507,883 \pm 500 \text{ J/mol}$ (1), the sulfur activity is given by

$$\log a_{\text{S}} = 1/2 [\log \{P_{\text{S}_2} (\text{Pa})/1.013 \times 10^5 (\text{Pa})\}] = -7.54 - \frac{2}{3} \log a_{\text{Al}} \quad [4]$$

Sulfur activities for alloy- Al_2S_3 equilibria were then calculated using the aluminum activity values and these evaluations are given in Table III.

An aluminum cation (or metallic) fraction of each phase is defined as

$$\xi_{\text{Al}} = \frac{g \text{ ions (atoms) of aluminum}}{g \text{ ions (atoms) of iron} + g \text{ ions (atoms) of aluminum}}$$

For the three-phase equilibrium, alloy + FeAl_2S_4 + Al_2S_3 , ξ_{Al} (alloy) was determined to be 0.059, corresponding to an activity of 3.9×10^{-4} . The corresponding sulfur activity was calculated to be 5.35×10^{-6} . It was not possible to evaluate the sulfur activity over the FeS + alloy + FeAl_2S_4 equilibrium because the free energy of formation of FeAl_2S_4 is unknown.

Figure 6 shows the sulfur activity equilibrium diagram, in a_{S} vs. ξ_{Al} , for the Fe-Al-S system at 1173 K. This diagram is semischematic and it has been compiled insofar as possible from the results given in Tables II and III. For clarity, dissociation pressures of the sulfides are also shown in this diagram.

Table III. The thermodynamic activity of Al in solid Fe-Al alloys (2) and the sulfur activities calculated from Eq. [4] for the alloy + Al_2S_3 equilibria at 1173 K

a/o Al	(ξ_{Al})		a_{Al} at 1173 K	$-\log a_{\text{S}}$
	$\frac{\eta_{\text{Al}}}{\eta_{\text{Al}} + \eta_{\text{Fe}}}$			
5	0.05		3.8×10^{-4}	
6	0.06		3.9×10^{-4}	5.27
10	0.10		8.1×10^{-4}	5.47
15	0.15		1.5×10^{-3}	5.65
20	0.20		2.5×10^{-3}	5.79
25	0.25		3.7×10^{-3}	5.91
30	0.30		5.5×10^{-3}	6.03
35	0.35		8.3×10^{-3}	6.15
40	0.40		1.4×10^{-2}	6.28
45	0.45		2.6×10^{-2}	6.47
50	0.50		5.5×10^{-2}	6.69
52	0.52		9.8×10^{-2}	6.86
60	0.60		9.8×10^{-2}	6.86
65	0.65		9.8×10^{-2}	6.86
67	0.67		1.3×10^{-1}	6.94
70	0.70		1.3×10^{-1}	6.94
75	0.75		4×10^{-1}	7.26
80	0.80		7×10^{-1}	7.42
100	1		1	7.54

The sulfur activity decreased from 1.2×10^{-4} imposed by the Fe-FeS coexistence to a lower value presently not determined associated with the univariant alloy + FeS + FeAl_2S_4 equilibrium. The fractions, ξ_{Al} , in each phase of this coexistence, are 0.0084, 0.012, and 0.566, respectively. The sulfur activity of the alloy + FeAl_2S_4 + Al_2S_3 coexistence was determined to be 5.35×10^{-6} . ξ_{Al} in each phase is 0.059, 0.658, and 0.992 respectively. FeAl_2S_4 equilibrated with alloys containing 0.84 to 5.86 a/o Al. The results indicate that Al_2S_3 exists with alloys containing greater than 5.86 a/o Al. Sulfur activity decreases with increasing aluminum contents of the alloy until it reaches 2.9×10^{-8} , corresponding to that of Al + Al_2S_3 equilibrium.

Summary

The ternary Fe-Al-S isotherm at 1173 K was constructed by determining the composition of equilibrated alloy and

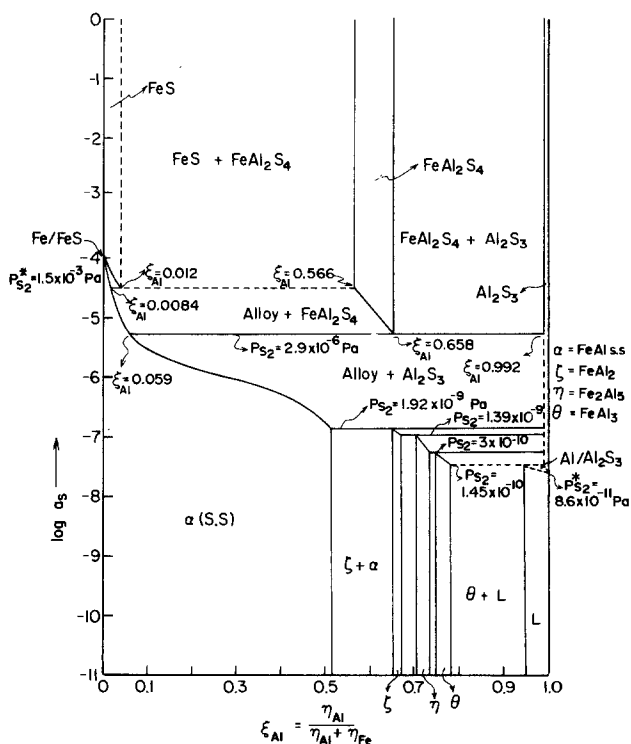


Fig. 6. The ternary equilibrium sulfur activity diagram at 1173 K, $\log a_{\text{S}}$ vs. Al cation (metallic) fraction. The dissociation pressures calculated for the sulfides are given by

$$a_{\text{S}} = \{P_{\text{S}_2} (\text{Pa})/1.013 \times 10^5 (\text{Pa})\}^{1/2}$$

sulfide phases. Equilibrium sulfur activities were determined for the alloy + FeAl_2S_3 + Al_2S_3 univariant equilibrium and alloy + Al_2S_3 coexistences. These results in conjunction with thermochemical data for Fe-Al alloys and Al_2S_3 were used to determine the equilibrium diagram of sulfur activity as a function of aluminum metallic fraction of each phase.

Acknowledgments

Financial assistance for this research by the Natural Sciences and Engineering Research Council of Canada is gratefully acknowledged. P. C. Patnaik wishes to acknowledge the award of a graduate scholarship in Metallurgy and Materials Science to carry out this research as a part of his Ph.D. studies at McMaster University.

Manuscript submitted April 19, 1984; revised manuscript received July 6, 1984.

McMaster University assisted in meeting the publication costs of this article.

REFERENCES

1. M. J. Ferrante, J. M. Stuve, H. C. Ko, and R. R. Brown, *High Temp. Sci.*, **14**, 91 (1981).
2. J. Eldridge and K. L. Komarek, *Trans. Metall. Soc. AIME*, **230**, 236 (1964).
3. P. Hultgren, P. D. Desai, D. T. Hawkins, M. Gleiser, and K. K. Kelly, "Selected Values of the Thermodynamic Properties of Binary Alloys," p. 156, American Society for Metals, Metals Park, OH (1973).
4. K. Nishida and T. Narita, *Bull. Fac. Eng. Hokkaido U.*, **81**, 1 (1976).
5. E. E. Hellstrom and R. A. Huggins, *Mater. Res. Bull.*, **14**, 127 (1979).
6. J. Flahaut, *Ann. Chim. (Paris)*, **63**, 632 (1952).

Preparation and Properties of Amorphous Boron Films Deposited by Pyrolysis of Decaborane in the Molecular Flow Region

K. Nakamura

Department of Chemistry, Nihon University, Sakurajosui Setagaya-ku, Tokyo 156, Japan

ABSTRACT

Boron films of 0.1-1.5 μm thickness have been prepared on sapphire, silicon, and tantalum as substrates by the pyrolysis of decaborane ($\text{B}_{10}\text{H}_{14}$) in the molecular flow region ($\leq 10^{-4}$ torr) and in a temperature range of 350°-1200°C. It is found that the deposition rate of the boron films is proportional to the decaborane partial pressure and the substrate temperature. Below 416°C, the deposition rate D is given as a function of the substrate temperature and partial pressure of decaborane. This relation is

$$D = 7.16 \times 10^6 \cdot P \cdot \exp(-39000/RT_s)$$

where T_s is the substrate temperature, P is the pressure of decaborane, and R is the gas constant. The apparent activation energy for the decomposition of decaborane is found to be 39 kcal/mol. X-ray and electron diffraction study indicates that the films are amorphous. The electrical conductivities vary from $3 \times 10^{-5} \text{ S} \cdot \text{cm}^{-1}$ at 77 K to $30 \text{ S} \cdot \text{cm}^{-1}$ at 1000 K, and the activation energy is 1.07 eV in the intrinsic temperature range (700-1000 K). The maximum value of thermoelectric power is about $420 \mu\text{V} \cdot \text{deg}^{-1}$ at 700 K, and its polarity is positive between 500 and 1000 K. The absorption coefficient, refractive index, and extinction coefficient of boron films are obtained from the measured transmittance and reflectance. The energy of the indirect allowed transition is estimated to be $1.28 \pm 0.08 \text{ eV}$.

Boron is one of the elemental semiconductors. However, the resistivity of boron is several hundred times larger than that of Si and Ge at room temperature. Although many studies (1-3) on the properties of boron have been done, the physical properties reported are not in agreement with each other because it is very hard to obtain high-purity bulk boron. However, we can obtain pure and uniform boron in film form. Boron films have been prepared by means of chemical vapor deposition (4-6) or vacuum evaporation using electron bombardment of boron (7-9). Croft (10) has obtained high-purity boron films by pyrolysis of diborane. However, diborane is a very dangerous gas which requires much care in handling. Pentaborane (B_5H_9 ; -46.5°C mp, 60°C bp) and decaborane ($\text{B}_{10}\text{H}_{14}$; 99.6°C mp, 213°C bp) can be used as alternative boron hydride sources. Decaborane is safer and more stable than pentaborane and diborane. Furthermore, decaborane has advantages as a source material for boron films because high purity decaborane is easy to obtain with a sublimation purification process.

Many studies on the electrical (6, 11, 12, 14) and optical (8, 9, 13, 14) properties of boron films prepared by vacuum evaporation (12, 13) and CVD (5, 14) have been reported. However, reported properties scatter widely (e.g., the values of electrical conductivity and optical gap energy at room temperature).

In this report, high quality boron films have been prepared by pyrolysis of decaborane in the molecular flow region at temperatures between 350° and 1200°C. The deposition mechanism is discussed in terms of the depen-

dence of the deposition rate on the substrate temperature and the impingement frequency of decaborane molecules onto the substrate surface.

The temperature dependencies of the electrical conductivity and of the thermoelectric power of the boron films deposited on sapphire substrates have been measured. The energy-band gap and optical constant ($n \cdot k$) of boron have been estimated from the results of the optical transmittance and reflectance in the visible and infrared spectral regions.

Experimental

The schematic diagram of the apparatus in this study is shown in Fig. 1. The vacuum chamber was evacuated by an oil diffusion pump system, and the ultimate pressure was 2×10^{-6} torr. Sapphire and silicon were used as the substrates. The substrate was fixed on the tungsten sheet heater (0.05 mm thickness) and was heated from 600° to 1200°C (Fig. 2). Tantalum sheet was also used as a substrate and was heated between 350° and 700°C by direct resistance heating. The sapphire substrate temperature was estimated from the heater temperature, which was measured with an optical pyrometer. The relation between the substrate and the heater temperatures was previously obtained. The tantalum substrate temperature was measured directly by a welded thermocouple.

Decaborane (Arfa Product) was sublimated by heating at about 70°C and was introduced to the vacuum chamber through a variable leak valve. Boron films were deposited on the heated substrate by thermal decomposition of

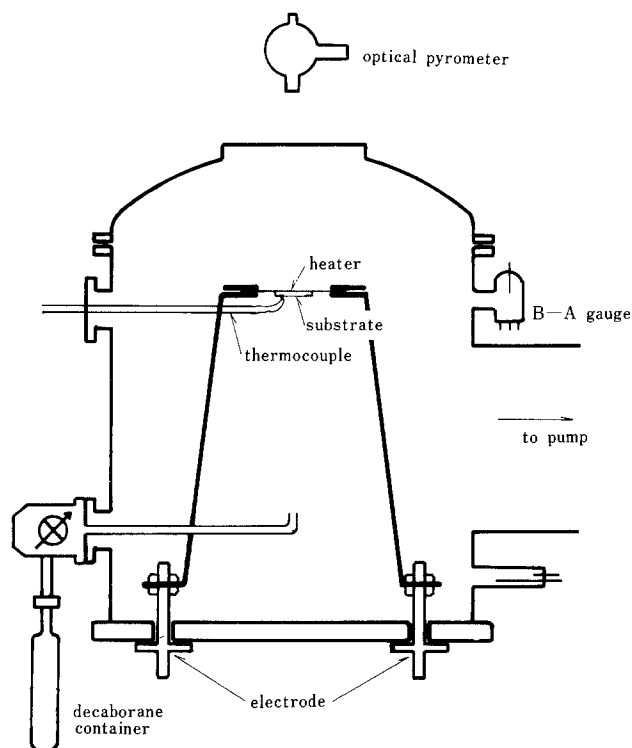


Fig. 1. Schematic diagram of the apparatus used for deposition of boron films by pyrolysis of decaborane.

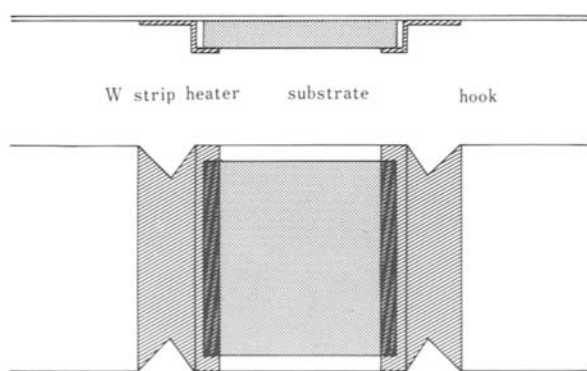


Fig. 2. Assembly of the substrate and the heater

the decaborane. The pressure of decaborane was measured as a corresponding of nitrogen pressure by a B-A type ionization gauge and was kept between 1×10^{-5} torr and 2×10^{-4} torr. Deposition time varied from 0.5-60 min, depending on the gas pressure and the substrate temperature. The thicknesses of the films on the sapphire substrates were measured with a multiple-beam interferometer and ranged from 442 to 4740 Å. In the case of the films deposited on tantalum, the film thickness could not be measured optically because of the rough surface of the tantalum substrate. The film thickness of the boron films on tantalum substrates was estimated from the measured x-ray fluorescence of boron deposited using EPMA with a 7 kV acceleration voltage, a 0.1A sample current, and a 100 μm beam-diameter. The relation between the x-ray intensity and the film thickness was previously obtained using boron films on a sapphire substrate.

The crystal structure of boron films was studied by reflection electron and x-ray diffraction techniques. The electrical conductivity and its temperature dependence were measured by a two-probe technique at temperatures ranging from 300 to 1000 K in vacuum. A gold film, deposited on the boron films by vacuum evaporation, was used as an electrode. Thermoelectric power of the films was measured by using a Pt-PtRh (10%) thermocouple

which was 0.2 mm in diameter. The distance between two thermocouples was 10 mm. The size of the boron films measured were $5 \times 13 \text{ mm}^2$, and the film thicknesses were 1.2 and 1.5 μm . The thermoelectric power could not be measured below 250°C because it was too small in comparison with the electrical noise in this temperature range.

The transmission and the reflection spectra of the boron films on sapphire were measured over a wavelength range of 200-2500 nm using a spectrophotometer MPS-50 (Shimadzu). In the transmission and the reflection measurements, an uncoated sapphire and an evaporated aluminum film were used as the references, respectively. Absorption coefficient, refractive index, and extinction coefficient of the boron films were calculated from the measured transmittance and reflectance at normal incidence.

Infrared transmittance at normal incidence on boron films deposited on high resistivity silicon wafers was measured in a wavelength range of 2.5-50 μm using an infrared spectrophotometer, DS-701G (Jasco).

Results and Discussion

Influence of the deposition parameters on the deposition rate.—The deposition rate of boron, D ($\text{\AA}/\text{s}$), is linearly dependent on the decaborane pressure, P (torr), as shown in Fig. 3, and is given as $D = 3.57 \times 10^{-3} \cdot P$ for substrate temperatures of 750° and 1000°C.

It is thought that the deposition rate of boron films obtained by pyrolysis of decaborane depends on the impingement frequency of decaborane onto the substrate. From gaseous molecular dynamics, the impingement frequency, S , of decaborane on the substrate surface is given as

$$S = P (M/2\pi RT_g)^{1/2} = 5.8 \times 10^{-2} \cdot P (M/T_g)^{1/2} \quad (\text{g}/\text{cm}^2 \cdot \text{s}) \quad [1]$$

where $R = 62.36 \text{ torr} \cdot \text{l}/\text{mol} \cdot \text{deg}$ is the gas constant, P is the decaborane pressure in torr, M is the molecular weight of decaborane, and T_g is the gas temperature considered to be at room temperature (*i.e.*, $T_g = 300 \text{ K}$).

The rate of chemisorption depends on the impingement frequency, S , of the decaborane molecules on the surface, the condensation coefficient, γ , and the fraction of collisions that take place at available sites $f(\theta)$, where θ is the fractional surface coverage. The rate of chemisorption, U is given as

$$U = S\gamma f(\theta) \exp(-E_c/RT_s) \quad [2]$$

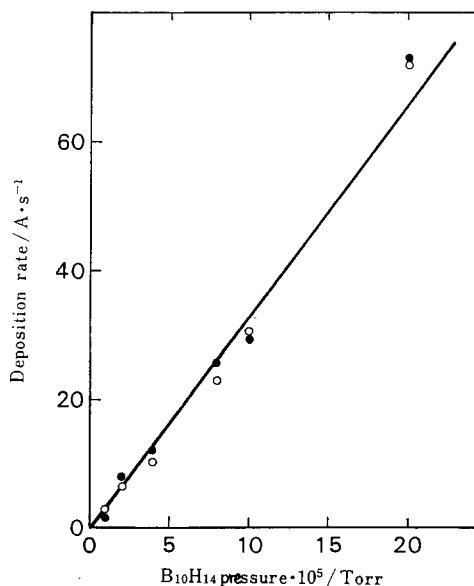


Fig. 3. Deposition rates of pyrolytic boron films as a function of $\text{B}_{10}\text{H}_{14}$ pressure. The films were deposited at substrate temperatures of $T_s = 750^\circ\text{C}$ (●) and $T_s = 1000^\circ\text{C}$ (○).

where T_s is the substrate temperature, and E_c is the activation energy for chemisorption.

As shown in Fig. 3, the deposition rate is independent of temperature, and the chemisorption is nonactivated; hence, the activation energy $E_c = 0$. Under the experimental conditions, we suppose that $f(\theta) \approx 1$ and $\gamma \approx 1$, hence, the rate of chemisorption is equal to the impingement frequency, S . The theoretical deposition rate, D_t , in this high temperature range is

$$D_t = 1.66 \times 10^{-2} \cdot P \quad (\text{cm/s}) \quad [3]$$

taking into account the ratio of boron weight to decaborane molecular weight (0.9) and the density of boron (2.0 g/cm^3). Comparison with the experimental values of Fig. 3 shows that D_t must be multiplied by a factor of 0.22. This factor is due to either $f(\theta)$, γ , or the sensitivity difference of decaborane and nitrogen in the ionization gauge.

Figure 4 shows the temperature dependence of the deposition rate of boron films in a temperature range of 350°C to 700°C at two decaborane partial pressures, 2×10^{-5} torr and 8×10^{-5} torr. In each case, the deposition rate increases steeply, with an increase in temperature of up to 416°C , and then saturates.

In the low temperature range, $T_s \leq 416^\circ\text{C}$, the activation energy is found to be 39 kcal/mol from the slope, and the deposition rate is given as

$$D = 7.16 \times 10^9 \cdot P \cdot \exp(-39000/R \cdot T_s) \quad (\text{cm/s}) \quad [4]$$

The saturated deposition rate above 416°C can be explained by Eq. [2]. The activation energy of 39 kcal/mol is in agreement with 41.4 kcal/mol (15) and $41.6 \pm 0.5 \text{ kcal/mol}$ (16), both reported for the activation energy of the decomposition of decaborane at temperatures below 250°C .

Characterization of the films (structure, impurities).—The x-ray diffraction pattern of a boron film deposited on sapphire at a substrate temperature of 700°C and a decaborane pressure of 2×10^{-5} torr for 15 min is shown in Fig. 5. The x-ray and electron diffraction analysis indicates that the films are amorphous.

The ESCA spectrum of the boron film deposited at a decaborane pressure of 4.4×10^{-5} torr and a substrate temperature of 700°C is shown in Fig. 6. Figure 6 shows

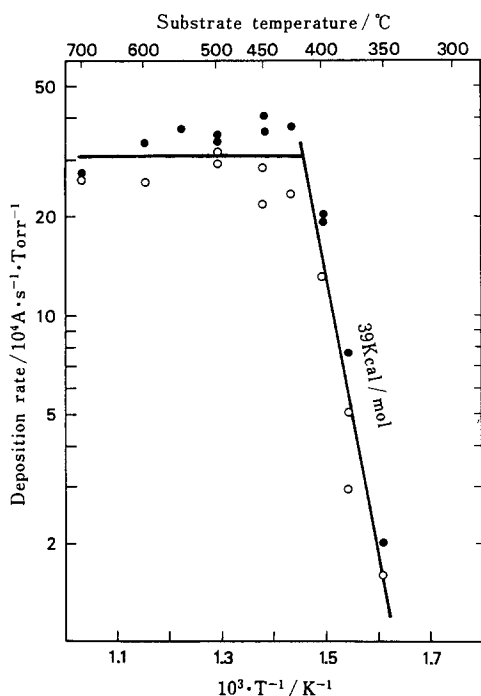


Fig. 4. Logarithm of the deposition rate divided by the decaborane pressure as a function of reciprocal absolute temperature of the substrate. The films were deposited at decaborane pressures of $P = 2 \times 10^{-5}$ torr (●) and $P = 8 \times 10^{-5}$ torr (○).

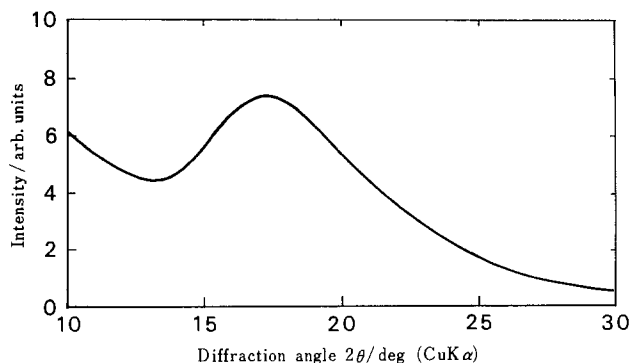


Fig. 5. X-ray diffraction pattern of a pyrolytic boron film

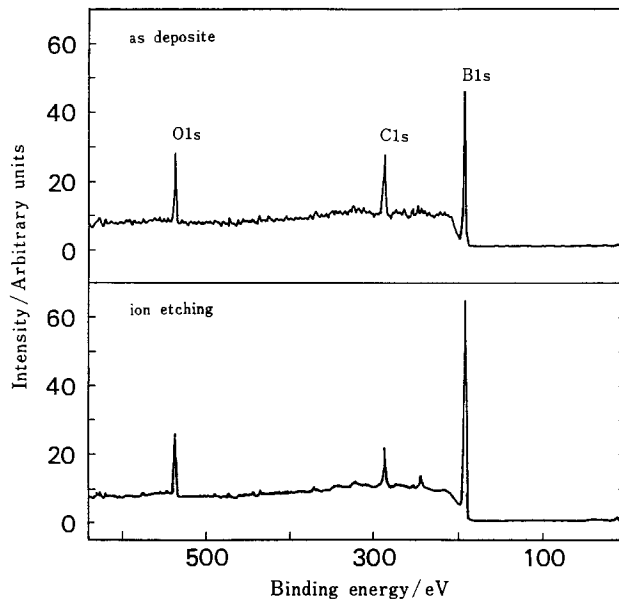


Fig. 6. ESCA spectra of a pyrolytic boron film

the spectrum of the film before and after ion etching. The peaks at the binding energies of 191, 288, and 512 eV correspond to boron 1s, carbon 1s, and oxygen 1s, respectively. The amounts of carbon and oxygen at the surface were estimated from the observed peak intensities multiplied by the photo-ionization cross-section, factor (B: 0.486, C: 1.00, O: 0.293) and are shown in Table I. The table shows that oxygen decreases little by ion etching, even though the apparent carbon content decreases to almost one third its original content. These results indicate that it is difficult to remove oxygen from the film surface by ion etching alone. The boron films were analyzed by EPMA because this method was not influenced by surface impurities. The amounts of impurities in three films deposited on sapphire substrates at decaborane pressures of 1.4×10^{-5} , 3.3×10^{-5} , and 4×10^{-5} torr are shown in Table II. This table shows that carbon decreases with increasing deposition rate. Oxygen impurities in boron films on sapphire substrates cannot be analyzed by EPMA because the primary electrons penetrate the film and extend into the oxygen bearing substrate. On the contrary, no oxygen was found in the films on tantalum substrates by EPMA. The EPMA and the ESCA analyses suggest that oxygen impurity localized near the surface is due to the exposing air, while carbon impurities are incorporated in the films from a residual gas.

Electrical properties.—The conductivities of boron films as a function of reciprocal absolute temperature are shown in Fig. 7. Conductivity varied from $3 \times 10^{-3} \text{ S} \cdot \text{cm}^{-1}$ at room temperature to $30 \text{ S} \cdot \text{cm}^{-1}$ at 1000 K . The conductivity at room temperature is in agreement with that for amorphous boron films deposited by CVD and vacuum evaporation ($1 \times 10^{-3} \text{ S} \cdot \text{cm}^{-1}$) (12), but much larger than that of single crystal ($\approx 10^{-6} \text{ S} \cdot \text{cm}^{-1}$) (17, 18).

Table I. ESCA data for a boron film deposited at a $B_{10}H_{14}$ pressure of 4.4×10^{-5} torr and a substrate temperature of 700°C

Sample	Intensity (arbitrary units)			C/B	O/B
	Boron	Carbon	Oxygen		
As deposited	95	28	6.1	0.298	0.065
After argon etching	131	12	5.7	0.092	0.044

Table II. Data for boron films analyzed by EPMA

$B_{10}H_{14}$ pressure (torr)	Deposition rate ($\text{\AA}/\text{s}$)	Characteristic x-ray intensity (CPS)		C/B
		Boron	Carbon	
2×10^{-5}	7	1740	18	0.0103
4×10^{-5}	14	1020	6	0.0059
1×10^{-4}	33	1320	4	0.0030

The conductivity decreases slightly with increasing deposition temperature and is not affected by the carbon impurities.

Generally, the conductivity of semiconductors in the intrinsic conduction region is written as

$$\sigma = \sigma_0 \exp(-E_g/kT) \quad [5]$$

where σ_0 is a constant, E_g the bandgap energy, k the Boltzmann constant, and T the absolute temperature. E_g can be determined from the slope of the straight line in the plot of $\log \sigma$ against $1/T$. By applying this method to Fig. 7, we obtained $E_g = 1.07$ eV. This value is in agreement with values reported for amorphous boron films (1.0-1.16 eV) (14, 19, 20), but is smaller than those for polycrystalline and single crystal boron (1.3-1.4 eV) (20-22). On the other hand, because the boron films obtained are amorphous,

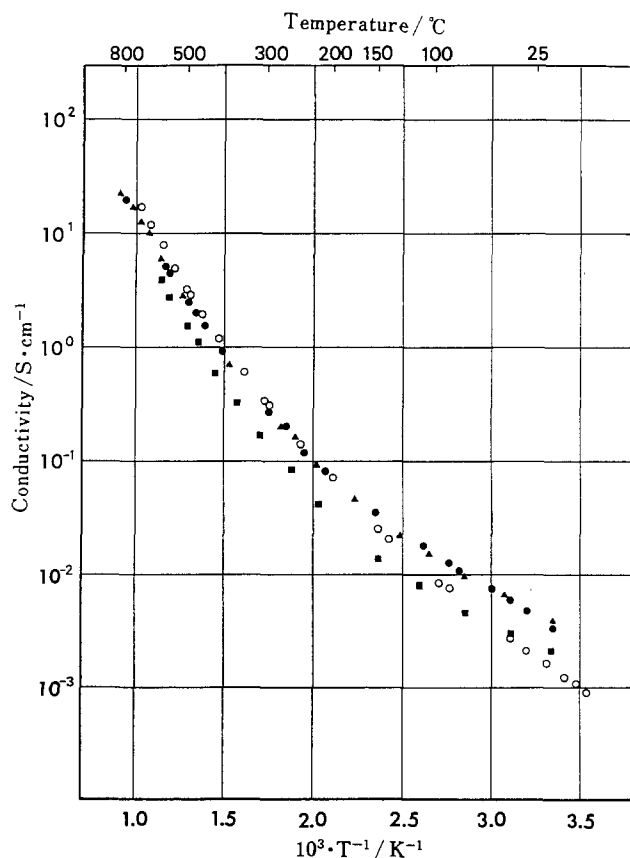


Fig. 7. Temperature dependence of the conductivity of pyrolytic boron films. The films were deposited at substrate temperatures and $B_{10}H_{14}$ pressures of $T_s = 700^\circ\text{C}$ and $P = 1.4 \times 10^{-5}$ torr (\blacktriangle), $T_s = 700^\circ\text{C}$ and $P = 2 \times 10^{-5}$ torr (\bullet), $T_s = 800^\circ\text{C}$ and $P = 3.3 \times 10^{-5}$ torr (\blacksquare), and $T_s = 750^\circ\text{C}$ and $P = 1.5 \times 10^{-5}$ torr (\circ).

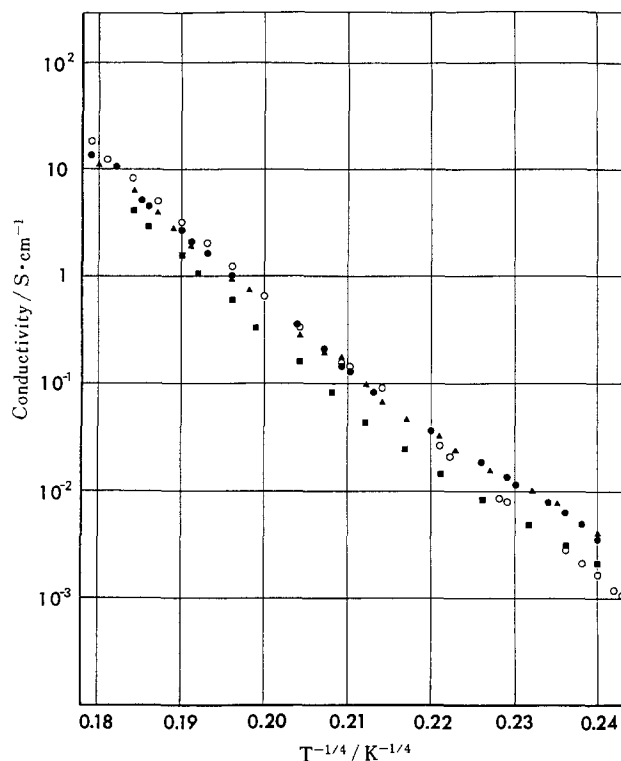


Fig. 8. Dependence of conductivity S on $T^{1/4}$; symbols correspond to those in Fig. 7.

the electric conduction is considered to be due to hopping conduction. Mott (23) has derived the equation for hopping conduction

$$\sigma = \sigma_0 \exp(-(T_0/T)^{1/4}) \quad [6]$$

where σ_0 and T_0 are constants.

The plots of $\log \sigma$ of the boron films as a function of $T^{1/4}$ are shown Fig. 8. The observed values show a good linear relation between $\log \sigma$ and $T^{1/4}$, and values of $\sigma_0 = 3.2 \times 10^{11}$ S·cm and $T_0 = 3.5 \times 10^{-8}$ K are obtained. According to Mott, T_0 is given as a function of the density of localized states at Fermi level, $N(E_F)$

$$T_0 = 16 \epsilon^3/kN(E_F) \quad [7]$$

where ϵ is the exponential decay factor of localized states ($\epsilon^{-1} \approx 5\text{\AA}$) (6), and k is the Boltzmann constant. From the value of T_0 and Eq. [7], $N(E_F) = 3.8 \times 10^{18}$ $\text{cm}^{-3} \cdot \text{eV}^{-1}$ is obtained. This value is in agreement with the value for amorphous boron films, 5×10^{17} - 10^{19} $\text{cm}^{-3} \cdot \text{eV}^{-1}$ (6), and the value for amorphous bulk, $\approx 10^{18}$ $\text{cm}^{-3} \cdot \text{eV}^{-1}$ (24). As mentioned above, the conduction of the boron films can be explained successfully by two conduction mechanisms. We cannot decide which mechanism is valid within our experimental accuracy.

Figure 9 shows the temperature dependence of the thermoelectric power of the films. All the films obtained show p-type conduction. The thermoelectric power increases rapidly from $107 \mu\text{V} \cdot \text{deg}^{-1}$ at 230°C to a maximum value of $400 \mu\text{V} \cdot \text{deg}^{-1}$ at 427°C ; it then decreases gradually to $310 \mu\text{V} \cdot \text{deg}^{-1}$ at 730°C . As the positive carrier concentration increases with increasing temperature, the thermoelectric power also increases with increasing temperature. However, at higher temperature, the thermoelectric power decreases with increasing temperature because the hole mobility decreases. The thermoelectric powers reported for bulk boron (17, 18, 25) show a large peak at a lower temperature, compared with those for the boron films we obtained ($420 \mu\text{V}$ at 700 K). These results can be explained by the assumption that the concentration of the impurities or defects in the boron films should be much higher than that in bulk boron. Middleton and Johnson have explained the same results for germanium by the higher concentration of aluminum (26).

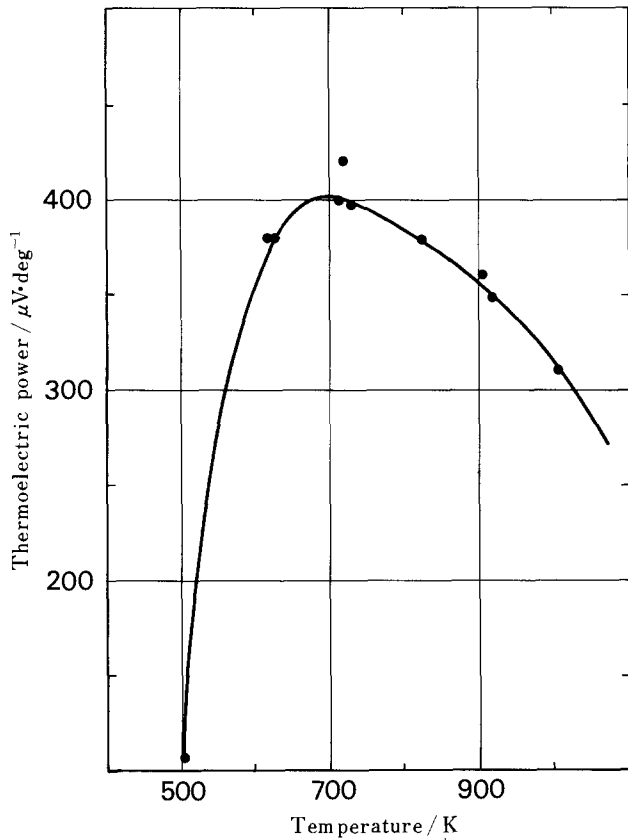


Fig. 9. Temperature dependence of the thermoelectric power

The figure of merit for thermoelectric materials, Z , is given as

$$Z = r^2\sigma/\kappa \text{ (deg}^{-1}\text{)} \quad [8]$$

where r is the thermoelectric power, σ is the electrical conductivity, and κ is the thermal conductivity. The thermal conductivity of boron is assumed to be $0.05 \text{ W}\cdot\text{cm}^{-1}\cdot\text{deg}^{-1}$ (27, 28).

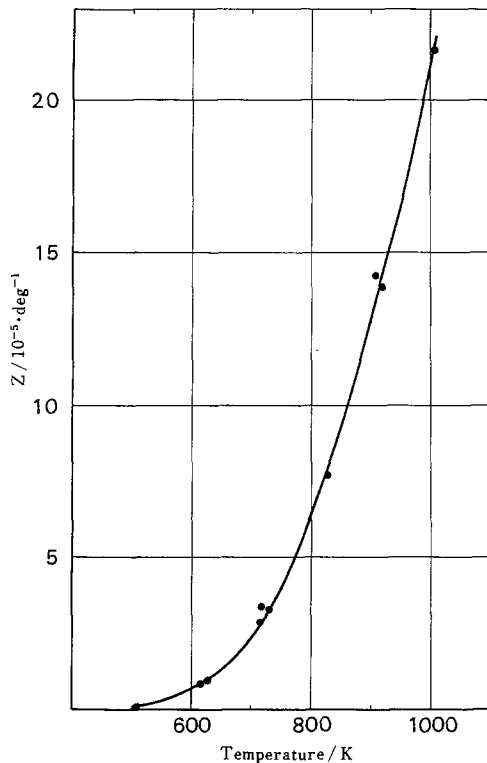


Fig. 10. EMF figure of merit Z of pyrolytic boron films as a function of absolute temperature.

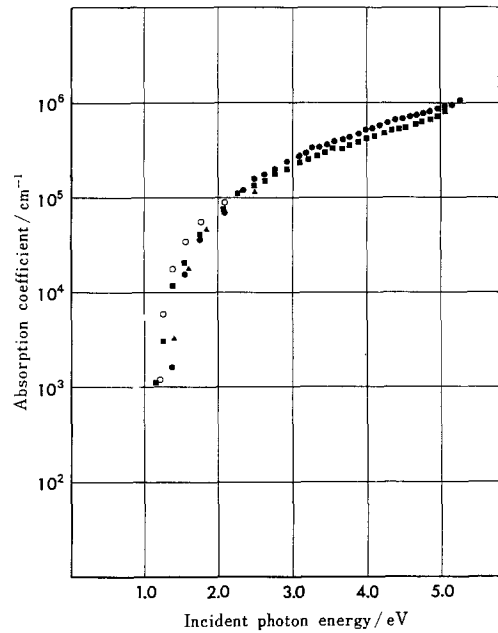


Fig. 11. Absorption coefficient of pyrolytic boron films as a function of incident photon energy.

However, the Z values of the boron films are smaller than those reported for the amorphous bulk material (29). A figure of merit higher than 10^{-3} deg^{-1} is required for the material of a practical thermoelectric converter. Figure 10 suggests that boron films deposited by pyrolysis of decaborane are useful for thermoelectric devices at over 2000 K.

Optical properties.—The absorption coefficient of the boron films, α , is shown in Fig. 11 as a function of incident photon energy, $h\nu$. The absorption coefficient increases rapidly at about 1.3 eV.

It is well known that boron is an indirect energy-gap type material. The absorption coefficient α near the ab-

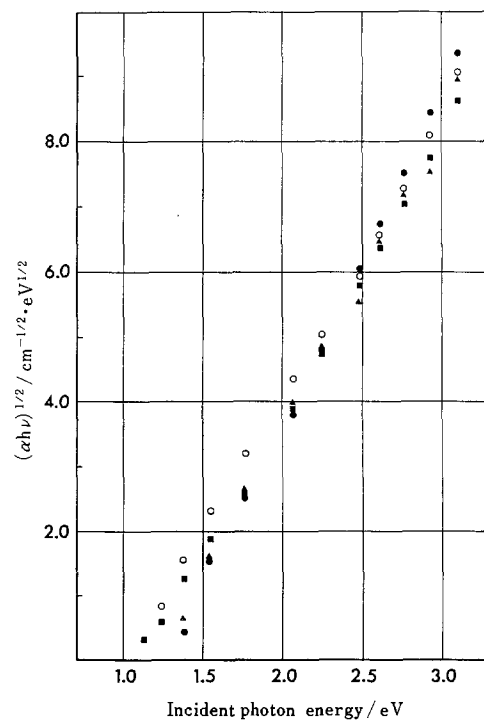


Fig. 12. The absorption edge fitted to the indirect allowed transition.

sorption edge E_g for the indirect allowed transition can be described as a function of the photon energy $h\nu$

$$\alpha h\nu \propto (h\nu - E_g)^2 \quad [9]$$

The variation of the square root of adsorption coefficient multiplied by photon energy $(\alpha h\nu)^{1/2}$ for the boron films with the incident photon energy is shown in Fig. 12. The figure shows that the boron film is an indirect energy-gap type material. The energy gap E_g is estimated to be 1.28 ± 0.08 eV by extrapolation of the linear part to the horizontal axis in Fig. 12. This value is larger than the value obtained by the electrical measurement (1.07 eV) and the values reported for amorphous films by Adirovich (19) and Morita (14).

The refractive index n and the extinction coefficient k of the boron films are shown as a function of wavelength in Fig. 13 and 14, respectively. These results agree well with the values obtained by Murphy (9) and Morita (14) for amorphous films deposited by vacuum evaporation. The hillock of the refractive index at the wavelength around $1 \mu\text{m}$ corresponds to the absorption edge. An increase in the extinction coefficient is also shown at wavelengths below $1 \mu\text{m}$.

Figure 15 shows the infrared transmission spectrum of the boron film deposited on a silicon substrate. As shown in Fig. 15, the absorption of the boron film in the IR spectral region increases at about $8 \mu\text{m}$ and reaches a maximum at $12.5 \mu\text{m}$. Blum (30) has studied the effect of impurities such as carbon and hydrogen on the infrared absorption of amorphous boron films and has shown that the narrow band at 2560 cm^{-1} observed in hydrogen-doped samples is due to B-H bond vibration. Also, the broad strong band from 1000 to 1200 cm^{-1} , which is correlated strongly with the amount of carbon in the films, is due to an overlapping and broadening of various B-C bond vibrations. Therefore, the absorption band from 8 to $12.5 \mu\text{m}$ observed in our films is not considered to be due to hydrogen and carbon impurities. Although many absorption bands caused by the complex crystal structure of boron have been reported, they are all in the wave-

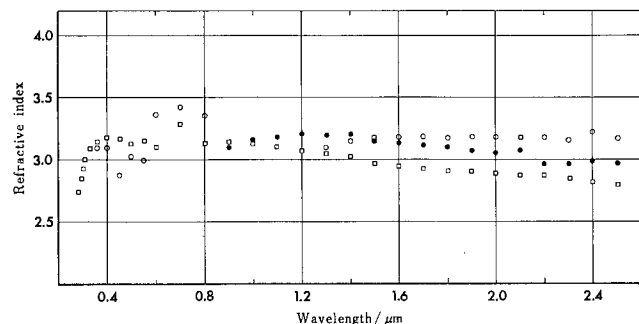


Fig. 13. Refractive index of pyrolytic boron films as a function of wavelength.

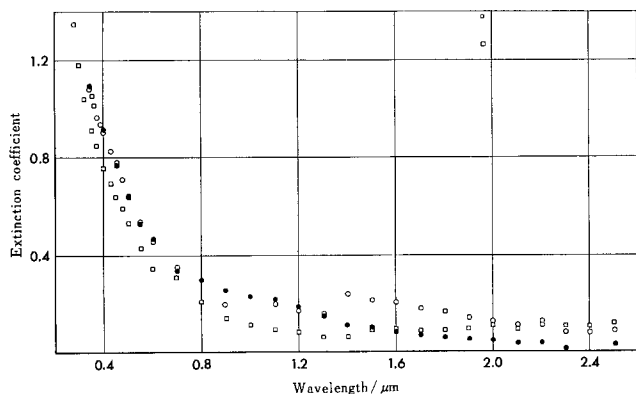


Fig. 14. Extinction coefficient of pyrolytic boron films as a function of wavelength.

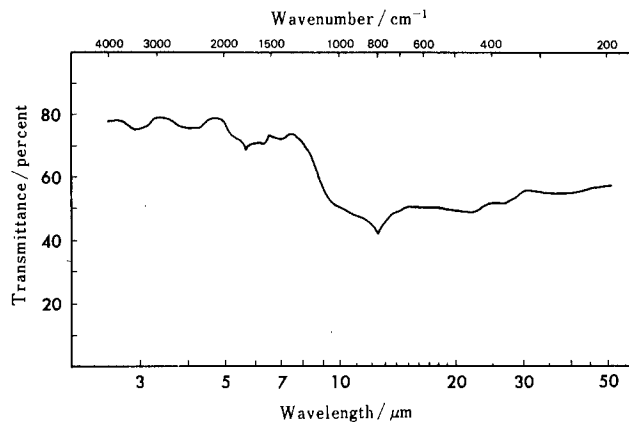


Fig. 15. Infrared transmission spectrum of a pyrolytic boron film deposited on a silicon substrate.

length region shorter than $8 \mu\text{m}$ (31). Werheit *et al.* (32, 33) have studied the optical properties of β -rhombohedral boron single-crystals in detail and have shown that absorption has a peak at $8 \mu\text{m}$. According to Decker (34), the absorption spectra of α -rhombohedral boron have absorption peaks at 18.2 , 10.9 , 9.3 , and $8.2 \mu\text{m}$. These absorption bands are not in agreement with those observed for boron films deposited by pyrolysis of the decaborane. On the basis of studies made by Golikova (21), it can be considered that the absorption at $12.5 \mu\text{m}$ is associated with the short-range lattice structure in the boron films.

Conclusion

Amorphous boron films have been deposited by pyrolysis of decaborane in the molecular flow region. On the assumption that the deposition rate of boron films is determined by the impingement frequency of the decaborane molecules onto the substrate surface, we have derived the equation for the deposition rate D at temperatures lower than 416°C . The equation, $D = 7.16 \times 10^9 \cdot P \cdot \exp(-39000/RT_s)$ (cm/s), explains the experimental results successfully.

Electrical conductivity of these boron films is $\approx 10^3$ larger than that for single-crystal boron and is in agreement with that for amorphous films deposited by CVD and vacuum evaporation. The influence of impurities on the conductivity is not clear. The activation energy for conduction of the boron films is estimated to be 1.07 eV in the intrinsic temperature range. The temperature dependence of the electrical conductivity can also be explained by a hopping conduction mechanism of amorphous materials. The plots of $\log \sigma$ against $T^{1/4}$ show a good linear relation, and the density of localized states at the Fermi level, $N(E_F)$, is estimated to be $3.8 \times 10^{18} \text{ cm}^{-3} \cdot \text{eV}^{-1}$. However, we cannot decide which mechanism is valid within our experimental accuracy.

The thermoelectric power of the boron films obtained shows a small peak at a higher temperature, compared with those for bulk boron. This may be attributed to the fact that the concentration of the acceptors in amorphous boron films is higher than that in boron crystals.

From the measurements of optical absorption, it is found that boron films are an indirect bandgap type material and have an energy gap of 1.28 ± 0.08 eV. The refractive indexes and the extinction coefficients of the boron films in the wavelength range of 0.27 - $2.5 \mu\text{m}$ were obtained. In the infrared spectral region, an absorption peak was observed at $12.5 \mu\text{m}$, which is considered to be associated with short-range order in the boron lattice.

Acknowledgments

The author would like to thank Professor K. Yoshimura and A. Itoh for suggesting this study and for their continuous encouragement. He wishes to express his thanks to S. Nakagawa, S. Misawa, and Dr. S. Gonda for helpful contributions and support of this work. Numerous valua-

ble and stimulating discussions with Professor A. Amano, Dr. S. Yoshida, and Dr. F. Shinoki are also acknowledged with many thanks.

Manuscript submitted Oct. 25, 1983; revised manuscript received May 15, 1984.

Nihon University assisted in meeting the publication costs of this article.

REFERENCES

- H. Werheit, *Festkoerperprobleme*, **10**, 189 (1970).
- O. A. Golikova, *Phys. Status Solidi A*, **51**, 11 (1979).
- W. C. Shaw, *Phys. Rev.* **107**, 419 (1957).
- L. Vandenbulke and G. Vuillard, *This Journal*, **123**, 278 (1976).
- J. O. Carlsson, *J. Less-Common Met.*, **70**, 69 (1980).
- M. Prudenziati, *Thin Solid Films*, **36**, 97 (1976).
- V. S. Postnikov, *J. Less-Common Met.*, **47**, 255 (1976).
- J. S. Lannin, *Solid State Commun.*, **25**, 363 (1978).
- A. M. Murphy, *J. Opt. Soc. Am.*, **57**, 845 (1967).
- W. J. Croft, *Mater. Res. Bull.*, **5**, 489 (1970).
- G. Caserta and A. Serra, *Thin Solid Films*, **20**, 91 (1974).
- C. Feldman, H. K. Charler, Jr., F. G. Statkiewicz, and J. Bohandy, *J. Less-Common Met.*, **47**, 141 (1976).
- K. Moorjani and C. Feldman, *Electron Technol.*, **3**, 265 (1970).
- N. Morita and A. Yamamoto, *Jpn. J. Appl. Phys.*, **14**, 825 (1975).
- H. C. Beachell and J. F. Haugh, *J. Am. Chem. Soc.*, **80**, 2939 (1958).
- A. J. Owen, *J. Chem. Soc.*, **1961**, 5438.
- J. Cueilleron, J. C. Viala, F. Thevenot, C. Brodhag, J. M. Dusseal, and A. Elbiach, *J. Less-Common Met.*, **59**, 27 (1978).
- H. Werheit and H. G. Leis, *Phys. Status Solidi*, **41**, 247 (1970).
- E. I. Adirovich and L. M. Gol'dshtein, *Sov. Phys. Semicond.*, **3**, 196 (1969).
- Sh. Z. Dzhmagidze, Yu. A. Mal'tsev, and R. R. Shvangiradze, *ibid.*, **2**, 320 (1968).
- O. A. Golikova, D. N. Mirlin, A. S. Umarov, and T. Khomidov, *ibid.*, **7**, 1091 (1974).
- A. Zareba and M. Maszkiewicz, *Phys. Status Solidi A*, **3**, K207 (1970).
- N. F. Mott, *J. Non-Cryst. Solids*, **1**, 1 (1968); *Philos. Mag.*, **19**, 835 (1969).
- A. A. Berezin, O. A. Golikova, M. M. Kazanin, T. Khomidov, D. N. Mirlin, A. V. Petrov, A. S. Umarov, and V. K. Zaitsev, *ibid.*, **16**, 237 (1974).
- G. Majini and M. Prudenziati, *Phys. Status Solidi A*, **5**, K129 (1971).
- V. A. Johnson and K. Lark-Horonitz, *Phys. Rev.*, **92**, 226 (1953).
- O. A. Golikova, V. K. Zaitsev, V. M. Orlov, L. S. Stilbans, and F. S. Tkalenko, *Phys. Status Solidi A*, **21**, 405 (1974).
- G. A. Slack, D. W. Oliver, and F. H. Horn, *Phys. Rev. B*, **4**, 1714 (1971).
- O. A. Golikova, V. K. Zaitsev, A. V. Petrov, L. S. Stil'bonds, and E. N. Tkalenko, *Sov. Phys. Semicond.*, **6**, 1488 (1973).
- N. A. Blum, C. Feldman, and F. G. Satkiewicz, *Phys. Status Solidi A*, **41**, 481 (1977).
- O. A. Golikova, *Sov. Phys. Solid State*, **11**, 1341 (1969).
- J. Jaumann and H. Werheit, *Phys. Status Solidi*, **33**, 587 (1969).
- H. Werheit, A. H. Ausen, and H. Binnenbruck, *Phys. Status Solidi B*, **51**, 115 (1972).
- B. F. Decker and J. H. Kasper, *Acta Crystallogr.*, **13**, 1030 (1960).

Electrical Properties of Organometallic Chemical Vapor Deposited GaAs Epitaxial Layers

Temperature Dependence

Douglas H. Reep*¹ and Sorab K. Ghandhi*

Department of Electrical, Computer, and Systems Engineering, Rensselaer Polytechnic Institute, Troy, New York 12181

ABSTRACT

Electrical characteristics are presented for unintentionally doped GaAs epitaxial films, grown by the pyrolysis of trimethylgallium (TMG) and arsine at atmospheric pressure. The depositions were carried out on (100) substrates, from 450° to 1050°C, for a wide variety of growth conditions. Growth rates and morphology have been presented elsewhere. Films grown at 1050°C were found to be p-type, with the hole concentration falling at lower growth temperatures. Conversion to n-type occurred for growth below 975°C, independent of the arsine overpressure. At still lower temperatures, the film became increasingly n-type, with a peak in free electron concentration occurring at 850°C. Further reduction in growth temperature resulted in lower electron concentrations until eventually the films became p-type at around 550°C, depending on the arsine overpressure. The electrical behavior of these films correlates well with predictions from the growth model and thus provides additional insight into the organometallic growth process.

Much attention has been paid recently to the growth of thin epitaxial layers of GaAs by the organometallic CVD technique. Promising results have been obtained with the use of these layers for optoelectronic (1, 2), microwave (3, 4), and high speed digital applications (4). In addition, organometallic CVD grown layers which approach the purity and electron mobility of the best layers produced by the chloride-based techniques have been reported (4). The organometallic technique has also generated much interest due to its flexibility and its apparent simplicity.

Little has been published in regard to the mechanisms of growth by this process, as compared to the halide and hydride growth systems. In fact, the growth of GaAs films by this technique is generally described as a simple pyrolysis of trimethylgallium (TMG) and arsine. However, many complex processes and intermediate reactions are involved, and the subject is far from understood at the present time.

Recently, based on experiments employing different substrate orientations [(100), (110), (111)Ga, and (111)As] performed over a wide range of temperatures (450°-1050°C), we have proposed (5, 6) a growth model for this process. A brief review of this model is as follows: the dis-

*Electrochemical Society Active Member.

¹Present address: General Electric Company, Electronics Laboratory, Syracuse, New York 13221.

sociation activation energy for the first, second, and third (Ga-CH₃) bonds is 59.5, 35.4, and 77.5 kcal/mol, respectively (7). This fact, together with an analysis of the rate constant data for this dissociation, leads to the conclusion that the rate limiter for the thermal decomposition of TMG is in all probability the breaking of the last (Ga-CH₃) bond. Studies of the decomposition of AsH₃, in like manner, lead to the conclusion that the primary surface-adsorbed arsenic species is (As-H). The growth model which we have described is the result of a Langmuir-Hinshelwood-type reaction involving these species. Although the actual reactions which take place are very complex, and are still the subject of much controversy, this relatively simple model fits the observed growth characteristics for a wide range of crystal orientations, reactant partial pressures, and growth temperatures. Thus, it serves as a useful starting point for developing further insight into the growth process. In this paper, we describe the electrical characteristics of these layers. It is shown that they, too, can be explained in terms of this growth model. Thus, they provide support for it and help in its further development.

Experimental Procedure

Epitaxial layers of GaAs were deposited by the pyrolysis of arsine and trimethylgallium (TMG), using hydrogen as the carrier gas. Anhydrous hydrogen chloride was available for *in situ* etching of the substrates prior to layer growth. Layer deposition was performed at temperatures from 450°-1050°C, for input TMG partial pressures ranging from 4.6 to 37 × 10⁻⁵ atm. The arsine flow was varied over a wide range, corresponding to AsH₃/TMG ratios of 4.7-75 at the reactor inlet. The hydrogen carrier gas flow through the reaction chamber was fixed at 5 l/min for all of the data reported here.

Single-crystal, semi-insulating GaAs substrates^{2,3} used in this study were (100) oriented or 3° off (100) towards the [110] direction, and were received lapped and chem-mechanically polished on one side. Prior to loading into the epitaxial reactor, the wafers were degreased sequentially in trichloroethylene, acetone, and methanol. A chemical polishing etch of 1 min duration in hot (60°C) Caro's etch (H₂SO₄:H₂O₂:H₂O = 3:1:1 by volume) produced mirror-like surfaces, and removed 15-25 μm of material from the substrate surface. The substrates were quenched in DI water immediately following removal from the Caro's etch, rinsed with methanol, and blown dry in filtered nitrogen.

The epitaxial reactor consisted of an atmospheric pressure, horizontal, RF-heated, cold wall system of the type described previously (8). Gases were delivered to the 50 mm id quartz reaction chamber through 316 stainless steel or Monel tubing. The substrate temperature was monitored with a Pt/Pt-13% Rh thermocouple, sheathed in quartz, and inserted into a well in the back of the graphite susceptor.

A 10% mixture of arsine⁴ in hydrogen was used in this work. TMG⁵ vapor was provided by bubbling hydrogen through this liquid, which was held at 0°C in a stainless steel bubbler. A 1% mixture of electronic-grade hydrogen chloride in hydrogen⁴ was available for *in situ* etching of the substrates. Ultrapure hydrogen carrier gas was obtained by passing commercial-grade hydrogen⁴ through a Pd-Ag alloy purifier. In all cases, the reactant gases were thoroughly mixed prior to entry into the reaction chamber.

The substrate wafers were loaded into the reactor after chemical etching and microscopic inspection of the surface. The reaction chamber was evacuated and purged with argon,⁴ followed by hydrogen gas. Next, the required flows of hydrogen and arsine were set. For experiments involving an *in situ* etch prior to growth, the susceptor

was heated and stabilized at the etch temperature (typically 945°C). After a period of 5 min, which was sufficient to remove any surface oxide left by the chemical cleaning procedure (9), the wafers were given an *in situ* etch of the type described previously (10). The temperature of the susceptor was then reset and allowed to stabilize at the growth temperature for 2 min prior to commencement of growth by the introduction of the TMG vapor.

For experiments where no *in situ* etch was performed, the susceptor was heated to the growth temperature⁶ and stabilized there for a period of 5 min, before the TMG flow was established. At the end of the growth interval, the TMG flow was terminated, and the system held at the growth temperature for an additional 3 min. The susceptor and substrates were then cooled to 200°C in the AsH₃/H₂ ambient, followed by an argon purge of sufficient duration for the susceptor to reach room temperature.

The growth rate of the epitaxial layer was determined either by weight change, in the case of no pregrowth *in situ* etch, or by cleaving and staining, followed by inspection with an optical microscope fitted for Nomarski differential interference contrast. Surface morphology was studied using scanning electron microscopy.

The free carrier concentration and mobility of the GaAs films were measured using the Hall effect. In particular, the van der Pauw technique was employed. All of the results presented are calculated directly from the Hall coefficient, following the common practice of assigning a unity value to the scattering factor (*i.e.*, $r_H = 1$). Ionized acceptor and donor concentrations were determined from the free carrier and mobility measurements (11) at liquid nitrogen temperature (77 K) for the n-type layers.

Results and Discussion

Only the (100) orientation was considered, because of the extreme difficulty of growing device-quality layers of other orientations by OMCVD. Moreover, a study of this orientation is of greatest interest, since it is commonly used in device fabrication. All of the (100) layers (oriented as well as misoriented) exhibited smooth, specular surfaces over the full range of deposition temperatures. Moreover, the morphology was found to be essentially in-

⁶A minimum of 700°C was used for the pregrowth heat-treatment, as this is sufficient to remove any traces of surface oxide (9). Thus, for the depositions performed below 700°C, the susceptor temperature was dropped (from 700°C) and allowed 2 min to stabilize at the growth temperature.

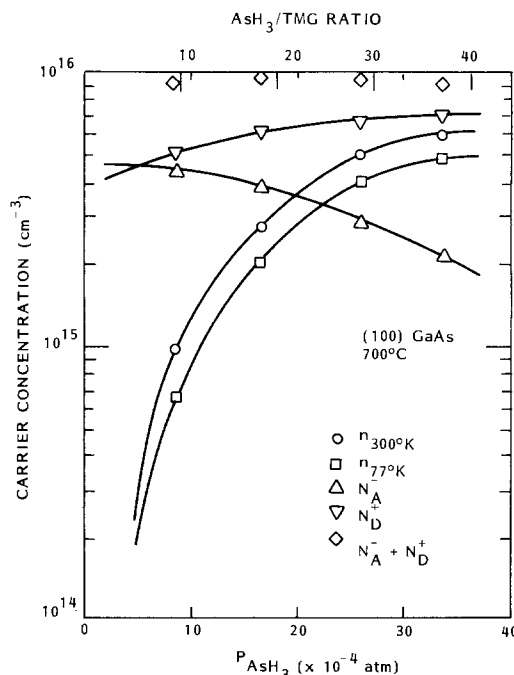


Fig. 1. Carrier concentration vs. p_{AsH_3} for (100) GaAs epitaxial layers grown at 700°C.

²Crystal Specialties, Incorporated, Monrovia, California 91016.

³Cambridge Instruments, Incorporated, Monsey, New Jersey 10952.

⁴Air Products, Tamaqua, Pennsylvania 19252.

⁵Alpha Products, Danvers, Massachusetts 01923.

dependent of the reactant flows over this temperature range, as was observed (6) for film growth at 700°C.

The majority of the epitaxial layers were grown for this investigation on substrates which were given no *in situ* etch, so that reliable growth rate data could be obtained. All of the data reported here were taken on layers which were 5-6 μm thick, so that the electrical measurements were not affected by the inclusion, or absence, of this etch step.

The electrical data reported here were made on samples grown using one lot of TMG and one cylinder of AsH_3 , so that meaningful comparisons could be made. In addition, the nature of the contaminants in the starting materials was first determined so that the results could be meaningfully interpreted.

Figure 1 shows the electrical properties of undoped samples grown at 700°C as a function of the arsine overpressure. Here, it is seen that N_D (the ionized donor concentration) increases with arsine pressure, where N_A (the ionized acceptor concentration) falls. These results are what would be expected if the primary contaminant in the starting chemicals came from column IV of the periodic table. Moreover, $(N_A + N_D)$ is independent of arsine pressure for these samples, indicating that the contaminant comes mainly from the TMG source, whose partial pressure was held constant for this series of experiments. Thus, to a first order, the inherent contaminant in the combination of starting chemicals used here can be attributed to column IV impurities⁷ related to the TMG, with relatively little contamination coming from the arsine. It is probable that silicon is this contaminant in our case, as this was detected by metallic impurity analysis.⁸ It has been shown that this dopant, although amphoteric, always results in n-type material in the OMCVD of GaAs (12).

We have proposed a growth model (5) based on the results of measurements made over a wide range of temperature, reactant partial pressures, and crystal orientations. Growth data, taken for the purpose of model development, is presented in Fig. 2 for the (100) orientation, and for AsH_3/TMG inlet pressure ratios from 9.3 to 36.9. A study of this figure, in the light of the growth model we have proposed, shows the following features: (i) at high temperatures (above the point A at 850°C), growth is limited by the desorption of (Ga-CH_3) from the surface since the presence of the methyl radical significantly reduces the effective Ga-As bond strength. The temperature at which the growth rate fall-off occurs is independent of the AsH_3/TMG ratio. (ii) At low temperatures, (below the point B at 600°C), the growth is limited by the decomposition of arsine, and by the increased desorption of (Ga-CH_3) resulting from this effect. (iii) Growth in the mid region, between A and B, is relatively independent of the temperature or the AsH_3/TMG ratio. Although this region is important from a device viewpoint, it sheds little light on the growth mechanism since diffusion through the boundary layer is the limiting factor, as opposed to surface dependent effects.

Figure 3 shows the electrical characteristics of layers grown on (100) GaAs for AsH_3/TMG ratios of 37, 19, and 9.3, respectively. (Here, the points A and B are the same as those indicated in Fig. 2.) As mentioned earlier, these divide the growth into three regions, which are now considered.

The high temperature region.—Here, falloff in carrier concentration (and peak value as well) occurs at the same temperature for all reactant partial pressure ratios. Even-

⁷As a point of interest, the usual situation at the present state of the art is that the TMG is considered to be relatively pure, and the contaminant is thought to come primarily from the arsine source. However, this was not the case with the sources used here. In fact, this controversy has received additional fuel recently with the identification of Ge as the dominant residual acceptor impurity in OMCVD GaAs, which as indeed traced to the TMG in at least one case (13).

⁸Contaminant data for TMG was 1 ppm Si, 2 ppm Al, and 1 ppm Fe with Mg and Zn not detectable. Data on the AsH_3 was not available.

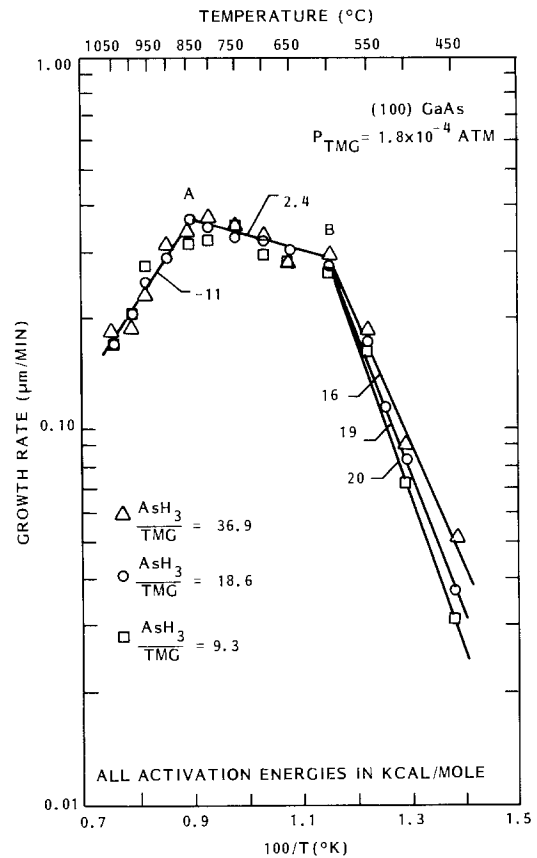
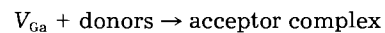


Fig. 2. Growth rate vs. reciprocal temperature for (100) GaAs epitaxial layers, as a function of P_{AsH_3} and for $P_{\text{TMG}} = 1.8 \times 10^{-4}$ atm.

tually, the layer becomes p-type, at a conversion temperature which is also independent of the AsH_3/TMG ratio. This behavior can be explained as follows: both the gallium and arsenic vacancy concentrations increase with increasing temperature, from thermodynamic considerations (14, 15). Additionally, however, the V_{Ga} increases because of increasing desorption of (Ga-CH_3) as postulated in our previous growth model; this in turn leads to increased acceptor formation, by the well-established complexing reaction of gallium vacancies and donors



which has been confirmed by various workers (15, 16). Results of their annealing experiments on n-doped GaAs are reproduced in Fig. 4, and indicate that acceptor formation by this reaction is significant and can result in converting the layers to p-type. Moreover, the acceptor concentration is not a function of the arsenic overpressure for the range of growth conditions ($p_{\text{AsH}_3} \approx 1-5$ torr) reported in this paper. Hence, we can expect the falloff in electron concentration, as well as the conversion temperature (n \rightarrow p) to be independent of p_{AsH_3} . Note that the data of Fig. 4 are for thermal annealing of bulk samples for long times (8-16h). We believe the analysis is applicable to this situation as well, since the layer growth is carried out in a strong excess arsine overpressure environment.

Our model leads us to conclude that this falloff in growth rate is primarily due to increased desorption of (Ga-CH_3) . As a result, carbon contamination is most probably not the dominant factor at elevated temperatures. This has been verified by secondary ion mass spectroscopy (SIMS) data taken on a layer grown at 1000°C, and shown in Fig. 5. Here, the carbon level in the sample is the same as that of the substrate (except for a small perturbation at the epi-substrate interface).⁹ Thus, the amount of carbon incorporated during growth at these el-

⁹Layers grown with an *in situ* HCl etch did not show this peak. All the SIMS results in this paper are for layer growth without this etch step.

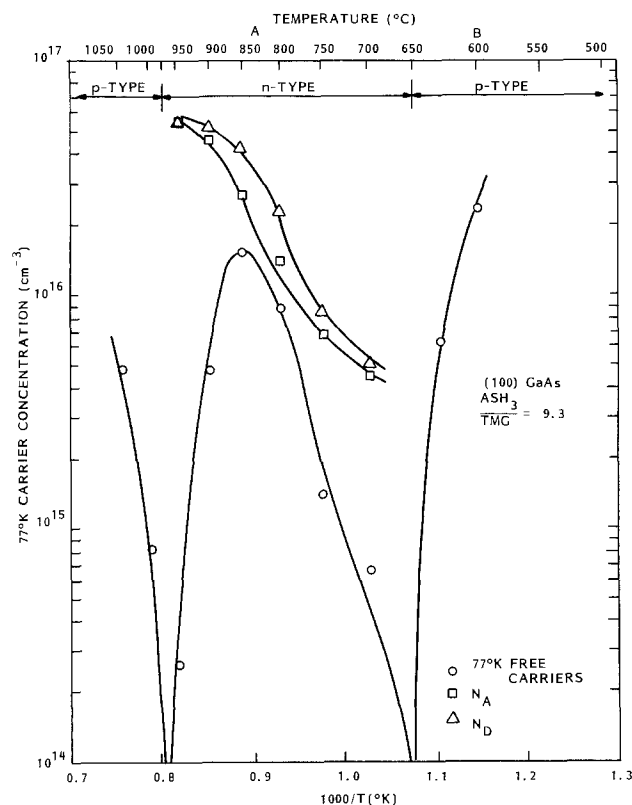
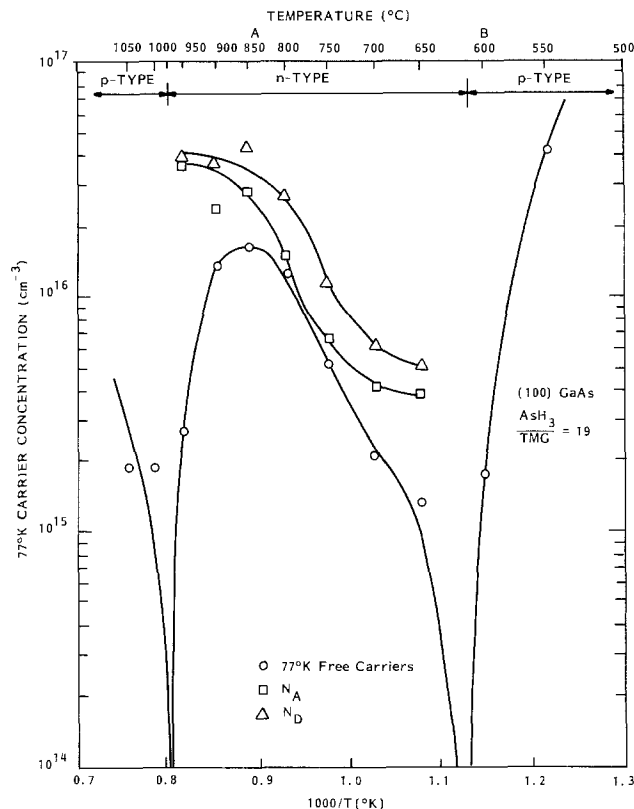
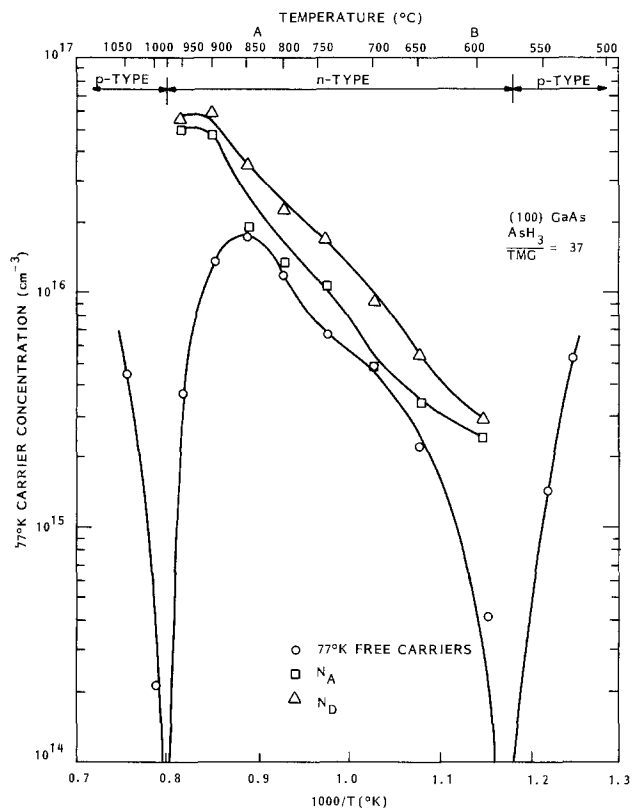


Fig. 3. 77 K carrier concentration vs. reciprocal temperature for (100) GaAs layers grown at $P_{\text{TMG}} = 1.8 \times 10^{-4}$ atm. a(top left): $P_{\text{AsH}_3} = 6.7 \times 10^{-3}$ atm. b(top right): $P_{\text{AsH}_3} = 3.3 \times 10^{-3}$ atm. c(left): $P_{\text{AsH}_3} = 1.7 \times 10^{-3}$ atm.

evated temperatures is below the detectability limit of the SIMS.

Low temperature region.—Here we note that the electron concentration falls for temperatures below A (Fig. 3a), with the layers eventually becoming p-type in the vicinity of, or slightly above, point B. This behavior differs from that in the high temperature region in many important respects. First, the $n \rightarrow p$ conversion point is a strong function of the arsine overpressure, and occurs at higher temperatures as p_{AsH_3} is decreased (Fig. 3b, 3c). Next, films grown at low temperatures are not entirely single

crystal in nature, with strong evidence of twinning noted by x-ray diffraction analyses (but were still shiny). Finally, there is direct evidence of a large amount of carbon incorporation in these films, as seen from the SIMS data of Fig. 6.

We believe that these observations can be explained as follows: the decomposition rate of arsine, and hence the arsenic overpressure, falls with falling temperature. This results in an increased residence time of (Ga-CH_3) on the surface of the slice, and an increased possibility of the strongly bonded carbon incorporating in the film. More-

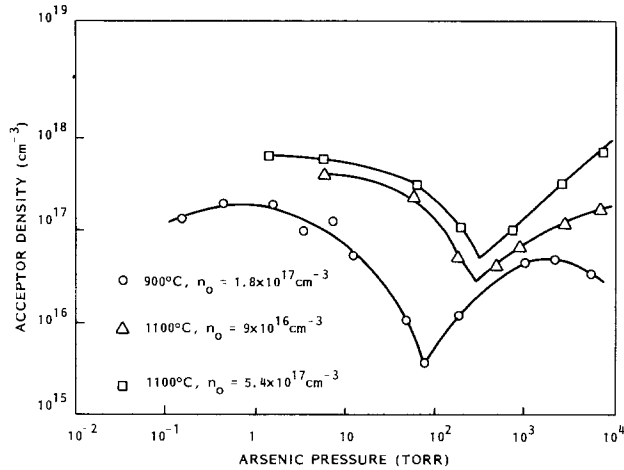


Fig. 4. Acceptor density in heat-treated n-type GaAs, as a function of arsenic overpressure, annealing temperature, and initial free electron concentration. After Ref. (15).

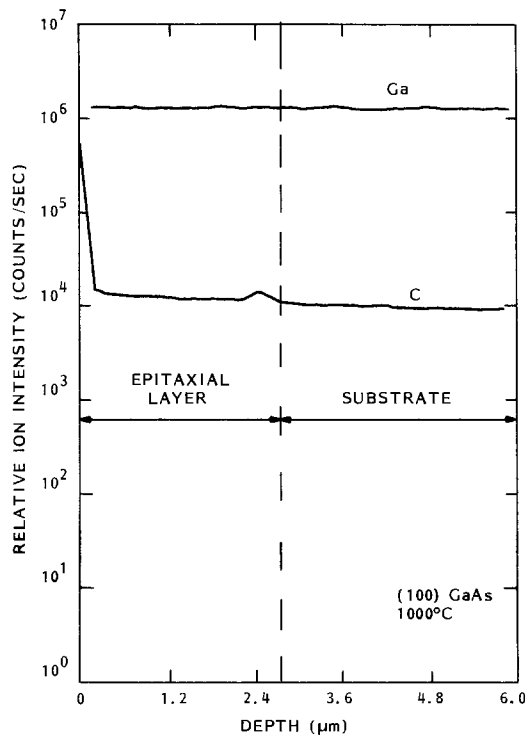


Fig. 5. SIMS trace of relative ion intensity for gallium and carbon vs. depth into sample, for a 2.7 μm thick (100) GaAs epitaxial layer grown at 1000°C.

over, the reduction in effective arsenic overpressure at these temperatures increases the possibility of incorporating this carbon into arsenic sites, (increased V_{As} in this case) where it behaves as an acceptor and, in sufficient concentration, causes the layers to grow p-type. Finally, following the reactant attachment scheme previously proposed (6), we expect the methyl radical to occupy an arsenic site until the (Ga-CH₃) bond is broken, again supporting the high probability of carbon acceptor incorporation for low temperature growth.

Mid temperature region.—Here, both N_A and N_D fall with temperature. However, growth occurs in an excess arsenic overpressure, so that there is a net reduction in ($N_D - N_A$) with falling temperature. We believe that this explains the change in carrier concentration that we note over this temperature region, consistent with other reports in the literature (4, 17). Note, however, that an analysis of electrical behavior in this region sheds little light on the growth model, since the actual growth process is limited by diffusion through the boundary layer at these tem-

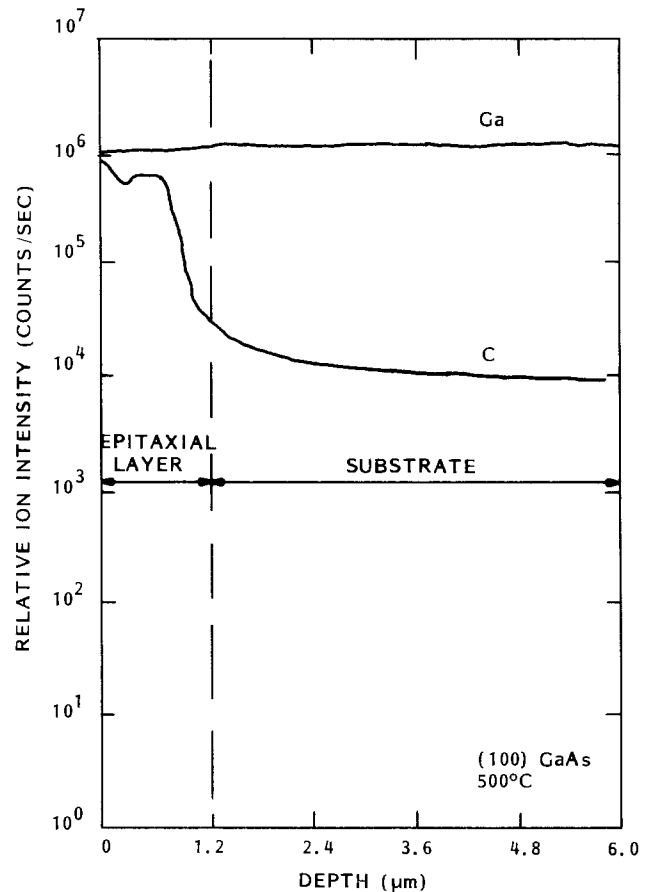


Fig. 6. SIMS trace of relative intensity for gallium and carbon vs. depth into sample for a 1.2 μm thick (100) GaAs epitaxial layer grown at 500°C.

peratures, and is independent of surface-related phenomena.

Summary

Gallium arsenide layers have been grown over a wide range of input reactant partial pressures, and for a broad range of deposition temperatures. Electrical properties of these layers have been measured, and are described in this paper. Reasons for their behavior with temperature and reactant partial pressure have been advanced; it has been shown that the observed behavior can be explained in terms of a growth model proposed earlier.

Conversion from n to p at high temperatures (> 975°C) is shown to result from an increased desorption of (Ga-CH₃) at these temperatures, and from acceptor formation by the gallium vacancy-donor reaction. Moreover, carbon incorporation is relatively unimportant at these temperatures, as compared to the complexing reaction.

It has also been shown that the electrical characteristics of films grown in the low temperature region shift from n → p type with falling temperature. This behavior can be explained by noting that arsine decomposition falls off at low temperatures, resulting in an increased possibility of carbon incorporation in the films. Evidence for this increased carbon incorporation is presented as well.

The electrical measurements thus support the growth model proposed earlier, and help to provide further insight into the growth process.

Acknowledgments

The authors wish to thank A. Hayner for manuscript preparation, and Dr. W. Katz, General Electric CRD, Schenectady, New York, for SIMS analysis. This work was supported by the Solar Energy Research Institute, Golden, Colorado, under Contract no. XS-0-9002-4. This support is gratefully acknowledged.

Manuscript submitted Feb. 6, 1984; revised manuscript received May 10, 1984.

Rensselaer Polytechnic Institute assisted in meeting the publication costs of this article.

REFERENCES

1. R. R. Bradley, *J. Cryst. Growth*, **55**, 223 (1981).
2. J. P. Andre, P. Guittard, J. Hallais, and C. Paiget, *ibid.*, **55**, 235 (1981).
3. M. Bonnet, N. Visentin, G. Bessonneau, and J. P. Duchemin, *ibid.*, **55**, 246 (1981).
4. T. Nakanisi, T. Udagawa, A. Tanaka, and K. Kamei, *ibid.*, **55**, 255 (1981).
5. D. H. Reep and S. K. Ghandhi, *This Journal*, **130**, 675 (1983).
6. D. H. Reep and S. K. Ghandhi, *J. Cryst. Growth*, **61**, 449 (1983).
7. M. G. Jacko and S. J. W. Price, *Can. J. Chem.*, **41**, 1560 (1963).
8. B. J. Baliga and S. K. Ghandhi, *This Journal*, **122**, 683 (1975).
9. M. Otsubo, T. Oda, S. Mitsui, and H. Miki, *ibid.*, **124**, 1970 (1977).
10. R. Bhat, B. J. Baliga, and S. K. Ghandhi, *ibid.*, **122**, 1378 (1975).
11. G. E. Stillman and C. M. Wolfe, *Thin Solid Films*, **31**, 69 (1976).
12. S. J. Bass, *J. Cryst. Growth*, **47**, 613 (1979).
13. G. E. Stillman, Personal communication (Jan. 1984).
14. R. M. Logan and D. T. J. Hurle, *J. Phys. Chem. Solids*, **32**, 1739 (1971).
15. D. T. J. Hurle, *ibid.*, **40**, 613 (1979).
16. J. Nishizawa, H. Otsuka, S. Yamakoshi, and K. Ishida, *Jpn. J. Appl. Phys.*, **13**, 46 (1974).
17. S. J. Bass and P. E. Oliver, in "Gallium Arsenide and Related Compounds, 1976," p.1, Institute of Physics Conference Series, Institute of Physics, London (1977).

Low Pressure Chemical Vapor Deposition of Tungsten on Polycrystalline and Single-Crystal Silicon via the Silicon Reduction

K. Y. Tsao^{1,*} and H. H. Busta^{**}

Gould Research Center, Rolling Meadows, Illinois 60008

ABSTRACT

High purity metallic tungsten films are deposited on phosphorus-doped and undoped polycrystalline and single-crystal silicon by the silicon reduction of WF_6 . Depositions are performed in a commercial LPCVD hot wall reactor at temperatures ranging from 310°-540°C. Film formation is self-limiting, meaning that after a given film thickness any further reaction between WF_6 and the underlying silicon is inhibited. Obtainable film thickness depends strongly on the doping condition of silicon and on surface preparation prior to LPCVD. Conventional wet chemical cleaning limits the maximum obtainable film thickness to approximately 400Å, whereas with a low power argon plasma treatment approximately 900Å thick films can be obtained reproducibly. The resistivity of these films is $18.3 \pm 4.5 \mu\Omega\text{cm}$. This corresponds to a minimum sheet resistance of the thickest films of approximately $2 \Omega/\square$. The depositions are completely selective; no detectable amount of tungsten can be observed on thermal field oxide.

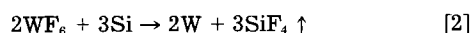
Low pressure chemical vapor deposition (LPCVD) of tungsten is currently under intense investigation for its potential application in VLSI circuits. These include shunting of polycrystalline silicon gate and interconnect lines with a lower resistivity tungsten film to reduce the interconnect RC time constant (1, 2), formation of a barrier between silicon and aluminum to reduce aluminum spike-induced failures (2, 4), planarization of the multilevel interconnect process (3, 4), low resistance contact formation to drain and source regions (1, 4), and formation of a Schottky barrier p-channel MOS transistor to form latch up-free CMOS (4).

An attractive feature of LPCVD tungsten is its selectivity. For appropriate deposition conditions, tungsten forms only on silicon and not on surrounding thermally grown SiO_2 . Thus, for polycrystalline gate shunting this eliminates one etching step in the processing sequence, as compared to shunting with a sputter-deposited silicide. However, some nucleation of tungsten can occur on thermally grown SiO_2 when films in excess of 2000Å are deposited (5) or when the SiO_2 is formed by sputter deposition, plasma-assisted CVD, or on borophosphosilicate glass (BPSG) (3).

Tungsten can be deposited via the hydrogen reduction of WF_6 (1-3, 6, 7, 9)



or the silicon reduction of WF_6 (3, 7-9)



With the hydrogen reduction, films of any thickness can be deposited, whereas with the silicon reduction the reaction ceases after formation of a given film thickness, because WF_6 cannot further react with the underlying silicon (9). Even in the hydrogen reduction, initial film growth proceeds via silicon reduction (3).

Since, according to reaction [2], 3 mol of silicon are needed to create 2 mol of tungsten, a certain thickness loss of silicon is experienced. It is given by

$$\frac{t_w}{t_{Si}} = \frac{2M_w \rho_{Si}}{3M_{Si} \rho_w} = 0.525 \quad [3]$$

and has to be taken into account during the device design stages. Here, t_w is the tungsten film thickness to be formed, t_{Si} the silicon thickness to be consumed, M_w , M_{Si} the molecular weights, and $\rho_w = 19.35 \text{ g/cm}^3$ and $\rho_{Si} = 2.33 \text{ g/cm}^3$ the densities of tungsten and silicon, respectively. Experimental verification of this fact is reported in Ref. (9).

In this paper, the LPCVD of tungsten using the silicon reduction method will be presented. The substrates are phosphorus-doped and undoped polycrystalline silicon and phosphorus-doped and undoped p-type single-crystal silicon.

The success of the LPCVD method in terms of obtaining reproducible films depends strongly on the surface preparation prior to film deposition (3) and hence on the native oxide characteristics (9). With the silicon reduction method, approximately 400Å thick films can be achieved at 350°C (3). By using standard wet chemical cleaning procedures we confirmed this result. With the addition of a low power argon plasma treatment, 900Å thick films can be deposited reproducibly with a sheet resistance of approximately $2 \Omega/\square$. Film properties as a

* Electrochemical Society Member Representative.

** Electrochemical Society Active Member.

¹ Current address: AT&T Teletype Corporation, Skokie, Illinois 60077.

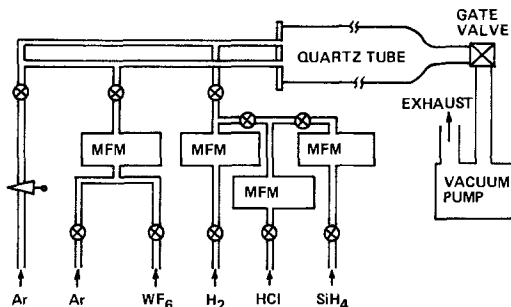


Fig. 1. Schematic of the LPCVD apparatus

function of the argon plasma treatment and deposition parameters such as WF_6 flow rate, deposition time, and deposition temperature will be presented in the following sections.

Experimental

The apparatus used for the depositions is a commercially available 4 in. hot-wall LPCVD quartz reactor whose plumbing system has been modified to allow Ar, WF_6 , H_2 , HCl, and SiH_4 to enter the system through mass flowmeters (MFM). This is indicated in Fig. 1. Not shown in Fig. 1 is a heating tape wrapped around the WF_6 cylinder, the gas lines, and the mass flowmeter. This is necessary to prevent the WF_6 from liquifying. The temperature of the WF_6 is controlled to provide a pressure of approximately 7-10 psi.

Argon is used as a carrier gas with a flow rate of 335 cm^3/min and a pressure of 0.3 torr. For most experiments, the WF_6 flow rate is 12.4 cm^3/min . In some cases, where the sheet resistance as a function of flow rate is determined, it is varied from 1.55 to 24.8 cm^3/min . Deposition temperatures range from 310° to 540°C.

Sample preparation consists of growing approximately 1000Å of thermal SiO_2 on 3 in. diam silicon wafers. Approximately 4500Å thick polycrystalline silicon is then deposited via LPCVD at 610°C. For the phosphorus-doped samples, doping is performed at 950°C in PH_3 for 50 min, resulting in a sheet resistance of approximately 24 Ω/\square .

The single-crystal (100) p-type wafers used in this work have a boron concentration of approximately $2 \times 10^{15} cm^{-3}$. Doping is performed at 950°C in PH_3 for 50 min. This is followed by an *in situ* nitrogen anneal for 10 min, which results in a sheet resistance of approximately 15 Ω/\square .

For selectivity studies, standard photolithographic methods are used to delineate the polycrystalline silicon lines into the appropriate patterns. After photoresist (AZ1450J) stripping, the samples are cleaned at 95°C for 10 min in a mixture of three parts H_2SO_4 and one part H_2O_2 . This is followed by a 6s 10:1 HF etch, followed by a DI rinse and nitrogen spin dry.

Loading of the samples takes place within several minutes after the argon plasma treatment. The LPCVD reactor is at deposition temperature and is purged with argon at approximately 3 liter/min. After loading and sealing, the system is pumped to approximately 0.03 torr and then refilled with argon to approximately 1 torr. This is followed by one more pumping and refilling cycle. The argon flow and chamber pressure are then adjusted to the appropriate values. WF_6 is then metered into the system. After deposition, the WF_6 flow is turned off and the system is allowed to cool to approximately 250°C, at which point the wafers are removed from the system.

A conventional stylus thickness monitor and the Auger elemental depth profiling technique are used for film thickness evaluations and a four-point probe for sheet resistance measurements. For the stylus measurements, a tungsten step is etched using positive photoresist or protective wax and an alkaline ferricyanide solution at room temperature to etch the tungsten. The solution consists of 5g $K_3Fe(CN)_6$, 5g KOH, and 100 ml DI water. All the

samples are being etched for 1 min. After tungsten etching, the photoresist or wax are being stripped.

Results and Discussion

Polycrystalline silicon substrates.—Surface plasma treatment.—Initial experiments have been performed using the H_2SO_4/H_2O_2 and HF clean prior to the tungsten deposition. Depending on the surface conditions, *i.e.*, ion implanted *vs.* nonimplanted, different sheet resistances for identical deposition parameters have been obtained. From this, it has been conjectured that formation of a uniform distribution of nucleation sites will aid in the initiation of the surface reaction. Several wet and dry surface treatments have been investigated, and good results have been obtained with a short, low power argon plasma treatment in a barrel plasma etching system from which the shielding tunnel is removed. Some of the results are shown in Fig. 2. It shows five samples deposited at 410°C for 5 min at a WF_6 flow rate of 12.4 cm^3/min . Sample A is a phosphorus-implanted (50 keV, $5 \times 10^{15} cm^{-2}$) polycrystalline silicon substrate, sample B is the same as A except it is annealed in N_2 at 1000°C for 30 min after the implantation, sample C is phosphorus-doped polycrystalline silicon, sample D is undoped polycrystalline silicon, and sample E phosphorus-doped p-type single-crystal silicon. Sheet resistances range from approximately 5 to 24 Ω/\square , indicating a strong sensitivity of film formation to surface conditions. Sample F is from the same wafer as sample C but is subjected to a plasma treatment at 2W for 5 min. The sheet resistance differences of the samples are caused by different film thicknesses. This has been experimentally confirmed by stylus measurements. The corresponding film thickness scale is indicated on the right side of Fig. 2.

The power dependence of the plasma treatment on film thickness formation (sheet resistance) is shown in Fig. 3. From 2 to 50W, no change in sheet resistance can be observed, indicating that even at the lowest power enough nucleation sites are being created on the polycrystalline surface for optimum film formation. Little dependence of sheet resistance on plasma treatment time in the range of 1-10 min is observed. Figure 4 shows the effect of a 2W, 5 min argon plasma treatment on the sheet resistance as a function of WF_6 flow rate for phosphorus-doped polycrystalline silicon. The top curve shows the results without the plasma treatment.

Below a flow rate of 6.2 cm^3/min , not enough WF_6 is supplied to fully react with the available silicon, thus

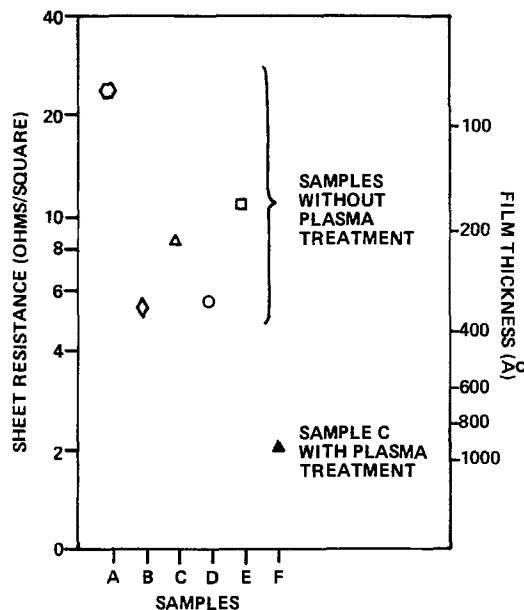


Fig. 2. Sheet resistance of tungsten films deposited on different samples with the silicon reduction method. Samples A to E are deposited without the plasma treatment. Sample F is part of the same substrate as sample C, but is being subjected to the plasma treatment.

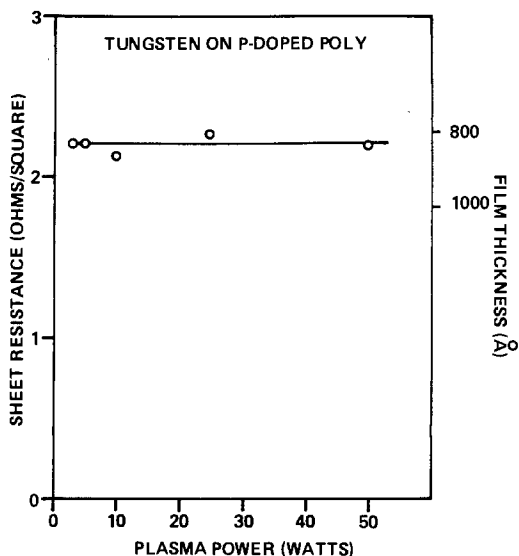


Fig. 3. Sheet resistance vs. argon plasma power for a phosphorus doped polycrystalline silicon sample. The tungsten deposition parameters are: 410°C, 5 min, WF_6 flow rate of 12.4 cm^3/min . The plasma treatment time per data point is 5 min.

causing thinner films. Above 6.2 cm^3/min , the difference in the sheet resistance between the treated and untreated samples is approximately a factor of three. This corresponds to a film thickness of approximately 900 Å for the treated and 300 Å for the untreated samples. Figure 5 shows the effect of a 2W, 5 min plasma treatment on sheet resistance as a function of the tungsten deposition time for phosphorus-doped polycrystalline silicon. The deposition is performed at a WF_6 flow rate of 12.4 cm^3/min . Otherwise, the same deposition parameters prevail as in Fig. 4. Very little dependence on deposition time is observed, indicating a self-limiting reaction. This is in agreement with the results presented in Ref. (9). Similar to Fig. 4, the difference in sheet resistances between the treated and untreated films is approximately a factor of 3, corresponding to thinner films (~300 Å) for the untreated samples. In addition to the possible creation of nucleation sites, the argon plasma treatment also changes the thickness of the discontinuous native oxide. Wafers removed

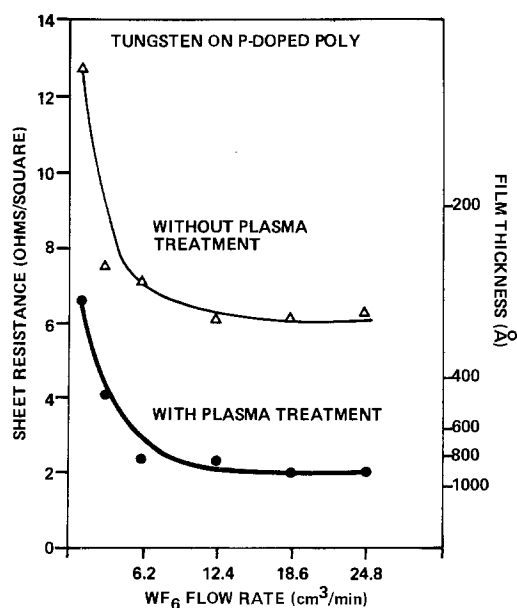


Fig. 4. Effect of the argon plasma treatment of sheet resistance (film thickness) for phosphorus-doped polycrystalline silicon as a function of WF_6 flow rate. The tungsten deposition parameters are: 410°C, 5 min, Ar pressure of 0.3 torr. Above a flow rate of 6.2 cm^3/min , the thickness of the treated films are approximately 1000 Å, those of the untreated films 330 Å.

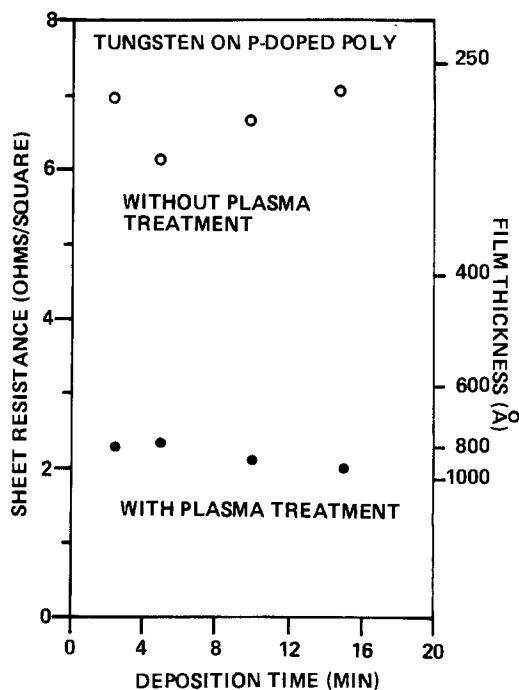


Fig. 5. Effect of the argon plasma treatment on sheet resistance as a function of tungsten deposition time for phosphorus-doped polycrystalline silicon. The tungsten deposition parameters are: 410°C, argon pressure of 0.3 torr, WF_6 flow rate of 12.4 cm^3/min .

from the storage container possess a native oxide of approximately $22 \pm 2 \text{ \AA}$ as measured with a Gaertner Scientific Instruments automatic ellipsometer. After cleaning and HF dip, this thickness is reduced to approximately $6 \pm 4 \text{ \AA}$. After the plasma treatment, the native oxide is approximately $14 \pm 4 \text{ \AA}$. At least qualitatively, this observation agrees with the discussion given in Ref. (9), where the argument is made that the thinner the native oxide the thinner a continuous tungsten film is formed, owing to a more homogeneous rate of reaction between WF_6 and silicon across the wafer surface. Similar results have been obtained with polycrystalline samples. Since the ellipsometer does not yield accurate results, the Auger technique has been used to estimate the thickness of the native oxide. HF-treated phosphorus-doped samples possess a discontinuous oxide of approximately 4-8 Å, which increases after the plasma treatment to approximately 8-16 Å. Results reported in the following sections are from substrates which have been subjected to a 2W, 5 min argon plasma treatment prior to tungsten deposition.

Deposition parameters.—Figure 6 shows resistance of tungsten/phosphorus doped polycrystalline silicon composite films at three different deposition temperatures as a function of deposition time. The data for the 367° and 419°C deposition temperatures show the self-limiting behavior, similar to the result shown in Fig. 5. At a deposition temperature of 469°C, the sheet resistance increases with deposition time. Stylus and Auger thickness measurements performed for the 5 and 30 min deposition time samples clearly indicate a decrease in the film thickness from approximately 330 to 235 Å during this time period. This result suggests a slow etching of the films (~4 Å/min) by WF_6 . Figure 7 shows the sheet resistance of tungsten/polycrystalline silicon composite films as a function of temperature for phosphorus-doped and undoped polycrystalline silicon. Deposition time in all cases is 20 min. In the undoped case, a shallow minimum is observed at approximately 420°C. Below this minimum, very little dependence on sheet resistance (film thickness) with deposition temperature is observed. Above the minimum, the sheet resistance increases from 2 to 4 Ω/\square . A strongly enhanced effect in terms of sheet resistance increase below and above a minimum is observed for the

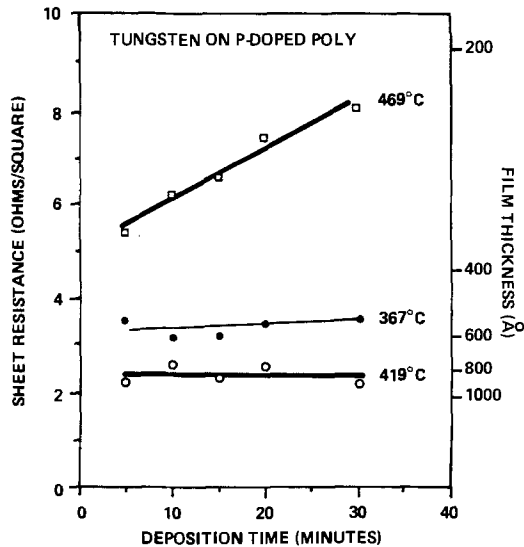


Fig. 6. Sheet resistance of tungsten/phosphorus-doped polycrystalline silicon composite films as a function of deposition time.

phosphorus-doped case, indicating a strong participation of phosphorus in the kinetics of film formation.

From stylus and Auger thickness measurements taken of several samples below, above, and at the minima of the two curves shown in Fig. 7, a film resistivity of $18.3 \pm 4.5 \mu\Omega\text{cm}$ was deduced. This is in good agreement with the data given in Ref. (4) for film thicknesses ranging from 200 to 900Å.

To investigate film surface morphology at different deposition temperatures, SEM micrographs have been prepared for samples deposited on phosphorus-doped polycrystalline silicon at 367°, 419°, and 469°C, and for a sample deposited on undoped polycrystalline silicon at 419°C. These samples are marked as A, B, C, and D in Fig. 7. Figure 8 shows the 367°C deposited film (A), which is approximately 460Å thick. Figure 9 shows the 419°C deposited film (B, 740Å), and Fig. 10 the 469°C deposited film (C, 250Å). As can be seen, the roughness of the tungsten film and of the polycrystalline interface increases with increasing film thickness. Figure 11 shows the 419°C

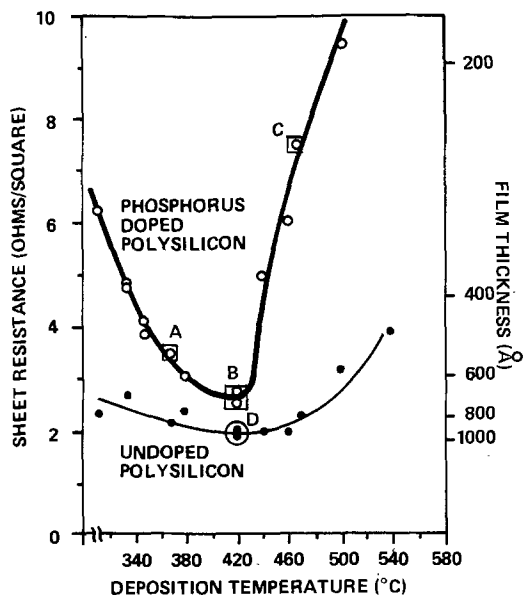


Fig. 7. Sheet resistance of tungsten/phosphorus-doped and undoped polycrystalline silicon composite films as a function of temperature. Film deposition time is 20 min. The thickness of the polycrystalline silicon is approximately 4500Å.

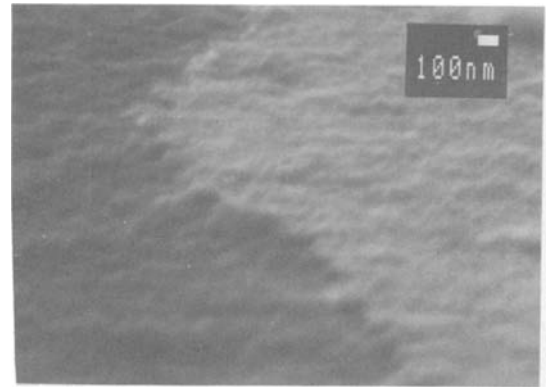


Fig. 8. SEM micrograph of a 460Å thick tungsten film deposited on phosphorus-doped polycrystalline silicon at 367°C. The film has been etched with the alkaline ferricyanide solution described in the "Experimental" section. This is sample A in Fig. 7.

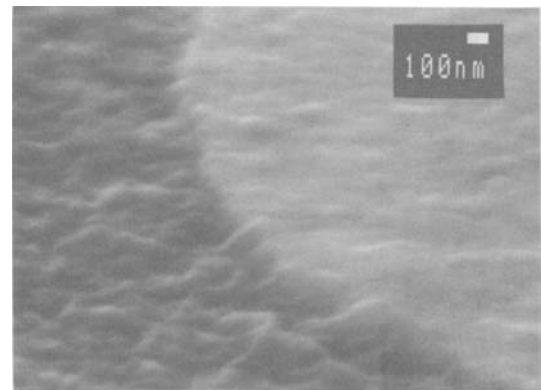


Fig. 9. SEM micrograph of a 740Å thick tungsten film deposited on phosphorus-doped polycrystalline silicon at 419°C. This is sample B in Fig. 7.

deposited film (D) on undoped polycrystalline silicon. The film thickness is 915Å. The roughness is similar to its doped counterpart (B). Auger elemental depth profiles (AEDP) of samples A, B, and C are shown in Fig. 12-14. Figure 12 shows the 367°C deposition temperature sample. Film thickness is defined at the 50% tungsten signal. The relatively broad interface between tungsten and polycrystalline silicon is an indication of film roughness, which, by taking the 10% and 90% points of the tungsten signal, is approximately equal to the film thickness. From Fig. 12, the consumption of polycrystalline silicon can also be deduced. According to Eq. [3], for a 460Å

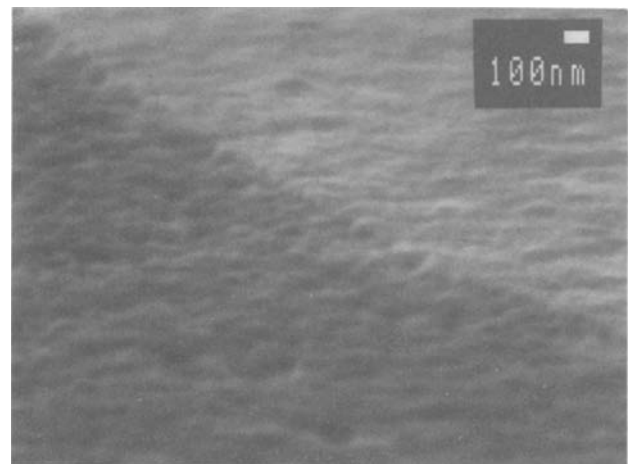


Fig. 10. SEM micrograph of a 250Å thick tungsten film deposited on phosphorus-doped polycrystalline silicon at 469°C. This is sample C in Fig. 7.

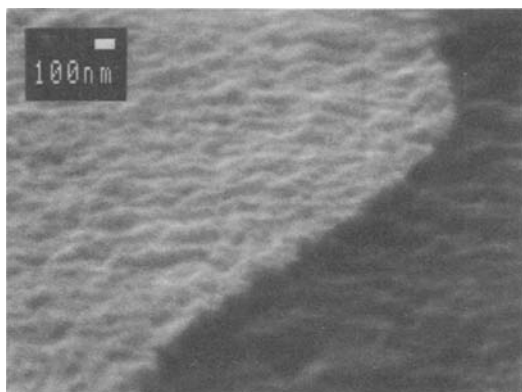


Fig. 11. SEM micrograph of a 915Å thick tungsten film deposited on undoped polycrystalline silicon at 419°C. This is sample D in Fig. 7.

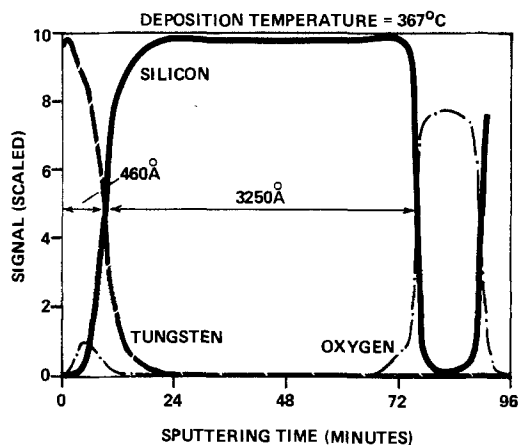


Fig. 12. Auger elemental depth profile of a tungsten/phosphorus-doped polycrystalline silicon/SiO₂ sandwich. The tungsten deposition is performed at 367°C. The deposition time is 20 min. This is sample A in Fig. 7.

thick tungsten film to be formed, approximately 900Å of silicon will be consumed. This then results in a thickness of the polycrystalline layer of $900 + 3250 = 4150\text{Å}$, in fair agreement with 4500Å, the initial polycrystalline layer thickness. Some uncertainty exists in defining the interface due to the film roughness. Figure 13 shows the 419°C deposition sample. The film thickness is 740Å, with a roughness of approximately the same value. Also, the consumption of the polycrystalline silicon, similar to the previous sample, can be seen. Figure 14 shows the 469°C deposition sample. The film is 250Å thick, and the interface is the smoothest of the three samples, which is in

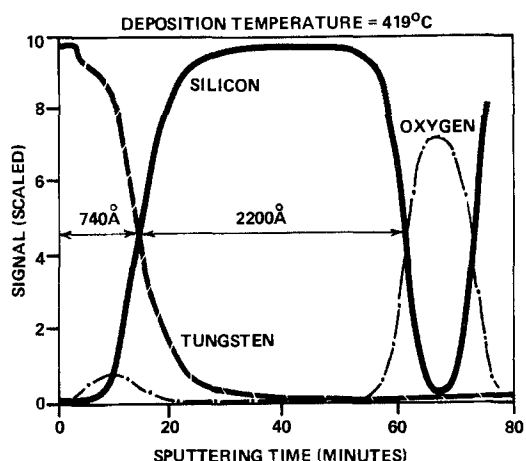


Fig. 13. Auger elemental depth profile of a tungsten/phosphorus-doped polycrystalline silicon/SiO₂ sandwich. The tungsten is deposited at 419°C. The deposition time is 20 min. This is sample B in Fig. 7.

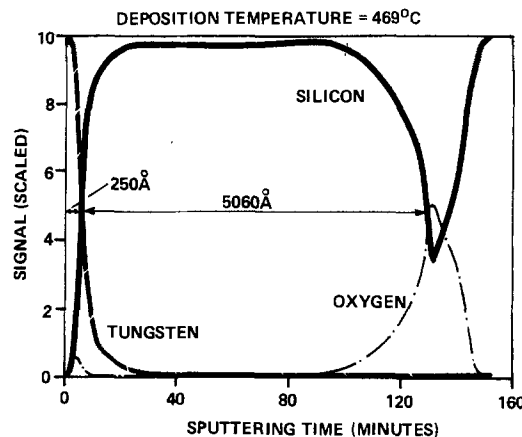


Fig. 14. Auger elemental depth profile of a tungsten/phosphorus-doped polycrystalline silicon/SiO₂ sandwich. The tungsten deposition is performed at 469°C. The deposition time is 20 min. This is sample C in Fig. 7.

agreement with the SEM micrographs shown in Fig. 8-10. In deducing the film thickness of these three samples, it was assumed that their density, and thus the sputtering rate, did not vary significantly from each other. From Fig. 12-14, it can be seen that some oxygen is incorporated into the films. A similar result is presented in Ref. (3). Assuming that this oxygen corresponds to the native oxide on the silicon surface prior to film formation (10), an estimate of its thickness can be performed. The area under the oxygen curve is determined and equaled to the height of the oxygen signal expected for SiO₂ times the thickness (sputtering time) of the to be determined native oxide layer. The height of the oxygen signal of SiO₂ is approximately 70% of the scaled signal scale. This can be seen in Fig. 12, where the polycrystalline silicon/SiO₂ interface is shown. The results yield approximately 30Å for sample A, 60Å for sample B, and 13Å for sample C. This agrees, at least qualitatively, with the conclusions made in Ref. (9) that film thickness and roughness depend strongly on the characteristics of the native oxide, with thinner tungsten films being formed for less native oxide. AEDP taken from other samples confirmed this observation: namely, that the oxygen incorporation is proportional to film thickness.

Figure 15 shows the SIMS phosphorus concentration profile of sample B in Fig. 7. Near the tungsten/polycrystalline silicon interface, the phosphorus concentration in

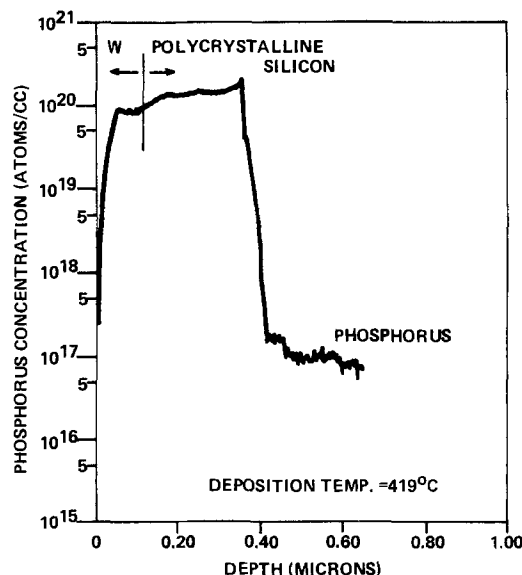


Fig. 15. Phosphorus concentration of a tungsten/phosphorus-doped polycrystalline silicon sample as measured by SIMS. The deposition temperature is 419°C. This is sample B in Fig. 7.

the tungsten film is approximately $1 \times 10^{20} \text{ cm}^{-3}$. The surface concentration is approximately $4 \times 10^{17} \text{ cm}^{-3}$. A similar profile has been obtained for sample A. Sample C exhibits a surface concentration of approximately $4 \times 10^{18} \text{ cm}^{-3}$. Within experimental error ($\pm 20\%$) the resistivity of the phosphorus containing tungsten films is not different from the undoped samples.

From the presented material it is clear that phosphorus takes an active part in tungsten film formation. From Fig. 7, it can be seen that at least two deposition mechanisms are present. For the undoped samples, the film thickness increases slightly, from 320° to 420°C , and then decreases from 420° to 540°C . A similar result is obtained for the films deposited on phosphorus-doped polycrystalline silicon except that it is accentuated. Film formation depends very strongly on the native oxide condition just prior to the WF_6 release into the LPCVD reactor. It is known that all the samples at the moment of insertion into the reactor have a native oxide of approximately 13 to 15 \AA . However, changes in oxide thickness can take place during pumpdown due to unavoidable oxygen traces present in the reactor. This change depends on temperature and sample doping conditions (11). This makes interpretation of the results shown in Fig. 6 and 7 difficult. Nevertheless, the results presented in these figures are very reproducible, sheet resistance across the 3 in. diam wafers do not vary by more than 5%. No film "cloudiness" or streaking phenomena are observed.

Single-crystal silicon substrates.—Similar results in terms of plasma treatment and film formation as described for polycrystalline substrates are obtained for p-type and phosphorus-doped p-type single-crystal substrates. Figure 16 shows the effect of the plasma treatment on n^+ -doped samples. Doping conditions are given in the "Experimental" section of this paper. The results are similar to Fig. 4, except that, without the plasma treatment, films of only approximately 200 \AA can be deposited under the given conditions of 410°C deposition temperature and a deposition time of 20 min. The sheet resistances of the plasma-treated samples (2W, 5 min) are almost identical to Fig. 4. Again, from stylus and Auger measurements, the thickness of the films has been obtained. The thickness scale is indicated on the right side of Fig. 16. The resistivity of the tungsten films is the same as of the tungsten films deposited on polycrystalline silicon, *i.e.*, $18 \mu\Omega\text{cm}$. Figure 17 shows the

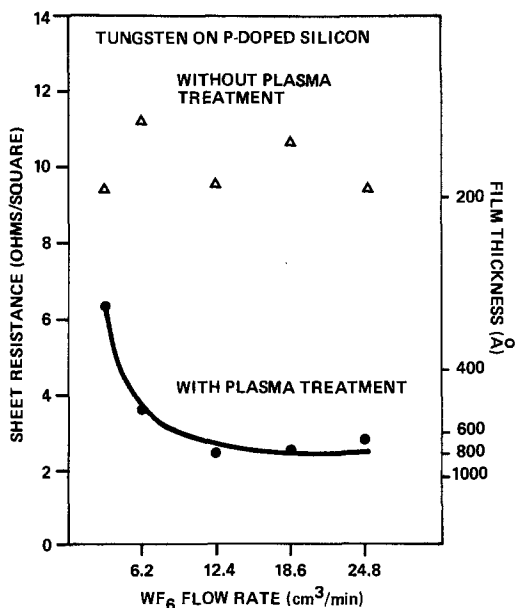


Fig. 16. Effect of the argon plasma treatment on sheet resistance for phosphorus-doped p-type single-crystal silicon as a function of WF_6 flow rate. The tungsten deposition parameters are: deposition temperature of 410°C , deposition time of 5 min, Ar pressure of 0.3 torr. Argon plasma treatment: 2W, 5 min.

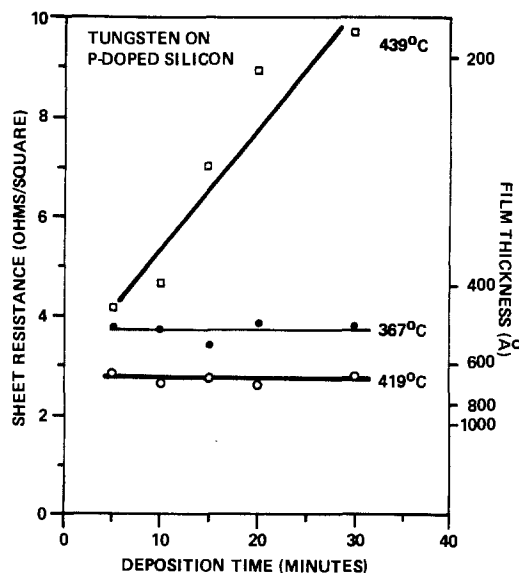


Fig. 17. Sheet resistance of tungsten deposited on phosphorus-doped p-type single-crystal silicon at three different deposition temperatures as a function of deposition time.

sheet resistance as a function of deposition time for n^+ -doped p-type samples. Strong similarity of the data with Fig. 6 is observed. For deposition temperatures of 367° and 419°C , the films form in less than 5 min after which film thickness is independent of deposition time. At a deposition temperature of 439°C , a strong decrease in film thickness from an initial value of approximately 500 \AA at 5 min to approximately 200 \AA at 30 min is observed. This again suggests etching of the films ($\sim 12 \text{ \AA}/\text{min}$) by WF_6 as a function of deposition time.

Figure 18 shows the sheet resistance for p-type single-crystal silicon as a function of temperature and for a film deposition time of 20 min. For the non-phosphorus-doped samples, very little change in sheet resistance and thus thickness is observed over the temperature range 330° - 460°C , which is similar to the undoped polycrystalline data given in Fig. 7. For the phosphorus-doped case, a minimum is reached at approximately 420°C . Above this minimum, a sharp increase in sheet resistance (decrease in film thickness) is observed. This decrease in film thickness is due to the onset of film etching above 420°C . The data in Fig. 18 are plotted for a deposition time of 20

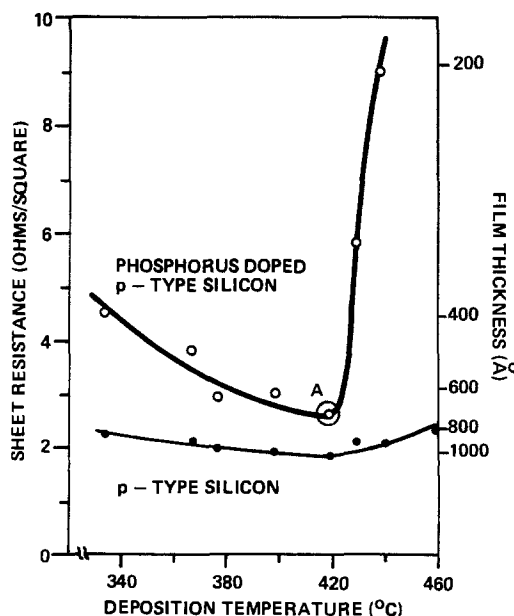


Fig. 18. Sheet resistance of tungsten deposited on phosphorus-doped p-type and on p-type single-crystal silicon as a function of temperature. Film deposition time is 20 min.

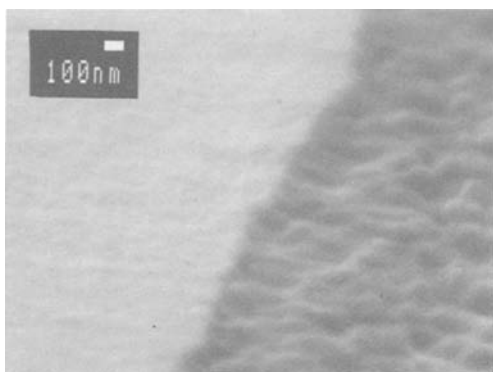


Fig. 19. SEM micrograph of a 670Å thick tungsten film deposited on phosphorus-doped single-crystal p-type silicon at 419°C. This is sample A in Fig. 18.

min. According to Fig. 17, at this time period, etching of the film is already taking place for a deposition temperature of 439°C. This behavior is similar to the data shown in Fig. 7. Insufficient data exist at this time to explain the accentuated increase in film thickness from 320° to 420°C of the phosphorus containing samples (Fig. 7 and 17).

Figure 19 shows the SEM micrograph of a 670Å thick tungsten film deposited on phosphorus-doped single-crystal p-type silicon at 419°C. This is sample A in Fig. 18. The degree of surface roughness at the W/Si interface is similar to Fig. 9 and 11. The surface roughness of the tungsten film is less, probably owing to the smoother initial surface of single-crystal vs. polycrystalline silicon.

Selectivity.—From AEDP, it is verified that tungsten deposited by the LPCVD method is 100% selective. Prior to tungsten deposition, 5 μm wide polycrystalline lines are photoshaped and etched on top of thermally grown SiO₂ regions, and no tungsten (< 10Å) can be detected. Selectivity has been observed for all deposition conditions reported in this paper.

Applications.—The primary purpose of this work has been to develop deposition conditions yielding low sheet resistance for a W/phosphorus-doped polycrystalline composite film to be used for IC gate and interconnects. The best results are obtained using a deposition temperature of 420°C. This results in a 700Å thick film with a sheet resistance of approximately 2.6 Ω/□ (see Fig. 7, upper curve). The initial polycrystalline silicon thickness has to be at least 4500Å. Below this value, film lifting due to the stress created by the tungsten film is observed. Note that approximately 1400Å of the polycrystalline silicon are consumed during the tungsten film formation.

For low resistance source/drain contact formation to n⁺ silicon, a temperature of 420°C gives the lowest resistance films. However, to avoid film encroachment at the Si/SiO₂ pattern edges (3, 12) a deposition temperature of 350°C is needed. This results in a sheet resistance of approximately 4 Ω/□. However, the suitability of this approach has to be investigated by electrical measurements. Due to the tungsten protrusions into silicon, excessive leakage currents might result for Schottky barrier structures and tungsten on shallow n⁺ source/drain structures.

Summary

Tungsten films have been deposited via the silicon reduction of WF₆ in a low pressure chemical vapor deposition system on phosphorus-doped and undoped polycrystalline silicon and on phosphorus-doped p-type

and undoped p-type single-crystal silicon. Deposition temperatures range from 310° to 540°C.

For the non-phosphorus-doped substrates (polycrystalline and single crystal), film thickness of approximately 200-400Å can be obtained using a H₂SO₄/H₂O₂, HF dip clean prior to film deposition. With the introduction of a low power argon plasma treatment, film thickness can be increased, for the same deposition conditions, to a maximum of approximately 900Å. This treatment increases the native oxide thickness of all samples from 6Å (chemical clean only) to 14Å. Over the temperature range, the thicknesses of the tungsten films deposited on undoped polycrystalline silicon range from 500 to 900Å, those deposited on lightly p-type doped silicon from 800 to 1000Å.

A drastically different behavior is observed for the phosphorus-doped substrates. Here, a maximum film thickness of approximately 700Å can only be reached at 420°C. Below this temperature, film thickness decreases to approximately 400Å at 340°C for both substrates. Above 420°C, film thickness reduces to 200Å at 500°C (on polycrystalline silicon) and at 440°C (single-crystal silicon). This decrease is due to etching of the films by WF₆, which is catalyzed by the presence of phosphorus.

Acknowledgments

The authors wish to thank R. Joy, AMI, for suggesting work on LPCVD tungsten, Professor K. Saraswat, Stanford University, for many helpful comments, A. Saxena, AMI, for alerting us to the encroachment problem, E. Butler, C. Strandberg, O. Wu, and J. Kao for the AEDP measurements, and A. Brandes and D. M. Chen for the SEM and stylus profilometer work.

Manuscript submitted Feb. 29, 1984; revised manuscript received June 1, 1984. This was Paper 97 presented at the Cincinnati, OH, Meeting of the Society, May 6-11, 1984.

Gould Research Center assisted in meeting the publication costs of this article.

REFERENCES

1. P. A. Gargini and I. Beinglass, *IEDM Tech. Dig.*, CH 1708-7/81, 54 (1981).
2. N. E. Miller and I. Beinglass, *Solid State Technol.*, **25**, 85 (1982).
3. T. Moriya, S. Shima, Y. Hazuki, M. Chiba, and M. Kashiwagi, *IEDM Tech. Dig.*, CH 1973-7/83, 550 (1983).
4. K. C. Saraswat, S. Swirhun, and J. P. McVittie, in "VLSI Science and Technology 1984," K. E. Bean and G. A. Rozgonyi, Editors, p. 409, The Electrochemical Society Softbound Proceedings Series, Pennington, NJ (1984).
5. K. Y. Tsao and H. H. Busta, Unpublished data.
6. N. E. Miller and I. Beinglass, *Solid State Technol.*, **23**, 79 (1980).
7. C. E. Morosanu and V. Soltuz, *Thin Solid Films*, **52**, 181 (1978).
8. E. K. Broadbent and C. L. Ramiller, Abstract 420, p. 657, The Electrochemical Society Extended Abstracts, Vol. 83-1, San Francisco, CA, May 8-13, 1983.
9. E. K. Broadbent and C. L. Ramiller, *This Journal*, **131**, 1427 (1984).
10. D. Pramanik, A. N. Saxena, O. K. Wu, G. G. Peterson, and M. Tanielian, *J. Vac. Sci. Technol.*, To be published.
11. C. P. Ho and J. D. Plummer, *This Journal*, **126**, 1516 (1979).
12. T. Moriya, K. Yamada, T. Shibata, H. Iizuka, and M. Kashiwagi, "1983 Symposium on VLSI Technology," Maui, HI, p. 96 (1983).

Charge Transfer via Interface States at Polycrystalline Cadmium Selenide Electrodes

Ron Haak* and Dennis Tench*

Rockwell International Science Center, Thousand Oaks, California 91360

Michael Russak

Grumman Aerospace Corporation, Bethpage, New York 11714

ABSTRACT

Polycrystalline cadmium selenide thin film electrodes prepared by coevaporation of the elements were investigated *in situ* by electrochemical photocapacitance spectroscopy (EPS) in aqueous basic electrolytes, with and without added polysulfide redox species. An interface state lying about 0.2 eV below the conduction bandedge was directly detected for material prepared at low substrate temperature and was demonstrated to mediate charge transfer between the semiconductor and the electrolyte.

Interface states are known to play an important role in charge transfer processes at both single-crystal and polycrystalline CdSe electrodes. For example, Fermi level pinning has been observed for n-CdSe in neutral sulfate electrolytes (1); for fast, one-electron redox species in nonaqueous electrolytes, the open-circuit voltage varies in a nearly ideal fashion as the redox potential is changed (over a limited range) (2). It has been proposed (3) that Fermi level pinning can result from interface-state densities as low as 10^{12} cm^{-2} . Interface-state effects in the thin-film n-CdSe/aqueous polysulfide system have been investigated by Rajeshwar (4). He reports that interface states associated with adsorbed sulfide ions mediate electron transfer and limit the open-circuit voltage; no change in V_{oc} was observed when the electrolyte composition was varied so as to change the redox potential over a 250 mV range.

In the present work, electrochemical photocapacitance spectroscopy (EPS) (5, 6) and ac impedance measurements were applied to further elucidate charge transfer processes associated with interface states at cadmium selenide electrodes prepared by coevaporation of the elements (7). Such thin film material was chosen for study because of its potential practical applications, *e.g.*, in photoelectrochemical cells. Results obtained previously for such electrodes in polysulfide electrolytes can be summarized as follows. Data are variable, but, in general, films prepared at low substrate temperatures ($\sim 100^\circ\text{C}$) yield higher photocurrents but lower open-circuit voltages ($\sim 100 \text{ mV}$ less) than those prepared at high substrate temperatures ($\sim 400^\circ\text{C}$) (8). For low substrate temperature films, the open-circuit voltage is increased by 50-100 mV and the fill factor is improved (with no loss in short-circuit photocurrent) when the electrode is soaked in ZnCl_2 solution and potential cycled (under illumination) in aqueous polysulfide (9). Based on Auger depth profile studies and impedance/polarization measurements, this improvement has been attributed to a negative shift in U_{FB} (flatband potential) caused by incorporation of Zn in the CdSe film.

Experimental Details

Thin film CdSe electrodes were prepared by vacuum coevaporation of Cd and Se from independently controlled sources, as described previously (7, 8). Two types of films were prepared (on titanium substrates). Low substrate temperature films were deposited at 100°C with a Se-to-Cd ratio in the vapor of 3:1. These films, which were only partially crystalline in the as-deposited state, were subsequently heat-treated at 400°C for 15 min in air to maximize their photovoltaic response. High substrate temperature films were deposited at 400°C with a Se-to-Cd ratio of 1:1. Although fully crystalline as deposited,

*Electrochemical Society Active Member.

these films still required heat-treatment at 450°C for 15 min for maximum photovoltaic output. After attachment of a wire lead to the titanium substrate with silver-epoxy resin, the electrode was sealed in Torr Seal® (Varian Associates, Palo Alto, California) so that the front (CdSe) face was exposed to the electrolyte. The geometric area of the electrodes ranged from 0.2-0.7 cm^2 . Before evaluation, films of both types were etched in 25% HNO_3 and dipped in polysulfide solution (0.1M S + 2.5M Na_2S + 1.0M KOH) to remove excess selenium from the surface.

The procedures and apparatus used to perform EPS measurements have been described previously (6). Impedance measurements were performed using the same apparatus.

Results and Discussion

For n-CdSe, which has a bandgap of 1.76 eV, four donor states (onsets at 1.04, 1.21,¹ 1.34, and 0.2 eV below the conduction bandedge) have been detected by EPS (10). As discussed in this earlier work, the 1.04 and 1.21 eV levels correspond to interface states associated with oxygen adsorption and play major roles in determining the electrical properties of CdSe devices. The 1.04 eV state predominates in aqueous solution and under vacuum conditions, resulting in a negative surface charge. At positive electrode potentials in acetonitrile solution, the 1.21 eV state occurs in higher concentrations, but can be electrochemically reduced to the 1.04 eV state at voltages near U_{FB} .

The 0.2 eV state in CdSe is of particular interest to the present work because it occurs in relatively high concentrations only in thin film materials prepared at low substrate temperature (100°C). As shown in Fig. 1a, this state ionizes at sufficiently positive electrode potentials and is detected as a sharp capacitance decrease beginning at about 1.5 eV (820 nm), corresponding to a transition from the valence band to the state. Such ionization, which increases the capacitance by increasing the positive charge at the interface (reduces the space charge thickness), is also reflected in Mott-Schottky plots as a sharp decrease in C^{-2} at more positive potentials. This is apparent above -0.5V in the plot given in Fig. 2; deviation from linearity, which apparently signals some ionization, is evident even at -0.7V . At potentials closer to U_{FB} , which according to Fig. 2 lies at -0.9V vs. SCE, the 0.2 eV state is nonionized in KOH solution and is, therefore, not detected. In this case, the capacitance is lower and the EPS spectrum (Fig. 1b) is similar to that for single-crystal electrodes; the 1.04 and 1.34 eV states are clearly evident, only slightly shifted in energy. As shown in Fig. 3, the 0.2 eV state is not detected at any appreciable concentration in coevaporated films prepared at high substrate temperature (400°C). This is an important result, indicating that the 0.2 eV

¹A slightly higher apparent onset is observed for this state in specimens having a high concentration of the 1.04 eV state.

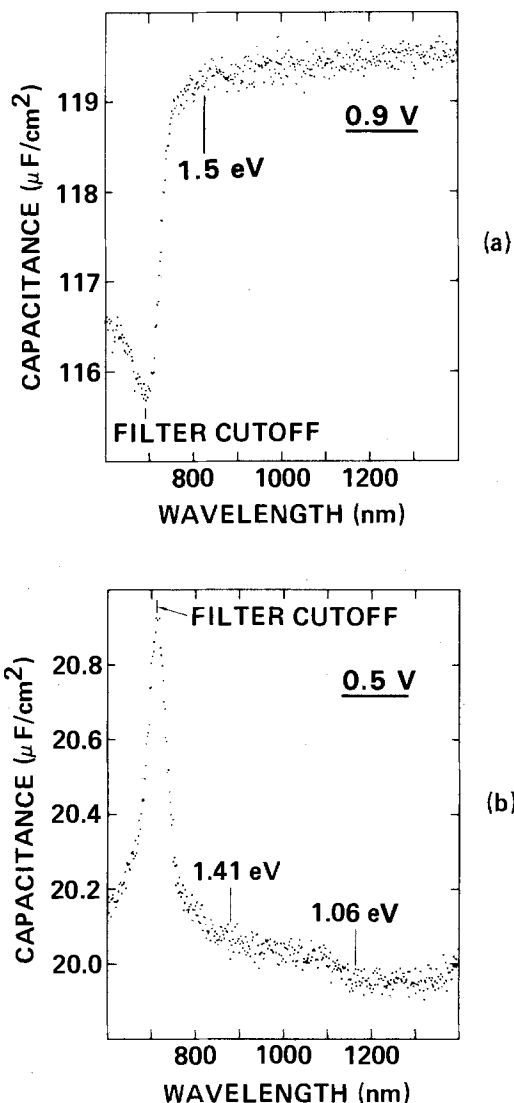


Fig. 1. EPS spectra (7 Hz) measured for a low substrate temperature film in 0.5M KOH at (a) 0.9V and (b) 0.5V vs. μ_{FB} .

level, by functioning as a charge transfer mediator/recombination center or by changing the interfacial potential distribution, is responsible for the observed limitations on the attainable open-circuit voltage for low substrate temperature material (8).

It should be mentioned that, as discussed previously (7), these thin film materials have a significant number of pinholes and cracks, through which a portion of the titanium substrate is exposed to the electrolyte. Thus, the measured capacitance includes a parallel contribution associated with the many small metal-electrolyte interfaces, which is likely to be large. In addition, the films are porous, so that the actual surface area of the electrode is much greater than the geometric area. Because of these combined effects, the capacitance values reported here tend to be large, even when the 0.2 eV state is nonionized. Hence, Mott-Schottky plots are of little value in determining carrier concentrations for these materials, but still provide useful information concerning the potential dependence of interfacial processes. Likewise, the absolute photocapacitance values reported have little quantitative significance.

Electrode porosity further complicates the situation by introducing frequency dispersion into the measured capacitance. Essentially, because of current distribution problems within pores, less of the surface of a porous electrode responds to the measurement perturbation at high frequencies, whereas the measured capacitance for an ideal planar electrode is frequency independent, that for an electrode with cylindrical pores that can

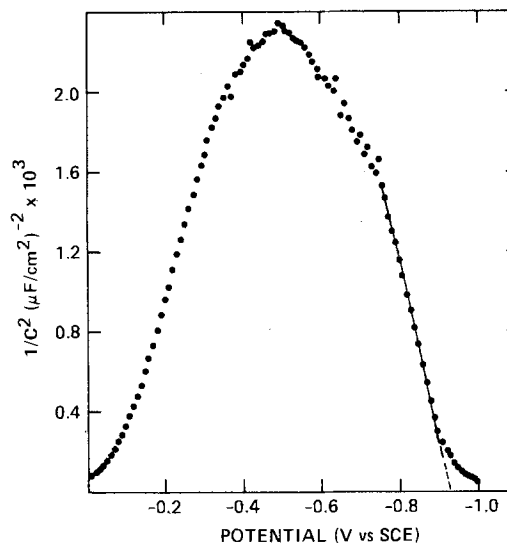


Fig. 2. Mott-Schottky plot (7 Hz) in 0.5M KOH for the same low substrate temperature CdSe electrode as in Fig. 1.

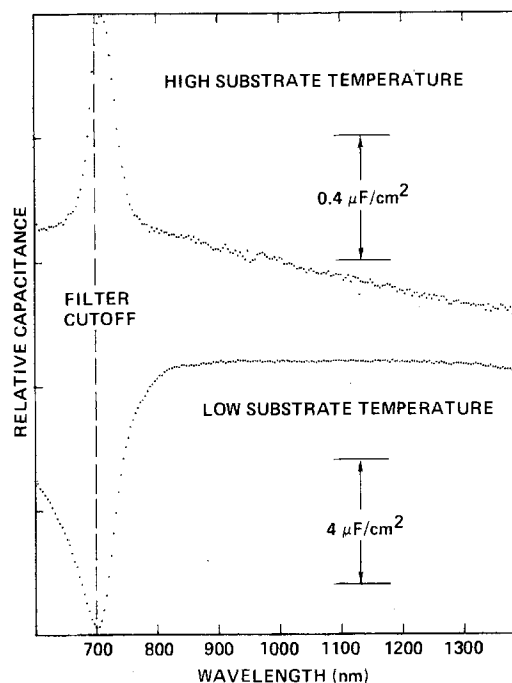


Fig. 3. EPS spectra (7 Hz) measured in 0.5M KOH at 1.0V vs. U_{FB} for coevaporated films prepared at low (100°C) and high (400°C) substrate temperatures.

be considered infinitely deep (in a given frequency range) decreases with increasing frequency. Specifically, the impedance for a porous electrode in this case is proportional to the square root of that for an ideal flat electrode (13). Consequently, low frequency measurements are preferable for porous electrodes because their capacitance behavior approaches that for ideal planar electrodes as the perturbation frequency is decreased. The relatively low perturbation frequencies used in the present work (7 and 70 Hz) were also chosen to provide optimum sensitivity to capacitance changes. Since it was not necessary, no attempt was made to normalize the data to permit determination of absolute densities of states.

The 0.2 eV state in CdSe apparently resides at the interface, since it is not observed for electrodes transferred from aqueous KOH to acetonitrile electrolytes, as shown in Fig. 4. An interface state is also consistent with the high associated EPS capacitance change (several $\mu F/cm^2$) and its potential dependence.

Because of the importance of the aqueous polysulfide for stabilization of CdSe photoanodes in photoelectro-

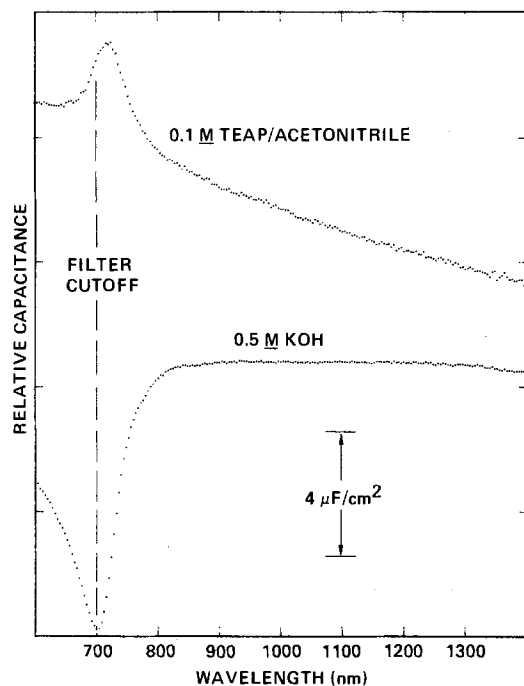


Fig. 4. EPS spectra (7 Hz) for the same low substrate temperature CdSe thin film electrode at 1.0V vs. U_{FB} in 0.5M KOH and in 0.1M tetraethylammonium perchlorate/acetonitrile solution.

chemical cells, appreciable effort was devoted to *in situ* investigation of various CdSe materials in the polysulfide electrolyte. Considerable quantitative variation in EPS results was observed from electrode to electrode (batch to batch), which can be attributed to differences in the material itself, since results for a given electrode were reproducible. In spite of the observed variation, some important general conclusions can be drawn from the data.

Exchange of electrons between the 0.2 eV state in CdSe and polysulfide species in solution is dramatically evident from the time dependence of the photocapacitance under intermittent illumination, as illustrated by the curves in Fig. 5. The response time for attainment of population/depopulation equilibrium for the state is on

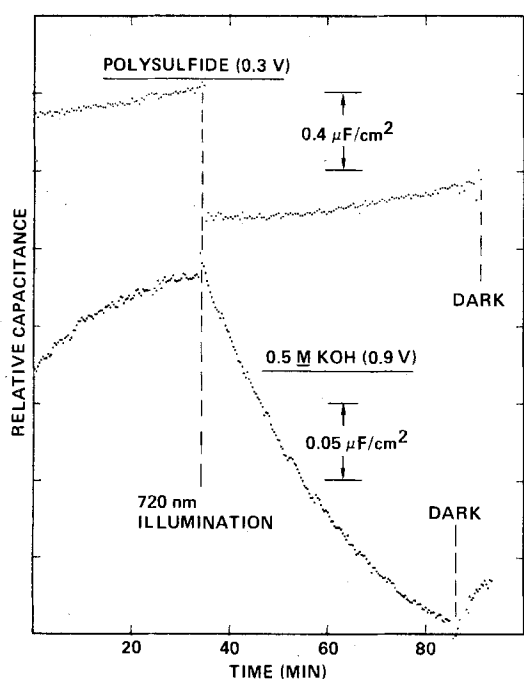


Fig. 5. Transient photocapacitance (7 Hz) for a low substrate temperature CdSe thin film electrode with and without 720 nm illumination in 0.5M KOH solution (0.9V vs. U_{FB}) and in polysulfide solution (0.3V vs. U_{FB}), i.e., 0.1M KOH + 2.5M Na_2S + 1.0M S.

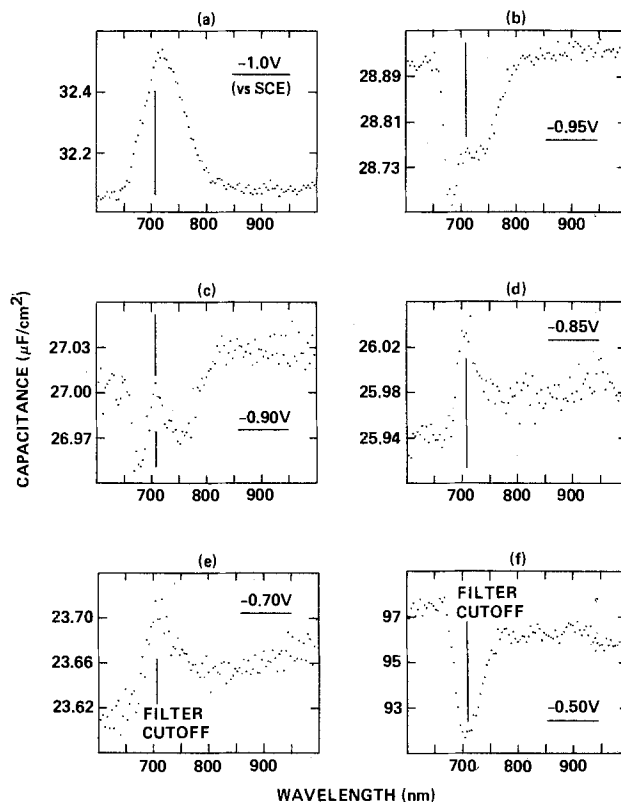
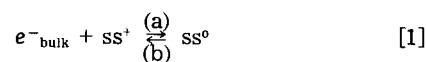


Fig. 6. EPS spectra (70 Hz) for a low substrate temperature n-CdSe electrode in polysulfide solution (0.1M KOH + 2.5M Na_2S + 1.0M S) at various electrode potentials: (a) -1.0; (b) -0.95; (c) -0.90; (d) -0.85; (e) -0.70; and (f) -0.50V vs. SCE.

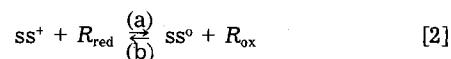
the order of hours in pure KOH solution, whereas in the presence of polysulfide, equilibrium is attained in less than 2s.

As is evident from the EPS spectra² in Fig. 6, the population of the 0.2 eV state in the presence of polysulfide is strongly dependent on the electrode potential. Ionized 0.2 eV states, which upon photoneutralization are reflected in a capacitance decrease beginning at 1.5 eV (820 nm), are not observed at -1.0V vs. SCE (Fig. 6a), are evident at -0.95 and -0.90V (Fig. 6b and 6c), are practically undetectable between -0.85 and -0.7V (Fig. 6d and 6e), but are present in very high concentration at -0.5V (Fig. 6f, note that absolute capacitance and photocapacitance are both large). It should be emphasized that all features of this complicated behavior are not observed for all specimens. This is not surprising since, as discussed below, the ionization/neutralization processes for the 0.2 eV state are complex and depend strongly on the density of states and U_{FB} , both of which vary appreciably from specimen to specimen.

The complex behavior illustrated in Fig. 6 can be understood in terms of interface-state (surface-state) reactions involving electron tunneling from the semiconductor bulk to ionized interface states (ss^+) or the reverse tunneling process from neutral interface states (ss^0), i.e.



and reactions involving the reduced (R_{red}) and oxidized (R_{ox}) redox species, i.e.



These reactions and the relative energies (approximately to scale) of the conduction band, semiconductor Fermi level, 0.2 eV interface states, and electrolyte redox level (E_R) are depicted for various bias voltages in Fig. 7. Based

²Note that the perturbation frequency in this case is 70 instead of 7 Hz; frequency dispersion effects are discussed below.

CdSe/POLYSULFIDE ENERGY LEVELS AT VARIOUS ELECTRODE POTENTIALS

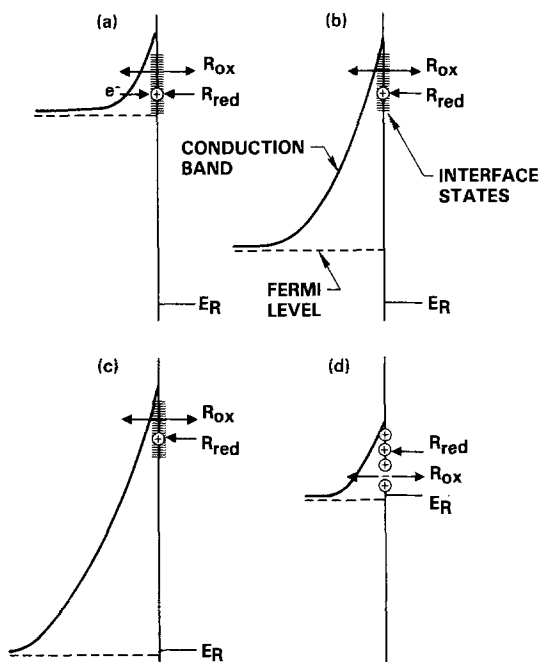


Fig. 7. Energy level diagrams for n-CdSe showing the relative positions of the conduction band, Fermi level, and polysulfide redox potential for $U_{FB} = -1.5V$ at various electrode potentials: (a) -1.1 ; (b) -0.95 ; (c) -0.8 ; and (d) $-0.5V$ vs. SCE.

on photocurrent onset and ac impedance measurements for single-crystal CdSe, U_{FB} is taken as $-1.5V$ vs. SCE, which is also consistent with the highest open-circuit voltage reported for this system ($0.7V$) (11) and a redox potential of $-0.8V$; apparent variations from this value for polycrystalline electrodes are discussed below. It should be kept in mind that exchange of electrons between the 0.2 eV interface state and polysulfide species is conclusively evident from the much faster time constant for both ionization and neutralization of the state in the polysulfide electrolyte compared to pure KOH solution (Fig. 5). For Fig. 7a-7c, all of the electrode potential drop is assumed to fall within the semiconductor space-charge region, which is consistent with the relatively low capacitance values.

Population of the interface states is determined by the relative rates of reactions [1a] and [2a] compared to [1b] and [2b], which in turn are influenced by the electrode potential. At potentials of less than about $0.4V$ vs. U_{FB} (Fig. 7a), interface states are filled by electron tunneling through the relatively thin space-charge layer (Eq. [1a]) and by reaction with reduced redox species (Eq. [2a]); although some cathodic dark current is observed, transfer of electrons to electrolyte species is relatively slow (compared to the tunneling/capture rates) at this electrode potential so that no ionized interface states are detected (Fig. 6a). It is important to note that even when the formal E_R value lies far below the interface-state energy, electron transfer from reduced redox species (filled states) is still possible since the energy barrier is greatly reduced by the high local electric field associated with ionized interface states and by specific orbital interactions between the redox species and interface states. Because of such localized effects, E_R in the vicinity of interface states is effectively shifted negatively. At somewhat more positive potentials (Fig. 7b), electron tunneling is suppressed (Fermi level too low) so that some ionized states exist in equilibrium with electrolyte redox species (Fig. 6b-6c). When the Fermi level reaches the electrolyte redox potential (Fig. 7c), net electron transfer from reduced electrolyte redox species to the semiconductor is thermodynamically favored and the ionized interface states are filled (Fig. 6d

and 6e). As the electrode potential is made sufficiently positive of the redox potential (Fig. 7d), a large fraction of the interface states ionize by electron tunneling to the semiconductor bulk (Eq. [2b]), so that a large fraction of the electrode potential drops across the electrolyte Helmholtz layer, increasing E_R relative to E_F and giving rise to an appreciable anodic dark current. In this case, the tunneling process is again relatively fast compared to interfacial charge transfer, so that the overall capacitance is large and a high density of ionized 0.2 eV interface states is detected (Fig. 6f).

The lower open-circuit voltage obtained for materials containing a high concentration of the 0.2 eV interface state can readily be explained within this model. That is, at potentials closer to U_{FB} than depicted in Fig. 7a, the Fermi level energy rises above that of the interface states, greatly increasing the probability of electron transfer to electrolyte species and, consequently, the cathodic dark current. In this case, the semiconductor bands cannot unbend further because of charge leakage to the electrolyte, so that a voltage loss, corresponding to the energy of the interface states below the conduction bandedge (0.2 eV), results. This is also reflected in photocurrent onset measurements, which yield apparent U_{FB} values for low substrate temperature films of typically $-1.3V$ vs. SCE rather than the $-1.5V$ obtained for single-crystal material. Values of U_{FB} measured for such films by the ac impedance method ranged from -1.0 to $-1.4V$, apparently reflecting, at least to some extent, variations in the density of ionized interface states. It should be mentioned that Reichman and Russak (8) have previously reported that Mott-Schottky plots are of questionable value in determining U_{FB} for thin film materials of this type.

The dark current-voltage behavior of thin-film CdSe electrodes correlates well with the EPS results and the proposed charge transfer model. Typical plots of log current vs. electrode potential for low and high substrate temperature electrodes are given in Fig. 8. High temperature films, for which the 0.2 eV state is not detected by EPS, exhibit very low forward and reverse dark currents (comparable to those observed for single-crystal electrodes) over a wide potential range. At $-1.0V$ vs. SCE, the dark current for low temperature films is an order of magnitude greater, presumably because of conventional electron tunneling associated with the decreased band bending (shift in U_{FB}) for this type of material (8). This is consistent with the energy level diagram in Fig. 7a. Also, the fact that the forward dark currents for the both types of materials have the same ideality factor (1.5) indicates a simple change in barrier height, i.e., a shift in U_{FB} for the low temperature material. In addition, the dark saturation current for the low temperature film is $8 \times 10^{-9} A/cm^2$, as compared to $9 \times 10^{-9} A/cm^2$ for the high temperature material, indicating that the former passes more current at the zero bias point. The anodic dark current under re-

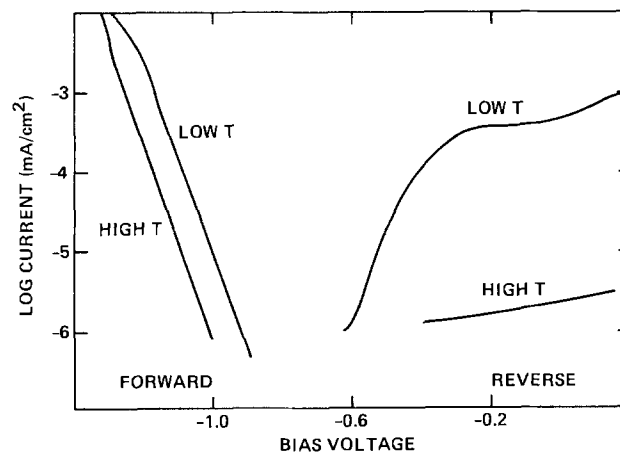


Fig. 8. Dependence of the dark current for low and high substrate temperature CdSe films in polysulfide electrolyte on the electrode bias potential (vs. SCE).

verse bias (-0.5V vs. SCE) is also much larger for the low temperature films, as expected from the proposed model (Fig. 7d).

Frequency dispersion of the photocapacitance also appears to reflect, in addition to porosity effects, the potential-dependent population/depopulation of the 0.2 eV interface state in aqueous polysulfide electrolytes. For example, in some relatively narrow potential regions, the photocapacitance decrease associated with this state was often much different in magnitude at the lower perturbation frequency (7 Hz) than at the higher frequency (70 Hz); in some cases, the 0.2 eV state was not observed at all at one of the frequencies. Such results indicate that the population of the interface state is affected by the perturbation voltage itself but only at sufficiently low frequencies for which electrons are induced to exchange between the state and electrolyte redox species or the semiconductor bulk (via tunneling). It should be mentioned that measurements of the photocapacitance frequency dispersion could ultimately yield rate constants for specific processes.

To further elucidate the role of the 0.2 eV interface state in charge transfer processes at n-CdSe electrodes, ac impedance measurements were performed over a broad frequency range (10,000 to 0.1 Hz), both in the dark and under illumination with 750 nm (1.65 eV) light. The data will be discussed in terms of the equivalent circuit given in Fig. 9, where R_s is the series resistance, C_p is the parallel capacitance, and R_{CT} is the charge-transfer resistance. Note that, ideally, C_p is a series combination of the space-charge (C_{sc}) and Helmholtz layer (C_H) capacitances, but in the present case there is also a contribution from the portion of the titanium substrate surface exposed to the electrolyte via pinholes and cracks in the CdSe film. In complex impedance plots of the imaginary (Z'') vs. real (Z') impedance components, generally R_{CT} is the diameter of the semicircle and $C_p = 1/2\pi f_m R_{CT}$, where f_m is the frequency at the maximum in the semicircle.

Complex impedance plots and calculated C_p and R_{CT} values for a low substrate temperature n-CdSe electrode in aqueous polysulfide at three electrode potentials are shown in Fig. 10, and the corresponding EPS spectra at two perturbation frequencies (7 and 70 Hz) are given in Fig. 11. At -1.0V, which is near U_{FB} , the semiconductor space-charge capacitance is relatively large and 0.2 eV states are readily filled via electrons tunneling from the semiconductor bulk. In this case, the 1.5 eV (820 nm) transition is not observed in the EPS spectrum for either frequency and well-defined semicircles, presumably associated with double layer charging and charge transfer/adsorption processes at the interface,³ are observed in the complex impedance plots. Although the subbandgap light (750 nm) has no appreciable effect on C_p , as expected when C_H is dominant, R_{CT} is decreased by almost a factor of two by such illumination. This effect is probably the result of electron-hole pair photogeneration, i.e., band tailing. Note that the presence of the 0.2 eV state might be expected to give rise to photocurrent band tailing associated with thermal emission of electrons photoexcited to

³Since no linear region, i.e., Warburg impedance, is observed, diffusional processes are apparently unimportant over the frequency range and light intensity studied.

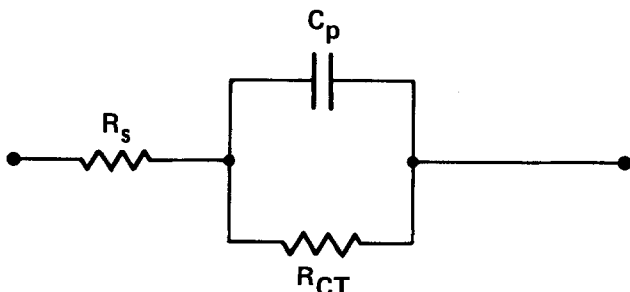


Fig. 9. Simple equivalent circuit for n-CdSe/polysulfide system

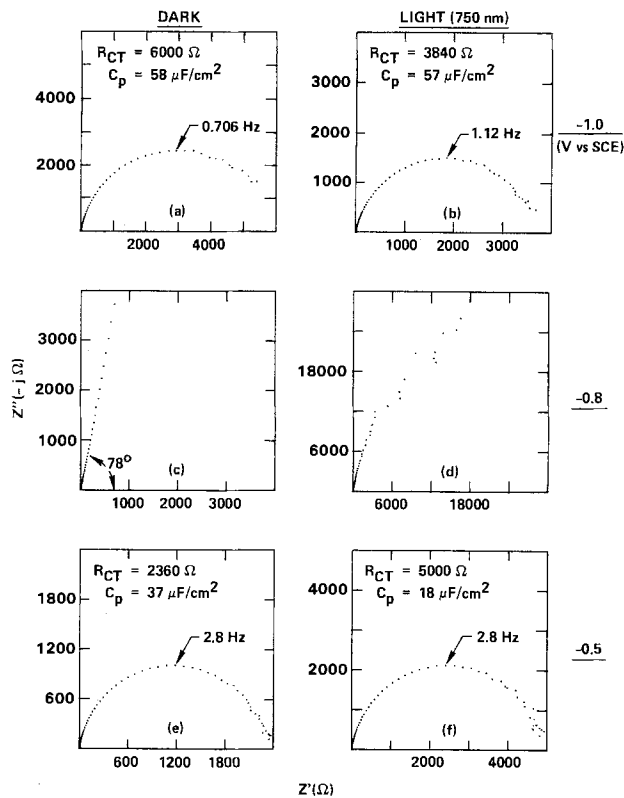


Fig. 10. Complex impedance plots for a low substrate temperature n-CdSe electrode at three bias potentials in polysulfide solution (0.1M KOH + 2.5M Na₂S + 1.0M S), with and without 750 nm illumination.

the state from the valence band. This would explain the long wavelength difference in the action spectra for low and high substrate temperature material given in Fig. 12.

At -0.8V vs. SCE, the situation is quite different. In this case, the 0.2 eV state is at least partially ionized and the 1.5 eV (820 nm) transition is observed in the EPS spectra (note that the magnitude of the capacitance decrease is smaller at the higher perturbation frequency). In the dark, the complex impedance plot is a straight line inclined at 78°, indicating that the impedance is dominated by a somewhat "leaky" capacitor (an ideal nonporous capacitor would yield an angle of 90°), presumably the space-

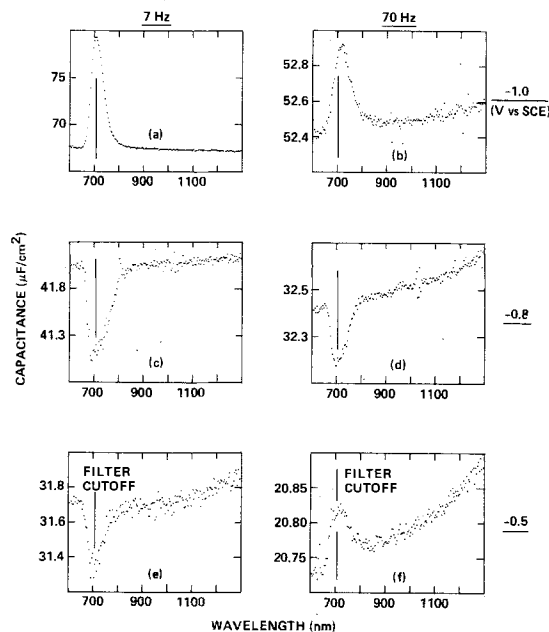


Fig. 11. EPS spectra (measured at 7 and 70 Hz) for n-CdSe at three bias potentials in polysulfide solution (same electrode and electrolyte as for Fig. 10).

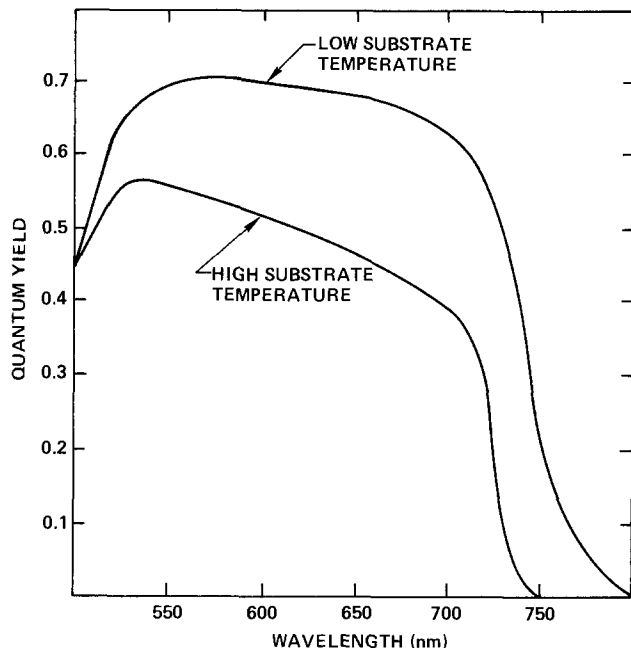


Fig. 12. Spectral response of low and high substrate temperature CdSe materials in polysulfide electrolyte at $-1.0V$ vs. SCE.

charge capacitance (C_{sc}). This is consistent with the model presented above, according to which electron tunneling from the semiconductor bulk to 0.2 eV interface states does not occur at this bias voltage so that interfacial charge transfer processes are subdued. With 750 nm illumination, the complex impedance plot exhibits significant curvature (the radius corresponding to $10^5 \Omega$), presumably associated with interfacial reaction of electrons photoexcited to the interface states. Since photogenerated holes are rapidly consumed at the interface, such interfacial reaction of electrons corresponds to charge-carrier recombination via electrolyte species. These results, therefore, provide strong evidence for the participation of the 0.2 eV state in recombination.

At $-0.5V$ vs. SCE, which is positive of the polysulfide redox potential, faradaic processes once again dominate the impedance, yielding a well-defined semicircle in the complex impedance plots. In this case, electrons are transferred from the reduced redox species to the interface states, then tunnel to the semiconductor bulk, resulting in an anodic dark current. The lower value of C_p compared to that at potentials near U_{FB} indicates a significant contribution from C_{sc} ; under illumination, which populates and thus reduces the density of ionized interface states, the contribution is larger (C_p is smaller). Illumination also increases R_{CT} in this case because fewer sites are available for interfacial charge transfer, i.e., states are filled via the 1.5 eV phototransition. In addition, neutralization of the 0.2 eV state effectively increases the space-charge layer thickness, as seen by the decrease in C_p , which will inhibit tunneling and thus increase R_{CT} . Although the 0.2 eV state is detected in the EPS spectrum at 7 Hz (as expected), it is not observed at 70 Hz. This is probably a consequence of the relative rates of tunneling and charge transfer and the effect the perturbation voltage has in populating/depopulating the state.

EPS was also used to investigate the mechanism by which zinc treatment improves the performance of n-CdSe photoanodes (9). Although this treatment (soaking in 0.1M $ZnCl_2$ solution) apparently reduces the concentration of the 0.2 eV interface state in some cases — results of one set of experiments are summarized in Table I — the effect is not consistently observed and is apparently related only incidentally to the performance improvement. This interpretation is consistent with the findings of Reichman and Russak (9) that Zn, which is incorporated in the CdSe lattice, improves the open-circuit voltage by shifting U_{FB} negatively.

Table I. Effect of $ZnCl_2$ treatment on photocapacitance change for 0.2 eV state in thin film CdSe

Electrode preparation	$\Delta C(\mu F/cm^2)^*$
Untreated (etched/cycled in polysulfide)	-0.80
30 min soak in 0.1M $ZnCl_2$	-0.70
Additional 30 min soak in $ZnCl_2$ solution	-0.60
4 days in $ZnCl_2$ solution	-0.47

* Measured at 7 Hz and 0.4V vs. U_{FB} .

Some speculation concerning the origin of the 0.2 eV state is in order. A chemical impurity seems unlikely, since the 0.2 eV state is observed in small concentrations even for single-crystal material. Also, secondary ion mass spectroscopy (SIMS) profiling of low substrate temperature films indicated that impurity levels are as low as those of the best high substrate temperature films, for which the 0.2 eV state is not detected by EPS. Since the concentration of the state in single-crystal material is enhanced by mechanical polishing, participation of a lattice defect is implied. This is consistent with the findings of Brillson (12) that the feature corresponding to the 0.2 eV state in surface photovoltage spectra is enhanced by argon bombardment. Frese (1) has inferred the presence of an interface state in CdSe centered about 0.2 eV below the conduction bandedge and attributed it to excess selenium. Although free Se would be expected to dissolve in aqueous polysulfide, a Se species bound to a lattice defect would appear to be a likely prospect as the origin of the 0.2 eV interface state. The occurrence of such a selenium-defect state would not be surprising, because as-deposited low temperature films contain a 3:1 molar ratio of Se to Cd and are only partially crystalline. It is only after heat-treatment and removal of excess Se that such films are crystalline and exhibit favorable photovoltaic characteristics. This type of defect is also consistent with our inference that this state shifts U_{FB} anodic by interfering with polysulfide adsorption, which should be favored on Cd sites but inhibited on Se.

Acknowledgments

This work was supported by the Solar Energy Research Institute (SERI) under Subcontract no. XE-2-02126-01 and XB-3-03108-01. The authors are also indebted to Dr. John Dick of SERI, who performed the SIMS profiling analyses.

Manuscript submitted Oct. 24, 1983; revised manuscript received May 14, 1984.

Rockwell International Science Center assisted in meeting the publication costs of this article.

REFERENCES

1. K. W. Frese, Jr., *J. Appl. Phys.*, **53**, 1571 (1982).
2. A. Aruchamy, J. A. Bruce, S. Tanaka, and M. S. Wrighton, *This Journal*, **130**, 359 (1983).
3. A. J. Bard, A. B. Bocarsly, F. F. Fan, E. G. Walton, and M. S. Wrighton, *J. Am. Chem. Soc.*, **102**, 3671 (1980).
4. K. Rajeshwar, *This Journal*, **129**, 1003 (1982).
5. R. Haak, C. Ogden, and D. Tench, *ibid.*, **129**, 891 (1982).
6. R. Haak and D. Tench, *ibid.*, **131**, 275 (1984).
7. M. A. Russak, J. Reichman, H. Witzke, S. K. Deb, and S. N. Chen, *ibid.*, **127**, 725 (1980).
8. J. Reichman and M. A. Russak, *ibid.*, **128**, 2025 (1981).
9. J. Reichman and M. A. Russak, *J. Appl. Phys.*, **53**, 708 (1982).
10. R. Haak and D. Tench, *This Journal*, **131**, 1442 (1984).
11. B. Miller, A. Heller, M. Robbins, S. Menezes, K. C. Chang, and J. Thompson, Jr., *This Journal*, **124**, 1019 (1977).
12. L. J. Brillson, *Surf. Sci.*, **69**, 62 (1977).
13. R. de Levie, in "Advances in Electrochemistry and Electrochemical Engineering," Vol. VI, P. Delahay, Editor, p. 329, Interscience, New York (1967).

Activity Coefficients of Electrons and Holes in Semiconductors

Mark E. Orazem^{*1} and John Newman^{**}

Materials and Molecular Research Division of Lawrence Berkeley Laboratory, and Department of Chemical Engineering, University of California, Berkeley, California 94720

ABSTRACT

Dilute-solution transport equations with constant activity coefficients are commonly used to model semiconductors. These equations are consistent with a Boltzmann distribution and are invalid in regions where the species concentration is close to the respective site concentration. A more rigorous treatment of transport in a semiconductor requires activity coefficients which are functions of concentration. Expressions are presented for activity coefficients of electrons and holes in semiconductors for which conduction- and valence-band energy levels are given by the respective bandedge energy levels. These activity coefficients are functions of concentration and are thermodynamically consistent. The use of activity coefficients in macroscopic transport relationships allows a description of electron transport in a manner consistent with the Fermi-Dirac distribution.

The concentrations of holes and electrons in a semiconductor are given by the Fermi-Dirac distribution (1, 2). A Boltzmann distribution is frequently used as an approximation to this distribution in statistical-mechanical analyses of semiconducting systems. Dilute-solution transport equations with constant activity coefficients, consistent with a Boltzmann distribution, are also used in characterizing the behavior of semiconducting systems. These approximate methods are popular because of their relative mathematical simplicity, but are invalid when electron or hole concentrations are close to the respective site concentrations in any region.

Calculation of individual ionic activity coefficients for electrons and holes has been proposed as a means of identifying the regions in which these approximations are justified. Rosenberg (3), Panish and Casey, Jr. (4, 5), and Hwang and Brews (6) have presented activity coefficients for electrons and holes that are functions of potential as well as concentration. Harvey (7) discusses the separation of the activity coefficient into parts due to chemical and electrical effects. Landsberg and Guy (8) present an activity coefficient based upon an Einstein relation that includes within it the nonidealities associated with the activity coefficient (9).

Activity coefficients are derived here that are functions of concentration. This derivation is independent of the Einstein relation. These activity coefficients are thermodynamically consistent and can be used to check the validity of the Boltzmann function as an approximation to the Fermi-Dirac distribution. These coefficients can also be used in the application of macroscopic transport equations to semiconducting systems in a way that is generally valid.

Theoretical Development

The electrochemical potential of a given species can arbitrarily be separated into terms representing a reference state, a chemical contribution, and an electrical contribution (10)

$$\mu_i = \mu_i^0 + RT \ln (c_i f_i) + z_i F \Phi \quad [1]$$

where Φ is a potential which characterizes the electrical state of the phase and can be defined in a number of ways. The potential used here is the electrostatic potential which is obtained through integration of Poisson's equation (11). Equation [1] can be viewed as the defining equation for the activity coefficient, f_i .

Under the assumption of a dilute solution, the flux of an individual species within the semiconductor is driven by a gradient of electrochemical potential

$$N_i = -c_i u_i \nabla \mu_i \quad [2a]$$

or

$$f_i N_i = -u_i RT \nabla (c_i f_i) - z_i u_i F (c_i f_i) \nabla \Phi \quad [2b]$$

where N_i is the flux of species i . Introduction of $A = c_i f_i e^{z_i F \Phi / RT}$ yields

$$f_i N_i = -u_i RT e^{-z_i F \Phi / RT} \nabla A \quad [3]$$

Under equilibrium conditions, $\nabla A = 0$, and

$$c_i f_i = A e^{-z_i F \Phi / RT} \quad [4]$$

where A is a constant. Under the assumption of a constant activity coefficient, Eq. [4] is consistent with a Boltzmann distribution.

The distribution of electrons in a semiconductor is characterized by the Fermi-Dirac function

$$\frac{n_i}{g_i} = [1 + \exp [(E_i - E_f) / RT]]^{-1} \quad [5]$$

where n_i is the number of electrons within an energy level E_i with degeneracy g_i . The Fermi energy E_f is a statistical parameter given the units of J/mol and defined as the energy at which the probability of occupancy of a state is one-half. The Fermi-Dirac distribution enters into the transport development (Eq. [2], [3], and [4]) through introduction of individual ionic activity coefficients: one for electrons and one for holes.

Through Fermi-Dirac statistics the concentration of conduction electrons is given by

$$n = \int_{E_c}^{\infty} \frac{N(E)}{1 + \exp [(E - E_f) / RT]} dE \quad [6]$$

and the concentration of holes by

$$p = \int_{-\infty}^{E_v} \left[1 - \frac{1}{1 + \exp [(E - E_f) / RT]} \right] N(E) dE \quad [7]$$

The concentrations defined above are consistent with the concentrations c_i used in Eq. [1]-[4]. If the distribution of available energy levels is narrow or RT is small, the valence and conduction electrons can be characterized by single-valued energy levels, E_v (the highest energy level of the valence band) and E_c (the lowest energy level of the conduction band), respectively. Thus

$$n = \frac{1}{1 + \exp [(E_c - E_f) / RT]} \int_{E_c}^{\infty} N(E) dE \quad [8]$$

or

$$n = \frac{N_c}{1 + \exp [(E_c - E_f) / RT]} \quad [9]$$

where N_c is the concentration of conduction-energy sites for electrons. A similar term, N_v , is defined as the concentration of valence-band sites.

From the definition of the electrochemical potential, the chemical activity

*Electrochemical Society Student Member.

**Electrochemical Society Active Member.

¹Present address: Department of Chemical Engineering, University of Virginia, Charlottesville, Virginia 22901.

$$a_i = c_i f_i \quad [10]$$

can be expressed as

$$a_i = \exp \left[\frac{\mu_i - \mu_i^0 - z_i \mathbf{F}\Phi}{RT} \right] \quad [11]$$

Note that the activity has units of concentration (see Eq. [1]). In Eq. [9], the concentration of conduction electrons is given as a function of the Fermi energy level. The energy E_c in this equation depends upon potential as

$$E_c = E_c^* + z_i \mathbf{F}\Phi \quad [12]$$

where E_c^* is a constant, independent of potential. The electrochemical potential of conduction electrons and the Fermi energy are related by an arbitrary constant

$$\mu_{e^-} = E_f + \mu_{e^-}^* \quad [13]$$

Equations [11] through [13] can be combined to yield

$$f_{e^-} = \frac{\exp[(\mu_{e^-}^* - \mu_{e^-}^0 + E_c^*)/RT]}{N_c} \left[\frac{1}{1 - n/N_c} \right] \quad [14]$$

where f_{e^-} is dimensionless. The secondary reference state quantities, E_c^* , $\mu_{e^-}^*$, and $\mu_{e^-}^0$, are chosen to allow the activity coefficient to approach unity as the concentration of conduction electrons approaches zero. Thus, the activity coefficient is obtained as a function of composition

$$f_{e^-} = \frac{1}{1 - n/N_c} \quad [15]$$

The activity coefficient of conduction electrons is equal to 2 for a dimensionless concentration n/N_c equal to 0.5.

A similar activity coefficient can be obtained for the holes as

$$f_{h^+} = \frac{1}{1 - p/N_v} \quad [16]$$

The assumption of unity activity coefficients is in harmony with the assumption of the Boltzmann limits to the Fermi-Dirac distribution. Use of the Fermi-Dirac distribution results in activity coefficients that are functions of concentration.

Discussion

Equations [15] and [16] are consistent with the form of the activity coefficients

$$f_{e^-} = \frac{N_c}{n} e^{(E_f - E_c)/RT} e^{\Delta E/RT}$$

presented by Hwang and Brews (6) and Landsberg and Guy (8). These authors include a term $e^{\Delta E/RT}$ for the shift in electron energy due to the occupation of energy levels above E_c at high electron concentrations (12). Under the assumption that $\Delta E = 0$, Eq. [15] is recovered by introduction of the Fermi-Dirac distribution function for electrons. Calculation of ΔE requires knowledge of the electron site distribution $N(E)$.

The activity coefficients defined above can be checked for consistency with the Fermi-Dirac function. Introduction of the activity coefficient presented for electrons in Eq. [15] into the respective Boltzmann distribution

$$n f_{e^-} = N_c e^{-(E_c - E_f)/RT} \quad [17]$$

recovers the Fermi-Dirac distribution

$$\frac{n}{N_c} = \frac{1}{1 + e^{(E_c - E_f)/RT}} \quad [18]$$

The same is true for the activity coefficient for holes.

A measure of internal thermodynamic consistency is obtained from the second cross-derivative of the Gibbs function, *i.e.*

$$\left(\frac{\partial \mu_i}{\partial c_k} \right)_{T,P,c_j \neq k} = \left(\frac{\partial \mu_k}{\partial c_i} \right)_{T,P,c_j \neq i} \quad [19]$$

where i and k represent components of the system that are not the solvent. This necessary condition for thermodynamic consistency is expressed for the system described here as

$$\frac{RT}{f_{e^-}} \left(\frac{\partial f_{e^-}}{\partial p} \right)_{T,P,n} = \frac{RT}{f_{h^+}} \left(\frac{\partial f_{h^+}}{\partial n} \right)_{T,P,p} \quad [20]$$

This condition is satisfied. (Equation [19] is properly stated in terms of mole numbers rather than concentrations. For the dilute systems involved here, lattice expansion is ignored, and the two are equivalent.)

Use of macroscopic relations for thermodynamics and transport in regions of nonzero electric charge density raises some interesting philosophical questions because transport and thermodynamic properties are not easily measurable as functions of composition including arbitrary departures from electroneutrality. Fortunately, the semiconductors of interest are extremely dilute compared to even dilute aqueous solutions, and theoretical expressions such as the Fermi-Dirac distribution can be used with some confidence. Note that individual ionic activity coefficients are here being introduced in regions of net charge.

The extreme dilution of the semiconductors is also a justification for using the simple transport Eq. [2a] rather than the multicomponent diffusion equation (10), which includes interactions of solute species, and for using the approximate thermodynamic test embodied in Eq. [19].

Conclusions

Activity coefficients are derived here that are functions of concentration. These activity coefficients are thermodynamically consistent and can be used to check the validity of the Boltzmann function as an approximation to the Fermi-Dirac distribution. These coefficients can also be used in the application of macroscopic transport equations to semiconducting systems.

The use of constant activity coefficients in modeling semiconductor systems is valid for dimensionless concentrations n/N_c and p/N_v less than 0.1. Use of the activity coefficients presented in Eq. [15] and [16] allows treatment of systems with dimensionless concentrations ranging from 0 to 1. This approach is restricted, however, by the assumption that valence- and conduction-band electrons are characterized by their respective bandedge energies. Relaxation of this assumption involves integration of Eq. [6] and [7] for a specific distribution of electron energy levels.

Acknowledgment

This work was supported by the United States Department of Energy under Contract no. DE-AC03-76SF00098 through the Director, Office of Energy Research, Office of Basic Energy Sciences, Chemical Sciences Division, and through the Assistant Secretary of Conservation and Renewable Energy, Office of Advanced Conservation Technology, Electrochemical Systems Research Division.

Manuscript submitted Nov. 21, 1983; revised manuscript received June 6, 1984.

The University of California assisted in meeting the publication costs of this article.

REFERENCES

1. A. S. Grove, "Physics and Technology of Semiconductor Devices," John Wiley and Sons, New York (1967).
2. S. M. Sze, "Physics of Semiconductor Devices," Wiley-Interscience, New York (1969).
3. A. J. Rosenberg, *J. Chem. Phys.*, **33**, 665 (1960).
4. M. B. Panish and H. C. Casey, Jr., *J. Phys. Chem. Solids*, **28**, 1673 (1976).
5. M. B. Panish and H. C. Casey, Jr., *ibid.*, **29**, 1719 (1968).
6. C. J. Hwang and J. R. Brews, *ibid.*, **32**, 837 (1971).
7. W. W. Harvey, *ibid.*, **23**, 1545 (1962).

8. P. T. Landsberg and A. G. Guy, *Phys. Rev. B*, **28**, 1187 (1983).
9. P. T. Landsberg, "Thermodynamics and Statistical Mechanics," Oxford University Press, Oxford, England (1978).
10. J. Newman, "Electrochemical Systems," Prentice-Hall, Englewood Cliffs, NJ (1973).
11. R. Parsons, in "Modern Aspects of Electrochemistry," Vol. 1, J. O'M. Bockris, Editor, Chap. 3, Academic Press, New York (1954).
12. F. A. Lindholm and J. G. Fossum, *IEEE Trans. Electron. Devices Lett.*, **ed1-2**, 230 (1981).

Technical Notes



Polarization Effects in Polyimides

G. Samuelson

Solavolt International, Phoenix, Arizona 85040

S. Lytle*

Motorola, Incorporated, Mesa, Arizona 85202

Polyimide is a class of high temperature, stable organic polymers that has found widespread use in the semiconductor industry. It has been used as an interlevel dielectric in multilevel discrete transistors (1), and as a final passivant (2). More recently, its role in silicon and aluminum MOS integrated circuits has been demonstrated (3).

Some limited-reliability data on polyimide films have been described in the literature. For example, the effect of incomplete cure on device performance was discussed by Gregoritsch (4). The via resistance and leakage current of a multilevel bipolar LSI chip was reported by Mukai *et al.* (5). Finally, the effects of ionic contamination and electrical conduction in polyimide was discussed by Brown (6).

The present work extends the discussion of charge instability within polyimide films by using standard C-V techniques to probe charge effects that are inherent in the polyimide film or are induced by certain processes. Evidence is presented to show that differences in inherent polarizability of several commercially available polyimides exist. Evidence is presented to show that absorbed water causes increases in the polarization time constants. It may be possible to distinguish different kinds of water, based on the fact that different dehydration conditions are required to restore the original time constants of polarization, depending on the relative humidity to which the polyimide film was exposed. Finally, evidence is presented to show that plasmas routinely used in the semiconductor industry may influence the polarization of polyimide films. For example, standard isotropic O₂ plasma etching of polyimide was shown to cause a decrease in the polarization time constant and activation energy.

Experimental

Polarization effects intrinsic to polyimide.—MIS structures were constructed of 8-12 Ωcm phosphorus-doped Si, 1000Å thermally grown MOS-quality SiO₂, 0.8-4.8μ polyimide (du Pont PI2545, PI2555, PI2562, PSH61453, and Hitachi PIQ-13), and 4000Å pure evaporated aluminum, patterned using conventional lithographic techniques. The resulting test wafer was subjected to a 200°C, 20 min dehydration bake immediately prior to measurement. The measurement system consisted of a Temprotronic TP350A thermally controlled chuck, an HP4275A LCR meter, and a Fluke 8502A multimeter. A "standard" room

temperature trace was performed at 100 kHz from -100V to +100V using a ramp rate of 1 V/s. The stress conditions used to compare measured ΔV_{FB} values against ΔV saturation calculated from classic polarization theory were -5V, 200°C, and 20 min, with cooling to room temperature under bias. At room temperature, the "standard" trace was repeated and the ΔV_{FB} measured. The stress conditions used to determine the time constants of polarization were -5V, 200°C, and times varying from 1 to 40 min, depending on the polyimide under test. Following stress, the MIS structure was cooled to room temperature under bias, the "standard" trace was repeated, and ΔV_{FB} was measured.

Humidity effects on polarization.—C-V analysis was performed on MIS structures which consisted of 4-7 Ωcm p-type Si substrates, 1000Å thermally grown MOS quality SiO₂, 1000Å CVD Si₃N₄, and 1.5μ polyimide, followed by 12 kÅ of sputtered Al-Cu-Si. An MDC computerized semiconductor measurement system consisted of a Boonton 72B capacitance meter, a HP7010B XY recorder, current monitors, and power supplies supported by an 8080S microcomputer system. Standard C-V traces of unstressed samples were made at room temperature over a voltage range of -75 to +25V at 1 MHz. Stressing was done at 225°C under a +5V bias for times ranging from 2 to 20 min. The MIS structure was brought to room temperature under bias, and the ΔV_{FB} was measured as a function of stress time. The time constant of polarization, τ, was calculated from the slope of the ln ΔV_{FB} vs. time curves for MIS structures exposed to various humidity ambients. 100% humidity ambient was achieved by placing wafers in an airtight wafer box with water. At no time was the water in contact with the polyimide. All other relative humidities were obtained by exposing wafers to the clean room ambient. Typically, control wafers were stored at 200°C at N₂.

Results and Discussion

Polarization effects vs. polyimide chemistry.—It has been noted by Brown (6) that charge effects in polyimide can cause inversion of underlying silicon and consequent undesired communication between doped areas. An effort was made to distinguish among the various commercially available polyimides with respect to charge instabilities by subjecting them to -5V, 200°C, and 20 min stress, conditions which mimicked realistic operating conditions for certain devices. The ΔV_{FB} of the stressed

*Electrochemical Society Active Member.

Table I. ΔV_{FB} measured and calculated for various polyamides

Polyamide	Thickness (μm)	ΔV_{FB} meas. (volts)	ΔV_{sat} (volts)	ΔV_{FB} meas./ ΔV_{sat}	ΔV_{FB} meas./ μm (volts/ μm)
PI2566	4.76	4	216.0	0.018	0.840
PI2562	0.79	18	35.9	0.501	22.800
PIQ-13	1.15	34	52.3	0.650	29.600
40%PSH					
61453	1.95	78	88.6	0.880	40.000
PI2545	1.68	80	76.4	1.000	47.600

profile was compared with the ΔV_{FB} of the unstressed profile. The results are presented as ΔV_{FB} , measured in Table I for numerous polyimides. The saturating shift was calculated from classic polarization theory where

$$\Delta V_{sat} = - (k_o x_p / k_p x_o) V_p^2$$

V_p is the polarizing voltage, k_o and k_p are the dielectric constants of oxide and polyimide, respectively, and x_p and x_o are the thicknesses of polyimide and oxide. The ratio of the ΔV_{FB} measured and the calculated ΔV saturation is a reflection of the relative polarizability of the polyimides tested, as is the parameter ΔV_{FB} measured/ μm . From Table I, it is clear that PI2566 is the least polarizable. du Pont PI2545 and PSH61453 are both rapid polarizers, and the other polyimides fall intermediately between these two extremes.

An attempt was made to measure the time constant of polarization. Figure 1 shows the C-V trace under $-5V$, 200°C stress for times varying from 1 to 15 min for PSH61453. The undulating C-V profiles made it difficult to measure a single meaningful time constant. An attempt was made to "freeze" out polarization events by reducing the stress temperature to as low as -10°C . Even under these conditions, the most rapid polarizers continued to exhibit nonlinear $\ln \Delta V$ vs. time curves. In fact, under conditions of no applied stress other than that imposed by the standard trace, considerable hysteresis in the C-V characteristics was observed for all polyimides, except for the slowest polarizer, PI2566. Figure 2 shows the comparable family of C-V traces for PI2566, also stressed at $-5V$ and 200°C , though now for 15-40 min. The family of curves exhibits uniform, conventional C-V behavior. A plot of $\ln \Delta V$ vs. time, as shown in Fig. 3, gives a straight line with correlation coefficient 0.984. The time constant τ was determined from the slope of the curve in Fig. 3 and the equation

$$\Delta V = \frac{K_o x_p}{K_p x_o} V_p (1 - e^{-t/\tau})$$

The calculated τ for PI2566 was 840 min.

Polarization effects due to absorbed water.—The specific contribution of water to polarization effects in poly-

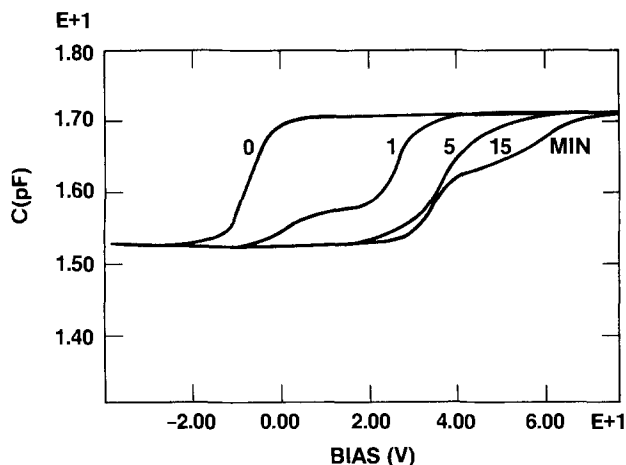


Fig. 1. C-V characteristics for PSH61453 stressed at $-5V$ and 200°C for 1-15 min.

imide films was studied. MIS structures using PIQ or PI2566 were "soaked" for varying times in either a clean room environment where the relative humidity varied from 17 to 35% or a 100% relative humidity environment. The structures were stressed at $+5V$ and 225°C following humidity exposure, and C-V profiles were measured as a function of stress time. Figure 4 is an example of the results for a MIS structure using PIQ and SiO_2 where the stress times were 2-16 min. The figure illustrates the typical finding that, initially, a rapid shift in ΔV_{FB} occurred which correlated directly with the relative humidity of the soak period. The term ΔV_{H_2O} was defined as the ΔV_{FB} that arose between the zero-stress C-V profile for a dehydrated film (the dotted line in Fig. 4) and the zero-stress C-V profile for a water-"soaked" film. The magnitude of ΔV_{FB} appeared to be a direct function of the relative humidity and the time of exposure to that humidity, as indicated in Fig. 5. The ΔV_{H_2O} occurred almost instantaneously upon temperature and bias stressing and disappeared following a 200°C , 30 min dehydration bake in dry N_2 . After ΔV_{H_2O} occurred, a family of C-V curves resulted, with continued stressing from which ΔV_{FB} values could be measured and used to calculate a time constant of polarization, τ . If such a time constant was measured as a function of exposure time in a 100% RH ambient, τ was seen to increase, as shown in Fig. 6 for PIQ MIS structures. Samples which exhibited increasing τ with time at 100%

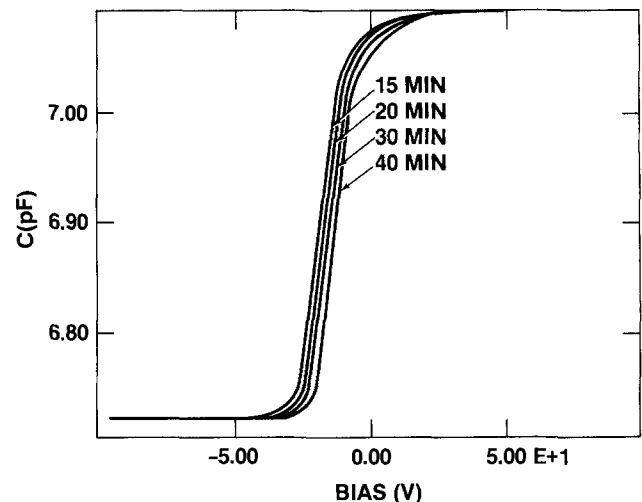


Fig. 2. C-V characteristics for PI2566 stressed at $5V$ and 200°C for 15-40 min.

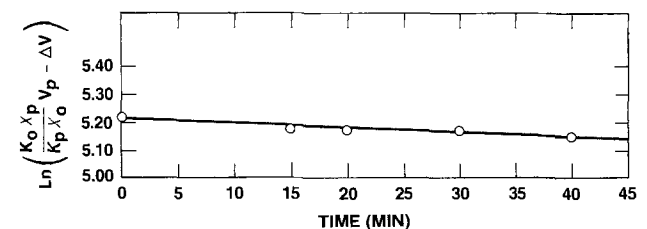


Fig. 3. $\ln \left(\frac{K_o x_p}{K_p x_o} V_p - \Delta V \right)$ vs. time for PI2566 stressed at $-5V$ and 200°C .

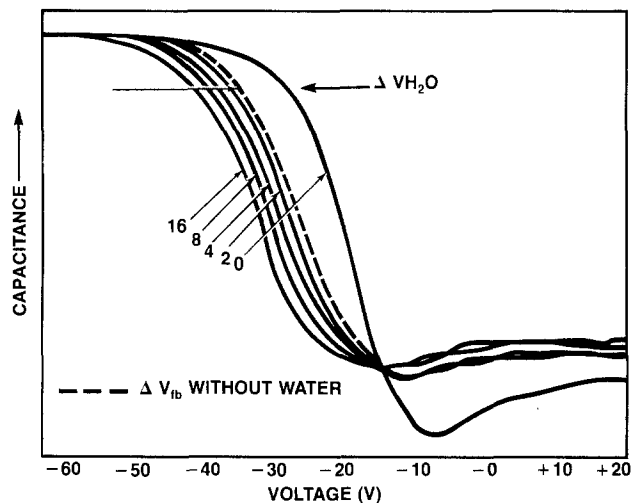


Fig. 4. C-V characteristics of PIQ-3 exposed to a 17% RH ambient for 22h and stressed at +5V and 225°C for 2-16 min.

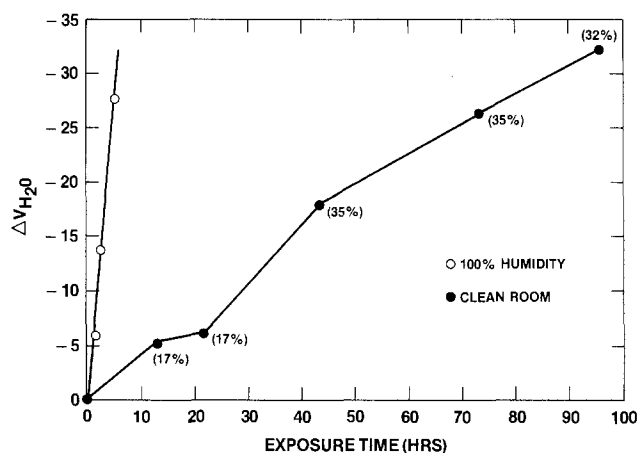


Fig. 5. Magnitude of ΔV_{H_2O} vs. exposed time for PIQ-13 at 100% RH and clean room humidity, varying as indicated in the parentheses.

RH did not revert to the original τ values following 200°C dehydration bake in dry N_2 atmosphere for as long as 72h. They did, however, revert to original τ values following 450°C dehydration bake in dry N_2 for 30 min. Such high temperature dehydration conditions were consistent with the release of H-bonded water. Samples exposed to lower relative humidities (i.e., 17-35%) for as long as 120h also

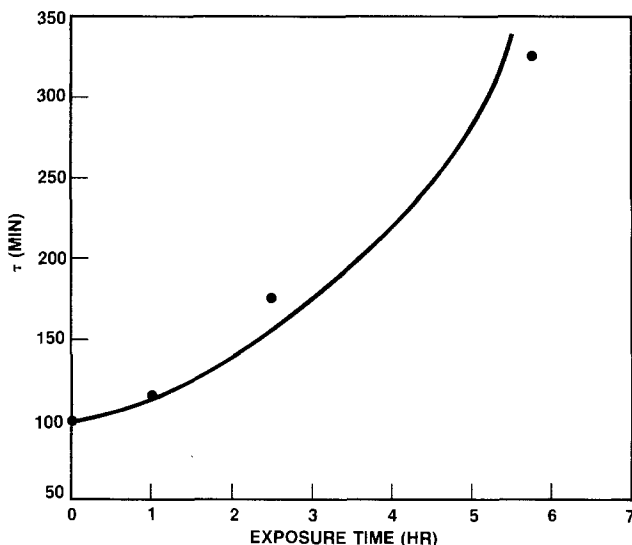


Fig. 6. The time constant of polarization for PIQ-13 as a function of exposure time to 100% RH conditions and +5V, 225°C stress conditions.

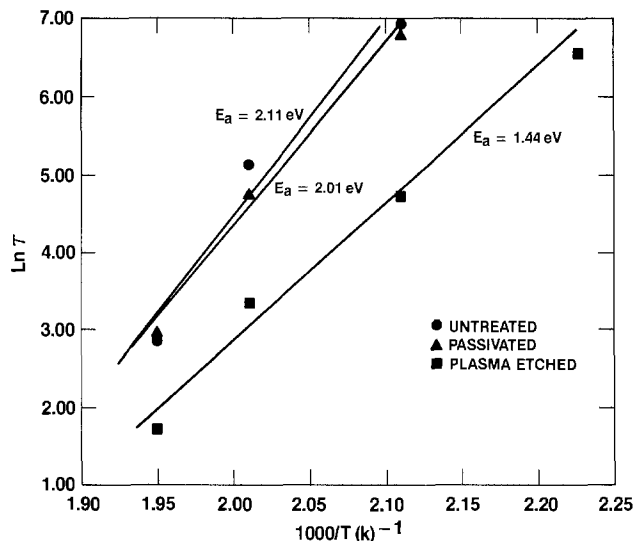


Fig. 7. Arrhenius plots for untreated, plasma-etched, and passivated PIQ-13 films.

exhibited increased τ values which reverted to original values on lower temperature, 200°C dehydration bake.

Processing effects on polarization.—A brief study was done to determine the effects of highly energetic UV irradiation associated with plasma processing on the polarization behavior of polyimide films. Two plasma processes were performed on deposited polyimide films: plasma etching of the polyimide film itself and passivation with a plasma-enhanced CVD film of silicon oxide.

Films with a thickness of $\sim 3.0 \mu m$ of cured PIQ-13 polyimide were etched to half their original thickness in a Dionex 3000 barrel reactor. Etching took place at 150°C and 0.5 torr in an O_2 plasma at 500W. The approximate etching time was 30 min. After etching, $1.5 \mu m$ of Al-Cu-Si was deposited, and C-V analysis was performed as previously described. For passivation, a 1000Å-thick film of plasma oxide was deposited on wafers which had $1.5 \mu m$ of cured PIQ-13 and Al-Cu-Si metallization. Passivation was performed in an AMT Plasma II reactor at 300°C and 0.3 torr. A plasma energy of 150W was used to react SiH_4 and N_2O in a carrier gas to form the silicon oxide film. Deposition time was approximately 5 min. The plasma oxide film was then selectively removed from the metal-patterned polyimide film, and C-V analysis was done.

Figure 7 shows Arrhenius plots for untreated, plasma-etched, and passivated PIQ films. While no significance beyond measurement error could be attributed to the differences in activation energy between the passivated film and the untreated control, there was a significant lowering of the activation energy for the plasma-etched film. In addition, this effect increased with increasing exposure and/or intensity of the plasma. This change in polarization could not be reversed by annealing the plasma-treated films at 450°C in N_2 for 1h.

Oxygen plasma treatments have been shown in the literature to affect other properties of polymer films, particularly in a 1-10 μm thick region at the surface. For example, general trends of increases in wettability and decreases in molecular weight have resulted for a number of different polymer films (8). Also, mechanical strength of surface layers has been altered as a result of exposing polypropylene to O_2 -containing and N_2O -containing plasmas (9). In general, the mechanism responsible for changes in these properties has been scissioning of polymer chains due to UV irradiation, with subsequent rapid termination of free radicals with oxygen (8). Such a mechanism may have been responsible for the changes in polarization behavior which occurred in the thin polyimide films studied.

Solvolt International assisted in meeting the publication costs of this article.

REFERENCES

1. K. Mukai, A. Saiki, S. Harada, and S. Shoji, International Electron Devices Meeting, p. 16 (1977).
2. A. Saiki, K. Mukai, S. Takahashi, K. Tamanaka, and S. Harada, "Reliability of Semiconductor Devices Using a Resin Insulation Structure," Hitachi Central Research Laboratories Bulletin, Japan.
3. R. Larsen, *IBM J. Res. Dev.*, **24**, 268 (1980).
4. A. Gregoritsch, Polyimide Passivation Reliability Study, Rel. Physics, 14th Annual Proceedings, 228 (1976).
5. G. Samuelson, *Organic Coatings and Plastics Chemistry*, **43**, 446 (1981).
6. G. Brown, Rel. Physics, 19th Annual Proceedings, Orlando, FL, 282 (1981).
7. E.H. Snow and M. E. Dumesnil, *J. Appl. Phys.*, **37**, 2123 (1966).
8. M. Hudis, "Plasma Treatment of Solid Materials," John Wiley and Sons, New York (1974).
9. H. Schonhorn, S. W. Ryan, and R. H. Hansen, *J. Adhesion*, **2**, 93 (1970).

Dependences of Magnetron-Sputtered SiO₂ Film Properties on Argon Pressure

Toshiaki Yachi and Tadashi Serikawa

Nippon Telegraph and Telephone Public Corporation, Musashino Electrical Communication Laboratory, 3-9-11 Midori-cho, Musashino-shi, Tokyo 180, Japan

Planar magnetron-sputtered SiO₂ films have been found to be desirable as insulating materials in integrated circuits, such as aluminum multilevel interconnections, because of their high deposition rates, very low deposition temperature, and good step coverage (1). Some studies on deposition rates and step coverage, as well as on applications for device fabrication, of such planar magnetron-sputtered SiO₂ films have been reported (2-5). However, dependences of the film properties on deposition conditions have yet to be made sufficiently clear (6). This note describes the dependences of the RF planar magnetron-sputtered SiO₂ film properties on argon pressure.

Experimental

SiO₂ film about 1 μm thick was deposited on (100)-oriented p-type 10 Ω cm resistivity silicon wafers of 3 in. diam by a RF planar magnetron sputtering apparatus with two targets. The system was pumped down to 3 × 10⁻⁴ Pa prior to in-bleeding of the argon, and sputtering was carried out at 0.3-2.0 Pa in argon. The barrel-type substrate holder, electrically at floating potential, had a 10 rpm rotation rate during deposition. The minimum spacing between the substrate and the target was 50 mm, and the targets used were 99.99% pure SiO₂ sheets, 5 × 15 in. and 1/8 in. thick. The RF forward power was held at 2.0 kW/target. The substrate temperature was also kept at 200°C. Some samples were annealed at 900°C for 20 min in nitrogen gas.

Film properties were evaluated by etching rate, transmission electron microscope (TEM) surface replica observation, and stress. Etching rates were determined by the film thickness decrease in 15:10:1 (H₂O:NH₄F:HF) buffered hydrofluoric acid solution at 30°C, which was measured by creating a step and then using the Talystep Height Reader. Film stresses were determined by comparing wafer curvatures before and after deposition, which were measured by the Newton rings method. Film densities were also measured by a gravimetric technique.

Results and Discussion

The SiO₂ film deposition rate vs. argon pressure is shown in Fig. 1. The deposition rate is maximum at 0.40 Pa. At an argon pressure above 0.40 Pa, the deposition rate decreases with regularity with an increase in argon pressure. The deposition rate at 2.00 Pa amounts to only about 60% of its maximum. At the higher pressures, this drop is due mainly to increased sputtered-particle scattering resulting from the discharge gas (7).

The dependence of the buffered HF etching rate on argon pressure is shown in Fig. 2, where the samples indica-

ted are deposited and annealed. The etching rates change markedly at the "critical pressure" of about 0.5 Pa. In the as-deposited samples, the etching rate of the film depos-

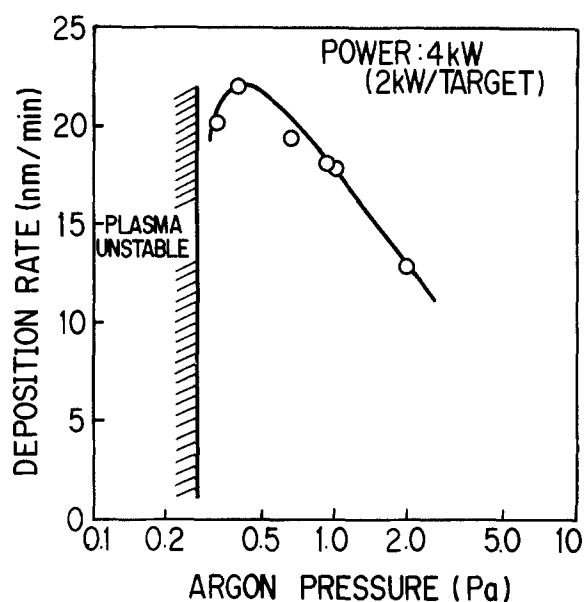


Fig. 1. SiO₂ film deposition rate vs. argon pressure

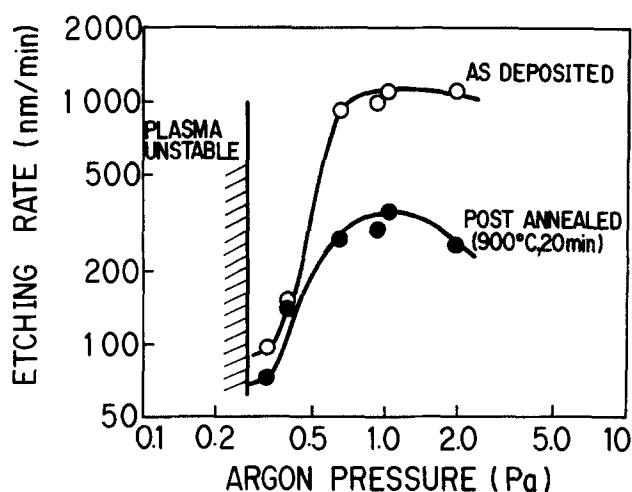


Fig. 2. SiO₂ film etching rates vs. argon pressure

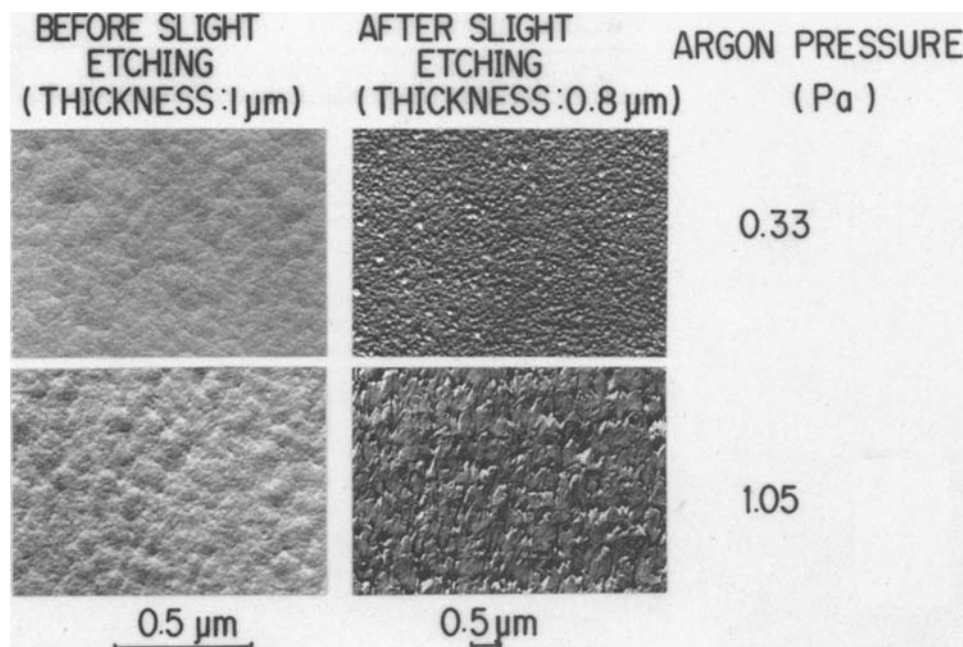


Fig. 3. TEM micrographs of as-deposited SiO₂ films.

ited at an argon pressure of 0.95 Pa is about 12 times greater than that for the film deposited at a pressure of 0.33 Pa. Although these etching rates are reduced over the entire argon pressure by annealing, the etching rate still exhibits a marked dependence on argon pressure.

TEM micrographs for as-deposited film before and after slight etching by buffered HF are shown in Fig. 3. Before slight etching the surfaces of the films deposited at both 0.33 and 1.05 Pa argon pressures show partial undulation. The surface of the film deposited at 1.05 Pa, however, has very small, shallow pits. The slightly etched film surfaces are markedly different for the two pressures. The film surface deposited at 0.33 Pa (below the critical pressure) shows comparatively shallow spherulike pits of about 0.1 μm diam, while the surface of the film deposited at 1.05 Pa (about the critical pressure) shows a deep leaflike roughness of about 0.5 μm overall.

TEM micrographs of annealed film before and after slight etching are also provided in Fig. 4. The films prior to etching indicate a scalelike surface, corresponding to the undulations in the as-deposited film surface. After

slight etching, the surface of the annealed film deposited at 0.40 Pa shows spherulike pits as in the as-deposited film, while the surface of the annealed film deposited at 2.00 Pa shows a marked roughness.

The SiO₂ film density also depends on the argon pressure. The density of film deposited at 0.33 Pa is 2.23 g/cm³, while the density of film deposited at 2.00 Pa is 2.10 g/cm³. Film density at 0.40 Pa corresponds to the thermally oxidized film density of 2.2 g/cm³ (8).

TEM micrographs and film density suggest that the marked increase in the etching rate of film deposited above the critical pressure arises mainly from the large amount of internal surface area associated with the microvoids present in these films.

The dependence of SiO₂ film intrinsic stress on argon pressure is shown in Fig. 5. The stresses are compressive. The stress also changes greatly at the critical pressure of about 0.5 Pa.

In a sputter deposition system the sputtered particles are emitted from the target, follow the cosine emission distribution and have an energy value of a few electron

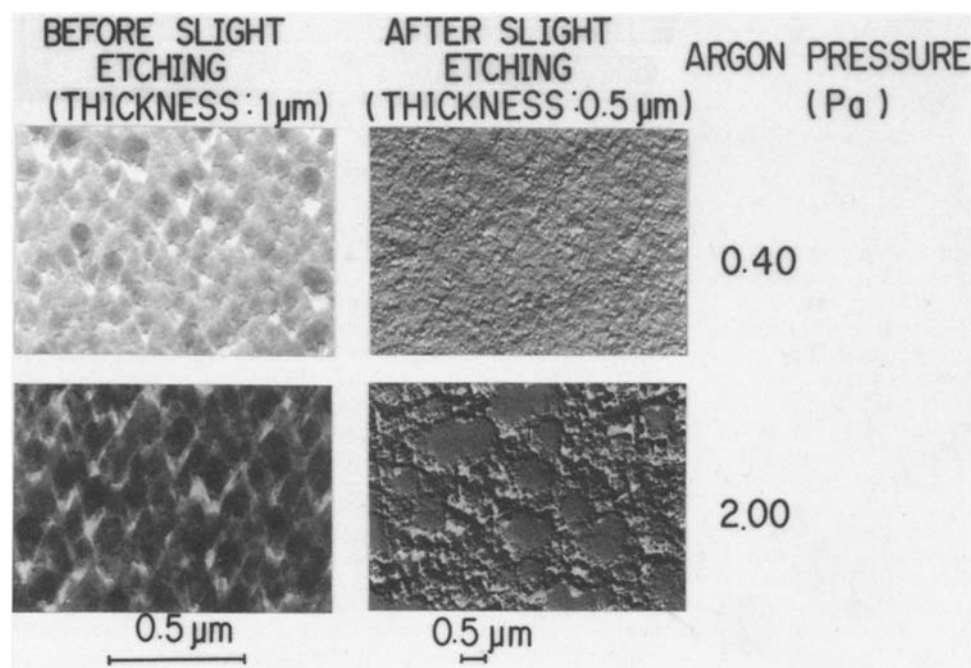


Fig. 4. TEM micrographs of annealed SiO₂ films.

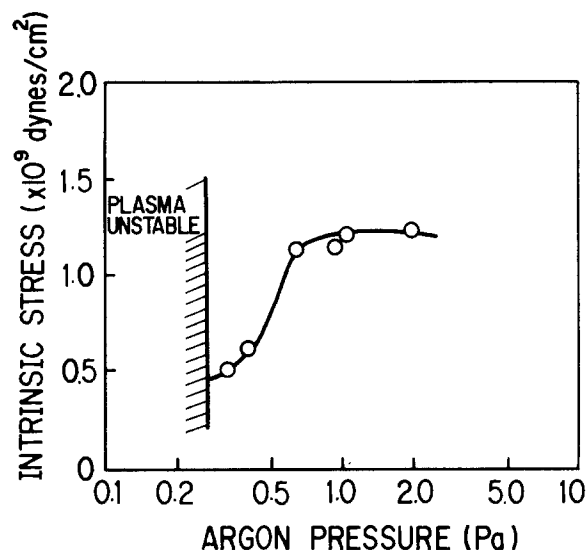


Fig. 5. SiO₂ film stress vs. argon pressure

volts (9). The energy of the emitted particles is reduced, and the direction of the particles changes as a result of gas-phase collisions with the argon atoms, as indicated in Fig. 1, and then reach the substrate. In this way, the energy of the sputtered particles is finally reduced so that it corresponds to the thermal energy of the gas.

Westwood calculated the distances which the particles travel normal to the sputtering target before their energies are reduced to the thermal energy of the gas. The distance increases with the mass and energy of the sputtered particle and with a decrease in argon gas pressure; for a 5 eV particle with a mass 60, the distance is about 8 cm at an argon pressure of 0.5 Pa (10).

The distance of 8 cm is near the space between the target and the substrate. At an argon pressure below the critical pressure 0.5 Pa, many SiO₂ particles reaching the substrate have an energy higher than the thermal energy of the gas. These SiO₂ particles with a higher energy migrate on the substrate; thus, the film contains few microvoids, and the film density increases. At an argon pressure above the critical pressure 0.5 Pa, however, the SiO₂ particle energy is thermalized before the particles reach

the substrate and the SiO₂ incident angle distribution is broad. This broad incident angle distribution produces a self-shadowing effect (11). The SiO₂ films contain microvoids, on account of both the low energy of the SiO₂ particle reaching the substrate and the self-shadowing effect. Thus, film density is low. Owing to etching along the microvoids, the films deposited at an argon pressure above the critical pressure 0.5 Pa have a markedly large etching rate. These microvoids can be partially removed by annealing.

In conclusion, the following results are demonstrated: (i) The SiO₂ films deposited below the critical pressure are dense (2.23 g/cm³) and have a low etching rate. (ii) The SiO₂ films deposited above the critical pressure contain many microvoids and film density decreases to 2.10 g/cm³. Moreover, the etching rate of the films deposited by buffered HF is 12 times greater than that of films deposited below the critical pressure. (iii) The stress of SiO₂ film is compressive and increases rapidly with the critical pressure.

Acknowledgment

The authors would like to thank A. Ishimoto and T. Wada for their valuable suggestions and encouragement.

Manuscript received June 11, 1984.

Nippon Telegraph and Telephone Public Corporation assisted in meeting the publication costs of this article.

REFERENCES

1. J. S. Chapin, *IBM J. Res. Dev.*, **18**, 37 (1974).
2. K. Urbanek, *Solid State Technol.*, **20**, 87 (1977).
3. R. A. Larsen, *IBM J. Res. Dev.*, **24**, 268 (1980).
4. T. Serikawa, *Jpn. J. Appl. Phys.*, **19**, L259 (1980).
5. T. Serikawa and T. Yachi, *This Journal*, **128**, 918 (1981).
6. K. Hara, Y. Suzuki, and Y. Taga, *Jpn. J. Appl. Phys.*, **18**, 2027 (1979).
7. S. Schiller, U. Heisig, and K. Goedicke, *Thin Solid Films*, **40**, 327 (1977).
8. A. S. Grove, "Physics and Technology of Semiconductor Devices," Chap. 2, John Wiley and Sons, Inc., New York (1967).
9. G. K. Wehner and G. S. Anderson, in "Handbook of Thin Film Technology," Chap. 3, L. I. Maissel and R. Glang, Editor, McGraw-Hill, New York (1970).
10. W. D. Westwood, *J. Vac. Sci. Technol.*, **15**, 1 (1978).
11. N. G. Nakhodkin and A. I. Shaldervan, *Thin Solid Films*, **10**, 109 (1972).

The Growth of Epitaxial Layers of Ga_{0.47}In_{0.53}As by the Vapor-Phase Epitaxy-Hydride Method Using a Gallium-Indium Alloy Source

Thomas E. Erstfeld and Kenneth P. Quinlan*

Rome Air Development Center, Solid State Sciences Division, Hanscom Air Force Base, Massachusetts 01731

Epitaxial structures of the ternary system, Ga_{0.47}In_{0.53}As, have found wide application in the fields of optoelectronic and microwave devices. These epitaxial layers have been prepared by various techniques: liquid-phase epitaxy (1), vapor-phase epitaxy (2), molecular beam epitaxy (3), and metal-organic chemical vapor deposition (4). All these methods have produced Ga_rIn_{1-r}As layers with room temperature mobilities in the 10,000 cm²/V-s range, with a high of 13,000 cm²/V-s for the liquid-phase epitaxy (3, 5-7). Carrier concentrations ranged from 10¹⁵ cm⁻³ to the mid-10¹⁶ cm⁻³.

The vapor-phase epitaxy (VPE) technique uses either AsCl₃ (chloride method) or AsH₃ (hydride method) as the source of arsenic. Higher mobilities have usually been achieved with the chloride method (8, 9) but the hydride method has many advantages that the chloride method

*Electrochemical Society Active Member.

lacks, e.g., ease of control, group V reactants are gaseous, etc. Most work with the VPE-hydride technique for the preparation of Ga_{0.47}In_{0.53}As have concentrated on the use of separate metallic sources for the group III elements with a double-barrel reactor. The use of an alloy source in the VPE-hydride technique offers two distinct advantages over the use of two separate metal sources: (i) the flow of hydrogen chloride over the source does not have to be as finely controlled as is necessary with separate metallic sources, and (ii) only a single-barrel reactor is needed. A study of the preparation of Ga_rIn_{1-r}As ternaries using an alloy source (Ga-In) with the VPE-hydride technique was carried out in order to evaluate the technique. This paper reports the effect of various parameters, e.g., source composition, hydrogen chloride pressure, deposition temperature, and operation time on the ternary compositions and growth rates.

The use of an alloy source for the preparation of $\text{Ga}_r\text{In}_{1-r}\text{As}$ by the VPE technique has been studied by a number of investigators. In 1965, Minden (10) used an alloy source of gallium and indium in a modified VPE-chloride method to prepare epitaxial layers of the ternary. Recently, Chatterjee *et al.* (11) studied the use of the alloy with a modified VPE-chloride technique and presented a thermodynamic model describing the system. They demonstrated that a low doped, lattice-matched gallium indium arsenide epilayer could be obtained in a reproducible and controlled manner. Kordos *et al.* (12) studied the growth of $\text{Ga}_r\text{In}_{1-r}\text{As}$ with the VPE-hydride system using a Ga-In alloy. Their results differ from those reported in this paper.

Experimental

The preparation of the epitaxial layers of the ternaries, $\text{Ga}_r\text{In}_{1-r}\text{As}$, was studied in the quartz reactor previously described (9). The quartz reactor has three temperature zones, source, mixing, and deposition, which are heated by "clam shell" resistance heaters. The reactor has three inlet flow systems for AsH_3/H_2 , HCl/H_2 , and H_2 . The flow rates are regulated by Tylan mass flow controllers. The reactants are the highest purity products obtainable: arsine (99.998%), as a 10% mixture in hydrogen (99.999%), hydrogen carrier gas (99.999%), hydrogen chloride (99.995%), indium (99.9999%), and gallium (99.9999%). The hydrogen carrier gas was further purified by a hydrogen purifier (Palladium Diffusion Process-Engelhard). The alloys were prepared by putting the appropriate amounts of the metals into a quartz boat. The masses of the alloys used varied between 99 and 107g. The surface areas of the alloys in the quartz boats were approximately 26 cm^2 . The alloys were prebaked for 50h in a hydrogen atmosphere before any runs were performed. This procedure as reported by Kordos *et al.* (12) lowers the carrier concentrations in the resulting epitaxial layers.

Compositions of the grown ternaries of $\text{Ga}_r\text{In}_{1-r}\text{As}$ were determined from Vegard's law plots of lattice constants *vs.* compositions. The lattice constants were determined by x-ray diffractometry with the $\text{CuK}\alpha$ irradiation using InP as an internal standard. Microprobe analyses verified this method of determining the composition. The growth rates were determined from the surface area of the substrate, mass of deposit, density of the ternary, and time duration of growth. The time of growth was usually 225 min.

The substrates were prepared from a liquid-encapsulated Czochralski (LEC)-grown InP(Fe-doped) boule. Slices were cut 3° off the (100) plane towards the (111) plane. The preparation of the InP substrates are described in Ref. (9).

Carrier concentrations (n) and mobilities (μ) were obtained from resistivity and Hall measurements at room temperature with the van der Pauw technique (13). A permanent magnet provided a field of 3 kG for the Hall measurements.

The residual compositions of the Ga-In alloys were determined by atomic absorption spectroscopy. The alloys for the analyses were remelted and quenched at 0°C to prevent formation of Ga-In solid solutions. During the course of a series of runs, the alloy becomes richer in indium content.

Results and Discussion

Various parameters were studied initially to determine the parameter values which produce high quality epitaxial layers with consistent growth rates. Superior quality epitaxial layers of the ternary, $\text{Ga}_r\text{In}_{1-r}\text{As}$, were obtained when the source, mixing, and deposition temperatures were 800°C , 850°C , and 700°C , respectively. The partial pressures of hydrogen chloride in these preliminary experiments were in the vicinity of 233 Pa. The partial pressure of AsH_3 was 1013 Pa, while the flow rate of hydrogen carrier gas was $980\text{ cm}^3/\text{min}$. The arsine and hydrogen were maintained at these values throughout the study. The x-ray diffractometry studies used for the determina-

tion of the lattice constants showed that the layers were normally of high quality and uniform composition. After these preliminary results were obtained, the determination of the alloy composition required to give a specific ternary composition of $\text{Ga}_r\text{In}_{1-r}\text{As}$ was undertaken. Growth rates of the ternary systems were determined as function of hydrogen chloride partial pressure and deposition temperature.

Figure 1 shows the composition of the ternary, $\text{Ga}_r\text{In}_{1-r}\text{As}$, obtained as a function of the alloy composition. The values depicted are for a deposition temperature of 700°C and a hydrogen chloride partial pressure of 233 Pa. The plot of the experimental data intersecting the $\text{Ga}_{0.47}\text{In}_{0.53}\text{As}$ composition line gives a value of 12.2 mole percent (m/o) gallium-87.8 m/o indium as the alloy necessary to prepare this ternary. The theoretical curve (Fig. 1) calculated from thermodynamic data shows that kinetic factors probably play a role in the deposition process. The differences between theory and experiment may not only be due to kinetic factors but may also be due to errors in the literature used in the calculation of thermodynamic values. Faktor and Haigh (14) have shown that errors in the literature can result in derived thermodynamic values that are inaccurate. Kordos *et al.* (12) reported that 7 m/o in the alloy produces the $\text{Ga}_{0.47}\text{In}_{0.53}\text{As}$ ternary. This large discrepancy between 7 m/o and that found in the present work (12.2 m/o) is not understood.

The compositions of the ternaries were studied as a function of the number of runs with an alloy. The plots obtained are shown in Fig. 2 and are typical of the ternary composition found for various alloys. Figure 2 shows the ternary compositions obtained from the two alloy compositions, 11.5 m/o Ga and 11.9 m/o Ga. The data show that the average composition of the ternaries exhibits a slight increase in the indium content as more runs are performed. An increase in the indium content of the ternary was expected since an analysis of an alloy after 30h of reaction time showed that the mole fraction of indium had increased by 4%. This is in agreement with the extrapolated value of 2% from the data of Chatterjee *et al.* (11). The data presented in Fig. 2 show that at least 14 samples lattice-matched to InP can be obtained with the same alloy.

Epitaxial layers with a value of $|\Delta a/a| < 10^{-3}$ are considered to be lattice-matched to InP. These values of $\Delta a/a$ correspond to $\text{Ga}_r\text{In}_{1-r}\text{As}$ layers that range in composition from $\text{Ga}_{0.45}\text{In}_{0.55}\text{As}$ to $\text{Ga}_{0.49}\text{In}_{0.51}\text{As}$. Inspection of Fig. 1 illustrates that alloy compositions with a gallium content between 11.9 and 12.9 m/o are capable of producing

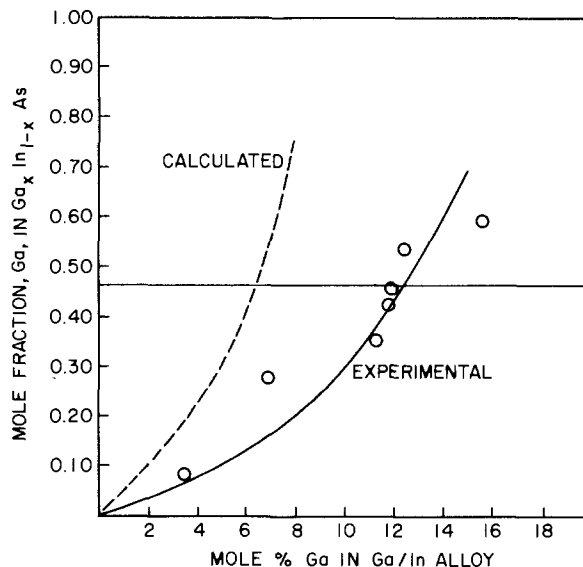


Fig. 1. Compositions of the ternaries, $\text{Ga}_r\text{In}_{1-r}\text{As}$, prepared from various alloy (Ga-In) mixtures. ---: Theory. \circ — \circ : Experimental. $\text{AsH}_3 = 1013\text{ Pa}$; $\text{HCl} = 233\text{ Pa}$; $\text{H}_2 = 980\text{ cm}^3/\text{min}$. Deposition temp. = 700°C ; mixing temp. = 850°C ; source temp. = 800°C .

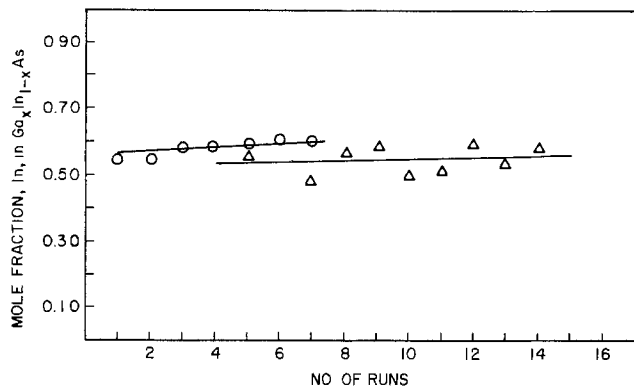


Fig. 2. Mole fraction of indium in $Ga_xIn_{1-x}As$ as a function of the number of runs. \circ — \circ : Alloy composition = 11.5 m/o Ga + 88.5 m/o In. \triangle — \triangle : Alloy composition = 11.9 m/o Ga + 88.1 m/o In. $AsH_3 = 1013$ Pa; $HCl = 233$ Pa; $H_2 = 980$ cm^3/min . Deposition temp. = $700^\circ C$; mixing temp. = $850^\circ C$; source temp. = $800^\circ C$.

$Ga_xIn_{1-x}As$ epitaxial that are lattice-matched to InP. The series of runs shown in Fig. 2 with an alloy composition of 11.9 m/o gallium produced epitaxial films that were lattice-matched to InP only one-third of the time. The values for the indium mole fraction in these samples ranged from 0.48 to 0.60, indicating the lack of reproducibility in these types of experiments. An important aspect of this type of work is depicted in these results, where a certain amount of scatter is observed in the composition of the epitaxial layers from one run to the next. This scatter may be attributed to the free radical nature of these reactions. Various workers (15) have shown that changes in the surfaces of a reactor greatly influence the course of free radical reactions. The surfaces of the reactors used for epitaxial growth undergo constant change when the different parameters of the system are varied. This scatter may account for the lack of observation of the increase in indium content for the ternaries obtained in the series of 25 runs reported by Kordos *et al.* (12).

The growth rates of the ternary, $Ga_xIn_{1-x}As$, were determined as functions of the source hydrogen chloride partial pressure and deposition temperature. Hydrogen chloride reacts with gallium and indium in the alloy to form $GaCl(g)$ and $InCl(g)$. The metal chlorides react with $As_4(g)$ at the InP-substrate surface in the deposition zone to form $Ga_xIn_{1-x}As$. The growth rates of various epitaxial layers grown from different alloy compositions as a function of HCl partial pressure are shown in Fig. 3. These results were obtained at a source temperature of $800^\circ C$ a mixing temperature of $850^\circ C$, and a deposition temperature of $700^\circ C$. The decrease in growth rate below ~ 233 Pa is probably due to the corresponding decrease in the concentration of the monochlorides of the group III elements being formed. The decrease in growth at HCl partial pressures greater than ~ 233 Pa may be due to the occupancy of the available arsenic adsorption sites by either the metallic monochlorides or hydrogen chloride molecules or both which inhibit the deposition reactions. This mechanism has been clearly described by Shaw (16, 17).

The maximum growth rates for the ternaries were obtained when the partial pressure of the hydrogen chloride was in the vicinity of 233 Pa. These growth rates for the various ternary compositions were investigated at $700^\circ C$ and $725^\circ C$, and the results are presented in Table I. The growth rate increases when the temperature is increased from 700° to $725^\circ C$, indicating that the growth is occurring in the kinetic-limited region. The table shows that the growth rates of $Ga_xIn_{1-x}As$ ternaries having indium mole fractions of 0.42-0.63 remain relatively constant at the two temperatures. These ternaries were prepared from alloy source compositions ranging from 15.9 to 11.1 m/o gallium. The ternaries, $Ga_{0.29}In_{0.71}As$ and $Ga_{0.08}In_{0.92}As$, produced from alloy sources of 6.9 and 3.2 m/o gallium, respectively, exhibited higher growth rates. InAs (18) has been shown to have a higher growth rate than GaAs (19)

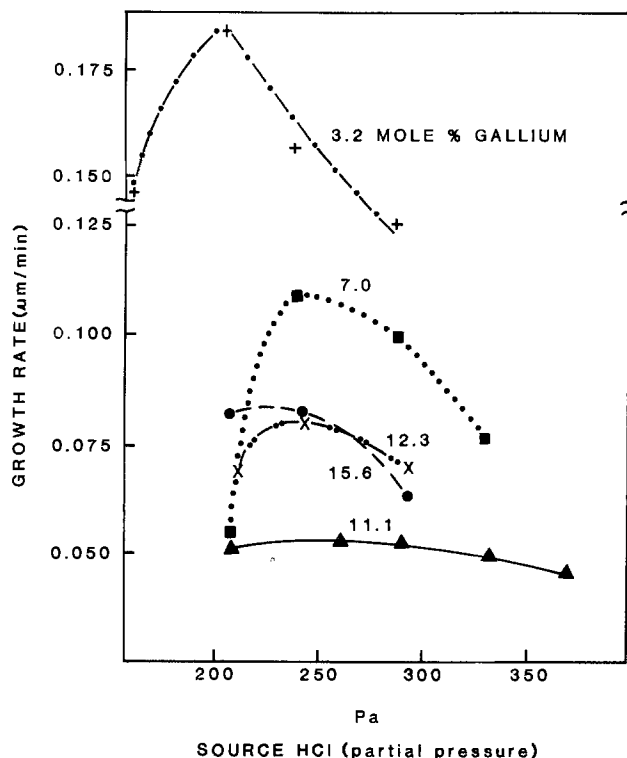


Fig. 3. Growth rate of epitaxial layers of $Ga_xIn_{1-x}As$ as a function of source HCl partial pressure using different alloys. $AsH_3 = 1013$ Pa; $H_2 = 980$ cm^3/min . Deposition temp. = $700^\circ C$; mixing temp. = $850^\circ C$; source temp. = $800^\circ C$. Compositions of layers prepared from the various alloys given in Table I.

in their homoepitaxial growth by the VPE-chloride technique.

Data showed that varying the partial pressure of the source hydrogen chloride had no effect on the composition of the epitaxial layer which is formed. This would be expected, because the ratio of $GaCl(g)$ to $InCl(g)$ would be independent of HCl partial pressures. No definite trend could be found in our work for the effect of deposition temperature on the composition of the epitaxial layer. Experiments carried out at $750^\circ C$ showed no effect on the composition. This was not surprising since the temperature coefficient of the compositional ratio of GaAs/InAs is very small (11). Kordos *et al.* (12) reported a 0.1% increase in gallium content of the ternary per degree.

The average energy of activation for the data presented in Table I is 170 kJ/mole. Activation energies of the formation of the epitaxial layers were obtained from Arrhenius plots of growth rates vs. reciprocal of the deposition temperatures. A value of 180 kJ/mol was found for the energy of activation for $Ga_{0.53}In_{0.47}As$ prepared from a 12.3 m/o Ga alloy. This value is in close agreement with the value of 44 kcal/mol (184 kJ/mol) reported by Hyder *et al.* (20). These authors used the VPE-hydride technique with separate metal sources.

Table I. Growth rates of $Ga_xIn_{1-x}As$ formed from various alloy compositions at two deposition temperatures. HCl partial pressure = 233 Pa, AsH_3 partial pressure = 1013 Pa, and H_2 flow rate = 980 cm^3/min . Source temp. = $800^\circ C$, mixing temp. = $850^\circ C$, and deposition temp. = 700° and $725^\circ C$.

Alloy composition (m/o Ga)	$Ga_xIn_{1-x}As$	Growth rate at $700^\circ C$ (μ/min)	Growth rate at $725^\circ C$ (μ/min)
15.6	$Ga_{0.58}In_{0.42}As$	0.08	0.13
12.3	$Ga_{0.53}In_{0.47}As$	0.08	0.14
11.9	$Ga_{0.46}In_{0.54}As$	0.08	0.12
11.5	$Ga_{0.43}In_{0.57}As$	0.08	0.11
11.1	$Ga_{0.37}In_{0.63}As$	0.05	0.11
7.0	$Ga_{0.29}In_{0.71}As$	0.11	—
3.2	$Ga_{0.08}In_{0.92}As$	0.19	—

Table II. Carrier concentrations (n) and mobilities (μ) of various ternaries at room temperature

Ternary	n (cm ⁻³)	μ (cm ² /V-s)
Ga _{0.56} In _{0.41} As	2.6×10^{15}	3982
Ga _{0.52} In _{0.48} As	4.4×10^{15}	4164
Ga _{0.51} In _{0.49} As	2.0×10^{15}	6601
Ga _{0.45} In _{0.55} As	2.4×10^{15}	5947
Ga _{0.41} In _{0.59} As	5.6×10^{15}	3064
Ga _{0.41} In _{0.59} As	3.4×10^{15}	7204
Ga _{0.40} In _{0.60} As	5.8×10^{15}	4991
Ga _{0.39} In _{0.61} As	8.4×10^{15}	3722

The carrier concentrations (n) and mobilities (μ) were determined for a series of samples and are reported in Table II. The results represent the average of a number of determinations for many of the ternaries. The carrier concentrations all fall in the vicinity of 4.0×10^{15} cm⁻³, while the mobilities range 3064-7204 cm²/V-s. A plot of the mobility vs. layer composition exhibits a curve with the appearance of two maxima. Whiteley and Ghandhi (21) reported a similar-type plot with less pronounced maxima and observed their highest mobility with a layer composition corresponding to Ga_{0.42}In_{0.58}As. The best values obtained in the present study for n and μ were 2.8×10^{15} cm⁻³ and 8852 cm²/V-s, respectively, for a sample whose composition was Ga_{0.41}In_{0.59}As. These higher mobilities when In > 0.53 have been attributed to less dislocation formation in layers under compressive stress (22). The present results compare favorably to the values previously reported: Kordos *et al.* (12) reported a value of 4000 cm²/V-s for the mobility for the Ga_{0.41}In_{0.59}As. Towe (23, 24) obtained a value of 9400 cm²/V-s for the mobility with a carrier concentration of 6.4×10^{15} cm⁻³ at room temperature for the composition Ga_{0.47}In_{0.53}As. Towe prepared the ternary with the VPE-hydride technique using two metal sources. Cheng and Cho (3) prepared Ga_{0.47}In_{0.53}As (Si-doped) by the MBE method and reported values of $\mu = 8500$ cm²/V-s and $n = 1 \times 10^{16}$ cm⁻³ at room temperature. A high value of 13,800 cm²/V-s for the mobility (with $n = 1.9 \times 10^{15}$ cm⁻³) at room temperature has been reported by Oliver and Eastman (6) for LPE prepared Ga_xIn_{1-x}As. The MOCVD technique for the growth of Ga_{0.47}In_{0.53}As used by Whiteley and Ghandhi (21) gave values of 5800 cm²/V-s and mid- 10^{16} cm⁻³ for μ and n at room temperature, respectively. These comparisons show that the system using the alloy source can be used to grow high quality Ga_xIn_{1-x}As epitaxial layers.

Recent analyses of the different techniques to grow epitaxial layers of the III-V compounds have shown that the roles of VPE, MOCVD, and MBE are expected to increase greatly (25) in the future. The present study shows that the VPE-hydride technique can be simplified by the use of an alloy source with no loss in the quality of the epitaxial layers. Further work with this system should give carrier concentrations and mobilities equal to those produced by the LPE technique.

Acknowledgments

The authors gratefully acknowledge the help provided by Jane A. Horrigan in performing x-ray analyses of these samples. Van der Pauw measurements were performed

by Joseph P. Lorenzo and Captain Kenneth J. Soda. Single-crystal InP substrates were grown and polished by Brian S. Ahern. The authors also wish to acknowledge the help and advice obtained from William D. Potter and John K. Kennedy through discussions with them. Finally, the authors wish to thank the team of A. K. Chatterjee, M. M. Faktor, M. H. Lyons, and R. H. Moss and the team of P. Kordos, P. Schumbera, M. Heyen, and P. Balk, both of whom were kind enough to send us preprints of their work on the growth of InGaAs from an alloy source.

Manuscript submitted Nov. 14, 1983; revised manuscript received June 11, 1984. This was paper 344 presented at the San Francisco, California, Meeting of the Society, May 8-13, 1983.

Rome Air Development Center assisted in meeting the publication costs of this article.

REFERENCES

1. N. Chand, A. V. Syrbu, and P. A. Houston, *Electron. Lett.*, **18**, 613 (1982).
2. N. Susa, Y. Yamauchi, H. Ando, and H. Kanbe, *Jpn. J. Appl. Phys.*, **19**, L17 (1979).
3. K. Y. Cheng and A. Y. Cho, *J. Appl. Phys.*, **53**, 4411 (1982).
4. J. S. Whiteley and S. K. Ghandhi, *This Journal*, **129**, 383 (1982).
5. S. Y. Narayan, T. P. Paczkowski, S. T. Jolly, E. P. Bertin, and R. T. Martin, *RCA Rev.*, **42**, 491 (1981).
6. J. D. Oliver and L. F. Eastman, *J. Electron. Mater.*, **9**, 693 (1981).
7. M. Razeghi, M. A. Poisson, P. Hirtz, B. de Cremoux, and J. P. Duchemin, Abstract I-2, p. 49, Electronic Materials Conference, Technical Abstracts, Colorado State University, Fort Collins, CO, June 23-25, 1982.
8. K. Fairhurst, D. Lee, D. S. Robertson, H. T. Parfitt, and W. H. E. Wilgoss, in "Proceedings of the 1980 NATO Sponsored InP Workshop, RADC-TM-80-07 (June, 1980)," Rome Air Development Center, Hanscom AFB, MA (1980).
9. T. E. Erstfeld and K. P. Quinlan, *J. Electron. Mater.*, **11**, 647 (1982).
10. H. T. Minden, *This Journal*, **112**, 300 (1965).
11. A. K. Chatterjee, M. M. Faktor, M. H. Lyons, and R. H. Moss, *J. Cryst. Growth*, **56**, 591 (1982).
12. P. Kordos, P. Schumbera, M. Heyen, and P. Balk, in "Proceedings of the International Conference on GaAs and Related Compounds," T. Sugano, Editor, p. 131, The Institute of Physics (Bristol), No. 63, Japan (1981).
13. L. J. van der Pauw, *Philips Res. Rep.*, **13**, 1 (1958).
14. M. M. Faktor and J. Haigh, *J. Cryst. Growth*, **58**, 291 (1982).
15. A. F. Trotman-Dickenson, "Gas Kinetics," p. 152, Academic Press, New York (1955).
16. D. W. Shaw, *This Journal*, **117**, 683 (1970).
17. D. W. Shaw, *J. Cryst. Growth*, **31**, 130 (1975).
18. O. Mizuno, H. Watanabe, and D. Shinoda, *Jpn. J. Appl. Phys.*, **14**, 184 (1975).
19. M. Makagawa and H. Ikoma, *ibid.*, **10**, 1345 (1971).
20. S. B. Hyder, R. R. Saxena, S. H. Chiao, and R. Yeats, *Appl. Phys. Lett.*, **35**, 787 (1979).
21. J. S. Whiteley and S. K. Ghandhi, *This Journal*, **130**, 1191 (1983).
22. B. I. Miller and J. H. McFee, *ibid.*, **125**, 1310 (1978).
23. E. Towe, *J. Appl. Phys.*, **53**, 5136 (1982).
24. E. Towe, M. S. Thesis, MIT, Cambridge, MA (1981).
25. J. M. Woodall, *Science*, **208**, 908 (1980).

Hot Wall Si-CVD at Reduced Pressures

C. Domínguez,¹ G. Pastor, E. Lora-Tamayo, and E. Domínguez

U.E.I. Microelectrónica, I.E.C. (C.S.I.C.), Madrid, Spain

In this technical note, results are given for silicon deposition in a hot-wall reactor at basic pressures of 10 and 76 torr and a temperature of 1223 K. Various initial gas mixtures were used (SiH_2 , $\text{Cl}_2/\text{HCl}/\text{H}_2$, $\text{SiH}_2\text{Cl}_2/\text{SiHCl}_3/\text{SiCl}_4/\text{HCl}/\text{H}_2$, $\text{SiHCl}_3/\text{H}_2$, and $\text{SiH}_2\text{Cl}_2/\text{H}_2$).

The system used for our experiments consisted of a reaction chamber, a vacuum system, and a gas system. The reaction chamber contained a 100 mm id quartz tube heated by a conventional diffusion furnace. The four heating zones this system provided guaranteed constant temperature over a length of 70 cm (with variations below 0.2%). The temperature profile was measured using a thermocouple (Pt-Pt 10% Rh) located inside the reactor under deposition conditions. The vacuum system consisted of a rotary pump in series with a variable-speed roots blower with a throttle valve. This provided a wide range of working pressures. The pressure was measured using two Baratron MKS pressure gauges, one for high ranges and one for low ranges. Chlorosilanes used for our experiments were SiH_2Cl_2 , SiHCl_3 , and SiCl_4 , as well as HCl and H_2 . Flow was measured and regulated using a mass-flow controller for gases and a vaporizer-type controller for liquid sources. All gases used were electronic-grade pure. For H_2 , a palladium cell purifier was used.

The depositions were made at a maximum flow of 2500 sccm, total pressures of 10 and 76 torr, and a gas temperature of 1223 K. Wacker Chemitronic silicon (100) wafers were placed vertically parallel or perpendicular to the gas flow, and no significant variations in the growth rate were observed.

The experiments were performed taking as a base the results obtained through a model (1) analogous to the one used by Sirtl and Hunt (2) and Van der Putte *et al.* (3). This program calculated the partial pressures of all the components of a gaseous mixture in equilibrium with solid silicon for the Si-H-Cl system. Results were obtained through the solution of a nonlinear system of equations generated by the application of the mass-action law to the formation reactions of the different components, starting from the elements. The pressure, temperature, and Cl/H ratio were used to define the composition of the gaseous phase.

To determine which type of thermodynamic equilibrium existed in the Si-H-Cl system, different series of experiments were performed, based on data provided by the model.

Series A: $\text{SiH}_2\text{Cl}_2/\text{HCl}/\text{H}_2$.—For the first group of experiments, a mixture of SiH_2Cl_2 , HCl, and H_2 was introduced into the system at the appropriate flow, under the equilibrium condition for each Cl/H ratio, and under successive situations of Si supersaturation at normal pressures of 10 and 76 torr. None of the experiments, despite having reached Si supersaturation levels [values above the equilibrium given by the model (1)] of close to 100%, revealed appreciable deposition or significant etching of the wafers. These results did not agree with model (1) for these conditions.

Series B: $\text{SiH}_2\text{Cl}_2/\text{SiHCl}_3/\text{SiCl}_4/\text{HCl}/\text{H}_2$.—These compounds were introduced simultaneously in the reactor in a proportion that anticipated this equilibrium (although the Si supersaturation was gradually increased). The experiments in this case continued to provide negative results.

Series C: $\text{SiH}_2\text{Cl}_2/\text{H}_2$.—Figure 1 shows the silicon growth rate for different SiH_2Cl_2 and H_2 flows (without HCl) at a

total pressure of 10 torr. Growth rates were much higher than those observed when HCl was present.

Series D: $\text{SiHCl}_3/\text{H}_2$.—Figure 2 shows the results of these experiments, together with those of SiH_2Cl_2 and H_2 at 76 torr. We found growth that was different from the series $\text{SiH}_2\text{Cl}_2/\text{H}_2/\text{HCl}$ under the same total pressure, temperature, and Cl/H ratio conditions. The crystalline structure was determined using x-ray diffraction, and polycrystalline silicon was obtained in every case.

It can be deduced from the analysis of prior experiments that, at equal or lower pressures of 76 torr, the growth rate is almost zero in the presence of HCl in the initial mixture and is considerably higher in the absence of HCl. Hence, the introduction of HCl in the initial mixture can be said to cause a drastic decrease of the growth rate.

We found that the growth rate, G , depends on the total flow in equilibrium, C_T^e , and on partial pressures of SiCl_2 , H_2 , P_{SiCl_2} , and P_{H_2} . The dependence can be expressed as

$$G = k(C_T^e)^\beta (P_{\text{SiCl}_2})^\gamma (P_{\text{H}_2})^\delta \quad [1]$$

where e expresses equilibrium values, k is a constant that depends on nucleation, and β , γ , and δ are exponents to be determined. Total flow in the equilibrium can be expressed as

$$C_T^e = C_{\text{SiCl}_2}^e + C_{\text{H}_2}^e \quad [2]$$

where $C_{\text{SiCl}_2}^e$ is equal to the initial dichlorosilane flow because, under experimental conditions, the equilibrium dissociation constant of equation

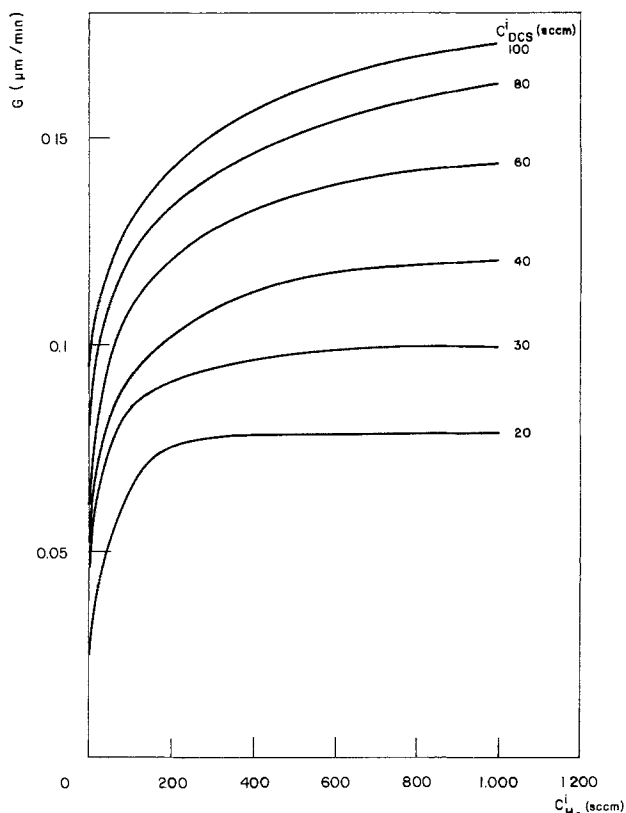
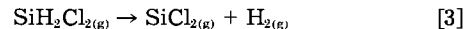


Fig. 1. Silicon growth rate under hydrogen flows for different dichlorosilane flows at 10 torr and 1223 K.

¹Present address: Department of Inorganic Chemistry, Complutense University, Madrid, Spain.

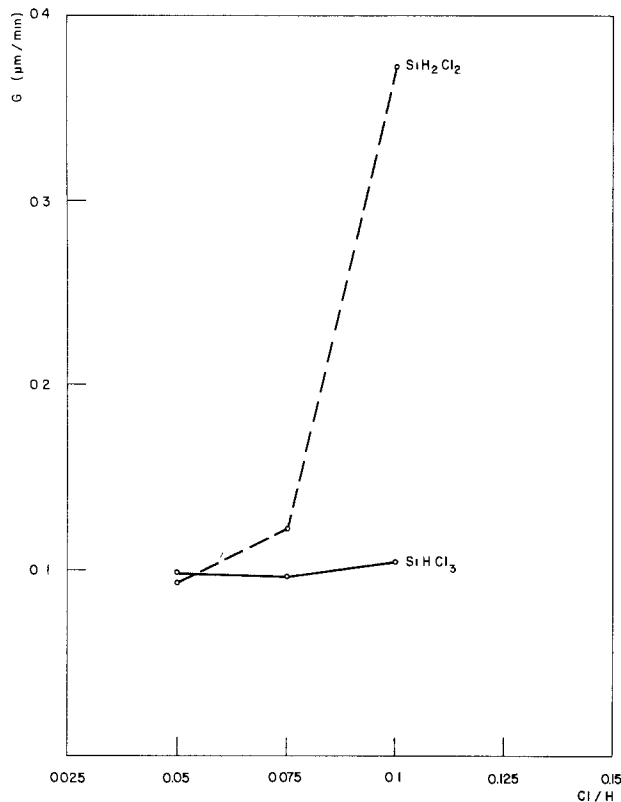


Fig. 2. Silicon growth rate under a Cl/H ratio for dichlorosilane-hydrogen and trichlorosilane-hydrogen at 76 torr and 1223 K.

is 3.322, and the degree of dissociation, without hydrogen and with it, is about 100%. $C_{H_2}^e$ is therefore

$$C_{H_2}^e = C_{H_2}^i + C_{DCS}^i \quad [4]$$

In other words, it is the sum of the initial hydrogen flows, i , and those obtained from the dissociation of

dichlorosilane as a result of the dissociation reaction [3]. Equation [1] can be expressed as

$$G = k' C_T^{e\beta} \left(\frac{C_{SiCl_2}^e}{C_T^e} \right)^\gamma \left(\frac{C_{H_2}^e}{C_T^e} \right)^\delta \quad [5]$$

where $(C_T^e)^\beta$ reflects diffusion dependence, and $(C_{SiCl_2}^e/C_T^e)^\gamma (C_{H_2}^e/C_T^e)^\delta$ reflects superficial adsorption of $SiCl_2$ and H_2 . The experimental values of the exponents are $\beta = 0.54$, $\gamma = 0.56$, and $\delta = 1$.

In summary, it has been confirmed that, at low pressures, the presence of HCl in the initial mixture produces silicon growth rates that are practically nil or negative for a supersaturation range of 0% to 120%. This result does not agree with the data based on the classic model of calculating the equilibrium for the Si-H-Cl system. In addition, a change in the silicon growth rate has been noted, according to the source of the silicon used in the initial mixture, so that a growth rate three times higher is obtained when SiH_2Cl_2/H_2 mixtures are used instead of $SiHCl_3/H_2$.

Finally, the silicon growth rate has been studied at a pressure of 10 torr and a temperature of 1223 K, with SiH_2Cl_2/H_2 mixtures and an LPCVD system modified in accordance with experimental conditions. The experimental results make it possible to determine the dependence of the silicon growth rate on the total flow and the partial pressures of $SiCl_2$ and H_2 in equilibrium. We have assumed that $SiCl_2$ comes mainly from the thermal decomposition of SiH_2Cl_2 .

Manuscript submitted Jan. 3, 1983; revised manuscript received May 25, 1984.

U.E.I. Microelectrónica IEC assisted in meeting the publication costs of this article.

REFERENCES

1. G. W. H. Staarink and F. Jakma, Private communication.
2. E. Sirtl, L. P. Hunt, and D. H. Sawyer, *This Journal*, **121**, 919 (1974).
3. P. Van der Putte, L. J. Giling, and J. Bloem, *J. Cryst. Growth*, **31**, 299 (1975).



Each issue of the **Journal** will have a section of "Comments." In this section, we provide a means via short pieces, *i.e.*, one column or less, to applaud, dispute, or otherwise discuss the papers published in the **Journal**. Space will be provided for one response by the paper's author(s) to each comment.

Since space available in each issue for the "Comments" section is limited; it is important to be concise.

Comments should be sent to the Editor, Dr. Norman Hackerman, President's Office, Rice University, P.O. Box 1892, Houston, TX 77251.

This is the second appearance of the "Comments" section.

Norman Hackerman
Editor

Sputter-Etching Planarization for Multilevel Metallization

H. Kotani, H. Yakushiji, H. Harada, K. Tsukamoto, and T. Nishioka
(pp. 645-648, Vol. 130, no. 4)

J. H. Thomas III and J. L. Vossen:¹ We should like to point out that the model employed by the authors for the variation of the sputtering yield with the angle of incidence of the bombarding ions is not applicable as a general model for all materials and bombarding species and energies.

The Sigmund theory² predicts a change in sputtering yield that rises as the angle of incidence increases, peaks, and then falls to zero at glancing incidence. The rate of increase and the angular position of the peak value depend upon the energy of the incident ions, the mass of the incident ion (as compared to the target atoms), and the target material. It has been verified both by computer simulation and experiment that the angle at which the peak sputtering yield occurs is between about 45° and 80°, depending on the conditions and materials involved.³

The authors' finding that the 45° facet angle developed in their experiment should be considered specific to the material being etched (SiO₂) and to the bombarding conditions used (which were not specified), and should not be extrapolated to other materials and bombarding conditions.

H. Kotani, H. Yakushiji, K. Tsukamoto, T. Nishioka,⁴ and H. Harada:⁵ We agree with the comments that the values of our results are specific and are not necessarily applicable to all materials and bombarding conditions. We consider the exact value of the facet angle in our experiments insignificant. It should be emphasized that the sputter etching in our experiment provides smooth surfaces and develops facets with angles of around 45°.

¹RCA Laboratories, Princeton, New Jersey 08540.

²P. Sigmund, *Phys. Rev.*, **184**, 383 (1969).

³P. D. Townsend, J. C. Kelly, and N. E. W. Hartley, "Ion Implantation, Sputtering and their Applications," p. 126, Academic Press, New York (1976); M. Kaminsky, "Atomic and Ionic Impact Phenomena on Metal Surfaces," pp. 159-163, Academic Press, New York (1965); H. H. Anderson and H. L. Bay, in "Sputtering by Particle Bombardment," Vol. 1, R. Behrisch, Editor, pp. 200-203, Springer-Verlag, Berlin (1981); C. M. Melliar-Smith and C. J. Mogab, in "Thin Film Processes," J. L. Vossen and W. Kern, Editors, pp. 523-525, Academic Press, New York (1978); J. P. Ducommun, M. Cantagrel, and M. Moulin, *J. Mater. Sci.*, **10**, 52 (1975); J. L. Vossen, *J. Phys. E*, **12**, 159 (1979); H. Dimigen, H. Luthje, H. Hubsch, and V. Convertini, *J. Vac. Sci. Technol.*, **13**, 976 (1976); P. G. Glöerson, *ibid.*, **12**, 28 (1975); H. Dimigen and H. Luthji, *Philips Tech. Rev.*, **35**, 199 (1975).

⁴Mitsubishi Electric Corporation, LSI Research and Development Laboratory, 4-1 Muzuhara, Itami, Hyogo 664, Japan.

⁵Mitsubishi Electric Corporation, Kitaitami Works, 4-1 Mizuhara, Itami, Hyogo 664, Japan.

Electrical Properties of Post-Annealed Thin SiO₂ Films

S. S. Cohen

(pp. 929-932, Vol. 130, no. 4)

P. A. Heimann:⁶ The author of this paper does not mention any checks for the presence of sodium, which might be present since the oxidations were done without HCl. In fact, the hysteresis of the C-V curves is in the direction which would be expected for mobile ions in the oxide. He assumes that this hysteresis is due to a layer of SiO at the oxide/silicon interface. However, stoichiometric SiO is not known to exist in the solid phase. The author does not give any reason for expecting that an oxygen-deficient layer (SiO_x) should contain "slow" charge trapping sites.

The author describes a cold trap for removing residual water from the oxygen, but he does not mention whether any other precautions were taken to keep water out. For instance, a double-walled quartz tube is often used to prevent atmospheric moisture from diffusing through the hot fused-silica furnace tube. Irene⁷ has shown that low concentrations of moisture can improve the breakdown voltages of thin oxides. This effect becomes probable for the very long annealing times described in this paper, so it is uncertain whether the improvement seen here is due to the annealing ambient or to trace moisture. This residual moisture could also affect the results of the second oxidation step, even if dry oxygen is being used.

The author might be underestimating the actual breakdown fields by choosing a breakdown definition of 1 μA. It is easy to pass currents much greater than 1 μA through thin oxides by Fowler-Nordheim tunneling without having catastrophic breakdown. The author should use a breakdown criterion that distinguishes between Fowler-Nordheim tunneling and irreversible breakdown.⁸ The breakdown histograms in his Fig. 3-5 probably should show higher breakdown fields.

S. S. Cohen:⁹ The following clarifications are provided to answer the comments made by P. A. Heimann about my paper.

1. Routine bias-temperature stress measurements were made in the course of the investigations to demonstrate that sodium was at a low level of $\approx 10^{10}$ cm⁻². Also, one who carefully reads the paper would notice that a re-oxidation treatment removed the observed hysteresis. Such a treatment is not known as capable of driving sodium out of the oxide film.

⁶AT&T Bell Laboratories, Murray Hill, New Jersey 07974

⁷E. A. Irene, *This Journal*, **125**, 1708 (1978).

⁸P. A. Heimann, *IEEE Trans. Electron Devices*, To be published.

⁹General Electric Company, Corporate Research and Development, Schenectady, New York 12301.

2. The possibility that water molecules made part of our ambient atmosphere was not ignored; it was clearly mentioned in the paper. The effects of these on the breakdown field was also discussed in view of Irene's paper.

3. Like most of the researchers in this field, we are well aware of the ability of thin SiO_2 films to withstand high level tunneling currents without suffering a destructive breakdown.¹⁰ We have, therefore, verified experimentally

that in our case a $1 \mu\text{A}$ current level could only be obtained after an irreversible breakdown of the MOS capacitors under study.

¹⁰D. A. Baglee and P. L. Sah, in "VLSI Electronics," Vol. 7, N. G. Einspruch, Editor, Academic Press, New York (1983); G. Gilenblat, D. M. Brown, C. A. Becker, and S. S. Cohen, "The Influence of Traps on the Conduction and Breakdown of the MOS Structure," General Electric Report no. 83CRD207 (1983).



Oxygen Reduction on Ruthenium Electrode Modified by Foreign Metal Adsorbates

R. R. Adžić, N. A. Anastasijević, and Z. M. Dimitrijević¹

Institute of Electrochemistry, ICTM and Center for Multidisciplinary Studies, University of Belgrade, Belgrade, Yugoslavia

Ruthenium is a metal of considerable importance in electrochemical technology, especially in combination with an oxidized Ti substrate as an electrocatalyst for Cl_2 evolution (1). A few studies of oxygen reduction on Ru(2) and RuOx/Ti (3) and RuO₂ (4) electrodes have been reported. Under certain conditions its activity for oxygen reduction is similar to that of the other noble metals (2). The oxidized surface of Ru, which would be encountered at potentials of practical oxygen cathodes, is completely inactive for O₂ reduction (2). This has been confirmed in the present work. Improving electrocatalytic properties of Ru for O₂ reduction appears interesting from both academic and practical viewpoints. In this work we have shown that a completely inactive surface of oxidized Ru can be modified by thallium and lead adsorbates in such a way as to show a pronounced activity for O₂ reduction. Also, these adsorbates catalyze O₂ reduction on the Ru surface which shows a high activity when cycled in the potential range encompassing H adsorption/absorption. The effects are of fundamental interest in developing an understanding of the relation of O₂ electrocatalysis to the surface oxide properties. They could furnish also some information on the properties of ruthenium oxides per se. Considering the importance of Ru as an electrode material these effects seem to have an applicative side.

Ru rod 99.999%, 4 mm diam x 6 mm was supplied by Metal Crystals Ltd, Cambridge, England. It was embedded in a Teflon holder to serve as a rotating electrode and polished in the standard way with a final polishing perfor-

med with 0.3 μm diamond paste. The solution, 0.1 M NaOH, was prepared from triply distilled water and "carbonate free" Barker's NaOH.

Fig. 1 gives a comparison of O₂ reduction on Ru and Ru modified by Tl adsorbate. An oxidized Ru surface, obtained by a repetitive cycling in the potential range (-) 0.7 V < E < 0.1 V does not show any activity for O₂ reduction. Almost identical curves have been obtained in the presence of N₂ or O₂ in this electrolyte. At high rotation rates a small reduction current is observed at the negative potential limit. Upon addition of Tl⁺ into the electrolyte the adatoms of Tl are formed at E = -0.6 V. At more positive potentials the Tl⁺ ions adsorb on the surface oxide layer. These two adsorbates change the properties of the oxide layer sufficiently to make it a good catalyst for O₂ reduction. A similar effect is caused by addition of Pb ions to the electrolyte (Fig. 2).

Fig. 3 shows O₂ reduction on Ru electrode when cycled in the potential range encompassing hydrogen adsorption/absorption. Under these conditions Ru shows a pronounced activity. This is in agreement with the data reported in reference (2). Tl adsorbates cause an enhancement of the reaction rate, causing a shift of half-wave potential by ~0.1 V. Oxygen reduction is strongly influenced by foreign metal adatoms obtained by underpotential deposition. The adatoms of Pb, Tl and Bi catalyze O₂ reduction on Au (5-9) and Pt (10). Besides adatoms, it has been shown that ions of the above metals, interacting with the oxidized layers of Au (6) and Pt (10), also cause a catalytic effect. This has been ascribed to the modification of the oxidized layers of Au and Pt which become better catalysts for O₂ reduction.

Permanent address: Institute of Chemical Power Sources, Belgrade, Yugoslavia.

Key words: oxygen reduction, ruthenium, modified surfaces, adatoms.

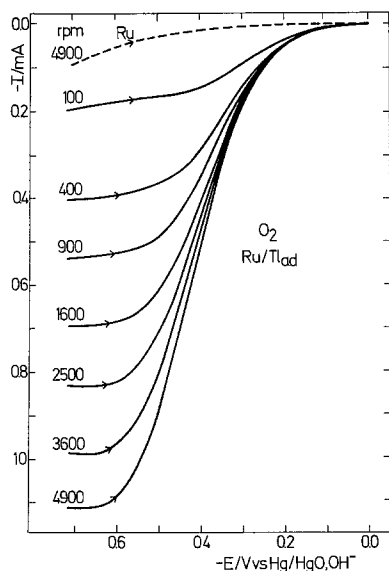


Fig. 1. O_2 reduction on Ru and Ru/Tl^{ad} in 0.1 M NaOH and 0.1 M NaOH + 1×10^{-4} M Tl⁺. Sweep rate 50 mVs⁻¹.

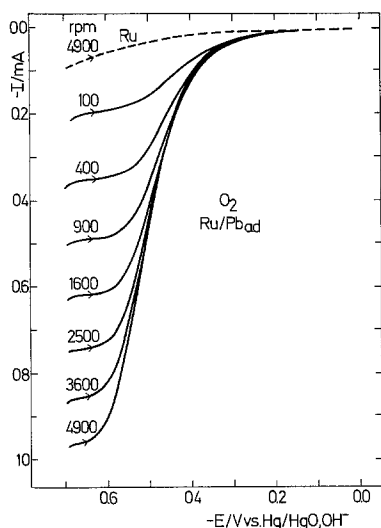


Fig. 2. Same as in Fig. 1 but for 1×10^{-5} M Pb²⁺ in 0.1 M NaOH.

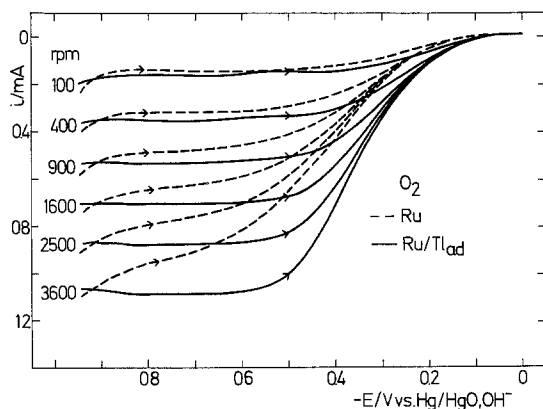


Fig. 3. Same as in Fig. 1 but for 1×10^{-5} M Pb²⁺ in 0.1 M NaOH and $E_{cat} = -0.95$ V.

These data show, for the first time, that foreign metal adatoms can modify an oxidized surface completely inactive for O_2 reduction and present further strong evidence of the modification of the oxide layer by ionic adsorption. Further work is in progress to determine the nature of the interaction of the oxidized Ru with foreign metals adsorbates, the extent of modification and kinetics and mechanism of O_2 reduction on such surface.

Acknowledgements: The authors are grateful to the Research Fund of the Republic of Serbia, Yugoslavia and the National Science Foundation, USA, grant No. YOR81/037, for financial support.

Manuscript submitted June 28, 1984; revised manuscript received August 27, 1984. References:

1. S. Trasatti and W.E. O'Grady in "Advances in Electrochemistry and Electrochemical Engineering" vol. 12, H. Gerischer and C. Tobias, Editors, pp 177-249, J. Wiley and Sons, Inc., New York (1982).
2. L. N. Nekrasov and E. I. Khruscheva, *Elektrokhimiya*, **3**, 166 (1967).
3. W.O. O'Grady, C. Iwakura, J. Huang and E. Yeager, In "Proceedings of the Symposium on Electrocatalysis", M. W. Breiter, Editor p. 286, The Electrochemical Society Inc., Princeton, N. J. (1974).
4. J. Horkans and M.W. Shafer, *This Journal*, **124**, 1202 (1977).
5. R.R. Adžić and A.R. Despić, *Zeit. Phys. Chem., N.F.*, **98**, 95 (1975).
6. R.R. Adžić, A.V. Tripković, N.M. Marković *J. Electroanal. Chem.*, **114**, 37 (1970).
7. R. Amadelli, N. Marković, R. Adžić and E. Yeager, *ibid*, **159**, 391 (1983).
8. J.D.E. McIntyre and W.F. Peck, *Proc. 3rd Symp. Electrode Processes*, pp. 332-349, The Electrochemical Society Inc. Pennington, N. J. (1979).
9. A. Zvetanova and K. Jüttner, *J. Electroanal. Chem.*, **119**, 149 (1981).
10. R. Amadelli, J. Molla and E. Yeager, *ibid*, **126**, 265 (1981).

A New Transition-Metal Penta-Chalcogenide Cathode for Secondary Lithium Cells

S. Okada, H. Ohtsuka, and T. Okada

Nippon Telegraph and Telephone Public Corporation, Ibaraki Electrical Communication Laboratory, Tokai, Ibaraki-ken, 319-11, Japan

INTRODUCTION

Low-dimensional van der Waals-bonded materials have been intensively studied for cathodes of secondary batteries based on rechargeable Li intercalation. In particular, transition-metal poly-chalcogenides, MX_n (M: transition-metal, X: chalcogen), have been supplying many candidates by combination of the elements (M,X) and stoichiometry (n). Dichalcogenides, typified by TiS_2 , exhibit relatively deep rechargeability and high rate capability due to the presence of straight Li diffusion pathways (1). On the other hand, higher chalcogenides such as $NbSe_3$ and $NbSe_4$ tend to exhibit highly specific capacities due to the presence of polychalcogen bonds which are reducible for Li intercalation (2).

Here, we report $ZrTe_5$ and $HfTe_5$ cathode properties in MX_5 for the first time. MX_5 ($ZrTe_5$ and $HfTe_5$) is the highest chalcogenide in MX_n and the atomic arrangement induces some expectation for a rechargeable high-capacity cathode material. MX_5 contains both layer and chain structures with the extra " X_2 " atoms linking the " MX_3 " chains into layers (3). These layers are weakly held together by van der Waals type forces. Correspondingly, a single crystal has cleavage properties along the a-c plane (X_2 -layer) with the longest dimension parallel to the a-axis (MX_3 -chain). Furthermore, $ZrTe_5$ and $HfTe_5$ show the lowest resistivity along the a-axis, $\sim 7 \times 10^{-4} \Omega cm$ at room temperature (4), and anisotropy in the a-c plane, $\rho_c / \rho_a = 2 \sim 3$, is quite small compared with that of typical MX_3 , e.g., 16 of $NbSe_3$ (5).

EXPERIMENTAL

MX_5 was synthesized from stoichiometric amounts of 99.9% Zr (99.8% Hf) and 99.999% Te by iodine vapor transport (5 mg per cc of the quartz ampule volume) in a $470 \sim 420^\circ C$ thermal gradient for a month. Most of the material were confirmed by X-ray powder

diffraction analysis as $ZrTe_5$ ($HfTe_5$) with the same lattice parameters given by Furuseth et al (3), that is, $a = 3.9876 \text{ \AA}$, $b = 14.502 \text{ \AA}$ and $c = 13.727 \text{ \AA}$ for $ZrTe_5$, $a = 3.9743 \text{ \AA}$, $b = 14.492 \text{ \AA}$ and $c = 13.730 \text{ \AA}$ for $HfTe_5$.

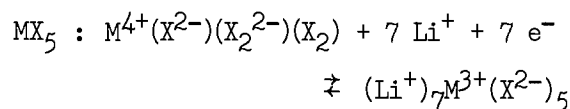
The cathode pellet (250 mg/cell) was prepared by mixing the sieved MX_5 powder (35 mesh) with carbon powder (Ketjen black) and polytetrafluoroethylene powder in a weight ratio of 78:20:2. The surface area of the cathode pellet in a coin type cell (23 mm diameter, 2 mm thickness) was 2 cm^2 . The Li content in each cell was 200 mAh. The electrolyte, used here, was 1M $LiClO_4$ -propylene carbonate/1,2-dimethoxyethane (1:1 vol%) with a water content of less than 50 ppm. The cell properties were measured galvanostatically and the open circuit voltages (OCV) were determined by discharge at regular intervals (discharging at 0.5 mA/cm^2 for 7 hr and resting for 50 hr). All set-up operations and measurements were carried out in a dry box filled with Ar gas.

RESULTS AND DISCUSSION

Figure 2 shows open circuit voltages and several discharge curves of $ZrTe_5$. Though the cell capacity above 1.5 V gradually decreased (260, 200, 100 and 50 Ah/kg) with an increasing current density (OCV, 0.5, 1.5 and 5 mA/cm^2), there are intrinsic similarities in each profile. In addition, the profiles of $HfTe_5$ agree with those of $ZrTe_5$.

This common $ZrTe_5$ and $HfTe_5$ behavior suggests that the MX_5 structure itself plays an important role in the cell reaction. The first plateau region on the open circuit voltage curve corresponds to 7 Li/ MX_5 (260 Ah/kg- $ZrTe_5$, 230 Ah/kg- $HfTe_5$), compared with 5 Li/ MX_4 (e.g., $NbSe_4$), 3 Li/ MX_3 (e.g., $NbSe_3$) and 1 Li/ MX_2 (e.g., $NbSe_2$) (6). The stoichiometry of Li/ MX_5 is accounted for by reduction of both the chalcogenide and the metal ions as follows;

Key Words: $ZrTe_5$, $HfTe_5$, Secondary Li cell, Intercalation.



Although the cell reaction mechanism beyond 7 Li/MX₅ is not clear, MX₅ cathodes show rechargeability for several cycles at least within this depth. The typical cycling behavior of ZrTe₅ at 1 Li/ZrTe₅ depth and 0.5 mA/cm² rate is given in Fig. 3. In terms of rechargeability, ZrTe₅ and HfTe₅ were also much the same. The cycle number was about 20 times to 2 Li/MX₅, but to 1 Li/MX₅ it exceeded 180 times. Commonly, most higher chalcogenides except NbSe₃ show over 100 cycles within the limits of 1 Li/MX_n. This good rechargeability to 1 Li/MX₅ may be mainly attributed to metal ion reduction/oxidation (M⁴⁺ ⇌ M³⁺) with Li intercalation/deintercalation.

In summary, the cathode properties of MX₅ are shown in Table I, compared with the other types of MX_n. It is worth while noting that the capacity of MX₅ reaches 7 Li/MX₅ for the 1.5 V cutoff, though a rechargeability of over 100 times is so far restricted to 1 Li/MX₅. This result involves a new possibility, that is, if a lighter MX₅ like TiS₅ can be synthesized and reacted with up to 7 Li in the same manner as ZrTe₅ or HfTe₅, the theoretical capacity is estimated to be 900 Ah/kg for TiS₅. Such MX₅ cathode properties are still open to future study.

ACKNOWLEDGEMENTS

The authors would like to thank Dr. A. Yamaji, C. Uemura, M. Kakuchi and A. Shibukawa for their helpful discussion. We are also grateful to Prof. T. Sambongi and Assistant Prof. M. Ido of Hokkaido University for their kind support.

REFERENCES

- 1) G.L. Holleck and J.R. Driscoll, *Electrochim. Acta*, **22**, 647(1977).
- 2) D.W. Murphy, F.A. Trumbore and J.N. Carides, *Electrochem. Soc.*, **124**, 325 (1977)
- 3) S. Furuseth, L. Brattas and A. Kjekshus, *Acta. Chem. Scand.*, **27**, 2367(1973)
- 4) S. Okada, T. Sambongi, M. Ido, Y. Tazuke, R. Aoki and O. Fujita, *J. Phys. Soc. Jpn.*, **51**, 460(1982)
- 5) N.P. Ong and J.W. Brill, *Phys. Rev.*, **B15**, 5265(1978)
- 6) D.W. Murphy and F.A. Trumbore, *J. Cryst. Growth.*, **39**, 185(1977)

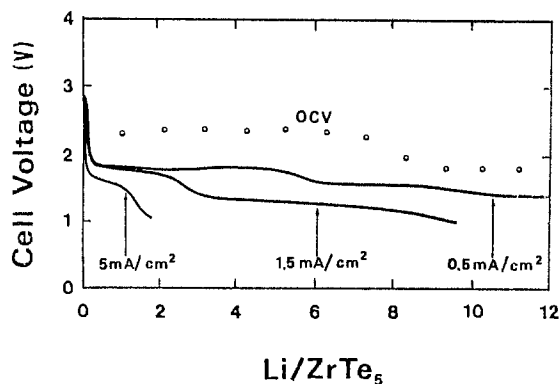


Fig. 1. Current dependence of ZrTe₅ discharge characteristics.

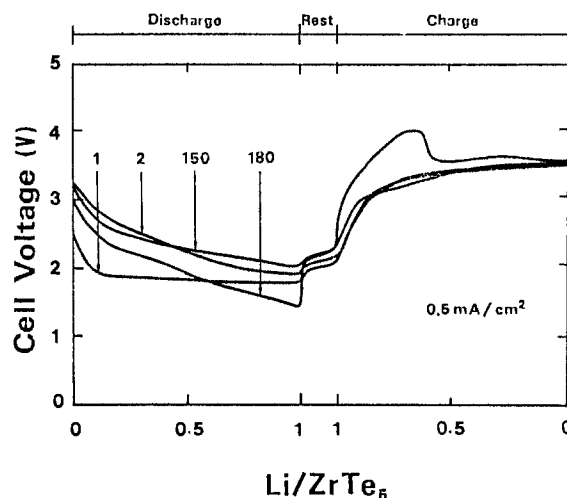


Fig. 2. Typical cycling behavior of ZrTe₅ at 1 Li/ZrTe₅ depth and 0.5 mA/cm² rate.

Table I. Approximate theoretical cathode capacities for MX_n.

Cathode	Li/mole ^{a)}	Ah/kg ^{b)}	Ah/cc ^{c)}
TiS ₂	1	240	0.8
NbSe ₃	3	240	1.6
NbSe ₄	5	330	-
ZrTe ₅	7	260	1.6
HfTe ₅	7	230	1.6

a: 1.5V cutoff

b: Calculated on the basis of MX_n weight.

c: Calculated on the basis of MX_n density.

Manuscript submitted August 21, 1984.
Nippon Telegraph and Telephone Public Corporation assisted in meeting the publication costs of this article.

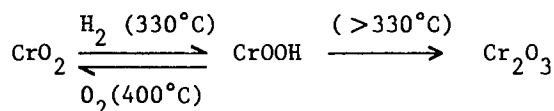
Electrochemical Conversion of CrO₂

D. Fousse, V. Jovancicevic,¹ and F. Tissier

Centre de Recherches du Fer Blanc, 57103 Thionville, France

Despite a number of interesting properties, such as ferromagnetism and "metallic" electrical conductivity ($10^4 \Omega^{-1} \text{cm}^{-1}$), CrO₂ is not well known by the electrochemists. This situation may be explained by relative chemical and electrochemical instability of the oxide and by difficulty in the preparation of the solid electrodes. One can suppose that its oxido-reduction properties (chromium valence IV) and/or metallic character can play a role in the electrocatalysis or in the chromate-passivated films behavior.

In the solid state chemistry, CrO₂ formed by the thermal decomposition of CrO₃ was extensively studied (1 - 3). In particular, the interconversion of CrO₂ to CrOOH and/or Cr₂O₃ was examined as a function of the temperature and is summarized by means of the equation :



The interconversion process was explained by the analogy between a tetragonal structure of CrO₂ and an orthorhombic distortion of rutile structure of CrOOH (2).

Besides, some literature results on the composition of the passive film on chromium (4) and chromate-passivated film on iron (5) allow to design a non-stoichiometric close to CrO₂ and a double layer chromium oxide structure, respectively. Nevertheless, a

1. Present address : Texas A & M University, College Station, Texas 77843

Key words : chromium dioxide, chromium-passivated film, electroconversion.

prevalent model of chromate passivation films is chromium trivalent oxide-hydroxide structure (6 - 8). In XPS spectroscopy, it is fairly difficult to obtain conclusive evidence of CrO₂ presence in the film since this compound is easily reduced to Cr₂O₃ by electron, ion or prolonged X-ray bombardment (9).

As a part of investigation on the composition of the electrolytically chromium coated steel (an industrial packaging material), the electrochemical behavior of CrO₂ in neutral NaH₂PO₄ (pH = 7) solution have been studied in the relation with those of Cr₂O₃ and Cr(OH)₃, using cyclic voltammetry. Considerable attention has been paid on the procedure of preparation of the oxide layers. The specimens were made from pressed (greater than 98 % pure) powder on platinum "soft" substrate to provide a 0.1 mm thin solid layer. The chromium dioxide (CrO₂) was obtained by courtesy of Kodak Pathé France.

The cyclic voltammograms on CrO₂ are shown in Fig. 1. In the region preceding oxygen evolution reaction at 0.35 V/SSE one can observe two characteristic features relative to CrO₂ layer ; an oxido-reduction process at about 0.2 V/SSE (sweep increasing currents) and a reduction process at - 0.2 V/SSE (sweep decreasing current) in the oxide. The "steady state" voltammetric curve obtained after ten sweeps (Fig. 1b) indicated that two steps reversible oxido-reduction reactions take place. No cathodic reduction peak at -0.2 V/SSE means that the transformation of the oxide produced in the course of the potential cycling is stopped. The same voltammogram was obtained with the previously potentiostatically reduced (- 0.2 V/SSE) CrO₂.

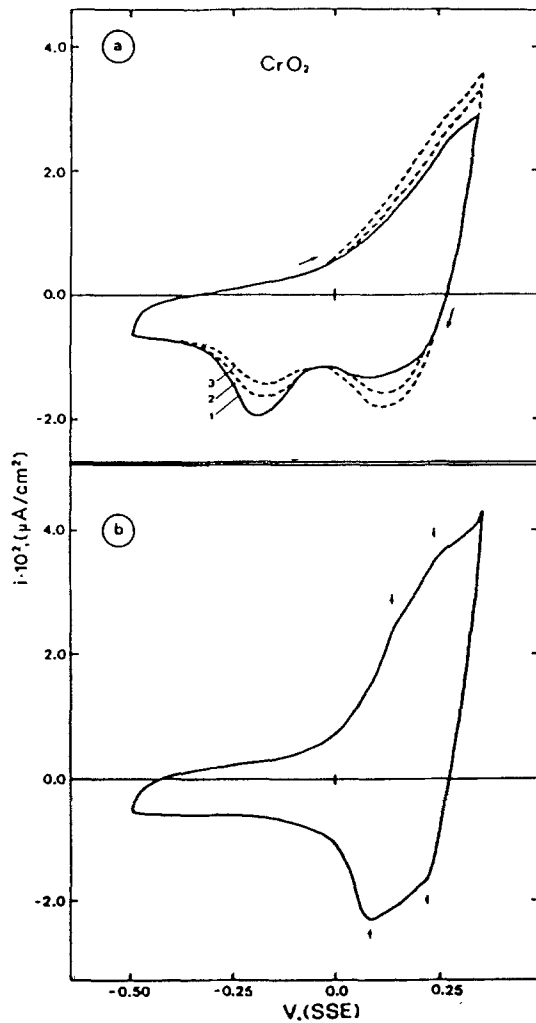
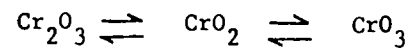
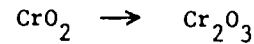


Fig. 1 : Cyclic voltammograms of CrO₂ for three first sweeps (a) and "steady state" curve after ten sweeps (b) ; scan rate = 20 mV/sec.

The double-peak feature of CrO₂ (arrows in Fig. 1b) was examined in relation with the cyclic voltammograms on Cr₂O₃ and Cr(OH)₃ oxides obtained in the same conditions (Fig. 2). Cr₂O₃ shows the same marked less than 0.05 V reversible double-anodic peak (second peak is more reversible than the first one). Conversely, Cr(OH)₃ presents only double layer behavior.

Two steps reversible oxidation of Cr₂O₃ can be assigned to the consecutive oxidation to CrO₂ and CrO₃.

Then the electrochemical conversion (Fig. 1) of CrO₂ can be summarized in terms of the following reactions :



the first one is irreversible reduction of CrO₂ and the second one is a reversible oxido-reduction of formed Cr₂O₃. The chromium dioxide participates in both reactions, as a bulk oxide and an intermediate oxide product, respectively. At the beginning of the cycling of the potential (Fig. 1a), the reduction of CrO₂ is produced at two different potentials separated by 0.35 V. One can assume that this difference is due to the different crystallographic structures of CrO₂.

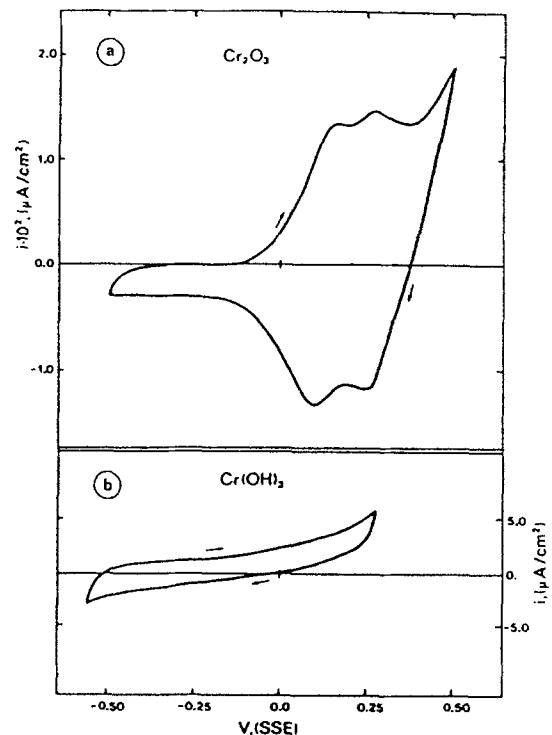


Fig. 2 : Cyclic voltammograms of Cr₂O₃ (a) and Cr(OH)₃ (b) ; scan rate = 20 mV/sec.

In this paper we give the evidence of the electrochemical stability of CrO₂ and the role that it can play as a component of the chromate passivation film. In the case of chromium coated steel a subsequent anodic oxidation allows to reduce the porosity of the chromium oxide film, more than by ten times (10). The improvement of the passivating properties may be ascribed

to the formation of the high conducting CrO_2 .

Besides, the metallic conductivity of CrO_2 and its electrochemical stability could be used to promote it, for example, as an electrocatalyst for oxygen evolution reaction.

REFERENCES

1. N.C. Tombs, W.J. Croft, J.R. Carter and J.F. Fitzgerald, *Inorg. Chem.*, 3, 1791 (1964).
2. I. Ikemoto, K. Ishii, S. Kinoshita, H. Kuroda, M.A. Alario-Franco and J.M. Thomas, *J. Solid State Chem.*, 17, 425 (1976).
3. R. Saes-Puche and M.A. Alario-Franco, *J. Solid State Chem.*, 38, 87 (1981).
4. A.M. Sukhotin, E.I. Antonovskaya and A.A. Pozdeeva, *Zh. Fiz. Khim.*, 36, 2368 (1962).
5. A.T. Vagramyan and D.N. Usachev, *Zh. Fiz. Khim.*, 32, 1900 (1958).
6. I. Inui, K. Saijyo and N. Shimizu, *Kinzoku Hyomen Gitjutsu*, 32, 80 (1981).
7. T. Hiroshi and K. Yoshitaka (Nippon Kokan K.K.), German Pat. 2,600,654 (1976).
8. S. Maeda, T. Asai, H. Omata and H. Okada, *Proceedings of 10th Congress on Metal Finishing, Interfinish 80*, ed. by S. Haruyama, p. 432, Kyoto (1980).
9. D. Fousse and F. Tissier, unpublished results.
10. V. Jovancicevic (Centre de Recherches du Fer Blanc), Patent applied for.

Manuscript submitted March 19, 1984.

Centre de Recherches du fer Blanc assisted in meeting the publication costs of this article.



Cation-Vacancy Model for MnO₂

Paul Ruetschi*

Leclanché S. A., 1400 Yverdon, Switzerland

ABSTRACT

A cation-vacancy model for electrochemically active manganese dioxides (γ -MnO₂ and ϵ -MnO₂) is presented. According to this model, the crystal structure, composed of closely packed O²⁻ ions which are octahedrally coordinated to Mn²⁺ ions, the [MnO₆] octahedra sharing edges and corners, contains [Mn] vacancies. Each vacancy is coordinated to, and electrostatically compensated by, four protons. The protons are present in the form of OH⁻ ions, these latter replacing O²⁻ in the lattice, without noticeable change in lattice parameters. Many hitherto unexplained phenomenological and experimental facts, relating to chemical composition (water content), density, electrochemical capacity, proton-transfer rate, electronic conductivity, and electrode potential of MnO₂, can be reconciled, and quantitatively predicted, on the basis of the present theory. In particular, electrochemical reactivity of MnO₂ in battery electrodes is shown to be due to the presence of cation vacancies in the lattice.

The large-scale use of MnO₂ for battery electrodes is continuing and is extending today also to nonaqueous lithium cells. Annual worldwide consumption for battery electrodes is now estimated at 400,000 tons. Although progress has been made in the characterization of MnO₂, with respect to structure and electrochemical behavior (1, 2), some aspects, relating in particular to the property called "electrochemical reactivity," remain unexplained. The reasons why certain forms of MnO₂, for instance, the γ and ϵ modifications, are highly reactive and may undergo electrochemical reduction at high rates, while other forms, for instance, the β modification, are relatively inactive, are still not fully understood (3).

The fact that the electrochemically active forms (γ - and ϵ -MnO₂) always contain in the crystal structure a considerable amount (typically 4% per weight) of "structural," "chemically bonded," or "combined" water, has been recognized for a long time (4-11). This structural water appears to be distributed over a wide range of "absorption energies" and can be removed progressively by heating to increasing temperatures in the range from about 100° to 400°C (12-17). It can thus be clearly distinguished from water which is physically adsorbed on the surface of the crystallites and which may be desorbed by applying vacuum at room temperature, or by heating without vacuum to just above 100°C. Chemisorbed water at the surface (surface OH⁻ groups) should have a binding energy approaching that of the structural bulk water. A large portion of the structural water may be removed by heating without apparent change in the x-ray powder diffraction patterns (18, 19). The presence of structural water influences not only electrochemical reactivity (4-9, 11, 20, 21), but also other properties, such as density (22, 23), electronic conductivity (14, 21, 24), and electrode potential (20, 25). However, to date, there is no clear understanding of the relation between water content and these properties.

The structural water in γ - and ϵ -MnO₂ modifications has been thought to be present, at least partially, in the form of OH⁻ ions, replacing O²⁻ in the lattice (7, 8, 19, 26-29). This requires, for charge balance, an equivalent number of Mn³⁺, replacing Mn²⁺ (30-34). However, there is, in total, always more structural water present than could be accounted for by the average state of oxidation (or val-

ency) of manganese. Thus, additional water, in the form of "interstitial" H₂O, or surface-adsorbed H₂O in a "high density state," or H₂O in "microcrevices" or "closed pores," was postulated. These explanations are unsatisfactory for the following reasons: "interstitial" water is not compatible with the accepted lattice structure of γ - or ϵ -MnO₂, in view of the dense packing of O²⁻ ions in these structures. The problem of how to locate interstitial H₂O has been struggled with by Freund *et al.* (35) and Parida *et al.* (36). Surface-adsorbed H₂O, or H₂O in microcrevices or closed pores, would not explain its influence on the physical bulk properties mentioned above. Chemisorbed H₂O at the surface, (as calculated from the BET area) could not account for the total quantity of structural water observed.

Koshiba and Nishizawa (37) proposed that a large number of "lattice dislocations" were present in γ -MnO₂, as well as structurally bonded water, associated with Mn²⁺ ions. The high electrochemical reactivity of γ -MnO₂ was attributed to the presence of such defects. However, the presence of Mn²⁺ in the lattice is unlikely, in view of its large size (Table I).

Recently, Burns (38, 39) suggested that naturally occurring and synthetic γ -MnO₂ phases, used in batteries, might contain lattice defects such as "stacking faults, dislocations, chain defects, multidimensional tunnels (for instance T(3, n) tunnels) and other irregular voids," and that "H₂O, impurity ions, etc., may be accommodated in such lattice defects." He also suggested that such defects might account for the high water content and the high electrochemical reactivity of γ -MnO₂. However, also relatively well-crystallized γ -MnO₂, in which the presence of

Table I. Ionic radii in MnO₂

Ion	Radius (Å)
O ²⁻	1.40
OH ⁻	1.37
Mn ⁴⁺	0.53
Mn ³⁺	0.645
Mn ²⁺	0.83

From Ref. (43). Values for CN (coordination number) = VI; HS (high spin); IR [effective ionic radii based on $r(\text{VIO}^{2-}) = 1.40\text{Å}$].

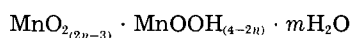
* Electrochemical Society Active Member.



large tunnels or voids has not been proven, shows a relatively high structural water content and a high electrochemical reactivity.

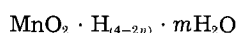
In a recent study, Turner and Buseck (40), using structure imaging by high resolution transmission electron microscopy (HRTEM) have demonstrated that naturally occurring nsutite (γ - MnO_2) contains T(1, 3) tunnels, as well as other structural defects and isolated larger voids or tunnels. However, it must be pointed out that T(1, 3) tunnels are too small to contain H_2O molecules and that larger voids or tunnels might not be present in sufficient number to account for the total quantity of structural water.

In view of the above facts, the presently accepted formula for MnO_2 (30-34)

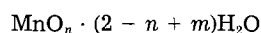


is unsatisfactory. It distinguishes between water in form of "acid" OH^- groups, associated with Mn^{3+} ions, and "neutral" water molecules, but gives no picture or explanation as to the physical state of the m "neutral" water molecules.

The above expression is formally equivalent to

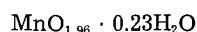


or



where n is the "degree of oxidation" ($2n$ = average valency) and where $(2 - n + m)$ represents the total structural water.

Preisler (14) reports for electrochemically deposited, fibrous ϵ - MnO_2 a composition (after drying for 2h at 120°C) of



This corresponds to $n = 1.96$ and $m = 0.19$. As Preisler points out, the value of n can only account for $(4 - 2n) = 0.08$ OH^- , that is, 0.04 moles of H_2O per mole of Mn, while an additional quantity of $m = 0.19$ moles of H_2O per mole of Mn would have to be present "interstitially." This is indeed not realistic from the crystallographic point of view, and a new explanation must, therefore, be found as to how this water can be present.

Lattice-Vacancy Model of γ - or ϵ - MnO_2

In this paper, I present a cation-vacancy model for MnO_2 . This model removes the previous lack of understanding concerning the state and quantity of structural water. The possibility, that cation vacancies could be present in MnO_2 , has been mentioned previously (3, 41), but, up to now, a complete and self-consistent vacancy model has not been developed.

My model is based on the following considerations.

1. Each manganese ion in the MnO_2 structure is octahedrally coordinated to six nearest oxygen ions, and each oxygen ion is coordinated to three nearest manganese ions. The (slightly distorted) MnO_6 octahedra are arranged in the crystal as to share edges and corners. Since O^{2-} ions are much larger than Mn^{4+} ions (Table I), the lattice resembles a dense packing (nearly hexagonally close-packed) of O^{2-} ions, with the small Mn^{4+} ions more or less orderly arranged in edge-shared MnO_6 octahedra-chains between O^{2-} layers (3, 19, 39, 42). This is the accepted crystallographic description.

2. A fraction x of Mn^{4+} ions is missing in the Mn^{4+} sublattice. Each empty Mn^{4+} site is, for charge compensation, coordinated to four protons, the latter being present in form of four OH^- ions. The OH^- ions replace O^{2-} in the lattice without significant volume change of the unit cell, the ionic radii of O^{2-} and OH^- being very similar (43). Normal unit cell parameters are thus maintained.

3. A fraction y of the Mn^{4+} ions are replaced by Mn^{3+} . This fraction determines the degree of oxidation (average valency) of the manganese ions. For each Mn^{3+} present, one proton is introduced for charge compensation. These

protons form further OH^- ions, replacing O^{2-} in the lattice. Substitution of Mn^{4+} by Mn^{3+} leads to lattice distortion (lattice expansion) and an increase in the volume requirement of the unit cell, as observed experimentally during electrochemical or chemical reduction (44-48).

4. The lattice is thus composed of O^{2-} , OH^- , Mn^{4+} , and Mn^{3+} ions, and Mn vacancies. All the structural water is present in form of OH^- ions, associated with either Mn vacancies, or Mn^{3+} ions. The vacancies are immobile. They will localize protons in surrounding OH^- groups. These protons can jump to adjacent O^{2-} sites, if they are being replaced at their previous location by introduction of further protons, as Mn^{4+} are being reduced to Mn^{3+} . Protons associated with Mn^{3+} are mobile.

5. The presence of Mn^{2+} in the lattice is considered unlikely on thermodynamic (49), as well as sterical grounds (46, 50).

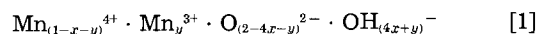
6. Surface-chemisorbed H_2O is considered to be present in form of surface OH^- groups. The surface is treated as a "continuous layer of Mn^{4+} vacancies," two "surface vacancies" being equivalent to one "interior vacancy" (regarding structural water).

7. Electronic conductivity arises from delocalized electrons, tunneling or hopping from one Mn^{4+} orbital to the next. Vacancies increase the tunneling distance.

In the following, I shall present the phenomenological predictions, which can be derived from this model, with respect to the chemical composition (water content), density, theoretical (maximum) electrochemical capacity, proton transfer rate, electronic conductivity, and electrode potential of electrochemically active (γ - and ϵ -) MnO_2 .

Chemical Composition (Water Content)

The proposed cation vacancy model leads to the following formula for manganese dioxide



The parameters x (fraction of vacancies) and y (fraction of Mn^{3+} ions) in expression [1] are related to the parameters n and m of the formula given in the above by the set of equations

$$x = \frac{m}{2 + m} \quad [2]$$

$$y = \frac{4(2 - n)}{2 + m} \quad [3]$$

and

$$n = \frac{4(1 - x) - y}{2(1 - x)} \quad [4]$$

$$m = \frac{2x}{1 - x} \quad [5]$$

Thus, the example cited above, a composition $\text{MnO}_{1.96} \cdot 0.23\text{H}_2\text{O}$ (structural water content 4.58%) corresponds to

$$x = 0.087$$

and

$$y = 0.073$$

This example illustrates how surprisingly large quantities of structural water may be explained by seemingly small vacancy fractions x . Preisler reported this composition to be typical for ϵ - MnO_2 (FEMD). Our interpretation implies that about one out of 12 Mn^{4+} would, for this material, be missing in the lattice (or would be situated at the surface), and about one out of 14 Mn^{4+} ions would be substituted by Mn^{3+} . For γ - MnO_2 (EMD and especially CMD), the structural water content, and thus the vacancy fraction x , would typically be somewhat smaller, but of the same order. In comparing expression [1] with other chemical formula for manganese dioxide, one has to keep in mind that expression [1] contains in total only $(1 - x)$ moles of manganese, while in the past the chemical composition was normally expressed per one mole of total manganese.

Using Eq. [1], the total structural water content may be expressed by

$$\% \text{H}_2\text{O} = \frac{18.016(4x + y)}{2 \text{ MW}}$$

where MW is the molecular weight of formula [1]. (MW depends on x and y .)

The above expression is plotted, for the cases $y = 0$ and $y = 0.10$ as a function of x , in Fig. 1.

A structural water content of 4%, for instance, would imply at $y = 0$ a vacancy fraction of $x = 0.092$, and at $y = 0.1$ a vacancy fraction of $x = 0.068$. From Fig. 1, one derives for $y = 0$ and $x < 0.1$ the following approximately linear relation between weight percent (w/o) H₂O and vacancy fraction x

$$\text{w/o H}_2\text{O} \approx 44x \quad [6]$$

Density

The crystallographic unit cell parameters a_0 , b_0 , and c_0 , of different MnO₂ modifications, and those of α -MnOOH, are listed in Table II.¹ Also shown in this table are unit cell volumes (v), stoichiometric numbers per unit cell volume (z), and x-ray densities (d) calculated with these unit cell parameters.

According to the present model, introduction of vacancies into the Mn⁴⁺ sublattice, and associated substitution of 4 O²⁻ by 4 OH⁻, does not lead to a noticeable change in lattice parameters. However, owing to missing Mn⁴⁺ ions, the density will decrease with increasing vacancy fraction x . The decrease of density with x may be calculated with

$$d = \frac{\text{MW}}{V}$$

where MW is the molecular weight of formula [1] and where V is its molecular volume.

For $y = 0$, the density varies then with x as follows

$$d = \frac{54.94(1 - x) + 32 + 1.008(4x)}{V_0}$$

This relation is plotted in Fig. 2 for $V_0 = 30.2 \text{ \AA}^3 \cdot 6.02 \cdot 10^{23} = 18.18 \text{ cm}^3$, corresponding to a density of 4.78 g/cm^3 at $x = 0$ (x-ray density of ramsdellite or ϵ -MnO₂, see Table II), and for $V_0 = (1/4) 118.3 \text{ \AA}^3 \cdot 6.02 \cdot 10^{23} = 17.805 \text{ cm}^3$, corresponding to a density of 4.88 g/cm^3 at $x = 0$ (x-ray density of γ -MnO₂, see Table II).

When calculating densities for $y > 0$, one must take into account lattice expansion, resulting from replacement of Mn⁴⁺ by the larger Mn³⁺ ions. The corresponding volume increase amounts empirically (44-48) to about $V(y) = V_0 + 3y$. For $y = 0.1$, the correction to V_0 is only about 1.7%, however, as illustrated in Fig. 2, it leads already to a measurable difference in density.

¹ Compiled with the help of R. Giovanoli, University of Bern, Bern, Switzerland.

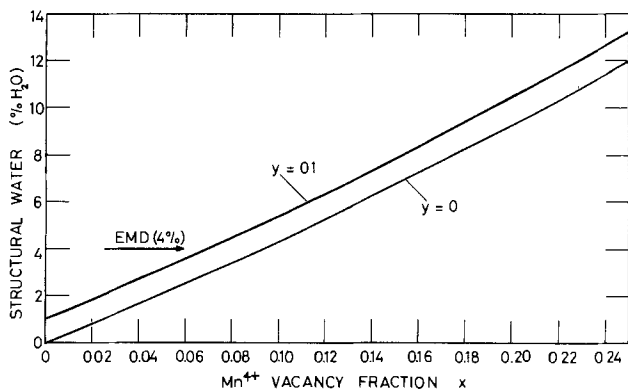


Fig. 1. Structural water content (%), as a function of Mn⁴⁺ vacancy fraction x .

Table II. Crystallographic unit cell parameters of MnO₂

Modification	Symmetry	a_0/b_0 (\AA)	c_0 (\AA)	v (\AA^3)	z	d (g/cm^3)
β -MnO ₂						
Pyrolusite	tetr.	4.40/—	2.87	55.3	2	5.22
MnO ₂						
Ramsdellite	orth.	4.53/9.27	2.87	120.5	4	4.79
γ -MnO ₂						
EMD and CMD	orth.	4.44/9.35	2.85	118.3	4	4.88
ϵ -MnO ₂						
FEMD	hex.	2.80/—	4.45	30.2	1	4.78
α -MnOOH						
Groutite	orth.	4.56/10.70	2.85	139	4	4.17

EMD: Electrolytic MnO₂.
CMD: Chemically prepared MnO₂.
FEMD: Fibrous, electrolytic MnO₂.

Combining the results of Fig. 1 and 2, one deduces readily a theoretical relation between water content and density, as presented in Fig. 3. This relation may be experimentally verified. For a structural water content of 4%, for instance, the theory predicts at $y = 0$ a density of 4.52 g/cm^3 for the ϵ -MnO₂ structure, and a density of 4.62 g/cm^3 for the γ -MnO₂ structure. Interestingly, the same values are calculated for $y = 0.1$. The calculated values are in excellent agreement with experimental pycnometric data (22, 23).

When removing structural water by means of heating, the density will increase, since \square vacancies would tend to "heal out" by cation self-diffusion (Mn⁴⁺ sublattice rearrangement). Protons will then be moving from the interior to the surface, where they would be leaving the crystal in form of H₂O, after combining with surplus O²⁻. It should be possible to follow experimentally the annealing of vacancies by HRTEM techniques (40).

Thermal treatment could, theoretically, lead also to the formation of \square vacancies in the O²⁻ sublattice

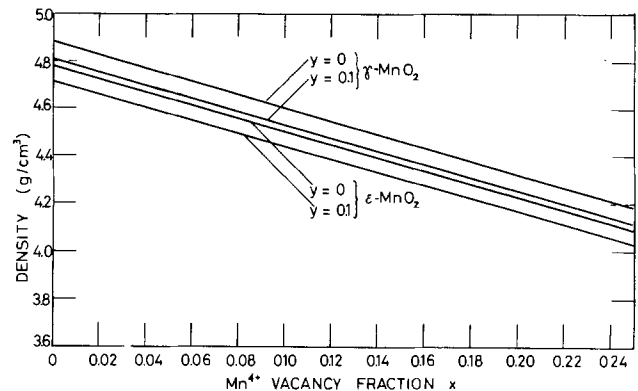


Fig. 2. Density as a function of Mn⁴⁺ vacancy fraction x for the ϵ - and γ -MnO₂ structures.

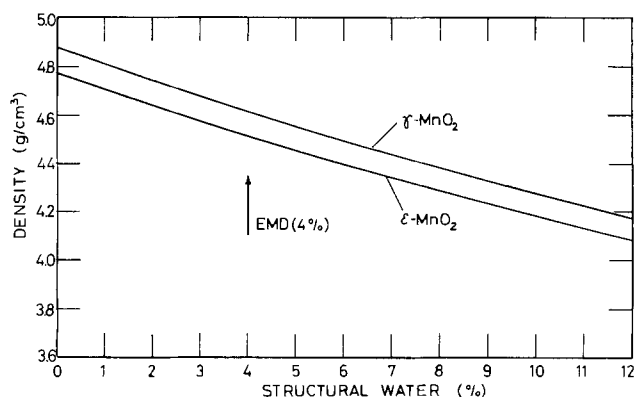
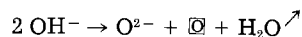


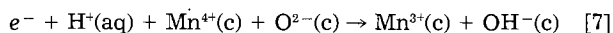
Fig. 3. Density as a function of structural water content



However, this process is likely to occur only at the surface of the crystal. Its influence on density would probably in any case be masked by the density increase due to cation (vacancy) diffusion.

Theoretical (Maximum) Electrochemical Capacity

The theoretical (maximum) electrochemical capacity deliverable per unit weight (C_w), or unit volume (C_v), calculated on the basis of expression [1] for a solid-state, one-electron reduction process [7], where (aq) and (c) designate "aqueous solution" and "crystalline" phase, respectively



is given by

$$C_w = \frac{(1-x-y) \cdot 26.80}{\text{MW}} \quad (\text{Ah/g})$$

and

$$C_v = C_w \cdot d \quad (\text{Ah/cm}^3)$$

C_w and C_v designate the capacity per unit of initial weight and per unit of initial volume of active material present.

The calculated values are plotted for $y = 0$ as a function of x in Fig. 4. This figure serves to illustrate that the theoretical maximum capacity must decrease with increasing x , that is, with increasing water content. This is a fact confirmed by practical experience. "Hydrous oxides," for example, containing up to 10% water, show notoriously poor capacity per unit weight or volume. In view of Fig. 2, the capacity is also predicted to decrease with decreasing density, which is also confirmed experimentally (51). This conclusion applies, of course, only when comparing MnO_2 materials containing no (or the same quantity) of heavy foreign ions. Figure 4 also shows that the capacity per unit volume decreases with increasing water content much more drastically than the capacity per unit weight.

While a high percentage of structural water is thus undesirable as regards to capacity, a certain amount of structural water is a necessity for a fast proton transfer, as discussed in the next section. In practice, most applications require that the capacity must be deliverable within a relatively short time. This is only possible if the proton-transfer rate is high.

Proton-Transfer Rate

The reduction of γ - or ϵ -manganese dioxide, according to reaction [7], involves the introduction of protons into the crystal lattice. This process occurs in a single phase, whereby the lattice expands with increasing degree of reduction (44-48). The "diffusion coefficient" for protons in MnO_2 has been reported to have a value of about

$$D = 6 \cdot 10^{-10} \text{ cm}^2/\text{s} \quad (52)$$

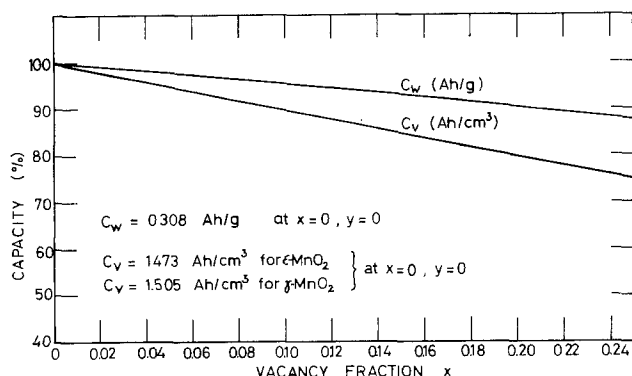


Fig. 4. Theoretical electrochemical capacity per unit weight (Ah/g) and per unit volume (Ah/cm³) as a function of Mn⁴⁺ vacancy fraction for $y = 0$ (undischarged state).

According to the present model, the OH^- ions incorporated into the lattice as a consequence of cation vacancies, will act as donors for and provide thus an initial concentration of protons for solid-state proton transfer. In terms of reaction-rate theory, one may then express the probability of proton transfer by

$$P_t = \nu \cdot [\text{OH}^-] \cdot [\text{O}^{2-}]$$

where ν is a "jump frequency," depending exponentially on temperature

$$\nu = \nu_0 \cdot \exp(-A_p/kT)$$

and where $[\text{OH}^-]$ represents the "concentration" of proton-occupied sites, and $[\text{O}^{2-}]$ the "concentration" of available, suitable empty sites for proton transfer.

If the $[\text{OH}^-]$ and $[\text{O}^{2-}]$ concentrations are expressed as number of ions per molecular volume, one derives in view of reaction [1]

$$[\text{O}^{2-}] = 2 - 4x - y \quad [8]$$

and

$$[\text{OH}^-] = 4x + y \quad [9]$$

The expression

$$[\text{OH}^-] \cdot [\text{O}^{2-}] = (4x + y) \cdot (2 - 4x - y)$$

is plotted in Fig. 5 as a function of x , for the condition $y = 0$. This figure serves to illustrate that the electrochemical reactivity of (undischarged) manganese dioxide increases with x , that is, with structural water content. The curve of Fig. 5, reaches a maximum at $x = 0.25$ and would decrease thereafter to zero at $x = 0.5$, as all the O^{2-} sites are occupied, even at $y = 0$.

In formulating the above expressions, it has been (temporarily) assumed that all the O^{2-} sites are sterically equivalent and equally accessible to protons during the reduction process. It has further been (boldly) assumed that all the protons, that is those in the OH^- ions coordinated to Mn vacancies, as well as those in the OH^- ions associated with Mn^{3+} ions, behave kinetically in an equivalent manner. This is not necessarily the case. For $y > 0$, the above expressions are thus, at best, a first approximation, if applicable at all.

It should also be remembered that, in total, not more than one proton per Mn^{4+} ion, that is not more than $(1-x)$ protons, can be taken up during single-phase reduction. In order to derive a measure for the overall rate of reduction, the rate of proton transfer would have to be multiplied with the fraction of Mn^{4+} ions present, that is with $(1-x-y)/(1-x)$.

The proton-transfer process shall now be detailed for the case of the ramsdellite structure. Two types of O^{2-} sites must here be distinguished: the "planar" and the "pyramidal" configuration, with respect to the three next-neighbor Mn^{4+} ions (53). It has been suggested by Maskell *et al.* (54) that only the "pyramidal" O^{2-} are suitable sites for proton-uptake. Protons introduced during reduction would thus occupy pyramidal sites only. The lat-

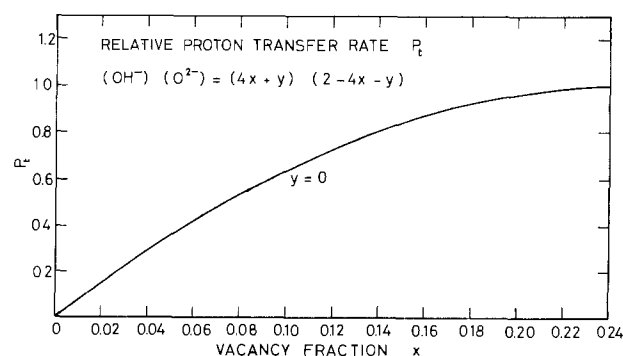


Fig. 5. Relative proton transfer rate in MnO_2 as a function of Mn⁴⁺ vacancy fraction x .

ter are arranged in strings along the [100] direction, along which the protons could be thought to move freely (direction vertical to the (001) plane).

However, protons present as a result of $\overline{\text{Mn}}$ vacancies, must occupy both, planar and pyramidal sites.

Depending on the spacial distribution of the four OH⁻ ions, present around a vacancy, either 1, 2, or 3 OH⁻ ions must occupy a pyramidal site. The remaining, free, accessible pyramidal sites are thus given by

$$[\text{O}^{2-}]_p = 1 - px - y \quad [10]$$

whereby p can assume values of 1, 2, or 3.

The number of pyramidal occupied sites becomes

$$[\text{OH}^-]_p = px + y \quad [11]$$

and the number of "planar" occupied sites is

$$[\text{OH}^-]_{pl} = (4 - p)x \quad [12]$$

These latter might play kinetically a particularly important role as proton "bridges," connecting neighboring strings of pyramidal occupied sites.

The proton transfer rate could thus be visualized as being proportional to

$$[\text{OH}^-]_{pl} \cdot [\text{OH}^-]_p \cdot [\text{O}^{2-}]_p \\ = (4 - p)x \cdot (px + y) \cdot (1 - px - y)$$

This expression is plotted in Fig. 6 as a function of x , for $p = 2$, and for several values of y as parameter. It is of importance to point out that for the case $p > 1$, the rate of proton transfer falls to zero before all the Mn⁴⁺ ions are reduced, because of the lack of free suitable O²⁻ sites. This might reduce the electrochemical capacity to a value smaller than that calculated theoretically (see previous section) on the basis of the Mn⁴⁺ ions present.

The cation vacancy model as developed in this paper sheds a completely new light on the property called "electrochemical reactivity." The reason, why γ -MnO₂ and ϵ -MnO₂ are electrochemically much more active than β -MnO₂ is shown to be due to the presence of $\overline{\text{Mn}}$ vacancies and a corresponding water content, providing an initial starting concentration of protons for the transfer process. In contrast, β -MnO₂ contains almost no vacancies and thus very little structural water. Electrochemical (and chemical) reactivity arises primarily from the presence of (proton-compensated) $\overline{\text{Mn}}$ vacancies, and not primarily from a special lattice structure, e.g., a pyrolusite-ramsdellite intergrowth lattice as assumed previously. This latter might, however, be particularly apt to contain and might possibly even be stable only in presence of vacancies.

Since the surface may be regarded as a "layer of vacancies," β -MnO₂ should also become reducible in a single phase, at least to some extent, if the surface is sufficiently large and if the crystallites are correspondingly small, e.g., only a few atomic layers thick.

Lattice expansion will certainly occur with less strain next to vacancies. In fact, Mn³⁺ present initially (in

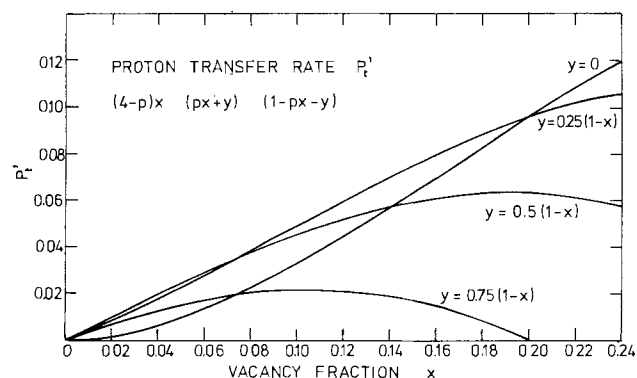


Fig. 6. Relative proton transfer rate as a function of Mn⁴⁺ vacancy fraction x for the special case of a ramsdellite structure.

nonreduced MnO₂) might in general be located adjacent to a vacancy (or in the surface). This is also borne out by the similarity in the values for x and y in the example discussed earlier.

The discontinuity in the lattice expansion, and in the distortion of MnO₆ octahedra, observed during reduction (46-48), at degree of reduction corresponding to about MnO_{1.75}, may reflect the greater strain required, as all the Mn⁴⁺ next to vacancies (or surfaces) are already reduced to Mn³⁺.

Electronic Conductivity

In this section, it will be shown how the experimental observation concerning the decrease of electronic conductivity with increase of structural water content (14, 21, 24) can be explained on the basis of the present vacancy model.

Manganese dioxide is an n-type semiconductor, with relatively high charge carrier concentration. For β -MnO₂, Euler *et al.* (55) reported a carrier concentration of $n = 10^{17} \text{ cm}^{-3}$ and Preisler (14) reported for γ -MnO₂ a value of $n = 1.5 \cdot 10^{16} \text{ cm}^{-3}$.

For electrochemical reduction, an electron, as well as a proton, must be available at the reaction site. In order to minimize ohmic voltage drops, and in order to achieve a discharge profile as uniform as possible, a high electronic conductivity is of advantage. According to a suggestion of Preisler (14), the probability of electron tunneling, and thus electronic conductivity σ , depends exponentially on the average electron tunneling distance, a_t , from one manganese orbital to another

$$\sigma = \sigma_0 \exp(-2\kappa a_t) \quad [13]$$

where σ_0 and κ are constants and a_t is the average tunneling distance (length of potential energy barrier). In a lattice containing $\overline{\text{Mn}}$ vacancies, the average, effective tunneling distance a_t will increase with increasing vacancy fraction x according to

$$a_t = a_0 \cdot \frac{1}{1-x} = a_0 (1 + x + x^2 + \dots) \quad [14]$$

For small values of x , one derives with Eq. [13] and [14]

$$\frac{d(\ln \sigma)}{dx} = -2\kappa \cdot a_0 \quad [15]$$

Since x is proportional to the water content, expression [6], Eq. [15] expresses the linear relation between logarithm of conductivity and water content, observed experimentally (14).

The relation

$$\frac{d(\log \sigma)}{d(\% \text{H}_2\text{O})} = \frac{-2\kappa}{44 \cdot 2.3} \cdot a_0 \quad [15a]$$

is plotted in Fig. 7, using the experimental results of Preisler (14).

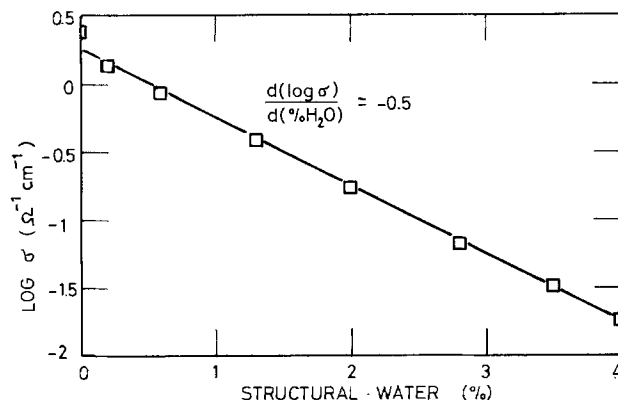


Fig. 7. Logarithm of electronic conductivity of MnO₂ as a function of structural water content. From the slope one calculates, with $a_0 = 2.85 \text{ \AA}$, from Eq. [15a] $\kappa = 8.9 \text{ \AA}^{-1}$ and from Eq. [18a] $\theta = 0.45 \text{ eV \AA}^{-1}$, or $10.3 \text{ kcal \AA}^{-1}$.

It is interesting to note that an equivalent expression to Eq. [15] and [15a] can also be derived from the Arrhenius relation for electronic conductivity (21)

$$\sigma = \sigma_0 \cdot \exp(-A_e/kT) \quad [16]$$

when assuming that the activation energy A_e depends linearly on the average transfer distance a_t for the electrons between neighboring manganese electronic orbitals

$$A_e = A_0 + \theta (a_t - a_0) \quad [17]$$

where θ is a factor relating activation energy to transfer distance and where a_0 is the transfer distance at $x = 0$. Then, with Eq. [14], [16], and [17], one has, for small values of x

$$\frac{d(\ln \sigma)}{dx} = -\frac{\theta}{kT} \cdot a_0 \quad [18]$$

and with Eq. [6]

$$\frac{d(\log \sigma)}{d(\%H_2O)} \approx \frac{-\theta}{kT \cdot 44 \cdot 2.3} \cdot a_0 \quad [18a]$$

It should also be pointed out that similar reasoning could be used to explain the drastic decrease of electronic conductivity with increasing y , that is with increasing degree of reduction. As Mn^{3+} ions are substituted for Mn^{4+} ions, the average tunneling distance a_t will increase. The density of (delocalized) electrons is presumably very low around Mn^{3+} ions. These latter might thus constitute "voids" for the conduction electrons and one would have, analogous with Eq. [14]

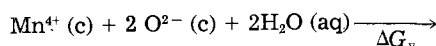
$$a_t = a_0 \cdot \frac{1}{1-x-y} \quad [19]$$

When introducing this expression into Eq. [13], one deduces a sharp decrease of conductivity with increasing y , that is increasing degree of reduction. At $y \rightarrow (1-x)$ the resistivity would, according to Eq. [19], reach infinity.

Electrode Potential

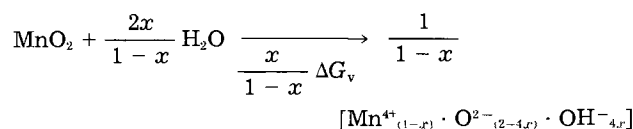
In the following, it shall first be discussed, how the free enthalpy of formation of a cation-deficient, electrochemically active (γ - or ϵ -) MnO_2 depends on the vacancy fraction x (and thus on the water content).

Let us consider a vacancy-formation process as follows



The free enthalpy of this reaction, ΔG_v , corresponds to the energy required to form 1 mol of \overline{Mn} vacancies under uptake of 2 mol of water.

When transforming 1 mol of vacancy-free (and water-free) MnO_2 into a cation-deficient oxide, having a vacancy fraction x , the above process would have to occur $x/(1-x)$ times



This transformation can be visualized as removal of a fraction x of Mn^{4+} ions from the interior of the crystal lattice, transport of the removed ions to the surface, and formation thereon of a corresponding quantity of $x/(1-x)$ mol of additional (defective) manganese dioxide, whereby the required protons and oxygen ions are stemming from the water taken up in the reaction.

When considering now vacancy formation in an oxide containing also Mn^{3+} ions, that is in an oxide having an average valency of

$$\frac{4(1-x-y) + 3y}{1-x} = \frac{4(1-x)-y}{1-x}$$

the free enthalpy of vacancy formation is a function of y . (Arguments that ΔG_v depends approximately linearly on y will be presented in a future publication.)

The free enthalpy of vacancy formation determines the electrode potential difference between a vacancy-free oxide and a cation-deficient oxide. If a single-phase, solid-state electrochemical reduction according to reaction [7] is potential determining (neutral or alkaline solutions), the electrode potential difference is obtained by differentiating the free enthalpy of vacancy formation with respect to y (54). One derives then, at constant y , the following dependence of the electrode potential on x

$$E_\gamma = E_{\gamma_0} - \frac{x}{1-x} \cdot \frac{1}{F} \cdot \frac{d(\Delta G_v)}{dy} \quad [20]$$

For small values of x , the electrode potential is then shown to depend linearly on x . In view of Fig. 1 and Eq. [6], the electrode potential is predicted to increase linearly with water content [$d(\Delta G_v)/dy$ being negative]

$$E_\gamma \approx E_{\gamma_0} - \frac{\%H_2O}{44} \cdot \frac{1}{F} \cdot \frac{d(\Delta G_v)}{dy} \quad [21]$$

This prediction is in agreement with the experimental results of Preisler (25).

In order to examine the question of how the electrode potential depends on y (the degree of reduction), it is helpful to depict the number of the various species present in the crystal lattice as a function of y . This is done in Fig. 8 for the case of $x = 0.1$.

Applying now methods of statistical thermodynamics, as suggested recently by Atlung *et al.* (56) and Maskell *et al.* (54, 57), and limiting the discussion to the configurational partition function, the cation-vacancy model leads to the following situation: at a fixed vacancy fraction x , there are in total $(1-x)$ Mn^{4+} sites available for distributing therein y Mn^{3+} ions (in effect distributing y electrons to transform Mn^{4+} to Mn^{3+} under lattice expansion). For each configuration, y protons can be distributed independently into $(2-4x)$ O^{2-} sites, if, according to Eq. [8], all the O^{2-} sites are equally available, or, on the other hand, into $(1-px-y)$ O^{2-} sites, if, according to Eq. [10], only the pyramidal oxygen sites are available for proton uptake during reduction. Neglecting interaction

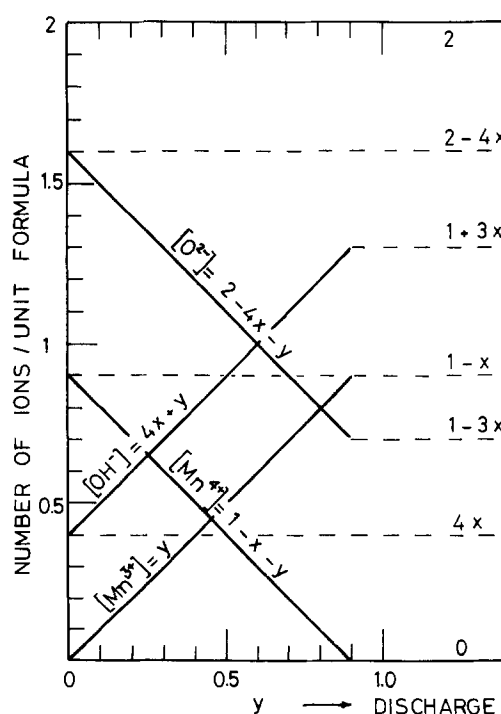


Fig. 8. Variation of $[Mn^{4+}]$, $[Mn^{3+}]$, $[O^{2-}]$, and $[OH^-]$ as a function of y , that is, as a function of discharge, for the case $x = 0.1$.

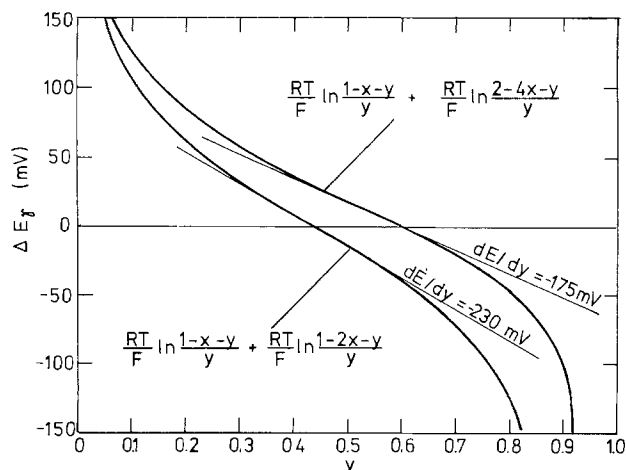


Fig. 9. Variation of electrode potential with y , (degree of reduction) according to Eq. [22] and [23], for $p = 2$ and $x = 0.08$.

terms, the following expressions are then derived for the electrode potential

$$E_{\gamma} = E'_{\gamma_0} + \frac{RT}{F} \ln \frac{1-x-y}{y} + \frac{RT}{F} \ln \frac{2-4x-y}{y} \quad [22]$$

or, respectively

$$E_{\gamma} = E''_{\gamma_0} + \frac{RT}{F} \ln \frac{1-x-y}{y} + \frac{RT}{F} \ln \frac{1-px-y}{y} \quad [23]$$

These equations, in which y may vary from 0 to $(1-x)$, or from 0 to $(1-px)$, respectively, are plotted in Fig. 9. These equations can fit the experimental results concerning the dependence of voltage on degree of reduction, as reported, for instance, by Kozawa (58), Maskell *et al.* (57), or Ohzuku and Hirai (59). A possible refinement of Eq. [22] or [23], including interaction energies, will be discussed in a future paper.

Conclusions

The cation-vacancy model for MnO₂, as presented in this paper, is able to quantitatively explain for the first time many aspects of MnO₂ electrochemistry, which have puzzled investigators in the past. In particular, the model predicts correctly the following observations regarding electrochemically active (γ - or ϵ -) MnO₂: (i) quantity of structural water, (ii) decrease of density with structural water content, (iii) decrease of theoretical electrochemical capacity (Ah/g and Ah/cm³) with structural water content, (iv) increase in proton-transfer rate (electrochemical reactivity) with structural water content, (v) decrease of electronic conductivity with structural water content, (vi) increase of electrode potential with structural water content, and (vii) dependence of electrode potential on degree of reduction.

The theory presented in this paper constitutes a breakthrough in our understanding of the physical, chemical, and electrochemical behavior of electrochemically active MnO₂. It will also have implications for the interpretation of the behavior of other oxide electrodes, for instance, PbO₂ and NiOOH.

Manuscript submitted Feb. 27, 1984; revised manuscript received June 27, 1984.

REFERENCES

1. "Proceedings of the Manganese Dioxide Symposium," Vol. 1, Cleveland 1975, A. Kozawa and R. J. Brodd, Editors, I.C. Sample Office, Cleveland, OH.
2. "Proceedings of the Manganese Dioxide Symposium," Vol. 2, Tokyo 1980, B. Schumm, H. M. Joseph, and A. Kozawa, Editors, I.C. Sample Office, Cleveland, OH.
3. P. Ruetschi, R. Giovanoli, and P. Bürki, in "Proceed-

- ings of the Manganese Dioxide Symposium," Vol. 1, Cleveland, 1975, A. Kozawa and R. J. Brodd, Editors, paper 1, p. 12, I.C. Sample Office, Cleveland, OH.
4. E. O. Jegge, *Trans. Electrochem. Soc.*, **53**, 71 (1928).
5. C. Drotschmann, "Moderne Primärbatterien," Nikolaus Branz, Editor, pp. 38, 39, Berlin-Schoeneberg, Berlin (1951).
6. K. Sasaki and A. Kozawa, *J. Electrochem. Soc. Jpn.*, **25**, 115, 273 (1957).
7. A. Kozawa, *This Journal*, **106**, 79 (1959).
8. W. C. Vosburgh, *ibid.*, **106**, 839 (1959).
9. A. Tvarusko, *ibid.*, **111**, 125 (1964).
10. R. F. Amlie and A. Tvarusko, *ibid.*, **111**, 496 (1964).
11. D. S. Freeman, P. F. Pelter, F. L. Tye, and L. L. Wood, *J. Appl. Electrochem.*, **1**, 127 (1971).
12. J. A. Lee, C. E. Newnham, and F. L. Tye, *J. Colloid Interface Sci.*, **42**, 372 (1973).
13. J. A. Lee, C. E. Newnham, F. S. Stone, and F. L. Tye, *ibid.*, **45**, 289 (1973).
14. E. Preisler, *J. Appl. Electrochem.*, **6**, 311 (1976).
15. K. Miyazaki, in "Proceedings of the Manganese Dioxide Symposium," Vol. 1, Cleveland 1975, A. Kozawa and R. J. Brodd, Editors, paper 6, p. 111, I.C. Sample Office, Cleveland, OH.
16. T. Yoshimori, M. Kato, K. Nippashi, and J. Murayama, in "Proceedings of the Manganese Dioxide Symposium," Vol. 2, Tokyo 1980, B. Schumm, H. M. Joseph, and A. Kozawa, Editors, paper 25, p. 369, I.C. Sample Office, Cleveland, OH.
17. T. Ohzuku, I. Tari, and T. Hirai, *Electrochim. Acta*, **27**, 1049 (1982).
18. H. Ikeda, T. Saito, and H. Tamura, in "Proceedings of the Manganese Dioxide Symposium," Vol. 1, Cleveland 1975, A. Kozawa and R. J. Brodd, Editors, paper 21, p. 384, I.C. Sample Office, Cleveland, OH.
19. R. Giovanoli, in "Proceedings of the Manganese Dioxide Symposium," Vol. 2, Tokyo 1980, B. Schumm, H. M. Joseph, and A. Kozawa, Editors, paper 7, p. 113, I.C. Sample Office, Cleveland, OH.
20. H. Bode, A. Schmier, and D. Berndt, *Z. Elektrochem.*, **66**, 586 (1962).
21. J. Brenet and P. Faber, *J. Power Sources*, **4**, 203 (1979).
22. D. M. Holton and F. L. Tye, in "Proceedings of the Manganese Dioxide Symposium," Vol. 2, Tokyo 1980, B. Schumm, H. M. Joseph, and A. Kozawa, Editors, paper 15, p. 244, I.C. Sample Office, Cleveland, OH.
23. A. J. Brown, F. L. Tye, and L. L. Wood, *J. Electroanal. Chem.*, **122**, 337 (1981).
24. K. A. Euler, *Naturwissenschaften*, **67**, 561 (1980).
25. E. Preisler, in "Proceedings of the Manganese Dioxide Symposium," Vol. 2, Tokyo 1980, B. Schumm, H. M. Joseph, and A. Kozawa, Editors, paper 12, p. 184, I.C. Sample Office, Cleveland, OH.
26. W. Feitknecht and W. Marti, *Helv. Chim. Acta*, **28**, 129 (1945).
27. O. Glemser and H. Meisiek, *Naturwissenschaften*, **44**, 614 (1957).
28. J. P. Gabano, B. Morignat, and J. F. Laurent, *Electrochem. Technol.*, **5**, 531 (1967).
29. R. M. Potter and G. R. Rossman, *Am. Mineral.*, **64**, 1199 (1979).
30. P. Brouillet, A. Grund, and F. Jolas, *C.R. Acad. Sci. Paris*, **257**, 3166 (1963).
31. L. Balevski, J. Brenet, G. Coeffier, and P. Lancon, *C.R. Acad. Sci. Paris*, **260**, 106 (1965).
32. G. Coeffier and J. Brenet, *Electrochim. Acta*, **10**, 1013 (1965).
33. J. P. Gabano, B. Morignat, E. Fialdes, B. Emery, and J. F. Laurent, *Z. Phys. Chem.*, **46**, 359 (1965).
34. J. Brenet, M. Cyrankowska, G. Ritzler, R. Saka, and K. Traore, in "Proceedings of the Manganese Dioxide Symposium," Vol. 1, Cleveland 1975, A. Kozawa and R. J. Brodd, Editors, paper 14, p. 276, I.C. Sample Office, Cleveland, OH.
35. F. Freund, E. Könen, and E. Preisler, in "Proceedings of the Manganese Dioxide Symposium," Vol. 1, Cleveland 1975, A. Kozawa and R. J. Brodd, Editors, paper 17, p. 328, I.C. Sample Office, Cleveland, OH.
36. K. M. Parida, S. B. Kanungo, and B. R. Sant, *Electrochim. Acta*, **26**, 435 (1981).
37. J. Koshiba and S. Nishizawa, in "Electrochemistry of Manganese Dioxide and Manganese Dioxide Batteries in Japan," Vol. II., K. Takahashi, S. Yoshizawa, and A. Kozawa, Editors, p. 85, US Branch Office of the Electrochemical Society of Japan, Cleveland, OH (1971).

38. R. G. Burns, "Battery Material Symposium, Vol. I," A. Kozawa, and M. Nagayama, Editors, p. 197, Brussels 1983, published by BMRA, Cleveland, OH (1984).
39. R. G. Burns and V. M. Burns, in "Proceedings of the Manganese Dioxide Symposium," Vol. 1, Cleveland 1975, A. Kozawa and R. J. Brodd, Editors, paper 16, p. 306, I.C. Sample Office, Cleveland, OH, "Proceedings of the Manganese Dioxide Symposium," Vol. 2, Tokyo 1980, B. Schumm, H. M. Joseph, and A. Kozawa, Editors, paper 6, p. 97, I.C. Sample Office, Cleveland, OH.
40. S. Turner and P. R. Buseck, *Nature*, **304**, 143 (1983).
41. J. P. Brenet, J. P. Gabano, and M. Seigneurin, 16. Congrès. Int. de Chimie Pure et Appliquée, Sedes, Paris 1957, p. 69.
42. P. M. de Wolff, J. W. Visser, R. Giovanoli, and R. Brüttsch, *Chimia*, **32**, 257 (1978).
43. R. D. Shannon, *Acta Crystallogr., Sect. A*, **32**, 751 (1976).
44. J. Brenet, P. Malesson, and A. Grund, *C.R. hebd. Séances Acad. Sci.*, **242**, 111 (1956).
45. W. Feitknecht, H. R. Oswald, and U. Feitknecht-Steinmann, *Helv. Chim. Acta*, **43**, 1947 (1960).
46. R. Giovanoli and U. Leuenberger, *ibid.*, **52**, 2333 (1969), in particular p. 2345.
47. W. C. Maskell, J. E. A. Shaw, and F. L. Tye, *Electrochim. Acta*, **26**, 1403 (1981).
48. W. C. Maskell, J. A. E. Shaw, and F. L. Tye, *J. Appl. Electrochem.*, **12**, 101 (1982).
49. P. Ruetschi, *ibid.*, **12**, 109 (1982).
50. R. Giovanoli and B. Balmer, *Chimia*, **37**, 424 (1983).
51. S. B. Kanungo, K. M. Parida, and B. R. Sant, *Electrochim. Acta*, **26**, 1147 (1981).
52. H. Kahil, F. Dalard, J. Guittou, and J. P. Cohen-Addad, *Surf. Technol.*, **16**, 331 (1982).
53. A. M. Byström, *Acta Chem. Scand.*, **3**, 163 (1949).
54. W. C. Maskell, J. E. Shaw, and F. L. Tye, *Electrochim. Acta*, **28**, 225 (1983).
55. K. J. Euler and T. Harder, *ibid.*, **26**, 1661 (1981).
56. S. Atlung and T. Jacobson, *ibid.*, **26**, 1447 (1981).
57. W. C. Maskell, J. E. Shaw, and F. L. Tye, *J. Power Sources*, **8**, 113 (1982).
58. A. Kozawa, "Power Sources," Vol. 7, J. Thompson, Editor, p. 485, Academic Press, London (1979).
59. T. Ohzuku and T. Hirai, Private communication.

A Rechargeable Battery Employing a Reduced Polyacetylene Anode and a Titanium Disulfide Cathode

Josip Čaja,^{*1} Richard B. Kaner,^{*} and Alan G. MacDiarmid^{*}

Department of Chemistry, University of Pennsylvania, Philadelphia, Pennsylvania 19104

ABSTRACT

Novel rechargeable battery cells have been constructed using a reduced form of the conducting organic polymer, polyacetylene, as the anode, the inorganic intercalating material, titanium disulfide as the cathode, and either 1.0M LiClO₄ in THF or 1.0M NaPF₆ in THF as the nonaqueous electrolyte. A feasibility study of the cells is described. It includes constant current discharge characteristics, stability, and rechargeability. The cells exhibited good stability and reversibility. Their performance was cathode limited, owing to the method used for fabricating the TiS₂ electrode.

Considerable interest has been shown during the past four years in the use of conducting organic polymers as electroactive materials (1). The prototype conducting polymer, polyacetylene, (CH)_x, can be reversibly oxidized or reduced electrochemically and has been studied primarily as a cathode-active material in rechargeable cells employing a lithium anode (2). Since the reduced form of (CH)_x, e.g., [Li_y⁺(CH)^{-y}]_x, is stable up to a reduction level of ~10 mole percent (m/o), i.e., y = 0.1, in an electrolyte of 1.0M LiClO₄ in tetrahydrofuran (3), it has potential for use as an anode-active material, in conjunction with a suitable cathode, in a rechargeable battery.

Inorganic intercalating materials, primarily titanium disulfide, TiS₂, have also been extensively studied as the cathode in rechargeable lithium cells (4, 5). The feasibility of combining an inorganic intercalating cathode, such as TiS₂, with a conducting organic polymer anode, such as reduced (CH)_x, is reported in the present study. A cell of this type has the advantage of avoiding the major problems associated with a lithium anode, specifically, reaction of the lithium electrode with the organic electrolyte and inadequate cycle life due to the growth of lithium dendrites.

The terms "doping," "intercalation," and "oxidation/reduction" have often been used interchangeably when referring to the process which increases the conductivity of an organic polymer, such as (CH)_x, by introducing small quantities of foreign species into the organic polymer matrix. In order to avoid confusion, it is desirable to distinguish between these three terms. The doping of an organic polymer, such as (CH)_x, is different from the doping of a classical semiconductor, such as silicon. If,

for example, a crystal of silicon is n-doped by replacing a silicon atom with a phosphorus atom (which has one valence electron more than Si), the phosphorus represents a negative site in so far as the crystal lattice is concerned, even if no charge transfer between silicon and phosphorus were to occur. However, the n-doping of a conducting organic polymer, such as (CH)_x, refers to the addition of a given number of electrons to the polymer chains together with a corresponding number of counter cations needed to maintain electrical neutrality. Conducting polymers generally require much higher doping levels than classical inorganic semiconductors in order to effect comparable electronic changes. Intercalation refers to the orderly insertion of a molecule or ion into the crystal lattice of a layered "host" material. Oxidation or reduction of the host material by either chemical or electrochemical means may occur during this process. Intercalation of lithium or sodium into TiS₂, for example, has been shown (5) to involve an almost complete electron transfer from the alkali metal with concomitant reduction of the TiS₂ to give species such as M_y⁺(TiS₂)^{-y} (y < 1; M = Li or Na). Throughout this paper, the incorporation of lithium or sodium cations into TiS₂ will be termed "intercalation," while the incorporation of lithium or sodium cations into (CH)_x will be termed "reduction."

When carrying out electrochemical studies on *trans*-polyacetylene, a semiconductor, it is important to note that pure, neutral (CH)_x can exhibit an open-circuit voltage, V_{oc}, lying in the range between 1.8V, below which significant reduction begins to occur, and 3.1V, above which significant oxidation begins to occur (6). These potentials are given with respect to the Li⁺/Li couple in 1.0M LiClO₄ in THF for the reduction reaction and in 1.0M LiClO₄ in propylene carbonate for the oxidation reaction. This variation in potential results from the slightly differ-

¹ Present address: Oak Ridge Precision Industries, Incorporated, Oak Ridge, Tennessee 37830.

^{*} Electrochemical Society Active Member.

ent ways in which the film has been previously stored or handled. The sensitivity of the potential to the previous history of the film is caused by the extremely small number of molecular orbitals (*i.e.*, density of states) lying between the highest filled pi bonding molecular orbital (at the top of the valence band) and the lowest empty pi antibonding molecular orbital (at the bottom of the conduction band) with which reduction or oxidation processes are associated. Thus, the transfer of an infinitesimally small number of coulombs into or out of the $(\text{CH})_x$ can lower its potential toward 1.8V or raise its potential toward 3.1V, respectively.

Experimental

Materials and reagents.—*cis*-Rich $(\text{CH})_x$ film was prepared as previously described (7). Tetrahydrofuran (THF) (Fisher Scientific Company) was freshly distilled from sodium benzophenone *in vacuo* and was used to make a 1.0M solution of LiClO_4 and a 1.0M solution of NaPF_6 . Anhydrous LiClO_4 (Alfa Ventron) was dried by melting under a dynamic vacuum. Anhydrous NaPF_6 (Aldrich Chemical Company) was dried by heating at 120°C under a dynamic vacuum for 24h. Titanium disulfide, TiS_2 , was synthesized directly from elemental titanium and sulfur in an evacuated, sealed silica hot/cold tube at 500°-900°C by chemical vapor transport (8). Lithium metal (Alfa Ventron) and sodium metal (J. T. Baker Company) were scraped with a knife in a dry argon atmosphere immediately before use. Glass filter paper (Reeve Angel 934AH), dried at 600°C for 24h, was employed as the separator.

Cell construction.—All measurements were performed using cells, shown in Fig. 1, constructed in a dry argon atmosphere by placing separators between the electrodes, squeezing the assembly into $4 \times 10 \times 50$ mm rectangular glass tubing (Vitro Dynamics, Incorporated), adding the electrolyte, freezing the cell contents with liquid N_2 , and sealing the cell under vacuum across the protruding electrode leads. The $(\text{CH})_x$ electrode was made from a 2.5 ± 0.1 mg strip of $(\text{CH})_x$ film (~ 0.7 cm²) mechanically pressed onto 52 mesh platinum gauze, to which had been spot welded a platinum wire lead. The lithium or sodium electrode was made by pressing a (~ 0.7 cm²) piece of 0.13 mm thick lithium ribbon or a (~ 0.7 cm²) strip of sodium into a 189 mesh nickel grid (Delker Corporation), to which had been spot welded a nickel-chromium wire lead. The TiS_2 electrode was made by pressing a TiS_2 /Teflon mixture in the form of a flat sheet (~ 0.1 mm thick) into the center of a nickel grid, to which had been spot welded a nickel-chromium wire lead. The TiS_2 /Teflon flat sheet was made by mixing and then pressing a two-to-one mixture, by weight, of TiS_2 powder and Teflon powder onto the bottom of a mortar by means of a pestle. The $(\text{CH})_x$ electrode was placed in the center of the cell with the TiS_2 electrode on one side and the alkali metal electrode on the other side. The electrodes were separated from each other by the glass filter paper separators.

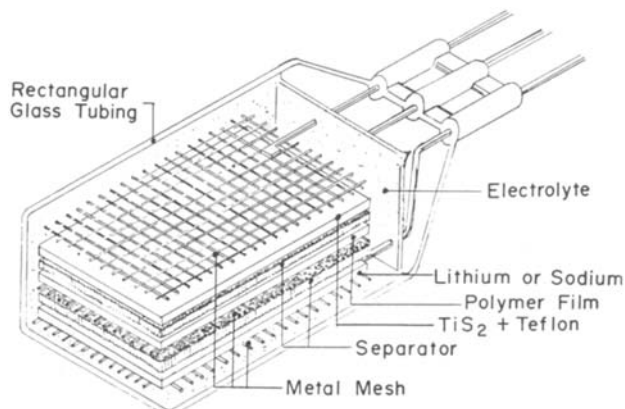


Fig. 1. Construction of the $[\text{M}_{0.10}^+(\text{CH})^{-0.10}]_r/\text{TiS}_2$ cell. Lithium or sodium metal serves as a reference electrode.

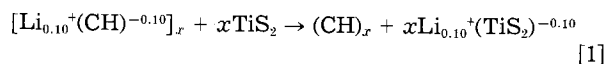
Preparation of the reduced polyacetylene anode.—The $[\text{M}_{0.10}^+(\text{CH})^{-0.10}]_r$ ($\text{M} = \text{Li}$ or Na) anode was prepared *in situ* in a cell of the type described above by electrochemically reducing the *cis*-rich $(\text{CH})_x$ to $[\text{M}_{0.10}^+(\text{CH})^{-0.10}]_r$ at a constant current of 0.1 mA (~ 2 m/o reduction/h) applied between the $(\text{CH})_x$ electrode and the alkali metal electrode. *cis*-Rich $(\text{CH})_x$ was used in the cell construction since it is more flexible than the *trans*-rich isomer. The reduced $(\text{CH})_x$ was then oxidized at a constant current of 0.1 mA until a voltage of ~ 2.4 V (*vs.* Li), characteristic of neutral $(\text{CH})_x$, was reached. Electrochemical reduction followed by oxidation back to neutral $(\text{CH})_x$ converts *cis*-rich $(\text{CH})_x$ to the more thermodynamically stable *trans*-rich $(\text{CH})_x$ (9). The *trans*-rich $(\text{CH})_x$ so formed was then reduced to a 10.0 m/o reduction level using the same conditions as described above and was permitted to stand for 12h, in order to permit diffusion of the alkali metal cations throughout the 200Å diam $(\text{CH})_x$ fibrils, before commencing with the electrochemical studies.

The $[\text{M}_{0.10}^+(\text{CH})^{-0.10}]_r$ ($\text{M} = \text{Li}$ or Na) obtained in this way and the TiS_2 electrode constituted the cell in its charged state. The alkali metal electrode thus served a dual role: first in the preparation of the reduced $(\text{CH})_x$ anode, and second as a reference electrode during the studies described below. All discharge studies were carried out to 0 V between the $(\text{CH})_x$ anode and the TiS_2 cathode and were performed at room temperature. All voltages are given with respect to a lithium or sodium reference electrode. The first discharge/charge cycle of each cell was ignored.

Results

Discharge/charge characteristics of $[\text{Li}_{0.10}^+(\text{CH})^{-0.10}]_r/\text{TiS}_2$ cells.—These studies were carried out on two $[\text{Li}_{0.10}^+(\text{CH})^{-0.10}]_r/\text{TiS}_2$ cells containing different molar ratios of $[\text{Li}_{0.10}^+(\text{CH})^{-0.10}]_r$ and TiS_2 . The use of different molar ratios permitted the final intercalation level, y , in $\text{Li}_y^+(\text{TiS}_2)^{-y}$, obtained after discharge, to be varied as desired. Cells of this type displayed an open-circuit voltage, V_{oc} , of ~ 1.65 V.

Use of a 1:1 molar ratio $[\text{Li}_{0.10}^+(\text{CH})^{-0.10}]_r/\text{TiS}_2$ cell.—The net electrochemical reaction taking place during the discharge process is given by Eq. [1]



The relationship between cell discharge voltage, V_d , and time for representative discharges to 0 V at constant currents of 0.2 and 0.1 mA are shown in Fig. 2, curves 1 and 2, respectively. Each charge was carried out first at a constant current to 1.8V and then at a constant applied potential of 1.8V for 48h. The 1.8V charging potential was used to complete the conversion of the electrode material to $[\text{Li}_{0.10}^+(\text{CH})^{-0.10}]_r$ and TiS_2 . Each cell discharge was completely reversible, as can be seen from Table I by comparing the coulombs involved in a discharge process,

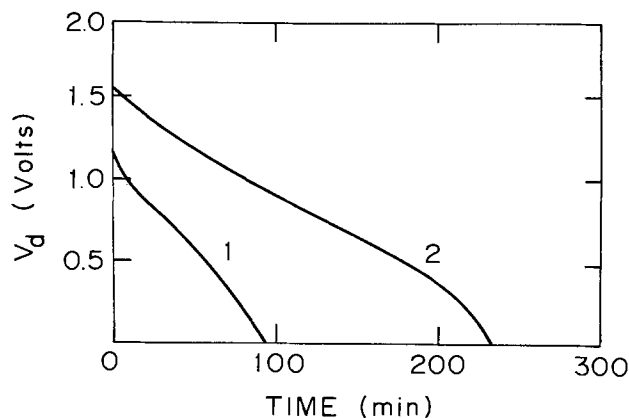


Fig. 2. Relationship between the discharge voltage, V_d and time, during the discharge of a 1:1 molar ratio $[\text{Li}_{0.10}^+(\text{CH})^{-0.10}]_r/\text{TiS}_2$ cell at 0.2 mA (curve 1) and 0.1 mA (curve 2).

Table I. Electrochemical characteristics of $[M_y^+(CH)^{-y}]_x/TiS_2$ cells

Molar ratio $[M_{0.10}^+(CH)^{-0.10}]_x/TiS_2$	Cell discharge reaction	Constant discharge current (mA)	Current density ^a (A/kg)	Calculated coulombs for 100% discharge ^b (C)	Discharge $Q_{(out)}$ ^c (C)	Extent of cell reaction when $V_d = 0$ V ^b (%)	Charge $Q_{(in)}$ ^d (C)	Average discharge voltage V_d (V)	Specific energy of reactant materials (Wh/kg) ^a
1:1	$[Li_{0.10}^+(CH)^{-0.10}]_x + xTiS_2 \rightarrow (CH)_x + xLi_{0.10}^+(TiS_2)^{-0.10}$	0.1	4.3	1.79	1.40	78	1.39	0.83	13.8
		0.2	8.6	1.79	1.15	64	1.12	0.56	7.5
10:1	$10[Li_{0.10}^+(CH)^{-0.10}]_x + xTiS_2 \rightarrow 10(CH)_x + xLi^+(TiS_2)^-$	0.1	16.6	1.86	0.91	49	0.89	0.65	27.1
4:1	$4[Na_{0.10}^+(CH)^{-0.10}]_x + xTiS_2 \rightarrow 4(CH)_x + xNa_{0.40}^+(TiS_2)^{-0.40}$	0.05	5.0	1.93	1.23	64	1.17	1.03	33.9
		0.2	19.9	1.93	0.96	50	0.73	1.00	26.5

^a Per kg of $[M_y^+(CH)^{-y}]_x$ and TiS_2 used in constructing a cell.

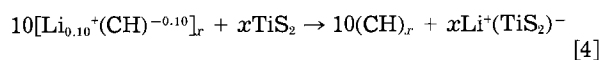
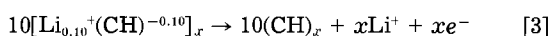
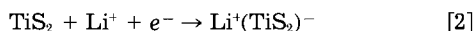
^b Based on the weights of $[M_y^+(CH)^{-y}]_x$ and TiS_2 used in constructing a cell. The number of moles of $[M_y^+(CH)^{-y}]_x$ used in constructing each cell was approximately the same.

^c $Q_{(out)}$ is the number of coulombs liberated during constant current discharge of the cell to 0 V.

^d The $[Li_{0.10}^+(CH)^{-0.10}]_x$ cells were charged at a constant potential of 1.8 V for 48h; the $[Na_{0.10}^+(CH)^{-0.10}]_x$ cell was charged at a constant potential of 1.9 V for 48h.

$Q_{(out)}$, to the coulombs involved in a charge process, $Q_{(in)}$. Note however, from the extent of a given cell reaction (Table I), that the discharge reactions were not entirely complete when 0 V had been reached. Additional discharge/charge cycles at 0.1 and 0.2 mA gave similar results.

Use of a 10:1 molar ratio $[Li_{0.10}^+(CH)^{-0.10}]_x/TiS_2$ cell.—The electrochemical reactions taking place at the TiS_2 cathode, the $[Li_{0.10}^+(CH)^{-0.10}]_x$ anode, and the net cell reaction during the discharge process of this cell are given by Eq. [2], [3], [4], respectively



The relationship between cell potential, V , and coulombs transferred, Q , during a 0.1 mA constant current discharge process and charge process is shown in Fig. 3, curves C and C', respectively. The respective TiS_2 and $[Li_{0.10}^+(CH)^{-0.10}]_x$ electrode potentials on discharge are given in Fig. 3, curves A and B. The corresponding potentials on charge are given in curves A' and B'. Curves A, B, and C correspond to Eq. [2], [3], and [4], respectively. The cell was then charged at a constant current of 0.1 mA for 1h. The charging was completed by applying a constant potential of 1.8 V for 48h.

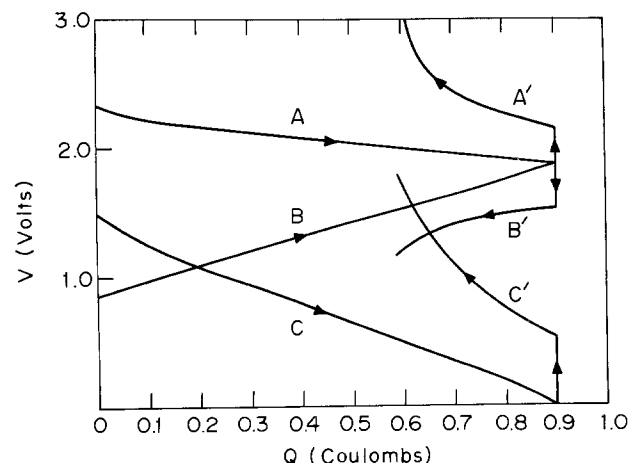
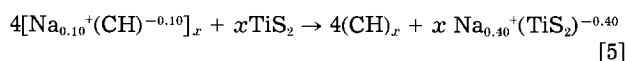


Fig. 3. The relationship between the voltage, V and the charge transferred, Q for the $Li_y^+(TiS_2)^{-y}$ cathode (vs. Li) (curves A and A'), the $[Li_y^+(CH)^{-y}]_x$ anode (vs. Li) (curves B and B'), and the 10:1 molar ratio $[Li_{0.10}^+(CH)^{-0.10}]_x/TiS_2$ cell (curves C and C') during 0.1 mA discharge and charge processes, respectively (see text).

The cell reaction was completely reversible, as can be seen from Table I by comparing the $Q_{(out)}$ and $Q_{(in)}$ values. Note, however, from the extent of a given cell reaction (Table I), that the discharge reaction was not entirely complete when 0 V had been reached. Additional discharge/charge cycles at 0.1 mA gave similar results.

Discharge/charge characteristics of a $[Na_{0.10}^+(CH)^{-0.10}]_x/TiS_2$ cell.—The studies were carried out on a 4:1 molar ratio $[Na_{0.10}^+(CH)^{-0.10}]_x/TiS_2$ cell. The net electrochemical reaction taking place during the discharge process is given by Eq. [5]



It has been reported that $Na_y^+(TiS_2)^{-y}$ undergoes a phase change at $y > \sim 0.4$ (10). Therefore, the present study has been restricted to $Na_y^+(TiS_2)^{-y}$ for $y < 0.4$, in which region the reaction given by Eq. [5] is believed to be reversible.

The relationship between cell discharge voltage, V_d , and time for representative discharges to 0 V at constant currents of 0.2, 0.1, and 0.05 mA are shown in Fig. 4, curves 1, 2, and 3, respectively. Each charge was carried out at a constant potential of 1.9 V for 48h. The 1.9 V charging potential was used to complete the conversion of the electrode materials to $[Na_{0.10}^+(CH)^{-0.10}]_x$ and TiS_2 .

The cell discharges at 0.05 and 0.1 mA were completely reversible, as can be seen from Table 1 by comparing the coulombs involved in a discharge process, $Q_{(out)}$, to the coulombs involved in a charge process, $Q_{(in)}$. However, the cell discharge at 0.2 mA was not completely reversible. Additional discharge/charge cycles at 0.05, 0.1, and 0.2 mA gave similar results.

Characteristics of the $[M_y^+(CH)^{-y}]_x/TiS_2$ cells.—Data from the studies described in the previous sections for the three cells investigated were used to compile the information in Table I. Included are the three cells containing $[M_{0.10}^+(CH)^{-0.10}]_x$ and TiS_2 in the molar ratios

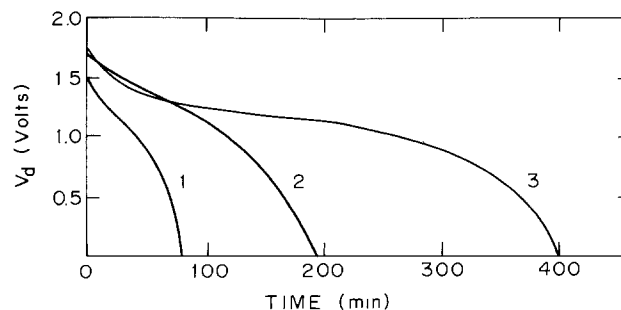


Fig. 4. The relationship between the discharge voltage, V_d and time, during the discharge of a 4:1 molar ratio $[Na_{0.10}^+(CH)^{-0.10}]_x/TiS_2$ cell at 0.2 mA (curve 1), 0.1 mA (curve 2), and 0.05 mA (curve 3).

1:1, 10:1, and 4:1 and their corresponding discharge reactions together with the number of coulombs calculated for 100% discharge, $Q_{\text{out, calc.}}$, of a cell if all the $[\text{M}_{0.10}^+(\text{CH})^{-0.10}]_r$ and TiS_2 employed in the cell construction underwent reaction. The coulombs liberated in the experimental discharge, Q_{out} , is given next, followed by the extent of the cell reaction, $[Q_{\text{out}}/Q_{\text{out, calc.}}]100$. An average discharge voltage, \bar{V}_d was calculated by integrating the area under each discharge curve, $(V_d \times Q_{\text{out}})$, (Fig. 2, curves 1 and 2; Fig. 3, curve C; Fig. 4, curves 1 and 3) and dividing this value by Q_{out} . Energy densities given in the table were obtained by integrating the area under each discharge curve, $(V_d \times Q_{\text{out}})$ and dividing this value by the combined weight of $[\text{M}_y^+(\text{CH})^{-y}]_r$ and TiS_2 employed in each cell construction. This value was then divided by 3600 to convert W-s/kg to W-h/kg.

Stability.—After the discharge/charge cycles described above were completed, the relationship between V_{oc} and time for the 4:1 molar ratio $[\text{Na}_{0.10}^+(\text{CH})^{-0.10}]_r/\text{TiS}_2$ cell was monitored and is shown in Fig. 5, curve 1. The cell showed an initial decrease from 1.75 to 1.64V during the first 15 days, followed by a very gradual decrease to 1.59V after 3 months. Its capacity on discharge after this time was 69% of that obtained from a discharge carried out immediately after completion of a charge cycle. The relationship between V_{oc} and time for the 10:1 molar ratio $[\text{Li}_{0.10}^+(\text{CH})^{-0.10}]_r/\text{TiS}_2$ cell is shown in Fig. 5, curve 2. This cell showed an initial decrease from 1.65 to 1.50V after 5 days, followed by a much more gradual decrease to 1.43V after 20 days. Its capacity on discharge after this time was 88% of that obtained from a discharge carried out immediately after completion of a charge cycle.

Discussion

Since, as described above, neutral $(\text{CH})_r$ can have a potential in the range 1.8-3.1V (*vs.* Li) and since $\text{Li}^+(\text{TiS}_2)^-$ has a potential of 1.9V (*vs.* Li), it is apparent that when a 10:1 molar ratio $[\text{Li}_{0.10}^+(\text{CH})^{-0.10}]_r/\text{TiS}_2$ cell is completely discharged to 0 V such that the electrodes attain the compositions $(\text{CH})_r$ and $\text{Li}^+(\text{TiS}_2)^-$, as given by Eq. [4], both electrodes will have a potential of 1.9V (*vs.* Li). Experimentally, this can be seen in Fig. 3, for the discharge of this cell to 0 V, by the intersection of curve A (the potential of the $\text{Li}_y^+(\text{TiS}_2)^{-y}$ cathode *vs.* Li) and curve B (the potential of the $[\text{Li}_{0.10(1-y)}^+(\text{CH})^{-0.10(1-y)}]_r$ anode *vs.* Li), which occurs at 1.9V (*vs.* Li). Although the potential of 1.9V (*vs.* Li) is consistent with the formation of $\text{Li}^+(\text{TiS}_2)^-$ and neutral $(\text{CH})_r$ the reaction is only 49% complete based on Q_{out} , the coulombs liberated during cell discharge and the weights of TiS_2 and $[\text{Li}_{0.10}^+(\text{CH})^{-0.10}]_r$ employed in the cell construction (see Table I). This is due to polarization of the $\text{Li}_y^+(\text{TiS}_2)^{-y}$ and $[\text{Li}_y^+(\text{CH})^{-y}]_r$ electrodes under the applied current densities and to incomplete diffusion of Li^+ ions from the surface of the TiS_2 to its interior and from the interior of the $(\text{CH})_r$ fibrils to its surface during the time in which the discharge studies were performed. These effects can readily be seen, for example, after the

10:1 molar ratio $[\text{Li}_{0.10}^+(\text{CH})^{-0.10}]_r/\text{TiS}_2$ cell was discharged to 0 V and then disconnected for 1 min. The V_{oc} increased to 0.3V as Li^+ ions diffused into the interior of the TiS_2 and toward the surface of the $(\text{CH})_r$ fibrils. These effects may be related, at least in part, to the fabrication of the TiS_2 electrodes' being poorer than that obtainable by the best state of the art procedures.

When comparing discharge cycles at different current densities for a given cell, it can be seen from Table I that the extent of cell reaction decreased with increasing discharge current density. This is consistent with increased polarization and less complete diffusion at higher current density discharges, which occurred in a shorter time period. Comparing the 1:1 and 10:1 molar ratio $[\text{Li}_{0.10}^+(\text{CH})^{-0.10}]_r/\text{TiS}_2$ cells at the same discharge current density (0.1 mA for 0.7 cm² of $(\text{CH})_r$), it can be seen that the extent of the cell reaction (78% *vs.* 49%, respectively) is less complete for the 10:1 molar ratio cell. This is consistent with the fact that both cells employed approximately the same amount of $(\text{CH})_r$ so that the 10:1 molar ratio cell contained only one-tenth the amount of TiS_2 . The correspondingly smaller surface area of TiS_2 will, therefore, increase the effects due to polarization.

The 1:1 and 10:1 molar ratio cell reactions were essentially reversible, as can be seen in Table I by comparing Q_{out} , the number of coulombs liberated during discharge, to Q_{in} , the number of coulombs involved during the charging process. Since these quantities were nearly the same in all cases, these reactions are considered to be essentially reversible even though they do not proceed to completion. The incompleteness of these reactions is believed to be due to incomplete diffusion during the time of the discharge, so that, in effect, the interior portions of the TiS_2 particles and the interior portions of the $(\text{CH})_r$ fibrils do not actively enter into the reaction processes.

Since the value of Q_{out} for the 0.05 mA discharge of the 4:1 molar ratio $[\text{Na}_{0.10}^+(\text{CH})^{-0.10}]_r/\text{TiS}_2$ cell, whose reaction is given by Eq. [5], was close to the value of Q_{in} (see Table I) obtained in the subsequent charge, this reaction may also be considered essentially reversible. However, when the discharge was carried out at the higher current of 0.2 mA, the value of Q_{out} was significantly larger than the value of Q_{in} . This may be due to the formation of some $\text{Na}_y^+(\text{TiS}_2)^{-y}$ ($y > 0.4$) phase at the surface of the TiS_2 , during the rapid discharge process, from which it is believed Na^+ ions may not be readily removed during the charging process (11).

In order to better understand the discharge curve shown in Fig. 3, curve C for the 10:1 molar ratio $[\text{Li}_{0.10}^+(\text{CH})^{-0.10}]_r/\text{TiS}_2$ cell, whose reaction is given by Eq. [4], a theoretical curve based on equilibrium data has been constructed. This theoretical curve, shown in Fig. 6, curve C, was constructed from (i) Fig. 6, curve A, which gives the equilibrium V_{oc} values of a $\text{Li}/\text{Li}_y^+(\text{TiS}_2)^{-y}$ cell as a function of increasing intercalation of Li^+ ions into the $\text{Li}_y^+(\text{TiS}_2)^{-y}$ ($0 \leq y \leq 1$) electrode as reported by Whittingham (12) and (ii) Fig. 6, curve B, which gives the equilibrium V_{oc} values of a $\text{Li}/[\text{Li}_{0.10}^+(\text{CH})^{-0.10}]_r$ cell as a function of decreasing reduction, *i.e.*, removal of Li^+ ions from the $[\text{Li}_y^+(\text{CH})^{-y}]_r$ ($0.1 \geq y \geq 0$) electrode, as we have reported previously (3). Curves A, B, and C in Fig. 6 correspond to the equilibrium potentials for the reactions given by Eq. [2], [3], and [4], respectively. The calculated equilibrium cell potential (Fig. 6, curve C) is thus based on the difference between curves A and B as given by Eq. [6]

$$V_{\text{cell}} = V_{\text{cathodic}} - V_{\text{anodic}} \quad [6]$$

Figure 6, curve C represents a hypothetical discharge carried out under no load, infinitely slowly, thus eliminating polarization and diffusion effects.

Figure 6, curve B' is an experimental curve obtained from a $\text{Li}/[\text{Li}_{0.10}^+(\text{CH})^{-0.10}]_r$ cell (employing 3.1 mg of $(\text{CH})_r$), when the $[\text{Li}_{0.10}^+(\text{CH})^{-0.10}]_r$ electrode was oxidized at a constant current of 0.17 mA/cm² of $(\text{CH})_r$ (3). If curve B' is combined with curve A using Eq. [6], then curve C'

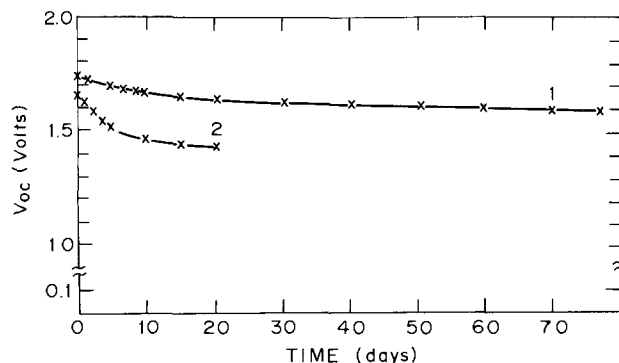


Fig. 5. Relationship between the open-circuit voltage, V_{oc} and time for a $[\text{Na}_{0.10}^+(\text{CH})^{-0.10}]_r/\text{NaPF}_6(\text{THF})/\text{TiS}_2$ cell (curve 1) and a $[\text{Li}_{0.10}^+(\text{CH})^{-0.10}]_r/\text{LiClO}_4(\text{THF})/\text{TiS}_2$ cell (curve 2).

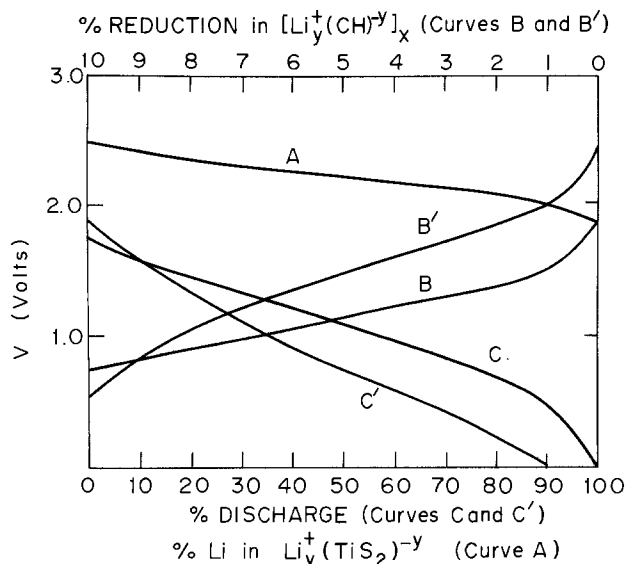


Fig. 6. Potential of: (A) $\text{Li}_y^+(\text{TiS}_2)^{-y}$ cothode vs. Li at equilibrium [Ref. (4)]; (B) $[\text{Li}_{0.10(1-y)}^+(\text{CH})^{-0.10(1-y)}]_r$ anode vs. Li at equilibrium [Ref. (3)]; (B') $[\text{Li}_{0.10(1-y)}^+(\text{CH})^{-0.10(1-y)}]_r$ electrode vs. Li during oxidation of $[\text{Li}_{0.10}^+(\text{CH})^{-0.10}]_r$ to $(\text{CH})_r$ [Ref. (3)]; (C) $[\text{Li}_{0.10(1-y)}^+(\text{CH})^{-0.10(1-y)}]_r/\text{Li}_y^+(\text{TiS}_2)^{-y}$ cell calculated at equilibrium; (C') $[\text{Li}_{0.10(1-y)}^+(\text{CH})^{-0.10(1-y)}]_r/\text{Li}_y^+(\text{TiS}_2)^{-y}$ cell calculated for discharge (see text).

is obtained. This gives a closer approximation than curve C to what could be expected experimentally during discharge of the 10:1 molar ratio $[\text{Li}_{0.10}^+(\text{CH})^{-0.10}]_r/\text{TiS}_2$ cell, since one of the curves (curve B') represents a discharge under actual load conditions.

Curve C in Fig. 6 is reproduced as curve 2 in Fig. 7. For comparative purposes, the experimental discharge curve for the 10:1 molar ratio $[\text{Li}_{0.10}^+(\text{CH})^{-0.10}]_r/\text{TiS}_2$ cell (Fig. 3, curve C) is reproduced as curve 1 in Fig. 7. It can be seen that these curves have a similar general shape, but that, owing to polarization and diffusion effects, the observed cell discharge reaction (curve 1, Fig. 7) is only 49% complete.

A theoretical V vs. Q curve based on equilibrium data has also been constructed for the 4:1 molar ratio $[\text{Na}_{0.10}^+(\text{CH})^{-0.10}]_r/\text{TiS}_2$ cell. This theoretical curve shown in Fig. 8, curve 2 is constructed from (i) equilibrium V_{oc} values of a $\text{Na}/\text{Na}_y^+(\text{TiS}_2)^{-y}$ cell as a function of increasing intercalation of Na^+ ions into the $\text{Na}_y^+(\text{TiS}_2)^{-y}$ ($0 \leq y \leq 0.4$) electrode as reported by Winn *et al.* (10) and (ii) equilibrium V_{oc} values of a $\text{Na}/[\text{Na}_{0.10}^+(\text{CH})^{-0.10}]_r$ cell as a function of decreasing reduction, *i.e.*, removal of Na^+ ions from the $[\text{Na}_y^+(\text{CH})^{-y}]_r$ ($0.1 \geq y \geq 0$) electrode (13).

For comparative purposes, the experimental discharge curve for the 4:1 molar ratio $[\text{Na}_{0.10}^+(\text{CH})^{-0.10}]_r/\text{TiS}_2$ cell (Fig. 4, curve 3) is reproduced as curve 1 in Fig. 8. From Fig. 8, it can be seen that the experimental curve also follows the general shape of the theoretical curve for the $[\text{Na}_{0.10}^+(\text{CH})^{-0.10}]_r/\text{TiS}_2$ cell, but, again, owing to polarization and diffusion effects, the observed cell discharge reaction (curve 1, Fig. 8) is only 64% complete.

Comparing the 10:1 molar ratio $[\text{Li}_{0.10}^+(\text{CH})^{-0.10}]_r/\text{TiS}_2$ cell data given in Fig. 7 with the 4:1 molar ratio $[\text{Na}_{0.10}^+(\text{CH})^{-0.10}]_r/\text{TiS}_2$ cell data given in Fig. 8, it is apparent that the potential of the $[\text{Li}_{0.10}^+(\text{CH})^{-0.10}]_r/\text{TiS}_2$ cell falls continually as the discharge reaction proceeds to completion, while the potential of the $[\text{Na}_{0.10}^+(\text{CH})^{-0.10}]_r/\text{TiS}_2$ cell decreases more gradually and then falls rapidly during the last ~10% of its discharge. This difference in the behavior of the cell potentials is consistent with the fact that the equilibrium potential of the $\text{M}_y^+(\text{TiS}_2)^{-y}$ electrode for differing values of y is dependent on the intercalant used with respect to a common reference (*e.g.*, vs. Li) (10, 12), while the potential of the $[\text{M}_y^+(\text{CH})^{-y}]_r$ electrode for differing values of y is independent of the dopant used (3, 13). Since the potential of $\text{Na}_y^+(\text{TiS}_2)^{-y}$ is greater than the potential of $\text{Li}_y^+(\text{TiS}_2)^{-y}$ for $y \leq 0.4$ vs. a common ref-

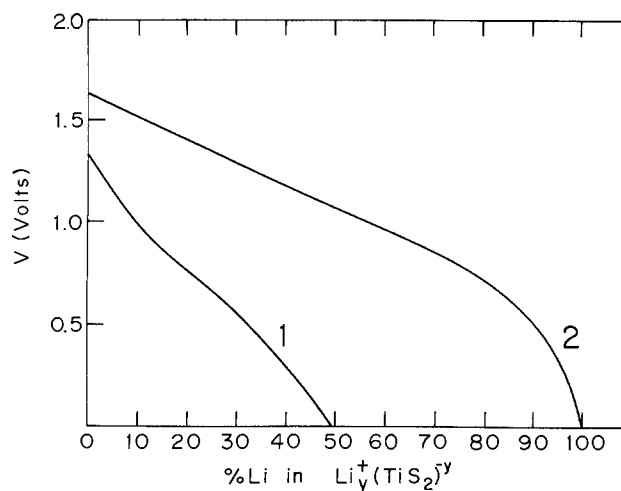


Fig. 7. Change in voltage of a 10:1 molar ratio $[\text{Li}_{0.10}^+(\text{CH})^{-0.10}]_r/\text{TiS}_2$ cell as a function of percent Li intercalation in $\text{Li}_y^+(\text{TiS}_2)^{-y}$ during a 0.1 mA discharge (curve 1) and at equilibrium (curve 2).

erence electrode (10, 12), the $\text{Na}_y^+(\text{TiS}_2)^{-y}$ electrode would therefore be expected to exhibit a larger potential than the $\text{Li}_y^+(\text{TiS}_2)^{-y}$ electrode, vs. a $[\text{M}_y^+(\text{CH})^{-y}]_r$ electrode. For example, at $y = 0.4$, the potential of a $\text{Na}_y^+(\text{TiS}_2)^{-y}$ electrode is 2.00V (vs. Na), *i.e.*, 2.33V (vs. Li),² while the potential of the corresponding $\text{Li}_y^+(\text{TiS}_2)^{-y}$ electrode is 2.20V (vs. Li). Also note that when $y = 0$, the V_{oc} of TiS_2 vs. Na is 2.3V, *i.e.*, 2.63V (vs. Li),² while the corresponding V_{oc} of TiS_2 vs. Li is 2.45V (see Table II).

The V_{oc} , theoretical energy density, and specific energy of reactant materials are given in Table II for each of the following cells: the 10:1 molar ratio $[\text{Li}_{0.10}^+(\text{CH})^{-0.10}]_r/\text{TiS}_2$ cell, the 4:1 molar ratio $[\text{Na}_{0.10}^+(\text{CH})^{-0.10}]_r/\text{TiS}_2$ cell, a $\text{Li}/\text{Li}_y^+(\text{TiS}_2)^{-y}$ cell, a $\text{Na}/\text{Na}_y^+(\text{TiS}_2)^{-y}$ cell, a $\text{Li}/[\text{Li}_y^+(\text{CH})^{-y}]_r$ cell, and a $\text{Na}/[\text{Na}_y^+(\text{CH})^{-y}]_r$ cell. The theoretical energy densities are based on the area under the equilibrium V_{oc} vs. Q curves for each reaction divided by the total weight of anode and cathode material employed in the cell construction. For example, the theoretical energy densities for the 10:1 molar ratio $[\text{Li}_{0.10}^+(\text{CH})^{-0.10}]_r/\text{TiS}_2$ cell and the 4:1 molar ratio $[\text{Na}_{0.10}^+(\text{CH})^{-0.10}]_r/\text{TiS}_2$ cell are obtained from the area under curve 2, Fig. 7 and curve 2, Fig. 8, respectively, and from the weights of $[\text{M}_{0.10}^+(\text{CH})^{-0.10}]_r$ and TiS_2 employed in each cell. The experimental energy densities are based on the area under a V_d vs. Q curve during a constant current discharge and the total weight of an-

² Assuming that the difference in the E_{red}^0 potential between Na (2.711V vs. SHE) and Li (3.045V vs. SHE), *i.e.*, 0.334V, will have approximately the same value in the electrolytes used in the present studies.

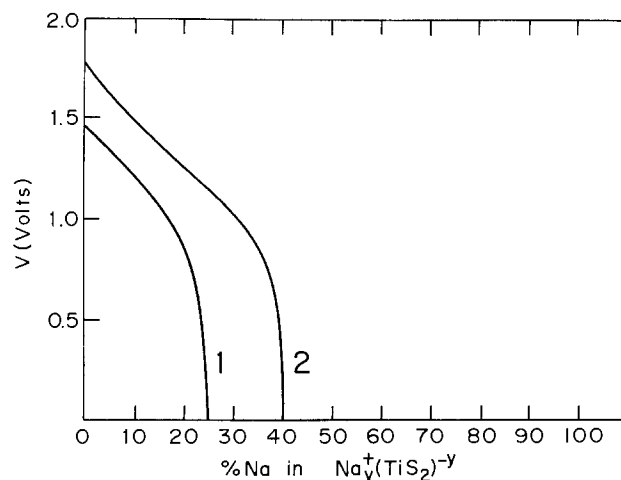


Fig. 8. Change in voltage of a 4:1 molar ratio $[\text{Na}_{0.10}^+(\text{CH})^{-0.10}]_r/\text{TiS}_2$ cell as a function of percent Na intercalation in $\text{Na}_y^+(\text{TiS}_2)^{-y}$ during a 0.05 mA discharge (curve 1) and at equilibrium (curve 2).

Table II. Energy densities of selected cells employing polyacetylene and titanium disulfide electrodes

Cell discharge reaction	V_{oc} (V)	Theoretical energy density (Wh/kg)	Discharge current density (mA/cm ²)	Specific energy of reactant materials (Wh/kg)
$10[\text{Li}_{0.10}^+(\text{CH})^{-0.10}]_x + x\text{TiS}_2 \rightarrow 10(\text{CH})_x + x\text{Li}^+(\text{TiS}_2)^-$	1.65	110.9 ^a	0.14	27.1 ^a
$4[\text{Na}_{0.10}^+(\text{CH})^{-0.10}]_x + x\text{TiS}_2 \rightarrow 4(\text{CH})_x + x\text{Na}_{0.40}^+(\text{TiS}_2)^{-0.40}$	1.80	78.9 ^a	0.14	30.1 ^a
$\text{Li} + \text{TiS}_2 \rightarrow \text{Li}^+(\text{TiS}_2)^-$	2.45	480 ^b	0.3	342 ^c
$0.40 \text{ Na} + \text{TiS}_2 \rightarrow \text{Na}_{0.40}^+(\text{TiS}_2)^{-0.40}$	2.3	166 ^c , 199 ^d	2.5	153 ^b
$0.10x \text{ Li} + (\text{CH})_x \rightarrow [\text{Li}_{0.10}^+(\text{CH})^{-0.10}]_x$	1.80	232 ^e	0.17	201 ^e
$0.10x \text{ Na} + (\text{CH})_x \rightarrow [\text{Na}_{0.10}^+(\text{CH})^{-0.10}]_x$	1.45	144 ^f	0.17	115 ^f

^a This work.^b Ref. (4).^c Calculated from data in Ref. (10).^d Calculated from data in Ref. (14).^e Ref. (3).^f Ref. (13).^g Ref. (15).^h Calculated from data in Ref. (11).

ode and cathode material employed in the cell construction. For example, the experimental energy densities for the 10:1 molar ratio $[\text{Li}_{0.10}^+(\text{CH})^{-0.10}]_x/\text{TiS}_2$ cell and the 4:1 molar ratio $[\text{Na}_{0.10}^+(\text{CH})^{-0.10}]_x/\text{TiS}_2$ cell are obtained from the area under curve 1, Fig. 7 and curve 1, Fig. 8, respectively, and from the weights of $[\text{M}_{0.10}^+(\text{CH})^{-0.10}]_x$ and TiS_2 employed in each cell.

The Li/TiS_2 and the $\text{Li}/(\text{CH})_x$ cells have significantly higher experimental energy densities than the corresponding Na/TiS_2 and $\text{Na}/(\text{CH})_x$ cells (see Table II). This is due to the lower atomic weight and higher reduction potential of lithium as compared to sodium. However, the $[\text{Na}_{0.10}^+(\text{CH})^{-0.10}]_x/\text{TiS}_2$ cell has an experimental energy density (30.1 Wh/kg, close to that of the $[\text{Li}_{0.10}^+(\text{CH})^{-0.10}]_x/\text{TiS}_2$ cell (27.1 Wh/kg). This is due to the higher potential of the $[\text{Na}_{0.10}^+(\text{CH})^{-0.10}]_x/\text{TiS}_2$ cell during discharge, as discussed above.

As can be seen in Fig. 3, curve C', the charging of the 10:1 molar ratio $[\text{Li}_{0.10}^+(\text{CH})^{-0.10}]_x/\text{TiS}_2$ cell could not be completed at a constant current of 0.1 mA. From Fig. 3, curve A', it can clearly be seen that the main cause of this is polarization of the TiS_2 electrode, resulting in a cathode-limited reaction. Thus, the applied charging current caused the $\text{Li}_y^+(\text{TiS}_2)^{-y}$ electrode potential to rise rapidly; the charging was therefore completed at a constant potential of 1.8V applied between the anode and the cathode.

Improved methods for constructing TiS_2 electrodes have allowed others to successfully cycle TiS_2 cathodes at high current densities (16, 17). Adopting some of these methods to the present cells could (i) improve the $[\text{M}_{0.10}^+(\text{CH})^{-0.10}]_x/\text{TiS}_2$ cells by enabling complete charging at high current densities and (ii) improve the energy densities by enabling the cell reactions to proceed further to completion. Improvements in fabricating the TiS_2 electrodes include a hot bonding technique (11), improved binders such as ethylenepropylene-diene terpolymer (16), and employing a reduced weight ratio of binder to TiS_2 . All these improvements have been shown to reduce polarization effects at the TiS_2 electrode and to improve its overall performance in a battery cell.

Improved electrolytes could be useful in the $[\text{M}_y^+(\text{CH})^{-y}]_x/\text{TiS}_2$ cells. For example, 1.0M LiAsF_6 in 2Me-THF has been shown to increase the recyclability of Li/TiS_2 cells (17). Since this electrolyte is compatible with the $[\text{Li}_y^+(\text{CH})^{-y}]_x$ electrode (18), it could be advantageously employed in a $[\text{Li}_{0.10}^+(\text{CH})^{-0.10}]_x/\text{TiS}_2$ cell.

Other intercalating inorganic materials might be substituted for TiS_2 as the cathode-active material in these cells. For example, the electrochemistry of the sulfides and selenides of vanadium, niobium, and tantalum and transition metal oxides such as V_2O_5 , MoO_3 , and MnO_2 , has been investigated (4). To determine which materials could be used in practical cells, theoretical V vs. Q curves, such as

those given in Fig. 7, curve 2 and Fig. 8, curve 2, should be constructed, and the electrochemical characteristics of those showing the most promise could be investigated.

Analogously, other conducting organic polymers might be substituted for polyacetylene as the anode-active material in these cells. Polyparaphenylene (19) and polyquinolines (20), both of which can be reduced electrochemically, are the most promising candidates.

Conclusions

This feasibility study of cells comprised of the conducting organic polymer anode—reduced polyacetylene and the inorganic intercalating cathode—titanium disulfide has shown some promise for practical cells. The major problems associated with lithium anodes are avoided. Two cells employing differing molar ratios of $[\text{Li}_{0.10}^+(\text{CH})^{-0.10}]_x$ and TiS_2 as anode- and cathode-active materials, respectively, and one cell employing a $[\text{Na}_{0.10}^+(\text{CH})^{-0.10}]_x$ anode and TiS_2 cathode have exhibited promising energy densities and electrochemical reversibility. Improvements in the fabrication of the TiS_2 electrode are needed to overcome the observed cathode limitations of the present cells. Other modifications, such as the use of new conducting organic polymer anodes or other inorganic intercalating cathodes, may show even greater technological promise.

Acknowledgments

The authors would like to thank Dr. T. Uchida and Dr. W. L. Worrell for preparation of the titanium disulfide and many helpful discussions. This study was supported by the Department of Energy, Contract No. DE-AC02-81-ER10832.

Manuscript submitted March 28, 1984; revised manuscript received July 20, 1984. This was Paper 145 presented at the Cincinnati, OH, Meeting of the Society, May 6-11, 1984.

The University of Pennsylvania assisted in meeting the publication costs of this article.

REFERENCES

- P. J. Nigrey, A. G. MacDiarmid, and A. J. Heeger, *J. Chem. Soc. Chem. Commun.*, 594 (1979); K. Kaneto, K. Yoshimo and Y. Unuishi, *Jpn. J. Appl. Phys.*, **22**, L567 (1983); see also Ref. (2, 3, 6, 13, 19, 20).
- P. J. Nigrey, D. MacInnes, Jr., D. P. Nairns, A. G. MacDiarmid, and A. J. Heeger, *This Journal*, **128**, 1651 (1981); K. Kaneto, M. Maxfield, D. P. Nairns, A. G. MacDiarmid, and A. J. Heeger, *J. Chem. Soc. Faraday Trans. I*, **78**, 3417 (1982); G. C. Farrington, B. Scrosati, D. Frydrych, and J. DeNuzzio, *This Journal*, **131**, 7 (1984).
- R. B. Kaner and A. G. MacDiarmid, *J. Chem. Soc. Fara-*

- day *Trans. I*, **80**, 2109 (1984).
- M. S. Whittingham, *Prog. Solid State Chem.*, **12**, 41 (1978).
 - B. G. Silbernagel and M. S. Whittingham, *J. Chem. Phys.*, **64**, 3670 (1976); B. S. Silbernagel and M. S. Whittingham, *Mater. Res. Bull.*, **11**, 29 (1976).
 - J. H. Kaufman, J. W. Kaufer, A. J. Heeger, R. B. Kaner, and A. G. MacDiarmid, *Phys. Rev. B*, **26**, 2327 (1982).
 - H. Shirakawa and S. Ikeda, *Polym. J.*, **2**, 231 (1971); H. Shirakawa, T. Ito, and S. Ikeda, *ibid.*, **4**, 460 (1973); T. Ito, H. Shirakawa, and S. Ikeda, *J. Polym. Sci. Polym. Chem. Ed.*, **12**, 11 (1974); *ibid.*, **13**, 1943 (1975).
 - M. S. Whittingham and J. A. Panella, *Mater. Res. Bull.*, **16**, 37 (1981).
 - T.-C. Chung, A. G. MacDiarmid, A. Feldblum, and A. J. Heeger, *J. Polym. Sci. Polym. Lett.*, **20**, 427 (1982).
 - D. A. Winn, J. M. Shemilt, and B. C. H. Steele, *Mater. Res. Bull.*, **11**, 559 (1976).
 - G. H. Newman and L. P. Klemann, *This Journal*, **127**, 2097 (1980).
 - M. S. Whittingham, *ibid.*, **123**, 315 (1976).
 - R. B. Kaner and A. G. MacDiarmid, *J. Chem. Soc. Faraday Trans. I*, To be published.
 - A. S. Nagelberg and W. L. Worrell, *J. Solid State Chem.*, **29**, 345 (1979).
 - G. L. Holleck and J. R. Driscoll, *Electrochim. Acta*, **22**, 647 (1977).
 - S. P. S. Yen., D. H. Shen, and R. B. Somoano, *This Journal*, **130**, 1107 (1983).
 - K. M. Abraham, J. L. Goldman, and D. L. Natwig, *ibid.*, **129**, 2404 (1982).
 - R. B. Kaner and A. G. MacDiarmid, Unpublished results.
 - L. W. Shacklette, R. L. Elsenbaumer, R. R. Chance, J. M. Sowa, D. M. Ivory, G. G. Miller, and R. H. Baughman, *J. Chem. Soc. Chem. Commun.*, 361 (1982).
 - A. H. Schroeder, Y. S. Papir, and V. P. Kurkov, Abstract 544, p. 822, The Electrochemical Society Extended Abstracts, Vol. 83-1, San Francisco, CA, May 8-13, 1983.

Methodology for Predictive Testing of Fuel Cells

D. N. Patel, H. C. Maru,* M. Farooque,* and C. H. Ware¹

Energy Research Corporation, Danbury, Connecticut 06810

ABSTRACT

A perturbation testing method has been developed and tested for predictive testing of fuel cells. This method involves application of small changes to the operating conditions of the cell in a predetermined sequence. The resultant response of the cell is then measured and statistically correlated with the corresponding test conditions. This method has been applied to the phosphoric acid fuel cell, and the effect of operating and cell-component variables on cell-performance degradation has been studied. A strong effect of the cell temperature and cathode potential on fuel-cell-performance degradation has been observed. A cell-performance degradation model has been formulated, and the unknown parameters in the model have been estimated by a regression analysis of the experimental data. A reasonable agreement between the fuel cell performance predicted by this model (derived from the perturbation experiments) and the unperturbed test data supports the applicability of the perturbation method.

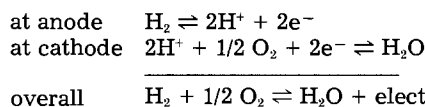
The phosphoric acid fuel cell being developed for electricity generation is expected to have a long operating life (typically 40,000h for use in utility power plants). A fuel cell aging model is therefore very useful in a cost-effective component evaluation and an optimization of design conditions minimizing the life-cycle cost. The techniques used most often in electrochemical studies for developing aging models are steady-state life testing and accelerated testing. Steady-state life testing of fuel cells offers limited information, is very expensive, and is time consuming. In accelerated testing, the cell is run at very severe operating conditions (e.g. a cell temperature of 200°C and a cathode voltage of 0.9V) to accelerate decay, and the large changes made in operating conditions to accelerate decay may cause a shift in the decay mechanism. Hence, the decay mechanism during accelerated testing may not be representative of design conditions. Accelerated testing is also expensive, as a large number of tests are required. This paper describes an alternative predictive testing approach—the perturbation testing technique—and describes its application to the phosphoric acid fuel cell (PAFC).

Theoretical

Perturbation testing technique.—This technique involves the investigation of a system response, utilizing small, careful changes in the operating conditions to ensure the representative behavior of the decay mechanism. It is an adaptation of "Evolutionary Operation" (EVOP) (1, 2), originally applied to optimization of plant operation. In this technique, changes are made in important variables of the plant to find conditions that would in-

crease its performance and provide the direction for further improvement. The changes are kept small to permit plant operation with an acceptable product. Because in the perturbation testing technique several perturbations in operating variables are applied to a single cell, fewer tests are required than in accelerated testing. Furthermore, perturbations on the same cell enable cell-to-cell, variation-free estimation of model parameters. Thus, the perturbation testing technique is cost effective, quick, and reliable.

Decay modes.—In this study, the perturbation testing technique is applied to phosphoric acid fuel cells (PAFC). The PAFC are operated in the temperature range of 165°-200°C. At temperatures lower than 165°C, the poisoning of the Pt catalyst by CO in the fuel increases, and at temperatures higher than 200°C, the material stability is affected. The basic reactions occurring in the PAFC are



The PAFC electrodes consist of platinum, carbon, and Teflon. The carbon support provides a conductive and highly dispersive base for the Pt (catalyst) crystallites; the Teflon mainly imparts hydrophobicity to the structure. The phosphoric acid (electrolyte stored in the matrix layer) provides a conductive path for H⁺ ions, and electricity is produced by an electrochemical reaction between H₂ from fuel and O₂ from air. The primary fuel for the PAFC is pure hydrogen. However, impure hydrogen (containing CO₂) may also be used as fuel.

Knowledge of possible decay modes and important parameters affecting the decay is desirable (and even essential to predict relative contributions of various decay

*Electrochemical Society Active Member.

¹Present address: World Energy Systems, Rocky Mount, VA 24151.

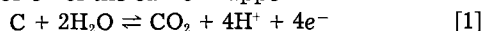
rates) in performing cost-effective and efficient predictive testing. The primary decay modes limiting the PAFC lives appear to be related to cathode performance decay (3). In this study, two primary decay modes are considered

A: Platinum deactivation (4)

- Catalyst surface area loss by platinum crystallite growth
- Platinum dissolution in the electrolyte

B: Increase in diffusion polarization

- Corrosion of the carbon support



- Teflon degradation

Possible secondary decay modes, such as anode poisoning, matrix-bubble pressure loss, and bipolar plate corrosion, are not studied. The electrolyte-loss decay mode is experimentally eliminated by providing a constant supply of electrolyte.

Experimental design.—Experimental variables which influence the cell-performance degradation through modes A and B are chosen next. Cell temperature, cathode potential, and average water partial pressure at cathode are selected as the operating variables (5). Catalyst loading and Teflon content of cathode are selected as the cell component (build) variables. The levels of these variables (see Table I) are decided after preliminary experiments. The criteria for the selection of levels is to have the "high" levels low enough to prevent material problems (and other problems) and to have the "low" levels high enough to provide a measurable decay in each perturbation period.

A variation on the Balanced Incomplete Block Design (BIBD) (6) has been selected for this study. The traditional application of an incomplete block design is one in which there are too many treatments (too many variables, which create the need for too many test runs) to be studied in a single block (a test cell, in this case). A balanced incomplete design is one in which every pair of treatments occurs the same number of times. One purpose of the perturbation experiments is to study the effects of cell operating and build variables on catalyst deactivation, which results in cell performance degradation. Since the catalyst utilization (effectiveness of the cathode catalyst) changes with time, the effects of variables has to be estimated in the presence of this uncontrolled variable (catalyst utilization). Hence, in the selected design, an important consideration is given to time. The balanced incomplete block designs permit the experimenter to obtain a small block of information which can be efficiently integrated into a large picture. The particular design chosen utilizes 2×2 factorial design as a block. BIBD is selected to obtain a snapshot of the effects of two variables (T and V_c) in a relatively short period of time (the 2×2 factorial) and then return to the same factorial design at a later time when catalyst utilization is different. The analysis of the results of each 2×2 factorial design yields the effects of the independent variables (T , V_c , P_{H_2O}) on decay rates. In addition, a comparison of these effects at two different catalyst utilization levels (different times) yields the mutual interaction between the operating variables and the catalyst utilization.

The use of a second block (2×2 factorial) at a later time does not only obtain the foregoing comparison. It is a vir-

Table I. Experimental variables and their levels

Levels	Operating variables			Build type	Cell component variables	
	T , °C	V_c , Volts	P_{H_2O} , kPa		CL, mg/cm ²	TFE, %
High	191	0.81	42	I	0.3	40
Center	184	0.77	35	II	0.6	40
Low	177	0.73	29	III	0.3	45
				IV	0.6	45

tual necessity to reduce the effect of changing catalyst utilization on the experimental results and, therefore, the estimates of the model coefficients. By making the second block a mirror image of the first, the confounding of catalyst utilization with operating variables can be eliminated if catalyst utilization is linear with time; if not, it can be reduced.

Balanced Incomplete Block Designs have another advantage. Unlike factorial designs, there is no test run with all variables at the most severe condition and at the least severe condition. By avoiding the most severe condition, material problems can be eliminated; by avoiding the least severe condition, a measurable decay can be obtained in a reasonable period of time.

A complete perturbation cycle is shown in Table II. The design is symmetrical with respect to Period 11. The operating sequence of the design consists of a 2×2 factorial in the cell temperature and cathode voltage, followed by single variable perturbation in water-vapor partial pressure. The fourth variable is assigned as a dummy variable to provide for orthogonal blocking in the design. This allows cell-to-cell, variation-free estimation of the model parameters.

It should be noted that this ($T \times V_c$, P_{H_2O}) is only one of three possible combinations. The other two combinations are

- 2×2 factorial in cathode voltage and water partial pressure, followed by single variable perturbation in cell temperature ($V_c \times P_{H_2O}$, T)
- 2×2 factorial in water partial pressure and cell temperature, followed by single-variable perturbation in cathode voltage ($P_{H_2O} \times T$, V_c)

If all three combinations are to be executed, too many test cells will be required. Also, the replicates are needed to estimate the experimental error. Hence, only one combination is used, and replicates are provided in the experiments to accomplish the objectives with a minimum number of test cells. The $T \times V_c$, P_{H_2O} combination is preferred because it offers $T \times V_c$ interaction, which may be stronger than $T \times P_{H_2O}$ and $V_c \times P_{H_2O}$ interactions.

The duration of the perturbation periods (Table II) are chosen after the preliminary experiments. They are selected to keep the change in catalyst utilization, CU , approximately equal in all periods in order to keep $\text{Var}(\ln r_u)$ comparable.

Testing

Test facility.—A test facility consisting of 22 high-quality test stands was designed and constructed for the pre-

Table II. A Complete cycle of BIBD with four variables (including one dummy variable)

Perturbation period	T	V_c	P_{H_2O}	Duration of period, days
1	O ^a	O	O	5
2	H ^a	H	O	4
3	L ^a	H	O	5
4	L	L	O	7
5	H	L	O	5
6	O	O	O	5
7	O	O	H	4
8	O	O	L	7
9	O	O	L	7
10	O	O	H	4
11	O	O	O	5
12	O	O	H	4
13	O	O	L	7
14	O	O	L	7
15	O	O	H	4
16	O	O	O	5
17	H	L	O	5
18	L	L	O	7
19	L	H	O	5
20	H	H	O	4
21	O	O	O	5

^a Variable levels: H-high; O-center; L-low.

dictive testing. Digital high-precision meters were used. The temperature controller for the cell had a dual set point: one to control cell temperature and the other to remove the load and to shut off the heating system when the temperature increased beyond a preset level. This protected the cell from excessive heating. For the oxidant, the facility provided air during the break-in period of the cell, O₂ during the perturbation runs, and an O₂-N₂ mixture during the limiting current measurements.

Perturbation testing.—Eighteen subscale cells (25 cm²) comprising the four buildtypes were assembled for the perturbation testing. Excellent reproducibility of the performance parameters was established (Table III) in the test cells to obtain statistically meaningful results. Cell-to-cell variation in the Ir-free performance fell within ± 5 mV for each buildtype. Perturbation testing was then initiated. The operating conditions established during the testing were

Pressure:	101 kPa (1 atm)
Temperature:	As required by the perturbation cycle
Cathode voltage:	
Fuel:	
Oxidant:	O ₂ [humidified, when required, to produce desired water partial pressure at cathode (see perturbation cycle)]
Fuel utilization:	75%
Oxidant utilization:	50%

The operating pressure, fuel (H₂) utilization, and oxidant utilization were maintained constant during the perturbation testing. The cell temperature, cathode voltage, and average water-vapor partial pressure at the cathode were maintained constant during each perturbation period. After each period, their values were changed to those corresponding to the next period (Tables I and II). The new period was initiated soon after the cells were stabilized at the new values. The catalyst loading and Teflon content at the cathode were kept approximately constant by using the same cell throughout the perturbation cycle.

Measurements made during the perturbation testing were

- Current, cell voltage, open-circuit voltage, and cell resistance (measured daily)
- Limiting current (measured at the beginning and the end of each perturbation period)
- Complete polarization measurements [measured when the cell was operating at center levels (at the end of periods 6, 11, 16, and 21)]

From these measurements, the current and the limiting current measurements were used in the data analysis. The rest of the measurements were taken for diagnostic purposes.

The planned 21 perturbation runs were completed in about 3000h. About 85% of the perturbation data obtained was used in the data analysis. The data from perturbation periods 20 and 21 for buildtypes III and IV, and from periods 18 through 21 for buildtypes I and II were not used in the analysis because of an unplanned disturbance in testing. This did not affect the data analysis because the lost data represented only 15% of the total.

Unperturbed testing.—Four base line cells of buildtype IV were operated constantly at centerpoint conditions to generate long-term base line performance data for evaluation of the aging model. The testing continued up to about 5500h.

Data Analysis

Computation of decay rates.—Catalyst utilization (CU) and limiting current density (i_L) are selected to represent the cell performance degradation via modes A and B, respectively. The limiting current-density data obtained during perturbation experiments are measured using dilute O₂ (4%O₂ + 96%N₂). The data, therefore, are corrected as follows

$$i_L (\text{corrected}) = i_L (\text{measured}) \times [P_{O_2} (\text{pert. cond.}) / P_{O_2} (i_L \text{ meas. cond.})]$$

Catalyst utilization values are computed from the cell current data and the limiting current data collected during perturbation tests, using the phosphoric acid fuel-cell performance model (see Appendix A). The performance model and the detailed computation procedure are given in Appendix A. Once the CU and i_L values are obtained for each perturbation period, $-dCU/dt$ and $-di_L/dt$ decay rates are computed using the least squares method. A typical decay plot is shown in Fig. 1. It can be observed that the effect of cell temperature and cathode voltage on Pt deactivation is predominant. Further discussion on this is presented later in the section.

Correlation of decay rates.—The correlation of decay rates with the corresponding operating conditions is then pursued. To begin with, a simple aging model is constructed

For platinum deactivation (mode A)

$$\tau_u = -\frac{dCU}{dt} = k_{u0} \exp(-E_u/RT) CU^{\alpha_u} \exp(\beta_u V_c/T) P_{H_2O}^{\gamma_u} \quad [2]$$

For increase in diffusion polarization (mode B)

$$\tau_i = -\frac{di_L}{dt} = k_{i0} \exp(-E_i/RT) i_L^{\alpha_i} \exp(\beta_i V_c/T) P_{H_2O}^{\gamma_i} \quad [3]$$

The above model is transformed to a logarithmic form for simplicity in correlating the decay rates. The detailed derivations are presented in Appendix B. The logarithmic form of the model is presented below

For platinum deactivation (mode A)

$$\ln \tau_u = \ln \tau_{u0} - E_u/R (1/T - 1/\bar{T}) + \alpha_u (\ln CU - \overline{\ln CU}) + \beta_u (V_c/T - \overline{V_c/T}) + \gamma_u (\ln P_{H_2O} - \overline{\ln P_{H_2O}}) \quad [4]$$

For increase in diffusion polarization (mode B)

$$\ln \tau_i = \ln \tau_{i0} - E_i/R (1/T - 1/\bar{T}) + \alpha_i (\ln i_L - \overline{\ln i_L}) + \beta_i (V_c/T - \overline{V_c/T}) + \gamma_i (\ln P_{H_2O} - \overline{\ln P_{H_2O}}) \quad [5]$$

Where

Table III. Reproducibility within a buildtype

Performance characteristics	Buildtype			
	I	II	III	IV
	0.3 mg/cm ² 40% TFE cells 110-115	0.6 mg/cm ² 40% TFE cells 116-118	0.3 mg/cm ² 45% TFE cells 107-109	0.6 mg/cm ² 45% TFE cells 101-106
Peak performance (Ir-free) at 200 mA/cm ² , mV	628 \pm 4	668 \pm 2	640 \pm 5	654 \pm 4
OCV, mV	921 \pm 3	930 \pm 0	922 \pm 3	925 \pm 5
O ₂ gain, mV	66 \pm 2	67 \pm 2	64 \pm 5	67 \pm 2
Cell resistance, m Ω	10 \pm 1	9 \pm 1	9 \pm 1	9 \pm 1

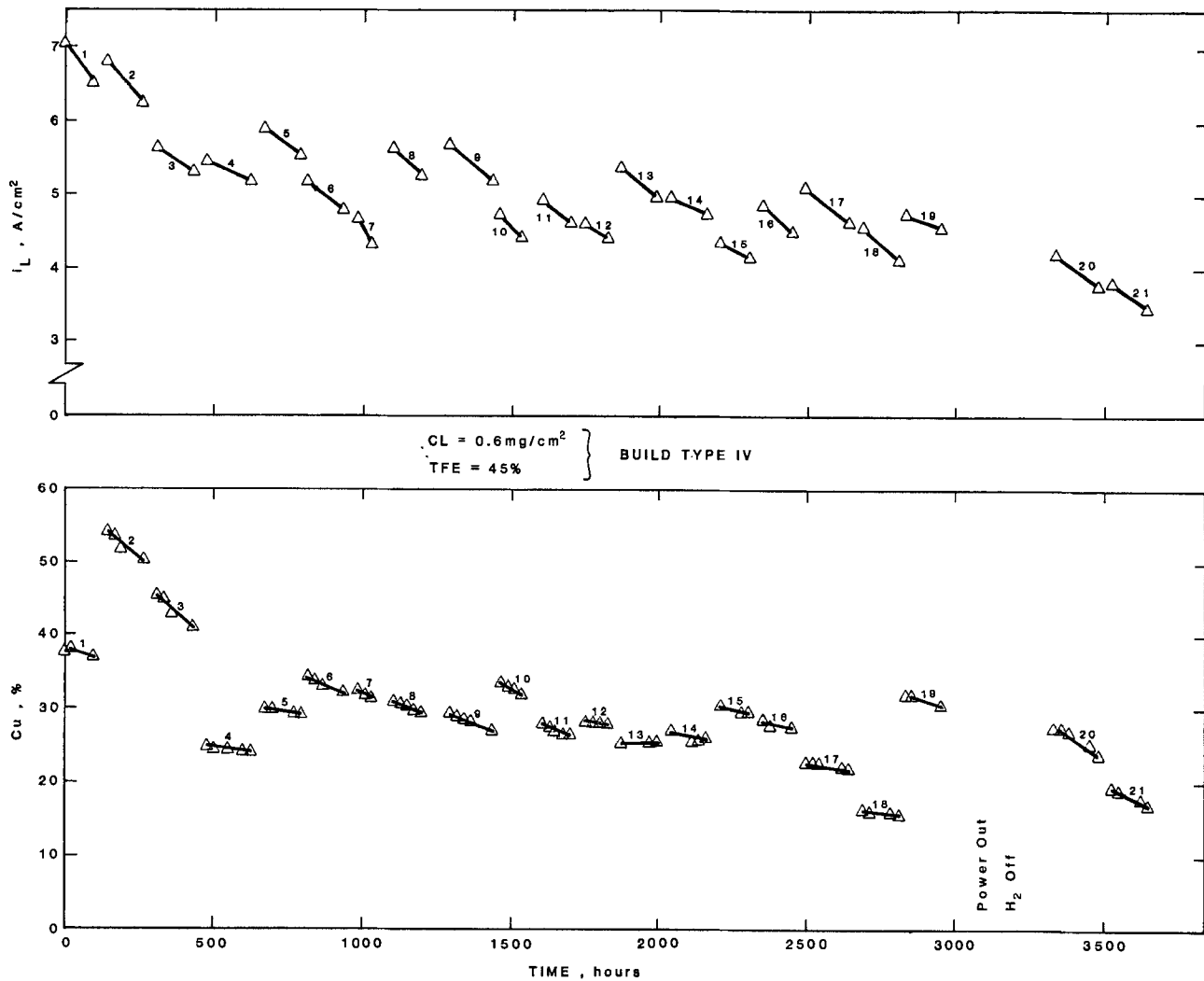


Fig. 1. Typical decay plot of a cell from buildtype IV

- CU = catalyst utilization
- k_{u0} = decay rate constant in mode A
- E_u = activation energy for the decay reaction in mode A
- R = universal gas constant
- T = absolute cell temperature
- V_c = cathode voltage
- P_{H_2O} = average partial pressure of water vapor at the cathode
- α_u = order of the decay reaction with respect to CU
- i_L = limiting current density
- k_{i0} = decay rate constant in mode B
- E_i = activation energy for the decay reaction in mode B
- α_i = order of the decay reaction with respect to i_L
- β_i, β_u = order of the decay reaction with respect to V_c
- γ_i, γ_u = order of the decay reaction with respect to P_{H_2O}
- r_u, r_i = decay rates via modes A and B, respectively
- r_{u0}, r_{i0} = decay rates when all variables at center level
- t = time

Initially, the average (for each period) of data from cells 101 to 106 (buildtype IV) is fitted to the logarithmic model by regression analysis. Though a good fit is obtained, a high uncertainty is observed in the estimated coefficients. To lower the uncertainty, data from individual cells (rather than average cell data) are fitted to the model. However, the F-test indicates a lack of fit. The residual analysis reveals a step change between periods 11 and 12 for a few cells (this upset is caused by an unplanned H₂ outage during these periods). The above data are excluded from further analysis. Also, the estimates of model coefficients and 95% confidence intervals show

that the CU, i_L , and P_{H_2O} terms are very small and have a high uncertainty. Hence, these terms are deleted from the model.

Finally, a good fit is obtained when data from the first six periods are fitted to the model. The model coefficients, standard deviations, and 95% confidence intervals are listed in Table IV. The last column in this table is the overall activation energy, which is a function of V_c . Although the estimates of $E_u, \beta_u, E_i,$ and β_i are statistically significant (because their mean value estimates are relatively much larger than the corresponding standard devi-

Table IV. Parameters estimated after excluding CU, i_L , and P_{H_2O} terms from regression equation

Buildtype IV (0.6 mg/cm ² cathode loading, 45% TFE)				
Parameter	$\ln r_{u0}$	E_u cal/g mol	β_u K/V	$E_{overall} = E_i - 0.77R\beta_i$ cal/g mol
Estimate	-4.309	16900	8100	4500
Std. error	0.078	5900	1100	6100
95% Conf. interval	±0.164	±12400	±2300	±12900
Based on $t_{0.025, 18} = 2.1$				
Parameter	$\ln r_{i0}$	E_i cal/g mol	β_i K/V	$E_{overall} = E_i - 0.77R\beta_i$ cal/g mol
Estimate	-5.551	18700	2900	5700
Std. error	0.087	6600	1200	6900
95% Conf. interval	±0.183	±13900	±2600	±14400

ations), when they are combined in an overall activation energy the two factors tend to cancel each other out, leaving a number which is relatively small compared to its standard deviation. This result, however, does not diminish the significance of the two parameters, E and β (see Table IV).

The strong effect of V_c on $-dCU/dt$ is analyzed for a proper interpretation. The voltage term ($\beta_u V_c/T$) of the decay model can be compared with the $\alpha F V_c/RT$ term from the Tafel equation. After multiplying both the terms by RT/V_c and after rearranging, α can be represented as $\beta_u R/F$. Based on $\beta_u = 8100 \text{ K/V}$ (see Table IV), α is computed to be 0.7, which agrees with α values obtained from the corrosion study of the Vulcan XC-72 carbon (used in this study as the catalyst support material) at ERC (unpublished work). It is an interesting result, because it suggests that the effectiveness (*i.e.*, activity and/or catalyst surface area) of the cathode catalyst is significantly affected by the cathode voltage, probably via carbon-support corrosion (see Eq. [1]).

The final form of the aging model for each of the four buildtypes is shown in Table V. The decay-rate equation accounting for the diffusion loss is discarded because the diffusion polarization is negligible for the test duration. The effects of the build variables are lumped in the decay-rate constants. A relative comparison of the decay-rate constants shows that the cathode with 0.6 mg/cm² Pt loading and 45% Teflon content decays much slower than the rest of the electrodes. This is expected because a cathode with higher Teflon content may be more resistant to acid attack and, hence, provide better wetproofing to prevent flooding. An evaluation of the model is discussed in the following section.

Table V. Final form of the aging model^a

• Buildtype I (0.3 mg/cm ² , 40% TFE)	$r_u = -dCU/dt = 0.0232 \cdot \exp[-10770(1/T - 0.0022)] \cdot \exp[6200(V_c/T - 0.0017)]$
• Buildtype II (0.6 mg/cm ² , 40% TFE)	$r_u = -dCU/dt = 0.0255 \cdot \exp[-3523(1/T - 0.0022)] \cdot \exp[7400(V_c/T - 0.0017)]$
• Buildtype III (0.3 mg/cm ² , 45% TFE)	$r_u = -dCU/dt = 0.0213 \cdot \exp[-9461(1/T - 0.0022)] \cdot \exp[5900(V_c/T - 0.0017)]$
• Buildtype IV (0.6 mg/cm ² , 45% TFE)	$r_u = -dCU/dt = 0.0134 \cdot \exp[-8505(1/T - 0.0022)] \cdot \exp[8100(V_c/T - 0.0017)]$

^a T - temperature, K; V_c - cathode voltage, V; CU - catalyst utilization, %; t - time, h.

Evaluation of the Aging Model

To evaluate the validity of the aging model (see Table V) the performance predicted by the model (for buildtype IV) is compared with the base line performance data. Because the model does not contain CU and i_l terms, it predicts a linear decay. The base line performance data shows an exponential decay. This indicates that the CU and i_l terms are necessary and should be included in the model. The model parameters are therefore re-estimated after including the CU and i_l terms. Though the F-test shows a good fit, the uncertainty in the estimates of the parameters increases because of the limited data available to estimate CU and i_l parameters (first six periods only).

Different values of the decay-rate constants and α within a 95% confidence interval are used to predict the

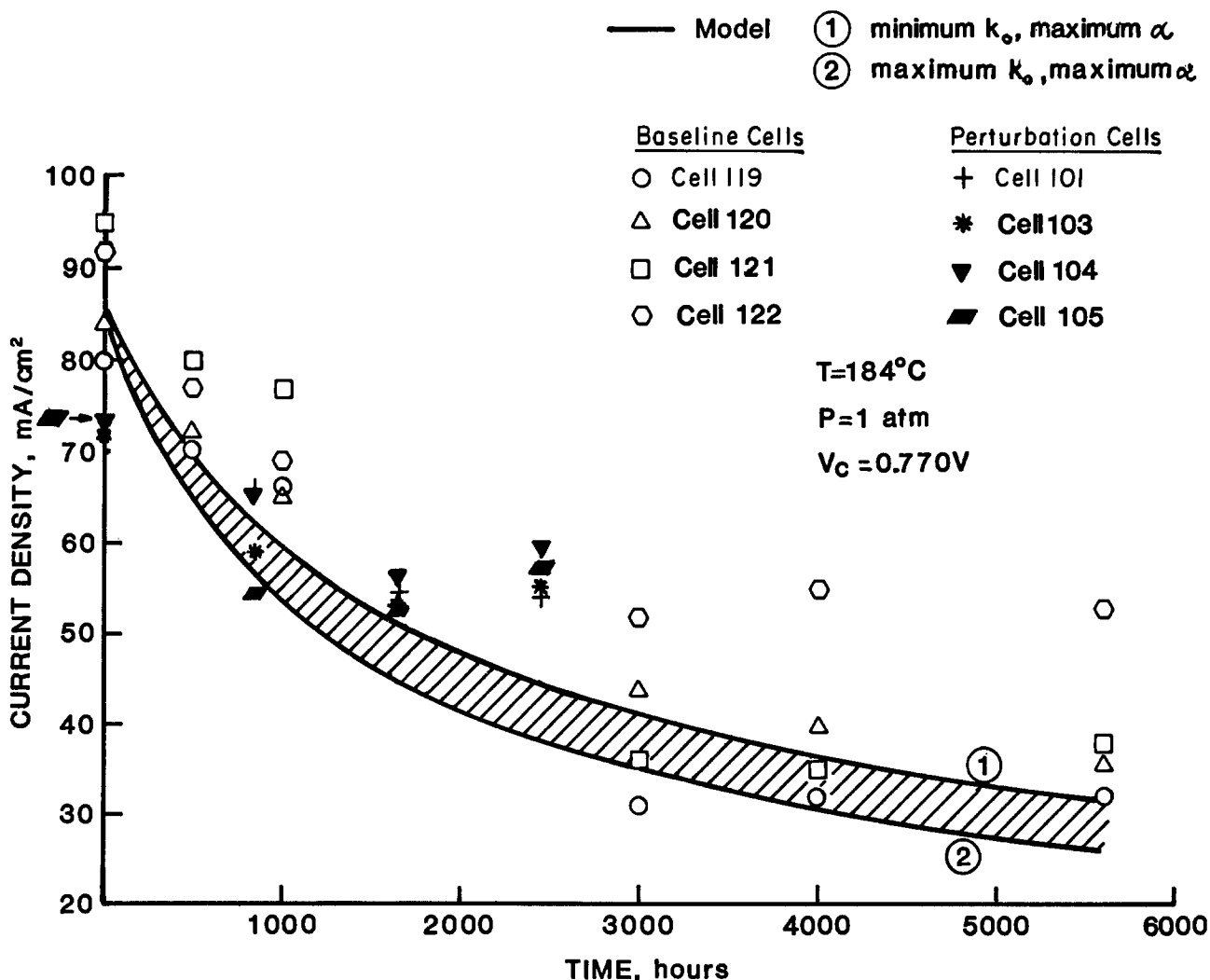


Fig. 2. Comparison of cell performance predicted by aging model derived from perturbation experiments, with unperturbed test data

performance. The minimum values of the decay-rate constants and the maximum values of α yield a reasonably good agreement between the predicted and the experimental curves (Fig. 2). The fact that parametric values for the best fit lie within the 95% confidence limits of the estimates supports the applicability of this approach. Because of a large uncertainty in the parametric values, however, it is weak evidence, and further experiments are needed to strengthen these findings.

Summary

A methodology for predicting long-term fuel-cell performance from short-term testing, utilizing a perturbation testing technique, has been developed and tested on phosphoric acid fuel cells. The initial series of perturbation tests appears to be reasonably successful. The perturbation levels and the periods selected are sufficient to obtain measurable decay. A reasonable agreement between the performance predicted by the simple aging model derived from the perturbation experiments and the unperturbed test data of base line cells supports the applicability of the perturbation technique and the methodology used. The methodology developed for perturbation testing of PAFC should be further refined and applied to other fuel cells, batteries, and electrochemical systems.

The following effects of the operating and cell-component variables on the phosphoric acid fuel-cell decay have been observed

- Cell temperature and cathode voltage are the dominant parameters in the platinum deactivation. The observed effect of cathode voltage on the activity and/or catalyst surface area of the cathode catalyst may be related to a corrosion of the carbon support.
- No significant effect of water partial pressure on cell decay is observed.
- The cathodes with 0.6 mg/cm² Pt loading and 45% Teflon content decay much slower than the electrodes having lower Pt loading and/or Teflon content.
- For the entire test duration, the limiting current density remains sufficiently high and, consequently, the diffusion polarization is found to be negligible.

Acknowledgments

This work was partially supported by DOE/NASA under Contract No. DE-AC05-79ET15381. The authors thank Dr. M. Lauver of the NASA Lewis Research Center for stimulating discussions.

Manuscript submitted June 12, 1982; revised manuscript received July 16, 1984.

Energy Research Corporation assisted in meeting the publication costs of this article.

APPENDIX A

Phosphoric Acid Fuel-Cell Performance Model and Estimation of Catalyst Utilization

Performance model.—The fuel cell terminal voltage, V , can be expressed as

$$V = E - Ir - \eta_{\text{anode}} - \eta_{\text{cathode}}^{\text{act}} - \eta_{\text{cathode}}^{\text{dif}} \quad [\text{A-1}]$$

In perturbation testing, cathode voltage, V_c , is kept constant during a period. Hence, substituting V_c for $V + Ir + \eta_{\text{anode}}$ in Eq. [A-1] gives

$$V_c = E - \eta_{\text{cathode}}^{\text{act}} - \eta_{\text{cathode}}^{\text{dif}} \quad [\text{A-2}]$$

where the Nernst potential or reversible EMF is

$$E = 1.2605 - 0.00025 T + RT/2F \ln (P_{\text{H}_2} P_{\text{O}_2}^{1/2} P_{\text{H}_2\text{O}}^{-1}) \quad [\text{A-3}]$$

activation polarization at cathode is

$$\eta_{\text{cathode}}^{\text{act}} = RT/F \ln (i \times (i_0 \times CL_0 \times SA_0 \times CU) - 1) \quad [\text{A-4}]$$

³Where, $CU = CU_0[(SA_0/SA_0)(CL_0/CL_0)]$ and $i_0 = 0.12 \exp(-12,795/RT) P_{\text{O}_2}^{3/4} P_{\text{H}_2\text{O}}^{1/2}$

and diffusion polarization at cathode is

$$\eta_{\text{cathode}}^{\text{dif}} = RT/2F \ln (i_L \times (i_L - i)^{-1}) \quad [\text{A-5}]$$

In the model, CL and SA are treated as the initial catalyst loading and initial surface area. Any changes in CL and SA with time, thus, are automatically lumped in the CU term.

Estimation of CU .—The Nernst potential, E , and diffusion polarization, $\eta_{\text{cathode}}^{\text{dif}}$, are computed by substituting i , i_L , T , P_{H_2} , P_{O_2} , and $P_{\text{H}_2\text{O}}$ (maintained constant during a perturbation period) in Eq. [A-3] and [A-5]. Activation polarization at the cathode, $\eta_{\text{cathode}}^{\text{act}}$, is then estimated by substituting E , $\eta_{\text{cathode}}^{\text{dif}}$, and V_c (kept constant during a perturbation period) in Eq. [A-2]. Finally, catalyst utilization, CU , is computed by substituting $\eta_{\text{cathode}}^{\text{act}}$, T , i , i_0 , CL_0 , and SA_0 , in Eq. [A-4].

APPENDIX B

Transformation to a Logarithmic Decay Model

The simple aging model represented by Eq. [2] and [3] (in the text) can be transformed to a logarithmic form below

$$\ln \tau_u = \ln k_{u0} - E_u/RT + \alpha_u \ln CU + \beta_u V_c/T + \gamma_u \ln P_{\text{H}_2\text{O}} \quad [\text{B-1}]$$

$$\ln \tau_i = \ln k_{i0} - E_i/RT + \alpha_i \ln i_L + \beta_i V_c/T + \gamma_i \ln P_{\text{H}_2\text{O}} \quad [\text{B-2}]$$

The most general logarithmic form is obtained by expanding $\ln \tau$ in a Taylor series in terms of $1/T$, $\ln CU$, $\ln i_L$, V_c/T , and $\ln P_{\text{H}_2\text{O}}$ about the center point

$$\begin{aligned} \ln \tau_u = & \ln \tau_{u0} + a_1 (1/T - \overline{1/T}) + a_2 (\ln CU - \overline{\ln CU}) \\ & + a_3 (V_c/T - \overline{V_c/T}) \\ & + a_4 (\ln P_{\text{H}_2\text{O}} - \overline{\ln P_{\text{H}_2\text{O}}}) + \frac{1}{2} a_{11} (1/T - \overline{1/T})^2 \\ & + \frac{1}{2} a_{22} (\ln CU - \overline{\ln CU})^2 + \frac{1}{2} a_{33} (V_c/T - \overline{V_c/T})^2 \\ & + \frac{1}{2} a_{44} (\ln P_{\text{H}_2\text{O}} - \overline{\ln P_{\text{H}_2\text{O}}})^2 + a_{12} (1/T - \overline{1/T}) \ln (CU - \overline{\ln CU}) \\ & + a_{13} (1/T - \overline{1/T}) (V_c/T - \overline{V_c/T}) + a_{14} (1/T - \overline{1/T}) (\ln P_{\text{H}_2\text{O}} \\ & - \overline{\ln P_{\text{H}_2\text{O}}}) \\ & + a_{23} (\ln CU - \overline{\ln CU}) (V_c/T - \overline{V_c/T}) + a_{24} (\ln CU - \overline{\ln CU}) \\ & (\ln P_{\text{H}_2\text{O}} - \overline{\ln P_{\text{H}_2\text{O}}}) + a_{34} (V_c/T - \overline{V_c/T}) (\ln P_{\text{H}_2\text{O}} - \overline{\ln P_{\text{H}_2\text{O}}}) \\ & + \text{higher order terms} \quad [\text{B-3}] \end{aligned}$$

Most general forms for $\ln \tau_i$ can be obtained similarly. However, quadratic, interaction, and higher order terms are neglected in order to have a simple linear model. The simplified model is

$$\ln \tau_u = \ln \tau_{u0} + a_1 (1/T - \overline{1/T}) + a_2 (\ln CU - \overline{\ln CU}) + a_3 (V_c/T - \overline{V_c/T}) + a_4 (\ln P_{\text{H}_2\text{O}} - \overline{\ln P_{\text{H}_2\text{O}}}) \quad [\text{B-4}]$$

and

$$\ln \tau_i = \ln \tau_{i0} + a_1' (1/T - \overline{1/T}) + a_2' (\ln i_L - \overline{\ln i_L}) + a_3' (V_c/T - \overline{V_c/T}) + a_4' (\ln P_{\text{H}_2\text{O}} - \overline{\ln P_{\text{H}_2\text{O}}}) \quad [\text{B-5}]$$

or

$$\ln \tau_u = \ln k_{u0} + a_1 \frac{1}{T} + a_2 \ln CU + a_3 V_c/T + a_4 \ln P_{\text{H}_2\text{O}} \quad [\text{B-6}]$$

and

$$\ln \tau_i = \ln k_{i0} + a_1' \frac{1}{T} + a_2' \ln i_L + a_3' V_c/T + a_4' \ln P_{\text{H}_2\text{O}} \quad [\text{B-7}]$$

Comparison of [B-6] and [B-7] with [B-1] and [B-2], respectively shows

$$a_1, a_1' = -E_u/R, -E_i/R$$

$$a_2, a_2' = \alpha_u, \alpha_i$$

$$a_3, a_3' = \beta_u, \beta_i$$

$$a_4, a_4' = \gamma_u, \gamma_i$$

Substituting the above relationships into Eq. [B-4] and [B-5] gives

$$\ln \tau_u = \ln \tau_{u0} - E_u/R (1/T - \overline{1/T}) + \alpha_u (\ln CU - \overline{\ln CU}) + \beta_u (V_c/T - \overline{V_c/T}) + \gamma_u (\ln P_{\text{H}_2\text{O}} - \overline{\ln P_{\text{H}_2\text{O}}}) \quad [\text{B-8}]$$

and

$$\ln \tau_1 = \ln \tau_{i_0} - E_i/R (1/T - 1/T) + \alpha_i (\ln i_i - \ln i_0) + \beta_i (V_c/T - \bar{V}_c/T) + \gamma_i (\ln P_{H_2O} - \ln \bar{P}_{H_2O}) \quad [B-9]$$

LIST OF SYMBOLS

CL_0	initial catalyst loading at cathode
CL_t	catalyst loading at time t
CU_0	initial catalyst utilization
CU	$CU_0 [(SA_t/SA_0) (CL_t/CL_0)]$
E	Nernst potential
E_i	activation energy for the decay reaction in mode B
E_u	activation energy for the decay reaction in mode A
F	Faraday's constant
I	current
i	current density
i_L	limiting current density
i_0	exchange current density
k_{i_0}	decay rate constant in mode B
k_{u_0}	decay rate constant in mode A
$P_{H_2}, P_{O_2}, P_{H_2O}$	average partial pressure of H_2 , O_2 , and H_2O at cathode, respectively
R	universal gas constant
r	internal resistance of cell
r_i	rate of decrease of i_i with respect to time
r_u	rate of decrease of CU with respect to time
SA_0	initial surface area of platinum
SA_t	surface area at time t
T	absolute cell temperature
t	time
V	cell terminal voltage

V_c	cathode voltage
α_i	order of the decay reaction with respect to i_i
α_u	order of the decay reaction with respect to CU
β_i, β_u	order of the decay reaction with respect to V_c
γ_i, γ_u	order of the decay reaction with respect to P_{H_2O}
η_{anode}	anode polarization
$\eta_{cathode}^{act}$	activation polarization at cathode
$\eta_{cathode}^{dif}$	diffusion polarization at cathode

REFERENCES

1. G. E. P. Box and N. R. Draper, "Evolutionary Operation: A Statistical Method for Process Improvement," Wiley, New York (1969).
2. G. E. P. Box, W. G. Hunter, and J. S. Hunter, "Statistics for Experimenters," pp. 362-367, Wiley, New York (1978).
3. H. C. Maru and L. Christner, "Phosphoric Acid Fuel Cell Cathode," in National Fuel Cell Seminar Abstracts, U.S. Department of Energy, Washington, DC (1978).
4. P. Bindra, S. Clouser, and E. Yeager, *This Journal*, **126**, (1979).
5. D. N. Patel, H. Maru, M. Farooque, and C. Ware, "Methodology for Predicting Long-Term Fuel Cell Performance from Short-Term Testing," Energy Research Corporation (1981).
6. C. Hicks, "Fundamental Concepts in the Design of Experiments," Holt, Rinehart and Winston, New York (1973).

Some Characteristics of PbO_2 Doped with Various Elements

A. Delmastro and M. Maja*

Dipartimento di Scienza dei Materiali ed Ingegneria Chimica, del Politecnico di Torino, 10129 Torino-Italia

ABSTRACT

The doping effect of various elements (Ag, As, Co, Ge, Mn, Ni, Sb, Se, Sn, Te, and Zn) on the O/Pb ratio, on morphology, and on self-discharge of alpha and beta lead dioxide have been investigated. These dopants increase the O/Pb ratio and, with the exception of As, Te, Sn, and Mn in the beta form, lower the self-discharge rate. The effects on the morphology are evident only for Ge and Sn at concentrations greater than 100 ppm in the solution.

It is well known that alloying elements in the lead of positive grids and inorganic compounds added to active material during manufacturing of plates of Pb-Ac batteries can affect the behavior of cells in various ways. The impurities in sulfuric acid used for plates' conversion and during battery service life can also have a noticeable influence (1). In fact, the alloying constituents of positive grids can enter the lattice of oxides that form during corrosion, thus influencing the electrical characteristics of contact between active material and the grid. Moreover, alloying elements that dissolve in electrolyte and the impurities of sulfuric acid can dope both allotropic forms of PbO_2 during cycling of the batteries, thereby promoting a stabilization of some structures and changing some active material properties.

Years ago, our research group began a systematic study concerning the electrochemical characteristics of alpha and beta lead dioxide doped with various elements. Some results regarding the influence of antimony have been reported (2, 3). In this work, the study is extended to other elements which can be present in lead-acid batteries, both as alloying constituents of grids and as impurities of electrolyte.

Studied in particular is the influence of Ag, As, Co, Ge, Mn, Ni, Sb, Se, Sn, Te, and Zn, inserted as doping ele-

ments in the lattice of lead dioxide, on stoichiometry deviation, crystal morphology, and self-discharge.

The effect of 24 contaminant ions on the gas generation rate of the lead-acid cell has been examined by Pierson *et al.* (4) in order to determine the permissible impurity concentration levels in a maintenance-free battery. They find that only five elements (As, Co, Ni, Sb, and Te) have a drastic effect on gassing during constant overcharge tests.

Mahato and Tiedemann (5) have studied the effect of trace As, Co, Ni, Sb, and Te ions on linear potential sweep curves of lead-acid battery electrodes. By considering the hydrogen and oxygen overvoltage change, these authors show the dangerous effects of As, Sb, and Te on negative plates and of Co and Ni on positive ones.

Experimental

According to the method referred to in the literature (6), various samples of the two allotropic forms of lead dioxide had been prepared. Alpha lead dioxide was electrodeposited on Pt electrodes from a 2M KOH solution saturated with PbO at a current density of 10 mA/cm². Beta lead dioxide was electrodeposited on Pt electrodes from a 0.5M lead-nitrate solution containing 0.15M nitric acid at a current density of 100 mA/cm². The solutions were stirred and maintained at 30°C.

* Electrochemical Society Active Member.

Doping of PbO₂ was achieved by adding to the pure electrodeposition solution known amounts of doping elements: As, Ge, Sn, Te, Sb, Se, and Zn for the alpha form; and Ag, As, Co, Ge, Mn, Ni, Sb, Se, Sn, Te, and Zn for the beta form. The doping elements were added to the solution as nitrates or as oxides dissolved in KOH. By increasing the concentration of some doping elements in the electrolyte above 100 ppm, the current efficiency for lead dioxide deposition abruptly decreased yielding powdery deposits (Fig. 1). For this reason, the maximum concentration of the studied elements was limited to 100 ppm. This finding was evidence of the influence of the considered elements.

After electrodeposition, the electrodes were washed in ammonium acetate and in distilled water; then they were dried in air. The influence of doping elements on the morphology of lead dioxide crystals was determined by observing with a scanning electron microscope (SEM) the surface of some anodic deposits obtained from solutions containing up to 200 ppm of dopant.

In order to determine the characteristics of the dioxide, the anodic layers were detached from the Pt substrates and carefully ground in a mortar to obtain a fine homogeneous powder. The phase purity and crystallinity of powder samples were tested by means of x-ray diffraction. The true surface area was determined by the standard BET method using nitrogen adsorption. A sample of the powder was analyzed to determine the amount of the doping element and the deviations from the stoichiometry (O/Pb ratio) of lead dioxide. The amount of doping elements was determined by means of inductively coupled plasma spectrophotometry, while the O/Pb ratio was measured by iodometric titration of active oxygen (7).

The self-discharge of lead dioxide was studied by measuring the oxygen evolution-rate at the rest potential of the dioxide in sulfuric acid, employing an apparatus similar to that described by Ruetschi (8). For this purpose, 1.5g of powder was introduced in a small glass tube for a microvolumetric gassing test; the tube was then filled with pure sulfuric acid having a density of 1.4 g/cm³ and was maintained at a temperature of 30° ± 0.05°C.

During these tests, which lasted 10 days, the amount of oxygen developed was periodically measured, and self-discharge equivalent currents of lead dioxide were calculated from the data collected.

Results and Discussion

Doping and stoichiometry deviation.—The analytical method employed to measure the stoichiometry of PbO₂ permits the determination of the amount of tetravalent lead ions in the lattice of this compound. The same method, applied to doped PbO₂, also takes into account the amount of doping elements having an oxidation number at which they behave as an oxidant in respect to chloride ions.

The doping elements considered in this work can have a variable valency, and the deposition potential of lead dioxide assures their codeposition with tetravalent lead ions in one of their oxidized states. Because the doping elements can have a different oxidation-number variation during the iodometric analysis, they do not behave the same way with respect to chloride ions. However, considering that the O/Pb ratio increase, calculated from the amount of doping elements present in the lattice at their highest oxidation number, will be markedly lower than the measured values, the O/Me ratio obtained by iodometric titration can be taken as the effective atomic ratio value of the doped dioxide.

In the case of pure alpha and beta forms, in agreement with the data reported in the literature (9), the analysis shows that their O/Pb ratios are equal to 1.87 and 1.93, respectively. These values for the doped lead dioxide will increase if the doping element, with an oxidation number greater than two, substitutes the bivalent lead ions in the lattice or occupies metal vacancies or if the lattice content of hydrogen or hydroxyl ions decreases as a consequence of doping.

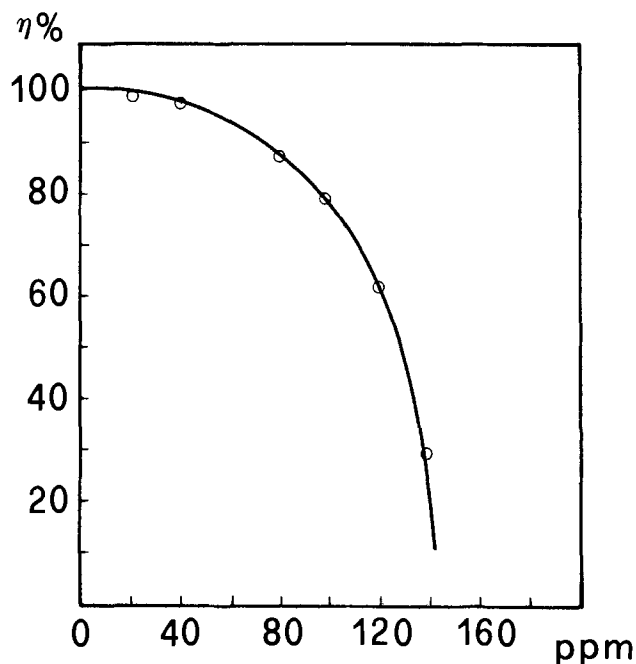


Fig. 1. Current efficiency for PbO₂ electrodeposition from solutions containing As³⁺ ions as impurity.

The data concerning the O/Pb ratio for the doped allotropic forms and the amount of doping elements in the lattice are reported in Fig. 2 and 3 and in Tables I and II. Under the same conditions of temperature, current density, and concentration of doping elements in the electrolyte, the ion which codeposits in the greatest amount in the alpha allotropic form is antimony, followed in decreasing order by Zn, Sn, Ge, Te, Se, and As. For the beta lead dioxide, the following decreasing series has been established: Sb, Ge, Te, Mn, As, Sn, Ag, Se, Co, Zn, and Ni. The results show that the O/Pb ratio for both the alpha and beta lead dioxide increases with the doping element amount in the lattice and that the increasing of the stoichiometry in the case of the alpha form is higher than that observed for the beta form. The alpha lead dioxide doped with Ge, Se, and Te presents an O/Pb ratio nearly equal to that of the pure beta form.

By comparing the amount of doping elements which can be codeposited with tetravalent lead ions from both alkaline and acid solutions (Table I) at the same concentration of doping ions added to the electrolyte used in anodic electrodeposition of PbO₂, it is possible to order these elements in the following decreasing series: Sb, Zn, Ge, Te, Sn, As, and Se.

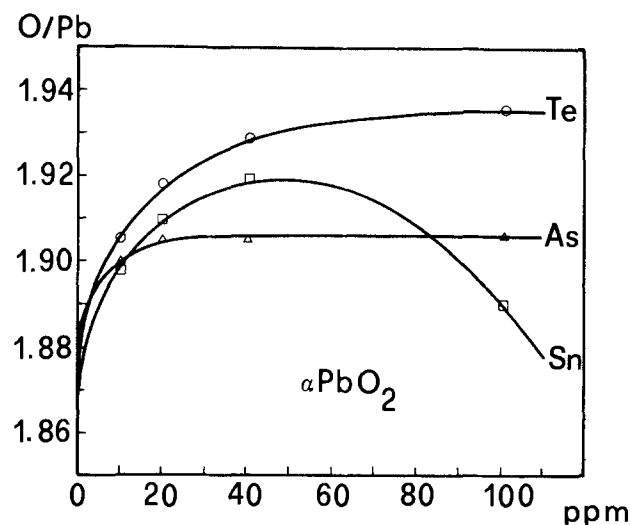


Fig. 2. O/Pb ratio vs. dopant content in the electrolyte

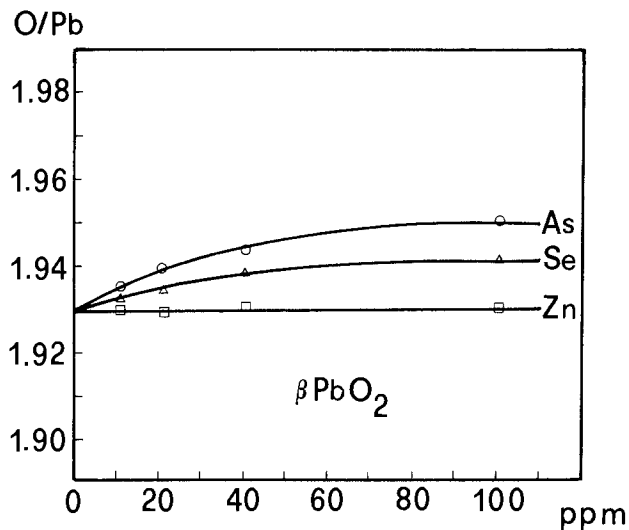


Fig. 3. O/Pb ratio vs. dopant content in the electrolyte

In order to ascertain the influence of the various dopants on the lead dioxide stoichiometry, the data corresponding to the same concentration of doping element in the PbO_2 lattice are compared. For this purpose, the experimental O/Pb ratio data are interpolated to calculate the value for a given dopant concentration (0.01%). The elements are ordered according to the following decreasing series: Te, Ge, Se, Zn, Sn, As, and Sb for the alpha lead dioxide; and Co, As, (Se, Sn, Mn, Zn), (Te, As, Ge), and Sb for the beta lead dioxide. It is interesting to observe the opposite positions occupied by As and Te in these series. The positions can only be explained by supposing that, according to the allotropic form, two different action mechanisms for these elements must be taken into account. Moreover, the great influence of the studied elements on the O/Pb ratio, compared with their concentration in the lattice, reveals that the stoichiometry deviation of the dioxide can be attributed to the decreasing of hydrogen and hydroxyl ions in the lattice as a consequence of doping.

By considering the above reported results, it is possible to determine that the major effect of Sb on the properties of alpha PbO_2 is strictly connected with the higher level of doping which may be obtained with this element.

Finally, SEM observation of electrodeposited anodic layers shows that, while the effect of the dopants is practically negligible in the case of beta PbO_2 , the elements codeposited with lead from solutions containing up to 100

Table II. Mean value of the O/Pb ratio for α and β PbO_2 for various concentrations of impurities in the solution

PbO_2	Impurity	Concentration of impurity in the solution			
		10 ppm	20 ppm	40 ppm	100 ppm
α	As	1.900	1.905	1.905	1.905
	Ge	1.915	1.920	1.925	1.925
	Sb	1.890	1.900	1.910	1.910
	Se	1.905	1.915	1.920	1.920
	Te	1.905	1.920	1.930	1.935
	Sn	1.900	1.910	1.920	1.890
	Zn	1.910	1.920	1.915	1.900
β	Ag	1.930	1.930	1.930	1.930
	As	1.935	1.940	1.945	1.950
	Co	1.930	1.930	1.935	1.940
	Ge	1.930	1.930	1.930	1.930
	Mn	1.930	1.935	1.940	1.940
	Ni	1.930	1.930	1.930	1.930
	Sb	1.930	1.930	1.930	1.930
	Se	1.930	1.935	1.940	1.940
	Sn	1.930	1.935	1.935	1.940
	Te	1.930	1.935	1.940	1.950
	Zn	1.930	1.930	1.930	1.930

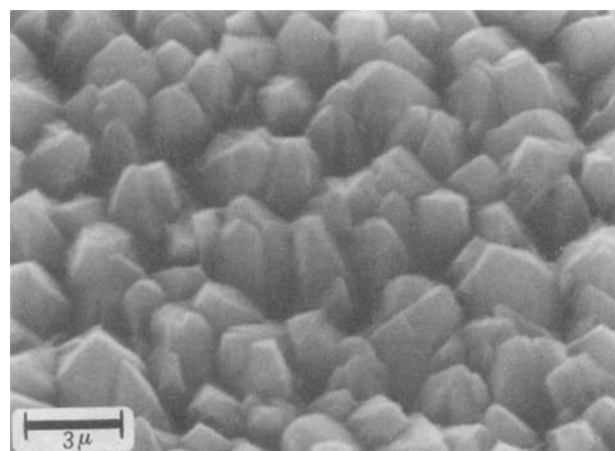
ppm of dopant cause a small reduction of the crystal size of alpha PbO_2 without substantially modifying the crystal morphology. A comparison of the structures of pure alpha PbO_2 and Ge- and Sn-doped alpha PbO_2 anodic layers is shown in Fig. 4-6.

For impurity concentration greater than 100 ppm, the current efficiency of PbO_2 electrodeposition decreases, as previously described, and the anodic layers formed are powdery. In the case of Ge- and Sn-doped alpha PbO_2 obtained from solutions containing impurity concentration of 200 ppm, the SEM observation of the anodic layers shows a "soap bubble" structure, as in the case of Sb-doped alpha PbO_2 (2). These results indicate that, generally, the impurities, entering the lattice of alpha PbO_2 , change the oxygen overpotential and the crystal morphology by increasing the active areas for the oxygen evolution. As a consequence, the oxygen evolution is the main process above a critical impurity concentration at which the PbO_2 anodic layers cannot form any more.

Self-discharge.—It is well known that lead dioxide is not thermodynamically stable in sulfuric acid solutions because of the high value of its standard potential of reduction with respect to the oxygen/hydroxyl ion couple. In spite of that, the reaction rate of self-discharge $\text{PbO}_2 + \text{H}_2\text{SO}_4 = \text{PbSO}_4 + \text{H}_2\text{O} + 1/2 \text{O}_2$ is very slow. Because the lead dioxide reduction occurs in sulfuric media at a very low overpotential, it is easy to forecast that the self-discharge reaction, in the absence of a reductive agent, is a process controlled by oxygen evolution. The recent developments in electrocatalysis concerning the oxygen evolution reaction on conductive oxides (10) take into ac-

Table I. Mean value of impurities percentage in α and β PbO_2 for various concentrations of impurities in the solution

PbO_2	Impurity	Concentration of impurity in the solution	
		40 ppm	100 ppm
α	As	0.0026	0.0071
	Ge	0.010	0.024
	Sb	0.188	0.480
	Se	0.0065	0.018
	Sn	0.021	0.045
	Te	0.0090	0.023
	Zn	0.105	0.252
β	Ag	0.011	0.032
	As	0.026	0.061
	Co	0.0041	0.0092
	Ge	0.044	0.115
	Mn	0.023	0.063
	Ni	Traces	Traces
	Sb	0.077	0.196
	Se	0.010	0.023
	Sn	0.018	0.041
	Te	0.036	0.088
	Zn	0.0012	0.0032

Fig. 4. SEM micrograph of pure αPbO_2 electrodeposited from KOH saturated with PbO , ($i_{\text{dep}} = 10 \text{ mA/cm}^2$, $T = 30^\circ\text{C}$).

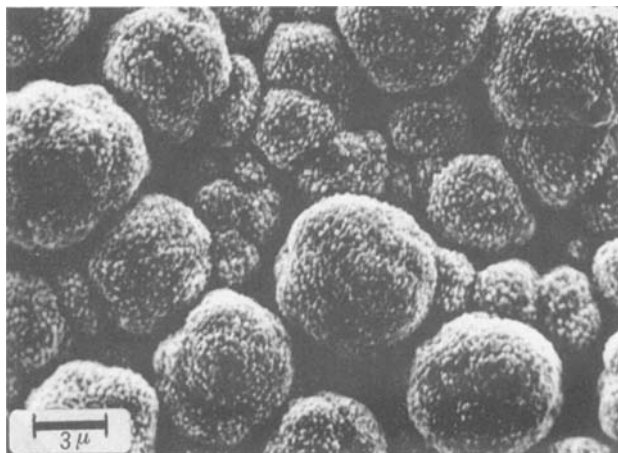


Fig. 5. SEM micrograph of α PbO₂ electrodeposited from KOH saturated with PbO, containing 200 ppm of Ge ($i_{dep} = 10 \text{ mA/cm}^2$, $T = 30^\circ\text{C}$).

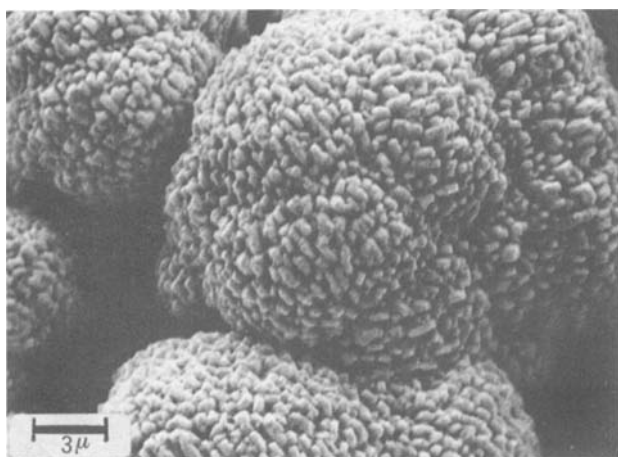


Fig. 6. SEM micrograph of α PbO₂ electrodeposited from KOH saturated with PbO, containing 200 ppm of Sn ($i_{dep} = 10 \text{ mA/cm}^2$, $T = 30^\circ\text{C}$).

count various parameters such as geometrical factor, adsorption and desorption energy of intermediates, O/Me ratio, and surface activity. This reaction is extensively studied in the case of PbO₂ electrodes.

Ruetschi *et al.* (11) shows that the kinetics of oxygen evolution on the two forms of lead dioxide are different for both Tafel slope (0.07 for the alpha form and 0.12 for the beta form) and exchange current density ($1.77 \cdot 10^{-16}$ and $6.2 \cdot 10^{-10} \text{ A/cm}^2$, respectively). Thus, while the overpotential differences become smaller at open circuit near the reversible potential of the dioxide/sulfate couple, the oxygen overvoltage on beta dioxide is higher than the value on the alpha form at high current density. On the other hand, Makrides (12) claims that no difference exists between the two forms if a nonporous film of the dioxide is deposited on Pt electrodes. The same results are also reported by Vuorio (13) and Hyvarinen (14). This disagreement can be resolved by considering the possibility that the alpha lead dioxide, in acid media, can transform to the more stable beta form.

The increase in activity of alpha lead dioxide with respect to beta has been attributed to different surface lattice spacing (10). Moreover, the position of lead dioxide on the "volcano curve" (10) indicates that the oxygen vacancies in the dioxide are responsible for its activity and that the decrease in nonstoichiometry, involving a weaker adsorption intermediate, produces a decrease of electrocatalytic activity of the dioxide. In regard to the surface activity, it must be pointed out that the physical-chemical methods used to measure the true surface of a specimen do not give information on the electrochemical

active surface which can otherwise be obtained by means of capacitance measurements. And finally, the literature refers to some evidence concerning the adsorbed species on lead dioxide (15). It is generally accepted that atomic oxygen, OH radicals, sulfate ions, and water molecules are present on the dioxide surface according to the applied potential.

In order to study the reaction rate of self-discharge, some microvolumetric determinations of oxygen evolved from a known amount of pure and doped lead dioxide ground and put into a sulfuric acid solution are carried out. Doped lead dioxide samples are prepared from solutions containing the same concentration of the doping element (100 ppm). They have different stoichiometry and various compositions, as it has been shown above. The specific area of the samples is reported in Table III.

It must be noted that while specific areas of alpha PbO₂ agree with the data in the work of Voss and Ruetschi (8, 16), the results for beta lead dioxide do not agree with the data in the literature. On the other hand, the tests show that the pure and doped beta allotropic forms, produced by anodic deposition and powdered as described above, have in all examined cases the same granulometry of the alpha form, but a lower BET area. Capacitance data obtained from impedance measurements on pure and antimony-doped alpha and beta electrodeposited PbO₂ seem to agree with BET data (17).

The collected experimental data, with daily measurements made for ten days, have been transformed using regression linear analysis, to the mean values of self-discharge current and self-discharge current density, as reported in Table III. For these data, varying behavior of doped alpha and beta lead dioxide occurs, and some remarks on the influence of the doping elements can be made. The values of self-discharge current density for the two pure lead dioxide forms are about the same. In the doped alpha form, all such values are smaller than those for the pure form. Whereas the dopants always decrease the self-discharge current for alpha PbO₂, three groups of elements having different effects can be depicted for doped beta PbO₂: As, Mn, and Sn increase the self-discharge current values, while Co and Te exhibit an almost null effect; and all the remaining elements show smaller values for self-discharge current density than in the case of the pure forms.

To study the effect of the doping elements on the self-discharge current density, some tests with lead dioxide specimens containing different concentrations of dopants are performed. In the range of dopant concentrations considered in this work, the results of these tests seem to in-

Table III. Surface area, oxygen evolution rate, and self-discharge current density for various doped PbO₂ samples, obtained from solutions containing 100 ppm of impurity, in H₂SO₄ ($d = 1.14$) at 30°C

PbO ₂	Impurity	BET area (m ² /g)	Oxygen evolution rate (μA)	Self-discharge current density (μA · 10 ⁻⁴ /cm ²)
α	—	0.48	6.74	9.36
	As	0.88	2.96	2.24
	Ge	0.67	7.31	7.27
	Sb	0.69	6.24	6.03
	Se	0.65	2.19	2.25
	Sn	0.54	1.49	1.84
	Zn	0.64	2.84	2.96
	β	—	0.24	3.47
Ag		0.38	1.89	3.32
As		0.28	7.04	16.76
Co		0.13	1.85	9.48
Ge		0.33	3.13	6.32
Mn		0.39	9.73	16.63
Ni		0.27	3.32	8.20
Sb		0.19	1.78	6.25
Se		0.23	2.70	7.83
Sn		0.30	8.77	19.48
Te		0.25	3.72	9.92
Zn		0.42	3.97	6.30

dicate a proportionality between the doping element concentration and the self-discharge current density.

As a consequence of interpolating the experimental data, the self-discharge current densities corresponding to the same concentration of dopants in the PbO_2 lattice (e.g., 0.01%) are calculated, and the following series is obtained, in which the elements are in a decreasing self-discharge current density order: As, Ge, Se, Te, Sn, Sb, and Zn with lowering effect in doped alpha PbO_2 ; Sn, As, and Mn with enhancing effect; Co and Te with negligible effect; and Zn, Se, Ag, Ge, and Sb with lowering effect in doped beta PbO_2 . It is interesting to note the opposite positions occupied by Zn and Ge in this series, the same approximate locations of Se in the sets, and the smallest values of self-discharge current density (always showed by lead dioxide doped with Sb).

Except for the results of beta PbO_2 doped with As, Mn, Sn, and Te, for which an increase in stoichiometry corresponds to a fairly important increase in self-discharge current density, the catalytic activity of oxygen evolution tends to reduce in all other cases when the O/Pb ratio values are increased. This agrees with recent discussions (10) on the electrocatalytic activity of the oxygen evolution process on oxides.

When comparing our results concerning the effect of Co and Ni with the literature data (5, 18) which report a decrease of the oxygen overvoltage when Ni and Co are added to the Pb-acid battery electrolyte, it appears that these impurities act according to a catalytic mechanism (18) involving the ions present in the solutions and not as a consequence of doping.

Conclusions

Some general conclusions can be drawn from the results discussed above.

- 1) By considering the dopants which can be present both in alpha and in beta PbO_2 , the alpha allotropic form incorporates greater amounts of Sb, Sn, and Zn, whereas the beta form incorporates greater amounts of As, Ge, Se, and Te.
- 2) The doping of alpha PbO_2 produces an increase in the O/Pb ratio which always corresponds to the decrease in oxygen evolution rate, according to ideas of electrocatalysis theory concerning the relation between oxygen overpotential and oxide stoichiometry.
- 3) Doping of beta PbO_2 produces a small increase in stoichiometry, and only in the case of Ag, Co, Ge, Ni, Sb, Se, and Zn is an increase in oxygen overpotential observed.
- 4) The greatest effect of doping elements on self-discharge current density occurs for Sn in the case of beta PbO_2 and for Ge in the case of alpha PbO_2 .

- 5) In regard to crystal morphology of PbO_2 , the effect of dopants on beta lead dioxide is practically negligible, whereas the elements codeposited with lead in the alpha form cause a small reduction of crystal size up to 100 ppm concentration; moderate variations of the crystal habitus of alpha PbO_2 occur at Ge and Sn concentrations greater than 100 ppm.

Acknowledgments

This work was supported by Consiglio Nazionale delle Ricerche (C. N. R., Rome). The authors thank Dr. R. Fratesi (Ancona University) for the chemical analyses.

Manuscript submitted Feb. 3, 1984; revised manuscript received July 9, 1984.

Politecnico di Torino assisted in meeting the publication costs of this article.

REFERENCES

1. G. Vinal, "Storage Batteries," p. 138, J. Wiley, New York (1955).
2. F. Caldara, A. Delmastro, G. Fracchia, and M. Maja, *This Journal*, **127**, 1869 (1980).
3. A. Boggio, M. Maja, and N. Penazzi, *J. Power Sources*, **9**, 221 (1983).
4. J. Pierson, C. Weinlein, and C. Wright, "Power Sources N.5," D. H. Collins, Editor, p.97, Academic Press, London (1975).
5. B. Mahato and W. Tiedemann, *This Journal*, **130**, 2139 (1983).
6. T. Sharpe, in "Encyclopedia of Electrochemistry of the Elements," A. J. Bard, Editor, Vol. 1, p. 305, M. Dekker, New York (1973).
7. "Scott's Standard Methods of Chemical Analysis," N. H. Furman, Editor, p. 675, D. Van Nostrand, New York (1950).
8. P. Ruetschi, J. Sklarchuk, and R. Angstadt, *Electrochim. Acta*, **8**, 333 (1963).
9. N. Bagshaw, R. Clarke, and B. Halliwell, *J. Appl. Chem.*, **16**, 180 (1966).
10. S. Trasatti and G. Lodi, in "Electrodes of Conductive Metallic Oxides," S. Trasatti, Editor, p. 600, Elsevier Scientific Publishing Company, New York (1981).
11. P. Ruetschi, R. Angstadt, and B. Cahan, *This Journal*, **106**, 547 (1959).
12. A. Makrides, *ibid.*, **113**, 1158 (1966).
13. V. Vuorio, *Suom. Kemistil.*, **34**, 179 (1961).
14. O. Hyvarinen, Thesis, Helsinki University of Technology, Helsinki, Finland (1972).
15. J. Carr and N. Hampson, *Chem. Rev.*, **72**, 679 (1972).
16. E. Voss and J. Freundlich, in "Batteries," D. H. Collins, Editor, p. 73, Pergamon Press, New York (1963).
17. M. Maja and N. Penazzi, Extended Abstracts 3-19, "Journées d'electrochimie '83," Paris (1983).
18. D. Koch, *Electrochim. Acta*, **1**, 32 (1959).

The Kinetics and Cyclability of Various Types of Polyacetylene Electrodes in Nonaqueous Lithium Cells

A. Padula and B. Scrosati*

Dipartimento di Chimica, University of Rome, Rome, Italy

M. Schwarz

Assoreni, 00015 Monterotondo, Rome, Italy

U. Pedretti

Assoreni, S. Donato Milanese, Milan, Italy

ABSTRACT

The electrochemical doping process of polyacetylene has been investigated in lithium cells using lithium perchlorate in propylene carbonate as the electrolytic solution. The kinetics and the cyclability of this process have been examined by cyclic voltammetry, charge-discharge curves, and EPR analysis. The results show that, for film-type polyacetylene electrodes, the kinetics are controlled by the diffusion of the dopant species throughout the polymer. This diffusion appears particularly slow from the bulk to the surface of the polymer so that constant-current charge-discharge cycles of polyacetylene film electrodes may sustain only low rates (*i.e.*, in the range of microamperes per square centimeter), and have a poor coulombic efficiency (*i.e.*, of the order of 50%). Much better performance is offered by foam-type polyacetylene electrodes, where the intrinsic high porosity produces an improved surface morphology, which in turn favors the diffusion of the dopant species. Indeed, constant-current, charge-discharge cycles at reasonably high rates (*i.e.*, in the range of milliamperes per square centimeter) and reasonably good coulombic efficiencies (*i.e.*, of the order of 85%), have been obtained with lithium cells using this type of polyacetylene electrodes.

Much interest has lately been devoted to polyacetylene (PA) films and to their application as electrodes in lithium-organic electrolyte batteries (1-4). However, the results so far published are somewhat controversial. MacDiarmid and co-workers (1, 5) have reported that PA can be oxidized and reduced with nearly 100% coulombic efficiency in the LiClO_4 -PC electrolyte and that this cycling process may be repeated several times (5). However, such high cycling efficiency was only obtained by a constant current charge followed by an extended, controlled-potential discharge. MacDiarmid and co-workers also reported that the electrochemically oxidized, PA-doped electrodes do not spontaneously lose their charge, thus showing very good stability and long shelf-life (1). Other authors have also observed that only about 50% of the charge stored in the oxidized PA can be recovered in a constant-current cycle, and the remainder is only accessible by the extended controlled-potential discharge (4, 6). But, they also presented convincing experimental indications that the electrochemically oxidized PA electrodes do suffer a considerable loss of charge upon standing in the nonaqueous electrolyte (4, 7).

Coulombic efficiency and stability are obviously crucial aspects in the characterization of electrode materials for batteries. Therefore, we have considered it important to carry out a systematic study on the electrochemical behavior of PA electrodes in nonaqueous electrolytes, in an attempt to clarify whether the apparently contradictory results are related to intrinsic properties of the polymer or to external, controllable factors, such as *cis-trans* conformation ratio, surface morphology, preparation technique, experimental procedure, and so forth.

In this paper, we discuss the kinetics and the cyclability of various types of PA electrodes in the LiClO_4 -propylene carbonate electrolyte, on the basis of cyclic voltammetry, polarization, and EPR studies.

Experimental

Shirakawa-type polyacetylene films about 0.005 cm thick were synthesized according to the procedure described by Ito *et al.* (8). The specific characteristics of these films are: (i) apparent density ranging from 0.7 to 0.9 g/cm³; (ii) specific conductivity in the range of 10^{-9} to

10^{-5} ($\Omega \cdot \text{cm}$)⁻¹, depending on the *cis-trans* conformation ratio.

The PA foam samples were prepared following the procedure recommended by Wnek *et al.* (9). Pressed foam samples about 0.1 cm thick were obtained using a gel as an intermediate synthetic step (9). The apparent density of these pressed samples was about 0.4-0.6 g/cm³, and their electrical characteristics, both in the undoped and in the doped state, were similar to those of the PA films.

The *cis-trans* ratio of all the PA samples was varied by temperature-induced polymerization.

In view of the sensitivity of PA to impurities, particular care was devoted to the preparation of the electrolyte solution, and to the assembly of the cell under controlled environmental conditions.

Propylene carbonate (PC), a Merck reagent-grade product, was distilled twice under vacuum and then percolated through activated alumina. Lithium perchlorate, LiClO_4 , a Ventron pure product, was used as received. The 1M LiClO_4 -PC electrolyte solution was prepared in a dry box and further purified by percolation through activated alumina.

The electrochemical measurements were carried out in a glass cell having three compartments separated by porous glass walls (4). The PA electrodes (approximately 1 cm² surface) were sandwiched in a platinum mesh and housed in the central compartment of the cell. The Li reference and Li counterelectrodes were located in the two side compartments. The lower part of the cell was first filled with a layer of activated alumina and then by approximately 10 cm³ of the LiClO_4 -PC solution.

The electrochemical stability of this solution was tested in the same cell using the platinum mesh as the indicator electrode.

All the experimental procedures were performed in a controlled-atmosphere dry box. Standard electrochemical equipment was used for the cyclic voltammetry and the polarization studies.

The EPR spectra were recorded on a Varian E-X4 band spectrometer with an ancillary temperature-control unit. The maximum hyperfrequency power was 5 mW. The experimental tests were performed on 100% *trans* PA samples in order to avoid isomerization effects on the EPR linewidth.

* Electrochemical Society Active Member.

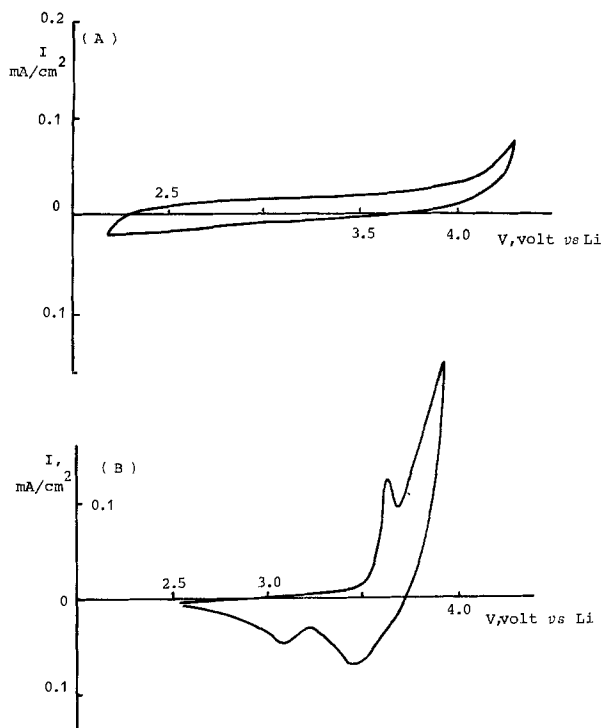


Fig. 1. A: cyclic voltammetry of the LiClO₄-PC electrolyte. (Pt mesh electrode.) B: cyclic voltammetry of a cis-rich PA film electrode in the LiClO₄-PC electrolyte. Scanning rate: 0.4 mV/s.

Results and Discussion

As already pointed out in the experimental section, particular care was devoted to the preparation and the purification of the LiClO₄-PC solution. Figure 1A shows the voltammetric response of a Pt mesh electrode in this electrolyte. The low residual current is a good indication of the purity of the electrolyte, whose reduction and oxidation voltage limits are about 2.5 and 4.0V, respectively, vs. Li.

The cyclic voltammogram of a cis-rich PA film electrode in the LiClO₄-PC electrolyte is shown in Fig. 1B. The voltammogram reveals two oxidation peaks, at about 3.6 and 3.8V, respectively, vs. Li. The two oxidation peaks suggest a two-stage mechanism for the electrochemical doping process of PA in LiClO₄-PC. Indeed, McKinney and Burrow (7), obtained a similar two-peak cyclic voltammogram of PA film electrodes in lithium perchlorate-sulfolane electrolyte and suggested the presence of two different sites in the PA structure available for the electrochemical p-doping process.

Figure 2 compares the cyclic voltammograms of the cis-rich PA film electrodes in LiClO₄-PC under different scanning rates. Notice that as the scanning rate increases, the separation between the peaks vanishes and finally only one peak becomes detectable. Furthermore, the increased scanning rate causes a decrease in the reversibility of the overall process. Therefore, the

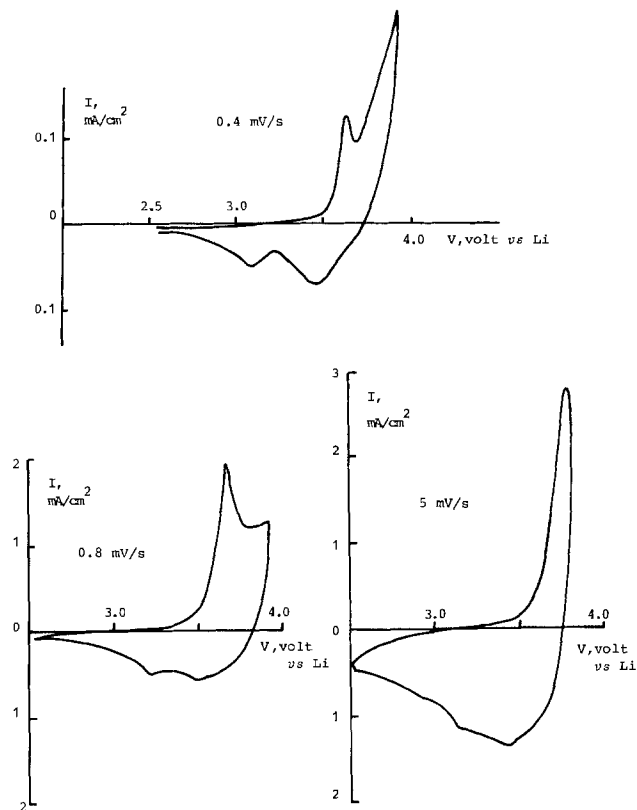


Fig. 2. Cyclic voltammetry of cis-rich PA film electrodes in the LiClO₄-PC electrolyte at various scanning rates.

voltammetric results indicate that the anodic charging (p-doping) process of PA in LiClO₄-PC is characterized by two steps, whose kinetics are strongly controlled by the diffusion of the dopant ClO₄⁻ species throughout the polymer.

In fact, Farrington *et al.* (4) and Abe *et al.* (10) have found two plateaus in the charging curve of a Li/LiClO₄-PC/PA cell. To the contrary, Kaneto *et al.* (2) reported the open-circuit potential of ClO₄⁻ doped, cis-rich PA electrodes increases smoothly with the doping level. This apparent difference may be explained by the diffusion-controlled kinetics of the electrochemical doping process of PA, whose characteristics can vary considerably with the experimental conditions.

On the basis of Fig. 2, one may reasonably expect that at high rates the charge curve of the Li/PA cell may reveal only one plateau and the charge-discharge coulombic efficiency may remain low. This is indeed what we have observed with cells using the same type of PA film electrodes to which Fig. 2 refers.

As illustrated in Fig. 3, the constant current charge-discharge cycles of these cells show a single-plateau charge curve and a poor coulombic efficiency (around 50%), even at moderate rates, such as 0.05 mA/cm². Low efficiency seems to be a typical characteristic of PA film electrodes; it remains around 50% for each constant-

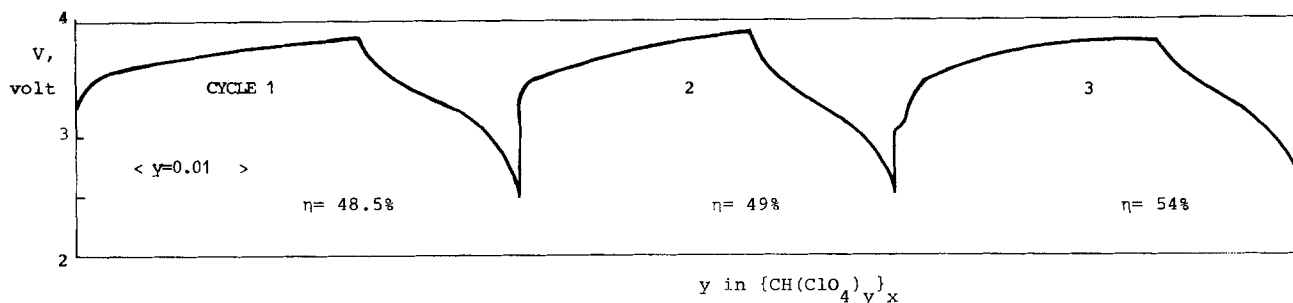


Fig. 3. Constant-current (0.05 mA/cm²) charge-discharge cycles of a Li/PA film cell at 25°C. The number of cycle and the coulombic efficiency (η) are indicated in the figure.

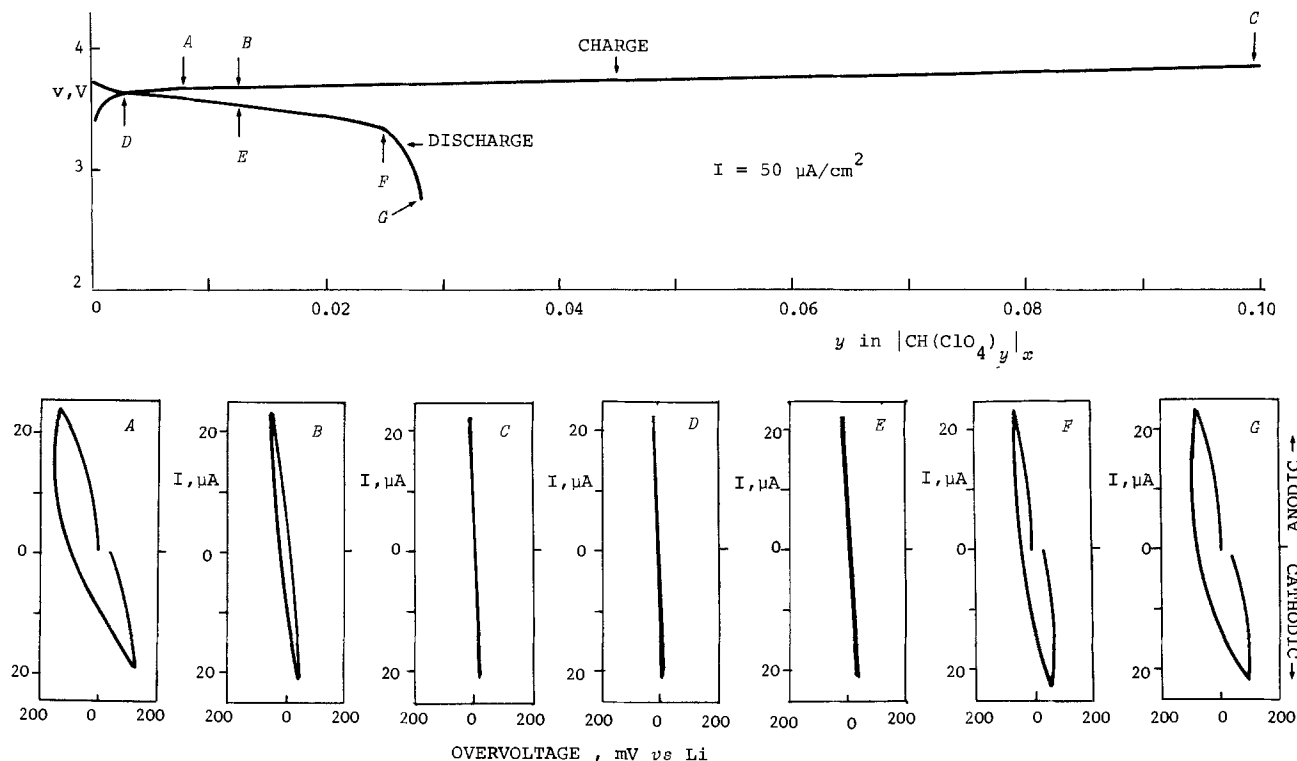


Fig. 4. Micropolarization tests of the PA film electrode at various stages of a constant-current ($0.05 \text{ mA}/\text{cm}^2$) charge-discharge cycle of a Li/PA cell.

current cycle and does not improve upon cycling. Similar results have been obtained by various other authors (2, 4,

6, 10), and thus it is reasonable to assume that the low coulombic efficiency of PA film electrodes in $\text{LiClO}_4\text{-PC}$

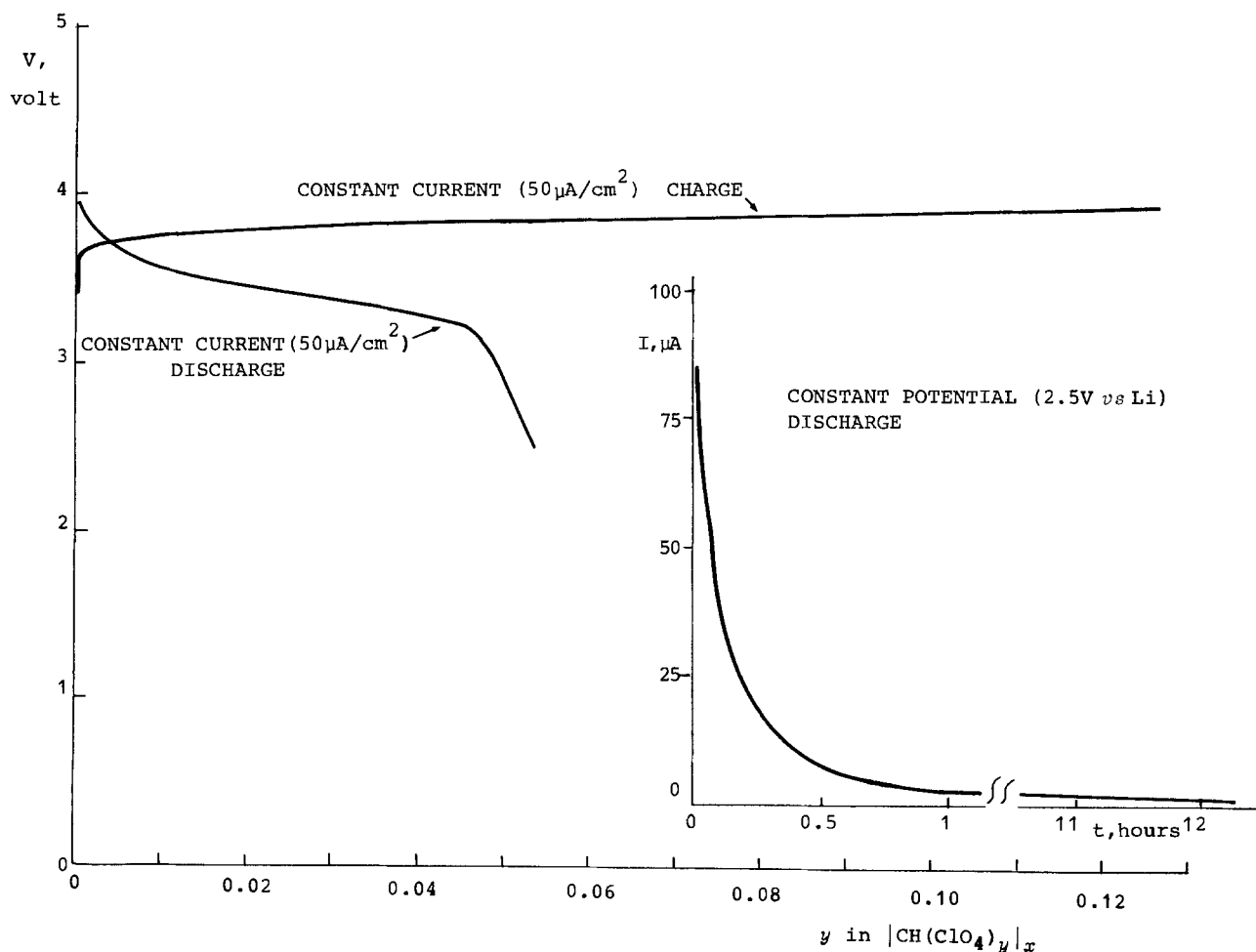


Fig. 5. Constant-current ($0.05 \text{ mA}/\text{cm}^2$) charge-discharge cycle of a Li/PA film cell. Only about 50% of the dopant species are removed by the discharge. Complete removal is obtained only by an extended, controlled-potential discharge.

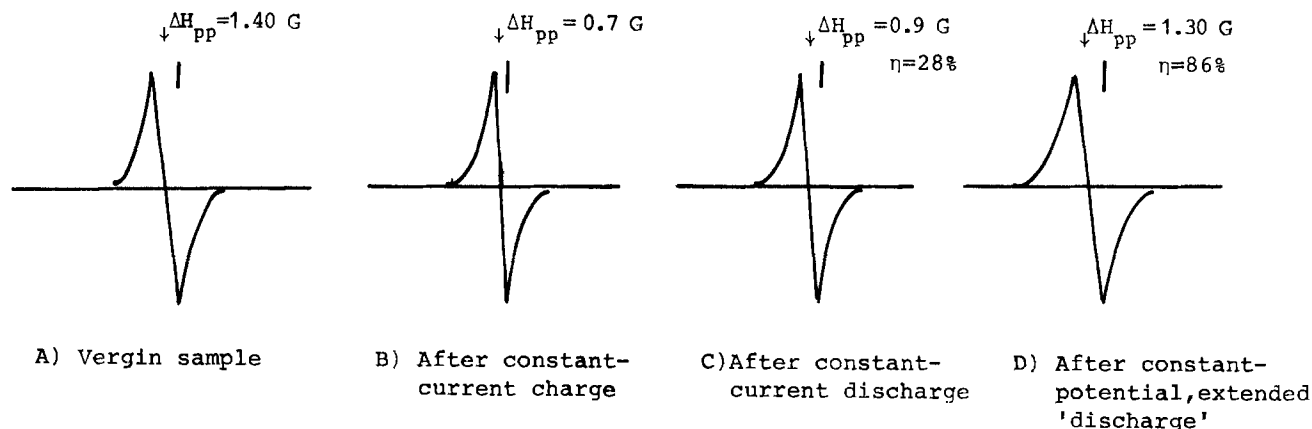


Fig. 6. EPR analyses of *trans*-rich PA film electrodes at various stages of a constant current charge and of a following constant current plus constant potential discharge process, of the type of that illustrated in Fig. 5. ΔH_{pp} = linewidth. η = percent of recovery of the original linewidth of the pristine sample.

is ascribable to the diffusion of the dopant ClO_4^- species, which appears especially slow from the bulk to the surface of the polymer.

In Fig. 4, micropolarization curves from the PA film electrodes at various stages of a constant current, charge-discharge cycle of the type discussed for Fig. 3 are shown. Fast kinetics and good reversibility (revealed by the linearity of the anodic and cathodic micropolarization scans), are obtained only during the last part of the charge and the beginning of the discharge. Apparently, only the dopant species residing near the surface of the polymer are easily removed by the constant-current discharge process. The remainder, which has diffused toward the bulk, is observed in the second oxidation step, and is not readily available; thus a poor coulombic efficiency is obtained over the entire cycle. The complete removal of the dopant species and therefore the full reversibility of the electrochemical PA doping process may be obtained only

by adding to the constant current discharge, an extended, controlled-potential (2.5V vs. Li) process, as illustrated in Fig. 5.

This conclusion is further supported by EPR analyses of the PA film electrodes, run at various stages in the cycle of Fig. 5. As shown in Fig. 6, the electrochemically doped PA samples after charge (B) show EPR spectra with a linewidth (ΔH_{pp}) narrower than that associable to the pristine sample (A). The EPR spectra related to the sample after the constant-current discharge (C) reveals only 25% recovery of the original linewidth. Only after the extended, controlled-potential process (D), does the recovery reach 86%. With constant potential, charge-discharge cycles, efficiencies on the order of 85%-95% have been obtained for Li/PA cells by various authors (2, 4). This type of cycling, however, does not appear very

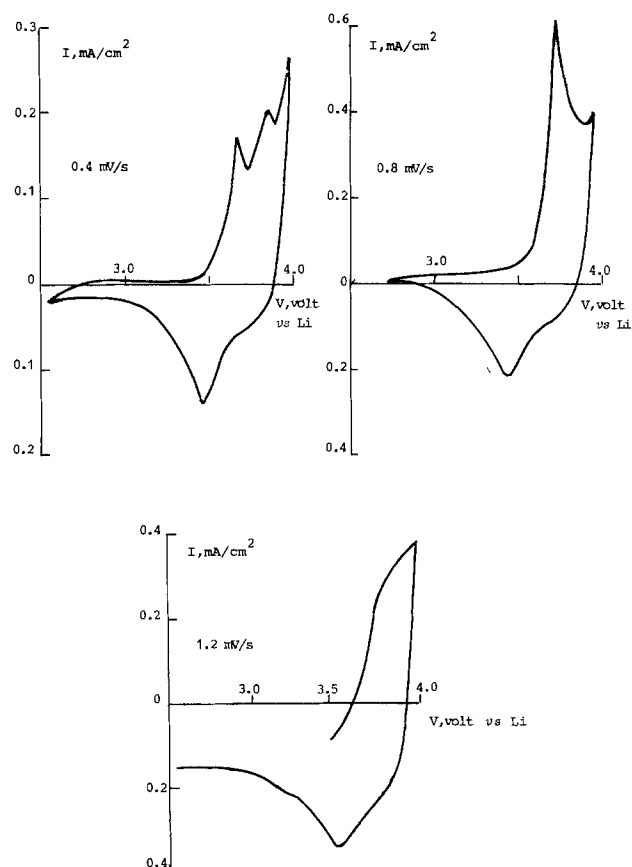


Fig. 7. Cyclic voltammetry of *trans*-rich PA film electrodes in the $\text{LiClO}_4\text{-PC}$ electrolyte at various scanning rates.

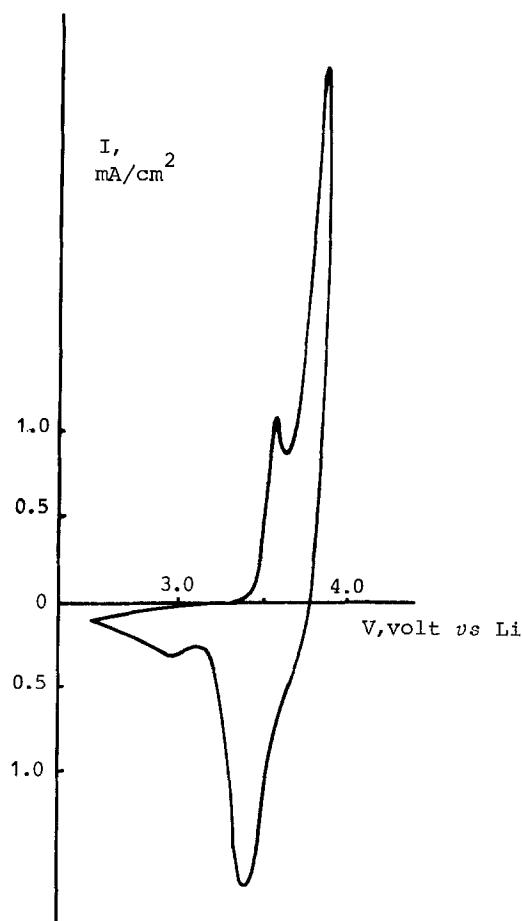


Fig. 8. Cyclic voltammetry of a *cis*-rich PA foam electrode in the $\text{LiClO}_4\text{-PC}$ electrolyte. Scanning rate: 0.4 mV/s.

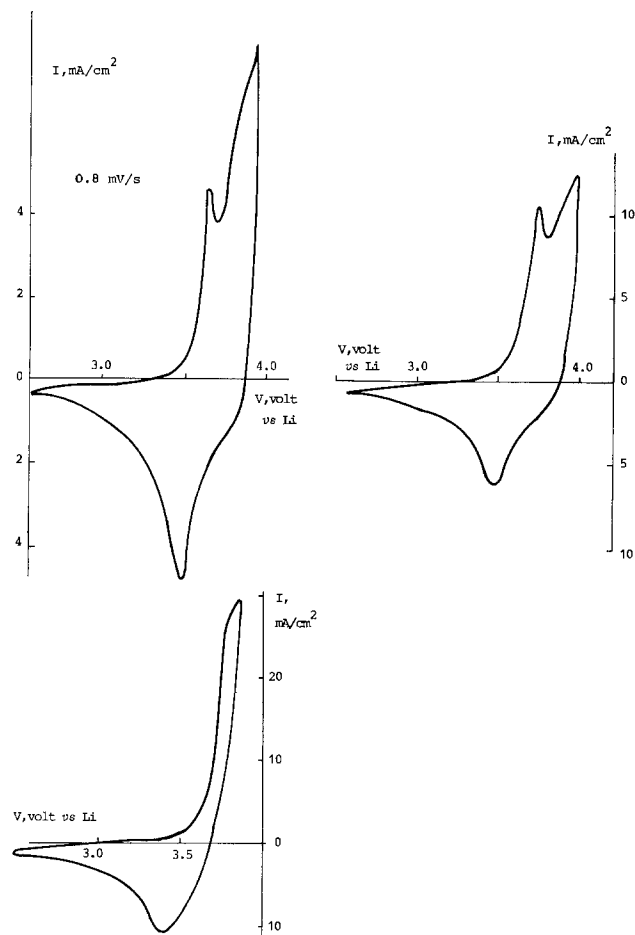


Fig. 9. Cyclic voltammety of *cis*-rich PA foam electrodes at various scanning rates.

useful in practice, where constant rates are generally required.

To determine whether the *cis-trans* conformation ratio of the polymer could be in part responsible for the kinetic limitation, we have considered the cyclic voltammety of *trans*-rich PA film electrodes. The results, obtained at various scanning rates, are shown in Fig. 7. The voltammetric response is similar to that observed for *cis*-rich electrodes (compare Fig. 2). Here again, the height of the first peak and the reversibility of the overall process depends on the scanning rate. Therefore, a poor coulombic efficiency for the *trans*-rich electrodes is to be expected in constant current, charge-discharge cycles, as was experimentally verified. The *cis-trans* ratio does not influence the kinetics of the electrochemical p-doping process of PA in the LiClO₄-PC solution. This is not surprising and is consistent with the fact that *cis-to-trans* isomerization takes place anyway during the electrochemical doping process, without apparently affecting its characteristics (11).

The kinetics may be more likely influenced by the morphology of the polymer, since diffusion of the dopants from the surface of the electrode seems to effect the efficiency so much. To investigate the role of the surface morphology on the electrochemical behavior of PA, we have considered the response of foam-type samples. In fact, the PA foam, even if retaining the typical mat-of-fibers structure of the PA film, has a much more extended surface area (9).

The cyclic voltammogram of a PA foam electrode in LiClO₄-PC, shown in Fig. 8, reveals the two typical oxidation peaks, at about 3.55 and 3.75V vs. Li, respectively. However, the response appears more reversible, both in terms of voltammetric peak resolution and current density, than the PA film electrodes under comparable conditions (compare Fig. 2B).

In Fig. 9 cyclic voltammety curves of foam PA electrodes are shown at various scanning rates. The behavior is again qualitatively similar to that of PA film electrodes (compare Fig. 2 and 7) since the increase in the scanning rate is accompanied by a broadening of the peaks. This, however, appears to be smaller in the case of the PA foam electrodes which, at high rate, assume the usual one-peak characteristic, but still maintain an acceptable degree of reversibility and a high current density response.

These results indicate that the kinetics of the electrochemical doping process of PA foam electrodes is still controlled by the diffusion of the dopant species in the polymer, but the extended surface allows reasonably high charge and discharge rates at good coulombic efficiencies.

This conclusion is further supported by examining the response of PA foam electrodes after prolonged charge-discharge cycles, obtained under diversified conditions both in terms of current density (ranging from 0.2 to 1.25 mA/cm²) and doping level (ranging from 0.5% to 4.2% mole percent [m/o]). The results, related to three different Li cells using the LiClO₄-PC electrolyte, are summarized

Table I. Charge-discharge characteristics of PA foam electrodes in Li cells with LiClO₄-PC electrolyte

Cycle no.	Charge current density (mA/cm ²)	Discharge current density (mA/cm ²)	Doping (m/o)	Coulombic efficiency (%)
Cell 1				
1	0.625	0.625	1.2	76
2	0.625	0.625	3.3	75
3	0.625	0.625	2.4	87
4	0.625	0.625	2.8	86
5	1.250	0.625	1.9	92
6	1.250	0.625	1.9	87
7	0.625	1.250	1.4	98
8	0.625	1.250	3.7	83
9	0.625	1.250	3.3	85
10	0.625	1.250	3.5	84
Cell 2				
1	0.5	0.5	1.0	45
2	0.5	0.5	1.9	72
3	0.5	0.5	2.8	67
4	0.5	0.5	2.4	84
5	0.5	0.5	2.8	84
6	0.5	0.5	2.6	88
7	0.5	0.5	3.1	83
8	0.5	0.5	3.3	83
9	0.5	0.5	3.8	81
10	0.5	0.5	4.2	81
11	0.5	0.5	3.8	81
12	0.5	0.5	4.1	83
13	0.5	0.5	3.4	84
Cell 3				
1	0.2	0.2	1.7	51
2	0.5	0.5	0.8	73
3	0.5	0.5	0.7	85
4	0.5	0.5	0.7	85
5	0.5	0.5	0.7	85
6	0.5	0.5	0.6	92
7	0.5	0.5	0.6	95
8	0.5	0.5	0.6	92
9	0.5	0.5	0.6	92
10	0.5	0.5	0.6	92
11	0.5	0.5	0.6	95
12	0.5	0.5	0.6	95
13	0.5	0.5	0.6	91
14	0.5	0.5	0.6	95
15	0.5	0.5	0.6	90
16	0.5	0.5	0.6	90
17	0.2	0.2	2.3	65
18	0.2	0.2	1.4	81
19	0.2	0.2	1.0	87
20	0.2	0.2	1.3	80
21	0.2	0.2	1.3	82
22	0.2	0.2	0.7	93
23	0.2	0.2	1.2	74
24	0.2	0.2	1.2	82
25	0.2	0.2	0.9	90
26	0.2	0.2	0.9	88
27	0.2	0.2	0.9	90
28	0.2	0.2	0.9	90
29	0.2	0.2	0.8	89
30	0.2	0.2	0.8	89

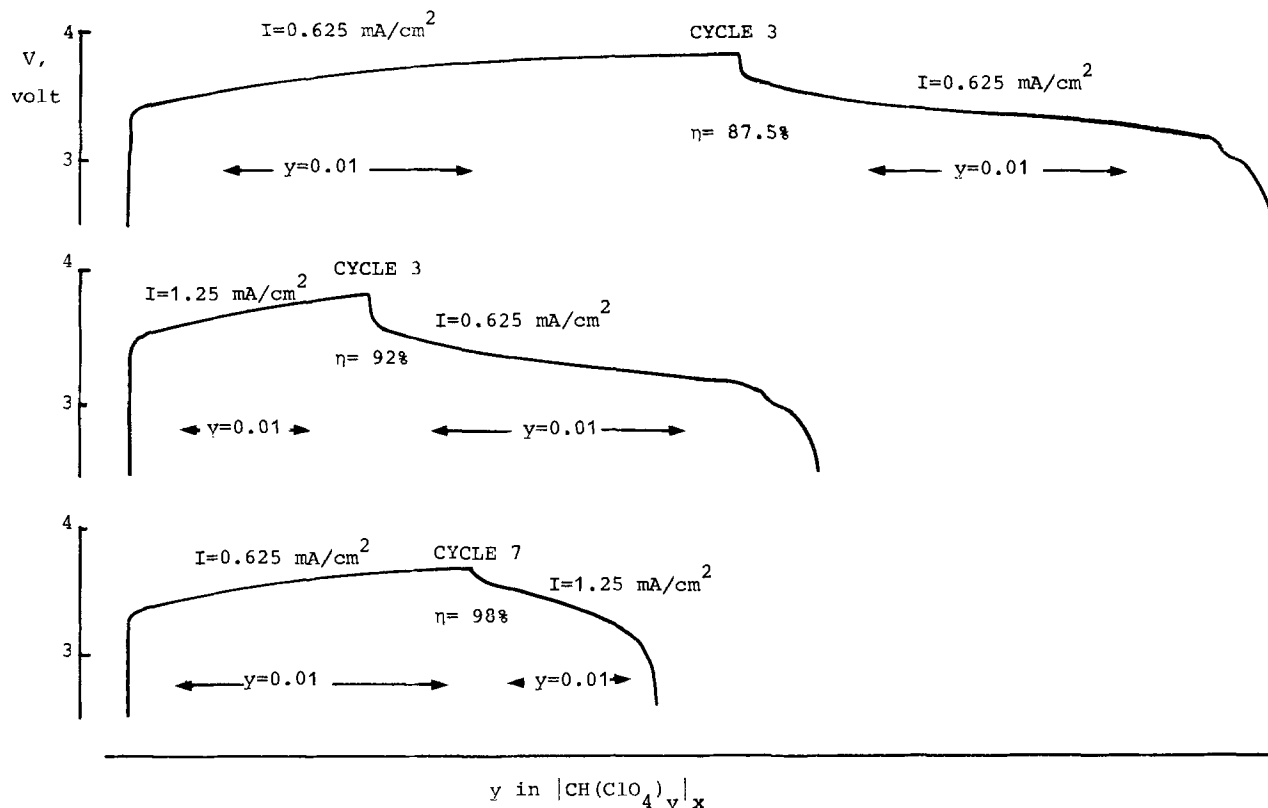


Fig. 10. Constant-current, charge discharge cycles of a Li/PA foam cell at 25°C. The number of cycle, the charge-discharge rates (mA/cm^2), and the coulombic efficiency (η) are indicated in the figure.

in Table I and illustrated in Fig. 10. The cycling behavior confirmed the voltammetric response, since the PA foam electrodes are indeed able to sustain comparatively high rates with reasonably good efficiencies.

This is clearly shown in Fig. 11, where the coulombic charge-discharge efficiencies obtained in each cycle of the three cells tested are progressively displayed. The first cycles generally have a lower efficiency than the following ones. This is not uncommon in lithium batteries; low initial coulombic efficiencies have often been reported for systems using intercalation electrodes. Such observations have been interpreted assuming that the initial intercalated species are strongly bound to the host structure and thus difficult to remove (12). These strongly bound species expand the layers of the

intercalating compound, thus facilitating further insertion and enhancing reversibility as the concentration increases (12). Since the electrochemical doping of PA may be regarded as similar to an intercalation process (4), a similar explanation may also hold in this case.

In contrast to what is observed with film-type electrodes, the efficiency of the foam type improves after the first cycles, as expected on the basis of the above-mentioned activating mechanism. After the two initial cycles, average coulombic efficiencies between 83% and 88% are obtained for the three Li/PA foam cells tested (see Fig. 11). These values, even if not yet completely satisfactory, are certainly much more encouraging in view of practical applications, than those reported for cells based on PA film electrodes, under comparable characteristics of cycling regimes and doping levels.

Conclusions

The above results show that the electrochemical p-doping process of PA in the $\text{LiClO}_4\text{-PC}$ electrolyte solution is controlled by the diffusion of the ClO_4^- dopant species in the polymer. For PA film electrodes, this diffusion appears particularly slow from the bulk to the surface, and this situation induces poor charge-discharge coulombic efficiencies for the Li/PA batteries.

Experimental results obtained by various authors (2, 4, 10, 13) confirm the kinetic limitation of the film electrodes. Slow diffusion may explain the drastic loss of capacity reported by various authors (4, 7) under open-circuit conditions. This effect may be related to the difficulty in removing the dopant species, which, upon standing, have diffused into the interior of the polymer electrode.

While the kinetic limitations of PA are independent of the *cis-trans* conformation ratio, the surface morphology does play a key role in the electrochemical doping process. Foam-type electrodes, which are characterized by a porous surface structure, can sustain much higher cycling rates and offer much better coulombic efficiencies than film-type electrodes, which are characterized by low porosity and smooth surfaces. Further study is certainly necessary to confirm this and to establish the long-term

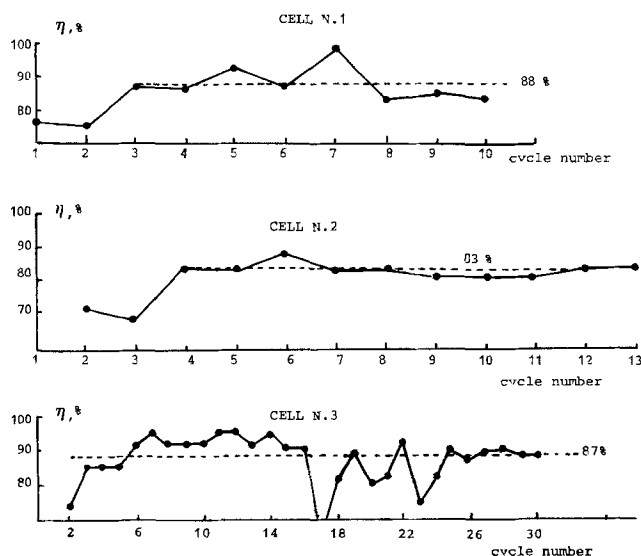


Fig. 11. Charge-discharge coulombic efficiency (η) of PA foam electrodes in the $\text{LiClO}_4\text{-PC}$ electrolyte, under the conditions listed in Table I.

behavior of the foam-type electrodes, especially in terms of a number and depth of cycles and stability. However, the results reported in this work, even if preliminary, allow us to infer that disordered, porous morphology should be preferred for polyacetylene if it is to be used as cathode in rechargeable lithium batteries.

Acknowledgments

This work has been carried out with the support of the Consiglio Nazionale delle Ricerche, Progetto Finalizzato Chimica Fine e Secondaria. One of us (A.P.) is grateful to AIRI for a Research Fellowship.

Manuscript submitted Feb. 13, 1984; revised manuscript received ca. July 27, 1984. This was Paper 70 presented at the Washington, DC, Meeting of the Society, October 9-14, 1983.

The University of Rome assisted in meeting the publication costs of this article.

REFERENCES

1. P. J. Nigrey, D. MacInnes, D. P. Nairns, A. G. MacDiarmid, and A. J. Heeger, *This Journal*, **128**, 1651 (1981).
2. K. Kaneto, M. Maxfield, P. Nairns, A. G. MacDiarmid, and A. J. Heeger, *J. Chem. Soc., Faraday Trans.*, **78**, 3417 (1982).
3. L. W. Shacklette, R. L. Elsenbaumer, and R. H. Baughman, "Proceedings of the International Conference on Conducting Polymers," Les Arcs, France, 1982.
4. G. C. Farrington, B. Scrosati, D. Frydrych, and J. deNuzzio, *This Journal*, **131**, 7 (1983).
5. A. G. MacDiarmid, K. Kaneto, M. Maxfield, D. P. Nairns, and A. J. Heeger, Abstract 25, p. 43, The Electrochemical Society Extended Abstracts, Vol. 82-2, Detroit, MI, Oct. 19-21, 1982.
6. B. Scrosati, A. Padula, and G. C. Farrington, *Solid State Ionics*, To be published.
7. B. L. Mackinney and R. G. Burrow, Abstract 559, p. 844, The Electrochemical Society Extended Abstracts, Vol. 83-1, San Francisco, CA, May 8-13, 1983.
8. T. Ito, H. Shirakawa, and S. Ikeda, *J. Polym. Sci., Polym. Chem. Ed.*, **12**, 11 (1974).
9. G. E. Wnek, S. C. W. Chien, F. E. Karasz, M. A. Druy, J. W. Park, A. G. MacDiarmid, and A. J. Heeger, *J. Polym. Sci., Polym. Lett. Ed.*, **17**, 779 (1979).
10. K. Abe, F. Goto, T. Yoshida, and H. Marimoto, Abstract 553, p. 836, The Electrochemical Society Extended Abstracts, Vol. 83-1, San Francisco, CA, May 8-13, 1983.
11. T. C. Chung, A. G. MacDiarmid, A. Feldblum, and A. J. Heeger, *J. Polym. Sci., Polym. Lett., Ed.*, **20**, 427 (1982).
12. B. Scrosati, *Electrochim. Acta*, **26**, 159 (1981).
13. F. G. Will, Abstract 554, p. 838, The Electrochemical Society Extended Abstracts, Vol. 83-1, San Francisco, CA, May 8-13, 1983.

Photoredox Reactions on Semiconductors at Open Circuit: A Single TiO₂ Electrode as a Model for Reactions in Particle Suspensions

Michael Neumann-Spallart

Institut de chimie physique, Ecole Polytechnique Fédérale de Lausanne, CH-1015 Lausanne, Switzerland

Octav Enea

Laboratoire de Chimie I, Université de Poitiers, F-86022 Poitiers, France

ABSTRACT

Optically and polarographically measured initial photoreduction rates of methylviologen on polycrystalline TiO₂ (anatase) electrodes at open circuit are shown to compare well with reduction rates calculated from the currents at the intersection of photocurrent and inverted dark current *i-E* curves. Such rates measured at single electrodes are then used to predict reduction rates on particle suspensions. The role of light intensity, pH, and platinization on reduction rates of various relays is discussed.

Redox reactions on illuminated semiconductor electrodes and on particle suspensions have been extensively studied in the last few years. One main interest lies in the photoelectrosynthetic applications, *i.e.*, the oxidation and reduction products that are formed by the charge carriers (electrons and holes) generated by light absorption in the semiconductor. In the case of a photoelectrochemical cell, one charge carrier is channeled through a wire to a counterelectrode which may be separated by an ionic conducting membrane. This is one of the main advantages of such a cell. The short-circuit current and, hence, the product formation rates can be measured and calculated from the current of the intersection of the anodic and cathodic current-potential (*i-E*) curves measured potentiostatically for the constituent electrodes of the cell (1).

Photoelectrosynthesis on semiconductor particle suspensions or colloids is less well understood because the individual reactions cannot be separately studied. The counterelectrode is directly attached to the photoelectrode (*e.g.*, in the form of a catalyst) or is identical to the latter. No electrical contact can be made on small particles, and the product formation rates can only be measured by chemical analysis. Interestingly, both products (reduction and oxidation) sometimes emerge from

the same (illuminated) surface; the same behavior has recently been seen in electrodes and 40 μm CdS particles embedded in a membrane (2).

In this work, we aim to predict product formation rates on single illuminated semiconductor electrodes suspended in solution and operated at open circuit from electrochemical measurements at the same electrode in a separate experiment. Such an electrode mimicks a semiconductor particle suspension consisting of only one large particle. We will use this principle to make the first attempts at a quantitative understanding of photoelectrosynthesis in semiconductor particle suspensions. Phenomenologically, in such suspensions, each particle consists of two short-circuited microelectrodes able to carry out a reduction and an oxidation. The concept has already successfully been applied in understanding corrosion phenomena (3) and redox catalysis by metallic particles (4). The idea is to extrapolate electrochemical data of macroelectrodes into the area of particle suspensions or colloids. If the material of the two electrodes is the same, and if one reaction only occurs under illumination, it is sufficient to study, in the dark and under illumination, on one electrode the current-potential (*i-E*) curves that are thought to be representative of the individual cathodic and anodic reactions. Product formation at a single sand-

wiched electrode under illumination (5) and the correlation between the deposition rate of silver (6) and reduction rate of methylene blue (7) and the currents in TiO_2 crystals have been reported in the literature.

Since redox reactions on semiconductors usually exhibit high overvoltage, much research has been done on the improvement of kinetics by attaching noble metal catalysts to the surface of semiconductor electrodes and powders (2, 8-11). New features can be observed because of the specific interaction of metals surface attached to the support (12, 13) or adsorption of relays on the catalyst (14). It is also the purpose of this work to explain on the basis of i - E curves whether (and if so, why?) catalytic deposits can increase product formation rates in the dark and under illumination. Experiments with TiO_2 (anatase) as the semiconductor and methylviologen as the relay will be reported, and the influence of various factors such as relay concentration, light intensity, and platinization on the rates of product formation will be investigated.

Experimental

n - TiO_2 (anatase) electrodes were prepared by thermal decomposition of TiCl_4 (10) on titanium sheets ($0.75 \text{ cm} \times 0.75 \text{ cm}$) cleaned with 30% HNO_3 /4% HF . The thickness of the TiO_2 layer, which was varied by varying the number of deposited layers prior to the final annealing procedure, was 10-40 μm , as estimated by weighing. Photoplatinization was carried out by UV irradiation ($\lambda > 350 \text{ nm}$, 8-80 min) in argon degassed solution ($\text{pH} = 2.43$) containing $8.2 \times 10^{-3} \text{ M K}_2\text{PtCl}_6$, at open circuit, in the absence of a deliberately added hole scavenger. One electrode was photoplatinized for 8 min at +0.342V, the potential initially established under irradiation at open circuit. From the integrated charge, a thickness of 20 \AA could be estimated, assuming a homogeneous layer. The morphology of the deposit will be discussed below. The back sides of the electrodes were insulated with plastic paint, unless otherwise indicated. TiO_2 powder "P 25" was obtained from Degussa.

The irradiation equipment consisted of a 450W Xe lamp (Oriel) operated at 22.2A, an 8 cm water filter (to remove IR light), a 350 nm cutoff filter (in its absence, direct photolysis of methylviologen occurred), a shutter, a slit, and the irradiation cell (shown in Fig. 1).

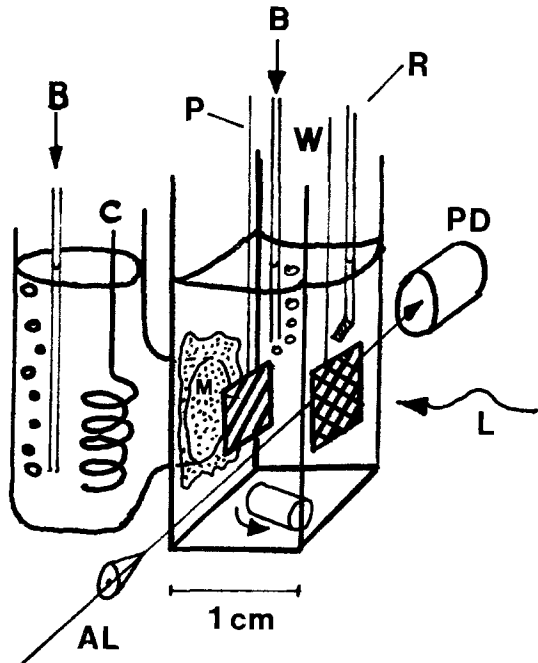


Fig. 1. Lower part of irradiation cell. (quartz) cell, W) working electrode (TiO_2), R) reference electrode, C) counterelectrode (Ti), P) electrode for polarographic detection of product (Pt), L) actinic light, AL) analyzing light, PD) photodiode, B) tube for bubbling with gas, M) separating membrane (cellulose).

Figure 1.—The total liquid volume was 2-3 ml. The solutions (made up in twice-distilled water, then filtered) were purged with Ar 4N8 (unless otherwise indicated) before and sometimes during the experiments, then they were stirred. Currents and potentials were measured with a Wenking POS 73 potentiostat. (All potentials are quoted vs. NHE.) Identical electrochemical pretreatment (potential at which the electrode is held before starting a scan, illumination, etc.) was necessary to obtain reproducible i - E curves in the region of the photocurrent onset. Production rates of reduced methylviologen, MV^+ , were measured by two ways: via its absorbance of light of a He-Ne laser at 632.8 nm ($\epsilon = 8060 \text{ M}^{-1} \text{ cm}^{-1}$); or by reoxidation on a polarographic detector electrode (Pt) held at 0V. The purpose of the latter method was to allow measurements of production rates in turbid solutions (particle suspensions) for which the same experimental setup was used. In front of the cell, a mask having the same surface and form as the TiO_2 electrodes used was attached to maintain the number of incident quanta.

Results

Figure 2.—Three types of measurements carried out at single n -type TiO_2 electrodes are compared in Fig. 2.

1) The i - E curves in the dark and under illumination have been recorded potentiodynamically, separately or simultaneously, using chopped light. i_d is the current for the reduction of the relay, MV^{2+} , in the dark, and i_d' is $-i_d$. i_i is the current under illumination, and the net photocurrent, i_{ph} , equals $i_i - i_d$.

2) A second experiment has been made at open circuit. The potential has been recorded as a function of time (E_t). When the light is switched on, the potential rapidly de-

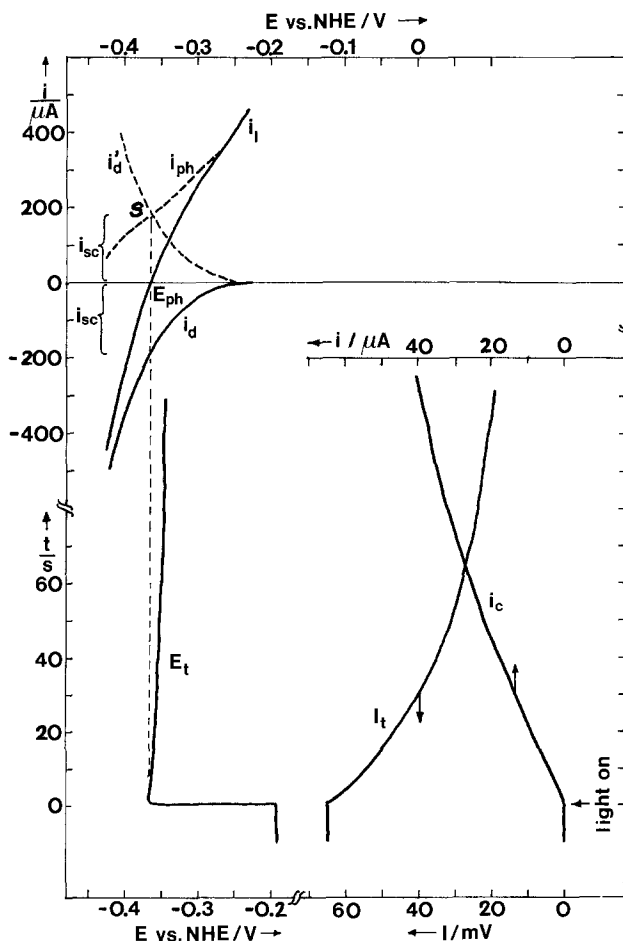


Fig. 2. Current-potential and photopotential- t curves and product formation rates for $\text{MV}^{2+}/\text{MV}^+$ on TiO_2 (anatase). 0.1 N NaOH , $6 \times 10^{-3} \text{ M MV}^{2+}$, Ar bubbling, stirring, $\lambda > 350 \text{ nm}$, scan rate -0.5 mV/s . i_t , i_c) intensity of transmitted analysis light and current on the polarographic detection electrode, respectively, as a function of time.

creases. Both charge carriers react on the surface of the electrode. When the photopotential, i_{ph} , is reached, the photocurrent (corresponding to an oxidation process carried out by holes in the valence band) equals the dark current (reduction of the relay), as indicated in Fig. 2 by the intersection point S, where $i_{ph} = -i_d = i_{sc}$. The production rate is then calculated from the current at the intersection

$$v_e = i_{sc}/F \quad [1]$$

For experiments where reduced methylviologen, MV⁺, is the reduction product, it turns out to be better to calculate i_{sc} using i_{ph} in the absence of the relay, since the photocurrents tend to decrease when MV⁺ is accumulated at slow scan rates. This also leads to the slow increase of E_t with time.

3) The increase in concentration of the photoproduct (MV⁺) is simultaneously measured photometrically (I_o) and polarographically (i_c). The current on the collector electrode, i_c , is proportional to the concentration of the reduced relay and can be calculated using the optical data (I_o)

$$v_a = \frac{V}{t\epsilon} \log \frac{I_o}{I_t} \quad [2]$$

Photoproduction rates tend to level off at prolonged irradiation time. The initial production rates V_{ap} and v_e are dependent on several factors, the influence of which on the individual (dark, light) i - E curves is shown in the following.

Figure 3.—There is a well marked dependence of production rates on concentration. The dark reactions which are thought to be responsible for this behavior are therefore recorded as a function of potential and relay concentration (Fig. 4).

Figure 4.—The dependence of plateau photocurrents on the TiO₂ electrodes on light intensity (I) is found to be linear in the range studied ($d \log i_{ph}(\text{plateau})/d \log I = 1$ over several orders of magnitude). A more complex dependence is expected for the currents at the intersection of inverted dark current i - E curves that occur in the falloff region of the photocurrent near the onset potential. As a consequence, the photopotential, E_{ph} , usually changes with the logarithm of the light intensity (18). This is also the case for "dry diodes." The photopotential of TiO₂/MV²⁺ shifts by 60 mV per decade of light intensity, as predicted for a one electron relay by Gomes *et al.* (18) (Fig. 5).

Figure 5.—At very high light intensities, the curve will reach a limiting value because the photopotential cannot

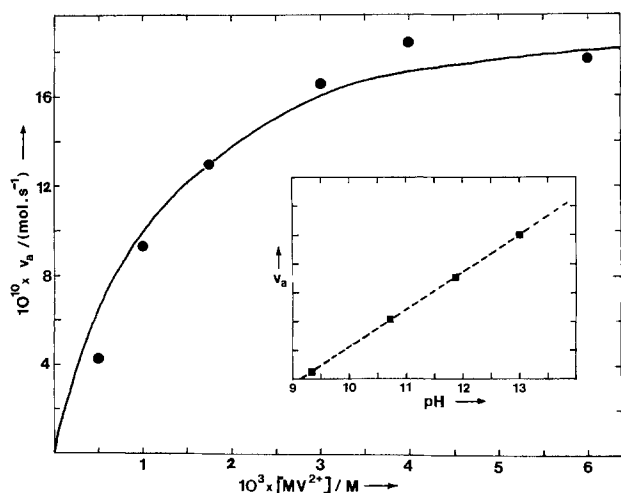


Fig. 3. Formation of MV⁺ as a function of MV²⁺. (●) data from optical measurements, (—) data calculated from i - E curves. 0.1N NaOH, Ar bubbling, stirring, $\lambda > 350$ nm. Insert: pH dependence of initial reduction rates at 6×10^{-3} M MV²⁺.

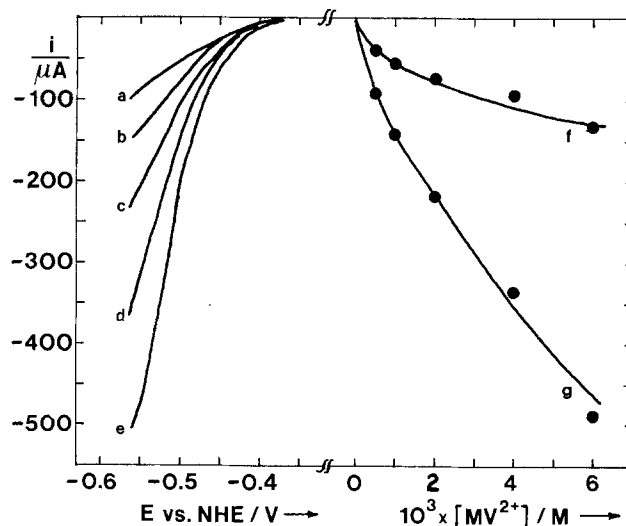


Fig. 4. Dependence of dark currents on relay concentration. Left side of diagram (i_d as a function of E for various concentrations of MV²⁺): 5×10^{-4} M (a); 1×10^{-3} M (b); 2×10^{-3} M (c); 4×10^{-3} M (d); 6×10^{-3} M (e). Right side: i_d as a function of [MV²⁺] at -0.482 V (f) and -0.557 V vs. NHE (g).

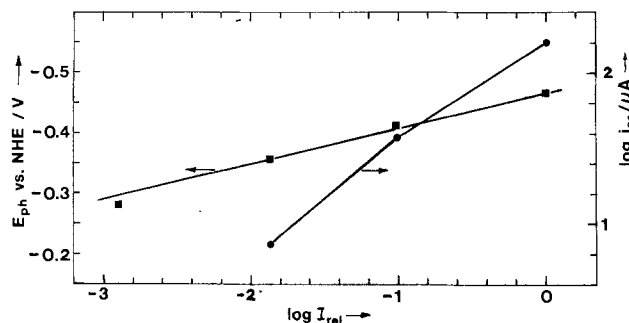


Fig. 5. Dependence of i_{sc} and photopotential, E_{ph} , on relative light intensity. 0.1N NaOH, 6×10^{-3} M MV²⁺, Ar bubbling, stirring. Light intensity varied by neutral density filters.

exceed the flatband potential. The intersection current at the photopotential which determines the photoproduction rate must therefore also show saturation behavior as shown in Fig. 5 (see also Fig. 7b below). At no value of the intensity does $d \log i_{sc}/d \log I$ reach 1, in contrast to plateau photocurrents.

Platinized TiO₂ electrodes show a markedly different behavior with respect to their i - E characteristics in the dark for various relays, but, also, the light curves are somewhat changed (Fig. 6).

Figure 6.—Only a small decrease (<10%) of the photocurrent is noticed in the plateau region. The relative decrease of photocurrents in the onset region (curves 7-10), however, is much more important. As with unplatinized electrodes, photocurrents decrease at high relay concentration. In Fig. 6, curves 9 and 6 intersect the baseline (continuation not shown), and the net effect becomes photocathodic.

In the presence of EDTA, H₂ is formed on platinized electrodes at a rate of 1.1×10^{-10} mol/s. Only trace quantities are detected without EDTA.

In Table I, data for production rates at a single TiO₂ electrode and for suspension of TiO₂ powder (same illumination area) are collected.

Discussion

First, the production rates on a TiO₂ electrode and the parameters influencing them will be discussed. The initial production rate $v_{a,0}$ compares well (Fig. 3) with values of the production rate v_a obtained from i - E curves on the same electrode. It thus seems possible to predict, from electrochemical data, production rates on electrodes at

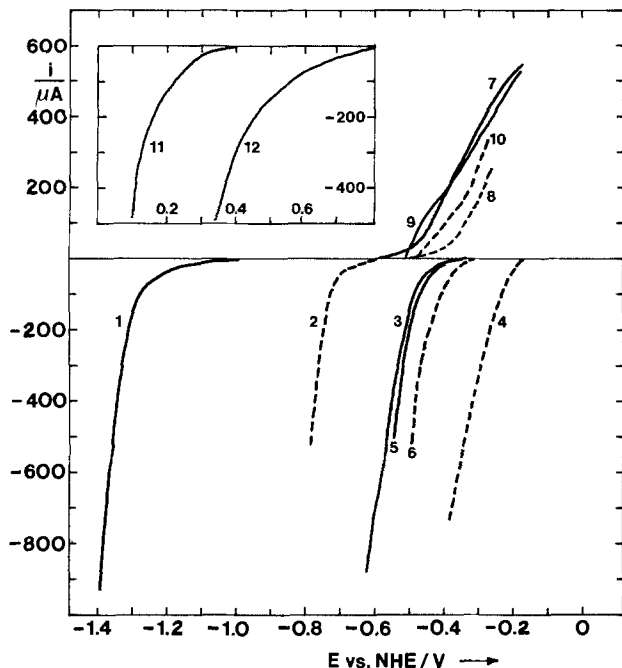


Fig. 6. Influence of platinumization of TiO_2 electrodes on i - E curves for various relays. (—) before platinumization, (---) after platinumization. 1, 2) Ar saturated solution, dark; 3, 4) oxygen saturated solution, dark; 5, 6) $6 \times 10^{-3} \text{M MV}^{2+}$, Ar saturation, dark; 7, 8) Ar saturated solution, light; 9, 10) $6 \times 10^{-3} \text{M MV}^{2+}$, Ar saturation, light; 11) Ar saturation, $8.2 \times 10^{-3} \text{M K}_2\text{PtCl}_6$, pH 2.43; 12) as 11, but scan recorded after 11. Scan rates: -0.5 mV/s for curves 1-10; -2 mV for curves 11 and 12, 0.1N NaOH; stirring.

open circuit. There are several factors responsible for the leveling off of the curves at high MV^{2+} . From Fig. 2, it can be seen that a doubling of reduction current will not result in a doubling of the current at the intersection point, for a purely geometrical reason (considering the given form of dark and light i - E curves).

Second, the dark reduction currents are not proportional to relay concentration. This effect has already been noticed by Memming *et al.* (15) on Fe_2O_3 and by Vandermolen *et al.* (16) on TiO_2 , and it is explained by the transfer of electrons to be occurring via surface states. Another reason for the leveling off of the rates calculated from i_{sc} is the decrease of the net photocurrents, i_{ph} , with increasing relay concentration. i_{ph} even becomes negative at sufficiently negative potential (Fig. 6). This has also been called "photocathodic" effect (17). However, before the net photocurrent turns cathodic, photoinduced reduction currents flow and lower i_{ph} . The contribution of this effect is relatively small for $\text{MV}^{2+}/\text{TiO}_2$ because intersection of i - E curves occurs at potentials where the photoreduction effect is of minor importance.

The dependence of production rates (insert Fig. 3) on pH can be explained as follows. A band shift of usually 59

Table I. Polarographically measured production rates of $6 \times 10^{-3} \text{M}$ methylviologen in 0.1N NaOH, $\lambda > 350 \text{ nm}$, Ar bubbling, stirring

Amount of TiO_2 (g/l)	Initial MV^+ production rate/(mol/s)
0.5	4.95×10^{-9}
2.5	7.29×10^{-9}
10.0	7.03×10^{-9}
Electrode	2.07×10^{-9}
	2.60×10^{-9} (a)
	3.00×10^{-9} (b)

(a) Value for electrode coated with TiO_2 on the back side.

(b) Calculated value for electrode with 4 times larger surface, but the same irradiated surface.

mV per pH unit is caused by the dissociation of surface OH groups on oxide semiconductors. Since the redox potential of methylviologen is independent of pH, the balance of reaction rates of injection of electrons from the reduced relay into the conduction band of the semiconductor and vice versa will depend on pH. From this, an attempt has been made to calculate the Fermi level of TiO_2 (as powder suspension) in redox systems at pH = 0, by flash photolysis (19) or by polarographic product analysis during illumination (20). However, the Fermi level is not always close to the potential of the conduction band edge, the value of which one usually obtains to characterize a semiconductor. Nor can a simple linear or logarithmic dependence for product formation rates or yields on pH be derived from theory. From the point of intersection of photocurrent potential curves, which shift 59 mV per pH unit toward more positive potentials, with dark current potential curves (i_a vs. E), it can be seen that the current and the production rate become zero at the pH where the onset of the i_{ph} - E curve occurs at the potential at which the dark current is zero. This potential may be identical to the redox potential of the relay, considering relative concentrations of oxidized and reduced form, if the relay shows rapid kinetics on the electrode, as it does for methylviologen [this is an exception for dark currents on semiconductors (21)]. Even then, if the experimentally measured reduction rates are initial rates, the Nernst potential changes rapidly in the beginning stages after the light is switched on, because the concentration of the reduced form of the relay is very small. This means that no reliable reference point is available to calculate the Fermi level.

For methylviologen on TiO_2 (anatase) electrodes, we find that the reduction rates become zero at pH 9 (insert, Fig. 3). Because no hole scavenger is employed, oxygen formed by valence band holes will start to consume MV^+ when it is accumulated. The reaction rate of oxygen with MV^+ certainly increases with decreasing pH, and we think that the fall off of reduction rates at relatively high pH [compared to a system in which a hole scavenger (acetate) is present (20)] is due to this back reaction. It is surprising that MV^+ is formed at all when a highly oxidizing anodic product is evolved. The reason might be that, shortly after switching on the light, photoproduct oxygen is adsorbed on TiO_2 and is reacted slower in this form with MV^+ being formed at other sites on the electrode and that the probability of reaction with MV^+ molecules already escaped into the solution will be smaller. Later, the leveling off of product formation is a consequence of the reaction of MV^+ with O_2 and valence band holes.

One of the most important factors influencing product formation is the presence of a catalyst on the semiconductor surface. This is mainly due to an influence on dark currents, as can be seen in Fig. 6. As expected, the reduction curve for water (curves 1, 2) shifts toward much more positive potentials (by 570 mV) when Pt is present at the surface. The shift for oxygen reduction (curves 3, 4) is smaller (250 mV), but still higher than that for the reduction of the one electron relay, methylviologen (60 mV, curves 5, 6). Undoubtedly, this effect is of catalytic nature for water and oxygen reduction, whereas the small shift for methylviologen reduction could be partially explained by the increase in surface when platinum is deposited. This has also been proposed by Kobayashi *et al.* (9). Preliminary experiments (electron micrographs) show that the metallic deposit is built up in the form of islands (preferentially at damaged areas). Generally, if no sites will be available where the electrolyte can reach the semiconductor surface, no photoeffect should occur, since a poreless metal film represents a perfect shunt for light-separated charges [ohmic contact provided, which is usually the case for Pt on TiO_2 (25)]. This has often been overlooked when discussing deposition on semiconductor surfaces. However, photodeposition can continue until almost the whole surface is covered (22). In the case of photodeposition of silver on WO_3 (23), photoactivity is

maintained, even when a visible deposit (plates perpendicular to the surface, as shown by electron micrograph) is present on the surface. An affirmation for nonhomogeneous coating lies in the fact that a rapidly decreasing overpotential is observed for the deposition of the first grains of metal on the surface [see also Ref. (8)]. During potentiostatic deposition of Pt in the dark (curves 11 and 12) and under illumination, the decrease in overpotential is caused by increasing dark reduction currents due to deposition on already existing sites (note that the i - E curve 12, obtained in the second scan for TiO₂ in K₂PtCl₆, lies 300 mV more positive than the one of the first scan, curve 11).

Photoreduction rates of methylviologen are not enhanced on platinized electrodes, although the dark reduction i - E curves shift toward more positive potentials. This is due to the decrease in photocurrents in the onset region, which is a result of metal islands serving as recombination centers for electrons and holes. The effect is also noted for a deposit of RuO₂ on WO₃ (24). Because of this, as little platinization as is necessary to obtain a catalytic deposit is recommended. The decrease in i_{ph} is smallest for the shortest platinization time used, 8 min. Note that at high relay concentration, the decrease in photocurrents is less pronounced (curves 8 and 10).

The situation is different for hydrogen generation on unbiased electrodes. From the current potential curves, it can be seen that there is no intersection of the inverted curve 1 (H₂O reduction on an unplatinized electrode) and curve 7. With a platinized electrode, the onsets of the curves 2 and 7 just touch each other, and hydrogen is detected only in trace amounts by gas chromatography. However, in the presence of a hole scavenger (EDTA), the curve i_{ph} vs. E (curve not shown) is shifted toward more negative potentials [transients which usually occur when the light is switched on or off are suppressed, probably due to the enhancement of the hole transfer rate and/or to specific binding in the form of a complex (26)], and the formation rate of hydrogen is corresponded to an intersection current of 20 μ A.

Comparison of reduction rates at single electrodes and particle suspensions.—The foregoing discussion of the influence of several parameters on product formation rates on unbiased electrodes using electrochemical data (i - E curves) shall now enable us to understand the photoelectrochemical performance of a semiconductor particle suspension that can be thought to consist of a high number of such electrodes (of much smaller surface, but exhibiting the same electrochemical features as a single macroelectrode). As would be expected from the doubling of the dark currents, the reduction rate of an electrode that is also covered on the back side with TiO₂ is already found to be higher (1.26 times, Table I). Even higher reduction rates are observed on illuminated powder suspensions (3.5 times, as compared to a single electrode) for > 2.5g TiO₂/l (the decrease in rate for amounts of TiO₂ < 2.5 g/l is due to the incomplete light absorption).

On a spherical particle, the surface available for dark reactions may be four times larger than its cross section because in a simplified approach, a light beam of cross section $r^2\pi$ would be entirely absorbed by a particle of radius r , surface $4r^2\pi$. However, as we have seen above (discussion of Fig. 1), an increase in dark current is not reflected in a proportional increase in current at the intersection of the i - E curves (a factor of 1.45 is calculated from the i - E curves for quadrupling the surface of the electrode; see data in Table I).

Refining the model, we must consider that light is also absorbed by particles lying partially in the shadow of the particles nearest to the window (for which the current density at a large part of the illuminated surface will be close to that on a flat single electrode), giving rise to smaller light currents, but making their entire surface available for the dark reaction.

Figure 7.—The total surface which can be used will thus be much higher, though the contribution is not addi-

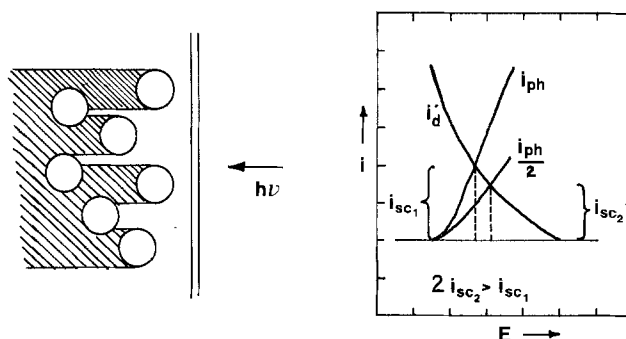


Fig. 7. Model for illumination of particle suspensions: (a, left) irradiation geometry; (b, right) i - E curves on particles, schematic.

tive, because the intersections of the i - E curves (i_{ph} and i_d') have to be calculated individually for each particle, and only the currents at the intersection points can be summed up (Fig. 7b). In any case, the following relation holds

$$i_{sc,t} = \sum_f f(I)_i m_i > f(I)_t \quad [3]$$

where $\sum_i I_i = I_t$, $i_{sc} = f(I)$ for constant particle surface and relay concentration. $i_{sc,t}$ is the total production current, I is the light intensity, I_i is the intensity at an individual particle, I_t the total absorbed light intensity, and m_i is the number of particles experiencing the light intensity I_i . The function f has a form like that in Fig. 5. From Eq. 3, it also follows that the same amount of light absorbed by smaller, therefore more transparent and more numerous (if total absorption is achieved in the vessel) particles should lead to higher reduction rates. In addition, light that is not entirely absorbed by the particle first hit (especially near the poles) will be absorbed by particles located at longer distance from the window. The derivation of an exact solution or analytical representation of the above problem is beyond the scope of this article, but we think that the above considerations can explain an increase in reduction rates like those observed in particle suspensions (compared to single electrodes). At the same number of quanta absorbed by the suspension as for the macroelectrode, the main topological difference is the fact that the light is absorbed by a great number of particles in the suspension, involving a larger total surface. The rates on single electrodes are of the same order of magnitude, which proves that the study of i - E curves on electrodes is a useful tool in predicting the possibility of reactions occurring in particulate systems and in predicting their rates.

Acknowledgment

We thank Mr. J. Desilvestro for helpful discussions.

Manuscript submitted Dec. 30, 1983; revised manuscript received Aug. 14, 1984.

REFERENCES

1. M. Neumann-Spallart and K. Kalyanasundaram, *Ber. Bunsenges. Phys. Chem.*, **85**, 1112 (1981).
2. T. Kobayashi, Y. Taniguchi, H. Yoneyama, and H. Tamura, *J. Phys. Chem.*, **87**, 768 (1983); D. Meissner, R. Memming, and B. Kastenig, *Chem. Phys. Lett.*, **96**, 34 (1983).
3. C. Wagner and W. Z. Traud, *Z. Elektrochem.*, **44**, 391 (1938); U. R. Evans, "The Corrosion and Oxidation of Metals," E. Arnold, Editor, London (1960).
4. M. Neumann-Spallart and K. Kalyanasundaram, *J. Phys. Chem.*, **86**, 2681 (1982); M. Neumann-Spallart, Submitted to *J. Chem. Soc. Faraday Trans. I*; D. S. Miller and G. McLendon, *J. Am. Chem. Soc.*, **103**, 6791 (1981); E. Sutcliffe and M. Neumann-Spallart, *Helv. Chim. Acta*, **64**, 2148 (1981); W. J. Albery, P. N. Bartlett, and A. McMahon, in "Photogeneration of Hydrogen," A. Harriman and M. A. West, Editors, p. 85, Academic Press, London (1982).
5. A. J. Nozik, *Appl. Phys. Lett.*, **30**, 567 (1977).
6. H. Hada, Y. Yonezawa, M. Ishino, and H. Tanemura, *J. Chem. Soc., Faraday Trans. 1*, **78**, 2677 (1981).

7. H. Yoneyama, Y. Toyoguchi, and H. Tamura, *J. Phys. Chem.*, **76**, 3460 (1972).
8. F. Möllers, H. J. Tolle, and R. Memming, *This Journal*, **121**, 1160 (1974).
9. T. Kobayashi, H. Yoneyama, and H. Tamura, *ibid.*, **130**, 1706 (1983).
10. J. S. Koudelka and J. Augustynski, *J. Phys. Chem.*, **86**, 4277 (1982).
11. H. Yoneyama, N. Nishimura, and H. Tamura, *ibid.*, **85**, 268 (1981).
12. J. Sanches, M. Koudelka, and J. Augustynski, *J. Electroanal. Chem.*, **140**, 161 (1982).
13. M. Koudelka and J. Augustynski, *J. Chem. Soc., Chem. Commun.*, p. 55 (1983).
14. O. Enea, Submitted to *Nouveau J. Chim.*
15. P. Iwanski, J. S. Curran, W. Gissler, and R. Memming, *This Journal*, **128**, 2128 (1981).
16. J. Vandermolen, W. P. Gomes, and F. Cardon, *ibid.*, **127**, 324 (1980).
17. H. R. Sprünken, R. Schumacher, and R. N. Schindler, *Ber. Bunsenges., Phys. Chem.*, **84**, 1040 (1980).
18. W. P. Gomes and F. Cardon, in "Semiconductor Liquid Junction Solar Cells," A. Heller, Editor, p. 120, The Electrochemical Society Softbound Proceedings Series, Princeton, NJ (1977).
19. D. Duonghong, J. Ramsden, and M. Grätzel, *J. Am. Chem. Soc.*, **104**, 2977 (1982).
20. M. D. Ward, J. R. White, and A. J. Bard, *ibid.*, **105**, 27 (1983).
21. J. Desilvestro and M. Neumann-Spallart, Personal communication.
22. T. Kobayashi, Y. Tanigushi, H. Yoneyama, and H. Tamura, *J. Phys. Chem.*, **87**, 768 (1981).
23. W. Erbs, J. Desilvestro, E. Borgarello, and M. Grätzel, *ibid.*, **88**, 4001 (1984).
24. J. Desilvestro, 4th Int. Conf. on Photochem. Conv. and Storage of Solar Energy, Jerusalem (1982).
25. G. A. Hope and A. J. Bard, *J. Phys. Chem.*, **87**, 1979 (1983).
26. J. Desilvestro, Personal communication.

Compositional Changes of Anolyte on Electrolyzing Stainless Steel in High Temperature Chloride Media

K. Tanno* and M. Aizawa¹

Department of Applied Chemistry, Faculty of Engineering, Iwate University, Ueda, Morioka 020, Japan

ABSTRACT

In connection with crevice corrosion of stainless steel in high temperature water, Type 304 stainless steel was anodically electrolyzed in 0.5N or 0.05N NaCl solution at temperatures up to 250°C with determination of compositional changes of the anolyte. Components of the steel dissolved as Fe²⁺, Cr³⁺, and Ni²⁺ and lowered the pH of the anolyte by hydrolysis of the dissolved ions. pH measured at room temperature decreased with increasing amounts of charge. During electrolysis at temperatures above 150°C, lower pH values and much more precipitates were obtained, and at 200° and 250°C hard films, which were mainly composed of CrOOH and scarcely dissolved in hot HCl, were formed on the specimens. In the electrolysis at 250°C, lower pH values were obtained in concentrated Cl⁻ solutions. These pH changes of the anolyte were well described with the experimental results of hydrolysis of Cr³⁺ solutions. At 200° and 250°C, local corrosion of the steel in the anolyte occurred.

Because of its technological importance, crevice corrosion of stainless steel in chloride media has been studied frequently and compositions of occluded solutions have been examined. Much evidence (1-3) shows that the occluded solution has a higher concentration of hydrogen ion and chloride ion than the bulk solution. Concentration of hydrogen ion is caused by hydrolysis of metal ions, and that of chloride ion is due to migration of the ion from the bulk solution due to an active-passive cell formed, respectively, inside and outside the crevice. Therefore, some authors (4) examined compositional changes of a simulated anolyte on electrolyzing stainless steel in chloride media.

However, most of these investigations have been conducted near room temperature, and there are few studies conducted at temperatures above 100°C, in spite of its practical importance. Taylor *et al.* (5-8) reported some results at 288°C relating to stress corrosion cracking of stainless steel in nuclear plants.

In the present study, compositional changes of electrolyte were examined when stainless steel specimens were dissolved anodically in chloride media at the temperature ranging from 25° to 250°C. In connection with the pH changes of the anolyte, hydrolysis of chromium chloride solutions at high temperatures were conducted.

Experimental

Electrolysis.—Austenitic stainless steel of Type AISI 304 was used for test specimens. All specimens were 1

mm thick, 10 × 10 mm in area, and have the following composition by percent weight: Cr = 18.77, Ni = 9.18, C = 0.08, Mn = 1.34, Si = 0.52, Mo = 0.19, and Fe to 100. They were mechanically polished with emery paper and washed with acetone and alcohol.

Figure 1 shows the electrolysis cell made of Teflon. The anodic and cathodic compartments are separated by a sintered SiC disk filter made of particles of an average size of 2 μm with a porosity of about 43%. The counter-electrode is platinum or Type 304 stainless steel plate. Sodium chloride solutions of 0.5 or 0.05N were used as electrolyte. Volumes of anolyte and catholyte were 30 and 175 cm³, respectively.

For electrolyses conducted above 100°C, this cell was set in an autoclave in the atmosphere and heated to definite temperatures. The electrolysis was performed at a constant current density of 12 mA/cm². After electrolysis, the autoclave was cooled and the anolyte and catholyte were filtered through no. 5C filter paper. Iron, chromium, and nickel were measured by atomic absorption spectrometry and chloride ion was determined by the Volhard method.

Hydrolysis.—In the experiment, 90 ml of 3.3 × 10⁻² mol/liter CrCl₃ solution with various concentrations of Cl⁻ in a titanium autoclave was heated to 150°, 200°, or 250°C for 24h, which is enough to get a steady state. The solution was then cooled quickly and filtered through a Millipore filter paper (pore size 0.8 μm), and pH and chromium content of the filtrate were measured. The composition of precipitate was examined by x-ray diffraction, IR spectrometry, and thermogravimetry. The test solutions were prepared from reagent-grade CrCl₃ and pure water,

*Electrochemical Society Active Member.

¹Present address: Hitachi Engineering Company, Limited, Hitachi 317, Japan.

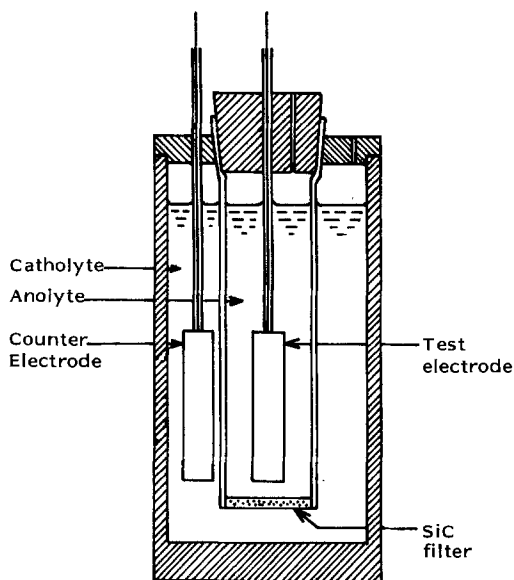


Fig. 1. Electrolysis cell

and their Cl^- contents were adjusted by adding reagent-grade NaCl.

Results and Discussion

Electrolysis.—Figure 2 shows enrichment of chloride ion in the anolyte with charge passed at various temperatures. Data at 200° and 250°C were omitted, as the diffusion of chloride ion from the anolyte to the catholyte was noticeable, as estimated from separate experiments. Chloride ion concentration increased proportionally to the charge and decreased slightly as the temperature rose, which led to slightly smaller transport numbers with temperature (9).

Figure 3 shows the pH of the anolyte at room temperature after electrolysis at various temperatures. The pH decreased almost logarithmically with charge. The pH of the anolytes electrolyzed at 25°, 50°, and 80°C were the same. However, those above 150°C decreased as the temperature of the electrolysis rose. The anolyte pH of the 0.5N solution electrolyzed at 250°C, showed a limiting value of 1.6 over the range of 13 C/ml. When 0.05N NaCl solution was used, the pH was higher than that of the 0.5N solution. As

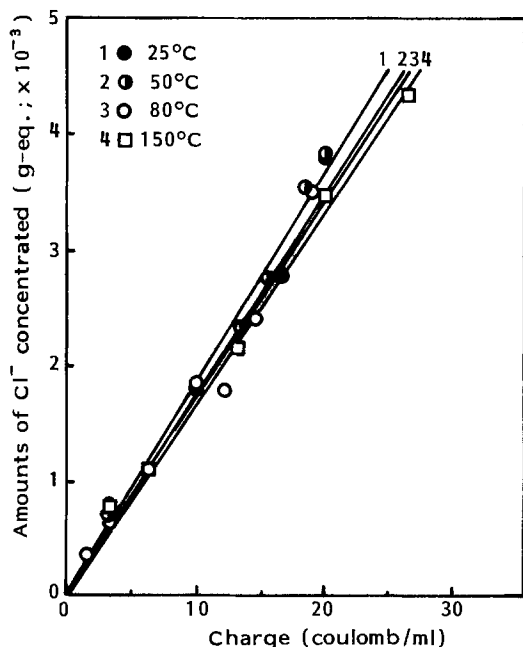


Fig. 2. Enrichment of chloride ion in the anolyte on electrolyzing stainless steel in 0.5N NaCl solution.

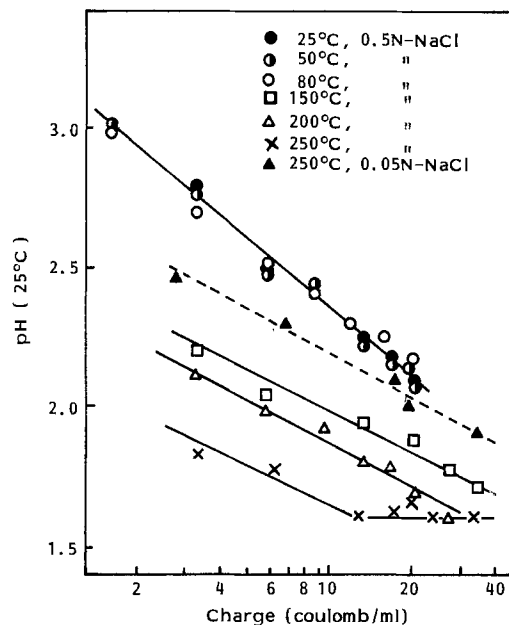


Fig. 3. Anolyte pH values on electrolyzing Type 304 stainless steel in NaCl solution.

for the appearance of the electrolytes and specimens after electrolysis, there were no visible precipitates nor films on specimens for electrolysis below 80°C, whereas there was some precipitate in the anolyte at 150°C, and there were considerable precipitate and hard films on specimens at 200° and 250°C. These films were hard to dissolve even in hot hydrochloric acid.

Figure 4 shows pH changes of the anolytes when they were held at room temperature after electrolysis at various temperatures. Whereas slight pH changes were observed in the anolytes electrolyzed at 80° and 150°C, pH of those electrolyzed at 200° and 250°C scarcely changed. The reason for this will be discussed later.

Table I shows amounts of metal existing in the anolyte and the catholyte after electrolysis equal to a charge of 20 C/ml. During electrolysis at 80°C, most of the dissolved metals existed in the anolyte, and a portion of that diffused into the catholyte through the SiC disk and precipitated there. Results at 25° and 50°C were similar. During electrolysis above 150°C, precipitates formed. As the temperature for the electrolysis increased, much more precipitation occurred. Moreover, at 200° and 250°C, hard films formed on the specimens, as described above.

Figure 5 shows amounts of metal dissolved during electrolysis in 0.5N NaCl solution, expressed as equivalents of Fe^{2+} , Cr^{3+} , and Ni^{2+} , respectively. Bold straight lines are calculated values from quantity of charge. As shown in Fig. 5a, both the measured and calculated values coincide at 150°C. So, it is ascertained that constituents of stainless steel dissolve as Fe^{2+} , Cr^{3+} , and Ni^{2+} in the experimental conditions. Results of electrolysis at 25°, 50°, and 80°C

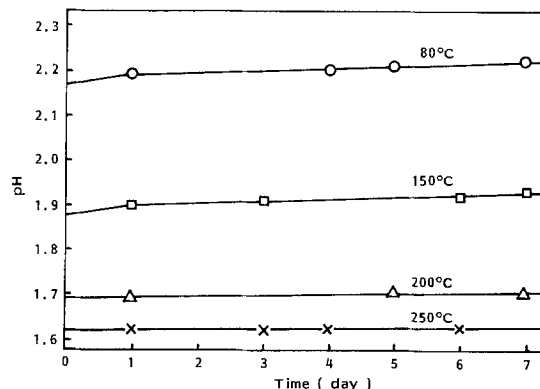


Fig. 4. Effect of time of room temperature on pH of the anolyte electrolyzed at various temperatures.

Table I. Amounts of metal in filtrates and precipitates

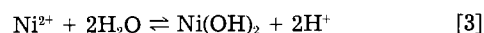
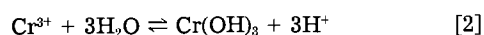
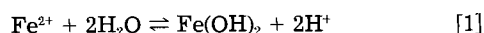
Electrolyte	Temp. (°C)	Fe (mol)		Cr (mol)		Ni (mol)	
		In filtrate	In ppt.	In filtrate	In ppt.	In filtrate	In ppt.
Anolyte	80	2.15×10^{-3}	—	5.3×10^{-4}	—	2.0×10^{-4}	—
	150	1.85×10^{-3}	9×10^{-6}	4.9×10^{-4}	1.9×10^{-5}	2.6×10^{-4}	1×10^{-6}
	200	1.75×10^{-3}	3.3×10^{-4}	4.7×10^{-5}	3.2×10^{-5}	2.9×10^{-4}	3.1×10^{-5}
	250	1.58×10^{-3}	3.4×10^{-4}	3×10^{-7}	6×10^{-6}	2.5×10^{-4}	1.7×10^{-5}
Catholyte	80	—	2.3×10^{-4}	—	3.7×10^{-5}	—	2.4×10^{-5}
	150	—	2.5×10^{-4}	—	1.9×10^{-5}	—	3.6×10^{-5}
	200	—	1.0×10^{-4}	—	1.7×10^{-5}	—	9×10^{-6}
	250	—	2.5×10^{-4}	—	2×10^{-6}	—	4.6×10^{-5}

Charge: 20 C/ml.
0.5N NaCl solution.

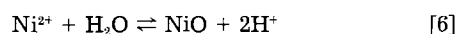
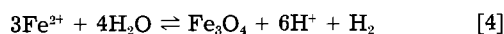
were the same. At 200°C (Fig. 5b), the measured values of Ni almost coincide with the calculated values, those of Fe were a little larger than the latter, but the measured values of Cr were significantly less than the calculated values. At 250°C, the measured values of Ni almost coincide with the calculated ones and the measured values of Fe were larger than the calculated ones up to about 20 C/ml and smaller above 20 C/ml (Fig. 5c). However, Cr was scarcely detected. Similar results were obtained for the 0.05N NaCl solution. From these results, it is assumed that the hard films formed on the specimen at 200° and 250°C contain mainly chromium compounds.

The hard films were removed by immersing the specimens in a boiling alkaline permanganate solution (NaOH 30 + KMnO₄ 2 + H₂O 68 weight percent [w/o]) for 2h, followed by an acidic hydrogen peroxide solution (conc. HNO₃ 25 + 35% H₂O₂ 5 + H₂O 70 w/o) for 3h at 60°C, and the specimens were weighed. A blank weight loss for this treatment was negligible. Figure 6 shows the results for specimens electrolyzed at 200° and 250°C. Whereas weight losses of specimens with film (line B) were smaller than those of the calculated values (line A) from the charges, weight losses after removing the films (line C) were larger. This larger weight loss after removing films might be due to a self-corrosion caused by low pH at the high temperatures.

Hydrolysis of Cr³⁺ solutions.—As for the hydrolysis of metal ions at temperatures below 100°C, there have been many studies (3, 4) connected with localized corrosion. Hydrolysis of metal ions lowers the anolyte pH mainly due to the hydrolysis of Cr³⁺ (reaction) [2]



However, hydrolysis products are oxides or oxyhydroxides in high temperature solutions. In the case of chromium, CrOOH was ascertained, as described later. So, the following equilibria were taken into account, and their equilibrium constants at 150°, 200°, and 250°C were calculated (Table II)



The calculation was conducted utilizing Criss and Cobble's entropy correspondence principle. The free energies and entropies for the substances were taken, whenever possible, from Latimer's and Pourbaix's compilations (10, 11). The heat capacities were taken from Kelley (12) and from Wicks and Block (13). The data for CrOOH, which was not available in these compilations, was taken from Lee's estimation (14). From the table, it is ascertained that the main factor of decreasing pH is the hydrolysis of Cr³⁺.

As the next step to understanding the pH changes of the anolyte, the hydrolysis of Cr³⁺ solutions was examined experimentally. Figure 7 shows the pH and the chromium

contents of the filtrates taken from the hydrolyzed 3.3×10^{-2} mol/liter Cr³⁺ solutions with various amounts of Cl⁻. As the temperature of hydrolysis increased, the pH of the filtrates decreased. As the Cl⁻ concentration increased, the pH of the filtrates treated at 200° and 250°C decreased, whereas the pH at 150°C increased. So, the differences of pH of the solutions treated at 150° and 250°C were larger in the more concentrated Cl⁻ solution. Chromium contents of the filtrates decreased with the temperature of hydrolysis and increased with the Cl⁻ concentration. In the case of 150°C and 3 mol/liter Cl⁻ concentration, the most chromium in the initial solution was found in the filtrate. But, the pH of the filtrate was 1.55, and this meant that the most of Cr³⁺ had hydrolyzed.

Figure 8 shows x-ray diffraction patterns of the precipitates. The precipitate obtained at 250°C was identified as CrOOH, while those at 200° and 150°C were amorphous. Infrared absorption spectra of the precipitates showed an absorption maximum at 3400 cm⁻¹ due to OH groups.

Figure 9 shows weight losses of the precipitates during thermogravimetric analysis. When the precipitates were heated to 500°C in an argon atmosphere, all of them gave Cr₂O₃. Assuming that the weight losses on heating were due to vaporization of water, repeated measurements showed that compositions of the precipitates obtained at 150°, 200°, and 250°C were CrOOH · (0-0.5)H₂O, CrOOH · (1-1.5)H₂O, and CrOOH · (1.5-2)H₂O, respectively.

Absorption spectra in the ultraviolet and visible region showed that the dissolved Cr³⁺ in the filtrate treated at high temperature existed as [Cr(H₂O)₆]³⁺, while those in the original solution as [Cr(H₂O)₆Cl₂]⁺ (15).

As the compositions of precipitates formed from hydrolysis of Cr³⁺ solutions were examined, the weight losses of the specimens with films in Fig. 6 were evaluated and compared with the measured values. Line D in Fig. 6b and lines E and F in Fig. 6a show weight losses of the specimens with film calculated from the lines C, assuming the film compositions as CrOOH, CrOOH · H₂O, and CrOOH · 2H₂O, respectively. As line B in Fig. 6a exists between line E and F and that in Fig. 6b near line D, it is assumed that the film formed at 250°C is composed of CrOOH with little or no water, and that formed at 200°C is CrOOH with one to two water molecules. These agree with the compositions of precipitates from Cr³⁺ solutions.

During electrolysis at 200° and 250°C, self-corrosion of the specimens was suggested to occur. Then, additional dissolution of Fe and Ni was calculated from weight loss due to the self-corrosion, the differences between lines A and C in Fig. 6, and the total dissolved Fe are shown as fine lines in Fig. 5b and 5c. In the case of Ni, the correc-

Table II. Equilibrium constants for the reactions [4]-[6]

Reaction	Temp. (°C)		
	150	200	250
[4]	2×10^{-19}	6×10^{-16}	4×10^{-14}
[5]	4.5	3×10	1.5×10^2
[6]	1×10^{-7}	2×10^{-6}	2×10^{-5}

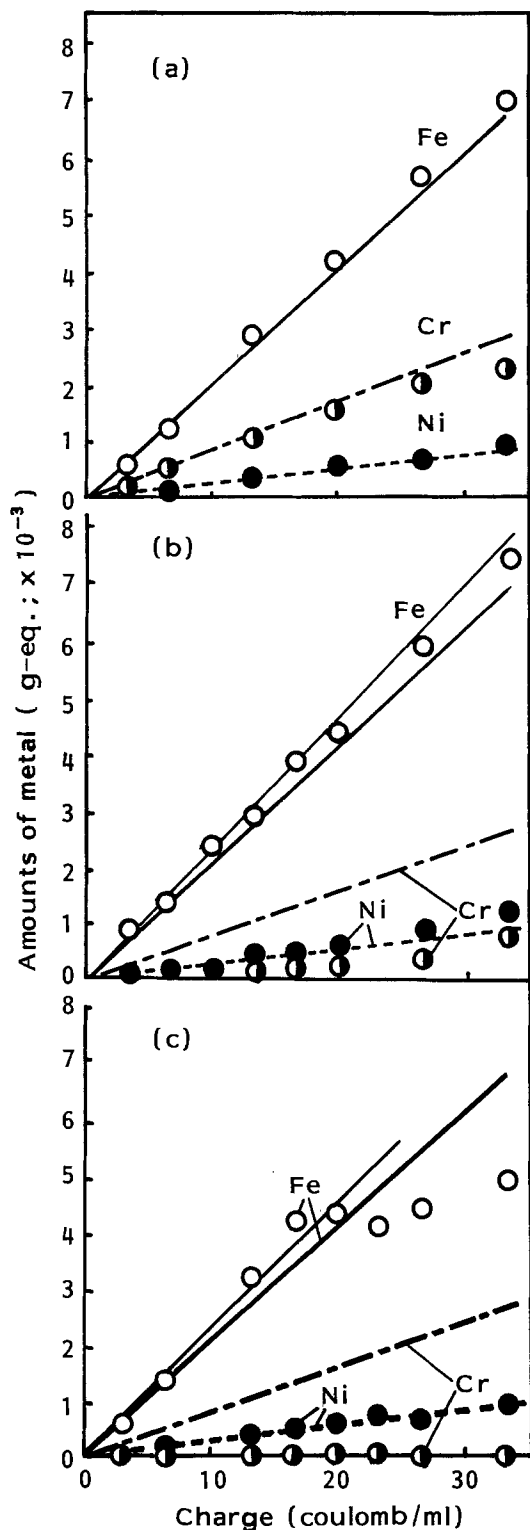


Fig. 5. Amounts of metal in solution after electrolyzing Type 304 stainless steel anode at (a) 150°, (b) 200°, and (c) 250°C in 0.5N NaCl solution (symbols are measured values plotted as Fe^{2+} , Cr^{3+} , and Ni^{2+} , bold lines are calculated values from the charges, and fine lines are calculated values of Fe corrected for self-corrosion).

tions were negligible. The results support the above assumption except for charges greater than 20 C/ml in Fig. 5c, where a part of the dissolved Fe might precipitate.

According to the knowledge of coordination chemistry (16), Cr^{3+} ion in aqueous solution forms aquo complexes and tends to hydrolyze and polymerize. Forms of complex in chloride media at room temperature are $[\text{Cr}(\text{H}_2\text{O})_6]^{3+}$, $[\text{Cr}(\text{H}_2\text{O})_5\text{Cl}]^{2+}$, and $[\text{Cr}(\text{H}_2\text{O})_4\text{Cl}_2]^+$, depending on the chloride concentration and history of the solution. The aquo complexes hydrolyze, behaving as acid like

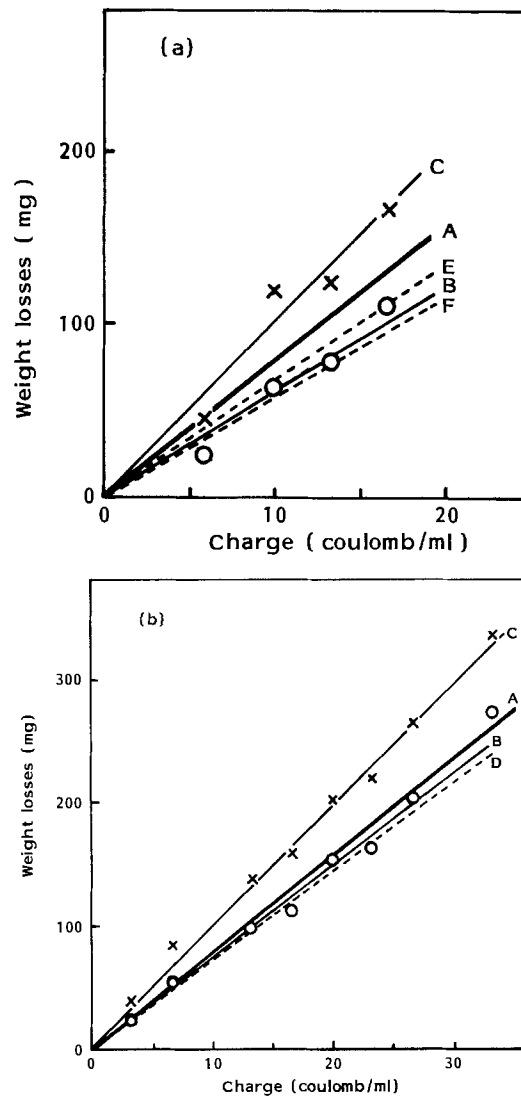
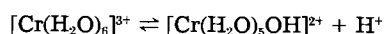
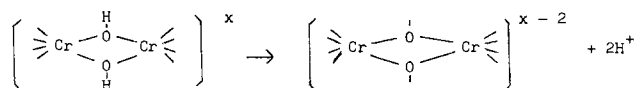


Fig. 6. Weight losses of specimens electrolyzed in 0.5N NaCl solution at (a) 200°C and (b) 250°C: \circ : Measured values with film; \times : Measured values without film. Line A: Calculated value from the charge as Fe^{2+} , Cr^{3+} , and Ni^{2+} . Line B: Fitted line for the measured values with film (\circ). Line C: Fitted line for the measured values without film (\times). Line D, E, and F: Assumed values with film composed of CrOOH , $\text{CrOOH} \cdot \text{H}_2\text{O}$, and $\text{CrOOH} \cdot 2\text{H}_2\text{O}$, respectively.

Heating shifts the equilibrium to the right, and more of the coordinated water molecules are converted to OH^- groups. Here, ololation and oxolation occur, resulting in formation of polynuclear complexes consisting of chains or rings of $\text{Cr}(\text{III})$ ions connected by bridging OH and O^- groups. Oxolation gives protons like



The ultimate consequences of ololation and oxolation are the formation of colloids and precipitates. Continued heating brings a remarkable decrease in reactivity of the colloids and precipitates.

This knowledge about aquo complexes is well suited to the observations in this study. The experimental results show that increasing temperature up to 250°C accelerates hydrolysis and polymerization, resulting in lower pH and more precipitates. The same phenomena were also observed for nickel and other metals (17). Acceleration of the hydrolysis of aquo complexes at high temperature is related to changes in the physical properties of water, and the most important change is the decrease of the dielectric constant (18).

Experimental results show that ololation or oxolation is inhibited in concentrated Cl^- media. Nevertheless, the

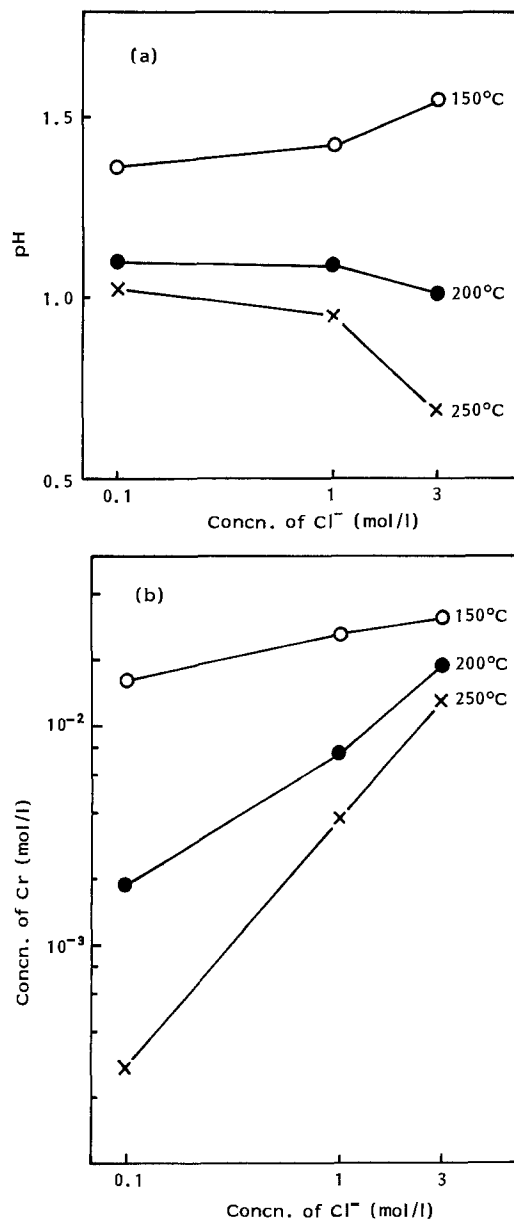


Fig. 7. pH (a) and Cr content (b) of the filtrates on hydrolyzing Cr^{3+} solutions at various temperatures. Initial concentration of Cr^{3+} : 3.3×10^{-2} mol/l.

pH of the filtrates is low. Generally, activity coefficients of H^+ are larger in concentrated Cl^- media, but those in 0.5N NaCl solution are not so large compared to those in 0.05N NaCl solution (19). The reason for such low pH in the concentrated Cl^- filtrate is not clear at present; further fundamental studies are needed.

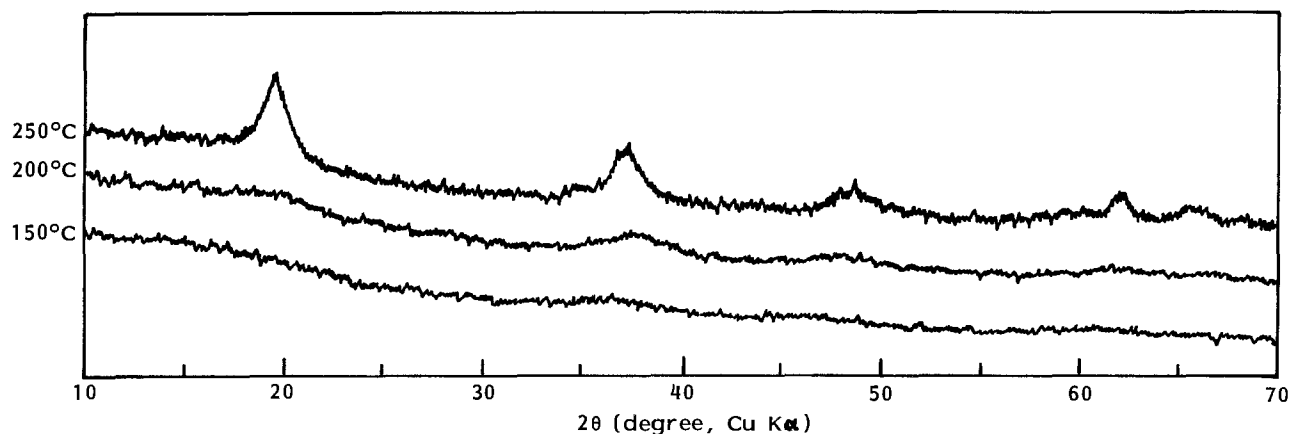


Fig. 8. X-ray diffraction patterns of precipitates

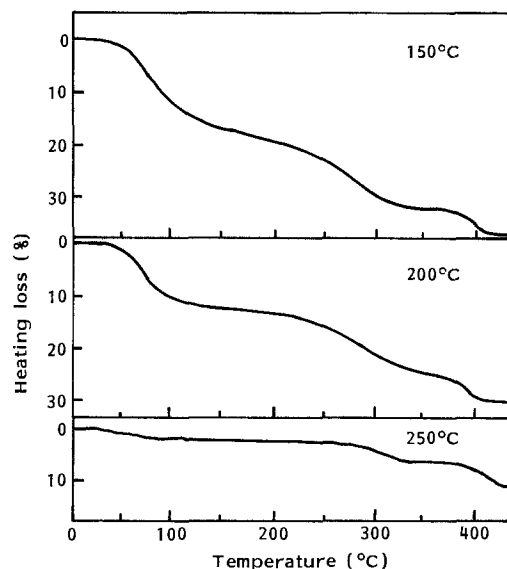


Fig. 9. Thermogravimetric analysis curves

Finally, the lower pH values of the anolyte electrolyzed at higher temperature (Fig. 3) are brought about by the accelerated hydrolysis and oxolation described above. When most Cr^{3+} ion is hydrolyzed and the activity coefficient of H^+ is constant with varying Cl^- concentration, the slope of pH against the log of charge should be -1 . Smaller slopes at higher temperature would be due to retardations of the hydrolysis in concentrated Cl^- solution, diffusion of H^+ into the cathodic compartment through the SiC disk during electrolysis and cooling, and consumption of H^+ by the local corrosion.

Conclusions

When Type 304 stainless steel specimens were electrolyzed anodically, the pH of the anolyte decreased with charge passed. As the temperature of electrolysis increased in the range above 150°C, lower pH values and more precipitates were obtained, and hard films were formed on the specimens at 200° and 250°C. The films were mainly composed of the hydrolysis product of chromium, CrOOH , which was the main factor for lowering the pH. During electrolysis at 250°C, lower pH values were obtained in concentrated Cl^- solution. These pH changes of the anolyte were well described with the experimental results of hydrolysis of Cr^{3+} solution. Heating of Cr^{3+} solutions at high temperatures accelerates hydrolysis and polymerization and brings low pH values.

Acknowledgments

The authors would like to thank Mr. S. Ishizuka, Mr. M. Keta, and Mr. S. Oikawa for helpful calculations and measurements and Mr. K. Nakamura of Hitachi Limited for providing the SiC disks used in this study.

Manuscript submitted Sept. 13, 1983; revised manuscript received July 19, 1984. This was Paper 69 presented at the Detroit, Michigan, Meeting of the Society, Oct. 17-21, 1982.

Iwate University assisted in meeting the publication costs of this article.

REFERENCES

1. Y. H. Lee, Z. Takehara, and S. Yoshizawa, *Corros. Sci.*, **21**, 391 (1981).
2. J. Mankowski and Z. S. Smialowska, *ibid.*, **15**, 493 (1975).
3. T. Suzuki, M. Yamabe, and K. Kitamura, *Corrosion*, **29**, 18 (1973).
4. H. Ogawa, M. Nakata, I. Ito, Y. Hosoi, and H. Okada, *Tetsu to Ko*, (*Iron and Steel, Japan*), **66**, 1385 (1980).
5. D. F. Taylor, *Corrosion*, **35**, 550 (1979).
6. D. F. Taylor and M. Silverman, *ibid.*, **36**, 447 (1980).
7. D. F. Taylor and M. Silverman, *ibid.*, **36**, 544 (1980).
8. D. F. Taylor and C. A. Caramihas, *This Journal*, **129**, 2458 (1982).
9. H. S. Harned and B. B. Owen, "The Physical Chemistry of Electrolyte Solutions," Reinhold, New York (1958).
10. W. M. Latimer, "Oxidation Potentials," p. 245, Prentice-Hall, Inc., New York (1952).
11. M. Pourbaix, "Atlas of Electrochemical Equilibria in Aqueous Solutions," p. 256, NACE, Houston, TX (1974).
12. K. K. Kelley, "Contributions to the Data on Theoretical Metallurgy XIII," U.S. Bureau of Mines Bulletin 584, U.S. Government Printing Office, Washington, DC (1960).
13. C. E. Wicks and F. E. Block, "Thermodynamic Properties of 65 Elements," U.S. Bureau of Mines Bulletin 605, U.S. Government Printing Office, Washington, D.C. (1963).
14. J. B. Lee, *Corrosion*, **37**, 467 (1981).
15. P. J. Elving and B. Zemel, *J. Am. Chem. Soc.*, **79**, 1281 (1957).
16. J. C. Bailar, H. J. Emeléus, R. Nyholm, and A. F. Trotman-Dickenson, "Comprehensive Inorganic Chemistry," Vol. 3, p. 666, Pergamon Press, New York (1973).
17. N. M. Nikolaeva, in "High Temperature High Pressure Electrochemistry in Aqueous Solutions," R. W. Staehle, D. de G. Jones, and J. E. Slater, Editors, p. 146, NACE, Houston, TX (1973).
18. R. C. Murray, Jr. and J. W. Cobble, in "Proceedings of the 41st International Water Conference," A. F. McClure and Y. Solomon, Editors, p. 295, Pittsburgh, PA (1980).
19. M. Takahashi, *Bōshokugijutsu (Corros. Eng. Jpn.)*, **21**, 199 (1982).

Nonlinear Current Response of Electrochemical Systems

Martin W. Kendig*

Rockwell International Science Center, Thousand Oaks, California 91360

ABSTRACT

Laplace analysis of the electrochemical response of an iron electrode in 1.0N H₂SO₄ containing 20 mM propargylic alcohol demonstrates the existence of a discontinuity in the potential at the inner Helmholtz plane (IHP) as a function of applied potential. This result is consistent with previous results reported by Lorenz and Mansfeld and demonstrates the utility of Laplace analysis for evaluating systems where adsorbed species give rise to discontinuous behavior of the effective potential at the IHP due to shielding by the adsorbed phase.

The Laplace transform of a current responding to an applied potential pulse can provide the frequency dependence of the electrochemical impedance (1), a function useful for the analysis of electrochemical kinetics. The Laplace transform is an integral transformation which takes a function of time into the frequency domain. The ratio of the Laplace transform of potential to that of the current, $\Delta E(s)/\Delta I(s)$, defines the frequency dependent electrochemical impedance $Z(s)$ by substituting $j\omega$ for the Laplace variable, s , where ω is the frequency (radian/s) and $j^2 = -1$. The assumptions involved in the definition of impedance include the assumption of causality and the assumption of linearity (2). Causality implies a cause and effect relationship between the respective current and potential variations ΔE and ΔI , and linearity requires the current transient, $\Delta I(t)$, to be proportional to the amplitude of the applied potential step. Electrochemical systems can meet these criteria for most cases through the careful control of experimental conditions. However, in the case of iron in dilute sulfuric acid containing propargylic alcohol (PGA) the current-potential behavior remains nonlinear down to very low potentials, as correctly analyzed by Lorenz and Mansfeld (3). Despite this presence of fundamental nonlinearities in certain electrochemical systems, transform analysis can provide a means for characterizing the electrochemical kinetics. Using this approach, the system iron in 1N H₂SO₄ containing 20 mM PGA has been analyzed to give details of the interfacial structure responsible for the nonlinear response.

Theoretical Considerations

In general, nonlinear current vs. potential behavior results from the fact that the free energy of activation for an

elementary charge-transfer process is proportional to the applied potential. Hence, the current varies exponentially with potential. This nonlinearity can always be excluded by using an appropriately small ΔE (< 10 mV) and is not the subject of this discussion. However, the existence of stored charge or the dielectric shielding of interfacial charge at the interface, produced by irreversible electro-sorption, can cause a discontinuity in the effective potential seen by the electroactive species at the inner Helmholtz plane (IHP) as a function of applied potential. Specific adsorption of molecular dipoles or ions can increase or decrease the potential of the IHP virtually independently of the electrode potential relative to a reference electrode (4). Such is the case of electrocrystallization when a sharp change in overvoltage occurs upon conversion of a surface phase (5). The anomalous dissolution of metals at cathodic potentials has been attributed to modification of the potential at the IHP due to shielding by adsorbed surface complexes (6). The model proposed here for this effect (Fig. 1) places an internal potential source, E_i , in series with the faradaic charge transfer resistance, R , and capacitance of the double layer, C . Usually E_i is insignificant or varies weakly with the applied potential, E , such that the potential fluctuation across R and C resulting from the external application of ΔE is identical, or at least varies linearly with ΔE . However, in the case that the potential at the IHP, that is, the internal potential E_i , contains a discontinuity at the potential E_0 where the pulse, ΔE , is applied as schematically shown in Fig. 1, a nonlinear ΔI vs. ΔE relationship follows. A discontinuity in the potential seen at the IHP as a function of electrode potential can lead to the apparent existence of a multiplicity of steady states (MSS) due to metastability resulting from a slow time dependence for the adsorption-desorption behavior which would extend the current

*Electrochemical Society Active Member.

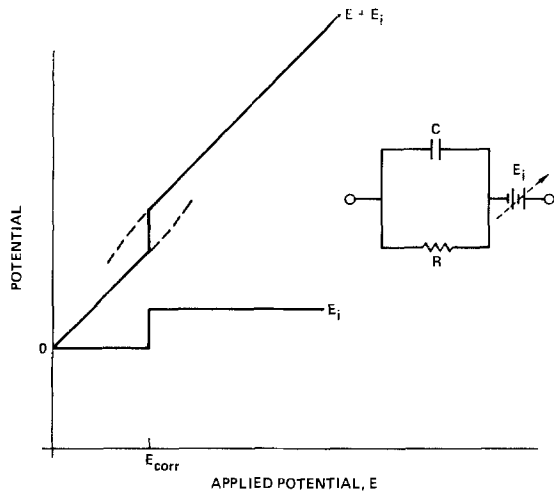


Fig. 1. Schematic for an electrochemical interface containing a discontinuity at the IHP as a function of applied potential.

voltage response along the dotted lines in Fig. 1. Analogous discontinuities in the potential at the IHP can also occur as a function of the chemical potential of surfactants where $\mu = \mu^0 + RT \ln a_s$, where a_s is the activity of the surfactant in the bulk solution. For example, discontinuities in the potential at the IHP as a function of inhibitor concentration can give rise to catastrophic transitions from one level of corrosion rate to the other across the discontinuity. These catastrophic transitions can occur as a function of time or location on the electrode surface and will cause the noted scatter in observed corrosion rates (7) or pitting (8), respectively. Sato uses a model containing a discontinuity in the IHP to explain passivity (9).

An electrochemical system with a discontinuity in the potential seen at the IHP influences the observed impedance behavior (3). The quantitative height of the discontinuity can be discerned, however, through Laplace analysis of the current responding to positive and negative pulses at E_0 across the discontinuity (Fig. 1). The analysis produces an observed effective impedance, $Z^{eff}(s)$ describing the electrochemical response, which provides a means for determining the magnitude of the discontinuity. Unlike a true impedance, $Z^{eff}(s)$ depends on the magnitude, ΔE , of the potential step.

An expression for $Z^{eff}(s)$ may be written in closed form, provided the contribution of ΔE_i to the total potential fluctuation ($\Delta E + \Delta E_i$), across the R and C takes an assumed time dependence. The transformation from the one state to the other at the discontinuity is assumed to result from a first-order process. Thus, upon stepping ΔE across the discontinuity (Fig. 1), $\Delta E_i(t)$ is assumed to take the following form

$$\Delta E_i(t) = E_i(1 - e^{-kt}) \quad [1]$$

The effective impedance $Z^{eff}(s)$ will be by definition $\Delta E(s)/\Delta I(s)$, where $\Delta I(s)$ is the transform of the observed current which flows across the RC network as a result of the application of $\Delta E(t) + \Delta E_i(t)$. Therefore

$$Z^{eff}(s) = \frac{\Delta E(s)}{\Delta I(s)} = \frac{\Delta E(s) Z(s)}{\Delta E(s) + \Delta E_i(s)} \quad [2]$$

where $Z(s)$ is the impedance of the RC network

$$Z(s) = R/(1 + RCs) \quad [3]$$

The Laplace transform of the pulse of amplitude ΔE gives $\Delta E(s)$ equal to $\Delta E/s$. Adding $\Delta E_i(s)$ to the transform of Eq. [1] and including the resulting $\Delta E(s) + \Delta E_i(s)$ into Eq. [2] gives

$$Z^{eff}(s) = \frac{(s + k)R}{\left(s + k\left(1 + \frac{\Delta E_i}{\Delta E}\right)\right)(1 + RCs)} \quad [4]$$

This analysis shows that Z^{eff} depends on ΔE . Furthermore, Z^{eff} has the same functional dependence on frequency as an equivalent circuit containing an inductance in series with a resistance, R, and in parallel with a capacitance, C_p

$$Z_{RLC} = \frac{R + sL}{1 + sC_p R + s^2} = \frac{P_1(s)}{P_2(s)} \quad [5]$$

where $P_n(s)$ is the nth-order polynomial function of s.

Experimental Approach

An iron specimen prepared as described previously (3) was held in a Stern holder and placed in a stagnant air-equilibrated 1N H_2SO_4 + 20 mM PA and allowed to equilibrate for a constant open-circuit potential. A Princeton Applied Research 173 potentiostat with a Model 176 coulometer was used to apply a ± 10 mV step about the corrosion potential. The current response was recorded on a fast responding strip chart recorder or a digital oscilloscope. The potential transform was taken as 0.010 V/s, where $s = -j\omega$ (radian/s), and the current response was estimated using the algorithm of Pilla (1) with the following modification. The Laplace integral between current points that increased with time were obtained by fitting the current-time curve at the interval $\{t_i, t_{i+1}\}$ to a cubic equation

$$I(t) = A_1 + A_2t + A_3t^2 + A_4t^3 \quad [6]$$

Hence, the integral, I_i of the interval

$$I_i = \int_{t_i}^{t_{i+1}} e^{-ts} I(t) dt = \sum_{j=1}^4 I_{ij} \quad [7]$$

could readily be calculated from evaluating the known integrals, I_{ij}

$$I_{ij} = \int_{t_i}^{t_{i+1}} A_j e^{-ts} t^{j+1} dt \quad [8]$$

using an established formula (10). The impedance, $Z(s)$, was calculated then as the transform of $I(t)$ [i.e., $I(s)$] divided by the respective transform of a 10 mV potential step.

Results and Discussion

Figure 2 shows a plot of the Laplace transformed data for a dummy cell consisting of a resistor R_p equal to 10,030 Ω in parallel with a capacitor C_p equal to 3138 μF both in series with a resistor R_s equal to 1002 Ω . The actual values for the impedance elements of the dummy cell were determined by conventional TFA analysis (11). The transformed data (solid circles) are superimposed on the calculated transform for the dummy cell (open circles), which demonstrates the validity of the transform. Significant errors can exist at the highest frequencies as a result of risetime of the potentiostat and current recorder. For this reason, frequencies $> 0.1/t_1$, where t_1 is the first time interval measured, have been ignored.

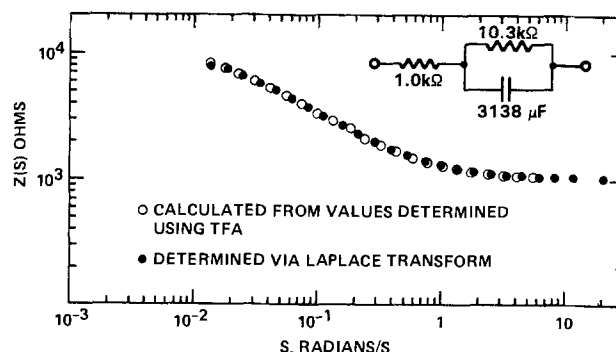


Fig. 2. Comparison of Laplace analysis with the transform calculated from the component values for a dummy cell determined using the TFA.

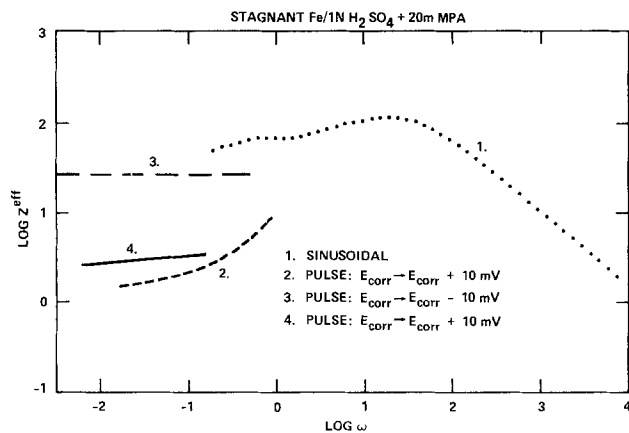


Fig. 3. Laplace transform and TFA impedance data determined for iron in stagnant 1N H_2SO_4 and 20 mM PGA.

The curves in Fig. 3 represent data for the observed impedance, Z^{eff} , of the iron in sulfuric acid-PGA solution. It must first be restated that these are not true impedances owing to the nonlinear nature of the system. As a result, Z^{eff} depends on the mode of measurement. Curve 1, for example, shows the impedance measured using the TFA. The region where the impedance increases with increasing frequency implies an inductive component. The low frequency Laplace transform analysis of the response to a 10 mV anodic potential pulse was obtained by computer analysis of a current transient and appears as curve 2 in Fig. 3. The time response of the recorder limits these data to low frequencies. Curve 2 shows a lower effective dc resistance than that indicated by curve 1. However, the Laplace analysis of a current response to a potential step, $\Delta E = 10$ mV cathodic to E_{corr} , shows no inductive behavior and a dc limit close to that obtained from the ac measurement (curve 3). The response to a second anodic potential pulse at a later time (curve 4) again represents a low dc resistance, but is only slightly higher than the previous response to an anodic pulse (curve 1), showing that there is a slow overall time dependence in the system behavior.

These results clearly indicate that the magnitude of ΔE influences the observed impedance as predicted by the model and observed by Lorenz and Mansfeld (3). The use of ac impedance analysis for inherently nonlinear systems, such as the PGA-inhibited Fe in sulfuric acid system, shows that care must be taken in defining the potential excitation which produces the current response. Despite the fact that true impedance can only result for linear systems, the true impedance R and C can, in principle, be extracted by using Eq. [4]. The effective impedances of 1.37 and 27.6 Ω evaluated for the limit as $s \rightarrow 0$ for $\Delta E = +10$ mV and $\Delta E = -10$ mV, respectively, and Eq. [4] allow calculation of the value for R as 3 $\Omega \cdot cm^2$, and ΔE_i due to the discontinuity as 9 mV. The value for ΔE_i is small, but represents a significant discontinuity since its magnitude compares with the ac modulation of ± 10 mV typically assumed to produce a linear response. A ΔE_i of 9 mV certainly is significant in light of its influence on the dc limits for Z^{eff} , which vary by over a factor of 10 de-

pending on whether the potential is pulsed in the positive or negative direction away from the open-circuit potential. Depending on the proximity of the electrokinetic plane of shear to the IHP, $E_i \cong E - \zeta$, where ζ is the zeta potential (12). Hence $\Delta E_i \cong -\Delta \zeta$. Since zeta potentials typically range between ± 50 mV, a difference of -9 mV represents a significant discontinuity in the zeta potential of the steel surface as a result of inhibitor desorption.

Summary

Electrochemical impedance in highly irreversible and nonlinear systems is not defined. However, the theoretical treatment presented here allows extraction of the true ac impedance from effective impedances obtained from Laplace transform of the current response of nonlinear systems. Furthermore, the model of a system undergoing an irreversible adsorption-desorption predicts an effective impedance containing an inductive component. The effective impedance depends on the amplitude of the applied-potential step. The present discussion explains the inductive behavior previously obtained for the system iron/ H_2SO_4 + PGA. The results are consistent with the presence of a discontinuity in the potential at the IHP of 9 mV as a function of applied electrochemical potential.

Acknowledgments

The author acknowledges support at Brookhaven National Laboratory by DOE for the development of the Laplace transform program used to analyze the data and the Rockwell International Science Center Industrial Research and Development program for support of the experimental work. The author gratefully acknowledges useful discussion with Dr. F. Mansfeld and Professor W. Lorenz.

Manuscript submitted July 25, 1983; revised manuscript received Feb. 24, 1984.

Rockwell International Science Center assisted in meeting the publication costs of this article.

REFERENCES

1. A. Pilla, *This Journal*, **117**, 467 (1979).
2. R. L. VanMeirhaeghe, E. C. Detoit, F. Cardon, and W. P. Gomes, *Electrochim. Acta*, **21**, 39 (1976).
3. W. J. Lorenz and F. Mansfeld, *Corros. Sci.*, **21**, 647 (1981).
4. K. Vetter, "Electrochemical Kinetics," pp. 78-79, Academic Press, New York (1967).
5. M. Fleischman and H. R. Thirsk, in "Advances in Electrochemistry and Electrochemical Engineering," Vol. 3, P. P. Delahay and C. W. Tobias, Editors, p. 123, Interscience, London (1963).
6. R. M. Lazorenko-Manevich and L. A. Sokolava, *Sov. Electrochem.*, **17**, 32 (1981).
7. C. Nathan, *Corrosion*, **14**, 193 (1958).
8. J. Osterwald, in "Corrosion and Corrosion Protection," R. P. Frankenthal and F. Mansfeld, Editors, p. 8, The Electrochemical Society Softbound Proceedings Series, Pennington, NJ (1981).
9. N. Sato, *Rev. Coat. Corros.*, **4**, 195 (1981).
10. Chemical Rubber Co., "Standard Mathematical Tables," 15th ed., S. M. Selby, Editor, p. 387, Eq. 398, CRC Press, Cleveland, OH (1967).
11. F. Mansfeld, *Corrosion*, **37**, 301 (1981).
12. A. Aveyard and D. A. Haydon, "An Introduction to the Principles of Surface Chemistry," Chap. 2, Cambridge University Press, London (1973).

Impedance Model for a Concentrated Solution

Application to the Electrodeposition of Copper in Chloride Solutions

Bernard Tribollet¹ and John Newman*

Department of Chemical Engineering, University of California, Berkeley, California 94720

ABSTRACT

From the Stefan-Maxwell equations, a model has been developed which describes the distribution of concentration of each species in the solution. This model has provision for an arbitrary number of simultaneous homogeneous and heterogeneous reactions and is used to treat the steady state and the impedance of an electrochemical interface. As an example, this method is applied to the anodic dissolution of a rotating disk of copper in chloride solutions.

The rate of many electrochemical processes is governed by the transport of reactant species to the electrode surface by diffusion and convection. The dilute-solution theory has been applied to many electrochemical problems and is adequate for analytic solution. The limits of application for the dilute-solution theory are not really clear, and these limits may be different for the steady state and the nonsteady state. Nevertheless, this theory breaks down in concentrated solution; first of all, because migration and diffusion fluxes must be defined with respect to some average velocity of the fluid, and the flux relations so defined must be consistent with this choice. In a concentrated solution, it is not only the solvent velocity which contributes to the average velocity.

A careful definition of transport properties also requires, except at infinite dilution, the application of the theory for concentrated solutions. In this theory, the dilute flux relation for each solute species is replaced by the multicomponent diffusion equation (1). This last equation involves many parameters, and an analytic solution is too complicated; but, if our aim is a numerical solution, it is possible to consider an analysis which includes variable physical properties and has provision for an arbitrary number of simultaneous homogeneous and heterogeneous reactions. This analysis should be able to deal with the steady state, and it was used with success for modeling silicon deposition on a rotating disk (2). In this paper, we use this model to treat not only the steady state but also the impedance of an electrochemical interface. The comparison of the numerical results from the theory for concentrated solutions with the analytic results from the dilute-solution theory allows one to define clearly the limits of this last theory.

The described method is applied to the anodic dissolution of a rotating disk of copper in chloride solutions. The rotating-disk electrode has been used in this study because the hydrodynamics and mass-transfer characteristics of this system are relatively well understood.

Theoretical Analysis

The multicomponent diffusion equation

$$\frac{c_i \nabla \mu_i}{RT} = \sum_{j \neq i} \frac{c_i c_j}{c D_{ij}} (v_j - v_i) \quad [1]$$

describes the motion of species i relative to the surrounding fluid. In this equation, μ_i is the electrochemical potential of species i and v_i is the velocity of species i (so that the flux density of species i is $N_i = c_i v_i$). The total concentration is $c = \sum_i c_i$, where the sum includes the solvent, and D_{ij} is a diffusion coefficient describing the interaction of species i and j ($D_{ij} = D_{ji}$).

Equation [1] is similar to the Stefan-Maxwell equation (3). By using the mole fraction

$$x_i = \frac{c_i}{c} \quad [2]$$

at constant temperature, the gradient of the electrochemical potential may be defined as

$$\nabla \mu_i = z_i F \nabla \Phi + RT \frac{\nabla x_i}{x_i} \quad [3]$$

where Φ is the electrostatic potential.

For a mixture of n species, the local mass-average velocity v is defined as

$$v = \frac{\sum_i \rho_i v_i}{\sum_i \rho_i} \quad [4]$$

The molar flux relative to the mass-average velocity v is

$$J_i = c_i (v_i - v) \quad [5]$$

With these parameters, the Stefan-Maxwell Eq. [1] becomes

$$x_i \frac{\nabla \mu_i}{RT} = \sum_{j \neq i} \frac{x_i J_j - x_j J_i}{c D_{ij}} \quad [6]$$

The number of independent equations with the form of Eq. [6] is one less than the number of species. If we consider the relation among the molar fluxes

$$\sum_i M_i J_i = 0 \quad [7]$$

we have a set of n equations which can be written in a matrix form

$$\frac{1}{RT} \begin{pmatrix} 0 \\ x_2 \nabla \mu_2 \\ \vdots \\ x_1 \nabla \mu_1 \\ \vdots \\ x_n \nabla \mu_n \end{pmatrix} = \begin{pmatrix} M_1 & \dots & M_k & \dots & M_n \\ \frac{x_2}{c D_{21}} - \sum_{j \neq 2} \frac{x_j}{c D_{2j}} & \dots & \frac{x_2}{c D_{2k}} & \dots & \frac{x_2}{c D_{2n}} \\ \vdots & & \vdots & & \vdots \\ \frac{x_1}{c D_{11}} & \dots & - \sum_{j \neq 1} \frac{x_j}{c D_{1k}} & \dots & \frac{x_1}{c D_{1n}} \\ \vdots & & \vdots & & \vdots \\ \frac{x_n}{c D_{n1}} & \dots & \frac{x_n}{c D_{nk}} - \sum_{j \neq n} \frac{x_j}{c D_{nj}} & \dots & \frac{x_n}{c D_{nn}} \end{pmatrix} \begin{pmatrix} J_1 \\ \vdots \\ J_k \\ \vdots \\ J_n \end{pmatrix} \quad [8]$$

or

$$\frac{1}{RT} x \nabla \mu = \underline{b} J \quad [9]$$

The material balance is described by

*Electrochemical Society Active Member.
¹Present address: Groupe de Recherche number 4 du CNRS, "Physique des Liquides et Electrochimie," associé à l'Université Pierre et Marie Curie, 75230 Paris Cedex 05, France.

$$\nabla \cdot J_i = \sum_l R_{i,l} - \nabla \cdot (vc_i) - \frac{\partial c_i}{\partial t} \quad [10]$$

$R_{i,l}$ is the net rate of production of species i by reaction l ; it is regarded as the difference between the rates of forward and backward rates and can be presented as

$$R_{i,l} = k_{if} \prod_j x_j^{\nu_{ji}} - k_{ib} \prod_j x_j^{-\nu_{ji}} \quad [11]$$

where k_{if} and k_{ib} are the rate constants for forward and backward reactions, respectively. The first product (Π) is over reactants ($\nu_{ji} > 0$) and the second product (Π) is over product species ($\nu_{ji} < 0$).

The law of conservation of mass can be expressed as (1)

$$\frac{\partial \rho}{\partial t} = - \nabla \cdot (\rho v)$$

When the density is constant in space and time, this expression reduces to

$$\nabla \cdot v = 0$$

This is frequently an adequate approximation for dilute liquid solutions. A solution without this approximation may be obtained, but it would be necessary to solve the Navier-Stokes equations and the conservation of mass equation together with the Stefan-Maxwell equations.

The inverse of Eq. [8] and so the flux expression is

$$J_i = \sum_{k=2}^n b_{ik}^{-1} \left(\nabla x_k + \frac{z_k F}{RT} x_k \nabla \Phi \right) \quad [12]$$

The divergence of the Stefan-Maxwell Eq. [6] is

$$\begin{aligned} \nabla^2 x_i + \frac{z_i F}{RT} \nabla x_i \cdot \nabla \Phi + \frac{z_i F}{RT} x_i \nabla^2 \Phi \\ = \sum_{j \neq i} \nabla \left(\frac{x_j}{cD_{ij}} \right) \cdot J_j - \nabla \left(\frac{x_j}{cD_{ij}} \right) \cdot J_i \\ + \sum_{j \neq i} \frac{x_j \nabla \cdot J_j - x_j \nabla \cdot J_i}{cD_{ij}} \end{aligned} \quad [13]$$

Since $\nabla \cdot J_i$ and J_i are given by Eq. [10] and [12], Eq. [13] becomes

$$\begin{aligned} \nabla^2 x_i + \frac{z_i F}{RT} \nabla x_i \cdot \nabla \Phi + \frac{z_i F}{RT} x_i \nabla^2 \Phi \\ - \sum_{j \neq i} \frac{x_j \sum_l R_{jl} - x_j \sum_l R_{il}}{cD_{ij}} + cv \cdot \sum_{j \neq i} \frac{x_j \nabla x_j - x_j \nabla x_i}{cD_{ij}} \\ + c \sum_{j \neq i} \frac{x_j \frac{\partial x_j}{\partial t} - x_j \frac{\partial x_i}{\partial t}}{cD_{ij}} - \sum_{j \neq i} \nabla \left(\frac{x_j}{cD_{ij}} \right) \\ \cdot \sum_{k=2}^n b_{jk}^{-1} \left(\nabla x_k + \frac{z_k F}{RT} x_k \nabla \Phi \right) \\ + \sum_{j \neq i} \nabla \left(\frac{x_j}{cD_{ij}} \right) \cdot \sum_{k=2}^n b_{ik}^{-1} \left[\nabla x_k + \frac{z_k F}{RT} x_k \nabla \Phi \right] = 0 \end{aligned} \quad [14]$$

The concentration dependence of D_{ij} may be taken into account in Eq. [14], if we know the concentration-dependence expression.

The relationship among the mole fractions is

$$\sum_i x_i = 1 \quad [15]$$

and the equation of electroneutrality is

$$\sum_i z_i x_i = 0 \quad [16]$$

With $n - 1$ equations of the form of Eq. [14] plus these two equations, we have a set of $(n + 1)$ equations with $(n + 1)$ unknowns (n mole fractions and Φ , the electrostatic potential). This set may be resolved with the corresponding boundary conditions set forth below.

1. Far from the disk, the composition approaches that of the bulk fluid, equilibrated with respect to homogeneous reactions.

2. At the interface, one or more heterogeneous reactions occur. A single-electrode reaction can be written in symbolic form as



Then the flux of a species is related to the partial current densities related to these heterogeneous reactions

$$J_i = - \sum_l \frac{s_{i,l}}{n_i F} i_l \quad [18]$$

and the total electrode current density is the sum of partial current densities ($i = \sum_l i_l$).

At the interface, Eq. [6] becomes

$$\begin{aligned} \nabla x_i = - \frac{z_i F}{RT} x_i \nabla \Phi \\ - \sum_{j \neq i} \frac{x_j \sum_l \frac{s_{j,l}}{n_j F} i_l - x_j \sum_l \frac{s_{i,l}}{n_i F} i_l}{cD_{ij}} \end{aligned} \quad [19]$$

The partial current densities can be expressed by the kinetic equation

$$\begin{aligned} \frac{i_l}{n_l F} = k_{al} \exp \left[\frac{(1 - \beta_l) n_l F}{RT} V \right] \prod_i x_i^{s_{i,l}} \\ - k_{cl} \exp \left[- \frac{\beta_l n_l F}{RT} V \right] \prod_i x_i^{-s_{i,l}} \end{aligned} \quad [20]$$

Again, the first product (Π) is for anodic reactants ($s_{i,l} > 0$ for $n_l > 0$), and the second product (Π) is for cathodic reactants ($s_{i,l} < 0$). Nonelectrochemical, heterogeneous reactions can be described similarly, but with no potential dependence and with $i_l/n_l F$ replaced by the rate of the heterogeneous reaction (in Eq. [18] as well as [20]).

At the electrode, $(n - 1)$ Stefan-Maxwell relations (Eq. [19]) are used together with the relationship between mole fractions (Eq. [15]) and the electroneutrality equation (Eq. [16]) in order to obtain $(n + 1)$ boundary conditions at the interface.

The steady-state solution may be obtained with $\partial x_i / \partial t = 0$. Then the transient solution may be obtained from the steady-state solution for a sinusoidal perturbation. If the amplitude of perturbation is low enough, each mole fraction may be written as

$$x_i = \bar{x}_i + \text{Re} \{ \tilde{x}_i \exp(j\omega t) \} \quad [21]$$

where \bar{x}_i is the steady-state solution and \tilde{x}_i is a complex function of distance from the disk.

By the same way the current and potential may be written as

$$i = \bar{i} + \text{Re} \{ \tilde{i} \exp(j\omega t) \} \quad [22]$$

$$V = \bar{V} + \text{Re} \{ \tilde{V} \exp(j\omega t) \} \quad [23]$$

The expression of the electrochemical impedance is independent of the choice of the regulation

$$\tilde{i} = \sum_l \tilde{i}_l \quad [24]$$

At the interface, Eq. [19] becomes

$$\begin{aligned} \nabla \bar{x}_i &= -\frac{z_i \mathbf{F}}{RT} \bar{x}_i \nabla \Phi - \frac{z_i \mathbf{F}}{RT} \bar{x}_i \nabla \phi \\ &- \sum_{j \neq i} \frac{\bar{x}_i \sum_l \frac{s_{j,l}}{n_l \mathbf{F}} \bar{i}_l - \bar{x}_j \sum_l \frac{s_{i,l}}{n_l \mathbf{F}} \bar{i}_l}{c D_{ij}} \\ &- \sum_{j \neq i} \frac{\bar{x}_j \sum_l \frac{s_{j,l}}{n_l \mathbf{F}} \bar{i}_l - \bar{x}_i \sum_l \frac{s_{i,l}}{n_l \mathbf{F}} \bar{i}_l}{c D_{ij}} \end{aligned} \quad [25]$$

For the nonsteady solution, with $2(n-1)$ equations of the form of Eq. [14] plus two equations of the form of Eq. [15] and two of the form of Eq. [16], we have a set of $2(n+1)$ real equations and two $(n+1)$ unknowns [$(n+1)$ for the real components and $(n+1)$ for the imaginary components]. This set may be resolved with the corresponding boundary conditions: (i) far from the disk, each concentration tends towards zero, and (ii) at the interface, $2(n-1)$ Stefan-Maxwell relations (Eq. [25]) are used together with the two relationships between mole fractions (Eq. [15]) and two electroneutrality equations (Eq. [16]).

The electrochemical impedance is defined as

$$Z = \frac{\bar{v}}{\bar{i}} = \frac{\bar{v}}{\sum_l \bar{i}_l} \quad [26]$$

From Eq. [20]

$$\bar{i}_l = n_l \mathbf{F} k_{al}$$

$$\begin{aligned} &\exp \left[\frac{(1-\beta) n_l \mathbf{F}}{RT} \bar{v} \right] \sum_l \left(s_{i,l} \bar{x}_i^{s_{i,l}-1} \bar{x}_i \prod_{j \neq i} \bar{x}_j \right) \\ &- n_l \mathbf{F} k_{cl} \exp \left[-\frac{\beta n_l \mathbf{F}}{RT} \bar{v} \right] \\ &\sum_l \left(-s_{i,l} \bar{x}_i^{-s_{i,l}-1} \bar{x}_i \prod_{j \neq i} \bar{x}_j \right) + R_{t,l}^{-1} \bar{v} \end{aligned} \quad [27]$$

with

$$R_{t,l}^{-1} = \sum_l R_{t,l}^{-1} \quad [28]$$

and

$$\begin{aligned} \frac{R_{t,l}^{-1}}{n_l \mathbf{F}} &= \frac{(1-\beta) n_l \mathbf{F}}{RT} k_{al} \\ &\exp \left[\frac{(1-\beta) n_l \mathbf{F}}{RT} \bar{v} \right] \prod_l \bar{x}_i^{s_{i,l}} \\ &+ \frac{\beta n_l \mathbf{F}}{RT} k_{cl} \exp \left[-\frac{\beta n_l \mathbf{F}}{RT} \bar{v} \right] \prod_l \bar{x}_i^{-s_{i,l}} \end{aligned} \quad [29]$$

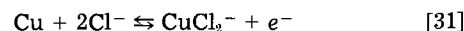
Then

$$\begin{aligned} Z &= R_t - \frac{R_t}{\bar{i}} \sum_l \left(n_l \mathbf{F} k_{al} \exp \left[\frac{(1-\beta) n_l \mathbf{F}}{RT} \bar{v} \right] \right. \\ &\quad \left. \sum_l (s_{i,l} \bar{x}_i^{s_{i,l}-1} \bar{x}_i \prod_{j \neq i} \bar{x}_j) - n_l \mathbf{F} k_{cl} \right. \\ &\quad \left. \exp \left[-\frac{\beta n_l \mathbf{F}}{RT} \bar{v} \right] \sum_l \left(-s_{i,l} \bar{x}_i^{-s_{i,l}-1} \bar{x}_i \prod_{j \neq i} \bar{x}_j \right) \right) \end{aligned} \quad [30]$$

Anodic dissolution of copper in chloride solutions.—At low current densities and for Cl^- concentration higher than 0.05M, copper dissolves anodically in acidic chloride

solution to form CuCl_2^- (4, 5). At high current densities, a mechanism involving the formation of CuCl and dissolution of this precipitate with the diffusion of CuCl_2^- has been suggested (5, 6). In this paper, we consider the case of low current densities for which there is a good agreement among the published experimental data (4-8); and we compare the results from the two models: infinitely dilute solution and concentrated solution.

Steady state



With this electrochemical reaction, Eq. [20] may be written as

$$\begin{aligned} \frac{i}{\mathbf{F}} &= k_a c_{\text{Cl}^-} \exp \left[\frac{(1-\beta) \mathbf{F}}{RT} V \right] \\ &- k_c c_{\text{CuCl}_2^-} \exp \left[-\frac{\beta \mathbf{F}}{RT} V \right] \end{aligned} \quad [32]$$

In the infinite dilution theory

$$\frac{i}{\mathbf{F}} = \frac{D_{\text{CuCl}_2^-}}{\delta_{\text{CuCl}_2^-}} (c_{\text{CuCl}_2^-} - c_{\text{CuCl}_2^-, \infty}) \quad [33]$$

$$\frac{i}{\mathbf{F}} = \frac{1}{2} \frac{D_{\text{Cl}^-}}{\delta_{\text{Cl}^-}} (c_{\text{Cl}^-} - c_{\text{Cl}^-, \infty}) \quad [34]$$

The expression of the current density may be obtained by solving this set of Eq. [32], [33], [34]. With the assumptions: $c_{\text{CuCl}_2^-, \infty} = 0$ and $c_{\text{Cl}^-, \infty} = c_{\text{Cl}^-}$, this expression is

$$\frac{i}{\mathbf{F}} = \frac{k_a c_{\text{Cl}^-} \exp \left\{ \frac{\beta \mathbf{F}}{RT} V \right\}}{1 + \frac{\delta_{\text{CuCl}_2^-}}{D_{\text{CuCl}_2^-}} k_c \exp \left\{ -\frac{(1-\beta) \mathbf{F}}{RT} V \right\}} \quad [35]$$

For the low rotation speeds

$$\frac{\delta_{\text{CuCl}_2^-}}{D_{\text{CuCl}_2^-}} k_c \exp \left\{ -\frac{(1-\beta) \mathbf{F}}{RT} V \right\} \gg 1 \quad [36]$$

and then

$$\frac{i}{\mathbf{F}} = \frac{D_{\text{CuCl}_2^-}}{\delta_{\text{CuCl}_2^-}} \frac{k_a}{k_c} c_{\text{Cl}^-} \exp \left\{ \frac{\mathbf{F}}{RT} V \right\} \quad [37]$$

and when the rotation speed tends towards infinity

$$\frac{i}{\mathbf{F}} \xrightarrow{\Omega \rightarrow \infty} k_a c_{\text{Cl}^-} \exp \left\{ \frac{\beta \mathbf{F}}{RT} V \right\} \quad [38]$$

Expression [35] is in good agreement with the experimental data given in Ref. (5, 7) and in particular with Smyrl's results (8). By using these last data we can determine the values of β , k_a , k_c , and $D_{\text{CuCl}_2^-}$

$$\beta = 0.5, k_a = 6 \text{ cm}^4/\text{s}, k_c = 10^{-3} \text{ cm/s},$$

and

$$D_{\text{CuCl}_2^-} = 5.4 \times 10^{-6} \text{ cm}^2/\text{s}$$

The value of D_{Cl^-} is given in Ref. (1): $D_{\text{Cl}^-} = 2.032 \times 10^{-5} \text{ cm}^2/\text{s}$; the values of k_a and k_c correspond to V relative to a saturated calomel electrode.

At first, we consider the case of low concentration in acidic chloride: $c_{\text{HCl}} = 0.1M$ and low potential $V = -0.205 \text{ mV/SCE}$.

From expression [35] we find $i = 0.00526 \text{ mA/cm}^2$ for $\Omega = 600 \text{ rpm}$ (10 Hz) and $T = 293.15 \text{ K}$ and by using the Stefan-Maxwell Eq. [2], the numerical integration gives 0.00527 mA/cm^2 . The agreement is very good, and the infinitely dilute solution theory may be used.

In Fig. 1 we give the mole fraction variation of each species vs. the distance from the electrode. These results were obtained from the integration of the Stefan-Maxwell Eq. [1].

In the second case, we consider a higher concentration in acidic chloride $c_{\text{HCl}} = 2.0M$ and a higher potential: $V = -0.085 \text{ mV/SCE}$. Expression [35] cannot be used because

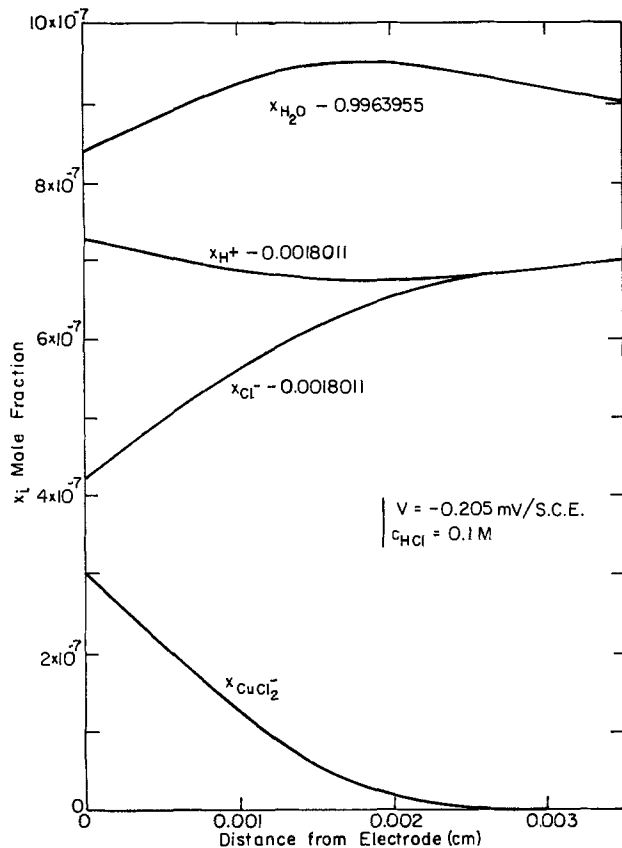


Fig. 1. Variations of the mole fraction of each species vs. the distance from the copper electrode. The concentration in HCl is 0.1M, and the potential is -0.205 mV/SCE.

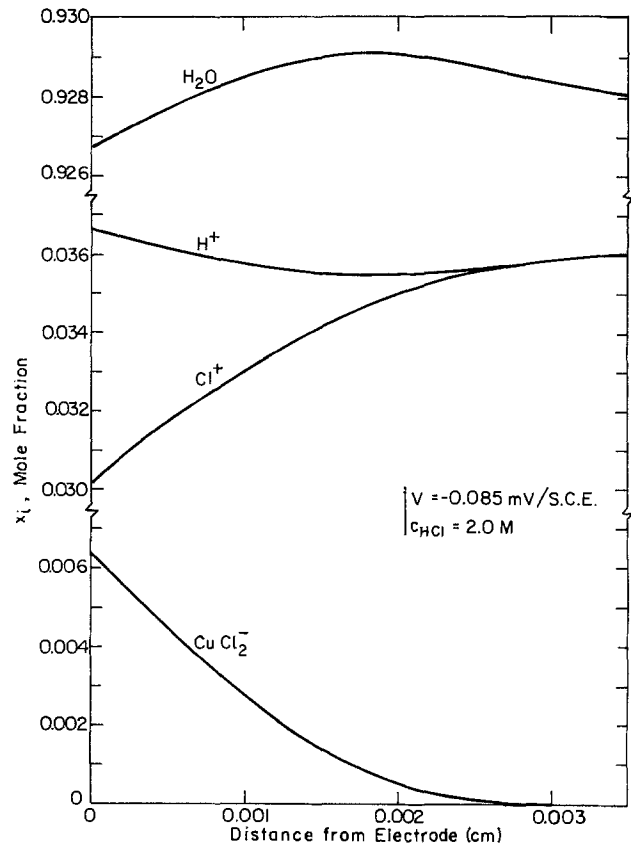


Fig. 2. Variations of the mole fraction of each species vs. the distance from the copper electrode. The concentration in HCl is 2.0M, and the potential is -0.085 mV/SCE.

the assumption $c_{Cl-i} = c_{Cl-\infty}$ is not valid. Therefore, we must solve the set of Eq. [32], [33], [34]; for $\Omega = 600$ rpm (10 Hz) and $T = 293.15$ K, we find $i = 115$ mA/cm², and by using the Stefan-Maxwell Eq. [1] $i = 119$ mA/cm². By using the numerical integration of the Stefan-Maxwell equation, we obtained the values of $\nabla\Phi$ and c_{Cl-s} , and thus we verified that the difference between the two previous results ($i = 115$ mA/cm² and $i = 119$ mA/cm²) is due to the effect of migration

$$D_{Cl-} c_{Cl-s} \frac{F^2}{RT} \nabla\Phi = 4 \text{ mA/cm}^2$$

In Fig. 2, we give the mole fraction variation of each species vs. the distance from the electrode. At the interface, the concentration of $CuCl_2^-$ is only five times less than the concentration of Cl^- ; that explains the effect of migration on the current.

The effect of the migration program [appendix C in Ref. (1)], or variations of it, could have been used with success here. The Stefan-Maxwell approach was used because we already had a nonelectrochemical version [silicon deposition (2)] with arbitrary homogeneous and heterogeneous reactions, and because of its ultimate validity when we get to problems (electropolishing, conditions of pitting corrosion), where even the viscosity and the pH of solution can vary dramatically near the electrode. We visualize adding surface coverages to the computer program at a later date.

Impedance.—For a low amplitude of perturbation, each variable may be written as in Eq. [21].

From Eq. [32]

$$\tilde{i} = R_t^{-1} \tilde{V} + 2 F k_a \bar{c}_{Cl-s} \exp \left[\frac{(1-\beta)F}{RT} \tilde{V} \right] \tilde{c}_{Cl-s} - F k_c \exp \left[-\frac{\beta F}{RT} \tilde{V} \right] \tilde{c}_{CuCl_2-s} \quad [39]$$

with

$$R_t^{-1} = \frac{(1-\beta)F^2}{RT} k_a \bar{c}_{Cl-s}^2 \exp \left[\frac{(1-\beta)F}{RT} \bar{V} \right] + \frac{\beta F^2}{RT} k_c \bar{c}_{CuCl_2-s} \exp \left[-\frac{\beta F}{RT} \bar{V} \right] \quad [40]$$

R_t is the usual charge-transfer resistance.

Equations [33] and [34] become

$$\tilde{i} = -F D_{CuCl_2-} \frac{\partial \tilde{c}_{CuCl_2-}}{\partial z} \Big|_{z=0} \quad [41]$$

$$\tilde{i} = \frac{1}{2} F D_{Cl-} \frac{\partial \tilde{c}_{Cl-}}{\partial z} \Big|_{z=0} \quad [42]$$

Then the faradaic impedance is

$$Z_f = R_t + Z_D \quad [43]$$

with

$$Z_D = R_t \left\{ 4 \frac{k_a \bar{c}_{Cl-s}}{D_{Cl-}} \exp \left[\frac{(1-\beta)F}{RT} V \right] \frac{\delta_{Cl-}}{-\theta'_{Cl-}(0)} + \frac{k_c}{D_{CuCl_2-}} \exp \left[-\frac{\beta F}{RT} V \right] \frac{\delta_{CuCl_2-}}{-\theta'_{CuCl_2-}(0)} \right\} \quad [44]$$

Z_D is the diffusion or convective Warburg impedance and $\{-1/\theta'(0)\}$ is the dimensionless convective Warburg impedance for the species i . The variation of $\{-1/\theta'(0)\}$ vs. the frequency was studied by several authors (9-11) with the assumptions of infinite dilution theory. If we assume $c_{Cl-i} = c_{Cl-\infty}$ and then $\tilde{c}_{Cl-i} = 0$, Eq. [44] becomes

$$Z_D = R_t \frac{k_c}{D_{CuCl_2-}} \exp \left\{ -\frac{\beta F}{RT} V \right\} \delta_{CuCl_2-} \left(-\frac{1}{\theta'(0)} \right)_{CuCl_2-} \quad [45]$$

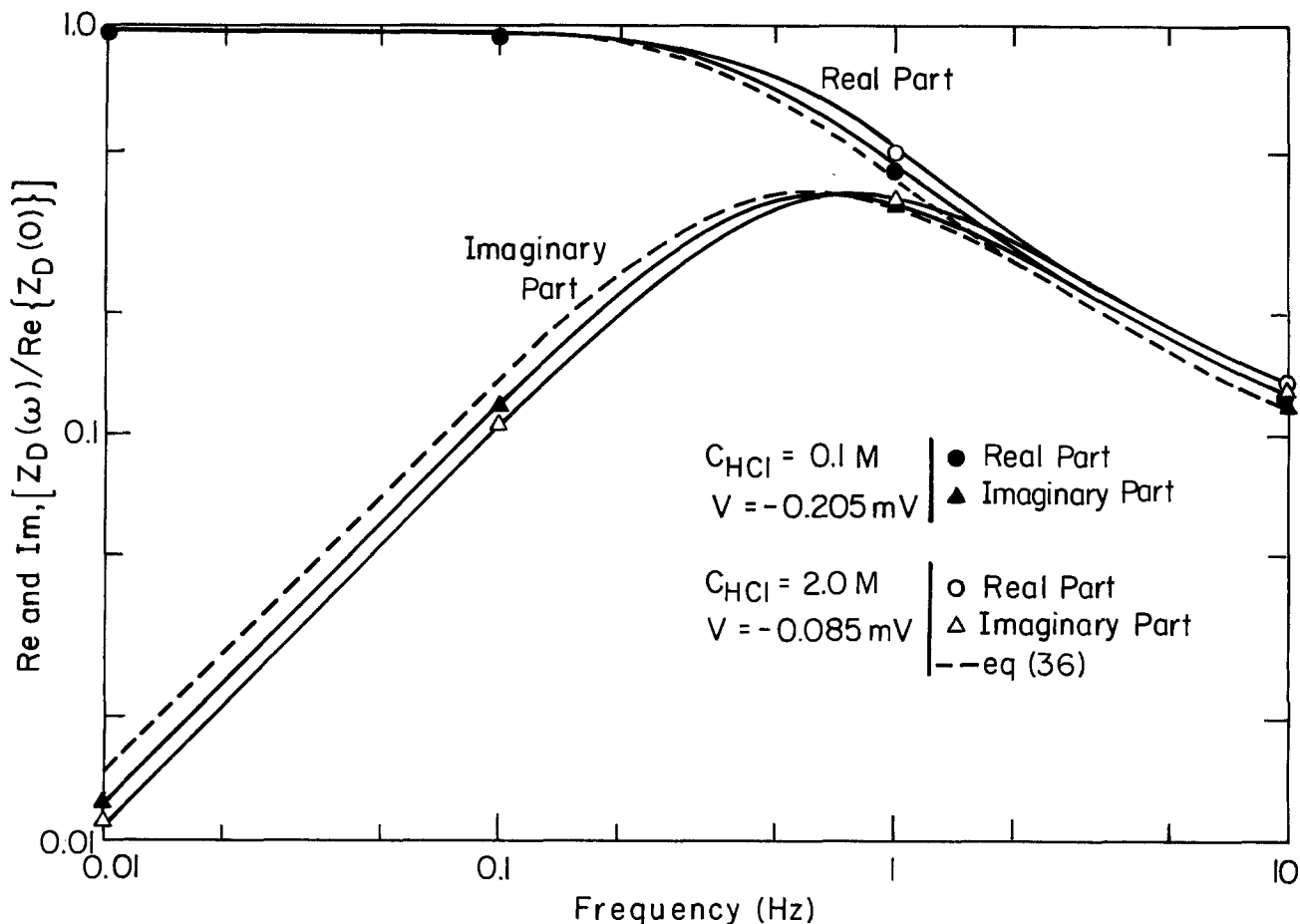


Fig. 3. Variation of the real and imaginary part of the normalized convective Warburg impedance for two particular conditions. ($c_{\text{HCl}} = 0.1\text{M}$ and $V = -0.205\text{ mV}$; and $c_{\text{HCl}} = 2.0\text{M}$ and $V = -0.085\text{ mV}$).

For $V = -0.205\text{ mV}$, $c_{\text{HCl}} = 0.1\text{M}$, and $\Omega = 600\text{ rpm}$ (10 Hz), the results from the infinite dilution theory (Eq. [45]) and the Stefan-Maxwell equation are very close. In Fig. 3, we have reported the variation of the real and imaginary part of the impedance vs. the frequency. In this figure, the curves from the concentrated solution theory and from the infinite dilution theory cannot be distinguished.

For $V = -0.085\text{ mV/SCE}$, $c_{\text{HCl}} = 2.0\text{M}$, and $\Omega = 600\text{ rpm}$, the results from the infinite dilution theory are given by Eq. [36] and are shown in Fig. 3 as a dashed line. The translation of this curve compared to the previous curve shows the effect of the Cl^- diffusion. The Schmidt number for CuCl_2^- is 1670, and for Cl^- is 4380, then the curve from Eq. [44] is identical to a curve from Eq. [45], corresponding to an apparent Schmidt number between 1670 and 4380 (here, approximately 2750).

When the frequency tends towards zero, the difference between the impedance derived from the infinite dilution theory and the impedance from the concentrated solution theory is 4%, in good agreement with the steady-state result. The variation of the dimensionless impedance derived from the concentrated solution theory is plotted in Fig. 3.

The curves are translated from the infinite dilution theory curves towards high frequency. In the concentrated-solution theory, the curves are identical to curve from Eq. [45], corresponding to an apparent Schmidt number of 1150, which is outside the average value of the CuCl_2^- Schmidt number and Cl^- Schmidt number. Then, in this case, the effect is very important, and an analysis of experimental data with the infinite-dilution theory (Eq. [44]) gives a wrong result for the Schmidt number determination.

Acknowledgment

This work was supported by the National Science Foundation through the United States-France Exchange

of Scientists Program with le Centre National de la Recherche Scientifique no. G050252.

Manuscript submitted Nov. 4, 1983; revised manuscript received June 21, 1984.

The University of California assisted in meeting the publication costs of this article.

LIST OF SYMBOLS

b	matrix defined by Eq. [8]
b_{ik}	element of matrix b
c	total concentration (mol/cm ³)
c_i	concentration of species i (mol/cm ³)
D_{ij}	diffusion coefficient for binary interactions (cm ² /s)
D_i	diffusion coefficient of species i (cm ² /s)
F	Faraday's constant (96,487 C/eq)
i	total current density (A/cm ²)
i_l	partial current density relative to reaction l (A/cm ²)
J_i	flux of species i relative to the mass average velocity (mol/cm ² s)
k_{a1}	anodic rate constant of heterogeneous reaction 1
k_{c1}	cathodic rate constant of heterogeneous reaction 1
k_{f1}	forward rate constant of homogeneous reaction 1
k_{b1}	backward rate constant of homogeneous reaction 1
m_i	molecular weight of species i (g/mol)
n_l	number of electrons involved in electrode reaction 1
N_i	flux of species i (mol/cm ² s)
R	universal gas constant (8.3143 J/mol K)
$R_{i,l}$	rate of homogeneous production of species i in the reaction mol/cm ³ s
R_t	charge transfer resistance relative to reaction 1 (Ω cm ²)
$*S_{i,l}$	stoichiometric coefficient species i in heterogeneous reaction 1
t	time (s)
T	temperature (K)
v	mass average velocity (cm/s)
v_i	velocity of species i (cm/s)
$*R_{t,l}$	charge transfer resistance relative to reaction 1 (Ω cm ²)

x_i	mole fraction of species i
z	axial distance from disk surface (cm)
z_i	charge number of species i
Z	electrochemical impedance ($\Omega \text{ cm}^2$)
Z_D	diffusion or convective Warburg impedance ($\Omega \text{ cm}^2$)
B_1	symmetry factor for reaction 1
δ	thickness of diffusion layer (cm)
$\{-1/\theta_i'(0)\}$	Dimensionless convective Warburg impedance to species i
μ_i	electrochemical potential of species i (J/mol)
ν_i	stoichiometric coefficient for species i in homogeneous reaction
ρ_i	mass of species i per unit volume (g/cm^3)
Φ	electrostatic potential (V)
ω	modulation frequency (Hz)
Ω	disk rotation speed (Hz)

Superscripts

(overbar)	steady state
(underline)	unsteady component

Subscripts

s	at surface
∞	in bulk solution

REFERENCES

1. J. Newman, "Electrochemical Systems," p. 239, Prentice Hall, Inc., Englewood Cliffs, NJ (1973).
2. R. Pollard and J. Newman, *This Journal*, **127**, 744 (1980).
3. R. B. Bird, W. E. Stewart, and E. N. Lightfoot, "Transport Phenomena," p. 570, J. Wiley and Sons, Inc., New York (1960).
4. W. H. Smyrl, in "Comprehensive Treatise of Electrochemistry," Vol. 4, J. O'M. Bockris, B. E. Conway, E. Yeager, and R. E. White, Editors, pp. 97-149, Plenum Press, New York (1981).
5. A. Moreau, *Electrochim. Acta*, **26**, 497 (1981).
6. R. S. Cooper and J. H. Bartlett, *This Journal*, **105**, 109 (1958).
7. M. Braun and K. Nobe, *ibid.*, **126**, 1666 (1979).
8. W. H. Smyrl, Paper 132 presented at the Electrochemical Society Meeting, Denver, CO, Oct. 11-16, 1981.
9. D. A. Scherson and J. Newman, *This Journal*, **127**, 110 (1980).
10. C. Deslouis, C. Gabrielli, and B. Tribollet, *ibid.*, **130**, 2044 (1983).
11. B. Tribollet and J. Newman, *ibid.*, **130**, 822 (1983).

Investigation of the Anodically Formed Passive Film on Iron by Secondary Ion Mass Spectroscopy

Oliver J. Murphy,* Tong E. Pou, and John O'M. Bockris*

Department of Chemistry, Texas A&M University, College Station, Texas 77843

Luis L. Tongson

Physics Department, Pennsylvania State University, Worthington Scranton Campus, Dunmore, Pennsylvania 18512

ABSTRACT

This paper reports SIMS analysis of passive layers. Pure Fe disks are used in borate buffers of $\text{pH} = 8.4$. Pre-electrolysis is carried out to remove trace impurities. Potential step control of the electrode is utilized. Two types of experiments are carried out. In one, passive layers are prepared and then exposed to chloride ions for various times. In the other, films are heated at various temperatures for preselected times. The passive layers subjected to these treatments are exposed to SIMS analysis. The distribution of OH^- with depth, from SIMS analysis, shows an exponential-like decrease away from the electrode/solution interface for passive films exposed to $0.5M$ buffered chloride solutions for various times or heated at a given temperature for a predetermined period of time. The OH^- peak heights at a fixed depth in passive layers decrease in a similar manner with increasing exposure time to chloride ions or with increasing annealing temperature for a given time period. Cl^- peak heights for films exposed to chloride ion-containing borate solutions increase rapidly for times up until breakdown, decrease sharply after breakdown, and then level off at times much longer than breakdown. O^- peak heights decrease exponentially with depth for samples exposed to chloride ions and decrease linearly for specimens annealed at various temperatures for a number of different times. Corresponding Fe^+ peak height data display a linear decrease with depth for chloride-treated films and an almost constant value for layers subjected to thermal treatments. Positive SIMS O^+ peak heights increase sharply for thermally treated films over a surface region of approximately 7\AA , remain constant in the bulk regions, and decrease rapidly in the film/metal interfacial regions. Homogeneous films are indicated with a thickness of about 25\AA . Detailed mechanistic discussions of the two principal models of passivity show that the results are in greater agreement with the amorphous hydrated polymeric oxide model than with the crystalline oxide model, in which water is considered only in terms of adsorbed water on the surface of the passive film.

Two kinds of approaches have been used in the past to characterize the passive film formed electrochemically on iron in neutral solutions (1, 2). The first includes *in situ* techniques such as ellipsometry (3, 4) and Mossbauer spectroscopy (5, 6). The second involves the use of high-vacuum spectroscopic methods such as electron diffraction (7, 8), XPS (9, 10), and Auger (11, 12). Both approaches have their drawbacks (difficulty of interpretation of Mossbauer spectra and the removal of the sample from its environment and potential control with *ex situ* techniques); however, a considerable wealth of information has been collected concerning the nature of the passive film.

At present, two models are utilized in interpreting the data obtained on passive films on iron (2, 13). In one view (7, 8, 14-16), the film is considered polycrystalline and an-

hydrous, the only water in the film being that adsorbed in the surface region (9, 17). Passivity in this model is understood in terms of the nature of the crystalline oxide present (either a duplex layer consisting of an inner layer of Fe_3O_4 and an outer layer of $\gamma\text{-Fe}_2\text{O}_3$ (7) or $\gamma\text{-Fe}_2\text{O}_3$ alone (8, 14)). In the second model (5, 18, 19), the passive layer is regarded as an amorphous hydrated ferric oxide represented by $\text{Fe}_2\text{O}_3 \cdot \text{H}_2\text{O}$ (12). According to this model, the bound water is the essential element in the passive film, cementing the polymeric iron oxide chains together (20). Passivity is understood in terms of the difficulty of lattice cation diffusion through the film as a result of the network formed by the bound water molecules.

A key problem to be resolved, therefore, is the location of hydrogen or hydrogen containing species, *e.g.*, OH^- and H_2O , in the passive layer. Secondary ion mass spectroscopy (SIMS) is uniquely suited for this problem be-

* Electrochemical Society Active Member.

cause of its ability to detect hydrogen and its isotopes in association with depth profiling. An early application of SIMS to this problem has given results which are inconclusive (9, 21, 22). Preliminary work in this laboratory (20, 23) shows the presence of water throughout the thickness of the passive layer and relates the loss of passivity in aggressive environments such as chloride solutions to displacement of the bound water molecules by the latter, eventually leading to pitting.

In this paper, a SIMS investigation of passive films on iron, both exposed and nonexposed to chloride ions, as well as those post-thermally treated in an inert gas atmosphere, is described.

Experimental

Working electrodes were iron disks (1 mm thick and 6 mm \times 6 mm square, 99.99% pure; Alfa Ventron Corp., Danvers, MA) mechanically polished to a mirror finish, washed with methanol and thrice-distilled water, dried, and stored *in vacuo*. Electrode specimens were prepared fresh with a fine-grade diamond paste prior to use. Samples were fixed in a Teflon electrode holder, as described previously (10). The counterelectrode was a piece of platinum gauze of an area about 100 times that of the iron disk working electrode and was situated in a manner to avoid depolarization of the latter. The reference electrode was a Hg/HgO, 1N KOH electrode.

Buffer solutions (pH = 8.4; 0.275M sodium tetraborate mixed with 0.15M boric acid) were made up, using thrice-distilled water and analytical-grade reagents. Prior to experimental runs, all solutions were pre-electrolyzed for about 15h at a current density of 20 $\mu\text{A cm}^{-2}$, using two large platinum gauze electrodes.

Air-formed oxide films on iron disks were removed by cathodic polarization at -0.74V (NHE) (24) for 30 min, followed by replacement of the contaminated borate electrolyte (from an attached reservoir) while maintaining the cleaned electrode surface under a nitrogen gas atmosphere. Electrodes prepared by this procedure were used afterward in experimental runs.

Passive films were formed in all cases by means of a potentiostatic step from the resting potential of the cleaned electrode to $+0.3\text{V}$ (NHE), the time of film growth being 50 min.

At this stage in one set of experiments, the solution of film growth was pressed out of the cell by means of nitrogen pressure and replaced with a chloride ion containing (0.5M) borate buffer solution from an attached reservoir. Passivated electrodes were exposed to this solution at the potential of film growth for various times prior to, during, and after breakdown. On completion of each experiment, the test solution was pressed out of the cell, quickly filled with thrice-distilled water from an attached reservoir, and released by nitrogen gas pressure. Washing with thrice-distilled water was repeated. The cell with the electrode still in place under a nitrogen gas atmosphere was placed in a glove box. On opening the cell, the electrode was removed, washed thoroughly again with thrice-distilled water, and transferred to a glass vial. The glass vials, which were filled with nitrogen gas, were carefully sealed with Teflon tape and a screw-on cap.

In another set of experiments, electrodes after film growth were put in a glove box as described above and placed individually in cleaned Pyrex glass tubes under a nitrogen gas atmosphere. The tubes were then placed in a furnace and heated at a number of temperatures for various times under a flowing inert gas atmosphere. On completion, tubes with specimens inside were returned to the glove box, and electrodes were removed and placed in glass vials.

Samples were opened under inert gas conditions and placed in the target chamber of a Gatan Model 591C SIMS-SIPS ion microprobe at the Materials Research Laboratory, Pennsylvania State University. In this instrument, the ion beam consists of a Colutron ion source, a Wein mass filter, and two electrostatic lenses. The ion gun chamber is pumped with a turbomolecular pump.

The target chamber can be evacuated to 10^{-10} torr with a second turbomolecular pump and titanium sublimation pump.

The typical operating parameters used in this work were probe ion beam $^{40}\text{Ar}^+$, beam voltage of 7 keV, beam current of 90 nA, and a sample chamber pressure during analysis of 5×10^{-9} torr. The ion beam of $\sim 70 \mu\text{m}$ in diameter was rastered over an area of 1.2×1.2 mm. The signal was gated, so the data were collected over a central area of 0.36×0.36 mm. The sputtering rate was found to be 0.3 \AA sec^{-1} , using a $102\text{\AA SiO}_2/\text{Si}$ standard. The sputtering rate for the passive film was taken to be the same as that for the SiO_2/Si material.

Results

A convenient measure of hydrogen containing species, including water, in passive films can be obtained from monitoring the negative SIMS OH^- peak heights with depth into the films. In Fig. 1, the OH^- peak height, which is related to water content as a result of OH^- ion formation from the fragmentation of water within the films on ion bombardment, is presented as a function of annealing temperature for passive films grown at $+0.3\text{V}$ (NHE) and subsequently annealed for 15 min at various temperatures in a flowing inert gas atmosphere.

The outer regions of the passive films (*i.e.*, where the aqueous solution is in contact with the films), for all temperatures, are richer in water than the bulk layers. In the former regions, an exponential-like decrease in water content can be observed from room temperatures of up to 200°C .

The OH^- peak heights for passive films formed at $+0.3\text{V}$ (NHE) and exposed afterward to a 0.5M chloride ion containing borate buffer solution at the latter potential for various times are shown in Fig. 2a for a number of film depths. Peak heights decrease sharply, particularly in the outer regions, for exposure times of up to 163s. At 163s, which is observed (20) to be the breakdown time for the passive film on iron under the experimental conditions employed, a minimum is to be noted in the OH^- peak heights for all depths. For exposure times greater than breakdown, namely 205 and 420s, an exponential-like increase in the OH^- peak heights occurs and is particularly large in the outer surface regions.

The corresponding Cl^- peak heights as a function of exposure time to chloride ions for the passive films described above are illustrated in Fig. 2b. Peak intensities increase sharply for exposure times up to breakdown, reach a maximum at breakdown, then decrease in an exponential-like manner. This behavior is opposite to that observed for the OH^- peak heights (Fig. 2a). Chloride ions penetrate into the interior of passive layers, up to the

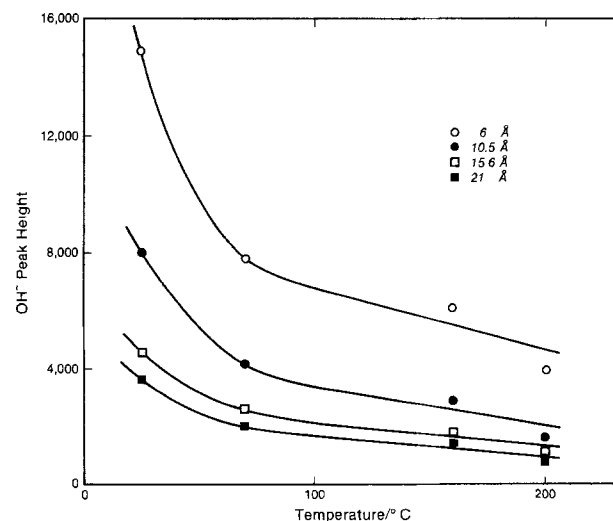


Fig. 1. Variation of OH^- peak height with annealing temperature for passive films formed in borate buffer solution at 0.3V (NHE) and then thermally treated in an inert gas atmosphere.

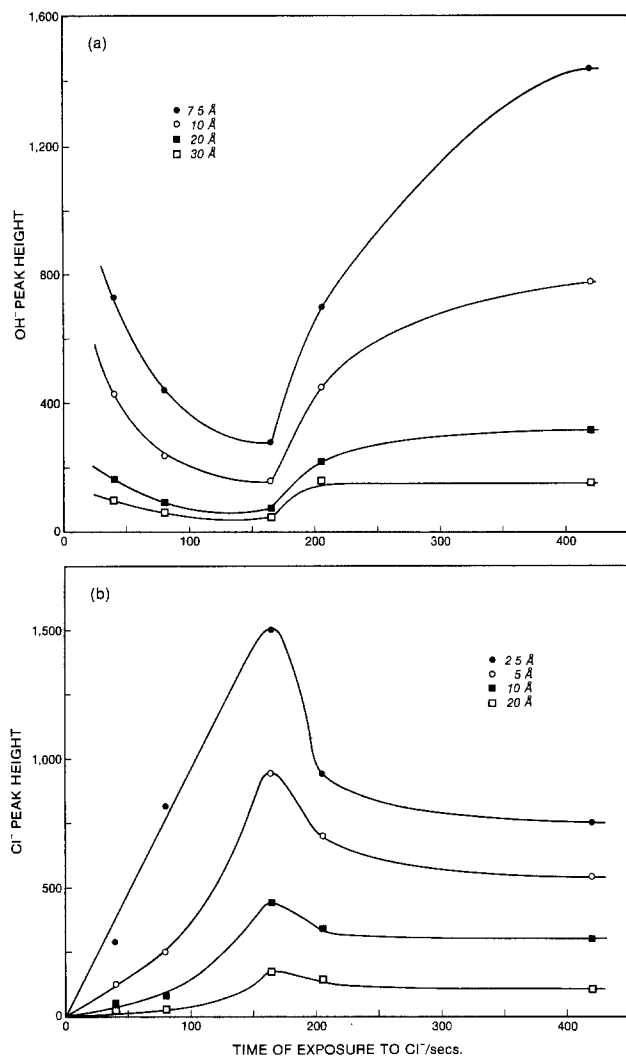


Fig. 2. (a) OH⁻ peak height as a function of the time of exposure to chloride ions for passive films formed in borate buffer solution at 0.3V (NHE) and then exposed to a chloride containing borate solution at this potential. (b) Variation of Cl⁻ peak height intensities with time of exposure to chloride ions for passive films formed in borate buffer solution at 0.3V (NHE) and then exposed to a 0.5M chloride containing borate solution at this potential for various times

metal/metal oxide interface. The local concentration of chloride ions is highest in the outer regions for all exposure times and decreases with depth into the films.

The treating of passivated iron specimens to chloride solutions or to annealing atmospheres also has an effect on the O⁻ peak heights, the latter being associated with lattice oxide ions. The latter are plotted as a function of depth in Fig. 3a for passive films annealed under an inert gas atmosphere at various temperatures for a number of different times. The oxide ion concentration decreases in a linear fashion in practically all cases, the decrease being lowest for those films annealed at the higher temperatures.

The Fe⁺ peak heights, obtained from positive SIMS, for the thermally annealed films are shown in Fig. 3b as a function of depth. After a sharp initial increase over the first 1-2 Å of the outer surface region, an approximately constant signal is obtained for all films throughout the bulk. At the metal/metal oxide interface (about 25 Å), a decrease in peak heights is observed.

The positive SIMS O⁻ peak heights arising from thermally treated passive films are illustrated in Fig. 3c as a function of depth into the films. A rapid signal increase occurs over the first 5-7 Å, followed by a plateau region which terminates as the metal/metal oxide interface is approached. Temperature effects are seen.

The variation of O⁻ peak heights with depth for passive films exposed to chloride ions for various times is pre-

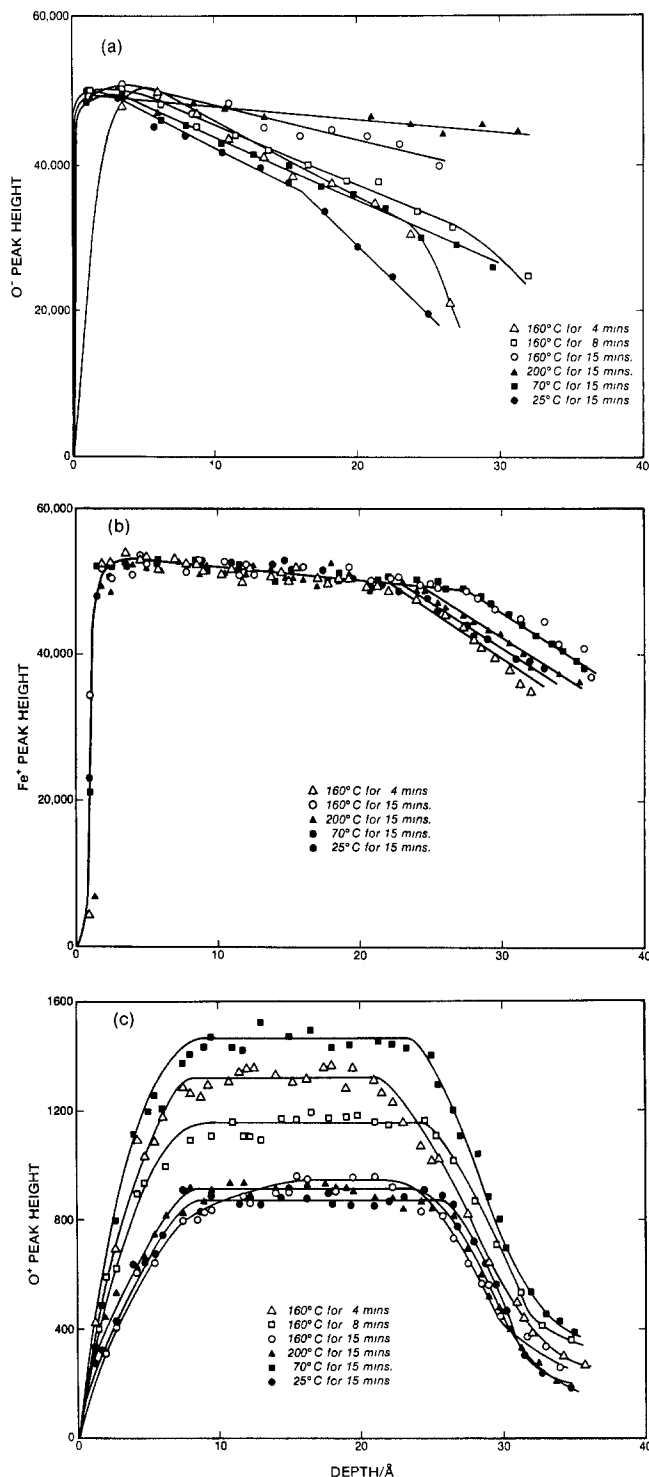


Fig. 3. (a) O⁻ peak height as a function of depth into passive films grown in borate buffer solutions at 0.3V (NHE) and then thermally annealed in an inert gas atmosphere at various temperatures for different times. (b) Fe⁺ peak height as a function of depth into passive films formed in borate buffer solution at 0.3V (NHE) and then thermally treated in an inert gas atmosphere. (c) O⁻ peak height as a function of depth into passive films which were thermally treated at a number of different temperatures for various times.

sented in Fig. 4. The profiles give rise to an initial sharp increase, followed by a sharp decrease in the outer surface regions of the films and, thereafter, a more gradual decrease in the bulk. A sharp drop in peak heights occurs in the interfacial region between the metal and the metal oxide. An increase in the O⁻ signal with exposure is observed at a given depth.

Fe⁺ data for films exposed to chloride solutions are presented in Fig. 5. Compared with the data in Fig. 3b, the outer surface regions in this case are much broader, of the

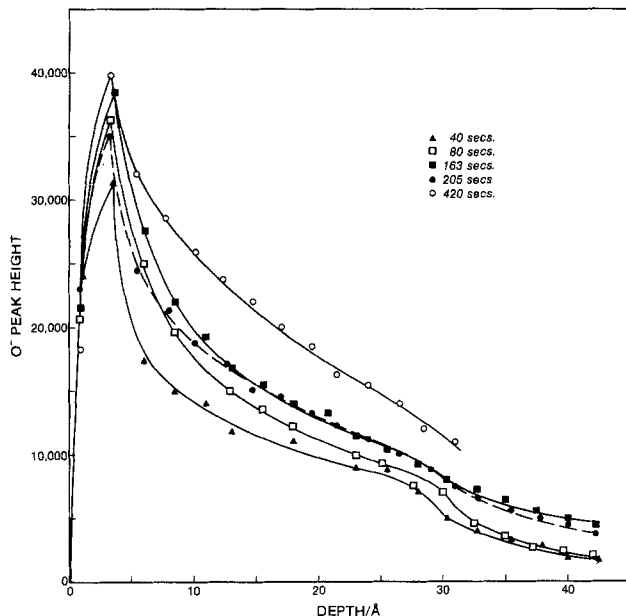


Fig. 4. Variation of O^- peak height with depth for passive films grown in borate buffer solutions at 0.3V (NHE) and then exposed to a chloride containing borate solution at this potential.

order of 1-7Å. Following an initial maximum at the latter depth, the Fe^+ signals decrease with depth, this being more pronounced for films with the shortest exposure time to chloride ions. Variations in ion yields per unit depth in the bulk and in the interfacial region are given in the inset in Fig. 5 as a function of exposure time.

Discussion

Effect of heating passive films.—*In situ* Mossbauer spectroscopy studies (5, 6, 25), *ex situ* Auger analysis under controlled conditions (12), and *ex situ* EXAFS investigations (26, 27) under an inert gas atmosphere support the hydrated amorphous polymeric ferric oxide nature of the passive film on iron. Data from Auger (12), tritium radiotracer measurements (28), and a recent combined XPS-ISS study (29) are consistent with a structure of the passive film corresponding to $Fe_2O_3 \cdot H_2O$. These observations are consistent with the formation of polymeric species and structures with oxy and hydroxy bridges on hydrolyzing ferric salts (30). However, electron diffraction data (8, 14), ellipsometric spectroscopy (4), and ac impedance studies (31) indicate that the passive film is composed of an anhydrous ferric oxide.

Naturally occurring and synthetic amorphous hydrated oxides of iron (III) subjected to thermal treatments in a variety of atmospheres have been well characterized (32-36). However, similar conditioning of thin passive oxide layers on iron has been little investigated (6, 37). Utilization of Mossbauer spectroscopy (6) reveals that thermally annealing passive films give rise to a change in the Mossbauer parameters: the parameters change from those typical of a hydrated amorphous polymeric ferric oxide film to those typified by anhydrous crystalline $\gamma-Fe_2O_3$. The SIMS analyses of thermally treated passive layers reported here (Fig. 1) can be interpreted along similar lines. Thermal expulsion of water takes place at temperatures of up to 200°C for weakly chemisorbed water and structural water from the outer surface regions and for structural or lattice-bound (38) water from the bulk of the films, giving rise to the formation of an anhydrous crystalline oxide, possibly $\gamma-Fe_2O_3$. This view may be compared with that concerning the dehydration behavior of a tungsten oxide hydrate, $WO_3 \cdot 1/3 H_2O$, which has been observed (39) to follow two steps: emission of adsorbed water, without a change in structure, followed by loss of structural water and the formation of anhydrous crystalline WO_3 .

The enthalpy, ΔH , associated with water removal from passive films, may be obtained from a van't Hoff type of

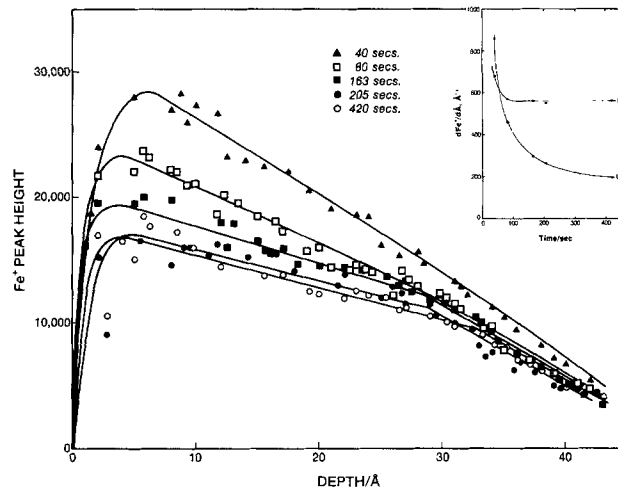
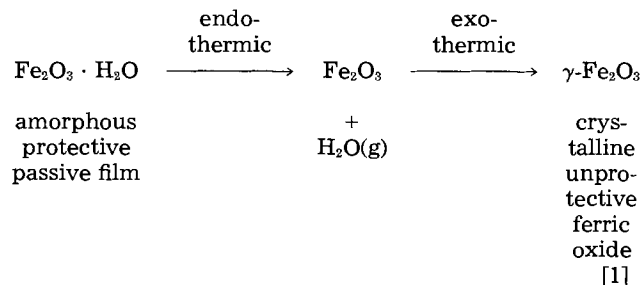


Fig. 5. Variation of Fe^+ peak height with depth for passive films exposed to 0.5M chloride containing borate buffer solutions for various times.

expression (40) by plotting the log of the OH^- peak heights (Fig. 1), which are proportional to the concentration of water, C_{H_2O} , in the layers, against the inverse of the absolute temperature. However, the qualitative nature of SIMS data (41) must be borne in mind, and any value of ΔH must be regarded as approximate.

From a plot of the relevant data (Fig. 6), $\Delta H \sim 2.0$ kcal mol^{-1} . This low value may be interpreted in terms of the hydrated polymeric oxide model of passivity in the following way: the amorphous Fe_2O_3 should be bonded in some fashion to H_2O , and after breaking this bond by thermal treatments, it is reasonable to expect a chemical bond strength to be involved, *i.e.*, a heat of reaction, ΔH , of the order of 20-100 kcal mol^{-1} . What actually happens is that, in the overall process, two compensating reactions are taking place—an endothermic bond-breaking reaction involving water removal and an exothermic crystallization reaction associated with the formation of a stable, anhydrous, crystalline lattice, probably $\gamma-Fe_2O_3$. These two compensating reactions can be represented by the equation



The heat of crystallization, given off during the formation of $\gamma-Fe_2O_3$, almost provides the heat required to expel water from passive layers—only 2 kcal mol^{-1} more are required. With this interpretation of events, the small calculated value of ΔH is rational.

With the crystalline oxide model of passivity, the low value of ΔH , 2 kcal mol^{-1} , could be understood in terms of the desorption of weakly adsorbed water on the outer surface of passive films, where the short-range forces involved are of the order of 1-10 kcal mol^{-1} . However, the distribution of water throughout the thickness of passive films (Fig. 1) strongly supports the first interpretation and the hydrated polymeric oxide model of passivity.

It must also be pointed out that the passivated samples, described in Fig. 1, are heated under a flowing inert gas atmosphere for only 15 min. In the case of many hydrated oxides or salts, a much longer thermal treatment of the order of 10-20h is needed to remove the last traces of bound water. For the passivated iron disks, the film thicknesses are low, approximately 30Å, so a shorter time

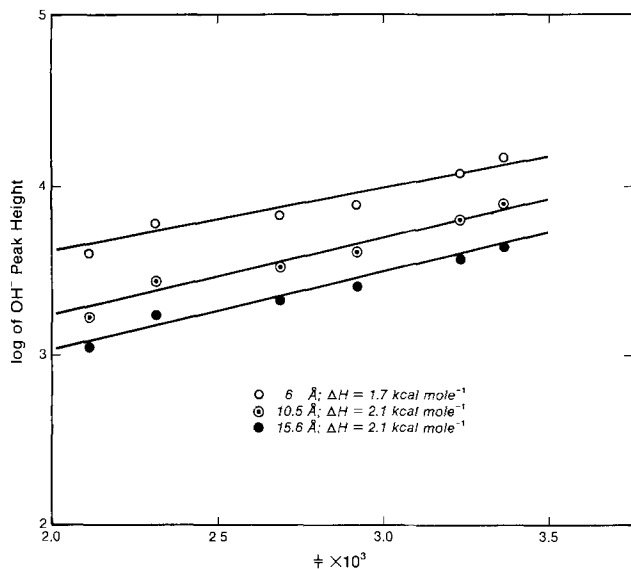


Fig. 6. Plot of log of OH⁻ peak height (relevant data taken from Fig. 1) vs. the inverse of the absolute temperature.

may suffice. However, the state of equilibrium achieved may not lie completely to the right of Eq. [1], i.e., in the purely crystalline state.

The O⁻ peak heights, which arise from lattice oxide ions, display for thermally treated films (Fig. 3a) a qualitative similarity to those of OH⁻, which give a measure of the water content (Fig. 1) with respect to depth into the films. The general tendency of O⁻ peak heights to decrease with increasing depth (Fig. 3a and 4) may result from a change in the oxide matrix with increasing annealing temperatures and give rise to differences in ion yields on performing SIMS analyses (42).

Effect of exposing passive films to chloride containing solutions.—An interesting comparison, with regard to the water content of passive films, can be made between thermally treated films (Fig. 1) and films exposed to chloride containing solutions (Fig. 2a). In Fig. 2a, the decrease of OH⁻ peak heights for exposure times of up to 163s is associated with events leading to breakdown of the passive films.

Figure 2b implies a permeation of chloride ions through the passive layer over a time period of about 160s. Using the relation (43)

$$\Delta^2 = 2Dt \quad [2]$$

and having $\Delta = 50\text{\AA}$ yield a value of the order of $10^{-15} \text{ cm}^2 \text{ s}^{-1}$ for the diffusion coefficient of chloride ions, D , through the passive film on iron. With the hydrated polymeric oxide model of passivity, it may be thought that the permeation occurs along certain paths (Fig. 7) where bound water molecules coordinated to lattice Fe³⁺ cations are located. Such a view is supported by the results shown in Fig. 2a and 2b, from which it can be seen that the progress of the chloride ions into the lattice is followed by a diminution of H₂O up to the critical time at which breakdown occurs. Penetration of chloride ions (but not nitrate ions) throughout the bulk of synthetic hydrated oxides of iron by expulsion of water molecules from the structures and by replacement by chloride ions was found to occur by Ellis *et al.* (44). Correspondingly, in mixtures consisting of a hydrated ferric oxide and goethite ($\alpha\text{-FeOOH}$) with KCN, rapid room temperature solid-state substitution reactions occur (45) involving replacement by cyanide ions of only the water molecules in the hydrated ferric oxide, the reaction going to completion. Rapidity of the reaction is attributed (45) to the greater π -acceptor properties of cyanide ion, as compared with water and the ease of CN⁻ diffusion due to the presence of water in the structure.

In the crystalline oxide model of passivity, chloride ion penetration may be accounted for in terms of ion ex-

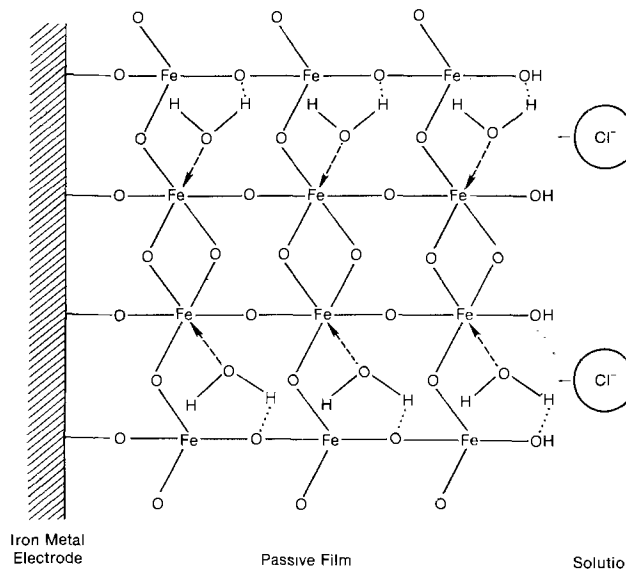


Fig. 7. Schematic representation of chloride penetration channels in terms of the amorphous hydrated polymeric oxide model of passivity.

change processes, e.g., Cl⁻ for lattice O²⁻ (46), via cation vacancies (47), or point defects (48). However, the correlation shown here between water content and chloride ion permeation through passive films (Fig. 2a and 2b) favors the hydrated polymeric oxide model.

The increase in OH⁻ peak heights after breakdown (about 160s) (*cf.*, Fig. 2a) may be thought to arise from the precipitation of corrosion products, e.g., Fe(OH)₂ or FeOOH, at the outer surface regions of the unprotective oxide film, as well as from porous plugs within the chloride ion permeation channels (Fig. 7). Using the solubility product of ferrous hydroxide, it can be shown that at a pH of 8.4 and at local current densities of 1 mA cm^{-2} , the solubility of Fe(OH)₂ will be exceeded. Precipitation of corrosion products in the outer film surface regions is supported by the enhanced OH⁻ peak heights obtained at a film depth of 7.5\AA (Fig. 2a), as compared with those observed at times well before breakdown.

The decreasing chloride ion peak heights observed for times after breakdown (Fig. 2b) could be due to chloride removal of some Fe³⁺ cations from within the film in the form of chloro complexes. Thus, the density of the resulting $\gamma\text{-Fe}_2\text{O}_3$ is likely to be substantially greater than that of the amorphous passive film. Support for the hypothesis of chloride removal of Fe³⁺ cations can be found by comparing the data presented in Fig. 3b and 5. A decrease in Fe³⁺ peak heights increasingly exposed to chloride ions (Fig. 5) is observed, whereas for passive films not exposed to chloride ions (Fig. 3b), almost constant Fe³⁺ peak heights are observed. Furthermore, the rotating ring-disk work of Heusler and Fischer (49) demonstrates the existence of Fe³⁺ species in solution after exposing passivated iron disks to chloride solutions.

The O⁻ peak profiles obtained for passive films exposed to chloride ions (Fig. 4) are similar in outline to those observed for thermally treated films (Fig. 3a) and, again, they indicate matrix effects. The increasing O⁻ ion yields at a given depth with increasing exposure time to chloride ions (Fig. 4) are probably due to a change in the oxide matrix (42) as a result of events leading to breakdown, subsequent corrosion, and corrosion product buildup on the outer surfaces.

Thickness and uniformity of passive films.—From the data presented in Fig. 3b, the interfacial region between the passive film and the underlying metal occurs at around $27 \pm 3\text{\AA}$. The lower Fe³⁺ ion yields in the interfacial regions are probably due to irregularities in the position of the metal/metal oxide interface and a change in the matrix in going from a predominantly oxide lattice to a metal one. Supporting evidence can be obtained from the related data shown in Fig. 5.

The change in ion yields per unit depth with time [(b) in the inset in Fig. 5] indicates that the bulk regions of chloride-exposed passive films undergo a change in cation environments with time of exposure to chloride ions. This is due to the aforementioned chloride removal and replacement of bound water and the chloride removal of some Fe^{3+} cations from the passive films. However, the almost constant ion yields obtained for exposure times greater than 200s indicate homogeneous layers for films after breakdown; this probably corresponds to $\gamma\text{-Fe}_2\text{O}_3$ (6).

The almost constant ion yields per unit depth with time of exposure of passive films to chloride ions in the metal/metal oxide interfacial region [(a) in the inset in Fig. 5] point to a uniform structure in this region for all films. This would correspond to the increasingly metallic region indicated at depths greater than 25Å. The same behavior is found for the interfacial region of thermally treated films (Fig. 3b).

The positive SIMS O^+ peak heights for passive films thermally treated (Fig. 3c) again indicate a passive film thickness of about 25Å. Also, the constant O^+ signal values, corresponding to the bulk of each film investigated, indicate homogeneous layers, though the layers differ from each other according to the degree of thermal treatment. Similar SIMS O^+ peak profiles are obtained for passivated iron disks exposed to chloride ions (29). A thickness of about 25Å for passive films grown under the conditions used compares very well with the ellipsometric data of Sato *et al.* (50) and Brusica *et al.* (51).

It is not at all obvious why the passive film treated at 25°C (Fig. 3c) should depart from the trend observed; it is unlikely that the matrix for this film is the same as that for films annealed at the highest temperatures, 160° and 200°C. This aspect requires further clarification.

Acknowledgments

Support of this work by the Department of the Interior (DOI) under grant no. 14-34-0001-9446 and by the Department of Defense (DOD) under grant no. N 0001480C0113 is gratefully acknowledged.

The authors are grateful to Mrs. Lynn McCartney-Murphy for her editing and typing of this manuscript.

Manuscript submitted January 16, 1984; revised manuscript received July 17, 1984.

Texas A&M University assisted in meeting the publication costs of this article.

REFERENCES

- M. Janik-Czachor, *This Journal*, **128**, 513C (1981).
- N. Sato and G. Okamoto, in "Comprehensive Treatise of Electrochemistry," Vol. 4., J. O'M. Bockris, B. E. Conway, E. Yeager, and R. E. White, Editors, p. 193, Plenum Press, New York (1981).
- A. K. N. Reddy and J. O'M. Bockris, "Ellipsometry in the Measurement of Surfaces and Thin Films," p. 229, N. B. S. Misc. Pub. 256, Washington, DC (1964).
- C. T. Chen and B. D. Cahan, *This Journal*, **129**, 17 (1982).
- W. E. O'Grady and J. O'M. Bockris, *Surf. Sci.*, **38**, 249 (1973).
- W. E. O'Grady, *This Journal*, **127**, 555 (1980).
- M. I. Nagayama and M. Cohen, *ibid.*, **109**, 781 (1962).
- K. Kuroda, B. D. Cahan, Gh. Nazri, E. Yeager, and T. E. Mitchell, *ibid.*, **129**, 2163 (1982).
- S. C. Tjong and E. Yeager, *ibid.*, **128**, 2251 (1981).
- D. L. Cocke, P. Nilsson, O. J. Murphy, and J. O'M. Bockris, *Surf. Interf. Anal.*, **4**, 94 (1982).
- M. Seo, J. B. Lumsden, and R. W. Staehle, *Surf. Sci.*, **42**, 337 (1974).
- R. W. Revie, B. G. Baker, and J. O'M. Bockris, *This Journal*, **122**, 1460 (1975).
- R. P. Frankenthal and J. Kruger, Editors, "Passivity of Metals," Electrochemical Society Corrosion Monograph Series, Princeton, NJ (1978).
- C. L. Foley, J. Kruger, and C. J. Bechtold, *This Journal*, **114**, 936 (1967).
- C. Wagner, *Ber. Bunsenges. Phys. Chem.*, **77**, 1090 (1973).
- J. W. Schultze, in "Passivity of Metals," R. P. Frankenthal and J. Kruger, Editors, Electrochemical Society Corrosion Monograph Series, Princeton, NJ (1978).
- H. T. Yolken, J. Kruger, and J. P. Calvert, *Corros. Sci.*, **8**, 103 (1968).
- G. Okamoto and T. Shibata, *ibid.*, **10**, 371 (1970).
- G. Okamoto, *ibid.*, **13**, 471 (1973).
- O. J. Murphy, J. O'M. Bockris, T. E. Pou, L. L. Tongson, and M. D. Monkowski, *This Journal*, **130**, 1792 (1983).
- J. O'M. Bockris, O. J. Murphy, and D. L. Cocke, *ibid.*, **129**, 1276 (1982).
- S. C. Tjong and E. Yeager, *ibid.*, **129**, 1276 (1982).
- O. J. Murphy, J. O'M. Bockris, T. E. Pou, D. L. Cocke, and G. Sparrow, *ibid.*, **129**, 2149 (1982).
- J. O'M. Bockris, M. Genshaw, and V. Brusica, *Symp. Faraday Soc.*, **4**, 177 (1970).
- J. Eldridge, M. E. Kordes, and R. W. Hoffman, *J. Vac. Sci. Technol.*, **20**, 934 (1982).
- G. G. Long, J. Kruger, D. R. Brack, and M. Kuriyama, *This Journal*, **130**, 240 (1983).
- G. G. Long, J. Kruger, D. R. Black, and M. Kuriyama, *J. Electroanal. Chem.*, **250**, 603 (1983).
- K. Kudo, T. Shibata, G. Okamoto, and N. Sato, *Corros. Sci.*, **8**, 809 (1968).
- T. E. Pou, O. J. Murphy, V. Young, J. O'M. Bockris, and L. L. Tongson, *This Journal*, **131**, 1243 (1984).
- S. Music, A. Vertes, G. W. Simmons, E. Czako-Nagy, and H. Leidheiser, *J. Colloid and Interface Sci.*, **85**, 256 (1982).
- B. D. Cahan and C. T. Chen, *This Journal*, **129**, 474 (1982).
- F. Watari, J. Van Landuyt, P. Delavignetti, and S. Amelincksi, *J. Solid State Chem.*, **29**, 137, 417 (1979).
- S. Yariv, E. Mendolovici, and R. Villalba, *J. Chem. Soc., Faraday Trans. 1*, **76**, 1442 (1980).
- S. Rajendran, V. Sitakara Rao, and H. S. Maiti, *J. Mater. Sci.*, **17**, 2709 (1982).
- A. K. Nikumbh, K. S. Rane, and A. J. Mukhedkar, *ibid.*, **17**, 2503 (1982).
- F. Watari, P. Delavignetti, J. Van Landuyt, and S. Amelincksi, *J. Solid State Chem.*, **48**, 49 (1983).
- J. R. Ambrose and J. Kruger, "Proc. Fourth Int. Congress Metallic Corrosion," p. 698, NACE, Houston (1973).
- V. P. Tayal, B. K. Srivastava, and D. P. Khandelual, *Appl. Spectros. Revs.*, **16**, 43 (1980).
- B. Terand, G. Nowogrocki, and M. Figlarz, *J. Solid State Chem.*, **38**, 312 (1981).
- P. W. Atkins, "Physical Chemistry," p. 268, Freeman & Co., San Francisco (1982).
- A. Benninghoven, C. A. Evans, R. A. Powell, R. Shimizu, and H. A. Storms, Editors, "Secondary Ion Mass Spectrometry SIMS-II," Vol. 9, Springer Series in Chemical Physics, Springer Verlag, New York (1980).
- N. Winograd, *Prog. Solid State Chem.*, **13**, 285 (1982).
- P. W. Atkins, "Physical Chemistry," p. 908, Freeman & Co., San Francisco (1982).
- J. Ellis, R. Giovanoli, and A. Stumm, *Chimia*, **30**, 194 (1976).
- S. Hoste, L. Verdonck, and G. P. Van der Kelen, *Bull. Soc. Chim. Belg.*, **91**, 597 (1982).
- J. Kruger, in "Passivity and Its Breakdown on Iron and Iron-Base Alloys," R. W. Staehle and H. Okada, Editors, p. 91, NACE, Houston (1974).
- M. J. Pryor, in "Localized Corrosion," R. W. Staehle, B. F. Brown, J. Kruger, and V. Agrawal, Editors, p. 2, NACE, Houston (1974).
- C. Y. Chao, L. F. Lin, and D. D. Macdonald, *This Journal*, **128**, 1187, 1194 (1981).
- K. E. Heusler and L. Fischer, *Werkst. Korros.*, **27**, 551, (1976); 697 (1976); 788 (1976).
- N. Sato, K. Kudo, and R. Nishimura, *This Journal*, **123**, 1419 (1976).
- J. O'M. Bockris, M. A. Genshaw, V. Brusica, and H. Wroblowa, *Electrochim. Acta*, **16**, 1859 (1971).

Corrosion Behavior of Magnetron Sputter-Deposited $[\text{Mo}_{0.6}\text{Ru}_{0.4}]_{82}\text{B}_{18}$ and $\text{Mo}_{82}\text{B}_{18}$ Amorphous Metal Films

R. M. Williams,* A. P. Thakoor,* and S. K. Khanna

Jet Propulsion Laboratory, California Institute of Technology, Pasadena, California 91109

W. L. Johnson*

W. M. Keck Laboratory for Engineering Materials, California Institute of Technology, Pasadena, California 91103

ABSTRACT

Amorphous metallic films of $\text{Mo}_{49}\text{Ru}_{33}\text{B}_{18}$ and $\text{Mo}_{82}\text{B}_{18}$ have been prepared by magnetron sputtering, and their corrosion behavior was investigated and compared with amorphous liquid-quenched $\text{Mo}_{49}\text{Ru}_{33}\text{B}_{18}$ and crystalline Mo in acidic and basic solutions. Sputtered $\text{Mo}_{49}\text{Ru}_{33}\text{B}_{18}$ showed lower corrosion rates compared with liquid-quenched $\text{Mo}_{49}\text{Ru}_{33}\text{B}_{18}$, owing to the superior surface smoothness and uniformity of the former. Amorphous $\text{Mo}_{82}\text{B}_{18}$ showed low corrosion rates in both acidic and basic aqueous solutions. Comparison of the corrosion properties of $\text{Mo}_{49}\text{Ru}_{33}\text{B}_{18}$ with $\text{Mo}_{82}\text{B}_{18}$ and Mo demonstrates the roles of the alloys' constituents. Ru significantly extends the passive region to high anodic potentials, but, at less anodic potentials, $\text{Mo}_{82}\text{B}_{18}$ has the lowest corrosion rate.

The extraordinary corrosion resistance exhibited by many amorphous metals (metallic glasses), owing to their chemical homogeneity, has led to much interest in their properties and applications. The majority of studies of their corrosion behavior have focused on materials produced by the widely employed liquid quenching technique, which yields samples in the form of powders, wires, foils, or ribbons. Amorphous metals can also be prepared by electroless or electrochemical deposition, solid-state diffusion reactions, and by a variety of vapor quenching techniques, in particular, sputtering. Sputtering techniques offer the greatest opportunity for variation of amorphous metal composition even beyond the bulk solubility limits, and are also attractive as a means for producing amorphous metals as protective coatings with good adhesion to substrates. The magnetron sputtering technique has met with increasing acceptance in large-scale industrial deposition applications owing to its high deposition rates, minimum substrate heating, ease of scale up, and extreme versatility (1). It is routinely used for commercial deposition of chromium and antireflection coatings on large area substrates. However, studies of the chemical corrosion behavior of sputter-deposited amorphous metallic films are quite limited. One study by Diegle and Merz comparing the corrosion resistance of triode sputter-deposited and liquid-quenched $\text{Fe}_{45}\text{Ni}_{30}\text{Cr}_2\text{V}_2\text{P}_{15}\text{B}_6$ and $\text{Fe}_{31}\text{Ni}_{30}\text{Cr}_{16}\text{V}_2\text{P}_{15}\text{B}_6$ concluded that the two amorphous materials were generally similar to the liquid-quenched samples in their corrosion behavior, but that the triode sputter-deposited film exhibited higher anodic current densities in some potential regimes and was thus somewhat inferior in its corrosion resistance (2). However, these authors did not discuss in detail the influence of surface roughness and bulk microstructure on the corrosion characteristics of these alloys.

We have undertaken a systematic and comparative study of the corrosion resistance of liquid-quenched and magnetron-sputtered early transition metal-based amorphous alloys in order to understand the role of alloy constituents and composition as well as bulk microstructure and surface features in determining corrosion properties. A second goal was the preparation of amorphous alloys, which are inaccessible by current liquid quenching technology, but could be readily prepared by magnetron sputtering. The amorphous alloy $(\text{Mo}_{0.6}\text{Ru}_{0.4})_{82}\text{B}_{18}$, or $\text{Mo}_{49}\text{Ru}_{33}\text{B}_{18}$, was selected for the comparative study because its physical properties have been thoroughly examined and because it has a comparatively high crystallization temperature (800°C), high mechanical strength, and thus represents a potentially important class of nonferrous-metal-based amorphous alloys derived from early

transition metals and metalloids (3). $\text{Mo}_{82}\text{B}_{18}$ was selected in order to demonstrate that this technique can be used to prepare refractory amorphous alloys, which cannot be prepared by liquid quenching. Moreover, the corrosion and thermal behavior of this alloy was expected to provide a useful comparison with $\text{Mo}_{49}\text{Ru}_{33}\text{B}_{18}$, allowing an improvement in our understanding of the effects of the individual constituents. The preparation of $\text{Mo}_{49}\text{Ru}_{33}\text{B}_{18}$, liquid-quenched and magnetron-sputtered amorphous metallic alloys, and the influence of sputtering parameters on microstructure and corrosion behavior of this alloy have already been briefly reported elsewhere (3-6). The corrosion behavior in acidic and basic aqueous solutions, as well as thermal properties of these alloys are reported here in more detail.

Experimental Details

Sputtering targets were fabricated by hot pressing thoroughly mixed powders (325 mesh) of high purity ($\geq 99.99\%$) elements in the desired composition at ~ 3000 psi and 1200°C. The hot-pressed targets were then machined to the exact size to fit the magnetron sputtering gun (Sputtered Films, Incorporated). Films 2-10 μm thick were deposited by magnetron sputtering onto precleaned glass or freshly cleaved mica substrates under conditions described elsewhere (3, 4, 5). Films were analyzed by energy dispersive analysis (EDS) and ion microprobe depth profiling in order to confirm uniformity of chemical composition. Differential thermal analysis (DTA) and differential scanning calorimetry (DSC) were carried out on the samples, scraped from the substrates, in order to measure temperatures at which relaxation and crystallization processes occur in the materials. X-ray diffraction patterns were measured before and after annealing experiments using either a powder diffractometer or a Guinier camera in order to unambiguously characterize the nature of transitions observed by DTA and DSC. The preparation and characterization of liquid-quenched $\text{Mo}_{49}\text{Ru}_{33}\text{B}_{18}$ alloys have been described previously (6). Electrodes for electrochemical studies were prepared by attaching leads to samples with indium-zinc solder, and covering leads and edges of the sample with epoxy. Potentiostatic and potentiodynamic polarization data were obtained in 1.0N aqueous solutions of HCl and H_2SO_4 , and 0.1N NaOH, using a Princeton Applied Research Model 173 potentiostat and a Model 376 log-current converter with Ag/AgCl and Hg/HgO reference electrodes in acidic and basic solution, respectively. Potentiodynamic data were collected at scan rates of 1-100 mV/s, but a 10 mV/s scan rate showed passivation behavior best. Potentiostatic measurements were made after holding the electrode at each potential in the passive region for 20-180 min, until a

* Electrochemical Society Active Member.

steady response was obtained. At potentials where corrosion was very rapid, measurements were made after 1-20 min since thin film integrity was short lived at high current densities. Corrosion measurements were also performed on liquid-quenched $\text{Mo}_{49}\text{Ru}_{33}\text{B}_{18}$ and molybdenum sheet (Alfa, 99.9%) for purposes of comparison.

Results and Discussion

$\text{Mo}_{49}\text{Ru}_{33}\text{B}_{18}$ films deposited under low pressures of argon gas ($\leq 5 \times 10^{-3}$ torr) exhibited a very smooth surface finish and a uniform tensile fracture cross section. Under higher Ar pressures ($35\text{--}75 \times 10^{-3}$ torr), the surface roughness increased and a distinct vertical columnar structure was seen in cross section. Scanning electron microscope photographs of the cross sections of films produced in both of these pressure ranges are shown in Fig. 1.

The films deposited under 5×10^{-3} torr Ar were slightly variable from batch to batch and displayed slightly different behavior when deposited on different substrate materials. Films deposited on glass substrates could be easily removed, intact, by immersion of the sample in concentrated HCl, but the films tightly coiled as they separated from the glass substrate, indicating high stress density in the as-deposited films. Films on mica substrates generally exhibited better adhesion and

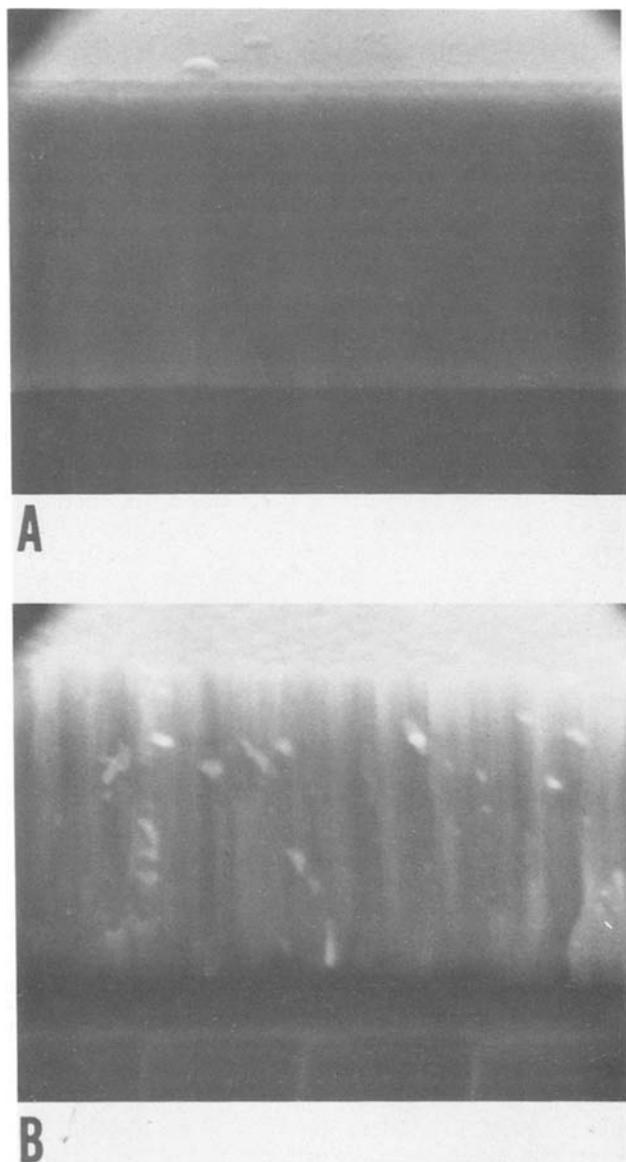


Fig. 1. Tensile fracture cross sections of $\text{Mo}_{49}\text{Ru}_{33}\text{B}_{18}$ films sputtered under Ar pressures of: $< 5 \times 10^{-3}$ torr (A), and $> 35 \times 10^{-3}$ torr (B). The films are each about $2.5 \mu\text{m}$ thick.

somewhat better corrosion resistance than most of the films deposited on glass. Clearly, complete optimization of the deposition process on different substrates must involve characterization of crystallinity and short-range order, microstructure, surface morphology, and the frozen-in internal, as well as interfacial stresses of the film. Figure 2 shows DTA plots for both liquid-quenched and magnetron sputter-deposited metallic amorphous alloys. Relaxation processes occur at 350° and 650°C for $\text{Mo}_{49}\text{Ru}_{33}\text{B}_{18}$ and $\text{Mo}_{82}\text{B}_{18}$, respectively. Crystallization occurs at $\sim 800^\circ\text{C}$ for $\text{Mo}_{49}\text{Ru}_{33}\text{B}_{18}$ and begins at $\sim 950^\circ\text{C}$ for $\text{Mo}_{82}\text{B}_{18}$ (3). X-ray powder diffraction patterns of the amorphous $\text{Mo}_{49}\text{Ru}_{33}\text{B}_{18}$ show broad, diffuse lines which shift slightly to shorter d spacings after relaxation. These peaks are further shifted and greatly sharpened after crystallization and the diffraction pattern became more complex. The diffuse diffraction pattern of $\text{Mo}_{82}\text{B}_{18}$ changes substantially after annealing for one day at 650°C without a significant increase in the distance over which order exists (7). Segregation as well as relaxation apparently occurs at 650°C , since three of the diffuse lines agree with the d spacings of Mo 110, 200, and 211 vectors within $1.5 \times 10^{-3}\text{\AA}$, and several new diffuse lines appear at 650°C , clearly indicating short-range structural changes. More new lines appear and all diffraction lines become sharp after annealing at 950°C for 20 min. The diffraction pattern of a sample annealed to 950°C was assigned to a mixture of crystalline Mo and a previously unknown Mo-B phase (8).

Annealing $\text{Mo}_{82}\text{B}_{18}$ at 650°C results in a decrease in the d spacing of the first strong diffraction peak, from 2.249\AA in the unannealed sample to 2.227\AA in the annealed sample, but this diffraction peak remains diffuse, even after annealing for 24h. These d spacings are clearly too small to be the nearest neighbor distances for Mo in an alloy, but are close to the 110 distance in crystalline Mo. Assuming short-range structure in $\text{Mo}_{82}\text{B}_{18}$ is similar to that in crystalline Mo, the nearest neighbor distance is 2.754\AA before annealing and 2.728\AA after annealing. There is no further change in this d spacing after annealing at 950°C for 20 min, but this and all other diffraction peaks sharpen, indicative of formation of long-range crystalline order in the sample. Similarly, sputtered $\text{Mo}_{49}\text{Ru}_{33}\text{B}_{18}$

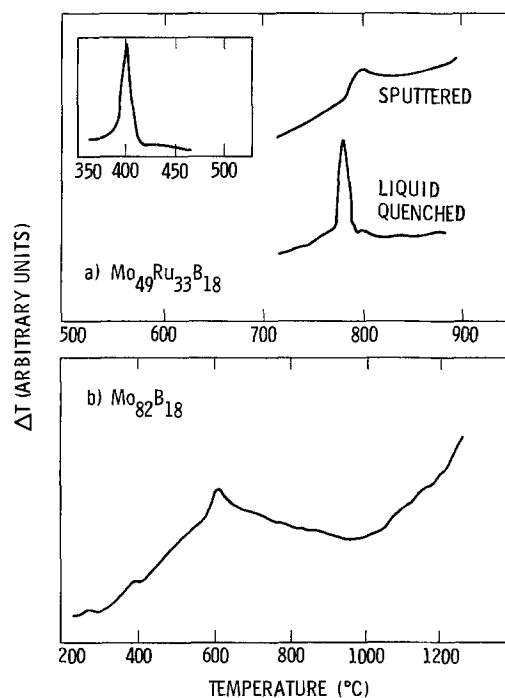


Fig. 2. (a): DTA plots showing crystallization exotherms of sputtered and liquid-quenched $\text{Mo}_{49}\text{Ru}_{33}\text{B}_{18}$ at $780^\circ\text{--}790^\circ\text{C}$. Inset shows DSC plot of sputtered films showing exotherm due to relaxation at 400°C . (b): DTA plot of $\text{Mo}_{82}\text{B}_{18}$ shows exotherm at 600°C due to relaxation/segregation and at $\geq 950^\circ\text{C}$ due to crystallization.

crystallizes at $\sim 790^\circ\text{C}$, but exhibits a thermal relaxation at 450°C , which is reflected in a decrease in the first nearest neighbor distance from 2.73 to 2.71 Å, the latter distance also being characteristic of liquid-quenched $\text{Mo}_{49}\text{Ru}_{33}\text{B}_{18}$.

Potentiostatic and potentiodynamic data are presented in Fig. 3-5. This data represents measurements on films prepared in argon at pressures less than 5×10^{-3} torr. Films prepared under these conditions were fairly reproducible and showed good passivation behavior, whereas films prepared at higher pressures or in the presence of nitrogen or oxygen showed higher corrosion rates at all potentials, and in some cases disintegrated immediately on contact with electrolyte solutions (5). The magnetron sputter-deposited films of $\text{Mo}_{49}\text{Ru}_{33}\text{B}_{18}$ showed passive behavior from ~ -0.4 to $\sim +1.1\text{V}$ in acid solutions (1.0N HCl and H_2SO_4), from ~ -0.6 to $\sim +0.4\text{V}$ in 0.1N NaOH. The presence of ruthenium, which is not oxidized until quite anodic potentials, results in a greatly reduced corrosion rate in $\text{Mo}_{42}\text{Ru}_{33}\text{B}_{18}$ in the range $+0.4$ to $+1.1\text{V}$ vs. Ag/AgCl. Corrosion studies of crystalline molybdenum-ruthenium alloys have also demonstrated the reduction of the corrosion rates in the range of $+0.4$ to $+1.1\text{V}$ vs. Ag/AgCl by addition of small percentages of ruthenium to molybdenum (9).

The first anodic passivation process at $\sim -0.2\text{V}$ vs. Ag/AgCl is common to $\text{Mo}_{49}\text{Ru}_{33}\text{B}_{18}$, $\text{Mo}_{82}\text{B}_{18}$, and crystalline Mo, and can be tentatively ascribed to formation of a passivation film containing Mo in mixed valent oxide of average oxidation state Mo^{+4} based on analogy to corrosion studies of other Mo containing alloys (9, 10). Likewise, the anodic process at $+0.4\text{V}$ vs. Ag/AgCl is common to all of the alloys and probably results in a Mo^{+5} - Mo^{+6} containing film.

This oxidation occurs at -0.3 to -0.4V vs. HgO/Hg in 0.1N NaOH, but at about $+0.2\text{V}$, potentiostatic current time curves show a minimum current of $\sim 10 \mu\text{A}/\text{cm}^2$ after several minutes, followed by a gradual increase to a steady-state current of $\sim 100 \mu\text{A}/\text{cm}^2$ after several hours. This may be explained by the high solubility of Mo^{+6} , i.e., as molybdate, in basic solution, and implies that the passive film is fairly completely converted to Mo^{+6} compounds at this potential. The highest potential anodic

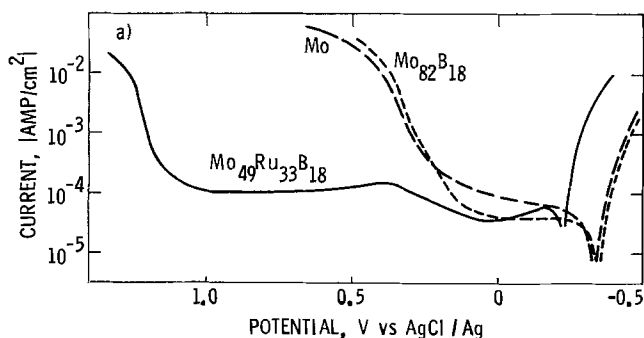


Fig. 3. Potentiodynamic polarization data for $\text{Mo}_{49}\text{Ru}_{33}\text{B}_{18}$ and $\text{Mo}_{82}\text{B}_{18}$ sputtered films and Mo in 1N H_2SO_4 . Scan rate: 10 mV/s.

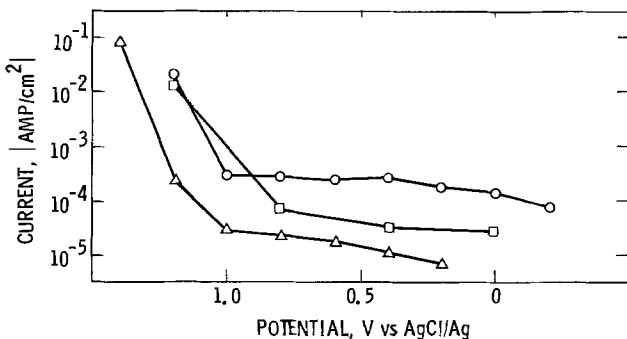


Fig. 4. Potentiostatic polarization data for $\text{Mo}_{49}\text{Ru}_{33}\text{B}_{18}$ in 1N HCl. (○): Liquid-quenched foil. (□): liquid-quenched foil, after polishing. (△): Sputtered film.

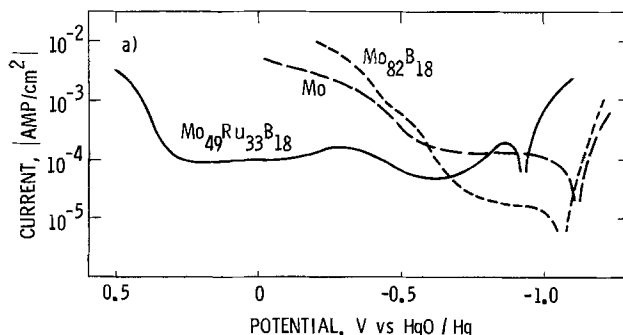


Fig. 5. Potentiodynamic polarization data for sputtered films of $\text{Mo}_{49}\text{Ru}_{33}\text{B}_{18}$, $\text{Mo}_{82}\text{B}_{18}$, and Mo in 0.1N NaOH. Scan rate: 10 mV/s.

process exhibited by $\text{Mo}_{49}\text{Ru}_{33}\text{B}_{18}$ occurs at a potential where no anodic waves are exhibited by $\text{Mo}_{82}\text{B}_{18}$ or Mo; it is presumably due to oxidation of Ru(O) to $\text{Ru}^{3+}/\text{Ru}^{4+}$. A brown-black film is observed to form at the onset of transpassive behavior at $\sim +1.0$ - 1.1 vs. Ag/AgCl, and gas evolution (presumably O_2) is only observed at still more anodic potentials. The lack of good resolution of waves in the voltammograms at scan rates of 1 to 100 mV/s is ascribed to the formation of a continuous range of mixed-valent molybdenum oxides. The potentiostatic and potentiodynamic behavior of magnetron-sputtered films and liquid-quenched foils of $\text{Mo}_{49}\text{Ru}_{33}\text{B}_{18}$ show similar corrosion responses, but the corrosion rate is somewhat greater for the liquid-quenched samples, as shown in Fig. 4. Polished samples of the liquid-quenched foils show a lower potentiostatic corrosion rate than unpolished samples, but the magnetron-sputtered films are still somewhat better. It appears that the very smooth, uniform surface of the sputtered films is responsible for its favorable corrosion response; the liquid-quenched samples, by contrast, have fairly rough surfaces. There is a small difference in the structure of liquid-quenched vs. sputtered $\text{Mo}_{49}\text{Ru}_{33}\text{B}_{18}$, as shown by the difference in the nearest neighbor spacing and minor differences in the thermal analytical data. However, since the differences in electrochemical behavior manifest themselves only in the magnitude of the currents observed, and polished liquid-quenched samples are not greatly different than sputtered samples, it is clear that most of the difference is due to surface uniformity. Amorphous $\text{Mo}_{82}\text{B}_{18}$ is similar to crystalline Mo in its corrosion response in acid 1.0N H_2SO_4 , but shows significantly lower anodic current density in the passive regime from -0.3 to $+0.3\text{V}$, and is also superior to amorphous $\text{Mo}_{49}\text{Ru}_{33}\text{B}_{18}$ within a limited potential regime.

In order to verify that pitting corrosion plays no important role in the corrosion of $\text{Mo}_{49}\text{Ru}_{33}\text{B}_{18}$ films, even in the transpassive regime several films were cycled from the passive regime to the active anodic corrosion regime and then taken to more cathodic potentials with agitation of the solution until the thick anodic film was dislodged. Invariably, the smooth mirror surface was retained for sputter-deposited films and no evidence of pitting corrosion was observed for either sputtered or liquid-quenched samples. In fact, the corrosion behavior of unpolished liquid quenched samples was improved by cycling in this manner, owing to an electropolishing effect, since no localized corrosion processes occurred, owing to the homogeneity of the bulk alloy.

Conclusions

Magnetron sputtering can be used to prepare amorphous alloys having compositions not easily accessible by liquid quenching techniques because existence of a deep eutectic of solid solubility is not a prerequisite. This technique may be especially useful for depositing protective coatings of amorphous metallic alloys with good adhesion as well as corrosion resistance. $\text{Mo}_{82}\text{B}_{18}$ is an example of such a high crystallization temperature alloy which has not yet been successfully prepared by liquid quenching.

Vapor-quenched amorphous metal films prepared under optimum deposition parameters show superior corrosion resistance, as compared with liquid-quenched samples, owing to the superior surface uniformity of the former. However, the sputtered films show poorer corrosion resistance if sputtering conditions which give rise to columnar deposits are used (5). The fundamental electrochemical reactions occurring during corrosion of liquid- and vapor-quenched amorphous alloys of similar composition are apparently identical since the potentials at which corrosion reactions are initiated are the same. The important differences between vapor-quenched (sputtered) and liquid-quenched amorphous alloys are due largely to the higher quenching rate, $\sim 10^{11}$ K/s for sputtering vs. $\sim 10^6$ K/s for liquid quenching. The liquid quenched samples have a possibility of inhomogeneity due to a cooling rate profile within the sample (11). Some chemical segregation is possible, and microstructural order may vary in the sample. Differences in composition have been observed between the top and bottom of liquid-quenched ribbons (12). More rapid quenching rates eliminate these diffusion-related inhomogeneities. These results are in basic agreement with the results of Diegle and Merz, who indicated that the thermal properties at their sputtered films of amorphous iron-based metallic alloys were virtually identical to the properties of melt-spun alloys and that the triode-sputtered films exhibited somewhat higher corrosion rates, but with overall corrosion behavior similar to the melt-spun alloys (2). It is apparent that vapor deposition techniques can yield films with widely varying corrosion behavior, depending on the deposition parameters employed and resultant variations in bulk and surface properties, such as microstructure, adhesion to substrate, and internal stress.

Magnetron sputtering offers a unique opportunity for synthesis of amorphous alloys of very refractory compositions, based on early transition metals and metalloids. Deposition of these alloys in adherent form on a variety of substrates is possible. Also, since compositions are not limited to those near eutectic compositions and quenching rates are high, systematic exploration and exploitation of a complete range of alloy compositions is possible. However, microstructure, thermal properties, and interfacial stress between film and substrate are all dependent on the deposition process, and understanding

and control of these properties of the films requires more detailed studies of the deposition process.

Acknowledgments

The research described in this paper was carried out at the Jet Propulsion Laboratory, California Institute of Technology, and was sponsored under a grant from the Caltech President's Fund, NASA Contract no. NAS7-918, and under contract no. DE-AI07-80ID12138 from the Department of Energy, Office of Industrial Programs, through an agreement with The National Aeronautics and Space Administration. We would like to thank Dr. M. Mehra, Professor S. Samson, and Dr. B. Carter for helpful discussions and assistance.

Manuscript submitted Feb. 6, 1984; revised manuscript received July 25, 1984.

The Jet Propulsion Laboratory assisted in meeting the publication costs of the article.

REFERENCES

1. J. A. Thornton, in "Deposition Technologies for Films and Coatings", R. Bunshah, Editor, p. 170, Nozes Publication, NJ. (1982); R. K. Warts, in "Thin Film Processes", J. L. Vossen and W. Kern, Editors, p. 167, Academic Press, New York, NY (1978).
2. R. B. Diegle and M. D. Merz, *This Journal*, **127**, 2030 (1980).
3. S. K. Khanna, A. P. Thakoor, R. F. Landel, M. Mehra, and W. L. Johnson, *App. Phys. Commun.*, **1**, 135 (1981).
4. M. Mehra, W. L. Johnson, A. P. Thakoor, and S. K. Khanna, *Solid-State Commun.*, **47**, 859 (1983).
5. A. P. Thakoor, S. K. Khanna, R. M. Williams, and R. F. Landel, *J. Vac. Sci. Technol. A*, **1**, 520 (1983).
6. W. L. Johnson and A. R. Williams, *Phys. Rev. B*, **20**, 1640 (1979).
7. A. J. C. Wilson, "X-Ray Optics," Methuen, London (1949).
8. JCPDS-Powder Diffraction File no. 6-0228, 6-0636, 6-0644, 6-0682, 20-1236, 25-0561.
9. S. Kabanov, T. Loboda, M. Raevskaya, and E. Sokolovskaya, *Vestn. Mosk. Univ. Ser. 2*, **21**, 77 (1980).
10. K. Asami, M. Naka, K. Hashimoto, and T. Masumoto, *This Journal*, **127**, 2130 (1980).
11. H. A. Daines, in "Amorphous Metallic Alloys," F. E. Luborsky, Editor, pp. 8-25, Butterworths, London (1983).
12. T. Devine, *This Journal*, **124**, 38 (1978).

Effect of Fluid Flow on Removal of Dissolution Products from Small Cavities

Richard C. Alkire* and David B. Reiser*¹

Department of Chemical Engineering, University of Illinois, Urbana, Illinois 61801

Robert L. Sani

Department of Chemical Engineering, University of Colorado, Boulder, Colorado 80302

ABSTRACT

The effect of fluid flow on transport of reaction products from dissolving cavities was investigated theoretically in order to establish regions of parameter space where the solution within the cavity may be above, or below, the saturation concentration. Situations where such phenomena are important include etching of masked devices and pitting corrosion. Steady laminar convective transport was analyzed in smooth-walled two-dimensional cavities (trenches) of several shapes. The fluid flow patterns within the cavities were obtained in the Stokes flow region. The convective diffusion problem was solved for values of the Peclet number between 1 and 500. Two types of boundary conditions were investigated: (i) uniform dissolution of the cavity surface, and (ii) uniform concentration along the cavity surface. Numerical calculations were carried out with a commercial, general-purpose finite element code. It was found that for $Pe \leq 1$, the entire cavity volume had a concentration in excess of 90% of the saturation value while for $Pe \geq 100$, the electrolyte within the cavity was substantially free of dissolution products.

Dissolution of small active sites on a surface exposed to flowing fluid will lead eventually to recession of the active surface below the surrounding plane, to formation of cavities occluded from the exterior flow region, and to secondary fluid flow patterns within the cavities. Situations where such phenomena are important include pitting corrosion, etching of masked device surfaces, electrochemical machining and electropolishing, and heat/mass transfer from rough surfaces. In general, the velocity of secondary fluid motion within cavities (*i. e.*, trapped eddies) will increase as the size of the cavity increases, that is, as dissolution proceeds. Therefore, in early stages of cavity formation, mass transport by diffusion may well control the rate of dissolution, but, as cavity size increases, transport by convection will increase and will eventually predominate over diffusion processes. Thus, the evolution of cavity shape is accompanied by a change in the controlling transport process. The purpose of this investigation was to study theoretically the effect of fluid flow on mass transfer within small cavities dissolving at such high rates that precipitation of dissolution products may occur.

While there are numerous applications of dissolution from small cavities, the present investigation evolved from a study of flow effects of pitting corrosion. General reviews of pitting are available (1-4) as are qualitative discussions of the effect of flow on corrosion (5-7). Efforts to model quantitatively the effect of fluid flow on corrosion have also recently been summarized (8).

Evidence that mass transport controls pitting corrosion of stainless steel (SS) has been reported by Isaacs (9) and by Rosenfeld *et al.* (10). Flow effects in pit-like geometries were studied by Beck (11) with the use of a flow channel, in one wall of which was an artificial cavity containing an electrode. It was found that fluid velocity influenced the dissolution rates of Al, Ti, and Fe electrodes. More recently, Beck and Chan (12) studied real pits on pure Fe and 304 SS in chloride solutions and found that there was a threshold velocity, above which fluid flow was important, and also a critical velocity, above which the current became limited by ohmic resistance rather than by convective transport. It was also found that stainless steel repassivated at flow rates above the (upper) critical velocity.

It has come to be generally recognized that the composition of solution within corrosion pits is substantially dif-

ferent from the exterior solution and, in particular, that salts of metal dissolution products may exceed saturation levels (13) and precipitate as metal salt films (10, 14-20). Based on transport equations, Beck and Alkire (21) predicted that the current density at small corrosion sites (10) could exceed 10^3 A/cm² and could therefore cause precipitation of salt films within 10^{-4} s following pit nucleation.

Weisbrod studied the repassivation of Fe, Co, and carbon steel in flowing sulfuric acid (22) and found that there was a critical velocity above which the specimens would not repassivate, a result which was opposite from that observed in chloride systems (12). It was found that the effect was due to rinsing off of precipitated sulfate salt films which formed on the surface during the repassivation sequence. Alkire and Cangelari (23) predicted theoretically the flow conditions under which such metal salt films would be rinsed away from a dissolving surface coplanar with the wall of a flow channel.

While a unified treatment of pitting corrosion has not yet emerged at the fundamental level, the foregoing discussion indicates that mass-transfer processes and precipitation of surface films are intimately coupled with the phenomenon. As a consequence, a general treatment of the effect of fluid flow past cavities within which salt films may precipitate would clearly be helpful.

The behavior of fluid flow (24-27) and of heat- and mass transfer (28-33) within cavities has been vigorously studied for a variety of geometries. In addition to pitting corrosion, there are many other processes where convective mass transfer from cavities controls the rate of dissolution (47), including electrochemical machining (34), chemical etching of masked device surfaces (35), heat- and mass transfer from rough surfaces (36), clot formation in flowing blood (37), and aerodynamic applications (38).

The goal of the present investigation was to develop an improved method of analysis which would be sufficiently robust that it could be expanded at a later time to include more factors than just mass transfer. The finite element method (FEM) was selected (39). The FEM has been applied to a small number of electrochemical applications to data (40-43), and has been found to be particularly effective for situations which involve curved boundaries and shape change.

Theoretical Information

The geometry of the systems studied in the present work are shown in Fig. 1. These geometries represent a range of shallow, cylindrical, and deep cavities. The uppermost diagram illustrates the general configuration un-

* Electrochemical Society Active Member.

¹Present address: Alcoa Laboratories, Alcoa Center, Pennsylvania 15069.

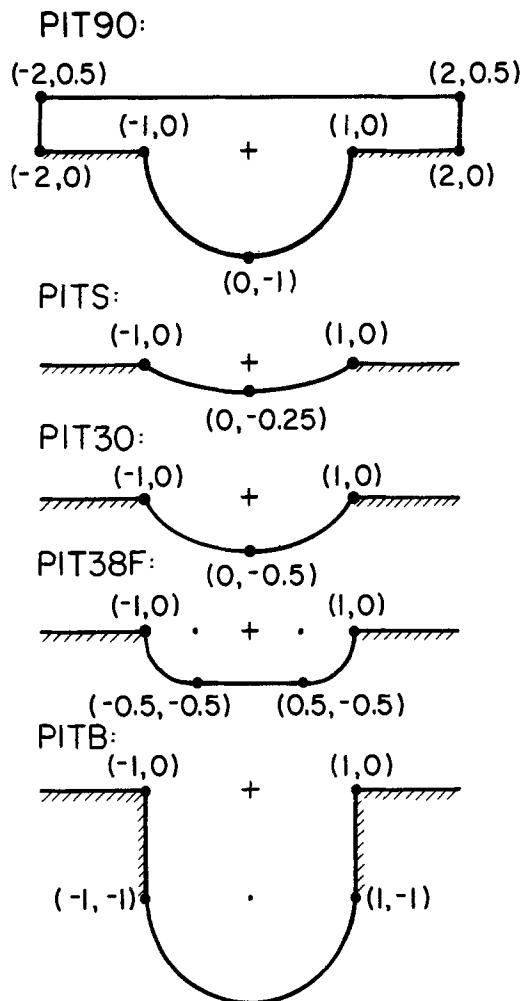


Fig. 1. Two-dimensional cavity geometries under study. The uppermost diagram illustrates the entire region over which solutions were obtained. The other diagrams depict the cavity shapes which were investigated, i.e., the lower surface of the region.

der study; a rectangular region in one wall of which is a two-dimensional semicircular cavity, or trench. Four other cavity configurations were also studied, as also shown in Fig. 1. Each cavity shape is specified by the coordinates with respect to the center cross given on the diagrams. While analysis of flow past an axisymmetric (hemispherical) cavity would be more representative of a real corrosion pit, the problem would then correspond to a three-dimensional situation which would increase computation cost and difficulty significantly. The present analysis of flow past a two-dimensional trench represents progress toward this goal.

Fluid enters the region through the left-hand boundary, flows past the cavity opening, and leaves through the right-hand boundary. The upper boundary of the region was set far enough away, for the region of interest in this study, that the fluid flow was a constant along its surface. The use of dimensionless equations and variables in this study enables the results to be applied to any system for which the configuration and assumptions are valid.

Dissolution occurs along the curved interior surface of the cavity. In Fig. 1, the hatched areas represent unreactive regions of the solid surface. The particular application to which this study was originally directed corresponded to dissolution of a small cavity on an otherwise passive metal immersed in flowing corrosive solution. For this reason, simplifying assumptions will be introduced in order to confine the scope of the assumptions to mass-transfer variables. The finite element method used in this study, however, is flexible and robust and could therefore be expanded in the future to include additional features.

Assumptions.—The cavity was assumed to have a smooth wall. Because interest was directed toward small cavities, the fluid flow in the immediate vicinity of the cavity wall was assumed to be laminar, although the possibility of turbulent flow at a distance was not precluded by the method of analysis. Further, constant property Stokes' flow was assumed ($Re < 0.1$). Since the Schmidt number for aqueous electrodes is approximately 2000, the range of Peclet numbers ($Pe = ReSc$) for which calculations are strictly valid is $Pe < 200$. In the results presented below, the interesting behavior was found to occur over the range $1 < Pe < 100$.

When a system is under mass-transfer control, other possible limitations are less important; therefore charge-transfer and ohmic resistance effects were neglected in this analysis, as was hydrolysis of solvated metal cations. It was assumed that the current efficiency for metal dissolution was 100% so that the local dissolution rate along the surface was proportional to the concentration gradient normal to the surface.

While dissolution causes gradual increase in cavity size, it was assumed that this process is slow enough that a pseudo-steady-state analysis of invariant cavity shapes would be useful. Indeed, it may be shown that the time constant for shape change is significantly longer than the time constant for fluid recirculation within the cavity.

Migration of dissolved metal species was assumed to be negligible owing to the presence of supporting electrolyte, and the physical properties of the system were assumed to be constant. These two assumptions may be questionable if the metal salt has a high solubility, since large metal ion concentrations can then arise within the diffusion region. The effect of migration of, say, divalent metal ions and divalent anions serves to increase the mass flux by a factor of up to two, depending upon the ratio of supporting cations to total anion concentration (44). However, an increase in concentration also serves to decrease the diffusion coefficient. Thus the two questionable assumptions tend fortuitously to offset each other (22).

Two mass-transfer situations were investigated. In the first, it was assumed that the surface was coated with a metal salt film so that the metal ion concentration immediately adjacent to the dissolving surface was assumed to be a constant, equal to the saturation concentration. In the second, the cavity was assumed to maintain a self-similar, semicircular shape during dissolution, according to which the dissolution rate was assumed to have the same value everywhere along the cavity surface.

Equations.—The dimensionless equation for Stokes' flow of a Newtonian fluid is

$$\nabla^2 U (=) Re \nabla P$$

where Re is the Reynolds number. With respect to Fig. 1, the following boundary conditions were used

$$\begin{aligned} U_y &= 0 \text{ on all boundaries} \\ U_x &= 0 \text{ on lower boundary} \\ U_x &= A \text{ on upper boundary} \end{aligned}$$

$$\frac{\partial U_x}{\partial x} = 0 \text{ on left- and right-hand boundaries} \quad [2]$$

These equations are independent of the concentration field and therefore may be solved to obtain the hydrodynamic flow and pressure field. Because the equations are linear in velocity, the results may be scaled to any value of Re for which the Stokes' approximation is valid.

The dimensionless equation of convective mass transfer is

$$UVC = \frac{1}{Pe} \nabla^2 C \quad [3]$$

where Pe is the Peclet number. Two cases of boundary conditions were investigated. In the first case, the surface was assumed to be covered with a metal salt, and the incoming fluid was assumed to contain no dissolved

metal salt

$$C = 1 \text{ on cavity surface}$$

$$C = 0 \text{ at } X = -2, \text{ where fluid enters} \quad [4]$$

$$\frac{\partial C}{\partial n} = 0 \text{ on other boundaries}$$

In the second case, the surface was assumed to dissolve at the same rate everywhere into a fluid which contained no dissolved metal salt.

$$\frac{\partial C}{\partial n} = -Sh \text{ on cavity surface}$$

$$C = 0 \text{ at } X = -2, \text{ where fluid enters} \quad [5]$$

$$\frac{\partial C}{\partial n} = 0 \text{ on other boundaries}$$

where Sh is the Sherwood number.

Method of solution.—The computer code used for calculations in this study was FIDAP, a versatile finite element code for solving fluid dynamics problems including convective heat-transfer applications. FIDAP solves transient or steady-state forms of the momentum and thermal energy equations in two- or three-dimensional finite element domains. The elements may be linear or quadratic elements of isoparametric form. The physical properties of the fluid may depend on time and fluid temperature, or may be constant. By using standard heat- and mass-transfer analogies, the program is also capable of solving problems of convective mass transfer. Boundary conditions can take on a variety of forms. Details of use of the program may be found in Ref. (45), as well as the appendixes of Ref. (46).

Referring to Fig. 1, configurations (a) and (b) were meshed with nine-noded quadratic elements, while the other configurations were meshed with eight-noded quadratic elements produced by the mesh generation package FIMESH (45). Table I gives mesh statistics and representative run times for solving the equations on a Cyber 175 computer. Since an out-of-core solver was used in the program, the central memory used by the program could be controlled by the user. In this study, 143,000 octal words of central memory were used for execution. It was found that computation costs were typically \$0.60/CPU second.

Results and Discussion

Hydrodynamic flow field.—The flow pattern in a cavity of given geometry needs to be determined only once for all Reynolds numbers in the Stokes regime. By substituting the Stokes solutions into the constant-property Navier-Stokes equations via the FIDAP algorithm, it was found that the norm of the error vector divided by the norm of the Stokes' solution vector was less than 0.2%. That is, inertial effects are negligible and the computed results are accurate. Table II provides input velocities (constant A in Eq. [2]), and the velocities at the center of the cavity mouth (u_0) which were used in normalizing the flow fields.

Table I. Mesh statistics and typical run times for FIDAP jobs

Geometry	Number of nodes	Number of elements	Run time for Stokes flow solution	Run time for convective-diffusion solution
PIT90	891	208*	20.70 CPU s	6.71 CPU s
PIT30	795	184*	14.14	5.20
PIT38F	537	160**	7.09	3.19
PITB	721	218**	13.15	4.90
PITS	393	116**	4.57	2.24

* Nine-noded elements.

** Eight-noded elements.

Table II. Characteristic velocities used in calculations

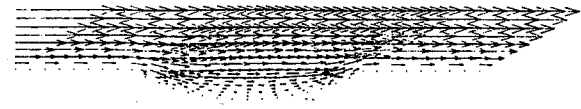
Pit	u input at $y = 0.5$	u calculated at (0, 0)
PIT90	5 radii/s	1.0221 radii/s
PIT30	5	0.7788
PIT38F	6	0.9551
PITB	5	1.2642
PITS	7	1.0449

Figure 2 illustrates the velocity vectors for the flow field in each of the cavity configurations under study. It was found that a single recirculating flow eddy existed in all but the shallowest cavity configuration. No secondary eddies were observed.

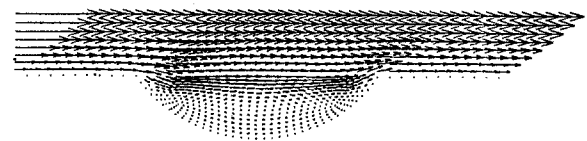
Concentration fields, constant concentration at cavity wall.—The solution of the convective diffusion equation for various values of Pe is shown in Fig. 3 in the form of metal ion concentration contour plots. The lettered contours correspond to lines of constant metal ion concentration, expressed in fractions of the saturation concentration, as given in the figure caption. Since the Peclet number contains both velocity and cavity size, the progression from Fig. 3(a) to Fig. 3(e) corresponds either to a sequence of increasing fluid flow, or to a sequence of increasing cavity sizes.

For $Pe = 1$ [Fig. 3(a)], the concentration contours near the top of the region are not realistic because the boundary condition on that surface forces the concentration gradients to the value of zero. However, modification in the

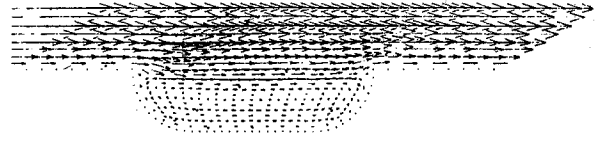
PITS



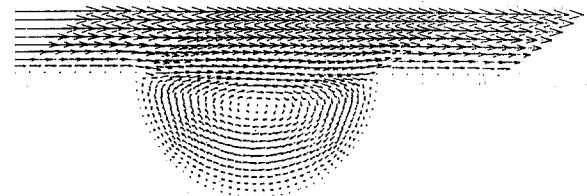
PIT30



PIT38F



PIT90



PITB

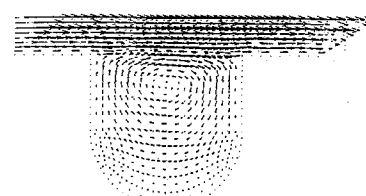


Fig. 2. Velocity vector flow field within various cavities. The arrow length is proportional to velocity.

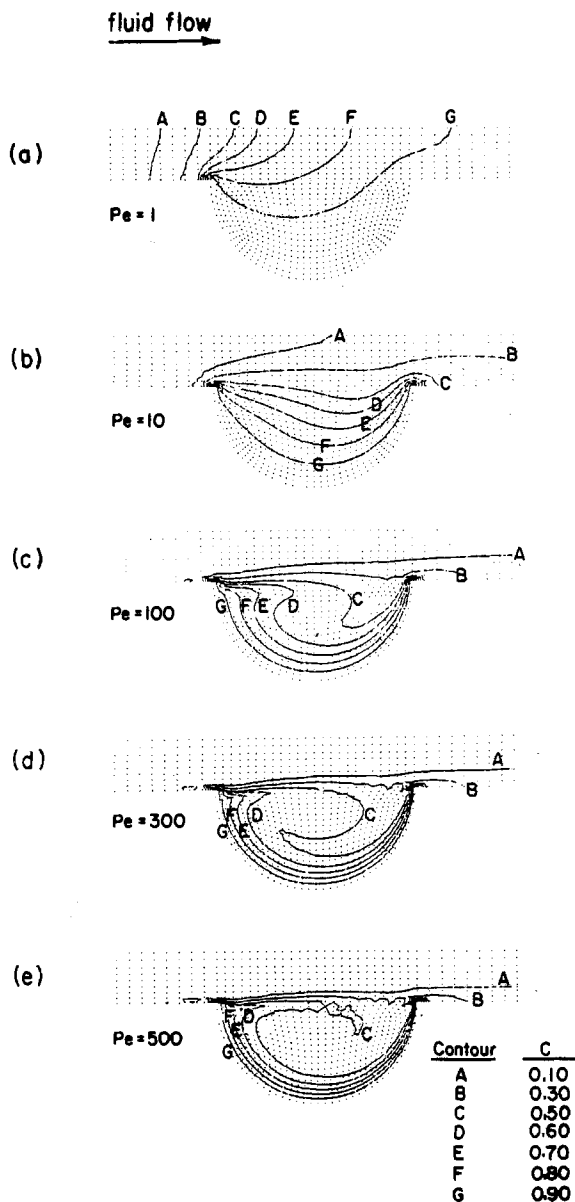


Fig. 3. Effect of Peclet number on metal ion concentration for PIT90 configuration when the concentration at the cavity wall is equal to the saturation value everywhere ($C = 1$). Equiconcentration contours are shown for various fractions of the saturation value as given in the accompanying key.

boundary condition on the upper surface would not be expected to change the observation that, for $Pe = 1$, the solution within the cavity is within 90% of the saturation concentration throughout. That is, the fluid flow external to the pit does not substantially influence the transport of dissolution products within the pit. Indeed, the contours A and B indicate clearly that there is substantial diffusion in the upstream direction, against the direction of fluid flow. Because the concentration field inside such pits is disrupted to only a minor extent by the action of fluid flow, it is concluded that very small pits are insensitive to external flow conditions even when there may be substantial superficial flow velocities outside the pit.

For $Pe > 1$, the metal ions were swept out the right-hand side of the region, and the anomalous behavior at the upper surface was not significant. For $Pe = 100$, Fig. 3(c), it may be seen that the electrolyte just outside the cavity mouth is essentially free of metal ions. That is, the effect of fluid flow has increased to substantial proportions. In addition, the effect of the recirculating flow pattern within the cavity can clearly be seen to influence the mass-transfer process.

For $Pe = 500$, the mesh size is too large for generation of smooth contours in the center of the cavity, a problem which could be eliminated by remeshing. The numerical jitter does not influence the observation that the concentration variation becomes confined to a thin region adjacent to the cavity surface.

Reference (46) contains additional results for other cavity configurations. These results indicate that the effect of recirculating flow becomes more pronounced as the pit becomes deeper, and that the influence of external flow on the ion concentration profile near the bottom of the pit decreases as the pit shape becomes deeper.

In all cases where there is a recirculating flow, the consequence is to cause the dissolution rate to have the greatest value along the downstream surface of the cavity. Such results are consistent, for example, with the experimental observation of "flow tails" in nickel pitting at high current densities under high electrolyte flow as seen in Fig. 5 of Ref. (34b) and Fig. 6 of Ref. (34c). In the shallowest cavity studied, there was no recirculation pattern, and the dissolution rate was highest at the upstream edge of the cavity.

Concentration profiles, constant flux at the cavity wall.—Under certain conditions, corrosion pits are known to exhibit hemispherical shapes, which implies that the dissolution rate is constant along the interior dissolving surface, a condition which may be simulated mathematically by the boundary conditions expressed in Eq. [5] above.

Figure 4 illustrates results for the semicircular cavity configuration for five values of Pe over the range 1-500 while holding Sh constant at 1.31. This sequence therefore corresponds to a variation of velocity while holding the average dissolution rate constant. The lettered contour lines indicate surfaces of constant concentration, expressed as fractions of the saturation concentration as given in the key associated with each figure. Since there is no physical limitation in the model on the value of the concentration, it is possible for the concentration to rise above the saturation value (1.0). For the conditions shown in Fig. 4, it may be seen that the entire cavity region contains supersaturated solution at $Pe = 1$, while for $Pe = 100$ the cavity region is everywhere below the saturation concentration. In addition, it may be seen that the region where the concentration is highest shifts from the downstream portions of the cavity surface (for small Pe) to the upstream region (for large Pe). In the shallowest cavity, where no recirculation eddy was present, the maximum concentration was always on the downstream portion of the cavity surface.

Similar concentration field plots are available for other cavity configurations in Ref. (46).

Critical flow conditions for salt film precipitation.—Based on the foregoing calculations, it is possible to map out generalized conditions under which saturation concentration will be found in cavities exposed to flowing fluid. For a cavity of certain shape experiencing electrolyte flow of a given velocity, there is a value of current density which must exist in order to sustain a saturated solution along the cavity surface. That is, for a given Pe , there exists some value of Sh which will result in $C_{max} = 1.0$ somewhere along the surface. In addition, there exists another value of Sh which will result in a $C_{max} \geq 1.0$ everywhere along the surface.

Figure 5 illustrates critical flow conditions for all of the cavity configurations investigated (46). For each configuration, two lines are indicated in the graph; the symbols in Fig. 5 represent values for which computations were carried out with use of Eq. [5]. The left-hand group of lines gives, for each of the five configurations, the critical conditions where the entire surface is below the saturation level everywhere along the cavity surface. Above and to the left of the line corresponds to flow conditions and dissolution rates where the solution at the cavity surface cannot exceed saturation. The right-hand group of lines gives, for the five configurations, the critical condi-

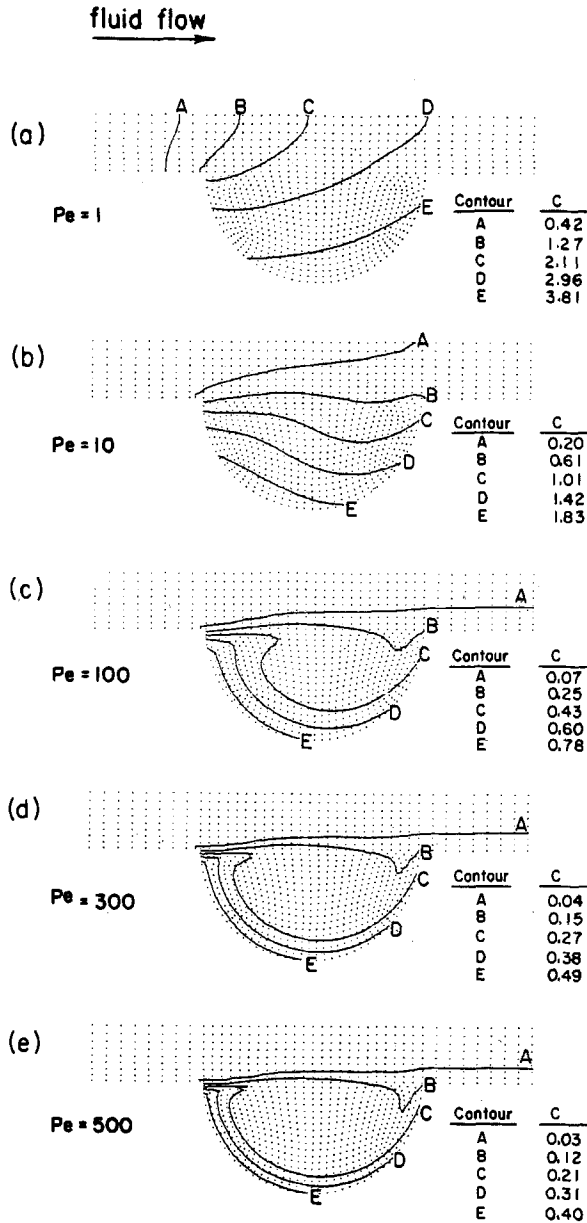


Fig. 4. Effect of Peclet number of metal ion concentration for PIT90 shape when the dissolution rate is constant over the cavity surface ($Sh = 1.31$). Equiconcentration contours are shown for various fractions of the saturation value as given in the keys associated with each figure.

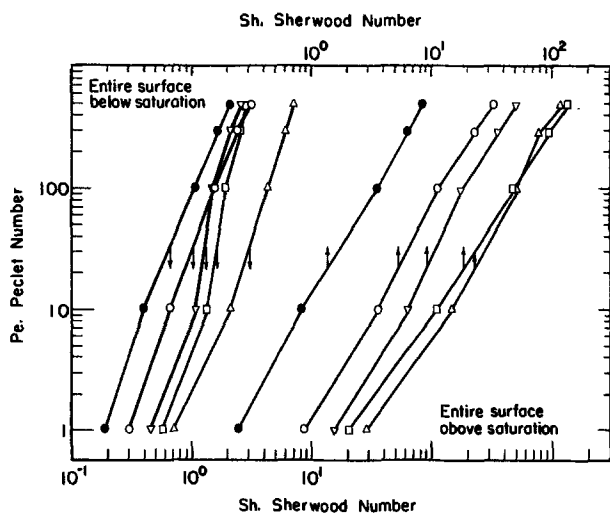


Fig. 5. Critical convective transport conditions for removal of dissolution products from cavities of various shapes. Δ : PIT38F. \square : PIT30. \circ : PIT90. \bullet : PITB.

tions where the entire surface is above the saturation level. Below and to the right of these lines corresponds to the region of parameter space where precipitation of dissolution products would be expected to occur.

In Fig. 5, the region between the two lines corresponds, for each configuration, to the region where some portion of the solution within the cavity would be at or above saturation (deep within the cavity interior), while other portions would be at or below saturation (nearer the cavity entrance).

Figure 5 illustrates that if a cavity is dissolving at a higher rate, it takes a higher flow rate to wash it out. Also, as a cavity becomes deeper, it becomes more difficult to rinse it out. For the configurations investigated, Fig. 5 indicates that an eightfold increase in depth to diameter (PITS vs. PITB) requires a fiftyfold increase in Pe to accomplish complete rinsing of the cavity. In addition, the geometry of the cavity entrance region influences the ease of rinsing: PIT30 and PIT38F are the same depth, but it takes a higher flow rate to rinse out PIT38F than PIT30.

Conclusions

A flexible, robust, commercially available finite element code has been used to predict mass-transfer behavior within cavities during dissolution in the presence of fluid flow. Analysis of the concentration distribution within small cavities has led to a general criterion for predicting conditions under which precipitation of sparingly soluble dissolution products may be expected to occur on the dissolving surface. Early stages of cavity growth were found not to be influenced by external flow owing to the small size of the cavity which impedes fluid circulation. As dissolution continues, however, fluid flow effects become increasingly significant and could eventually rinse out the cavity.

Situations where such phenomena are important include etching of masked surfaces and also pitting corrosion. Disruption of electrolyte in the interior of corrosion pits has been linked by other investigators to the repassivation of active pits, particularly in chloride solutions. It may thus be anticipated that a young corrosion pit would grow to a certain size, at which it would become susceptible to being washed out and thus repassivated. If such a pit were not completely rinsed out while relatively shallow, then it may partially passivate, in the entrance region, but remain active in the more remote regions. Such events could thus lead to evolution of steadily deeper and thus more shielded configurations, which would be increasingly more difficult to repassivate by rinsing. The analysis presented here gives a limiting case of performance against which the behavior of real systems may be compared.

Hydrodynamic strategies for corrosion prevention have not been fully explored to date. The damage of materials by corrosion in the presence of impingement, erosion, wear, cavitation, and other flow-related phenomena represents a research field of vital importance. Of special value would be improved understanding of flow conditions under which inexpensive materials of construction could be used with confidence in corrosive environments.

Acknowledgments

This research was supported by the National Science Foundation (Grants ENG 76-83379 and CPE 80-08947), with further assistance for D.B.R. from an IBM Predoctoral Fellowship, and from the Gulf Oil Foundation. Dr. Michael Engelman, University of Colorado, Boulder, Colorado, assisted in development of numerical procedures.

Manuscript submitted Oct. 5, 1983; revised manuscript received June 15, 1984.

The University of Illinois assisted in meeting the publication costs of this article.

LIST OF SYMBOLS

- c concentration (gmol/cm)
 C concentration (c/c_{sat} , dimensionless)
 D diffusion coefficient (cm^2/s)
 F Faraday's constant, (96,500 C/eq)
 i current density on cavity surface (A/cm^2)
 l_0 half-width of cavity opening (cm)
 n number of electrons participating in electrode reaction
 \hat{n} unit normal vector
 p pressure (g/cm^2)
 P pressure, ($p/\rho u_0^2$, dimensionless)
 Pe Peclet number ($l_0 u_0 / D$, dimensionless)
 Re Reynolds number ($u_0 l_0 \rho / \mu$, dimensionless)
 Sh Sherwood number ($il_0 / n F c_{\text{sat}} D$, dimensionless)
 u_0 velocity at center of cavity opening (cm/s)
 \underline{u} velocity vector, (cm/s)
 \underline{U} velocity (u/u_0 , dimensionless)

Greek characters

- μ viscosity ($\text{g}/\text{cm} \cdot \text{s}$)
 ρ fluid density (g/cm^3)

Subscripts

- max maximum value
 sat saturation value

REFERENCES

- S. Szklarska-Smialowska, *Corrosion*, **27**, 223 (1971).
- S. Szklarska-Smialowska, in "Localized Corrosion," R. W. Staehle *et al.*, Editors, p. 312, NACE-3, Houston (1974).
- J. R. Galvele, in "Passivity of Metals," R. P. Frankenthal and J. Kruger, Editors, p. 285, The Electrochemical Society Monographs Series, Princeton, NJ (1978).
- M. Janik-Czachor, *This Journal*, **128**, 513C (1981).
- F. L. LaQue, in "Corrosion Handbook," H. H. Uhlig, Editor, p. 383, John Wiley and Sons, New York (1948).
- F. L. LaQue, "Marine Corrosion," p. 138, John Wiley and Sons, New York (1975).
- B. C. Syrett, *Corrosion*, **32**, 242 (1976).
- B. T. Ellison and C. J. Wen, *AIChE Symp. Ser.*, **77**, 204, 161 (1981).
- H. S. Isaacs, *This Journal*, **120**, 1456 (1973).
- I. L. Rosenfeld, I. S. Danilov, and R. N. Oranskaya, *ibid.*, **125**, 1729 (1978).
- T. R. Beck, *Corrosion*, **33**, 9 (1977).
- T. R. Beck and S. G. Chan, *ibid.*, **37**, 665 (1981).
- H. Kaesche, *Z. Phys. Chem.*, (N. F.), **32**, 87 (1962).
- T. R. Beck, *This Journal*, **120**, 1317 (1973).
- K. J. Vetter and H.-H. Strehblow, in "Localized Corrosion," R. W. Staehle *et al.*, Editors, p. 240, NACE, Houston (1974); *Ber. Bunsenges. Phys. Chem.*, **74**, 1024 (1970).
- J. W. Tester and H. S. Isaacs, *This Journal*, **122**, 1438 (1975).
- H. J. Engell, *Electrochim. Acta*, **22**, 987 (1977).
- Yu. A. Popov and Ya. M. Kolotyarkin, *Zh. Fiz. Khim.*, **51**, 3121 (1979); Yu. A. Popov, Y. V. Alekseev, Ya. M. Kolotyarkin, and A. A. Vasil'ev, *ibid.*, **51**, 1729 (1978).
- R. Alkire, D. Ernberger, and T. R. Beck, *This Journal*, **125**, 1382 (1978).
- N. Sato, *ibid.*, **129**, 260 (1982).
- T. R. Beck and R. C. Alkire, *ibid.*, **126**, 1662 (1979).
- K. R. Weisbrod, Ph.D. Thesis, University of Illinois, Urbana, IL (1981).
- R. Alkire and A. Cangelari, *This Journal*, **130**, 1252 (1983).
- C. R. Burggraf, *J. Fluid Mech.*, **24**, Part 1, 113 (1966).
- M. Takematsu, *J. Phys. Soc. Jpn.*, **21**, 1816 (1966).
- F. Pan and A. Acrivos, *J. Fluid Mech.*, **28**, Part 4, 643 (1967).
- S. A. Trogon and D. D. Joseph, *J. Non-Newtonian Fluid Mech.*, **10**, 185 (1982).
- H. W. Townes and R. H. Sabersky, *Int. J. Heat Mass Transf.*, **9**, 729 (1966).
- E. L. Jarrett and T. L. Sweeney, *AIChE J.*, **13**, 797 (1967).
- A. D. Gosman *et al.*, "Heat and Mass Transfer in Recirculating Flows," Academic Press, New York (1969).
- J. L. Duda and J. S. Vrentas, *J. Fluid Mech.*, **45**, 247, 261 (1971).
- S. Taneda, *J. Phys. Soc. Jpn.*, **46**, 1935 (1979).
- H. K. Kuiken, *J. Engr. Math.*, **12**, 129 (1978).
- (a) M. Datta and D. Landolt, *This Journal*, **122**, 1466 (1975); (b) *Electrochim. Acta*, **25**, 1255 (1980); (c) *ibid.*, **25**, 1263 (1980); (d) *This Journal*, **129**, 1889 (1982).
- G. Goosen and J. Van Ruler in, "Proceedings of the 9th World Conference on Metal Finishing," Interfinish 1976, Amsterdam.
- T. C. Reiman and R. H. Sabersky, *Int. J. Heat Mass Transf.*, **11**, 1083 (1968).
- J. F. Stevenson, *J. Appl. Mech.*, **40**, 355 (1973).
- R. E. Chilcott, *Int. J. Heat Mass Transf.*, **10**, 783 (1967).
- O. Zienkiewicz, "The Finite Element Method in Engineering Science," 2nd Ed., McGraw-Hill, New York (1971).
- R. C. Alkire, T. Bergh, and R. L. Sani, *This Journal*, **125**, 1981 (1978).
- R. Sautebin, H. Froidevaux, and D. Landolt, *ibid.*, **127**, 1096 (1980).
- R. Sautebin and D. Landolt, *ibid.*, **129**, 946 (1982).
- R. Alkire and D. Reiser, *Electrochim. Acta*, **28**, 1309 (1983).
- J. S. Newman, "Electrochemical Systems," p. 358, Prentice-Hall, Englewood Cliffs, NJ (1973).
- M. Engleman, "FIDAP Users Manual," Computer Applications International, S. A. (1981).
- D. B. Reiser, Ph.D. Thesis, University of Illinois, Urbana, IL (1983).
- J. K. Aggarwal and L. Talbot, *Int. J. Heat Mass Transf.*, **22**, 61 (1979).

Structural Studies of Electroless Thin Co-P Films¹

R. O. Cortijo and M. Schlesinger

Department of Physics, University of Windsor, Windsor, Ontario, Canada N9B 3P4

ABSTRACT

The microstructure of thin electroless Co-P films is studied using electron microscopy with radial distribution function (RDF) analysis of electron diffraction patterns. It is concluded that, depending on metalizing bath chemistry, films may grow with their component crystallites, having their c-axis prefer to be perpendicular to the plane of the film. No evidence of an fcc phase is found in these films.

Chemically (electroless) deposited thin cobalt film (Co-P) can be considered as a binary system of cobalt and phosphorus. They have been regarded as a potential digital recording medium ever since their discovery by Brenner and Riddell (1). For recording applications, one seeks a thin layer ($\sim 500\text{\AA}$) with appropriate magnetic properties. In Co-P, the magnetic properties are strongly dependent

¹ Work supported by the Natural Sciences and Engineering Research Council of Canada.

upon the microstructure, and the microstructure, in turn, is markedly influenced by the plating conditions and the substrate.

In the past (2), the nucleation and growth of Co-Ni-P and Co-P films have been studied. It has been found that mixed cobalt-nickel films form an fcc structure like nickel. This is not surprising, as it is known to be one of the simplest systems formed by cobalt, and nickel can form a complete series of solid solutions with fcc cobalt.

Of more complexity are the results pertaining to Co-P. It has been conjectured that the films constitute a mixture of fcc and hcp phases and that increasing the phosphorus content tips the balance toward the hcp phase.

The aim of the present work is to elucidate the nature of the microstructure of thin Co-P. Here, transmission electron microscopy, electron diffraction, and reduced radial distribution curves are employed. It is concluded that thin Co-P deposits on Formvar form microcrystals possessing an hcp structure which has a degree of preferred orientation dependent on the phosphorus content. No evidence for the presence of an fcc phase, as stated previously, has been found.

Experimental

Films in this investigation were grown on microscope slide glasses coated with Formvar (4g polyvinylformal in one liter of ethylene dichloride). Standard sensitizing (Sn II), activating (Pd II), and metalizing (as in Ref. 2) procedures were followed in their preparation. The films were floated off the glass substrate in distilled water. They were subsequently placed in the sample holder of a JEOL Model JEM-100CX electron microscope. The electron microscope was operated at 100 kV, and electronmicrographs and selected area diffraction patterns (camera length of 236 mm) were recorded photographically.

The diffraction patterns were scanned by a microdensitometer whose output was fed into an ADC of a PDP 11/03 minicomputer. The reduced radial distribution functions (RDF) were obtained as described recently (3, 4). A combined smoothing and averaging technique was used to reduce random noise errors. A number of procedures were adopted to eliminate the effects of systematic errors. We will present reduced RDF curves given by

$$G(r) = 8\pi \int_0^{\infty} i(s) \sin(2\pi sr) ds$$

with

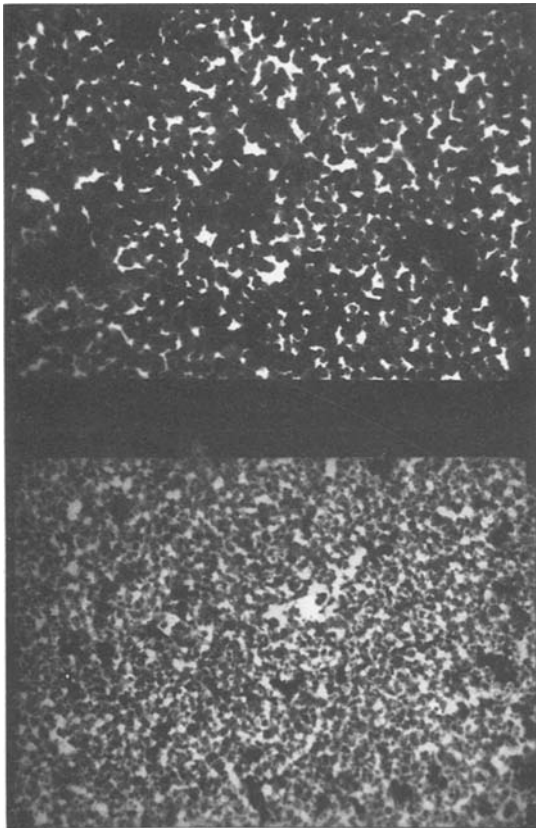


Fig. 1. Electron micrographs of two Co-P films: (bottom) sample grown with 10 g/l hypophosphate; (top) sample grown with 5 g/l hypophosphate (magnification = $\times 14,000$).

$$s = \frac{2 \sin \theta}{\lambda}$$

where $i(s)$ is the reduced interference function.

Results and Discussion

In Fig. 1, we present electron micrographs corresponding to two (out of a dozen or so on which measurements were carried out) typical samples. One has grown in a metalizing bath with a sodium hypophosphite ($\text{NaH}_2\text{PO}_2 \cdot \text{H}_2\text{O}$) content of 10 g/l and the other has grown in a bath containing 5 g/l sodium hypophosphite. In Fig. 2 we present their respective selected area diffraction (SAD) curves after subtracting the background in the SAD patterns. This background is due to nonelastic collisions and, as it has the form of a slowly varying function, the procedure for its elimination is rather simple. We have indicated the Miller (hkl) indexes on the different peaks (rings).

In Table I we summarize the hkl and corresponding $d(\text{\AA})$ values of the curves in Fig. 2, along with the corresponding bulk cobalt values. These values are determined directly from the photographic plates, using a traveling microscope, and the curves in Fig. 2 represent the densitometer's output. The former is a somewhat more sensitive method; it yields, for instance, a value for a (002) ring, while no such peak is identifiable on the corresponding SAD curve (Fig. 2a). A close comparison of Fig. 2a and 2b shows differences in the relative intensities of some peaks. One such difference is between the (101) peak and stronger (100) peak in 2a and the (100) peak and stronger (101) peak in 2b. Another difference is between

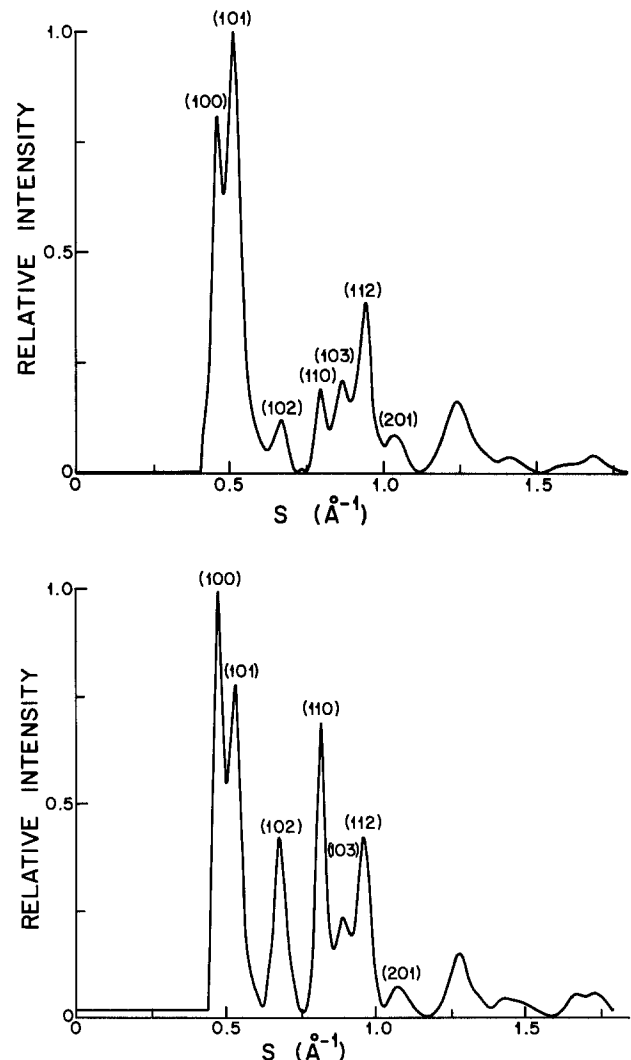


Fig. 2. Diffraction patterns corresponding to the films shown in Fig. 1: (a) phosphorus rich sample; (b) phosphorus poor sample.

Table I. Spacing [$d(\text{\AA})$] values corresponding^a to SAD curves in Fig. 2

hkl	$d(\text{\AA})$ High P	$d(\text{\AA})$ Low P	$d(\text{\AA})$ Bulk Co
100	2.162	2.127	2.165
002	2.038		
101	1.913	1.883	1.910
102	1.478	1.482	1.480
110	1.249	1.234	1.252
103	1.148	1.135	1.149
112	1.068	1.048	1.066
201	1.045		1.047

^a Values in table were determined directly from photographic plates.

the relative intensities of the (110) and, say, the (112) peaks.

It is proposed that curve 2a is an hcp structure with random crystallite orientation. It is further proposed that 2b is an hcp structure with crystallites, where the c -axis prefers to be (but is not exclusively) perpendicular to the plane of the films. These proposals are based on a number of considerations. In Fig. 2b, it is the peaks with index $l = 0$ that are observed to be enhanced. These are the reflections from planes having no intercept (*i.e.*, parallel) with the c -axis. These planes are expected to be in "grazing angle" position relative to the electron beam, being more likely to fulfill the Bragg condition if our proposal is valid. It is the same consideration which should explain the complete absence of the (002) reflection (see Table I) from the low P content film, because it represents a plane perpendicular to the c -axis.

In order to lend further support to our proposal and rule out the possibility that Fig. 2b represents the existence of an fcc phase, we have carried out a series of experiments in the electron microscope. The film corresponding to Fig. 2b was tilted by 45° in the sample holder, and its SAD was recorded. Next, it was rotated and tilted about the z and y axes, respectively, by 45° , and its SAD was recorded again; the process continued as such. Eight pictures were taken making sure that the SAD was taken each time exactly from the same film area. Figure 3 is the average (background subtracted) of these eight SAD patterns. Note that, now, the relative intensities more closely resemble those of Fig. 2a, *i.e.*, the proposed case of a random orientation of crystallites. The reduced RDF from the curves of Fig. 2a and Fig. 3 have been calculated and found to be very similar, as shown in Fig. 4a and 4b, respectively. Specifically, both indicate a nearest neighbor distance of 2.5\AA and a second nearest neighbor distance of 4.0\AA . These values agree well with the cobalt bulk values of $a = 2.507\text{\AA}$ and $c = 4.070\text{\AA}$. From Table I, one can also

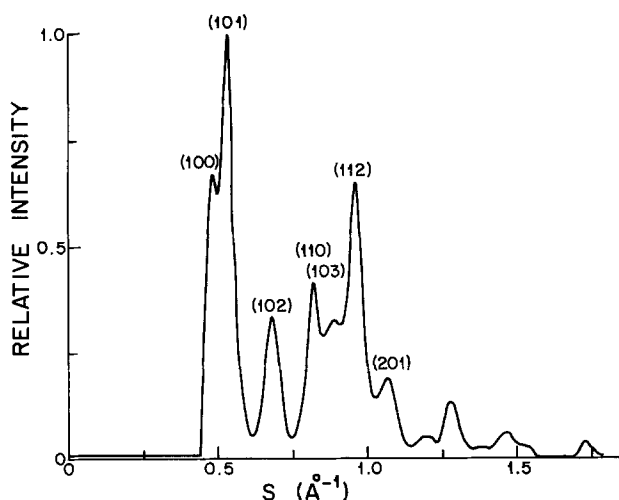


Fig. 3. Diffraction pattern of the phosphorus poor sample, taken as an average of eight different film orientations.

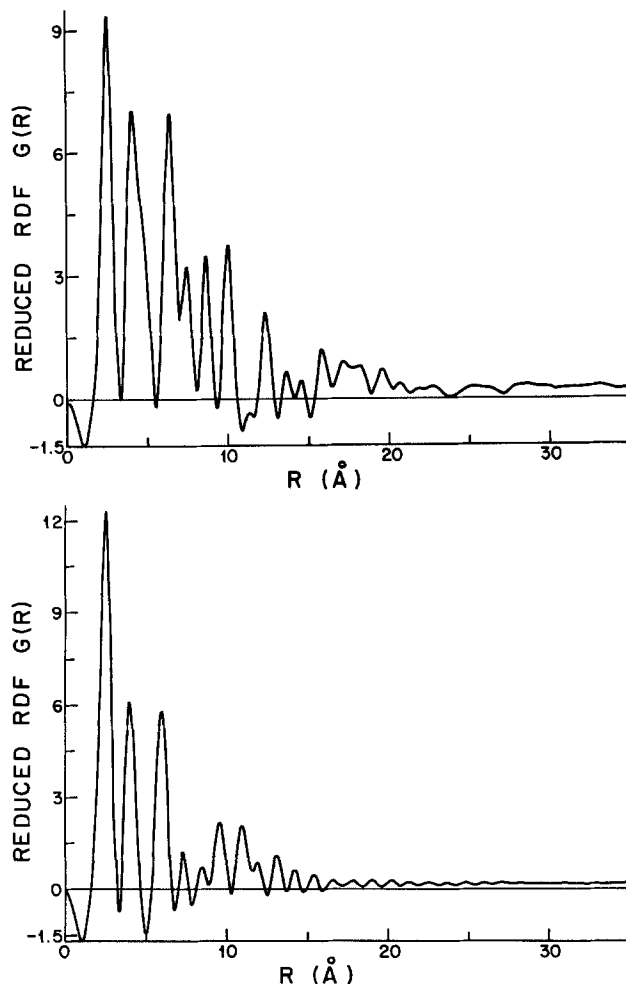


Fig. 4. Reduced radial distribution curves: (a) calculated from Fig. 2(a); (b) calculated from Fig. 3.

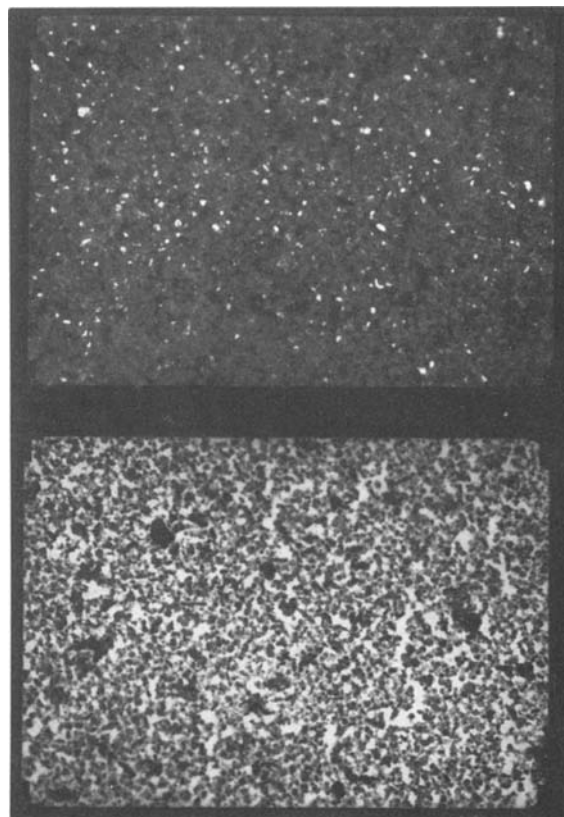


Fig. 5. Electron micrographs of a phosphorus poor Co-P film: (bottom) bright field; (top) dark field (magnification = $\times 20,000$).

infer a set of values as follows. For the P-rich sample, $a = 2.497\text{\AA}$ and $c = 4.081\text{\AA}$; for the P-poor film, $a = 2.482\text{\AA}$ and $c = 3.980\text{\AA}$.

Finally, a crystallite size range can also be inferred from either the RDF or the diffraction patterns. Figure 4a would seem to correspond to a "long" range order of about 15\AA . The further peaks tend to smear out, indicating a lack of longer range order or that any further points are usually beyond a given crystallite. Figure 4b corresponds to a range of order of about 20\AA . It is perhaps not surprising that the sample richer in phosphorus possesses a slightly shorter order range (3) (smaller crystallites). The diffraction patterns yield a very nearly identical crystallite size value of about 18\AA for both samples. This is inferred from the width of the Bragg diffraction peak Δs and its relation to the crystallite size (3, 4). The nearly equal crystallite sizes of phosphorus rich and phosphorus poor samples should be contrasted with their markedly different metal island sizes, as seen in Fig. 1a and 1b. The difference between metal island and crystallite size is best illustrated by a dark field electron micrograph. Figure 5a is the bright field and 5b the dark field electron micrograph of a phosphorus poor Co-P film. The dark field is due to the (110) reflection, and it clearly shows the sizes of component crystallites to be much less than the sizes of metal islands.

Conclusion

Electroless-plated cobalt films should be considered α -cobalt with a hexagonal lattice composed of crystallites about 20\AA in size. These create groups forming metal islands. Depending on phosphorus content, films may

grow with their component crystallites, having their c-axis prefer to be perpendicular to the plane of the film. It is noteworthy that in the low-phosphorus deposit, the $\langle 0001 \rangle$ direction is already preferentially perpendicular to the surface in the very early stages of deposition. Frieze *et al.* (5) have performed experiments similar to the present ones, but they have not analyzed the electron diffraction patterns in the way this work does or found that thicker deposits produced in an electrolyte with the same hypophosphite concentration also have a $\langle 0001 \rangle$ texture. Co-P deposits produced in solutions with higher hypophosphite concentration have a $\langle 1010 \rangle$ texture. Finally, no evidence is found for the presence of β -cobalt with fcc lattice. Nor do the films exhibit the presence of cobalt phosphide phases such as Co_2P with orthorhombic lattice. Electrodeposited films do show (6) its presence after heat treatment.

Manuscript submitted June 18, 1984; revised manuscript received August 17, 1984.

University of Windsor assisted in meeting the publication costs of this article.

REFERENCES

1. A. Brenner and G. E. Riddell, *Nat. Bur. Stand.*, **3**, 31 (1946).
2. S. L. Chow, N. E. Hedgecock, M. Schlesinger, and J. Rezek, *This Journal*, **119**, 1614 (1972).
3. R. O. Cortijo and M. Schlesinger, *ibid.*, **130**, 2341 (1983).
4. R. O. Cortijo and M. Schlesinger, *Solid State Commun.*, **49**, 283 (1984).
5. A. Frieze, R. Sard, and R. Weil, *This Journal*, **115**, 586 (1968).
6. J. G. M. de Lau, *J. Appl. Phys.*, **41**, 5355 (1971).

Electrochemical Etching of the Semiconductor Lead Tin Telluride

Patrick G. Barber*

Longwood College, Farmville, Virginia 23901

Roger K. Crouch*

NASA-Langley Research Center, Hampton, Virginia 23665

ABSTRACT

Convective currents during the Bridgman growth of a compound semiconductor lead to temperature fluctuations at the solid-liquid interface. These temperature fluctuations in turn lead to microscopic compositional variations in the solid. Electrochemical principles have been applied to develop three etches which delineate the variations in the compound semiconductor, lead tin telluride, and allow optical studies of the growth kinetics of this material. Use of these etches has shown periodic lines during the initial growth, with indications of oscillatory instabilities developing in later stages of growth, and, finally, complete breakdown of the interface.

With the increased use of remote sensing systems utilizing infrared detectors, there is a need for materials suitable for large area arrays. One material that possesses properties suitable for such detectors is the narrow bandgap semiconductor, lead tin telluride ($\text{Pb}_{1-x}\text{Sn}_x\text{Te}$), which can be prepared as an infrared detector in which the peak detectivity can be chosen to be any wavelength from 5 to $17\ \mu\text{m}$ by changing the ratio of the lead to the tin (1). As part of NASA's Microgravity Science Program at Langley Research Center, studies are being carried out on the effects of convection on microscopic inhomogeneities in the compound semiconductor lead tin telluride (LTT). Crystals have been grown in quartz ampuls using the Bridgman technique (2). Natural convection during the growth of this material results in temperature fluctuations at the solid-liquid interface, which consequently results in microscopic variations in the composition of the solid as the growth progresses. Since these fluctuations are small, accurate quantitative analysis of the resulting crystals is difficult. The development of

etching techniques which delineate these variations making optical studies possible are very desirable.

The literature provides several chemical etches for materials like LTT. These chemical etches are typically solutions of strong, corrosive chemicals, such as concentrated nitric acid, hydrofluoric acid, liquid bromine, hydrobromic acid, or concentrated potassium hydroxide (3-8). Such corrosive etches do attack the LTT, but they do not do so selectively, so that the fine interface demarcations are not made visible reproducibly and reliably. This report describes the development of a mild etching procedure for LTT by applying electrochemical principles. Three different solutions were successfully used for this particular application, but the procedure may have more general applicability in the semiconductor industry and in materials research. Etches do not have to be corrosive reagents to be effective.

Experimental

A review of the thermodynamics quickly reveals why strong, corrosive reagents could not be used for LTT.

*Electrochemical Society Active Member.

Chemical reagents that solubilize the component ions of LTT create a thermodynamic dilemma, for once the metallic cations and telluride anions are in solution, they should react with each other to form the respective metals. The standard electrode potentials, shown in Tables I and II, indicate that these reactions should go to completion, since the equilibrium constants are very large. Consequently, as fast as strong corrosive etchants dissolve the semiconductor surface, the component ions react in solution to form a precipitate that plasters over the surface to be viewed in the optical microscope. The fact that the surface features are sometimes more visible after a light polishing than immediately after etching tends to support this hypothesis. Such a polishing procedure, using strong, corrosive reagents, is not reproducible or reliable.

Electrochemical procedures were applied to selectively dissolve the lead and tin tellurides and, at the same time, quickly sweep away the resulting ions before the subsequent chemical reactions forming the obscuring deposits can occur. Electrochemical cells were set up as shown in Fig. 1, and mild chemical etching solutions were used. The particular geometry of the cell did not appear to be crucial, for reproducible results were obtained on samples regardless of whether the platinum cathode was vertical or horizontal, whether it was near or far from the surface of the sample, or whether the sample itself was vertical or horizontal. The usual configuration of having the sample horizontal and the cathode vertical was selected for ease of assembly. The position of the platinum contact on the sample was not critical. Contacts were made at different sites on the LTT surface and at the edge of the sample. Reproducible patterns occurred in all cases. To enhance the removal of the solvated ions from the surface of the semiconductor and to retard their subsequent self-oxidation and reduction, the ionic strength of the solution was increased, thus reducing the thickness of the electrical double layer. Chelating agents were also added to the solution to tie up the liberated ions. This did prevent further chemical reactions and reduced the deposit formed back over the semiconductor surface.

Three mild electrochemical etching solutions were developed for lead tin telluride. The compositions of these solutions are given in Table III. The colloidal sulfur, mild Norr (composition 1 in Table III), and ethylenediamine tetraacetic acid (EDTA) solutions gave the most informative and reproducible results on the samples of LTT. The mild Norr was developed by reducing the concentration

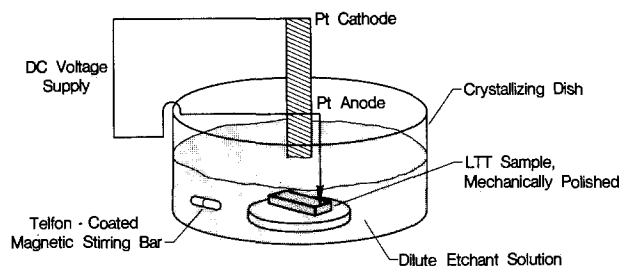


Fig. 1. Electrochemical cell for etching lead tin telluride

of the corrosive reagents in that etch described in the literature. The other two solutions were developed by considering the inorganic and electrochemical factors described in the previous paragraph. Sulfur will react quickly with both lead and tin to form precipitates; and the rationale was that if these elements formed precipitates with sulfur, they would not be available to form the obscuring plaster on the surface of the semiconductor. The EDTA solution was developed using the ability of this chelating reagent to complex with lead and tin ions in solution. If the ions were locked in an inorganic complex, they would not be as readily available to react with the telluride ions and to form the plaster. All three of these rationales lead to successful solutions.

The procedure followed in all cases was the same even though the sample orientations and etching solutions were changed. The LTT single crystals were in the form of cylindrical boules when they were removed from the Bridgman furnace. These were cut into slices along their long axis, and they were mounted and carefully polished using a series of decreasing grit sizes from 600 grit to 0.05 μm as the final mechanical polish. The sample was then polished on a soft cloth using an alkaline, silica solution. These samples were placed one at a time in an electrochemical cell, shown in Fig. 1, and arranged in such a way that the sample was the anode and the ribbon of platinum was the cathode. A magnetic stirring bar assured rapid mixing in the solution, which covered the sample. A small voltage was applied, on the order of 1-3V, and the current was monitored. Currents were normally kept at values less than 50 mA. Within these current and voltage limits, the exact current density did not appear to be critical in developing the etch patterns, since these patterns seemed to be independent of sample size and voltage. Etch rates and current densities were not measured. Samples were etched for approximately 1 min. Then the power supply was turned off, at which time, due to the decay characteristics of the power supply, a reversed current flow of about 5 mA was observed for approximately 2-4s. The current would again rise to about 15 mA for 1-2s before decaying back to zero in about ten more seconds. However, if the voltage applied to the sample initially was too large, the solution itself would begin to electrolyze, and the desired surface features would be obscured by

Table I. Thermodynamics of Pb^{2+} and Te^{2-}

Oxidation: $\text{Te}^{2-}(\text{aq}) \rightarrow \text{Te}(\text{s}) + 2\text{e}^-$	E° 0.92V
Reduction: $\text{Pb}^{2+}(\text{aq}) + 2\text{e}^- \rightarrow \text{Pb}(\text{s})$	-0.13V
$\text{Pb}^{2+}(\text{aq}) + \text{Te}^{2-}(\text{aq}) \rightarrow \text{Pb}(\text{s}) + \text{Te}(\text{s})$	0.79V
$\Delta G^\circ = -nFE^\circ = -2 \times 23,060 \times 0.79$ $= -36.3 \text{ kcal mol}^{-1}$	
$\Delta G^\circ = -RT \ln K$ $\ln K = 61.4 \text{ at } T = 298 \text{ K}$ $K = 1/[\text{Pb}^{2+}][\text{Te}^{2-}] = e^{61.4} \approx 10^{27}$	

Table II. Thermodynamics of Sn^{2+} and Te^{2-}

Oxidation: $\text{Te}^{2-}(\text{aq}) \rightarrow \text{Te}(\text{s}) + 2\text{e}^-$	E° 0.92V
Reduction: $\text{Sn}^{2+}(\text{aq}) + 2\text{e}^- \rightarrow \text{Sn}(\text{s})$	-0.14V
$\text{Sn}^{2+}(\text{aq}) + \text{Te}^{2-}(\text{aq}) \rightarrow \text{Sn}(\text{s}) + \text{Te}(\text{s})$	0.78V
$\Delta G^\circ = -nFE^\circ = -2 \times 23,060 \times 0.78$ $= -36.1 \text{ kcal mol}^{-1}$	
$\Delta G^\circ = -RT \ln K$ $\ln K = 60.9 \text{ at } T = 298 \text{ K}$ $K = 1/[\text{Sn}^{2+}][\text{Te}^{2-}] = e^{60.9} \approx e^{26}$	

Table III. Electrochemical etching solutions

- Alkaline ferricyanide
70 ml distilled water
30 ml 95% ethanol
0.5g KOH (pH 12.5 \pm 0.4)
2.6g $\text{K}_3\text{Fe}(\text{CN})_6$
The clear, yellow solution may be used for a few days until the color darkens.
- Colloidal sulfur
50 ml distilled water
50 ml Kodak fixer
0.5 ml 12M HCl
After stirring, the solution should be creamy-white with an opaque cloudiness due to the colloidal sulfur.
- Ethylenediamine tetraacetic acid (EDTA)
80 ml distilled water
20 ml ethanol
0.3g EDTA-disodium salt
0.2g KOH
0.2g hydroquinone (optional)

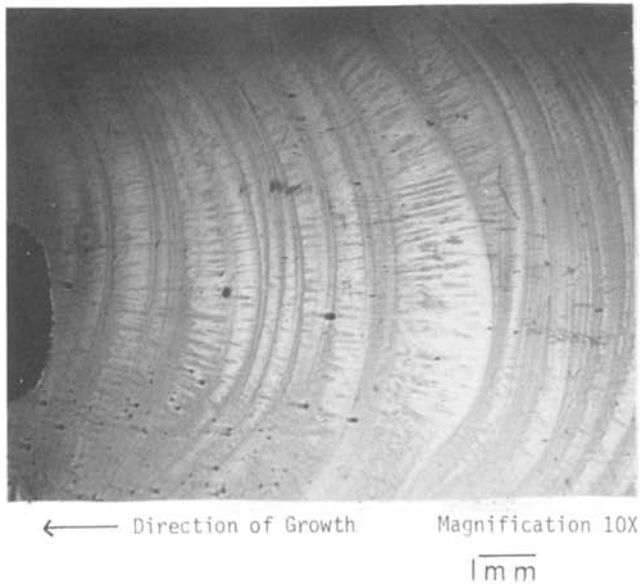


Fig. 2. Etched sample showing apparent melt-regrowth patterns and initial interface breakdown.

the plaster coat. These steps were repeated until the desired degree of etching was achieved. A successful etching could easily be monitored visually while regulating the applied voltage.

Results

Use of these electrochemical etching procedures have revealed microscopic inhomogeneities in samples grown in a thermally unstable Bridgman configuration. Examples of the etch patterns are shown in Fig. 2 and 3. These patterns were reproducible in the sense that an etched sample could be polished and etched again and the same patterns would appear. The patterns seem to indicate that an oscillatory growth occurs in the sample and that the solid-liquid interface is concave into the solid. As the growth progresses, oscillatory perturbations begin to occur along the interface, and eventually the interface appears to break down completely. A more complete description and analysis of the crystal growth and morphology will be published later.

Concluding Remarks

Electrochemical principles have been combined with thermodynamics and inorganic chemistry to develop a new etching procedure for the compound semiconductor lead tin telluride. These etches have been shown reproducibly to enhance microscopic inhomogeneities in LTT and to offer the potential of studying interface

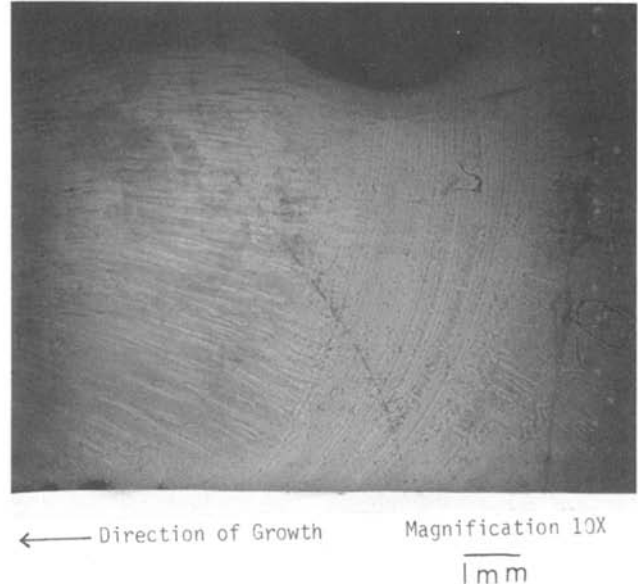


Fig. 3. Etched sample showing apparent breakdown of interface

growth kinetics. It is believed that the same principles used in the development of these etches can also be used in the development of etches for other semiconductor materials.

Manuscript submitted April 27, 1984; revised manuscript received July 9, 1984. This was Paper 507 RNP presented at the Washington, DC, Meeting of the Society, Oct. 9-14, 1983.

NASA assisted in meeting the publication costs of this article.

REFERENCES

1. S. G. Parker and R. E. Johnson, in "Preparation and Properties of Solid State Materials," Vol. 6, W. R. Wilcox, Editor, pp. 45-47, Marcel Dekker, Inc., New York (1981).
2. Roger K. Crouch, A. L. Fripp, W. J. Debnam, Jr., and I. O. Clark, in "Advances in Ceramics—Materials Processing in Space," Vol. 5, B. J. Dunbar and E. Lense, Editors, pp. 186-194, The American Ceramic Society, Inc., Columbus, OH (1983).
3. M. K. Norr, *This Journal*, **109**, 433 (1962).
4. M. K. Norr, *ibid.*, **113**, 621 (1966).
5. A. R. Calawa, T. C. Harman, M. Finn, and P. Youtz, *Trans. Met. Soc. AIME*, **242**, 374 (1968).
6. J. F. Butler and T. C. Harman, *This Journal*, **116**, 260 (1969).
7. W. Rollis, R. Lee, and R. J. Eddington, *Solid State Electron.*, **13**, 75 (1970).
8. T. C. Harman, *J. Non-Metals*, **1**, 183 (1973).

Photoelectrochemical Study of SnS₂ in Aqueous Solution

A. Katty, B. Fotouhi, and O. Gorochov

Laboratoire de Physique des Solides, CNRS, 92195 Meudon, France

ABSTRACT

n-Type SnS₂ with a layered structure has been grown by chemical vapor transport using phosphorus as doping agent. It has a resistivity of 1 Ω cm and an energy gap of 2.2 eV. It is characterized by very low dark current under anodic polarization. The material is not stable under prolonged illumination in aqueous acidic and basic solutions. However, the stability can be improved considerably in acidic solutions containing potassium iodide. The voltammograms under illumination indicate that the photocurrent onset potential, particularly in alkaline solutions, depends on redox reagents used. Photopotentials do not vary as expected with different redox couples.

Metal dichalcogenides have been the subject of intensive work during the past six years (1-14). Among these materials, WSe₂ and MoSe₂ have received most attention. Characterization of new materials continues; some of them might be durable and efficient materials. Among metal dichalcogenides, tin sulfide has not yet received attention in photoelectrochemistry, but has been characterized by reflection data. The energy gap is given as 2.21 eV for the first indirect transition (15-16). At higher energies (ca. 2.88 eV) a direct transition is reported.

SnS₂ has a CdI₂-type C₆ structure (D_{3d}³ - P3̄m1) composed of planes of hexagonal close packed S atoms interleaved with planes of Sn atoms to give the stacking sequence S—Sn—S S—Sn—S in c direction of the unit cell. This C₆ structure is characterized by adjoining planes of weakly bound S atoms allowing a cleavage in [001] direction. Sn has in this structure a characteristic sixfold octahedral coordination (17).

The semiconducting nature of SnS₂ has been predicted assuming that Sn forms a resonating sp^{3d} bonds. Calculated electronic band models have shown a good agreement with optical reflectivity spectra and confirm the existence of an indirect gap around 2.2 eV (15-16). The conduction band as well as the valence band should exhibit essentially s-p like character.

Experimental

SnS₂ single crystals doped with phosphorus were grown by chemical vapor transport method in a closed silica tube. The transporting agents were bromine and iodine. The temperature of the transport and growth zones were, respectively, 600° and 530°C. Yellow reddish crystals (~3 × 3 × 0.1 mm) were obtained both with bromine and iodine within a week.

The tube initially contained stoichiometric amounts of tin and sulfur plus 5 atomic percent (a/o) of phosphorus. Microprobe analysis, however, indicate that the amount of phosphorus incorporated in the crystal bulk was less than 0.5%. The excess phosphorus stayed either unreacted in the tube or distributed in some crystals as a black localized phase (dark points).

Typical transport properties (from resistivity and Hall voltage) at room temperature were a resistivity of ~ 1 Ω cm and a carrier density of 5 × 10¹⁷ cm⁻³.

Electrochemical measurements were performed using standard potentiostatic system and a classical three-electrode cell. A 75W tungsten halogen lamp was used as light source. Samples were illuminated by monochromatic light (λ = 480 nm) using a Jobin-Yvon H20 monochromator. The lock-in amplifier method was used to perform capacitance measurements between 200 and 1500 Hz. Analytical-grade chemicals and deionized water were used for the preparation of the solutions.

Contacts were achieved by using Ga/In eutectic and Johnson Matthey silver paste. Samples were mounted on a copper plate and then insulated by Dow Corning glue.

All potentials are referred to the saturated calomel electrode.

Electrochemical Results

Figure 1 demonstrates the behavior of an n-type SnS₂ single crystal in the dark and under illumination in solutions of three different pH values. The electrode shows nearly perfect blocking characteristics over all pH values in the dark, the dark current being equal to 10⁻⁷ A cm⁻² over a wide range of potentials. Under illumination, the photocurrent onset depends on the pH of the solution. It shifts to more negative potentials as the pH of the solution increases. The photocurrent onset potential in solutions of sulfuric acid pH = 0, KCl pH = 5.5, KOH pH = 14 are, respectively, + 0.2V, 0V, and -0.35V.

Capacitance measurements also indicate that the flat-band potential shifts to more negative values with increasing pH of the solution. Mott-Schottky plots are linear and are extrapolated to the same potential independent of frequency (between 200 and 1500 Hz). Figure 2 shows the Mott-Schottky plots in acidic and basic media. The corresponding slope gives a carrier number of 3.7 × 10¹⁷ cm⁻³ (assuming ε = 10), which is in agreement with Hall measurements.

When redox couples such as Fe(CN)₆^{4-/3-} and I⁻/I₂ are added to the alkaline solution, a shift in photocurrent onset potential is observed. For instance, in alkaline solutions, the addition of Fe(CH₃)₆^{4-/3-} and I⁻/I₂ shifts the photocurrent onset to a more positive value, whereas the addition of S²⁻/S₂⁼ produces a negative shift. The photocurrent onset in solutions containing I⁻/I₂ and Fe(CN)₆^{4-/3-} is at -250 mV; for the one containing S²⁻/S₂⁼ it is at -450 mV (Fig. 3).

In acidic solutions, the addition of I⁻/I₂ produces a negative shift of the photocurrent onset potential (Fig. 4), whereas other couples, such as Fe(CN)₆^{4-/3-}, Fe^{2+/3+}, do not have any effects.

Capacitance measurements (18) also indicate a shift in flatband positions (a positive shift in alkaline solutions containing I⁻/I₂ and Fe(CN)₆^{4-/3-} and a negative shift in acidic solution containing I⁻/I₂). Table I shows the photopotential values obtained in a molar solution of sulfuric acid in the presence of different redox reagents. These values remained almost unchanged in different redox media.

SnS₂ is not stable in aqueous acidic and basic solutions and decomposes gradually under prolonged anodic polarization (4h at +1V) and white light illumination (≈ 200 mW cm⁻²). Decomposition products were a yellow layer, which covered the electrode surface and was proved to be elemental sulfur by x-ray analysis, and dissolved tin, which was found by the analysis of the solution.

The decomposition reaction can be prevented when I⁻ is present in acidic solutions.

The addition of I⁻ in sufficiently high concentration (0.1M) to the acidic solution improves to a great extent the stability of the electrode. The oxidation of iodide to triiodide in an argon-purged solution can be observed during the photoelectrolysis as the solution's color changes to reddish brown. The experiment was performed in a cell in which the counterelectrode was separated by a glass frit. The solution was bubbled with argon

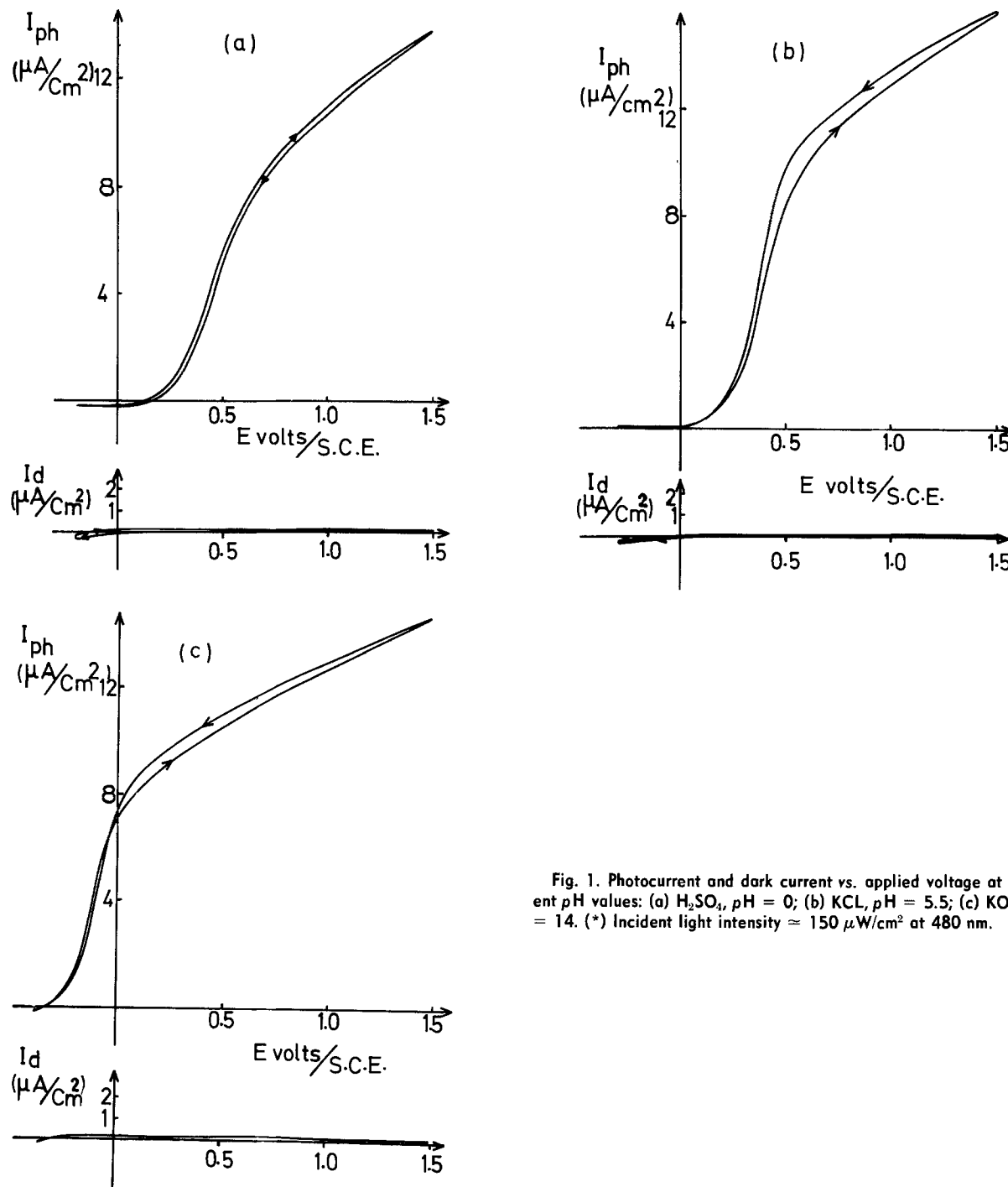


Fig. 1. Photocurrent and dark current vs. applied voltage at different pH values: (a) H_2SO_4 , pH = 0; (b) KCl, pH = 5.5; (c) KOH, pH = 14. (*) Incident light intensity = $150 \mu W/cm^2$ at 480 nm.

for several hours before the addition of KI. The electrode was polarized at +1V ($V_{FB} = 0.05V$) under white light ($\approx 200 mW cm^{-2}$). The current, after initial variation, remained constant during the experiment (Fig. 5), and no change on the electrode surface was observed.

The analysis of the solution did not show any trace of tin. The triiodide formed during the photoelectrolysis was titrated potentiometrically with sodium thiosulfate, and its concentration corresponded within the experimental

error to 95% of the total charge produced during the experiment. Table II shows, at pH = 0 and 14 with and without addition of I^- , the percentage of total charge consumed in electrode photodecomposition reaction calculated from the ratio of the concentration of dissolved tin found in the solution and the total charge produced during the experiment.

It is noted that Ce^{3+} and $Fe(CN)_6^{4-}$ do not improve the electrode stability.

Table I. Photopotential values obtained for 1M H_2SO_4 in the presence of various redox couples

Redox couples	Photovoltage
I^-/I_2	0.205V
$Fe(CN)_6^{4-\beta-}$	0.218V
$Fe^{2+/\beta+}$	0.204V
Br^-/Br_2	0.200V
$Ce^{3+/\beta+}$	0.300V

Table II. Total charge consumed

Medium	Dissolved tin
	Total charge produced
H_2SO_4	41
$H_2SO_4 + 0.1M IK$	<1
KOH	100
KOH + 0.1M IK	57

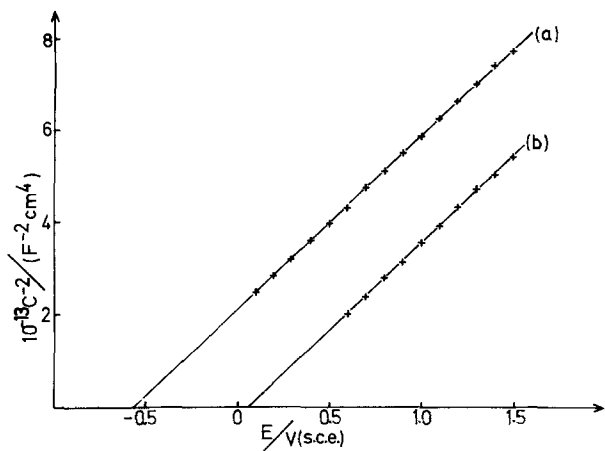


Fig. 2. Mott Schottky plots (a) in 1M KOH, and (b) in 1M H₂SO₄.

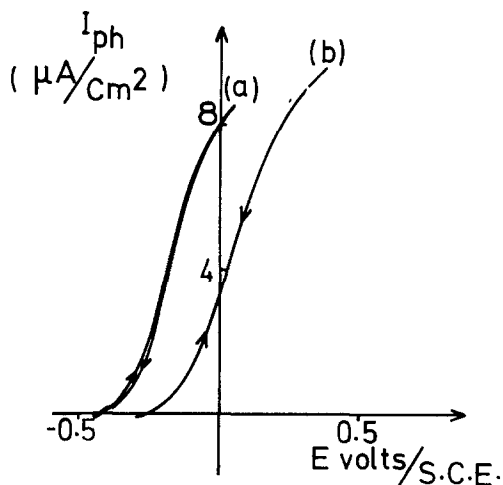


Fig. 3. Photocurrent vs. applied voltage in a KOH solution (pH = 14): (a) containing S²⁻/S₂²⁻; (b) containing I⁻/I₂.

The spectral dependence of the photocurrent at constant photon flux is shown in Fig. 6. Using the general theoretical relation between the photocurrent and light energy (19), assuming that I_{ph} is directly proportional to α and that L_p is small

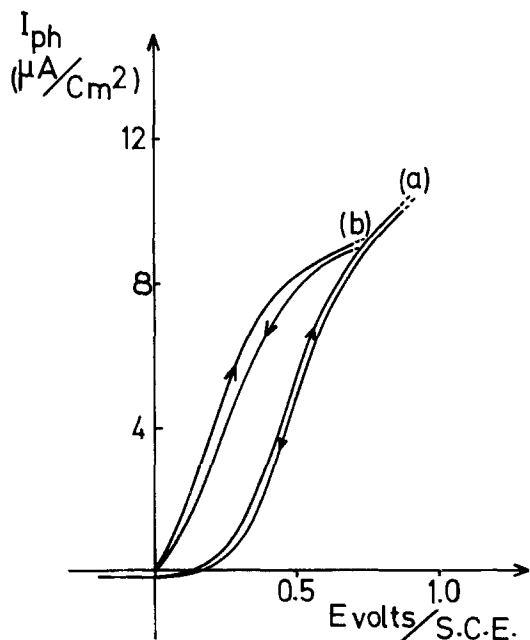


Fig. 4. Photocurrent vs. applied voltage (a) in 1M H₂SO₄ and (b) in 1M H₂SO₄ + 0.05M I⁻ and 0.001M I₂.

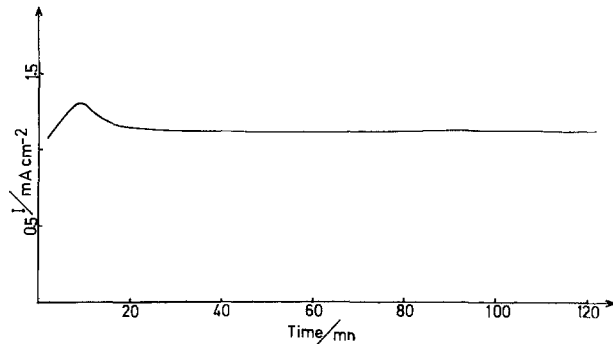


Fig. 5. Photocurrent variation as a function of time at constant potential (+1V/SCE) in 1M H₂SO₄ + 0.1 KI.

$$h\nu I_{ph} \propto (h\nu - E_g)^{n/2}$$

where $n = 1$ for a direct gap and $n = 4$ for an indirect gap, the linear extrapolation of $(h\nu I_{ph})^{1/2}$ as a function of $h\nu$ yields the value of 2.21 eV as the first indirect transition.

The relative energy scheme for SnS₂ and redox potentials of the couples in H₂SO₄ and KOH can be constructed (Fig. 7).

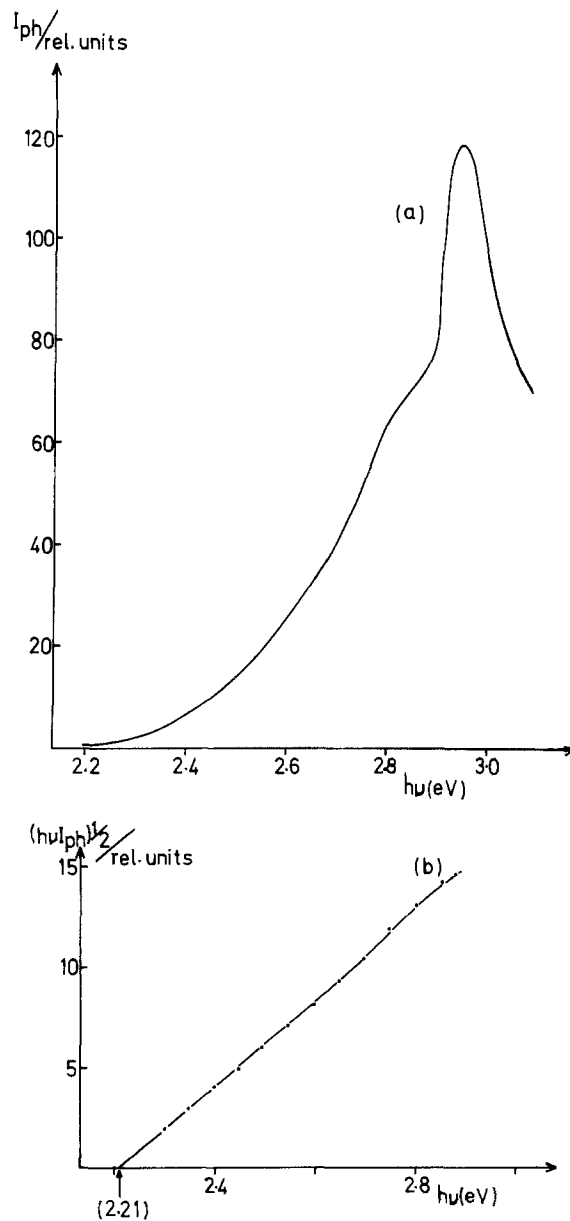


Fig. 6. Spectral response of SnS₂ in 1M H₂SO₄: (a) I_{ph} vs. light energy and (b) $(h\nu I_{ph})^{1/2}$ vs. light energy (at different scale).

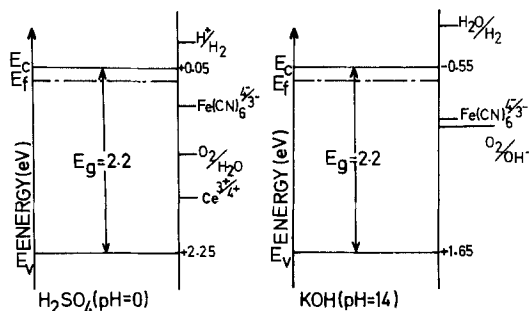
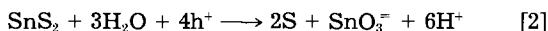
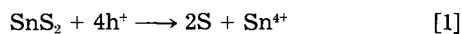


Fig. 7. Energy scheme of SnS₂ in H₂SO₄ (pH = 0) and in KOH (pH = 14).

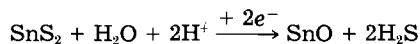
As it can be seen from Fig. 7, hydrogen couple redox potential is situated above the conduction band edge. At cathodic polarizations (ca. more negative than -0.3V), hydrogen evolution does not take place and the cathodic current is mostly due to the electrode decomposition. This leads to the formation of hydrogen sulfide and a black layer on the surface of the electrode. X-ray analysis indicates that this layer corresponds to the formation of tin oxide (SnO).

Discussion

The voltammograms, in the dark, indicate that tin sulfide is characterized by very low anodic current. The first indirect transition determined from the spectral response is in complete agreement with values found in the literature. This value corresponds to 2.2 eV. Although oxygen evolution under illumination is energetically possible (Fig. 7), photoinduced holes are partly consumed in the electrode-decomposition reaction in acidic solutions, while in KOH the decomposition rate is much higher. The decomposition product is a yellow layer which covers the electrode surface. X-ray analysis indicates that the layer is composed primarily of elemental sulfur. However, dissolved tin was found in the solutions, which indicates that tin passes into the solution both in acidic (pH = 0) and basic (pH = 14) media. The following anodic decomposition reactions, in acidic and basic solutions, respectively, can be considered



It seems that the decomposition mechanism of tin sulfide is similar to that of ZrS₂, for which the anodic decomposition product is also elemental sulfur (20). In contrast, the cathodic decomposition mechanism is not the same. In the case of ZrS₂, for example, hydrogen sulfide and zirconium metal are the cathodic decomposition products in acidic solution (20); in the case of SnS₂, the cathodic decomposition product is hydrogen sulfide and the lower oxide of tin (SnO). The following reaction may be considered as the cathodic decomposition reaction in acidic solutions



SnO is also formed during the cathodic polarization in basic solutions, but it dissolves (probably oxidizes to SnO₃⁻) when the polarization is stopped.

As it has been already mentioned, the oxidation of iodide to triiodide is the main photoanodic reaction in acidic solutions, and therefore considerable improvement is obtained in the stability of the electrode.

An interesting feature of Fig. 5, which shows the variation of current under anodic bias of SnS₂ in acidic solution containing I⁻, is the increase in photocurrent at first before further stabilization. This may be caused by the negative flatband shift due to the production of triiodide. The gradual formation of I₃⁻ during the electrolysis and its accumulation shifts the flatband potential to more negative values, and the photocurrent increases at first.

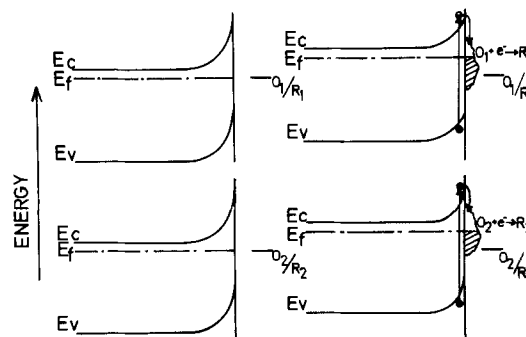


Fig. 8. Energy scheme of SnS₂ in the dark and under illumination. The role of surface states in preventing the flattening of the bands is illustrated.

The peak disappears when iodine is intentionally added to the solution before experiment.

The addition of I⁻/I₂ to acidic solution also shifts the photocurrent onset potential to a more negative value. The negative shift of the flatband position due to the adsorption of triiodide ion (21, 22) has already been shown in the case of MoSe₂ and MoS₂. The phenomenon has been interpreted by the introduction of a large number of acceptor states on the surface. Our results indicate that the same behavior can be assumed in the case of SnS₂. The introduction of surface states with accumulation of negative charge on the surface provokes changes in the field of the Helmholtz double layer. On the contrary, the addition of other couples such as Fe^{2+/3+} and Fe(CN)₆^{4-/3-} has no effect on the photocurrent onset potential and the flatband position.

The addition of redox reagents such as I⁻/I₂ and Fe(CN)₆^{4-/3-} to alkaline solutions provokes a positive shift of the photocurrent onset potential. But, the shape of the photocurrent voltage curve remains unchanged, and the decomposition of the electrode is the main photoanodic reaction. The positive shift of the photocurrent onset potential arises from the dependence of the flatband position on the above redox agents. The flatband potential is more positive in alkaline solutions containing I⁻/I₂ and Fe(CN)₆^{4-/3-} and it becomes more negative in those containing S²⁻/S₂²⁻ (23). The positive shift in flatband position has been discussed elsewhere (18), and it has been shown that the shift arises from the interaction of the oxidized form of the redox couples with the negatively charged surface states. On the contrary, S²⁻/S₂²⁻ couple increases the negative charge on the surface.

Shifts in photopotentials can be explained either by band edge movement or by the existence of surface states close to the conduction band edge (Fig. 8). Electrons which are excited into the conduction band fall into these surface states and prevent the flattening of the band. A similar effect was observed with ZrS₃ (24). Surface states below the conduction band edge should also be responsible for the existence of cathodic dark currents when solutions contain redox reagents. At all pH values, when solutions contained redox reagents, a cathodic dark current was observed at potentials positive to the flatband position.

Conclusion

It has been demonstrated that SnS₂ doped with phosphorus has a diode-like behavior. Under illumination, the electrode is not stable in acidic and basic media and the photoelectrochemical reactions are mostly due to the decomposition of the semiconductor. However, the electrode can be stabilized in acidic solutions containing iodide. The main photoanodic reaction in this case is the oxidation of iodide to triiodide.

Acknowledgments

The authors would like to thank H. Ezzaouia for helpful discussions and C. Bahezre for microprobe analysis.

Manuscript submitted Dec. 16, 1983; revised manuscript received Aug. 13, 1984.

CNRS assisted in meeting the publication costs of this article.

REFERENCES

1. H. Tributsch, *Z. Naturforsch.*, **322**, 972 (1977).
2. H. Tributsch and J. C. A. Bennett, *J. Electroanal. Chem. Interfacial Electrochem.*, **81**, 97 (1977).
3. H. Tributsch, *Ber. Bunsenges. Phys. Chem.*, **81**, 361 (1977); *ibid.*, **82**, 169 (1978).
4. H. Tributsch, *This Journal*, **128**, 1261 (1981).
5. H. J. Lewerenz, A. Heller, and F. J. Di Salvo, *J. Am. Chem. Soc.*, **102**, 1877 (1980).
6. S. Menezes, F. J. Di Salvo, and B. Miller, *This Journal*, **127**, 1751 (1980).
7. F.-R. F. Fan, H. S. White, B. L. Wheeler, and A. J. Bard, *J. Am. Chem. Soc.*, **102**, 5142 (1980); *This Journal*, **127**, 518 (1980).
8. H. S. White, F.-R. F. Fan, and A. J. Bard, *ibid.*, **128**, 1045 (1981).
9. G. Nagasubramanian and A. J. Bard, *ibid.*, **128**, 1055 (1981).
10. D. Canfield and B. A. Parkinson, *J. Am. Chem. Soc.*, **103**, 1279 (1981).
11. M. S. Wrighton and L. F. Schneemeyer, *J. Am. Chem. Soc.*, **101**, 6496 (1979); *ibid.*, **102**, 6946 (1980).
12. L. F. Schneemeyer, M. S. Wrighton, A. Stacy, and M. J. Sienko, *Appl. Phys. Lett.*, **36**, 701 (1980).
13. J. Gobrecht, H. Tributsch, and H. Gerischer, *This Journal*, **125**, 2085 (1978).
14. P. G. P. Ang and A. F. Samuels, in "Third International Conference on Photochemical Conversion and Storage of Solar Energy," Book of Abstracts, p. 473, Solar Energy Research Institute, Golden, CO (1980).
15. D. L. Greenway and R. Nitsche, *J. Phys. Chem. Solids*, **26**, 1445 (1965).
16. G. Domingo, R. S. Itoga, and C. R. Kannewurf, *Phys. Rev.*, **143**, 536 (1966).
17. H. Krebs, "Fundamentals of Inorganic Crystal Chemistry," p. 223, McGraw-Hill, London (1968).
18. B. Fotouhi, A. Katty, and R. Parsons, *J. Electroanal. Chem.*, To be published.
19. F. Stern, *Solid State Phys.*, **15**, 299 (1963).
20. H. Tributsch, "Structure and Bonding," p. 189, Vol. 49 of Solar Energy Materials, Springer-Verlag, Berlin (1981).
21. W. Kautek and H. Gerischer, *Electrochim. Acta*, **12**, 1771 (1981).
22. J. A. Turner and B. A. Parkinson, *J. Electroanal. Chem.*, **150**, 611 (1983).
23. A. B. Ellis, S. W. Kaiser, J. M. Bolts, and M. S. Wrighton, *J. Am. Chem. Soc.*, **99**, 2839 (1977).
24. O. Gorochoy, A. Katty, N. Le Nagard, C. Levy-Clement, A. Redon, and H. Tributsch, *This Journal*, **130**, 1301 (1983).

Electrodialytic Water Splitting

Conversion of Dilute Sodium Acetate or Acetic Acid into Concentrated Acid

John Kassotis and Harry P. Gregor

Department of Chemical Engineering and Applied Chemistry, Columbia University, New York, New York 10027

Frederick P. Chlanda

Allied Corporation, Corporate Research Group, Morristown, New Jersey 07960

ABSTRACT

Electrodialytic water splitting is an energy-efficient and inexpensive means to produce relatively concentrated solutions of weak acids and bases from feed solutions of the corresponding salts. With contaminated feedstreams, ultrafiltration is a necessary prerequisite. A 6% solution of sodium acetate was readily resolved into 35% acetic acid and about 8% sodium hydroxide. The degree of concentration achieved is determined by the electro-osmotic coefficients of the ions involved. This process can also serve to concentrate relatively dilute solutions of weak acids and weak bases, ones too weak to be capable of concentration by direct electrodialysis. The water splitting process has unusual advantages for the treatment of the products of fermentation in closed-loop systems.

The extensive development of ion-exchange membranes has led to increased interest in the phenomenon of water splitting. In the electrodialytic processes when a critical current density is reached wherein the concentration of electrolyte at the membrane surface approaches zero, the water in or at the membrane surface starts to dissociate at a rate such that the transport of hydrogen and hydroxyl ions in opposite directions becomes significant. This phenomenon was first observed by Bethe and Toropoff (1, 2), who observed that equal amounts of acid and base were produced, presumably from water.

The development of bipolar membranes and their study has led to several rather detailed analyses of water splitting processes. It also became evident that bipolar membrane systems could be used for the production of acids and bases from neutral solutions. Accordingly, the preparation of bipolar membranes of industrial utility has been a topic of study for some years. For a bipolar membrane to be useful industrially, the following properties must be realized: high permselectivity; stability and efficacy under high current densities; stable physical properties; and low ohmic resistance.

Several techniques have been employed. Frilette (3) fused monopolar membranes together and used them in

electrodialytic processes. De Korosy (4) made bipolar membranes from a single sheet of polyethylene by sulfochlorination from one side and amination from the other. Benjamin *et al.* (5) improved the cementation technique. Most recently, Liu *et al.* (6-12) prepared bipolar membranes which have demonstrated operational characteristics suitable for large-scale utilization.

Benjamin (13) studied three different applications of bipolar water splitting membranes: namely, the preparation of KOH and HCl from KCl, of Mg(OH)₂ and H₂SO₄ from MgSO₄, and the decomposition of ammonium bicarbonate to form CO₂ and ammonia. It was found that in the production of 0.2N KOH and HCl the coulombic efficiency was 90%. In the production of Mg(OH)₂ and H₂SO₄ current efficiencies fell to 85% and 65%, respectively, attributed to the low mobility of the large bisulfate ion. Fused monopolar membranes were used in these studies.

Chang (14) evaluated the feasibility of electrodialytic water splitting for the conversion of ferrous chloride-HCl pickling solutions into the insoluble hydroxide and free acid, and demonstrated feasibility at the laboratory level. Chang (15) also applied water splitting to the conversion of hydroxylamine hydrochloride into hydroxylamine nitrate.

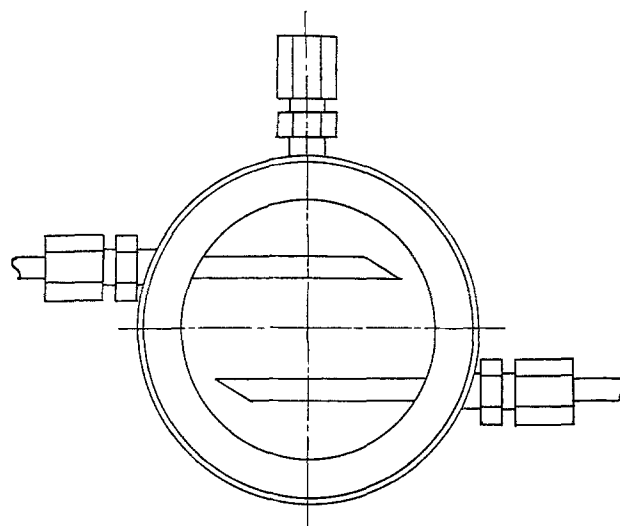
Chlanda *et al.* (11) characterized the Allied bipolar membranes by producing 1N HCl and NaOH from NaCl at a current efficiency of 93% for the base and 80% for the acid. Most of the loss in efficiency was attributed to leaks in the flanking monopolar membranes.

Experimental

Preparation of bipolar membranes.—The fused bipolar membranes deteriorate after prolonged use due to their separation, probably as a result of electro-osmotic forces. Improved bipolar membranes were made using the gluing technique of Benjamin and Chang, wherein Ionac MC3470 and MA3475 membranes of the heterogeneous monopolar type were used. A solution of linear polystyrenesulfonic acid in DMF was applied as a thin film across each surface face, and the two fused together for 3 min in a hydraulic press at 200° F and 2000 psi pressure, the optimal conditions.

Measurement of electrolysytic and water splitting efficiencies.—A batch recirculating device (Fig. 1) was employed to determine water splitting efficiencies; it had six cells (Fig. 2) in series, each connected to individual 2 × 15 in. Pyrex cylinders calibrated for volume measurement. Four compartments (two for feed and one each for base and acid delivery) had individual micropumps, and the two end electrode compartments had a joint feed stream and pump. For water splitting, the membranes used were, from left to right in Fig. 1, + (cation permeable), +, - + (bipolar), - (anion permeable), +. Two cell compartments had an in-line heat exchanger to maintain stream at 25°-35°C. Prior to each experiment, distilled water was circulated to test for leaks because no materials can be lost if accurate current efficiencies are to be calculated. Solutions were prepared with reagent-grade chemicals and deionized water.

After the insertion of feed solutions, circulating pumps were started, and their rheostats regulated for proper flows and cell liquid levels. Zero time samples were taken for analysis and then current was passed with the voltage properly adjusted. The device was operated for the time intervals necessary to achieve a given concentration charge, then current was stopped, samples of acid



POLYPROPYLENE: 4" OD X 3" ID X 1"
FITTINGS: POLYPROPYLENE TUBE FITTINGS 1/4" ID
TUBING: POLYETHYLENE 1/4" OD X 1/8" ID

Fig. 2. Cell compartment

and base were taken, and volume changes recorded. The base concentration was maintained near 0.5M to keep diffusible losses low; different initial concentrations of acetic acid were used to allow one to measure membrane efficiency over a wide range of concentrations.

When straightforward concentration by electrolysis (ED) was desired, one concentrate cell was used between two feed cells, with the membrane sequence: +, +, -, +.

There are several fermentation routes to make acetic acid. In one, the almost pure acid is produced at the 3%-10% levels, depending upon the feedstock, organism, and rate of fermentation desired. In general, rates of conversion decrease with increasing product concentration, owing to product inhibition. Jeffries (16) and Omstead (17) have shown that when product levels are kept well below the maximum which can be attained, fermentation rates are substantially increased, often as much as five-fold. In the anaerobic digestion of primary sewage sludge, for example, Naughton (18) obtained detention times 0.1 of the usual (1.5 cf. 15 days) by the use of concomitant ultrafiltration.

Wang (19) has shown that biomass is an effective feedstock to produce at neutral pH levels 6% or 0.73M sodium acetate, corresponding to 4.4% acetic acid. It is usually converted to glacial acetic acid by treatment with sulfuric acid; solvent extraction then removes the acid which is concentrated by distillation.

Thus, there are several possible routes to glacial acetic acid by the use of membrane processes, including the straightforward electrolysytic concentration of acetic acid or that of sodium acetate, but little is gained by concentrating the salt.

Results

Electrolysytic concentration of acid.—A feed of 4.8% acetic acid was electrolysytically concentrated at 17.3 mA/cm² with AMV and CMV membranes of the Asahi Glass Company at 35°C. The concentration of acid was carried to the 19.8% level (Table I). The current efficiency was fairly high ini-

Table I. Electrolysytic concentration of acetic acid with AMV/CMV membranes

Time (h)	HAC (%)	Cell volume (ml)	Current efficiency (%)
0	4.8	230	—
5	9.0	280	96
10	11.6	330	71
20	15.8	440	72
30	18.7	520	62
35	19.8	560	53

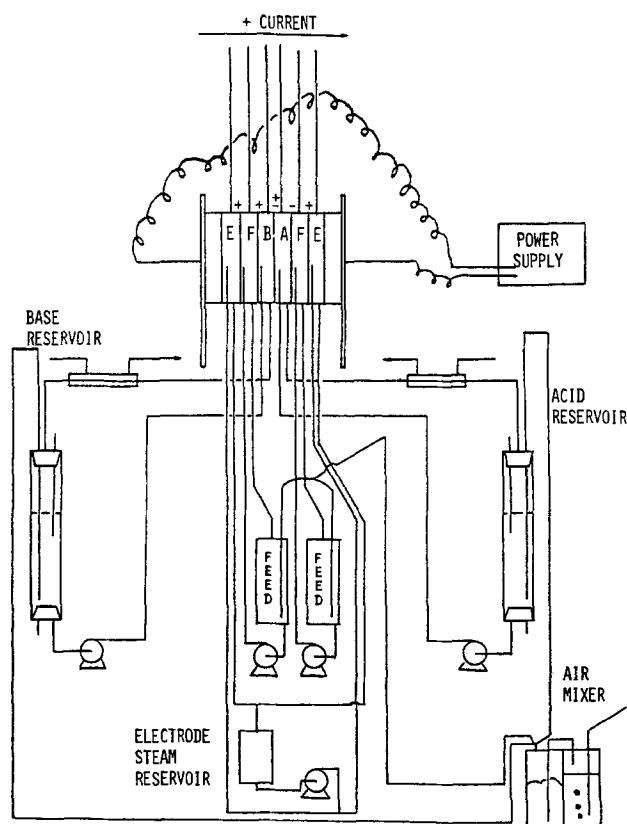


Fig. 1. Laboratory cell and auxiliary equipment

tially; it fell to 53% when approximately 20% acetic acid is reached.

The transport efficiency of acetic acid is influenced by the electro-osmotic water carried along with the acid which dilutes it in the concentrate stream; it is lowered by back-diffusion of acid. Water splitting taking place at the surface of the anion-permeable membrane in the dilute solution feed lowers current efficiency, where generated hydroxide ions pass through the membrane, with hydrogen ions going into the deionate.

Asahi Glass membranes are among the tightest available commercially. When looser Ionac membranes were employed at 20 mA/cm² and starting with 0.6% acid, when a concentration of 4.9% was reached the current efficiency fell to 27%. Thus, the nature of the membranes used is important.

The extent of electroolytic water splitting is appreciable here because the concentration of ionized species in solution is low. For example, in 0.73M acetic acid at the 4.4% level, the concentration of hydrogen ions is 0.0038M and its specific resistance 667 Ω-cm. Water splitting could be minimized by operating at low current densities, but this increases the relative contribution of back-diffusion and makes for increased equipment costs.

The limiting current before water splitting is readily calculated from Nernst-Planck as equal to $2DC/\delta$, where D and C are diffusion coefficient and concentration of transported species and δ the boundary layer thickness. Since the diffusion coefficient of acetate is 1×10^{-5} cm²/s at a concentration of 0.004M and a boundary layer thickness of 100 μm (as measured in these cells), the limiting current density is 0.8 mA/cm². With high convection the boundary layer resistance can be lowered by two-thirds, but a current of 2.4 mA/cm² requires too much investment in equipment.

The rate of back-diffusion of acid through the much more permeable cation membrane is readily calculated.

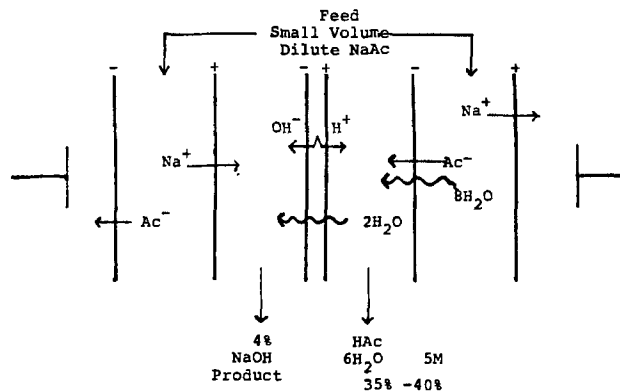


Fig. 3. Electrolytic water splitting to convert salts of organic acids into bases and organic acids.

For a membrane thickness of 200 μm and an effective diffusion coefficient of acetic acid in it of 10^{-6} cm²/s, if the concentration of acetic acid on one side is 20% acid and zero on the other, the flux is 1.5×10^{-7} mol/cm² s, corresponding to a current of 15 mA/cm². It is evident, therefore, that a high current density must be employed, something precluded by the low concentration of ionized species present and resultant water splitting. Thus, we cannot use a low current density nor a high one.

Conversion of sodium acetate to acetic acid.—Consider electroolytic water splitting in a bipolar cell (Fig. 3). Because of the high mobility of the hydroxide ion, we do not allow the concentration of the base stream to rise above 0.5M, but raise the concentration of acetic acid in its product stream as high as possible. If a high concentration of base is desired, conventional ED can produce 15%-40% base, depending on the membrane used.

In the initial series of experiments, cemented Ionac bipolar membranes were employed at a current density of

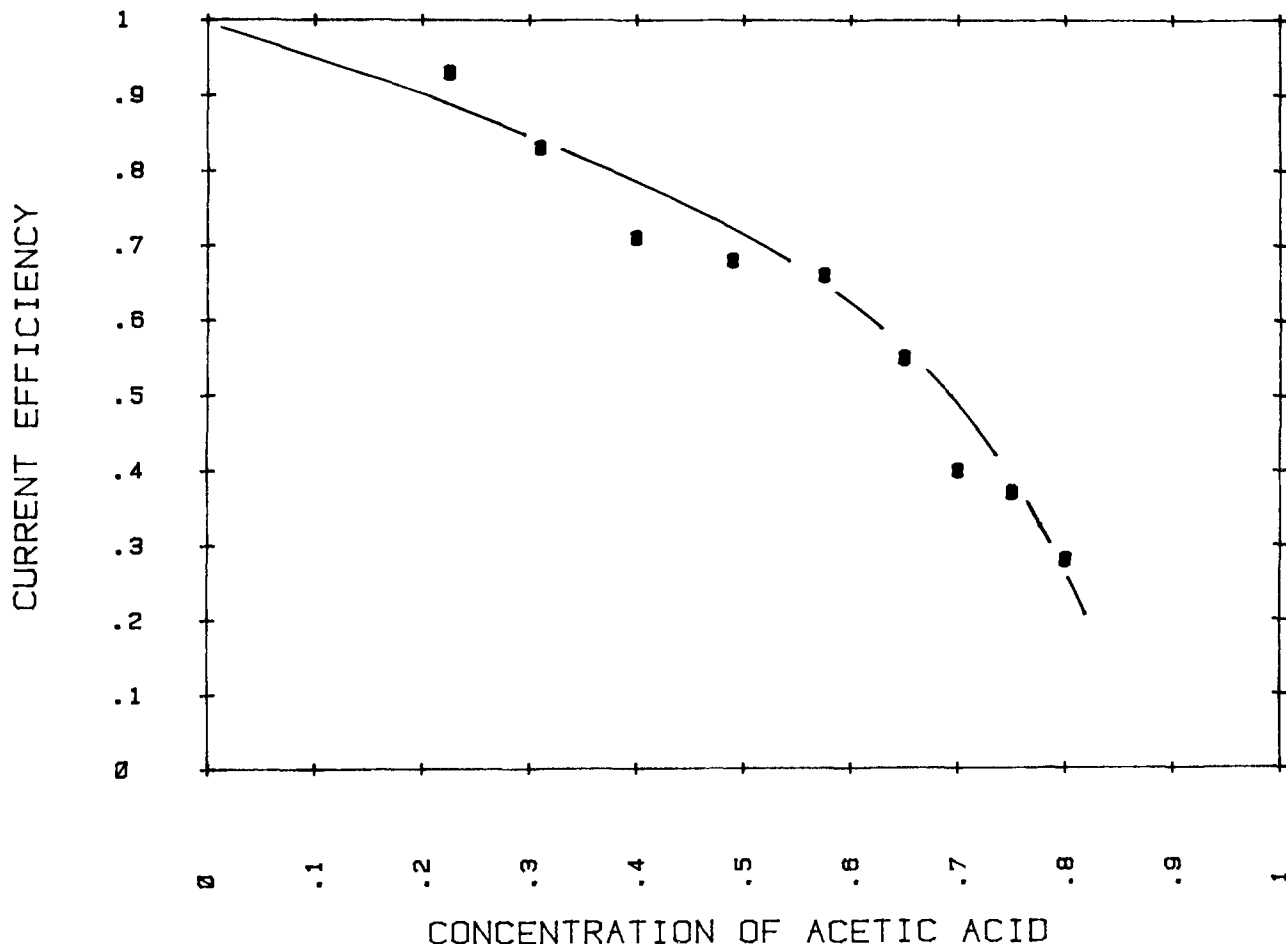


Fig. 4. Conversion of 6% sodium acetate feed to acetic acid by fused ionac bipolar membranes at 20 mA/cm²

Table II. Current-voltage characteristics of allied bipolar membrane

Current (A)	ΔE Membrane and solution (V)	Membrane* (V)
0.05	0.84	0.72
0.10	1.02	0.79
0.20	1.31	0.85
0.40	1.85	0.93
0.60	2.36	0.99
0.80	2.86	1.03
1.00	3.36	1.08
1.20	3.84	1.10

Cell of area 11 cm² with 0.5M sodium sulfate at room temperature.

* Calculated by subtracting calculated solution resistance from total resistance.

20 mA/cm². Monopolar membranes of the Ionac variety were used. Figure 4 shows that the current efficiency was high when a dilute solution of acid was obtained, but it fell to about 27% when 5% acid was reached. Varying the current density to higher and lower values did not lead to improved current efficiencies, probably because the heterogeneous monopolar Ionac membranes show a rather large leak to acetate and acetic acid.

The allied bipolar membrane was first measured as to its current-voltage characteristics in a similar 11 cm² cell between 0.5M sodium sulfate solutions at room temperature and at 0.05-1.2A current. The voltage drop across the membrane and solution and across the solution itself was measured, and that across the membrane was calculated. Probe electrodes inserted in the two solutions flanking the membrane were used. The voltage drop across the membrane increased from 0.7 to 1.1V as the current density was varied by a factor of about 24, as shown in Table II. The decrease in membrane resistance with increasing current is typical for bipolar membranes which act like p-n junctions in generating current carriers proportional to current density. This membrane was designated ACBM-3 bipolar membrane, its preparation is given in Chlanda *et al.* (11), and its properties were quite similar or identical with those of Ref. (6-12).

The water splitting conversion of 6% sodium acetate was performed in the 11 cm² cell, starting with 0.5 NaOH and 6% acetic acid in the product compartments. A constant current density of 109 mA/cm² was maintained, and the flanking membranes were the C322 (similar to ones of AMF) and the ASV membranes of the Asahi Glass Company. To reduce the overall IR drop in the receiving acid compartment, small amounts of sodium acetate were added to the acid product compartment initially. Some sodium acetate also entered this compartment due to the leak of salt.

In a first run (Table III), acetic acid was concentrated from 6.00% to 7.54% at a current efficiency of 89.7%. Subsequently, the acid product stream was raised to 27.3%, and the current efficiency remained fairly high through-

Table IV. Initial and final concentrations of sodium acetate in concentrated acetic acid

M_{is}	M_{fs}	X_{fs}	M_{fa}
0.01090	0.0870	0.9520	1.690
0.00992	0.1067	0.9665	3.067
0.00548	0.0920	0.9975	4.550
0.00513	0.0958	0.9800	4.150

M_{is} : initial molar concentration of salt in acid.

M_{fs} : final molar concentration of salt in acid.

X_{fs} : final mole fraction of salt in acid.

M_{fa} : final molar concentration of acid.

out. However, the current efficiency fell to 38% when a concentration of 36.6% acetic acid was reached by initial addition, probably because the maximum concentration of acid that could be reached (as dictated by electro-osmotic transport of water) was exceeded. Table IV gives salt levels in acid product stream.

A final series of steady-state experiments was performed, wherein the process was continued until a constant concentration of acid in the product stream was reached. In water splitting, the device "pumps" both acid and water (plus a small amount of salt) into the product stream; if this is allowed to overflow, a steady-state concentration is obtained. Table V gives results at 1.2A for the 11 cm² cell, at 109 mA/cm² or 101 A/ft². The maximum level of acid reached in ten separate experiments varied from 33% to 41% acetic acid.

Discussion

Water splitting technologies can convert fermentation product streams of salts of weak acids into solutions of base, with the acids in a concentrated solution. The highest level of acid obtainable is dictated by electro-osmotic water transport across the anion-permeable membrane. For a given ion, the electro-osmotic coefficient is primarily a function of the effective pore diameter of the membrane, and increases rather sharply with pore size. The anion-permeable membranes used here had osmotic coefficients of 8 mol of water per Faraday; finer pore membranes allowing but 5-6 mol of water could be developed to obtain a 50% acid solution, one which is probably the upper limit.

There are few limitations to this process. The upper MW level of permeating solutes is about 500. The concentration of the feedstock plays no role other than to dictate the IR drop across the feed compartment. If dilute feedstocks must be employed, they can be readily concentrated by membrane processes at low cost to the point where the overall cost of the process is minimized. For example, solutions of salts of organic acids at the 1000-5000 mg/liter levels and produced by the fermentation of sewage sludge under membrane-facilitated conditions have been treated first by ultrafiltration to remove fouling components, then by reverse osmosis for concen-

Table III. Water splitting with allied bipolar membrane for elapsed intervals of 4000s

V_{ai} (ml)	V_{af} (ml)	M_{ai}	M_{af}	M_{bi}	M_{bf}	V_{bi} (ml)	V_{bf} (ml)	CE (%)
148.8	155.4	1.012	1.256	0.5425	0.8160	146.5	145.3	0.897
152.4	157.8	1.885	2.092	0.531	0.792	147.1	150.9	0.861
146.4	153.0	1.480	1.690	0.520	0.795	140.5	144.1	0.840
149.07	157.19	2.954	3.061	0.531	0.808	135.65	139.87	0.820
141.05	149.4	2.933	3.067	0.505	0.815	132.6	136.3	0.890
142.7	150.6	4.475	4.550	0.505	0.795	135.1	138.7	0.938
133.1	137.3	6.101	6.036	—	—	—	—	—

a: Acid stream.

b: Base stream.

V: Volume of cell solution (ml).

M: Concentration in cell (molar).

i: Initial.

f: Final.

CE: Current efficiency.

Table V. Steady-state concentrations of acetic acid produced by water splitting

No.	NaAc feed (%)	HAc (%)	CE (%)
1	28.4	32.9	0.90
2	23.9	35.0	0.92
3	7.5	40.0	0.94
4	8.6	40.8	0.99
5	9.6	39.7	0.97
6	10.7	40.0	0.98
7	11.8	38.6	0.96
8	12.7	37.7	0.93
9	13.6	37.5	0.96
10	14.5	36.2	0.98

tration, and then by water splitting to produce concentrated acids.

Reliable costs for this process can be estimated. For a relatively small plant producing 1000 gal/h of a 6% sodium acetate feed, a plant having a total area of about 800 ft² effective area for each of the three membrane types would be required, operating at a current density of 100 A/ft². The investment costs would be approximately \$50,000; larger plants cost somewhat less. These are total plant costs including the power source, module and pumps but not interest on investment. For this small plant, the cost of device per square foot of cell area was taken as \$62.50; according to Liu *et al.* (8), one having an area of 18,750 ft² costs \$28.50 per ft², so appropriate consideration was given to the economies of scale which prevail in this field.

For this plant, the production of 35% acetic acid is about 0.1 lb/s. Taking the standard amortization rate of this equipment (5 yr average, 3 on membranes and 7 on the remainder) the total equipment cost would be approximately 0.2¢/lb of acid. With power at 5¢/kWh and with a dilute feed (0.5%) requiring a total voltage of 3V, the cost is 3.4¢/lb acetic acid. With a more concentrated feedstock of the type studied here (3%-10% salt) and electricity at 3.5¢/kWh, the voltage drop is 2V and the power required is approximately 1.6¢/lb of acid produced.

The water splitting process can be applied to a wide range of electrolytes of different kinds for the double purpose of converting these into their corresponding acids and bases and also producing concentrated product streams. The current efficiencies obtainable and the maximum current densities which can be utilized depend upon the nature and concentration of the feed substances. In the present study, the relatively large molecular size of the acetic acid product and its relatively low diffusivity through the membranes allowed for a high current efficiency, with little loss of acid by diffusion. If the product were formic acid, somewhat higher losses would be encountered, as would occur if ammonia were the base produced. Solutes of higher molecular weight, particularly those which are poorly ionized in the acid or base form, make for the highest current efficiencies and the smallest losses by diffusion.

Water splitting can also serve to concentrate weak electrolytes. As was observed, the electrochemical concentration of acetic acid was impractical. Somewhat stronger acids such as malic acid can be electrochemically concen-

trated to up to 30% efficiently from a 5% feedstock as demonstrated by Liu (20).

The concentration of dilute acetic acid to the 35%-40% level by electrochemical water splitting can be readily achieved. The acid feedstock is first neutralized and the salt used as feed, with the base recycled for neutralization of feed. At a feed level of 1000 GPM of 4.4% acetic acid (the same molarity as 6% sodium acetate), the membrane plant has the same area and cost as with salt conversion.

If a product stream entirely free of excess sodium acetate were desired, straightforward electrochemical with little loss of free acid would reduce it to the 0.01M or 500 mg/liter level. Or, direct cation exchange using a strong acid regenerant would remove all traces of sodium and produce pure acid at nominal cost.

Acknowledgments

This work was supported in part by two research contracts from the United States Department of Energy, the first from the Office of Energy from Municipal Wastes (DF-AC 01-78CS-20400), the second through the Solar Energy Research Institute (XB-9-8161-1); the authors express their thanks for this support. We also thank Allied Corporation for its cooperation and permission to use its facilities.

Manuscript submitted Aug. 1, 1983; revised manuscript received May 16, 1984.

Columbia University assisted in meeting the publication costs of this article.

REFERENCES

1. A. Bethe and T. Toropoff, *Z. Phys. Chem.*, **88**, 686 (1914).
2. A. Bethe and T. Toropoff, *ibid.*, **89**, 597 (1915).
3. V. Frilette, *J. Phys. Chem.*, **60**, 435 (1956).
4. F. DeKorossy, *Isr. J. Chem.*, **3**, 22 (1965).
5. B. Benjamin, K. Brennen, and H. P. Gregor, To be published.
6. G. J. Dege and K. J. Liu, U.S. Pat. 4,024,043 (1977).
7. L. T. C. Lee, G. J. Dege, and K. J. Liu, U.S. Pat. 4,057,481 (1977).
8. K. Nagasubramanian, F. P. Chlanda, and K. J. Liu, *J. Memb. Sci.*, **2**, 109 (1977).
9. K. J. Liu, F. P. Chlanda, and K. Nagasubramanian, *ibid.*, **3**, 57 (1978).
10. K. J. Liu, K. Nagasubramanian, and F. P. Chlanda, *ibid.*, **3**, 71 (1978).
11. F. P. Chlanda, L. T. C. Lee, and K. J. Liu, U.S. Pat. 4,116,889 (1978).
12. G. J. Dege and K. J. Liu, U.S. Pat. 4,140,815 (1979); K. Mani and F. P. Chlanda, U. S. Pat. 4,391,680 (1983).
13. B. Benjamin, Dr. Eng. Sci. Thesis, Columbia University, New York (1975).
14. Y. Chang, Dr. Eng. Sci. Thesis, Columbia University, New York (1979).
15. Y. Chang and H. P. Gregor, *IEC Process Design Dev.*, **20**, 361 (1981).
16. T. W. Jeffries, D. R. Omstead, R. R. Cardenas, and H. P. Gregor, in "Biotechnology and Bioengineering Symposium," no. 8, p. 37 (1979).
17. D. R. Omstead, T. W. Jeffries, R. Naughton, and H. P. Gregor, in "Bioengineering and Biotechnology Symposium," no. 10, p. 247 (1980).
18. R. Naughton, M. S. Thesis, Columbia University, New York (1981).
19. D. Wang, Personal communication.
20. K. J. Liu, F. P. Chlanda, and H. P. Gregor, To be published.

A Homogeneous/Agglomerate Model for Molten Carbonate Fuel Cell Cathodes

H. R. Kunz,* L. J. Bregoli, and S. T. Szymanski

United Technologies Corporation, Power Systems Division, South Windsor, Connecticut 06074

ABSTRACT

A molten carbonate fuel cell cathode model was developed which enables the estimation of performance as a function of cathode electrolyte content. This model is neither a thin film nor a conventional agglomerate model, but involves the calculation of the effective agglomerate diameter, porosity, tortuosity, and number based on knowledge of the electrode's pore spectrum and electrolyte content. Calculated electrode performance and experimental results are compared for cathodes of different pore spectra over a range of electrolyte contents.

The cathode of present molten carbonate fuel cells consists of porous, lithiated nickel oxide, which, during operation, is partially filled with electrolyte. Its structure consists of microporous nickel oxide particles clustered to form macropores, as shown in Fig. 1. The degree of saturation of the cathode with electrolyte depends upon the total amount of electrolyte in the cell and the pore-size distributions and volumes of the cell anode, cathode, and matrix. When good performance is being attained, the larger electrode pores are open to allow gas-phase diffusion of reactants into the cathode and reduce the path length for liquid-phase diffusion. Enough electrolyte is present to facilitate the electrochemical reactions and ionic conduction. Good electronic conductivity should be provided by the catalyst particles.

Such an electrode configuration has been modeled in the past using a thin film model (1-3), whereas a cylindrical agglomerate model would be more appropriate (4-6). Both of these approaches, however, are deficient in that neither the electrolyte film thickness nor the agglomerate diameter is known with any accuracy, and they are frequently used as fitting parameters to the experimental data. The uncertainties are compounded when the performance is desired as a function of the amount of electrolyte in the electrode. In order to avoid these uncertainties, a new model was developed, which is basically a cylindrical agglomerate model with the agglomerate diameter, number, porosity, and tortuosity calculated from a knowledge of the pore size distribution and electrolyte content.

In conjunction with the theoretical analysis, experimental performance data were obtained for four cathodes of different pore structure using a half-cell rig containing a reference electrode. Electrolyte was added and removed from these cathodes to obtain performance as a function of electrolyte content. These experimental results were used to evaluate the capabilities of the model.

Theory

If an electrode is completely filled with electrolyte and a gas pressure is applied in excess of the liquid pressure, liquid is forced out of the electrode into adjacent liquid containing regions. Most of the PdV work done in this expulsion increases the vapor-liquid interfacial free energy, σdA . This relationship is used to determine the surface area of a porous body using mercury intrusion porosimetry (7). Here P is the pressure difference between the gas and liquid, V is the volume of the gas in the electrode, σ is the surface tension, and A is the vapor-liquid interfacial area. This is not an exact relationship in this case because of solid-gas and solid-liquid interfacial free energies, the effect of vapor-liquid interfacial curvature on the free energy, the effect of film thickness on surface free energy, chemical effects, and the process by which the electrode is filled. However, if the electrolyte is considered to completely wet the catalyst and form a relatively thick film, the equality of PdV and σdA may provide an

*Electrochemical Society Active Member.

equation which enables the prediction of gas-liquid interfacial area. If this area is known and the cylindrical agglomerate concept is retained, this area becomes the gas surface area of all the agglomerates.

An assumption must be made that the measured pore-size distribution is suitable for use in this analysis. Most pore spectra are obtained using mercury intrusion porosimetry, in which nonwetting mercury is forced into the porous body. In the fuel cell case, a wetting liquid is wicked into or forced from the body, which results in somewhat different pore spectra, since hysteresis effects are known to be present in pore spectra.

Agglomerate properties.—If all of the above assumptions are made, the agglomerate radius, number, and po-

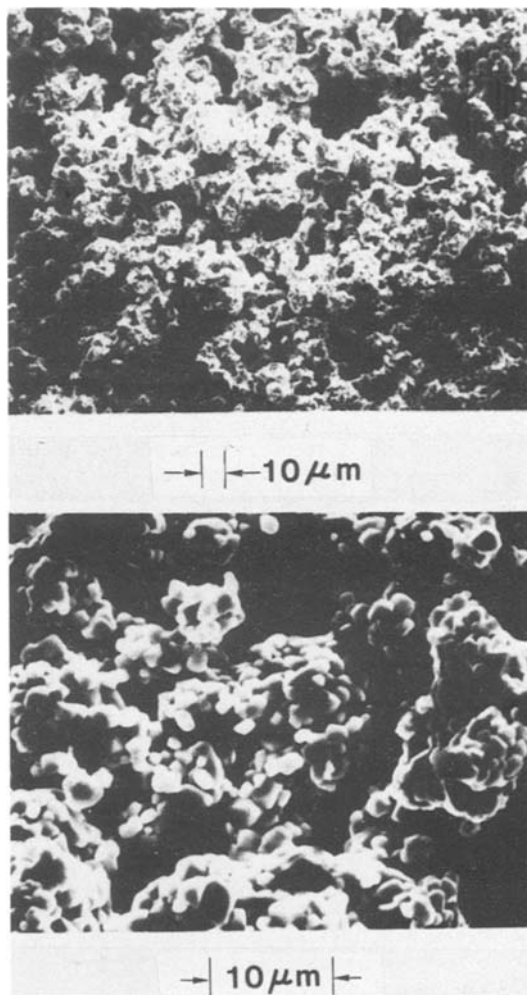


Fig. 1. Scanning electron micrograph of oxidized cathode

rosity can be calculated from the pore spectrum as follows

$$(P_G - P_L) dV = -\sigma dA \quad [1]$$

where V is now the volume of liquid in the electrode. Since

$$(P_G - P_L) = 2\sigma/r \quad [2]$$

it follows that

$$dA = 2dV/r \quad [3]$$

where $r(V)$ is the pore radius on the pore-size distribution graph. Therefore

$$A = \int_{V_{\text{filled}}}^{V_{\text{total}}} \frac{2dV}{r} \quad [4]$$

V_{total} is the total void volume of the electrode and V_{filled} is the volume of electrolyte in the electrode.

For a cylindrical agglomerate

$$A/V_{\text{filled}} = (2Nr_o \pi \tau_E \delta \theta) / (N\pi r_o^2 \tau_E \delta \theta) \quad [5]$$

where N is the number of agglomerates, r_o the agglomerate radius, τ_E the agglomerate tortuosity, θ the porosity, and δ the electrode thickness.

Then

$$A/V_{\text{filled}} = 2/r_o \quad [6]$$

Eliminating A between Eq. [4] and [6] yields

$$r_o = V_{\text{filled}} \int_{V_{\text{filled}}}^{V_{\text{total}}} \frac{dV}{r} \quad [7]$$

This equation can be used to obtain the agglomerate radius from the pore-size distribution curve.

The number of agglomerates, N , is calculated assuming the agglomerates are cylindrical using the equation

$$N = (V_{\text{filled}} + V_{\text{solid}}) / (\pi r_o^2 \tau_1 \delta) \quad [8]$$

where V_{solid} is the volume of solid in the electrode. The agglomerate porosity, θ , is

$$\theta = V_{\text{filled}} / (V_{\text{filled}} + V_{\text{solid}}) \quad [9]$$

and the tortuosity for ionic migration, τ_1 , is

$$\tau_1 = [(V_{\text{total}} + V_{\text{solid}}) / V_{\text{filled}}]^{0.75} \quad [10]$$

using an Archie's law relationship (8) found to hold for molten carbonate fuel cell matrices. These equations predict that the radius of the agglomerate decreases and the number of agglomerates increases as the electrolyte content of the electrode is decreased. This is due to the increase of the vapor-liquid interfacial area. The model also predicts that the porosity of the agglomerates decreases from the overall porosity of the electrode when it is completely filled to zero when it is empty of electrolyte.

Agglomerate model description.—Figure 2 is an idealized illustration of the model. The agglomerates are assumed to consist of an array of right-circular cylinders of radius r_o in which nickel oxide catalyst particles and electrolyte are homogeneously dispersed. The agglomerate radius and number are calculated by Eq. [7] and [8], respectively, for a specified pore spectrum and electrolyte content. During steady-state operation, reactant gases at the surface of the cylinder dissolve in the electrolyte and diffuse radially with simultaneous reaction on the catalyst particles. Ionic current is assumed to conduct only in the axial direction.

Additional assumptions include the following: (i) electrolyte is saturated with reactant gas at the gas-electrolyte interface, (ii) all activities are equal to concentrations (i.e., all activity coefficients are assumed equal to one), (iii) transport parameters are constant, and (iv) the electrode operates at a uniform temperature.

The model includes the effects of activation polarization, liquid-phase diffusional resistance in the electrolyte,

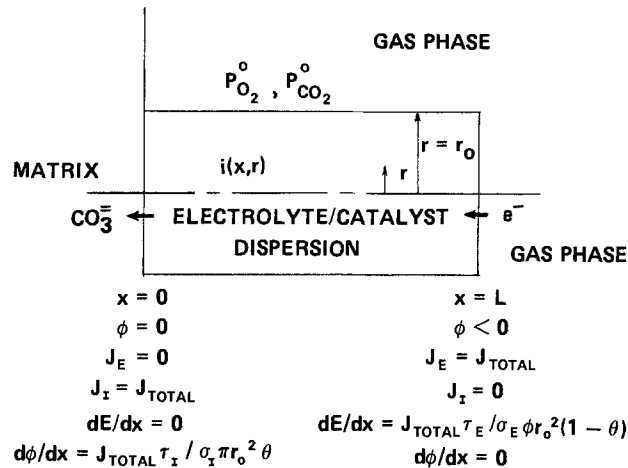
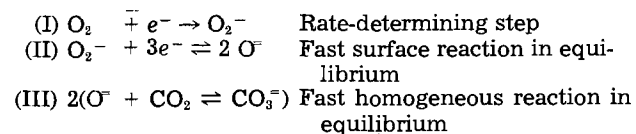


Fig. 2. Homogeneous/agglomerate model

ionic resistance in the electrolyte, and electronic resistance in the nickel oxide structure. Gas-phase diffusional losses were not considered. Previous results indicate that these losses may be significant (6). For a given overall electrode current density, the model calculates the axial variation of electrode and electrolyte potentials and the radial and axial variations of reactant concentrations and local current density.

Mechanism.—The geometric configuration presented above was used with the following reaction sequence occurring within the agglomerate.



The correct mechanism to use for an actual fuel cell cathode is uncertain at this time (9), so this mechanism was used to evaluate the concept of the homogeneous/agglomerate model. The above reaction sequence assumes that oxygen dissolves as molecular oxygen. In the actual case, molecular oxygen dissolves as superoxide and peroxide if these dissolution reactions are adequately fast. The relative contents of superoxide and peroxide depend on the electrolyte and oxidant composition and the relative rates of the dissolution reactions. The rate of homogeneous reaction (III) may also be slow enough to be controlling.

Activation polarization.—Using the above reaction sequence, the local current per unit of real catalyst surface area, $i(x, r)$ is

$$i(x, r) = i_o \left\{ \left(\frac{P_{CO_2}^o}{P_{CO_2}} \right)^2 \exp \left[\frac{(3 + \beta)F\eta}{RT} \right] - \left(\frac{P_{O_2}}{P_{O_2}^o} \right) \exp \left[\frac{-(1 - \beta)F\eta}{RT} \right] \right\} \quad [11]$$

where i_o is the exchange current density (A/cm^2), $P_{CO_2}^o$, $P_{O_2}^o$ the bulk gas partial pressures at the gas/agglomerate interface, P_{CO_2} , P_{O_2} the equivalent reactant partial pressure at the reaction site, η the local overpotential (V), and β the symmetry factor for rate-determining step.

The exchange current density is given by

$$i_o = k(T) [P_{O_2}^o]^{3/4 + \beta/4} [P_{CO_2}^o]^{-1/2 - \beta/2} \quad [12]$$

where $k(T)$ is the cathodic rate constant for the rate-determining step and is a function of temperature.

In this analysis, the reference state is taken to be that of the local conditions along the agglomerate under load. Hence $P_{CO_2}^o/P_{CO_2}$ and $P_{O_2}^o/P_{O_2}$ are measures of the liquid-phase diffusional polarization.

The overpotential $\eta(x)$ is defined as

$$\eta(x) \equiv E(x) - \phi(x) - E_{o/c} = E(x) - \phi(x)$$

$$-\frac{RT}{2F} \ln \left[\left(\frac{P_{CO_2}^o}{0.67} \right) \left(\frac{P_{O_2}^o}{0.33} \right)^{1/2} \right] \quad [13]$$

where $E(x)$ is the potential of the electrode solid (V), $\phi(x)$ the electrolyte potential (V), and $E_{o/c}$ the reversible or open-circuit potential measured relative to a 2:1 $CO_2:O_2$ reference (V).

Liquid-phase diffusional polarization.—To determine the liquid-phase diffusional losses, the following approach is taken. Assuming Henry's law to hold for both oxygen and carbon dioxide

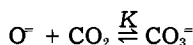
$$P_{CO_2}/P_{CO_2} = H_{CO_2} P_{CO_2}^o/[CO_2] \quad [14]$$

and

$$P_{O_2}/P_{O_2}^o = [O_2]/H_{O_2} P_{O_2}^o \quad [15]$$

where factors in brackets represent molar concentrations and H is Henry's law constant.

Since step (III) in the overall mechanism is in equilibrium at all points within the agglomerates according to the equation



$$K = (CO_3^-)/(O^-) P_{CO_2} = (CO_3^-)^o/(O^-)^o P_{CO_2}^o$$

Therefore

$$P_{CO_2}/P_{CO_2} = [CO_2]^o/[CO_2] = (O^-) (CO_3^-)^o/(O^-)^o (CO_3^-)$$

The mole fractions are related to molar concentrations by the molar density, D_M

$$(O^-) = [O^-]/D_M$$

Since $(CO_3^-)^o/(CO_3^-) = 1$, then

$$P_{CO_2}/P_{CO_2} = [CO_2]^o/[CO_2] = [O^-]/[O^-]^o \quad [16]$$

The $[O^-]/[O^-]^o$ factor can be determined by taking into account the oxygen and carbon atom fluxes through the agglomerate

$$\begin{aligned} \text{O atom flux } 5 \cdot 2D_{O_2} \frac{\partial [O_2]}{\partial r} + D_{O^-} \frac{\partial [O^-]}{\partial r} \\ + 2D_{CO_2} \frac{\partial [CO_2]}{\partial r} + 3D_{CO_3^-} \frac{\partial [CO_3^-]}{\partial r} = 0 \end{aligned} \quad [17]$$

$$\text{C atom flux } 5 \cdot D_{CO_2} \frac{\partial [CO_2]}{\partial r} + D_{CO_3^-} \frac{\partial [CO_3^-]}{\partial r} = 0 \quad [18]$$

where D is the diffusion coefficient of a species.

Differentiating Eq. [16]

$$\frac{\partial [O^-]}{\partial r} = \frac{-[O^-]^o [CO_2]^o}{[CO_2]^2} \frac{\partial [CO_2]}{\partial r} \quad [19]$$

Substituting Eq. [18] and [19] into [17], simplifying, and then integrating between limits yield

$$[CO_2] = \frac{(\alpha - \epsilon) + \sqrt{(\epsilon - \alpha)^2 + 4\gamma\beta}}{2\gamma} \quad [20]$$

where

$$\alpha = \{D_{CO_2}[CO_2]^o - D_{O^-} [O^-]^o\}/2D_{O_2}$$

$$\beta = D_{O^-} [CO_2]^o [O^-]^o / 2D_{O_2}$$

$$\gamma = D_{CO_2} / 2D_{O_2}$$

$$\epsilon = [O_2]^o - [O_2]$$

$$[O^-]^o = D_M H_{CO_2} / K [CO_2]^o = D_M / KP_{CO_2}^o$$

Equation [20] expresses $[CO_2]$ only as a function of $[O_2]$ and a series of constants.

Substituting Eq. [14], [15], and [20] into [11] results in an expression for the current density $i(x, r)$ which is a function only of $[O_2]$ at a fixed value of x .

The diffusion of dissolved oxygen through the agglomerate with simultaneous consumption due to current generation is given by the steady-state continuity equation using Fick's law

$$\frac{\partial^2 [O_2]}{\partial r^2} + \frac{1}{r} \frac{\partial [O_2]}{\partial r} + \frac{\tau_1 S_g \rho (1 - \theta) i(x, r)}{nFD_{O_2} \theta} = 0 \quad [21]$$

with boundary conditions

$$\frac{\partial [O_2]}{\partial r} = 0 \text{ at } r = 0, [O_2] = [O_2]^o = H_{O_2} P_{O_2}^o \text{ at } r = r_o$$

where $n = 4$, the number of electrons in the overall reaction, S_g is the surface area of catalyst (cm^2/g), and ρ is the catalyst density (g/cm^3).

Equation [11] can then be substituted into [21], resulting in a second-order, nonlinear, partial differential equation. The solution of this equation in conjunction with Eq. [16] and [20] gives $[O_2]$, $[O^-]$, $[CO_2]$, and i as functions of r and x for a given value of η .

Ohmic effects.—The electrolyte potential, ϕ , is taken as zero at $x = 0$, the matrix side of the electrode, and decreases as x increases. $d\phi/dx$ reaches 0 at the end of the agglomerate on the gas side of the electrode.

The effect of the ohmic potential gradient within the electrolyte can be taken into account by relating the ionic current, J_i , developed in the axial direction in the agglomerate, to the ohmic potential gradient in the electrolyte by Ohm's law

$$J_i = \frac{\sigma_1 \pi r_o^2 \theta}{\tau_1} \frac{\partial \phi}{\partial x} \quad [22]$$

Because of the current generated by the electrochemical reaction

$$dJ_i/dx = -2\pi S_g \rho (1 - \theta) \int_0^{r_o} i r dr \quad [23]$$

where σ_1 = ionic conductivity, $\Omega^{-1} cm^{-1}$.

Differentiating Eq. [22] and setting it equal to Eq. [23] yields

$$\frac{d^2 \phi}{dx^2} = \frac{-2\tau_1 S_g \rho (1 - \theta)}{\sigma_1 \tau_o^2 \theta} \int_0^{r_o} i r dr \quad [24]$$

The total current generated for the entire agglomerate, J_T , can be found by evaluating Eq. [22] at $x = 0$

$$\left. \frac{d\phi}{dx} \right|_{x=0} = \frac{J_T \tau_1}{\sigma_1 \pi r_o^2 \theta} \quad [25]$$

J_T is the overall current, I , divided by the number of agglomerates of radius r_o .

As stated above

$$\phi|_{r=0} = 0 \quad [26]$$

$$\left. \frac{d\phi}{dx} \right|_{x=L} = 0 \quad [27]$$

At each point along the agglomerate, the sum of the ionic current, J_i , and the electronic current, J_E , must be equal to the total current

$$J_T = J_i + J_E \quad [28]$$

at

$$x = 0 \quad J_i = J_T, J_E = 0; \text{ at } x = L, J_i = 0, J_E = J_T$$

The change in the electrode solid potential, E , with distance is related to the electronic current by

$$\frac{dE}{dx} = \frac{J_E \tau_E}{\sigma_E \pi r_o^2 (1 - \theta)} \quad [29]$$

where σ_E = electrode conductivity, $\Omega^{-1} cm^{-1}$.

Substituting Eq. [28] into [29] gives

Table I. Pore spectra characteristics of four pre-oxidized nonlithiated cathodes

Cathode designation	Thickness (mil)	Porosity (fraction)	Surface area (m ² /g)	Mean pore diameter (μm)
A	21	0.40	0.9	0.74
B	30	0.39	0.4	2.25
C	35	0.60	0.3	16.00
D	30	0.48	1.5	2.95

$$\frac{dE}{dx} = \frac{J_T \tau_E}{\sigma_E \pi r_0^2 (1 - \theta)} - \frac{\tau_E \sigma_1 \theta}{\tau_1 \sigma_E (1 - \theta)} \frac{d\phi}{dx} \quad [30]$$

From Eq. [25] and [27] it follows that

$$\left. \frac{dE}{dx} \right|_{x=0} = 0 \quad [31]$$

$$\left. \frac{dE}{dx} \right|_{x=L} = \frac{J_T \tau_E}{\sigma_E \pi r_0^2 (1 - \theta)} \quad [32]$$

The values of $E(x)$ and $\phi(x)$ are calculated by the above equation and used in Eq. [13] and [11].

Experiments

Performance data were obtained on four cathodes fabricated by sintering nonlithiated nickel oxide powders. The thicknesses, porosities, surface areas, and mean pore sizes of these cathodes are shown in Table I. The surface areas listed there were obtained by mercury intrusion porosimetry. Pore spectra are shown in Fig. 3. As can be seen, the properties of these cathodes were considerably different. For each of these cathodes, the cathode potential was measured as a function of current density in a half-cell apparatus using 62 mole percent (m/o) Li₂CO₃, 38 m/o K₂CO₃ electrolyte, and 67 m/o CO₂, 33 m/o O₂ oxidant. The use of this gas composition eliminated gas-phase diffusional losses, which were not included in the model. Electrolyte was added and removed from these cathodes to obtain data as a function of electrolyte content using the techniques described in Ref. (6). Post-test analyses of the electrodes were used to verify the electrolyte contents.

Results

The performance characteristics of the four cathodes are shown in Fig. 4-7, where the overpotential at 160 mA/cm² is plotted as a function of the percentage of the open pore volume that is filled with electrolyte (percentage fill). Because of excessive polarization, the "estimated" point shown in Fig. 6 was obtained by a small extrapolation of the overpotential vs. current density sweep curve to 160 mA/cm². The arrows on the lines connecting the data points indicate the sequence used in obtaining the data. In some cases, a considerable hysteresis in performance is evident.

The mathematical model described in this report was fit to each of the experimental data curves using a value for symmetry factor determined in a previous study. The

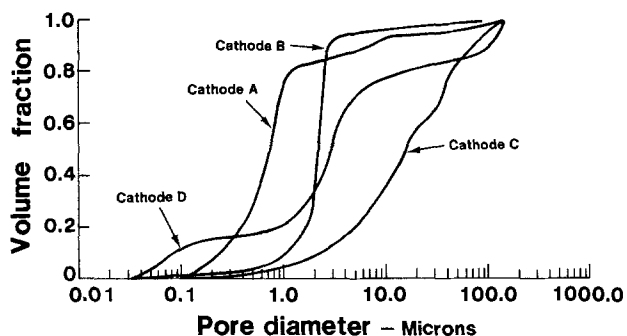


Fig. 3. Pore spectra characteristics of four preoxidized nonlithiated cathodes.

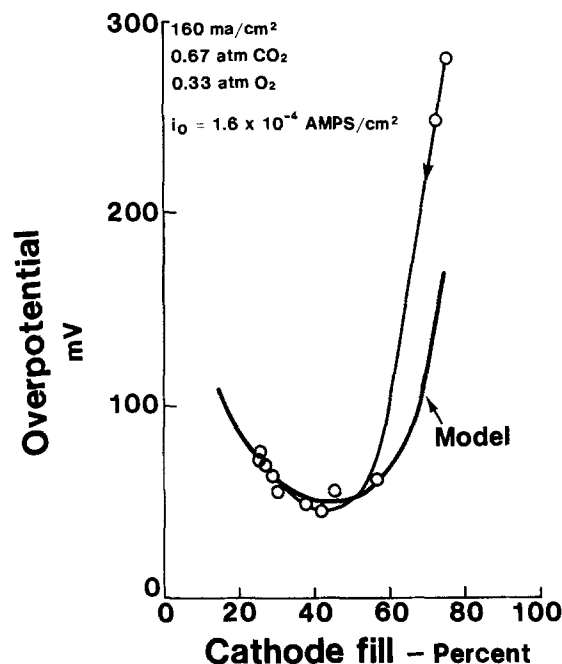


Fig. 4. Performance characteristics of cathode A

three diffusion coefficients (D_{CO_2} , D_{O_2} , and $D_{O^{2-}}$) and exchange current density were used as fitting parameters.

In the investigation that was conducted to define the symmetry factor, experimental performance data from a 10.8 cm² molten carbonate cell were compared to the results of a thin film model using the same rate-determining step as the present model. The analysis was a modification of that presented in Ref. (2). Best agreement was obtained using a value of β equal to zero. This unlikely value for β is an indication that further studies are needed on the reaction mechanism.

The same diffusion coefficients were found to result in good agreement in all cases

$$D_{CO_2} = 8.8E-7, D_{O_2} = 1.7E-6, D_{O^{2-}} = 3.4E-6 \text{ cm}^2/\text{s}$$

These diffusion coefficients have not been measured but are about the values that might be expected based on the specie ionic radii and the diffusion coefficient of Ni²⁺,

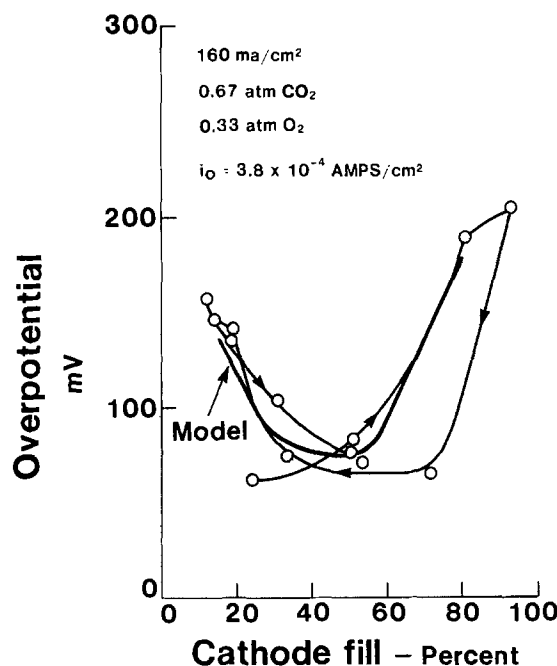


Fig. 5. Performance characteristics of cathode B

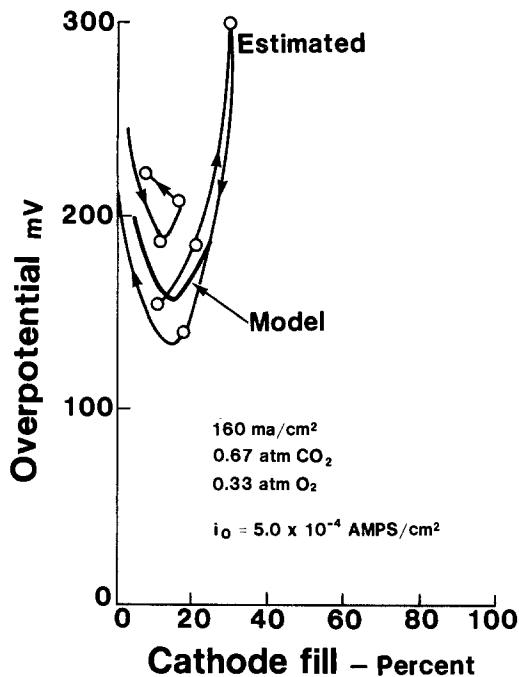


Fig. 6. Performance characteristics of cathode C

which has been measured as $4.86 \times 10^{-6} \text{ cm}^2/\text{s}$ (10) and estimated to be $1.2 \times 10^{-5} \text{ cm}^2/\text{s}$ (11).

The values obtained for the exchange current densities are presented in Table II. Although the same value of exchange current density was not obtained for all four cathodes, the values are considered to be nearly equal considering the hysteresis present in the performance curves and the accuracy with which the surface areas were determined.

Cathode C, which had the smallest mean pore size and low porosity, was very intolerant to percentage fill and had much higher overpotential at optimum fill.

In order to demonstrate the features of the present model, the agglomerate properties were calculated for cathode A over a range of percentage fills. The changes in the agglomerate number and agglomerate radius as a function of the percentage of cathode void filled with electrolyte are shown in Fig. 8. Here, the number of ag-

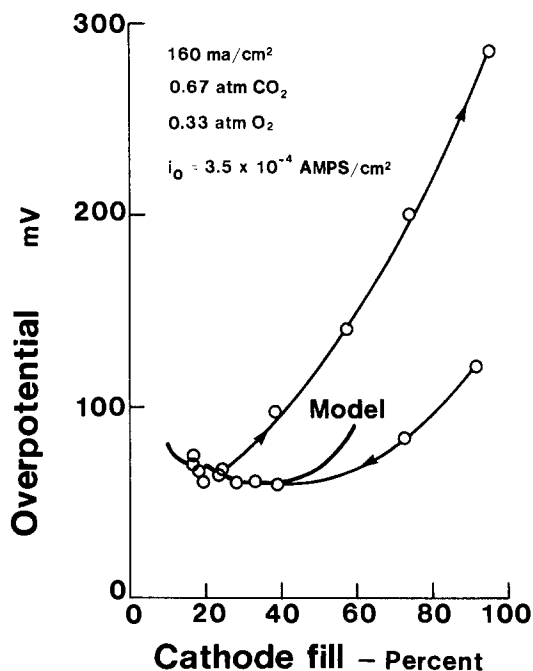


Fig. 7. Performance characteristics of cathode D

Table II. Exchange current densities of four pre-oxidized nonlithiated cathodes

Cathode A	$1.6 \times 10^{-4} \text{ A/cm}^2$
Cathode B	$3.8 \times 10^{-4} \text{ A/cm}^2$
Cathode C	$5.0 \times 10^{-4} \text{ A/cm}^2$
Cathode D	$3.5 \times 10^{-4} \text{ A/cm}^2$

glomerates decreases by seven orders of magnitude as the percentage fill increases from 10% to 90%. However, the radius increases by four orders of magnitude over the same fill range.

Figure 9 illustrates the effect of electrolyte content on the relative agglomerate diameter. The relative agglomerate diameter is defined as the ratio of the calculated agglomerate diameter to the pore diameter obtained from a pore spectra curve at a given fill state. For the case of the cathode A, the ratio is less than or equal to one for electrolyte contents below 40%. As the electrode continues to fill, the ratio rapidly increases beyond this point. Since the number of agglomerates decreases and the agglomerate radius increases with electrolyte content, greater liquid-phase diffusional polarization results. At the same time, the agglomerate porosity is increasing, as shown in Fig. 10, and ionic tortuosity is decreasing, as shown in Fig. 11. These decreases would tend to reduce ohmic losses. At a fill state of approximately 40%-50%, these effects balance out, resulting in an optimum in performance as presented in Fig. 4.

Reference (6) indicates that the current density of an *in situ* oxidized nickel cathode structure at optimum elec-

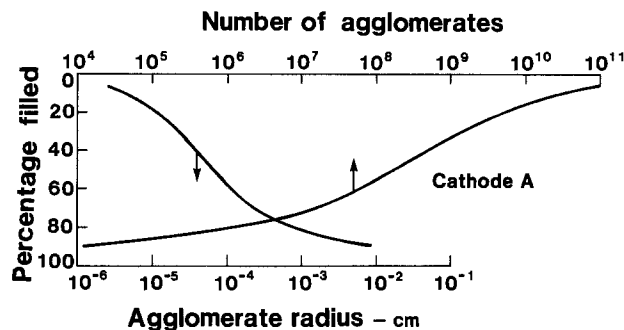


Fig. 8. Effect of electrolyte content on number of agglomerates and agglomerate radius.

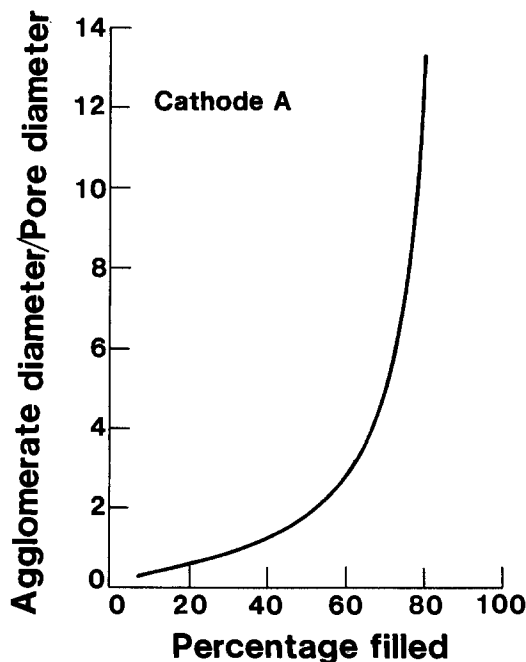


Fig. 9. Effect of electrolyte content on relative agglomerate diameter

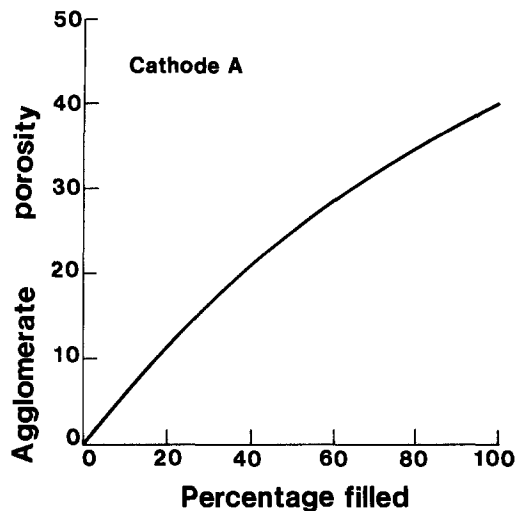


Fig. 10. Effect of electrolyte content on agglomerate porosity

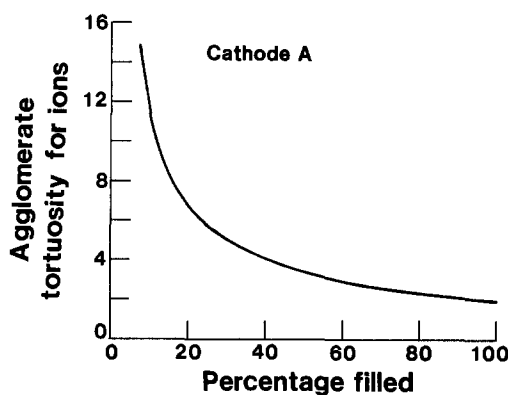


Fig. 11. Effect of electrolyte content on agglomerate ionic tortuosity

tolerance to percentage fill both increase as the cathode thickness increases, the tolerance of the cathode to electrolyte content increases greatly as the thickness of the cathode is increased. This feature is of great significance in molten carbonate fuel cells, since loss of electrolyte is a major cause for performance decay.

Calculations were also performed using the present model and the structure of cathode A to determine the electrolyte volume tolerance as a function of the cathode thickness. These results are shown in Fig. 14. As can be seen, not only does the cathode overpotential decrease initially as the cathode is thickened, but also the volume tolerance increases. Since the electrolyte volume and tol-

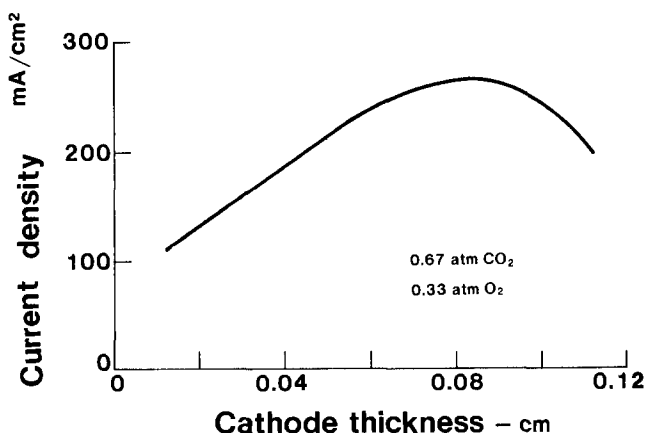


Fig. 12. Current at a 60 mV overvoltage as a function of electrode thickness (6).

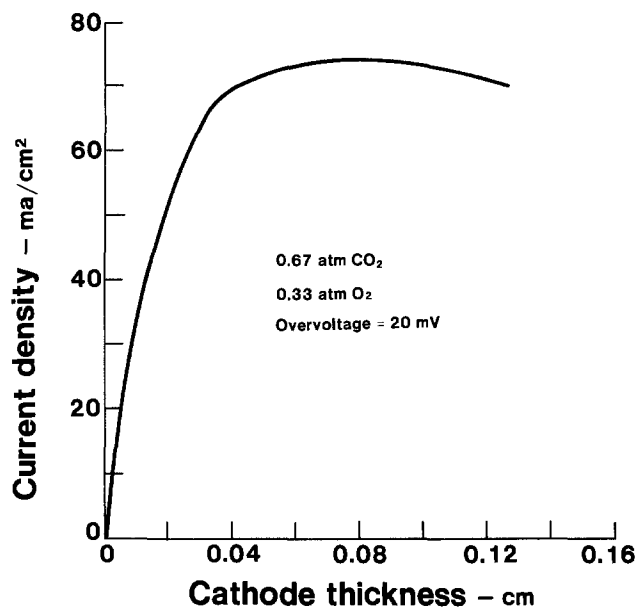


Fig. 13. Calculated variation of performance with thickness for cathode A.

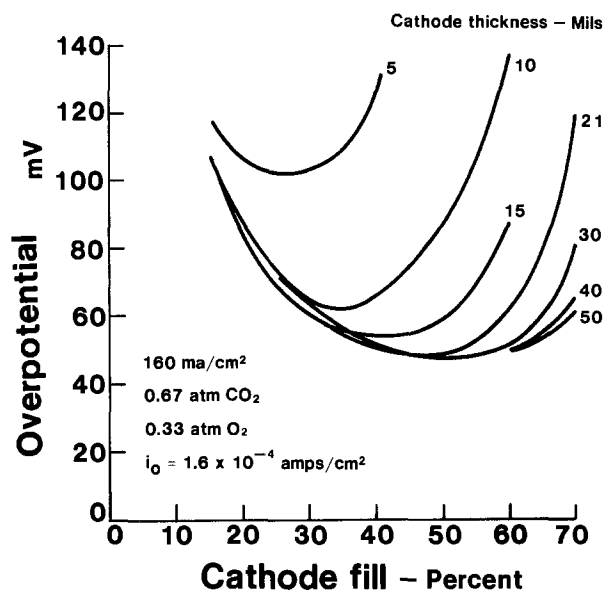


Fig. 14. Calculated performance characteristics of cathode A at various thicknesses.

erance to percentage fill both increase as the cathode thickness increases, the tolerance of the cathode to electrolyte content increases greatly as the thickness of the cathode is increased. This feature is of great significance in molten carbonate fuel cells, since loss of electrolyte is a major cause for performance decay.

Conclusions

The homogeneous/agglomerate model of fuel cell cathodes was found to suitably describe the performance characteristics of cathodes as a function of electrolyte content and cathode thickness. These results indicate that an optimum electrolyte content is present in a cathode, with the tolerance of the cathode to electrolyte content depending upon the cathode structure. An optimum thickness also exists for a cathode of given pore structure, with that optimum thickness providing a higher degree of electrolyte volume tolerance than cathodes thinner than the optimum. Further modeling is required in order to account for the true reaction process in a cathode so the effects of reactant composition and pressure can be predicted and further electrode optimization performed.

Acknowledgments

This work was done at the Fuel Cell Operations of Power Systems Division. The fabrication of the electrodes used in this program was sponsored by the Department of Energy under Contract DE-AC01-79ET15440 and is gratefully acknowledged. The authors also appreciate the contributions of T. E. Swarr for this electrode fabrication and W. H. Ray for the performance of the experiments.

Manuscript submitted July 29, 1983; revised manuscript received June 13, 1984. This was Paper 343 presented at the Detroit, Michigan, Meeting of the Society, Oct. 17-21, 1983.

United Technologies Corporation assisted in meeting the publication costs of this article.

LIST OF SYMBOLS

A	Vapor-liquid interfacial area (cm^2)
D_i	Liquid-phase diffusion coefficient of component i (cm^2/s)
D_M	Molar density of electrolyte (gmol/cm^3)
E_{OIC}	Open-circuit potential measured relative to a 2:1 $\text{CO}_2\text{:O}_2$ reference electrode (V)
$E(x)$	Potential of electrode solid (V)
F	Faraday's constant, (96,487 C/eq.)
H_i	Henry's law constant for component i ($\text{mol}/\text{atm cm}^3$)
i_0	Exchange current density (A/cm^2)
$i(x, r)$	Local current density (A/cm^2)
J_E	Electronic current (A)
J_I	Ionic current (A)
J_T	Total current generated in agglomerate (A)
K	Equilibrium constant for $\text{CO}_2 + \text{O}^- \rightleftharpoons \text{CO}_3^-$ reaction
$k(T)$	Temperature dependent cathodic rate constant ($(\text{atm})^{0.25} \text{A}/\text{cm}^2$)
L	Length of agglomerate (cm)
N	Number of agglomerates
n	Number of electrons in overall reaction
P_i	Equivalent reactant partial pressure at the reaction site (atm)
P_G	Gas pressure (dyne/cm^2)
P_L	Liquid pressure (dyne/cm^2)
P_i^0	Bulk gas partial pressure of component i at gas/agglomerate interface (atm)
R	Gas constant ($8.3176 \text{ J}/\text{gmol K}$)
r	Radial distance in agglomerate and pore radius (cm)
r_0	Agglomerate radius (cm)

S_g	Surface area of catalyst (cm^2/g)
T	Temperature (K)
V	Liquid volume (cm^3)
V_{filled}	Volume of electrolyte in electrode (cm^3)
V_{solid}	Volume of solid in electrode (cm^3)
V_{total}	Total void volume of electrode (cm^3)
x	Axial distance of agglomerate (cm)
β	Symmetry factor for rate-determining step
δ	Electrode thickness (cm)
$\eta(x)$	Local overpotential (V)
θ	Agglomerate porosity, fraction
ρ	Catalyst density (g/cm^3)
σ	Surface tension of electrolyte (dyne/cm)
σ_F	Electrode conductivity ($\Omega^{-1} \text{cm}^{-1}$)
σ_I	Ionic conductivity ($\Omega^{-1} \text{cm}^{-1}$)
τ_E	Agglomerate tortuosity
τ_I	Ionic tortuosity
$\phi(x)$	Electrolyte potential (V)
(CO_2)	Mole fraction of CO_2 in electrolyte
$[\text{CO}_2]$	Molar concentration of CO_2 in electrolyte (gmol/cm^3)

REFERENCES

1. S. T. Szymanski and H. R. Kunz, in "Proceedings of Molten Carbonate Fuel Cell Workshop," Oak Ridge National Laboratory, Oak Ridge, TN (1978).
2. S. T. Szymanski, Abstract 38, p. 101, The Electrochemical Society Extended Abstracts, Vol. 76-2, Las Vegas, NV, Oct. 17-22, 1976.
3. G. Wilemski, *This Journal*, **130**, 118 (1983).
4. G. Wilemski and A. Gelb, Abstract 381, p. 628, The Electrochemical Society Extended Abstracts, Vol. 82-1, Montreal, Que., Canada, May 9-14, 1982.
5. C. Y. Yuh and J. R. Selman, Abstract 382, p. 629, The Electrochemical Society Extended Abstracts, Vol. 82-1, Montreal, Que., Canada, May 9-14, 1982.
6. L. H. Bregoli and H. R. Kunz, *This Journal*, **129**, 2711 (1982).
7. Yu. A. Chizmanzhev and Yn. G. Chirkov, "Comprehensive Treatise of Electrochemistry," Vol. 6, Chap. 5, Plenum Press, New York (1983).
8. R. E. Merideth and C. W. Tobias, in "Advances in Electrochemistry and Electrochemical Engineering," Vol. 2, C. W. Tobias, Editor, p. 15, Interscience, New York (1966).
9. W. M. Vogel, S. W. Smith, and L. J. Bregoli, *This Journal*, **130**, 574 (1983).
10. N. Kh. Tumanova, *Ukr. Khim. Zh.*, **30**, 684 (1964).
11. W. M. Vogel, L. J. Bregoli, H. R. Kunz, and S. W. Smith, Paper 386 presented at the Electrochemical Society Meeting, Montreal, Que., Canada, May 9-14, 1982.

Conductivity of the LiBF_4 /Mixed Ether Electrolytes for Secondary Lithium Cells

Yoshiharu Matsuda,* Masayuki Morita, and Tooru Yamashita

Department of Industrial Chemistry, Faculty of Engineering, Yamaguchi University, Tokiwa-dai, Ube, Yamaguchi, Japan

ABSTRACT

Electrolytic conductivity of LiBF_4 has been studied in the mixed system of 1,3-dioxolane with 1,2-dimethoxyethane or with tetrahydrofuran. Relative permittivity (dielectric constant) of the solvents suggested the formation of associated ion pairs in the systems, but the conductivity measured was higher than that expected from the viewpoint of ionic association. Conductivity maxima were observed in the solutions containing about 1:1 (by volume) mixed solvents. Viscosities of the solvent and the solution were also measured, and their contribution to the conductivity change with the solvent composition was discussed. Solute concentration dependence of the molar conductivity was specific for the ether solutions. Apparent activation energy for conduction, which was determined by the temperature dependence of the conductivity, varied with LiBF_4 concentration. Structural specificity of the mixed ether solutions was discussed with these parameters and ^1H NMR spectra of the solutions.

In the development of secondary lithium cells, the choice of a suitable electrolyte system is of great importance (1). It is necessary to secure as high an electrolytic conductivity as possible in order to obtain high charge and discharge currents in practical secondary cells.

* Electrochemical Society Active Member.

Mixed solutions of propylene carbonate (PC) with 1,2-dimethoxyethane (DME), γ -butyrolactone (BL) with tetrahydrofuran (THF), and the like have been used as the solvent of the electrolytic solution in primary lithium cells (2-5). One of the reasons for this is that the improvement of electrolytic conductivity has been realized by

using these mixed solvents (6, 7). However, Besenhard and Eichinger (8) reported that solutions containing PC as a main component were not suited for the electrolytes of secondary lithium cells, because the reaction of the solvents with active Li deposited during charge lowered the cycling efficiency of the Li electrode. Koch and Young (9) pointed out that aliphatic cyclic ethers like THF, which do not have reactive C=O bonds, were better solvents for the secondary cells. Recently, Koch *et al.* (10, 11) showed that 2-methyltetrahydrofuran (2-MeTHF) was much less reactive toward Li than THF, and that higher Li cycling efficiency was obtained in 2-MeTHF containing LiAsF₆. Other ethers (or acetals) such as DME (12, 13), 1,3-dioxolane (DOL) (12-15), and polymethoxy-methanes (16) have also been proposed as the solvents of secondary lithium cells. Sometimes mixed solvents have been used to improve solubility of electrolytic salts. For instance, mixed systems of diethylether (DEE)-THF (17, 18), DEE-DME (18), DEE-DOL (18), THF-DME (19), DME-DOL (12, 13, 19), and THF-2-MeTHF (20) have been examined.

Up to the present, basic properties of these electrolytic solutions, which might relate to the charge-discharge performance of the cell, have not been clarified, except for the solution stability. The authors have studied physico-chemical properties of mixed systems of PC-THF (21, 22), PC-DME (23-25), and BL-THF (26) for primary lithium cells. The mixing effects of the solvents on the conductance and the ionic behavior in the mixed systems were discussed. This paper is concerned with the mixed ether solutions of DOL-THF and DOL-DME as the solvents of secondary lithium cells. Ether-based electrolytes should have different properties from those of PC- or BL-based electrolytes for the primary cells. It is necessary to consider the ionic behavior in the mixed ether solutions since solvent mixing effects on the charge-discharge characteristics of Li and TiS₂ electrodes were really observed in DOL-THF containing lithium tetrafluoroborate (LiBF₄) (27). Polarization of Li and TiS₂ electrodes in LiBF₄/DOL-THF was smaller than that in LiBF₄/DOL or LiBF₄/THF, and the charge-discharge curves of the Li electrode in the mixed electrolyte solution showed stable potential-change during the cycle (27). It has been reported that salts of Lewis acids such as LiAsF₆ decompose DOL (1, 28) and that the use of LiBF₄ lowers cycling efficiency of Li in THF (9). These faults in the use of DOL and LiBF₄, however, would be overcome by mixing ether solvents. The mixed LiBF₄ (1 mol dm⁻³)/DOL-THF solution did not practically polymerize, and the Li cycle efficiency in that solution did not appreciably lower with increase in the cycle number (27). In this work, the electrolytic conductivity of LiBF₄ was measured in the mixed solutions of DOL-THF and DOL-DME. The relation between the conductance and other properties such as viscosity, permittivity, and NMR spectra of the solutions was investigated, and the ionic behavior in the mixed ether systems was discussed.

Experimental

The solvents, DME (Mitsubishi Petrochemical) and THF (Toyo Soda Manufacturing) were purified by the methods described previously (24-26). DOL (Tokyo Kasei Kogyo) was refluxed over CaH₂ for 48h and then fractionally distilled at 75°C. The fraction was stirred over metallic Na for 48h, degassed under reduced pressure, and then distilled at 75°C again (27). LiBF₄ (Morita Chemical Industries, >98%) was used as a supporting electrolyte after drying under reduced pressure at 80°C for 24h. For comparison, LiClO₄ (Ishizu Pharmaceutical) was also used.

The electrolytic conductivity was measured with an impedance bridge using 10 kHz ac (bridge: DRZ-2M, Ando Electric; oscillator: Model 417RC, Kikusui Electronics; synchroscope: DS5016, Iwatsu Electric). The viscosity was measured with a modified Ostwald viscometer or with a B-type (rotator-type) viscometer (BL-type, Tokyo Keiki). The relative permittivity (dielectric constant) was determined by a bridge method using 10 kHz ac (bridge:

TR-1C; oscillator: WBG-9; detector: BDA-9, Ando Electric). The NMR spectra of the solvents and the solutions were measured under 100 MHz field. These measurements were mainly carried out at 30°C, except for temperature dependence experiments. In most cases, the data will be graphically described with marks of appropriate size in which standard deviations of individual points are included.

Results and Discussion

In general, electrolytic solutions with high conductance should be realized when solvents with high permittivity and low viscosity are used (29). Ether solvents have low viscosity but have low permittivity, compared with PC or BL. Figure 1 shows the relative permittivity, ϵ_r , against the solvent composition, in mole percent (m/o), for the mixed systems of DOL-THF and DOL-DME at 30°C. The relative permittivity decreased almost linearly with DOL concentration in the solvent for both systems, though a little deviation from linearity was observed in DOL-DME. In these mixed ether systems, an additive property of each solvent determines almost the relative permittivity of the mixed solvent. This is similar to the results obtained for the mixed systems containing PC (22, 23, 25).

According to the ion association model by Bjerrum (30), the critical distance for ion-pair formation, q , is given by Eq. [1]

$$q = \frac{|z_i z_j| e^2}{8\pi\epsilon_0 \epsilon_r kT} \quad [1]$$

where ϵ_0 is the permittivity of a vacuum, z 's are charge numbers of ions, and other symbols have their usual meanings. For a 1:1 electrolyte in DOL-THF and DOL-DME, q 's were calculated, and the results are shown in Table I. The values are about four times larger than those in the PC-based electrolytes, which are 0.5-1 nm in DME (or THF) concentration of 0%-70% (22, 25). The degree of association is given by Eq. [2] (30, 31)

$$1 - \alpha = \frac{4\pi Nc}{1000} \int_a^q \exp\left(\frac{|z_i z_j| e^2}{4\pi\epsilon_0 \epsilon_r kT} \frac{1}{r}\right) r^2 dr \quad [2]$$

where α is the degree of dissociation, a is the distance of closest approach of two ions, r is the distance from the center of ion j , N is the Avogadro constant, and c is the molar concentration of the salt. The degree of association, $1 - \alpha$, was calculated as a function of α . The results are

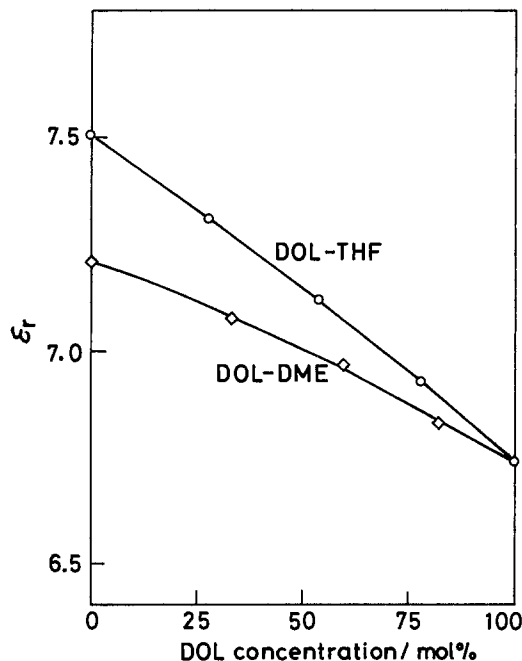


Fig. 1. Relative permittivity (ϵ_r) of the mixed solvent at 30°C

Table I. Relative permittivity (ϵ_r) and critical distance for ion-pair formation (q) in DOL-THF and DOL-DME systems at 30°C

vol% DOL	DOL-THF		DOL-DME			
	mol% DOL	ϵ_r	q/nm	mol% DOL	ϵ_r	q/nm
0	0.0	7.51	3.67	0.0	7.21	3.83
25	28.1	7.31	3.77	33.3	7.08	3.89
50	53.9	7.12	3.87	60.0	6.97	3.95
75	77.8	6.97	3.98	81.8	6.83	4.07
100	100.0	6.74	4.09	100.0	6.74	4.09

shown in Fig. 2. The a in the LiBF₄ solution was not practically determined, but would be less than 1 nm for a moderate concentration of the electrolyte (22, 25, 27). Thus, the relatively large values of q in DOL-THF and DOL-DME suggest that the ion-pair formation, or the ion association, is liable to occur in these systems.

Figures 3 and 4 show the viscosities, η , of the solvents and of the 1 mol dm⁻³ LiBF₄ solutions, respectively. The variations of the solvent viscosity deviated slightly in the negative direction from straight lines which correspond to the additive property. The viscosities of the electrolytic solutions also varied nonlinearly with the solvent compositions, and increased markedly in high DOL concentration regions. These are similar to the results obtained in mixed systems of PC-DME and PC-THF (22, 23, 25), but the values in the present systems are much smaller than those in the PC-based systems. This fact means that the present systems would be preferable to the ionic mobility than the PC-based systems.

The molar conductivities, Λ , of the 1 mol dm⁻³ LiBF₄ solutions at 30°C are shown in Fig. 5. The conductivity in the mixed solvent was higher than that in each pure solvent. The conductivity became maximum at about 40 m/o DOL in DOL-DME and at about 60 m/o DOL in DOL-THF. The DOL-DME solutions had much higher conductivity than the DOL-THF solutions. The maximum conductivities were 4.1 and 2.5 S cm² mol⁻¹ in DOL-DME and DOL-THF, respectively. These values were higher than those expected from the relative permittivity of the solvents. It is considered that ionic behavior in these ether systems could not be expressed by Bjerrum's classical model. As shown in Fig. 2, low permittivity of the solvents seemed to lead to extremely high degree of association, if Bjerrum's model is adopted. However, the observed molar conductivity suggested that considerable amounts of mobile ions exist in these ether-based electrolytes. The degree of dissociation, α , can also be estimated from the ratio of Λ and Λ_0 (Λ_0 : molar conductivity under the infinite dilution condition). In the present systems, however, Λ_0 of LiBF₄ was not determined because of complicated concentration dependence of Λ , which will be mentioned later. Thus, α of LiBF₄ in mixed DOL-DME or

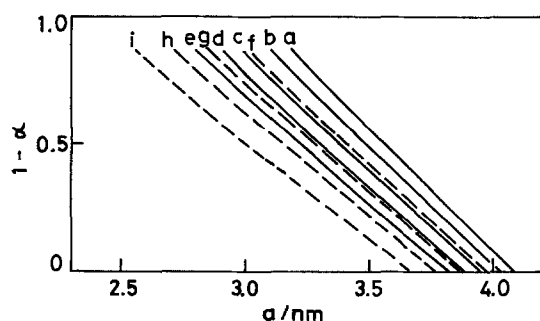


Fig. 2. Variation in the degree of association with the distance of closest approach in DOL-DME and DOL-THF. Curve a: DOL(100). Curve b: DOL(82)-DME(18). Curve c: DOL(60)-DME(40). Curve d: DOL(33)-DME(67). Curve e: DME(100). Curve f: DOL(78)-THF(22). Curve g: DOL(54)-THF(46). Curve h: DOL(28)-THF(72). Curve i: THF(100). Figures in parentheses indicate mole percent of the components.

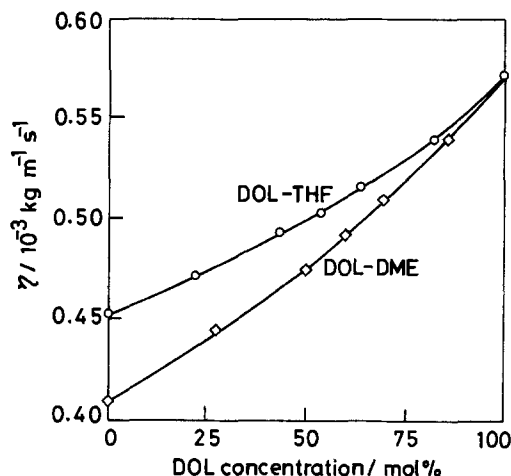


Fig. 3. Viscosity (η) of the solvent at 30°C

DOL-THF could not be discussed quantitatively. As DME and THF have high donicities (32), Li⁺ ion would be firmly solvated by coordination in the DME- or THF-based electrolyte. This is one of the reasons for which the present electrolyte systems show considerably high conductance in spite of the low permittivity of the solvents. As another contribution to the high conductance in these ether-based electrolytes, the formation of conductive ion triplets was also taken into account, which will be discussed in a later part of this section.

Figure 6 shows the molar conductivities of 1 mol dm⁻³ LiClO₄ solutions. The conductivity maxima were observed in these solutions like in the LiBF₄ solutions. The conductivity of LiClO₄/DOL-DME and LiClO₄/DOL-THF were 9.1 and 4.9 S cm⁻² mol⁻¹, respectively, which were about twice those of the LiBF₄ solutions. However, these LiClO₄ solutions containing DOL would not be suited for practical use, owing to the possibility of explosion (33).

Sometimes DEE has been mixed with THF, DME, DOL, and 2-MeTHF for the purpose of raising LiAsF₆ solubility (17, 18). However, the conductivity decreased gradually with increasing DEE concentration in LiAsF₆/DEE-THF (17). The variations in the molar conductivities of LiBF₄/DEE-THF and LiBF₄/DEE-DOL are shown in Fig.

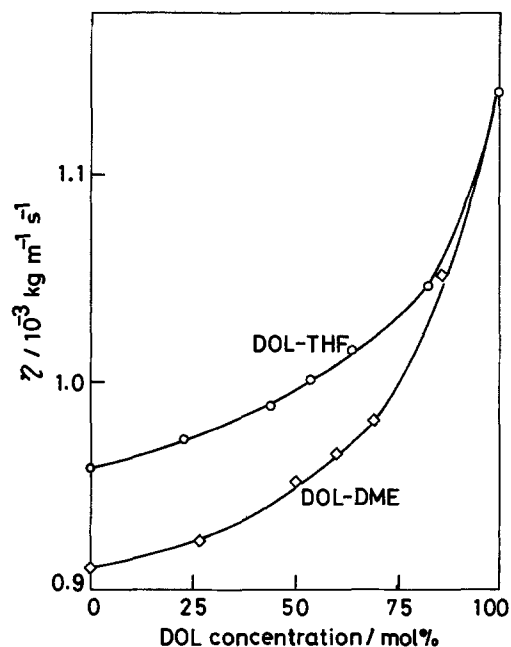


Fig. 4. Viscosity (η) of the mixed solution containing 1 mol dm⁻³ LiBF₄ at 30°C.

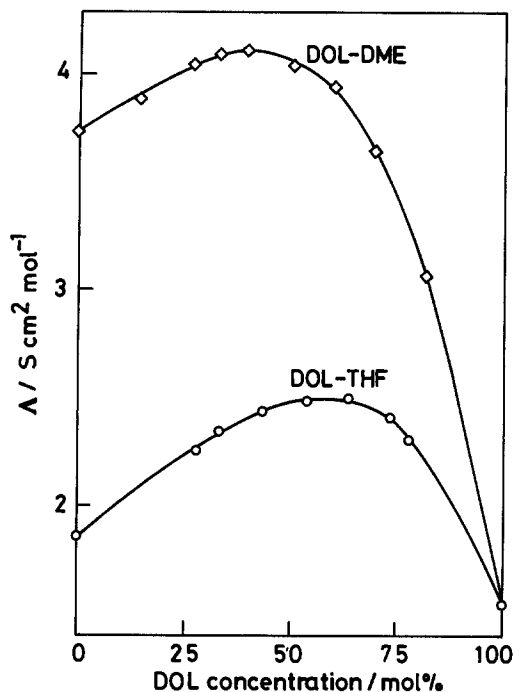


Fig. 5. Molar conductivity (Λ) of the mixed solution containing $1 \text{ mol dm}^{-3} \text{ LiBF}_4$ at 30°C .

7. Solubility of LiBF_4 decreased by DEE addition and it became less than 1 mol dm^{-3} at 75 m/o DEE in DEE-THF and at 25 m/o DEE in DEE-DOL. The molar conductivities of LiBF_4 were relatively low in the DEE-based solutions, and no conductivity maximum was observed either in DEE-THF or in DEE-DOL, in contrast to DOL-DME and DOL-THF. On the other hand, it has been reported that, in 2-MeTHF-THF, the conductivity of LiAsF_6 varied almost linearly with THF concentration (20). Thus, the conductivity maxima observed in the present mixed-

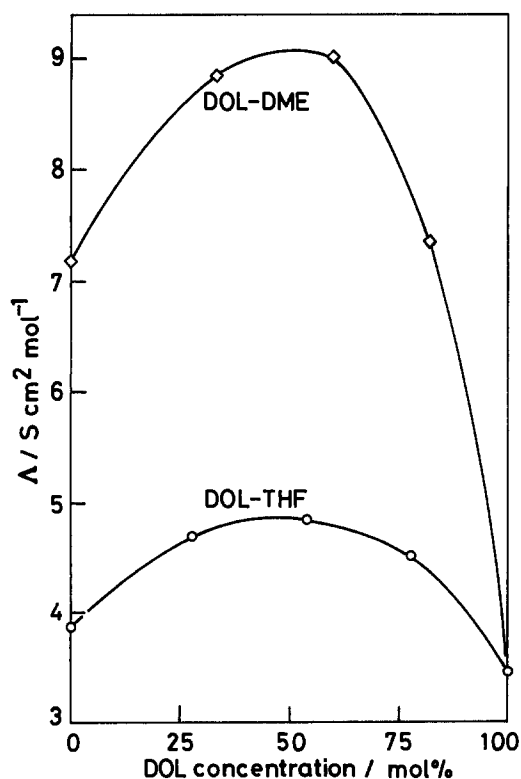


Fig. 6. Molar conductivity (Λ) of the mixed solution containing $1 \text{ mol dm}^{-3} \text{ LiClO}_4$ at 30°C .

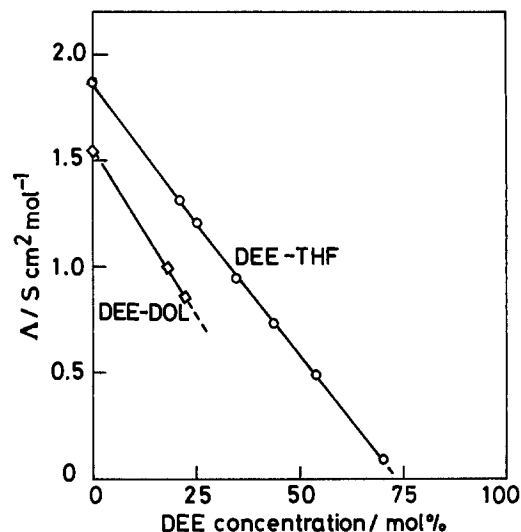


Fig. 7. Molar conductivity (Λ) of the diethylether (DEE)-based solution containing $1 \text{ mol dm}^{-3} \text{ LiBF}_4$ at 30°C .

ether systems might be peculiar to such systems as DOL-DME and DOL-THF.

Figure 8 shows Walden products, $\Lambda\eta$, for $1 \text{ mol dm}^{-3} \text{ LiBF}_4$ in DOL-DME and DOL-THF, as a function of solvent composition. The Walden products had also maxima in the mixed solvents. This is probably due to changes in size of the ions with solvent composition. In general, the size of solvated ion is closely associated with donor and acceptor properties of the solvent (34). The donicity (DN) of solvent is concerned in the solvation of cation and the acceptor number (AN) of the solvent determines the solvation of anion. The DN and AN of DOL have not been measured, but it can be assumed that they are not greatly different from those of dioxane (DO) whose structure is analogous to that of DOL. According to Gutmann's data (32), the order of DN becomes $\text{DME}(24) > \text{THF}(20.0) > \text{DOL}(\text{DO}: 14.8)$ and the order of AN is $\text{DOL}(\text{DO}: 10.8) > \text{DME}(10.2) > \text{THF}(3.9)$. This suggests that, in the systems of DOL-DME and DOL-THF, DME and THF acting as donors mainly interact with Li^+ ion, and DOL acting as an acceptor mainly interacts with the anions. These differences in the donor and acceptor properties of the solvents probably cause the conductivity maxima observed in the mixed solvents and the difference in the conductivity between the solutions of LiBF_4 and LiClO_4 .

The molar conductivities at -20°C are shown in Fig. 9. The conductivities of the LiBF_4 solutions did not appreci-

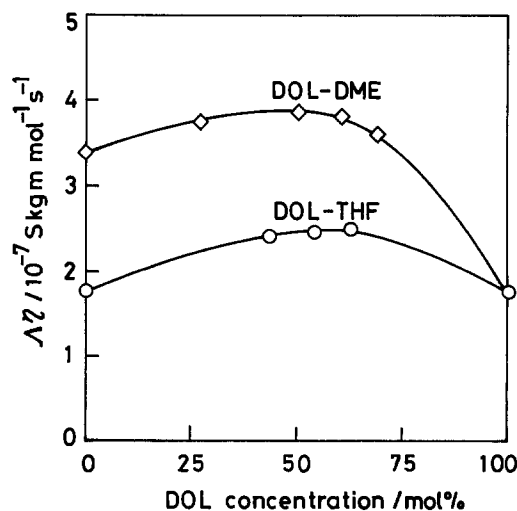
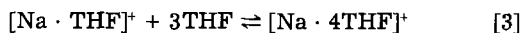


Fig. 8. Walden product ($\Lambda\eta$) for the mixed solution containing $1 \text{ mol dm}^{-3} \text{ LiBF}_4$.

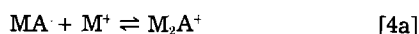
ably lower at low temperature. Their maximum values at -20°C are 70%-80% of those at 30°C . This is probably due to low viscosity of the ether solvent even at -20°C . The relatively high conductance of these electrolytes at low temperature is a very attractive property from the standpoint of practical use. Abraham and Goldman (20) have examined mixed 2-MeTHF-THF system in order to gain high conductance of the LiAsF₆ solution even at low temperature.

Figure 10 shows the LiBF₄ concentration dependence of the molar conductivity at 30°C . The mixed solvents used here are DOL-DME (1:1 volume = 60 m/o DOL) and DOL-THF (1:1 volume = 54 m/o DOL). Specific conductances, κ , of 3 mol dm⁻³ LiBF₄ were 9×10^{-3} S cm⁻¹ in DOL-DME and 6×10^{-3} S cm⁻¹ in DOL-THF. In the present systems shown in Fig. 10, the profiles of the concentration dependence were similar to each other. The molar conductivity in the low concentration range did not linearly vary with a square root of LiBF₄ concentration. That is, the conductivity variation did not follow the Onsager equation as shown in strong electrolytes. LiBF₄ in these solvents acted as a weak electrolyte, and accurate estimates of Λ_0 were impossible. In every case, a maximum of the molar conductivity appeared in the high concentration range of 1.0-1.5 mol dm⁻³. Similar variations in molar conductivity have been reported in sodium tetrabutylaluminate (NaAlBu₄)/THF (35) and LiBF₄/THF (36). These phenomena might be interpreted by some changes in the conduction mechanism from high concentration to low concentration. On the basis of molecular weights of the solvents and densities of the solutions, the concentration of solvent in the 1 mol dm⁻³ LiBF₄ solution was estimated to be 10-15 mol dm⁻³. This means that the molar ratio of the solvent molecule to Li⁺ ion in the 3 mol dm⁻³ LiBF₄ solution would be about 4-5:1.

In the NaAlBu₄/THF solution, the following equilibrium has been proposed (35)



At low Na⁺ concentration, Na⁺ ion is solvated by four THF molecules and forms a stable 1:4 complex. The fraction of the 1:1 complex increases with increasing Na⁺ concentration because of lowering in the relative concentration of free THF. Similar equilibria would be present in the LiBF₄/THF system (37). If the solvation number at low concentration is different from that at high concentration, the ionic mobility should be markedly influenced by the electrolyte concentration. On the other hand, it is believed that equilibria between nonconducting ion pairs and conductive ion triplets, such as Eq. [4], are present in solvents of relative permittivity below 10 (36, 38).



James (36) suggested that the maximum at 1.0-1.5 mol dm⁻³ in molar conductivity of LiBF₄/THF was associated with these equilibria and with the sharply increased solution viscosity at high concentration. Consequently, it is possible that two above-mentioned effects, i.e., change in solvation of Li⁺ ion and conversion of ion pairs to ion triplets, exist in the present mixed ether systems.

Temperature dependence of the molar conductivity was measured in the range of 20°C - 40°C . Typical Arrhenius plots are shown in Fig. 11. The conductivities increased normally with increasing temperature in the solutions of high LiBF₄ concentration (1.5 mol dm⁻³). At low LiBF₄ concentration (0.01 mol dm⁻³), however, the slopes of the plots had opposite sign. This means that the conductivities of the low concentration solutions have negative activation energies. The apparent activation energies for conduction were calculated from the

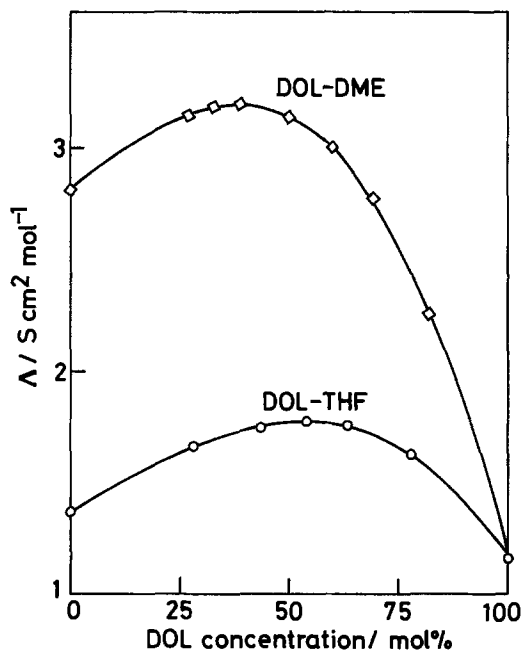


Fig. 9. Molar conductivity (Λ) of the mixed solution containing 1 mol dm⁻³ LiBF₄ at -20°C .

slopes of the $\log \Lambda$ vs. T^{-1} plots for the LiBF₄ concentration of 0.01, 0.05, 1.0, and 1.5 mol dm⁻³. Reasonable values from the viewpoint of ionic motion were obtained in 1.5 mol solutions [4.16 kJ mol⁻¹ for THF, 4.77 kJ mol⁻¹ for DME, 4.43 kJ mol⁻¹ for DOL-THF(1:1), 4.48 kJ mol⁻¹ for DOL-DME(1:1)]. The activation energy tended to decrease with decreasing LiBF₄ concentration. At 0.05 and 0.01 mol dm⁻³, the calculations gave negative activation energies. It was impossible to interpret the negative energies quantitatively, but the drops in the activation energy with lowering salt concentration were probably due to the equilibria for the Li⁺ ion solvation and/or for the ion pair-ion triplet conversion. It was thought that ion conduction occurred mainly in the forms of the 1:1 complex, $[\text{Li} \cdot \text{THF}]^+$, and/or of the ion

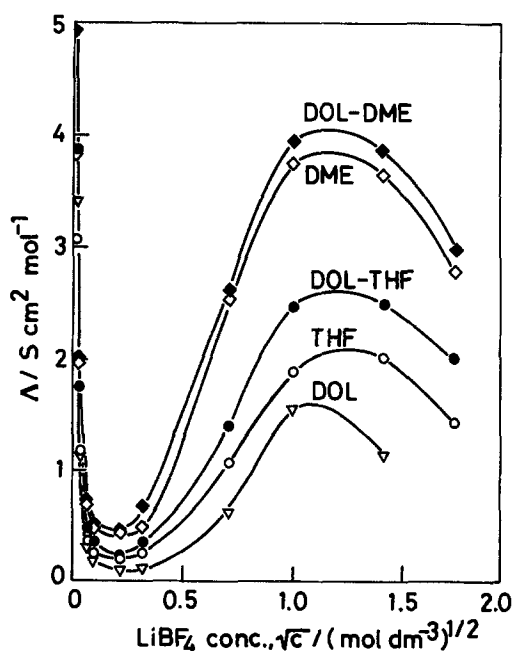


Fig. 10. LiBF₄ concentration dependence of Λ in DOL, THF, DME, and their mixed systems at 30°C . ∇ : DOL. \circ : THE. \diamond : DME. \bullet : DOL-THF (1:1 volume = 54 m/o DOL). \blacklozenge : DOL-DME (1:1 volume = 60 m/o DOL).

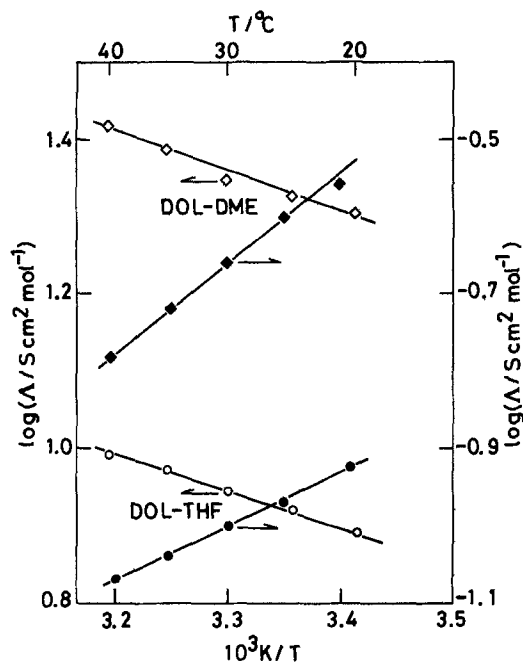


Fig. 11. Typical Arrhenius plots of molar conductivity of the LiBF_4 solution. \circ , \bullet : DOL-THF (1:1 volume = 54 m/o DOL). \diamond , \blacklozenge : DOL-DME (1:1 volume = 60 m/o DOL). \circ , \diamond : $1.5 \text{ mol dm}^{-3} \text{ LiBF}_4$. \bullet , \blacklozenge : $0.01 \text{ mol dm}^{-3} \text{ LiBF}_4$.

triplets, $[\text{Li}_2\text{BF}_4]^+$ and $[\text{Li}(\text{BF}_4)_2]^-$, in the solutions of high LiBF_4 concentration. At lower concentrations, the equilibria should be displaced, so that the components of 1:4 complex and/or the ion pairs increased with decreasing LiBF_4 concentration. Thus, it was considered that the negative activation energies appeared since the equilibria are dependent on temperature.

The ^1H NMR spectra of the mixed ether solutions were measured, so as to obtain further information on the solution structure. Typical spectra of the mixed solvents and the effects of LiBF_4 concentration on the spectra are shown in Fig. 12 and 13 for DOL-DME and DOL-THF, respectively. The spectra shifted to the lower field (higher δ values) at high LiBF_4 concentration (1.5 mol dm^{-3}). Similar results have been reported in the case of the spectra of $\text{LiB}(\text{CH}_3)_4$ ($0.5\text{--}2.2 \text{ mol dm}^{-3}$)/DOL system (14). These changes in the proton chemical shifts to the lower magnetic field show that the increase in electrolyte concentration increases the number of the solvated ether molecules where the electron density around the proton is reduced by the solvation or the complex formation. The changes in the chemical shifts of DME were larger than those of DOL in DOL-DME. The shift of α -proton in THF (c in Fig. 13) changed most remarkably in DOL-THF. It is presumed that DME or THF solvates to Li^+ ion more strongly than DOL does, though the magnitude of the change in the chemical shift does not quantitatively correspond to the strength of the coordination bond. These results are consistent with the previous discussion based on the donicities and acceptor numbers of the solvents. It is thought that the contribution of the solvation or the ion-solvent interactions to the conductivity play a large part in the ether-based electrolyte like the present systems. However, further information concerning their solvation chemistry is required.

Summary

Electrolytic conductivity and other physicochemical properties were measured for LiBF_4 solutions of DOL-THF and DOL-DME mixed systems. The results obtained are summarized below.

1. In spite of low permittivities of the solvents, the conductivities of the solutions were moderately high.

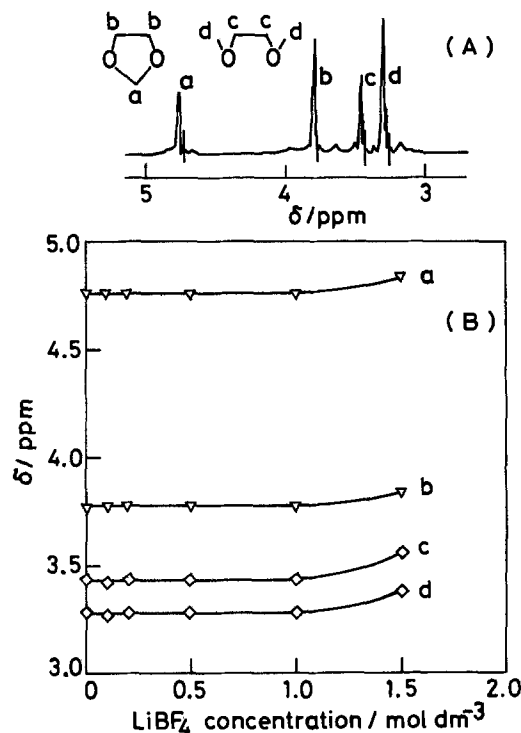


Fig. 12. ^1H NMR spectrum of the DOL-DME mixed system (1:1 volume = 60 m/o DOL). (A): a typical spectrum of the solvent. (B): LiBF_4 concentration dependence of the proton chemical shifts in DOL-DME.

2. The maximum conductivities were obtained in the solutions consisting of the mixed solvents (about 1:1 by volume).

3. The salt concentration dependence and the temperature dependence of the molar conductivity suggested that

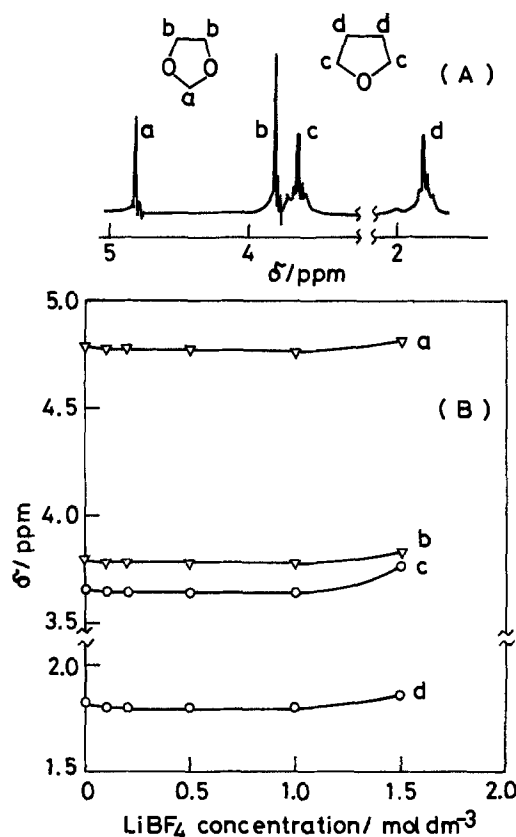


Fig. 13. ^1H NMR spectrum of the DOL-THF mixed system (1:1 volume = 54 m/o DOL). (A): A typical spectrum of the solvent. (B): LiBF_4 concentration dependence of the proton chemical shifts in DOL-THF.

the solvation of Li⁺ ion and/or the ion-pair formation varied with salt concentration.

4. The changes in the proton chemical shifts which were probably caused by the coordination of the solvents to Li⁺ ion were observed in the solutions of high LiBF₄ concentration.

Acknowledgments

We wish to thank Dr. S. Fujisaki and Mr. K. Yamada for NMR measurements. We are grateful to Japan Securities Scholarship Foundation (no. 249) for partial support of this work.

Manuscript submitted Jan. 9, 1984; revised manuscript received July 10, 1984.

Yamaguchi University assisted in meeting the publication costs of this article.

REFERENCES

1. K. M. Abraham and S. B. Brummer, in "Lithium Batteries," J. P. Gabano, Editor, Chap. 14, p. 371, Academic Press, London (1983).
2. H. Ikeda, T. Saito, and H. Tamura, *Denki Kagaku*, **45**, 314 (1977).
3. H. Ikeda, S. Ueno, T. Saito, S. Nakaido, and H. Tamura, *ibid.*, **45**, 391 (1977).
4. M. Fukuda and T. Iijima, in "Progress in Batteries and Solar Cells," Vol. 1, A. Kozawa *et al.*, Editors, p. 26, JEC Press Inc., Cleveland, OH (1978).
5. M. Broussely, U.S. Pat. 4,129,691 (1978).
6. R. Jasinski, *Electrochem. Technol.*, **6**, 28 (1968).
7. T. Saito, H. Ikeda, Y. Matsuda, and H. Tamura, *J. Appl. Electrochem.*, **6**, 85 (1976).
8. J. O. Besenhard and G. Eichinger, *J. Electroanal. Chem.*, **68**, 1 (1976), and references therein.
9. V. R. Koch and J. H. Young, *This Journal*, **125**, 1371 (1978).
10. V. R. Koch and J. H. Young, *Science*, **204**, 499 (1979).
11. J. L. Goldman, R. M. Mank, J. H. Young, and V. R. Koch, *This Journal*, **127**, 1461 (1980).
12. J. W. Johnson and M. S. Wittingham, *ibid.*, **127**, 1653 (1980).
13. J. W. Johnson and A. H. Thompson, *ibid.*, **128**, 932 (1981).
14. L. P. Klemann and G. H. Newman, *ibid.*, **128**, 13 (1981).
15. L. P. Klemann and G. H. Newman, *ibid.*, **129**, 230 (1982).
16. J. S. Foos and J. McVeigh, *ibid.*, **130**, 628 (1983).
17. V. R. Koch, J. L. Goldman, C. J. Mattos, and M. Mulvaney, *ibid.*, **129**, 1 (1982).
18. K. M. Abraham, J. L. Goldman, and D. L. Natwig, *ibid.*, **129**, 2402 (1982).
19. M. Eisenberg, *Electrochim. Acta*, **26**, 955 (1981).
20. K. M. Abraham and J. L. Goldman, *J. Power Sources*, **9**, 239 (1983).
21. Y. Matsuda and H. Satake, *Denki Kagaku*, **47**, 743 (1979).
22. Y. Matsuda, M. Morita, and K. Kosaka, *ibid.*, **51**, 119 (1983).
23. Y. Matsuda and H. Satake, *This Journal*, **127**, 877 (1980).
24. Y. Matsuda, H. Nakashima, M. Morita, and Y. Takasu, *ibid.*, **128**, 2552 (1981).
25. Y. Matsuda, M. Morita, and K. Kosaka, *ibid.*, **130**, 101 (1983).
26. Y. Matsuda, Y. Yamamoto, and M. Morita, *Denki Kagaku*, **49**, 653 (1981).
27. Y. Matsuda, M. Morita, and K. Takata, *This Journal*, **131**, 1991 (1984).
28. P. G. Glugla, in "Power Sources for Biomedical Implantable Applications and Ambient Temperature Lithium Batteries," B. B. Owens and N. Margalit, Editors, p. 407, The Electrochemical Society, Softbound Proceedings Series, Princeton, NJ (1980).
29. R. Jasinski, in "Advances in Electrochemistry and Electrochemical Engineering," Vol. 8, P. Delahey and C. W. Tobias, Editors, p. 253, Interscience, New York (1971).
30. N. Bjerrum, *K. Danske Vidensk. Selsk.*, **7**, No. 9 (1926); R. A. Robinson and R. H. Stokes, "Electrolyte Solutions," p. 392, Butterworths, London (1959).
31. G. H. Nancollas, "Interactions in Electrolyte Solutions," p. 16, Elsevier, New York (1966).
32. V. Gutmann, *Electrochim. Acta*, **21**, 661 (1976).
33. G. H. Newman, R. W. Francis, L. H. Gaines, and B. M. L. Rao, *This Journal*, **127**, 2025 (1980).
34. V. Gutmann, "The Donor-Acceptor Approach to Molecular Interactions," Chap. 7, Plenum Press, New York (1978).
35. C. N. Hammonds and M. C. Day, *J. Phys. Chem.*, **73**, 1151 (1969).
36. S. D. James, *J. Chem. Eng. Data*, **23**, 313 (1978).
37. S. Tobishima and A. Yamaji, *Electrochim. Acta*, **28**, 1067 (1983).
38. R. Fernandez-Prini, in "Physical Chemistry of Organic Solutions," A. K. Covington and T. Dickinson, Editors, p. 564, Plenum Press, New York (1973).

Electrode Kinetics of Fuel Oxidation at Copper in Molten Carbonate

S. H. Lu* and J. R. Selman**

Department of Chemical Engineering, Illinois Institute of Technology, Chicago, Illinois 60616

ABSTRACT

Copper appears to be a promising anode material for the molten carbonate fuel cell, as an alternative to nickel. Therefore, polarization data have been obtained for oxidation of fuel gases on a fully immersed copper rod. The electrode-kinetic parameters have been determined using the potential-step technique. The reaction mechanism on copper appears to be similar to that on nickel, and the exchange current density only slightly less than that on nickel. The importance of a correct extrapolation technique to obtain the time-zero current response is emphasized.

In molten carbonate fuel cell (MCFC) development, exploration of suitable materials for the electrode is a persistent effort. A good electrode material must be cheap, stable, durable, and compatible with other cell components. After testing, many materials in terms of performance and stability, and surveying the availability and cost of each prospective material for commercialization, the

*Electrochemical Society Student Member.

**Electrochemical Society Active Member.

conclusion is that no one material shows definite superiority over the others in all respects. The decision is a tradeoff and depends on what is critical with respect to its use: whether high catalytic activity is necessary; whether the cost of material is a primary consideration; whether the worldwide supply/demand is the first concern; etc.

The currently used anode material is porous sintered nickel, stabilized with 2-10 weight percent (w/o) chromium to inhibit sintering. These nickel anodes exhibit

good, stable electrochemical performance. However, nickel-based anodes are relatively high cost components. In addition, questions arise regarding the availability of nickel in the quantities required for commercialization of MCFC power plants. Exploratory polarization data for hydrogen oxidation have shown relatively little dependence on the nature of the metal (1, 2).

Copper is presently being considered as an alternative anode material based upon its greater domestic availability, significantly lower cost, and expected chemical stability in the fuel cell anode environment. The objective of this work was to ascertain the electrode-kinetic suitability of copper as an alternative anode material. Since extensive data were available for nickel (3), a comparative study was made of copper and nickel, using the same techniques and procedures in both cases.

Apparatus and Procedure

The experiments were conducted in a hermetically sealed cylindrical closed-end alumina tube (AD-998, nominally 99.8% recrystallized Al_2O_3), containing an alumina crucible (Coors Porcelain Company, Golden, Colorado) of 250 ml capacity. The crucible was hung on Pt-Pd hooks from alumina supports fitted with pierced baffles to minimize temperature gradients. The whole assembly was suspended from a metal header attached to a leveling table and placed in a vertical tubular furnace. After assembly, the crucible rested on a piece of alumina firebrick placed at the bottom of the outer alumina jacket. The most important feature of the apparatus was its vacuum tightness; otherwise, the gas composition above the melt, and consequently the electrode potentials, would become inaccurate, owing to effects such as the diffusion of air from outside, as well as thermal dissociation of the molten carbonates. The apparatus was rendered vacuum tight by means of O-rings between the alumina jacket and the stainless steel header. Similarly, the outer sheaths of the working and reference electrodes, and the gas bubbler tube were sealed by O-rings.

The configuration of the cell is shown in Fig. 1. The working electrodes were made of pure nickel and copper rods. The nickel and copper were Marz grade with purity of 99.995% and 99.999%, respectively (Materials Research Corporation, Orangeburg, New York). The dimensions of the electrodes were measured by micrometer to within ± 0.01 mm. The surface area was 4.25 ± 0.05 cm². The rod was threaded at the center and screwed to a lead wire of the same material, which was sheathed in an alumina tube constructed in such a way as to prevent meniscus effects. The working electrode was completely immersed in the melt which was about 5 cm deep. The counterelectrode was a gold sheet fitted as an inner liner of the alumina crucible so as to surround entirely the working electrode and, thus, ensure uniform current distribution. A gold wire in equilibrium with a 33.3% O_2 -66.7% CO_2 gas mixture inside an alumina tube served as the reference electrode. Electrolyte in the tube communicated with the bulk melt through a tiny hole (0.038 cm diam) at the bottom of the tube. Since the tube was pressed against the flat bottom of the crucible, diffusive and convective mixing between the reference and the bulk electrolyte was restricted. The end of the gold wire was ca. 2.5 cm above the bottom of the tube; this location was found to be very important to ensure stable potential readings. The reference gas mixture was supplied through the inner alumina tube (which also carried the gold wire) and escaped through the annulus between the inner and outer tubes of the electrode. The flow rate was kept at 2 ml/min. Two reference electrodes with separate gas supplies were used as an insurance against accidental occurrence of plugging and instability. Under normal conditions, their readings were within 2 mV of each other.

Electrolyte mixtures were prepared from Li_2CO_3 and K_2CO_3 (Fisher analytical reagent). The composition used in this study was 62 mole percent (m/o) Li_2CO_3 , 38 m/o K_2CO_3 . The melting point of this eutectic mixture is 761 K (488°C). Fuel gas mixtures were purchased premixed from

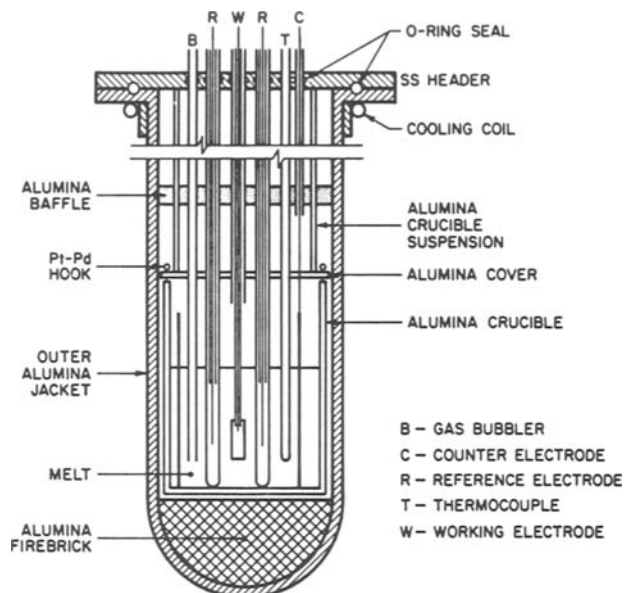


Fig. 1. Configuration of cell

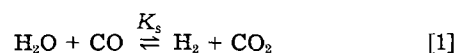
Matheson Gas Company (Joliet, Illinois); the gas compositions were verified by gas chromatographic analysis. The fuel flow rate was kept at 50 ml/min, adjusted by pressure regulators and capillary flowmeters. Humidification of the inlet gas was performed by passing it through a column of water in a large tube, and from there to the gas bubbler in the working electrode compartment. The saturator efficiency was checked by gas-chromatographic analysis of the humidified gas, as reported previously (3). The gas line from the humidifier to the bubbler was kept at 403 K (130°C) to prevent condensation of water. A long nickel wire was inserted in the gas line to facilitate the water-gas shift reaction.

The whole apparatus was heated up slowly (100°C/h). Because of the tendency of the melt to creep along the surfaces in direct contact with the molten carbonate, care was taken to turn on the reference and fuel gases before the melting point was reached; if this was not done, plugging of the tubes was likely to occur. A Universal Programmer (Model 175, Princeton Applied Research, Princeton, New Jersey) was used to control the potentiostat (Wenking, Model ST72, Gerhard Bank Elektronik, Germany). The output voltage was monitored by a Fluke Type 8020A Digital Voltmeter (John Fluke Company, Seattle, Washington). Steady-state currents were recorded on an Omnigraphic 2000 X-Y recorder (Houston Instrument, Austin, Texas). The transient response following a potential step was displayed on a Nicolet Explorer II Digital Oscilloscope (Nicolet Instrument Company, Madison, Wisconsin), which has a risetime of 50 ns or less with 5 μV resolution.

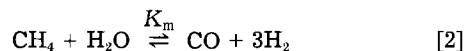
Feed Gases and Their Equilibrium Potentials

In accordance with the envisaged application of the molten carbonate fuel cell, five typical fuel gases (4) were chosen for these experiments, ranging from high Btu to very low Btu. These feed gases were produced from various initially dry mixtures by saturation with water at different dewpoints. Dewpoints were chosen in such a way as to prevent carbon formation at lower temperatures encountered by the gas during heating to cell temperature.

Two reactions are involved in establishing the equilibrium compositions of these gas mixtures: the water-gas shift reaction



and the steam reforming reaction



Their equilibrium constants

$$K_s = \frac{P_{\text{H}_2} P_{\text{CO}_2}}{P_{\text{CO}} P_{\text{H}_2\text{O}}}$$

and

$$K_m = \frac{P_{\text{CO}} P_{\text{H}_2}^3}{P_{\text{CH}_4} P_{\text{H}_2\text{O}}} \quad [3]$$

can be found in the literature [$K_s = 1.96$, $K_m = 2.68$ at 923 K (650°C)] (5). The compositions of the dry gas mixtures, the compositions corresponding to complete shift equilibrium and those corresponding to simultaneous equilibrium of the shift and the steam reforming reactions, are listed in Table I. The open-circuit potentials based on these gas compositions, as well as the experimentally measured open-circuit potentials are shown in Table II. The observed open-circuit potentials are in good agreement with the theoretical values obtained, assuming simultaneous equilibrium of the shift and the steam reforming reactions (6).

Steady-State Results

Steady-state polarization curves for high Btu fuel gas at nickel and at copper in $\text{Li}_2\text{CO}_3/\text{K}_2\text{CO}_3$ eutectic at 923 K (650°C) are shown in Fig. 2 and 3, respectively. In these figures, measurements made under conditions of continuous bubbling (50 ml/min) are compared to those made in the quiescent melt. Nickel supports a higher current density than copper at the same polarization. In both cases, much higher current densities are obtained with the melt subjected to continuous bubbling. The difference is obvious even in the low polarization region (20 mV). This demonstrates that the electrode process is under partial diffusion (mixed) control. The persistent presence of diffusion control in the anode process can be explained either by depletion of the reactant (H_2) or buildup of the re-

Table I. Gas composition before and after equilibrium, assuming steam reforming and/or gas shift reactions

	H_2	H_2O	CO	CO_2	CH_4	N_2
Initially dry gas						
High Btu (53°C)*	0.80	—	—	0.20	—	—
Intermediate (71°C)	0.74	—	—	0.26	—	—
Low Btu 1 (71°C)	0.213	—	0.193	0.104	0.011	0.479
Low Btu 2 (60°C)	0.402	—	—	0.399	—	0.199
Very low Btu (60°C)	0.202	—	—	0.196	—	0.602
Shift equilibrium						
High Btu	0.5914	0.2366	0.0964	0.0756	—	—
Intermediate	0.4385	0.3845	0.0651	0.1119	—	—
Low 1	0.2147	0.2497	0.0616	0.1405	0.0075	0.3220
Low 2	0.2305	0.2884	0.0930	0.2281	—	0.1600
Very low	0.1277	0.2303	0.0348	0.1229	—	0.4843
Shift and steam reforming						
High Btu	0.5546	0.2667	0.0819	0.0772	0.0196	—
Intermediate	0.4278	0.3937	0.0621	0.1119	0.0046	—
Low 1	0.2300	0.2409	0.0674	0.1384	0.0013	0.3220
Low 2	0.2273	0.2903	0.0915	0.2290	0.0014	0.1606
Very low	0.1274	0.2304	0.0347	0.1229	0.0001	0.4845

* Temperatures in parentheses are humidification temperatures.

Table II. Open-circuit potentials for various feed gases with respect to 33% O_2 -67% CO_2 reference electrode (mV)

Gas	Experimental	Shift only	Shift and methane
High Btu	-1116 ± 3	-1121.5	-1113.3
Intermediate Btu	-1071 ± 2	-1074.6	-1072.7
Low Btu 1	-1062 ± 3	-1054.3	-1059.1
Low Btu 2	-1030 ± 2	-1032.2	-1031.2
Very low Btu	-1040 ± 3	-1042.2	-1042.1

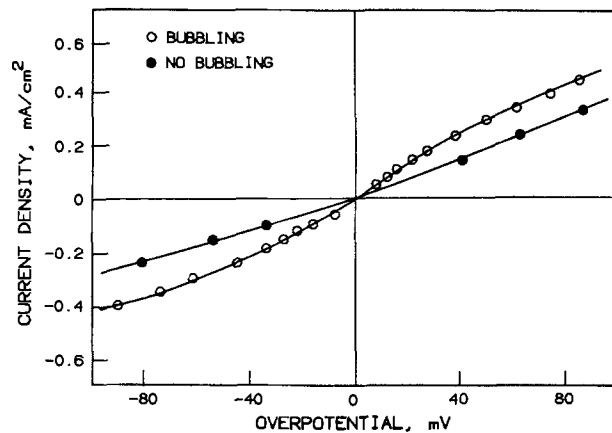


Fig. 2. Steady-state polarization curve for high Btu gas (55% H_2) at nickel in Li/K eutectic at 923 K (650°C).

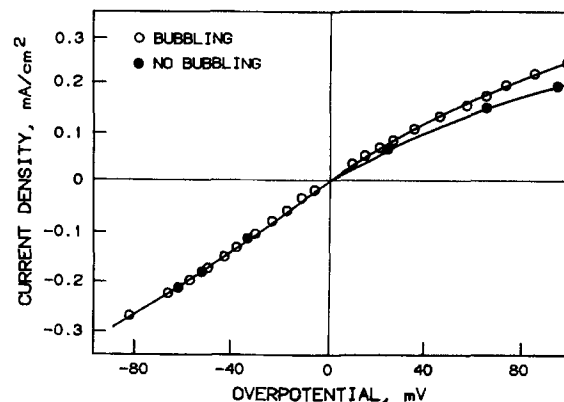


Fig. 3. Steady-state polarization curves for high Btu gas (55% H_2) at copper in Li/K eutectic melt at 923 K (650°C).

action products (H_2O and CO_2) near the electrode surface, or both. Equating activation overpotentials to steady-state potentiostatic measurements would give too low a value for the exchange current density. Near-equilibrium resistances (7), composed of kinetic and mass-transfer effects if ohmic potential drop is neglected, can be calculated from the current densities at a total polarization of 20 mV under identical conditions of continuous bubbling

$$R_{\text{Ni}} = \frac{\Delta \eta}{\Delta i} = 1.4 \times 10^2 \Omega\text{-cm}^2$$

$$R_{\text{Cu}} = \frac{\Delta \eta}{\Delta i} = 3.3 \times 10^2 \Omega\text{-cm}^2$$

The resistance for nickel is lower than that of copper. Under the same hydrodynamic conditions, the mass-transfer contributions to these resistances are equal ($RT/nF i_{\text{lim}}$). Comparing the above resistances, nickel appears to support a larger exchange current density than copper.

Potential-Step Transient

Technique and interpretation.—The potential step technique with appropriate IR compensation has been proven to be valid for separating activation (kinetic) and mass-transfer effects under mixed control conditions (3). In the cell configuration used here, an appreciable distance separates the reference and working electrodes (Fig. 1). The ohmic resistance (typically 5Ω) causes a potential drop which contributes significantly to the controlled potential. In order to control the potential drop across the working electrode/solution interface accurately, one must resort to an IR-compensation technique. An external voltage divider was used to pick up part of the voltage at the current recording terminal of the potentiostat, and feed this back into one of the potentiostat control inputs. The

positive feedback voltage was then adjusted until the system became almost unstable. This resulted in a maximum obtainable compensation of the ohmic resistance, which was confirmed by the current interruption technique. A typical oscilloscope trace obtained using this technique is shown in Fig. 4. The effect of positive feedback can be seen, where the upper trace is with compensation, and the lower one without. With appropriate IR compensation, the capacitive current can be clearly distinguished from the faradaic current; it has become negligible at 0.2 ms (Fig. 4).

Determination of the kinetic parameters of an electrode reaction by the potential step technique generally involves two difficulties, namely (i) superposition of activation and diffusion polarization in the presence of a double-layer charging current, and (ii) occurrence of a multistep reaction mechanism.

Upon application of a potential step to the working electrode, direct observation of the faradaic current is at first prevented by the double-layer charging current which, however, as noted above, decays rapidly. Therefore, if one only uses data points obtained after a period of time long enough for the charging current to become negligible, and makes a plot of current density vs. some appropriate function of time, then the activation current, free from the effects of mass transfer, may be obtained by backextrapolation of the transient current to time zero.

The second difficulty cannot be overcome by experimental means, and will be discussed in some detail below. First, however, an important aspect of the treatment of potential-step data needs to be considered.

An analytical solution is available only for first-order kinetics involving a single reacting species and product (8). The current-time relationship for the reaction



is, as shown by Gerischer and Vielstich

$$i = i(0) \exp(\lambda^2 t) \operatorname{erfc}(\lambda \sqrt{t}) \quad [5]$$

Here $i(0)$ is the "kinetic" current density corresponding to the potential step, η , and the expression for λ can be found in Ref. (8). For small time periods, this solution can be linearized

$$i = i(0) \left(1 - \frac{2}{\sqrt{\pi}} \lambda \sqrt{t} \right) \quad \text{for } \lambda \sqrt{t} < 1 \quad [6]$$

Thus, the current density is a linear function of \sqrt{t} for small time periods, and \sqrt{t} appears to be the appropriate simple function of time for backextrapolation to $i(0)$. Several papers discuss the criteria of satisfactory extrapolation, and possible improvements (9, 10). However, in the literature, two other techniques of extrapolation are found. They were devised either for ease of use, or for assumed high precision. These techniques are: (i) linear extrapolation. This technique, adopted by Ang and Sam-

mells, (3) is the easiest way to process the data. The near-linear initial section of the oscillogram following decay of capacitive current is selected and extrapolated back to time zero, which yields $i(0)$. (ii) Analysis in Laplace space. Some authors have analyzed their experimental data in Laplace space (11). This has certain advantages of accuracy and versatility, as it utilizes the entire time span of the transient and avoids approximation (12). It should be especially useful in cases where the inverse Laplace transformation cannot be performed, or where the inverse form can only be handled by approximation.

To compare the results obtained by these techniques with the simple \sqrt{t} extrapolation, the time variation of current density following a potential perturbation of +100 mV from the rest potential, is treated by each of the three methods. Figure 5 shows the oscillogram of the current density and the results of linear and \sqrt{t} extrapolation. The kinetic current, $i(0)$, is obtained by extrapolating currents between 0.3 and 0.5 ms to time zero. The trace of the \sqrt{t} extrapolation, bending up near $t = 0$, yields a higher kinetic current than does linear extrapolation. In this particular case, the results are 100.5 and 76.4 mA/cm², respectively.

In the case of Laplace-space analysis, although the data span the entire period of 0-1s, the first charging-free datum point is at $t = 0.8$ ms. Since the current density is weighted by an exponential function in the Laplace transformation, neglecting the initial portion of the transient will cause a significant error. Although analysis in Laplace space utilizes more points in the transient, the precision of this approach is limited by the double layer charging period. To remedy this problem, currents before 0.8 ms were generated by \sqrt{t} extrapolation and included in the integration. The results are shown in Fig. 6. The kinetic currents for three time intervals are 47.9, 104.7, and 291.0 mA/cm², respectively. Linearity is satisfied for all cases, but the kinetic currents are very sensitive to the time interval used for extrapolation. Comparing methods of reducing potential-step data, we conclude that: (i) Extrapolation vs. t (linear) yields too low a value of $i(0)$, (ii) extrapolation vs. \sqrt{t} (theory) yields satisfactory values of $i(0)$ if the time interval is 0.3-0.5 ms, and (iii) Laplace-transform taken over 0.2-1000 ms yields $i(0)$ identical with extrapolation vs. \sqrt{t} , but including data at less than 0.2 ms yields too high a value of $i(0)$.

Application to nonlinear kinetics.—Strictly speaking, the procedures described above are valid only for a generalized redox reaction Eq. [4]. Although such a reaction can take place in any number of chemical and electrochemical elementary steps, one of these is assumed to be rate determining so that the current is determined solely by semi-infinite linear diffusion of the reactant and product of this step, and by the first-order kinetics of the step. It is also assumed that: (i) none of the species taking part in the reaction sequence is strongly adsorbed on the electrode surface, and (ii) the intermediates are not diffusing

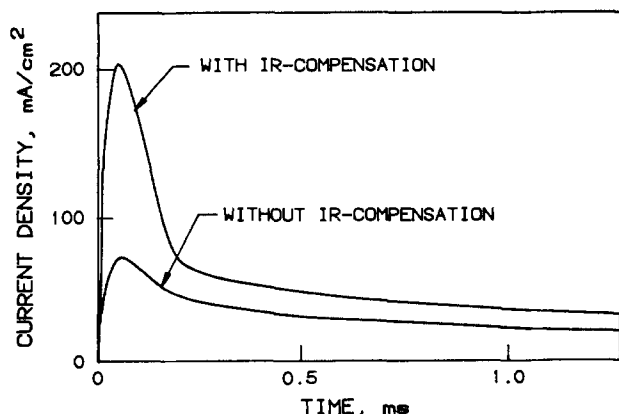


Fig. 4. Variation of current with time at a copper electrode. The upper trace is with IR-compensation, the lower one without compensation.

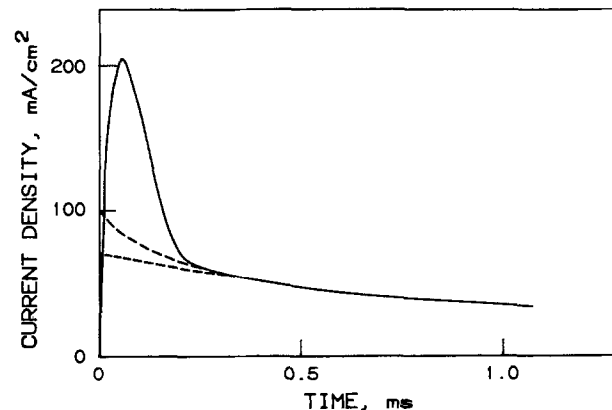


Fig. 5. Extrapolation of potential-step response vs. \sqrt{t} (upper) or t (lower).

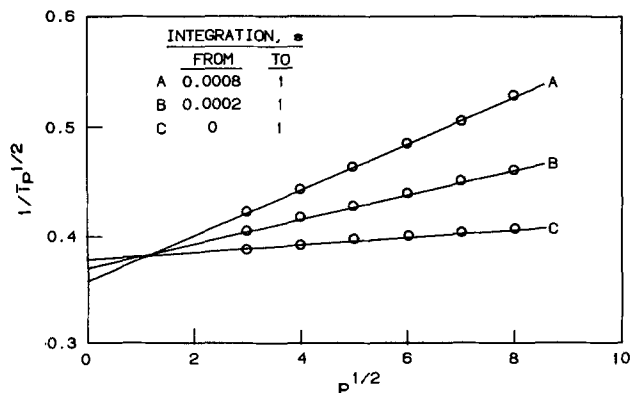


Fig. 6. Analysis of data in Laplace space

into the bulk solution. However, many reactions involve multiple components and multistep charge transfers. These kinetic complications frequently generate fractional reaction orders for reactants and products (3). Clearly, the previous procedures are not *ipso facto* applicable directly to potential step data for such a case. A more extensive analysis should be made. This analysis may well lead to a different but more appropriate technique for data treatment technique; or, on the other hand, it may show that the basic features of the Gerischer-Vielstich analysis (8) are applicable.

To investigate the effect of fractional reaction order on the current-time behavior, consider a general electrode reaction



where p and q are reaction orders for S_r and S_o , respectively. At $t = 0$, a potential step is applied to the working electrode. Following the same procedures as Newman (13), the boundary value problem can be described by the following equations

$$\frac{\partial C_o}{\partial t} = D_o \frac{\partial^2 C_o}{\partial x^2}, \quad \frac{\partial C_r}{\partial t} = D_r \frac{\partial^2 C_r}{\partial x^2} \quad [8a, 8b]$$

with the boundary and initial conditions

$$C_o(x, 0) = \bar{C}_o, \quad C_r(x, 0) = \bar{C}_r \quad [9a, 9b]$$

$$C_o(\infty, t) = \bar{C}_o, \quad C_r(\infty, t) = \bar{C}_r \quad [10a, 10b]$$

$$pD_o \left(\frac{\partial C_o}{\partial x} \right)_{x=0} + qD_r \left(\frac{\partial C_r}{\partial x} \right)_{x=0} = 0 \quad [11]$$

$$i = \bar{i}_o \left[\left(\frac{C_r}{\bar{C}_r} \right)^p \exp \left(\frac{\alpha n F}{RT} \eta \right) - \left(\frac{C_o}{\bar{C}_o} \right)^q \exp \left(- \frac{(1-\alpha)nF}{RT} \eta \right) \right] \quad [12]$$

Here x is the distance from the electrode surface, \bar{C}_o and \bar{C}_r are the initial concentrations of the substances S_o and S_r , respectively, D_o and D_r are the respective diffusion coefficients, and α is the symmetry factor. η is the overall overpotential which consists of surface (η_s) and concentration (η_c) overpotentials. \bar{i}_o is the exchange current density at the bulk concentration.

Equations [8]-[12] have been solved numerically assuming the following set of parameters for illustration purposes

$$D_r = D_o = 1.0 \times 10^{-5} \text{ cm}^2/\text{s}, \quad \bar{C}_r = 1.0 \times 10^{-5} \text{ mol/cm}^3\text{-atm}$$

$$\bar{C}_o = 4.0 \times 10^{-6} \text{ mol/cm}^3\text{-atm}, \quad \eta = 0.1V, \quad \bar{i}_o = 10 \text{ mA/cm}^2$$

$$T = 923 \text{ K}, \quad n = 1$$

The following procedure is used to obtain the systematic errors caused by the linear and the square-root-of-time extrapolations. Data points (i - t pairs) are generated by solving Eq. [8]-[12] for the time span 0.3-0.5 ms. The initial current (current at $t = 0$) is then obtained from these data points by either linear or \sqrt{t} extrapolation. The true and extrapolated initial currents are compared to obtain the systematic errors.

The numerical method which was employed in solving Eq. [8]-[12] has been described by Feldberg (14). The accuracy of this numerical approach was demonstrated by comparing the numerical results with the analytical solutions in the case of $p = q = 1$, and the results differed by less than 0.02%. The systematic errors caused by the two extrapolation procedures for various values of p and q are evaluated and listed in Table III. The maximum error found for square-root-of-time extrapolation is about 3%. However, the value estimated by linear extrapolation is more than 10% lower than the exact value. This result is not surprising; in the conventional trial-function expansion method for solving the differential equations, the known solution of a simplified problem is often used as a first approximation (15), since it usually has similar behavior in a limited range. In the present case, since the linearized form (Eq. [6]) is a good approximation for the first-order reaction, it is reasonable to assume that the same functional form (\sqrt{t} dependence at short times) is applicable to the case of fractional reaction orders.

Table III. Numerical solutions for various values of fractional reaction order p , assuming $p = q$, and relative errors caused by two extrapolation procedures

$t/p \rightarrow$	0.3	0.4	0.5	0.6	0.7	0.8	0.9	1.0
0.30	1.31735	1.29889	1.27574	1.24829	1.21699	1.18234	1.14486	1.10506
0.32	1.31657	1.29753	1.27367	1.24541	1.21323	1.17764	1.13920	1.09845
0.34	1.31581	1.29621	1.27167	1.24263	1.20960	1.17311	1.13376	1.09211
0.36	1.31507	1.29493	1.26973	1.23994	1.20609	1.16874	1.12852	1.08601
0.38	1.31435	1.29369	1.26785	1.23733	1.20269	1.16452	1.12346	1.08012
0.40	1.31366	1.29248	1.26602	1.23480	1.19939	1.16043	1.11856	1.07445
0.42	1.31298	1.29131	1.26425	1.23234	1.19619	1.15646	1.11382	1.06895
0.44	1.31232	1.29016	1.26252	1.22995	1.19308	1.15261	1.10922	1.06363
0.46	1.31167	1.28904	1.26083	1.22761	1.19006	1.14886	1.10476	1.05847
0.48	1.31104	1.28795	1.25918	1.22534	1.18711	1.14522	1.10042	1.05347
0.50	1.31042	1.28688	1.25757	1.22312	1.18423	1.14166	1.09620	1.04860
				Exact value				
$i(0)$	1.34152	1.34137	1.34117	1.34092	1.34063	1.34030	1.33992	1.33950
			\sqrt{t} — Extrapolation and relative error					
$i(0)$	1.34116 (0.03%)	1.34015 (0.09%)	1.33814 (0.23%)	1.33471 (0.46%)	1.32945 (0.83%)	1.32191 (1.37%)	1.31176 (2.10%)	1.29862 (3.05%)
			t — Extrapolation and relative error					
$i(0)$	1.32758 (1.04%)	1.31661 (1.85%)	1.30252 (2.88%)	1.28537 (4.14%)	1.26523 (5.62%)	1.24217 (7.32%)	1.21637 (9.22%)	1.18795 (11.31%)

$i(0)$ = Initial current density (10^{-2} A/cm 2).
 t = Time (ms).

This investigation, therefore, leads to the conclusion that the square root of time is an appropriate form for short time extrapolation, even in the case of fractional reaction orders. The value obtained by the linear extrapolation is likely to be too low. The conclusions of this analysis are applied in the following sections.

Results.—Kinetic parameters for the hydrogen-oxidation reaction on nickel have been reported previously by Ang and Sammells (3). Some of their measurements were repeated in this work, using the same procedure as these authors, for a more direct comparison with the data at copper. Exchange current densities for high and intermediate-Btu gases at nickel electrode were measured. The kinetic current, $i(0)$, was obtained by linear extrapolation of the current between 0.3 and 0.5 ms, to time 0. In this manner, the activation polarization curve was obtained in the -100 to $+100$ mV overpotential region; from this, the Allen-Hickling plot was constructed and the exchange current density calculated. At least three measurements were taken at each overpotential, and sufficient time was allowed to let the open-circuit potential return to normal (usually 15 min). The measurements were taken in the absence of gas bubbling. The raw data were fed into a regression analysis program to get the mean value and the standard deviation. Exchange current densities for high and intermediate-Btu fuel gas were 37 and 44 mA/cm², respectively. These values compare well with those of Ang and Sammells, who obtained 35 and 42 mA/cm², respectively, under the same experimental conditions and using the same potential-step technique.

However, if the dependence of current density is assumed to be with the square root of time, in agreement with the theory, the extrapolation leads to higher values of i_0 at nickel than given by Ang and Sammells. The exchange current densities at nickel are 51 and 59.5 mA/cm² for high and intermediate Btu gases. The corresponding Allen-Hickling plot for intermediate Btu fuel at nickel is shown in Fig. 7.

The true (activation) polarization curve and Allen-Hickling plot at copper in the Li/K eutectic at 923 K (650°C), using intermediate Btu fuel, are shown in Fig. 8 and 9, respectively. For this gas composition, the i_0 value at copper was found to be 28.7 mA/cm². Five different gas compositions ranging from high Btu to very low Btu fuel gas were thus measured. The corresponding i_0 values are tabulated in Table IV.

From the known values of the exchange current density for the five different gas compositions, the dependence of the exchange current density, i_0 , on fuel composition can be determined. Since equilibrium conditions exist in the melt, the CO content can be determined from the respective concentrations of H₂, CO₂, and H₂O, using the equilibrium constants. The dependence of exchange current density on gas composition is assumed to be

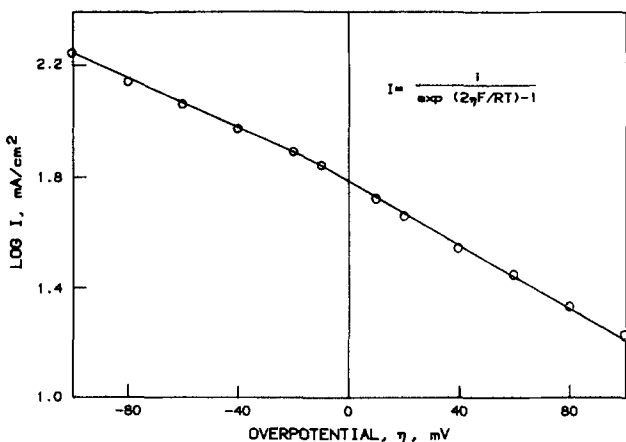


Fig. 7. Allen-Hickling plot for nickel electrode in Li/K eutectic with intermediate Btu fuel (42.8% H₂). Assumed: $\alpha_a + \alpha_c = 2$.

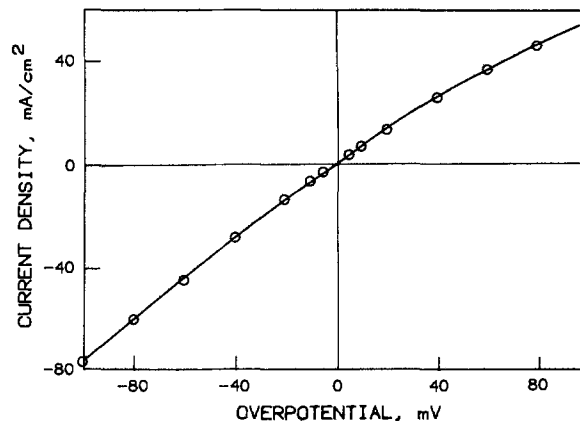


Fig. 8. Activation polarization for copper in Li/K eutectic with intermediate Btu fuel (42.8% H₂) at 923 K (650°C).

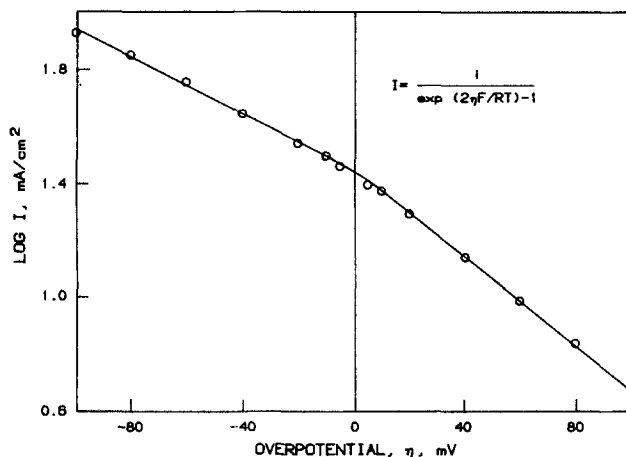


Fig. 9. Allen-Hickling plot for copper in Li/K eutectic with intermediate Btu fuel (42.8% H₂) at 923 K (650°C). Assumed: $\alpha_a + \alpha_c = 2$.

$$i_0 = i_0^0 [\text{H}_2]^a [\text{CO}_2]^b [\text{H}_2\text{O}]^c \quad [13]$$

where i_0^0 is the standard exchange current density (mA/cm²) at 1 atm partial pressure of each reactant.

Using the i_0 values at copper obtained with fuel gas compositions corresponding to high, intermediate, low, and very low Btu, and assuming shift equilibrium, Eq. [13] has the parameters

$$i_0^0 = 69.50 \pm 2.28 \text{ mA/cm}^2, a = 0.34 \pm 0.01 \\ b = 0.13 \pm 0.01, c = 0.31 \pm 0.02 \quad [14]$$

If both steam reforming and shift equilibria are assumed, one finds

$$i_0^0 = 71.12 \pm 2.14 \text{ mA/cm}^2, a = 0.33 \pm 0.01 \\ b = 0.14 \pm 0.01, c = 0.33 \pm 0.02 \quad [15]$$

The difference is not significant, as is to be expected for one atmosphere pressure data. Ang and Sammells reported for the nickel electrode

$$i_0^0 = 104.7 \text{ mA/cm}^2, a = 0.26, b = 0.28, c = 0.18 \quad [16]$$

Table IV. Exchange current densities, i_0 , and transfer coefficient, α_c , for copper in Li/K melt at 923 K (650°C) using various feed gases

Feed gas	i_0 (mA/cm ²)	α_c
High Btu	26.6 ± 0.41	1.31
Intermediate Btu	29.2 ± 0.37	1.31
Low Btu 1	21.1 ± 0.23	1.33
Low Btu 2	23.4 ± 0.23	1.30
Very low Btu	16.6 ± 0.24	1.27

The standard exchange current density for copper is lower than that for nickel. However, if one corrects the data of Ref. (3) for the underestimation caused by linear extrapolation, the actual value of the standard exchange current density at nickel may be as high as 138 mA/cm² at 923 K (650°C).

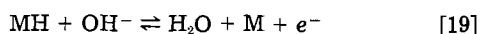
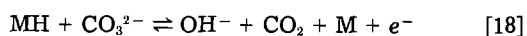
The kinetic results at both nickel and copper indicate that the anodic activation polarization of anode is very small in the molten carbonate fuel cells; also, the electrode metal has little effect on the polarization. These results are consistent with the low anode polarization of lab-scale (3 cm²) cells using a porous copper anode [fabricated by Gould laboratories and stabilized at IGT (16)].

Discussion and Conclusions

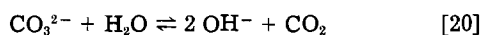
The exchange current density at copper measured in this study is very encouraging from a practical point of view. The standard value (i_0) of 71.1 mA/cm² at 923 K (650°C), is of the same order of magnitude as, but somewhat lower than, that for nickel. The previously determined value of i_0 at nickel appears to underestimate the actual value due to an inappropriate extrapolation technique; it may be as large as 138 mA/cm² at 923 K (650°C).

This study confirms the electrode-kinetic suitability of copper as an alternative anode material to nickel. Performance studies of porous copper anodes in small cells at IGT have led to the same conclusion.

Several reaction mechanisms have been considered to interpret the dependence of i_0 on gas composition (17). Ang and Sammells suggest that a good representation of their experimental results, Eq. [16], is given by



In deriving the theoretical expression for the current, they assume that Eq. [18] is the rate-determining step, and thus the preceding and following steps are in quasiequilibrium. It should be noted that the proposed mechanism also assumes that the reaction steps must take place consecutively and that the intermediates do not diffuse toward or away from the electrode surface. Since the intermediate hydroxide ions are quite stable in molten carbonate, their concentration may be determined from the hydrolysis equilibrium



The hydrolysis constant of reaction [20] is reported to be $K_h = 1.79 \times 10^{-4}$ for 923 K (650°C) (18). Because of the existence of an appreciable amount of OH⁻ ions in the melt, the rate of reaction [19] is not limited by the rate of supply of OH⁻ ions from reaction [18]. Under the circumstances, a more rigorous analysis of the anodic process requires the treatment of reactions [18] and [19] as simultaneous reactions rather than as consecutive steps of a simple reaction. Also, separate conservation equations must be set up for each species to account for their diffusion, and possibly convection. If reaction [18] occurs rather slowly, most of the OH⁻ ions consumed in reaction [19] are produced by reaction [20] and the reaction rate, *i.e.*, the current density, will have a strong dependence on H₂O partial pressure. As observed experimentally (see Eq. [15]),

the exchange current density is more sensitive to H₂O than to CO₂.

Equation [7] represents a general overall reaction on the electrode. This simplified form was used to show the applicability of the extrapolation scheme to fractional kinetics. As a matter of fact, an electrode kinetic analysis must consider the overall reaction in terms of several elementary steps. Such an analysis is complicated by the need to account for the transport process and kinetics for each step. This rigorous approach, in which complications from the multistep mechanism and the diffusion of multiple components are taken into consideration, will be discussed in a follow-up paper (19).

Acknowledgment

This work was supported by the Electric Power Research Institute, Palo Alto, California, under Contract RP-1085-2, and carried out at the Institute of Gas Technology, Chicago, Illinois. The authors thank Dr. A. J. Appleby for helpful discussions. The interest and cooperation of Dr. T. D. Claar, Mr. E. H. Camara, and others on the IGT staff are gratefully acknowledged.

Manuscript submitted Aug. 8, 1983; revised manuscript received April 4, 1984. This was Paper 375 presented at the Montreal, Quebec, Canada, Meeting of the Society, May 9-14, 1982.

The Illinois Institute of Technology assisted in meeting the publication costs of this article.

REFERENCES

- L. P. Klevtsov, G. G. Arkhipov, and G. K. Stepanov, *Sov. Electrochem.*, **3**, 785 (1967).
- "Advanced Technology Fuel Cell Program" Project 114-2 Interim Report, pp. 3-8, Nov., 1977, EPRI EM-576, United Technologies, Inc., South Windsor, CT.
- P. G. P. Ang and A. F. Sammells, *This Journal*, **127**, 1287 (1980).
- "Fuel Cell Research on Second-Generation Molten Carbonate Systems" Project 8984 Final Status Report, Vol. I., Institute of Gas Technology, Chicago, IL (1977).
- Catalyst Division, Chemetron Corp., "Physical and Thermodynamic Properties of Elements and Compounds." GC 245-3-373, Rev. 4, Louisville, KY (1972).
- W. M. Vogel and C. D. Iacovangelo, *This Journal*, **124**, 1305 (1977).
- A. C. Riddiford, *J. Chem. Soc.*, 1175 (1960).
- K. J. Vetter, "Electrochemical Kinetics—Theoretical Aspects," pp. 362-365, Academic Press, New York, (1967).
- D. J. Kooijman, *J. Electroanal. Chem.*, **18**, 81 (1968).
- K. B. Oldham and R. A. Osteryoung, *ibid.*, **11**, 397 (1966).
- D. D. Macdonald, "Transient Techniques in Electrochemistry," pp. 62-63, Plenum Press, New York (1977).
- H. S. Wroblowa and N. Gupta, Abstract A34, 32nd I. S. E. Meeting, Cavtat, Yugoslavia, September 1981.
- J. Newman, "Electrochemical Systems," p. 388, Prentice-Hall, Englewood Cliffs, NJ (1973).
- S. W. Feldberg, *J. Electroanal. Chem.*, **3**, 199 (1969).
- R. Caban and T. W. Chapman, *Chem. Eng. Sci.*, **36**, 849 (1981).
- T. D. Claar and R. A. Donado, Institute of Gas Technology, Chicago, IL, Private Communication (1981).
- "Fuel Cell Research on Second Generation Molten Carbonate Systems," Project 9105 Final Technical Report, P. 2-97, Institute of Gas Technology (1979).
- B. K. Andersen, Ph.D. Thesis, Technical University of Denmark, Lyngby, Denmark (1975).
- S. H. Lu and J. R. Selman, Submitted to *This Journal*.

Bench Scale Experiment of Recovery of Chlorine from Waste Gas

F. Hine*

Nagoya Institute of Technology, Nagoya, Japan 466

M. Nozaki and Y. Kurata

Tsukishima Kikai Co., Ltd., Chuo-ku, Tokyo 104

ABSTRACT

A bench scale experiment with a 50A cell equipped with a Nafion membrane has been conducted. Electrolyte is a mixture of HCl and CuCl₂. Chlorine is generated at the graphite anode, and cupric chloro-complex ions are reduced at the graphite cathode. The catholyte effluent is sent to the packed tower, where the cuprous ions are oxidized by chlorine in the waste gas. The cost evaluation for chlorine production in full-scale plants of various sizes is also described.

It is estimated that 2-3% of the chlorine produced by brine electrolysis is being wasted by the liquefaction unit as a dilute gas because the cell gas contains a small amount of oxygen, nitrogen, hydrogen, and others, depending on the cell design and the operating conditions of the electrolyzers and the liquefaction plant. Although most waste gas is treated by caustic soda solution to convert it into hypochlorite, it would be profitable if concentrated chlorine could be recovered. Hooker has developed an adsorption-desorption process using pressurized water, whereas Diamond Shamrock uses chlorinated solvents such as carbon tetrachloride (1, 2).

Hine *et al.* has studied electrolysis of the mixed solution of CuCl₂ and HCl where chlorine is liberated from the anode and cupric chloro-complex ions are reduced at the cathode. The catholyte leaving the cell is oxidized in a separate reactor by waste chlorine and recycled to the electrolytic cell (3, 4). This process consumes a relatively small amount of electricity because the decomposition voltage and the anodic and cathodic overvoltages are small. The chemical reactions involved in this process are relatively simple and have already been clarified (5-8).

This paper deals with a bench scale experiment of the electrolytic process with a 50A cell. The cost estimation for 0.5-5.0 ton-Cl₂/day units is also discussed.

Outline of the Process

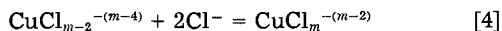
The electrolytic cell is equipped with the graphite anode and cathode, and a Nafion membrane is located between them. The electrolytic solution consists of a mixture of 6M HCl and 1.5M CuCl₂, in which cupric ions may form chloro-complex CuCl_m^{-(m-2)}. The chloride ions are oxidized at the anode (reaction [1]), and cupric chloro-complex ions can also discharge as a side reaction (reaction [2])



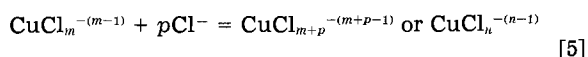
At the cathode, cupric ions are reduced into cuprous



where *m* is the coordination number of Cl⁻ with respect to a cupric ion, its possible number in 6M HCl being 3. Tetrachloro-complex is a stable form of cuprous ions (5). Consequently, reactions [2] and [3] are followed by the homogeneous reactions [4] and [5] in the anode and cathode compartments, respectively



and

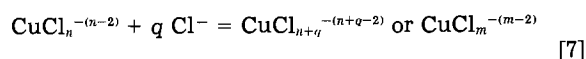
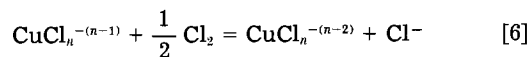


where *n* is the coordination number of Cl⁻ with respect to a cuprous ion.

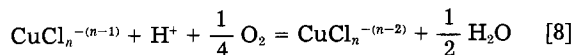
*Electrochemical Society Active Member.

Although the Nafion membrane rejects the anions, H⁺ can pass through the membrane from the anode side to the cathode side. It causes depletion of HCl in the anode compartment, whereas the HCl concentration in the cathode compartment increases during electrolysis.

The catholyte liquor leaving the cell is sent to the oxidation tower, and it reacts with the waste gas containing chlorine. A possible reaction is



Also, reaction [8] may take place because the waste gas contains air or oxygen, as well as chlorine (7)



Polarization Studies

It is well known that an oxide-coated Ti anode such as DSA is the best selection for chlor-alkali cells because of its low chlorine overvoltage and corrosion resistance in concentrated NaCl solutions. An oxide-coated Ti anode composed of 1 part RuO₂ and 2 parts TiO₂ in mole ratio (OCTA, hereafter) was prepared and electrolyzed in a mixed solution of 6M HCl and 1.5M CuCl₂ at 100 A/dm². The chlorine overvoltage remained low for about 3 months, then after 6 months the oxide layer degraded and the overvoltage increased considerably. The service life was extended somewhat by addition of a third element such as Ir.

However, the graphite anode was resistant to concentrated HCl, and its chlorine overvoltage was acceptably low, *e.g.*, about 0.1V at 20 A/cm². Also, the chlorine overvoltage was lowered by addition of cupric ions in concentrated HCl solutions, as shown in Fig. 1, though its mechanism was unclear. Consequently, graphite was used as the anode material. The Ti screen and/or perforated electrodes coated with noble metal oxide were also examined in some cases for the convenience of the cell design.

The main reaction at the cathode was the conversion of cupric chloro-complex ions into cuprous ions, as shown by reaction [3]. However, copper deposition could have taken place and been troublesome if the cathode was polarized more negative than 0V vs. SCE. The cathodic polarization curves of various materials are shown in Fig. 2. The rotating-disk electrode was used because the cathodic process under consideration was diffusion-controlled. Because an undivided cell was employed, a part of the chlorine generated from the anode was reduced at the Pt cathode at the potentials more negative than 0.5V vs. SCE and was also controlled by diffusion. The cathodic reduction of cupric chloro-complex ions (reaction [3]) took place at the same potential range. This reaction

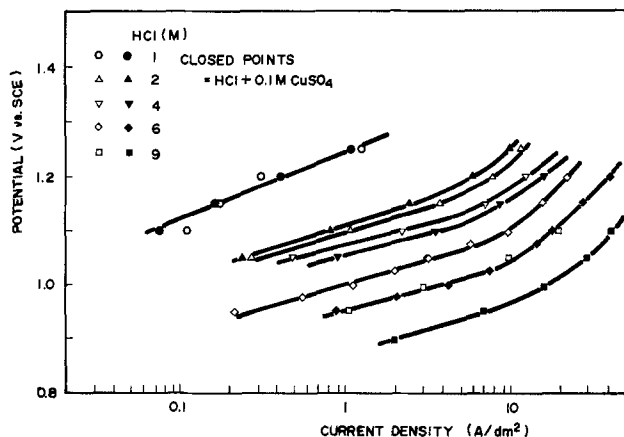


Fig. 1. Polarization curves of the graphite anode in HCl solutions with and without CuSO_4 at 40°C .

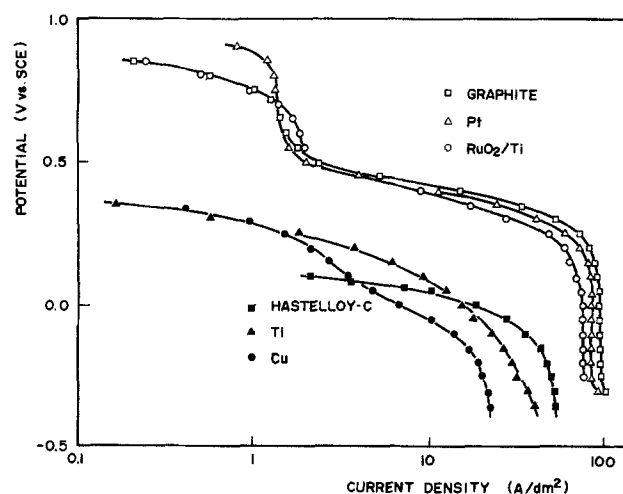


Fig. 2. Polarization curves of various cathode materials in $6\text{M HCl} + 1.5\text{M CuCl}_2$ at 70°C .

was limited by mass transfer. Further polarization would have caused copper deposition on the cathode.

A fresh oxide-coated Ti electrode showed almost the same behavior as the Pt cathode, but the oxide coating was degraded gradually by cathodic reduction. Other metallic specimens such as Cu, Ti, and Hastelloy C were corroded, even when they were polarized cathodically from their static potential in the solution under discussion.

Graphite was, of course, corrosion resistant, and its cathodic polarization was the same as that of the Pt cathode. Consequently, a graphite cathode was considered to be the best selection.

Bench Scale Experiment

The flowsheet of the bench scale experiment with a 50A cell was almost the same as that of the fullscale plant illustrated in Fig. 11, with some exceptions. The electrolytic solution was pumped to the anode and cathode compartments. The catholyte effluent was sent back to the reservoir. However, chlorine gas was separated from the anolyte before return to the electrolytic reservoir. A part of the electrolytic solution was circulated between the reservoir and the oxidation tower. The dilute gas was sent to the bottom of the tower, and its tail gas was brought to the wash tower to remove traces of acid mist and chlorine. The dilute gas was prepared with chlorine generated at the anode; hence, a very small amount of chlorine from the cylinder (an additional source) was required during the experiment.

The electrolytic cell made of Lucite resin was 50 mm wide and 515 mm high and had a flange 30 mm wide. The cell was equipped with a pair of graphite electrodes with a Nafion membrane between them. The cathode was sec-

tioned to determine the current distribution along the electrode. The anode was also sectioned for convenience of preparation and fabrication.

The catholyte oxidizer was a Lucite resin column of 10 cm diam and 100 cm height packed with Raschig rings of 1 cm diam and 1 cm height. The total height of the packings was about 60 cm. It was excessively large in capacity, compared with the cell capacity for convenience of experiment.

A beaker-shaped cell of 89 mm id and 145 mm height was used to investigate absorption of chlorine into the electrolytic solution (Fig. 3). The solution level was 80 mm. The solution and the gas in the test cell were agitated by their respective paddles. The mixed gas of N_2 and Cl_2 was sent to the cell at a given flow rate, and the tail gas was washed out by caustic liquor. The solution was pipetted out and titrated intermittently to obtain the absorption rate.

Results and Discussion

The chlorine evolution reaction is stimulated by Cu^{2+} , as described above (see Fig. 1). An example of the polarization curves of the graphite anode positioned in a vertical cell is shown in Fig. 4. The anode overvoltage is almost independent of the location along the vertical electrode. The Tafel slope of the anodic polarization curve is about 130 mV/decade in the range of 0.2-65.0 A/dm^2 , suggesting that the main reaction is Cl^- -to- Cl_2 oxidation controlled by charge transfer. (In reaction [2], it is accompanied with the chlorine evolution from cupric chloro-complex ions to some extent.)

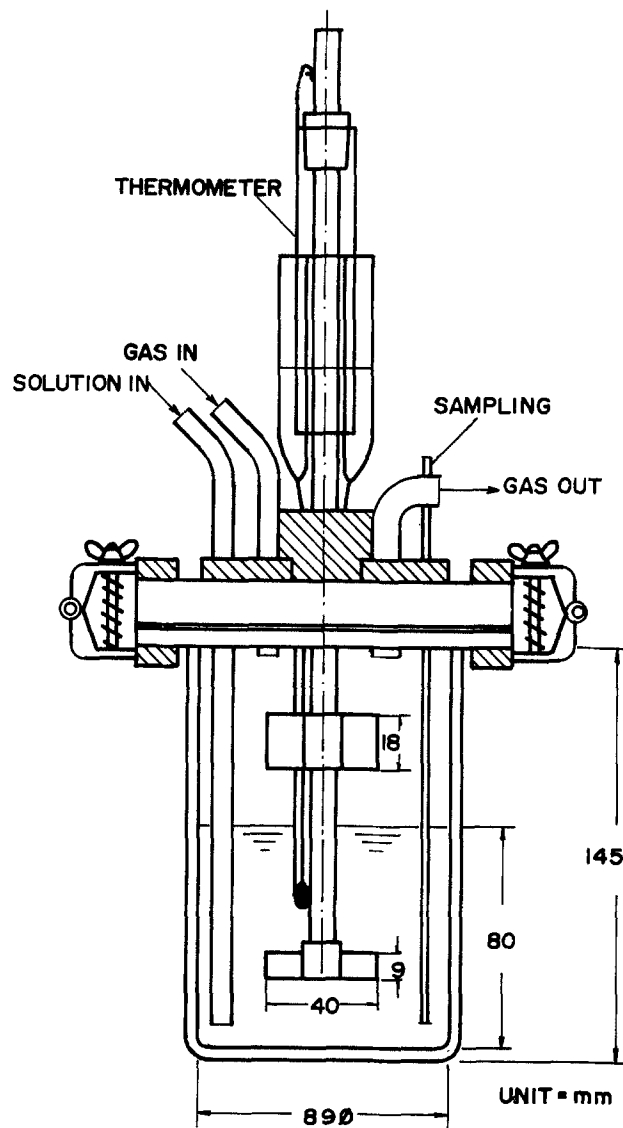


Fig. 3. Setup for gas absorption

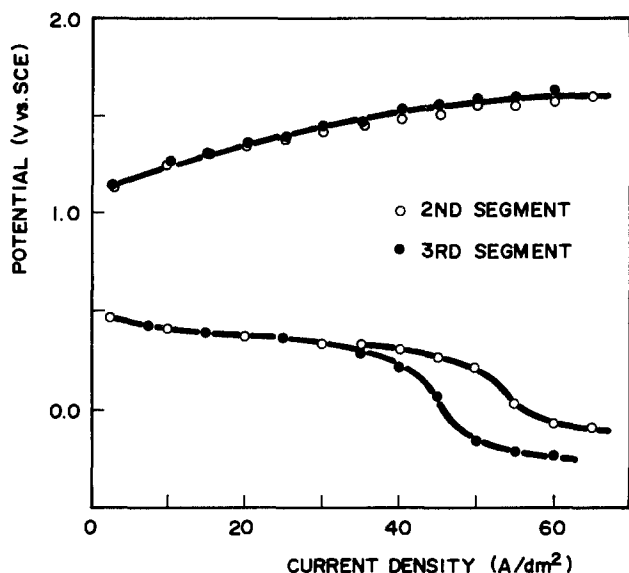


Fig. 4. Examples of the polarization curves of the graphite electrodes in 6M HCl + 1.5M CuCl₂ at 70°C. Flow rate: anolyte = 10 cm/sec; catholyte = 31 cm/sec.

The Tafel slope of the cathode process is about 120 mV/decade in the potential range of up to 0.3V vs. SCE and, hence, charge transfer of cupric ions to cuprous ions is assured. However, the diffusion limiting current density appears when the cathode potential becomes more negative than 0.3V. The limiting current density depends on its distance from the catholyte inlet or the location of the catholyte inlet, probably due to change in thickness of the diffusion layer along the vertical electrode.

The current density at a given potential is a linear function of the flow rate, as shown in Fig. 5. The results of previous work with a small electrode of 4 cm diam and 5 cm height are also illustrated; they represent very large current densities created by a rapid flow of catholyte in a small cell (4). A rotating-disk cathode enables the limiting current density to increase to more than 90 A/dm², as shown in Fig. 2. These results show that designing the cathode compartment so that it yields sufficient flow is

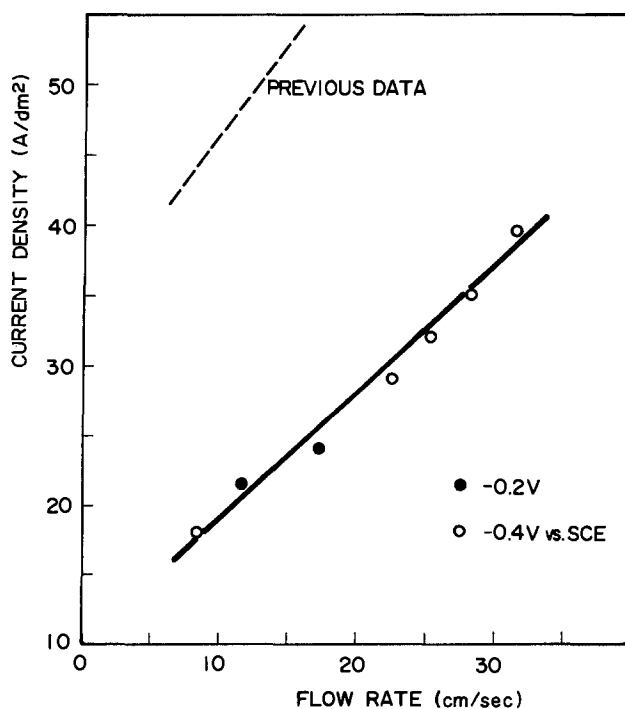


Fig. 5. Current density vs. flow rate curves in 6M HCl + 1.5M CuCl₂ at 70°C.

necessary in operating the cell, without trouble of copper deposition, in high ranges of current density.

Further experiments have been conducted to obtain design data such as limiting current density and solution conductivity. The summary of the results is as follows. First, the higher the solution temperature, the larger the current density at a given potential. For example, at -0.2V vs. SCE, the current density is 20 A/dm² at 51°C and 31 A/dm² at 70°C. Second, the current density increases with the increase of the Cu²⁺ concentration up to the solubility of CuCl₂ in HCl solution. The solubility of CuCl₂ in 6M HCl at room temperature is about 1.5M. Third, the HCl solution of about 6M in concentration shows the maximum conductivity, depending on the solution temperature. The electrical conductivity of the mixed solution of HCl and CuCl₂ decreases almost linearly with the increase of the CuCl₂ concentration (7, 8).

The voltage drop through the Nafion membrane in the mixed solution of HCl and CuCl₂ is low, compared with that in the solutions composed of alkali metal chloride, as shown in Fig. 6; this is due to a large permeability of H⁺ through the membrane. The Nafion membranes do not allow any anion to pass through. Accordingly, the current efficiencies for the anode and cathode processes are sufficiently high.

Figure 7 shows an example of the V-A curves. The voltage balances at both 20 and 40 A/dm² are as follows

	At 20 A/cm ²	At 40 A/dm ²
Decomposition voltage	0.60	0.60
Anode overvoltage	0.20	0.35
Cathode overvoltage	0.10	0.20
Solution IR-drop	0.10	0.20
Membrane IR-drop	0.15	0.30
Bubble effect	0.05	0.10

Terminal voltage 1.20V 1.75V

Along with the decomposition voltage, the membrane IR-drop and the anode overvoltage are major factors. The slope of the V-A curve becomes large when the current density exceeds 50 A/dm², due to delay of the cathode

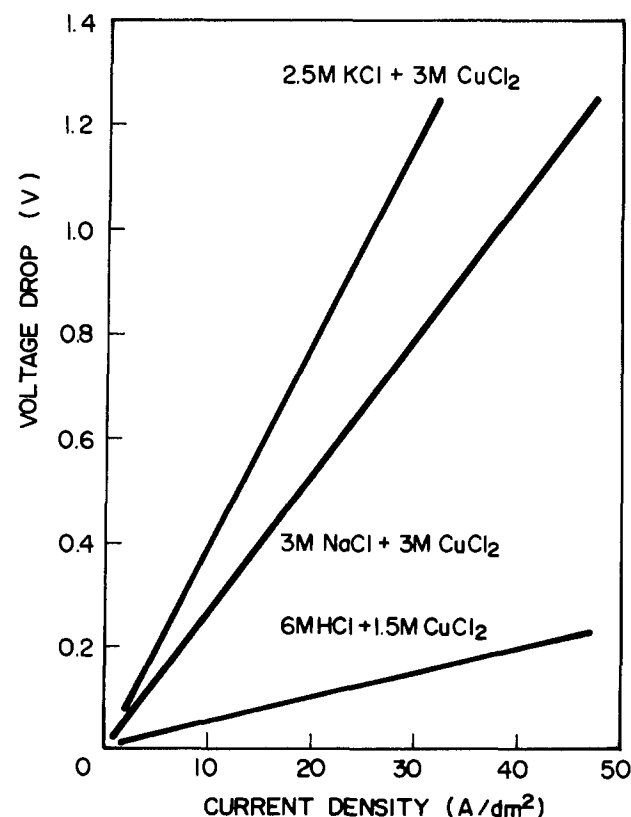


Fig. 6. Voltage drop of Nafion 390 in various solutions at 70°C

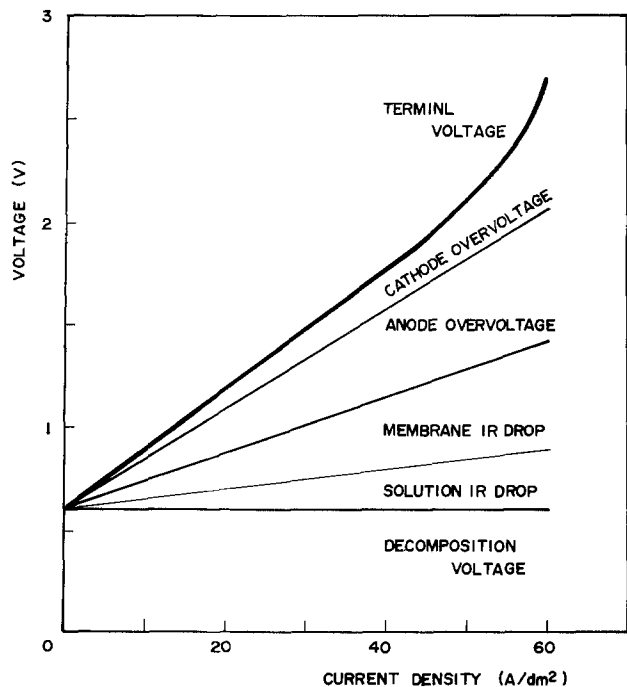


Fig. 7. An example of the voltage breakdown of the chlorine recovery cell. Electrolyte = 6M HCl + 1.5M CuCl₂ at 70°C. Anode-to-cathode gap = 4 mm.

process. The chlorine current efficiency is in the range of 92-98%, with an average of 95%. Almost all the electrolytic current is carried by H⁺, and the remainder (about 1%) are covered by Cu²⁺. The water transport is 2 mol for 1F.

Experiments on the gas absorption are conducted with a Lucite cell having a paddle agitator (shown in Fig. 3). The area of the gas-solution interface is 62.2 cm², and the solution volume is 500 cm³. The size of the paddles located in the gas and solution phases is varied to estimate the absorption characteristics at the interface.

The chlorine absorption rate is unchanged during a 30 min period, as shown in Fig. 8, and is a function of the chlorine partial pressure and the paddle size in the solution. However, the paddle size in the gas phase is a small factor in the absorption rate. Consequently, the chlorine absorption in the mixture of HCl and CuCl₂ is controlled by mass transfer through the liquid-side boundary layer at the gas-solution interface. Absorption of chlorine into the solution containing cuprous ions is associated with chemical reaction [6], and its rate is large compared with the rate of physical absorption of chlorine in HCl single

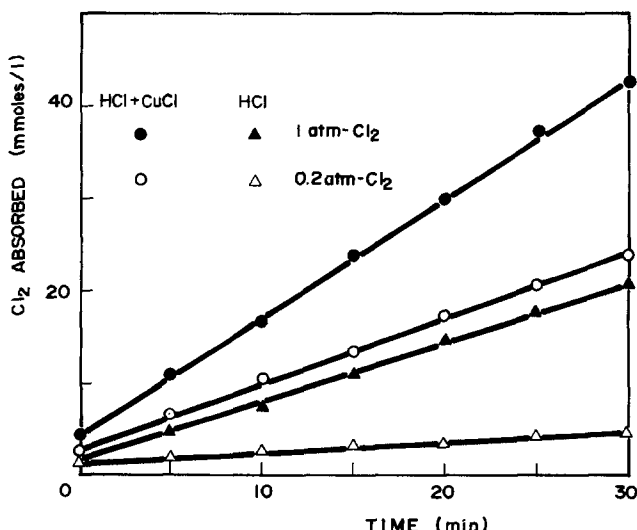


Fig. 8. Chlorine concentration vs. time curves in 6M HCl with and without CuCl (0.1M). Rotating speed = 200 rpm.

solution. The Hatta number γ (see Eq. [19]) is 1.7 at 1 atm of chlorine partial pressure and is 5.6 at 0.2 atm.

Levenspiel *et al.* (9) classifies the processes of gas absorption with chemical reaction into eight types and describes the experimental method for evaluating the regime of the process.

The features of chlorine absorption into the mixture of HCl and CuCl are as follows: the process is fast because gas absorption is associated with chemical reaction [6]; the absorption rate is almost linear with chlorine partial pressure; the absorption rate is almost independent of the volume of liquid and the flow rate of gas; however, absorption of chlorine is stimulated by agitation of liquid. Consequently, it is assured that the reaction is instantaneous, occurring within the liquid-side boundary layer, and that the process is diffusion controlled (*i.e.*, Regime A of Levenspiel's classification).

Figure 9 illustrates the gas-solution interface under discussion. Assume that Henry's law

$$C = H p \tag{9}$$

is applicable in this case. The rate equation for the reaction



is thus represented as follows

$$v = \frac{D_G}{X_G} (p - p_i) \quad (\text{gas}) \tag{11}$$

$$= \frac{D_L}{\beta X_L} C_i \quad (\text{A in solution}) \tag{12}$$

$$= \frac{\alpha D_L}{(1 - \beta) X_L} \frac{C_B}{b} \quad (\text{B in solution}) \tag{13}$$

where

$$\alpha = \frac{D_L'}{D_L} \tag{14}$$

Substituting Eq. [9] into Eq. [11] and applying the addition theorem for fractional equations, we have

$$v = \frac{H p + \frac{\alpha C_B}{b}}{\frac{H X_G}{D_G} + \frac{X_L}{D_L}} \tag{15}$$

Since the first term of the denominator in Eq. [15] is negligible compared with the second term, the equation can be simplified

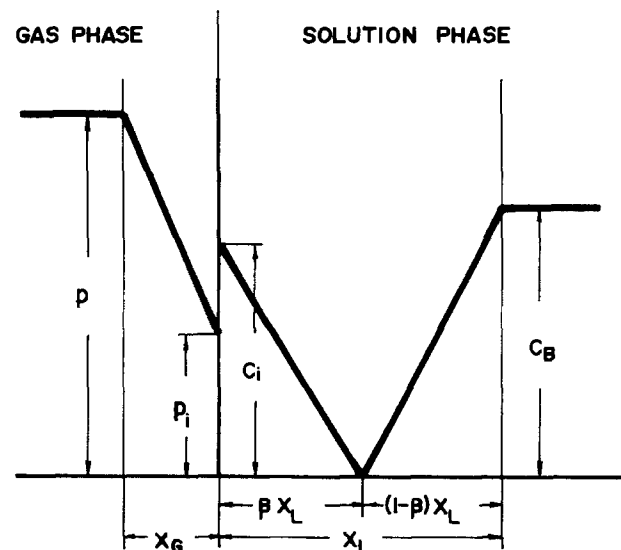


Fig. 9. Profile of the gas-solution interface

$$v = K_L C^* \left(1 + \frac{\alpha C_B}{b C^*} \right) \quad [16]$$

where

$$K_L = \frac{D_L}{X_L} \quad [17]$$

and

$$C^* = H p \quad [18]$$

The bracketed term on the right side of Eq. [16] is the Hatta number γ , which represents the acceleration of gas absorption with chemical reaction

$$\gamma = 1 + \frac{\alpha C_B}{b C^*} \quad [19]$$

The Hatta number can be obtained as a ratio of the slope of the absorption *vs.* time curve for the mixed solution to that for the single solution of HCl. From the data plotted in Fig. 8, γ is estimated to be 5.6 at 0.2 atm of chlorine partial pressure and 1.7 at 1 atm.

The experiment is conducted with a mixed solution of 6M HCl and 0.1M CuCl under various pressures of chlorine, and the results shown in Fig. 10 are obtained. The absorption rate is proportional to $(C^* + \alpha C_B/b)$ and, hence, Eq. [16] is valid.

A Pt rotating-disk cathode is operated to obtain the diffusion coefficient D_L of dissolved chlorine in HCl solution. The Levich equation (10)

$$i = 0.62 n F D_L^{2/3} \nu^{-1/6} \omega^{1/2} (C_o - C_s) \quad [20]$$

is used, where i is the current density, n is the number of charge transfer, and F is the Faraday constant. An estimated D_L is 1.9×10^{-5} cm²/s. With $\gamma = 5.6$ at $p_{Cl_2} = 0.2$ atm, $C_{CuCl} = 0.1$ M/l, and $H = 4.6 \times 10^{-5}$ mol/cm³ atm, the ratio of diffusion coefficients, α , is evaluated to be 0.85. Therefore, the diffusion coefficient of cuprous ion D_L' is 1.6×10^{-5} cm²/s. Since γ is significantly larger than unity under the conditions employed here, the chlorine partial pressure is a small factor in the absorption rate. Also, the absorption rate is almost independent of the CuCl₂ and HCl concentrations and the solution temperature. These experimental results are useful for designing the chlorine absorption tower.

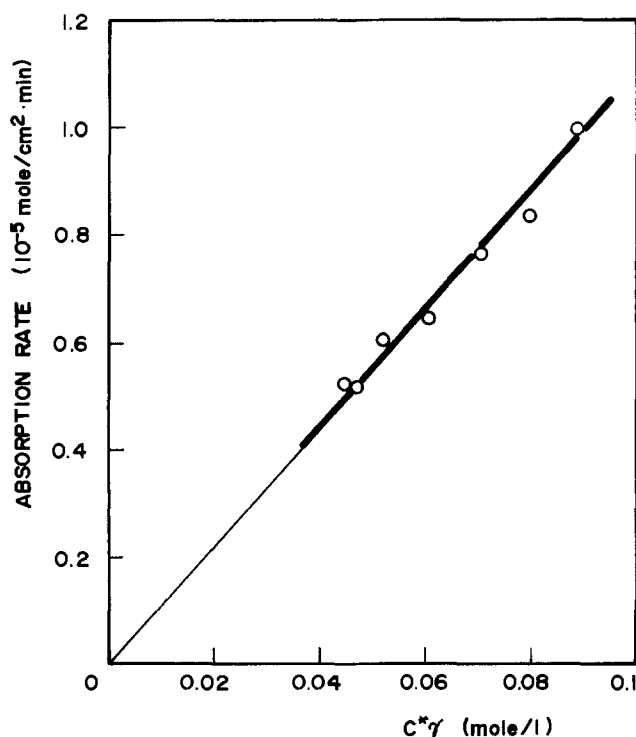


Fig. 10. Absorption rate vs. concentration curve

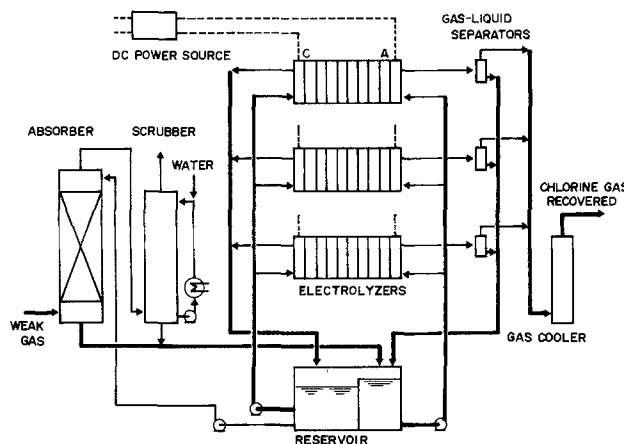


Fig. 11. Flowsheet of the electrolytic chlorine recovery system

Figure 11 shows the flowsheet of the process. The electrolyzer consists of 22 bipolar cells of 1.5 kA in a series connection, and the capacity is 1 ton of chlorine per day. The nominal current density is low (15-20 A/dm²) to lower the cell voltage, *i.e.*, 1.1-1.3V for each cell or 25-30V terminal voltage. The system is composed of an adequate number of these stacks. For example, 3 stacks are installed as a 3 ton-Cl₂/day plant.

The electrolytic solution is pumped to the anode and cathode compartments. Chlorine gas generated at the anode is separated from the anolyte and cooled. The anolyte and the catholyte are sent back to the reservoir. A part of the electrolytic solution is pumped to the absorption tower, where cuprous chloride is oxidized to cupric chloride by chlorine in the waste gas. The inert gas leaving the chlorine absorption tower is washed with water prior to purge. The system has been designed to be operated in the temperature range of 50-70°C. However, the higher the temperature is, the lower the cell voltage is, and the water balance in the system varies with the operating temperature. The overall chlorine current efficiency is assumed to be an average of 95%. The dc electric power consumption is 890-950 kWh/ton-Cl₂, depending on the current density, the cell voltage, and the operating temperature. Also, additional ac power is required for pumping and gas blowing.

Because the system is small and the terminal voltage of the rectifier is low compared to a modern chlor-alkali cell plant, the conversion efficiency of the rectifier is somewhat low. Assuming that the overall efficiency of the power supply system, including rectifier, transformer, and auxiliaries, is 85-87%, the ac power consumption for electrolysis is estimated to be 1050-1120 kWh/ton-Cl₂.

Cost Estimation

The investment cost and the operating cost of the full-scale plant (shown in Fig. 11) in the range of 0.5-5.0 ton-Cl₂/day capacity have been evaluated on a Japanese money basis. The calculation for two plants, 1 ton/day and 3 ton/day, have been conducted in detail. The specifications employed are as follows

Plant capacity	0.5-5.0 ton-Cl ₂ /day
Flowsheet	shown in Fig. 11 with some exceptions
Electrolyzer	filterpress, bipolar type, plastic
Electrodes	graphite anode and cathode
Separators	Nafion 315
Number of cells	22 cells/stack
Capacity of each stack	1 ton-Cl ₂ /day
Amperage	1.5 kA
Terminal voltage	26.5V
Current efficiency	95%

An appropriate number of stacks are installed in a plant having a capacity of more than 1 ton/day. These stacks can be operated in parallel or in series, depending on the

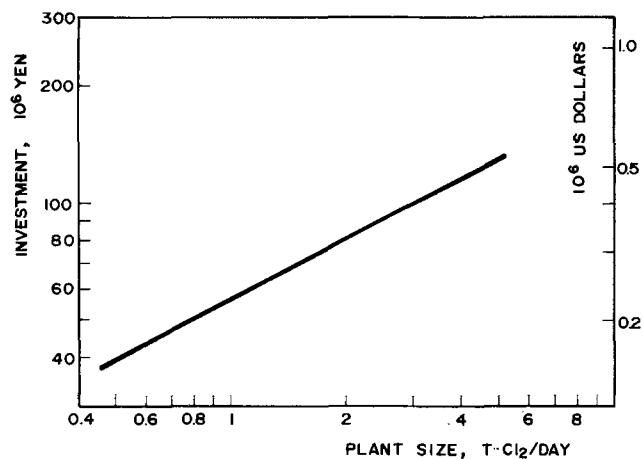


Fig. 12. Investment cost as a function of the plant size

plant situation and other factors. For a small plant, such as 0.5 ton/day, a half-size electrolyzer composed of 11 cells is used. The capacity can also be controlled by changing the amperage in a range of 1-2 kA.

It is well known that the investment J for an electrochemical process plant of capacity P is represented as follows (11)

$$J = J_0 P^a i^b \quad [21]$$

where J_0 is the investment cost for a plant having unit capacity, i is the current density, a is the Williams coefficient, and b is also a coefficient. It is clear that the fixed charge in the manufacturing cost is decreased with increased current density because the coefficient b is negative, but the cell voltage and, hence, the electric power cost are increased. Consequently, there is an optimum current density which depends on investment, price of electricity, and other factors such as cell design and operating conditions other than current density. Under the present situation, an optimum current density is estimated to be about 20 A/dm².

The Williams coefficient for the cell room area including electrolyzers, rectifiers, and the busbar system is 0.83-0.84, which is significantly larger than the approximate 0.6 for the nonelectrochemical processes. In other words, the scale merit of an electrochemical process plant is relatively small (11). However, the coefficient for the total investment of the electrolytic chlorine recovery process under discussion is also small, 0.51-0.53, as shown in Fig. 12, because the installation, aside from the electrolyzers and the power supply, is large and is a weak function of the plant size.

The manufacturing cost of 1 ton of chlorine has been calculated with several assumptions in mind

Depreciation	On the fixed instalment method for 7 years
Life of membranes	2 years
Maintenance cost	10% of the fixed charge
Price of electricity	15 yen/kWh

The fixed charge and the manufacturing cost per unit ton of chlorine are shown in Fig. 13 as functions of the plant size in ton-Cl₂/day. Other costs such as overhead and laboratory must be added if required. Since replacement of the membranes is a large factor, extension of the service life must be considered to reduce the manufacturing cost of chlorine.

The estimated cost is 53,000 yen (\$214) and 43,000 yen (\$174) per ton of chlorine in the 1 ton/day and 3 ton/day

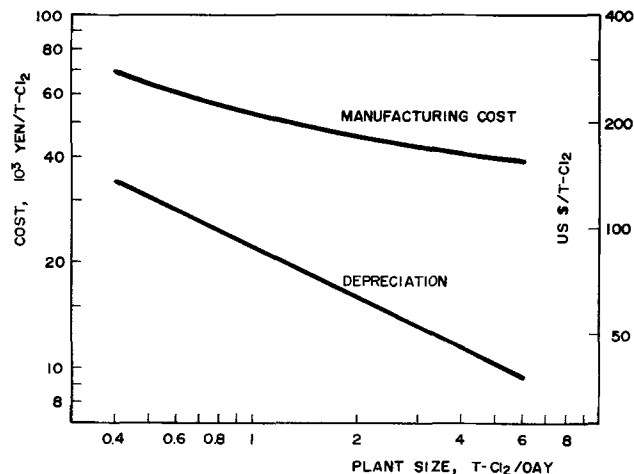


Fig. 13. Manufacturing cost and depreciation as functions of the plant size.

plants, respectively, which would be competitive with the brine electrolysis. A very small plant, such as 0.5 ton/day or less, is not economical and, hence, the waste gas should be washed out by caustic soda solution and the chlorine recovered as hypochlorite. Although the manufacturing cost decreases with increase in plant capacity, the cell configuration and the plant layout must be considered for further reduction of the fixed charge when the plant size is larger than 5 tons per day.

Acknowledgments

This program was supported by Hooker Denka Co., Tokyo, a joint venture of Hooker Chemical and Tsukishima Kikai. The authors acknowledge Tim Fukunaga of Hooker, now Olin Technology Center, and Dr. M. Yasuda, Nagoya Institute of Technology, for their discussions and suggestions. The authors also thank Tsukishima Kikai Co., Ltd., Tokyo, for publication permission.

Manuscript submitted March 20, 1984; revised manuscript received July 20, 1984. This was Paper 233 presented at the Cincinnati, Ohio, Meeting of the Society, May 6-11, 1984.

Tsukishima Kikai Co., Ltd., assisted in meeting the publication costs of this article.

REFERENCES

- H. A. Sommers, *Chem. Eng. Prog.*, **61**, 94 (1965).
- T. A. Liederbach, Paper 236 presented at the AIChE-Canadian Soc. Chem. Eng. Joint Meeting, Vancouver, B.C., September 1973.
- F. Hine and M. Yasuda, *This Journal*, **119**, 1057 (1972).
- F. Hine, M. Yasuda, and M. Higuchi, in "Chlorine Bicentennial Symposium," T. Jeffrey, P. Danna, and H. Holden, Editors, p. 278, The Electrochemical Society Softbound Proceedings Series, Princeton, NJ (1974).
- F. Hine and K. Yamakawa, *Electrochim. Acta*, **13**, 2119 (1968).
- F. Hine and K. Yamakawa, *ibid.*, **15**, 769 (1970).
- F. Hine, S. Yoshizawa, K. Yamakawa, and Y. Nakane, *Electrochem. Technol.*, **4**, 555 (1966).
- F. Hine and K. Yamakawa, Paper 184 presented at the Electrochemical Society Meeting, Cleveland, Ohio, May 1-6, 1966.
- O. Levenspiel and J. H. Godfrey, *Chem. Eng. Sci.*, **29**, 1723 (1974).
- V. G. Levich, "Physicochemical Hydrodynamics," p. 69, Prentice-Hall, Englewood Cliffs, NJ (1962).
- F. Hine, *Electrochem. Technol.*, **6**, 69 (1968).

Electrochemical Evidence of a Possible Route for the Metabolism of Oltipraz 5-(2-Pyrazinyl)-4-Methyl-1,2-Dithiole-3-Thione

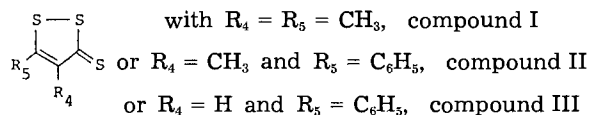
J. Moiroux and S. Deycard

Laboratoire Chimie Analytique, Faculté Pharmacie, Université René Descartes (Paris V) 75270 Paris Cedex 06, France

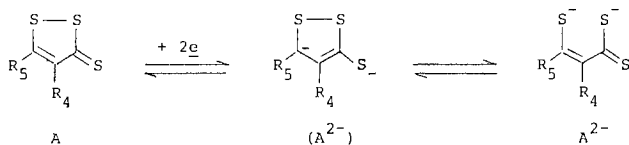
ABSTRACT

The presence of the 5-pyrazinyl substituent induces some noticeable changes in the reaction pathways accompanying the electrochemical reduction of oltipraz compared with the behavior of dithiole-thiones, which do not possess such a substituent and are not endowed with antischistosomal activity. First, electrochemical techniques ascertain the transient formation of the radical anion resulting from the reversible addition of one electron to oltipraz in aprotic media. Second, the electrochemical two-electron reduction, under anaerobic conditions, yields a mixture of dianionic isomers which can be protonated one, two, and even three times. In the protonated species which also exist in isomeric forms and are not starting materials for the regeneration of oltipraz through oxidation, both the dithiole-thione and pyrazinyl rings are reduced. In the presence of air or methylating reagent, the two-electron reduction products are transformed into pyrrolo [1,2-a] pyrazine derivatives, which are some of the major metabolites of oltipraz.

In a previous paper (1), we reported a detailed analysis of the electrochemical behavior of 1,2-dithiole-3-thiones (1,2-dithio-4-cyclopentene-3-thiones) variously substituted at positions 4 and 5



The polarographic behavior of those dithiole-thiones noted A in N,N-dimethyl-formamide (DMF) depends on the nature of substituent R_4 . When R_4 is a methyl group, a two-electron ($2e$) cathodic wave is observed. When R_4 is H, two, apparently $1e$, cathodic waves are observed. The first can be ascribed to a reversible monoelectronic reduction yielding an organomercurial. The second, in fact, corresponds to the occurrence of the same $2e$ cathodic process as observed when R_4 is a methyl group. The $2e$ process occurs at ca. -1050 mV vs. aqueous SCE¹, and this potential does not markedly depend on the nature of R_4 and/or R_5 . The $2e$ reduction product is either a cyclic dianion noted (A^{2-}) when R_4 is H and R_5 a phenyl group, or a mixture of (A^{2-}) and the open form of the dianion noted A^{2-} when R_4 and/or R_5 is a methyl group. The redox couple (A^{2-})/A exhibits reversible behavior at the mercury electrode.



The three dithiole-thiones, I, II, and III, mentioned above are of no remarkable pharmaceutical interest, but oltipraz [5-(2-pyrazinyl)-4-methyl-1,2-dithiole-3-thione, i.e., with $R_4 = \text{CH}_3$ and $R_5 = 2\text{-pyrazinyl}$] has a well-established antischistosomal activity (2-4). As an evaluation of a limited number of oltipraz analogs, including compound II, revealed among dithiole-thiones rather stringent structural requirements for antischistosomal activity (4), we examined the electrochemical behavior of oltipraz in order to see if changes in the electrochemical behavior could be related to structural changes and antischistosomal effects.

The present paper deals with the electrochemical reduction of oltipraz, 5-(2-pyrazinyl)-1,2-dithiole-3-thione, i.e., the oltipraz analog in which $R_4 = \text{H}$ instead of CH_3 and 5-(2-pyrazinyl)-4-methyl-1,2-dithiole-3-one, which is the ketone analog of oltipraz. The working electrode was a platinum electrode and the solvent was either DMF or acetonitrile (ACN). The excitation and measurement techniques used included electrochemical ones such as volt-

¹ In this paper, all potentials are referred to the potential of the aqueous saturated KCl calomel electrode (SCE).

ammetry at the rotating or stationary disk electrode (RDE or SDE, respectively) and potential step chronoamperometry and spectroscopic techniques such as UV-visible and IR absorption spectrophotometries and ¹H NMR spectrometry.

The analysis of the reduction pathways may be of pharmaceutical interest since the primary metabolite of oltipraz is a product resulting from the reduction of the drug (5).

Experimental

Materials.—Oltipraz and its two analogs were generously provided by Rhône-Poulenc-Santé and used without further purification. DMF, ACN, and deuterated solvents were obtained from Merck and used as received unless otherwise specified. Tetraethylammonium bromide (TEAB) from J. T. Baker was recrystallized twice from tert-butanol. A stock solution of 0.1M tetrabutylammonium hydroxide (TBAH) in isopropanol was obtained from Fluka and stored under nitrogen. For dehydration of solvents prior to electrochemical measurements we followed a procedure given in the literature (6) using neutral alumina (Merck 90, 0.063-0.200 mm). Thin layers or columns of Silicagel 60 from Merck have been used for chromatographic separations, the eluent being (v/v) toluene/acetone (95/5). Other reagent-grade chemicals were obtained from Prolabo.

Electrodes.—For voltammetry and potential step chronoamperometry, the working electrode was the platinum disk of a Tacussel EDI rotating electrode connected to a Tacussel CONTROVIT servocontrol electronic amplifier. For controlled potential electrolysis, the working electrode was a large platinum disk (8 cm diam).

For polarography, the working dropping mercury electrode was obtained with a Tacussel CMT 10/24 capillary. The drop-time was controlled by a Tacussel MPO 3 drop-knocker.

The counterelectrode was a platinum Tacussel Pt 33/88 electrode for voltammetry and chronoamperometry and a platinum foil for controlled-potential electrolysis.

The potentials were measured against an aqueous SCE using a two-part salt bridge.

Apparatus.—We used a three-compartment water-jacketed cell whose counter and reference electrode compartments were filled with the background solution (0.1M TEAB in DMF or ACN) and whose temperature was 25°C.

Electrochemical measurements were made with a Tacussel PRG 5 multipurpose polarograph, with a built-in iR drop compensation device, which was also used simply as a rapid-response potentiostat working under the control of a Tacussel GSTP function generator for cyclic voltammetry and potential step chronoamperometry. Current-potential curves were recorded on a Tacussel EPL 2 recorder or a Tektronix 5111 storage os-

cilloscope with voltage-amplifier 5 A 15 N and time-base 5 B 10 N (for current-time curves) plug-ins. A Tacussel PRT 30-01 potentiostat, a Tacussel IG 5 N electronic integrator, and a general purpose milliammeter were used for controlled potential electrolysis.

UV-visible and IR absorption spectra were obtained with a Varian DMS 90 (plus a Sefram TGM 164 X-Y recorder) UV-visible spectrophotometer and a Perkin Elmer 167 IR spectrophotometer.

In order to avoid the contact of electrolyzed solutions with air during spectrophotometric measurements, a cell for circulation (optical path length 0.1 cm) located in the spectrophotometer communicated with the electrochemical cell through a Teflon hose on the one side and with a vacuum pump on the other side, and the electrolyzed solution was sucked up into the spectrophotometric cell.

^1H NMR spectra were obtained with a Bruker Spectrospin 270 MHz spectrometer thanks to the skills of M. Belleney.

Results and Discussion

Voltammetry at the RDE.—A well-defined cathodic wave corresponding to the reduction of oltipraz appears in the voltammogram in the 0 to -1300 mV potential region, the solvent being either DMF or ACN and the rotation frequency N of the RDE being 10 Hz. A plot of E (potential) vs. $\log [i/(i_1 - i)]$, where i_1 is the limiting plateau current and i the current at potential E , is linear with a slope of -62 mV (DMF and ACN) almost as expected theoretically for a reversible $1e$ transfer. The value of i_1 compared with that of the first cathodic wave of 9-fluorenone under the same experimental conditions confirms the occurrence of a monoelectronic transfer. The value of the ratio $i_k/N^{1/2}$ does not depend on N as long as N is higher than 4 Hz in DMF or 7 rps in ACN, but increases with decreasing N when N becomes lower than 4(DMF) or 7(ACN) Hz.

Cyclic voltammetry at the SDE.—When oltipraz is dissolved in DMF the cyclic voltammogram is as expected theoretically for a reversible $1e$ transfer even when the potential sweep rate v is as low as 0.1 V s^{-1} . When the solvent is ACN, such a behavior is observed only when v is higher than 4 V s^{-1} . The ratio $i_{p,c}/v^{1/2}$ increases with decreasing v when v is lower than 4 V s^{-1} ($i_{p,c}$ being the peak height of the cathodic peak) and the chemical reversibility of the system diminishes accordingly.

Occurrence of ECE mechanism.—The observed increase in $i_{p,c}/v^{1/2}$ with decreasing v as well as the increase in $i_k/N^{1/2}$ with decreasing N mentioned above strongly suggests the occurrence of an ECE mechanism in which the radical anion resulting from the first electron addition can be involved in a chemical step yielding a species more reducible than oltipraz (7, 8). We also used potential step chronoamperometry at the SDE for the study of the kinetics of this process. In the following, i_k designs the measured value of the current and i_d the value of the current corresponding to the occurrence of a $1e$ reversible and diffusion-controlled transfer under the same experimental conditions whatever the technique is, i.e., the notation i_k is used in place of $i_{p,c}$ or i_1 .

Potential step chronoamperometry of a DMF solution of 9-fluorenone was used as a means of determination of the effective electrode area A , the estimation of the diffusion coefficient of 9-fluorenone in DMF being 6.9×10^{-6} $\text{cm}^2 \text{s}^{-1}$ (9). In the case of oltipraz, the plot of i_k vs. $t^{-1/2}$ is reproduced in Fig. 1a, t being the time elapsed since the potential was stepped from a value at which oltipraz is not reduced to a value corresponding to the plateau of the cathodic wave in the RDE voltammogram. i_k is proportional to $t^{-1/2}$ at short times, i.e., when the process is monoelectronic, and then the diffusion coefficient D of oltipraz can be determined with the help of the Cottrell equation. The knowledge of A and D enables us to compute i_d for SDE cyclic voltammetry and RDE voltammetry, the kinematic viscosities of DMF and ACN being taken as 0.84 and 0.44 cS, respectively (10).

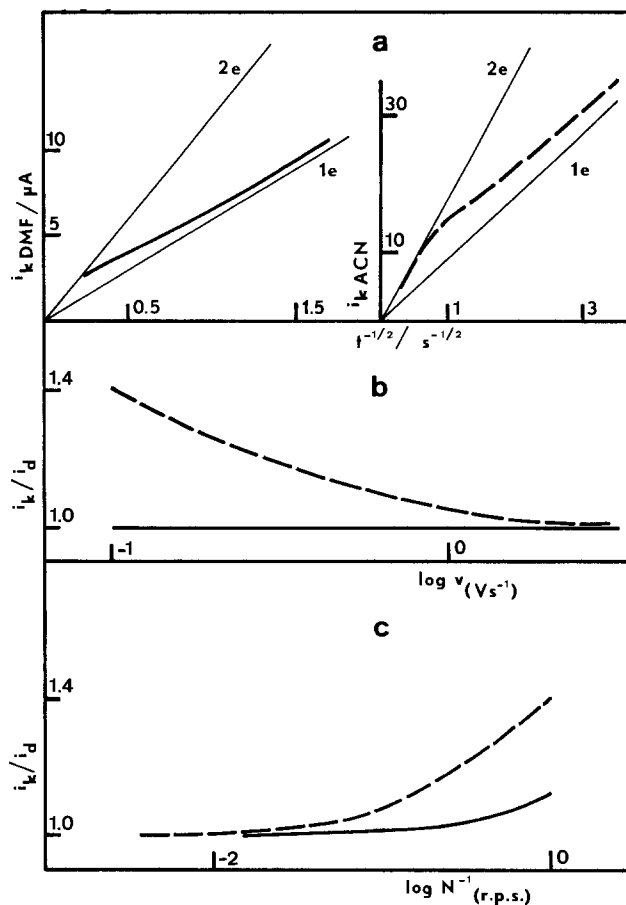


Fig. 1. Reduction of oltipraz. Variations of i_k/i_d as observed by means of potential step chronoamperometry (a) and cyclic voltammetry (b) at the SDE, and RDE voltammetry (c). Oltipraz concentration $C = 1$ mM in either DMF (continuous lines) or ACN (discontinuous). For b, $i_d = 268 AD^{1/2}v^{1/2}C$ (13) and for c, i_d is given by the Levitch equation.

Besides the $i_k-t^{-1/2}$ plot, plots of i_k/i_d vs. $\log v$ or $\log N^{-1}$ are reproduced in Fig. 1 (b and c). All these plots can be readily compared to the working curves given in the literature (8, 11, 12) for each technique in the case of an ECE mechanism when the chemical step consists of a first- (or pseudo-first) order irreversible reaction. Assuming that the preceding condition is fulfilled, the rate constant k of the chemical reaction can be determined. We obtained data which are gathered in Table I. As can be seen, there is no significant dependence of k upon the oltipraz concentration C , a result which justifies the assumption concerning the order of the chemical reaction. It also appears that the three different techniques give comparable values for k .

Altogether, several results suggest that the intermediate chemical reaction is almost certainly the protonation of the radical anion. The proton donor is probably the residual water, the amount of which is roughly equivalent in commercial DMF and ACN, and it has already been reported that, under such conditions, ACN behaves as a more acidic medium than DMF (14). Addition of water up to 10% does not modify the kinetics of the reaction but cyclic voltammetric reversibility is obtained even at v as low as 0.1 V s^{-1} when the commercial ACN is dehydrated with neutral alumina prior to electrochemical measurement. Besides, addition of one electron to the oltipraz analog in which $R_a = \text{H}$ (see Appendix A) produces a radical anion which is less basic and then the rate of the intermediate chemical reaction is much slower. It has not been possible to check out that addition of protons actually increases the rate of the chemical reaction since such an addition causes the occurrence of catalytic hydrogen discharge giving rise to signals which superimpose upon the one due to the reduction of oltipraz thus hampering meaningful measurements. An ECE mechanism con-

Table I. Reduction of oltipraz. Data obtained by means of SDE potential step chronoamperometry and cyclic voltammetry, and RDE voltammetry (effective electrode area: $A = 4.0 \times 10^{-2} \text{ cm}^2$)

Techniques	DMF				ACN			
	$E_1^{o,a}$ (mV)	D^b (cm^2s^{-1})	$k^{c,d}$ (s^{-1})	$k^{c,e}$ (s^{-1})	$E_1^{o,a}$ (mV)	D^b (cm^2s^{-1})	$k^{c,d}$ (s^{-1})	$k^{c,e}$ (s^{-1})
Potential step chronoamperometry		7.5×10^{-6}	0.10	0.08		18.0×10^{-6}	1.0	0.8
Cyclic voltammetry	-925				-1000		1.4	1.2
RDE voltammetry	-915		0.15	0.10	-1000		0.9	1.0

^a Precision ± 5 mV.

^b Precision $\pm 0.5 \times 10^{-6}$ (DMF) and 10^{-6} (ACN).

^c Precision ± 0.03 (DMF), ± 0.3 (ACN).

^d Oltipraz concentration $C = 1$ mM.

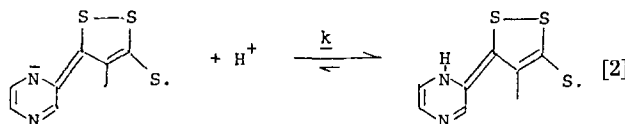
^e $C = 0.2$ mM.

sisting of the following steps, denoted [1], [2], and [3], seems likely

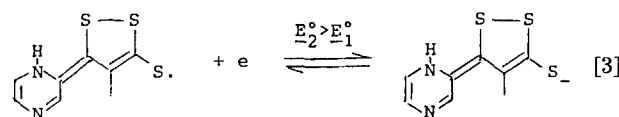


E_1^o can be determined by means of SDE cyclic voltammetry and RDE voltammetry when v and N , respectively, are large enough to overrun the protonation of the radical anion and numerical data are reported in Table I.

The radical anion can exist in many resonant forms since the delocalization of the negative charge and the unpaired electron can be extended to the pyrazine ring. That is probably the reason why such a radical anion is much more stable than the one resulting from the 1e reduction of a dithiole-thione bearing a 5-methyl or 5-phenyl substituent. In the latter case, direct 2e transfer was observed and we found no electrochemical evidence of transient formation of a radical anion (1).



The backward reaction of the above equilibrium is probably slow, since it implies the heterolytic cleavage of the N-H bond and it can account for the irreversible behavior appearing at low v in the cyclic voltammograms when the solvent is ACN.



Disproportionation of the protonated radical can actually occur instead of reaction [3] as long as such a disproportionation is faster than reaction [2], which must remain the rate-determining step since the overall process obeys first-order kinetics.

The 2e reduction product can exist in various resonant forms and tautomers. This point will be discussed later in the section assigned to the characterization of the 2e reduction products.

Controlled-potential electrolysis.—An exhaustive reduction of oltipraz by means of electrolysis at a controlled potential corresponding to the plateau of the cathodic wave appearing in the RDE voltammogram involves $n = 2.10 \pm 0.05$ e per molecule of oltipraz. Such a result confirms the effect of the time scale upon the nature of the electrochemical process, since the reduction proceeds according to a 2e process at the time scale of an exhaustive electrolysis, while only a 1e process is observed by means of RDE and SDE voltammetries, at least when N and v are not too small.

At the beginning of the electrolysis, the solution turns very dark due to the transient production of the radical anion. We have not been able to perform sufficiently fast

spectrophotometric measurements so as to record the UV-visible absorption spectrum of the radical anion whose half-life time is about 7s in DMF and 0.7s in ACN, according to the values of k given in Table I. We have only established that the spectrum of the radical anion in DMF exhibits an absorption maximum around 450 nm with a molar absorptivity greater than that of oltipraz at the same wavelength. However, the absorption spectrum of the radical anion of oltipraz probably does not differ markedly from that of the radical anion of 5-(2-pyrazinyl)-1,2-dithiole-3-thione, which is much less basic and can be prepared and characterized easily (see Appendix A). The UV-visible absorption spectrum of the latter is reproduced in Fig. 2.

Slightly different results were obtained in DMF and ACN. In the following, DMF solutions will be considered first, but before doing so it must be said that the results did not depend on the nature of the working electrode. For example, we checked out that exhaustive electrolysis at a mercury pool gave the same products as when the working electrode was a platinum disk. In the present paper, we do not report the results obtained at the dropping mercury electrode (polarography and cyclic voltammetry), because the signals were then very complex and poorly defined, owing to the occurrence of catalytic discharges related to surface reactions, which were strongly potential dependent.

Characterizations and reactivities of the 2e reduction products of oltipraz.—When the exhaustive electrolysis is carried out in DMF, the absorption spectrum of oltipraz

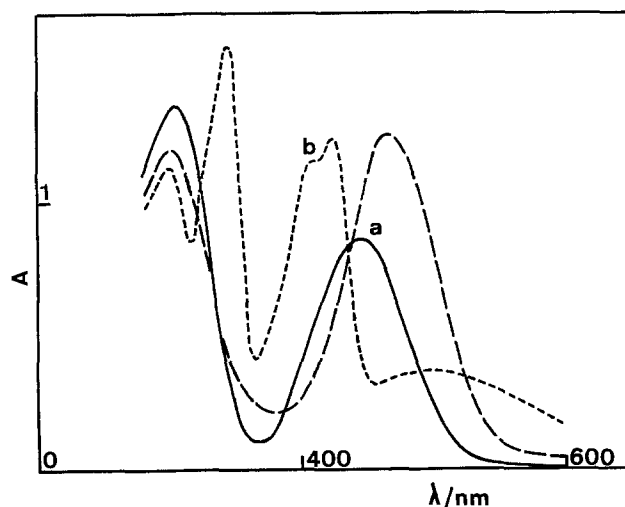


Fig. 2. UV-visible absorption spectra of oltipraz and its 2e reduction products in DMF. Curve a (—): oltipraz. Curve b (---): absorption spectrum of the exhaustively electrolyzed solution, 2e per molecule of oltipraz having been transferred. (— · —): Radical anion resulting from the 1e reduction of 5-(2-pyrazinyl)-1,2-dithiole-3-thione. Oltipraz concentration $C = 1$ mM, cell thickness: 0.1 cm; background: 0.1M TEAB in DMF.

(curve a in Fig. 2) is replaced by the absorption spectrum noted b in Fig. 2. Spectrum b is stable as long as the solution is not put in contact with air.

After injection of concentrated perchloric acid into the exhaustively electrolyzed solution, the absorption spectrum becomes analogous to spectrum c (Fig. 3) provided that the total concentration of added acid is $2C$ or more in the bulk, C being the initial concentration of oltipraz. When the concentration of added perchloric acid is lower than $2C$, the absorption spectrum is a mixture of spectra b and c, i.e., no spectrum is observable which could be ascribed to the formation of a monoprotated species. Once the solution has been acidified, it is not possible to reobtain spectrum b upon addition of an excess of a base as strong as TBAH. A spectrum similar to spectrum d (Fig. 3) is obtained instead. Moreover shifting from spectrum c to spectrum d, and vice versa, can easily be made by adding base or acid to the solution. Such a result ascertains that spectra c and d are the absorption spectra of an acid and its conjugated base, respectively. In that process, isosbestic points appear at 335, 380, and 470 nm (Fig. 3), and quantitative additions of strong acid and base show that the acid-base reaction involves the transfer of only one proton.

When the solutions corresponding to spectra c and d are left in contact with air, they undergo slow transformations, the half-reaction time being 100h for the acidic solution and 5h for the basic solution. In both cases, the ultimate products are identical. This common final product does not absorb appreciably at wavelengths greater than 420 nm but exhibits a flat absorption band around 350 nm (ϵ_{\max} being ca. $5500 M^{-1} cm^{-1}$) and a shoulder at 310 nm preceding a large increase in the absorbance at shorter wavelengths. In the following, the spectrum of this product will be called spectrum e (not shown in the figures). Besides, it is not possible to oxidize electrochemically the acidic and basic compounds whose absorption spectra are spectra c and d. However, the polarograms (dropping mercury electrode) of these solutions exhibit anodic waves which are typical of the oxidation of mercury in the presence of thiol or thiolate groups. The heights of such waves decrease markedly when the solutions are left in contact with air till their absorption spectra become like spectrum e.

When the solution corresponding to spectrum b is left in contact with air, the sharp absorption bands at 345 and 405-425 nm disappear as fast as oxygen diffuses through

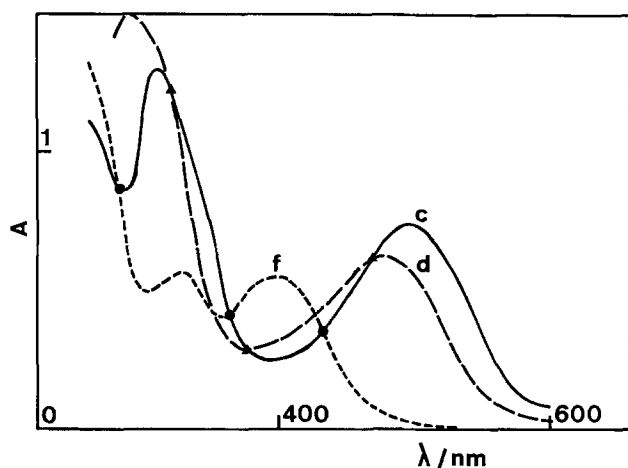


Fig. 3. UV-visible absorption spectra of the $2e$ reduction products of oltipraz in ACN depending on the amounts of perchloric acid or TBAH which have been added to the exhaustively electrolyzed solution. Same conditions as in Fig. 2. Curve c (—): the total concentration of added acid is $2C$. Curve d (---): after addition of TBAH at a total concentration $\cong C$ to the solution whose spectrum is curve c. Curve f (-·-·-): after addition of perchloric acid at a total concentration $\cong C$ to the solution whose spectrum is curve c. ▲: Isosbestic points appearing during the change from spectrum c to spectrum d. ●: Isosbestic points appearing during the change from spectrum c to spectrum f.

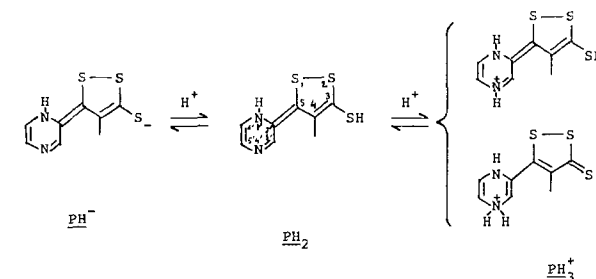
the solution. In the end the absorption spectrum is a linear combination of spectra a (around 40%) and e (around 60%). Electrochemical reoxidation of the solution whose absorption spectrum is spectrum b can be performed at a controlled potential of -700 mV at the mercury pool electrode or at -100 mV (i.e., with an overpotential of ca. 900 mV) at the large platinum disk. Then the oxidation product is oltipraz.

Controlled-potential electrolysis carried out in ACN yields very similar results except for the following points: (i) spectrum d is obtained directly after exhaustive electrolysis, i.e., spectrum b is never recorded, at least when we operate under the same experimental conditions as when DMF is the solvent, particularly when the initial oltipraz concentration C is 1 mM. If C is greater than 5 mM, sharp absorption bands characteristic of spectrum b are superimposed on spectrum d in the spectrum of the exhaustively electrolyzed solution. (ii) When C is greater than 1 mM, the compound, whose absorption spectrum is c (Fig. 3), partially precipitates. Then, the crystalline red solid can be isolated by filtration, washed with ACN, dried and used for chemical analysis and 1H NMR spectroscopy after dissolution in deuterated solvents (DMF, DMSO, and pyridine). (iii) While spectrum c can be obtained as in the case of a DMF solution, a new species is formed in ACN when perchloric acid is added at a concentration higher than $2C$. Spectrum f (Fig. 3) is recorded when the bulk concentration of added perchloric acid is $3C$ or more. Shifting from spectrum c to spectrum f (either way) can be made easily by adding one equivalent of strong acid or base, isosbestic points appearing at 280, 365, and 430 nm (Fig. 3).

Methylation of the $2e$ reduction product of oltipraz can be achieved in DMF or ACN by adding pure methyl iodide (or dimethylsulfate) to the exhaustively electrolyzed solution. In both cases, the methylation is total when the concentration of methyl iodide introduced amounts to $2C$ or more. The UV-visible absorption spectrum of the methylated solution exhibits a band at $\lambda_{\max} = 350$ nm ($\epsilon_{\max} = 5500 M^{-1} cm^{-1}$) and two maxima of equal heights at 302 and 312 nm ($\epsilon = 5700 M^{-1} cm^{-1}$). This spectrum is similar to spectrum e, but most of all it is strikingly identical with that of the primary metabolite of oltipraz (5, 15). That the methylation of the $2e$ reduction product of oltipraz produces metabolites of the drug is confirmed by the isolation of the methylated products and 1H NMR and mass spectroscopy (see Appendix B).

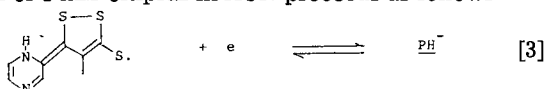
Reaction pathways.—In order to justify the spectrophotometric changes which accompany the additions of strong acid or base to the exhaustively electrolyzed solution, it seems reasonable to assume that spectra b (Fig. 2) c, d, and f (Fig. 3) are the absorption spectra of dianionic, neutral (diprotonated), monoanionic (monoprotonated), and cationic (triprotonated) species, respectively.

As the structure of the diprotonated product (noted PH_2) can be established by means of 1H NMR spectroscopy (see Appendix B), the most probable structures of the monoprotonated (PH^-) and triprotonated (PH_3^+) products are as follows

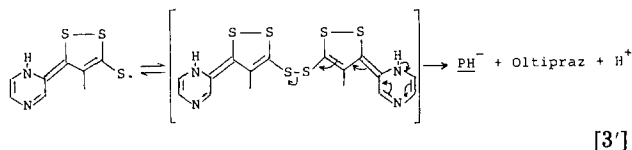


The formation of the thione tautomeric form of PH_3^+ is likely since it can justify correctly the 100 nm hypsochromic shift which results from the protonation of PH_2 (Fig. 3). As PH_2 (see Appendix B), PH^- , and PH_3^+ can exist in isomeric (z, e) forms. TBAH is too weak a base, in either DMF or ACN, to deprotonate PH^- .

Therefore, we can consider that the electrochemical reduction of 1 mM oltipraz in ACN proceeds as follows



or



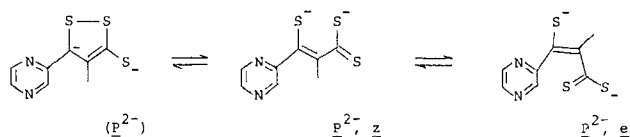
and depending on addition of perchloric acid



A solution of PH^- is obtained only when the amount of available protons is sufficient. It is not the case when the solvent is DMF, since DMF is less acidic than ACN as already noticed apropos of the kinetics of radical anion protonation, and it is no more the case when the initial concentration of oltipraz is higher than 5 mM in ACN. Under the latter circumstances, the basicity of the medium increases significantly as the electrolysis progresses towards completion and exhaustive electrolysis produces dianionic species. When the experiment is carried out in DMF, the dianionic species predominate markedly (spectrum b of Fig. 2).

The strong absorption band which appears at 345 nm in spectrum b is characteristic of the open form denoted P^{2-} of the dianion (1), while the twin bands at 405-425 nm are

probably due to the production of the cyclic form noted (P^{2-}) of the dianion.



The absorbance appearing at 500 nm and above in spectrum b of Fig. 2 can also be ascribed to the presence of P^{2-} (1). Similar equilibria between the cyclic and open forms of the dianionic $2e$ reduction products of 4,5-dimethyl-1,2-dithiole-3-thione and 4-methyl-5-phenyl-1,2-dithiole-3-thione have been described in a previous paper (1). We also showed that the dianionic $2e$ reduction products could be electrochemically oxidized at the mercury electrode at potentials no more positive than -700 mV, the oxidation yielding the original dithiole-thione, while the electrochemical oxidation is less easy at the platinum electrode, owing to large overpotential. However, when the dianionic $2e$ reduction products of oltipraz are left in contact with air, only a partial regeneration of oltipraz is obtained, its extent corresponds roughly to the amount of (P^{2-}) existing at the equilibrium before oxidation. In the cases of 4,5-dimethyl-1,2-dithiole-3-thione and 4-methyl-5-phenyl-1,2-dithiole-3-thione, the regeneration of the original dithiole-thiones through air oxidation were practically total. When left in contact with air, the open dianionic $2e$ reduction product of oltipraz yields the compound denoted ($\text{P}'\text{H}$)₂, whose absorption spectrum is spectrum e.

As mentioned in the previous section of this paper related to the reactivities of the $2e$ reduction products, (P^{2-}), P^{2-} , or PH^- can be methylated, and most of the methylated derivatives are metabolites of oltipraz denoted ($\text{P}'\text{CH}_3$)₂ (65%) and $\text{P}'(\text{CH}_3)_2$ (25%) (see also Appendix B).

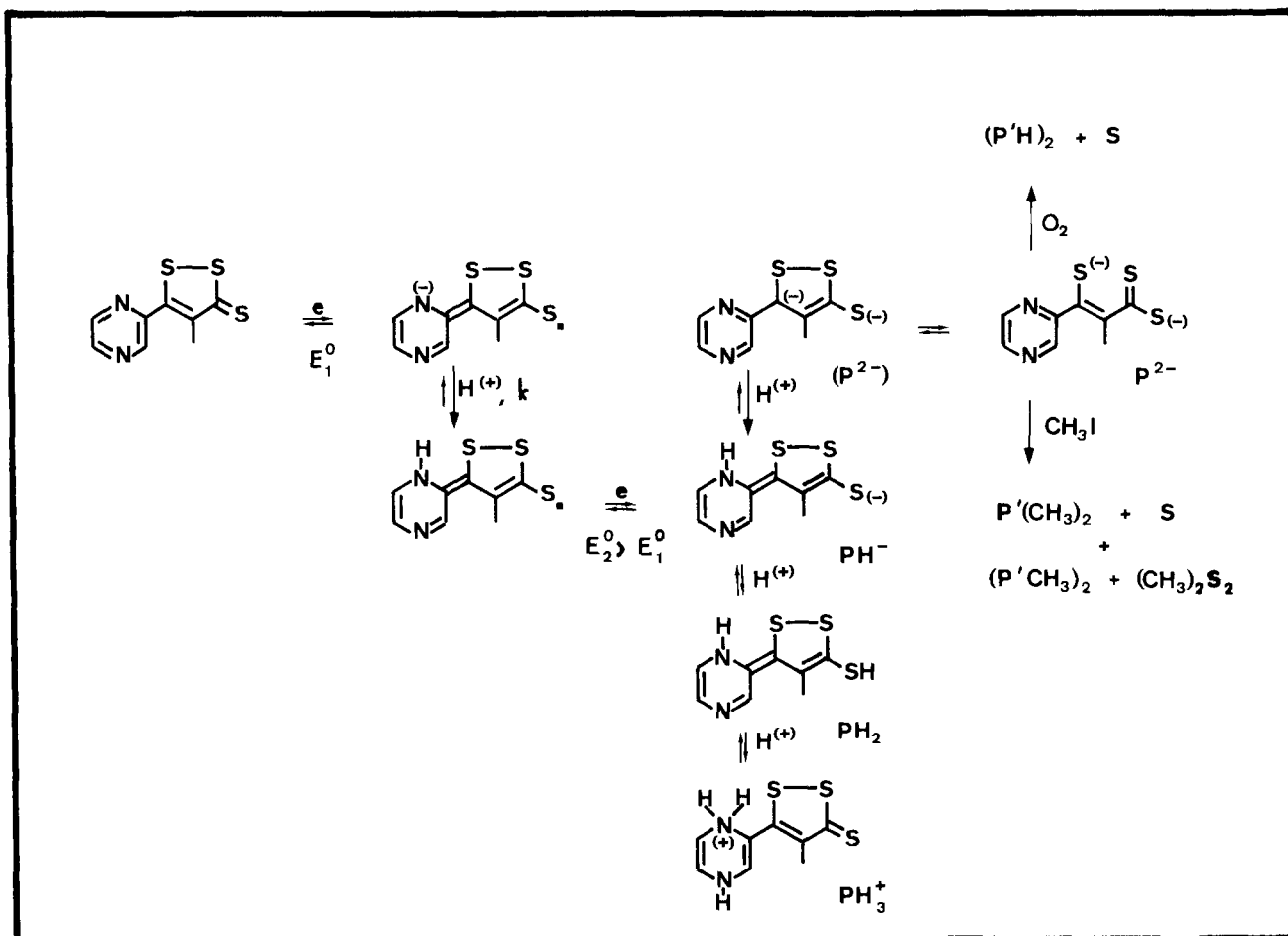
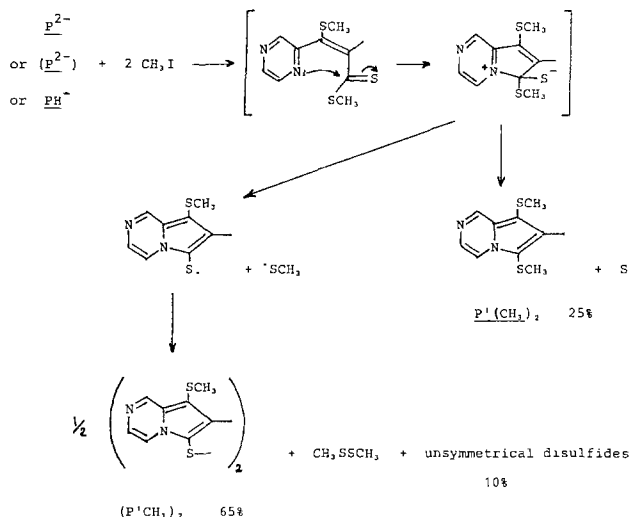
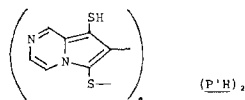


Fig. 4. Reaction path for the electrochemical reduction of oltipraz and possible transformations of the $2e$ reduction products in the presence of protons, oxygen and/or methylating reagent. Most of the compounds can exist in resonant and/or isomeric forms. The structures of the pyrrolo(1,2-a)pyrazine derivatives denoted ($\text{P}'\text{H}$)₂, $\text{P}'(\text{CH}_3)_2$ and ($\text{P}'\text{CH}_3$)₂ are given in the text.

The following mechanism for the obtention of these derivatives is likely



The methylation is the driving force for such a process. A similar driving force is oxygen, since P^{2-} , (P^{2-}) , and PH^+ are ultimately transformed into $(\text{P}'\text{H})_2$ when left in contact with air.



As shown in Appendix B, $(\text{P}'\text{H})_2$ has the same pyrrolo[1,2-a]pyrazine structure as $(\text{P}'\text{CH}_3)_2$, thiol substituents replacing the methylthio groups at positions 8, 8'.

Conclusion

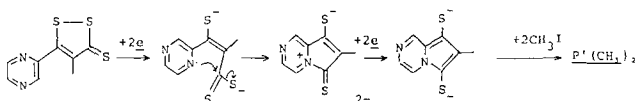
Figure 4, then, represents the state-of-the-art knowledge concerning the electrochemical reduction of oltipraz and the reactivity of its $2e$ reduction products in the presence of protons, oxygen, and/or methylating reagent.

In comparison with the electrochemical behavior of other dithiolethiones, which was reported in a previous paper (1), it appears that the influence of the pyrazinyl substituent is twofold.

1. The lifetime of the radical anion produced by the addition of one electron is considerably increased, a result which may be of biological interest if the antischistosomal activity is relevant to a radical mechanism.

2. The $2e$ reduction product can undergo complex transformations which involve the pyrazinyl ring and cannot occur when the latter is not present. It is particularly interesting to observe that these transformations yield the ultimate products noted $(\text{P}'\text{H})_2$, $\text{P}'(\text{CH}_3)_2$, or $(\text{P}'\text{CH}_3)_2$, which have been found among the metabolites of oltipraz isolated according to the procedures described in Ref. (5).

Before the electrochemical study was carried out, the latter result was far from evident, since the production of $\text{P}'(\text{CH}_3)_2$, for instance, could be considered at first glance as implying a $4e$ process like the following one



3. The presence of the methyl substituent at position 4 of the dithiole ring is not decisive since the reduction reaction pathway at the platinum electrode is not modified when it is replaced by a hydrogen, the only changes consisting in the lower basicity of the radical anion and the predominance of the cyclic form of the dianionic $2e$ reduction product (see Appendix B). However, 5-(2-pyrazinyl)-4-methyl-1,2-dithiole-3-one is reduced electrochemically according to a reaction pathway which differs markedly from that of oltipraz but is similar to those of dithiole-thiones (or one) having no pyrazinyl substituent (Appendix A). Besides, it is interesting to notice that

5-(2-pyrazinyl)-1,2-dithiole-3-one is not endowed with any antischistosomal activity, even though it is one of the metabolites of oltipraz (5).

Acknowledgment

The authors thank the CNRS, which helped support the work described (Equipe de Recherche Associée 950, "Synthese et Electrochimie de Composés d'Intérêt Biologique," plus a grant from the P.I.R.M.E.D.). We are also very grateful to Dr. Jolles, Dr. Messer, and Dr. Barreau for mass spectra and fruitful discussion.

Manuscript submitted Feb. 22, 1984; revised manuscript received July 9, 1984. This was Paper 352 presented at the Cincinnati, Ohio, Meeting of the Society, May 6-11, 1984.

APPENDIX A

Electrochemical Behavior of 5-(2-Pyrazinyl)-1,2-Dithiole-3-Thione

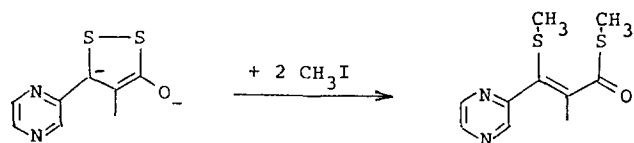
At the platinum electrode, the reduction of this oltipraz analog proceeds according to a pattern entirely similar to that of oltipraz. $2e$ reduction products having the same structures are obtained before and after addition of various amounts of perchloric acid to the exhaustively electrolyzed solution. Methylation or air-oxidation yield the compounds with pyrrolo [1,2-a] pyrazine skeletons analogous to $\text{P}'(\text{CH}_3)_2$ and $(\text{P}'\text{H})_2$. Since the electron donating effect of the methyl-4 substituent is missing, the radical anion produced upon $1e$ reduction is much less basic than in the case of oltipraz. As a result, its rate of protonation in DMF or ACN is so slow that preparing a solution of radical anion is possible when the controlled-potential electrolysis is stopped after transfer of a quantity of electricity amounting to $1e$ equivalent per molecule of the parent compound. The UV-visible absorption spectrum of the $1e$ reduced solution is reproduced in Fig. 2. Electrochemical or air oxidations of this radical anion regenerate the original oltipraz analog.

At the mercury electrode, the polarographic behavior of 5-(2-pyrazinyl)-1,2-dithiole-3-thione is identical to that of 5-phenyl-1,2-dithiole-3-thione, a dithiole-thione not substituted at the C-4 position of the dithiole ring. Such a behavior has been described and analyzed in a previous paper (1). The first monoelectronic cathodic wave occurring at -675 mV corresponds to the production of an organomercurial which can be prepared by means of controlled-potential electrolysis and has the same characteristics as the one obtained in the case of 5-phenyl-1,2-dithiole-3-thione (1). The second cathodic wave, at -1070 mV, corresponds to the $2e$ reduction, i.e., to the production of a mixture of the analogs of (P^{2-}) and P^{2-} . The suppression of the electron donating effect of the 4-methyl substituent renders the cyclic form markedly predominant (90%), as observed previously with other dithiole-thiones (1).

Electrochemical Behavior of

5-(2-Pyrazinyl)-4-Methyl-1,2-Dithiole-3-One

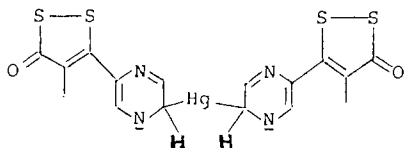
The electrochemical behavior of this oltipraz analog is identical with that of 5-phenyl-1,2-dithiole-3-one, which has been already reported (1). At the platinum electrode, only the $2e$ reduction is observable and it requires an overpotential of ca. -120 mV. The $2e$ reduction product prepared by means of controlled potential electrolysis is the following cyclic dithiole dianion



whose methylation results in ring opening. The methylated $2e$ reduction product has been isolated and its structure confirmed by means of ^1H NMR spectroscopy. No evolution yielding the formation of a pyrrolo[1,2-a]pyrazine skeleton can be obtained.

At the mercury electrode, the reversible $2e$ reduction occurs at -1080 mV. A $1e$ reduction producing an organomercurial is observable at -860 mV. However, the absence of the characteristic absorption band at ca. 400 nm in the UV-visible absorption spectrum (1) shows that it is not the carbon atom at position 5 of the dithiole ring which is bound to mercury, as occurred in the case

of 5-phenyl-1,2-dithiole-3-one. Thus, the structure of the organomercurial is probably



APPENDIX B

The derivatives resulting from the methylation of the 2e reduction products can be isolated as follows. After stoichiometric methylation of the exhaustively electrolyzed solution of oltipraz in ACN, ACN is evaporated under vacuum. The remaining solid is washed with acetone, in which the solubility of TEAB is very low. Acetone is removed under vacuum from the solution containing the methylated derivatives, and the remaining solid is recrystallized twice in water and dried under vacuum. The signals appearing in the ^1H NMR spectrum are identical with those given in the literature (5) for the metabolite of oltipraz which has the same structure and formula as $P'(\text{CH}_3)_2$, the solvent being deuterated DMSO, *i.e.*: 2.20 ppm [S, $-\text{SCH}_{3(8)}$]; 2.23 ppm [S, $-\text{SCH}_{3(6)}$]; 2.40 ppm [S, $-\text{CH}_{3(7)}$]; 7.75 ppm [D, $J = 5.2$ Hz, $-\text{H}_{(3)}$]; 8.37 ppm [D, $J = 1.5$ and $J = 5.2$ Hz, $-\text{H}_{(4)}$]; 8.92 ppm [D, $J = 1.5$ Hz, $-\text{H}_{(1)}$]; where S and D stand for singlet and doublet, respectively. However, the result of chemical analysis is: (experimentally found) C: 50.5%, N: 12.7%, S: 29.8%; (calculated) C: 53.5%, N: 12.5%, S: 28.6%. The disagreement between calculated and observed elemental analysis concerning particularly the carbon percentage suggests that the isolated solid is actually a mixture of compounds having similar spectral characteristics. This assumption can be confirmed by means of thin layer chromatography, and two major products can be separated by means of column chromatography. Then, chemical analysis gives for the first one (25%); C: 53.5%; N: 12.5%; S: 28.6%; and for the second one (65%); C: 51.7%; N: 13.4%; S: 30.6%. The preceding results indicate that the production of $P'(\text{CH}_3)_2$ amounts to only 25%. The elemental analysis of the second compound is in good agreement with the formula of $(P'\text{CH}_3)_2$, and its obtention is confirmed by the determination of a molecular weight of 418 by means of mass spectroscopy. The remaining products (10%), which have not been isolated, are probably unsymmetrical disulfides.

Isolation of PH_2 has been described in the text. There are many tautomers which can be considered as possible structures for PH_2 . However, all those containing a thione group are to be rejected for a number of reasons: a thione would be reducible at a not too negative potential, but no corresponding polarographic wave is observed, while the anodic wave characteristic of a thiol group appears in the polarogram, as already mentioned in the text. The band due to C=S vibration (16) cannot be found in the IR absorption spectrum. Besides, the persistency of a strong absorption band at ca. 500 nm (spectrum c, Fig. 3) indicates that the dithiole ring is not destroyed (1). When all the preceding arguments are taken into consideration, it is possible to make the following assignments concerning the ^1H NMR spectrum of PH_2 , which has been dissolved successively in deuterated ACN, DMF, DMSO and pyridine: [2.13 ppm S, $-\text{CH}_{3(4,z)}$]; 2.34 ppm [S, $-\text{CH}_{3(4,e)}$]; 7.23 ppm [D, $J = 5.2$ Hz, $-\text{H}_{(6,z)}$]; 7.29 ppm [D, $J = 5.5$ Hz, $-\text{H}_{(6,e)}$]; 7.48 ppm [S, $-\text{H}_{(3'e)}$]; 8.04 ppm [D, $J = 5.2$ Hz, $-\text{H}_{(5'z)}$ and/or e]; 8.3 ppm [S, $-\text{H}_{(3'e)}$]; where the subscripts z and e indicate the

type of isomeric z or e form concerned. According to the integration trace, the amount of z isomer is roughly twice that of e isomer. A broad peak which can be ascribed to the proton bound to a nitrogen atom appears at ca. 11.7 ppm. The result of chemical analysis is: (experimental) C: 41.8%; N: 11.8%; S: 35.8%; (calculated) C: 41.6%; N: 11.6%; S: 38.4%.

PH_2 , which has been isolated can be dissolved again in ACN, the PH_2 concentration being 1 mM or less, and acidified stoichiometrically with perchloric acid in order to produce PH_3^+ . The crystalline salt PH_3^+ , ClO_4^- can be gathered up after evaporation of the solvent under vacuum. The protonation (quaternarization) of a nitrogen atom, which causes the hypsochromic shift of the main visible absorption band from 475 to 400 nm (from spectrum d to spectrum f in Fig. 3), is corroborated by the IR absorption spectrum of the crystal dispersed into KBr since absorption bands appear in this spectrum at ca. 2800 and 1100 cm^{-1} , which are characteristic of $-\text{N}^+\text{H}_2$ (17) and ClO_4^- , respectively.

When the solution of PH_2 in deuterated DMF has been left in contact with air for one week, PH_2 is totally transformed into $(P'\text{H})_2$, which still bears thiol substituents according to its polarographic behavior. The structure proposed in the text for $(P'\text{H})_2$ is in agreement with the following assignments concerning its ^1H NMR spectrum: 1 ppm [S, $-\text{CH}_{3(8)}$]; 8.22 ppm [D, $J = 5.0$ Hz, $-\text{H}_{(3)}$]; 8.72 ppm [D, $J = 5.0$ Hz, $-\text{H}_{(4)}$]; 9.27 ppm [S, $-\text{H}_{(1)}$]. The decrease in the chemical shift of $-\text{CH}_{3(8)}$ of $(P'\text{H})_2$ compared with that of $-\text{CH}_{3(8)}$ of $P'(\text{CH}_3)_2$ results from the formation of the disulfide bond (5). The formation of a sulfoxide would provoke an increase in the chemical shift of $-\text{CH}_{3(8)}$ (5).

REFERENCES

1. J. Moiroux, S. Deycard, and M. B. Fleury, *J. Electroanal. Chem.*, **146**, 313 (1983).
2. J. P. Leroy, M. Barreau, C. Cotrel, J. Jeanmat, M. Messer, and F. Benazet, *Curr. Chemother.*, **1**, 148 (1978).
3. J. P. Leroy and M. Barreau, *Abst. Joint Mtg. Roy. Soc. of Trop. Med. Hyg. and Swiss Soc. Trop. Med. and Parasitol.*, p. 40, Basel, Switzerland (1980).
4. E. Bueding, P. Dolan, and J. P. Leroy, *Res. Commun. Chem. Pathol. Pharmacol.*, **37**, 293 (1982).
5. A. Bieder, D. Decouvelaere, C. Gaillard, H. Depaire, D. Heusse, C. Ledoux, M. Lemar, J. P. Leroy, L. Raynaud, C. Snozzi, and J. Gregoire, *Arzneim. Forsch. Drug Res.*, **33**, 1289 (1983).
6. O. Hammerich and V. D. Parker, *Electrochim. Acta*, **18**, 537 (1973).
7. R. S. Nicholson and I. Shain, *Anal. Chem.*, **37**, 178 (1965).
8. L. S. Marcoux, R. N. Adams, and S. W. Feldberg, *J. Phys. Chem.*, **73**, 2611 (1969).
9. E. Ahlberg, B. Swensmark, and V. D. Parker, *Acta Chem. Scand.*, **B34**, 53 (1980).
10. C. K. Mann, in "Electroanalytical Chemistry," Vol. 3, A. J. Bard, Editor, p. 128, M. Dekker, New York (1969).
11. G. S. Alberts and I. Shain, *Anal. Chem.*, **35**, 1859 (1963).
12. R. S. Nicholson and I. Shain, *ibid.*, **37**, 190 (1965).
13. R. S. Nicholson and I. Shain, *ibid.*, **36**, 706 (1964).
14. C. P. Andrieux and J. M. Saveant, *J. Electroanal. Chem.*, **33**, 453 (1971).
15. J. P. Corbet, J. M. Paris, and C. Cotrel, *Tetrahedron Lett.*, **23**, 3565 (1982).
16. J. Fabian and R. Mayer, *Chem. Ind.*, 1962 (1966).
17. L. J. Bellamy, "The Infra-Red Spectra of Complex Molecules," p. 259, Methuen, London (1962).

Fundamental Electrochemical Studies of Polyacetylene

J. H. Kaufman, T.-C. Chung, and A. J. Heeger

Institute for Polymers and Organic Solids, University of California at Santa Barbara, Santa Barbara, California 93106

ABSTRACT

We report an electrochemical and *in situ* optical study of doping processes in polyacetylene. Electrochemical voltage spectroscopy (EVS) is used to characterize the energies of charge injection and removal, as well as the kinetics of these processes. *In situ* optical spectroscopy provides complementary information on the energy of the electronic states where charge is stored (after injection). The EVS results provide a measurement of the energy gap; from these electrochemical data, we infer $E_g \cong 1.5$ eV, in good agreement with that obtained by other methods. The observation of hysteresis in the electrochemical cycle, and the associated increase in the midgap optical absorption upon doping, are both indicative of the formation of states in the bandgap. The resolution available with the EVS technique allows precise determination of both the energy and number of these states. The results demonstrate that the injected charge is stored in the form of charged solitons (chemical potential E_g/π , with respect to midgap) and not a random distribution of impurity states throughout the gap, nor polaron states near the bandedge. The observation of 300 ppm charge removal precisely at midgap provides a detailed verification of Kivelson's model of charge transport via intersoliton electron hopping. Kinetics studies performed both at low and high dopant levels reveal that ionic diffusion rates under load (current carrying conditions) are two orders of magnitude faster than free ionic-diffusion rates. This anomaly is explained in terms of electric field enhancement of the ionic diffusion in $(CH)_x$.

The discovery of rechargeable storage batteries (1,2) made from synthetic metals such as polyacetylene has stimulated detailed experimental studies of these materials using electrochemical techniques (3-8). The precise control of dopant levels available through electrochemistry and the ability to reversibly dope and undope the polymer offer unique advantages to fundamental scientific studies and to material characterization from a technological point of view.

Owing to the simplicity of its structure, polyacetylene is often considered the prototype conducting polymer (9). In electrochemical studies, experiments employing $(CH)_x$ as the active electrode demonstrated the utility of conducting polymers as an electroactive class of materials (1-8). By applying an external voltage to an electrochemical cell with $(CH)_x$ as one electrode, the chemical potential of the polymer can be shifted across the bandgap, and the polymer can be electrochemically oxidized or reduced (4). Microscopically, the $(CH)_x$ fibrils expand to admit the dopant ions between polymer chains, and charge transfer occurs without damage to the structure (10). Both oxidation and reduction are reversible even at fairly high concentrations (above 4%). Though the morphology (9) of $(CH)_x$ may differ in detail from that of other conducting polymers, the electrochemical techniques and concepts developed in studies of polyacetylene may be universally applied to this whole class of new materials.

In this paper, we report an electrochemical and *in situ* optical study of doping processes in polyacetylene. Electrochemical voltage spectroscopy (EVS) is used to characterize the energies of charge injection and removal, as well as the kinetics of these processes. At low doping levels, the results demonstrate a unique hysteresis in the cell voltage *vs.* charge relation, which we interpret as charge injection via polarons and charge removal via solitons. At higher doping levels, the voltage *vs.* charge shows a change in slope, and the hysteresis vanishes for rapid charge cycles. Kinetics studies performed at both low and high dopant levels reveal that ionic diffusion rates under load (current carrying conditions) are two orders of magnitude faster than free-diffusion rates. This anomaly is explained in terms of electric field enhancement of ionic diffusion in $(CH)_x$.

Experimental Techniques

Electrochemical voltage spectroscopy (EVS).—Computer-controlled electrochemical voltage spectroscopy is a convenient method for precise *V vs. Q* measurements of an electrochemical cell at quasiequilibrium (4) (see Fig. 1). The external power supply serves to vary the electrochemical potential difference between the $(CH)_x$ electrode and the lithium electrode. When carrying out an experiment, the cell first is allowed to equilibrate at some ini-

tial voltage V_0 , measured with respect to the lithium reference electrode. After stepping the voltage by an amount dV , the cell current (i_c) is monitored by the voltage drop across a series resistor (R) and decreases with time as the cell approaches equilibrium. When i_c falls below a preset minimum value, i_c^{\min} , (chosen to be small enough to insure quasiequilibrium conditions), the current is integrated, yielding the charge dQ that flowed on raising the cell voltage from V_0 to $(V_0 + dV)$. This procedure is repeated until a preset maximum voltage is reached. The sign of dV is then reversed, and the voltage is stepped back to V_0 . At each voltage, the differential charge that flowed (dQ_j) at the voltage $V_j = V_0 + jdV$ and the derivative dQ/dV are stored on disk. The derivative may be integrated to obtain a plot of *V vs. Q*, which in turn may be integrated to find the energy density of the cell. The derivative dQ/dV is the incremental charge capacitance of the battery.

The information obtained from EVS is very similar to that obtained from cyclic voltammetry (12). Both the derivative dQ/dV *vs.* *V* (from EVS) and *i vs. V* (from cyclic voltammetry) measure the number of charges transferred as a function of energy. There are, however, some important differences. The minimum current in the EVS method can be made arbitrarily small so that the entire system is in diffusion equilibrium. In cyclic voltammetry, the electrode reactants and products are considered to be in equilibrium if the kinetics of charge transfer are rapid compared to mass-transport rates (12). The method, therefore, probes the surface of the polymer where concentrations are related to cell voltage by the Nernst equation. Since the total charge accommodated on the surface [of a $(CH)_x$ fibril, for example] is orders of magnitude less than the charge capacity of the bulk, the resolution of the cyclic voltammetry method is orders of magnitude less than EVS. By sacrificing speed, features corresponding to parts per million of charge can routinely be resolved with EVS. The integrated EVS data, *V vs. Q*, is equivalent to a constant current charge discharge at $i_c = i_c^{\min}$. However, since $i_c^{\text{avg}} \gg i_c^{\min}$, data collection is much faster than the corresponding constant current method. In summary, (fast) cyclic voltammetry probes surface only, whereas (slow) EVS more truly reflects the response of the total polymer structure (interior plus surface). Thus, EVS represents a probe of the thermodynamics of the charge-discharge process.

Nonequilibrium effects such as I^2R loss and overpotentials do not contribute to the EVS data for conducting polymer electrodes. The unimportance of I^2R loss follows directly from the fact that all data are acquired at i_c^{\min} , which can be made arbitrarily small. The absence of overpotential effects in the EVS data of conducting polymers follows from an examination of the electrochemical

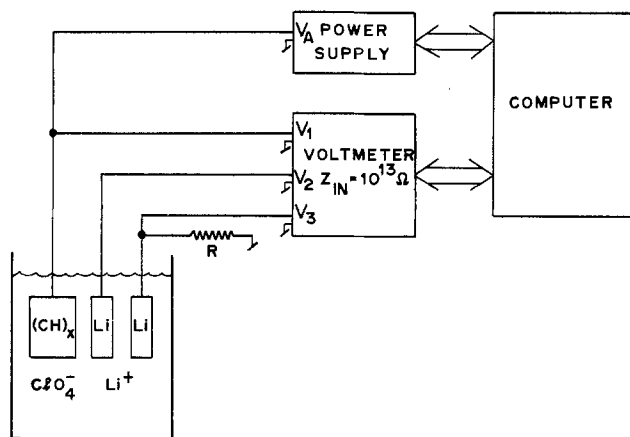
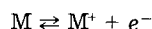


Fig. 1. Schematic diagram of computer-controlled instrumentation for electrochemical voltage spectroscopy (EVS); $V = V_1 - V_2$, $i = V_3/R$.

reactions. In a conventional electrochemical cell with two metal electrodes, the equilibrium cell voltage, V_e , is determined by the difference in chemical potentials of the metals. A double layer of ions at each electrode generates a potential barrier for each half-cell reaction. In equilibrium, at each electrode



and no current flows in the cell. When an overpotential $\Delta V = V_{app} - V_e$ is applied, the barrier heights at each electrode change and the half-cell reactions proceed at a rate determined by the activation energies at the barriers. The current through the cell as a function of applied overpotential is described by the Butler-Volmer equation (12). In such a cell (where the chemical potentials of the two metal electrodes do not change during charge or discharge), the current does not decay with time so EVS would not be a useful technique. In the case of a polymer electrode, however, the material dopes as current flows, and the chemical potential of the polymer changes until the equilibrium potential reaches the applied potential. At this point (where the EVS data are taken), the overpotential is rigorously zero. The double-layer barrier and all other contributions to the activation energy (e.g., ionic diffusion) determine the rate at which the polymer reaches equilibrium, but since all measurements are made arbitrarily close to equilibrium, they do not affect the EVS data.

Cell construction.—A battery cell is constructed by pressing $(CH)_x$ film (0.1 mm thick \times 1 cm²; 3 mg) onto platinum mesh to act as the working electrode. Lithium metal (surface scraped clean and then embedded in nickel mesh) acts as the counterelectrode and is separated from the $(CH)_x$ by a kiln-dried piece of glass filter paper. A second (identical) lithium electrode is used as the reference electrode. Basic activated alumina serves to scavenge impurities. One molar (1M) $LiClO_4$ -tetrahydrofuran is added as the electrolyte-solvent system for n-type doping, while 1M $LiClO_4$ -propylene carbonate is used for p-type doping. Prior to use, the $LiClO_4$ is melted under dynamic vacuum. Tetrahydrofuran (Fisher Scientific Company) is kept in sodium benzophenone, while propylene carbonate (Aldrich Chemical Company) is spin-band distilled and stored over lithium chips. The cell is encased in rectangular glass and sealed under vacuum across platinum wires, which are spot welded to the electrodes.

Although resolution at the ppm level is routinely available with the EVS technique, cell purity at this level is difficult to achieve. For example, impurities can lead to side reactions causing charge flow at cell voltages within the energy gap of *trans*- $(CH)_x$. In this case, the intrinsic charge-transfer processes might be masked.

When more rigorous cleaning procedures were required, a special three-armed apparatus was constructed

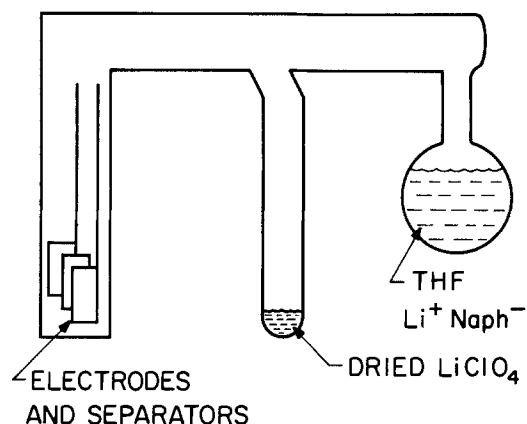


Fig. 2. Three-armed apparatus used for construction of rigorously clean electrochemical cells. This construction allowed extensive washing of the cell electrodes (and separators) while under vacuum.

(Fig. 2), which allowed washing of the cell electrodes (and separators) while under vacuum. The first arm, made of rectangular glass, contains the electrodes and leads. The second arm contains dried $LiClO_4$, and the third arm contains purified THF with $Li^+ Naph^-$ in solution. The apparatus was first evacuated, and then pure THF was vacuum distilled into the electrode arm. After washing, the THF was poured back into the arm containing the $Li^+ Naph^-$ solution (which serves to scavenge any impurities taken out in the washing step). This process was repeated a number of times. Pure THF was then vacuum distilled into the arm containing $LiClO_4$, and the electrolyte was transferred into the electrode arm. The rectangular glass was then twice sealed across the wire leads, and the sealed electrochemical cell removed from the apparatus.

Experimental Results: Charge Injection into the Electronic Band Structure

Figure 3 shows dQ/dV vs. V as obtained from EVS data. The derivative dQ/dV is plotted vs. V for injection of n- and p-type dopants. The integrated EVS data (i.e., V vs. Q) for charge injection and removal (p-type) is shown in Fig. 4. These data were obtained with 0.02V steps at $i_c^{min} = 1 \mu A/mg$. A threshold for n-type charge injection is observed at $1.75 \pm 0.05V$ (referenced to lithium). Hysteresis is evident; final charge removal occurs at $2.40 \pm 0.05V$. The threshold for p-type injection occurs at $3.05 \pm 0.05V$, and again final charge removal is at $2.40 \pm 0.05V$.

The thresholds for charge injection can be understood in terms of the band structure of *trans*- $(CH)_x$. Polyacetylene in its undoped state is a semiconductor

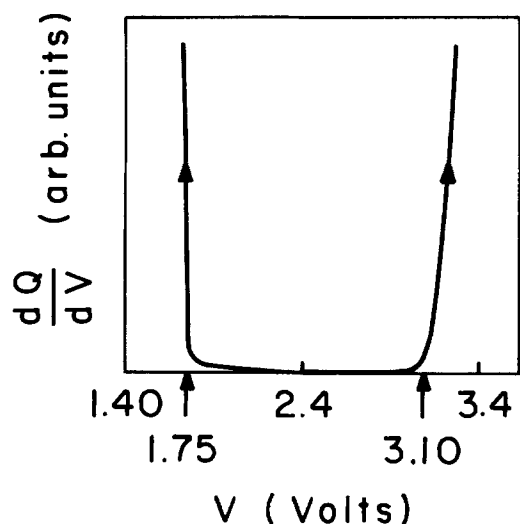


Fig. 3. dQ/dV vs. V as obtained from EVS data; injection n- (reducing) and p-type (oxidizing) dopants are shown.

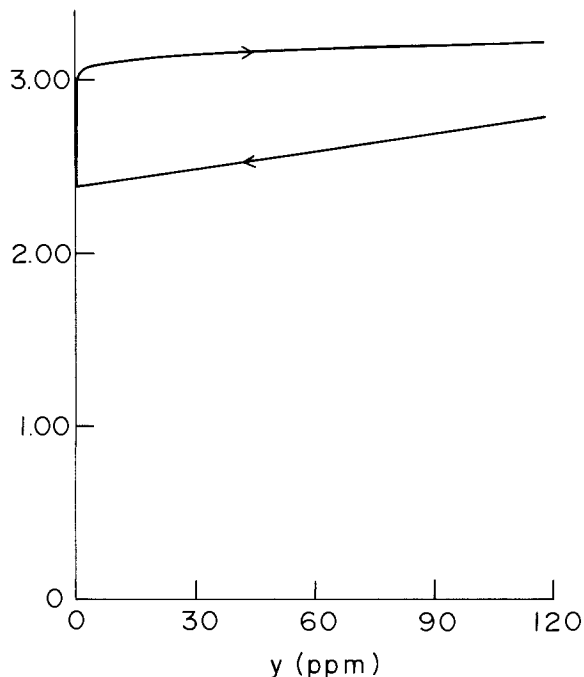


Fig. 4. V vs. y for charge injection and removal using p-type dopant with scale expanded to show ppm resolution.

with the electronic chemical potential at midgap. By applying an external potential between the $(\text{CH})_x$ working electrode and a Li counterelectrode in an electrochemical cell, it is possible to counterbalance the difference in chemical potential between $(\text{CH})_x$ and Li to allow injection into the available states of the polymer (see Fig. 5). If there are no localized states in the bandgap, no charge will flow until the chemical potential is at an energy equal to a bandedge of *trans*- $(\text{CH})_x$ where states are available. Thus, the band structure of $(\text{CH})_x$ determines the threshold for charge injection (n- or p-type). At an applied voltage V_p° , holes are injected into the $(\text{CH})_x$ electrode. Similarly, at a lower applied voltage V_n° , electrons are injected into the $(\text{CH})_x$ electrode. Structural relaxation around the injected charges will lead to polaron bound states (13, 14) below the bandedge and, thereby, an apparent energy gap (for charge injection) that is somewhat smaller than that determined by optical absorption (9, 15). The formation of a structural distortion is not a novel phenomenon in the context of charge injection into molecules. Structural relaxation after oxidation or reduction lowers the free energy of the molecule (or macromolecule) and is, therefore, thermodynamically favorable. Similarly, in semiconducting polymers, charge injection is expected to be followed by a localized structural distortion, *i.e.*, a polaron.

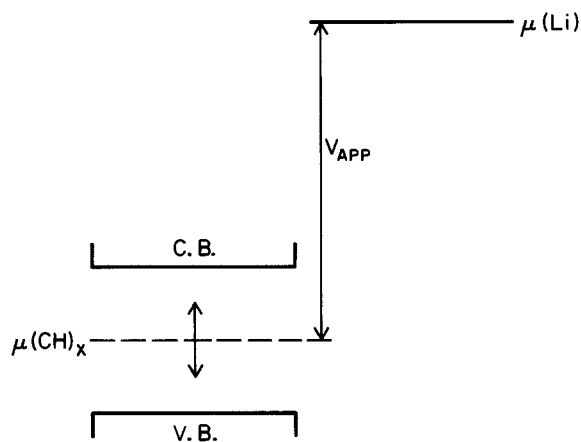


Fig. 5. Schematic band diagram relating injection threshold voltages to valence and conduction bandedges of *trans*- $(\text{CH})_x$.

The difference between injection energies for electron or hole creation is defined to be equal to the electronic energy gap $E_g = 2\Delta$, assuming a rigid band picture for the electronic structure. From optical absorption of the undoped polymer, one finds $E_g = 2\Delta \sim 1.5$ eV. Allowing for structural relaxation around the injected charge to form polarons, one would predict

$$V_p^\circ - V_n^\circ = 2E_p = (4\sqrt{2}/\pi)\Delta \cong 1.34 \text{ eV} \quad [1]$$

Experimentally, one finds (see Fig. 3)

$$(V_p^\circ - V_n^\circ) = 1.3 \text{ eV}$$

in good agreement with Eq. [1]. The implied value for the energy gap, $E_g \cong 1.5$ eV, is therefore consistent with that obtained from optical-absorption measurements.

Though injection occurs near the bandedge, charge removal occurs at lower energy. The observed hysteresis is independent of set voltage limits and step size (though smaller step size increases resolution). Figure 6 shows the EVS data for n-type charge injection (curve B) and charge removal (curve A). The small amount of charge injected in the shoulder between 2 and 1.75V is due to residual impurities or defects; curve C shows the injection data from a cell with an even cleaner injection edge for comparison. This same "impurity shoulder" is evident in the charge removal data as well.

In order to clearly observe the important features of Fig. 6, it is essential to have a cell construction which is rigorously clean. An example of the kind of data obtained under more routine conditions is shown in Fig. 7. In this case, the cell was constructed in a controlled atmosphere dry box, but the rigorous cleaning procedures were not carried out. In the initial cycle, charge flow begins even at midgap. On subsequent cycles, the injection curves clean up somewhat, with a more clearly defined edge appearing below 2V. The successive behavior (first cycle through fourteenth cycle) implies that impurities can be at least partially cleaned up in the cell through side reactions. However, after many cycles, both the injection edge and the midgap peak become broadened and more difficult to detect, suggesting that electrochemical cycling in-

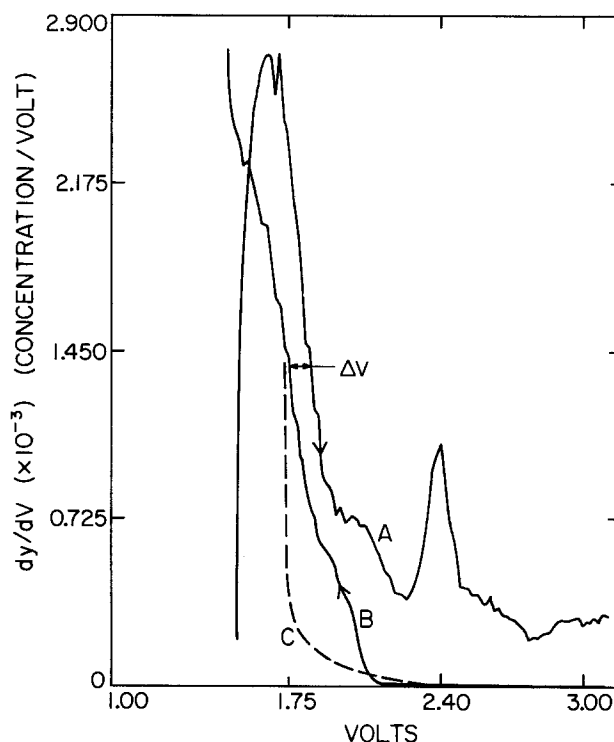


Fig. 6. dQ/dV vs. V showing hysteresis in voltages for n-type charge removal (curve A) and charge injection (curve B). Curve C shows the injection data from a cell with an even cleaner edge for comparison. The data are plotted as dQ/dV , where y is the dopant concentration in the $(\text{CH})_x$ electrode.

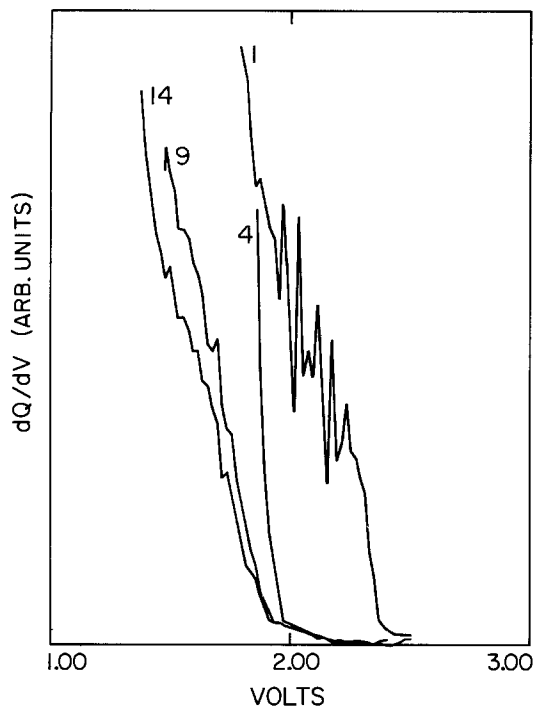


Fig. 7. dQ/dV vs. V for an electrochemical cell showing the effect of impurities. The numbers (1, 4, 9, 14) refer to the number of cycles. Successive oxidation and reduction removes impurity effects (through side reactions) leading to a relatively clean injection below 2 eV (see text).

duces significant disorder in $trans-(CH)_x$. By extensive experimental studies on many cells, we have been able to sort out the impurity or imperfection related features (*i.e.*, extrinsic) such as the weak shoulder near 2.0V in Fig. 6.

Ignoring the impurity shoulder, we observe a single process for charge injection which occurs at about 1.75V. Note in particular that there is no detectable injection at midgap (2.4V). There are, however, two distinct modes for charge removal. Most of the charge is removed in the large peak which extends up to about 1.9V. A second peak at 2.4V (relative to Li) corresponds quantitatively to the removal of the final 300 ppm of charge at midgap.

The temperature dependence of the hysteresis has also been measured. Between $T = 21^\circ\text{C}$ and $T = 44^\circ\text{C}$, the hysteresis was found to be independent of temperature for $I^{\text{min}} \sim 2 \mu\text{A/mg}$ and below. Since Fickian diffusion rates are inversely proportional to temperature, the observed independence is a good indication of diffusion equilibrium below the metal-insulator transition (9). The ionic mobility is given by

$$\mu = e\tau/M = eD_0/k_B T \quad [2]$$

where M is the mass of the ion. Therefore

$$\tau = MD_0/kT \quad [3]$$

A 20°C change in temperature would result in a significant change in τ . Since the current is exponentially dependent on temperature, so is the concentration

$$c = \int j(t) dt \sim c_0 e^{-t/\tau}$$

If the system were diffusion limited, at each voltage step one would have $t \ll \tau$. Then $e^{-t/\tau} \sim 1 + t/\tau + \dots$. A 10% change in τ would, therefore, result in a 10% change in concentration at a given voltage. Alternatively, since the voltage *vs.* charge relation can be approximated by a power law (10)

$$V \sim A + Bc^\gamma \quad [4]$$

For $\gamma \sim 2/3$, a 10% change in τ (from ΔT of 20°C , ignoring any temperature dependence of D_0) would result in an 8% change in voltage or approximately 16% increase in hysteresis on lowering the temperature by 23 K. This is certainly a lower limit, since typically one expects D_0 to be

activated and thus strongly temperature dependent. The corresponding change in apparent concentration would certainly show up in the electrochemical-voltage spectrograph. Since no change of this magnitude is evident, it follows that $t > \tau$ and that the system is in diffusion equilibrium.

Discussion of Charge Injection and Removal Energies

Su *et al.* (16) demonstrated that the lowest energy-charge configuration for a polyacetylene chain is a collection of soliton-antisoliton pairs corresponding to bond-alternation domain walls in the $(CH)_x$ crystal lattice. Since in polyacetylene there is one π electron per carbon atom, each domain wall has associated with it a nonbonding localized state which by symmetry lies at the center of the energy gap (Fig. 8). Since this electronic state can hold zero, one, or two electrons, the soliton (electronic state plus structural distortion) can have charge 0 or $\pm 1e$, where e is the electron charge.

The soliton-antisoliton pairs that are created by doping store an energy equal to the soliton-creation energy (16-19), $E_s = (2/\pi)\Delta$, where $2\Delta = E_g$ is the energy gap. Thus upon adding a pair of electrons (reduction) the charge is accommodated in two negative solitons and the increase in free energy is $(2/\pi)\Delta$ per negative soliton. Consequently, in n-doped (reduced) $trans-(CH)_x$ at dilute concentrations, the chemical potential is at $\mu_n = +(2/\pi)\Delta$ with respect to midgap. Similarly, by a completely symmetrical argument, for p-doped (oxidized) $trans-(CH)_x$ the chemical potential is at $-(2/\pi)\Delta$ with respect to midgap. At higher concentrations, additional contributions arise from charge-charge interactions and from the change in electronic structure when the energy gap closes to form a true metal (~ 5 mole percent [m/o]) (10, 29). This analysis of the chemical potential in the dilute regime ignores a variety of additional contributions (see Appendix A) and it ignores the contribution from the configurational entropy; $S = k_B \ln W$, where W describes the number of independent ways in which N_s solitons can be arranged on a chain of N carbon atoms (see Appendix B). These additional contributions are small in magnitude (and independent of concentration), so that they are not important to the interpretation of the EVS data.

In addition to these "doping induced" soliton pairs, polyacetylene contains approximately ~ 300 ppm of permanent defects which originate during isomerization (9). These states can become charged; again, the associated defect levels would reside at midgap. Since the defect corresponding to the isomerization-induced neutral soliton is permanent, the charged soliton stores no energy. Consequently, the last ~ 300 ppm of charge should come out at a cell voltage corresponding to placing the chemical potential of the Li counter at the neutral point, *i.e.*, 2.4V (see next section).

These experiments establish the open-circuit voltage of neutral $trans-(CH)_x$ *vs.* Li to be 2.4V. This value is consistent with the measured difference in work functions. From photoemission studies (20) of $trans-(CH)_x$, the work function was found to be 4.5 eV, whereas the handbook value

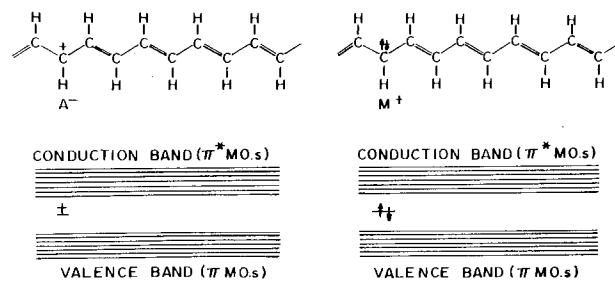
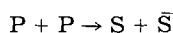


Fig. 8. Schematic diagram of positive and negative bond alternation domain walls (solitons) in $trans-(CH)_x$. Each domain wall has associated with it a nonbonding state at the center of the energy gap. The soliton is positive if this state is empty, and negative if this state is doubly occupied. The diagram is schematic; the actual domain wall in $trans-(CH)_x$ is spread over about 12-15 carbon atoms.

for lithium metal is about 2.4 eV. Additional contributions are discussed in Appendix B.

Charge injection into the polymer is necessarily a non-equilibrium process since injection via the lower energy soliton state cannot take place. Injection directly into solitons is inhibited by a topological constraint: solitons must be made in pairs (16-19), whereas electrons (or holes) are injected at the electrode singly and in an uncorrelated manner. Moreover, even in the event of a fluctuation with simultaneous injection of a pair of electrons (or holes), the direct process is exponentially small since it requires a significant lattice distortion simultaneous with the electronic transition below the bandedge (21). Precisely the same features have been shown to dominate the photogeneration of solitons in polyacetylene (22). Thus, charge is injected into the band states (or associated polaron states) of the polymer, and the injection threshold should occur near the bandedge. After injection, the lattice distortions which lead to soliton formation take place through the reaction



where P denotes polaron and S and \bar{S} denote soliton and antisoliton, respectively. The injected charge is stored in the midgap soliton states. This has been proved experimentally through *in situ* optoelectrochemical spectroscopy (10) and through photoinduced absorption (23). Charge removal, on the other hand, takes place from the doped polymer in which the chemical potential is determined by the charged solitons, as defined above. The essential point is that once formed, the solitons can exist in any one of the three charged states (positive, neutral, or negative) (16-19), so that charge can be removed from the solitons one at a time. Thus, one expects charge injection (electrons) to occur at approximately the polaron energy (13, 14), $E_p = \sqrt{2}(2/\pi)\Delta$ (see Eq. [1]), charge removal to occur at the chemical potential, $\mu_n = E_s = (2/\pi)\Delta$. For hole injection and removal, the argument is the same: injection at $-\sqrt{2}(2/\pi)\Delta$ and removal at $\mu_p = -(2/\pi)\Delta$ (note that all energies are measured with respect to midgap). This hysteresis is evident in the data of Fig. 4 and 6. Moreover, the same hysteresis has been observed in the intensity of the midgap transition as a function of applied voltage during *in situ* optical studies (10). Thus, both the EVS data (4) and the optoelectrochemical data (10) indicate charge injection near the bandedge, but charge storage and removal from the states at midgap.

Integration of the data from Fig. 6 (curve A) yields the voltage as a function of charge (Fig. 9). The dashed lines in the figure represent idealized charge injection (via polarons at energy E_p) and charge removal (via solitons at energy $E_s = (2/\pi)\Delta$). From Fig. 6 and 9, we infer $E_p \cong 0.65$ eV (*i.e.*, the difference between midgap, 2.4V, and charge injection, 1.75V). From the observed hysteresis in the main charge injection-removal edge, ΔV on Fig. 6, we find $E_p - E_s \cong 0.1-0.15$ eV, implying $E_s \cong 0.5-0.55$ eV. $E_s = (2/\pi)\Delta$, this value leads to $2\Delta = 1.6-1.8$ eV, in close agreement with the 1d energy gap as obtained from studies of the pressure dependence of the optical absorption (15). Note that although most of the charge comes out at about 0.5-0.6V above (or below) midgap, the final ± 300 ppm of charge is removed precisely at midgap. This final charge removal is due to the neutral soliton defects and is discussed in detail in the next section.

The principal quantitative uncertainty in the above analysis is the role of three-dimensional effects resulting from interchain coupling (15, 24). Although relatively small, studies of the pressure dependence (15) of the interband absorption edge have shown that the energy gap is reduced from the 1d value by about 0.2-0.4 eV. Thus, although the soliton level remains rigorously at midgap in the presence of relatively weak interchain coupling, the injection threshold will be sensitive to interchain interaction. Consequently, the value inferred above for E_p (1d) may be too small by about 0.1 eV.

The interpretation of soliton states as the source of hysteresis in polyacetylene electrochemical cells requires an

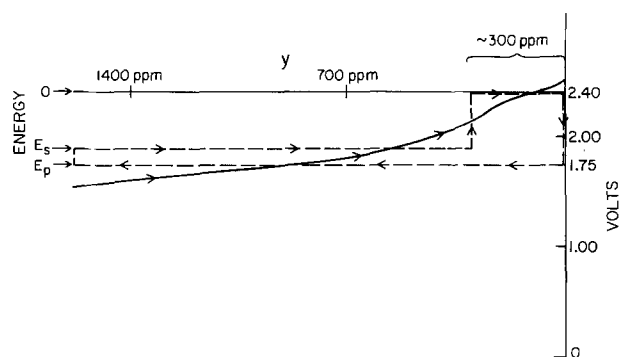


Fig. 9. Q vs. V during charge removal (the integral of curve A in Fig. 6). The dashed lines represent idealized charge injection (at the polaron energy, E_p) and charge removal (at the soliton energy, E_s). The final 300 ppm will come out (from the soliton defects) at midgap, as predicted by the Kivelson mechanism. The inset shows a full cycle (n-type) to higher doping levels.

understanding (and dismissal) of other energy loss processes. Dissipation of energy through the cell internal resistance is eliminated through the use of a reference electrode (through which no current flows) and arbitrarily small minimum currents. Since the cell internal resistance is typically $\sim 100\Omega$, and since measurements were taken at $i_c^{\min} \sim 10^{-6}$ A, the voltage difference on charging and discharging would be $\Delta V \sim 10^{-4}$ V, truly negligible. The fact that data have been obtained with 100% coulombic efficiency rules out irreversible chemical reactions. Finally, factors limiting mass-transport rates were considered. Detailed measurements of ionic diffusion rates will be discussed in the "Optical Spectroscopy" section below. The results demonstrated electric field enhancement of ionic diffusion greater than 2 orders of magnitude. By insuring that the resting time at each voltage step was longer than the measured ion-transport rate, diffusion equilibrium was achieved. The hysteresis, therefore, can only be due to relaxation of the charged polymer state into a lower energy state after charge injection. The formation of soliton-antisoliton pairs seems to be the only relaxation mode with sufficient energy to account for the observed hysteresis in the main charge-removal peak (Fig. 6).

Charge Transport at Dilute Levels: the Kivelson Mechanism

The data of Fig. 6 show that ~ 300 ppm are removed in a narrow range about midgap (the charge removal peak in Fig. 6 has a full width of about 0.2V, centered at 2.4V). This demonstration of the removal of 300 ppm of charge precisely at midgap is important in understanding transport phenomena in lightly doped polyacetylene. Kivelson (25) proposed that, in lightly doped *trans*-(CH) $_x$, phonon-assisted electron hopping among soliton midgap states could be the dominant mechanism of charge transport. A key feature of the Kivelson mechanism (which distinguishes it from other hopping models that do not involve solitons) is that transport of charge occurs through energetically equivalent levels which are at gapcenter. This is to be contrasted, for example, with polaron hopping models, which involve excitation from localized states near the bandedge into band states. A critical test of the transport in *trans*-(CH) $_x$, therefore, is to establish the energy of the localized states that dominate the transport in the dilute regime (5). The EVS data (Fig. 6) give a direct measure of this energy and establish it to be precisely at midgap, as predicted by the Kivelson mechanism.

The EVS data, dQ/dV vs. V , may be thought of as an infinitely slow cyclic voltammogram (see the "Experimental Technique" section). Although the principal charge removal peak is observed in cyclic voltammetry experiments, the smaller midgap peak has never been reported. This is due to the small amount of charge removed at midgap and to the nonequilibrium effects inherent in cyclic voltammetry when ionic diffusion rates

become very slow. Since the EVS method has the resolution to detect parts per million of charge, and since the measurements can be made arbitrarily close to diffusion equilibrium, the data are not diffusion limited.

The removal of ~300 ppm of charge at midgap (see the previous section) follows directly from the Kivelson mechanism. We note, however, that charge injection directly into these neutral solitons is not observed, even though they exist in the neutral polymer. The Kivelson mechanism requires electron hopping between energetically equivalent states. Therefore, in the process of charge injection, the neutral soliton midgap states in the bulk of the $(\text{CH})_x$ electrode are not accessible since there are no Li^+ ions in the bulk material. As a result, electron hopping through the "midgap" states is inhibited by the inequivalence of the site energies. Thus, these levels will become charged at midgap only after initial charge injection (at the surface) into a band (or polaron) state with the charge subsequently migrating to and falling into the lower energy midgap state, as described in detail in the previous section. During charge removal, since the Li^+ ions are distributed into the polymer, electronic charge can hop between the equivalent midgap states, diffusing to the contact where it can be removed at midgap. The Li^+ ions will, of course, follow and return into the electrolyte. Therefore, the injection and transport of electronic charge into the neutral soliton defect states is inhibited by the site inequivalence, whereas the transport and subsequent removal of charge from these states proceeds via the Kivelson mechanism. The charge removal peak at 2.4V and the hysteresis are evident in Fig. 6.

Ionic Diffusion in *trans*-(CH)_x: Field Enhancement

A detailed study of mass transport in polyacetylene was conducted to determine its contribution (if any) to the observed hysteresis, as well as to study field-enhancement phenomena (26). By modifying the EVS experiment to store the current *vs.* time information (as opposed to just the integrated charge), the ionic diffusion rate can be measured as a function of energy and dopant concentration (under current carrying conditions). Alternatively, by measuring the recovery of the open-circuit voltage after a period of constant current charging (or discharging), the free diffusion rate can be measured (6, 27). In both experiments, the signal (after a short transient) is found to decay exponentially with time, indicating that the diffusion

obeys Fick's law. An example of the EVS current decay is shown in the inset to Fig. 10.

Figure 10 shows the diffusion time constant (τ) as a function of voltage for charging (removal of Li ions). The time constant is observed to rise from ~250s at 1V to ~1000s at the bandedge. In the bandgap, τ rapidly increases to ~3000s. These values are to be compared with the measured free diffusion rates of ~12h (40,000s). Assuming cylindrical geometry for the $(\text{CH})_x$ fibrils, the diffusion constant can be obtained from the exponential decay time (28)

$$D_0 = r_0^2 / [(2.405)^2 \tau_0] \quad [5]$$

where r_0 is the fibril radius ~100Å. From this expression, a time constant of 12h corresponds to a diffusion constant $D_0 \sim 4 \times 10^{-18} \text{ cm}^2/\text{s}$. A time constant ~400s corresponds to $D_0 \sim 4 \times 10^{-16} \text{ cm}^2/\text{s}$.

The apparent paradox between free-diffusion rates of 40,000s and rates ~400s under current carrying conditions was resolved in a publication by Kaufman *et al.* (26). The presence of a small driving potential (or a load) causes current to flow and generates a large electric field within the fibrils. This field dramatically increases the ion-transport rate when the electronic screening length is on the order of a fibril radius. Under current carrying conditions, this theory accounts for the observed enhancement of two orders of magnitude or more.

Since the minimum current in the EVS method can be made arbitrarily small, it is possible to wait at each voltage step a time much longer than the field-enhanced diffusion time. By measuring the diffusion rate, one can adjust the minimum current so that the cell is always in diffusion equilibrium when measurements are made. However, above some doping level (y_0), the polymer becomes sufficiently highly conducting that the electronic screening length may become much less than a fibril radius. At this point, field enhancement would cease to be effective, and the time required to achieve diffusion equilibrium would increase toward its unenhanced value. In this regime, a film uniformly doped to y_0 would exhibit "metallic" behavior; there would be no electric field in the fibril, and charge transfer would occur at the surface. The V *vs.* Q relation should resemble that of an electrolytic capacitor exhibiting linear behavior with no hysteresis. Since charge transfer above y_0 occurs primarily at the surface, diffusion times (as measured by the decay of the

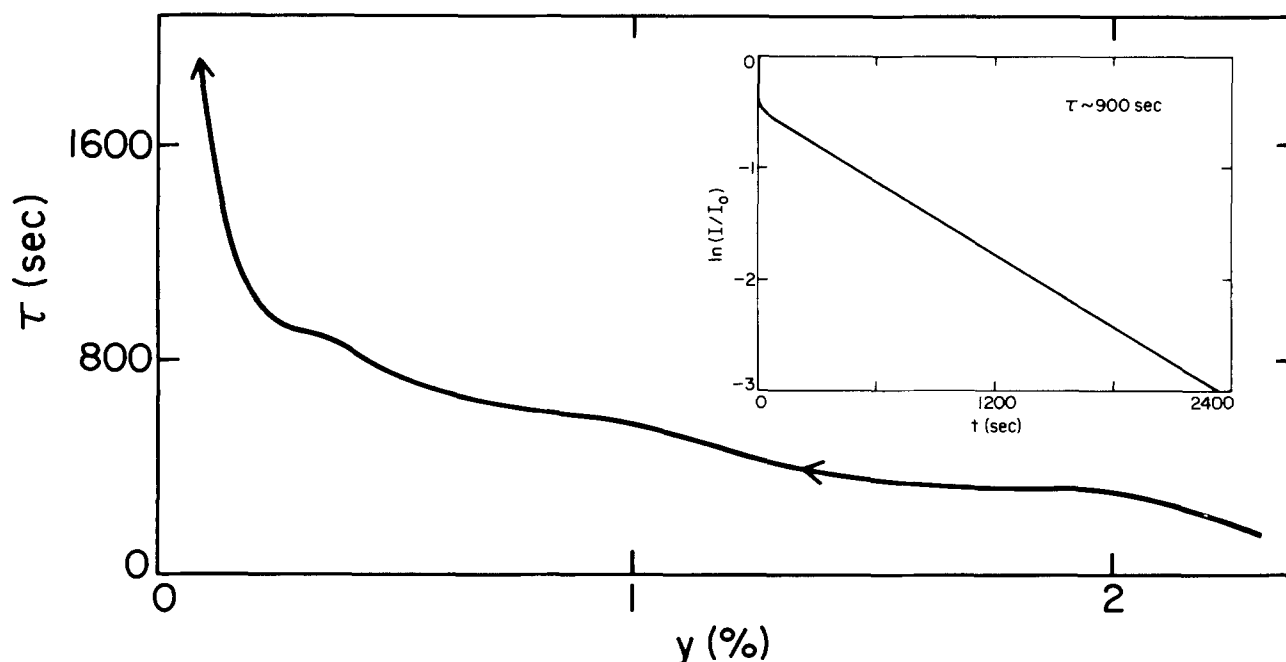


Fig. 10. Diffusion time, τ vs. V , for charge removal (i.e., oxidation of *n*-doped material). Observed diffusion rates under load are two orders of magnitude faster than free diffusion. The inset shows the exponential decay of the cell current (over ~3 orders) after a 0.10V change in applied voltage.

cell current) would represent surface diffusion rates only and should decrease in the highly conducting regime. If the polymer were doped nonuniformly (by a "fast" cycle, for example), the surface of a fibril could become highly conducting before the bulk. It would, therefore, be possible to observe pseudometallic behavior at a concentration even less than y_0 .

A series of experiments were performed to investigate the effects of electronic screening length on diffusion as discussed above. Figures 11 and 12 show the time constant τ and the voltage V plotted together as a function of dopant concentration y (at $I_{\min} = 2\mu\text{A/mg}$). The voltage vs. charge relation in Fig. 11 shows a change in slope (kink) at $y \sim 2\%$. At the same concentration, the time constant decreases. Figure 12 shows a voltage kink at $y \sim 1\%$ and a corresponding decrease in τ . Though the voltage kink and decreases in τ occur at different doping concentrations in the two cycles, both features occur at the same voltage ($V \sim 1.25\text{V}$). Figure 13 shows an EVS cycle taken at voltages $V < 1.25\text{V}$ ($y > y_0$). This short (and comparatively fast) cycle demonstrates vanishingly small hysteresis and linear V vs. Q relation past the 1.25V kink. All these effects are consistent with retarding of ionic diffusion rates in the highly conducting regime. The absence of hysteresis for fast cycles and the decrease in τ indicate charge transfer at the fibril surface. Slow cycles, even in the highly conducting material, would involve free diffusion (without field enhancement) of the dopants into the polymer, driven by concentration gradients. We note that this interpretation of the change in kinetics is associated with the loss of electric-field enhancement (when the electrical conductivity becomes sufficiently high that the screening length is less than a typical fibril dimension). This appears to occur at a concentration somewhat below that required for the microscopic electronic structure transition, as evidenced by closure of the energy gap and the onset of Pauli susceptibility. The latter takes place at $y \approx 5\text{ m/o}$ (29, 30).

As is evident in Fig. 11 and 12, the concentration above which the change in kinetics occurs is sample dependent. However, the onset of this behavior occurs at the same voltage ($\sim 1.25\text{V}$). Since voltage is uniquely related to dopant concentration on the fibril surface (where contact is made to the polymer), the actual concentration at which the change in kinetics is observed appears to be unique for a uniformly doped film. There are a number of possible explanations for the sample dependence of the concentration. Different sample preparations may result in different characteristic fibril diameters, and different isomerization conditions may effect the conductivity of the doped polymer. Variations in cell construction result in different internal resistances, which, in turn, can effect doping kinetics. The primary effect, however, is probably polymer degradation after multiple cycling. As the electrochemical cell is repeatedly cycled to high dopant levels (which is necessary to "clean up" impurities

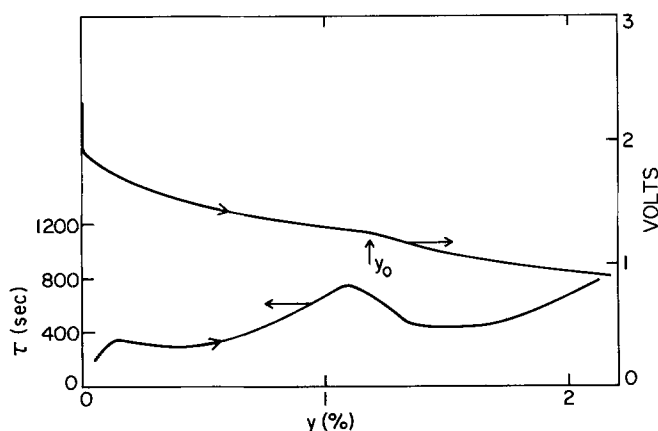


Fig. 11. Diffusion time, τ vs. y , for n-type injection. τ has a local maximum where V vs. y changes shape (see text).

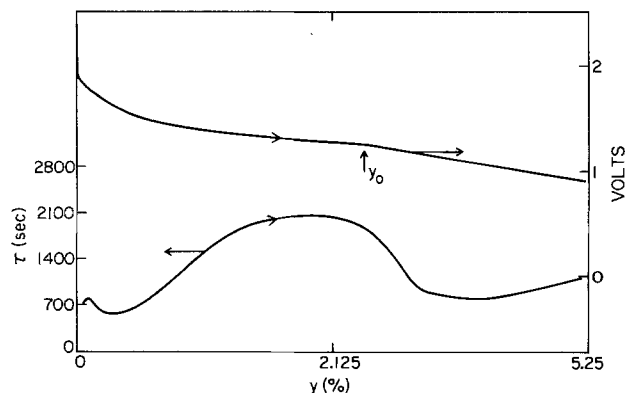


Fig. 12. Diffusion time, τ vs. y , as in Fig. 11, but for a different cell (see text).

so 100% coulombic efficiency is achieved) disorder occurs in the $(\text{CH})_x$ chains. This results in a decrease in the effective mass of crystalline polymer in the cell. Initial cycles which sometimes exhibit $\sim 60\%$ charge loss may indicate polymer mass loss on the same order. If the calculated mass is twice the actual mass in a particular cell, doping levels computed from coulombs transferred would be reduced by a factor of two.

Optical Spectroscopy of Doped $(\text{CH})_x$: Charge Storage in Midgap States

As shown in the "Discussion of Charge Injection" section, charge is injected near the bandedge and stored in the midgap electronic states associated with the bond-alternation domain walls. *In situ* optoelectrochemical experiments have been previously reported (10), which demonstrated the charge storage in the midgap states through doping induced optical transitions between the midgap state and the bandedge (see Fig. 14). In these earlier *in situ* experiments, the doping was p-type, using ClO_4^- as the counterion. As doping proceeds, the midgap absorption appears, centered near 0.65-0.75 eV with an intensity which increases monotonically in proportion to the dopant concentration. We show here that these spectroscopic features are independent of dopant species and independent of whether the doping is p-type (oxidation) or n-type (reduction).

Figure 14 shows optical absorption spectra for polyacetylene doped with different species (Na, Li, Bu_4N , ClO_4^-) at $y \sim 1\%$. The Na samples were chemically doped, the others electrochemically (using *in situ* opto-EVS technique). The similarity between these data proves conclusively that the optical spectra of *trans*- $(\text{CH})_x$ depends only on the properties of the doped polymer, and not on the particular dopant species.

The midgap optical absorption provides direct evidence for charged soliton states in doped polyacetylene. Independent evidence has been obtained from the doping in-

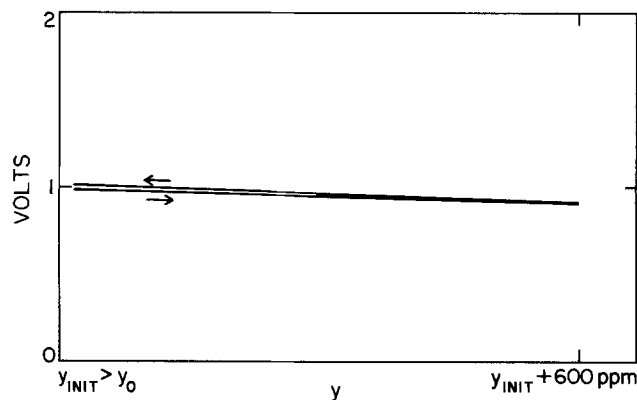


Fig. 13. V vs. Q exhibits no hysteresis in highly conducting regime (see text).

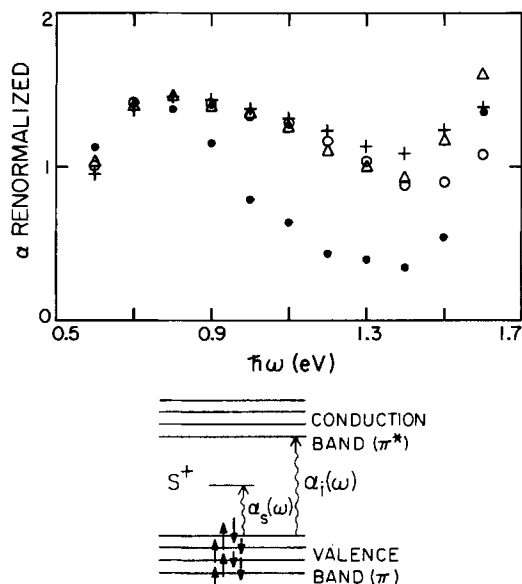


Fig. 14. Near-IR absorption spectra showing the midgap transition for *trans*-(CH)_x doped with Na⁺ (○), Li⁺ (Δ), Bu₄N⁺ (•), and ClO₄⁻ (+). The inset is a schematic band diagram showing the midgap and interband transitions.

duced modes (31) which appear in the midinfrared associated with the local vibrational modes of the charged bond-alternation domain wall. Again, these mid-IR modes are independent of dopant (9) and show characteristic shifts after deuteration (32): (CD)_x compared to (CH)_x. That all of these spectroscopic features are associated with charged solitons has been unambiguously proven through a series of photoinduced absorption (22, 23, 33) and photoinduced ESR measurements (34).

The remarkable oscillator strength associated with these doping induced spectroscopic features arises directly from the spatial extent of the charge-storage state. Whereas one might anticipate that the ratio of oscillator strengths would be equal to the dopant concentration, a detailed theoretical analysis shows that for dilute concentrations the midgap transition is enhanced by a factor of about (2*l*), where (2*l*) is the full width of the bond-alternation domain wall and *a* is the carbon-carbon spacing along the (CH)_x chain (10). Since (2*l*) ≅ 14, this enhancement of the soliton transition makes it observable even at highly dilute dopant concentrations. A complete analysis of the strength of the midgap transition is included in the work of Feldblum *et al.* (10), who find the results to be in good quantitative agreement with theory.

Conclusion

The combined application of optical and electrochemical methods to the study of polyacetylene demonstrates an important technique for studying conducting polymers in general. By providing complementary information on the transition energies and joint density of states (from optical absorption) and the energies at which these (bandgap) states are created, transported, and destroyed (through EVS techniques), it is possible to study many properties not directly accessible by other methods. In the case of polyacetylene, we have been able to use the EVS technique to measure the energy gap. The resulting value, *E_g* ≅ 1.5eV, is in good agreement with that obtained by other methods. The subsequent observation of hysteresis in the electrochemical cycle, and an increase in the midgap optical absorption upon doping, are both indicative of the creation of bandgap states. The resolution available in the EVS technique allowed precise determination of both the energy and number of these states. The results demonstrated that the injected charge was stored in the form of charged solitons [chemical potential (2/π)Δ] and not some random distribution of impurity states throughout the gap or polaron states near the bandedge.

The demonstration that 300 ppm of charge is removed precisely at midgap provided a detailed verification of Kivelson's model of charge transport via intersoliton electron hopping.

Finally, kinetics studies (*τ vs. y*) were used to quantify the anomaly between slow free-diffusion rates and dramatically enhanced diffusion under conditions of current flow (*i.e.*, high current and power densities). With precise data available, a theory was developed to explain the observed enhancement quantitatively. The local maximum in *τ vs. y*, the change in slope of *V vs. y*, and the vanishing of the hysteresis — all occurring at a common concentration — provided insight into ionic transport in the highly conducting regime. All the above effects follow directly from a reduced screening length and vanishing electric field in the fibrils. Since this "metallic" behavior (and the slow free diffusion) allow greater dopant concentration near the surface, the large current levels obtainable from highly doped polyacetylene electrochemical cells is also understood.

Acknowledgments

We thank Professor J. R. Schrieffer for suggesting the solution to the bead problem as a means of calculating *Ω_{config}* for solitons. We are grateful to Dr. A. Kapitunlik and Dr. Esther Conwell for many helpful discussions. This work was supported by the Office of Naval Research.

Manuscript submitted Nov. 23, 1983; revised manuscript received July 30, 1984.

The University of California assisted in meeting the publication costs of this article.

APPENDIX A

Corrections to the Electronic Free Energies

In the discussion and analysis of the "Charge Transport" section, we assumed that the measured EVS injection and removal voltages are determined only by the differences in electrochemical potentials for electrons in Li and *trans*-(CH)_x. There are, however, many contributions to the free energy of charge injection and removal in an electrochemical cell. In particular, one must include the free-energy change associated with removing a Li atom from the metal electrode and taking it into solution, and the free-energy change between dopant ions in solution and in the oxidized or reduced polymer. The true chemical potential, *μ* = ∂*F*/∂*N*, must include all such solution energies.

Such contributions to the free energy can be accounted for by consideration of each half-cell reaction. The chemical potential of Li is the sum of the single electron contribution (*μ_{Li}^e*) and the solution energy for Li ions (*E_{Li⁺→Li}*).

$$\mu_{\text{Li}} = \mu_{\text{Li}}^e + E_{\text{Li}^+ \rightarrow \text{Li}} \quad [\text{A-1}]$$

Similarly, the chemical potential of (CH)_x is written as a sum of electronic and solvation contributions. For p-type doping

$$\mu_{(\text{CH})_x}^{\text{p,d}} = \mu_{\text{p,i}}^{\text{h}} + E_{\text{A}^- \text{sol-pol}} \quad [\text{A-2}]$$

where *μ_{p,i}^h* is the electronic energy for hole injection into the valence band and *E_{A⁻sol-pol}* is the energy change on taking the negative dopant ion A⁻ (in our case, ClO₄⁻) from the electrolyte into the polymer. For p-type undoping

$$\mu_{(\text{CH})_x}^{\text{p,u}} = \mu_{\text{p,r}}^{\text{h}} + E_{\text{A}^- \text{sol-pol}} \quad [\text{A-3}]$$

where *μ_{p,r}^h* is the electronic energy for the removal (electron injection) from the soliton levels in the gap. Similarly, for n-type doping and undoping

$$\mu_{(\text{CH})_x}^{\text{n,i}} = \mu_{\text{n,i}}^e + E_{\text{D}^+ \text{sol-pol}} \quad [\text{A-4}]$$

$$\mu_{(\text{CH})_x}^{\text{n,u}} = \mu_{\text{n,r}}^e + E_{\text{D}^+ \text{sol-pol}} \quad [\text{A-5}]$$

where *E_{D⁺sol-pol}* is the energy change on taking the positive dopant ion D⁺ (in our case, Li⁺) from the electrolyte into the polymer. The electronic contributions are defined as follows: *μ_{n,i}^e* is the electronic energy from electron injection into the conduction band, and *μ_{n,r}^e* is the electronic energy for electron removal from the soliton levels in the gap. The complexity of equations arises because the elec-

tronic chemical potential of *trans*-(CH)_s can be moved across the gap by doping. The various specific electronic energies are summarized in Table A-I.

The above equations can be combined to predict the voltage for charge injection and removal in the dilute regime (where dopant-dopant interactions are unimportant). For p-type doping oxidation occurs at (see Table A-I)

$$-eV_{(\text{ox})}^p = (E_{\text{VB}} + E_{\text{ClO}_4^{\text{sol-pol}}}) - (\mu_{\text{Li}}^e + E_{\text{Li}^+ \rightarrow \text{Li}}) \quad [\text{A-6}]$$

The voltage at which the p-doped material is reduced to neutral

$$-eV_{(\text{red})}^p = (\mu_{s_0} + E_{\text{ClO}_4^{\text{sol-pol}}}) - (\mu_{\text{Li}}^e + E_{\text{Li}^+ \rightarrow \text{Li}}) \quad [\text{A-7}]$$

For n-type doping, reduction occurs at

$$-eV_{(\text{red})}^n = (E_{\text{CB}} + E_{\text{Li}^{\text{sol-pol}}}) - (\mu_{\text{Li}}^e + E_{\text{Li}^+ \rightarrow \text{Li}}) \quad [\text{A-8}]$$

and final oxidation of n-doped material to neutral occurs at

$$-eV_{(\text{ox})}^n = (\mu_{s_0} + E_{\text{Li}^{\text{sol-pol}}}) - (\mu_{\text{Li}}^e + E_{\text{Li}^+ \rightarrow \text{Li}}) \quad [\text{A-9}]$$

Note that the relative sign of the solvation energies does not change on switching from oxidation to reduction because the process (solvation) is reversible and conserves energy.

In the "Experimental Techniques" section, we identified the difference between electron injection and hole injection energies with the energy gap. From Eq. [A-6] and [A-8], we find

$$-e(V_{(\text{red})}^n - V_{(\text{ox})}^p) = (E_{\text{CB}} - E_{\text{VB}}) + (E_{\text{Li}^{\text{sol-pol}}} - E_{\text{ClO}_4^{\text{sol-pol}}}) = E_g + (E_{\text{Li}^{\text{sol-pol}}} - E_{\text{ClO}_4^{\text{sol-pol}}}) \quad [\text{A-10}]$$

This difference gives the energy gap only if the difference in solvation energies, $(E_{\text{Li}^{\text{sol-pol}}} - E_{\text{ClO}_4^{\text{sol-pol}}})$, is negligible. This quantity can be obtained directly from experiment; using Eq. [A-7] and [A-9]

$$-e(V_{(\text{ox})}^n - V_{(\text{red})}^p) = E_{\text{Li}^{\text{sol-pol}}} - E_{\text{ClO}_4^{\text{sol-pol}}} \quad [\text{A-11}]$$

As shown in the "Experimental Techniques" section, final charge removal for both n- and p-type doping occurs at the same voltage (2.4V) to an accuracy of better than 0.05V. Thus, $(E_{\text{Li}^{\text{sol-pol}}} - E_{\text{ClO}_4^{\text{sol-pol}}}) \leq 0.05\text{V}$ and

$$-e(V_{(\text{red})}^n - V_{(\text{ox})}^p) \cong E_{\text{CB}} - E_{\text{VB}} \equiv E_g \quad [\text{A-12}]$$

The fact that the difference in solvation energies (Eq. [A-11]) is vanishingly small can be rationalized on very general grounds. The absolute energy difference between an ion screened in a conducting electrolyte and an ion screened in a conducting polymer depends on the dielectric constants of the polymer and electrolyte and on the charge distributions around the ion in the two environments. Since the dielectric constants are similar and since the screening charge distribution are similar, the energies, $E_{\text{Li}^{\text{sol-pol}}}$ and $E_{\text{ClO}_4^{\text{sol-pol}}}$ are both small and of the same magnitude. Thus the difference (Eq. [A-11]) is negligible.

Since in our experiments n- and p-doping experiments were carried out in different solvents (THF and PC, respectively) the value of the Li solvation energy $E_{\text{Li}^+ \rightarrow \text{Li}}$ would differ in the two cases. The difference equations should therefore include a term $(E_{\text{Li}^+ \rightarrow \text{Li}}^{\text{THF}} - E_{\text{Li}^+ \rightarrow \text{Li}}^{\text{PC}})$. This difference is also expected to be small for the same reasons outlined above. Since Eq. [A-12] is empirically zero (to within the resolution of the experiment), the inclusion of this and any other higher-order term does not affect the

Table A-I. Electronic chemical potentials of polyacetylene (taking midgap as the zero of energy)

$\mu_{n,i}^e = E_{\text{CB}} \equiv \Delta$.
$\mu_{n,r}^e = (2/\pi) \equiv \mu_{n,-}$ for soliton generated by charge transfer (reduction).
$\mu_{n,r}^e = 0 \equiv \mu_{s_0}$ for the 300 ppm soliton defects in the as-grown polymer.
$\mu_{n,i}^h = 0 \equiv \mu_{s_0}$ for the 300 ppm soliton defects in the as-grown polymer.
$\mu_{n,r}^h = -(2/\pi)\Delta \equiv \mu_{s,+}$ for solitons generated by charge transfer (oxidation).
$\mu_{n,i}^h = E_{\text{VB}} \equiv -\Delta$.

In the above, we have for simplicity ignored the polaron contribution to the electron and hole injection energies (see "Experimental Techniques" section).

final result. We therefore conclude that the difference in injection energies provides a direct measure of the energy gap (reduced by the polaron lattice-relaxation energy).

APPENDIX B

Contribution of the Configurational Entropy

The configurational entropy associated with placing N_s ion soliton pairs in polyacetylene may shift the chemical potential of the doped polymer as measured by EVS. The magnitude of this shift can be computed analytically.

The number of distinguishable ways to put N_s ions in a polymer with N available sites is

$$\Omega_{\text{ion}} = \binom{N}{N_s}$$

For a given configuration of ions, there is only one distinguishable way to place N_s solitons near N_s ions on a given chain: s s s --- with each s or s associated with one of the ions. Although there are two types of chains, the system is assumed to be either in the A phase or the B phase because of the broken symmetry. So, the total number of ways to place N_s soliton-ion pairs in the polymer is

$$\Omega_{\text{config}} = \binom{N}{N_s} \quad [\text{B-1}]$$

This contribution to the chemical potential (using Stirling's approximation) is

$$\mu_{\text{config}} = kT(d \ln \Omega / dN_s) = kT \ln (c/[1-c]) \quad [\text{B-2}]$$

where c is the concentration of ions (solitons) and $kT \sim 1/40$ eV at room temperature.

It is possible to modify Eq. [B-1] to include the finite width (l) of the N_s solitons. The correct combinatorial expression in the discrete limit [appropriate to a *trans*-(CH)_s chain] is

$$\Omega_{\text{config}} = l^{N_s} \binom{N/l}{N_s} \quad [\text{B-3}]$$

where $(N/l N_s)$ is the number of ways to place N_s rods (with fixed origin) of length la on a chain of length Na ; and l^{N_s} is the number of ways to fix an origin on N_s rods of length la . This expression for Ω_{config} also gives a contribution to the chemical potential of the form of Eq. [B-2].

This problem can also be solved in the continuum limit ($1 \ll N_s \ll N$) by considering the solitons to be solid beads on a ring (periodic boundary conditions). The total number of configurations for N_s beads of length la on a ring of circumference Na (where a is the lattice spacing) is the sum (or integral) of the possible configurations of each of the beads, i.e.

$$\Omega_{\text{config}} = \int_{\text{bead } N_s} \dots \int_{\text{bead } 1} \frac{dx_1}{a} \dots \frac{dx_{N_s}}{a}$$

where x_i is the position of the i^{th} bead. The first bead can be placed from the origin, 0, to the end of the second bead x_2 (less one bead length la). Then

$$\int_0^{x_2-la} \frac{dx_1}{a} = \left(\frac{x_2 - la}{a} \right) / 1!$$

$$\int_{la}^{x_3-la} \frac{x_2 - la}{a} \frac{dx_2}{2} = \frac{\left(\frac{x_3 - 2la}{a} \right)^2}{2!}$$

$$\int_{2la}^{x_4-la} \frac{\left(\frac{x_3 - 2la}{a} \right)^2}{2!} \frac{dx_3}{a} = \frac{\left(\frac{x_4 - 3la}{a} \right)^3}{3!}$$

etc. Therefore

$$\Omega_{\text{config}} = \int_{(N_s-1)a}^{Na-la} \frac{\left(\frac{x_{N_s-1} - (N_s-1)la}{a} \right)^{N_s-1}}{(N_s-1)!} \frac{dx_{N_s}}{a} \quad [\text{B-4}]$$

$$\Omega_{\text{config}} = \frac{(N_s - lN)^{N_s}}{N_s!}$$

Note that the results given in Eq. [3] and [4] are equivalent so long as $lN_s \ll N$, i.e., so long as the concentration is low enough to avoid significant overlap.

Conwell (35) deduced a slightly different expression for Ω_{config} ; she found

$$\Omega_{\text{config}} = \frac{1}{2^{N_s-1}} \frac{l^{N_s} \left(\frac{N}{2l} - 1 \right)^2}{\left(\frac{N}{2l} - \frac{N_s}{2} \right)^2 \left(\frac{N_s}{2} \right)^2} \quad [\text{B-5}]$$

which for $l = 1$ is identical to the expression found by Baughman and Moss (36)

$$\Omega_{\text{config}} = \frac{1}{2^{N_s-1}} \left(\frac{N/2}{N_s/2} \right)^2 \quad [\text{B-6}]$$

However, the factor 2^{N_s-1} is not correct. Since solitons (or antisolitons) can be centered on any site, even or odd (37), the correct counting procedure is given by Eq. [B-1] and [B-3].

To understand how the logarithmic dependence of μ_{config} (see Eq. [B-2]) affects the electrochemical potential as measured by EVS, we must first note that "neutral" $(\text{CH})_x$ has a charge carrier concentration (presumably charged solitons) on the order of 10^{18} cm^{-3} (i.e., $\sim 10^{-4}$ per carbon atom) due presumably to impurities which arise during synthesis. The most probable source of these carriers is from reaction of the $(\text{CH})_x$ chain with residual catalyst. With the inclusion of a concentration c_0 of such "ions," the configuration contribution to the chemical potential can be written

$$\mu_{\text{config}} = kT \ln \left\{ \frac{c + c_0}{1 - (c + c_0)} \right\} \\ \sim kT \ln \{c + c_0\}$$

where $c_0 \sim 10^{-4}$. This lifts the divergence at $c = 0$ (where Stirling's approximation is invalid anyway). The maximum value of μ_{config} occurs at $c = 0$, where the configurational contribution to the chemical potential is $\sim 0.25V$. However, since μ_{config} depends only on soliton number (or concentration) and is independent of sign, the shift of the electrochemical potential is in the same direction for n- and p-type dopants. The injection thresholds are

$$\mu_p^0 = \Delta_0 + \mu_{\text{config}} = \Delta_0 + kT \ln (c + c_0)$$

and

$$\mu_n^0 = -\Delta_0 + \mu_{\text{config}} = -\Delta_0 + kT \ln (c + c_0)$$

The difference in injection thresholds is still

$$\mu_p^0 - \mu_n^0 = 2\Delta_0$$

At low dopant concentrations, the logarithmic concentration dependence of μ_{config} may affect the shape of the V vs. Q curves (for n- and p-type dopants), but it in no way affects the injection thresholds as measured by EVS.

In the above discussion, changes in solvent concentration were neglected. For n-type doping, this is certainly valid, as the change in solvent concentration is rigorously zero. Then

$$\mu = dF/dN = 0 \quad (dN = 0)$$

For p doping there is a slight concentration dependence. One can estimate this by considering the chemical potential of N_i ions in a solvent with \bar{N} "available sites." The solution may be found in Landau and Lifschitz's "Statistical Physics." The result is

$$\mu_{\text{sol}} \sim kT[\ln(c_i) - c_i]$$

where c_i is the ion concentration in solution. On removing N_s of the N_i ions from the solution and transferring them to the polymer, the chemical potential of the solution changes by an amount

$$\delta\mu_{\text{sol}} = kT[1/c_i - 1] \delta c_i$$

where $\delta c_i = N_s/\bar{N}$. For a solution containing 10^{21} ions, removing 10^{19} ions to dope a 1 mg film to $\sim 10\%$ results in a change in chemical potential of the solution of 3×10^{-4} eV; truly a negligible effect.

REFERENCES

- P. J. Nigrey, D. McInnes, Jr., D. P. Nairns, A. G. MacDiarmid, and A. J. Heeger, *This Journal*, **128**, 1651 (1981).
- D. McInnes, Jr., M. A. Druy, P. J. Nigrey, D. P. Nairns, A. G. MacDiarmid, and A. J. Heeger, *J. Chem. Soc. Chem. Commun.*, 317 (1981).
- P. J. Nigrey, A. G. MacDiarmid, and A. J. Heeger, *ibid.*, 594 (1979).
- J. H. Kautman, J. W. Kauter, A. J. Heeger, R. Kaner, and A. G. MacDiarmid, *Phys. Rev. B*, **26**, 2327 (1982).
- J. H. Kaufman, T.-C. Chung, and A. J. Heeger, *Solid-State Commun.*, **47**, 585 (1983).
- R. Kaner, A. G. MacDiarmid and A. J. Heeger, Paper 27 presented at The Electrochemical Society Meeting, Detroit, MI, Oct. 17-21, 1982; P. J. Nigrey, A. G. MacDiarmid, and A. J. Heeger, in "Proceedings of the International Conference on Low Dimensional Conductors," Boulder, Colorado, August 1981 (unpublished).
- L. W. Shacklette, R. L. Elsenbaumer, and R. H. Baughman, *J. Phys.*, **44**, 559 (1983); M. Armand, *ibid.*, **44**, 551 (1983); F. Beniere, D. Boils, H. Canepa, J. Franco, A. Corre, and J. P. Louboutin, *ibid.*, **44**, 567 (1983).
- T. Nagatomo, T. Hanna, C. Yamamoto, K. Negishi, and O. Omoto, *Jpn. J. Appl. Phys.*, **22**, L275 (1983).
- S. Etemad, A. J. Heeger, and A. G. MacDiarmid, *Ann. Rev. Phys. Chem.*, **33**, 443 (1982); and references therein.
- A. Feldblum, J. H. Kaufman, S. Etemad, A. J. Heeger, T.-C. Chung, and A. G. MacDiarmid, *Phys. Rev. B*, **26**, 815 (1982).
- A. H. Thompson, *Physica (Utrecht)*, **99B**, 100 (1980); *Phys. Rev. Lett.*, **40**, 1511 (1978).
- A. J. Bard and L. R. Faulkner, "Electrochemical Methods," John Wiley and Sons, New York (1980); J. O'M. Bockris and D. M. Drazic, "Electrochemical Science," Barnes & Noble Books, New York (1972).
- S. A. Brazovskii and N. N. Kirova, *Sov. Phys. JETP Lett.*, **33**, 4 (1981).
- D. K. Campbell and A. R. Bishop, *Phys. Rev. B*, **24**, 4859 (1981).
- D. Moses, A. Feldblum, E. Ehrenfreund, A. J. Heeger, T.-C. Chung, and A. G. MacDiarmid, *ibid.*, **26**, 3351 (1982); and references therein.
- W.-P. Su, J. R. Schrieffer, and A. J. Heeger, *Phys. Rev. Lett.*, **42**, 1698 (1979); *Phys. Rev. B*, **22**, 2099 (1980).
- H. Takayama, Y. R. Lin-Lin, and K. Maki, *ibid.*, **21**, 2388 (1980).
- S. A. Brazovskii, *JETP Lett.*, **28**, 656 (1978); *ibid.*, **78**, 677 (1980).
- M. J. Rice, *Phys. Lett.*, **A**, **71**, 152 (1979).
- W. R. Salaneck, H. W. Gibson, E. W. Plummer, and B. H. Tonner, *Phys. Rev. Lett.*, **49**, 801 (1982).
- J. P. Sethna and S. Kivelson, *Phys. Rev. B*, **26**, 3513 (1982).
- G. B. Blanchet, C. R. Fincher, T. C. Chung, and A. J. Heeger, *Phys. Rev. Lett.*, **50**, 1938 (1983).
- G. B. Blanchet, C. R. Fincher, and A. J. Heeger, *Phys. Rev. Lett.*, **51**, 2132 (1983).
- P. M. Grant, *Phys. Rev. B*, **26**, 6888 (1982).
- S. Kivelson, *ibid.*, **25**, 3798 (1982).
- J. H. Kaufman, E. J. Mele, R. Kaner, and A. J. Heeger, *This Journal*, **130**, 571 (1983).
- K. Kaneto, M. Maxfield, D. P. Nairns, A. G. MacDiarmid, and A. J. Heeger, *J. Chem. Soc. Faraday Trans.*, **78**, 3417 (1982).
- W. Jost, "Diffusion in Solids, Liquids and Gases," Academic Press, New York (1960).
- S. Ikehata, J. Kaufer, T. Woerner, A. Pron, M. A. Druy, A. Sivak, A. J. Heeger, and A. G. MacDiarmid, *Phys. Rev. Lett.*, **45**, 1123 (1980).
- T.-C. Chung, A. Feldblum, A. J. Heeger, and A. G. MacDiarmid, *J. Chem. Phys.*, **74**, 5504 (1981).
- C. R. Fincher, M. Ozaki, A. J. Heeger, and A. G. MacDiarmid, *Phys. Rev. B*, **19**, 4140 (1982).
- S. Etemad, A. Pron, A. J. Heeger, A. G. MacDiarmid, E. J. Mele, and M. J. Rice, *ibid.*, **23**, 5137 (1981).
- Z. Vardeny, J. Orenstein, and G. L. Baker, *Phys. Rev. Lett.*, **50**, 2032 (1983).
- J. D. Flood, *et al.*, *Solid-State Commun.*, **44**, 1055 (1982); J. D. Flood and A. J. Heeger, *Phys. Rev. B*, **28**, 2356 (1983).
- E. Conwell, *ibid.*, In press.
- R. Baughman and J. Moss, *J. Chem. Phys.*, **77**, 12 (1982).
- A. J. Heeger and J. R. Schrieffer, *Solid-State Commun.*, **48**, 207 (1983).

Primary Current Distribution and Resistance of a Slotted-Electrode Cell

Mark E. Orazem^{*,1} and John Newman^{**}

Materials and Molecular Research Division, Lawrence Berkeley Laboratory, and Department of Chemical Engineering, University of California, Berkeley, California 94720

ABSTRACT

The primary current distribution and the resistance of a cell containing a slotted electrode were calculated using numerical methods coupled with the Schwarz-Christoffel transformation. Results are presented and compared to asymptotic solutions. An approximate analytic expression for the cell resistance is presented.

Primary current and potential distributions apply when the surface overpotential can be neglected and the solution adjacent to the electrode can be taken to be an equipotential surface. Calculation of a primary current distribution and resistance represents a first step toward analyzing and optimizing an electrochemical system. The cell resistance calculated can be coupled with calculations including mass-transfer and kinetic effects to optimize approximately a given cell configuration. The objective of this work is to calculate the primary current distribution and resistance of a cell containing a slotted electrode.

Calculation of the primary current and potential distributions involves solution of Laplace's equation, $\nabla^2\Phi = 0$, which is not trivial, even for relatively simple geometries. The method of images (1), separation of variables (2), and superposition (3, 4) have been used to solve Laplace's equation for a number of systems. A review of analytic solutions has been presented by Fleck (5).

The Schwarz-Christoffel transformation (6-8) is a powerful tool for the solution of Laplace's equation in systems with planar boundaries. This method was used by Moulton (9) to derive the current distribution for two electrodes placed arbitrarily on the boundary of a rectangle. Hine *et al.* (10) used this method to describe the primary current distribution for two plane electrodes of infinite length and finite width confined between two infinite insulating planes, perpendicular to but not touching the electrodes. Wagner (11) presented the primary and secondary current distribution for a two-dimensional slot in a planar electrode. Newman (12) has presented the primary current distribution for two plane electrodes opposite each other in the walls of a flow channel. These solutions made use of the Schwarz-Christoffel transformation.

Application of the Schwarz-Christoffel transformation is generally limited by the ability to generate solutions to the resulting integrals. Analytic solutions allow calculation of the primary current and potential distribution throughout the cell but are possible for a limited number of system geometries. Numerical evaluation of these integrals allows calculation of both the primary current distribution along the electrodes and the cell resistance.

Cell Geometry

A cell geometry is presented in Fig. 1 which may be well suited for photoelectrochemical applications. This cell contains a slotted semiconductor with the semiconductor-electrolyte interface open to illumination. A glass cover plate protects the cell. Sunlight passes through the cover plate and the electrolyte to illuminate the semiconductor surface. Electrical current flows from the semiconductor surface to the counterelectrode through the slots of the semiconductor. This configuration has the advantages that no shadows are cast upon the semiconductor, reaction products can be separated, absorption of light by the electrolyte can be minimized, and

*Electrochemical Society Student Member.

**Electrochemical Society Active Member.

¹Present address: Department of Chemical Engineering, University of Virginia, Charlottesville, Virginia 22901.

an enhanced-surface-area counterelectrode (perhaps a porous electrode) can be used.

The slotted electrode cell can be sectioned and, under the assumption that the cell width W (in the direction perpendicular to the plane of the paper in Fig. 1b) is large as compared to the spacing between slots, has the electrochemical characteristics of the two-dimensional cell presented in Fig. 2a. Here, the cell has been turned from Fig. 1b so that illumination now comes from the right in Fig. 2a; the semiconductor electrode is represented by AB , the counterelectrode by EF , and all other boundaries of the cell are considered to be insulators. The lines DE and BC and FG represent two planes of symmetry in the cell in Fig. 1b; one plane bisects the semiconductor electrode, and the other bisects the slot.

The coordinate system of Fig. 2a is transformed through an intermediate half-plane t (see Fig. 2b) to a coordinate system (Fig. 2c) in which Laplace's equation can be solved easily.

Theoretical Development

The primary current distribution along the electrodes and the cell resistance can be calculated through application of the Schwarz-Christoffel transformation. Complex coordinate systems are used; thus

$$z = z_r + jz_i$$

The cell was assumed to be symmetric about $z_r = 0$. The approach presented below, however, could be easily extended to relax this assumption.

The z coordinate system is related to the t coordinate system of Fig. 2b by

$$z = \int_0^t \frac{(a2s - t^2)^{1/2}}{(b^2 - t^2)^{1/2}(c^2 - t^2)^{1/2}(d^2 - t^2)^{1/2}} dt \quad [1]$$

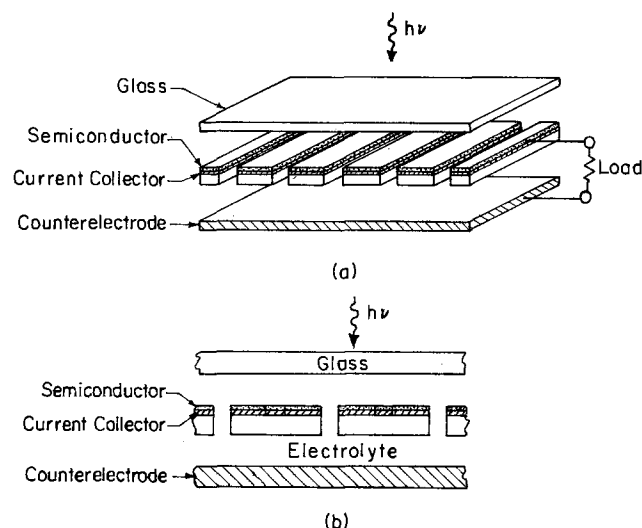


Fig. 1. Schematic diagram of the slotted-semiconductor photovoltaic cell

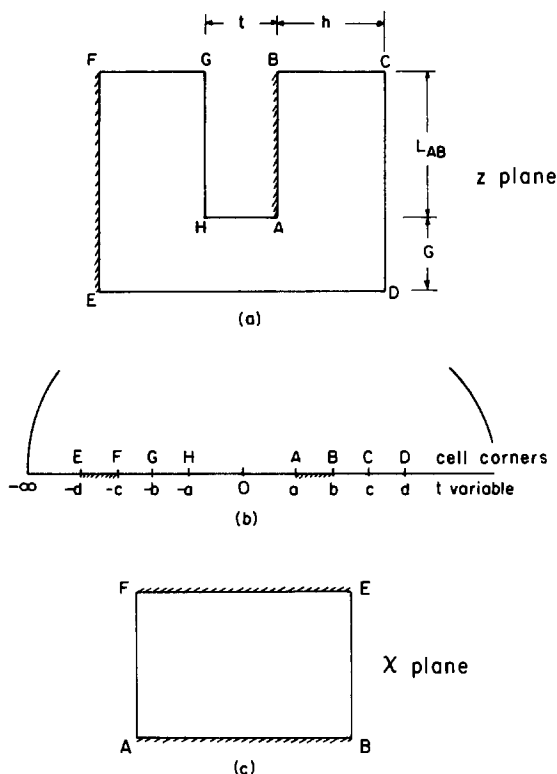


Fig. 2. Schematic diagram of the sectioned cell with coordinate systems: (a) $z = z_r + jz_i$, (b) $t = t_r + jt_i$, and (c) $\chi = \chi_r + j\chi_i$.

where a , b , c , and d are the values of t corresponding to z values of A , B , C , and D , respectively. Through the assumption of symmetry about $z_r = 0$, the values $-a$, $-b$, $-c$, and $-d$ correspond to z values of H , G , F , and E , respectively. The electrodes AB and EF correspond to ab and $-c-d$ in the t plane. Along the electrode AB (ab), this transformation can be expressed by

$$\left. \frac{dz_r}{dt_i} \right|_{ab} = jf(t_r) \quad [2a]$$

where

$$f(t_r) = \frac{(a^2 - t_r^2)^{1/2}}{(b^2 - t_r^2)^{1/2}(c^2 - t_r^2)^{1/2}(d^2 - t_r^2)^{1/2}} \quad [2b]$$

These equations will be used to calculate the derivative of the potential at the electrodes; z_r is the direction normal to the electrode in the z plane, and t_i is the direction normal to the electrode in the t plane.

The variable χ (see Fig. 2c) is related to the t plane by the Schwarz-Christoffel transformation

$$\chi = \int_a^t \frac{1}{(t-a)^{1/2}(b-t)^{1/2}(c-t)^{1/2}(d-t)^{1/2}} dt \quad [3]$$

Along the electrode ab , Eq. [3] can be expressed as

$$\left. \frac{d\chi_i}{dt_i} \right|_{ab} = g(t_r) \quad [4a]$$

where

$$g(t_r) = \frac{1}{(t_r - a)^{1/2}(b - t_r)^{1/2}(c + t_r)^{1/2}(d + t_r)^{1/2}} \quad [4b]$$

Equations [2] and [4] are also valid at the electrode EF ($-c-d$). The variable χ_i is normal to the electrode in χ space, and t_i is, as above, normal to the electrode in t space.

The potential in the χ system is

$$\Phi = \frac{\chi_i}{\chi_{i,\max}} V \quad [5]$$

where V is the cell potential difference and $\chi_{i,\max}$ is the separation between electrodes in χ space. The current density is related to the potential derivative at the electrodes. In the χ system, this derivative is given by

$$\left. \frac{\partial \Phi}{\partial \chi_i} \right|_{-c-d} = \left. \frac{\partial \Phi}{\partial \chi_i} \right|_{ab} = \frac{1}{\chi_{i,\max}} V \quad [6]$$

The potential derivative at the electrode ab in the t system is

$$\left. \frac{\partial \Phi}{\partial t_i} \right|_{ab} = \left. \frac{\partial \Phi}{\partial \chi_i} \right|_{ab} \left. \frac{\partial \chi_i}{\partial t_i} \right|_{ab} \quad [7]$$

and the potential derivative in the z system is given by

$$\left. \frac{\partial \Phi}{\partial z_r} \right|_{ab} = \left. \frac{\partial \Phi}{\partial t_i} \right|_{ab} \left. \frac{\partial t_i}{\partial z_r} \right|_{ab} \quad [8]$$

Substitution of Eq. [2a], [4a], [6], and [7] into Eq. [8] and similar manipulations for the $-c-d$ electrode yield the potential derivative along the electrodes ab and $-c-d$ in the original z coordinate system as functions of t_r

$$\left. \frac{\partial \Phi}{\partial z_r} \right|_{ab} = \frac{g(t_r)}{f(t_r)} \frac{V}{\chi_{i,\max}} \quad [9a]$$

and

$$\left. \frac{\partial \Phi}{\partial z_r} \right|_{-c-d} = \frac{g(t_r)}{f(t_r)} \frac{V}{\chi_{i,\max}} \quad [9b]$$

respectively.

The current distribution along the electrode AB is therefore given by

$$i(z_i) = \frac{g(t_r)}{f(t_r)} \int_a^B \frac{g(t_r)}{f(t_r)} dz_i \quad [10]$$

A similar expression results for the electrode EF . The dimensionless primary cell resistance is

$$W\kappa R = \frac{\chi_{i,\max}}{\int_a^B \frac{g(t_r)}{f(t_r)} dz_i} \quad [11]$$

where R is the actual cell resistance. The primary current distribution and the cell resistance for this system are functions of only three geometric ratios and were obtained numerically. Values of A , B , C , and D in the z plane corresponding to a , b , c , and d in the t plane were obtained through numerical integration of Eq. [1] (13). The value of $\chi_{i,\max}$ was obtained through numerical integration of Eq. [3] between the limits of a and $-d$. The values of t_r corresponding to given values of z were calculated through numerical integration of Eq. [1] and were used to calculate the values of $f(t_r)$ and $g(t_r)$.

Results

The calculated primary current distribution is presented below and compared to current distributions obtained from asymptotic solutions of Laplace's equation. The result most useful for cell design, however, is the cell resistance.

Primary current distribution.—The primary current distributions on the AB and EF electrodes are presented in Fig. 3. This distribution is characterized by three geometric ratios, chosen here to be $t/G = 0.25$, $h/G = 1$, and $L/h = 2.5$, where L is the length of the AB electrode and the insulating wall, t is the thickness of the protruding electrode assembly, G is the gap between the front edge of the AB electrode and the insulating wall, and h is the separation between the lines AB and CD (and, by symmetry, EF and GH) (see Fig. 2a). The current distributions of the two electrodes have been superimposed. The current density is infinite at A and is finite at B , E , and F .

Asymptotic forms of the current distribution can be derived and compared to the calculated current distribu-

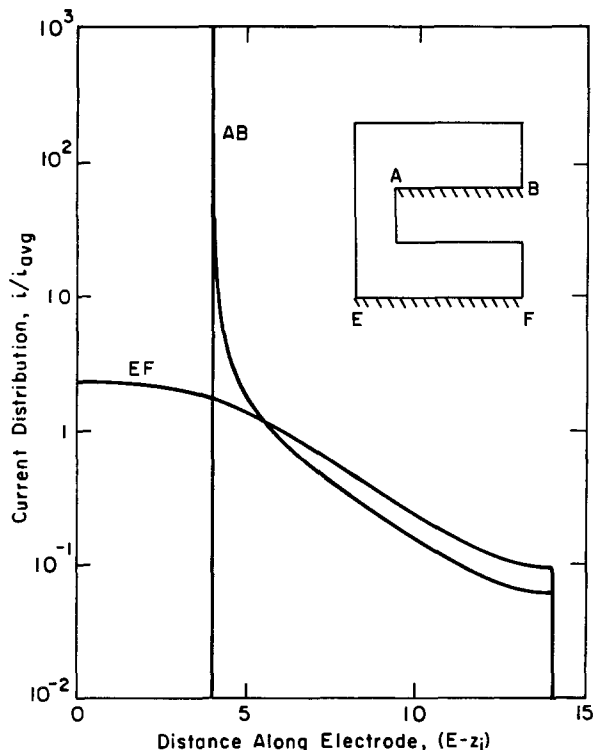


Fig. 3. Current distribution along the AB and EF electrodes for $L/h = 2.5$, $t/G = 0.25$, and $h/G = 1$.

tion. The current distribution close to the edge of an electrode adjoining an insulator with an angle α is

$$\frac{i(z_i)}{i_{avg}} = \text{const.} \frac{\pi}{2\alpha} (Q - z_i)^{\pi/2\alpha - 1} \quad [12]$$

where Q is the point of intersection of the electrode and insulator. At A , where α is $3\pi/2$, the current density is proportional to $(A - z_i)^{-2/3}$, and at B , E , and F , the current density is independent of $(Q - z_i)$. The current density is seen in Fig. 3 to approach a constant value at both edges of the EF electrode and at the far edge of the AB electrode. The current distribution along the AB electrode is presented in a log-log format in Fig. 4. The behavior close to the edge is emphasized, and the expected $-2/3$ power dependence on $(A - z_i)$ is observed.

Far from the gap, the asymptotic form for the current distribution is

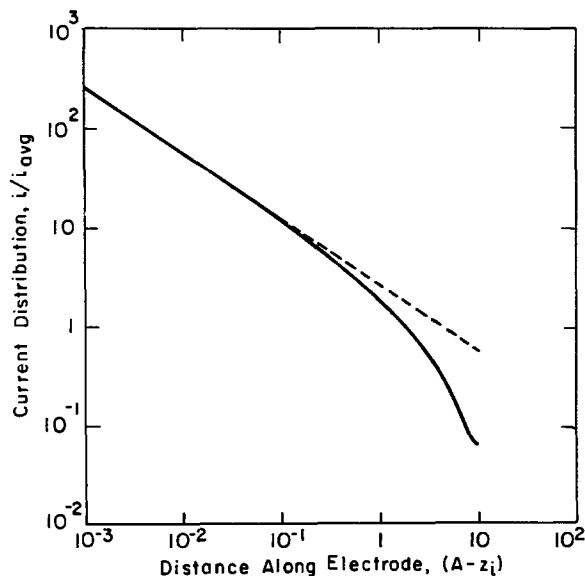


Fig. 4. Current distribution along the AB electrode compared to the asymptotic solution for $L/h = 2.5$, $t/G = 0.25$, and $h/G = 1$.

$$\frac{i(z_i)}{i_{avg}} = \text{const.} \nu \cosh [\nu (z_i - z_{i,max})] \quad [13]$$

where

$$\nu = \frac{\pi}{2h}$$

The calculated current distributions for the AB and the EF electrodes presented in Fig. 3 show agreement with this form for values of $E - z_i$ greater than about 7.5. The curves have the same shape in this region but are displaced vertically, attesting to the need for a different coefficient ("const.") for the two electrodes.

Primary cell resistance.—The primary cell resistance R can be expressed in terms of a dimensionless group $W\kappa R$. The dimensionless primary cell resistance for this system is a function of three geometric ratios, as described in the previous section. In the limit that the thickness t approaches zero, the resistance approaches a value that is independent of t/G . The cell resistance can therefore be expressed as the sum of the resistance for t/G equal to 0, $W\kappa R_0$, and a dimensionless correction term, Δ

$$W\kappa R = W\kappa R_0 + \Delta \quad [14]$$

The resistance $W\kappa R_0$ is presented in Fig. 5 as a function of L/h with h/G as a parameter. For all values of h/G , the dimensionless resistance in Fig. 5 approaches a constant value as L/h becomes greater than 2. The additional electrode length is relatively inaccessible and does not contribute much to current flow (see Fig. 3). For all values of h/G , the resistance approaches infinity with $[-1/\pi \ln(L/h)]$ as L/h approaches zero. The resistance increases with h at constant L and G because the distance between the electrodes AB and EF increases.

The resistance correction term, Δ , can be considered to be the additional resistance due to a finite (nonzero) electrode thickness t . Δ is presented in Fig. 6 as a function of t/G with L/h as a parameter. This term is independent of h/G and is only a very weak function of L/h . The correction term is given by the upper line in Fig. 6 for $L/h > 1$ and by the lower line in Fig. 6 for $L/h < 0.01$. The slope for $t/G > 0.5$ has the value 1, as anticipated from the asymptotic solutions for t/G approaching infinity.

The cell resistance for a given configuration can be obtained from Fig. 5 and 6 with Eq. [14]. The cell resistance is smallest when the gap (G) is large, the height (h) is small, and the electrode length (L) is large. An approximate analytic expression for the cell resistance can be obtained by interpolation of asymptotic solutions to Eq. [11]. The correction term for a finite electrode thickness can be expressed by

$$\Delta = t/G + \Delta_1 \quad [15]$$

The resistance of the cell with a zero electrode thickness is given by

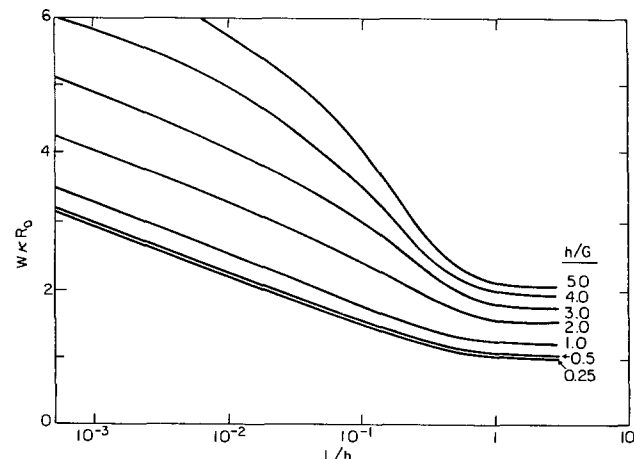


Fig. 5. Dimensionless cell resistance with t/G equal to zero as a function of L/h with h/G as a parameter.

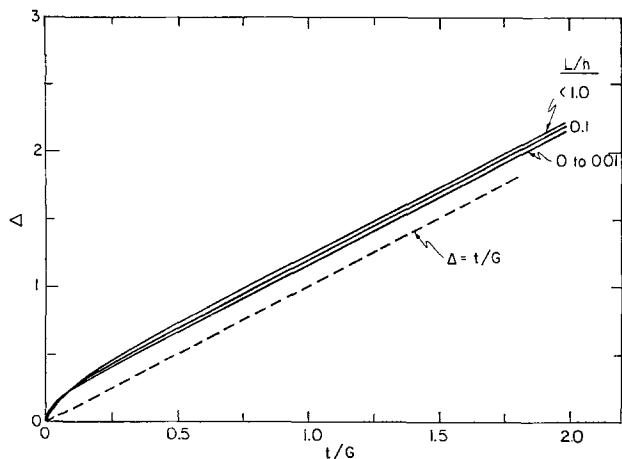


Fig. 6. Dimensionless correction to the cell resistance as a function of t/G with L/h as a parameter.

$$W\kappa R_0 = \frac{1}{\pi} \ln \left[\frac{16 \left(1 + \frac{c}{b}\right)}{\left(1 - \frac{c}{d}\right)} - (32 - e^\pi) \right] + \Delta_0 \quad [16]$$

where

$$\frac{b}{c} = \tanh \left\{ \frac{\pi}{2} \left[\frac{\left(\frac{L}{G}\right)^4}{\left(1 + 2\frac{L}{G}\right)^2} + \left(\frac{L}{h}\right)^4 \right]^{0.25} \right\} \quad [17]$$

$$\left(1 - \frac{c}{d}\right) = 2 \frac{\sinh^2\left(\frac{x}{2}\right)}{\cosh(x)} \quad [18a]$$

and

$$x = \frac{4 \cos\left(\frac{\pi}{2} \frac{L}{L+G}\right) e^{-\frac{\pi}{2} \frac{h}{L+G}}}{\cosh\left(0.3 \frac{\pi}{2} \frac{L}{h}\right)} + \frac{\frac{\pi}{2} \frac{G}{h}}{\cosh^2\left(1.2 \frac{\pi}{2} \frac{h}{L+G}\right)} \quad [18b]$$

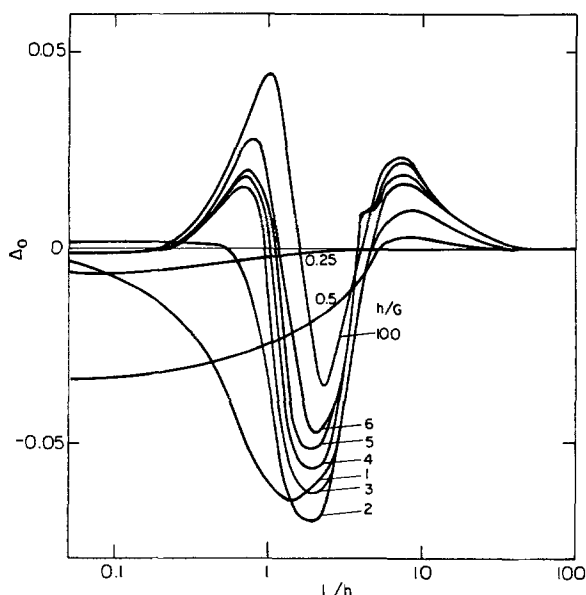


Fig. 7. Dimensionless correction to Eq. [16] for a resistance of a cell with $t/G = 0$.

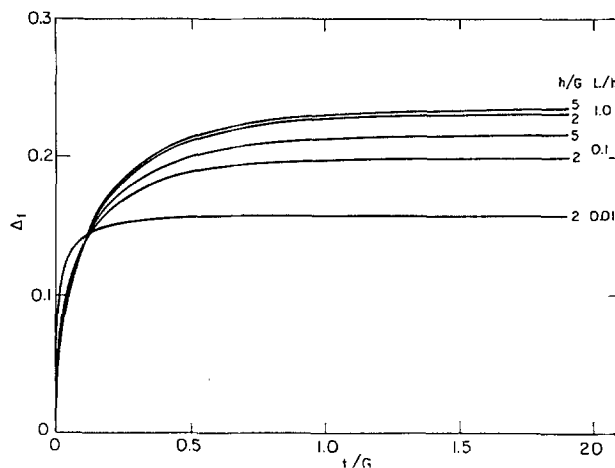


Fig. 8. Dimensionless correction to Eq. [15] for the contribution of t/G to the cell resistance.

The term Δ_0 in Eq. [16] is presented in Fig. 7 as a function of L/h . This term amounts to less than 5% and approaches a constant value as L/h approaches infinity and as L/h approaches zero. The term Δ_1 in Eq. [15] is presented in Fig. 8.

The effect of the cell resistance in the photoelectrochemical cell proposed, in the "Cell Geometry" section must be balanced with the need for a large semiconductor area open to illumination. Optimal design of this cell requires a large number of narrow slots (13, 14). The resistance of such a cell with $h/G = 10$, $L/h = 0.5$, and $t/G = 20$, can be expressed in terms of Eq. [14], [15], and [16] as

$$W\kappa R = W\kappa R_0 + \Delta_0 + t/G + \Delta_1 \quad [19]$$

$$W\kappa R = 2.9891 + 0.0148 + 20. + 0.2$$

The error in neglecting the correction terms, Δ_0 and Δ_1 , is 0.93%.

Conclusions

The primary resistance of a slotted-electrode cell was obtained by numerical integration coupled with the Schwarz-Christoffel transformation. An approximate analytic expression is also presented for the cell resistance. The slotted-electrode cell design may be well suited for photoelectrochemical devices for solar energy conversion. For optimal solar cell designs, the cell resistance can be expressed as the sum of $W\kappa R_0$ (given by Eq. [16]) and the simple parallel-plate term t/G .

Acknowledgment

This work was supported by the United States Department of Energy under Contract no. DE-AC03-76SF00098 through the Director, Office of Energy Research, Office of Basic Energy Sciences, Chemical Sciences Division, and through the Assistant Secretary of Conservation and Renewable Energy, Office of Advanced Conservation Technology, Electrochemical Systems Research Division.

Manuscript submitted June 24, 1983; revised manuscript received April 16, 1984.

The University of California assisted in meeting the publication costs of this article.

LIST OF SYMBOLS

G	distance between edge of AB electrode and the center of the gap (cm)
h	separation between electrode AB and cover plate CD (cm)
i	current density (mA/cm ²)
j	$\sqrt{-1}$
L	half-length of AB electrode (cm)
R	cell resistance (Ω)
t	thickness of AB electrode assembly (cm)
V	cell potential (V)
W	cell width in direction with no variations (cm)

Greek characters

α	angle at corner of electrode and insulating wall (radians)
Δ	cell resistance correction associated with a finite value of t/G
Δ_0	error term in Eq. [16]
Δ_1	error term in Eq. [15]
κ	conductivity (mho/cm)
Φ	electrical potential (V)

Subscripts

avg	average
i	imaginary
o	value with $t/G = 0$
r	real

REFERENCES

- C. Kadper, *Trans. Electrochem. Soc.*, **78**, 353 (1940); *ibid.*, **82**, 153 (1942).
- J. Newman, *This Journal*, **113**, 501 (1966).
- J. J. Miksis, Jr. and J. Newman, *ibid.*, **123**, 1030 (1976).
- P. Pierini and J. Newman, *ibid.*, **126**, 1348 (1979).
- R. N. Fleck, M. S. Thesis, University of California, Berkeley, CA (1964).
- R. V. Churchill, "Complex Variables and Applications," 2nd Ed., McGraw-Hill, New York (1960).
- E. T. Copson, "An Introduction to the Theory of Functions of a Complex Variable," Oxford University Press, London (1935).
- F. Bowman, "Introduction to Elliptic Functions with Applications," John Wiley and Sons, New York (1953).
- H. F. Moulton, *Proc. London Math. Soc. Ser. 2*, **3**, 104 (1905).
- F. Hine, S. Yoshizawa, and S. Okada, *This Journal*, **103**, 186 (1956).
- C. Wagner, *Plating*, **48**, 997 (1961).
- J. Newman, in "Electroanalytical Chemistry," Vol. 6, A. J. Bard, Editor, p. 187. Marcel Dekker, Inc., New York (1973).
- M. E. Orazem, Ph.D. Thesis, University of California, Berkeley, CA (1983).
- M. E. Orazem and J. Newman, *This Journal*, To be published.

Photodissolution Kinetics of n-GaAs in 1M KOH and Calculation of the Stabilization by Se^{2-}

Effect of the Ru^{3+} Surface Treatment

P. Allongue and H. Cachet

Groupe de Recherche no. 4 du CNRS, "Physique des Liquides et Electrochimie," associé à l'Université Pierre et Marie Curie, 75230 Paris Cedex 05, France

ABSTRACT

We present a method for obtaining the photodissolution kinetics of n-GaAs in 1M KOH. It is based upon the simultaneous measurement of photocurrent and impedance. It is shown that an accurate determination of the band bending is absolutely necessary to obtain the actual kinetic constants. In fact, the semiconductor bandedges shift toward positive potentials when illumination is increased. In addition, a potential-dependent surface charge variation is responsible for another voltage drop in the Helmholtz layer which modifies the band bending. This is shown by the surface-state capacitance C_{ss} (V), which presents sharp variations in applied potential. According to the current expression, $J_{\text{corr}} = k_{\text{corr}} p_s^2$, a value of $k_{\text{corr}} = 5.7 \times 10^{-27}$ mA cm⁴ is found to be independent of the photon flux, the surface orientation, and the ruthenium treatment. This value is used to estimate the stabilization coefficient s of the n-GaAs/1M ($\text{Se}^{2-}/\text{Se}_2^{2-}$) + 1M KOH junction. A value of s close to 100% is found. We then discuss the ruthenium treatment in selenide solution, where energetic conditions for charge transfer are changed through surface-charge modifications. Our calculations show an improvement of both cell performances and stability, as expected, when the electrode is Ru treated. Moreover, the effect of Ru^{3+} cations upon the impedance data suggests that the flatband potential shift is linked to chemical surface modifications, prior to corrosion. This is confirmed by the fact that k_{corr} is not photon-flux dependent. Finally, we examine whether the bonds (GaAs) with one electron might be responsible for the bandedge shift and the C_{ss} (V) behavior of the n-GaAs/1M KOH junction. The case of the Se^{2-} stabilized junction is also discussed.

For many years, the photocorrosion process at illuminated n-type III-V semiconductor electrodes in contact with aqueous electrolytes has been extensively studied in view of possible photoelectrochemical (PEC) application for solar energy conversion. A number of articles deal with the corrosion mechanism itself (1, 2) or with the competition between the photocorrosion of the semiconductor and the oxidation of a redox couple in solution (3-5). Until now, very little, to our knowledge, has been done to estimate the photocorrosion kinetic constants (6, 7).

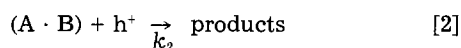
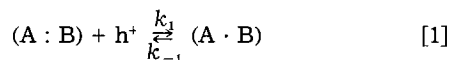
At first, it was stated that for all n-type semiconductor electrodes, except Ge, holes are entirely responsible for the photocorrosion reaction (1). For example, for GaAs, six charges per molecule of GaAs are consumed. It is shown also for III-V semiconductors that the stabilization coefficient, defined as the fraction of the photocurrent associated with the oxidation of the redox couple over the total photocurrent, is light-intensity dependent (3, 4). This very important result led workers to study the different mechanisms for explaining the competition between the semiconductor and redox couple photo-oxidations (1-5). These studies show that the corrosion process can be de-

scribed by a two-step reaction, each one involving a hole. The first one is rate limiting while the second one is considered as very fast. Cardon *et al.* (3) developed a very general kinetic scheme assuming the first corrosion step can be reversible or not, the transfer upon the redox couple direct or indirect, and the intermediates mobile or motionless. These assumptions lead, for III-V semiconductors, to $s = f(y/j)$ or $s = f(y^2/j)$ relationships, where y is the redox concentration and j the total photocurrent. Unfortunately, it seems difficult to connect unambiguously experimental facts to these resulting equations. If a mechanism may be deduced from such equations, the number of parameters does not reasonably allow one to reach a kinetic constant for the corrosion. This quite extensive analysis was applied to n-GaP and n-InP electrodes (3). However, Frese and co-workers (4) and, more recently, Gerischer (5) presented very similar models for the corrosion-stabilization mechanism of n-GaAs and n-GaP, respectively.

In fact, all these models can be reduced to a mechanism that focuses on the breaking of a single surface bond, involving two electrons, as the one of Frese *et al.*, although it is known that six holes are consumed per mole-

cule of GaAs. It means that when a surface bond is completely broken, the corresponding atoms are more weakly linked to the semiconductor lattice and are attacked much faster than those having their three complete bonds. Thus, the breaking of the two last bonds is implicit and the first breaking is the rate-limiting mechanism of photocorrosion.

We retain the model of Frese *et al.*, which is appropriate to determine a kinetic constant, because parameters are very few and have a physical meaning. As it is necessary for the discussion, we briefly summarize the main points of this model and the signification of the involved rate constants. The photodissolution process is described by the two following reactions, where A and B denote the two compounds of the semiconductor



In Eq. [1], a photogenerated hole h^+ is captured by a two-electron surface bond (A : B) leading to the creation of a radical like (A · B). This step is supposed reversible. This means that the complete bond may be regenerated by the capture of an electron. The second reaction is assumed irreversible and fast because the bonding energy E_{SR} associated with the radical is very weak compared to the lattice bond energy. The first step is an activated hole capture between the top of the valence band E_V and the energy E_{SB} of a two-electron surface bond (Fig. 1). The rate constant k_1 is given by

$$k_1 = \langle q\sigma_1 v d \rangle (A : B) \exp\left(-\frac{(E_V - E_{SB})}{kT}\right) \quad [3]$$

where q is the electronic charge ($q > 0$), σ_1 the capture cross section for holes, v the thermal velocity for holes (1.7×10^7 cm/s), d a reaction length, and (A : B) the volume density of the two-electron surface bonds, which are likely to undergo corrosion. The reverse reaction is a hole exchange between the valence band and the energy level E_{SB} . If E_{SB} is close to E_V , one gets for the rate constant k_{-1}

$$k_{-1} = \langle q\sigma_1 v d \rangle N_V \quad [4]$$

where N_V is the valence-band-state density.

The second step is responsible for the corrosion current corresponding to the release of Ga^{3+} and As^{3+} ions to solution (2b). This is only indicative of the oxidation state of gallium and arsenic atoms, whereas the actual chemical entities may involve solvated ions or oxide or hydroxide compounds. This last step is a simple hole capture by the surface state connected with the radical (A · B). The corresponding energy of a one-electron bond is expected to be much weaker than a two-electron bond, which is why E_{SR} is higher in the bandgap than E_{SB} (Fig. 1). The capture rate constant k_2 is

$$k_2 = \langle q\sigma_2 v d \rangle \quad [5]$$

Under stationary conditions, $d(A \cdot B)/dt = 0$, and assuming first-order kinetics for all reactive species, one gets the corrosion current J_{corr} which arises from the transfer of Ga^{3+} and As^{3+} to solution

$$J_{corr} = k_1 p_s^2 / (k_{-1} k_2 + p_s) \quad [6]$$

where p_s is the hole concentration at the surface.

As mentioned above, kinetic constant investigations for photocorrosion has been neglected, while the stabilization coefficient was extensively studied, mainly by rotating ring-disk electrode. The aim of this paper is to estimate the photocorrosion rate constants for n-GaAs in 1M KOH. We intend to compare our results for photodissolution to the previous kinetics determination we made for n-GaAs in 1M KOH + 1M (Se²⁻/Se₂²⁻) (8). Through stabilization coefficient calculations, we show that our experimental method, based upon simultaneous impedance

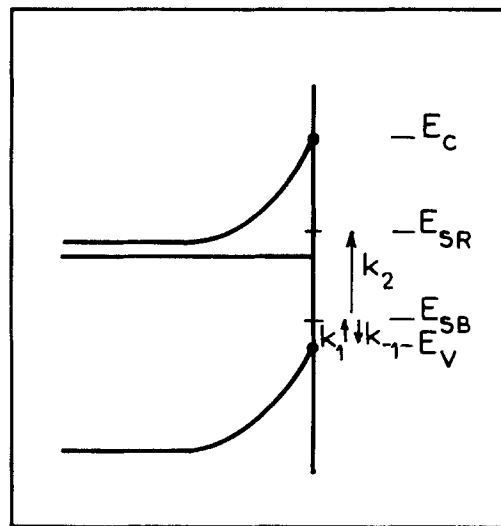


Fig. 1. Energy diagram of an n-type III-V semiconductor/electrolyte PEC junction. The energy levels E_{SR} and E_{SB} associated with (A · B) and (A : B) bonds are reported. The currents associated with Eq. [1] and [2] are represented.

and current measurements in order to determine the actual band bending at any bias, is self-consistent. Furthermore, the effect of the ruthenium treatment is studied and discussed in terms of surface modifications. At last we try to see if the model of Frese *et al.* can be used to interpret impedance results for corrosion and for the stabilized junction.

Experimental and Analysis Procedure

Undoped n-type (2.3×10^{16} cm⁻³; <100> orientation) and (1.4×10^{16} cm⁻³; <111> orientation) GaAs single crystals are purchased from MCP Limited and RTC, respectively. After polishing, semiconductor electrodes are etched with a (H₂SO₄; H₂O₂; H₂O) (2V; 1V; 1V) mixture. All measurements are made in a classical three-electrode electrochemical cell. All potentials refer to the saturated calomel reference (SCE). Ruthenium treatment is performed as follows: the freshly etched electrode is dipped in 1M KOH + 1M (Se²⁻/Se₂²⁻) electrolyte for a few minutes, rinsed with water, then dipped in an acidic 0.1M HCl + 10⁻²M RuCl₃ solution for a few minutes, and water rinsed before being employed for photoelectrochemical experiments (9). A 100W quartz-halogen lamp is used for illumination and light intensity is changed with neutral filters and measured with a MACAM TR 3010 radiometer. The given light intensities, in the following, are measured before the light flux comes into the PEC cell. Stationary I-V curves and impedance measurements are performed under potentiostatic conditions. Impedance analysis has been presented elsewhere (8), but as it is important for kinetics studies, we emphasize the band bending determination in the next paragraph.

We will not describe once again the way impedances are analyzed; one should refer to our previous paper for the significance of C_{ss} (V) and C_{sc} (8); C_{sc} is the space-charge capacitance, and C_{ss} (V) is associated with surface-charge variations. The main point is that these capacitances are C_H dependent, C_H being the Helmholtz capacitance. According to the equivalent electrical scheme we use (8), two cases may exist: (i) when $C_{ss} \ll C_{sc}$, as it is the case in the linear part of the Mott-Schottky plot, the series combination of C_{sc} and C_H is measured. (ii) When C_{ss} is much greater than C_{sc} , the series combination of C_{ss} and C_H is measured. This happens under illumination for potentials close to -1.25 V/SCE (see Fig. 5).

Consequently, the slope β of the experimental Mott-Schottky plot ($C_{sc}^{-2} = \beta V_b$) and the C_{ss} (V) curve are C_H dependent. The aim is to determine the real band bending V_b of the semiconductor at each potential V , for a given C_H .

From capacitance measurements, the band bending V_b can be derived from the following differential equation (10)

$$dV_b/dV = C_H/(C_{sc} + C_{ss} + C_H) \quad [7]$$

If we integrate this equation between two potentials close to each other, one gets the variation δV_b^i of the band bending when V varies from V^i to $V^i + \delta V^i$. δV_b^i and δV^i are no longer infinitesimal, but are now finite variations, and the following relation holds

$$\delta V_b^i = \delta V^i \cdot C_H/(C_H + C_{sc}^i + C_{ss}^i) \quad [8]$$

where C_{sc}^i and C_{ss}^i are the space-charge and the surface-state capacitances, respectively, at the potential V^i . If we repeat this procedure for each potential V^i , one may reach the total variation of V_b for any variation of the applied potential. Thus V_b^i is known with respect to an additive constant V_b^0

$$V_b^i = V_b^0 + \sum_{j=1}^i \delta V_b^j \quad [9]$$

where V_b^i is the effective band bending of the semiconductor at the potential V^i , and V_b^0 the additive constant corresponding to the band bending at $V = V^0$.

We then compare, for a given V_b^0 , at each potential, the experimental C_{sc}^{-2} value and the quantity $\beta V_b(V)$, β being the experimental slope of the Mott-Schottky plot, and V_b defined by Eq. [7]. Doing this, we may: (i) check that Eq. [7] is valid, and (ii) determine V_b^0 and then $V_b(V)$ at each potential.

Using this procedure for I-V curve analysis of n-GaAs/selenide junctions, we found that C_H should take a value close to $2.8 \mu\text{F}/\text{cm}^2$ to obtain the best fit between experimental and calculated I-V characteristics (11). In the case of the n-GaAs/1M KOH interface, C_H represents the series combination of the Helmholtz and the oxide overlayer capacitances. In fact, in 1M KOH electrolyte, the surface is covered by a very thin As_2O_3 layer that does not exist when K_2Se is put in solution (Fig. 2) (12). Moreover, direct observation of nuclear reactions allowed us to estimate the O_2 quantity at the surface (13). It appears that the As_2O_3 thickness is about 10-20Å (12). Taking $\epsilon \sim 10$ and a thickness of 10Å, one gets $C_{ox} = 8.8 \mu\text{F}/\text{cm}^2$, C_{ox} being the surface-oxide capacitance.

For calculations, we take $C_H = 2 \mu\text{F}/\text{cm}^2$. This value is obtained by the same procedure as for n-GaAs/selenide junctions. Note that this value is close to the series combination of $C_{ox} = 8.8 \mu\text{F}/\text{cm}^2$ and $C_H = 2.8 \mu\text{F}/\text{cm}^2$.

Results

Figure 3 presents $C_{sc}^{-2}V$ Mott-Schottky plots for an n-GaAs(100)/1M KOH PEC junction in the dark and under various illuminations. As for n-GaAs/selenide junctions (8, 11), these curves are straight lines, almost parallel, and shifted toward positive potentials as light intensity is in-

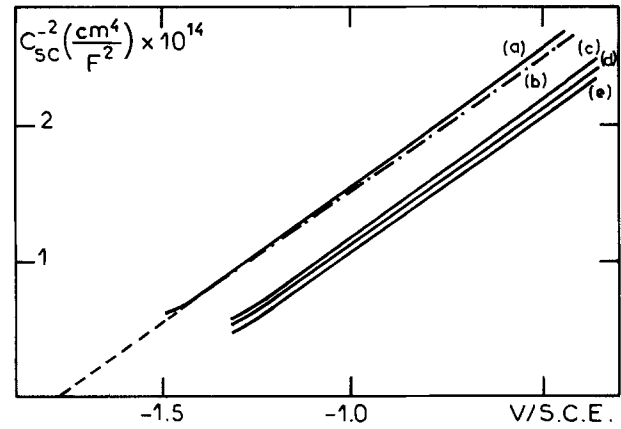


Fig. 3. Mott-Schottky plots for the n-GaAs/1M KOH junction in the dark and under the various illuminations. Curve (a): in dark. Curve (b): in dark, after a photocorrosion current flowing through the junction ($I = 1 \text{ mA}/\text{cm}^2$ for 1h). Curves (c), (d), and (e); under 1, 5, 20 mW/cm^2 illumination.

creased. In the dark, the flatband potential $V_{FB} = -1.85 \text{ V/SCE}$, is independent of the surface orientation. This result is in good agreement with other publications (14). For potentials anodic of -1.2 V/SCE , the semiconductor bands are pinned and a pseudo-flatband potential V_{FB}^* under illumination can be defined as the intercept of the $C_{sc}^{-2}V$ straight line with the V axis. Moreover, this shift is reversible. The bandedges return to their initial positions when light is cut off, although the slope of the Mott-Schottky plot is slightly changed (Fig. 3, curve b). This latter point may be the consequence of a change of the geometrical surface due to surface corrosion. Under illumination and for potentials cathodic of -1.2 V/SCE , all the curves slightly deviate from their linear part; the same behavior is observed in the dark around -1.5 V/SCE . The variations of the flatband potential shift $\Delta V_{FB} = V_{FB}^* - V_{FB}$ as a function of the saturation current density is reported in Fig. 4. It can be seen that ΔV_{FB} presents a step for very low illumination and then a regular variation with light intensity. Furthermore, ΔV_{FB} tends to an asymptotic value of $\sim 0.380 \text{ V}$, similar to the one found for n-GaAs/selenide junctions (11).

Surface charge variations are evidenced by the surface-state capacitance $C_{ss}(V)$ curves under illumination (Fig. 5). These data are characterized by a sharp peak located around -1.25 V/SCE , and its height increases with increasing light intensity. In the dark, the peak disappears. This behavior recalls the one of n-GaAs/selenide junctions. Note that measurements are not performed for potentials cathodic of -1.35 V/SCE to avoid any chemical modification of the surface: our surface observations show that the As_2O_3 oxide layer, which results from the

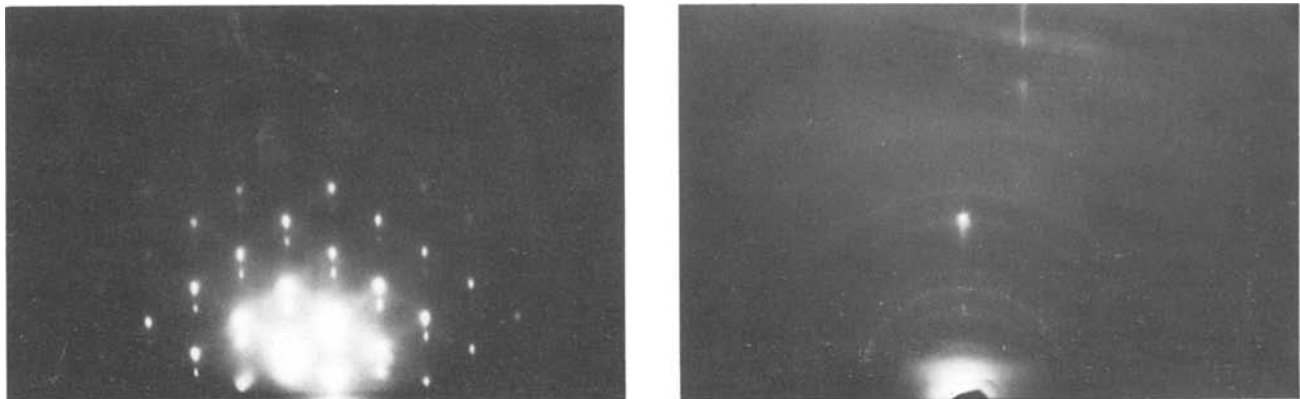


Fig. 2. RHEED observations of an n-GaAs surface in contact with 1M KOH. a(left) Freshly etched electrode; points represent the single-crystal diffraction pattern. b(right): The same electrode after photodissolution for 2h ($V = -1.0 \text{ V/SCE}$; $I = 1 \text{ mA}/\text{cm}^2$); the rings have been identified to those of As_2O_3 (12).

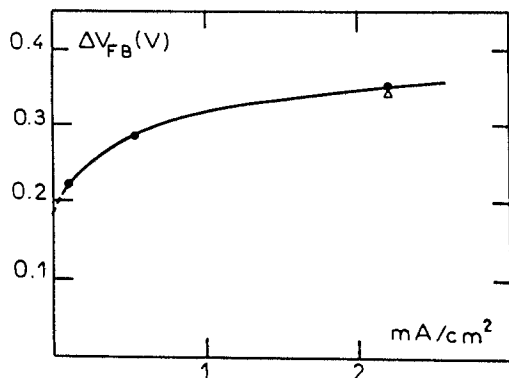


Fig. 4. Flatband potential shift $\Delta V_{FB} = V_{FB} - V_{FB}^*$ as a function of the saturation current density. (●): n(100) orientation. (△): n(111) orientation.

photocorrosion process, can be reduced by hydrogen evolution (12).

In Fig. 4, the flatband potential shift ΔV_{FB} for an n(111) GaAs electrode is also reported. This value is almost on the curve corresponding to the (100) electrode, showing no particular effect of the orientation. In addition, this parameter is not crucial for the photocorrosion process of n-GaAs. This fact is confirmed by Fig. 6, which presents very similar I-V curves for n(100) (curve a) and n(111) (curve d) GaAs in the same pure photocorrosion conditions in 1M KOH under 20 mW/cm².

The ruthenium treatment is only sensitive over the flatband potential in the dark, which is now $V_{FB} = -1.78$ V/SCE. This value is slightly more positive than that of the untreated electrode, indicating that the surface has gained positive charges as Ru^{3+} . However, the I-V curves and the V_{FB}^* are independent of this treatment (Fig. 6, curves e and f). On the contrary, this treatment is quite important for n(100) GaAs/selenide junctions, as is revealed by our preliminary results. The I-V characteristics, Mott-Schottky plots and surface-state capacitance are modified. As reported by Parkinson *et al.* (9), it is confirmed that the fill factor is greater for treated electrodes (Fig. 7), while the open-circuit voltage remains little changed. This is to be connected to capacitance measurements. In the dark, the flatband potential is $V_{FB} = -1.91$ V/SCE, while under 22 mW/cm² the pseudo-flatband potential becomes $V_{FB}^* = -1.85$ V/SCE (Fig. 8). As a result, the bandedge shift $\Delta V_{FB} = 0.06$ V is much smaller for treated electrodes. For untreated ones the values are, respectively: $V_{FB} = -2.06$ V/SCE, $V_{FB}^* = -1.79$ V/SCE, and $\Delta V_{FB} = 0.270$ V. Correlatively, the peak in C_{ss} (V) keeps almost the same location but it is lowered (Fig. 9).

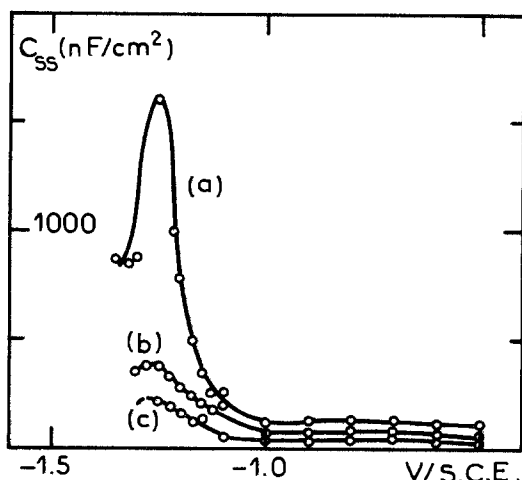


Fig. 5. Surface-state capacitance C_{ss} (V) curve of an n-GaAs/1M KOH junction under various illuminations. Curve (a): 20 mW/cm². Curve (b): 5 mW/cm². Curve (c): 1 mW/cm².

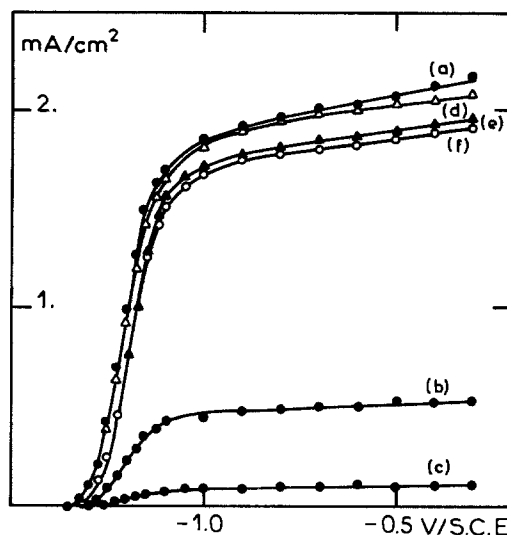


Fig. 6. Experimental and calculated I-V characteristics of n-GaAs/1M KOH junctions under various levels of illumination and for various electrodes. (●), (▲), (○), (△): Experimental data. (—): Calculated curves according to the complete model. (●): n(100) orientation, untreated electrode. Parameters are: $\alpha = 26,000$ cm⁻¹; $V_{FB} = -1.85$ V/SCE; $L = 0.2$ μm; $\tau = 1.45 \times 10^{-10}$ s; $N_D = 2.3 \times 10^{16}$ cm⁻³; $\sigma_1 = \sigma_2 = 10^{-15}$ cm² (with these values $k_{-1} = 2.72 \times 10^{-12}$ mA cm). Curves (a), (b) and (c): $k_{corr} = 5.7 \times 10^{-27}$ mA cm⁴ ($k_1 = 5 \times 10^{-8}$ mA cm). (△): n(111) orientation, untreated electrode. Parameters are those of curve (a), except: $L = 0.25$ μm; $\tau = 2.42 \times 10^{-10}$ s; $N_D = 1.4 \times 10^{16}$ cm⁻³. Curve (d): $k_{corr} = 8.0 \times 10^{-27}$ mA cm⁴ ($k_1 = 7 \times 10^{-8}$ mA cm). (▲) and (○): untreated and ruthenium treated n(100) electrodes, respectively. Curve (e): Parameters are those of curves (a), (b), and (c), except $k_{corr} = 0.8 \times 10^{-27}$ mA cm⁴ ($k_1 = 7 \times 10^{-9}$ mA cm). $V_{FB}^* = -1.50$ V/SCE. Curve (f): Parameters are those of curve (e), except: $V_{FB} = -1.78$ V/SCE, $k_{corr} = 1.14 \times 10^{-27}$ mA cm⁴ ($k_1 = 1 \times 10^{-8}$ mA cm), $V_{FB}^* = -1.50$ V/SCE.

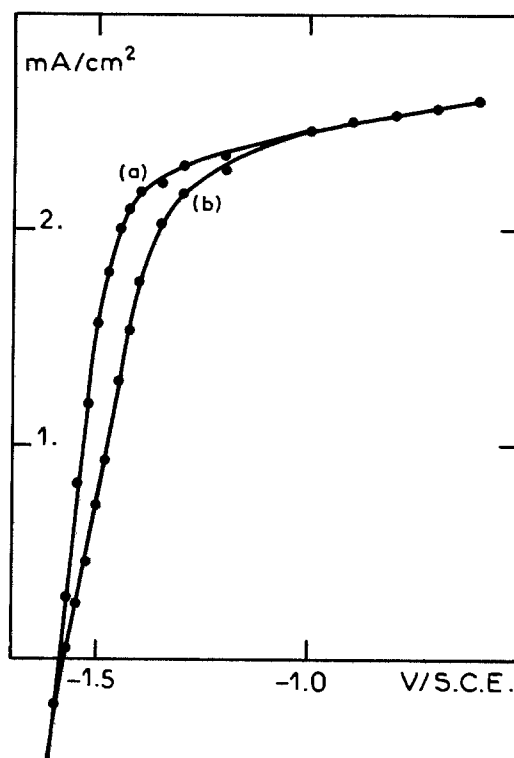


Fig. 7. I-V characteristics of an n-GaAs/(Se²⁻/Se₂²⁻) junction under ~30 mW/cm² illumination. (●): Experimental data. (—): Calculated curves according to the model of Ref. (8). Curve (a): ruthenium-treated electrode. Parameters are: $\alpha = 26,000$ cm⁻¹; $L = 0.2$ μm; $\tau = 1.45 \times 10^{-10}$ s; $N_D = 2.3 \times 10^{16}$ cm⁻³; $V_{FB} = -1.91$ V/SCE; $V_{FB}^* = -1.85$ V/SCE; $\lambda = 1$ eV; $V_{redox} = -0.96$ V/SCE; $V_{oc} = 0.62$ V; FF = 0.64. Curve (b): untreated electrode. Parameters are those of curve (a), except: $V_{FB} = -2.06$ V/SCE; $V_{FB}^* = -1.79$ V/SCE; $V_{oc} = 0.62$ V; FF = 0.52.

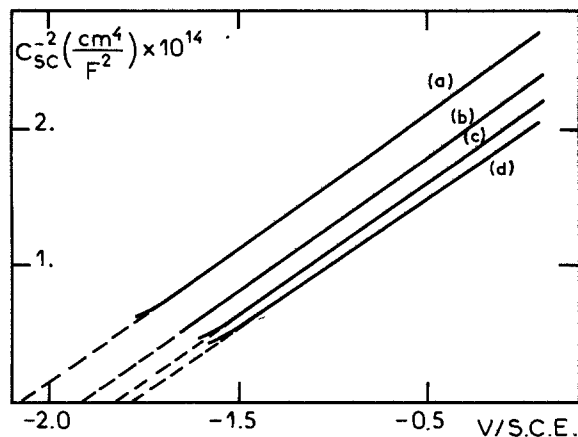


Fig. 8. Mott-Schottky plots for an n-GaAs/(Se²⁻/Se²²⁻) junction in the dark and under ~ 30 mW/cm² illumination. Curves (a) and (d): untreated electrode in dark and under illumination, respectively; $\Delta V_{FB} = 0.270$ V. Curves (b) and (c): ruthenium-treated electrode in the dark and under illumination, respectively; $\Delta V_{FB} = 0.06$ V.

Discussion

In a previous paper, we dealt with the detailed analysis of the photoresponse of a n-type semiconductor/electrolyte liquid junction, assuming a direct hole transfer upon the reduced species in solution (8). The transfer rate constant being defined, we calculated the surface hole concentration through the balance between photogenerated holes and holes which disappear because of recombination (at the surface and in the space-charge region) or because they cross the interface towards solution. In this paper, the same method is used. We only have to change the hole-transfer current upon the redox couple J_p (8) by the expression of the photocorrosion current J_{corr} (Eq. [6]) in Eq. [24] of Ref. (8). The other currents only concern the

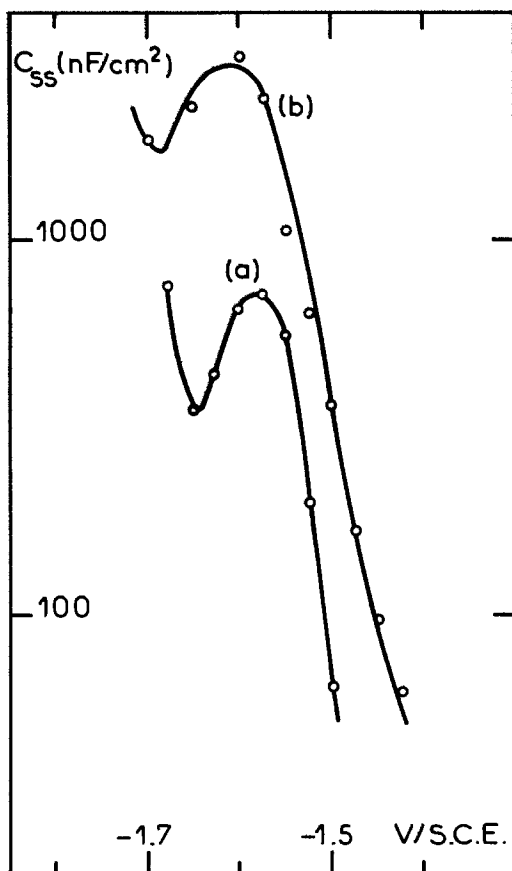


Fig. 9. Surface-state capacitance C_{ss} (V) curves for n-GaAs/(Se²⁻/Se²²⁻) liquid junctions under ~ 30 mW/cm² illumination. Curve (a): ruthenium-treated electrode. Curve (b): untreated electrode.

semiconductor itself and thus have not to be modified, except the surface recombination current. For this latter, the complete analogy of the surface-state capacitance C_{ss} (V) results between the two systems, stabilized or not, allows one to think that this current is negligible. In the following, we do not take it into account.

Kinetic rate constant determination.—As before, all parameters (V_{FB} , V_b (V), . . .) are predetermined by impedance and current measurements (8), except for the ratio $k_1 k_2 / k_{-1}$, which is the only adjustable parameter in the present analysis of the photocorrosion I-V curves. In fact, according to the model of Frese *et al.*, it appears that $k_{-1} k_2 = N_V \sigma_1 / \sigma_2 \gg p_s$ at any bias for the illumination range we use. Thus J_{corr} reduces to Eq. [10]

$$J_{corr} = \frac{k_1 k_2}{k_{-1}} p_s^2 = k_{corr} p_s^2 \quad [10]$$

In the following, we will attempt to discuss the different constants that are included in k_{corr} within the framework of our impedance results. For the moment, we assume that Eq. [10] is valid and that k_{corr} is an adjustable parameter.

Under various illuminations, we try to fit, in the best way, the calculated I-V curve to the experimental one. Of course, in this analysis, we take into account the band-edge shift (Fig. 3) to estimate the band bending V_b of the semiconductor. Taking the pseudo-flatband potential V_{FB}^* as the reference for V_b , e.g., $V_b = V - V_{FB}^*$, where V is the applied potential, we obtain a good match (Fig. 10, curve a). But under illumination, for potentials close to -1.25 V/SCE, the Mott-Schottky plots present a slight deviation with respect to their linear part (Fig. 3). This experimental fact can be interpreted by a slower variation of V_b with respect to the applied potential V , owing to surface-charge variations (Eq. [7]). Calculating V_b with all the capacitances of the equivalent circuit, we find a better fit between calculated and experimental I-V curves, and we are also able to represent the Mott-Schottky plots. The calculated photocurrent rise is less abrupt and more representative of the observed behavior (Fig. 10, curve b). Moreover, the value of k_{corr} is found to be much smaller than in the case of the simple analysis (Fig. 10). In the following, the complete analysis is performed to determine the actual V_b at each potential.

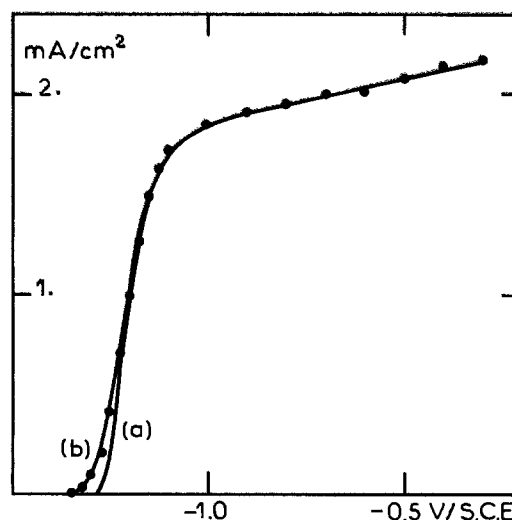


Fig. 10. Comparison between calculated and experimental I-V curves for the n-GaAs/1M KOH junction under 20 mW/cm² illumination. (●): Experimental data. (—): Calculated curves according to the model of Frese *et al.* Different methods to calculate V_b are considered. Parameters are: $\alpha = 26,000$ cm⁻¹; $L = 0.2$ μ m; $\tau = 1.45 \times 10^{-10}$ s; $V_{FB} = -1.85$ V/SCE; Curve (a): $V_{FB}^* = -1.50$ V/SCE. V_b is taken as: $V_b = V - V_{FB}^*$. $k_{corr} = 1.1 \times 10^{-25}$ mA cm⁴. Curve (b): The complete calculation of the band bending V_b is performed at every potential. $k_{corr} = 5.7 \times 10^{-27}$ mA cm⁴.

For an n-type GaAs (100) electrode, we obtain $k_{\text{corr}} = 5.7 \times 10^{-27}$ mA cm⁴ under any illumination (Fig. 6, curves a, b, c). In fact, during the photodissolution process, charges are transferred to atoms of the semiconductor itself. Thus the relative bandedge position with respect to a reference in solution does not play any role upon the kinetic constant k_{corr} . This point is well verified experimentally. The corrosion model, its quadratic dependence in p_s , and our band bending analysis are then found to be justified. Consequently, all studies based only upon capacitance data in the dark are erroneous. The latter would lead to a light intensity-dependent constant k_{corr} , and the resulting values would be much smaller than ours. The stabilization coefficient calculation further reinforces our analysis.

Physically, the potential for the onset of the photocorrosion hole current is the potential where a critical surface hole concentration is reached. For a given p_s , the required V_b becomes smaller when the illumination increases. Thus, the flatband potential shift with illumination makes k_{corr} independent of the photon flux. This remark leads us to believe that the bandedge shift could be linked to steps that precede corrosion itself. The last step (corrosion) does not occur if the hole transfer upon the redox species is more favorable, as it is the case with Se²⁻ electrolytes (8, 11). These intermediate steps should be then understood as chemical modifications at the surface through interactions between holes trapped in surface bonds and the solvent (11, 15).

In the case of n(111) GaAs electrodes, we found $k_{\text{corr}} = 8.0 \times 10^{-27}$ mA cm⁴. This value is very similar to the one obtained for n(100) electrodes and confirms that photocorrosion process in 1M KOH is not strongly affected by surface orientation. However, the surface morphology of a photocorroded n-GaAs (100) electrode in 1M KOH shows a slight variation in corrosion rate for different crystallographic planes (Fig. 11) (12, 16). A difference of a few percent is sufficient to produce such a pattern.

Last, the case of n(100) ruthenium-treated electrodes has been examined. We find $k_{\text{corr}} = 1.14 \times 10^{-27}$ mA cm⁴ and 0.8×10^{-27} mA cm⁴ for the treated and untreated electrodes (Fig. 6, curves e and f). These latter values are close to each other and confirm the previous determination of k_{corr} . In fact, if we consider the extreme sensitivity of k_{corr} with respect to the band bending estimate, it can be concluded that the ruthenium treatment and the surface orientation have no significant influence upon the photodissolution rate of GaAs in 1M KOH. It is worth noting that a 10 mV change in the determination of V_b may modify k_{corr} by a factor 2. In the dark, flatband potential measurements give $V_{\text{FB}} = -1.85$ and -1.78 V/SCE for the untreated and the treated electrodes, respectively. These

values indicate the surface has gained Ru³⁺ chemisorbed ions. It is well known that Ru³⁺ ions are incorporated at the surface defects (9). In spite of this remark, our analysis shows that the ruthenium treatment has no influence upon the photocorrosion kinetics of GaAs. This may be explained by the observed generalized attack (4, 12) (Fig. 11). The initial Ru³⁺ defect passivation is not sufficient to prevent corrosion because the defects are not preferred sites for corrosion. Under heavy photocorrosion conditions, Ru³⁺ ions are removed from the electrode. This is confirmed by the identical values of V_{FB}^* found for treated and untreated electrodes (Fig. 6, curves e and f).

Stabilization coefficient (case of untreated electrodes).—Evaluation of the rates of the reactions of photodissolution of the semiconductor and photo-oxidation of the redox couple allows one to estimate the stabilization coefficient of the n-GaAs/(Se²⁻/Se₂²⁻) junction. The parameters we use in our calculations are those of the stabilized junction (particularly bandedge positions). As above, the current J_p of Ref. (8) is replaced by $J_p + J_{\text{corr}}$ in Eq. [24] of Ref. (8). The stabilization coefficient is then $s = J_p/(J_p + J_{\text{corr}})$. When arriving at the surface, a hole may be transferred to solution either directly to be reduced species (Se²⁻) or through Ga³⁺ and As³⁺ ions as these leave the surface upon photocorrosion. In the second case, the hole current crosses the surface state E_{SR} .

Calculations have been performed with the data of the n-GaAs/(Se²⁻/Se₂²⁻) cell given in Ref. (11) for various levels of illumination. With $k_{\text{corr}} = 5.7 \times 10^{-27}$ mA cm⁴, our largest and least favorable value, we obtain a stabilization coefficient $s > 95\%$ (see Table I). This means that less than 5% of the total photocurrent is a corrosion current. Moreover, it is found that s increases when the light intensity is lowered or when the current is reduced through the applied potential at a given illumination (Fig. 12), as expected from theory (3): s varies between 95% and better than 97% when the illumination decreases from 50 to 1.5 mW/cm² (see Table I). It is worth noting that with a value of k_{corr} deduced from curves e and f (Fig. 6), s would be about 99%. In spite of the extreme sensitivity of k_{corr} to V_b , our finding of s is close to being 100% and is a very positive result that supports our current- and impedance-based analysis. This result also agrees with the one of Chang *et al.*, who performed weight loss experiments for the same cell (17): they found $s = 99.9\%$ for the n-GaAs/(Se²⁻/Se₂²⁻) junction under 70 mW/cm² solar illumination. The slight difference between the two results may come from the surface preparation (4) or from the Se²⁻ concentration (17). When the regeneration of the (A · B) bond by the redox species (3) is considered, the calculated stabilization is only improved of a few tenths of a percent. Figure 13 shows the electrode surface after

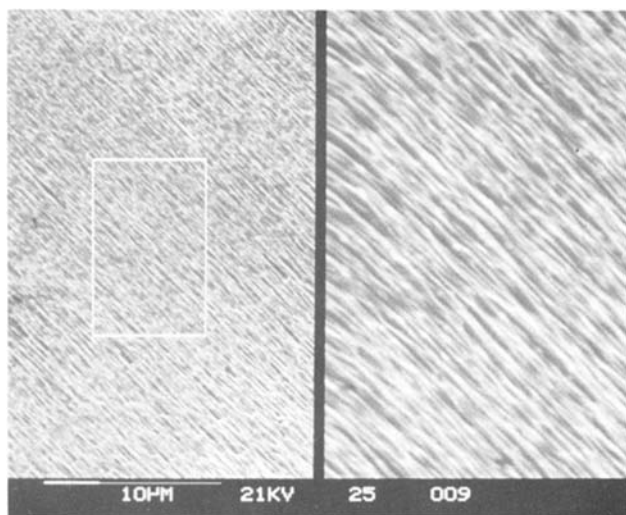


Fig. 11. SEM picture of the surface of the electrode of Fig. 2b. The entire surface is attacked, but the rate of attack depends slightly on the crystallographic planes.

Table I. Stabilization coefficient s calculated for various electrodes in contact with (Se²⁻/Se₂²⁻) under various illuminations ($V_{\text{redox}} = -0.96$ V/SCE)

Light intensity ^e (mW/cm ²)	I^b (mA/cm ²)	$k_{\text{corr}} = 5.7 \times 10^{-27}$ mA cm ⁴	s^a $k_{\text{corr}} = 10^{-27}$ mA cm ⁴
50 ^c	4.310	0.940	0.987
22 ^c	1.845	0.950	0.989
9 ^c	0.723	0.968	0.993
1.5 ^c	0.113	0.970	0.994
30 ^d	2.458	0.975	0.994

^a $s = J_p/(J_p + J_{\text{corr}})$ is calculated under short-circuit conditions (i.e., $V = V_{\text{redox}}$). Calculations have been performed for two values of k_{corr} corresponding to the extreme values obtained for all the studied samples.

^b I is the current density crossing the junction n-GaAs/(Se²⁻/Se₂²⁻) at $V = V_{\text{redox}}$.

^c Untreated electrode [parameters are those of Fig. 2a, curves a, b, c, and d of Ref. (11)].

^d Ruthenium-treated electrode (parameters are those of Fig. 7, curve a).

^e Light intensity is measured before the flux enters into the PEC cell.

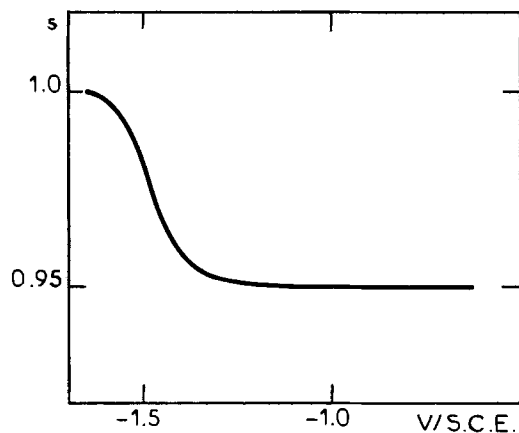


Fig. 12. Evolution of the calculated stabilization coefficients with potential for an n-GaAs/(Se²⁻/Se₂²⁻) junction under 22 mW/cm² ($k_{\text{corr}} = 5.7 \times 10^{-27}$ mA cm⁴ is used in calculation).

passage of photocurrent through the n-GaAs/(Se²⁻/Se₂²⁻) interface. The surface remains smooth, showing again that Se²⁻ is very efficient in stabilizing the GaAs in 1M KOH.

Ruthenium-treated electrodes in contact with K₂Se.—Heller *et al.* showed that there is an improvement of the solar energy conversion efficiency of the n-GaAs/(Se²⁻/Se₂²⁻) PEC cell when the electrode is ruthenium treated. Figure 7 confirms this fact: the fill factor is increased and the I-V characteristics are improved. A reduction of the surface recombination velocity by Ru treatment has been stated by Nelson *et al.* (18). The fact that C_{ss} (V) capacitances are lowered for treated electrodes might be further evidence for this phenomenon (Fig. 9). However, we do not think that this result explains all of the improvement in cell performance.

Our calculations, for untreated electrodes as well as for treated ones, show that the recombination current at the very surface is much smaller than the photocurrent as soon as the potential is positive of -1.55 V/SCE. Thus it appears that surface recombinations have little influence upon the I-V characteristics of our PEC cell. According to our model for the photocurrent, the Ru treatment mainly increases the exchange current $J_{p,0}^{**}$ [see Ref. (8)] through modifications of the energetic conditions of the charge transfer: $V_{\text{FB}}^* = -1.85$ V/SCE is found instead of -1.78 V/SCE for untreated electrodes (Fig. 8). One may then think that ruthenium has two effects; a newly discovered catalytic effect upon the hole transfer kinetics, and the reported reduction of the surface recombination (9, 18). Thus, the stabilization is better than for untreated electrodes under a given illumination (see Table I). This

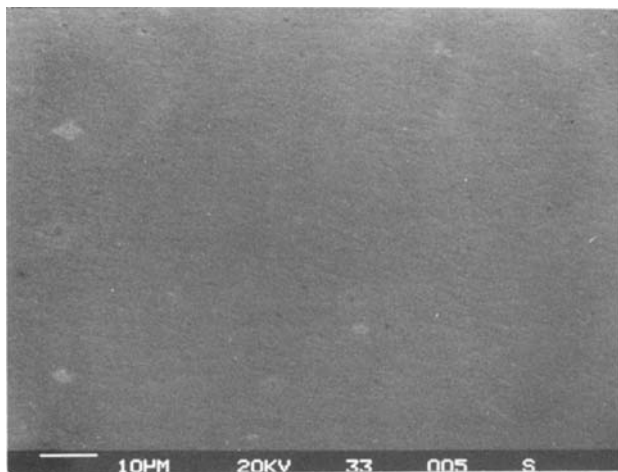


Fig. 13. SEM picture of the surface of an n(100) electrode after passing a 3 mA/cm² photocurrent for 2h through the n-GaAs/1M (Se²⁻/Se₂²⁻) junction. $V_{\text{redox}} = -0.95$ V/SCE.

agrees with experiment (19). The fact that the Ru-treatment is persistent (9) requires, however, explanation. We also observe that the I-V curves and the Mott-Schottky plots (V_{FB}^*) remain stable for hours, *i.e.*, that the surface concentration in Ru³⁺ ions is constant with time. This means that Ru³⁺ ions are either able to form quickly new bonds with the lattice atoms to saturate their own reactive bonds (formed by corrosion) or that they chemisorb again as soon as they are removed from the surface. In both cases, the main idea is the ability of Ru³⁺ ions to move laterally on the surface if the corrosion rate is sufficiently reduced (this is not possible under rapid photocorrosion).

Our impedance results show that the Ru chemisorption reduces both fast and slow surface-state densities at the n-GaAs/(Se²⁻/Se₂²⁻) interface: the surface-state capacitances C_{ss} (V) (fast states) are lower, and ΔV_{FB} (slow states) is smaller than for untreated electrodes (Fig. 9 and 8, respectively) (11). These states may originate in chemical interactions between the solvent and the semiconductor, as is the case between GaAs and a metal in Schottky barriers (20-22). The pH dependence of V_{FB} for GaAs (23) suggests that OH groups in solution are involved in such interactions. Surface atoms which are likely to form these chemical bonds with OH groups are "isolated" from solution by the Ru treatment, because the reactive bonds are saturated. Thus, the state densities are smaller. Finally, the correlation between the experimental improvement of the stabilization by Ru and the smaller observed ΔV_{FB} seems to confirm that ΔV_{FB} is linked to the formation of corrosion intermediates (see the above discussion about corrosion).

The model.—According to the model of Frese *et al.*, we obtained $k_{\text{corr}} = 5.7 \times 10^{-27}$ mA cm⁴, thus $k_1 = 5 \times 10^{-8}$ mA cm with $\sigma_1 = \sigma_2 = 10^{-15}$ cm² ($N_V = 8.7 \times 10^{18}$ cm⁻³ for GaAs). Knowing that corrosion is generalized, *i.e.*, (A : B) $\sim 10^{15}$ cm⁻², one gets $E_{\text{SB}} = E_V + 0.075$ eV (Eq. [3]). This value is very close to the top of the valence band at the surface and is in good agreement with the fact that intrinsic surface states which are moved out of the bandgap then move back when surface agents are present (20, 21).

We have tried to see if this model is able to interpret our impedance results [ΔV_{FB} and C_{ss} (V)]. As reaction [1] is a surface hole trapping, it is interesting to examine if the one-electron (A · B) surface bond formation could give rise to the C_{ss} (V) peak and ΔV_{FB} .

Kinetic analysis only gives information about k_{corr} . But, k_{corr} may be written (Eq. [4], [5], and [10])

$$k_{\text{corr}} = \frac{k_1}{N_V} \frac{\sigma_2}{\sigma_1} \quad [8]$$

Moreover, at stationary conditions, one gets

$$(A \cdot B) = \frac{k_1}{N_V} p_s \quad [9]$$

Without changing k_{corr} and thus p_s , it is possible to modify the calculated (A · B) concentration, by multiplying k_1 by a given factor and dividing σ_2/σ_1 by the same one. Figure 14 presents our results when $k_1 = 5 \times 10^{-6}$ mA cm and $\sigma_2/\sigma_1 = 10^{-2}$ ($\sigma_1 = 10^{-15}$ cm²; $\sigma_2 = 10^{-17}$ cm²). The C_{ss} (V) curve in 1M KOH is well accounted for by this calculation, and E_{SB} is slightly changed. However, as for n-GaAs/(Se²⁻/Se₂²⁻) cells, the entire surface charge variation is insufficient to promote the whole ΔV_{FB} .

If now we take these values of σ_1 , σ_2 , and k_1 to estimate the stabilization coefficient on the n-GaAs/(Se²⁻/Se₂²⁻) junction, we find that: (i) s is unchanged because k_{corr} remains equal to 5.7×10^{-27} mA cm⁴; (ii) under these conditions, calculations show that (A · B) is divided by about 10. Correspondingly, the surface-charge relaxation, owing to the variations of the concentration (A · B) gives too small a contribution to represent the experimental C_{ss} (V) curve. This mechanism does not explain either ΔV_{FB} or

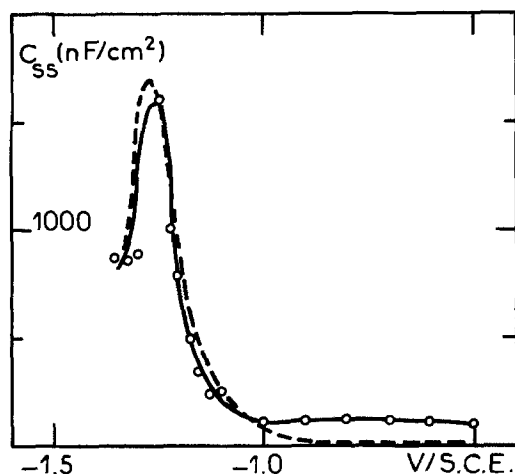


Fig. 14. Calculated surface-state capacitance C_{ss} (V) curve, assuming that the variations of the surface bonds ($A \cdot B$) are responsible for the surface charge relaxation at the n-GaAs/1M KOH interface. (—○—): Experimental data. (---): Calculated curve. Parameters are those of Fig. 5, curve a, except: $k_1 = 5 \times 10^{-6}$ mA cm; $\sigma_1 = 10^{-15}$ cm²; $\sigma_2 = 10^{-17}$ cm² (k_{corr} remains unchanged at 5.7×10^{-27} mA cm²).

the C_{ss} (V) peak in the case of the selenide-stabilized junction. The origin of these states remains to be found.

Conclusion

The present study shows the following points.

1. Self-consistent results are obtained for the photocorrosion and the stabilization of the studied junction. Our band bending calculations appear to be sufficiently precise and realistic to yield the real rate constants, as well as the stabilization coefficient.

2. The results on the Ru-treated electrodes confirm that reaction intermediates are responsible for the flatband potential shift under illumination. These intermediates are not formed when Ru^{3+} is chemisorbed, i.e., after the reactive semiconductor bonds are saturated with Ru^{3+} .

3. The model for the photocorrosion allows one to obtain the right stabilization coefficient of the n-GaAs/selenide junction, but does not account for all our impedance data. Under rapid photodissolution conditions, the unsaturated surface bond concentration ($A \cdot B$) may account for the C_{ss} (V) peak. This latter hypothesis does not apply for the stabilized junction, where we invoke other states (11).

Our study describes, for the first time, that Ru^{3+} ions have a double role: they improve the photoresponse and stability of the n-GaAs/(Se^{2-}/Se_2^{2-}) PEC cell, not only by reducing the surface-state density, but also by improving the transfer kinetics upon the redox species in solution. The latter point appears to be the most important.

Acknowledgments

The authors wish to thank Dr. B. Agius (Groupe de Physique des Solides, Université Paris VII) and Dr. M. Froment ("Physique des Liquides et Electrochimie" du

CNRS) for surface studies. This work was supported by the GRECO 130061 of CNRS.

Manuscript submitted Jan. 23, 1984; revised manuscript received July 17, 1984.

CNRS assisted in meeting the publication costs of this article.

REFERENCES

1. R. Memming and G. Schwandt, *Electrochim. Acta*, **13**, 1299 (1968).
2. (a) H. Gerischer and W. Mindt, *ibid.*, **13**, 1329 (1968); (b) H. Gerischer, *Ber. Bunsenges. Phys. Chem.*, **69**, 578 (1965).
3. D. Vanmaekelbergh, W. P. Gomes, and F. Cardon, *This Journal*, **129**, 546 (1982); *J. Chem. Soc. Faraday Trans. I*, **79**, 1391 (1983).
4. K. W. Frese, Jr., M. J. Madou, and S. R. Morrison, *This Journal*, **128**, 1527 (1981); *J. Phys. Chem.*, **84**, 3172 (1980).
5. H. Gerischer and M. Lübke, *Ber. Bunsenges. Phys. Chem.*, **87**, 123 (1983).
6. W. Lorenz and B. Wolf, *Electrochim. Acta*, **28**, 191 (1983).
7. R. Tenne, H. Flaischer, B. Vainas, N. Müller, G. Hodes, J. Manassen, D. Lando, Y. Mirovsky, and D. Cahen, in "Photoelectrochemistry: Fundamental Processes and Measurement Techniques." W. L. Wallace, A. J. Nozik, S. K. Deb, and R. H. Wilson, Editors, p. 172, The Electrochemical Society Softbound Proceedings Series, Pennington, NJ (1982).
8. P. Allongue, H. Cachet, and G. Horowitz, *This Journal*, **130**, 2352 (1983).
9. B. A. Parkinson, A. Heller, and B. Miller, *ibid.*, **126**, 954 (1979).
10. K. W. Frese, Jr. and S. R. Morrison, *ibid.*, **126**, 1235 (1979).
11. P. Allongue, Thesis, Université Paris VI, Paris (1984).
12. P. Allongue, H. Cachet, and M. Froment, p. 719, Extended Abstracts of the 34th Meeting of I.S.E., Erlangen (RFA) (1983).
13. G. Amsel, J. P. Nadai, E. d'Artemare, D. David, E. Girard, and J. Moulin, *Nucl. Inst. Meth.*, **92**, 489 (1971); F. Abel, G. Amsel, M. Bruneaux, C. Cohen, and A. l'Hoir, *Phys. Rev. B*, **12**, 4617 (1975).
14. P. Janietz, R. Weiche, J. Westfahl, R. Landsberg, and R. Dehmow, *J. Electroanal. Chem.*, **106**, 23 (1980).
15. Y. Nakato, A. Tsumura, and H. Tsubomura, *This Journal*, **127**, 1502 (1980).
16. P. A. Kohl, C. Wolowdiuk, and F. W. Ostermayer, Jr., *ibid.*, **130**, 2288 (1983).
17. K. C. Chang, A. Heller, B. Schwartz, S. Menezes, and B. Miller, *Science*, **196**, 1097 (1977); A. Heller and B. Miller, *Electrochim. Acta*, **25**, 29 (1980).
18. R. J. Nelson, J. S. Williams, H. J. Leamy, B. Miller, H. C. Casey, Jr., B. A. Parkinson, and A. Heller, *Appl. Phys. Lett.*, **36**, 76 (1980).
19. A. Heller, Private communication.
20. W. E. Spicer, P. W. Chye, P. R. Skeath, C. Y. Su, and I. Lindau, *J. Vac. Sci. Technol.*, **16**, 1422 (1979).
21. D. Bolmont, P. Chen, V. Mercier, and C. A. Sebenne, *Physica*, **117B**, **118B**, 816 (1983).
22. L. J. Brillson, *Phys. Rev. Lett.*, **40**, 260 (1978); *J. Vac. Sci. Technol.*, **16**, 1137 (1979).
23. W. H. Laflere, F. Cardon, and W. P. Gomes, *Surf. Sci.*, **59**, 401 (1976).

Annealed Single-Crystal Cadmium Selenide Electrodes in Liquid Junction Solar Cells

S. Wessel, A. Mackintosh, and K. Colbow

Department of Physics, Simon Fraser University, Burnaby, British Columbia, Canada V5A 1S6

ABSTRACT

I-V characteristics, voltage dependence of the quantum efficiency, and spectral response were compared for annealed single-crystal CdSe photoanodes. Annealing in cadmium atmosphere improved the overall solar response considerably, while annealing under vacuum revealed a poor response for photon energies larger than 1.8 eV and a high quantum efficiency for near-bandgap energies. This behavior may be attributed to electron-hole pair generation from interbandgap states and a large density of minority carrier recombination centers near the crystal surface, owing to a high nonstoichiometry and a selenium layer at the surface. Annealing in selenium atmosphere resulted in very poor solar response caused by compensation. Simultaneous illumination of the electrodes with a He-Ne laser strongly enhanced the quantum efficiency for vacuum-annealed crystals for near-bandgap photons. We attribute this to electron trapping in the selenium-rich surface, with a resulting increase in depletion-layer width in the cadmium selenide.

The quantum efficiency spectral response of an ideal semiconductor photoelectrochemical solar cell will exhibit a flat behavior for photon energies moderately larger than the bandgap, independent of illumination intensity. Recombination centers within the bulk of the semiconductor and at its surface can substantially reduce the photocurrent and thus the quantum efficiency in a nonlinear fashion, while photogenerated carrier losses in the depletion region are usually small (1, 2). For highly doped semiconductors ($> 10^{18} \text{ cm}^{-3}$), the space-charge region becomes smaller than the absorption length for near-bandgap photon energies, which will thus lead to generation of minority carriers (holes for n-CdSe) in the bulk of the semiconductor with increased probability of loss by recombination (3). Carriers photogenerated by high energy photons will originate near the surface, where large losses of photocurrent may arise from a high density of surface recombination centers. In a two-beam experiment using a He-Ne laser (6328Å) as a dc pumping source, it was found that the spectral dependence of the quantum efficiency obtained with a weak, modulated measuring beam was very sensitive to the presence of carrier recombination centers (1).

We analyzed and compared various annealed crystals by single- and double-beam photocurrent spectroscopy. In this paper, we present data for vacuum-, cadmium-, and selenium-annealed single-crystal CdSe and give a possible explanation for the large change in spectral response of the vacuum-annealed crystals.

Experimental

Precut and polished C-plate single-crystal CdSe (batch A) and a raw ingot of CdSe (batch B) were obtained from Cleveland Crystals, Cleveland, Ohio. The conductivities of batch A and B were $0.3 \Omega \text{ cm}$ and $2 \text{ M}\Omega \text{ cm}$, respectively. The ingot was cut and polished into C-plates. The crystals were annealed for 6h at 600°C under vacuum, or in sealed evacuated quartz tubes in the presence of selenium or cadmium. The crystals were then mounted on a copper disk with an In-Ga (25:75) eutectic and silver dag for ohmic contact and sealed in a plexiglass disk with Devcon epoxy.

Prior to testing, all samples were etched for 1 min in a 50% H_2O_2 and glacial acetic acid solution in the ratio of 1:3. Light entered the test cell through a quartz bottom window, allowing $\sim 3 \text{ mm}$ of electrolyte between the window and the CdSe electrode, which was faced by a large Pt counterelectrode ring (25 cm^2). In all cases, the sulfide/polysulfide redox electrolyte was unstirred and consisted of 1M NaOH , $2\text{M Na}_2\text{S}$, 1M S , and 0.01M Se . N_2 gas continuously flushed the system since the electrolyte is sensitive to oxygen. The spectral response of the electrodes was obtained under short-circuit conditions using a 100W tungsten halogen lamp, the output of which was chopped at 20 Hz, followed by a Jarrel-Ash grating

monochromator with 8 nm resolution, and a Princeton Applied Research lock-in amplifier (Model HR-8). The illumination intensities were corrected for electrolyte absorption and at the crystal surface they were measured to be $20\text{-}40 \mu\text{W cm}^{-2}$. In the two-beam experiment, a He-Ne laser (Spectra Physics Model 133) served as an intense pumping source, with a weak, modulated probing beam obtained from the monochromator. The irradiance on CdSe from the laser was 1 mW cm^{-2} .

The current-voltage (I-V) characteristics of the electrodes were determined in the dark and under 100 mW cm^{-2} white light illumination from a 100W tungsten halogen lamp by adjusting the bias voltage. The change in quantum efficiency (η) with forward bias voltage was measured using the lock-in amplifier and a Spectra-Physics Model 125 He-Ne laser source (14 mW cm^{-2}).

Anodization of the electrodes was achieved in saturated KCl by 30 min white light illumination (100 mW cm^{-2}), while connected through a 100Ω load.

Results and Discussion

It is known that annealing of polycrystalline CdSe under vacuum liberates selenium from the surface, leaving a cadmium-rich sample behind (4, 5). While in polycrystalline samples selenium would escape via grain boundaries, it is plausible that in single crystals the selenium diffuses through the crystal surface, resulting in a selenium-rich surface layer over a nonstoichiometric CdSe crystal, which is indicated by a reddish color. This gives rise to bulk defects and a surface barrier associated with a high density of surface states. The polysulfide redox electrolyte would readily dissolve the Se° surface layer; however, the rate of dissolution is strongly reduced by the addition of 0.01M Se° to our electrolyte.

Figure 1 presents the current-voltage characteristics of cadmium and vacuum-annealed single-crystal CdSe. While the total current of the two different samples are similar, the dark currents (Fig. 1b) show very different behavior: the dark current increases rapidly at approximately 1500 mV forward bias for vacuum-annealed single crystals and between 500 and 600 mV for cadmium-annealed samples. This may be accounted for by the presence of a surface barrier to electron flow arising from the selenium-rich surface which breaks down at high forward bias. This is in agreement with a model proposed by Frese (6-8) for anodized single-crystal surfaces.

It can be seen in Fig. 1a that the decrease in current density of the cadmium-annealed crystals is primarily determined by its dark current, while the vacuum-annealed samples do not depend on dark current. For both samples, the decrease in current density for low forward bias indicates a blocking barrier for holes at the surface (9).

El Guibaly *et al.* (9) associated this behavior with surface states acting as hole trapping sites and becoming ion-

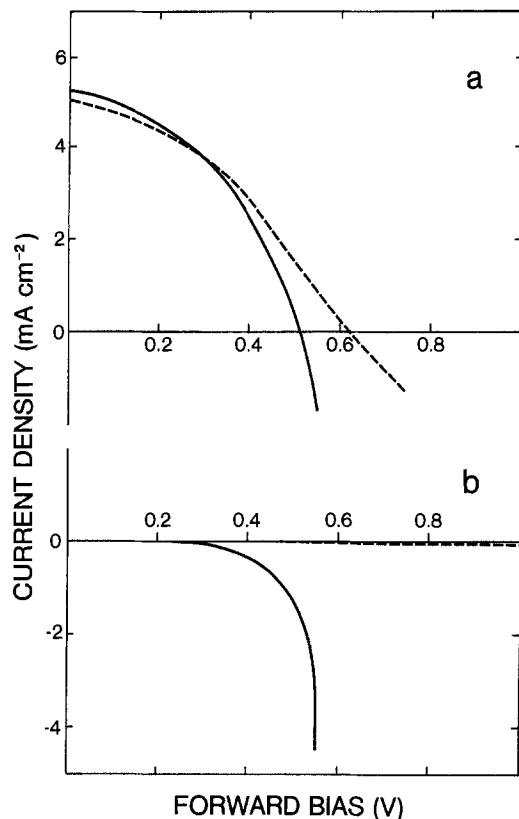


Fig. 1. *i*-*V* characteristics for 100 mW cm^{-2} white light irradiation (a) and in the dark (b) for annealed single-crystal CdSe in Cd-atmosphere (—) and under vacuum (---).

ized with illumination, thus reducing the amount of band bending. As seen from Fig. 1a, the vacuum-annealed single crystals show a larger open-circuit voltage than the

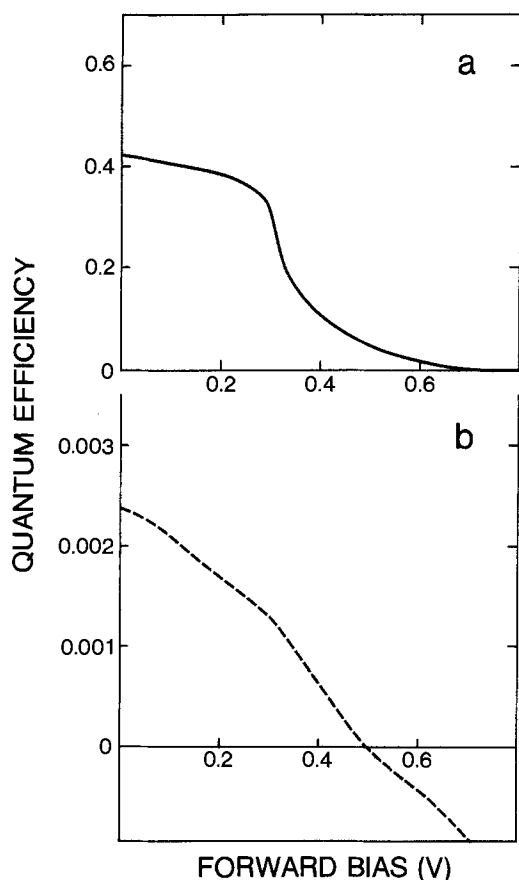


Fig. 2. Voltage dependence of the quantum efficiency at 632.8 nm (14 mW cm^{-2} He-Ne laser) for single-crystal CdSe annealed (a) in Cd atmosphere and (b) under vacuum.

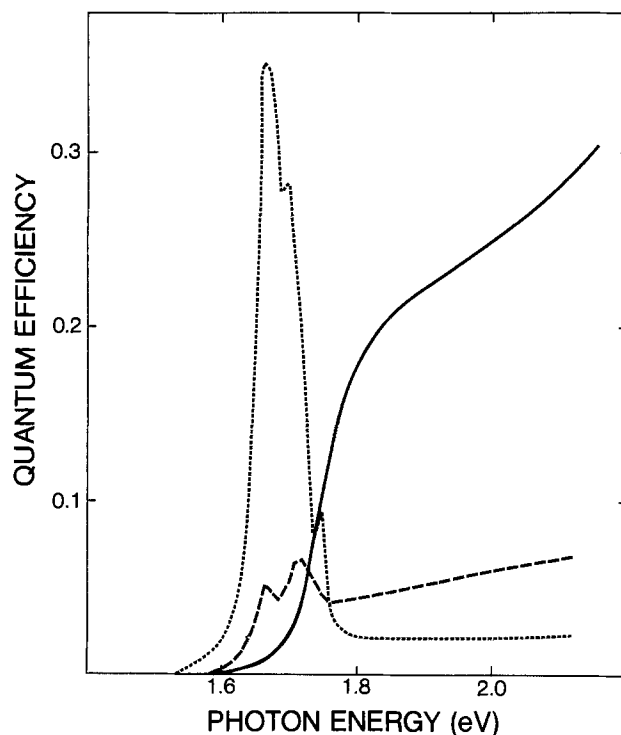


Fig. 3. Spectral response of single-crystal CdSe (batch A) for Cd-annealed (—) and vacuum-annealed electrodes without (---) laser pumping and the vacuum-annealed electrode under laser pumping (···). Actual efficiencies of the dashed and dotted curve is one-half as shown.

Cd-annealed samples, which may result from larger band bending or a different shift of the bandedges, consistent with electron-hole pair generation within the Se-rich surface and immobilization of electrons in the selenium layer (6-8).

Figure 2 shows the behavior of the quantum efficiency at 632.8 nm with applied forward bias. The current direction of the vacuum-annealed single crystal (Fig. 2b) reverses for voltages larger than the open-circuit voltage. A possible explanation is that as the bands of the CdSe flatten at large forward bias, additional photogenerated holes in the selenium may accumulate at the CdSe/Se interface and are injected into the CdSe crystal, where they recombine with electrons; thus, more e-h pairs recombine than were photogenerated in CdSe.

The cadmium-annealed sample gave the same "normal" spectral response (Fig. 3) as an untreated single crystal (3) (not shown), but with a six-fold increase in quantum efficiency (see Table I), with and without laser pumping. However, vacuum annealing of the CdSe crystals did not improve the overall solar response; in fact, it

Table I. Quantum efficiencies at 2.00 eV and at the peak response ($\approx 1.7 \text{ eV}$) with and without laser pumping for variously treated single crystals of CdSe

Crystal batch	Treatment	Laser off		Laser on		
		Quantum efficiency (%)	Quantum efficiency (%)	Quantum efficiency (%)	Quantum efficiency (%)	
		2.00 eV	1.71 eV	2.00 eV	1.66 eV	
A	Etched	4		4		
	Cd-annealed					
	etched	24		24		
	anodized	30		30		
	24h later	37		37		
Vacuum-annealed	etched	3	3	0.1	21	
	anodized	5	6	0.1	21	
	24h later	12	11	0.1	94	
	B	Etched	16		16	
		Cd-annealed	50		50	
Vacuum-annealed		0	1	0	47	
Se-annealed		0.1		0.1		

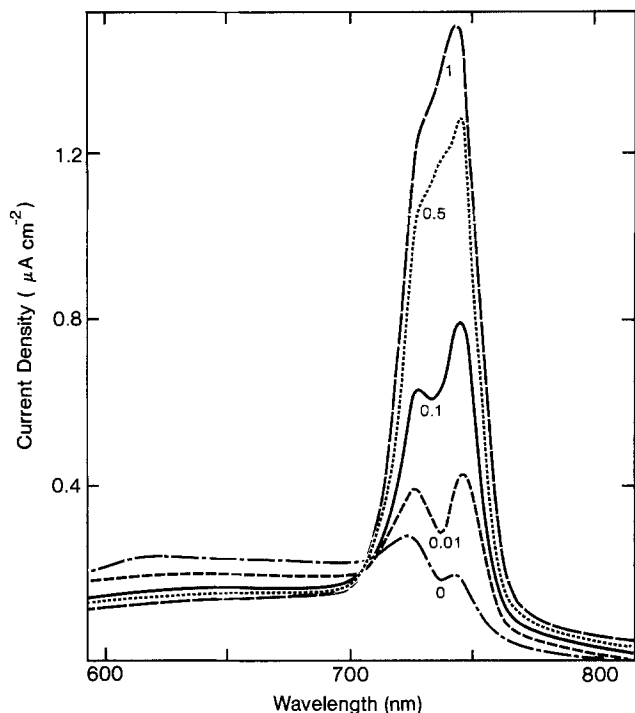


Fig. 4. Short-circuit current wavelength response of vacuum-annealed CdSe (batch A) with simultaneous laser pumping for different laser intensities as shown in milliwatts per square centimeter.

showed a rather unusual spectral behavior, which became more pronounced with laser pumping: a double peak in the photocurrent spectrum at 1.66 and 1.71 eV near the bandedge of CdSe, and a lower, nearly constant response for photon energies larger than 1.8 eV. With laser pumping, the efficiencies near the bandgap increase substantially, while the efficiency decreases and reaches a low value for high energy photons. Heller *et al.* (2) observed similar, but much less pronounced, behavior for

single-crystal CdSe with peaks at 1.64 and 1.69 eV. They ascribed these peaks to states within the bandgap owing to imperfections near the semiconductor surface acting as carrier traps and recombination centers, which would lead to changes in the photoresponse, particularly for light absorbed near the semiconductor surface. It seems plausible that the observed peaks arise from photon absorption and electron-hole generation involving inter-bandgap states. Photons of energy larger than 1.8 eV are strongly absorbed near the surface, resulting in a reduced quantum efficiency due to recombination via the large density of surface states. Laser pumping would result in the filling of traps near the CdSe/selenium interface and an increased quantum efficiency. Amorphous selenium has a bandgap of 2.05 eV (10) just above the laser energy of 1.96 eV. Amorphous selenium at the surface with a large concentration of cadmium will likely show strong absorption at the laser energy. If electrons are trapped in the selenium-rich surface layer, while the light generated holes diffuse away (6-8), a larger band bending will be produced in the CdSe and thus a larger depletion width. The increased number of electrons near the surface will decrease the quantum efficiency for electron-hole pairs generated by high energy photons, owing to increased recombination probability, and the increased depletion width will give an increased quantum efficiency for holes generated by near-bandgap photons, which create hole-electron pairs deeper into the crystal. This would then also explain why carrier generation from the 1.66 eV impurity levels becomes more efficient with increasing laser intensity (Fig. 4). At a laser intensity of $\sim 0.7 \text{ mW cm}^{-2}$ the photocurrent saturates, giving rise to the same response as for 1 mW cm^{-2} laser pumping, consistent with a slow transfer velocity of holes to the electrolyte (9, 11) with resulting photocorrosion.

Figure 5 shows the spectral response of anodized, Cd- and vacuum-annealed CdSe. The grown Se layer was found to be $\sim 0.27 \mu\text{m}$ thick for both samples as calculated from integrated photocurrent measurements (6-8). While the Cd-annealed samples again reveal the same behavior with and without laser pumping (Fig. 5a), the

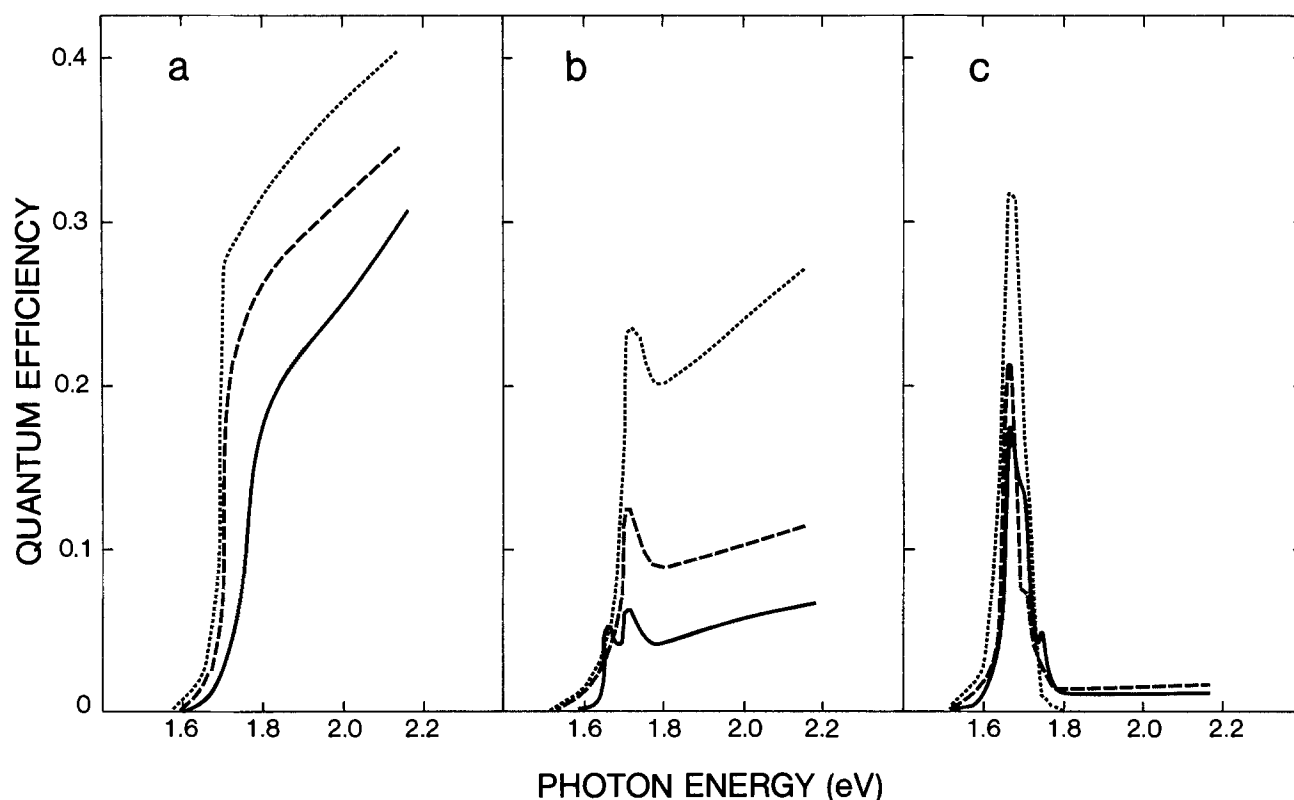


Fig. 5. Spectral response of single-crystal CdSe (batch A) for etched electrodes (—), and anodized electrodes after 1/2 h (---) and 24h (· · ·) in redox electrolyte. All curves in graph b show twice and the dotted line in graph c one-third the actual efficiencies.

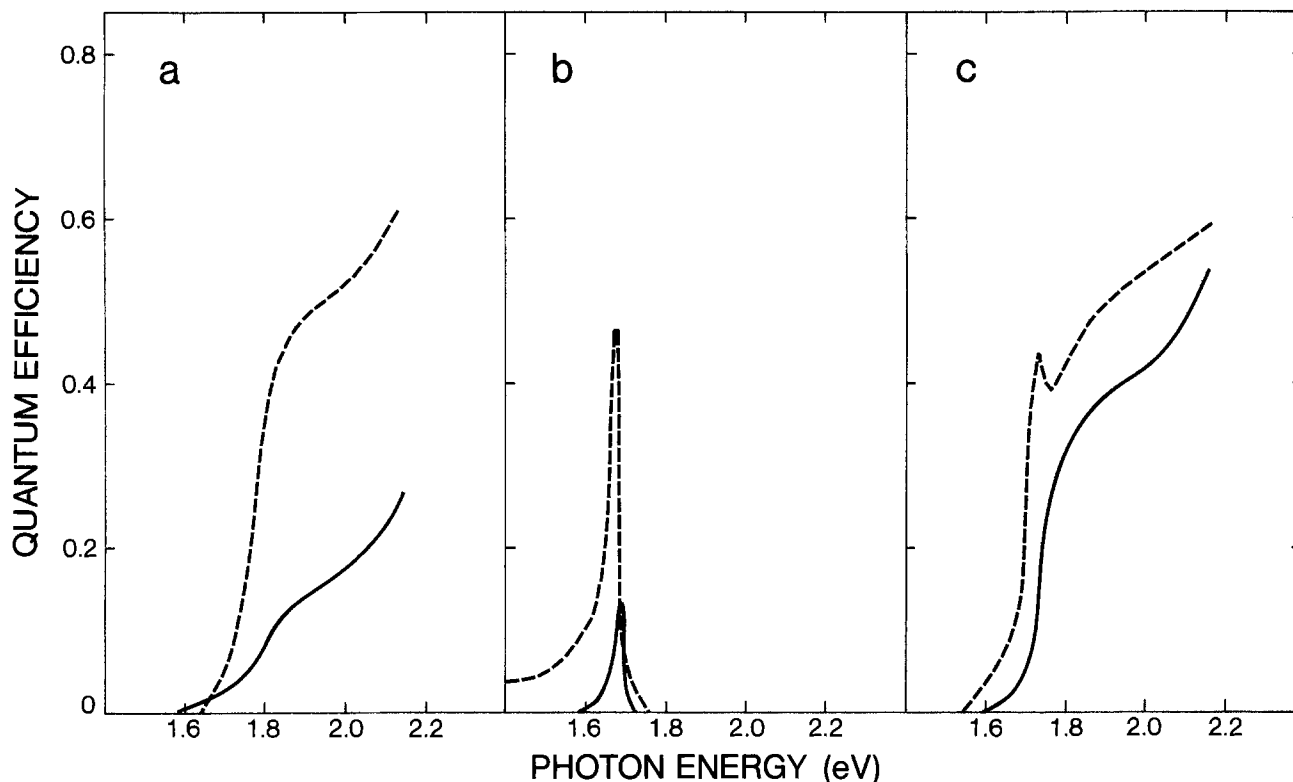


Fig. 6. Spectral response of single-crystal CdSe (batch B). Graph a shows the behavior of untreated (—) and Cd-annealed (---) electrodes; graphs b and c vacuum- and selenium-annealed CdSe, respectively, with (---) and without (—) laser pumping. The solid line in graph b shows ten times and both curves in graph c 500 times the actual efficiencies.

vacuum-annealed anodized crystals (Fig. 5b, 5c) show a similar response as etched vacuum-annealed crystals. The overall increase in quantum efficiency of anodized samples is most likely caused by improved surface condition due to photoetching. Similar results were obtained by Frese (8), showing an increased quantum efficiency near the bandedge for anodized CdSe electrodes. For selenium thicknesses of 0.24 and 0.36 μm , the response substantially decreased for wavelengths smaller than 630 nm (1.96 eV) and was associated with photon absorption in the selenium layer. Our results show a smaller decrease in quantum efficiency for the high energy photons, indicating that our selenium layer may in fact be thinner than calculated, or porous (12).

Leaving the anodized samples for 24h in redox electrolyte under short-circuit conditions improves the quantum efficiency, which indicates that the selenium layer dissolves, thus leaving a photoetched CdSe surface behind. The double-peak feature of the vacuum-annealed sample (Fig. 5b) disappears upon anodizing, and only the 1.71 eV peak remains visible. Upon laser pumping (Fig. 5c), the quantum efficiency peak shifts again to 1.66 eV. This would indicate that the 1.66 eV peak is due to a deep interband state which is essentially not affected by photoetching.

Figure 6 presents various heat-treatments for batch B single-crystal CdSe. Again, the spectral response of the quantum efficiency is considerably improved for Cd-annealed samples compared to untreated single crystals (Fig. 6a). They show a "normal" spectral response and reveal identical results with and without laser pumping. The untreated crystals show some band tailing, which seems to disappear upon Cd annealing. The vacuum-annealed single crystals (Fig. 6b) show one peak only at 1.71 eV with very low quantum efficiency. Photons with energy larger than ~ 1.8 eV do not show any measurable photoresponse, indicating a strong absorption in the selenium-rich surface layer of the crystal and/or a larger density of hole trapping sites at and near the surface. Upon laser pumping, again only one peak is observed which shows strong band tailing and a large 50-fold increased quantum efficiency at 1.66 eV. Figure 6c presents

selenium-annealed CdSe crystals. While the quantum efficiency is extremely small, the crystals show a "normal" behavior, with a bandgap of 1.74 eV. With laser pumping, the bandedge shifts towards lower energies, giving rise to a small peak at 1.74 eV. Annealing in selenium atmosphere may compensate the semiconductor, since selenium would act as an electron acceptor, resulting in a low effective donor density and a large number of carrier traps.

Table I summarizes and compares the observed quantum efficiencies for highly energetic photons (2.0 eV) and the observed peak efficiency at 1.71 eV (without laser pumping) and 1.66 eV (with laser pumping) for the untreated and annealed CdSe single crystals.

Conclusions

A satisfactory model to account for our data as well as previous work suggests that vacuum annealing of CdSe single crystals produces a selenium-rich surface and a large density of bulk defect states, probably due to selenium interstitials. This results in an unusual spectral response: namely, high quantum efficiency in two distinct bands below the CdSe absorption edge (1.74 eV) and decreased efficiency for highly absorbed light due to large recombination near the semiconductor surface. Simultaneous pumping with a strong He-Ne laser enhances these unusual spectral characteristics, which may be accounted for by assuming that the laser light is strongly absorbed in the larger bandgap selenium surface, where electron trapping leads to a larger band bending and thus increase of the depletion layer in the CdSe. This, as well as hole injection from the CdSe/selenium interface, would lead to an improved quantum efficiency for below bandgap photon energies.

One may be tempted to attribute the laser enhancement to a photoconductivity effect, that is, a lowering of the series resistance by penetrating light (≈ 745 nm), which does indeed occur for the high resistance vacuum-annealed samples. However, the observed photoconductivity reduced the series resistance by $\approx 40\%$; this is not sufficient to account for our data.

Acknowledgments

We would like to thank Dr. S. R. Morrison from Simon Fraser University and Dr. A. Heller, AT&T Bell Laboratories, Murray Hill, New Jersey, for useful discussions.

Manuscript submitted April 5, 1984; revised manuscript received July 6, 1984.

Simon Fraser University assisted in meeting the publication costs of this article.

REFERENCES

1. A. Heller, K. C. Chang, and B. Miller, *J. Am. Chem. Soc.*, **100**, 684 (1978).
2. A. Heller, K. C. Chang, and B. Miller, *This Journal*, **124**, 697 (1977).
3. K. Colbow, D. H. Harrison, and B. L. Funt, *ibid.*, **128**, 547 (1981).
4. A. Reisman, M. Berkenblit, and M. Witzten, *J. Phys. Chem.*, **66**, 2210 (1962).
5. K. T. L. de Silva, D. J. Miller, and D. Haneman *Solar Energy Mater.*, **4**, 233 (1981).
6. K. W. Frese, Jr., *J. Appl. Phys.*, **53**, 1571 (1982).
7. K. W. Frese, Jr., *Appl. Phys. Lett.*, **40**, 275 (1982).
8. K. W. Frese, Jr., *This Journal*, **130**, 28 (1983).
9. F. El Guibaly and K. Colbow, *J. Appl. Phys.*, **52**, 5247 (1981).
10. E. A. Davis, *J. Non-Cryst. Solids*, **4**, 107 (1970).
11. F. El Guibaly and K. Colbow, *J. Appl. Phys.*, **54**, 6488 (1983).
12. W. M. Sears and S. R. Morrison, *J. Phys. Chem.*, **88**, 976 (1984).

Correlation of the Photoelectrochemistry of the Amorphous Hydrogenated Silicon/Methanol Interface with Bulk Semiconductor Properties

Chris M. Gronet and Nathan S. Lewis*

Department of Chemistry, Stanford University, Stanford, California 94305

George W. Cogan, James F. Gibbons, and Garret R. Moddel

SERA Solar Corporation, Santa Clara, California 95054

Harold Wiesmann

Vactronic Laboratory Equipment, Inc., East Northport, New York 11731

ABSTRACT

Semiconductor/liquid junctions derived from 0.5 μm thick films of amorphous hydrogenated silicon, a-Si:H, have been investigated in CH_3OH solvent. The a-Si:H films consist of a weakly doped n-type layer over a 200 \AA n⁻-a-Si:H layer on a stainless-steel substrate. The low series resistance and high ratio of minority carrier collection length to film thickness in this arrangement allows a study of the properties of semiconductor/liquid interfaces with minimal interference from bulk resistance losses. We find that a-Si:H anodes in 0.02M ferrocene, $\text{FeCp}_2/0.5 \text{ mM FeCp}_2^+/1.5\text{M LiClO}_4/\text{CH}_3\text{OH}$ solutions exhibit poor short-circuit quantum yields and low fill factors with 632.8 nm irradiation, but that these junctions display internal quantum yields of close to unity and high fill factors with short wavelength ($\lambda < 450 \text{ nm}$) irradiation. Photons absorbed within a distance comparable to the minority carrier collection length are efficiently collected, and the fill factors and quantum yields under such conditions are insensitive to increases in photocurrent density over a range of 0.1-2 mA/cm². Solar-simulated irradiation (88 mW/cm²) from a ELH-type tungsten-halogen lamp in the a-Si:H/0.02M $\text{FeCp}_2/0.5 \text{ mM FeCp}_2^+/1.5\text{M LiClO}_4/\text{CH}_3\text{OH}$ system yields open-circuit photovoltages of 0.75-0.85V, short-circuit photocurrents of 6-7 mA/cm², and photoelectrode efficiencies for conversion of light to electricity of 2.7%-3.3%. Photovoltages with the acetylferrocene⁺⁰ redox system are among the highest reported for any a-Si:H surface barrier system, and can exceed 0.85V under AM1 illumination conditions. Variation in the redox potential of the solution leads to changes in open-circuit photovoltage in accord with theory, and does not yield evidence for pinning of the a-Si:H Fermi level by interface states or by surface oxides over the potential range investigated. The observed photoelectrochemical behavior of these a-Si:H films is consistent with documented bulk transport and carrier collection properties of a-Si:H, and does not show evidence for series resistance losses, unusual spectral response characteristics, or recombination sites at the semiconductor/liquid junction. Manipulation of the electronic properties of the a-Si:H films can thus lead to improved energy conversion parameters and a clearer picture of the chemistry at the a-Si:H/liquid interface.

To elucidate the fundamental chemistry at the semiconductor/liquid interface, we have studied photoelectrodes having liquid contacts derived from nonaqueous solvents. Nonaqueous solvents largely circumvent the photocorrosion and photopassivation processes prevalent in aqueous solution (1-4), and thus provide media which are suitable for reproducible, controlled investigations of the semiconductor/liquid interface. Unfortunately, most semiconductor/liquid combinations in nonaqueous solvents have been reported to exhibit low solar energy conversion efficiencies and generally rather poor interface properties (3-9). The major cause of this behavior has been assigned to interface states at the semiconductor/liquid junction (10-14). These

states can act as recombination sites, and thereby lead to low quantum efficiencies and fill factors. Also, these states may serve to pin the surface Fermi level and lead to less than ideal photovoltages at the semiconductor/liquid interface (13, 14).

Of major concern, however, must be the correct assignment of properties to the semiconductor/liquid interface as distinguished from those that are simply electronic properties of the semiconductor itself or artifacts of the method of measurement of current-voltage characteristics. Recent investigations on common semiconductor substrates, such as n-type Si (15) and n-type GaAs (16), have demonstrated that proper attention to bulk electrode properties and control of interfacial chemistry can lead to efficient nonaqueous semiconductor/liquid junctions.

* Electrochemical Society Active Member.

tion systems. We have thus turned our attention to thin film materials, such as amorphous hydrogenated silicon (a-Si:H), in an attempt to extend these principles to a wider class of semiconductor materials.

We report herein new data on the photoelectrochemistry of a-Si:H/liquid junctions in nonaqueous solvents. Notably, our results demonstrate that such interfaces exhibit little evidence of recombination sites at the semiconductor/liquid interface which would act to decrease the short-circuit quantum efficiency or to produce unusual wavelength response characteristics. We find that inefficiencies can be ascribed primarily to transport properties in the semiconductor material itself. Control of these parameters can thus lead to improvements in the properties of a-Si:H/liquid junctions. We observe that properly designed semiconductor/liquid combinations with a-Si:H can exhibit internal quantum yields for electron flow which are close to unity over a substantial portion of the solar spectrum. In addition, we observe open-circuit photovoltages and photoelectrode efficiencies for conversion of visible light to electricity which are comparable to the best reported values for any surface barrier device fabricated with similar a-Si:H material. An important conclusion of our study is that substantial progress in improving the photocurrent response of a-Si:H/liquid junctions will require improvements in electronic properties of the bulk material itself rather than improvements in the properties of the semiconductor/liquid interface.

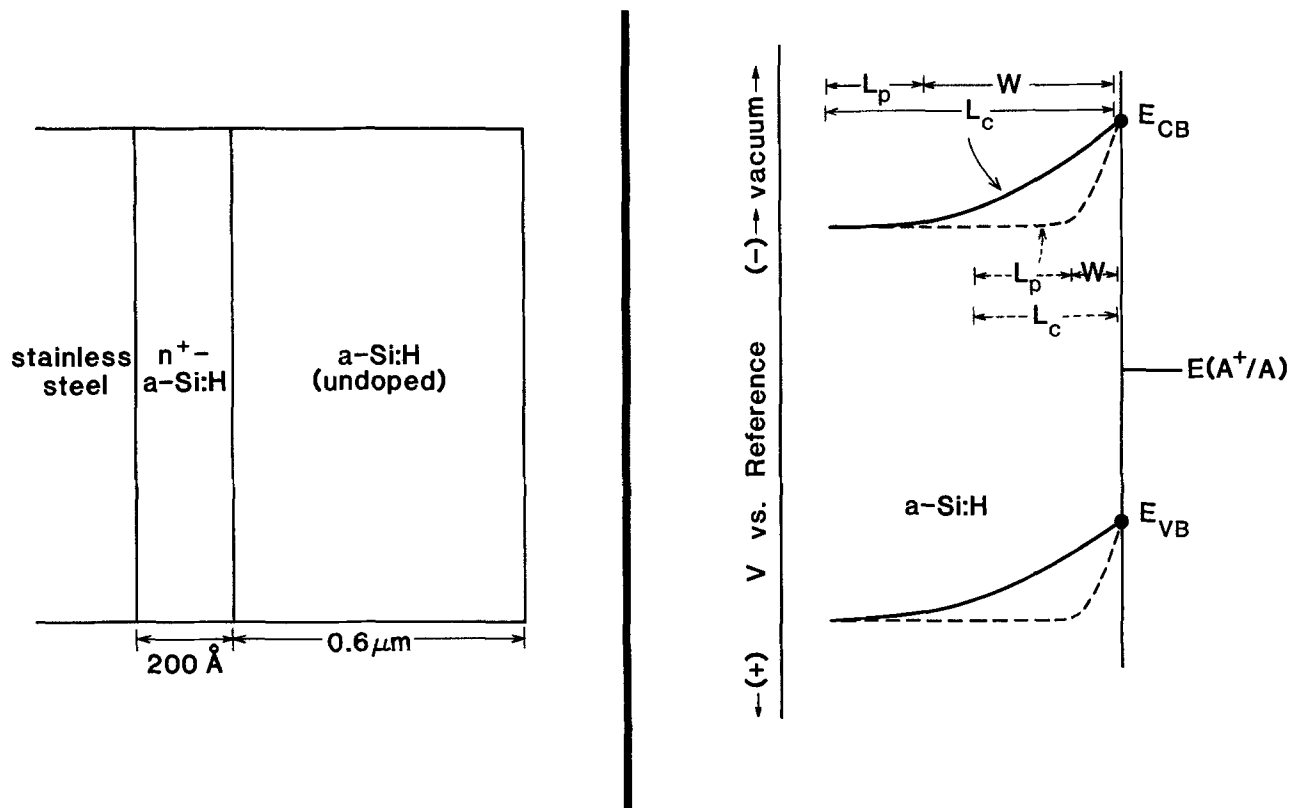
Electronic Properties of a-Si:H

Amorphous hydrogenated silicon, a-Si:H, has been the subject of intense study for application in terrestrial photovoltaic and photoelectrochemical devices (17-20). This material can be produced by a number of methods (21-23) which yield thin films which are either p-type, "intrinsic," or n-type. In contrast to single-crystal silicon, a-Si:H

films possess a strong optical absorption resembling that of a direct gap semiconductor having a bandgap at 1.7 eV (25). The overlap of the absorption spectrum of a-Si:H with the solar spectrum, as well as the ease of deposition of the material itself, are attractive features of these films. An especially critical property in a-Si:H is the relatively short hole-diffusion length. Doping of the film has generally been found to decrease the hole-diffusion length substantially (25-26); thus the preferred structure for photoanode applications consists of a relatively thin, heavily doped n-type layer followed by a thicker "intrinsic" layer (usually weakly n-type), as shown in Scheme I.

Another important property of a-Si:H is that over $2 \mu\text{m}$ of the material is required to absorb essentially all visible light with energy greater than 1.7 eV. However, film thicknesses significantly below this value are employed in practical solar cells at present. This is because of the low value of the hole-diffusion length, which is typically $0.2\text{-}0.7 \mu\text{m}$ in intrinsic a-Si:H films of the highest quality currently available (27). Thicker films would absorb more light, but electron-hole pairs created at depths large compared to the collection length (at most the sum of the diffusion length and the depletion width) would not be collected and would recombine in the bulk material. Also, the increased series resistance of relatively thick a-Si:H films could produce poor fill factors. Thus, use of relatively thick films would require a detailed analysis of bulk-transport properties in order to isolate those features originating from the semiconductor/liquid interface.

In this study, we have employed $0.5\text{-}0.6 \mu\text{m}$ thick a-Si:H films which have been plasma deposited on a reflecting substrate, stainless steel. The film thickness is on the order of the minority-carrier collection length, L_c , and the reflection of light by the substrate provides an additional pass for light of long wavelengths, effecting increased carrier creation within a distance L_c of the interface. Series resistance losses due to excess bulk thickness have been



Scheme I. Left: Representation of the thin film a-Si:H photoelectrode structure. The contact to the stainless steel substrate is provided by a 200\AA thick n⁺-a-Si:H film, followed by a $0.5\text{-}0.6 \mu\text{m}$ thick layer doped weakly n-type. The situation will result in photoanode behavior qualitatively similar to conventional single-crystal photoanodes. Right: Interface energetics for two different light intensities at a-Si:H/liquid interfaces. The collection length, L_c , is the sum of the minority carrier diffusion length, L_p , plus the depletion region thickness, W . Contraction of the depletion width in a-Si:H with increasing light intensity (---) leads to a decrease in L_c at a fixed voltage bias, and yields poor charge collection for light which penetrates deeply into the a-Si:H film. The fill factor and short-circuit quantum yield of these interfaces is thus sensitive to both the intensity and wavelength of light incident on the a-Si:H film.

minimized without sacrifice of light absorption within a distance L_c of the surface. Our films provide an opportunity for detailed examination of the properties of the semiconductor/liquid junction. Information concerning the significance of recombination sites at the semiconductor/liquid interface has been obtained from suitable variations in incident light wavelength and intensity, as well as from photocurrent-voltage properties.

Experimental

Experimental techniques and procedures have been described previously (15). CH_3OH was distilled from Mg prior to use; no other precautions concerning exclusion of air or water were found necessary to obtain reproducible photocurrent-voltage characteristics. All current-voltage curves were obtained under potentiostatic control of the working electrode vs. a Pt reference electrode, and thus represent photoelectrode efficiencies which measure the properties of the a-Si:H photoanode. These values cannot be compared directly with two electrode solar cell efficiencies without actual fabrication of such devices.

The a-Si:H films were prepared by RF decomposition of silane, and were all prepared at HT Products by H. Wiesmann. The stainless-steel substrate was maintained at 220°C , with a deposition rate of 1.5 \AA/s . A 200 \AA thick n-doped layer was deposited from silane with 1% phosphine, and was then followed by a nominally intrinsic $0.5\text{--}0.6 \text{ \mu m}$ layer of a-Si:H. Infrared absorption measurements indicate that film deposition under these conditions yields a-Si:H with 15% hydrogen content; thus the stoichiometry of our material does not differ substantially from samples used in previous liquid junction studies (9). Slight compositional differences between these samples and previous results (9) do not affect an interpretation of our results, because we obtained excellent agreement with previous data when our a-Si:H samples were tested under experimental conditions identical to those described in other studies.

Photoanodes were fabricated by bonding the stainless-steel substrate to a coil of Cu wire with Ag paint. Insulation from the liquid was obtained with ordinary epoxy resin. Typical photoelectrode areas exposed to the elec-

trolyte were $0.1\text{--}0.4 \text{ cm}^2$. All electrodes were etched for 10s in 5% aqueous HF and washed with CH_3OH immediately before use. Reflectance spectra were obtained by use of spectral response apparatus previously described (15), with reflected light determined by a calibrated Si detector from United Detector Technologies, Incorporated. Spectral response and Schottky barrier measurements were performed using apparatus at SERA Solar, and all other data was collected at Stanford using techniques described previously (15, 16).

Open-Circuit Photovoltage Measurements to Probe Interface Kinetics

We have performed cyclic voltammetry and steady-state current-voltage experiments with outer-sphere redox couples in order to establish trends in photovoltages for the a-Si:H/ CH_3OH interface. The data are summarized in Fig. 1, which indicates the photovoltages, V_{oc} , obtained for a-Si:H films in contact with various redox couples, A^+/A . At sufficiently negative potentials, as in the cyclic voltammetry for (N,N'-dimethyl-4,4'-bipyridinium) $^{2+/+}$ (Fig. 1a), we observe dark oxidations and dark reductions near the formal potential of the redox couple, indicating no appreciable photovoltage for this system (10). The (N,N'-dimethyl-4,4'-bipyridinium) $^{2+/+}$ redox system does exhibit anodic photocurrent, and the photovoltage [as determined by the difference in anodic peak potential between an a-Si:H photoanode and a Pt electrode (3, 10)] is 0.2V under 100 mW/cm^2 of tungsten-halogen irradiation. The dark reductions at a-Si:H films have not been reported in other nonaqueous solvents, and indicate substantial room temperature dark conductivity in this particular sample of a-Si:H material (likely owing to tailing of phosphorus dopant into the intrinsic layer). Accurate values of the conduction band edge position would require measurement of the barrier height, not the photovoltage (28, 29); however, the data do allow us to conclude that E_{CB} is more negative than -0.7V vs. SCE in CH_3OH solvent.

We have also employed steady-state photocurrent-voltage techniques to complement the cyclic voltammetry V_{oc} measurements. All experiments were per-

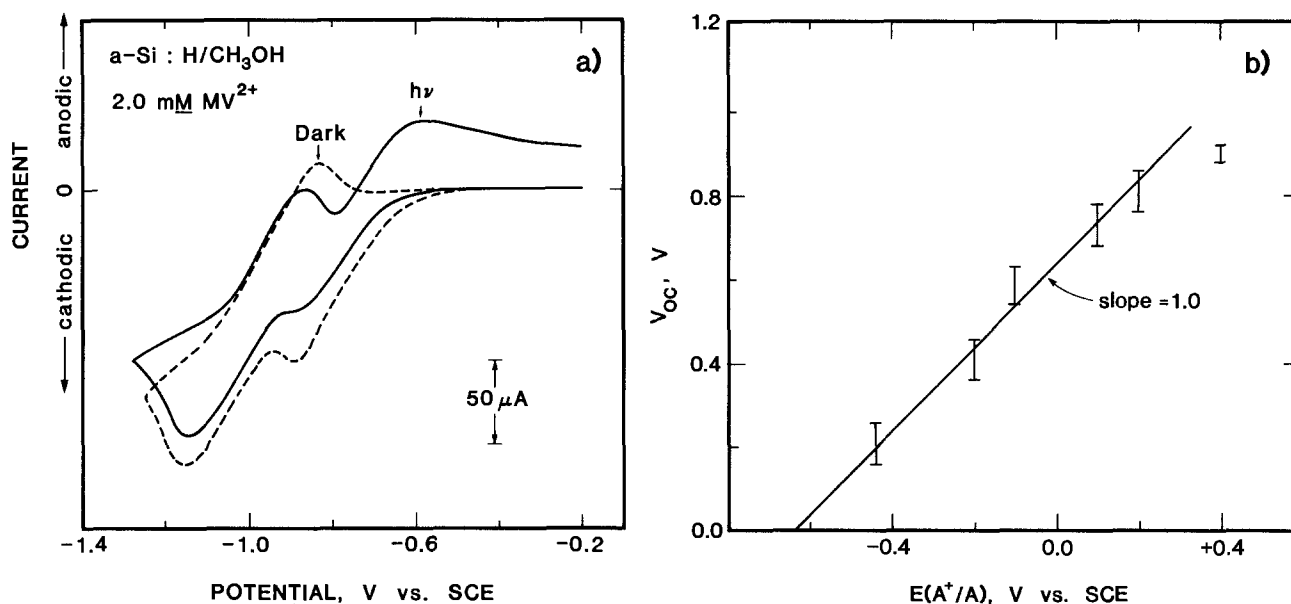


Fig. 1. (a) Cyclic voltammetry (100 mV/s) of a-Si:H films in 1.0M KCl/ CH_3OH with 2.0 mM N,N'-dimethyl-4,4'-bipyridinium (MV^{2+}) dichloride added. Irradiation is 100 mW/cm^2 provided from a tungsten-halogen lamp, and is expanded uniformly over the entire electrode surface. The $\text{MV}^{2+/+}$ couple exhibits enhanced oxidation currents in the light, while $\text{MV}^{+/0}$ shows both oxidation and reduction currents in the dark. Cathodic peaks at a Pt foil electrode under the same conditions are at -0.50V vs. SCE for $\text{MV}^{2+/+}$ and -1.00V vs. SCE for $\text{MV}^{+/0}$. Substantial room temperature conduction in a-Si:H can be obtained due to tailing of phosphorus dopant from the n^+ layer into the undoped region of the film. (b) Open-circuit photovoltage for the a-Si:H/ CH_3OH interface as a function of solution redox potential. Cell potentials, including redox couples, with $E(\text{A}^+/\text{A})$ in V vs. SCE, are as follows: N,N'-dimethyl-4,4'-bipyridinium $^{+/0}$ (-0.95V); N,N'-dimethyl-4,4'-bipyridinium $^{2+/+}$ (-0.45V); $[\eta^5\text{-C}_5(\text{CH}_3)_5]_2\text{Fe}^{+/0}$ (-0.21V); N,N,N',N'-tetramethylphenylenediamine $^{+/0}$ (-0.11V); 1,1'-dimethylferrocene $^{+/0}$ ($+0.10\text{V}$); ferrocene $^{+/0}$ ($+0.20\text{V}$); acetylferrocene $^{+/0}$ ($+0.39\text{V}$). All determinations were in 1.0M LiClO₄ except for the N,N'-dimethyl-4,4'-bipyridinium system, which required 1.0M KCl for solubility. Measurements are the result of several independent determinations for a number of anodes.

formed with irradiation from a tungsten-halogen lamp, and the solutions contained sufficiently high concentrations of electroactive material to preclude significant photodecomposition processes on the time scale of the measurement. In each cell, the light intensity was adjusted to yield typical AM1 short-circuit photocurrent densities for this a-Si:H of 6-7 mA/cm². V_{oc} values obtained through a high impedance voltmeter or from the onset of anodic photocurrent in a steady-state current-voltage scan were in excellent agreement. We observe a linear dependence of V_{oc} vs. $E(A^+/A)$ over a wide (1.0V) potential range, with a slope of V_{oc} vs. $E(A^+/A)$ of 1.0 ± 0.2 (Fig. 1b). The data are thus in accord with the ideal model for the semiconductor/liquid interface (30), and do not yield evidence for gap states which pin the surface Fermi level to yield a relatively low photovoltage. While the V_{oc} values do seem to level off at very positive potentials, photoanodic decomposition processes prevented further variation in the solution potential. For A-acetyl ferrocene, the V_{oc} of 0.88-0.91V at light levels equivalent to 6-7 mA/cm² photocurrent densities for A = acetylferrocene are among the highest values of V_{oc} reported for any a-Si:H surface barrier device (17, 19, 31).

Cyclic voltammetry measurements of a-Si:H anodes in C₂H₅OH solvent are reported to yield nonideal behavior of V_{oc} vs. $E(A^+/A)$ (9). Photoanodic decomposition processes at low concentrations of redox couples and relatively high water content can lead to low values of V_{oc} in cyclic voltammetric experiments, and this is responsible for the discrepancy between our new dependence of V_{oc} vs. $E(A^+/A)$ and a previous study of a-Si:H in C₂H₅OH solvent. Cyclic voltammetric scans with our a-Si:H samples yield excellent agreement with previously reported data (9) in C₂H₅OH and yield similar data in CH₃OH solvent. However, a direct interpretation of these experiments is hindered by concurrent decomposition processes, as is evidenced by the disparity between cyclic voltammetric V_{oc} (0.57V) and steady-state V_{oc} photocurrent-voltage data (0.75V) for the ferrocene⁺⁰ system in previous studies (9). The high concentrations of electroactive reagents and minimal faradaic currents in the direct open-circuit photovoltage determinations (Fig. 1) minimize these complications, and yield an internally consistent set of data which indicate a substantially different dependence of V_{oc} vs. $E(A^+/A)$.

Our new data also modify the basic interpretation of the causes of junction nonideality in the a-Si:H system. We note that a slope of only 0.42 for V_{oc} vs. $E(A^+/A)$ has been found by cyclic voltammetry for p-i a-Si:H cathodes in aqueous solution (32). In addition, metal/semiconductor Schottky barriers with a-Si:H have been reported to yield a slope of V_{oc} vs. metal work function of 0.52 (33). This slope in Schottky systems has been attributed to the presence of interface states with a density of 10^{13} cm⁻²eV⁻¹

(33). Within this framework, it has been proposed (32) that the native a-Si:H surface oxide is the source of interface states, and that this oxide results in nonideal behavior at all of these a-Si:H interfaces. Our data (Fig. 1b) indicate ideal behavior [slope of V_{oc} vs. $E(A^+/A) = 1.0 \pm 0.2$] for a-Si:H/CH₃OH interfaces, and demonstrate that systems with surface oxides present can indeed exhibit ideal junction behavior in the proper system.

Our a-Si:H/liquid junction ideality data can be easily rationalized within the framework of past direct comparisons of liquid interfaces to Schottky systems. We have previously demonstrated that the chemistry of the semiconductor/contact junction can play a large role in determining interface kinetics, and that under identical illumination conditions, semiconductor/liquid interfaces with n-Si, n-GaAs_{1-x}P_x ($0 < x < 1$), and n-GaAs exhibit higher values of V_{oc} than do direct Schottky contacts with metals such as Pt or Au (15, 16, 34). Surfaces which exhibit a high density of gap states at metal contacts may not possess similar interface states at liquid junctions. For example, surface pinning in Si Schottky systems can be related to metal-silicide formation (35), and pinning in n-GaAs systems can be assigned to formation of Ga/metal alloys or formation of surface defects upon deposition of the metal barrier (36). There would appear to be few documented examples where the behavior of Schottky contacts successfully correlates with the behavior of liquid junctions. Consistently, immersion of a-Si:H in liquid systems (Fig. 1b) can yield ideal V_{oc} vs. $E(A^+/A)$ behavior and large photovoltages with no direct relation to Schottky barrier data.

Photocurrent-Voltage Characteristics of a-Si:H/CH₃OH Interfaces

We observe several novel effects in the photocurrent-voltage behavior of our a-Si:H films. These effects should be general for low L_c material, and have been observed for metal/semiconductor barriers with a-Si:H (37), but have not been previously noted for a-Si:H in contact with a liquid electrolyte. Previous work (9) on the a-Si:H/liquid interface has suggested that a source of inefficiency may be the use of relatively thick a-Si:H layers, and concurrently suggests that thinner samples may yield improved quantum efficiencies and fill factors since the field could extend across the entire material. Within the framework of Scheme I, it is apparent that if bulk collection difficulties are indeed the sole source of inefficiency, the use of shorter wavelength irradiation should yield improved cell behavior for any thickness of sample. However, substantial wavelength effects on the fill factor and short-circuit quantum efficiency, which would confirm the proposed suggestion, were not observed (9). In fact, exactly the opposite behavior was found, and 454.4 or 514.5 nm light gives lower observed quantum yields than does 632.8 nm light. Furthermore, no improvements in fill factor were observed with white light irradiation as compared to 632.8 nm irradiation, and little or no improvement in efficiency was observed with shorter wavelength excitation sources.

In contrast, we observe here substantial improvements in the photocurrent-voltage characteristics of the semiconductor/liquid interface with decreases in the wavelength of the excitation light source. Our data indicate that measurements of the photocurrent-voltage properties of a-Si:H at a single wavelength of light, especially light with energy near the absorption edge, are insufficient to identify the nature of the kinetics at the a-Si:H/liquid interface. We assign the previous declines in fill factor and quantum efficiency with decreasing photon wavelength not to a fundamental property of the a-Si:H/liquid interface, but rather to a combination of series resistance losses and to solution absorption of light. If these losses are minimized, the behavior of a-Si:H/alcohol interfaces can be consistently understood within the framework of the known bulk properties of a-Si:H.

Figure 2 displays the photocurrent-voltage characteristics as a function of the excitation wavelength of a-Si:H

Table I. Photocurrent-voltage parameters vs. photon wavelength for the a-Si:H/CH₃OH interface

λ (nm) ^a	Input (mW/cm ²)	Φ_{sc} ^b	V_{oc}	V_{pmax} ^c	η (%) ^d
632.8	5.46	0.18	0.69	0.54	3.4
632.8	11.9	0.16	0.73	0.56	3.2
632.8	25.1	0.16	0.77	0.54	3.2
514.5	1.86	0.46	0.64	0.50	6.8
514.5	3.27	0.47	0.66	0.52	7.6
514.5	5.30	0.44	0.68	0.52	7.1

^a Input at 632.8 nm is from a beam expanded He/Ne laser; input at 514.5 is from a beam expanded Ar ion laser.

^b Quantum yield for electron flow at short circuit.

^c Voltage at the maximum power point.

^d Maximum energy conversion efficiency for monochromatic light to electricity, uncorrected for cell reflection losses or solution absorption. Data are for one particular a-Si:H sample, and were obtained in a stirred 5.0 mM FeCp₂/0.5 mM FeCp₂⁺/1.0M LiClO₄/CH₃OH solution. The potential of the cell was measured as +0.20V vs. SCE. Efficiencies at other wavelengths are a compromise between variations in quantum yield and fill factor, as depicted in Fig. 2 and 3.

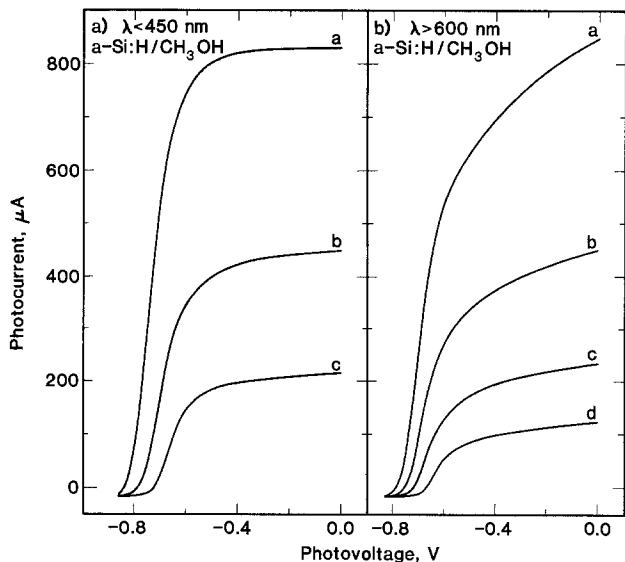


Fig. 2. Photocurrent-voltage properties of a-Si:H films (0.35 cm^2) in contact with stirred $10 \text{ mM FeCp}_2/0.5 \text{ mM FeCp}_2^+/1.0 \text{ M LiClO}_4/\text{CH}_3\text{OH}$ solution. The optical path length through the solution is 2 mm . The photocurrent-voltage curves are scanned at 50 mV/s , and potentials were measured vs. a Pt reference electrode poised at the cell potential through a 0.2 mm od Luggin capillary. (a) Photocurrent-voltage properties with irradiation of $\lambda < 450 \text{ nm}$ obtained from a 200 W Hg lamp equipped with a short pass filter. Curves b and c were obtained with neutral density filters transmitting 50% and 25% of the light intensity available in curve a. (b) Photocurrent-voltage properties under identical cell conditions as in Fig. 2a, but irradiation is far $\lambda > 600 \text{ nm}$ from a ELH-type tungsten halogen lamp equipped with a 600 nm long pass colored-glass filter. Curves c and d were obtained with 50% and 25% transmittance neutral density filters from the irradiation level in curve b; curve a has the light intensity adjusted to provide similar photocurrent density to curve a in Fig. 2a. Note the pronounced decline in fill factor in Fig. 2b relative to the collection properties displayed in Fig. 2a.

films in contact with a $1.0 \text{ M LiClO}_4/10.0 \text{ mM ferrocene (FeCp}_2)/0.5 \text{ mM FeCp}_2^+/\text{CH}_3\text{OH}$ solution. With excitation of $\lambda > 600 \text{ nm}$ (Fig. 2b, Table I), we observe low short-circuit quantum yields which decline with increasing light intensity. In addition, the fill factor is 0.50 at very low current density and shows a decline with increasing light intensity. Higher values of photocurrent density than displayed in Fig. 2b, as obtained with $\lambda > 600 \text{ nm}$ from a filtered tungsten-halogen lamp, yield even poorer fill factors and quantum efficiencies. These photocurrent-voltage characteristics generally resemble those reported previously for a-Si:H films in $\text{C}_2\text{H}_5\text{OH}$ solution with 632.8 nm excitation (9), except that the lower series resistance of the $\text{CH}_3\text{OH}/1.0 \text{ M LiClO}_4$ electrolyte (15) and the lower bulk resistance in the $0.5 \mu\text{m}$ film leads to better fill factors in our system.

In contrast, Fig. 2a displays the photocurrent-voltage behavior of the a-Si:H/ $10.0 \text{ mM FeCp}_2/0.5 \text{ mM FeCp}_2^+/\text{CH}_3\text{OH}$ interface when irradiated with light of $\lambda < 450 \text{ nm}$ (obtained from a 200 W Hg lamp equipped with a 450 nm short pass filter). We observe significantly higher fill factors, which do not degrade even at photocurrent densities threefold higher than the onset of decline with the $\lambda > 600 \text{ nm}$ light. In addition, with minimal solution absorption, the quantum efficiency for carrier collection with 450 nm light is over twice the value obtained at 632.8 nm (*vide infra*). Thus, both the short-circuit quantum yield and fill factor of these a-Si:H/liquid junctions are dependent upon incident photon energy.

Previous studies have speculated that a decline in fill factor with increasing photocurrent density observed with 632.8 nm irradiation might be due to surface recombination sites at the a-Si:H/liquid interface, or perhaps due to series resistance losses associated with the photoconductivity property of the a-Si:H films (9, 32).

The improvements in our photocurrent-voltage responses with excitation by higher energy photons rule out both of these possibilities in our system. We find that our observations are consistent with the transport and absorption properties of a-Si:H, and we conclude that the behavior of a-Si:H/liquid junctions is dominated by these processes.

In a-Si:H films irradiated with sufficiently short wavelengths, such that the penetration depth $\alpha(\lambda)^{-1}$ is on the order of 100 nm or less (24), essentially all of the photogenerated holes will be collected at the junction, resulting in high short-circuit quantum efficiencies. In addition, fill factors should be high, provided that series resistance losses from the use of excessively thick a-Si:H films and highly resistive electrolytes are minimal. As depicted in Fig. 2a, these expectations are in excellent agreement with the photocurrent-voltage characteristics for irradiation of the a-Si:H/ $\text{CH}_3\text{OH}/\text{FeCp}_2^+/\text{FeCp}_2$ interface with light of wavelength less than 450 nm .

The situation for 632.8 nm excitation is substantially different. The $\alpha(\lambda)^{-1}$ in a-Si:H of 632.8 nm light is typically $1\text{--}2 \mu\text{m}$ (24); thus, low quantum efficiencies should be expected, since only a fraction of the carriers will be created within a collection length of the interface. Use of material with thicknesses greater than L_c may lead to increased light absorption, but will not necessarily produce substantial increases in photocurrent flow. Quantum yields with 632.8 nm light are rather modest even with our film geometry (Table I), and we conclude that increases in quantum efficiency at this wavelength will require fabrication of material with larger collection lengths, rather than passivation of surface states.

We have noted above that the fill factor at a specific photocurrent density is dependent on the wavelength of the incident photons (31). This can be understood by considering the factors which determine the fill factor of a semiconductor/liquid junction, with emphasis upon the particular electronic properties of a-Si:H. The hole-collection length usually is the depletion width, W , plus the diffusion length, L_p ; thus, only holes produced at depths comparable to $L_p + W$ will diffuse to the depletion region where the built-in field can sweep them to the junction.¹ a-Si:H differs from its crystalline counterparts in that L_p is on the order of, and sometimes less than, W (25-29). Application of an external potential to bias the cell from open circuit towards short circuit will serve to increase the field-assisted drift, and thus will lead to collection lengths, and hence photocurrents, which are a strong function of applied voltage. Additionally, in a-Si:H, L_c is known to decrease with increasing light intensity, due to a contraction of the depletion region under illumination (38). Thus, the fill factor should be dependent upon both the light intensity and the penetration depth of the light as compared to $L_p + W$, with shorter wavelengths of light yielding improved photocurrent-voltage characteristics (Fig. 2, 3; Table I).

Clearly, a complete description of the a-Si:H/liquid interface must take these bulk effects into account in order to interpret the photocurrent-voltage data. Quantitative descriptions of the light intensity and potential dependence of the fill factors are being developed, and should yield information concerning carrier transport in a-Si:H similar to that produced by the established surface photovoltage technique. The stability of a-Si:H films in the nonaqueous $\text{FeCp}_2^+/\text{FeCp}_2/\text{CH}_3\text{OH}$ solvent should provide a distinct advantage over the aqueous redox system presently used for these surface photovoltage measurements (38). In this regard, the study of liquid junctions may aid in developing improved techniques for characterizing a-Si:H films, as well as a-Si:H interface properties.

¹ In our discussion of collection lengths, we have implicitly assumed that the hole mobility is sufficiently large that all carriers created in the depletion region are collected. Under this condition, $L_c = L_p + W$. However, if the hole mobility is sufficiently small, drift alone will dictate the collection length, and L_c may then only be a fraction of W . Our data can be accommodated within the framework of either of these two conditions.

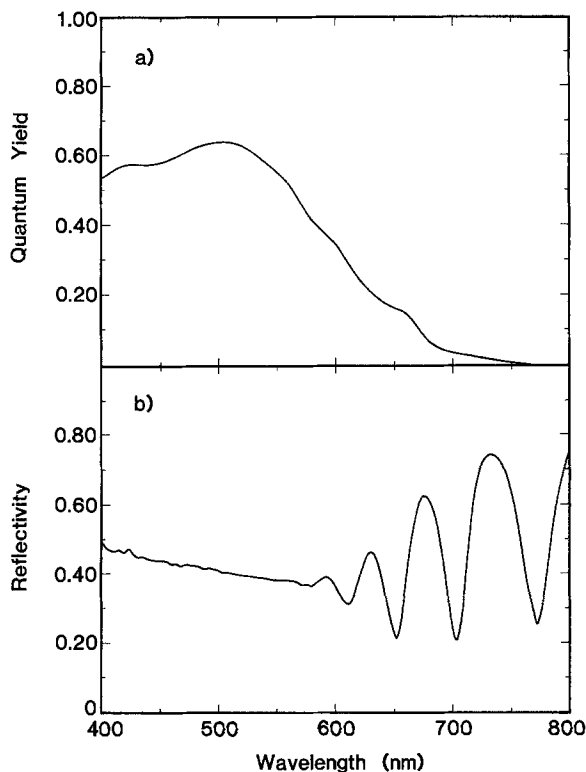


Fig. 3. (a) Short-circuit quantum yield vs. photon wavelength for the a-Si:H/5.0 mM FeCp₂/0.5 mM FeCp₂⁺/1.0M LiClO₄/CH₃OH interface. Optical path length through the solution is 1 mm, and the light intensity is approximately 1 mW/cm². (b) Reflectivity spectrum at an air interface of an a-Si:H film on a Pd-coated n-Si substrate. The interference fringes for $\lambda > 600$ nm arise from the 0.5 μ m film thickness.

Spectral Response Characteristics of a-Si:H/Liquid Junctions

The spectral response of short-circuit photocurrent *vs.* photon wavelength lends further credence to the notion that the electronic properties of a-Si:H dominate the photoelectrochemical behavior. The spectral response data for a-Si:H/CH₃OH/5.0 mM FeCp₂/0.5 mM FeCp₂⁺ are depicted in Fig. 3. In addition, a reflectivity spectrum of a similar a-Si:H film on a substrate of Pd-coated single-crystal silicon is displayed for reference in Fig. 3b. The spectral response data have been obtained at short-circuit conditions (1 mm optical path length through the solution), with an average light intensity of 1 mW/cm². As discussed above, the quantum yields obtained for long wavelength excitation at these light intensities will be somewhat higher than differential quantum yields under solar photon fluxes. The measurement in Fig. 3a is based upon light incident upon the photoelectrochemical cell, and is not corrected for solution absorption or optical reflection losses. For excitation with short-wavelength photons, we observe high quantum yields for electron flow, >0.55 . Reference to the reflectivity spectrum at the a-Si:H/air interface (Fig. 3b) indicates that the effective index of refraction of this a-Si:H film at 450 nm is 4.8 (39). Using a value for the index of refraction of 1.0M LiClO₄/CH₃OH of 1.35 (40), we calculate that reflective losses from the air/glass/solvent/a-Si:H interfaces will amount to approximately 30% of the incident light. Thus, quantum yields corrected for reflection are greater than 0.8, and would approach unity if corrections for solution absorption were also included.

The effect of small carrier collection lengths in a-Si:H is demonstrated by a comparison of the spectral response curves in the 600-700 nm region to the reflectivity data. In this wavelength region, the absence of interference fringes and the known increase in absorption coefficient with wavelength indicate increasing absorption by the

a-Si:H film; however, in the same wavelength region, the short-circuit quantum yield declines noticeably. Long wavelength photons penetrate too deeply into the film to be efficiently collected because of the modest collection lengths of these particular samples of a-Si:H. Thus, low short-circuit quantum yields and low fill factors for excitation of a-Si:H with 632.8 nm light do not necessarily result from recombination sites at the semiconductor/liquid interface, but can be assigned to carrier transport and optical-absorption properties of the material itself.

We note that typical p-i-n solid-state devices show a decline in short-circuit quantum efficiency with short-wavelength excitation because of high recombination rates in the doped layers near the surface (25). However, liquid junctions should benefit from the efficient collection of carriers generated near the interface, and need not possess the surface dead layer present in p-i-n-type systems. In addition, a liquid junction may not exhibit metal/semiconductor interfacial stress, which can induce recombination sites and cause declines in the spectral response for short-wavelength excitation. Ideal semiconductor/liquid junctions should not show a decline in short-circuit quantum efficiency with high energy excitation unless bulk resistivity effects influence majority-carrier collection. Previous investigations of n⁺-i-a-Si:H films in C₂H₅OH/FeCp₂ liquid junctions indicate that the short-circuit quantum yield decreases when the excitation wavelength is changed from 632.8 nm to 514 or 454 nm (9). Recent work on p-i type a-Si:H films in liquid junctions also reveals this effect, and the assumption of low series resistance in these films has led to the suggestion that a decline in short-wavelength response is an intrinsic property of the a-Si:H/liquid interface (32). Different preparations of a-Si:H films could produce different interface properties; however, reference to the spectral response characteristics in Fig. 3 demonstrates that a-Si:H/liquid junctions can exhibit internal quantum yields near unity, and that a decline in spectral response characteristics at short wavelengths is not apparent with our a-Si:H samples under these conditions.

Excessive series resistance losses, especially for majority carriers in p-i a-Si:H films, can lead to decreases in short-circuit quantum yield at short-excitation wavelengths. With excitation of $\lambda < 500$ nm, we can assign reduced quantum efficiencies in our low resistance n⁺-i a-Si:H/liquid junctions to solution absorption of light, and not to recombination at the semiconductor/liquid interface or to the a-Si:H material itself. Figure 4 depicts the spectral response parameters of a-Si:H films as a function of the concentration of FeCp₂ in CH₃OH solvent. We observe that the quantum yield declines severely at short wavelengths, owing to excessive solution absorption, even at relatively modest levels of FeCp₂ and with relatively short optical path lengths through the solution (0.5-1.0 mm). Addition of small amounts of the highly absorbing FeCp₂⁺ makes the effect more pronounced. Absorption spectra indicate that 0.070M FeCp₂ in C₂H₅OH in a 2.0 mm thickness absorbs 43% of the light at 514 nm and 97% at 454 nm, and that accurate quantum yields based on photons incident on the a-Si:H electrode surface in these solutions would require extremely short path lengths. Minimization of these losses does not yield evidence for low quantum efficiencies, and yields improved behavior for the a-Si:H/liquid junctions.

Efficiency Parameters for the a-Si:H/FeCp₂/FeCp₂⁺/CH₃OH System

The photocurrent-voltage characteristics under simulated solar illumination of a-Si:H films in 20.0 mM FeCp₂/0.5 mM FeCp₂⁺/1.5M LiClO₄/CH₃OH are depicted in Fig. 5. Even with the relatively poor long wavelength response of our particular a-Si:H samples and substantial solution absorption for $\lambda < 500$ nm, at 88 mW/cm² of ELH-type tungsten-halogen irradiation, we observe a short-circuit photocurrent density of 7-8 mA/cm². Under these

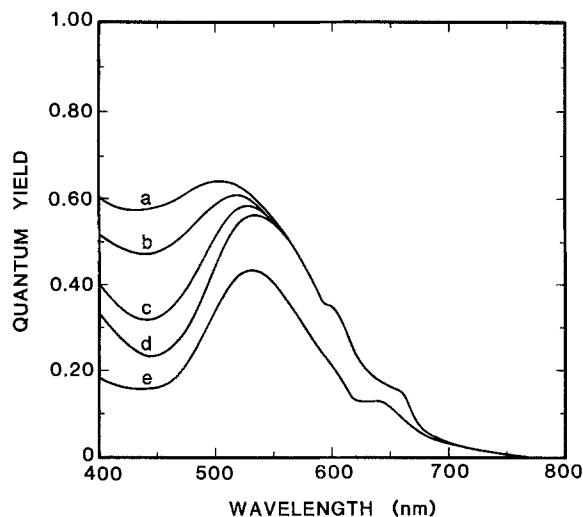


Fig. 4. Short-circuit quantum yield vs. photon wavelength for a-Si:H/CH₃OH junctions at varying concentrations of FeCp₂. The optical path length through the solution is 1.5 mm, and the electrode is maintained at short circuit vs. a Pt counterelectrode. Initial FeCp₂⁺ concentration is 0.5 mM; curve (a) has 5.0 mM FeCp₂. In curve (b), 13.3 mM FeCp₂ is present, in (c) 25.4 mM FeCp₂, in (d) 43.4 mM FeCp₂, and (e) contains 40.0 mM FeCp₂ with 2.0 mM FeCp₂⁺ in solution.

conditions, we observe open-circuit photovoltages of 0.75-0.85V and fill factors of 0.5-0.6, with typical photoelectrode efficiencies for conversion of optical energy to electricity of 2.7%-3.3%. On identical samples of a-Si:H, Schottky barriers fabricated with nominally 50Å thick Pt films yield short-circuit currents of 5-7 mA/cm² and efficiencies of 1%-2%. We attribute the variation in short-circuit current to differences in transmittance of Schottky barriers and liquid junctions, while the lower efficiency of the Schottky contacts arises from a lower V_{oc} . Open-circuit photovoltages on the best surface barrier devices with high quality a-Si:H can be 0.85V (31) at AM1 irradiation levels, which is comparable to the value we observe with the acetylferrocene^{+/0} redox system in our unoptimized liquid junctions. We note that an improve-

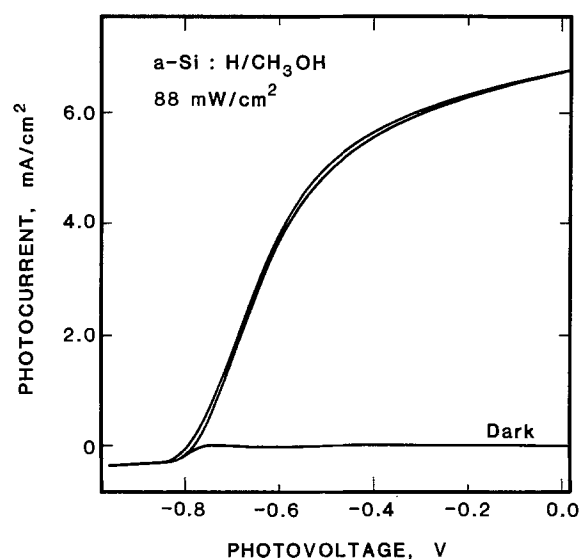


Fig. 5. Photocurrent-voltage characteristics of (50 mV/s) of an a-Si:H film in 20.0 mM FeCp₂/0.5 mM FeCp₂⁺/1.5M LiClO₄/CH₃OH solution. The solution is stirred, and potentials are measured vs. a Pt reference electrode at the cell potential (+0.18V vs. SCE). Irradiation is 88 mW/cm² from an ELH-type tungsten-halogen source, and optical path length through the solution is minimized in order to avoid substantial light absorption losses (Fig. 4).

ment in material quality of our a-Si:H samples would yield substantial increases in photocurrent owing to improved quantum efficiencies in the 600-700 nm region of the spectrum. In addition, the fill factor under ELH irradiation is a combination of the relatively poor long-wavelength response and the good short-wavelength parameters, and is also expected to improve with better electronic transport properties in the a-Si:H. With a collection length of 1.0 μm and fill factors similar to those depicted in Fig. 2a, we calculate that a-Si:H/liquid junction cells would yield photoelectrode efficiencies for conversion of sunlight to electricity of over 5% without further optimization of the system. These values are comparable to efficiencies obtained with a-Si:H surface-barrier-type systems, and would compare favorably to the highest efficiencies obtained for single-crystal silicon semiconductor/liquid junctions under solar conditions (15). It would thus appear that the a-Si:H/liquid interface is not the limiting factor in development of efficient a-Si:H/liquid junctions, but that control and improvement of the electronic properties of the a-Si:H films are the dominant factors at present.

The high quality of the a-Si:H/liquid interface observed in this study is consistent with other recent descriptions of photoelectrodes in nonaqueous solvents (15, 16, 34), and implies that systematic design and study of efficient photoelectrochemical systems in nonaqueous solvents may be possible with a variety of materials. We have demonstrated that a-Si:H/CH₃OH/FeCp₂/FeCp₂⁺ junctions can exhibit high quantum efficiencies for electron flow, large photovoltages, and excellent photocurrent-voltage characteristics under the proper conditions. Successes with properly prepared single-crystal photoelectrode substrates strongly suggest that future challenges in the area will arise from the chemistry of grain boundaries and recombination sites in polycrystalline materials at liquid junctions, where the unique chemistry at semiconductor/liquid interfaces should allow manipulation of recombination sites through simple chemical processes.

Acknowledgment

We thank L. Christel of SERA Solar Corporation for valuable discussions and supply of computer programs, and Jeff Marks of Stanford University for the use of the arc lamp source. We also thank Professor M. S. Wrighton of MIT for generously supplying a preprint describing work on p-i a-Si:H.

Manuscript submitted Oct. 26, 1983; revised manuscript received Nov. 4, 1983.

REFERENCES

1. A. J. Bard and M. S. Wrighton, *This Journal*, **124**, 1706 (1977).
2. M. S. Wrighton, *Acc. Chem. Res.*, **12**, 303 (1979).
3. P. A. Kohl and A. J. Bard, *J. Am. Chem. Soc.*, **99**, 7531 (1977).
4. M. E. Langmuir, M. A. Parker, and R. D. Rauh, *This Journal*, **129**, 1705 (1982).
5. J. M. Bolts and M. S. Wrighton, *J. Am. Chem. Soc.*, **101**, 6179 (1979).
6. P. A. Kohl and A. J. Bard, *This Journal*, **126**, 603 (1979).
7. L. Fornarini, F. Stirpe, and B. Scrosati, *ibid.*, **129**, 1155 (1982).
8. D. C. Bookbinder, N. S. Lewis, M. G. Bradley, A. B. Bocarsly, and M. S. Wrighton, *J. Am. Chem. Soc.*, **101**, 7721 (1979).
9. G. S. Calabrese, M. S. Lin, J. Dresner, and M. S. Wrighton, *ibid.*, **104**, 2412 (1982).
10. L. F. Schneemeyer and M. S. Wrighton, *ibid.*, **101**, 6496 (1979).
11. M. S. Lin, N. Hung, and M. S. Wrighton, *J. Electroanal. Chem.*, **135**, 121 (1982).
12. A. J. Bard, F.-R. F. Fan, A. S. Gioda, G. Nagasubramanian, and H. S. White, *Disc. Faraday Soc.*, **70**, 19 (1980).
13. A. B. Bocarsly, E. G. Walton, M. G. Bradley, and M. S. Wrighton, *J. Electroanal. Chem.*, **100**, 283 (1979).

14. A. J. Bard, A. B. Bocarsly, F.-R. F. Fan, E. G. Walton, and M. S. Wrighton, *J. Am. Chem. Soc.*, **102**, 3671 (1980).
15. C. M. Gronet, N. S. Lewis, G. Cogan, and J. Gibbons, *Proc. Natl. Acad. Sci. U.S.A.*, **80**, 1152 (1983).
16. C. M. Gronet and N. S. Lewis, *Appl. Phys. Lett.*, **43**, 115 (1983).
17. A. H. Mahan and J. L. Stone, *Solar Cells*, **7**, 398 (1983).
18. T. Skotheim, I. Lundstrum, A. E. Delahoy, F. J. Kompas, and P. E. Vanier, *Appl. Phys. Lett.*, **40**, 281 (1982).
19. R. Williams, *J. Appl. Phys.*, **50**, 2848 (1979).
20. Y. Avigal, D. Cahen, G. Hodes, J. Manassen, B. Vaines, and R. A. G. Gibson, *This Journal*, **128**, 1209 (1980).
21. D. E. Carlson, *Solar Energy Mater.*, **3**, 503 (1980).
22. W. Paul and D. A. Anderson, *ibid.*, **2**, 229 (1981).
23. M. Hirose, *J. Phys. C*, **42**, 705 (1981).
24. G. D. Cody, C. R. Wronski, B. Abeles, R. B. Stephous, and B. Brooks, *Solar Cells*, **2**, 227 (1980).
25. P. Viktorovitch, G. Moddel, J. Blake, S. Oquz, R. L. Weisfield, and W. J. Paul, *J. Phys. C*, **42**, 455 (1981).
26. Y. Tawada, K. Tsuge, M. Kondo, M. Okamoto, and Y. Hanakawa, *J. Appl. Phys.*, **53**, 5273 (1982).
27. T. McMahon, in "Proceedings of the 16th IEEE Photovoltaics Specialists Conference," p. 1389, IEEE, New York (1982).
28. S. J. Fonash, "Solar Cell Device Physics," Academic Press, New York (1981).
29. S. M. Sze, "Physics of Semiconductor Devices," John Wiley and Sons, New York (1981).
30. H. Gerischer, *J. Electroanal. Chem.*, **58**, 263 (1975).
31. D. E. Carlson, C. R. Wronski, A. R. Trianao, and R. E. Daniel, in "Proceedings of the 12th IEEE Photovoltaics Specialists Conference," p. 893, IEEE, New York (1976).
32. D. J. Harrison, G. S. Calabrese, A. J. Ricco, J. A. Dresner, and M. S. Wrighton, *J. Am. Chem. Soc.*, **105**, 4213 (1983).
33. D. E. Carlson, D. R. Wronski, J. I. Pankove, P. J. Zancucchi, and D. L. Stoebler, *RCA Rev.*, **38**, 211 (1977); C. R. Wronski, D. E. Carlson, and R. E. Daniel, *Appl. Phys. Lett.*, **29**, 602 (1976).
34. C. M. Gronet and N. S. Lewis, *Nature (London)*, **300**, 733 (1983).
35. R. Purtell, J. G. Clabes, G. W. Rubloff, B. R. Ho, and F. J. Himpel, *J. Vac. Sci. Technol.*, **17**, 1019 (1980).
36. W. E. Spicer, I. Lindau, P. R. Skeath, and C. Y. Su, *ibid.*, **17**, 1019 (1980).
37. C. R. Wronski, *IEEE Trans. Electron Devices*, **ed-24**, 35 (1977).
38. A. Moore, *Appl. Phys. Lett.*, **40**, 403 (1981).
39. J. D. Jackson, "Classical Electrodynamics," 2nd Ed., p. 312, John Wiley and Sons, New York (1975).
40. "CRC Handbook of Chemistry and Physics," R. C. Weast, Editor, CRC Press, Cleveland, OH.

Blockage of the Active Sites of a Platinum Electrode

Influence of Dissolved Molecular Oxygen on the Time Dependence of Blockage in the Methanol/Electrolyte/Rotating Disk Electrode System

Albert Marie de Ficquelmont and May Marie de Ficquelmont-Loïzos¹

Institut de Topologie et de Dynamique des Systèmes, Université Paris VII, associé au CNRS, 75005 Paris, France

ABSTRACT

The MeOH/0.1M NaClO₄/Pt system is investigated in aerated and deaerated medium, by analyzing the $I(t)$ output signals for a single gating input potential signal $[SII(t)]$ and for a sequence of two isochronic gating input signals $[DII(t)]$ separated by a varying time $\Delta\tau$ in open circuit, under the same conditions ($U = +750$ mV/SCE; $\omega = 12.5$ rps; $\theta = 25^\circ\text{C}$; electrode pretreatment = polishing plus sonication). Analysis (in $\ln I - \ln t$ coordinates) of the $I(t)$ signals resulting from an $SII(t)$ of 600s shows that the current decays to $I = 0$ as a function of time through three nearly linear sections, much more slowly in aerated medium. For $DII(t)$, the current increases as a function of $\Delta\tau$ up to a plateau. These results are interpreted in terms of two types of adsorption: a hard one (species strongly bound to the substrate), and a soft one (weakly bound species). Dissolved O₂ is shown to act as a blockage inhibitor through a mechanism based on the following hypotheses: (i) competition between MeOH and O₂ adsorptions leading to sites occupied by oxygen admolecules, (ii) dissociative chemisorption of MeOH, on bare Pt sites and on Pt(Ad-O₂) sites without segregation, with the same stepwise dehydrogenation mechanism. With these hypotheses, the blocking adsorbates, whatever their nature, are more labile on Pt(Ad-O₂) sites, due to a higher oxidation state of the carbon atom therein, thus explaining the two types of adsorption observed.

The interest of methanol as a solvent (in organic chemistry, chemical kinetics, or electro-organic synthesis) and as a fuel in fuel cells is no longer to be demonstrated. From this last point of view, methanol electro-oxidation in acidic or alkaline aqueous media, *i.e.*, the water/methanol + electrolyte/electrode system, has been widely investigated. However, only few studies deal directly with the methanol/electrolyte/electrode system (1-3) and the role of the blockage of the electrode active sites therein. The latter is known to exist in methanol oxidation in acidic medium (4), in contrast with alkaline medium (5), and constitutes a very important obstacle to the development of methanol-air fuel cells (6). It is important to specify that blockage means, in general, any decrease in the number and the reactivity of the active sites.

We present here a study on the blockage of the active sites for the simple system MeOH/NaClO₄/Pt. We shall also show the role of dissolved molecular oxygen, which has a marked influence on the interface topography

(number and nonrandom distribution, at the atomic level, of the active sites), as was shown for metal systems (titanium or iron) in sulfuric acid (7, 8). To our knowledge, the role of dissolved oxygen on the behavior of the electrode in methanol has not previously been investigated; only deaerated media have been considered.

We study here the response of a rotating disk electrode to a potential pulse input. This response depends on the interface topography, *i.e.*, (i) on parameters inherent in the electrode itself (nature, structure, shape, pretreatment etc.), (ii) on parameters inherent in the medium (concentration, temperature, viscosity, hydrodynamic conditions, diffusion phenomena, etc.), and (iii) on the type of reaction mechanisms taking place at the interface (8, 9).

Experimental

The supporting electrolyte (0.1M) was sodium perchlorate (Merck proanalysis), dried at 150°C under vacuum. Methanol (Baker Absolute) was distilled over Prolabo 99.8% magnesium turnings in order to eliminate water and metallic impurities. Measurements performed with undistilled solvent have indeed shown blockage occur-

¹Present address: CNRS, E.R. 248, "Instrumentation et Dynamique Cardiovasculaire," Hôpital Broussais, 75674 Paris Cedex 14, France.

ring more rapidly. The solutions were aerated by dry atmospheric air in thermodynamic equilibrium with methanol without bubbling. Deaeration was performed by argon bubbling (Air-Liquide N55) saturated with methanol of cell composition. During the measurements, in order to avoid a perturbation of the fluid flow and bubbles at the electrode surface, bubbling was stopped, but an overpressure of methanol-saturated argon was maintained over the solution. Under these conditions, solvent evaporation was negligible. Between two measurements, argon bubbling was maintained. The efficiency of deaeration was regularly verified through the current variation of oxygen reduction from aerated to deaerated medium (e.g., at -0.6V , from $300\ \mu\text{A}$ to less than $3\ \mu\text{A}$ on the average at a rotation speed $\omega = 0$). The currents depend of course on the atmospheric pressure. Note that oxygen is far more soluble in methanol than in water, leading to more important currents (current densities ten times higher).

Measurements were performed, at $+25^\circ\text{C} \pm 0.1^\circ\text{C}$, using a classical three-electrode system and a hemispherical one-compartment and double-wall cell (solution volume = 125 ml). The working electrode was the cross section of a platinum cylinder (0.5 cm diam) inserted in a Teflon thermoshrinkable sheath (overall diameter of the electrode = 1 cm). The counterelectrode was a large, hemispherical iridium-coated platinum grid. The reference electrode was a removable double-compartment calomel electrode in saturated $\text{KCl}(\text{MeOH})$. $I(t)$ curves were recorded potentiostatically (home-built potentiostat, solid or mercury contactor according to the range of ω), and $I(U)$ curves under potential sweep conditions. The electrode rotation speed was measured to $\pm 1\%$ photoelectrically (home-built frequency meter). The rotating disk electrode (RDE) was mirror polished with $3\ \mu\text{m}$ diamond paste for 150s then sonicated for 450s in methanol of cell composition. The RDE and the glassware were rinsed with the distilled methanol.

Results

The RDE behavior has been examined through the current-time $I(t)$ curves recorded, in laminar flow (10), at different values of the potential U and of the rotation speed ω (ranging from 6.25 to 100 rps), both in aerated and in deaerated medium. This behavior is exemplified here by the results relative to $U = +750\ \text{mV/SCE}$ and $\omega = 12.5\ \text{rps}$. Since any change in the initial and boundary conditions is liable to lead to a different mathematical expression of the output signal, we have always operated as follows: after pretreatment (polishing and sonication), the RDE was rotated in the solution before the counterelectrode circuit was closed.

The potential of $+750\ \text{mV/SCE}$ corresponds (Fig. 1) to a range between oxygen reduction and an oxidation step (prewave at an average value of $1.2\ \text{V/SCE}$). The initial forward trace is very reproducible with a polished RDE, but is affected by blockage during consecutive sweeps, as is the case in sulfuric acid (4). On the contrary, the backward trace markedly varies with the experimental conditions. The prewave at 1.2V is to be compared with the one observed for $\text{NaClO}_4\text{-MeOH}$ under other experimental conditions, which was attributed to the oxidation of the solvent and not to that of the supporting electrolyte (3). The cathodic processes correspond to the reduction of dissolved O_2 and Na^+ [solvated in MeOH (11)].

The $I(t)$ output signal corresponds to the following conditions: on circuit closure, the potential is held at a fixed value over a time interval T and is zero before and after T (open circuit). Further information on the RDE behavior was provided by the $I(t)$ curves recorded after open-circuit exposure. To this end, two isochronic $I(t)$ signals recorded at a given U and separated by a time $\Delta\tau$ on open circuit ($U = 0$) were compared (Fig. 2). The RDE was pretreated for the first signal only; the hydrodynamic conditions were held all over (RDE immersed and rotated at the same ω); $\Delta\tau$ was varied from some fractions of a second to 1 or 2h. The input signals are obviously of the

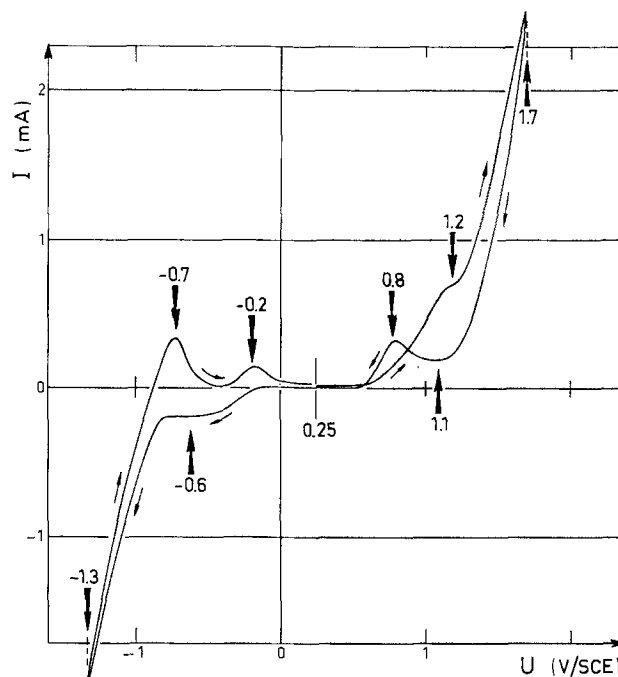


Fig. 1. Linear sweep voltammogram for 0.1M NaClO_4 in aerated methanol. [$\omega = 0$; sweep rate = $600\ \text{mV/min}$; RDE treatment: $3\ \mu\text{m}$ diamond paste polishing (150s) + sonication (450s); $\tau = 25^\circ\text{C}$; ϕ RDE = $0.5\ \text{cm}$]. Scale: 1 unity = $200\ \mu\text{A}$ or $200\ \text{mV}$.

gating pulse type, and will be denoted hereafter, for the sake of convenience, as $S_{II}(t)$ for the single and $D_{II}(t)$ for the double gating pulse.

Experimental $I(t)$ curves for an $S_{II}(t)$ input signal.—The experimental $I(t)$ curves exhibit (Fig. 2) in both media a very important impulse (D_1) followed by a rapid and continuous decrease down to a zero or at least a very low current value, when $t \rightarrow \infty$ (fall of 99% even at U 's at which I is important on the $I(U)$ curve). The shape of the signal is different from the one given, for example, by the oxidation of the methanol residue on platinized platinum in sulfuric acid (12). The fact that no stationary current is reached and the very fast decay of I are indicative of blocking phenomena taking place very rapidly at the RDE surface.

The part of the signal at very short times is the consequence of the circuit closure, the charge of the double-layer capacitance, the transfer function of the device, and the mass transfer of species arriving at the electrode under the influence of the electric field (although the hydrodynamic steady state was attained before circuit closure, since the RDE was rotated before U was applied).

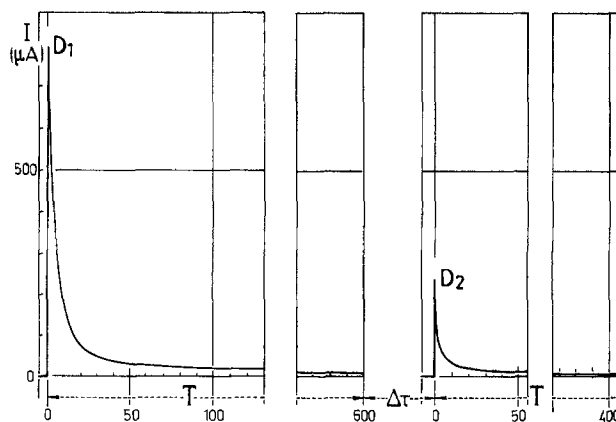
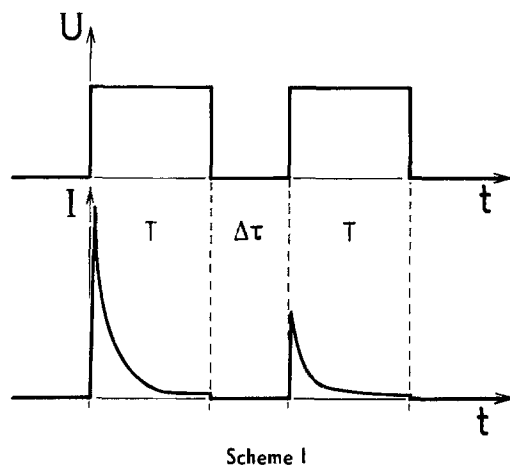


Fig. 2. Experimental $I(t)$ output signal recorded after RDE treatment [$S_{II}(t)$ input signal] and after open-circuit exposure during a time $\Delta\tau$ [$D_{II}(t)$ input signal] for 0.1M NaClO_4 in aerated methanol. [$U = +750\ \text{mV/SCE}$; $\omega = 12.5\ \text{rps}$; $\theta = 25^\circ\text{C}$; ϕ RDE = $0.5\ \text{cm}$; $T = 600\text{s}$].



Scheme I

The ascending part of the impulse reaches a maximum value at 0.18–0.20s after circuit closure and is therefore located within the time range for mass transfer.

The descending part of $I(t)$ is not a simple exponential over the duration T of the input signal, since the $\ln t$ vs. t curve is similar to $I(t)$, i.e., $\ln I$ nonlinear vs. t . Its analysis in $\ln I - \ln t$ coordinates reveals the existence of three nearly linear sections, both in aerated and deaerated medium (Fig. 3, curves A and B), as was observed in the case of the formation of oxide layers on iridium from sulfuric acid (13). The number of sections (three) is relative to a time T of 600s, but another number may be revealed when the observation time is varied. In deaerated medium, the second section is less extended, the instant value of I is lower, the slopes are higher, and the transition times (defined at the intersections of the tangents) are shorter. In Fig. 3, the ratios of the slopes are 2.5 for the first and 1.1 for the second and third sections; the ratios of the transition times are 1.2 for the first to the second section and 1.5 for the second to the third section.

Experimental $I(t)$ curves for a $DII(t)$ signal.—By increasing $\Delta\tau$ (Fig. 2), a sharp increase of I followed by a plateau is observed, as shown by the values D_2 of the maximum in the second $I(t)$ signal (Fig. 4). This behavior is revealed in both media, whatever the value of ω , but the height of the plateau is markedly lower in the absence of dissolved molecular oxygen (5% instead of 30% in aerated medium). Owing to our procedure, the values of D_1 and D_2 are obviously coupled, and therefore the ratio D_2/D_1 has been plotted in order to take account of this coupling.

In aerated medium, analysis of the second $I(t)$ curve leads to two linear sections only at low $\Delta\tau$ values (Fig. 5, curve 1 for $\Delta\tau = 1.95$ s). When $\Delta\tau$ is increased, the shape of the curves becomes more and more similar to that of the initial curve (three sections), i.e., the one with the pretreated RDE (curve 0). In deaerated medium, the behavior

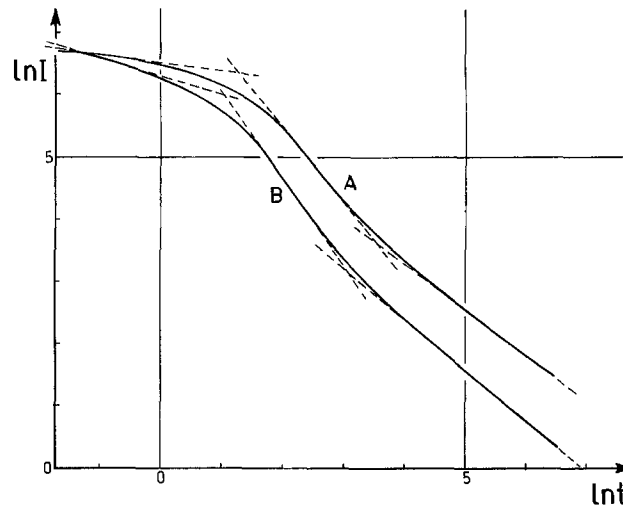


Fig. 3. Comparison between aerated (A) and deaerated (B) medium on the $I(t)$ curves, expressed in $\ln I - \ln t$ coordinates, recorded for an $s\Pi(t)$ input signal, for 0.1M NaClO_4 in methanol. [$U = +750$ mV/SCE; $\omega = 12.5$ rps; $\theta = 25^\circ\text{C}$; ϕ RDE = 0.5 cm; $T = 600$ s.]

observed shows similarities but also differences, since low $\Delta\tau$ values do lead to two sections only (Fig. 6, curve 1) whereas the third section starts to appear at higher values, but not as clearly as in aerated medium. In addition, the gap between curve 0 and the other curves is far more important in deaerated medium for a given $\Delta\tau$, as shown by curve 4 in Fig. 5, curve 2 in Fig. 6 ($\Delta\tau = \text{ca. } 30$ s in both cases), and Fig. 7 ($\Delta\tau = \text{ca. } 60$ s).

Influence of the RDE pretreatment.—The results presented here are relative to average current values, because of a scattering over a Gaussian curve (shown up on the values of D_1). This scattering can be due partly to the pretreatment of the RDE. It is indeed known that a change in the pretreatment of the electrode (chemical, thermal, physical, electrochemical methods, or combinations of these) gives rise to different results on adsorption phenomena (14). Moreover, a simple change in the grade of the abrasive paper used in mechanical polishing also leads to marked differences in the blockage (8). More expectedly, a change in the potential sequence during an electrochemical treatment leads to significant modifications of the adsorption process and the oxidation of the resulting adsorbates in $\text{MeOH-H}_2\text{SO}_4$ medium (15, 16).

In the present case, using always the same type of pretreatment and the same grade of diamond paste, we have shown that certain parameters characterizing our technique play an important part in the current measured, even if the overall shape of the curves remains unchanged. Thus, the polishing time t_p of the RDE has a marked influence, as shown by D_2 values (Fig. 8), and a correlation can be established between D_1 , D_2 , and t_p ac-

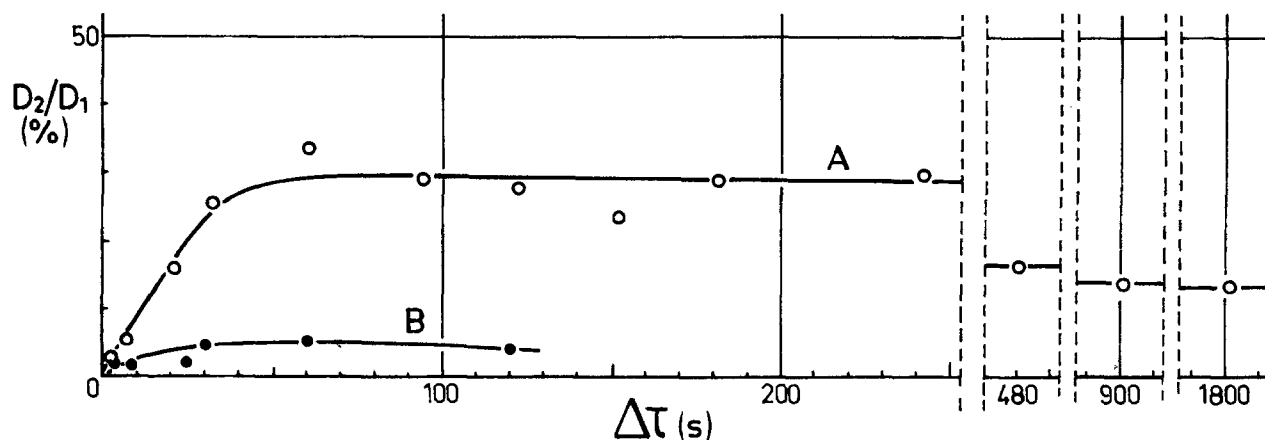


Fig. 4. Influence of the open-circuit exposure time ($\Delta\tau$) on the height of the second impulse (D_2) in $DII(t)$ for aerated (A) and deaerated (B) 0.1M NaClO_4 -methanol solution. [$U = +750$ mV/SCE; $\omega = 12.5$ rps; $\theta = 25^\circ\text{C}$; ϕ RDE = 0.5 cm; $T = 600$ s.]

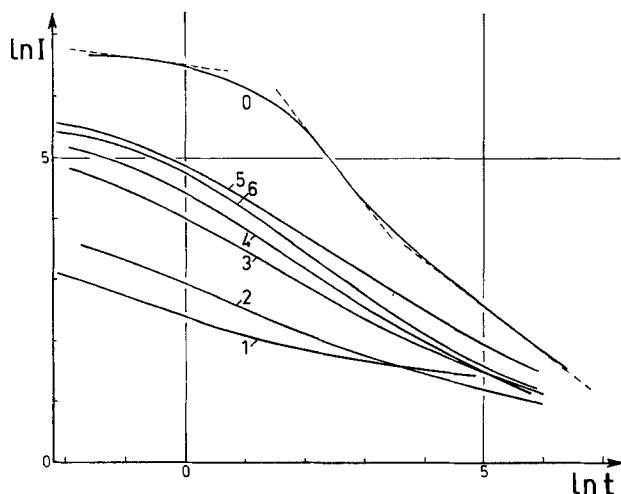


Fig. 5. Modification of the second $I(t)$ signal in $DII(t)$ after open-circuit exposure over a time $\Delta\tau$ for 0.1M NaClO_4 in aerated methanol. [$U = +750$ mV/SCE; $\omega = 12.5$ rps; $\theta = 25^\circ\text{C}$; ϕ RDE = 0.5 cm; $T = 600\text{s}$.] Curves: 0: initial curve (first signal); 1: $\Delta\tau$ (s) = 1.95; 2: $\Delta\tau = 6.18$; 3: $\Delta\tau = 19.97$; 4: $\Delta\tau = 31.51$; 5: $\Delta\tau = 40.63$.

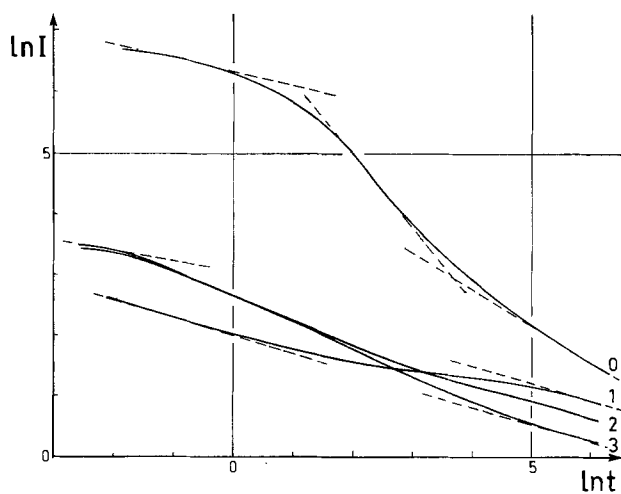


Fig. 6. Modification of the second $I(t)$ signal in $DII(t)$ after open-circuit exposure over a time $\Delta\tau$ for 0.1M NaClO_4 in deaerated methanol. [$U = +750$ mV/SCE; $\omega = 12.5$ rps; $\theta = 25^\circ\text{C}$; ϕ RDE = 0.5 cm; $T = 600\text{s}$.] Curves: 0: initial curve (first signal); 1: $\Delta\tau$ (s) = 3.24; 2: $\Delta\tau = 30.32$; 3: $\Delta\tau = 60.19$.

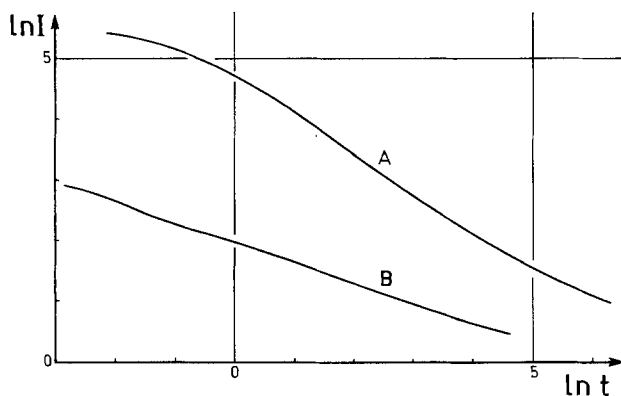


Fig. 7. Comparison between aerated (A) and deaerated (B) medium through the $\ln I - \ln t$ curves for the second signal in $DII(t)$ after open-circuit exposure over a time $\Delta\tau$ of 60s, for 0.1M NaClO_4 in methanol. [$U = +750$ mV/SCE; $\omega = 12.5$ rps; $\theta = 25^\circ\text{C}$; ϕ RDE = 0.5 cm; $T = 600\text{s}$.]

according to the working time of the RDE (Fig. 9). This may be due to the fact that successive polishings can assign different weights, during time, to the planes (100), (110), and (111) of the polycrystalline surface constituting the

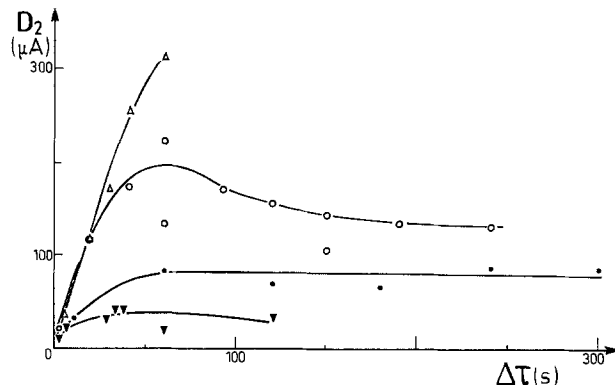


Fig. 8. Influence of the RDE polishing time ($\phi = 0.5$ cm) on the value of the second impulse in $DII(t)$ for 0.1M NaClO_4 in aerated methanol, as a function of the time Δt in open-circuit. [$U = +750$ mV/SCE; $\omega = 12.5$ rps; $\theta = 25^\circ\text{C}$; $T = 600\text{s}$.]

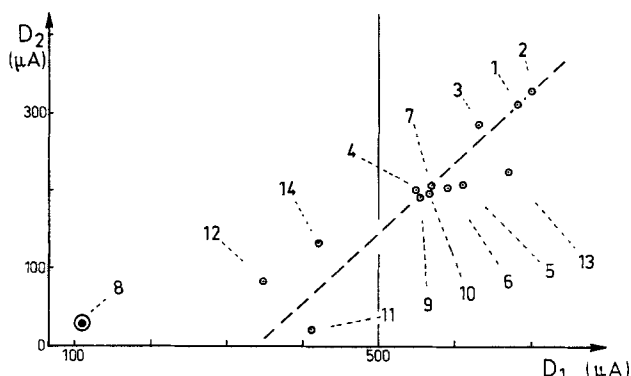


Fig. 9. Relationship between the values of the first (D_1) and the second (D_2) impulse in $DII(t)$ and the RDE polishing time ($\phi = 0.5$ cm) for 0.1M NaClO_4 in aerated methanol. (The working time of the RDE increases from point 1 to point 10.) [$U = +750$ mV/SCE; $\omega = 12.5$ rps; $\theta = 25^\circ\text{C}$; $T = 600\text{s}$.] Polishing time t_p (point) (s): 150(1); 10(2); 10(3); 10(4); 30(5); 30(6); 30(7); 0(8); 30(9); 60(10); 60(11); 120(12); 130(13); 130(14).

RDE, and to the fact that methanol adsorption may depend on this weight. The latter indeed takes place differently in H_2SO_4 (4) but similarly in NaOH medium (5). But this interpretation is to be ruled out, since, not only the medium is neutral here, but also the size of the grains of the Pt employed is such that the distribution of the crystal orientations remains unchanged whatever the polishing plane. Therefore, this combined influence of t_p and the working time can be explained by the existence of adsorbates strongly bound to the substrate which cannot be entirely eliminated after a certain working time by successive polishings with the same t_p (e.g., 150s).

Discussion

In the literature, methanol electro-oxidation on platinum has been investigated over two directions mainly (separate study of MeOH electroadsorption and electro-oxidation of the residue or simultaneous study of the adsorption-oxidation). In general, unstirred and deaerated media were investigated, and different types of working electrodes were used (poly- or monocrystalline, wire, plate, and, more seldomly, rotating disk), as well as various electrochemical conditions and different electrode pretreatments. The nature of the intermediates in water has been shown to depend on the experimental conditions, i.e., the pH, the MeOH concentration, the structure of Pt, and, more particularly, the potential (15, 17-20). The adsorbed intermediates acceptedly formed up in aqueous methanol through stepwise dehydrogenation can be: $^*\text{CH}_2\text{OH}$; $^*\text{CHOH}$; $^*\text{COH}$; $^*\text{C} = \text{O}$, $^*\text{C} = \text{O}$ (16, 18, 19, 21), in addition to OH_{ads} (22). The species which admittedly poisons the electrode is $^*\text{COH}$ [see, e.g., Ref. (6, 18, 23)] bound to three Pt sites through carbon

(6, 24) or *CHO bound to a single Pt (25). However, an *in situ* IR investigation has shown, under certain conditions, the presence of *C=O and *C≡O to the exclusion of *COH (21). In addition, multimolecular layers have been assumed to form (12, 16, 26), and the existence of a weakly bound species has long been subject to discussion (12, 27, 28).

The MeOH/NaClO₄/Pt stirred medium: existence of two types of adsorption.—In the present work, the hydrodynamic conditions established by the RDE ensure (i) a continuous contact of the solid-liquid interface with the bulk of the fluid, (ii) a constant renewal of the fluid adjacent to the RDE surface, and (iii) shearing stresses and a flux density more important than in unstirred medium. Taking account of the recirculations that can exist even in laminar flow (29), the organization of the fluid within the Levich layer is higher at the interface than in the solution bulk or in unstirred medium. The increased flux density (and, hence, shorter intermolecular distances) enhances the possibility of physical adsorption. Adsorption phenomena will be more organized, especially as the fluid can penetrate into the stagnant viscous layer of Lewis (30) as organized aggregates coming from the bulk of the flow (31, 32). Subsequently, when the potential is applied, electroadsorption and/or electro-oxidation will be generated, possibly in several steps as is the case in water, leading to the blockage of active sites.

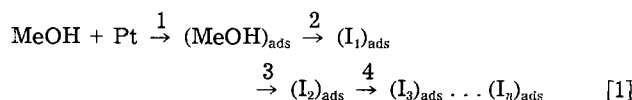
In addition, owing to the continuous mass supply (and departure) maintained by stirring, various types of bondings, more or less strong, between the substrate and the adsorbates can be expected. This is supported by our results on the behavior in open circuit of a previously blocked RDE, *i.e.*, the fact that the current (D_2) increases but only up to a limit which always remains lower than the value (D_1) measured with a pretreated RDE (Fig. 4). This is indicative of the existence of two types of adsorption: a "hard" one (species strongly bound to the substrate) and a "soft" one (weakly bound species). In that case, one (or several) of the blocking species seems to be removed, partly or totally, by circuit opening, and the other (or the others) remains adsorbed, even if the RDE is withdrawn from the solution after blockage. The current decrease at very high $\Delta\tau$'s can be explained by a further adsorption in open circuit (Fig. 4, at 480-1800s). The dual character of the adsorption is also confirmed (Fig. 5 and 6) by the $\ln I$ vs. $\ln t$ curves for the second $I(t)$ signal in $DI(t)$. At low $\Delta\tau$ values, the curves exhibit two linear sections only; now, considering our procedure, they still correspond to a nearly total blockage of the active sites. When $\Delta\tau$ is more and more increased, the weakly bound species are eliminated under open circuit, thus liberating active sites on which the phenomenon relative to curve 0 (presence of three sections) can again take place, at least partly, since the RDE is not entirely regenerated (curves always under curve 0).

The MeOH/NaClO₄/Pt stirred medium: influence of dissolved molecular oxygen.—In pure methanol, the species liable to adsorb and lead to blockage phenomena are the entities initially present in the medium (and species derived from them subsequently): (i) CH₃OH (neutral medium here); (ii) ClO₄⁻ [analogy with anion adsorption during methanol oxidation in aqueous medium (33)]; Na⁺ should not interfere at the anodic potential used; (iii) residual H₂O [its initial concentration is low (less than 1%) with respect to the critical threshold determined for the influence of water (or at least its detection) as a function of the supporting electrolyte (1, 2)]; (iv) dissolved O₂ in aerated or residual O₂ in deaerated medium. In what follows, we shall consider CH₃OH and O₂ only, given the significant differences observed between the two media, and shall not take account of the possible influence of the other entities (ClO₄⁻ and H₂O), since their initial concentrations are the same in both media.

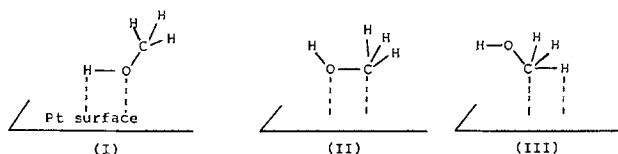
The existence of three sections in the $\ln I$ vs. $\ln t$ curves traduces changes in the regime of the system, each of them being related to a different adsorption regime tak-

ing place with a different kinetic law. It is, however, difficult to establish a direct relationship between the number of species involved and the presence of three nearly linear sections. As a matter of fact, the complexity of the $I(t)$ curve in various coordinates (no linear part in $\ln I$ vs. t among others) is indicative of a complex adsorption process (of order other than 0 or 1), in which would intervene several species in each section, for instance, and/or isotherms other than the Langmuir isotherm. In addition, an interaction between adsorption kinetics and mass transfer was shown here, since the slopes and the transition times for the three sections depend on ω (see Table I).

Deaerated medium.—Since the amount of residual O₂ is very low (residual current at -600 mV/SCE about 100 times lower than in aerated medium), the results observed are mainly due to MeOH. We can assume that the latter forms (i) first, weak bondings (of the physical adsorption type) with the substrate, which are favored by stirring, thus leading to a structure we denote by (MeOH)_{ads}, and (ii) then stronger bondings (of the strong chemisorption type), thus leading to irreversible (17) dehydrogenation and/or electro-oxidation steps. As in water, we can assume a stepwise mechanism through the formation of several adsorbates or groups of adsorbates (I)_{ads} (Eq. [1])



In Eq. [1], three possible structures, (I), (II), or (III), can be considered for (MeOH)_{ads}. These will undergo dissociative chemisorption depending on the energies involved, *i.e.*, on the bond energies and the energies of formation of adsorbate-substrate bondings relatively to the value of the potential. For instance, at certain U values, (II) and (III) can be more favored than (I), since the O—H bond is more difficult to break than C—H or C—O, assuming that the bond energies in Pt—H and Pt—C are similar.



In reaction [1], the number, nature, and subsequent evolution of the adsorbates will depend on the experimental conditions as is the case in water. Therefore, various species can arise from side-reactions and adsorb and/or react according to their environment, *i.e.*, to the neighboring species adsorbed at the RDE surface or the bulk species. For example, depending on the starting structure of (MeOH)_{ads}, (I)_{ads} can be

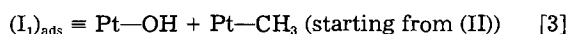
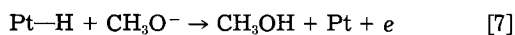
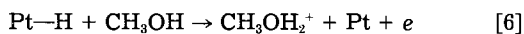
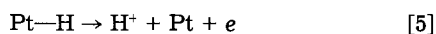


Table I. Influence of mass transfer on the slopes and the transition times from one section to another for an $SII(t)$ input signal in 0.1M NaClO₄ in aerated methanol.
 $U = +750$ mV/SCE; $\theta = 25^\circ\text{C}$; ϕ RDE = 0.5 cm

ω (rps)	Slopes in the $\ln I$ - $\ln t$ curves			Transition time (s)	
	First section	Second section	Third section	First → second section	Second → third section
16	-0.45	-1.07	-0.75	2.72	21.3
25	—	-1.06	-0.67	—	27.1
49	-0.25	-0.82	-0.55	1.43	40.0
81	-0.28	-0.89	-0.65	1.16	50.4
100	-0.22	-0.77	-0.59	0.70	60.3

Another example is given by adsorbed hydrogen, which can be more or less strongly bound to the substrate as in the case of Fe or Ti in acidic aqueous medium (7, 34) and react with other entities adsorbed at the surface or coming from the solution bulk on account of the conditions for constant renewal of the interface. In this last case, Pt—H would react with CH_3OH or with CH_3O^- , solvated by five solvent molecules (11), arising from the autoprotolytic equilibrium of methanol in neutral medium. Therefore, the current observed can result from one (or all) of the possible reactions for the elimination of adsorbed hydrogen atoms, *i.e.*



Reaction [5] is invoked in aqueous medium where atomic hydrogen can adsorb at coverage fractions almost as important as those of methanol (35-38). Side reactions can take place between Pt—H and adsorbed species, *e.g.*, Pt— CH_3 , Pt—OH, Pt— CH_2OH , Pt—H, $(\text{CH}_3\text{OH})_{\text{ads}}$, etc., thus liberating platinum sites without current production.

Starting from $(\text{I}_1)_{\text{ads}}$, dissociative chemisorption (steps 2, 3, 4, ...) will proceed provided the various energies involved be at the adequate level. In $(\text{I}_1)_{\text{ads}}$ mainly will be implied the carbon containing species Pt— OCH_3 , Pt— CH_3 , and Pt— CH_2OH . Thus, among the $(\text{I}_2)_{\text{ads}}$'s, may exist: $(\text{Pt})_2\text{—CHOH}$; among $(\text{I}_3)_{\text{ads}}$: $(\text{Pt})_3\text{—COH}$; among $(\text{I}_4)_{\text{ads}}$: $(\text{Pt})_3\text{—CO—Pt}$, which can evolve to give $(\text{Pt})_2\text{—C} \equiv \text{O}$, then $\text{Pt—C} \equiv \text{O}$.

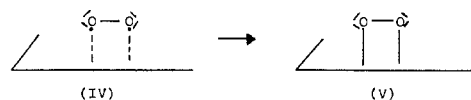
The foregoing shows that it is very difficult to determine which species are formed up under our conditions and block the RDE, but it can be accepted that they are directly bound to the substrate (Pt), in contrast to the aerated medium.

Aerated medium.—Since the same experimental conditions are used, the blockage inhibition, the RDE regeneration, and the differences in the $\ln I$ vs. $\ln t$ curves must be caused by the presence of dissolved molecular oxygen. It is known that oxygen can bring modifications to the bulk solvent and to the interface. The presence of a gas can indeed modify the order and hence the structure of methanol with respect to degassed medium (39). Rigorously speaking, the deaerated medium here is not degassed (due to argon bubbling), but it is probable that methanol is modified differently by two gases of different natures (air and argon). Such a difference is also observed in the case of the effect of supporting electrolytes on methanol structure (40). At the level of the interface, adsorption of oxygen (molecular or atomic) is expected to bring changes in: (i) the platinum surface as was shown for solid-gas (41) and for solid-liquid interfaces (42-45); (ii) the interface topography (8, 9); and (iii) the adsorption-desorption kinetics of other species without changing the overall mechanism (46).

The structure of adsorbed (molecular or atomic) oxygen is influenced by the experimental conditions. Several types of platinum oxide arising from water dissociation have been considered in aqueous medium (47), particularly during the dynamic aging of oxygen containing electrosorbed layers in acidic (48, 49) or alkaline (50) medium. In the case of O_2 adsorption at the solid-gas interface, the existence of two types of surface oxygen on Pt(100) has been shown: chemisorbed oxygen and a platinum oxide (41, 51). In addition, the structure of the oxygen adlayer depends on the method of formation of the substrate (41).

Considering our results, we shall assume that dissolved molecular oxygen does adsorb at the anodic potential used. Taking account of the electron structure of oxygen and platinum, O_2 adsorption would take place on two neighboring platinum atoms through the unpaired electrons in the π^* antibonding molecular orbitals of oxygen and the unpaired electron in the 5d orbital of platinum, thus leading to (IV) and (V). Such a bonding requires a

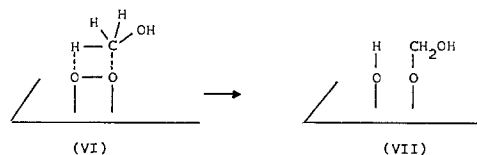
lower energy than does the complete dissociation of the O_2 molecule.



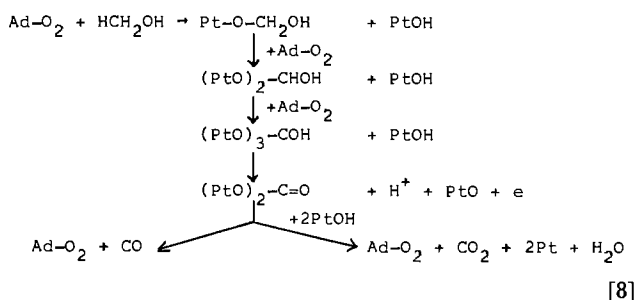
Structure (V), denoted hereafter by Ad—O_2 , corresponds stoichiometrically to a Pt_2O_2 platinum oxide in which the O/Pt ratio is the same as in PtO (one of the possible forms of adsorbed oxygen from water) or Pt—O (adsorbed oxygen atoms). We shall make no assumptions on the thickness of the oxygen adlayer which can exceed one monolayer (50, 52), the possible diffusion of O_2 into the metal lattice, the anisotropy of the crystal planes of platinum towards the adsorption of simple molecules (53), or the mobility of surface platinum atoms under the influence of oxygen (54, 55).

Accepting oxygen adsorption under our conditions, we can reasonably consider that there is a competition between O_2 and MeOH adsorptions. At this stage, arises the question on methanol adsorption at a surface partaken between bare substrate [Pt (subs)] and Ad—O_2 sites. Two cases can be distinguished: (i) methanol adsorbs both on Pt(subs) and Ad—O_2 , and (ii) methanol adsorbs on Pt(subs) only.

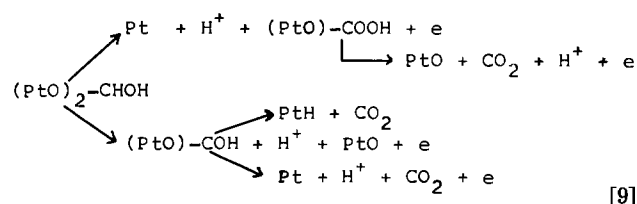
First case: no segregation between Pt(subs) and Ad—O_2 sites.—In this case, the dissociative chemisorption of CH_3OH also proceeds on Ad—O_2 , hence on a partially modified RDE, according to a stepwise mechanism, *i.e.*, through a sequence of dehydrogenation steps similar to reaction [1] proposed for the deaerated medium or for aqueous media in the literature. For example, starting from (III), the first step is



Since other Ad—O_2 sites are liable to be present in the vicinity of Pt— $\text{O—CH}_2\text{OH}$ [at the solid-gas interface, oxygen adsorbs on Pt(111) in islands (56)], the following steps can be considered

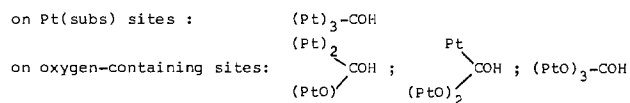


As in deaerated medium, the $(\text{I}_1)_{\text{ads}}$'s can undergo several side reactions with neighboring groups such as Pt—OH, Pt—H [resulting from the adsorption of MeOH on Pt(subs)], etc., thus liberating active sites. It is to be noted that decarboxylation can occur at any stage of the various steps, *e.g.*



In that way, the mechanism is to be compared with the one proposed for formaldehyde electro-oxidation on oxygen adsorbing adatoms on Pt in aqueous medium through a parallel path without obstruction by the COH poison (57).

In reaction [8], $\ast\text{COH}$ is fixed on three PtO sites, but other possibilities can be considered according to the environment [presence of Pt(subs) or Ad—O₂ sites] in the steps leading to $\ast\text{COH}$



From the foregoing, it may be concluded that the higher currents observed in aerated medium result from several concomitant facts, listed below.

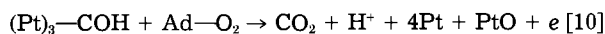
1. In all adsorbates on PtO (from Ad—O₂), the carbon atom is in an oxidation state, as defined in Ref. (58), higher than in the corresponding adsorbates on Pt(subs) and is hence more labile. For example, taking a value -1 for each bond to H and Pt, and +1 for each bond to O, as for C atoms covalently bonded in organic molecules, the carbon atom in PtO—CH₂OH is in an oxidation state two units higher than in Pt—CH₂OH. In the various structures for $\ast\text{COH}$, the oxidation state varies from -2 to +4; therefore, the same adsorbate (e.g., $\ast\text{COH}$, $\ast\text{C} \equiv \text{O}$), or $\ast\text{C} \equiv \text{O}$) can undergo different subsequent reactions, depending on its environment and the experimental conditions. Similarly, a higher oxidation state is reached more rapidly in aerated medium.

2. The Pt—OH adsorbate, which is thought to be indispensable for the electro-oxidation in aqueous medium [e.g., Ref. (6)], is formed simultaneously to (PtO)₃—COH, whereas in deaerated methanol it can only be formed through the dissociative chemisorption of (II), hence less easily.

3. The oxidizing effect of Pt—OH is more readily performed on species such as (PtO)₃—COH than on (Pt)₃—COH, owing to the oxidation states of C in such entities. Consequently, Pt and PtO sites will be liberated more easily in aerated medium.

As for the dual character of the adsorption, whether the poison is the same or not on Pt(subs) and on PtO and whatever its nature, it becomes a hard adsorbate when fixed on Pt(subs) and a soft one when fixed on PtO (via Ad—O₂), owing to the difference of the oxidation states. In the stepwise mechanism, a part of the Ad—O₂ sites would be recovered, and, therefore, O₂ can be considered as playing a double role, i.e., as a catalyst and as an oxidizer. However, this does not prevent the RDE from being blocked, since the sites liberated are in turn subjected to the MeOH/O₂ competition, and their number continues thereby to decrease with time. This interpretation also holds for the deaerated medium, owing to the presence of residual O₂ and of air-oxygen adsorbed during the pre-treatment of the RDE.

Second case: segregation between Pt(subs) and Ad—O₂ sites.—If such a segregation is assumed, i.e., MeOH adsorption on Pt(subs) only, then the mechanism on Pt(subs) would be reaction [1], but with the possibility of oxidation by oxygen at any step. For example, considering an island-type topography (56), the (Pt)₃—COH poison could be oxidized at the island boundaries by oxygen adsorbed on neighboring Pt(subs) sites as follows



This process is to be compared with the mechanism proposed in the case of oxygen adsorbing adatoms on Pt which enhance methanol or formaldehyde electro-oxidation (38, 57). Such a mechanism would, of course, account for the higher current values in aerated medium, but would explain less readily the existence of two types of adsorption, and should, therefore, be ruled out in the present case.

Manuscript submitted Feb. 7, 1984; revised manuscript received July 24, 1984.

CNRS assisted in meeting the publication costs of this article.

REFERENCES

- G. Belanger, *This Journal*, **123**, 818 (1976).
- C. Iwakura, T. Hayacki, S. Kikkawa, and H. Tamura, *Electrochim. Acta*, **17**, 1085 (1972).
- G. Sundholm, *J. Electroanal. Chem.*, **31**, 265 (1971).
- J. Clavilier, C. Lamy, and J. M. Leger, *ibid.*, **125**, 249 (1981).
- C. Lamy, J. M. Leger, and J. Clavilier, *ibid.*, **135**, 321 (1982).
- B. D. McNicol, *ibid.*, **118**, 71 (1981).
- A. Caprani and Ph. Morel, *J. Appl. Electrochem.*, **7**, 65 (1977).
- A. Caprani, I. Epelboin, and Ph. Morel, *J. Less-Common Metals*, **69**, 37 (1980).
- A. Caprani, *Appl. Surf. Sci.*, **2**, 13 (1978), and references therein.
- Yu. V. Pleskov and V. Yu. Filinovskii, "The Rotating Disk Electrode," pp. 18-20, Engl. Transl. by Consultants Bureau, New York (1976).
- W. L. Horgenson, B. Bigot, and J. Chandrasekhar, *J. Am. Chem. Soc.*, **104**, 4584 (1982).
- B. I. Podlovchenko and R. P. Terukhova, *Elektrokhimiya*, **9**, 273 (1973).
- B. D. Kurnikov and Yu. B. Vasil'ev, *ibid.*, **9**, 1203 (1973).
- T. Biegler, *Aust. J. Chem.*, **26**, 2571 (1973).
- R. E. Smith, H. B. Urbach, J. H. Harrison, and N. L. Hatfield, *J. Phys. Chem.*, **71**, 1250 (1967).
- D. Pletcher and V. Solis, *Electrochim. Acta*, **27**, 775 (1982).
- T. Biegler, *J. Phys. Chem.*, **72**, 1571 (1968).
- V. S. Bagotzky, Yu. B. Vassiliev, and O. A. Khazova, *J. Electroanal. Chem.*, **81**, 229 (1977), and references therein.
- B. I. Podlovchenko and R. P. Petukhova, *Elektrokhimiya*, **10**, 489 (1974).
- F. Kadirgan, B. Beden, J. M. Leger, and C. Lamy, *J. Electroanal. Chem.*, **125**, 89 (1981).
- B. Beden, C. Lamy, A. Bewick, and K. Kunimatsu, *ibid.*, **121**, 343 (1981).
- O. A. Khazova and Yu. B. Vasil'ev, *Elektrokhimiya*, **10**, 606 (1974).
- A. Capon and R. Parsons, *J. Electroanal. Chem.*, **44**, 1 (1973).
- P. Sidheswaran, *J. Electrochem. Soc. India*, **26**, 33 (1977).
- M. Watanabe and S. Motoo, *J. Electroanal. Chem.*, **60**, 259 (1975).
- A. Wieckowski, J. Sobkowski, and I. Szamrej, *Rocz. Chem.*, **48**, 77 (1974).
- S. S. Beskorovainaya, Yu. B. Vasil'ev, and V. S. Bagotzki, *Elektrokhimiya*, **8**, 376 (1972).
- M. W. Breiter, *Discuss. Faraday Soc.*, **45**, 79 (1968).
- G. Guiffant, Ph.D. Thesis, Université Paris VII, Paris (1982).
- W. K. Lewis, *Ind. Eng. Chem.*, **8**, 825 (1916).
- R. Higbie, *Trans. A.I.Ch.E.*, **31**, 365 (1935).
- P. V. Danckwerts, *Ind. Eng. Chem.*, **43**, 1460 (1951).
- G. Belanger, *Can. J. Chem.*, **50**, 1891 (1972).
- A. Caprani and Ph. Morel, *J. Less-Common Metals*, **56**, 223 (1977).
- V. M. Kamath and H. Lal, *J. Electroanal. Chem.*, **19**, 137, 249 (1968).
- P. Sidheswaran and H. Lal, *ibid.*, **34**, 173 (1972).
- B. I. Podlovchenko and E. P. Gorgonova, *Dokl. Akad. Nauk. SSSR*, **156**, 673 (1964).
- P. Sidheswaran, *J. Electrochem. Soc. India*, **28**, 27 (1979).
- G. A. Alp'er, V. N. Afanas'ev, and G. A. Krestov, *Zh. Fiz. Khim.*, **53**, 499 (1979).
- W. R. Snyder, Ph.D. Thesis, FL (1977).
- M. A. Barteau, E. I. Ko, and R. J. Madix, *Surf. Sci.*, **102**, 99 (1981).
- J. Clavilier, D. Armand, R. Durand, and R. Faure, Paper presented at the 32nd I.S.E. Meeting, Dubrovnik/Cavtat, Yugoslavia, Sept. 1981.
- J. Clavilier, R. Faure, G. Guinet, and R. Durand, *J. Electroanal. Chem.*, **107**, 205 (1980).
- J. Clavilier, R. Durand, G. Guinet, and R. Faure, *ibid.*, **127**, 281 (1981).
- J. Clavilier, D. Armand, and B. L. Wu, *ibid.*, **135**, 159 (1982).

46. A. Caprani and J. P. Frayret, *ibid.*, **138**, 155 (1982).
 47. J. P. Hoare, "The Electrochemistry of Oxygen," Chap. II, Interscience, New York (1968).
 48. N. R. de Tacconi, J. O. Zerbino, M. E. Folquer, and A. J. Arvia, *J. Electroanal. Chem.*, **85**, 213 (1977).
 49. M. W. Folquer, J. O. Zerbino, N. R. de Tacconi, and A. J. Arvia, *This Journal*, **126**, 592 (1979).
 50. M. Y. Duarte, M. E. Martins, and A. J. Arvia, *Anal. Asoc. Quim. Argent.*, **70**, 525 (1982).
 51. C. G. Vayenas, C. Georgakis, J. Michels, and J. Tormo, *J. Catal.*, **67**, 348 (1981).
 52. R. J. Berry, *Surf. Sci.*, **76**, 415 (1978).
 53. R. W. McCabe and L. D. Schmidt, *ibid.*, **66**, 101 (1977).
 54. J. Clavilier, R. Durand, G. Guinet, and R. Faure, *J. Electroanal. Chem.*, **69**, 317 (1976).
 55. R. M. Ishikawa and A. T. Hubbard, *ibid.*, **69**, 317 (1976).
 56. R. A. Shigeishi and D. A. King, *Surf. Sci.*, **75**, L379 (1978).
 57. S. Motoo and M. Shibata, *J. Electroanal. Chem.*, **139**, 119 (1982).
 58. J. B. Hendrickson, D. J. Cram, and G. S. Hammond, "Organic Chemistry," 3rd Ed., p. 739, McGraw-Hill, New York (1970).

An Aluminum Acid-Base Concentration Cell Using Room Temperature Chloroaluminate Ionic Liquids

C. J. Dymek, Jr.,* J. L. Williams,* and D. J. Groeger

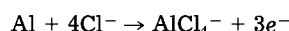
The Frank J. Seiler Research Laboratory, United States Air Force Academy, Colorado Springs, Colorado 80840

J. J. Auburn*

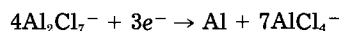
Office of Naval Research, Arlington, Virginia 22217; AT&T Bell Laboratories, Murray Hill, New Jersey 07974

ABSTRACT

Mixtures of 1-methyl-3-ethylimidazolium chloride (MEICl) and aluminum chloride are molten salts at room temperature and below. Acidic melts, which contain AlCl_3 mole fraction (N) greater than 0.5, can be used as catholytes, with basic melts ($N < 0.5$) as anolytes, in a concentration cell using Al plate electrodes and a microporous polypropylene separator. Gravimetric analysis of electrodes indicates that the anode reaction is



and the cathode reaction is

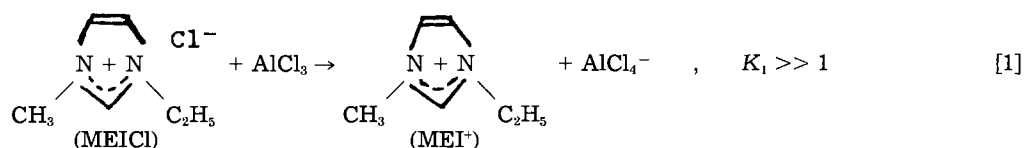


The open-circuit potential for the cell

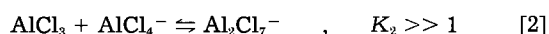


is 1.38V, and the voltage remains above 1.0V at constant current discharge of 1-3 mA for 6 cm² Al electrodes. Coulometry is combined with gravimetric and compositional analysis (using NMR spectroscopy) of the electrolytes to estimate transport numbers.

Researchers at the Frank J. Seiler Research Laboratory have discovered a chloroaluminate salt which is liquid at room temperature and below (1). This salt is formed by mixing 1-methyl-3-ethylimidazolium chloride (MEICl) with AlCl_3 , with both solids at room temperature, as shown by



When AlCl_3 is added to MEICl in less than stoichiometric amount (*i.e.*, N in the melt is less than 0.5), the anions in the melt are AlCl_4^- and Cl^- . Such mixtures are basic because Cl^- acts as a Lewis base in these melts. When $N > 0.5$, the process



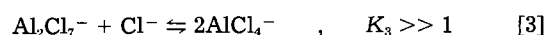
occurs, and the anions are AlCl_4^- and Al_2Cl_7^- . Such melts are acidic because Al_2Cl_7^- acts as a Lewis acid. K_1 and K_2 have not been measured yet for these melts. However, the values of K_1 and K_2 for the analogous system, $\text{NaCl}/\text{AlCl}_3$, have been determined to be 3.2×10^{-11} and 3×10^4 , respectively, at 175°C (2). Because preliminary studies in our laboratory show that the MEICl/ AlCl_3 melts have

*Electrochemical Society Active Member.

significantly lower vapor pressure (due to AlCl_3) than $\text{NaCl}/\text{AlCl}_3$ melts at the same temperatures, it can be assumed that K_1 and K_2 for the MEICl/ AlCl_3 melts are even larger than for the $\text{NaCl}/\text{AlCl}_3$ melts. The anion mole fraction of each ion as a function of N is shown in Fig. 1.

These curves are calculated from the stoichiometry of Eq. [1] and [2]. These dependencies are similar to those for *n*-butyl pyridinium chloride/aluminum chloride (3) and to a lesser extent to those for alkali metal chloride/aluminum chloride melts at elevated temperature (2).

The acid-base properties of chloroaluminate melts are best understood in terms of the equilibrium



Since K for this reaction is large, about 10^{16} (4), acid melts and basic melts can be combined as catholytes and anolytes in concentration cells with relatively high potentials, using aluminum electrodes and an appropriate separator. A schematic of such a cell, in which the electrolytes are $N = 0.33$ and $N = 0.60$ melts, is shown in Fig. 2. The

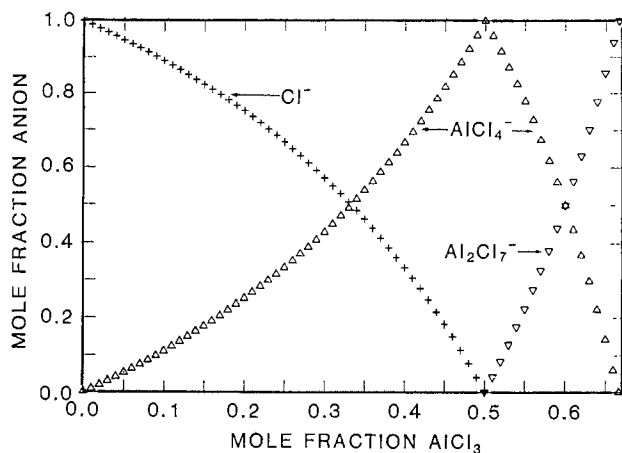
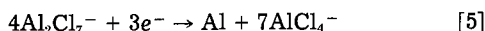
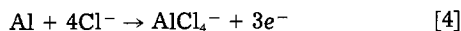


Fig. 1. Mole fractions of anions in melts vs. mole fraction of AlCl_3 in melt.

species in the dashed boxes are shown with coefficients that indicate their relative amounts in these melts. These coefficients represent the stoichiometric amounts required to generate three equivalents of electrons if the cell discharges according to the anode and cathode reactions shown in Eq. [4] and [5]



Directions of transport of charge by MEI^+ , AlCl_4^- , and Al_2Cl_7^- are indicated by the dashed arrows in Fig. 2.

Three aspects of concentration cell performance are investigated to determine if the picture of the basic cell electrochemistry shown in Fig. 2 is valid. Gravimetric analysis of the electrodes is correlated to measured charge passed, cell open-circuit potential is compared to the predicted potentials based on previous obtained cyclic voltammograms (5), and measured specific energies are compared to values obtained from calculations based on the Fig. 2 model (6). Knowledge of the quantities of MEI^+ in the anolyte before and after discharge of a measured number of coulombs also allows us to estimate the external (relative to the separator) transport numbers for MEI^+ , AlCl_4^- , and Al_2Cl_7^- .

Experimental

All melts were prepared as reported previously (1). All operations described below were done in an Ar-atmosphere dry box. The concentration cells were constructed by sandwiching each component — anode, separator, and cathode — between Teflon gasket/spacers and clamping the package together. Electrodes (0.25 mm-thick 99.999%

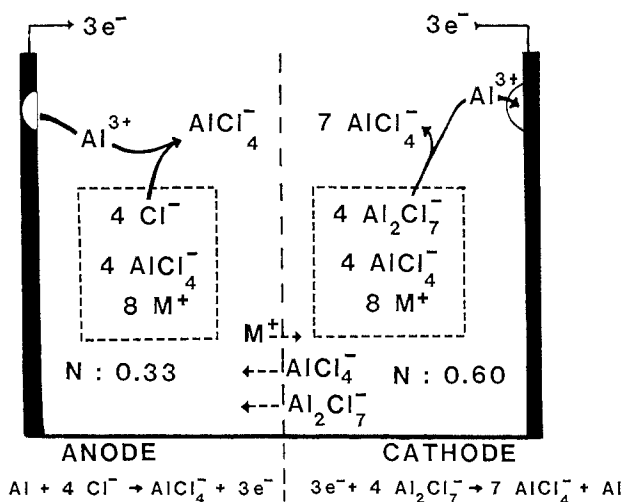


Fig. 2. Schematic diagram of concentration cell

Al [Alfa Products] with about 6 cm^2 active area) were abraded with carborundum paper to remove oxides, rinsed with acetonitrile, dried, and weighed before cell assembly. The separator, Celgard® 4510 microporous polypropylene film, was also preweighed. The electrodes were 1.0 cm apart in the assembled cell, which was weighed before and after each electrolyte was added (about 2.5g [$\sim 2.0 \text{ ml}$] anolyte, $N = 0.37$, and 3.5g [$\sim 2.8 \text{ ml}$] catholyte, $N = 0.60$). A Mettler AE163 electronic balance in the dry box was used for all weighing. Within a few minutes of assembly, the cell was connected to a PAR 173 Potentiostat/Galvanostat with a PAR 179 Coulometer. The cells were discharged at controlled current, and the voltage was recorded on a chart recorder connected to the PAR 173 summing amplifier output. At various times during discharge, voltage/current behavior was recorded by varying the constant current. Following discharge, which is usually to about 0.5V from a load voltage of over 1.0V, the electrolytes were removed (this included wiping parts of the cell in contact with them) to determine final anolyte and catholyte masses. The final mole fractions of the anolyte samples were determined using an NMR technique (7). Final electrode masses were obtained after they were rinsed with acetonitrile and blotted dry. The final separator mass was also recorded. Because we observed that acidic melts wetted the separator much more effectively than basic melts, the gain in separator mass was added to the final catholyte mass. To insure this was the case, the separator was positioned so that its rougher, more porous surface faced the catholyte; the smoother side faced the anolyte.

Results

Cell discharges.—Cyclic voltammograms of Al in acid melts and in basic melts are shown in Fig. 3. The difference in potential between reduction to Al in $N = 0.60$ melt [a reversible process (8)] and oxidation of Al in $N = 0.40$ melt (an irreversible process) lies between 1.2 – 1.5V. The open and circuit potentials of our cells fall in this range, as indicated by the discharge curves in Fig. 4. Thus, reduction and oxidation of Al appear to be the dominant electrode processes in the concentration cell, as expected.

The fairly long time (about 10-15h) required for the cell to achieve maximum voltage under load is due to the slow rate at which a dry separator is wetted by the melt. This process can be accelerated by discharging at low currents during the first several minutes after the cell is connected. When a separator wetted with melt (from use in an earlier run) is used in the cell, the maximum load voltage is achieved in about 30 min. The slopes of V vs. I plots at various times during discharge are plotted against the charge, Q , in Fig. 5 for some representative cells. Comparison of the plots for the discharges using dry and

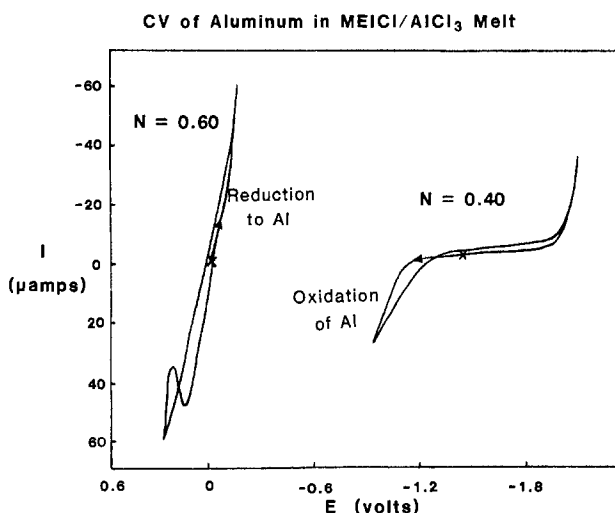


Fig. 3. Cyclic voltammograms of Al in acid melts and in basic melts [reproduced from Ref. (5)].

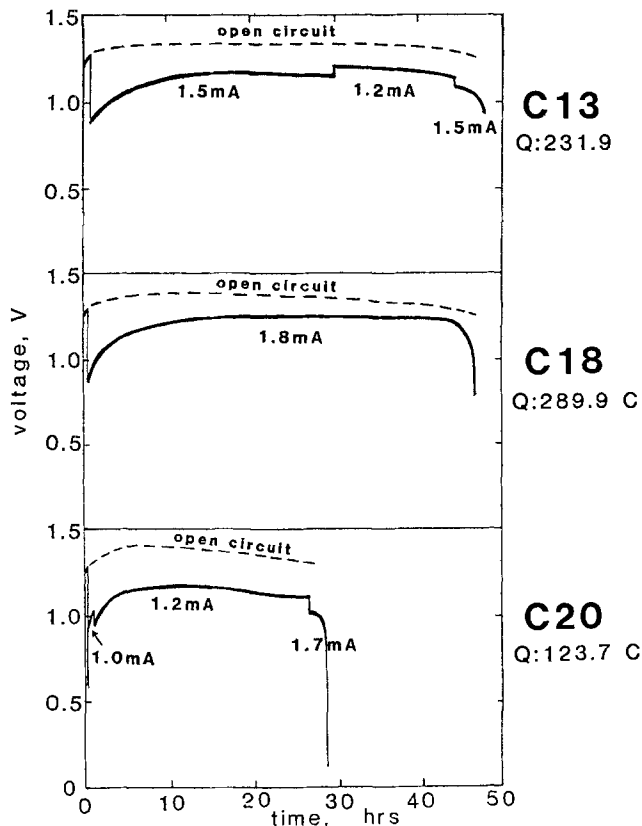


Fig. 4. Sample discharge curves for concentration cells

prewetted separators demonstrates the effect of the separator resistance on the load voltage.

Electrode analysis.—That Al oxidation and deposition are the electrode reactions is confirmed by the gravimetric analysis of the cell electrodes shown in Table I. Values for the predicted charge, Q_{calc} , based on Eq. [4] and [5] are calculated from the mass changes in the anode and cathode. The averages of the two calculated values, $Avg Q_{calc}$, are in reasonably good agreement with the measured values, Q_{meas} . In each cell, the reason for the lack of exact agreement is that the loss in mass of each of the electrodes is slightly more than can be attributed to the electrode reactions shown in Eq. [4] and [5]. If we assume that a certain amount of corrosion of both anode and cathode occurs during discharge, we can obtain Q_{calc} values that equal Q_{meas} . These deduced corrosion losses are listed in Table I. This is probably a good assumption, in view of the results of a separate gravimetric analysis of Al corro-

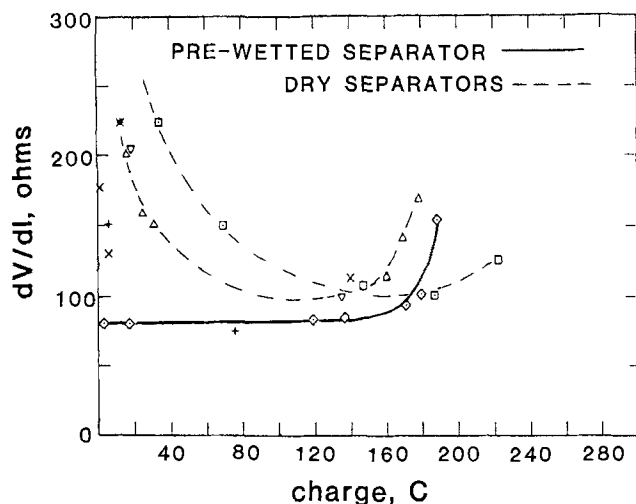


Fig. 5. Slopes of V vs. I plots for various cells as a function of charge passed.

sion in $N = 0.37$ melts and in $N = 0.60$ melts, as shown in Fig. 6. Several strips of Al with areas equal to our electrode areas (in contact with electrolyte) are either abraded or etched with 15% HF in 5% HNO_3 . These are submersed in melts for various times and then rinsed with acetonitrile, blotted dry, and reweighed. Each point in Fig. 6, except for the first in each run, is the average of weightings of more than one strip (up to 10 for the last points); hence, the initial increase in mass observed in some runs is real, if unexplained at this point. While this indicates that further studies are required to understand the effect of impurities and other initial reactions on the Al surface, it is clear that the deduced corrosion losses of the concentration cells are similar to the corrosion losses measured for the Al strips which are simply submersed in the melts. Molten chloroaluminate salts are very sensitive to moisture (9), so the initial high corrosion rate in these submersed strips is probably due to impurities caused by water contamination. The much slower steady-state corrosion rate of aluminum in acidic melts and in basic melts is equivalent to $0.2 \mu A/cm^2$. These steady-state rates are obtained from the averages of slopes of linear fits of points after 200h (the solid lines in Fig. 6). Thus, it appears that virtually all of the corrosion loss in the concentration cells is due to reactions of Al with impurities in the melts.

Scanning electron micrographs of the aluminum anode and cathode surface are shown in Fig. 7. It appears that aluminum is etched uniformly and with minimal pitting. The deposited aluminum is crystalline and uniform, with no evidence of dendritic growths, and it adheres strongly to the electrode surface. This strong adherence of Al de-

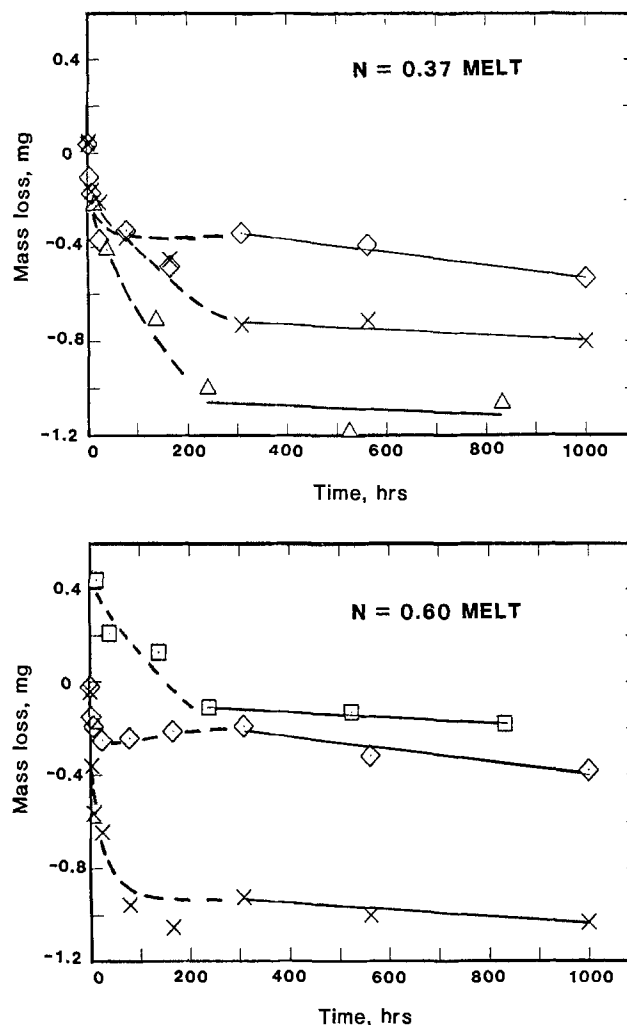


Fig. 6. Results of gravimetric analysis of aluminum corrosion on strips of aluminum soaked in 0.37 melt (a, top) and 0.60 melt (b, bottom).

Table I. Gravimetric analysis of concentration cell electrodes

Cell	$\Delta m, g (\pm 0.00010)$		Avg $Q_{calc.}$ C (± 1)	$Q_{meas.}$ C (± 0.5)	Deduced corrosion loss, mg (± 0.10)	
	Anode	Cathode			Anode	Cathode
C-7	-0.02185	0.02116	231	228.5	0.55	0.14
C-8	-0.02326	0.02318	249	243.6	0.04	0.04
C-9	-0.01879	0.01760	195	189.1	1.16	0.03
C-10	-0.02810	0.02694	295	289.0	1.16	0.00
C-13	-0.02273	0.02132	236	231.9	1.12	0.29
C-14	-0.01932	0.01818	201	199.2	0.75	0.38
C-18	-0.02846	0.02526	288	289.9	1.44	1.76
C-19	-0.01003	0.00935	104	105.3	0.22	0.46
C-20	-0.01187	0.01095	122	123.7	0.34	0.58
C-21	-0.01322	0.01227	137	139.7	0.20	0.75

posited from acidic melts has also been observed to occur on Al, C, W, Fe, and Pt at rates of up to 20 mA/cm² (8).

Specific energies.—Specific energies of the cells are calculated from the following equation

SP EN (W-h/kg) =

$$\frac{(V)(Q, eq)(26.8 \text{ A-h/eq})}{[\text{mass anolyte} + \text{mass catholyte} + \Delta \text{mass anode}]} \quad [6]$$

where V is the average load voltage and Q is the total measured charge in equivalents. The results from the 10 cells which are analyzed are presented in Table II, along with the calculated specific energies. Five cells with capacities (in terms of total charge passed per grams anolyte, Q/M-ALY, in Table II) less than 85 C/g were discarded, generally because electrolyte had leaked through the Teflon seals. The average load voltage in the discharge of these cells is 1.1V, and the average ratio of mass catholyte to mass anolyte is 1.5. Theoretical specific energies (based on the Fig. 2 model) are calculated (6) for the case of cells with $N = 0.37$ melts and $N = 0.60$ melts, 1.1V load voltages, and 1.5 electrolyte mass ratios for various transport numbers. The results of these calculations are compared in Fig. 8 to the experimental results for the ten cells.

Table II. Specific energies in concentration cells

Cell	Q/M-ALY [C/g]	SPEC ENE [Wh/kg]
C-7	90.57	11.71
C-8	92.24	11.71
C-9	95.65	11.57
C-10	96.33	12.94
C-13	90.03	12.81
C-14	87.20	10.39
C-18	92.44	12.58
C-19	93.16	10.07
C-20	100.11	11.65
C-21	107.59	9.71
Average:		11.51
Std. dev.:		1.07

Transport numbers.—Transport numbers are calculated from the measured charge and measured changes in anolyte mass and N . The number of moles of MEI⁺ in the anolyte can be calculated from both N and the mass of the anolyte, which are measured before and after the discharge.

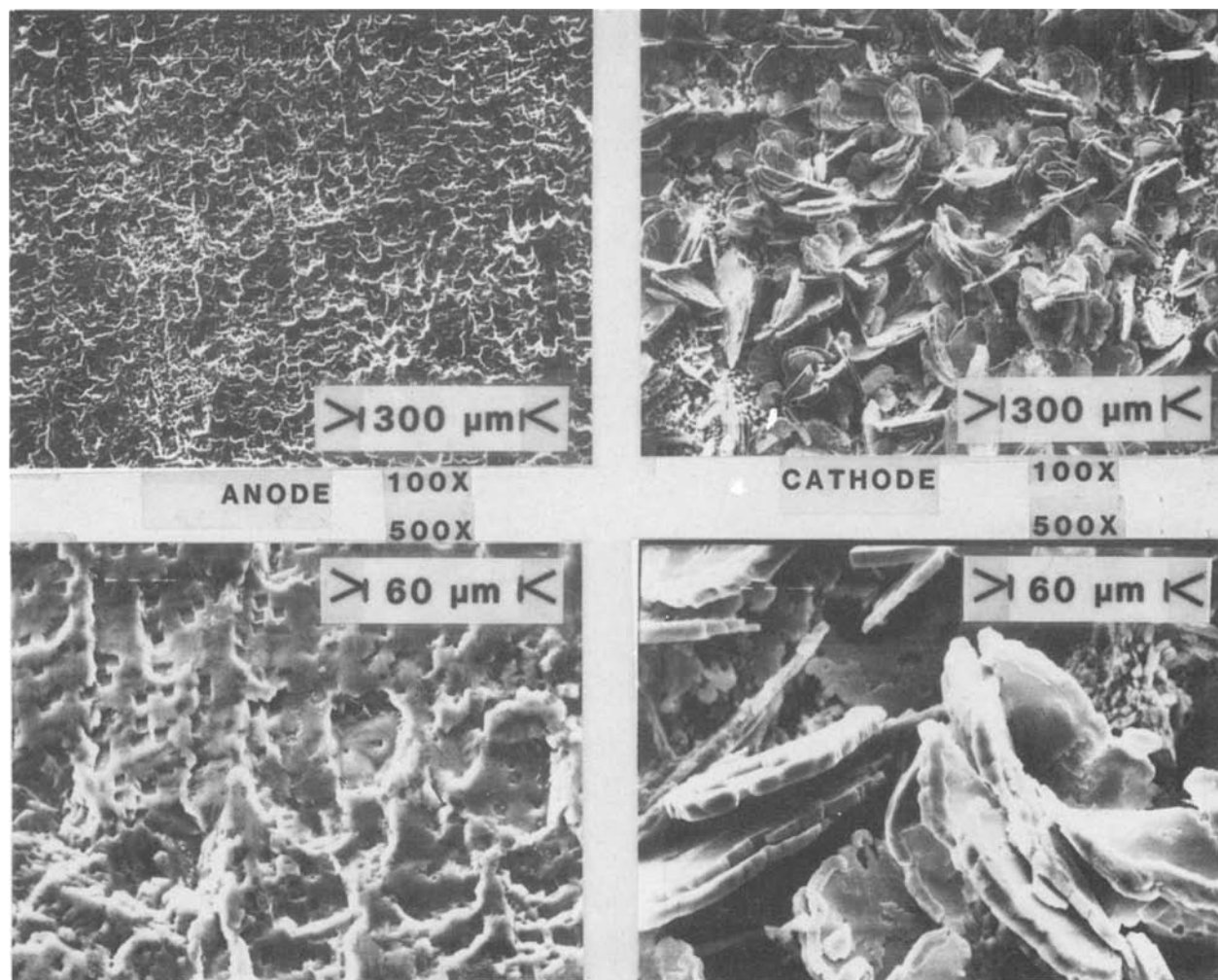


Fig. 7. Scanning electron micrographs of aluminum anodes and cathodes from concentration cells

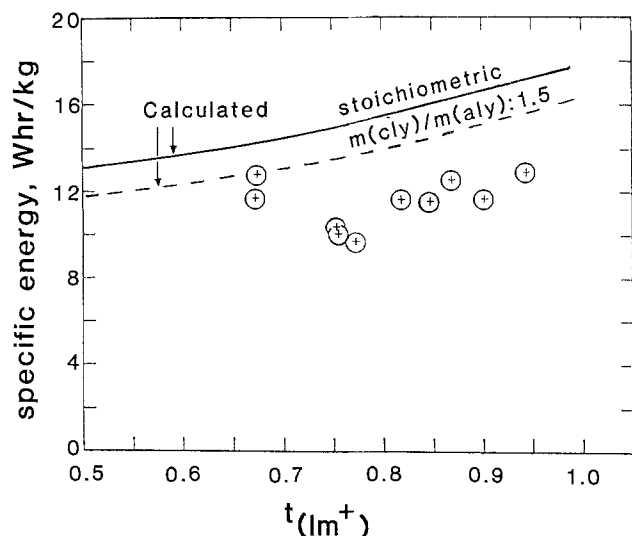


Fig. 8. Experimental values, +, of specific energies and transport numbers, t_+ , of concentration cells (from Table II); calculated values for cell with $N = 0.37$ and $N = 0.60$ melts and load voltage of 1.1V.

The change in moles of MEI^+ in the anolyte can thus be calculated, then divided by the equivalents of charge passed, to give an estimate of t_+ . Since $t_+ + t_{-4} + t_{-7} = 1$, where t_{-4} and t_{-7} are the transport numbers for AlCl_4^- and Al_2Cl_7^- , respectively, we can get t_{-4} from the change in mass of the anolyte as follows

$$\Delta m (\text{anolyte}) = \frac{Q (\text{meas})}{96,487} [-t_+ MW(\text{MEI}^+) + t_{-4} MW(\text{AlCl}_4^-) + (1 - t_+ - t_{-4}) MW(\text{Al}_2\text{Cl}_7^-)] \quad [7]$$

where the MW's are the molecular weights of the species designated in parentheses. Then t_{-7} is obtained as $(1 - t_+ - t_{-4})$. The transport numbers calculated in this way are listed in Table III.

We can also calculate transport numbers from the change in Cl^- content in the anolyte, a value which is also determined from both the initial and final mass and N of the anolyte. In each discharge, the loss of Cl^- is larger than that calculated from the measured charge using the assumed anode reaction (Eq. [4]). The excess loss in Cl^- is assumed to be due to the reaction shown in Eq. [3], where the Al_2Cl_7^- is transported into the anolyte. Thus, the Δ mol Cl^- (excess) is equated to mol Al_2Cl_7^- transporting charge. This is divided by the measured charge, giving t_{-7} . Then t_{-4} can be obtained from

$$\Delta m (\text{anolyte}) = \frac{Q (\text{meas})}{96,487} [-(1 - t_{-7} - t_{-4}) MW (\text{MEI}^+) + t_{-4} MW (\text{AlCl}_4^-) + t_{-7} MW (\text{Al}_2\text{Cl}_7^-)] \quad [8]$$

The transport numbers obtained in this way are virtually identical to those obtained from Δ mol MEI^+ and Eq. [7].

Table III. Transport numbers in concentration cells

Cell	t_+	t_{-4}	t_{-7}
C-7	0.67	0.08	0.25
C-8	0.90	-0.30	0.40
C-9	0.85	0.10	0.05
C-10	0.95	-0.29	0.35
C-13	0.68	-0.04	0.36
C-14	0.75	-0.29	0.53
C-18	0.87	-0.11	0.24
C-19	0.76	0.14	0.10
C-20	0.82	-0.01	0.20
C-21	0.77	0.21	0.02
Average:	0.80	-0.05	0.25
Std. dev.:	0.09	0.18	0.15

Discussion

The acid-base cell described here appears to behave according to the simple model shown in Fig. 2. The reversible deposition of aluminum from acidic (AlCl_3 rich) catholyte proceeds by a $3e^-$ Al process that is coulometrically balanced by irreversible dissolution of the aluminum negative electrode in basic (MEI^+ rich) anolyte. Delivered specific energies are close to those calculated (based on the model) for complete discharge to neutral melt.

Minor deviations in electrode mass changes are adequately explained by small corrosion losses. Long term corrosion rates, after removal of impurities, appear to be slow and about equal in acid melts and in basic melts. Further studies are required to determine if the steady-state corrosion rates obtained in the submerged strip experiments may be influenced by formation of passivating surfaces on the aluminum. Variability of corrosion rates in acid melts may be due to variations in contamination by trace amounts of water. Corrosion in basic melts may be related to irreversible reduction of the imidazolium cation by aluminum metal (8).

The majority of ionic conduction in the melt is accomplished by the organic cation, MEI^+ . The transport number for the acidic anionic species, Al_2Cl_7^- , appears to be larger than the number for the neutral anionic species, AlCl_4^- . The transport number for MEI^+ of 0.80 ± 0.09 calculated from electrode and electrolyte compositional changes in the concentration cells, is in reasonable agreement with the values of 0.72 ± 0.03 obtained by Hussey and Øye (10). Hussey and Øye also find that the transport numbers for the anions depend on the acidity of the melts, with Al_2Cl_7^- dominating in more acidic melts and AlCl_4^- dominating at near-neutral melts in approximately direct relation to their concentrations. Further work has shown that t_+ (MEI^+) is 0.70 ± 0.03 , in basic and neutral melts, with Cl^- and AlCl_4^- sharing in the transport of the remaining charge (11).

Acidic melts react slowly with the microporous polypropylene separator used in these experiments. The extent and nature of melt diffusion through the separator is unknown. However, based on the relative consistency of our results and on agreement with the expected model, it is probably a minor effect. Reactivity of polypropylene with acidic melts may be dependent on impurities such as water in the melt or separator. This may account in part for the large standard deviations observed for anion transport numbers, as small errors in the electrolyte weighing give rise to fairly large errors in the anion transport numbers. It must also be noted that we have calculated these transport numbers as if they were independent of concentration. While this appears to be valid for the MEI^+ based on other studies (10, 11), it is probably not true for the anionic species. Lacking the strict control of concentrations required in traditional methods for determining transport numbers, the data from the concentration cells give, at best, rough estimates of "average" transport numbers for the anions in the concentration range spanned during cell discharge.

Variable amounts of impurities (especially those derived from reactions with H_2O) in the melts probably account for the scatter in the observed aluminum electrode weight changes. This is indicated by the fact that the deduced corrosion losses (Table I) are variable and not correlated with the charge passed.

Conclusions

Low-specific-energy, aluminum acid-base concentration cells using ambient-temperature chloroaluminate ionic liquids have been discharged close to their theoretical limits. Relatively flat constant-current discharge curves at current densities of up to 0.5 mA/cm^2 have been obtained at 1.0-1.3V. Analysis of electrode mass changes and electrolyte compositional changes accompanying discharge show that aluminum is reduced from acidic melts and oxidized in basic melts, by a $3e^-$ process. Transport

numbers determined by these experiments show that the MEI^+ cation is the principal charge carrying species.

Acknowledgments

The authors wish to acknowledge support from Mr. Lloyd Pflug, FJSRL, in the NMR analysis; Ms. Katherine Ciemiecki, AT&T Bell Labs, in providing the SEM photos of the electrodes; Lt. Col. Armand A. Fannin, Jr., FJSRL, in the development of programs used in the calculations and data handling; and John Wilkes, Fred Reynolds, and Lowell King, FJSRL, in many helpful discussions of the results.

Manuscript submitted May 14, 1984; revised manuscript received July 13, 1984.

The United States Air Force Academy assisted in meeting the publication costs of this article.

REFERENCES

1. J. S. Wilkes, J. A. Levisky, R. A. Wilson, and C. L. Hussey, *Inorg. Chem.*, **21**, 1263 (1982).
2. R. J. Gale and R. A. Osteryoung, *ibid.*, **18**, 1603 (1979).
3. A. A. Fannin, Jr., L. A. King, and D. W. Seegmiller, *This Journal*, **119**, 801 (1972).
4. R. A. Osteryoung, Paper 781 presented at The Electrochemical Society Meeting, San Francisco, CA, May 8-14, 1983.
5. B. J. Piersma and J. S. Wilkes, "Electrochemical Survey of Selected Cations and Electrode Materials in Dialkylimidazolium Chloroaluminate Melts," FJSRL-TR-82-0004, Frank J. Seiler Research Laboratory, USAF Academy, CO 80840, September, 1982.
6. C. J. Dymek, Jr., "Specific Energies of Concentration Cells Using Room Temperature Chloroaluminate Molten Salts," FJSRL-TR-83-0013, Frank J. Seiler Research Laboratory, USAF Academy, CO 80840, November, 1983.
7. J. S. Wilkes, J. A. Levisky, J. L. Pflug, C. L. Hussey, and T. B. Scheffler, *Anal. Chem.*, **54**, 2378 (1982).
8. J. A. Wilkes and J. J. Auburn, Abstract 242, The Electrochemical Society Extended Abstracts, Vol. 83-2, Washington, DC, Oct. 9-14, 1983.
9. C. R. Boston, in "Advances in Molten Salt Chemistry," J. Braunstein, G. Mamantov, and G. P. Smith, Editors, Chap. 3, Plenum Press, New York (1971).
10. C. L. Hussey and H. Øye, *This Journal*, **131**, 1621 (1984).
11. C. J. Dymek, Jr. and L. A. King, 35th Meeting of the International Society of Electrochemistry, Berkeley, CA, Aug. 5-10, 1984.

The Electrochemistry of Colloidal Semiconductor Particles

Theory

W. John Albery,* Philip N. Bartlett, and John D. Porter*¹

Department of Chemistry, Imperial College, London, England SW7 2AY

ABSTRACT

The distribution of majority carriers in a collection of colloidal semiconductor particles is calculated. The kinetics of electron transfer from such particles to a macroscopic electrode are considered. Although each particle may have hundreds of electrons, the kinetics are shown to obey the simple equations of classical electrochemistry, such as the Tafel relation. The effect of illuminating the particles and photogenerating majority carriers is also considered. Again, the classical results for the photoelectrochemistry on a transparent rotating disk electrode are obtained, providing that account is taken of the much slower diffusion of the particles.

Colloidal semiconductors have attracted considerable attention (1, 2) as possible systems for utilizing solar energy. Their advantages include good adsorption of the solar energy and a large surface area for carrying out chemical reactions. To trap the energy, electron-transfer reactions have to take place on the surface of the particle for both the minority and majority carriers. An understanding, therefore, of electron-transfer processes at the surface of these particles is important for the design, characterization, and optimization of these systems. In this paper, we first discuss the distribution of electrons among a system of colloidal particles. Unlike a simple ionic reactant, where the charge is the same on each ion, a collection of colloidal particles will contain different numbers of electrons. It is interesting to explore this distribution function and to find out the dispersion about the mean number of electrons per particle. Second, we report theoretical results for electron transfer from colloidal particles to a macroscopic electrode. A new theoretical description is necessary because when the colloidal particle reaches the surface of the electrode, several hundred electrons may be transferred. We prove that, although these particles, containing large numbers of reactant electrons, are very different from normal one-electron species, nevertheless, many of the results of classical electrode kinetics, such as the Tafel relation, are found to hold. Having described the kinetics at the electrode surface, we next combine these results with the convective diffusion equation for mass transfer to derive

expressions for the current at a rotating disk electrode. We show that the classical Koutecky-Levich equation applies to the system. Experimentally, the system has been investigated using the optical rotating disk electrode (ORDE), and again we show that the rotation speed dependence of the photocurrent is similar to that for classical systems. In the subsequent paper (3), the theoretical model and results will be tested using results from n-type colloidal TiO_2 and CdS . Throughout this paper, therefore, we will consider n-type particles.

Distribution of the Number of Majority Carriers Between the Particles

In the subsequent paper (3), we will show that the number of majority carriers (electrons in our case) per particle may vary from three or four up to several hundred. With these small numbers, the number of electrons per particle will not be the same for every particle; there will be a distribution about some mean number. We start by calculating that distribution. We assume first that majority carriers are generated by thermal and/or photonic processes with a rate constant k_g/s^{-1} and, second, that the loss of majority carriers, described by the rate constant k , is first order in the number of majority carriers per particle. This second assumption is particularly appropriate for small particles ($\sim 50\text{\AA}$) where field effects are small; for larger particles, complications may arise from the space charge. In the steady state, the flux generating a particle with, say, m electrons in it from a particle with $m - 1$ electrons must balance the loss of an electron from the particle with m electrons to form a particle with $m - 1$ electrons. Writing the concentration of particles with m electrons as

*Electrochemical Society Active Member.

¹Present address: AT&T Bell Laboratories, Murray Hill, New Jersey 07974.

c_m and similarly c_{m-1} for the particle with $m - 1$ electrons, we have

$$k_g c_{m-1} = k m c_m$$

Applying this recurrence relation successively, we obtain

$$c_m = \frac{c_0 (k_g/k)^m}{m!} \quad [1]$$

The concentration c_0 is fixed by summing all the c_m to give the total concentration of particles in the system, c_p

$$c_p = \sum_0^{\infty} c_m = c_0 \exp(k_g/k) \quad [2]$$

We can also find the average number of electrons per particle, \bar{n}

$$\bar{n} = c_p^{-1} \sum_0^{\infty} m c_m = (k_g/k) \exp(-k_g/k)$$

$$\sum_{m=1}^{\infty} (k_g/k)^{m-1} / (m-1)! = (k_g/k) \quad [3]$$

Substitution of Eq. [2] and [3] in Eq. [1] gives

$$\frac{c_m}{c_p} = \frac{(\bar{n})^m \exp(-\bar{n})}{m!} \quad [4]$$

which is the Poisson distribution (4). Inspection shows that c_m is at a maximum when $m = \bar{n}$. For values of \bar{n} greater than 10, we can use the fuller form of Stirling's approximation

$$\ln(m!) \approx m \ln m - m + 1/2 \ln(2\pi m)$$

to give

$$\frac{c_m}{c_p} \approx \frac{\exp[-\bar{n}(\chi \ln \chi + 1 - \chi)]}{(2\pi \bar{n} \chi)^{1/2}} \quad [5]$$

where

$$\chi = m/\bar{n} \quad [6]$$

Comparison of the results from Eq. [4] and [5] shows that the approximation holds to within 1% for $\bar{n} \geq 10$. As in Eq. [4], c_m/c_p has a maximum value when $m = \bar{n}$ or $\chi = 1$

$$(c_m/c_p)_{\max} = (2\pi \bar{n})^{-1/2} \quad [7]$$

For \bar{n} greater than 500, Eq. [5] reduces to a Gaussian distribution. It is interesting to calculate the width of the distribution in terms of m or its normalized counterpart χ (Eq. [6]) at half-height. For the range $10 \leq \bar{n} \leq 1000$, we find that to within 1%

$$(\Delta m)_{1/2} = 2.36 (\bar{n})^{1/2} \quad [8]$$

and

$$(\Delta \chi)_{1/2} = 2.36 (\bar{n})^{-1/2} \quad [9]$$

In view of Eq. [7], these results are not surprising; in fact, the product $(\Delta m)_{1/2} (c_m/c_p)_{\max} = 0.94$, which is close to unity. Figure 1 shows plots of $(\Delta m)_{1/2}$ and $(\Delta \chi)_{1/2}$ as a function of \bar{n} . The distribution function (c_m/c_p) is also shown for $\bar{n} = 10, 100$, and 1000. It can be seen that as \bar{n} increases the absolute width of the distribution, $(\Delta m)_{1/2}$, increases but that the normalized parameter $(\Delta \chi)_{1/2}$ decreases, giving a sharper peak.

These results hold for both the dark and when the particles are illuminated. We are always dealing with a distribution of particles with different numbers of majority carriers.

Electrode Kinetics

Turning next to the electrode kinetics, the crucial difference between the electrochemistry of a colloidal particle and an ordinary species is that the number of elec-

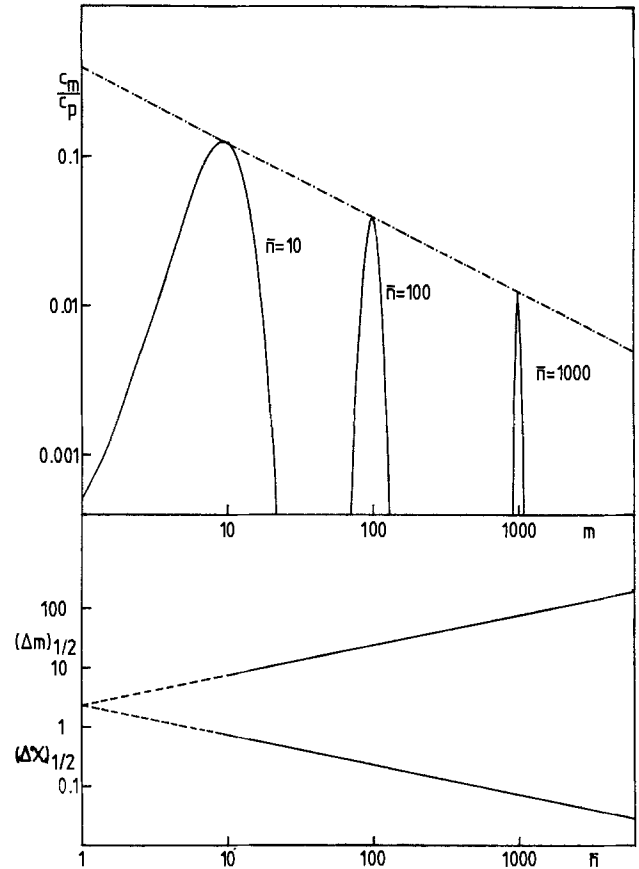


Fig. 1. Distribution functions calculated from Eq. [15] for the number of electrons per particle, m . Each curve is labeled with the average number of electrons per particle, \bar{n} . The broken line shows the locus of the maximum as calculated from Eq. [7]. The widths of the distribution peaks at half-height are plotted according to Eq. [8] and [9] in the lower half of the diagram.

trons transferred from each particle to the electrode may be large and will depend upon the potential of the electrode. In Fig. 2, we depict the model for an encounter of a particle with an electrode. We describe the transport of the particle to the electrode with the mass-transfer coefficient k_D' (5) where

$$k_D' = D_p/X_D$$

D_p is the diffusion coefficient of the particle, and X_D is the diffusion layer thickness of the electrode. For a rotating disk electrode, the Levich equation gives (6, 7)

$$X_D = 0.643 D_p^{1/3} \nu^{1/6} W^{-1/2} \quad [10]$$

where ν is the kinematic viscosity and W is the rotation speed in Hz. Hence, the flux of particles arriving at the electrode is given by

$$j_0 = k_D' c_p$$

For the moment, we assume that each particle has n electrons (majority carriers) in the conduction band; we will return to the effects of the distribution function below. We further assume that the rate constant for the transfer of an electron from the particle to the electrode is proportional to the number of electrons in the conduction band

$$k_m' = k_1' (n - m + 1)$$

where k_1' describes the transfer of the last electron from the conduction band of the particle at this particular electrode potential. We further assume that the potential distribution between the particle and the electrode and within the particle is not effected by the successive electron transfers. Our previous work showed (8) that, in many cases, particles are so small that field effects are small and, often, a constant potential distribution is found within the particle.

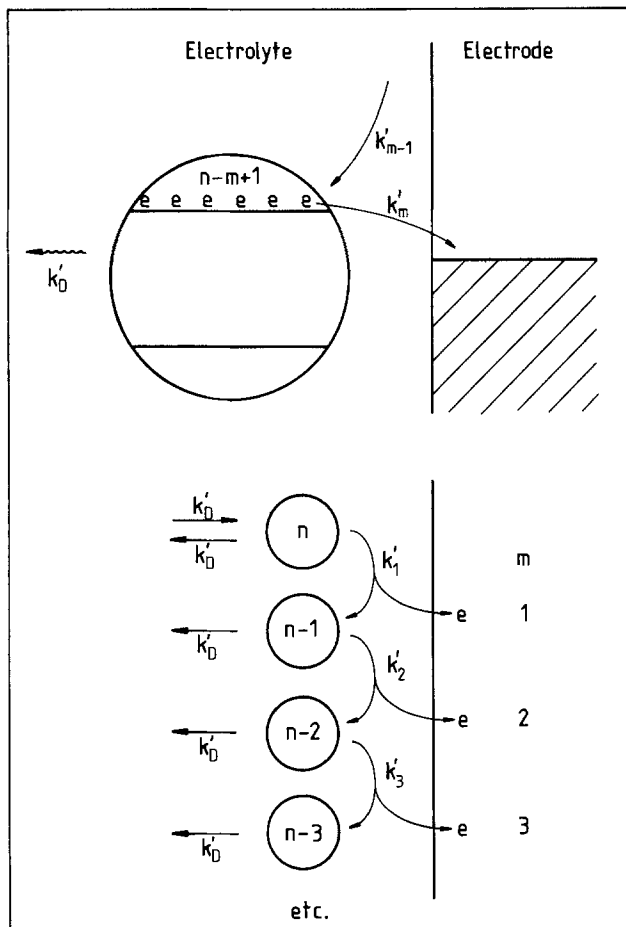


Fig. 2. Kinetic scheme for the successive transfer of electrons from a colloidal particle to a macroscopic electrode.

With these assumptions, we consider the cascade process depicted in Fig. 2. Summing the transfer of electrons for each partition, we obtain for the total flux of electrons

$$\frac{j_e}{j_0} = \sum_{m=1}^{m=n} \prod_{i=0}^{i=m-1} \frac{1}{1 + \lambda(n-i)} = S_n \quad [11]$$

where $\lambda = k'_D/k'_i$. The successive terms $\lambda/(n-i)$ describe the partition between leaving the surface and transferring another electron.

The series may be summed up by the method of induction. We assume that the sum S_n is given by

$$S_n = n/(1 + \lambda) \quad [12]$$

Then

$$S_{n+1} = \left(1 + \frac{\lambda}{n+1}\right)^{-1} (1 + S_n) \quad [13]$$

Substitution of Eq. [12] in Eq. [13] gives

$$S_{n+1} = (n+1)/(1 + \lambda)$$

For $n = 1$

$$S_1 = 1/(1 + \lambda)$$

and hence Eq. [12] holds for all values of n . We therefore obtain the gratifyingly simple result that

$$j_e/j_0 = n/(1 + k'_D/k'_i) \quad [14]$$

This equation has exactly the same form as the current voltage curve for a single-electron transfer. This is because in our model each electron has the chance $k'_i/(k'_i + k'_D)$ of being transferred at the electrode. As long as k'_i is independent of the number of electrons in the conduction band, it makes no difference whether the electrons all

come together in one big particle or each comes separately on its own little ion. Hence, although the electrons will be distributed among the particles as shown in Fig. 1, there will be no complications in the observed kinetics arising from this effect. We can also conclude that for this model the Tafel relation and the Koutecky-Levich equation should hold. The limiting current i_L , for large values of k'_i is given by

$$i_L = nFAk'_Dc_p \quad [15]$$

Under these conditions all the electrons in the conduction band are removed, and the current is limited by the arrival of the particles at the electrode surface.

Although the electrode kinetics of the particles give similar equations to those for simple ions, it is interesting to use Eq. [11] to explore the details of the cascade process depicted in Fig. 2. For this purpose, we use the variables y and χ , which describe the flux of electrons compared to the limiting flux and the number of electrons compared to the total number in the conduction band

$$y = j_e/j_0n$$

and

$$\chi = m/n$$

Then from Eq. [11] considering the contribution, δy , from each successive transfer, we have

$$\delta y_m = \delta y_{m-1} [1 + \lambda(n-m+1)]^{-1} \quad [16]$$

Next we assume that n is a reasonably large number, so that

$$\delta\chi = n^{-1} \ll 1$$

Then, providing m is not too close to n , we can write from Eq. [16]

$$\begin{aligned} \delta y_{m-1}/\delta y_m &\approx 1 + \lambda(n-m) \approx [1 + (n-m)^{-1}]^\lambda \\ &= \left[\frac{n-(m-1)}{n-m} \right]^\lambda \end{aligned} \quad [17]$$

when $m \rightarrow 1$, $\delta y_0 \rightarrow 1/n$, corresponding to the transfer of a single electron at the first encounter.

Hence, we find that to satisfy Eq. [17]

$$\begin{aligned} \delta y_m &\approx n^{-1} (1 - m/n)^\lambda \\ &= \delta\chi (1 - \chi)^\lambda \end{aligned}$$

or

$$dy/d\chi \approx (1 - \chi)^\lambda \quad [18]$$

It is satisfactory that integration of this equation with respect to χ from $\chi = 0$ (no electrons transferred) to $\chi = 1$ (all the electrons transferred) gives, for the total flux of electrons described by y

$$y = (1 + \lambda)^{-1} = S_n/n$$

This result agrees with Eq. [14] and justifies the approximation used in deriving Eq. [17]. (It is interesting that there is no error in the approximation for the particular case of $\lambda = 1$.) Figure 3 shows plots of Eq. [18] for different values of λ . The curves describe the fraction of particles that survive to deliver the m th electron in the cascade process. Thus for low values of λ , corresponding to fast electrode kinetics, most particles survive to the bitter end and lose all their electrons. However, for large values of λ , few electrons are transferred before the particles diffuse back into the solution.

Differentiation of Eq. [18] gives a distribution function, f , for the number of electrons delivered by the particles

$$f = -d^2y/d\chi^2 = \lambda(1 - \chi)^{\lambda-1} \quad [19]$$

Again, it is satisfactory that integration by parts of this equation shows that the total flux of electrons is given by

$$\int_0^1 \chi f d\chi = (1 + \lambda)^{-1} = S_n/n$$

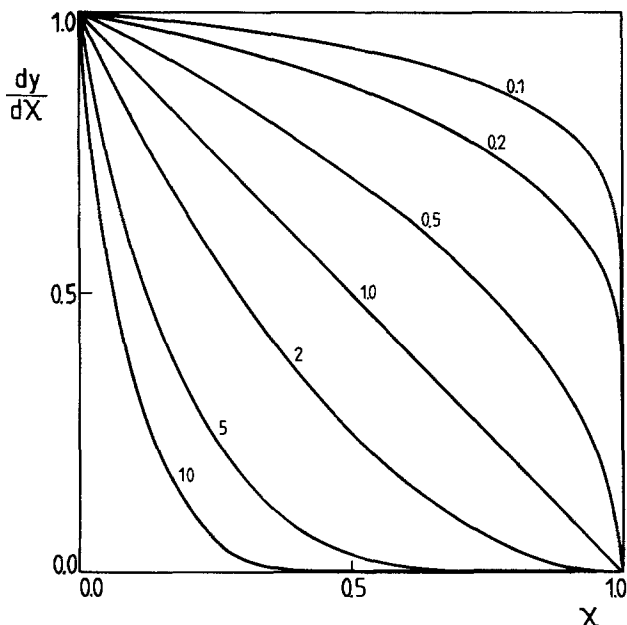


Fig. 3. Curves calculated from Eq. [18] showing the fraction of particles that remain at the electrode to deliver the m th electron where $\chi = m/n$. Each curve is labeled with its value of λ , which in Eq. [11] compares the transport and electrode kinetics.

Curves for the function, f , given by Eq. [19] for different values of λ are shown in Fig. 4. For large values of λ (slow electrode kinetics), the particles transfer few electrons, while for small values of λ (fast electrode kinetics), many particles lose all their conduction-band electrons. It is interesting that for $\lambda = 1$ a completely flat distribution is found, so that some particles lose no electrons, while an equal number lose all their electrons. This distribution

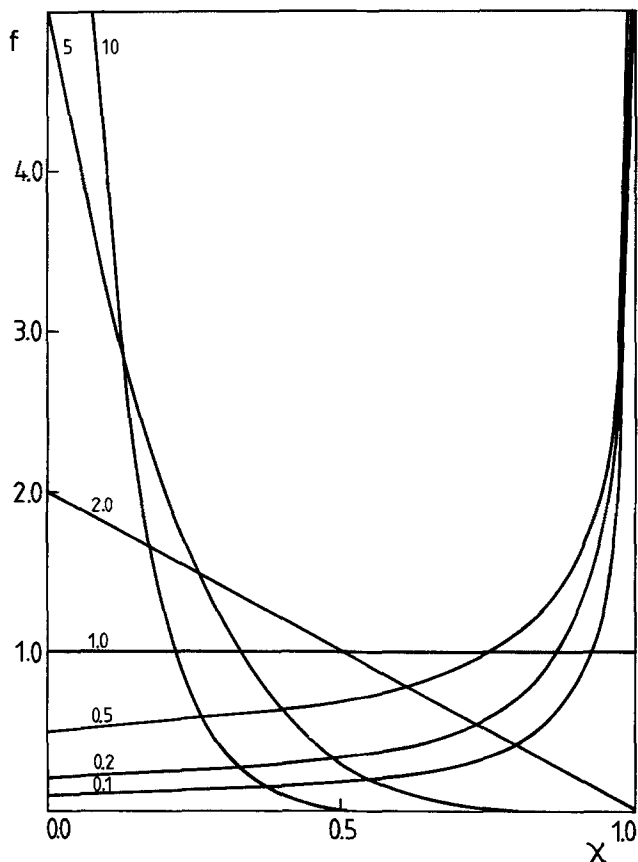


Fig. 4. Distribution curves, calculated from Eq. [19], showing the fraction of the electrons in the conduction band delivered by the particles to the electrode. Each curve is labeled with its value of λ .

imposed by the irreversible reaction is very different from the peaked distribution of the unperturbed system (Fig. 1).

The Convective Diffusion Equation

While the section above considers the electrode reaction, we now consider the convective diffusion equation for the system of particles as they diffuse towards a rotating disk electrode.

We can write a convective diffusion equation for a particle containing m electrons in the conduction band of concentration c_m

$$\text{Tr}(c_m) + k_g c_{m-1} - k m c_m + k(m+1)c_{m+1} - k_g c_m = 0 \quad [20]$$

In this equation the operator Tr describes the diffusion and convection terms for a rotating disk electrode

$$\text{Tr} = D_p \frac{\partial^2}{\partial x^2} + C x^2 \frac{\partial}{\partial x} \quad [21]$$

where x is the distance normal to the electrode and (9)

$$C = 8.0W^{2/3}\nu^{-1/2} \quad [22]$$

As described above, the first-order rate constant k_g describes electron promotion either by thermal or by photonic processes, and the rate constant k describes the loss of electrons from the conduction band by a process which is first order in the electron concentration. There will be an equation similar to Eq. [20] for each value of m . We now multiply each equation by its value of m and sum the set of equations to obtain the simple result that

$$\text{Tr}(c_e) + k_g c_p - k c_e = 0 \quad [23]$$

where c_e , the total concentration of electrons in the conduction band, is given by

$$c_e = \sum_{m=0}^{\infty} m c_m$$

and where, as in Eq. [2], c_p is the concentration of particles.

This result shows that the transport of the whole system of particles may be treated by the usual convective diffusion equation using c_e as the variable. For an irreversible reaction, the boundary condition at the electrode surface is given by

$$j_e = D_p \left[\frac{\partial c_e}{\partial x} \right]_0 = k' c_e$$

where k' is an electrochemical rate constant. This result again confirms the analysis from the cascade model; the simple Tafel and Levich relations will apply to the system of particles.

In Eq. [20], when one uses the ORDE, the generating rate constant k_g can be made up of a thermal contribution, k_T , and a photonic contribution

$$k_g = k_T + (I_0/\epsilon_p) \exp(-x/X_e) \quad [24]$$

where I_0 is the irradiance at the electrode surface

$$X_e = (\epsilon_p c_p)^{-1}$$

and ϵ_p is the molar extinction coefficient (in natural logarithms) of the particles treated as a species in solution of concentration c_p .

In terms of bulk properties

$$X_e \approx (\epsilon_B c_{FU} V)^{-1}$$

where ϵ_B is the extinction coefficient of the bulk material, c_{FU} is the concentration of formula units, and V is the molar volume. Just as k_g is split in Eq. [24] into two contributions, so c can be split into the thermal contribution $(c_e)_T$, giving rise to the dark current and the photogenerated contribution $(c_e)_{hv}$ giving rise to the photocurrent. The variable $(c_e)_{hv}$ obeys the same differential equation as a photogenerated product, such as leucothionine, and so all

of the results we have previously deduced for the ORDE can be applied to the colloidal system (10-12).

In particular, when the absorption length, X_c , is much longer than the thickness of the diffusion layer, so that the diffusion layer is uniformly illuminated, and when the photogenerated electrons are stable with respect to their passage across the diffusion layer, we obtain (10) the following result for the limiting photocurrent

$$(i_{hv})_L = \phi A F I_0 (X_D/X_c) \quad [25]$$

Finally, we summarize our conclusions below.

1. The distribution of majority carriers in a system of colloidal particles obeys the Poisson distribution (see Fig. 1).

2. A collection of particles, each with n electrons, will transfer electrons to an electrode as shown in Fig. 2, giving distribution functions shown in Fig. 3 and 4.

3. Despite the complex behavior in conclusions (1) and (2), providing that the electrochemical rate constant is independent of the number of electrons in the conduction band, the Tafel relation will be obeyed.

4. The rotating disk convective diffusion equation for a system of particles can be solved and the Koutecky-Levich relation will be obeyed.

5. Similarly, a system of illuminated particles obeys the simple equations for the optical rotating disk electrode.

In the subsequent paper, these theoretical results will be tested using experimental results from n-type TiO_2 and CdS.

Acknowledgments

We thank the 1851 Commissioners and NSERC (Canada) for Research Fellowships for P. N. B. and J. D. P., re-

spectively. This is a contribution from the Oxford Imperial Energy Group.

Manuscript submitted Feb. 21, 1984; revised manuscript received Aug. 3, 1984.

AT&T Bell Laboratories assisted in meeting the publication costs of this article.

REFERENCES

1. K. Kalyanasundaram, E. Borgarello, and M. Grätzel, *Helv. Chim. Acta*, **64**, 362 (1981).
2. D. Duonghong, J. Ramsden, and M. Grätzel, *J. Am. Chem. Soc.*, **104**, 2977 (1982).
3. W. J. Albery, P. N. Bartlett, and J. D. Porter, *This Journal*, **130**, 2896 (1984).
4. H. Margenau and G. M. Murphy, "The Mathematics of Physics and Chemistry," p. 438, Van Nostrand, Princeton, NJ (1968).
5. W. J. Albery, "Electrode Kinetics," p. 58, Clarendon Press, Oxford, England (1975).
6. W. J. Albery, "Electrode Kinetics," p. 53, Clarendon Press, Oxford, England (1975).
7. V. G. Levich, "Physicochemical Hydrodynamics," p. 68, Prentice Hall, Englewood Cliffs, NJ (1962).
8. W. J. Albery and P. N. Bartlett, *This Journal*, To be published.
9. W. J. Albery and M. L. Hitchman, "Ring-Disc Electrodes," p. 12, Clarendon Press, Oxford, England (1971).
10. W. J. Albery, M. D. Archer, and R. G. Egdell, *J. Electroanal. Chem.*, **82**, 199 (1977).
11. W. J. Albery, W. R. Bowen, F. S. Fisher, and A. D. Turner, *ibid.*, **107**, 1 (1980).
12. W. J. Albery, P. N. Bartlett, W. R. Bowen, F. S. Fisher, and A. W. Foulds, *ibid.*, **107**, 23 (1980).

The Electrochemistry of Colloidal Semiconductor Particles

Experiments on CdS and TiO_2

W. John Albery,* Philip N. Bartlett, and John D. Porter*¹

Department of Chemistry, Imperial College, London, England SW7 2AY

ABSTRACT

Results are presented for the dark electrochemistry and photoelectrochemistry of CdS and TiO_2 colloidal particles studied with the optical rotating disk electrode (ORDE). The electron-transfer reactions between the particles and the electrode are found to be irreversible. However, in agreement with theoretical predictions, the kinetics obey both the Tafel and Levich relations. Several hundred electrons may be transferred on each encounter between a particle and the ORDE. Added halide ions are shown to be good scavengers for photogenerated holes. Results for the quantum efficiencies for the photogeneration of majority carriers are reported.

In the previous paper (1), we derived various theoretical relations for the electrochemistry and photoelectrochemistry of colloidal particles of semiconductors such as TiO_2 and CdS. In this paper, we report experimental results designed to test the model presented and the relations derived. These results were obtained using the optical rotating disk electrode (ORDE) (2-4). This electrode consists of a quartz rod, the end of which is coated with tin oxide to form a transparent electrode. Light is shone down the rod through the electrode and then into the solution. The rotation of the electrode imposes known transport by convection and diffusion on the species reacting on the electrode. In this case, the species are the colloidal semiconductor particles. We report results on the dark electrochemistry of the particles and on the photocurrents observed when the particles are illuminated. Experiments have also been carried out in the presence of different halide ions, which scavenge the photogenerated holes. The kinetics of this process are shown to obey the Stern-Volmer quenching law.

*Electrochemical Society Active Member.

¹Present address: AT&T Bell Laboratories, Murray Hill, New Jersey 07974.

Experimental

The apparatus and ORDE have been described previously (5). The radius of the electrode used in this work was 2.03 mm. The light source was a Thorn 250W quartz halogen slide projector lamp. Because of the small currents involved (\sim nA), a special potentiostat was constructed, which used commutating operational amplifiers, and which was powered by dry cells.

All chemicals were of analytical reagent grade. The TiO_2 colloids were made by the method of Henglein (6), which involves the hydrolysis of titanium tetraisopropoxide. We made two modifications to the method. First, we carried out the hydrolysis in $0.05 \text{ mol dm}^{-3} \text{ HClO}_4$ under nitrogen, rather than in HCl under air; this was to avoid the incorporation of Cl^- or oxygen into the particles. Second, the isopropanol, formed by the hydrolysis, was removed as an aqueous azeotrope by a three-stage rotary evaporation. The particles were used without the addition of any support material, such as polyvinylalcohol. The CdS colloids were made by the method of Grätzel (7), which involves the reaction of $\text{Cd}(\text{NO}_3)_2$ with H_2S . For the same reasons as discussed above, in our

method, we dissolved CdO in HClO_4 and performed the reaction with H_2S under nitrogen. For both colloids the size of the particles was determined by light scattering using a Cary 14 spectrophotometer. The diameters of the TiO_2 and CdS particles were 2.5 and 8.0 nm, respectively. In addition, transmission electron microscopy was performed on the TiO_2 particles, and a mean diameter of less than 6 nm was found.

All potentials were measured and are reported with respect to the saturated calomel electrode (SCE). All experiments were carried out at 25°C. Experiments with TiO_2 particles were carried out in 0.05M dm^{-3} HClO_4 ; the concentration of TiO_2 was 10 mM dm^{-3} . Experiments with CdS particles were carried out in a solution containing 10 mM dm^{-3} KClO_4 and 10 mM dm^{-3} sodium hexametaphosphate; the concentration of CdS was 5 mM dm^{-3} .

Results and Discussion

Dark electrochemistry.—Typical current voltage curves for the transfer of electrons from the conduction band of TiO_2 and of CdS to a macroscopic electrode in the dark are shown in Fig. 1. Because the currents were so small, the voltammograms were obtained point by point. It is clear that the electron-transfer reactions are very irreversible. The flatband potentials for TiO_2 and CdS may be estimated from their bulk values (8) to be approximately -0.6 and -0.8V, respectively. Hence, overvoltages of some 800-1000 mV are required to drive the electron-transfer reaction to the macroscopic electrode.

Next, we consider the variation of the limiting current, i_L , from the particles with the rotation speed of the electrode. Equation [15] of our previous paper (1) shows that these currents should obey the Levich equation

$$i_L = nFAD_p W^{1/2} c_p / X_{D,W=1} \quad [1]$$

where n is the number of electrons in the conduction band, A is the area of the electrode, D_p is the diffusion coefficient of the particles, W is the rotation speed (Hz), c_p is the concentration of the particles, and $X_{D,W=1}$ is the thickness of the diffusion layer for $W = 1$ Hz. From the Levich equation (9)

$$X_{D,W=1} = 0.643\nu^{1/6} D_p^{1/3} \quad [2]$$

Figure 2 shows typical results for CdS, and it can be seen that the limiting currents vary linearly with the square root of the rotation speed. The intercept probably arises

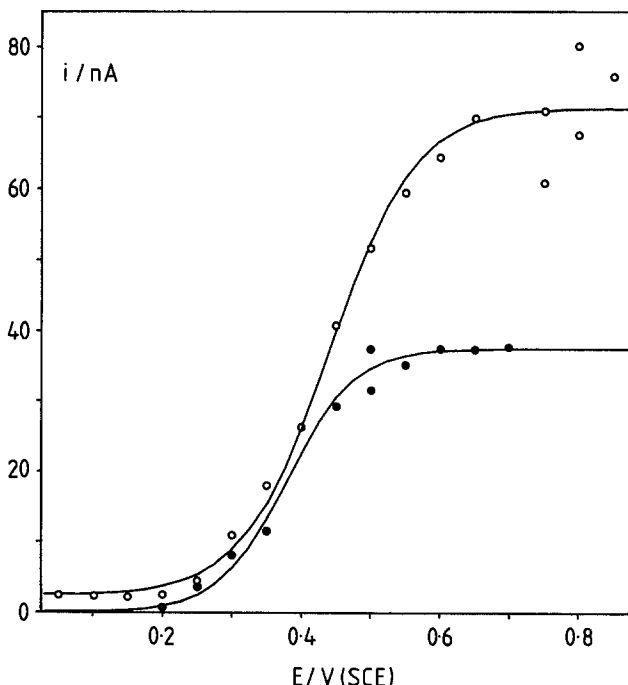


Fig. 1. Typical current voltage curves in the dark for CdS (o) and TiO_2 (●) colloids

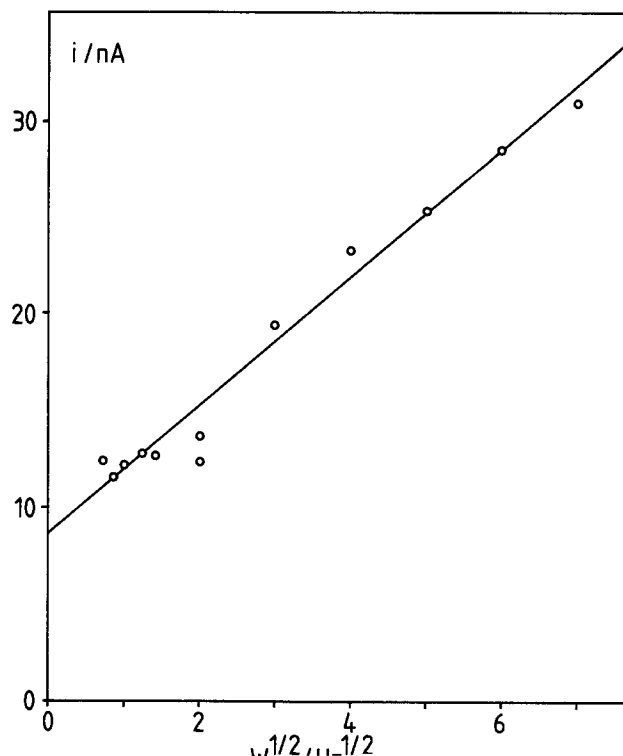


Fig. 2. Limiting dark currents for CdS plotted according to Eq. [1] against the square root of rotation speed ($W^{1/2}$).

from background currents or offset currents from the amplifiers. From the Stokes-Einstein equation (10), and the radius of the particles, we estimate that

$$D_p/\text{cm}^2\text{s}^{-1} = 4 \times 10^{-7} \quad [3]$$

From the bulk density (11) and the radius, we find that each particle contains about 5×10^8 atoms of Cd; hence, in our solution

$$c_p/\mu\text{M dm}^{-3} = 0.9$$

Using this value, the value of D in Eq. [3], the gradient of the plot in Fig. 2, and Eq. [1], we find that the number of electrons in the conduction band of a single particle is

$$n = 4$$

This corresponds to a doping density of $1.6 \times 10^{19} \text{ cm}^{-3}$, which seems reasonable, considering that the particles were prepared in the absence of halide and oxygen. Similar results were found for the TiO_2 particles.

Next, we turn to the irreversible electrode kinetics on the rising part of the current voltage curve in Fig. 1. Equation [14] or our previous paper (1) shows that

$$i_L/i = 1 + k_D'/k_1' \quad [4]$$

where

$$k_D' = D_p W^{1/2} / X_{D,W=1}$$

and k_1' is the electrochemical rate constant for the transfer of a single electron from the conduction band of a particle to the macroscopic electrode. Equation [4] can be rearranged to give

$$\ln(i_L/i - 1) = \ln(k_D'/k_{1,E=0}') - \alpha E \quad [5]$$

where E is the potential of the macroscopic electrode.

Figure 3 shows a typical plot of Eq. [5] for CdS in the dark. A reasonably straight line is obtained, showing that the electrode kinetics of the colloidal particles obey the Tafel relation. Similar results are found for TiO_2 . However, the values of the transfer coefficient, α , are somewhat smaller than usual, being 0.40 and 0.34 for TiO_2 and CdS, respectively. It might be thought that these results, coupled with the irreversibility of the reaction, are those

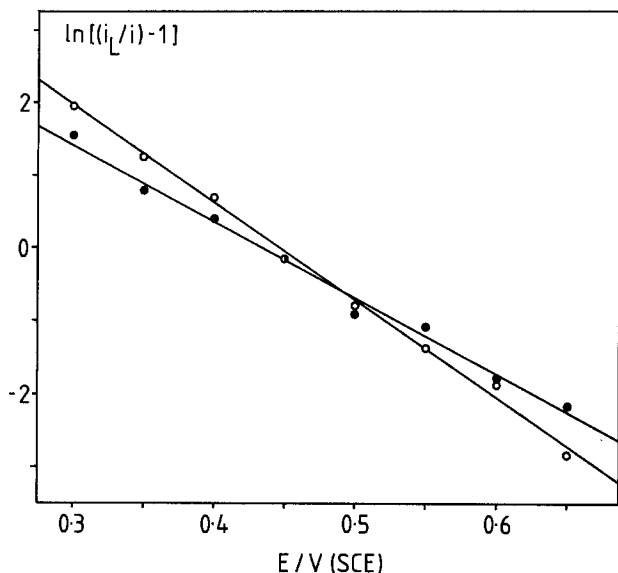


Fig. 3. Corrected Tafel plots (Eq. [5]) for CdS in the dark (o) and under illumination (o).

that would be expected for such a reaction being driven hard by the electrode potential (12). However, solvent reorganization will not be relevant to this type of transfer between two massive entities, and the traditional Marcus picture (13) is not applicable. With negligible solvent reorganization, one might have expected instead that the electron-transfer reactions would have been very rapid. The observed irreversibility may arise from the mutual repulsion of the double layers, so that the transfer of the electron resembles that in a metal insulator semiconductor junction.

Photoelectrochemistry.—Having characterized the dark electrochemistry, we now report what happens when the ORDE is illuminated. Figure 4 shows typical results obtained with CdS. It can be seen that the photocurrent voltage curve has a similar shape to the dark current voltage curve. This is in agreement with the theoretical model, where all the conduction band electrons have the same electrode kinetics. The rising part of the photocurrent

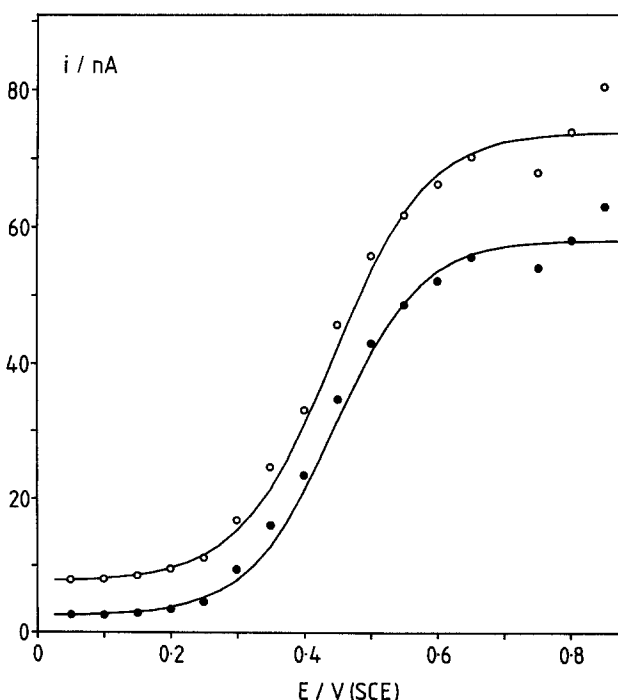


Fig. 4. Typical current voltage curves for a CdS colloid in the dark (o) and under illumination (o).

voltage curve can be plotted according to the Tafel relation given in Eq. [5]; the results are shown in Fig. 3. Similar values of the electrochemical rate constant and of α are found.

Turning to the limiting photocurrent, we find that these currents decrease with increasing rotation speed. This behavior is to be expected if the photogenerated electrons are kinetically stable in their passage across the diffusion layer (1). Under these conditions, the photogenerated electrons are either transferred to the electrode or are lost to the bulk of the solution as the particles are swept on their way by the radial convection. Equation [25] of our previous paper (1) states that

$$(i_{hv})_L = FA\phi I_0(X_{D,w=1}/X_e) W^{-1/2} \quad [6]$$

where ϕ is the quantum efficiency for the photogeneration of holes that leave the particle giving stable conduction band electrons, I_0 is the irradiance at the electrode surface, and X_e is the absorbance length (3), describing the Beer-Lambert profile of the incoming light (1)

$$X_e = (\epsilon_p c_p)^{-1} \quad [7]$$

Figure 5 shows typical results for the limiting photocurrents for CdS plotted, according to Eq. [6] against $W^{-1/2}$. A good straight line is obtained. The small intercept is caused by photocurrents generated at the electrode surface. Thus, these results again confirm the theoretical results of our previous paper.

From the gradient, we find that the value of ϕ , the quantum efficiency, is 2×10^{-3} . Hence, we may conclude that under these conditions, where there is no scavenger for photogenerated holes in the solution, the main process is recombination of the holes and electrons inside the particle. The photogenerated electrons that survive to reach the electrode do so because the holes have been removed, and then they are safe in their tiny particle. We cannot identify the reaction that removes the holes; it may be corrosion or it may be reaction with trace electron donors. However, it is clear that this value of ϕ sets an upper limit on the corrosion rate.

Comparing the size of the photocurrent to that of the dark current, we can estimate a typical number of conduction band electrons which are transferred per particle in the light. For a rotation speed of 1 Hz, the number is 20. Under these conditions the particles take about a second to cross the diffusion layer, where they are in the light.

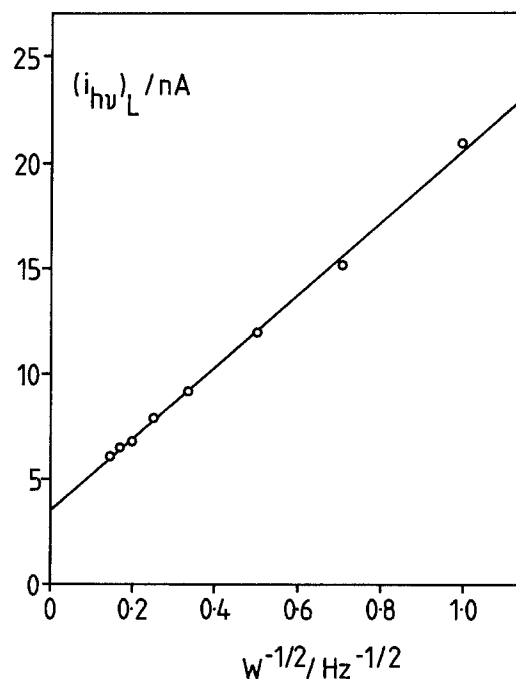


Fig. 5. Limiting photocurrents for CdS plotted according to Eq. [6] against $W^{-1/2}$.

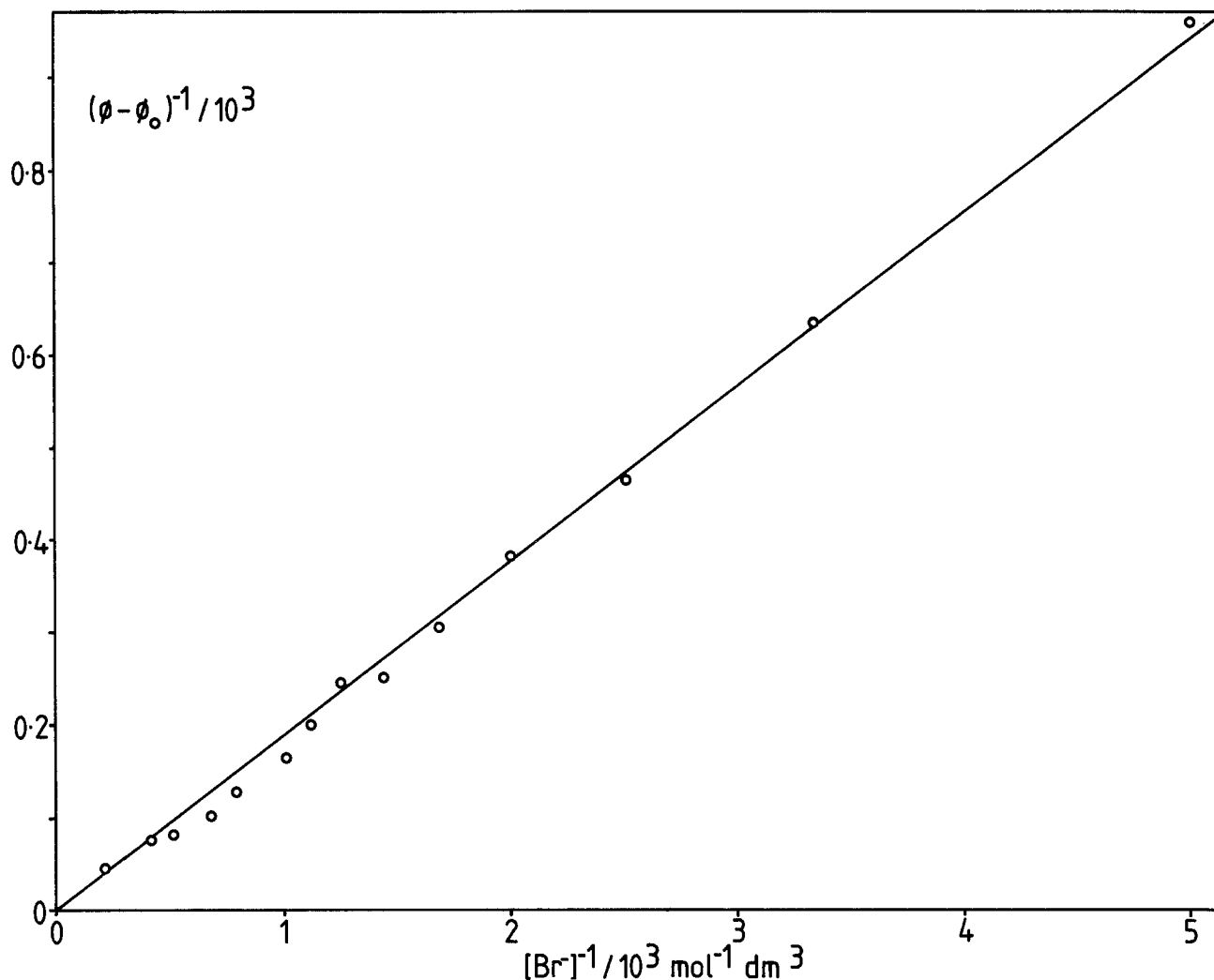


Fig. 6. Stern-Volmer analysis according to Eq. [8] of the scavenging of photogenerated holes in CdS by Br^- . Note the scale on the y axis, which means that an intercept of unity is indistinguishable from zero.

During this passage they are hit by a photon every 0.1 ms, which with ϕ equal to 2×10^{-3} , generates the 20 photoelectrons that finally reach the macroscopic electrode.

We have also measured the action spectrum of the photocurrent and have found it to be identical to the absorption spectrum of bulk CdS.

For TiO_2 , the photocurrents were smaller by an order of magnitude, and so less time was spent on this system. However, the limiting photocurrents did decrease with increasing rotation speed, and the general behavior was similar to CdS.

Effect of added halide ions.—We found that the photocurrents for CdS could be dramatically increased by adding Br^- . The rotation speed dependence was similar to that in Fig. 5. We therefore conclude that the action of the Br^- is to increase ϕ by scavenging the photogenerated holes out of the particles, before they recombine with the electrons. If this is the case, then the usual Stern-Volmer equation should apply, and we can write, as shown in the Appendix

$$(\phi - \phi_0)^{-1} = 1 + k_R/k_S[\text{Br}^-] \quad [8]$$

where ϕ_0 is the quantum efficiency in the absence of Br^- , k_S describes the scavenging of a hole by Br^- , and k_R de-

scribes the recombination of a hole inside the particle. Figure 6 shows that this modified Stern-Volmer relation is indeed obeyed. Similar plots were found for Cl^- and I^- . Results for the ratios of rate constants are collected in Table I. It can be seen that Br^- is a much more efficient scavenger than either Cl^- or I^- . These results suggest that Br^- systems are to be preferred for solar energy conversion. At the largest concentration of Br^- used in this work (4.5 mM dm^{-3}), ϕ was 0.022, and 270 electrons were being transferred on each encounter of a particle with the macroscopic electrode.

The study of the electrochemistry of colloidal particles with the ORDE can therefore determine the number of electrons in the conduction band, the quantum efficiency of their generation, and their lifetime. All of these parameters are fundamental to an understanding of the behavior of such systems and their possible application to solar energy conversion.

Acknowledgments

We thank the 1851 Commissioners and NSERC (Canada) for Research Fellowships for P. N. B. and J. D. P., respectively. This is a contribution from the Oxford Imperial Energy Group.

Manuscript submitted Feb. 21, 1984; revised manuscript received Aug. 3, 1984.

AT&T Bell Laboratories assisted in meeting the publication costs of this article.

APPENDIX

In this Appendix, we derive the modified Stern-Volmer relation in Eq. [8]. We assume that a photogenerated hole may recombine with a rate constant, k_R , or it may be

Table I. Scavenging of holes from CdS particles

Halide ion	$(k_S/k_R)/\text{dm}^3 \text{ mol}^{-1}$
Cl^-	0.074 ± 0.011
Br^-	5.2 ± 0.1
I^-	0.093 ± 0.009

lost from the particle with a rate constant $k_0 + k_s [\text{Br}^-]$, where k_0 describes the processes in the absence of Br^- and k_s describes the scavenging by Br^- . We then find that

$$\phi = \frac{k_0 + k_s [\text{Br}^-]}{k_R + k_0 + k_s [\text{Br}^-]}$$

$$\phi_0 = k_0 / (k_R + k_0)$$

and

$$\frac{1}{\phi - \phi_0} = \frac{k_0 + k_R}{k_R} \left[1 + \frac{k_0 + k_R}{k_s [\text{Br}^-]} \right] \quad [9]$$

Now $\phi_0 \ll 1$ and so $k_0 \ll k_R$. With this assumption, Eq. [9] simplifies to give Eq. [8].

REFERENCES

1. W. J. Albery, P. N. Bartlett, and J. D. Porter, *This Journal*, **130**, 2892 (1984).
2. W. J. Albery, M. D. Archer, and R. G. Egdell, *J. Electroanal. Chem.*, **82**, 199 (1977).
3. W. J. Albery, W. R. Bowen, F. S. Fisher, and A. D. Turner, *ibid.*, **107**, 1 (1980).
4. W. J. Albery, P. N. Bartlett, W. R. Bowen, F. S. Fisher, and A. W. Foulds, *ibid.*, **107**, 23 (1980).
5. W. J. Albery, W. R. Bowen, F. S. Fisher, and A. D. Turner, *ibid.*, **107**, 11 (1980).
6. A. Henglein, *Ber. Bunsenges. Phys. Chem.*, **86**, 241 (1982).
7. D. Duonghong, J. Ramsden, and M. Grätzel, *J. Am. Chem. Soc.*, **104**, 2977 (1982).
8. W. P. Gomes and F. Gordon, *Prog. Surf. Sci.*, **12**, 155 (1982).
9. V. G. Levich, "Physicochemical Hydrodynamics," p. 68, Prentice Hall, Englewood Cliffs, NJ (1962).
10. R. A. Robinson and R. H. Stokes, "Electrolyte Solutions," p. 44, Butterworths, London (1959).
11. B. R. Pamplin, in "CRC Handbook of Chemistry and Physics," R. C. Weast, Editor, p. E-103, CRC Press, Cleveland, OH (1979).
12. R. R. Dogonadse, in "Reactions of Molecules at Electrodes," N. S. Hush, Editor, p. 135, John Wiley and Sons, London (1971).
13. R. A. Marcus, *Ann. Rev. Phys. Chem.*, **15**, 155 (1964).



Breakdown Phenomena During the Growth of Anodic Oxide Films on Zirconium Metal

Influence of Experimental Parameters on Electrical and Mechanical Breakdown

Francesco Di Quarto, Salvatore Piazza, and Carmelo Sunseri

Istituto di Ingegneria Chimica, Università di Palermo, 90128 Palermo, Italy

ABSTRACT

Different aspects of the breakdown phenomena observed during the growth of anodic films on zirconium metal in aqueous solutions have been investigated. Two different mechanisms of breakdown are suggested as a result of the experimental observations. A mechanical breakdown, which is dependent upon the logarithm of the anodizing current density, has been observed in carbonate and sulfate solutions at low concentrations of salt or acid and/or low anodizing current densities. The appearance of small fissures in the ZrO_2 films is related to this type of breakdown. An electrical breakdown was observed in sulfamic acid solutions as well as in sulfate and carbonate solutions at high salt or acid concentrations and/or high current densities. In the case of electrical breakdown, the first spark voltage showed a significant dependence upon the value of current density only in carbonate and sulfate anion containing solutions. A possible explanation for this dependence is suggested in agreement with Christov's model, taking into account also the incorporation of anions into the films. The different influences of the electrolytic solutions upon both types of breakdown are presented and discussed.

Breakdown phenomena in solids have been the subject of research for many years (1, 2) because of the practical importance of solid dielectrics (2). In the case of dry systems, a reasonable agreement exists on the possible explanations of the breakdown phenomena (1-4). In wet systems, and particularly in MOE (metal-oxide-electrolyte) systems, further complications arise from the electrolyte interface. In this case, besides the influence of the dielectric thickness and magnitude of electric field, it is necessary to take into account other variables such as: (i) nature of the solutions and their resistivity; (ii) anodizing current density; (iii) incorporation of electrolytic species into the oxide films; (iv) parasitic side reactions at the oxide/electrolyte interface; and (v) existence of mechanical stresses during the growth of the films.

Owing to the possible influence of all these parameters in determining the breakdown phenomena in a MOE system, it has been very difficult to develop a theoretical model which could explain the general behavior of the breakdown for different MOE systems. In the case of the growth of anodic films on valve metals two different types of breakdown can be envisaged, according to the different experimental findings and the interpretative models proposed by different authors (5-16).

A mechanical breakdown has been suggested in those cases where a mechanical failure due to stress is the cause of the arrest of growth of the films. In this case, although the existence of stresses during the growth of the films is widely accepted (5-13), the agreement about the source of these stresses is less general. It has been attributed to: (i) hydration and dehydration of the films (5-6); (ii) presence of impurities (7) and flaws (8-10); (iii) a Pilling-Bedworth ratio (molar volume of the oxide/molar volume of the metal) higher than unity, or, more generally, changes in volume due to the conversion of metal to oxide (11-12); and (iv) electrostrictive effects (13). The influence of the electrolytic solution on this last type of breakdown has been predicted theoretically by Sato (13).

An electrical breakdown has been proposed in those cases where the arrest of growth process seems related to

the onset of phenomena of electronic conduction in the films with consequent light emission phenomena and/or gas evolution at the oxide/electrolyte interface.

Previous studies (14, 15) have excluded for breakdown possible mechanisms such as crystallization and thermal heating due to the Joule effect. On the contrary, it has been suggested that crystallization is a result of the breakdown. The hypothesis (16) that only solid-state properties of the oxide films control the breakdown phenomena has been definitely discarded, while it has been suggested that the main source of electrons is the oxide/electrolyte interface (14, 17, 18, 22).

In this work, we present some experimental results on the breakdown phenomena observed during the growth of ZrO_2 anodic films in different solutions and at various current densities.

In particular, we will show how the different kinds of breakdown observed on ZrO_2 films follow different phenomenological relationships. The influence of the anodizing parameters on both types of breakdown will be discussed on the basis of the available theories of breakdown in MOE systems.

Experimental

Zirconium of purity 99.8%+ (Goodfellow Metals, Cambridge, England) was used. Rods were sealed to Teflon cylinders with epoxy resin (TorrSeal, Varian Associates) or forced into heated Teflon cylinders (4.5 mm id). The area exposed to the electrolytic solution was 0.196 cm². The surface exposed to the solution was mechanically polished before each experiment with very fine abrasive papers, ultrasonically cleaned in distilled water, and then chemically etched. The chemical etching was in $HF:H_2O:HNO_3$ mixture (1:4:2 in volume) (8). During the etching, the electrode was rotated at constant rotation speed so that a better finish of the electrode surface was obtained.

The electrodes were anodized galvanostatically by using a Keithley Model 227 constant current generator. The cell voltages were measured by a digital multimeter and

the V_{cell} vs. time curves (V - t curves) were recorded on a X, Y, t recorder. Surface inspection, before and after the anodization, was made with a scanning electron microscope.

The counterelectrode was a Pt wire or a Zr foil. Solutions were prepared from analytical-grade reagents. All experiments were carried out at room temperature.

Experimental Results

The different types of breakdown phenomena were classified on the basis of the galvanostatic growth curves as well as of the morphological analysis performed by electron microscopy. In Fig. 1, we show three typical anodic growth curves, which display the different behavior observed during the anodization of zirconium electrodes in various electrolytes and in a range of current densities between 2 and 32 mA cm⁻². The slope of the growth curves changed with the c.d., with the electrolytic solutions, and with the film thickness, as reported in previous work (19). Curves 1a and 1b were typical of anodization processes performed, respectively, in NH₂SO₃H (0.1-1.5M) and in 1N H₂SO₄ solutions at any current density of anodization.

By decreasing the concentration of the anion and the anodizing current density in sulfate containing solutions the shapes of the growth curves became similar to that of curve 1c. The behavior depicted in Fig. 1c was typical of films grown in 0.1M Na₂CO₃ solution at any c.d. In 0.5M carbonate solution, the growth curves showed a behavior similar to that depicted in Fig. 1b at high anodizing current densities ($i \geq 8$ mA cm⁻²), while the behavior displayed in Fig. 1c was observed at low c.d.

The main difference between curves a, b, and c of Fig. 1 is the appearance in the last one of a shoulder well below the onset of sparking phenomena. The appearance of the shoulder also marked the beginning of a second straight-line behavior in the growth curve having a lower slope. It must be mentioned that the slope of the growth curves after the shoulder was related to the anodizing current

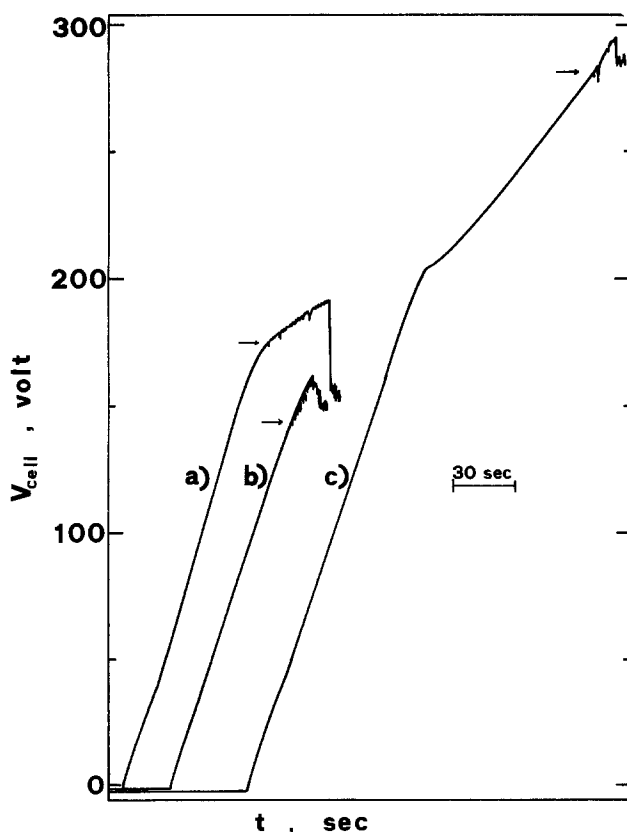


Fig. 1. Growth curves for films grown on zirconium metal at $i = 8$ mA cm⁻² in different solutions: (a) 1M NH₂SO₃H; (b) 1N H₂SO₄; (c) 0.1N H₂SO₄. The arrows mark the first spark occurrence.

density. In particular, the second slope was about one-half of the initial one in both solutions.

Using electron microscopy it was possible to associate the appearance of the shoulder in the V - t curves with the presence in the anodic films of very small fissures as shown in Fig. 2 (see also Fig. 5).

The presence of these fissures did not stop the growth of the films. The subsequent decrease of slope in the growth curves is interpreted in terms of the onset of a mechanical breakdown in the films well before the start of the sparking phenomenon. The cell voltage at which this phenomenon appears is defined as "mechanical breakdown voltage" (V_{mb}). The V_{mb} values were found to follow a relationship

$$V_{\text{mb}} = A_{\text{mb}} + B_{\text{mb}} \log i \quad [1]$$

where A_{mb} and B_{mb} are constants which depend on the electrolytic solution. As reported in Fig. 3, the coefficients A_{mb} and B_{mb} depend mainly upon the kind of anion in the solution, while the pH of electrolytic solution seems to have a negligible effect on both coefficients. A deviation from the behavior depicted in Eq. [1] was observed at high current densities in 0.1N H₂SO₄ solution.

In order to get more information on different aspects of the mechanical breakdown some experiments were focused on the dependence of V_{mb} upon the film thickness in various solutions.

For carbonate solutions, a nearly constant film thickness was calculated at the breakdown voltages both from the interference colors and by using the kinetic parameters of Fromhold's theory previously obtained for 0.5M Na₂CO₃ solutions (19).

In the range of c.d. reported in Fig. 3a, the film thickness at the different V_{mb} values was equal to about 4000Å. In the case of sulfate anion containing solutions the film thickness at the breakdown voltages generally increases with c.d., as reported in Table I.

An exception to this was the films formed in 0.1N H₂SO₄ solution for $i \geq 8$ mA cm⁻². For these films, a nearly constant critical thickness of about 3500Å was estimated on the basis of the interference colors of the films.

In Fig. 4, we show an electron micrograph typical of films with anodic growth curves similar to curves 1a and 1b in Fig. 1. Anodizing processes producing these curves showed all the features typical of the sparking phenomena (light emission, cell-voltage oscillations, noise) already described in the literature for different MOE systems [Ref. (17) and references therein]. As shown in Fig. 4, the surfaces of the electrodes are free of fracture, but in some areas a certain texture can be observed. Anodic films grown in similar conditions did not show such textured regions if the anodization process was stopped be-

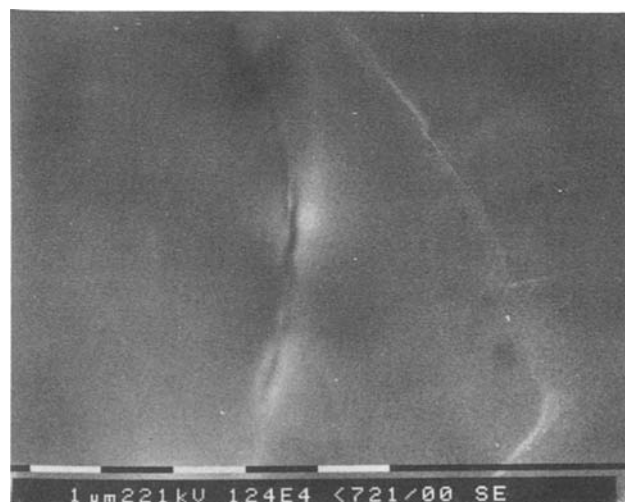


Fig. 2. SEM micrograph of a film grown in 0.1N Na₂CO₃ at $i = 16$ mA cm⁻² after the appearance of shoulder in the growth curve.

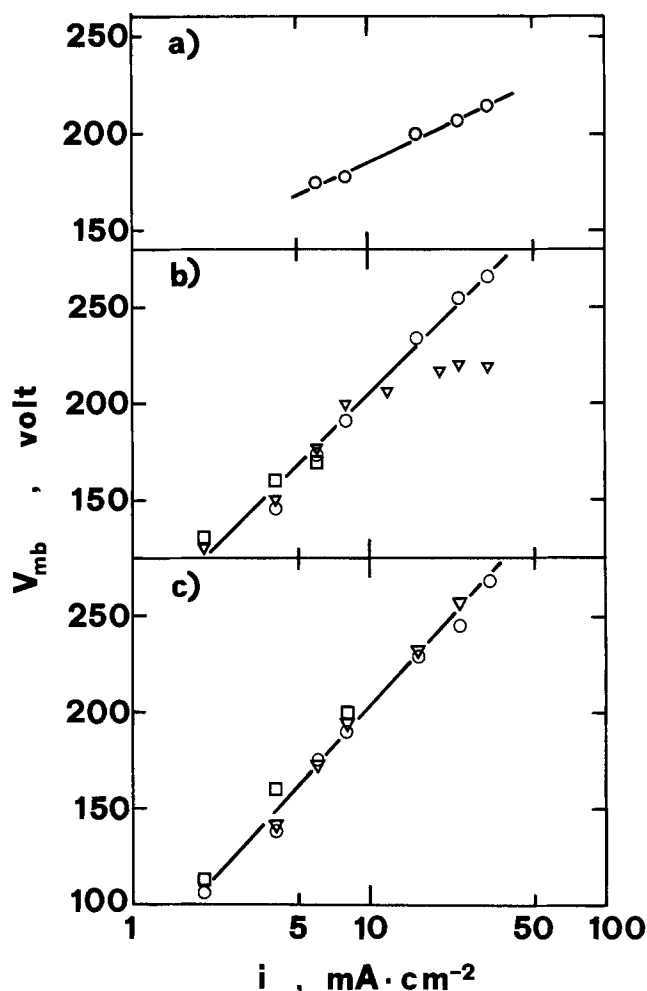


Fig. 3. Voltage of mechanical breakdown vs. anodizing current density for films grown in various solutions: (a) 0.1M Na_2CO_3 ; (b) H_2SO_4 (circles: 0.05N; triangles: 0.1N; squares: 0.5N); (c) K_2SO_4 (circles: 0.05N; triangles: 0.1N; squares: 0.5N).

fore the onset of sparking. X-ray analysis, performed on foils not chemically etched but anodized in the same solutions, showed clear evidence of crystallization only after prolonged sparking. We think the texture identifies thicker crystalline areas. These results must be taken with caution, because it is known from the literature that the crystallization of ZrO_2 films is strongly affected by the nature of the solution, the anodization technique, the thickness of the film, and the initial surface treatment (12, 20).

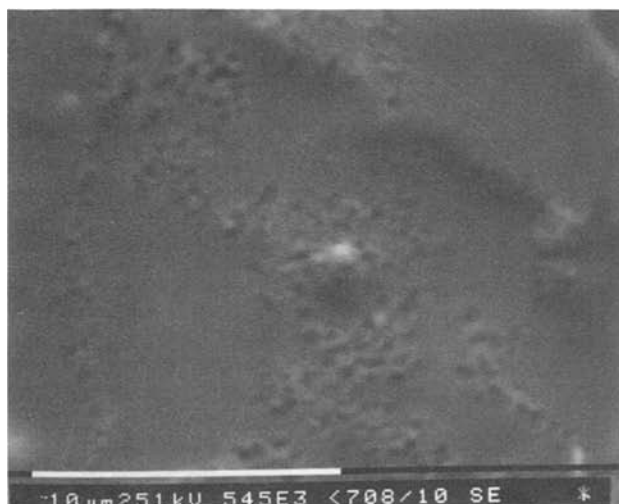


Fig. 4. SEM micrograph of a film grown in 1M $\text{NH}_2\text{SO}_3\text{H}$ at $i = 16 \text{ mA cm}^{-2}$ above the first spark voltage.

Table I. Film thickness values at the breakdown voltage calculated by means of Fromhold theory (26) (L_c^{calc}), and estimated on the basis of the interference colors (L_c^{exp}), for films grown in different solutions at various c.d.'s. A mean refractive index equal to 2.2 was assumed for the estimation of L_c^{exp}

i (mA cm^{-2})	H_2SO_4 0.05N		K_2SO_4 0.1N	
	L_c^{exp} (\AA)	L_c^{calc} (\AA)	L_c^{exp} (\AA)	L_c^{calc} (\AA)
24	4000	3970	3900	4000
16	3750	3820	3700	3800
12	3600	3630	—	—
8	3250	3380	3300	3420
6	3150	3210	—	—
4	2800	2830	2700	2760

* The kinetic parameters are assumed equal to those already published for 0.1N H_2SO_4 solution (19).

The sparking phenomenon could be observed also in the case of fractured films as shown in Fig. 5. In this case, the sparking seems to occur preferentially along the edges of the fissures.

The values of the cell voltage at which sparking began (V_{FS}) were identified either by visual inspection or from the first oscillation recorded in the galvanostatic $V-t$ curves (see Fig. 1). This V_{FS} value was reproducible, and the V_{FS} values used here are the average for different experiments performed under similar conditions (a very small influence of the surface finish was observed).

In Fig. 6, we report the dependence of V_{FS} on the value of current density for different electrolytic solutions. A constancy in the V_{FS} value is observed in sulfamic acid solutions, while a linear dependence on c.d. value is observed for carbonate and sulfate solutions. Moreover, the linear dependence is valid, regardless of the kind of anodic growth curves obtained, that is, types a, b, c in Fig. 1.

In Fig. 7, is reported the dependence of V_{FS} on the resistivity of the electrolytic solutions. As reported for other MOE systems (21-24) the experimental values (at a fixed i) follow a relationship

$$V_{\text{FS}} = a + b \log \rho \quad [2]$$

where a and b are constants and ρ is the resistivity of the electrolytic solution. For films grown in $\text{NH}_2\text{SO}_3\text{H}$ solutions, the a and b values are independent of the anodizing current density values according to the results of Fig. 6. In the case of sulfate containing solutions, the a and b constants are dependent on the anodizing current as reported in Table II.

In Table III, we report the estimated film thicknesses and the average electric fields at the first spark voltages for different sulfamic acid solutions at various c.d.'s.

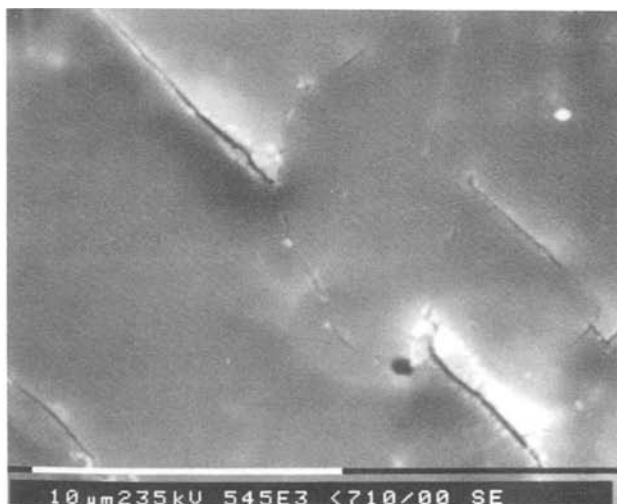


Fig. 5. SEM micrograph of a film grown in 0.1N H_2SO_4 at $i = 8 \text{ mA cm}^{-2}$ above the first spark voltage.

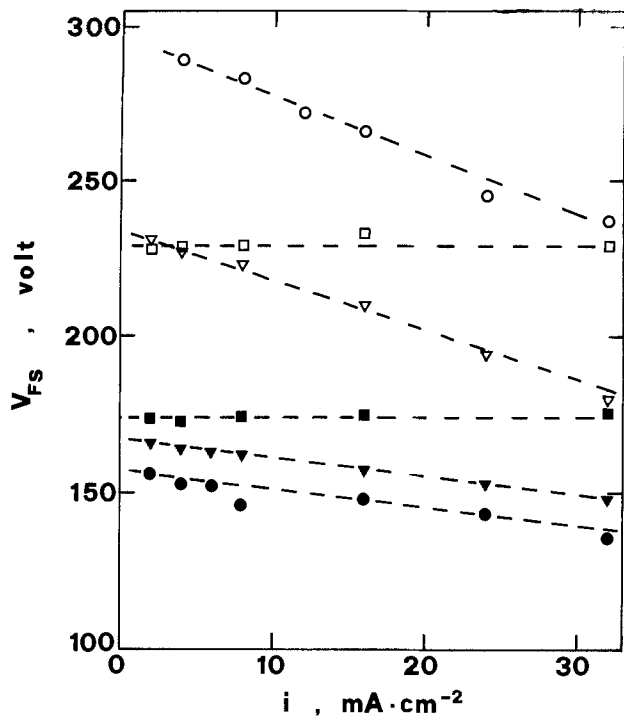


Fig. 6. First spark voltage vs. anodizing current density for films grown in: (○) 0.1N H₂SO₄; (□) 0.1M NH₂SO₃H; (▽) 1N Na₂CO₃; (■) 1M NH₂SO₃H; (▼) 1N K₂SO₄; (●) 1N H₂SO₄.

Discussion

The experimental results outlined here for the Zr/ZrO₂/electrolyte system provide new information on the breakdown of anodic oxide films grown in various electrolytic solutions. We stress the fact that two different kinds of phenomena are involved in the breakdown of the system. They are not mutually exclusive, but these two phenomena are governed by experimental parameters in different ways.

In the solutions where mechanical breakdown occurs, the most important parameter in determining the V_{mb} value seems to be the anodizing current density. This influence can be explained by assuming that mechanical failure of the films occurs when a critical thickness, L_c , is reached at which the internal stresses exceed the

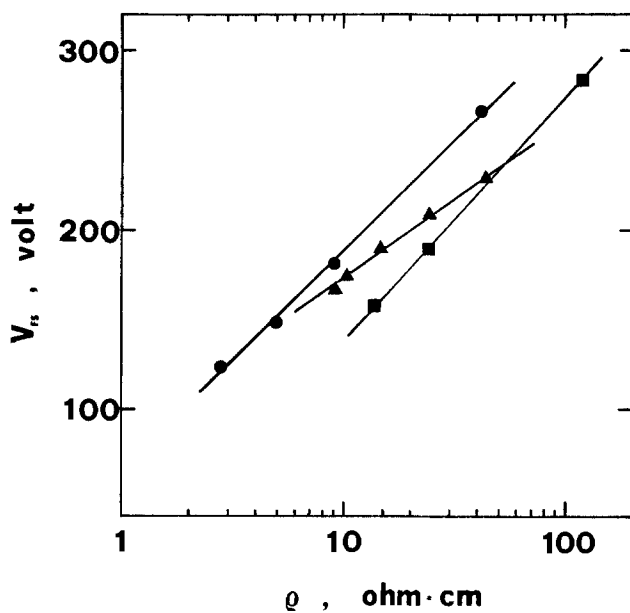


Fig. 7. First spark voltage vs. electrolyte resistivity for films grown in: (●) H₂SO₄ at $i = 16 \text{ mA cm}^{-2}$; (■) K₂SO₄ at $i = 16 \text{ mA cm}^{-2}$; (▲) NH₂SO₃H at $2 \leq i \leq 32 \text{ mA cm}^{-2}$.

Table II. Values of the a and b constants of Eq. [2] for films grown in sulphate and sulphamate containing solutions at different current densities

Electrolyte	i (mA cm ⁻²)	a (V)	b (V)
H ₂ SO ₄	32	71	102
H ₂ SO ₄	24	74.3	104.5
H ₂ SO ₄	16	66.5	122.6
H ₂ SO ₄	8	58.5	137
H ₂ SO ₄	6	54.7	140
H ₂ SO ₄	4	60	140.6
K ₂ SO ₄	32	5.2	120.1
K ₂ SO ₄	24	15.7	122
K ₂ SO ₄	16	-6.3	143.4
K ₂ SO ₄	8	-15.1	154
K ₂ SO ₄	6	-8.3	153.5
NH ₂ SO ₃ H	2-32	81	90

Table III. Thickness of film and "average" electric fields, calculated by means of Fromhold theory (26) at the first spark voltage, for films grown in NH₂SO₃H solutions. The kinetic data, E_0 , and E^* , were those reported in Ref. (19) for the 0.1M solution, while in the case of 1M solution, they were calculated in the same manner as in Ref. (19).

Electrolyte	i (mA cm ⁻²)	D_{FS} (Å)	$\bar{E} = V_{FS}/D_{FS}$ (MV cm ⁻¹)
0.1M NH ₂ SO ₃ H	32	3950	5.79
0.1M NH ₂ SO ₃ H	16	4020	5.69
0.1M NH ₂ SO ₃ H	8	4100	5.58
0.1M NH ₂ SO ₃ H	4	4380	5.22
1M NH ₂ SO ₃ H	32	2910	5.97
1M NH ₂ SO ₃ H	16	3000	5.79
1M NH ₂ SO ₃ H	8	3120	5.58

mechanical strength of the film. The critical thickness is related to the breakdown voltage by

$$V_{mb} = \bar{E} \cdot L_c \quad [3]$$

where \bar{E} is the average anodizing electric field strength.

According to this hypothesis, the internal stresses must increase with the film thickness. This appears in conflict with the results of Leach and co-workers (8, 12), which show nearly constant stresses in ZrO₂ films formed on chemically etched Zr anodized above 80V in ammonium borate as well as in carbonate solutions. Moreover, they have shown that the stresses measured at different c.d.'s decrease with increasing c.d. in a range of current densities analogous to that exploited in our measurements. It must be stressed, however, that in our experimental conditions bending was biaxial rather than uniaxial (8, 12).

If the results obtained by Leach and co-workers are representative of the behavior of ZrO₂ films grown in our conditions, an explanation is needed for the mechanical breakdown of ZrO₂ films in the presence of a constant compressive stress. We suggest that the stress distribution normal to the surface of the film is not uniform, but rather changes with thickness in such a way that the average value remains constant.

In this frame, the results obtained in sulfate solutions are quite well explained by saying that, according to Leach *et al.*, greater mean stresses and anodizing ratios ($\Delta D/\Delta V$) combine to lower the V_{mb} values at low c.d.'s.

In the case of breakdown at constant film thickness (0.1N H₂SO₄ solution at $i \geq 8 \text{ mA cm}^{-2}$ and carbonate solution), the interpretation of the mechanical breakdown requires further hypothesis about the effect of anion incorporation on the mechanical properties of ZrO₂ films grown in these solutions. We suggest that the level of impurity content into the films lowers the mechanical strength of these films. This suggestion is based on the following findings: (i) in sulfamic acid solutions, where the incorporation phenomenon has been supposed to be absent (19), higher film thicknesses were reached without appearance of mechanical breakdown (compare Tables I and III), (ii) according to Leach and Pearson [see

Fig. 5 and 6 of Ref. (12)], lower compressive stresses are observed in carbonate solution in a range of c.d. where higher anion incorporation occurs (27); as reported in Fig. 5 of Ref. (12), the compressive stress measured in carbonate solution at the critical thickness is halved by increasing c.d. from 6 to 10 mA cm⁻², and (iii) according to our results, the mechanical breakdown occurs in carbonate solution at constant thickness ($L_c \cong 4000\text{\AA}$) for films grown at $i \geq 6$ mA cm⁻², which is the range of c.d. where a steep increase of carbonate incorporation has been observed (27).

The same interpretative hypothesis could explain the experimental findings in 0.1N H₂SO₄ solution at $i \geq 8$ mA cm⁻², if the dependence of internal stresses upon c.d. is supposed to be analogous to that observed in ammonium borate and carbonate solutions. Further investigations on these aspects are necessary before reaching a firm conclusion.

The different values of A_{mb} and B_{mb} obtained for films grown in different electrolytic solutions should reflect the complex role played by the electrolyte in the kinetics of growth as well as in the mechanical properties of the films due to the incorporation of anions. A more quantitative analysis of the experimental data should need a knowledge of the laws of variation of internal stresses with oxide thickness in each solution at each current density.

At this point, it is important to note that the observed absence of any influence of the resistivity of the electrolytic solution on V_{mb} values suggests that no direct effect should be assigned to the solution in determining the mechanical breakdown of ZrO₂ anodic films, although an indirect effect can arise through the anion incorporation phenomenon (27, 28). By taking into account all of these findings, it would appear that the most likely source of stresses during the growth of these films at the metal/oxide interface is the volume change accompanying oxide formation. A Pilling-Bedworth ratio higher than unity [$V_{molar}^{ZrO_2}/V_{molar}^{Zr} = 1.56$ (29)] and a very low transport number of cation (30) suggest the existence of compressive stresses inside the films. The increase, with increasing film thickness, of local stresses to a critical value which should be dependent only on the bulk properties of ZrO₂ films, then causes the mechanical failure of the films. In fact, the above-mentioned absence of influence of the solution resistivity seems to exclude any effect of the interfacial tension on the mechanical breakdown of the investigated systems.

For the sparking phenomena, the experimental results fall into one of two groups, according to the nature of the electrolytic solution: (i) nonincorporating solutions [sulfamic acid solutions (19, 31)] in which there is no influence of the anodizing current density on the V_{FS} values, and (ii) incorporating solutions [sulfate and carbonate containing solutions (27)] which show a clear influence of the anodizing current density on V_{FS} values.

A linear dependence of V_{FS} on the logarithm of the solution resistivity was found experimentally for both kinds of solutions.

According to the electron ionization avalanche mechanism, an increase of the internal electric field and/or the dielectric film thickness enhances the multiplication of electrons which are injected at the cathode (in MOE systems, the oxide/electrolyte interface). This is in qualitative agreement with the results in sulfamic acid solutions, where sparking occurred with thinner films in the presence of a higher anodizing electric field (see Table III).

The strong influence on the V_{FS} values of the electrolytic solution, which is reflected in the V_{FS} vs. $\log \rho$ relationship, suggests that the electron injection levels at the oxide/electrolyte interface affect the sparking phenomenon. A quantitative analysis of sparking phenomena requires a knowledge of the laws governing electronic injection at this interface for each MOE system. However, a preliminary analysis on the basis of Ikonopisov's model (17) of electrical breakdown for MOE systems shows that

present experimental results are in agreement with the essential features of this model. In fact, both the nearly constant values of V_{FS} with the ionic current density and the V_{FS} vs. $\log \rho$ relationship agree with the theoretical predictions of the model. However, the discrepancies between the model and the experimental results obtained in sulfate and carbonate containing solutions (chiefly the strong dependency of V_{FS} on the anodizing current) could be associated with the incorporation of sulfate and carbonate anions (27, 28) which could modify the solid-state properties of the anodic films.

It has been reported that: (i) the amount of anion incorporation in ZrO₂ anodic films is strongly dependent on the c.d. and the local pH of solution (12, 27); (ii) the value of dielectric constant decreases with increasing anion incorporation (19, 33, 34).

These facts help explain the results in Fig. 6 for carbonate and sulfate solutions if we recall that according to Ikonopisov's model (17) the electron injection level at the oxide/electrolyte interface controls the V_{FS} value. Moreover, in the model recently proposed by Christov (18) the electronic current injected at this interface can be written

$$i_{el} = i_0 \exp \alpha \left(\frac{\bar{E}}{\epsilon_i} \right)^{1/2} \quad [4]$$

where i_0 and α are constants which depend only on the temperature and on the oxide/electrolyte interface and ϵ_i is the dielectric constant of the film.

Perhaps the main effect of anion incorporation is to decrease ϵ_i and hence increase the electron injection level at the oxide/electrolyte interface in such a way as to make the dependence of V_{FS} on the applied current density more pronounced. According to this, the results of Fig. 6 suggest that the influence of c.d. on anion incorporation should be stronger in more dilute acidic solutions (0.1N H₂SO₄) as well as in concentrated neutral solutions of carbonate. In this last case, a very strong influence of the c.d. on the incorporation phenomenon has been reported (27).

Conclusions

The results of this work illustrate the complex nature of the breakdown processes in MOE systems. It has been shown that both "mechanical" and "electrical" breakdown can occur during the anodization process. Each type of breakdown occurs in a different way and depends on the anodizing parameters in a different way. In the case of ZrO₂/electrolyte systems, it has been shown that the conditions favoring electrical breakdown are high c.d. and/or low electrolytic resistivity. The appearance of electrical breakdown is always associated with a rapid end to film growth. In the case of mechanical breakdown, although the rate of film growth is decreased, a second linear but slower dV/dt relationship is observed, until sparking eventually puts an end to film growth.

The phenomenon of mechanical breakdown suggest fracture brought about by critically large internal stresses, associated with the volume increase when metal is converted to oxide.

The incorporation of anion, which affects mechanical breakdown through a mechanism of relaxation of internal stresses (11) and by changing the mechanical strength of the films, is thought to influence the electrical breakdown of the films in such a manner as to increase the electronic injection current at the oxide/electrolyte interface.

A better knowledge of the electron injection process at this interface during the film growth seems necessary for improving the quantitative agreement between experimental data and theoretical analysis of the sparking phenomena.

Acknowledgments

This work has been partially supported by C.N.R. (Rome) and M.P.I. (Rome). Part of this work has been performed by S. Piazza in partial fulfillment of the require-

ments for the Chemical Engineering degree at the University of Palermo, March 1981.

Manuscript submitted June 21, 1983; revised manuscript received Aug. 1, 1984.

The Università di Palermo assisted in meeting the publication costs of this article.

REFERENCES

1. A. Güntherschultze, *Phys. Z.*, **24**, 212 (1923).
2. H. Frölich, *Rpt. Prog. Phys.*, **6**, 143, (1939), and references therein.
3. F. Forlani and N. Minnaja, *Phys. Status Solidi*, **4**, 311 (1964).
4. J. J. O'Dwyer, *This Journal*, **116**, 239 (1969).
5. D. A. Vermilyea, *ibid.*, **110**, 345 (1963).
6. R. S. Alwitt, A. J. Breen, and J. S. L. Leach, in "Oxide-Electrolyte Interfaces," R. S. Alwitt, Editor, p. 265, The Electrochemical Society Softbound Proceedings Series, Princeton, NJ (1973).
7. S. F. Bubar and D. A. Vermilyea, *This Journal*, **113**, 892 (1966).
8. L. C. Archibald and J. S. L. Leach, *Electrochim. Acta*, **22**, 15 (1977).
9. L. C. Archibald and J. S. L. Leach, *ibid.*, **22**, 21 (1977).
10. V. R. Howes, *Corros. Sci.*, **14**, 491 (1974).
11. D. H. Bradhurst and J. S. L. Leach, *This Journal*, **113**, 1245 (1966); *ibid.*, **113**, 1284 (1966).
12. J. S. L. Leach and B. R. Pearson, in "Proceedings of the 7th International Congress on Metallic Corrosion," p. 151, Rio de Janeiro (1978).
13. N. Sato, *Electrochim. Acta*, **16**, 1683 (1971).
14. J. Yahalom and J. Zahavi, *ibid.*, **16**, 603 (1971).
15. J. Yahalom, in "Oxide-Electrolyte Interfaces," R. S. Alwitt, Editor, p. 288, The Electrochemical Society Softbound Proceedings Series, Princeton, NJ (1973).
16. A. K. Vijn, *Corros. Sci.*, **11**, 411 (1971).
17. S. Ikonopisov, *Electrochim. Acta*, **22**, 1077 (1977).
18. S. G. Christov, *J. Electroanal. Chem.*, **105**, 275 (1979).
19. F. Di Quarto, S. Piazza, and C. Sunseri, *This Journal*, **130**, 1014 (1983).
20. B. Cox, *ibid.*, **117**, 654 (1970).
21. S. Ikonopisov, A. Girginov, and M. Machkova, *Electrochim. Acta*, **24**, 451 (1979).
22. A. Güntherschultze and H. Betz, "Electrolyt-Kondensatoren," pp. 116-122, Technischer Verlag Herbert Cram, Berlin (1952).
23. G. C. Wood and C. Pearson, *Corros. Sci.*, **7**, 119 (1967).
24. F. J. Burger and J. C. Wu, *This Journal*, **118**, 2039 (1971).
25. N. Cabrera and N. F. Mott, *Rpt. Prog. Phys.*, **12**, 163 (1949).
26. A. T. Fromhold, Jr., *This Journal*, **124**, 538 (1977).
27. G. T. Rogers, P. H. G. Draper, and S. S. Wood, *Electrochim. Acta*, **13**, 251 (1968).
28. J. C. Banter, *This Journal*, **114**, 508 (1967).
29. N. Baba, *J. Less-Common Met.*, **43**, 295 (1975).
30. J. A. Davies, B. Domeij, J. P. S. Pringle, and F. Brown, *This Journal*, **112**, 675 (1965).
31. R. Piontelli, in "Symposium Proceedings on Sulphamic Acid and its Electrometallurgical Applications," Milan, May 1966, pp. 175, 437, Associaz. Ital. Metall., Milano (1966); L. Peraldo Bicelli, *ibid.*, pp. 19-27.
32. L. Young, *Trans. Faraday Soc.*, **55**, 632 (1959).
33. F. Di Quarto, A. Di Paola, and C. Sunseri, *This Journal*, **127**, 1016 (1980).
34. J. J. Randall, W. J. Bernard, and R. R. Wilkinson, *Electrochim. Acta*, **10**, 183 (1965).

Plasma Etching of Oxygen Containing Titanium Silicide Films

F.Y. Robb*

Motorola, Incorporated, Process Technology Laboratory, SRDL, Phoenix, Arizona 85008

ABSTRACT

Anisotropic etching of titanium silicide is essential if its low resistivity gate properties are to be utilized on scaled MOS devices. CCl_4 and CF_4 plasmas, as well as ion milling, were used to etch composite titanium silicide/polysilicon films, with each displaying definite drawbacks. CCl_4 plasmas yielded rough etching and etch residue, presumably due to the high oxygen content of the silicide film and the relatively high selectivity (low oxide etch rate) of the etch. CF_4 reactive ion etching and ion milling produced smooth etching but lacked the selectivity to stop on thin underlying gate oxides. A combination of these processes, however, provided successful anisotropic patterning of such structures. A nonselective, smooth etching CF_4 reactive ion etch was used to etch through the silicide layer, followed by a higher selectivity Cl_2 plasma etch through the underlying polysilicon down to the thin gate oxide.

Anisotropic etching of titanium silicide is essential if its low resistivity is to be utilized on scaled MOS devices.

Increases in packing density and complexity of MOS devices have increased the importance of the interconnect technology (1, 2). With the sheet resistance of even the most heavily doped polysilicon greater than $15 \Omega/\square$, the advantages of further scaling will soon be offset by the interconnect resistance at the gate level. The selection of a lower resistivity gate material, together with the shortening of interconnect lengths by circuit designers, is essential in order to take advantage of the higher switching speeds of scaled down devices.

The low resistivity refractory metal silicides, with sheet resistances over an order of magnitude lower than polysilicon (3, 4), offer an attractive alternative. Replacing polysilicon entirely with the silicide, however, entails major changes in device design and processing and, perhaps most importantly, introduces an interface at the gate oxide of questionable stability. Thus, the more conservative approach has been to replace enough of the doped polysilicon with the silicide to achieve the desired resistance goal, but not so much as to cause a change in the ef-

fective metal-semiconductor work function (and thereby gate threshold voltage).

Since titanium silicide (TiSi_2) has one of the lowest resistivities of the refractory metal silicides, very low resistivity titanium polycide gates can be achieved. In fact, a titanium polycide structure of 1500\AA of silicide over 1500\AA of polysilicon has a composite resistance of 1 to $2 \Omega/\square$ (5), more than an order of magnitude lower than straight doped polysilicon.

The etchability of titanium silicide is, of course, one of the prime processing considerations. Anisotropic etching is essential in order to produce the fine patterns required for scaled MOS devices.

Little information is available on the etching of titanium silicide. Wang *et al.* (6) have reported the successful use of chlorine plasma etching for the patterning of composite TiSi_2 /polysilicon gate structures, but found an extreme sensitivity to contamination in the film and required that the oxygen level in the film be less than 0.5%. In practice, obtaining such a low oxygen content in titanium silicide films is difficult and perhaps unnecessary, as resistances as low as $1 \Omega/\square$ have been obtained on films containing 5% oxygen (5).

* Electrochemical Society Active Member.

The plasma-etch characteristics of oxygen containing titanium silicide films is the subject of the present study. CCl_4 and CF_4 reactive ion etching, as well as ion milling, will be detailed and contrasted. Successful anisotropic etching could not be accomplished in any one-step etch; it required two etch steps. The first step used a low silicon-to-oxide etch-rate ratio to etch smoothly through the oxygen containing silicide. The second step, in contrast, utilized a high silicon-to-oxide etch-rate ratio to pattern the underlying polysilicon and stop on the thin gate oxide.

Experimental

Etch systems.—Several different etch systems were used in this study.

CCl_4 plasma etching was studied in a single-wafer planar reactor. The top electrode was powered (13.56 MHz), while the etching wafer was placed on the lower grounded electrode. An upper-to-lower electrode-area ratio of 2 to 1 was utilized. All surfaces exposed to the plasma were passivated with an anodized aluminum coating. Wafer cooling was provided by a cold (10°C) plate physically affixed to the lower electrode. A gas mixture of 8 sccm CCl_4 , 7 sccm Ar, 8 sccm N_2 , and 3 sccm H_2 , at $300\ \mu\text{m}$ with $1\ \text{W}/\text{cm}^2$ was used. This process was developed for anisotropic etching of N^+ polysilicon.

CF_4 etching was performed in two reactors.

Initial CF_4 studies utilized a laboratory-scale diode configured reactor. The wafers were positioned on the smaller powered (13.56 MHz) electrode, while the outer chamber walls acted as the grounded anode. The chilled (10°C) cathode, which held nine 3 in. substrates, was covered with a thin silicon plate to minimize metallic contamination. A flow rate of 7 sccm CF_4 , with a $100\ \mu\text{m}$ pressure, and $0.55\ \text{W}/\text{cm}^2$ was used.

The temperature dependence of CF_4 etching was measured in a Perkin-Elmer Omni-Etch Cornerstone single-wafer etcher, where the wafers were physically clamped to a temperature-controlled lower electrode. The system had a powered (200 kHz) porous graphite top electrode. A flow rate of 50 sccm CF_4 , with a $800\ \mu\text{m}$ pressure, and $1.5\ \text{W}/\text{cm}^2$ was used.

The Cornerstone was also used for low frequency Cl_2 plasma etching of polysilicon in the second step of the two-step polycide etch process. Process conditions used were 100 sccm Cl_2 , $800\ \mu\text{m}$ pressure, $0.7\ \text{W}/\text{cm}^2$, and a 5°C lower electrode. No undercutting of even highly doped N^+ polysilicon was observed.

All plasma-etch systems used standard rotary pumps and maintained base pressures of between 20 and $40\ \mu\text{m}$. Mass flowmeters were used to monitor gas flow and pressure was measured with capacitance manometers.

Ion milling was performed in the Veeco Microetch system, which utilized a 10 in. diffusion pump and a Kaufman-type ion gun. Typical milling conditions were $0.4\ \text{mA}/\text{cm}^2$, 600V, and 9.0×10^{-4} torr argon pressure. Milling angles between 0° and 15° were studied.

Sample preparation and analysis.—Titanium silicide films were cosputtered in a Sputtered Films, Incorporated, Research System with a Ti:Si ratio of 1:2.2. At this composition, the resistivity after anneal was about $17\ \mu\Omega \cdot \text{cm}$.

Auger electron spectroscopy (AES), in conjunction with sputter profiling, was used to analyze the samples as a function of depth. As shown in Fig. 1, deposited films were uniform, incorporated an atomic oxygen concentration of about 5%, and had a native oxide thickness of between 50 and $100\ \text{\AA}$. After anneal, the bulk oxygen content decreased slightly, as apparently some of the oxygen diffused to the surface to react with Ti or Si. The surface oxide thickness after anneal was about twice that of the nonannealed films.

Unannealed pure titanium films, sputter-deposited in the same system, were etched for comparison. AES profiling showed a similar oxygen content and native oxide as for the unannealed silicide.

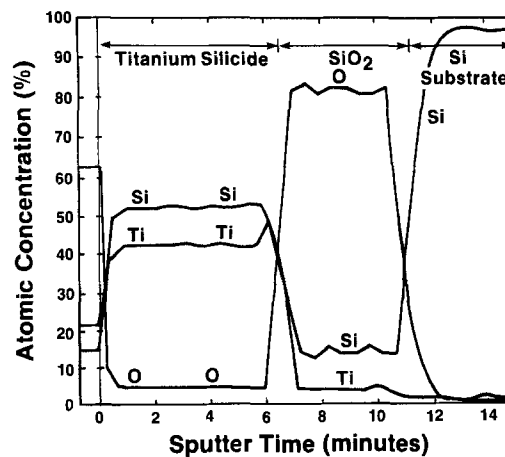


Fig. 1. Auger depth profile of an as-deposited $\text{TiSi}_{2.2}$ film. This film was deposited directly on thermal oxide.

The TiSi_2 film was typically $1500\text{--}2000\ \text{\AA}$ thick and deposited directly on a $2000\ \text{\AA}$ thick polysilicon film. Underlying the polysilicon was gate oxide. The polysilicon was phosphorus doped via either standard ion-implantation techniques or by 950°C PH_3 diffusions. In most cases, no annealing of the $\text{TiSi}_2/\text{poly}$ was done prior to etch, although where specified a 950°C , 30 min N_2/H_2 anneal was utilized. On these samples, a $1000\ \text{\AA}$ CVD oxide cap was deposited on top of the silicide to stop out-diffusion of phosphorus from the underlying polysilicon. The cap was removed via CHF_3 reactive ion etching after photoresist masking but before subsequent polycide etching.

KTI II and AZ-1350J positive photoresists, as well as trilevel (7, 8) plasma oxide/HPR-204 masks, were used to produce patterned samples.

Analytical techniques.—Silicide and resist rates were calculated from etch depth measurements made on the Tencor 10-0020 Alpha Step. Polysilicon and oxide rates were calculated from thickness measurements made on an IBM 7840 Film Thickness Analyzer.

The surface roughness as a function of the etch technique was quantified with reflectance data from the IBM 7840. The reflectance of each sample was measured and plotted as a function of wavelength from 4300 to $7000\ \text{\AA}$. In order to simplify data reporting, an "average" reflectivity was calculated from the maximum and minimum reflectances, as shown below

$$R = \frac{R_{\text{max}} + R_{\text{min}}}{2}$$

All reflectivities are reported as a percentage of an evaporated aluminum standard measured at the same time.

Cross-sectional scanning electron micrographs (SEM's) of patterned samples were utilized to determine etch anisotropy.

AES was used to analyze the cleanliness of etched surfaces.

Results and Discussion

CCl_4 etching.—Table I summarizes the etch data from the single-wafer etcher. The unannealed silicide etched at about the same rate as polysilicon, whereas the annealed silicide etched about 20% more slowly. In addition, the pure titanium etch rate was considerably higher than that of either polysilicon or the silicide. The fast titanium rate was unexpected, considering the reported volatilities of the expected etch products. SiCl_4 , the more volatile product, has a vapor pressure of 1 torr at -63.4°C , while TiCl_4 has a similar vapor pressure at -13.9°C (9).

A simple evaporation model allows an estimate of the maximum TiSi_2 etch rate achievable from evaporation only. The model assumes thermal equilibrium, so that the number of molecules condensing must equal the number evaporating. From simple kinetic theory, the number condensing is assumed to be $1/4 n\bar{v}$, where n is the num-

Table I. CCl_4 plasma etch data from the single-wafer etcher with 8 sccm CCl_4 , 7 sccm argon, 8 sccm N_2 , and 3 sccm H_2 , a 300 μm pressure and 1 W/cm^2

Film	Etch rate ($\text{\AA}/\text{min}$)	Etch residue	Anisotropy* (with resist mask)
Titanium silicide			
Unannealed	2300	Dense	Good
Annealed	1800	Moderate	Good
Polysilicon	2200	None	Excellent (undoped) Good (N^+ poly)
Titanium	3400	Dense	Good
Thermal SiO_2	350	—	—
Positive resist	800	—	—

* "Excellent" means zero undercut with 50% overetch. "Good" means zero undercut with 10% overetch and slight notching with 50% overetch. "Fair" means very slight undercut with 10% overetch.

ber of molecules per cubic centimeter and \bar{v} is the average molecular speed. Using this model and the above vapor-pressure data, a maximum TiSi_2 etch rate of $10^7 \text{\AA}/\text{min}$ is calculated. The poor agreement with the measured etch rate of 2300 $\text{\AA}/\text{min}$ indicates that evaporation is not the rate-limiting step of the etch mechanism.

Figure 2 shows composite titanium silicide/polysilicon films etched in the CCl_4 process. The anisotropy of the CCl_4 etch was good, with no undercutting observed for a 10% overetch and only very slight notching with a 50% overetch. Etch residue, however, plagued the etch. The

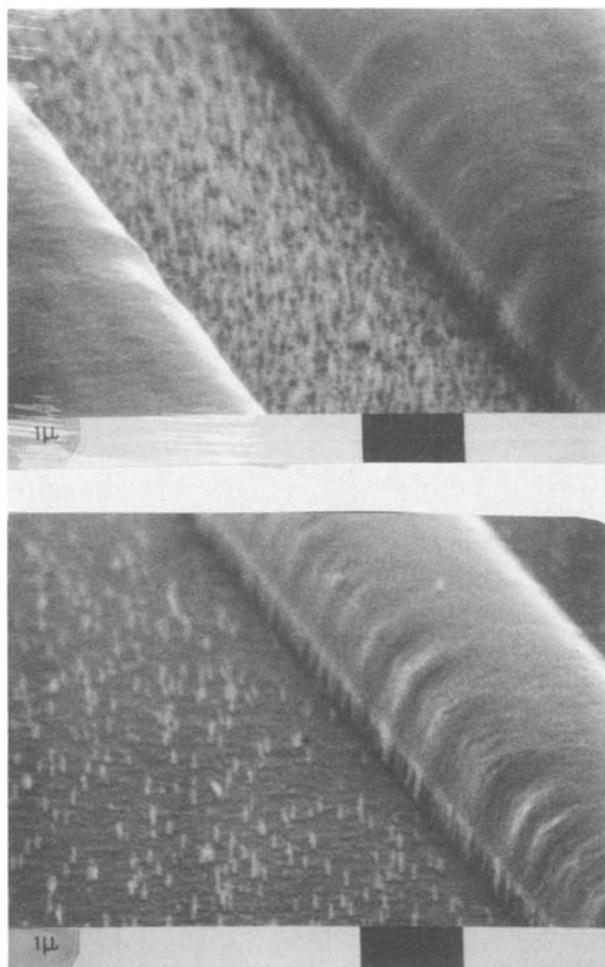


Fig. 2. Composite 2 k\AA titanium silicide/2 k\AA polysilicon films etched in the CCl_4 process. The bottom film was annealed and etched in CHF_3 to remove its CVD oxide cap, before the CCl_4 etch. Both samples were given a 10% overetch. The resist mask remains to demonstrate anisotropy.

residue was presumed to be simply unetched polysilicon, since Auger analysis of etched surfaces found only silicon, oxygen, and carbon. Because N^+ poly was used for the polycide gate, the residue provided conductive paths and was therefore unacceptable. Although longer overetches somewhat reduced the residue height and density, the thin underlying gate oxide prohibited this.

The etch residue was attributed to rough etching of the TiSi_2 layer. Reflectivity, which provides a quantitative measure of the roughness is plotted as a function of etch depth in Fig. 3. Within experimental error, no differences can be seen between the unannealed silicide and pure titanium films. Both became extremely rough as etching proceeded. This roughness, which was then replicated into the underlying polysilicon layer, resulted in the etch residue. The annealed silicide, surprisingly, etched much more smoothly. In addition, the reflectivity of virgin polysilicon as a function of depth is also plotted for comparison and shows that polysilicon films by themselves etched quite smoothly.

The rough etching was attributed to both the presence of a native oxide and to the relatively high oxygen content of titanium containing films. Auger analysis revealed that all the titanium containing films had more than an order of magnitude more oxygen than polysilicon. In addition, although the thickness of the native oxide on both polysilicon and unannealed TiSi_2 films was comparable (50 \AA), the oxide on the silicide contained titanium. The "toughness" of titanium oxide is well known to ion millers (10), as it is reported to have one of the lowest known milling rates.

The relatively low oxide etch rate of the CCl_4 process meant submicron sized "oxide" inclusions in/on the film would act as micromasks, blocking etching of the underlying material. Rough etching, and ultimately etch residue, would result.

The role of the bulk vs. surface oxide was separated by comparing the two samples shown in Fig. 2. The annealed sample, which was given a CHF_3 pre-etch to remove its CVD oxide cap (and would also remove any native oxide), showed a much cleaner etched surface than the unannealed sample. A similar CHF_3 pre-etch of unannealed films also produced cleaner etching. Since both films still yielded etch residues even after native ox-

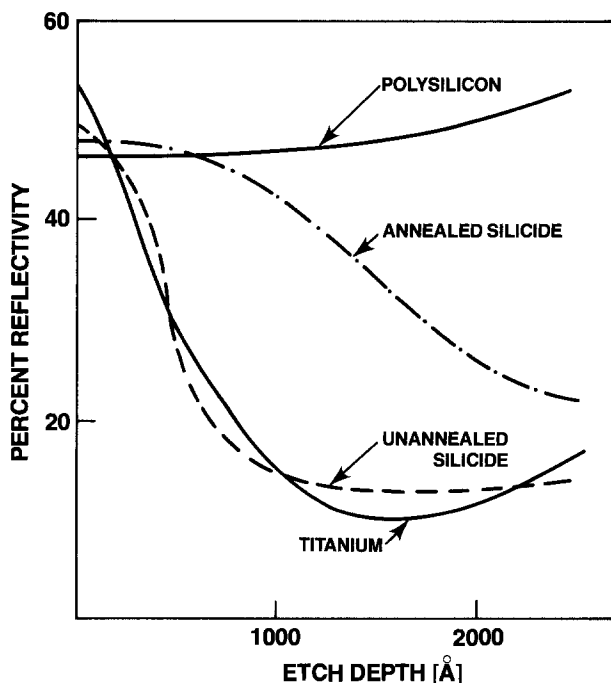


Fig. 3. Reflectivity as a function of etch depth for the CCl_4 plasma etch. The silicide films were 2 k\AA titanium silicide/2 k\AA polysilicon. The polysilicon and pure titanium films were 4 k\AA and deposited directly on 1 k\AA gate oxide.

ide removal, however, bulk oxides as well as surface oxides contribute.

The use of lower selectivity etches (those with higher oxide etch rates) to eliminate the rough etching and etch residues is expanded below. Both ion milling, with silicon-to-oxide selectivities on the order of 1/1, and CF_4 reactive ion etching, where the selectivity was even less than 1/1, are considered.

Ion milling.—Argon ion milling was investigated as a function of the incidence angle as it was varied from 0° to 15° . Within experimental error, the etch rates of titanium silicide, silicon dioxide, and positive resist did not vary with angle in this range and were 170, 200, and $125 \text{ \AA}/\text{min}$, respectively. In addition, the silicide rate did not depend on whether the film was annealed prior to etch.

The low selectivity ion milling produced much smoother etching than with CCl_4 , as evidenced by a comparison of Fig. 3 and 4. Unlike the CCl_4 etch, however, annealed silicides etched more roughly than unannealed silicides. This rougher etching was attributed to the already rougher surface of the annealed silicide before etch. The well-known milling rate dependence on angle (10) would cause a rough surface to further roughen as etching proceeds.

Trenching and shadowing during the milling of actual titanium silicide features prohibited its successful use, despite its much smoother etching in open areas. A 0° incidence angle produced severe trenching along etched features. As the angle was raised from 0° to 15° , the severity of the trenching decreased, with trenching only present around isolated features at 15° . Shadowing, or slower etching between closely spaced features, however, appeared with increasing intensity as the angle was increased from 5° to 15° . Thus samples milled at 15° showed both shadowing and trenching depending on the geometry/pitch of the etching features. In short, an optimum set of conditions, one where neither trenching nor shadowing occurred, could not be found.

CF_4 etching.—Reactive ion etching with fluorine containing gases was also studied as a means of reducing the silicon-to-oxide selectivity in order to produce smooth etching of titanium containing films. Both CHF_3 and CF_4 plasmas were characterized, but since the trends/results of each were similar, only the CF_4 data will be discussed here.

Table II lists the etch rates, surface smoothness during etch, and the anisotropy obtained when utilizing a CF_4 reactant in the diode-configured reactor. The silicide etched at the same rate as polysilicon but faster than pure titanium. In addition, both thermal oxide and positive photoresist etched faster than titanium silicide and polysilicon, limiting any practical application.

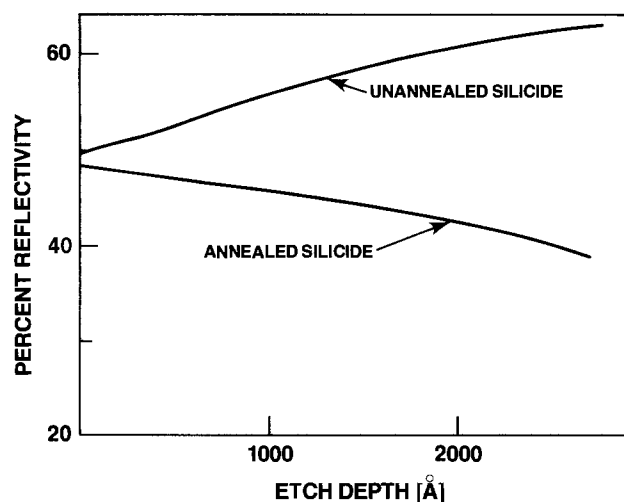


Fig. 4. Reflectivity as a function of etch depth for argon ion milling of 2 k\AA titanium silicide/ 2 k\AA polysilicon. The reflectivity was independent of milling angle, within the 0° - 15° range studied.

Table II. CF_4 etch data from the laboratory-scale diode reactor with 7 sccm CF_4 , $100 \text{ }\mu\text{m}$ pressure and $0.55 \text{ W}/\text{cm}^2$

Film	Etch rate ($\text{\AA}/\text{min}$)	Etch texture	Anisotropy* (with resist mask)
Titanium silicide			
Unannealed	120	Smooth	Excellent
Annealed	130	Rough	Excellent
Polysilicon	125	Smooth	Good-Fair
Titanium	60	Smooth	Excellent
Thermal SiO_2	445	—	—
Positive resist	250	—	—

* See Table I for anisotropy definitions.

The anisotropy of titanium containing films etched in CF_4 was excellent. No undercutting was ever seen for titanium silicide, while polysilicon films were undercut somewhat during extended overetches. This lower reactivity of titanium films in CF_4 is attributed to the low volatility of the expected product, TiF_4 . No vapor pressure data is available on TiF_4 , as it is reported in the literature simply as a white solid having a density of $2.8 \text{ g}/\text{ml}$ which sublimates at 284°C (11).

This low volatility is, however, evidenced by the strong temperature dependence of the CF_4 etch rate of titanium silicide. Figure 5 shows data collected in the single-wafer CF_4 plasma etch. No measurable etching occurred with the wafer clamped to a 5°C electrode, while the etch rate increased from 950 to $1350 \text{ \AA}/\text{min}$ as the temperature was increased from 25° to 60°C .

The reflectivity as a function of etch depth for CF_4 etching in the diode-configured reactor is shown in Fig. 6. The unannealed silicide and pure titanium films etched very smoothly, as evidenced by the flat reflectivity. The annealed silicide, however, etched quite roughly. This trend is similar to, although more dramatic than, that observed for ion milling (see Fig. 4). The reason for the rough etching after annealing is not clear, but may be simply that, as for ion milling, the rougher surface on annealed films "facets" during etching due to an angle dependence of the etch rate.

Figure 7 compares the surface roughness of partially etched annealed and unannealed polycide samples. In addition to the obvious differences in surface texture, the SEM inspection showed no undercutting of the silicide or any problems such as trenching or shadowing.

The reverse selectivity of the fluorine-based processes makes them unsuitable for complete etching of a polycide structure. Calculations show that polysilicon-to-oxide selectivities of at least 10/1 are needed for successful etching over thin (150\AA) gate oxide. Etches with selectivities that high, however, produced rough etching of oxygen containing $TiSi_2$. The solution is a two-step etch. The first step requires a low selectivity to oxide to etch

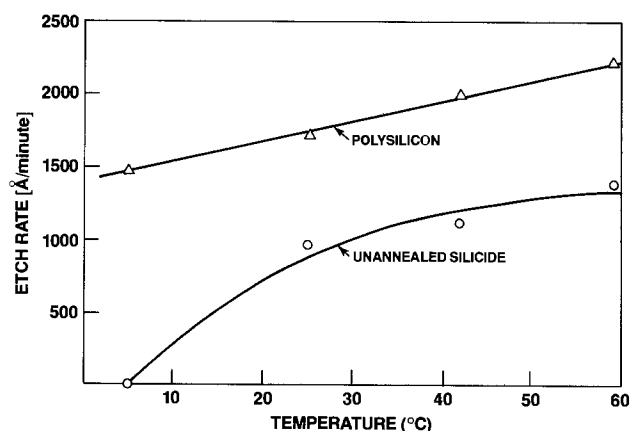


Fig. 5. The titanium silicide and polysilicon etch rates as a function of temperature in the Perkin-Elmer Cornerstone CF_4 etch process.

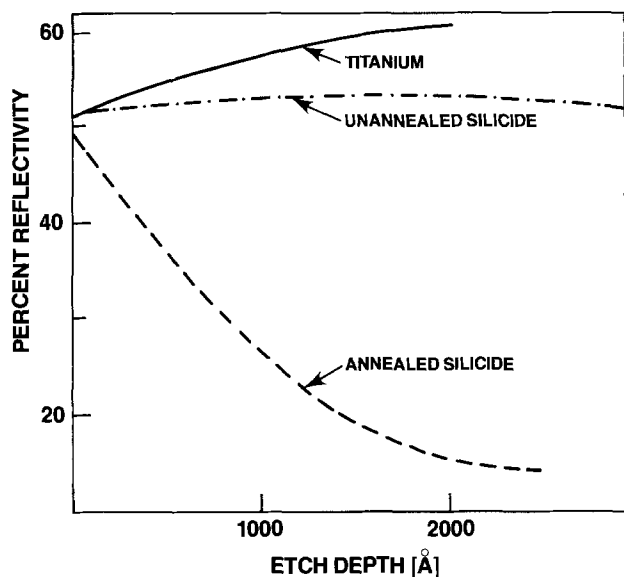


Fig. 6. Reflectivity as a function of etch depth for CF_4 reactive ion etching. The silicide films were $2 \text{ k}\text{\AA}$ titanium silicide/ $2 \text{ k}\text{\AA}$ polysilicon. The titanium film was $4 \text{ k}\text{\AA}$ and deposited directly on gate oxide.

smoothly through the silicide, the second a high selectivity to oxide to stop at the thin underlying gate oxide.

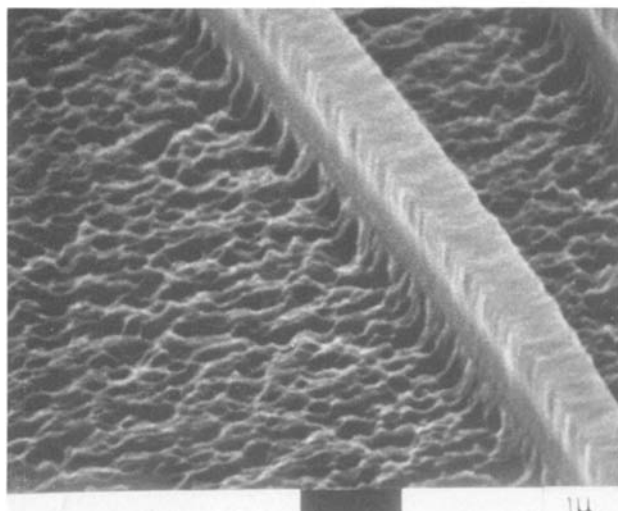
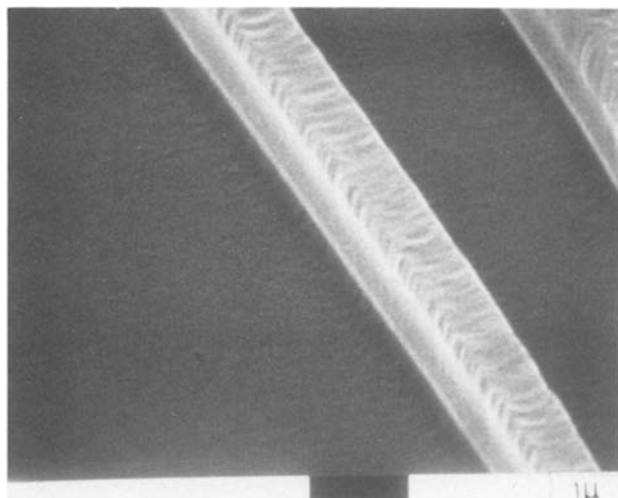


Fig. 7. Composite $2 \text{ k}\text{\AA}$ titanium silicide/ $2 \text{ k}\text{\AA}$ polysilicon films partially etched (stopped in the poly layer) in CF_4 in the laboratory scale diode reactor. The bottom film was annealed before etch. The photoresist remains on both samples.

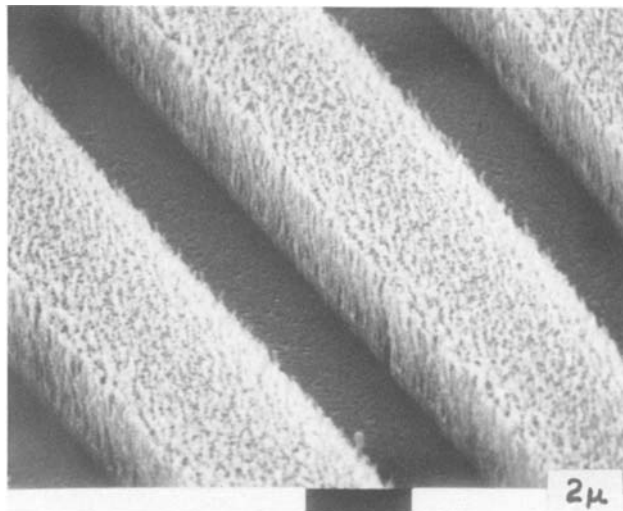


Fig. 8. Unannealed $2 \text{ k}\text{\AA}$ titanium silicide/ $2 \text{ k}\text{\AA}$ polysilicon film etched via a two-step process. Step one utilized a CF_4 reactive ion etch through the silicide. Step two was a Cl_2 plasma polysilicon etch. The photoresist remains to demonstrate anisotropy.

Two-step etching.—This section details a specific two-step etch of unannealed titanium polycides. The first step was a CF_4 reactive ion etch through the silicide, stopping in the polysilicon. The second step was a low frequency Cl_2 plasma etch of the underlying polysilicon. Figure 8 shows a sample etched via this process. Anisotropic etching with very little etch residue resulted.

The two-step etch, however, also had drawbacks. The first was simply that it was a two-step two-reactor process. A successful one-step process would certainly be more desirable. The second was that the etch selectivity with respect to photoresist was extremely poor, owing to the CF_4 etch, where resist was removed at more than twice the rate of the silicide. Trilevel resist processing (7, 8) was utilized, however, to produce the very thick sub-micron-sized resist patterns needed to mask this two-step process. In this manner, titanium polycide gates as small as $0.5 \mu\text{m}$ have been produced.

Certainly other two-step etch processes should work equally well. Chlorine-based plasmas produced smooth etching of oxygen containing TiSi_2 , when the silicon-to-oxide selectivity was reduced to less than 2/1. Higher power densities, lower pressures, and hydrogen addition were combined to produce the low selectivity needed for the first step in a two-step, one-reactor etch. In addition, the resist-removal rate in the "all-chlorine" etch was substantially less than with CF_4 .

Conclusions

Successful anisotropic etching of oxygen containing titanium silicide/polysilicon films could not be achieved in conventional one-step plasma etches. Selective, anisotropic chlorine-based plasmas produced unacceptably rough etching of the titanium silicide, presumably because "oxide" micromasks in/on the silicide block etching of the underlying material. Although the low selectivity of either CF_4 reactive ion etching or ion milling enabled smooth etching of unannealed silicide, the inability to stop on underlying gate oxide limited any practical application. A two-step etch, utilizing a low selectivity etch to smoothly "mill" through the silicide, followed by a high selectivity etch of the polysilicon down to the thin gate oxide, produced residue-free anisotropic etching of oxygen containing titanium polycide films.

Acknowledgments

The author wishes to thank Dr. Clarence Tracy for his helpful comments and suggestions during the etch evaluations, and for his review of this paper. Also, the film deposition and analysis performed by Carl Aspin and

Jerry Adams, and Auger analysis by Mike Kottke were greatly appreciated.

Manuscript submitted April 11, 1984; revised manuscript received Aug. 6, 1984.

Motorola, Incorporated, assisted in meeting the publication costs of this article.

REFERENCES

1. R. H. Dennard, F. H. Gaensslen, H. Yu, V. L. Rideout, E. Bassous, and A. R. LeBlanc, *IEEE J. Solid State Circuits*, **se-9**, 256 (1976).
2. J. D. Meindl, K. N. Ratnakumar, L. Gerzberg, and K. C. Saraswat, in "IEEE International Solid State Circuits Conference, Digest of Technical Papers,"

- L. Winner, Editor, p. 36, IEEE, New York (1981).
3. S. P. Murarka, *J. Vac. Sci. Technol.*, **17**, 769 (1980).
4. L. Mohammadi, *Solid State Technol.*, **1**, 65 (1981).
5. C. Aspin, Unpublished data.
6. K. L. Wang, T. C. Holloway, R. F. Pinizzotto, Z. P. Sobczak, W. R. Hunter, and A. F. Tasch, *IEEE Trans. Electron Devices*, **ed-29**, 547 (1982).
7. J. M. Moran and D. Maydan, *Bell Syst. Tech. J.*, **58**, 1027 (1979).
8. D. Maydan, *J. Vac. Sci. Technol.*, **17**, 1164 (1980).
9. "Handbook of Chemistry and Physics," 50th ed., W. C. Weast, Editor, pp. D-143, D-144, The Chemical Rubber Co., Cleveland, OH (1969).
10. S. Somekh, *J. Vac. Sci. Technol.*, **13**, 1003 (1976).
11. "Encyclopedia of Chemical Technology," 2nd ed., Vol. 20, p. 388, Interscience, New York (1967).

Thermal Diffusion Effects in Chemical Vapor Deposition Reactors

Joel P. Jenkinson and Richard Pollard*

Department of Chemical Engineering, University of Houston, Houston, Texas 77004

ABSTRACT

A mathematical model that describes the behavior of chemical vapor deposition reactors with well-defined hydrodynamics has been extended to include the effects of multicomponent thermal diffusion. The influence of thermal diffusion on the deposition rate is dependent on the deposition system and on the operating conditions of the reactor. For production of silicon by reduction of silicon tetrachloride in excess hydrogen, deposition rates are typically lowered by 15-20%. However, for deposition of boron from boron trichloride and hydrogen, thermal diffusion can raise growth rates by approximately 7% when concentrated inlet gas mixtures are used.

Chemical vapor deposition (CVD) processes are widely used in the manufacture of electronic materials and in the formation of surface coatings. Several theoretical descriptions of CVD systems have been proposed (1-15). However, the complex nature of the coupled multicomponent transport phenomena and reaction kinetics has necessitated the incorporation of many assumptions into these models. As a result, the physical factors that control the behavior of CVD reactors are only partially understood. In particular, the role and relative importance of thermal diffusion in CVD processes is a subject of controversy. Some workers feel that it can be neglected (12), whereas others state that it needs to be considered because temperature gradients are large and because there are substantial differences in the molecular weights of the reactants (13). An approximate model based on constant binary thermal diffusion ratios indicates that deposition rates could be altered significantly (15, 16). However, an order of magnitude analysis suggests that the opposite is true (12). A detailed investigation is needed to clarify the specific effects of thermal diffusion on the behavior of CVD processes.

In this paper, a previous analysis (10, 15) of CVD reactors is extended to include multicomponent thermal diffusion. Comparisons of simulations with and without thermal diffusion terms in the heat and mass transport equations are used to illustrate the effects of thermal diffusion on the performance of CVD reactors. Quantitative results are obtained for two representative CVD systems: deposition of silicon at a rotating disk, using SiCl_4 in excess hydrogen (17); and deposition of boron from BCl_3 and hydrogen, using an impinging jet apparatus (18).

Analysis

A steady-state model for CVD systems with an arbitrary number of chemical species has been developed previously (10, 15). The analysis includes multicomponent transport phenomena, variable physical properties, finite interfacial velocity, and simultaneous homogeneous and heterogeneous reactions. The governing equations are summarized in Table I. For laminar flow in geometries

such as the rotating disk or impinging jet, Eq. [5] and [6] can be transformed into a set of ordinary differential equations, and the problem becomes one-dimensional. Also, at atmospheric pressure, it is reasonable to neglect pressure variations across the diffusion layer (10) and, hence, to use only two Navier-Stokes relations (Eq. [5]). Boundary conditions for the velocity components v_r and v_θ are dependent on the flow system (10, 15). However, the axial velocity v_z at the substrate surface is determined by the heterogeneous reaction rates, as indicated by Eq. [11]. Surface compositions are obtained with Eq. [1] and [3]. Far from the substrate, the inlet gas is assumed to be at equilibrium at the inlet gas temperature.

When thermal diffusion is included in the analysis, the multicomponent diffusion equation for an isobaric system becomes (19)

$$c_i \nabla \mu_i = RT \sum_{k \neq i} \frac{c_i c_k}{c_T \mathfrak{D}_{ik}} \left[v_k - v_i + \left(\frac{D_k^T}{\rho_k} - \frac{D_i^T}{\rho_i} \right) \nabla \ln T \right] \quad [12]$$

The last term on the right-hand side of Eq. [12] represents the contribution of the temperature gradient to mass transport. The method for calculating values of the multicomponent thermal diffusion coefficients D_i^T is given in the Appendix. If gas behavior is ideal, Eq. [12] may be rewritten in dimensionless form as

$$\nabla x_i - k_i^T \nabla \ln T = \sum_{k \neq i} \frac{(x_i J_k - x_k J_i)}{D_{ik}} \quad [13]$$

where D_{ik} is a dimensionless diffusion coefficient for binary interactions defined by

$$D_{ik} = c_T \mathfrak{D}_{ik} / c_{\infty} v_z \quad [14]$$

and k_i^T is a dimensionless multicomponent thermal diffusion ratio given by

$$k_i^T = \sum_{k \neq i} \frac{(x_i M_i D_k^T - x_k M_k D_i^T)}{M_i M_k c_{\infty} v_z D_{ik}} \quad [15]$$

*Electrochemical Society Active Member.

Table I. Governing equations for CVD processes (10, 15). Description of steady-state equations for system with n species in gas phase: [1] multicomponent diffusion equation; [2] material balance; [5] Navier-Stokes equation of motion for Newtonian fluid; [6] continuity equation; [7] ideal gas equation of state; [9] thermal energy equation; [10] law of mass action to predict homogeneous production rates (equation used to eliminate R_i in Eq. [2] and [9]); [11] boundary condition for axial velocity at surface due to heterogeneous reactions.

Variable	Equation	Number of equations	Equation number
\underline{J}_i	$x_i \left(\nabla \mu_i - \frac{M_i \nabla p}{\rho} \right) = \sum_{k \neq i} \frac{x_i \underline{J}_k - x_k \underline{J}_i}{c_T \mathcal{D}_{ik}}$	$n - 1$	[1]
x_i	$\nabla \cdot \underline{J}_i = R_i - c_T \underline{v} \cdot \nabla x_i + c_i \underline{v} \cdot \nabla \ln \bar{M}$	$n - 1$	[2]
—	$\sum_i x_i = 1$	1	[3]
—	$\sum_i M_i \underline{J}_i = 0$	1	[4]
v_r, v_θ, v_z	$\rho \underline{v} \cdot \nabla \underline{v} = -\nabla p + \rho \underline{g} + \nabla \cdot \left[\mu \nabla \underline{v} + \mu (\nabla \underline{v})^T - \frac{2}{3} \mu \underline{I} \nabla \cdot \underline{v} \right]$	3	[5]
p	$\nabla \cdot (\rho \underline{v}) = 0$	1	[6]
c	$p = c_T R T$	1	[7]
ρ	$\rho = \bar{M} c_T$	1	[8]
T	$c_T \bar{C}_p \underline{v} \cdot \nabla T = \nabla \cdot (k \nabla T) + \underline{v} \cdot \nabla p - \sum_i (\underline{J}_i \cdot \nabla \bar{H}_i + \bar{H}_i R_i)$	1	[9]
R_i	$R_i = -\sum_{l=1}^{l_h} \nu_{il} \left(k_{lf} \prod_i x_i^{\nu_{il}} - k_{lb} \prod_i x_i^{-\nu_{il}} \right)$ $\nu_{il} > 0 \quad \nu_{il} < 0$	n	[10]
$(v_z)_s$	$(v_z)_s = -\sum_i \sum_{l=1}^{l_s} M_l s_{il} \left(k_{lf} \prod_i x_i^{\nu_{il}} - k_{lb} \prod_i x_i^{-\nu_{il}} \right) \theta_{vl}^{\nu_{il}}$ $s_{il} > 0 \quad s_{il} < 0$	1	[11]

For a two-component system, Eq. [15] reduces to the binary thermal diffusion ratio (20), $k^T = (\rho/c_T^2 M_1 M_2) (D_1^T / \mathcal{D}_{12})$. The sum of k_i^T or D_i^T over all the species is zero, i.e.

$$\sum_i D_i^T = \sum_i k_i^T = 0 \quad [16]$$

Consequently, for a system with n species, there are $n - 1$ independent values of D_i^T or k_i^T .

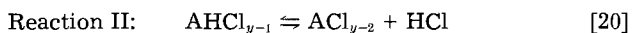
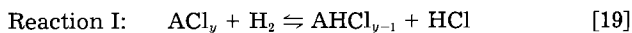
The steady-state thermal energy equation also needs to be modified to account for the temperature changes induced by thermal diffusion of the species. For an ideal gas mixture in which viscous energy dissipation can be neglected, Eq. [9] becomes

$$c_T \bar{C}_p \underline{v} \cdot \nabla T = \nabla \cdot (k \nabla T) - \sum_i (\underline{J}_i \cdot \nabla \bar{H}_i^* + \bar{H}_i^* R_i) - \nabla \cdot q^{(x)} \quad [17]$$

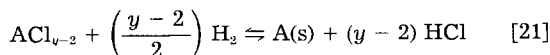
for an isobaric system. The Dufour energy flux $q^{(x)}$ is given by

$$q^{(x)} = -\sum_i \frac{D_i^T}{\rho_i} c_i \nabla \mu_i = -RT \sum_i \frac{D_i^T}{\rho_i} \nabla x_i \quad [18]$$

For the examples of CVD of silicon and boron considered here, the chemical reactions are taken to be



Reaction III:



where A represents either silicon ($y = 4$) or boron ($y = 3$). Reactions I and II can occur in the gas phase as well as at the substrate surface. In each example, five gas-phase species are present: H_2 , HCl , ACl_y , AHCl_{y-1} , and ACl_{y-2} . Thermal diffusion is accounted for by replacing Eq. [1]

and [9] in Table I with Eq. [13] and [17], respectively. The governing equations are solved numerically by a finite difference technique (19).

Results and Discussion

In general, thermal diffusion effects are directly related to the temperature gradient and to the relative magnitudes of the molecular weights of the species in the system. Motion toward the hot substrate surface is enhanced for smaller molecules and retarded for larger molecules. Consequently, local compositions and reaction rates are altered. The influence of thermal diffusion on the behavior of two CVD systems is described below. In both cases, the Dufour term in Eq. [17] is always several orders of magnitude smaller than the other terms in the equation and has a negligible effect on the results.

Silicon deposition at a rotating disk.—The production of silicon from silicon halides and hydrogen is an example of a CVD process that generally uses excess reducing agent. The results presented here are for an inlet gas mixture with 1 mole percent (m/o) SiCl_4 .

Figure 1 illustrates the predicted effects of thermal diffusion on steady-state composition variations across the mass-transfer boundary layer adjacent to the substrate surface. If thermal diffusion is included in the analysis, silicon compounds reach the surface less easily and transport of HCl from the surface is facilitated. As a result, the surface compositions of these species are reduced. Away from the substrate, these compositions are increased and the diffusion layer thickness becomes slightly larger. The maxima for the intermediates SiHCl_3 and SiCl_2 are shifted to larger values of ζ . Also, a small maximum for x_{SiCl_4} is shown near $\zeta = 12$. In this region, movement of SiCl_4 toward the disk is restricted by thermal diffusion, but the local temperature is too low for homogeneous decomposition of SiCl_4 to occur.

Equation [16] indicates that thermal diffusion cannot move all molecules in the same direction. Therefore, the effects on the chloride compounds are balanced by the effects on the hydrogen, which moves to the disk more easily. Composition profiles for hydrogen are not shown in

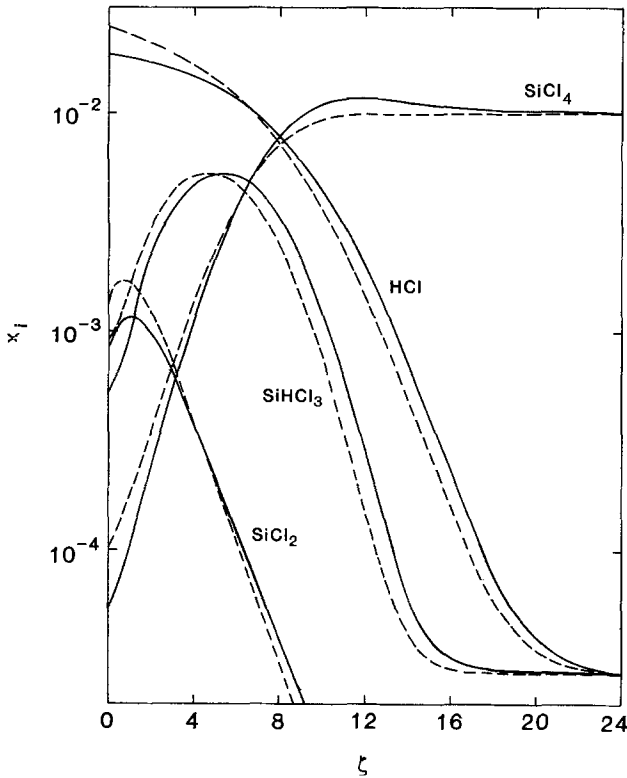


Fig. 1. Composition profiles, with and without thermal diffusion effects (solid lines and broken lines, respectively), in diffusion layer adjacent to substrate surface for CVD of silicon at a rotating disk. $T_s = 1473$ K, $T_\infty = 298$ K, $p_\infty = 1.013 \times 10^5$ N/m², $x_{SiCl_4}^\infty = 0.01$, $\Omega = 12.57$ rad/s, $\theta_{v1} = 1$. Kinetic parameters are as in Fig. 1 of Ref. (10).

Fig. 1 because it is present in excess and mole fraction variations are small. However, the surface composition x_{H_2} is raised by thermal diffusion and, in order to satisfy Eq. [3], it slightly exceeds the inlet value of 0.99. Also, the hydrogen profile shows a small minimum near $\zeta = 12$, where the compositions of the other species are larger.

For the operating conditions used in Fig. 1, the variations of some physical properties are shown in Fig. 2. Small but noticeable changes occur when thermal diffusion is included in the analysis. These changes can be attributed to the modifications in the composition profiles because the temperature profile is essentially unchanged by thermal diffusion. Figure 3 indicates that the changes

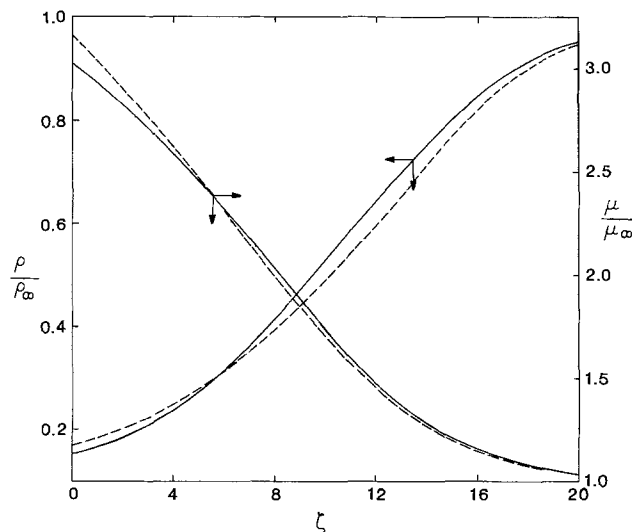


Fig. 2. Dependence of viscosity and density on distance from surface, in rotating disk system for silicon CVD with and without thermal diffusion effects (solid lines and broken lines, respectively). Parameter values are as in Fig. 1. $\mu_\infty = 9.602 \times 10^{-5}$ g/cm s; $\rho_\infty = 1.536 \times 10^{-3}$ g/cm³.

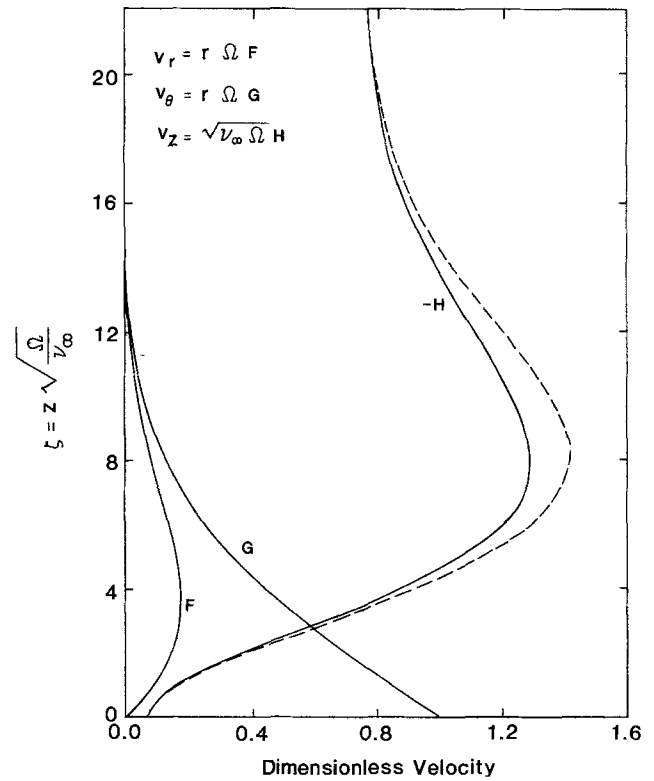


Fig. 3. Velocity profiles for silicon deposition at a rotating disk with and without thermal diffusion effects (solid lines and broken lines, respectively). Parameter values are as in Fig. 1.

in the local density and viscosity of the fluid reduce the minimum in the dimensionless axial velocity H but do not alter the radial or angular velocity profiles.

The effects of thermal diffusion on the dimensionless silicon deposition rate S are illustrated in Fig. 4. The kinetic parameters used in the simulations are chosen to match the shape of the experimentally observed temperature dependence of the deposition rate (10, 17). The model predicts that, for the range of surface temperatures considered, thermal diffusion does not alter the shape of the curve significantly, but S is lowered by approximately

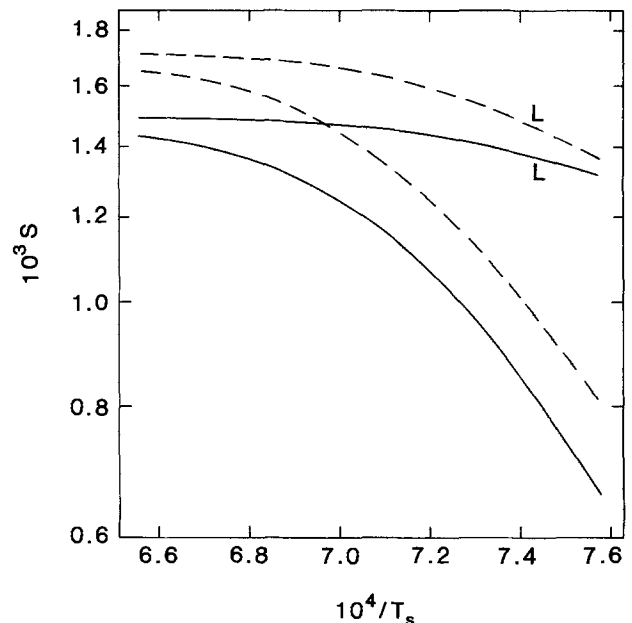


Fig. 4. Temperature dependence of dimensionless deposition rates for deposition of silicon at a rotating disk with and without thermal diffusion effects (solid lines and broken lines, respectively). Parameter values are as in Fig. 1. Curves marked L are thermodynamic-mass-transfer limits.

15%-20%. The lower HCl mole fraction near the surface (see Fig. 1) favors a higher deposition rate. However, this is overshadowed by the lower surface compositions of the silicon halides which reduce the forward rates of the reactions.

Dimensionless surface fluxes N_i' are related to local dimensionless reaction rates r_i' by

$$N_i' = - \sum_1 s_{i1} r_1' \quad [22]$$

For the reaction mechanism considered here (Eq. [19]-[21]), the dimensionless deposition rate S is given by $-\sum_k N_k'$, where the sum k is over the silicon compounds.

In this example, the rate of heterogeneous reaction II (Eq. [20]) is negligible (10) and, hence, the deposition rate simplifies to $-N_5'$, where the subscript 5 represents SiCl_2 . For an inlet gas mixture with 1 m/o SiCl_4 , the use of binary transport equations gives results that are typically within 7% of those obtained with the multicomponent diffusion relations (21). Therefore, the deposition rate can be approximated by

$$S = D_{5,H_2} x_5 (\nabla \ln x_5 + \alpha^T \nabla \ln T)_s - \frac{x_5 c_T H_s}{c_\infty} \quad [23]$$

where α^T is a binary thermodiffusion factor (22) and H_s is the axial velocity at the substrate surface

$$H_s = \frac{c_\infty \sum_1 M_1 N_1'}{\rho} \quad [24]$$

With a substrate temperature of 1473 K, the surface value of α^T is 1.2, and inclusion of the second term on the right-hand side of Eq. [23] reduces S by approximately 8%. The deposition rate changes by a larger percentage (see Fig. 4) because the SiCl_2 composition gradient at the surface becomes slightly less positive when thermal diffusion is incorporated into the analysis (see Fig. 1).

Also shown in Fig. 4 are two curves representing the thermodynamic-mass-transfer limits (10) with and without the inclusion of thermal diffusion effects. These limits represent maximum dimensionless deposition rates obtained as the reaction rate constants approach infinity and the local gas compositions approach their equilibrium values. The effects of thermal diffusion under these conditions are similar to those obtained with finite kinetic parameters: motion of reactants to the substrate is retarded and the deposition rate is reduced. The change is greater at higher surface temperatures because the temperature gradient is larger.

Simulations were repeated with different values of the bulk gas temperature T_∞ in the range of 20°-400°C. As T_∞ is increased, the thermal boundary layer thickness decreases; but the temperature gradient near the surface and the role of thermal diffusion, do not change appreciably.

Boron deposition via an impinging jet.—Chemical vapor deposition of boron represents an example where relatively concentrated mixtures of the gaseous reactants are used. The mole fraction of BCl_3 in the BCl_3/H_2 inlet gas is usually between 0.1 and 0.6 (18). As a result, the mole fractions of the intermediate species are higher than in CVD of silicon and the multicomponent nature of the system is more evident.

Composition profiles for typical reaction conditions are shown in Fig. 5. With thermal diffusion terms included in the model, mole fractions of the chlorides are lower at the surface. Further from the substrate, compositions are predicted to be higher and, hence, species diffusion layers are thicker. With $x_{\text{BCl}_3}^0 = 0.4$, values of k_i^T are positive for all species except hydrogen. However, thermal diffusion coefficients D_i^T for the lighter chlorides, HCl and BCl, are

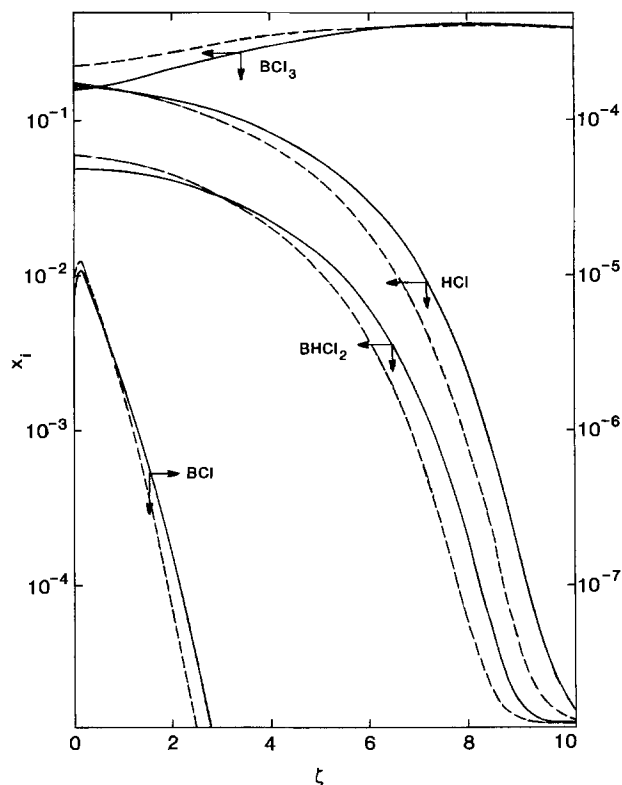


Fig. 5. Composition profiles, with and without thermal diffusion effects (solid lines and broken lines, respectively), in diffusion layer adjacent to reaction surface for boron deposition in the impinging jet system. $T_s = 1373$ K, $T_\infty = 298$ K, $p_\infty = 1.013 \times 10^5$ N/m², $x_{\text{BCl}_3}^0 = 0.40$, $a = 417$ s⁻¹. Kinetic parameters are as in Fig. 2 of Ref. (15).

negative (see Fig. A-2). This is in contrast to the silicon deposition example, where k_i^T and D_i^T have the same sign. This difference in the effect of thermal diffusion on the motion of intermediate size molecules can be associated with the relative numbers of large and small species in the gas phase and the balancing constraint of Eq. [16].

Physical property variations across the boundary layer are modified by thermal diffusion, and the temperature gradient near the surface is slightly reduced. Also, the axial velocity at a given location in the impinging jet system is lower, but the radial velocity component is not changed noticeably.

The influence of thermal diffusion on dimensionless boron deposition rate is illustrated in Fig. 6 and 7. Figure 6 indicates that, with $x_{\text{BCl}_3}^0 = 0.4$, the deposition rate is generally raised by thermal diffusion. With the sequence of reactions given by Eq. [19]-[21], each value for $-S$ can be equated to the sum of the dimensionless surface fluxes N_i' of the boron compounds. The absolute magnitude of the BHCl_2 flux is largest because the composition of BCl is very low near the substrate and because significant homogeneous decomposition of BCl_3 takes place (15). Inversion of the Stefan-Maxwell equations shows that, for a concentrated gas mixture, the flux of BHCl_2 cannot be determined from the composition gradient of BHCl_2 alone. However, the increase in deposition rate with thermal diffusion is consistent with the less negative surface mole fraction gradient for BHCl_2 shown in Fig. 5. At high jet mass flow rates (large values of a) and high surface temperatures, thermal diffusion increases the deposition rate less and, in extreme cases, lower values for S are predicted.

Figure 7 shows the influence of inlet gas composition on S for a specific jet mass flow rate. With large values of $x_{\text{BCl}_3}^0$, thermal diffusion raises the dimensionless deposition rate by 6%-8%. As the inlet composition of BCl_3 is reduced, the direction of the thermally induced motion of HCl and BCl is altered. The signs of D_i^T for HCl and BCl change at $x_{\text{BCl}_3}^0$ values of approximately 0.28 and 0.33, re-

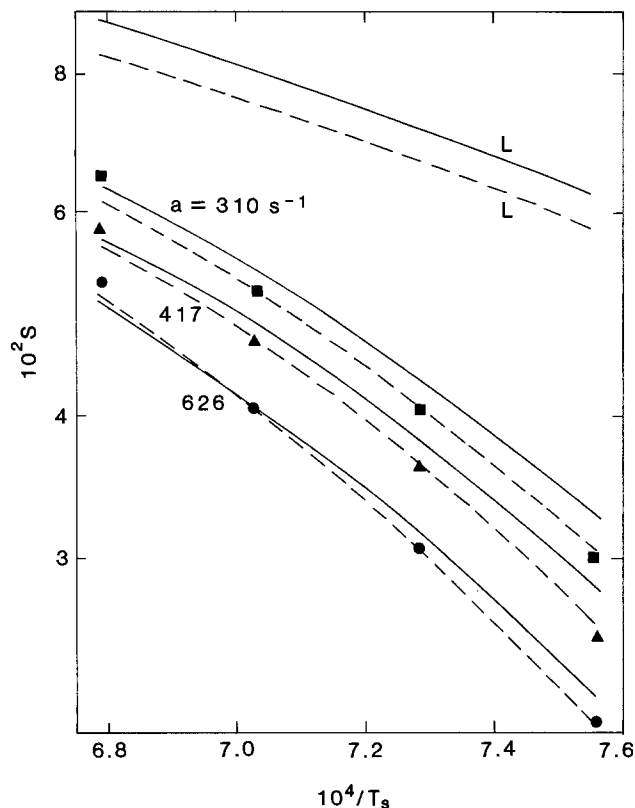


Fig. 6. Dependence of dimensionless boron deposition rate on substrate temperature, with and without thermal diffusion effects (solid lines and broken lines, respectively). Experimental data (18): $\bullet \sim a = 310 \text{ s}^{-1}$, $\blacktriangle \sim a = 417 \text{ s}^{-1}$, $\blacksquare \sim a = 626 \text{ s}^{-1}$, with other parameters as in Fig. 5. Curves marked L are thermodynamic-mass-transfer limits.

spectively. At lower inlet compositions, the deposition process is more closely analogous to CVD of silicon: thermal diffusion retards the motion of all boron com-

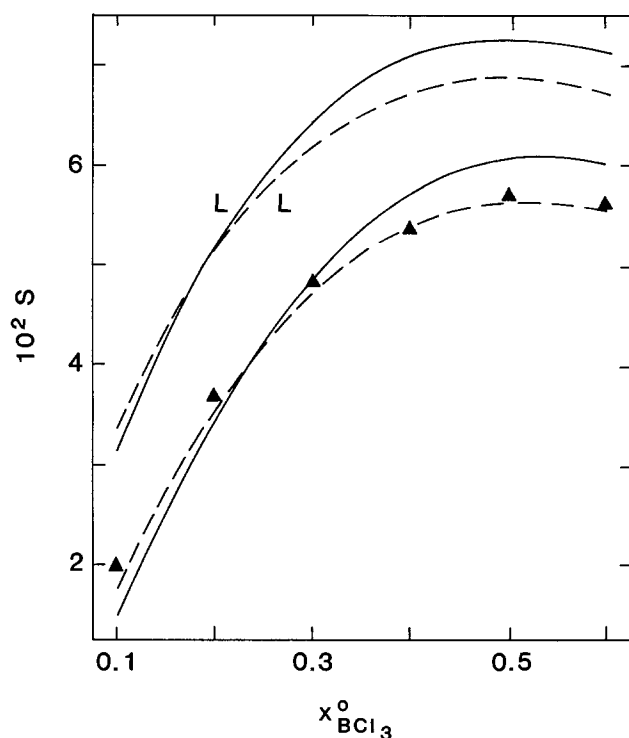


Fig. 7. Dependence of dimensionless boron deposition rate on inlet gas composition, with and without thermal diffusion effects (solid lines and broken lines, respectively). Parameter values are as in Fig. 5. Experimental data (18): $\blacktriangle \sim a = 102 \text{ s}^{-1}$ at $x^0_{\text{BCl}_3} = 0.4$. Curves marked L are thermodynamic-mass-transfer limits.

pounds toward the heated substrate, and it is predicted that thermal diffusion will lower the deposition rate.

The match of the data given by the lower dashed curve in Fig. 7 uses a Langmuir-Hinshelwood model with adsorption of BCl_3 to represent the heterogeneous kinetics (15). With thermal diffusion, local compositions are modified; this can affect the fraction of vacant adsorption sites available, as well as the forward and backward terms in the rate expression. However, the change in shape of the curve for the thermodynamic-mass-transport limit is similar to the change predicted for the case with finite kinetic parameters. This suggests that the influence of thermal diffusion is dictated primarily by the transport processes, rather than by effects associated with the reaction kinetics.

The changes in the shapes of the theoretical curves caused by incorporation of thermal diffusion into the analysis have implications concerning the identification of rate-limiting steps in the process. In Fig. 6 and 7, modified kinetic parameters or rate equations would be needed to provide a satisfactory match between the experimental data and the theoretical predictions that include thermal diffusion effects. For the boron deposition example, it is anticipated that adsorption terms in the rate expressions may be modified but that the relative importance of homogeneous and heterogeneous reactions will not be changed significantly.

Conclusions

A one-dimensional model that describes the coupled transport phenomena and reaction kinetics of CVD reactors has been extended to include the effects of multicomponent thermal diffusion. The role of thermal diffusion in CVD processes has been elucidated by studies of two systems: silicon deposition at a rotating disk and boron deposition using an impinging jet apparatus. The model predicts that numerical changes in the deposition rate associated with thermal diffusion are different in the two cases. For growth of silicon from a dilute mixture of 1 m/o SiCl_4 in hydrogen, deposition rates are lowered by 15%-20%. In contrast, thermal diffusion can raise the boron deposition rate by approximately 7% if high inlet compositions of BCl_3 are used. However, with larger quantities of hydrogen in the feed stream, the boron deposition rate is lowered and the system behavior becomes more analogous to the silicon deposition example. The analysis also shows that the Dufour energy flux in the thermal energy equation is not important in CVD reactors.

Acknowledgment

This work was supported by the National Science Foundation (Grant no. CPE-8203554).

Manuscript submitted April 30, 1984; revised manuscript received Aug. 8, 1984.

APPENDIX

Calculation of Thermal Diffusion Coefficients

Multicomponent thermal diffusion coefficients may be calculated using the Chapman-Enskog kinetic theory of gases. The method presented here, based on the Lennard-Jones potential function, is adapted from the book by Hirschfelder *et al.* (23).

The second-order approximation¹ for the multicomponent thermal diffusion coefficient for species *i* is given by

¹The first-order approximation, which uses only the first term in the Sonine polynomial expansion, results in zero-valued thermal diffusion coefficients. For this reason, thermal diffusion is often referred to as a second-order effect.

$$D_i^T = x_i \sqrt{\frac{M_i k T}{2}} \begin{vmatrix} Q_{11}^{00} & Q_{12}^{00} & \dots & Q_{1n}^{00} & Q_{11}^{01} & Q_{12}^{01} & \dots & Q_{1n}^{01} & 0 \\ Q_{21}^{00} & Q_{22}^{00} & \dots & Q_{2n}^{00} & Q_{21}^{01} & Q_{22}^{01} & \dots & Q_{2n}^{01} & 0 \\ \vdots & \vdots & \ddots & \vdots & \vdots & \vdots & \ddots & \vdots & \vdots \\ Q_{n1}^{00} & Q_{n2}^{00} & \dots & Q_{nn}^{00} & Q_{n1}^{01} & Q_{n2}^{01} & \dots & Q_{nn}^{01} & 0 \\ Q_{11}^{10} & Q_{12}^{10} & \dots & Q_{1n}^{10} & Q_{11}^{11} & Q_{12}^{11} & \dots & Q_{1n}^{11} & R_{11} \\ Q_{21}^{10} & Q_{22}^{10} & \dots & Q_{2n}^{10} & Q_{21}^{11} & Q_{22}^{11} & \dots & Q_{2n}^{11} & R_{21} \\ \vdots & \vdots & \ddots & \vdots & \vdots & \vdots & \ddots & \vdots & \vdots \\ Q_{n1}^{10} & Q_{n2}^{10} & \dots & Q_{nn}^{10} & Q_{n1}^{11} & Q_{n2}^{11} & \dots & Q_{nn}^{11} & R_{n1} \\ \delta_{11} & \delta_{12} & \dots & \delta_{1n} & 0 & 0 & \dots & 0 & 0 \end{vmatrix} \begin{vmatrix} Q_{11}^{00} & \dots & Q_{1n}^{00} & Q_{11}^{01} & \dots & Q_{1n}^{01} \\ \vdots & \ddots & \vdots & \vdots & \ddots & \vdots \\ Q_{n1}^{00} & \dots & Q_{nn}^{00} & Q_{n1}^{01} & \dots & Q_{nn}^{01} \\ Q_{11}^{10} & \dots & Q_{1n}^{10} & Q_{11}^{11} & \dots & Q_{1n}^{11} \\ \vdots & \ddots & \vdots & \vdots & \ddots & \vdots \\ Q_{n1}^{10} & \dots & Q_{nn}^{10} & Q_{n1}^{11} & \dots & Q_{nn}^{11} \end{vmatrix} \quad [A-1]$$

where n is the number of species in the system. The elements of the determinants are given by

$$Q_{ij}^{00} = 8 \sum_{k=1}^n \frac{x_k M_k}{\sqrt{M_i M_j} (M_i + M_j)} [x_i M_i (\delta_{ij} - \delta_{jk}) - x_j M_j (1 - \delta_{ik})] \Omega_{ik}^{(1,1)} \quad [A-2]$$

$$Q_{ij}^{01} = -8 \left(\frac{M_i}{M_j}\right)^{3/2} \sum_{k=1}^n \frac{x_i x_k M_k^2}{(M_i + M_k)^2} (\delta_{ij} - \delta_{kj}) \left[\Omega_{ik}^{(1,2)} - \frac{5}{2} \Omega_{ik}^{(1,1)} \right] \quad [A-3]$$

$$Q_{ij}^{10} = \left(\frac{M_i}{M_j}\right) Q_{ij}^{01} \quad [A-4]$$

$$Q_{ij}^{11} = 8 \left(\frac{M_i}{M_j}\right)^{3/2} \sum_{k=1}^n \frac{x_i x_k M_k}{(M_i + M_k)^3} \left\{ (\delta_{ij} - \delta_{kj}) \left[\frac{5}{4} (6M_j^2 + 5M_k^2) \Omega_{ik}^{(1,1)} - 5M_k^2 \Omega_{ik}^{(1,2)} \right] + M_k^2 \Omega_{ik}^{(1,3)} + (\delta_{ij} + \delta_{jk}) 2M_j M_k \Omega_{ik}^{(2,2)} \right\} \quad [A-5]$$

$$R_{im} = \delta_{m1} \frac{15}{4} x_1 \sqrt{2kT/M_i} \quad [A-6]$$

$$\delta_{ij} = \begin{cases} 1 & i = j \\ 0 & i \neq j \end{cases} \quad [A-7]$$

The collision integrals $\Omega_{ik}^{(l,s)}$ for the Lennard-Jones (6-12) potential function are related to dimensionless integrals $\Omega_{ik}^{(l,s)*}$ by (20-24)

$$\Omega_{ik}^{(l,s)*} = \frac{\Omega_{ik}^{(l,s)} \sqrt{2\pi m_{ik} N_A / kT}}{\frac{1}{2} (s+1)! \left[1 - \frac{1}{2} \left(\frac{1+(-1)^s}{1+1} \right) \right] \pi \sigma_{ik}^2} \quad [A-8]$$

where σ_{ik} is the collision diameter and m_{ik} is the reduced mass, given by

$$m_{ik} = \frac{M_i M_k}{M_i + M_k} \quad [A-9]$$

Values for $\Omega_{ik}^{(l,s)*}$ have been tabulated as a function of kT/ϵ_{ik} (20, 23, 25, 26).

The equations above indicate that the thermal diffusion coefficients are dependent on the compositions and molecular weights of the species and on the temperature. Figures A-1 and A-2 show typical values of local thermal diffusion coefficients for CVD of silicon and boron, respectively. Comparison of these figures with the corresponding composition profiles (Fig. 1 and 5) illustrates the strong composition dependence of the thermal diffusion coefficients. It should be noted that for a dilute system (i.e., silicon deposition) values of D_i^T/ρ_i for the minor species are approximately equal, and the function $D_i^T/\rho_i T$ varies by less than an order of magnitude across the diffusion layer.

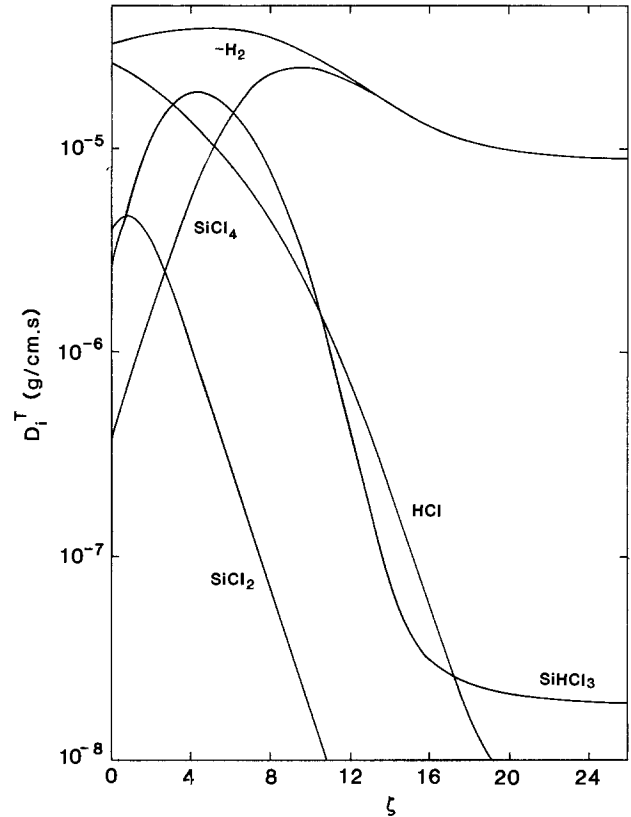


Fig. A-1. Typical absolute values of thermal diffusion coefficients in the diffusion layer adjacent to the reaction surface for silicon deposition in the rotating disk system. Minus sign denotes negative thermal diffusion coefficient for that species. Parameter values are as in Fig. 1.

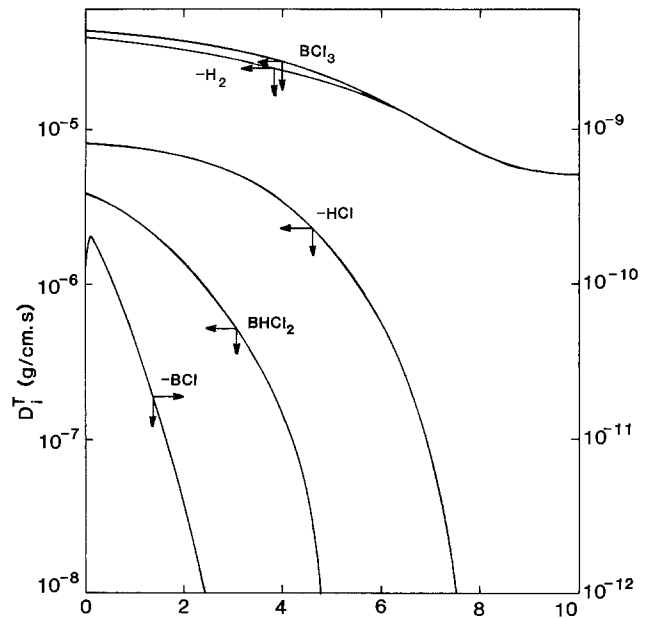


Fig. A-2. Typical absolute values of thermal diffusion coefficients in the diffusion layer adjacent to the reaction surface for boron deposition in the impinging jet system. Minus signs denote negative thermal diffusion coefficients for those species. Parameter values are as in Fig. 5.

LIST OF SYMBOLS

- a hydrodynamic constant in impinging jet system (proportional to mass flow rate of jet stream) (s^{-1})
- c_i concentration of species i (mol/cm^3)
- c_T total concentration (mol/cm^3)
- c_∞ bulk total concentration (mol/cm^3)

\tilde{C}_p = $\sum_i x_i \tilde{C}_{pi}$, molar heat capacity of mixture (J/mol K)
 \tilde{C}_{pi} molar heat capacity of species i (J/mol K)
 \mathcal{D}_{ik} diffusion coefficient for binary interactions (cm²/s)
 D_{ik} dimensionless diffusion coefficient for binary interactions
 D_i^T thermal diffusion coefficient for species i (g/cm s)
 F dimensionless radial velocity
 G dimensionless angular velocity
 H dimensionless axial velocity
 \bar{H}_i partial molar enthalpy of species i (J/mol)
 \bar{H}_i^* molar enthalpy of ideal gas (J/mol)
 I unit matrix
 \bar{J}_i flux of species i relative to mass average velocity (mol/cm² s)

J_i = $J_i/c_x \sqrt{\nu_x \lambda}$, dimensionless flux
 k Boltzmann constant (used in Appendix) (1.3806×10^{-23} J/K)

k thermal conductivity (W/cm K)
 k_i thermal conductivity of species i (W/cm K)
 k_{1f} forward rate constant for reaction 1
 k_{1b} backward rate constant for reaction 1
 k^T dimensionless binary thermal diffusion ratio
 k_i^T dimensionless multicomponent thermal diffusion ratio for species i , defined by Eq. [15]

l_h number of homogeneous reactions
 l_s number of surface reactions
 m_{ik} reduced mass as defined by Eq. [A-9]
 M_i molecular weight of species i
 \bar{M} = $\sum_i M_i x_i$, average molecular weight
 n number of species in gas phase
 n_l exponent for θ_{vl} in surface reaction 1
 N_i flux of species i (mol/cm² s)

N_i' $N_i/c_x \sqrt{\nu_x \lambda}$, dimensionless flux of species i
 N_A Avogadro's number (6.023×10^{23} per g mol)
 p gas pressure (N/m²)
 Pr Prandtl number

$q^{(x)}$ Dufour energy flux, defined by Eq. [18] (J/cm² s)
 $Q_{ij}^{mm'}$ parameters defined by Eq. [A-2]-[A-5]
 r radial distance (cm)
 r_1' dimensionless rate of reaction 1
 R universal gas constant (8.3143 J/mol K)
 R_{im} parameters defined by Eq. [A-6]
 R_i rate of homogeneous production of species i (mol/cm³ s)

s_{il} stoichiometric coefficient for species i in heterogeneous reaction 1 (positive for reactants, negative for products)
 S = actual deposition rate/ $c_x \sqrt{\nu_x \lambda}$, dimensionless deposition rate

T temperature (K)
 v mass average velocity (cm/s)
 \bar{v}_r radial velocity (cm/s)
 v_θ angular velocity (cm/s)
 v_z axial velocity (cm/s)
 $(v_z)_s$ axial velocity at surface given by Eq. [11] (cm/s)
 x_i mole fraction of species i
 z axial distance from surface

Greek Symbols

δ_{ij} Kronecker delta defined by Eq. [A-7]
 ϵ_{ij} maximum energy of attraction between molecules i and j (J)
 ζ = $z \sqrt{N/\nu_x}$, dimensionless axial distance
 θ_k dimensionless kinetic parameters for boron deposition ($k = 1-5$)
 θ_{vl} adsorption/desorption parameter for surface reaction 1, see Ref. (15)
 λ hydrodynamic parameter (corresponds to rotation

rate Ω for rotating disk system and to parameter a for impinging jet apparatus) (s⁻¹)
 μ fluid viscosity (g/cm s)
 μ_i chemical potential of species i (J/mol)
 ν_{il} stoichiometric coefficient for species i in homogeneous reaction 1 (positive for reactants, negative for products)
 ν_x bulk kinematic viscosity (cm²/s)
 ρ fluid density (g/cm³)
 σ_{ik} collision diameter for Lennard-Jones potential (cm)
 Ω rotation rate of disk (rad/s)
 $\bar{\Omega}_{ik}^{(l,s)}$ collision integral
 $\bar{\Omega}_{ik}^{(l,s)*}$ dimensionless collision integral

Superscripts

* ideal gas
 \star dimensionless quantity
 $-$ partial molar quantity
 T transpose (in Eq. [5])

Subscripts

s at surface
 ∞ in bulk

REFERENCES

1. W. H. Sheperd, *This Journal*, **112**, 988 (1965).
2. S. E. Bradshaw, *Int. J. Electron.*, **23**, 381 (1967).
3. D. R. Olander, *Ind. Eng. Chem. Fundam.*, **6**, 188 (1967).
4. F. C. Eversteyn, P. J. W. Severin, C. H. J. van der Brekel, and H. L. Peek, *This Journal*, **117**, 925 (1970).
5. J. Bloem, *ibid.*, **117**, 1397 (1970).
6. R. Takahashi, Y. Koga, and K. Sugawara, *ibid.*, **119**, 1406 (1972).
7. V. S. Ban and S. L. Gilbert, *J. Cryst. Growth*, **31**, 284 (1975).
8. C. W. Manke and L. F. Donaghey, *This Journal*, **124**, 561 (1977).
9. J. Korec, *J. Cryst. Growth*, **46**, 362 (1979).
10. R. Pollard and J. Newman, *This Journal*, **127**, 744 (1980).
11. J. Subrahmanyam, A. K. Lahiri, and K. P. Abraham, *ibid.*, **127**, 1394 (1980).
12. M. L. Hitchman, *J. Cryst. Growth*, **48**, 394 (1980).
13. J. Jůza and J. Čermak, *This Journal*, **129**, 1627 (1982).
14. M. E. Coltrin, R. J. Kee, and J. A. Miller, *ibid.*, **131**, 425 (1984).
15. M. Michaelidis and R. Pollard, *ibid.*, **131**, 860 (1984).
16. J. Bloem and L. J. Giling, in "Current Topics in Materials Science," Vol. 1, E. Kaldis, Editor, p. 214, North Holland, Amsterdam (1977).
17. K. Sugawara, *This Journal*, **119**, 1749 (1972).
18. L. Vandenbulcke and G. Vuillard, *ibid.*, **124**, 1931 (1977).
19. J. S. Newman, "Electrochemical Systems," Prentice-Hall, Engelwood Cliffs, NJ (1973).
20. R. B. Bird, W. E. Stewart, and E. N. Lightfoot, "Transport Phenomena," John Wiley, New York (1960).
21. R. Abber, M.S. Thesis, University of Houston (1984).
22. K. E. Grew and T. L. Ibbs, "Thermal Diffusion in Gases," Cambridge University Press, London (1952).
23. J. O. Hirschfelder, C. F. Curtiss, and R. B. Bird, "Molecular Theory of Gases and Liquids," Wiley, New York (1954).
24. S. Chapman and T. G. Cowling, "The Mathematical Theory of Nonuniform Gases," Cambridge University Press, London (1970).
25. J. O. Hirschfelder, R. B. Bird, and E. L. Spotz, *J. Chem. Phys.*, **16**, 968 (1948).
26. J. O. Hirschfelder, R. B. Bird, and E. L. Spotz, *Chem. Rev.* **44**, 205 (1949).

Prediction of Spatial Patterns of Oxygen Precipitation in Silicon

G. Markovits, E. E. Hearn, M. V. Kulkarni,* and B. J. Elliott¹

IBM Corporation, East Fishkill Facility, Hopewell Junction, New York 12533

ABSTRACT

This work demonstrates a correlation between the initial resistivity pattern and the final precipitation pattern in silicon wafers. The correlation allows prediction of the final precipitation pattern by measuring of the initial resistivity pattern prior to any thermal donor annihilation by thermal processing. By using a simple change in the form of the thermal cycle, this precipitation pattern can be forced into a positive or negative image of the initial resistivity pattern. Time domain reflectometry and cathodic hydrogen generation ("bubble test") are two nondestructive methods used to characterize the state of the electrically active donor complexes; both methods are described here.

Oxygen precipitation in silicon wafers during device fabrication is an important factor in final product yields. The role of oxygen begins during crystal growth and plays a key part through all phases of processing. It can act as a getterer of heavy metal ions, thereby increasing product yield, or it can cause device killing defects. Usually oxygen effects are measured after one or more heat cycles. However, oxygen effects can be monitored, predicted, and therefore controlled before being exposed to any heat cycles.

This paper describes how to predict the oxygen precipitation pattern found after thermally processing silicon wafers. Prediction is made by measuring the wafer resistivity before any heat-treatment and by comparing the resistivity pattern to the infrared absorbance pattern after heat-treatment. Also, the nondestructive detection schemes and heat-treatment conditions are described; we show how they reinforce each other's being able to predict where oxygen will precipitate in wafers after heat-treatment.

Materials and Equipment

100 mm diam wafers are processed from boron-doped crystals of 11-24 Ω -cm resistivity. The wafers have an orientation of [100], are 675 μ m thick, and are chem-mech polished on both sides. These samples are taken from ingots grown in Czochralski-type crystal pullers.

Thermal Donor Determination

Kaiser and Keck (1) have shown that oxygen can be introduced into p-type silicon during growth. This oxygen can be incorporated in two forms during growth: one is the solid solution interstitial oxygen; the other is the electrically active formed donor complex. In p-type silicon, the latter form tends to compensate the intended boron dopant. It is possible to convert large areas of the silicon to n-type, depending on the relative concentrations of boron and oxygen thermal donors (2). The net effect of the electrical activity of these interactions can be measured by resistivity techniques (3). Two nondestructive methods are used to obtain this information. Most of the available techniques require some contact with the sample and are likely to damage the sample.

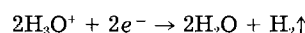
The first technique is time domain reflectometry [TDR] (4). Essentially, this method uses a miniature radarlike set, with the wafer surface acting as a reflecting target. By analyzing the magnitude, shape, and duration of the reflected 2.3 GHz signal, the impedance of the target can be determined. Through a novel modification of capacitively coupling the signal source to the wafer, this device becomes a contactless tool suitable for point-to-point measurements on a wafer. This technique is called capacitively coupled time domain reflectometry [CCTDR] (5) and is schematically shown in Fig. 1. CCTDR has its limitations. In this experiment, the equipment was reasonably accurate over a limited range of 5-500 Ω -cm. This limitation is acceptable. A comparison of

a CCTDR scan and a stepped four-point probe scan on the same sample reveals that the CCTDR captures all of the salient features (see Fig. 2).

It should be emphasized that this study is strictly phenomenological. Thus, the CCTDR is adequate, and, most importantly, it avoids introducing damage which, in subsequent processing, might propagate and influence oxygen precipitation.

The second method is the cathodic generation of hydrogen, referred to as "the bubble test." First reported by Markovits (6), this technique is described here. A silicon wafer is reverse-biased at 5V in a cell that allows the back side of the wafer to be the cathode and the front side to be the anode. Figure 3 shows that the wafer's front side contacts the anode through an electrolyte of 2% H₂SO₄. The wafer back side is vacuum sealed, and it contacts the cathode by carbon impregnated wool.

The silicon (wafer) acts as a catalyst while the water molecule and its associated hydrogen ion reduce and provide the extra electron to free the hydrogen gas, as in



At any place there is a higher probability of electron

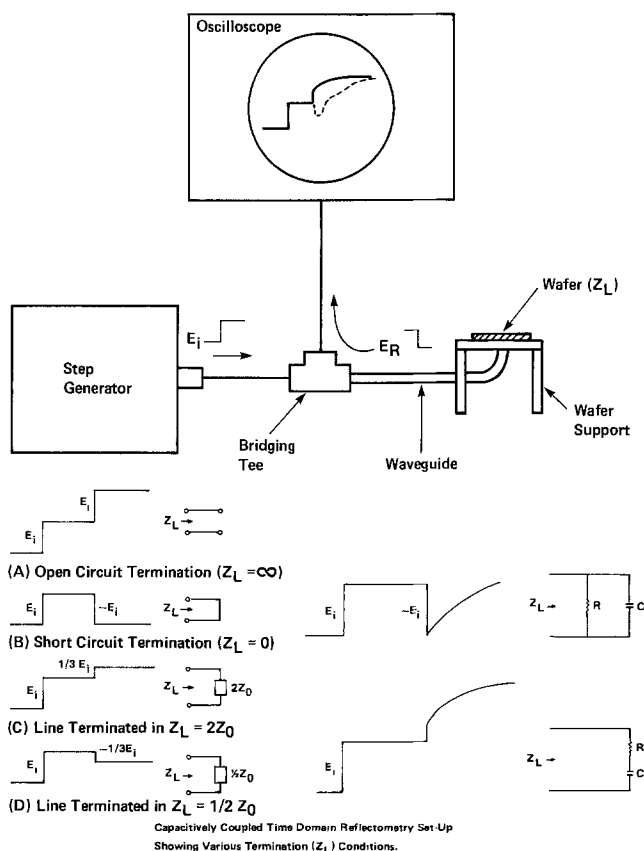


Fig. 1. Coupled time domain reflectometry schematic

*Electrochemical Society Active Member.

¹Present address: Hewlett-Packard, San Jose, California.

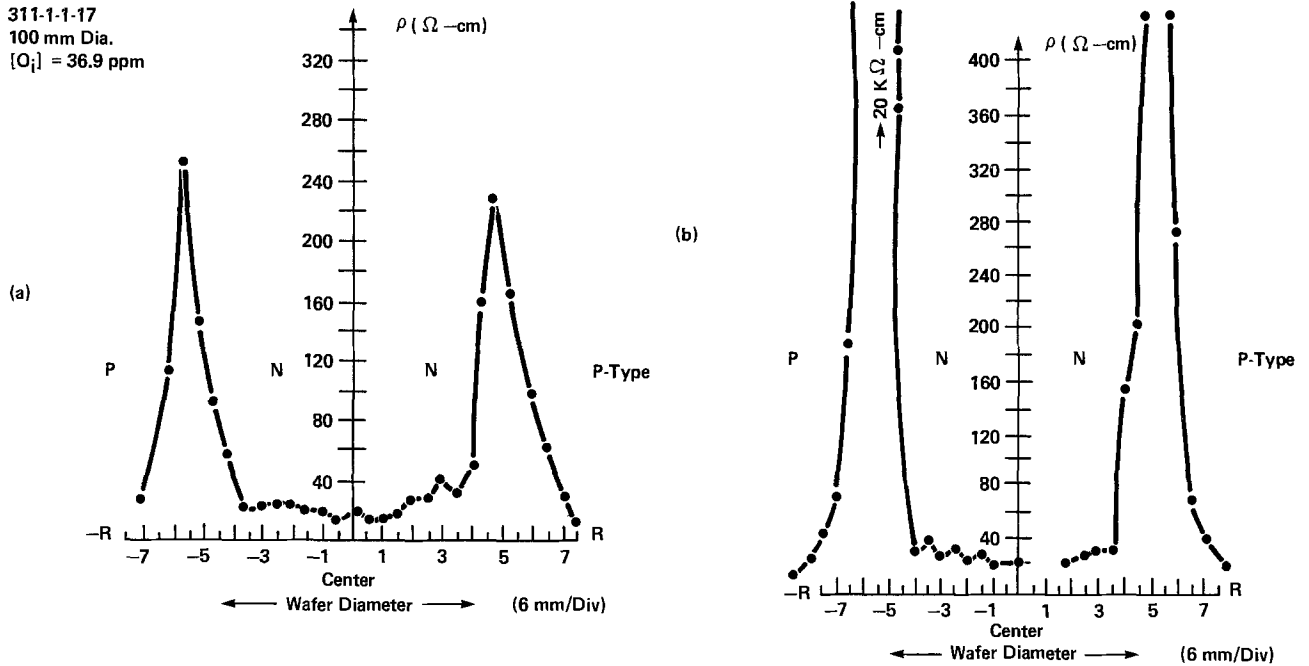


Fig. 2. CCTDR scan (a) and stepped four-point probe scan (b) on same sample.

transfer from the semiconductor to the electrolyte, hydrogen is formed at a proportionately higher rate. This can occur as a result of p-n junctions, damage, dirt, excessive light.

An ohmic contact exists between the dilute sulfuric acid and the n-type regions of the wafer. In contrast, the p-type regions produce a condition like that of a reverse-biased junction. The resulting current variation across the sample reflects the change in conductivity from p to n. This variation in current density is reflected by variations in hydrogen production at the silicon surface. Hydrogen bubbles adhere to the silicon surface by surface

tension. When illuminated obliquely, they can be photographed to provide a record of the conductivity changes

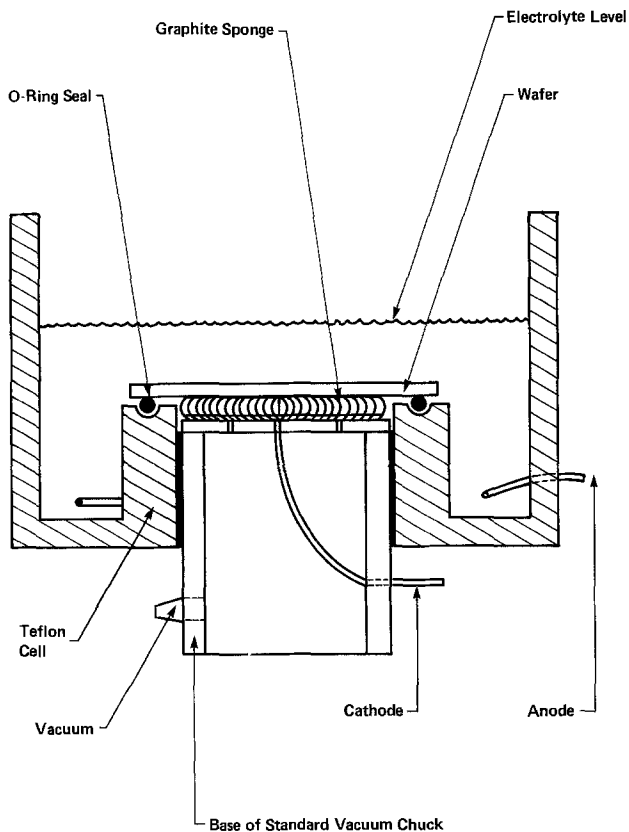


Fig. 3. Apparatus used for wafer "bubble test"

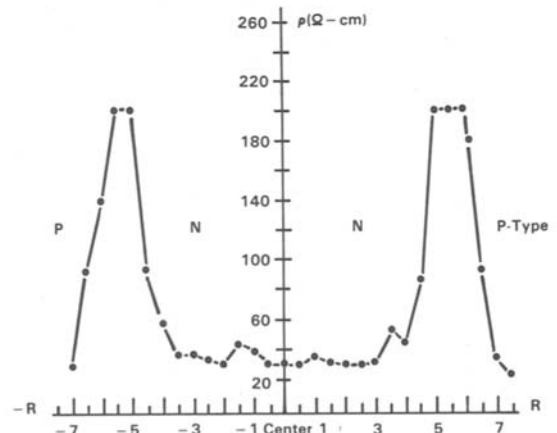
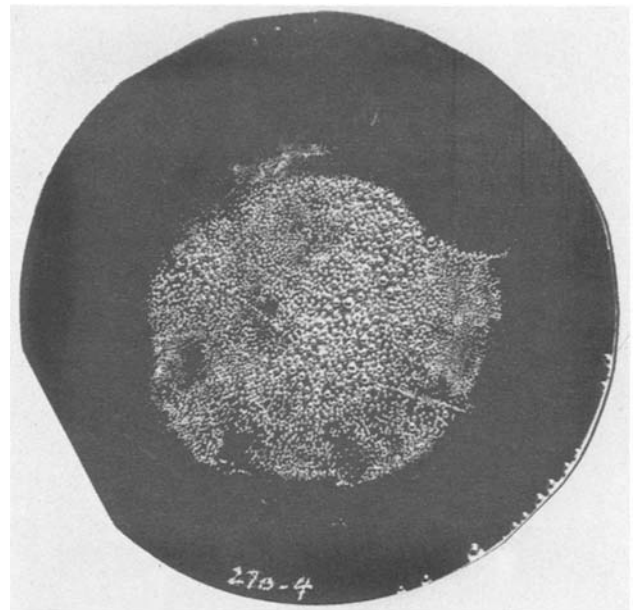


Fig. 4. Hydrogen bubble pattern (top) and CCTDR pattern for crystal seed end (bottom).

across the wafer. For a totally p-type wafer, visible hydrogen bubbles are absent.

The conductivity-type changes revealed by the cathodically generated hydrogen pattern are checked in two ways: the first is with a hot probe (7), which confirms that it is only the n-type regions that generate the visible amounts of hydrogen; the second check is made with a copper stain, which preferentially plates out on n-type regions. This essentially confirms the results of the other two methods. It also is applied to a beveled sample to confirm that the surface conductivity-type pattern is continuous through the bulk.

Interstitial oxygen concentration measurement.—The interstitial oxygen concentration is determined by the infrared absorption method. Absorption due to an 1107 cm^{-1} interstitial oxygen wave number peak is measured, at the sample location, on the double-side polished wafers, using a Fourier transform spectrometer with a beam spot size of less than 6 mm in diameter. The silicon lattice contribution is removed by using an oxygen-free floating-zone wafer reference. The concentration of oxygen is calculated from these measurements using a calibration plot generated from three similar wafers that are accurately measured for oxygen content by the ASTM method (8). Because oxygen precipitates also generate absorption peaks quite close to the 1107 cm^{-1} interstitial oxygen peaks (9), we use a point-to-point subtraction method to determine the contribution of interstitial oxygen to the composite spectrum. The resolution used for most of the measurements is 8 cm^{-1} . The time of measurement is

chosen so that the standard deviation for the precision of the measurement is about 0.5 ppma of oxygen. The decrease in interstitial oxygen is solely attributed to its precipitating to form SiO_x complexes of various kinds. As precipitation progresses, absorption traces of the different spectra are made so that it is possible to monitor development of different oxygen precipitate forms (9).

Thermal treatment of our samples occurs in a Thermco Brute American furnace equipped with a Tylan GP481 flow controller. A quartz liner and polysilicon boats are used. Experimental samples are sandwiched in the center of a group of 20 dummy wafers. This is done to further ensure that the thermal environment of all experimental samples will be identical, even during heat-up and cool-down phases of the cycle. The ambient for our thermal cycles is nitrogen.

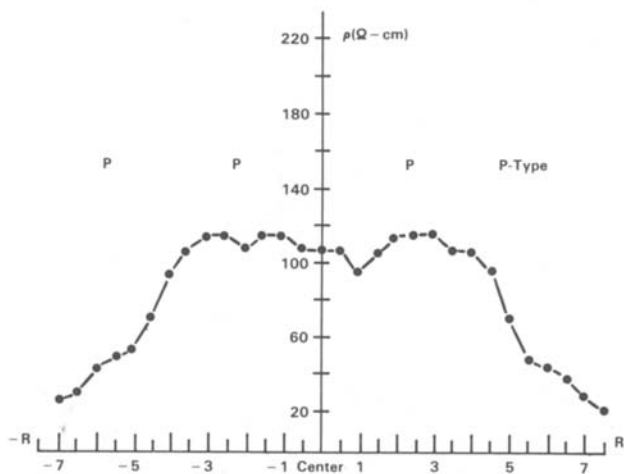
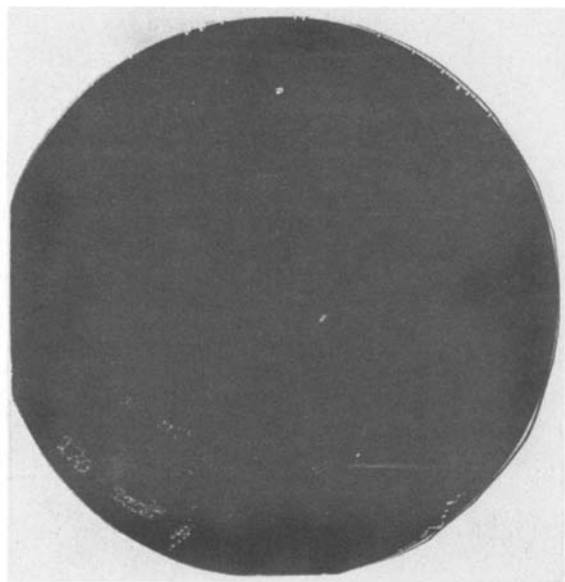


Fig. 5. Cathodic generation test result (top) and CCTDR pattern for bottom (nonseed) end of crystal (bottom).

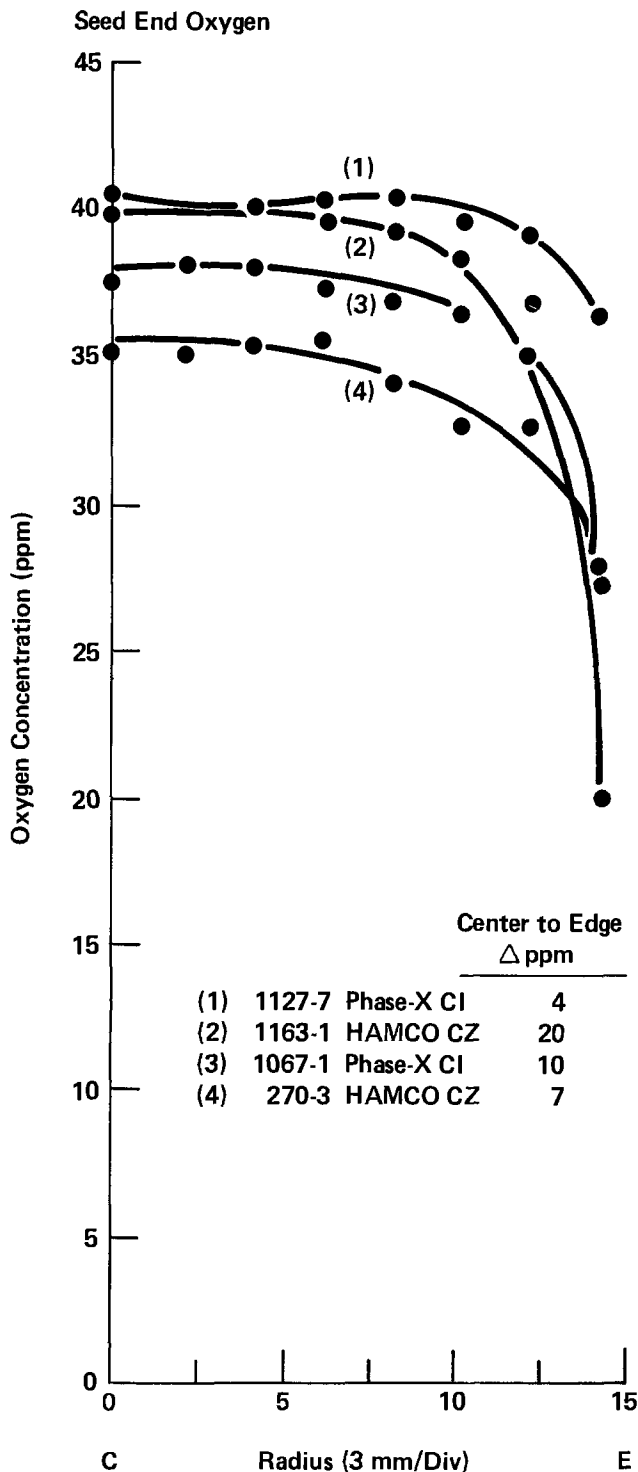


Fig. 6. Oxygen concentration profile at seed end of crystal

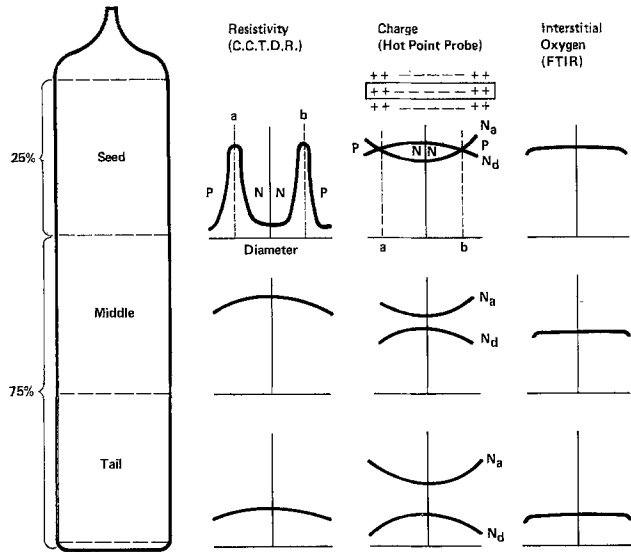
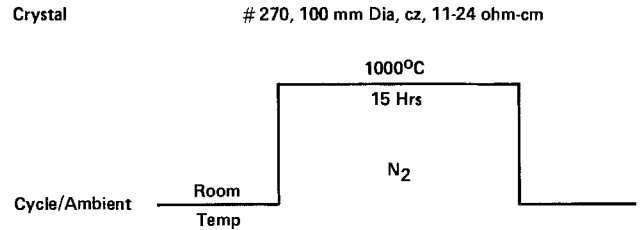


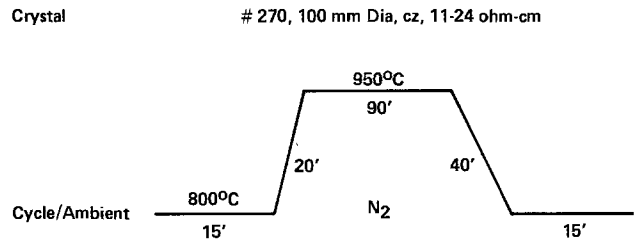
Fig. 7. Schematic summary of raw wafer characteristics

Experiment and Results

Initial characterization.—Two broad classes of wafers exist, according to their initial resistivity and conductivity-type patterns. The group exhibiting conductivity-type patterns is referred to as the character group; the remainder is referred to as the characterless group. There is also a correlation between the character/characterless conductivity groups before heat-treatment and the character/characterless precipitation groups after heat-treatment. Examples of the character and characterless patterns are shown in Fig. 4 and 5. Simple patterns, as in Fig. 4, are typical for the first 20-30% of most crystals. This is the seed end of the crystal, and it usually contains the greatest oxygen concentration. However, it is not oxygen concentration alone that determines whether or not the conductivity-type patterns will exist. For the last 70-80% of the crystal, we find no conductivity-type patterns. The thermal donor concentration is always less than the intended boron dopant; it is not invariant across the sample. Figure 5 shows the result of the cathodic genera-



(a) Isothermal Anneal Cycle



(b) Totally Ramped Cycle

Fig. 8. (a) Isothermal anneal cycle, and (b) totally ramped cycle

tion test for such wafers. The CCTDR traces corresponding to the bubble test are also shown in Fig. 4 and 5.

In contrast to the initial resistivity patterns, the initial interstitial oxygen concentration is uniform. In most samples, the concentration varies by only one or two parts per million until within approximately 6 mm from the edge, at which point it decreases more drastically in some of the seed end samples. An example of typical initial oxygen concentration profiles is given in Fig. 6.

The overall oxygen range, as determined by center readings on each sample, is 24-43 ppm. The group of samples with initial resistivity character span a range of 34-43 ppm, while the characterless group has a range of 24-38 ppm. This overlap of oxygen concentration demonstrates that the initial resistivity character is a function of more than the oxygen concentration. This is further supported in later experiments where lower oxygen content crystals are found to extend the range of the character

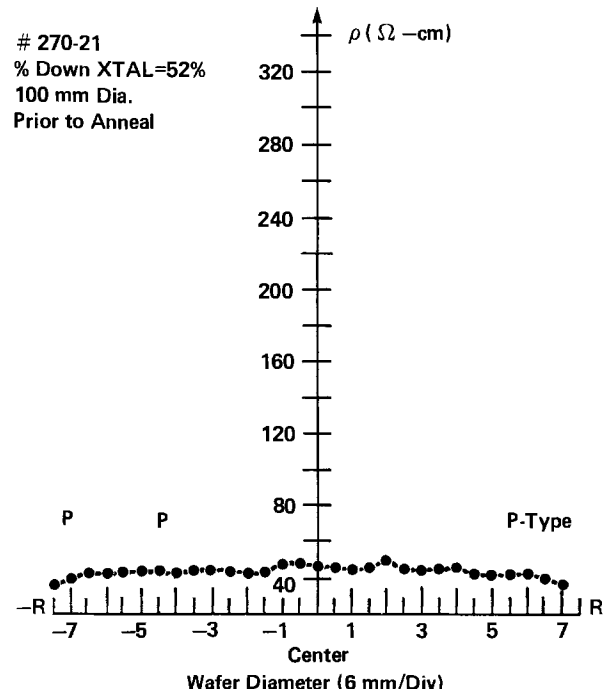
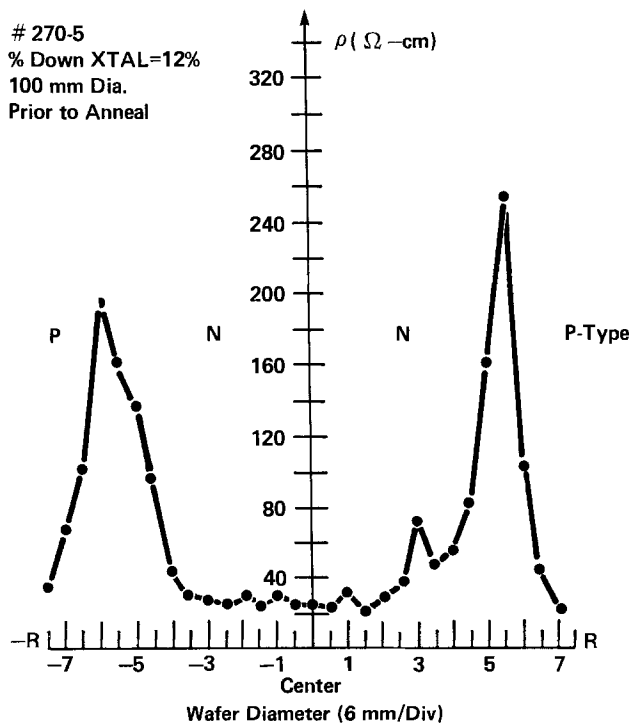


Fig. 9. Initial resistivity, prior to thermal donor anneal, vs. wafer diameter. Measurement made by time domain reflectometry.

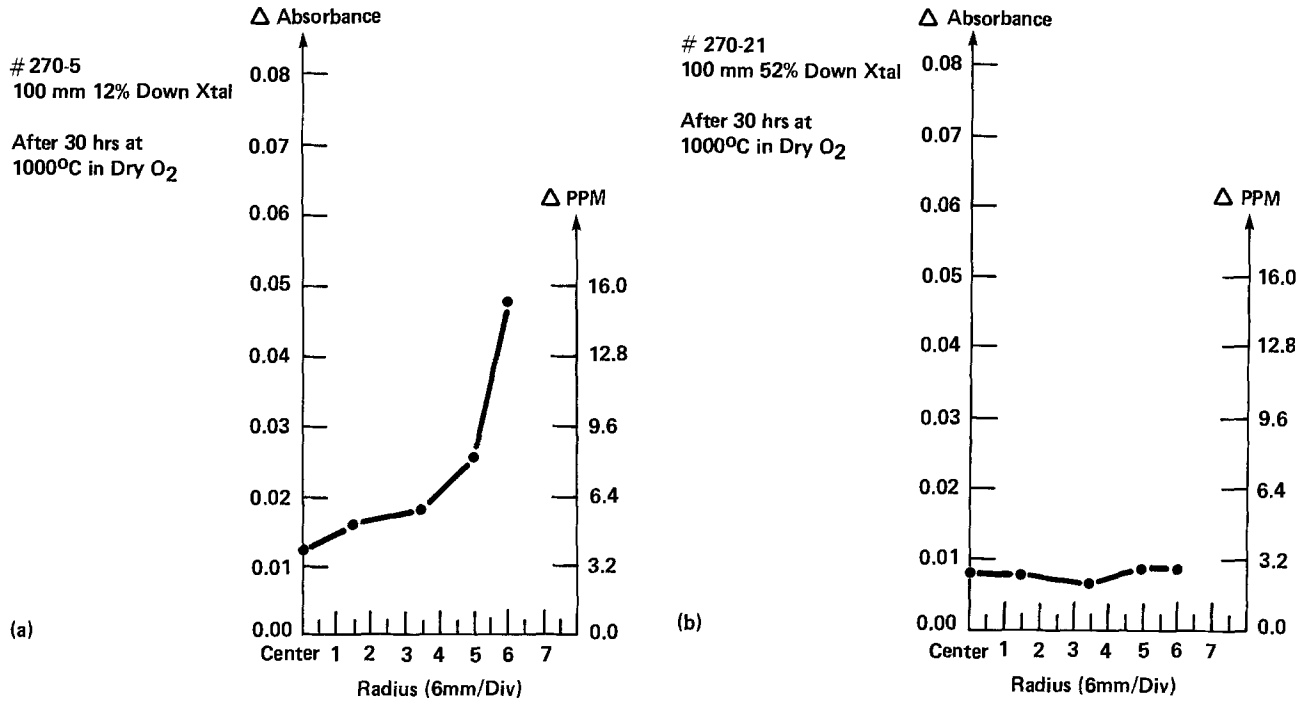


Fig. 10. Oxygen precipitation vs. radius for two samples

group down to 27 ppm. It appears that the dominant factor is the axial position within a crystal and, therefore, the thermal history during crystal growth, rather than absolute oxygen level.

A schematic summary of the raw wafer characteristics is presented in Fig. 7. In the as-grown material, the thermal donor concentration varies from seed to tail. This results in producing annular conductivity-type patterns in the first third or less of the crystal.

Post Thermal Processing

Isothermal anneals.—Samples are divided into groups and subjected to two different thermal cycles. The first cycle is isothermally annealed to 1000°C in nitrogen for a period of 15h. Insertion and withdrawal times are done within 20s for each cycle. The second cycle form is ramped up and down from an end cap temperature to a

peak of 950°C. The peak temperature is maintained for a period of 90 min. Details of the two cycles are shown in Fig. 8. Each thermal cycle form is populated with wafers from both the character and characterless groups, as de-

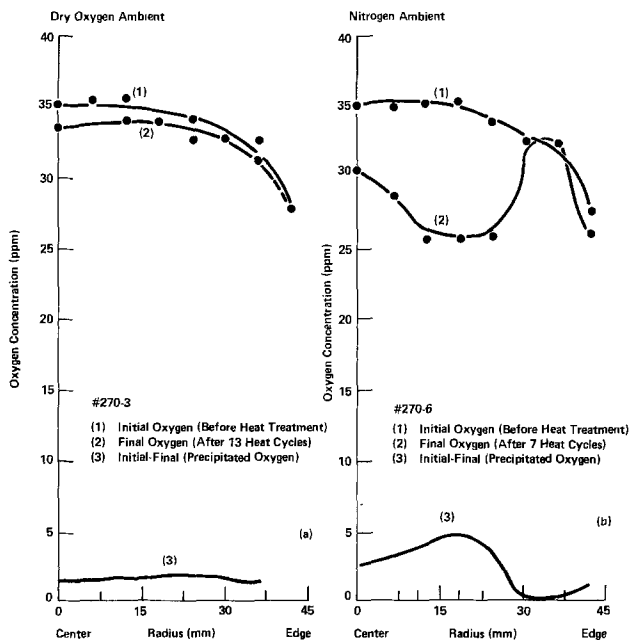


Fig. 11. Interstitial oxygen precipitation vs. crystal radius for characterless and character samples after ramped thermal cycles.

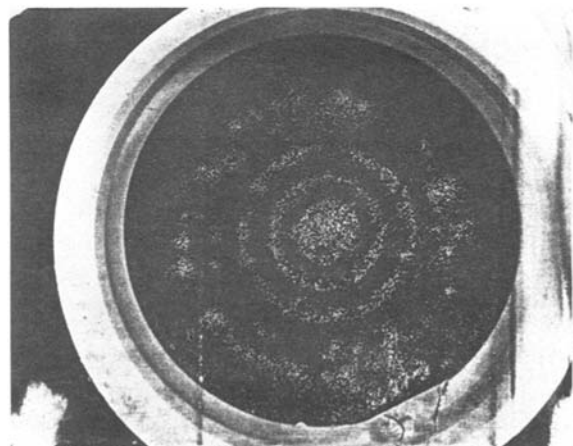
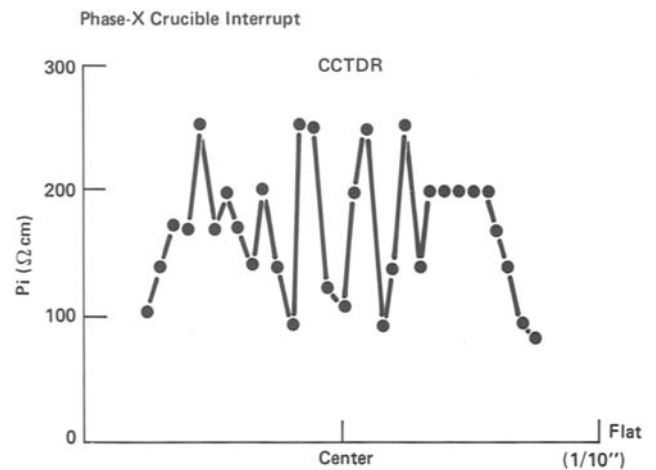


Fig. 12. Pattern obtained by cathodic generation of hydrogen on a seed-end wafer. Areas (bottom) covered by hydrogen bubbles are of n-type conductivity.

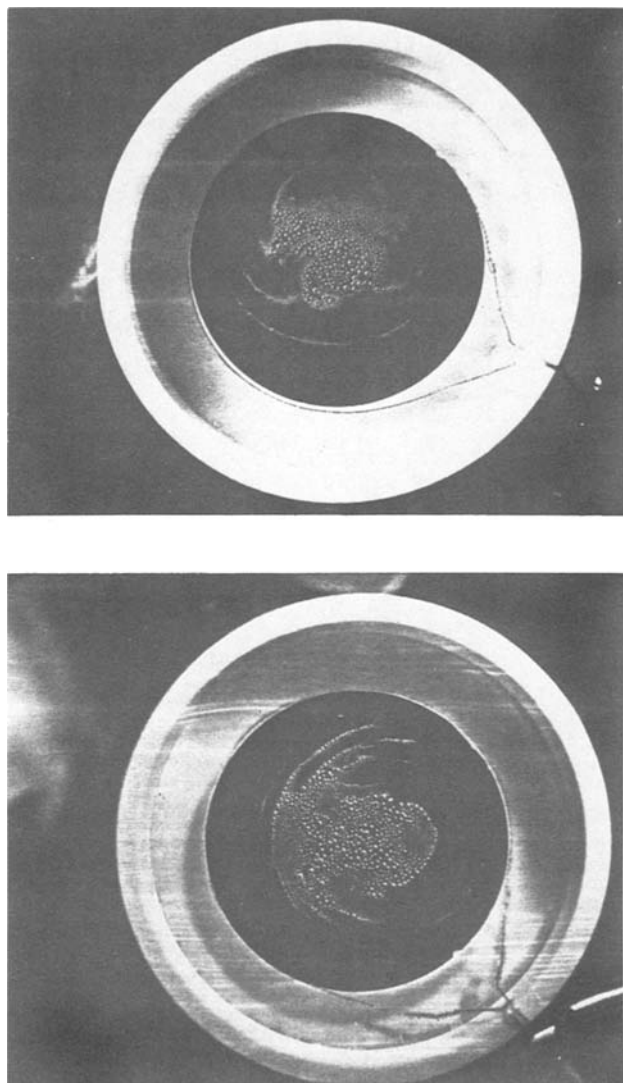


Fig. 13. Examples of complex nonsymmetric patterns before heat-treatment.

terminated by initial resistivity patterns. The ambient in all cases is nitrogen.

Sample numbers 270-5 and 270-21 in Fig. 9 come from the character and characterless groups, respectively. Figure 9 contains the respective CCTDR traces before the isothermal heat-treatment. Sample 270-5 displays the simple annular pattern, *i.e.*, an n-type central disk surrounded by an intrinsic ring which is surrounded by a p-type ring.

Figure 10 is a plot of the amount of precipitated oxygen *vs.* radius. It is obtained by subtracting the post thermal processing measurements from the initial raw wafer measurements. A ring of precipitation occurs in sample 270-5. The little precipitation that occurs in sample 270-21 is quite uniform.

Ramped heat cycles.—Results for samples subjected to ramped thermal cycling are consistent, yet quite different. They are similar, in that the group with initial resistivity character also has character in its final precipitation pattern, whereas the initially characterless group does not. The results are quite different from those of the isothermal experiment because the “sign” of the correlation has inverted. Where earlier we find that the maxi-

mum precipitation occurs in the intrinsic ring, with relatively less in the central disk, we now find the central disk to be the more heavily precipitated region.

Samples 270-6 and 270-3 are subjected to seven thermal cycles of the ramped form; they represent a character and a characterless sample, respectively. The hydrogen bubble pattern and CCTDR trace of sample 270-6 before heat-treatment appear the same as shown in Fig. 4. The initial and final oxygen concentrations *vs.* radius are plotted in Fig. 11. Both thermal cycle types are populated with samples from the same crystals. What we discover is that a wafer with initial resistivity character can be forced to precipitate in either the disk or the ring by proper selection of the thermal cycle form.

These experiments are repeated with similar results on material from five other crystals. In all cases, a correlation exists in form between the initial resistivity pattern and the final precipitation pattern. The causes and effects of these heat cycles are the subject of Hearn *et al.* (10) and are omitted here.

Other examples of variation of the theme of simple patterns (Fig. 4) are shown in Fig. 12 and 13. Multiple rings spaced by alternating intrinsic regions (n-i-p-i-n) result in a typical swirl pattern, as seen by the bubble test before heat-treatment (Fig. 12). Noncentrosymmetric rings are also seen in the bubble test before heat-treatment. Again, these same patterns remain after heat-treatment, as detected by x-ray topography, etching, and infrared absorbance measurements.

The measured initial oxygen concentration in some of these complex samples lacks a corresponding variation in oxygen concentration, which is sometimes used to explain the patterns. However, the initial oxygen concentration is always uniform within a few parts per million until it is within a few millimeters of the sample edge.

Summary

This work demonstrates a correlation between the initial resistivity pattern and the final oxygen precipitation pattern in silicon wafers. This correlation enables one to predict the final oxygen precipitation pattern by simply measuring the initial resistivity pattern prior to any thermal donor annihilation by thermal processing.

A complex relationship between oxygen thermal donors, the intended acceptors, and the final precipitation sites is suggested. This is demonstrated by using a simple change in the thermal cycle form to force an oxygen precipitation pattern into either a positive or negative image of the initial resistivity pattern.

REFERENCES

1. W. Kaiser and P. H. Keck, *J. Appl. Phys.*, **28**, 882 (1957).
2. C. S. Fuller, Ditzenberger, Hannay, and Buehler, *Phys. Rev.*, **96**, 833 (1954).
3. C. Kittel, “Introduction to Solid State Physics,” p. 375, John Wiley & Sons, New York (1971).
4. “Time Domain Reflectometry,” Hewlett-Packard Application Note no. 62 (1964).
5. B. J. Elliott, IBM Report RC6077, IBM Research Center, Yorktown Heights, NY (1976).
6. G. Markovits, Paper 543 presented at The Electrochemical Society Meeting, Los Angeles, CA, Oct. 14-19, 1978.
7. ASTM F42-64T Method A, “Standard Methods of Test for Conductivity Type of Extrinsic Semiconductor Materials,” Philadelphia, PA (1967).
8. ASTM F45-64T, “Annual Book of ASTM Standards,” Philadelphia, PA (1968).
9. K. Templehoff, F. Spielberg, and R. Gleichman, *Semicond. Silicon*, **77**, 585 (1977).
10. E. W. Hearn, G. Markovits, and M. V. Kulkarni, *Semicond. International*, **4**, 101 (1981).

Interaction of H₂O with Si(111) and (100)

Critical Conditions for the Growth of SiO₂

G. Ghidini¹ and F. W. Smith

Department of Physics, City College of New York, New York, New York 10031

ABSTRACT

The reactions of H₂O with the clean Si(111) and (100) surfaces have been studied at high temperatures (890°-1350°C) for H₂O pressures between 7×10^{-5} and 4×10^{-1} torr. The critical conditions involving H₂O pressure and substrate temperature which are necessary for the growth of SiO₂ have been determined, and are consistent with a thermodynamic model modified to include effects due to H₂O dissociation and SiO desorption. In addition to clean (active) and SiO₂-covered (passive) surface regions, an intermediate region is observed and is proposed to be related to a thin, nonpassivating Si_xO_yH_z film on the Si surface.

Passivating films of SiO₂ can be grown on Si via the reaction of H₂O with the clean Si surface at high temperature (1-3). The SiO₂ layers grown via the H₂O + Si reaction are more protective and can be grown more rapidly than those prepared via the comparable O₂ + Si reaction (3). Information concerning the critical conditions for growth of SiO₂ via the reaction of H₂O with Si is thus of considerable technological interest, as well as being important for aiding in our understanding of gas-surface interactions and thin film growth processes.

Our previous study (4) of the O₂ + Si reaction has indicated that the processes of O₂ dissociation on and SiO desorption from the Si surface are crucial for determining the critical conditions for the growth of SiO₂. Analogous processes will influence the H₂O reaction, with the additional factor of the presence of hydrogen on the surface to be considered.

We report here on a study of the reactions of H₂O with the clean Si(111) and (100) surfaces, which has been undertaken to determine the critical conditions for growth of SiO₂. We will first summarize some previous studies both of the growth of thick SiO₂ films via the H₂O + Si reaction and of the adsorption and dissociation of H₂O on Si. Experimental details are then presented, followed by the results of this study for the critical growth conditions, SiO₂ growth features, and parameters characterizing the dissociation of H₂O and desorption of SiO. These results will be discussed in terms of a thermodynamic model modified to take into account H₂O dissociation and SiO desorption. Finally, the presence of a thin, nonpassivating Si_xO_yH_z layer on the Si surface under certain experimental conditions is proposed.

Background

Growth rates of films of SiO₂ produced via the reaction of Si with H₂O have been analyzed in terms of the linear-parabolic model (5), with rate constants for both the linear and parabolic regimes observed to be at least an order of magnitude larger than those observed for the corresponding O₂ + Si reaction. The linear rate constant k_{LIN} reflects the reaction occurring between the oxidizing species and Si at the Si-SiO₂ interface. In the case of H₂O (and H₂O + O₂) oxidation, the enhancement of k_{LIN} has been proposed to be due to the "catalytic" effect of hydrogen on the oxidation reaction (1, 6). One possible mechanism for this "catalytic" effect is the weakening of Si-Si bonds at the interface for those Si atoms bonded to H, thus facilitating oxygen atom insertion. Hydrogen may play an analogous role in the initial stages of the interaction of H₂O with the clean Si surface, which would then be an important factor for determining the critical conditions for the growth of SiO₂.

The initial adsorption of H₂O on Si at room temperature has been the topic of several recent experimental investigations (7-10). It seems clear that the H₂O molecule is adsorbed on Si with the oxygen atom bonding to the surface Si (7, 8). The removal of gap states (associated with the

dangling bonds at the surface) is readily achieved via H₂O adsorption on Si, indicating a strong interaction. Whether the adsorption is initially molecular or dissociative at room temperature appears to depend critically on the structure of the Si surface (8-10). It has been found (9) that the sticking coefficient at room temperature for adsorption and decomposition of H₂O is unity on Si(100) and about 10^{-2} on Si(111)-(7 × 7). In the same work, evidence has been seen for SiH and SiOH groups on the Si surface at room temperature, with further dissociation leading to the reaction SiOH → Si-O-Si + SiH by 150°C, and finally H₂ desorption by 330°C. Other workers claim that H₂O adsorbs molecularly at room temperature if the surface is smooth, but dissociates if the surface is disordered (8). Dissociative adsorption of H₂O on Si at room temperature has recently been predicted theoretically (11).

A study of the critical conditions for the oxidation of Si via the H₂O + Si(111) reaction has been carried out by Maguire and Augustus (12) for $P(\text{H}_2\text{O}) < 8 \times 10^{-4}$ torr and $T_s < 1000^\circ\text{C}$. They used Auger electron spectroscopy to detect the presence of oxygen bound to the Si surface at room temperature following the high temperature H₂O + Si reaction. Their results will be discussed in more detail below.

Experimental

These reactions of H₂O with Si(111) and (100) have been carried out in the UHV system described previously (4), using the same experimental procedures for determining the critical growth conditions. Briefly, the Si substrates studied were supported in Mo clamps in the UHV chamber and cleaned thermally *in situ* via treatment at 1350°C. The H₂O used was distilled, deionized, and further purified via repeated freezing in liquid nitrogen and subsequent evacuation in order to remove volatile impurity gases. The H₂O was stored in a glass cylinder and admitted to the UHV chamber via a bakeable leak valve. $P(\text{H}_2\text{O})$ was measured above 10^{-3} torr via a Pirani gauge, while below 10^{-3} torr an ionization gauge was used.

By varying both $P(\text{H}_2\text{O})$ and the substrate temperature T_s , different regions of etching via SiO production (active surface) and SiO₂ growth (passive surface) on the Si surface were observed using an optical pyrometer. The pyrometer also served to measure T_s at the boundaries between the different regions which are present at the same time on the Si surface due to the temperature gradient along the sample. It was determined that in addition to regions of clean surface (region I, etching) and SiO₂ growth (region III), there existed on the Si surface an intermediate region II which was still active but which had a different emissivity and "grainier" appearance than the clean Si surface of region I. Details of these three regions are presented below.

Following the reactions, the samples were examined using optical and scanning electron microscopy. The boundary on the Si surface between regions II and III was quite sharp and showed growth features similar to those observed for the O₂ + Si reaction. The boundary be-

¹Present address: SGS, Agrate Brianza, Milano, Italy.

tween regions I and II was much less distinct and showed no distinctive growth or etching features. Nevertheless, it was observed reproducibly *in situ* for several different samples via the optical pyrometer.

Results

In Fig. 1 are presented our results for the critical conditions for growth of SiO₂ via the reaction of H₂O with both the Si(111) and (100) surfaces. At the highest values of $P(\text{H}_2\text{O})$ and lowest values of T_s , the surface is covered with SiO₂ (region III in Fig. 1), while at the lowest $P(\text{H}_2\text{O})$ and highest T_s , the surface remains clean via the production of SiO and H₂ (region I). Unlike the case of the O₂ + Si reaction, where only regions analogous to I and III were observed, for H₂O + Si we observe an intermediate region with surface structure and emissivity differing from the other regions. In this intermediate region, etching continues as SiO and H₂ are still produced via the reaction of H₂O with the Si surface. We will discuss this intermediate region in more detail below. The dashed line in Fig. 1 labeled $P_c(\text{O}_2)$ represents our previous results (4) for O₂ + Si, where only a single boundary was observed.

In Fig. 2 are shown SiO₂ growth features in the shape of pyramids whose square bases are rotated by 45° with respect to the [100] axes of the Si(100) substrate. This type of growth feature has previously been observed (4) for the O₂ + Si(100) reaction, and has been proposed to be the result of the epitaxial growth of the high temperature cubic form of SiO₂, β -cristobalite, specifically on Si(100), where there is only a 7% lattice constant mismatch when the two lattices are rotated by 45°, as observed in Fig. 2. We note that the growth features shown in Fig. 2 consist of only a thin [estimated (4) thickness of about 100Å], passivating layer of SiO₂ protecting the Si core of the pyramid. One

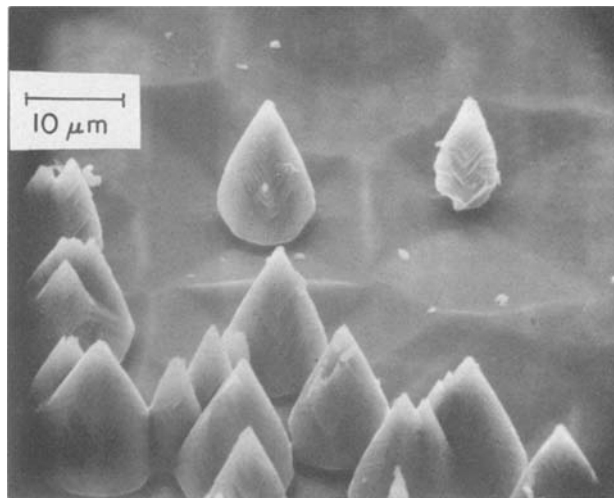


Fig. 2. SEM micrograph of SiO₂ growth features formed via the reaction of H₂O with Si(100) at $P(\text{H}_2\text{O}) = 0.15$ torr and $T_s = 1085^\circ\text{C}$. The growth features, pyramids whose square bases are rotated by 45° with respect to the Si [100] axes, sit in depressions whose sides are parallel to the [100] axes.

new result observed for H₂O + Si(100), and also illustrated in Fig. 2, is the association of the pyramidal growth features with square depressions whose sides are parallel to the Si[100] axes. No such depressions were observed for the O₂ + Si(100) case.

As for O₂ + Si and several other reactions previously studied [e.g., C₂H₄ + Si (13), C₂H₂ + Si (14), NH₃ + Si (14)], the observed boundaries between different surface regions indicated in Fig. 1 can be expressed in terms of a critical pressure via

$$P_c(\text{H}_2\text{O}, T_s) = P_0 \exp(-\Delta E/k_B T_s) \quad [1]$$

For the H₂O + Si(100) reaction, we find $P_0 = 2.3 \times 10^{13}$ torr and $\Delta E = 3.9$ eV from the straight line drawn for the upper boundary in Fig. 1, while for the lower boundary we find $P_0 = 5.6 \times 10^7$ torr and $\Delta E = 3.0$ eV. Our results for H₂O + Si(111) are consistent with the above Si(100) results, but are not as complete and are somewhat more scattered. For $P(\text{H}_2\text{O}) < 1 \times 10^{-3}$ torr (or $T_s < 950^\circ\text{C}$), we note that the boundary between regions II and III falls below the straight line drawn in Fig. 1. This result will be discussed below.

The reaction of H₂O in regions I and II of Fig. 1 leads to rapid etching of the Si surface via the production of volatile SiO molecules. An important parameter influencing the critical growth conditions is $S(\text{H}_2\text{O} \rightarrow \text{SiO})$, which gives the probability that an incident H₂O molecule adsorbs on the Si surface, dissociates, and reacts to form an SiO molecule, which eventually desorbs. The incoming flux of H₂O is determined from the H₂O pressure via the kinetic theory expression

$$R(\text{H}_2\text{O}) = P(\text{H}_2\text{O})N_0/(2\pi M(\text{H}_2\text{O})RT_g)^{1/2} \quad [2]$$

where N_0 is Avogadro's number, $M(\text{H}_2\text{O}) = 18$, R is the gas constant, and $T_g = 300$ K. The outgoing flux of SiO molecules is given by $R(\text{SiO}) = v_e \rho(\text{Si})$, where v_e is the experimentally measured etching velocity and $\rho(\text{Si})$ is the atomic density of Si. Values of $S(\text{H}_2\text{O} \rightarrow \text{SiO}) = R(\text{SiO})/R(\text{H}_2\text{O})$ determined from $P(\text{H}_2\text{O})$ and v_e are given in Table I for three groups of samples: samples at the upper boundary between regions II and III; samples near the lower boundary; and samples in region II. We note that the highest values of $S(\text{H}_2\text{O} \rightarrow \text{SiO})$, 0.016-0.029, are observed in region II.

Further evidence for the dramatic effects of etching via SiO production can be seen when the oxidant pressure falls below the critical value for the growth of SiO₂. The etching process then dominates and the pyramidal SiO₂-covered growth features can be undercut (see Fig. 3).

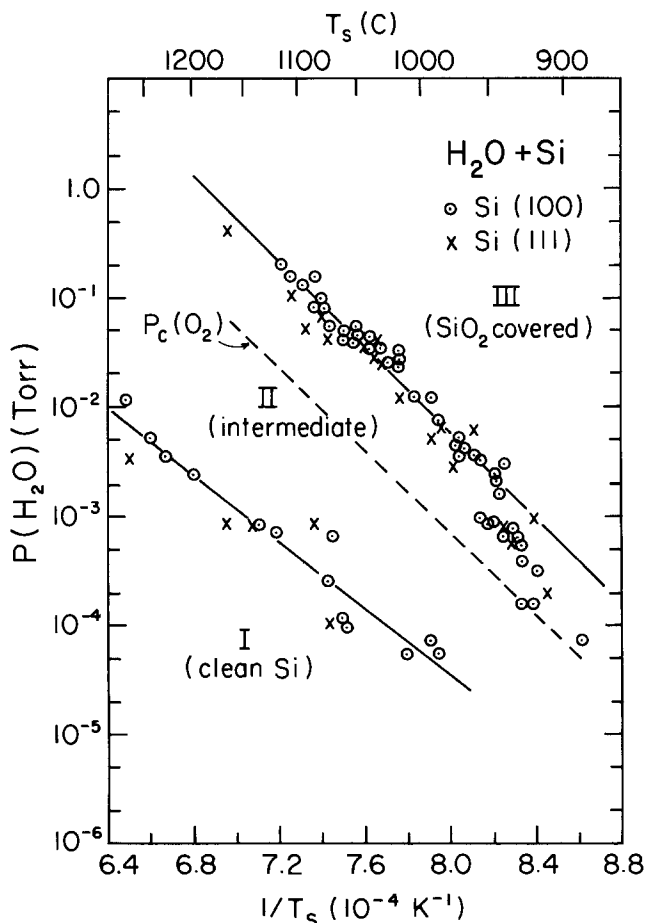


Fig. 1. The critical conditions for the growth of SiO₂ via the reaction of H₂O with Si(111) and (100). $P(\text{H}_2\text{O})$, water vapor pressure; T_s , substrate temperature. Previous results obtained for the O₂ + Si reaction are indicated by $P_c(\text{O}_2)$.

Table I. Parameters for the reaction of H₂O with Si

Sample no.	P (H ₂ O) (torr)	T _s (K)	v _e (Å/s)	S (H ₂ O → SiO)	S _{SiO}
<u>At upper boundary</u>					
5 (100)	6.4 × 10 ⁻⁴	1215	16	0.027	0.081
6 (111)	1.6 × 10 ⁻³	1215	14	0.0093	0.071
6 (100)	4.7 × 10 ⁻²	1323	370	0.0084	0.13
14 (100)	5.5 × 10 ⁻²	1333	500	0.0096	0.13
2 (100)	8.4 × 10 ⁻²	1355	480	0.0061	0.078
8 (111)	2.2 × 10 ⁻¹	1399	740	0.0036	0.048
<u>At lower boundary</u>					
38 (100)	6.0 × 10 ⁻³	1630	19	0.0034	
15 (100)	8.1 × 10 ⁻³	1538	54	0.0071	
16 (100)	3.2 × 10 ⁻²	1503	180	0.0059	
<u>In region II</u>					
39 (100)	6.0 × 10 ⁻³	1424	88	0.016	
25 (100)	7.0 × 10 ⁻³	1352	190	0.029	

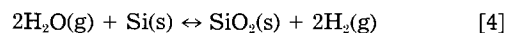
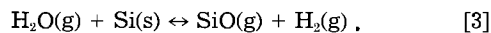
Discussion

In order to understand the upper boundary of Fig. 1, separating the intermediate region II from region III of SiO₂ growth at higher values of P(H₂O), we will first consider the thermodynamics of the reactions involved. The



Fig. 3. SEM micrograph of a pyramidal SiO₂ growth feature formed via the reaction of O₂ with Si(100) at P(O₂) = 1.8 × 10⁻² torr and T_s = 1090°C. The pyramid is undercut at its base via the etching reaction producing SiO.

net reactions which are important for the interaction of H₂O with Si under our experimental conditions are



Reactions [3] and [4] proceed to the right under our experimental conditions, with free energy changes ΔG₃ and ΔG₄ both less than zero. Reaction [3] dominates in regions I and II, while reaction [4] dominates in region III of Fig. 1.

Noting that 2ΔG₃ - ΔG₄ = ΔG₅, we find that reactions [3] and [4] will proceed at the same rate, per incident H₂O molecule, when reaction [5] is in equilibrium, i.e., when ΔG₅ = 0. The equilibrium SiO vapor pressure P_{eq}(SiO, T_s) for reaction [5], measured for ΔG₅ = 0, also determines the maximum rate at which SiO can be produced by reaction [3]. This maximum rate is given by

$$R_{\text{max}}(\text{SiO}, T_s) = S_{\text{SiO}} P_{\text{eq}}(\text{SiO}, T_s) N_A / (2\pi M(\text{SiO}) RT_s)^{1/2} \quad [6]$$

Here S_{SiO} is the vaporization coefficient for SiO on Si at temperature T_s (15). The critical conditions for growth of SiO₂ via the H₂O + Si reaction are attained when S(H₂O → SiO)R(H₂O), the rate at which H₂O molecules react to form SiO, is equal to R_{max}(SiO, T_s). The critical value for P(H₂O) is thus given, using Eq. [2] and [6], by

$$P_c(\text{H}_2\text{O}, T_s) = \left(\frac{S_{\text{SiO}}}{S(\text{H}_2\text{O} \rightarrow \text{SiO})} \right) \left(\frac{M(\text{H}_2\text{O})T_s}{M(\text{SiO})T_s} \right)^{1/2} P_{\text{eq}}(\text{SiO}, T_s) \quad [7]$$

Apart from a factor of 1/2, this is equivalent to the expression previously derived (4) for the O₂ + Si case. Using P_{eq}(SiO, T_s) = (3.08 × 10¹¹ torr) exp(-3.54 eV/k_BT_s) measured experimentally (16) and our measured values of S(H₂O → SiO) given in Table I, we assume Eq. [7] to be correct and thus obtain the values of S_{SiO} also listed in Table I from our measured results for P_c(H₂O, T_s). Once again, as for the case of O₂ + Si, we find S_{SiO} < 1, indicating that the vaporization of SiO from the Si surface is somewhat retarded.

The curvature, or bending down, of the boundary between regions II and III, which is evident in Fig. 1 for P(H₂O) < 1 × 10⁻³ torr and T_s < 950°C, can be seen from the results presented in Table I to be consistent with both an increase in S(H₂O → SiO) and a decrease in S_{SiO} in this region. This bending down of the boundary corresponds to an enhancement of region III of SiO₂ production and likely results from an increased coverage of the surface with adsorbed SiO molecules which would cause reaction [5] to tend to proceed in the reverse direction, i.e., 2SiO(ads) → SiO₂(s) + Si(s). Alternatively, a lower value of S_{SiO} implies that the SiO molecules remain on the surface longer before desorption, thus increasing the probability of their being further oxidized by incoming H₂O molecules via the reaction H₂O(g) + SiO(ads) → SiO₂(s) + H₂(g). The increased coverage by adsorbed SiO molecules results both from the increased rate of H₂O reaction (i.e., higher S(H₂O → SiO) and from the decreased vaporization of SiO from the surface (i.e., lower S_{SiO}). It is not clear why SiO molecules remain on the Si surface longer for T_s < 950°C, but it may be related to an increased coverage of the surface by hydrogen. The reaction 2H(ads) → H₂(g) is an activated one and if it goes more slowly for T < 950°C, then preferred sites for SiO desorption may be blocked by adsorbed hydrogen.

Thus we conclude that the thermodynamic model for P_c(H₂O, T_s), Eq. [7], as modified to include effects due to H₂O dissociation and SiO desorption, adequately represents the critical conditions for growth of SiO₂ via the H₂O + Si reaction with the parameters S(H₂O → SiO) and S_{SiO} listed in Table I. That this statement also holds for the case of the O₂ + Si reaction was not so clear previously (4), when average values of S(O₂ → SiO) and S_{SiO} were used instead of the observed pressure- and temperature-dependent ones. The kinetic growth etching model presented previously (4) to describe the development of

the SiO₂ growth features is still valid, but should not be considered to be an improvement on the thermodynamic model.

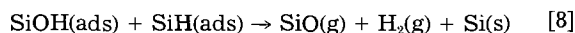
As mentioned previously, Maguire and Augustus (12) have also studied the initial interaction of H₂O with Si at high T_s (up to 1000°C) and low P(H₂O), up to 8 × 10⁻⁴ torr. Our results for P_c(H₂O, T_s) agree qualitatively with theirs, although they did not observe three regions of interaction, such as we have indicated in Fig. 1. Their results for P_c(H₂O, T_s) show more scatter than ours and lie between our lower and upper boundaries, with a slope, or activation energy, of 2.5 eV, as compared with our result of 3.9 eV for the upper boundary. For P(H₂O) approaching 1 × 10⁻⁴ torr, our results merge with those of Maguire and Augustus. From a study of pumping speed, they determined the initial sticking probability of H₂O on Si to be about 10⁻³, somewhat lower than our result, S(H₂O → SiO) = 0.0034-0.029.

We note from Fig. 1, which includes our previous results for P_c(O₂, T_s) for the O₂ + Si reaction, that for a given oxidant pressure, SiO₂ is stable on the Si surface for higher values of T_s for the O₂ + Si reaction than for the H₂O + Si reaction. In other words, P_c(O₂, T_s) is less than P_c(H₂O, T_s) for T_s > 950°C. It is apparent that this results from the fact that S(O₂ → SiO) is greater than S(H₂O → SiO), (0.027-0.061) for O₂ as compared with (0.0034-0.029) for H₂O. We note that S_{SiO} values are comparable for the two reactions, (0.059-0.19) for O₂ and (0.048-0.13) for H₂O. Thus, per incident molecule, more SiO is produced on the Si surface for the O₂ + Si case, increasing the likelihood of further oxidation to SiO₂. The lower value of S(H₂O → SiO) as compared to S(O₂ → SiO) may result from the fact that two bonds in the case of the H₂O molecule must be broken before an oxygen atom is available to form an Si-O-Si bridging bond, where in the case of O₂ the breaking of a single bond generates two reactive oxygen atoms. We note that O=O and H-OH bonds are of essentially equal strength (17), 5.0 eV.

From Table I, it can be seen that S(H₂O → SiO) is generally a decreasing function of P(H₂O), an effect which may be related to the increasing coverage of the Si surface by SiOH and SiH groups, which could block further adsorption of incident H₂O molecules.

Our results indicate that the Si surface is more reactive to O₂ than to H₂O as far as the production of SiO and the initial growth of SiO₂ are concerned, in contrast to the observed more rapid growth of thick SiO₂ films in H₂O. The existence of region II, extending down to the lower boundary in Fig. 1, apparently does signal a type of enhanced reactivity of H₂O with Si. The existence of three surface regions for H₂O + Si, as compared with only two for O₂ + Si seems likely to be due to the presence of hydrogen on the surface in SiOH and SiH groups in the former case. We will now discuss the possibility of a thin, nonpassivating Si_xO_yH_z layer on the Si surface in region II.

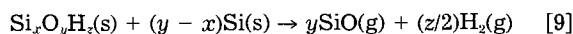
In region I, when incident H₂O molecules dissociate on the Si surface, SiOH and SiH groups are formed initially. If P(H₂O) is low enough and T_s high enough, the SiOH groups will be unstable and the following reaction



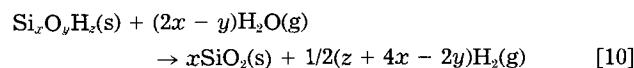
will proceed readily, leading to rapid etching and the maintenance of a clean Si surface. As P(H₂O) increases or T_s decreases, the coverage of the Si surface by SiOH and SiH groups will increase. A "catalytic" effect of hydrogen in this situation could be the weakening of Si-Si back bonds to the extent that an Si_xO_yH_z layer, with O atoms in both bridging and nonbridging configurations, could form on the Si surface well before the generation of SiO has reached its maximum value given by Eq. [6]. Also, it has been stated (18) previously that an SiOH group on the Si surface can stabilize a neighboring Si-O-Si bond. This effect may also aid in the formation of an Si_xO_yH_z layer. Thus, a thin, nonpassivating Si_xO_yH_z layer could exist for values of P(H₂O) lower than those which would lead to the formation of a passivating SiO₂ layer.

The continuing (nonuniform) etching of the underlying Si through this Si_xO_yH_z layer via the production of SiO could lead to the rougher, "grainier" surface observed in region II. The possible existence of this Si_xO_yH_z layer has been inferred from the fact that the emissivity observed in region II differs from that of the SiO₂ layer and of the clean Si surface. An analogous situation has recently been reported (19) for the case of an amorphous Si_xH_z layer observed using similar procedures on the surface of Si during SiH₄ CVD. A semipassive surface layer has also previously been inferred (20) to exist on the surface of SiC during reaction with oxygen atoms and molecules.

The Si_xO_yH_z layer proposed here for region II is not expected to be stable, but rather to exist on the Si surface only in semiequilibrium both with the underlying Si and the incoming flux of H₂O. For lower P(H₂O) or higher T_s (i.e., region I), the layer would disappear via a reduction reaction



while for higher P(H₂O) or lower T_s, approaching region III, oxidation to SiO₂ would occur



Unfortunately, thermochemical data for such an Si_xO_yH_z layer are not available, and the kinetics of its formation are not clear, so that a model for the critical P(H₂O) for the lower boundary, separating regions I and II, does not seem possible at this time.

The square depressions in which the pyramidal SiO₂ growth features are found (see Fig. 2) are likely to be caused by enhanced etching of the Si substrate in this region. The mechanism for this enhanced etching is not clear, although one possibility may be that H₂O molecules incident on the SiO₂-covered pyramid which stick and dissociate cannot all be consumed by the reaction producing SiO₂ (typical SiO₂ film growth rates are only on the order of 0.1 Å/s (1), compared to etching velocities v_e, which are typically (10-1000) Å/s, see Table I). Thus, there may be a considerable flux of OH groups (or even H₂O molecules) diffusing down the sides of the pyramids to the Si substrate. Such a flux should result in an enhancement of the etching via SiO production, thus explaining the presence of the square depressions surrounding the pyramids. This effect could be negligible for the O₂(g) + Si(s) reaction because of the smaller diffusion velocity of O₂ (or O) on the SiO₂ layer and the lower sticking coefficient on SiO₂ (21). Enhanced etching due to SiH_x (x = 1-4) production is very unlikely on thermodynamic grounds.

Conclusions

We have determined experimentally the critical conditions for growth of SiO₂ on the clean Si(111) and (100) surfaces for values of T_s between 890° and 1350°C and P(H₂O) between 7 × 10⁻⁵ and 4 × 10⁻¹ torr. These results are consistent with a thermodynamic model for SiO₂ growth, which has been modified to account for the dissociation of H₂O on and desorption of SiO from the Si surface. The presence on the Si surface for certain values of P(H₂O) and T_s of a thin, nonpassivating Si_xO_yH_z film has been inferred. Further experiments are required to confirm the presence of this Si_xO_yH_z film.

Acknowledgments

We wish to thank Dr. J. Osinchak and Mr. J. Downey for taking the SEM micrographs. Thanks also to Dr. E. A. Irene for many helpful discussions. The support of the U.S. Department of Energy under Contract no. DE-AC02-79ER10438 is greatly appreciated.

Manuscript received May 9, 1984.

City College of New York assisted in meeting the publication costs of this article.

REFERENCES

1. T. Nakayama and F. C. Collins, *This Journal*, **113**, 706 (1966).
2. W. A. Pliskin, *IBM J. Res. Dev.*, **10**, 198 (1966).
3. E. A. Irene, *This Journal*, **125**, 1708 (1978).
4. F. W. Smith and G. Ghidini, *ibid.*, **129**, 1300 (1982).
5. B. E. Deal and A. S. Grove, *J. Appl. Phys.*, **36**, 3770 (1965).
6. E. A. Irene, *This Journal*, **121**, 1613 (1974).
7. K. Fujiwara, *Surf. Sci.*, **108**, 124 (1981); *J. Chem. Phys.*, **75**, 5172 (1981).
8. D. Schmeisser, F. J. Himpsel, and G. Hollinger, *Phys. Rev. B*, **27**, 7813 (1983); D. Schmeisser, *Surf. Sci.*, **137**, 197 (1984).
9. H. Ibach, H. Wagner, and D. Bruchmann, *Solid-State Commun.*, **42**, 457 (1982).
10. Y. J. Chabal, *Phys. Rev. B*, **29**, 3677 (1984).
11. S. Ciraci and H. Wagner, *ibid.*, **27**, 5180 (1983).
12. H. G. Maguire and P. D. Augustus, *Phys. Status Solidi A*, **17**, 101, (1973).
13. F. W. Smith, *Surf. Sci.*, **80** 388 (1979).
14. F. W. Smith, and B. Meyerson, *Thin Solid Films*, **60**, 227 (1979).
15. For a definition and discussion of the physical meaning of the vaporization coefficient, see: G. M. Rosenblatt, in "Treatise on Solid State Chemistry," Vol. 3, N. Hannay, Editor, Plenum Press, New York (1976).
16. O. Kubachewski and T. G. Chart, *J. Chem. Thermodyn.*, **6**, 467 (1974).
17. "Handbook of Chemistry and Physics," R. C. Weast, Editor, pp. F-177, F-183, The Chemical Rubber Co., Cleveland, OH (1971).
18. A. G. Revesz, *This Journal*, **126**, 122 (1979).
19. A. M. Beers and J. Bloem, *Appl. Phys. Lett.*, **41**, 153 (1982).
20. D. E. Rosner and H. D. Allendorf, *J. Phys. Chem.*, **74**, 1829 (1970).
21. R. S. McDonald, *J. Am. Chem. Soc.*, **79**, 850 (1957).

Properties of Magnetron-Sputtered Silicon Nitride Films

T. Serikawa and A. Okamoto

Nippon Telegraph and Telephone Public Corporation, Musashino Electrical Communication Laboratory, Midoricho, Musashino-shi, Tokyo, 180 Japan

ABSTRACT

Films 100-200 nm thick have been deposited at 200°C by reactive sputtering of a silicon target in nitrogen-argon mixtures using an RF planar magnetron system. Film properties were examined in reference to nitrogen partial pressure and sputtering gas pressure. At nitrogen partial pressure higher than a certain pressure, silicon nitride films are deposited. Properties of silicon nitride films are remarkably dependent on sputtering gas pressure. By controlling the pressure, silicon nitride films have been synthesized with 1.7-200 nm/min etching rate in buffered HF, 2.97-2.28 g/cm³ density, 1.97-1.82 refractive index, 5×10^9 - 1×10^9 dyne/cm² compressive intrinsic stress and 5.5×10^6 - 3.5×10^6 V/cm breakdown voltage. High density, low etching rate films deposited under optimized sputter conditions act as an efficient barrier to oxygen diffusion in oxygen atmospheres at high temperature. In addition, it was demonstrated from MOS device characteristics that the silicon nitride films are free from contaminants and can be successfully applied to device fabrication.

Silicon nitride films are very important in semiconductor device fabrication because they afford a good moisture and contamination barrier (1, 2). Great effort has been made to investigate the formation and characterization of the film (2). For formation of silicon nitride films, chemical vapor deposition (CVD) has most widely been in use (2, 3). The method, however, has a disadvantage in regard to its high substrate temperature. Certain process schemes in device fabrication require that silicon nitride films be deposited at low substrate temperature. To meet this requirement, a plasma-assisted CVD has been recently developed (3-5). This method uses mixtures of SiH₄ and NH₃ in the same manner as the CVD method. As a result, the silicon nitride films are contaminated with hydrogen, which degrades device characteristics (6, 7). However, in sputtering, films are deposited at low substrate temperature and are free from hydrogen contamination. These advantages make sputtering a potentially attractive method to deposit silicon nitride films.

Sputtered silicon nitride films have commonly been deposited in nitrogen mixed gases using a diode-type system (8-11). This system has the disadvantage of small deposition rate and substrate heating due to plasma exposure. However, in the recently developed magnetron system, lower substrate temperatures are still obtainable, even when deposition rates are significantly higher (3). This combination of higher rates and lower temperature can improve sputter deposition economics. However, there have been only a few reports on silicon nitride film deposition by magnetron sputtering. Moreover, the magnetron system is different from the diode-type system in some respects (12).

This paper describes the preparation and properties of silicon nitride films made by reactive sputtering, using

an RF planar magnetron apparatus in reference to sputter conditions. Also, it was demonstrated that the film deposited under optimized conditions is applicable as an oxidization mask in a wet oxygen atmosphere at high temperature for MOS device fabrication.

Experimental

Sputtering apparatus and film deposition.—Film depositions were carried out with a 13.56 MHz RF magnetron sputtering apparatus, shown in Fig. 1 (13). An RF electrode is mounted in a bell jar so that the target materials are sputtered onto a barrel-type rotatable substrate holder. The 5 × 15 in. silicon target (99.999% pure), 0.25 in. thick was mechanically clamped to a water-cooled RF electrode. The minimum spacing between the target and the substrate holder was 50 mm. The target could be covered with a movable shutter mounted approximately 25 mm in front of the target. The bell jar was made of stainless steel, but the holder and shutter were made of titanium.

The sputtering system was evacuated to less than 2×10^{-4} Pa before a baffle valve above the diffusion pump was throttled. Nitrogen-argon mixtures were admitted to the system. After presputtering was carried out for 10 min, the shutter was removed to deposit films ranging in thickness from 100 to 200 nm on 3 in. diam silicon and aluminum substrates. The main deposition parameters were nitrogen partial pressure and sputtering gas pressure. The sputtering conditions are listed in Table I.

Measurements.—Films were evaluated on the basis of infrared absorption spectra, film composition, etching rate, film density, surface texture, refractive index, resistivity, breakdown voltage, and film stress. In addition,

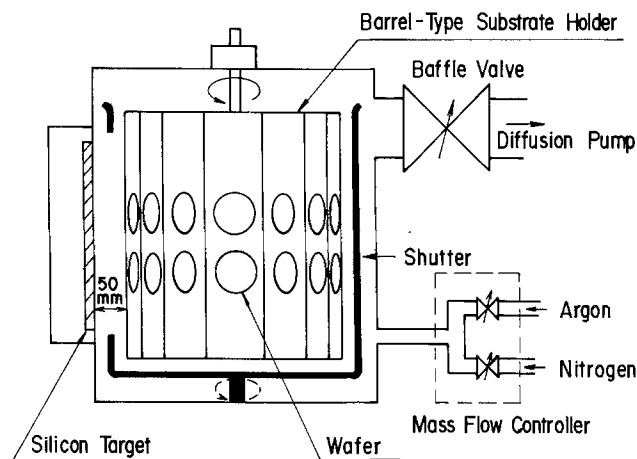


Fig. 1. The RF planar magnetron sputtering apparatus

thermally oxidized films were analyzed by Auger electron spectroscopy (AES) to determine depth profiles.

Film compositions were measured using x-ray microanalysis and the Lorentz-Lorenz relationship. Film densities were measured by a gravimetric technique. Etching rates were calculated from etching depth in 30°C buffered hydrofluoric acid [100 ml (50% HF) + 860 ml (40% NH_4F)] and etching time. The etched depths were measured by a roughness tester (TalystepTM). Surface textures of as-deposited and slightly etched in 30°C buffered hydrofluoric acid for 5s were observed by transmission electron microscopy of a carbon replica. Resistivities and breakdown voltages were measured using an MIS capacitor, which had a 500 μm diam aluminum electrode-silicon nitride film-silicon substrate structure. Film stresses were calculated from silicon substrate curvature measured by the Newton-ring method (14).

MOS device fabrication.—MOS transistors and capacitors were fabricated using the reactively sputtered silicon nitride films as a local oxidation (LOCOS) mask on silicon substrates (15). The silicon substrates used were boron-doped p-types with a (100) orientation and 4 $\Omega\text{-cm}$ resistivity. SiO_2 films 60 nm thick were thermally grown on the substrates. Next, 150 nm thick silicon nitride films were deposited on SiO_2 films. After patterning silicon nitride films and SiO_2 films, thick SiO_2 films were formed for field isolation by thermal oxidation for 370 min in wet oxygen atmosphere at 1000°C. After removing the silicon nitride film patterns and underlying SiO_2 films, gate SiO_2 films were thermally grown to 60 nm thick. MOS devices were completed through additional fabrication steps: gate electrodes for poly-Si film, source/drain electrodes, intermediate SiO_2 films, and aluminum interconnections. Finally, all devices were annealed in forming gas for 20 min at 450°C.

Results and Discussions

Preparation and properties.—**Nitrogen partial pressure effect.**—Figure 2 shows changes in deposition rate and film composition as a function of nitrogen partial pressure. In the pressure range lower than 0.12 Pa, decrease in deposition rate is small, but deposition rate decreases abruptly near 0.15 Pa. Nitrogen concentration saturates at a pressure higher than 0.1 Pa. The infrared absorption spectrum for film deposited at 0.28 Pa nitrogen partial pressure is shown in Fig. 3. Absorptions at 840 and 460 cm^{-1} are peculiar to silicon nitride (2, 6), and are representative

Table I. Sputtering conditions

Sputtering power	3.0 kW
Substrate temperature	200°C
Sputtering gas pressure	0.3 ~ 6.7 Pa
Sputtering gas flow rate	100 sccm
Substrate holder rotation rate	10 rpm
Background pressure	$< 2 \times 10^{-4}$ Pa

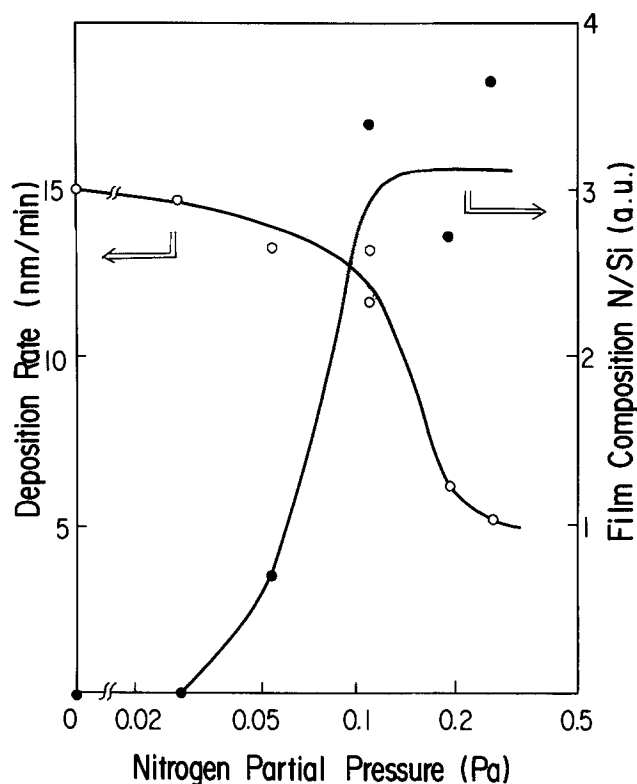


Fig. 2. Changes in deposition rate and film composition by nitrogen partial pressure. Sputtering gas pressure was 0.56 Pa. Film compositions for films deposited on aluminum substrates were measured by x-ray microanalysis.

of all films deposited at higher than 0.1 Pa partial pressures. No additional peaks were observed between 400 and 2000 cm^{-1} .

In reactive sputtering of targets like silicon, three possible nitrogen reaction sites can be considered: (i) at the target surface, (ii) on the substrate, and (iii) during transfer from target to substrate (16). The last can be neglected because silicon nitride films are deposited even at 0.12 Pa nitrogen partial pressure at which collision with nitrogen is unity. In the magnetron system, the discharge intensity is localized close to the target so that the substrates are located in a less chemically reactive environment (17). At low nitrogen partial pressure, insufficient nitrogen is available to form a silicon nitride on the target surface.

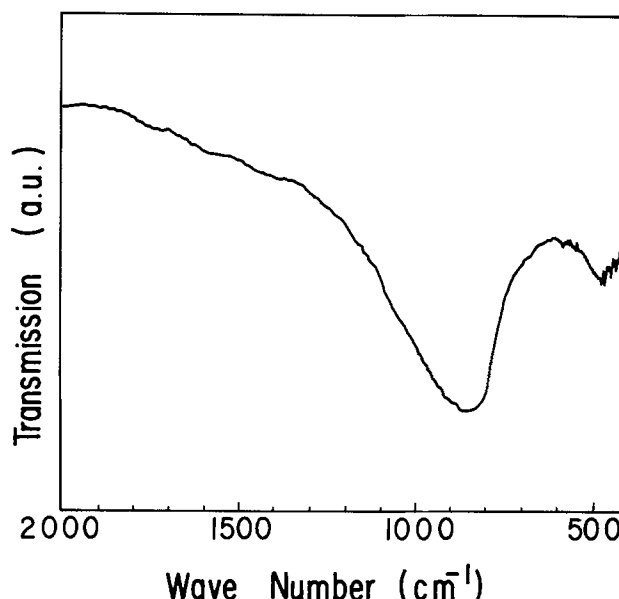


Fig. 3. Infrared absorption spectrum for film deposited at 0.28 Pa nitrogen partial pressure, where sputtering gas pressure was 0.56 Pa.

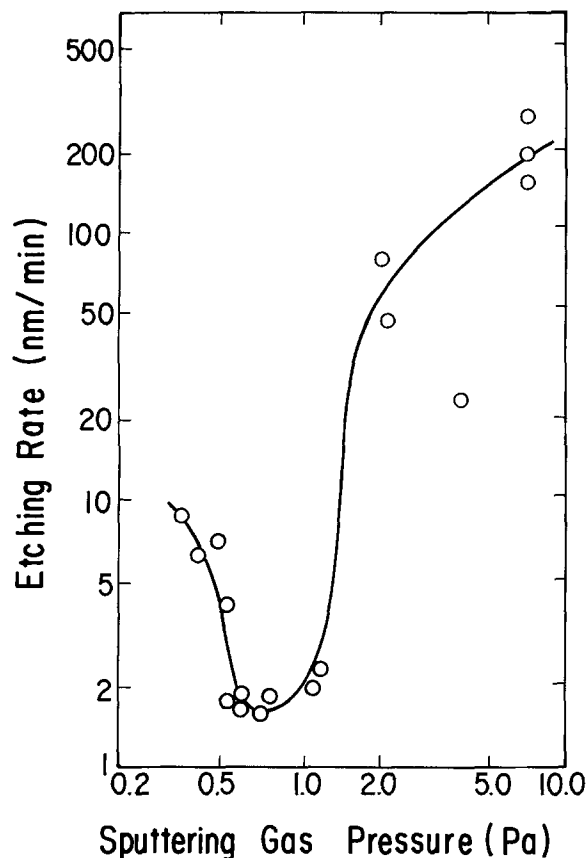


Fig. 4. Change in etching rate as a function of sputtering gas pressure. Sputtering gas composition was 50% nitrogen-50% argon.

Only when nitrogen partial pressure reaches a value near 0.15 Pa is sufficient nitrogen available to form silicon nitride on the target (17, 18). This formation on the target reduces deposition rate, since the sputtering rate for silicon nitride is less than that for silicon. Moreover, silicon nitride films are obtained, as shown in Fig. 2 and 3.

Sputtering gas pressure effect.—Etching rate in buffered HF showed a marked dependence on sputtering gas pressure, as seen in Fig. 4. Etching rate is smallest near 0.6 Pa and increases drastically at 1.2 Pa. Figure 5 shows changes in film density, refractive index, and film composition at different sputtering gas pressures. Film compositions were calculated from measured film density and refractive index using Lorentz-Lorenz correlation (19). At 0.56 Pa, film density and refractive index reach maximums of 2.97 g/cm³ and 1.97, respectively. Film composition N/Si changes from 1.42 to 1.15 as a result of increasing sputtering gas pressure. Figure 6 shows surface textures of as-deposited and slightly etched films at 0.3, 0.56, and 6.7 Pa sputtering gas pressure. In the 6.7 Pa as-deposited films, 100 nm diam irregularities are observed and many microvoids a few nanometers in diameter are observed. In contrast to the relatively smooth surfaces of as-deposited films, the slightly etched film surfaces are markedly different. The film at 0.56 Pa is the smoothest. In the film at 6.7 Pa, the surface becomes very irregular.

Figure 7 illustrates typical current-voltage characteristics for films deposited at 0.3, 0.56, and 6.7 Pa. Films at 0.3 and 0.56 Pa exhibit linear $\ln I$ vs. $V^{1/2}$ plots indicative of a Poole-Frenkel conduction mechanism, whereas $\ln I - V^{1/2}$ data for the films at 6.7 Pa invariably exhibit curvature when plotted in the same manner. Arrows in the figure indicate breakdowns of the films. High density films at 0.56 Pa show high breakdown voltage. Films at 0.3 Pa have low breakdown voltage, in spite of a linear $\ln I$ vs. $V^{1/2}$ relationship.

Silicon nitrides formed on target are sputtered with an energy spectrum having a strong peak at a few electron

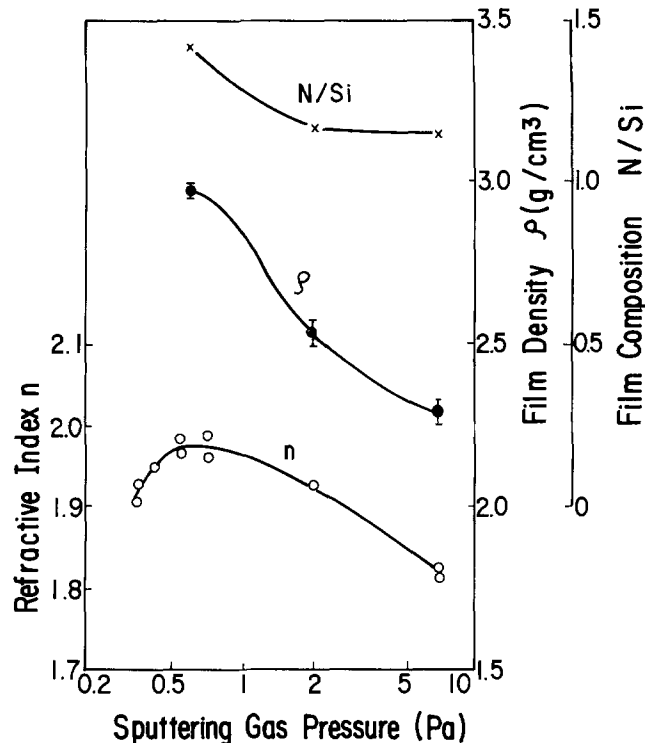


Fig. 5. Changes in film density, refractive index, and film composition by sputtering gas pressure. Sputtering gas composition was 50% nitrogen-50% argon.

volts (20). Sputtered materials lose their energies and directions through collisions with argon and nitrogen, and are finally thermalized to the average gas energy (21). Before thermalization, the materials travel normal to the target surface. However, after thermalization, oblique and horizontal incident components are mixed in an incident angular distribution of sputtered materials (22). As shown in Fig. 4, etching rates change drastically at 1.2 Pa. At 1.2 Pa, the thermalization distances, which the sputtered materials travel before thermalization, are 40 and 65 mm at initial energies of 5 and 1000 eV, respectively (21). Therefore, thermalized materials are in the majority on a substrate 50 mm from the target.

Reducing sputtered material energy results in the attenuation of (i) surface mobility of deposited atoms and (ii) re-emission of weakly bound atoms, which are in unfavorable positions for achieving optimum density (3, 11). Also, after thermalization, oblique and horizontal components increase in incident angular distribution (21, 22). Sputtered materials with oblique and horizontal components are shadowed by irregularities on substrate and growing film (22, 23). Because surface mobility and re-emission are attenuated, the areas shadowed by the components remain, resulting in microvoid formation, as shown in Fig. 6. Consequently, at a sputtering gas pressure higher than 1.2 Pa, silicon nitride films with microvoids are deposited, resulting in abnormal etching rates, low resistivity, and low breakdown voltage.

By decreasing sputtering gas pressure from 0.56 Pa, etching rate increases and film surface texture becomes irregular again, as seen in Fig. 4 and 6. Substrate surfaces are negatively self-biased against plasma in RF sputtering (3). The self-biased potential increases with decreasing pressure (3). In the magnetron sputtering system used in this study, the potential was nearly constant at -8V for pressures higher than 1 Pa, but increased markedly for low pressure and reached -20V at 0.4 Pa. Consequently, at lower pressures, growing film surfaces are bombarded by argon and nitrogen positive ions with higher energies. These energetic ion bombardments enhance re-emission and surface diffusion of depositing atoms. However, the bombardments lead to surface irregularities. The irregularities on growing film promotes the self-shadowing ef-

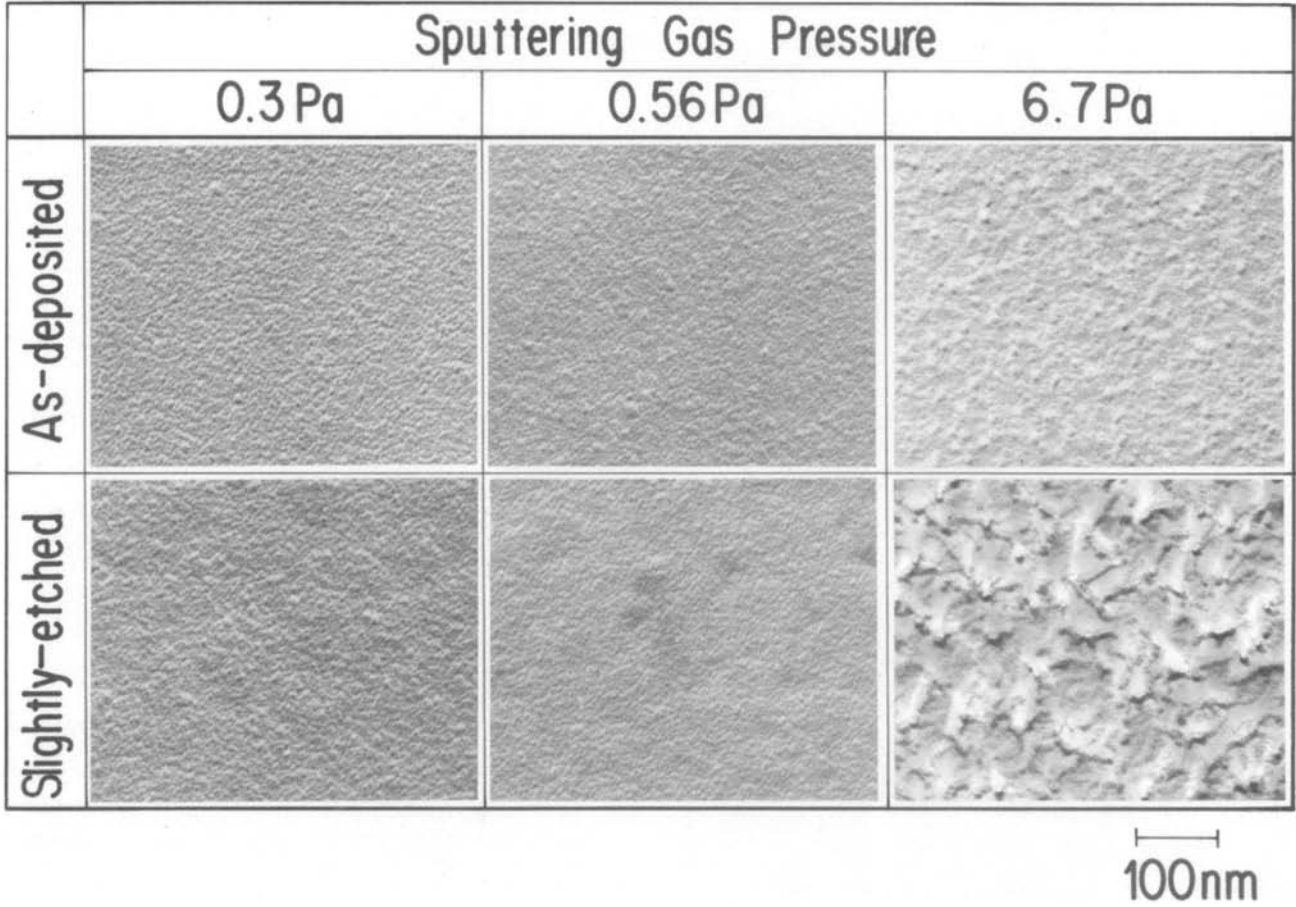


Fig. 6. Transmission electron micrographs of as-deposited and slightly etched films deposited at 0.3, 0.56, and 6.7 Pa sputtering gas pressures.

fect. The self-shadowing effect overshadows enhanced re-emission and surface diffusion. Consequently, silicon nitride films are deposited with high etching rates and

low refractive index. Degradation for film property deposited at low pressure results from energetic argon and nitrogen ion bombardments. This fact is clarified further by application of RF biases to the substrate through a capacitor. The dc self-biased potential was adjusted to -20V. In the entire sputtering gas pressure range, the etching rate for films deposited under RF bias is greater than that for films deposited in the absence of applied bias. For example, silicon nitride films deposited at 0.56

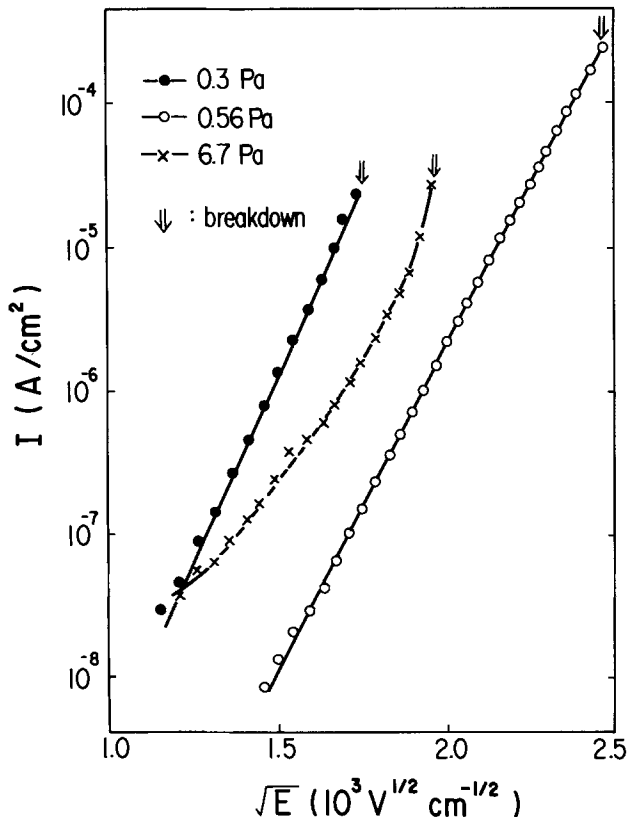


Fig. 7. Current-voltage characteristics for silicon nitride films deposited at 0.3, 0.56, and 6.7 Pa.

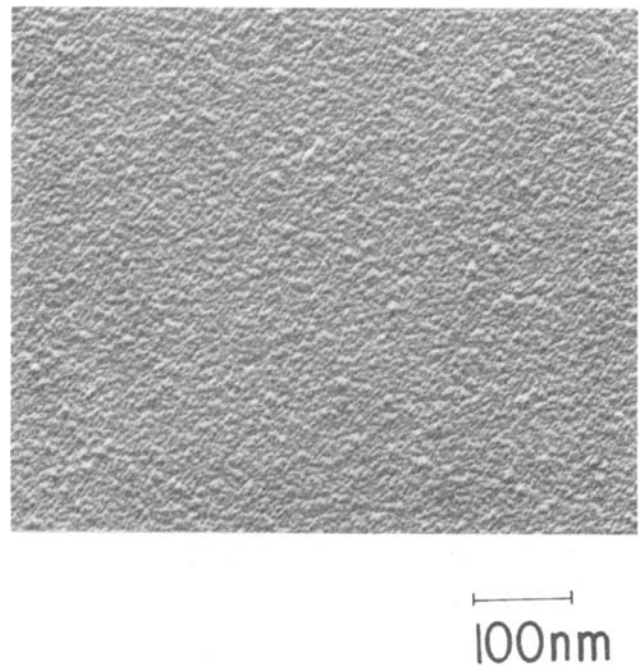


Fig. 8. Transmission electron micrograph of film deposited under RF bias at 0.56 Pa.

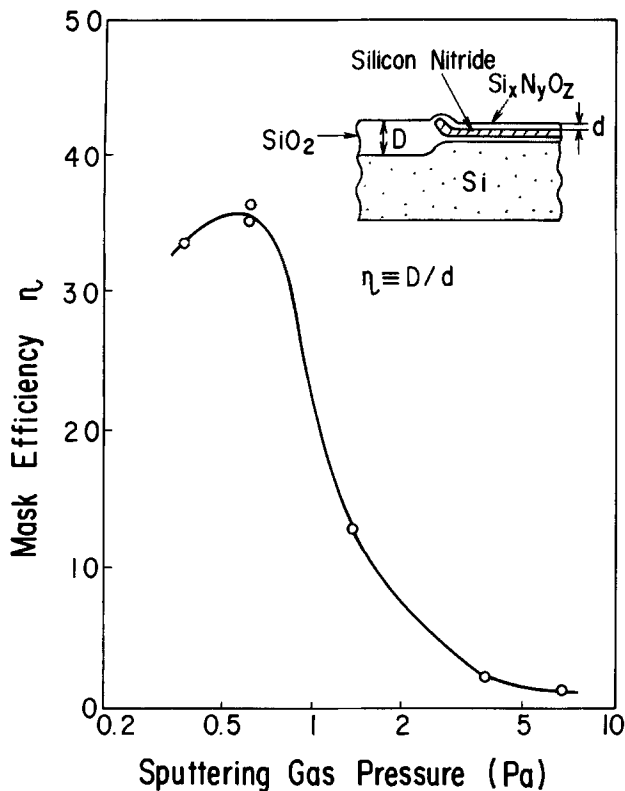


Fig. 9. Change in mask efficiency as a function of sputtering gas pressure.

Pa under an RF bias show 5.0 nm/min, which is greater than 1.7 nm/min in films without bias. In addition, as shown in Fig. 8, the electron micrograph reveals that biased sputtered films are more irregular than film without bias. Growing films are bombarded by argon and nitrogen ions accelerated due to dc self-biased potential, resulting in film property degradation. It was anticipated, on the basis of surface irregularities and the self-shadowing effect, that films deposited at low pressure and biased sputtered films exhibit poor film properties. For surface irregularization by energetic ion bombardments, the mechanisms assumed to be responsible are either nonuniform re-emission or etching by the bombardments. More work is needed to clarify this.

Intrinsic stresses are indicated as compressive for all silicon nitride films. The stress decreases with increasing sputtering gas pressure.

Properties of silicon nitride films deposited at 0.56 and 6.7 Pa are summarized in Table II.

Application to MOS device fabrication.—Figure 9 indicates mask efficiency for silicon nitride films deposited at various sputtering gas pressures. The mask efficiency was defined as D/d , as shown in the inset in the figure, where d and D are thermally oxidized thicknesses on silicon nitride and (100) oriented silicon substrate, respec-

Table II. Silicon nitride film properties

	0.56 Pa	6.7 Pa
Film density	2.97 g/cm ³	2.28 g/cm ³
Refractive index	1.97	1.82
Film composition	1.42	1.15
N/Si		
Infrared absorption peak	840 cm ⁻¹ , 460 cm ⁻¹	900 cm ⁻¹ , 460 cm ⁻¹
Etching rate (30°C BHF)	1.7 nm/min	200 nm/min
Breakdown voltage	5.5×10^6 V/cm	3.5×10^6 V/cm
Resistivity ($E: 3 \times 10^6$ V/cm)	$3 \times 10^{11} \Omega \cdot \text{cm}$	$3 \times 10^{10} \Omega \cdot \text{cm}$
Stress	5×10^9 dyne/cm ² (Compressive)	1×10^9 dyne/cm ² (Compressive)

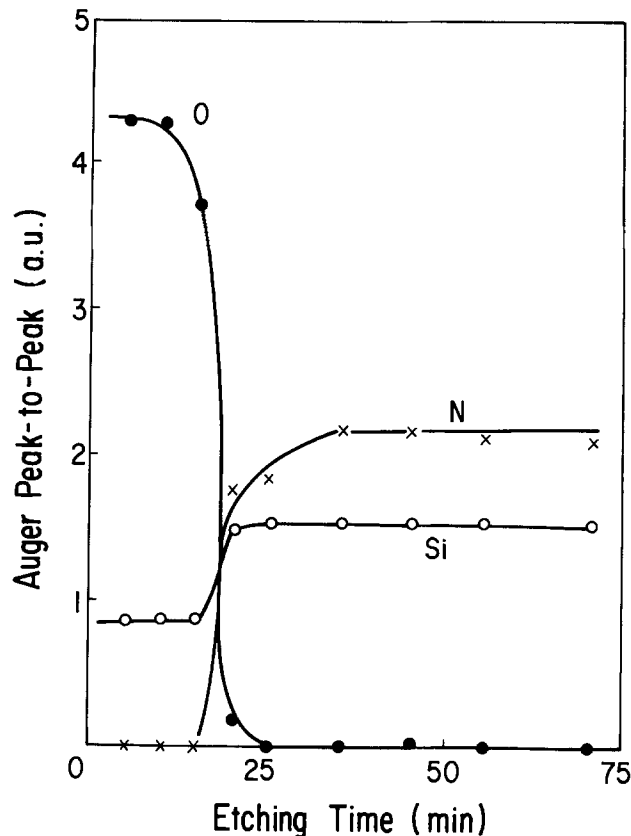


Fig. 10. Auger electron spectrum peak profile for thermally oxidized silicon nitride films for 370 min at 1000°C in wet oxygen atmosphere. Film was deposited at 0.56 Pa.

tively. Thermal oxidation was carried out for 370 min in a wet oxygen atmosphere at 1000°C, where D was about 1 μm . Mask efficiency markedly depends on sputtering gas pressure in the same manner, as shown in Fig. 4 and 5. Moreover, mask efficiency reaches a maximum at 0.56 Pa, where high density and low etching rate films are deposited. Figure 10 shows Auger depth profile after film oxidation, when film was deposited at 0.56 Pa. An oxygen peak is observed only at less than 25 min etching time.

Owing to high density in film deposited at 0.56 Pa, the film acts as an effective barrier against oxygen, as seen in Fig. 10. Moreover, mask efficiency is as great as 35. However, low density films are easily oxidized, showing low mask efficiency (Fig. 9).

Figure 11 shows breakdown voltage characteristics for gate SiO_2 films 60 nm thick. The characteristic distribution has a peak at 7.8 MV/cm and high breakdown voltage. In Fig. 12, change in threshold voltage in a MOS transistor is shown as a function of substrate voltage. The calculated curve uses 3.5×10^{15} 1/cm³ acceptor-type boron concentration and -0.9 V as work function difference between the poly-Si electrode and the silicon substrate (24, 25). Threshold voltages agree with calculations. Also, field effect mobility in the transistor in Fig. 12 is greater than 700 cm²/V·s. The MOS transistor characteristics mean that neither oxide charge in gate SiO_2 films nor surface state at Si-SiO₂ interface are generated when magnetron-sputtered silicon nitride films are used. Figures 9, 11, and 12 show that silicon nitride film deposited under optimized condition is successfully applicable to MOS device fabrication without contamination and degradation in MOS device.

Conclusions

Silicon nitride films were deposited at 200°C by reactive sputtering of a silicon target in a nitrogen-argon mixture using an RF planar magnetron system. Films properties, composition, etching rate, film density, stress, and breakdown voltage, were measured. Experiments demon-

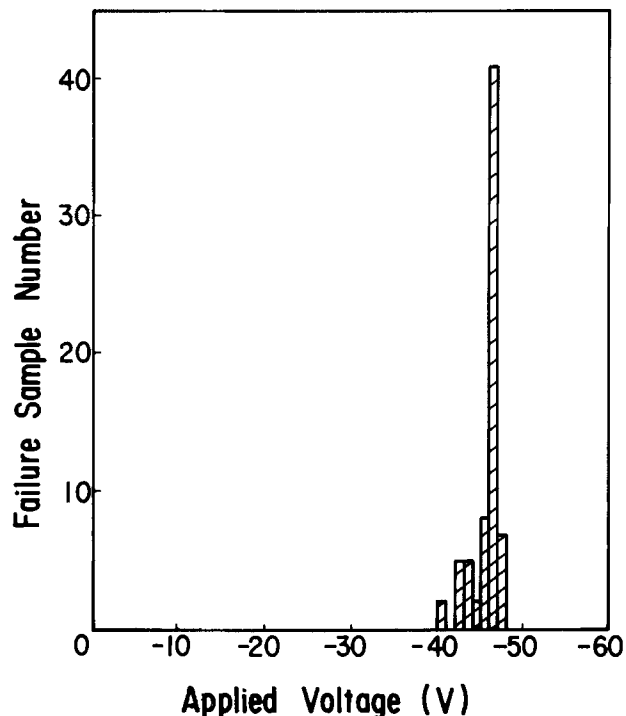


Fig. 11. Breakdown voltage characteristics for gate SiO_2 film 60 nm thick

strated that film properties displayed remarkable dependence on sputtering gas pressure. Under proper sputtering conditions, good quality silicon nitride films with high density and low etching rate can be deposited. Moreover, it was demonstrated that the silicon nitride films act as an efficient barrier to oxygen diffusion and are successfully applicable to MOS device fabrication. However, by adjusting sputtering conditions, films with microvoids are deposited. The film formation mechanism was discussed on the basis of self-shadowing of deposited atoms owing to irregularities on growing film surfaces.

Acknowledgment

The authors wish to express their sincerest thanks to A. Ishimoto for his valuable suggestions and encouragement.

Manuscript submitted Nov. 7, 1983; revised manuscript received ca. Aug. 3, 1984.

Nippon Telegraph and Telephone Public Corporation assisted in meeting the publication costs of this article.

REFERENCES

1. J. A. Amick, G. L. Schnable and J. L. Vossen, *J. Vac. Sci., Technol.*, **14**, 1053 (1977).
2. C. E. Morosanu, *Thin Solid Films*, **65**, 171 (1980).
3. J. L. Vossen and W. Kern, "Thin Film Processes," Academic Press, New York (1978).
4. R. C. G. Swann, R. R. Mehta, and T. P. Cage, *This Journal*, **114**, 713 (1969).
5. A. K. Sinha, J. J. Levinstein, T. E. Smith, G. Quintana, and S. E. Haszko, *ibid.*, **125**, 601 (1978).
6. E. A. Taft, *ibid.*, **118**, 1341 (1971).

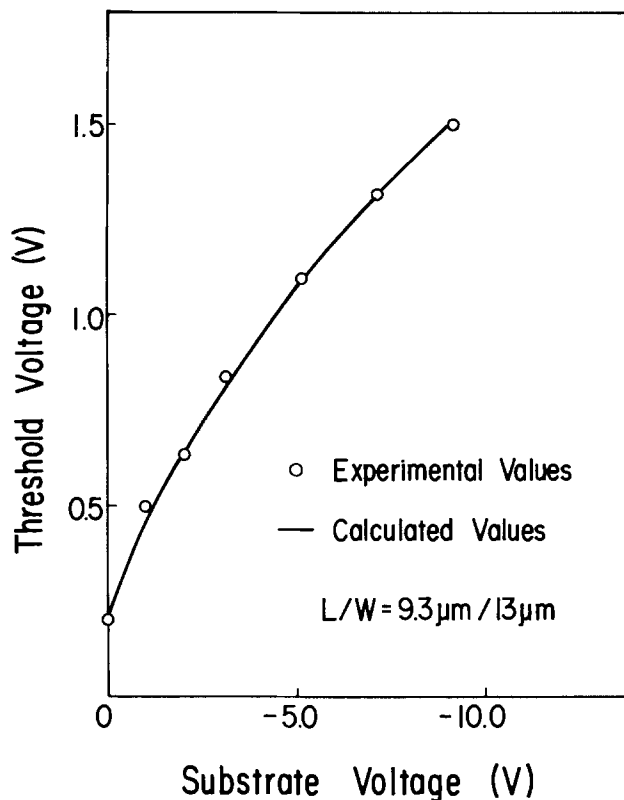


Fig. 12. Change in threshold voltage for MOS transistors as a function of substrate voltage. Channel length and width are 8.5 and 13 μm , respectively. Threshold voltages were measured using turn-on voltages in transconductance-gate voltage curves in the saturation region.

7. R. C. Sun, J. T. Clemens, and J. T. Nelson, in "IEEE 18th Proceedings on Reliability Physics," p. 244, IEEE, New York (1980).
8. S. M. Hu and L. V. Gregar, *This Journal*, **114**, 826 (1967).
9. A. M. Stephens, J. L. Vossen, and W. Kern, *ibid.*, **123**, 303 (1976).
10. C. J. Mogab and E. Lugujo, *J. Appl. Phys.*, **47**, 1302 (1976).
11. C. J. Mogab, P. M. Petroff, and T. T. Sheng, *This Journal*, **122**, 815 (1975).
12. S. Schiller, *Thin Solid Films*, **64**, 455 (1979).
13. T. Serikawa and A. Okamoto, *ibid.*, **101**, 1 (1983).
14. R. Glang, R. Holmund, and R. Rosenberg, *Rev. Sci. Instrum.*, **36**, 7 (1965).
15. J. A. Appels, E. Kool, M. M. Paffen, J. J. Schatroje, and W. C. G. Wavkuylen, *Philips Res. Rept.*, **25**, 118 (1970).
16. A. J. Stirling and W. D. Westwood, *Thin Solid Films*, **7**, 1 (1971).
17. S. Maniv and W. D. Westwood, *J. Appl. Phys.*, **51**, 718 (1980).
18. J. Heller, *Thin Solid Films*, **17**, 163 (1973).
19. A. K. Sinha and E. Lugujo, *Appl. Phys. Lett.*, **32**, 245 (1978).
20. M. W. Thompson, *Philos. Mag.*, **18**, 377 (1968).
21. W. D. Westwood, *J. Vac. Sci. Technol.*, **15**, 1 (1978).
22. T. Serikawa *ibid.*, **17**, 582 (1980).
23. J. A. Thornton, *ibid.*, **11**, 666 (1974).
24. T. W. Hickmott, *J. Appl. Phys.*, **48**, 723 (1977).
25. P. P. Wang and O. S. Spencer, *IBM J. Res. Dev.*, **19**, 530 (1975).

Interaction Between Ti and SiO₂

C. Y. Ting, M. Wittmer,* S. S. Iyer,* and S. B. Brodsky

IBM T. J. Watson Research Center, Yorktown Heights, New York 10598

ABSTRACT

We have investigated the interaction between Ti and SiO₂ in the temperature range of 400° to about 1000°C. The reaction proceeds in a layer-by-layer fashion and consists of SiO₂ reduction followed by the formation of a Ti-rich silicide at the interface. At higher temperatures, a Ti-rich oxide is formed near the surface. The reaction starts at approximately 400°C, and the loss of SiO₂ becomes significant above 500°C. A strong interaction between Ti and SiO₂ takes place at 700°C and above. The thicker the SiO₂, the higher resistance it has to degradation due to elevated temperature effects.

The performance and density of today's MOS integrated circuits are further improved by scaling down the physical dimensions of the individual circuit elements. It follows from the MOS scaling laws that the miniaturization process reduces the length of interconnect lines by the scaling factor and their cross-sectional area by the square of that factor. Consequently, the resistance of polycrystalline silicon lines increases with the scaling factor. However, the area of ohmic contacts is reduced by the square of the scaling factor, which results in an increase of the contact resistance by the square of that factor. The above resistance increases give rise to excessive RC time constants and IR voltage drops which may offset the speed advantages gained by scaling the MOS technology to smaller feature sizes.

Recently, refractory metals and their silicides have found an increased interest as means to reduce both the contact resistance and the high resistance of poly-Si lines and diffusion layers. Specifically, VLSI technology makes use of Ti in contact structures (1, 2) and self-aligned TiSi₂ in both source/drain and gate areas (3, 4). If Ti is employed in oxide windows for ohmic contacts and Schottky diodes, it is likely to be in connection with the field oxide as well. However, any reaction between Ti and SiO₂ during postmetal annealing at 400°-450°C could degrade the device performance. However, self-aligned TiSi₂ over poly-Si lines and diffusion layers is formed at higher temperatures, around 600°-700°C. The unreacted Ti over the field oxide is removed in a subsequent step. Any residue on the oxide as a result of the interaction of Ti with SiO₂ during self-aligned TiSi₂ formation presents a potential hazard to the performance of the device. Therefore, the Ti/SiO₂ interaction has to be minimized. For this purpose, it is imperative to study the interaction between Ti and SiO₂.

The reactions of thin films of Ti, V, and Nb with SiO₂ substrates was first investigated by Kräutle *et al.* (5). They found that, upon annealing a Ti film on SiO₂ at 800°C for 2h in vacuum, a bilayer structure is formed, consisting of a surface layer of Ti with about 50% oxygen and a layer beneath of mostly Si and Ti in the ratio Si:Ti = 0.62. They were unable to identify the compounds formed. Our goal was to study in detail the interaction between Ti and SiO₂ in order to determine its implications on device performance. For that purpose, we carried out both thin film analysis and electrical measurements on MOS capacitors. The results of this paper extend very well those of two recent photoelectron spectroscopy studies on low coverages of Ti and SiO₂ to the case of thin films, as they are used in integrated circuits.

Experimental

The Si substrates used in this work were <100> oriented and p-type doped. A 1000Å thick SiO₂ layer was grown on 10 Ω cm Si substrates in a dry-wet-dry oxidation sequence at 1000°C with HCl addition to the oxygen gas. Thinner SiO₂ layers up to 350Å were grown on 2 Ω cm material in dry oxygen with HCl addition. Blanket layers of 1000Å Ti were evaporated in a diffusion-pumped system from a resistively heated source. The base pressure

Electrochemical Society Active Member.

prior to evaporation was better than 2×10^{-7} torr, and the evaporation rate was 10 Å/s. During evaporation, the substrates were maintained at a temperature of 150°C. Titanium MOS capacitors were prepared by evaporating circular Ti dots of 0.8 mm diam through a metal mask.

Samples of the blanket-deposited wafer as well as of the MOS capacitors were subsequently annealed for various times at temperatures ranging from 400° to about 1000°C in Ar. The Ar gas was purified in a hot Ti sponge filter prior to purging of the annealing furnace. The thin films were analyzed with Rutherford backscattering spectrometry (RBS) (6) and glancing angle x-ray diffractometry. Both leakage current and C-V measurements were used in the investigation of the Ti-MOS capacitors.

Other samples of the blanket-deposited wafer were first annealed at temperatures between 500° and 800°C and then stripped of the unreacted Ti in an etching solution which attacks neither titanium silicide nor SiO₂ (3). The thickness of the remaining SiO₂ layer was then measured with optical interferometry. Finally, SIMS analysis was used to determine a possible Ti diffusion into the SiO₂.

Results

Thin film analysis.—A set of samples with 1000Å Ti on 1000Å SiO₂ was annealed for 30 min in 100°C steps from 400° to about 1000°C. The RBS spectra of these samples are summarized in Fig. 1. From this figure, it is clearly seen that the Ti signal is well separated from the Si signal, whereas the oxygen signal is superimposed on the Si signal. This is due to the difference in atomic mass of these elements. The energies for scattering of the ⁴He⁺ particles from surface positions of the elements are indicated by the vertical arrows marked Ti, Si, and O.

The spectra for the as-deposited sample and the samples annealed up to 600°C are practically identical and

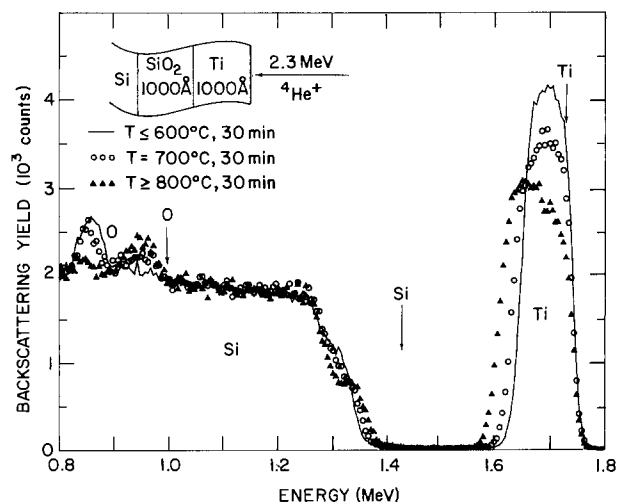


Fig. 1. 2.3 MeV ⁴He⁺ spectra of 1000Å thick Ti layers on 1000Å thick SiO₂ annealed under various conditions. The vertical arrows mark the surface position of the corresponding elements.

represented by the solid line in Fig. 1. The oxygen and silicon signals of the SiO₂ layer are displaced to energies below their corresponding surface position because of the energy loss of the ⁴He⁺ particles in the overlying Ti film. Diffusion of Ti into the SiO₂ is not observed under these annealing conditions. Upon annealing at 700°C, two changes in the RBS spectrum (open circles) can be discerned. First, the height of the Ti signal has dropped and a second oxygen peak near the surface position of oxygen has appeared. This indicates that a significant amount of oxygen has dissolved in the Ti film. Second, the width of the Ti signal has increased and the Si signal extends now to higher energies. This signifies that Ti and Si at the original Ti/SiO₂ interface have reacted with each other and formed a mixed layer. Heat-treatments at 800°C and higher yield RBS spectra typical of the one represented by the filled triangles in Fig. 1. It is clearly seen that most of the oxygen from the SiO₂ layer is now distributed in the Ti layer and that the Ti and the Si have mixed extensively. Finally, we find from Fig. 1 that within the accuracy of RBS the area under the oxygen peaks is preserved, indicating that the oxygen in the Ti layer originates mainly from the decomposed SiO₂ layer.

Strong interactions occur between the Ti and the SiO₂ at high temperatures. This is demonstrated in Fig. 2, which shows the RBS spectrum of a sample annealed at 900°C for 30 min. It is apparent from the step in the Ti signal at 1.7 MeV in Fig. 2 that the original SiO₂/Ti structure has been transformed into a different bilayer structure. The uppermost layer contains Ti and O₂ in the ratio Ti:O = 2:3. This can be inferred from the heights of the Ti and O₂ signals near their surface positions. In a similar fashion, we can determine the composition of the layer beneath. It consists mostly of Ti and Si in the ratio of Ti:Si = 5:3. A thin interfacial layer of the original SiO₂ remains between the Ti-Si mixed layer and the Si substrate, as indicated in Fig. 2. The drop of the oxygen signal between the surface position "s" and interface position "i" indicates that the Ti-Si mixed layer contains only a small amount of oxygen.

We used glancing angle x-ray diffraction to identify the compounds formed in the interaction between Ti and SiO₂. Figure 3 shows the diffraction spectrum of a sample which has been annealed at 800°C for 30 min. Most of the diffraction lines can be ascribed to two compounds, Ti₅Si₃ or Ti₅Si₄, with the exception of one line which can only be identified as the (121) diffraction of Ti₅Si₃. Thus, we conclude from the x-ray analysis that the compound formed is the metal-rich silicide Ti₅Si₃. This result is in excellent agreement with the composition of the compound determined by RBS. The result is also in good agreement with the atomic ratio of Si and Ti reported by Kräutle *et al.* (5).

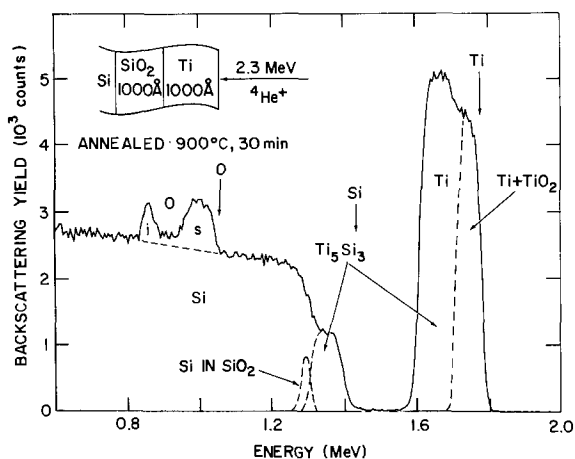


Fig. 2. 2.3 MeV ⁴He⁺ RBS spectrum of a Si/1000Å SiO₂/1000Å Ti sample following a heat-treatment for 30 min at 900°C. The contributions of the various compounds to the overall spectrum is indicated by the dashed lines, and the vertical arrows mark the surface positions of the corresponding elements.

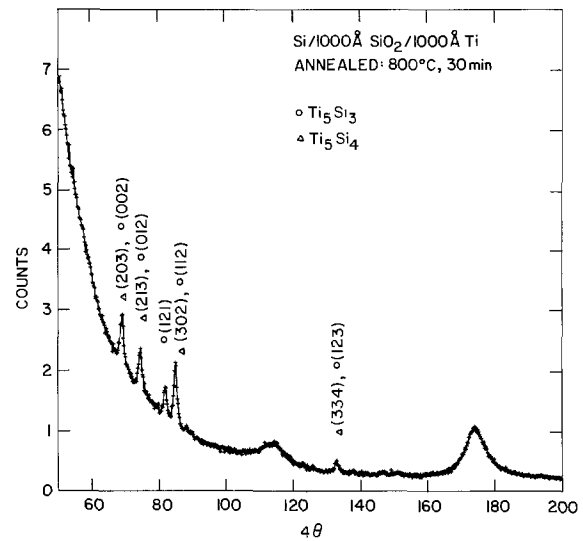


Fig. 3. Glancing angle x-ray diffraction pattern obtained with Cu K α radiation from a Si/1000Å SiO₂/1000Å Ti sample after annealing for 30 min at 800°C, identifying the compound Ti₅Si₃. The broad diffraction peaks are artifacts of the x-ray equipment.

The broad diffraction peaks in Fig. 3 are artifacts of the x-ray equipment.

We cannot identify the Ti-oxide phase from the x-ray spectra of Fig. 3. The number of diffraction lines we obtained from this as well as other samples is insufficient to determine which of the many possible Ti-oxide compounds are formed. From RBS analysis alone one would speculate that Ti₂O₃ is the compound in question. However, we believe that in this temperature range rutile TiO₂ is formed in the presence of some unreacted Ti.

MOS capacitor measurements.—The breakdown voltage of the Ti-MOS capacitors prepared with a 1000Å thick Ti layer was measured before and after various heat-treatments. We defined the breakdown voltage as the voltage at which the leakage current surpassed 50 μ A. The histograms of the capacitors as a function of breakdown voltage for oxide thicknesses of 100, 200, and 350Å are shown in Fig. 4. Histograms are shown before any heat-treatment of the capacitors and after a maximum permissible time-temperature cycle that the capacitors were able

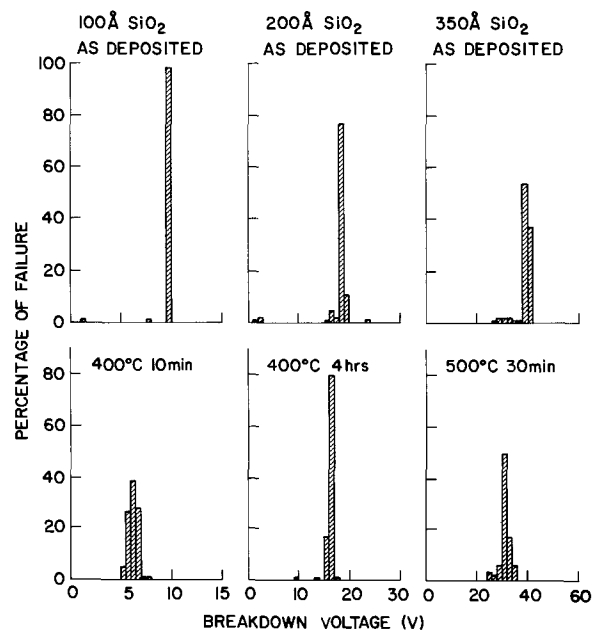


Fig. 4. Distribution of Ti-MOS capacitors as a function of breakdown voltage for oxide thicknesses of 100, 200, and 350Å. Distributions are shown before and after a heat-treatment at 400° and 500°C, respectively.

to withstand: namely, 10 min at 400°C for 100Å SiO₂, 4h at 400°C for 200Å SiO₂, and 30 min at 500°C for 350Å SiO₂. Two features are apparent from Fig. 4. First, the width of the distributions is small and is not altered in a marked way by the annealing process. This indicates that the integrity of the MOS structure is maintained. Second, the breakdown voltage is shifted to lower voltages after the annealing process. This points to either a thinning of the SiO₂ layer and/or increase of the dielectric constant of SiO₂. We could not measure the breakdown voltage for thicker oxide layers because the voltage was too high for our instrumentation. In this case, we measured only the leakage current.

The leakage current of Ti-MOS capacitors with 1000Å thick oxide layer is stable for heat-treatments of 30 min up to 600°C. This is shown in Fig. 5, which illustrates the dependence of the leakage current of a typical capacitor on applied bias. The small peak at 0 V is due to charging of the capacitor. After a heat-treatment of 30 min at 700°C, a pronounced increase in leakage current is observed on some of the capacitors. The I-V characteristic differed strongly from one capacitor to another upon annealing at 700°C. An example is shown in Fig. 5. It seems that the capacitor is about to fail at that temperature. However, after annealing the capacitors for 30 min at 800°C and above the I-V characteristics turned out to be consistent among the capacitors investigated. A typical example is shown in Fig. 5. The asymmetry of the leakage current on the polarity of the applied bias is remarkable and is indicative of a rectifying behavior. We believe that in this temperature range the Ti has completely decomposed the oxide layer, thereby destroying the MOS capacitor and forming a low barrier Schottky diode with the Si substrate. Titanium-MOS capacitors prepared on 350Å thick oxide layers were destroyed after a heat-treatment at 600°C for 30 min.

We have also investigated the Ti-MOS capacitors with C-V measurements. The high frequency (1 MHz) C-V characteristics of capacitors with a 350Å thick oxide layer are shown in Fig. 6. The C-V characteristics are well behaved for as-deposited capacitors and capacitors which have been annealed for 30 min up to 500°C. However, it is obvious from Fig. 6 that the capacitance in accumulation increases with increasing annealing temperature. In addition, a reduction in flatband voltage is noticeable in Fig. 6 upon annealing of the capacitors, in accordance with the increase in accumulation capacitance. Both effects can be explained by a thinning of the oxide layer due to Ti-SiO₂ interaction and/or an increase of the dielectric constant of the SiO₂. Diffusion of Ti into the SiO₂ is not expected to increase the dielectric constant because Ti in SiO₂ will be bound to oxygen, forming a semiconducting titanium oxide. Therefore, the above effects are likely to be due to a thinning of the oxide layer. Finally, Fig. 6 indicates that heat-treatments of 600°C and higher essentially

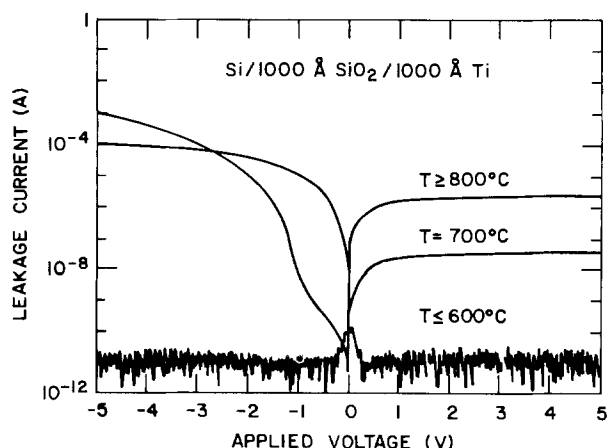


Fig. 5. Leakage current vs bias for Ti-MOS capacitors with a 1000Å thick oxide layer following heat-treatments for 30 min at various temperatures. Note the asymmetry of the I-V characteristic on the polarity of the applied bias.

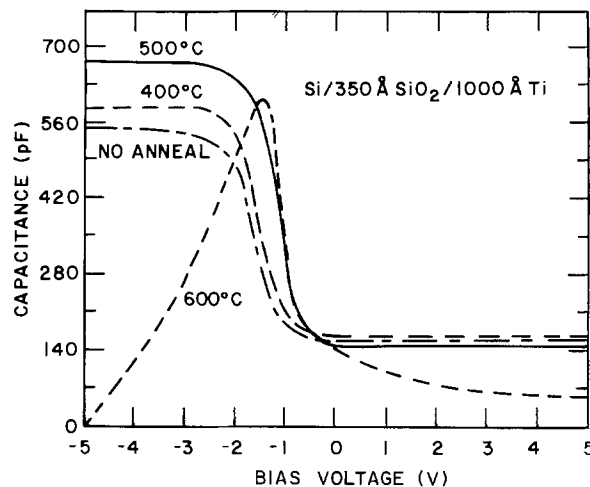


Fig. 6. High-frequency (1 MHz) C-V characteristics of Ti-MOS capacitors with a 350Å thick oxide before and after annealing for 30 min at various temperatures. Note the change in accumulation capacitance and flatband voltage with annealing temperature.

short the MOS capacitors prepared with a 350Å thick oxide layer. For MOS capacitors prepared with a 1000Å thick SiO₂, shorting occurred during heat-treatments at 700°C.

Investigations of the oxide layer.—So far, it seems that the electrical properties of the oxide layer beneath the titanium silicide are not altered by the Ti-SiO₂ interaction. The steep trailing edges of the Ti signals in the RBS spectra of Fig. 1 and 2 indicate that the silicide-oxide interface is sharp. In addition, a noticeable Ti diffusion into the SiO₂ has not been observed with RBS. To further substantiate these facts, we have investigated the properties of the oxide layer beneath the reaction interface in detail.

First, we measured the thickness of the SiO₂ layer after the interaction between Ti and SiO₂. For that purpose, we annealed Ti films on SiO₂ at temperatures between 500° and 800°C. The unreacted Ti was then etched away (3), and the thickness of the remaining oxide was measured with optical interferometry. Table I lists the amount of oxide consumed by the Ti-SiO₂ interaction for various annealing conditions. It is clear from Table I that the amount of SiO₂ lost depends on both annealing temperature and time. The amount of SiO₂ lost during the 500°C heat-treatment corresponds to the increase of the accumulation capacitance at 500°C, as shown in Fig. 6. For annealing temperatures of 700°C and above, the SiO₂ surface acquires a metallic luster and the measurement of the loss of SiO₂ with optical interferometry became difficult. We tried to analyze the nature of the metallic luster with ESCA, but were unable to detect foreign elements within its resolution limit. However, a SEM investigation revealed tiny residues on the surface of the SiO₂, as shown in the micrograph of Fig. 7. The spherically shaped residues are about 300Å diam and cover only about 0.5% of the SiO₂ surface. Therefore, ESCA could not detect them. We were not able to determine the composition of the res-

Table I. Loss of oxide during the reaction between Ti and SiO₂ in argon ambient

Temperature (°C)	Heat-treatment Time (min)	Loss of oxide (Å)
500	30	55
550	30	90
550	60	105
550	90	110
550	120	115
600	30	150
700	30	*
800	30	*

* Sample surface exhibits metallic luster.

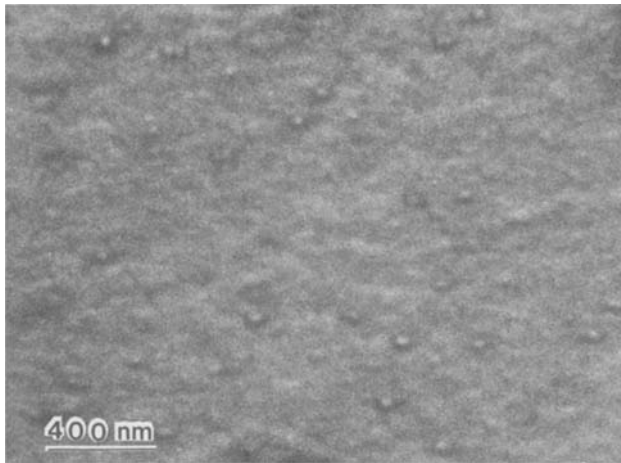


Fig. 7. SEM micrograph of a Si/1000Å SiO₂/300Å Ti sample following a heat-treatment for 30 min at 800°C and stripping of the Ti-silicide on unreacted Ti. A thin Au layer has been evaporated to prevent charging up of the SiO₂ Layer.

ides. It is possible that they consist of a metal-rich titanium silicide such as Ti₅Si₃ because they were not removed by the selective etching solution.

The loss of SiO₂ during interaction between Ti and SiO₂ is consistent with the RBS profiles of oxygen shown in Fig. 1 and the increase of the accumulation capacitance observed in Fig. 6. These facts rule out Ti diffusion into the SiO₂. We also performed SIMS analysis of the SiO₂ layer after stripping of the Ti-silicide to further support the absence of Ti diffusion. The analysis revealed that a possible Ti concentration in the SiO₂ must be below the sensitivity of SIMS for Ti ($< 10^{15} \text{ cm}^{-3}$).

Finally, we have prepared Al-MOS capacitors on 1000Å thick SiO₂ layers which had been reacted with the Ti at 700°C for 30 min and subsequently stripped of the silicide and any unreacted Ti. For comparison, we have also prepared Al-MOS capacitors on unreacted SiO₂ layers. The thickness of the Al dots was 7000Å. The high frequency (1 MHz) C-V characteristics of the capacitors, which are shown in Fig. 8, are well behaved in both cases, irrespective of the 700°C heat-treatment. The accumulation capacitance for the capacitors on reacted SiO₂ is 50 pF higher than for those on unreacted SiO₂. This corresponds to a reduction of the oxide thickness of about 200Å, which is in good agreement with the observed oxide loss given in Table I. Thus, we are confident to rule out Ti diffusion into the SiO₂ during the heat-treatments.

Discussion

It is observed in general that the interactions between thin films of refractory metals and plain Si substrates yield silicon-rich silicides. In the case of Ti films on Si, the formation of the monosilicide TiSi is observed around 500°C and the disilicide TiSi₂ is formed at 600°C or higher temperatures (7). This is in contrast to the present results of the interaction between Ti and SiO₂. Here, a metal-rich silicide, Ti₅Si₃, is formed at the Ti-SiO₂ interface. The silicon needed for the silicide formation originates from SiO₂, which is decomposed by the Ti-SiO₂ interaction. The oxygen which is freed by this interaction is dissolved in the Ti and at higher temperatures reacts with the Ti to form an oxide layer near the surface. The oxide layer is metal rich and consists presumably of TiO₂ and unreacted Ti.

These conclusions are in basic agreement with those presented by Krättele *et al.* (5). However, our investigation of Ti-MOS capacitors revealed the onset of the Ti-SiO₂ interaction at 400°C, which is below the temperature for conventional Ti-silicide formation. Krättele *et al.* (5) claimed that refractory metals react with SiO₂ at temperatures which are about 200°C higher than the temperature to form the corresponding silicide with Si. This discrep-

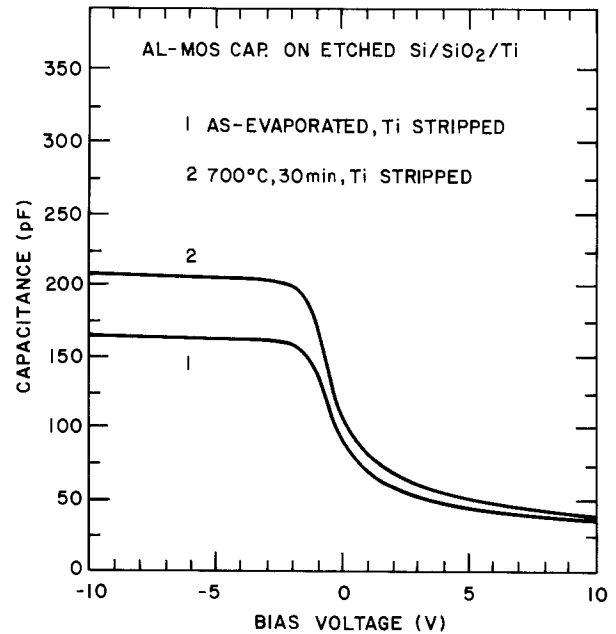


Fig. 8. High-frequency (1 MHz) C-V characteristics of Al-MOS capacitors fabricated on etched Si/SiO₂/Ti substrates. Two cases are shown, one for substrates with Ti stripped after evaporation and one for substrates with Ti stripped after reaction with SiO₂ at 700°C for 30 min.

ancy is not surprising because their methods of analysis were restricted to RBS and x-ray diffraction. As shown in Fig. 1, RBS does not detect any interaction between Ti and SiO₂ below 600°C. There is also a remarkable analogy between the interaction of Ti and SiO₂ and that of Ti and Si₃N₄. Borisov *et al.* (18) reported that mixtures of Ti and Si₃N₄ powders reacted at temperatures below 1330°C to form Ti₅Si₃ and TiN compounds.

It seems that the Ti-SiO₂ interface is a very reactive one. Titanium atoms at the interface have a strong tendency to reduce neighboring Si-O bonds and to form new Ti-O and Ti-Si bonds. At this point, it is instructive to compare our results with the findings of two recent photoelectron spectroscopy investigations of the Ti/SiO₂ interface (9, 10). It is reported that the presence of SiO₂ at the Si surface has a significant effect on the reaction of Ti and Si, and, more important, that the thickness of the SiO₂ determines the end products of the reaction. The evaporation of Ti onto thin layers ($< 20\text{Å}$) of SiO₂ at room temperature was found to break Si-O bonds and to rebond the free oxygen atoms to Ti atoms (10). This reactivity of the Ti is reflected in its excellent adhesion to insulators, in particular SiO₂ and Si₃N₄. The formation of silicides is not observed during evaporation of Ti onto SiO₂. Annealing at moderate temperatures (300°-400°C) changes the bonding of the Ti from Ti-O to Ti-Si and produces a stable silicide phase. For thin oxide layers, the silicide is similar to that formed with a clean Si substrate (9, 10).

It is the combination of both processes, the reduction of SiO₂ and the low temperature interfacial reaction with Si, which mark the reliability of Schottky barriers and the low resistivity of ohmic contacts prepared with Ti. However, the reactivity of the Ti/SiO₂ interface is a disadvantage when the preservation of thin SiO₂ layers is important. This is specially the case for gate oxides and regions of thinner field oxide around device oxide windows. Heat-treatments above 400°C cause a noticeable reduction of the oxide thickness, owing to the Ti-SiO₂ interaction. The excess oxygen probably forms a solid solution with the unreacted Ti. As the Ti-SiO₂ reaction proceeds during extended or higher temperature heat-treatments, the oxygen concentration in the Ti increases. When it exceeds the solid solubility limit, a Ti-rich oxide forms, in agreement with the photoelectron spectroscopy results of Ti on thick SiO₂ layers (9).

We have not found any indication of Ti diffusion into the SiO₂ during heat-treatments up to 800°-900°C. The

photoelectron spectroscopy studies of the Ti/SiO₂ interface (9, 10) were also unable to detect diffusion of Ti beyond the mixed interfacial layer amounting to a few monolayers. Thus, we conclude that the diffusivity of Ti in SiO₂ is very low. This is also expected from the fact that Ti is very reactive and reduces quickly many oxide compounds. As a consequence, the interface between evaporated Ti and SiO₂ is very sharp and stays relatively sharp during subsequent heat-treatments up to 700°C. This is beneficial to the application of Ti in the manufacture of integrated-circuit elements.

Conclusions

We have studied the interaction between Ti and SiO₂ during thermal annealing in the temperature range of 400° to about 1000°C. The results show that Ti reacts in a limited fashion with SiO₂ at temperatures of 700°C and below, but strong interactions take place at higher temperatures. At high temperatures, the reaction mechanisms consist of the decomposition of SiO₂ by the Ti metal and the formation of a Ti-rich silicide, Ti₅Si₃, at the interface and a Ti-rich oxide, presumably a mixture of Ti and TiO₂, near the surface. Below 700°C, the reaction results in a net loss of the SiO₂ and exhibits a sharp interface, characteristic of a layer-by-layer growth process. However, we have not observed diffusion of Ti into the SiO₂ during the interaction.

The application of a Ti-based metallurgy to silicon devices requires special attention. The use of Ti or Ti silicides in contact structures and interconnects should be of no concern as long as the oxide thickness is greater than 350Å and the post-metal heat-treatment is performed at a temperature not exceeding 400°-450°C. However, in the case of self-aligned TiSi₂, the formation temperature of the silicide should be kept below 700°C in order to prevent excessive Ti-SiO₂ interactions. Also, the field oxide should have a thickness of at least 1000Å. Besides these

restrictions, which are not severe at all, there is no reason why the full advantage of the application of Ti or Ti-silicide metallurgies to device manufacturing cannot be taken.

Manuscript submitted May 2, 1984; revised manuscript received July 12, 1984. This was Paper 77 presented at the Cincinnati, Ohio, Meeting of the Society, May 6-11, 1984.

IBM Corporation assisted in meeting the publication costs of this article.

REFERENCES

1. C. Y. Ting and B. L. Crowder, *This Journal*, **129**, 2590 (1982).
2. C. Y. Ting and M. Wittmer, *Thin Solid Films*, **96**, 327 (1982).
3. C. Y. Ting, S. S. Iyer, C. M. Osburn, G. J. Hu, and A. M. Schweighart, in "VLSI Science and Technology 1982," C. J. Dell'Oca and W. M. Bullis, Editors, p. 224, The Electrochemical Society Softbound Proceedings Series, Pennington, NJ (1982).
4. C. K. Lau, Y. C. See, D. B. Scott, J. M. Bridges, S. M. Perna, and R. D. Davies, *IEDM Tech. Dig.*, 714 (1982).
5. H. Kräutle, W.-K. Chu, M.-A. Nicolet, J. W. Mayer, and K. N. Tu, in "Applications of Ion Beams to Metals," S. T. Picraux, E. P. EerNisse, and F. L. Vook, Editors, p. 193, Plenum Press, New York (1974).
6. W.-K. Chu, J. W. Mayer, and M.-A. Nicolet, "Backscattering Spectrometry," p. 89, Academic Press, New York (1978).
7. K. N. Tu and J. W. Mayer, in "Thin Films—Interdiffusion and Reactions," J. M. Poate, K. N. Tu, and J. W. Mayer, Editors, p. 359, John Wiley and Sons, New York (1978).
8. Yu. S. Borisov, A. L. Borisova, Yu. A. Kocherzhinskii, and E. A. Shishkin, *Poroshk. Metall. (Kiev)*, **3**, 63 (1978).
9. M. A. Taubenblatt and C. R. Helms, *J. Appl. Phys.*, **53**, 6308 (1982).
10. R. Butz, G. W. Rubloff, and P. S. Ho, *J. Vac. Sci. Technol. A*, **1**, 771 (1983).

Low Energy Proton Beam Lithography with a Thin Oxygen-Etch Barrier Layer

H. Hiraoka*

IBM Research Laboratory, San Jose, California 95193

ABSTRACT

Low energy protons in the several keV energy range have very limited penetration depths into polymer films. This limitation necessitates the use of very thin oxygen-etch barrier layers and of dry image development by oxygen reactive ion etching. For negative tone images, the etch-barrier layers were deposited patternwise by proton-beam-induced polymerizations of organo-metallic compounds, followed with dry image development by oxygen reactive ion etching. For positive tone images, the etch-barrier layers were deposited (prior to patternwise exposure to proton beams) on top of polymer films by plasma polymerizations of organo-metallic compounds, or by evaporation or sputtering of certain metals. Hydrogen atoms and/or protons react with metal atoms in the etch barrier layers to yield volatile metal hydrides, making the exposed areas more vulnerable to oxygen reactive ion etching, and providing positive tone images after image development. Sub-keV electrons can replace low energy protons for fabrications of positive-tone polymer images. In these processes, almost any kind of carbonaceous polymer film can be used as the imaged material. With a bright ion gun available, the exposure times could be less than a second, yielding high aspect ratio and high resolution polymer patterns.

Ion beam lithography does not suffer from the proximity effect, which is one of the most serious problem of electron beam lithography with electron energy of 20-30 keV (1). The very limited penetration depths of ions, however, require high acceleration energies of ions (for example, 150 keV proton beams), to be useful for lithographic applications (2). Associated with high energy ion beams, there are many problems to be considered. With the use of very thin oxygen etch barrier layers deposited from the vapor phase, as in plasma polymerization or by sputtering

or evaporation, a few keV proton beams can be utilized successfully to delineate high resolution positive-tone polymer images, as described later.

Shallow ion implantation [gallium ion (3), indium ion (4), silicon ion (5)] into resist films has been reported to fabricate negative-tone polymer images. An organic semiconductor film was used to avoid charge buildup with scanning indium ion (4). In all these shallow ion implantations for reducing oxygen plasma etch rates, high doses of ion beams (1×10^{15} Si ion/cm²) are required to obtain reasonably thick polymer images. In a similar way as in ion implantations, thin oxygen-etch barrier layers can be

*Electrochemical Society Active Member.

deposited patternwise in ion-beam-induced polymerization onto the exposed surfaces of polymer films during proton-beam exposures. As opposed to the ion-implantation method, no charge build-up problem appears and high sensitivity is possible.

Experimental

Proton-beam exposures.—Proton-beam exposures were carried out through a stencil mask with a cold cathode ion source, a 2-30 Magmiller ion gun from Commonwealth Scientific Company. At a typical hydrogen pressure of 4×10^{-5} torr, the proton-beam current density was 1.5×10^{-7} A/cm² at 4 keV, resulting in a dose of 5×10^{-4} C/cm² for a 60 min exposure period. The stencil masks used are the same ones reported for electron-beam proximity printing (6). The spacings between the mask and resist layers are about 200 μ m.

Electron-beam exposures.—Sub-keV electron-beam exposures were carried out through a stencil mask with a Varian scanning Auger electron gun operating in a raster scan mode. With a beam current of 25 μ A, the electron dose was about 1×10^{-4} C/cm² for an exposure period of 60 min.

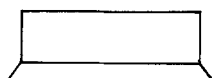
Dry image development.—Polymer images were developed by oxygen reactive ion etching. After proton- or electron-beam exposures, wafers with polymer films were placed in a reactive ion etching system, which was a parallel-plate diode system with a cathode of 12 in. diam. Under typical experimental conditions, images were developed at an oxygen pressure of 0.12 torr with a power density of 0.34 W/cm² at a bias potential of -300V. Image development times varied from 15 to 60 min, depending upon a film thickness and a kind of polymer films; PMMA films without oxygen etch barrier layers have an etch rate of 1 μ m/10 min.

Negative-Tone Polymer Patterns

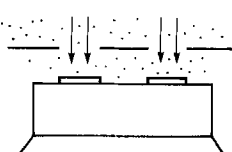
For fabrication of negative-tone images, thin oxygen-etch barrier layers were deposited through a stencil mask in ion-beam-induced polymerizations during proton-beam exposures on top of polymer films; images are developed afterwards by oxygen reactive ion etching. Figure 1 shows the process. The thickness of the deposited oxygen-etch barrier layers is not so critical as in the case for positive-tone polymer images; the thickness could be as thick as 1000 Å , but there is a lower limit of about 150 Å , as discussed below for the fabrication of positive-tone images.

Many organo-silicon compounds and organo-tin compounds can be used as the etch-barrier forming materials as long as they have sufficient vapor pressure; for example, tetravinylsilane, hexamethyldisiloxane, hexamethyl-

1. Polymer film deposition; cure prior to the next step for polyimides:



2. Patternwise exposures to H⁺ beams in presence of vaporous organo-metallic compounds at pressures less than 5×10^{-5} torr:



3. Image developments by oxygen RIE:

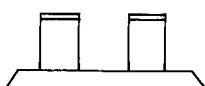


Fig. 1. Negative-tone pattern fabrication by proton beam induced polymer deposition of organo-metallic compounds.

disilazane, tetramethyltin. Halogenated aromatic compounds like hexafluorobenzene can also be deposited as an etch-barrier layer on top of PMMA films. The etch-barrier layers made of hexafluorobenzene deposited in proton-beam-induced polymerization has a graphitic polymer structure, based on its ESCA data, which explains the relatively high etch resistance under our RIE conditions.

The monomer vapor inlet tube was located 12 in. away from the ion source, about 2 in. above the mask and resist/wafer assembly. Because polymer deposition on top of the stencil mask cannot be avoided, it is essential to remove deposited polymer films from the mask surface after certain times of deposition; this cleaning has been carried out in a CF₄/oxygen plasma without any deterioration of the mask.

A typical example of the results obtained by this method is shown in Fig. 2. Polyamic acid films were deposited on a silicon wafer from vapors of 1,2,4,5-benzene-tetracarboxylic anhydride (PMDA) and of 4-aminophenyl ether (ODA) (7). After curing the polyamic acid films at 250°C for 30 min in air, the polyimide films formed were subjected to patternwise exposures of proton beams through the mask, as described earlier. During the proton-beam exposure, tetravinylsilane vapor was introduced through the inlet tube located above the mask-polyimide film assembly; the partial pressure of the silane was 2×10^{-5} torr as measured at a distant location, and the hydrogen pressure was 3×10^{-5} torr. The exposure period was 60 min, corresponding to 5.4×10^{-4} C/cm² with 1.5×10^{-7} A/cm² ion density. After patternwise deposition of the etch-barrier layer, the mask was removed from the mask-polyimide film assembly. Polymer images were developed by oxygen reactive ion etching: development time was 15 min at an oxygen pressure of 0.12 torr, with power density of 0.34 W/cm² and a bias potential of -300V. SEM pictures of the polyimide patterns are shown in Fig. 2 together with a partial image of the mask used. The thickness of the oxygen etch barrier layer deposited was 0.1 μ m. Figure 3 shows the thermal stability of the polyimide patterns; (a) polymer images prior to heating, and (b) and (c) polyimide patterns after heat-treatment at 450°C for 30 min in vacuum, revealing no thermal flow of a half- or a quarter-micron-sized polyimide images. In a similar way as described for polyimide images, we have been successful in obtaining negative tone high resolution and high aspect ratio polymer patterns made of PMMA, cresol-formaldehyde novolac resins, and poly(p-hydroxystyrene).

Positive-Tone Polymer Images

The positive tone polymer pattern fabrications consist of three processes: first, deposition of very thin oxygen etch barrier layers on top of polymer films; second,

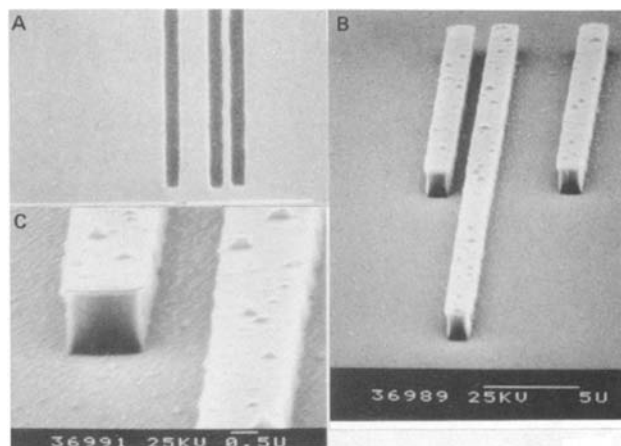


Fig. 2. Negative-tone polyimide (PMDA-ODA) made by the process outlined in Fig. 1. (a): A part of a stencil mask. (b) and (c): The polyimide patterns obtained.

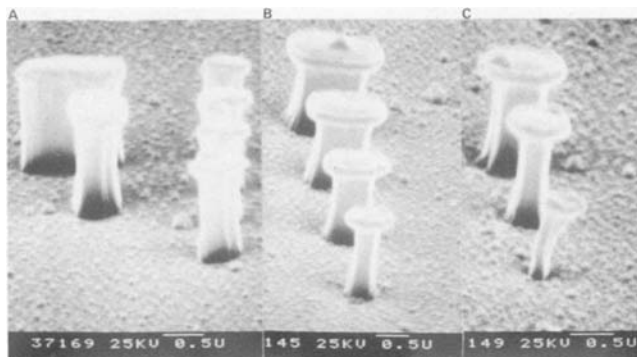


Fig. 3. Thermal stability of dry processed-polyimide patterns. (a): Prior to heat-treatment. (b) and (c): After heat-treatment at 450°C for 30 min in vacuum after dry development.

patternwise exposure of polymer films with thin etch barrier layers to proton beams; and third, image developments in oxygen reactive ion etching, as shown in Fig. 4.

Thin oxygen-etch barrier layers were deposited from the vapor phase on top of polymer films in plasma polymerizations of organo-metallic compounds. Another method used was evaporation or sputtering of certain metals. In either case, the control of the thickness of the etch barrier is extremely important. This control was realized with a quartz crystal microbalance (8). Assuming unit density of the etch barrier layers, the thickness must be in the range of 150-250Å. With thinner barrier layers, the thinning of unexposed areas appears, yielding poor quality polymer patterns. With thicker etch barriers, the images cannot be developed, even after prolonged oxygen reactive ion etching.

Plasma polymerized organo-metal films.—The same kind of organo-silicon and organo-tin compounds described in the preceding section have been used in plasma polymerization to form oxygen etch barrier layers: tetra vinylsilane, hexamethyldisilazane, hexamethyldisiloxane, and tetramethyltin. A monomer vapor was introduced into the tail end of an argon or helium glow discharge, and thin plasma polymerized organo-metal films were deposited onto polymer surfaces on silicon substrates located about 5 in. away from the monomer inlet. The deposition was usually completed within 30-60s at about 0.5 torr total pressure, while the amount of deposited films was carefully monitored with a microbalance to a film thickness of 150-250Å.

Polymer films with thin oxygen-etch barrier layers were then exposed to 3-5 keV proton beams through a stencil mask with a beam dose ranging from 2×10^{-4} to 1×10^{-3} C/cm². With the present Magmiller ion gun, these doses corresponded to 20-80 min exposure periods. With a

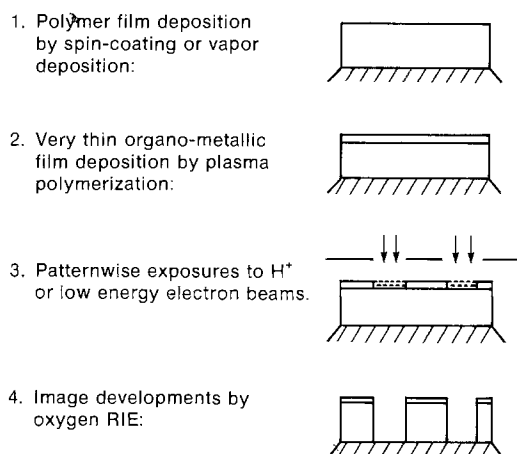


Fig. 4. Positive-tone polymer patterns fabricated by low energy proton beams with the use of thin oxygen-etch barrier layers made of organo-metallic films.

brighter ion source which is now commonly available, this exposure time should be less than 1s. During proton exposures, protons and/or hydrogen atoms reacted with silicon or tin to yield volatile metal hydrides, as discussed later.

After proton-beam exposures, faint color changes appeared in the exposed areas, but the thickness loss never exceeded a few hundred angstroms. Polymer images were then developed by oxygen reactive ion etching; RIE conditions were as already described.

Typical examples of the polymer patterns obtained are shown in Fig. 5. Figure 5a consists of positive-tone polyimide patterns with plasma-polymerized thin tetra vinylsilane layers as the oxygen-etch barrier. These polyimide films were made from vapor-deposited polyamic acid, as previously described. A narrow line (1.5 μm) was delineated completely with vertical wall profiles on 1.3 μm thick polyimide film. The present technique successfully provides fine lines narrower than 1.5 μm, with high resolution in an all dry process.

A charge buildup trouble appeared, however, in the delineation of larger-sized patterns. It was difficult to develop the inner areas of larger images completely, and sometimes the images were developed in the form of a ring like a doughnut, as shown in Fig. 5b and 5c. Figure 5b is a PMMA pattern with plasma-polymerized tetra vinylsilane film as an oxygen etch barrier; 4 keV proton beams impinged onto the silane film through the stencil mask used for images shown in Fig. 2a. As opposed to the other cases, however, island bars with vertical wall profiles were formed inside the developed areas. A 3 μm

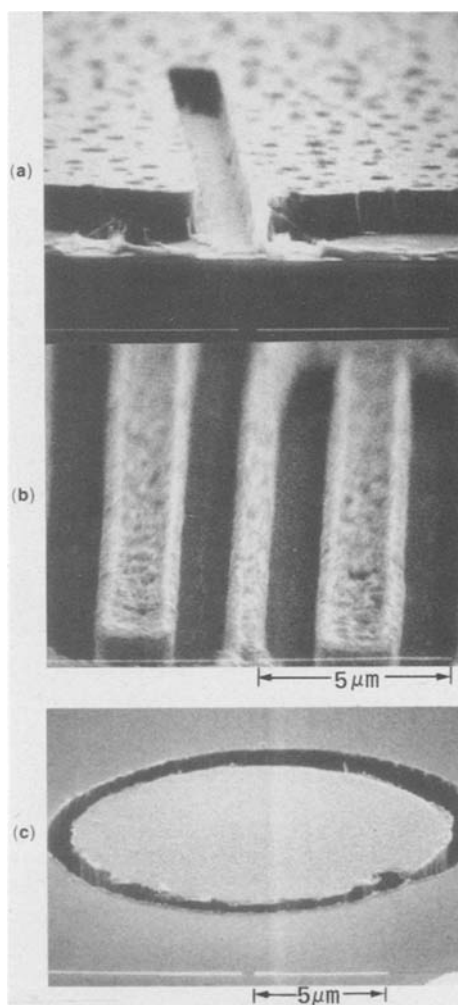


Fig. 5. Positive-tone images of polyimides (a) and (c), or PMMA (b) imaged by 5 keV proton-beam exposures onto polymer films with thin oxygen-etch barrier layers made of plasma polymerized tetra vinylsilane, and subsequently developed by oxygen reactive ion etching.

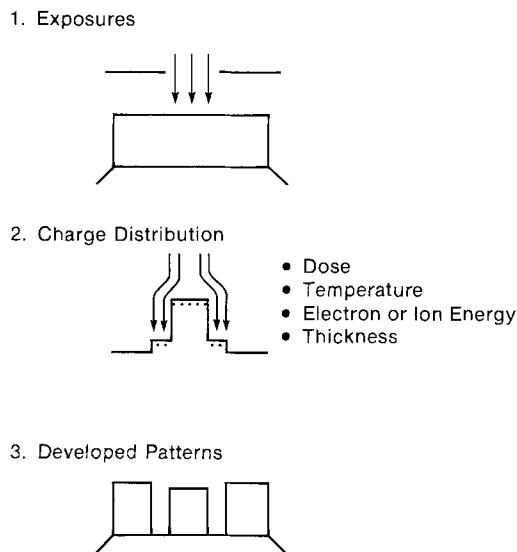


Fig. 6. Trapped charge mechanism for doughnut-shaped pattern formation.

wide mask image appeared as a $5\ \mu\text{m}$ wide rectangular hole with a $2.3\ \mu\text{m}$ wide island bar. Figure 5c shows positive-tone polyimide images of a circular hole, which was made by impinging 4 keV proton beams onto plasma-polymerized tetravinylsilane film and subsequent oxygen reactive ion etching for image developments. The inside island should not appear if there were no charge buildup. The height of the inside island depends upon the degree of charge buildup, which was in turn determined by proton-beam dose, proton energy, substrate temperature, and film thickness. The $1.5\ \mu\text{m}$ wide channel delineated by polymer films was completely developed by oxygen reactive ion etching with surrounding vertical walls. Figure 6 illustrates schematically how these doughnut-shaped patterns were formed by proton charge trapped in the films. Although the polarity should be opposite, low energy electron beams of 800-1000 eV energy generated similar patterns from trapped electrons, as described below.

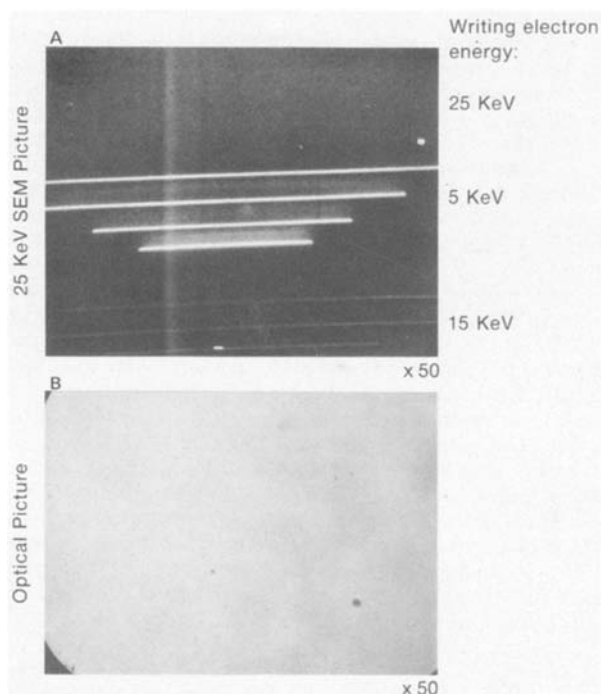


Fig. 7. Images of trapped low energy electrons in PMMA. (a): 25 keV SEM picture of trapped electrons. (b): Optical picture of the exact same areas of (a).

Sub-keV electron beam exposures.—Low energy electron beam lithography has been reported with focused scanning electron beams with an electron energy below 5 keV (9). Either thin polymer films like PMMA or inorganic resist films have been used; troubles associated with trapped low energy electrons have never been reported. In low energy scanning electron microscopy, no metal coatings are required because of the rapid dissipation of impinging electrons via surfaces. However, as shown in Fig. 7, electrons with 5 keV energy were trapped more efficiently in polymer films than those of 15 or 25 keV energies. In Fig. 7, electrons were scanned on polymer surfaces with equal doses ($\sim 5 \times 10^{-4}\ \text{C/cm}^2$) at 5, 15, and 25 keV. Although there were no images seen optically as shown in Fig. 7b, traces of scanned electrons were seen in SEM pictures of Fig. 7a taken with 25 keV scanning electrons for the same area, particularly the clear traces of 5 keV electrons because of their trapped charge. These images disappeared in heating, or on standing for long times in air, by charge leakage via surfaces and/or through media.

After PMMA films bearing thin oxygen etch barriers were exposed to 5 keV scanning electron beams, attempts were made to develop images by oxygen reactive ion etching. Hollow images were formed, however, in these conditions, as shown in Fig. 8b and 8c, indicating that the electron energy was deposited inside the film, but not very much in the etch barrier layers. With electrons of lower energies of 800-1000 eV, images were developed "from top to bottom" by oxygen reactive ion etching, as shown in Fig. 8a. With such a low energy as 800 eV, however, the doughnut-shaped patterns reported in the preceding section on proton beam exposures were obtained, as

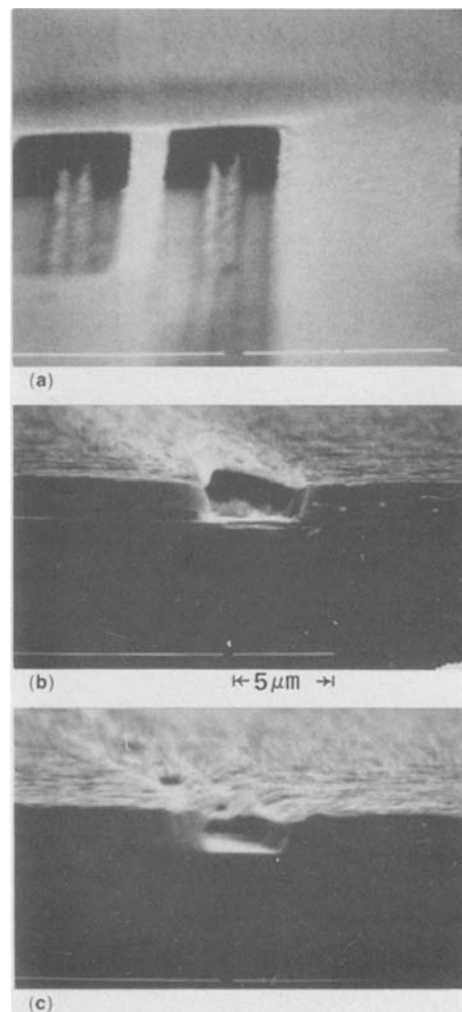


Fig. 8. Positive-tone images of PMMA by 800 eV electron beams (a) or by 5 keV scanning electron beams (b) and (c).

shown in Fig. 9 for large area delineation. The charge buildup is again responsible to these images. In these electron-beam exposures of PMMA films, considerable amounts of hydrogen atoms were formed (10), and these hydrogen atoms are expected to react with silicon atoms to make the exposed areas more vulnerable to oxygen reactive ion etching.

Thin metal films.—The charge buildup problem encountered in the delineation of large patterns in polymer films with insulating plasma polymerized organo-metal films could be avoided in several ways. One way is the use of neutralizing thermal electrons flooding polymer surfaces during proton-beam exposures; most ion sources available have a built-in neutralizer. Another way is to use conducting oxygen etch barrier layers, as reported here. High energy proton beams do not cause this charge buildup problem. Certain metal hydrides are well known for their volatility; for example, SiH_4 , SnH_4 , AlH_3 , Ga_2H_6 , and Ge_2H_6 . When low energy proton beams impinged onto thin metal films, metal films were removed by formation of metal hydrides such as SiH_4 or SnH_4 . Preferential removal of Si atoms or Sn atoms from organo-metal films have been demonstrated with ESCA, as discussed later.

Thin metal films, such as aluminum, bismuth, tin, or other volatile hydride forming metals, were deposited by evaporation or by sputtering onto polymer surfaces; the thickness is critical and must be in the range described above. Subsequent processes are exactly the same as the ones in the preceding section. During image development by oxygen reactive ion etching, the metal films in unexposed areas were converted to metal oxides, which were readily removed in a mild acidic solution.

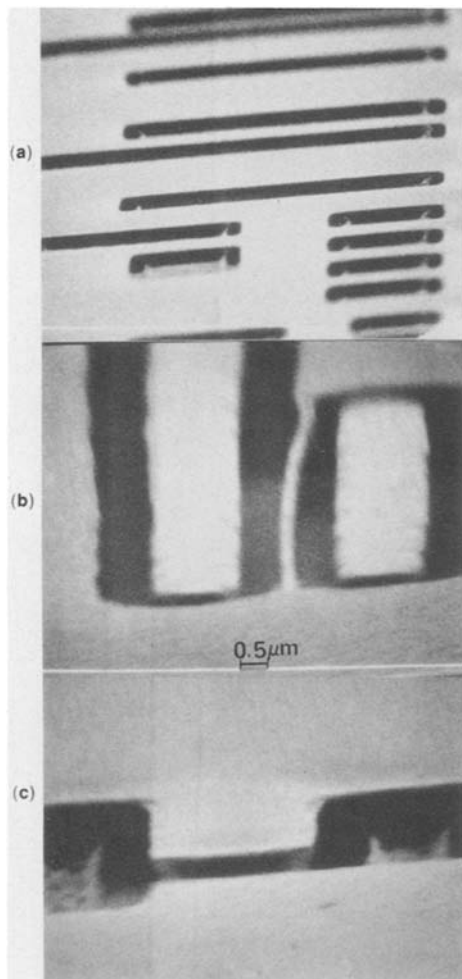


Fig. 9. Positive-tone images of PMMA generated by 800 eV electron-beam exposures. The polymer films have thin oxygen-etch barrier layers made of plasma-deposited tetravinylsilane.

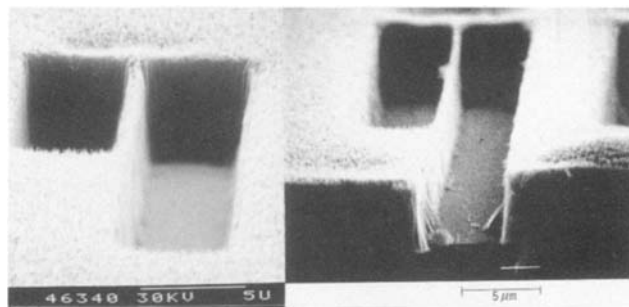


Fig. 10. Thin bismuth films on top of PMMA were exposed to 4 keV proton beams through a stencil mask, followed by oxygen reactive ion etching for positive-tone image development.

Figure 10 shows 5 μm thick positive tone PMMA patterns. The images were made with thin bismuth films deposited on top of the polymer films, exposed to 4 keV proton beams through a stencil mask, then developed by oxygen reactive ion etching. The bismuth oxide was dissolved in a mild hydrochloric acid. Even the presence of thin bismuth metal films could not prevent a small amount of degradation of PMMA during the oxygen reactive ion etching, resulting in somewhat rough surfaces of PMMA patterns after development. The roughness extended about a few thousand angstroms into 5 μm thick polymer films. With other polymer films, such as polyimide or novolac resin films, this kind of surface degradation never took place during image development. The polymer patterns with 0.5 μm wide and 5 μm high vertical-wall profiles are obtained in this way without any charge buildup, as shown in Fig. 10.

Hydrogen reactive ion etching lithography.—In the preceding sections, proton beams with 3-5 keV energy have been used to delineate polymer images by impinging onto thin oxygen-etch barrier layers and making the impinged areas vulnerable to oxygen reactive ion etching. We do not know exactly how deep these protons penetrate through to the polymer films, although a Monte Carlo calculation predicted about 1000 \AA with 4 keV proton. However, our result that the etch barrier has to be less than 250 \AA to obtain developable images indicates the proton-penetration depth could be less than the calculated extent (11). We also do not know that the active species is a proton or a neutral hydrogen atom, or both. We learned, however, that the etch resistance of the oxygen-etch barrier layers was markedly diminished once the barrier layers were exposed to hydrogen reactive ion etching even for a short period. In our RIE conditions of 0.15 torr and -300V bias potential, neutral hydrogen may play a significant role. PMMA films bearing plasma polymerized tetravinylsilane layers were exposed to hydrogen reactive ion etching for a short period (1 min) through a stencil mask, as had been done with proton beams, followed by image development by oxygen reactive ion etching. The resulting polymer patterns are shown in Fig. 11. In contrast to the images shown in Fig. 5, no doughnut-shaped patterns are obtained in this case, although the same oxygen-etch barrier layer was employed. The difference may have originated from the contribution of neutral hydrogen atoms (hydrogen pressure: 5×10^{-5} torr vs. 0.1 torr in RIE), or because of the different proton energies (4 keV vs. 0.3 keV in RIE). The very shallow penetration of 300 eV protons may help charge leakage via surfaces. The polymer patterns obtained have vertical wall profiles with 6 μm high, but fine images could not be fabricated, probably because of the poor directionality of the proton beams under our RIE conditions.

Discussion

The results described in the preceding sections clearly demonstrate feasibility of thick submicron polymer pattern fabrications with high aspect ratios using low energy proton beams. The present processes depend upon the

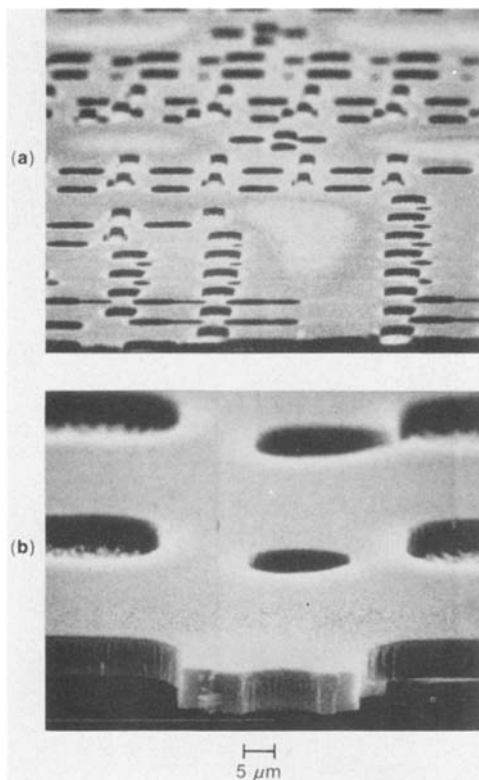


Fig. 11. Positive-tone images of PMMA generated by hydrogen reactive ion etching.

use of thin oxygen-etch barrier layers; the images were made in this thin oxygen-etch barrier layer, and oxygen reactive ion etching extended the thickness of patterned images. This mechanism for micropattern generations is different from the "top down" development mode for nitrocellulose resist films, which is a sensitive, self-developing resist under low energy argon ions beams or pulsed UV laser radiations (12). Our technique for micropattern generation does not depend upon the nature of the imaged films, as shown in the examples of PMMA and polyimide, but the role of thin oxygen etch barrier layers is very important. The thickness of the barrier layers is related with the penetration depth of low energy proton beams. The reactivity of a proton and/or a hydrogen atom with a metal atom of the etch-barrier layers determines a proton dose required for image development.

The selective removal of metal atoms from plasma polymerized organo-metal films by proton beams or by hydrogen reactive ion etching is shown in Fig. 12. The ESCA data of the plasma polymerized tetramethyltin films has the core level signals of $\text{Sn}_{3\text{D}3/2}$ and $\text{Sn}_{3\text{D}5/2}$ at 494 and 495 eV, respectively, and the $\text{C}_{1\text{S}}$ core level signal at 284 eV. After 20 min exposure of the plasma polymerized films to hydrogen RIE, the $\text{Sn}_{3\text{D}}$ signals diminished to 10% of their original intensities, whereas the $\text{C}_{1\text{S}}$ core level signal intensity did not change at all, indicating the initial preferential removal of tin atoms. Further exposure to the hydrogen reactive ion etching removed the carbon signal along with the Sn signals; the immediate increase of the oxygen signal after the hydrogen RIE was caused by oxygen attachment to the exposed polymer surfaces, and a signal at 308 eV may arise from an inorganic substrate material. Similarly, silicon and other metal atoms were removed from thin oxygen-etch barrier layers by proton beams, leaving the exposed areas vulnerable to oxygen RIE.

The penetration depth of low energy proton beams is limited from a few hundred angstroms to 1000Å. An extension of the Monte Carlo calculation indicates about 1000Å as the projected range of 4 keV proton beams in PMMA. Although the range of proton beams inside organo-metal films is not known, our experimental requirement that the etch barrier thickness must be within

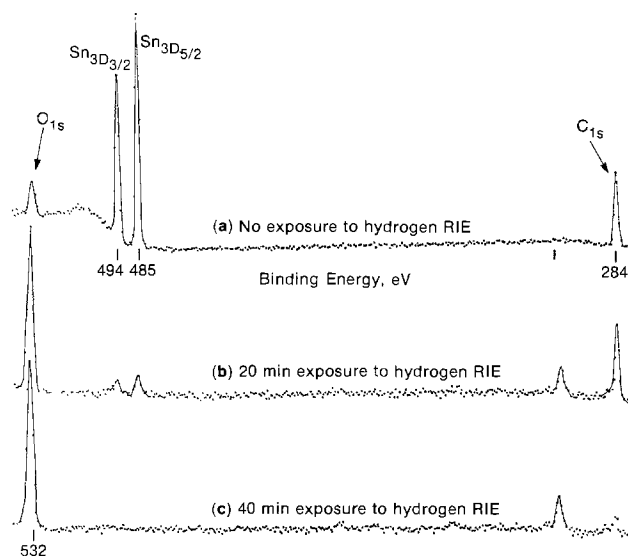


Fig. 12. Removal of Sn from plasma polymerized tetramethyltin films by hydrogen reactive ion etching.

250Å to get developable images indicates that the penetration depth of the proton beams must be far shallower in the etch-barrier layers than expected from the projected range in PMMA.

After the proton-beam exposures, there are only faint color changes in the exposed areas, but the thinning in the exposed areas was so shallow that the measurement was very difficult, probably within 100Å. The only way to develop images after patternwise removal of the etch-barrier layer by proton beams is oxygen reactive ion etching, which does not erode unexposed areas of the oxygen-etch barrier.

Summary

Low energy proton beams in several keV energy ranges, which are readily available for ion milling and other processes, have been used successfully for the fabrication of high resolution polymer patterns in both negative and positive tones. The proton exposures were carried out through a stencil mask used for the proximity electron printing process. Very thin oxygen etch barrier layers are required because of the limited penetration depths of proton beams. For negative-tone images, etch barriers are deposited in H^+ -beam-induced polymerization of organo-metal compounds. For positive-tone images, etch barriers are deposited by plasma polymerization or by sputtering or evaporation of certain metals prior to patternwise exposures. Charge buildup, which appeared in large pattern delineation, can be avoided by the use of thin metal films as etch barriers, or possibly by flooding the polymer surfaces with thermal electrons. Images are developed by oxygen reactive ion etching, and almost any kind of carbonaceous polymer films can be used as the imaged materials.

Acknowledgment

The author thanks a German IBM research and development group for stencil masks used in this study. He also thanks Dr. R. Yang for vapor deposited polyamic acid samples.

Manuscript submitted April 2, 1984; revised manuscript received Aug. 6, 1984.

IBM Corporation assisted in meeting the publication costs of this article.

REFERENCES

1. M. Parik, *J. Vac. Sci. Technol.*, **15**, 927 (1978); see also D. F. Kyser and C. H. Ting, *ibid.*, **16**, 1959 (1980).
2. B. Rensch, R. L. Seliger, G. Csanky, R. D. Olney, and H. L. Stover, *ibid.*, **16**, 1897 (1979).
3. H. Kuwano, K. Yoshida, and S. Yamazaki, *Jpn. J. Appl. Phys.*, **19**, L619 (1980).

4. T. Venkatesan, G. N. Taylor, A. Wagner, B. Wilkens, and D. Barr, *J. Vac. Sci. Technol.*, **19**, 1379 (1981).
5. I. Adesida, J. D. Chinn, L. Rathbun, and E. D. Wolf, *ibid.*, **21**, 666 (1982).
6. H. Bhlen, J. Greschner, J. Keyser, W. Kulcke, and P. Nehmiz, *IBM J. Res. Dev.*, **26**, 568 (1982).
7. J. Duran and D. Haarer, *IBM Tech. Discl. Bull.*, **20**, 1552 (1977).
8. J. W. Coburn, "Applications of Piezoelectric Quartz Crystal Microbalance," C. Lu and A. Czanderna, Editors, pp. 221-249, Elsevier, Amsterdam (1983).
9. K. J. Polasko, Y. W. Yau, and R. F. W. Pease, in "Sub-micron Lithography," Proceedings of SPIE Meeting," Vol. 333, P. D. Blais, Editor, p. 76, SPIE Bellingham, WA (1982).
10. H. Hiraoka, *IBM J. Res. Dev.*, **21**, 121 (1977).
11. L. Karapiperis, I. Adesida, C. A. Lee, and E. D. Wolf, *J. Vac. Sci. Technol.*, **19**, 1259 (1981).
12. M. W. Geis, J. N. Randall, T. F. Duetsch, P. D. DeGraff, K. E. Krohn, and L. A. Stern, Paper presented at 1983 International Symposium on Electron, Ion and Photon Beams, American Vacuum Society, Electron Devices Group of IEEE, and The Electrochemical Society, Los Angeles, CA, May 1983, *J. Vac. Sci. Technol. B*, **1**, 1178 (1983).

Internal Gettering in Bipolar Process

Effect on Circuit Performance and Relationship to Oxygen Precipitation Kinetics

L. Jastrzebski,* R. Soydan, B. Goldsmith,¹ and J. T. McGinn

RCA Laboratories, Princeton, New Jersey 08540

ABSTRACT

The effect of internal gettering on circuit performance has been studied for I^2L and linear logic bipolar circuits. The gettering has been introduced by controlled precipitation of oxygen in silicon wafers during processing, and its effect has been measured as reduction of circuit leakage current, which has been reflected in yield improvement. The efficiency of internal gettering has been found to be a strong function of the amount of precipitated oxygen and precipitate's morphology. It has also been found that the same factors affect the mechanical strength (warpage) of silicon wafers. The best gettering and yield improvement was obtained for relatively low amounts of precipitated oxygen (about 10 ppm), which resulted in the desired precipitate's morphology. An increase in the amount of precipitated oxygen decreased the gettering efficiency and also reduced the mechanical strength of the silicon wafers. The present work showed that, in addition to well-known factors, such as the interstitial oxygen concentration in virgin wafers, oxygen-precipitation kinetics during bipolar processing is strongly affected by other factors, such as concentration of nucleation centers for oxygen precipitation. They control the rate of oxygen precipitation and precipitate's morphology. Since the concentration of these centers is related to the crystal-growth conditions, differences in precipitation kinetics are found in the wafers provided by various commercial suppliers. This can lead to unusual results. For instance, lower amounts of precipitated oxygen have been found in wafers with an initial oxygen concentration of 40 ppm than in wafers with 28 or 31 ppm coming from different suppliers. We believe that our results clearly demonstrate that internal gettering after optimization can be used to improve circuit yield in bipolar processing lines.

The one most important material problem associated with the use of silicon wafers in LSI and VLSI circuits is control of crystallographic defects formation, which is closely related to the oxygen-precipitation kinetics during processing (1-3). Defects present in the device active area, especially those decorated by heavy metals (4, 5), would give dark current generation sites, which could cause functionality failure or excessive leakage in integrated circuits (1). However, defects present in the bulk of a silicon wafer would have a beneficial effect on circuit performance by acting as a gettering site for contamination, which otherwise would precipitate in the active area of the circuit leading to defect formation and/or decoration (1-3, 6-8).

Oxygen present in silicon affects the formation of oxygen precipitates, stacking faults, dislocations, and thermal donors (1, 2). During the defect-generation process, oxygen can play a positive (dislocation pinning and internal gettering) or a negative (thermal donor generation, poorer mechanical strength, and precipitates in the device active area) role (1). Even in the same state and at the same point in processing, oxygen can be both an asset and a liability, as in the case of SiO_2 precipitates that introduce sites for internal gettering but also lower the mechanical strength, resistance to warpage, of silicon wafers (9).

In order to be able to use internal gettering successfully on production lines, it is essential to balance the amount of oxygen in different states during the circuit-fabrication process in such a way that will simultaneously result in efficient internal gettering and good mechanical strength of the silicon wafers. This can be achieved by controlling the oxygen-precipitation process.

*Electrochemical Society Active Member.

¹Present address: RCA Solid State Division, Findlay, Ohio 45840.

In addition to the amount of precipitated oxygen, the morphology of the precipitates has the strong influence on the efficiency of internal gettering. Conditions exist under which an efficient gettering action and an excellent mechanical strength, resistance to warpage, of silicon wafers in the presence of a relatively low density of oxygen precipitates can be achieved (6). To obtain the desired density and morphology of oxygen precipitates in processed wafers, control of the oxygen-precipitation kinetics during bipolar processing and the relationship of kinetics to the as-grown wafer characteristics become important issues.

It has been well documented that the oxygen-precipitation kinetics are controlled by the interstitial oxygen concentration in the as-grown wafers (10). Two models of nucleation and growth, homogeneous and heterogeneous (1), for oxygen precipitation have been proposed. The homogeneous precipitation model (11, 12) assumes that the driving force for oxygen precipitation is oxygen supersaturation in the crystal during processing, which is a function of the interstitial oxygen concentration. The homogeneous precipitation process is spontaneous. If precipitation is homogeneous, it should be similar in different crystals with different contents of impurities or point defects but the same oxygen content and thermal history. It has been shown that the presence of carbon at high levels (10^{17} cm^{-3}) (13), and variations in the cooling schedule of the crystal after the crystal growth (14), affect oxygen precipitation kinetics during subsequent processing. These data indicate that the oxygen precipitation process can also be heterogeneous (*i.e.*, precipitation of oxygen driven by oxygen supersaturation; nucleation occurs not spontaneously but around nucleation sites already present in the crystals). Heterogeneous nucleation occurs during the growth of the silicon crystal or during the postgrowth process. In addition to foreign impurities,

nucleation sites can be formed by complexes of point defects (15). The formation of these sites during the crystal-growth process is not well understood and is controlled, usually, on a semi-empirical basis. It would appear that the extent to which oxygen-precipitation kinetics will be homogeneous or heterogeneous in nature during processing depends on the concentration of the nucleation sites for oxygen precipitates in the silicon crystal (1).

Because of the differences in equipment and growth procedures used, one can expect that the concentration of nucleation sites in silicon wafers can significantly differ in material obtained from various, commercial, silicon wafer suppliers. Therefore, large differences in the oxygen-precipitation kinetics could be expected in wafers with similar oxygen and carbon concentration coming from different suppliers. This work has been aimed towards providing a link between oxygen-precipitation kinetics, which has been observed during bipolar device processing, and characteristics of virgin wafers. In addition, the goal of this work is to present the relationships which exist between the density and morphology of precipitated oxygen, and (i) the efficiency of internal gettering and (ii) the mechanical strength of the silicon wafer during bipolar processing.

Experimental Procedure

(100) silicon wafers (3 in. diam) were bought from five commercial suppliers. The wafers were p-type (boron-doped) 4-11 Ω cm and 500 $\mu\text{m} \pm 50 \mu\text{m}$ thick. They have been divided into nine categories, according to supplier, interstitial oxygen concentration, degree of back-side damage (group 5), and the density of nucleation centers (group 1). Parameters of different groups of wafers are compared in Table I. Wafers from each group covered approximately 5 ppm range of oxygen concentration. In most instances, two groups of wafers with similar oxygen concentrations, but coming from different suppliers, were available. In addition to interstitial oxygen concentration in virgin wafers, carbon concentration and the concentration of noninterstitial oxygen have also been determined (16). To study the effect of carbon on the oxygen-precipitation process, the wafers from group 3 have been divided into two subgroups containing different carbon concentrations, less than 0.5 ppm and between 1 and 2 ppm. Some wafers from each group have been exposed to preannealing at 800°C for 16h in N_2 prior to processing to enhance the precipitation process. Subsequently, wafers have been introduced into two bipolar fabrication processes used to make linear bipolar logic circuits and I^2L circuits. The time/temperature schedules are presented in Fig. 1. In the initial stage, the processes differ for the I^2L and linear bipolar circuits in the duration of the pocket deposition (a ½h vs. 1h at 1250°C, respectively). The next significant difference between these two pro-

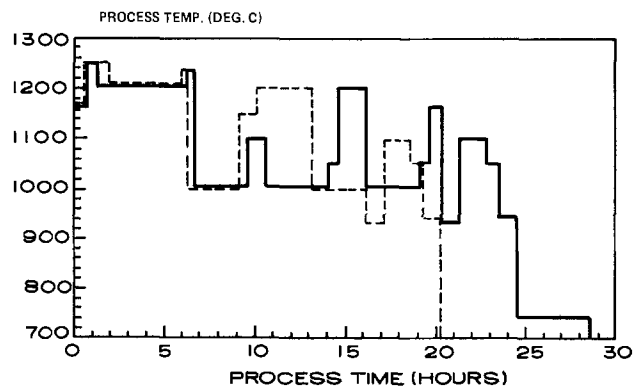


Fig. 1. Temperature/time of I^2L and analog processes

cesses takes place after about 10h of high temperature processing during base diffusion. At this time, the linear bipolar circuits are exposed to a higher temperature than the I^2L circuits. Also, the I^2L process is about 5h longer than the linear bipolar.

The interstitial oxygen and carbon concentration for each group of wafers have been measured after each high temperature step. The amount of oxygen precipitated during processing in each group of wafers has been determined by comparing the interstitial oxygen concentration in the processed blank wafers (which did not receive diffusions) to the amount of interstitial oxygen in the virgin wafers. The morphology of the oxygen precipitates has been studied by Nomarski microscopy after Wright etching of cleaved wafers. It has been verified that the blank wafers and the wafers with circuits had similar defect morphology. Bulk defects in some of the wafers were also examined using TEM.

The mechanical strength of the wafers has been determined by measuring their bow during and after completion of processing. Statistically, wafers from different groups have been exposed to identical stress forces during processing; therefore, one can assume that their bow will be a good qualitative indication of resistance to deformation/mechanical strength of silicon. About 3000 wafers have been processed.

Results

Circuit performance.—To easily separate the effect of internal gettering on circuit performance, the circuit types chosen for this study were such that printing of critical photolithographic dimensions have not been limited by wafer warpage. Usually slip has been localized to the regions at the edge of the silicon wafer which did not contain working circuits. It was thus felt that the circuit yield was not affected by the slip.

Table I. Parameters of as-grown wafers

Group ^a	Interstitial oxygen (ppm)			Noninterstitial oxygen in as-grown (ppm)	Carbon concentration (ppm)
	20	30	40		
1-1 ^b		—		None	1-3.5
1-2		—		≈1.5	1-3.5
2-1	—			None	None
2-2		—		None	0.3-0.6
3-1	—			≈2	0.6-1.0
3-2		—		≈3	< 2 ^c
4			—	None	0.3-0.8
5-1 ^d		—		None	None
5-2		—		None	None

^a First number corresponds to supplier.

^b According to supplier 1, group 1-2 had higher precipitation rate than 1-1.

^c Two subgroups: (i) carbon less than 0.5 ppm, and (ii) carbon 1-2 ppm.

^d Group 5-1 had 3 μm back-side damage, group 5-2 had 10 μm back-side damage.

The effectiveness of internal gettering has been measured directly by its impact on circuit yield. The observed yield increase caused by internal gettering has been traced directly to the improvement of leakage current distribution (soft junction leakage) in the analog bipolar circuits. This is shown in Fig. 2, where the leakage current distribution for two types of wafers, internally gettered wafers (group 1-2 and 1-1) and wafers without intentional internal gettering (standard), are compared. Owing to gettering action of the oxygen precipitates in the wafer interior, impurities are removed from the device active area, which decreases the probability of defect formation (*e.g.*, iron needles which cause emitter collector pipes) and the decoration of already present crystallographic defects (*e.g.*, edge dislocation). As a result of the reduction of the density of electrically active defects, the statistical distribution of leakage current is improved. Excessive leakage current in the analog circuits is the major mechanism limiting yield, and, therefore, internal gettering resulted in yield improvement. As a result of the improved statistical distribution of leakage current, variations of the yield from wafer to wafer in the lots of processed wafers has been also improved. In the I^2L circuit, a relationship between leakage current and yield is not as straightforward as for the analog circuit, and had to be established on a statistical basis. In this case, the most likely cause of circuit performance degradation is functionality failure caused by excessive leakage current of individual small transistors. This is probably related to the presence of collector-emitter pipes. Figure 3 presents a relationship between yield (arbitrary units) and the percentage of devices in which total leakage exceeds 3.0 mA level. Although a one-to-one correlation does not exist as for the analog circuits, a trend can be clearly observed.

The yield improvement observed for various groups of wafers in the I^2L circuits and the analog circuits has been measured through extended periods of time, during which the contamination level in the processing line showed significant fluctuations. The yield improvement, which is presented in Table II, is measured by two factors: (i) a ratio of yield loss due to an excessive leakage in the internally gettered *vs.* standard wafers (CZ wafers with oxygen concentration between 25-40 ppm which did not have any intentional internal gettering) which were processed at the same time (the lowest values correspond

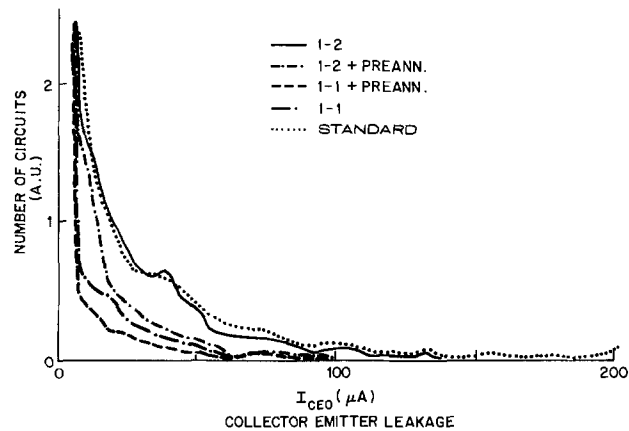


Fig. 2. Leakage distribution for analog circuits made on standard and internally gettered wafers (1-1-I, 1-2).

to the best improvement), which measures the improvement caused by gettering for a given contamination level in the line, and (ii) normalized yield loss, which is the ratio between observed yield loss for a given group of wafers to the lowest yield loss observed in gettered silicon during the time of the experiment, and which gives a certain base line to which the efficiency of internal gettering can be referred (the most efficient gettering for group 4 has the normalized yield of one). The normalized yield should be used essentially as a measure of gettering efficiency, while the ratio of yield loss shows how much yield improvement can be expected over the wafers which do not have any intentional internal gettering. This ratio is also a good measurement of contamination level in the line. For high level of contamination this ratio will be small; for a clean line, this ratio will be close to one. In order to estimate the effect of internal gettering on the yield of bipolar circuits, the normalized yield and the ratio of yield losses should both be considered since the impact of internal gettering on circuit performance can depend on the contamination level present in the processing line. For instance, for low levels of contamination (lot 1-1-II) internal gettering in wafers 1-1 have been sufficient to remove defects from the active area, achieving a normalized

Table II. Efficiency of internal gettering; yield improvement (see text) and the amount of precipitated oxygen during I^2L and analog processes

Group	Preheat-treatment		Initial interstitial oxygen (PMMA)	Yield loss due to leakage			Precipitated oxygen	
	Yes	No		% Experiment % Standard	Normalized to lowest loss observed	I^2L Normalized to lowest loss	Analog	I^2L
1-1-I	X	X	30-34	0.46	2.7	1.12	19	19
				0.31	1.8			20
1-1-II		X	30-34	0.93	1.15			
1-2	X	X	30-35	0.6	3.5		21	
				1.1	6.1			22
2-1	X	X	22-25	1.1	2.0		2	6
							9	10
2-2	X	X	24-28	1.4	2.7		3	5
								14
3-1	X	X	22-26	1.4	2.5	1.46	6	11
								3.4
3-2	X	X	27-29	0.83	1.6	1.22	15	18
				0.73	1.3			3.1
4	X	X	37-42	0.54	1.0	1.0	10	8
				1.2	2.2			23
5-1	X	X	30-33	0.84	1.3		8	12
								16
5-2	X	X	30-32	1.05	1.65	1.25	13	11
								16

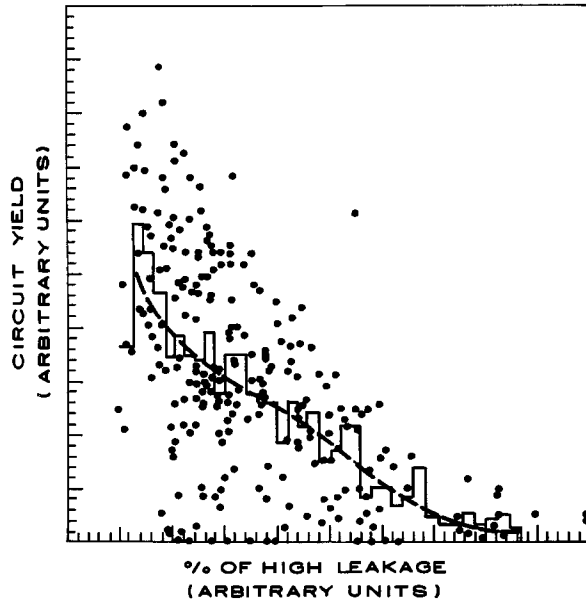


Fig. 3. I^2L circuit yield vs. percentage of highly leaky circuits (exceeding 3 mA).

yield loss of 1.15, which is close to the best values obtained, although the improvement over standards was relatively low (ratio of yield loss 0.93). When the contamination level increased, the gettering action was not strong enough to remove the majority of contamination from the circuit area, and, therefore, the significant yield reduction took place (normalized yield loss 2.7): A large improvement over standard product has, however, been observed in this case (ratio of yield loss: 0.46). An enhancement of gettering action in these wafers due to preannealing (group 1-1) resulted in a significant increase in the yield (normalized yield loss: 1.8) and the larger difference *vs.* the standard wafers (ratio of yield loss: 0.31 *vs.* 0.46). For group 4, the best results were obtained for all contamination levels. The value 0.54 given for the yield loss is an average of the values obtained over an extended period of time when contamination level showed significant fluctuations, ranging from low (time at which 1-1-I was being processed) to high (1-1-II being processed). For I^2L circuits which have been processed through shorter periods of time, with all wafers encountering similar levels of contamination, only the normalized yield loss has been given in Table II.

It is apparent that large differences in the efficiency of internal gettering have been observed between the different groups. The similar trends in the efficiency of internal gettering for the different groups of wafers are visible for I^2L as well as for analog circuits. The effect of preannealing on the efficiency of internal gettering is not straightforward: for group 1-1 and 3-2, a beneficial effect was observed, while for group 4, a detrimental effect occurred. It has to be pointed out that carbon for group 3-2 does not influence gettering efficiency. Two subgroups of wafers, one with carbon concentration between 1-2 ppm and other less than 0.5 ppm, showed similar gettering efficiency. Also, the effect of back-side damage is not clear. Wafers with 10 μm back-side damage (group 5-2) showed slightly less efficient gettering than the same wafers with 3 μm back-side damage (group 5-1). As will be discussed later, these differences are most likely attributed to differences in the oxygen-precipitation kinetics observed in these wafers, and not to differences in gettering caused by the back-side damage.

For a given circuit type, the efficiency of internal gettering is related to the density of precipitated oxygen and the precipitate morphology. The amount of precipitated oxygen during the two processes, together with the interstitial oxygen concentration in the as-grown wafers for different groups of wafers, is also presented in Table II. The gettering efficiency for analog circuits (normalized

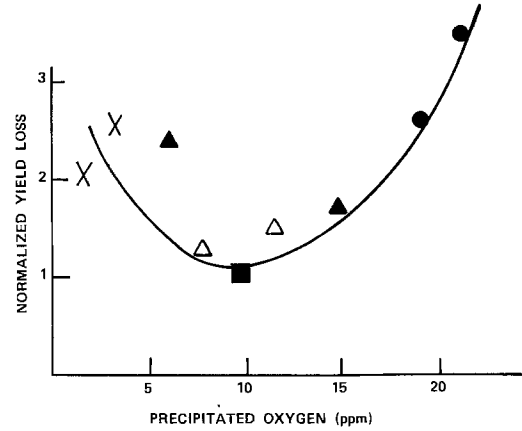


Fig. 4. Normalized yield loss (see test) as a function of amount of precipitated oxygen after completion of the analog process (wafers without preannealing) ●: Group 1. ×: Group 2. ▲: Group 3. ■: Group 4. △: Group 5.

yield) is plotted in Fig. 4 as a function of the amount of precipitated oxygen present after processing. The most efficient gettering takes place around 10 ppm of precipitated oxygen (group 4). When the amount of the precipitated oxygen increases beyond this point, the efficiency of gettering decreases. As it will be discussed later, this phenomena is most likely related to the effect of precipitate's morphology on gettering action. It has to be pointed out that the denuded-zone depth is very similar for all groups of wafers. As shown on Table III, it seems that preannealing does not significantly alter the depth of denuded zone. The effect of preannealing on the efficiency of internal gettering is not straightforward. It seems that, for the groups 3-2 and 1-1, preannealing improves yield in the analog circuits, while it deteriorates yield in the wafers from group 1-2 during the analog process and groups 3-1 and 3-2 during the I^2L process. The deterioration of the yield after the preannealing was attributed to an increase of the number of defects in the denuded zone, which propagated through the epilayers to device active regions, causing functionality failures.

The two typical types of bulk defects observed in the wafer's interior after completion of the analog circuits are shown in Fig. 5. It is quite apparent that the morphology of oxygen precipitates is different for these two groups. The wafers in which the amount of precipitated oxygen after processing does not exceed 11 ppm (groups 2, 4, 5) usually have a low density of large, bulk stacking faults (see Fig. 5c). The wafers with the higher amount of precipitated oxygen (groups 1 and 3) have a high density of small stacking faults and precipitates (see Fig. 5a). It has been observed that if the preannealing does not significantly change the concentration of precipitated oxygen in a wafer (groups 1 and 3-2), no change in the precipitate morphology will occur during preannealing (Fig. 5a and 5b). In the wafers in which preannealing significantly increases the concentration of precipitated oxygen (all other groups), a significant change in precipitate morphology is apparent (Fig. 5c and 5d). Preannealing causes the formation of a high density of the small bulk precipi-

Table III. Denuded zone width after analog processing (μm)

Supplier	No preheat-treatment	Preheat-treated
1-1	54	59
1-2	54	60
2-1	70	50
2-2	50	60
3-1	45	55
3-2	50	50
4	50	50
5-1	54	50
5-2	58	45

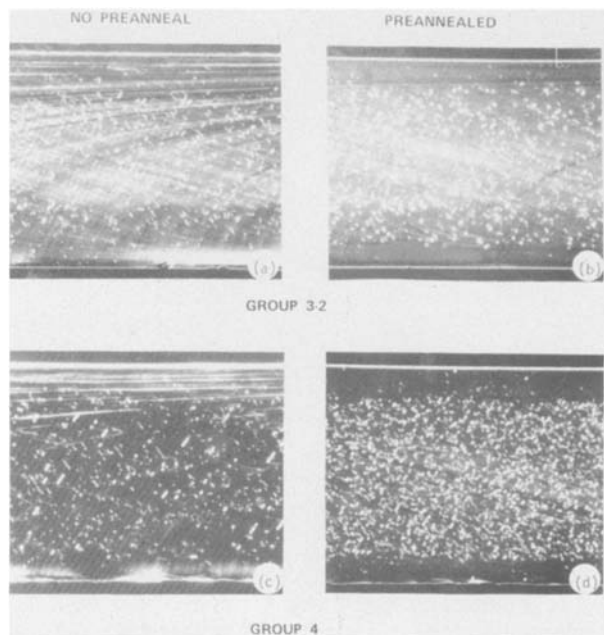


Fig. 5. Morphology of oxygen precipitates after completion of the processing for groups 4 and 3-2 (a and c, no preannealing, b and d, preannealed).

tates (Fig. 5d) which are not present in the nonpreannealed wafers with low amounts of precipitated oxygen (Fig. 5c) and are similar to those observed in pre- (Fig. 5a) and nonpreannealed (Fig. 5b) wafers with the higher amounts of precipitated oxygen. An increase of the amount of precipitates and a change of their morphology in the preannealed wafers has detrimental effects upon the efficiency of internal gettering. An example is seen in group 4, where the preannealing deteriorated the normalized yield loss from 1 to 2.2 while the amount of precipitated oxygen increased from 10 to 20 ppm. The increase in the efficiency of internal gettering in the case of preannealing for groups 1-1 and 3-2 analog process should probably be attributed to the stronger gettering action (higher concentration of precipitated oxygen) during the initial processing steps (see below). Although the amount of precipitated oxygen differs slightly for the I^2L and the analog process, the morphology of precipitates for each group, subjected to these two processes, is similar.

Warp/mechanical strength.—The histogram of the warpage distribution in the wafers from group 1-1, 4, 3-1, and 3-2 after the completion of the analog processing is presented in Fig. 6. The best mechanical properties have been observed in wafers from group 4, which have the highest interstitial oxygen concentration in both the as-grown states (40 ppm) and after completion of processing (29 ppm). Preannealing of these wafers significantly increases the amount of precipitated oxygen, changes the precipitate morphology, and catastrophically decreases resistance to warpage (see dashed line).

It seems that mechanical properties are different for the two different ranges of precipitated oxygen. When the amount of precipitated oxygen is relatively low (below 10-12 ppm), the observed variations in the mechanical strength between the different groups of wafers could be explained by the larger relative changes in the interstitial oxygen concentration. For about 10 ppm of precipitated oxygen, wafers with 29 ppm of interstitial oxygen warped less than wafers with 13 ppm of interstitial oxygen (compare group 4 and 3-1). It seems that for low concentrations of precipitated oxygen (not exceeding 10-12 ppm), a small change in the amount of precipitated oxygen does not significantly affect the mechanical strength of the silicon wafer. In the group 3-1, a change of oxygen concentration due to preannealing by about 5 ppm was not reflected in a noticeable change of warpage.

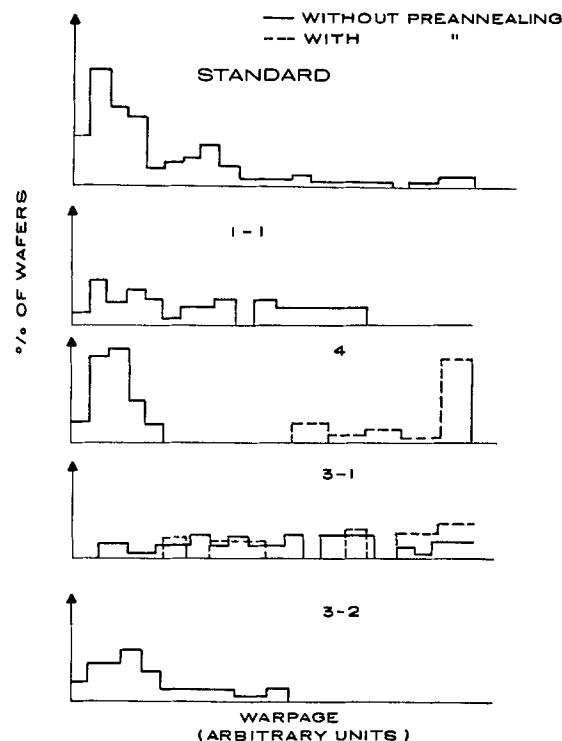


Fig. 6. Histogram of warpage in the wafers from different groups after completion of analog process.

For the high range, when the amount of precipitated oxygen exceeds 10 ppm, a small change in the amount of precipitated oxygen does affect the mechanical strength. For wafers with 12-13 ppm of interstitial oxygen, mechanical strength is reduced when the amount of precipitated oxygen increases from 15 to 20 ppm (compare 3-2 and 1-1). At the present stage, it is not clear why the small change in the high concentration of precipitated oxygen has such a dramatic effect upon warpage while the same change for a low concentration of precipitated oxygen has far less noticeable effect. It seems that for the case of the high amount of precipitated oxygen, change in the interstitial oxygen concentration has less effect on mechanical properties than do changes in the amount of precipitated oxygen. A comparison of mechanical properties of group 1-1 (12 ppm of interstitial oxygen, 20 ppm of precipitated oxygen) to group 4 after preannealing (17 ppm of interstitial and 23 precipitated oxygen) shows that an improvement in the mechanical strength due to 5 ppm increase in the interstitial oxygen concentration can be totally offset by 3 ppm increase in the amount of precipitated oxygen. These data clearly indicate that the mechanical strength of silicon wafers is related to the amount of precipitated and interstitial oxygen, although the observed relation is not straightforward.

It seems that there are two ranges of precipitated oxygen which influence mechanical strength differently during bipolar process. In the low range (up to 10-12 ppm of precipitated oxygen), changes in the amount of precipitated oxygen do not significantly influence wafer warpage. For the high range, a slight increase in the amount of precipitated oxygen significantly decreases the mechanical strength. This effect is probably related to the change of the oxygen-precipitated morphology. For the low range, a significant amount of the defects are long stacking faults often reaching 10 μm in length, which do not seem to have a strong effect upon mechanical strength. In the high range, in addition to small stacking faults, a much higher density of oxygen precipitates resulting in small etch pits is also present. These defects seem to significantly deteriorate mechanical properties.

The beneficial effect of oxygen on mechanical strength of silicon has been attributed usually to dislocation pinning by oxygen in the form of complexes (17, 18) or at in-

terstitial positions (19). However, oxygen precipitates which act as sources of dislocation loops were shown to deteriorate the mechanical strength of silicon (1). It seems that, for high concentrations of precipitated oxygen (above 11 ppm), the deteriorating mechanical properties correlate well with the amount of precipitated oxygen. It also would appear that the extent of dislocation pinning is well characterized by the measure of interstitial oxygen. It has to be pointed out that the present analysis is simplified since it discusses only the effects of two variables, the concentration of precipitated and interstitial oxygen, and is not able to distinguish between the effects which oxygen in complexes or different forms of precipitates would have on the mechanical properties.

Precipitation kinetics.—One can expect that the differences in the internal gettering observed for different groups of wafers are related to the differences in the oxygen-precipitation kinetics which took place during processing. Figures 7-11 present the interstitial oxygen concentration measured in the processed wafers after each high temperature step during I^2L bipolar process. The reduction in the interstitial oxygen concentration is plotted as a function of processing steps.

Micrographs of typical defects observed in the wafer interior after initial oxidation and completion of the process are also included in Fig. 7-11. The samples have been classified by the supplier, and each plot includes wafers which also received preheat-treatment prior to processing. Figures 7-11 show two types of trends: (i) a gradual decrease in the concentration of the interstitial oxygen through practically all processing steps (groups 2, 4, 5) or (ii) a sharp decrease in the interstitial oxygen concentration during the few initial processing steps (prior to isolation deposition and drive). This was observed in all the preannealed wafers and the wafers from groups 1 and 3. It has to be pointed out that the initial interstitial concentration of oxygen in silicon wafers will not determine which type of precipitation kinetics will be observed during processing and, therefore, will not determine the total amount of precipitated oxygen after completion of the process. The slow kinetics has been observed for all inter-

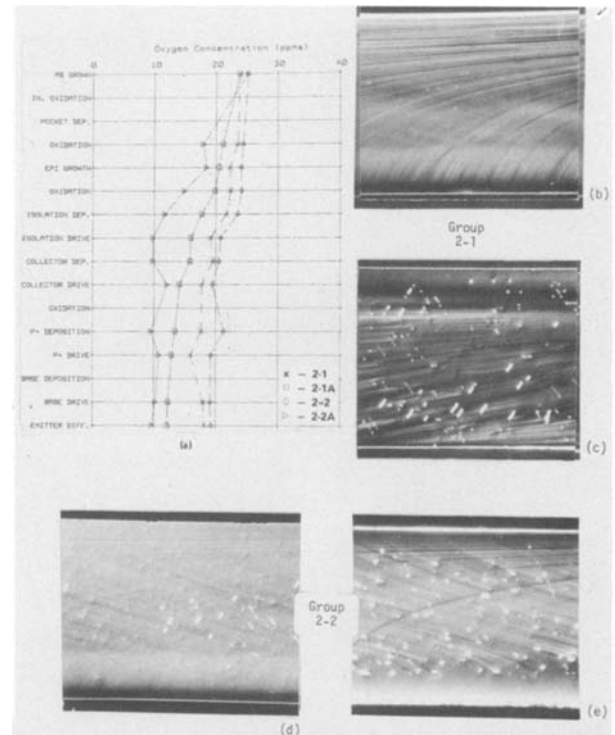


Fig. 8: a: Change in the interstitial oxygen concentration during I^2L processing observed in the wafers from groups 2-1 and 2-2 (2-1, 2-2, no preannealing; 2-1A, 2-2A, after preannealing). b, d: Precipitate morphology after initial oxidation in groups 2-1 (b) and 2-2 (d). c, e: Precipitate morphology after completion of process in groups 2-1 (c) and 2-2 (e).

stitial oxygen concentrations [i.e., in the wafers with the highest (group 4) as well as the lowest (group 2-1) concentration of the interstitial oxygen], while the rapid precipi-

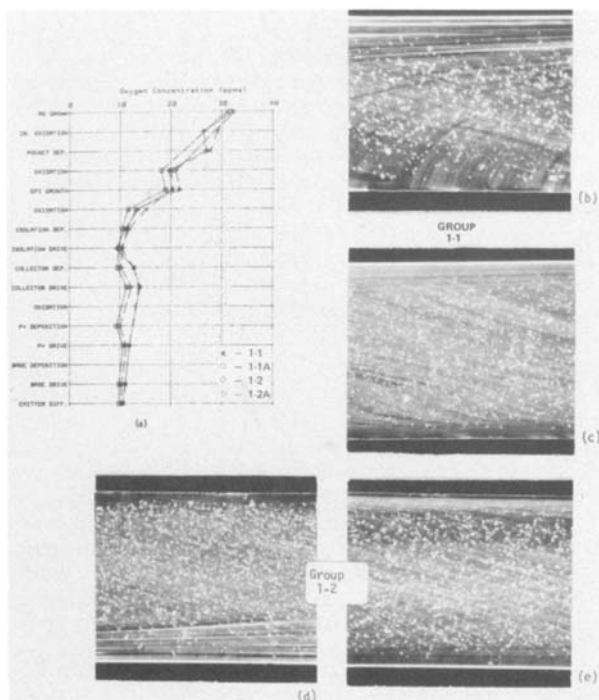


Fig. 7a: Change in the interstitial oxygen concentration during I^2L processing observed in the wafers from groups 1-1 and 1-2 (1-1, 1-2 no preannealing; 1-1A, 1-2A, after preannealing). b, d: Precipitates morphology after initial oxidation in groups 1-1 (b) and 1-2 (d). c, e: Precipitate morphology after completion of the process in groups 1-1 (c) and 1-2 (e).

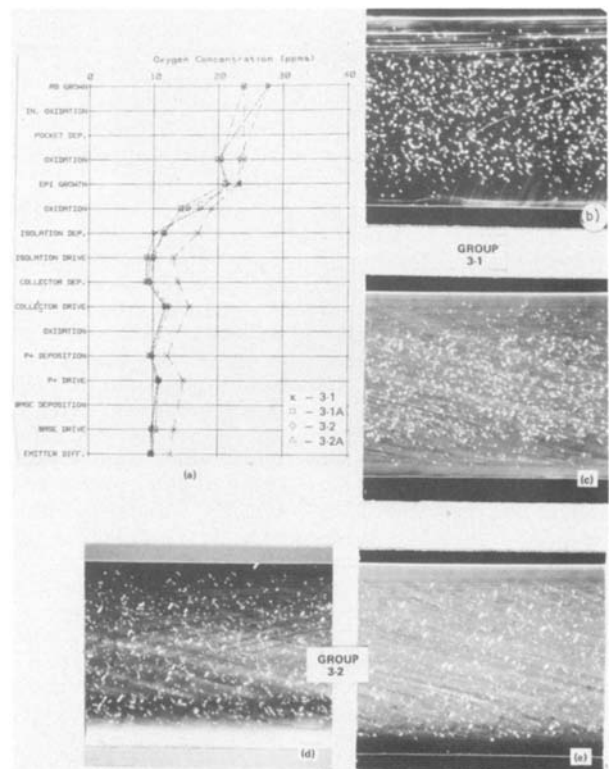


Fig. 9: a: Change in the interstitial oxygen concentration during I^2L processing observed in the wafers from groups 3-1 and 3-2 (3-1, 3-2 no preannealing; 3-1A, 3-2A, after preannealing). b, d: Precipitate morphology after initial oxidation in groups 3-1 (b) and 3-2 (d). c, e: Precipitate morphology after completion of process in groups 3-1 (c) and 3-2 (e).

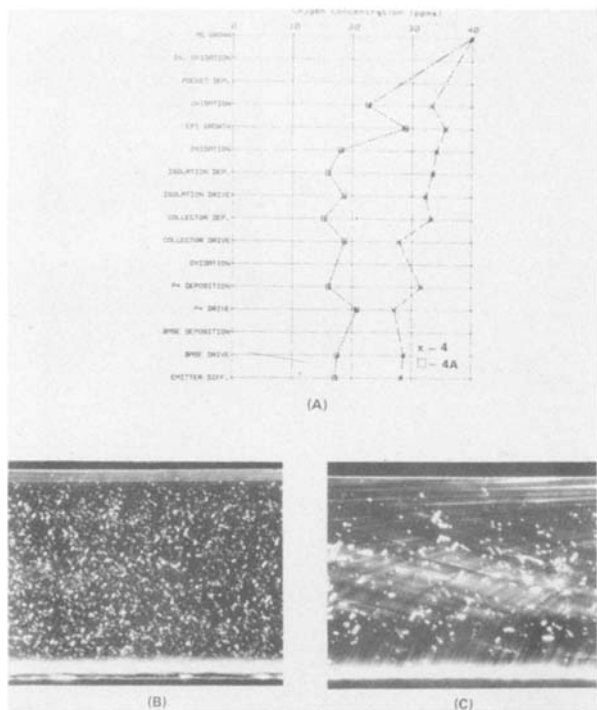


Fig. 10. a: Change in the interstitial oxygen concentration during I^2L processing observed in the wafers from group 4 (4, no preannealing; 4A, after preannealing). b: Precipitate morphology after initial oxidation in group 4. c: Precipitate morphology after completion of processing in group 4.

tation has been observed mostly in the wafers which initially had certain trace amounts of the oxygen in a noninterstitial form (see Table I).

The amount of oxygen precipitation which takes place during the analog and I^2L processes for different groups of wafers is compared in Table II. The amount of precipitated oxygen during these two processes is very similar, although the amount of oxygen precipitated during I^2L process is slightly higher (about 2 ppm). For the wafers with the lowest oxygen content (groups 2-1 and 3-1), the difference in the amount of precipitated oxygen during these two processes is the largest.

The morphology of oxygen precipitates after the initial steps and completion of the process is quite different for different groups of wafers (Fig. 7-11). The observed differences in morphology correspond to the differences in the rate of oxygen precipitation for the various groups of wafers. It seems that the slower precipitation kinetics results in a relatively low density of large oxygen precipitates and stacking faults, while the rapid precipitation process gives a high density of small precipitates and stacking faults. As has been discussed before, preannealing changes the oxygen precipitation kinetics from slow to rapid; the amount and morphology of bulk precipitates will also change (see groups 2, 4, 5). For wafers with rapid precipitation kinetics, preannealing does not have a pronounced effect on the amount and morphology of bulk precipitates. The morphology of the precipitates after completion of the process was usually similar to the morphology observed after the initial processing steps. Only wafers with the highest oxygen concentration (group 4) were an exception; their defect morphology at the beginning of the process was similar to that of groups 1 and 3, and to groups 2 and 5 after completion of the process.

The amount of precipitated oxygen and precipitate morphology have been affected by the degree of mechanical damage present on the back of the wafers. The wafers with 10 μm damage had more precipitated oxygen during analog process than 3 μm damaged wafers. This indicates that mechanical damages accelerate the precipitation process in group 5.

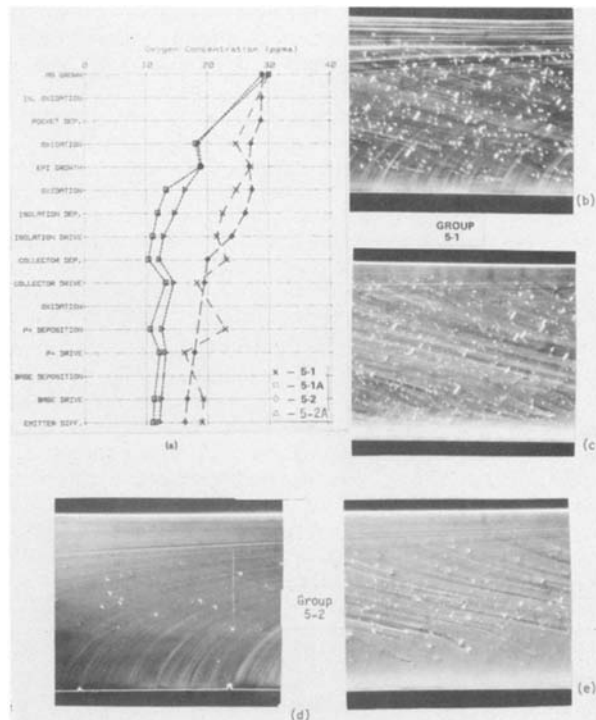


Fig. 11. a: Change in the interstitial oxygen concentration during I^2L processing observed in the wafers from groups 5-1 and 5-2 (5-1, 5-2, no preannealing; 5-1A and 5-2A, with preanneal). b, d: Precipitate morphology after initial oxidation in groups 5-1 (b) and 5-2 (d). c, e: Precipitate morphology after completion of process in groups 5-1 (c) and 5-2 (e).

A comparison of the precipitates in the wafers from group 3 with various carbon levels did not show any substantial differences. From this, it appears that, for the rapid kinetics (group 3), carbon at the level up to 2 ppm does not influence the oxygen-precipitation process.

Some variations in the amount of precipitated oxygen and precipitate morphology have been observed in the wafers belonging to the same group as well as across individual wafers. In the latter case, the most noticeable differences were in precipitation density and morphology between the edges and center of the wafer or a striation-type distribution of precipitates in the wafer. In most instances, these differences in precipitate's density were not related to the differences in the oxygen or carbon concentrations across the wafer. Because oxygen and carbon concentration did not show any appreciable variations, it was assumed that the observed changes in the precipitate's density were caused by nonuniform distribution of nucleation centers for oxygen precipitation (1) in the wafers.

Microcharacterization of defects.—The etching study provides quantitative information about the defect density and their distribution in the wafers, but does not evaluate the microscopic defect structure. To investigate differences in the microdefect structure in the wafers with slow and rapid precipitation kinetics, samples from group 4 and group 3-2 were examined using TEM. The preliminary results showed large differences in the microscopic nature of stacking faults in these two groups of wafers (Fig. 12). As is shown in Fig. 12a, stacking faults in the wafers from group 3-2 are usually not decorated with precipitates, while those from group 4 showed more complex structures (Fig. 12b). The stacking faults from group 4 has several distinguishing characteristics: (i) the stacking faults appear in segmented form, (ii) dislocations are observed at numerous locations along the fault, and (iii) numerous precipitates decorate the fault.

The segmentation of the stacking fault, shown in Fig. 12b, is a result of the formation of additional stacking faults along slip planes parallel to the original fault. As

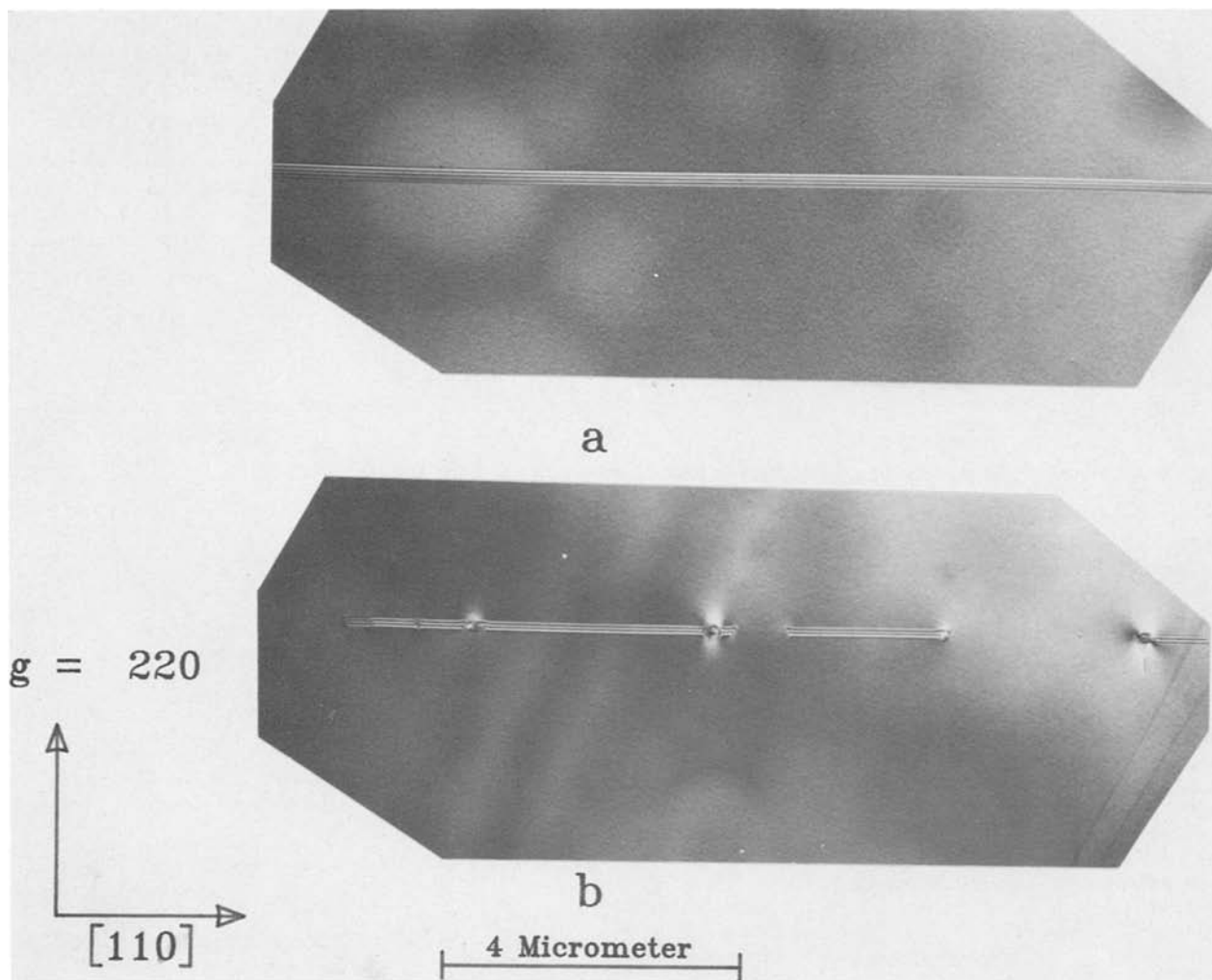


Fig. 12. Comparison of typical defects observed by TEM in groups 3-2 (a) and group 4 (b)

the electron beam passes through successive, closely spaced faults, it undergoes a phase shift of $\pm 2\pi/3$ at each fault (20). If the electron beam passes through $3n$ stacking faults each resulting in the same sign of the phase shift, the characteristic fringe structure of the fault will be absent. Stacking faults are bounded by partial dislocations. In overlapping faults, a partial dislocation will then delineate the boundary across which a phase shift will occur. A total phase shift of zero will occur every two dislocations if the signs of the shifts at the dislocations are opposite or every third dislocation, if the signs are the same. Both of these occur in Fig. 12b.

A total of seven precipitates may be seen along the various segments of the stacking fault in Fig. 12b, while the bulk of the silicon is relatively free of such defects. The high density of precipitates along the fault clearly indicates that their nucleation occurred preferentially after the formation of the initial stacking fault. What is not clear is whether or not the formation of the additional overlapping faults and associated dislocations (those other than initial fault and bounding dislocation) preceded or followed the nucleation of precipitates. The presence of numerous precipitates situated along the stacking fault indicates that the precipitation process took place after the stacking fault was formed. It is not clear at the present stage why the microstructure of the stacking faults in Fig. 12 differs. These differences can be caused by fundamental differences in the stacking faults' nucleation process in the two groups of wafers or be related to the time during processing when stacking faults have been generated in these two groups of wafers. According to data on the oxygen precipitation, it seems that the stacking faults' formation process in group 4 was

gradual, while in group 3-2 it took place abruptly during a few initial processing steps.

In addition to precipitates which have formed on stacking faults, larger faceted precipitates (see Fig. 13) have been observed away from stacking faults. Microdiffraction from the regions containing the faceted precipitates shows only silicon matrix spots. This suggests that the precipitates are either amorphous or coherent with the silicon matrix. Ponce *et al.* (21) have examined similar precipitates using high resolution lattice imaging techniques. Their results indicate that these precipitates are amorphous and the faceting is a consequence of matrix effects within the silicon crystal.

Energy dispersive x-ray spectroscopy performed with a windowless detector showed that the precipitates formed outside the stacking faults contained only oxygen and silicon, when precipitates formed at the stacking faults often have heavy metals (see Fig. 14) associated with them. This result indicates that the gettering of contaminations during internal gettering is carried out by stacking faults; other defects play a secondary role in the gettering process.

Discussion

Oxygen precipitation kinetics and gettering.—Surprising differences have been observed when the oxygen precipitation kinetics between various groups of wafers have been compared. Two types of precipitation kinetics have been observed during the bipolar processes: a slow, gradual decrease in the interstitial oxygen concentration through all processing steps (groups 2, 4, and 5), and a sharp, fast change during the few initial processing steps (prior to the isolation drive) (groups 1, 3, and all the preannealed wafers).

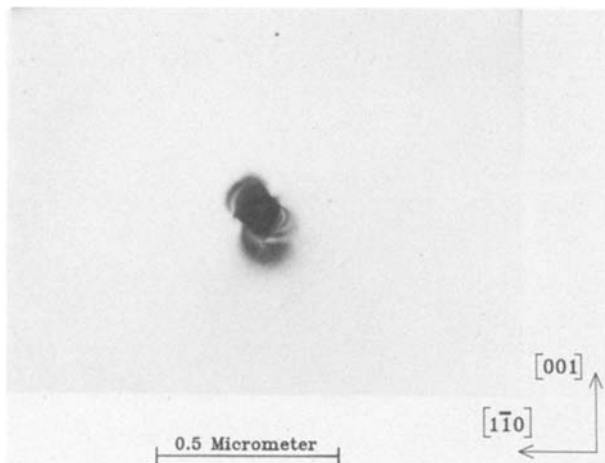


Fig. 13. Large-faced precipitates found away from stacking faults

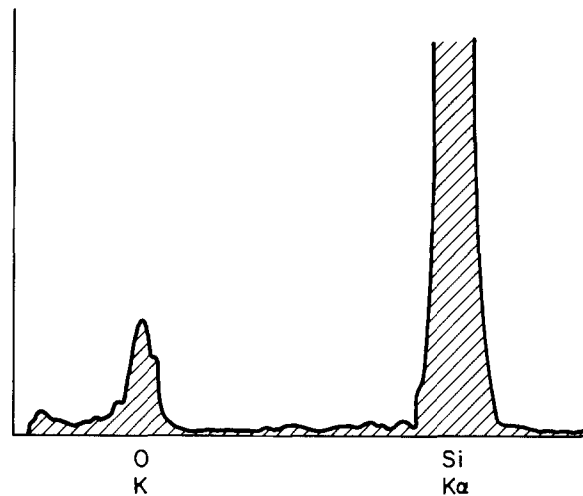
Oxygen supersaturation during processing is not the main factor controlling precipitation kinetics in various groups of wafers. For instance, group 4 with the initial oxygen concentration of 40 ppm exhibits slow precipitation kinetics, giving about 10 ppm of precipitated oxygen, while for the same process for a lower oxygen concentrations, of 28 ppm group 3-2, a faster precipitation kinetics resulted in 18 ppm of precipitated oxygen. Therefore, the specification of the oxygen content in as-grown wafers is not sufficient to predict the wafer behavior during processing. The differences for the two types of precipitation kinetics have been reflected in the character of the oxygen precipitate's morphology, and the amount of precipitated oxygen; (e.g., compare wafers from group 5 and 1 with apparently identical initial characteristics in terms of interstitial oxygen concentration but visible differences in precipitates' morphology). These differences are visible after the initial processing steps and are preserved through the entire process.

It seems that one of the factors affecting the mechanism of oxygen precipitation is the amount of oxygen in noninterstitial state in the virgin wafers. The rapid kinetic occurs if oxygen is present in noninterstitial sites in the as-grown wafers, while slower kinetic is typical for wafers with interstitial oxygen. Group 3-1 and 2-1 had similar initial oxygen concentration (24 ppm), but the amounts of precipitated oxygen after completion of the P^2L process were 11 and 6 ppm, respectively. Initially, the wafers from group 3-1 had about 2 ppm of oxygen in noninterstitial sites, while the wafers from group 2-1 had none. These data indicate that silicon crystals which have the same grown-in interstitial oxygen concentration can behave differently during processing if different growth procedures, giving different levels of noninterstitial oxygen, were used during the crystal-growth process.

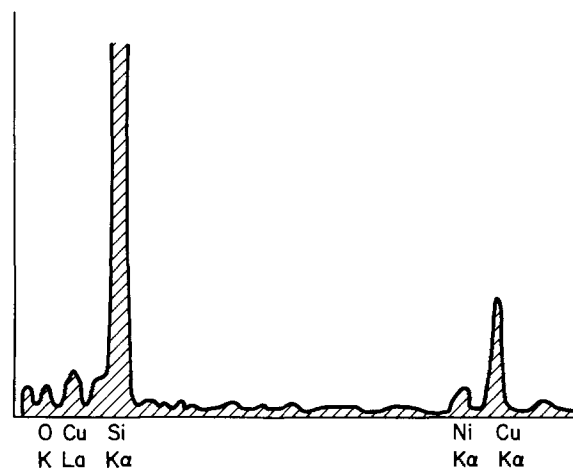
Preannealing seems to convert a slow precipitation mechanism into a rapid mechanism, by introducing oxygen into noninterstitial state. However, preannealing does not significantly influence the precipitation character in wafers in which precipitation would have otherwise undergone the rapid process. Nucleation centers in these wafers are already provided by noninterstitial oxygen introduced during the crystal-growth process. In the case when the oxygen-precipitation process occurs rapidly, a carbon concentration of up to 2 ppm does not affect the precipitation kinetics (group 3 wafers).

Mechanical damage on the back side of the wafers can influence the precipitation process, as demonstrated for group 5. For the slow precipitation process, mechanical damages slightly accelerate oxygen precipitation.

Noticeable differences in precipitation kinetics have been observed for two bipolar processes which differ slightly in temperature but significantly in the time duration of high temperature steps (see Fig. 1). The differences were largest for the wafers with the lowest oxygen



(a)



(b)

Fig. 14. Energy dispersive spectra (EDS) taken from (a) faceted precipitate—notice only oxygen and silicon signal—and (b) precipitate found on a stacking fault. Heavy metal is clearly associated with precipitate.

concentration (lowest supersaturation). The higher amounts of precipitates usually observed during the P^2L process than during the analog process can be explained by the longer processing time during the P^2L process. At these longer times, more oxygen was able to diffuse to the precipitates, thus contributing to their growth.

Differences in the precipitation kinetics observed in the wafers belonging to the same group are most likely related to the differences in the concentration of nucleation centers for oxygen precipitation, which were introduced by point defect complexes (15) during the crystal-growth process.

The bulk oxygen precipitates and stacking faults generated during the bipolar process have been used successfully to reduce defect density which results in a reduction of leakage current and, therefore, a yield improvement of bipolar circuits. The efficiency of internal gettering is not only dependent on the total amount of precipitated oxygen during processing, but is also strongly affected by the precipitate morphology. The most efficient gettering for various contamination levels in the processing line has been achieved by about 10 ppm of postprocessing, precipitated oxygen, which formed large stacking faults. Any attempt to increase the amount of precipitated oxygen above this value results in the reduction of the gettering efficiency. It seems that the increase in the amount of precipitated oxygen results always in change of defect morphology from low density, large, bulk stacking faults

and precipitates to high density, small stacking faults and precipitates. The preliminary TEM data indicate that the microstructures of these bulk defects are also quite different, with large stacking faults acting as good gettering sink for heavy metals. In addition to the adverse effect on the gettering efficiency, the increase in the amount of precipitated oxygen seems to adversely effect the mechanical strength of silicon wafers.

It is remarkable that the best efficiency of internal gettering and resistance to warpage has been observed for the same wafers (group 4). These wafers had the highest initial interstitial oxygen concentration and exhibit the slow oxygen-precipitation kinetics during the bipolar process. This resulted in about 10 ppm of the precipitated oxygen forming large, precipitate decorated stacking faults. It seems that this morphology and density of precipitated oxygen is small enough not to cause serious degradation of the wafer strength but sufficiently large to provide efficient gettering.

Summary

We believe that our results clearly demonstrate that internal gettering can be used to improve circuit yield in bipolar processing lines. The oxygen-precipitation process has to be carefully adjusted to obtain the desirable morphology and the optimum density of precipitates to provide an efficient gettering action. Simultaneously, the amount of oxygen in a state which results in dislocation pinning and ensures good mechanical strength and resistance to warpage of silicon wafers must be achieved. These results can only be accomplished with a well-controlled oxygen-precipitation process.

The present work shows that, in addition to the well-known factors, such as the interstitial oxygen concentration in virgin wafers, oxygen-precipitation kinetics during bipolar processing is also strongly affected by an additional factor which could be related to the concentration of nucleation centers. These centers are generated by the oxygen in noninterstitial sites or point-defect complexes present in virgin wafers. The concentration of these centers is related to the crystal-growth conditions, and is different in silicon from various commercial suppliers. It should be pointed out that the nature and formation of these centers is not well understood. The development of the more complete understanding will require an extensive basic study of the relationship between formation of nucleation centers and the phenomena taking place during crystal growth. For practical application, a reproducible and controllable precipitation rate is required, which implies that in addition to oxygen content the concentration and the nature of the nucleation centers must be precisely controlled. In most instances, only the concentration of interstitial oxygen, and sometimes carbon, is specified in commercial silicon wafers. Therefore, one has to realize that to achieve controllable precipitation kinetics during bipolar processing the density of nucleation sites in silicon also has to be controlled on a reproducible basis by the crystal growers. Only then will processing

engineers be able to take full advantage of the benefits of internal gettering in production lines.

Acknowledgments

The authors would like to thank R. Metzl for writing the computer programs used in generating plots and histograms, and Dr. G. W. Cullen for his critical review of this paper.

Manuscript submitted Jan. 9, 1984; revised manuscript received June 29, 1984.

RCA assisted in meeting the publication costs of this article.

REFERENCES

1. L. Jastrzebski, *IEEE Trans. Electron Devices*, **ed-29**, 475 (1982).
2. C. W. Pearce, in "Semiconductor Silicon 1981," H. R. Huff, R. J. Kriegler, and Y. Takeishi, Editors, p. 705, The Electrochemical Society Softbound Proceedings Series, Pennington, NJ (1981).
3. J. E. Lawrence and H. R. Huff, in "VLSI Electronics Microstructure Science," Vol. 5, N. C. Einspruch, Editor, p. 55, Academic Press, New York (1982).
4. L. Jastrzebski, P. A. Levine, W. A. Fisher, A. D. Cope, E. D. Savoye, and W. N. Henry, *This Journal*, **128**, 885 (1981).
5. L. Jastrzebski and J. Lagowski, *ibid.*, **128**, 1957 (1981).
6. B. Goldsmith, L. Jastrzebski, and R. Soydan, in "Defects in Silicon," W. M. Bullis and L. C. Kimerling, Editors, p. 142, The Electrochemical Society Softbound Proceedings Series, Pennington, NJ (1983).
7. S. Kishino, Y. Matsushita, and M. Kanamono, *Appl. Phys. Lett.*, **35**, 213 (1979).
8. K. Yasutake, M. Vmemo, and H. Kawabe, *ibid.*, **37**, 789 (1980).
9. F. Shimura, H. Tsuya, and T. Kawamura, *This Journal*, **128**, 1579 (1981).
10. K. Wada, N. Inone, and K. Kohra, *J. Cryst. Growth*, **49**, 749 (1980).
11. J. Osaka, N. Inone, and K. Wada, *Appl. Phys. Lett.*, **36**, 288 (1980).
12. P. E. Freeland, K. A. Jackson, C. W. Lowe, and J. R. Patel, *ibid.*, **30**, 31 (1977).
13. See, for example, F. Shimura, H. Tsuya, and T. Kawamura, *This Journal*, **128**, 1578 (1981).
14. H. Nakanishi, H. Koda, H. Hirata, and K. Hoshikawa, *Jpn. J. Appl. Phys.*, **19**, 561 (1980).
15. S. M. Hu, *J. Appl. Phys.*, **52**, 3974 (1981).
16. L. Jastrzebski, P. Zanzucchi, D. Thebault, and J. Lagowski, *This Journal*, **129**, 1638 (1982).
17. S. M. Hu and W. J. Patrick, *J. Appl. Phys.*, **46**, 1869 (1975).
18. S. M. Hu, *Appl. Phys. Lett.*, **31**, 53 (1977).
19. See, for example, S. Takasu, in "Proceedings of the 3rd Microelectronic Measurement Technology Seminar," p. V-53, Benwill Publishing Corporation, Boston, MA (1981).
20. P. B. Hirsch, A. Howie, R. B. Nicholson, D. W. Pashley, and M. J. Whelan, "Electron Microscopy of Thin Crystals," p. 244, Butterworth, Washington, DC (1965).
21. F. A. Ponce, T. Yamashita, and S. Hahn, in "Defects in Silicon," W. M. Bullis and L. C. Kimerling, Editors, p. 105, The Electrochemical Society Softbound Proceedings Series, Pennington, NJ (1983).

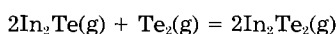
Analysis and Thermodynamics of the Vapor Phase over Liquid InTe at 1106 ± 2 K

Raman S. Srinivasa* and Jimmie G. Edwards**

Department of Chemistry, University of Toledo, Toledo, Ohio 43606

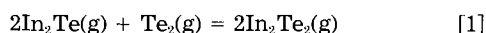
ABSTRACT

The vapor phase over InTe(l) at 1106 ± 2 K was analyzed by an isothermal total exhaustion experiment with a Knudsen-cell mass spectrometer. In^+ , In_2^+ , Te^+ , Te_2^+ , InTe^+ , In_2Te^+ , InTe_2^+ , and In_2Te_2^+ were observed. The appearance potentials of In^+ , In_2^+ , Te^+ , InTe^+ , In_2Te^+ , InTe_2^+ , and In_2Te_2^+ were 7.7, 9.6, 9.9, 8.6, 8.3, 8.2, and 7.6V, respectively, with an uncertainty of 0.3V. The fragment ions and their precursors were identified in three ways: (i) their appearance potentials were compared with those in the literature; (ii) the slopes of the plots of ionic intensities vs. time were compared; and (iii) all ions were assumed to be parents; hypothetical equilibrium constants for several vapor-phase reactions involving the hypothesized gaseous precursors were checked for time-dependent trends and, where possible, compared with literature data. From these three tests, we found that almost all of In^+ , In_2^+ , Te^+ , InTe^+ , and In_2Te^+ came from $\text{In}_2\text{Te}(\text{g})$, almost all of Te_2^+ came from $\text{Te}_2(\text{g})$, and almost all of InTe_2^+ and In_2Te_2^+ came from $\text{In}_2\text{Te}_2(\text{g})$. Thus, it was found that the vapor phase was composed of $\text{Te}_2(\text{g})$, $\text{In}_2\text{Te}(\text{g})$, and $\text{In}_2\text{Te}_2(\text{g})$. The mass spectrometer was calibrated with integrated ion intensities and the analysis of the fragmentation processes. Partial pressures of the vapor species were derived from ionic intensities. The equilibrium constant for the reaction



was found to be $(1.81 \pm 0.10) \times 10^{-3} \text{ Pa}^{-1}$. The standard enthalpy of the above reaction at 298 K was $-310.9 \pm 0.5 \text{ kJ}$.

The study of indium telluride is of interest because of its application in solid-state devices: nuclear radiation detectors (1), photoconductors (2), and heterojunction devices (3-4). Knowledge of the chemistry and thermodynamics of the gas phase over indium tellurides will be useful in the preparation of such devices by vapor-phase growth. In this paper, we report our analysis of the vapor phase over InTe(l) at 1106 ± 2 K and thermodynamics of the reaction



Colin and Drowart (5) studied the gas-phase equilibria among indium tellurides by mass spectrometry in the temperature range 1093-1234 K with a single Knudsen cell and in the range 1198-1557 K with a double cell in a double oven. They observed Te^+ , Te_2^+ , In^+ , InTe^+ , In_2Te^+ , InTe_2^+ , and In_2Te_2^+ . They measured the appearance potentials of these ions. On the basis of the appearance potentials, they concluded that in their single-cell experiments In^+ and Te^+ were composed of both parent and fragment ions. All other ions were parent ions. They took the vapor phase over liquid In_2Te_3 to be composed of $\text{In}(\text{g})$, $\text{Te}(\text{g})$, $\text{Te}_2(\text{g})$, $\text{InTe}(\text{g})$, $\text{In}_2\text{Te}(\text{g})$, $\text{InTe}_2(\text{g})$, and $\text{In}_2\text{Te}_2(\text{g})$ and calculated partial pressures from the ion intensities.

We carried out an isothermal total exhaustion experiment on InTe(l). From the relationships between ion intensities as functions of time and from the appearance potentials, we could identify the fragment ions and their parent ions. On the basis of our understanding of the fragmentation processes in this system, we found that the vapor phase over InTe(l) consists of $\text{Te}_2(\text{g})$, $\text{In}_2\text{Te}(\text{g})$, and $\text{In}_2\text{Te}_2(\text{g})$ and analyzed the thermodynamics of the gas-phase reaction [1].

Experimental

InTe(s) was prepared by heating the high-purity elements in vacuum-sealed Vycor tubes. A Nuclide 12-90 HT Knudsen-cell mass spectrometer was used to analyze the vapor from the Knudsen cell. A movable shutter was used to focus the molecular beam from the Knudsen cell into the ionization chamber of the mass spectrometer and to discriminate against background gases. The Knudsen cell was heated by radiation from electrically heated tungsten filaments. The cell and the filaments were surrounded by tantalum radiation shields. The temperature of the sample was measured with a Leeds and Northrup, disapp-

earing filament, optical pyrometer focused on a black-body hole in the bottom of the Knudsen cell.

A sample of $9.39 \pm 0.05 \text{ mg}$ of InTe(s) was evaporated completely at 1106 ± 2 K, while the intensities of the ions were measured as functions of time. The sample was contained in a graphite Knudsen cell whose effective orifice area was $1.08 \pm 0.03 \text{ mm}^2$. Intensity measurements were made at m/e values of 115 (In^+), 130 (Te^+), 230 (In_2^+), 241 (InTe^+), 256 (Te_2^+), 360 (In_2Te^+), 371 (InTe_2^+), and 486 (In_2Te_2^+). The electron multiplier gain at m/e of 202 (Hg^+) was measured at room temperature before the evaporation of the sample.

In separate experiments with samples of InTe(s) from the same preparation batch, ionization efficiency curves were obtained for all ions whose precursors originated from the Knudsen cell and for Hg^+ , CO_2^+ , and H_2O^+ , which were background ions. The appearance potentials of the background ions above and that of Te_2^+ were used to calibrate the voltage axis. Weighted least squares analysis was carried out to obtain the calibration curves. During the same experiments, the electron multiplier gains of all ions, including $^{202}\text{Hg}^+$, were measured.

Partial pressures in the Knudsen cell were related to ion intensities with the equation

$$p_i = kT \sum_j \frac{I_{ij}^+}{\sigma_i \gamma_j f_j} \quad [2]$$

in which p_i is the partial pressure of i th precursor, I_{ij}^+ is the ion intensity of j th fragment of i th precursor, σ_i is the ionization cross section of i th precursor leading to j th fragment, γ_j is the electron multiplier gain of j th ion, f_j is the isotopic fraction of the observed ion, T is the temperature, and k is the instrument transmission factor

$$k = g \left[\frac{2\pi R}{T} \right]^{1/2} \left[AW \sum_i M_i^{1/2} \sum_j \frac{\int_0^t I_{ij}^+ dt}{\sigma_i \gamma_j f_j} \right]^{-1} \quad [3]$$

where g is the mass of the sample, M_i is the molecular weight of i th precursor, t is the time, t' is the time at which the sample was completely vaporized, A is the area of the orifice, and W is its transmission probability.

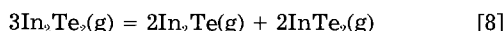
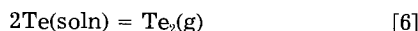
The atomic ionization cross sections are those of Mann (6). Ionization cross sections of In_2 , Te_2 , InTe , In_2Te , and InTe_2 were taken to be 0.8 times the sum of the ionization cross sections of the atoms. Ionization cross section of In_2Te_2 was taken to be 0.8 times that of InTe . Lacking dependable values of ionization cross sections for the

*Electrochemical Society Student Member.

**Electrochemical Society Active Member.

various fragmentation processes, we assumed the ionization cross section of the precursor to be independent of the subsequent fragmentation events. This assumption had the effect of removing the subscript j from σ_{ij} in Eq. [2] and [3].

The fragmentation processes in this system were analyzed in three ways. In the first method, ionic intensities were plotted as functions of time, and their slopes were compared to identify those ions with a common precursor. In the second method, the appearance potentials of the ions were analyzed to find the fragment ions and the parent ions. In the third method, we assumed that all ions were parents and ion intensities were used to calculate partial pressures of the hypothetical gaseous precursors with Eq. [2] and [3]. This assumption had the effect of removing summations over j , there being but one ion from each precursor. With these hypothetical partial pressures, equilibrium constants were calculated for the following hypothetical reactions



and for reaction [1]. The reaction quotients were checked for their trends with time and, where possible, compared with equilibrium constants from the literature.

The standard enthalpy of the vapor-phase reaction [1] was calculated from partial pressures, temperature, and Gibbs energy functions $\phi^\circ(T)$ with the equation (8)

$$\Delta H^\circ(298 \text{ K}) = RT [\Delta \phi^\circ(T)/R + \ln(K_1 \times \text{Pa}) + 11.526] \quad [9]$$

where K_1 is the equilibrium constant, in units of Pa^{-1} , for reaction [1], and the last term accounts for the fact that the standard pressure is 1 atm. Gibbs energy functions of $\text{In}_2\text{Te}_2\text{(g)}$ and $\text{In}_2\text{Te(g)}$ were those of Colin and Drowart (5), and that of $\text{Te}_2\text{(g)}$ was taken from Hultgren *et al.* (10).

Results

In^+ , In_2^+ , Te^+ , Te_2^+ , InTe^+ , In_2Te^+ , InTe_2^+ , and In_2Te_2^+ were observed. Their intensities measured as electron currents at the electron multiplier output, and corrected for the isotopic fraction, during the total exhaustion experiment are shown in Fig. 1. In this figure, region I corresponds to a period during which the temperature of the Knudsen cell was raised sharply to a steady-state value of $1106 \pm 2 \text{ K}$. Regions II and III correspond to a period during which the Knudsen cell was at constant temperature. In region II, the ion intensities varied continuously with time till a point of discontinuity occurred at $75.5 \pm 0.5 \text{ min}$ from the beginning of heating. At this point of discontinuity, In^+ intensity dropped by a factor of ~ 15 , Te^+ intensity by a factor of ~ 60 , In_2Te^+ intensity by a factor of ~ 100 , and In_2^+ intensity by a factor of ~ 15 . The intensities of Te_2^+ , InTe_2^+ , and In_2Te_2^+ dropped below the sensitivity of the instrument. The variation of ion intensities in region II fell into three distinct groups. The curves which represented the variation of In^+ , In_2^+ , Te^+ , InTe^+ , and In_2Te^+ were parallel, and those of InTe_2^+ and In_2Te_2^+ were parallel. The curve which represented the variation of Te_2^+ with time was unique. In region III, In^+ and Te^+ continuously decreased to a value of about a thousandth of their maximum intensities. At this stage, the variation of ion intensities with the shutter position suggested that the gaseous precursors were originating from the radiation shields and not from the Knudsen cell.

Table I gives the appearance potentials, electron multiplier gains, and cross sections of the ions. Column 1 gives the list of ions observed, column 2 the appearance potentials from this work, and column 3 the appearance potentials of these ions from the literature. The literature values are those reported for parent ions. Column 4 gives

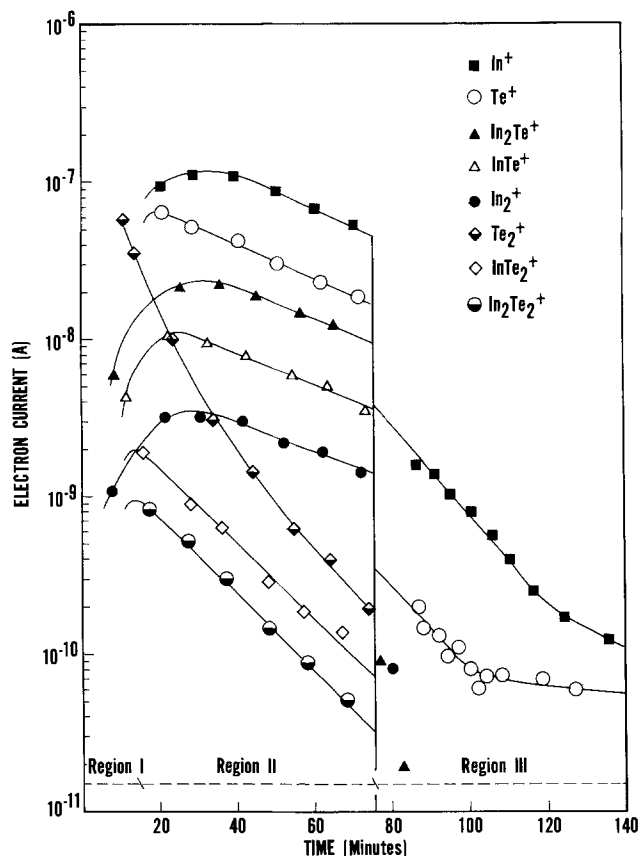


Fig. 1. Variation of ion intensities, measured as the electron currents at the electron multiplier output, and corrected for the isotopic fractions, with time.

the electron multiplier gains of the ions. The electron multiplier gain for $^{202}\text{Hg}^+$ remained constant between experiments. Column 5 gives the ionization cross sections of the ions.

Ion intensities read from Fig. 1 at regular intervals are given in Table II. Column 1 gives the times and columns 2-9 give the ion intensities of Te_2^+ , Te^+ , In^+ , In_2^+ , InTe^+ , In_2Te^+ , InTe_2^+ , and In_2Te_2^+ , respectively.

The instrument transmission factor calculated with Eq. [3] and the assumption that all ions were parents was $9.88 \times 10^{-11} \text{ Pa m}^2 \text{ A}^{-1} \text{ K}^{-1}$. Table III gives the hypothetical equilibrium constants for reactions [4]-[8] and [1]. Column 1 gives the time. Columns 2 and 4 give the partial pressures of In(g) and $\text{Te}_2\text{(g)}$, respectively. Columns 3 and 5 give the equilibrium constants for the dimerization of In(g) and Te(g) , respectively. Column 6 gives the equilib-

Table I. Appearance potentials, electron multiplier gains, and ionization cross sections

Ion	Appearance potentials (V)		Electron multiplier gain	Ionization cross section ($\times 10^{20}/\text{m}^2$)
	This work ^a	Literature ^b		
Te_2^+	c	8.8 (5) 8.7 \pm 0.5 (12)	1.62×10^5	11.7
Te^+	9.9	9.00 ± 0.01 (11)	1.59×10^5	7.31
In^+	7.7	5.8 (5) 5.786 ± 0.01 (11)	1.82×10^5	6.74
In_2^+	9.6	5.8 (5) 5.8 ± 0.3 (11)	1.19×10^5	10.8
InTe^+	8.6	7.6 (5)	1.34×10^5	11.5
In_2Te^+	8.3	7.1 (5)	1.62×10^5	16.6
InTe_2^+	8.2	8.9 (5)	9.84×10^4	17.1
In_2Te_2^+	7.6	7.2 (5)	2.80×10^5	18.4

^a Uncertainty in this work is estimated to be 0.3V.

^b Literature values given are those reported for parent ions. In Ref. (5), uncertainty in AP is 0.5V.

^c Te_2^+ was used as a calibrant.

Table II. Ion intensities^a as functions of time

Time (min)	Electron current (nA)							
	Te ₂ ⁺	Te ⁺	In ⁺	In ₂ ⁺	InTe ⁺	In ₂ Te ⁺	InTe ₂ ⁺	In ₂ Te ₂ ⁺
10	57.4	—	—	1.92	7.91	2.52	—	—
20	12.1	65.5	108	3.53	11.6	17.6	1.31	0.716
30	4.39	50.5	114	3.73	10.4	24.7	0.766	0.413
40	1.86	39.3	106	3.03	7.87	21.7	0.448	0.237
50	0.886	31.3	85.7	2.31	6.25	17.2	0.262	0.136
60	0.464	24.2	68.5	1.81	4.84	13.1	0.156	0.078
70	0.242	19.2	55.4	1.41	3.78	10.6	0.094	0.044
75.5	0.172	16.2	48.4	1.26	3.35	9.04	0.069	0.032
80	—	0.282	2.77	0.08	—	0.05	—	—
90	—	0.146	1.41	—	—	—	—	—
100	—	0.081	0.79	—	—	—	—	—
110	—	0.071	0.42	—	—	—	—	—
120	—	0.067	0.22	—	—	—	—	—
130	—	0.063	0.14	—	—	—	—	—
140	—	0.060	0.11	—	—	—	—	—

^a Ion intensities are those measured as electron currents at the electron multiplier output and corrected for the isotopic fractions.

rium constant for reaction [8]. Column 7 gives the equilibrium constant for reaction [1]. The bottom two rows give the equilibrium constants from the literature and their source. The literature values of the equilibrium constants of reactions [4] and [6] are the vapor pressures of pure indium and pure tellurium because the solution laws and concentrations of the system are unknown.

The instrument transmission factor, k , calculated with the hypotheses that all In⁺, Te⁺, In₂⁺, InTe⁺, and In₂Te⁺ came from In₂Te(g), all In₂Te₂⁺ and InTe₂⁺ came from In₂Te₂(g), and all Te₂⁺ came from Te₂(g), was 1.27×10^{-10} Pa m² A⁻¹ K⁻¹. Thermodynamics of reaction [1] derived on the basis of the above hypotheses are in Table IV. Column 1 gives the time, and columns 2 to 4 give the partial pressures of Te₂(g), In₂Te(g), and In₂Te₂(g), respectively. Column 5 gives the equilibrium constant of reaction [1], and column 6 gives the ΔH° (298 K) for this reaction derived by the third-law method. The average ΔH° (298 K) was -310.9 ± 0.5 kJ.

Discussion

We reached five conclusions: (i) the chemical system we studied can be thought of as a solution of tellurium in an indium-rich liquid; (ii) the vaporization of this liquid is incongruent; (iii) almost all of In⁺, In₂⁺, Te⁺, InTe⁺, and In₂Te⁺ came from a single precursor, In₂Te(g); (iv) almost all of Te₂⁺ came from Te₂(g); and (v) almost all of In₂Te₂⁺ and InTe₂⁺ came from a common precursor, In₂Te₂(g).

The standard enthalpy of reaction [1] at 298 K from this work is -310.9 ± 0.5 kJ. The uncertainty in our data is the standard deviation of the mean. The overall uncertainty is estimated to be less than 10 kJ. From the results of Colin and Drowart, we calculated -298 ± 33 kJ for the same reaction.

The variation of ionic intensities with time in Fig. 1 for the three groups of ions were different and indicated that the vapor-phase composition was changing during evaporation. Hence, the vaporization was incongruent. In a two-component system with a changing vapor composition, there should be but one condensed phase. We took this phase to be a solution of tellurium in an indium-rich liquid. During the vaporization of such a liquid, the activity of tellurium should be decreasing, while the activity of indium should be increasing. We observed that the intensity of Te₂⁺ was falling more rapidly than those of the indium containing ions and of Te⁺. The slow decrease in the intensities of indium containing ions was attributed to the decreasing surface area of the sample.

The three groups of curves in the plots of ionic intensity vs. time indicated that there were three molecular precursors in this system. Each precursor gives rise to one group of ions. The curves for In⁺, In₂⁺, Te⁺, InTe⁺, and In₂Te⁺ were parallel and indicated that these ions had a common precursor. This common precursor can be thought of as a species present in the gaseous phase or the condensed phase. If the precursor were to be present in the gaseous phase, and if we assume that we observed all parent ions, then In₂Te(g) would be the common precursor of In⁺, In₂⁺, Te⁺, InTe⁺, and In₂Te⁺. If the precursor were to be present in the condensed phase, then this precursor during vaporization should produce In(g), In₂(g), Te(g), InTe(g), and In₂Te(g), and these, in turn, should produce the corresponding ions. We ruled out this possibility by tests described later in this section.

The curves for In₂Te₂⁺ and InTe₂⁺ were parallel and indicated that In₂Te₂(g) would be the common precursor. The curve for Te₂⁺ was unique and indicated that Te₂(g) would be its precursor.

Appearance potentials provided additional support to the hypothesis of three gaseous precursors over InTe(l). The appearance potential of In₂Te₂⁺ agreed with that in the literature for the parent ion, within the uncertainty limits. The appearance potential of InTe₂⁺ was lower than that in the literature, but higher than the appearance potential of In₂Te₂⁺. The appearance potential of In⁺, In₂⁺, Te⁺, InTe⁺, and In₂Te⁺ were higher than the ones in the literature for parent ions. The appearance potentials of In₂⁺,

Table III. Hypothetical equilibrium constants and literature values

Time (min)	K_p/Pa	K_p/Pa^{-1}	K_p/Pa	K_p/Pa^{-1}	K_p/Pa	K_p/Pa^{-1}
20	9.62×10^{-1}	3.24×10^{-2}	6.98×10^{-2}	1.84×10^0	9.94×10^1	6.76×10^{-3}
30	1.02×10^0	3.04×10^{-2}	2.53×10^{-2}	1.12×10^{-1}	3.45×10^2	3.16×10^{-3}
40	9.44×10^{-1}	2.89×10^{-2}	1.07×10^{-2}	7.86×10^{-2}	4.85×10^2	3.17×10^{-3}
50	7.63×10^{-1}	3.36×10^{-2}	5.11×10^{-3}	5.91×10^{-2}	5.50×10^2	3.48×10^{-3}
60	6.10×10^{-1}	4.14×10^{-2}	2.68×10^{-3}	5.15×10^{-2}	5.98×10^2	3.76×10^{-3}
70	4.94×10^{-1}	4.92×10^{-2}	1.40×10^{-3}	4.27×10^{-2}	7.96×10^2	3.49×10^{-3}
75.5	4.31×10^{-1}	5.76×10^{-2}	9.92×10^{-4}	4.08×10^{-2}	8.09×10^2	3.61×10^{-3}
Literature value	1.51×10^{-1}	3.06×10^{-2}	2.00×10^4	2.73×10^0	—	—
Ref.	(10)	(13)	(10)	(10)	—	—

Table IV. Thermodynamics of reaction [1]

Time (min)	Partial pressure (Pa)			$K_1 \times \text{Pa}$	$\Delta H^\circ(298 \text{ K})/\text{kJ}$
	Te ₂ (g)	In ₂ Te(g)	In ₂ Te ₂ (g)		
20	8.97×10^{-2}	1.04×10^0	1.24×10^{-3}	1.58×10^{-3}	-309.8
30	3.25×10^{-2}	1.06×10^0	7.23×10^{-3}	1.43×10^{-3}	-308.9
40	1.38×10^{-2}	8.89×10^{-1}	4.21×10^{-3}	1.63×10^{-3}	-310.1
50	6.57×10^{-3}	7.11×10^{-2}	2.46×10^{-3}	1.82×10^{-3}	-311.1
60	3.44×10^{-3}	5.59×10^{-1}	1.45×10^{-3}	1.96×10^{-3}	-311.8
70	1.79×10^{-3}	4.49×10^{-1}	8.68×10^{-4}	2.09×10^{-3}	-312.4
75.5	1.27×10^{-3}	3.90×10^{-1}	6.36×10^{-4}	2.09×10^{-3}	-312.4

Te⁺, and InTe⁺ were higher than that of In₂Te⁺ and indicated that these three ions could be the fragments of In₂Te⁺. The appearance potential of In⁺ was lower than that of In₂Te⁺ and indicated that a part of In⁺ came from a different source.

The various gaseous species inside the Knudsen cell should be at equilibrium. The equilibrium constants for vapor-phase reactions should be independent of the time at which the partial pressures were measured, and the values should be comparable to literature data. The reaction quotients of reactions [5], [7], and [8] failed these tests. The reaction quotients for the incongruent vaporization of indium and tellurium from the homogenous condensed phase showed variations with time because of variations in their activities and sample surface area. The partial pressure of In(g) over liquid InTe was about seven times that over pure indium and showed that the major source of In⁺ was fragmentation processes. The partial pressure of Te₂⁺ at its maximum value was lower than that over pure tellurium, as expected. The equilibrium constant for the dimerization of indium showed variations with time, and its value was higher than the literature value by four orders of magnitude. The dimerization constant for Te(g) showed large variations with time. Large variations in the equilibrium constant for reaction [8] showed that such an equilibrium did not exist in the Knudsen cell. The hypothetical equilibrium constant for reaction [1] remained constant. These tests with reaction quotients provided additional support in the identification of fragment ions and the ruling out of the possibility that all ions are parents and the precursor is the condensed phase. The fact that the reaction quotient of reaction [1] remained constant, $(1.81 \pm 0.10) \times 10^{-3} \text{ Pa}^{-1}$, in spite of large variations in the partial pressures of Te₂(g), In₂Te(g), and In₂Te₂(g) confirmed conclusions (iii)-(v) above.

Acknowledgment

This work was supported by the National Science Foundation under Grant no. CPE8103676.

Manuscript submitted June 27, 1984; revised manuscript received Aug. 17, 1984.

The University of Toledo assisted in meeting the publication costs of this article.

REFERENCES

1. V. M. Koshkin, L. P. Galchinetskii, V. N. Kulik, G. K. Gusev, and V. A. Ulmanis, *Atom. Energy*, **42**, 290 (1977).
2. W. Takuo and F. Shinji, *Japan Kokai*, **76**, 11585 (1976); C. A. 85:278482.
3. S. Fujwara, T. Chikamura, and M. Fukai, *J. Cryst. Growth*, **61**, 567 (1983).
4. A. Shahar, M. Oran, and A. Zusbman, *J. Appl. Phys.*, **54**, 2477 (1983).
5. R. Colin and J. Drowart, *Trans. Faraday, Soc.*, **64**, 2611 (1968).
6. J. B. Mann, *J. Chem. Phys.*, **46**, 1646 (1967).
7. R. T. Grimley in "The Characterization of High Temperature Vapors," J. L. Margrave, Editor, p. 225, John Wiley and Sons, New York (1967).
8. D. Cubicciotti, *J. Phys. Chem.*, **70**, 2410 (1966).
9. R. Haque, A. S. Gates, and J. G. Edwards, *J. Chem. Phys.*, **73**, 6301 (1980).
10. R. Hultgren, P. D. Desai, D. T. Hawkins, M. Geiser, K. K. Kelley, and D. D. Wagman, "Selected Values of the Thermodynamic Properties of the Elements," American Society For Metals, Metals Park, OH (1973).
11. H. M. Rosenstock, D. Sims, S. S. Schroyer, and W. J. Webb, "Ion Energetics Measurements. Part I. 1971-73," NSRDS-NBS-66 (1980).
12. J. Drowart, G. Exteen, and A. Vander Auwera-Mahieu, *J. Phys. Chem.*, **71**, 4130 (1967).
13. J. Drowart, G. DeMaria, and M. G. Ingram, *J. Chem. Phys.*, **31**, 1076 (1959).

Process Modeling of n-Type Doping in Gallium Arsenide

J. K. Dhiman and K. L. Wang*

Department of Electrical Engineering, School of Engineering and Applied Science, University of California, Los Angeles, California 90024

ABSTRACT

Empirical models have been developed for predicting the carrier distributions after ion implantation and annealing process steps used in GaAs device fabrication. The present models predict the carrier distributions for n-type GaAs using Si and Se as the dopants. The simulation is done by using the atomic profile and activation efficiency models developed in this study. These models are based on SIMS and measured carrier concentration profile studies reported in the literature. The model for atomic distribution provides a gaussian profile for Si and a joined half-gaussian one for Se using the projected range and standard deviation parameters obtained from SIMS studies. The effect of radiation enhanced diffusion is taken into account. Impurity diffusion during annealing for temperatures up to 920°C for Si and 1000°C for Se is neglected. Volumetric concentration has been properly chosen as a canonical parameter for obtaining activation efficiency. The universal activation efficiency plots for each dopant species give percentage activation efficiency as a function of atomic concentration (cm^{-3}) at different annealing temperatures.

GaAs is rapidly emerging as an important alternative material in high speed digital and microwave monolithic integrated-circuit applications (1, 2). The rapidly improving technology of GaAs FET's is making a major impact on a wide range of microwave power and digital circuits. Direct ion implantation into bulk-grown semi-insulating GaAs with or without an epitaxially grown buffer layer has become a mainstream technology for GaAs FET fabrication. The characteristics of GaAs devices strongly depend on the carrier concentration profile which results from ion implantation and subsequent annealing. Therefore, a model for predicting carrier concentration profiles is needed to facilitate the processing of GaAs devices. Most of the experimental work using Cr-doped HB mate-

rial reported so far does not give consistent results in the low doping range. This is because of the strong dependence of the doping on the initial Cr content in the substrate material (3). Moreover, the experimental data available in the literature are not systematic enough for the purpose of constructing a theoretical model. The decision was, therefore, made to develop empirical models based on the available experimental data. These models will give a first-order estimate of the carrier concentration profile and will serve the needs for all practical purposes.

In GaAs device processing, ion implantation is normally used to dope the channel, and the source and drain regions of MESFET's where n-type dopants such as silicon (group IV) and selenium (group VI) have been most extensively used. Owing to the limited availability of ex-

*Electrochemical Society Active Member.

perimental data for other species, this study models Si and Se impurities only.

Approach

The basic approach taken for modeling the ion implantation and annealing steps of GaAs device processing for obtaining the carrier distribution is to generate the impurity atomic profile first. Then the activation efficiency plots as a function of atomic concentration (N) are constructed, as it has been widely found that activation efficiency is a function of N , the volumetric concentration (cm^{-3}), rather than the integrated quantity, fluence. Other important process variables that will be considered are categorized as follows: (i) ion-implantation variables: energy (E), fluence (ϕ), and implantation temperature (T_i); (ii) thermal annealing variables: capped or controlled atmospheric technique (CAT), annealing temperature (T_E); type of substrate materials used: Cr-doped HB, VPE, LEC, LPE.

It has been assumed that the electrical activation efficiency (η) is a function of impurity atomic concentration (cm^{-3}) and not of any other implantation variables such as ion energy and fluence separately. The volumetric concentration thus becomes a canonical parameter for computing η . Activation efficiency (η) is defined as the fraction of implanted impurity atoms, which shows electrical activation, *i.e.*, the ratio of carrier concentration n (cm^{-3}) to atomic concentration N (cm^{-3}).

Development of Basic Empirical Models

Model for atomic profile.—According to the LSS theory, the atomic impurity profile for an amorphous GaAs substrate is gaussian (49). Its parameters, *i.e.*, projected range (R_p) and standard deviation (ΔR_p), are only a function of energy of the implanted impurity. However, in practice, these parameters can be a function of other implantation variables such as implantation temperature. Owing to the complicated functional dependence of these parameters on the implantation conditions, the experimental data from secondary ion mass spectrometry (SIMS) studies rather than theoretical values were used to obtain the distribution parameters for calculating atomic distributions of Si and Se impurities.

Silicon atomic profile.—The dependence of R_p and ΔR_p on implant energy (E) for Si obtained from SIMS studies (4-8) has been found to be independent of substrate material, implant temperature up to 400°C, and annealing procedures with temperatures up to 920°C for 20 min. These parameters are tabulated in Tables I and II and plotted as a function of implant energy in Fig. 1. The relationships between R_p , ΔR_p , and E are fitted with empirical mathematical formulas, which in turn are used to generate atomic profiles. The least squares spline fit of cubic polynomials obtained in different ranges of energy gives the relationships of R_p and ΔR_p with E . The atomic profile

Table I. Projected range (μm) at different implant energies (keV) taken from different studies

Energy (keV)	(7)	Ref. (5)	(6)
40	0.0396		
50		0.040	0.0485
60	0.0691		
100			0.088
120	0.1216		
150		0.140	0.1464
200	0.1807		0.1778
250			0.2202
280	0.2587		
300		0.280	0.2836
400	0.3945	0.375	0.3871
500	0.5272		0.5203
600	0.6560		
700	0.7477		
800	0.8308		
900	0.9000		
1000	0.9743		
1200	1.0972		

Table II. Projected standard deviation (μm) at different implant energies (keV) taken from different studies

Energy (keV)	(7)	Ref. (5)	(6)
40			
50	0.0218		0.0277
60		0.026	
100	0.0442		0.0490
120			
150	0.06422	0.0680	0.0709
200			0.0869
250	0.1000		0.1052
280			
300	0.1202	0.1180	0.1253
400		0.1330	0.1321
500			0.1652
600	0.1747		
700	0.1863		
800	0.1901		
900	0.1954		
1000	0.2000		
1200	0.2220		

is assumed to be gaussian for $E < 700$ keV and a joined half-gaussian or Pearson's distribution for $E > 700$ keV based on the results of SIMS study (7).

Selenium atomic profile.—After reviewing the SIMS results for Se implants, the following conclusions were arrived at: (i) atomic profile is independent of substrate material type, annealing methods used, and annealing temperature up to 1000°C for a period of 15 min (9-11), (ii) diffusion length (\sqrt{Dt}) during implantation is a complex function of implant energy, fluence, and temperature due to radiation-enhanced diffusion (9-13), and (iii) use of a joined half-gaussian distribution rather than a normal gaussian better approximates the deeper side of the as-implanted profile (14).

Based on the above-mentioned facts, the following procedure has been adopted for modeling the atomic distribution. A two-dimensional diffusion equation can be solved using a finite element method. By knowing the implant time (t) and using a half-gaussian distribution (49) as the initial condition, the diffusion coefficient (D) can be obtained. However, if the product Dt is small, the resulting profile due to radiation-enhanced diffusion can be approximated simply by another joined half-gaussian

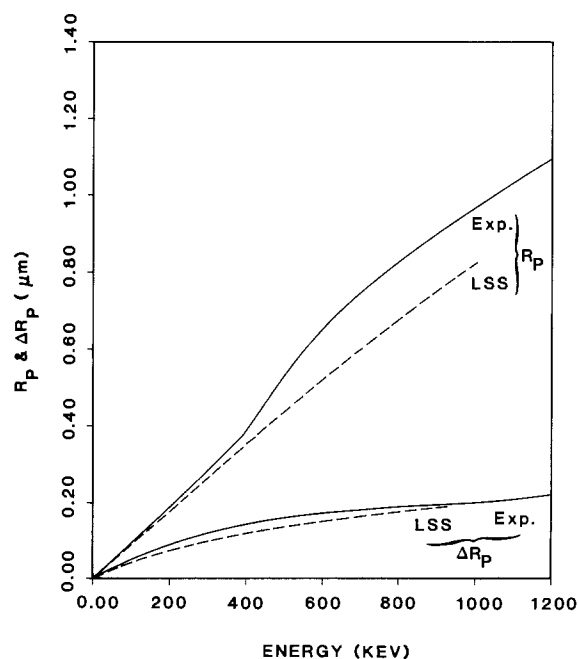


Fig. 1. Projected range (R_p) and standard deviation (ΔR_p) as a function of energy from LSS theory and the empirical fit of experimental (SIMS) data from Ref. (5-7).

having a lower peak as given by Eq. [1]. Therefore, the diffusion length (\sqrt{Dt}) may be calculated from the peak of the as-implanted profile (N_{\max}) by using Eq. [2].

$$N(x) = \frac{\phi}{[2\pi(\Delta R_p^2 + 2Dt)]^{1/2}} \exp - \frac{(x - R_p)^2}{2(\Delta R_p^2 + 2Dt)} \quad [1]$$

and

$$Dt = \frac{1}{2} \left[\frac{1}{2\pi} \left(\frac{\phi}{N_{\max}} \right)^2 - (\Delta R_p)^2 \right] \quad [2]$$

In Eq. [2], the description of the broadening of the distribution function using diffusion length \sqrt{Dt} (cm) is valid because it is found to be almost independent of implant time with a given fluence (10).

In addition to the available SIMS data, published carrier concentration profile results (28, 34, 35, 37, 53) were used to obtain Dt for the range of implant energy in which SIMS data are lacking. In the latter case, only carrier profiles having peak carrier concentration between $2E17$ and $3E17$ cm^{-3} obtained from high purity epitaxial samples were utilized. In this doping range, the effect of thermal conversion, if any, is very small. Furthermore, the activation efficiency in this doping range is independent of the annealing temperature and is known to be approximately 94%-97%. Thus, the atomic distributions can be obtained directly from the measured carrier profiles. This approach appears to provide correct Dt as a function of energy for those cases in which the corresponding SIMS data are not available.

The data from the SIMS and carrier concentration studies done at $T_i \geq 150^\circ\text{C}$ are used to evaluate Dt data and the results are plotted in Fig. 2. Based on our procedure of using the peak of the diffused profile, Dt is found to be independent of fluence but increases as E increases. The atomic profile can then be generated from the factor $(\Delta R_p^2 + 2Dt)^{1/2}$, knowing the peak value and assuming that the profile remains half-gaussian after diffusion. This procedure has led to a program step for obtaining the as-implanted Se atomic profile.

Model for electrical activation efficiency.—Activation efficiency (η) can be obtained if both the carrier and atomic concentration profiles are available. Most of the work published to date provides only the carrier profiles. However, in such cases the atomic profile of Si and Se can be generated for the work that reported only carrier profiles using the procedure to be described in the subsequent section. The carrier concentration data used in this study were taken from the results of either C(V) measurements or a series of etching and Hall measurements:

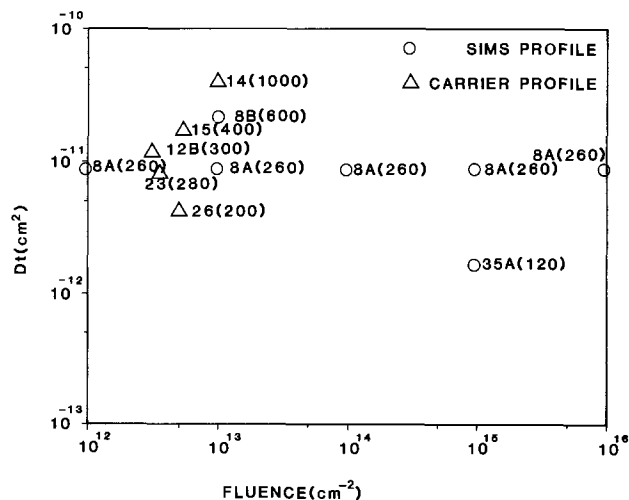


Fig. 2. Plot of diffusion length square (Dt) vs. fluence (ϕ) of Se in GaAs as a function of implant energy obtained from atomic and carrier profile studies. Numbers within parentheses are the implant energy (keV).

In principle, η should be obtained as a function of N for the entire range of the distribution. Owing to the steep nature of the gaussian profile, an accurate alignment of the peaks of atomic and carrier profiles is essential for correctly obtaining η in the tail portion of the distribution, where a small shift of the gaussian peak position can result in a large difference in η . It is difficult to determine the actual peak position of the carrier profile accurately because its apparent peak position may not be the true one. This difficulty in determining the peak position may be due to the thermal conversion of the substrate, error in measurements, or smearing of the peak that can be caused by decreasing activation near the peak concentration regions. Additionally, the thermal conversion can affect the carrier concentration profile markedly in the lower concentration regions. In order to avoid any significant error caused by the above-mentioned sources, only one data point per carrier profile corresponding to the maximum carrier concentration (n_{\max}) was used and the η was calculated as the ratio of n_{\max} to N_{\max} .

Some experimental studies which reported only the conductivity measurements of the implanted samples were also utilized in our study. In such cases, sheet carrier concentration (N_s) cm^{-2} was obtained from the measured conductivity (σ_s) and sheet mobility (μ_s) of the implanted samples from ($\sigma_s = q\mu_s N_s$). The effective electrical activation efficiency (η_s) obtained as the ratio of N_s to the implant fluence has been plotted against the peak atomic concentration (N_{\max}). However, η_s obtained this way is lower than the true η because of the steep nature of the gaussian profile (15). The problem of evaluating the appropriate correction for each η_s data point is nontrivial. These uncorrected data points were, therefore, used for providing some simple guidelines in the regions where volumetric activation data are not available. These data points have been shown moved up with arrows in Fig. 3 and 4.

In order to obtain the activation efficiency, only reproducible data were used. These data were obtained from the work including the use of various substrate materials (VPE, LEC, Cr-doped HB). No distinction was made for using different annealing methods, *i.e.*, Si_3N_4 or AlN capping, or controlled atmospheric technique.

Silicon activation efficiency.—The activation efficiency of Si impurity was found to be independent of implant temperature (12, 17) and therefore the data for low and high implant temperatures were both used together. Similarly, annealing time and annealing method (capped or CAT) for Si implantation (43, 54) were not considered as variables. The resulting activation data were compiled and plotted in Fig. 3, on which the points with an up-arrow distinguish the values of η_s from η according to the

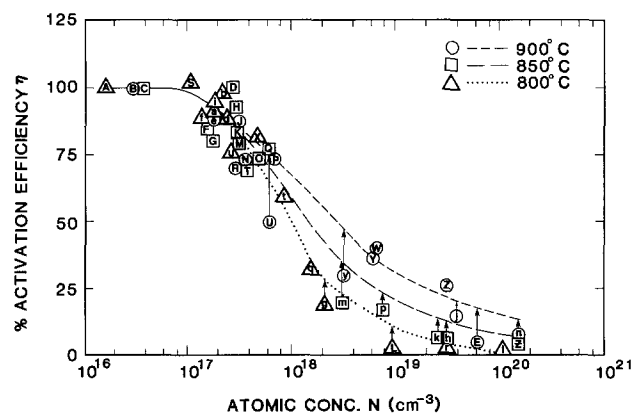


Fig. 3. Universal activation plots for Si impurity in GaAs annealing at $T_A = 800^\circ, 850^\circ, 900^\circ, 950^\circ\text{C}$. Data points having letters represent the references: A, b = (5); B, C, Z, R, T, e, k, m, y = (12); D, u = (8); E, P, W = (27); F, O, d = (43); G = (44); H = (46); I = (50, 7); J = (47); K = (48); L = (50); M, P, k = (7); N = (45); Q = (49); S, X, a, f, i, q, t, u = (42); U, Y = (49); V = (52); g = (17); h, j, r = (51); n, Z = (52).

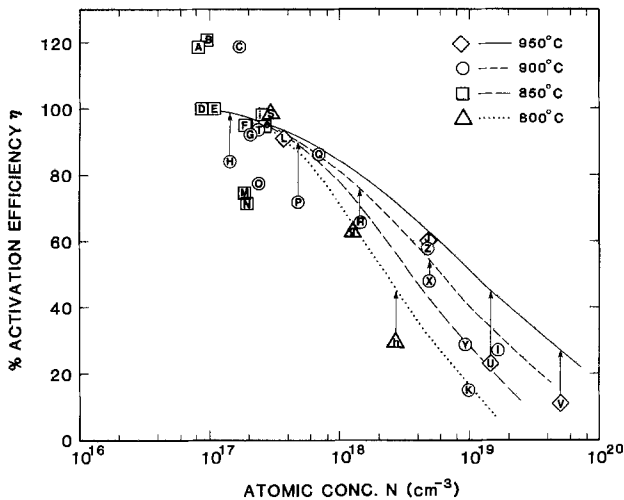


Fig. 4. Universal activation plots for Se impurity in GaAs annealed at $T_A = 800^\circ, 850^\circ, 900^\circ, 950^\circ\text{C}$. Data points having letters represent the references: such as A = (29); B, F, = (32); C, S, = (32); D, N = (30); B, E = (31); F = (32); G, Q = (36); H, J, R, P, U, X, Z = (12); I = (21, 41); K, O, Y = (38); M = (26); T = (53); V = (11); i = (34); e = (35); g = (39); h = (17). Low activation for K, Y, O is due to low annealing time used.

different calculating procedures described in the previous section. A 100% activation in the low doping concentration region is not obtained from Cr-doped HB material. The scattering of the data in the low doping region ($N < 3 \times 10^{17} \text{ cm}^{-3}$) is indicative of possible doping compensation or thermal conversion arising from the redistribution of Cr or Mn. For high purity VPE material, another study (5) shows an actual 100% activation in the low doping concentration. As the doping level increases beyond $1E17 \text{ cm}^{-3}$, η decreases, probably because of the combined effect of defects generated, amphoteric property of doping, and the solid solubility limitations.

The activation efficiency, η , of Si, in general, appears to be independent of annealing temperature, T_A , in the low doping region ($N \approx 3 \times 10^{17} \text{ cm}^{-3}$). However, η becomes increasingly dependent on annealing temperature and time as the implant dose increases, *i.e.*, as the implanted region approaches the amorphous phase. Analytical expression was used to fit these empirical data between η and N for different T_A used.

Selenium activation efficiency.—The η of Se was found to depend markedly on implant temperature (12, 13, 16-22). The data for all implant temperature greater than 150°C were used together because of insufficient number of data points available for each temperature and because of the small dependence of η on T_i in the temperature region. The annealing method and time (19) were not considered as variables. The activation data were plotted in Fig. 4 similar to the Si case. Again, some scattering of data for $N < 3 \times 10^{17} \text{ cm}^{-3}$ is indicative of thermal conversion of the Cr-doped material used. In this doping level, η decreases for similar reasons as for the Si case (22). The η of Se is again independent of T_A in the low doping region ($N \approx 3 \times 10^{17} \text{ cm}^{-3}$). However, η becomes increasingly dependent on T_A as N increases. A higher activation efficiency is generally observed for Se as compared to the Si case for the same doping level. This increase in η for Se may be attributed to the lack of amphoteric behavior of Se impurity. Solid solubility at different temperatures is used to limit the maximum value of the calculated carrier concentration when exceeded. The data of solid solubility used are the average from the two studies (24, 36), being $7.75E18$ and $1.64E19 \text{ cm}^{-3}$ for 900° and 950°C , respectively. For 850°C annealing, the value is $2.56E18 \text{ cm}^{-3}$ from another study (24).

The least squares spline fit of cubic polynomials was used as for the Si case to represent the relationship of η and N for different T_A .

Generation of Carrier Distribution

A computer program was developed for generating the carrier profiles resulting from Si or Se impurity implantation. The details follow.

Silicon carrier distribution.—The program generates an atomic profile using Eq. [1] when an implant energy (E) and a fluence (ϕ) are given. In Eq. [1], $D = 0$ is assumed, while R_p and ΔR_p are calculated for a given E from the empirical equation discussed in the "Silicon atomic profile" section. By using the activation efficiency *vs.* N relationship described in the "Silicon activation efficiency" section, the carrier concentration n (cm^{-3}) as a function of depth (μm) can be computed. An example is illustrated in Fig. 5.

Selenium carrier distribution.—The as-implanted atomic profile is assumed half-gaussian (see the "Selenium atomic profile" section) and its maximum value calculated by knowing the factor $(\Delta R_p^2 + 2Dt)^{0.5}$. The Dt can be obtained from Fig. 2, in which a linear interpolation between the available experimental data point is applied. The R_p and ΔR_p are obtained from the LSS theory (49). Since the diffusion of Se impurity during annealing is negligible, the as-implanted profile is identical to the final impurity profile. By knowing η as a function of N (see the "Selenium activation efficiency" section), the resulting carrier distribution can be calculated as a function of depth.

Applicability of the Present Models

In order to achieve a good activation and reproducibility of the doping process, the substrate material used in the direct ion-implantation step should meet certain requirements. Different qualification criteria of the substrate material have been employed from time to time (26, 27).

The present process model should only be applied to the qualified substrate material in the following range of the process variables: (i) annealing method: cap (Si_3N_4 , AlN), CA, ACCA having $P_{\text{AsH}_3} \approx 3$ torr; (ii) annealing temperature used: $< 920^\circ\text{C}$ for Si and $< 1000^\circ\text{C}$ for Se; (iii) annealing time: 10-30 min; (iv) implant temperature: $\approx 150^\circ\text{C}$ for Se impurity.

The model is a simplified one, owing to the complex nature of the problem and lack of enough data for the large number of process variables. If the above conditions

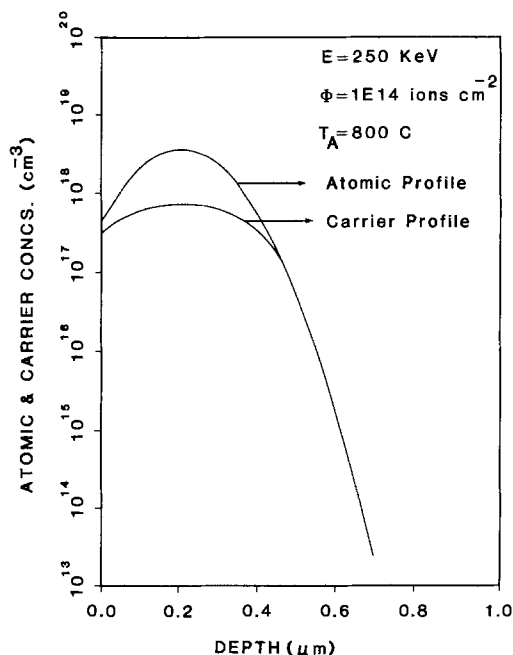


Fig. 5. Atomic and carrier profiles of Si in the high doping level for the process variables given above using the empirical models developed in the present study.

are not met by the process variables, the present model has to be modified.

Conclusion

Empirical models have been developed for simulating the implantation and annealing steps used for doping GaAs with Si and Se. The modeling efforts in the present research has led to the recognition of important process variables which affect the atomic distribution and the activation efficiency of the implanted impurities. The first-order effect of radiation-enhanced diffusion for Se has been modeled. The diffusion effect due to high annealing temperatures normally employed can be neglected. The compilation of the activation data has led to the establishment of universal plots for each dopant which are different for each annealing temperature.

The empirical models can be updated from time to time with the availability of more experimental data. The deeper side of the profile will be better approximated by using Pearson's distribution as more experimental SIMS data become available. Other more exact formulation of radiation-enhanced diffusion and the diffusion of impurity during annealing can be incorporated in the future. The effect of other process variables, *i.e.*, annealing time, detailed effect of the ambient used for annealing can be modeled in future.

In essence, the present study will serve as a foundation for future development of more realistic and comprehensive process models.

Acknowledgments

The authors would like to thank the TRW/U.C. Micro program for their support of this work. In addition, we wish to express our appreciation for cooperation of TRW management, Dr. R. Kagiwada and R. Fairman and H. Hennecke.

Manuscript submitted Feb. 27, 1984; revised manuscript received July 20, 1984.

The University of California assisted in meeting the publication costs of this article.

REFERENCES

- R. C. Eden and B. M. Welch, in "VLSI," D. F. Barbe, Editor, Springer-Verlag, Berlin (1980).
- W. R. Wissemann and J. G. Oakes, *IEEE Trans. Electron Devices*, **ed-28**, 133 (1981).
- G. M. Mizutani, T. Honda, S. Ishida, and Y. Kawasaki, *Solid State Electron.*, **25**, 885 (1982).
- M. Feng, V. K. Eu, H. Kanber, and W. B. Henderson, *J. Electron. Mater.*, **10**, 973 (1981).
- D. H. Lee, R. M. Malbon, and J. M. Whelan, in "Ion Implantation in Semiconductors," S. Namba, Editor, p. 115, Plenum Press, New York (1974).
- D. H. Lee and R. M. Malbon, *Appl. Phys. Lett.*, **30**, 327 (1977).
- S. G. Liu, E. C. Douglas, C. W. Magee, F. Kolondra, and S. Jain, *ibid.*, **37**, 79 (1980).
- M. Feng, S. P. Kwok, V. K. Eu, and B. W. Henderson, *J. Appl. Phys.*, **52**, 2990 (1981).
- R. G. Wilson and D. M. Jamba, *Appl. Phys. Lett.*, **39**, 715 (1981).
- A. Lidow, J. F. Gibbons, V. R. Deline, and C. A. Evans, Jr., *ibid.*, **32**, 149 (1978).
- R. L. Chapman, C. C. John, J. P. Donnelly, and B. Y. Tsauro, *ibid.*, **40**, 805 (1982).
- J. P. Donnelly, W. T. Lindley, and C. E. Hurwitz, *ibid.*, **27**, 41 (1975).
- T. Inada and T. Suqiyama, *J. Appl. Phys.*, **52**, 6986 (1981).
- A. Lidow, J. F. Gibbons, V. R. Deline, and C. A. Evans, Jr., *Appl. Phys. Lett.*, **32**, 15 (1978).
- G. Dearnaley, J. H. Freeman, R. S. Nelson, and J. Stephen, "Ion Implantation," Elsevier, New York.
- A. Lidow, J. F. Gibbons, V. R. Deline, and C. A. Evans, Jr., *Appl. Phys. Lett.*, **51**, 4130 (1980).
- D. E. Davies, J. K. Kennedy, and C. E. Ludington, *This Journal*, **122**, 1374 (1975).
- R. Zucca, B. M. Welch, P. M. Asbeck, R. C. Eden, and S. I. Long, in "Semi-insulating III-V Materials," p. 335, Nottingham, England (1980).
- A. W. Livingstone, P. A. Leigh, N. McIntyre, I. P. Hall, J. A. Bowie, and P. J. Smith, *Solid State Electron.*, **26**, 19 (1983).
- H. Kanber, M. Feng, V. K. Eu, R. C. Rush, and W. B. Henderson, *J. Electron. Mater.*, **11**, 1083 (1982).
- I. R. Sanders, A. H. Peake, and R. K. Surridge, in "Semi-insulating III-V Materials," p. 349, Nottingham, England (1980).
- Y. Kushiuro and T. Kobayoshi, in "Ion Implantation in Semiconductors," S. Namba, Editor, p. 67, Plenum Press, New York (1975).
- A. K. Rai, R. S. Bhattacharya, and P. P. Pronko, *Appl. Phys. Lett.*, **41**, 1086 (1982).
- A. Lidow, J. F. Gibbons, V. R. Deline, and C. A. Evans, Jr., *ibid.*, **32**, 572 (1979).
- R. S. Bhattacharya, P. P. Pronko, Y. K. Yeo, A. K. Rai, Y. S. Park, and J. Narayan, *J. Appl. Phys.*, **53**, 4821 (1982).
- R. D. Fairman and J. R. Oliver, in "Semi-insulating III-V Materials," p. 83, Nottingham, England (1980).
- J. Kasahara, M. Arai, and N. Watanabe, *This Journal*, **126**, 1997 (1979).
- J. A. Higgins, R. L. Kuvass, F. H. Eisen, and D. R. Chen, *IEEE Trans. Electron Devices*, **ed-25**, 587 (1978).
- A. A. Immorlica and F. H. Eisen, *Appl. Phys. Lett.*, **29**, 94 (1976).
- H. A. Higgins, F. Eisen, B. Welch, G. Robinson, and W. Hill, in Institute of Physics Conference Series 33b, p. 237, Institute of Physics, London (1977).
- S. I. Long, B. M. Welch, R. Zucca, P. M. Asbeck, C. P. Lee, C. G. Kirkpatrick, F. S. Lee, G. E. Kalelin, and R. C. Eden, in "Semi-insulating III-V Materials," p. 135, Nottingham, England (1980).
- F. N. Favennec, L. Henry, and H. L. Haridon, *Solid State Electron.*, **21**, 705 (1978).
- C. A. Stottle, in "Semi-insulating III-V Materials," p. 93, Nottingham, England (1980).
- G. M. Martin, in "Semi-insulating III-V Materials," p. 13, Nottingham, England (1980).
- R. K. Surridge and B. J. Sealy, *Electron. Lett.*, **13**, 233 (1977).
- C. L. Anderson, K. V. Vaidyanathan, H. L. Dunlap, and G. S. Kamath, *This Journal*, **127**, 925 (1980).
- T. Inada, S. Kato, T. Hara, and N. Toyoda, *J. Appl. Phys.*, **50**, 4466 (1979).
- B. J. Sealy, R. K. Surridge, S. S. Kular, and K. G. Stephens, in Institute of Physics Conference Series 46, p. 476, Institute of Physics, London (1979).
- A. Ezis, D. V. Morgan, and M. J. Howes, *Nucl. Instrum. Meth.*, **182/183**, 705 (1979).
- K. Gamo, T. Inada, S. Krekeler, and J. W. Mayer, *Solid State Electron.*, **20**, 213 (1977).
- T. Inada, H. Miwa, S. Kato, E. Kobayashi, T. Hara, and M. Mihara, *J. Appl. Phys.*, **52**, 6128 (1981).
- T. Onuma, T. Hirao, and T. Sugawa, *ibid.*, **52**, 6128 (1981).
- T. Onuma, T. Hirao, and T. Sugawa, *This Journal*, **129**, 837 (1982).
- H. M. Hobgood, W. Eldridfe, D. L. Barrett, and R. N. Thomas, *IEEE Trans. Electron Devices*, **ed-28**, 140 (1981).
- M. Kuzuhara, M. Kohzu, and Y. Takayama, *Appl. Phys. Lett.*, **41**, 755 (1982).
- J. Kasahara, M. Arai, and N. Watanabe, *J. Appl. Phys.*, **50**, 8229 (1979).
- M. Arai, K. Nishiyama, and N. Watanabe, *Jpn. J. Appl. Phys.*, **20**, L124 (1981).
- J. Kasahara and N. Watanabe, *ibid.*, **19**, 11, L679 (1980).
- J. F. Gibbons, W. S. Johnson, and S. W. Mylroie, "Projected Range Statistics," Dowden, Hutchinsonson, and Ross (1975).
- H. Krautle, *Nucl. Instrum. Meth.*, **182/183**, 625 (1981).
- J. L. Tandon, M. A. Nicolet, W. F. Tseng, F. H. Eisen, S. U. Campisano, G. Foti, and E. Rimini, *Appl. Phys. Lett.*, **34**, 597 (1979).
- T. Miyazaki and M. Tamura, in "Ion Implantation in Semiconductors," Chernw, Editor, p. 41, Plenum Press, New York (1975).
- J. C. C. Fan, J. P. Donnelly, C. O. Bozler, and R. L. Chapman, in Institute of Physics Conference Series 45, p. 472, Institute of Physics, London (1979).
- S. Nojima, *J. Appl. Phys.*, **53**, 5028 (1982).

Boltzmann-Matano Analysis of Boron Profiles in Silicon

C. Kim,* Z-Y. Zhu,¹ R-I. Kang, and K. Shono*

Faculty of Science and Technology, Sophia University, Kioicho-7, Chiyoda-ku, Tokyo 102, Japan

ABSTRACT

Boltzmann-Matano analysis of the boron profiles in silicon diffused from the boron-excess BN film was carried out, and the boron diffusivity was obtained as a function of the local concentration. Boron diffusivity in silicon can be described by the diffusion model, which considers both effects of the charged monovacancy-impurity interaction and the internal electric field. The prefactors in the simplified expressions of x , Q , and R_s as a function of the surface concentration normalized to the intrinsic carrier concentration at the diffusion temperature were obtained by the numerical analysis of the diffusion equation, including the concentration-dependent diffusivity.

A general theory of impurity diffusion in silicon was proposed by Hu and Schmidt (1). They formulated the concentration dependent diffusivity involving both effects of the impurity-vacancy interaction and the internal electric field. The arsenic diffusivity reported by Fair and Tsai (2) is in good agreement with the theoretical prediction, and the arsenic profiles are coincident with the approximate solution of diffusion equation with the concentration-dependent diffusivity.

For the case of boron, Fair summarized the diffusivity data obtained from BN disk and B₂O₃ box source diffusions and concluded that the boron diffusion was dominated only by the interaction of charged monovacancy and boron ion, without the electric field effect (3). However, the effect of internal electric field is clearly apparent in the diffusivity data by Matsumoto *et al.*, who employed boron-doped oxide as the diffusion source (4). It seems that the diffusivity data reported are not yet sufficient to discuss the mechanism of boron diffusion in silicon.

Boron-excess BN film deposited on a silicon surface and encapsulated with thin Si₃N₄ film acts as a boron-diffusion source. The surface concentration is kept constant during the diffusion heat-treatment and can be controlled in the high concentration from 2×10^{18} cm⁻³ to the solid solubility as a function of deposition temperature of the BN film (5). It has also been confirmed that silicon boride is not formed at the interface of silicon and BN film (6). By using the boron-excess BN film as a diffusion source, Boltzmann-Matano technique (7) can be employed for the analysis of boron profile over a wide range of the surface concentration.

This paper describes the boron diffusivity as a function of the boron concentration. The prefactors in the simplified expressions of x , Q , and R_s of boron-diffused layer in silicon will be discussed.

Experimental

Substrates used in the experiment were mirror-finished n-type silicon having a resistivity of 4-5 Ω-cm and (100) orientation. The boron-excess BN films as the boron source were deposited on the silicon wafers by use of the experimental apparatus schematically described in Ref. (8) and a quartz tube with the internal width 35 mm, height 25 mm, and length 400 mm. The gaseous flow conditions were 50 cm³/min of 1% B₂H₆ in N₂, 70 cm³/min of NH₃, and 2000 cm³/min of N₂, and the deposition temperature was in the range of 440°-720°C. The Si₃N₄ film was successively deposited on the BN film, under the gaseous flow conditions of 20 cm³/min of 5% SiH₄ in N₂, 70 cm³/min of NH₃, and 2000 cm³/min of N₂ at 720°C. Resultant thicknesses of the BN and the Si₃N₄ films were 50 and 30 nm, respectively. Heat-treatment for boron diffusion was carried out at the temperature range of 990°-1200°C in a nitrogen atmosphere. After the heat-

treatment, the Si₃N₄ and the BN films were removed by etching in HF and in H₃PO₄, respectively.

An analyzed spreading resistance profile is in good agreement with the incremental sheet resistivity profile except near the surface, and the difference between the junction depth obtained from spreading resistance profiles and that determined with drilling and staining technique is within the range of $\pm 5\%$ (9). In this investigation, we have mainly employed spreading resistance method in order to determine the boron profiles in terms of the carrier concentrations. In addition, incremental sheet resistance technique was used to correct the profiles near the surface. The four-point probe method and the spherical drilling and staining technique were used for measurements of the sheet resistance and the depth of diffused layers.

Results and Discussion

Profiles and diffusivity.—By using a concentration factor α introduced by Hu and Schmidt (1), the diffusion equation can be written as, in one-dimensional form

$$\frac{\partial \alpha}{\partial t} = \frac{\partial}{\partial x} \left\{ D(\alpha) \frac{\partial \alpha}{\partial x} \right\} \quad [1]$$

where $\alpha = C/2n_i$, C is the local concentration of boron, and n_i is the intrinsic carrier concentration at the diffusion temperature, given in Ref. (10) as

$$n_i^2 = 1.5 \times 10^{33} T^3 \exp \left(- \frac{1.21}{kT} \right) \quad [2]$$

$D(\alpha)$ in Eq. [1] is the concentration-dependent diffusivity expressed as

$$D(\alpha) = D_i \frac{1 + \beta (\alpha + \sqrt{\alpha^2 + 1})}{1 + \beta} (1 + \alpha/\sqrt{\alpha^2 + 1}) \quad [3]$$

where β is the phenomenological coefficient in the value of 19 for boron (11), and D_i is the intrinsic diffusivity at the diffusion temperature.

Figure 1 shows the boron profiles in silicon. The local concentration C is normalized by the surface concentration C_s , and the distance from surface is by $(4D_i t)^{1/2}$. The solid lines correspond to the numerical solutions of Eq. [1], with the normalized surface concentration by the intrinsic carrier concentration C_s/n_i , ranging from 0.4 to 12.0. The boron profile with the normalized surface concentration C_s/n_i of 0.4 fits on the theoretical curve for $C/C_s > 0.01$, but the profile at the diffusion front is retarded from the theory. The retardation of boron diffusion is observed only when the surface concentration C_s is lower than the intrinsic carrier concentration n_i (9). For $C_s/n_i > 1$, the boron profiles agree well with the theoretical curves, and the shape becomes steeper with increasing C_s/n_i .

The boron diffusivity obtained as the results of Boltzmann-Matano analysis on the profiles is described in Fig. 2 and 3 as a function of the local concentration. The surface concentration C_s is in the range of $4 \times 10^{19} - 2.4 \times 10^{20}$

*Electrochemical Society Active Member.

¹On leave from Institute of Microelectronics, Tsinghua University, Peking, China.

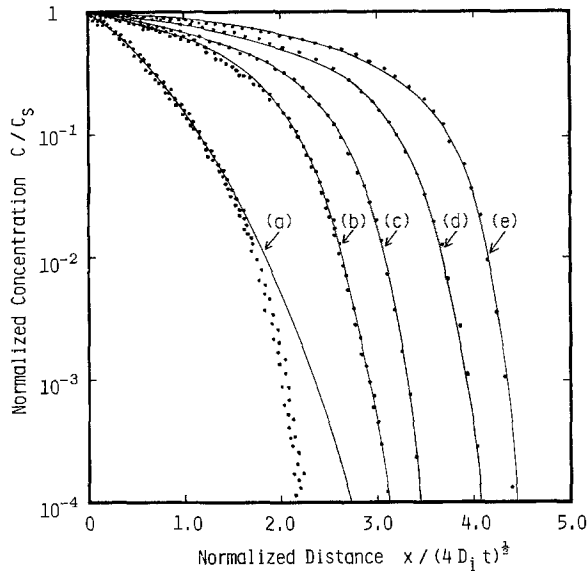


Fig. 1. Normalized boron profiles in silicon. The normalized surface concentration C_s/n_i is (a) 0.4, (b) 2.8, (c) 4.4, (d) 8.2, and (e) 12.0.

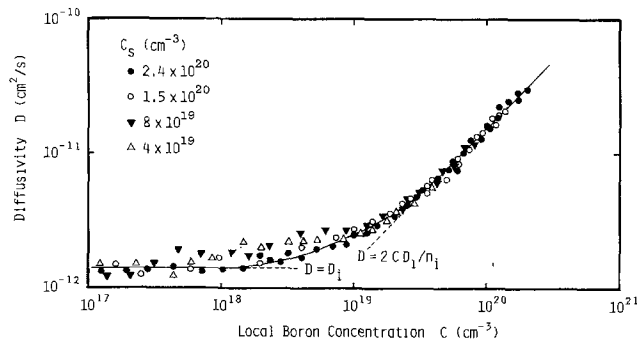


Fig. 2. Boron diffusivity at 1200°C as a function of the local concentration.

cm^{-3} . The relationship of the boron diffusivity and the local concentration agrees very closely with the theoretical relation of Eq. [3], shown as the solid curves in the figure, and is independent of the surface concentration in the given range. The diffusivity is coincident with the intrinsic value D_i at $C \ll n_i$ and is proportional to $2CD_i/n_i$ for $C > n_i$. The boron diffusivity at the temperature range of 990°-1200°C is shown as a function of the local boron concentration in Fig. 3. An excellent agreement of the experimental values on the theoretical curves is found at the given temperature range.

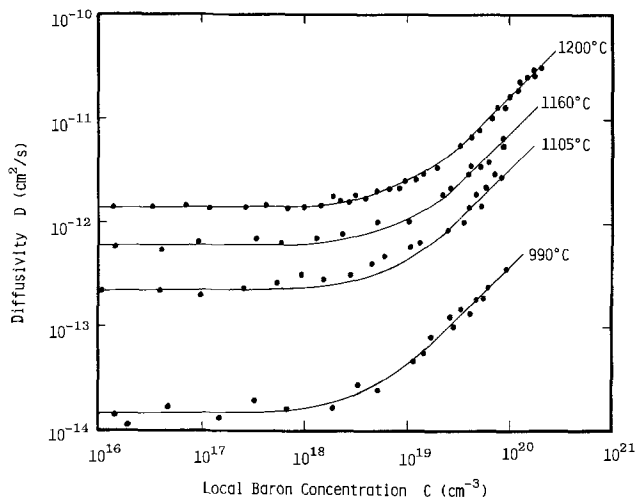


Fig. 3. Boron diffusivity in temperature range of 990°-1200°C as a function of the local concentration.

From the experimental results shown in Fig. 1-3, it can be concluded that the boron diffusion in silicon is clearly described with the diffusion theory proposed by Hu and Schmidt, except the diffusion front with the surface concentration C_s is lower than the intrinsic carrier concentration n_i .

Prefactors of x_i , Q , and R_s .—Approximate solutions of Eq. [1] have been driven in polynomial form by Guo (12) and Wang and Lo (13), and a fitting function of the experimental boron profiles has been proposed by Fair (3). Their works are commonly based upon the assumption that the boron profiles would be independent of the surface concentration and could be uniquely described as a function of the distance from surface normalized by the diffusion depth taken at $C(x_i) = 0.01C_s$. By use of the approximate profiles, they gave also simplified expressions of the diffusion depth x_i , the total diffused boron Q , and the sheet resistance R_s in the following form

$$x_i = K_j \sqrt{D_s t} \quad [4]$$

$$Q = K_q C_s x_i \quad [5]$$

and

$$R_s = K_r / (C_s x_i) \quad [6]$$

where the surface diffusivity $D_s = 2D_i C_s/n_i$ for $C_s > n_i$, and the hole mobility in diffused layer was approximated as $55 \text{ cm}^2/\text{Vs}$ in derivation of Eq. [6]. The prefactors K_j , K_q , and K_r are given as the constant in their reports, where K_j and K_q are dimensionless.

Figure 4 shows the numerical solutions of Eq. [1] in terms of the normalized profile. The diffusion depth was taken at $C(x_i) = 10^{-4} C_s$, because the range of background concentration is 10^{15} - 10^{16} cm^{-3} in the conventional CMOS and bipolar IC fabrication. The normalized profiles are clearly dependent on the normalized surface concentration C_s/n_i for the values less than 10, even though they are almost independent of C_s/n_i for larger than 10. In order to obtain x_i , Q , and R_s in the whole range of the surface concentration between the intrinsic carrier concentration and the solid-solubility, their prefactors must be described as a function of the normalized surface concentration.

The prefactors obtained as the results of numerical analysis of Eq. [1] are shown as the solid curves in Fig. 5. In the calculation of K_r , the hole mobility was fixed as a constant of $55 \text{ cm}^2/\text{Vs}$. For $C_s/n_i < 10$, the prefactors depend strongly on the normalized surface concentration

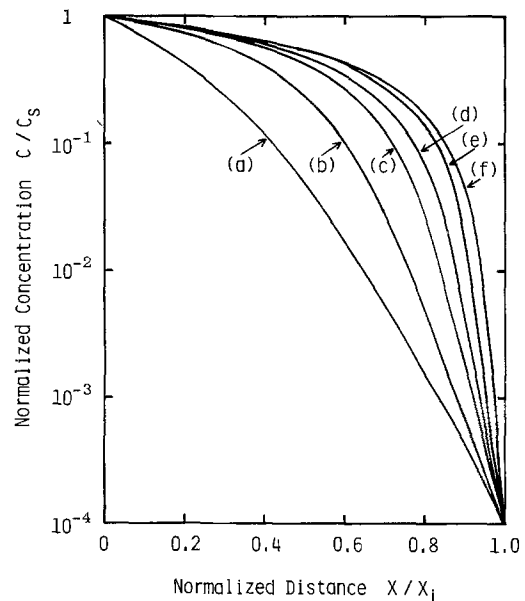


Fig. 4. Numerical solutions of diffusion equation with concentration-dependent diffusivity. The normalized surface concentration C_s/n_i is (a) 0, (b) 1.6, (c) 3.8, (d) 5.6, (e) 11.1, and (f) 16.6.

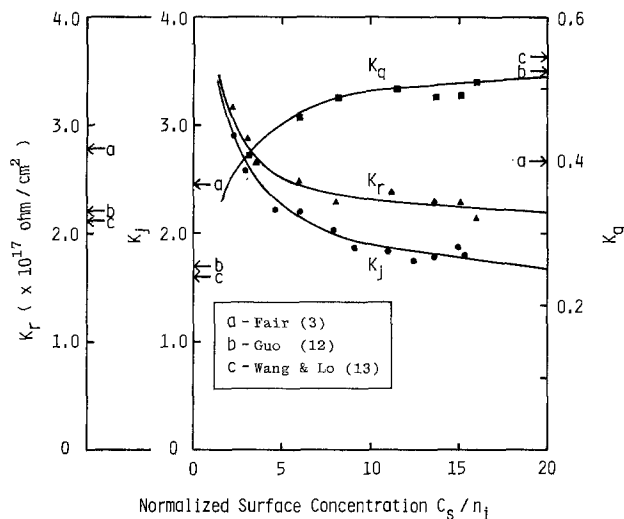


Fig. 5. Prefactors K_j , K_q , and K_r as a function of normalized surface concentration C_s/n_i .

C_s/n_i , where K_r and K_j decrease and K_q increases with the increase of C_s/n_i . For $C_s/n_i > 10$, all prefactors depend linearly and weakly on the normalized surface concentration. Experimentally obtained values of K_j , K_q , and K_r are also plotted in the same figure and fit well with the solid curves.

In Fig. 5, the values of prefactors reported in the previous papers are also indicated on the scales. The prefactors reported by Guo and also by Wang and Lo are comparable with those of the work only for $C_s/n_i \approx 20$. This means that their expression of the profile and the prefactors are in good approximation only for the solid-solubility boron diffusion. In order to determine the prefactors, Fair has used the experimental data where the surface concentration distributed in a wide range, and attempted to express the data with a universal relationship. Therefore, the prefactors by Fair might be considered as a mean value for the adopted data.

Conclusions

Boltzmann-Matano analysis was carried out on the boron profiles in silicon diffused from the boron-excess BN film, and the boron diffusivity was obtained as a function of the local concentration. For the boron diffusion with the surface concentration higher than the intrinsic carrier concentration at the diffusion temperature, the diffusivity can be described by the diffusion model which considers both effects of the charged vacancy-impurity interaction and the internal electric field. The prefactors in the simplified expressions of x_j , Q , and R_s were given by the numerical analysis of the diffusion equation including the concentration-dependent diffusivity and described as a function of the surface concentration normalized by the intrinsic carrier concentration.

Acknowledgment

The authors would like to thank Mr. M. Yabuki, who supported the numerical analysis.

Manuscript submitted April 23, 1984; revised manuscript received July 30, 1984.

Sophia University assisted in meeting the publication costs of this article.

REFERENCES

1. S. M. Hu and S. Schmidt, *J. Appl. Phys.*, **39**, 4272 (1968).
2. R. B. Fair and J. C. C. Tsai, *This Journal*, **122**, 1689 (1975).
3. R. B. Fair, *ibid.*, **122**, 800 (1975).
4. S. Matsumoto, Y. Ishikawa, Y. Shirai, S. Sekine, and T. Niimi, *Jpn. J. Appl. Phys.*, **19**, 217 (1980).
5. C. Kim, B.-K. Sohn, and K. Shono, *This Journal*, **131**, 1384 (1984).
6. K. Shono, T. Kim, and C. Kim, *ibid.*, **127**, 1546 (1980).
7. C. Matano, *Jpn. Phys.*, **8**, 109 (1933).
8. M. Hirayama and K. Shono, *This Journal*, **122**, 1671 (1975).
9. C. Kim, *ibid.*, **131**, 885 (1984).
10. R. G. Mazur and D. H. Dickey, *ibid.*, **113**, 255 (1966).
11. D. D. Warner and C. L. Wilson, *Bell Syst. Tech. J.*, **59**, 1 (1980).
12. S. F. Guo, *This Journal*, **127**, 2506 (1980).
13. W.-S. Wang and Y.-H. Lo, *IEEE Trans. Electron Devices*, **ed-30**, 1828 (1983).

Metal Impurities near the SiO₂-Si Interface

Akira Ohsawa,* Kouichirou Honda, and Nobuo Toyokura

Fujitsu Laboratories Limited, Nakahara-ku, Kawasaki, Japan

ABSTRACT

The behavior of metal impurities (Cu, Fe, Cr, and Ni) near the SiO₂-Si interface during dry O₂ and O₂/HCl oxidation was studied by means of defect etching and secondary ion mass spectroscopy methods using intentionally metal-contaminated silicon wafers. Redistribution of metal impurities resulting from a thermal oxidation is different for each metal. Copper diffused into the silicon, showing concentration peaks 0.3-1.2 μm from the interface, and tended to be rejected by the silicon dioxide. Iron accumulated at the interface, while chromium tended to accumulate in the oxide having a lower concentration in silicon. Gettering ability using O₂/HCl oxidations was excellent for copper, but poor for iron and chromium impurities. Copper and iron impurities precipitate in the silicon near the interface, but chromium and nickel impurities do not.

The dielectric-breakdown strength of silicon dioxide is directly related to the reliability of MOS LSI devices because of the thin oxide layers they use. Breakdown strength was reported to be reduced by metal-decorated stacking faults in the silicon substrate at the SiO₂-Si interface (1). The authors reported that stacking faults did not reduce the breakdown strength, but metal precipitates in the silicon substrate did (2, 3). Gettering of metals (Cu, Fe, and Au) in the silicon substrate by annealing in ambients with HCl was studied by Green *et al.* (4). Gettering of met-

als (Cu, Fe, Cr, Co, and Ni) through silicon dioxide was also performed by annealing in dry oxygen with 1% HCl using a 950°-1250°C ramp cycle (5). The redistribution of gold during the growth of an oxide was reported on contaminated silicon wafers (6). However, it is necessary to understand the behavior of metals near the SiO₂-Si interface during thermal oxidation to fabricate highly reliable devices. In this study, we intentionally contaminated silicon wafers by ion implantation of Cu, Fe, Cr, and Ni. The behavior of these metals near the SiO₂-Si interface during oxidation was studied on the wafers by defect etching and secondary-ion mass spectroscopy (SIMS) methods.

*Electrochemical Society Active Member.

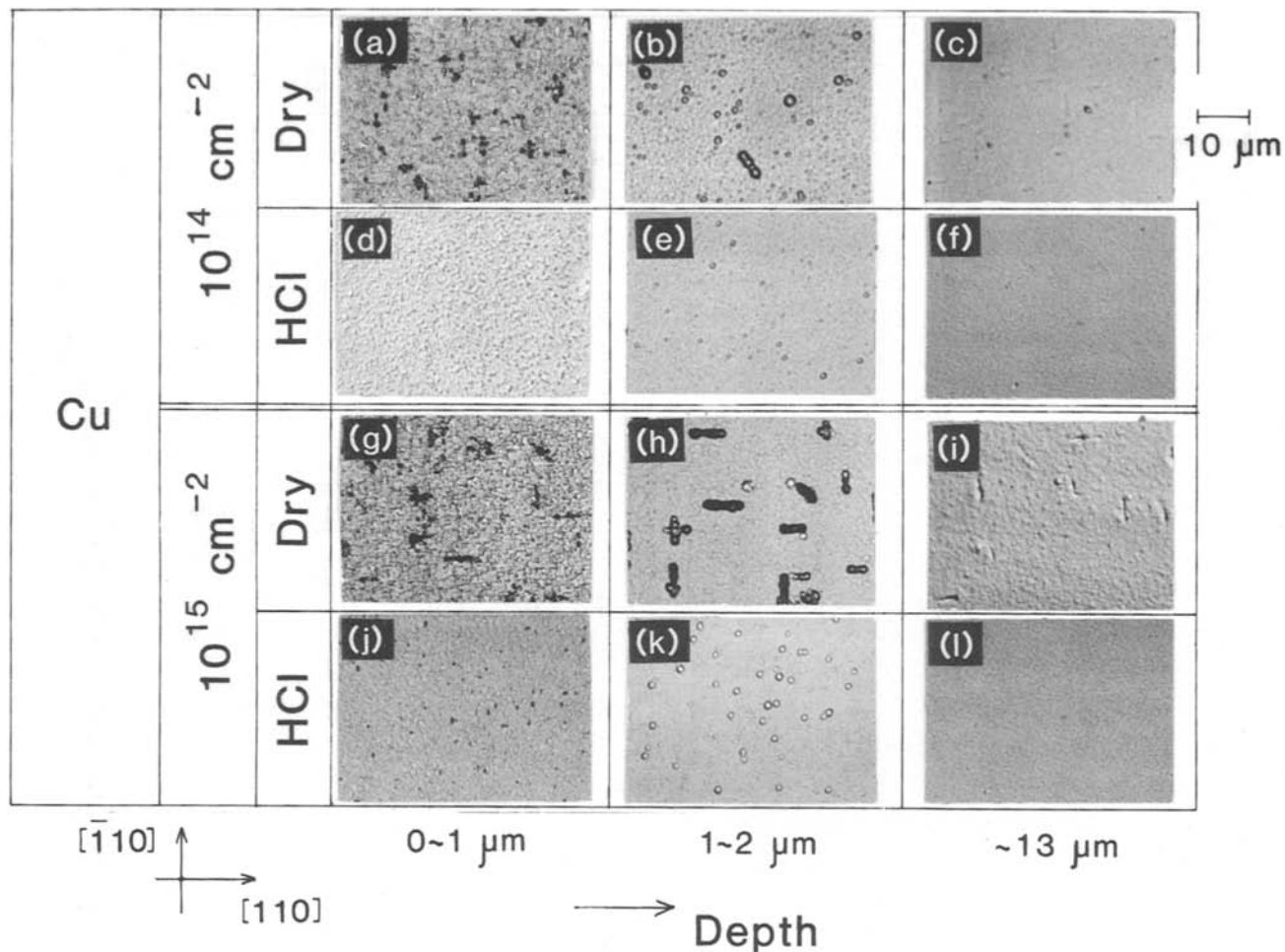


Fig. 1. Depth profiles of etch pits in silicon substrates from the SiO₂-Si interface. The samples are Cu⁺ doses of 10¹⁴ and 10¹⁵ cm⁻², and are oxidized in dry O₂ (Dry) and in O₂/HCl (HCl).

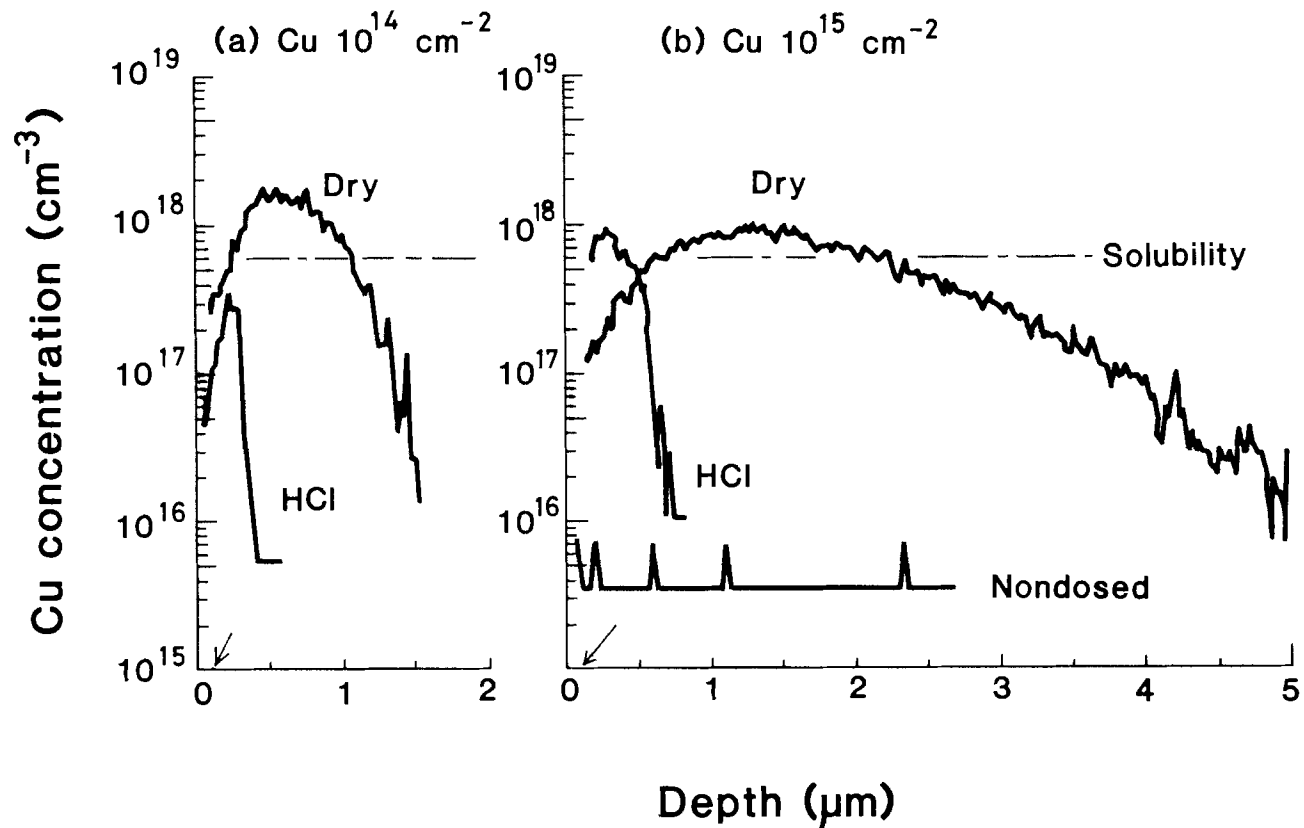


Fig. 2. SIMS depth profiles of Cu in the samples of (a) 10¹⁴ cm⁻² and (b) 10¹⁵ cm⁻² Cu⁺ implanted, then oxidized in dry O₂ (Dry) and in O₂/HCl (HCl). The profile of a control (Nondosed) sample is shown for reference.

Experimental

Boron-doped, 10 Ω-cm (100), Czochralski-grown silicon wafers, 500 μm thick, were used for this experiment. Cu⁺, Fe⁺, Cr⁺, and Ni⁺ ions were implanted in the wafers using 100 keV through 50 nm dry oxide films. The doses were 10¹³, 10¹⁴, and 10¹⁵ cm⁻² for Cu⁺ and Fe⁺ ions, and 10¹³ and 10¹⁴ cm⁻² for Cr⁺ and Ni⁺ ions. After removing the filter oxide films, gate oxides were grown in dry O₂ (24 nm thick) and in O₂/HCl (30 nm thick) at 1050°C, then annealed in N₂ at 1100°C for 20 min. Portions of the sample were Secco etched (7) for 1 min to observe any crystal defects in the silicon at the SiO₂-Si interface. Other portions were etched with HF-HNO₃ (1-20), then Secco etched to observe the depth profile of crystal defects.

The primary ion ¹⁶O₂⁺ was used for secondary ion mass spectroscopy (SIMS) measurements. Profiling was initiated from the oxide surface and continued across the interface into the silicon. The secondary ⁶³Cu⁺, ⁵⁶Fe⁺, ⁵²Cr⁺, or ⁵⁸Ni⁺ ions were monitored at the slow Si sputter rate of 0.115-0.225 nm/s. ¹⁸O⁻ and ¹¹B⁺ were monitored at the same time. The depth resolution was about 20 nm. The metal data were reduced to concentration by comparison with doped standards (metal ion-implanted silicon). The redistribution of metal impurities near the SiO₂-Si interface was determined. The secondary ⁶³Cu⁺ ions were also monitored at a fast Si sputter rate of 2.84 nm/s into the silicon to a depth of 5 μm. The redistribution of Cu impurities in the silicon was determined.

Results and Discussion

Cu impurities.—Figure 1 shows the depth profiles of etch pits in silicon substrate. The samples are for Cu⁺ doses of 10¹⁴ and 10¹⁵ cm⁻², which were oxidized in dry O₂ (Dry) and in O₂/HCl (HCl). No defects were observed in the samples of 10¹³ cm⁻² dose, and the samples are not shown in the figure. No pits or only traces of pits were

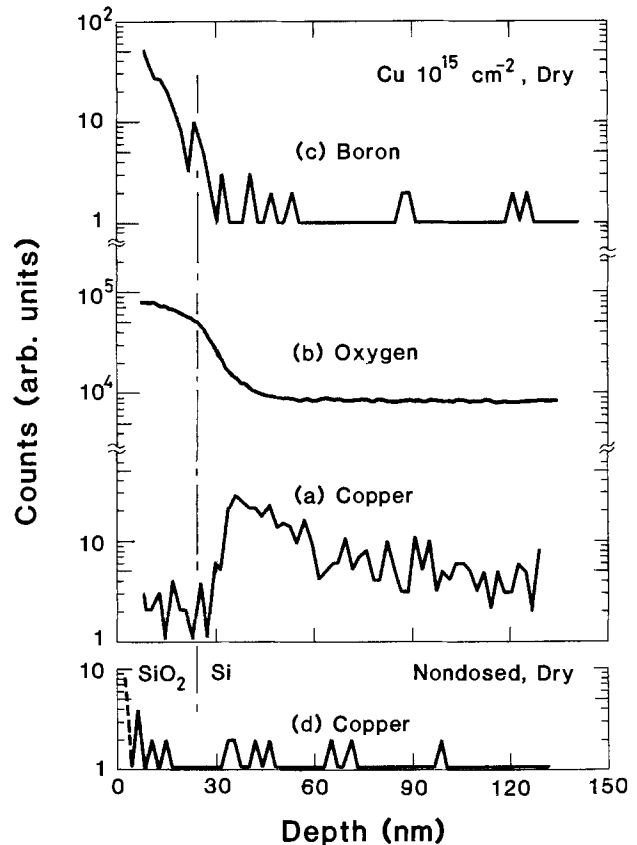


Fig. 3. SIMS depth profiles for (a) copper, (b) oxygen, and (c) boron at the SiO₂-Si interface for samples of 10¹⁵ cm⁻² Cu doses and Dry oxidation. (d) is a copper profile for a control (Nondosed, Dry) sample.

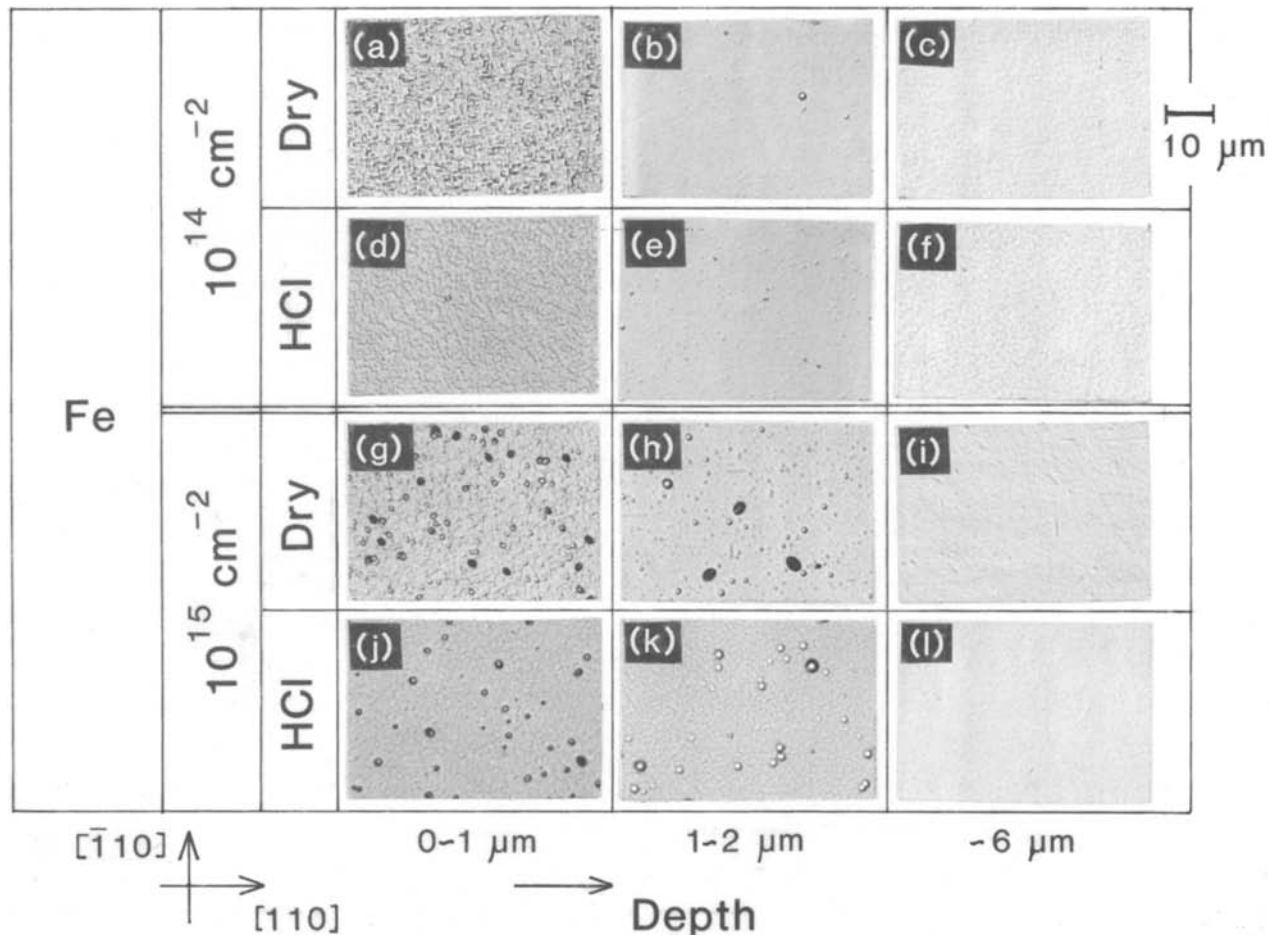


Fig. 4. Depth profiles of etch pits in silicon from the SiO₂/Si interface. The samples are Fe⁺ doses of 10¹⁴ and 10¹⁵ cm⁻², and are oxidized in dry O₂ (Dry) and in O₂/HCl (HCl).

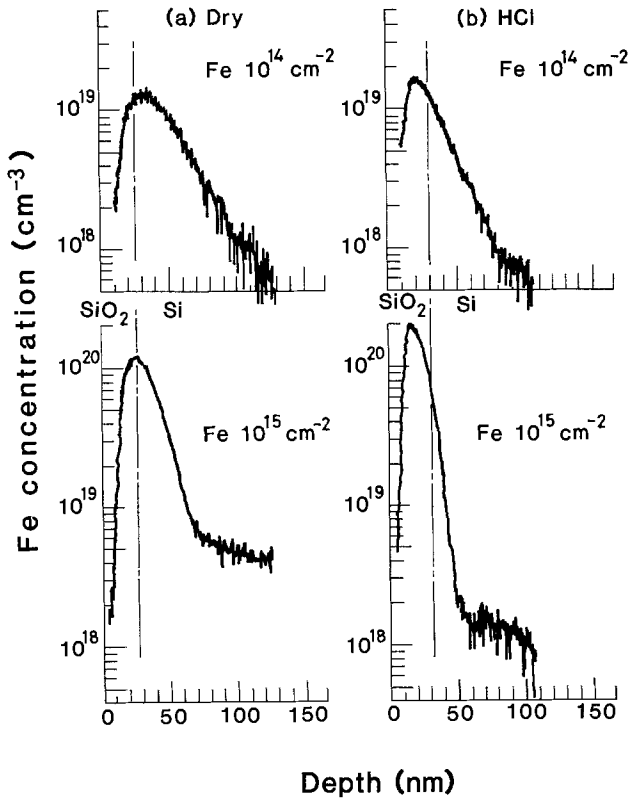


Fig. 5. SIMS depth profiles of Fe in the samples oxidized in dry O₂ (a) Dry and in O₂/HCl (b)HCl for Fe⁺ doses of 10¹⁴ and 10¹⁵ cm⁻².

observed at the depth of 13 μm, but black-line and S pits (8, 9) on a rough background were observed near the SiO₂-Si interface. The rough background was due to stacking faults generated by implantation damage and oxidation (2). The black-line pit is a Cu precipitate colony and is along <110> directions (2). The line pits are 3-8 μm long and 8 × 10⁵ cm⁻² in density for samples (g) and (h), and are shorter than the 2 μm 3 × 10⁶ cm⁻² pits in samples (a) and (j). S pit densities are 10⁶ cm⁻² in sample (b), 8 × 10⁵ cm⁻² for sample (e), 2 × 10⁵ cm⁻² for sample (h), and 2 × 10⁶ cm⁻² for sample (k). The difference caused by the oxidation methods is clear: there are larger Cu precipitates in the dry samples, but smaller ones or S pits in the HCl samples. This suggests getting of Cu due to HCl oxidation.

Figures 2(a) and 2(b) shows SIMS depth profiles of Cu for samples (a) 10¹⁴ cm⁻² and (b) 10¹⁵ cm⁻² Cu⁺-implanted and followed by dry O₂ (Dry) and O₂/HCl (HCl) oxidations. The profile of control sample is shown for reference in Fig. 2(b). The level indicated by a chain line is the solid solubility at 1100°C (10), which is the last and highest annealing temperature. The depth profile of Cu in the implanted state shows a sharp peak just left of 0.1 μm, indicated by an arrow in the figure. The sharp distribution is redistributed by oxidation at 1050°C, and subsequent annealing at 1100°C to yield the depth profiles seen in Fig. 2(a) and 2(b). The profiles of Fig. 2 are very different: (a) between dry and HCl oxidation, and (b) between 10¹⁴ and 10¹⁵ cm⁻² dose. The HCl oxidation redistributes Cu shallower in silicon than the dry oxidation. HCl oxidation lowers the Cu concentration, as shown in Fig. 2(a). The higher dose distributes Cu wider and deeper in silicon. The first result clearly shows a getting of Cu from the

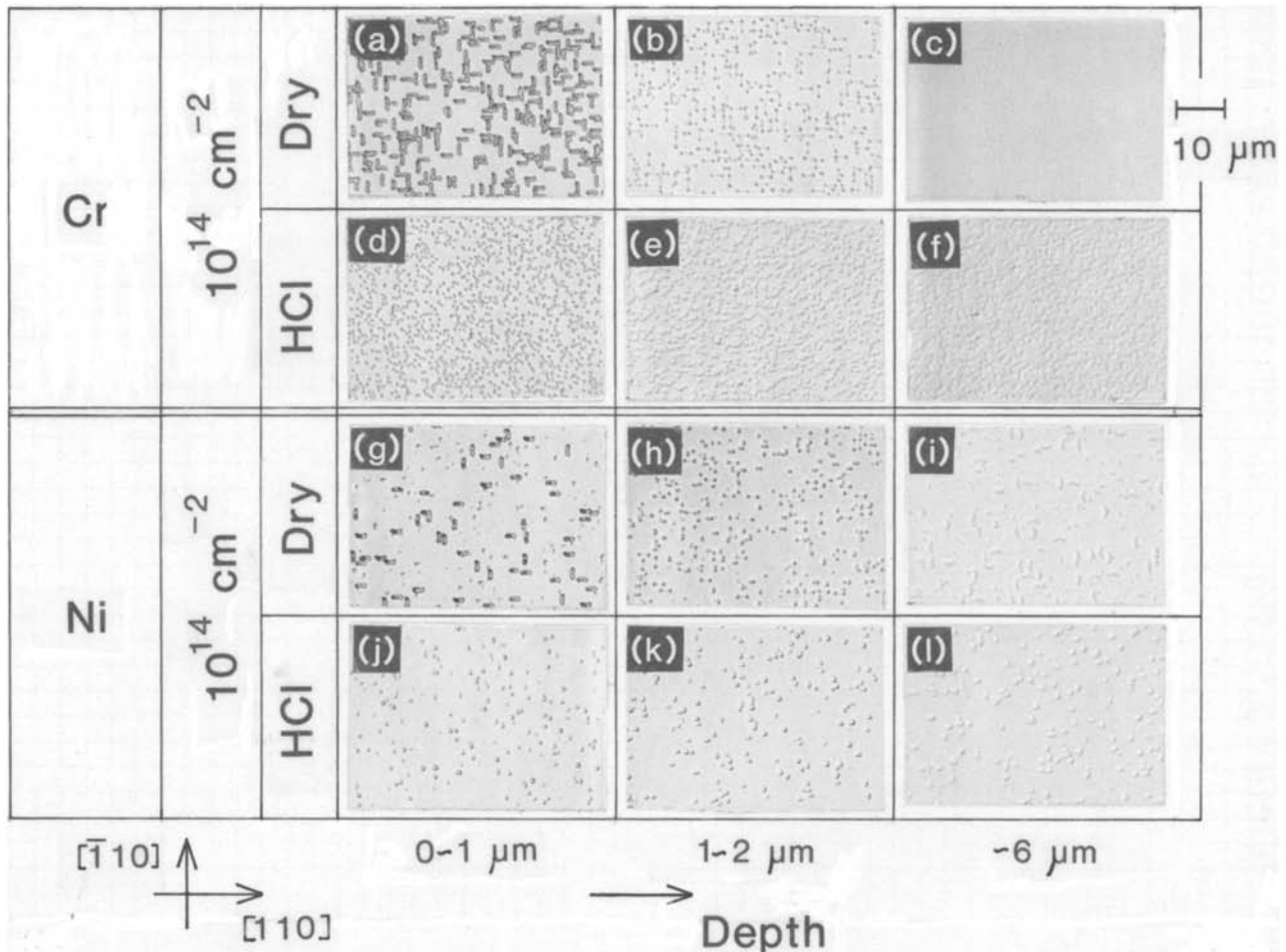


Fig. 6. Depth profiles of etch pits in silicon from the SiO₂-Si interface. The samples are Cr⁺ or Ni⁺ dose of 10¹⁴ cm⁻², and oxidized in dry O₂ (Dry), and in O₂/HCl (HCl).

surface due to HCl oxidation. The second result shows re-distribution of Cu is not caused by simple diffusion during the oxidation and subsequent annealing. We must take into account the effects of copper impurities: (i) outdiffusion through the oxide layer, (ii) segregation at the SiO₂-Si interface resulting from thermal oxidation, and (iii) interaction with the crystal defects.

Figure 3 shows SIMS depth profiles of (a) copper, (b) oxygen, and (c) boron near the SiO₂-Si interface. The sample had 10¹⁵ cm⁻² Cu⁺ implanted followed by dry O₂ oxidation. The profile for copper in the control sample is also shown for reference in (d). The position SiO₂-Si interface was estimated relative to an oxide thickness of 24 nm, and is indicated as a chain line in the figure. A segregation of copper impurities at the interface is shown in Fig. 3(a), and the one for boron is shown in Fig. 3(c). Copper is rejected from the oxide and accumulates near the interface about 30 nm in the silicon. Using segregation coefficient *m*, the ratio of equilibrium concentration in the silicon to that of silicon dioxide (11), *m* for copper is larger than 1. Boron migrates into the oxide as shown in Fig. 3(c). This tendency is consistent with other reports (12, 13).

Fe impurities.—The depth profiles of etch pits in silicon substrate are shown in Fig. 4. The samples are for Fe⁺ doses of 10¹⁴ and 10¹⁵ cm⁻², which were oxidized in dry O₂ and in O₂/HCl. No defects were observed for samples of 10¹³ cm⁻² dose. As shown in the figure, no pits were observed at the depth of 6 μm. Black pits on rough backgrounds were observed near the SiO₂-Si interface in Fig. 4(g), 4(h), and 4(j) for 10¹⁵ cm⁻² dose. In Fig. 4(h) of 10¹⁵

cm⁻² and the Dry sample, faint line pits along <110> directions were also observed. These black and line pits were confirmed to be Fe precipitates by transmission electron microscopy and energy dispersive x-ray spectroscopy (14). S pits are seen in Fig. 4(g), 4(h), 4(j), and 4(k) of 10¹⁵ cm⁻² implanted samples, but less than those in Fig. 4(a), 4(b), 4(d), and 4(e) of 10¹⁴ cm⁻² implanted samples. The defect generation is different between 10¹⁴ and 10¹⁵ cm⁻² dose, but the difference due to oxidation methods Dry and HCl is small. This suggests that iron impurities are not getterd by HCl oxidation.

Figures 5(a) and 5(b) show SIMS depth profiles for Fe impurities near the SiO₂-Si interface. Figure 5(a) is the sample oxidized in dry O₂ (Dry), and Fig. 5(b) that oxidized in O₂/HCl (HCl) for Fe⁺ doses of 10¹⁴ and 10¹⁵ cm⁻². The interfaces were estimated from the oxide thickness of 24 nm (Dry) and 30 nm (HCl), and are indicated by the chain line in the figure. The characteristics of Fe profiles are as follows: (i) the peak concentration increases from 1-2 × 10¹⁹ to 1-2 × 10²⁰ cm⁻³ proportionally to doses of 10¹⁴-10¹⁵ cm⁻²; (ii) the iron impurities do not diffuse into silicon, but accumulate up at the interface. The peak position is at the interface for Dry [Fig. 5(a)] samples, and at 10-15 nm deep into SiO₂ from the interface for HCl samples [Fig. 5(b)]; (iii) oxidation in O₂/HCl apparently does not lower peak concentration, rather, it sharpens the profile. Iron impurities could have a harmful effect on device reliability, because they tend to accumulate in the active region of the devices (15).

Cr and Ni impurities.—The depth profiles of etch-pits in silicon substrate are shown in Fig. 6 for samples of Cr⁺

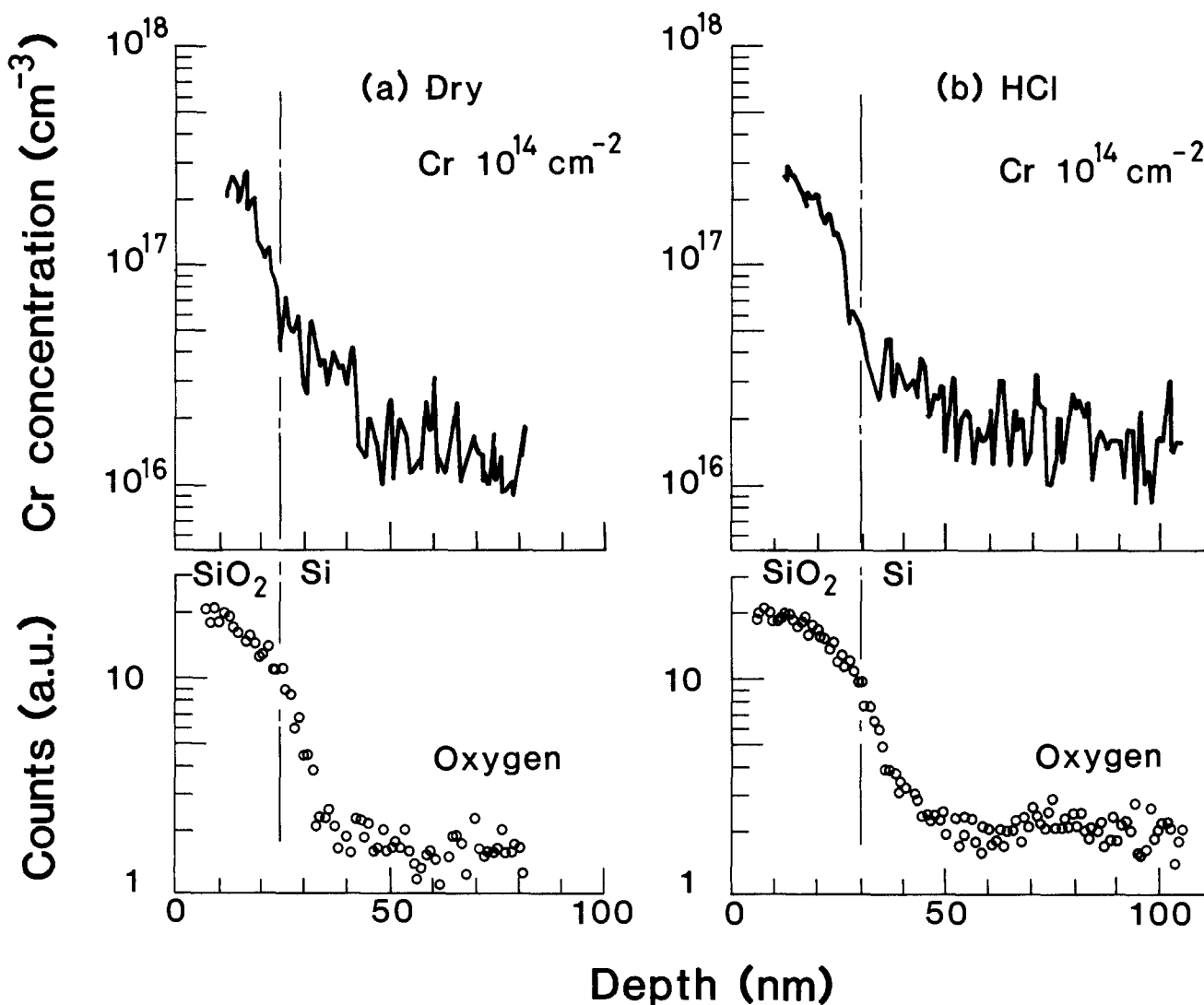


Fig. 7. SIMS depth profiles of chromium and oxygen for the samples oxidized in dry O₂ (a) Dry and in O₂/HCl (b) HCl for Cr⁺ dose of 10¹⁴ cm⁻².

and Ni⁺ doses of 10¹⁴ cm⁻² oxidized in dry O₂ (Dry) or O₂/HCl (HCl). No defects were observed for the 10¹³ cm⁻² dose samples. The depth profiles for Cr⁺- and Ni⁺-implanted samples resemble each other, but are very different from those for the Cu⁺- and Fe⁺-implanted samples (Fig. 1 and 4). Metal precipitates and S pits were not observed in the Cr⁺- and Ni⁺-implanted samples in Fig. 6. The stacking faults were observed only near the SiO₂-Si interface. The stacking faults are about 2 μm long and 2 × 10⁷ cm⁻² in density in Fig. 6(a) Cr Dry, smaller than 0.5 μm and 6 × 10⁷ cm⁻² in Fig. 6(d) Cr HCl, 1-2 μm long and 9 × 10⁶ cm⁻² in Fig. 6(g) Ni Dry, and smaller than 1 μm and 10⁷ cm⁻² in Fig. 6(j) Ni HCl. The rough backgrounds observed in Fig. 1 and 4 were not observed in Fig. 6 because of the low stacking fault density. The stacking fault is smaller and higher in the HCl, than in the Dry. Because of metal (Cr or Ni) decoration, the stacking faults are thick at the interface in Fig. 6(a) and 6(g).

Figures 7(a) and 7(b) show SIMS depth profiles of Cr impurities and oxygen near the SiO₂-Si interface. Figure 7(a) shows the samples oxidized in dry O₂ (Dry), and Fig. 7(b) those oxidized in O₂/HCl (HCl) for Cr⁺ doses of 10¹⁴ cm⁻². The interface was estimated from the oxide thickness, and is indicated as a chain line. The characteristics of Cr profiles are as follows: (i) chromium segregates out of the silicon and accumulates in the silicon dioxide; this suggests that the segregation coefficient resulting from thermal oxidation is larger than 1; (ii) the difference between Dry [Fig. 7(a)] and HCl [Fig. 7(b)] oxidation is very small. This suggests that the HCl oxidation cannot getter Cr impurities.

Summary

The behavior of metal impurities (Cu, Fe, Cr, and Ni) near the SiO₂-Si interface during dry O₂ and O₂/HCl oxidations was studied by means of etching and SIMS methods using intentionally metal-contaminated wafers. Copper and iron impurities precipitate in the silicon near the interface, but chromium and nickel impurities do not. Redistribution of the metal impurities resulting from the thermal oxidation is different for each metal. Copper diffuses deep into the silicon and shows concentration peaks

at a depth of 0.3-1.2 μm from the interface, and tends to be rejected by the silicon dioxide. Iron accumulates up at the interface. Chromium tends to accumulate in the oxide and has a low concentration in silicon. Gettering ability due to O₂/HCl oxidation is very different for each metal. The ability is excellent for copper, but poor for iron and chromium impurities.

Manuscript submitted April 9, 1984; revised manuscript received Aug. 13, 1984.

Fujitsu Laboratories Limited assisted in meeting the publication costs of this article.

REFERENCES

1. P. S. D. Lin, R. B. Marcus, and T. T. Sheng, *This Journal*, **130**, 1878 (1983).
2. K. Honda, A. Ohsawa, and N. Toyokura, *Appl. Phys. Lett.*, To be published.
3. C. W. Pearce and V. C. Kannan, in "Defects in Silicon," W. M. Bullis and L. C. Kimerling, Editors, p. 396, The Electrochemical Society Softbound Proceedings Series, Pennington, NJ (1984).
4. J. M. Green, C. M. Osburn, and T. O. Sedgwick, *J. Electron. Mater.*, **3**, 579 (1974).
5. L. E. Katz, P. F. Schmidt, and C. W. Pearce, *This Journal*, **128**, 620 (1981).
6. T. A. O'Shaughnessy, H. D. Barber, and E. L. Heasell, *ibid.*, **123**, 1560 (1976).
7. F. Secco D'Aragonna, *ibid.*, **119**, 948 (1972).
8. D. Pomerantz, *J. Appl. Phys.*, **38**, 5020 (1967).
9. W. T. Stacy, D. F. Allison, and T.-C. Wu, in "Semiconductor Silicon 1981," H. R. Huff and R. J. Kriegler, Editors, p. 344, The Electrochemical Society Softbound Proceedings Series, Pennington, NJ (1981).
10. H. F. Wolf, "Silicon Semiconductor Data," p. 155, Pergamon Press, Oxford, England (1969).
11. A. S. Grove, "Physics and Technology of Semiconductor Devices," p. 69, John Wiley and Sons, New York (1967).
12. L. E. Katz in "VLSI Technology," S. M. Sze, Editor, p. 157, McGraw-Hill, New York (1983).
13. J. W. Colby and L. E. Katz, *This Journal*, **123**, 409 (1976).
14. K. Honda, A. Ohsawa, and N. Toyokura, To be submitted.
15. P. J. Ward, *This Journal*, **129**, 2573 (1982).

X-Ray Investigation of Boron- and Germanium-Doped Silicon Epitaxial Layers

H.-J. Herzog

AEG-Telefunken, Forschungsinstitut, D-7900 Ulm, Germany

L. Csepregi and H. Seidel

Fraunhofer-Institut für Festkörpertechnologie, D-8000 München 60, Germany

ABSTRACT

The lattice strain in highly boron-doped, highly germanium-doped, and simultaneously boron-and-germanium-doped epitaxial layers was investigated by means of x-ray techniques. The lattice-contraction coefficient was determined for both impurities, and was found to be 5 × 10⁻²⁴ cm³/atom for boron and -6.2 × 10⁻²⁵ cm³/atom for germanium doping. A simple linear superposition of calculated or experimentally determined lattice-contraction coefficients obtained for layers doped with boron vs. those doped with germanium does not yield satisfactory results in estimating the germanium concentration necessary for strain compensation in highly boron-doped layers. Strain-compensated dislocation-free epitaxial layers were fabricated with a boron concentration of 1 × 10²⁰ atom/cm³, using a germanium concentration of 1 × 10²¹ atom/cm³.

Highly boron-doped layers are becoming increasingly important in the fabrication of three-dimensional structures in silicon, such as micromechanical devices, sensors, or masks for x-ray as well as ion-beam lithography (1-3). Since silicon layers with boron concentrations

higher than 1 × 10²⁰ atom/cm³ have extremely low etch rates with certain anisotropic selective etchants, these layers are very useful for accurate control of the etching process, taking advantage of their etch stopping properties (4). The most widely used etchants providing these

features are solutions of KOH and water or ethylenediamine, pyrocatechol, and water.

The incorporation of boron at such concentration levels causes a significant lattice mismatch between the doped layer and the undoped substrate, resulting from the smaller covalent radius of boron compared to that of silicon. This lattice mismatch induces high strain and, in thicker layers, misfit dislocations as well (5). In some applications, such as for lithography masks, a certain tensile strain is often desired to avoid out-of-plane distortions due to thermal effects (3); however, strain is disadvantageous in structures such as pressure sensors, owing to the significantly reduced sensitivity (6). In both cases, films with well-defined strain levels are desirable, while crystal defects such as dislocations are generally undesirable.

In order to eliminate strain as well as dislocation generation in highly boron-doped silicon films, codoping with a strain counterbalancing element of a larger covalent radius has been proposed (7, 8). Germanium was found to be a suitable element, owing to its advantageous properties, such as high solubility and electrical inactivity. However, quantitative experimental data concerning the degree of strain compensation when using germanium as a codopant have not been available up to now.

In this work, the concentration dependence of the strain in silicon layers doped with boron, germanium, or both simultaneously, has been investigated. The goal was to fabricate highly boron-doped, strain-compensated, dislocation-free layers with the help of these data.

Lattice Mismatch and Lattice-Contraction Coefficient

The incorporation of dopants in a silicon epitaxial layer contracts or expands the lattice of the layer relative to that of the undoped silicon substrate. This lattice mismatch is expressed as

$$\eta = \frac{\Delta a}{a_{\text{Si}}}$$

where a_{Si} is the lattice constant of silicon and Δa is the change in lattice constant induced by the dopant. It has been determined that thin films, or layers with small mismatch, are strained in a purely elastic manner to match the substrate lattice. With increasing lattice registry, the film strain ϵ_f increases until a "critical mismatch" is reached, the value of which depends on the film thickness. Beyond this value, the film strain ϵ_f decreases, since the generation of misfit dislocations becomes the dominant process in the accommodation of the lattice mismatch (9, 10). This means that in the subcritical range, the film strain ϵ_f is equal to the mismatch value η , whereas beyond the critical value, the film strain is lower than the mismatch value.

In the range of purely elastic accommodation, the film strain ϵ_f depends linearly on the dopant concentration C (11)

$$\epsilon_f = \beta C \quad [1]$$

where β is the lattice-contraction coefficient. Obviously, when misfit dislocations participate in mismatch accommodation, Eq. [1] is no longer valid. Two different equations for calculating β exist, based on a linear model and a volumetric model, (12, 13)

$$\beta_1 = \left[1 - \frac{r_{\text{dop}}}{r_{\text{Si}}} \right] N^{-1} \quad [2]$$

$$\beta_v = \frac{1}{3} \left[1 - \left(\frac{r_{\text{dop}}}{r_{\text{Si}}} \right)^3 \right] N^{-1} \quad [3]$$

where r_{dop} and r_{Si} are the covalent radii of the dopant and silicon atoms, respectively, and N is the density of lattice sites in silicon.

Substitution of Pauling's covalent radii (14) ($r_{\text{Si}} = 1.17\text{\AA}$, $r_{\text{B}} = 0.88\text{\AA}$, and $r_{\text{Ge}} = 1.22\text{\AA}$) yields the following results for β_1 and β_v

	Boron	Germanium
β_1 [cm^3/atom]	4.96×10^{-24}	-8.55×10^{-25}
β_v [cm^3/atom]	3.83×10^{-24}	-8.92×10^{-25}

These values can be inserted into Eq. [1] in order to calculate the germanium-to-boron concentration ratio necessary to match the lattices of the epitaxial layer and the undoped substrate. One obtains 5.8:1 or 4.4:1 for this ratio, depending on whether Eq. [2] or Eq. [3] is used.

Experimental Techniques

Silicon wafers with (100) orientation, a diameter of 3 in, and 1-10 Ω cm resistivity were used for the experiments. Their nominal thickness was 380 μm ; however, the precise thickness of each wafer was measured prior to deposition. The epitaxial layers were deposited in a barrel-type vertical reactor (AMC-7000, made by Applied Materials), employing the $\text{SiH}_2\text{Cl}_2\text{-B}_2\text{H}_6\text{-GeH}_4\text{-H}_2$ chemical system. The growth temperature and the growth rate were 1080°C and 0.9 $\mu\text{m}/\text{min}$, respectively. The final thickness of the epitaxial layers was $5 \pm 0.2 \mu\text{m}$.

The boron concentration of the deposited layers was measured by determining the wavelength of the plasma-resonance minimum in the infrared spectrum (15). The composition of the germanium-doped layers was determined by the methods of backscattering and channeling with helium ions (16).

Measurement Techniques

X-ray topography and curvature measurement.—A strained film on a substrate causes bending of the wafer. The strain-induced curvature of a silicon wafer can be measured with high accuracy using x-ray diffraction (17). We employed a Lang transmission camera with Mo-K α radiation, as described in Ref. (10).

The relationship between the measured curvature k , the lattice film strain ϵ_f , the thickness of the epitaxial layer t_f , and that of the substrate t_s , is given by the equation

$$k = 6\epsilon_f \frac{t_f}{t_s^2} \quad [4]$$

assuming thin layer ($t_f \ll t_s$) and equal elastic constants of film and substrate (18, 19). Using Eq. [4], the film strain ϵ_f can be obtained from the curvature k as a function of the dopant concentration.

As mentioned above, Eq. [1] is only valid when misfit dislocations do not contribute to the accommodation of lattice mismatch. X-ray transmission topography measurements were carried out (with the same Lang camera as for the curvature measurements) on all wafers to determine the presence of misfit dislocations.

Rocking curves.—Small differences between the lattice constants of the epitaxial layers and the substrate can be measured with high accuracy by means of x-ray rocking-curve analysis, where two reflections at different Bragg angles are obtained, one from the substrate, the other from the layer. In order to verify and supplement the results of the curvature measurements, rocking curves were taken from samples where plastic relaxation through misfit dislocations had not occurred. As a consequence, the mismatch value η is expected to be equal to the elastic film strain. For this analysis, a double-crystal diffractometer in the (+, -) mode with Cu-K α radiation was employed. As the monochromator, a (100)-oriented silicon crystal in the (422)^R setting was used (20), and rocking curves from the specimen crystals were taken using different (hkl) reflecting planes. However, in order to determine the lattice constant of the layer in the relaxed state, the tetragonal distortion of the epitaxial lattice has to be taken into account (21-23). Because of this tetragonal distortion, two Bragg-angle splittings $\Delta\theta_1$ and $\Delta\theta_2$ can be recorded when x-rays are diffracted on one set of inclined (hkl) planes under two specimen positions relative to the x-ray path. In order to determine the lattice mismatch as a function of angle difference in the rocking curves, the calculation procedure given in detail by Halliwell (23) was used.

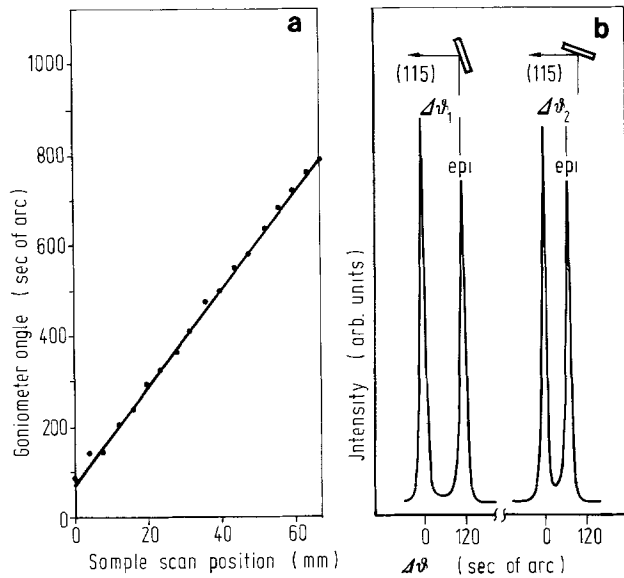


Fig. 1. Results of x-ray measurements on an epitaxial silicon layer with a boron concentration of 5×10^{19} atom/cm³. Diagram a (left) yields a curvature radius of 19.1m. Rocking curves for the two reflections on the same (115) crystal plane for the same sample are shown in diagram b (right).

Results and Discussion

Boron-doped layers.—The investigated epitaxial layers had a boron concentration between 2×10^{19} and 1.5×10^{20} atom/cm³. As a typical result, a curvature measurement (Fig. 1a) and a set of rocking curves (Fig. 1b) are shown for a wafer covered with a 5×10^{19} atom/cm³ boron-doped epitaxial layer. As expected, the wafer is under tensile stress, and exhibits spherical curvature. The calculated elastic film strains ϵ_f obtained by both methods are in excellent agreement, and indicate a value of 2.5×10^{-4} . The film strain ϵ_f as a function of the boron concentration is shown in Fig. 2. Up to the "critical strain" value, the film strain increases linearly with increasing boron concentration. For epitaxial layers with a thickness of $5 \mu\text{m}$, the critical strain amounts to 5.5×10^{-4} , corresponding to a boron concentration of 1.1×10^{20} atom/cm³. Above this critical value, a rapid increase in the density of misfit dislocations occurs, and ϵ_f drops considerably. This is confirmed by x-ray topographs, as shown in Fig. 3. Below the critical strain, no, or only a few, misfit dislocations are found (Fig. 3a and 3b); however, a dense net of

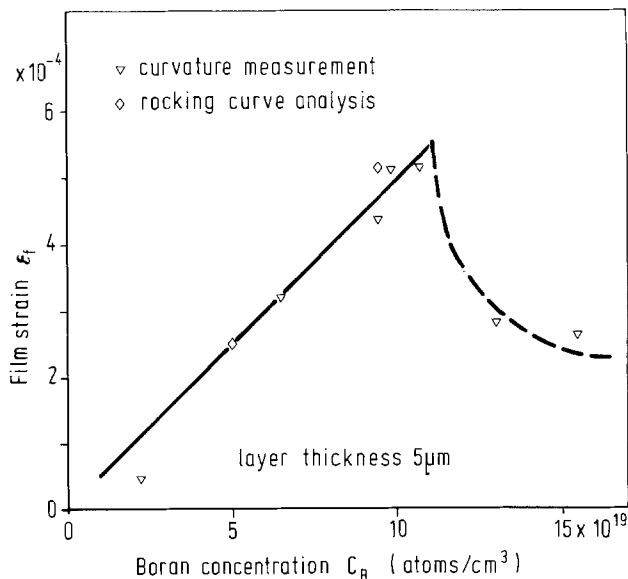


Fig. 2. Film strain ϵ_f as a function of the boron concentration C_B , obtained by curvature measurements and rocking-curve analysis.

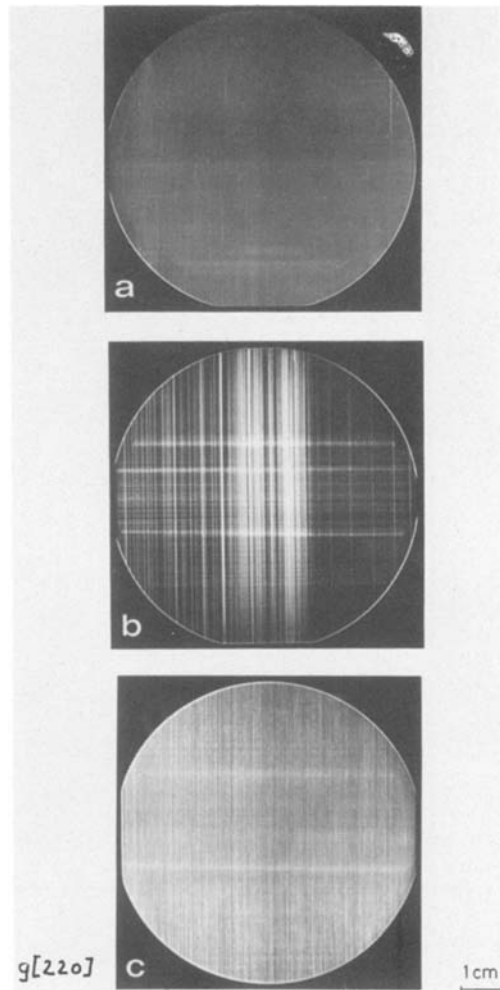


Fig. 3. X-ray transmission topographs of epitaxial layers with boron concentrations of 5×10^{19} atom/cm³ (a), 8×10^{19} atom/cm³ (b), and 1.5×10^{20} atom/cm³ (c).

misfit dislocations is observed in the region above the critical strain (Fig. 3c). The blurred horizontal lines are artifacts of the measurement technique, and do not represent actual crystal defects. The slope of the straight line in Fig. 2, where the strain is only elastically accommodated, corresponds to a lattice-contraction coefficient of $\beta_B = 5 \times 10^{-24}$ cm³/atom. This value agrees well with the results reported by McQuhae and Brown (5.2×10^{-24} cm³/atom) (12) and by Horn (5.6×10^{-24} cm³/atom) (24), but is higher than that reported by Pearson and Bardeen (2.5×10^{-24} cm³/atom) (25) or by Cohen (2.3×10^{-24} cm³/atom) (11).

Germanium-doped layers.—The x-ray analysis of the germanium-doped layers was carried out the same as that for boron. The germanium concentration was determined in all samples by means of the Rutherford backscattering and channeling techniques. Lattice-location experiments such as that shown in Fig. 4 indicated that the germanium atoms are situated on substitutional sites, even at concentrations around 1×10^{21} atom/cm³. In Fig. 5, the result of a curvature measurement and a set of rocking curves are shown for a wafer with a germanium concentration of 4×10^{20} atom/cm³. The dependence of the film strain ϵ_f on the germanium content for a layer thickness of $5 \mu\text{m}$ is shown in Fig. 6. As expected, the films are under compression. In this case too, there is an initial region of linearly increasing film strain with increasing germanium concentration, followed by predominant relaxation of lattice mismatch through misfit dislocations. This behavior is also confirmed by the x-ray topographs, which appear very similar to those obtained for boron-doped wafers. For the $5 \mu\text{m}$ thick layers, the critical strain amounts to -5×10^{-4} ,

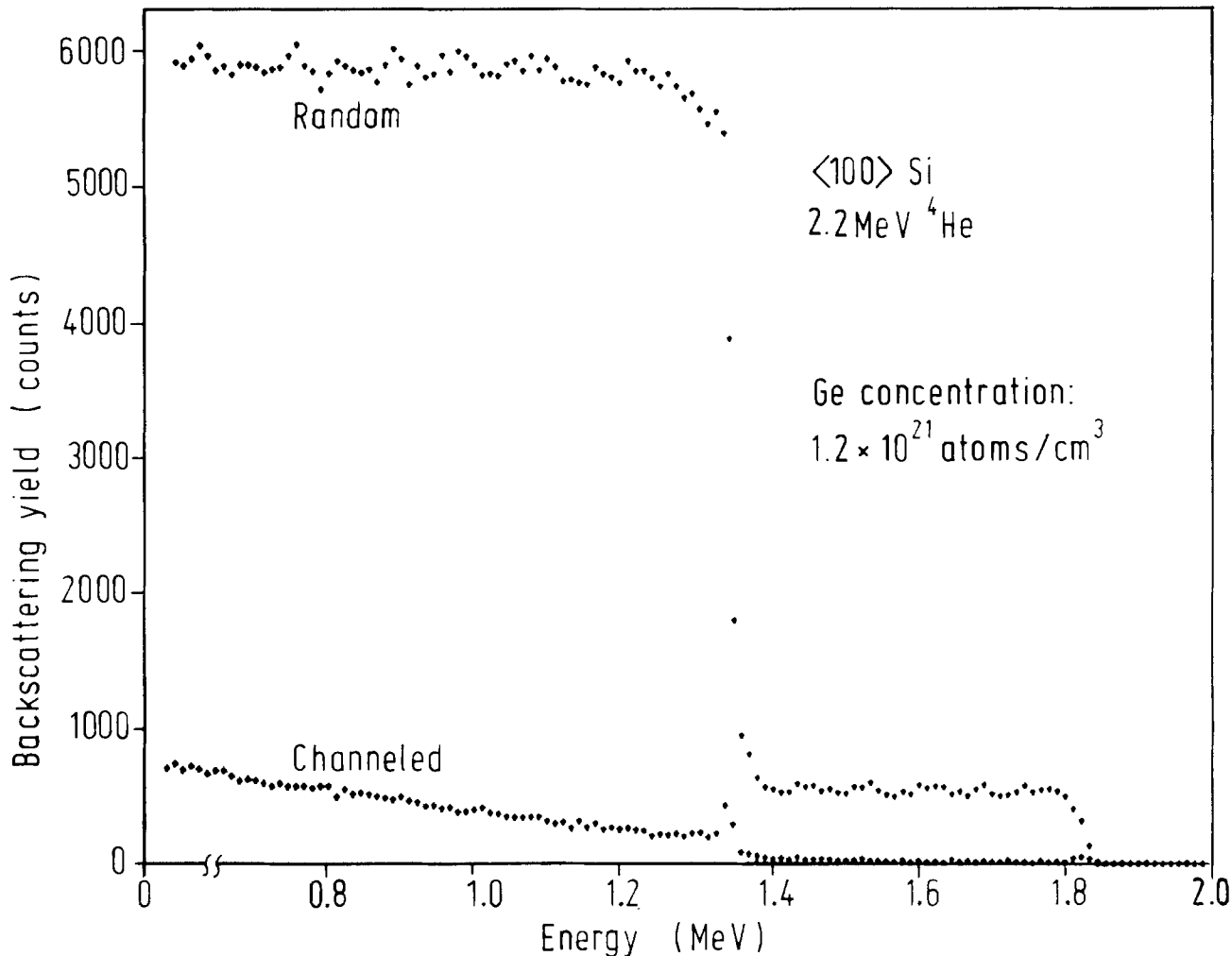


Fig. 4. Backscattering spectra for 2.2 MeV ⁴He ions incident on a highly germanium-doped sample in the random and channeling directions, with a detector angle of 135°.

corresponding to a germanium concentration of 8×10^{20} atom/cm³. The slope of the straight portion of the curve in Fig. 6 yields a contraction coefficient of $\beta_{Ge} = -6.2 \times 10^{-25}$ cm³/atom. This experimentally determined value is considerably smaller than the lattice-contraction coefficient

calculated by means of Eq. [2] and [3]. This behavior may be partly explainable in terms of a deviation from Vegard's law in germanium-silicon solid solutions, as reported by Dismukes *et al.* (26).

Boron/germanium codoped layers.—For the investigation of the strain-compensation effect, the boron-

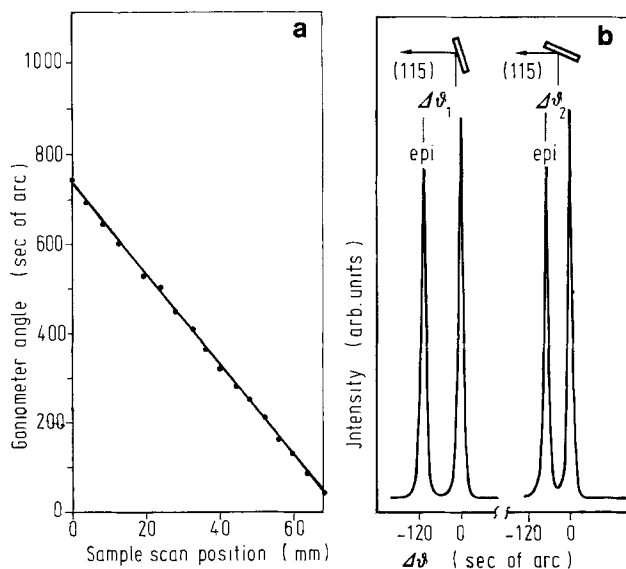


Fig. 5. Results of x-ray measurements on an epitaxial silicon layer with a germanium concentration of 4×10^{20} atom/cm³. Diagram a (left) yields a curvature radius of -20.2 m. Rocking curves for the two reflections on the same (115) crystal plane for the same sample are shown in diagram b (right).

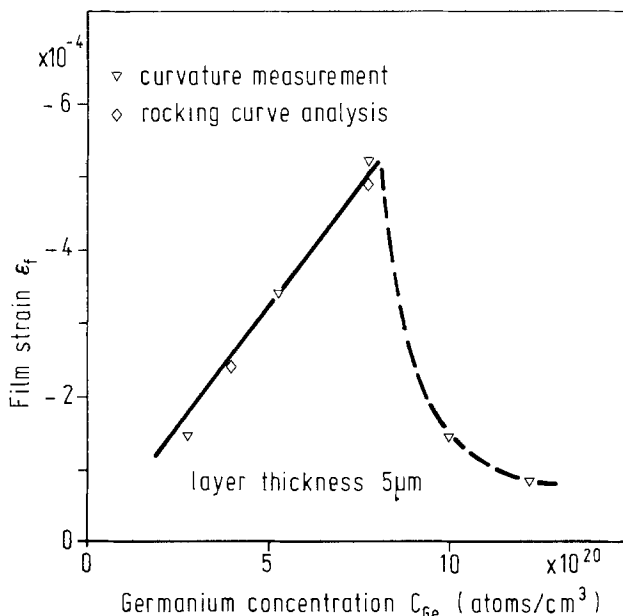


Fig. 6. Film strain ϵ_f as a function of the germanium concentration C_{Ge} , obtained by curvature measurements and rock curving analysis.

concentration level in the $5\ \mu\text{m}$ thick layers was held constant at $C_B = 1 \times 10^{20}\ \text{atom/cm}^3$. The film strain ϵ_f was measured for several germanium concentrations ranging from 2 to $10 \times 10^{20}\ \text{atom/cm}^3$. The solid line in Fig. 7 shows the film strain, obtained by curvature measurements and rocking-curve analysis, as a function of the germanium concentration. As expected, the film strain decreases with increasing germanium codoping, indicating that strain compensation takes place. From the experimental curve in Fig. 7, the germanium concentration for a strain-free layer containing $1 \times 10^{20}\ \text{atom/cm}^3$ boron is found to be $\sim 1.1 \times 10^{21}\ \text{atom/cm}^3$. For the above boron concentration, Eq. [2] and [3] predict complete strain compensation at germanium doping levels of $4.4 \times 10^{20}\ \text{atom/cm}^3$ or $5.8 \times 10^{20}\ \text{atom/cm}^3$, respectively, as indicated by the dashed lines a and b in Fig. 7. A linear superposition of the experimental lattice-contraction coefficients β_B and β_{Ge} obtained for layers doped with only one element predicts a required germanium concentration of $8 \times 10^{20}\ \text{atom/cm}^3$ for a strain-free layer (line c in Fig. 7), which is slightly above the value used by Black *et al.* (6). This deviation from the experimentally obtained value for codoped layers ($1.1 \times 10^{20}\ \text{atom/cm}^3$) indicates that changes in lattice constant induced by simultaneous doping with the two elements are not independent of each other, and that a linear superposition is not allowable.

X-ray topographs taken from wafers with different levels of germanium codoping are shown in Fig. 8. Some misfit dislocations are still observable in Fig. 8a and 8b, with a decrease in density correlated with increasing germanium concentration. The epitaxial layers in Fig. 8a and 8b have germanium concentrations of $2 \times 10^{20}\ \text{atom/cm}^3$ and $6 \times 10^{20}\ \text{atom/cm}^3$, respectively. Above a germanium codoping level of $7 \times 10^{20}\ \text{atom/cm}^3$, the wafers are completely free of misfit dislocations. Figure 8c shows a topograph of a wafer close to the point of complete strain compensation, with a germanium concentration of $9.8 \times 10^{20}\ \text{atom/cm}^3$.

Conclusions

Measurements of doping induced lattice strain and misfit dislocations by means of x-ray diffraction, for highly boron-doped and highly germanium-doped epitaxial silicon layers, yielded the following results.

The lattice-contraction coefficient β was found to be $5 \times 10^{-24}\ \text{cm}^3/\text{atom}$ for boron and $-6.2 \times 10^{-25}\ \text{cm}^3/\text{atom}$ for germanium single-doped layers. The experimental result for boron doping shows a very good agreement with previously reported values (12, 23), as well as with the linear calculation model. The germanium coefficient, however,

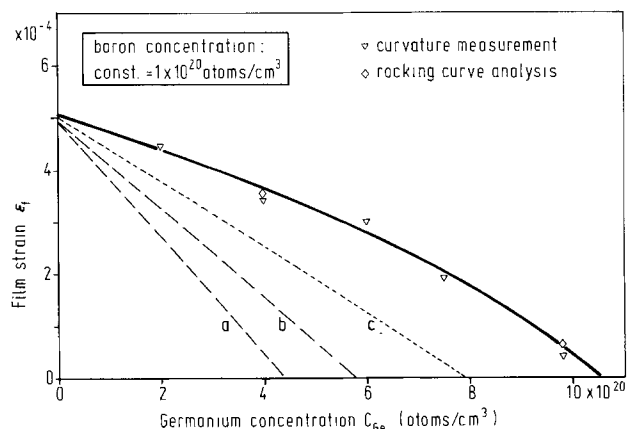


Fig. 7. Film strain ϵ_f of boron-and-germanium-codoped epitaxial layers as a function of the germanium concentration. The boron concentration is kept constant at $1 \times 10^{20}\ \text{atom/cm}^3$. The solid line shows the experimental results. The broken lines indicate the strain compensation, calculated by a linear superposition of experimental (line c) and theoretical (lines a and b) lattice-contraction coefficients for single-doped layers.

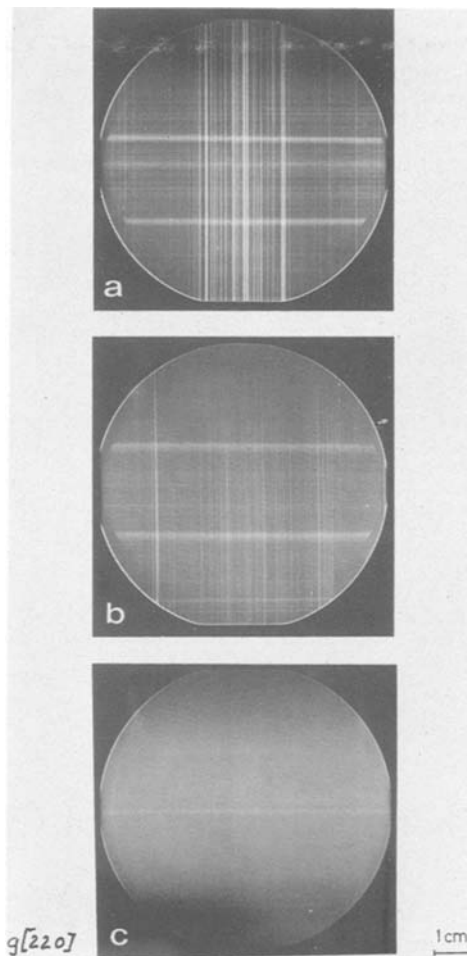


Fig. 8. X-ray topographs of epitaxial layers doped simultaneously with boron and germanium. The boron concentration is kept constant at a level of $1 \times 10^{20}\ \text{atom/cm}^3$. The germanium concentration varies from $2 \times 10^{20}\ \text{atom/cm}^3$ (a), over $6 \times 10^{20}\ \text{atom/cm}^3$ (b), to $1 \times 10^{21}\ \text{atom/cm}^3$ (c).

deviates from the values calculated by the linear and volumetric models.

The value of critical mismatch in epitaxial layers $5\ \mu\text{m}$ thick is 5.5×10^{-4} in the case of boron and 5×10^{-4} in the case of germanium doping, corresponding to concentration levels of 1.1×10^{20} and $8 \times 10^{20}\ \text{atom/cm}^3$, respectively. When the dopant concentration is increased to a level above the critical mismatch, the film strain decreases and the actual lattice mismatch is accommodated mainly by misfit dislocations. Below this critical mismatch, there are no, or only a few, misfit dislocations.

The boron-induced film strain can be reduced by codoping with germanium. Surprisingly enough, however, it was found that strain compensation in codoped layers is not obtained at the concentration predicted by linear superposition of the results for boron and germanium single-doped layers.

Using the experimental data given in this paper, it is not only possible to compensate the strain in highly boron-doped epitaxial layers, but also to adjust it to a certain desired level.

Two problems remain to be clarified. First, the experimental lattice-contraction coefficient of germanium in silicon is considerably lower than the calculated value. Second, the strain predicted by linear superposition of the experimentally determined lattice-contraction coefficients for single-doped epitaxial layers does not agree with the results for codoped layers.

Acknowledgments

The authors would like to thank Dr. E. Kasper for many helpful discussions, as well as for his valuable comments

on the manuscript. The assistance of E. Fencel, R. Niessl, and J. Weidhaas is gratefully acknowledged. This work was supported by the Ministry of Research and Development of the Federal Republic of Germany, under Contract no. NT 2604.

Manuscript submitted Feb. 16, 1984; revised manuscript received Aug. 7, 1984.

AEG-Telefunken assisted in meeting the publication costs of this article.

REFERENCES

1. K. Petersen, *Proc. IEEE*, **70**, 420 (1982).
2. E. Spiller and R. Feder, in "X-Ray Optics — Applications to Solids," H. J. Queisser, Editor, p. 35, Springer Verlag, Berlin (1972).
3. I. Bartelt, C. McKenna, and C. Slayman, Abstract 277, p. 454, The Electrochemical Society Extended Abstracts, Vol. 82-1, Montreal, Que., Canada, May 9-14, 1982.
4. H. Seidel and L. Csepregi, Abstract 123, p. 194, The Electrochemical Society Extended Abstracts, Vol. 82-1, Montreal, Que., Canada, May 9-14, 1982.
5. H. J. Queisser, *J. Appl. Phys.*, **32**, 1776 (1961).
6. I. F. Black, D. E. Cullen, and T. W. Grudowski, *ibid.*, **32**, 192 (1961).
7. T. H. Yeh and M. L. Joshi, *This Journal*, **116**, 73 (1969).
8. Y. T. Lee, N. Miamoto, and I. Nishizawa, *ibid.*, **122**, 530 (1975).
9. J. H. van der Merwe, in "Single-Crystal Films," M. H. Francombe and H. Sato, Editors, p. 139, Pergamon Press, Oxford, England (1964).
10. E. Kasper and H.-J. Herzog, *Thin Solid Films*, **44**, 357 (1977).
11. B. G. Cohen, *Solid State Electron.*, **10**, 33 (1967).
12. K. G. McQuhae and A. S. Brown, *ibid.*, **15**, 259 (1972).
13. J. E. Lawrence, *This Journal*, **113**, 819 (1966).
14. L. Pauling, "The Nature of the Chemical Bond," p. 256, 3rd ed., Cornell University Press, Ithaca (1960).
15. ASTM Standards F 398-77, 798 (1979).
16. W. K. Chu, J. W. Mayer, and M. A. Nicolet, "Backscattering Spectrometry," Academic Press, New York (1978).
17. G. A. Rozgonyi and D. C. Miller, *Thin Solid Films*, **31**, 185 (1976).
18. A. Brenner and S. Senderoff, *J. Res. Natl. Bur. Stand.*, **42**, 105 (1949).
19. F. K. Reinhart and R. A. Logan, *J. Appl. Phys.*, **44**, 3171 (1973).
20. M. Renninger, *Z. Naturforsch. A*, **16**, 1110 (1961).
21. K. Ishida, J. Matsui, T. Kamejima, and J. Sakuma, *Phys. Status Solidi A*, **31**, 255 (1975).
22. W. J. Bartels and W. Nijman, *J. Cryst. Growth*, **44**, 518 (1978).
23. M. A. G. Halliwell, in "Microscopy of Semiconducting Materials 1981," A. G. Cullis and D. C. Joy, Editors, p. 271, Institute of Physics Conference Series 60, Institute of Physics, Bristol, England (1981).
24. F. H. Horn, *Phys. Rev.*, **97**, 1521 (1955).
25. G. L. Pearson and J. Bardeen, *ibid.*, **75**, 865 (1949).
26. J. P. Dismukes, L. Ekstrom, and R. J. Paff, *J. Phys. Chem.*, **68**, 3021 (1964).

Photoluminescence of Chemical Bath Deposited CdS Films

M. Gracia-Jiménez, G. Martínez,¹ J. L. Martínez, E. Gómez, and A. Zehe²

Departamento de Física, Instituto de Ciencias de la Universidad de Puebla, Apdo. Postal J-48, Puebla, Pue., Mexico

ABSTRACT

Photoluminescence spectra of chemical bath deposited CdS films have been taken. It is shown that the emission line reaching from 0.8 to 2.4 eV depends on the stoichiometry of the films. The stoichiometry is controlled either by changing the pH of the working solution during the deposition process or by carrying out a thermal annealing in air on the films. The most stoichiometric CdS films present a green edge emission line which persists even at room temperature. This line is identified as a radiative transition between a Cd complex and an S vacancy.

Current interest in direct energy conversion devices has led to renewed research on different fabrication techniques in order to elaborate a simple, low cost, low energy consumption technology for fabricating such devices. Recently, there has been a great deal of interest in studying the optical properties of spray-pyrolyzed CdS (1). However, the chemical bath deposition technique, which has many of the advantages claimed for the better known spray deposition technique (2), should offer the prospect of better control over the preparation process because of the slower rate of formation of the film (3). It is the aim of this work to report that this material has a photoluminescence spectrum which depends strongly on the fabrication parameters in the chemical bath and that the most stoichiometric films display photoluminescence spectra reported in single crystal CdS material (4).

Experimental

The CdS films were fabricated by the chemical bath deposition technique (CBD) suggested by Kaur *et al.* (3). Briefly, it consisted of preparing thin CdS films by decomposing thiourea [(NH₂)₂CS] in an alkaline solution of salt of the corresponding cation. This process, which involves a controllable chemical reaction at a low rate by adjusting the pH and the temperature of the working so-

lution, allows maintaining the stoichiometry constant for any ratio of anions and cations. The working solution consisted of preparing three aqueous solutions, thiourea (1M), Cd sulfide (1M), and ammonium hydroxide (0.7-15.0M), in deionized water (DI). We prepared several thin film CdS samples on Corning glass substrates; each was prepared with different molar concentrations of ammonium hydroxide. In Table I, we show the amounts of NH₄OH employed in the solutions and the resulting pH measured for each prepared sample. Half a slice of each sample was subjected to thermal annealing in air at 350°C for 20-60s. Spectra of the photoluminescence of the "as-prepared" and annealed samples were taken by mounting them on a cold finger of a Displex system and were held at temperatures ranging from 10 to 300 K. These samples were photoexcited by the 488 nm line of a Spectra Physics cw Ar ion laser. Luminescence spectra were analyzed by a Zeiss SPZ monochromator and recorded by a lock-in technique in a HP X-Y plotter.

Results

The stability plots of ion concentration *vs.* pH of the depositing reactants in the working solution are obtained by the method reported by Martínez (5). These results are shown in Fig. 1. From this, we can distinguish two regions: one in which the amount of S⁻² ions exceeds the amount of Cd⁺² ions in the prepared films (region I) and in which the corresponding pH values are <11.5; and another in which films are prepared with pH values of

¹Present address: Department of Electrical Engineering, University of Arizona, Tucson, Arizona 85721.

²Present address: Sektion Physik, Technische Universität Dresden, 8027 Dresden, Germany.

Table I. pH of working solution as function of the molarity (M) of $(\text{NH}_4)\text{OH}$ in H_2O

Sample no.	Molarity of $(\text{NH}_4)\text{OH}$	pH measured
1	0.5	9.4
2	1.0	10.1
3	1.5	10.4
4	3.0	11.3
5	4.5	11.5
6	6.0	11.5
7	7.5	11.7
8	9.0	11.5
9	10.5	11.9
10	12.0	11.9
11	13.5	11.9
12	15.0	11.9

>11.5 (region II). The excess of Cd^{2+} ions is easily seen from Fig. 1. In films whose pH is approximately the calculated value of pH 11.5, one could expect to get the most stoichiometric films. The measured values of pH for the samples prepared with the method mentioned above are shown in Table I.

The luminescence spectra of three different samples held at 10 K are shown in Fig. 2. The samples prepared with characteristics shown in region I of Fig. 1 (pH < 11.5, sample 1) show a characteristic spectrum consisting of a broad line (640 meV, half-width) centered around 1.68 eV (curve A, Fig. 2). A similar broad spectrum is recorded for those CdS films displaying the characteristics of region 2 (pH > 11.5, sample 11). This Fig. 1 spectrum is centered around 1.70 eV and is a little broader than that in Fig. 2 (720 meV, curve C). However, films whose preparation method was at pH = 11.5 show distinct spectra, compared to those mentioned above (sample 4). These spectra consist of a similar featureless broad line ("red"), centered also at 1.68 eV, with a half-width of 620 meV and an addi-

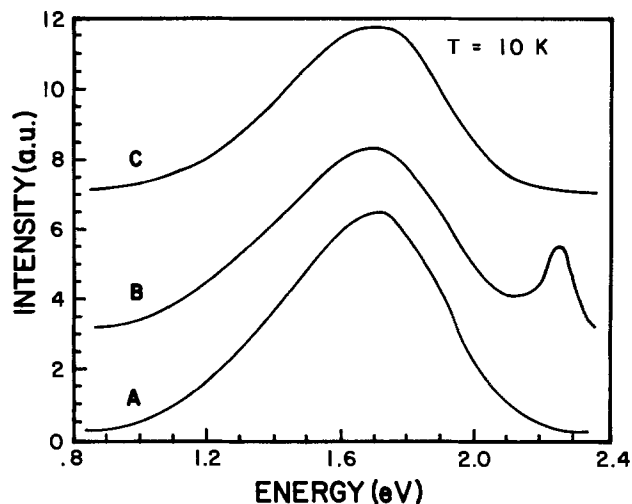


Fig. 2. Luminescence spectra for samples 1 (A), 4 (B), and 11 (C) under Ar laser excitation (488 nm), held at 10 K.

tional "green" edge line centered at 2.255 eV with a narrow half-width of 180 meV (curve B, Fig. 2).

In Fig. 3a and 3b, the temperature dependence and the characteristic green luminescence line intensity are shown. The green line intensity is reduced by a factor of 10, but it does not vanish at 300 K. The peak position, on the other hand, shows a clear maximum at about 80 K (2.265 eV at 80 K, compared to 2.255 eV at 10 K and 150 K). In Fig. 4, we show $\log(\text{intensity})$ vs. $1/T$ dependence of the green radiative transition. Two somewhat clear regions of different inclination are apparent, the one in the high tem-

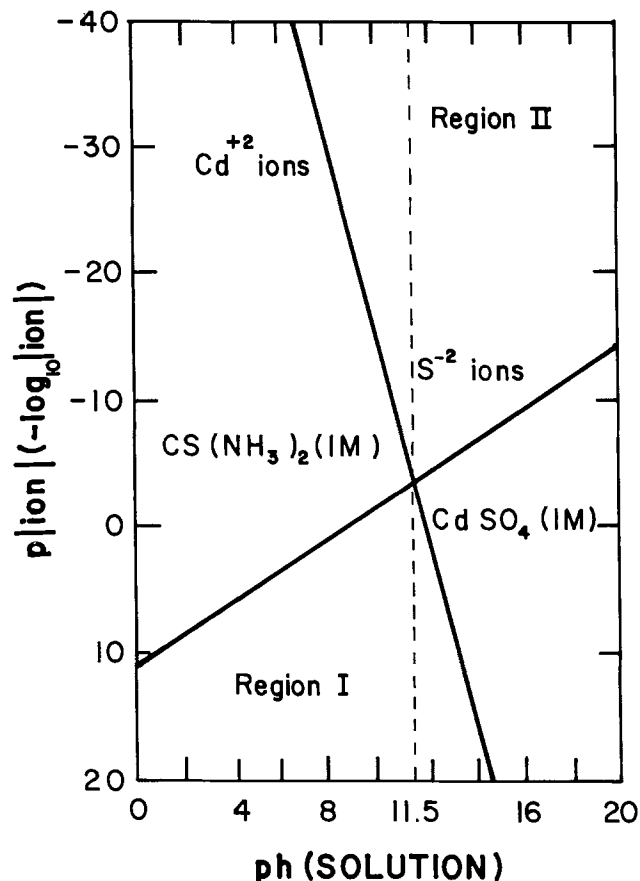


Fig. 1. Stability plots of sulfur and cadmium ion concentration vs. pH of the working solution.

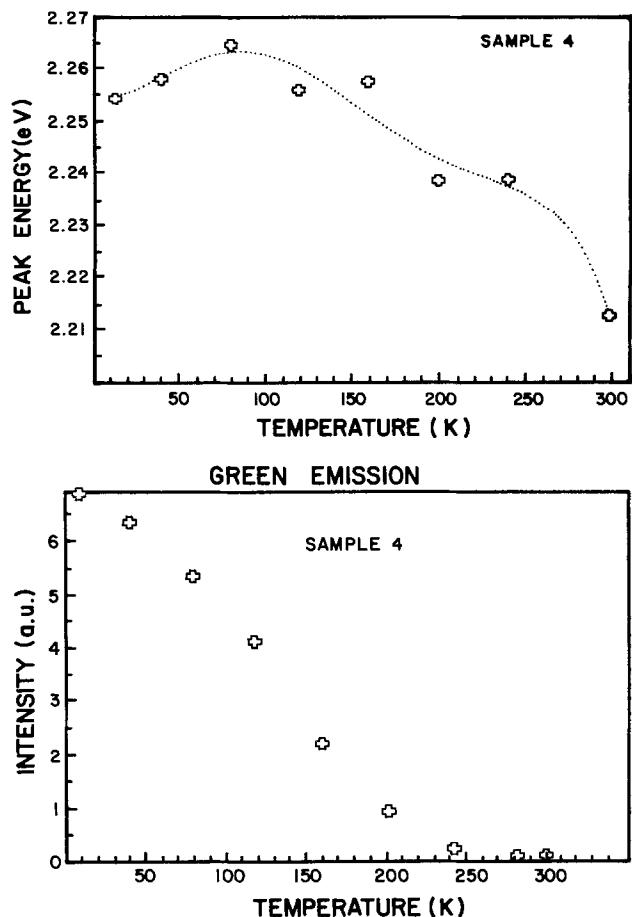


Fig. 3. (a, top) Luminescence green peak energy value vs. temperature for sample 4; (b, bottom) luminescence green intensity value vs. temperature for sample 4.

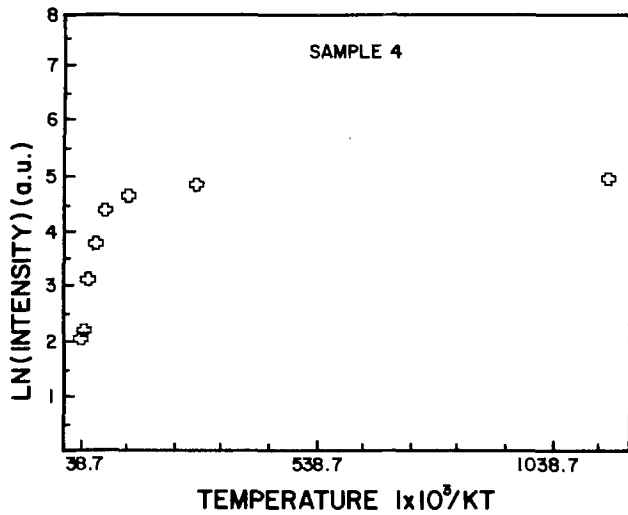


Fig. 4. Log of intensity vs. $1/\text{temperature}$ of the green luminescence of sample 4.

perature region resulting in an activation energy of 6.19 meV and the other resulting in an activation energy of 0.103 meV. We have assumed that this calculation contains an $\exp(E/KT)$ dependence of the green luminescence peak with temperature.

For comparison, we display in Fig. 5a and 5b the temperature behavior of the red luminescence band intensity and the peak position of sample 4 for the same region of temperature. We also include samples 1 and 11, which do not present the green line. A similar run is found for all samples below 200 K, but whereas the peak energy de-

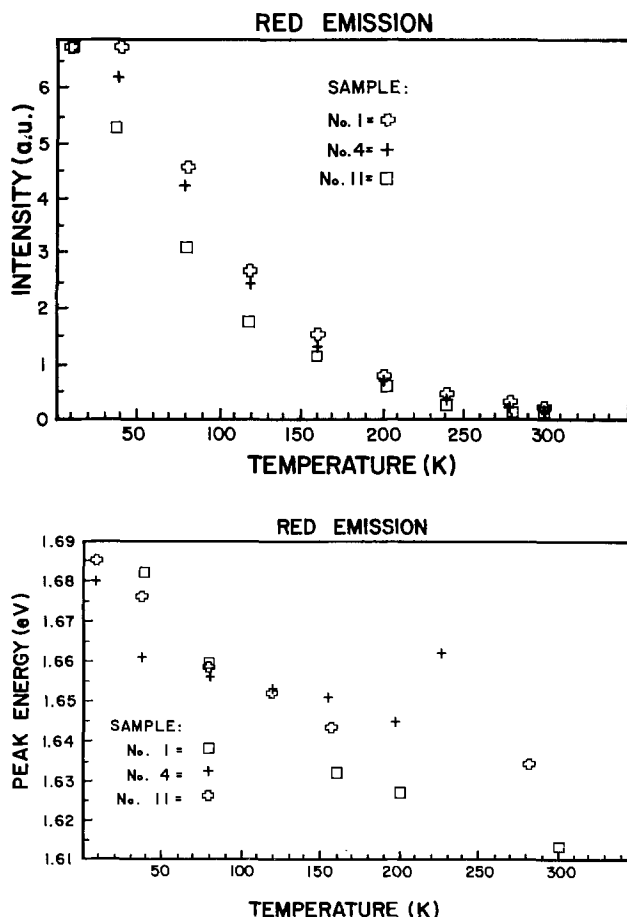


Fig. 5. (a, top) Intensity vs. temperature variation of the red emission for samples 1 (θ), 4 (\blacklozenge), and 11 (\blacksquare), with a 488 nm excitation line; (b, bottom) luminescence red peak energy value vs. temperature for samples 1 (\blacksquare), 4 (\blacklozenge), and 11 (\circ).

creases continuously for samples 1 and 11 with increasing temperature, the peak energy position of sample 4 increases above 200 K. Also, in Fig. 6 we show the spectra lines of sample 2 "as-prepared" with a 30s annealing in air at 400°C. Both show the red broad line, but a green small line tends to appear for the annealed sample.

Discussion

Broad photoluminescence at 1.65 eV has been reported in surface-damaged and electron-irradiated single-crystal CdS and identified with a complex sulfur interstitial (4). In our CBD CdS samples, one would expect to find similar defects and luminescence sites in dislocations and stacking faults of polycrystalline films. It is found that CBD generates films with numerous stacking faults (6). We believe that this situation helps cause radiative recombination channels in our CBD films whose method of preparation has almost no influence over the broad red emission line. Samples prepared with pH around 11.5, on the other hand, show characteristic green edge emission lines (the most stoichiometric films); the behavior of the red line is modified only for the case of this type of sample, e.g., sample 4. A high energetic recombination channel underlying the broad red emission line starts gaining efficiency at 200 K, causing a blue shifting of the overall peak position of the line (see Fig. 5a). A similar argument holds for the abrupt decrease of the peak energy position of sample 11 at 300 K.

For the case of "as-prepared" and annealed samples, we detect a modification in the spectra of the films. Samples whose preparation was at pH < 11.5 are able to show an increase in a green emission band after thermal annealing. The opposite is true for samples whose pH is > 11.5; they do not show any modification of the overall intensity line and the peak energy position. It is known that thermal annealing of CBD films in air evaporates the excess sulfur ions in the films because of their high vapor pressure (compared with the Cd ions). Thus, samples with concentrations of S-ions greater than that of Cd ions during preparation are thermally "annealed," and they present a modification of the spectra emission line. The samples whose Cd ion concentration is greater than S ion concentration during preparation are thermally annealed and do not show any change in the spectral emission line. There seems to exist two ways of achieving films which present a green emission line: selecting a pH whose Cd ion and S ion concentrations are equal; or selecting thermally annealed samples whose S ion concentration exceeds the Cd ion concentration. Only for these cases have we found the green emission line which has been related to a complex transition between cadmium and sulfur vacancies present in dislocated single CdS crystals (7).

The overall room temperature photoluminescence of the CBD CdS films grown with pH 11.5 is higher than that of single crystal CdS. The same behavior has been reported by Feldman and Dusiman (1) for spray pyrolyzed CdS, with no explanation for it. From our point of view, such behavior might be possible when taking into ac-

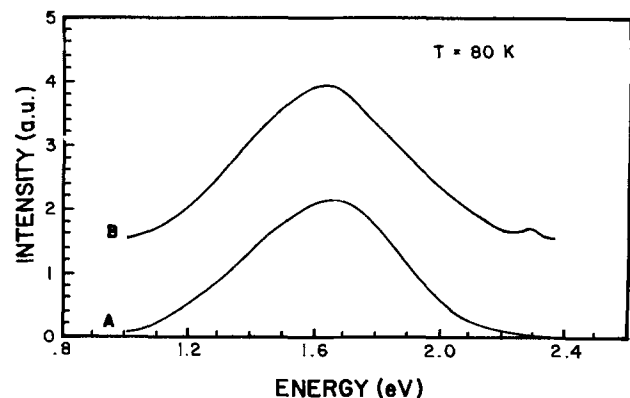


Fig. 6. Luminescence spectra for sample 2, held at 80 K for as-prepared (A) and annealed-in-air at 400°C for 30s (B).

count existing electric fields between microcrystallites of optically excited films, which cause an acceleration of the radiative recombination process, as compared with the nonradiative processes always present in single and polycrystalline material. A detailed experimental study of this behavior is still in progress, and electroluminescence excitation seems the appropriate means. At the same time, it should be possible to make clear whether the large room temperature green photoluminescence is a sufficient indication of a high efficient electroluminescence device.

Summary

In this work, we have shown that CBD CdS films prepared with approximately equal amounts of Cd and S ions give films whose green emission persists up to room temperature. There are two ways to achieve this situation: by preparing films whose pH value of the working solution corresponds to equal amounts of Cd and S ion concentrations; or by thermally annealing samples whose S ion concentration exceeds the Cd ion concentration. The mechanism for red luminescence is not affected by these processes. The green emission line is strongly influenced

by this situation. We have tried to identify the green emission line with a complex transition between Cd and S ion vacancies present in dislocated films.

Acknowledgment

This work was supported by DIGICSA-SEP and CONACYT (PCCB-101238), México.

Manuscript submitted Oct. 17, 1983.

REFERENCES

1. B. J. Feldman and J. A. Dusiman, *Appl. Phys. Lett.*, **37**, 1092 (1980).
2. N. R. Pavaskar, C. A. Menezes, and A. P. B. Sinha, *This Journal*, **124**, 743 (1977).
3. I. Kaur, D. K. Pandya, and K. L. Chopra, *ibid.*, **127**, 943 (1980).
4. C. N. Elsby and J. M. Messe, *J. Appl. Phys.*, **43**, 4818 (1972).
5. G. Martínez, Submitted to *This Journal*.
6. N. K. Abrikosov, V. F. Bankina, L. V. Poretskaya, and L. E. Shelimova, "Semiconducting II-VI and V-VI Compounds," Plenum Press, New York (1969).
7. H. Mitsuhashi, H. Komura, and J. Chikawa, in "II-VI Semiconducting Compounds," D. Thomas, Editor, p. 179, W. A. Benjamin Inc., New York (1967).

Photoelectric Properties of ITO/CdS/Surfactant Aluminum Phthalocyanine/Au Solar Cells

M. F. Lawrence, J. P. Dodelet,* and L. H. Dao*

Institut National de la Recherche Scientifique-Energie, Varennes, Quebec, Canada J0L 2P0

ABSTRACT

A heterojunction solar cell made by sequential electrodeposition of CdS and a surfactant aluminum phthalocyanine, (SAIPc), onto ITO (Nesatron) conductive glass, has been analyzed. Barrier formation occurs upon light absorption and is related to "doping" of the organic pigment by trapped electrons. When the cell is illuminated with white light, all the band bending occurs in the phthalocyanine, and two mechanisms are at work in relation to current production. The optimum thickness for the CdS and SAIPc layers was found to be 4000 and 2500Å, respectively. The photovoltaic characteristics of the optimized cell, under an illumination of 50 mW cm⁻², were: $J_{sc} = 0.33 \text{ mA cm}^{-2}$, $V_{oc} = 0.46\text{V}$, $ff = 0.3$, and $\eta = 0.09\%$. From capacitance measurements a density of $N \sim 3 \times 10^{17}$ charge carriers/cm³ was calculated, and the barrier parameters were: $w_0 \sim 300\text{Å}$ and $V_0 \sim 0.5\text{V}$. To illustrate how the junction changes with "doping" of the organic layer by photogenerated electrons, an energy level diagram of the proposed model is presented.

For years now, solar cell research has been primarily concerned with finding efficient devices that are easily fabricated, utilizing low cost durable materials. This task has led to the consideration of, among other things, the possibility of employing organic semiconductors as a substitute for some of the more expensive inorganic materials. With this in mind, determining the electrical and photoelectrical characteristics of the most promising organic molecules (phthalocyanines, merocyanines, porphyrines, squaryliums, etc.), became a major priority in the hope of discovering one with all the right qualities.

These organic pigments exhibit p-type conductivity (1-4), and the first devices fabricated with them were of the Schottky barrier type, using metals such as aluminum, indium, or chromium to establish a blocking contact. Lately, cells incorporating an organic-inorganic heterojunction have attracted attention in regard to their potential for eventual use in energy conversion. Phthalocyanine-type molecules, because of their environmental stability, their high absorption in the visible region, and their relatively good photoconductive properties, have emerged as one of the main organic substances to be used conjointly with inorganic n-type semiconductors like CdS and ZnO (5) to form heterojunctions.

Hor *et al.* (6) have developed a CdS/trivalent metal-phthalocyanine device with a conversion efficiency of 0.22% under AM2 illumination of 75 mW cm⁻², which is

*Electrochemical Society Active Member.

one of the largest values obtained for devices using organic photoconductors at high light intensity. A conversion efficiency of 0.5% has also been attained with a CdS/polyacetylene photovoltaic cell under AM1 irradiation (7). These results are quite modest compared to the > 9% conversion efficiency obtained with the CdS/Cu₂S cell (8), but, nevertheless, many aspects of organic-inorganic systems remain to be clarified; they deserve further investigation.

In our own effort, we have undertaken the fabrication and analysis of a heterojunction cell built up by sequential electrodeposition of CdS and a surfactant aluminum phthalocyanine (SAIPc) onto Nesatron conductive glass. This metal-phthalocyanine, unlike those commonly used (MgPc, CuPc, ZnPc, H₂Pc, etc.) and usually deposited by vacuum sublimation, has the interesting property of forming a positively charged colloid when put in an iso-octane + n-butanol mixture, permitting its electrodeposition on top of the CdS layer. This practical deposition technique of organic compounds was first performed by Tang and Albrecht (9) using microcrystalline Chl *a*, which forms a positively charged colloid in 3-methylpentane or iso-octane. Dodelet *et al.* (10) have subsequently applied the method to SAIPc in making an Al/SAIPc/Ag photovoltaic cell, where stability and conversion efficiency were found to be seriously hampered by the accumulation of electrons trapped in Al₂O₃ at the Al/SAIPc interface. Besides providing a simple and rapid way of film deposi-

tion, this technique allows the coverage of large surfaces, making it particularly well suited for an eventual practical application.

The main goal of this article is to describe our cell's behavior and to report on its characteristics and its optimization through variation of the semiconductor layer thicknesses. The experiments show that, when the cell is illuminated with white light, all the band bending occurs in the phthalocyanine and two mechanisms are at work in relation to current production. The information gained sheds more light on the organic and inorganic semiconductors separate functions, on how they combine to produce power, and provides a deeper understanding of the model proposed for organic-inorganic heterojunction devices (11).

Experimental

The CdS was deposited electrochemically onto Nesatron conductive glass of 82% transparency (indium-tin-oxide coating, P.P.G. Industries), according to the method described by Baranski and Fawcett (12). The cadmium chloride, elemental sulfur, and dimethylsulfoxide were reagent grade and used without further purification. The procedures by which the surfactant aluminum phthalocyanine (SAIPc) shown in Fig. 1 was synthesized and electrodeposited have been described previously (10). The SAIPc film thickness was varied from ~ 400 to 3700\AA , depending on the amount of SAIPc in the iso-octane + n-butanol mixture, and the CdS layer was varied from ~ 1000 to 5500\AA , depending on the electrodeposition time. Figure 2A shows a picture of a 2000\AA thick CdS film and Fig. 2B is a 2500\AA SAIPc film taken with an ETEC Autoscan scanning electron microscope. The CdS films have surfaces that are quite smooth up to thicknesses of about 6000\AA , above which the layer becomes cracked by the appearance of numerous crevices. The SAIPc films are less smooth and gradually become rougher as they get thinner. Nevertheless, reasonable films are obtainable down to about 400\AA (13). Film thicknesses were measured with a Dek-Tak surface profile measuring system (Sloan). The heterojunction cells were completed by the evaporation under vacuum ($\leq 5 \times 10^{-7}$ torr, Varian Cryostack 8) of a gold collecting (0.5 cm^2) and guard electrode (99.9% pure from Alfa).

The cells are installed in a Faraday cage, where they could be irradiated through the Nesatron with monochromatic light from a 650W tungsten-halogen lamp (Schoeffel) passing through a Kratos monochromator (Schoeffel), or/and with white light from a Kodak Ektagraphic slide projector (300W tungsten-halogen lamp). Because of the detrimental effect oxygen has on cell performance (see "Results and Discussion" section), the cells were analyzed while under N_2 atmosphere. The light intensity was

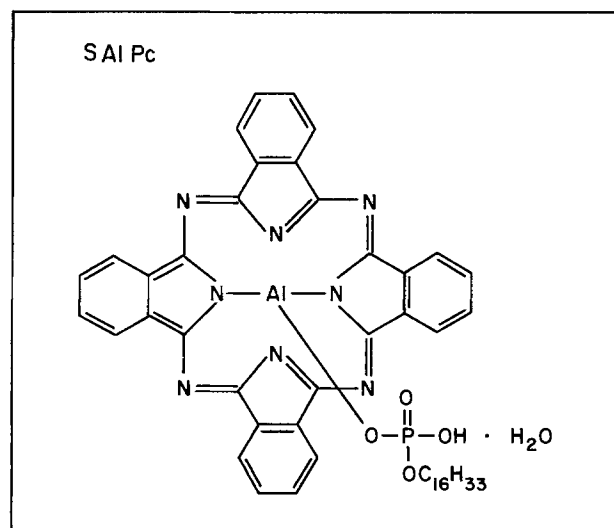


Fig. 1. SAIPc molecular structure

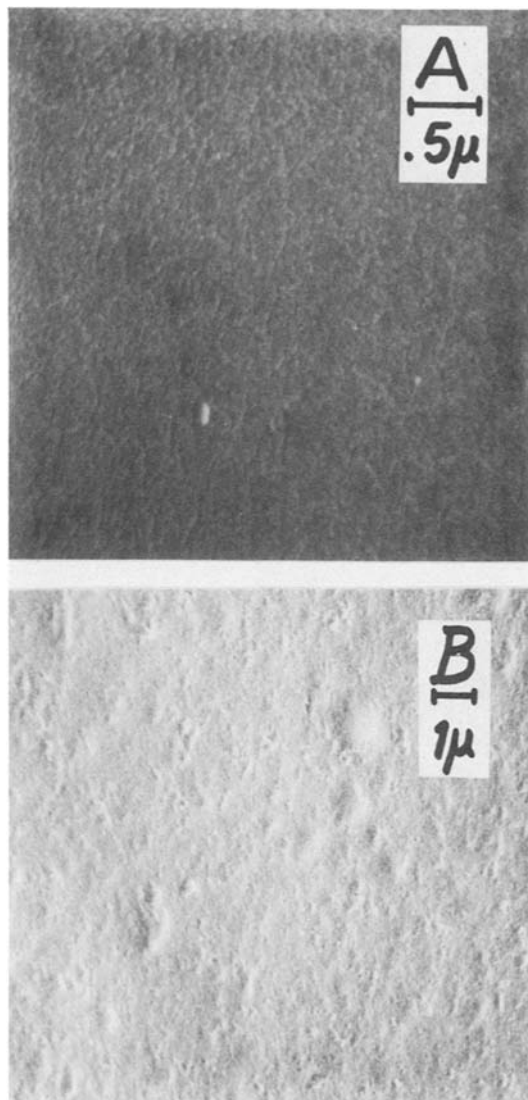


Fig. 2. SEM photographs of (A) a 2000\AA thick electrodeposited CdS layer and (B) a 2500\AA thick electrodeposited SAIPc layer.

varied by interposing neutral density filters (Oriol Corporation) and measured with a United Detector Technology 21A power meter equipped with a Radiometric filter. The intensities reported correspond to light incident on CdS. Filters (Oriol Corporation) having different cut-on and cut-off wavelengths were used in order to illuminate the cells with isolated parts (blue light or red light only) of the visible spectrum emanating from the slide projector. Currents and voltages generated by the cells were measured with a Keithley Model 616 electrometer. Capacitance measurements were performed according to the discharge method using a setup similar to the one described by Popovic (14). The absorption spectra were obtained with a Hitachi Model 100-60 spectrophotometer.

Results and Discussion

J-V characteristics.—Figure 3 shows the J-V curves of a typical CdS/SAIPc cell, corresponding to three important stages of measurement in which cell behavior is found to be different. The first curve is obtained by measuring the dark J-V characteristics of a freshly prepared cell, not yet exposed to light. At this stage, all of the cells exhibit very little rectification and their behavior is mostly resistive. The second stage (curve 2), involving the J-V measurement under white light illumination, clearly demonstrates that the rectifying properties appear as a result of light absorption. In the third stage, the J-V curve is taken in the dark, immediately after illumination, and the rectifying qualities of the cell are still present but have al-

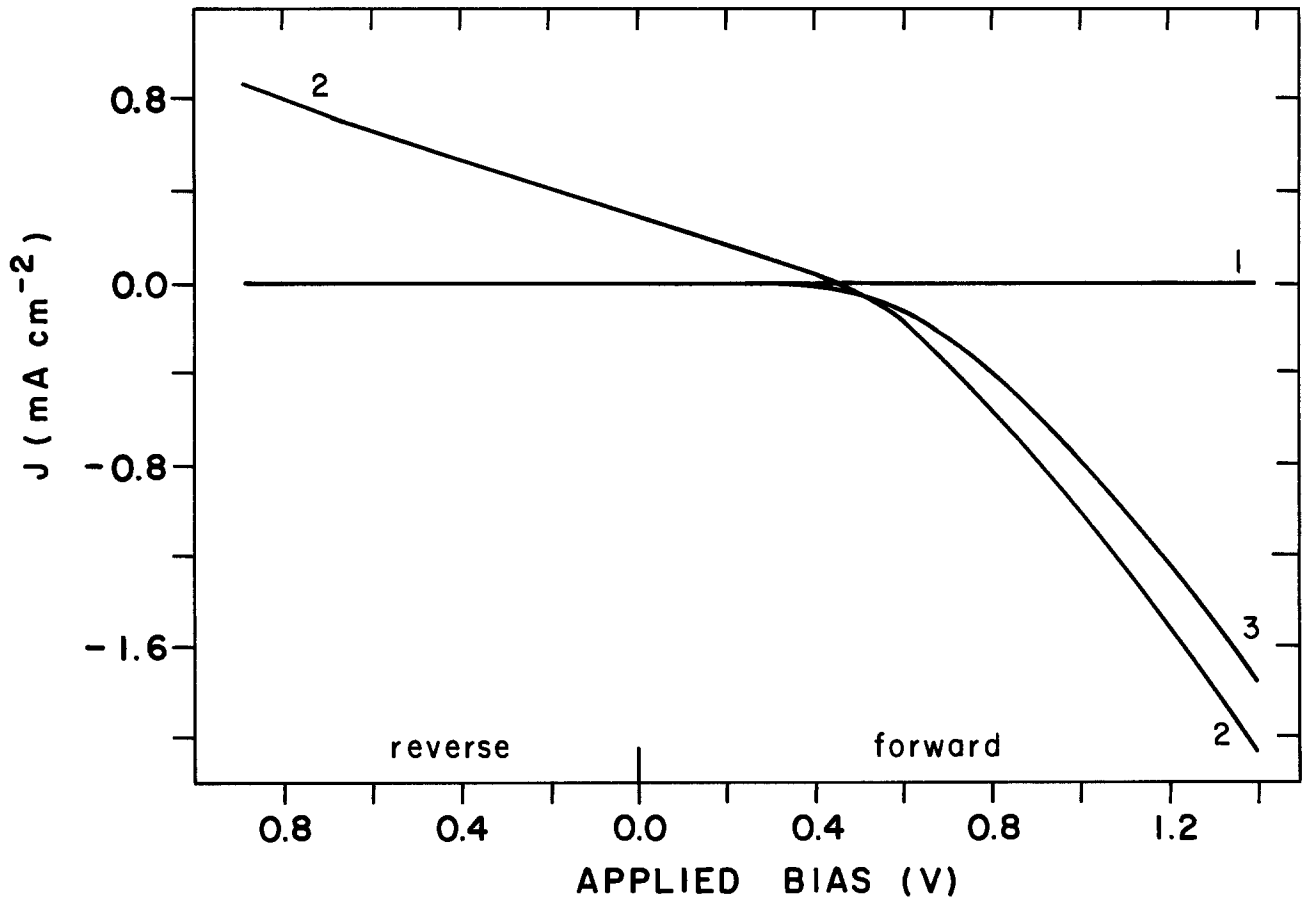


Fig. 3. J-V characteristics of CdS-SAlPc cell. Curve 1: first stage, in the dark. Curve 2: second stage, under white light illumination (50 mW cm⁻²). Curve 3: third stage, in the dark, after illumination.

ready begun to decay. Now, if after illumination, the cells are kept in the dark long enough (from 8h to 5 days, depending on the SAlPc film thickness), they gradually regain their initial resistive behavior. From that point, putting them again through the same three respective steps yields the same result. Wagner and Loutfy (11) obtained an identical result with a NESACdS/MgPc/Au cell before and during illumination, but the behavior of the device, in the dark after illumination, was not mentioned.

Figure 4A shows the semilogarithmic plots of the forward dark current *vs.* applied voltage (curves 1 and 3 of Fig. 3) and provides additional information concerning the state of the cell before and after illumination. The J-V data of a cell in the first stage (before illumination and very little rectification) cannot be fitted to the modified Schottky equation (15)

$$J = J_0 [\exp e(V - JR_s)/nkT - 1] + (V - JR_s)/R_{sh} \quad [1]$$

where J_0 , n , R_s , R_{sh} , and e are the reverse saturation current, the diode quality factor, the series resistance, the shunt resistance, and the electronic charge, respectively. J is the measured dark current, and V the forward applied voltage (positive potential on gold electrode). Rectification's being practically absent implies that the device at this point is not a diode, or that, at most, it is a very poor one and therefore Eq. [1] is not suited for its description. The data, however, fit reasonably well to an ohmic relation

$$J = \frac{V}{R} \quad [2]$$

which is more appropriate for the description of an essentially resistive device. Curve 1 of Fig. 4A (left axis) was calculated with Eq. [2] taking $R = 0.16 \text{ M}\Omega$. The J-V data of the same cell in the third stage (immediately after illumination, with rectification) can be fitted quite well to Eq. [1] using values of $J_0 = 8.2 \times 10^{-8} \text{ A cm}^{-2}$, $n = 2.85$, R_s

$= 415 \Omega$, and $R_{sh} = 1 \text{ M}\Omega$ (curve 3 of Fig. 4A, right axis). $R_{sh} = 1 \text{ M}\Omega$ was calculated from the slope of the reverse bias characteristics. Figure 4B illustrates how the open-circuit

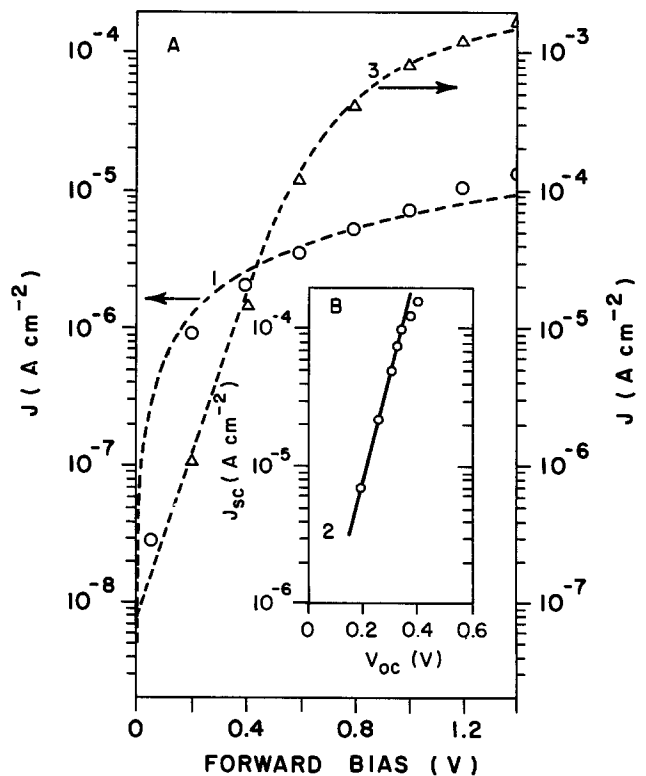


Fig. 4. A: J-V forward bias characteristics in the dark corresponding to curves 1 and 3 of Fig. 3. B: J_{sc} vs. V_{oc} for light intensities ranging from 0.7 to 18 mW cm⁻² (second stage).

voltage V_{oc} and the short-circuit current J_{sc} at light intensities ranging from 0.7 to 18 mW cm^{-2} (second stage) follow the relation

$$V_{oc} = \frac{nkT}{e} \ln \left(\frac{J_{sc}}{J_0} + 1 \right) \quad [3]$$

From the plot of $\log J_{sc}$ vs. V_{oc} , we find $n = 2.2$ and $J_0 = 2.7 \times 10^{-7} \text{ A cm}^{-2}$. Comparing these parameters with those obtained for the same cell immediately after illumination (curve 3, Fig. 4A) shows that the diode is at its best in the presence of light.

The J-V characteristics indicate the following: when the CdS and SAIPc are first brought together to form a heterojunction, the amount of free carriers in SAIPc is too little at this stage, and the result is a diode with poor rectification. Light absorption in SAIPc causes the formation of excitons that dissociate into electron-hole pairs. Because some of the electrons are rapidly trapped in SAIPc, mobile holes are left for conduction. Consequently, the pigment takes on a p-type semiconducting behavior, which permits, in the presence of nearly degenerate electrodeposited CdS (16), the formation of a nonideal Schottky barrier diode. The voltage developed at the barrier, therefore, corresponds to the difference between the Fermi levels of CdS and SAIPc when the system is illuminated and not to the difference between their respective Fermi levels when both materials are at equilibrium in the dark. Immediately after illumination (third stage), the captured electrons start escaping from their traps only to recombine with the holes present at that point in the SAIPc layer. This has the effect of transforming the organic pigment from its light-induced semiconducting character back to its initial, more insulating state, and causes the gradual decrease of the diode's rectifying capability. This mechanism, involving "doping" of the pigment by trapped electrons has also been mentioned in the case of chlorophyll α (17, 18). At the end of this article, an energy band diagram is presented to give a more detailed description of the barrier formation upon illumination.

Action and absorption spectra.—Figure 5A presents the absorption spectra of CdS (broken line) and SAIPc (solid line). Figure 5B shows the action spectra of three cells having different thicknesses of CdS for which the SAIPc film thickness has been kept constant at 2000Å. In the red part of the action spectrum (520 to 800 nm), where the absorption is due to SAIPc, the action spectra for all three cells are identical and correspond to the absorption spectrum of SAIPc. In the blue region, however (400 to 520 nm), the absorption by CdS has a marked effect on the resulting action spectrum. We have also noticed that when the cells are illuminated with red light only (≥ 600 nm), the photocurrent decreases quite rapidly and continues to do so unless a certain amount of blue light (430 nm) is added. This noteworthy observation, and what occurs in the blue region of Fig. 5B, can be explained by assuming the existence of two mechanisms responsible for current production.

Under white light illumination, electron-hole pairs are formed simultaneously in both semiconductors. The major mechanism at work for current production involves the recombination, at the junction, of electrons from the SAIPc conduction band with holes from the CdS valence band, leaving extra electrons in the CdS and extra holes in SAIPc to be recuperated. Blue light is essential, because the holes it generates in CdS are needed to balance the photocurrent. When the photocurrent produced with red light only (≥ 600 nm) is balanced with just the right amount of added blue light (430 nm), we find

$$\frac{N_{(e)}}{N_{(ph)}} = 0.7 \pm 0.1 \quad [4]$$

where $N_{(e)}$ is the total number of electrons collected per second and $N_{(ph)}$ is the total number of blue photons absorbed in the CdS within a distance from the phthalocyanine not exceeding the diffusion length of holes in CdS

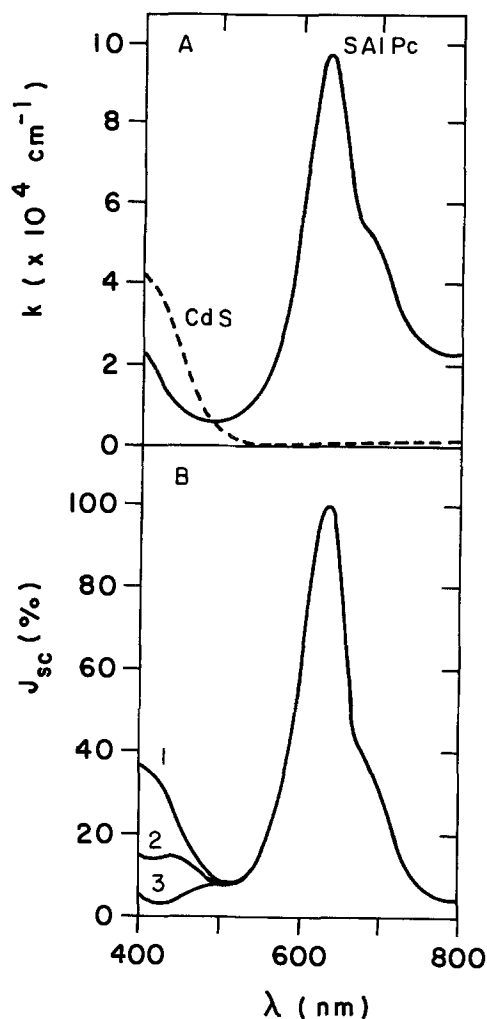


Fig. 5. A: Absorption spectra of SAIPc (full line) and CdS (broken line). B: Normalized action spectra of three cells having different CdS thicknesses. Curve 1: 1100Å. Curve 2: 2300Å. Curve 3: 4400Å. SAIPc thickness is 2000Å.

(*vide infra*). $N_{(e)}/N_{(ph)}$ represents an efficiency for the conversion of minority carriers from SAIPc to majority carriers in CdS.

In Fig. 5B, the effect CdS thickness has on the photocurrent generated in the blue part of the action spectra provides us with evidence for a second mechanism in relation to current production. It is important here to note that the action spectra are given as a percentage normalized at the maximum in the red (634 nm). If we assume that the CdS acts only as a filter for blue light, it is possible to calculate for each CdS thickness (taking into consideration the absorption coefficients of both semiconductors) what the action spectra would be from 400 to 520 nm, if the phthalocyanine was the only one to contribute currentwise. Subtracting these calculated action spectra from their corresponding spectra in Fig. 5B, we find that the CdS layer is responsible for $70\% \pm 10\%$ (independent of its thickness) of the overall photocurrent measured in the region where it absorbs. This would imply another mechanism of current production, however secondary, involving a direct injection of holes from the CdS valence band into the SAIPc valence band.

In an additional experiment, we have measured the cell V_{oc} when irradiated with red light only (≥ 600 nm), therefore, giving the voltage developed uniquely in the SAIPc. If the cell is illuminated with a red light intensity at which the maximum V_{oc} is obtained from SAIPc, the subsequent addition of blue or white light does not increase the measured potential, indicating that the band bending is entirely located on the phthalocyanine side of the junction. These results agree with findings already reported in the literature (11, 19), and they are expected since the

electrodeposited CdS is a nearly degenerate semiconductor.

The information gained by probing the heterojunction with isolated parts of the visible spectrum (blue or red light) permits us to determine how both semiconductors participate in this cell. Unlike completely inorganic devices (20), heterojunctions of this type behave rather like Schottky barrier cells where the organic layer acts as absorber-generator and simultaneously contains the built-in voltage region which allows the generated minority carriers to be collected and converted to majority carriers in the inorganic layer. The CdS, in this case, serves as a blocking contact and also contributes directly to the photocurrent.

The action spectra in Fig. 5B were obtained for a constant photon flux, with a maximum energy of 0.2 mW cm⁻² incident on the CdS layer at 634 nm. Quantum efficiencies at the maximum in the red (634 nm) vary between 6% and 11%, calculated according to

$$\phi(\%) = \frac{100 J_{sc} h\nu}{eI} \quad [5]$$

where $h\nu$ is the photon energy at 634 nm and I is the 634 nm light intensity incident on the CdS layer. Considering only the major mechanism for current production described previously, the requirement of balanced electron-hole pair production in both halves of the junction means, in fact, that the maximum quantum efficiency of this system is 50%.

Cell optimization.—In an attempt towards cell optimization, the semiconductor layers were varied in thickness starting with CdS. Figure 6 shows the variation of current density as a function of CdS thickness under white light illumination (8 mW cm⁻²). The optimum thickness, which corresponds to the diffusion length of holes in the electrodeposited CdS, was found experimentally to be ~ 4000Å. The full line in Fig. 6 (right axis) is the fraction of light, F , absorbed in CdS within a distance from the SAlPc not exceeding the hole diffusion length. F is calculated taking into account the absorption of light in CdS at a specific wavelength (400 nm) and using 4000Å as the diffusion length of holes in the inorganic semiconductor. For CdS thicknesses $\leq 4000\text{\AA}$, we have

$$F = [1 - \exp(-\alpha d)] \quad [6]$$

and for thicknesses $> 4000\text{\AA}$

$$F = [1 - \exp(-\alpha d)] - [1 - \exp\{-\alpha(d - \Lambda_h)\}] \\ = \exp(-\alpha d) \times [\exp(\alpha \Lambda_h) - 1] \quad [7]$$

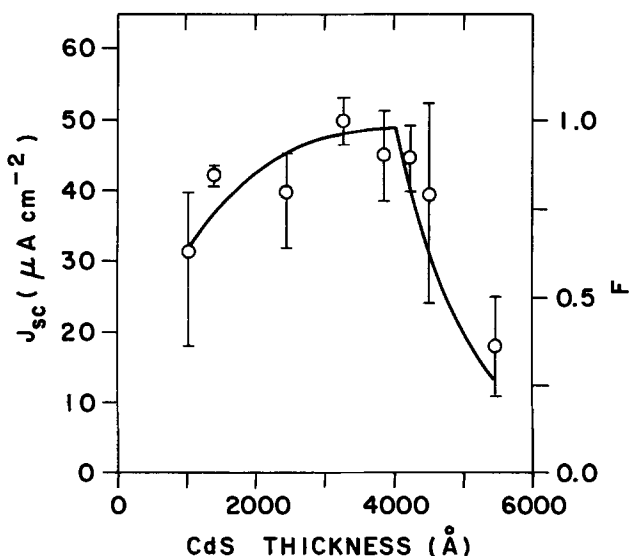


Fig. 6. Short-circuit current density, J_{sc} , vs. CdS thickness (left axis). Fraction of light, F , absorbed in CdS within a distance from SAlPc not exceeding the hole diffusion length ($\Lambda_h = 4000\text{\AA}$) vs. CdS thickness (right axis). Also indicated are the maximum and minimum experimental values obtained.

where α is the absorption coefficient for CdS at 400 nm (see Fig. 5A), which we have found to be $9.7 \times 10^4 \text{ cm}^{-1}$ ($2.30259 \times 4.2 \times 10^4 \text{ cm}^{-1}$), d is the total CdS layer thickness, and $\Lambda_h = 4000\text{\AA}$, the hole diffusion length in the CdS. Wagner and Loutfy (11), taking $\alpha \sim 10^5 \text{ cm}^{-1}$, at 520 nm (which seems large for CdS at that wavelength), estimated a Λ_h of 1000Å. The fit of the calculated curve to the experimental points using $\Lambda_h = 4000\text{\AA}$ is reasonably good.

Figure 7 illustrates the variation of cell efficiency, η , vs. the organic layer thickness measured under white light illumination of 20 mW cm⁻². The CdS layer of these cells was kept at the optimum thickness of ~ 4000Å. Cell efficiency is calculated with the expression

$$\eta(\%) = \frac{100 J_{sc} V_{oc} ff}{I_T} \quad [8]$$

where ff is the cell fill factor and I_T is the white light intensity incident on CdS. Typical values of ff were found to be ~ 0.3. A maximum efficiency of ~ 0.1% was attained at a SAlPc thickness of ~ 2500Å.

The absorption of visible light by the organic pigment results in exciton formation. The excitons are capable of diffusing a certain length (Λ) across the SAlPc layer before they decay or dissociate into charge carriers which can be collected readily, if they are formed in the space-charge region, or if the excitons form outside at a distance $\leq \Lambda$ and diffuse into the space-charge region. The width of the depletion region at zero applied bias being w_0 , the active region extends over a distance of $w_0 + \Lambda$. In photoelectrochemical cells using SAlPc (13), a maximum value of ~ 250Å was found for Λ , which agrees with $\Lambda \sim 300\text{-}500\text{\AA}$ obtained for $x\text{-H}_2\text{Pc}$ (21, 22).

Figure 8 shows the efficiency variation (right axis), open-circuit voltage and short-circuit current density variation (left axis) with I_T for an optimized cell. The light exponent, γ , appearing in the expression

$$J_{sc} \propto I_T^\gamma \quad [9]$$

has a value of ~ 0.9. The sublinear dependence of J_{sc} on I_T is related to the distribution of traps for holes in the phthalocyanine (23). This effect, combined with the fact that V_{oc} reaches a constant value at ~ 20 mW cm⁻², causes the efficiency to decrease at greater intensities. An efficiency of ~ 0.09% at a 50 mW cm⁻² white light illumination compares well to $\eta = 0.10\%$ obtained with ITO/CdS/ZnPc/Au and $\eta = 0.066\%$ for ITO/CdS/MgPc/Au at the same light intensity (24). The best result for heterojunction devices of this type, however, was reached with an ITO/CdS/ClAlPc/Au cell having a conversion efficiency of 0.22% at an AM2 illumination of 75 mW cm⁻² (6).

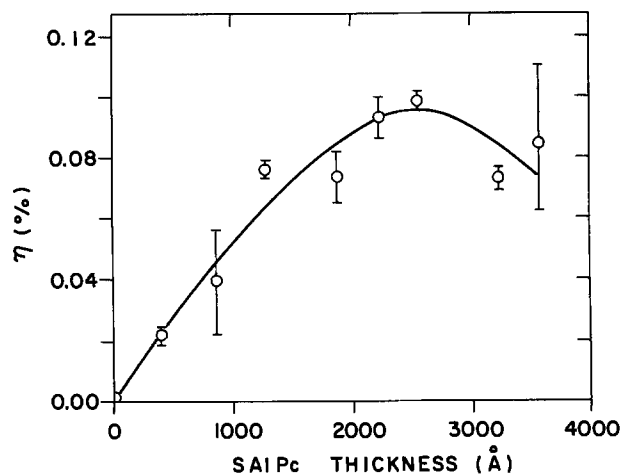


Fig. 7. Power conversion efficiency, η , vs. SAlPc thickness. Also indicated are the maximum and minimum experimental values obtained.

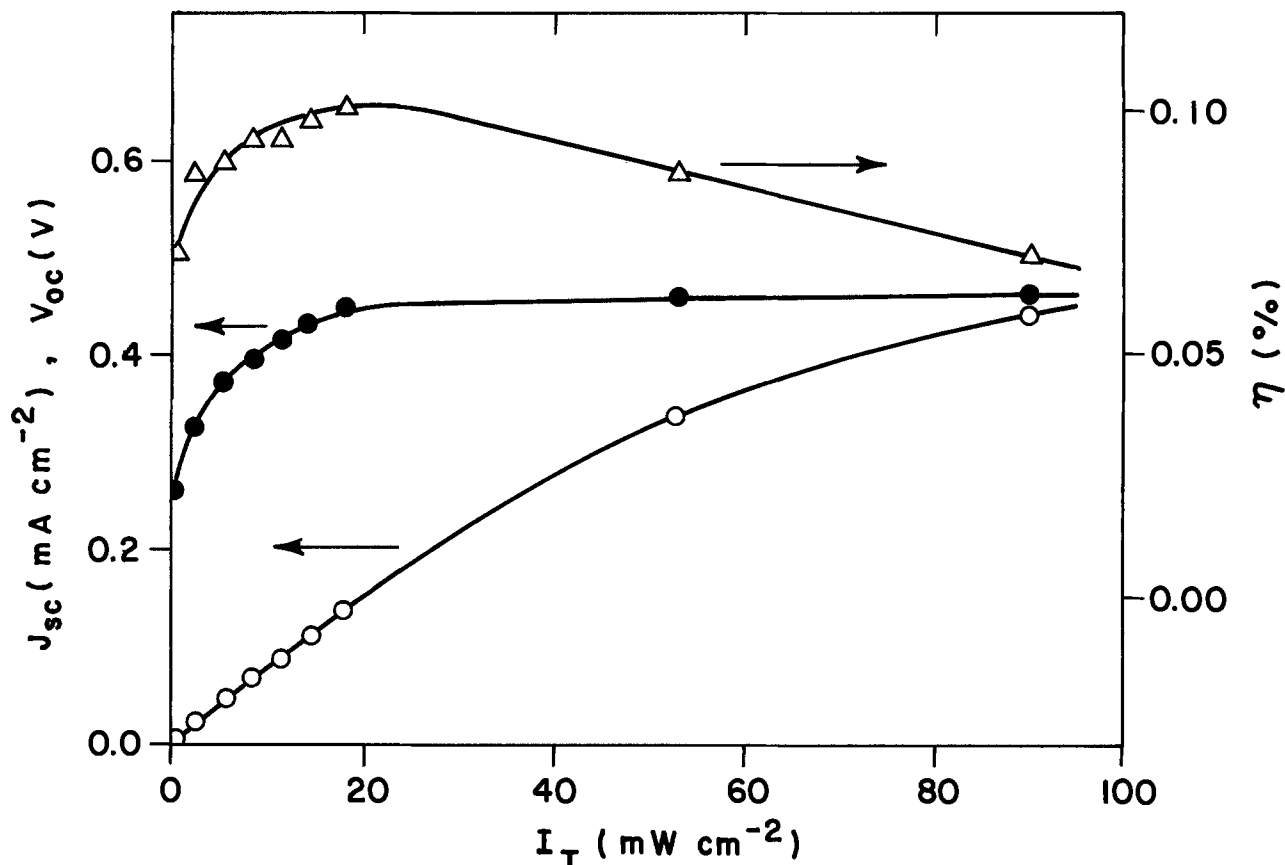


Fig. 8. Short-circuit current density, J_{sc} , open-circuit voltage, V_{oc} , (left axis) and power conversion efficiency, η , (right axis) vs. white light intensity incident on CdS, I_T .

Capacitance measurements.—The capacitor discharge technique consists in measuring the total accumulated charge, Q_i , after the cell has been biased with a voltage V . The result is

$$C_i = Q_i/V \quad [10]$$

where C_i is the integral capacitance. The accumulated charge, when external voltage V is applied to an ideal or MIS Schottky barrier, can be expressed by (14)

$$Q_i = \left(1 + \frac{V}{V_0}\right)^{1/2} Q_0 - Q_0 \quad [11]$$

where $Q_0 = AeNw_0 = A(2e\epsilon\epsilon_0NV_0)^{1/2}$ is the amount of charge accumulated in the barrier at zero bias, A the sample area, e the electronic charge, ϵ the SAIPc dielectric constant, ϵ_0 the vacuum permittivity, N the density of majority carriers, and V_0 and w_0 are the built-in voltage and barrier width at zero applied bias. Since the CdS/SAIPc heterojunction behaves like a Schottky barrier (while under illumination or immediately after), we assume the application of the present theory to be justified. Equation [11] can be rewritten in the more convenient form

$$\frac{1}{C_i} = \frac{1}{C_0Q_0} Q_i + \frac{2}{C_0} \quad [12]$$

where $C_0 = Q_0/V_0$. From the slope, $1/C_0Q_0$, and the intercept, $2/C_0$, obtained by plotting $1/C_i$ vs. Q_i , the different barrier parameters V_0 , w_0 , and N can be estimated. Substituting Eq. [11] in the definition of the integral capacitance (Eq. [10]), we obtain

$$\frac{C_i}{C_0} = \left(\frac{V_0}{V}\right) \left[\left(1 + \frac{V}{V_0}\right)^{1/2} - 1\right] \quad [13]$$

For small applied biases ($V \ll V_0$), Eq. [13] becomes

$$C_i = 1/2 C_0 \quad [14]$$

and under this condition, determining Q_i permits (when

V_0 and N are known) the direct evaluation of w_0 , the barrier width at zero applied bias.

As was the case in the J-V experiments, capacitance measurements performed before and after illumination provide valuable results. For a freshly prepared device, not yet exposed to light (or a cell kept in the dark long enough after illumination), the capacitance dependence on applied voltage does not resemble the typical dependence of depletion layer capacitance on applied voltage for p-n junctions and Schottky barriers (25). At this stage, the values found for w_0 when Q_i is measured at $V \ll V_0$ (0.01V), correspond quite closely to the thickness of the SAIPc layer of the cell, if $\epsilon = 4.3$ is assumed for SAIPc. A dielectric constant of 4.25 has been reported for α -H₂Pc (26). This indicates that, before illumination, the density of mobile charge carriers in the organic layer must be quite low and, because of the high resistivity of phthalocyanines compared to CdS, the cell behaves like a simple capacitor with the SAIPc as dielectric. A similar behavior was observed by Skotheim *et al.* (19) for an Au/merocyanine/TiO₂ sandwich cell in the dark.

Furthermore, to obtain a suitable plot of $1/C_i$ vs. Q_i (Fig. 9), it was necessary to illuminate the cells before each measurement of Q_i in the dark at a specific reverse applied V . This is consistent with the behavior indicated by the J-V results. The significant band bending at the p-n junction appears with the onset of light, and measuring Q_i at $V \ll V_0$ immediately after illuminating the cell with white light, yields the barrier width at zero applied bias, w_0 . By determining C_i at $V = 0.01V$, we found w_0 to be independent of the CdS thickness and to vary only with SAIPc thickness. This helps in confirming a model with virtual absence of band bending in CdS, and where all of the built-in potential develops across the phthalocyanine film. From the $1/C_i$ vs. Q_i plots (as described by Eq. [12]), typical values of $N \sim 3 \times 10^{17} \text{ cm}^{-3}$, $w_0 \sim 300\text{\AA}$, and $V_0 \sim 0.5V$ were obtained for the optimized cells (CdS $\sim 4000\text{\AA}$ and SAIPc $\sim 2500\text{\AA}$). These results are in accordance with $N \sim 10^{18} \text{ cm}^{-3}$, $w_0 \sim 200\text{-}250\text{\AA}$, and $V_0 \sim 0.6V$ found by Ghosh *et al.* for an Al/MgPc/Ag Schottky barrier cell (1).

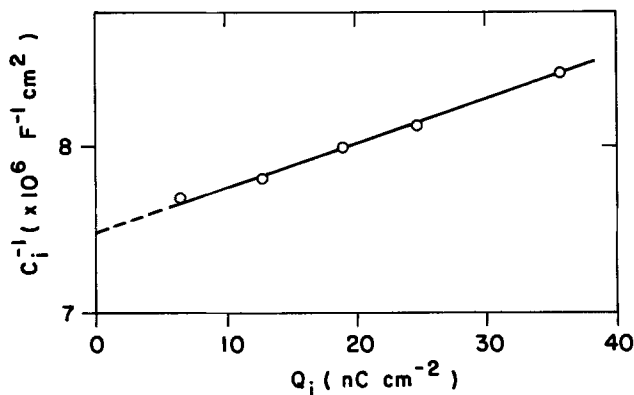


Fig. 9. Reciprocal integral capacitance, C_i^{-1} , vs. total accumulated charge, Q_i , at different applied reverse biases.

If the collected charges are the result of excitons dissociating in w_0 only, the active region of the cell would therefore correspond to $w_0 + \Lambda \sim 550\text{\AA}$. Figure 7 shows, however, that the efficiency increases up to a SAIPc thickness of at least 2000\AA , leaving $\sim 1500\text{\AA}$ in excess of $w_0 + \Lambda$ unaccounted for, which also contributes to the total efficiency. A possible explanation would be that the minority carriers created in the bulk of SAIPc might be capable of migrating towards the space-charge region over a distance of $\sim 1500\text{\AA}$, or a participation by triplet excitons may be involved.

ITO/CdS/SAIPc/Au cells are much more stable than the Al/Al₂O₃/SAIPc/Ag cells already investigated (10), but their photovoltaic properties still decrease slowly during illumination. Under 90 mW cm^{-2} white light, J_{sc} typically drops to $\geq 70\%$ of its initial value after 10h of irradiation. A smaller drop is observed if the irradiation power is reduced.

Water vapor and atmospheric gases also have an influence on the cell characteristics. J_{sc} (and V_{oc}) decreases when atmospheric air is replaced by dry air, but increases when atmospheric air or dry air is replaced by dry N₂. J_{sc} decreases also by wetting N₂. This indicates, first of all, that water vapor has a positive influence on J_{sc} only in the presence of O₂ and, second, that O₂ by itself has a negative effect on J_{sc} .

The conjugated effect of water vapor and O₂ on J_{sc} has already been mentioned for Al/Al₂O₃/chlorophyll *a*/Ag cells (27), but the dry N₂ effect is quite puzzling. O₂ is known to reversibly adsorb on phthalocyanines (28). The decrease of J_{sc} when O₂ is present could be explained by the formation of surface states on SAIPc, through which the photogenerated electrons and holes could recombine. This reaction would be in competition with the main mechanism for current production in the cell. The effect of O₂ could also be explained by again assuming the participation of triplet excitons in photocurrent generation. These excitons would be quenched by O₂, therefore reducing the overall photoactivity of the cells.

The influence of water vapor and gases was not investigated further, and, as indicated in the experimental section, all the measurements were performed in dry N₂ environment.

Energy band diagram for barrier formation.—Figure 10 shows the energy band diagram of the optimum ITO/CdS/SAIPc/Au cell in the dark, before (or in the dark long enough to be at equilibrium) and immediately after illumination. For CdS, the value of E_c is at 4.50 eV below the vacuum level and $E_g = 2.42\text{ eV}$ (29). Being a nearly degenerate semiconductor with $N = 10^{18}\text{ cm}^{-3}$ (16), electrodeposited CdS has a Fermi level located at $\sim 0.06\text{ eV}$ below E_c (4.56 eV below vacuum). With experiments described elsewhere (13), using photoelectrochemical cells having a SAIPc/Fe(CN)₆^{3/4-} electrolyte junction, a value of $E_{FB} = 5.05\text{ eV}$ vs. vacuum was found for the flatband energy of SAIPc, which corresponds to the Fermi level's location immediately after "doping by illumination. The

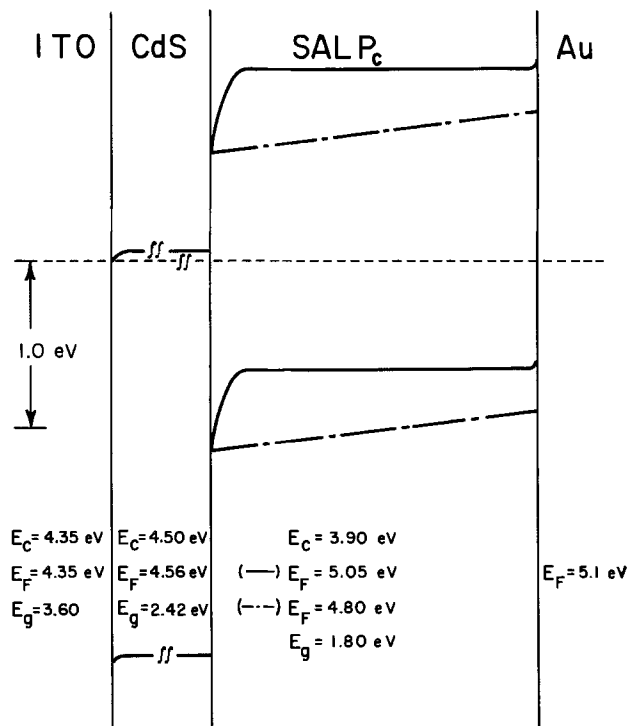


Fig. 10. Energy band diagram of the optimum ITO/CdS/SAIPc/Au cell in the dark. The solid line represents SAIPc band bending immediately after illumination; the dash-dotted line represents SAIPc band bending before the first illumination or in the dark long enough after illumination to be at equilibrium.

equalization of the CdS and SAIPc Fermi levels, therefore, results in a built-in potential of $5.05 - 4.56 = 0.49\text{V}$. This is in good agreement with $V_0 = 0.50$ obtained from the capacitance-voltage measurements. In order to position the SAIPc valence band relative to its Fermi level, we have used a value reported by Loutfy (30) for metal-free phthalocyanine. With studies of current-voltage variations, Loutfy found that the H₂Pc Fermi level lies at 0.65 eV above the valence band. For the bandgap of SAIPc, the value of 1.8 eV reported for AlPc⁺ (31) is employed. The ITO and Au energy level positions appearing in Fig. 10 were obtained from Ref. (32) and (33), respectively. The energy diagram, of course, is only accurate to the extent of how well the physical quantities borrowed from the literature for H₂Pc and AlPc⁺ apply to SAIPc.

When the cell is left long enough in the dark after illumination, the depletion width increases from its minimum length of 300\AA until it eventually attains the SAIPc film thickness (2500\AA in optimum cells). This increase results from the recombination of electrons with mobile holes, which causes N in SAIPc to diminish. N_t , the majority charge-carrier density when the system has returned to equilibrium, can be estimated in the following manner. In the dark, immediately after light-induced doping, SAIPc contains $N_i = 3 \times 10^{17}\text{ cm}^{-3}$ majority carriers and the cell at this stage has a series resistance $R_{si} = 415\Omega$. After having been in the dark for a few days, the cell's series resistance increases to $R_{sf} = 160\text{ k}\Omega$. If it is assumed that SAIPc is mostly responsible for R_s and that the mobility of majority carriers stays constant, we may write

$$\frac{\rho_i}{\rho_f} = \frac{e\mu N_f}{e\mu N_i} = \frac{R_{si}}{R_{sf}} \quad [15]$$

where ρ is the resistivity of the sample, μ is the mobility and N is the density of majority charge carriers, R_s is the series resistance, and the index *i* and *f* refer, respectively, to the initial (immediately after illumination) and final (at equilibrium) stage in the dark. From Eq. [15], we obtain $N_f \approx 8 \times 10^{14}\text{ cm}^{-3}$. This decrease of N implies that the Fermi level moves from its position at $\sim 0.65\text{ eV}$ above the valence band towards the middle of the forbid-

den bandgap. At most, the Fermi level of SAIPc can move from 5.05 eV to $1/2 (E_c + E_v) = 4.80$ eV below vacuum, which yields a V_0 of $|4.80 - 4.56| = 0.24$ V. This change is represented in the diagram of Fig. 10.

Conclusion

We have presented evidence that, for this CdS/SAIPc heterojunction solar cell, the mechanism related to barrier formation is initiated by light absorption in the organic layer. Subsequently, the trapping of electrons dopes the organic pigment and transforms it into a p-type semiconductor, which, in the presence of CdS, permits the formation of a Schottky barrier. Even though all of the band bending occurs in the phthalocyanine, the CdS, nevertheless, contributes directly to the overall photocurrent. The presence of these electron traps in SAIPc is of primary importance. Without them, the pigment could not behave as a semiconductor. This is also the case with other organic materials, such as chlorophylls, for example.

Future work on this subject will be directed towards the determination of the energy levels associated with the "doping" electron traps in SAIPc and the description of their nature. Future work will also be concerned with the enhancement of power conversion efficiency by selectively doping each of the materials with appropriate electron donors (for CdS) and acceptors (for SAIPc). The technique of film deposition presently in use seems well suited for the accomplishment of this task because it permits the simultaneous electrodeposition of the semiconductor and the dopant.

Acknowledgments

This work was supported by an FCAC and a CRSNG grant. Technical assistance of A. Joly from IREQ for the electron microscopy is greatly appreciated.

Manuscript submitted Jan. 3, 1984; revised manuscript received July 31, 1984. This was Paper 365 presented at the Washington, DC, Meeting of the Society, Oct. 9-14, 1983.

The Institut National de la Recherche Scientifique-Energie assisted in meeting the publication costs of this article.

REFERENCES

1. A. K. Ghosh, D. L. Morel, T. Feng, R. F. Shaw, and C. A. Rowe, Jr., *J. Appl. Phys.*, **45**, 230 (1974).
2. A. K. Ghosh and T. Feng, *ibid.*, **49**, 5982 (1978).
3. F. J. Kampas and M. Gouterman, *J. Phys. Chem.*, **81**, 690 (1977).
4. V. Y. Merritt and H. J. Hovel, *Appl. Phys. Lett.*, **29**, 414 (1976).
5. H. J. Wagner and R. O. Loutfy, *Solar Cells*, **5**, 331 (1982).
6. A. M. Hor, R. O. Loutfy, and C. K. Hsiao, *Appl. Phys. Lett.*, **42**, 165 (1983).
7. M. Cadene, M. Rolland, M. Aldissi, and M. Badie, *Comm. Eur. Communities [Rep] EUR 8042*, 848 (1982).
8. J. A. Bragagnolo, A. M. Barnett, J. E. Phillips, R. B. Hall, A. Rothwarf, and J. D. Meakin, *IEEE Trans. Electron Devices*, **ed-27**, 645 (1980).
9. C. W. Tang and A. C. Albrecht, *Mol. Cryst. Liq. Cryst.*, **25**, 53 (1974).
10. J. P. Dodelet, H. P. Pommier, and M. Ringuet, *J. Appl. Phys.*, **53**, 4270 (1982).
11. H. J. Wagner and R. O. Loutfy, *J. Vac. Sci. Technol.*, **20**, 300 (1982).
12. A. S. Baranski and W. R. Fawcett, *This Journal*, **127**, 766 (1980).
13. D. Bélanger, J. P. Dodelet, L. H. Dao, and B. A. Lombos, *J. Phys. Chem.*, **88**, 4288 (1984).
14. Z. Popovic, *Appl. Phys. Lett.*, **34**, 694 (1979).
15. M. Bujatti, *Proc. IEEE*, **53**, 397 (1965).
16. A. S. Baranski, M. S. Bennett, and W. R. Fawcett, *J. Appl. Phys.*, **54**, 6390 (1983).
17. G. A. Gorker and I. Lundström, *ibid.*, **49**, 686 (1978).
18. I. Lundström, G. A. Corker, and M. Stenberg, *ibid.*, **49**, 701 (1978).
19. T. Skotheim, J. M. Yang, J. Otvos, and M. P. Klein, *J. Chem. Phys.*, **77**, 6144 (1982).
20. A. M. Barnett and A. Rothwarf, *IEEE Trans. Electron. Devices*, **ed-27**, 615 (1980).
21. E. R. Menzel and R. O. Loutfy, *Chem. Phys. Lett.*, **72**, 522 (1980).
22. R. O. Loutfy, C. K. Hsiao, and R. Ho, *Can. J. Phys.*, **61**, 1416 (1983).
23. H. Meier "Organic Semiconductors," p. 321, Verlag Chemie, Weinheim, Germany (1974).
24. A. M. Hor and R. O. Loutfy, *Can. J. Chem.*, **61**, 901 (1983).
25. S. M. Sze "Physics of Semiconductor Devices," p. 370, Wiley-Interscience, New York (1969).
26. M. A. Abkowitz and A. I. Lakatos, *J. Chem. Phys.*, **57**, 5033 (1972).
27. J. P. Dodelet, J. Le Brech, and R. M. Leblanc, *Photochem. Photobiol.*, **29**, 1135 (1979).
28. S. C. Dahlberg, *Appl. Surf. Sci.*, **14**, 47 (1982-1983).
29. A. L. Fahrenbuch and R. H. Bube, "Fundamentals of Solar Cells," p. 427, Academic Press, New York (1983).
30. R. O. Loutfy, *Phys. Status Solidi A*, **65**, 659 (1981).
31. A. Giraudeau, F. R. F. Fan, and A. J. Bard, *J. Am. Chem. Soc.*, **102**, 5137 (1980).
32. F. Decker, J. Melsheimer, and H. Gerisher, *Isr. J. Chem.*, **22**, 195 (1982).
33. "Handbook of Chemistry and Physics," 58th Ed., R. C. Weast, Editor, CRC Press, Cleveland, OH (1977-1978).

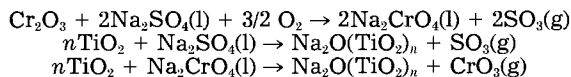
Chemical Reactions Involved in the Initiation of Hot Corrosion of IN-738¹

G. C. Fryburg, F. J. Kohl, and C. A. Stearns

National Aeronautics and Space Administration, Lewis Research Center, Cleveland, Ohio 44135

ABSTRACT

Sodium-sulfate-induced hot corrosion of preoxidized IN-738 was studied at 975°C, with emphasis on processes occurring during the long induction period. Thermogravimetric tests were run for predetermined periods of time, after which one set of specimens was washed with water to give information about water-soluble metal salts and residual sulfate. A second set of samples was cross-sectioned dry and polished in a nonaqueous medium. Element distributions within the oxide scale were obtained from electron microprobe x-ray micrographs. Evolution of SO₂ was monitored throughout the thermogravimetric tests. Kinetic studies were performed for several pertinent processes, and rate constants were obtained for the following chemical reactions



Recently, we reported on the chemical reactions involved in the initiation of Na₂SO₄-induced hot corrosion of the nickel-base alloys B-1900 and NASA-TRW VIA (1), which derive their oxidation resistance from the formation of a thin continuous oxide layer composed largely of α-Al₂O₃. It was shown that, after an induction period, hot corrosion was initiated by basic fluxing of the protective Al₂O₃ layer by the liquid Na₂SO₄ deposit. This was followed by a catastrophic attack resulting from acidic fluxing of the remaining oxide layer by a Na₂MoO₄·MoO₃ molten phase that had formed underneath the oxide layer.

Unlike B-1900 and VIA, the alloy IN-738 derives its oxidation resistance from a protective layer composed largely of Cr₂O₃. This superalloy is of special interest because of its widespread use, both coated and uncoated, in gas turbine engines (2, 3). This position of prominence is due not only to its good mechanical properties, but also to its superior hot corrosion resistance.

The Na₂SO₄-induced hot corrosion of IN-738 between 825° and 1000°C had been studied by several investigators (3-13). Depending on test conditions, either the alloy had not displayed hot corrosion, or hot corrosion had been preceded by a long induction period, during which the corrosion rate was similar to that in simple oxidation. Most of these studies had emphasized hot corrosion kinetics or the morphology of the corrosion scale. Less effort had been devoted to the important processes occurring during the long induction period. These processes were emphasized in this study. We used the same techniques employed in our studies of B-1900 and VIA and, in addition, performed rate studies on several of the simple processes thought to be important in the hot corrosion of IN-738. This work complemented recent research on the effects of temperature and oxide scale thickness on the hot corrosion of IN-738 (13).

Experimental

Specimens of alloy IN-738 were obtained from commercial sources and given conventional heat-treatments. The composition was nominal for IN-738 (weight percent (w/o): Cr, 16.0; Al, 3.4; Ti, 3.4; Co, 8.5; Mo, 1.7; W, 2.6; Ta, 1.7; Nb, 0.9; Zr, 0.1; C, 0.17; Ni, balance) (7). Test samples' dimensions were 0.3 × 1.0 × 2.5 cm. All surfaces were glass-bead blasted to give a uniform matte finish and were scrupulously cleaned.

All samples were preoxidized at 975°C in 1 atm of slowly flowing oxygen for 24h. Hot corrosion was induced by coating the preoxidized samples with about 3 mg cm⁻² of Na₂SO₄; this was followed by isothermal oxidation at 975°C in a vertical tube furnace. Oxygen flowed downward at 126 cm min⁻¹ (620 ml min⁻¹) in the 2.5 cm

diam quartz furnace tube. Continuous weight change measurements were made with a Cahn R-100 microbalance and corrected for flow and buoyancy effects. The concentration of product SO₂ was measured continuously with a Thermoelectron-Pulsed Fluorescent Analyzer specific to SO₂, whose detection capability extended from 0.01 to 50.0 ppm.

One set of reacted samples was cross-sectioned for morphological examination of the corrosion scale by light microscopy and electron microprobe techniques. Reaction products were identified from elemental x-ray micrographs and x-ray diffraction analyses, as reported previously (7). A second set of samples was washed with hot water to extract soluble species, and the wash solutions were analyzed for metal cations and/or anions by atomic absorption techniques. Residual sulfate was determined by ion chromatography.

Results and Discussion

A typical weight gain curve for IN-738 during preoxidation at 975°C, showing typical parabolic kinetics, is presented in Fig. 1. Elemental x-ray micrographs of a typical oxidized sample (Fig. 2), preoxidized for 24h, show that the compact oxide is about 10 μm thick and is composed primarily of Cr₂O₃, with considerable amounts of TiO₂. Tentacle-like internal oxides of Al₂O₃ are observed below the Cr₂O₃ layer, extending 30 μm into the substrate. Tantalum and, possibly, niobium oxides are found beneath the Cr₂O₃-TiO₂ layer. Titanium and chromium have depletion zones about 30 μm thick. Little or no nickel or molybdenum appear in the oxide layer. *In situ* high temperature x-ray diffraction (15) was performed to identify the

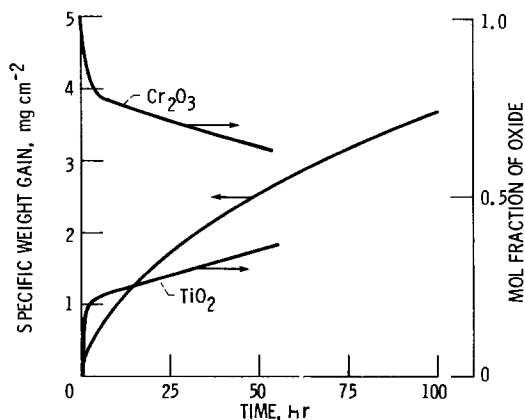


Fig. 1. Typical specific weight gain for isothermal oxidation of IN-738 at 975°C in flowing oxygen and for mol fraction of Cr₂O₃ and TiO₂ in scale, as a function of time.

¹A more detailed account of this work can be found in NASA TP-2319 (1984).

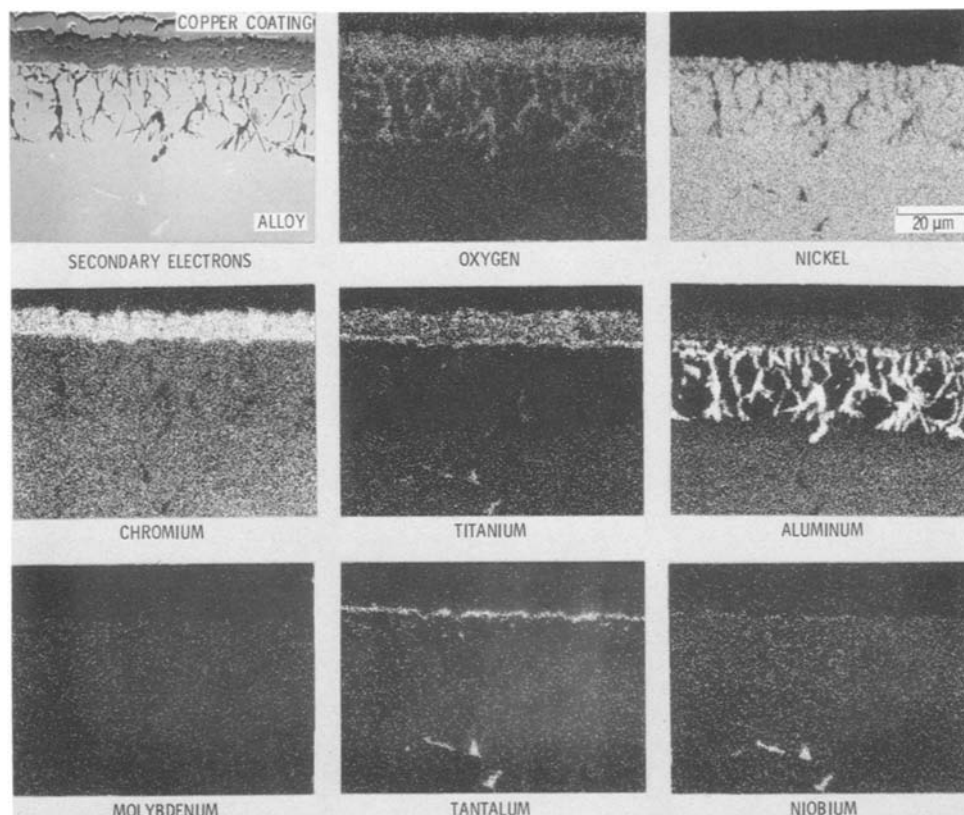


Fig. 2. Secondary electron and x-ray micrographs of IN-738 specimen preoxidized at 975°C for 24h in flowing oxygen

oxides formed during isothermal oxidation and to roughly calculate their relative amounts. The results for Cr_2O_3 and TiO_2 presented in Fig. 1 show that the oxide layer formed in 24h is about 75 mole percent (m/o) Cr_2O_3 and 25 m/o TiO_2 .

Thermogravimetric analysis.—A typical hot corrosion curve for preoxidized IN-738 is shown in Fig. 3a. The hot corrosion process for this alloy is characterized by a rather long induction period. The duration of this period is a function of alloy composition, preoxidation treatment, test temperature, and amount of Na_2SO_4 applied (7). An examination of Fig. 3a indicates that the induction period is about 55h and that the corresponding specific weight gain is 5 mg cm^{-2} . If the specific weight gain during the latter part of the induction period is plotted on an expanded scale, it is seen that the specimen corrodes at a linear rate from 15 to 55h, an indication that the oxide formed is not protective in the usual sense. The linear corrosion rate is $0.14 \text{ mg cm}^{-2} \text{ h}^{-1}$, about four times the oxidation rate at 24h during preoxidation.

The induction period is followed by a period of rapidly accelerating corrosion until, at about 60h, attack becomes catastrophic and rapid linear weight gain which continues until about 75h is displayed. By this time, most of the specimen is consumed and is covered with a voluminous, porous, greenish-black oxide (Fig. 4). Most of the attack occurs on the bottom half of the specimen, owing to "slumping" of the liquid Na_2SO_4 .

Sulfur dioxide evolution.—Sulfur dioxide evolution results are shown in Fig. 3b for a typical specimen. The SO_2 product concentration rises rapidly when beginning a run to about $3.4 \pm 0.25 \text{ ppm cm}^{-2}$ (25 ppm), generally within the first 5-10 min of reaction, then it decreases to about 0.27 ppm cm^{-2} (2 ppm) at 4h and to $<0.0027 \text{ ppm cm}^{-2}$ (<0.02 ppm) at 20h. No further SO_2 is detected until the specimen starts corroding catastrophically. Then, the SO_2

level rises slowly to about $0.014 \text{ ppm cm}^{-2}$ (0.1 ppm) at 80h and decreases to 0.02 ppm at 110h.

Analysis of water soluble elements.—Water-soluble compounds are extracted from reacted specimens for chemical analysis. Tests times ranging from 5 min to 100h are normalized to the weight-gain time scale by matching each individual weight gain with the curve given in Fig. 3a. The quantities of various species, reported in Fig. 3c, are normalized to the initial quantity of Na_2SO_4 of 0.168 mmol. The S^{-2} concentrations in the specimens are also shown in Fig. 3c as a function of time.

The amount of SO_4^{-2} recovered drops rapidly to 10% of its original value in 12.5h and to ~ 0 after 25h. The applied sodium ($1/2 \text{ Na}^+$) is completely recovered for times of up to about 5h, after which it rapidly decreases to $\sim 30\%$ of its original value at 30h, persists to $\sim 40\text{h}$, rises to 0.07 mmol at 75h, then falls sharply and levels out at ~ 0.01 mmol. A large quantity (0.11 mmol) of soluble chromium (CrO_4^{-2}) is formed. The soluble chromium rises rapidly to a peak at $\sim 10\text{h}$, then falls in a nearly linear manner until about 30h, subsequently decreasing slowly to a small value after about 60h. Soluble molybdenum (MoO_4^{-2}), which is assumed to come from Na_2MoO_4 , appears at $\sim 10\text{h}$ and increases linearly through the induction period to >0.02 mmol at 55h. It increases more rapidly during catastrophic corrosion, peaks at 0.06 mmol at 75h, and decreases rapidly to 0.01 mol at 90h. Soluble tungsten (WO_4^{-2}) is detected at about the same time as the soluble molybdenum, but increases more slowly than molybdenum and peaks at 40h.

The solutions are also analyzed for soluble aluminum, titanium, tantalum, niobium, and nickel. Soluble aluminum, an important feature in the hot corrosion of B-1900 and VIA, is not detected here. Only soluble nickel is found, at levels less than 0.01 mmol, during the period of catastrophic corrosion. Sulfur is found in the 5 and 10h

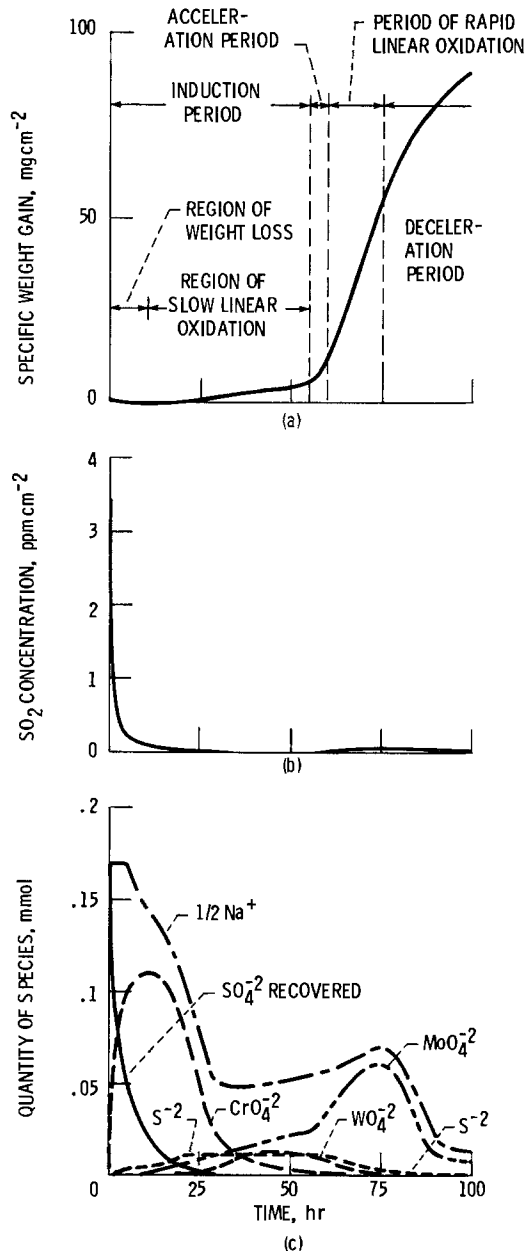
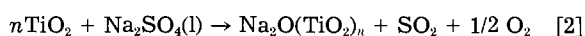
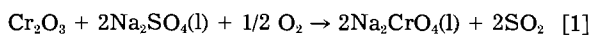


Fig. 3. Preoxidized IN-738 corroded with $3 \text{ mg cm}^{-2} \text{ Na}_2\text{SO}_4$ at 975°C in slowly flowing oxygen: (a) typical specific weight change; (b) concentration of SO_2 evolved as a function of time; and (c) quantity of water soluble species found remaining.

specimens at 0.004 mmol . The value rises to 0.01 mmol at 20h , remains constant until after 60h , and decreases to 0 at 100h .

If the loss of sulfate is due to reaction with Cr_2O_3 and TiO_2 in the scale, there should be a direct proportionality between the SO_2 evolved and the sulfate reacted, as shown by the reactions



Cumulatively evolved SO_2 quantities are obtained by numerically integrating the concentrations over time. These values are compared with the sulfate reacted in Fig. 5. A direct relationship does exist between the two quantities, but the quantity of SO_2 evolved is only about 35% of the quantity of sulfate reacted. This discrepancy arises because some SO_2 is converted to SO_3 in and below the reaction zone. Since the SO_3/SO_2 ratio is characteristic of a temperature lower than that in the reaction zone, accurate theoretical correction for its presence is precluded. The

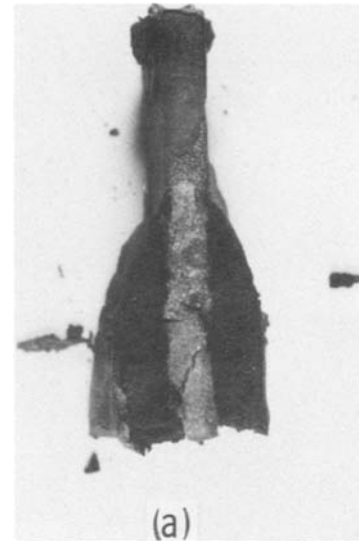


Fig. 4. Typical IN-738 specimen after corrosion with $3 \text{ mg cm}^{-2} \text{ Na}_2\text{SO}_4$ for 100h at 975°C in slowly flowing oxygen (edge view with oxide scale intact).

direct relationship between evolved SO_2 and the reacted sulfate lends credence to the occurrence of reactions [1] and/or [2] in the early part of the hot corrosion process.

Microprobe analysis.—Samples from specimens tested for 5 min – 90h are prepared for microprobe examination. All of the samples are examined carefully in several different areas, and only the most pertinent micrographs will be discussed.

The appearance of the 5 min sample is similar to that of the preoxidized sample (Fig. 2), but radical changes occur in 5h (Fig. 6). Most of the original continuous Cr_2O_3 - TiO_2 layer is removed, and islands of the alloy, with most of the Cr , Al , and Ti leached out, protrude along the surface. The outer oxide layer is still primarily Cr_2O_3 and TiO_2 , but is no longer continuous, and depletion of chromium in the alloy is more pronounced. Sodium seems to be associated with the chromium and/or the titanium. X-ray micrographic observations in 5 and 10h samples are complicated by formation of a void that encircles most of the sample cross section between the oxide layer and the copper coating. It is believed that the void develops during polishing by removal of a large drop of Na_2CrO_4 which is observed visually on the specimens after testing. The chromium micrograph in Fig. 6 indicates the presence of chromium in the void and an almost continuous Cr_2O_3

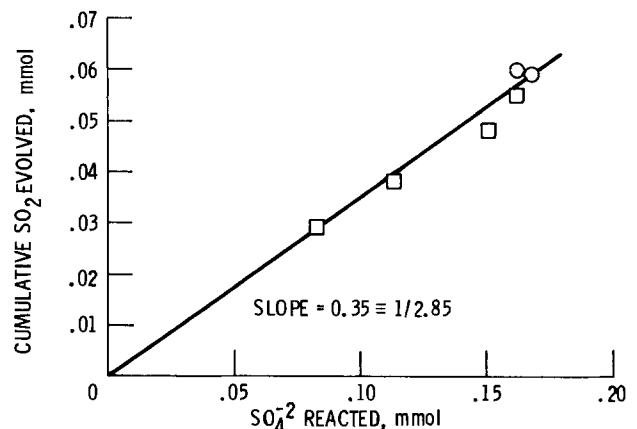


Fig. 5. Relationship between cumulative quantity of SO_2 evolved and quantity of sulfate reacted during hot corrosion of IN-738 at 975°C .

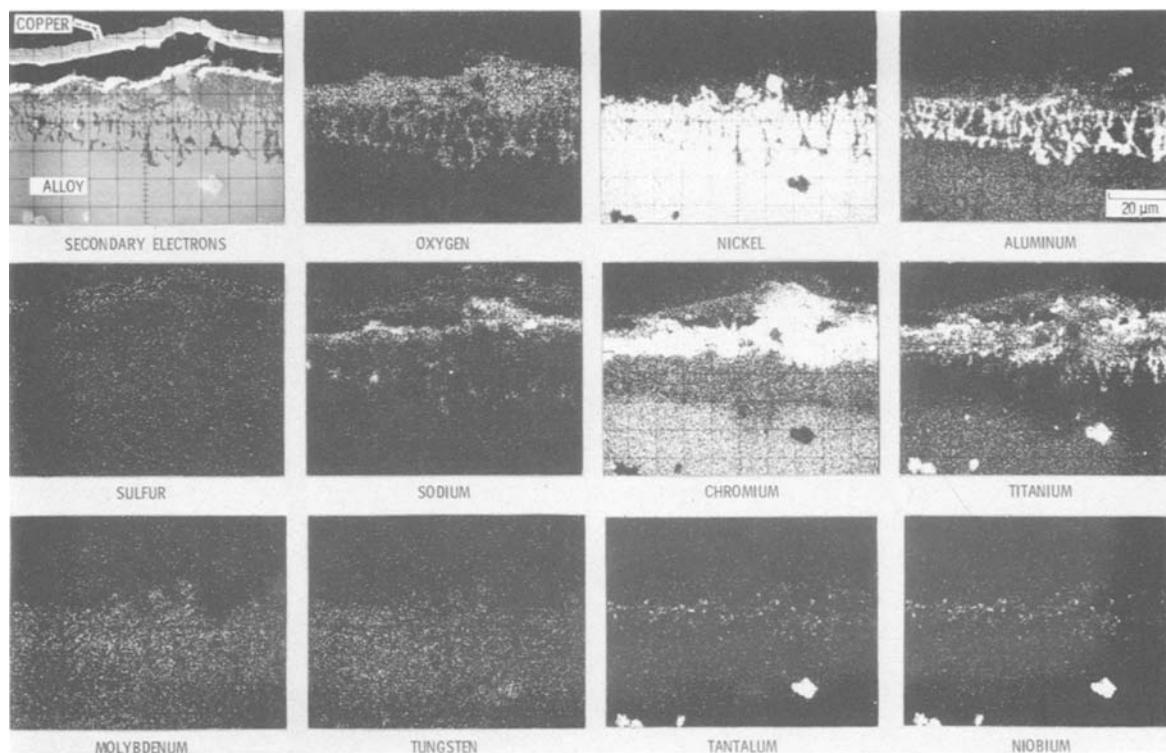


Fig. 6. Secondary electron and x-ray micrographs of preoxidized IN-738 specimen corroded at 975°C with 3 mg cm⁻² Na₂SO₄ for 5h

layer on the sample, though the secondary electron micrograph clearly shows a noncontinuous Cr₂O₃ layer. Light micrographs are not affected by the presence of the void, and they show the discontinuous Cr₂O₃-TiO₂ layer unambiguously (Fig. 7). Micrographs of the 10h sample resemble those of the 5h sample.

For the 20h sample, the micrographs (Fig. 8) show reforming of a 20-30 μm thick oxide scale. The oxide advances into the region of Al₂O₃ tentacles and is primarily Cr₂O₃ and TiO₂, with scattered NiO and engulfed Al₂O₃. The depletion zones for Cr and Ti are wider and more depleted. Chromium sulfides appear near the bottom of the depletion zone and probably in the upper portion, as well. Sodium remains associated with Cr and Ti along the outer edge of the sample. Some areas of sodium within the scale are associated with tantalum and/or niobium and are probably either NaTaO₃ or NaNbO₃, formed from the original Ta and Nb carbides. Sodium is also associated with tantalum and niobium oxides found along the bottom edge of the scale. Molybdenum and tungsten are associated with the isolated Ni-Co islands between the Al₂O₃ tentacles in the scale.

The micrographs of the 30h sample (Fig. 9) show continued growth of the Cr₂O₃-TiO₂-Al₂O₃-NiO scale. "Ghosts" of the Al₂O₃ tentacles appear near the bottom of the scale. Nickel oxide becomes more prominent along the outer edge of the oxide layer. Sodium is still distributed in the scale and associated with tantalum and niobium. Sulfur is at the bottom of the depletion zone and on grain boundaries; it is associated primarily with titanium. An area of MoO₃-WO₃ appears at the bottom of the scale near the left side.

In the 40h sample, the oxide is about 30-35 μm thick, with some areas up to 60 μm thick (Fig. 10). It appears that the leached Ni-Co islands oxidize. At the lower edge of the oxidized islands are isolated areas of MoO₃-WO₃, which must have originated from the Mo and W in solution in the Ni-Co islands. The composition of the scale is similar to that of the 30h sample, but the sodium seems to

be tied up as NaTaO₃/NaNbO₃, and little or no sulfur is in evidence.

In the 48h sample, a large fraction of the oxide is 60 μm thick (Fig. 11) and has a morphology similar to that of the thick area of the 40h sample. The MoO₃-WO₃ areas on the bottom edge of the scale are still discrete, but so numerous as to be virtually continuous. Although some sodium is combined with the Ta and Nb, some is also associated with the MoO₃-WO₃ areas, probably as Na₂MoO₄ and/or Na₂WO₄. Sulfur occurs in small concentrations in the MoO₃-WO₃ areas. NiO is observed in the oxidized islands and along the outer edge of the scale.

Most of the oxide layer in the 56h sample is similar to the 48h sample presented in Fig. 11. In two locations, MoO₃-WO₃ areas merge to form a molten phase, probably composed of MoO₃-WO₃ and Na₂MoO₄-Na₂WO₄ (Fig. 12). The sulfides are engulfed by the molten phase, and sodium is distributed throughout the entire oxide layer and the molten phase. The oxide scale is 80-90 μm thick and is composed of all the metallic components of the alloy, except molybdenum and tungsten. The striated or layered structure is characteristic of that found when acidic fluxing occurs (reaction [1]; Fig. 14). The 62, 68, and 77h samples all show an increasing occurrence of areas similar to those in the 56h sample.

In the 90h sample, the molten phase under the scale decreases in prominence. In some areas, the molten MoO₃-WO₃/Na₂MoO₄-Na₂WO₄ is converted to solid NiMoO₄-NiWO₄, as identified by x-ray diffraction (Fig. 13). Most of the thick oxide scale peels off the sample, revealing the NiMoO₄-NiWO₄ layer. This layer exhibits a great deal of cracking because of the NiMoO₄ phase transformation or cooling. Sodium is no longer observed with the molybdate; it diffuses deep into the alloy where it combines with tantalum and niobium located in internal carbides.

Rate determinations of pertinent processes.—To interpret the above results, measurements of the rates of several pertinent physical and chemical processes are re-

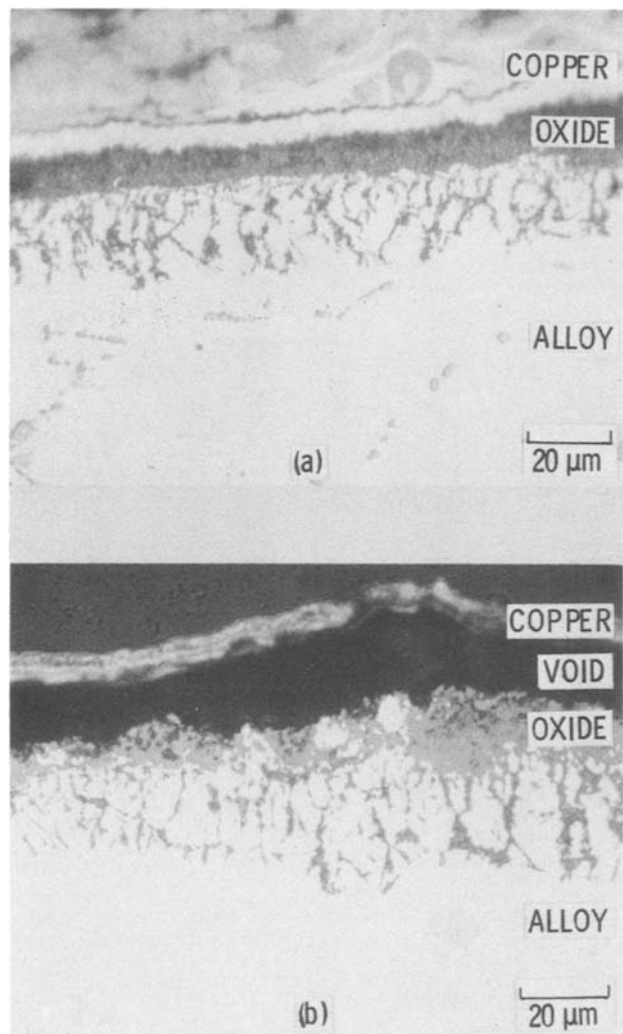


Fig. 7. Light micrographs of IN-738 specimens: (a) preoxidized for 24h at 975°C; and (b) preoxidized for 24h and corroded at 975°C with 3 mg cm⁻² Na₂SO₄ for 5h.

quired. Some of these processes have been investigated, and they allow reasonable conclusions to be drawn regarding the hot corrosion of IN-738.

Evaporation of Na₂SO₄ and Na₂CrO₄.—3 mg cm⁻² deposits of Na₂SO₄ or Na₂CrO₄ are air brushed onto coupons the same size as the oxidation specimens. Gold coupons are used for Na₂SO₄ (16), and platinum is used for Na₂CrO₄. The weight loss at 975°C is determined under the same experimental conditions as in the hot corrosion tests. Weight losses are monitored for periods of up to 100h and are linear in time. After the tests, the cooled coupons are water-washed, and the resulting solutions are analyzed for sodium and either SO₄⁻² or CrO₄⁻². The analyses agree well with the measured weight losses. In addition, the pH's of the wash solutions are measured and are found to agree well with pH values of prepared solutions of the respective salts. This agreement of pH values

indicates that no dissociative vaporization occurs. The bare coupons have no weight loss, showing that no reactions occur between them and the salts. The rates of evaporation are given in Table I, where it is seen that Na₂CrO₄ evaporates about 1.5 times more rapidly than Na₂SO₄.

Rate of reaction of Na₂SO₄ with the pure oxides Cr₂O₃ and TiO₂.—To measure the individual rates of reactions [1] and [2], pure Cr₂O₃ and TiO₂ layers are reacted using the same experimental conditions as for hot corrosion of IN-738. The Cr₂O₃ sample is made by preoxidizing a coupon of pure chromium at 975°C. The TiO₂ sample is made by plasma spraying high purity TiO₂ onto a platinum coupon and annealing in oxygen at 975°C for 2h. The amounts of TiO₂ and Cr₂O₃ are more than are required for complete reaction with Na₂SO₄.

Results for a Cr₂O₃ specimen, tested for 2.5h, are shown in Fig. 14. The specific weight increases initially, followed by a loss during the period when SO₂ and SO₃ are being evolved rapidly. Finally, a slow increase occurs because of further oxidation of the Cr coupon. The concentration of evolved SO₂ rises rapidly to 4.3 ppm cm⁻² and then falls at a fast, though decreasing rate. Based on the results of Fig. 5, the low value for the concentration of SO₂ at the end of the experiment indicates that the reaction between Cr₂O₃ and Na₂SO₄ is mostly completed. This conclusion is supported by the chemical analyses of the water-wash solutions (Table II), which show that 94% of the SO₄⁻² reacts during the experiment. The quantity of CrO₄⁻² formed equals the quantity of SO₄⁻² reacted, as expected (Table II, column 7). The ratio of SO₂ evolved to SO₄⁻² reacted is 0.40, similar to (but slightly larger than) that obtained in the hot corrosion experiments (Fig. 5).

To calculate a rate constant for reaction [1] from the data shown in Fig. 14, we have assumed that the reaction is first order with respect to the concentration of SO₄⁻². Therefore, the kinetics should be described by the equation

$$\log(C_0/C) = k_1 t / 2.303 \quad [3]$$

where k_1 is the first-order rate constant, C is the concentration of SO₄⁻² at time t , and C_0 is the initial concentration of SO₄⁻². The concentration of SO₄⁻² can be obtained from the cumulative SO₂ at any time using the relationship shown in Fig. 5. From the values of residual SO₄⁻² so obtained, a plot of $\log C$ vs. t is constructed (Fig. 15). The data follow a straightline relationship reasonably well for the first 2h, during which 95% of the sulfate is reacted. The first-order rate constant is $k_1 = 1.55\text{h}^{-1}$ (Table I).

The specific weight of the TiO₂ sample falls at a constant rate throughout the experiment after an initial 4h period (Fig. 16) and levels off at 24h, at which time virtually all of the Na₂SO₄ has reacted. The concentration of SO₂ evolved is approximately constant throughout the experiment, with an average value of 0.145 ppm cm⁻². The observed weight loss can be correlated with the expected evolution of SO₂ during the experiment, as indicated by reaction [2]. There should also be a weight gain of the TiO₂-Pt coupon resulting from the formation of Na₂O(TiO₂)_n. The results presented in the last line of Table II correlate well with the behavior predicted by reaction [2]. Analysis of the water-wash solution indicates that all of the SO₄⁻² applied has reacted (Table II, columns 3, 4, and 6). The ratio of SO₂ evolved to SO₄⁻² re-

Table I. Rates of pertinent processes

System	Evaporation rate (mmol cm ⁻² h ⁻¹)	First-order rate constant, k_1 (h ⁻¹)	Zero-order rate constant, k_0 (mmol cm ⁻² h ⁻¹)
Na ₂ SO ₄ (l) → Na ₂ SO ₄ (g)	1.0 × 10 ⁻⁴		
Na ₂ CrO ₄ (l) → Na ₂ CrO ₄ (g)	1.5 × 10 ⁻⁴		
Cr ₂ O ₃ + 2Na ₂ SO ₄ (l) + 3/2 O ₂ → 2Na ₂ CrO ₄ (l) + 2SO ₃ (g)		1.55	
n TiO ₂ + Na ₂ SO ₄ (l) → Na ₂ O(TiO ₂) _n + SO ₃ (g)			1.25 × 10 ⁻³
n TiO ₂ + Na ₂ CrO ₄ (l) → Na ₂ O(TiO ₂) _n + CrO ₃ (g)			5.9 × 10 ⁻⁴

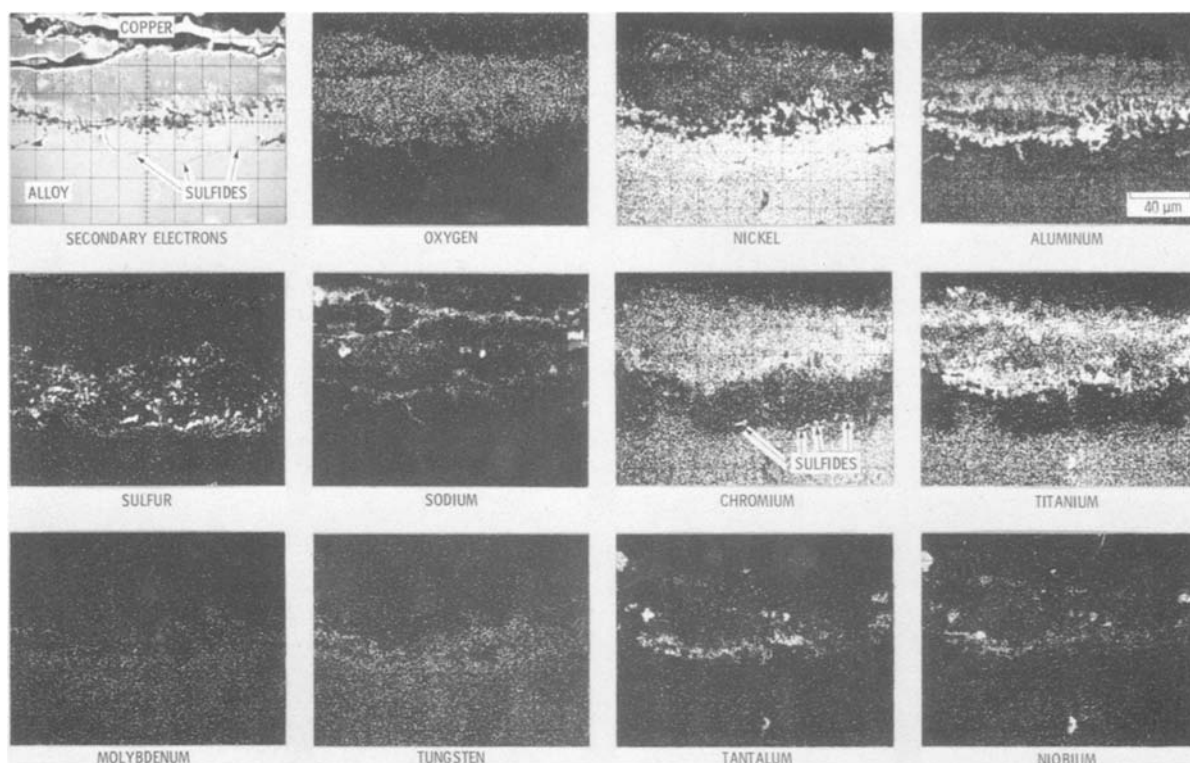


Fig. 8. Secondary electron and x-ray micrographs of preoxidized IN-738 specimen corroded at 975°C with 3 mg cm⁻² Na₂SO₄ for 20h

acted is 0.335 (Table II, column 9). The total weight loss expected from SO₂ + SO₃ evolution during the experiment agrees with the experimental value given in column 11. The expected overall weight gain of the coupon after the experiment, resulting from Na₂O(TiO₂)_n formation

(column 12), agrees well with the experimental value given in column 13. After the experiment, the coupon is examined by x-ray diffraction. Unreacted TiO₂ and the compound Na₂Ti₃O₁₁, the most stable form of sodium titanate, are identified.

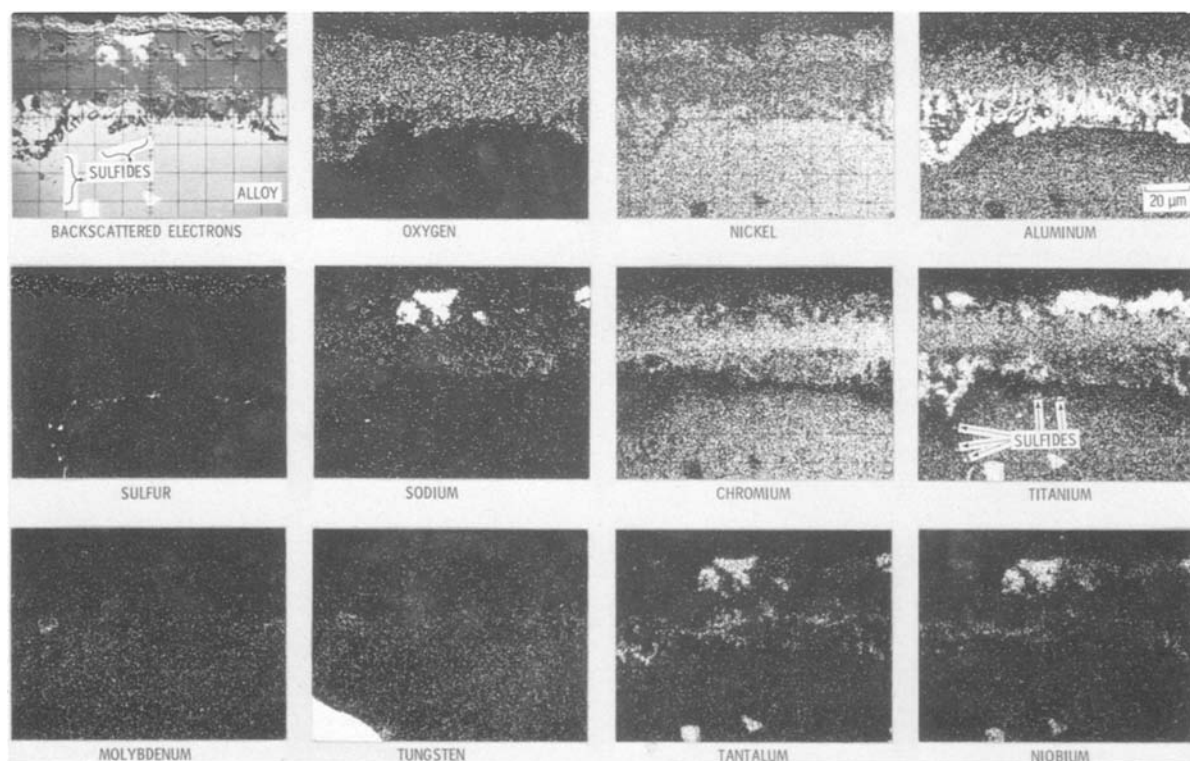


Fig. 9. Back-scattered electron and x-ray micrographs of preoxidized IN-738 specimen corroded at 975°C with 3 mg cm⁻² Na₂SO₄ for 30h

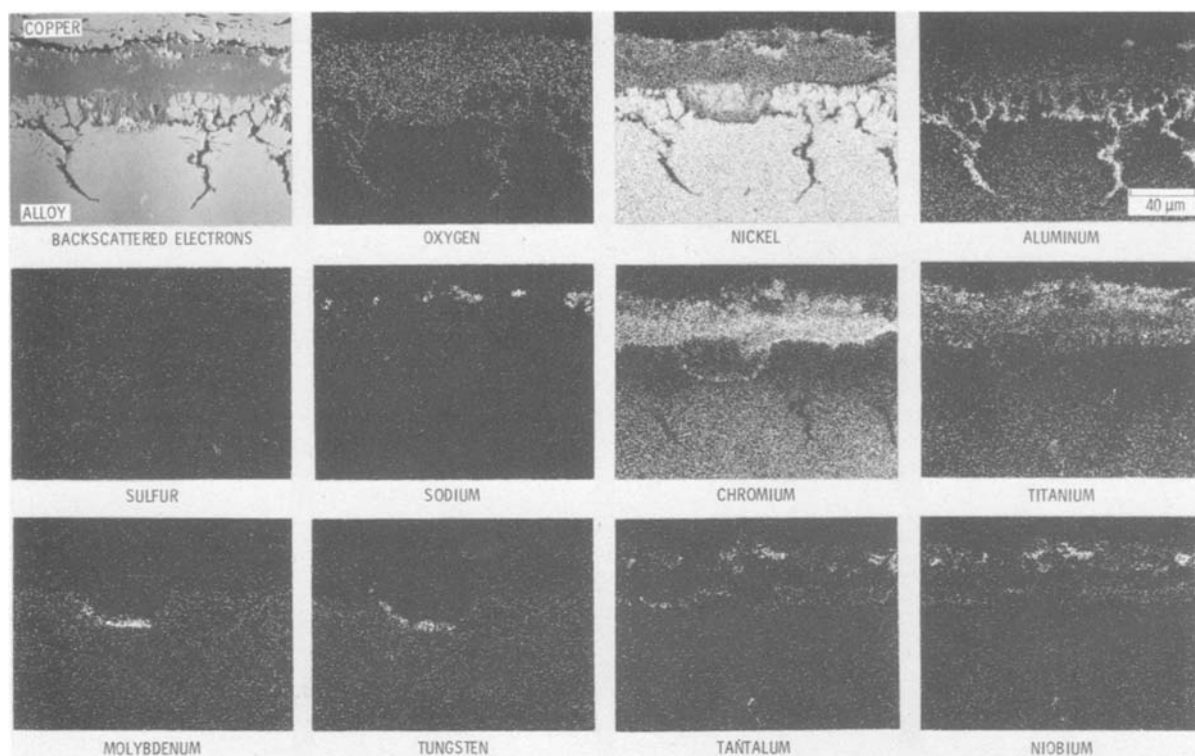


Fig. 10. Back-scattered electron and x-ray micrographs of preoxidized IN-738 specimen corroded at 975°C with 3 mg cm⁻² Na₂SO₄ for 40h

The kinetics of reaction [2] are characteristic of a zero-order reaction, for which

$$C_0 - C = k_0 t \quad [4]$$

where k_0 is the zero-order rate constant, C is the concentration of sulfate at time t , and C_0 is the initial concentra-

tion of sulfate. Because the weight loss of the sample is equivalent to the SO₄⁻² reacted, Fig. 16 is a plot of C vs. t , and the slope of the straight line gives $k_0 = 5.9 \times 10^{-4}$ mmol cm⁻² h⁻¹ (Table I).

The rate constants in Table I can be used to calculate the relative rates of Na₂SO₄ reactions with Cr₂O₃ and TiO₂

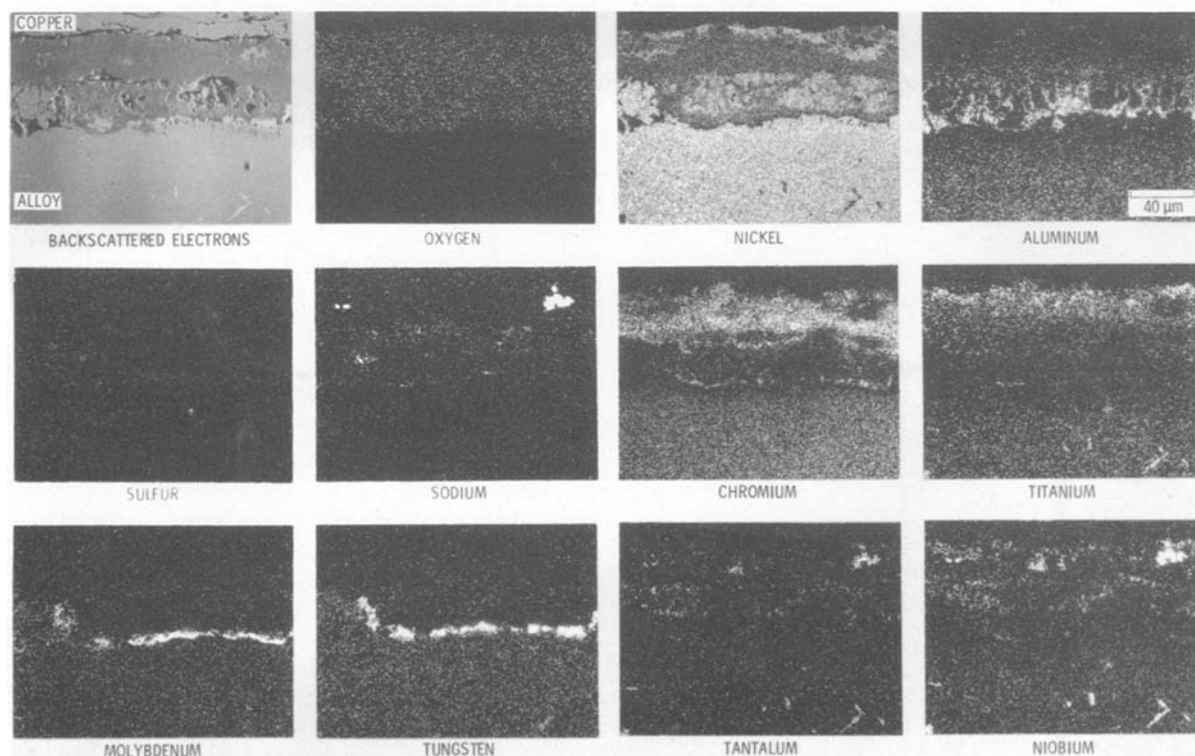


Fig. 11. Back-scattered electron and x-ray micrographs of preoxidized IN-738 specimen corroded at 975°C with 3 mg cm⁻² Na₂SO₄ for 48h

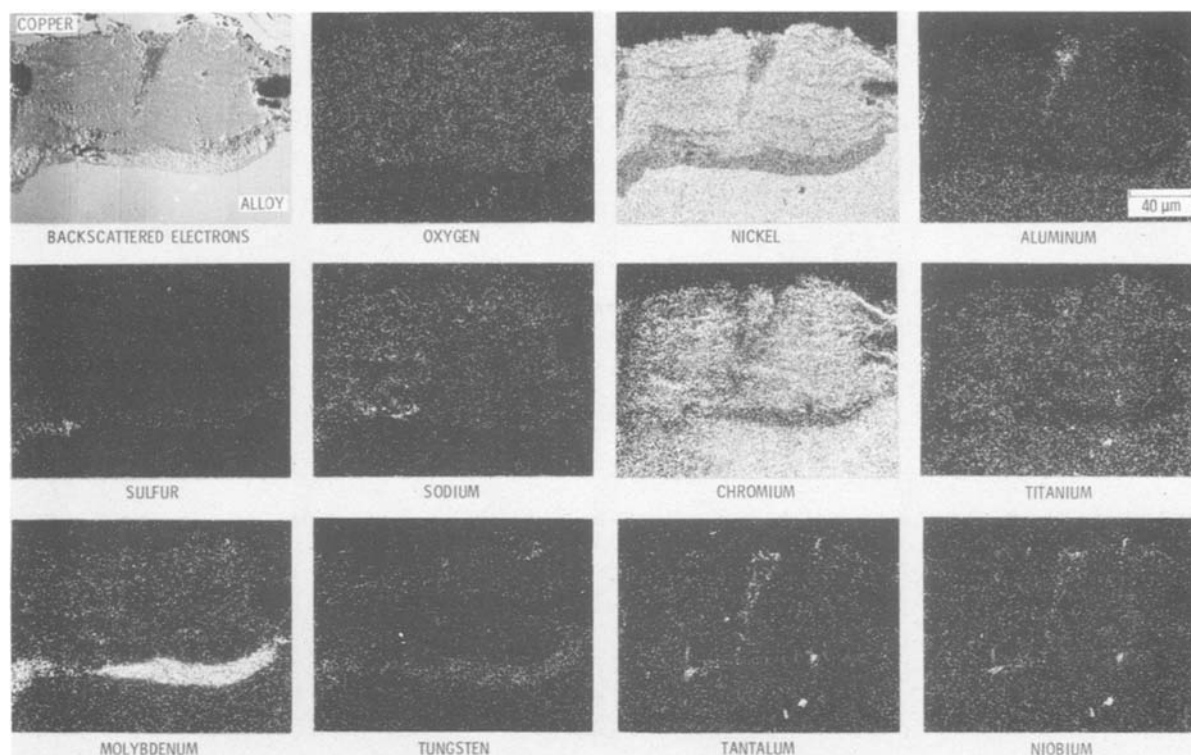


Fig. 12. Back-scattered electron and x-ray micrographs of preoxidized IN-738 specimen corroded at 975°C with $3 \text{ mg cm}^{-2} \text{ Na}_2\text{SO}_4$ for 56h

during hot corrosion. The rate of reaction [1] can be determined using the SO_4^{-2} curve in Fig. 3c. The zero-order rate constant for reaction [4] is multiplied by 7.5 cm^2 , a typical area for the IN-738 specimens.

Results of these calculations in Table III show that the Na_2SO_4 should react much more rapidly with Cr_2O_3 than with TiO_2 on IN-738. The Cr_2O_3 reaction rate is initially 30 times faster than the TiO_2 rate, and when the SO_4^{-2} is half

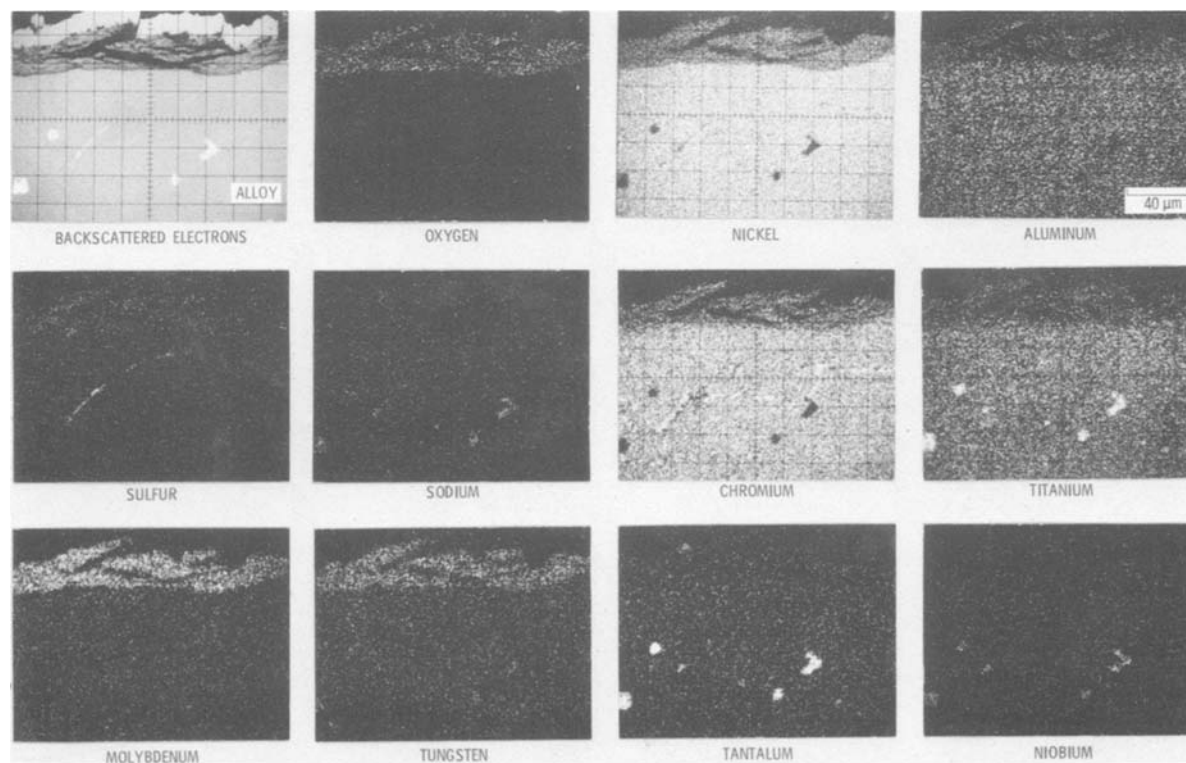


Fig. 13. Back-scattered electron and x-ray micrographs of preoxidized IN-738 specimen corroded at 975°C with $3 \text{ mg cm}^{-2} \text{ Na}_2\text{SO}_4$ for 90h

Table II. Mass balance results of oxide-Na₂SO₄ reactions

1	2	3	4	5	6	7	8	9	10	11	12	13
Reactant system	Test duration (h)	SO ₄ ⁻² applied (mmol)	SO ₄ ⁻² recovered (mmol)	SO ₄ ⁻² reacted (mmol)	Fraction SO ₄ ⁻² reacted	CrO ₄ ⁻² analysis (mmol)	SO ₂ evolved (mmol)	Ratio of SO ₂ evolved to SO ₄ ⁻² reacted	Calc'd -ΔW _{SO₃} (mg)	Expt'l -ΔW (mg)	Calc'd ΔW _{Na₂O} (mg)	Expt'l ΔW (mg)
Cr ₂ O ₃ on Cr	2.5	0.0656	0.00385	0.0617	0.94	0.0615	0.0247	0.40	NA	NA	NA	NA
TiO ₂ on Pt	29.0	0.169	0	0.169	1.0	NA	0.057	0.335	13.5	14.3	10.5	10.1

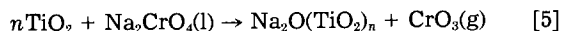
Table III. Relative reaction rates of Na₂SO₄ with Cr₂O₃ and TiO₂ at various times during the hot corrosion of IN-738

Time (h)	Residual SO ₄ ⁻² (mmol)	Fraction residual SO ₄ ⁻²	R(Cr ₂ O ₃) (mmol min ⁻¹)	R(TiO ₂) ^a (mmol min ⁻¹)	$\frac{R(\text{Cr}_2\text{O}_3)}{R(\text{TiO}_2)}$
0.0	0.168	1.0	4.4 × 10 ⁻³	1.5 × 10 ⁻⁴	29
0.5	0.135	0.80	3.5 × 10 ⁻³	1.5 × 10 ⁻⁴	23
1.0	0.117	0.70	3.0 × 10 ⁻³	1.5 × 10 ⁻⁴	20
2.0	0.092	0.55	2.4 × 10 ⁻³	1.5 × 10 ⁻⁴	16
2.5	0.085	0.50	2.2 × 10 ⁻³	1.5 × 10 ⁻⁴	15
5.0	0.054	0.32	1.5 × 10 ⁻³	1.5 × 10 ⁻⁴	10
7.5	0.035	0.21	9.1 × 10 ⁻⁴	1.5 × 10 ⁻⁴	6.1
10.0	0.025	0.15	6.5 × 10 ⁻⁴	1.5 × 10 ⁻⁴	4.3
12.5	0.017	0.10	4.4 × 10 ⁻⁴	1.5 × 10 ⁻⁴	2.9

^a Calculated for a specimen area of 7.5 cm².

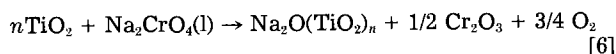
gone after 2.5h, the factor is still 15. The rates do not become comparable until virtually all of the SO₄⁻² has reacted. Thus, most of the Na₂SO₄ applied to the IN-738 specimens should react primarily with the Cr₂O₃ in the preoxidized scale.

Rate of reaction of Na₂CrO₄ with TiO₂.—Considerable Na₂CrO₄ is formed in the initial stage of hot corrosion, which can evaporate and/or react with other oxides present on the preoxidized IN-738 specimens. The rate of the reaction



is studied.

The oxide CrO₃ should volatilize rapidly at 975°C (17). However, because of boundary layer considerations, some fraction may back-reflect to the hot specimen (18), decomposing on contact and resulting in redeposition of Cr₂O₃. For these molecules, the net reaction is



The specimens used are made by plasma spraying TiO₂ onto Pt coupons and annealing in oxygen for 2h at 975°C. The Na₂CrO₄ at 3 mg/cm² is air-brushed onto the speci-

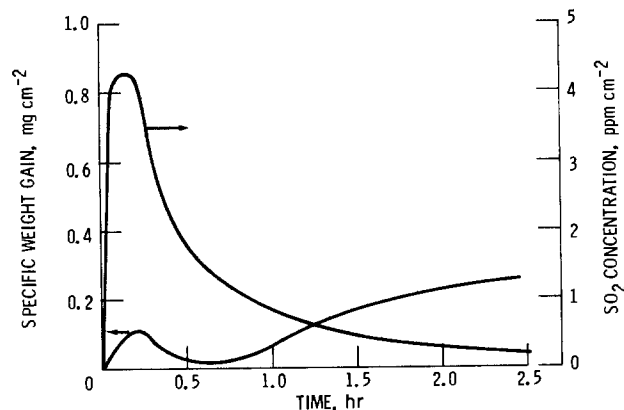


Fig. 14. Specific weight gain and concentration of SO₂ evolved per unit specimen area as a function of time for preoxidized chromium corroded at 975°C in flowing oxygen with 3 mg cm⁻² Na₂SO₄ (sample area = 2.9 cm²).

mens. Experimental methods similar to those used in the hot corrosion experiment are used.

Samples tested up to 14h exhibit a steady, constant decrease in specific weight, similar to that exhibited in Fig. 16 for the reaction of TiO₂ with Na₂SO₄. The rate of weight loss is calculated to be 4.1 × 10⁻² mg/cm² h⁻¹, corrected for Na₂CrO₄ evaporation. The constant rate of weight loss indicates that the reaction of TiO₂ with Na₂CrO₄ is of zero order.

The overall rate constant of reaction of Na₂CrO₄ with TiO₂ can be calculated from the results of the chromium analyses of the water-wash solutions. These data give a value for the rate constant k₀ of 9.55 × 10⁻² mg cm⁻² h⁻¹ or 5.9 × 10⁻⁴ mmol cm⁻² h⁻¹, both corrected for Na₂CrO₄ evaporation. This value is given in Table I for comparison with the rate constant from reaction [4]. Using the value of 9.55 × 10⁻² mg Na₂CrO₄ cm⁻² h⁻¹ for the reaction and using the experimental value for the rate of weight loss, 4.1 × 10⁻² mg cm⁻² h⁻¹, we deduce that 60% of the Na₂CrO₄ reacts by reaction [5] and that 40% reacts by reaction [6]. The overall weight gain of the coupon resulting from Na₂O(TiO₂)_n formation corroborates these percentages. As in the reaction with TiO₂ and Na₂SO₄, x-ray diffraction analysis shows the presence of Na₂Ti₅O₁₁ on the coupons after the experiment, and the water-wash solutions yield soluble sodium equivalent to the unreacted Na₂CrO₄.

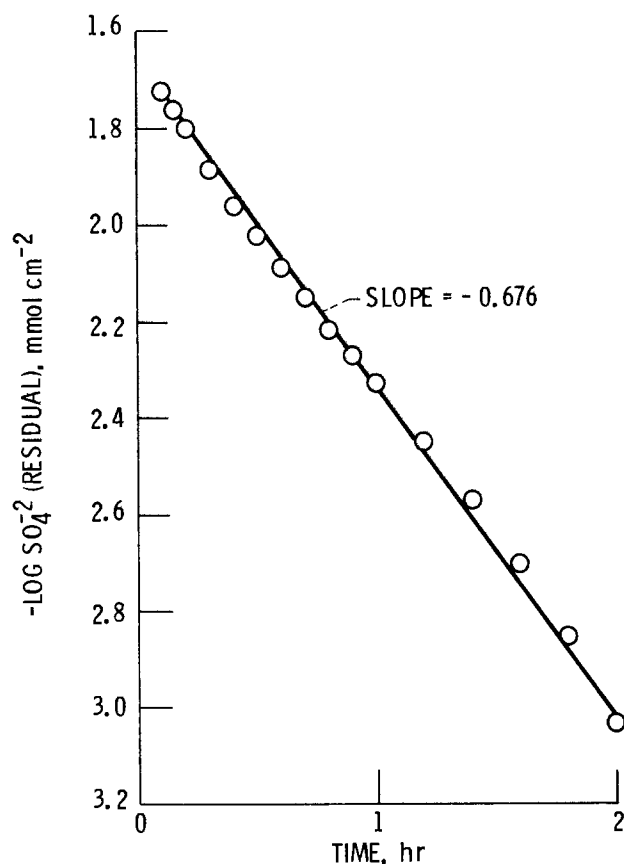


Fig. 15. First-order reaction rate plot for preoxidized chromium specimen corroded at 975°C in flowing oxygen with 3 mg cm⁻² Na₂SO₄.

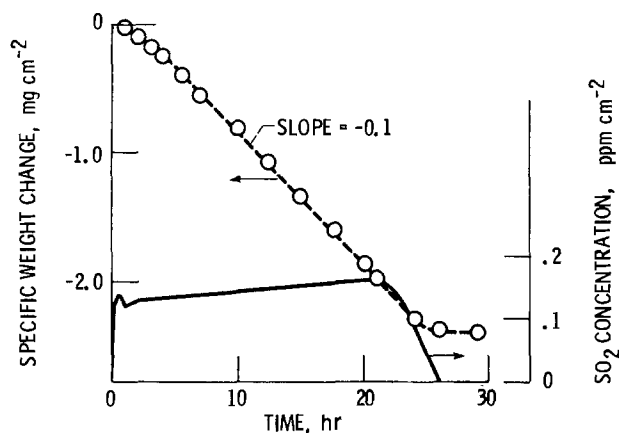


Fig. 16. Specific weight change and concentration of SO_2 evolved per unit specimen area as a function of time for plasma-sprayed TiO_2 corroded at 975°C in flowing oxygen with 3 mg cm^{-2} Na_2SO_4 (sample area = 5.8 cm^2).

Chemical Mechanisms

The results obtained in the present studies of Na_2SO_4 -induced hot corrosion of IN-738 can be explained in terms of the sequence of reactions presented in Table IV. The time periods listed in this table are defined in Fig. 3a.

The initial oxide fluxing reactions are generally discussed with reference to thermodynamic stability diagrams such as those for the Cr-O-S, Ti-O-S, Mo-O-S, and W-O-S systems shown superimposed on a diagram for the Na-O-S system at a temperature of 975°C (Fig. 17a, b, c, and d). The diagrams are constructed by using the FACT computer program (19), and they show the phases that are in equilibrium with gas mixtures having specified pressures of O_2 and SO_3 . The dashed vertical line in the diagrams is the boundary where $\log a_{\text{Na}_2\text{O}} = \log P_{\text{SO}_3}$ in Na_2SO_4 , and it is representative of "neutral" Na_2SO_4 at 975°C .

Examination of Fig. 17 shows that the oxides of all four elements should be converted to the appropriate sodium salts in neutral Na_2SO_4 under 1 atm of oxygen and that the most stable sodium salts under high SO_3 pressure (or low oxide ion activities) are Na_2MoO_4 and Na_2WO_4 .

Although these diagrams have been used extensively to interpret hot corrosion behavior in terms of the chemical reactions involved, their usefulness is limited because

they give no kinetic information. The interpretation of our results will be based largely on the results of the kinetic studies described in a previous section.

Induction period, region of weight loss (0-10h).—Immediately upon bringing the test specimens to temperature, the Na_2SO_4 melts and reacts with the Cr_2O_3 to form Na_2CrO_4 and SO_3 ([a], Table IV). The early occurrence of this reaction is substantiated by the evolution of SO_2 (Fig. 3b), the appearance of water-soluble chromium (Fig. 3c), and the rapid drop in residual SO_4^{2-} (Fig. 3c). This behavior is predicted by the stability diagram for chromium (Fig. 17a), and kinetic studies of [a], Table IV, indicate that Cr_2O_3 and Na_2SO_4 should react rapidly until all Na_2SO_4 is consumed. The 0.11 mmol of Na_2SO_4 that reacted with the Cr_2O_3 in the first 10h of hot corrosion is equivalent to removal of all of the Cr_2O_3 from the bottom 2/5 of the specimen; this agrees with observations of "slumping" of the liquid reactants.

After an incubation period of about 5h, the TiO_2 on the specimen begins to react with the Na_2SO_4 and forms water-insoluble $\text{Na}_2\text{O}(\text{TiO}_2)_n$, ([b], Table IV), as evidenced by the drop in soluble sodium beginning at this time (Fig. 3c). This behavior is also predicted by the stability diagram for titanium (Fig. 17b). Our kinetic studies also demonstrate that [b], Table IV, should occur, though at a much slower rate than the Na_2SO_4 - Cr_2O_3 reaction.

Comparison of the SO_2 concentrations in Fig. 3b for IN-738 and in Fig. 14 for Cr_2O_3 indicates that the reaction with the alloy continues for 20-25h; the reaction with Cr_2O_3 is effectively completed in 2.5h. The lowered activity of the Cr_2O_3 in the oxide mixture relative to that of pure Cr_2O_3 may account for the difference. This difference precludes quantitative interpretation of the IN-738 kinetic data, and it appears that kinetic data for reactions of Na_2SO_4 with known mixtures of Cr_2O_3 and TiO_2 are required.

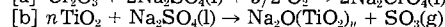
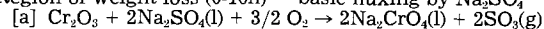
In the first 10h of corrosion of IN-738, Na_2SO_4 is mostly consumed by reaction with the protective oxide scale on the alloy. The Cr_2O_3 - TiO_2 scale is removed from the bottom half of the specimen by this basic fluxing (Fig. 6). The weight loss observed during this period results from evolution of SO_3 + SO_2 from the sample as a result of the reactions.

Induction period, region of slow linear oxidation (10-55h).—A result of the reaction between Cr_2O_3 and Na_2SO_4 during the first 10h of corrosion is the formation of Na_2CrO_4 (Fig. 3c). The Na_2CrO_4 is liquid at 975°C , and it covers the surface of the specimen. Examination of Fig.

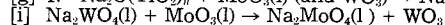
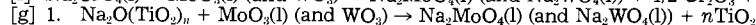
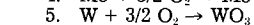
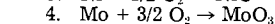
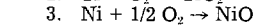
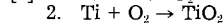
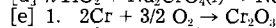
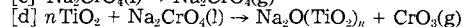
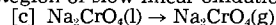
Table IV. Corrosion mechanism

Induction period (0-55h)

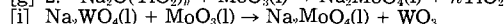
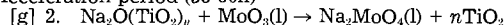
Region of weight loss (0-10h) — basic fluxing by Na_2SO_4



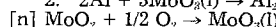
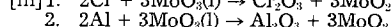
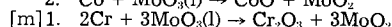
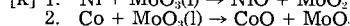
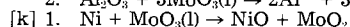
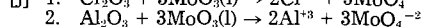
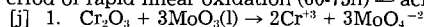
Region of slow linear oxidation (10-55h)



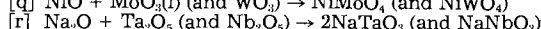
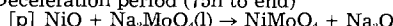
Acceleration period (55-60h)



Period of rapid linear oxidation (60-75h) — acidic fluxing



Deceleration period (75h to end)



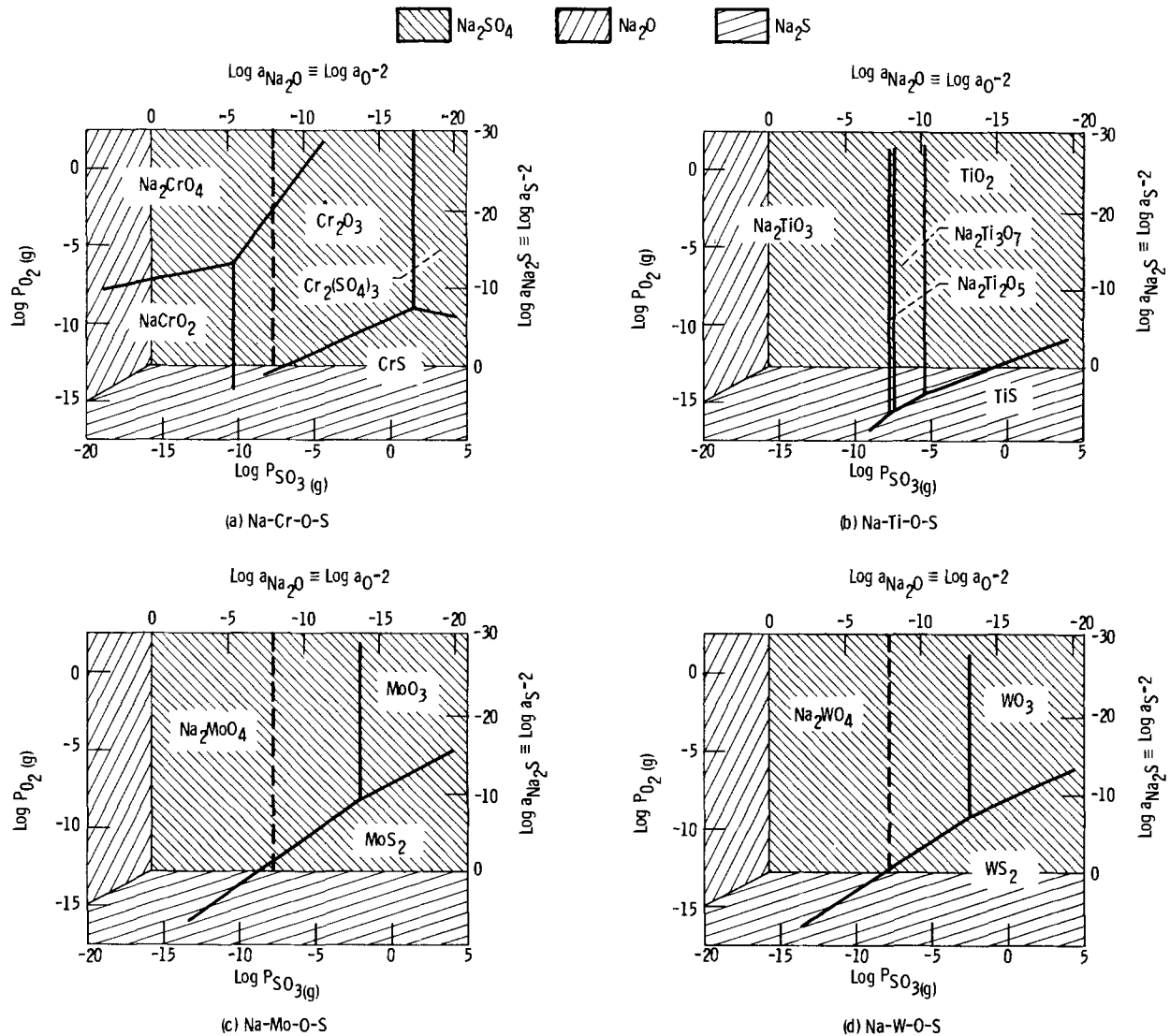


Fig. 17. Thermodynamic phase stability diagrams at 975°C. The Cr-, Ti-, Mo-, and W-O-S diagrams are superimposed on the Na-O-S diagram. The dashed line is drawn where $\log a_{\text{Na}_2\text{O}} = \log P_{\text{SO}_3(\text{g})}$.

3c shows that soluble chromium and soluble sodium disappear rather rapidly between 15 and 30h. We can calculate a linear disappearance rate for these species of 7.7×10^{-4} mmol $\text{cm}^{-2} \text{h}^{-1}$.

The soluble sodium and chromium can be lost by evaporation of Na_2CrO_4 and/or reaction with TiO_2 ([d], Table IV). The sum of the rates of these two processes (Table I) is 7.4×10^{-4} mmol $\text{cm}^{-2} \text{h}^{-1}$, which agrees with the rates of disappearance of soluble sodium and chromium. We may conclude that the loss of Na_2CrO_4 depicted in Fig. 3c can mostly be accounted for, 20% by vaporization and 80% by reaction with TiO_2 .

The rapid reaction between Cr_2O_3 and Na_2SO_4 during the first 10h of corrosion results in the removal of most of the protective oxide scale. The alloy then begins a slow reoxidation that lasts until the end of the induction period ([e1]-[e5], Table IV). This is verified by the nearly linear weight gain displayed in Fig. 3a for this time period and by the growth of the oxide layer observed in Fig. 8-12. The reformed oxide is not protective in the usual sense, though the rate of oxidation is relatively slow; this is indicated by the fact that the weight increase is linear rather than parabolic. The inability of the alloy to produce a protective oxide scale probably results from the large depletion of chromium resulting from preoxidation, reoxidation, and sulfide formation near the bottom of the depletion zone (20).

The most important development during the reoxidation period is the gradual growth of areas of MoO_3 - WO_3 along the lower edge of the oxide layer. Soluble Mo and

W arise from reaction between MoO_3 - WO_3 and Na_2CrO_4 ([f], Table IV). As the Na_2CrO_4 is converted to $\text{Na}_2\text{O}(\text{TiO}_2)_n$ by [d], Table IV, soluble Mo and W arise from reaction of the oxides with $\text{Na}_2\text{O}(\text{TiO}_2)_n$ ([g1], Table IV). Some of the recovery of soluble sodium after 40h is probably due to this reaction. The micrographs of Fig. 10 and 11 show how the MoO_3 - WO_3 areas develop. After the reformed oxide layer reaches a thickness of about 30 μm , the underlying isolated Ni-Co islands are leached of all active elements, except molybdenum and tungsten. Further oxidation of the specimen oxidizes these islands. The molybdenum and tungsten dissolved in the islands also oxidize and are found on the interface between the oxidized islands and the alloy. The presence of sodium, often found in the MO_3 - WO_3 areas, effects a lowering of the melting point of MoO_3 - WO_3 by formation of Na_2MoO_4 - Na_2WO_4 and also reduces the effective vapor pressure (1). Toward the latter part of this period, the soluble tungsten starts to decrease, probably by [i], Table IV, as a result of the slightly greater thermodynamic stability of Na_2MoO_4 , as compared with Na_2WO_4 (Fig. 17c and d).

The period from 10h to the end of the induction period, 55h, is a time in which the alloy slowly reoxidizes to form an oxide scale about 60 μm thick. This oxide is nonprotective, and numerous discrete areas of MoO_3 - WO_3 / Na_2MoO_4 - Na_2WO_4 are formed along the lower edge.

Acceleration period (55-60h).—The corrosion process begins to accelerate at about 55h (Fig. 3a), and the amount of soluble molybdenum increases markedly (Fig. 3c). This

results from an increase in the rate of formation of Na_2MoO_4 by [g2] and [i], Table IV, probably because of the considerable quantity of MoO_3 that accumulates along the oxide scale. This amount of Na_2MoO_4 effects melting of some discrete $\text{MoO}_3\text{-WO}_3/\text{Na}_2\text{MoO}_4\text{-Na}_2\text{WO}_4$ areas into a large molten phase (21). In Fig. 12, the molten oxide phase can be seen migrating across the sample, disrupting and fluxing the scale above it. The oxide above the $\text{MoO}_3\text{-WO}_3/\text{Na}_2\text{MoO}_4\text{-Na}_2\text{WO}_4$ is striated and layered, typical of acidic fluxing. Most of the oxide layer is still similar to that shown in Fig. 11, with discrete areas of $\text{MoO}_3\text{-WO}_3/\text{Na}_2\text{MoO}_4\text{-Na}_2\text{WO}_4$.

Period of rapid linear oxidation (60-75h).—Beyond 60h, the quantity of Na_2MoO_4 increases rapidly (Fig. 3c) as more of the discrete oxide areas merge into large molten masses below the oxide scale. Finally, in the 77h sample, the large molten phase of $\text{MoO}_3\text{-WO}_3/\text{Na}_2\text{MoO}_4$ has become the major feature of the scale. This development promotes acidic fluxing of the oxide scale by [j1] and [j2], Table IV. Bornstein *et al.* (22) have shown that Al_2O_3 exhibits an extremely rapid rate of dissolution in molten MoO_3 at 900°C. A major breakup of large areas of the oxide scale occurs and exposes the alloy surface. Rapid oxidation of the alloy ensues and produces a large porous oxide scale, as shown in Fig. 4. The rate of oxidation is nearly $3 \text{ mg cm}^{-2} \text{ h}^{-1}$, about 20 times larger than the rate observed in the induction period. The molten oxide phase appears to attack the alloy itself, possibly by [k] and [m], Table IV, which have been calculated to be thermodynamically favored. Reactions such as these have first been suggested by Leslie and Fontana (23) and have been discussed more recently by Peters, Whittle, and Stringer (24).

The acidic fluxing is self-sustaining, and it accounts for the linear nature of the attack. The self-sustaining feature may have resulted from the cyclic operation of [j1] and [j2], Table IV, and their reverse reactions. After solution of the oxides in the molten $\text{MoO}_3\text{-WO}_3/\text{Na}_2\text{MoO}_4$ phase, the metal cations diffuse to the outer zone of the melt, where they reoxidize by the higher oxygen potential. The cycle repeats as the alloy is consumed. The cyclic behavior of acidic fluxing can be explained more quantitatively by the Rapp-Goto model (25), in which attack is explained in terms of a negative solubility gradient of the corrosion product across the molten phase. The striated appearance of the oxide (Fig. 12) is a result of the cyclic nature of the attack. Table IV, [k] and [m], are also capable of exhibiting cyclic behavior through reoxidation of MoO_2 at the outer zone of the melt ([n], Table IV).

The small amount of SO_2 observed during this period must have resulted from oxidation of the sulfur in the molten oxide phase. This conclusion is supported by the observation that the sulfur content of the test specimens drops from the 50h sample to the 75h sample.

Deceleration period (75h to end).—At ~75h, a deceleration of the corrosion rate is observed (Fig. 3a); it results from conversion of the molten $\text{MoO}_3\text{-WO}_3/\text{Na}_2\text{MoO}_4$ to solid $\text{NiMoO}_4\text{-NiWO}_4$ by [p] and [q], Table IV, and is accompanied by a rapid decrease in both the soluble molybdenum and sodium (Fig. 3c). The formation of these stable nickel compounds eliminates the molten oxide phase that causes acid fluxing. Figure 3c shows that the Na_2MoO_4 is reduced at 90h to a value below the one at which the catastrophic attack begins at 55h. An area where the transformation to $\text{NiMoO}_4\text{-NiWO}_4$ occurs is shown in Fig. 13. Here, $\text{NiMoO}_4\text{-NiWO}_4$ is found along the oxide alloy interface, and no evidence of a molten phase is present.

Other aspects.—The formation of sulfides has not been included in Table IV, though sulfides certainly form early in the corrosion process (Fig. 3c and 8). Although this sulfide formation leads to degradation of the alloy, it is considered to be of secondary importance in the overall mechanism. It does contribute to the depletion of chromium and to the resulting inability of the alloy to form a

protective oxide scale during the induction period. Finally, the formation of NaTaO_3 and NaNbO_3 ([r], Table IV) has not been discussed. This is an important reaction in some alloys, as discussed previously (26), because NaTaO_3 seems to act as a sink for Na_2O and, thus, it inhibits the formation of Na_2MoO_4 . However, it has not been effective in IN-738 because of the low concentration of tantalum and niobium.

Concluding Remarks

We have shown that the induced hot corrosion of IN-738 is initiated by basic fluxing of the protective $\text{Cr}_2\text{O}_3\text{-TiO}_2$ scale and that the fluxing reaction continues as long as Na_2SO_4 is available. Reoxidation of the alloy is not able to produce a protective scale because chromium is depleted from the exterior surfaces. A slow linear oxidation ensues, during which $\text{MoO}_3\text{-WO}_3$ builds up along the oxide-alloy interface. Gradually, MoO_3 reacts with Na_2CrO_4 and $\text{Na}_2\text{O}(\text{TiO}_2)_n$ to form Na_2MoO_4 , which lowers the melting point of the $\text{MoO}_3\text{-WO}_3$ areas. Large areas of the molten phase $\text{MoO}_3\text{-WO}_3/\text{Na}_2\text{MoO}_4$ are formed, and these areas effect acidic fluxing of the oxide scale and result in catastrophic attack of the alloy. The attack eventually slows down as Na_2MoO_4 and $\text{MoO}_3\text{-WO}_3$ are converted to their corresponding nickel salts, but the alloy specimen is largely destroyed by this time.

The Na_2SO_4 has two main effects in this mechanism of hot corrosion: it removes the protective $\text{Cr}_2\text{O}_3\text{-TiO}_2$ scale; and it supplies sodium that eventually forms Na_2MoO_4 , which initiates melting of the $\text{MoO}_3\text{-WO}_3$ areas. Therefore, any method of removing the scale should cause hot corrosion if sodium is available. In contrast, if sodium is extracted after scale removal, no hot corrosion should occur. With reference to the first effect, Bourhis and St. John (6) find that, in Na_2SO_4 -induced hot corrosion tests at 900°C, alloys forming a protective Cr_2O_3 layer are not susceptible to accelerated attack. However, if the oxide scale is removed by abrasion, heavy corrosion occurs. We have performed tests in which the preoxidation scale is removed by water quenching and the specimen is coated with 2 mg cm^{-2} of Na_2CrO_4 to supply a source of sodium. The specimen is oxidized at 975°C, and catastrophic hot corrosion occurs in 60h, a time not much different from our normal induction period. With reference to the second effect, a normal hot corrosion test is stopped after 10h, by which time the protective oxide scale has been largely fluxed. The specimen is cooled and water-washed. This removes the Na_2CrO_4 that has formed and any Na_2SO_4 that has not reacted. The oxidation is then reinitiated and continued for times of up to 200h. Although a long period of reoxidation ensues, no catastrophic hot corrosion occurs.

The corrosion mechanism postulated here includes several new ideas and new processes. We have demonstrated that the Na_2SO_4 fluxes the $\text{Cr}_2\text{O}_3\text{-TiO}_2$ scale until all of the Na_2SO_4 is consumed. Generally, it has been believed that reaction [1] results in the Na_2SO_4 becoming so "acidic" that the Cr_2O_3 becomes stable in the Na_2SO_4 and the reaction ceases (27). We have shown that Na_2CrO_4 reacts with TiO_2 to form $\text{Na}_2\text{Ti}_2\text{O}_{11}$, and that both of these compounds react with $\text{MoO}_3\text{-WO}_3$ to form the low-melting-point compounds Na_2MoO_4 and Na_2WO_4 . We have also shown that acidic fluxing is caused by a molten $\text{MoO}_3\text{-WO}_3$ oxide phase containing Na_2MoO_4 , instead of a molten Na_2SO_4 phase "acidified" by dissolved $\text{MoO}_3\text{-WO}_3$ (28). In addition, we have suggested that the molten $\text{MoO}_3\text{-WO}_3/\text{Na}_2\text{MoO}_4$ phase can attack the components of the alloy itself by a form of basic fluxing involving MoO_3 and MoO_2 .

Two methods of preventing hot corrosion of the alloys which principally form Cr_2O_3 protective scales are suggested by this research: increasing the chromium content of the alloy; and replacing the molybdenum and, possibly, the tungsten with tantalum or niobium. This latter suggestion has been made previously (1, 26). It appears that in IN-738, in which there is a small initial amount of

molybdenum, catastrophic corrosion can be eliminated by this replacement.

Application of the corrosion mechanism postulated here to the problem of hot corrosion of IN-738 in gas turbine engines is complicated by the widely different environmental conditions encountered in service. Although the mechanism is based on laboratory results, we feel the same processes are involved in practice, but the relative importance of the various processes may be quite different. The rate of evaporation of Na_2CrO_4 will be considerably higher in the high-velocity flow environment of a gas turbine. As compared with our tests, this should decrease the formation of Na_2MoO_4 and lengthen the induction period for catastrophic corrosion. However, repeated engine cycling and attendant spallation would accelerate chromium depletion and probably shorten the induction period. Possibly, the overriding factor is that in an operating gas turbine, the Na_2SO_4 is deposited more or less continuously. If the salt level is high, as in a marine environment, the Na_2SO_4 will probably effect catastrophic hot corrosion. But if the salt level is low, as in a power generating turbine, the high rate of vaporization of Na_2CrO_4 and MoO_3 may prevent catastrophic hot corrosion entirely. A quantitative evaluation of these many complex processes is not possible at this time.

It is necessary to stress the importance of using kinetic data when interpreting hot corrosion processes. Until now, interpretation has been based on thermochemical Pourbaix diagrams. Such diagrams have been invaluable, but their usefulness is limited because they give no kinetic information. In addition, the environment in a gas turbine is hardly an equilibrium system. Even if the SO_3 pressure is maintained at some constant value, SO_3 is only one of the products being evolved in the reaction between Na_2SO_4 and Cr_2O_3 . The Na_2CrO_4 also evaporates, as we have shown, at the rate of $1.5 \times 10^{-4} \text{ mmol cm}^{-2} \text{ h}^{-1}$. In the high-velocity environment of a gas turbine, this rate would be increased markedly.

Unfortunately, little kinetic data are available for reactions of the type involved in hot corrosion. We have studied three such reactions ([a], [b], and [d], Table IV), but our investigation has been limited. The need for more extensive information of this type is imperative in the proper interpretation of hot corrosion phenomena.

Acknowledgments

The authors would like to thank Frank M. Terepka for obtaining the electron microprobe data. Warren F. Davis and Constance S. Buchar are thanked for performing the chemical analyses. We would also like to thank Dr. Reza Haque and Dr. Ajay K. Misra for running some of the later hot corrosion tests.

Manuscript submitted April 4, 1983; revised manuscript received July 27, 1984.

NASA assisted in meeting the publication costs of this article.

REFERENCES

- G. C. Fryburg, F. J. Kohl, C. A. Stearns, and W. L. Fielder, *This Journal*, **129**, 571 (1982).
- F. D. Lordi, "Advanced Materials and Coatings," Gas Turbine Reference Library, GER 182N, General Electric Co., Schenectady, NY (1980).
- J. M. Ferguson, RD/L/N 73-80, Central Electricity Research Laboratories, CEGB, Leatherhead, Surrey, England (1980).
- K. Page and R. Taylor, in "Deposition and Corrosion in Gas Turbines," A. B. Hart and A. J. B. Cutler, Editors, p. 350, J. Wiley and Sons, New York (1973).
- D. M. Johnson, D. P. Whittle, and J. Stringer, *Corros. Sci.*, **15**, 721 (1975).
- Y. Bourhis and C. St. John, *Oxid. Met.*, **9**, 507 (1975).
- G. C. Fryburg, F. J. Kohl, and C. A. Stearns, in "Properties of High Temperature Alloys," Z. A. Foroulis and F. S. Pettit, Editors, p. 585, The Electrochemical Society Softbound Proceedings Series, Princeton, NJ (1976).
- E. Erdős and E. Denzler, in "Behavior of High Temperature Alloys in Aggressive Environments," I. Kirman *et al.*, Editors, p. 455, Petten, The Netherlands, The Metals Society, London (1979).
- P. Cavalotti, U. Ducati, D. Columbo, and D. Donzelli, in "Behavior of High Temperature Alloys in Aggressive Environments," I. Kirman *et al.*, Editors, p. 513, Petten, The Netherlands, The Metals Society, London (1979).
- C. J. Grant, *Br. Corros. J.*, **14**, 26 (1979).
- T.-T. Huang, Ph.D. Thesis, Univ. of Pittsburgh (1979).
- J. M. Ferguson, RD/L/2113N81, Central Electricity Research Laboratories, CEGB, Leatherhead, Surrey, England (1981).
- R. Haque, F. J. Kohl, G. C. Fryburg, C. A. Stearns, and W. L. Fielder, in "High Temperature Materials Chemistry," D. D. Cubicciotti and D. L. Hildenbrand, Editors, p. 240, The Electrochemical Society Softbound Proceedings Series, Princeton, NJ (1982).
- G. C. Fryburg, F. J. Kohl, and C. A. Stearns, NASA TN D-8388 (1977).
- R. G. Garlick and C. E. Lowell, NASA TM X-2796 (1973).
- F. J. Kohl, C. A. Stearns, and G. C. Fryburg, in "Metal-Slag-Gas Reactions and Processes," Z. A. Foroulis and W. W. Smeltzer, Editors, p. 649, The Electrochemical Society Softbound Proceedings Series, Princeton, NJ (1975).
- C. A. Stearns, F. J. Kohl, and G. C. Fryburg, *This Journal*, **121**, 945 (1974).
- G. C. Fryburg and H. M. Petrus, *ibid.*, **108**, 496 (1961).
- C. W. Bale, A. D. Pelton, and W. T. Thompson, "F*A*C*T User's Guide," McGill University/École Polytechnique, Montreal, Quebec, Canada (1979).
- C. J. Spengler and R. Viswanathan, *Met. Trans.*, **3**, 161 (1972).
- E. M. Levin, C. R. Robbins, and H. F. McMurdie, "Phase Diagrams for Ceramists," pp. 95, 144, The American Ceramic Society, Columbus, OH (1964).
- N. S. Bornstein, M. A. DeCrescente, and H. A. Ruth, *Met. Trans.*, **4**, 1799 (1973).
- W. C. Leslie and M. G. Fontana, *Trans. A.S.M.*, **41**, 1213 (1949).
- K. R. Peters, D. P. Whittle, and J. Stringer, *Corros. Sci.*, **16**, 791 (1976).
- R. A. Rapp and K. S. Goto, in "Molten Salts," J. Braunstein and J. Selman, Editors, The Electrochemical Society Softbound Proceedings Series, Princeton, NJ (1981).
- G. C. Fryburg, C. A. Stearns, and F. J. Kohl, *This Journal*, **124**, 1147 (1977).
- J. A. Goebel, F. S. Pettit, and G. W. Goward, *Met. Trans.*, **4**, 261 (1973).
- C. S. Giggins and F. S. Pettit, Pratt and Whitney Report No. FR 11545, Final Report on AFOSR Contract No. F44620-76-C-0123 (1979); AD-A072645.

Gaseous Sulfidation of Pure Molybdenum at 700°-950°C

Bom Soon Lee¹ and Robert A. Rapp*

Department of Metallurgical Engineering, The Ohio State University, Columbus, Ohio 43210

ABSTRACT

The kinetics and mechanism of sulfide scale growth on pure molybdenum have been investigated in an elemental sulfur (S_2) atmosphere and in an H_2S/H_2 gas mixture over the temperature range of 700°-950°C. Below about 800°C, linear kinetics were observed, and at higher temperatures the kinetics were parabolic. The surface orientation of the metal affected the sulfidation mode and rate, and the MoS_2 scale showed a strong epitaxial relationship with the metal at all temperatures. For the low temperature linear kinetics, a sulfide crystal nucleation step is believed to be rate limiting. In the high temperature parabolic regime, the diffusion of sulfur ions through the scale is the rate-limiting step. After the scale reaches some critical thickness, Mo_2S_3 crystals form beneath the MoS_2 scale, which slows the reaction somewhat. The parabolic rate constants for sulfidation in H_2S/H_2 gas mixtures at high temperatures were about one order of magnitude higher than those in elemental sulfur at the same sulfur activity.

The practical importance of the sulfidation of metals and alloys has become apparent because of the increasing utilization of metals at high temperatures in industrial atmospheres containing sulfur and its compounds. The increased use and conversion of low-grade fossil fuels and the introduction of sodium-sulfur batteries, etc., have made high temperature sulfidation problems even more frequent.

Many investigators have studied the sulfidation resistance of the metals iron, nickel, cobalt, and copper, as well as their alloys with chromium. In each case, the high concentrations and mobilities of point defects in the sulfide scales yield relatively high scaling rates. However, some previous studies of molybdenum sulfidation which reported slow scaling rates (1-3) in either S_2 or H_2S have been limited to narrow ranges of temperatures and sulfur activity or H_2S/H_2 gas ratios, and a comprehensive mechanistic study is not available.

Dutrizac (1) investigated the thermogravimetric kinetics of the sulfidation of Mo in pure sulfur vapor for sulfur pressures ranging from 0.03 to 300 torr. Dutrizac obtained linear kinetic curves for the temperature range 415°-550°C for $P_{S_2} > 20$ torr. At lower P_{S_2} , parabolic kinetics were obtained for approximately half the experiments. Dutrizac concluded that the linear sulfidation kinetics of Mo are controlled by some reaction step occurring at either the MoS_2 /gas or the Mo/MoS_2 interface. The kinetic rate was insensitive to changes in sulfur pressures in excess of 20 torr, but the sulfidation rate decreased at lower sulfur pressures. The mechanism of scale growth was not detailed, and hexagonal MoS_2 was reported as the only reaction product formed under all conditions.

Gerlach and Hamel (2) obtained parabolic sulfidation curves for reactions in H_2S/H_2 gas mixtures at 900°-1050°C. Curve markers were used, and it was concluded that the inward diffusion rate of the sulfur ion is higher than the outward diffusion rate of the Mo ion in MoS_2 , which was the only corrosion product reported. To calculate the activation energy for sulfidation, they used a constant H_2S/H_2 ratio for each temperature rather than a constant sulfur activity (P_{S_2}). Slope changes were observed in parabolic plots of weight change vs. time, but the authors did not elaborate.

Fueki *et al.* (3) studied the sulfidation of Mo in H_2/H_2S gas mixtures at 800°-950°C. They obtained parabolic kinetic curves, but the rate constants differed from those of Gerlach and Hamel (2). Again, a constant H_2S/H_2 gas ratio (1:1) was used for each temperature to calculate the activation energy for sulfidation.

The objectives of this research were to determine kinetic information for the sulfidation of pure Mo over a wide range of sulfur activities and temperatures and to clarify the mechanisms of sulfidation. The experiments were conducted in elemental sulfur vapor and in H_2S/H_2

gas mixtures. Kinetic results from these two environments were compared for the same sulfur activity (P_{S_2}).

Thermodynamics of Mo-S system.—Several sets of thermodynamic data are available for the Mo-S system. The data of Larson and Elliott (4) for ΔG_f° (MoS_2) in combination with those of Hager and Elliott (5) for ΔG_f° (Mo_2S_3) would indicate that Mo_2S_3 is not stable at temperatures below 1400°C. However, Young *et al.* (6) reported the formation of Mo_2S_3 on a Ni-Mo alloy at 700°C. The data of Stubbles and Richardson (7) show the existence of Mo_2S_3 in the phase stability diagram of Fig. 1. Suzuki *et al.* (8) also confirmed a narrow band of Mo_2S_3 stability.

Experimental Apparatus, Materials, and Procedure

A quartz-spring² TGA balance system shown in Fig. 2 was used for kinetic measurements of molybdenum sulfidation. The total length of the reaction tube was about 150 cm; the lower part of the tube was connected to an isothermal reservoir of pure liquid sulfur, which was heated to generate the desired sulfur vapor pressure. The silicone-greased standard taper joint connection was heated about 30°C higher than the sulfur reservoir to avoid sulfur condensation. A cathetometer outside the reaction chamber was used to monitor the weight gain of the specimen by measuring the elongation of the quartz

²Worden Quartz, Houston, Texas. Sensitivity: 40 $\mu g/0.01$ mm. Maximum load: 2g.

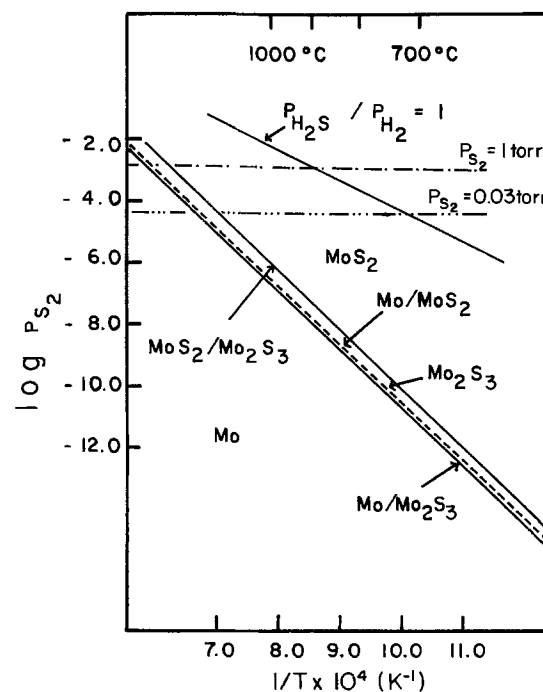


Fig. 1. Phase stability diagram for Mo-S system

*Electrochemical Society Active Member.

¹Present address: Department of Nuclear Energy, Brookhaven National Laboratory, Upton, New York 11973.

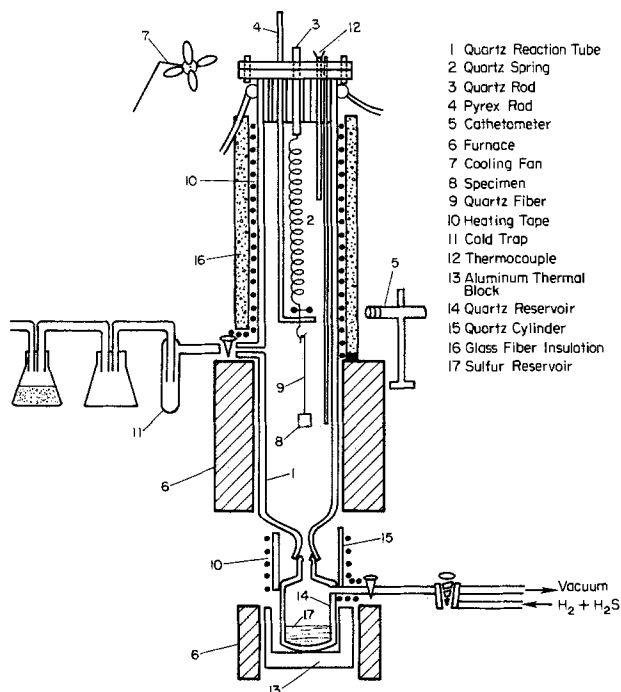


Fig. 2. Schematic drawing of experimental setup for molybdenum sulfidation study.

spring. A Pyrex rod was used to lower or raise the specimen.

For initial experiments in H_2S/H_2 gas mixtures, convection caused severe fluctuations in the spring because of the large temperature gradient between the spring column ($200^\circ C$) and the main furnace ($800^\circ-950^\circ C$). This noise problem was reduced significantly by inserting several quartz cylinders inside the reaction chamber (not shown in Fig. 2) to induce downward flow of gas around the specimen and to increase the resistance to the gas flow.

Sublimed sulfur (Mallinckrodt) was used to generate sulfur vapor. Prepurified H_2 gas (NCG Industrial Gas) and H_2S gas (Matheson) were used. Thin (0.25 mm) cold-rolled sheet of 99.97% Mo with $3\text{ }\mu\text{m}$ average grain size from Alfa Chemical Company was cut into $2 \times 3\text{ cm}$ specimens for elemental sulfur experiments and $1 \times 5\text{ cm}$ for H_2S/H_2 gas experiments. Molybdenum sheet with equiaxed grains, $5\text{ }\mu\text{m}$ average grain size, was received from Climax Molybdenum Company. The purity of this annealed molybdenum sheet was about 99.97%, with impurities of about 70 ppm C, 80 ppm O, 48 ppm Si, and 23 ppm Al.

For some experiments, the shiny as-received (as-rolled) surface was degreased with a detergent and warm water; for other experiments, specimens were ground to 600 grit paper, polished with $3\text{ }\mu\text{m}$ alumina, and washed with detergent and warm water. To investigate the effects of surface finish and grain size on the reaction kinetics, four different surfaces were studied: as-rolled coupons (Alfa Products) and annealed specimens (Climax) were used in the as-received condition or with a ground and polished surface.

During kinetic runs, the thermally insulated tube surrounding the spring was heated to a constant temperature above the dew point for the sulfur vapor. The spring constant was calibrated to be $39.9\text{ }\mu\text{g}/0.01\text{ mm}$ for a tube temperature of $25^\circ C$, and $42\text{ }\mu\text{g}/0.01\text{ mm}$ for a tube temperature of $200^\circ C$. To avoid oxide formation on the specimen during its residence in the tube prior to the experiment, the system was evacuated to about 10^{-5} torr while the sulfur reservoir was brought to temperature. Then the specimen was lowered into the hot zone. A quartz specimen submitted to the same procedure did not indicate any weight gain in 2h.

In the elemental sulfur experiments, gaseous sulfur consisted mainly of S_2 species at the experimental tem-

peratures ($700^\circ-950^\circ C$). These experiments were conducted in the viscous pressure regime so that the pressure inside the chamber was uniform throughout. The total vapor pressure above the liquid sulfur was calculated using the equation obtained by Meisen and Bennet (9). For the experiments in H_2S/H_2 gas mixtures, the gas ratio was adjusted to provide an equivalent P_{S_2} of 1 torr at each temperature.

Results and Discussion

Elemental sulfur experiments at $700^\circ-800^\circ C$.—Figure 3 is a plot of the sulfidation kinetics for the annealed Climax Mo specimen at $750^\circ C$, $P_{S_2} = 0.03$ torr, which shows representative kinetic behavior for the lower temperatures. The most important characteristic of the kinetics is that the sulfidation rate of Mo is low, $< 0.3\text{ mg}/\text{cm}^2$ over many hours reaction time. The curve is initially linear, but after about $0.15\text{ mg}/\text{cm}^2$ weight gain (scale thickness: $\sim 0.6\text{ }\mu\text{m}$), much slower approximately parabolic period II kinetics are initiated. Period III is comprised of repeated parabolic weight gains and interruptions. During period III, a vibration of the spring was detected occasionally, which may indicate sudden release of stress by scale fracture. This kinetic behavior was common for studies in the temperature range $700^\circ-800^\circ C$, as shown also in Fig. 4 and 5.

Figure 6 is an Arrhenius plot of the initial linear sulfidation rate constants for four different specimens. The as-rolled Alfa specimen exhibited apparent parabolic behavior at $800^\circ C$, and the linear rate constant was calculated from the first five data points; the resulting point on Fig. 6 falls between the two lines. The activation energy for linear sulfidation calculated from this plot is $103 \pm 21\text{ kJ}/\text{mol}$, which is identical with the $103 \pm 13\text{ kJ}/\text{mol}$ obtained by Dutrizac (1), who established linear scaling rates for S_2 reactions at $415^\circ-550^\circ C$. As seen in Fig. 6, the as-received Alfa specimens have the highest linear kinetic rates, and the other specimens react more slowly.

X-ray diffraction patterns were made from unreacted Mo surfaces to identify any differences which might re-

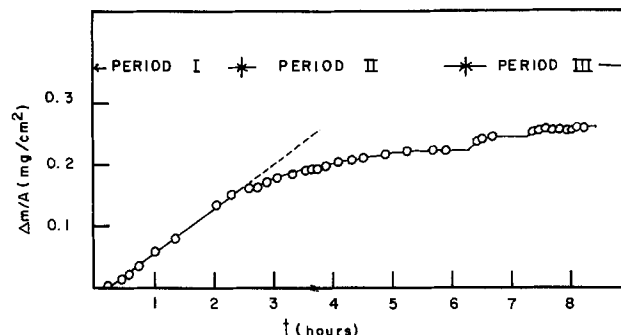


Fig. 3. Sulfidation kinetics for annealed Climax Mo specimen at $750^\circ C$, $P_{S_2} = 0.03$ torr.

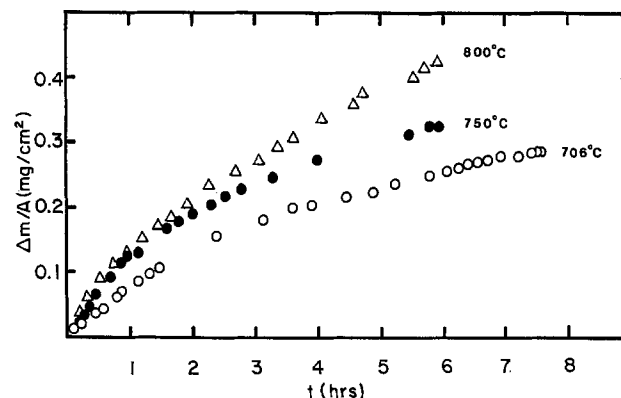


Fig. 4. Sulfidation kinetics for as-rolled Alfa Mo specimen. $P_{S_2} = 0.03$ torr.

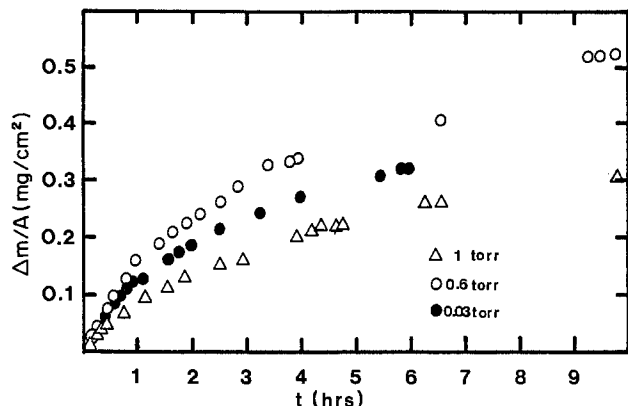


Fig. 5. The effect of P_{S_2} on sulfidation kinetics for as-rolled Alfa Mo specimen at 750°C.

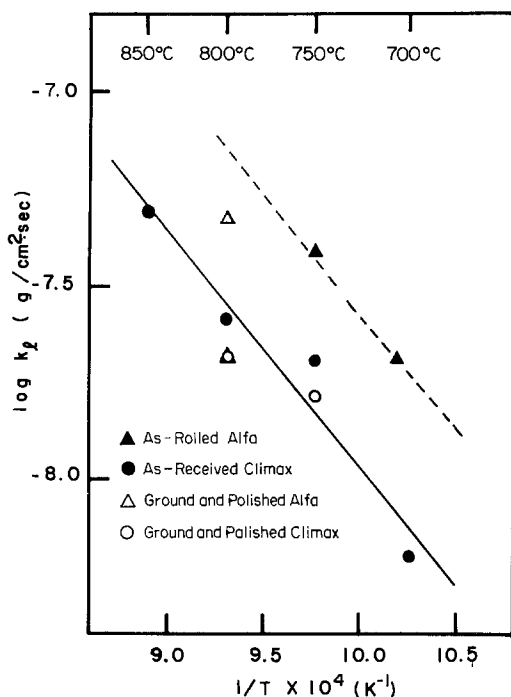


Fig. 6. Arrhenius plot for the initial linear sulfidation of molybdenum specimens with four different surfaces. $P_{S_2} = 0.03$ torr.

late grain orientation to the observed kinetics. For the as-rolled Alfa specimen, the $\{110\}$ peak which is expected to exhibit the highest intensity was very weak, and the $\{200\}$ and $\{211\}$ peaks were very strong. Thus, the surface of this specimen exhibited a strong rolled texture with $\{100\}$ and $\{211\}$ planes predominantly normal to the surface. The as-received surface of the Climax specimens showed a strong $\{110\}$ peak, and indicated a lesser degree of preferred orientation. A ground and polished Alfa specimen showed the strongest peak from $\{110\}$ planes, so that this surface preparation removed the outermost oriented grains. This information and the kinetic results in Fig. 6 show that the orientation of the Mo surface grains affects the sulfidation rate. This will be discussed in detail later.

As shown in Fig. 6, polished Alfa and Climax specimens of different grain sizes exhibited the same sulfidation rate. Figure 7 shows a cross section of a specimen sulfidized at 800°C. The thickness of the fine-grained columnar scale is uniform, and the grain boundaries of the metal do not show any preferential attack, which is consistent with the independence of rate on grain size.

Scale morphology.—According to the x-ray diffraction patterns, MoS_2 was the only product phase formed at lower temperatures. The scale morphology changed as the reaction temperature was increased, but the scale al-

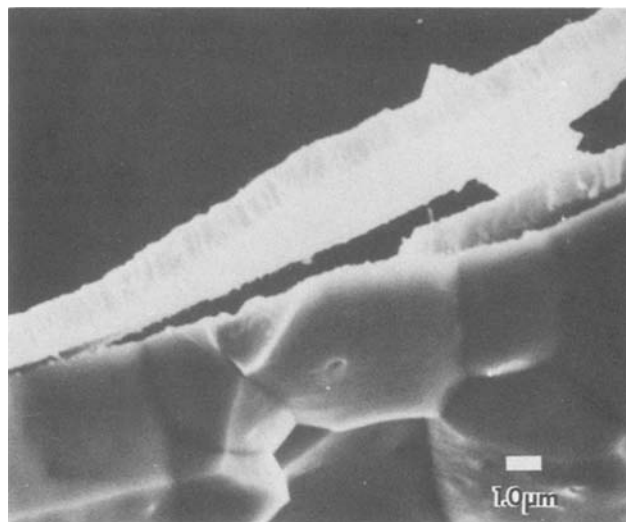


Fig. 7. MoS_2 scale on ground and polished Mo surface of fractured Climax Mo specimen. $T = 800^\circ C$, and $P_{S_2} = 0.03$ torr.

ways exhibited a uniform thickness with small columnar aggregate grains, as shown in Fig. 8, where the scale was fractured intentionally to show its cross section. The MoS_2 scale was always tightly adherent, and no spalling occurred.

Scratches on the initial metal surface remained evident at the surface of the scale after sulfidation. This feature represents evidence that sulfur is the mobile species in the scale (inward diffusion), so that new scale forms at the metal/scale interface. Further evidence for inward diffusion of sulfur is shown in Fig. 9, where the eccentric corner morphology shown is characteristic of inward diffusion for the oxidant and scale formation at the metal/scale interface. For example, this morphology is commonly observed in the high temperature oxidation of the refractory metals niobium and tantalum.

A marker experiment was also conducted by evaporating gold onto the surface of a molybdenum specimen before reaction. After the sulfidation, the particulate gold markers remained at the scale/gas interface, providing further evidence for the inward diffusion of sulfur.

Orientation of sulfide crystals.—An x-ray diffractometer pattern was made from a specimen after sulfidation at 800°C in $P_{S_2} = 0.03$ torr for 66h. The MoS_2 pattern should exhibit the highest peak for $\{001\}$ at $14.75^\circ (2\theta)$, but this peak was absent. Instead, the $\{101\}$ and $\{100\}$ MoS_2 planes from the pyramidal and prism planes, respectively,

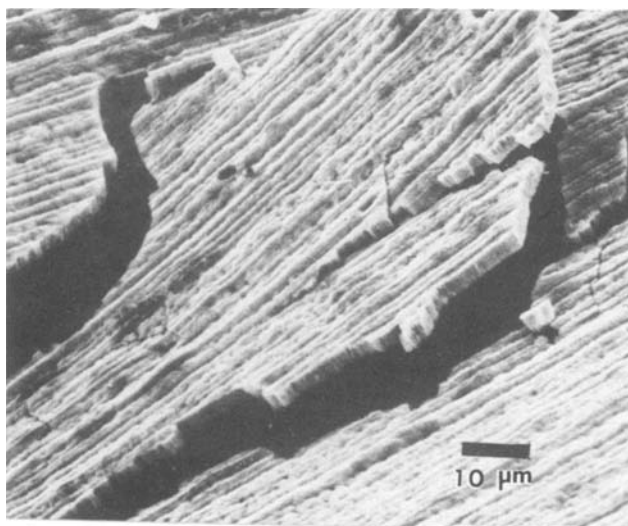


Fig. 8. MoS_2 scale on as-rolled Mo specimen sulfidized at $T = 800^\circ C$ and $P_{S_2} = 0.03$ torr.

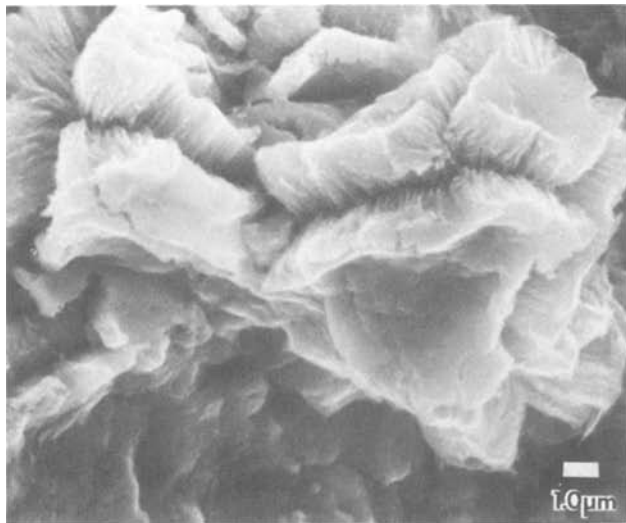


Fig. 9. Edge of the sulfidized Alfa Mo specimen, $T = 800^\circ\text{C}$ and $P_{\text{S}_2} = 0.03$ torr 14h.

showed strong peaks. The absence of the $\{001\}$ peak in the diffraction pattern is caused by the preferred orientation of MoS_2 crystals; in this case, the basal $\{001\}_{\text{MoS}_2}$ planes are preferentially oriented normal to the Mo grains with $\{100\}$ preferred texture as drawn schematically in Fig. 10. This epitaxial relation is described by $\{100\}_{\text{MoS}_2} \parallel \{100\}_{\text{Mo}}$ and $\langle 001 \rangle_{\text{MoS}_2} \perp \langle 100 \rangle_{\text{Mo}}$. This arrangement is favored, because the lattice parameter "a" of MoS_2 is an excellent match with that for Mo, and the lattice parameter "c" of MoS_2 is almost exactly four times that of "a" for Mo. Clearly, there are two equivalent, but incompatible, epitaxial MoS_2 orientations on Mo.

Another x-ray diffraction pattern was made from the back side of the scale (metal/scale interface) by removing the scale using adhesive tape, and again the peak from the basal planes for MoS_2 , $\{001\}_{\text{MoS}_2}$, was absent. A sample of the scale was scraped from a reacted specimen and powdered; in this case, the expected $\{001\}_{\text{MoS}_2}$ peak appeared.

The size of the individual sulfide crystallites of the low temperature MoS_2 scale ranged from 0.1 to 0.2 μm as shown in Fig. 11a. Thus, the columnar scale observed in surface and cross-sectional views does not represent individual grains, but rather the columns are comprised of thousands of small crystallites, as shown in the schematic diagram of Fig. 11b.

Dependence of scaling kinetics on P_{S_2} .—For 750°C , the plot of $\log k_1$ vs. $\log P_{\text{S}_2}$ showed a slope of 0.06, so that the sulfidation rate is essentially independent of the sulfur activity within the range of P_{S_2} studied (0.03 ~ 0.06 torr). At 750°C , for $P_{\text{S}_2} = 1$ torr, the kinetics were not linear, but approximately parabolic. As will be explained later, the kinetics at 750°C , in $P_{\text{S}_2} = 1$ torr fit the high temperature mechanism.

Proposed mechanism.—From the kinetic studies and the epitaxial microcrystalline nature of the MoS_2 sulfide scale, a mechanism for low temperature molybdenum sul-

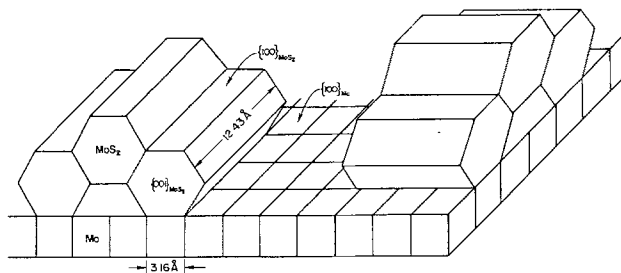


Fig. 10. Schematic diagram of the MoS_2 growing epitaxially on the $\{100\}$ surface of Mo.

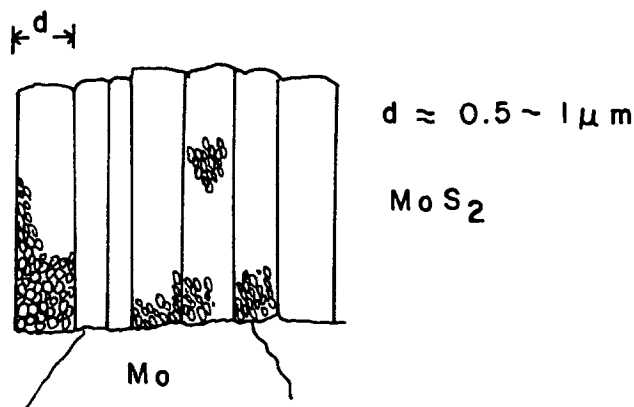
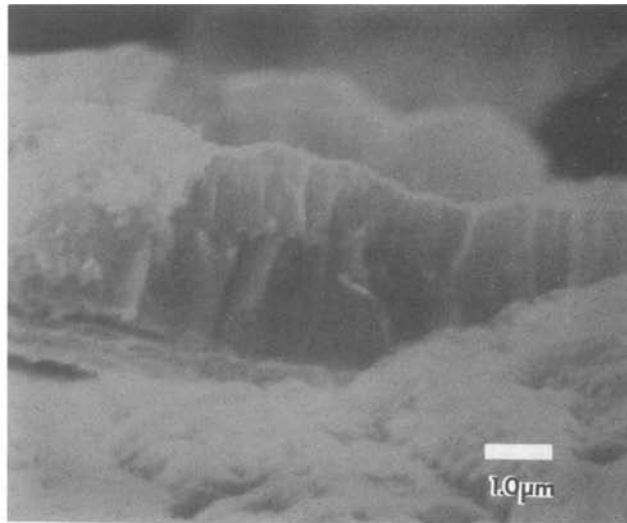


Fig. 11. a (top): MoS_2 scale formed on as-rolled Alfa Mo specimen reacted at $T = 800^\circ\text{C}$ and $P_{\text{S}_2} = 0.03$ torr for 14h. b (bottom): Schematic diagram of the columnar MoS_2 scale.

fidation can be suggested. As demonstrated by the Au markers and the retention of surface markings, sulfur is transported through the MoS_2 scale to form new crystals at the Mo/ MoS_2 interface.

When one $\{100\}$ grain of Mo reacts with sulfur at the Mo/ MoS_2 interface, MoS_2 grains of two equivalent, but incompatible, epitaxial orientations can be formed, as shown in Fig. 10. Because of the impossibility of intergrowth between adjoining MoS_2 crystals of equivalent but incompatible epitaxial orientations on the same Mo grain, MoS_2 grain growth is very restricted as basal planes of some grains impinge on prism planes of others. This grain impingement results in a very fine MoS_2 grain size and the requirement for continuous nucleation at the metal/scale interface. The MoS_2 nucleation rate, \dot{N} , can be calculated in terms of the linear gravimetric rate constants k_1 , plotted in Fig. 6. Let us assume that the scale is comprised of cubic MoS_2 grains with a side length equal to δ . Then the nucleation rate is given by

$$\dot{N} = k_1 \bar{V}_{\text{MoS}_2} / 64 \delta^3 \quad [1]$$

where \bar{V}_{MoS_2} is the molar volume of MoS_2 . For a k_1 value of 3×10^{-8} ($\text{g}/\text{cm}^2\text{s}$), δ equal to 10^{-5} cm, and $\bar{V}_{\text{MoS}_2} = 33.3$ cm^3/mol ; \dot{N} equals 1.6×10^7 $\#/\text{cm}^2\text{s}$.

With emphasis on the importance of sulfide nucleation at the metal/scale interface, the rate-limiting step(s) for each of the three periods in Fig. 3 will be discussed.

Period I, initial linear kinetics.—The Pilling-Bedworth ratio ($\bar{V}_{\text{MoS}_2}/\bar{V}_{\text{Mo}}$) in Mo sulfidation is about 3.5. Thus, for a MoS_2 crystal to form, or for an existing crystal to grow at the metal/scale interface, the previously formed sulfide crystallites must be pushed out or extruded toward the surface, a deformation which should introduce micro-

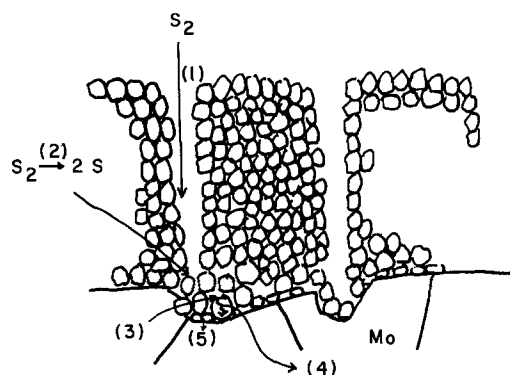
cracks in the scale. These microcracks are presumably generated almost continuously, so that even the innermost scale can be considered faulted. The mismatch between two adjoining crystallites of equivalent epitaxy but differing orientation maintains a microcrystalline grain size.

To form new crystallites at the Mo/MoS₂ interface, or to grow existing sulfide crystals, the steps illustrated in Fig. 12 should be involved. It is assumed that the MoS₂ scale contains microcracks everywhere. Because the arrival flux of S₂ molecules in the gas phase is adequate to support the observed kinetics, one of the steps 1 to 5 in Fig. 12 should be the rate-limiting step: (1) the transport of sulfur molecules along the microcracks of the scale, (2) the dissociation of diatomic sulfur molecules to form adsorbed atomic sulfur, (3) the reduction of internally adsorbed atomic sulfur, (4) the diffusion of S²⁻ through one or several MoS₂ crystals near the metal/scale interface, and (5) the nucleation of new crystallites after crystalline impingement has locally halted crystallite growth.

If the rate-limiting step were step 1, the dissociation of the molecular gas (S₂), the sulfidation rate should increase with the square root of the gas pressure. But the linear kinetic rate constant was virtually independent of P_{S₂}. In the much more rapid sulfidation of other transition metals (Fe, Ni, Co, Cr, etc.) at the same temperatures, the dissociation of molecular sulfur and the reduction step offer trivial hindrance to the rapid scaling kinetics, so the steps 2 and 3 should not be limiting here. The linear rate extends to the start of the reaction when the initially formed scale is quite thin and easily fractured; then the diffusion of S²⁻ should not be rate limiting either. Thus, sulfide nucleation at the metal/scale interface, as affected by the two epitaxial orientations of the sulfide to the substrate, must be the rate-limiting step for the initial linear sulfidation kinetics. This difficult nucleation step can be envisioned as requiring a significant local rearrangement of the metal/scale interface with a resultant large strain energy requirement for a relatively small Gibbs energy driving force.

Period II.—After a weight gain of 0.13-0.16 mg/cm² (scale thickness: 0.5-0.7 μm), the sulfidation kinetics are no longer linear, but change to slower parabolic kinetics. As a scale increases in thickness, its mechanical strength should increase, at least by the sintering of adjacent MoS₂ crystallites. Thus, after some critical thickness of the scale is reached, it becomes more difficult to fracture the scale, so that the diffusion of sulfur ions through the compact inner scale becomes important in limiting the sulfidation rate.

However, sometimes period II also exhibits linear kinetics with a rate which is lower than that for period I.



- (1) Sulfur Molecules Reach the Reaction Site
- (2) Sulfur Molecules Dissociate to Atomic Sulfur
- (3) Sulfur Atoms are Reduced: $S + 2e^- = S^{2-}$
- (4) Short Distance Diffusion of S²⁻
- (5) Sulfur Ions Nucleate a New Crystallite

Fig. 12. Illustration of series reaction steps for the MoS₂ scale growth

With the realization that very small weight changes are being measured, and with the presence of gross edge and corner heterogeneities (Fig. 9), a precise explanation may not be justified. However, the period II is a transition period from linear I to parabolic III kinetics.

Period III.—Period II is concluded by a cracking of the scale, which is followed by clearly parabolic kinetic behavior. In period III, a compact inner scale forms at the interface of Mo and MoS₂, and the diffusion of sulfur ions through the inner scale becomes the rate-limiting step. As a result, period III shows parabolic behavior until the increased thickness and the decreased plasticity of the MoS₂ scale prevents further plastic deformation, so that scale fracturing occurs again and the cycle repeats. Such a mechanism is also observed in the oxidation of niobium, *i.e.*, at steady state, parabolic kinetic segments have been correlated to the repeated cracking of a compact inner scale (10). Because of the hexagonal layered structure of MoS₂, sulfide ion diffusion can only occur between {001} layers, not normal to them. But for the low temperatures and fine grain sizes of this study, grain boundary diffusion may be more important than lattice diffusion anyway.

Elemental sulfur experiments at higher temperatures (850°-950°C).—**Kinetics.**—At temperatures higher than 850°C, and at 750°C for P_{S₂} = 1 torr, the scaling behavior was clearly parabolic with time. Initially, the plots of Δm/A vs. t^{1/2} showed straight lines; then, after the scales reached some thickness, the slope changed to lower values. After that stage, the scaling behavior was described by sequences of weight gains and interruptions, as was the case for period III of the low temperature curves.

Figures 13-15 show representative kinetic results for different temperatures and values of P_{S₂}. Figure 16 is an Arrhenius plot for the parabolic sulfidation of Alfa as-rolled Mo specimens. The activation energy for sulfidation was 147 kJ/mol (35.2 kcal/mol). The results from H₂S/H₂ gas mixture experiments noted in Fig. 16 will be discussed later.

Morphology and scale composition.—The scale morphology at the scale/gas interface at higher temperatures differs significantly from that observed at lower temperature. As shown in Fig. 17, the scale appears to be compact and not fractured. When scales formed with linear kinetics at temperatures lower than 800°C were spalled by bending the specimens, bare metal with metallic color was revealed. However, when the scales formed at higher temperatures were similarly detached, the underlying metal was not bare, but showed a very thin layer of gray color with a slight gold tone. Upon bending the sulfidized specimen, the outermost layer (MoS₂) cracked eas-

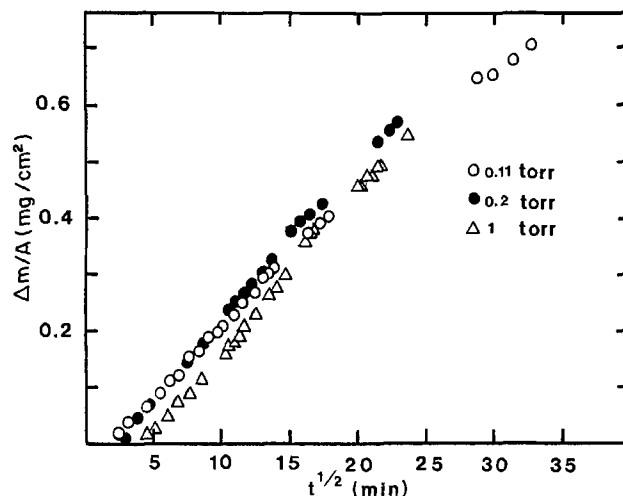


Fig. 13. Sulfidation kinetics for as-rolled Alfa Mo specimens at 850°C

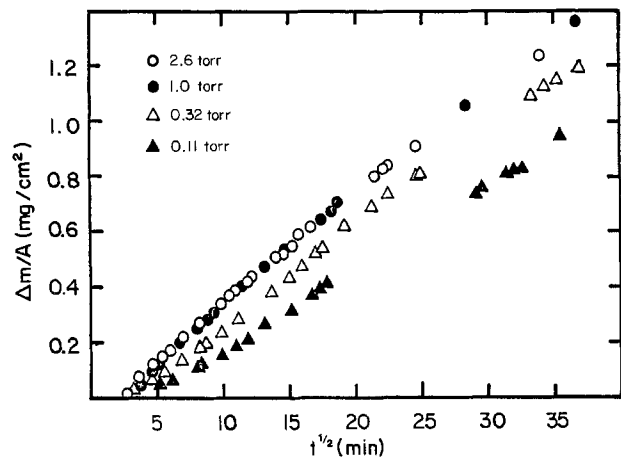


Fig. 14. Sulfidation kinetics for as-rolled Alfa Mo specimens at 900°C

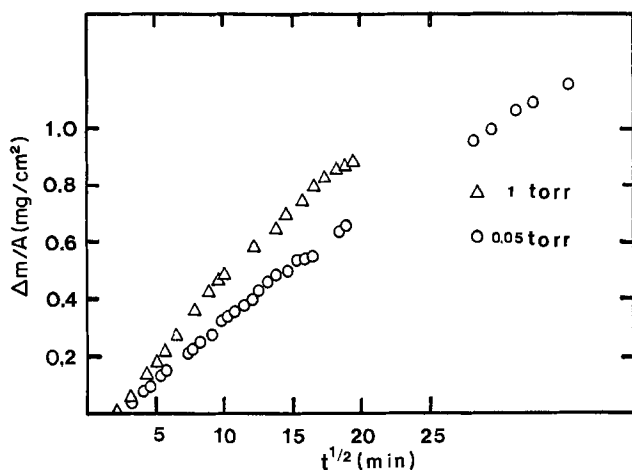


Fig. 15. Sulfidation kinetics for as-rolled Alfa Mo specimens at 950°C

ily and could be removed. However, the innermost layer was tightly adherent to the metal.

Figure 18 shows the fractured cross section of a scale formed at 950°C in $P_{S_2} = 0.05$ torr. The outer scale exhibits a laminated or layered structure, while the inner scale ex-

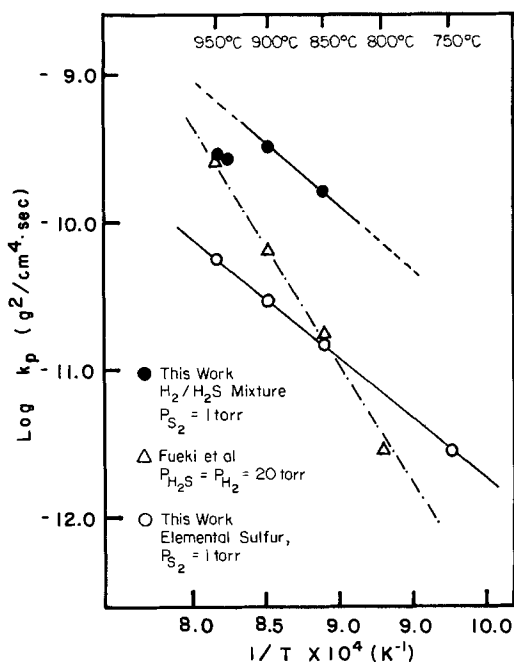


Fig. 16. Arrhenius plot for the parabolic sulfidation of Mo in elemental sulfur and in H_2/H_2S gas mixtures.

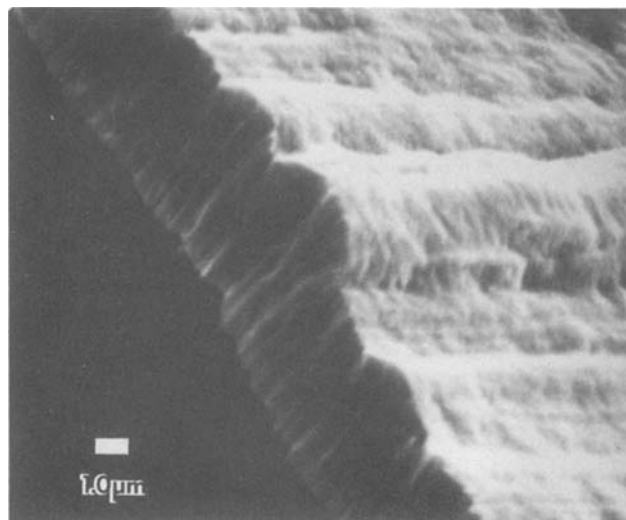


Fig. 17. MoS_2 scale of Alfa Mo specimen reacted at 900°C in $P_{S_2} = 0.11$ torr.

hibits a blocky equiaxed structure. Adhesive tape was applied to the surface of the MoS_2 scale, and the specimen was bent several times; the MoS_2 scale was successfully removed, leaving only the inner scale adherent to the metal, as shown in Fig. 19. An x-ray diffraction pattern was made from the inner layer using $Cu K\alpha$ radiation and a Ni filter, and this phase was identified as Mo_2S_3 . Refer to Ref. (11) for more details.

Previous investigators have not reported the existence of an Mo_2S_3 inner scale beneath the MoS_2 scale in sulfidation, but the formation of Mo_2S_3 is not surprising. As shown in the phase stability diagram in Fig. 1, for all temperatures, there exists a narrow regime of $\log P_{S_2}$ where Mo_2S_3 is stable. At 945°C and a sulfur pressure of 0.0076 torr, only Mo_2S_3 was formed. For these conditions, a marker experiment was conducted with the Au evaporation technique previously described, and the gold markers remained on the surface of Mo_2S_3 , indicating inward diffusion of sulfur in this phase.

The dependence of the parabolic rate constant on P_{S_2} .—As shown in Fig. 13-15, high temperature sulfidation in S_2 vapor obeyed parabolic kinetics. Figure 20 is a plot of k_p vs. $\ln P_{S_2}$ for three different temperatures, 850°, 900°, and 950°C. The parabolic rate shows a small dependence on P_{S_2} at low sulfur activities, but becomes independent of P_{S_2} above $P_{S_2} = 1$ torr.

Mechanism of high temperature sulfidation of Mo in S_2 vapor.—The slope of the plot of $\Delta m/A$ vs. $t^{1/2}$ decreases

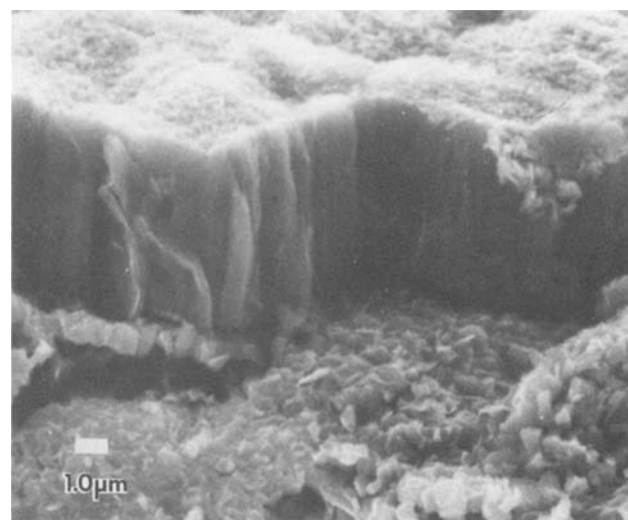


Fig. 18. Cross section of a scale formed on as-rolled Mo specimen reacted at 950°C in $P_{S_2} = 0.05$ torr for 21h.

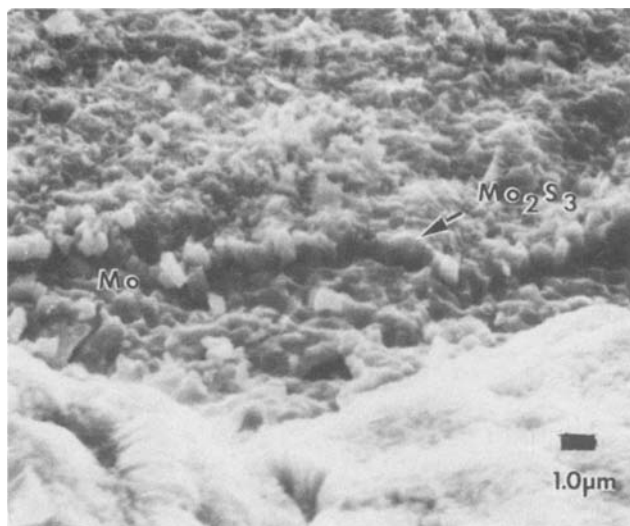


Fig. 19. Inner scale formed at 950°C in $P_{S_2} = 0.05$ torr

somewhat after some scale has formed, as shown in Fig. 13-15. This phenomenon was also observed by Gerlach and Hamel (2) and Fueki *et al.* (3), but was not explained. From the results of the current study, it seems this slope change is caused by the formation of Mo_2S_3 . The growth rate of Mo_2S_3 was found to be slower than that for MoS_2 (11), so that the formation of an Mo_2S_3 inner layer should reduce the overall sulfidation rate.

At the beginning of a high temperature sulfidation experiment, *e.g.*, at $P_{S_2} = 0.03$ torr, MoS_2 forms initially. As the parabolic sulfidation progresses, the Mo/MoS_2 interface should maintain a local metastable equilibrium with a P_{S_2} value higher than the equilibrium P_{S_2} for Mo/MoS_2 coexistence. But after the MoS_2 scale grows to some critical thickness, Mo_2S_3 is nucleated at the Mo/MoS_2 interface.

Gerlach and Hamel's results (2) showed a reduction in parabolic kinetics after ~30 min at 951°C in 0.10 $H_2S/0.90 H_2$, while the slope did not change up to ~90 min in 0.50 $H_2S/0.50 H_2$ at 953°C. In terms of the present hypothesis, the critical MoS_2 scale thickness for the formation of Mo_2S_3 must be larger for a higher P_{S_2} , *i.e.*, for a higher MoS_2 growth rate.

The parabolic kinetics for sulfidation of pure molybdenum at temperatures above 850°C indicate that the diffusion of sulfur ions through a compact sulfide scale is the rate-limiting step. Indeed, parabolic kinetics are also expected for the diffusion-limited growth of a layered scale comprised of two phases (12). The question remains whether bulk diffusion or grain boundary diffusion (for pure or doped compounds) through the inner compact scale is rate limiting.

Suzuki *et al.* (8) have recently reported on the compositions of $MoS_{2.6}$ equilibrated in H_2S/H_2 mixtures at 750° and 950°C. Each sulfide is sulfur deficient; point defects are associated with the nonstoichiometry in Mo_2S_3 , but no defect was proposed for MoS_2 . Especially for the layered hexagonal MoS_2 lattice, the intercalation (doping) for hydrogen ions between the layers must be considered. Frivaz and Mooser (13) reported that MoS_2 is an n-type semiconductor, but the temperature range of experimentation only reached 700 K and the specimens were not equilibrated to any sulfur activity. The exact modes of sulfur ion diffusion and electrical conduction remain uncertain.

In the oxidation of metals to form a pure, compact n-type semiconducting oxide scale whose growth is limited by volume diffusion, the ideal Wagnerian parabolic scale growth rate is predicted to be nearly independent of the oxidant gas pressure. This theoretical expectation results because the equilibrium concentration of anion vacancies in the scale at the metal/scale interface is many orders of magnitude higher than that in equilibrium with

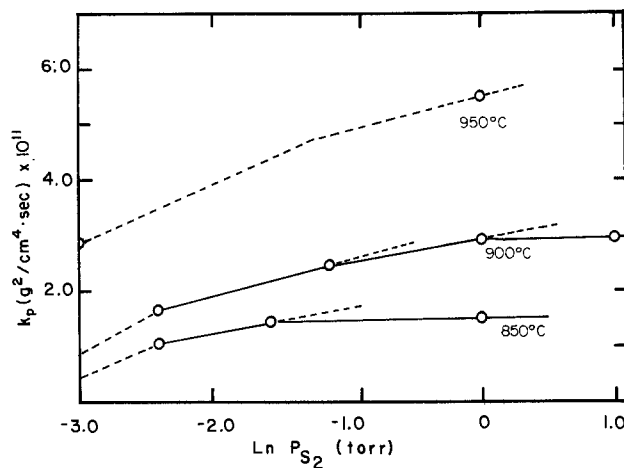
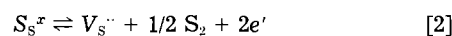


Fig. 20. P_{S_2} dependence of the parabolic rate constant

the gas phase when a large Gibbs energy change is involved for forming a highly stable oxide. Then in that case, *e.g.*, for ideal parabolic oxidation of refractory metals, the change in defect concentration gradient resulting from a change in the oxidant activity is negligible, and thus k_p is predicted to be virtually independent of imposed P_{O_2} .

This independence of the parabolic rate on oxidant pressure is valid only when the ambient oxidant pressure is several orders of magnitude higher than the equilibrium oxidant activity at the metal/scale interface. As shown in Fig. 1, for the sulfidation of pure Mo, a gaseous S_2 pressure of 0.03 torr is only about two orders of magnitude higher than the MoS_2/Mo_2S_3 equilibrium sulfur activity at 950°C, so the change in the point defect concentration gradient caused by a change in P_{S_2} should not be negligible here.

Let us assume a simple and ideal point defect model³ applicable for both MoS_2 and Mo_2S_3



$$K = [V_s^{\cdot\cdot}] (P_{S_2})^{1/2} [e']^2 / [S_s^x] \quad [3]$$

where, for electrical neutrality

$$[e'] = 2[V_s^{\cdot\cdot}] \quad [4]$$

The incorporation of the constant $[S_s^x]$ into K provides

$$K = 4[V_s^{\cdot\cdot}]^3 (P_{S_2})^{1/2} \quad [5]$$

so that

$$[V_s^{\cdot\cdot}] = K' (P_{S_2})^{-1/6} \quad [6]$$

For low concentrations of $V_s^{\cdot\cdot}$, the ionic conductivity, σ_{ion} , or the diffusivity, D_s , should be proportional to $[V_s^{\cdot\cdot}]$. Then

$$\sigma_{ion} \propto D_s \propto K' P_{S_2}^{-1/6} \quad [7]$$

Wagner's rational rate constant becomes

$$k \propto k_p \propto K' \{ (P_{S_2}^i)^{-1/6} - (P_{S_2}^o)^{-1/6} \} \quad [8]$$

where $P_{S_2}^i$ and $P_{S_2}^o$ are the equilibrium P_{S_2} values at the metal/scale and scale/gas interfaces, respectively.

If we plot k_p vs. $\ln P_{S_2}^o$, the slope will be

$$\frac{dk_p}{d \ln P_{S_2}^o} = \frac{d}{d \ln P_{S_2}^o} K' \{ (P_{S_2}^i)^{-1/6} - (P_{S_2}^o)^{-1/6} \} \quad [9]$$

$$= \frac{P_{S_2}^o d}{d P_{S_2}^o} K' \{ (P_{S_2}^i)^{-1/6} - (P_{S_2}^o)^{-1/6} \} \quad [10]$$

$$= \frac{K'}{6} \{ (P_{S_2}^o)^{-1/6} \} \quad [11]$$

³The defect notation of Kröger and Vink (14) has been used to denote doubly ionized anion vacancies, $V_s^{\cdot\cdot}$, and excess electrons, e' .

The slopes of the curves for three temperatures in Fig. 20 are indeed in rather good agreement with the prediction of Eq. [11]. As the external $P_{S_2}^0$ increases, the slope decreases; as the temperature increases, the slope increases because K' of Eq. [6] increases at higher temperatures. The dependence of k_p on the ambient $P_{S_2}^0$ is consistent with a change in the point defect concentration gradient in response to a change in $P_{S_2}^0$.

If grain boundary sulfur diffusion were the rate limiting diffusion step, the diffusivity of sulfur through grain boundaries also would depend on $P_{S_2}^0$, but no prediction of mathematical dependence is possible. The slope of the k_p vs. $\ln P_{S_2}^0$ plot might also be valid for grain boundary diffusion. Since the melting point for MoS_2 is reported as 1185°C, temperatures of 850°-950°C would seem sufficiently high for bulk diffusion in the sulfides to dominate the transport step. However, the very fine grain size of the scale would favor grain boundary diffusion. After weighing these factors, volume diffusion of sulfur ions over anion vacancies is suggested to be the rate-limiting step for the parabolic sulfidation of Mo.

Sulfidation of pure Mo in H_2S/H_2 gas mixture.—To test further the conclusion that the growth of the two-layered Mo_2S_3/MoS_2 scale at high temperatures occurs according to a classical Wagnerian sulfur ion diffusion-limited mechanism, a few experiments were conducted in H_2S/H_2 gas mixtures, as summarized in Fig. 16. For temperatures of 850°, 900°, and 950°C, the H_2S/H_2 ratio was adjusted so that the equilibrium activity of S_2 was held constant at 1 torr. In the absence of extraneous effects, such as the hydrogen doping of the sulfide scale, classical parabolic oxidation theory involving local equilibrium at the scale/gas interface would predict that the kinetics should depend only on the sulfur activity in the gas phase, not on the nature of the molecular oxidant species. However, the parabolic sulfidation rates for H_2S/H_2 runs reported in Fig. 16 are about a factor of ten higher than those for the molecular S_2 experiments at 850° and 900°C, and a factor of five higher at 950°C. However, for H_2S/H_2 experiments at 940° and 950°C, a dark green deposit accumulated in the cool section of the reaction tube. X-ray diffraction provided a peak corresponding to the principal MoS_2 peak. Thus, some evaporation of the MoS_2 scale (probably as MoS_3 vapor) may have reduced the rate constant reported for 950°C. The parabolic rate constant for 950°C for Fueki *et al.* (3) was lower than that from this work, probably because they used a different gas mixture ($P_{H_2} = P_{H_2S} = 20$ torr, $P_{S_2} = 2$ torr) in a closed system, while in this study, the P_{H_2S}/P_{H_2} was adjusted to achieve $P_{S_2} = 1$ torr in a flowing system, with $P_{H_2} = 0.575$ and $P_{H_2S} = 0.425$.

The more rapid sulfidation rates in H_2S/H_2 gases cannot be explained by an easier molecular dissociation of H_2S compared to S_2 because the kinetics are parabolic, demonstrating diffusion-limited kinetics. A reasonable explanation for higher rates in H_2S/H_2 compared to those in S_2 at the same sulfur activity is that the sulfide scale was doped by hydrogen. Stoltz and Wagner (15) discussed the possible doping of oxides with hydrogen (and water vapor) both as H^+ and as H^- species. Zelouf and Simkovich (16) explained an increased sulfidation rate for Fe to form FeS in terms of an increase in cation vacancy concentration with dissolved interstitial protons for variable P_{H_2} at fixed P_{H_2S}/P_{H_2} . No previous defect studies for MoS_2 and Mo_2S_3 are available to interpret a possibility or mechanism for hydrogen doping. But the open-layered structure of MoS_2 suggests that some intercalation or substitution of solutes is possible. For an increase in the bulk anion vacancy concentration of Mo sulfides, a dopant hydrogen ion would need a negative net charge, *e.g.*, either as an interstitial H_i^- or as a substitutional ion at an anion site H_s^- . Because of the very large size of the negative hydrogen ion ($R = 2.08\text{\AA}$ for six-fold coordination), the substitutional ion would be favored. This model should lead to an electrical neutrality condition of $[H_s^-] = 2[V_s^-]$ when the dopant content exceeds the concentration of native defects in the pure sulfides. Support for this interpreta-

tion must await further experimentation, preferably by electrical conductivity measurements. From Fig. 16, the higher sulfidation rate at 900°C for $P_{S_2} = 1$ torr with $P_{H_2} = 380$ torr from this study compared to $P_{S_2} = 1$ torr with $P_{H_2} = 20$ torr from Fueki *et al.* (3) is also consistent with hydrogen doping. Likewise, the relative drop in the hydrogen doping effect for 950°C compared to the extrapolation of the 850° and 900°C behavior would suggest that the native defects at 950°C are not exceeded to the same extent by dopant-generated defects as the temperature is increased.

Summary and Conclusions

The kinetics and mechanism of sulfide scale growth on pure molybdenum have been investigated in an elemental sulfur (S_2) atmosphere and in H_2S/H_2 gas mixtures for the temperature range of 700°-900°C.

The following conclusions were reached:

1. Below about 750°C, time-independent (linear) kinetics were observed; the linear scaling rate was on the order of 10^{-8} g/cm²s. The activation energy for the linear sulfidation kinetics is 103.4 ± 21.2 kJ/gm mol.
2. For temperatures of 850°C and higher, parabolic scaling behavior was observed, with rate constants on the order of 10^{-11} g²/cm⁴s. The activation energy for the parabolic sulfidation kinetics is about 148 kJ/mol.
3. For all experimental temperatures, the sulfide scales had a uniform thickness and a columnar morphology. The MoS_2 crystals have a strong epitaxial relationship with the metal. The surface orientation of the metal affected the sulfidation rate.
4. For the linear kinetics, a sulfide crystal nucleation step is believed to be rate limiting. The microcrystalline nature of the scale caused by the two equivalent but incompatible epitaxial orientations of MoS_2 crystals on Mo introduces scale porosity.
5. For parabolic behavior, a bulk diffusion process of sulfur ions is the rate-limiting step. After the scale reaches some thickness, Mo_2S_3 crystals form beneath the MoS_2 scale and the kinetics are reduced somewhat.
6. The parabolic rate constants of sulfidation in H_2S/H_2 gas mixtures were about one order of magnitude higher than those for elemental sulfur, possibly because of hydrogen doping (intercalation or substitution) of the MoS_2 scale.

Acknowledgments

This research was sponsored by the DOE Materials Science Program, Division of Physical Research under Grant no. 79ER10404. The Climax annealed molybdenum sheet was kindly provided by William Hagel.

Manuscript submitted Dec. 5, 1983; revised manuscript received Aug. 13, 1984.

Ohio State University assisted in meeting the publication costs of this article.

REFERENCES

1. J. E. Dutrizac, *Can. Metall. Quar.*, **9**, 449 (1970).
2. J. Gerlach and H. J. Hamel, *Metall.*, **23**, 1006 (1969); *ibid.*, **24**, 488 (1970).
3. K. Fueki, H. Ishibashi, and T. Mukaiba, *J. Electrochem. Soc. Jpn.*, **30**, E-23 (1962).
4. H. R. Larson and J. F. Elliott, *Trans. Met. Soc. AIME*, **239**, 1713 (1967).
5. J. P. Hager and J. F. Elliott, *ibid.*, **239**, 513 (1967).
6. D. T. Young, W. W. Smeltzer, and T. S. Kirkaldy, *Oxid. Met.*, **7**, 3 (1973).
7. T. R. Stubbles and F. D. Richardson, *Trans. Faraday Soc.*, **56**, 1460 (1960).
8. Y. Suzuki, T. Uchida, M. Wakihara, and M. Taniguchi, *Mater. Res. Bull.*, **16**, 1085 (1981).
9. A. Meisen and H. Bennet, *Hydrocarbon Proc.*, **58**, 131 (1979).
10. J. S. Sheasby, *This Journal*, **115**, 695 (1968).
11. B. S. Lee, Ph.D. Thesis, The Ohio State University, Columbus, OH (1980).
12. G. J. Yurek, J. P. Hirth, and R. A. Rapp, *Oxid. Met.*, **8**, 265 (1974).

13. R. Fivaz and E. Moosen, *Phys. Rev.*, **163**, 743 (1967).
 14. F. A. Kroger and H. J. Vink, "Solid State Physics," Vol. 3, F. Seitz and D. Turnbull, Editors, Academic Press, New York (1956).
 15. S. Stolz and C. Wagner, *Ber. Bunsenges. Phys. Chem.*, **70**, 781 (1966).
 16. S. Zelouf and G. Simkovich, *Trans. Met. Soc. AIME*, **245**, 875 (1969).

Solid-State Electrochemical Study of In-Sb Liquid Alloys

T. J. Anderson*

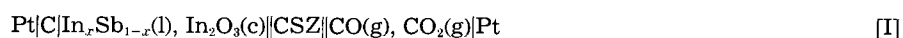
Department of Chemical Engineering, University of Florida, Gainesville, Florida 32611

L. F. Donaghey

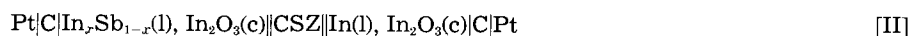
Chevron Research Company, Richmond, California 94802

ABSTRACT

The indium activity in liquid In-Sb solutions is measured in the following high temperature solid-state galvanic cells



and



The measurements indicate a moderate negative deviation from ideal solution behavior and are in close agreement with previous studies. The results are compared with the available calorimetric and phase-diagram determinations and are found to be consistent with them. An expression for the standard Gibbs energy of formation of solid InSb is presented that is consistent with the direct EMF measurements, calorimetric studies, reported phase diagram, and results of this study. The nonrandom two-liquid theory is found to adequately represent the liquid mixture thermodynamic data.

Indium antimonide is the only existing intermetallic compound in the In-Sb system; it exhibits a high electron mobility and presents the lowest bandgap energy of the group III-V semiconducting compounds (1-3). The pure compound and mixed crystals containing InSb are of current interest as host materials for a variety of solid-state electronic devices (4-7). As the chemical processing of these materials often involves the melt and the analysis of such processes frequently assigns an equilibrium boundary condition, knowledge of the solid-liquid phase diagram is important. Furthermore, the phase fields for uninvestigated multicomponent systems can be estimated from consideration of the binary limits alone. The interpolation of the multicomponent phase diagrams between the binary edges generally involves use of a solution model to describe the composition and temperature dependence of the excess Gibbs energy. The success of a model should be determined by its ability to represent not only the binary-phase diagram, but also the mixture enthalpy and entropy. With this objective in mind, solid-state electrochemical measurements of the In activity in In-Sb melts are reported and an analysis of the available phase-diagram and thermochemical information for both the mixture and pure compound is presented.

A considerable number of experimental characterizations of the thermodynamic properties for the In-Sb system have been reported. Presented in Table I is the melting temperature of InSb, $T_f[\text{InSb}]$, as determined by several investigators. It is noted that InSb is the only III-V compound having T_f below that of a component element [Sb]. Also shown in Table I is a summary of the enthalpy of fusion of InSb, $\Delta H_f^\circ[\text{InSb}]$. As can be seen, there exists a maximum difference of 13.3 kJ · mol⁻¹ in the reported values of $\Delta H_f^\circ[\text{InSb}]$. The mixing of pure In and pure Sb produces a negative enthalpy change as determined calorimetrically by several investigators (15, 23-28). The different measurements are in good agreement, with the published range for the maximum exothermic enthalpy of mixing, ΔH^M , of 2345-3725 kJ · mol⁻¹ for temperatures in the range of 910-1184 K. The enthalpy of mixing is not a symmetric function of composition; the maximum exo-

thermic ΔH^M is located in the reported range $x_{\text{In}} = 0.55-0.61$. The more recent results of Rosa *et al.* (28), obtained at five temperatures in the same calorimeter, indicate that the maximum ΔH^M shifts to a lower magnitude at increased Sb content as the temperature is increased. The phase diagram for the In-Sb system has been reported by several investigators (15, 19, 22, 29) who found a simple eutectic on the Sb-rich side of the compound at a composition of $x_{\text{Sb}} = 0.682$ and a temperature of 767 K. The In-InSb eutectic is practically degenerate, having a melting temperature approximately 1 K below that of pure In at a composition $x_{\text{Sb}} = 0.007$.

Of primary importance in the understanding of solid-liquid phase equilibria in III-V compounds and solid solutions is an accurate description of the liquid-phase solution behavior. The multicomponent solid solutions are often nearly ideal, but the liquid phase for most III-V systems shows negative deviations from ideal behavior. The calculation of liquidus temperatures proves to be sensitive to the model employed for the liquid-phase thermodynamics. As these models are generally based on a formulation of the excess Gibbs energy of the mixture, a direct determination of the composition dependence of

Table I. Comparison of the reported melting temperature and enthalpy of fusion of InSb

$T_f[\text{InSb}]/\text{K}$	$\Delta H_f^\circ[\text{InSb}]/\text{kJ} \cdot \text{mol}^{-1}$	Ref.
798 ± 3	37.7 ± 12.6	(8)
—	46.9	(9)
—	46.9 ± 1.7	(10)
797 ± 1	47.8 ± 0.8	(11)
800 ± 3	48.1 ± 1.7	(12)
803	48.5	(13)
—	48.5 ± 2.9	(14)
—	48.7 ± 1.0	(15)
—	49.4 ± 1.7	(16)
—	51.0 ± 2.1	(17)
798	51.0	(18)
798	—	(19)
798.4 ± 0.3	—	(20)
809	—	(21)
813	—	(22)

*Electrochemical Society Active Member.

the Gibbs energy of mixing, ΔG^M , would aid in the assessment of various proposed models. To date, there have been three experimental determinations of component activities in liquid In-Sb solutions. Terpilowski (30) measured In activities in an electrochemical cell using a double bromide salt and found negative deviations throughout the entire composition range. Similarly, Hoshino *et al.* (31), using a double iodide salt concentration cell, measured In activities that were in fair agreement with the results of Terpilowski. As is often the case with this method, the excess enthalpies and entropies reported in these two studies were quite different, and further discrepancies are found when compared to calorimetric data. Furthermore, Terpilowski (30) and Hoshino and co-workers (31) assumed that the In ions transported in the fused salt electrolytes were monovalent; this assumption directly affects the activity calculated from the measured cell EMF.

The possible uncertainty in the In oxidation state for these cells prompted Chatterji and Smith (32) to investigate the activity of In with a galvanic cell using a solid oxide electrolyte in which In ions are known to be trivalent and the transported oxygen ion divalent. Four compositions were studied, all of which were in the In-rich portion of the phase field, where this technique is not as reliable. In addition, Chatterji and Smith (32) used air as the reference electrode, thus requiring knowledge of the Gibbs energy of forming indium sesquioxide from the elements. Therefore, a second electrochemical cell was evaluated using a mixture of pure In metal and indium sesquioxide as the working electrode and air as the reference electrode. The resulting logarithm of the indium activity is then proportional to the difference in the measured EMF of the above two types of cells. This difference is small in value (6.5-37 mV for the compositions studied) compared to the measured EMF's of the two individual cells (920-1160 mV) and includes the uncertainties of two experiments, though the possible errors are probably systematic and cancel. A third-law analysis indicated the expression for $G_r^\circ[\text{In}_2\text{O}_3]$ of Chatterji and Smith (33) to be inconsistent with other available thermodynamic data (34).

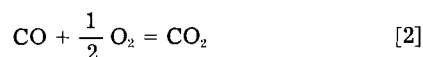
For these reasons, the following solid-state electrochemical cells were investigated



In both cells, the working electrode consisted of the mixture of a liquid In-Sb alloy at the composition of interest and the most stable oxide, indium sesquioxide. In the first cell type, the reference oxygen partial pressure was established with a mixture of CO + CO₂ of known composition, while the second cell type utilized pure liquid indium and its stable oxide as the reference electrode. The open-circuit potential, E , of concentration cell [I] can be related to the indium activity, a_{In} , by the following expression

$$a_{\text{In}} = (p_{\text{CO}_2}/p_{\text{CO}})^{-3/2} \exp \{3FE/RT - 3\Delta G^\circ[\text{CO}-\text{CO}_2]/2RT + \Delta G_r^\circ[\text{In}_2\text{O}_3]/2RT\} \quad \text{[1]}$$

where $p_{\text{CO}_2}/p_{\text{CO}}$ is the ratio of the partial pressure of CO₂ to that of CO in the reference gas mixture, $\Delta G^\circ[\text{CO}-\text{CO}_2]$ is the standard Gibbs energy change for the reaction



and $\Delta G_r^\circ[\text{In}_2\text{O}_3]$ is the standard Gibbs energy change for the formation of 1 mol of indium sesquioxide.

Cell type II gives the simple relationship between the measured cell voltage and temperature to the indium activity

$$\ln a_{\text{In}} = -3FE/RT \quad \text{[3]}$$

The first cell is advantageous in that the gaseous reference electrode provides a more reversible electrode and

generally serves as a better buffer for oxygen. Thus, temperature coefficients of these cells were found to be in closer agreement with calorimetric values, though the calculated activities are subject to uncertainty in not only the temperature and measured voltage but also in $p_{\text{CO}_2}/p_{\text{CO}}$, $\Delta G^\circ[\text{CO}-\text{CO}_2]$ and $\Delta G_r^\circ[\text{In}_2\text{O}_3]$. In addition, the use of the CO-CO₂ reference electrode is superior to air since the O₂ partial pressure can be adjusted to closely match that established in the working electrode. However, the use of pure In-In₂O₃ as a reference electrode is advantageous in that the only errors involved are those associated with the measurement of the voltage and temperature. Thus, in this study, indium activities were measured in liquid solutions with antimony by means of the oxygen-ion conducting solid electrolyte, calcia-stabilized zirconia. Both the investigation of solutions throughout the entire composition range and the use of a solid oxide electrolyte should eliminate possible ambiguities in the oxidation state of the In ion that was assumed by earlier workers employing a halide-based concentration cell.

Experimental

A complete description of the experimental design and procedure has been given previously (34-36). Extreme care was taken to minimize the oxygen content of the inert gas blanket. Data acquisition was automated with a microcomputer system. The alloys were formed by mixing powdered InSb (Orion Chemical Company, 325 mesh, 99.999% purity) with either pure antimony (Cominco American, high purity, lot EM 2139) or pure indium (Orion Chemical Company, 325 mesh, 99.999% purity, lot no. 2449) to obtain the desired composition. Indium sesquioxide (Alfa Inorganics, 99.999% purity) was placed on top of the alloy or the pure indium in each cell. The CO-CO₂ reference gas mixture (22.169 ± 0.02% CO₂, 2.349 ± 0.02% CO, and balance Ar) was a primary standard procured from Matheson Gas Products.

When a new alloy composition was formed by adding pure elemental material to a previously studied composition, it was found to give inconsistent results. This inconsistency was apparent in a changing EMF temperature coefficient as the temperature was cycled and was probably due to incomplete mixing. Thus, for each composition studied, an alloy was synthesized from the pure elements.

Results

The open-circuit equilibrium potential for cells [I] and [II] was measured throughout a predetermined temperature range, and the results are plotted in Fig. 1 and 2. The EMF measured for cells using the CO-CO₂ gaseous mixture as the reference electrode is shown in Fig. 1, while Fig. 2 depicts the more direct measurements employing the pure metal reference electrode. Only the measurements made in the final temperature cycle are shown. It was found that several cycles were required before reproducible EMF temperature variations were obtained. As can be seen, the measured potentials are linear in temperature over the range investigated.

The activity of indium was calculated with Eq. [1] or [3] at 973 K using linear regression coefficients for the straight lines shown in Fig. 1 and 2. These results are given in Table II, along with the antimony activity calculated by integration of the Gibbs-Duhem equation. Also listed in Table II are the corresponding activity coefficients, γ_{In} , and the resulting molar Gibbs energy of mixing, ΔG^M . The partial molar enthalpy of In calculated from the temperature dependence of the cell potential exhibited considerable scatter, particularly with use of the pure metal/metal oxide reference electrode. Similar scatter was observed in the results for the gallium activity in Ga-Sb melts (36). This inconsistency is common in these types of measurements and does not reflect on the primary results of EMF measurements-Gibbs energy changes. The results of the activity measurements are graphically shown in Fig. 3 and depict a negative deviation from ideal solution behavior. Shown for comparison are the molten salt electrolyte results of Terpilowski (30)

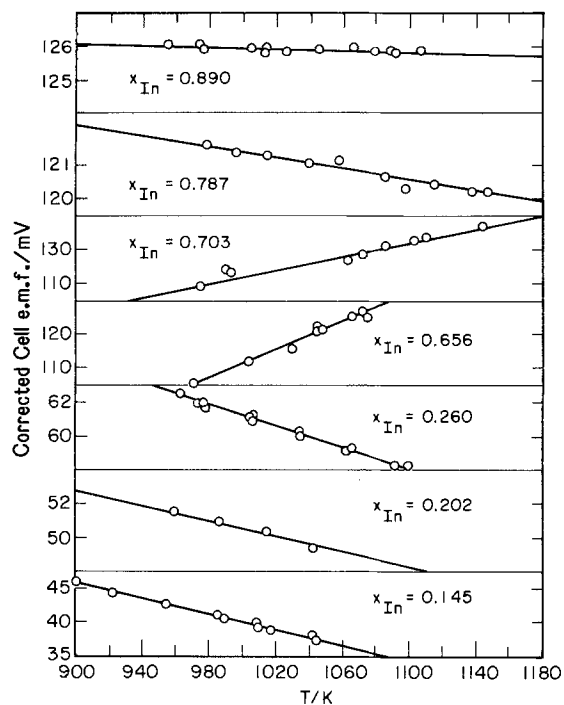


Fig. 1. Experimental cell voltages as a function of temperature for cell type [I]. Least squares line shown.

at 923 K and of Hoshino *et al.* (31) at 900 K and also the solid oxide electrolyte results of Chatterji and Smith (32) at 973 K. As can be seen, the results of all four investigations are in relatively good agreement. The results of the molten salt electrolyte work shows a slightly more negative deviation in component-rich solutions than this work, though the difference is within the experimental error involved.

The smoothed values for the indium and antimony activities are indicated by the solid lines in Fig. 3 and are combined to give ΔG^M , which is plotted as a function of composition in Fig. 4. Also summarized in Fig. 4 is the experimental enthalpy of mixing as measured by several investigators (23-26). The primary results of this work can be combined with the primary results of the calorimetric investigators to produce the entropy of mixing, ΔS^M . Shown in Fig. 4 is ΔS^M calculated from ΔG^M presented

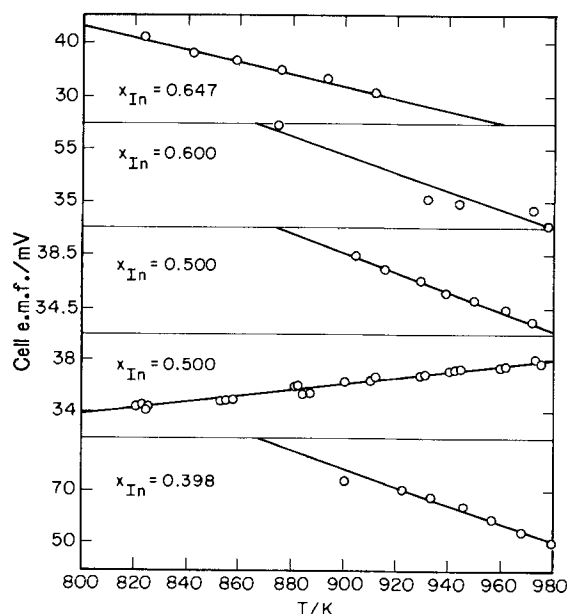


Fig. 2. Experimental cell voltages as a function of temperature for cell type [II]. Least squares line shown.

Table II. Summary of thermodynamic data for In-Sb liquid alloys derived from EMF measurements at 973 K

Cell	x_{In}	a_{In}	γ_{In}	a_{Sb}	γ_{Sb}	$-\Delta G^M$ (kJ · mol ⁻¹)
[I]	0.145	0.051	0.352	0.828	0.968	9.59
[I]	0.202	0.072	0.356	0.741	0.929	12.47
[I]	0.260	0.106	0.408	0.659	0.890	14.43
[I]	0.656	0.435	0.663	0.158	0.459	19.11
[I]	0.703	0.544	0.774	0.107	0.360	17.66
[I]	0.787	0.760	0.966	0.043	0.197	14.34
[I]	0.890	0.915	1.028	0.012	0.110	9.15
[II]	0.398	0.142	0.357	0.475	0.789	19.82
[II]	0.500	0.265	0.530	0.343	0.685	19.40
[II]	0.500	0.261	0.522	0.343	0.685	19.52
[II]	0.600	0.364	0.607	0.218	0.544	19.67
[II]	0.647	0.418	0.646	0.166	0.471	19.39

here and from two of the ΔH^M determinations. For comparison, the ideal entropy of mixing is plotted; the excess entropy of mixing can be seen to be nearly zero in the composition range $0.0 < x_{In} < 0.4$ and positive in more indium-rich solutions.

Discussion

Calculation of the phase diagram.—The In-Sb binary phase diagram is well known, and thus a convenient check of the consistency of the available solution thermodynamic data is a calculation of the liquidus. The conditions of solid-liquid equilibrium stipulate equivalence of the temperature, pressure, and component chemical potentials in both phases, subject to the constraint of an equal number of lattice sites for In and Sb in the solid compound. Neglecting any pressure dependence, the combination of these requirements results in the following simple relationship between the liquidus composition, x_{In} , and temperature, T_l

$$x_{In}(1 - x_{In}) = \exp [\vartheta_{InSb}(T_l)] / \Gamma_{InSb}(x_{In}, T_l) \quad [4]$$

The ϑ_{InSb} term is the reduced reference state chemical potential change and is defined by

$$\vartheta_{InSb} = (\mu_{InSb}^o - \mu_{In}^o - \mu_{Sb}^o) / RT \quad [5]$$

where μ_i^o is the standard state chemical potential for the solid compound InSb or the liquid components In and Sb. The quantity Γ_{InSb} is a measure of the deviation of the liquid solution from ideal behavior at the liquidus temperature and composition of interest and is simply the product of the liquid-phase component activity coefficients, γ_i

$$\Gamma_{InSb} = \gamma_{In}\gamma_{Sb} \quad [6]$$

Choosing the standard state for all species to be the pure component at the temperature, pressure, and state of

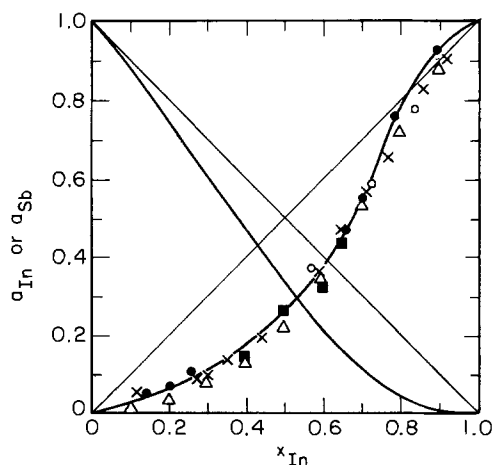


Fig. 3. The activity of indium and antimony in the liquid mixture: (—) 973 K, smoothed, this study; (●) this study, gas reference electrode; (■) this work, metal reference electrode; (○) Chatterji and Smith (32); (X) Hoshino *et al.* (31); (Δ) Terpilowski (30).

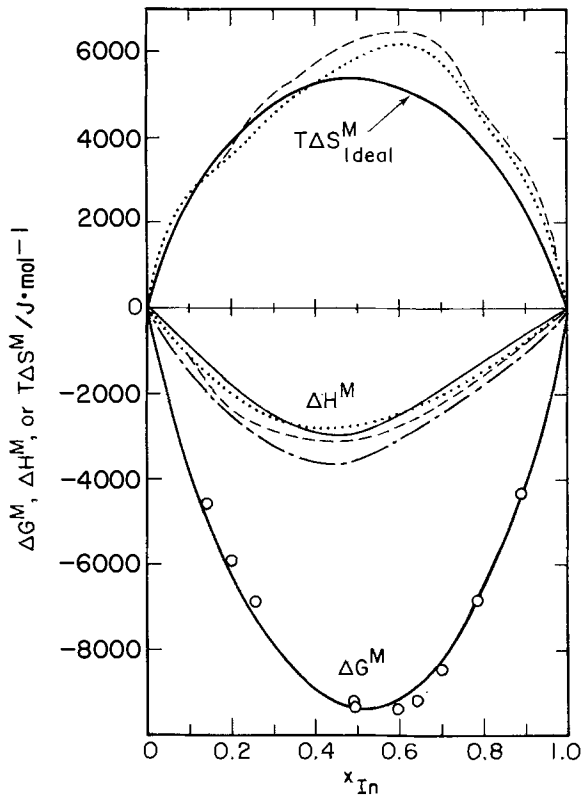


Fig. 4. Gibbs energy, enthalpy and entropy of mixing for In-Sb liquid alloys at 973 K. ΔG^M : (o) this study. ΔH^M : (----) Wittig and Gehring (23), (.....) Yazawa *et al.* (24), (—) Vecher *et al.* (25), (— · —) Itagaki and Yazawa (26).

aggregation of interest, ϑ_{InSb} is simply the molar Gibbs energy difference between the solid compound and the pure liquid elements and is made dimensionless upon division by RT . Several paths of state change can be formulated to estimate this molar Gibbs energy change, each requiring a different data base. One such sequence, first proposed by Wagner (37) and later applied to III-V binary systems by Vieland (38), is to change the temperature of the pure compound from the one of interest, T , to $T_f[\text{InSb}]$, melt the compound, subcool the resulting equimolar mixture to T , and separate the solution into the pure elements. The resulting expression for ϑ_{InSb} is

$$\vartheta_{\text{InSb}} = \ln \left[\frac{\gamma_{\text{In}}[T, x = 0.5] \gamma_{\text{Sb}}[T, x = 0.5]}{4} \right] - \frac{\Delta S_f^\circ[\text{InSb}]}{R} \left(\frac{T_f[\text{InSb}]}{T} - 1 \right) + \frac{1}{RT} \int_T^{T_f[\text{InSb}]} \frac{\Delta C_p}{T} dT \quad [7]$$

Here, ΔC_p is the molar heat capacity difference between the stoichiometric liquid and the compound. Substituting this relationship into Eq. [4], neglecting the ΔC_p term [$\Delta C_p = 5.52 \text{ J} \cdot \text{mol}^{-1} \cdot \text{K}^{-1}$ at $T_f[\text{InSb}]$ (11)], and explicitly indicating the principal temperature dependence of the activity in terms of the relative partial molar enthalpy, $\Delta \bar{H}_i$, and entropy, $\Delta \bar{S}_i$, results in the following equation for the liquidus temperature

$$T_l = \frac{\Delta H_f^\circ[\text{InSb}] + \Delta \bar{H}_{\text{In}}[x] + \Delta \bar{H}_{\text{Sb}}[x] - \Delta \bar{H}_{\text{In}}[x = 0.5] - \Delta \bar{H}_{\text{Sb}}[x = 0.5]}{\Delta S_f^\circ[\text{InSb}] + \Delta \bar{S}_{\text{In}}[x] + \Delta \bar{S}_{\text{Sb}}[x] - \Delta \bar{S}_{\text{In}}[x = 0.5] - \Delta \bar{S}_{\text{Sb}}[x = 0.5]} \quad [8]$$

A second expression for the reduced standard state chemical potential difference represents the molar Gibbs energy change of the following process: solid InSb is reduced to the natural elements at the temperature of interest (the reverse formation reaction), followed by a thermal sequence similar to that used in the previous analysis but applied to Sb since the melting temperature of Sb, $T_f[\text{Sb}]$, is above that of InSb. The expression for ϑ_{InSb} is

$$\vartheta_{\text{InSb}} = \left\{ \Delta G_f^\circ[\text{InSb}, T] - \Delta S_f^\circ[\text{Sb}][T_f[\text{Sb}] - T] - \int_T^{T_f[\text{Sb}]} \frac{\Delta C_p[\text{Sb}]}{T} dT \right\} / RT \quad [9]$$

Here $\Delta G_f^\circ[\text{InSb}, T]$ is the standard Gibbs energy of formation of InSb at the temperature of interest and $\Delta C_p[\text{Sb}]$ is the heat capacity difference between liquid and solid Sb. Substituting this expression for ϑ_{InSb} into Eq. [4], while again neglecting the $\Delta C_p[\text{Sb}]$ term [$\Delta C_p[\text{Sb}] = 0.42 \text{ J} \cdot \text{mol}^{-1} \cdot \text{K}^{-1}$ at $T_f[\text{Sb}]$ (39)], yields the alternative expression for the liquidus temperature

$$T_l = \frac{\Delta H_f^\circ[\text{InSb}] - \Delta H_f^\circ[\text{Sb}] - \Delta \bar{H}_{\text{In}}[x] - \Delta \bar{H}_{\text{Sb}}[x]}{\Delta S_f^\circ[\text{InSb}] - \Delta S_f^\circ[\text{Sb}] - \Delta \bar{S}_{\text{In}}[x] - \Delta \bar{S}_{\text{Sb}}[x]} \quad [10]$$

In this relationship $\Delta H_f^\circ[\text{InSb}]$ and $\Delta S_f^\circ[\text{InSb}]$ represent the standard enthalpy and entropy of formation of InSb, respectively. Comparing Eq. [8] and [10], it is evident that the "formation" expression (Eq. [10]) is a more critical test of the consistency between the solution properties and the measured liquidus, as the liquid mixture information required in Eq. [10] is relative to the pure components, while, in Eq. [8], it is relative to the stoichiometric liquid. However, the enthalpy of fusion and melting temperature required in Eq. [8] are directly measurable, whereas the standard enthalpy and entropy of formation are generally obtained from the temperature dependence of $\Delta G_f^\circ[\text{InSb}, T]$ and thus subject to more uncertainty.

The InSb phase diagram shows simple eutectic behavior in the Sb-rich portion. Equating the chemical potential of Sb in the liquid mixture to that of pure solid Sb, and using the same sequence developed in Eq. [7] to determine the reduced standard state chemical potential change but applied to solid Sb, results in

$$T_l = \frac{\Delta H_f^\circ[\text{Sb}] + \Delta \bar{H}_{\text{Sb}}[x]}{\Delta S_f^\circ[\text{Sb}] + \Delta \bar{S}_{\text{Sb}}[x]} \quad [11]$$

As in Eq. [10], the $\Delta C_p[\text{Sb}]$ term is assumed to be negligible.

Given in Table III are the results of calculating the liquidus temperatures with either the "fusion" (Eq. [8]) or "formation" (Eq. [10]) expressions. The partial molar enthalpies of the components were obtained from the calorimetric enthalpy of mixing investigations of Yazawa *et al.* (24), and the partial molar entropies of the components were calculated from the measured component activities from this work. The smoothed values of the component activities used in these calculations are also listed in Table III. A melting temperature for InSb of 800 K was used in conjunction with the experimental enthalpies of fusion listed in Table I to calculate the liquidus temperatures with the "fusion" equation. The values of $\Delta H_f^\circ[\text{InSb}]$ used were the smallest (8) and largest (18) experimental determinations, along with the selected value of $49.4 \text{ kJ} \cdot \text{mol}^{-1}$ (16). There are four EMF studies of the standard Gibbs energy of formation of solid InSb available in the literature (40-43). The standard enthalpy and entropy of formation of InSb, required in the "formation" equation, can be determined from the temperature dependence of these measurements. The value for $\Delta H_f^\circ[\text{Sb}]$ was taken from Hultgren *et al.* (39) as $19,870 \text{ J} \cdot \text{mol}^{-1}$, and $T_f[\text{Sb}]$

was assumed to be 904 K. Table IV gives the liquidus temperatures determined from Eq. [11], using the smoothed activity measurements of this work and also of Terpilowski (30) and Hoshino *et al.* (31). Also found in Tables III and IV are the liquidus temperatures determined by assuming that the solutions exhibit ideal behavior. Finally, these results are compared with the experimental liquidus temperatures as determined by Liu and

Table III. Comparison of the liquidus temperatures, T_l (K), in the In-Sb system

x_{Sb}	0.1	0.2	0.3	0.4	0.5	0.6	0.7	Ref.
Smoothed $a_{In}(973\text{ K})$	0.915	0.785	0.538	0.378	0.262	0.180	0.112	$\Delta H_f^\circ(\text{InSb})$
Smoothed $a_{Sb}(973\text{ K})$	0.010	0.048	0.114	0.218	0.335	0.470	0.605	or
Method	$T_l(\text{K})$							$\Delta G_f^\circ(\text{InSb})$
Fusion	541.4	676.9	747.2	790.2	800.0	794.0	761.9	(8)
Fusion	596.9	707.5	760.5	792.7	800.0	795.6	771.7	(18)
Fusion	591.3	704.5	759.4	792.5	800.0	795.5	770.7	(16)
Formation	576.6	687.3	741.6	774.3	781.7	777.2	752.8	(40)
Formation	582.3	697.8	754.4	788.5	796.3	791.6	766.1	(41)
Formation	585.1	698.4	653.6	786.9	794.5	789.9	765.0	(42)
Formation	597.2	705.9	758.1	789.5	796.6	792.3	768.9	(43)
Ideal	701.8	753.0	779.9	793.8	798.2	793.8	—	—
Experimental	607.2	699.3	756.9	787.6	798.2	788.6	774.3	(19)

Table IV. Comparison of the liquidus temperatures, T_l (K), in the In-Sb system rich in Sb

x_{Sb}	0.7	0.8	0.9	Ref.
Smoothed $a_{In}(973\text{ K})$	0.112	0.062	0.021	a_{In}
Smoothed $a_{Sb}(973\text{ K})$	0.605	0.754	0.884	
Method	$T_l(\text{K})$			
Eq. [11]	755.2	815.6	863.6	This work
Eq. [11]	730.5	797.0	860.1	(30)
Eq. [11]	765.7	819.5	866.5	(31)
Ideal	796.6	833.6	869.4	—
Experimental	774.3	825.1	867.7	(19)

Peretti (19). The results of these calculations using the "fusion" equation in conjunction with the smoothed activity measurements of this study, $\Delta H_f^\circ[\text{InSb}] = 49.4\text{ kJ} \cdot \text{mol}^{-1}$ (16), and the enthalpy of mixing of Yazawa *et al.* (24) are graphically displayed in Fig. 5. For comparison,

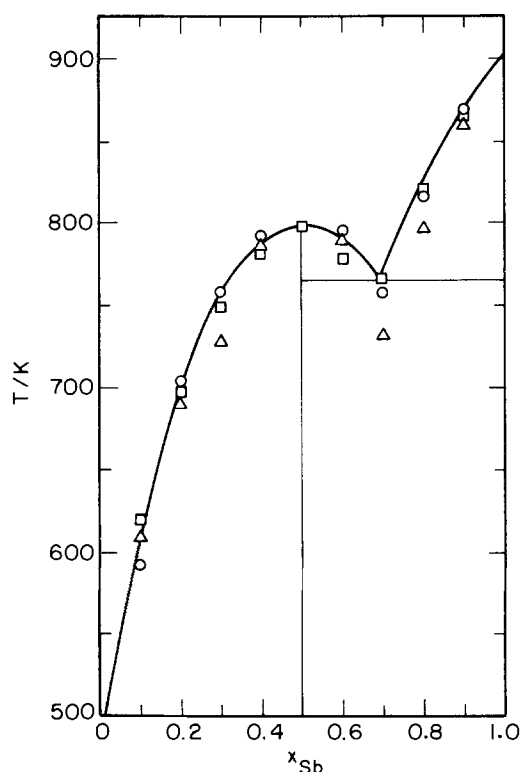


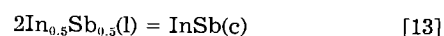
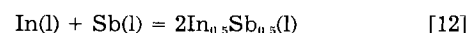
Fig. 5. Liquidus temperatures for the In-Sb system calculated from Eq. [8] and [11]. (o): This study. (Δ): Terpilowski (30). (\square): Hoshino *et al.* (31). (—): Experimental results of Liu and Peretti (19).

Fig. 5 also shows the liquidus temperatures calculated from the actual activity measurements of Terpilowski (30) and the smoothed values of Hoshino *et al.* (31). The results of Chatterji and Smith (32) were obtained over an insufficient composition range to be compared.

Several conclusions can be made from these calculations. First, the negative deviation observed in the various EMF measurements is supported by these calculations, as is seen by comparing the calculated liquidus temperatures with the ideal temperatures. The enthalpy of fusion reported as $37.7\text{ kJ} \cdot \text{mol}^{-1}$ (8) appears to be too low, and the use of the experimental $\Delta H_f^\circ[\text{InSb}]$ range of $46.9\text{--}51.0\text{ kJ} \cdot \text{mol}^{-1}$ give liquidus temperatures consistent within the experimental error for at least one of the three activity measurements. The results of this study tend to support a higher value of $\Delta H_f^\circ[\text{InSb}]$; the results of Terpilowski support the lower $\Delta H_f^\circ[\text{InSb}]$ values. It is noted that the use of different enthalpy of mixing data has a negligible effect on the calculated temperatures. Finally, the results in the antimony-rich region indicate that the activities of this work and of Hoshino *et al.* (31) are in close agreement, while the work of Terpilowski (30) yields considerably lower liquidus temperatures.

A more stringent test of the thermodynamic consistency of the various data is found in using the formation equation. Figure 6 shows the liquidus temperatures calculated using the results of Sirota and Yushkevich (42), Abbasov and Mamedov (40), and Terpilowski and Trzebiatowski (43) for the standard enthalpy and entropy of formation and the smoothed activities of this work. Of the four experimental values for $\Delta H_f^\circ[\text{InSb}]$ and $\Delta S_f^\circ[\text{InSb}]$ available, the values given by Nikol'skaya *et al.* (41) and Sirota and Yushkevich (42) are in good agreement. As can be seen, fairly close agreement is observed, though the use of the values of Abbasov and Mamedov (40) yielded significantly lower temperatures. Again for comparison, the formation liquidus temperatures were calculated with the molten salt EMF activity measurements. Figure 7 depicts the results of using either the results of Terpilowski (30) or Hoshino *et al.* (31) in conjunction with the extremum for $\Delta H_f^\circ[\text{InSb}]$ and $\Delta S_f^\circ[\text{InSb}]$ (40, 43). The results of Terpilowski (30) show considerable discrepancy with the reported phase diagram, while good consistency is found with the results of this study or of Hoshino *et al.* (31) and with use of the lowest values of $\Delta H_f^\circ[\text{InSb}]$ and $\Delta S_f^\circ[\text{InSb}]$ (43).

Gibbs energy of formation of InSb(c).—An alternate expression for $\Delta G_f^\circ[\text{InSb}]$ can be derived using the results of this study as follows. Consider the following reaction scheme



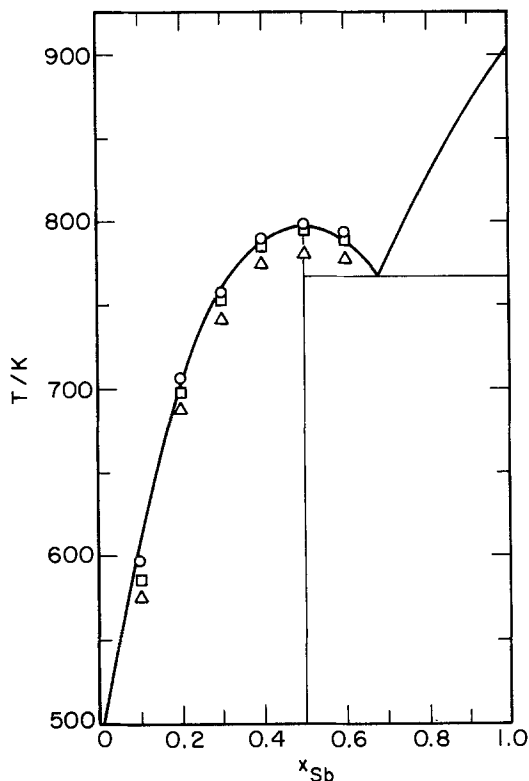


Fig. 6. Liquidus temperatures for the In-Sb system calculated from Eq. [10] and the results of this study. The standard enthalpy and entropy of formation of InSb taken from: (o) Terpilowski and Trzebiatowski (43), (□) Sirota and Yushkevich (42), (△) Abbasov and Mamedov (40). The solid line represents the experimental results of Liu and Peretti (19).

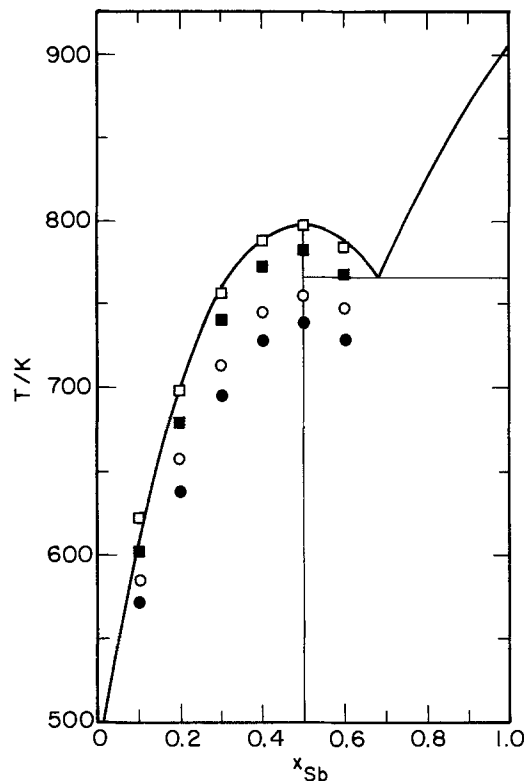


Fig. 7. Liquidus temperatures for the In-Sb system calculated from Eq. [10] and the EMF activity measurements of: (o) Terpilowski (30), (□) Hoshino *et al.* (31). The standard enthalpy and entropy of formation of InSb taken from: open, Terpilowski and Trzebiatowski (42); closed, Abbasov and Mamedov (40). The solid line represents the experimental results of Liu and Peretti (19).

The Gibbs energy change for the first reaction is simply the Gibbs energy change upon mixing equal moles of In and Sb. The Gibbs energy change for reactions [13] and [14] can be approximated by

$$\Delta G^{\circ}[13] = -\Delta H_f^{\circ}[\text{InSb}]\{1 - T/T_f[\text{InSb}]\} \quad [15]$$

$$\Delta G^{\circ}[14] = \Delta H_f^{\circ}[\text{Sb}]\{1 - T/T_f[\text{Sb}]\} \quad [16]$$

where the small temperature dependence of the enthalpy and entropy of fusion of InSb and Sb has been neglected. Upon summation of the above reactions, the overall reaction is found to be the desired formation reaction, and the standard enthalpy and entropy of formation are given by

$$\Delta H_f^{\circ}[\text{InSb}] = 2\Delta H^{\text{M}}[x = 0.5] + \Delta H_f^{\circ}[\text{Sb}] - \Delta H_f^{\circ}[\text{InSb}] \quad [17]$$

and

$$\Delta S_f^{\circ}[\text{InSb}] = 2\Delta S^{\text{M}}[x = 0.5] + \Delta H_f^{\circ}[\text{Sb}]/T_f[\text{Sb}] - \Delta H_f^{\circ}[\text{InSb}]/T_f[\text{InSb}] \quad [18]$$

By using the results of Yazawa *et al.* (24) for $\Delta H^{\text{M}}[x = 0.5]$, the enthalpy of fusion as given by Blachnik and Schneider (16), the results of this study to determine $\Delta S^{\text{M}}[x = 0.5]$, and by taking $\Delta H_f^{\circ}[\text{Sb}]$, $T_f[\text{Sb}]$, and $T_f[\text{InSb}]$ as given previously, the following equation is derived for $\Delta G_f^{\circ}[\text{InSb}]$

$$\Delta G_f^{\circ}[\text{InSb}] = -35,220 + 25.54(T/\text{K}) \text{ J} \cdot \text{mol}^{-1} \quad [19]$$

Table V summarizes the various results reported for the standard enthalpy and entropy of formation of solid InSb. The values determined by molten salt EMF studies are given for the average temperature of those measurements. Also listed are two high temperature calorimetric investigations of the standard formation enthalpy which are in excellent agreement with Eq. [19]. For comparison, the standard entropy derived from the equimolar activity results of the two molten salt studies (30, 31) is also given.

There are several different ways to test the consistency of these various results. The primary result of the EMF formation work is the Gibbs energy of formation of InSb. Thus the derived expressions should produce $\Delta G_f^{\circ}[\text{InSb}]$ values in close agreement with the EMF values. Table VI lists two values of $\Delta G_f^{\circ}[\text{InSb}]$ calculated from the derived equations and are compared to the measured results. As can be seen, the equations derived using the activity measurements of this work and of Hoshino *et al.* (31) are within the range of experimental error for the EMF results and the range produced by varying the enthalpy of fusion of InSb and enthalpy of mixing. The result found

Table V. Summary of results for the standard enthalpy and entropy of formation of InSb

Method	$-\Delta H_f^{\circ}(\text{InSb})$ (kJ · mol ⁻¹)	T (K)	Ref.
EMF	34.17	703	(40)
EMF	33.30 ± 1.67	703	(41)
EMF	37.66 ± 1.76	703	(43)
EMF	34.39	703	(42)
Calorimetric	36.15 ± 0.17	723	(44)
Mass spectroscopic	34.31	798	(45, 16)
Calorimetric	35.42 ± 0.84	750	(13)
Eq. [19]	35.22	—	(This work, 16, 24, 39)

Method	$-\Delta S_f^{\circ}(\text{InSb})$ (J · mol ⁻¹ · K ⁻¹)	T (K)	Ref.
EMF	25.48	703	(40)
EMF	23.26 ± 2.09	703	(41)
EMF	28.70 ± 1.67	703	(43)
EMF	24.77	703	(42)
Eq. [19]	25.54	—	(This work, 16, 24, 39)
Derived	22.32	—	(30, 16, 24, 39)
Derived	26.11	—	(31, 16, 24, 39)

Table VI. Summary of the Gibbs energy of formation of InSb

Method	$-\Delta G_f^\circ[\text{InSb}]$ (kJ · mol ⁻¹)		Ref.
	643 K	763 K	
Eq. [19]	18.80	15.73	This work
Derived	20.87	18.19	
Derived	18.43	15.30	
EMF	17.78	14.73	
EMF	18.34	15.56	(41)
EMF	18.47	15.50	(42)
EMF	19.20	15.76	(43)

in using the activity studies of Terpilowski (30) gives Gibbs energies which are too low.

A second consistency test involves a third law calculation of $\Delta H_f^\circ[\text{InSb}]$ from the following relationship

$$\Delta H_f^\circ[\text{InSb}, 298.15 \text{ K}]$$

$$= T \left\{ - \left[\frac{\Delta G_f^\circ[\text{InSb}, T] - \Delta H_f^\circ[\text{InSb}, 298.15 \text{ K}]}{T} + \frac{\Delta G_f^\circ[\text{InSb}, T]}{T} \right] \right\} \quad [20]$$

The first term on the left is the free energy function and can be calculated from

$$- \left[\frac{\Delta G_f^\circ[\text{InSb}, T] - \Delta H_f^\circ[\text{InSb}, 298.15 \text{ K}]}{T} \right] = \Delta S_f^\circ[\text{InSb}, 298.15 \text{ K}] + \Delta_f^\circ[S(T) - S[298.15 \text{ K}]] - \Delta_f^\circ[H(T) - H[298.15 \text{ K}]]/T \quad [21]$$

Thus, the free energy function, calculated from both low and high temperature heat capacities, can be combined with the Gibbs energy of formation of InSb from the various sources to give a calculated value of $\Delta H_f^\circ[\text{InSb}, 298.15 \text{ K}]$. The calculated result can then be compared to that measured independently by calorimetry. Taking the high temperature heat capacity of In from Hultgren *et al.* (39), for Sb from Glassner (46), and for InSb from Lundin *et al.* (13) and the absolute entropy for the elements from Hultgren *et al.* (39) and for InSb from Renner (47), and combining this with the values of $\Delta G_f^\circ[\text{InSb}, T]$ yield the results shown in Fig. 8. The results using measurements of the four EMF formation studies are given by the solid lines and are compared with the

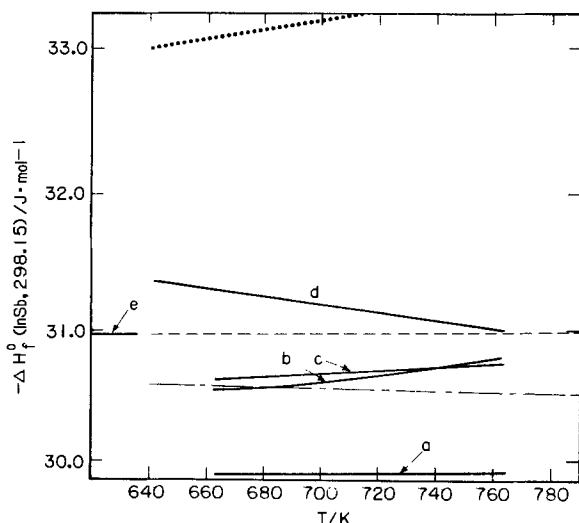


Fig. 8. Standard enthalpy of formation of InSb at 298.15 K obtained by a third-law analysis with $\Delta G_f^\circ[\text{InSb}, T]$ of: a, Abbasov and Mamedov (40); b, Nikol'skaya *et al.* (41); c, Sirota and Yushkevich (42); d, Terpilowski and Trzebiatowski (43). (---): Eq. [19]. (.....): Derived, Terpilowski (30). (— — —): Derived, Hoshino *et al.* (31). e: Selected value of $\Delta H_f^\circ[\text{InSb}, 298.15 \text{ K}]$, Hultgren *et al.* (12).

Table VII. Summary of the standard enthalpy of formation of InSb at 298.15 or 273 K

Method	$-\Delta G_f^\circ[\text{InSb}]$ (kJ · mol ⁻¹)	Ref.
Tin solution calorimetry	29.04 ± 0.59	273 K (18)
Tin solution calorimetry	30.64 ± 0.84	273 K (13)
Calculated	30.54	273 K (48, 49)
Calorimetry	28.45 ± 2.51	298 K (50)
Calorimetry	32.55 ± 0.33	298 K (51)
Calculated	30.96 ± 0.84	298 K (11, 12)

value selected by Hultgren *et al.* (12) though the direct measurements available in the literature show considerable scatter as summarized in Table VII.

Although the results of these calculations are not definitive, the derived expression for $\Delta G_f^\circ[\text{InSb}]$ using the data of Terpilowski (30) gives values which are low. It is noted that the expression derived with the results of this work give constant values of the calculated $\Delta H_f^\circ[\text{InSb}, 298.15 \text{ K}]$ as required.

As a final comparison, the phase diagram for In-Sb is again calculated using the standard enthalpy and entropy given by Eq. [19]. These results are presented in Fig. 9, and it is found that the activity measurements of this work and of Hoshino *et al.* (31) give excellent agreement between the calculated and experimental phase diagram. The liquidus temperatures calculated with the data of Terpilowski (30) are low. It should be noted that this method requires the melting temperature of the compound to be predicted exactly. Similar liquidus temperature calculations with the other derived equations again gave excellent agreement, thus supporting the composition dependence commonly reported for the activity. In

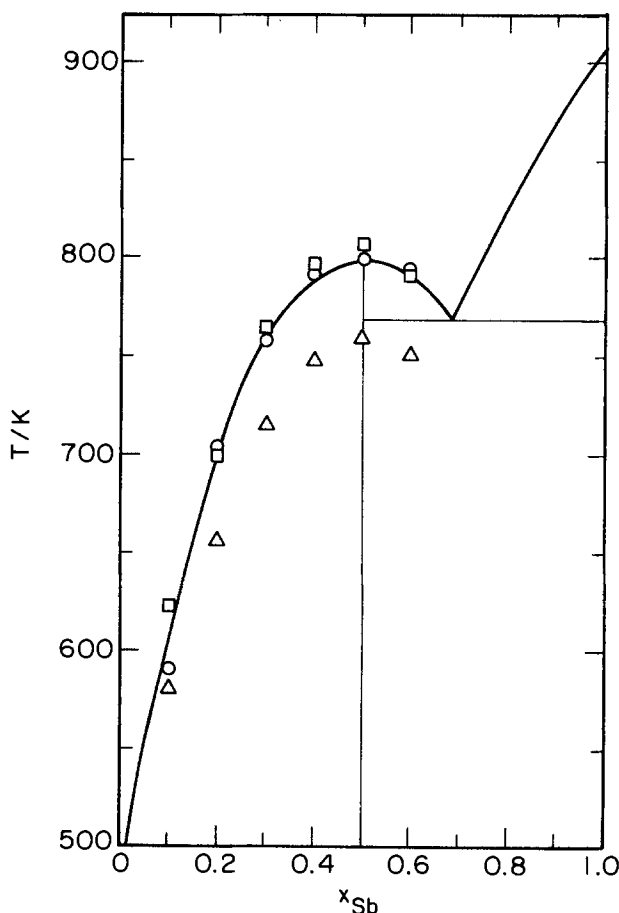


Fig. 9. Liquidus temperatures for the InSb system calculated from Eq. [10] and [19]. (a): This study. (Δ): Terpilowski (30). (□): Hoshino *et al.* (31). The solid line represents the experimental results of Liu and Peretti (19).

summary, it can be concluded that the expression for $\Delta G_f^\circ[\text{InSb}]$ derived here, Eq. [19], is consistent with other available Gibbs energy determinations, with calorimetric results, and with the reported phase diagram.

A solution model for representing the results.—An equimolar liquid solution of In and Sb exhibits unusual properties near the melting temperature. These properties include anomalous values for the heat capacity (11), viscosity (52), and velocity of sound (53) for temperatures up to 20 K above the melting temperature. Direct x-ray scattering curves for liquid InSb have been measured at 813 K (54, 55) and result in a radial distribution function having a first maximum at 3.2 Å, with a corresponding coordination number of 5.7. Crystalline InSb, on the other hand, exhibits a maximum at 2.80 Å and has a coordination number of 4, thus indicating that the zinc-blende structure is not retained upon melting. In addition, an examination of the radius of the first coordination sphere for both the pure liquid elements and the liquid solution establishes that the nearest neighbors in InSb are atoms of different kinds. Thus, the atoms in liquid InSb tend to form unlike pairs and may even form covalent clusters in a small temperature range above $T_f[\text{InSb}]$.

These considerations suggest that any solution model to be used for the description of the liquid-phase nonidealities of In-Sb mixtures must account quantitatively for the effects of nonrandomness of the thermochemical properties. In addition, the model should adequately represent not just a particular quantity but all of the pertinent data, in this case, the measured component activities along with the reported binary-phase diagram and enthalpy of mixing. The ability of several solution models to meet these criteria has been examined; the details of this comparison are provided elsewhere (56). With the use of a data base consisting of the liquidus measurements of Liu and Peretti (19), the enthalpy of mixing data of Rosa *et al.* (28), and the In activity measurements of this work along with those of Hoshino *et al.* (31) and Chatterji and Smith (32), it was shown that the nonrandom two-liquid (NRTL) equation (57) provided the most consistent representation of the In-Sb liquid phase. The activity coefficient of In as given by the NRTL equation is

$$\ln \gamma_{\text{In}} = x_{\text{Sb}}^2 \left\{ \tau_{21} \left(\frac{\exp(-\alpha_{12}\tau_{21})}{x_{\text{In}} + x_{\text{Sb}} \exp(-\alpha_{12}\tau_{21})} \right)^2 + \tau_{12} \frac{\exp(-\alpha_{12}\tau_{12})}{(x_{\text{Sb}} + x_{\text{In}} \exp[-\alpha_{12}\tau_{12}])^2} \right\} \quad [22]$$

The numerical values of the adjustable parameters were determined by a maximum likelihood algorithm (58) and found to be $\tau_{12} = 3.039 \times 10^3/(T/\text{K}) + 0.913$, $\tau_{21} = -839.6/(T/\text{K}) - 1.823$, and $\alpha_{12} = 0.315$. The standard deviations as estimated by the algorithm were $\sigma_{\tau_1} = 4.8 \text{ K}$, $\sigma_{\Delta H_m} = 134 \text{ J} \cdot \text{mol}^{-1}$, $\sigma_{\alpha_{12}} = 0.016$, and $\sigma_{\tau_{12}} = 0.008$.

Conclusions

Component activities in liquid solutions containing In and Sb were measured with a solid-state galvanic cell and were found to give moderate negative deviations from ideal behavior. The measured activities showed close agreement with other reported EMF activity measurements and support the assumption that the indium ion is monovalent in the fused salt electrolytes used in previous studies. The system exhibited a negative enthalpy of mixing having a maximum near $x_{\text{Sb}} = 0.42$. The combination of these results showed a significant positive excess entropy of mixing. Comparison of the reported phase diagram (19) with various thermodynamic results indicated that the results of Hoshino *et al.* (31) and of this work were consistent, whereas the work of Terpilowski (30) showed marked discrepancies. Furthermore, these calculations supported a value of the enthalpy of fusion of InSb of $49.4 \text{ kJ} \cdot \text{mol}^{-1}$. A new expression for the standard Gibbs energy of formation of solid InSb was derived, with the standard enthalpy and entropy given by

$-35.22 \text{ kJ} \cdot \text{mol}^{-1}$ and $-25.54 \text{ J} \cdot \text{mol}^{-1} \cdot \text{K}$, respectively. This result was shown to be consistent with the available $\Delta G_f^\circ[\text{InSb}]$ determinations, the calorimetric investigations, the reported phase diagram, and the activity measurements of this study. Liquid-phase x-ray scattering investigations suggested the tendency of pairing between In and Sb atoms. This observation was quantified with the aid of the nonrandom two-liquid theory. Thus, it can be concluded that the high temperature thermodynamic properties for the solid and liquid In-Sb system are experimentally well defined and consistent.

Acknowledgments

This research was supported by the National Science Foundation, Materials Division, Ceramics Program under grant number DMR-8012684 and the U.S. Department of Energy. The authors are grateful for the helpful discussions and guidance of Dr. L. Brewer.

Manuscript received Feb. 22, 1984.

REFERENCES

- H. Welker, *Z. Naturforsch.*, **7a**, 744 (1952).
- H. Welker, *ibid.*, **8a**, 248 (1953).
- R. G. Breckenridge, R. F. Blunt, W. R. Hosler, H. P. R. Fredricks, J. H. Becker, and W. Oshinsky, *Phys. Rev.*, **96**, 571 (1954).
- A. Heime and H. Pagnia, *Appl. Phys.*, **15**, 79 (1978).
- H. Sewell and J. C. Anderson, *Solid State Electron*, **18**, 641 (1975).
- T. Yoshida, K. Miyazaki, and K. Fujisawa, *Jpn. J. Appl. Phys.*, **14**, 1987 (1975).
- F. Nakajima and M. Kobayashi, *ibid.*, **17**, 149 (1978).
- D. Richman and E. F. Hockings, *This Journal*, **112**, 461 (1965).
- R. H. Cox and M. J. Pool, *J. Chem. Eng. Data*, **12**, 247 (1967).
- N. H. Nachtrieb and N. Clement, *J. Phys. Chem.*, **62**, 876 (1958).
- B. D. Lichter and P. Sommelet, *Trans. Metall. Soc. AIME*, **245**, 99 (1969).
- R. Hultgren, P. D. Desai, D. T. Hawkins, M. Gleiser, and K. K. Kelley, "Selected Values of the Thermodynamic Properties of Binary Alloys," American Society for Metals (1973).
- C. E. Lundin, M. J. Pool, and R. W. Sullivan, Denver Research Report AFORL-63-156 (1963).
- L. Garbato and F. Ledda, *Thermochim. Acta*, **19**, 267 (1977).
- K. Itagaki and A. Yazawa, *Trans. Jpn. Inst. Metals*, **18**, 825 (1977).
- R. Blachnik and A. Schneider, *Z. Anorg. Alleg. Chem.*, **372**, 314 (1970).
- L. A. Mechkovskii, A. A. Savitskii, V. F. Skums, and A. A. Vecher, *Russ. J. Phys. Chem.*, **45**, 1143 (1971).
- W. F. Schottky and M. B. Bever, *Acta Metallurg.*, **6**, 320 (1958).
- T. S. Liu and E. A. Peretti, *Trans. Am. Soc. Metals*, **44**, 539 (1952).
- J. Bednar and K. Smirous, *Czech J. Phys.*, **5**, 546 (1955).
- S. A. Pogodin and S. A. Dubinskii, *Izv. Sektora Fiz. Khim. Analiza, Inst. Obshch. Neorg. Khim. Akad. Nauk SSSR*, **17**, 204 (1949).
- V. M. Glazov and D. A. Petrov, *Izv. Akad. Nauk SSSR Otd. Tekhn. Nauk*, **4**, 125 (1958).
- F. E. Wittig and E. Gehring, *Ber. Bunsenges. Phys. Chem.*, **71**, 29 (1967).
- A. Yazawa, T. Kawashima, and K. Itagaki, *J. Jpn. Inst. Metals*, **32**, 1288 (1968).
- A. A. Vecher, E. I. Voronova, L. A. Mechkovskii, and A. S. Skoropanov, *Russ. J. Phys. Chem.*, **48**, 584 (1974).
- K. Itagaki and A. Yazawa, *Nippon Kinzoku Gakkai-Shi*, **38**, 880 (1975).
- B. Predel and G. Oehme, *Z. Metallkd.*, **67**, 826 (1976).
- C. J. Rosa, N. Rumpf-Bolz, F. Sommer, and B. Predel, *ibid.*, **71**, 320 (1980).
- R. N. Hall, *This Journal*, **110**, 385 (1963).
- J. Terpilowski, *Arch. Hutn.*, **4**, 355 (1959).
- H. Hoshino, Y. Nakamura, M. Shimoji, and K. Niwa, *Ber. Bunsenges. Phys. Chem.*, **69**, 114 (1965).
- D. Chatterji and J. V. Smith, *This Journal*, **120**, 770 (1973).
- D. Chatterji and J. V. Smith, *J. Am. Ceram. Soc.*, **55**, 575 (1972).
- T. J. Anderson and L. F. Donaghey, *J. Chem. Thermodyn.*, **9**, 603 (1977).

35. T. J. Anderson and L. F. Donaghey, *ibid.*, **9**, 617 (1977).
36. T. J. Anderson, T. L. Aselage, and L. F. Donaghey, *ibid.*, **15**, 927 (1983).
37. C. Wagner, *Acta Metall.*, **6**, 309 (1958).
38. L. J. Vieland, *ibid.*, **11**, 137 (1963).
39. R. Hultgren, P. D. Desai, D. T. Hawkins, M. Gleiser, K. K. Kelley, and D. D. Wagman, "Selected Values of the Thermodynamic Properties of the Elements," American Society for Metals (1973).
40. A. S. Abbasov and K. N. Mamedov, *Isz. Akad. Nauk Azerb. SSR Ser. Fiz Mt. Tekhr. Nauk.*, **3**, 86 (1970).
41. A. N. Nikol'skaya, V. A. Geiderikh, Ya. I. Gerasimov, *Dokl. Akad. Nauk SSSR*, **130**, 1074 (1959).
42. N. N. Sirota and N. N. Yushkevich, "Chemical Bonds in Semiconductors," N. N. Sirota, Editor, p. 95, Consultants Bureau, New York (1967).
43. J. Terpilowski and W. Trzebiatowski, *Bull. Acad. Poln. Sci. (Chim.)*, **8**, 95 (1960).
44. O. J. Kleppa, *J. Am. Chem. Soc.*, **77**, 897 (1955).
45. G. De Maria, J. Drowart, and M. G. Inghram, *J. Chem. Phys.*, **31**, 1076 (1959).
46. A. Glassner, Argonne National Laboratory Report ANL-5760 (1957).
47. T. Renner, *Solid State Electron.*, **1**, 39 (1960).
48. A. K. Jena, M. B. Bever, and M. D. Banus, *Trans. Metall. Soc. AIME*, **239**, 1232 (1967).
49. A. K. Jena, M. B. Bever, and M. D. Banus, *ibid.*, **239**, 725 (1967).
50. A. Schneider, H. Klotz, J. Stendel, and G. Strauss, *Pure Appl. Chem.*, **2**, 13 (1961).
51. S. N. Gadzhiev and K. A. Sharifov, *Dokl. Akad. Nauk SSSR*, **136**, 1339 (1961).
52. V. M. Glazov, S. N. Chizhevskaya, and N. N. Glagoleva, "Liquid Semiconductors," Plenum Press, New York (1969).
53. V. M. Glazov, A. A. Aivazov, and U. I. Timoshenko, *Sov. Phys. Solid State*, **18**, 1236 (1976).
54. H. Krebs, H. Weyand, and M. Haucke, *Angew. Chem.*, **70**, 468 (1958).
55. R. Buschert, I. G. Geib, and K. Lark-Horovitz, *Bull. Am. Phys. Soc.*, **1**, 111 (1956).
56. T. J. Anderson, T. L. Aselage, and K. M. Chang, submitted to *CALPHAD* (1984).
57. H. Renon and J. M. Prausnitz, *A.I.Ch.E. J.*, **14**, 135 (1968).
58. H. I. Britt and R. H. Leucke, *Technometrics*, **15**, 233 (1973).

Thermal Stresses in Heteroepitaxial Beta Silicon Carbide Thin Films Grown on Silicon Substrates

H. P. Liaw^{*1} and R. F. Davis

Department of Materials Engineering, North Carolina State University, Raleigh, North Carolina 27695

ABSTRACT

Microcracks were observed in epitaxial β -SiC thin films grown on (111) Si substrates by chemical vapor deposition (CVD) from SiH_4 and C_2H_4 entrained in H_2 . A one-step process and a more commonly used two-step process were employed. The latter was comprised of an initial chemical conversion of the Si surface, via the deposition of C alone and a subsequent deposition of both C and Si to form the β -SiC film. In contrast, no cracks were revealed in the β -SiC film grown on (100) Si by using either process. However, the growth of high quality, reproducible films occurred only when the two-step technique was used. The resulting thermal stresses in the β -SiC films deposited on both (111) and (100) Si substrates were calculated. The tensile strength of the deposited single-crystal films was estimated to be in the range of 1.88×10^8 - 3.36×10^8 N/m². Possible solutions to minimize crack initiation and growth will be discussed.

The achievement of epitaxial growth of single crystal thin films depends as critically on the substrate material as it does on the growth technique or environment employed during the growth. The ideal substrate for the vapor-phase epitaxial growth of the cubic (zinc blende structure) β -SiC films is obviously a single crystal of the same material, primarily because of the exact matching of the lattice constant and the coefficient of thermal expansion. However, the few β -SiC single crystals currently available (usually obtained from the reaction of molten Si with its graphite container) are very small in size, irregular in shape, and highly twinned. Nominally hexagonal α -SiC single crystals have been successfully employed as substrates in CVD processes below 1873 K (1, 2). However, they are uncommon (usually obtained from a commercial Acheson furnace), small in size, irregular in shape, and, most importantly, they normally contain significant quantities of Al and/or N, which are electrically active in SiC. If the deposition temperatures exceed 1873 K, α -SiC becomes the predominant phase which grows on these crystals (1, 2). Therefore, in order to obtain electronic quality β -SiC single-crystal thin films of larger area, it is presently necessary to employ foreign substrates.

In choosing foreign substrates for heteroepitaxial film growth, one must carefully consider the physical and chemical compatibility between the deposited film and the substrate. Differences in crystalline nature, lattice constant, melting point, vapor pressure, and coefficient of thermal expansion are all of vital importance in the at-

tainment of an epitaxial film. To meet these requirements, the number of potential substrate materials is normally very limited.

Silicon, although not a perfect candidate material, is the next logical choice as a substrate for the epitaxial growth of β -SiC films. It has been employed in this capacity by a number of workers (3-21) because it is chemically compatible with SiC and can be obtained in single-crystal form in ultrahigh purities at reasonable cost. It has also been used in the β -SiC deposition research described herein. However, it does have some major limitations which must be surmounted in order to grow these films in single-crystal form.

One of the constraints associated with the use of Si for the growth of SiC is the maximum deposition temperature's being limited by the melting temperature of Si (≈ 1693 K). Another problem is the thermal tensile stresses introduced into the film upon cooling from the high deposition temperature. Thermal stresses and resultant fracture have also been observed in several other heteroepitaxial film and substrate combinations, e.g., Si or AlN on sapphire (22, 23) and Si on spinel (24). The following paragraphs discuss the results of the characterization and calculations of the residual stresses present in the β -SiC film/Si substrate combination after cooling to room temperature.

Film Growth

The single-crystal Si substrates employed in this research were n-type and p-type, with reported resistivities in the range of 37-420 Ω -cm and 10-50 Ω -cm, respectively. All were 1° or 6° off axis from the (100) plane and 2° or 4° off axis from the (111) plane.

^{*}Electrochemical Society Active Member.

¹Present address: Advanced Micro Devices, Incorporated, Sunnyvale, California 94086.

A cold-wall, RF-heated, barrel-type CVD system containing a SiC-coated graphite susceptor was employed for the deposition. The chamber pressure, gas flow rates, and temperature were independently and electronically controlled to prevent fluctuations in nucleation rate. Reproducible β -SiC films were obtained by a two-step process. Initially, C was deposited on and reacted with the Si substrate to form an approximately 15 nm thick chemically converted layer containing Si and C in progressively varying ratios as a function of depth.² This was followed by the deposition of both Si and C to form the β -SiC films. This procedure allowed epitaxy of the films on the off-axis oriented (111) and (100) Si substrates.

The chemical conversion noted above was conducted from room temperature to a temperature above 1523 K³, using a 1 sccm flow of C₂H₄ (ethylene) in a 3000 sccm flow of H₂ under a total pressure of 0.1 MPa. The β -SiC deposition was conducted within the temperature range of 1590-1610 K, using 2, 1, and 3000 sccm flow rates for SiH₄, C₂H₄, and H₂, respectively, under a total pressure of 0.1 MPa⁴. The final thickness of the deposited β -SiC films was in the range of $1.0-7.5 \times 10^{-6}$ m, depending on the duration of the deposition.

The existence of the epitaxial growth of β -SiC as the only SiC polytype and the single crystallinity of these deposited films were determined by Laue transmission and pole figure x-ray diffraction procedures, as well as reflection and transmission electron diffraction. The characterization of the surfaces and the results of the fracture process caused by thermal stresses during cooling were conducted using optical and scanning electron microscopy techniques. Details of the equipment, instrumentation, and employment of these procedures are presented in Ref. (25).

Results

At the outset of this research, deposition of β -SiC on (111) and (100) Si was conducted without the initial chemical conversion process. Although the resulting films were usually monocrystalline, especially if deposited at the higher growth temperatures, the surfaces of the films were frequently unacceptable in terms of growth pit density and roughness and were nonreproducible. This was especially true of films grown on (100) Si. Additional problems were prevalent in the (111) films.

As the conditions for the occurrence of epitaxy and single crystallinity of the β -SiC films grown on (111) Si were improved by judicious changes in the deposition parameters, microcracks began to be observed in the films, as shown in Fig. 1. The presence of a converted (111) layer often mitigated the severity and depth of the fracture process, but did not prevent it. These cracks were determined to be along the $\langle 110 \rangle$ and to be parallel to two of the sides of the triangles, which formed in the Si surface at the initiation of the deposition and which frequently migrated through the film. Crack lines were seldom found in the third direction. This cracking in the films was also frequently seen to extend into the Si substrate, as revealed in Fig. 2. At no time was crack formation observed in the β -SiC films grown on (100) Si substrates, regardless of the process method employed. However, the only reproducible films of sufficient quality for microelectronic purposes were grown on chemically converted (100) Si, as described in Ref. (25).

Figure 3 contains an SEM micrograph of the fractured cross section of the β -SiC film and the (111) Si substrate. The fracture lines shown in the Si were realized as a result of the fracture process used to prepare the SEM

²An extensive characterization study of this converted layer is now ongoing and will be reported in the near future.

³The temperature of chemical conversion varies with time because the susceptor is heated rapidly from room temperature and does not reach equilibrium during the conversion process.

⁴Although it is common, especially in the chemical deposition of polycrystalline SiC, to use a methylchlorosilane as the input gas, these gases decompose into C and Si containing gases which decompose at different rates in the temperature range employed in the present research. As a result, SiC and free Si or free C are normally produced.

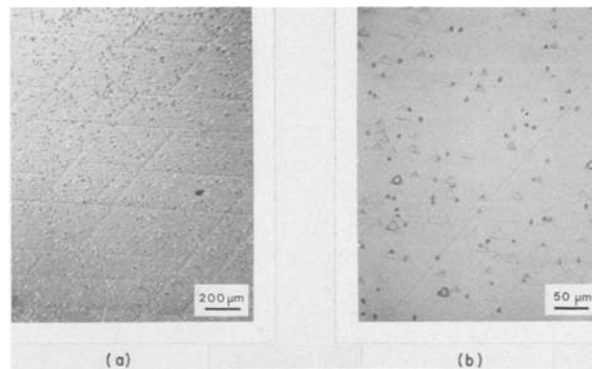


Fig. 1. Crack lines on the top surface of a (111) β -SiC thin film grown on a (111) Si substrate using the two-step process. (a) reveals the density of the crack lines, and (b) shows that the crack lines are parallel to the sides of the triangular surface defects.

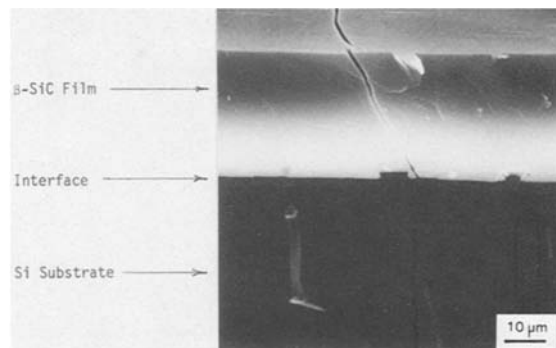


Fig. 2. An example of a crack generated during cooling as a result of thermal stresses at the (111) β -SiC/(111) Si interface. Note the extension of this fracture through the film, as well as into the substrate.

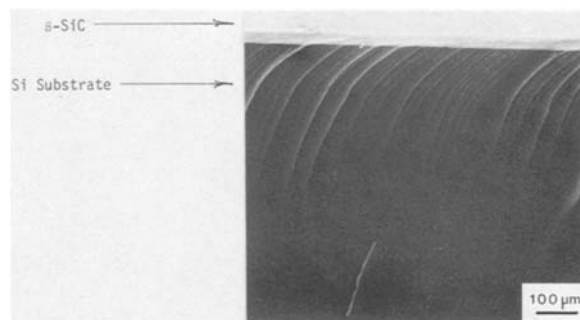


Fig. 3. SEM micrograph of a fracture cross-section of the (111) β -SiC grown on (111) Si substrate. Note the increasing curvature of the Si fracture lines resulting from the increasing compressive stresses in this material as one gets nearer the Si/SiC interface. Similar results are found in (100) Si substrates.

sample; however, their curvature is indicative of the residual compressive stresses present at room temperature in this material, especially near the Si/SiC interface. Additional higher magnification SEM pictures taken in cross section from the left (Fig. 4a) and right (Fig. 4b) sides of the same sample show the considerable but opposite curvature of the fracture lines resulting from the tensile stresses in the (111) β -SiC film. The degree of bending of the fracture lines is an indication of the relative magnitudes of the stresses in the film and in the substrate.

Another indication of the stress which the SiC film experiences after cooling is revealed by the satellite spots along the zone axes in the transmission Laue pattern shown in Fig. 5 and 6. The samples for Laue studies were prepared by selectively etching a 0.01m diameter center area of the Si substrate, using a mixture of HF and HNO₃.

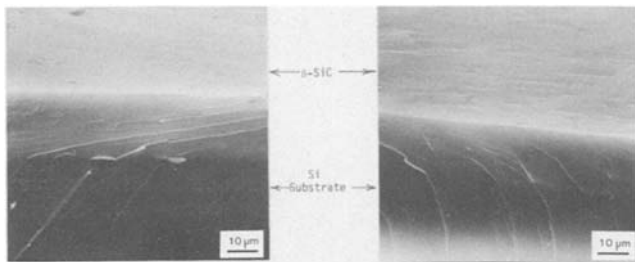


Fig. 4. The top surface and the fracture cross section of an epitaxial β -SiC thin film grown on a (111) Si substrate. (a) is taken from the left-hand side of the sample, and (b) is taken from the right-hand side of the same sample. Similar but less curved fracture lines are found in (100) Si and (100) β -SiC substrates and films. Bar = 10 μ m.

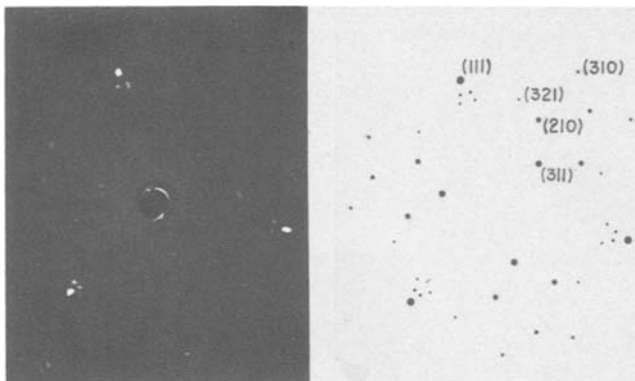


Fig. 5. (a) x-ray transmission Laue pattern and (b) the indexes of the resulting spots of an epitaxial β -SiC film grown on a (111) Si substrate.

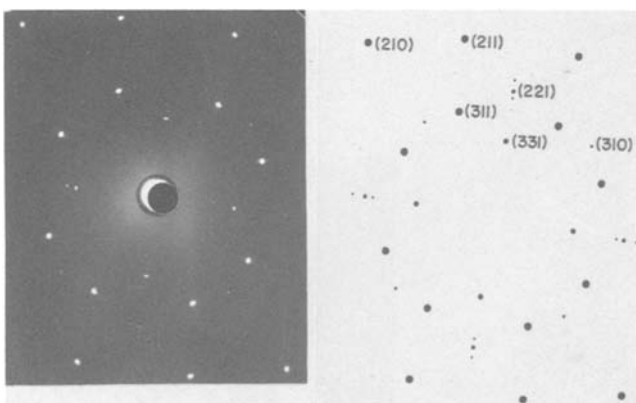


Fig. 6. (a) x-ray transmission Laue pattern and (b) the indexes of the resulting spots of an epitaxial β -SiC film grown on a (100) Si substrate.

The remainder of the substrate was covered in an acid insoluble mounting wax which could be removed with acetone. A residual stress was maintained in the film, as shown in the Laue patterns. The films were found to be transparent, with a light yellowish color typical of high purity crystals and films of this material.

It is obvious that the Laue spots for the (111) and (100) β -SiC films have the characteristic 3-fold and 4-fold symmetries, respectively. Because of the difficulty of printing the entire patterns, the additional but weaker spots, plotted from the x-ray negative, are shown in Fig. 5b and 6b. Most of the spots could have been routinely indexed. However, the (111) pattern contained twelve spots, in three groups of four which were very close to the (111) spots which were more difficult to identify. Further investigations showed that these satellite-like spots were on three zone axes and on two rings which corresponded to the (111) β -SiC reflections from the K_α and K_β characteristic radiations of the Cu target. Normally, bending of

crystallographic planes as a result of residual stresses causes streaks along the zone axis. However, because a Cu target was used to produce the "white" radiation, wherever the reflection from the characteristic radiation satisfied Bragg's law, a spot occurred instead. Thus, these satellite spots note the existence of residual stresses in the grown (111) film.

The (100) pattern also contained extra spots very close to the (221) spots. In this case, it was determined that the extra spots were on two zone axes and on two rings which corresponded to the (220) β -SiC reflections from the K_α and K_β characteristic radiations of the Cu target. Again, this indicated the existence of curved planes, which formed as a result of stresses in the (100) β -SiC films.

Discussion

In choosing a substrate for thin film growth, it is desirable to have one which contracts the same as or more than the film after cooling from the deposition temperature. This will normally prevent cracking because the film is either unstressed or in compression. Unfortunately, as shown in Table I, the thermal expansion coefficient of β -SiC is greater than that of Si; thus, upon cooling, the resulting film will be in tension, as noted above, which is the stress state which leads to extended crack formation in brittle materials, as shown in Fig. 1 and 2. In the present system, this is compounded by the fact that the expansion coefficient for β -SiC increases with temperature to a greater extent than Si.

As also shown in Table I, there is an additional very large lattice mismatch of $\approx 25\%$ between β -SiC and Si. This may be accommodated by the creation of a large number of misfit dislocations at the interface. However, the pile-up of these dislocations can result in the accumulation of extra half-planes and the formation of additional microcracks.

The thermal stress (σ_f) in the CVD film can be calculated using the following equation (28)

$$\sigma_f = \Delta\alpha \cdot \Delta T \left(\frac{E}{1 - \nu} \right) \quad [1]$$

where $\Delta\alpha$ is the difference in the coefficient of thermal expansion between the film and the substrate, ΔT is the difference between the growth temperature and the room temperature, E is the Young's modulus of the film, and ν is the Poisson's ratio of the film.

It has been proven by Brantley (29) that the effective elastic constants, $E/(1 - \nu)$, are invariant for all directions within the (100) and the (111) planes. They can be expressed as

$$\left(\frac{E}{1 - \nu} \right)_{(111)} = \frac{6}{4S_{11} + 8S_{12} + S_{44}} \quad [2]$$

and

$$\left(\frac{E}{1 - \nu} \right)_{(100)} = \frac{1}{S_{11} + S_{12}} \quad [3]$$

Table I. Lattice constant and the coefficient of thermal expansion for β -SiC (26) and Si (27)

Properties	β -SiC	Si
Lattice constant (nm)	0.4359	0.5430
Coefficient of thermal expansion (cm/cm K)	3.8×10^{-6} at 473 K 4.3×10^{-6} at 673 K 4.8×10^{-6} at 873 K 5.2×10^{-6} at 1073 K 5.8×10^{-6} at 1273 K 5.5×10^{-6} at 1673-2073 K	2.5×10^{-6} at 300 K 3.1×10^{-6} at 400 K 3.5×10^{-6} at 500 K 3.8×10^{-6} at 600 K 4.1×10^{-6} at 700 K 4.3×10^{-6} at 800 K

where S_{ij} are the values of the elastic compliance. Sometimes, the elastic stiffness values (C_{ij}) are readily available instead of S_{ij} values for certain materials. The conversion of the C_{ij} values to the S_{ij} values can be achieved according to the following equations

$$S_{11} = \frac{C_{11} + C_{12}}{(C_{11} - C_{12})(C_{11} + 2C_{12})} \quad [4]$$

$$S_{12} = \frac{-C_{12}}{(C_{11} - C_{12})(C_{11} + 2C_{12})} \quad [5]$$

and

$$S_{44} = \frac{1}{C_{44}} \quad [6]$$

Table II provides the values of elastic stiffness and compliance for both β -SiC (26) and Si (29). The invariant values of $E/(1 - \nu)$ for directions within the (111) and (100) planes are summarized in Table III. Values for Si are also listed for reference in Table III.

If we take the average coefficient of thermal expansion of β -SiC in the temperature range of 293-1673 K to be $4.9 \times 10^{-6} \text{ K}^{-1}$ and that of Si to be $3.9 \times 10^{-6} \text{ K}^{-1}$, the estimated thermal stress using the above equations, in the β -SiC film will be $3.36 \times 10^8 \text{ N/m}^2$ on a (111) Si substrate and $1.88 \times 10^8 \text{ N/m}^2$ on a (100) Si substrate, assuming the growth temperature is 1603 K. It is clear that using a (100) Si substrate instead of a (111) Si substrate will reduce the thermal stress in a β -SiC film by almost half. Because the β -SiC films on a (111) Si substrate contain cracks and those on a (100) Si substrate do not, the tensile strength of the deposited single crystal β -SiC thin films is estimated to be in the range of 1.88×10^8 - $3.36 \times 10^8 \text{ N/m}^2$. Furthermore, it has been reported by Bradt *et al.* (30) that the tensile strength for NC 203 hot-pressed polycrystalline SiC⁵ is approximately $3.10 \times 10^8 \text{ N/m}^2$. Although possibly fortuitous, this is in agreement with the calculated range of values for the parameter for the pure β -SiC single-crystal films grown in this research.

The off-axis orientation of the (111) Si substrates may also affect the magnitude of the resulting thermal stresses in the β -SiC film. It has been found in this study that Si wafers sliced at an angle of 4° off the (111) orientation have less cracks than similar wafers at an angle of 2° off this orientation. The exact reason for this phenomenon is

⁵Norton Company, Worcester, MA. This material contains approximately 1.5% Al_2O_3 as a sintering aid, 2.5%W from the comminution process, and $\leq 0.05\%$ each of Ti, Co, Ca, and Mg. It fractures in a transgranular mode.

Table II. Values of elastic stiffness^a and compliance^b for both β -SiC and Si

	β -SiC	Si
C_{11}	2.89	1.657
C_{12}	2.34	0.639
C_{44}	0.554	0.7956
S_{11}	1.256	0.768
S_{12}	-0.562	-0.214
S_{44}	1.805	1.26

^a In units of 10^{11} N/m^2 .

^b In units of 10^{-11} N/m^2 .

Table III. Calculated values for the effective elastic constant^a $E/(1 - \nu)$ for both β -SiC and Si

	$(E/(1 - \nu))$ (111)	$(E/(1 - \nu))$ (100)
β -SiC	2.572	1.441
Si	2.290	1.805

^a In units of 10^{11} N/m^2 .

not known at this time. However, it may be related to the fact that Young's modulus has the largest value along the (111) direction.

The use of long cooling times (up to 3.6×10^3 s) after deposition does not solve the problem of cracking. The use of thinner Si substrates has also been recognized as a possible solution because thermal stresses can be partially relieved by warping of the entire substrate/film combination. However, it proves experimentally difficult to obtain a sufficiently thin substrate (estimated to be the same order of the grown film) which can be handled to conduct the additional processing steps necessary for device fabrication. Moreover, a slight pressure from the back side of the deposited sample will tend to break the film. Therefore, the use of very thin substrates is not a desirable approach to solving the problem of crack initiation in this system.

Deleterious lattice misfit effects can often be reduced by using compositionally graded layers (31) to change the lattice constant, in either small abrupt steps or in a continuous manner, from its initial value (which typically matches the substrate) to that of its final value. This method necessitates the existence of a wide range of solid solutions among the various components in the substrate and the thin film system. It has been used extensively in depositing III-V semiconductor materials. Unfortunately, no solid solution between Si and C exists which could be used to produce a graded layer for this purpose. Furthermore, it has been reported (32) that in order to grow a truly crack-free structure which is under tension (*e.g.*, $\text{GaAs}_{0.6}\text{P}_{0.4}$ on GaAs), it is necessary to use a graded region about $30 \mu\text{m}$ in thickness. This is impractical because the total thickness of the desired epitaxial film is usually much less than $30 \mu\text{m}$ and is difficult in our RF-heated system because the temperature of the growth surface decreases as the film thickness increases.

As inferred above, if a foreign substrate must be employed, the most viable solution for the crack initiation problem in the present research should be the use of a substrate with a coefficient of thermal expansion equal to or larger than that of β -SiC to ensure that the film will be unstressed or under only slight compression after cooling. Sapphire (Al_2O_3) is one material which falls into this category, with the coefficient of thermal expansion being $8.40 \times 10^{-6} (\text{K}^{-1})$ at 25° - 800°C (33). However, Al_2O_3 tends to decompose slightly at the temperatures normally employed for the epitaxial growth of β -SiC, and it may result in autodoping of the growing film (Al is a p-type dopant in SiC). Thus, its usefulness may be limited.

Summary

Single-crystal thin films of β -SiC have been successfully grown on (100) Si using a two-step process of initial chemical conversion of the Si surface via a Si-C reaction and subsequent deposition of both Si and C from SiH_4 and C_2H_4 , respectively, carried in H_2 . Similar procedures using (111) Si substrates result in microcracking formation in the films after cooling. Characterization by optical microscopy and SEM x-ray diffraction techniques reveal the extent of microcracking and residual stress in the substrate/thin film system. Subsequent thermal stress calculations reveal that the stress in the (100) β -SiC films is approximately half that in the (111) films. Furthermore, because of the absence of microcracking in the (100) films, the tensile strength of these films is estimated to be between 1.88 and $3.36 \times 10^8 \text{ N/m}^2$.

Acknowledgments

The authors wish to thank Dr. H. H. Stadelmaier for valuable discussion. The support of the Office of Naval Research, via Grant no. N00014-79-C-0121, is also gratefully acknowledged.

Manuscript submitted May 7, 1984; revised manuscript received July 30, 1984.

North Carolina State University assisted in meeting the publication costs of this article.

REFERENCES

- G. Gramberg and M. Koniger, *Solid-State Electron.*, **15**, 285 (1972).
- H. Matsunami, S. Nishino, M. Odaka, and T. Tanaka, *J. Cryst. Growth*, **31**, 72 (1975).
- W. G. Spitzer, *Powder Metall. Int.*, **12**, 141 (1980).
- D. M. Jackson, Jr., and R. W. Howard, *Trans. Metall. Soc. AIME*, **233**, 468 (1965).
- H. Nakasima, T. Sugano, and H. Yanai, *Jpn. J. Appl. Phys.*, **5**, 874 (1966).
- K. E. Bean and P. S. Gleim, *This Journal*, **114**, 1158 (1967).
- I. H. Khan and R. N. Summergrad, *Appl. Phys. Lett.*, **11**, 12 (1967).
- J. E. Spruiell, "Chemical Vapor Deposition of Silicon Carbide from Silicon Tetrachloride-Methane-Hydrogen Mixtures," ORNL-4326 (1968).
- I. H. Khan, *Mater. Res. Bull.*, **4**, S285 (1969).
- P. Rai-Choudhury and N. P. Formigoni, *This Journal*, **116**, 1440 (1969).
- A. S. Brown and B. E. Watts, *J. Appl. Cryst.*, **3**, 172 (1970).
- A. J. Learn and I. H. Khan, *Thin Solid Films*, **5**, 145 (1970).
- K. E. Haq and I. H. Khan, *J. Vac. Sci. Technol.*, **7**, 490 (1970).
- K. A. Jacobson, *This Journal*, **118**, 1001 (1971).
- J. Mercier and C. Roussel, in "Third International Conference on CVD," F. A. Glaskin, Editor, p. 426, American Nuclear Society, Hinsdale, IL (1972).
- K. Kuroiwa and T. Sugano, *This Journal*, **120**, 138 (1973).
- C. J. Mogab and H. J. Leamy, *J. Appl. Phys.*, **45**, 1075 (1974).
- S. Nishino, H. Matsunami, and T. Tanaka, *Jpn. J. Appl. Phys.*, **14**, 1833 (1975).
- H. Matsunami, S. Nishino, and T. Tanaka, *J. Cryst. Growth*, **45**, 138 (1978).
- M. Balog, A. Reisman, and M. Berkenblit, *J. Electron. Mater.*, **9**, 669 (1980).
- S. Nishino, Y. Hazuki, H. Matsunami, and T. Tanaka, *This Journal*, **127**, 2674 (1980); S. Nishino, J. A. Powell, and H. A. Will, *Appl. Phys. Lett.*, **42**, 460 (1983).
- D. J. Dumin, *J. Appl. Phys.*, **36**, 2700 (1965).
- W. M. Yim and E. J. Stofko, *This Journal*, **119**, 381 (1972).
- C. C. Wang, G. E. Gottlieb, G. W. Cullen, S. H. McFarlane III, and K. H. Zaininger, *Trans. Metall. Soc. AIME*, **245**, 441 (1969).
- H. P. Liaw, Ph.D. Thesis, North Carolina State University, Raleigh, NC (1982); H. P. Liaw and R. F. Davis, Submitted to *This Journal*.
- J. W. Faust, Jr., in "Silicon Carbide—1973," R. C. Marshall, J. W. Faust, Jr., and C. E. Ryan, Editors, p. 668, University of South Carolina Press, Columbia, South Carolina (1974).
- "Handbook of Tables for Applied Engineering Science," R. E. Bolz and G. L. Ture, Editors, p. 249, CRC Press, Boca Raton, FL (1972).
- H. Schlotterer, *Solid-State Electron.*, **11**, 947 (1968).
- W. A. Brantley, *J. Appl. Phys.*, **44**, 534 (1973).
- R. C. Bradt, S. D. Hartline, J. A. Coppola, G. Weaver, and R. A. Alliegro, in "Silicon Carbide—1973," R. C. Marshall, J. W. Faust, Jr., and C. E. Ryan, Editors, p. 367, University of South Carolina Press, Columbia, South Carolina (1974).
- G. H. Olsen, M. S. Abrahams, C. J. Buiocchi, and T. J. Zamoski, *J. Appl. Phys.*, **46**, 1643 (1975).
- T. Y. Wu, *This Journal*, **121**, 1357 (1974).
- G. W. Cullen, *J. Cryst. Growth*, **9**, 107 (1971).

Technical Note



Densified Deposited Oxide Films for Surface Passivation

Wendell D. Eades, Anthony M. McCarthy,* and Richard M. Swanson**

Stanford Electronics Laboratories, Stanford University, Stanford, California 94305

Deposited silicon dioxide films have been investigated as an alternative to thermal oxide for passivation of the silicon surface. These films are of interest in the fabrication of solar cells and integrated circuits because they offer decreased junction movement and good interface properties without thickness constraints (1, 2). We have investigated the possibility of hybrid deposited-thermal silicon dioxide films, and we have compared them to both solely thermal and solely deposited oxide films.

Samples were fabricated from a quartered n-type Czochralski-grown <100> silicon wafer with a doping of $6 \times 10^{14} \text{ cm}^{-3}$. A back-side predeposition of phosphorous was performed to ensure good ohmic contact for electrical measurements. All samples were given an RCA clean (3), including a 50:1 HF dip immediately preceding the final rinse, prior to the first deposition or oxidation. Sample 1 was thermally oxidized at 1000°C for 90 min in O_2 with a 2% HCl ambient derived from trichloroethane (4), and annealed in argon at that temperature immediately afterwards. Sample 2 was oxidized at 1000°C for 20 min in a low partial pressure oxygen ambient (2% O_2 , 0.5% HCl in argon). After an anneal in argon at the oxidation temperature, it was brought to 850°C and pulled slowly. The thermal oxide thickness was 100Å. Silicon dioxide was then deposited in an Applied Materials AMS-2600

Table I. Oxide thickness, flatband voltage, and midgap interface state densities for the four types of oxide investigated

Sample	Oxide type	Oxide thickness (Å)	Midgap interface trap density ($\text{cm}^{-2} \text{eV}^{-1}$)	Flatband voltage (V)
1	Thermal	905	1.1×10^9	-0.03
2	Deposited on thermal	910	1.0×10^9	-0.01
3	Deposited	830	1.4×10^9	0.14
4	Thermal under deposited	1060	1.2×10^9	0.00

Table II. Generation lifetime summary for the four types of oxide investigated

Sample	Oxide type	Average lifetime (μs)	Standard deviation
1	Thermal	318	14
2	Deposited on thermal	197	23
3	Deposited	660	149
4	Thermal under deposited	528	33

* Electrochemical Society Student Member.

** Electrochemical Society Active Member.

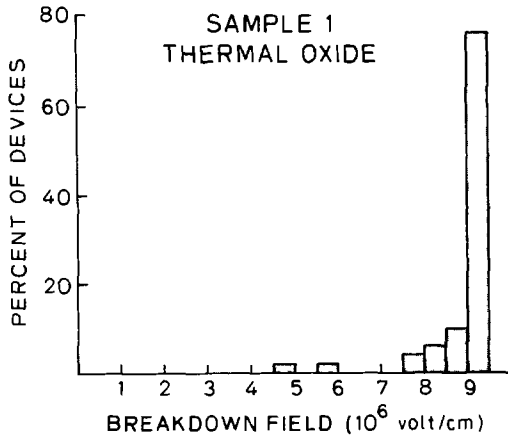


Fig. 1. Oxide breakdown field values for thermal oxide grown at 1000°C in O₂ with 2% HCl.

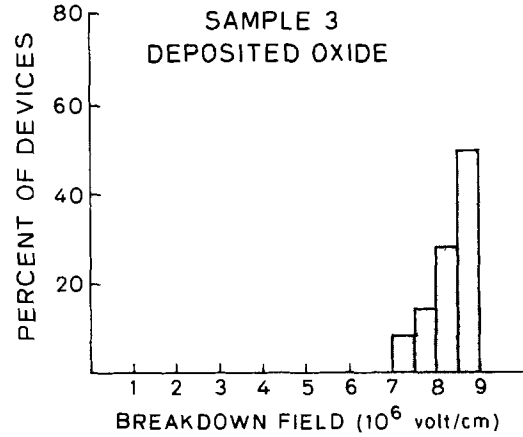


Fig. 3. Oxide breakdown field values for oxide deposited onto a bare silicon surface and densified in argon at 1000°C.

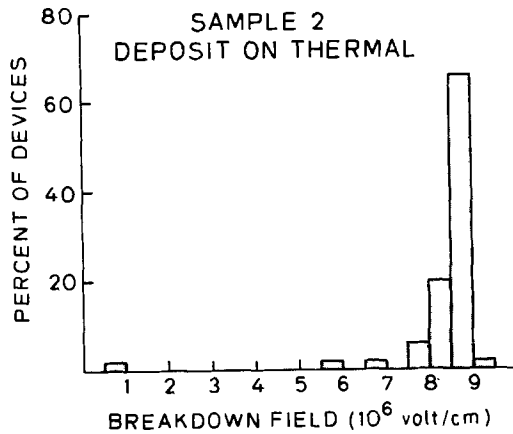


Fig. 2. Oxide breakdown field values for oxide deposited on top of a previously grown 100Å film and then densified in argon at 1000°C.

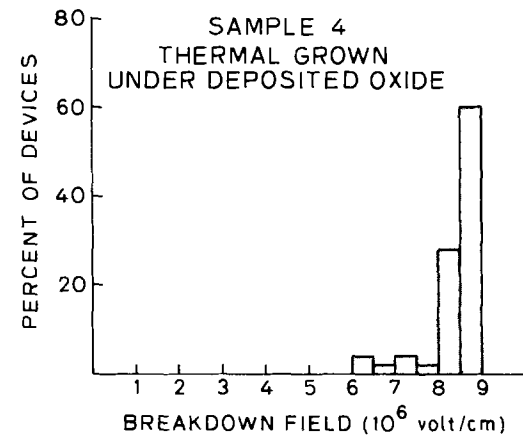


Fig. 4. Oxide breakdown field values for thermal oxide grown at 1000°C in O₂ with 2% HCl underneath a previously deposited oxide film.

Silox Reactor at a temperature of 450°C and atmospheric pressure. Flow rates used were 90 liter/min N₂, 350 cm³/min O₂, and 35 cm³/min SiH₄. This oxide was then densified (1) in argon for 20 min at 1000°C. For sample 3, about 1200Å of oxide was deposited onto bare silicon and later densified at 1000°C in argon for 20 min. Sample 4 also received 1200Å of deposited oxide onto a bare surface, but was densified and thermal oxide grown underneath it simultaneously. The densification/oxidation was performed at 1000°C for 15 min in O₂ with a 2% HCl ambient. An anneal in argon followed. At the conclusion of each sample's argon anneal, it was cooled to 650°C (3°-6°C/min) in argon and pulled slowly to avoid the possibility of quenched-in defects (5). Following removal of any oxide on the back sides of the samples, 1 μm of aluminum was deposited on both sides of the wafers by E-beam evaporation. Capacitors of area 0.0036 cm² were defined photolithographically following a postmetallization anneal in forming gas.

Oxide thickness, flatband voltage, and the density of interface traps were measured using the high-low frequency capacitance method (6). The results for typical capacitors are presented in Table I. The densified deposited oxide has slightly less positive fixed charge than the other samples, all of which have a thermally grown oxide right at the interface. Interface trap densities for all samples were in the 1-2 × 10⁹ cm⁻² eV⁻¹ range. Using the error analysis of Nicollian and Brews (6), we estimate error bars of 1 × 10⁹ cm⁻² eV⁻¹ for the midgap interface state densities. Hence, the densities measured here must be considered equal to within the accuracy of the method.

Measurements of the generation lifetime of the samples were made using the modified linear sweep method (7), as implemented in the program GLiP4 (8). No correction was made for the perimeter current contributions. Aver-

age values and standard deviations for the lifetime are given in Table II. The deposited oxide sample shows the greatest mean lifetime, but it also has the poorest uniformity. Comparison of the oxide preparation conditions suggests the presence of HCl is a critical factor in uniformity. With regard to average lifetime, we note the samples receiving a thick deposited oxide initially (samples 3 and samples 4) had a higher value than those thermally oxidized initially (1 and 2).

Oxide breakdown measurements were also performed on all samples. The voltage was increased at a rate of 50 V/s, and the breakdown voltage was defined to be the bias at which the leakage current first exceeded 2 μA. Fifty capacitors spaced over a 1 cm² area in the center of each wafer were probed in order to obtain a distribution of values. To compare the intrinsic breakdown strength of each form of oxide, we discarded the five worst values on each sample and calculated the average breakdown field and standard deviation, σ . The thermal oxide was found to have both the greatest average breakdown field (8.9 MV/cm) and the tightest distribution ($\sigma = 0.2$ MV/cm) and the densified deposited oxide the poorest average (8.4 MV/cm) and worst scatter ($\sigma = 0.4$ MV/cm). Both hybrid oxide samples had averages of 8.6 MV/cm and standard deviations of 0.3 MV/cm. Histograms of all measured data are presented in Fig. 1-4.

Based on the results presented here, we conclude that the growth of a thin layer of thermal oxide underneath a previously deposited oxide film is a promising alternative to thermal oxide for thick film high lifetime applications. Furthermore, improved uniformity and higher throughput could likely be achieved using low pressure rather than atmospheric deposited oxide, and merits investigation.

Acknowledgment

This research was sponsored by the Electric Power Research Institute.

Manuscript submitted April 5, 1984; revised manuscript received Aug. 3, 1984.

Stanford University assisted in meeting the publication costs of this article.

REFERENCES

1. T. M. Hall, Engineer's degree thesis, Stanford University, Stanford, CA (1981).
2. W. A. Pliskin and H. S. Lehman, *This Journal*, **112**, 1013 (1965).
3. W. Kern and D. A. Puotinen, *RCA Rev.*, 187 (1970).
4. E. J. Janssens and G. J. Declerck, *This Journal*, **125**, 1696 (1978).
5. K. L. Wang, *ibid.*, **125**, 1664 (1978).
6. E. H. Nicollian and J. R. Brews, "MOS Physics and Technology," Chap. 8, p. 331, John Wiley and Sons, New York (1982).
7. R. F. Pierret and D. W. Small, *IEEE Trans. Electron Devices*, **ed-22**, 1051 (1975).
8. W. D. Eades, J. D. Shott, and R. M. Swanson, *ibid.*, **ed-30**, 1274 (1983).



COMMENTS

Each issue of the **Journal** will have a section of "Comments." In this section, we provide a means via short pieces, *i.e.*, one column or less, to applaud, dispute, or otherwise discuss the papers published in the **Journal**. Space will be provided for one response by the paper's author(s) to each comment.

Since space available in each issue for the "Comments" section is limited; it is important to be concise.

Comments should be sent to the Editor, Dr. Norman Hackerman, President's Office, Rice University, P.O. Box 1892, Houston, TX 77251.

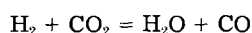
Norman Hackerman
Editor

The Equilibrium Constant for the Reaction $H_2S + 3H_2O + (Li_{0.66}K_{0.34})CO_3 \rightleftharpoons 4H_2 + CO_2 + (Li_{0.66}K_{0.34})SO_4$ at Elevated Temperature

S. W. Smith and S. M. Kapelner
(pp. 405-407, Vol. 130, no. 2)

David A. Shores and Mary L. Orfield:¹ The subject paper has described an experimental study of the sulfation of molten 62%Li₂CO₃-38%K₂CO₃ by reaction with H₂S (in the ppm range) in a mixture of H₂-H₂O-CO-CO₂. The compositions of both the gas and the salt were analyzed. From these data, along with thermodynamic data from the literature, the authors have calculated the Gibbs energy of formation of 0.66Li₂SO₄-0.34K₂SO₄. However, their results and the calculated values of Gibbs energy may be questioned on two issues: (i) the gas compositions reported in their Table II do not correspond to equilibrium mixtures, and (ii) mole fractions have been used to represent activities in the molten salt mixtures.

In their experimental arrangement, the authors attempted to ensure that the gas equilibrated with the salt and that the gas itself reach equilibrium. The predominant species in the gas are H₂-H₂O-CO-CO₂; *i.e.*, the concentration of other species, such as H₂S, reaction products from H₂S, or vaporized salt species, are quite small in comparison with the major species. Therefore, the equilibrium represented by the water-gas-shift reaction.



may be used to check approximately whether the measured gas compositions correspond to equilibrium at the temperature of the gas-salt reaction. Values of the equilibrium constant for the above reaction were calculated from well-established thermodynamic data² at the temperatures of the gas-salt reaction. They are shown in Table I. Also listed in Table I are values of the equilibrium constant calculated from the experimental gas compositions in Table II of Smith and Kapelner's paper. The experimental equilibrium constants are significantly different from the expected values. The former correspond to equilibrium at temperatures far below the temperatures of the

¹Corrosion Research Center, University of Minnesota, Minneapolis, Minnesota, 55455.

²E. T. Turkdogan, "Physical Chemistry of High Temperature Technology," Chap. 1, Academic Press, New York (1980).

Table I. Equilibrium constants for the water-gas-shift reaction

Run	Temp. (°F)	Calculated K_{eq}	Measured K_{eq}
1	1096	0.324	2.15×10^{-3}
2	1200	0.434	5.74×10^{-3}
3	1200	0.434	5.74×10^{-3}
4	1200	0.434	6.63×10^{-3}
5	1200	0.434	6.07×10^{-3}
6	1306	0.564	2.32×10^{-2}

gas-salt reactions (in the range 300°-550°F). One possible explanation is that in withdrawing samples of gas for analysis the water-gas-shift reaction continued within the nickel tube as the gas cooled down to room temperature. In any case, the gas compositions listed in Smith and Kapelner's Table II are not appropriate to the reaction being studied, but appear to have been used to calculate the equilibrium constant listed in Table I.

The existence of compounds in the binary phase diagrams of K₂CO₃-Li₂CO₃ and K₂CO₃-K₂SO₄ suggest that activity coefficients in the salt mixtures under consideration will not be unity. However, the authors have used mole fractions to represent activities in the equilibrium constants listed in Table I. Indeed, from the work of Pelton *et al.*,³ one can estimate the activity coefficient of K₂CO₃ for the melt in run 3 (Table I) to be 0.033. Using such data,³ one can also calculate the Gibbs energy of formation for the liquid mixture 0.66Li₂SO₄-0.34K₂SO₄, taking activity coefficients into account. To cite one example, the value obtained at 649°C (1200°F), 252,200 cal/mol, is significantly smaller than the comparable value, 272,700 cal/mol, reported in Smith and Kapelner's Table III. In view of these criticisms, the derived values of the Gibbs energy of formation of 0.66Li₂SO₄-0.34K₂SO₄ are questionable. The values calculated from the data of Pelton *et al.*³ appear to be more reliable.

S. W. Smith and S. M. Kapelner:⁴ In the discussion of Shores and Orfield above, the calculated values of the Gibbs free energy are questioned on the bases that the gas compositions do not correspond to equilibrium mixtures and that mole fractions were used in place of activities. Some comment on each of these questions is in order.

The gas mixtures indeed were not in equilibrium, and no attempt was made to reach equilibrium. On the contrary, the experimental apparatus was designed to minimize the shift reaction by keeping the stainless steel inlet tube as short as practicable. It had been shown earlier by Vogel⁵ that several feet of tubing is needed to reach equilibrium in this temperature region. Additionally, it was expected that poisoning by adsorbed H₂S on the surface of the tube would further reduce the amount of shift. The measured compositions indicated that the maximum shift was only a few percent, as expected. Gas samples were taken through 99.98% Al₂O₃ tubes as well as the Ni tubing reported in the paper without altering the results. It was on this basis that the measured gas compositions (essen-

³A. D. Pelton, C. W. Bale, and P. L. Lin, "Calculation of Thermodynamic Equilibria in the Carbonate Fuel Cell," Vol. 1, Final report to the U. S. Department of Energy, Contract no. DE-AC02-79ET15416, May 1981.

⁴United Technologies Corporation, Power Systems Division, South Windsor, Connecticut 06074.

⁵W. M. Vogel and C. D. Iacovangelo, *This Journal*, **124**, 305 (1977); W. M. Vogel, Personal communication.



tially the same as the input compositions) were used to calculate the values reported in our Table III.

With respect to the use of mole fractions to represent activities in the calculation of the equilibrium constants, there is no doubt that when reliable values for activities are available they should be used to calculate thermodynamic constants. If the activities are sufficiently well known over the range of the experiment, it would be appropriate to use them to recalculate the tabulated equilibrium constants. It should be pointed out, however, that the practical use of data of this type is usually to calculate the sulfate/carbonate composition for a given set of experimental conditions. If $K_{(\text{act})}$ is known, the composition may be calculated over any range where the activities are available. If $K_{(\text{mol})}$ is known, the correct composition may also be calculated, but one is at hazard if attempting to extend the range much beyond the original data.

Pore Size Distribution in Porous Silicon Studied by Adsorption Isotherms

G. Bomchil, R. Herino, K. Barla, and J. C. Pfister
(pp. 1161-1164, Vol. 130, no. 7)

V. P. Bondarenko, A. M. Dorofeev,⁶ and L. V. Tabulina:⁷

In the paper under discussion, the adsorption isotherms method was used to investigate porous silicon. Interesting experimental data on specific surface and pore size distribution are presented. However, the interpretation of these results is ambiguous; therefore, it is necessary to make some remarks.

The BJH method⁸ was used by the authors to determine pore size distribution in the porous silicon. By this method, the distribution is obtained from the desorption isotherms, a technique valid only for cylindrical pores.⁹ For porous silicon, interpretation of the experimental results is difficult, owing to the complex, noncylindrical shape of pores. In fact, as shown in their Fig. 2, the desorption isotherm (for example, for a porous silicon sample, corresponding to a forming current density of 80 mA/cm²) is sharper than the adsorption one. Isotherms of this shape are typical for pores with narrow regions.^{9,10} Analyzing the experimental data,¹¹ we can infer that the above-mentioned narrow regions are located near the surface of the porous silicon layer, e.g., the pores are bottle-like. In our opinion, the decrease of the apparent density of porous silicon through the thickness (their Fig. 5) is an additional argument for bottle-like shaped pores.

We have found that plasma etching of porous silicon up to the depth of 1 μm helps to achieve the equilibrium pressure value more rapidly during the isotherm procedure. Obviously, it may be explained by the removal of the subsurface dense layer of porous silicon.

Considering the facts above, we can assume that the pore size distribution shown in their Fig. 4 yields reliable information for the subsurface layer, but not for the entire volume of the porous silicon.

Another point concerns the electrolyte composition for silicon anodic treatment. Ethanol-aqueous hydrofluoric solution was used as electrolyte rather than the conventional aqueous solutions. Actually, the use of an alcoholic electrolyte results in a better homogeneity of the porous silicon layer. However, the results of our experience lead us to assert that the proposed electrolyte is not suitable for long-term use. Analysis allows us to conclude that electrolyte which has volatile solvents change in time be-

cause of evaporation. Moreover, gas evolution and the increase of electrolyte temperature at high forming current density result in enhanced alcohol evaporation.

The last point is connected with the specific surface value of porous silicon samples. As seen in their Fig. 2, the adsorption isotherm of the porous silicon sample, corresponding to the forming current density of 240 mA/cm², is located higher than the one of 80 mA/cm². However, the higher adsorption corresponds to the higher specific surface.⁹ It contradicts the data of their Table I, where the specific surface 205 m²/cm² for the sample treated at $j = 240$ mA/cm² and 225 m²/cm² for $j = 80$ mA/cm² are presented.

G. Bomchil, R. Herino,¹² and J. L. Ginoux:¹³ The comments by Boudarenko, Dorofeev, and Tabulina (BDT) on our paper are much appreciated. In particular, the contradiction that they point out between the results in Table I and isotherms presented in our Fig. 2 allow us to realize that a normalization error in the plot of the adsorbed nitrogen volumes V_{N_2} was present, so that the adsorbed gas scales were not the same for each curve. Exact quantitative results are obtained when all plotted values of V_{N_2}/V_p are multiplied by a factor (the sample weight), which is 1.19 for the sample formed at 80 mA/cm² (full line) and 1.75 for the sample formed at 240 mA/cm² (dotted line). Corrected curves are shown on Fig. 1, and are in agreement with data presented in Table I and Table II in the original paper.

The main point of the BDT remarks concerns the relation between the isotherm shape and the geometrical pore shapes. Let us briefly recall that in the classical classification,¹⁴ type A isotherms correspond to cylindrical pores (radius r_n) open at both ends. However, tubular tubes containing widened parts where radius r_w is less

¹²CNET-CNS, 38243 Meylan Cedex, France.

¹³Laboratoire d'Adsorption et de Réaction de Gaz sur Solides, Institut National Polytechnique de Grenoble, 38402 St. Martin d'Heres, France.

¹⁴S. J. Gregg and K. S. W. Sing, "Adsorption, Surface Area and Porosity," p. 117, Academic Press, New York (1982).

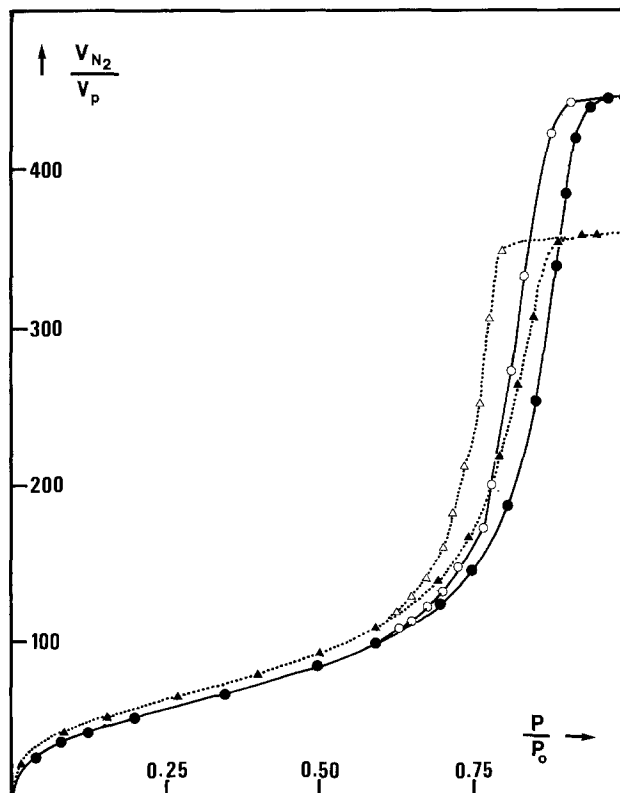


Fig. 1. Adsorption isotherms of two porous silicon samples, corresponding to a forming current density of 240 mA/cm² (full line) and 80 mA/cm² (dotted line). Adsorbed gas volume V_{N_2} (cm³) are plotted relative to the geometrical volume of porous material (cm³).

⁶Department of Microelectronics, Minsk Radioengineering Institute, 220069 Minsk, USSR.

⁷Institute of General and Inorganic Chemistry, Byelorussian Academy of Sciences, 220073 Minsk, USSR.

⁸E. P. Barrett, L. G. Joyner, and P. P. Halenda, *J. Am. Chem. Soc.*, **73**, 373 (1951).

⁹S. Gregg and K. Sing, "Adsorption, Specific Surface, Porosity," Mir, Moscow (1970).

¹⁰R. M. Barrer, N. McKenzie, and J. S. S. Reay, *J. Colloid. Sci.*, **11**, 479 (1956).

¹¹T. Unagami, *This Journal*, **127**, 476 (1980); V. A. Labunov, I. L. Baranov, and V. P. Bondarenko, *Thin Solid Films*, **64**, 479 (1979); Y. Arita, *Proc. Int. Conf. Thin Solid Films, Nagoya*, 222 (1978).

than $2r_n$ or complex pores system consisting of randomly connected tubes of various diameters will exhibit the same shape of isotherm. On the other hand, type E is characteristic of ink-bottle-shaped pores, with $r_n < 2r_w$. For type A isotherms, the desorption branch is commonly used for the determination of the pore radius distribution. For type E isotherms, Everett¹⁵ concludes that the adsorption branch is to be preferred. In the case of porous silicon, the obtained isotherms present an intermediate shape between type A and E; this suggests that we are in presence of neither perfect cylindrical pores, nor ink-bottle-shaped pores. Anyway, referring to Mikhail and Robens,¹⁶ it is very difficult to classify an actual pore system on the only basis of the theoretical isotherm shapes.

As stated in our paper, the pore radius distributions were obtained from the desorption branch of the isotherm by using the BJH analysis. The same calculations were performed using the adsorption branch, but results were not plotted as this analysis leads to pore sizes smaller just by 10% and presents the same relative behavior for the radius distribution of the different samples. From a practical point of view, the use of the adsorption or desorption branch of the isotherm leads to the same classification of porous silicon samples prepared in different electrochemical conditions.

Coming back to the actual pore shapes, we believe that our porous silicon samples consist in a complex system of interconnected tubular pores, with a few proportions of widened parts where $r_w > 2r_n$. Two arguments can support this description. First, it appears that the radius corresponding to the maximum of the distribution curves is only 15-30% less than the value of the most frequent pore radius defined by $r = 2V_s/S_{BET}$, where V_s is the porous volume and S_{BET} the surface area of the sample. This indicates that our samples are mostly formed by cylindrical pores with similar radius. In addition, the presence of hysteresis loops in our isotherms indicates that these tubular pores are interconnected. A second argument is given by transmission electron microscopy (TEM) cross-sectional photographs of porous layers that we have recently obtained.¹⁷ An example is shown Fig. 2, where details of the sample structure can be seen, with empty spaces appearing black in the porous structure. The sample, prepared at a current density of 80 mA/cm², presents pores with a mean orientation perpendicular to the surface and to the interface with bulk silicon. Pore dimensions are quite uniform along the whole thickness of the layer. This is confirmed by other observations near the surface or in other parts of the sample which present the same pore dimensions. The structure is not formed by perfect silicon rods and cylindrical holes, but presents a distribution of lateral branches. The length of these branches is no more than a few times the pore diameter. Only from TEM observations, a quite narrow pore size distribution can be expected, with diameters ranging between 50 and 100Å, which is in excellent agreement with the value determined by adsorption isotherms.

BDT description of porous silicon appears quite different from ours, as they assume the presence of very narrow necks located near the surface of the layer. As such surface sublayer cannot be seen by TEM or inferred from isotherms, we have performed plasma etching of porous samples in the same way as reported by BDT. Porous silicon samples 20 μm thick were prepared in exactly the same electrochemical conditions, and then etched in a SiF₆ plasma down to 1.6 and 6.6 μm. After analysis in the same conditions, no difference can be seen in the isotherms obtained for etched and unetched samples: the ra-

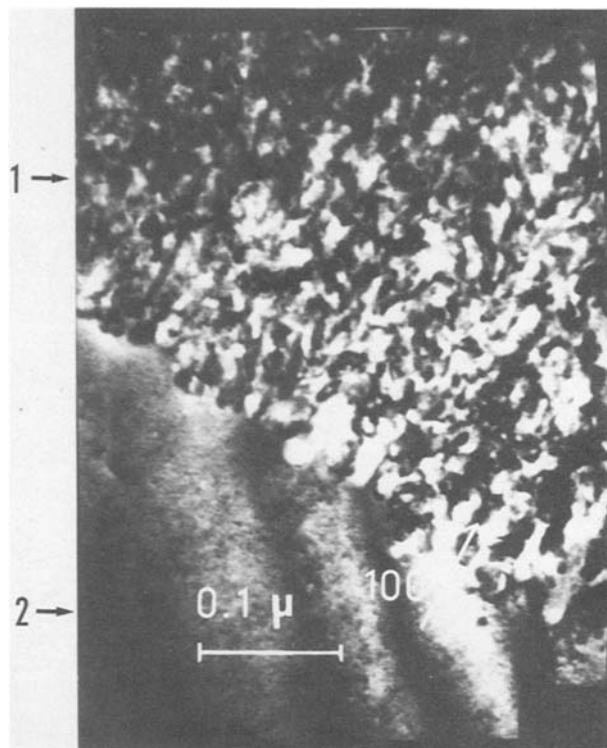


Fig. 2. TEM dark field cross-sectional photograph of the porous silicon film (1) and the silicon substrate (2).

dius distribution does not change with depth. Moreover, we did not observe any differences in kinetics and time required to reach the equilibrium pressure. Consequently, the results presented in our paper do yield reliable information for the whole volume of the porous layer. The assumption of ink-bottle-shaped pores in our samples can be rejected. The slight decrease with depth in the porous silicon density which was observed only in the case of the lowest current density (10 mA/cm²) cannot be related to drastic changes in the pore dimensions.

Consequently, it seems that the differences between our measurements and that of BDT have to be related to the preparing conditions of the samples. The porous layers obtained in alcoholic electrolytes present much better homogeneity and crystalline quality than layers prepared in conventional aqueous electrolytes.¹⁸ Conversely to BDT experience, we have found no difficulties using alcoholic electrolytes, providing that elementary precautions are taken: the cell is covered, the electrolyte is changed for each sample, the solution is carefully stirred. A crude calculation indicates that gas evolution during electrolysis cannot evaporate noticeable quantities of ethanol, even if the gas is saturated. However, at the highest current density, the electrolysis times are quite short, and the slight increase of the electrolyte temperature which occurs does not provoke drastic changes in the electrolyte composition. In our opinion, there are only advantages in using alcoholic solutions in the preparation of porous silicon layers.

Electrochemistry of Coal Slurries

II. Studies on Various Experimental Parameters Affecting Oxidation of Coal Slurries

Patrick M. Dhooge and Su-Moon Park
(pp. 1029-1036, Vol. 130, no. 5)

H. G. Linge:¹⁹ Dhooge and Park have analyzed the kinetics of coal oxidation from the anode current (*i*) of slurried coal in ferric sulfate or ceric sulfate anolytes (total metal

¹⁹CSIRO Division of Mineral Chemistry, Perth Laboratories at W.A.I.T., Bentley 6102, Australia.

¹⁵D. H. Everett, in "Characterization of Porous Solids," S. J. Gregg, K. S. W. Sing, and H. F. Stoeckli, Editors, p. 229, Soc. Chem. Ind., London (1979).

¹⁶R. S. Mikhail, and E. Robens, "Microstructure and Thermal Analysis of Solid Surfaces," John Wiley and Sons, New York (1983).

¹⁷R. Herino, A. Perio, K. Barla, and G. Bomchil, *Mater. Lett.*, To be published.

¹⁸K. Barla, R. Herino, G. Bomchil, J. C. Pfister, and A. Freund, *J. Cryst. Growth*, To be published.

ion concentration C). Their analysis and conclusion are invalid, since the coal oxidation is a mediated electrolysis reaction in these analytes.^{20,21} The anode current is therefore primarily determined by the anolyte concentration (C_r) of Fe(II) or Ce(III)

$$i = F k_a A C_r \quad [1]$$

where F is the Faraday constant, k_a a first-order rate constant, and A the anode area. For a limited time interval, the rate of coal oxidation (R_o) is dependent only on coal characteristics and the anolyte redox potential^{20,21}

$$R_o = R_c w (C_o/C_r)^\beta \quad [2]$$

where R_c is a coal characteristic, w the coal weight, C_o the anolyte concentration of Fe(III) or Ce(IV), and the fraction β is an apparent charge-transfer coefficient. The anode current is a different function than R_o of the system parameters, even at steady state when $R_o = F^{-1}i$. This is seen by combining Eq. [1] and [2] with $C = C_o + C_r$, providing the general relationships

$$\begin{aligned} i &= Z ((I - i)/i)^\beta \\ Z &= F R_c w \\ I &= F k_a A C \end{aligned} \quad [3]$$

where Z is a coal characteristic and I a system characteristic. I equals the maximum i value attainable when all anolyte iron (cerium) is present as Fe(II) and Ce(III) but is not directly dependent on the coal properties.

Simplified analytical solutions to Eq. [3] are possible for (i) high and (ii) low coal reactivities in the anolyte.

By high coal reactivity, we mean that sufficient to limit any buildup of oxidant from the electrode reaction. Hence, $C_r \sim C$, $i \sim I$ in Eq. [3] and, therefore

$$i = I(1 - [I/Z]^{1/\beta}) \quad [4]$$

valid for $Z > I$, which provides a more explicit definition of "reactive" coal.

By low coal reactivity, we mean that enabling significant buildup of oxidant until $C_o \sim C$, i.e., $i < I$ in Eq. [5]. Therefore

$$i = Z^{1/\beta+1} I^{\beta/\beta+1} \quad [5]$$

valid for $Z < I$, which provides a more explicit definition of "unreactive" coal.

Inspection of Eq. [4] reveals immediately that i is practically independent of Z for reactive coals, especially for small β values. Coal type and weight have then little influence on the anode response, but i is almost proportional to anode area and anolyte metal concentration; i can also be sensitive to the slurry stirring rate at high anode potentials when anodic mass-transport control prevails. Evidently, these dependences provide false information on the coal oxidation kinetics, since Eq. [2] is not directly dependent on any of these terms.

Equation [5] shows that the coal properties have a significant influence on i for low coal reactivities ($Z < I$), but the experimental dependence of i on coal weight here is attenuated and less sensitive than in Eq. [2]. This explains why i "saturates" with increasing slurry density for some coals (Dhooze and Park), even though R_o is always directly proportional to w (see Eq. [2]). i is also still dependent on I . Again, significant increases in i can result from this term, even though the coal oxidation kinetics are not directly affected. However, compared to Eq. [4], the influence of A and C is attenuated via the fractional power $\beta/(\beta + 1)$, and the effect of increasing these variables diminishes progressively.

For any given coal, Eq. [4] must ultimately break down, because I can be arbitrarily increased at least threefold, e.g., by changing C from 10^{-3} to $1M$. The condition $Z > I$ reverses when $C > R_c w/k_a A$, and Eq. [5] is therefore the more general solution of Eq. [3], valid for a wide range of

coal reactivities in sufficiently concentrated analytes. This is the reason why the i - C curves for reactive coals tend to be linear only in dilute analytes, but this experimental trend cannot be used to justify a first-order mechanism for the coal oxidation reaction. Similarly, considerable caution has to be exercised in the mechanistic interpretation of the experimental anode-current activation energy.

Su-Moon Park and David E. Stilwell:²² The comments offered by Dr. Linge are based on his misconceptions in using electrochemical relationships. We would like to point out that his comments refer more to our first paper on the subject,²³ than that which he cited.

First, Linge stated that our analysis was invalid since the coal oxidation is a mediated electrolysis reaction. We wish to point out that we were the first to reach the conclusion that coal oxidation is a mediated or catalytic process, based on our extensive experimental data.²³ Electrochemists have been known to call them: redox, electron shuttle, catalytic, or mediated reaction mechanisms, but these all refer to the same phenomenon. This is a rather minor point, and we wish to make it clear that our analysis and conclusions cannot be invalid simply because we did not use the same terminology as he did.

Our more important comments pertain to the invalidity of the equations evoked by Linge. First of all, Eq. [1] in his comment is only valid in the mass-transfer limiting region where k_a should be more properly replaced by m_o , the mass-transfer coefficient. At smaller overpotentials, the well-known Butler-Volmer equation must be employed with simplification only possible after reasonable assumptions have been made regarding overpotential and mass-transfer considerations, i.e.

$$i = i^0 \left[\frac{C_{O(O,t)}}{C_O^*} \exp\left(\frac{-\alpha n F}{RT} \eta\right) - \frac{C_{R(O,t)}}{C_R^*} \exp\left\{\frac{(1-\alpha)n F}{RT} \eta\right\} \right]$$

where i^0 is the exchange current, C_o and C_r are concentrations of the oxidant and reductant, respectively, at the electrode surface at any time, t , and in the bulk, expressed by subscript (O, t) and superscript*, respectively, η is the overpotential, and α is the transfer coefficient. Of course, i^0 is related to the charge-transfer coefficient, k^0 , by a relation, $i^0 = n F A k^0 (C_o)^{1-\alpha} (C_r)^\alpha$.

Since Linge did not specify any conditions, we can only assume that Eq. [1] refers to a mass-transfer limiting current. If not, then this alone causes us to question any subsequent equations that are based on its use. Under mass-transport-controlled conditions, Eq. [1] can be used to estimate the concentration of electroactive reductant, i.e., Fe^{2+} or Ce^{3+} in this case. Here, k^0 is the heterogeneous standard rate constant for charge transfer in centimeters per second.

Equation [2] in his comments does not appear in one of the references cited by Linge for its source;²¹ we have no ready access to his other reference.²⁰ One can write down a relation as Eq. [2] provided that coal particles are regarded as electrodes to transfer electrons to the solution species, i.e., Fe^{3+} or Ce^{4+} in this case. Then R_c should contain parameters related to the exchange current between coal and the solution species. One should, however, include the reverse current term as shown in the above Butler-Volmer equation, unless it is assumed that the polarization controlled by the ratio of C_o/C_r is in the Tafel region. Yet, Anthony and Linge²¹ ran their experiments near the equilibrium potential, the conclusion of which became the basis of Linge's current comments. Equations [1] and [2] cannot be combined, since they are based on different assumptions and also they are not correct.

We therefore wish to point out that one can derive any equations, but they may not have any physical meaning

²⁰D. A. J. Swinkels *et al.*, NERDDC Research Report, Contract no. 80/0210, B. H. P. Central Research Laboratories, Shortland, N.S.W., 2307, Australia (July 1981, April 1982, January 1984).

²¹K. E. Anthony and H. G. Linge, *This Journal*, **130**, 2217 (1983).

²²Department of Chemistry, University of New Mexico, Albuquerque, New Mexico 87131.

²³P. M. Dhooze, D. E. Stilwell, and S.-M. Park, *This Journal*, **129**, 1719 (1982).

unless assumptions made are met in the experiments. Take Eq. [3] in Linge's comment. The equation appears perfectly valid algebraically, but it has absolutely no physical meaning. Consider, for example, that at constant Z and I , the right-hand side of the equation decreases with increasing i , while the left-hand side increases. This necessitates changes in supposedly constants, Z and I . Any discussions based on this equation would, therefore, be invalid.

In summary, we are pointing out two reasons for invalidity of Eq. [3] in Linge's comment. First, Eq. [1] and [2] are valid only under the experimental conditions specified above. Second, these two equations cannot be combined to obtain Eq. [3]. The major confusion in deriving Eq. [3] came from the indiscriminate use of rate constants; charge-transfer rate (k^0), first-order reaction rate (k_a here?), and mass-transfer rate (m_o) are all different from each other. We have seen how Eq. [3], resulting from this combination, does not carry any physical significance. We welcome Dr. Linge's sending any literature/documents/data that detail the derivation of equations used in his comments. Our points made in this reply

can be found in any standard textbooks of electrochemistry.^{24,25}

Finally, we wish to make comments concerning our analysis and conclusions based on our data. Our techniques for obtaining kinetic data were based either on the current-time profile of Fe^{2+} oxidation at controlled potentials in a stirred solution before and after perturbation by coal or on a steady-state approximation. Here, we assumed that rates of reaction between coal slurries and an oxidant are rate limiting, and thus the rate of Fe^{2+} generation, monitored by the anodic current in the mass-transfer region, should approximate the rate of reactions between Fe^{3+} and coal.

In conjunction with these comments, we request that authors in *This Journal* cite, whenever possible, only literature that is readily available and that editors and referees see to it that this is observed. Also, when a mathematical relation is used, "conventional" symbols should be used and assumptions made should be fully specified.

²⁴A. J. Bard and L. R. Faulkner, "Electrochemical Methods," Chap. 3, John Wiley and Sons, New York (1981).

²⁵J. O'M. Bockris and A. K. N. Reddy, "Modern Electrochemistry," Vol. 2, Chap. 8, Plenum Press, New York (1973).



Surface Phenomena in Composite Electroless Coatings Containing Polycrystalline Diamond

N. Feldstein* and T. S. Lancsek

Surface Technology, Inc., Princeton, New Jersey 08540

Composite electroless coatings have been accepted as commercial coatings primarily due to the resulting outstanding wear characteristics. A survey of the state of the art and its evolution was recently published (1).

Due to the autocatalytic nature of electroless plating compositions it has been stipulated (2) that the particles which are to be dispersed within the electroless plating bath and then codeposited must be non-catalytic and inert in order to prevent the homogeneous decomposition of the electroless plating compositions. Examination (1) of composite electroless coating generally reveals a uniform dispersion of the particulate matter within the metallic matrix, with some particles exposed from the outer surface of the composite.

There does not appear to be any specific orientation in the exposure of the particles, nor does there appear to be any orderly fashion as to the degree by which these particles are exposed above the surface.

In an extensive examination of particulate matter for potential composite electroless coatings, Christini et al (3) noted that diamond, particularly polycrystalline diamond, has a tendency to form metallic sites onto exposed diamond particles in isolated regions. The degree of this tendency was found (3) to be dependent upon plating conditions and the nature of the plating bath chosen (e.g., nickel-boron vs. nickel-phosphorous).

Though diamond exists in various forms, polycrystalline diamond produced by a shock synthesis method (4) has found several commercial applications as applied in composite electroless coatings, stemming from several unique characteristics achieved with this form of diamond in comparison to others. The successful commercial adaptation of this specific form of

diamond has resulted in additional interest as to the non-catalytic properties and inertness of this polycrystalline form of diamond when used along with electroless plating baths.

The present method provides a new approach to the examination of discrete polycrystalline diamond exposed from the metallic matrix. This new method appears to be effective even though the number of exposed diamond particles has been reduced due to commercial practices. The new method is based upon the interaction of previously prepared composites with electroless plating baths which are free of any particles, and observation of the resulting surface roughness.

EXPERIMENTAL PROCEDURE

Miscellaneous coated substrates with exposed particles of polycrystalline diamond in an electroless nickel matrix were used as a test vehicle. These substrates were contacted with an electroless nickel plating bath (nickel-phosphorous type). The degree of overcoat thickness was varied by varying the plating time; the resulting surface roughnesses were monitored. Roughness measurements were conducted using a Surf-Indicator, product of Gould, Inc., El Monte, California. Fig. 1 represents the resulting roughness measurements. In all cases, the initial roughness increased, leading to a leveling-off phenomenon. The electroless plating baths chosen for use in this study were all commercially available baths, and their use was in accordance with the specification of the supplier.

Table I demonstrates the results of applying the overcoat onto two plated discs, both containing an electroless nickel composite polycrystalline diamond. Disc A is a

*Electrochemical Society Active Member.

commercial product which was smoothed subsequent to the plating step; in so doing, a significant amount of the outer diamonds resulting from the plating operation were removed. Disc B is a laboratory-prepared disc, also containing the polycrystalline form of diamond with a smoothing operation subsequent to the plating. The diamond size (4 micron) chosen for Disc B in Table I is the same as that chosen in the substrate preparation for Fig. 1. It should be noted that 10 minutes of overcoating results in about 3.5 microns of thickness.

Though the smoothing operation removes a significant amount of exposed particles and also lowers the surface roughness, a few particles are still present and exposed from the outer surface (Ref. 1, Fig. 8).

Examination of the results for Disc A in Table I shows a slight tendency for the initial roughness to increase with no major effect thereafter up to about 5 minutes of overcoat. A similar trend appears to take place for Disc B. In none of the cases examined is there any initial tendency for the roughness to decrease with overcoat variations. Therefore, it is believed that the observed tendency demonstrates that the diamond used (polycrystalline diamond) is, in fact, catalytic and not inert, probably due to sites which lead to the deposition of electroless nickel onto them. These sites are of catalytic nature, and it is these sites that may have partially contributed to Christini et al's (3) observation as to the phenomenon of nucleation bonding. In any event, the presence of such catalytic sites would lead to the random metallic build-up.

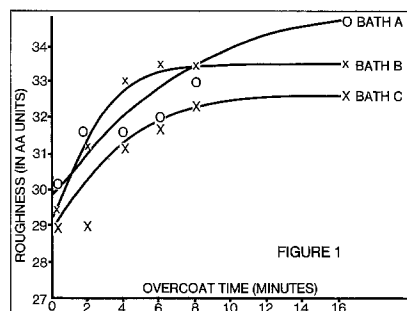
SUMMARY AND CONCLUSIONS

Based upon roughness measurements with varied coating thicknesses of electroless nickel composition, it has been demonstrated that the exposed particles (polycrystalline diamond) provide catalytic tendency which results in the plating of the diamonds. At times the plating onto the diamond particles is in preferential rate to the plating onto the nickel matrix, thereby resulting in an increase in the initial surface roughness. No

change in surface roughness corresponds to a precise replication of the composite surface with the electroless layer free of the particulate matter. In either case, no initial decrease in surface roughness has been observed which would account for a selective "fill-in" by the secondary layer between exposed particles. Selective "fill-in" could only take place if the exposed polycrystalline diamond particles are truly non-catalytic and inert. It is conceivable that the catalytic sites associated with the polycrystalline diamond may be due to its unique morphology and/or residual transition metals used in its synthesis (5,6). The present observations and conclusion are further supported by previous observations that diamond, particularly the polycrystalline form, has the tendency to decompose electroless plating baths (2,3,7).

Table I. Roughness Measurements of Composite Coatings Previously Smoothed

	Roughness	
	Disc A	Disc B
Control (no overcoat)	16.6 AA	14.7 AA
2 min. overcoat	19.3 AA	14.9 AA
5 min. overcoat	16.2 AA	14.2 AA
10 min. overcoat	14.9 AA	14.3 AA



REFERENCES

1. Feldstein et al, Metal Finishing, No. 8, p. 35 (1983).
2. Metzger et al, U.S. Patents 3,753,667, and 3,617,363.
3. Christini et al, U.S. Patent Reissue 29,285.
4. Cowan et al, U.S. Pat. 3,401,019.
5. M. Seal, Industrial Diamond Review, March, p. 104 (1968).
6. R. Komanduri, Proceeding, Diamond-Partner in Productivity, p. 174 (1974).
7. J. Lukschandel, Trans. Inst. Metal Finishing, p. 118 (1978).

Manuscript submitted October 1, 1984. Surface Technology, Inc., assisted in meeting the publication costs of this article.

Molecular Beam Epitaxial Growth on Radiation-Heated Substrates

S. C. Palmateer, B. R. Lee, and J. C. M. Hwang*

General Electric Company, Electronics Laboratory, Syracuse, New York 13221

Growth of epitaxial layers on GaAs substrates without indium-mounting is essential for improvements in throughput of a molecular beam epitaxy (MBE) system. The elimination of indium-mounting will also improve backside morphology and avoid any indium incorporation in GaAs/AlGaAs layers during molecular beam epitaxial growth.

We have succeeded in growing GaAs epilayers on 2" wafers by radiation heating of the substrate. A coating of Ti/W (~3000Å thick) is sputtered on the backside of the GaAs wafer prior to epitaxial growth. The wafer is loosely held in a ring-shaped holder with molybdenum clips. Figure 1 illustrates the substrate holder arrangement. The temperature variation across a 2" wafer is $\pm 15^\circ\text{C}$, as shown in Figure 2. The temperature response of the wafer is excellent compared to heating through a 2" molybdenum block using indium mounting. This fast temperature response is important for the growth of heterostructures containing both GaAs and AlGaAs layers; the temperature of the wafer can be ramped from 600°C (for GaAs growth) to 700°C (for AlGaAs growth) within 3 seconds. The morphology of epilayers grown on radiation heated wafers is comparable to the morphology of epilayers grown on substrates mounted with indium.

Figure 3 shows a plot of theoretical⁽¹⁾ and experimental 77K mobility for n-type (Si-

doped) GaAs. Solid circles represent epilayers grown on indium mounted wafers, while open circles are mobilities measured on radiation heated wafers. Comparable 300K and 77K mobilities are obtained using both heating techniques. Hall measurements done across a 2" wafer show excellent uniformity ($\pm 5\%$) in carrier concentration and mobility. 4K photoluminescence measurements across a wafer are uniform and comparable in intensity to wafers grown on indium mounted substrates.

Figure 4 shows a plot of four electrochemical profiles done across a 2" wafer. These measurements exhibit excellent doping (d) and thickness (t) uniformity ($\pm 2\%$) across a 2" wafer.

Field effect transistors are being processed to compare uniformity of device characteristics; the results will be reported elsewhere.

ACKNOWLEDGEMENTS

We would like to acknowledge the help of Shirley J. Nitzke for the Ti/W sputtering.

REFERENCES

- (1) C.M. Wolfe and G.F. Stillman, Appl. Phys. Lett., 27, 564 (1979).

*Electrochemical Society Active Member.

Manuscript submitted September 6, 1984.

General Electrical Company assisted in meeting the publication costs of this article.

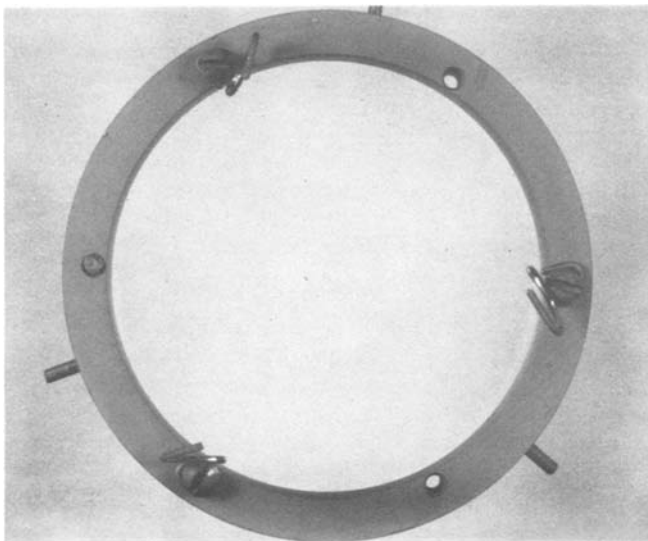


Fig. 1. Substrate holder arrangement.

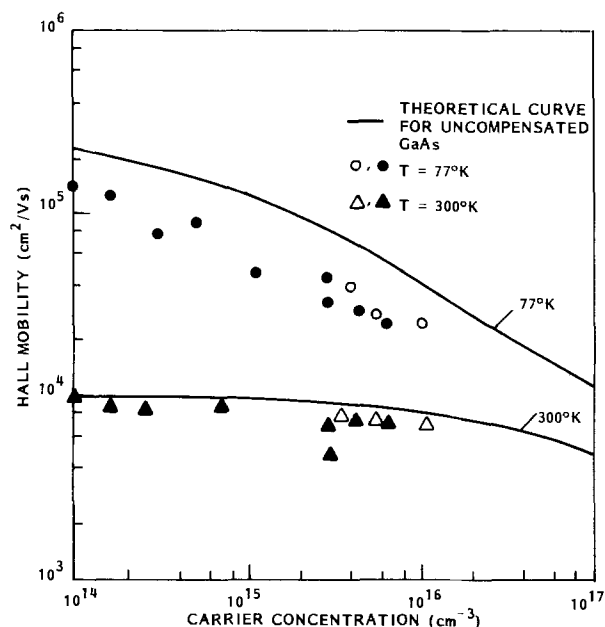


Fig. 3. Plot of theoretical and experimental 77K mobility versus carrier concentration for n-type (Si-doped) GaAs. Solid points -- indium-mounted wafers. Open points -- radiation heated wafers.

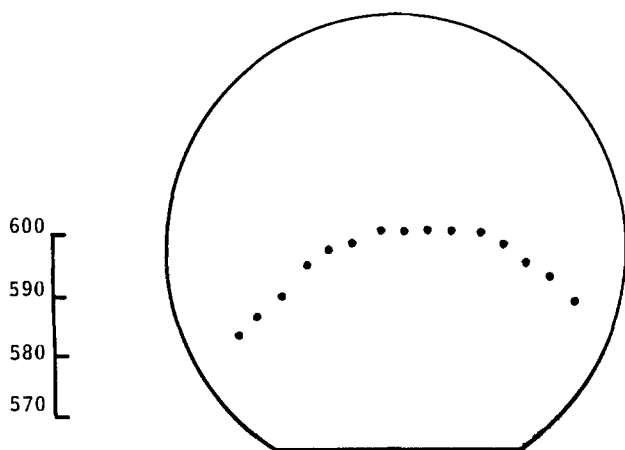


Fig. 2. Temperature uniformity plot.

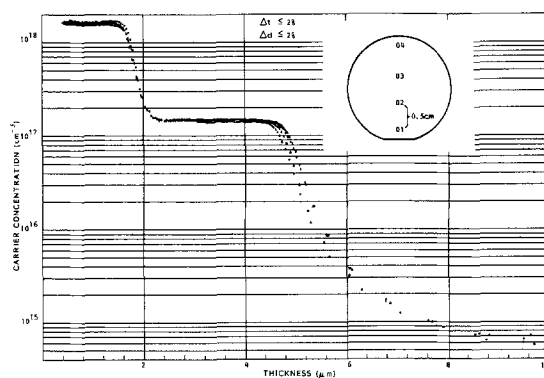


Fig. 4. Doping concentration as a function of depth from the surface of a GaAs layer grown with the substrate rotated at 4 RPM. Four traces were measured on different spots of the wafer as indicated. The structure consisted of a 1 micron undoped GaAs buffer, a 0.36 micron $\sim 1.5 \times 10^{17}$ at/cm Si-doped layer and a 0.20 micron $\sim 2 \times 10^{18}$ at/cm grown on a semi-insulating Si substrate. The Si cell was ramped between the two doped regions.

Heterojunction by Photoelectrochemical Surface Transformation: n:CuInSe₂/p-CuISe₃Se⁰

S. Menezes**, H.-J. Lewerenz*, and G. Betz

Hahn-Meitner-Institut für Kernforschung Berlin,
Bereich Strahlenchemie, D-1000 Berlin 39, Federal Republic of Germany

K. J. Bachmann*

Department of Chemistry, North Carolina State University, Raleigh, North Carolina 27650

R. Kötz

Brown, Boveri & Cie, Baden, Switzerland

Heterojunction formation by photoelectrochemical alteration of semiconductor surfaces is reported. Growth of a new semiconducting phase at the n-CuInSe₂/I⁻-I₂-Cu⁺ interface is achieved by controlling electrochemical parameters. The interfacial layer is identified as CuISe₃Se⁰ and exhibits p-type conductivity. Under illumination the interphase mediates efficient charge transfer between CuInSe₂ and the I⁻/I₂ redox couple while inhibiting semiconductor dissolution.

Current interest in CuInSe₂ systems from its exceptional optoelectronic properties, resulting in the development of efficient solid state (1) and photoelectrochemical (2) solar cells. Performance of the latter pivots on the growth of an interfacial layer induced by specific electrolyte composition, resulting in a substrate-film-electrolyte structure. In this note we explore the location of the photoactive junction and the circumstances leading to the CuInSe₂ surface transformation.

Interfacial films were grown on back ohmic contacted, epoxy insulated and etched (112) faces of n-CuInSe₂ by operation as photoanodes in an electrolyte consisting of 1 M I⁻, 0.05 M I₂, 0.02 M CuI and 2 M HI. This involved, cyclic polarization of the electrode between the potential limits of short circuit and open circuit or leaving it at the maximum power point. Film quality was monitored by the photocurrent-voltage output. Generally 3 - 4 intermediary etches were required to optimize the film performance.

Scanning electron micrographs of the electrochemically treated CuInSe₂ electrodes show that a polycrystalline film consisting of randomly oriented, flat, hexagonal crystallites is grown on the CuInSe₂ substrate (3). Crystallite sizes range between 2 - 5 microns. A cross-section of a cleaved electrode evidences that the film does not penetrate deeper than 2 microns into the substrate even after pro-

key words: Semiconductor Interfaces, Solar Energy, Photoelectrochemistry

longed operation (5 weeks) in a solar cell, but appears to completely cover the substrate growing into microscopic cavities.

The distinct crystallite geometry suggests that a chemically well defined compound is grown at the CuInSe₂/electrolyte interface. X-ray diffraction analysis of the crystallites identifies the new phase as consisting of mainly CuISe₃ and up to 30 % elemental Se. No evidence for formation of polycrystalline CuI was found.

Chemical reactions of illuminated CuInSe₂ with the electrolyte constituents obviously transform the semiconductor surface to generate the CuISe₃-Se⁰ phase. In the absence of Cu⁺ in the electrolyte, elemental Se⁰ and triangular crystallites of CuI have been detected on photocorroded CuInSe₂ surfaces (3). CuI is partly soluble in iodide solution forming CuI₂⁻. Addition of Cu⁺ to the solution probably raises the surface concentration of CuI₂⁻ to a critical value required to initiate CuISe₃ film growth. CuISe₃ crystals have been previously prepared by reacting stoichiometric mixtures of CuI and Se in HI medium under hydrothermal conditions (4). The reactants employed in the hydrothermal synthesis of CuISe₃ are thus provided by the electrolyte and the semiconductor components in our cell while the reaction enthalpy is probably supplied by the photopotential.

Fig. 1 compares UPS energy distribution curves, N(E) of the untreated CuInSe₂ single crystal and the CuInSe₂/CuISe₃-Se⁰ structure, with the Fermi levels E_F aligned to the edges of the valence band. E_Vⁿ and E_V^p for the two samples differ by 0.65 eV. |E_Vⁿ - E_V^p| is 0.85 eV for CuInSe₂ and 0.2 eV for the film. With a bandgap, E_g^p of 2 eV for CuISe₃ (5) and for Se (6), the film is thus a p-type semiconductor. Measurement of the relative work functions, φ, of the two samples with the vacuum levels aligned also indicate that the E_F's differ by 0.65 V. Hence E_Vⁿ(CuInSe₂) = E_V^p(film). Adding the electron affinity, χⁿ of 4.58 eV (7) to the E_gⁿ of 1 eV for CuInSe₃ the absolute value of E_V^p is estimated to be 5.58 eV.

The energetics of the structure are given in Fig. 2. Experimental and literature values for various electronic parameters indicated with superscripts n and p refer to n-CuInSe₂ and p-CuISe₃-Se⁰, respectively. An estimate for the work function of the I⁻-I₂-Cu⁺-HI electrolyte of $\phi^e=5.1$ eV is obtained by adding the measured redox potential of +0.2 V (SCE) to the more recent value of (NHE)=4.7 eV (8). Comparison of E_F^n , E_F^p and ϕ^e yields a potential of at least 0.65 eV at the substrate/film junction and of 0.2 eV ($\Delta\phi$) at the film/electrolyte interface. This implies a p-n junction between the solids and a rectifying junction at the electrolyte contact. The spectral response and the anodic photocurrent, however, attest the light absorption and photogeneration of h⁺ in the n-CuInSe₂ (2,3). A barrier at the film/electrolyte interface would impede h⁺ transfer to I⁻. The high quantum efficiency and the photovoltage of 0.42 V (2) argue against such a barrier and suggest that the principal potential drop occurs in the p-n junction with the electrolyte providing an ohmic contact. Interactions between the semiconductor and electrolyte upon immersion may account for the energetic difference, $\Delta\phi$, as the scheme in Fig. 2 disregards the effects of pH and specific adsorption.

References

1. J.L. Shay, S.Wagner, and H.M. Kasper, Appl. Phys. Lett., 27, 89 (1975).
2. S.Menezes, H.J.Lewerenz, and K.J.Bachmann, Nature, 305, 615 (1983).
3. K.J.Bachmann, S.Menezes, R.Kötz, M.Fearheily, and H.J.Lewerenz, Surface Sci., 138 (1984).
4. A.Rabenau, H.Rau and G.Rosenstein. Z.Anorg. Allgem. Chem., 374, 43 (1970).
5. A. Rabenau and H. Rau, Solid State Commun. 1, 1281 (1969).
6. W.H. Strehlow and E.L. Cook, J. Phys. Chem. Ref. Data, 2, 183 (1973).
7. K.J. Bachmann, E.Buehler, J.C.Shay, and S.Wagner, Appl. Phys. Lett., 29, 121 (1976).
8. R.Gomer and G.Tryson, J.Chem.Phys., 66, 4413 (1977).

Manuscript submitted July 7, 1984.

Hahn-Meitner-Institut für Kernforschung
Berlin assisted in meeting the publication costs of this article.

*Electrochemical Society Active Member.

** Electrochemical Society Student Member.

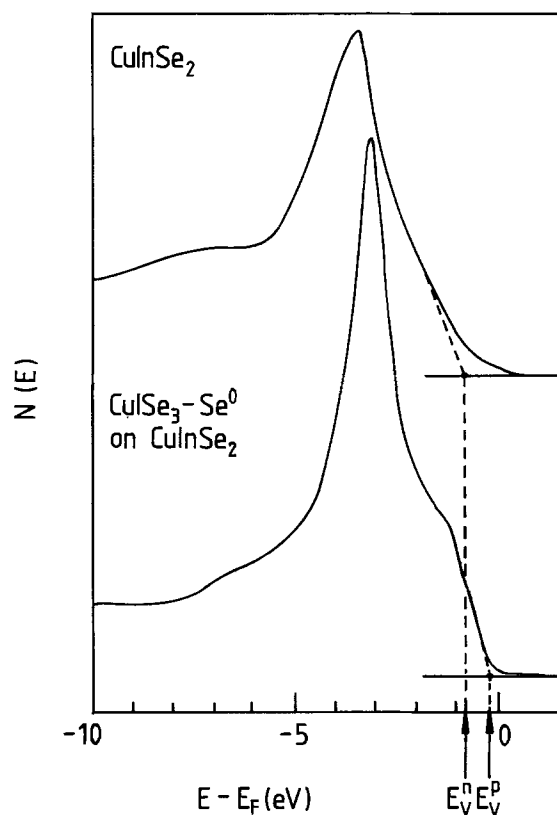


Fig.1 Energy distributions $N(E)$ obtained by UPS using He(II) excitation ($h\nu = 41.8$ eV).

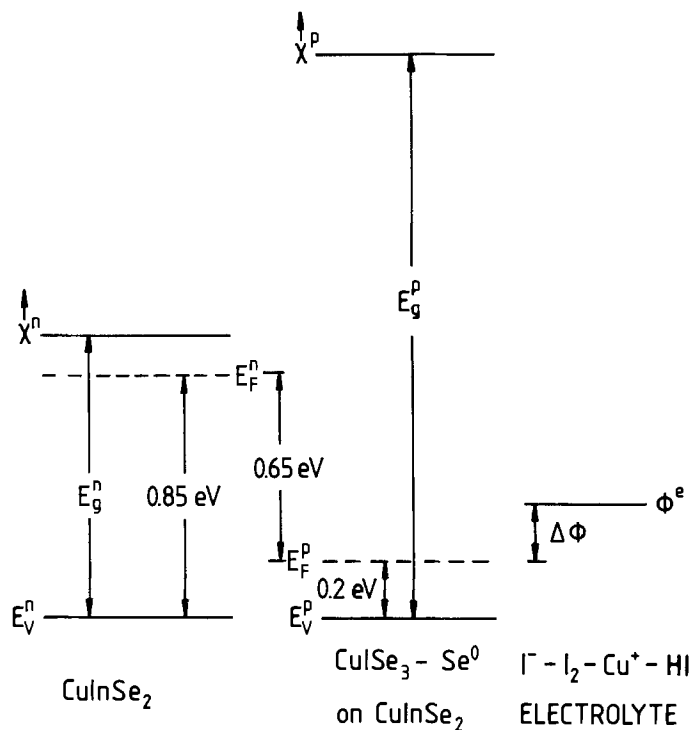


Fig.2 Schematic of energy levels of n-CuInSe₂, p-CuISe₃ and redox electrolyte.

Adsorption of Thiourea on Passivated Iron

An Infrared Spectroscopy and Radiotracer Study

J. O'M. Bockris,* M. A. Habib,* and J. L. Carbajal

Department of Chemistry, Texas A&M University, College Station, Texas 77843

Since adsorption of thiourea markedly influences the inhibition of electrochemical corrosion (1), it is important to know the extent and variation of thiourea adsorption with potential of the corroding object. We report here the adsorption of thiourea on iron as measured by the in-situ Fourier Transform Infrared Spectroscopy and by parallel measurements by means of radiotracers.

An iron rod (99.9995%) of 0.6 cm diameter clad with heat shrinkable teflon tube was used as the electrode for the IR study. The electrode surface exposed to a solution film of about 1μ thick was of 0.6 cm diameter. A Digilab FTS-20E spectrometer system was used. Detailed optical arrangements and experimental procedures are reported elsewhere (2). The counter and reference electrodes were a Pt coil and a calomel electrode, respectively.

For the radiotracer technique, a glass scintillator NE901 of 3 mm thick and 3 cm diameter with a 3000 Å thick vacuum deposited layer of iron was used as a working electrode. C^{14} labeled thiourea obtained from ICN radiochemicals, was used in a buffer borate solution of pH = 8.4.

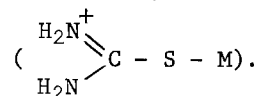
A cathodic pretreatment for the iron at -0.74 V (NHE) for 30 minutes was followed by a potential step to 0.3 V where the passive film was grown for 50 minutes (3). The passive film was about 20-30 Å thick.

The electrode was potentiostatically polarized in the region of -0.2 V to 1.1 V NHE at an interval of 200 mv and IR spectra were recorded at each potential. The spectra reported here were obtained by subtracting from the spectra at various potentials, the reference spectra at -0.2 V; the spectra are thus termed differential spectra.

For the radiotracer measurements, the radioactive signal from C^{14} of adsorbed thiourea is guided by a light pipe placed behind the scintillator to a photomultiplier (EMI 9635QB) connected to a multichannel

analyzer (EG&G 7100). The number of counts detected by the multichannel analyzer was recorded as a function of potential and was converted to surface excess (4).

In Fig. 1, the differential IR spectra of adsorbed thiourea at various potentials are shown. IR peaks at 1652, 1616, 1506, 1458, and 1385 cm^{-1} are found to vary with electrode potential. The peak at 1652 and the broad band at 1616 cm^{-1} correspond to the N-H scissoring (bending) vibration (5). The peak observed at 1506 cm^{-1} corresponds to the N-C-N stretching vibration (5). This peak is shifted from 1407 cm^{-1} in free thiourea to 1506 cm^{-1} in adsorbed state due to an increased double bond character of the carbon to nitrogen bond (5) as the thiourea molecule is expected to adsorb with its sulfur end toward the metal (6),



The peak at 1458 cm^{-1} also corresponds to the 1417 cm^{-1} band of free thiourea and thus can be assigned to the NH_2 rocking vibration and N-C-N and C=S stretching vibration (5). The nature of vibrations is changed slightly on adsorption through the sulfur atom.

The area under the peaks corresponds to the amount of adsorbed thiourea on the electrode. The integrated peak areas are plotted as a function of potential in Fig. 2. Areas under all the above mentioned peaks except the broad band at 1616 cm^{-1} are found to increase to a maximum at 0.9 V with increase of potential in the anodic direction. With further increase of potential above 0.9V, the peak areas except that of 1616 cm^{-1} increase with increase of anodic potential and becomes constant above 1.1 V. This signifies adsorbed thiourea molecules.

In the active region, i.e., at potentials lower than -0.2 V, due to corrosion of iron, no regular or reproducible spectra were obtained.

From the radiotracer measurements, the adsorption of thiourea on passive iron is also found to pass through a maximum at 0.9 V (Fig. 2). The maximum area of the IR peaks for the electrode at 0.9 V are normalized with respect to the maximum coverage determined by the radiotracer method at 0.9 V. Variations of the adsorption of thiourea with electrode potential as determined by the FTIR and radiotracer method are in reasonable agreement above 0.4 V. The discrepancy at potentials < 400 mV may be due to the difference in the strength of $(\text{NH}_2)_2\text{CS-Fe}$ interaction with potential. It is well known that amplitude of the observed absorption band will vary with the molecular orientation, being zero when the dipole derivative is parallel to the surface and giving a maximum value when it is perpendicular (7). Thus, the orientation of the adsorbed thiourea at the potential (0.9 V) where the IR absorption bands are normalized to surface excess value by the radiotracer, will change and hence affect the integrated area of the absorption band as the potential of the electrode is changed. The radiotracer method, of course, is insensitive to these orientational changes. The area of the peak at 1616 cm^{-1} , unlike other peak areas, does not decrease with increase of potential above 0.9 V, and the radiotracer measurements show a decrease beyond 0.9 V; but when all the peak areas are added together and plotted as a function of potential, a net decrease beyond 0.9 V is observed.

In-situ FTIR spectroscopic method combined with radiotracer measurements allow quantitative determination of the potential dependent adsorption of thiourea on passivated iron from an aqueous solution.

REFERENCES

1. Y.V. Fedorov, M.V. Uzlyuk and V.M. Zelenin, *Zaschita Metal.*, **6**, 311 (1970).
2. M.A. Habib and J.O'M. Bockris; *J. Electrochem. Soc.*, submitted for publication (1984).
3. T.E. Pou, O.J. Murphy, V. Young, J.O'M. Bockris and L.L. Tongson; *J. Electrochem. Soc.*, **131**, 1243 (1984).
4. E.A. Blomgren and J.O'M. Bockris, *Nature*, **186**, 305 (1960).
5. A. Yamaguchi, R.B. Penland, S. Mizushima, T.J. Laane, C. Curran and J.V. Quagliano; *J. Am. Chem. Soc.*, **80**, 527 (1958).
6. H. Wroblowa and M. Green; *Electrochim. Acta*, **8**, 679 (1963).
7. A. Bewick and B.S. Pons in "Advances in Infrared and Raman Spectroscopy", eds. R.E. Hexter and R. Clark, Heyden and Son, London (1984).

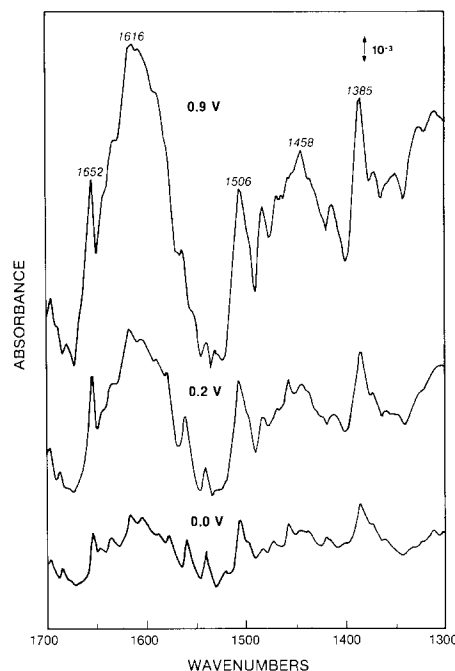


Fig. 1: Differential IR Spectra of Thiourea adsorbed on Fe electrode at various potentials, with respect to that at a reference potential of -0.2 V (solution = Borate buffer, $\text{pH} = 8.4$)

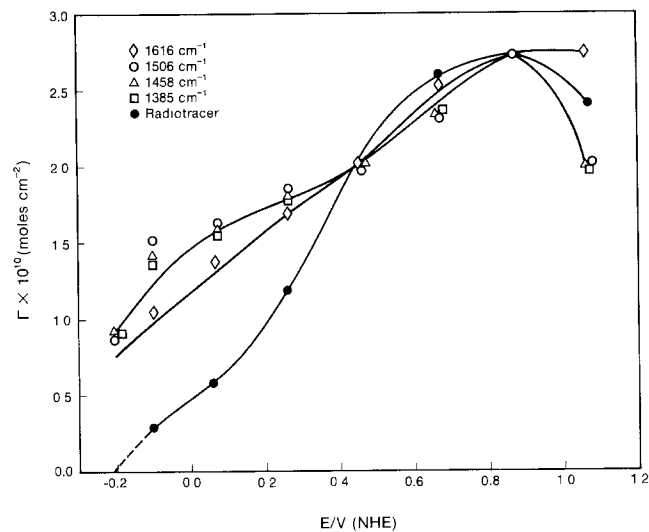


Fig. 2: Surface Concentration, Γ , of Thiourea as a function of potential by the radiotracer and the FTIR methods.

*Electrochemical Society Active Member.
Manuscript submitted July 9, 1984.
Texas A&M University assisted in meeting the publication costs of this article.